

Life-Cycle of Structures and Infrastructure Systems

Editors

Fabio Biondini and Dan M. Frangopol



LIFE-CYCLE OF STRUCTURES AND INFRASTRUCTURE SYSTEMS

Life-Cycle of Structures and Infrastructure Systems collects the lectures and papers presented at IALCCE 2023 - The Eighth International Symposium on Life-Cycle Civil Engineering held at Politecnico di Milano, Milan, Italy, 2-6 July, 2023. This Open Access Book contains the full papers of 514 contributions, including the Fazlur R. Khan Plenary Lecture, nine Keynote Lectures, and 504 technical papers from 45 countries.

The papers cover recent advances and cutting-edge research in the field of life-cycle civil engineering, including emerging concepts and innovative applications related to life-cycle design, assessment, inspection, monitoring, repair, maintenance, rehabilitation, and management of structures and infrastructure systems under uncertainty. Major topics covered include life-cycle safety, reliability, risk, resilience and sustainability, life-cycle damaging processes, life-cycle design and assessment, life-cycle inspection and monitoring, life-cycle maintenance and management, life-cycle performance of special structures, life-cycle cost of structures and infrastructure systems, and life-cycle-oriented computational tools, among others.

This Open Access Book provides both an up-to-date overview of the field of life-cycle civil engineering and significant contributions to the process of making more rational decisions to mitigate the life-cycle risk and improve the life-cycle reliability, resilience, and sustainability of structures and infrastructure systems exposed to multiple natural and human-made hazards in a changing climate. It will serve as a valuable reference to all concerned with life-cycle of civil engineering systems, including students, researchers, practitioners, consultants, contractors, decision makers, and representatives of managing bodies and public authorities from all branches of civil engineering.



Taylor & Francis

Taylor & Francis Group

<http://taylorandfrancis.com>

PROCEEDINGS OF THE EIGHTH INTERNATIONAL SYMPOSIUM ON LIFE-CYCLE CIVIL
ENGINEERING (IALCCE 2023), 2-6 JULY 2023, POLITECNICO DI MILANO, MILAN, ITALY

Life-Cycle of Structures and Infrastructure Systems

Edited by

Fabio Biondini

Department of Civil and Environmental Engineering, Politecnico di Milano, Milan, Italy

Dan M. Frangopol

*Department of Civil and Environmental Engineering, ATLSS Engineering Research Center,
Lehigh University, Bethlehem, PA, USA*



CRC Press

Taylor & Francis Group

Boca Raton London New York Leiden

CRC Press is an imprint of the
Taylor & Francis Group, an **informa** business

A BALKEMA BOOK

First published 2023
by CRC Press/Balkema
4 Park Square, Milton Park, Abingdon, Oxon, OX14 4RN

and by CRC Press/Balkema
2385 NW Executive Center Drive, Suite 320, Boca Raton FL 33431

CRC Press/Balkema is an imprint of the Taylor & Francis Group, an informa business

© 2023 selection and editorial matter, Fabio Biondini & Dan M. Frangopol; individual papers, the contributors

The right of Fabio Biondini & Dan M. Frangopol to be identified as the authors of the editorial material, and of the authors for their individual papers, has been asserted in accordance with sections 77 and 78 of the Copyright, Designs and Patents Act 1988.

The Open Access version of this book, available at www.taylorfrancis.com, has been made available under a Creative Commons Attribution-Non Commercial-No Derivatives 4.0 license.

Although all care is taken to ensure integrity and the quality of this publication and the information herein, no responsibility is assumed by the publishers nor the author for any damage to the property or persons as a result of operation or use of this publication and/or the information contained herein.

British Library Cataloguing-in-Publication Data
A catalogue record for this book is available from the British Library

Library of Congress Cataloging-in-Publication Data

A catalog record has been requested for this book

ISBN: 978-1-003-32302-0 (ebk)

DOI: 10.1201/9781003323020

Table of contents

Preface	xli
Acknowledgments	xliii
Symposium Organization	xliv
Organizing Association	xlix
 <i>FAZLUR R. KHAN PLENARY LECTURE</i>	
Making bridges sustainable <i>E. Brühwiler</i>	3
 <i>KEYNOTE LECTURES</i>	
Probabilistic life-cycle performance assessment of corroded concrete structures: Core technologies to predict the remaining service life <i>M. Akiyama & D.M. Frangopol</i>	21
The structural life of a Cathedral and the worksites of the Duomo di Milano <i>F. Canali & D. Coronelli</i>	33
Field and laboratory tests for corrosion assessment of existing concrete bridges <i>M. Carsana, E. Redaelli & F. Biondini</i>	45
Bayesian assessment of existing concrete structures: Exploiting the full power of combined information <i>R. Caspele & W. Botte</i>	57
Safety assessment of civil infrastructure assets subjected to extreme events <i>M. Ghosn</i>	69
Digital transition in asset management of bridges – Advantages and challenges <i>J.S. Jensen</i>	81
Life-cycle sea-crossing bridge operation under strong winds in severe weather <i>H.-K. Kim, H.-Y. Cheon & S. Kim</i>	90
Resilient structures: Materials Components Systems <i>M.P. Sarkisian</i>	98
Risk and decision-making for extreme events: What terrorism and climate change have in common <i>M.G. Stewart</i>	109

MINI-SYMPOSIA

MS1: Component reuse in structures and infrastructures

Organizers: *O. Iuorio & C. Fivet*

The design and development of a demountable and reconfigurable segmented fan concrete shell flooring system	119
<i>M. Nuh, J. Orr & R. Oval</i>	
Can we reuse plasterboards?	127
<i>S. Kitayama & O. Iuorio</i>	
Re-use of existing load-bearing structural components in new design	135
<i>R.P.H. Vergoossen, G.J. van Eck & D.H.J.M. Jilissen</i>	
Quality assurance process for reuse of building components	142
<i>A. Räsänen & J. Lahdensivu</i>	
Calculating embodied carbon for reused structural components with laser scanning	149
<i>B.S. Byers, M. Gordon, C. De Wolf & O. Iuorio</i>	
Reuse of existing reinforced concrete beams: Exploration of residual mechanical characteristics and measure of environmental impact	157
<i>A. Lachat, A. Feraille, T. Desbois & A.S. Colas</i>	
Designing with recovered precast concrete elements	165
<i>T.S.K. Lambrechts, F.J. Mudge, S.N.M. Wijte & P.M. Teuffel</i>	
Building structures made of reused cut reinforced concrete slabs and walls: A case study	172
<i>N. Widmer, M. Bastien-Masse & C. Fivet</i>	
Reuse of fibrous tectonics as the secondary structure of the facade system	180
<i>A. Ahmadnia, C. Monticelli, S. Viscuso & A. Zanelli</i>	
Properties and durability of recycled concrete with mixed granulates: Application for infrastructures	188
<i>C. Paglia, C. Mosca & E.G. Cordero</i>	
Behavior of bolted shear connectors for demountable and reusable UHPC-formed composite beams	195
<i>H. Fang</i>	

MS2: Smart condition assessment of railway bridges

Organizers: *T. Bittencourt, R. Calçada, D. Ribeiro, H. Carvalho, M. Massao & P. Montenegro*

A monitoring based digital twin for the Filstal bridges	205
<i>A. Lazoglu, H. Naraniecki, I. Zaidman & S. Marx</i>	
An application of drive-by approach on a railway Warren bridge	213
<i>L. Bernardini, A. Collina, C. Somaschini, K. Matsuoka & M. Carnevale</i>	
Optimal design and application of 3D printed energy harvesting devices for railway bridges	221
<i>J.C. Cámara-Molina, A. Romero, P. Galvín, E. Moliner & M.D. Martínez-Rodrigo</i>	
Smart condition monitoring of a steel bascule railway bridge	229
<i>J. Nyman, P. Rosengren, P. Kool, R. Karoumi, J. Leander & H. Petursson</i>	

A Bayesian bridge model update with complex uncertainty under high-speed train passages <i>K. Matsuoka, D. Mizutani, C. Somaschini, L. Bernardini & A. Collina</i>	237
Computational analysis of a reinforced concrete railway bridge considering the soil-structure interaction <i>A.L. Gamino, R.R. Santos, T.N. Bittencourt, M.M. Futai & H. Carvalho</i>	244
Drive-by damage detection methodology for high-speed railway bridges applying Mel-frequency cepstral coefficients <i>E.F. Souza, T.N. Bittencourt, I. Ames, D. Ribeiro & H. Carvalho</i>	252
Evaluation of corroded reinforced concrete railway bridge subjected to concrete cracking under uncertainty <i>L.S. Moreira, T.N. Bittencourt, M.M. Futai & H. Carvalho</i>	260
Structural reliability analysis of vehicle-bridge interaction based dynamic response for a high-speed railway bridge <i>I. Ames, T.N. Bittencourt, M.M. Futai, A.T. Beck & E.F. Souza</i>	268
 MS3: Integrating life-cycle engineering concepts into community resilience and decision-support	
<i>Organizers: J. van de Lindt, J. Padgett, A.R. Barbosa & N. Makhoul</i>	
Resilience and the use of life-cycle cost analysis in civil engineering in the US <i>T. Neimeyer, B. Parsons, L. Champion, A. Kane & L. Orsenigo</i>	279
The value of multi-criteria decision analysis for asset management <i>J. Bödefeld & F. Marsili</i>	287
Toward enhancing community resilience: Life-cycle resilience of structural health monitoring systems <i>N. Makhoul & R. Kromanis</i>	295
The life-cycle of a community for physical-social interdependent resilience impacted by policy decisions following tornado hazards <i>W. Wang, J.W. van de Lindt, S. Hamideh & E. Sutley</i>	303
Impact of modeling uncertainty on seismic life-cycle cost analysis of RC building under mainshock-aftershock sequences <i>S.P. Rayjada, J. Ghosh & M. Raghunandan</i>	311
Sensitivity analysis on resilience components throughout the lifecycle of an asset <i>N.K. Stamataki & D.V. Achillopoulou</i>	319
A Markovian framework to model life-cycle consequences of infrastructure systems in a multi-hazard environment <i>K. Otárola, L. Iannacone, R. Gentile & C. Galasso</i>	325
Integrating life-cycle analysis into civil infrastructure resilience decision making: Illustrative application to seismic resilience modeling of US communities <i>M. Roohi, J. Li & J.W. Van de Lindt</i>	333
Smart resilience: Capturing dynamic, uncertain and evolving lifecycle conditions <i>R. Rincon & J.E. Padgett</i>	341

MS4: Vibration-based structural health monitoring, damage identification and residual lifetime estimation

Organizers: E. Reynders, G. Lombaert, E. Chatzi & C. Papadimitriou

Structural damage estimation using short-time Fourier transform and improved convolution neural networks 351

C. Shi, Y. Aoues, R. Troian, D. Lemosse & H. Bai

Dynamic characteristic study of a heritage structure in Tiruchirappalli city using operational modal analysis 359

S. Anjuna, N. Radhakrishnan & G. George

Optimal design of a vibration-based sensor network for bridge monitoring 367

M.F. Yilmaz, K. Ozakgul & B.O. Caglayan

Indirect bridge damage detection using frequencies identified from vibrations of a single two-axle vehicle 374

Z. Li, W. Lin & Y. Zhang

Small-scale damage detection of bridges using machine learning techniques and drive-by inspection methods 383

Y. Lan, Z. Li, Y. Zhang & W. Lin

Structural health monitoring of the KW51 bridge based on detailed strain mode shapes: Environmental influences versus simulated damage 391

D. Anastasopoulos, K. Maes, G. De Roeck, G. Lombaert & E.P.B. Reynders

Dissipated hysteretic energy reconstruction for high-resolution seismic monitoring of instrumented buildings 399

M. Roohi, E.M. Hernandez & D.V. Rosowsky

Follow-up assessment of a prestressed concrete road bridge based on dynamic bridge behaviour – analysis of structural integrity and evaluation of maintenance condition 407

T. Reimoser, R. Veit-Egerer, A. Schmitt & Y. Benitz

Laboratory validation of an arduino based accelerometer designed for SHM applications 415

S. Komarizadehasl, E. Delgado, G. Ramos, J. Turmo & J.A. Lozano-Galant

Pre-posterior effectiveness of modal extraction techniques for vibrational tests design 422

A. Lotti, D. Tonelli, S. Zorzi, D. Zonta & E. Tubaldi

MS5: Life-cycle performance assessment of civil engineering systems

Organizers: M. Akiyama, D.M. Frangopol & H. Matsuzaki

Structural reliability assessment of RC shield tunnels with nonuniform steel corrosion 433

Z. He & C. He

Life-cycle analysis of aging structures based on reliability approach 439

S. Joshi, A. Thorat, H. Dehadray & M. Tundalwar

Baseline digital twin models for key performance management of prefabricated bridges 447

C.S. Shim, G.T. Roh, M.U. Kang & Y.H. Lee

Analysing the impact of local factors on the life-cycle of metallic bridge girders 453

G. Calvert, M. Hamer, L. Neves & J. Andrews

Quantifying the effects of long duration ground motions on the lifetime seismic losses of aging highway bridges	461
<i>S. Shekhar, B. Panchireddi & J. Ghosh</i>	
Seismic demand hazard assessment for RC bridges considering cumulative damage over time	469
<i>D. Herrera & D. Tolentino</i>	
Development of maintenance systems for bridge members	477
<i>K. Kwon, Y. Choi & J.S. Kong</i>	
Durability analysis and optimization of a prestressed concrete bridge strengthened by a fiber reinforced concrete layer	485
<i>S. Schoen, P. Edler, G. Meschke & S. Freitag</i>	
Multivariate inspection of German steel civil infrastructure using autonomous UAS	493
<i>D. Thomas, M. Gündel, A. Wickers, M. Alpen & J. Horn</i>	
A lifecycle analysis approach to the impact of green roofs on the structural and thermal performances of buildings	501
<i>S. Kalantari, M.R. Rashedi, R. Ehsani & F.M. Tehrani</i>	
Deep learning-based life-cycle system reliability assessment of asphalt pavement	509
<i>J. Xin, D.M. Frangopol & M. Akiyama</i>	
Climate change impact on the integrity of structures and infrastructure in mountainous or hilly areas	515
<i>Y. Tsompanakis, N. Makrakis, P.N. Psarropoulos & D.M. Frangopol</i>	
Assessing life-cycle seismic fragility of corroding reinforced concrete bridges through dynamic Bayesian networks	523
<i>F. Molaioni, Z. Rinaldi & C.P. Andriotis</i>	
 MS6: Smart maintenance and AI applications	
<i>Organizers: H. Furuta, N. Catbas & Y. Nomura</i>	
Bolt axial force detection using deep learning based on vision methods	533
<i>Y. Chen, J. Lai, G. Hayashi & T. Yamaguchi</i>	
Proposal of deep learning ensemble method for phased array ultrasonic testing for tube-to-tubesheet weld of heat exchange	541
<i>H. Hattori, J. Murakami, N. Shinmura, K. Shinoda, M. Abe, T. Katayama, R. Ioka & T. Wada</i>	
Innovative methods for the inspection of hydraulic structures	548
<i>A. Seiffert & J. Bödefeld</i>	
Behaviour of corroded bridge bearing and full-bridge modeling	555
<i>A. Hiraoka, G. Hayashi & T. Yamaguchi</i>	
Damage identification of corroded arch bridge using vibration characteristics and rotational angle	562
<i>K. Akahoshi, G. Hayashi, Y. Chen & T. Yamaguchi</i>	
Identification of spalling in concrete structures by a hammering test using autoencoder	570
<i>H. Emoto, N. Fukui, Y. Iitaka & S. Kanazawa</i>	

Corrosion progress detection in steel bridge from vehicle-mounted camera images based on deep learning	578
<i>S. Ozaki, Y. Nomura, H. Furuta, H. Yamazaki & Y. Yamato</i>	
Development of a cable inspection robot for cable-stayed bridges	584
<i>K. Kawamura, W. Zheng & M. Shiozaki</i>	
Application of cluster analysis and Markov chain model for network-level highway infrastructure management	592
<i>A. Amir & M. Henry</i>	
Digital twin-oriented maintenance: A hybrid finite element and surrogate model approach for predicting the excavation-induced tunnel displacement	600
<i>Y. Gu, L. Zhang, Q. Ai, X. Jiang & Y. Yuan</i>	
Development of simple fatigue crack propagation monitoring using IoT	608
<i>T. Ishikawa, N. Matsumoto & K. Komon</i>	
Detection of debonding of CFRP bonded steel members using the AE method	615
<i>M. Mizutani, T. Ishikawa & Y. Fujii</i>	
Condition-based maintenance of fatigue-sensitive structures using model predictive control	623
<i>S. Kong, R. Cao, J. Cheng & Y. Liu</i>	
A deep learning-based corrosion prediction model for paint-coated steel with defects	631
<i>F. Jiang & M. Hirohata</i>	

MS7: Non-deterministic model updating for structural health monitoring of existing structures

Organizers: M. Kitahara, M. Broggi, M. Beer & T. Kitahara

System identification and damage assessment of benchmark model H	641
<i>G.S. Wang, C.W. Lo & F.K. Huang</i>	
Updating simplified jack-up model using basin test data	649
<i>J.X. Cao, S.T. Quek, S.L. Zhang, C. Zhang, M.B. Cai & M. Si</i>	
Application of unscented transformation for Bayesian updating	657
<i>T. Shuku & T. Kitahara</i>	
Environmental influence on structural health monitoring systems	662
<i>J.-H. Bartels, M. Kitahara, S. Marx & M. Beer</i>	
Distribution-free stochastic model updating with staircase density functions	670
<i>M. Kitahara, T. Kitahara, S. Bi, M. Broggi & M. Beer</i>	
Efficient posterior estimation for stochastic SHM using transport maps	678
<i>J. Grashorn, M. Broggi, L. Chamoin & M. Beer</i>	
Evaluating the minimum cross-section thickness of a conveyor support structure member	686
<i>Y. Yang, D. Ogawa, T. Nagayama, S. Kato, K. Hisazumi & T. Tominaga</i>	
Scenario-oriented analysis of bridges subjected to non-deterministic combined seismic actions based on finite element modeling	694
<i>S. Yamamoto, G. Shoji & M. Ohsumi</i>	
Probabilistic-based model updating on a prestressed concrete box girder	701
<i>X. Zhou, D. Chen & C.-W. Kim</i>	

Applicable schemes for the Vehicle-Bridge Interaction System Identification method <i>K. Yamamoto & R. Shin</i>	709
Risk-based resilience assessment framework for thermal power plants after a catastrophic seismic event <i>A. Yuyama, G. Shoji & Y. Kajitani</i>	717
Non-deterministic seismic damage detection of road infrastructure analysing image training database <i>R. Kondo & G. Shoji</i>	725
MS8: Resilience and sustainability of steel based hybrid building structures in the life-cycle environment	
<i>Organizers: D. Dubina, F. Dinu & V. Ungureanu</i>	
Life-cycle assessment of cold formed steel buildings: Main influential materials and parameters <i>O. Iuorio & A. Gigante</i>	735
The new construction products regulation: Opportunity or barrier for reused constructional steel? <i>P. Hradil, L. Fülöp, M. Wahlström & C. del Castillo</i>	743
A comparative life-cycle assessment of structural composite steel-concrete floor systems – A case study <i>I. Lukačević, A. Rajić, V. Ungureanu & R. Buzatu</i>	751
Sustainability and seismic resilience of hybrid lightweight residential buildings <i>D. Dubina, V. Ungureanu & M. Mutiu</i>	759
Influence of fastening systems on the ultimate capacity of steel- faced sandwich wall panels under transverse loads <i>F. Dinu, C. Neagu, S. Lindiri & M. Senila</i>	767
Simplified assessment of the cyclic performance of steel constructions in aggressive environments <i>A. Milone & R. Landolfo</i>	775
Multi-hazard robustness assessment of seismic resistant multi-story steel frame buildings <i>D. Dubina, F. Dinu & J. Dominiq</i>	783
Laser scanning technology for the evaluation of damage in complex building envelopes after extreme load events <i>P.C. Zdrengha, F. Dinu, S. Herban & C. Neagu</i>	791
Design strategies for reusable structural components in the built environment <i>F. Kavoura & M. Veljkovic</i>	799
MS9: Recent development IoT- and ICT-based infrastructure inspection and management	
<i>Organizers: C. Kim, V. Sarhosis, M. Noori & Y. Zhang</i>	
A computer vision-based identification of natural frequency of a pole structure and damage detection <i>D. Kawabe & C.-W. Kim</i>	809

A framework for digital twinning of masonry arch bridges <i>I.B. Muhit, D. Kawabe, D. Loverdos, B. Liu, Y. Yukihiro, C.-W. Kim & V. Sarhosis</i>	817
Quality analyses of crowdsourced smartphone trips for bridge dynamic monitoring <i>T.J. Matarazzo, I. Dabbaghchian, L. Cronin, S.N. Pakzad, S.S. Eshkevari, H. Yin, R. Lassman, P. Santi & C. Ratti</i>	825
Remote ambient vibration-based scour monitoring system <i>S. Kitagawa, H. Yano, C.-W. Kim & D. Kawabe</i>	833
The ratio of stress amplitudes between two directions around welded part of trough rib in orthotropic decks with fatigue cracks <i>R. Saita, M. Ueno, Y. Sugimoto & H. Onishi</i>	841
Ambient-vibration-based operational modal analysis and cable tension estimation in the long-term SHM of a cable-stayed bridge <i>W.J. Jiang, C.-W. Kim & K. Ono</i>	849
Uncertainty quantification of modal properties using half year monitoring data of a plate girder bridge <i>Y. Goi & C.-W. Kim</i>	857
Study on estimation of reaction force based on vibration measurement of girders <i>I. Kim, S. Watanabe, Y. Goi, Y. Kitane, K. Sugiura & N. Okubo</i>	865
Change in vibration characteristics of steel poled structure with damage <i>M. Kato, Y. Goi, Y. Kitane, K. Sugiura & Y. Adachi</i>	872
 MS10: Advances in life-cycle earthquake engineering	
<i>Organizers: L. Capacci, M. Akiyama, F. Biondini & D.M. Frangopol</i>	
Review of advances in life-cycle seismic risk and resilience of bridges and bridge networks <i>L. Capacci, F. Biondini & D.M. Frangopol</i>	883
Agile analysis of life-cycle damage cost of concrete frame structures under earthquake <i>J.M. Bairán & M. García</i>	892
Methodology for determining optimal countermeasure for bridges under seismic and tsunami hazards <i>H. Ishibashi, M. Akiyama & S. Koshimura</i>	899
Seismic damage control of bridges with deteriorated seismic isolation bearings by rupture of anchor bolts <i>H. Matsuzaki</i>	906
Probabilistic resilience assessment of aging bridge networks based on damage disaggregation and stationary proposal importance sampling <i>L. Capacci, F. Biondini & A.S. Kiremidjian</i>	914
Dynamic characteristic of geodesic domes with different location of mass <i>D. Bysiec, T. Maleska & A. Janda</i>	923
Life-cycle benefits of seismic protection using a novel active mass damper <i>C. Fontana, M. Caruso, R. Pinho, F. Menardo, G. Rebecchi & A. Bussini</i>	931
Decision-making procedures for optimal seismic-energy integrated retrofitting of buildings <i>M. Caruso, R. Pinho, R. Monteiro & R. Couto</i>	939

MS11: Life-cycle asset management and the complexity of socio-environmental-technical transitions

Organizers: A. Hartmann, M. Hertogh, J. Bakker & H. Roebers

Multi-stakeholder service life design for rail level crossings <i>Y. Shang, R. Binnekamp & A.R.M. Wolfert</i>	949
Preference-based service life design of floating wind structures <i>H.J. van Heukeelum, A.C. Steenbrink, O. Colomé, R. Binnekamp & A.R.M. Wolfert</i>	957
A life-cycle assessment framework for pavement management considering uncertainties <i>A. Vargas-Farias, J. Santos, A. Hartmann & F. Van der Pijl</i>	965
To replace or not to replace: A model for future functional performance of bridges <i>S.C.A. Mooren, A. Hartmann & S. Asgarpour</i>	973
The end-of-life of bridges: Integrating functional, technical and economic perspective <i>A. Hartmann & J.D. Bakker</i>	981
How to estimate costs of replacement for an aging infrastructure, a Dutch case study <i>G.A. De Raat</i>	989
Plannability of maintenance in life-cycle decision making for infrastructure <i>J.D. Bakker & R. Treiture</i>	995
Predictive twin for steel bridge in The Netherlands <i>G.A. de Raat, J.D. Bakker, G.T. Luiten, J.H. Paulissen, B.Q. de Vogel, H. Scholten & S. de Graaf</i>	1003

MS12: Advanced strengthening and retrofitting solutions for existing concrete structures

Organizers: N. Randl & E. Rossi

Numerical investigation of the effects of graphene on the mechanical properties of fibre reinforced cementitious matrix composite <i>X.M. Zhu, M.N. Su & Y.C. Wang</i>	1013
Experimental behavior of FRCM-confined concrete under high temperature <i>F. Faleschini, C. Pellegrino & K. Toska</i>	1021
Retrofit of RC bridge half-joints: Applications and remarks with emphasis on post-tension techniques <i>G. Santarsiero, V. Picciano, A. Masi & G. Ventura</i>	1029
Enhancing Textile Reinforced Concrete materials by admixing short dispersed fibres <i>E. Rossi & N. Randl</i>	1037
Shear strengthening with F/TRC: Experimental investigation on real scale RC beams <i>E. Rossi & N. Randl</i>	1044
State of the art in flexural prestressing of RC members with SMA materials <i>J. Rogowski & R. Kotynia</i>	1050
FRP shear dowels - Experimental investigation <i>Đ. Čairović, M. Zlámal, J. Venclovský & P. Štěpánek</i>	1058
Bond behavior of CFRP-concrete systems using toughened epoxies <i>D.V. Achillopoulou, A. Kosta, A. Montalbano & F. Choffat</i>	1065

The effect of fatigue loading on the behavior of externally bonded CFRP-to-concrete joints using the grooving method	1073
<i>M. Khorasani, G. Muciaccia & D. Mostofinejad</i>	
Externally applied textile reinforced systems on RC members: Innovative and sustainable materials and techniques	1081
<i>F. Bencardino & R. Curto</i>	
Experimental investigation on strengthening of RC members with HSC overlays	1089
<i>N. Randl & M. Steiner</i>	
Innovative shear strengthening with post-installed undercut anchors	1097
<i>N. Randl, P. Harsányi & J. Kunz</i>	

MS13: Safety and durability of high-performance structures

Organizers: X. Gu & Q. Yu

Evolution of seismic fragility of reinforced concrete columns subjected to corrosion	1107
<i>Y. Liu, W.P. Zhang, X.L. Gu & Y. An</i>	
Experimental study on water absorption in unsaturated concrete	1115
<i>J. Fang, C. Jiang & X.L. Gu</i>	
Monitoring electrochemical chloride extraction process by testing chloride ion contents in electrolyte	1122
<i>C. Song, C. Jiang & X.L. Gu</i>	
Experimental study on stress recovery behavior of Fe-SMA subjected to multi-activation	1127
<i>Q.Q. Yu, Z. Y. Chen, X.L. Gu, X.W. Xiao, W.P. Zhang & Y.H. An</i>	
SMFL-based probability distribution of minimum cross-sectional areas of corroded steel bars	1134
<i>J.L. Qiu, W.P. Zhang, Q.Q. Yu & Z.P. Chen</i>	
Reliability analysis considering epistemic uncertainties with small initial sample and successive updating data	1141
<i>Y. Fei, Y. Jiang, Y. Leng, L. Wang, Z. Chen</i>	
Numerical simulation of freeze-thaw damage deterioration of concrete in cold region	1149
<i>J. Jiang, Y. Wang, Z. Liu & Z. Chen</i>	
Smart aggregate-based automated concrete stress monitoring via deep learning of impedance signals	1158
<i>J.T. Kim, Q.B. Ta, Q.Q. Pham, N.L. Pham & T.C. Huynh</i>	

MS14: Coupled chemical, physical, and mechanical processes in cementitious materials for short- and long-term behavior of R.C. and P.C. structures

Organizers: G. Di Luzio, R. Wan-Wendner, M. Alnaggar & J. Vorel

LCA assessment related to the evolution of the earthquake performance of a strategic structure	1169
<i>D. di Summa, A. Marcucci, M. Nicolò, F. Martignoni, A. Carrassi, L. Ferrara & N. De Belie</i>	
The influence of the expansive site of delayed ettringite formation on the anisotropy of expansion evaluated by mesoscale discrete model	1177
<i>M. Fujishima, T. Miura & H. Nakamura</i>	

Chemo-physics and mechanics of RC for behavioral simulation in micro-seconds to years <i>K. Maekawa, K. Iwama & Y. Takahashi</i>	1185
Temperature dependent modelling approach for early age behavior of printable mortars <i>A. Robens-Radermacher, J.F. Unger, A. Mezhev & W. Schmidt</i>	1193
Experimental study on effect of winter curing conditions on mechanical properties of concrete <i>F.L. Li, W.L. Lu, W.Q. Peng, Y.D. Tang & L.F. Xu</i>	1201
Hygro-thermo-chemo-mechanical coupled discrete model for the self-healing in Ultra High Performance Concrete <i>A. Cibelli, L. Ferrara & G. Di Luzio</i>	1209
Crack healing under sustained load in concrete: An experimental/numerical study <i>G. Di Luzio, A. Cibelli, S.M.J. Al-Obaidi, S.M.I. Radwan, M. Davolio, L. Ferrara, R. Wan-Wendner & Y. Wang</i>	1217
Homogenized mesoscale discrete model for coupled multi-physical analysis of concrete <i>J. Eliáš & G. Cusatis</i>	1225
Early-age cracking in concrete slabs with FRP reinforcement <i>J.E. Bolander, H. Roghani & A. Nanni</i>	1233
Toward distinguishing the chemical, physical, and wetting-drying sulfate attack on concrete <i>I.A.N. Omrani, M. Koniorczyk & D. Bednarska</i>	1241

MS15: Deconstruction and reuse of steel and lightweight metal structures

Organizers: M. Kuhnhenne & P. Kamrath

Requirements for gutting and demolition cost index <i>H. Kesting & M. Helmus</i>	1249
Numerical determination of the wrinkling stress of steel polyurethane sandwich panels for reuse scenarios <i>K. Janczyk & M. Kuhnhenne</i>	1257
Allowable strength estimation of vertical members used for system scaffolds considering reusability <i>N.G. Jang, J.H. Won, S.S. Ko, J.K. Bong & D.H. Chung</i>	1265
Limits of reuse of steel <i>P. Kamrath</i>	1270
The deconstruction of a steel based single story hall <i>P. Kamrath</i>	1278
On the development of regulations for the increased reuse of steel structures <i>H. Bartsch, F. Eyben, J. Voelkel & M. Feldmann</i>	1287
RFID-based traceability system for constructional steel reuse <i>P. Hradil, K. Jaakkola & K. Tuominen</i>	1295
Environmental and economic impact of steel industrial buildings made of reclaimed elements <i>R. Buzatu, V. Ungureanu & P. Hradil</i>	1303

MS16: Assessment of existing masonry arch bridge infrastructure

Organizers: M. Gilbert, G. Cardani, T. Boothby & D. Coronelli

- Optimal strengthening of masonry arch bridges with externally bonded reinforcing layers 1315
M. Bruggi & A. Taliervo
- Static and seismic assessment of Ponte delle Capre, a masonry arch bridge 1323
F. Casarin, S. Bellin, M. Mocellini & R. Fabris
- Damage accumulation in the structural life and assessment of masonry bridges 1331
T.E. Boothby & D. Coronelli
- Three-dimensional limit analysis of barrel arch bridges 1338
D. Coronelli & M.C. Giangregorio
- The reinforced arch method for the life of the ancient bridge of Omegna 1344
L. Jurina, E.O. Radaelli & D. Coronelli
- Numerical investigation of 3D response characteristics of masonry bridges by detailed mesoscale masonry models 1352
M.S. El Ashri, S. Grosman, L. Macorini & B.A. Izzuddin
- Experimental investigation of the effect of masonry infill on the performance of masonry arch bridges 1360
S. Amodio, M. Gilbert & C.C. Smith
- Multi-fidelity modelling of masonry arch bridges under traffic loading 1368
S. Grosman, Q. Fang, L. Macorini & B.A. Izzuddin
- Analysis of masonry arch bridges using multi-scale discontinuity layout optimization 1376
L. He, N. Grillanda, J. Valentino, M. Gilbert & C.C. Smith
- The role of history in the structural assessment of a multi-span masonry arch bridge 1384
G. Zani, P. Martinelli, G. Cardani & M. di Prisco
- Stochastic load-carrying capacity assessment of brick masonry arch bridges 1392
B. Liu, I.B. Muhit & V. Sarhosis
- New UK guidance for the assessment of masonry arch bridges 1400
M. Gilbert, C.C. Smith & S. Amodio

MS17: Recent advance in seismic protection systems: Design, modeling and testing strategies of traditional and innovative solutions

Organizers: A. Pavese & M. Furinghetti

- Prestressed lead damper for seismic protection of structures 1411
V. Quaglino, C. Pettoroso, E. Bruschi & M. Sartori
- Nonlinear analysis of base isolated buildings with curved surface sliders including over-stroke displacements 1419
F.C. Ponzo, A.D. Cesare & N. Lamarucciola
- Effects of wear on the friction coefficient of a curved surface slider 1427
V. Quaglino, E. Bruschi, E. Çavdar, G. Özdemir, V. Karuk & U. Özcamur
- Effects of rubber shear modulus variability on the seismic response of isolated bridges 1435
M. Marra & S. Silvestri

Prediction of the response of a lead-core rubber bearing using machine learning <i>T. Zhelyazov, S. Ólafsson & R. Rupakhety</i>	1443
Experimental assessment of anti-seismic devices performance <i>A. Pavese, S. Reale & M.J. Fox</i>	1450
Vulnerability assessment of bridges within the Italian highway network <i>S. Reale, A. Pavese & M. Furinghetti</i>	1458
Life-Cycle Assessment (LCA) of fiber-reinforced reclaimed-rubber seismic isolators <i>F. Cilento, D. Losanno, C. Menna, C. Ciriello & F. Parisi</i>	1466
Definition of a design procedure of seismic isolation systems based on rubber bearings <i>M. Furinghetti</i>	1474
Inverse design of isolated structures using predicted FEMA P-58 decision variables <i>H.G. Pham & T.C. Becker</i>	1481
Seismic behaviour of building using damage-avoidance shearwall hold-downs <i>L. Budi</i>	1489
MS18: Safety and maintenance of masonry arch bridges: diagnostic, monitoring, modelling, risk analysis and retrofit interventions	
<i>Organizers: F. Cannizzaro, N. Cavalagli, C. Chisari, B. Pantò, F. Scozzese, P. Zampieri & M. Zizi</i>	
Preliminary investigation on the response sensitivity of masonry arch bridges subjected to scour <i>F. Scozzese, A. Dall'Asta & E. Tubaldi</i>	1499
A methodology to derive scour fragility functions for masonry arch bridges <i>G.D. Di Dieco, M. Pregolato & A.R. Barbosa</i>	1507
Experimental modal analysis and finite element model updating of a historical masonry arch bridge <i>M. Morici, V. Nicoletti, G. Leoni & F. Gara</i>	1515
Influence of site effects on the seismic vulnerability of masonry arch bridges <i>Ö. Saygılı & J.V. Lemos</i>	1523
Computational strategy for the design of monitoring for masonry arch bridges using DIC procedures <i>S. Grosman, Q. Fang, L. Macorini & B.A. Izzuddin</i>	1530
Influence of uncertain mechanical parameters on the load-bearing capacity of multi-span masonry arch bridges <i>M. Zizi, C. Chisari & G. De Matteis</i>	1538
Simplified analysis on multiring masonry arch bridges <i>R. Piazzon, P. Zampieri & C. Pellegrino</i>	1546
Effects of changing temperature in the vibration-based model updating of a masonry bridge <i>P. Borlenghi, A. Saisi & C. Gentile</i>	1552
Numerical approaches to assess the load capacity of FRCM strengthened masonry bridges <i>D. Santinon, P. Zampieri, C. Pellegrino, D. Ricci, F. Iodice, A. Vecchi & F. Iacobini</i>	1560
3D collapse mechanisms of masonry bridges subjected to horizontal actions <i>L. Niero, P. Zampieri & C. Pellegrino</i>	1567

Near-collapse deformed configuration of masonry arch bridges <i>G. Stagnitto & P. Zampieri</i>	1574
Safety checking at point and section level of masonry arch bridges <i>G. Stagnitto, R. Siccardi, M. Ghioni & P. Zampieri</i>	1582
Discrete Macro-Element structural assessment of a railway masonry arch bridge subjected to pier settlements <i>D. Rapicavoli, F. Cannizzaro, S. Caddemi & I. Calì</i>	1590

SPECIAL SESSIONS

SS1: Climate change effects on life-cycle safety, reliability, and risk of structures and infrastructure systems

Organizers: F. Biondini, Z. Lounis & M. Ghosn

Framework for life-cycle tsunami risk assessment considering sea-level rise effects due to climate change <i>A.K. Alhamid, M. Akiyama, K. Aoki, S. Koshimura & D.M. Frangopol</i>	1601
Life-cycle design of concrete highway bridge decks under climate change <i>H. Shirkhani, Z. Lounis & J. Zhang</i>	1609
Climatic design data for buildings and infrastructure under changing climate in Canada <i>H. Shirkhani & Z. Lounis</i>	1617
Life-cycle structural reliability of RC bridge piers under corrosion in a changing climate <i>G.V. Nava, L. Capacci, F. Biondini & L. Casti</i>	1625
Risk based life-cycle planning for flood-resilient critical infrastructure <i>S.S. Palic, I. Stipanovic, E. Ganic, M. Kosic, A. Anzlin, M. Bacic, M.S. Kovacevic & K. Gavin</i>	1634
Equitable climate adaptation framework for levees <i>A. Mohammed & F. Vahedifard</i>	1642

SS2: SHM for life-cycle informed management of degrading structures

Organizers: M.P. Limongelli, P. Gardoni, S. Thöns & D. Lu

Integration of information quality assessment in bridge resilience management <i>N. Makhoul & M.P. Limongelli</i>	1653
Optimum inspection scheduling of steel storage tanks based on past ultrasonic thickness measurements <i>S.A. Faroz, M.S. Khan & S. Ghosh</i>	1661
The role of life-cycle civil engineering practices in smart and sustainable cities <i>M.D. Lepech, A.S. Kiremidjian & K.H. Law</i>	1669
Value of information under random decision, model, and measurement errors <i>Z.Y. Mir Rangrez, J. Ghosh, S. Ghosh & C. Caprani</i>	1677
A review on low-cost sensors compatible with open-source platforms used for life-cycle monitoring of civil structures <i>M. Komary, S. Komarizadehasl, J. Turmo, F. Lozano, J.A. Lozano-Galant & X. Ye</i>	1685

On the utilization of multiple information for the integrity management of deteriorating systems 1693
G. Costa, M.P. Limongelli & S. Thöns

SS3: Monitoring of structures for informed decision making

Organizers: A. Strauss & D.M. Frangopol

Recent progress developing a rating framework for evaluating SHM for bridge scour 1705
P.J. Vardanega, G. Gavriel & M. Pregnolato

Predicting the usefulness of monitoring information for structural evaluations of bridges 1713
N. Bertola & E. Brühwiler

Monitoring and data informed approaches for the condition assessment of existing structures 1721
E. Apostolidi, M.F. Granzner, A. Strauss & R. Geier

A novel low-cost inclinometer sensor based on fusion technology for structural health monitoring applications 1729
M. Komary, A. Alahmad, S. Komarizadehasl, J. Turmo, J.A. Lozano-Galant & Y. Sun

Sensor monitoring for engineering structures: Applications to tunnels 1737
A. Strauss, F. Sattler, B. Täubling-Frueux, C. Seywald, H. Neuner, V. Kostjak & D.M. Frangopol

Digital twins for bridges – concept of a modular digital twin based on the linked data approach 1745
T. Zinke, S. Reymer, S. Kosse, P. Hagedorn, M. König, F. Wedel, S. Schneider, S. Marx, S. Nieborowski & S. Windmann

SS4: Artificial intelligence-based life-cycle management of infrastructure systems

Organizers: Y. Dong, D.M. Frangopol & X. Lei

Sustainability-informed intelligent management of aging civil infrastructure systems with emphasis on bridge networks 1755
X. Lei, Y. Dong & D.M. Frangopol

Meta-learning method for efficient time-variant reliability analysis of deteriorating structures 1763
T. Gao, J. Cheng, Y. Liu, M. Cheng & D.M. Frangopol

Optimization of sewer flushing programs: A deep reinforcement learning approach 1770
A. Keshvari Fard & X.-X. Yuan

Carbon emission reduction in railway maintenance using reinforcement learning 1778
J. Sresakoolchai & S. Kaewunruen

Intelligent monitoring and control method of the life-cycle cable-stayed bridge with steel-concrete composite beam 1786
G.W. Yao, G.F. Zhang, S.Y. Li, Y.F. Wu, E.G. Jiang & Y.D. Zhu

Integrating unstructured data analytics and BIM to support predictive maintenance 1794
S. Sobhkhiz & T. El-Diraby

SS5: Concrete damage assessment using coda waves

Organizers: C. Gehlen, E. Niederleithinger, J. Timothy & T. Kränkel

- Ultrasonic monitoring of large-scale structures - input to engineering assessment 1805
N. Eppe, C.A. Sanchez-Trujillo & E. Niederleithinger
- A new technique to detect altered stresses in tendons early 1813
N. Sträter, F. Clauß, M.A. Ahrens & P. Mark
- Comparison of structural analysis results with coda wave interferometry measurements 1821
S. Grabke & K.-U. Bletzinger
- About the separation of impacts on coda waves in concrete 1827
F. Diewald
- A virtual lab for damage identification in concrete using coda waves 1834
G. Vu, G. Meschke, J.J. Timothy & E.H. Saenger
- The hydration of cement paste: Thermodynamics driven multi-scale modeling of elastic properties and coda wave interferometry based monitoring 1842
E. Jäggle, J.J. Timothy, F. Diewald, T. Kränkel, C. Gehlen & A. Machner

SS6: Life-cycle redundancy, robustness, and resilience indicators for aging structures and infrastructure systems under multiple hazards

Organizers: F. Biondini & D.M. Frangopol

- Financial risk assessment of flexible infrastructure systems 1853
N. Acuña-Coll & M. Sánchez-Silva
- Time-dependent assessment of corrosion impact on R/C members 1861
M. Calò & G. Gabbianelli
- Resilience-based optimal management of aging bridge networks under mainshock-aftershock sequences 1869
L. Jafari, L. Capacci, F. Biondini & M. Khanmohammadi
- Risk-based optimal life-cycle maintenance of post-tensioned concrete bridges considering accuracy of inspection methods in structural model updating 1877
M. Taeb, A.B. Mehrabi & K. Lau
- Seismic safety assessment of “Palácio do Itamaraty” at Brasília reliability-based 1885
P.Q. Rodrigues, J.C. Pantoja & P.S.T. Miranda

SS7: Bridge weigh-in-motion systems and applications to structural health monitoring

Organizers: S. Mustafa & D. Cantero

- Bridge weigh-in-motion to support SHM 1895
D. Cantero
- Bayesian-based bridge influence line identification and uncertainty estimation 1903
S. Mustafa, I. Yoshida & H. Sekiya
- Bridge weigh-in-motion: Feedback on various types of bridges 1911
F.B. Cartiaux, V. Le Corvec, J. Semiao & A. Brouste

Estimation of remaining fatigue life of railway bridges using measurements from the WIM system	1919
<i>M. Zakharenko, G.T. Frøseth & A. Rönquist</i>	
Bridge-weigh-in-motion by strain of transverse stiffener and heavy-truck traffic characteristics in Fukuoka area, Japan	1927
<i>E. Yamaguchi, Y. Furusato, R. Nakamura & K. Horiuchi</i>	
Deep sensor-fusion approach to vehicle detection on bridges using multiple strain sensors	1935
<i>H.T. Vuong, A. Takasu & T.P. Doan</i>	
SS8: Performance, safety, and cost of civil infrastructure in a life-cycle context	
<i>Organizers: Y. Li, P. Yuan, Y. Dong & D.M. Frangopol</i>	
Masonry design for extended life-time usage by implementing joint behaviour	1945
<i>T. Molkens, J. Smits, S.V. Hout & R. Meuleman</i>	
Data-driven life-cycle risk assessment of bridge networks using Bayesian network	1953
<i>M. Cheng & H.O. Gao</i>	
Risk-based life-cycle loss assessment using statistical moments	1961
<i>Y. Zhang & Y. Li</i>	
Effects of high temperature on web crippling strength of lean duplex stainless steel tubular sections	1967
<i>Y. Cai, C.-C. Lee, S.-L. Mak, L. Wang & F. Zhou</i>	
Risk-based fatigue assessment of orthotropic steel decks	1975
<i>J. Heng, Y. Dong, C. Baniotopoulos & S. Kaewunruen</i>	
Life-cycle management of offshore wind deteriorating structures under ship collision accidental events	1983
<i>P. Salazar L., J. Morán A., P. Rigo & P.G. Morato</i>	
SS9: Risk-based prioritization and monitoring of bridges for road infrastructure management in Lombardy region, Italy	
<i>Organizers: F. Biondini, M.P. Limongelli, C. Gentile & M. Belloli</i>	
Static monitoring of a masonry arch bridge: Evaluating the effects of changing environment	1993
<i>P. Borlenghi, C. Gentile, M. D'Angelo & F. Ballio</i>	
Structural health monitoring of bridges based on GNSS	2001
<i>S. Bianchi, L. Capacci, M. Anghileri, F. Biondini, G. Rosati, G. Cazzulani, S. Barindelli & S. Caldera</i>	
Remote monitoring of a concrete bridge through InSAR and GNSS measurements	2009
<i>O. Lasri, P.F. Giordano, M. Previtali & M.P. Limongelli</i>	
How to prioritize bridge maintenance using a functional priority index	2017
<i>M. Arena, G. Azzone, V.M. Urbano, P. Secchi, A. Torti & S. Vantini</i>	

SS10: Deterioration modeling of concrete, rebar, steel and bond performance

Organizers: X. Gao, X. Ren & J. Li

Analysis of mechanical behavior of bond between plain rebar and concrete 2027

X. Gao, Y. Yu, C. Su & J. Li

Residual bearing capacity of corrosion-damaged reinforced concrete columns with annular cross sections 2035

Y. Jiang, H.-P. Chen & W.B. Li

Steel liner corrosion and its effects on the leak-tightness of the nuclear containment structure 2043

X.B. Li, X.Y. Wu & J.X. Gong

Influence of combined corrosion of carbonation and cyclic loading on reinforced concrete beams 2051

L.X. Zhu, Z.J. Zhou, Y.Q. Tian & C.R. Chen

SS11: BRIDGE|50: Experimental testing and model validation for life-cycle design and assessment of RC/PC bridges

Organizers: F. Biondini, F. Tondolo, S. Manto & C. Beltrami

Large-scale experimental testing of 50-year-old prestressed concrete bridge girder 2061

P. Savino, A. Quattrone, D. Sabia, B. Chiaia, F. Tondolo, M. Anghileri, F. Biondini & G. Rosati

Experimental tests for mechanical characterization of prestressed concrete bridge deck beams 2069

M. Anghileri, G. Rosati, F. Biondini, P. Savino & F. Tondolo

Experimental campaign for corrosion assessment of 50-year-old PC deck beams 2077

M. Carsana, E. Redaelli, D.O. Valoti & F. Biondini

Experimental validation of nonlinear finite element analysis of PC bridge deck beams based on the results of full-scale load tests 2085

M. Anghileri & F. Biondini

Dynamic response of PC bridge beams under different damages 2093

D. Sabia, A. Quattrone, P. Savino & F. Tondolo

SS12: Exploiting digitalization in the intervention planning for transportation infrastructure

Organizers: B.T. Adey, S. Moghtadernejad, S. Chuo & H. Mehranfar

Decentralized control-based intervention policies for road networks 2103

Y. Nakazato, D. Mizutani & T. Nagae

Efficient early estimates of bridge interventions: Costs, required possession times and associated failure risks 2112

H. Mehranfar, B.T. Adey, S. Chuo & S. Moghtadernejad

Estimation of bridge component condition states with varying data availability 2120

S. Chuo, B.T. Adey, H. Mehranfar & S. Moghtadernejad

State-of-the-art in the use of responsive systems for the built environment 2128

J. Suo, C. Martani, A.G. Faddoul, S. Suvarna & V.K.T. Gunturu

Digital twins in construction practice – A use case driven implementation based on existing theory 2136
T. Zinke, C.P. Schimanski, D. Schäfer, M. Rowsell & R. Schumann

SS13: Strengthening and rehabilitation of steel bridges

Organizers: X. Jiang, X. Qiang & Z. Lv

Numerical analysis of weld throat crack of rib-to-deck reinforced by bonding angle steel 2147

Z.L. Lv, X. Jiang, X.H. Qiang, H.L. Wu & J.M. Ding

Flexural behavior of prestressed concrete beams strengthened with external CFRP tendons 2154

L.L. Chen, X.H. Qiang, X. Jiang & P. Liu

Rehabilitation of cracked diaphragm cutouts in steel bridge using Fe-SMA 2162

Y.P. Wu, X.H. Qiang, X. Jiang, H.L. Wu & J.M. Ding

Numerical study on the mechanical behavior of Fe-SMA/steel hybrid joints based on cohesive zone modeling 2170

Y. Shu, X.H. Qiang, X. Jiang, Q.L. Zhang & H.L. Wu

Full-scale experimental study on strengthened riveted gusset joints 2178

S. Wang, Q. Su, B. Liu, X. Jiang, L. Chen & C. Zhang

SS14: Data management and analysis for predictive maintenance of aging infrastructure

Organizers: F. Schmidt, M. Rasol & L.F.M. Sanchez

Weather condition effect on the road surface friction: A preliminary assessment based on sensor data 2187

M. Rasol, F. Schmidt & S. Ientile

Prediction of recovery time of infrastructure functionalities after an earthquake using machine learning 2195

B. Derras & N. Makhoul

Condition assessment and management protocols for concrete infrastructure affected by internal swelling reactions: Challenge and research needs 2203

R. Medeiros, A. Bergmann & L.F.M. Sanchez

The efficiency of laboratory test procedures for assessing field performance of concrete against Alkali-Aggregate Reaction (AAR) 2211

A. Bergmann, R. Medeiros & L.F.M. Sanchez

Digital twins for civil infrastructure: A case study on the Clifton suspension bridge (Bristol, UK) 2219

M. Pregnolato, S. Gunner, E. Voyagaki, R. de Risi, G. Gavriel, P. Tully, N. Carhart, T. Tryfonas & C. Taylor

SHM analysis for damage detection using time series analysis methods 2227

F. Schmidt, F. Chabi & J.-F. Bercher

SS15: Reinforced concrete-to-concrete interfaces: experiments and modelling

Organizers: V. Palieraki & S. Cattaneo

- Effect of size on the shear strength between old to new concrete interface 2237
S. Cattaneo & M. Scamardo
- Experimental behavior of interfaces with anchors to thin overlays 2245
E. Oikonomopoulou, V. Palieraki, E. Vintzileou & G. Genesio
- Calculation of the interface resistance in RC construction using different codes 2253
V. Palieraki, E. Vintzileou & S. Cattaneo
- Performance-based design of new concrete walls for building seismic rehabilitation 2261
S.M. Alcocer & B. Moctezuma
- Composite action in tunnel linings by use of shear connectors in concrete interfaces 2269
K. Mitroulis, N. Mellios, P. Spyridis & K. Bergmeister

SS16: Risk-informed life-cycle management of bridges

Organizers: I. Venanzi, M.P. Limongelli & U. Alibrandi

- SHM-informed management of bridges in a life-cycle perspective 2279
L. Ierimonti, F. Mariani, I. Venanzi & F. Ubertini
- Integration of MCDM-based regional flood hazard indexing with the Cerema guidelines for risk assessment of riverine bridges 2287
M. Loli, G. Kefalas, S. Dafis, S.A. Mitoulis & F. Schmidt
- Assessment as to the best strategies for the maintenance of existing bridges 2295
A. Contardi & G. Pasqualato
- The possibility of data integration of drive-by monitoring and direct bridge monitoring 2303
M. Miyagi, R. Shin, E. Mudahemuka & K. Yamamoto

SS17: BIM-based sustainability considerations in infrastructure construction

Organizer: M. König

- Potential of holistic asset information management 2313
A. Buttgereit, M. Block, D. Gogolin & S. Gomolluch
- Towards environmental design decision-making for infrastructure planning using parametric BIM 2321
J. Hofmeyer, K. Forth, S. Esser & A. Borrmann
- BIM-based EPD adaption in the context of ecological sustainability and municipal infrastructures 2329
J. Maibaum, M. Block, M. König & A. Wachsmann
- Element approach for BIM-based life-cycle modeling of bridges 2337
M. Müller, T. Zinke & T. Ummenhofer

SS18: Optimization of inspection, monitoring and maintenance strategies for existing concrete structures

Organizers: R. Caspeele, W. Botte, G. Lombaert & A. Strauss

- Inspection and assessment of PT structures: Results from application to an existing bridge 2347
I. Mazzatura, S. Caprili, W. Salvatore, J.R. Casas, M. Gammino, F. Ferrari & A. Piscini
- Non-destructive and partially destructive test locations in RC structures: A combined spatial optimisation and Bayesian updating approach 2355
S. Karmakar, S. Ghosh, D. Saha & S.A. Faroz
- FL decision system to choose the best maintenance strategy depending on condition 2363
F. Binder, N. Hlebec, U. Schneck & A. Strauss
- Probability-based service life design of repair mortar overlay in case of chloride-induced depassivation risk 2371
K. Van Den Hende, S. Helderweirt, W. Botte, S. Matthys, R. Caspeele & G. Lombaert
- Early detection of corrosion in reinforced concrete using ultrasonic-guided waves 2379
N. Habbaba, S. Mustapha & Y. Lu
- The use of corrosion rates for the identification of damaged zones in a football stadium and efficacy of surface inhibitors as repair method 2387
C. Andrade, J.J. Muñoz & J.R. Rosell

SS19: Sustainability of steel production chain

Organizers: H. Gervasio & M.M. Sesana

- Net-zero and lightweight steel technologies for the construction sector: Overview and case studies in Italy 2397
M.M. Sesana
- Life-cycle assessment of light steel frame buildings: A systematic literature review 2405
G. Marrone, M. Imperadori & M.M. Sesana
- Building life-cycle assessment considering different structural materials 2413
J.H. de Paula Filho, M. Charlier & M. D'Antimo
- Optimised steel structures for a low carbon future 2421
M. D'Antimo
- The contribution of low carbon steel to the decarbonization of the building sector 2429
H. Gervasio, L. Simões da Silva & M. D'Antimo

SS20: Advances in performance and life-cycle design of green structural materials for a more sustainable environment

Organizers: B. Belletti, P. Bernardi & A. Sirico

- Use of coarse recycled concrete aggregates and vitrified MSW ash in eco-concrete design 2439
P. Plaza, C. Medina, A. Sirico, B. Belletti, P. Bernardi & J. Sánchez
- Vitrified beads as aggregate replacement for sustainable cementitious materials 2447
B. Belletti, P. Bernardi, S. Ravasini, A. Sirico, D. Milanese, C. Sciancalepore, M. Malavasi & A. Cortese

Mechanical strength and environmental sustainability of EAF concrete <i>F. Faleschini, D. Trento, M.A. Zanini, C. Pellegrino, V. Ortega-López & A. Santamaria</i>	2455
Sustainable design of lightened reinforced concrete flat slabs in coastal environment <i>A.J. Sánchez-Garrido, I.J. Navarro & V. Yepes</i>	2463

SS21: Durability of reinforced concrete structures and infrastructures under changing climate conditions

Organizers: S. Kessler, F. Marsili, P. Croce & F. Landi

Exploratory analysis of the impact of natural hazards on road infrastructure in the Philippines <i>M. Adarne, A. Amir & M. Henry</i>	2473
Prediction of R.C. bridge deterioration under changing environmental conditions <i>F. Landi, P. Croce, F. Marsili & S. Kessler</i>	2481
Life-cycle assessment of R.C. bridge components based on cluster analysis and stochastic process <i>F. Marsili, S. Keßler & F. Landi</i>	2489
Corrosion effects of RC bridges considering the climate change impact <i>M. Zucca, M.L. Puppio, F. Mistretta, F. Landi, P. Formichi & P. Croce</i>	2497

SS22: Life-cycle and sustainability of precast concrete structures

Organizers: B. Dal Lago, H. Rodrigues & P. Negro

Seismic response analysis of precast structures retrofitted with dissipation devices, including qualitative assessment of environmental impact <i>F. Cavalieri, D. Bellotti, M. Caruso & R. Nascimbene</i>	2507
Aggregates for innovative use in precast concrete panels: State of the Art and perspectives <i>M.L. Puppio, F. Coccu, A. Usman, M. Valdés, A. Frattolillo, M. Sassu & L. Casali</i>	2515
Environmental impact reduction of precast multi-storey buildings by crescent-moon seismic dampers hidden in beam-column joints <i>L. Casali, B. Dal Lago, A. Fulco & M. Mezzi</i>	2523
Life-cycle assessment of coal mining wastes upcycling <i>S. Muller, F. Lai, M. Nucci, E. Segù, R. Crane, W. Nash, A. Wrana, B. Bezak & L. Ferrara</i>	2531

SS23: Shaping development planning processes for infrastructure systems under future uncertainty

Organizers: B.T. Adey, A. Elvarsson & O. Román

The value of accelerating the infrastructure planning process <i>A.B. Elvarsson, B.T. Adey & O. Roman</i>	2541
Stakeholder inclusive port development planning for an uncertain future <i>M. Eskafi & G.F. Ulfarsson</i>	2549
Probabilistic circular economy assessment for infrastructures considering time-variant influencing factors <i>H. Lei, W. Wang, C.Q. Li & W. Yang</i>	2557

Data-driven infrastructure systems design for uncertainty, sustainability, and resilience <i>M.-A. Cardin, A. Mijic & J. Whyte</i>	2565
Evaluating design modifications on a building portfolio considering future uncertainty and multiple stakeholders <i>C. Martani, N. Calen & B.T. Adey</i>	2573
Exploratory modelling for transport infrastructure planning under future uncertainty <i>O. Roman, A.B. Elvarsson & B.T. Adey</i>	2580
SS24: Functional end-of-life framework applied to hydraulic structures	
<i>Organizers: E.J. Hamerslag, E. van Baaren & A. Bakker</i>	
Embedding functional performance in asset management of hydraulic structures <i>E.J.F. Hamerslag & A.M.R. Bakker</i>	2591
Assessing the functional end of life of critical hydraulic structures in The Netherlands <i>A.M.R. Bakker, E.S. van Baaren, E.J.F. Hamerslag & C.J.J. Bodelier</i>	2598
Framework functional performance hydraulic structures <i>E.S. van Baaren, J. Bredeveld, N.J.M. ten Harmsen van der Beek, T. O'Mahoney, N. Kramer, H. Berger & A. Barneveld</i>	2605
Determining the future functional requirements of a pumping-weir station with the help of data-analysis <i>L. van Gijzen & A.M.R. Bakker</i>	2612
SS25: The process of decarbonization: from ideation to specification	
<i>Organizers: D. Shook & M. Sarkisian</i>	
Resilience through superelasticity <i>D. Shook, M.P. Sarkisian & C. Horiuchi</i>	2623
Design of the urban sequoia tower <i>M.P. Sarkisian, E. Long, A. Beghini, K. Micallef & S. Jaberansari</i>	2631
Achieving net zero embodied carbon: The SE2050 program and its impact on structural design <i>C. Horiuchi, M. Stringer & N. Wang</i>	2639
Quantifying and specifying decarbonization in buildings <i>N. Wang, D. Shook, K. Chang & E. Leung</i>	2646
Carbon optimization of hybrid material structures <i>M.P. Sarkisian, D. Shook, A. Zha & C. Horiuchi</i>	2653
SS26: Structural resilience in bridge engineering: Method, theory, and practice	
<i>Organizers: A. Chen, X. He & X. Ruan</i>	
A study on the mutual effect on fatigue damage of orthotropic steel decks and pavements <i>B. Wang, D.L. Wang, R. Ma & A.R. Chen</i>	2663
Modeling of coarse aggregate based on 3D point cloud and spherical harmonics <i>J.J. Zhang & Z.C. Pan</i>	2670

Bridge tower aesthetic assessment using convolutional neural network 2678
D.L. Wang, Y. Ning, C. Xiang & A.R. Chen

Influence of different curing condition on seismic performance of reinforced concrete bridge piers 2686
Q.P. Wen, L.L. Wen, L.L. Feng, D.T. Ya & F.X. Lin

SS27: Practical applications and value of advanced computational and probabilistic modelling in life-cycle engineering

Organizers: P. Bocchini, A. Strauss & H. Sousa

Semi-probabilistic assessment of concrete bridge exploiting additional data from experiments and numerical analysis 2697
L. Novák, D. Novák, M. Cao & R. Pukl

Probabilistic structural assessment of RC bridges under corrosion based on efficient simulation methods 2705
F. Padovani, L. Capacci & F. Biondini

Life-cycle assessment of Tunnel Boring Machine (TBM) segments of a new tunnel: Carbonation attack and sulfate attack 2714
F.T. Torabian, I. Vangelisti & C. Beltrami

Holistic assessment-framework for railway noise barrier constructions 2722
M.F. Granzner, A. Strauss & M. Reiterer

SS28: Use of SHM and NDE for decision making

Organizers: N.M. Apaydin, F.N. Catbas & B. Briseghella

The state-of-the-art in health monitoring of long-span cable supported bridges in Turkey 2731
O. Çetindemir, A.C. Zülfikar & N.M. Apaydin

Informed assessment of structural health conditions of bridges based on free-vibration tests 2739
M. Mazzeo, D. De Domenico, R. Santoro & G. Quaranta

The effect of road roughness on vehicle-bridge interaction modeling 2746
A. Aloisio, R. Alaggio, A. Contento & B. Briseghella

Influence of different debonding gap types on mechanical performance of axially compressed CFST stub columns with same debonding arc-length ratio 2754
J.Q. Xue, J.P. Huang, L.Q. He, B. Briseghella & A. Contento

Dynamic assessment of a stress-ribbon CFST arch bridge with SHM and NDE 2762
J.P. Huang, L.Q. He, J.Q. Xue, S.N. Zhou, B. Briseghella, C. Castoro, A. Aloisio & G.C. Marano

Bridge maintenance prioritization by using multi-criteria decision analysis 2770
H. Silimanotham & M. Henry

SS29: Durability and structural assessment of fiber reinforced strengthening materials and strengthened structures

Organizers: F. Micelli, C. Papanicolaou, B. Ghiassi & M. Leone

- Freeze/thaw effects on the performances of FRCM strengthened reinforced concrete beams 2781
S. Verre & M. Guglielmi
- Interface experimental behavior between basalt-FRCMs and natural stones 2789
G. Bramato, M. Leone & M.A. Aiello
- Tensile behavior of a glass FRCM composite with textile lap splice exposed to freeze-thaw cycles 2796
A.S. Calabrese, V. Bertolli, P. Colombi, T. D'Antino & C. Poggi
- Effect of salt crystallization on the bond behavior of glass FRCM-masonry joints 2804
V. Bertolli, A. Cagnoni, A.S. Calabrese, P. Colombi & T. D'Antino
- On the behaviour of FRCM fibres in saturated alkaline solution 2812
M. Canestri, F. Ferretti, E. Sassoni & C. Mazzotti
- Durability of CRM reinforcements 2820
F. Micelli, A. Franco, R. Greppi & M.A. Aiello

SS30: Durability of sustainable reinforced concrete for civil engineering structures

Organizers: M. Carsana & E. Redaelli

- Performance and environmental analysis of Reclaimed Asphalt Pavement (RAP) concrete produced in industrial environment 2831
G. Masi, A. Michelacci, S. Manzi, A. degli Esposti, B. De Pascale, A. Bonoli & M.C. Bignozzi
- Life extension of existing steel reinforced structures by simple cathodic protection techniques for sustainable durability 2839
G. Sergi
- Corrosion of rebars in concrete: Comparison of preventative measures 2847
F. Bolzoni, A. Brenna, S. Beretta, M. Ormellese, M.V. Diamanti & M.P. Pedeferra
- Role of concrete and reinforcement characteristics to increase the service life of structures 2855
M.C. Alonso
- Durability performance indicators for service life analysis and quality control 2863
F. Moro & R.J. Torrent

SS31: Structural health monitoring and asset management of infrastructures

Organizers: S. AlSanad & J. Parol

- Measuring heavy traffic using alternative systems in an urban environment 2873
M.L. Soudijn, S. van Rossum & A. de Boer
- Improving the resolution and accuracy of low-cost Arduino-based accelerometers 2881
S. Komarizadehasl, G. Ramos, J. Turmo, J.A. Lozano-Galant, V. Torralba & M. Haiying
- Preventive SHM for asset management: A case study on the Mont-Blanc tunnel 2888
F.B. Cartiaux & B. Prudhomme
- Characteristics of ultrasonics guided waves in timbers under moisture and temperature 2896
R. Yassine & S. Mustapha

Asset management – Towards adaptive resilient infrastructures 2904
S. AlSanad & J. Parol

SS32: Corrosion-induced structural damage and prevention measures for reinforced concrete infrastructure

Organizers: S. Yang, F. Tang & W. Zhang

Corrosion and bond behavior of silicate dioxide particle modified enamel coated steel bar 2911
F. Tang, Y. Kuang, H. Cui & Z. Lin

Non-destructive investigation of corrosion in reinforced concrete structures and modelling the structural degradation 2918
S.T. Yang, F. Zhang, Z. Yin & X. Xi

Chloride transport properties of Portland cement and limestone systems 2925
Z.L. Jiang, Z. Dong, C.Q. Fu, Y.J. Pan & Y.C. Wang

Simplified analytical method for moment-curvature response of corroded prestressed concrete beams 2933
S. Ravasini, L. Franceschini & B. Belletti

Structural behavior of PC beams under simultaneous corrosion and sustained loads 2941
F.F. Bico, M. Bartoli, F. Di Carlo, A. Meda, F. Molaioni & Z. Rinaldi

Random field analysis of corrosion of steel in the artificial marine atmosphere 2949
W.P. Zhang, X.L. Gu, Q.Q. Yu & J. Chen

SS33: Life-cycle and sustainability performance of fastenings

Organizers: P. Spyridis, G. Muciaccia, K. Bergmeister, T. Pregartner, R. Piccinin & T. Sippel

Installation, structural, and sustainability characteristics of direct fastening in textile reinforced concrete plates 2959
P. Spyridis, J. Orlowsky & K. Bergmeister

Redundancy of concrete fastenings under combined fatigue and corrosion – A probabilistic study on catenary system installations 2967
S. Kessler, N. Mellios, A. Takriti & P. Spyridis

Long term assessment of bonded anchors with two different methods, Findley extrapolation vs. time-to-failure approach 2975
I. Boumakis, K. Nincevic, R. Piccinin, R. Wan-Wendner, T. Pregartner & K. Bergmeister

Impact of concrete age and aggregate type on anchor load performance 2983
K. Nincevic, R. Piccinin, I. Boumakis, T. Pregartner & R. Wan-Wendner

Impact of end-of-life stage in cradle-to-cradle LCA analysis of timber and timber-hybrid buildings 2991
L. Corti & G. Muciaccia

GENERAL SESSIONS

Organizers: F. Biondini & D.M. Frangopol

Shear strength assessment of FRP pre-tensioned concrete beams 3001
A. Mari, E. Oller, J. Murcia-Delso, J.M. Bairán & N. Duarte

Life-cycle cost of CFRP and steel prestressed concrete elements <i>J.M. Bairán, J. Murcia-Delso, N. Duarte, E. Oller & A. Mari</i>	3009
Numerical analysis of short-term performance of CFRP new composite anchorage <i>S. Y. Sun</i>	3017
Preliminary assessment on the effects of longitudinal cracks on carbonation-induced corrosion <i>N. Russo, M. Gastaldi, F. Lollini, L. Schiavi & A. Strini</i>	3025
Numerical evaluation on electrical resistivity of hardened cement paste using 3D pore model based on X-ray micro-CT images <i>K. Kawaai & T. Nishida</i>	3033
Coupled deterioration by freeze-thaw and chloride salt on mill-cut steel fiber reinforced concrete <i>S. Liu, Y. Liu, Y. Li, L. Fan & Z. Yang</i>	3041
Construction of hydrogen pipeline utilizing communication pipeline and experimental study on its utilization <i>T. Ishikawa & K. Itasaka</i>	3049
Modelling the thermal response of firestop sealant exposed to standard fire <i>Z. Ye, A.K. Abu, C.M. Fleischmann & R.P. Dhakal</i>	3054
Dynamic chain reaction analysis of a cable-stayed bridge by sudden loss of stays considering cable corrosion <i>Y. Aoki, H. Tsunoda, T. Akiyama, H. Gotou & S. Nakamura</i>	3062
Revisiting shape/size effect formulation of EUROCODE 2 for structural concrete members <i>S. Abdo, R. Wan-Wendner, R. Caspeele, S.C. Seetharam & Q.T. Phung</i>	3070
Guided tour of the pathological manifestations found at Rossio's historical train station <i>C. Carvalho, N. Bento & A. Silva</i>	3078
Non-destructive evaluation for voids under airport pavement concrete in-situ <i>T. Nishida, F. Izu, Y. Kobayashi, M. Aizawa & K. Kawaai</i>	3086
How to better exploit the use of LCA analysis for Ultra High Performance Concrete (UHPC) through a constitutive law which integrates chloride and sulfate attack <i>D. di Summa, F. Soave, M. Davolio, S.M.J. Al-Obaidi, L. Ferrara & N. De Belie</i>	3094
Durability of residential construction in a marine environment <i>I.N. Robertson</i>	3102
Predicting the military load class from bridge data with a multilayer perceptron <i>M. Haslbeck, J. Flotzinger & Th. Braml</i>	3110
Elaboration of a truncated probability function for the Young's modulus of concrete <i>M. Haslbeck & Th. Braml</i>	3118
The impact of surface aspect ratio on the embodied energy, embodied carbon, and embodied water of a building structure <i>M.K. Dixit & P. Pradeep Kumar</i>	3126
Performance assessment of existing prestressed concrete bridges utilizing distributed optical fiber sensors <i>H. Burger, T. Tepho, O. Fischer & N. Schramm</i>	3134

Life-cycle assessment of crack repair systems for fire-damaged concrete <i>R.M. Galano, R.S. Chan & J.M. Ongpeng</i>	3142
Rehabilitation of underground garages – defining a cost function for use in the decision-making process <i>J.M. Lozano Valcarcel, C. Gehlen, T. Kränkel, A. Schiessl-Pecka, J.D. Cassiani & S. Kessler</i>	3150
The potential for direct reuse of precast concrete slabs in buildings with “wet” joints <i>P.S. Halding & K. Negendahl</i>	3158
Life-cycle assessment of concrete hollow blocks and autoclaved aerated concrete blocks <i>J.M. Ongpeng & M.V. Umali</i>	3166
Temperature effect on static and quasi-static bridge measurements <i>K. Dakhili, T. Kebig, M. Schäfer, M. Maas, M. Bender & A. Zürbes</i>	3174
Robot-BIM integration for underground canals life-cycle management <i>H. Pourhosseini, F. Zahedi & J.M. Sardroud</i>	3182
Life-cycle cost analysis of possible solutions for converting existing single-family house into nZEB <i>C. Marincu & D. Dan</i>	3190
End-of-life rule checking for transport infrastructure: The case of navigation locks <i>K.E. Bektas & I.E. Ozer</i>	3198
Environmental and economic assessment of service life extending repairs for a concrete silo <i>N. Renne, A. Audenaert, M. Buyle & B. Craeye</i>	3206
Foundation for risk-based asset management for storm surge barriers <i>Y. Kharoubi, M. van den Boomen, M.J.C.M. Hertogh & J. van den Bogaard</i>	3214
Lessons learned from past earthquakes for horizontally curved bridges <i>E. Namlı & T. Öztürk</i>	3222
Using the USGS database to study parameter uncertainty when assessing pier scour using the HEC-18 framework <i>G. Gavriel, M. Pregolato & P.J. Vardanega</i>	3230
Time-variant reliability analysis of corroded steel girder <i>Y. Wang, W. Wang, C.Q. Li & W. Yang</i>	3238
Quantification of the effect of corrosion on the compressive membrane action in restrained hollow core slabs <i>T. Thienpont, W. De Corte, R. Van Coile & R. Caspeele</i>	3244
Bayesian pre-estimation of bridge life-cycle costs <i>T. Vagdatli, K. Petrousatou, P. Panetsos, Z. Barmpa & N. Fragkakis</i>	3252
A service value predictive system of componentized infrastructure assets <i>K. Petrousatou, T. Vagdatli, M. Voutsis, P. Panetsos & Z. Barmpa</i>	3260
Powder wastes from concrete recycling as a sustainable source of calcium carbonate mineral admixture <i>K.M. Masunaga & T. Iyoda</i>	3268
Travel time gains VS time constancy - An irresolvable contradiction? <i>M. Hoffmann</i>	3276

Reliable estimation of investment and life-cycle costs from road projects to single road assets <i>M. Hoffmann & V. Donev</i>	3284
Legal governance for BIM – rights management and lawful data use <i>B. Weber & M. Achenbach</i>	3292
Advanced life-cycle assessment of reinforced concrete bridges using digital twin concept <i>J. Rymeš, J. Červenka, M. Herzfeldt & R. Pukl</i>	3300
Sustainable reuse of public real estate assets meeting structural, conservation and territorial needs <i>G. Concu, D.R. Fiorino & E. Pilia</i>	3308
Evaluation of low-velocity impact damage in metal/composite layered structure <i>S. TerMaath, B. Ingling, J. Noland & D. Hart</i>	3316
Development of high durable precast PC deck with ultra-high-strength fiber-reinforced concrete layer <i>H. Hayashi, Y. Yasukawa, N. Oba & K. Sasaki</i>	3324
Development of digital rules for optimal auto-routing design of pipe <i>S.-E. Park, S.-W. Choi & E.-B. Lee</i>	3332
Structural response of corroded concrete columns with different rebar confinements under cyclic compressive loading <i>H.O. Aminulai, N.S. Ferguson & M.M. Kashani</i>	3340
Structural behaviour of axially loaded corroded low-strength RC columns with different confinement ratios <i>H.O. Aminulai, N.S. Ferguson & M.M. Kashani</i>	3348
Impact of as-recorded mainshock-aftershock excitations on seismic fragility of corrosion-damaged RC frames <i>E.A. Dizaj, M.R. Salami & M.M. Kashani</i>	3356
Seismic fragility analysis of nonuniformly corroded irregular RC bridges <i>E.A. Dizaj, M.R. Salami & M.M. Kashani</i>	3364
Study on the applicability of repairing rubber bearing covers by resurface vulcanization in the field <i>A. Matsumoto, R. Takahara, T. Imai & W. Abe</i>	3372
Application of BIM in design review processes for buildings <i>M. Achenbach, P. Rivas & B. Weber</i>	3380
A basic study on the evaluation of the protective effect of silane-based impregnation on mortar using electrochemical impedance spectroscopy <i>S. Nagaoka, K. Nakayama & M. Iwanami</i>	3388
Life-cycle of existing asphalt to build new highway foundation pavements: Environmental procedures according to new Italian standards, geotechnical and durability performance assessments, construction methods <i>M. Biasioli, F.T. Isfahani, D. Giometti, C. Beltrami, G. Piovano, F. Vergano & M. Marino</i>	3396
Infrastructure asset management and the role of structural health monitoring <i>A. AlBanwan, A. AlFoudari & R. AlBehbehani</i>	3404

Inclusion of Stochastic Petri-net models on a risk-based tool for the maintenance of road drainage systems	3412
<i>L.G. Rodrigues, L.C. Neves, J. Wallis, R. Brook & K. Morosiuk</i>	
Rehabilitation, strengthening and life-cycle assessment of an historical water channel Cavour masonry bridge crossing Cervo River after an extreme flood erosion at foundation pier causing massive settlement and large structural damages	3420
<i>C. Beltrami, M. Capalbo, G. Giacalone, M. Vittone, G. Comaita, I. Vangelisti, F.T. Isfahani, F. Damiani, R. Salomone, L. Casti, J. Salvioni, D. Cagliani, F. Burlone, M. Fossati & M.F. Carera</i>	
High performance computing methods for concrete surface damage identification and prevision in service highways tunnel concrete linings	3428
<i>I. Vangelisti, C. Beltrami & G. Rozza</i>	
Experimental study on quantification of carbon dioxide adsorption by different cement types and mix proportions	3436
<i>T. Iyoda, E. Ishikawa & Y. Ikeo</i>	
Value of information for a rational experimental and testing budget applied to a regional old Italian bridges database	3444
<i>I. Vangelisti & C. Beltrami</i>	
Multi-risk analysis methodology for evaluating climate change impacts at different scales	3452
<i>F.V. De Maio, R. Valsecchi, S. Osmani, C. Solari & P. Basso</i>	
Evaluation of the safety factor in masonry buildings as acceleration varies: A quick approach	3460
<i>E. Garavaglia</i>	
Attack of aggressive carbon dioxide on hardened Portland and blast furnace slag cement paste	3468
<i>F. Wagemann, F. Schmidt-Döhl & A. Rahimi</i>	
Big data in construction project management: The Colombian northeast case	3476
<i>S. Zabala-Vargas, M. Jiménez-Barrera, L. Vargas-Sánchez & M. Jaimes-Quintanilla</i>	
Numerical analysis of prestressed sleepers affected by expansive mechanisms	3484
<i>R.P. Randi, L.M. Trautwein, D.J.M. Mariata, L.F.M. Sanchez & A.C. Santos</i>	
The probabilistic fatigue life of plain concrete under low-frequency stress reversal loading	3492
<i>E.C. Ferreira, P. Sotoudeh, G. Fiorillo & D. Svecova</i>	
Influence of different coarse aggregate types on porosity and various properties in concrete	3500
<i>N. Matsuda & T. Iyoda</i>	
Visual inspection of bridges and tunnels in Italy: By experience made with different owners and methods to a new proposal for a better and more efficient inspection procedures	3508
<i>R. Salomone, F. Damiani, M. Vittone, M. Scarsi Napolitano, I. Vangelisti, G. Giacalone, A. Bombace, M. Brescia, M. Rabbia & C. Beltrami</i>	
Inspection of highway retaining walls and geotechnical sites, state of the art in Italy and possible proposals for improving procedures and effectiveness	3516
<i>M.S. Napolitano, D. Bonassi, R. Morè & C. Beltrami</i>	
Using shape optimization and principal stress line based stiffness improvement of thin-shell structure and reduce construction costs	3523
<i>Y.X. Sun, Y.Y. Yang, L.J. Leu & K. Yamamoto</i>	

Numerical verification of vehicle-bridge interaction system identification using a 3D models <i>E. Mudahemuka, S. Ryota & K. Yamamoto</i>	3531
Parametric study of the vehicle-bridge interaction system identification method <i>R. Shin, Y. Okada & K. Yamamoto</i>	3539
Influence of various admixture materials on pore structure and mass transfer characteristics <i>R. Yahiro & T. Iyoda</i>	3547
Research on the anti-sliding performance of cable clamps in an irregular elliptical suspen- dome structure <i>H.J. Wang, X.D. Ren, S.W. Xiao, L. Li & B. Luo</i>	3554
Lessons learned from highway tunnels inspection, analysis, assessment and refurbishment works <i>A. Damiani, E. Crippa & M. Rabbia</i>	3562
Deterministic and probabilistic damage calculation of offshore wind turbines considering the low-frequency fatigue dynamics <i>N. Sadeghi, P. D'Antuono, K. Robbelein, N. Noppe, W. Weijtjens & C. Devriendt</i>	3570
Developing a cost-control and project-planning based implementation of circular construction in temporary works: A framework of core supportive technologies <i>F. Tizzani, P. Herthogs & R. Stouffs</i>	3578
Life-cycle assessment of buried water-transmission concrete mains <i>H. Yáñez-Godoy & S.M. Elachachi</i>	3586
Shear strength investigation of carbon fiber reinforced polymer strips-wrapped concrete beams with regression analysis and experiments <i>P. Fan, H.F. He, S.S. Cheng, S.S. Guo & C. Liu</i>	3594
Multi-criteria assessment of reinforced limestone powder concrete slabs and columns <i>A. Radović, H. Hafez, N. Tošić, S. Marinković & A. De la Fuente</i>	3602
Development of life-cycle inventory for timber products to support the circular economy in construction <i>S. Ge, P.J. McGetrick, C. O'Ceallaigh & A.M. Harte</i>	3610
Life-cycle assessment and sensitivity analysis of a clayey sediment-based geopolymer concrete <i>L. Monteiro, H. Yáñez-Godoy, J. Saliba & N. Saiyouri</i>	3618
Research on calculation method of creep and shrinkage effects of steel-concrete-Ultra-High- Performance Concrete (UHPC) composite bridge considering construction process <i>X.G. Ma, D.W. Zhang, H.W. Ling, H.J. Shen, S.S. Guo & C. Liu</i>	3626
Interactive visualization of uncertain embodied GHG emissions for design decision support in early stages using open BIM <i>K. Forth, A. Borrmann & A. Hollberg</i>	3634
Port facilities asset management: Coping with aging infrastructure and constrained budgets on the long term <i>H. Voogt</i>	3642
Modeling and characterization strategy as a basis for improved prediction of concrete fatigue degradation in wind power plants <i>A. Baktheer, M. Aguilar, H. Becks, M. Classen, J. Hegger & R. Chudoba</i>	3649

Sustainability concept of design of concrete bridges based on LCA <i>B. Vlasatá, J. Pešta, C. Fiala, P. Hájek & M. Novotná</i>	3656
Fundamental experiments for monitoring water leakage of underground structures using plastic optical fibers <i>H. Zhang, Z. Liu, X. Ma, J. Qian & S. Akutagawa</i>	3664
Effects of structural rehabilitation on modal parameters of the Marlo Bridge <i>B. Siedziako, T.S. Nord & A. Fenerci</i>	3672
Simulation of chloride ingress into aging surface-coated concrete <i>C. Yoshii, F. Biondini, M. Iwanami & K. Nakayama</i>	3680
Embedded fibre optical strain monitoring of a bio-composite bridge <i>M. Weil, Y. Bel-Hadj, W. Weijtjens, C. Devriendt, Y.-A. Janssens & E. Voet</i>	3688
Dissipative steel and steel-concrete composite beam-to-column joints <i>G. Skarmoutsos & U. Kuhlmann</i>	3696
Seismic and energetic renovation of existing masonry buildings by innovative FRLM composite materials <i>D. Pugliese, V. Alecci, S. Galassi, A.M. Marra & M. De Stefano</i>	3704
Development of a method for resource-efficient structural maintenance of reinforced concrete buildings based on digital BIM models <i>J.-I. Jäkel, L. Kloesgen, T. Koenig, K. Klemt-Albert, H. Morgenstern & M. Raupach</i>	3712
Cost-optimization based generalized target reliabilities for reinforced concrete slab exposed to fire <i>F. Put, R.K. Chaudhary, A. Lucherini, B. Merci & R. Van Coile</i>	3720
Sensitivity of the seismic response to the modelling variables defining constitutive models of reinforced concrete frames <i>G. Karaki</i>	3728
Effect of concrete age on the reliability of existing reinforced concrete columns <i>L.C.R. Castro & S.M.C. Diniz</i>	3736
A microservice for evaluating resilience of water distribution network <i>X.Y. Yu, Y.N. Xu, F. Liu & X. Zhou</i>	3744
Project management and life-cycle cost evaluation using infrastructure-building information modeling techniques: A railway infrastructure design case study <i>M. Pasetto & G. Giacomello</i>	3752
A non-Gaussian algorithm to simulate the earthquake motion phase difference <i>T. Sato</i>	3760
Health monitoring of long-span bridges using deep learning driven by sensor measured and numerical response data <i>Z. Xue, W. Sebastian & D. D'Ayala</i>	3769
Progressive collapse behavior of RC frames subjected to reinforcement corrosion <i>L.C. Ding, Y.B. Peng & J.B. Chen</i>	3777
Numerical simulation of non-Fick moisture diffusion of pultruded GFRP bolt connection <i>Y. Sun, Y. Liu, X. Wang & H. Xin</i>	3785

A methodology for the service life estimation of timber structures <i>D. Marranzini, G. Iovane, L. Cascini, R. Landolfo, M. Nicoletta & B. Faggiano</i>	3793
Multi-scale structural integrity assessment of a series of identical components in cultural-heritage structures: The case of the Clifton suspension bridge <i>R. De Risi, T. Moody, E. Voyagaki, S. Gunner, M. Pregolato, N. Grilli & C. Taylor</i>	3800
Assessment of energy redistribution of structural collapse under seismic loads using wavelet transforms <i>N.S.D. Farhan, J. Lu, W.A. Altabey, Z. Wu, A. Silik & M. Noori</i>	3808
Application of infrared thermography in civil engineering: Limits and drawbacks <i>D. Meloni, G. Sechi & G. Concu</i>	3816
Soundness evaluation of small-scale bridge decks with portable FWD tests <i>T. Sasaki, A. Tsuboi, Y. Sugimoto, H. Kakeda & H. Onishi</i>	3824
Rut depth estimation by distortion analysis of images taken by an in-vehicle camera <i>W. Gao, K. Xue, T. Nagayama, B. Zhao, D. Su, K. Xue & B. Zhao</i>	3832
M-integral applied to fatigue life prediction in notched elastic-plastic material <i>Z.J. Zhang & Q. Li</i>	3840
Dynamic performance of connection between frame-structure and jacked caisson <i>X.Z. Lan, W.F. Wu, C. Li & Y. Yuan</i>	3848
Robustness of RC girder bridges: The case of half-joint bridges <i>P. Martinelli, M. Colombo & M. di Prisco</i>	3856
Research on imaging technology of concrete bridge bottom apparent disease detection based on machine vision <i>S.G. Cao, X.Y. Li, Y. Pan, J.L. Fu & H. Tian</i>	3864
Semi-probabilistic methods for the assessment of existing concrete structures: An overview <i>L. Casti, F. Schmidt, F. Biondini & N. Makhoul</i>	3872
Digital fatigue test of rib-to-deck welded joint details in orthotropic steel deck <i>P.Y. Li, C.S. Wang, Y. Li & D.D. He</i>	3880
Nonstructural performance improvements for seismic resilience enhancement of modern code-compliant buildings <i>M.R. Joo & R. Sinha</i>	3888
Fatigue performance simulation of UHPFRC composited deck for steel truss girder bridge <i>C.H. Zhu, L. Duan, C.S. Wang, P.Y. Li, Z. Kang & J. Kang</i>	3896
Redundancy, importance, and robustness analyses for damage scenarios of bridges <i>S. Sarmiento, J. González-Libreros, G. Sas, I. Björnsson & S. Thöns</i>	3904
Structural behavior of composite truss girder with thicker concrete deck at side span in a cable-stayed bridge <i>M.Y. Yang, C.S. Wang, Y.Q. Li & Y.C. Feng</i>	3913
Assessment of mechanical properties for ancient timber through visual and ND methods <i>S. Verre, G.F. Cauteruccio, G. Fortunato, A.A. Zappani, L. Ombres, M. Brunetti, M. Nocetti, N. Ruggieri, M. Togni, D. Marranzini, G. Iovane & B. Faggiano</i>	3920

Failure analysis of ageing RC bridges: The cases of the Polcevera viaduct and the Capriogliola bridge	3927
<i>N. Scattarreggia, A. Orgnoni, G.M. Calvi, R. Pinho, D. Malomo & M. Moratti</i>	
Digital fatigue test of flange-web welded details in guideway girders	3935
<i>C.S. Wang, X.G. Zhou, Y.Z. Wang & M.Y. Yang</i>	
3-D segmentation of concrete spalling in point cloud using unsupervised clustering and plane fitting	3943
<i>Y. Zhang & B. Xia</i>	
Fatigue assessment of complex welded connection in the large-span steel truss suspension bridge	3951
<i>G. Y. Xie, S.L. Ding, H.J. Liu & C.S. Wang</i>	
Life-cycle and evolution of tunnel equipment	3959
<i>G. Nodiroli, M. Katterbach, P. Klaus & D. Tillet</i>	
A multi-phase survey approach for post-tensioned prestressed concrete bridge decks	3967
<i>I. Mazzatura, S. Caprili, W. Salvatore, A. Lupoi & A. Ficociello</i>	
Super resolution of multi-channel ground penetrating radar volume data by zero-interpolated 3D kirchhoff migration	3975
<i>T. Imai & T. Mizutani</i>	
Crack growth suppression effect of SFRC overlay for root-deck fatigue in orthotropic steel deck	3983
<i>M.J.B. Uaje & J. Murakoshi</i>	
Refined perception and management of ring-wise deformation information for shield tunnels based on point cloud deep learning and BIM	3991
<i>W. Lin, X. Xie, B. Zhou, P. Li & C. Wang</i>	
Structural model updating of an existing concrete bridge based on load testing and monitoring data	3999
<i>A. Agredo Chávez, J. Gonzalez-Libreros, L. Elfgren, G. Sas, L. Capacci & F. Biondini</i>	
Demolition of a 65-year-old box-girder prestressed concrete bridge located in Northern Sweden	4007
<i>C. Daescu, J. Gonzalez-Libreros, C. Wang, L. Elfgren, G. Sas, L.B. Nilsson, T. Larsson & P. Simonsson</i>	
Experimental study on constitutive law of stainless steel under multiaxial stress	4015
<i>E. Horisawa, K. Sugiura, Y. Kitane & Y. Goi</i>	
Structural behavior of UHPC transition segment of wind tower without ordinary reinforcement under serviceability limit state	4023
<i>L.R. Lin, X. Zhang, X.G. Wu, X. Wang, X.S. Zhang & H. Wang</i>	
Applications of drone inspection and use of strain-hardening cementitious composites (ECC/SHCC) in lowering carbon footprint and lifecycle cost of bridges	4029
<i>D.K. Mishra, P. Ranjan, H. Sun, J. Yu & P.L. Ng</i>	
Chloride-attack fragility curve: The probability of failure is estimated at a life expectancy	4037
<i>J.H. Kim, T.H. Han & D.J. Jeong</i>	
A review on electrodeposition repair of cracked reinforced concrete	4043
<i>Q. Zhang, Q. Chen & H. Yang</i>	

The economic evaluation method of a foamed ceramics external wall panel based on full life-cycle theory	4051
<i>Z.W. Cao, H.B. Fang & L. Tian</i>	
Mechanical performance of steel plate combination beam bridge with clustered shear studs considering slip effect	4057
<i>Y.L. Yi, W.Y. Meng, N.N. Huo & X. Ruan</i>	
Risk-based prioritization of earthquake performance of RC buildings in Turkey by rapid visual scanning	4065
<i>M. Özdemir</i>	
Chloride ingress of concrete structure considering the effect of early-age shrinkage	4072
<i>Y. Li, X. Ruan, T. Li & W.Y. Dou</i>	
Seismic performance evaluation of masonry infilled RC frame retrofitted with BRBs	4078
<i>R. Chelapramkandy, J. Ghosh & F. Freddi</i>	
LCA and EPD need digitalization	4086
<i>U.R. Panmuti</i>	
Using monetization to harmonize life-cycle assessment and life-cycle cost analysis for green public procurement of pavement projects	4092
<i>B. Moins, D. Hernando, W. Van den bergh & A. Audenaert</i>	
Digital twins and sensor monitoring for alpine engineering structures: Applications for tunnels	4100
<i>A. Strauss, A. Beigel, F. Sattler, B. Täubling-Fruleux, C. Seywald, H. Neuner, V. Kostjak & D.M. Frangopol</i>	
Life-cycle and sustainability impact of composite and combined concrete tunnel linings	4107
<i>P. Spyridis & K. Bergmeister</i>	
Assessing highway bridge scour reliability and risk under changing floods	4115
<i>N. Devineni & M. Ghosn</i>	
Positive effects of aligned steel fiber using the electro-magnetic field on flexural behavior of reinforced UHPC beams	4123
<i>Y.M. Xiong, M. Yang, H. Shi & J. Zhao</i>	
Service-life extension of transport infrastructure through structural health monitoring	4131
<i>M. Domaneschi, R. Cucuzza, L. Martinelli & M. Noori</i>	
Service-life extension of transport infrastructure through structural control	4139
<i>L. Martinelli, M. Domaneschi, R. Cucuzza & M. Noori</i>	
Digital Twin - solution in the digital age for improving critical infrastructure resilience to extreme events	4147
<i>M.Q. Tran, H.S. Sousa, E. Texeira, J.C. Matos & H.T. Dang</i>	
Flood Vulnerability Index (FVI) of infrastructures for reducing adverse flood events	4155
<i>M.Q. Tran, H.S. Sousa, E. Texeira & J.C. Matos</i>	
Structural modeling and dynamic testing of high-speed railway bridges	4163
<i>M. Anghileri, L. Capacci, F. Biondini, L. Bernardini, C. Somaschini & M. Belloli</i>	
Seismic base isolation of Palazzo Partigiani in Perugia	4171
<i>F. Parisi, T. Zordan & A. Romano</i>	
Author index	4179



Taylor & Francis

Taylor & Francis Group

<http://taylorandfrancis.com>

Preface

Structures and infrastructure systems need to comply with the continuously increasing demand from societal, political, economic, and environmental needs associated with aging, deterioration processes, and other multiple natural and human-made hazards affecting civil infrastructure facilities. To respond to these needs, civil engineering is undergoing a profound change towards a life-cycle-oriented design and maintenance philosophy where the system performance is considered as time-dependent and the desired levels of target performance are addressed over the entire life-cycle taking into account the effects of aging and deterioration processes, time-variant loadings, and maintenance and repair interventions, among others. This transition is at the heart of civil engineering and is promoting and guiding a considerable amount of research and relevant advances in the fields of modeling, analysis, design, inspection, monitoring, repair, maintenance, and rehabilitation of deteriorating civil engineering systems. To support this process, after a series of International Workshops on Life-Cycle Analysis and Design of Civil Engineering Infrastructure Systems, IALCCE - The International Association for Life Cycle Civil Engineering was created in 2006 (<https://www.ialcce.org>).

IALCCE covers all aspects of life-cycle assessment, design, maintenance, rehabilitation and monitoring of civil engineering systems. The objective of the Association is to promote international cooperation in the field of life-cycle civil engineering for the purpose of enhancing the welfare of society. Currently, IALCCE includes over 800 individual members from 66 countries and over 30 collective members. Seven International Symposia have been organized since the foundation of IALCCE. The inaugural IALCCE Symposium was held in Varenna, Lake Como, Italy, in June 2008, under the auspices of Politecnico di Milano. Following IALCCE 2008, a series of Symposia have been organized in Taipei, Taiwan (IALCCE 2010), Vienna, Austria (IALCCE 2012), Tokyo, Japan (IALCCE 2014), Delft, The Netherlands (IALCCE 2016), Ghent, Belgium (IALCCE 2018), and Shanghai, China (IALCCE 2020). These events have been very successful, both technically and academically, and IALCCE Symposia have become established events in the field of life-cycle civil engineering. It was therefore considered fruitful to continue this landmark series and celebrate the 15th Anniversary of IALCCE Symposia where they were initiated by bringing together recent advances and cutting-edge research in the field of life-cycle civil engineering and related topics at the Eighth International Symposium on Life-Cycle Civil Engineering (IALCCE 2023), held at Politecnico di Milano, Milan, Italy, 2-6 July, 2023 (<https://ialcce2023.org>).

IALCCE 2023 has been organized on behalf of IALCCE under the auspices of Politecnico di Milano. The interest of the international civil engineering community in the activities covered by IALCCE has been confirmed by the significant response to the IALCCE 2023 call for papers. In fact, over 750 abstracts from more than 50 countries were received by the Symposium Secretariat, and approximately 70% of them were selected for final publication as technical papers and presentation at the Symposium within mini-symposia, special sessions, and general sessions. Contributions presented at IALCCE 2023 cover recent advances and cutting-edge research in the field of life-cycle civil engineering, including emerging concepts and innovative applications related to life-cycle design, assessment, inspection, monitoring, repair, maintenance, rehabilitation, and management of structures and infrastructure systems under

uncertainty. Major topics covered include: life-cycle safety, reliability, risk, resilience and sustainability, life-cycle damaging processes (aging of structures, deterioration modeling, durable materials, earthquake and accidental loadings, fatigue and damage, fire and high temperatures, marine and severe environments, structure-environment interaction, global warming and climate change effects), life-cycle assessment and design (design for durability, failure analysis and risk prevention, structural robustness, lifetime structural optimization, long-term performance analysis, performance based design, service life prediction, uncertainty modeling, value of information, life-cycle structural safety, time-variant reliability, functionality and resilience, risk and sustainability), life-cycle monitoring, maintenance, and management (damage identification, field testing and proof loading, health monitoring, inspection and evaluation, robotic and aviation-based techniques, BIM techniques, maintenance strategies, rehabilitation techniques, strengthening and repair, structural integrity, asset management, infrastructure resilience, risk-based prioritization), life-cycle performance of special structures (bridges and viaducts, high-rise buildings, hydraulic structures, off-shore structures, precast systems, roof systems, runway and highway pavements, tunnels and underground structures), life-cycle cost of structures and infrastructure systems (decision making processes, human factors, life-cycle cost models, project management, risk-lifetime analysis and optimization, whole life costing), and life-cycle-oriented computational tools (artificial intelligence methods, evolutionary procedures, heuristic techniques, mathematical optimization, soft-computing methods, survival models and simulation), among others.

Life-Cycle of Structures and Infrastructure Systems collects the lectures and papers presented at IALCCE 2023. This Open Access Book contains the full papers of 514 contributions, including the Fazlur R. Khan Plenary Lecture, nine Keynote Lectures, and 504 technical papers from 45 countries. It provides both an up-to-date overview of the field of life-cycle civil engineering and significant contributions to the process of making more rational decisions to mitigate the life-cycle risk and improve the life-cycle safety, reliability, redundancy, robustness, resilience, and sustainability of structures and infrastructure systems exposed to multiple natural and human-made hazards in a changing climate. The Editors hope that this volume will serve as a valuable reference to all concerned with life-cycle of civil engineering systems, including students, researchers, practitioners, consultants, contractors, decision makers, and representatives of managing bodies and public authorities from all branches of civil engineering.

Fabio Biondini and Dan M. Frangopol
Chairs, IALCCE 2023

Milan and Bethlehem, April 2023

Acknowledgments

The Editors are extremely grateful to all people who contributed to the organization of the IALCCE 2023 Symposium and to the production of this Open Access Book. Particularly, the Editors would like to express their sincere thanks to all the authors for their contributions, to the members of the Steering Committee, International Scientific Committee, and National Advisory Committee for their role in ensuring the highest scientific level of the Symposium, and to the members of the Local Organizing Committee for the time and efforts dedicated to make IALCCE 2023 a successful event.

Moreover, the Editors wish to thank all organizations, institutions, and authorities that offered their patronage. At the institutional level, a special acknowledgment has to be given to the Politecnico di Milano, for organizing and co-sponsoring this Symposium along with the International Association for Life-Cycle Civil Engineering (IALCCE), as well as to the Department of Civil and Environmental Engineering for endorsing and supporting the Symposium organization.

Finally, the Editors wish to express their warmest appreciation to Mattia Anghileri, Adriano D'Iorio, and Francesco Marino, for their effective teamwork and dedication in supporting the editorial activities. Special thanks are due to Andrea Bertoni, Stella Pennini, and Gaia Gorini, who professionally managed the Organizing Secretariat with outstanding expertise, commitment, and enthusiasm, and Marco Guerini for his valuable contribution in designing and developing the Symposium website.



Taylor & Francis

Taylor & Francis Group

<http://taylorandfrancis.com>

Symposium Organization

SYMPOSIUM CHAIRS

Fabio Biondini *Politecnico di Milano, Milan, Italy*
Dan M. Frangopol *Lehigh University, Bethlehem, PA, USA*

INTERNATIONAL STEERING COMMITTEE

Dan M. Frangopol (Chair) *Lehigh University, Bethlehem, PA, USA*
Mitsuyoshi Akiyama *Waseda University, Tokyo, Japan*
John Andrews *University of Nottingham, Nottingham, UK*
Alfredo H.-S. Ang *University of California, Irvine, CA, USA*
Jaap Bakker *Rijkswaterstaat, Utrecht, The Netherlands*
Konrad Bergmeister *University of Natural Resources and Life Sciences, Vienna, Austria*
Fabio Biondini (Ex Officio) *Politecnico di Milano, Milan, Italy*
Robby Caspeeel *Ghent University, Ghent, Belgium*
Airong Chen *Tongji University, Shanghai, China*
George Deodatis *Columbia University, New York, NY, USA*
Armen Der Kiureghian *University of California, Berkeley, CA, USA*
Dan Dubina *University of Timisoara, Timisoara, Romania*
Bruce Ellingwood *Colorado State University, Fort Collins, CO, USA*
Allen C. Estes *California Polytechnic State University, San Luis Obispo, CA, USA*
Luis Esteva *Universidad Nacional Autonoma de Mexico, Mexico City, Mexico*
Hitoshi Furuta *Kansai University, Osaka, Japan*
Michel Ghosn *The City College of New York/CUNY, New York, NY, USA*
Ho-Kyung Kim *Seoul National University, Seoul, South Korea*
Jerome Lynch *Duke University, Durham, NC, USA*
Pier Giorgio Malerba *Politecnico di Milano, Milan, Italy*
Robert Melchers *The University of Newcastle, Callaghan, Australia*
Torgeir Moan *Norwegian University of Science and Technology, Trondheim, Norway*
Terry Neimeyer *KCI, Sparks, MD, USA*
Mark Sarkisian *Skidmore, Owings & Merrill LLP, San Francisco, CA, USA*
Luc Taerwe *Ghent University, Ghent, Belgium*
Man-Chung Tang *T. Y. Lin International, San Francisco, CA, USA*
Jin-Guang Teng *The Hong Kong Polytechnic University, Hong Kong, China*

INTERNATIONAL SCIENTIFIC COMMITTEE

Fabio Biondini (co-Chair)	<i>Politecnico di Milano, Milan, Italy</i>
Alfredo H-S. Ang (co-Chair)	<i>University of California, Irvine, CA, USA</i>
Sreenivas Alampalli	<i>Stantec, Albany, NY, USA</i>
Sotirios Argyroudīs	<i>Brunel University London, London, UK</i>
Túlio N. Bittencourt	<i>University of Sao Paulo, Sao Paulo, Brazil</i>
Paolo Bocchini	<i>Lehigh University, Bethlehem, PA, USA</i>
Eugen Brühwiler	<i>Ecole Polytechnique Fédérale de Lausanne, Lausanne, Switzerland</i>
Joan R. Casas	<i>Technical University of Catalonia, Barcelona, Spain</i>
F. Necati Catbas	<i>University of Central Florida, Orlando, FL, USA</i>
Eleni Chatzi	<i>ETH Zurich, Zurich, Switzerland</i>
Minghui Cheng	<i>Cornell University, Ithaca, NY, USA</i>
Paulo Cruz	<i>University of Minho, Guimaraes, Portugal</i>
Donald W. Davies	<i>Magnusson Klemencic Associates, Seattle, WA, USA</i>
Nele De Belie	<i>Ghent University, Ghent, Belgium</i>
David De Leon	<i>Universidad Autonoma del Estado de Mexico, Toluca, Mexico</i>
Sofia Diniz	<i>Federal University of Minas Gerais, Minas Gerais, Brazil</i>
Panos Diplas	<i>Lehigh University, Bethlehem, PA, USA</i>
You Dong	<i>The Hong Kong Polytechnic University, Hong Kong, China</i>
Dan M. Frangopol (Ex-Officio)	<i>Lehigh University, Bethlehem, PA, USA</i>
Paolo Gardoni	<i>University of Illinois at Urbana-Champaign, Urbana, IL, USA</i>
Rade Hajdin	<i>University of Belgrade, Belgrade, Serbia</i>
Petr Hajek	<i>Czech Technical University, Prague, Czech Republic</i>
Ichiro Iwaki	<i>Nihon University, Sendai, Japan</i>
Sunyong Kim	<i>Wonkwang University, Iksan, South Korea</i>
Chul-Woo Kim	<i>Kyoto University, Kyoto, Japan</i>
Anne S. Kiremidjian	<i>Stanford University, Stanford, CA, USA</i>
Chun-Qing Li	<i>RMIT University, Melbourne, Victoria, Australia</i>
Zoubir Lounis	<i>National Research Council Canada, Ottawa, Canada</i>
Antonio Mari Bernat	<i>Technical University of Catalonia, Barcelona, Spain</i>
Jose Matos	<i>University of Minho, Guimaraes, Portugal</i>
Ayaho Miyamoto	<i>Yamaguchi University, Ube, Japan</i>
Luis Neves	<i>University of Nottingham, Nottingham, UK</i>
Drahomir Novak	<i>Brno University of Technology, Brno, Czech Republic</i>
André D. Orcesi	<i>Cerema, Champs-sur-Marne, France</i>
Jamie Ellen Padgett	<i>Rice University, Houston, TX, USA</i>
Alessandro Palermo	<i>University of Canterbury, Christchurch, New Zealand</i>
Kok Kwang Phoon	<i>National University of Singapore, Singapore</i>
Han Roebers	<i>Provincie Noord Holland, Haarlem, The Netherlands</i>
Xin Ruan	<i>Tongji University, Shanghai, China</i>
Mauricio Sanchez-Silva	<i>Los Andes University, Bogota, Colombia</i>
Mohamed Soliman	<i>Oklahoma State University, Stillwater, OK, USA</i>
John Dalsgaard Sorensen	<i>Aalborg University, Aalborg, Denmark</i>
Bill F. Spencer	<i>University of Illinois, Champaign, IL, USA</i>
Mark G. Stewart	<i>University of Technology Sydney, Ultimo, NSW, Australia</i>

Daniel Straub	<i>Technical University of Munich, Munich, Germany</i>
Alfred Strauss	<i>University of Natural Resources and Life Sciences, Vienna, Austria</i>
Yiannis Tsompanakis	<i>Technical University of Crete, Crete, Greece</i>
David Yang	<i>Portland State University, Portland, OR, USA</i>
Victor Yepes	<i>Universitat Politecnica de Valencia, Valencia, Spain</i>

NATIONAL ADVISORY COMMITTEE

Andrea Prota (co-Chair)	<i>University of Naples Federico II</i>
Gianpaolo Rosati (co-Chair)	<i>Politecnico di Milano</i>
Anna Saetta (co-Chair)	<i>IUAV University of Venice</i>
Antonietta Aiello	<i>University of Salento</i>
Nadia Baldassino	<i>University of Trento</i>
Beatrice Belletti	<i>University of Parma</i>
Fabio Biondini (Ex-Officio)	<i>Politecnico di Milano</i>
Gian Michele Calvi	<i>IUSS Pavia</i>
Maddalena Carsana	<i>Politecnico di Milano</i>
Dario Coronelli	<i>Politecnico di Milano</i>
Maurizio Crispino	<i>Politecnico di Milano</i>
Pietro Croce	<i>University of Pisa</i>
Francesca Da Porto	<i>University of Padua</i>
Andrea Dall'Asta	<i>University of Camerino</i>
Mario De Stefano	<i>University of Florence</i>
Marco di Prisco	<i>Politecnico di Milano</i>
Liberato Ferrara	<i>Politecnico di Milano</i>
Paolo Franchin	<i>Sapienza University of Rome</i>
Elsa Garavaglia	<i>Politecnico di Milano</i>
Iunio Iervolino	<i>University of Naples Federico II</i>
Lidia La Mendola	<i>University of Palermo</i>
Sergio Lagomarsino	<i>University of Genoa</i>
Pier Giorgio Malerba	<i>Politecnico di Milano</i>
Giuseppe Marano	<i>Politecnico di Torino</i>
Angelo Masi	<i>University of Basilicata</i>
Claudio Modena	<i>University of Padua</i>
Roberto Nascimbene	<i>IUSS Pavia</i>
Emidio Nigro	<i>University of Naples Federico II</i>
Roberto Paolucci	<i>Politecnico di Milano</i>
Alberto Pavese	<i>University of Pavia</i>
Maria Rosaria Pecce	<i>University of Naples Federico II</i>
Carlo Pellegrino	<i>University of Padua</i>
Giovanni Plizzari	<i>University of Brescia</i>
Zila Rinaldi	<i>University of Rome Tor Vergata</i>
Paolo Riva	<i>University of Bergamo</i>
Walter Salvatore	<i>University of Pisa</i>
Mauro Sassu	<i>University of Cagliari</i>
Marco Savoia	<i>University of Bologna</i>
Enrico Spacone	<i>University of Chieti-Pescara</i>
Francesco Tondolo	<i>Politecnico di Torino</i>
Filippo Ubertini	<i>University of Perugia</i>

LOCAL ORGANIZING COMMITTEE

Mattia Anghileri (co-Chair)	<i>Politecnico di Milano</i>
Luca Capacci (co-Chair)	<i>Politecnico di Milano</i>
Grigor Angjeliu	<i>Politecnico di Milano</i>
Silvia Bianchi	<i>Politecnico di Milano</i>
Lorenzo Casti	<i>Université Gustave Eiffel, Champs-sur-Marne, France</i>
Marco Cervio	<i>Politecnico di Milano</i>
Andrea Consiglio	<i>Politecnico di Milano</i>
Adriano D'Iorio	<i>Politecnico di Milano</i>
Enrique Ibarra Martinez	<i>Politecnico di Milano</i>
Leila Jafari	<i>Politecnico di Milano</i>
Ruiqi Luo	<i>Politecnico di Milano</i>
Nisrine Makhoul	<i>Politecnico di Milano</i>
Angelo Marchisella	<i>Politecnico di Milano</i>
Francesco Marino	<i>Politecnico di Milano</i>
Giuseppe V. Nava	<i>Politecnico di Milano</i>
Francesco Padovani	<i>Amplia Infrastructures, Milan</i>
Zhibin Wang	<i>Politecnico di Milano</i>
Sicong Xie	<i>Politecnico di Milano</i>
Chihiro Yoshii	<i>Politecnico di Milano</i>

SYMPOSIUM SCIENTIFIC SECRETARIAT

Adriano D'Iorio, Enrique Ibarra Martinez, Francesco Marino
Department of Civil and Environmental Engineering
Politecnico di Milano
Piazza Leonardo da Vinci, 32
20133 Milan, Italy

SYMPOSIUM ORGANIZING SECRETARIAT

Andrea Bertoni, Stella Pennini, Gaia Gorini
LAAN & Incentives Congressi e Formazione
Via Gerolamo Savoldo, 11/b
25124 Brescia, Italy

SYMPOSIUM WEBSITE

<https://ialce2023.org>

ORGANIZING ASSOCIATION



IALCCE
International Association for Life-Cycle Civil Engineering

ORGANIZING INSTITUTION



POLIMI
Politecnico di Milano
Milan, Italy

SUPPORTING PUBLIC AUTHORITIES



Ministero delle Infrastrutture e dei Trasporti
Ministry of Infrastructures and Transport



Agenzia del Demanio
Italian Public Property Agency



Regione Lombardia
Lombardy Regional Administration



Regione Piemonte
Piedmont Regional Administration



Comune di Milano
Milan Municipality



CNI
Consiglio Nazionale degli Ingegneri
National Council of Italian Engineers



Ordine degli Ingegneri della Provincia di Milano
Association of Engineers of the Province of Milan

PATRONAGES



ACI
American Concrete Institute



AICAP
Italian Association of Reinforced and Prestressed Concrete
Associazione Italiana Calcestruzzo Armato e Precompresso
Rome, Italy



ATLSS
Advanced Technology for Large Structural Systems Engineering
Research Center
Lehigh University, Bethlehem, PA, USA



BOKU
University of Natural Resources and Life Sciences
Vienna, Austria



CISM
International Centre for Mechanical Sciences
Udine, Italy



CTE
Italian Society of Building Engineers
Collegio dei Tecnici della Industrializzazione Edilizia
Milan, Italy



fib
The International Federation for Structural Concrete



IABMAS
International Association for Bridge Maintenance And Safety



IABMAS Italy
Italian National Group of IABMAS
International Association for Bridge Maintenance And Safety



IALCCE NL
Dutch National Group of IALCCE
International Association for Life-Cycle Civil Engineering



JAEE
Japan Association for Earthquake Engineering



JCI
Japan Concrete Institute



JSCE
Japan Society of Civil Engineers



RCEAS
P.C. Rossin College of Engineering and Applied Science
Lehigh University, Bethlehem, PA, USA



ReLuis
Italian Network of the University Laboratories of Seismic
Engineering
Rete Nazionale dei Laboratori di Ingegneria Sismica e Strutturale



TU Delft
Delft University of Technology
Delft, The Netherlands



UGhent
Ghent University
Ghent, Belgium



WASEDA
Faculty of Science and Engineering
Waseda University
Tokyo, Japan

IALCCE EXECUTIVE BOARD

Dan M. Frangopol (President)	<i>Lehigh University, Bethlehem, PA, USA</i>
Alfredo H.-S. Ang (Hon. President)	<i>University of California, Irvine, CA, USA</i>
Harald Budelmann (Vice-President)	<i>Technical University of Braunschweig, Braunschweig, Germany</i>
Hitoshi Furuta (Vice-President)	<i>Kansai University, Osaka, Japan</i>
Fabio Biondini (Secretary General)	<i>Politecnico di Milano, Milan, Italy</i>
Mitsuyoshi Akiyama	<i>Waseda University, Tokyo, Japan</i>
Jaap Bakker	<i>Rijkswaterstaat, Utrecht, The Netherlands</i>
Airong Chen	<i>Tongji University, Shanghai, China</i>
Shi-Shuenn Chen	<i>National Taiwan University of Science and Technology, Taipei, Taiwan</i>
Donald W. Davies	<i>Magnusson Klemencic Associates, Seattle, WA, USA</i>
Sofia Diniz	<i>Federal University of Minas Gerais, Belo Horizonte, Brazil</i>
Luis Esteva	<i>National University of Mexico, Mexico City, Mexico</i>
Leo Klatter	<i>Rijkswaterstaat, Utrecht, The Netherlands</i>
Mark P. Sarkisian	<i>Skidmore, Owings & Merrill LLP, San Francisco, CA, USA</i>

IALCCE SECRETARIAT

Prof. Fabio Biondini
Department of Civil and Environmental Engineering
Politecnico di Milano
Piazza Leonardo da Vinci, 32
20133 Milan, Italy

IALCCE WEBSITE

<https://www.ialcce.org>

FAZLUR R. KHAN PLENARY LECTURE



Taylor & Francis

Taylor & Francis Group

<http://taylorandfrancis.com>

Making bridges sustainable

E. Brühwiler

EPFL (Ecole Polytechnic Fédérale de Lausanne) and BridgIng Consultant, Lausanne, Switzerland

ABSTRACT: Lack of incentives mainly explains why the implementation of novel methods and technologies in bridge engineering practice is generally postponed by the engineering community despite the urgent need to advance also bridge engineering to meet the objectives of sustainability. Novel engineering methods and technologies are presented in this paper to extend the service duration of existing bridges while meeting the requirements of modern use. Accurate determination of bridge behavior using data from in-situ measurements and long-term monitoring of traffic action effects allow to verify realistically the structural and fatigue safety of bridges. If interventions are necessary, a targeted use of advanced high-performance materials such as UHPFRC allows to rehabilitate and strengthen effectively reinforced concrete bridges. This approach follows the principle of sustainability to preserve material resources and their grey energy that are already in use, thereby limiting greenhouse gas emissions to a minimum when requalifying and adapting existing bridges to future use.

1 INTRODUCTION

1.1 *Sustainability and existing bridges*

Civil engineers will be called upon to find solutions to mitigate the unpredictable effects of the climate change on people. Currently, civil engineers are still primarily trained to build new structures without learning how to consider *concretely* the principles of sustainability of constructions. A turning point in the education of engineers and practicing engineers is urgently needed. To soften the effects of the climate change on people, greenhouse gas emissions must be radically reduced. It is obvious that rehabilitation, adaptation and modification of existing structures and bridges must be given first priority. We must value the existing and avoid the still commonly practiced “demolition-replacement” approach including high material consumption and high greenhouse gas emissions, and also loss of cultural values.

Civil Engineers are trained to build new structures. These “new builders” are only partially or not at all competent to engineer existing structures. That’s why, methods of new construction are applied to existing bridges under the title “re-calculation” and interventions are designed using code provisions for new structures. But an existing bridge exists ! A stress in a rebar can be measured directly. It does not have to be “re-calculated”, which, due to significant model uncertainties, leads to unrealistic though over-conservative results.

In addition, “new builders” describe a bridge that is f.ex. 60 years in use, as an “old” bridge that - like humans - has a “lifespan” of 80 to 100 years. But bridges are not living beings and have thus no “lifespan” and no “remaining life”. Bridges are useful objects, bind enormous amounts of resources and heavily burden the environment. In outstanding cases, bridges are also built culture. For economic reasons alone and out of respect for the environment, bridges should in principle be preserved for as long as people use trains and road vehicles. Bridges (and other structures) are not consumer goods to be thrown away and, at best, recycled. The profession has yet to be “converted” to the engineering of existing structures!

1.2 *Engineering of existing structures*

“Engineering of existing structures” requires an own approach as it implies to precisely determine the capacity and structural resistance of an existing structure with respect to its intended use and exposure. This process is called “updating”. The basic methodology is to collect systematically and specifically detailed information on the existing structure, by non-destructive testing methods and measurements (monitoring). In this way, the determinant variables related to the loading action effects and the resistance of structural elements are determined as realistically as possible. This procedure is not new and in principle already permitted by standards. However, it is rarely used because practicing engineers are not trained or competent to do so.

“Engineering of existing structures” has the goal to show that existing structures can be subjected to higher loads by exploring and exploiting often available load-bearing reserves while meeting the safety requirements. Only when all possibilities for updating the bridge have been exhausted and the requirements for structural safety and usability can still not be met, interventions to strengthen structural elements are necessary. The extent of the intervention and the consumption of resources should thereby be as limited as possible. New technologies and high-performance building materials are often effective means to achieve this goal.

“Engineering of existing structures” also implies “Baukultur” (building culture) and knowledge of the history of structural engineering. But most engineers have yet to develop their sensitivity for questions of cultural values of structures and the preservation of monuments of various degrees of importance. Accordingly, the subject of building culture should be part of the basic competences of structural engineers.

“Engineering of existing structures” is needed to avoid cost-intensive or even unnecessary interventions, which are often the result of incomplete know-how of structural engineers and lack of sufficient information about the existing structure.

1.3 *Standards for engineering of existing structures*

When dealing with existing structures, the “new builders” among structural engineers apply standards valid for the design of new structures. This is a problematic approach as standards for new structures are obviously not applicable to existing structures. Only some provisions may be analogously applied to existing structures.

Over the last 30 years, a methodology inherent to existing structures has evolved, presented at numerous scientific and professional conferences, and successfully applied in many existing bridge cases. However, it has not yet been fully adopted in practice by the majority of structural engineers. This is explained by the fact that there are no standards available which practicing engineers can rely on.

For this reason, the Swiss Society of Engineers and Architects (SIA) elaborated a series of standards exclusively devoted to the engineering of existing structures, published in January 2011 as SIA269 Standards (Brühwiler et al. 2012). This pioneering initiative may still be considered as unique worldwide. Switzerland is a country with well-developed built infrastructure, and the enforcing of these standards led to a marked improvement of engineering projects related to existing structures, implying significant socio-economic benefits and reducing the environmental impact of structures.

In Europe, CEN-TC 250-SC 10 is elaborating a standard, entitled “Basis of structural and geotechnical assessment of existing structures” (CEN-TC 250-SC10, 2022), which relies on contents of the Swiss SIA269 Standard. This initiative can be interpreted as a “memorandum of understanding” that standards for existing structures are needed. However, this European standard is currently limited to basic principles and still requires time and discussions to achieve agreement among all member countries.

Worldwide, in many countries there seem to be no concerns about existing bridges being exposed f.ex. to higher traffic loading or deteriorating bridge condition. Commonly, in these countries, engineering of existing structures is limited to condition assessment, and invasive methods often implement “demolition-replacement” projects, implying high construction

costs and high environmental impacts. As a consequence, the need to introduce standards for the engineering of existing structures is not prevailing in these countries.

Overall, the situation related to the engineering of existing structures is unsatisfactory and still rather unprofessional, which is also the result of the traditional conservatism of structural engineers that, as “new builders”, underestimate the significance of engineering of existing structures.

1.4 Outline

After this review of the current situation of the engineering of existing structures based on the authors rich practical experience in Switzerland and worldwide, this paper contains two main parts:

- Chapter 2 presents recent research findings by the author and his research team in the domain of *monitoring-based verification* of existing structures. Rational ready-to-use engineering methods are deduced to investigate as precisely as possible *action effects* (f.ex. due to traffic loading) on bridge structures, while current structural engineering is more at ease in the determination of ultimate resistance of structural elements.
- Chapter 3 is a brief overview of the current state-of-knowledge of the *UHPFRC Technology* to rehabilitate and strengthen existing bridges, as mostly developed and implemented in practice by the author and his research team.

Both domains follow the goal to radically *preserve existing bridges* and to follow the principle of sustainability of continued use of material resources and their grey energy, thereby limiting greenhouse gas emissions to a minimum when adapting bridges to future use.

2 MEASUREMENT AND MONITORING BASED VERIFICATION OF FATIGUE AND STRUCTURAL SAFETY

2.1 Methodology

2.1.1 Basic approach

The modern approach to existing structures is based on “updating”, which means collecting and exploiting detailed in-situ information from the existing structure while reducing uncertainties in structural parameters (Brühwiler et al. 2012). The controlling parameters are determined as precisely as needed following a stepwise procedure with increasing focus on details.

The structural safety verification is finally performed using updated values, called examination (or assessment) values. The notion of degree of compliance n is introduced in the deterministic verification of the structural safety:

$$n = \frac{R_{d,updated}}{E_{d,updated}} \quad (1)$$

where $R_{d,updated}$ and $E_{d,updated}$ are the examination values of resistance and action effect, respectively. The degree of compliance is a numerical statement showing the extent to which an existing structure fulfils the structural safety requirements. This formulation not only gives the information whether the structural safety is fulfilled. It also indicates by how much the verification is fulfilled (or not). The latter is necessary for the evaluation of results and in view of the planning of interventions.

2.1.2 Non-destructive evaluation

In a first step, examination (often called: assessment) of existing structures is typically conducted using construction drawings (if available), information on materials and visual inspection. While a broad range of sensing and monitoring technologies have been developed over the last decades, *non-destructive evaluation (NDE)* is still rarely used for the condition survey and safety verification of existing bridges. NDE techniques include both *non-destructive testing (NDT)* and *structural performance (or: “health”) monitoring (SPM)* (Bertola et al. 2022) (Figure 1):

- In NDT, instruments and sensors are deployed temporarily to measure the response due to a known stimulus, to determine structural (e.g., location of reinforcing bars, element thickness, etc.) and material properties (e.g., modulus of elasticity and strength) as well as characteristics of structural behavior (e.g., rigidity, deformation, deflections). Techniques include ground penetrating radar (GPR), ultrasonic testing (UST), acoustic emission (AE), rebound hammer testing or load testing.

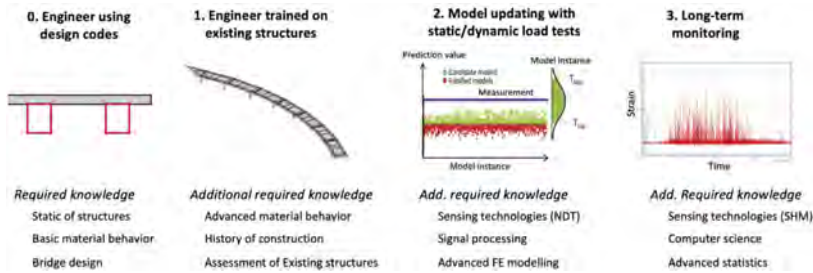


Figure 1. Stepwise procedure with increasing refinement, from Step 0 to 3, for the examination of existing structures with the associated training required, taken from (Bertola et al. 2022).

- In SPM, sensors are mounted in targeted locations of the bridge structure to collect strain and temperature data over rather long time using periodically sampled response measurements. SPM data are useful to describe condition changes and monitor degradation processes. Stress histograms due to traffic loading, temperature induced stress and changes of material and geometric properties are monitored. This data is then analyzed to support the fatigue and structural safety verifications of existing bridges.

Most sensor data such as deformations, strains and accelerations are indirect measures of material and structural properties and behavior. Therefore, data interpretation is indispensable, and in-situ measurements often must be complemented by advanced structural analysis. Calibrated finite-element (FE) models are needed to provide accurate data on structural behavior and capacity.

Although NDE information may lead to more sustainable and cost-effective management of existing infrastructure, it requires additional training for structural engineers that are usually not included in current curricula (Figure 1).

2.1.3 Practicability of NDE, in-situ measurements and monitoring

The verification of structural safety must thus be based on in-situ measurements of actual structural behavior, rather than theoretical design-based engineering values. Several ways to measure, monitor, and analyze structural behavior are possible and should be carefully selected based on the objectives of monitoring, case study, sensor availability and training of engineers.

The advent of cheap and high storage capacity hardware in recent years means that direct measurement of action effects in structural elements via structural monitoring is now a viable option. On purpose tailored compact monitoring equipment is a rational and ready-to-use tool of reasonable cost that can be used on a routinely basis by bridge engineers commissioned to perform an examination of an existing bridge. In this way, structural monitoring becomes as self-evident for engineers as f.ex. the routinely use of software tools implementing Finite Element models.

Obviously, current practitioners' perception of monitoring as being complex, costly and not always providing useful results needs to be challenged and altered. Researchers have a responsibility to support practice.

2.2 Risk-based bridge inspection

The visual inspection of existing bridges is a critical step in bridge safety verification, as the detection and quantification of damage must be accurate, reliable and useful to conduct

realistic examination of existing bridges. Often, a condition value ranging from 1 to 5 is given to each bridge. As only element-based degradations are currently considered in bridge-condition evaluations, inaccurate assessments of global structural safety are also provided by bridge inspectors.

A risk-based methodology provides a more objective and reliable examination of the bridge condition based on visual-inspection data. Degradation states of bridge elements are coupled with element-failure consequences on the global structural safety in risk analysis. Risk-based methodologies have been proposed in the past and are even in use. However, it is crucial to validate them in the field in order to have them accepted by practice.

A recent case study of a strategic road involving sixty bridges was conducted to assess bridge conditions applying a novel risk-based methodology based on visual inspections (Bertola & Brühwiler 2023). The study revealed that including element-failure consequences in bridge-condition assessments supports more accurate evaluations of the impacts of damage on the global structural safety, leading to more objective decisions on management actions and interventions. Analyses of four damaged bridges showed that traditional inspection methods often lead to over-pessimistic assessments in terms of structural damage, and this can lead to unnecessary or excessive rehabilitation interventions.

2.3 *Updating traffic action effects by structural monitoring*

In recent years, monitoring has offered a significant complement or even alternative to traditional analytical safety verification approaches. However, there still remains a lack of guidance for the use of monitored data in structural safety verification. Often, relatively short time frames of monitoring are used. Additionally, temperature effects often have a significant influence on the structural response which requires adequate consideration.

2.3.1 *Duration of monitoring*

The duration of monitoring has an important influence on predicted characteristic action effects and is thus of first importance regarding reliability of data. In order to determine if a monitoring campaign is sufficiently long to obtain a reliable extreme value estimate of the action effect, a case study of a highway bridge in Switzerland, with one year of continuous high-frequency measurements, was analyzed by means of several approaches (Treacy et al. 2014). The focus was on direct measurement of the traffic action effects in the bridge's deck slab steel reinforcement bars. A comprehensive statistical approach for determination of site- and element-specific extreme traffic action effects was conducted.

The study showed that the time required to capture stable record behavior in the deck slab rebars is highly dependent on element location and orientation, as well as the local traffic composition. The behavior of the predicted extreme values was strongly influenced by the record accumulation behavior for daily maximum measured strains. Single extreme events significantly higher than the average daily maxima had a strong effect on the extreme value predictions.

2.3.2 *Fatigue and temperature effects*

The results of 28-month-long monitoring of a slab portion of a highway viaduct using strain gauges and thermocouples were investigated (Sawicki & Brühwiler 2020). The post-tensioned reinforced concrete structure was strengthened with a layer of UHPFRC (see Chapter 3). Strain gauges were used to measure stress values in the bottom layer of reinforcement bars in the slab, while thermocouples recorded the global behavior of the structure due to ambient temperature variation (Figure 2).

The study revealed that the stress variation due to the thermal action can be as large as the response due to traffic action, even in a massive structure. Monitoring data was analyzed for fatigue and structural safety verification and compared with traditional re-calculation on Level 1, showing that assessment by re-calculation is highly conservative, leading to significant overestimation of structural action effects.

The fatigue safety of existing bridges may be assessed using data from monitoring. This data is then used to assess fatigue due to the past traffic and to extrapolate to the future service duration using traffic scenarios as given by the bridge owner. Due to the randomness of

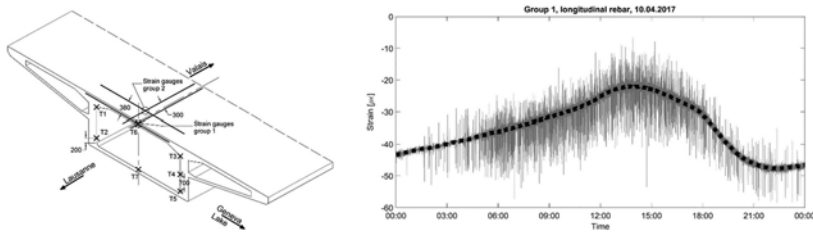


Figure 2. Left: Scheme of monitoring with strain gauges on rebars and thermocouples (T1–T7) (dimensions in mm); right: Strain recorded during 1 day on group 1 longitudinal rebar; filtered-out “thermal wave” is shown with dotted line, taken from (Sawicki & Brühwiler 2020).

traffic loading, there exists a likelihood of over- and under-estimation of potential fatigue damage in the case of short-term monitoring campaigns. As a consequence, the influence of monitoring duration on the obtained results must be known.

To investigate this research question, datasets collected during long-term (>3 years) monitoring campaigns of two bridges were analyzed (Sawicki & Brühwiler 2022). The two road bridges had different nature of traffic: a two-lane highway viaduct with heavy traffic, and a bridge with a bi-directional regional traffic. The deck slabs of both bridges were monitored using strain gauges installed on reinforcement bars. The daily, seasonal and year-to-year measured traffic action effects were analyzed, and a theoretical equivalent fatigue damage was calculated.

The resampling method was used for the simulation of possible short-term monitoring campaigns during the period considered, with different order of heavy vehicles arriving. The Extreme Value Theory served to answer what is the required monitoring duration for reliable results. Methods to consider the monitoring duration in fatigue damage calculations were proposed and validated.

In order to verify the efficiency of the UHPFRC strengthening (see Chapter 3) and to further evaluate its long-term performance, a structural monitoring campaign was implemented, relying on low-cost, yet easily deployable, sensors, including a suite of accelerometers, strain gauges, temperature and humidity sensors (Martin-Sanz et al. 2020). The monitoring data was first processed by means of standard modal analysis methods as well as non-stationary time-series analysis tools. In a second step, a Finite Element model of the system was built and updated, and subsequently exploited to deliver a comparison between the original and strengthened structure using reliability analysis, confirming the efficiency of the UHPFRC strengthening.

2.3.3 NDT of bridge deck condition

RC bridge deck condition was monitored during one year by means of AE (acoustic emission) permanent measurements (Bayane & Brühwiler 2020). The study has shown that the structural response and characteristics of the slab under operational and environmental loading can be investigated within reasonable postprocessing work and statistical analyses. AE measurements allowed to identify the nature of cracking activity in the concrete slab as a function of traffic loading and ambient temperature variation. The method was validated on combining the AE and strain gauge measurements, performed on a bridge deck slab in service for 60 years, providing finally useful information for structural and fatigue safety evaluation.

2.3.4 Monitoring-based examination value

The examination value of the railway traffic action effect was calculated from long-term monitoring data without resorting to load models and structural analysis (Grigoriou & Brühwiler 2016). Monitoring data was obtained from measurements on a short span RC slab bridge. The action effect is represented by the distribution of its maxima per train passage. The end tail of the distribution was modelled by a shifted exponential distribution, and the examination value was calculated by extreme value theory, using additionally a confidence upper bound in order to consider the monitoring duration.

The monitoring-based safety verification procedure was developed through probabilistic modelling and reliability calculations, based on failure probabilities per freight train incident

(and not per unit of time). The duration of the monitoring period, in terms of the number of recorded freight train incidents, was considered in the examination value of the action effect by means of a confidence upper bound.

On the other hand, the annual variation of temperature had a significant indirect effect on the traffic action effect and, unless monitoring was performed over several years, the uncertainty related to this effect can only be considered by empirical factors.

The relatively simple semi-probabilistic method gave results close to the more complex FORM. For the six-month monitoring campaign, the uncertainty from the limited duration of monitoring resulted in an increase of the examination value by 18%. This increase could possibly be reduced to 10% for a one-year monitoring period and to 6% for two years.

2.3.5 *Dynamic action effects*

All previously described and other bridge measurement campaigns confirmed that there is no notable dynamic amplification of road and rail traffic effects on structural bridge elements like slabs or rail track system, if stress and strain are directly measured on relevant rebar and concrete as well as steel element locations. The plausibility of this significant finding can be explained by simple dynamic models (Ludescher & Brühwiler 2009).

Consequently, no dynamic amplification factor needs to be considered on Level 1 verifications by re-calculation using traffic load models, while on advanced level monitoring-based examinations eventual dynamic effects are implicitly included in the measurement results.

2.4 *Updating permanent actions*

In the case of massive bridge structures like the ones in reinforced concrete, often more than 60% of the total action effect on structural elements is due to permanent actions (consisting of the self-weight of the structure and equipment (f.ex. pavement)). In extreme cases, permanent actions represent 80% of the total examination value of action effect.

As a consequence, NDT is required to provide precise data of structural dimensions, in particular thickness of structural elements and pavement, and the volumetric load of materials, to update the characteristic value of permanent actions.

Updating by means of NDT reduces uncertainties which in turn provides the basis to update also the load factor for permanent action, in the framework of the basic deterministic safety verification. Application of the well-known semi-probabilistic method has shown to be an effective mean to update permanent actions effects, while adequately respecting safety requirements.

2.5 *Structural identification and value of information*

The monitoring of existing bridges has the potential to improve bridge management. Monitoring data help identify unknown model-parameter values. Then, this information is used to accurately evaluate bridge condition and behavior, such as to predict reserve capacity and fatigue resistance, avoiding invasive interventions or replacement. This model-updating method is called structural identification.

The benefits of structural identification depend on the selected monitoring system, including sensor types, number of sensors and device locations. As these choices are usually made using engineering judgment and qualitative metrics, the selected measurement systems may be sub-optimal, leading to a low cost-benefit ratio of bridge load testing and monitoring.

Methodologies now exist to design optimized measurement systems based on their cost-benefit ratio. Such a methodology has been suggested and validated by means of a composite steel-concrete bridge in Switzerland (Bertola et al. 2022, Bertola & al. 2023). It was found that a rational methodology to design measurement systems helps to reduce the number of sensors without compromising the information gain, thus significantly improving the cost-benefit of bridge load testing and monitoring.

Monitoring data from several sources can be used to develop accurate physics-based models and Error-domain model falsification (EDMF) (Goulet & Smith 2013) to analyze measurements, enabling accurate identification of structural parameters necessary f.ex. to verify fatigue safety of existing bridges (Bayane et al. 2021).

2.6 *Training in engineering of existing structures*

Structural engineers today are still educated mainly to design new structures. Engineers are thus often ill-equipped to deal with maintenance and preservation of existing structures.

Consequently, educational programs should be modernized and developed to the engineering of existing structures. Such programs would still include certain basic structural engineering courses (like structural mechanics) but also elaborate on structural behavior and material properties, and how these can be determined by means of NDT and SPM, in sum referred to as non-destructive evaluation NDE. Because these tools are traditionally not included in the structural engineering curriculum, a new set of basic interdisciplinary skills from the domains of mechanical and electrical engineering, as well as computer science (data analysis, signal processing, etc.), need to be acquired by the students.

Measurement-informed approaches for structural analysis require training beyond traditional structural engineering backgrounds. Engineers must understand the potential of sensor devices in terms of data collection and signal processing. Moreover, model updating requires building refined FE models to accurately predict structural behavior under in-situ conditions. When long-term monitoring measurements are collected, very large data sets need to be analyzed and interpreted, which requires special training. Statistical and data science tools, such as machine learning, could be appropriately used to f.ex. differentiate signal from noise.

3 REHABILITATION AND STRENGTHENING USING UHPFRC

3.1 *Introduction*

Construction of reinforced concrete bridges is very successful because it is cheap. However, the problems of insufficient durability are known for several decades. Rehabilitation of bridges in reinforced concrete using traditional methods implies high intervention and user costs which represent a heavy burden for national economies and the environment. Nevertheless, there is no end of RC bridge construction in view... ! Many bridge engineers and the profession do not seem to care about this problem and are not motivated to make progress !

UHPFRC stands for Ultra-High-Performance Fiber Reinforced Cementitious Composite materials. UHPFRC is composed of cement and other reactive powders, additions, hard fine particles, low amount of water, admixtures and very high amount of relatively short and slender steel fibers. The composition of UHPFRC is optimized with respect to compaction of particles leading to a waterproof material up to a tensile strain of about 0,1 %. The tensile strength of UHPFRC typically is about 12 MPa and the material shows significant strain-hardening behavior in tension. UHPFRC has compressive strength higher than 140 MPa. UHP(FR)C is nowadays used in many countries, mostly in the domain of new construction (Graybeal et al. 2021).

The author and his team have developed the UHPFRC rehabilitation and strengthening technology over the last 25 years by means of scientific research and applications (Bertola et al. 2021, Brühwiler 2019). In Switzerland (8,7 million inhabitants, area of 41'000 km²) there are currently more than 350 reinforced concrete structures, mainly bridges, that have been improved using the UHPFRC Technology, since 2004. This is the by far highest UHPFRC application rate in the world with respect to the size of the country.

The main reason for this successful implementation of a new technology in practice is that compared to traditional methods using concrete, mortar and epoxy coatings, the UHPFRC Technology is economic in terms of costs and material use, allows for an accelerated construction process and provides durable structures for further use reducing or eliminating maintenance costs.

By applying a UHPFRC reinforcement and waterproofing layer, the use of an existing RC bridge can continue. In this way, new requirements of use are accommodated in an economical, environmentally friendly and socially responsible manner. The UHPFRC Technology is also particularly suitable for bridges of high cultural values, since interventions are usually not visible.

3.2 Principles of UHPFRC-concrete composite elements

UHPFRC is used as a high-performance building material to improve existing bridges in traditional reinforced concrete with the aim of remedying, through a targeted supplement with UHPFRC, the known deficiencies of reinforced concrete.

3.2.1 Concept

The basic idea of reinforcing structural RC bridge elements with UHPFRC is to monolithically connect a 25 to 80 mm thick UHPFRC layer with the RC cross-section. The resulting UHPFRC-concrete composite element consists of a RC cross-section and a layer of UHPFRC or R-UHPFRC (incorporating steel reinforcement bars) according to Figure 3. The term “strengthening” used here includes the increase in resistance and rigidity of structural bridge elements. At the same time, the UHPFRC layer also provides the protection function by a watertight barrier to shield reinforced concrete from direct contact with water and chloride ions.

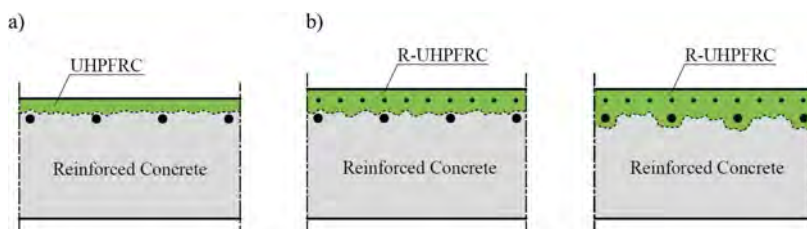


Figure 3. Basic configurations of the UHPFRC-concrete composite construction: a) protective function and increase in rigidity under service conditions, b) protective function and increase in element rigidity and ultimate resistance (rebars in the RC may be integrated or not in the R-UHPFRC layer).

The essentials of UHPFRC-concrete composite behavior can be summarized as follows:

3.2.2 Behaviour in bending

When in tension, the R-UHPFRC layer principally acts as an added flexural reinforcement chord for the RC member. Both the steel rebars and the UHPFRC contribute to the structural resistance. RC beams strengthened with a R-UHPFRC layer show significant increase in elastic stiffness and ultimate resistance when compared to the initial RC member.

The bond between UHPFRC and concrete is obtained by preparing the concrete substrate surface by high pressure water jetting or sand blasting. The concrete substrate has to be wetted and needs to be moist when the layer of UHPFRC is cast. This surface preparation provides a full bond between the UHPFRC and the concrete substrate with monolithic behaviour.

The plastic post-peak rotation capacity of strengthened RC beams is maintained with an appropriate design of the rebars in the UHPFRC layer. The structural behaviour in terms of moment – curvature relation and the ultimate bending resistance are calculated using the conventional sectional model, extended to account for the R-UHPFRC layer in the monolithic section (Figure 4).

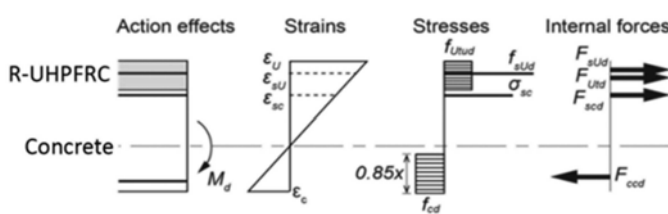


Figure 4. Plane section analysis for ultimate bending resistance.

When subjected to compressive stresses, the R-UHPFRC layer acts as a compression flange but the high UHPFRC compressive strength can usually not be fully exploited. This is because the

compressive strength of the adjacent concrete below the UHPFRC layer often is three to six times lower, and thus concrete would crush prior to the UHPFRC reaching its compressive strength.

3.2.3 Behaviour in combined bending and shear

Testing of R-UHPFRC – RC composite beams revealed that the addition of a layer of R-UHPFRC delays the formation of the inclined shear crack in the concrete section. For many geometric configurations, the R-UHPFRC layer modifies the failure mode from well-known RC shear failure with little deformation to a ductile flexural failure mode.

A shear failure is observed in a composite section only for specific geometric and material configurations. Due to the experimentally observed failure mechanism, the ultimate shear resistance is composed of the contributions due to concrete web crushing, vertical steel reinforcement yielding and a two hinge-bending mechanism of the R-UHPFRC layer. Accordingly, analytical expressions have been deduced to calculate the ultimate shear strength of RC slabs and beams strengthened by a R-UHPFRC layer.

3.2.4 Fatigue behaviour

Bending fatigue tests on R-UHPFRC – RC composite elements revealed the existence of a fatigue limit at 10 million cycles at a fatigue stress level of about 50 % of the ultimate static resistance of the R-UHPFRC – RC beams. Consequently, fatigue design rules for R-UHPFRC – RC members under bending fatigue need to account for steel rebar and UHPFRC fatigue resistances. Fatigue stresses are calculated using an elastic sectional model similar to the one shown in Figure 4.

3.2.5 Design provisions

Rational design provisions for the application and implementation of R-UHPFRC in structural engineering are given in the Swiss Standard SIA 2052 (SIA2052 2016) which is still the only UHPFRC Standard explicitly treating the application of UHPFRC for the enhancement of existing concrete structures. Is the experts basic education as “new builders” the reason why other code committees don’t integrate the engineering of existing structures in their UHP(FR)C codes ?

3.3 Design concepts to improve bridges

Obviously, UHPFRC should generally be used as a material to rehabilitate and restore damaged reinforced concrete elements, thereby replacing the use of inferior materials like repair mortars or epoxy coatings. In the following, concepts are presented to increase structural resistance of R-UHPFRC improved RC bridges:

3.3.1 Project objective 1: Restoring and increasing the resistance of bridge deck slabs

Bridge deck slabs made of reinforced concrete are subject to particularly high loading due to environmental influences and traffic loads. Accordingly, there is a high demand for intervention to restore and increase the structural resistance of deck slabs.

Figure 5 shows the basic strengthening concept of bridge deck slabs by applying a R-UHPFRC layer to the existing concrete slab. Bridge deck slabs carry loads and forces mainly in the transverse direction. Correspondingly, a distinction is made between the sagging moment zone (positive bending moments) and the hogging moment zone (negative bending moments) above the webs of beams or box girders.

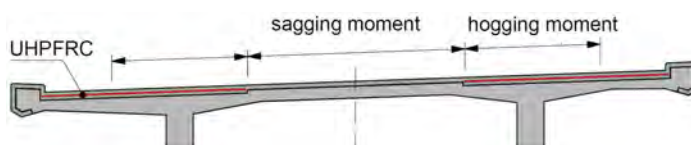


Figure 5. Concept of increasing the resistance of the original RC deck slab by means of the R-UHPFRC layer forming a strong R-UHPFRC tension chord in the hogging moment zone.

The concept is to significantly increase the flexural resistance in the hogging moment zone by forming a strong R-UHPFRC tension chord allowing for moment redistribution from the sagging to the hogging moment zone at ULS (ultimate limit state) according to the plasticity theory, given that the UHPFRC layer under compression in the sagging moment zone only leads to a comparatively small increase in the flexural resistance.

The R-UHPFRC tension chord must be compensated by a correspondingly strong compression zone. In order to ensure the balance of the tensile and compressive forces resulting in the bending cross-section, the effective concrete compressive strength is exploited, which has usually increased considerably (i.e. by 20 to 50 % compared to the 28-day compressive strength) during the bridge's service duration usually of several decades. This well-known time-dependent increase in strength is estimated using analytical expressions given in scientific literature and standards, and verified by means of non-destructive testing on the structure. In this way, strengthening of the compression zone can often be avoided.

By creating a R-UHPFRC tension chord, the ultimate shear resistance is also greatly increased in the hogging moment zone, such that the shear force check is usually fulfilled easily. By the R-UHPFRC reinforcement, the slab rigidity is significantly increased, which greatly reduces fatigue stresses in the steel reinforcement bars and in the concrete. The fatigue safety check is therefore usually fulfilled with margins.

3.3.2 Project objective 2: Increasing the resistance of bridge girders

The targeted use of R-UHPFRC, in particular as a R-UHPFRC tension chord, enables a significant increase in the load-bearing capacity of bridge girders in the longitudinal direction without significantly increasing permanent actions (by the additional R-UHPFRC layer) and without the intervention becoming visible. For this purpose, a modification of the static system is usually appropriate. Two basic principles are described as follows.

Principle 1: Reinforcement of continuous beams by means of a R-UHPFRC layer

In statically indeterminate systems such as continuous beams, the bending resistance in the hogging moment zone is greatly increased by the formation of a strong R-UHPFRC tension chord in order to be able to carry out a plastic moment redistribution from the sagging to the hogging moment zones at ULS, similar to the concept related to deck slabs (Figure 6). However, this moment redistribution is only possible if the bending cross-sections are sufficiently ductile, which must be verified. For this purpose, a non-linear finite element analysis is often useful if the empirical rules of standards are not satisfactory.

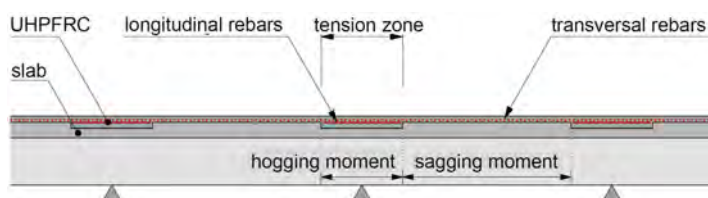


Figure 6. Principle of increasing the ultimate resistance of reinforced concrete bridge girders using a R-UHPFRC layer with the formation of a strong R-UHPFRC tension band in the support area.

This principle is efficient in that an increase in the load-bearing capacity (ultimate resistance) of 15 to 30% (and in extreme cases up to 50%) can be obtained. In this way, for example, severe damage such as failure of prestressing cables due to corrosion can be compensated without having to install costly additional tendons.

As in the sagging moment zone of a bridge girder, the R-UHPFRC layer only leads to a small increase of the flexural resistance, a need for additional reinforcement of the tension zone at the bottom of simple and continuous beams can be accommodated for by CFRP (carbon fiber reinforced plastics) lamellas on the underside of the bottom flange or by additional external posttensioning tendons.

Principle 2: Creation of hyperstatic systems by force-locked closure of dilation joints

For existing short and medium span RC bridges with lengths up to 80m, all dilatation joints can be eliminated using UHPFRC. Force-fit joint closure leads to hyperstatic systems. Particularly, the structural behavior of the modified abutments needs to be investigated applying recent knowledge in the area of integral RC bridge structures. In the case of existing bridges, the dilatation movement to be considered is limited to that due to changes in temperature alone, since girder deformation due to final shrinkage and creep of the existing concrete is negligible.

Bridges consisting of a series of simple beams that are force-fitted monolithically in the support zone by R-UHPFRC, are converted into a continuous beam and are thus analyzed like continuous beams according to Principle 1.

Figure 7a shows the concept of joint closure in the abutment area of a single span beam. In the case of pier-like abutments with large dimensions, a frame structure can be created. By modifying the end zones of the beam to frame corners, the bending stress is redistributed from the sagging zone to the frame corners and thus relieved. By installing the R-UHPFRC tension chord in the abutment zones and a UHPFRC layer over the entire deck, the dilatation joints are eliminated and the reinforced concrete is protected from chlorides and water.

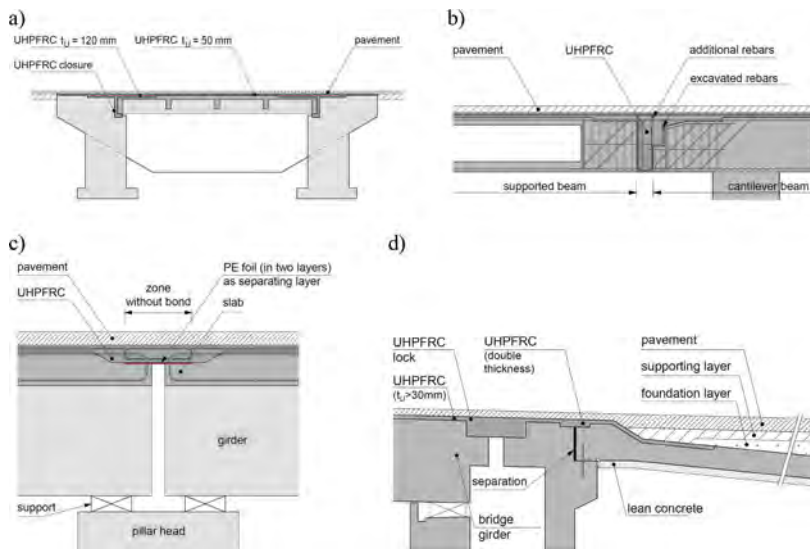


Figure 7. Principle of UHPFRC joint closure: a) in the abutment zones of a single span bridge to create a half-frame, b) force-locked Gerber joint, c) partial joint closure for beam chains, also called “link slab”, and d) creation of a semi-integral bridge end.

Figure 7b shows the constructional detail of a force-locked Gerber joint, which is bending- and shear resistant. The UHPFRC lock is anchored into the existing RC bridge structure with rebar inserts on both sides.

In the case of single span girders in series, the partial joint closure at the level of the deck slab shown in Figure 7c can be suitable. A relatively massive unbonded slab in R-UHPFRC, called “link slab”, is anchored in the adjacent RC deck slabs to connect two adjacent bridge girders by a continuous deck slab. The length of the connecting UHPFRC slab is designed such that temperature related deformations are absorbed by deformation of the “link slab”. The static functioning of the original simple beams is not modified by this intervention. This “link slab” principle can also be implemented in the transition from the bridge to the road for dilatations up to ± 10 mm.

Figure 7d shows the design of a semi-integral abutment by means of a R-UHPFRC lock connecting the bridge deck slab to the transition (or approach) slab, thereby waterproofing the bridge end zone and eliminating the dilation joint above the bridge bearing and thus a major bridge damage situation.

By forming force-locked UHPFRC connections, the structure is stiffened, which usually increases structural resistance. Obviously, the entire strengthened structure and in particular the UHPFRC-locked zone must be analyzed accordingly and the force flow in the modified structure must be carefully verified.

3.4 Three selected recent applications

Among numerous UHPFRC application projects with involvement of the author in conceptual design, dimensioning, project proof and quality control, three recent projects are selected and briefly described in the following:

3.4.1 Riddes Viaduct

The 1.2 km long road viaduct (Figure 8a) consisting of a twin continuous box girder in post-tensioned concrete built in 1976 is a major overpass over a railway line, highway and a river.



Figure 8. a) UHPFRC ready mix plant next to the Riddes Viaduct, b) UHPFRC casting on the deck slab.

RC damage including corrosion of prestressing tendons and steel rebars as well as alkali-aggregate reaction lead to a significant deficit in structural resistance. Strengthening intervention was urgently needed. The objective of the intervention was to over-strengthen the girder for flexural resistance to accommodate for (1) potential loss of 1/3 of post-tensioning, (2) 30% AAR-related forecasted concrete strength reduction and (3) local damage of the deck slab.

The R-UHPFRC intervention method was found to be most cost-effective and rapid to rescue the viaduct's post-tensioned concrete structure. The concept and design of strengthening was following the principle shown in Figure 6 and the design provisions of the Swiss UHPFRC standard (SIA 2052, 2016) including detailed non-linear FE analyses. The UHPFRC layer was cast in 2021 on the deck slab of the viaduct using a casting machine (Figure 8b).

3.4.2 Aare Bridge Schinznach

This 120 m long three span road bridge for bi-directional road traffic and with a pedestrian walkway was built in 1954. This bridge belongs to the first generation of steel-concrete composite bridges and has significant cultural values.

The cross section consists of two main steel girders and the RC deck slab. The RC slab showed ordinary steel rebar corrosion damage, and the pedestrian walkway had to be widened to accommodate for future user demand. In addition, examination of the composite structure and the deck slab revealed deficits in structural capacity and thus structural strengthening was required.



Figure 9. a) View of the steel-concrete composite bridge after R-UHPFRC strengthening, b) casting of UHPFRC with immediate application of curing compound.

The strengthening consisted in adding a 60mm thick layer of UHPFRC incorporating steel reinforcement bars in orthogonal directions to waterproof and protect the RC slab as well as to increase the resistance of the slab in the transverse direction and the hogging moment capacity over the piers in the longitudinal direction. The UHPFRC casting works were realized in two days in Summer 2022 (Figure 9b).

The R-UHPFRC strengthening was optimized such that strengthening of the two steel girders could be avoided, reducing the intervention on the main structure in steel to the renewal of the corrosion protection coating only.

3.4.3 Viaducts Pont d'Ouche

Built as part of a vast motorway program in the 1960s, the 504 m long Pont d'Ouche twin viaducts are one of the major elements of the A6 motorway in France (Figure 10a). At the time of their construction, they were unique by its geometric characteristics, since built entirely in curves and in slope, and by the structure being made up of prestressed prefabricated isotatic beams with spans of 36m with cast-in-place connecting slabs. This rational structural system for RC viaducts, which was very often realized in France and worldwide, allowed realization in a record time of 20 months and the inauguration of the viaducts in October 1970.

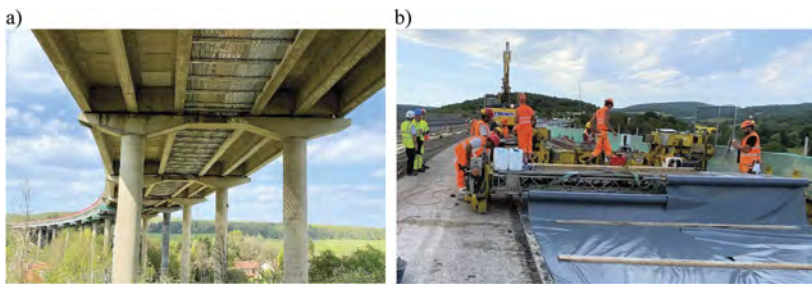


Figure 10. a) View of the twin viaduct structure with triple PC-girder cross section, b) casting of UHPFRC and curing with a plastic foil.

Installation of a robust water proofing layer in UHPFRC, repair of rebar corrosion damage and structural strengthening of the slab zone near the curbs to resist possible vehicle impact forces on the new vehicle retaining system, were the main reasons for realizing the UHPFRC project. The UHPFRC layer on the deck slab of the first viaduct was cast in 2022 using a casting machine (sure 10b). The same UHPFRC intervention will be realized in 2023 on the adjacent viaduct.

3.5 UHPFRC Technology and sustainability

The two most efficient materials in the building industry, steel and cement, are currently criticized as being particularly harmful to the environment. This ignores the fact that it depends on how these building materials are used. UHPFRC contains relatively high quantities of

cement and steel, so that the energy input and greenhouse gas emissions per kg of UHPFRC are high compared to most other building materials.

Nevertheless, the principles of sustainability can be well respected through the targeted use of UHPFRC. This is because UHPFRC is a high-performance building material with which the required technical performance of structures is achieved with small material quantities. In addition, “eco”-UHPFRC mixtures have already been developed (Hajiesmaeili et al. 2021), allowing for a reduction of the environmental impact of the UHPFRC material alone. Also, UHPFRC can be decomposed and recycled.

When dealing with existing structures, the use of UHPFRC leads to: “*Improve instead of replace!*” UHPFRC technology is able to rehabilitate and strengthen, actually to salvage, existing RC structures. In this way, material resources and grey energy already in use are further utilized, thanks to a relatively small amount of UHPFRC. The existing structure is valorized and upgraded in an economic manner.

4 CONCLUSION

Engineering of existing bridges comprises accurate determination of structural behavior and targeted use of advanced materials for improvement of structural performance with the ultimate goal of limiting construction intervention to a strict minimum while extending the service duration and thus limiting “life cycle costs”.

Two basic novel engineering methods and technologies were described to preserve existing bridges and to improve them to accommodate to the requirements of future utilization:

- NDE (non-destructive evaluation) is ready to be used in engineering practice to determine accurately traffic action effects with the goal to achieve realistic structural and fatigue safety verifications of existing bridges.
- If interventions are necessary, the UHPFRC Technology provides effective solutions to rehabilitate and strengthen existing bridges with little use of materials to upgrade them for future utilization.

These methods and technologies have already been successfully applied in practice, demonstrating their effectiveness. Recently, the Swiss Federal Roads Office has published a documentation to facilitate the use of the UHPFRC Technology for the preservation existing and the construction of new engineering structures of the road infrastructure (FEDRO 2023).

The presented approach follows the principle of sustainability to preserve material resources and their grey energy that are already in use, thereby limiting greenhouse gas emissions to a minimum and thus *making bridges sustainable*.

REFERENCES

- Bayane, I. & Brühwiler, E. 2020. Structural condition assessment of reinforced-concrete bridges based on acoustic emission and strain measurements, *Journal of Civil Structural Health Monitoring* No 10, 1037–1055. <https://doi.org/10.1007/s13349-020-00433-0>.
- Bayane, I., Pai, S.G.S., Smith, I.F.C., Brühwiler, E. 2021. Model-based interpretation of measurements for fatigue evaluation of existing reinforced-concrete bridges, *ASCE Journal of Bridge Engineering*, 26 (8):04021054 [https://doi.org/10.1061/\(ASCE\)BE.1943-5592.0001742](https://doi.org/10.1061/(ASCE)BE.1943-5592.0001742).
- Bertola, N.J., Bayane, I., Brühwiler, E. 2022. Cost-benefits evaluation of a monitoring system for structural identification of existing bridges, *Proceedings, 11th International Conference on Bridge Maintenance, Safety and Management (Barcelona IABMAS2022 July 11- 15,2022)*, edited By Joan Ramon Casas, Dan M. Frangopol, Jose Turmo.
- Bertola, N.J., Henriques, G., Schumacher, T., Brühwiler, E. 2022. Engineering of Existing Structures: The Need and Place for Non-destructive Evaluation, *Proceedings, NDT-CE 2022: The International Symposium on Nondestructive Testing in Civil Engineering (NDT-CE) Zurich*, August 16-18, 2022.
- Bertola, N.J., Schiltz, P., Denarié, E., Brühwiler, E. 2021. A review of the use of UHPFRC in bridge rehabilitation and new construction in Switzerland, *Frontiers in Built Environment, Special Series:*

- Advanced Structural Upgrading of Bridges, Structures and Infrastructures*, Submission, Volume 7, Article 769686. <https://doi.org/10.3389/fbuil.2021.769686>.
- Bertola, N.J., Reuland, Y. & Brühwiler, E. 2023. Sensing the structural behavior: A perspective on the usefulness of monitoring information for bridge examination. *Front. Built Environ.* 8:1045134. <https://doi.org/10.3389/fbuil.2022.1045134>.
- Bertola, N.J. & Brühwiler, E. 2023. Risk-based methodology to assess bridge condition based on visual inspection, *Structure and Infrastructure Engineering*, 19:4, 575–588. <https://doi.org/10.1080/15732479.2021.1959621>.
- Brühwiler, E. 2020. UHPFRC technology to enhance the performance of existing concrete bridges, *Structure and Infrastructure Engineering*, 16:1, 94–105, <https://doi.org/10.1080/15732479.2019.1605395>.
- Brühwiler, E., Vogel, T., Lang, T., Lüchinger, P. 2012. Swiss standards for existing structures, *Structural Engineering International*, IABSE Zurich, 22(2):275–280. <https://doi.org/10.2749/101686612X13291382991209>.
- CEN-TC 250-SC 10, 2022, Draft Standard: Basis of structural and geotechnical assessment of existing structures, version dated 2022- 12-02.
- FEDRO 2023. Documentation: UHPFRC for the preservation and construction of structures of the road infrastructure (author: E.Brühwiler), Swiss Federal Roads Office, Bern, Switzerland (in German and French).
- Goulet, J.A., Smith, I.F.C. 2013. Structural identification with systematic errors and unknown uncertainty dependencies, *Computers & Structures*, Vol. 128, p.251–258. <https://doi.org/10.1016/j.compstruc.2013.07.009>.
- Graybeal, B., Brühwiler, E., Kim, B.-S., Toutlemonde, F., Voo, Y. and Zaghi, A. 2020. International Perspective on UHPC in Bridge Engineering, *ASCE Journal of Bridge Engineering* 25:11, 16 p. [https://doi.org/10.1061/\(ASCE\)BE.1943-5592.0001630](https://doi.org/10.1061/(ASCE)BE.1943-5592.0001630).
- Grigoriou, V., Brühwiler, E., Monitoring-based safety verification at the Ultimate Limit State of fracture of the RC slab of a short span railway underpass, *Journal of Structural Safety*, Vol. 60, 2016, pp. 16–27. <https://doi.org/10.1016/j.strusafe.2016.01.002>.
- Hajiesmaeili, A., Hafiz, M.A. & Denarié, E. 2021. Tensile response of Ultra High Performance PE Fiber Reinforced Concretes (PE-UHPFRC) under imposed shrinkage deformations. *Mater Struct* 54, 114. <https://doi.org/10.1617/s11527-021-01621-0>.
- Ludescher, H. & Brühwiler, E. 2009. Dynamic amplification of traffic loads on road bridges, *Structural Engineering International*, 19:2, 190–197. <https://doi.org/10.2749/101686609788220231>.
- Martín-Sanz, H., Tatsis, K., Dertimanis, V.K., Avendaño-Valencia, L.D., Brühwiler, E., Chatzi, E. 2020. Monitoring of the UHPFRC strengthened Chillon viaduct under environmental and operational variability, *Structure and Infrastructure Engineering*, 16:1, 138–168. <https://doi.org/10.1080/15732479.2019.1650079>.
- Sawicki, B. & Brühwiler, E. 2022. Quantification of influence of monitoring duration on measured traffic action effects on fatigue of RC deck slabs of road bridges, *Structure and Infrastructure Engineering*, 18:10-11, 1442–1456. <https://doi.org/10.1080/15732479.2022.2059527>.
- Sawicki, B. & Brühwiler, E. 2020. Long-term strain measurements of traffic and temperature effects on an RC bridge deck slab strengthened with an R-UHPFRC layer. *Journal of Civil Structural Health Monitoring*, 10, 333–344. <https://doi.org/10.1007/s13349-020-00387-3>.
- Treacy, M.A., Brühwiler, E., Caprani, C.C. 2014. Monitoring of traffic action local effects in highway bridge deck slabs and the influence of measurement duration on extreme value estimates, *Structure and Infrastructure Engineering*, 10:12, 1555–1572. <https://doi.org/10.1080/15732479.2013.835327>.

KEYNOTE LECTURES



Taylor & Francis

Taylor & Francis Group

<http://taylorandfrancis.com>

Probabilistic life-cycle performance assessment of corroded concrete structures: Core technologies to predict the remaining service life

Mitsuyoshi Akiyama

Waseda University, Tokyo, Japan

Dan M. Frangopol

Lehigh University, Bethlehem, Pennsylvania, USA

ABSTRACT: Predicting the performance and remaining service life of deteriorated reinforced concrete (RC) structures based on observational information obtained by means such as visual inspection and monitoring remains a very challenging task in the structural engineering community and the subject of this keynote paper. After experimentally studying the process of steel corrosion and the subsequential impact that corrosion has on the structural performance and integrity of deteriorated RC structures, it was determined that existing numerical simulation techniques need to be improved to reproduce the phenomena observed. With the application of machine learning techniques, the mechanical properties of concrete and rebar and their bonding over the entire RC structure should be determined quantitatively to replicate the observational information. In addition, new inspection technologies, such as those that use drones, must be utilized to obtain required observational information more efficiently. To address this challenging task, it is of vital importance to further integrate various advanced technologies and properly consider the uncertainties involved in the estimation and evaluation of each stage of deterioration and its propagation. In this study, a probabilistic framework for estimating the structural performance of corroded RC structures using observational information is presented using the associated core technologies in the literature, which include: (a) X-ray and digital image processing techniques to understand spatial steel corrosion, the product generated from corrosion and the associated crack width distributions, (b) the finite element method to simulate the structural performance and cracking behavior of corroded RC members, (c) the stochastic simulation technique to reproduce the characteristics of spatial steel corrosion variation, and (d) Bayesian updating and machine learning methods to estimate the degradation state from observational information as an inverse problem. For illustrative purposes, the effect of the observed corrosion-induced crack width distribution on the probability density function of the structural capacity of corroded RC beams is investigated based on the proposed framework.

1 INTRODUCTION

For RC members located in an aggressively corrosive environment, structural degradation due to chloride attack depends on several uncertainties associated with the predictions of mechanical and environmental stressors (Akiyama et al. 2011, 2012, 2014, 2020; Biondini et al. 2006, 2008, 2016). It is important to further develop probabilistic life-cycle design and assessment methods for RC structures in harsh environments (e.g., chloride-laden environments). Over the past decades, many studies have been performed to evaluate the reliability of newly constructed RC structures. Mori & Ellingwood (1993) proposed a framework to estimate reliability-based service life for corroded concrete girders. Frangopol et al. (1997) developed the reliability assessment method of RC girders being damaged due to corrosion and investigated the influences of steel corrosion on both flexure and shear reliabilities. Stewart et al. (1998) presented the time-dependent reliability method

of analyzing RC bridge decks, which is used to investigate the long-term deterioration of RC bridge decks generated from the application of deicing salts as well as from exposure to a marine environment. Enright and Frangopol (1998, 1999) and Yang et al. (2004) predicted the service life of existing deteriorating concrete bridges using time-variant reliability, Bayesian updating and life-time functions. Biondini et al. (2004) presented a novel approach of durability analysis and service life assessment for deteriorating concrete structures, where the mechanical damage was coupled to the diffusion process caused by the use of aggressive environmental agents, modeled by cellular automata, and was evaluated by the application of suitable laws of material degradation.

A key to assessing the performance of existing RC structures under uncertainty is gathering and utilizing observational information obtained through visual inspection and monitoring and the spatial modeling of material properties. Observational information can help reduce epistemic uncertainties associated with the prediction of structural performances. Assuming the uniform corrosion of steel over the entire structure results in overestimating its structural performance and in underestimating the associated corrosion cracking and spalling extents of the covering concrete (Zhu et al. 2014). Several probabilistic models used to reproduce the spatial variation in steel corrosion in RC members have been proposed in the literature (e.g., Stewart 2004; Lim et al. 2016, 2017; Zhang 2019). The spatial variability associated with steel corrosion is caused by several uncontrollable parameters such as the spatial distribution of the aggregate and porous zone of the steel-concrete interface, concrete mixing and casting methods. Structural details such as the concrete cover and rebar diameter also contribute to the variability in the generation of steel corrosion. These factors are the genesis of uncertainty associated with steel corrosion and the corresponding corrosion crack width. Since cracks stemming from the corrosion process are caused by pressure from the expansion of the corrosion products generated by steel corrosion, there should exist a strong positive correlation between the width of corrosion cracks and the amount of corrosion of rebars. Theoretically, if the width of corrosion cracks can be measured, it should be possible to estimate the amount of steel corrosion and to estimate the load-bearing capacity of deteriorated RC members. However, it is still extremely difficult to estimate the load-bearing capacity from observational information on corrosion cracks due to the influence of the aforementioned uncontrollable parameters.

To solve this problem, it is necessary to study the following issues:

- understand the occurrence of steel corrosion and the associated distribution and shape of corrosion products along the cross-sectional and longitudinal directions of RC members;
- model the complex nonlinear relationship between corrosion cracks and rebar corrosion, e.g., by machine learning;
- develop artificially deteriorated RC members using stochastic simulation and numerical analysis based on the experimental evidence and use as a database for subsequent training of machine learning programs, since the acquisition of experimental data using deteriorated RC members is time consuming and costly;
- perform a reliability assessment that considers the various uncertainties involved in the acquisition of observational information compared to the performance of RC members; and
- use new techniques that can efficiently acquire observational information.

This study presents a framework for estimating the structural performance of corroded RC members using observational information with the core technologies. These technologies include: (a) X-ray and digital image processing techniques, (b) FE methods, (c) stochastic simulation techniques, and (d) Bayesian updating and machine learning methods. In an illustrative example, the probabilistic density function (PDF) associated with the flexural capacity of corroded RC beams based on the corrosion-induced crack width distribution is estimated.

2 FLOWCHART FOR PREDICTING THE REMAINING SERVICE LIFE OF DETERIORATED CONCRETE STRUCTURES

Figure 1 depicts the flowchart for predicting the remaining service life of deteriorated concrete structures using core technologies based on information provided via inspection. The

proposed procedure consists of two phases. In Phase I, steel weight loss and crack width distributions obtained from RC beams are experimentally investigated. The measured distributions of steel weight loss for the corroded RC members are applied to generate a dataset of the steel weight loss distributions using a two-dimensional (2D) stochastic simulation method. The crack width distributions are developed by the three-dimensional (3D) FE model using the dataset of the simulated steel weight loss distributions.

In Phase II, the datasets of steel weight loss and crack width distributions that were synthesized in Phase I were then used to train the machine learning model. Based on the trained machine learning model with the observed inspection results (e.g., corrosion crack width) obtained from the RC structures analyzed, the distributions of steel weight loss inside the members are predicted. Finally, the PDF of the structural capacity for aging RC members was estimated by performing a Monte Carlo simulation (MCS)-based 3D FE analysis.

The following Sections 2 to 6 introduce the experimental and analytical approaches related to Phases I and II. Section 7 presents a case study of performance evaluation of aging RC structures by using experimental evidence, stochastic simulation, FE analysis, and machine learning.

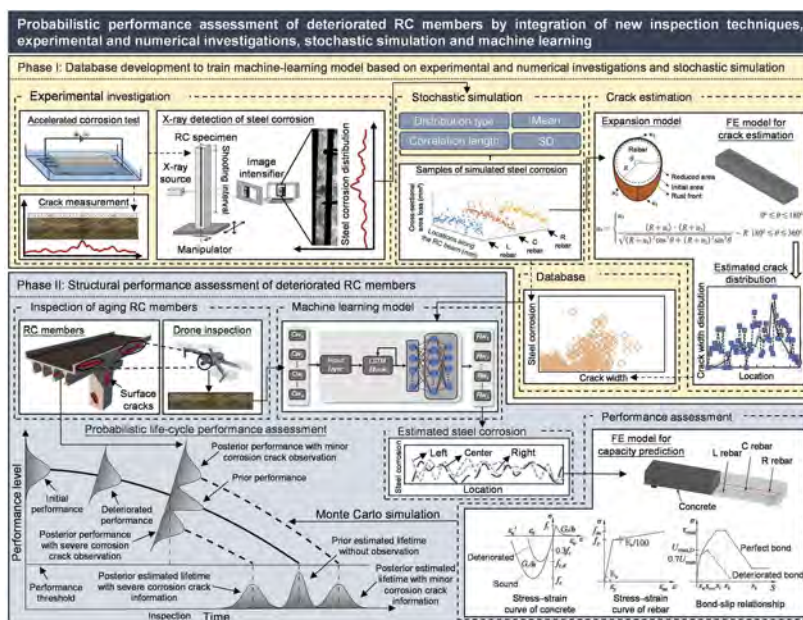


Figure 1. Flowchart for predicting the remaining service life of deteriorated concrete structures.

3 X-RAY AND DIGITAL IMAGE PROCESSING TECHNIQUE

It is essential to develop advanced measurement methods to detect and understand the spatio-temporal variability of nonuniform steel corrosion distributions. In recent years, obtaining information on the spatial steel corrosion of corroded RC members has become the focus of researchers (Lim et al. 2016, 2017; Gu et al. 2018; Zhang et al. 2019). Various methods, including weighing steel loss due to corrosion, measuring with Vernier calipers, drainage methods, and 3D scanning, have been applied to measure steel corrosion. However, since these methods require certain specimens to be demolished and removed to quantify the evolution of the steel corrosion in RC members, there is a high potential for experimental error owing to the difficulty in controlling for repeatable experimental conditions and other uncertainties.

To understand the development of steel corrosion and its spatial variability over time, continuous monitoring of steel corrosion based on a nondestructive evaluation technique is necessary. Akiyama & Frangopol (2012) demonstrated that an X-ray apparatus was a suitable tool for continuously investigating the weight loss of corroded rebar. Lim et al. (2017) further combined

X-ray and image processing techniques to monitor steel corrosion embedded in RC specimens. The nonuniform steel corrosion distribution along corroded rebars can be detected at different stages during the corrosion process. The steel weight loss per 5-mm length of rebar is determined by taking the average of each value of steel weight loss for each viewing angle as follows:

$$R_w = \frac{1}{k} \sum_{n=1}^k \frac{(W_{\theta_n} - W'_{\theta_n})}{W_{\theta_n}} \times 100\% \quad (1)$$

where R_w is the steel weight loss per 5-mm length of rebar, W_{θ_n} and W'_{θ_n} are the weights of the structurally intact sections and corroded sections of the steel rebars, respectively, and k is the number of viewing angles used (i.e., $k = 8$). A more detailed description of the method and analysis are given by Lim et al. (2017).

The general procedure applied in this study to investigate the nonuniformity of steel corrosion, as well as an example of the measured steel weight loss distribution of the rebar in a corroded RC specimen, are shown in Figure 2. Due to the shortage of experimental data, the obtained measurement results of steel weight loss are applied to the stochastic simulation method to generate a database of corrosion products and steel weight loss. This database is then utilized to obtain the crack width, using the 3D FE method, for training the machine learning model.

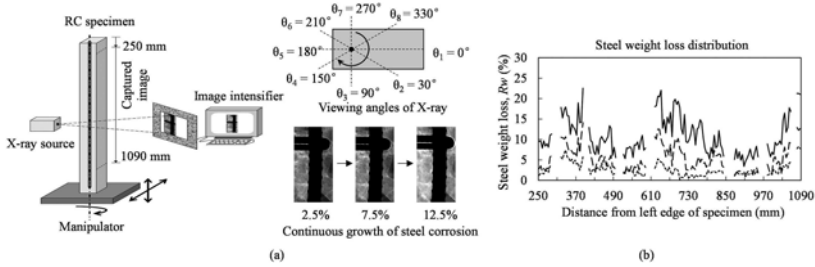


Figure 2. (a) Continuous evaluation of steel corrosion by X-ray and image processing techniques and (b) an example of the measured steel weight loss distribution.

4 TIME-DEPENDENT RELIABILITY ASSESSMENT OF CORRODED RC MEMBERS WITH STOCHASTIC SIMULATION

4.1 Stochastic simulation

Several methods are commonly utilized to generate random fields based on statistical information, such as covariance matrix decomposition (CMD) (Zhang et al. 2020; Ali et al. 2017), the spectral representation method (SRM) (Ma et al. 2020; Srivaranun et al. 2021), Karhunen–Loève expansion (KLE) (Wu et al. 2020) and the local average subdivision (LAS) method (Fenton et al. 1990). Among the stochastic simulation methods, SRM is a versatile method in terms of representing steel corrosion in RC members. The SRM can be utilized to simulate Gaussian and non-Gaussian random fields, univariate (UV) and multivariate (MV) random fields, and multidimensional random fields. The SRM for the simulation of UV and MV Gaussian random fields was introduced by Shinozuka & Jan (1972).

Further developments for the simulation of UV Gaussian random fields were proposed by Shinozuka & Deodatis (1991, 1996). For the simulation of UV non-Gaussian random fields, Yamazaki & Shinozuka (1988) proposed the SRM-based iterative methodology according to a target non-Gaussian spectral density function (SDF) and a target non-Gaussian marginal cumulative density function (CDF). Their method is based on Grigoriu’s translation field theory (Grigoriu et al. 1995). Since the methodology proposed by Yamazaki & Shinozuka (1988) was later confirmed to have less-than-ideal accuracy, Deodatis & Micaletti (2001) proposed some modifications using a “compatibility check” to confirm whether the target non-Gaussian SDF and the prescribed non-Gaussian marginal CDF are compatible. Their proposed method dramatically improved the accuracy of the simulation.

Shields & Deodatis (2011) developed the SRM-based iterative technique for generating UV non-Gaussian random fields. The proposed algorithm is conceptually much simpler and more computationally efficient. The applications of the UV non-Gaussian SRM have contributed to, for example, simulation of the corrosion process of steel beams (Christou et al. 2014) and simulation of the damage levels of bridges (Bocchini et al. 2011).

4.2 Life-cycle reliability assessment with stochastic simulation

Probabilistic concepts have been employed due to numerous sources of uncertainty in the degradation model, and the extent of damage is quantified by considering the spatial variability of the various parameters. Life-cycle reliability analysis of deteriorated RC structures should be performed in combination with stochastic simulation. A stochastic spatial-time-dependent analysis of chloride-induced corrosion in large RC structures was performed by Papakonstantinou & Shinozuka (2013). Spatial variation in the respective variables was represented by uni-variate, two-dimensional stochastic fields, simulated by the SRM. Shafei & Alipour (2015) developed an FE framework-based life-cycle prediction model of corrosion-affected RC members. Gaussian and non-Gaussian random fields were created using the SRM to consider the stochastic process of steel corrosion, which was used to reflect the spatial and temporal variability in material properties, structural properties, and exposure conditions.

Based on the experimental data (i.e., steel weight loss distributions identified by X-ray and digital image processing, as shown in Figure 2), Srivaranun et al. (2021) presented an application of the 2D stochastic simulation method using the SRM for estimating the reliability of aging RC structures that considered the effect of the interaction of corrosion pits among multiple tensile rebars. The interaction of corrosion pits among tensile rebar is represented by a transverse correlation parameter of steel weight loss distributions. To apply the SRM and simulate the MV random field, the Gaussian cross-spectral density matrix (CSDM) needs to be determined and should consider the cross-correlation of the corrosion in each component of the tensile rebar. The Gaussian CSDM of spatial steel weight loss distributions, $\mathbf{S}(\kappa)$, is expressed as follows (Deodatis et al. 1996):

$$\mathbf{S}(k) = \begin{bmatrix} S_{11}(k) & S_{12}(k) & \cdots & S_{1m}(k) \\ S_{21}(k) & S_{22}(k) & \cdots & S_{2m}(k) \\ \vdots & \vdots & \ddots & \vdots \\ S_{m1}(k) & S_{m2}(k) & \cdots & S_{mm}(k) \end{bmatrix} \quad (2)$$

where m is the number of spatial steel weight loss distributions, which is the same as the number of tensile rebars in the RC structure; κ is the wavenumber; and $S_{ij}(\kappa)$ represents the cross-SDF values, which is defined as:

$$S_{ij} = \gamma_{ij}(k) \sqrt{S_{ii}(k)S_{jj}(k)}, \quad i, j = 1, 2, \dots, m \quad (3)$$

where

$$\Delta k = \frac{\kappa_u}{N} \quad (4)$$

$$k = n\Delta k, \quad n = 0, 1, 2, \dots, N - 1$$

$S_{ii}(\kappa)$ and $S_{jj}(\kappa)$ are the auto-SDF of steel weight loss in rebars i and j , respectively; $\gamma_{ij}(\kappa)$ is the coherence function of steel weight loss between rebars i and j ; κ_u is the upper cutoff wavenumber beyond which the spectral density can be assumed to be zero; and N is a parameter defining the number of discretization points in the wavenumber domain. N is related to the number of discrete locations in a simulated steel weight loss distribution of a single rebar (M) because of the following anti-aliasing requirement: $M \geq 2N$.

Based on the measured steel weight loss distributions of the rebars in the RC specimen, the auto-SDF, $S_{ii}(\kappa)$, and coherence function, $\gamma_{ij}(\kappa)$, are determined empirically (Bendat & Piersol 2011). By considering the transverse correlation of the measured steel weight loss between

rebars i and j , a negative exponential functional form of the coherence function, $\gamma_{ij}(\kappa)$, is obtained by using the following equation:

$$\gamma_{ij}(k) = \exp\left(-\frac{k\sqrt{d_{ij}}}{2\pi C_3}\right) \quad (5)$$

where d_{ij} is the distance between rebars i and j ; and C_3 is the parameter associated with the degree of transverse correlation of steel weight loss distributions.

Based on the Gaussian CSDM, $S(\kappa)$, and the parameters of the standard deviation of steel weight loss and mean steel weight loss, the MV random field of steel weight loss for m corroded rebars can be simulated. The detailed procedure for simulating the MV random field using the SRM was provided in Bocchini (2008). Figure 3 presents the effect of the transverse correlation parameter C_3 on the simulated spatial steel weight loss distributions in the RC slab specimen with three tensile rebars assuming mean steel weight loss (MRW) = 10%. $C_3 = 0.05$ was determined experimentally. For comparative purposes, a value of $C_3 = 0.005$ was also used. As shown in Figure 3, the transverse correlation among the steel weight loss distributions of the three tensile rebars depends on the transverse correlation parameter C_3 . By applying the SRM to simulate the spatial steel weight loss distributions in MV random fields, the effects of the interaction of corrosion pits among tensile rebars can be considered.

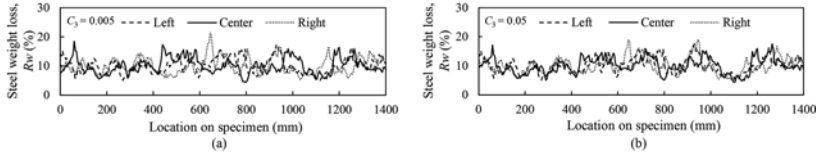


Figure 3. Effect of the transverse correlation parameters (a) $C_3 = 0.005$ and (b) $C_3 = 0.05$ on the spatial steel weight loss distributions in the RC slab specimen assuming $MRW = 10\%$.

Numerical models that can account for the varying spatial amount of rebar corrosion in RC structures and for the associated material property of concrete and bond strength are necessary to evaluate structural performance. Simple cross-sectional analysis cannot provide good agreement with the test results from loading of RC beams (Zhang et al. 2020). The 3D FE method used to assess deteriorated RC structures is discussed in the following section.

5 FE CONSIDERING THE EFFECT OF STEEL CORROSION

The FE method is now widely used for investigating the structural performance of corroded RC structures. Cornelli et al. (2004) investigated the structural behavior of corroded RC beams by using FE analysis to deepen the understanding of the damage caused by corrosion and to appropriately evaluate the actual safety level of RC structures. The analyses performed in their study indicated that corrosion affects both the strength and the ductility of a structure. They pointed out that the bond conditions should be carefully assessed and modeled to predict the structural ductility, which is intimately associated with the mode of failure and, consequently, with the ultimate bearing capacity. El Maaddawy et al. (2005) proposed a new stress-slip model to predict the bond strengths of corroded beams at different levels of damage based on published data. Biondini et al. (2015) presented a three-dimensional RC beam finite element model for nonlinear analysis of concrete structures that are exposed to corrosion. Their formulation allows to model the damaging effects of uniform and pitting corrosion in terms of a reduction in the cross-sectional area of corroded rebars, a reduction in the ductility of reinforcing steel, deterioration of concrete strength and the presence of spalling in the concrete cover. The proposed model was validated with experimental results of RC specimens corroded with both accelerated and natural corrosion.

Both strength and ductility were affected mainly due to variability in the cross-sectional area loss of rebar along its length (François et al. 2013). It is essential to consider the effect of spatial steel corrosion when simulating the performance of corroded RC members. Lim et al. (2016)

developed a two-dimensional FE model that considered the variability in steel corrosion to simulate the responses of the corroded RC beams. Due to the difficulty in implementing the actual variability in steel corrosion in the numerical model, an alternative approach was applied by modeling the corroded rebar over a determined length based on the average cross-sectional area loss, together with empirical coefficients, to account for the reduction in strength and ductility of the corroded rebar attributed to the irregular cross-sectional area loss from corrosion along the length of the rebar. Lim et al. (2016) reported that with the residual bond stress–slip curve proposed by Kallias & Rafiq (2010), the results obtained from the FE model were in good agreement with those from a loading test performed on corroded RC beams.

Zhang et al. (2020) conducted FE analysis to investigate the effects of localized corrosion and the correlation of the steel corrosion distribution between adjacent rebars on the structural behavior of corroded RC beams. By comparing the computational results to experimental results, they concluded that the 3D FE model could better predict the behavior of the corroded RC beams than the 2D FE model, especially when the beam had a small correlation coefficient of cross-sectional area loss of rebar in the transverse direction.

6 INVERSE ANALYSIS: BAYESIAN UPDATING VS. MACHINE LEARNING

The corrosion-induced crack width can be the clearest visual indicator (Akiyama et al. 2010) to quantify the damage state of corroded RC structures. Many researchers have attempted to link the corrosion crack width and the amount of rebar corrosion. However, as mentioned previously, their relationship is unclear, making it difficult to accurately evaluate performance using the crack widths. There are two methods to evaluate the structural performance of existing RC members given corrosion crack information: Bayesian updating and machine learning methods.

6.1 *Bayesian updating*

It is well known that maintenance and repair decisions should be made based on inspection data and the results of performance prediction models (Frangopol et al. 2008). The models used to assess the deterioration status of RC members must be updated over time to revise the maintenance strategy based on how the structure is actually behaving in its lifespan. Within recent decades, several procedures have been presented for updating performance prediction models based on inspection results by applying the Bayesian updating method.

Akiyama et al. (2010) established a procedure to update time-dependent reliability using visual inspection (i.e., crack width and chloride concentration) for an existing RC slab in a marine environment by a particle filter (PF)-based method assuming the uniform distribution of reinforcement corrosion. To overcome this oversimplified assumption associated with steel corrosion, Srivaranun et al. (2022) proposed a framework for updating time-dependent reliability by incorporating the effect of the spatial corrosion distribution. The random variables associated with the corrosion prediction model, which are spatially correlated, are simulated in the random field context for the life-cycle reliability estimation. The random fields of the associated random variables are updated using the PF-based method. Jia et al. (2023) presented an inference framework for a stochastic volatility model conditioned on the time-dependent deflection of pre-stressed concrete (PC) bridges. In this framework, the augmented state space includes the full ranges of the unobserved state variables affecting the time-dependent deflection of PC bridges, which is modeled via the Wiener process. To utilize the latent structure of the stochastic volatility model, a cyclic Markov chain Monte Carlo (MCMC) sampler was proposed to draw samples from the joint posterior distribution of the unobserved state variables and volatility parameters.

6.2 *Machine learning*

Machine learning-based approaches have gained attention owing to their ability to simulate the complex physical process required for structural assessment. For instance, the feed-forward multi-layer perceptron (MLP) model, a classic artificial neural network (ANN), has been widely used in the field of civil engineering since it can identify complicated nonlinear relationships between inputs and outputs (Khandel et al. 2021; Most et al. 2007; Haddad et al. 2021; Xin et al. 2021).

The long short-term memory (LSTM) model, as an extension of the recurrent neural network (RNN), has the advantage of predicting data sequences by learning over long time sequences and retaining memory (Yu et al. 2020). Compared with empirical and mechanical models, it is expected that machine learning-based methods could provide a better solution for conducting inverse analysis that utilizes inspection information for the assessment of structural performance.

Recently, several researchers have developed machine learning and probabilistic-based approaches for estimating the steel weight loss distribution using the inspection information of the corrosion-induced crack width distribution. Zhang et al. (2021) adopted an LSTM network, as shown in Figure 4(a), to predict distribution possibilities of steel corrosion in RC beams with a single rebar due to the output sequence information from the LSTM model, which was then used to train a predictive model from the datasets of 1D spatial distributions of steel corrosion and the corresponding corrosion crack width. However, it was numerically and experimentally confirmed that rust expansion in corroded RC beams with multiple rebars can reduce the widths of corrosion cracks on the propagating concrete surface for adjacent rebars (Cheng et al. 2018). To consider the potential effect of multiple tensile rebars on the relationship between steel corrosion and corrosion crack width, a machine learning model (e.g., pix2pix, as shown in Figure 4(b)) capable of handling steel corrosion and corrosion cracks distributed in 2D space (Srivaranun et al. 2023) is needed. This model will be presented in the case study in the following section.

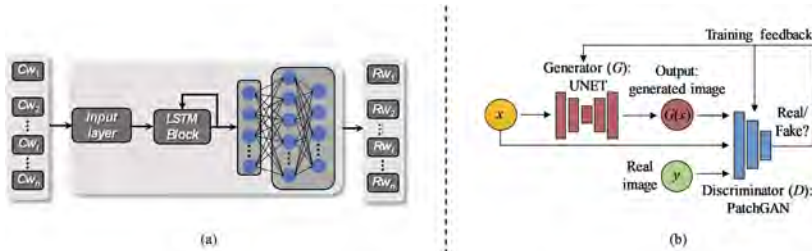


Figure 4. Flow diagram describing the training process of the (a) LSTM and (b) pix2pix models.

7 ILLUSTRATIVE EXAMPLE

An illustrative example of the probability-based structural performance assessment of corroded RC beams using machine learning is presented herein. Experimental data of steel weight loss and crack width distributions obtained from RC specimens were collected continuously during corrosion tests by both X-ray and image processing techniques, as introduced in Section 3.

A 3D FE model for estimating the corrosion-induced crack, as shown in Figure 5(a), was developed and then verified by the experimental results of crack width distributions for corroded RC beams. The elliptical corrosion expansion model proposed by Yuan & Ji (2009), shown in Figure 5(b), was utilized in this study to calculate the corrosion product thickness (u_θ), which was imposed on the holes to simulate the expansion stress on the concrete due to the formation of corrosion products. By inputting the steel weight loss distribution into the 3D FE model, numerical results of the distribution of the corrosion crack width were obtained and then verified by comparing those results to the experimental results.

A dataset with a certain number of samples is necessary for training the machine learning model. Due to the limited amount of experimental data of corroded RC beams available, the datasets of steel weight loss and crack width distributions were synthesized. Because steel corrosion over the length of RC beams was spatially distributed and subjected to several uncertain parameters and environmental factors, steel weight loss distributions were simulated by random field theory using statistical parameters. The measurement results of steel weight loss distributions for corroded RC beams were applied to obtain statistical parameters and then to generate the dataset of steel weight loss distributions in the 2D random field. Based on the generated steel weight loss distribution, the dataset of the corresponding crack width distributions was developed using the verified 3D FE model.

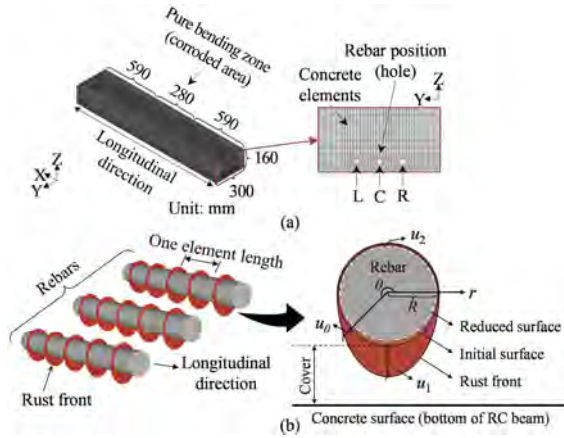


Figure 5. (a) 3D FE model for estimating the distributions of the corrosion crack width for the RC beam and (b) illustration of the mechanism of corrosion-induced stress expansion on concrete in the longitudinal direction and around the rebar cross section.

As a machine learning model, the pix2pix network is used to train the predictive model for the corrosion of RC beams. The flow diagram describing the training process of the pix2pix network is shown in Figure 4(b). The PDF of the flexural capacity for RC beams was estimated based on the predicted corrosion distributions by using MCS-based 3D FE analysis. Model errors associated with machine learning and FE modeling were taken into account. Figure 6 presents the estimation results of histograms and fitting lognormal PDF of the flexural capacity and the corresponding loading test result. It can be confirmed that the framework of the probability-based structural performance assessment using machine learning presented in this study can provide relevant and quantitative information on the possible deterioration level of aging RC structures based on the observational corrosion-induced crack width distribution.

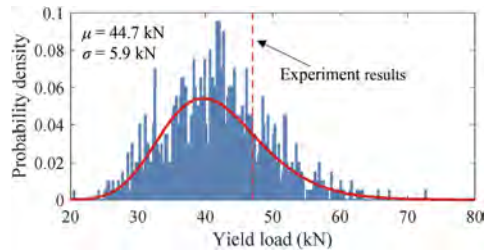


Figure 6. PDF of the flexural capacity of multiple rebar beams using observational corrosion-induced crack width distribution and corresponding loading test results (dashed line).

8 CONCLUSIONS

The following conclusions are drawn:

1. A framework for predicting the life-cycle performance of deteriorating RC members using inspection information by integrating new inspection techniques, experimental and numerical investigations, stochastic simulation and machine learning is presented. The associated state-of-the-art existing core technologies in the literature were comprehensively introduced.
2. As an illustrative example, the PDF of the flexural capacity of deteriorated RC beams was obtained, given the corrosion crack widths, and distributed in two-dimensional space. The machine learning model pix2pix was trained using the artificial database of deteriorated RC beams constructed by stochastic simulation. 3D FE model analysis was performed repeatedly in the MCS to obtain the PDF of the flexural capacity, and model uncertainties were taken into account.

This study presents a load-bearing capacity estimation using corrosion crack widths. Recently, load tests on bridges have also been conducted (Lantsoght et al. 2022), and structural performance can be evaluated using the results of these tests. In addition, optimization can be incorporated into the framework presented in this study to provide an optimal maintenance strategy for deteriorated RC structures, which should be addressed in the future (Frangopol 1995, Frangopol et al. 1997; Yang & Frangopol 2018).

ACKNOWLEDGMENTS

This work was supported by JSPS KAKENHI grant number 19H00813, Japan Construction Information Center (JACIC) grant number 2021-1.

REFERENCES

- Akiyama, M., & Frangopol, D. M. (2012). Estimation of steel weight loss due to corrosion in RC members based on digital image processing of X-ray photogram. In *Life-Cycle and Sustainability of Civil Infrastructure Systems: Proceedings of the Third International Symposium on Life-Cycle Civil Engineering (IALCCE'12)* (p. 389). Vienna: CRC Press.
- Akiyama, M., & Frangopol, D. M. (2014). Long-term seismic performance of RC structures in an aggressive environment: Emphasis on bridge piers. *Structure and Infrastructure Engineering*, 10(7), 865–879.
- Akiyama, M., Frangopol, D. M., & Ishibashi, H. (2020). Toward life-cycle reliability-, risk- and resilience-based design and assessment of bridges and bridge networks under independent and interacting hazards: emphasis on earthquake, tsunami and corrosion. *Structure and Infrastructure Engineering*, 16(1), 26–50.
- Akiyama, M., Frangopol, D. M., & Matsuzaki, H. (2011). Life-cycle reliability of RC bridge piers under seismic and airborne chloride hazards. *Earthquake Engineering & Structural Dynamics*, 40(15), 1671–1687.
- Akiyama, M., Frangopol, D. M., & Suzuki, M. (2012). Integration of the effects of airborne chlorides into reliability-based durability design of reinforced concrete structures in a marine environment. *Structure and Infrastructure Engineering*, 8(2), 125–134.
- Akiyama, M., Frangopol, D. M., & Yoshida, I. (2010). Time-dependent reliability analysis of existing RC structures in a marine environment using hazard associated with airborne chlorides. *Engineering Structures*, 32(11), 3768–3779.
- Ali, A., Lyamin, A. V., Huang, J., Sloan, S. W., & Cassidy, M. J. (2017). Undrained stability of a single circular tunnel in spatially variable soil subjected to surcharge loading. *Computers and Geotechnics*, 84, 16–27.
- Bendat, J. S., & Piersol, A. G. (2011). *Random data: analysis and measurement procedures*. John Wiley & Sons.
- Biondini, F., & Frangopol, D. M. (2008). Probabilistic limit analysis and lifetime prediction of concrete structures. *Structure and Infrastructure Engineering*, 4(5), 399–412.
- Biondini, F., & Frangopol, D. M. (2016). Life-cycle performance of deteriorating structural systems under uncertainty. *Journal of Structural Engineering*, 142(9), F4016001.
- Biondini, F., & Vergani, M. (2015). Deteriorating beam finite element for nonlinear analysis of concrete structures under corrosion. *Structure and Infrastructure Engineering*, 11(4), 519–532.
- Biondini, F., Bontempi, F., Frangopol, D. M., & Malerba, P. G. (2004). Cellular automata approach to durability analysis of concrete structures in aggressive environments. *Journal of Structural Engineering*, 130(11), 1724–1737.
- Biondini, F., Bontempi, F., Frangopol, D. M., & Malerba, P. G. (2006). Probabilistic service life assessment and maintenance planning of concrete structures. *Journal of Structural Engineering*, 132(5), 810–825.
- Bocchini, P. (2008). Probabilistic approaches in civil engineering: generation of random fields and structural identification with genetic algorithms. PhD thesis, University of Bologna.
- Bocchini, P., & Frangopol, D. M. (2011). A stochastic computational framework for the joint transportation network fragility analysis and traffic flow distribution under extreme events. *Probabilistic Engineering Mechanics*, 26(2), 182–193.
- Cheng, X., Su, Q., Ma, F., Liu, X., & Liang, X. (2018). Investigation on crack propagation of concrete cover induced by non-uniform corrosion of multiple rebars. *Engineering Fracture Mechanics*, 201, 366–384.

- Christou, V., & Bocchini, P. (2014). An efficient methodology that simulates a multi-dimensional non-Gaussian field to evaluate the effect of the spatial distribution of corrosion in a steel beam. In *Structures Congress 2014* (pp. 1059–1069).
- Coronelli, D., & Gambarova, P. (2004). Structural assessment of corroded reinforced concrete beams: modeling guidelines. *Journal of structural engineering*, 130(8), 1214–1224.
- Deodatis, G. (1996). Simulation of ergodic multivariate stochastic processes. *Journal of Engineering Mechanics*, 122(8), 778–787.
- Deodatis, G., & Micaletti, R. C. (2001). Simulation of highly skewed non-Gaussian stochastic processes. *Journal of Engineering Mechanics*, 127(12), 1284–1295.
- El Maaddawy, T., Soudki, K., & Topper, T. (2005). Analytical model to predict nonlinear flexural behavior of corroded reinforced concrete beams. *ACI Structural Journal*, 102(4), 550.
- Enright, M.P., & Frangopol, D.M. (1998). Service-life prediction of deteriorating concrete bridges. *Journal of Structural Engineering*, 124 (3), 309–317.
- Enright, M.P., and Frangopol, D.M. (1999). Condition prediction of deteriorating concrete bridges using Bayesian updating. *Journal of Structural Engineering*, 125(10), 1118–1124.
- Fenton, G. A., & Vanmarcke, E. H. (1990). Simulation of random fields via local average subdivision. *Journal of Engineering Mechanics*, 116(8), 1733–1749.
- François, R., Khan, I., & Dang, V. H. (2013). Impact of corrosion on mechanical properties of steel embedded in 27-year-old corroded reinforced concrete beams. *Materials and Structures*, 46(6), 899–910.
- Frangopol, D.M. (1995). Reliability – based optimum structural design. Chapter 16 in *Probabilistic Structural Mechanics Handbook*, C. Sundararajan, ed., Chapman & Hall, New York, 352–387.
- Frangopol, D. M., Lin, K. Y., & Estes, A. C. (1997). Reliability of reinforced concrete girders under corrosion attack. *Journal of Structural Engineering*, 123(3), 286.
- Frangopol, D. M., Strauss, A., & Kim, S. (2008). Bridge reliability assessment based on monitoring. *Journal of Bridge Engineering*, 13(3), 258–270.
- Frangopol, D. M., Dong, Y., & Sabatino S. (2017). Bridge life-cycle performance and cost: analysis, prediction, optimization and decision-making. *Structure and Infrastructure Engineering*, 13(10), 1239–1257.
- Grigoriu, M. (1995). Applied non-gaussian processes: Examples, theory, simulation, linear random vibration, and MATLAB solutions (Book). *Englewood Cliffs, NJ: Prentice Hall, Inc, 1995*.
- Gu, X., Guo, H., Zhou, B., Zhang, W., & Jiang, C. (2018). Corrosion non-uniformity of steel bars and reliability of corroded RC beams. *Engineering Structures*, 167, 188–202.
- Haddad, R., & Haddad, M. (2021). Predicting fiber-reinforced polymer-concrete bond strength using artificial neural networks: A comparative analysis study. *Structural Concrete*, 22(1), 38–49.
- Jia, S., Akiyama, M., Han, B., Xie, H., & Frangopol, D. M. (2023). Structural identification via the inference of the stochastic volatility model conditioned on the time-dependent bridge deflection. *Structural Safety*, 100, 102279.
- Kallias, A. N., & Rafiq, M. I. (2010). Finite element investigation of the structural response of corroded RC beams. *Engineering Structures*, 32(9), 2984–2994.
- Khandel, O., Soliman, M., Floyd, R. W., & Murray, C. D. (2021). Performance assessment of prestressed concrete bridge girders using fiber optic sensors and artificial neural networks. *Structure and Infrastructure Engineering*, 17(5), 605–619.
- Lantsoght, E.O.L., Yang, Y., & Veen, C.V.D. (2022). Multi-level decision-making strategy for preparation of proof load and failure tests. *Engineering Structures*, 252, 113672.
- Lim, S., Akiyama, M., & Frangopol, D. M. (2016). Assessment of the structural performance of corrosion-affected RC members based on experimental study and probabilistic modeling. *Engineering Structures*, 127, 189–205.
- Lim, S., Akiyama, M., Frangopol, D. M., & Jiang, H. (2017). Experimental investigation of the spatial variability of the steel weight loss and corrosion cracking of reinforced concrete members: novel X-ray and digital image processing techniques. *Structure and Infrastructure Engineering*, 13(1), 118–134.
- Ma, L., Bocchini, P., & Christou, V. (2020). Fragility models of electrical conductors in power transmission networks subjected to hurricanes. *Structural Safety*, 82, 101890.
- Mori, Y., & Ellingwood, B. R. (1993). Reliability-based service-life assessment of aging concrete structures. *Journal of Structural Engineering*, 119(5), 1600–1621.
- Most, T., & Bucher, C. (2007). Probabilistic analysis of concrete cracking using neural networks and random fields. *Probabilistic Engineering Mechanics*, 22(2), 219–229.
- Papakonstantinou, K. G., & Shinozuka, M. (2013). Probabilistic model for steel corrosion in reinforced concrete structures of large dimensions considering crack effects. *Engineering Structures*, 57, 306–326.

- Shafei, B., & Alipour, A. (2015). Application of large-scale non-Gaussian stochastic fields for the study of corrosion-induced structural deterioration. *Engineering Structures*, 88, 262–276.
- Shields, M. D., Deodatis, G., & Bocchini, P. (2011). A simple and efficient methodology to approximate a general non-Gaussian stationary stochastic process by a translation process. *Probabilistic Engineering Mechanics*, 26(4), 511–519.
- Shinozuka, M., & Deodatis, G. (1991). Simulation of stochastic processes by spectral representation. *Applied Mechanics Reviews*, 44(4), 191–204.
- Shinozuka, M., & Deodatis, G. (1996). Simulation of multi-dimensional Gaussian stochastic fields by spectral representation. *Applied Mechanics Reviews*, 49(1), 29–53.
- Shinozuka, M., & Deodatis, G. (1996). Simulation of multi-dimensional Gaussian stochastic fields by spectral representation.
- Shinozuka, M., & Jan, C. M. (1972). Digital simulation of random processes and its applications. *Journal of Sound and Vibration*, 25(1), 111–128.
- Srivaranun, S., Akiyama, M., Bocchini, P., Christou, V., Frangopol, D. M., Fukushima, H., & Masuda, K. (2021). Effect of the interaction of corrosion pits among multiple tensile rebars on the reliability of RC structures: Experimental and numerical investigation. *Structural Safety*, 93, 102115.
- Srivaranun, S., Akiyama, M., Masuda, K., Frangopol, D. M., & Maruyama, O. (2022). Random field-based reliability updating framework for existing RC structures incorporating the effect of spatial steel corrosion distribution. *Structure and Infrastructure Engineering*, 18(7), 967–982.
- Srivaranun, S., Akiyama, M., Yamada, T., Frangopol, D. M., & Xin, J. (2023). A novel combined experimental-machine learning approach to estimate the probabilistic capacity of RC beams with spatially correlated rebar corrosion in transverse and longitudinal directions. *Engineering Structures*, 279, 115588.
- Stewart, M. G. (2004). Spatial variability of pitting corrosion and its influence on structural fragility and reliability of RC beams in flexure. *Structural Safety*, 26(4), 453–470.
- Stewart, M. G., & Rosowsky, D. V. (1998). Time-dependent reliability of deteriorating reinforced concrete bridge decks. *Structural Safety*, 20(1), 91–109.
- Wu, Y. C., & Zhi, P. (2020). Reliability assessment of RAC chloride concentration using Karhunen–Loève expansion with digital-image kernels. *Construction and Building Materials*, 245, 118352.
- Xin, J., Akiyama, M., Frangopol, D. M., Zhang, M., Pei, J., & Zhang, J. (2021). Reliability-based life-cycle cost design of asphalt pavement using artificial neural networks. *Structure and Infrastructure Engineering*, 17(6), 872–886.
- Yamazaki, F., & Shinozuka, M. (1988). Digital generation of non-Gaussian stochastic fields. *Journal of Engineering Mechanics*, 114(7), 1183–1197.
- Yang, D. Y., & Frangopol, D. M. (2018). Probabilistic optimization framework for inspection/repair planning of fatigue-critical details using dynamic Bayesian networks. *Computers & Structures*, 198, 40–50.
- Yang, S-I., Frangopol, D.M., & Neves, L.C. (2004). Service life prediction of structural systems using lifetime functions with emphasis on bridges. *Reliability Engineering & System Safety*, 86 (1), 39–51.
- Yu, C., Qi, X., Ma, H., He, X., Wang, C., & Zhao, Y. (2020). LLR: Learning learning rates by LSTM for training neural networks. *Neurocomputing*, 394, 41–50.
- Yuan, Y., & Ji, Y. (2009). Modeling corroded section configuration of steel bar in concrete structure. *Construction and Building Materials*, 23(6), 2461–2466.
- Zhang, M., Akiyama, M., Shintani, M., Xin, J., & Frangopol, D. M. (2021). Probabilistic estimation of flexural loading capacity of existing RC structures based on observational corrosion-induced crack width distribution using machine learning. *Structural Safety*, 91, 102098.
- Zhang, M., Nishiya, N., Akiyama, M., Lim, S., & Masuda, K. (2020). Effect of the correlation of steel corrosion in the transverse direction between tensile rebars on the structural performance of RC beams. *Construction and Building Materials*, 264, 120678.
- Zhang, M., Song, H., Lim, S., Akiyama, M., & Frangopol, D. M. (2019). Reliability estimation of corroded RC structures based on spatial variability using experimental evidence, probabilistic analysis and finite element method. *Engineering Structures*, 192, 30–52.
- Zhu, W., & François, R. (2014). Corrosion of the reinforcement and its influence on the residual structural performance of a 26-year-old corroded RC beam. *Construction and Building Materials*, 51, 461–472.

The structural life of a Cathedral and the worksites of the Duomo di Milano

F. Canali

Veneranda Fabbrica del Duomo di Milano, Milan, Italy

D. Coronelli

Politecnico di Milano, Milan, Italy

ABSTRACT: The life of Milan Cathedral is described with the evolution of the structural system and the restorations carried out throughout the centuries. The organization of the Veneranda Fabbrica del Duomo di Milano is outlined, with the latest restoration interventions. The case study of the construction and restorations of the Tiburio with its supporting pillars is analyzed, from the initial design to the dramatic damage in the 20th century. The rebirth of the Cathedral was the fruit of restorations preserving the structural identity of the monument up to the present. The conclusions address the study of damage and maintenance and repair operations of monumental heritage buildings within a life cycle perspective, in relation to the underlying societal values.

1 INTRODUCTION

The Cathedral of Milan represents an example of a century long structural life, characterised by a long construction and ongoing restoration history. A central event along the period of time between the start of the Fabbrica in 1386 and the present is the risk of collapse of the Tiburio and the “rebirth” - as defined by the former Architect of the Fabbrica, Carlo Ferrari da Passano (1988) - that occurred in the 20th century.

Novel approaches in life-cycle assessment, maintenance planning, and optimal design of structural systems (Biondini and Frangopol, 2016) foresee their extension to built heritage. Historic structures must be restored according to general conservation criteria (Roca, 2011). Also the safety of people and the integrity of the possible artistic contents pose certain requirements on structural reliability. While facing these two main challenges, the design and the management of such a specific activity has to often deal with uncertainties of the most intimate static and mechanical behavior of the monument. The result is a complex engineering problem aiming to optimal solutions which, while granting the reliability requirements, cause the minimum possible alteration to the original features of the structure. And, as a matter of fact, the experience acquired day after day on the scaffoldings and while designing, should be preserved as a most valuable knowledge increase by the means of specific organisations established in order to take care of the monument through the centuries.

The case-study of the structural life of the Tiburio of the Cathedral is here presented to link this history to central topics of life cycle assessment: the damage of existing structures, its evolution in time, restoration interventions and the safety requirements of historic buildings for their present function. Moreover this case demonstrates that the conservation or the restoration of a heritage property can be oriented to preserve its authenticity (Roca 2011).

The Veneranda fabbrica del Duomo is described as the active institution carrying out the operations needed for the preservation of the life of the Cathedral. Whereas modern design

and scientific concepts aim to a reference design service life of 50 or 100 years, heritage constructions often span a 5 to 10 times longer lifetime. Thus the survey and modelling of deterioration and time-variant structural performance meet a different temporal dimension, encompassing a past and often complex structural evolution. In addition these differences highlight the importance of maintenance within a life-cycle perspective, and the social and moral values of a society determining rules for this process.

2 THE FABBRICA DEL DUOMO AND THE TIBURIO RESTORATION CASE STUDY

2.1 *The Veneranda Fabbrica del Duomo*

The singular history of this institution is such that a brief summary is necessary. The Fabbrica of the Duomo of Milan (Venerable as dating back to the late XIV century) is the institution responsible for the conservation and development, as well as the maintenance of the cathedral. This is an ecclesiastical body endowed with legal authority by ancient statutory determination, for the purpose of worship and religion. It excludes all profit making activities.

There is a Board of Directors composed of 7 members who remain in office for 3 years, one of whom is elected President. Two are appointed by the diocesan ordinary and 5 by the ministry of the Interior, with the consent of the Archbishop.

Needless to say works of such entity, today as in the past demand large resources. In the course of its history the Fabbrica has been sustained by the donations of citizens, and by the introits of an important real estate patrimony formed by the numerous bequests made by those wishing to be remembered as associated with this great undertaking. The yields from these properties providing the necessary funds for the realization of such works arising from time to time.

However in the early years of the xviii century this efficient system of self-support fell victim, so to say, of History. On his arrival in Milan Napoleon, finding the Cathedral far from completion ordered the Fabbrica to sell of the entire property patrimony in order to speedily obtain the necessary resources in order to complete the facade.

There followed a very difficult period, with the Fabbrica obliged to recur to the Administrative Authority of the time for financial support, receiving which, to greater or lesser extent according to the interlocutors they were faced with, and within the historical context. Today faced once more with dramatic urgency to find new forms of financial support, for the first time in over 600 years the “Infinite Fabbrica” would run the risk of closure. From the tickets sold for guided tours and entry to the Terrazze in particular, together with specific fundraising campaigns (Adopt a spire, Adopt a statue) an adequate answer to the difficulties has been found.

As in every operative organisation the personnel employed on the front line (the 3 work sites, and the assistance to visitors and tourists) depend on the support of others to organise the work (from management to planning, to personnel and to logistics). The Fabbrica counts circa 200 employees subdivided in the following areas (Table 1).

The particular maintenance work on the cathedral can only be carried out by direct control of skilled workers of the Veneranda Fabbrica. There are approximately 100 people divided between 3 worksites, that of the Candoglia quarry, the marble carvers and the cathedral worksite, employees of the Institute founded by the Duke of Milan, Gian Galeazzo Visconti, in 1387; and from that time engaged, up to 1965, in the construction and particular maintenance (from 1842 to this day) of the cathedral.

The components of the Fabbrica work in the closest coordination, a delay in the chain of purchases has immediate effect on the possibility to proceed with work on the scaffolds; while unsatisfactory programming on the sites may compromise the visits of the faithful or visitors.

An error in daily consultation of the archives may compromise the research of scholars, or the necessary verifications regarding the worksites. Each of the areas listed above has its own work plan and procedures codified from time back, so that it is sought to combine the original procedures while keeping up to date, as regards the management profile. this is also true for all the extraordinary organisms of the Fabbricerias, Italian and European. Between which there is an ever growing network of contacts and the sharing of knowledge (see section 4).

Table 1. Fabbrica del Duomo - Areas of activity.

Administration	Technical activities	Culture	Tourism	Communication	Services
Private fundraising Advisory board	Technical office	Arts, Culture Museum	Monumental Complex Visitor service	Press and com- munications office	Safety measures
International Patrons of the cathedral	Candoglia quarry	The Archive - Library	Ticket office	Press office	Security Area
Raising of public funds and institutional relations	Marble worksite	Musical chapel	Fast track Cathedral shop	Digital communication	Security General services.
Public funds and calls International relations and European projects	Cathedral The San Gottardo in corte church	Cultural events and activities	Guided tours	Photo and Video shooting	
Real Estate and Purchases		Department of Education			

2.2 The restoration of the Tiburio

March 2016 saw the start to erect scaffolding around the cathedral Tiburio. Despite delays caused by the SaRs-CoV-2 epidemic the intensity and precision of the work to date indicate the possible completion of this very demanding restoration by the end of 2024.



Figure 1. The scaffolding for the Tiburio restoration.

A few figures may serve to understand the complexity of the undertaking:

- 3.600 tons weight of the tiburio developed over 55 metres height, supported within the span of a system of 4 arches.
- The absence of precise mechanical and geometrical data about the nature and function of the supporting arch system, which was conceived and realised during the mid XV century and the first 20 years of the XVI (see section 3).
- A 35 year period during which the conception and the actuation of the supporting structural system was conceived.
- A workforce consisting of 96 men a day on the scaffolding.

- 480 man hours to mount and erect it.
- 1.750 man hours estimated for the restoration work
- 72 hours topographical monitoring calculated to control the the functionality of the structural system during restoration work.
- 8 load cells installed and controlled daily to govern the weight distribution of the provisional structure on the architecture of the tiburio.
- 95 man days to consult the Archives with an end to obtain necessary information for the development of the work
- 6 million euro the estimated cost of the intervention.
- 20 cubic metres of Candoglia marble for substitution and 200 cubic metres of marble restored in situ at a medium height of 75 m from the cathedral square.
- 76 marble statues restored

The ensuing activities required a workforce which at the lowest level received a 2 year formation period before they could operate with a certain degree of autonomy, in a team type formed by 3 men, one of whom being the supervisor.

It was possible to develop the work by virtue of a series of hoisting towers, designed for the purpose and constantly checked and maintained by specialised personnel, and with the additional efficiency of the site store depot, while operating right in the heart of Milan’s historic centre.

3 HISTORY AND STRUCTURAL LIFE OF THE DUOMO

The great Milan cathedral (il Duomo) is a most imposing monument built in the Gothic style. Construction began in 1386. Late Gothic (the French style born some 200 years previously), was adopted more from political and economic motives than from architectural sensibilities. Almost as if to say that the social and economic field of reference was that north of the Alps.

The fact of being the 4th largest cathedral in the world for extension, and the 3rd in height, for the internal dimensions of the main nave, make it a very particular structure. The vertical system from floor to the terraces is built of buttresses, walls and piers of brick and blocks of serizzo, faced with Candoglia marble. The vaults are made of brick, with Candoglia ribs; the lateral buttressing is provided by diaphragm walls and iron ties (Coronelli et al., 2015). The upper part, from the terraces to the summit of the great spire, entirely built of Candoglia marble. This is a crystalline marble only extracted from the quarry of the same name as the town at the entrance to Val d’Ossola. Beautiful as it is to behold the marble presents structural problems: the presence of pyrite, plus the iron ties used over the centuries to join the units, frequently provoke sudden internal fracturing.

The history of the construction is here described underlining the different phases in time, followed by restoration. The sources used are mainly the writings of Ferrari da Passano (1988), Architect of the Fabbrica del Duomo from 1964 to 1988; these are based on this Author’s experience and the Annales of the Fabbrica del Duomo, a unique record of the worksite activities from 1386 to the present. A description of the overall structural configuration can be found in Coronelli et al. (2015).

3.1 Construction history

3.1.1 The Apse

The construction started in 1386 with the apse proceeding from East to West, containing the choir. The geometry of the apse (Figure 2) is a half octagon in plan, covered by a half dome with triangular cells, and six interior pillars supporting the half dome are placed along the perimeter. These members together with six vertical buttresses, support five quadripartite vaults of trapezium shape in the deambulatory. Here the apse is closed by large decorated windows. The dimensions of these openings together with the slenderness of the buttresses raised the concern of the French consultant Mignot, that originated a documented controversy (Ferrari da Passano, 1988). The statements of the constructors underlined the key role of pointed arches and iron ties for the stability.

The choir is flanked by the sacristies on either side with perimetral walls, connected to the buttresses on the exterior perimeter, constituting a firm system with lateral load bearing capacity, that was the first part of the construction.

The following part constructed was the crossing with a structure with one nave and two aisles very similar to that of the longitudinal body, with a main nave and four aisles. The buttressing is provided by diaphragm walls and lateral buttresses walls, combined with iron ties (Coronelli et al., 2015).

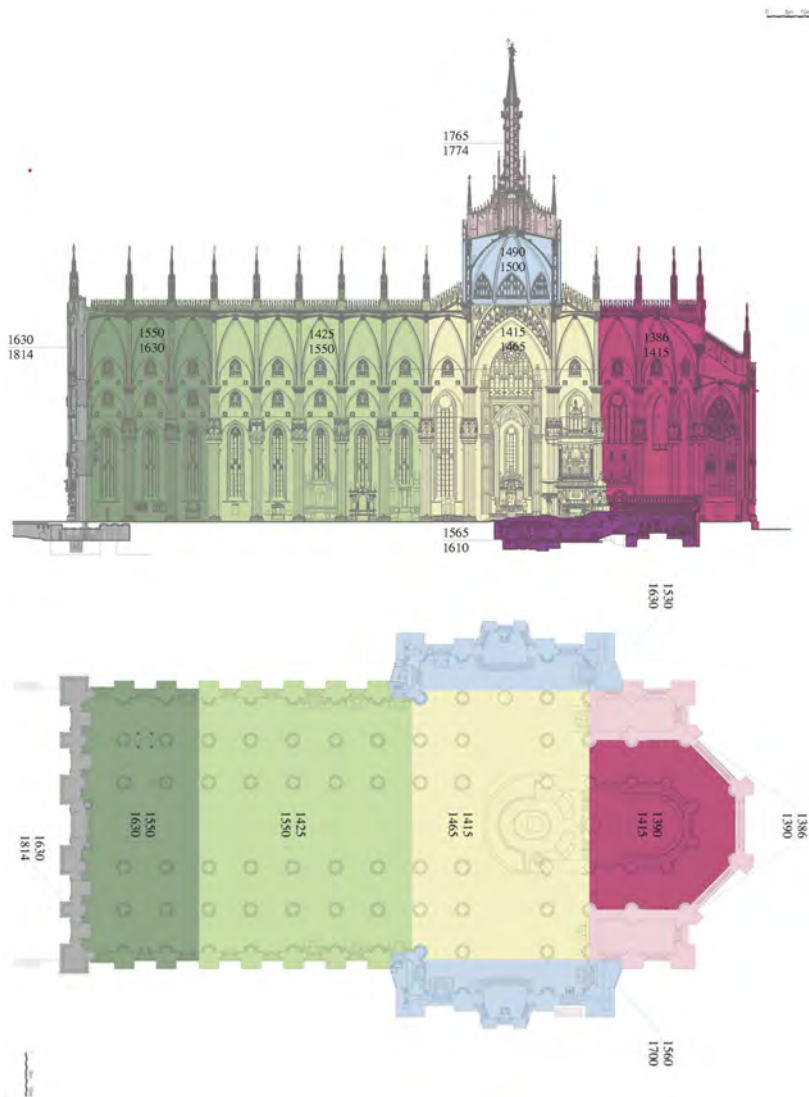


Figure 2. Parts of the Cathedral and years of construction.

3.1.2 The Tiburio and Dome

The construction of the tiburio began with foundations and four pillars slightly larger than those of the other vertical members. At the beginning of the 15th century these were built, supporting the four 19.6m span pointed arches, the walls above the arches, the pendentives and the decorations. The choir backed by the apse, the transepts and the first bay of the nave and aisles surrounded this part of the fabric.

The discussion developed with foreign and Italian experts including Leonardo Da Vinci and Bramante amongst others. The solution adopted was proposed by Lombard personalities, first Giovanni Solari from 1452 and then Guiniforte Solari, who took the lead of the construction starting from 1459. This consists of four semi-circular arches hidden behind the walls above the pointed arches (Figure 3). Conceptually these act as load-relieving arches for the pointed arches.

The intrados radius is 8,6 m, a great depth and width of the cross section, ensuring a wide load path for the loads of the dome: at the crown 160 by 180cm, and increasing moving towards the supports. The cross-section is obtained with voissiors in radial position, in a ring of constant depth (1,6m). Above this blocks are laid horizontally, reaching an extrados drawn by a circular line with a radius of nearly 18m and a centre at the springing line of the pointed arches. The material used is serizzo, a strong metamorphic stone quarried in Lombardy and Val d'Ossola.

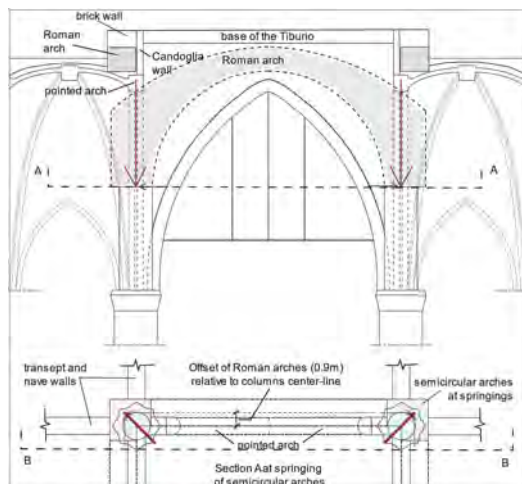


Figure 3. Arches supporting the Tiburio.

The choice was made to build the arches supported on the pillars of the crossing, without demolishing the walls above the pointed arches; hence the arches lie in an off-set position (Figure 3, plan view) (Ferrari da Passano and Brivio, 1967). This layout increases the eccentricity of the reactions of the arches on top of the pillars (Ferrari da Passano, 1988).

As a consequence very relevant problems arose in the construction after the removal of the centering, as the pillar tops were displaced outwards under the arch thrusts. The ties of the Gothic arches below were all broken. The structures surrounding the Tiburio were damaged. As a consequence the construction was stopped around year 1470.

The system at the time was bearing only the weight of the new Roman arches and the masonry walls above. The arches were buttressed against the surrounding structure of the transepts, choir and nave. The walls in the choir and sacristies in particular definitely played a role in the lateral stability. Despite the damage the structure reached a new equilibrium that was the basis for the future of the construction.

This was undertaken under the guidance of Amadeo and Dolcebuono, and the dome was completed in year 1500. The whole structure was supported by the system of Gothic and Roman arches described above and is based on an octagonal geometric scheme, leading to concentrating the load on the drum in eight locations, interior to the span of the arches below.

The dome (Figure 4) was built with the same characteristics of the existing construction – the half-dome of the apse in particular, with the same arches and vaults (Ferrari da Passano and Brivio, 1967). The plan is octagonal, connected to the square of the crossing with pendentives. The dimensions are the same of the apse with a span of 32 braccia (19,2 m), and the crown at 19,2m from that of the pointed arches of the crossing. The interior vaults are made of brick, with eight cells, and Candoglia marble ribs meeting in a central ring of brick and marble. Walls made

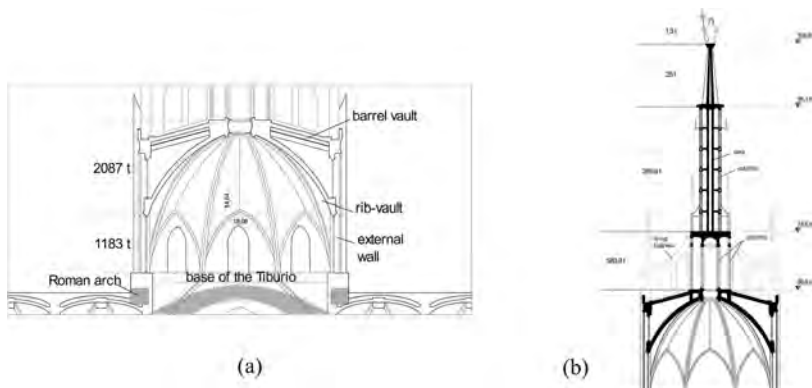


Figure 4. (a) Structure and weight of the Tiburio and Dome and (b) Tiburio with the main Spire.

of brick in vertical planes bear on the base and extend radially above each rib, creating a fan and connecting at the central ring. Barrel vaults span between adjacent radial walls at the top, to support the stone roof, and creating a chamber above the dome inner vaults. This is the same scheme used for the double vaults to support the roof above the naves (Coronelli et al, 2015).

The dome is enclosed within exterior vertical walls, along the perimeter of the octagon. Windows open at two levels, one looking into the interior of the church and the other into the chambers between the two vault systems. The walls connecting in the vertexes of the octagon form eight vertical members, with spires placed at their top. The weight of the walls sums with the forces transferred by the dome at the supports, bearing on the base of the Tiburio. The outwards components of these forces are balanced by steel ties lying in the horizontal octagonal ring at the base of the dome. The vertical components are transferred by vertical walls onto the semi-circular arches of the crossing.

Thus, following the history of the construction, the intensity and distribution of the loads on the semi-circular arches changed between years 1490 and 1500 with the construction of the tiburio, with increasing vertical forces and lateral thrusts on the underlying pillars. But further stages and changes were still to take place.

3.1.3 The main spire and gugliotti

The project to build a spire to crown the building dates back to the beginning of the construction (Ferrari da Passano, 1988). The main spire, “la Gran Guglia” was built in the 18th century, after studies to ascertain the safety for the underlying construction (Brivio and Repishti, 1998).

The final design (Figure 4b) was presented by Francesco Croce in 1764. Its base is at the level of 65,6m and reaches 104,9m at the feet of the statue of the Madonna. The spire is a rather light structure, with a central marble cylindrical tube, and pillars on the outer perimeter. All the stone works are connected by a complicated system of iron ties, with longitudinal elements within the central void and transverse fastenings. The total weight bearing on the top of the tiburio is 884 tons.

The four gugliotti (Figure 1) are small towers with spires at the top, placed on the roof at the four corners of the square corresponding to the perimeter of the crossing. The first was built between 1507 and 1518 and the others followed much later in the second half of the 19th century. Their position corresponds to the pillars of the crossing, and their load flows directly onto these members. The overall axial force of each pillar increases by 100-150 tons, less than 5% of the total axial load, approximately equal to 3000 tons at the base of each pillar. Nevertheless significant damage showed in these vertical members with cracking of the outer Candoglia ring. This led to the closing of the Duomo at the end of the 19th century for restoration works, showing that these members were already close to their safety limit at the time.

3.2 Restoration history

Any action aiming to the conservation or the restoration of a heritage property should be oriented to preserve its authenticity (Roca 2011). In this perspective, this section provides a synthesis of the

main structural restoration works related to the Tiburio and the piers of the crossing in the period ranging from the end of the 19th century until today. These have been the object of detailed reports by Ferrari da Passano and Brivio (1967) and Ferrari da Passano (1988).

The size of the cross-section, and the type and quality of construction were at the origin of the distress in the piers of the crossing. The cross-section is made of an outer ring of Candoglia marble; the thickness of this part is varying without a precise rule along the height. The interior is filled with mixed materials, including serizzo blocks, brick and mortar. The building of the Tiburio in the 16th century and then of the main Spire in the 18th century added high loads on these members. The configuration of the Roman arches caused eccentricity of these loads and lateral displacements of the pier.

In the second half of the 19th century, the piers of the crossing showed signs of severe damage. This indicates that the load effects were such to approach critical conditions for these members. Restorations were carried out extracting the damaged voissiors, filling with lead the inner voids, and replacing new marble units.

In the 20th century the soil water table was lowered by 20m between 1950 and 1970 by the industrial water consumption in Milano. The soil subsidence caused settlements of the foundations. Measurements of the differential settlements over a period of 5 years from 1965 to 1970 showed rates higher than 1mm/year between points at 20m distance (Ferrari da Passano, 1988).

A survey of the piers in the crossing (Figure 5) and in the choir showed compression cracks in the blocks of the outer Candoglia skin, with an approximately vertical orientation. Monitoring showed a dramatic progression of phenomena, with crack widths were increasing in time and the formation of new damage and spalling of parts of the units.

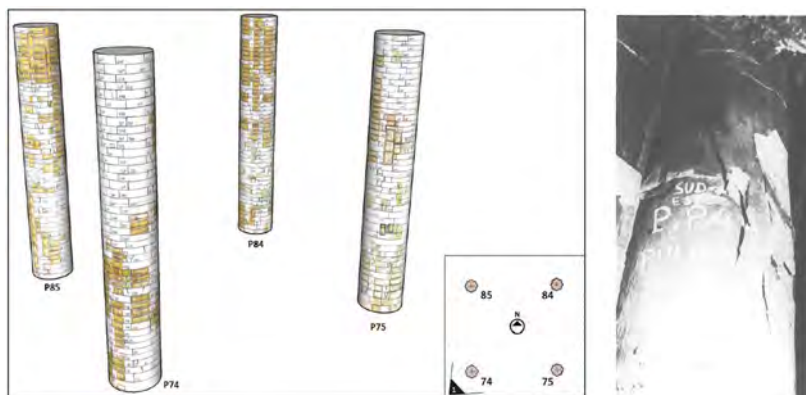


Figure 5. Survey before restoration: sketch of deterioration pattern of blocks and photograph of cracking.

To face the emergency a commission was formed in 1965 by the Fabbrica del Duomo and the Politecnico di Milano. The piers of the crossing were provisionally encased in reinforced concrete, while those of the choir with a steel structure. A geotechnical study showed that the load bearing capacity of the foundations was not the cause of the phenomena, whereas the settlements were compatible with a theoretic calculation of the effects of subsidence.

The interpretation of the conditions was carried out at the ISMES laboratory, resorting to a scaled experimental model of the whole Tiburio with the surrounding vaults and supporting vertical members (Ferrari da Passano and Oberti, 1983). Imposing differential foundation settlements, a redistribution of forces with overloading of the northern piers with respect to the southern was shown (Ferrari da Passano, 1988).

To stop the causes of the phenomena, the use of water was banned from industries surrounding the central part of Milan, hence stopping the lowering of the water table. This in turn gradually stopped the ground settlements.

The study of a restoration technique then started. Scaled masonry models of the piers were built and tested (Ferrari da Passano and Oberti, 1983). The solution adopted for the four

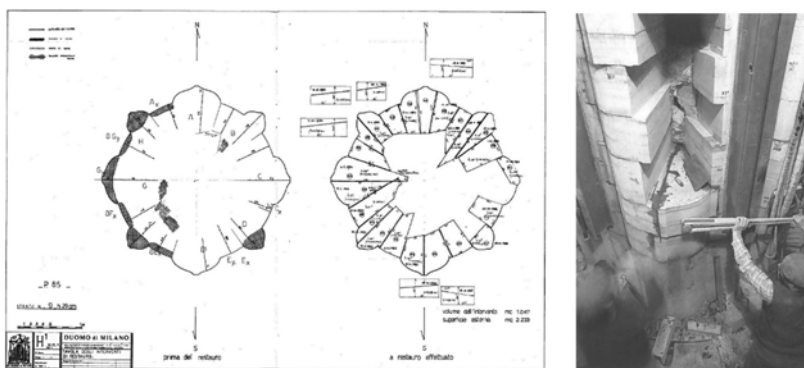


Figure 6. Survey and restoration: damaged and replaced units.

main piers of the crossing, proposed by the Architect of the Veneranda Fabbrica, Carlo Ferrari da Passano, was inspired by the concept of maintaining the identity of the Cathedral by preserving its original structure.

After a detailed survey of the thickness of the outer Candoglia ring and of the damaged units (Figure 6), these were gradually replaced with new pieces of the same material and profile, penetrating deeper radially in to the core of the pier and thus providing an increased resistance. To provide safety to the operations, the reinforced concrete outer skin was gradually removed, exposing only the parts being restored. By 1980 the four piers supporting the Tiburio appeared sound again.

Another intervention on the Tiburio structure was the placing of steel ties connecting the four piers of the crossing, anchored within the walls of the transepts. These correspond to the original design of the crossing, where iron ties had been used before the failure caused during the construction of the Tiburio (see Section 3.1). Finally, displacement monitoring on relevant points of the building began, and has been carried out with a period of six months up to today, highlighting essentially stable conditions.

It must be remarked that these choices reflect the concepts on the relation between structure and authenticity outlined by Roca (2011). The conditions of the piers were successfully improved by the restoration works described in this section; these members have been now in service for more than thirty years, and the elegance of the cathedral was restored (Figure 7).

Explanation of these past phenomena though was only partial. The experimental scaled model (Ferrari da Passano and Oberti, 1983) being elastic, made of materials obtained with epoxy resins, lead to estimates of the redistribution of loads with the ground settlements. These events could be examined and understood more deeply by numerical analysis with nonlinear constitutive models for the materials (Roca et al., 2013; Angjeliu et al., 2020). Another aspect to which attention should be devoted are creep effects (Binda, 2008). The effect of soil settlements evolution in time should be included. Thus a more thorough explanation of the phenomena that nearly led to the collapse of the Tiburio could be reached, and the present and future evolutions followed.

The last step in the 21st century is the restoration of the Tiburio (see Section 2). With the scaffolding in position maintenance operations have been carried out on the sculpture and decorations. Units of masonry of the walls above the supporting arches has been replaced, and the mortar beds maintained. The ties connecting this system have been inspected, showing good conditions.

4 INSPECTION AND MAINTENANCE

4.1 *The technical table of the Italian Fabbricerie*

One of the main aims of a restoration of a heritage structure is ascertaining the safety of people using or visiting the structure, with the possible risks limited to acceptable levels (Roca, 2011). Following the dramatic incident in Florence, in the Santa Croce cathedral, on the 20th October 2017, the leading technicians of the principal Italian Fabbricerie within AFI (Associazione Fabbricerie Italiane) decided to confront one another on their respective experiences and activities, to discuss

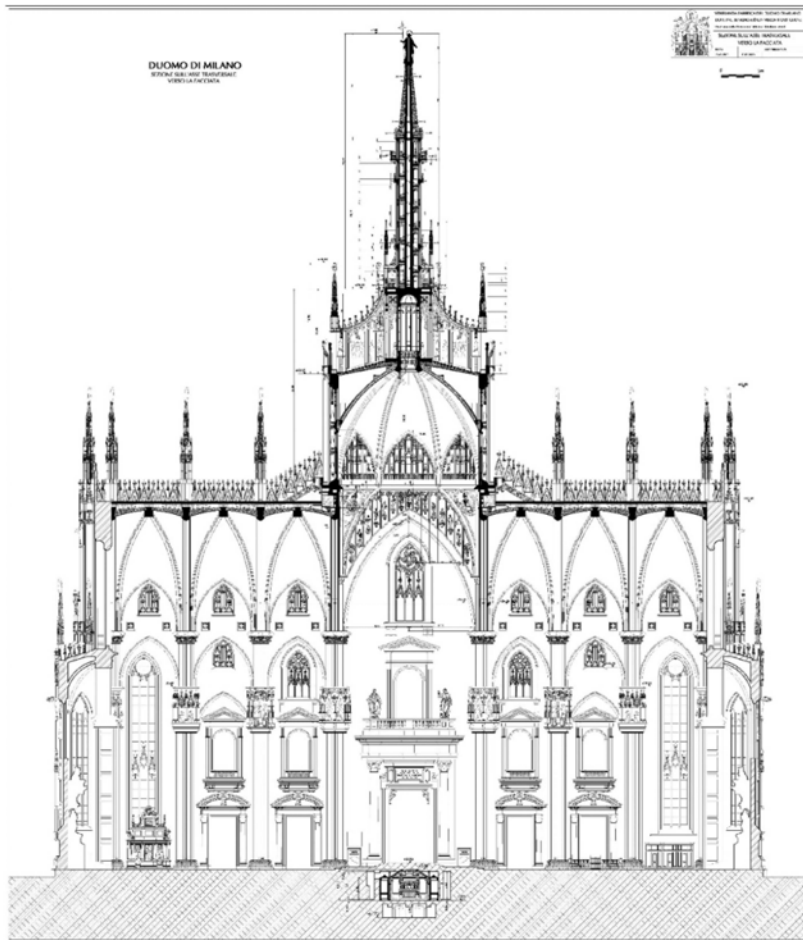


Figure 7. Section of the crossing.

the possibility of defining a code of practice for maintenance of such complex architectural organisms. For 18 months of monthly encounters and consultations, a document was formulated to underline the fundamental importance of periodical inspections; defining the operational modalities and criteria for the management and programming of the same inspections and verifications on all the elements at quota, characteristic of every monumental fabric, the degradation of which could present a danger to the public and private incolumity.

This was considered to be the prime, inexorable object to be reached, propedeutic to the definition of a code for programmed maintenance, to which each Fabbrica should comply according to the capacities and economical and financial possibilities of each.

To follow, a resume of the chief considerations which emerged in conclusion of the Technical table, regarding both the content and necessary action to be taken, in order to render the guidelines for inspection of cathedrals, fully operative.

4.2 *The conclusions of the AFI 2018-2019 activities*

With reference to public safety precautions, each Fabbrica possesses specifications which make it different, and has specific problems. Even though the type of problem is similar. Those of a structural nature (overloading, cracking, settlements etc.) being too different in the various cases must however be dealt with and resolved by each single Fabbrica.

On the other hand damage to decorative elements such as tiling, plaster or stone fragments of various dimensions, are a common phenomenon, constituting possible negative consequences for safety, and are by no way inferior to the structural problems.

Therefore it was agreed that in order to confront these problems from the safety point of view, monitoring of the architectural surfaces is fundamental. This can be undertaken essentially, by periodical visual inspection, eventually from hoists, or by workers specialised in operating at heights; the frequency and modality varying from case to case.

Each inspection is to be documented graphically, illustrating the area (prospects or parts of these, covering, characterising elements etc) and the architectonic or decorative elements of which they are composed or characterised by. The amount of detail will vary naturally, for each monumental fabric, but may also vary within the structure, as each possess intrinsic characteristics.

The evaluation must furnish a quantitative result, not only the conceptual. To this end the technical table has elaborated a procedure which, on the basis of inspection results, (that is the state of conservation in the inspected area), the estimated duration of the manufactured components of the same, and of the level of risk relative to its exposition, must report the degree of alert and establish the frequency of verifications to be made. To complete the evaluation it is essential to establish the expected duration of the manufacture defining the architectural surface, distinguished according to form, material and exposition.

5 CONCLUSIONS

In a life cycle analysis perspective, the study highlighted the description of damage, its evolution in time and the study of the causes. Two aspects that differentiate the structure of heritage buildings from modern construction are the higher uncertainties related to the geometrical complexity and of the materials effectively used. The case of the piers in the crossing of Milan Cathedral is emblematic with the differences between external and internal geometry and materials.

A specific type and pattern of mechanical damage, showing in the 19th and 20th century, related to overloading of the piers and their masonry texture, has been documented. This shows the need for the development of numerical structural and constitutive models capable of predicting effects of masonry creep in relation to different materials and textures. The engineering problem, tackled by the experts of the time, leading to successful restoration intervention and a true rebirth of the Cathedral at the end of the last century has been described.

The 21st century restoration activities on the Tiburio show the solution of a different type of damage, of relevant importance for monumental buildings and their present use. Operations carried out to maintain the decorations and sculptures, contemporarily provide means to avoid dramatic accidents, that have been the object of a technical discussion table of the Italian Fabbricerie.

When the concept of maintenance of the cultural patrimony assumes the aspect of physical care to an architecture (that is, to any expression of the building capacity of Man) the study of the best way to fulfil such an arduous task is enriched by certain, perhaps surprising observations for those who do not habitually frequent the scaffolding of a building site, or the tables at which restoration projects, or the economic aspects and financing of such, are planned.

One of the observations which is brought to the attention of those studying these processes, regards the realization that the significance of testimonies that vert on the cultural patrimony is seen to be in the majority of cases centered on a single case, independently of its nature or dimensions, be it a commemorative monument or building. Single constructions, were erected in the distant past, using building techniques and suffer the effects not only of the times when they were erected but also of the regional uses to which they were put, so that when faced with their conservation we have little information, or few designs to describe their constitution.

The knowledge and experience gathered by whomsoever has done conservation work on these goes to form a valuable capital, allowing to consider the best way to invest in the sector. Knowledge is often gained from past errors, or from verifications made during the intervention, or from fortunate intuition during the course of the works; this together with the experience gained, leading inevitably to an affection towards the object, as well as satisfaction over

a successful intervention, or a desire to improve on this when not entirely successful at a first attempt. It is natural that we strive toward improvement in our professional practice.

How are we to avoid the loss of such capital? How to make it more fruitful? By the formation of a group of persons essentially drawn from skilled operators, for the constant maintenance of a chosen cultural object. A group of workers, of varied experience, according to the specifics of the monument, to acquire in depth and transmit the method of intervention, increasingly gaining understanding of the nature and characteristics of the same, and with a greater knowledge measure the resources necessary. Such a group to be composed, as fore-said, of skilled workers: that is to say, artisans specialized in the sector, allowing for them to develop and investigate modalities for the intervention, and to be in a condition in which to dedicate themselves with serenity, to the monument in question, without having to submit to managerial impositions.

The management, for commercial reasons and bearing in mind the above mentioned difficulties incurred in intervention (unusual techniques of the times, lack of specific technical information, etc.) must find an economic balance which however could sometimes penalize the quality of the intervention. Small scale public or private administrations, as well as great cultural institutions such as Museums or Foundations could make the most of their most significant assets, finding in an economy of scale solutions to questions of costs and benefits.

The permanent maintenance group must certainly be enriched by the indispensable contribution of the design engineers; but these may be autonomous professionals, accustomed to operating in the market. The commissioning body must formulate clearly the request to supervise activities of the workforce, while taking a long view, as the planning of the maintenance operations at the very best will be projected for tens of years, and for centuries to come. Therefore inevitably a period beyond that of individual involvement. An unimaginable stimulus this, to give of one's best.

ACKNOWLEDGEMENTS

The Authors are grateful to Prof. Fabio Biondini and the IALCCE Association for the invitation to present the keynote lecture outlined in this paper.

REFERENCES

- Angeliu, G., Coronelli, D., Cardani, G. 2020. Development of the simulation model for Digital Twin applications in historical masonry buildings: The integration between numerical and experimental reality. *Computers and Structures*. 238 (3).
- Binda, L. 2008. *Learning from failure. Long term behaviour of heavy masonry structures*. WIT press: pp 228.
- Biondini, F., Frangopol, D. 2016. Life-Cycle Performance of Deteriorating Structural Systems under Uncertainty: Review. *J. Struct. Eng.* 142(9): F4016001
- Brivio E., Repishti, F. 2003 ... e il Duomo toccò il cielo. *I disegni per il completamento della facciata e l'invenzione della guglia maggiore tra conformità al gotico e razionalismo matematico*. Skira, Ginevra, Milano: 224 pp (in Italian).
- Coronelli, D., Caggioni, B., Zanella, F. The Cathedral of Milan: the structural history of the load bearing system." *International Journal of Architectural Heritage*, 5, 510–528. 2015.
- Ferrari da Passano C., Brivio E. 1967. Contributo allo studio del Tiburio del Duomo di Milano, alcune considerazioni maturate a seguito dei lavori di restauro", *Arte Lombarda*, I semestre: 5–29.
- Ferrari da Passano, C. 1988. *Il Duomo rinato*. Vigevano: Diakronia. 136 pp.
- Ferrari da Passano, C., Oberti, G. 1983 Reconstruction des Structures du Dôme de Milan. IABSE Symposium on *Strengthening of Building Structures – Diagnosis and Therapy*, Venezia, 277–286.
- Roca, P. Restoration of historic buildings: conservation principles and structural assessment. *Int. J. Materials and Structural Integrity*, Vol. 5, Nos. 2/3, 2011 151
- Roca, P., Cervera, M., Pelà L., Clemente R., Chiumenti M. 2013. Continuum FE models for the analysis of Mallorca Cathedral. *Engineering Structures* 46: 653–670.

Field and laboratory tests for corrosion assessment of existing concrete bridges

M. Carsana & E. Redaelli

Department of Chemistry, Materials and Chemical Engineering, Politecnico di Milano, Milan, Italy

F. Biondini

Department of Civil and Environmental Engineering, Politecnico di Milano, Milan, Italy

ABSTRACT: Many existing Reinforced Concrete (RC) structures built around the middle of the last century have now reached the end of service life and require maintenance interventions to repair degradation-induced damage, especially due to steel corrosion. The conservation of existing structures and infrastructural facilities is therefore a relevant and urgent problem, particularly bridges and viaducts in view of their social and economic importance. In order to correctly define the restoration interventions and fulfill safety, robustness, and durability requirements, it is necessary to inspect RC structures and assess the state of degradation of materials and corrosion of embedded steel. This paper is aimed at contributing to effective methods, procedures, and criteria for corrosion assessment of existing RC bridges and viaducts. To this purpose, the results of inspections and diagnostics carried out on structural members of bridges subjected to corrosion and exposed to different environmental conditions and microclimates will be presented by focusing on in-field non-destructive testing as well as on chemical, physical and microstructural analyses.

1 INTRODUCTION

Structures and infrastructure systems are exposed to aging and deterioration processes. Among other structures, many existing Reinforced Concrete (RC) bridges built around the middle of the last century have now reached the end of service life and require significant maintenance interventions to repair damage, especially due to concrete degradation and corrosion of steel reinforcement (Bertolini 2008, Biondini & Frangopol 2016). The conservation of existing structures and infrastructural facilities such as bridges and viaducts, that due to their social and economic importance, are included among the most critical assets of cultural heritage, is therefore a relevant and urgent problem. In order to correctly define the restoration interventions and fulfill safety, robustness, and durability requirements, it is necessary to monitor RC structures and assess their state of degradation paying special attention to corrosion of embedded steel and related concrete damage (Bertolini et al. 2013, Biondini & Frangopol 2019).

Maintenance of existing RC structures is an important challenge that may be coped with through suitable criteria, methods and procedures for structural condition assessment. The developments and results presented in this paper are part of the contributions to this field given in recent years by a synergy of research activities ongoing at Politecnico di Milano within the mCD Concrete Durability group of the Department of Chemistry, Materials and Chemical Engineering on corrosion assessment and Department of Civil and Environmental Engineering on life-cycle of bridges and viaducts. After analyzing the mechanisms of corrosion of steel in RC structures and the main factors affecting corrosion, the paper describes methods and procedures for structural condition assessment of RC bridges, with emphasis on characterization of corrosion damage of the materials. Special attention is paid to field non-destructive testing as well as sampling of materials in order to perform laboratory tests including both chemical and microstructural analyses on concrete, complemented by electrochemical

tests on steel reinforcement. To this purpose, the results of inspections carried out on structural members of bridges or viaduct subjected to corrosion and exposed to different exposure conditions and microclimates are presented, including some selected results obtained within the BRIDGE|50 research project (Carsana et al. 2022). This project is carried out by Politecnico di Milano and Politecnico di Torino in collaboration with several public authorities and private companies to investigate the residual structural performance of a 50-year-old concrete bridge recently dismantled in Italy (Biondini et al. 2020, 2021, Savino et al. 2023). A set of 29 precast prestressed beams and two pier caps are stored in a testing site at Politecnico di Torino for non-destructive testing, full-scale load tests, and extraction of a large number of samples from the tested structural elements for laboratory tests. Figure 1 provides an example of corrosion-induced degradation of a pier cap of the viaduct before dismantling. Figure 2 shows a series of deck beams (Figure 2a) and a pier cap (Figure 2b) stored in the testing site.



Figure 1. Corrosion-induced degradation of a pier cap of the bridge before dismantling (Biondini et al. 2020).

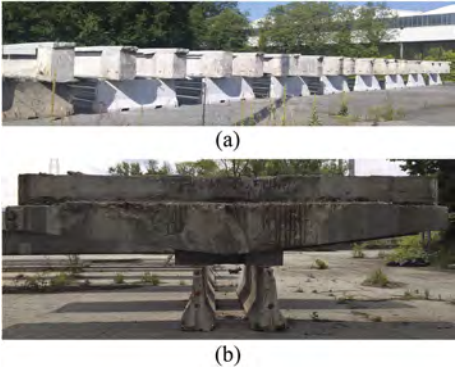


Figure 2. Bridge elements stored in the testing site: (a) deck beams; (b) pier cap (Biondini et al. 2020).

2 CORROSION IN RC STRUCTURES

Experience has shown that corrosion is frequently the main cause of degradation of RC over time. As a consequence of the typical urban or industrial exposure conditions of RC bridges and viaducts, they often suffer damage due to carbonation-induced corrosion of reinforcement and/or chloride-induced corrosion if exposed to de-icing salts or marine environments. Moreover, on high-strength steel used in prestressed concrete under very specific conditions, hydrogen embrittlement can also occur. Figure 3 shows the typical evolution in time of corrosion in RC structures, adapted from Tuutti (1982), due to carbonation-induced corrosion (black line), chloride-induced corrosion (orange line), and hydrogen-induced stress corrosion cracking (red line).

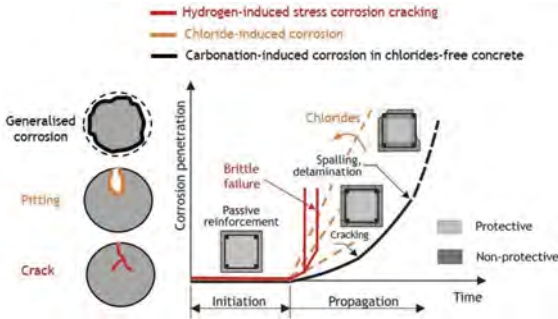


Figure 3. Evolution of the degradation of a RC element due to corrosion (adaptation of Tuutti’s diagram).

2.1 Mechanism of corrosion and consequences

Steel in concrete is normally protected by the alkaline solution contained in the pores of the hydrated cement paste (with pH values higher than 13) which promotes passivation, i.e. the spontaneous formation of a thin oxide film on the surface of the steel. Passivation guarantees negligible corrosion rate (i_{corr}) values, typically lower than 1 mA/m^2 , corresponding to a depletion of about $1 \text{ }\mu\text{m/year}$ (Bertolini et al. 2013), regardless of the presence of oxygen and moisture in the concrete pores.

Corrosion on the steel bars takes place if the passive film is removed or is locally damaged. This usually occurs due to carbonation of concrete or chloride penetration. Carbonation is the neutralization of alkalinity of concrete due to carbon dioxide in the atmosphere. It brings about a drop in the pH of concrete from alkaline values to neutrality, with consequent loss of stability of the passive film on the steel bars. Consequently, rebars can corrode, if oxygen and moisture are available. Chloride ions may locally break the passive film even in alkaline concrete. This occurs when chloride ions, which are contained for instance in seawater or in common de-icing salts, penetrate the concrete cover and reach a critical threshold level at the depth of the reinforcement. Pitting corrosion thus initiates and may propagate if moisture and oxygen are available at the steel surface. Corrosion of steel bars in chloride-contaminated concrete is usually more severe than carbonation-induced corrosion, leading to much higher corrosion rates for given conditions of moisture content and temperature.

Although carbonation and chloride penetration are the most frequent causes of corrosion initiation in RC structures, it is worth recalling that, under specific circumstances, other forms of corrosion could take place. DC stray currents may promote corrosion initiation or propagation, e.g. in structures of railway networks (Bertolini et al. 2007), whilst high strength steels used in pre-stressed concrete may be highly vulnerable to the effects of corrosion (Page & Page 2007). In fact, corrosion can have serious consequences when it occurs in pre-stressed or post-tensioned concrete structures. Due to high loads applied to the tendons or bars and low fracture toughness that characterize the high strength steels, the consequences of corrosion attacks are more dangerous than in the case of conventional reinforced structures. As a matter of fact, even tiny localized attacks can determine the failure under service of tendons or bars. In the case of pre-tensioned structures, as shown in Figure 4, corrosion can be brought about by the penetration of carbonation or chlorides through the concrete cover (Figure 4a), while in post-tensioned structures corrosion usually arises as a consequence of ineffective filling of ducts with cement grouts (Figure 4b) or other protective materials. Under specific conditions, localized attacks (Figure 4c) can degenerate into cracks promoted by hydrogen embrittlement and brittle failure can take place.

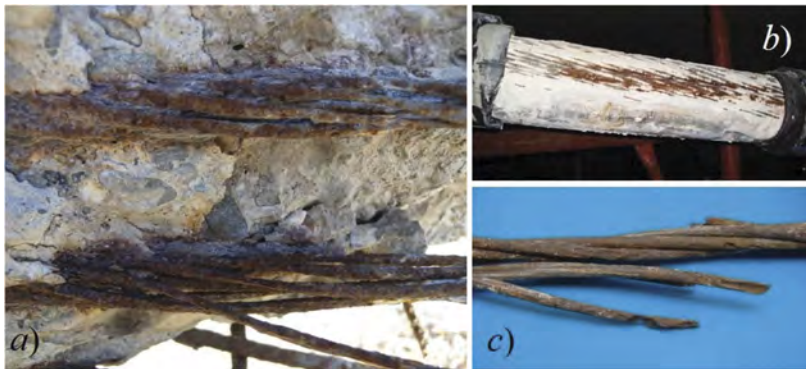


Figure 4. Examples of (a) strand conditions in pre-stressed beam (Carsana et al. 2021), (b) segregated grout in the external post-tensioning tendons in contact with strand with severe corrosion attacks (Carsana & Bertolini 2015), and (c) localized corrosion attacks.

2.2 *Factors affecting corrosion*

Many factors can influence the corrosion behavior of steel in RC structures. They are related mainly with aggressiveness of exposure conditions, concrete quality, and thickness of concrete cover (Bertolini 2008). Environmental aggressiveness is a function of numerous factors not always independent of each other, such as humidity of the environment and its variability in time and place (the latter connected with macroclimate and local microclimatic conditions), presence of chlorides and oxygen, and temperature.

In case of carbonated concrete that does not contain chlorides, rebars can corrode if oxygen and moisture are available. Corrosion rate of steel increases as the moisture of concrete increases (Bertolini et al. 2013), and only when the moisture content approaches saturation the corrosion rate decreases due to lack of oxygen.

Chloride-induced corrosion occurs when chloride ions penetrate the concrete cover and reach a critical threshold level at the depth of the reinforcement. In presence of chlorides, the environment may be aggressive if the R.H. remains above 50% (or even 40% if the chloride content is very high and hygroscopic chlorides such as magnesium or ammonium chloride are present). Aggressiveness increases with humidity, chloride content, and temperature.

The resistance of RC elements against corrosion strongly depends on quality of concrete. The penetration of carbon dioxide and chlorides depends on the permeability of concrete. All factors that promote a dense, low-porosity microstructure of the cement paste (e.g. low water/cement ratio, careful placing, compaction and curing), allow obtaining a concrete with high resistance to carbonation and chlorides penetration (Bertolini 2011).

In addition to concrete quality, also a minimum value of concrete cover has to be prescribed. An increase in the thickness of the concrete cover increases the barrier to the various aggressive species moving towards the reinforcement and increases the time for corrosion initiation.

3 INSPECTION PROCEDURES

Regular inspection of RC structures and infrastructural facilities is fundamental to detect signs of deterioration and, if necessary, application of remedial measures in an early stage of damage. There are many reasons why inspection or condition assessment of RC structures are performed. Firstly, inspection activity is part of management operations of many large-scale structures (Carsana et al. 2023b, Bertolini et al. 2011). Based on the observation of signs of deterioration, a proper follow up can be taken before damage is too large. Structures with damage due to incidents, such as fires and collisions, need to be inspected for establishing proper corrective measures. Damaged RC structures need to be repaired in order they can reach the expected service life or prolong the residual lifetime (Bertolini et al. 2016). With respect to corrosion damages, a condition assessment of the structure has to be performed in order to find the optimum repair solution and to avoid further corrosion problems in the future. This evaluation consists into preliminary visual inspections (§3.1) that should allow for planning other detailed survey (§3.2 and §3.4).

3.1 *Visual inspections*

Visual inspection is the preliminary step in any survey. It should give a first indication of the nature of degradation problems and the extent of damages. Figure 5 shows typical effects of concrete degradation and steel corrosion, which may affect serviceability and safety of RC structures. Cracking, spalling or delamination of the concrete cover may take place due to tensile stresses induced by corrosion products growing at the steel surface, especially in case of inadequate thickness of concrete cover (Figure 5a). Further problem that is often observed on RC structures is the concrete segregation (Figure 5b). Evidences of macro-voids observed on the concrete surface suggest that concrete has not been properly compacted during casting phases. This phenomenon may cause premature corrosion initiation with consequent

detachments. Thus, prevention of steel corrosion should be further developed as the concrete is mixed, placed, compacted and cured. Moreover, even simple design details should be taken into account in order to prevent significant degradation of RC structures. Such significant signs can often be observed in those parts of the structural elements that were exposed to wetting (Figure 5c) in absence of adequate systems of collection of water coming mainly from the bridge platform.

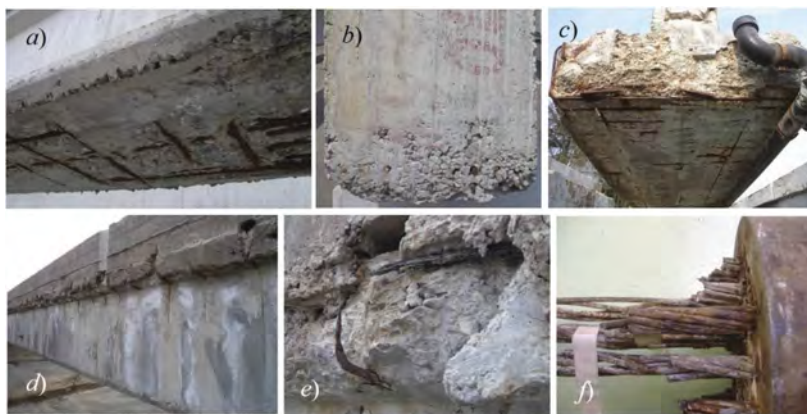


Figure 5. Effects of steel corrosion and concrete degradation: (a) cracking and spalling or delamination; (b) concrete segregation; (c) degradation of structural parts exposed to wetting; (d) efflorescence; (e) pitting corrosion; (f) corrosion of steel strands at the anchor head.

Visual inspection can highlight the presence of signs of degradation due to phenomena of efflorescence for the use of de-icing salts (Figure 5d). In the case of chloride-induced pitting corrosion, the cross-section of the reinforcing bars can significantly be reduced (Figure 5e) and thus the mechanical characteristics of structural members, including load-bearing capacity, ductility, and fatigue strength, may be affected, even before any cracking takes place in the concrete cover. Visual observation could also concern corrosion of external post-tensioning tendon (Figure 5f).

3.2 *Non-destructive tests*

Visual inspection is often combined with several non-destructive tests (NDTs), as shown in Figure 6. NDTs include Schmidt rebound hammer and ultrasonic pulse tests carried out on concrete surface of structural elements to estimate mechanical properties and, in this way, detect the possible presence of zones where the concrete is unsound. Examples of frequency distributions of concrete strength, estimated through the Schmidt rebound hammer test for different structural elements, i.e., a pier cap, a box beam, and an I-beam investigated after dismantling of the viaduct (Figure 1), are illustrated in Figure 7. Additional NDT results can be found in Anghileri et al. (2021).

Average values of concrete strength around 50-55 MPa have been found, confirming a comparable design strength for concrete used to realize these different elements. Anyway, the wide range of variation of values measured on the pier cap highlights the possible presence of weak zones, such as those close to cracking and spalling of concrete surface (Figure 1).

As far as NDTs are concerned, the measure of concrete cover by magnetic-type instrument is also essential in order to explain why some areas of a structure are corroding and to identify those of future corrosion risk. In fact, low cover will favor the onset of corrosion because carbonation or chlorides reach the rebars more rapidly. Figure 8 shows the frequency distributions of concrete cover of the outermost reinforcement (stirrup bars) and internal longitudinal rebars of a RC element and it highlights the variability associated with this parameter.



Figure 6. Examples of non-destructive tests: (a, b), electrochemical inspection techniques; (c) concrete cover measurement; (d, e) Schmidt rebound hammer and ultrasonic pulse tests.

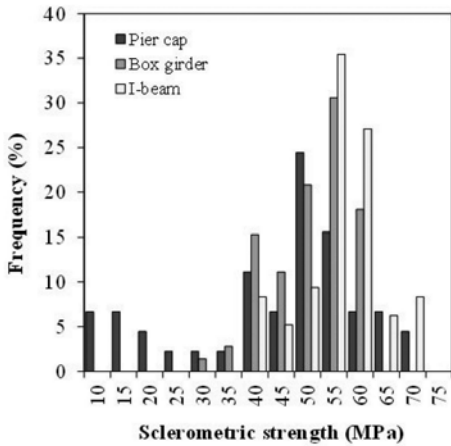


Figure 7. Frequency distribution of concrete strength estimated by means of Schmidt rebound hammer test (Carsana et al. 2022).

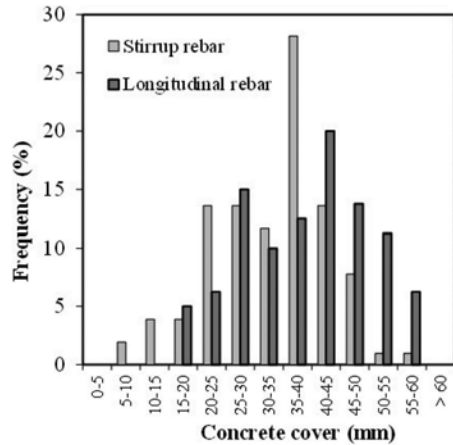


Figure 8. Frequency distribution of concrete cover thickness measured onsite for stirrups and longitudinal steel bars of a RC element.

Since corrosion is an electrochemical process, electrochemical techniques are most suited to assess the corrosion state of the reinforcement, to highlight corrosion sites and to monitor the corrosion propagation. Potential mapping is the only widely recognized and standardized NDT for assessing the corrosion state of rebars in concrete structures. To facilitate the interpretation of half-cell potential measurements of large bridge elements (Elsener 1995, Elsener et al. 2003), the most suitable approach of representing the data has been found to be a color map of the corrosion potential field (E_{corr}) based on the criterion of the American Standard ASTM C876 (1991), as shown in Figure 9a. According to this criterion, for $E_{corr} > -200$ mV vs CSE (Copper Sulphate Electrode) the probability of corrosion is less than 10% while for $E_{corr} < -350$ mV vs CSE the probability of corrosion is higher than 90%. However, the interpretation of the corrosion potential is not so obvious because the concrete cover and its resistivity, in addition to the actual corrosion potential of the steel, influence the readings at the concrete surface at the inspection time. Important information can be obtained by combining results from half-cell potential mapping and resistivity measurements. Figure 9b shows the relationship between the corrosion potential of steel and the electrical resistivity of concrete measured on a box beam.

The regions with very negative corrosion potentials and low electrical resistivities represent wet corroding zones, where steel bars are in contact with carbonated or/and chloride-contaminated concrete, while those with positive potentials and high resistivity indicate dry conditions and passive zones. The points where low resistivity yet positive potential are measured can be interpreted as the areas at risk of future corrosion. Electrochemical inspection techniques include also corrosion rate measurement carried out by means of polarization resistance method (Bertolini et al. 2013), which presents some difficulties when performed onsite (Andrade & Alonso 2004).

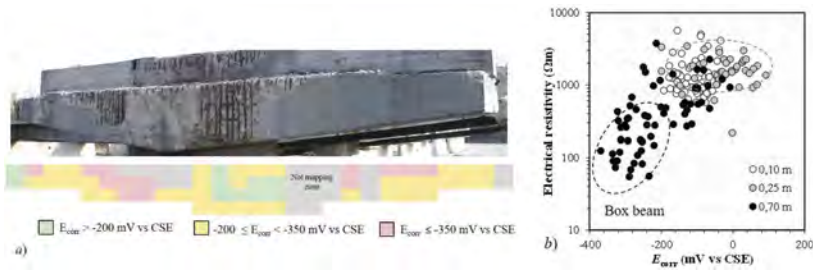


Figure 9. (a) Half-cell potential contour map. (b) Corrosion potential of steel reinforcement vs concrete electrical resistivity measured at different depths from top of a box beam (Carsana et al. 2020).

Certainly, the interpretation of available electrochemical parameters should be associated with further analyses aimed at assessing the actual state of steel bars embedded in concrete. In particular, concrete samples should be collected during inspection phase in order to evaluate also the carbonation depth and chloride content of concrete at the time of measurement and to predict future deterioration of the structure or to assess residual lifetime.

3.3 Sampling

Based on visual inspections, several zones of the structural elements of a bridge can be located for sampling. Inspection, condition assessment and prediction of the future service life require information both on concrete and on steel reinforcement. Thus, different types of samples have to be collected (Figure 10). Such samples are dedicated to several types of analyses that may help in the characterization of concrete, steel reinforcement and their resistance to aggressive agents.



Figure 10. Different sampling procedures during onsite inspections: (a) concrete fragments, (b) concrete cores, (c) concrete powders, and (d) samples of steel reinforcement.

3.4 Laboratory analyses

3.4.1 Carbonation depth

For determining carbonation depth it is essential to spray freshly broken concrete surfaces with a phenolphthalein solution (pH indicator) which will remain colorless where concrete is carbonated, while it will turn pink where concrete is still alkaline (Figure 11). The depth of carbonation can be measured also by spraying the same solution on concrete powders that are collected by drilling at increasing depth with a tip. The latter method is slightly less accurate than taking a concrete core, but it is less invasive as well. Usually the square-root formula is used to describe the penetration of carbonation in concrete ($d = k \cdot t^{0.5}$, where k is carbonation coefficient that is a function of concrete and environmental conditions). For real structures exposed to atmosphere (Bertolini et al. 2013) k ranges between 2 and 15 $\text{mm}/\text{y}^{0.5}$ (indicatively $2 < k < 6$ for concrete of low porosity, and $k > 9$ for highly porous concrete). Based on results obtained from inspection of deck beams after 53 years (Carsana et al. 2023), it has been observed that the carbonation depth shows a certain variability due to different local properties of concrete. In fact, carbonation depth measured on a core collected next to a segregation

zone is higher than that obtained on a sample cored in an undamaged zone of the same front. Figure 12 shows the progress in time of the carbonation depth for the values of k obtained for the investigated deck beams with and without segregation (respectively equal to 3.2 and 6.2 $\text{mm}/\text{y}^{0.5}$, grey lines). It can be deduced that the carbonation depth is less than 22-23 mm (average thickness of concrete cover of ordinary reinforcement in the deck beams) after 50 years only if k ranges between 2 and 3.2. This means that 22-23 mm of concrete cover for ordinary rebars in the inspected beams lead to an initiation time of over 50 years only in dense concrete. Strands, which are in depth at an average cover depth of 40 mm, are protected after 50 years in a concrete with k equal to 3.2 only in absence of segregation.

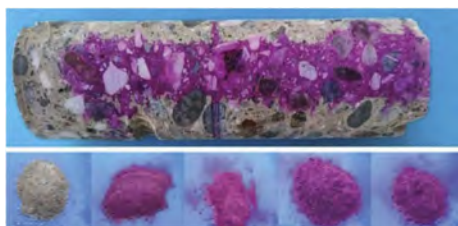


Figure 11. Phenolphthalein test on concrete core and concrete powders.

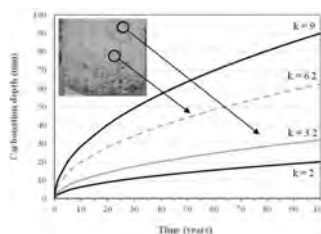


Figure 12. Carbonation depth vs time and carbonation coefficient k .

3.4.2 Chlorides content

Chlorides can be transported in concrete from the environment due to seawater exposure or to de-icing salts. Thus, chloride depth profiles should be determined in order to value the actual chloride level at the reinforcement and possible corrosion initiation and propagation. Chlorides contents can be measured by different methods. It is preferable to carry out laboratory tests which are more accurate than field tests (Colleparidi 1995). Figure 13 shows the chloride profiles measured on concrete samples after being digested in hot nitric acid for several type of deck beams inspected after 53 years of service life (Figure 1). The chloride content, measured by means of potentiometric titration, has been expressed as percentage of the dry concrete. Chloride profiles have been interpolated based on the “erf function” obtained from the analytical solution of the one-dimensional Fick’s second law of diffusion (Colleparidi et al. 1972). From Figure 13 it can be observed that the chloride profile measured on a pier cap overcome the critical chlorides threshold for carbon steel (0.05-0.125% in mass of concrete)

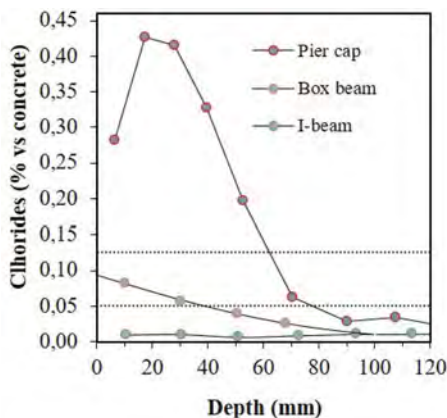


Figure 13. Chlorides profiles on bridge elements: I-beam, box beam, pier cap (Carsana et. al 2023). Dotted lines indicate critical chloride thresholds.

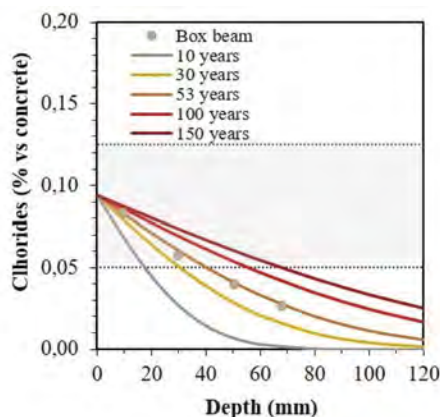


Figure 14. Chlorides profiles calculated after different time of exposure (10-100 years), based on experimental data from a box beam (Figure 13).

also far beyond typical minimum concrete cover thickness (for example 20 mm) with maximum values of 0.42% vs concrete mass. Conversely, for deck beams the risk of chlorides-induced corrosion shall be considered low at inspection time. In fact, chlorides content is below critical chlorides threshold at any concrete depth.

The diffusion equation considered to fit experimental data can be also used for the evaluation of the initiation time of corrosion. As shown in Figure 14, by assuming constant exposure conditions, the evolution with time of the chlorides profile in concrete can be evaluated.

3.4.3 Physical, microstructural and chemical analyses

To predict future deterioration of RC elements of bridges and viaducts due to corrosion phenomena, several measurements of the electrochemical parameters in time are usually needed in order to take into account daily and seasonal variations due to change in temperature and relative humidity. However, if this is not feasible, the interpretation of the available data deriving from electrochemical techniques can be improved by measuring physical properties of cores and samples collected from inspected structure (such as density in dry and water-saturated conditions and water absorption). In fact, it is well known that the electrical resistivity of concrete and cement paste depends on pore volume and pore-size distribution of cement paste, the pore-water composition and moisture content. Depending on exposure conditions and chemical and microstructural properties of concrete, resistivity can vary of several orders of magnitude. For instance, Figure 15 shows the relationship between the moisture content of concrete and its resistivity, obtained from laboratory tests on cores taken from transversal (T) and longitudinal (L) fronts of some deck beams of the viaduct shown in Figure 1. Resistivity of these cores has been measured in different conditions: “as received”, after (o during) wetting and drying.

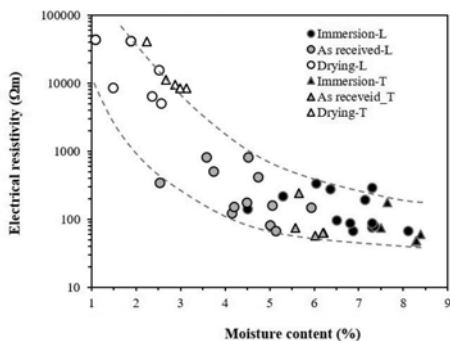


Figure 15. Electrical resistivity vs moisture content measured on some concrete cores taken from several deck beams of the viaduct shown in Figure 1.

Moreover, to investigate the composition, microstructure, and thus the protection given by concrete (or grout in case of post-tensioning tendons) to embedded steel, further laboratory analyses can be carried out on selected samples. Firstly, X-ray diffraction analysis is performed in order to identify crystalline compounds of cementitious materials or corrosion products. The ICP-OES technique by plasma emission spectrometry is used to analyze the elemental composition of concrete or grout and of reinforcement in terms of oxides. Finally, the microstructure of concrete samples, grout or reinforcement can be also observed under stereomicroscope and environmental scanning electron microscope with an EDS X-ray spectrometer (Carsana & Bertolini 2016).

As an example, Figure 16 shows evidence of phenomena of efflorescence on a concrete sample collected from the surface of a box beam, by means of stereo-microscope and scanning electron microscope. In particular, Figure 16b shows the morphology of crystallization products and highlights main elements such as sodium (Na), sulfur (S) and oxygen (O) and traces of chlorine (Cl), thus confirming the presence of chloride and sulfate salts.

As far as steel reinforcements are concerned, by analyzing a polished section of a rebar with stereo-microscope and scanning electron microscope, as shown in Figure 17, its microstructure and the thickness of the oxide layer can be estimated.

Stereo-microscope and scanning electron microscope allow also to observe fracture surfaces of samples of steel. For instance, Figure 18 shows the failure of a wire, which took place in correspondence of a localized corrosion attack. At the scanning electron microscope (SEM), the fracture surface, where it is not masked by corrosion products, seems ductile and characterized by the presence of elongated dimples (Carsana & Bertolini 2015). Microstructural observations allow to investigate on the possible presence of hydrogen-induced stress corrosion cracks, as reported in Carsana & Bertolini (2015).

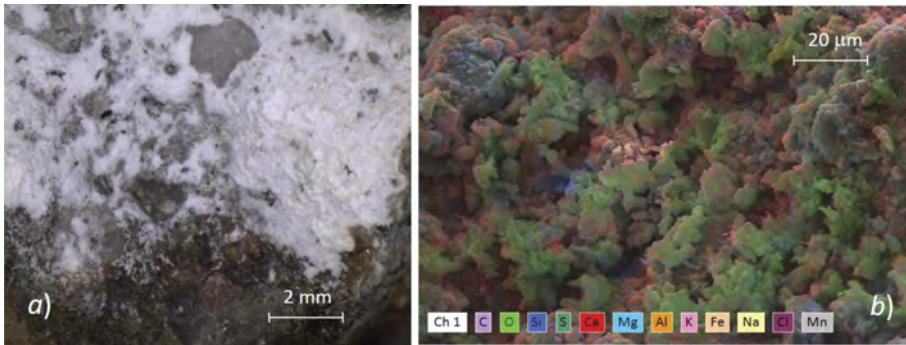


Figure 16. (a) Stereo-microscope and (b) SEM images with EDS map of concrete sample collected from surface of a box beam of the viaduct shown in Figure 1.

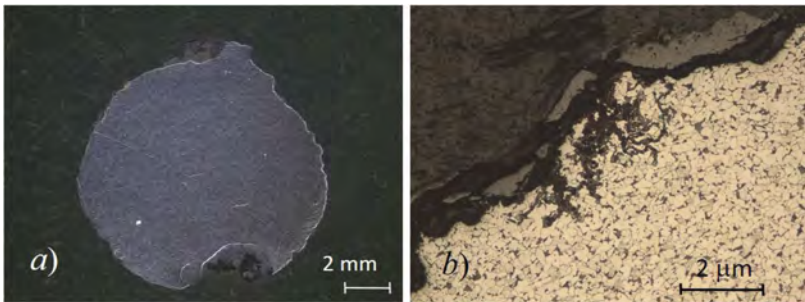


Figure 17. (a) Stereo-microscope image and (b) metallographic section of a steel rebar.

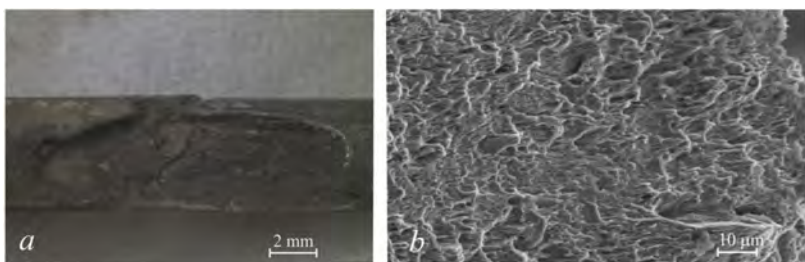


Figure 18. (a) Stereo-microscope image of the two parts of a broken wire and (b) SEM image of the ductile fracture surface (Carsana & Bertolini 2015).

4 CONCLUSIONS

The paper has introduced some of the key aspects of inspection procedures for corrosion assessment of RC bridges and viaducts. Methodologies and results from several field and laboratory tests have been presented and exemplified, illustrating the procedures and tools available in order to perform both chemical and microstructural analyses on concrete, complemented by electrochemical tests on steel reinforcement.

A summary of the results of recent studies and research investigations carried out by the authors have been presented. In particular, a wide campaign of investigations has been considered to evaluate statistically various electrochemical, physical and microstructural parameters of real scale elements. These outcomes, in agreement with the results reported by many other researchers, have allowed defining a procedural approach aimed at assessing the state of materials degradation and corrosion conditions of structural members with emphasis on bridge structural components. These investigations have highlighted mainly the effects of both carbonation and chlorides-induced corrosion on reinforcing and prestressing steel of concrete structural elements and how to consider the results of surveys for preliminary evaluating the evolution with time of such degradation phenomena. The collected data will also be used in future research investigations for the development of database and inventories for condition evaluation and structural assessment and of the life-cycle performance and residual lifetime of in-service structures and infrastructure facilities.

ACKNOWLEDGEMENTS

BRIDGE|50 is a research project based on a research agreement among universities, public authorities, and private companies. Members of the Management Committee: S.C.R. Piemonte (President); Politecnico di Milano (Scientific Coordinator); Politecnico di Torino (Scientific Responsible of the Experimental Activities); Lombardi Engineering (Secretary); Piedmont Region; City of Turin; Metropolitan City of Turin; TNE Torino Nuova Economia; ATI Itinera & C.M.B.; ATI Despe & Perino Piero; Quaranta Group. BRIDGE|50 website: <http://www.bridge50.org>

* * *

This keynote paper is dedicated to the memory of prof. Luca Bertolini and prof. Pietro Pedefferri.

REFERENCES

- Andrade, C., Alonso, C., 2004. Test methods for on-site corrosion rate measurement of steel reinforcement in concrete by means of the polarization resistance method, *Materials and Structures*, 37, 623–643.
- Anghileri, A., Savino, P., Capacci, L., Bianchi, S., Rosati, G., Tondolo, F., Biondini, F. 2021. Non destructive testing and model validation of corroded PC bridge deck beams. *1st Conference of the European Association on Quality Control of Bridges and Structures (EUROSTRUCT 2021)*, Padua, Italy, August 29 - September 1, 2021. In: Pellegrino, C., Faleschini, F., Zanini, M.A., Matos, J.C., Casas, J.R., Strauss, A. (Eds.) *Lecture Notes in Civil Engineering*, 200, 2022, Springer.
- ASTM C876-91, 1991. *Standard test method for half-cell potential of reinforcing steel in concrete*, American Society for Testing and Materials.
- Bertolini, L., Carsana, M., Pedefferri P., 2007. Corrosion behaviour of steel in concrete in the presence of stray current. *Corrosion Science*, 49(3), 1056–1068.
- Bertolini, L., 2008. Steel corrosion and service life of reinforced concrete structures. *Structure and Infrastructure Engineering*, 4(2), 123–137.
- Bertolini, L., 2011. A tribute to Pietro Pedefferri's contribution to the knowledge on corrosion of steel in concrete and its prevention. *Materials and Corrosion*, 62(2), 96–97.
- Bertolini, L., Carsana, M., Gastaldi, M., Lollini, F., Redaelli, E., 2011. Corrosion assessment and restoration strategies of reinforced concrete buildings of the cultural heritage. *Materials and Corrosion*, 62(2), 146–154.

- Bertolini, L., Elsener, B., Pedefferri, Redaelli, E., Polder, R., 2013. *Corrosion of Steel in Concrete: prevention, diagnosis, repair*, Weinheim, Germany, Wiley.
- Bertolini, L., Carsana, M., Gastaldi, M., Lollini, F., Redaelli, E., 2016. Corrosion of steel in concrete and its prevention in aggressive chloride-bearing environments. *International Conference on Durability of Concrete Structures (ICDCS 2016)*, June 30 - July 1, 2016.
- Biondini, F., Frangopol, D.M., 2016. Life-cycle performance of deteriorating structural systems under uncertainty: Review, *Journal of Structural Engineering*, ASCE, 142(9), 1–17.
- Biondini, F., Frangopol, D.M., (Eds.), 2019. *Life-cycle design, assessment and maintenance of structures and infrastructure systems*, American Society of Civil Engineers (ASCE), Reston, VA, USA.
- Biondini, F., Manto, S., Beltrami, C., Tondolo, F., Chiara, M., Salza, B., Tizzani, M., Chiaia, B., Lencioni, A., Panseri, L. & Quaranta, L., 2020. BRIDGE|50 research project: Residual structural performance of a 50-year-old bridge, *10 International Conference on Bridge Maintenance, Safety and Management (IABMAS 2020)*, June 28-July 2, 2020 (postponed to April 11- 15,2021), Sapporo, Japan. In: Yokota, H., Frangopol, D.M. (Eds.), *Bridge Maintenance, Safety, Management, Life-Cycle Sustainability and Innovations*. CRC Press/ Balkema, Taylor & Francis Group, London, UK.
- Biondini, F., Tondolo, F., Manto, S., Beltrami, C., Chiara, M., Salza, B., Tizzani, M., Chiaia, B., Lencioni, A., Panseri, L. & Quaranta, L., 2021. Residual structural performance of existing PC bridges: Recent advances of the BRIDGE|50 research project. *1st Conference of the European Association on Quality Control of Bridges and Structures (EUROSTRUCT 2021)*, Padua, Italy, August 29 - September 1, 2021. In: Pellegrino, C., Faleschini, F., Zanini, M.A., Matos, J.C., Casas, J.R., Strauss, A. (Eds.) *Lecture Notes in Civil Engineering*, 200, 2022, Springer.
- Carsana, M., Bertolini, L., 2015. Corrosion failure of post-tensioning tendons in alkaline and chloride-free segregated grout: a case study. *Structure and Infrastructure Engineering*, 11(3), 402–411.
- Carsana, M., Bertolini, L., 2016. Characterization of segregated grout promoting corrosion of post-tensioning tendons. *Journal of Materials in Civil Engineering*, ASCE, 28 (4),04016009, 1–9.
- Carsana, M., Biondini, F., Redaelli, E., Valoti, D.O., 2021. On site-corrosion characterization of 50-year-old PC deck beams. *1st Conference of the European Association on Quality Control of Bridges and Structures (EUROSTRUCT 2021)*, Padua, Italy, August 29 - September 1, 2021. In: Pellegrino, C., Faleschini, F., Zanini, M.A., Matos, J.C., Casas, J.R., Strauss, A. (Eds.) *Lecture Notes in Civil Engineering*, 200, 2022, Springer.
- Carsana, M., Biondini, F., Redaelli, E., Valoti, D.O. 2022. Corrosion assessment of 50-year-old PC deck beams. *11th International Conference on Bridge Maintenance, Safety and Management (IABMAS 2022)*, Barcelona, Spain, July 11- 15, 2022. In: Casas, J.R., Frangopol, D.M., Turmo, J. (Eds.), *Bridge Safety, Maintenance, Management, Life-Cycle, Resilience and Sustainability*. CRC Press/ Balkema, Taylor & Francis Group, London, UK.
- Carsana, M., Redaelli, E., Valoti, D.O., Biondini, F., 2023. Experimental campaign for corrosion assessment of 50-year-old PC deck beams. *Eighth International Symposium on Life-Cycle Civil Engineering (IALCCE 2023)*, Milan, Italy, July 2-6, 2023.
- Carsana, M., Gastaldi, M., Redaelli, E., 2023b. A case study on corrosion conditions and guidelines for repair of a reinforced concrete chimney in industrial environment, *Structure and Infrastructure Engineering*, 19(3), 366–377.
- Colleparidi, M., Marcialis, A., Turriziani, R., 1972. Penetration of chloride ions into cement pastes and concretes. *Journal of American Ceramic Society*, 55, 534.
- Colleparidi, M., 1995. Quick method to determine free and bound chlorides in concrete, *International Rilem Workshop "Chloride penetration into concrete"*, Saint Rémy lès Chevreuse, October 15-18, 1995.
- Elsener, B., Andrade, C., Gulikers, J., Polder, R., Raupach, M., 2003. Recommendation on half-cell potential measurements, *Materials and Structures*, 36, 461–471.
- Elsener, B., Böhni, H., 1995. Condition evaluation of reinforced concrete bridges - The benefits of potential mapping, *International Conference on Structural Faults and Repair*, London, UK, 47–52.
- Page, C.L., Page, M.M., 2007. *Durability of concrete and cement composites*, Woodhead Publishing Series in Civil and Structural Engineering.
- Savino, P., Tondolo, F., Sabia, D., Quattrone, A., Biondini, F., Rosati, G., Anghileri, M., Chiaia, B., 2023. Large-scale experimental static testing on 50-year-old prestressed concrete bridge girders. *Applied Sciences*, 13(834), 1–22.
- Tuutti, K., 1982. *Corrosion of steel in concrete*. Doctoral Thesis, Division of Building Materials, Swedish Cement and Concrete Research Institute, Stockholm, Sweden.

Bayesian assessment of existing concrete structures: Exploiting the full power of combined information

R. Caspeele & W. Botte
Ghent University, Ghent, Belgium

ABSTRACT: When assessing existing concrete structures, an adequate prediction of the time-dependent structural performance is crucial. Unfortunately, the degradation process is associated with large uncertainties and when executing additional investigations and measurements, significant model and measurement uncertainties play a dominant role in the reliability-based performance prediction. Bayesian updating techniques provide a unique engineering tool to adequately combine and fully exploit the power of combined available information, enabling to make inferences where classical statistical approaches fail. Among others, uncertainties on degradation parameters and variables in structural reliability calculations can be updated on the basis of combined information from measurements, monitoring and visual inspections. Even the effect of quality control can be taken into account. Consequently, these updated uncertainties can be taken into account in full-probabilistic structural reliability calculations, or partial factors for the structural verification can be adjusted according to the posterior probabilistic models. In this contribution, the integration of these approaches into the practical assessment process is briefly explained and an outlook is given on future engineering challenges to integrate such approaches further in the life-cycle assessment of existing concrete structures.

1 INTRODUCTION

An increasing amount of the current activities in the construction sector are oriented towards the assessment of existing structures and the associated repair and upgrading interventions. Although the last decennia significant progress has been made to analytically and numerically simulate the degradation process of concrete structures and their associated structural performance prediction in time, structural engineers are challenged to deal with the large uncertainties involved. Besides a typical lack of information, the degradation processes are associated with large uncertainties and when executing additional investigations and measurements, significant model and measurement uncertainties play a dominant role in the reliability-based performance prediction. Intentions to generalize and internationally fix variables and parameters involved in the assessment of existing concrete structures appear difficult to achieve. Hence, a solution to this problem is rather to be found in the application of Bayesian updating techniques that enables to take into account the specific situation of the structure and its environment. This Bayesian updating provides a unique engineering tool to adequately combine and fully exploit the power of combined available information, enabling to make inferences where classical statistical approaches fail.

After revisiting some basics on Bayesian approaches, it is explained and illustrated how Bayesian updating techniques provide an undeniable advantage in several steps of the assessment process. It is explained how degradation models whose parameters generally are difficult to find consensus about, can gradually be updated when more information becomes available. Variables in structural reliability calculations can be updated on the basis of direct as well as indirect measurement data. Sources of information contained in different types of measurements or even visual inspections can be combined in order to make much more informed inferences and to reduce

uncertainties in the reliability-based performance assessment, compared to when such data is analysed separately. Even, although often forgotten, the positive effect of quality control can be taken into account when assessing the structural reliability. After updating the uncertainties of the variables involved, these posterior distributions can be taken into account in full-probabilistic structural reliability calculations, or partial factors used in semi-probabilistic assessment approaches can be adjusted on the basis of updated uncertainties (fib 2016). Finally, the paper ends with an outlook to future engineering challenges to integrate such approaches further in the life-cycle assessment of existing concrete structures.

2 BAYESIAN INFERENCE

The basic theory behind Bayesian statistics dates already from 1763 with the famous paper (posthumously published) by the reverend Thomas Bayes in order to solve the question how to assess the probability of a certain value of not observable quantities, given a set of related measurements. Note that this is exactly the challenge we are often faced with as structural engineers. However, it is only the last decennia that this Bayesian point of view is used extensively due to the advances in computational abilities and the development of more efficient numerical algorithms to solve the mathematical difficulties associated with Bayesian statistics. Many fields of research have recognized the importance of Bayesian statistics, which has led to new research perspectives, for sure also in the field of structural engineering. Although already common practice to tackle research challenges, the methodology has still not yet fully found its way into practical applications by practitioners where frequentistic approaches still dominate statistical inference to deal with uncertainties. A challenge ahead is hence to make the *Bayesian way of thinking* more accessible.

The Bayesian definition of the probability $P[A]$ of an event A is formulated as a degree of belief that A will occur. Hence, Bayesian inference probabilities are a measure of our state of knowledge about nature, not a measure of nature itself (Gregory 2005). The degree of belief can hence be a reflection of the state of mind of the individual person in terms of experience, expertise and preferences. In this respect the Bayesian interpretation of probability is subjective. However, this subjective nature is not a big issue, as we can require that observers with the same amount of information should come to the same conclusion (Verdoolaege 2006). More specifically, it is possible to suppose as little as possible and *let the data speak for themselves* by using non-informative priors. However, the ability to include prior information is of large importance in structural engineering problems, especially when confronted with limited data.

The Bayes' theorem to calculate the probability P of an event E_i given the observation A (i.e. the posterior probability of E_i) is given by Equation (1):

$$P[E_i|A] = \frac{P[A|E_i]P[E_i]}{P[A]} \quad (1)$$

where $P[E_i|A]$ is called the posterior probability of E_i , $P[A|E_i]$ is often referred to as the likelihood (i.e. the probability of observing a certain outcome given a certain cause) and $P[E_i]$ is called the prior probability of the event E_i (i.e. prior to the knowledge about event A). Hence, Bayes' theorem enables to update probabilities, based on new information.

In case of continuous distributions, the continuum formulation of Bayes' theorem can be used. Consider a random variable X which has a probability density function $f_X(x|\theta)$ depending on a parameter vector θ . In case new information becomes available, the prior distribution function $f'_{\Theta}(\theta)$ of the parameters θ can be updated towards a posterior distribution function $f''_{\Theta}(\theta)$ (Gelman et al. 2004):

$$f''_{\Theta}(\theta) \equiv f(\theta|\mathbf{I}) = \frac{L(\theta|\mathbf{I}) \cdot f'_{\Theta}(\theta)}{\int L(\theta|\mathbf{I}) \cdot f'_{\Theta}(\theta) d\theta} = c \cdot L(\theta|\mathbf{I}) \cdot f'_{\Theta}(\theta) \quad (2)$$

where c is a normalizing constant, $L(\theta|\mathbf{I})$ is the likelihood function, i.e. the likelihood of the parameters θ based on the new information \mathbf{I} . Assume for example that n independent results x_i are observed, then the likelihood associated with this new information is given by the probability:

$$L(\theta|\mathbf{I}) \equiv L(\theta|x_1, \dots, x_n) = \prod_{i=1}^n f_X(x_i|\theta) \quad (3)$$

In case of correlated observations, the likelihood can be extended to a multivariate distribution including the correlation between variables.

In contrast to the classical or frequentistic approach, prior information can be taken into account through the prior density function of the parameters, i.e. $f_{\theta}(\theta)$. The way in which this influences the posterior density function is depending on the relative importance of the prior information compared to the new information (i.e. the likelihood function). In order to *let the data speak for themselves* most often non-informative or vague priors are used, which maximize the information provided by the likelihood function (see e.g. Box & Tiao 1973, Gelman et al. 2004)

When calculating the posterior distribution, computational difficulties arise due to the necessary evaluation of high-dimensional integrals. This was the main obstacle for the use of Bayesian methods in the previous century. Together with the advances in computational efficiency, a group of so-called Markov Chain Monte Carlo methods (MCMC) were developed (see e.g. Gelman et al. 2004) for the numerical determination of the posterior probabilities.

3 APPLICATION OF BAYESIAN UPDATING TECHNIQUES IN THE ASSESSMENT OF EXISTING CONCRETE STRUCTURES

3.1 *The Bayesian way of thinking in all steps of the assessment and rehabilitation process*

The assessment process commonly consists of several steps, encompassing condition assessment, performance prediction, monitoring, performance updating and an optimization of interventions (Figure 1). Uncertainties are involved in all of these steps, and Bayesian updating can play a role in each of the steps to adjust lacking knowledge when more information becomes available.

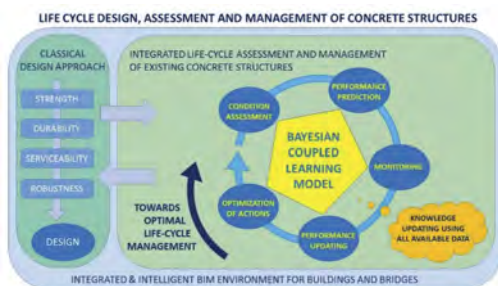


Figure 1. Principle of life-cycle design, assessment and management of concrete structures and the place of Bayesian approaches to update within and in-between all aspects.

In particular, parameters that are difficult to be fixed in general (e.g. degradation parameters such as diffusion coefficients and carbonation resistance, environmental conditions, direct and indirect costs, etc.), can be updated when more information becomes available and as such bypass the often occurring conundrum when trying to fix model parameters in general for all cases.

Moreover, while often forgotten, also the interaction between the different steps in the assessment process plays an important role when updating uncertainties and the combination of this kind of information can lead to a significant improvement of the posterior uncertainties. Monitoring data can for example also be used to update degradation models used in the condition assessment. Structural analysis models can be extended by random fields that enable to update degradation models and their spatial variability – which is often not quantitatively accounted for as most models are 1D models – when test and monitoring data becomes available.

In the following, several more specific aspects on how to exploit Bayesian updating in the framework of assessment of existing concrete structures are highlighted.

3.2 Updating variables in structural reliability calculations

3.2.1 Updating of variables on the basis of direct associated measurements

Bayesian updating methods based on prior information are already widely applied for the assessment of existing concrete structures (see e.g. Strauss et al. 2008). In case of the assessment of concrete strength, quantitative prior knowledge on concrete strength distributions can be found in literature (see e.g. Rackwitz 1983), and similarly for other variables (see e.g. JCSS 2001). Prior information can for example be modelled, based on normal-gamma or lognormal-gamma distributions. These types of distributions are natural conjugate priors for updating the mean and standard deviation of the normal or lognormal concrete strength distribution, which enables to find simple analytical expressions for updating the parameters of the strength distribution function in a Bayesian framework. When for example the characteristic concrete strength has to be estimated from a limited number of test samples, the use of a combined vague-informative prior is of particular interest (Caspellee & Taerwe 2012). Prior knowledge on the standard deviation can be taken into account, leading to a reduction in the standard deviation of the predictive strength distribution and a more realistic estimation of the characteristic concrete strength in cases where only a limited number of test results are available. A similar approach can be followed for other variables.

3.2.2 Data from in-situ static load tests

Data obtained from static load tests can be used to update the probabilistic distributions of variables which are of significant importance when assessing the behaviour of concrete structures. Such static load tests can be executed in situ on (part of) the structure or in laboratory on representative elements which have been taken from the structure to be assessed. In such cases, the observed data $\bar{\mathbf{d}}$ can according to (Simoen et al. 2015) be written as:

$$\bar{\mathbf{d}} = M(\boldsymbol{\theta}) + \boldsymbol{\eta}_G + \boldsymbol{\eta}_D \quad (4)$$

where, $M(\boldsymbol{\theta})$ is a model with input parameters $\boldsymbol{\theta}$ used to predict the data $\bar{\mathbf{d}}$, $\boldsymbol{\eta}_G$ is a modelling error and $\boldsymbol{\eta}_D$ is the measurement error. Assuming a normal distribution with zero mean and covariance matrices $\boldsymbol{\Sigma}_D$ and $\boldsymbol{\Sigma}_G$ for the latter, the likelihood can be expressed as:

$$L \sim (\det(\boldsymbol{\Sigma}_D + \boldsymbol{\Sigma}_G))^{1/2} \exp\left(-\frac{1}{2} F_{ML}\right) \quad (5)$$

where F_{ML} is the maximum likelihood function, which can be formulated as:

$$F_{ML} = (M(\boldsymbol{\theta}) - \bar{\mathbf{d}})^T (\boldsymbol{\Sigma}_D + \boldsymbol{\Sigma}_G)^{-1} (M(\boldsymbol{\theta}) - \bar{\mathbf{d}}) \quad (6)$$

When looking into the incorporation of information of monitoring data based on static load tests on infrastructure, the approach followed in (Vereecken et al. 2023) illustrates the possibility to use the data of strains and displacements collected during a static load test on a reinforced concrete slab bridge in Amsterdam (The Netherlands) to update the spatial distribution of the stiffness of the deck along the bridge (Figure 2). In case of strains and considering $\boldsymbol{\Sigma}_G = \mathbf{0}$, the likelihood function can be rewritten as (Vereecken et al. 2022b):

$$F_{ML} = \sum_{j=1}^N \frac{1}{\sigma_\varepsilon^2} (\bar{\varepsilon}_j - \varepsilon_j(\boldsymbol{\theta}))^2 \quad (7)$$

where N is the number of measurements, σ_ε is the standard deviation of the measurement error, $\bar{\varepsilon}_j$ are the measured strains and $\varepsilon_j(\boldsymbol{\theta})$ are the strains obtained from a numerical model with input parameters $\boldsymbol{\theta}$.

In (Vereecken et al. 2023), the aim was to determine the best posterior model based on MCMC in combination with surrogate modelling in order to limit the computational cost. Therefore, the influence of different models for the prediction error, as in (Simoen et al. 2013),

the model bias, and the influence of different definitions of the stiffness of the structural model, was investigated on an actual engineering structure. Bayesian-based model selection was performed both based on log evidence and posterior predictive capabilities. As an example, the posterior distributions of the stiffness along the deck of the bridge is illustrated in Figure 2 for two models: one adopting two possibilities for the stiffness (cracked and uncracked) and one adopting for more flexibility in the stiffness distribution along the length. A more flexible model for the stiffness distribution was found to be preferred over a model allowing less spatial variability.

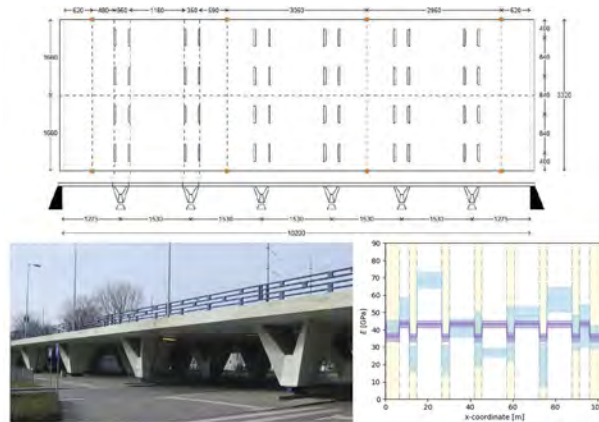


Figure 2. Picture, top and side view of bridge 705 with its main dimensions in [cm] (Rozsas et al. 2022) and posterior distribution of the stiffness along the deck for two *situations*: 2 discrete stiffness distributions (purple) and a spatially variable stiffness distribution (blue). The solid/dashed line represents the posterior mean and the hatched area represents the posterior 90% HDI (Vereecken et al. 2023).

3.2.3 Data from laboratory static load tests

Bayesian updating can also play a significant role when analysing results from a limited number of (e.g. large-scale) tests. In this regard, the approach developed in (Botte et al. 2021) is of particular interest, adopting a two-step Bayesian framework in combination with non-linear finite element modelling in order to assess the remaining prestress and associated uncertainties in post-tensioned concrete beams from the 1940's. In the first step, the distributions of material characteristics such as the compressive strength, tensile strength, Young's modulus and density of concrete as well as the Young's modulus of the prestressing steel were updated using MCMC and based on direct measurements of those properties. Prior information was selected from the JCSS Probabilistic Model Code (JCSS 2001) based on historical documentation regarding the design. Considering these updated distributions for the material properties, a vague prior distribution of the remaining prestress was consecutively updated based on the information obtained from large-scale load tests in laboratory. In particular the cracking moment, moment of reopening of cracks and behaviour in the non-linear branch of the load-displacement diagram contain in that regard very valuable information, since these depend significantly on the remaining prestress level.



Figure 3. Static load test on a primary beam and the corresponding posterior distribution of the remaining prestress including the 90% HDI (Botte et al. 2021).

3.2.4 Ambient vibration data

Model-based structural health monitoring is often executed through vibration-based finite element model updating. It is based on the assumption that local structural damage results in a local reduction of stiffness. The presence of damage can be detected, located and quantified (Simoen et al. 2015). The natural frequencies identified in a modal test only provide global information, whereas localization of damage requires the identification of mode shape displacements. However, mode shapes are usually characterized by a larger identification uncertainty and they are not extremely sensitive to moderate changes in structure stiffness (Simoen et al. 2015). Hence, additional properties can be measured which are more sensitive to changes in stiffness, such as modal flexibilities (Catbas et al. 2008), modal curvatures (Pandey et al. 1991) and modal strain energies (Jaishi & Ren 2007).

In case eigenvalues and mode shapes are used in a Bayesian model updating procedure and considering $\Sigma_G = \mathbf{0}$, the likelihood function can be written as:

$$F_{ML} = \sum_{j=1}^N \frac{(\bar{\lambda}_j - \lambda_j(\boldsymbol{\theta}))^2}{\sigma_{\lambda_j}^2} + \sum_{j=1}^N \frac{(\bar{\phi}_j - \phi_j(\boldsymbol{\theta}))^2}{\sigma_{\phi_j}^2} \quad (8)$$

where N is the number of modes considered, $\bar{\lambda}_j$ and $\bar{\phi}_j$ are the measured eigenvalues and mode shape vectors and $\sigma_{\lambda_j}^2$ and $\sigma_{\phi_j}^2$ are the standard deviations of the error related to the measured frequency and mode shape respectively.

3.2.5 Visual inspections

Visual inspections are the most frequently occurring types of inspections since these are relatively simple to execute. These inspections provide rough indications whether there is a risk related to human safety or whether there are any alarming time-dependent evolutions in the structural behaviour. Regarding corrosion, the most important visual observations are the presence of rust stains, corrosion cracks or concrete spalling. If any of these signs are present, it can be concluded that the reinforcement at that location has started to corrode. In Figure 4 it is illustrated how visual observations can influence the distribution of the initiation period. If at t_{insp} it is observed that rust stains are present, the initiation time T_i should be lower than t_{insp} . Hence, the distribution of the initiation time can be updated as follows (Botte, 2017):

- In case inspection reveals that corrosion has initiated at some point in time before t_{insp} :

$$F''_{T_i}(t) = \frac{F'_{T_i}(t)}{F'_{T_i}(t_{insp})} \quad (9)$$

- In case inspection reveals corrosion has not yet initiated at t_{insp} :

$$F''_{T_i}(t) = \frac{F'_{T_i}(t) - F'_{T_i}(t_{insp})}{1 - F'_{T_i}(t_{insp})} \quad (10)$$

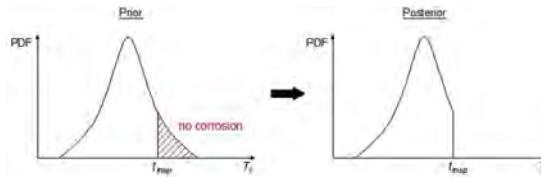


Figure 4. Influence of a visual observation of corrosion on the PDF of the initiation period.

In addition, this visual data can be used to supplement the static and/or dynamic data as it – through the application of the Bayesian updating approach – can lead to inferences on the origin of the stiffness reduction. Furthermore, models to predict the crack width or time to

cracking can be updated based on the observed crack locations or crack widths according to the approach which will be explained in section 3.3. It should be pointed out that visual inspections can also suffer significantly from operator bias. If such bias is present, this bias should and can be accounted for when evaluating the information from the visual inspections.

3.2.6 Combining different sources of information

Each of the mentioned test methods and corresponding data types has its advantages and limitations. Nevertheless, in a Bayesian context, the different types of data can be combined in a smart way in order to optimize the assessment procedure. A possible solution consists of first localizing the critical elements of the structure based on the modal data so that these can be prioritized when strain data are collected under proof-loading. Combining the data of both measurements will lead to reduced identification uncertainties when compared to the case where the measurements are considered separately. A conceptual illustration of the advantage of combining both sources of information is provided in Figure 5.

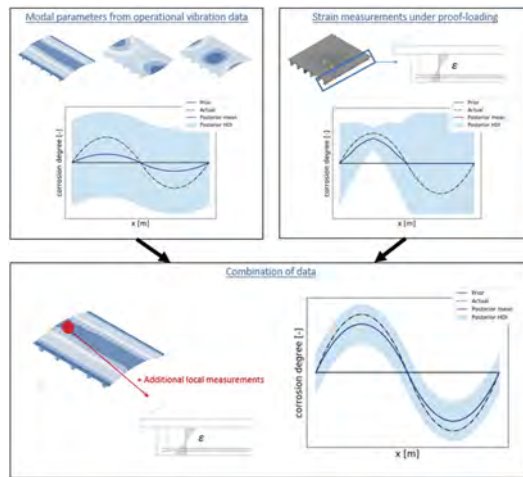


Figure 5. Concept of updating the corrosion degree based on strain data from proof-loading and modal data from ambient acceleration measurements and the improved predictability considering both sources of information (Vereecken et al. 2022b).

In (Vereecken 2022a) the advantage of updating on the basis of combined information with or without the information from visual observations is illustrated in relation to the posterior distribution of the corrosion degree of reinforcement in a concrete beam, see Figure 6.

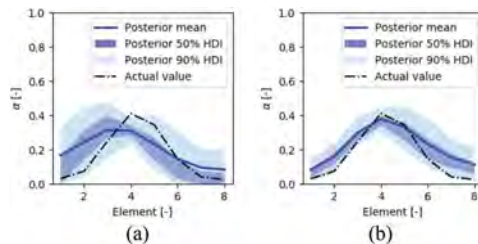


Figure 6. Posterior corrosion degree of a simply supported beam when measuring the strains under proof loading (a) without visual observation, (b) with visual observation of rust stains. For more detailed information, see (Vereecken 2022a).

3.3 Updating of degradation models

The principle provided by Bayes' rule can also be applied in regression analysis. This way, previously obtained information regarding regression parameters of degradation models can be

updated towards posterior distributions of the regression parameters, taking into account experimental data. The fact that prior information can be taken into account, moreover enables to make sure that relevant regression models can be obtained even in case of very limited information, which provides a significant advantage compared to other statistical approaches.

Assume that the true value of the response variable \tilde{y} can be predicted by a mathematical or numerical model $M(\cdot)$ which is a non-linear function of R regression parameters β_i and depends on a vector \mathbf{x} which represents a m -dimensional set of input parameters. If this model would be perfect and the true values $\tilde{\mathbf{x}}$ are exactly known, this model would predict the true response value \tilde{y} . However, due to the existence of uncertainties, the true value is given by:

$$\tilde{y} = y + \varepsilon = M(\mathbf{x}) + \varepsilon \quad (11)$$

where the error term is usually considered as a realization of a Gaussian random variable with mean 0 and standard deviation σ_ε , representing the measurement and model uncertainties.

If N independent test results y_i are available for the response variable of N sets of corresponding input parameters \mathbf{x}_i , the likelihood of the experimental data can in general be written as:

$$L(y_1, \dots, y_N | \mathbf{x}_1, \dots, \mathbf{x}_N) = \prod_{i=1}^N \frac{1}{\sigma_\varepsilon} \phi\left(\frac{y_i - M(\mathbf{x}_i)}{\sigma_\varepsilon}\right) \quad (12)$$

where $\phi(\cdot)$ is the probability density function of the standard normal distribution.

Based on the Bayesian principle, the prior information is given as the joint prior distribution $f'_B(\sigma_\varepsilon, \beta_1, \dots, \beta_R)$ regarding the standard deviation σ_ε of the error term and the regression parameters $(\beta_1, \dots, \beta_R)$. This prior distribution can be updated towards a posterior distribution, using the likelihood function, i.e.:

$$f''_B(\sigma_\varepsilon, \beta_1, \dots, \beta_R) = c \cdot f'_B(\sigma_\varepsilon, \beta_1, \dots, \beta_R) \cdot L(y_1, \dots, y_N | \mathbf{x}_1, \dots, \mathbf{x}_N) \quad (13)$$

where c is a normalizing constant.

When now considering again the situation with degradation models, a common discussion relates to fixing model parameters for the corrosion propagation phase in concrete. Rather than trying to fix these parameters in general for all cases, this Bayesian regression approach can be incorporated in the updating process when additional information becomes available. Consider for example the empirical model to predict the corrosion rate presented in (Vu & Stewart 2000) and (Stewart and Suo 2009):

$$M(\mathbf{x}) = i_{corr}(t_p) = i_{corr}(1) \cdot a \cdot t_p^b \quad (14)$$

$$i_{corr}(1) = \frac{d \cdot (1 - WC)^e}{C} \quad (15)$$

where t_p is the propagation time, $i_{corr}(1)$ is the corrosion rate at the start of corrosion propagation, WC is the water-cement ratio, C is the concrete cover, and a , b , d and e are regression parameters (with default values $a = 0.85$, $b = -0.3$, $d = 27$ and $e = -1.64$ according to (Stewart and Suo 2009)). In case N measurements of the corrosion rate $i_{corr,j}$ and associated input vectors $\mathbf{x}_j = (WC, C, t_p)_j$ are available, the likelihood function (12) and posterior distribution (13) yield respectively:

$$L(i_{corr,1}, \dots, i_{corr,N} | \mathbf{x}_1, \dots, \mathbf{x}_N) = \prod_{j=1}^N \frac{1}{\sigma_\varepsilon} \phi\left(\frac{i_{corr,j} - M(\mathbf{x}_j)}{\sigma_\varepsilon}\right) \quad (16)$$

$$f''_B(\sigma_\varepsilon, a, b, d, e) = c \cdot f'_B(\sigma_\varepsilon, a, b, d, e) \cdot L(i_{corr,1}, \dots, i_{corr,N} | \mathbf{x}_1, \dots, \mathbf{x}_N) \quad (17)$$

The likelihood and probability distributions can simply be added to the likelihood and distribution in relation to other variables and updated together. Prior information can moreover be based on literature data (such as mentioned for this specific case) or be based on vague prior information or information based on expert judgement. Finally, it is also important to notice that in case the corrosion rate is not measured directly, indirect measures may be used as for example corrosion

degrees, deflections, crack widths, etc. to infer indirectly about the corrosion rates. In such case also the model uncertainties or model parameters can be taken into account in the likelihood function and the updating can be performed together with all other uncertainties. In doing so the power of Bayesian updating is fully exploited in a way that is not comparable to other statistical methods.

3.4 Updating on the basis of information from quantitative quality control

The most important objective of quality control is to verify whether the delivered product or service complies with the specifications requested by the client. In general, quality control has a favourable effect due to the fact that the existence of quality requirements (such as conformity criteria) compels producers to deliver high quality products in order to avoid rejection by quality assessment. This effect has an influence on the probabilistic modelling of e.g. concrete properties of accepted concrete lots and also influences the structural reliability analysis of concrete structures. Bayesian approaches can be used to quantify this effect (Caspeele & Taerwe 2013).

For an assumed property (e.g. the concrete strength distribution) and for a given conformity criterion, one can calculate the probability that a concrete lot, characterized by a fraction defectives θ , is accepted. This probability is called the probability of acceptance and denoted as P_a . An example of such an operating characteristic curve is shown in Figure 7 in case of conformity criteria for concrete strength.

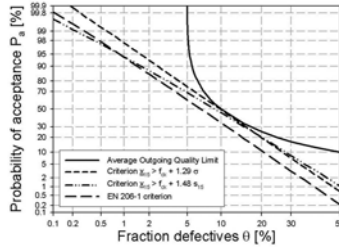


Figure 7. OC-line corresponding to different conformity criteria (Caspeele et al. 2014).

The filter effect of a conformity criterion is related to the probability of acceptance associated to the applied conformity control scheme. Due to the lower acceptance probability of a strength population with a high fraction defectives, the population of strength distributions shifts towards lower fractions defectives (which correspond to a higher quality with respect to e.g. concrete strength). Bayesian statistics provide the probabilistic framework for updating the (strength) distribution after conformity control, thus enabling to quantify the so-called filter effect, as follows:

$$f_{\theta,o}(\theta) = \frac{P_a(\theta) f_{\theta,i}(\theta)}{P_a(\theta) f_{\theta,i}(\theta) d\theta} \quad (18)$$

with $f_{\theta,i}(\theta)$ the prior distribution of the fraction defectives in incoming lots (designated 'i') and $f_{\theta,o}(\theta)$ the posterior distribution of the fraction defectives in outgoing or accepted lots (designated 'o'). In case of structural reliability calculations, it is however more relevant to update the parameters of the strength distribution (i.e. the mean and standard deviation of e.g. the concrete strength). In (Caspeele et al. 2014) a semi-analytical approach was developed to assess the filtering effect of complex conformity criteria accounting for autocorrelation between consecutive test results. Consider the following model for the concrete compressive strength X :

$$X = X_m + X_l \quad (19)$$

where X_m is a quantity describing the variation of the mean strength of different lots, i.e. X_m is normally distributed with mean μ_m and standard deviation σ_m , and X_l is a quantity describing the variation of the strength within a certain concrete lot, i.e. X_l is normally distributed with mean 0 and standard deviation σ_l . The mean and standard deviation of the offered (incoming) lots can be written as Equations (20) and (21) respectively:

$$\mu_i = \mu_m \quad (20)$$

$$\sigma_i = \sqrt{\sigma_m^2 + \sigma_l^2} \quad (21)$$

After conformity control, the posterior density function of X_m is given by:

$$f_o(x_m) = \frac{\frac{1}{\sigma_m} \phi\left(\frac{x_m - \mu_m}{\sigma_m}\right) P_a(x_m | \dots)}{\int_{-\infty}^{\infty} \frac{1}{\sigma_m} \phi\left(\frac{x_m - \mu_m}{\sigma_m}\right) P_a(x_m | \dots) dx_m} \quad (22)$$

where $\phi(\cdot)$ is the probability density function of the standard normal distribution and $P_a(x_m | \dots)$ is the probability that a concrete lot with mean strength x_m is accepted by the conformity criteria.

Further, the posterior predictive distribution of the concrete strength can then be calculated according to Equation (23) in case of the model outlined in Equations (19)–(22):

$$f_o(x) = \int_{-\infty}^{\infty} f(x|x_m, \sigma_l) \cdot f_o(x_m) dx_m = \int_{-\infty}^{\infty} \frac{1}{\sigma_l} \phi\left(\frac{x - x_m}{\sigma_l}\right) \cdot f_o(x_m) dx_m \quad (23)$$

where $f(\cdot)$ is the prior probability density function of X .

In (Caspele et al. 2014) and (Caspele 2014), the influence of quality control of concrete on structural reliability has been assessed based on the procedure outlined above. It was shown that due to conformity control, a more uniform reliability is obtained in function of the incoming fraction defectives. Thus, conformity control reduces the dependency of the reliability index with respect to the parameter uncertainties of concrete strength distributions. In Figure 8a, the filter effect is illustrated for the reliability of a concrete column subjected to compression. Similar results were obtained in (Botte et al. 2017) in case of conformity control of reinforcing steel. The influence of the latter on the reliability of a concrete beam subjected to bending is shown in Figure 8b.

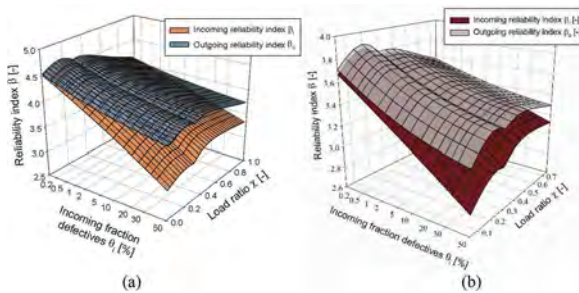


Figure 8. Influence of conformity control on the reliability index of a concrete (a) column subjected to compression and (b) beam subjected to bending: incoming and outgoing reliability indices β_i and β_o as a function of incoming fraction defectives θ_i and load ratio χ .

4 OUTLOOK

From the above overview it is clear that Bayesian updating techniques provide a unique tool for engineers in order to incorporate additional direct and indirect information about structures in all steps of the life-cycle assessment framework. Nevertheless, several challenges remain to be tackled the coming decades in order to bring these new developments into practical applications and convey the *Bayesian way of thinking* into everyday engineering practice.

At the research level, more efforts need to be undertaken to develop easy-to-use engineering tools that enable to disguise the often complex numerical and probabilistic calculations and simulations that are involved. There is an urgent need for the development of commercial FEM software for structural analysis that enables to incorporate localized information about the structure such as

measured concrete properties, monitoring data, durability parameters, etc. and automatically integrate this in a Bayesian calculation scheme enabling to make spatial predictions of the structural behaviour. Further, it is also necessary to orient research efforts to the quantification of suitable prior information in relation to measurement and model errors, as the current vague information that is available on this matter prevents more accurate posterior prediction of the structural behaviour. Especially in relation to degradation processes, research should step away from the intention of proposing generally applicable probabilistic models for the degradation process (which is very case specific) and orient towards updating degradation models along the lifetime of the structure.

At the level of practical applications, efforts should be oriented to develop a suitable assessment framework incorporating these Bayesian updating techniques. The optimization of investments in testing, monitoring and interventions is feasible with such techniques (see e.g. Vereecken et al. 2020) and should be more intensively exploited in order to come to cost-efficient, but adequate structural assessment and rehabilitation. There is an urgent need to step away from prescribing an extensive testing program without looking at the Value of Information (VoI) this data provides for the structural analysis to be performed. Frequently, investments in testing and monitoring can more adequately be spent if the VoI is properly considered, i.e. by quantifying the influence of the additional information on the posterior uncertainties and the associated decision making through a pre-posterior analysis (see e.g. Vereecken et al. 2021). Finally, in order to exploit the updating feasibilities during the lifetime, efforts and investments during the exploitation of the structures should be oriented to more frequent material testing rather than only making point-wise investigations and assessments in time. In this way, the Bayesian updating of the life-cycle performance becomes more effective and a more accurate estimation of the end of lifetime can be obtained.

5 CONCLUSIONS

Bayesian updating techniques have proven to be of undeniable importance when requiring to incorporate different sources of information into the assessment process of concrete structures. Although the last decennia significant progress has been made to analytically and numerically simulate the degradation process of concrete structures and their associated structural performance prediction in time, dealing with the large uncertainties involved requires the use of updating techniques that enable to incorporate direct and indirect information from inspection, testing and monitoring when these become available. Moreover, the combined integration of this information into the performance prediction proves to enable much more accurate predictions compared to the situation when this data is analysed separately. Also the need to step away from classical ad-hoc testing approaches and the formulation of testing and measurement campaigns considering the Value of Information is stressed. Further, it was also identified that several challenges still remain in relation to the development of such Bayesian updating methodologies, not least the quantification of suitable prior information as well as the values of model and measurement uncertainties to be considered. The integration of these approaches into the practical assessment process is however proven to be feasible and an outlook was presented on challenges to be tackled in the coming years in order to integrate such approaches further in commercial FEM software. As such, a more accessible and easy-to-use platform can be created in order to introduce the *Bayesian way of thinking* in all steps of the life-cycle assessment process of concrete structures.

ACKNOWLEDGEMENTS

The financial support from FWO-Flanders on the FWO SBO project lifeMACS “Multi-layer Bayesian life-cycle Methodology for the Assessment of Existing Concrete Structures” is highly appreciated (FWO-SBO project S001021N).

REFERENCES

Botte, W. (2017). Quantification of Structural Reliability and Robustness of New and Existing Concrete Structures Considering Membrane Action. PhD Dissertation, Ghent University, Ghent, Belgium.

- Botte, W., Vereecken, E., Taerwe, L., & Caspeele, R. (2021). Assessment of posttensioned concrete beams from the 1940s: large-scale load testing, numerical analysis and Bayesian assessment of prestressing losses. *Structural Concrete*, 22(3),1500–1522.
- Botte, W., Veyt, C., & Caspeele, R. (2017). Evaluation of conformity criteria for reinforcing steel properties. In C. Bucher, B. R. Ellingwood, & D. M. Frangopol (Eds.), *Safety, Reliability, Risk, Resilience and Sustainability of Structures and Infrastructure (ICOSSAR2017)* (pp. 1411–1420).
- Box G., Tiao G. (1973). *Bayesian inference in statistical analysis*. USA: Addison-Wesley Publishing Company.
- Caspeele, R. (2010). Probabilistic evaluation of conformity control and the use of Bayesian updating techniques in the framework of safety analyses of concrete structures. PhD dissertation, Ghent University, Ghent, Belgium.
- Caspeele, R. (2014) From quality control to structural reliability: where Bayesian statistics meets risk analysis. *Heron*, Vol. 59, No. 2/3, 79–100.
- Caspeele, R. & Taerwe, L. (2012). Bayesian assessment of the characteristic concrete compressive strength using combined vague–informative priors. *Construction and Building Materials*, 28, 342–350
- Caspeele, R., & Taerwe, L. (2013). Numerical Bayesian updating of prior distributions for concrete strength properties considering conformity control. *Advances in Concrete Construction*, 1(1),85–102
- Caspeele, R., Sykora, M., & Taerwe L. (2014). Influence of quality control of concrete on structural reliability: assessment using a Bayesian approach. *Materials and Structures*. 47(1-2), 105–116
- Catbas, F. N., Gul, M. & Burkett, J. L. (2008). Damage Assessment Using Flexibility and Flexibility-Based Curvature for Structural Health Monitoring. *Smart Materials and Structures* 17(1), 015024.
- fib (2016) *Bulletin 80: Partial factor methods for existing concrete structures*. Technical Recommendation. 2016, ISBN 978-2-88394-120-5.
- Gelman A. (2004) *Bayesian Data Analysis*. 2nd ed. USA: Chapman & Hall/CRC.
- Gregory P. (2005) *Bayesian Logical Data Analysis for the Physical Sciences*. Cambridge University Press, The Netherlands.
- Jaishi, B., & Ren, W. X. (2007). Finite element model updating based on eigenvalue and strain energy residuals using multiobjective optimization technique. *Mechanical Systems and Signal Processing*, 21(5),2295–2317.
- JCSS (2001). Probabilistic Model Code. <https://www.jcss-lc.org/jcss-probabilistic-model-code/>.
- Pandey, A., Biswas, M., & Samman, M. (1991). Damage detection from mode changes in curvature. *Journal of Sound and Vibration*, 145(2),321–332.
- Rackwitz, R. (1983). Predictive distribution of strength under control. *Matériaux Constr.* 16, 259–267.
- Rózsás, Á., Slobbe, A., Martini, G., & Jansen, R. (2022). Structural and load parameter estimation of a real-world reinforced concrete slab bridge using measurements and Bayesian statistics. *Structural Concrete*, 23 (6),3569–3600.
- Simoen, E. (2013). Uncertainty quantification in finite element model updating. PhD Dissertation, KU Leuven, Leuven, Belgium.
- Simoen, E., Papadimitriou, C., & Lombaert, G. (2013). On prediction error correlation in Bayesian model updating. *Journal of Sound and Vibration*, 332(18),4136–4152.
- Simoen, E., De Roeck, G., & Lombaert, G. (2015). Dealing with Uncertainty in Model Updating for Damage Assessment: A Review. *Mechanical Systems and Signal Processing* 56: 123–49.
- Stewart, M.G. & Suo, Q. (2009). Extent of spatially variable corrosion damage as an indicator of strength and time-dependent reliability of RC beams. *Engineering Structures* 31(1),198–207.
- Strauss, A., Frangopol, D.M., Kim, S. (2008). Use of monitoring extreme data for the performance prediction of structures: Bayesian updating. *Engineering Structures*, 30, 3654–66.
- Verdoolaege G. (2007). Bayesian integrated determination of the ion effective charge via Bremsstrahlung and charge exchange spectroscopy in Tokamak plasmas. PhD thesis, Ghent University, Ghent, Belgium.
- Vereecken, E., Botte, W., Lombaert, G., & Caspeele, R. (2020). Bayesian decision analysis for the optimization of inspection and repair of spatially degrading concrete structures. *Eng. Struct.*, 214: 111028
- Vereecken, E., Botte, W., Lombaert, G., & Caspeele, R. (2021). Vol-Based Optimization of Structural Assessment for Spatially Degrading RC Structures. *Applied Sciences*, 11, 4994
- Vereecken, E. (2022a). Applied Bayesian pre-posterior and life-cycle cost analysis for determining and optimizing the value of structural health monitoring for concrete structures. Ghent University. Faculty of Engineering and Architecture, Ghent, Belgium.
- Vereecken, E., Botte, W., Lombaert, G., & Caspeele, R. (2022b). A Bayesian inference approach for the updating of spatially distributed corrosion model parameters based on heterogeneous measurement data. *Structure and Infrastructure Engineering*, 18(1),30–46
- Vereecken, E., Botte, W., Lombaert, G., & Caspeele, R. (2023). Influence of the correlation model on the failure probability of a reinforced concrete beam subjected to spatially variable corrosion. *Structure and Infrastructure Engineering*, 19(4),510–524
- Vu, K.A.T. & Stewart, M.G. (2000). Structural reliability of concrete bridges including improved chloride-induced corrosion models. *Structural Safety* 22(4),313–33.

Safety assessment of civil infrastructure assets subjected to extreme events

M. Ghosn

The City College of New York, The City University of New York, New York, USA

ABSTRACT: Civil infrastructure systems are exposed to various types of human-made, environmental, and climatic hazards within their service lives. Reliability-based approaches and probabilistic risk-informed methods have long been used for assessing the safety of such systems and developing design standards and specifications to account for the random nature of these hazards, their intensities and rates of occurrence, and possible compounding effects. Specifically, current design standards provide reliability-calibrated design load maps and tables as well as load combination factors for use in engineering practice during a structure’s safety check process. These maps and associated procedures are based on historical data assuming that the underlying processes are unchanging over time where observed variations in the historical data are only random oscillations around underlying stationary statistical properties. However, ageing processes, growth in economic activities, and climate change are causing increases in the frequencies and intensities of human-made and environmental hazards, raising the risk to infrastructure systems and their users.

This presentation reviews the fundamental principles behind structural code developments and their underlying assumptions. It also examines analytical methods to assess the safety of structural systems accounting for the nonstationary nature of hazards. The presentation discusses approaches for adjusting current structural design specifications in view of anticipated climate change scenarios. A numerical example illustrates the application of these approaches during the safety assessment and the design of structural systems.

1 INTRODUCTION

The failure of civil infrastructure systems is associated with severe safety and financial consequences to their users, owners, and the surrounding community. For these reasons, the design and construction of structural systems must meet strict criteria stipulated in design codes and standards. As explained in NEHRP (2020), “structures designed according to modern codes are targeted to have low probabilities of collapse when extreme hazards occur while ensuring that construction costs remain within a level that does not discourage development. A critical function of code writing authorities is finding a proper balance between these conflicting considerations”.

Because assessing the potential for structural collapse is difficult, traditional structural design processes are mostly based on checking the safety of each individual member of a structural system for a single limit state or one failure mode at a time. However, structures are composed of many members, each of which may fail in a different mode and the reliability of the structural system is a function of the reliability of all its components. The target performance is set in design codes to minimize risk which provides a means to consider the performance of structural members or that of the system including the probability of structural failure, P_f , which is defined as the probability of exceeding a pre-defined limit state and the resulting consequences where in the most basic formulation, Risk is considered to be the product of the probability of failure and the consequences of failure (Ang and Tang, 2006):

$$\text{Risk} = P_f \times \text{consequence of failure} \quad (1)$$

It is most common to express the consequence of failure in terms of costs. These may include direct costs, such as the cost of replacing or repairing the structure and loss of life, as well as indirect and user costs including downtime, economic losses, environmental, societal, and political costs. The expression for risk, or the probability of loss due to damage caused by a single or multiple hazards, can be conceptually presented as:

$$Risk = P(loss) = \sum_H \sum_D \sum_{LS} P(loss|D)P(D|LS)P(LS|H)P(H) \quad (2)$$

where *loss* is any appropriate loss metric; $P(H)$ is the probability of occurrence of an input intensity level of a hazard within a structure's service period; $P(LS|H)$ is the conditional probability of exceeding a structural limit state, *LS*, given the hazard intensity, *H*; $P(D|LS)$ is the conditional probability of a damage state, *D*, given the exceedance of the structural limit state, *LS*; and $P(loss|D)$ is the conditional probability of a loss given the damage state, *D*.

The last two terms which express the probability of reaching a limit state define the probability of failure which itself can be conceptually presented as:

$$P_f = \sum_H P(LS|H)P(H) \quad (3)$$

For the probabilistic assessment of structural members, P_f gives the probability that capacity represented by strength capacity, *R*, is less than demand represented by the applied load effects, *S*, or the probability that the limit state function $Z=R-S$ is less than zero (Ang & Tang, 2006, Melchers & Beck, 2018):

$$P_f = \Pr(Z < 0) = \Pr(R < S) \quad (4)$$

where the load effect, *S*, is related to the maximum hazard intensity, H_T , that may occur within the service life, *T*, of the structure. The relationship between load effect and the maximum hazard can be represented through an Influence Function, $IF(\dots)$, such that $S=IF(H_T)$ represents the structural analysis process that converts hazard intensities into applied load effects such as bending moments, shearing forces, curvatures, or displacements.

Depending on methods of structural analysis and the ease of their implementation, it has been traditional to use different limit states for different applications. For example, for the analysis of most hazards, ASCE 7 (2021) and most structural design codes and standards require assessing the structural response of individual members such that the limit state function in Eqs. 3 & 4 represents the margin of safety between a member's resistance and applied load effect. On the other hand, seismic design may consider the probability of structural collapse allowing for nonlinear structural behavior and the associated redistribution of forces between components.

As expressed in Eq. (3), evaluating the probability of failure, whether failure is set in terms of member limit state or in terms of structural collapse, involves a three-step process: 1) establishing a hazard curve, which expresses the rates at which different amplitudes of a hazard are exceeded; 2) developing a fragility curve for the structure, each point of which represents the conditional probability of failure given that a certain amplitude of the hazard has occurred, $P(LS|H)$; and 3) Integrating the hazard and fragility curves to compute the unconditional probability of structural failure, P_f . The safety assessment process is based on evaluating the probability distribution of the maximum hazard intensity expected to occur within the base line service life of the structure. For example, for buildings the base line service life is usually set at 50 years while for bridges it is set at 75 years (ASCE, 2021; AASHTO, 2020).

Design codes specify load and resistance factors and magnitudes of hazards for use in the design process to ensure that structural members designed according to the specifications provide a minimum risk of failure related to a pre-set probability of failure or a target reliability index, β , defined as:

$$\beta = -\Phi^{-1}(P_f) \quad (5)$$

where $\Phi^{-1}(\dots)$ is the inverse of the cumulative normal probability distribution function.

For example, ASCE 7 sets the target probability of member failure for most buildings under gravity loads at $P_f=0.135\%$ in 50 years or at $\beta=3.0$. For other buildings categories, the target reliability index varies between $\beta=2.50$ to 3.50 . For bridges, the target reliability index is $\beta=3.5$ for a 75-year design period. These criteria were set based on extensive reliability analyses of previous generation of structural systems that demonstrated that the best performing structural systems provided this level of reliability in the respective base-line service lives (50-yr and 75-yr). By calibrating the target reliability to the successful performance of previous generation of structures, the target probability of failure in a service life reflects the risk level tolerated by society giving indirect consideration of cost, safety, and our ability to adequately characterize safety. Thus, the explicit calculation of risk is avoided.

While the reliability analysis in Eqs. 3 and 4 involves the probability distribution of the maximum expected hazard within the base line service life, H_T , the intensities of the design hazards are usually expressed in terms of return periods, T_R , also known as Mean Recurrence Intervals (MRI). The return periods are set in the codes for use during the calculation of the nominal resistance of structural members. These return periods are calibrated based on the annual probability of exceedance. In fact, recognizing the large uncertainties in estimating hazard intensities, scientists and engineers have represented yearly maximum hazards with cumulative probability distribution functions, $F_{H1}(\dots)$, using historic data on hazard frequencies and intensities. In many cases, Gumbel or Generalized Extreme Value (GEV) distribution functions have been adopted because they modeled the distributions of yearly maximum hazards quite well.

The cumulative distribution for the maximum hazard event in a period of time T depends on the number of loading events, N , that occur during this period of time. These events are designated as $H_1, H_2, \dots H_N$. The maximum of these N events, call it H_T , is represented by:

$$H_T = \max_{i=1}^N (H_i) \quad (6)$$

The probability that H_T is smaller than some value, h , implies that each of $H_1, H_2, \dots H_N$ is smaller than h . Assuming the events are statistically independent, the cumulative probability distribution of H_T , $F_{H_T}(\dots) = P(H_T < h)$ can be obtained from:

$$F_{H_T}(h) = F_{H_1}(h) \times F_{H_2}(h) \times \dots \times F_{H_N}(h) \quad (7)$$

If one assumes that the probability distributions of the annual maximum events are stationary represented by the same CDF so that $F_{H_1}(h) = F_{H_2}(h) = \dots = F_{H_N}(h)$, Eq. (7) reduces to:

$$F_{H_T}(h) = [F_{H_1}(h)]^N \quad (8)$$

While Eq. (7) is always valid assuming independence, Eq. (8) is only valid if in addition the CDF are identical, which implies that the process generating the hazard is stationary.

When the distribution $F_{H1}(h)$ is that of the maximum yearly event, the number of events, N , used in Eq. 8 is equal to the number of years in the structure service period and $N=T$. The calculation of the probability of failure and the reliability index can then proceed for different possible member resistances using Eqs. 4. The process is described as shown in Figure 1 where the maximum load effect increases assuming a stationary distribution of the load effects. The resistance that produces a reliability index equal to the target is subsequently used to calibrate a Load and Resistance Factor Design (LRFD) equation that takes the form:

$$\phi R_n = \sum \gamma_i S_{ni} \quad (9)$$

where R_n is the nominal member resistance, ϕ is the resistance factor, γ_i is the load factor for load i and S_{ni} is the nominal design load effect of hazard i where $S_{ni} = IF(H_n^*)_i$, with H_n^* being the design intensity of hazard i . The calibration of the load factors and H_n^* seek to ensure that Eq. 4 leads to reliability index values equal to the target for the entire applicable range of structure dimensions.

For environmental and climatic hazards, the design hazard intensity H_n^* are typically expressed in terms of the probability, $1/T_R$, that the design hazard is exceeded in any

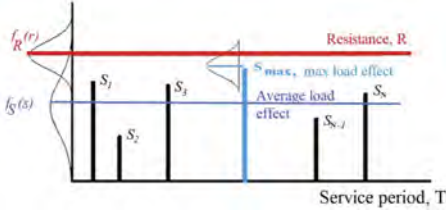


Figure 1. Safety assessment process for stationary conditions.

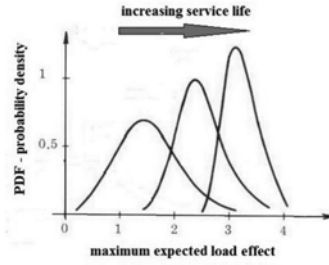


Figure 2. Variation of probability distribution of hazards with service life.

given year, in which T_R is the return period or the Mean Recurrence Interval (MRI). Thus, the distribution of the yearly maximum value is used to determine the nominal value for a design hazard, H_n^* , such that:

$$H_n^* = F_{H_1}^{-1}\left(1 - \frac{1}{T_R}\right) \quad (10)$$

where $F_{H_1}^{-1}(\dots)$ is the inverse of the cumulative probability distribution function (CDF) of the yearly maximum hazard intensity, H_1 .

T_R in Eq. (10) may or may not coincide with the base line design life of the structure. If T_R is equal to the base line design life (e.g. 50 or 75-years), the live load factor γ_i is usually associated with a factor greater than 1.0 to ensure that Eq. (9) leads to designs that meet the target reliability index. In fact, Eqs. (10) and (8) indicate that if T_R is equal to the base line service life, the probability that the hazard will exceed the design hazard will be equal to 63.2% which would lead to an unacceptably high probability of failure unless a relatively high load factor is applied. For example, early versions of wind-resistant design standards specified 50-year design wind speed contour maps with a load factor equal to 1.6 for the design of ordinary building occupancies. Design standards that assign the same return period to define the amplitude of a nominal load without considering the probabilistic nature of other design variables are said to follow a *uniform hazard* approach.

More recently, it was determined that the presence of regional variations in the probability distributions of environmental and climatic hazards meant that the target reliability index was not uniformly achieved when the return period coincided with the base line design life. Instead, it was determined that using a live load factor $\gamma_i=1.0$ with high return periods led to more uniform reliability indices for the different regions in the US and the range of structural types. For example, McAllister et al. (2018) observed that achieving the target reliability levels $\beta = 2.5$, $\beta = 3.0$, $\beta = 3.25$ and $\beta = 3.5$ for the wind design of buildings as set in ASCE 7 (2021) would require respectively return periods of 300 years, 700, years, 1700 years and 3000 years for the four building categories whose member failure is not sudden and does not lead to wide-spread progression of damage. Table 1 summarizes the relationship between the target reliabilities and the return periods specified in ASCE 7 associated with a load factor equal to 1.0.

Table 1. Return periods for wind design load in ASCE-7 for members whose failure is not sudden and does not lead to wide-spread progression of damage.

Basis Period	Target reliability	Return period
50 years	$\beta = 2.50$	300 yrs
50 years	$\beta = 3.00$	700 yrs
50 years	$\beta = 3.25$	1700 yrs
50 years	$\beta = 3.50$	3000 yrs

2 APPLICATIONS TO CLIMATE CHANGE

As explained in Section 1 and illustrated in Figure 1, current structural design standards are based on the assumption that environmental and climatic hazards are stationary and that any observed oscillations in their intensities are natural random variations around stationary statistical parameters. Existing research indicates that due to climate change, the intensities of several types of climatic hazards will increase over time in various regions of the world. As a matter of fact, over the past few years, an international team of climate scientists, economists and energy systems modelers have built a range of “pathway” scenarios that examine how global society, demographics and economics might change over the current century. These scenarios, known as the “Shared Socioeconomic Pathways” (SSPs) are associated with future CO₂ and other global greenhouse gas emissions. Climate scientists are using these SSPs as inputs for developing climate models as described in the Intergovernmental Panel on Climate Change (IPCC, 2022).

Table 2. Shared Socio-economic Pathways, SSPs, and associated temperature changes, IPCC (2022).

SSP	Scenario	Estimated (2041–2060)	Estimated (2081–2100)	Very likely (2081–2100)
SSP1-1.9	very low GHG emissions: CO ₂ emissions cut to net zero around 2050	1.6 °C	1.4 °C	1.0 – 1.8
SSP1-2.6	low GHG emissions: CO ₂ emissions cut to net zero around 2075	1.7 °C	1.8 °C	1.3 – 2.4
SSP2-4.5	intermediate GHG emissions: CO ₂ emissions around current levels until 2050, then falling by 2100	2.0 °C	2.7 °C	2.1 – 3.5
SSP3-7.0	high GHG emissions: CO ₂ emissions double by 2100	2.1 °C	3.6 °C	2.8 – 4.6
SSP5-8.5	very high GHG emissions: CO ₂ emissions triple by 2075	2.4 °C	4.4 °C	3.3 – 5.7

Table 2 lists the five IPCC pathways and the corresponding temperature rise relative to pre-industrial times. As shown in Table 1, every SSP is also associated with a “Representative Concentration Pathway” (RCP) value that predicts how concentrations of CO₂ in the atmosphere will change in the future as a result of human activities. The numerical values of these RCPs (1.5, 2.6, 4.5, 7.0 and 8.5) refer to greenhouse gas emissions and concentrations and their combined radiative forcing in Watt/m² in the year 2100. Figures 3 and 4, extracted from the IPCC report, illustrate how the CO₂ concentrations are expected to change over the years and their respective global warming estimates by the year 2100 relative to 1986-2005 period. Although, the IPCC (2022) report did not give precise estimates of the likelihoods of the scenarios, it described the most severe scenario SSP5-8.5 as highly unlikely, SSP3-7.0 as unlikely, and SSP2-4.5 as likely. In addition to using these RCP’s to project future changes in temperature, they are used as bases for projecting future changes in the intensities of various climatic hazards such as precipitations, and wind which can be subsequently used to study the effect of future climate-related hazards, such as sea level rise, floods, wind storms and hurricanes, rain, snow and ice, on structures and infrastructure systems.

Global warming is expected to lead to significant changes in several hazards such as sea level rise, precipitation, hurricanes, storm surges and floods that inflict severe risk on society and civil infrastructure systems. Yet, current structural design codes and standards assume that past history is sufficient to describe future events and the data used to obtain the probability distributions of the relevant hazards for reliability assessment and design purposes as expressed in Eqs. (8) and (10) are based on historic data. The assumption is that any oscillations in observed extreme events are due to natural variations and that the past will represent the future. However, as schematically presented in Figure 5, global warming may be causing severe changes in both the expected maximum intensities of future events and the confidence

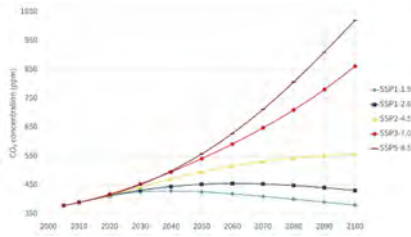


Figure 3. Atmospheric CO₂ concentrations by SSP across the 21st century (IPCC, 2022).

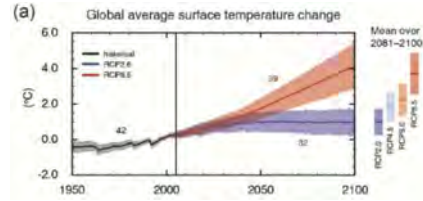


Figure 4. Projection of temperature change for RCP 2.6 and 8.5 scenarios (IPCC, 2022).

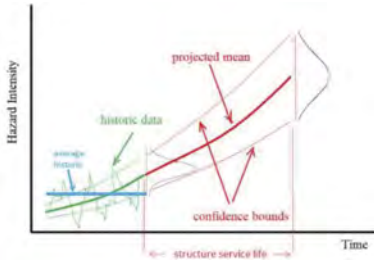


Figure 5. Schematic representation of non-stationary hazard intensity.

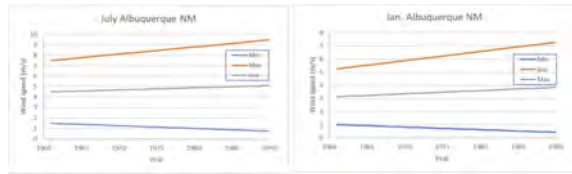


Figure 6. Observed differences in Jan. & July’s maximum and minimum wind speeds (Klink, 1999).

bounds in our estimates. The reduced confidence is not only due to the random nature of hazards but also to the limited ability of climate science to model future changes and the large uncertainties in predicting society’s response to the scientific community’s dire warnings about the need to reduce greenhouse gas emissions to reduce climate change trends.

Ongoing studies are providing information on expected changes in global climate and related hazard levels, as well as assessments of uncertainties associated with the projection of future climatic hazards. However, one should note that most climate science studies seek only to project typical trends in hazard intensities which would give the “average load effect” illustrated in the solid lines of Figure 4 rather than analyzing the trends in the extreme events which form the bases for structural design and safety assessment as explained earlier. As an example, Figure 6 extracted from the data by Klink (1999) illustrates how historic maximum and minimum monthly 1-minute wind speeds in different directions leading to practically no change in the mean wind speed in Albuquerque, New Mexico. Hence, as shown in Figure 1, providing trends on potential changes in the mean values of any hazard could be misleading when it comes to analyzing the ability of our infrastructure to sustain future extreme events. Therefore, much work is still needed to coordinate between what climate science reports are providing as compared to the needs of the structural engineering community.

If available, projections of changes in the extreme intensities of relevant hazards during the base line service life of structural systems, can be used to implement the same uniform risk concepts described in Section 1 for the safety assessment of structures and the adjustment of current design standards to account for the effect of changing climatic hazards.

3 ILLUSTRATIVE FLOOD WALL DESIGN EXAMPLE

A simple example is provided to illustrate how the analysis of climate hazard data, specifically riverine flooding, would be performed for the safety assessment of a flood wall to account for changes in flood intensities over time. As explained in Section 1, evaluating the safety of structures exposed to potential riverine floods requires a hazard assessment process that models the maximum intensity of the hazard over the service life of the structure accounting for future

changes in the hazard. This can be done using two approaches: 1) performing a direct study of historical changes of extreme floods at a given river location over time, modeling the correlation of these changes to other controlling factors such as CO₂ emissions, as well as changes in temperature and precipitations over time and performing a statistical projection of these factors to estimate future floods, or 2) modeling changes in the primary climate parameters such as temperature and precipitation and using these models to project their influence on flooding hazards at the specified location using a combined topographical/hydrological/hydraulic model. The first approach requires the availability of a long historical record at specific locations of all the pertinent climatic factors, the availability of future projections of the basic primary climate factors and assumes that the correlation between observed maximum floods and the primary factors will continue at the same historic trend. The second approach requires an integrated model that relates the intensity of the riverine floods to the underlying climate parameters (Xue et al., 2018).

Because at this stage future projections of floods are not readily available for either of the statistical or the integrated model, in this example we use historical data on hydraulic discharge rates collected for the Schoharie Creek USGS Station 01350000 at Prattsville, NY (Molodecka, et al. 2020) to describe how the safety assessment of a flood wall can be undertaken for cases where flooding hazards are changing over time.

The statistical analysis of the historic upward trend in the maximum yearly flood event shown in Figure 7 indicates that the maximum yearly discharge rate starting with the year 1908 can be modeled as a Gumbel distribution with a location parameter, u_t , and a scale parameter, β_t , both of which are observed to have increased over time. A statistical analysis shows that both u_t and β_t are linearly increasing over time, t , measured in years, such that:

$$u_t = 10,371 + 51.71 * t \quad (11)$$

$$\beta_t = 5,869 + 43.30 * t \quad (12)$$

where the discharge rate is in ft³/sec (1ft³/sec = 0.0283168 m³/s). The data plotted in Figure 7 show that the rate of change for the location parameter per year equals 0.50%/year and for the scale parameter it is 0.74%/yr.

Maximum hydraulic events used in design are usually represented by the flood having a return period $T_R=100$ years. If the Gumbel distribution is used in Eq. (10) for a return period $T_R=100$ years, using the statistics of the first year, the design flood would have a discharge rate equal to 37,332 ft³/sec (1,057 m³/sec). Table 3 compares the results obtained for the maximum 100-year discharge rate assuming stationary (Eq. 9) or nonstationary (Eq. 8) models based on the statistical models in Eqs. (11) and (12). The calculations show that the application of Eq. 8 would produce a probability distribution for the maximum 100-year flood that can be approximated by a Gumbel distribution. Thus, accounting for the increase in the flood discharge rates over the 100 years beginning in 1908 leads to an expected maximum discharge rate equal to 57,000 ft³/sec (1,614 m³/sec) with a coefficient of variation (COV) of 20.3%. This value is 40% higher than the one predicted assuming no change over the years as implied in Eq. (9).

The data plotted in Figure 7 indicate that the calculated expected maximum 100-year discharge rate covers all the actual measured peaks in the 100-year period starting in 1908 except for the data from the 2011 Hurricane Irene when the discharge rate is almost six standard deviations above the mean, presenting an anomaly to the statistical trends observed over the period of data collection. It has been observed that the high discharge rate was due to the combination of heavy precipitations from another storm that coincided with Irene. Table 3 also shows that even under stationary assumptions, the flood with 100-yr return period for this river data would underestimate the mean value of the maximum 100-year flood by about 9%. As shown in the last two rows of the table, using the end year's data to conservatively develop design standards to account for climate change, as some researchers have advocated, would lead to over-conservative designs. Alternatively, using the average yearly statistics would underestimate the maximum flood rate by about 5%.

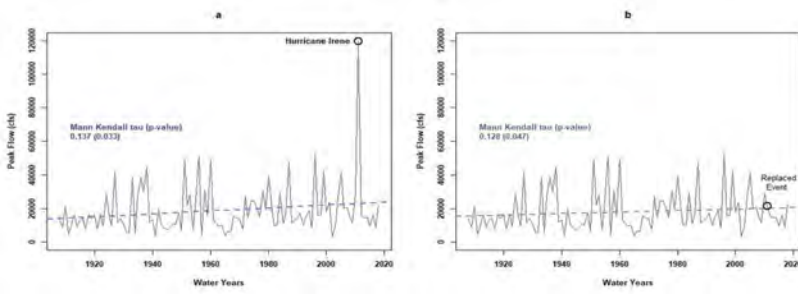


Figure 7. Analysis of historical trends for Schoharie Creek peak streamflow (a) with and (b) without the effect of hurricane Irene. (Molodecka, et al. 2020).

The effects of riverine floods on structures are related to: 1) flood depth, 2) flood velocity, 3) structural exposure, and 4) type and depth of their foundations. Good estimates of flood depth and velocity are obtained based on flood discharge rate data as well as the topographical profile of the river and flooded zone and the type of soils in the vicinity of the structure using computationally intensive or sometimes simplified hydraulic models (Xue et al.; 2018; Ghosn, et al. 2003). As an example, the discharge rate, Q , at a cross-section of a river is computed by dividing the cross-section into “ n ” elements (Genc et al., 2015):

$$Q = \sum_{i=1}^n U_i d_i \Delta w_i \quad (13)$$

where U_i , d_i and Δw_i are the mean velocity, mean flood depth and width in cross sectional element, i , respectively. The flow velocity can be estimated from Manning’s equation:

$$U_i = \frac{R_i^{2/3} S_i^{2/3}}{n_i} \quad (14)$$

where $R_i = A_i/P_i$ is the hydraulic radius of section i of the channel with A_i being the cross section area, and P_i the wetted perimeter; S_i is the friction slope, which is equal to the bed slope for a steady uniform flow; n_i is Manning’s coefficient.

Given a value for Q , the solution of Eqs. (13) and (14) leads to the determination of the flood depth and velocity in each flooded sub-area of width Δw_i . As shown in Figure 8, the flood depths and velocities are used to study hydraulic effects of a flood on a structure which are of two types: 1) hydraulic forces on structural components and foundations, and 2) foundation scour. (Lagasse et al., 2013).

Flood water pressure at each point of a submerged structural component is due to hydrostatic and hydrodynamic effects, such that:

$$p = \rho g z + \frac{1}{2} \rho a U^2 \quad (15)$$

where ρ is the density of water, g is the gravity, z is the depth below the water surface at the point where the pressure is evaluated, U is the average water velocity and a is a drag coefficient or shape factor.

The structure may also be subject to impact forces from debris carried by a flooded river. However, the difficulty of determining the type of debris being carried may require the consideration of various site-specific scenarios. A more complex situation arises when openings between different structural elements (or different structures) are obstructed by large size debris causing a blockage of water flow which can itself collect smaller debris resulting in a debris jam. The blockage adds to the forces applied on the structural elements at contact debris-structure areas.

Table 3. Comparison of projected 100-year maximum flood rates for stationary and nonstationary cases.

Case	Yearly Dist., Location ft ³ /sec	Yearly Dist., Scale ft ³ /sec	Yearly Mean ft ³ /sec	Yearly Standard dev. ft ³ /sec	Mean of 100-yr max. ft ³ /sec	Std. dev of 100-yr max. ft ³ /sec	COV of 100-yr max.	100 yr return Q _r , ft ³ /sec
Stationary with stats. from year 1908	10,371	5,869	13,754	7,517	40,745	7,517	18.4%	37,332
Stationary with average stats. 1908-2007	12,938	7,808	17,560	10,271	54,438	10,271	18.9%	49,775
Stationary w stats. from year 2007	15,505	10,155	21,366	13,024	68,130	13,024	19.1%	62,218
Nonstationary					57,000	11,548	20.3%	

NB: 1,000 ft³/sec = 28.32 m³/sec

Ignoring the effects of debris related forces, a simple free body diagram of a submerged structural component may be represented as shown in Figure 8 where d_w is the water depth. The structure may fail due to bending or shearing forces or due to general equilibrium instability, or from foundation scour.

In this simplified example, we demonstrate the analysis of the effect of the static water pressure on a hypothetical reinforced concrete flood wall that is built in the flood plain of the Schoharie River at Prattsville, NY in the vicinity of the site where the data of Eq. (11) and (12) were collected. The schematics of the flooded area and the protective flood wall are shown in Figure 9.

The hydraulic static force and the corresponding moment at the base of the flood wall per unit wall width will be respectively equal to $F = \rho g d_w^2 / 2$ and $M = \rho g d_w^3 / 6$ where d_w is the height of the water level in the flood plain. According to the USGS web site, <https://fim.wim.usgs.gov/fim/>, the implementation of Eqs. (11) and (12) with the site specific values of river channel dimensions, bed slope, and Manning coefficient lead to a rating curve that can be approximated by the following relationship between the total flood depth, d , in feet and the discharge rate Q in ft³/sec:

$$d = 12\text{ft} + d_w = 0.66 Q^{0.31} \quad (16)$$

where 12 ft is the overtopping water depth in the channel.

The design and safety assessment of the flood wall must consider various failure modes including shear and bending moment failures, sliding and overturning, foundation failures, etc. In this example, we demonstrate the design and reliability analysis for bending moment at the base of the concrete flood wall. The required moment capacity per unit wall width is obtained as:

$$0.9 M_{cap} > 1.6 \rho g d_w^3 / 6 \quad (17)$$

where $\phi = 0.9$ is the resistance factor and $\gamma_w = 1.6$ is the load factor. As shown in Table 3, assuming that the engineer ignores the effects of climate change, the design flood corresponding to a 100-year return period is obtained as $Q_{design} = 37,332$ ft³/sec, leading to water depth at the wall level equal to 5.25 ft. Using the specific weight for water equal to 62.4 lb/ft³, the required moment capacity per unit width is obtained as $M_{cap} = 2.675$ kip-ft/ft.

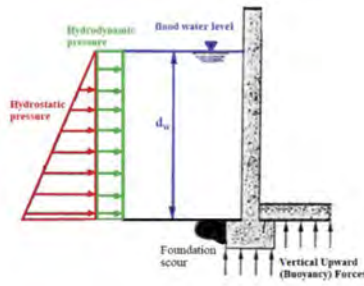


Figure 8. Free Body diagram of a submerged simple structure.

Table 3 shows that a yearly maximum discharge rate $Q_f=13,754 \text{ ft}^3/\text{sec}$ yields a 100-year maximum discharge rate $Q_{100}=40,745 \text{ ft}^3/\text{sec}$ with a standard deviation= $7,517 \text{ ft}^3/\text{sec}$. This yields a mean value for $d_w= 5.67 \text{ ft}$ and a COV= 17% . Given a bias equal to 1.14 and a COV= 13% for the bending strength of reinforced concrete members, the probability of failure for a wall built to meet the $M_{cap}=2.675 \text{ kip-ft/ft}$ is equal to $P_f=16.3\%$ or a reliability index $\beta = 0.98$. This low reliability index associated with a design discharge rate obtained for a 100-year return period that has a probability of occurrence equal to 63.2% is a reflection of the cubic power for the depth in Eq. (14) indicating that a live load factor of 1.6 is not adequate even without considering climate change.

As shown in Table 3, accounting for climate change, the 100-year maximum discharge rate has a mean $Q_{100}=57,000 \text{ ft}^3/\text{sec}$ with a standard deviation= $11,548 \text{ ft}^3/\text{sec}$. The probability of failure for a wall built to meet the $M_{cap}=2.675 \text{ kip-ft/ft}$ obtained for the stationary case is equal to $P_f=78.2\%$ or a reliability index $\beta = -0.78$. Raising the reliability index to $\beta = 0.98$ obtained for the stationary assumption will require a design moment capacity $M_{cap} = 6.20 \text{ kip-ft/ft}$ which is associated with a design depth $d_w=6.95 \text{ ft}$ or a design discharge rate $Q_{design} = 50,945 \text{ ft}^3/\text{sec}$. This design discharge corresponds to a probability of exceedance in a 100-yr period equal to 66.7% . If one uses the probability of exceedance of 63.2% to define the design discharge rate, then Q_{design} would have been $51,805 \text{ ft}^3/\text{sec}$ which is less than 2% more conservative than what is required to give the same reliability index as that obtained when the river is not exposed to climate change. The 63.2% probability of exceedance is equivalent to the probability obtained if the process were stationary and where the design load is obtained from the hazard having a return period $T_R=100$ years.

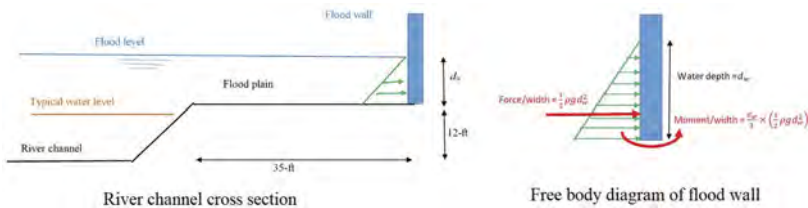


Figure 9. Schematic representation of river cross section and floodwall free body diagram.

4 IMPLICATION FOR DEVELOPMENT OF DESIGN STANDARDS

The theoretical review presented in Sections 1 and 2 about the process of developing structural design standards and specifications and how the effect of climate change can be accounted for during the development of the next generation of standards along with the simple illustrative example presented in Section 3, present important observations worthy of consideration.

4.1 *Inapplicability of return periods*

Current standards for the design of bridges, buildings and other structures specify design load intensities for climatic hazards (e.g. temperature, snow, wind, floods) based on return periods presented in maps or tables that account for pertinent regional differences. The design load S_{ni}^* for return period, T_R , has a probability of being exceeded in any one year equal to $1/T_R$ (e.g. = $1/50$) but has 63.2% probability of exceedance in T_R years. The high probability of exceedance necessitates the application of load factors or else the use of return periods significantly higher than the base line service life that would lead to much lower probabilities of exceedance (e.g. 700 years for a 5-year base line service life) so that the design of structures for wind loads achieve a target reliability index $\beta = 3.0$. However, the concept of using return periods imply that the hazards are stationary and that their statistical parameters do not change over time and that their probability density functions over the years are well represented by that of a single year. Hence, in view of climate change, the concept of using return periods to define design loads is no longer applicable. Instead, codes and standards should calibrate design loads based on the probability of occurrence of a maximum hazard in the specified base line service life.

4.2 *Alternative approaches for defining hazard maps*

Given the inapplicability of specifying return periods for design hazards when the hazards are not stationary, it is recommended that design standards develop hazard contour maps based on the target reliability and base line service period. For example, instead of providing wind maps for 300 years, 700, years, 1700 years and 3000 years return periods, the maps should provide contours of hazard intensities that achieve specified target reliabilities in base line service periods. Specifically, code writers could develop load hazard maps in terms of a target reliability index and design period basis rather than in terms of specific return periods and label these maps accordingly (e.g. $\beta = 2.5$ in 50-years, $\beta = 3.0$ in 50-years, $\beta = 3.25$ in 50-years and $\beta = 3.5$ in 50-years).

In the meantime and until such design hazard maps are developed, the numerical example presented in this paper as well as others presented by Ghosn & Ellingwood (2022) demonstrate that engineers can adjust a design performed using existing standards and design hazard by simply scaling up the required design capacity in the inverse ratio of the design load calculated using current hazard maps to the a load value obtained from a hazard that has an intensity with the same implied probability of exceedance within the specified base line service life. Eq. (7) in this paper provides an approach to find this hazard intensity. Of course, this would require the availability of projections describing how the maximum hazard intensities would be changing over the specified base line service life, which for many hazards may not yet be available. In fact, due to computer limitations and other factors, climate scientists have been traditionally projecting average trends rather than extreme events.

It is also observed that using the hazard data from the most conservative year as the basis for defining the design intensity as many researchers have recently proposed would lead to very conservative designs which may lead to unjustifiable high costs for rehabilitating existing structures or designing new structures. Such tendencies to be over-conservative are likely be rejected by developers and infrastructure owners because of the implied additional costs. More importantly, an excessive over-conservatism could lead to the rejection of any future consideration of the problem.

5 CONCLUSIONS

This paper reviewed how the safety and reliability of structures exposed to climatic hazards that may be changing due to global warming should be analyzed to maintain a uniform and consistent levels of risk and reliability. The concepts are applied in a numerical example demonstrating the safety analysis of a wall designed to protect from riverine floods. The example illustrates how a structure's safety may be affected by increases in river discharge rates over time. The simple example demonstrates that maintaining the same target reliability level set in

current design standards would require a major change in the specified design flood loads. For the particular case analyzed, it appears that using a design flood that achieves the same probability of exceedance within the specified base line service life of the structure as that obtained from current standards if climate change effects are ignored, would lead to reliability levels similar to those currently specified. Specifically, if one uses for design flood the discharge rate that has 63.2% probability of exceedance within a 100-year period accounting for climate change, the reliability index would be similar to the one obtained by using in design the flood corresponding to a 100-year return period assuming stationary flood discharge rates. This situation appears to be valid as long as the COV of the maximum design-life-flood under climate change remains reasonably close to the COV for the stationary condition. Additional work is needed to verify the validity of this observation for various limit states and conditions.

REFERENCES

- AASHTO (2020) *LRFD Bridge Design Specifications*, American Association of State Highway and Transportation Officials, Washington DC.
- Ang, A. H-S & Tang, W. H. (2006) *Probability Concepts in Engineering: Emphasis on Applications to Civil and Environmental Engineering*, 2nd Edition, Wiley.
- ASCE, 2021. *Minimum Design Loads for Buildings and Other Structures*, ASCE/SEI 7-22. American Society of Civil Engineers, Reston, Virginia.
- Genç, O., Ardiclioglu, M., and Agralioglu, N. (2015). "Calculation of mean velocity and discharge using water surface velocity in small streams." *Flow Measurement and Instrumentation*, 41, 115–120.
- Ghosn, M. & Ellingwood, B.R. (2022). Risk-based Design and Safety Assessment of Structures in a Changing Climate. *Proc., Int. Assoc. for Bridge Maintenance and Safety, (IABMAS 2022)*. Barcelona, Spain, July, 2022.
- Ghosn, M. et al. (2016) Reliability-Based Performance Indicators for Structural Members, *Journal of Structural Engineering*, Vol. 142-9.
- Ghosn, M., Moses, F. & Wang J., 2003, *Design of highway bridges for extreme events*, NCHRP Report 489 Transportation Research Board, the National Academies, Washington DC. USA
- IPCC (2022) *Climate Change 2022: Impacts, Adaptation, and Vulnerability. Contribution of Working Group II to the Sixth Assessment Report of the Intergovernmental Panel on Climate Change* Cambridge University Press, UK and New York, NY, USA, 3056 pp. <https://doi.org/10.1017/9781009325844>.
- Klink, K. (1999) Trends in mean monthly maximum and minimum surface wind speeds in the coterminous United States, 1961 to 1990, *Climate Research*, Vol. 13: 193–205.
- Lagasse, P. F., Ghosn, M., Johnson, P.A., Zevenbergen, L. W., Clopper, P. E., (2013) *Risk-based approach for bridge scour prediction*, NCHRP report, the National Academies, Washington DC. USA
- McAllister, T.P., Wang, N., Ellingwood, B.R., (2018) Risk-Informed Mean Recurrence Intervals for Updated Wind Maps in ASCE 7-16, Technical Notes, *ASCE Journal of structural engineering*, Vol. 144, issue 5, May 2018.
- Melchers, R.E. and André T. Beck (2018) *Structural Reliability Analysis and Prediction*, 3rd edition, John Wiley & Sons Ltd. DOI:10.1002/9781119266105
- Molodecka, V., Devineni, N., & Ghosn, M. (2020). Effect of climate change on reliability of bridges under threat from flood-related scour, American Geophysical Union, Fall Meeting 2020, abstract #GC092-08.
- NEHRP, 2020, (National Earthquake Hazards Reduction Program) *Recommended Seismic Provisions for New Buildings and Other Structures (FEMA P-2082-2) 2020 Edition Volume II: Part 3 Resource Papers*, the National Institute of Building Sciences Washington, D.C. 2020
- Xue, X., Wang, N., Ellingwood, B.R. and Zhang K. (2018). "The impact of climate change on resilience of communities vulnerable to riverine flooding." In *Climate Change and its Impacts: Risks and Inequalities*, Chapter 8: 129–144 (ISBN 978-3-319-77544-9), Springer.

Digital transition in asset management of bridges – Advantages and challenges

J. Sandager Jensen

COWI A/S, Kongens Lyngby, Denmark

ABSTRACT: Operation and Maintenance (O&M) of bridges are undergoing a digital transformation, and with better technical and more cost-beneficial equipment (drones, sensors, software, etc.), the digital transition accommodates environmental, economic, and technical benefits. Today, most inspections of civil structures are done on-site challenged by traffic restrictions, difficult access- and working conditions, and high initial costs (lift, rope access, etc.). With high-quality RGB - and thermal imagery captured by drones etc., a Reality Model or a visual Digital Twin of the structure may be created, and a Virtual Inspection can be carried out revisiting the structure when needed. The thermal imagery is used in combination with the RGB photo to detect hidden defects in the structure such as delaminations, honeycombing and water ingress. In asset management, the key interest is to find the optimal point in time to repair or replace structural elements considering the Key Performance Indicators (KPIs) that are important to the asset manager or operator. Combining the Reality Model with Artificial Intelligence (AI) for damage detection and monitoring data from implemented sensors on a web-based platform might be the solution to find the optimal point in time for repair, increase the level of safety (for bridge users and O&M personnel), and minimize traffic disturbance. Working with a Reality Model may also decrease the level of subjectivity and increase the level of transparency in decision-making as well as provide efficient means of communication. Despite the many advantages, some challenges remain. They are related to e.g., the reality capture process, AI training, data processing, -presentation, and -integration (also with data-enriched 3D BIM models for recent bridges) in current asset management systems.

1 INTRODUCTION

In general, there has been a great focus on the Operation and Maintenance (O&M) of bridges the recent years originating from e.g., bridge collapses, environmental advancement; ‘repair instead of replacing’, and the attention to service life and Life Cycle Cost of structures and materials.

Asset managers of bridges perform or outsource visual inspections of bridges. The traditional inspections are challenged by e.g., traffic restrictions, high initial costs (rope access, platform, lift, etc.), subjectivity and consistency in documentation (Moore et al., 2001), and access - and working conditions. The inspections are usually reported using condition rating, which is a somewhat ‘weak’ measure loosely correlated to safety and serviceability (COST TU1406, 2018).

The construction sector’s digital maturity was reported as very low back in 2016 (McKinsey 2016). When compared to other industries there seems to be great potential in terms of both technical and economic benefits of the digital transition in the construction sector, and O&M is no exception.

The use of Unmanned Aerial Vehicles (UAVs) has accelerated in the construction sector the recent years, and with high-quality sensors (e.g., thermos cameras) and improved software, it is possible to establish detailed 3D Reality Capture Models and carry out a Virtual Inspection. RGB photogrammetry is used with Artificial Intelligence (AI) to detect visual defects e.g., cracks, spalling, corrosion, etc. (Avendaño et al., 2022) and thermal imagery is used to detect hidden defects e.g., delamination, repairs, and water ingress. UAV-based photogrammetry

has proven safe, cost –, and technically efficient on multiple bridge projects with the use of both RGB – and thermal imagery (Linneberg et. al. 2022).

The digital transition and market within asset management is rapidly improving, and this paper provides a review of three case studies the last five years and a look at the prospects within virtual inspections and the digitalization of O&M.

2 ASSET MANAGEMENT OF BRIDGES

In Denmark, bridge managers are obligated to perform principal inspections every sixth year. The inspections are mostly outsourced to consultancy companies performing a visual inspection of the bridge which is cost-effective when performed by qualified personnel. The inspectors should be able to acknowledge when to upgrade the principal visual inspection to a special inspection to detect non-visible defects, perform load capacity assessment, proof-loading, etc.

The observations from the principal inspections are translated into a condition rate for each structural element class (intermediate piers, abutment, pavement, bearings, etc.) by following a manual and are documented in a report including selected photos. The inspector also provides a timing and cost estimates of needed repair or replacement works. The asset manager plans for future repair work based on this principal inspection report.

The condition rating is a somewhat “weak” measure loosely correlated to safety and serviceability, and ref. (COST TU1406, 2018, Linneberg, 2020) proposes a transition from condition to performance assessment using one or several Key Performance Indicators (KPIs). For the asset manager, the key interest is to find the ‘optimal point in time’ for the repair and replacement work of structural elements considering a range of KPIs. The COST TU1406 project (COST TU1406, 2018) has defined a set of orthogonal (non-overlapping) KPIs relevant for bridge management considering the service life of the bridge:

Reliability (fit for purpose or probability of structural failure, operational failure, or any other failure mode), *Availability* (proportion of time the system is in a functioning condition), *Safety* (minimizing or eliminating the harm to people, i.e. loss of life and limb and not structural failure), *Economy* (minimizing the long-term costs of maintenance activities), and *Environment* (sustainability, minimizing the harm to the environment) (Linneberg et al., 2022).

The KPIs can be translated into monetary units to set up different maintenance scenarios with adjacent long-term costs to find the ‘optimal point in time’ being the lowest long-term cost (Linneberg et al., 2022). Considering the monetary units, the ‘optimal point in time’ could be identified using a risk-based analysis, ranking different maintenance scenarios considering likelihood and monetized consequences.

Many portfolios Bridge Management Systems (BMS) cannot accommodate the integration of Structural Health Monitoring Systems (SHMS), load situations, and defect modelling in 3D which is key input to the decision-making considering multiple KPIs. Such improvement of the current portfolio BMS incl. full integration of a risk-based management system considering multiple maintenance scenarios (and KPIs) is technically challenging and costly. Therefore, the digital transition is only improved gradually.

3 REALITY CAPTURE MODELS AND VIRTUAL INSPECTIONS

3.1 Introduction

One of the important first steps towards the digital transition within bridge management is to establish a Reality Capture Model or Virtual Twin. The model is created from photogrammetrically processed images efficiently collected using camera-mounted UAVs. Establishing a detailed 3D mesh model which in combination with high-quality RGB – and thermal images creates the Reality Capture Model used for visual (virtual) inspections.

It requires domain knowledge within reality capture (data collection, flight plans, light conditions, data processing, etc.) and within bridge condition assessment (vulnerable zones,

damage mechanisms, resolution needed for defect finding, etc.) to establish a detailed 3D model suitable for visual (virtual) inspections.

3.2 *Workflow of virtual inspections*

When the Reality Capture Model is established, it is imported into COWI Virtual Inspection or similar commercial software. Artificial Intelligence (AI) is applied to detect common defects and damages e.g., cracks, corrosion, spalling, graffiti etc. The damages are then reviewed by an experienced engineer to sort the damages. The AI models are in general trained with the mindset, that false positives are accepted (they are sorted out later during the manual visual inspection), but a false negative of a given size or in vulnerable regions (e.g., shear cracks in bridge half joints) is not accepted. In addition, it is important to use AI models that are trained for similar damage types and image resolution.

The manual visual (virtual) inspection is then carried out, and all significant damages are registered and annotated directly in the model. The thermal imagery is used as a supplement to the RGB photos and can identify areas with temperature changes at the surface of the concrete e.g., delamination, certain cracks and joints, concrete repair, and water ingress which may not be visible on RGB photos.

Some of the benefits of having a Reality Capture Model are that it can have multiple viewers, several specialists can be consulted during the inspection process, the structure can be revisited when needed, and all the annotated damages and defects can be reported to the asset manager within the model and as conventional reports summarizing finding.

The asset manager is provided with a 3D Reality Capture Model with annotated damages and defects. The model may be used to plan future repairs and replacements of structural elements, for daily operation, and assist contractors before repairs and replacements.

3.3 *Introduction to case studies*

Three case studies from Denmark emphasize the development within use and integration of UAVs and Reality Capture Models from 2018 to 2022. The New Little Belt Bridge project consists of a UAV-based Reality Capture Model and handheld thermographic screening of the concrete approach spans. The Faroe Bridges project consists of several UAV flights to establish a Reality Capture Model of both bridges, RGB photogrammetry of concrete emergency walkways and both RGB – and thermal imagery of all concrete piers.

In the pilot project of the Queen Alexandrines Bridge, UAVs captured RGB photogrammetry and thermal imagery in one flight, and a complete virtual inspection is completed on the Reality Capture Model in COWI Virtual Inspection software.

In only five years the process is improved, and the Reality Capture Models become easier to establish due to high-quality sensors. The use of UAV for inspection purposes maximize availability and reduce the time on-site, especially when access is difficult e.g., bridges across water or deep valleys.

3.4 *The New Little Belt Bridge*

The New Little Belt Bridge connects Funen and Jutland in Denmark. The bridge opened to traffic in 1970 and is built as a six-lane highway connection with a total length of 1,700 m, and with a main span of 600 m between the two pylons and with a clearance from the sea of 44 m (Linneberg et al., 2022).

The bridge is owned and operated by the Danish Road Directorate. COWI A/S has provided consultancy services related to the operation and maintenance of the bridge. The New Little Belt bridge is shown in Figure 1. In 2018, the Danish Road Directorate commissioned COWI A/S to perform a safety inspection of selected concrete approach spans. The key concern was delamination of the superstructure to recreation-al areas below the bridge in relation to public safety. A Reality Capture Model was established using UAV-based RGB photogrammetry and is shown in Figure 2.



Figure 1. The New Little Belt Bridge.



Figure 2. Reality capture of approach spans at the New Little Belt Bridge.

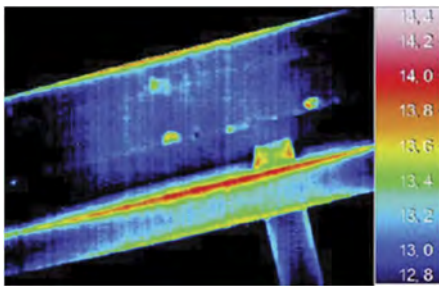


Figure 3. Potential areas with delaminated concrete (thermography at 10 m distance).



Figure 4. Delaminated concrete removed.

The second investigation comprised a handheld thermographic screening from 2--10 m distance from the concrete surface to find delaminated areas. The areas with delaminations were confirmed and removed by contractors from an under-bridge inspection gantry. An example of an identified area is shown in thermography Figure 3, and the removed concrete from same identified area is shown in Figure 4. Defects that were not captured during the visual inspection were also identified.

3.5 *The Faroe Bridges*

The Faroe Bridges connect Falster and Zealand across the Faroe Island in Denmark. The bridges opened to traffic in 1985 and is carrying four lanes of highway traffic. The connection consists of a cable stayed bridge in South from Falster to Faroe with a length of 1,726 m and a main span of 290 m with a clearance from the sea of 26 m and a concrete beam bridge (orthotropic steel box girder) in North from Faroe to Zealand with a total length of 1,596 m and a clearance from the sea of 20 m (Linneberg et al. 2022).

The bridge is owned and operated by the Danish Road Directorate. COWI A/S has provided consultancy services related to the operation and maintenance of the bridge. The Cable stayed bridge is shown in Figure 5. In 2020, the Danish Road Directorate commissioned COWI A/S to establish a Reality Capture Model of both bridges to be used for operation in general and for presentation of principal inspection of concrete emergency walkways (more than 6.5 km) and bridge piers (34 in total).

In total four UAV flights were performed: The first flight established reference points. The second flight established RGB photogrammetry for the whole model. The third flight established close-up photos of emergency walkways. The fourth flight established close-up photos incl. thermal imagery of all bridge piers.

The Reality Capture Model was imported into COWI Virtual Inspection software, and a visual inspection is carried out using both RGB – and thermal imagery. Examples of two areas with defects are identified in RGB – and thermal imagery in Figures 6 and 7. After a virtual visual inspection, an inspection of six bridge piers using rope access were carried out.

The inspectors found the same significant defect (delaminated areas of similar size) as the virtual inspection alongside minor defects as cracking and poor in-situ grouting of voids from the removal of scaffolding. In addition, the virtual inspection identified few defects in the splash zones not accessible to rope access.



Figure 5. The Faroe Bridges (Cable Stayed Bridge in South).

3.6 *The Queen Alexandrines Bridge*

The Queen Alexandrines Bridge, also known as the Moen Bridge, connects Zealand with Moen in Denmark. The bridge opened to traffic in 1943 and is carrying two lanes of traffic and two pedestrian walkways with a total length of 745,5 m, and a main span of 127,5 m with a clearance from the sea of 26 m (The Danish Road Directorate, 2022). The construction is an open arch bridge with five approach spans cast in reinforced concrete on each side of the main arch span constructed in steel.



Figure 6. Potential areas with delaminated concrete (verified by rope-access personnel).



Figure 7. Potential areas with delaminated concrete - captured using thermography.

The bridge is owned and operated by the Danish Road Directorate. COWI A/S has provided consultancy services related to the operation and maintenance of the bridge. The Queen Alexandrines Bridge is shown in Figure 8. In 2022, the Danish Road Directorate commissioned COWI A/S to establish a reality capture model of one approach span and integrate the model in COWI Virtual Inspection as part of a pilot project for visual inspections.

The Reality Capture Model of the bridge is based on both RGB – and thermal imagery captured simultaneously with the use of a drone without any traffic restrictions.

The Reality Capture Model is imported into COWI Virtual Inspection, and a principal inspection is carried out using annotations in the model to illustrate visible damages e.g., cracks, spalling, organic growth, graffiti, etc. The annotations are directly linked to the specific area of the model and are easy to revisit to e.g., consult or verify with a specialist.

Thermal imagery identifies areas with possible delamination that have a temperature difference down to 0.1-0.2 degrees Celsius compared to the surrounding structure. Three identified areas are shown in the RGB photo in Figure 9 and thermography in Figure 10. Two areas located in the bottom of the concrete arch show concrete repair works, and another area close to the granite parament show delamination on the thermal imagery. The identified areas were subsequently verified by contractors with a hammer test and repaired as part of a larger maintenance project on the pile caps in 2022 and 2023.

The Danish Road Directorate can access the model and hereby get full documentation of the bridge related to the principal inspection. A screen dump from the COWI Virtual Inspection software is shown in Figure 11.

The Reality Model may also be used to e.g., annotate daily operation jobs for operation personnel, plan future repair works, etc. The model creates a solid foundation for collaboration with all stakeholders incl. owners, contractors, and consultants without being present at the bridge site and without possible traffic restrictions.



Figure 8. The Queen Alexandrines Bridge.



Figure 9. RGB photo of potential delaminated areas on concrete bridge pier.

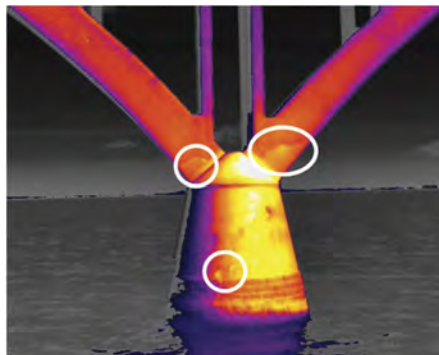


Figure 10. Thermography of potential delaminated areas on concrete bridge pier.

4 ADVANTAGES AND CHALLENGES

4.1 *Virtual inspections*

Working with virtual inspections proposes many advantages related to the reality capture process, the inspection itself, and future use of the Reality Capture Model. Using UAVs leads to reduced traffic disturbance and a short time on site which overall reduce the initial cost e.g., truck mounted under bridge inspection units, rope access, lifts, etc. for visual inspections.



Figure 11. Screen dump of one approach span in COWI Virtual Inspection software.

The COWI Virtual Inspection platform allows multiple specialists to take part in the visual inspection leading to transparency in decision-making and less subjectivity. The bridge is inspected with well-rested personnel, and it is possible to revisit structural elements to look for repetition patterns in defects. The asset manager is provided with full photo-realistic 3D documentation of the bridge and with a Reality Capture Model providing an efficient means of communication with various stakeholders incl. operational personnel.

Though many advantages have been pointed out, some challenges remain: The data collecting process still requires highly trained personnel to establish a detailed photo-realistic 3D model and depends on the quality of sensors (cameras etc.), traffic laws, and restrictions when flying with UAVs, flight plans, lighting conditions, weather, and temperature (when using thermal imagery).

The implementation of the Reality Capture Model in ‘codified’ procedures and manuals, and in current BMS software remains one of the greater challenges.

4.2 Future perspectives

Companies specialized in asset management have acknowledged the great potential for digitalization within Operation and Maintenance (O&M), and UAVs, AI models, and Bridge Management systems are rapidly improving.

When delivering a new bridge, BIM models can be handed over as part of the As-built information if specified by contract requirements. At the same time, a ‘Birth Certificate’ of the bridge (incl. a Reality Capture Model) should be established and linked to the BIM model. This model ‘environment’ may later be supplemented with information from O&M incl. sensor data in a complete asset management system to predict repairs and replacements of structures.

Furthermore, new types of drones that can “bump” into obstacles when capturing images and thereby get close to full coverage of the bridge structure including e.g., tight spaced areas, hangers, and bearings has been developed. UAV’s can fly autonomously, and soon AI-assisted flying will be implemented e.g., a drone being a part of the daily operations and inspections fully integrated into the asset management system and updating the adjacent Reality Capture Model.

5 CONCLUSIONS

Operation and Maintenance (O&M) of bridges are undergoing a digital transformation, and with better technical and more cost-beneficial equipment (drones, sensors, software, etc.), the digital transition accommodates environmental, economic, and technical benefits.

Combining the newest UAV technology (incl. carry-on equipment) and trained AI-based models with the knowledge of experienced engineers is one of the keys to success toward a digital transition of bridge inspections and their relation to bridge management.

Data processing requires domain knowledge to establish a detailed Reality Capture Model suitable for visual virtual inspections. Digitalization in general comes with a cost and requires certain competences within an organization to be a part of the digital transition.

With improved sensors, software, and autonomously UAVs, the data collection -and integration process becomes less time consuming and more cost beneficial. Virtual inspections performed on Reality Capture Models delivers less subjectivity and full 3D documentation in an improved workflow with full transparency. In addition, UAV-based inspections increase bridge availability, increase safety for bridge users and workers – with less environmental impacts from emissions.

The workflow of Virtual Inspections is tested and improved over three bridges presented in this paper with both RGB and thermal imagery to detect visual and certain non-visual (hidden) defects. It is important to calibrate virtual inspection results with manual hands-on inspections.

The integration of the Reality Capture Model within the principal inspection regime improves workflow and supports finding the ‘optimal point in time’ to repair and replace structural elements considering multiple Key Performance Indicators for bridge owners and operators.

ACKNOWLEDGEMENTS

A huge thanks to the Danish Road Directorate, for allowing us to work with the three bridges presented in this paper. We look forward to future collaboration when expanding the pilot project on the Queen Alexandrines Bridge to include a full virtual principal inspection of the bridge in 2023.

REFERENCES

- Avendaño, J. C., Leander, J., Karoumi, R., 2022, Image based inspection of concrete cracks using UAV photography, *IABMAS 2022*.
- COST TU1406, 2018, Hajdin, R., Kusar, M., Masovic, S., Linneberg, P., Amado, J., Tanasic, N., WG3 Technical report, Establishment of a Quality Control Plan, ISBN: 978-86-7518-200-9.
- Linneberg, P., 2020, From condition to performance assessment of bridges – The challenge, *IABMAS 2020*.
- Linneberg, P., Jensen, F. M., Hartwich, E. D., Holt, P., 2022, Unmanned Aerial Vehicle (UAV) supported bridge inspections, *IABMAS 2022*.
- McKinsey Global Institute, 2016, Digital Europe: Pushing the frontier, capturing the benefits, www.mckinsey.com/mgi.
- Moore, M, et al., 2001, Reliability of Visual Inspection for Highway Bridges, *FHWA-RD-01-020*.
- The Danish Road Directorate, 2022, Dronning Alexandrines Bro, *Dronning Alexandrines Bro (vejdirektoratet.dk)*.

Life-cycle sea-crossing bridge operation under strong winds in severe weather

Ho-Kyung Kim & Hyeong-Yun Cheon
Seoul National University, Republic of Korea

Sejin Kim
University of Michigan, USA

ABSTRACT: This study addresses the challenge of maintaining the stability of running vehicles on sea-crossing bridges in the presence of strong side winds. To ensure safety, bridge operators often limit speed or close bridges when wind speeds reach predetermined criteria. However, critical wind speeds vary from bridge to bridge due to influential factors such as geometrical shape and road surface conditions. This study proposes a framework to determine critical wind speeds, considering rain or icing road conditions during severe weather. The study also reports on two overturning accidents on double-deck suspension and cable-stayed bridges and extends the procedure to probabilistic risk assessment for the bridge's lifetime. The results provide guidelines for bridge operators to balance driving safety and mobility in hazardous weather conditions.

1 INTRODUCTION

The Korean peninsula is frequently affected by typhoons, and the over 90 cable-supported sea-crossing bridges in the region are often subjected to strong side winds. While most bridges are closed at wind speeds above 25 m/s on a 10-minute average, speed control protocols vary based on bridge-specific experiences or benchmarks. However, bridge operators face challenges in taking timely actions, such as bridge closure, due to the need for advanced discussion with the police department and site preparation, coupled with unpredictable fluctuations in wind speed (Lim et al. 2022). Additionally, vehicle speed control or bridge closure protocols may not be relevant for specific bridges (Kim et al. 2022a, b, Kim et al. 2021, Kim et al. 2020, Kim et al. 2016).

This paper presents two case studies of bridges, a suspension bridge (GAB) and a cable-stayed bridge (SHB), which experienced rollover accidents in almost the same locations. The study applied a risk assessment procedure to determine the root cause of the accidents and compared potential measures to mitigate the risk index.

The study emphasizes that a comprehensive vulnerability assessment of driving safety on sea-crossing bridges must consider several factors, including bridge geometry, wind and traffic data, and road surface conditions during severe weather, throughout the life cycle of the bridge. The results of the study highlight the importance of such assessments in ensuring the safety of vehicles on cable-supported bridges during strong side winds and can provide guidance for bridge operators in developing effective strategies for managing the safety of sea-crossing bridges considering different road surface conditions.

2 EXAMINED BRIDGES

2.1 GAB – a double-deck suspension bridge

Figure 1 provides an overview of GAB, including its main span and approach spans. Notably, the lower deck at the approaching spans, marked in Figure 1(a), was the exact location of

consecutive rollover accidents that occurred in 2012, with only an hour interval between them. After identifying the corner points along the approaching spans as vulnerable spots, a risk assessment framework needs to be employed to determine the root cause of the consecutive roll-over accidents that occurred at this location.

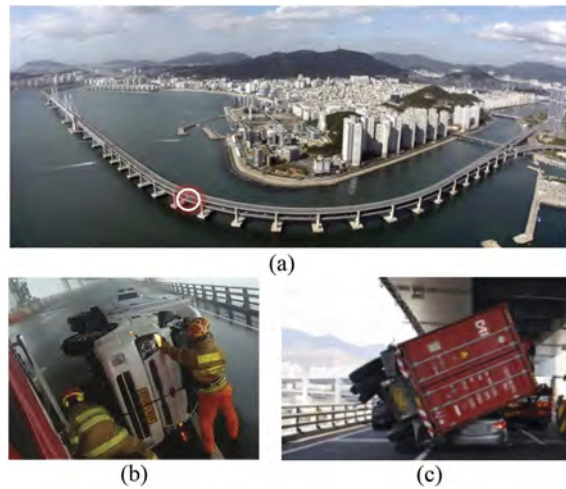


Figure 1. GAB (a) bridge overview (b) A roll-over accident (c) Another roll-over accident.

2.2 SHB – a cable-stayed bridge with approach spans with a transition region

Figure 2(a) provides an overview of the SHB, including its main and approach spans, while Figure 2(b) shows a sudden change in deck width at the transition region. A rollover accident occurred in 2012 at this location, as illustrated in Figure 2(c). CCTV footage revealed that all vehicles hesitated to cross the transition spots and the overturned truck had come to a stop just before the accident. These observations suggest that the transition region was indeed vulnerable to accelerated wind conditions.

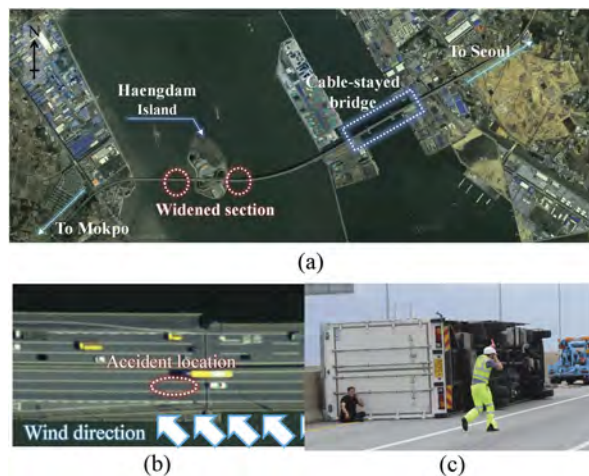


Figure 2. SHB (a) bridge overview (b) transition region (c) A roll-over accident.

3 RISK ASSESSMENT FRAMEWORK

Figure 3 shows the risk assessment framework for the root cause analysis and mitigation strategy for the whole life. The framework includes a wind tunnel test, vehicle analysis, wind-environment analysis with long-term wind data, fragility analysis, and risk assessment.

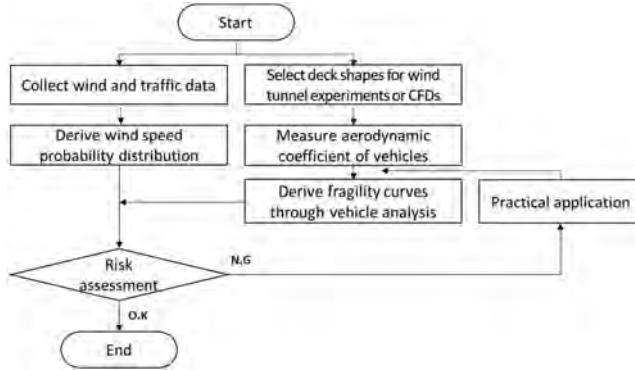


Figure 3. Risk assessment framework (KBRC 2021).

3.1 Wind tunnel test

A wind tunnel test was conducted using scaled-down bridge and vehicle models to estimate aerodynamic coefficients, which considered the effect of girder shape. Six different aerodynamic loads acting on the vehicle models were measured on each traffic lane using a small-size six-axis load cell. A special jig system (shown in Figure 4(a)) was used to measure the coefficients according to the incident wind angle by rotating the bridge model from -40° to $+40^\circ$ along the vertical axis (as shown in Figure 4(b)). The variations of aerodynamic coefficients for all wind directions were obtained through sine curve fitting (Figure 4(c)).

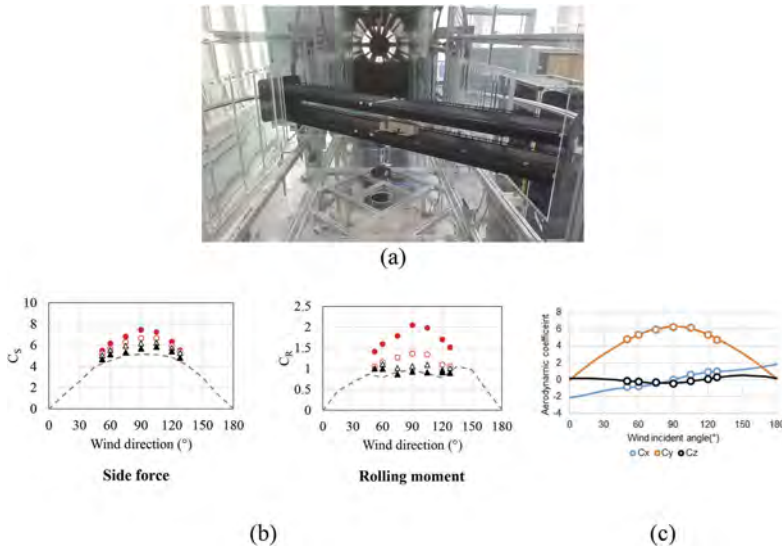


Figure 4. (a) Wind tunnel test using jig (b) measured coefficients (c) fitted coefficients result.

3.2 Critical wind speed curves (CWCs)

The authors used a dynamic simulation of running vehicles to estimate the critical wind speeds (CWCs) of vehicles. This was done using software such as TruckSim/CarSim and Simulink, which allowed for the simulation of vehicle models, running speeds, wind conditions, road geometries, and surface conditions. The quasi-static procedure (Batista & Perkovič 2014, Kim & Kim 2019) was also adopted for simplicity, and critical wind speeds were estimated by considering two accident types: rollover and side slip.

The CWCs were estimated based on the tire reaction forces and calculated for both the main and approach spans. Figure 5 shows a sample of the estimated CWCs for a truck on the lower deck of an approaching span of the GAB when the vehicle speed is restricted to under three different speeds. The traffic control wind speed can be determined for all vehicle types by selecting the lowest value of CWC.

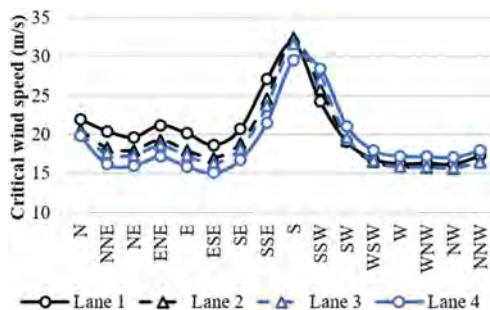


Figure 5. Example of dangerous wind speed curves according to Speed Limit (vehicle type: truck, accident probability: 5%).

3.3 Risk assessment

The authors estimated the risk index by analyzing the wind environment using long-term wind data collected from nearby weather stations. The probability distribution functions of wind speed were evaluated for 16 wind directions. Based on the previously estimated CWCs, the annual accident occurrence frequency (NE) was calculated.

$$N_E = 365 \times A \times Q_d \times R_v \times R_L \times \sum_{i=0}^{16} P_i \times P_{E|dir=i} \quad (1)$$

where Q_d is the annual average daily traffic, R_v is the vehicle type ratio, and R_L is the ratio of traffic volume for traffic lanes. A is the modification factor, which can be smaller than 1.0 considering the empty and closed container vehicle ratios. P_i is the ratio of the occurrence frequency of wind speed by the wind direction and can be calculated through wind environment analysis. $P_{E|dir=i}$ is the accident probability for the i -th wind direction and can be calculated based on the driving restriction wind speed applied to the bridge.

4 RISK REDUCTION STRATEGY DURING THE WHOLE LIFE OPERATION

4.1 The GAB

A series of wind tunnel tests demonstrated the wind tunneling effect, revealing an acceleration in wind speed between the upper and lower decks (Kim et al. 2020). This effect was found to be more pronounced in the approaching spans that lacked truss members between decks. The increased vehicle side force and rolling moment at the lower deck were identified as the primary causes of the consecutive rollover accidents in 2012. Analysis results indicated that the truck was the most vulnerable vehicle type, with an annual accident frequency risk index of 0.34.

To reduce the risk index, traffic control measures following Table 1 can be implemented as an effective solution (Kim et al. 2022b). While the construction of a windscreen on the vulnerable point of the bridge would be demanding, it is a viable option with the limited range required for the corner part of the approach span when the dominant wind direction is included in the risk assessment. Figure 6 illustrates the effectiveness of the windscreen in reducing the risk index, with the second bar indicating the windscreen case for one side of the road and the third bar for both sides (Kim et al. 2022b). However, after another recent rollover accident, the bridge owner has temporarily reduced the speed limit for wind speed.

Table 1. Proposal for improvement of traffic control strategy for the GAB.

	Response	Wind speed (existing)	Wind speed (improved)
Level 0	Speed limit 110 km/h	0~14 m/s	0~16 m/s
Level 1	Speed limit 80 km/h	14~21 m/s	16~19 m/s
Level 2	Speed limit 50 km/h	21~25 m/s	19~22 m/s
Level 3	Bridge closure	25 m/s~	22 m/s~

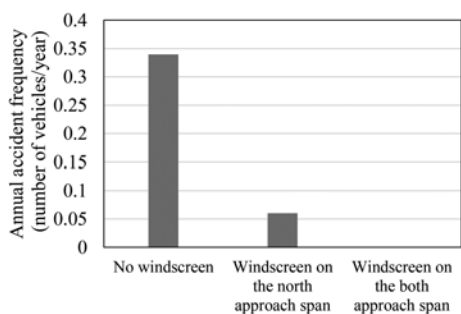


Figure 6. Changes in the risk index of the truck according to the installation location of the windscreen.

4.2 The SHB

A series of wind tunnel tests were conducted to understand the variation of wind speed at the transition region. The structural details, including the double installation of roadside barriers, induced an acceleration in wind speed over the open deck, increasing the side force and roll-over moment three to four times that of the general approach spans. To adhere to the Korean guideline (KBRC 2021), the proposed risk assessment procedure suggested lowering the traffic control wind speed by 1~3 m/s, as shown in Table 2 (Kim et al. 2022b).

Figure 7 demonstrates the risk index based on the traffic control plans for the transition section, where the risk index decreases with the decrease of the restricted wind speed. It is more meaningful to adopt the second or third plan instead of the first one, which has no significant difference from the current one (Kim et al. 2022b). Moreover, a windscreen installation in the transient region could be more effective from a mobility standpoint, as indicated in Figure 8.

Table 2. Proposal for improvement of traffic control strategy for the SHB.

Response	10-minute-average wind speed		
	Strategy 1 (-1 m/s)	Strategy 2 (-2 m/s)	Strategy 3 (-3 m/s)
Level 0	Speed limit 80 km/h	14 m/s	
Level 1	Speed limit 50 km/h	19 m/s	17 m/s
Level 2	Bridge closure	24 m/s	22 m/s

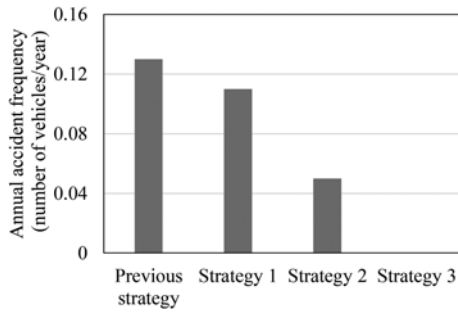


Figure 7. Changes in the risk index according to the improvement plan for the SHB.

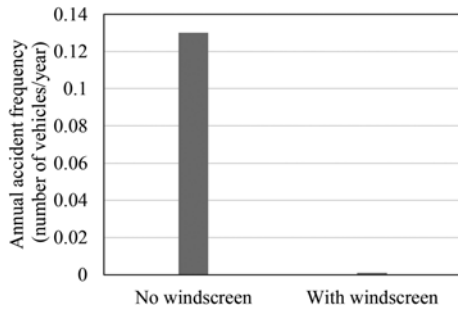


Figure 8. Changes in the risk index according to the windscreen installation on the transition section.

5 EFFECT OF ROAD CONDITIONS IN A SEVERE WEATHER

5.1 Measuring road surface roughness coefficients in severe weather conditions for GAB

Given the significant impact of road surface roughness coefficients on vehicle stability, Busan Infrastructure Corporation measured them during rainy conditions. Specifically, we analyzed the relationship between hydroplaning depth and the corresponding surface roughness coefficients measured on GAB, as illustrated in Figure 9. The field measurements of the roughness coefficients were conducted seven times between May and November 2020. Our findings indicate that the roughness coefficients decreased from 0.8-0.85 to 0.60-0.70, depending on the rainfall intensity. Notably, when the hydroplaning depth exceeded 2 mm, the roughness coefficients stabilized at 0.6.

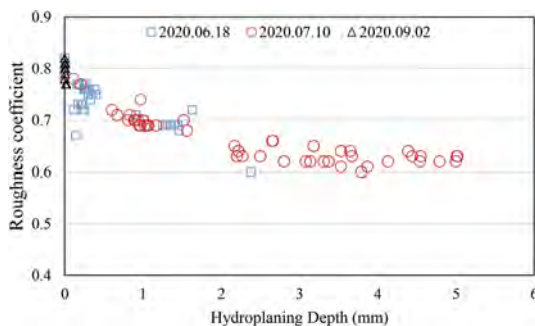


Figure 9. Hydroplaning depth and measured road surface roughness coefficients.

5.2 Traffic control wind speed according to road surface conditions

To facilitate our analysis, we assumed the roughness coefficient to be 0.85 under dry conditions, 0.50 under wet conditions, and 0.20 under icing conditions, as we did not have access to direct measurements of the latter. Figures 10 and 11 demonstrate how the varying road surface conditions affected the critical wind speed (CWC) at two different driving speeds: 80 km/hr. and 40 km/hr. Our analysis revealed that the surface conditions significantly impacted CWCs, particularly for passenger vehicles, which were more susceptible to road conditions. For instance, at a driving speed of 80 km/hr., the CWC decreased from 22 m/s to 17 m/s and 7 m/s for wet and icing conditions, respectively. Conversely, the truck was less affected, with the CWC decreasing from 14 m/s to 14 m/s and 8 m/s under the same conditions. This difference can be attributed to surface conditions primarily affecting side slip accidents.

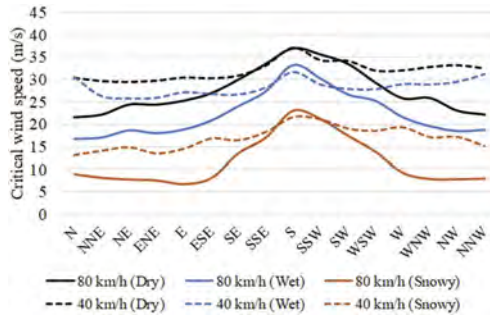


Figure 10. CWCs of passenger cars for three road conditions and two vehicle speeds on the lower deck of GAB.

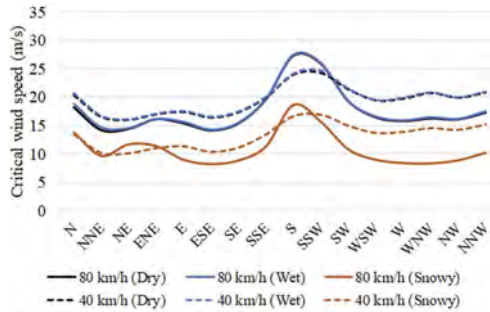


Figure 11. CWCs of trucks for three road conditions and two vehicle speeds on the lower deck of GAB.

6 CONCLUSIONS

This study highlights the significance of employing a probabilistic risk assessment procedure to determine the appropriate traffic control strategy for ensuring the safety of crossing vehicles during strong side winds. Our proposed risk assessment framework successfully identified the root causes of the rollover accidents that occurred on two examined bridges. Interestingly, we found that the vulnerable spots were not always in the main span of the sea-crossing bridges with high altitudes and more exposure to open space. Instead, weak spots were identified in the approach span, contrary to our initial expectations. Our analysis indicated that the geometrical characteristics of the bridge deck, particularly double deck configuration and road width transition regions along the sea-crossing bridges, were the most influential parameters that affected the risk of overturning accidents. Additionally, the evaluation of long-term wind

speed, with consideration of wind direction, was found to be an essential component of the assessment. These findings emphasize that traffic control or bridge closure during strong side winds should be determined for each bridge, considering its geometry, alignment, traffic volume, wind environment, and road conditions in severe weather conditions at the site for the entire lifespan of the bridge. We proposed traffic control strategies for the examined bridges. However, considering the bridge's serviceability and the driving mobility of bridge users, we recommend the use of a windscreen for vulnerable spots as a long-term operational measure for the bridge's life cycle.

ACKNOWLEDGMENT

This research was supported by a Grant (RS-2023-00250727) from the Ministry of Land, Infrastructure and Transport of the Korean Government. The authors thank Principal Engineer Young-Kook Kim, the Bridge Management Team leader of Busan Infrastructure Corporation, for field-measured wind and roughness data and his comments on this study.

REFERENCES

- Batista, M. and Perkovič, M. 2014. A simple static analysis of moving road vehicle under crosswind. *Journal of Wind Engineering and Industrial Aerodynamics* 128.
- Kim S.J., Seyedi M.R., and Kim H.K. 2022a. Risk Assessment of Wind-Induced Vehicle Accidents on Long-Span Bridges Using Onsite Wind and Traffic Data. *Journal of Structural Engineering* 148(10).
- Kim H.K., Cheon H.Y., and Kim S.J. 2022b. Probabilistic Assessment of Vehicle Driving Safety under Strong Winds – Cause Investigations on Two Sea-Crossing Bridges. *Proc. IABSE Congress*, Nanjing September 2022. Zurich: IABSE.
- Kim S.J., Lim J.Y., and Kim H.K. 2021. Decision framework for traffic control on sea-crossing bridges during strong winds. *Journal of Bridge Engineering* 26(8).
- Kim S.J., Shim J.H., and Kim H.K. 2020. How wind affects vehicles crossing a double-deck suspension bridge. *Journal of Wind Engineering and Industrial Aerodynamics* 206.
- Kim S.J., and Kim H.K. 2019. Feasibility of a quasi-static approach in assessing side-wind hazards for running vehicles. *Applied Science* 9(16).
- Kim S.J., Yoo C.H., and Kim H.K. 2016. Vulnerability assessment for the hazards of crosswinds when vehicles cross a bridge deck. *Journal of Wind Engineering and Industrial Aerodynamics* 156.
- Korea Bridge Design and Engineering Research Center (KBRC). 2021. *Guidelines for Securing Driving Safety for Cable-supported Bridge under Strong Winds*. Seoul National University.
- Lim J.Y., Kim S.J., Kim H.K., and Kim Y.K. 2022. Long Short-Term Memory (LSTM)-based wind speed prediction during a typhoon for bridge traffic control, *Journal of Wind Engineering and Industrial Aerodynamics* 220.

Resilient structures: Materials | Components | Systems

Mark P. Sarkisian

Partner, Skidmore, Owings & Merrill, San Francisco, CA, USA

ABSTRACT: Materials, components, and systems are all essential to creating resilient structural systems. Historical, materials have been used based on technologies of the time including an understanding of mathematics, physics, and engineering. Modest-strength materials, when assembled creatively can provide significant resistance to gravity and lateral loads. When intelligently placed, these materials can form structures that are even self-stabilizing during construction without the need for forming systems. Structural components designed for maximum life and performance can transform brittle structures into those with ductility where damage can be reduced when subjected to extreme loadings such as those created from seismicity. Structural systems can be comprised of multiple types of materials and can be assembled into efficient structures at all scales. New advancements in design include super-elastic materials that can be used to dissipate energy during seismic events and even provide self-centering of structures after strong ground motions.

Several building examples will be described and presented. These examples will be based on fundamental concepts of life-cycle engineering including ideas that help reduce embodied carbon through initial construction and long-term behavior. Ideas include structures that incorporate seismic isolation, friction fuse devices, and even new concepts using Shape Memory Alloys (SMA).

1 INTRODUCTION

Resilience is arguably the most important aspect of life-cycle civil engineering. Even though code-based design inherent provides a reasonable approach to resilient structures primarily due to a life-safety considerations, it falls short of achieving optimal performance in areas of risk especially those with high potential seismicity. For example, many buildings in Christchurch, New Zealand were designed to recent building codes and proved to be life-safe during the 2011 earthquake. However, many buildings were significantly damaged and proved to be unfit for continued operation even with a magnitude earthquake of 6.3 on the Richter Scale. These buildings were demolished as a result causing significant financial loss and major disruptions to businesses in the city of Christchurch (Figure 1).

Environmental impacts due to the emission of carbon dioxide and carbon dioxide equivalents has proven to be an important consideration in life-cycle civil engineering. The carbon associated with building construction is perhaps the most significant contributor accounting for approximately 50% of emitted carbon when considering initial construction and building operations (Figure 2). Approximately one half of these emissions are associated with initial construction and embodied. Urban developments around the world can sometimes occur over a limited period of time.

Without careful planning, these developments (Figure 3) can have enormous impact on the emission of carbon not just during the initial construction but throughout the development's life where resilient materials, components, and systems are important to minimize impact. In areas of environment risks (ie. seismicity), the amount of embodied carbon can significantly increase over time due to the need for repairs or in extreme cases demolition and new construction.



Figure 1. Damage and demolition of buildings - Christchurch, New Zealand due to the 2011 earthquake.

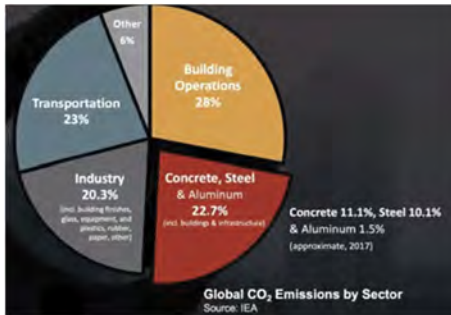


Figure 2. Global carbon dioxide emission by sector.



Figure 3. Aerial photograph – Lima, Peru.

2 MATERIALS

For thousands of years, mankind has invented ways of using materials based on a specific understanding of applications known at the time. First developed for shelter and later of a wide range of uses, structures incorporated ingenuity that was largely informed by construction trial and error and near-term/long-term environmental conditions. Structures originally were constructed by found materials (i.e. stone) and later by fabricated materials. In early applications using fabricated materials, raw materials used were largely those resourced directly from the earth such as clay. These materials could be fired for increased strength and when used in pure compression with modest loads, could be used for large structures (Figure 4).

Within the last few hundred years, masonry has been widely used in major structures in Europe and in many of those structures, timber vaults were used to span significant distances. Timber vaults are unique since these structures are typically constructed without formwork (geometric guides only) and are self-stabilizing (Figure 5).

The disadvantage to these structures is they typically perform poorly in significant seismic events where masonry materials are subjected to tension and cyclic loadings. A major earthquake in April 2015 in Nepal led schools, constructed of brick or stone, to collapse (Carroll, 2015). Techniques to retrofit these buildings so that they can withstand seismic loading are strongly needed. While reinforcement attempts have increased over the last decades (Foraboschi, 2004) (Shrive, 2006) (Ramaglia, 2016), the reinforcement of buildings made from solid masonry, such as brick, stone, adobe blocks and hollow clay tile, remains an ill-mastered technique for which no standard procedure has been developed. SOM research done in



Figure 4. Stacked masonry – Lima, Peru. Figure 5. Masonry timbrel vault construction.

collaboration with the University of Alcalá, Madrid and Taller de Bóvedas has resulted in more highly resilient timbrel vaults when subjected to lateral loading while using modest materials such as fiberglass to reinforce the masonry.

Analysis of arches, a segment of idealized vaults, focused on the onset of mechanisms when four hinges are formed. Analysis and physical testing considered unreinforced and reinforced masonry vaults (Figure 6).



Figure 6. Masonry arches on shake table – reinforced on left, unreinforced on right.

Given that the supports of the arch were pinned in the numerical model, predicted collapse would occur when two hinges form within the arch. Lateral analyses of unreinforced arches when subjected to lateral acceleration using frame elements is shown in Figure 7.

The distance e between the centroid of the section and the location of the force resultant in the section is given by the following formula: $e = \frac{M}{P}$ (1), where M is the strong axis bending moment and P is the axial force. Therefore, the condition for a hinge to form is represented by the following formula: $e \geq \frac{h}{2}$ (2), where h is the section height.

The unreinforced arch was originally considered for a unidirectional lateral acceleration starting at 0.1g. Using equation (2), the first hinge was predicted to appear at an acceleration of 0.2g between elements 7 and 8. Collapse was predicted at 0.23g, when a second hinge formed between elements 2 and 3 and the original hinge moved to the joint between bricks 8 and 9 (Figure 7).

To validate the predicted hinge locations, the bricks were modelled as shell elements and the stress distribution in the shell elements was evaluated. Similar to the frame element model, the interface between bricks was modelled as a continuum. In this model, compressive stresses were

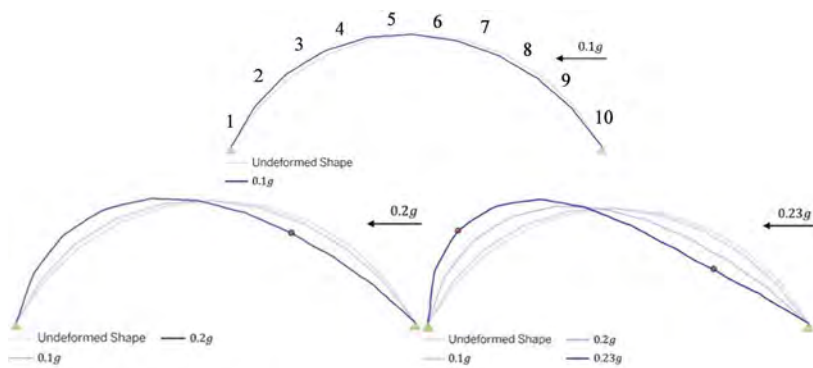


Figure 7. Masonry arch deformation at 0.1g, 0.2g, and 0.23g (numbers indicate frame element labels and red circles indicate hinges).

concentrated on one the side of the section at the hinge locations. On the other side of the section, tensile stresses were observed, indicating that the adjacent brick sections had separated. The stress distribution and the predicted hinge locations at 0.23 g is presented in Figure 8.



Figure 8. Stress distribution in arch 1 at 0.23g.

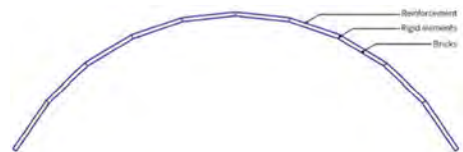


Figure 9. Extrados – reinforced arch.

Reinforcement was introduced into the model with another layer of elastic frame elements offset from the elements representing the bricks (Figure 9). The reinforcement elements were assigned low values of inertial stiffness so that they mainly resisted axial loads. The two layers of frame elements were connected through rigid frame elements. The deformation at a similar level of acceleration was found to be more pronounced for the unreinforced arch than it was for the extrados-reinforced arch (Figure 10). When collapse occurred in Arch 1 with the formation of two hinges within the span, the reinforcement in Arch 2 prevented hinges from forming on the intrados, allowing it to resist higher levels of acceleration.

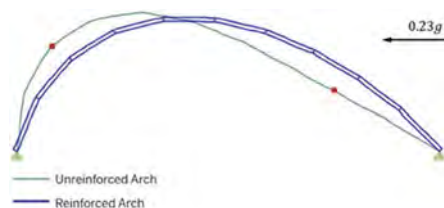


Figure 10. Deformation comparison between the unreinforced arch (green) and the extrados – reinforced arch (blue) under 0.23g.

In addition to the improved lateral load resilience of modestly reinforced masonry arches, principles of structural optimization were applied to the masonry vaults. For the installation of works at the College of Architecture Madrid (COAM), density optimization was applied to a structure that was built as part of the exhibition. The goal was to create a timber vault that could minimize the use of materials and therefore embodied carbon. Construction would be faster since less materials would be placed. The concept of the vault was one that could be

scales to larger structures when carbon emissions associated with materials and construction would be much more significant. Topology optimization analyses led to mapping of states of stress with areas in red having highest compressive stress and areas in light blue where stress was minimal, and material could be removed (Figure 11).

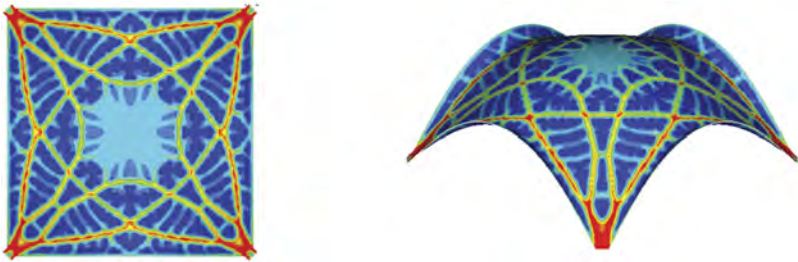


Figure 11. Topology optimization of masonry timber vault.



Figure 12. Constructed masonry timber vault indicating material removal and overall geometry.

Skilled, increasingly rarely available labor to build such vaults led to imagining that geometrically specific, self-stabilizing structures could be built with an automated process where three-dimensional space could be defined, and the material could be placed by robots. Alternate materials, still exhibiting good compressive characteristics, could be used to replace conventional masonry elements. SOM collaborated with Princeton University to create a glass vault assembled jointly by robots and humans. The structure was built using two robots placed on a platform to avoid arm interference and allowing for the placement of glass block material in predetermined three-dimensional space (Figure 13).

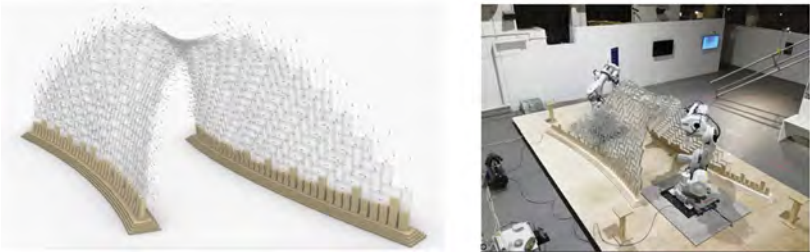


Figure 13. Geometric definition and constructed self – stabilized glass vault.

3 COMPONENTS

The original request for proposal (RFP) for the design-build Long Beach California Civic Center Project (Figure 14) stated four design objectives for a design level seismic event – 1. Experience few or no injuries; 2. Reoccupy the new facility within a week; 3. Have full functionality within 30 days; and 4. Experience less than 5% financial loss (as compared to the replacement value). For a public facility this criterion was a welcomed framework for resilient design. Initial ideas led to concepts of replacement traditional plastic yielding mechanisms of shear wall cores with an innovative concept of using a central base bearing at the base of core walls to allow for controlled mechanisms to occur during a seismic event while limiting damage.

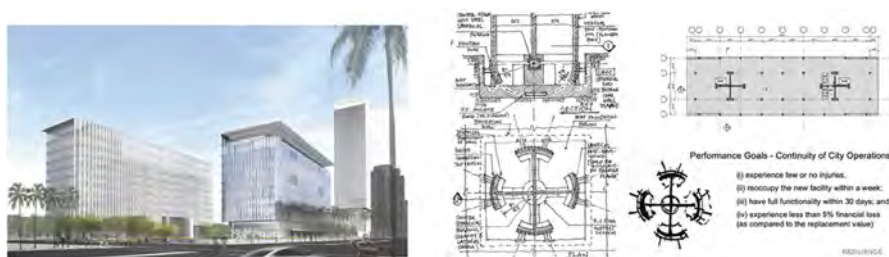


Figure 14. Rendering of Long Beach civic center project with core wall bearing concept.

For cost and schedule reasons, the final design included a creative alternative idea that used a more conventional approach where staggered openings in core walls were used so no link beams were required, therefore eliminating damage for these otherwise sacrificial elements during a seismic event. In addition, non-structural components were carefully considered for seismic displacement. For instance, partition walls typically did not span between each floor level but were otherwise interconnected only at the base of walls allowing for tops to move freely.

Advancements to friction joints within seismic resistance structures have led to an innovative approach to increase seismic resilience of the Sanyi Irotech Towers in Guangzhou (Figure 15). Seismic fuses were introduced into offset exterior braced frames. The fuses use bolted friction connections designed to slip during a major earthquake while protecting the base building material from plastic deformations/permanent damage. This resilient system does not move during typical service conditions when the towers are subjected to wind and moderate seismic events.

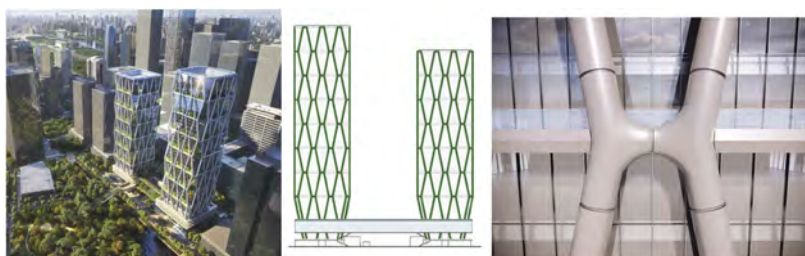


Figure 15. Rendering, idealized frame elevation, and enlarged view of offset frame joint.

High strength slip-critical bolts and steel friction shims are used to create the fused joints within the frame. Slip is considered through vertical slip in the joints. Conventional steel building components are used in each joint and the structural frame is exposed without cladding (Figure 16).

The combination of structural steel and heavy timber is a solution to reducing seismic mass while providing a ductile lateral load-resisting system. As part of the Long Beach Civic Center Project, a public library name the Billie Jean King Library was designed and built. This ultra-low

carbon structure was built over an existing parking structure where load was balanced through the removal of heavy landscaping and the addition of a lightweight steel and timber structure.

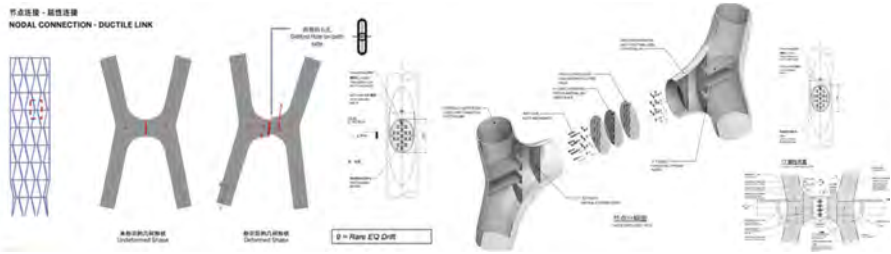


Figure 16. Modeled movement and components of frame friction joints.

This approach resulted in only modest seismic upgrades to the existing parking structure while creating long-span, flexible library spaces above. Steel braced frames and steel columns are interconnected with repetitive timber construction used for all of the floor systems (Figure 17).

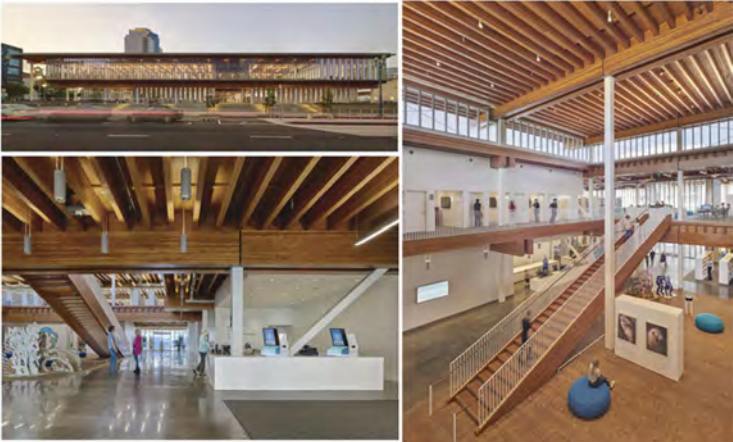


Figure 17. Combination of steel and timber – Billie Jean King library.

Components were further developed in the recently designed County Office Building 3 (COB3) Project for San Mateo County (Figure 18). Structural steel was also incorporated into



Figure 18. COB3 project under construction and typical beam-to-column connection detail.

the timber structure with wood typically used for columns instead of steel. Connections were prefabricated and proved to be essential to the rapid on-site assembly. Instead of conventional steel braced frames, unbonded steel braces were used in the core areas for seismic resistance. These braces can be replaced after a significant seismic event.

4 SYSTEMS

The Cathedral of Christ the Light in Oakland (Figure 19), California is an excellent example of a resilient, low embodied carbon structure. Seismic isolation is central to the design approach with the timber and steel structure supported on stainless steel friction pendulum bearings.

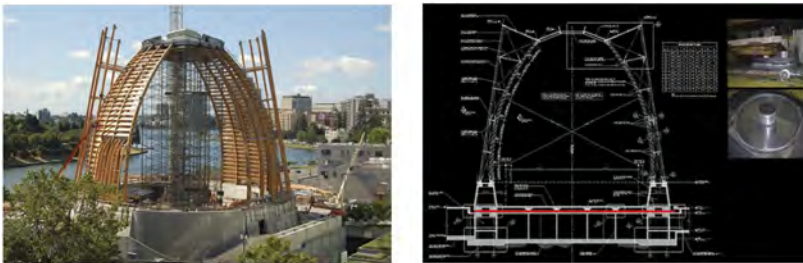


Figure 19. The cathedral of Christ the light under construction and the seismic isolation design.

A similar systematic approach was used for the design of Los Angeles County Museum of Art (LACMA) expansion project in collaboration with architect Peter Zumthor. This structure, currently under construction, consists of long cantilevers (up to 25 meters) as well as a clear span condition at the existing Wilshire Blvd. Seismic isolation is used to protect the artwork and create a resilient structure that is designed to minimize and damage due to potentially high seismicity.



Figure 20. Rendering and cross-section of structure for the LACMA museum.

The superstructure consists for reinforced concrete ribs and post-tensioning that sandwiches and top and bottom slab systems. Slabs are also post-tensioned. Art House walls interconnect the floor framing sandwich systems at the exhibition floor and the roof. Art Tower reinforced concrete shear wall cores house services and support the framing systems and are ultimately supported on 3 meter-diameter friction pendulum bearings. Post-tensioning is also used in the art house walls to transfer gravity loads from the framing to the Art Tower walls (Figure 21).

Significant advancements have been made for framed systems for all building structures. Based on the concept of the Michell Truss, the theoretically most correct and efficient use of materials in a cantilevered structure when subjected to lateral loads, several design

advancements have been made. Instead of concentrically braced frames, those that consist of a high-waisted asymmetrical system results in a more efficient structure achieving target strength and displacements with far less material. 800 West Fulton Market in Chicago (Figure 22) incorporates this system. A steel brace frame provides the lateral system for an otherwise reinforced concrete structure.

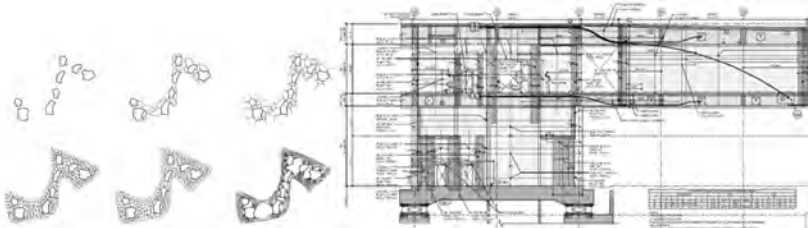


Figure 21. LACMA framing system concepts and cross section of wall system.



Figure 22. Lateral frame concept and final construction of 800 West Fulton Market, Chicago.

The important attribute to the Michell Truss concept is its application to horizontal framed structures such as the pedestrian bridge for Emery Cancer Center in Atlanta, Georgia (Figure 23). This concept can be used for pedestrian or vehicle bridges as well as long-span floor framing systems that can be used in repetition structures of all heights.

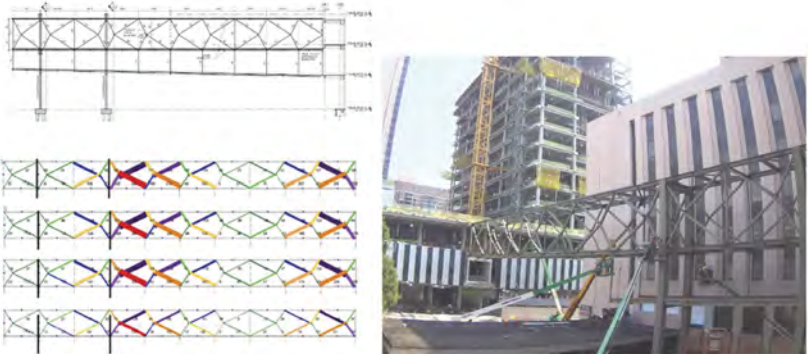


Figure 23. Emery cancer hospital pedestrian bridge drawing, analysis, and on-site photograph.

Bracing systems with seismic fuses provide an excellent solution to creating ductility in a potentially otherwise non-ductile seismic system. For the University of California, Berkeley, Bechtel Engineering Center fuses are introduced into the perimeter steel tension-only bracing system. What is unique about the system for the Bechtel Center is that the fuses are comprised

of super elastic Shape Memory Alloy (SMA) devices (Figure 24). The overall concept is to create an ultra-lightweight structure that is supported on an existing reinforced concrete building while minimizing any seismic retrofit to the existing building. The SMA devices deform during an extreme seismic event, dissipate energy, and then act to restore the building to its original position after the event (Figure 25).



Figure 24. UC Berkeley Bechtel center rendering and location SMA seismic fuses.

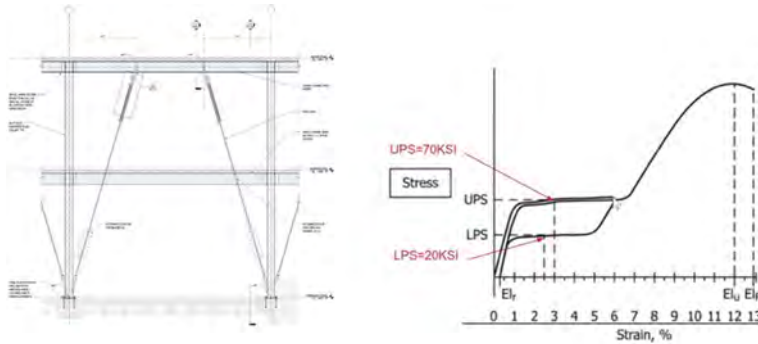


Figure 25. SMA Fuses – Elevation drawing and stress – strain relationship of material.

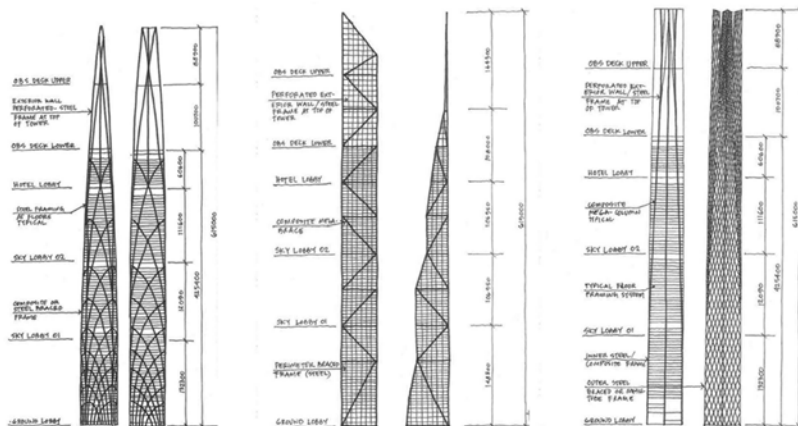


Figure 26. Structural system concept sketches for the Grand Rama tower – Bangkok.

5 CONCLUSION

Resilient design can be accomplished at all scales. Careful considerations of materials, components, and systems are all essential to efficient, low-carbon emitting structures that optimally perform over a projected building life. Combined concepts are important and when designing structures at great scale all attributes can be combined with great benefits. Mapping natural force flows is important resulting in structures that are elegant and potentially expressive (Figure 26).

REFERENCES

- Carroll, C. (2015, April 30). How Impoverished Nepal Can Rebuild for the Next Earthquake. Retrieved from National Geographic. <http://news.nationalgeographic.com/2015/04/150430-nepal-earthquake-rebuilding-construction-science/>.
- Foraboschi, P. (2004). Strengthening of Masonry Arches with Fiber-Reinforced Polymer Strips. *Journal of Composites for Construction* 8(3). [https://doi.org/10.1061/\(ASCE\)1090-0268\(2004\)8:3\(191\)](https://doi.org/10.1061/(ASCE)1090-0268(2004)8:3(191)).
- Ramaglia, G. (2016). Seismic Strengthening of Masonry Vaults with Abutments Using Textile-Reinforced Mortar. *Journal of Composites for Construction* 21(2). [https://doi.org/10.1061/\(ASCE\)CC.1943-5614.0000733](https://doi.org/10.1061/(ASCE)CC.1943-5614.0000733).
- Shrive, N. (2006). The Use of Fibre Reinforced Polymers to Improve Seismic Resistance of Masonry. *Construction and Building Materials* 20(4): 269–277. <https://doi.org/10.1016/j.conbuildmat.2005.08.030>. *Construction and Building Materials*, 269-277.

Risk and decision-making for extreme events: What terrorism and climate change have in common

M.G. Stewart

University of Technology, Sydney, Australia

ABSTRACT: Terrorism and climate change debates are often characterized by worst-case thinking, cost neglect, probability neglect, and avoidance of the notion of acceptable risk. This is not unexpected when dealing with extreme events. However, it can result in a frightened public, costly policy outcomes, and wasteful expenditures. The paper will describe how risk-based and cost-benefit approaches are well suited to infrastructure decision-making in these uncertain environments.

1 INTRODUCTION

Cyclones, earthquakes, tsunami and floods are natural hazards that cause significant loss of life, and economic and social losses. Added to this are ‘man-made’ hazards such as climate change and terrorism. These hazards are low probability - high consequence events which in recent times are more commonly referred to as ‘extreme events’. There is much hyperbole in the media and other sources that terrorism and more recently climate change are (or can be) reaching dangerous levels, are apocalyptic, or even existential. This characterisation of extreme events can result in a frightened public, costly policy outcomes, and wasteful expenditures. Hence, extreme events illicit extreme reactions – risk aversion, probability neglect, cost neglect, worst-case thinking – that may distort the decision-making process in an effort by policy makers to be seen to be ‘doing something’ irrespective of the actual risks involved.

Terrorism and climate change are extreme events of much interest. They can engender fear in the community, and predictions of impending doom are often overstated. Many terrorism and climate change ‘risk’ and ‘risk management’ reports dwell on lists of vulnerabilities and consequences. There is seldom mention of probabilities, or quantitative measures of vulnerability, or the likelihood of losses. While useful for initial risk screening, intuitive and judgement-based risk assessments are of limited utility to complex decision-making since there are often a number of climate or threat scenarios, adaptation or counterterrorism options, limited funds and doubts about the cost-effectiveness of protective measures. In this case, the decision-maker may still be uncertain about the best course of action. For this reason, there is a need for sound system and probabilistic modelling that integrates the performance of infrastructure systems with the latest developments in stochastic modelling, structural reliability, and decision theory.

Civil Engineering infrastructure such as houses, buildings, bridges, roads, pipelines, dams, etc. are vulnerable to terrorism and climate change. Over the past century building standards have been developed and continually improved – with the prevention of building collapse and catastrophic loss (ultimate limit state) the main driver for change. And while uncertainties and knowledge gaps still exist, disaster risks in the developed world are, in general, at an acceptable level. Hence, new infrastructure is, in general, built to modern codes of practice and so are less vulnerable to these extreme events. However, risks are generally higher for ageing or deteriorating infrastructure.

Risk-based approaches are well suited to optimising decisions related to extreme events (e.g., Stewart and Rosowsky 2022), in this case, climate adaptation strategies and counterterrorism measures. Stochastic methods may be used to model threat likelihood, vulnerability, resilience, effectiveness of protective strategies, exposure, and costs. Probabilistic terrorism risk assessment methods have been developed to assess the risks of terrorism, and effectiveness of risk reducing

measures (Mueller and Stewart 2011, 2015). Risk-based assessments of climate adaptation measures have also been developed (e.g., Bastidas-Arteaga and Stewart 2019). While the jargon may differ, the decision support approaches to counterterrorism and climate adaptation measures have much in common, as are the challenges. This paper aims to draw out these issues in more detail, with a particular focus on the pitfalls often encountered when assessing the threats, hazards, vulnerabilities and consequences of counter-terrorism measures, and climate change mitigation and adaptation.

2 CLIMATE ADAPTATION ENGINEERING

In recent years climate change seems to have displaced terrorism as the extreme event of most concern to public and governments. There is increasing research that takes into account the changing climate risks and life-cycle costs in engineering to reduce carbon emissions and/or reduce the vulnerability or increase the resiliency of infrastructure – this may be referred to as ‘climate adaptation engineering’. Climate adaptation engineering is defined as measures taken to:

- (i) reduce CO₂ emissions during the life cycle of design, construction, operation and end-of-life of infrastructure that may include decarbonisation measures such as more sustainable (low carbon) materials, enhanced operation efficiency (e.g., more thermally efficient buildings), and changes to inspection and maintenance regimes, and/or
- (ii) reduce the vulnerability or increase the resiliency of built infrastructure to storms, floods, fire, heat and other climate hazards, this may include, for example, enhancement of design standards (higher design loads or flood levels), retrofitting or strengthening of existing structures, or use of hazard resistant materials such as fire-resistant cladding.

Figure 1 shows a schematic to help illustrate the concept of climate adaptation engineering.

The political imperative to “act” on climate change is to reduce CO₂ emissions with a recent push for renewable energy, electric vehicles and other sustainability measures. However, while these measures are needed, their impact on the near to mid-term climate-related losses is miniscule. Whereas measures to reduce vulnerability and enhance resiliency of infrastructure provides a more immediate reduction in climate-related losses.

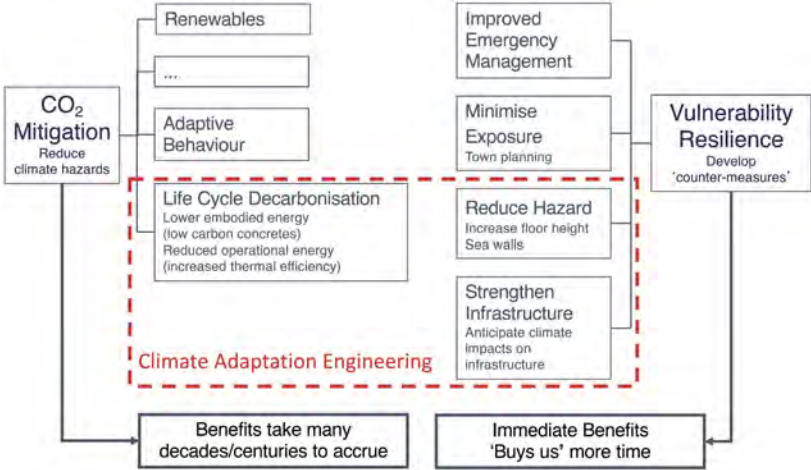


Figure 1. Illustration of climate adaptation engineering.

3 DECISION CHALLENGES: TERRORISM AND CLIMATE CHANGE

There are a number of issues and questions related to controversial and emotive issues such as terrorism, climate change, and other extreme events, and are discussed as follows.

3.1 *Worst-case thinking*

The media are replete with stories and articles that the world has never been more dangerous, and this is exacerbated by worst-case thinking and hyperbole expressed by many climate change and terrorism experts. In 2008, Department of Homeland Security (DHS) Secretary, Michael Chertoff proclaimed the “struggle” against terrorism to be a “significant existential” one. In 2021 U.S. President Joe Biden said that climate change poses a “global existential crisis”. These are not isolated examples, as similar remarks have been made by Boris Johnson, the United Nations General Secretary, and other world leaders and senior government officials. However, with the exception of all-out nuclear war or an asteroid impacting earth, other threats existential to humanity are hard to fathom.

If business as usual predictions are biased towards impending doom, then this justifies any response no matter the cost in loss of civil liberties, quality of life, and treasure. It can lead to wasteful expenditures for a threat or hazard that is possible, not probable. Sunstein (2007) notes that “For public officials no less than the rest of us, the probability of harm matters a great deal, and it is foolish to attend exclusively to the worst-case scenario”. A more rational approach is to focus on estimating the likelihood of costs and benefits when assessing the need for protective measures. This of course, is the essence of risk assessment.

Worst-case thinking can also lead to excessive spending on programs with little benefit, and ignoring other programs with large benefits. The current U.S. budget for domestic homeland security is approximately \$120 billion per year (Stewart and Mueller 2018). Mueller and Stewart (2011) estimated that U.S. counter-terrorism costs are 5-75 times higher than any benefits – i.e., one dollar buys less than 20 cents in benefits. A panel of more than 40 international experts assembled by Bjorn Lomborg found that a \$2 billion investment could save more than 1.5 million lives by expanded immunisation coverage and community-based nutrition programs (Lomborg 2009). Hence, if a miserly \$2 billion were redirected from the homeland security budget to these more effective risk reducing measures, the likelihood and consequences of terror attacks would hardly change, but 300 to 60,000 more lives would be saved.

3.2 *Cost neglect*

While it is not difficult to list threats and vulnerabilities, what is more challenging is to ascertain the cost to reduce these threats and vulnerabilities. And to decide who pays, and when. There is a notion that safety is infinitely good, and no cost is too high. There is no attempt to compare costs against benefits.

For example, it is not unusual for books on counter-terrorism to provide exhaustive lists of vulnerabilities and the need for enhanced security measures such as explosive detection systems, surveillance cameras, armed guards, etc. – yet often there is no entry for cost in the index (for examples see Mueller and Stewart 2011).

3.3 *Probability neglect*

Many analysts base their findings on threats or scenarios that they assume will occur. There is no consideration of the likelihood of a terrorist attack, that a specific CO₂ emission scenario will occur, or that adaptation will be effective. For example, a U.S. 2014 climate risk assessment report predicts trillions in dollars of damage due to climate change for the business as usual scenario – i.e., the U.S. continues in its current path assuming a RCP8.5 (known more recently as SSP8.5) emission scenario (Risky Business 2014). This IPCC emissions scenario assumes that emissions will continue unabated for the next 85 years including 6.5 more coal being used in 2100 as it is today¹. This is very much a worse-case scenario, and might be better characterised as unrealistic and implausible as it ignores that CO₂ mitigation measures will be implemented, that adaptation measures are implemented, or the impact of improved or game-changing technologies.

1. A more realistic scenario is RCP 2.6 – this corresponds to the Paris Agreement which aims to hold the increase in the global average temperature to below 2 degrees Celsius above pre-industrial levels.

Sunstein (2003) terms this as ‘probability neglect’ and that “people’s attention is focused on the bad outcome itself, and they are inattentive to the fact that it is unlikely to occur.” There is no certainty with predictions, nicely summed up by physicist Niels Bohr: “Prediction is very difficult, especially if it’s about the future.”

3.4 *Opportunity costs*

Policy-makers that act before they carefully consider the implications of their actions can result in undesirable outcomes which are often referred to as ‘opportunity costs’. For example, increased delays and added costs at U.S. airports due to new security procedures provide incentive for many short-haul passengers to drive to their destination rather than flying, and, since driving is far riskier than air travel, the extra automobile traffic generated has been estimated to result in 500 or more extra road fatalities per year (Blalock et al. 2007). Using DHS-mandated value of statistical life of \$7.5 million (Robinson et al. 2010), this equates to a loss of \$3.75 billion per year.

A CO₂ mitigation strategy that reduces economic growth, particularly in developing countries, may reduce their ability to adapt and other indirect impacts. In the 50 years since 1970, the natural hazard fatality rates have reduced by over 90% for low income countries (Ritchie et al. 2022a). This shows that economic development is a key driver in reducing the impact of natural hazards, and climate change mitigation or adaptation measure that reduce economic growth may have a significant opportunity cost.

Further, according to the charity ActionAid, the increased use of industrial biofuels (fuels made on an industrial scale from agricultural crops) have been a major cause of the food and hunger crisis in the developing world – filling an SUV with one tank of biofuel requires over 450 pounds of corn, which contains enough calories for a person for a year (ActionAid 2010). Rising energy costs also mostly affects the poor.

3.5 *Acceptable risk*

The notion of acceptable risk is rarely raised in public discussions. The world is not risk free. The generally accepted level of annual fatality risk is 1 in a million (e.g. Stewart and Melchers 1997). The probability that an American will be killed by a hurricane stands at about one in 7 million per year, and one in 2.8 million per year for a heat-related death. The probability that an American will be killed by a terrorist in the United States, with the events of 2001 included in the count, stands at about one in 4 million per year (Mueller and Stewart 2015), and is one in 39 million since 9/11. In Western Europe the odds are higher at one in 9 million, but still considerable lower than one in a million. The annual likelihood worldwide that a person will be killed in an airliner by a terrorist is approximately 1 in 320 million for the period since 9/11. To put some of these data in context, a person would need to fly once per day for 30,000 years before being involved in a terrorist attack (Stewart and Mueller 2018). By comparison, an American’s chance of being killed in an automobile crash is about one in 9,500 a year, the chance of being a victim of homicide is about one in 20,000, and the chance of being killed by lightning is one in 10 million (Stewart and Mueller 2018). How much should we be willing to reduce a risk, and is the risk reduction worth the cost?

In the past decade, the chance of being killed in a natural disaster in the United States is one in a million per year, in Western Europe is one in 500,000. However, for the world the odds are significantly higher at one in 150,000 per year (Ritchie et al. 2022b). In the 50 years since 1970, the natural hazard fatality rates have reduced globally by 75%, and by over 90% for low income countries (Ritchie et al. 2022a).

The above data shows that the world is not becoming any more dangerous or vulnerable. There is evidence to suggest that the opposite holds true – it can be argued that the world has never been healthier, wealthier and more educated leading to more resilient societies that can better cope with natural and manmade disasters (for a full discussion see Stewart 2022). While vulnerabilities remain, people and infrastructure are showing increased resilience. Though staggering losses may still occur, they can be ameliorated with targeted strategies to reduce vulnerability, increase resilience or reduce exposure of infrastructure and people to extreme events.

4 LIFE CYCLE ANALYSIS

The decision challenges discussed in the previous section are also mostly relevant for life-cycle analysis for civil engineering infrastructure. These include:

4.1 *Opportunity costs*

Direct costs to an asset owner or manager are, in general, relatively straightforward to estimate for design, construction maintenance, repair, etc. However, opportunity costs are normally harder to quantify and require awareness of unintended impacts to a community. For example, opportunity costs may be considerable if a road or bridge is closed for maintenance and repair, such as delayed response by ambulances reducing the odds of timely life-safety interventions, or occurrence of an extreme hazard (earthquake, bushfire) will hinder emergency vehicle access and safe evacuation routes for residents.

4.2 *Probability neglect*

The world is not deterministic. The timing and severity of natural hazards, loads, deterioration, maintenance, repair, etc. associated with the life-cycle of infrastructure are highly variable and uncertain. Added to this is the uncertainty and incomplete knowledge of how infrastructure is vulnerable and damaged by these hazards, and the ability for economic or societal infrastructure to be resilient and for communities to recover. Infrastructure comprises of interlinked sectors and networks which adds uncertainty about how the performance of each component affects overall system behaviour.

Uncertainty and incomplete knowledge may be modelled by probabilistic (stochastic) methods. It provides a normative measure of uncertainty that may be quantified from field, laboratory or historical data and/or advanced computer simulation models. While the former can help ascertain past or current vulnerabilities and resiliency, it has very little predictive capability if the network or system changes over time to suit increases in demand and shifting community demographics, or if the infrastructure degrades over time, or if the likelihood or severity of natural hazards increases due to climate change. These stochastic methods allow risk to be quantified, such as the likelihood and extent of infrastructure damage and recovery for future scenarios of hazard, vulnerability or resiliency.

An area of particular difficulty for decision-making is where the potential consequences are extremely large or severe yet the probability of these consequences actually occurring is estimated to be extremely low. These are termed “low probability – high consequence” events or hazards, or more recently, as “extreme events”. As discussed above, a probabilistic risk analysis based on sound system and probabilistic modeling is well suited to predicting life saving and damage risks for extreme events. This probabilistic framework provides practical guidance; for example, developing disaster risk reduction measures, safety and load rating assessment of bridges, asset management of pipelines, tunnel safety from vehicle fires, safety cases for offshore platforms and chemical process plants, reliability of electricity infrastructure, and it underpins the development of safety factors and design loads for civil engineering design codes and standards. The next section will describe how risk-based decision support may be applied to life-cycle assessment of infrastructure.

The outcomes of probabilistic risk analysis include: (i) likelihood and extent of infrastructure damage and losses to the owner, users, community and other stakeholders, (ii) influence that infrastructure resiliency has on the time to renewal and follow-on consequences and losses, (iii) effect of risk mitigating measures on predicted damage and losses, and (iv) cost-benefit or similar decision analysis used to assess the probability that a decision option (risk mitigating measure) will yield a benefit to one or more stakeholders. The robustness of decisions can be explored through scenario and sensitivity analyses. Since the outcomes of a probabilistic risk assessment can affect significantly the safety and operations of infrastructure, it is important that an independent and critical review be conducted by recognised experts, and the findings discussed at workshops involving all stakeholders.

Not surprisingly, learned academies such as the Royal Academy of Engineering (RAE) and the Australian Academy of Technological Sciences and Engineering (ATSE) understands the importance of probabilistic thinking: “Regulations and design standards are evidently in need of revision to reflect the uncertain climatic conditions that will be experienced in coming decades, setting probabilistic standards rather than absolute requirements for performance” (RAE 2011) and “The Academy considers evidence-based tools, such as probabilistic risk assessments. . . to be fundamental for building resilience into Australia’s future planning processes” (ATSE 2022). However, they note an understandable concern: “The lack of understanding of probabilistic scenarios by politicians and the media could be particularly problematic” (RAE 2011). This is an ongoing challenge to the engineering profession, where engineers need to explain probabilistic concepts to the government, media and the public in a way that allows for more informed and rational decision-making.

5 RISK-BASED DECISION SUPPORT

Decision criteria for extreme events are typically based on (i) annual fatality risk, and (ii) cost-effectiveness of protective measures. Risk for a system exposed to a threat is

$$E(L) = \sum \Pr(T)\Pr(H|T)\Pr(D|H)\Pr(L|D)L \quad (1)$$

where $\Pr(T)$ is the annual probability that a specific threat will occur (a terrorist attack, an emission scenario), $\Pr(H|T)$ is the annual probability of a hazard (wind, heat, explosion) conditional on the threat, $\Pr(D|H)$ is the probability of damage or other undesired effect conditional on the hazard (also known as vulnerability or fragility) for the baseline case of no extra protection (i.e. ‘business as usual’), $\Pr(L|D)$ is the conditional probability of a loss (economic loss, loss of life, etc.) given occurrence of the damage (resilience), and L is the loss or consequence if full damage occurs. In some cases, ‘damage’ may equate to ‘loss’ and so a vulnerability function may be expressed as $\Pr(L|H)$ which is equal to the product $\Pr(D|H)\Pr(L|D)$. The summation sign in Equation (1) refers to the number of possible threats, hazards, damage levels and losses. If the loss refers to a monetary loss, then $E(L)$ represents an economic risk. If the loss refers to fatalities, then $E(L)$ represents an annual fatality risk (AFR).

If we modify Equation (1) where ΔR is the reduction in risk caused by protective measures (e.g., climate adaptation or counterterrorism measures) then expected loss after protection is

$$E_{\text{protect}}(L) = \sum (1 - \Delta R)E(L) - \Delta B \quad (2)$$

where ΔR is the reduction in risk caused by the protective measure, $E(L)$ is the ‘business as usual’ expected loss (risk) given by Equation (1), and ΔB is the co-benefit such as reduced losses to other hazards, increased energy efficiency of new materials, etc. If there is an opportunity cost associated with a new measure, then ΔB becomes a negative value. Protective measures should result in risk reduction (ΔR) that may arise from a combination of reduced likelihood of the hazard, damage states, safety hazards and and/or people exposed to the safety hazard.

The challenging aspect of risk-based decision theory is predicting values of $\Pr(T)$, $\Pr(H|T)$, $\Pr(D|H)$, $\Pr(L|D)$ and ΔR . This information may be inferred from expert opinions, scenario analysis, and statistical analysis of prior performance data, as well as system and reliability modelling. Since there is uncertainty associated with such predictions, the use of probability distributions to describe mean, variance and distribution type is recommended.

If the AFR lies in the generally tolerable region (e.g., 1×10^{-4} to 1×10^{-6}) then several criteria may be used to assess if the benefits of protective measures exceed their cost:

1. Net Present Value (NPV)
2. Probability of cost-effectiveness or $\Pr(\text{NPV} > 0)$

The ‘benefit’ of a protective measure is the reduction in damages or losses associated with the protective strategy, and the ‘cost’ is the cost of the protective strategy. The net benefit or net present value (NPV) is equal to benefit minus the cost. The decision problem is to maximise the net present value

$$NPV = \sum E(L)\Delta R + \Delta B - C_{\text{protect}} \quad (3)$$

where C_{protect} is the protection cost including opportunity costs that reduces risk by ΔR . Figure 2 shows how protective costs increase with risk reduction, while benefits increase. The optimal protection occurs when NPV is a maximum, leading to optimal risk reduction. Relevant is what level of expenditure and risk reduction gives the greatest benefit and when does the law of diminishing returns kick in. The first dollars spent on protective measures are likely to be worthwhile, even if the last is not.

The above discussion is related to the concept of life-cycle cost analysis for infrastructure where design, construction, operation, failure, and end of use costs are summed and the optimal configuration selected based on minimal life-cycle cost or other decision criteria.

Governments and their regulatory agencies normally exhibit risk-neutral attitudes in their decision-making as described by the above equations. Utility theory can be used if the decision maker wishes to explicitly factor risk attitudes such as risk aversion or proneness into the decision process (e.g. Stewart et al. 2011, Qin and Stewart 2021).

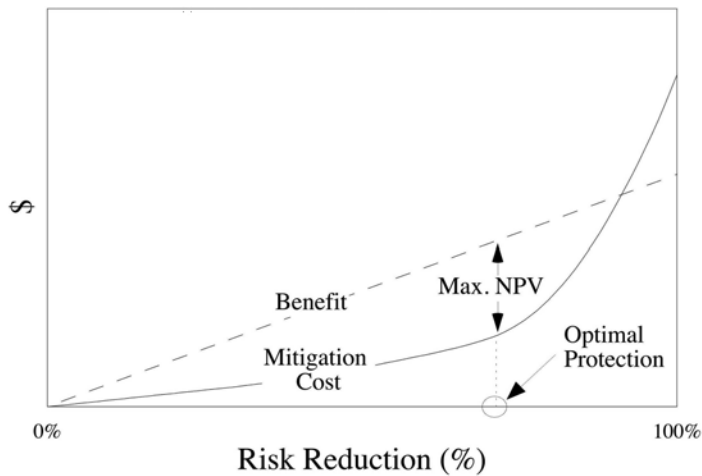


Figure 2. Schematic of net present value (NPV) showing optimal protection.

If parameters $\text{Pr}(T)$, $\text{Pr}(H|T)$, $\text{Pr}(D|H)$, $\text{Pr}(L|D)$, L , ΔR , ΔB and/or C_{protect} are random variables then the output of the analysis (NPV) is also variable. This allows confidence bounds of NPV to be calculated, as well as the probability that an adaptation measure is cost-effective denoted herein as $\text{Pr}(NPV > 0)$. If $NPV > 0$ then there is a net benefit and so the protective measure is cost-effective. Other notations and formulae can be used to provide optimal protection, but ultimately these also mostly rely on maximising NPV.

If the probability that a specific threat will occur $\text{Pr}(T)$ is too unreliable, then a decision analysis based on scenario analysis where threat probability is decoupled from Equation (1) provides an alternative decision-making criteria based on expected costs. The above equations can be generalised for any time period, discounting of future costs and more detailed time-dependent cost and damage consequences.

Threat, vulnerability, loss and protective costs are subject to considerable uncertainty due to lack of available data and models. For this reason, calculations of risks, costs and benefits will be imprecise. Hence, a ‘break-even’ analysis may be useful where minimum threat probability, minimum risk reduction or maximum protective cost necessary for protective measures to be cost-effective is selected such that there is 50% probability that benefits equal cost – i.e. $\text{mean}(NPV) = 0$. For example, if the actual cost of protection exceeds the predicted break-even value, then protection is not cost-effective. Decision-makers can then judge whether a protective strategy meets these break-even values.

Ultimately however, the outcomes of risk-informed decision analysis will be to inform decision makers as not all decisions can be made on technical merits alone. It also helps to inform government, infrastructure asset and network owners and operators, community and individuals of the trade-offs between risk, benefits and cost when making decisions on how best to protect communities.

6 CONCLUSIONS

Terrorism and climate change are extreme events that engender fear and anxiety in the community. Policy makers are also susceptible to these emotions. Risk-based approaches are suitable to assess the acceptability of risks, and the cost-effectiveness of measures to reduce terrorism and climate impact risks.

REFERENCES

- ActionAid (2010), *Meals per Gallon: The impact of industrial biofuels on people and global hunger*, ActionAid UK, London, United Kingdom.
- ATSE (2022), *Building a Resilient Australia*, Position Statement, Australian Academy of Technological Sciences and Engineering, Melbourne, Australia, October.
- Bastidas-Arteaga, E. and Stewart, M.G. (2019), *Climate Adaptation Engineering: Risks and Economics for Infrastructure Decision-Making*, Elsevier, Oxford, U.K.
- Blalock, G., Kadiyali, V. and Simon, D.H. (2007) The Impact of Post- 9/11 Airport Security Measures on the Demand for Air Travel. *Journal of Law and Economics* 50(4) November: 731–755.
- Lomborg, B. (2009). *Global Crises, Global Solutions*, Cambridge University Press, UK.
- Mueller, J. and Stewart, M.G. (2011) *Terror, Security, and Money: Balancing the Risks, Benefits, and Costs of Homeland Security*. Oxford University Press, Oxford and New York.
- Mueller, J. and Stewart, M.G. (2015) *Chasing Ghosts: The Policing of Terrorism*. Oxford University Press, Oxford and New York.
- Qin, H. and Stewart, M.G. (2021), Risk perceptions and economic incentives for mitigating windstorm damage to housing, *Civil and Environmental Engineering Systems*, 38(1),1–19.
- RAE (2011), *Engineering the Future: Infrastructure, Engineering and Climate Change Adaptation – ensuring services in an uncertain future*, The Royal Academy of Engineering, London.
- Ritchie, H., Rosado, P. and Roser, M. (2022a), Natural Hazards, Published online at OurWorldinData.org. <https://ourworldindata.org/grapher/decadal-average-death-rates-from-natural-disasters?country=~Low-income-countries> (accessed 8 January 2023).
- Ritchie, H., Rosado, P. and Roser, M. (2022b), Natural Hazards, Published online at OurWorldinData.org. https://ourworldindata.org/grapher/decadal-average-death-rates-from-natural-disasters?country=~OWID_WRL (accessed 8 January 2023).
- Risky Business (2014), Risky Business: The Economic Risks of Climate Change in the United States. RiskyBusiness.org, June 2014.
- Robinson, L.A., Hammitt, J.K., Aldy, J.E., Krupnick, A. and Baxter, J. (2010) Valuing the risk of death from terrorist attacks. *Journal of Homeland Security and Emergency Management* 7(1).
- Stewart, M.G. and Melchers, R.E. (1997) *Probabilistic Risk Assessment of Engineering Systems*. London. Chapman & Hall.
- Stewart, M.G., Ellingwood, B.R. and Mueller, J. (2011) Homeland Security: A Case Study in Risk Aversion for Public Decision-Making. *Int. Journal of Risk Assessment and Management* 15(5/6):367–386.
- Stewart, M.G. and J. Mueller. 2018. *Are We Safe Enough? Measuring and Assessing Aviation Security*, Elsevier, New York.
- Stewart, M.G. and Rosowsky, D.V. (2022), *Engineering for Extremes: Decision-making in an Uncertain World*, Springer, Cham, Switzerland.
- Stewart, M.G. (2022), Systems Thinking Averts Apocalypses Now and in the Future: Why we should always look on the bright side of life, *Civil Engineering and Environmental Systems*, 39(3): 188–204.
- Sunstein, C.R. (2003), Terrorism and Probability Neglect. *J. of Risk and Uncertainty*. 26(2–3):121–136.
- Sunstein, C.R. (2007), *Worst-Case Scenarios*. Harvard University Press, Cambridge, MA.

MINI-SYMPOSIA

MSI: Component reuse in structures and infrastructures

Organizers: O. Iuorio & C. Fivet



Taylor & Francis

Taylor & Francis Group

<http://taylorandfrancis.com>

The design and development of a demountable and reconfigurable segmented fan concrete shell flooring system

M. Nuh & J. Orr

University of Cambridge, Cambridge, UK

R. Oval

Princeton University, Princeton, USA

ABSTRACT: The structural floor of typical concrete frame buildings contributes a significant portion to the total embodied carbon of the superstructure by its sheer mass. In addition, the monolithic nature of in-situ concrete and the frequent use of grouting for prefabricated components result in structures which are often difficult to disassemble, creating barriers towards reuse. We present a novel segmented thin-shell concrete flooring system which facilitates component reuse and reconfiguration compatible with a circular economy for construction. By leveraging the funicular potential of shell structures and the geometry of masonry fan vaults, a lightweight materially efficient flooring system which can be disassembled without the need to cut through concrete or grout is proposed. Fabrication and assembly of a scale prototype spanning 2 m by 2 m were carried out as a proof-of-concept, leveraging digital fabrication techniques to create the curved vault profile.

1 INTRODUCTION

The construction industry contributes an estimated 38% of worldwide energy and process-related emissions (United Nations Environment Programme, 2020), emphasising the need for increased efforts to reduce the environmental impact of our built environment. A potential means which has gained renewed interest for reducing the carbon impact of building structures is the reuse of structural building components to extend their lifespan. However, various projects which implement concrete reuse have often faced challenges in terms of making them economical (Durmisevic, 2019; Eklund et al., 2003; Glias, 2013; Roth, 2005; te Dorsthorst & Kowalczyk, 2005); having to cut away sections manually is a labour-intensive process which typically leads to increased cost premiums, making it an economically unattractive practice.

We present a novel flooring system which is designed for disassembly, component reuse, and reconfigurability. Concrete segments can be assembled without the use of any grout through a compression-dominated segmentation plan. A geometry inspired by masonry fan vaults facilitates this segmentation while also allowing reconfiguration to span different distances. This paper will detail the design conceptualisation and form-finding approach for the shell, the potential for reconfigurability in the context of a circular economy of construction, the fabrication and assembly of a quarter-scale prototype, and, lastly, a sustainability assessment of the flooring system.

2 CONCEPTUAL AND STRUCTURAL DESIGN

A segmented shell flooring system offers several advantages related to carbon savings compared to conventional flat slab concrete flooring. Firstly, the funicular nature of a shell (i.e., mainly acting in compression) is highly compatible with brittle materials with low tensile capacity such as plain concrete. As such, less concrete is needed to span distances and there is no need to embed steel reinforcement within the concrete to resolve tensile stresses. Rather, the thrust of the vault can be resolved externally, either through buttresses (as is the case in Gothic cathedrals) or through external ties, creating a physical separation between the materials which

is conducive for disassembly and reuse. Secondly, segmentation allows for accurate prefabrication of the curved components, thereby reducing the amount of on-site concrete required. This leads to less material wastage due to the more controlled factory environment compared to on-site casting. Lastly, the compressive nature of the shell combined with the segmentation allows for dry joints under compression between segments. This facilitates disassembly as there is no need to manually cut out elements using saws or to remove grouting. As a trade-off, the complexity lies in the assembly and disassembly process of the shell which is more involved compared to the fabrication of prismatic formwork or assembly of prefabricated flat slabs.

The use of dry joints in segmented shells for flooring systems is not a novel concept: a 3D sand-printed floor using 5 discrete segments has been prototype (Rippmann et al., 2018) and a nine-segment concrete floor demonstrator spanning a 4.5 m by 4.5 m bay (Oval et al., 2023) all validates that it is a structurally feasible system. However, the primary focus of these prototypes was not on the potential for disassembly and circularity of the structure; the segmentation was typically a by-product of size constraints imposed by transportation or digital fabrication print area limitations. Reconfiguration of the structure to span different distances was also not considered as it is challenging for a form-found shell; changing the distance spanned will affect membrane action and introduce bending unless the curvature of the structure is adjusted.

To further leverage the disassembly potential of a segmented concrete shell for circularity, therefore increasing its lifespan and reducing its environmental impact, the form-finding and segmentation plan of the shell must be taken into consideration. The two are intimately interlinked to each other as the shape of the shell will affect the ‘optimal’ locations of interfaces. The criteria for an optimal interface were defined as follows:

1. Compression dominated to avoid opening of interfaces and hinge formation, and
2. Minimal shear forces along the surface of the interface to avoid slipping.

To satisfy both criteria, it follows that interfaces should be oriented with their normal aligned with the principal compressive stress direction.

2.1 *Fan vault concept*

The masonry fan vault presents a base for the shell geometry which allows for a simple segmentation plan that is both optimal and allows for reconfigurability. The geometry of the fan vault is characterised by surfaces of revolutions which form conoids which may intersect with one another, with the central region (if there are any) filled by a spandrel—a shallow or flat segment acting as a keystone. The manner in which the conoids intersect with each other defines the class of fan vault (Bagi, 2021). Here, we are mainly interested in fan vaults where the conoids do not intersect with each other, to avoid trimming segments that would become harder to reuse. The surface of revolution also allows for increased repetition of segments along the hoop direction, facilitating prefabrication and modularity.

Membrane analysis can be performed to determine a state of stresses on the conoids following plasticity’s lower-bound theorem (Heyman, 1967), shown in Figure 1. Taking a strip along the conoid and applying a radially symmetric load at the top, the analysis shows that, with a sufficiently large spandrel load, the structure experiences no tensile stresses. In this radially symmetric load case, the compressive stresses flow along the strip direction with the other principal stress direction found along the hoop-wise direction of the conoids, providing an evident and simple segmentation plan. While the true loading clearly does not take the form of a constant, radially symmetric load, this provides a good starting point for the segmentation plan. In addition, the locations of interfaces having minimal shear forces will inevitably vary depending on the loading due to asymmetric load cases, making optimisation of a segmentation plan against one load case an unproductive exercise. The shear which will be present in the interfaces can be minimised by the inclusion of interlocking shear keys between segments to resist slippage. Staggering can also aid in this, although was not considered for this design as it introduces complexity to the fabrication process.

The spandrel and the conoid of the fan vault inspired shell can be separated into two parts of the system, allowing them to be uncoupled to span different distances, as shown in Figure 2. Shorter distances can be spanned by removing the sections of the upper conoids and

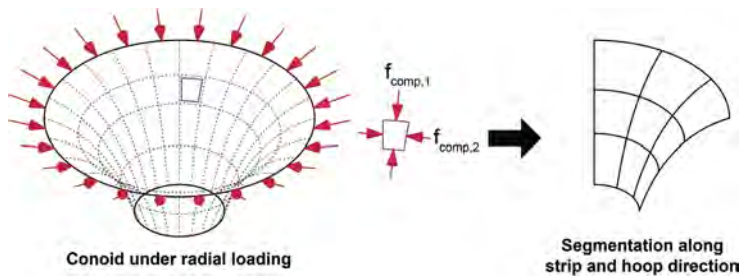


Figure 1. Conoid membrane analysis of the fan vault informing the segmentation plan for the shell.

installing a new spandrel while larger distances can be spanned by installing a larger spandrel. For the latter, the increased loading may not be sufficiently resisted by the conoids. In such cases, it may be necessary to reinforce the conoids (e.g., using carbon fibre plates or wraps) unless the shell was already pre-designed for a larger span. Note that if a different distance is to be spanned, this requires the fabrication of a new spandrel, leading to waste. However, the flexibility the system affords for future reuse cases may prove beneficial; while it has been suggested that a *form follows availability* approach should be taken for a design using reused components (Brütting et al., 2019), increased flexibility in the distance spanned allows designers more freedom in the final form and may lower the barrier towards reuse.

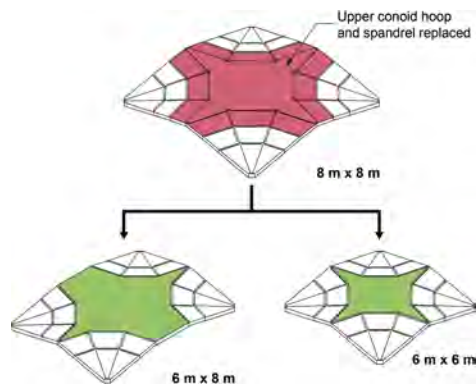


Figure 2. Reuse of a segmented fan concrete shell to span different bay sizes.

2.2 Form finding and structural optimisation

Form finding of the segmented fan concrete shell was performed by firstly parametrising the geometry into the thicknesses at various locations and the curve profile of the conoid, illustrated in Figure 3. This was performed in the Grasshopper visual programming environment (Rutten et al., 2007). The shape of the curve was controlled by a Bézier curve with 4 control points, with the two endpoints set by the shell width and depth. The coordinates for the Bézier curve's profile were limited to the upper triangle to ensure a concave profile. The thickness in the conoid was allowed to vary linearly (against the u-direction shown in Figure 3) from the base to the top and a separate constant thickness was allowed for the spandrel. The span of this shell was set as a constant 8 m and the distance from the mid-depth of the spandrel to the mid-depth of the conoid base was set to 800 mm. This was selected as a representative span and depth, although different spans can be easily optimised for using the same approach. Segmentation along the strip direction was done every 1 m as this is assumed to provide a sufficiently small resolution for reconfiguration purposes while avoiding too many segmentations which results in a lower structural capacity. As it is envisioned that the smallest distance between columns will be at least 4 m, the segments in a 2 m vicinity from each corner were merged. M24 steel ties were connected at the corners to resolve the horizontal thrust of the shell.

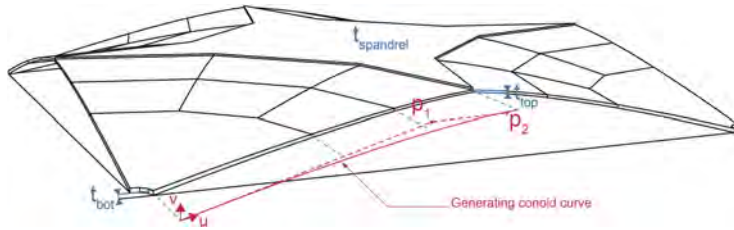


Figure 3. Parametrized geometry model.

Using the shell geometry parametrised into 7 variables (with the two points deconstructed into their coordinate values), a finite element model in Karamba3D (Preisinger & Heimrath, 2014) was created using shell elements to ensure that the element stresses are within the material limits and that the shell is stable. In addition to the gravitational loading, a uniform imposed load of 1 kPa and a live load of 1.5 kPa were applied. The lower live load was selected based on work by Orr (2018) which suggested it is a more representative loading for a typical office building. Various area loading was applied to the shell and preliminary investigations show that the uniform live load case was likely to be critical. As such, optimisation was carried out based on that load case.

A unique modelling approach for the interfaces was taken, inspired by one developed for a rigid body analysis (Galassi et al., 2018). At the interface, stiff beam elements are connected to nodes located at the extreme fibre locations. The beams are removed if tensile forces are transmitted across the nodes, allowing 1) a hinge to form at the interface and 2) the segments to fully detach themselves. The beam elements are added back in if the nodes are detected to penetrate each other, signifying a closing of the interface. The use of a stiff beam element is due to the lack of rigid links in Karamba3D. Analysis was performed by incrementally increasing the loading by 10% for a linear elastic model where the interface elements were modified for each iteration. Note that this is not a non-linear analysis, but rather a set of linear elastic analyses where the previous analysis informs the state of the joints of the next. As such, it will not fully capture the behaviour of the structure, especially in cases where many hinges form as the model will exhibit large rotations and displacements. A fully non-linear analysis incorporating contact behaviour using commercial software such as 3DEC and LS-DYNA is expected to be able to capture the behaviour of the shell. However, the long computation time is not conducive for optimisation purposes, often taking several days to compute a single shell.

The Wallacei Grasshopper plugin (Makki et al., 2021), which implements the NSGA-II multi-objective evolutionary algorithm (Deb et al., 2002) was used to optimise the shell against two objectives: maximised buckling load factor and minimised mass (which was used as a surrogate metric for the embodied carbon of the structure). Once the algorithm converged, a set of Pareto front solutions was obtained which provides a minimum mass structure given a certain buckling load factor. Due to the limitations of the linear elastic analysis used, as well as to account for manufacturing tolerances, a candidate with a large buckling load factor of 10 (the properties of which are tabulated in Table 1) was selected for the basis of design for the fabricated quarter-scale prototype spanning 2 m by 2 m. As the thicknesses of the quarter-scale prototype were quite thin (being merely 18 mm at the top of the conoid), all the thicknesses were doubled to accommodate fabrication process tolerances and prevent significant damage from storage and handling.

3 FABRICATION

Fabrication of variable-thickness curved concrete shells poses challenges on two fronts: the manufacturing of the formwork and the deposition of the material. The Automated Robotic Concrete Spraying fabrication process (Nuh et al., 2022) was developed to address these challenges and was used to fabricate the curved conoid segments (Figure 4). Using a target spraying surface constructed using a wooden frame and a shape-reconfigurable pin-bed, a robot arm connected to a glass fibre reinforced concrete (GFRC) spraying station deposits the

Table 1. Selected candidate from form finding optimisation.

	Selected candidate's properties
<i>Objective values</i>	
Mass	10.8 t
Buckling load factor	10.2
<i>ULS stress and utilisation</i>	
Steel tie	489 MPa (67.7%)
GFRC tensile	3.34 MPa (87.3%)
GFRC compressive	4.93 MPa (23.7%)
<i>Variables [full-scale geometry]</i>	
Conoid thickness – bottom [t_{bot}]	100 mm
Conoid thickness – top [t_{top}]	75 mm
Spandrel thickness [$t_{spandrel}$]	86 mm
Bézier point 1 [p_1]	(1.94, 0.43) m
Bézier point 2 [p_2]	(3.48, 0.70) m

material where it is required. The shear keys were formed by including their negatives within the wooden frame. As the spandrel was of a flat profile, it was not manufactured using this process and was instead cast in a conventional manner using wooden formwork. Further details regarding the GFRC mix can be found in Nuh et al. (2022) and the unreinforced spandrel was cast using a standard C30/37 class concrete mix.



Figure 4. Digital fabrication setup (left) used to fabricate the sprayed GFRC conoid segments (right).

4 ASSEMBLY AND DISASSEMBLY

The assembly of the segmented fan concrete shell requires that all pieces are placed in their correct position before being decentred. As opposed to masonry structures which often require intricate falsework and scaffolding due to the large number of bricks, the shell's larger segments mean that telescopic props and standard scaffolding can be used to position the structure as needed. The addition of shear keys also aids in the erection process as they align adjacent segments together. A similar method was used to great effect by Oval et al. (2023) to assemble their nine-segment shell demonstrator.

The detailed procedure for the assembly of the prototype shell is as follows, also illustrated in Figure 5:

1. Position all segments in their appropriate location using props and jacks,
2. Tighten the steel ties to resolve the horizontal thrust from the shell's self-weight, and
3. Remove the props.

For the prototype, the fabrication tolerances of the hand-made wooden side frames were found to be lacking. This resulted in gaps between segments, which ranged from effectively flush to 1 cm (i.e., approximately 2% of their size), hindering solid contact and arch action formation. Therefore, fine sand was added between the interfaces prior to tightening the steel

ties. This was found to sufficiently stabilise the shell while still being demountable. The fully assembled shell is shown in Figure 6.

The disassembly process of the shell follows the same procedure as the assembly process but in reverse; by adding props and slightly pushing on the segments, the tie can be safely loosened, and the segments lifted off one by one.

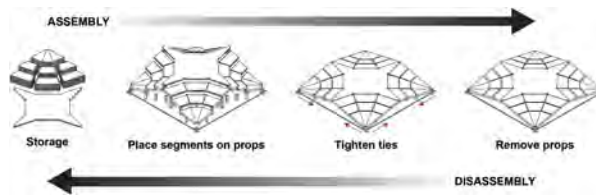


Figure 5. Assembly and disassembly process for the shell.



Figure 6. The prototype segmented fan concrete shell during assembly (left) and fully assembled (right).

5 SUSTAINABILITY ASSESSMENT

The embodied carbon impacts from *cradle-to-gate* (Modules A1 to A3 of the BS EN 15798 life cycle stages) of various flooring systems were compared to provide a quantitative comparison of their carbon impact. The selected flooring systems compared are:

1. Flat concrete slab,
2. BubbleDeck (a voided hollow deck system), and
3. Segmented fan concrete shell.

Combined embodied carbon factors for the relevant materials are tabulated in Table 2. For this analysis, the flat concrete slab, BubbleDeck, and the flat spandrel of the segmented shell were designed using C30/37 class concrete with 35% cement replacement and reinforcement bars having a yield stress of 500 MPa. The design was based on an 8 m by 8 m bay under the same loading as the segmented shell based on Eurocode 2 for the flat slab and recommendations from the BubbleDeck manufacturer for the voided hollow deck system (BubbleDeck, 2006). The HDPE bubble thickness used to form the BubbleDeck voids was assumed to be 5 mm. Excluded from the calculation is the raised flooring—which will be used to create a level surface for the shell like the demonstrator shell by Oval et al. (2023)—as it is assumed that all flooring systems will include them to accommodate services. The resulting masses and the embodied carbon equivalents of the three flooring systems are tabulated in Table 3.

The analysis shows that the segmented fan concrete shell has a lower embodied carbon impact compared to the other options, albeit only a 13.6% saving compared to the reference flat slab. This is mainly due to the high embodied carbon of the GFRC mix which has a high proportion of cement. This saving can be further increased by using larger aggregates and by adding cement replacement as binder. Conversely, the 8 m by 8 m span used to design the flat slab and BubbleDeck are not optimal spans for those systems; shorter spans have been shown to reduce the initial embodied carbon contribution of these reinforced concrete systems (Drewniok, 2020) making them potentially competitive with the segmented fan concrete shell. However, one clear benefit of

Table 2. Cradle-to-gate embodied carbon factors of materials.

Material	Embodied carbon factor kgCO ₂ e/kg
C30/37 with 35% cement replacement ¹	0.103
Reinforcement bars/steel ties ²	0.76
HDPE ³	1.93
Plywood formwork ⁴	0.681
<i>GFRC components</i>	
Cement ⁴	0.832
Sand ⁴	0.00747
Polycure FT [curing agent] ^{4,5}	1.67
Flowaid FT [super plasticizer] ⁴	1.88
Pumpaid FT [thixotropic pumping aid] ^{4,5}	1.67
Alkali resistant glass fibre ⁶	3.00
Combined GFRC mix	0.626

1 (Institut Bauen und Umwelt e.V, 2018)

2 (UK CARES, 2020), steel ties assumed to have similar values to reinforcement bars

3 (Hammond & Jones, 2011)

4 (Hammond & Jones, 2020)

5 Taken from average factor of concrete admixtures

6 (Granta Design Ltd, 2018)

Table 3. Mass and embodied carbon equivalent per floor area of various flooring systems.

	Mass and embodied carbon equivalent Kg/m ² and kgCO ₂ e/m ²					
	<i>Flat slab</i>	<i>BubbleDeck</i>		<i>Segmented fanconcrete shell</i>		
Concrete	587.5	60.5	431.2	44.4	49.5	5.10
Reinforcement bars/ steel ties	40.8	31.0	38.6	29.4	1.50	1.14
HDPE	-	-	12.28	23.7	-	-
GFRC	-	-	-	-	128.1	80.2
Plywood formwork*	12.96	8.83	12.96	8.83	0.416	0.283
Total	628 (ref.)	100.3 (ref.)	482 (-23%)	106.3 (+6%)	179.1 (-71%)	86.7 (-13%)

* Based on a nominal weight of 720 kg/m³ using 18 mm plywood.

the shell is the large mass savings of 71% over the baseline flat slab. This can result in drastic savings in the material of the columns and footings of the structure, leading to further carbon savings elsewhere in the structure. In addition, the potential for reconfiguration and design for reuse for different spans remains a strong benefit of the shell system for sustainability reasons.

6 CONCLUSIONS

The segmented fan concrete shell presented is a novel concrete flooring system which is designed for reuse in a circular economy. Using the revolution geometry of the fan vault provides a simple segmentation plan which facilitates reconfiguration into different spans. The quarter-scale prototype demonstrates that the system is structurally sound and can be assembled and disassembled using simple props.

To validate the modelling approach as well as investigate the structural capacity and reconfigurability of the system, an experimental testing program is currently underway. Further

work is required to reduce the tolerance of the segments to provide better contact at interfaces for future prototypes. Lastly, further improvements to the mix design of the GFRC material can lead to further reductions to the cradle-to-gate embodied carbon of the structure.

REFERENCES

- Bagi, K. (2021). Statics of fan vaulting: Current state of knowledge and open issues. *Proceedings of the Royal Society A: Mathematical, Physical and Engineering Sciences*, 477(2246), 20200893. <https://doi.org/10.1098/rspa.2020.0893>.
- Brütting, J., Senatore, G., & Fivet, C. (2019). Form Follows Availability – Designing Structures Through Reuse. *Journal of the International Association for Shell and Spatial Structures*, 60(4), 257–265. <https://doi.org/10.20898/j.iaass.2019.202.033>.
- BubbleDeck. (2006). *BubbleDeck Span Guide*. BubbleDeck.
- Deb, K., Pratap, A., Agarwal, S., & Meyarivan, T. (2002). A fast and elitist multiobjective genetic algorithm: NSGA-II. *IEEE Transactions on Evolutionary Computation*, 6(2), 182–197. <https://doi.org/10.1109/4235.996017>.
- Drewniok, M. P. (2020). *Relationships between building structural parameters and embodied carbon. Part 1: Early-stage design decisions* (ENG-TR.013). University of Cambridge.
- Durmisevic, E. (2019). *The Super Circular Estate project Journal N° 3*. Urban Innovative Actions.
- Eklund, M., Dahlgren, S., Dagersten, A., & Sundbaum, G. (2003). *The Conditions and Constraints for Using Reused Materials in Building Projects*. 287.
- Galassi, S., Misseri, G., Rovero, L., & Tempesta, G. (2018). Failure modes prediction of masonry voussoir arches on moving supports. *Engineering Structures*, 173, 706–717. <https://doi.org/10.1016/j.engstruct.2018.07.015>.
- Glias, A. (2013). *The ‘Donor Skelet’: Designing with reused structural concrete elements* [MSc]. TU Delft.
- Granta Design Ltd. (2018). *The Cambridge Engineering Selector EduPack 2018* (18.1.1). Granta Design. www.grantadesign.com/industry/products/ces-selector/
- Hammond, G., & Jones, C. (2011). *Embodied Carbon—The ICE Database*.
- Hammond, G., & Jones, C. (2020). *Embodied Carbon—The ICE Database*.
- Heyman, J. (1967). Spires and fan vaults. *International Journal of Solids and Structures*, 3(2), 243–257. [https://doi.org/10.1016/0020-7683\(67\)90073-X](https://doi.org/10.1016/0020-7683(67)90073-X).
- Institut Bauen und Umwelt e.V. (2018). *Environmental Product Declaration: UK manufactured generic ready-mixed concrete*.
- Makki, M., Showkatbakhsh, M., & Song, Y. (2021). *Wallacei: An evolutionary and Analytic Engine for Grasshopper 3D* (2.65). <https://www.wallacei.com/>
- Nuh, M., Oval, R., Orr, J., & Shepherd, P. (2022). Digital fabrication of ribbed concrete shells using automated robotic concrete spraying. *Additive Manufacturing*, 59, 103159. <https://doi.org/10.1016/j.addma.2022.103159>.
- Orr, J. (2018). *Minimising Energy in Construction*. University of Cambridge.
- Oval, R., Nuh, M., Costa, E., Madyan, O. A., Orr, J., & Shepherd, P. (2023). A prototype low-carbon segmented concrete shell building floor system. *Structures*, 49, 124–138. <https://doi.org/10.1016/j.istruc.2023.01.063>.
- Preisinger, C., & Heimrath, M. (2014). Karamba—A Toolkit for Parametric Structural Design. *Structural Engineering International*, 24(2), 217–221. <https://doi.org/10.2749/101686614X13830790993483>
- Rippmann, M., Liew, A., Van Mele, T., & Block, P. (2018). Design, fabrication and testing of discrete 3D sand-printed floor prototypes. *Materials Today Communications*, 15, 254–259. <https://doi.org/10.1016/j.mtcomm.2018.03.005>
- Roth, L. (2005). *Reuse of construction materials—Environmental performance and assessment methodology* [PhD]. Linköpings universitet.
- Rutten, D., McNeel, R., & others. (2007). *Grasshopper3D*. Robert McNeel & Associates.
- te Dorsthorst, B. J. H., & Kowalczyk, T. (2005). State of Deconstruction in the Netherlands. In *Deconstruction and Materials Reuse—An International Overview* (Vol. 300). in - house publishing.
- UK CARES. (2020). *Environmental Product Declaration: Carbon Steel Reinforcing Bar (secondary production route—Scrap)*, Sector Average.
- United Nations Environment Programme. (2020). *2020 Global Status Report for Buildings and Construction: Towards a Zero-emission, Efficient and Resilient Buildings and Construction Sector*. United Nations Environment Programme.

Can we reuse plasterboards?

S. Kitayama & O. Iuorio
University of Leeds, Leeds, UK

ABSTRACT: Gypsum turns plaster when it is dehydrated, and it returns to gypsum when it is hydrated. Because of this, gypsum is 100 % recyclable in theory. However, in reality, only 4% (in mass) of the plasterboard is from recycled plasterboard. This is because of the substances, other than fresh gypsum from quarries, to make plasterboard, and the current demolition methods that cause material contamination. The current practice of manufacturing, construction, and deconstruction of plasterboard necessitates significant resource extraction and carbon emissions, and the situation is unlikely to change in the foreseeable future. Reusing, instead of recycling, construction material is effective in reducing resource extraction and carbon emissions, however, it has not been investigated at all for plasterboard. Thus, this paper explores the potential and feasibility of reusing plasterboard used for exterior infill walls, which is made of plasterboards and an increasingly used façade construction method in the UK.

1 INTRODUCTION

Exterior lightweight infill walls (see Figure 1) are increasingly used in building façade construction in the UK (SCI, 2019a). These walls are often replaced during the refurbishment of buildings to adapt spaces to new functions or to comply with new energy efficiency or humidity control targets (Morgan & Stevenson, 2005). The replacement typically occurs every 30 years (ARUP, 2022), even though most of the components could maintain their good performance generally much longer than 30 years.

The authors of this article have recently evaluated the carbon emission from the exterior lightweight infill wall construction/deconstruction, using lifecycle assessment procedures (RICS, 2017) of an actual building (located in the Greater Manchester area, UK). The authors found that the construction and deconstruction of exterior lightweight infill walls could contribute significantly to the amount of carbon emission (more than 20% of embodied carbon emitted from the entire building). Thus, the authors have investigated the potential of disassembly of infill wall components for future reuse.

The earlier work by the authors investigated the potential for the disassembly and reuse of lightweight cold-formed steel (CFS) members within the infill wall (Kitayama and Iuorio, 2022). The steel frame members in infill walls are the major contributor to the carbon emission from the construction and deconstruction of infill walls. However, the exterior infill walls are made up of, not only steel frames, but several other components, including internal plasterboards, cavity insulation, external plasterboard, external insulation, and cladding. The contributions of carbon emissions from the construction and deconstruction of these components are significant. Also, the current practice of construction and deconstruction of any of these components has not established circular practice (i.e., reuse or energy-efficient recycling). Moreover, past research and practice focused on recycling to improve the efficient use of materials and carbon reduction, however, a significant improvement in material use and carbon reduction from recycling has not been achieved and will not be achieved in the foreseeable future.

Reusing, instead of recycling, construction material can be effective in reducing resource extraction and carbon emissions, however, it has not been investigated at all for plasterboard, which is one of the main components of infill walls. Thus, this paper first examines the potential for the disassembly and reuse of gypsum plasterboard based on available publications, including journal articles, technical reports, Environmental Product Declarations (EDPs) and other company documents. The examination follows the order of lifecycle stages specified in BS EN 15978 (BSI, 2011), which are: product stage, construction process stage, use stage, and end-of-life stage. Subsequently, the feasibility of disassembly and reuse of plasterboard is discussed by looking at three different aspects: connections between plasterboard and steel profiles, available experimental data, and construction methods used for infill walls.

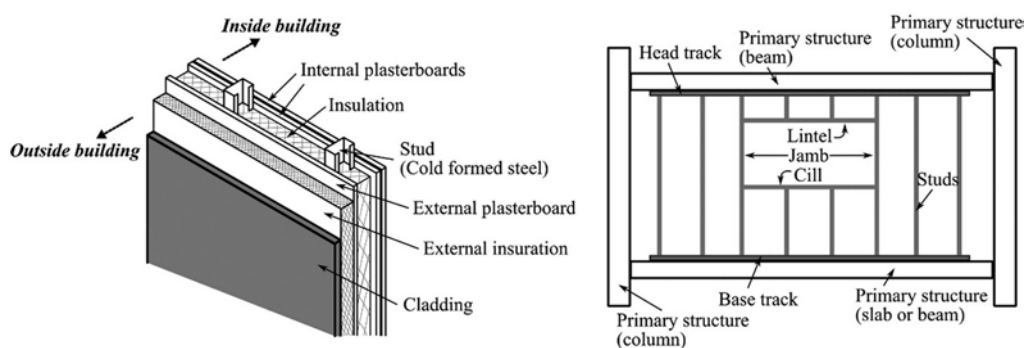


Figure 1. Exterior infill wall: (left) notations of infill wall components; (right) notations of lightweight cold-formed steel members and surrounding primary structure.

2 LIFECYCLE STAGES OF PLASTERBOARD

2.1 Product stage

According to Etex's EDP (Etex, 2018), the product of plasterboard consists of plasterboard (94.8%), paper liner (3.6%) and additives (1.6%). Among the 94.8% of the plasterboard, 36% is from mineral quarrying, 60% is from by-products from a coal-burning power station, and 4% is from recycled plasterboard (Etex, 2018). The rate of recycled gypsum in new plasterboards is limited to only 4%. This is due to the presence of impurities, introduced with the use of additives and the lining paper. There is an ongoing research program in the UK and abroad that aims to increase the recycled gypsum content in new plasterboards by increasing the purity rate of the collected gypsum waste (Erbs et al., 2018; Castro-Díaz et al., 2021). However, usually, the development and implementation of new technologies take a long time (Allwood et al., 2019).

2.2 Construction process stage

For the construction of exterior infill walls, the plasterboards are fixed to the studs of a lightweight steel frame, using self-drilling screws (Siniat, 2021). Screws are used at a minimum of 13mm from cut edges. The screws for the infill wall linings are used at a maximum distance of 300 mm (Siniat, 2021). The plasterboards should not be screwed to the head track, to avoid compromising the free movement relative to the structure (SCI, 2019a). One or two plasterboards are used for the internal linings for the infill walls depending on the designed performance for fire resistance, sound and heat insulations, and strength to wind load and cladding weight.

2.3 Use stage

The plasterboards do not need maintenance, repair, replacement, or refurbishment during the use stage. Plasterboards can be used in UK and European buildings for 50-60 years (Etex,

2018, 2021). While the expected life of the plasterboards is long (50-60 years), the infill walls, of which plasterboards are parts, are usually replaced every 30 years (ARUP, 2022) during the refurbishment of the building to adapt spaces to new functions or to comply with new energy efficiency or humidity control targets. The warranty period of plasterboard for some prefabricated types of infill walls is 30 years (Etex, 2020) but the warranty may be set to target the typical replacement period and it is not representative of the plasterboard's actual functional period. Indeed, warranties issued by manufacturers are often much shorter in their lifetime than the expected service life (Hartwell et al., 2021).

2.4 *End-of-life stage*

Most of the plasterboards (83% in mass) are landfilled or recycled and used for other purposes (e.g., agriculture), and the rest (17%) is sent for recycling to manufacture new plasterboard (Etex, 2018). Landfilling the plasterboard generates hydrogen sulphide, a toxic and foul-smelling gas, and incinerating the plasterboard results in the release of sulphur gas, a contributor to acid rain formation (Ndukwe & Yuan, 2016). In the UK, the method of landfilling plasterboard waste is getting stricter (DEFRA, 2010), and the landfill tax is increasing (DEFRA, 2013). Among the 83% of plasterboards that are either sent to landfilled or reused, the rate of landfilled plasterboard is declining due to the agreement with all stakeholders to reduce the waste sent to landfill (Jiménez-Rivero & García-Navarro, 2017). The low rate of recycling (17%) is due to the impurities of the collected plasterboard. The amount of recyclable post-consumer plasterboard may be increased when the plasterboard is dismantled and segregated from other wastes at the deconstruction site (Jiménez-Rivero, 2016).

In summary, the rate of recycled plasterboard in newly manufactured plasterboard is very low and the technology to increase it is still under development, the amount of landfilled plasterboard needs to be reduced due to the cost and detrimental environmental effect, and plasterboard used for infill walls can be used longer (50-60 years) than they are typically used for (30 years). The first two demonstrates the necessity of alternative way of improving resource efficiency and reducing carbon emissions from recycling and landfilling plasterboard. The third point demonstrates the potential of plasterboard being reused to extend the life of the plasterboard that is used in place. It is also clear that for the reuse of plasterboard to be practical and implemented in the near future, the technology must already exist or, at most, minor modifications of current technologies need to be conceived, as the development and implementation of totally new technologies take time (Allwood et al., 2019).

3 CAN WE REUSE PLASTERBOARD?

The reuse of plasterboard is beneficial as it can reduce the carbon emission from the production of the plasterboard. It also reduces the extraction of gypsum from quarries. Thus, we want to know if the plasterboards can be reused. In this section, the feasibility of reusing the plasterboard is discussed from three aspects: (i) Connections in plasterboard, (ii) Experiment of plasterboard, and (iii) prefabricated systems to respond to the question, "Can we reuse plasterboard?"

3.1 *Connections in plasterboard*

To disassemble and reuse plasterboards, the connections between the board and light steel frames need to be disconnected. As described in the previous section, the connections are made using screws between the plasterboard and studs, and between the plasterboard and base track. The connections need to have sufficient stiffness and strength to stabilise the infill wall. According to the company EDPs, the screws can be removed, and other screws can be used at the same location where the hole already exists, although some repair actions may be necessary. This is because when the screws are used in the pre-existing screw holes, the stability

of the screw may be weak and needs to strengthen the connection. Specifically, the manufacturer of weather defence board (external plasterboard) recognises the situation when the screws are used at the pre-existing screw holes, “Multiple attempts to fix a screw may create holes, inspect for holes carefully and seal” (Siniat, 2021).

When it is not feasible to remove the screws between the plasterboard and steel frame members due to the difficulty in finding their locations (e.g., the screws are not visible because the wallpapers hide them), the plasterboard may be locally cut to find the connections. This is deemed possible as there is an established repair method of plasterboard for up to certain areas of damage. The manufacturer of plasterboard specified the following repair options for different levels of damage (Siniat, 2021):

- Small areas of damage, up to 15mm x 15mm and a maximum of 3mm deep, may be patched using Siniat Fire Rated Silicone Sealant or Siniat Weather Defence™ Joint Tape.
- Areas up to 300mm x 300mm and a maximum of 5mm deep, may be filled with Siniat Aquamix water-resistant compound.
- An area larger than 300mm x 300mm or if the board has been perforated by damage must be replaced. Additional metal noggins or straps may be required to support the board.

The EDP for the internal plasterboard from the same company also states that a certain amount of damage is repairable (Etex, 2019): “Mechanical damage can be repaired using jointing compound, due to the easy repair associated with the plasterboards and without any adverse effects on function. Plasterboards can be easily replaced with new boards in the event of more extensive damage.”

Other methods may be introduced to ease the separation of plasterboard from the steel frames, for example, by developing a connection between the plasterboard and steel frame using a hooking or hanging mechanism, developing easily detachable adhesives, or using dot snap fasteners, Velcro strips, or magnetic strips. These connections need to be satisfactory to the essential structural functions of the infill walls, i.e., support the weight of the cladding and resist the shear and pull-out force induced by wind load. However, developing and implementing such new ideas in the practice may take time.

3.2 *Experiment of plasterboard*

The material properties of various types of plasterboards and the strength, stiffness and ductility of connections between plasterboard and lightweight cold-formed steel members have been investigated by many researchers (Iuorio 2009, 2017; Chen et al., 2016; Petrone et al., 2016; Ye et al., 2016; Selvaraj & Madhavan, 2019a; Abeyasiriwardena et al., 2021; Kyprianou et al., 2021; Stergiopoulos et al., 2022). The lightweight wall systems (plasterboard attached to either stud-only or studs and tracks) were also experimentally investigated by many (Bewick, 2013; Vieira et al., 2013; Liu et al., 2014; Peterman et al., 2014; Petrone et al., 2016; Landolfo et al., 2019; Selvaraj & Madhavan, 2018, 2019b; Kyprianou et al., 2021; Peiris & Mahendran, 2022).

The experimental results provide the material properties of the plasterboard and the strength of the walls (plasterboard + lightweight steel frame members). The information about the elastic range indicates that the wall systems or wall components are undamaged, therefore if carefully disassembled, they could be in a suitable condition for reuse. Recent research on structural members, other than exterior walls, at the connections of beam-to-slab, beam-to-column, and column-to-column, used the experimental results, in terms of the relationship between the deformation and strength, to discuss the feasibility of reusing the connected members (Uy et al, 2017.). These studies set 40% of the ultimate (peak) strength as the limit of reusability of the structural members. The 40% of the ultimate (peak) strength corresponds to the elastic deformation of the structural systems being deformed or stressed without damage. This type of experimental investigation, or re-evaluation of existing experimental results, provides further guidance on the feasibility of reusing the infill wall systems or plasterboards. A guideline document may be developed based on these test results to facilitate the reuse of plasterboard and wall systems. For other popular structural members, such as structural steel, for example, a guideline for assessment, testing and design of reclaimed members

exists (SCI, 2019b). According to this, straightness, loss of section, signs of damage, signs of fire exposure, plastic strain, etc. are checked for reuse of structural steel members. Similarly, a guideline document could be developed for the assessment of plasterboard panels for the determination of re-usability.

3.3 Prefabricated systems

Infill walls are often site assembled from lightweight cold-formed steel members that are delivered cut-to-length, followed by installation of plasterboard and other components (see Figure 1), or can be prefabricated as storey-high units (SCI, 2012). The disassembly of prefabricated, modules, in general, provides great opportunities for the refurbishment and reuse of modules or the recycling of materials and components used in the modules (SCI, 2001). Figure 2 shows the photos of prefabricated infill walls (SCI, 2008). Figure 3 presents the prefabricated panelised infill walls that were used in the construction of a school building in the Greater Manchester area, UK.

There are several advantages of using the prefabricated, panelised infill walls over other ways of constructing infill walls, such as (a) enhanced safety of installation workers (installation from inside the structure, reducing working externally at height), (b) reduced costs (reduced mast climber and scaffolding requirements; the crane is not necessary), and (c) reduced site waste.



Figure 2. Installation of lightweight infill wall in a primary structural frame (images from SCI, 2008), (left): Prefabricated infill wall with cladding, windows, and light steel frame, and (right) prefabricated infill wall with exterior plasterboard, windows, and light steel frame.



Figure 3. Prefabricated panelised infill wall with exterior plasterboard (photos taken by the authors on December 2021 in the Greater Manchester area, UK).

3.4 *Can we reuse plasterboard?*

Based on the discussions in this section, the authors consider that the plasterboards can be reused, and this can be done today. The reuse of plasterboard is done at the usual refurbishment time that takes place after 30 years of building construction. Currently, the plasterboard is reported to be functional for about 50-60 years, so the plasterboards can be reused once. Primarily, there are two ways of reusing the plasterboard: (a) removing plasterboard from steel frames and using it to construct another infill wall (or any other systems, i.e., internal partition walls, ceilings, etc.), and (b) keeping them attached to the steel frames and reusing the infill walls as prefabricated walls (see Figures 2 and 3). For (b), the plasterboards do not need to be separated from the steel frames. As discussed in the previous sections, any damage caused by the removal of plasterboard or prefabricated infill walls, or transportation processes, can be repaired by the existing technologies by manufacturers. In case the prefabricated infill walls are reused in other buildings, the size (width and height) of primary frames (steel or reinforced concrete frames) may be different from that of the original one. This is not a problem because the height and width of the infill walls are adjustable (i.e., the connection between studs and head track are adjustable; there are some spaces between the stud and column of the primary frame that are filled by insulation). Due to the advantages discussed in Section 3.3, prefabricated panelised infill walls may be most feasible for reusing plasterboard.

4 CONCLUSIONS

This paper first discussed the potential of reusing plasterboard. It showed that currently the rate of recycled plasterboard in the newly manufactured plasterboard is very low, the amount of landfilled plasterboard needs to be reduced, and plasterboard used for infill walls can be used longer than they are typically used. It then discussed the feasibility of reusing the plasterboard, looking at the feasibility of disassembling current connection systems, available experimental data, and prefabricated systems. Based on the developed analysis, the authors conclude that plasterboards have a high potential and feasibility to be reused, and the reuse of plasterboards can be done using existing technologies. Additionally, the authors consider that the prefabricated panelised infill walls are most suitable for the reuse of plasterboard due to their size and construction method. In the future experimental tests will be developed to provide further evidence of feasibility.

ACKNOWLEDGEMENT

This research is funded by EPSRC through the Interdisciplinary Circular Economy Centre for Mineral-Based Construction Materials from the UK Research and Innovation (EPSRC Reference: EP/V011820/1). The authors thank Etex for sharing the information regarding the topic in this paper.

REFERENCES

- Abey Siriwardena, T., Peiris, M., Mahendran, M. 2021. Local in-plane strength and stiffness of stud-to-sheathing fastener connections in LSF wall panels. *Thin-Walled Structures*. 160: 107383.
- Allwood, J., Azevedo, J., Clare, A., Cleaver, C., Cullen, J., Dunant, C.F., Fellin, T., Hawkins, W., Horrocks, I., Horton, P., Ibell, T., Lin, J., Low, H., Lupton, R., Murray, J., Salamanti, M., Serrenho, A. C., Ward, M., Zhou, W. 2019. Absolute zero: Delivering the UK's climate change commitment with incremental changes to today's technologies. Available online: <https://doi.org/10.17863/CAM.46075> [Accessed: 31-October-2022].
- ARUP. 2022. Carbon footprint of façades: significance of glass. Available online: <https://www.arup.com/perspectives/publications/research/section/carbon-footprint-of-facades-significance-of-glass> [Accessed: 31-October-2022]

- Bewick B.T., O’Laughlin C.G., Williamson E.B. 2013. Evaluation of Conventional Construction Techniques for Enhancing the Blast Resistance of Steel Stud Walls. *Journal of Structural Engineering*. 139(11): 1992–2002.
- British Standards Institution (BSI). 2011. BS EN 15978 Sustainability of construction works - Assessment of environmental performance of buildings - Calculation method. London, United Kingdom. 64p.
- Castro-Díaz, M., Osmani, M., Cavalaro, S., Needham, P., Thompson, J., Elliott, S., Parker, B., Lovato, T., & Jalland, D. 2021. Gypsum purification for improved recycling. Available online: <https://iceberg-project.eu/gypsum-purification-for-improved-recycling/> [accessed: 9-November-2022]
- Chen, W., Ye J., Chen, T. 2016. Design of cold-formed steel screw connections with gypsum sheathing at ambient and elevated temperatures. *Applied Sciences*. 6(9): 248.
- Department for Environment Food and Rural Affairs (DEFRA). 2010. Environmental Permitting Guidance - The Landfill Directive For the Environmental Permitting (England and Wales) Regulations. Version 3.1. Nobel House 17 Smith Square London SW1P 3JR.
- Department for Environment Food and Rural Affairs (DEFRA). 2013. Plasterboard Sustainability Action Plan. 2nd Annual Report 2013. Nobel House 17 Smith Square London SW1P 3JR.
- Erbs, A., Nagalli, A., Querne de Carvalho, K., Mymrin, V., Hermes Passig, F., & Mazer, W. 2018. Properties of recycled gypsum from gypsum plasterboards and commercial gypsum throughout recycling cycles, *Journal of Cleaner Production*. 183: 1314–1322.
- Etex. 2018. Environmental product declaration for GTEC plasterboard. BREG EN EPD No.: 000204; Publisher: Building Research Establishment (BRE). Available online: https://www.greenbooklive.com/filelibrary/EN_15804/EPD/BREGENEPD000204.pdf [accessed: 13-June-2022].
- Etex. 2019. Environmental product declaration. EPD-ETX-20180169-ICA1-EN; Publisher: Institut Bauen und Umwelt e.V. Available online: <https://epd-online.com/PublishedEpd/Detail/10957> [accessed: 13-June-2022]
- Etex. 2020. Thruwall solutions for the building envelope. Available online: <https://etex-bp.co.uk/wp-content/uploads/2022/02/ETEX-Thruwall-Solutions-Brochure-02-2020-1.pdf> [accessed: 19-November-2022]
- Etex France Building Performance. 2021. Environmental product declaration. Weather Defence BD 20 mm. Registration number: 0274023082021; Programme operator: INIES Environmental and health references data for the building. Available online: <https://www.base-inies.fr/iniesV4/dist/consultation.html> [accessed: 30-September-2022]
- Fiorino, L., Pali, T., Bucciero, B., Macillo, V., Terracciano, M.T., & Landolfo, R. 2017. Experimental study on screwed connections for sheathed CFS structures with gypsum or cement-based panels. *Thin-Walled Structures*. 116: 234–249.
- Fiorino, L., Pali, T., Landolfo, R. 2018. Out-of-plane seismic design by testing of non-structural lightweight steel drywall partition walls. *Thin-Walled Structures*. 130: 213–230.
- Hartwell R, Macmillan S, Overend M. 2021. Circular economy of façades: Real-world challenges and opportunities. *Resources, Conservation & Recycling*. 175: 105827.
- Iuorio, O. 2009. Design procedures for cold-formed steel housing in seismic area, PhD thesis, University of G. D’Annunzio, IT.
- Jiménez-Rivero, A. 2016. Gypsum Waste Management in the European Union: Towards a Circular Economy for the Construction Sector. Doctoral Thesis. Technical University of Madrid.
- Jiménez-Rivero, A. & García-Navarro, J. 2017. Exploring factors influencing post-consumer gypsum recycling and landfilling in the European Union. *Resources, Conservation and Recycling*. 116: 116–123.
- Kitayama, S., & Iuorio, O. 2022. Design for de-construction of lightweight infill wall systems. The Eighth International Conference on Structural Engineering, Mechanics and Computation (SEMC 2022). 5-7 September 2022, Cape Town, South Africa.
- Kyprianou C, Kyvelou P, Gardner L, Nethercot DA. 2021. Characterisation of material and connection behaviour in sheathed cold-formed steel wall systems – Part 1: Experimentation and data compilation. *Structures*. 30: 1161–1183.
- Kyprianou C, Kyvelou P, Gardner L, Nethercot DA. 2021. Experimental study of sheathed cold-formed steel beam–columns. *Thin-Walled Structures* 166: 108044.
- Landolfo R, Pali T, Bucciero B, Terracciano MT, Shakeel S, Macillo V, Iuorio O, Fiorino L. 2019. Seismic response assessment of architectural non-structural LWS drywall components through experimental tests. *Journal of Constructional Steel Research*. 162
- Liu P., Peterman KD, Schafer BW. 2014. Impact of construction details on OSB-sheathed cold-formed steel framed shear walls. *Journal of Constructional Steel Research* 101: 114–123.
- Morgan, C., & Stevenson, F. 2005. Design for deconstruction: SEDA Design Guides for Scotland: No. 1. Scottish Ecological Design Association.

- Ndukwe, I. & Yuan, Q. 2016. Drywall (gyproc plasterboard) recycling and reuse as a compost-bulking agent in Canada and North America: A review. *Recycling*. 1: 311–320.
- Peiris M, Mahendran M. Experimental investigation and design of sheathed LSF wall panels under eccentric axial compression. *Thin-Walled Structures*. 176: 109328.
- Peterman KD., Schafer BW. 2014. Sheathed Cold-Formed Steel Studs under Axial and Lateral Load. *Journal of Structural Engineering*. 140(10): 04014074.
- Petrone C., Magliulo G., Lopez P., Manfredi G. 2016. Bulletin of the New Zealand Society for Earthquake Engineering. 49(1): 125–137.
- Petrone C., Magliulo G., Manfredi G. 2016. Mechanical Properties of Plasterboards: Experimental Tests and Statistical Analysis. *Journal of Materials in Civil Engineering*. 28(11):04016129.
- RICS (Royal Institution of Chartered Surveyors). 2017. Whole life carbon assessment for the built environment. 1st edition, November. RICS professional standards and guidance. London, UK.
- Selvaraj, S., & Madhavan, M. 2018. Studies on Cold-Formed Steel Stud Panels with Gypsum Sheathing Subjected to Out-of-Plane Bending. *Journal of Structural Engineering*. 144(9): 04018136.
- Selvaraj, S., & Madhavan, M. 2019a. Sheathing braced design of cold-formed steel structural members subjected to torsional buckling. *Structures*. 20:489–509.
- Selvaraj S., & Madhavan M. 2019b. Sheathing Bracing Requirements for Cold-formed Steel Wall Panels: Experimental Investigation. *Structures*. 19: 258–276.
- Steel Construction Institute (SCI). 2001. Modular construction using light steel framing. Design of residential buildings. SCI Publication. P302. Silwood Park, Ascot, UK.
- Steel Construction Institute (SCI). 2008. Best practical in steel construction, Residential buildings. Guidance for architects, designers & constructors. SCI Publication. Silwood Park, Ascot, UK.
- Steel Construction Institute (SCI). 2012. Light steel infill walls. Light steel framing and modular construction. Technical information sheet. ED013. Silwood Park, Ascot, UK.
- Steel Construction Institute (SCI). 2019a. Design and installation of light steel external wall systems. SCI Publication. ED017. Silwood Park, Ascot, UK.
- Steel Construction Institute (SCI). 2019b. Structural Steel Reuse - Assessment, testing and design principles. SCI Publication. P427. Silwood Park, Ascot, UK.
- Siniat. 2021. Drywall manual. Plasterboard systems for partitions, ceilings and wall linings. Available online: https://www.siniat.co.uk/en-gb/uk/drywall-manual/?page=1&page_size=12&sort=Id&sort_type=desc [Accessed: 9-November-2022]
- Siniat. 2021. Weather defence™ brochure. Available online: <https://www.siniat.co.uk/-/dam/weather-defence-brochure-aug-2021.pdf/pi48561/original/weather-defence-brochure-aug-2021.pdf?v=-1053309165> [Accessed: 14-November-2022]
- Uy B, Patel V, Li D, Aslani F. (2017). “Behaviour and design of connections for demountable steel and composite structures.” *Structures*. 9: 1–12.
- Ye J., Wang X, Zhao M. 2016. Experimental study on shear behavior of screw connections in CFS sheathing. *Journal of Constructional Steel Research*. 121: 1–12.
- Vieira LCM, Schafer BW. 2013. Behavior and Design of Sheathed Cold-Formed Steel Stud Walls under Compression. *Journal of Structural Engineering*. 139(5): 772–786.

Re-use of existing load-bearing structural components in new design

R.P.H. Vergoossen, G.J. van Eck & D.H.J.M. Jilissen

Royal HaskoningDHV, Rotterdam, South Holland, The Netherlands

ABSTRACT: One of the main contributions to meet the goals of circularity, i.e. reduce Carbon emissions and use of primary materials, is the re-use of load bearing structural components from existing structures into new structures. In the last years, as a result of the Dutch Concrete Act, different projects on re-use of structural components in new structures are executed in the Netherlands. On the other hand, the first steps in eliminating the barriers for a shift from linear to circular design and construction have been taken. One of these steps is the drafting of guidelines and codes (CB'23, NTA Steel, CROW-CUR guideline for concrete and National Annexes to Eurocodes) to make re-use of existing load-bearing components in new structures possible within the Dutch Building Act. Disseminating of knowledge through publicizing lessons-learned from executed projects is another. In this paper both points are described, with a focus on Dutch infrastructures (bridges and overpasses). Not only the technical challenges will be addressed but also the mutual influence of architectural design, road design and social safety on circular design with re-use of structural components. A framework is proposed for investing in more material and/or costs including environmental costs for easier and cheaper deconstruction depending on the most likely envisioned lifespan of the structure with regard to maintenance costs.

1 INTRODUCTION

The Dutch construction industry is believed [Ministry 2016] to use approximately half of all raw materials and 40% of the total energy in the Netherlands. Additionally, the industry is a major contributor to waste production, accounting for up to 40%, as well as CO₂ emissions, at almost 35%. The Dutch Concrete Agreement [Ministry 2018], supported by the Dutch government, states that CO₂ emissions must be reduced with 49% compared to 1990 and that all concrete waste must be recycled in new concrete by 2030. Innovations in the construction sector are needed to achieve these goals. One of the solutions is to reuse structural elements from bridges/overpasses to be demolished and to use them in new structures to be built. It sounds simple, though it isn't done in practice. From a study [Donker 2021] it was concluded a few barriers are present.

2 FIRST BARRIER: NO GUIDELINES

One of the key barriers is the lack of standards and guidelines for the reuse of structural elements. For example, the Eurocodes are currently fully focused on new construction. However, from the Building Act, a construction to be erected must often comply with it, or deviations must be made in agreement with the authority. Various guidelines (CB'23 [Platform CB'23 2020], NTA Steel [NTA 8713 2023], CROW-CUR guideline for concrete [CUR-Aanbeveling 127 2021]) have been drawn up to provide guidance. A draft version of the CUR guideline for the reuse of structural

elements [CROW-CUR, 2023] is already available. Which should eventually lead to guidelines for reuse in the National Annexes of the Eurocodes. In international connection with the new FIB modelcode 2020 end-of-life scenarios and re-use are for the first time in history (pre)codified.

Deconstruction of structural elements from an existing structure currently costs (far) more than traditional demolition. This means that there must be a party that makes a pre-financing, extra investment, to dismantle the elements instead of crushing them into concrete aggregate. A contractor is often commissioned to demolish an existing viaduct and build a new one. For the contractor, the reuse of constructive elements and making an extra investment is therefore only interesting if it is certain that the elements can be reused or sold in the foreseeable future. At the same time, when a new viaduct is being built, one wants to be certain that these reused elements will be released in time and that they can be provided with a quality declaration (assurance of delivery) after disassembly and, if necessary, modification and repair. In addition, both parties benefit from knowing whether, and in what capacity, the elements can be reused. For this, a structural assessment must be carried out, which also requires pre-financing. When a client in a country or region has a large part of the (main) infrastructure, it is obvious that the pre-financing and matchmaking is done by the client. The client can stimulate dismantling and reuse through contracts and has an overview of constructions that will expire and where new constructions are required.

At the moment there is no stock of deconstructed elements. When elements are deconstructed from various bridges and overpasses over time, a stock is built up. Ideally, this stock will consist of various elements with different lengths, angles of skew and load bearing capacities. In this way, the elements can be most efficiently matched to the preconditions of the new overpass to be built.

3 THE SECOND BARRIER: DISSEMINATING OF KNOWLEDGE

Reuse of concrete components in new construction has already been applied in various projects in recent years [Küpfer 2023]. However, the reuse of structural elements in new bridges has not been done before.

Rijkswaterstaat, the Dutch Ministry of Infrastructure, has asked the market through a Strategic Business Innovation Research (SBIR) assignment to come up with ideas for Circular Viaducts in order to achieve its goal of being climate neutral and fully circular by 2030. The consortium with Royal HaskoningDHV with reuse of prefab girders was chosen by an independent assessment committee to realize a tested prototype after the feasibility study showed it was feasible.

In Groningen, a large-scale conversion of the southern ring road is taking place. The contractor had been commissioned to demolish the viaduct KW21 Europaplein. Instead of demolishing the entire viaduct and grinding it into aggregate, it was decided, in the context of circular construction, to reuse the 26 prefabricated prestressed girders from the main spans.



Figure 1. Deconstruction of prefab girders in Groningen (left) and girders in temporary storage (right).

A temporary access bridge (Oling 5) had to be built at the location of a temporary residential area in Appingedam (near Groningen). Seven girders from the former Groningen viaduct were used for this. But before the girders could be reused, the girders were stripped of the in-situ deck and the tooth support in a temporary storage facility. The original design was based on three shorter spans. To be as circular as possible, the design has been adapted to the available beams from Groningen. The access bridge now consists of a single span, retaining the original beam length of 18.2m. In addition to the beams, the tubular piles, sheet piles and H-profiles for the substructure have also been reused. In short, only the in-situ deck and the handrail were new for this bridge.



Figure 2. Temporary access bridge Oling 5: reused girders, sheet piles and purlins.

Within the SBIR project the project team was looking for a project in which a new overpass has to be constructed. Project partner Dura Vermeer has been awarded the tender of the replacement of the 60-year-old overpass Hoog Burel over the A1 motorway. The tender design consisted of a fully new overpass with 4 spans and an angle of skew of 30 degrees. The project team of Liggers2.0 went looking to several projects in construction if girders were to be demolished with lengths that could fit. In the project Southern Ring Road Groningen such an overpass was found. But that overpass had girders of 13 m and 19 m (with half joints) were the overpass Hoog Burel needed girders of 34 m and 14.4 m. The contact demands of the new overpass Hoog Burel were such that the length of the girders wasn't allowed to change. Therefore, it was decided to investigate if the main spans of 19 m could be shortened to the desired length of 14.4 m. One of the challenges was that the original shop drawings of the girders from the overpass in Groningen were lost. Another challenge was that because of the demands of the number of construction joints, the girders had to be supported indirectly to provide sufficient vertical support reaction for the bearings to resist horizontal forces and movements. All actions to prove that the girders could be adapted and fulfill the structural safety requirements of a new structure are described in [Vergoossen 2022]. In order to prove the quality of the elements, tests on bored cylinders were performed in the laboratory. Strength (both compression and tensile splitting), chloride ingress, carbonation and alkali-aggregate reaction were tested. All tests showed very high performance with almost zero ingress of aggressive agents after 40 years. Based on these results a remaining service life of hundreds of years is predicted according to FIB modelcode on service life design [CEB-FIP fib 2006]. As these are one of the first elements which are being reused these tests were performed as part of a the SBIR pilot project to demonstrate that the remaining service life generally is no problem for these elements. In the future less or no tests are required. The girders were placed under a large audience from Rijkswaterstaat and Ligger2.0 project partners. These girders are the first re-used girders within the acreage of Rijkswaterstaat. Although, it was proven that the girders can be adapted this project was far from ideal from a circularity viewpoint. As the girders had to be shorten for about 30% of their original length, and the skew angle had to be increase from 8 to 30 degrees. Also, the indirect support resulted in a lot of extra engineering

work and some extra reinforcement and extra roughening of the webs of the girders. On the other hand, because of the many extra challenges in this project, it can be said that because all these challenges were successfully solved all girders can be adapted. Despite all these modifications still a huge environmental saving in terms of CO₂-eq of 96% has been achieved when compared purely to newly-cast girders.

A previous case study [Vergoossen 2021] has shown that a saving of more than 40% CO₂-eq can be achieved when looking at a viaduct by only reusing girders instead of making new girders. As 26 girders were dismantled and 16+7=23 girders were used in the above-described project, still three girders are available. Although, there were some promising contacts for a new pedestrian bridge, it was decided to keep these girders into storage. Therefore, these girders were transported to the Urban Miner facility in 's Gravendeel of project partner Dura Vermeer. The girders are also placed at the digital marketplace Bridgebank, so interested parties can find the properties of the girders. The project partners of Ligger2.0 are currently investigating a new pilot bridge where the original inverted-T-beams are transformed into H-beams, which can be connected together with transversely post-tensioned prestressing without bond. In that way a fully re-useable structure can be made, without waste and the need of sawing or drilling.

During the feasibility phase of the SBIR project, the project team of Liggers2.0 investigated which structures with girders were to be demolished in the next years. One of these structures was planned to be demolished before the submission date of the tender. The project team reacted agile and decided to invest into the dismantlement of 6 of the 40 girders, as an option for a pilot project if the project was awarded. On the other hand, the dismantlement helped the feasibility study as it proved it is possible to save girders from demolition. Although the project was awarded, the girders weren't suitable for the above-mentioned project Hoog Burel. So, the project team went on searching for another possible location.



Figure 3. Placing the reused girders in Hoog Burel.

That was found to be the new bridge in the provincial road N386. In that road a new water and fauna underpass had to be designed. The reference design consisted of a two-span bridge with spans of 10 m. As the existing girders from the overpass in the A9 Motorway had a length of 22 m it was decided to change the design into a single span of 21.5 m. On this way even extra width of the fauna and a better water run-off could be made. As there were only 6 girders saved and the width of the N386 needed 8 girders to fit, the new structures will consist of a combination of 2 new girders and 6 re-used ones. In this contract the project partner Haitsma Beton, which is the largest prefabrication producer of the Netherlands, will produce

the two new girders as well as deliver the 6 re-used girders as a client delivery to the contractor. The project is planned to be constructed this year.

Contractor Dura Vermeer deconstructed a 45-year-old pedestrian overpass in the city of Zoetermeer. The I-girders were in such a good shape that it was decided to save these girders and put them into a storage. For a project for a new sports facility in Amsterdam near the Johan Cruijf Arena a new temporary pedestrian bridge was planned. That project was also awarded to Dura Vermeer. Therefore, together with Royal HaskoningDHV it was decided to design the new bridge based on the available I girders from the overpass in Zoetermeer. After the completion of the design, the total project unfortunately was stopped because of lack of funds for the total project. Therefore the design still only exists on paper. The girders are still in a storage and the availability of the girders is made publicly via the platform Bridgebank www.bruggenbank.nl.



Figure 4. a) former pedestrian overpass Zoetermeer (left) and b) girders in storage (right).

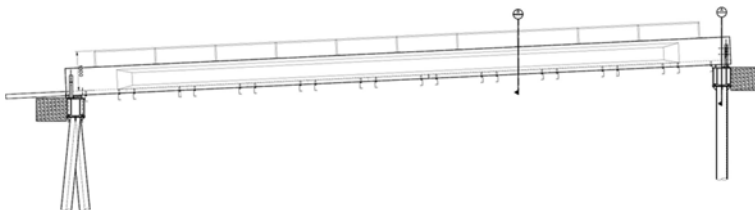


Figure 5. Longitudinal section of the design with the reused girder.

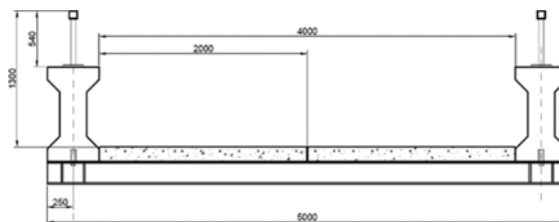


Figure 6. Cross-section of the design with the reused girder.

For the Floriade in Almere three new pedestrian bridges were needed. It was decided that these bridges should be designed as circular as possible. It was proposed by Dura Vermeer to build one of these bridge as a ‘second life bridge’. Shortly before the Floriade project started, Dura Vermeer was commissioned to remove the pedestrian overpass “Bolgerijnse Kade” over motorway 27. It was decided to re-use four of the main girders in the new bridge at the Floriade. The other elements of the Floriade bridge also consisted of re-used elements [Doorn 2021]. The other six girders are placed in a storage and their availability is made publicly by the Bridgebank.

Together with Rijkswaterstaat and the consortium Closing the Loop, who was also awarded a SBIR pilot overpass, the partners of Liggers2.0 are investigating the re-use of up to 1500 girders which are to be demolished within the A9 motorway project. The first success is that about 40 girders are dismantled for re-use of an overpass over the A76 for Rijkswaterstaat. Another success is that a letter of intent between Rijkswaterstaat and the province of Noord-Holland was signed to dismantle at least 32 girders for two new bridges in de provinciale road N201. A feasibility study is conducted to structural assess all the girders if they can fulfill the demands for new structures in new motorways for Rijkswaterstaat. As the costs of dismantlement usually are much higher than demolition, someone has to invest in the dismantlement. In many cases at that time there isn't any assurance that the girders can be re-used. To gain more assurance the first step is to perform structural assessments to check if the girders can meet the requirements. In some cases, a second step is to perform laboratory tests on drilled cylinders from the structure to assess the ingress of carbonation and chlorides and the susceptibility of Alkali-Aggregate-reaction within the concrete. Although for most of the prefabricated pretensioned concrete girders there aren't any serious deterioration mechanisms as the concrete strength and quality is very high and therefore the concrete is very dense.

4 DISCUSSION

In addition to the assessment level for new construction from the Eurocodes, the Netherlands has from the Dutch standard NEN 8700 the levels for reconstruction, usage and disapproval for assessing existing structures. The lack of a specified level for reuse has led to a discussion as to which level should be maintained for reused structural elements. The divisions that can be made here are everything at new construction level (Eurocodes), loads and partial safety factors at new construction level (Eurocodes) with the capacity following the NEN 8700 for existing structures (add shear capacity of concrete share and stirrups), and loads and partial safety factors reconstruction level (NEN 8700) with the capacity following the NEN 8700 again. First, one could always assume new construction. If this level cannot be met, the capacity according to NEN 8700 can be assumed. In this way, the safety philosophy of the design (reliability index) is maintained. Based on the FIB model code 2020 one could use the principle of "economic value" for decision-making. For example, in the case of an inverted T-girder with an in-situ deck where the deck is not removed, one could assume that the reconstruction level is used. Structurally, nothing changes to the element and the economic investment is relatively limited. In practice, the in-situ deck will have to be removed in order to obtain a single bridge deck again after casting a new in-situ deck on site and due to the mediocre quality of the old concrete. In that case, structural changes do occur in the element to be reused and a relatively large investment must be made. The most economic value is then obtained by making the relatively small additional investment to meet the assessment level for new structures.

The structural design of an overpass or bridge is generally determined by conditions like the road layout, the desired location and number of supports (and therefore the length of the spans), the maximum length of the structure and the construction height of the deck. One is used to designing a construction and ordering the structural elements project-specifically. From the design point of view the highest efficiency is achieved with "taylor fit" elements. Reused elements must then be modified to be used in a new bridge or overpass. In addition, there is a good chance that newly produced project-specific elements will have to be adapted for future reuse. The most circular would be to reuse elements as they are deconstructed. This means that one has to design with the elements that are available. This does depend on the stock and the contract requirements of the owner of the construction to be deconstructed. In addition, a contractor prefers to reuse elements as quickly as possible in order to save on storage costs.

5 CONCLUSIONS

The various projects described in this paper show that it is very well possible to reuse structural elements from existing overpasses in new overpasses to be built, both demand and

supply driven. It is possible to modify elements to enable application within the design of the structure to be realized. However, it is most circular to reuse elements with only minimal adjustments, so this is preferable. This means that one has to design based on the elements that are or will become available.

In many cases, reused structural elements are still more expensive than the traditional demolition and production of new elements. Costs for deconstruction, storage and modification can still be optimized. The reuse of structural elements does make a significant contribution to the circularity goals. In this way a contribution is made to moving away from the throw-away society.

REFERENCES

- Donker, J. Identifying and subducting the key barriers of reusing precast girders in Dutch overpasses, Master thesis Delft University of Technology 2021.
- Doorn, E. van, Lukassen, R., Meijdam, J., A second life bridge (een tweede leven brug in Dutch), 2021. CEMENT vakblad voor betonconstructies, no. 3 2021.
- Platform CB'23, www.platformcb23.nl (partly in English)
- Nederlandse Technische Afspraak (NTA), NTA 8713: Hergebruik constructiestaal, 2023
- CROW-CUR, CUR-Aanbeveling 127: Beton met betongranulaat als fijn en/of grof toeslagmateriaal, 2021 (in Dutch)
- CROW-CUR, CUR-richtlijn: Hergebruik constructieve elementen, 2023 (in Dutch)
- Küpfer, C., Bastien-Masse, M., Fiver, C., Reuse of concrete components in new construction projects: Critical review of 77 circular precedents, 2023, Journal of Cleaner Production Volume 383
- Ministry of Infrastructure and the Environment, Ministry of Economic Affairs. Nederland circulair in 2050. Rijksbreed programma Circulaire Economie (The Netherlands circular in 2050. National program circular economy), The Hague, Ministry of Infrastructure and the Environment, 2016 (in Dutch)
- Ministry of Infrastructure and Water Management et al, Betonakkoord voor duurzame groei (Concrete-agreement for Sustainable growth), Nootdorp, 2018 (in Dutch).
- Vergoossen R., Van Eck G., Jilissen D., Re-using existing prefabricated prestressed concrete girders in new bridges, 2022, IABSE Symposium Prague 2022 p554–p561
- CEB-FIP fib, Model Code for Service Life Design, 2006, bulletin 34
- Vergoossen R., Van Eck G., Bakker, R., Re-using existing prefabricated prestressed concrete girders, 2021, IABSE Symposium Ghent 2021 p215–p222

Quality assurance process for reuse of building components

A. Räsänen & J. Lahdensivu

Tampere University, Tampere, Finland

ABSTRACT: Reusing building components has generated discussion increasingly. Current guidelines and practices are not suitable for the reuse process, and therefore new guidelines need to be developed. With new guidelines the quality of reuse can be ensured. The quality assurance process can be divided in five different stages including pre-deconstruction audit, structural condition investigation, deconstruction design and deconstruction, demands for redesign in new building and product approval and authorization. In the process, overall perspective of the building and its structures is required. This can be achieved by studying old documents and doing structural condition investigation. With the results, more exact information about the structural properties of the building components can be obtained. These results can be used in redesigning the components and in product approval. Also, the quality of the deconstruction stage needs to be ensured in order to avoid any effects on the structural properties of reusable building components.

1 INTRODUCTION

Construction industry consumes a vast amount of natural resources globally. In addition to natural resources, construction industry produces over 35 % of the EU's total waste generation. Also, greenhouse gas (GHG) emissions are estimated to be 5-12 % of total national GHG emissions. GHG emissions includes material extraction, manufacturing of new construction products, construction and renovation of buildings. Therefore, saving natural resources is one essential means of curbing climate change. (European Commission 2022)

In a Finnish apartment building carbon footprint from construction materials is average 26 % of the whole life cycle of the building. Most of the carbon footprint consist of energy consumption, which is approximately 63 %, since buildings requires heating during cold periods and cooling in hot periods in Finland. The carbon footprint of the whole service life may differ from this average value in individual cases, because it depends on energy efficiency of the building, carbon footprint of the energy production and the materials used in the building. (Ymparisto 2016) Currently zero-energy buildings have become more common and the emissions of energy production have been decreased. Therefore, the material emissions of the whole life cycle increase in proportion to the emissions of a whole building. Construction product industry has developed several construction products by which the carbon footprint of buildings can be decreased. With low-carbon concrete the carbon footprint of an usual apartment building can be decreased 34 % (Lahdensivu & Lahdensivu 2021). Reusing building components is one potential way to decrease the carbon footprint even more, because the carbon footprint of a product stage (A1-A3) is zero according to Finnish national guideline (Kuittinen 2019). According to German studies carbon footprint (A1-A3) of reused concrete elements is between 3 and 5 % (Mettke 2010). The product stage A1-A3 includes material supply, transport and manufacturing according to information modules of assessment of environmental, social and economic performance of the construction works in European standard SFS-EN 15643:2021.

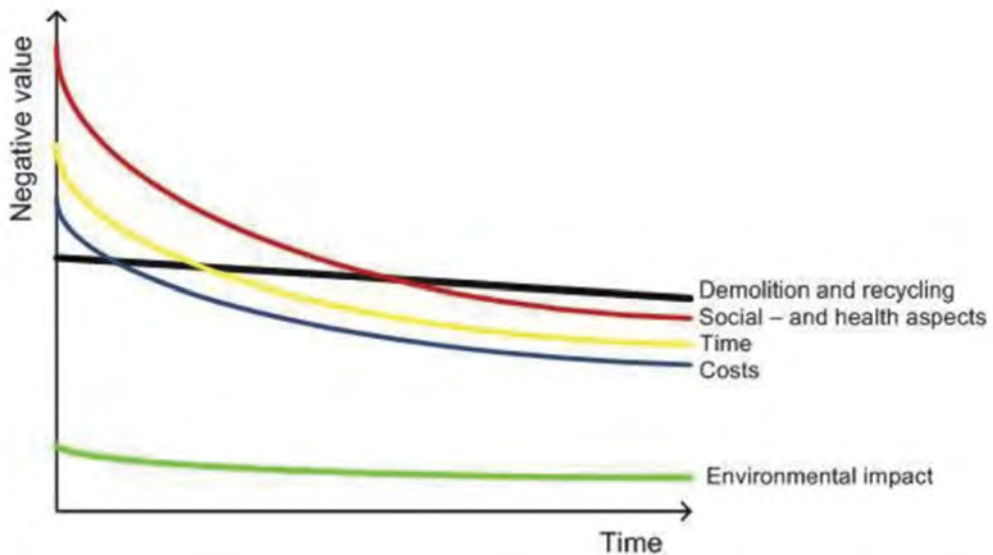


Figure 1. The progress of negative values for reuse of hollow-core slabs in the future compared to demolition and recycling (Naber 2012, p. 135).

Buildings are designed to service several decades. In Finland facades are designed typically for 50 years while frame and foundation structures are designed to service at least 100 years. However, industrial and office buildings have been demolished notably under designed service-life, typically after 20 to 40 years (Huuhka & Lahdensivu 2014). Therefore, building components have several decades of service-life left at demolition stage and potential for reuse.

According to European Union's directive 2008/98/EC of 19 November 2008 on waste and repealing certain Directives, reuse, recycling and other material recovery of construction and demolition waste should have been increased to a minimum of 70 % by weight by 2020. This varies between EU's member countries, but the most common way is using the waste as a substitutive material in land construction or as an aggregate in concrete. However, recycling is inferior to reusing in waste hierarchy in 2008/98/EC. Also, by reusing building components, for example concrete components, the carbon footprint and energy consumption can be decreased 96-98 % compared to a new product (Mettke 2010, ReCreate 2022).

Reuse of building components have been studied previously by several researchers (Mettke 2010, Lahdensivu et al. 2015, Huuhka et al. 2018, van den Brink 2020, RE:Source 2021, Zhu et al. 2022). From previous studies it can be concluded that reusing is possible. However, a main challenge found in previous studies is quality assurance process (Re:Source 2021, Zhu et al. 2022). The challenge includes especially ensuring safety and healthiness of the reusable building components and methods for investigate these.

Building components may deteriorate or material properties may change in-use. Also, the components may get damaged in deconstruction. Several national guidelines for condition assessment of façade structures have been developed (Lahdensivu et al. 2019, Lahdensivu et al. 2021), but for load-bearing structures there are no as united whole guidelines. This structural assessment is an essential stage for reuse process of building components since the properties and reusable components can be discovered before deconstruction. A problem is a lack of established practices of reuse, which increases negative values as costs, time, environment impact and social factors of reuse. These negative values may increase higher than in recycling and new construction. In the future after getting more utilized practices, negative values are assumed to decrease lower than demolition and new construction (Figure 1). (van den Brink 2020)

This paper presents a concept of quality assurance process for reuse of pre-cast concrete elements. The aim of the study is to create a practical process which can be used to ensure the quality of the reuse of building components. The current quality assurance processes are for

new construction and for example in concrete industry these are for concrete batching. However, the properties of concrete vary in time and the properties in old structures may differ from the age of batching. Therefore, new processes need to be developed for old reusable components. The process in this study is supposed to promote the reuse of building components by providing a base for development of practices. This process will be developed during the Reusing precast concrete for a circular economy (ReCreate) project by using it in practice.

2 REUSE PROCESS

Several different further actions may be done after building's service life. The further action depends on the owner's decision of what is the future of the plot or the building. The decision may be maintenance, repair or upgrading works, demolition or deconstruction for reuse of building components. The deconstruction process differs significantly from usual demolition and new construction as far as designing and building practices. (Bertino et al. 2021)

Reuse process can be divided in four different stages: deconstruction, transport, storage and building. All these stages differ from new construction and should be considered in the reuse process as they increase the challenges of reusing without established practices. (Bertino et al. 2021) The current challenges in the whole reuse process are costs, design, regulation, market and deconstruction. The costs may be three to five times higher in reuse than in new construction, because deconstruction and design stages being unusual and thus taking more time (Rakhshan et al. 2020). Furthermore, the costs in reuse process may be lower than in new construction if labor costs are small and the deconstructed components have demand (da Rocha & Sattler 2009). In addition to these challenges, one of the main challenges, which must not be forgotten, is the quality assurance of the reusable building components as mentioned in the introduction. The quality assurance process will be discussed further in the following section.

3 QUALITY ASSURANCE PROCESS

There are several different stages in quality assurance process. Each of these stages are essential to consider in reuse process for safe and reliable reuse of building components. The process starts before deconstruction and ends to product approval after the deconstruction of the building. General flow diagram of the quality assurance process is illustrated in Figure 2.

3.1 *Pre-deconstruction audit*

Before deconstruction stage, it is essential to decide what needs to be done with the building. The decision may be to maintain the current building by renovating or deconstruct the building and reuse the components in a new building. Regardless of the decision, the properties of structures should be assessed in both cases. Only the scope and extent of investigation vary. There are no any strict rules for decision-making as the decision varies between individual cases, but before the decision, the structures of the building should be always studied. This study can also be helpful and support the decision-making.

Overall, at this stage it is essential to get a general overview of the building and its structures. This can be done by studying design basis, previous inspections and maintain records and occurred irregularities to get information about the properties and factors as dimensions, environment, joints etc. that affect to service life, deconstruction work and reusability of the structures. This stage is also known as pre-deconstruction audit.

3.2 *Structural condition investigation*

One of the essential stage in reuse process is to ensure reusability of building components. This includes mechanical properties for structural capacity design, durability properties for

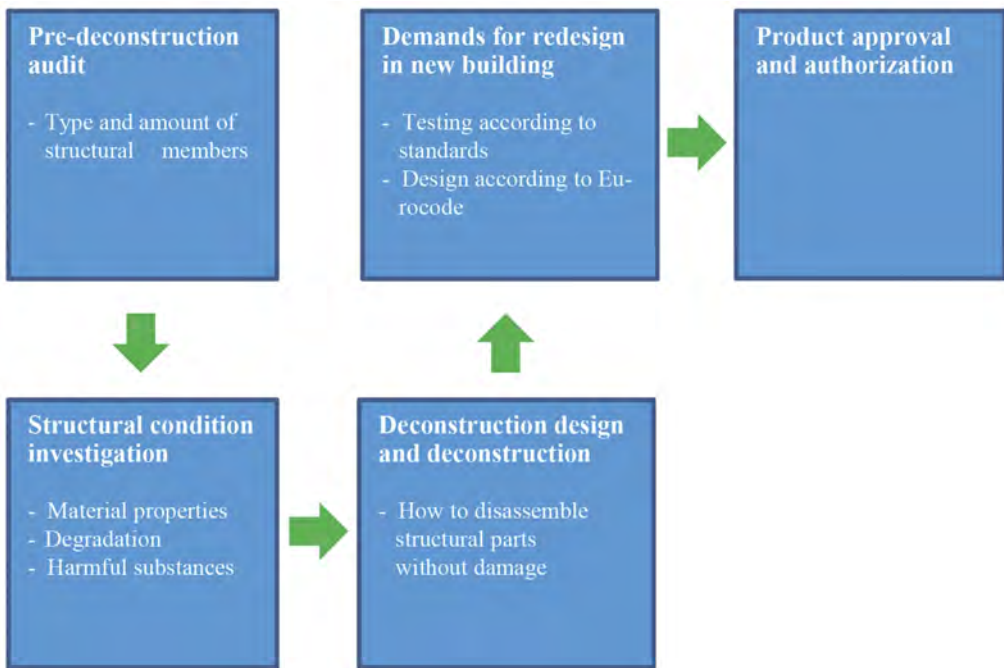


Figure 2. Quality assurance process for reuse of building components.

service-life assessment and hazardous substances for safe and healthy deconstruction work and reuse. These affects to the design process for a new building as well as to the product approval and authorization before the reuse. The properties can be assessed by structural condition investigation and assessment.

For a successful condition assessment, careful pre-planning is required. In the pre-planning it is essential to decide test methods, sampling spots and sample size for each test. Decision-making for testing reusable building components differs from usual condition assessment of a building, since the components are going to be redesigned according to current requirements and standards. For condition assessment of a building, the minimum performance requirement can be decided by the owner of the building, but in the reuse process, the minimum performance requirement is defined in standards and design guidelines for a new building. Thus, representative of test results, reliability of testing and threshold values for different deterioration mechanisms are emphasized in the structural condition investigation of reusable building components.

To get reliable and representative results, it is important to know every factor affecting to the results. For example, different non-destructive test methods (NDT) for testing bricks have uncertainty, and it is therefore important to select the right methods and sample sizes for each property (Räsänen et al. 2022). Also sampling spot and sampling should be considered in pre-planning, since they have a significant influence for example on the testing results in concrete structures (Haavisto et al. 2021). In addition to these examples mentioned above, other factors as location of the sampling spot and used equipment should be considered as well depending on the structure and building.

Threshold values for corrosion of reinforcement in concrete, for example, needs to be decided according to the demands from new building. The testing procedure needs to be as accurate as possible, since the threshold value is essential information for the service-life assessment. This procedure varies for different deterioration mechanisms. Therefore, it is very important to know if there are any ongoing deteriorating and what is the primary deterioration mechanism to be investigated and assessed. Deterioration mechanisms are not the only

thing, since the components are going to be redesigned. The most important thing being the structural properties as strength and stiffness. These are the essential information for design and therefore the values for these must be as accurate as possible.

To achieve accurate results, on-site inspection is required. Visual inspections, non-destructive testing and destructive testing should be done to get a representative picture of all the structures. Using these methods mentioned above alone or together, this representative picture can be achieved. After having the results of the tests, the results need to be analyzed and assessed by a qualified person who can identify any factors of uncertainty.

3.3 *Deconstruction design and deconstruction*

Deconstruction process relates to occupational safety and is therefore essential stage in the quality assurance process. This requires thorough design process where every affecting factor to the occupational safety need to be considered. In the reuse process, it is also essential to design the deconstruction so that the properties of the building components are not being affected. The factors are for example deconstruction order, working method, support structures, lifting equipment and joints of the structures.

Before actual deconstruction work, the condition investigation results need to be assessed at general level. The reason for this is that possible damages before and after deconstruction must be separated so that the main reason and influence of the damage on the properties of structure can be assessed. At least visual inspection is required before and after deconstruction. Also, need for further investigations must be clarified, if needed.

In addition to the deconstruction of the building, storage and transport conditions must be considered. These conditions may have significant effect on the properties of structures, and it is essential factor. For example, in-door structures may have problems with freeze-thaw durability in cold climates if they are not protected sufficiently from moisture or cold air. Further investigations and assessment are required if there are any doubts of deterioration during storage or transportation.

3.4 *Demands for redesign in new building*

As mentioned before, reusable building components are designed according to current standards and guidelines. The values for these can be determined by condition investigation and assessment which cannot be over-emphasized in the reuse process. In the redesign of the components, reliability of the results from condition investigation is essential and needs to be considered by the designer. The reused building components cannot risk sustainability of the new building.

The current design equations may not represent the real performance in the structure, if the structure has been damaged. Thus, the factors in the design equations may require adjustment in the redesign stage. The way how these factors have been influenced by the damage need to be investigated and assessed. This requires expertise to understand the design equations and factors which may have been affected. In addition to the design equations, the joints may require full demolition, or they may be damaged during deconstruction, and therefore new joints and details may be needed. This may require more creative thinking because typical joints in new construction may not be practicable with reused components.

In addition to the structural properties, the designer must understand the meaning of fire and sound insulation of the structures. The requirements for these have changed during time, and reusable components may not fulfill these requirements without any improvement. All these demands must be considered for reusable components as in new construction with new components.

These factors affecting to the redesign of the reusable building components are just a few examples from several affecting factors. This indicates that there are several challenges in the reuse process, and it requires a lot of understanding to consider all the affecting factors. Also experience from practice will point out the typical challenges in the redesign stage in the future.

3.5 Product approval and authorization

Currently CE marking is required for new materials and components in EU. However, this is only for products manufactured after 2013, and therefore, for reusable building components manufactured before that, the CE marking is not required. Local and national authorities may still require product approval for ensuring safe reuse. This can be done by following each stage of the quality assurance process in Figure 2.

For a product approval it is highly recommended to create a document from each stage which can be used as an aid for proving the usability of the reused components. In these documents the results and decisions need to be stated. The documents are also helpful for designer who tries to figure out the uncertainty of the material properties and select the usable property value in design. Therefore, any uncertainty in different stages need to be considered in the documentation.

4 CONCLUSIONS

The quality assurance process of reusable building components has several stages. Each of these stages needs to be done with care, since they affect to the next steps and the whole process. The pre-deconstruction audit is important to get a general picture of the building and reusable components. This is an aid for designing structural condition investigation and assessment stage, which is a very important stage in the whole process. By the results of the condition investigation, the reusability of the components can be ensured. The requirements for the condition investigation comes from the demands from the new building because the building need to be designed according to the current standards and guidelines. To ensure that the components satisfy the demands for the new building, the deconstruction needs to be taken with care. In addition to the components, occupational safety is an essential perspective at this stage. At the end of the process, reusability of the building components can be ensured by following these stages above.

FUNDING

The study was conducted in the Reusing precast concrete for a circular economy (ReCreate) project. The project has received funding from the European Union Horizon 2020 research and innovation programme under grant agreement No 958200.

REFERENCES

- Bertino, G., Kisser, J., Zeilinger, J., Langergraber, G., Fischer, T. & Österreicher, D. 2021. Fundamentals of building deconstruction as a circular economy strategy for the reuse of construction materials. *Applied sciences* 11(3). 31 p. <https://doi.org/10.3390/app11030939>.
- Da Rocha, C-G. & Sattler, M. 2009. A discussion on the reuse of building components in Brazil: an analysis of major social, economical and Legal Factors. *Resources, Conservation and Recycling* 54. Pp. 104–112. <https://doi.org/10.1016/j.resconrec.2009.07.004>.
- Directive 2008/98/EC. Directive of the European Parliament and of the Council of 19 November 2008 on waste and repealing certain Directives. *Official Journal of the European Union*. 22 November 2008. Accessed 29 November 2022. ELI: <http://data.europa.eu/eli/dir/2008/98/oj>.
- European Commission. 2022. Buildings and construction. European Commission website. [Online]. Accessed 24 November 2022. https://single-market-economy.ec.europa.eu/industry/sustainability/buildings-and-construction_en.
- Haavisto, J., Husso, A. & Laaksonen, A. 2020. Compressive strength of core specimens drilled from concrete test cylinders. *Structural Concrete* 22(1). 13 p. <https://doi.org/10.1002/suco.202000428>.
- Huuhka, S. & Lahdensivu, J. 2014. A statistical and geographical study on demolished buildings. *Building Research an Information* 44(1). 24 p. DOI: <https://doi.org/10.1080/09613218.2014.980101>.

- Huuhka, S., Köliö, A., Annala, P. & Poti, A. 2018. Puurakenteiden uudelleenkäyttömahdollisuudet (*Reuse possibilities of timber structures*). In Finnish. *Tampere University of Technology. Architecture & Civil Engineering*. Research Report 165. 66 p. <https://urn.fi/URN:ISBN:978-952-15-4075-2>.
- Kuittinen, M. 2019. Rakennuksen vähähiilisyiden arviointimenetelmä (*Method for the whole life carbon assessment of buildings*). In Finnish. *Publications of the Ministry of the Environment* 2019:22. 54 p. <http://urn.fi/URN:ISBN:978-952-361-029-3>
- Lahdensivu, E. & Lahdensivu, J. 2021. Decreasing carbon footprint of block of flats – concrete technology possibilities. *Nordic concrete Research* 64. Pp. 129–144. DOI: <http://dx.doi.org/10.2478/ncr-2021-0006>.
- Lahdensivu, J., Huuhka, S., Annala, P., Pikkuvirta, J., Köliö, A. & Pakkala, T. 2015. Betonielementtien uudelleenkäyttömahdollisuudet (*Reuse possibilities of pre-cast concrete panels*). In Finnish. *Tampere University of Technology. Department of Structural Engineering*. Research report 162. 78 p. <https://urn.fi/URN:ISBN:978-952-15-3461-4>.
- Lahdensivu, J., Weijo, I., Ruuska-Jauhijärvi, K. & Pyy, H. 2019. Betonijulkisivun kuntotutkimus (*Condition assessment of concrete facade*). In Finnish. 4th edition. *Concrete Association of Finland*. 136 p.
- Lahdensivu, J., Köliö, A., Pakkala, T., Lemberg, A-M., Eronen, M. & Hyrynen, S. 2021. Muurattujen ja rapattujen julkisivujen kuntotutkimus (*Condition assessment of masonry and plastered facades*). In Finnish. *Concrete Association of Finland*. 180 p.
- Mettke, A. 2010. Material- und Productrecycling – am Beispiel von Plattenbauten (*Material and Product Recycling – Using the Example of Prefabricated Buildings*). Habilitation Thesis. In German. Cottbus. *Brandenburg University of Technology*. urn: nbn:de:kobv:co1-opus4-46133.
- Naber, N. 2012. Reuse of hollow core slabs from office buildings to residential buildings. Master's Thesis. *Delft University of Technology*. Faculty of Civil Engineering and Geosciences. 259 p. <http://resolver.tudelft.nl/uuid:a04416b7-e8c0-499d-81c7-48c51b5e7fda>.
- Rakhshan, K., Morel, J-C., Alaka, H & Charef, R. 2020. Components reuse in the building sector – A systematic review. *Waste management & research* 38(4). Pp. 347–370. <http://dx.doi.org/10.1177/0734242X20910463>.
- ReCreate. 2022. KTH presents its pilot building made of recycled concrete. [Online]. Accessed 29 November 2022. <https://recreate-project.eu/2022/06/10/kth-pilot-building-recycled/>.
- RE:Source. 2021. Rivningsobjekt – från kostnad till resurs (*Demolition object – from cost to resource*). In Swedish. Final Report. 37 p. <https://resource-sip.se/projektdatabas/>.
- Räsänen, A., Huuhka, S., Pakkala, T. & Lahdensivu, J. 2022. Methods for evaluating the technical performance of reclaimed bricks. *Case Studies in Construction Materials* 17. 19 p. <https://doi.org/10.1016/j.cscm.2022.e01504>.
- SFS-EN 15643:2021.2021. Sustainability of construction works. Framework for assessment of buildings and civil engineering works. *Finnish Standards Association SFS*. Helsinki, Finland. 42 p.
- Van den Brink, G.J. 2020. Designing with recovered precast concrete elements. A study on the possibilities of reusing structural precast concrete elements, from disassembled office buildings, in new apartment building. Master's Thesis. *TU Eindhoven*. Innovative structural engineering and design. 2019 p. <https://research.tue.nl/en/studentTheses/designing-with-recovered-precast-concrete-elements>.
- Ymparisto. 2016. Tiekartta rakennusmateriaalien hiilijalanjäljen vähentämiseksi valmisteilla (*A roadmap for decreasing carbon footprint of construction materials in preparation*). Announcement of the Ministry of Environment. In Finnish. [Online]. Accessed 29 November 2022. https://www.ymparisto.fi/fi-FI/Kulutus_ja_tuotanto/Tiekartta_rakennusmateriaalien_hiilijala%2840813%29.
- Zhu, Y., Lonka, H., Tähtinen, K., Anttonen, M. Isokääntä, P., Knuutila, A., Lahdensivu, J., Mahiout, S., Mäntylä, A-M., Raimovaara, M., Rantio, T., Santonen, T. & Teittinen, T. 2022. Purkumateriaalien kelpoisuus eri käyttökohteisiin turvallisuuden ja terveellisuuden näkökulmasta (*Suitability of demolition materials for different applications from safety and health point of view*). In Finnish. *Prime Minister's Office*. 161 p. <http://urn.fi/URN:ISBN:978-952-383-253-4>.

Calculating embodied carbon for reused structural components with laser scanning

B.S. Byers, M. Gordon & C. De Wolf
ETH Zurich, Zurich, Switzerland

O. Iuorio
University of Leeds, Leeds, UK

ABSTRACT: The global warming potential (GWP) of reused building elements can be evaluated based on two variables: structural material quantity (SMQ) and embodied carbon coefficient (ECC). The volume of the SMQ can often be unknown, however, and it is not clear how to best estimate the ECC of a reused element. This paper illustrates a method for extracting the volume of reused metal structural elements to calculate their GWP in buildings that lack documentation. The authors use laser scanning and voxelization to extract the volume and a method based on the Swiss Society of Engineers and Architects (SIA) 2032 norms for calculating the GWP of reused materials. The reality capture method is accurate enough to approximate structural material volume, although it requires exposed structures. The results are important for building managers to understand the relative environmental impact savings from reused versus new building elements.

1 INTRODUCTION

New structural design methods are needed to achieve many industrial and governmental goals for sustainable construction. In the closed material system of planet Earth, it is imperative to be more efficient with building resources and to understand how to use what is already available. Circular construction and the reuse of building elements is a growing approach for minimizing environmental impacts through lowering embodied emissions in the product stage of the construction process. One approach for measuring embodied emissions is through measuring global warming potential (GWP), a sub-factor of a traditional life cycle assessment. There are existing methods for measuring GWP in new projects but measuring GWP in the current building stock is limited due to a dearth of as-built drawings and further information on existing building stock. Two challenges prevent understanding of how reused building components affect the net environmental impact: no consensus on a method currently exists for calculating the GWP of reused components, and documentation is usually lacking the volume and material data of existing components in buildings. From these issues, the research question arises: how can we extract the estimated volume of metal structural elements to calculate their GWP in buildings with no documentation?

1.1 *Review: Reality capture for reuse and volume estimation*

Reality capture technologies, such as Lidar laser scanning and photogrammetry (photographic image analysis), are increasingly used in the architecture, engineering, and construction industry for applications such as construction progress monitoring (Dimitrov and Golparvar-Fard 2014, Bosché *et al.* 2015), continuous site inspection (Hutter *et al.* 2018), interior mapping (Tchapmi *et al.* 2017), and scan-to-BIM (Pătrăucean *et al.* 2015, Iglesias *et al.* 2019). Although work is emerging on reality capture for circular construction (Xiong *et al.* 2022), building component volume estimation has yet to be thoroughly explored (Xu *et al.* 2021).

A common volumetric application of Lidar is for estimating volume change over time in planar surfaces by integrating point-to-point distances (Puente *et al.* 2013). Similar bulk volume estimation, such as for stockpiles or excavation, is built from the summation or integration of a resulting digital surface model (Manish *et al.* 2022). For geometries with clear axes, volumes are estimated through a series of slices and profiles along their length (Chang *et al.* 2017, Terryn *et al.* 2022). For more complex geometries, volumes are read from an intermediate mesh, generated, for example, by Delauney triangulation (Zhang and Yang 2019), convex hulls and alpha shapes (Terryn *et al.* 2022), or Poisson surface reconstruction (Ma *et al.* 2020). Voxel-based (volumetric cubic grid) approaches have been applied in domains with irregular density complexity (Kim *et al.* 2016). Finally, additional domain information may be integrated, such as by combining surface segmentation with associated material volumes for typical building typologies, such as the depth of different materials in walls (Heisel *et al.* 2022). Due to the difficult geometry of the web and flanges of structural metal, a voxel-based approach is best suited and explored in this paper.

1.2 *Review: Calculating embodied carbon of reused components*

One output from the life cycle assessment of structures is the GWP, measured in carbon dioxide equivalent emissions (CO₂-eq). Embodied carbon is the sum of greenhouse gas emissions released outside of the operation stage. It is used interchangeably with GWP in this paper, as both measure the relative impact of a given greenhouse gas on global warming. Existing research has explored how to measure the embodied carbon values of specific building structures to aid early design-stage decisions (De Wolf *et al.* 2014, Iuorio *et al.* 2015). An exposition of relative environmental savings in reusing steel elements demonstrates environmental savings and the relatively low impact of transportation (Brütting, Vandervaeren, *et al.* 2020). A consensus is lacking, however, on how to best calculate and compare the environmental impact of reused building elements (Hoxha and Fivet 2018, De Wolf *et al.* 2020).

This research focuses on the reuse of structural metal components due to the existing research precedent, modularity, and ease of disassembly. Although structural steel typically consists of a very high amount of recycled content (Iuorio *et al.* 2019), there are continuing efforts to focus on component reuse to remove the added energy demands of melting and recasting. Validation of the process of reusing steel components can be found in various case study analyses (Pongiglione and Calderini 2014, Drewniok *et al.* 2017).

1.3 *The contributions of the work*

How to best assess environmental impact for reused building elements is not agreed upon, but reusing structural building elements has undoubted environmental benefits. This research aims to use Lidar scanning to collect data for estimating volume and GWP savings of in-situ reused structural elements relative to new elements. As mesh-based analysis methods have low accuracy and would be difficult to use for this domain, a voxel-based volume estimation method is explored, compared to ground truth volumes, and after testing on a site with known structural volumes applied to a more difficult site. The results of this research will contribute to a growing body of knowledge on the relative environmental impacts of reusing steel building components as well as how component volume calculations can be supplemented with laser scanning.

2 CASE STUDY DESCRIPTION

This research examines two different structures of reused structural elements, the first being a recent steel construction with known structural volumes used as a baseline for the volume estimation techniques. The Kopfbau Halle 118 building (K118) is a building expansion project in Winterthur, Switzerland completed in 2021 under the architecture firm Baubüro in situ AG. Reusing structural and facade materials in the expansion reduced the carbon footprint from construction by around 60%. K118 uses a standard steel girder system with a maximum span of 8.5 m, 1.4 m on center, and a total floor plan area of 230.4 m². Prior work in (Brütting, Senatore, *et al.* 2020) looked into the design process using the same stock of steel elements used in K118.

The second structure is in the Grand Café Horta in Antwerp, Belgium, which includes a unique iron portal frame structure in art nouveau style. The café's Art Nouveau Room contains nine cast iron portal frames of differing heights and degrees of completeness, and three half-portals originally designed by the architect Victor Horta from 1895–1899 for the Maison de Peuple. Documentation of the frame is limited. The original Maison du Peuple was deconstructed in 1965, and the trusses were eventually reused in the construction of the Art Nouveau Room in 2000. The current structure is 46.1 m long, 16.3 m wide, and 10.5 m high. Each truss is an open web non-continuous portal frame, spaced 5.2 meters apart. Although the design styles and materials differ, these buildings were chosen because they both had exposed frames of reused structural metal and the developed method can be used on both to explore GWP.

3 METHODOLOGY

3.1 *Data collection and processing*

The volume estimation strategy of structural metal for the embodied carbon calculation employed here covers three main steps. First, raw point cloud data is collected using terrestrial Lidar scanners. This data is then classified and segmented to separate only the points representing the metal structure. Automated segmentation was considered outside this study's scope; the clouds were manually segmented to correspond to the best possible output from automated segmentation. Lastly, the subset of the cloud is geometrically analyzed to produce the final volume estimation

3.1.1 *Approach for K118*

One floor of the K118 building was selected as the test site, wherein most of the steel structure was left exposed with relatively little interior clutter (Figure 1). Scanning was conducted using a Leica RTC360 Lidar scanner. 24 captures were taken over two hours, with a total raw cloud size of 102 million points. The manufacturer software Leica Cyclone was used for registration. Reflection noise was cleaned by manual cropping, and no downsampling was performed as it may have induced aliasing errors with the voxel analysis strategy. The cloud was manually segmented to produce a test cloud containing only the steel points, resulting in 10 million points for analysis (Figure 1). The ground truth steel volume was derived from the original construction drawings, extracted from a model produced with Revit.



Figure 1. Interior view (left) and captured point cloud (right) for K118 (edited for steel visibility).

3.1.2 *Approach for Café Horta*

The Art Nouveau Room was captured using a RIEGL VZ-400i terrestrial laser scanner. The space was captured across 32 scans in two hours, producing a raw point cloud of 580 million points. The manufacturer software RiSCAN Pro 2.0 was used for registration. The cloud was manually cleaned and segmented to retain the iron portals. This site contained more prevalent occlusions both at the bases of the trusses and near the ceiling, which the estimation method does not attempt to account for. This resulted in a cloud of 39.9 million points for analysis (Figure 2).

There was significantly less accessible documentation for this site than for K118. The baseline 3D model was instead based on existing historic modeling work drawing on a combination of



Figure 2. Café Horta, interior view (left), captured point cloud after steel segmentation (right).

archival documentation and on-site photogrammetry (Van Laere 2003, Vaeck 2006, De Prins 2016). Typical details were then adapted to the changes in base height along the length of the site.

3.2 Point cloud volume extraction

Given the concave complexity and prevalence of self-occlusions in metal structural geometry, the visible points were directly measured using a voxelization method. Herein, the total space was divided into equal cubic volumes, which were considered filled if they contained any scanned points. The sum of these volumes was considered the raw volume value. The point clouds were pre-rotated to align the major walls to the world axes to reduce aliasing errors. The size of the voxel grid is critical to this estimation, and a range of possible sizes was evaluated between 1 mm and 100 mm. As the ideal size was found to correlate closely with the average web and flange thickness, a heuristic was determined wherein the operator would manually measure a typical element as input. Figure 3 demonstrates the influence of voxel size selection. The middle example is similar to the determined voxel sizes used for the test sites.



Figure 3. Example beam point cloud voxelization: (left to right) under sized, usefully sized, and oversized.

3.3 Global warming potential calculations

Full life cycle assessments are broad in inventory requirements and impact assessment scope, but focusing the assessment to a single impact factor, GWP, increases accessibility for industry to make informed decisions about relative carbon footprint of building materials (Bala *et al.* 2010, De Wolf *et al.* 2014, 2020). Cradle-to-gate GWP of structures can be calculated by multiplying two variables: structural material quantity (SMQ) and embodied carbon coefficients (ECC), as demonstrated in Equation (1) below (De Wolf *et al.* 2014):

$$SMQ (kg_m/m^2) * ECC (kg_{CO_2e}/kg_m) = GWP (kg_{CO_2e}/m^2) \quad (1)$$

SMQ can be calculated from the volume of material, the density of the material, and the floor area of the structural system. The ECCs, in this case, capture only the embodied emissions in the product life cycle stages A1–A3 (SIA 2020). ECCs differ depending on the data source. To stay consistent with the chosen environmental impact method and location for one of the buildings, the ECCs used are from the Swiss KBOB (Koordinationskonferenz der Bau- und Liegenschaftsorgane der öffentlichen Bauherren) database.

The method for calculating the GWP of reused components is not straightforward. Research done by De Wolf *et al.* (2020) compares six different environmental impact allocation methods for building components reused over n life cycles. This paper used one method derived from the Swiss Society of Engineers and Architects (SIA) 2032 norms to demonstrate the GWP reduction

associated with reusing building components. The adapted SIA 2032 method compares the total time of use to the time of expected use (design use) as a factor for the ECC. For calculating the environmental allocation of previous life cycle(s), one takes the percentage of actual use over design use. For the current life cycle, if combined actual use has exceeded design use, then the allocation is zero. If combined actual use is less than design use, then the allocation is proportional to the projected remaining years of actual use over design use.

Additionally, using the SIA 2032 norms, all building components have a maximum of 60 years of design use (SIA 2020). This value is arbitrary and may not correspond to actual life cycle but helps normalize comparisons. The first life cycle of the Café Horta structure was in use for 66 years until it was dismantled in 1965. Its second life cycle (in use since 2000) equates to an extra 22 years at the time of this study. The structural steel used in K118 was only in use for 15 years in its first life cycle and has been in use since 2021 for its second life cycle. Therefore, considering a 60-year design life, significant GWP is allocated in the reused K118 building elements due to its very short initial life span.

4 RESULTS

4.1 Validation of the volume estimation approach

While testing voxel sizes between 1 mm and 100 mm, 10 mm was found to produce the least error for K118. This roughly correlates with the typical web and flange size on site, matching the chosen heuristic measurement. The density of structural steel is approximately 7850 kg/m^3 , thus the total mass of steel reused in the K118 site is approximately 13,229 kg. In the Grand Café Horta site, the best voxel size was found to be 7 mm, likewise in the range of flange sizes present on the site. The best-estimated volume from existing records was calculated at 4.168 m^3 , while the best voxel volume estimate was 3.771 m^3 . However, the volume from estimated records had lower confidence due to less documentation. Table 1 shows a summary of the volume values extracted from documentation of both buildings compared to the estimated volume from the scanning method, plus a percentage error.

Table 1. Comparison of estimated and calculated structural metal volume.

	Raw Point Count	Segmented Point Count	Volume from Documentation	Volume from Scan	Volume Error
Project	millions	millions	m^3	m^3	%
K118	102	10.2	1.698470	1.685224	0.78
Café Horta	580	39.9	4.168164	3.771370	9.51

4.2 Results from GWP analysis

4.2.1 SMQ calculation

For the structural material quantities, information had to be collected not only on the total volume of the structural metals but also on the floor plan area and material density. The floor

Table 2. Structural material quantities per project.

Project	Location	Structural Material	Material Density	Total Volume	Floor Plan	SMQ
			kg/m^3	m^3	m^2	kg/m^2
K118	Switzerland	Steel	7850	1.69847	230.4	57.87
Café Horta	Belgium	Cast Iron	7300	4.16816	751.4	40.49

plans from the architects of K118 and some general information on the Café Horta building were used to calculate the floorplan. The results can be seen in Table 2 below:

4.2.2 GWP results for new material verse reused

Following Equation 1, the GWP of the structures assuming new material was used and calculated by multiplying the ECC and SMQ of the materials. The ECC values used for the GWP calculation are drawn from the 2022 life cycle assessment data published by KBOB. The product stage emissions for steel profiles are 0.731 kg CO₂-eq/kg_m, and the product stage emissions for cast iron are 2.1 kg CO₂-eq/kg_m. Note the emissions for cast iron are based off current production values, likely, the impact from the original manufacturing at the end of the 18th century would be worse. The resulting GWP calculations for the structural systems assuming new components were used are reported below in Figure 4. The GWP values assuming new building components are 42.30 kg CO₂-eq/m² for K118 and 85.04 kg CO₂-eq/m² for Café Horta. Figure 4 shows the calculated GWP of the actual structures with reused components with the method adapted from SIA 2032. The GWP values of the actual reused building components are 31.73 kg CO₂-eq/m² for K118 and 0.00 kg CO₂-eq/m² for Café Horta. Reusing elements reduces GWP by 25% and 100% for K118 and Café Horta, respectively.

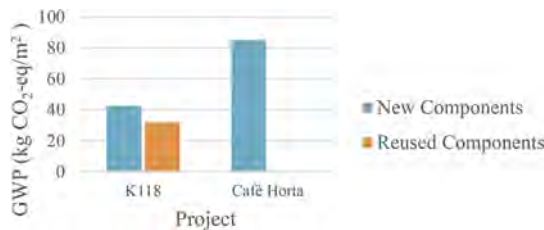


Figure 4. Global warming potential for new and reused components per project.

5 DISCUSSION

The estimation method achieves good accuracy in a setting with strong point coverage on all surfaces for K118. The voxel method's reliance on visible areas and lack of extrapolation necessitates taking many scans on site to avoid high occlusion scenes. While the method would not be strongly affected by small amounts of noise in the segmentation, consistent confusion by the model would quickly compound across the entire cloud. The effects of high occlusion were evident in the higher error for Café Horta, and the unseen points are consistent with the volume underestimation, which probably contributed to the 9.51% error. Additionally, though the chosen 7 mm voxel size falls within the set of flange sizes for this site, increasing component variation typically necessitates increasingly frequent spot checks for verification.

The design specifics also affect the necessity of the method. While a single-story space with standard components such as K118 could be measured and calculated manually, structures with significant height and complexity would be less tenable and benefit more from automation.

A thorough embodied carbon analysis of reused building elements should account for other stages in the life cycle. Hidden carbon costs include intermediate transportation and potential remanufacturing, which are neglected when using the SIA 2032 method for reuse. However, research demonstrates transportation has a relatively low impact on the total embodied carbon of building components (Seo *et al.* 2015, De Wolf *et al.* 2018, Brütting, Vandervaeren, *et al.* 2020).

The use of the adapted SIA 2032 method prioritizes reusing building components that have already served longer lifespans: when the predicted service life is surpassed, GWP impacts on additional life cycles are nullified. The calculations within this paper show that with the chosen allocation method, the reuse of the Café Horta structural elements contributed no additional environmental impact, thus incentivizing its reuse and preserving cultural heritage. In contrast, the beams in K118 were only in use for about 15 years, thus allocating more GWP to

its recent life cycle. Lastly, although the chosen structures for this work are both exposed metal frames, **a 1-to-1 comparison of GWP between the buildings is not reasonable** because material choice affects the ECC, the intended structural use case and optimization are different.

5.1 Limitations of the approach

Although the findings of the proposed approach are promising, there are some limitations in the method. Laser scanning requires the structural components to be visible, but the elements are encased in many structural systems, thus preventing this approach. In addition, the developed technique for volumetric analysis contains opportunities for human error during the scanning, spot checks, and manual segmentation. Lastly, our approach was only used for homogenous materials; calculating GWP for hybrid structural systems would be more complex.

6 CONCLUSION

This paper demonstrated how to calculate the environmental savings from reused structural metal without prior documentation on the components. Lidar scanning helped capture the point cloud of exposed structural elements and develop a method to extract the component volume. (Previous literature focused on using Lidar as a method for tracking more raw material volumes, but Lidar had not been used for component volume extraction.) The second part of this paper conducted a GWP analysis of the scanned components and compared the savings of carbon dioxide equivalent emissions from reusing the components relative to using new components of the same volume. The latter work supplements existing literature by providing case-study applications and demonstrates the impacts of reusing structural components.

The calculation of material volume partially informs post hoc embodied carbon analyses of structures with lost or no prior documentation. This work aims to inspire future work on models based on artificial intelligence (AI) for structural point cloud segmentation and volume estimation for a more rapid analysis of buildings. Future research will focus on the automation and error resistance of the process. Deep learning approaches, currently applied for various interior classes, can be evaluated for automatic classification and segmentation of structural elements in different contexts. Semantic analysis of the voxel grid may allow for automatic calculation of the ideal voxel size without manual spot checks, as well as the detection and mitigation of occlusion areas. This work successfully demonstrates a reality capture workflow to estimate in-situ building component volumes in order to calculate GWP savings from reusing components.

REFERENCES

- Bala, A., Raugei, M., Benveniste, G., Gazulla, C., and Fullana-i-Palmer, P., 2010. Simplified tools for global warming potential evaluation: when ‘good enough’ is best. *The International Journal of Life Cycle Assessment*, 15 (5), 489–498.
- Bosché, F., Ahmed, M., Turkan, Y., Haas, C.T., and Haas, R., 2015. The value of integrating Scan-to-BIM and Scan-vs-BIM techniques for construction monitoring using laser scanning and BIM: The case of cylindrical MEP components. *Automation in Construction*, 49, 201–213.
- Brütting, J., Senatore, G., Schevenels, M., and Fivet, C., 2020. Optimum Design of Frame Structures From a Stock of Reclaimed Elements. *Frontiers in Built Environment*, 6.
- Brütting, J., Vandervaeren, C., Senatore, G., De Temmerman, N., and Fivet, C., 2020. Environmental impact minimization of reticular structures made of reused and new elements through Life Cycle Assessment and Mixed-Integer Linear Programming. *Energy and Buildings*, 215, 109827.
- Chang, W.-C., Wu, C.-H., Tsai, Y.-H., and Chiu, W.-Y., 2017. Object volume estimation based on 3D point cloud. *In: 2017 International Automatic Control Conference (CACCS)*. 1–5.
- De Prins, M., 2016. La Maison du Peuple by Victor Horta : a structural analysis for the reconstitution. Université libre de Bruxelles.
- De Wolf, C., Brütting, J., and Fivet, C., 2018. Embodied Carbon Benefits of Reusing Structural Components in the Built Environment. Presented at the PLEA 2018 HONG KONG.

- De Wolf, C., Hoxha, E., and Fivet, C., 2020. Comparison of environmental assessment methods when reusing building components: A case study. *Sustainable Cities and Society*, 61, 102322.
- De Wolf, C., Iuorio, O., and Ochsendorf, J., 2014. Structural Material Quantities And Embodied Carbon Coefficients: Challenges And Opportunities. In: *Proceedings of the 5th Annual School of Architecture Symposium*. Portland State University, Portland, OR, USA, 309–328.
- Dimitrov, A. and Golparvar-Fard, M., 2014. Vision-based material recognition for automated monitoring of construction progress and generating building information modeling from unordered site image collections. *Advanced Engineering Informatics*, 28 (1), 37–49.
- Drewniok, M.P., Dunant, C.F., Allwood, J.M., and Cullen, J.M., 2017. Successful steel reuse in the UK – key aspects why it happened.
- Heisel, F., McGranahan, J., and Boghossian, A., 2022. ScanR: A composite building scanning and survey method for the evaluation of materials and reuse potentials prior to demolition and deconstruction. In: *IOP Conference Series: Earth and Environmental Science*. IOP Publishing, 012012.
- Hoxha, E. and Fivet, C., eds., 2018. Environmental Benefits when Reusing Load-Bearing Components in Office Buildings: A Case Study. In: *Proceedings of the PLEA 2018 Conference*. Presented at the 34th PLEA Conference, ‘Smart & Healthy within the 2 degree limit’.
- Hutter, M., Diethelm, R., Bachmann, S., Fankhauser, P., Gehring, C., Tsounis, V., Lauber, A., Guenther, F., Bjelonic, M., Isler, L., Kolvenbach, H., Meyer, K., and Hoepflinger, M., 2018. Towards a Generic Solution for Inspection of Industrial Sites. In: M. Hutter and R. Siegwart, eds. *Field and Service Robotics*. Cham: Springer International Publishing, 575–589.
- Iglesias, J.L., Severiano, J.A.D., Amorocho, P.E.L., Val, C.M. del, Gómez-Jáuregui, V., García, O.F., Royano, A.P., and González, C.O., 2019. Revision of Automation Methods for Scan to BIM.
- Iuorio, O., Napolano, L., Fiorino, L., and Landolfo, R., 2019. The environmental impacts of an innovative modular lightweight steel system: The Elissa case. *Journal of Cleaner Production*, 238, 117905.
- Iuorio, O., Wolf, C.D., and Ochsendorf, J., 2015. Embodied carbon of long span roofs. *Proceedings of IASS Annual Symposia*, 2015 (4), 1–11.
- Kim, E., Lee, W.-K., Yoon, M., Lee, J.-Y., Son, Y., and Abu Salim, K., 2016. Estimation of Voxel-Based Above-Ground Biomass Using Airborne LiDAR Data in an Intact Tropical Rain Forest, Brunei. *Forests*.
- Ma, J., Song, R., Han, T., Sanchez-Azofeifa, A., and Basu, A., 2020. Poisson Surface Reconstruction from LIDAR for Buttress Root Volume Estimation. In: T. McDaniel, S. Berretti, I.D.D. Curcio, and A. Basu, eds. *Smart Multimedia*. Cham: Springer International Publishing, 463–471.
- Manish, R., Hasheminasab, S.M., Liu, J., Koshan, Y., Mahlberg, J.A., Lin, Y.-C., Ravi, R., Zhou, T., McGuffey, J., Wells, T., Bullock, D., and Habib, A., 2022. Image-Aided LiDAR Mapping Platform and Data Processing Strategy for Stockpile Volume Estimation. *Remote Sensing*, 14 (1), 231.
- Pătrăucean, V., Armeni, I., Nahangi, M., Yeung, J., Brilakis, I., and Haas, C., 2015. State of research in automatic as-built modelling. *Advanced Engineering Informatics*, 29 (2), 162–171.
- Pongiglione, M. and Calderini, C., 2014. Material savings through structural steel reuse: A case study in Genoa. *Resources, Conservation and Recycling*, 86, 87–92.
- Puente, I., Solla, M., Gonzalez, H., and Arias, P., 2013. Validation of mobile LiDAR surveying for measuring pavement layer thicknesses and volumes. *NDT & E International*, 60, 70–76.
- Seo, S., Kim, J., Yum, K.-K., and McGregor, J., 2015. Embodied carbon of building products during their supply chains: Case study of aluminium window in Australia. *Resources, Conservation and Recycling*.
- SIA, 2020. SIA 2032:2020 Graue Energie - Ökobilanzierung für die Erstellung von Gebäuden.
- Tchapmi, L., Choy, C., Armeni, I., Gwak, J., and Savarese, S., 2017. SEGCloud: Semantic Segmentation of 3D Point Clouds. In: *2017 International Conference on 3D Vision (3DV)*. Presented at the 2017 International Conference on 3D Vision (3DV), 537–547.
- Terryn, L., Calders, K., Bartholomeus, H., Bartolo, R.E., Brede, B., D’hont, B., Disney, M., Herold, M., Lau, A., Shenkin, A., Whiteside, T.G., Wilkes, P., and Verbeeck, H., 2022. Quantifying tropical forest structure through terrestrial and UAV laser scanning fusion in Australian rainforests. *Remote Sensing of Environment*, 271, 112912.
- Vaeck, K., 2006. Digitale architectuuranalyse: Horta’s Volkshuis gereconstrueerd. KU Leuven.
- Van Laere, K., 2003. Studie en computersimulatie van Horta’s Volkshuis (1899). Ghent University.
- Xiong, Z., Gordon, M., Byers, B., and De Wolf, C., 2022. Reality capture and site-scanning techniques for material reuse planning. Presented at the IASS Annual Symposium and Asia-Pacific Conference on Spatial Structures: Innovation, Sustainability and Legacy (IASS/APCS 2022), 88.
- Xu, Y., Tong, X., and Stilla, U., 2021. Voxel-based representation of 3D point clouds: Methods, applications, and its potential use in the construction industry. *Automation in Construction*, 126, 103675.
- Zhang, W. and Yang, D., 2019. Lidar-Based Fast 3D Stockpile Modeling. In: *2019 International Conference on Intelligent Computing, Automation and Systems (ICICAS)*. 703–707.

Reuse of existing reinforced concrete beams: Exploration of residual mechanical characteristics and measure of environmental impact

A. Lachat & A. Feraille

Navier, École des Ponts, University Gustave Eiffel, CNRS, Marne-la-Vallée, France

T. Desbois

Cerema, University Gustave Eiffel, UMR MCD, Sourdun, France

A.S. Colas

GERS-RRO, University Gustave Eiffel, University Lyon, Lyon, France

ABSTRACT: With a view to developing reuse, reinforced concrete beams were retrieved from a deconstructed building, and tested by 3-point bending tests in order to measure their residual strength. With a residual strength of about 70% of the presumed initial strength in the worst case, deconstruction by beam sawing appears to be an interesting solution for the recovery of deconstructed buildings. For a low resistance loss, LCA of these solutions highlights that the reused beam has globally less impact than a new beam. Additional studies need to be conducted to increase the robustness of these conclusions.

1 INTRODUCTION

Scientific literature shows that the building materials sector is the third most CO₂-emitting industrial sector in the world and in the European Union. Parrot (2002) states that the building materials sector is responsible for 10% of total anthropogenic greenhouse gas (GHG) emissions, the majority of which being related to concrete manufacturing.

Moreover, concrete is a material that is extensively used around the world, particularly in the construction industry. In France in 2018, more than 40 million cubic meters of ready-mix concrete (RMC) were produced, representing 6.8% more than in 2010 (UNICEM & SNBPE 2020).

In order to mitigate the resource-intensive consumption of this sector (and all sectors in general), waste hierarchy has been introduced by European Union since 2008 (European Parliament 2008). It prioritizes reuse of waste over recycling. Hence, reuse seems to be the best waste recovery method and is promoted by governments. Moreover, scientific literature identifies numerous examples of reuse in history (Benoit et al. 2018; Ghyoot et al. 2018).

The reuse in buildings affects lots of parts, from the interior installation to the structural work while passing (in a non-exhaustive way) by the frontages, the joineries, the grounds, the partitions and the technical elements. Nevertheless, the reuse of structural elements are less common (Küpfer & Fivet 2021).

For cast-in-place concrete elements (and more broadly, structural concrete elements), reuse is an “exceptional practice”. However, for reasons of deconstruction in dense urban areas, “careful dismantling” (Küpfer & Fivet 2021) techniques have been developed.

In this context, concrete seems to be a strategic candidate for reuse: its manufacture has a high environmental impact and it is widely used. Thereby the objective is to reduce the quantity of waste, as well as the use of natural resources (aggregates and cement) which induces reduction of GHG emissions from natural resources production.

This study aims to show to what extent reuse of reinforced-concrete structures from deconstruction is environmentally friendly.

First, an exploratory study on the residual strength of a deconstructed beam is undertaken: two beams are subjected to a 3-point bending test. Then, a Life Cycle Assessment (LCA) of different scenarios of beams construction is carried out, allowing to compare a reused beam to a new beam with the same functional unit (same resistance).

2 DETERMINATION OF THE RESIDUAL RESISTANCE OF A DECONSTRUCTED CONCRETE BEAM

To evaluate the environmental impact through the LCA, a functional unit has to be defined in order to compare end of life scenarios. Consequently, the mechanical resistance of structure deconstructed should be preliminary determined. This exploratory study is based on a case study of a cast-in-place concrete beam which has been deconstructed from a building under renovation in France (Figure 1). No particular protocol is set up in relation to a deconstructed beam for landfill for this case study.

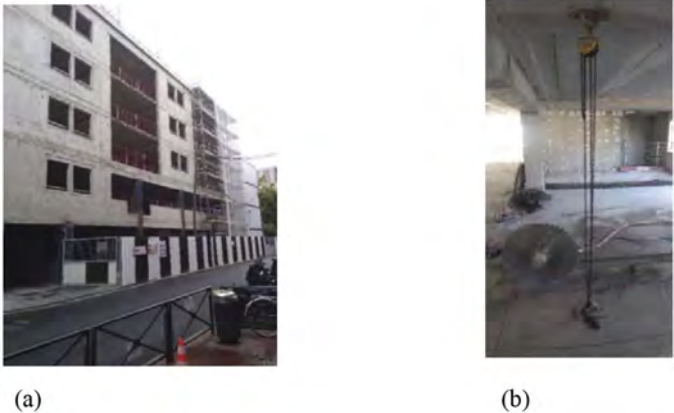


Figure 1. Picture of the building during partial dismantling (a), dismantling process of the concrete beams (b) (pictures A. Lachat).

2.1 3-point bending test

The objective of this study is to obtain a first value of loss of resistance of such element and to determine the behavior of a deconstructed element from loading to failure (elastic and plastic limits, and cracking mechanism). To this end, 3-point bending tests were carried out (Figure 2) using a hydraulic press of 450 kN at the Navier Laboratory. Figure 3 presents the beam on the test device.

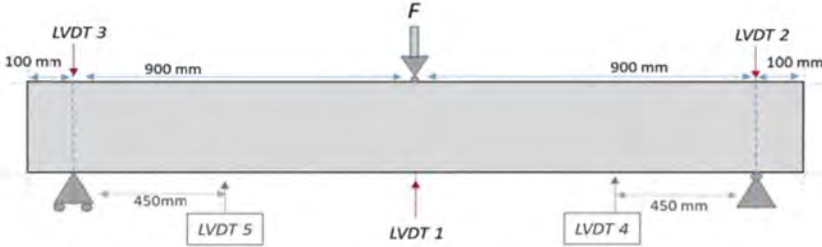


Figure 2. Instrumentation diagram of the 3-point bending test.

The instrumentation of the device is as follows:

- The force F applied by the cylinder, measured by the press;
- The deflection f at the center of the beam and at two points halfway between the center and the supports, measured by Linear Variable Differential Transformer (LVDT) displacement transducers with a stroke of 2 cm (LVDT 1, 4 and 5);
- The parasitic displacements at the supports (LVDT 2 and LVDT 3).

This test provides an estimation of the residual strength of the beam. The force-displacement curve is shown in Figure 4. Three unloading were performed during the test.

The curve is consistent with the bending studies performed on new elements (Ajdukiewicz & Kliszczewicz 2007, Omary et al. 2014) and theoretical studies (Fleury & Mouterde 2019, Mosley et al. 1996). Three main phases can be identified:

- **Quasi-elastic phase** (phase 1): At low loading, concrete and steel materials are in the linear elastic domain. The shear force is taken up by the vertical reinforcement (frames). During this phase, the displacement is almost reversible.
- **Elastic steel phase** (phase 1 bis): Cracks appear and propagate within the beam. The deflection becomes more important. The displacements are irreversible; a residual deflection is observed after unloading. The cracks are oriented at about 45° , reflecting the combined shear force and bending moment.
- **Plastics steel phase** (phase 2): The cracks widen more strongly and the deflection increases more significantly. Tensile reinforcements go through a plastic phase.
- **Beam failure**: In the face of tensile cracking, the compressed concrete section becomes too small. The concrete cracks in compression at the level of the upper fiber. The beam gradually loses strength.



Figure 3. Picture of the instrumented test device (picture A. Lachat).

Beam failure appears at 426 kN, compared with the theoretical value 494 kN (according to the EN 1992-1-1 standard (EUROCODE 2 2005)). The loss of resistance is at most of 14% for this beam. This value represents an upper bound due to uncertainty on the quality of the reinforcing steel (if $R_e = 500\text{MPa}$). For a more probable value of steel resistance ($R_e = 450\text{MPa}$), the loss of resistance of the beam is only 8%. The same test was carried out with a similar beam, and the upper bound loss was less than 30% (the uncertainties regarding the layout of reinforcing steel were higher). These tests (resistance and durability) show that deconstructed beams have an interesting mechanical potential for reuse. The implementation of a rigorous protocol for deconstruction, transport and reconstruction would allow for the reliability and optimization of the residual strength.

2.2 Carbonation test

In addition to the residual strength evaluation, phenolphthalein tests were performed in order to assess the durability of the beam. These tests consist in measuring punctually the progress of carbonation on the beams, and thus to estimate the risk of corrosion.

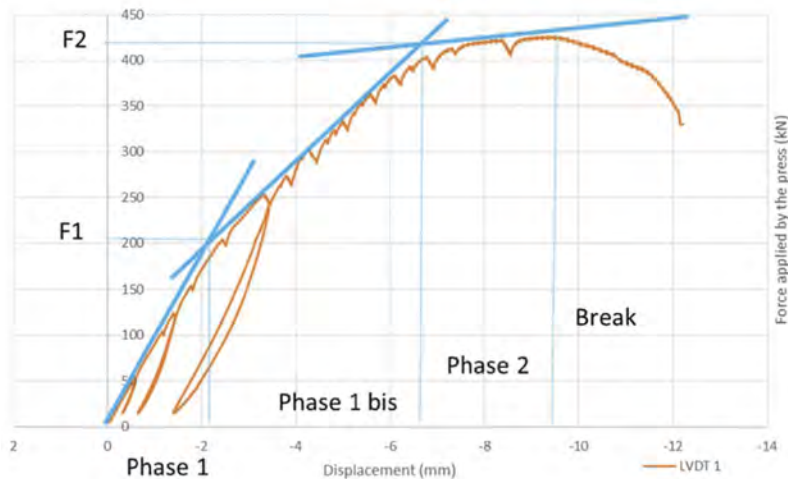
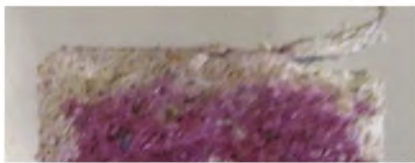


Figure 4. Value of the force applied as a function of the displacement for the central LVDT sensor and highlighting of phases.

The phenolphthalein test is carried out on the exposed faces of the beam: top face (ground side) (Figure 5a) and bottom face (ceiling side of the lower floor) (Figure 5b). It can be seen on these photographs that the carbonate section (none colored) is very small: less than 0.5 mm. However, the coating of the reinforcement is 2 cm which leaves a margin of evolution of the carbonation of more than 1 cm before there is a risk of initiation of corrosion.



(a)



(b)

Figure 5. Photograph of phenolphthalein tests: (a) surface mortar, upper part of the beams (on the flooring side); (b) concrete on the underside of the beam (on the false ceiling side) (test realization: Cerema; pictures: A. Lachat).

3 EVALUATION OF ENVIRONMENTAL IMPACT

The exploratory mechanical study presented in the previous section enabled to prove that reuse of concrete structures (concrete beams) is mechanically feasible, and to quantify the corresponding loss of resistance. Evaluation of the environmental impacts is consequently now achievable. Reuse solution will be compared with a new construction solution.

3.1 Materials and methods

The objective of this part is to compare, resorting to the Life Cycle Assessment (LCA), these three following fictitious beams:

- A reused beam, named *Breu* (Beam reused),
- A new constructed beam made from raw materials, named *Bvir* (virgin),
- A new constructed beam made with recycled aggregates, named *Brec* (recycled).

The functional Unit chosen is “to construct/ install a beam allowing to cross a span of 1.80 m and to support a maximum load (point in its center) equal to that of the reused beam (426 kN) for a minimum life span of 50 years”.

The value of resistance is extracted from the case study detailed in section 2. We use the most probable loss of resistance i.e. 8%. New beams are designed according to EUROCODE 2 (2005) and the height of the beam is fixed at 0.36 m.

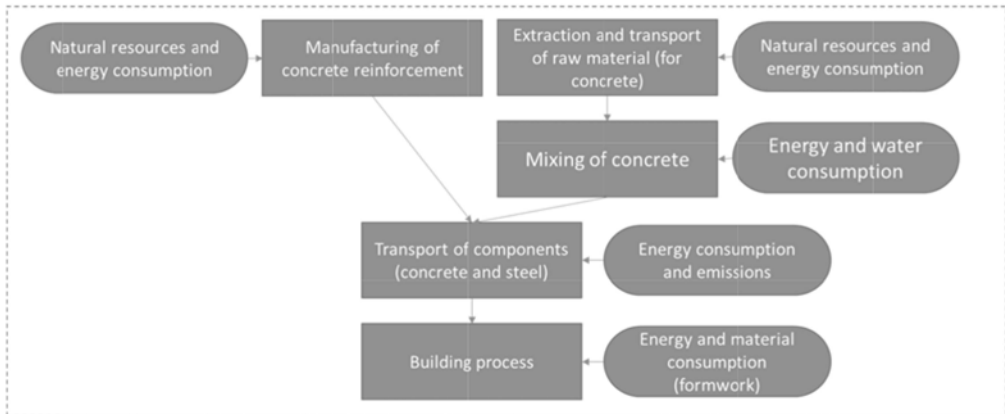


Figure 6. Boundaries of the system for the construction of a new beam from new or recycled aggregates.

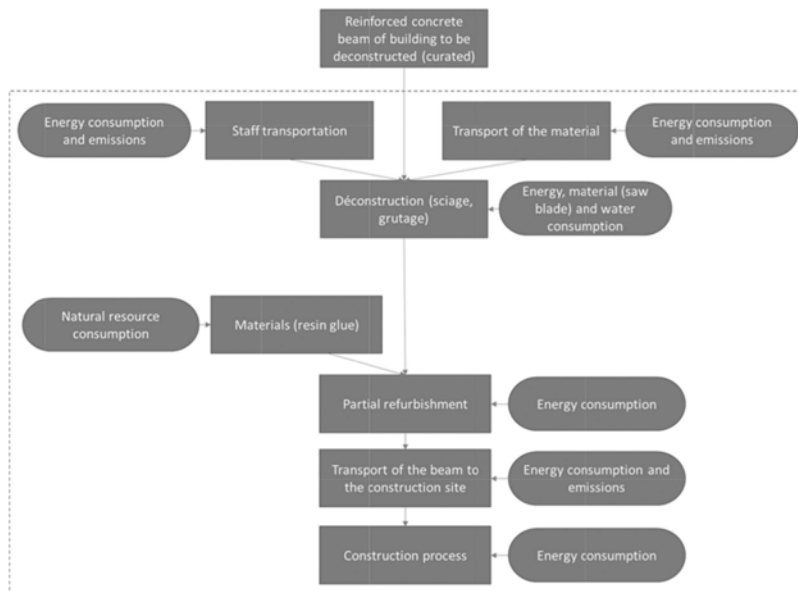


Figure 7. Boundaries of the system for the dismantling and the construction of a reused beam.

The LCA model is constructed according the standard NF EN 15804 and the impact method is NF EN 15804+A1/CN. Modeling is made on the software OpenLCA 1.10 applied on the database Ecoinvent 3.5.

System boundaries are represented on the Figure 7 for the new constructed beams and the Figure 7 for the reused beam.

The intermediate processes are derived from:

- Data from the deconstruction sites of the beams to be re-used;
- Ben Fraj & Idir (2017) for the recycling of aggregates and concrete;
- The SNBPE’s BETie tool (product declaration sheet generator) for new beam construction;
- Bertin (2020) and Brière (2016) for additional data on reuse.

3.2 Results

Results of this LCA are presented on the Figure 8. Reuse solution is the least impacting solution for 5 out of 9 indicators: *soil and water acidification, climate change, water pollution, depletion of abiotic resources (fossils + elements)*. For climate change, the reuse scenario is more than 50% less impactful than the most impactful scenario (new with recycled aggregate) and 50% less impactful than the virgin scenario. Nevertheless, the reuse scenario has a biggest impact on the *photochemical ozone formation* indicator by more than 10% compared to the other scenarios (about 20%). For the three remaining indicators: *ozone depletion, air pollution and eutrophication*, the reuse scenario is of the same order of magnitude as the recycled scenario, taking into account a 10% uncertainty.

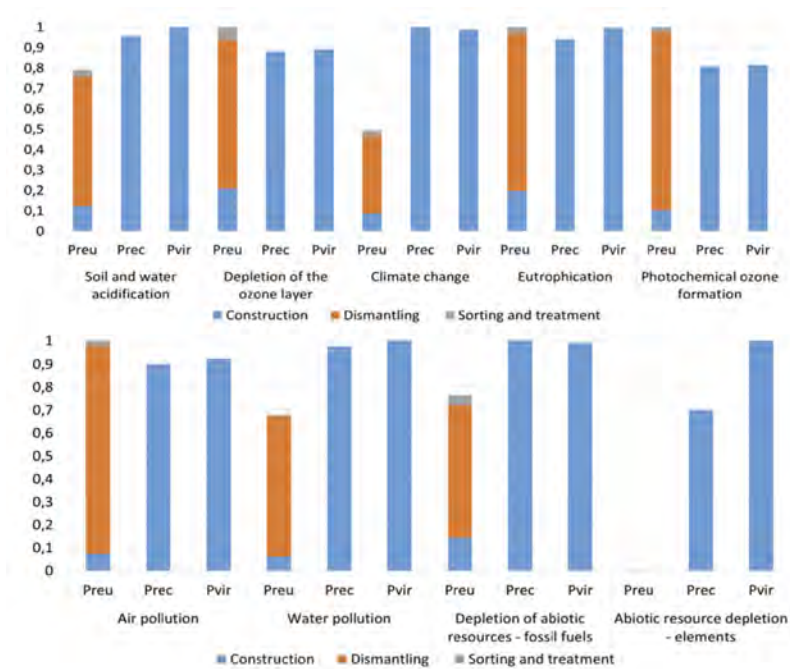


Figure 8. Relative impact of the three scenarios according to NF EN 15804+A1 impact indicators.

Thus, it can be said that the reuse of reinforced concrete structural beam seems beneficial for most indicators. However, it is necessary to conduct more studies to determine the loss of strength of the beam after deconstruction. Indeed, if the loss is too high, the fabrication of the new beam (with less material) could be equivalent to the reused beam. This is the subject of a sensitivity study in section 3.3.

The impact for the reuse scenario is mostly related to the end of life of the structure within the previous building (sorting and treatment). The construction phase contributes at most 24% of the total impact (for the *water pollution* indicator). This is consistent with the principle of reuse which, by definition, requires limited reconditioning. Consequently, in order to limit

the impact of reuse scenario, it is necessary to think about the deconstruction phase and in particular on the impact of sawing (or more broadly of the dismantling method).

3.3 Sensibility analysis

Previously, it has been highlighted that, for some indicators, the reused beam is not more virtuous than the new beam. However, the impact of the new beam is strongly linked to the manufacturing of the beam and in particular to its formulation. Thus, the impact may vary if the geometry or the required resistance changes. This sensitivity analysis aims at highlighting the consequences on the result of a modification of the residual resistance of the reused beam (and thus a new beam with different dimension). This is all the more important as the loss of resistance currently used is linked only to a single feedback.

Two alternative scenarios have therefore been constructed:

- *Bvir 0% loss*: a very optimistic scenario where there is no loss when the beam is reused. The equivalent new beam is therefore built identically to the reused beam during its first life (beam resistance of 463 kN).
- *Bvir 15% loss*: a pessimistic scenario where the loss of resistance is almost doubled (15% loss) (beam resistance of 393 kN).

The results of these scenarios are presented on Figure 9. Very strong variations are observed, especially for the scenario without loss of resistance where the increase in *climate change* can reach 50% for the virgin beams. Moreover, with this scenario (*Bvir 0% loss*), reuse becomes less impactful or equal for all indicators (equivalent impact for *photochemical ozone formation*). The scenario with a 15% loss in resistance makes the new beam more competitive with the reused beam.

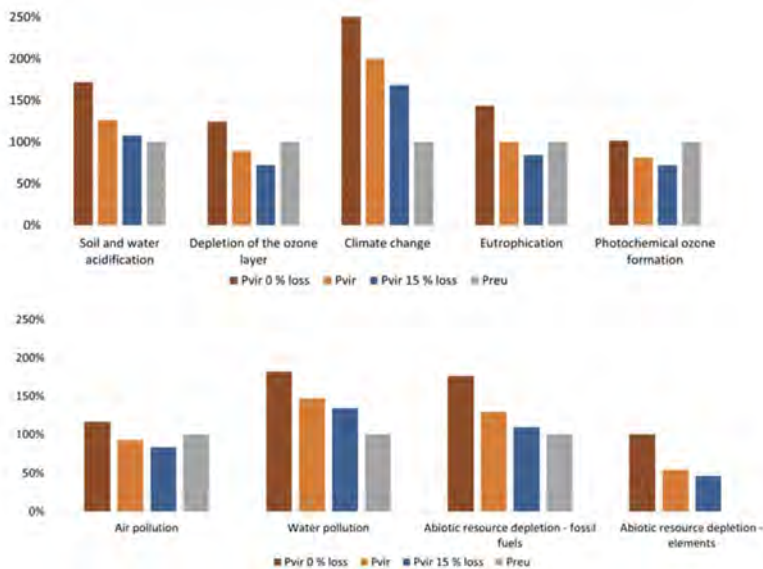


Figure 9. Sensitivity analysis on the strength loss of the reused beam, relativized according to the reused solution except for the last indicator (*Bvir* = 8% loss).

Thus, the new beam becomes less impactful for *eutrophication* and equivalent for *water pollution*. This scenario remains significantly more impactful for the *climate change* indicator. For this indicator, equivalence could be reached for a loss of resistance of about 30%.

The determination of the strength loss has a strong influence on the environmental benefit of the reuse. It is therefore important to determine the residual strength of a reused beam as accurately as possible, which requires a more detailed technical study.

4 CONCLUSION

In order to develop reuse, 3-point bending tests were undertaken on reinforced concrete beams from a deconstructed building in order to measure their residual strength. With a residual strength of about 70% of the initial strength in the worst case, deconstruction by beam sawing appears to be an interesting solution for the recovery of deconstructed buildings.

For low resistance loss, LCA of these solutions highlights the fact that the reused beam has globally less impact than a new beam particularly for the *climate change* indicator but there is a transfer of impact for *water pollution* and *photochemical ozone formation*. Nevertheless, the good result is highly depending on the dismantling process and the loss of resistance.

The reuse of reinforced concrete structural elements is therefore a potential alternative to concrete recycling. Additional studies, including a broader experimental campaign on existing beams and a focus on the influence of the dismantling process, need to be conducted to increase the robustness of the results presented here.

REFERENCES

- Ajdkiewicz, A.B. & Kliszczewicz, A.T. 2007. Comparative Tests of Beams and Columns Made of Recycled Aggregate Concrete and Natural Aggregate Concrete. *Journal of Advanced Concrete Technology* 5, 259–273.
- Ben Fraj, A. & Idir, R. 2017. Concrete based on recycled aggregates – Recycling and environmental analysis: A case study of paris' region. *Construction and Building Materials* 157, 952–964.
- Benoit, J., Saurel, G., Billet, M., Laurenceau, S. & Bougrain, F. 2018. REPAR #2 - le réemploi passerelle entre architecture et industrie, Bellastock, CSTB, ADEME. ed.
- Bertin, I. 2020. Conception des bâtiments assurant leur réversibilité, leur déconstruction et leur réemploi, méthodologie de suivi et évaluation environnementale sur les cycles de vie (PhD Thesis). Paris Est.
- Brière, R. 2016. Etude ACV des chantiers de démolition en vue de la préservation des ressources : focus sur les procédés de transport et de décharge (PhD thesis). Paris Est.
- EUROCODE 2 2005. Calcul des structures en béton Partie 1-1 : Règles générales et règles pour les bâtiments. (NF EN 1992-1-1). AFNOR.
- European Parliament 2008. Directive 2008/98/EC of the European Parliament and of the Council of 19 November 2008 on waste and repealing certain Directives, OJ L.
- Fleury, F & Mouterde, R. 2019. *Comprendre simplement- la résistance des matériaux*, 3ème édition. Editions Le Moniteur.
- Ghyoot, M., Devlieger, L., Billet, L. & Warnier, A. 2018. Déconstruction et réemploi - Comment faire circuler les éléments de construction, Rotor. ed, Presse polytechnique et Universitaire Romande, Lausanne.
- Küpfer, C. & Fivet, C. 2021. *Déconstruction sélective - Construction Réversible: recueil pour diminuer les déchets et favoriser le réemploi dans la construction*. EPFL. ed. Zenodo.
- Mosley, W.H., Hulse, R. & Bungey, J.H. 1996. *Reinforced concrete design to EuroCode 2 (EC2)*, Basingstoke: Macmillan.
- Omary, S., Wardeh, G., Ghorbel, E. & Gomart, H. 2014. Comportement à la flexion des poutres en béton armé à base de graviers recyclés.
- Parrot, L. 2002. Cement, concrete and sustainability. A report on the progress of the UK cement and concrete industry towards sustainability, British Cement Association - Publication Index | NBS. British Cement Association.
- UNICEM & SNBPE, 2020. L'industrie française du béton prêt à l'emploi - édition 2020 (data 2018).

Designing with recovered precast concrete elements

T.S.K. Lambrechts, F.J. Mudge, S.N.M. Wijte & P.M. Teuffel

Technical University of Eindhoven, Eindhoven, The Netherlands

ABSTRACT: In The Netherlands, two shortcomings of the country's building stock have become increasingly prevalent in recent years: high vacancy rates of office buildings (8.2% as of 2022) and a high demand for residential buildings (shortage of up to 315,000 dwellings as of 2022). This paper investigates how the reuse of whole precast concrete elements from office buildings can lead to more sustainable residential building designs. As a case study, suitable 'donor' office buildings and an apartment building design are identified. First, the apartment building design is modified to employ as many suitable recovered elements as possible (while maintaining the original building geometry). This leads to a 69% reduction of new concrete used and a 46% reduction of CO₂ output. Second, the design is adjusted to an optimal grid layout for maximal component reuse. This further improves the outcome to 90% and 60% respectively.

1 INTRODUCTION

The construction industry is considered to be a major contributor to global environmental degradation (Bossink & Brouwers, 1996) – responsible for 42% of annual worldwide natural resource consumption and 30-40% of solid waste generation (de Wit et al., 2020)(Jin et al., 2019). Within the construction sector, the production of concrete requires more raw materials and generates more CO₂ emissions than any other sub-sector (Herczeg & Klaassens, 2014). The production of cement generates 8% of the CO₂ emission by humans (Florea, 2016).

While downcycling concrete (e.g., using crushed concrete in road layer works or as coarse aggregate in new concrete) is a common practice, this does not prevent new concrete and more particular new cement from being used in construction (Durmisevic Elma., 2006). Therefore, it is more effective to reuse the material for the same function or in the highest possible value function. Keeping elements in their original shape may prevent the need for certain steps of the preparation and production process, however, this may cause challenges for conventional transport and storage equipment and processes. This paper investigates possibilities for making the concrete sector more sustainable by exploring the possibilities for reuse of pre-fabricated structural concrete elements.

Previous literature provides inspiration towards this goal. The first case where structural concrete elements were reused on a large scale was in Gothenburg, Sweden, in 1984 where elements from apartment buildings were reused in the construction of freestanding homes (Huuhka et al., 2019). Similarly, in 1986 the five top floors of a residential building in Middelburg, The Netherlands, were deconstructed and the elements used for new housing (Coenen et al., 1990). Another project in The Netherlands took place in Maassluis in 2000, which revealed substantial synchronization issues between deconstruction and reconstruction, thus indicating a need for a set process for determining which buildings are optimal to deconstruct and what the optimal deconstruction process is.

In The Netherlands, there is a relatively high vacancy of office buildings (8.2% as of 2022) (Verhaegh, 2022), while there is a pressing need for housing (shortage of up to 315,000 dwellings as of 2022) (Ministerie van binnenlandse zaken en koninkrijksrelaties, 2022). The best option to increase the number of houses is to transfer office buildings to apartment buildings.

The second best option is to disassemble vacant office buildings and reuse the harvested structural concrete elements in the structure of new apartment buildings. The case study discussed in this paper presents two design approaches for reusing such elements.

2 DESIGN APPROACH

In this study a re-design approach consisting of 8 steps has been developed and is summarized below:

1. Inventory of office buildings: The re-design process starts with an inventory of possible donor buildings. In this case it regards office buildings, which consist of structural precast concrete elements that are (or are expected to become) out of use in the near future. For this study, four office buildings (A to D), located in the Amstel III office park in Amsterdam, are considered. Due to low occupancy, the municipality of Amsterdam launched a project, where a substantial number of office buildings are going to be transformed to residential buildings.
2. Inventory of structural components: An inventory is created containing the precast concrete structural elements from the attained donor buildings. All structures of the four donor buildings use hollow-core slabs (HCS) as floor elements, three of them use precast beams and load bearing façade elements, of which two also use precast columns and walls. The remaining in-situ concrete elements are not considered for reuse. The available number of elements, derived from the inventory can be seen in Table 1.

Table 1. Inventory of available elements in four office buildings.

Building	Beam	Column	Wall	Façade	Slab
A	45	72	50	115	430
B	0	0	0	515	1169
C	138	60	34	131	686
D	84	84	0	0	165

3. Apartment design: An already existing apartment design with 19 units and three stories has been selected and used as the basis for the re-design of the building with a structure consisting of recovered structural elements. To make the process a little bit more challenging in terms of structural stability, the number of stories has been increased from three in the original design to five. The relatively regular floor layout can be seen in Figure 1.

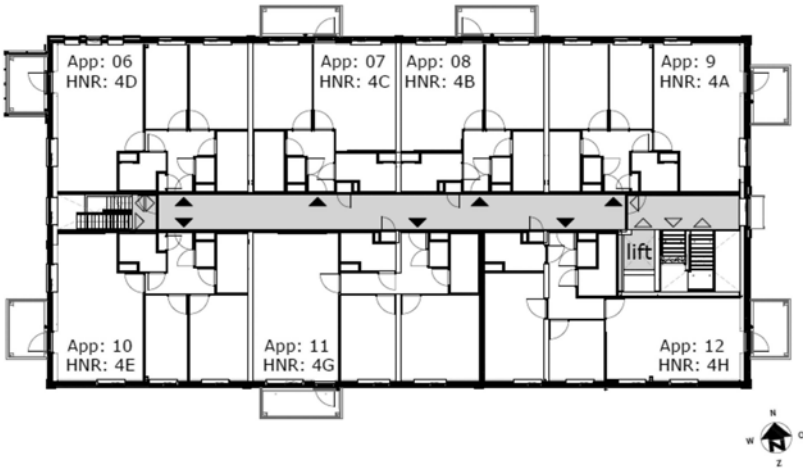


Figure 1. Floor layout of apartment design (de Alliantie, 2019).

4. Determination of the structural characteristics of the apartment: The key structural requirements, such as spans of floor and stability system are determined.
5. Selection of suitable elements: An investigation based on step 4 is carried out, in which the suitable elements from the donor building(s) are selected. A distinction will be made between elements which meet the requirements, elements that need adaptations, and elements not suitable for re-use.
6. Start of re-design approach: This step has a more detailed focus on the structural requirements. A distinction can be made between the following two approaches:
 - a. Using recovered elements and following the intended design as close as possible
 - b. Using recovered elements and adapting the intended design to maximize the number of re-used elements
7. Re-evaluate the design: Once the initial implementation of re-used elements has been made, the whole design needs to be checked again as the elements influence the other parts of the building (e.g., extra load due to bigger dimensions of recovered elements).
8. Redesign 2: The final step entails the iteration of steps 6 and 7 to further maximize reuse potential and eliminate possible problems.

3 CASE STUDY

3.1 Available office buildings

The information on the four office buildings is retrieved from Alexandros Glias's master dissertation (Glias, 2013). The buildings range from three to eight floors and were built between 1983 and 1988.

3.2 Apartment design

The apartment design is based on a three-story apartment building in Eemnes. The structure consists of precast concrete walls and HCS. Stability is ensured by the walls, core and diaphragm action of the floors. As mentioned previously, the re-design consists of five floors instead of three.

3.3 Goals

The main goal is to put the two design approaches into practice in a case study. The first re-design approach is to match the original apartment building design as closely as possible. This makes it unlikely that a suitable replacement for every precast concrete element will be found or the need for large adaptations rises and the missing pieces will be filled in with newly constructed elements.

Table 2. Goals of design approach.

Aspect	Redesign approach 1	Redesign approach 2
Structural quality	The reused concrete structure is technically possible and full fills requirements with respect to safety and serviceability.	
Material use	Significant reduction in new material used.	Even larger reduction in new material used.
	Significant reduction of construction waste.	Even larger reduction in construction waste.
CO ₂ emissions	Significant reduction in CO ₂ emissions in total process.	Even larger reduction in CO ₂ emissions in total process.
Architectural Design quality	Equal architectural design quality to original design.	

In the second approach, the focus lies on achieving an even larger reduction in the use of new concrete, construction waste and CO₂ emissions. This is done by increasing the amount of re-used concrete and limiting element adaptation, by allowing for small alterations of the design grid geometry without compromising on layout functionality or structural integrity.

3.4 Reused elements

In both design approaches it is considered that recesses in wall elements can be partially or fully filled by applying concrete block masonry. Table 3 provides an overview of the number and type of elements that can be used based on the first design approach. From the hollow core slabs, 264 of the 365 are reused elements, originating from office B and office D. The HCS from office B were used in the roof and ground floor as they were only suitable for this. The HCS from office D will serve for the floors in between, leaving 92 HCS unaccounted for, for which newly constructed elements have to be used. The design requires 80 load-bearing wall elements, building A can supply 46 elements, leaving only four not viable for this design. New wall elements have to be used for the 34 remaining. Building B has 74 suitable façade elements, the remaining 36 have to be newly constructed. The main reason remaining elements were not suitable for reuse in this design, is that they do not meet the required dimensions and load capacity.

Table 3. Overview of reused elements for redesign one (reused/available).

Element	Required	Recovered				Total	New
		Office A	Office B	Office C	Office D		
Slabs	365	0/430	112/1169	0/686	152/165	264	92
Walls	80	46/50	n.a.	0/34	n.a.	46	34
Beams	0	0/45	n.a.	0/138	0/84	0	0
Columns	0	0/72	n.a.	0/60	0/84	0	0
Façade	110	0/115	74/515	0/131	n.a.	74	36

In the second redesign approach, reusing HCS is prioritized as those are the elements with the largest volume of concrete, thus contributing most to the CO₂ emissions when creating new elements. HCS reuse can be improved by taking less suitable slabs from another building and allowing minor changes to the layout of the planned building. In this second approach, slight alterations to the window sizes and positions were allowed, leading to significantly higher reuse ratio. Both redesigns of the apartment building can be seen in Figure 2 below.

Table 4 provides an overview of the number of recovered elements resulting from the redesign with the second approach. The number of HCS has increased to 333 elements, which will be sufficient for the whole building. All 50 of the wall elements from building A will be reused, leaving 30 to be filled in by new elements. The reuse of façade elements has increased significantly, going from 74 elements to 150 elements. Thus only 21 new façade elements will be constructed

3.5 Comparison to original design

The two design approaches are both compared to the original design on the amount of new concrete used and CO₂ emissions. Redesign based on the first approach uses 69.4% less new concrete while also using less concrete in total, this due to the possibility for thinner walls and floors. It has to be noted that using thinner walls and floors could require additional sound- and thermal insulation. Approach two uses 89.6% less new concrete than the original apartment design and 65.9% less new concrete than redesign one. The largest amount of concrete reduction originates from the increased reused of HCS and façade elements. Values used for the determination of percentage of concrete used can be seen in the Table 5. The values include concrete blocks to fill the openings in the walls and mortar used for the connections.

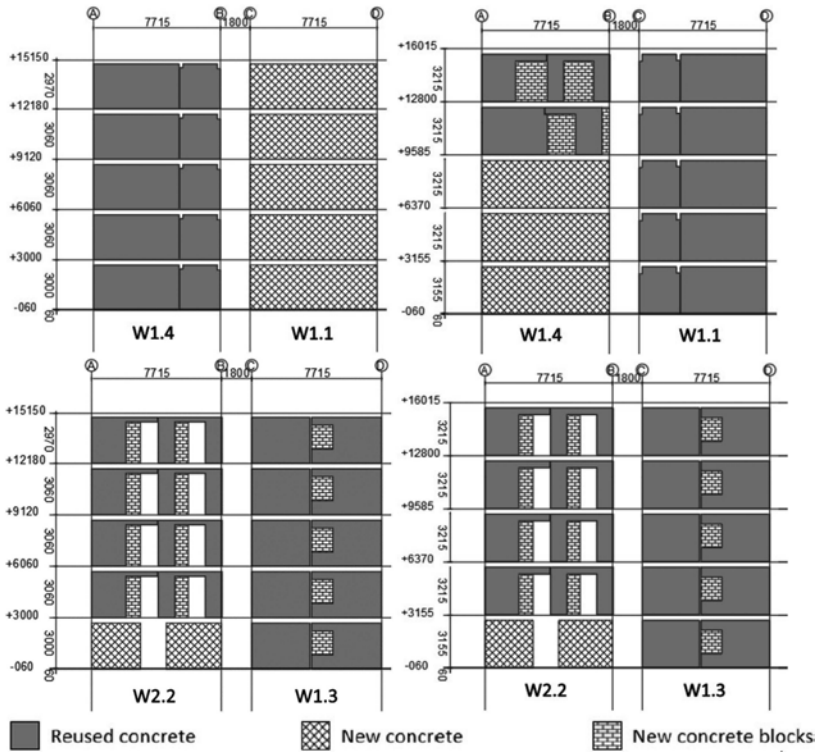


Figure 2. Configuration of façade elements in approach one (left) and approach two (right).

Table 4. Overview of reused elements for redesign two.

Element	Required	Recovered					Total	New
		Office A	Office B	Office C	Office D			
Slabs	333	0/430	333/1169	0/686	0/165	333	0	
Walls	80	50/50	n.a.	0/34	n.a.	50	30	
Beams	0	0/45	n.a.	0/138	0/84	0	0	
Columns	0	0/72	n.a.	0/60	0/84	0	0	
Façade	171	0/115	150/515	0/131	n.a.	150	21	

Table 5. Concrete usage in different design approaches.

Design	Reused/new	Concrete
		m3
Original	Reused	-
	New	1452.6
Redesign 1	Reused	886.2
	New	463.2
Redesign 2	Reused	1085.5
	New	152.6

In terms of CO₂ emissions, approach one saves 21.5% of CO₂ emissions at the end of life of the office building and 46.2% in the creation of the apartment building. Approach two saves 34.9% and 60.9% CO₂ emission respectively. The largest savings are made in both the demolition and production phase, and not so much in the construction phase. As previously mentioned, the HCS's cause most of the CO₂ emissions - this is also the case for transport emissions. For transport emissions, a hypothetical distance of 50 km is assumed between the deconstruction site and the building site for the apartment building. Values used for the determination of CO₂ emissions used can be seen in the Table 6.

Table 6. CO₂ emissions in different design approaches.

	Original design	Redesign 1	Redesign 2
Time	Ton CO ₂ equivalent	Ton CO ₂ equivalent	Ton CO ₂ equivalent
Creation of apartment	390.7	306.4	253.8
End of life of office building	489.5	263.0	191.2

3.6 Recommendations for general design approach

Based on the case study some recommendations for the general design approach can be derived. Giving precedence to reusing as many HCS as possible over other elements could provide benefits as HCS have the largest impact on material use and CO₂ emissions. Second, allowing for the window size and positions to be altered, could increase the number of façade elements that are reused, and limit their adaptation. Allowing alteration of the floor height to match the available façade and wall elements could prevent the need for adaptations, which will also allow for more finishing options such as a floating floor. Lastly, in some cases, limiting the reuse to not include odd-shaped elements could prevent the building process from becoming too complicated. An important note is that these recommendations, and all suggestions made in this paper, should be judged on a case-to-case basis.

4 CONCLUSION

From the literature study it can be concluded that concrete element reuse is possible, but remains to be optimized. Reusing precast concrete elements can lead to significant reduction in new concrete and steel whilst also reducing the amount of waste generated in the demolition process, which all contributes to a substantial reduction in CO₂ emissions. It is important to limit transport distances of reclaimed elements to further reduce the CO₂ emissions.

Creating a completely new design to optimize the reuse of available elements is favoured over redesigning an already existing design. However, this is not always possible, allowing for small adaptations in dimensions of elements and positions of openings could substantially increase the reuse capacity.

After the initial load calculation, the reused elements are chosen, these are unlikely to have the exact same dimensions of the elements of the initial calculation. Thus, it is necessary to perform a secondary load calculation after the element selection to check the influence of the elements. The creation of a list or database of available elements with their relevant properties would be beneficial to the design process.

ACKNOWLEDGEMENTS

I would like to acknowledge Bart van den Brink, he did the fundamental research on which this paper is based (van den Brink, 2020). Also, Rijk Blok who sadly passed away but was the supervisor for both Bart van den Brink and myself.

REFERENCES

- Bossink, B. A. G., & Brouwers, H. J. H. (1996). Construction Waste: Quantification and Source Evaluation. *Journal of Construction Engineering and Management*, 122(1), 55–60. [https://doi.org/10.1061/\(asce\)0733-9364\(1996\)122:1\(55\)](https://doi.org/10.1061/(asce)0733-9364(1996)122:1(55))
- Coenen, M., Lentz, G., & Prak, N. (1990). *De kop is eraf*.
de Alliantie. (2019). *Zuidpolder Eemnes*.
- de Wit, M., Hoogzaad, J., & von Daniels, C. (2020). *Circularity Gap report 2020*.
- Durmisevic Elma. (2006). *Transformable building structures. Design for disassembly as a way to introduce sustainable engineering to building design & construction*. [s.n.].
- Florea, M. V. A. (2016). *Advances in Cement and Concrete Technology in Africa*. www.tue.nl/taverne
- Glias, A. (2013). *The “Donor Skelet” Designing with reused structural concrete elements*. www.tudelft.nl
- Herczeg David, McKinnon Leonidas Milios, M., & Klaassens Katarina Svatikova Oscar Widerberg Rotterdam, E. (2014). *Resource efficiency in the building sector*. www.ecorys.nl
- Huuhka, S., Caldenby, C., & Asam, C. (2019). *Architectural transformation of disadvantaged housing areas*.
- Jin, R., Yuan, H., & Chen, Q. (2019). Science mapping approach to assisting the review of construction and demolition waste management research published between 2009 and 2018. In *Resources, Conservation and Recycling* (Vol. 140, pp. 175–188). Elsevier B.V. <https://doi.org/10.1016/j.resconrec.2018.09.029>
- Ministerie van binnenlandse zaken en koninkrijksrelaties. (2022). *Het statistisch woningtekort nader uitgelegd*. <https://www.volkshuisvestingnederland.nl/onderwerpen/berekening-woningbouwopgave#:~:text=Er%20zijn%20in%202021%20circa,gesproken%20over%20het%20statistisch%20woningtekort>.
- van den Brink, G. (2020). *Designing with recovered precast concrete elements A study on the possibilities of reusing structural precast concrete elements, from disassembled office buildings, in new apartment buildings*.
- Verhaegh, J. (2022, July 4). *Leegstand kantoren op historisch laag niveau*. <https://www.cushmanwakefield.com/nl-nl/netherlands/insights/historisch-lage-leegstand-kantorenmarkt#:~:text=Jan%20Verhaegh%20%E2%80%A2%2004%2F07%2F2022&text=Dit%20blijkt%20uit%20de%20nieuwste,niveau%20in%2020%20jaar%20tijd>.

Building structures made of reused cut reinforced concrete slabs and walls: A case study

N. Widmer, M. Bastien-Masse & C. Fivet

Ecole Polytechnique Fédérale de Lausanne (EPFL), Fribourg, Switzerland

ABSTRACT: Reuse of reinforced concrete (RC) components reduces construction's environmental impacts and waste. Rather than crushing the concrete of an obsolete structure, its components are saw cut and later reassembled in a new structure. The theoretical feasibility of this method is demonstrated through a case study: the design of a residential building structure that reclaims cast-in-place RC components from two 60-year-old office buildings scheduled for demolition. Parts of the source buildings are allocated to an optimal position in the target building using an algorithm that minimizes the need for strengthening. Construction details are developed for the slab-wall connections and the bracing system. An alternative conventional cast-in-place RC design is proposed for comparison, as well as a hybrid design balancing environmental and cost savings with technical readiness. The assessment of the designs confirms that reusing RC components allows saving up to 75% of greenhouse gas emissions for similar costs, as long as demolition and disposal of obsolete source material are considered.

1 INTRODUCTION

Concrete is the most commonly used building material and the related production of cement is responsible for at least 9% of global CO₂ emissions (Monteiro et al. 2017). Cement and concrete production also consume large quantities of raw materials such as gravel, sand and limestone, which, in combination with an increasing concrete demand, will most likely lead to a shortage of these natural resources in the near future (Habert et al. 2010).

Meanwhile, construction and demolition waste correspond to about one third of all waste in Europe (Zhang et al. 2022) of which about 30% is concrete rubble (Giorgi et al. 2018). Nowadays, the demolition of buildings is usually not due to structural deficiencies but to changes of requirements – e.g. new functions, use intensification, or improved energy efficiency. During demolition, concrete is most often crushed and used as backfilling material (Zhang et al. 2022) or as a substitution for natural aggregates in a new, so-called recycled concrete. However, because both need similar amounts of cement, CO₂ emissions for recycled concrete are comparable to those for a conventional mix, especially if the rubble has to be transported over long distances before use (Marinkovic et al. 2010, Knoeri et al. 2013).

To reduce the detrimental environmental impacts (DEI) of concrete construction, the service life of existing structural components should be extended as much as possible through maintenance, renovation and strengthening. When none of these options are feasible anymore, deconstruction and component reuse is preferable to demolition. Reuse involves carefully dismantling the structure into smaller elements that are then reassembled in a new structure. This strategy delays the waste production and significantly reduces the need for new materials and the related CO₂ emissions.

Since the 1980s, there have been several examples where prefabricated concrete components were deconstructed and reused in new structures, many of which demonstrate a major reduction in DEI (Küpfer et al. 2022). The reuse of components extracted from cast-in-place reinforced

concrete (RC) structures is much less common. Recently, a pedestrian bridge named Re:Crete has been built from 25 reused blocks sawed out from concrete walls of a building undergoing renovation (Devènes et al. 2022). For this specific project, a 75% reduction in CO_{2eq} emissions was calculated when compared to a recycled concrete alternative.

Through a case study, this paper demonstrates the theoretical feasibility of constructing a residential *target* building with pre-existing cast-in-place RC components. The components are reclaimed from two *source* buildings that are expected to be demolished soon. The paper is organized as follows. Section 2 presents the design process specific to a RC-component-reuse project. The resulting design for the case study is given in section 3 including new construction details developed for connections. In addition to the reuse design, a conventional concrete construction alternative is developed, as well as a hybrid solution balancing environmental and cost savings with technical readiness. The alternatives are compared and assessed in terms of CO_{2eq} emissions and construction costs in section 4. Section 5 highlights the main conclusion of this work.

2 DESIGN METHODOLOGY

2.1 Design process

Figure 1 shows the 11 steps of the process for designing a load-bearing system from reclaimed cast-in-place RC components, including the required iterations. Step 1 consists in analyzing the source buildings to obtain the structural capacity of the different components available for reuse – e.g. bending-moment resistance for different slab parts and normal force resistance for walls and columns. In parallel, the floor plan of the target structure is defined and used to fix a preliminary load-bearing system – i.e. the layout of vertical load-bearing elements and the boundary conditions (step 2). The live loads are specified according to the space use while dead loads are set based on assumed structural thicknesses.

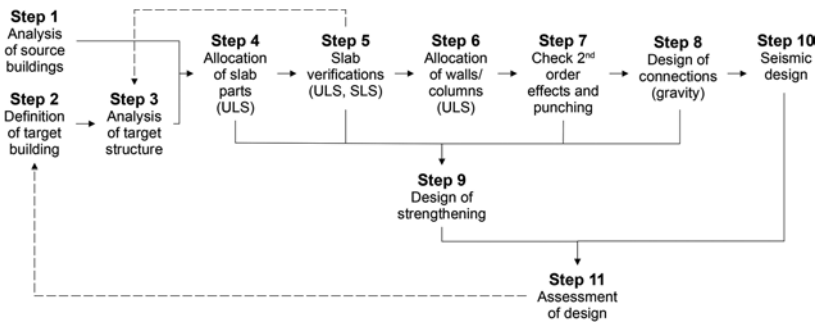


Figure 1. Selected design process.

In step 3, the target slab is divided into parts which are sought to be built in one piece – i.e. the position of joints in the target structure is defined. Different types of joints are considered, allowing or not the transmission of bending-moments or shear-forces (continuous, hinged, free, etc.). A Finite Element Model (FEM) of the target structure is created and joints are placed between the parts corresponding to their boundary condition. The action effects are calculated, which corresponds to the minimal resistance requirement of the target slab.

Subsequently, the dismantling and reassembly of floor slabs is planned. An algorithm is used in step 4 to allocate parts of the source slabs to the parts of the target slab defined in step 3. The allocation criterion is to minimize areas where structural strengthening is required to satisfy the bending-moment-resistance requirement at Ultimate Limit State (ULS). The shear-force-resistance requirement at ULS and deflections at the Serviceability Limit State (SLS) are subsequently checked in step 5. Deflections should not be larger than the limits fixed in in-force

design codes. In case the shear-force resistance of the allocated slab is insufficient or deflection limits are not met, the slab is either strengthened or the load-bearing system is modified – e.g. by adding supports or changing the type of joints to remove hinges. The latter is a first iteration looping between step 5 and step 3. Changing the load-bearing system will modify action effects and the corresponding resistance requirements for the target slab. Therefore, the allocation of source parts (step 4) should be redone to find a satisfactory solution.

If walls and columns are also sought to be built from reclaimed components, a similar approach as for slab parts is followed. The list of available vertical load-bearing parts made in step 1 is updated in step 6 to take into account the results of step 4. On top of the walls available in the source structures, parts of the source slabs which were not used to reassemble the target slab are considered as available stock for wall elements. This available stock is then allocated to a position in the target building according to structural resistance. Then, columns are checked for second order effects and punching resistance of the reassembled slab is also verified (step 7).

After allocation of all structural components, connections and the required strengthening of the slab are designed in steps 8 and 9 to resist gravity-action effects. Connections should ensure the force transmission conditions chosen for the joints in the structural model. Finally, the lateral bracing system is designed to resist seismic loads in step 10.

Once the structural design of the target structure is completed, it is assessed in step 11 regarding different criteria – e.g. DEI and construction costs (cf. section 2.2). If performance is not satisfactory, the design is modified at different stages, particularly by modifying the desired target structure to make better use of the available stock of reclaimed components.

2.2 *Assessment*

2.2.1 *Functional unit and system boundaries*

Life-cycle and cost assessments are dependent on a predefined functional unit and limits of the analysis. For this paper, the functional unit is the load-bearing system of one story – i.e. the RC slab with its vertical supports (RC columns and walls) – in the new target structure. Non-structural elements are not taken into account.

For the purpose of comparison, different design alternatives are developed and assessed: conventional construction with new materials; construction with reused structural components; hybrid construction. For all alternatives, processes related to the construction of the new building and the production of new materials are considered in the system. The end-of-life of the source buildings is taken into account as well. This is especially relevant for projects where existing buildings are to be demolished prior to the construction of a new building – i.e. a replacement project. For the variants applying reuse, all processes related to the deconstruction of building parts to be reused are included as well as those related to the demolition and disposal of the remaining material. For the conventional variant, the demolition and disposal of the entire source buildings is accounted for. The operation, maintenance, and end-of-life stages of the new target structure are not considered in the system. Moreover, construction processes expected to be the same for all variants – e.g. cranes, site specific installations, foundations, etc. – are excluded from the comparative assessment.

2.2.2 *Life Cycle Assessment*

In order to evaluate the environmental impacts of reusing structural RC elements, a comparative Life Cycle Assessment (LCA) is conducted (International Organization for Standardization 2006). LCA has been previously applied to evaluate reductions of DEI when reusing structural elements (Yeung et al. 2017, Brütting et al. 2020a, b, Devènes et al. 2022).

As introduced in section 2.2.1, the analysis includes the product stage and the construction process stage of the project (construction stages A1-A5) as well as the end-of-life of the source buildings (construction stages C1-C4) according to the European standard for Life Cycle Assessments (CEN 2011). The impacts associated with recycling materials or reusing components are allocated to the final product resulting from the processes, i.e. following a cut-off approach (Schrijvers et al. 2016).

In this paper, the global warming potential (GWP) is chosen as the indicator for comparing the variants, expressed in kilograms of equivalent carbon dioxide ($\text{kgCO}_{2\text{eq}}$). Emission factors for the different processes are mainly taken from the Swiss LCA database (KBOB 2022).

2.2.3 Construction costs

In order to evaluate the economical implications of reusing RC components, costs for dismantling the source structure and constructing the target structure are estimated for all variants. For this paper, unit prices for the reference year 2021 are used. They are mainly estimated from construction companies' bids, engineering office experience and average prices published in the Swiss Construction Price Index (FSO 2021).

3 CASE STUDY

3.1 Source and target buildings

The two source structures for the case study are cast-in-place RC slab-and-column systems of office buildings located on a former industrial site in the city of Basel, Switzerland, Figure 3. They were constructed in the late 1950's and are now destined to be dismantled following the urban re-qualification of the district.

The target building is shown in Figure 2. It is a 6-story residential building with an area of 606 m^2 per floor and a total height of 17.1 m above the ground. It is to be located on the same site as the source buildings.

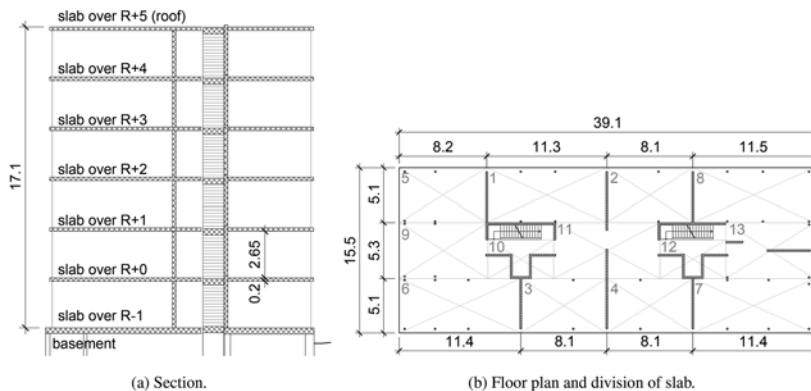


Figure 2. Target building.

3.2 Design alternatives

For the sake of comparison, three different design alternatives are developed. The first one, “Reuse”, includes as many reclaimed RC components as possible. The details of this design are given in section 3.3. The second design alternative, “Conventional”, instead uses only newly cast-in-place RC and is used as a reference for conventional construction methods. The third alternative, “Hybrid”, is a combination of both variants that favors a simplified construction process for the bracing system: slabs and vertical supports are made of reclaimed components except for the bracing walls, i.e. the walls of the cores, that are made from new cast-in-place RC.

3.3 Reuse-driven design

3.3.1 Slab design

Figure 2b shows the division of the target floor slab into parts (step 3 of the design process, see Figure 1). For each part, a component of the source building must be allocated (step 4 of the design process, see Figure 1).

Figure 3 shows the floor plan of the considered source buildings. Color zones correspond to different bending-moment resistances which are used as an input for the allocation algorithm. Each zone is characterized by four values – i.e. positive and negative resisting bending-moment in x- and y-direction respectively. The final sawing position for every part allocated to the target slab, obtained after the design iterations, are also shown.

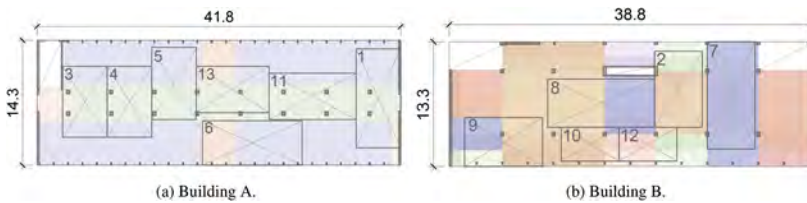


Figure 3. Distribution of bending-moment resistance across the source slabs and final sawing layout.

3.3.2 Strengthening and connection details

For the Reuse design variant of this case study, a layer of 20 to 35 mm of Ultra-High Performance Fiber Reinforced cementitious Composite (UHPFRC) is used to provide structural strengthening when necessary as well as continuity at the connections. The composite material is commonly used for rehabilitation of existing structures and allows bending as well as shear strengthening of the slab in all directions simultaneously (Habel et al. 2006, Bastien-Masse & Brühwiler 2016). The zones of the target building requiring a UHPFRC-layer are shown in Figure 4a. The blue zones illustrate bottom reinforcement, while the red zones are top reinforcement.

In the structural model of the target building, slabs are considered to be continuous over walls, meaning that there are negative bending moments over the supports. Therefore, as shown in Figure 4b., a layer of UHPFRC is applied on the upper surface of the slab in the joint region to transfer the tensile force from one slab element to the other.

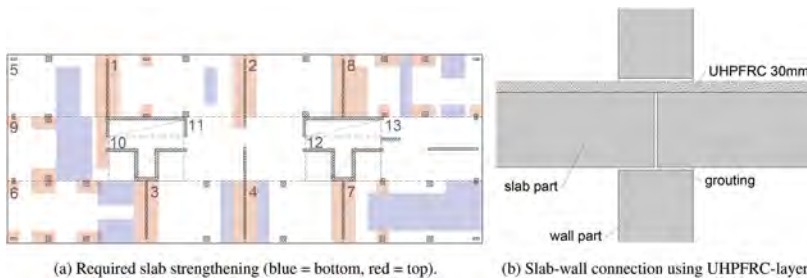


Figure 4. Slab strengthening and slab-wall connection.

3.3.3 Lateral bracing system

The city of Basel, Switzerland, where the case study is located, has the second highest seismic risk in the country. Therefore, an adequate seismic design is required. For the Reuse design, bracing walls to resist seismic loads are sought to be built from reclaimed components as well. The analysis shows that the reclaimed components do not provide a sufficient cross-sectional resistance to resist lateral forces. Therefore, another bearing system is suggested, where each bracing wall is built as a truss system over the height of the whole building, as shown in Figure 5a. A compression strut forms in the reclaimed concrete walls, which is deviated by ties at each slab level. The connection between the walls is done as shown in Figures 5b, c, so that new reinforcement bars embedded inside cast-in-place concrete are introduced in between the reclaimed wall components as vertical and horizontal ties.

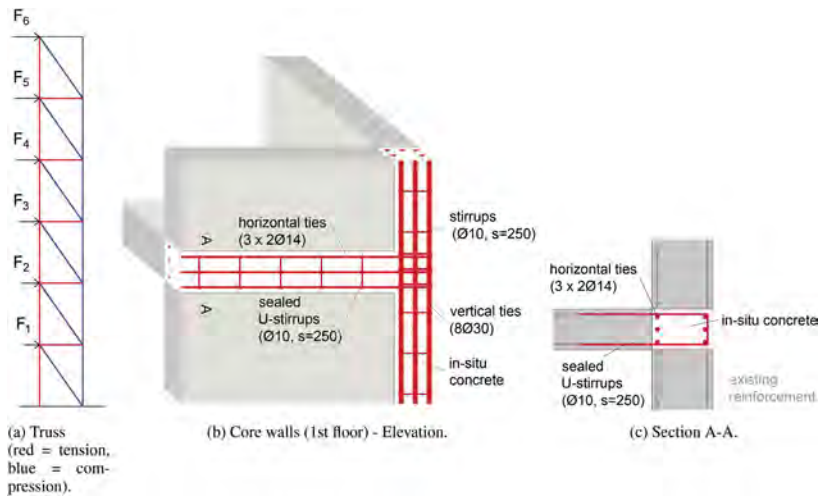


Figure 5. Design of new bracing system with reclaimed concrete walls to resist lateral forces.

4 ASSESSMENT RESULTS

4.1 Life Cycle Assessment

Figure 6 shows the comparison of the GWP for the three design variants. It is assumed that the components to reuse are stored on the same site as the deconstruction of the source buildings and the construction of the target structure. Therefore, no transportation of reclaimed elements is considered for the Reuse and Hybrid design variants.

If the demolition of the source buildings is not considered, greenhouse gas emissions of the Reuse and Hybrid variants are respectively 77% and 73% lower than those of the Conventional variant. If the end-of-life is included in the LCA, ratios become 75% for the Reuse variant and 72% for the Hybrid variant. The Hybrid variant is slightly less favorable in terms of GWP than the Reuse variant due to the larger quantity of newly poured concrete. For both variants using reclaimed materials, the largest share of GWP is caused by the UHPFRC structural strengthening of the slab which amounts to about 60-70%.

4.2 Construction costs

Figure 7 shows the comparison of the estimated construction costs for the three variants, with a $\pm 15\%$ precision. The ratio of costs between variants differs significantly depending on whether the end-of-life of the source buildings is taken into account or not. If the costs of demolishing the source buildings are attributed to a different project than the construction of the target building, then the costs of the Reuse and Hybrid variants are respectively 54% and 56% higher than for the Conventional variant.

However, if the end-of-life of the source buildings is included in the analysis, demolition and material disposal drive up the costs of the Conventional variant to a level comparable to the variants applying reuse. Under these assumptions, the Reuse and Hybrid variants have costs within the $\pm 15\%$ precision range of those for the Conventional variant.

For the Reuse and Hybrid variants, the biggest share of costs is due to the deconstruction of the components to reuse, i.e. related to sawing (30-40%) and to lifting components with a crane (10-20%). New materials needed for the bracing system only amount to around 2-3% of total costs.

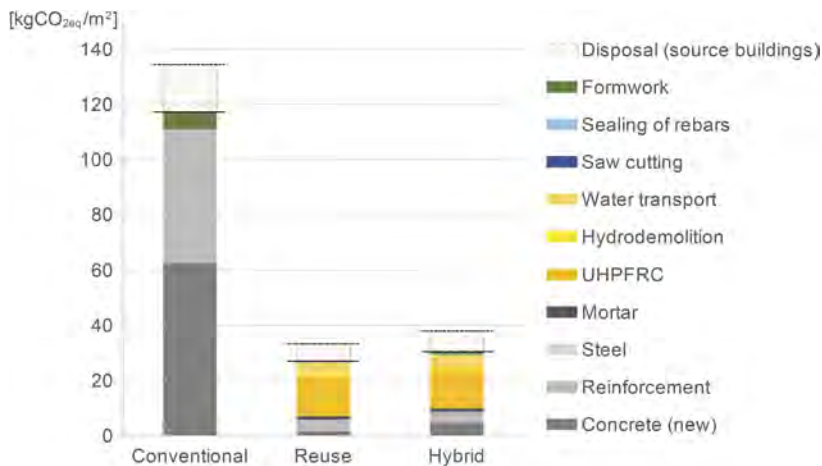


Figure 6. Comparison of global warming potential per floor area for different design alternatives.

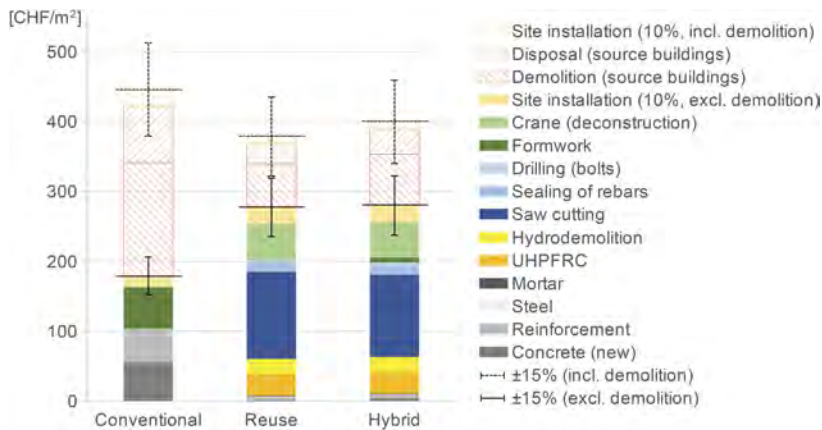


Figure 7. Comparison of construction costs per floor area for different design alternatives.

5 DISCUSSION AND CONCLUSION

The aim of this study is to investigate the technical feasibility as well as the benefits in terms of environmental impacts and costs of reusing RC components from obsolete structures in new constructions. To this end, the load-bearing structure of a residential building is designed with reclaimed cast-in-place RC components mined from two given source buildings. The final design is compared to an equivalent, conventionally built structure using new cast-in-place RC.

The study proves that technical solutions are available to design the structural system of a building floor from reclaimed cast-in-place RC elements. It is found that by reusing structural components greenhouse gas emissions are reduced by 75% compared to conventional construction techniques. Integrating a limited amount of newly cast-in-place RC in a structure mostly made from saw cut parts simplifies the construction process and at the same time achieves a similarly low level of global warming potential. In terms of construction costs, estimations show that reusing RC components competes with conventional construction methods only if the demolition and disposal of the source buildings are included in the analysis.

These are promising results, as they clearly show the potential of reuse to reduce the DEI of RC construction for a similar range of costs. Especially in times of supply bottlenecks and increasing material prices, when costs of conventional construction tend to increase, reuse becomes an interesting alternative that is beneficial not only from an ecological but also from a financial point of view. Yet, more studies like the present one are needed to support a widespread application of RC component reuse.

ACKNOWLEDGMENTS

This work was supported by the Ecole Polytechnique Fédérale de Lausanne (EPFL) through an ENAC Cluster grant 2022.

REFERENCES

- Bastien-Masse, M. & Brühwiler, E. 2016. Contribution of R-UHPFRC Strengthening Layers to the Shear Resistance of RC Elements. *Structural Engineering International* 26: 365–374.
- Brütting, J. & Vandervaeren, C. & Senatore, G. & De Temmerman, N. & Fivet, C. 2020a. Environmental impact minimization of reticular structures made of reused and new elements through Life Cycle Assessment and Mixed-Integer Linear Programming. *Energy and Buildings* 215: 109827.
- Brütting, J. & Senatore, G. & Schevenels, M. & Fivet, C. 2020b. Optimum design of frame structures from a stock of reclaimed elements. *Frontiers in Built Environment* 6(57): 1–18.
- Devènes, J. & Brütting, J. & Küpfer, C. & Bastien-Masse, M. & Fivet, C. 2022. Re:Crete – Reuse of concrete blocks from cast-in-place building to arch footbridge. *Structures* 43: 1854–1867.
- European Committee for Standardization (CEN). 2011. *EN 15978 Sustainability of construction works – Assessment of environmental performance of buildings – Calculation method*.
- Federal Statistical Office (FSO). 2021. *Schweizerischer Baupreisindex - Durchschnittliche Einheitspreise in der Schweiz und in den Grossregionen*.
- Giorgi, S. & Lavagna, M. & Campioli, A. 2018. Guidelines for Effective and Sustainable Recycling of Construction and Demolition Waste. In E. Benetto & K. Gericke & M. Guiton (eds), *Designing Sustainable Technologies, Products and Policies: From Science to Innovation*. Cham: Springer.
- Habel, K. & Denarié, E. & Brühwiler, E. 2006. Structural Response of Elements Combining Ultrahigh-Performance Fiber-Reinforced Concretes and Reinforced Concrete. *Journal of Structural Engineering* 132(11): 1793–1800.
- Habert, G. & Bouzidi, Y. & Chen, C. & Jullien, A. 2010. Development of a depletion indicator for natural resources used in concrete. *Resources, Conservation and Recycling* 54(6): 364–376.
- International Organization for Standardization. 2006. *ISO 14040 Environmental management — Life cycle assessment — Principles and framework*.
- Knoeri, C. & Sanyé-Mengual, E. & Althaus, H.-J. 2013. Comparative LCA of recycled and conventional concrete for structural applications. *The International Journal of Life Cycle Assessment* 18(5): 909–918.
- Koordinationskonferenz der Bau- und Liegenschaftsorgane der öffentlichen Bauherren (KBOB). 2022. *Ökobilanzdaten im Baubereich 2009/1:2022*.
- Küpfer, C. & Bastien-Masse, M. & Fivet, C. 2022. Reuse of concrete components in new construction projects: review of 77 circular precedents. *Journal of Cleaner Production*.
- Marinković, S. & Radonjanin, V. & Malešev, M. & Ignjatović, I. 2010. Comparative environmental assessment of natural and recycled aggregate concrete. *Waste Management* 30(11): 2255–2264.
- Monteiro, P.J.M. & Miller, S.A. & Horvath, A. 2017. Towards sustainable concrete. *Nature Materials* 16(7): 698–699.
- Schrijvers, D.L. & Loubet, P. & Sonnemann, G. 2016. Developing a systematic framework for consistent allocation in LCA. *The International Journal of Life Cycle Assessment* 21(7): 976–993.
- Yeung, J. & Walbridge, S. & Haas, C. & Saari, R. 2017. Understanding the total life cycle cost implications of reusing structural steel. *Environment Systems and Decisions* 37(1): 101–120.
- Zhang, C. & Hu, M. & Di Maio, F. & Sprecher, B. & Yang, X. & Tukker, A. 2022. An overview of the waste hierarchy framework for analyzing the circularity in construction and demolition waste management in Europe. *Science of The Total Environment* 803: 149892.

Reuse of fibrous tectonics as the secondary structure of the facade system

A. Ahmadnia, C. Monticelli, S. Viscuso & A. Zanelli

Politecnico di Milano, Milan, Italy

ABSTRACT: Fibrous structures are structures that are made of fiber-reinforced polymer (FRP) composites. Their excellent mechanical properties, in addition to their low densities, can result in a lightweight structure. However, there are some obstacles that prevent them from being used more widely: high material and manufacturing costs, end of life (EoL), plus optimizing their design and fabrication procedures to be used on a building scale, like they have been used efficiently in the aerospace and automobile industries. The current recycling process for FRP can cause a huge loss in mechanical properties and be costly. The goal of this study is to reuse the entire continuous fiber-reinforced polymer composite with minimal loss in mechanical properties, so the current use of thermosets has to be changed to thermoplastic. The secondary structure of a façade system is intended to replace existing bulk structural systems and scale up the FRP composite to the building scale.

1 INTRODUCTION

1.1 *History of FRPs in industry*

Owens Corning was the first to introduce glass fiber in 1935, kicking off the fiber-reinforced polymer (FRP) industry. Following World War II, the burgeoning petrochemical industry made available glass fiber embedded in polymeric resins; as a result, high-strength, high-stiffness structural fibers were combined with low-cost, light-weight, environmentally resistant polymers to create a composite with better mechanical properties and durability than the constituents alone (Bakis et al., 2002). Moreover, due to the demands of World War II, the FRP industry transitioned from research to manufacturing. Bill Tritt prototyped and tested a totally composite body car built of glass fiber-reinforced polymer composite (GRP) in the 1940s. In the 1950s, manufacturing innovation continued with the developments of pultrusion, vacuum bag molding, and large-scale filament winding. Later, fibers with higher stiffness, strength, and density, such as boron, aramid, and carbon, were used for high-performance applications in space exploration, aerospace, and air travel, as well as the defense industry (Bakis et al., 2002). High-performance fibers were initially too expensive to be employed in other applications; as a result, work began in the 1970s to reduce the cost of high-performance fibers (Bakis et al., 2002). As the cost reduced and the defensive market waned, the use of FRP as a new material in the renewal of infrastructure increased at the end of the 1980s and the beginning of the 1990s. Furthermore, lots of funding opportunities were devoted to industries and governments around the world (Bakis et al., 2002). Figure 1. represents a summary of the history of fiber-reinforced polymers in industry.

1.2 *History of FRPs in architecture and construction*

Fiber-reinforced polymers have been used in architecture since the second half of the twentieth century (Dambrosio et al., 2020). After World War II, a large portion of the polymer output was made available for non-military uses. In 1955, the Radome, an enclosure for a radar station, was mounted in Washington according to Richard Buckminster Fuller’s geodesic dome idea (Knippers et al., 2012). This enclosure had to be a free metal structure, which led to the first assemblies made entirely of synthetic materials. Buckminster Fuller continued to work on polymer geodesic domes, building the “Fly’s Eye Dome” in 1970. The Monsanto Chemical

Company approached MIT in 1954 with the concept of building an entirely polymer-based dwelling. A year later, MIT published “Plastics in Housing,” a study that outlined how the house of the future would look (Knippers et al., 2012). The main motivations for adopting polymers in construction were flexibility for changing families, ease of relocation for increased mobility, and cost-effective housing for the developing middle class. All of these features were to be exhibited in a project that could be easily assembled and modified to fit varied plan layouts and local conditions (Knippers et al., 2012).

Fiber-reinforced polymer structural forms are one of the most common uses in the building and structural industries. The pultrusion method was utilized to create the structural shapes of the fiber-reinforced polymer. Via the pultrusion technique, the fiber-reinforced polymer has been employed in structural, non-structural, and electrical applications. Before the 1970s, the development of small-sized commodities for non-structural and electrical purposes was the main focus (Bakis et al., 2002). Since the 1970s, pultruded structural shapes have been used for primary load-bearing systems. The use of pultruded structural shapes of fiber-reinforced polymer in the design and construction of pedestrian bridges, such as the long cable-stayed Aberfeldy Footbridge in Scotland, is also evident (Bakis et al., 2002).

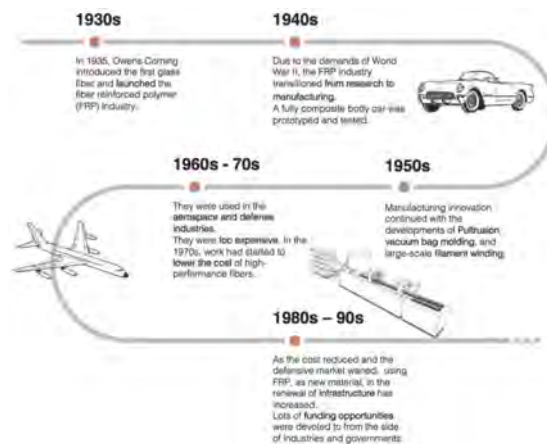


Figure 1. History of FRPs.

2 MATERIAL INVESTIGATION

2.1 Fiber-reinforced polymer composite (FRP)

FRP composites are high-strength, lightweight, with great fatigue resistance, a high elastic modulus, and low thermal expansion and corrosion resistance (Liu et al., 2015). Besides, they can be ductile (depending on the type of matrix), but they are anisotropic materials (Waimer et al., 2013), which means they present different behaviors in different directions. Since an FRP composite contains a reinforcement (fiber, 60%) embedded in a matrix (polymer, 40%) (Figure 2.) (Liu et al., 2015; Bhargava, 2004), it primarily exhibits the mechanical properties of the fiber in the fiber direction, i.e., relatively high strength and modulus. On the other hand, it exhibits the mechanical properties of the polymer and resin in the direction perpendicular to the fiber axis, i.e., relatively low strength and modulus (Liu et al., 2015).

The matrix of FRP can be a thermoplastic, elastomer, or thermoset. Because of its high mechanical strength, epoxy, a thermoset polymer, is often employed as the matrix material in fiber-reinforced polymer composites (Boon et al., 2021). Although making a thermosetting composite is a simple operation, the long curing cycle of thermosets will increase the manufacturing cost (Boon et al., 2021). On the other hand, fiber-reinforced thermoplastic polymer composites take substantially less time to make because of their fast consolidation cycles; they also offer higher toughness, a longer shelf life, are easier to repair, and can be recycled

(Arhant et al., 2019). The high melt viscosity of thermoplastics can cause non-homogenous impregnation of reinforcement during the infusion process (the process of producing FRTP). The melt flow index must be considered when using thermoplastic polymers. According to the standards ASTM D1238 and ISO 1133, it is defined as a measure of the resistance to flow (viscosity) of the polymer melt at a given temperature under a given force for a predetermined period of time. It has a direct relationship with the flow of thermoplastic and an indirect relationship with viscosity. A thermoplastic epoxy resin (TP-EP) that combines the benefits of thermoset and thermoplastic resins was recently created (Nishida et al., 2018).

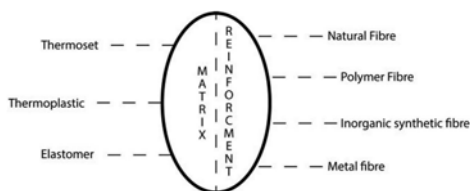


Figure 2. Reinforcement/Matrix in FRP composite.

2.2 Market share of FRPs

Fiber-reinforced polymer composites (FRP) have been in use since the 1930s, but they are now gaining popularity in the structure and construction industries (Bakis et al., 2002). FRPs are frequently used in place of metals in construction as well as in the military, energy, transportation, chemical, and electric power industries because of their high strength, light weight, and low maintenance requirements (Xue et al., 2022). Glass fiber-reinforced polymer composites (GFRP) and carbon fiber-reinforced polymer composites (CFRP) as two inorganic synthetic fibers are mostly common in different industries. In 2021, the global market for carbon fiber-reinforced plastic (CFRP), according to Statista, will be worth about 8.2 billion dollars. The size of the global market for carbon fiber-reinforced plastic is anticipated to reach approximately \$13.1 billion in 2027. The market for carbon fiber (CF) is expanding at a fast rate of 10%–12% annually due to the growing use of CF in aerospace, wind turbine blades, and other industrial applications (Xue et al., 2022). Glass fibers (GFs) were in high demand globally in 2019 (5.26 million tons), and it is anticipated that they will continue to lead the composite materials market (Xue et al., 2022). This shows an increased use of these materials in the construction industry. An investigation shows that the market share distribution of fiber-reinforced polymers in the construction industry is about 26 percent (Zyjewski et al., 2017).

While carbon fiber-reinforced plastics (CFRPs) are primarily used in the aerospace, wind power, sporting goods, and automobile manufacturing industries, glass fiber-reinforced plastics (GFRPs) are more commonly used in construction, transportation, industrial applications, electronic products, and other fields (Xue et al., 2022).

2.3 State of the art in recycling and reusing of FRPs

The disposal and burning of FRP will no longer be permitted due to the new regulation (the “green deal”) (Kang et al., 2021). Additionally, recycling has economic and energy advantages; for instance, recycling carbon fibers uses between 80% and 98% less energy than producing virgin fibers (Ghanbari et al., 2021). Consequently, recycling and reusing FRP have become more popular these days. However, due to the combination of two materials in FRP composite, recycling is a challenge (Rybicka et al., 2016). The thermosetting continuous FRP, which is considerably more prevalent than thermoplastic, can be recycled by thermal, chemical, and mechanical processes (Freedden et al., 2022). Thermal and chemical strategies are focusing on the separability of reinforcement and matrix to recover the fibers alone (Freedden et al., 2022). The mechanical strategy for recycling results in a loss of mechanical properties because the continuous FRP is shredded (Freedden et al., 2022). These techniques are extremely expensive, so they are routinely utilized for recovering carbon fiber, and mechanical recycling is mostly used for glass fiber-reinforced polymer (GFRP) composites (Rybicka et al., 2016). Thermal recycling strategy causes approximately 80%

of GFRP strength losses; however, this figure is only about 10% for carbon fiber-reinforced polymer composites (CFRP) (Pender et al., 2019).

There are a few examples and strategies for reusing the entire fiber and thermosetting matrix composite. Bus stops, benches, and children's playgrounds constructed from recycled wind turbine blades are a few isolated examples. The large amounts of End-of-Life (EoL) material cannot be recycled or reused using these methods (Freeden et al., 2022).

Recently, two case studies for reusing and recycling FRP were investigated in the industry. The first is a reuse plan that was designed for the canopy of i-mesh at Expo Dubai. This canopy was designed by Werner Sobek Company and constructed by i-mesh Company by utilizing glass fiber reinforcement and a thermoplastic elastomer matrix. The system contains a set of patterns that are connected to each other and can be separated by certain lines. They plan to take away the canopy after the Expo exhibition and use it as the shading system for the courtyard of a middle-eastern country, which is suffering from the huge amount of light from the sun. Figure 3-Right presents the i-mesh canopy during Expo 2020 Dubai, and Figure 3-Left shows the reuse plan after the exhibition. This reuse potential, though only focusing on the reuse of the panels, can be useful for using the systems again; however, in this case, it is not possible to come back to the level of material filaments, so it can reduce the design potentiality because of these restrictions.



Figure. 3. I-mesh reuse plan.

Cygnat Textkimp's (cygnat-textkimp.com) waste recycling uses superheated steam to gently remove a range of polymers from filters and related production equipment, allowing raw material waste to be reused in your manufacturing process. Using a combination of superheated steam pressure swings or compression and decompression cycles, frozen polymer is removed from contaminated components and assemblies. The process takes place in a controlled environment contained within a custom-designed pressure vessel. The components are enclosed in a pressure vessel, and the pressure is rapidly decreased by opening the blowdown valves. Depending on the polymer type, temperatures above 250 °C will melt or soften the polymer, and a degree of hydrolysis will occur. When under pressure, the steam will penetrate fissures in the polymer, where it condenses as superheated water. On decompression, it boils, instantly cracking the polymer and carrying away broken particles along with the softened, degraded polymer fragments from the outer faces. The pressure swing cycle is then repeated at frequent intervals and controlled automatically with no detrimental effect on the integrity of the filter media or metal structure.

3 EXISTING GAPS AND RESEARCH AIMS

In the previous century, the consumption of building materials has increased dramatically, and the weight of the materials used for the structures is more than half that of the other systems involved. As a result, deconstruction wastes (Ng et al., 2015) and the use of virgin materials (Herrmann et al., 2018) have increased in the construction sector, and their fate cannot be landfill or burning.

The excellent mechanical properties of FRP, in addition to their low densities, can result in a lightweight structure as a result. However, there are some obstacles that prevent them from being used more widely: high material and manufacturing costs, end of life (EoL) in general,

plus optimizing their design and fabrication procedures to be used on a building scale, like they have been used efficiently in the aerospace and automobile industries. Given the size of the market and the anticipated rise in waste generation over the coming years, it is critical that composite products are properly managed when they reach the end of their useful lives.

Besides, current research in the state of the art shows that these materials have been used primarily for temporary lightweight structures (primarily pavilions, shells, and membranes) in recent years. However, the IntCDC and ITKE at the University of Stuttgart presented a possible concept of having fibrous structures on a building scale at the Biennale di Venezia 2021 (Maison Fibre), but there is still a long way to go. Older case studies show the use of these materials at the building scale, but with design, structure, and fabrication processes that are mostly similar to the traditional procedures that have been used for other structural materials like steel (for example, pultruded structural shapes). However, FRP has its own specific mechanical properties and behavior that must be taken into account.

This paper aims to reuse the entire continuous fiber-reinforced polymer composite with minimal loss of mechanical properties, necessitating a switch from thermosets to thermoplastics. A secondary structure for the facade system is designed to take the place of current bulk structural systems and scale up the FRP composite to building scale.

4 RESEARCH METHODOLOGY

According to the standard BS 8887-2:2009, “reusing” is the operation by which a product is put back into use for the same purpose at its end-of-life. In order to reuse the material after the end-of-life of a system, its design must be disassembled and reversible to return to its original situation (Gorgolewski, 2017). In the case of fiber-reinforced polymer composites, disassembly is defined as the separation between the joints that connect the fibrous structure to the context, and reversibility can be defined as the ability to unwind and wind the spool of fiber-reinforced polymer composite without losing any mechanical or physical properties. “Reusing of Fibrous Tectonics” consists of three related but distinct fields: material, computational design, and digital fabrication. Its concept can be summarized in Figure 4.

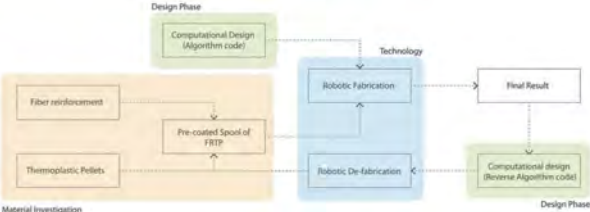


Figure 4. Research overview.

4.1 Fiber-reinforced thermoplastic polymer composites (FRTPs)

Although thermoset resins are more frequently used in fiber-reinforced polymer composites than thermoplastic resins, this study will use a thermoplastic resin. The pre-impregnated fiber-reinforced thermoplastic polymer composite (FRTP) is used in the research project, and an elastomer thermoplastic matrix has been used to feed the disassembly and reversibility, which are essential for the reusing process. The research project also makes use of the FRTP in the form of roving, which is a bundle of straight strands wound onto spools (Figure 5). However, the aim of this research is only to reuse the materials, but the use of thermoplastic matrix can bring about the possibility of recycling for future development. The unwinding and winding processes are made simpler by the composite’s increased flexibility as a result of the use of elastomer thermoplastic resin. The FRTP spools have already been impregnated and manufactured in the factory. According to the mechanical properties of the FRTP, a design and optimization process is run to reach the final shape of the structure.



Figure 5. Spool of fiber-reinforced thermoplastic polymer composite.

4.2 Form-finding process and fibrous pattern generation

An integral component of this project, which investigated the material’s reusability, was the form-finding procedure. In this study, the form-finding procedure was restricted to the generation of straightforward random patterns. For instance, no two consecutive points could be on the same side of the frame, and each loop had to have four points (mullion or transom). It is significant to note that no load was taken into account when finding the form. Because this is a lab-scale project, the paper’s main emphasis is on reusability. The points were exported in order to be imported for the fabrication part after choosing the fibrous pattern. In Figure 6, the code used to generate the pattern in the Grasshopper can be seen.

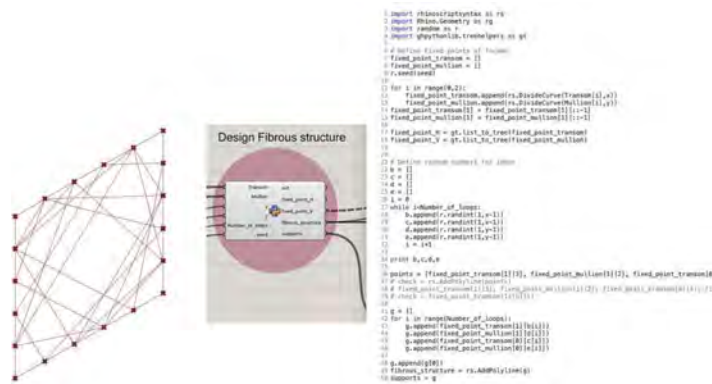


Figure 6. Fibrous pattern generation through grasshopper.

4.3 Lab-scale robotic fabrication system for in-situ fabrication and de-fabrication

The current use of industrial-type robots is primarily suitable for off-site and prefabrication of building components (Dörfler et al., 2019), which can increase the cost of transportation and the total cost in general. However, robotic technology in architecture brings greater freedom, the ability to fabricate intricate shapes and geometries (Dörfler et al., 2019), and improves the sustainability, efficiency, and productivity of building construction. The vertical-robotic system is inspired by the Polargraph drawing robot (<http://www.polargraph.co.uk/>), which includes three different yet connected subgroups. The material subgroups consist of spools of pre-impregnated fiber-reinforced elastomer polymer composite that are flexible enough to unwind and are used to fabricate the secondary structure of the façade system plus the tensioning system. The hardware subgroups, which included two motors, an electronics setup, and an Arduino, moved the end-effector (which is just responsible for fiber placement in this research) to wind the continuous fiber-reinforced thermoplastic polymer (FRTP) composite in the exact place according to the data that came from the design subgroups. The design subgroup is responsible for changing the data coming from the design and optimization process into data that can be read by hardware subgroups. Figure 6 presents the scheme of in-situ robotic fabrication on a façade.

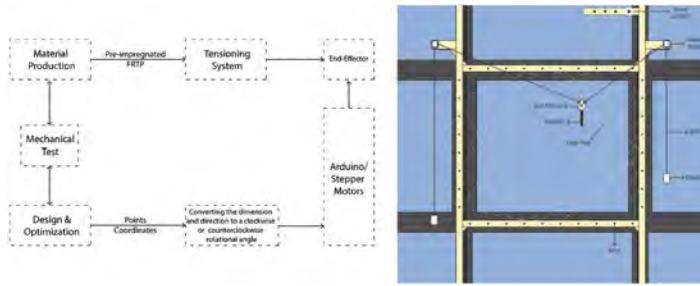


Figure 7. Robotics sub-groups.

During the form-finding process, each loop, which can be a rectangle, is considered a linear connection between four anchor points (two on the mullions and two on the transoms). The final solution of the form-finding process can be summarized in point coordinates, which represent the index of anchor points, respectively. These coordinates will be translated into angles that can be read by the Arduino and implemented by motors. The design subgroup considers any two points in a row as the direction of movement and changes the points' coordinates to the radius that is readable for the stepper motor. No load has been considered in the form-finding process. The difference between the fabrication process and the de-fabrication process is the order of anchor points. In fabrication, the order should be from the point with index 0 to the point with index -1, whereas in de-fabrication, the order should be reversed. Contrary to the de-fabrication process, which uses an additional servo motor to help wind the fiber-reinforced polymer composite back onto the spool, a tensioning system is utilized in the fabrication process since the fiber-reinforced polymer composite has to be pre-tensioned before the filament winding technique. Figure 8 shows the fabrication diagram of one loop of fibrous structure for the facade system. The result of this research has been prototyped at 1:1 scale in the laboratory as an internal secondary structural system for façade to test the reliability and functionality of the methodology exclusively for the fabrication and de-fabrication processes.

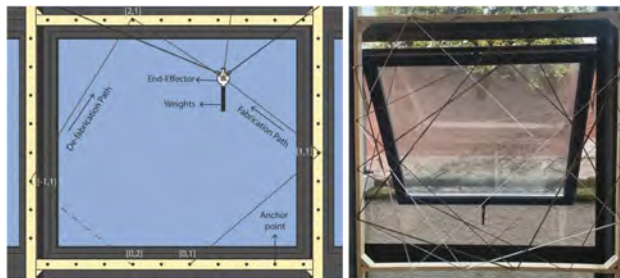


Figure 8. Fabrication diagram + final result - * [Index of point, Number of loop].

5 CONCLUSIONS

In order to overcome the difficulties and restrictions associated with using FRP composites in building-scale applications, this paper introduces a novel strategy that involves incorporating a design approach that emphasizes reusability, end-of-life, and environmental impact into the fabrication workflow of a fibrous structure for the secondary structure of a facade. In-situ fabrication is made possible by the suggested robotic system, opening up new avenues for the construction industry. This strategy may help to advance sustainability in the field of fibrous tectonics by using an elastomer thermoplastic matrix for the FRP composite. This study makes a contribution to the field by providing a fresh viewpoint on the use of FRP composites and outlining a potential fix for the environmental problems that currently prevent their use in large-scale construction projects.

This paper is part of a research project conducted at Politecnico di Milano's TextilesHUB laboratory with the collaboration of the i-mesh company, and it focuses primarily on the lab-scale prototyping.

REFERENCES

- Arhant, M., Davies, P. 2019. 2-Thermoplastic matrix composites for marine applications. In *Marine Composites*; Pemberton, R., Summerscales, J., Graham-Jones, J., Cambridge: Woodhead Publishing; pp. 31–53.
- Bakis, C.E., L.C. Bank, V.L. Brown, E. Cosenza, J.F. Davalos, J.J. Lesko, A. Machida, S.H. Rizkalla, & T.C. Triantafillou. 2002. fiber reinforced polymer composites for construction; state-of-the-art review. *journal of composites for construction* 6(2): 73–87
- Bhargava, A.K. 2004. *Engineering Materials: Polymers, Ceramics and Composites*. New Delhi, India: Prentice-Hall of India Pvt. Ltd.
- Boon, Y.D.; Joshi, S.C.; Bhudolia, S.K. 2021. Review: Filament Winding and Automated Fiber Placement with In Situ Consolidation for Fiber Reinforced Thermoplastic Polymer Composites. *Polymers*. BS 8887–2:2009 Standard (2009). *Design for manufacture, assembly, disassembly and end-of-life processing*. Terms and definitions.
- Dambrosio, N., Zechmeister, C., Bodea, S., Koslowski, V., Gil, P. M., Rongen, B., Knippers, J. & Menges, A. (2019). BUGA FIBRE PAVILION: Towards an architectural application of novel fiber composite building systems. *39th ACADIA Conference 2019*. The University of Texas at Austin School of Architecture, Austin, Texas.
- Dörfler, K., Hack, N., Sandy, T. et al. 2019. Mobile robotic fabrication beyond factory conditions: case study Mesh Mould wall of the DFAB HOUSE. *Construction Robot.* (3): 53–67.
- Ghanbari, A, Seyedin, S, Nofar, M, Ameli, A. 2021. Mechanical properties and foaming behavior of polypropylene/elastomer/recycled carbon fiber composites. *Polymer Composites*. (42): 3482–3492.
- Gorgolewski M. 2017. *Resource Salvation: the Architecture of Reuse*, Oxford: Wiley Blackwell.
- Herrmann, C., Dewulf, W., Hauschild, M., Kaluza, A., Kara, S., & Skerlos, S. 2018. Life cycle engineering of lightweight structures. *C I R P Annals*. 67(2): 651–672. <https://doi.org/10.1016/j.cirp.2018.05.008>.
- Kang, D, Lee, J-M, Moon, C, Kim, H-I. 2021. Improvement in mechanical properties of recycled polypropylene composite by controlling the length distribution of glass fibers. *Polymer Composites*. (42) 2171–2179.
- Knippers, J.; Cremers, J.; Gabler, M.; Lienhard, J. 2012. *Construction Manual for Polymers + Membranes*. Berlin: Walter de Gruyter.
- Liu, Y.; Zwingmann, B.; Schlaich, M. 2015. Carbon Fiber Reinforced Polymer for Cable Structures—A Review. *Polymers* (7): 2078–2099. <https://doi.org/10.3390/polym7101501>
- Ng, W.Y., & Chau, C.K. 2015. New Life of the Building Materials- Recycle, Reuse and Recovery. *Energy Procedia* (75): 2884–2891.
- Nishida, H., Carveli, V., Fujii, T. & Okubo, K. 2018. Thermoplastic vs. thermoset epoxy carbon textile composites. *IOP Conf. Series: Materials Science and Engineering*. (406).
- Pender, K. and Yang, L. 2019. Investigation of catalyzed thermal recycling for glass fiber-reinforced epoxy using fluidized bed process. *Polymer Composite* (40):3510-3519. <https://doi.org/10.1002/pc.25213>.
- Rybicka, J., Tiwari, A. and Leeke, G.A. 2016. Technology readiness level assessment of composites recycling technologies. *Journal of Cleaner Production* (112 -Part 1):1001–1012.
- Von Freeden, J., Erb, J., Schleifenbaum, M. 2022. *Polymer Composite*. 43(4): 1887.
- Waimer, F., La Magna, R., Reichert, S., Schwinn, T., Menges, A. & Knippers, J.. In: Gengnagel C, editor. *Rethink. Prototyping, proc. des. model. symp.* Berlin: Verlag der Universität der Künste Berlin; 2013. p. 277–90.
- Xue X., Liu S.Y., Zhang Z.Y., Wang Q.Z., Xiao C.Z. 2022. A technology review of recycling methods for fiber-reinforced thermosets. *Journal of Reinforced Plastics and Composites*;41(11-12):459–480.
- Żyjewski, A., Chróścielewski, J., & Pyrzowski, Ł. 2017. The use of fibre-reinforced polymers (FRP) in bridges as a favourable solution for the environment. *9th Conference on Interdisciplinary Problems in Environmental Protection and Engineering EKO-DOK 2017*, 17, 102–110.

Properties and durability of recycled concrete with mixed granulates: Application for infrastructures

C. Paglia, C. Mosca & E. Giner Cordero

Institute of Materials and Constructions, Mendrisio, Switzerland

ABSTRACT: In the last decades recycled concrete was widely investigated. The reuse of crushed cementitious aggregates allows to close a loop towards a circular economy. In this concern, the cement-based materials are particularly important, because of their worldwide use. The addition of recycled concrete aggregates to produce new concrete is done for many applications in the building sector. Properties such as the compressive strength or the durability issues are attained with an adequate mix proportion and quality of the components. On the other hand, the concrete produced with mixed granulates, such as ceramics, stone and cementitious wastes as main ingredients, still remains an issue to clarify. This work analyzes the main inert components that may be collected in regional recycling centers and preliminary reviews the properties and the durability of recycled concrete that may be produced with a variable content of the components. This allows to better identify the possible uses of such recycled concrete for the infrastructures: embedding, support, basements, or structural.

1 INTRODUCTION

The sustainability is a wide topic that involves numerous building aspects that are linked to the life cycle and the environmental declaration of the products (Norm EN 15804:2021). The re-use of building materials became an important issue in the last decades. The enormous production of inert material waste during construction, such as for instance tunnel break aggregates or excavation as well as the demolition of built infrastructures triggered new finding and possibilities to recycle the mass. This was particularly investigated in the case of lack or reduction of disposal spaces. Many types of inert waste are considered in the building sector, such as recycled concrete aggregates, milled asphalt granulates, excavation or fluvial material, quarry debris, cementitious dusts, various type of ashes (Siddique et al. 2018). Most of the material tends to be re-used as broken coarse aggregates, while fine cementitious aggregates are still a limiting factor, that needs to be further investigated (Norm SIA 2030, 2021). On the other hand, cementitious binder alternatives in partial substitution of Portland cement try to focus on the geographical and geological availability and to reduce the burning temperature down to 800 °C and the CO₂ production, such as for LC3 cements (Scrivener et al. 2018).

In this work, the main focus was given to overview the recycled concrete produced with mixed inert granulates, although a brief indicative application was also treated for recycled concrete with cementitious aggregates. The aim is to further clarify the possible application of such an inhomogeneous material consisting of a mixed granulated recycled concrete, that nowadays is still widely disregarded in relevant engineering infrastructures and brought to disposal. In this concern, clear technical guidelines, compulsory requirements and financial support from the public administration may help to trigger a market for these type of recycled materials (OECD, 2017).

Nonetheless, every step must be followed by appropriate material quality controls.

2 RECYCLED CONCRETE

The recycled concrete aggregates (RCA) are largely used for low grade infrastructures, as a landfilling material or for road bases. This in spite of the fact that, the main mechanical properties, such as a useful compression strength can be easily achieved with an appropriate percentage of addition. This occurs also when the origin of the demolished cementitious material is unknown (Paglia et al. 2021).

The durability performance needed a longer investigation time (ACI Committee 555 2001), and it is still a matter of discussion. This is mainly caused by the microcracks present in the old mortar during the demolition processes and the high porosity (Xiao et al. 2021). The mortar remains the weakest zone for recycled concrete (Etxeberria et al. 2007); (Corinaldesi et al. 2009). At high level of RCA aggregate substitution from 50 to 100 % the durability properties, such as the chloride permeability is questionable [Kou et al. 2013]; (Kanellopoulos et al. 2014). The use of mineral admixture, such as fly ash or silica fume, have a positive effect (Kaur et al. 2021). In this concern, the reduction of the amount of adhered old mortar on the aggregates exhibited an improvement of the performance (Dimitriou et al. 2018). In addition, the CO₂ pre-treatment of waste hydrated cement paste (Mehdizadeh et al. 2022), the carbonation of concrete fines particles (Ho et al. 2021) and the wet carbonation of concrete fines, in order to obtain supplementary cementitious material with high pozzolanicity (Shen et al. 2022), appear to give interesting results. Nonetheless, with known high quality original concrete, that means, by clarifying if it is coming from a building or a bridge and with an appropriate mixing proportion not higher than 50 % of the recycled aggregates, it is possible to prepare a recycled concrete that complies with the main durability requirements (Paglia et al. 2022). By increasing the recycling cycles, the durability properties, such as the freeze/thaw resistance, the chloride ion permeability coefficient and the carbonation depth decreased (Zhu et al. 2019). This also takes place by multi-recycling of coarse aggregate (Ebrau et al. 2018). However, with the appropriate mix design and quality control it appears possible to achieve a 50 years structural concrete live span for each recycling cycle.

3 RECYCLED CONCRETE WITH MIXED GRANULATES

3.1 *The local issue and material source*

The concrete is a common source of recycled cementitious material, that derives from the construction demolition waste. Even more present are unsorted debris mixed materials, that comes from the demolition or from excavation (Figure 1 left). The variation of the components is relatively high. Some material supply to the disposal centers are particularly enriched in ceramic thin tiles (Figure 1 centre-left). This is a result from the demolition of internal part of buildings. In addition, drywall may be present in the debris. This latter component may cause potential expansion issues, when reused in concrete, due to the sulphate that interacts with the aluminate component of the cements. An increase in the ceramic brick and roofing tile elements (centre-right) and crushed fine-grained component (right).



Figure 1. Unsorted mixed debris (left), increase white ceramic tile's component (left-centre), higher brick and roofing tile elements (centre-right) and crushed fine-grained component (right).

tile elements may also be observed (centre-right). The crushing of all the elements to a fine-grained aggregate component < 22 mm (Figure 1 right) may create the conditions for the waste components to be recycled within the cementitious material. It must also be said that, within these mixed materials, wood, plastic and metallic wastes have also to be sorted out in order to get inert inorganic materials.

The geographic location and building culture may also influence the type of mixed materials picked up from the different demolition sites. In spite of the advised selective demolition, that needs to be applied in order to better separate some of the main components, different type of materials enter the actual disposal sites. This is mainly caused by the absence of a market for these type of mixed granulates. Consequently, there is a lack of such materials in the recycling sites and the materials are mainly brought to disposal.

In this concern, a log-term monitoring up to at least one year will be done to identify the type of debris present in the disposal sites. The main components will be identified and an evaluation of the separation possibilities will be investigated.

3.2 *Properties and durability of the concrete*

In order to define a recycled concrete a RC-M type, the content of mixed granulates (M) must be at least 10 % by mass. This percentage derives from a geographic local requirement (Norm SIA 2030:2021). The concrete produced with a mixture of clay stones and carbonate-rich sand debris needed a higher amount of water, because of the higher porosity and water adsorption (Leemann, et al. 1999). A reduction of the modulus of elasticity in structural tests was also found (Olia et al. 2000); (Hoffmann et al. 2006). The density was also lower as compared to natural stone components. The porosity of a mixture with an addition of 60 % by weight mixed granulates exhibited a porosity around 17 %. A little higher as compared to concretes mixed with 90 % recycled concrete aggregates and 30 % recycled concrete with 30 % mixed aggregates. All these latter mixes showed compressive strength on cubes above 45 Mpa after 28 days. On the other hand, the durability, especially the freeze/thaw resistance did not often reach the requirements [Hoffmann, 2006].

3.3 *The ceramic component*

Bricks are among the most used construction materials. Several old buildings in the recent decades were demolished and the availability of such debris increased (Li et al. 2016). Brick waste can be considered an eco-friendly material due to its chemical stability and inert behaviour. It appears that, the use of bricks in form of fine grained dust and added in substitution of cement, exhibits a pozzolanic activity and has a positive effect on strength and durability of concrete when the crushed bricks are added up to 20 % by weight. The pozzolanic activity of bricks derives from its production and chemical composition. Clays are exposed to fire at high temperatures and the main chemical composition indicates a content of SiO_2 , Al_2O_3 and CaO (Wild et al.1997). The crystallinity of the minerals (Walker et al. 2011) and the particle size may inhibit the pozzolanicity (Komnitsas et al. 2015). On the contrary, the use of bricks as coarse aggregate adversely affects the concrete property. This is caused by the porosity contained in the bricks and the addition in concrete should be limited only to contribute to a local environmental improvement (Wong, 2018). Nano brick powder was also added in replacement of cement up to 10 % and the 20 % substitution of sand aggregates improved the mechanical properties (Abbas et al. 2021). While the substitution of maximum 20 % brick aggregates has a similar effect on creep as with conventional concrete with natural aggregates (Gayarre et al. 2019). Bricks have a brittle behaviour and when added in form of aggregates they may increase the fragility of the concrete. This property will be tested in our mixtures. In addition, crushed brick components exhibit a strong angular component. This fact adversely affects the workability of the fresh cementitious blends. The workability and pumpability are reduced. These negative consequences must be faced with adequate chemical additives.

A first characterization of the chemical composition of bricks was done with SEM-EDX device at 15 kV. They exhibit SiO_2 , Al_2O_3 as main components and Na_2O for the solid bricks

(Table 1). The perforated bricks may exhibit CaO contents up to 50 % by weight as already observed (Wild et al. 1997). Occasionally FeO and MgO are also present up to 10 %.

Table 1. Main chemical composition of the solid brick.

Element Number	Element Symbol	Element Name	Atomic Conc.	Weight Conc.	Oxide Symbol	Stoich. Weight Conc.
6	C	Carbon	1.139	0.701		
8	O	Oxygen	68.518	56.156		
11	Na	Sodium	2.804	3.303	Na ₂ O	5.230
13	Al	Aluminum	8.260	11.411	Al ₂ O ₃	25.334
14	Si	Silicon	18.157	26.126	SiO ₂	65.652
16	S	Sulfur	0.000	0.000	SO ₂	0.000
17	Cl	Chlorine	0.000	0.000		
20	Ca	Calcium	1.121	2.302	CaO	3.784

The SEM investigation of the microstructure exhibits more platy phases and less porosity for the solid bricks (Figure 2 left) as compared to the perforated bricks (Figure 2 right). However, the pores are clearly visible in both cases and the microstructure partially assumes a sponge-like morphology. Pores are present in such materials (Wong et al. 2018) and may inhibit the use as coarse aggregates.

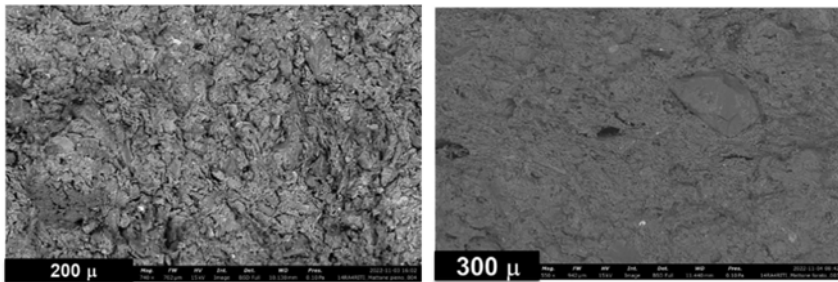


Figure 2. Overview of the bricks microstructure in the BSD mode.

In addition, the microstructure of the grinded particles of the solid bricks was investigated. They showed a predominant angular shape, rarely platy or elongated (Figure 3 left). The preliminary study of the particle in contact with water up to 24 hours shows an initial hydration reaction to form a relatively amorphous mass (Figure 3 right), although in this brick type the low CaO content does not allow the pozzolanic activity of the materials (Walker et al. 2011); (Komnitsas et al. 2015) to act and form a stiff gel.

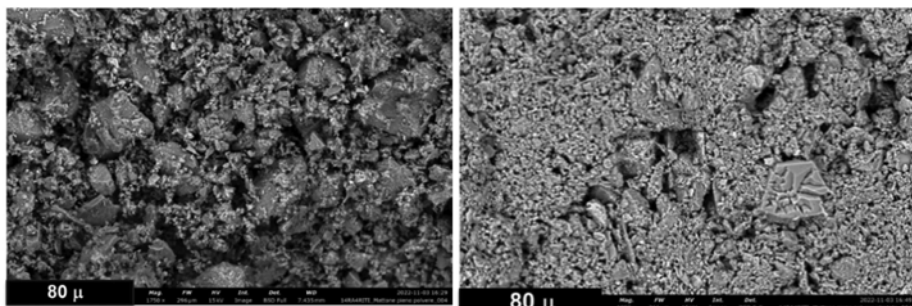


Figure 3. Solid bricks particles prior (left) and after (right) the contact with water up to 24 hours.

Ceramic waste recycled aggregates mainly composed of SiO_2 and Al_2O_3 and derived from sanitary installations are used as fine or coarse substitutions. Generally, the workability is decreased with the addition of such a component, while the mechanical properties and the durability tend to increase if 20 % addition is not exceeded (Magbool et al. 2022). The ceramic waste is used to replace the cement, due to the pozzolanic reactivity and as an aggregate replacement. In both cases, the mechanical performance and the durability was reported to increase also with 40 % substitution degree (Gautam et al. 2021). Durability, in particular chloride ion penetration, appears to be reduced, while the resistance to sulphate attack, resistance to abrasion and the electrical resistivity were reported to increase (Meena et al. 2022). This later parameter may help in reducing the corrosion susceptibility of reinforced concrete, but this fact still needs to be further clarified.

3.4 Application

At the moment, several low grade applications are thought for recycled concrete with cementitious aggregates (Figure 4). The experimental mixtures prepared with mixed granulates or with sorted single components such as brick, tiles or ceramic waste must clarify the possible uses of such concrete RC-M material for the orange parts of the infrastructures. The aim is to identify appropriate mix design that will allow such applications. In this concern and in the case of positive performance of the recycled cementitious RC-M concrete blends, the public sector will impose the use of such material and will create the premise for the development of a local market and the necessity for the recycling companies to collect such mixed waste material and sell it to the concrete producers.

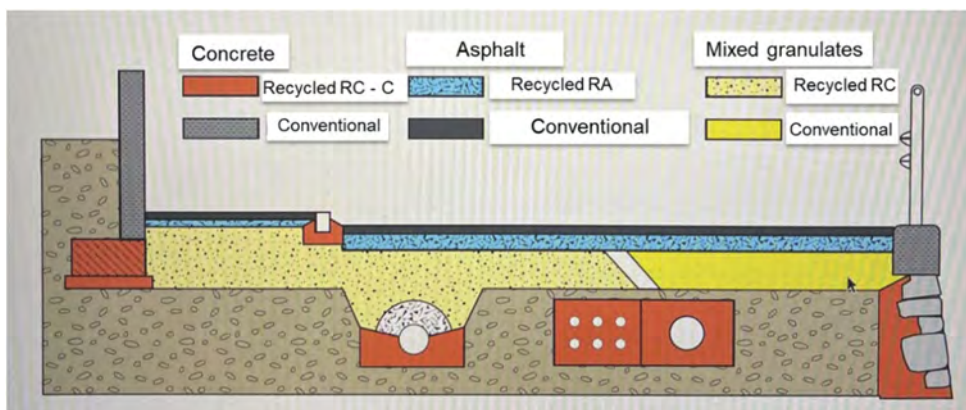


Figure 4. Uses of recycled components for the application in infrastructures.

The unsorted mixed material is actually collected into the disposals is considered not adequate to be reused in concrete. The significant inhomogeneity of the mixed components added to concrete does not allow a reliable production of material with adequate constant behaviour. Its quality would need to be constantly monitored. An unthinkable highly costs for the clients and the producers. On the other hand, more clear specifications or guidelines about the mix design, the mechanical as well as the durability parameters required by the different infrastructural applications may ease the use of a recycled concrete with the partial addition of some type of mixed granulated or single components.

3.5 Prospectives

The recycling of materials is an actual and big concern in the construction industry. At this stage it is necessary to deal with the old way to plan the buildings and the infrastructure. In

the past, often the multiple combination of materials created high performance construction systems from the point of view of the mechanical properties. On the other hand, the durability was mainly considered in the last decades and the reuse and recycling topics only arised in the recent years. This fact suggests another way of thinking when planning the future built environment.

At this stage we still need to deal with the old construction multiple systems. Consequently, during the demolition mixed debris are often present on sites. The demolition waste needs to be separated during the demolition process. If not possible, the separation of some main components is increasingly required in order to recycle high quality materials with known properties. In this regard, the use of some single components or the addition within concrete may be possible. Although further investigations must be done to clarify the influence on the mechanical, physical, chemical, durability and recycling properties of the recycled single components within the concrete. These are some of the aspects that will be clarified in our future work.

4 CONCLUSIONS

Mixed construction demolition debris are widely present in todays building sector. Mixed inert materials, such as excavation and demolition waste must find a better and high technological way to be reused or recycled. The addition of some single components within concrete can be done, while the addition of the mixed granulates has to be questioned. In fact, it is necessary to separate the main components of the mixed debris and better characterize their microstructure and function as a coarse or fine component within cementitious blends. Concrete with the addition of single debris components may be a more reliable way to recycle them. Especially brick or ceramic elements appear to have a change to be added within concrete as a fine pozzolanic addition. In addition, in a further recycle process, it would not be necessary to separate them, because of the similar inorganic nature of the concrete. Furthermore, the higher quality of the recycled material may be used for more technological application and not simply as a filler or protection materials for infrastructure.

ACKNOWLEDGEMENTS

The authors would like to thank the technicians of the Institute of materials and construction SUPSI for sample preparation and testing.

REFERENCES

- Abbas Z. K. & Abbood A., The influence of incorporating recycled brick on concrete Properties. *The 4th International Conference on Engineering Sciences (ICES 2020)*, IOP 1067, 2021.
- Abreu V., Evangelista L. & de Brito J., The effect of multi-recycling on the mechanical performance of coarse recycled aggregates concrete, *Construction and Building Materials* (188): 480–489, 2018.
- ACI Committee 555, *Removal and Reuse of Hardened Concrete*, 2001.
- Corinaldesi V. & Moriconi G., Behaviour of cementitious mortars containing different kinds of recycled aggregate, *Construction building materials* (23): 289–294, 2009.
- Dimitriou G., Savva P & Petrou M.F., Enhancing mechanical and durability properties of recycled aggregate concrete, *Construction and Building Materials* (158): 228–235, 2018.
- Etxeberria M., Vázquez E., Mari A. & Barra M., Influence of amount of recycled coarse aggregates and production process on properties of recycled aggregate concrete, *Cement concrete research* (37): 735–742, 2007.
- Gautam L., Jain J. K., Kalla P. & Choudhary S., A review on the utilization of ceramic waste in sustainable construction, *Products, Materials Today: Proceedings* (43): 1884–1891, 2021.
- Gayarre F. L., González J. S., López-Colina Pérez C., Serrano López M. A., Ros P.S. & Martínez-Barrera G., Shrinkage and creep in structural concrete with recycled brick. *Aggregates, Construction and Building Materials* (228), 2019.

- Ho H.J., Iizuka A., Shibata E., Tomita H., Takano A. & Endo T., *Utilization of CO₂ in direct aqueous carbonation of concrete fines generated from aggregate recycling: Influences of the solid–liquid ratio and CO₂ concentration*, *Journal of Cleaner Production* 312, 2021.
- Hoffmann C. & Huth O., *Swiss federal testing laboratories*, EMPA, November 2006.
- Kanellopoulos A., Nicolaides D. & Petrou M. F., Mechanical and durability properties of concretes containing recycled lime powder and recycled aggregates, *Construction building materials* (53): 253–259, 2014.
- Kaur G., Singh S.P. & Kaushik S.K., Reviewing some properties of concrete containing mineral admixtures, *Indian Concrete Journal*: 35–51, 2012.
- Komnitsas K., Zaharaki, D., Vlachou, A., Bartzas, G., Galetakis, M., Effect of synthesis parameters on the quality of construction and demolition wastes (CDW) geopolymers. *Advanced powder technology* 26 (2), 2015.
- Kou S.C. & Poon C.S., Long-term mechanical and durability properties of recycled aggregate concrete prepared with the incorporation of fly ash, *Cement concrete composite* (37): 12–19, 2013.
- Leemann A. & Olbrecht H., Concrete with mineral construction debris, *Tec* 21: 9–12, 1999.
- Li H., Dong, L., Jiang, Z., Yang, X. & Yang, Z., *Study on utilization of red brick waste powder in the production of cement-based red decorative plaster for walls*. *J. Clean. Prod.* 133, 2016.
- Magbool H. M, Utilisation of ceramic waste aggregate and its effect on Eco-friendly concrete: A review. *Journal of Building Engineering* (47), 2022.
- Meena R. V., Jaina J. K., Chouhan H. S. & Beniwal A. S., Use of waste ceramics to produce sustainable concrete: A review, *Cleaner Materials* (4), 2022.
- Mehdizadeh H., Cheng H.B38, Mo K.H. & Ling T.H, Upcycling of waste hydrated cement paste containing high-volume supplementary cementitious materials via CO₂ pre-treatment, *Journal of Building Engineering* (52), 2022.
- Norm EN 15804, Environmental product declaration, 2021.
- Norm SIA 2030, Concrete with recycled granulates, 2021.
- Olia S., Static load tests on concrete and recycled concrete beams. *Swiss Federal Testing Laboratories*, EMPA- Test report 840'031, 2000.
- Paglia C., Antonietti S. & Mosca C., Recycling cementitious aggregates in the building field, FTAL Conference 2021, *Sustainable smart cities and regions*, 28-29 October, Lugano, Switzerland, 2021.
- Paglia C., Paderi M., Mosca C. & Antonietti S., The recycling of a concrete with known properties to reproduce a durable material for the civil engineering infrastructure, *International meet on civil, structural and environmental engineering*, 23-26 Mai, Munich, Germany, online, Civilmeet 2022.

Behavior of bolted shear connectors for demountable and reusable UHPC-formed composite beams

H. Fang

University of Leeds, Leeds, West Yorkshire, UK

ABSTRACT: Steel-concrete composite beams are widely applied in the design and construction of bridges and buildings. Due to the urgent need for the transformation towards sustainability and net-zero, developments of innovative composite systems with improved life-cycle sustainability such as lower embodied carbon and the potential for reuse after the end-of-life stage are required. To address this challenge, this study aims to contribute to the development of the composite beams with the ultra-high performance concrete (UHPC) proven with lower life-cycle embodied carbon than conventional concrete and the high-strength steel (HSS) bolts as the shear connection that facilitates demountability and reuse to reduce the production of new materials and the associated carbon footprint. The behavior of HSS bolts embedded in UHPC slabs is investigated experimentally. The resistance, load-slip responses and failure modes of the HSS bolts are presented and discussed. The suitability of design approaches for shear connection in conventional concrete slab for the HSS bolt shear connection in UHPC slab is also assessed and discussed.

1 INTRODUCTION

Steel and concrete composite structural systems have been widely applied in the construction of various infrastructures owing to the outstanding structural performance compared with the reinforced-concrete or pure steel structures (Johnson 2004; Fang et al. 2023; Wang et al. 2023). Among different types of composite structural systems, steel-concrete composite beams with optimal material efficiency for load bearing are commonly used in medium- and high-rise building and bridges (Johnson 2004; Rehman et al. 2016). With the need to transit towards low-carbon construction and sustainability, reducing the embodied carbon of the structural systems in the life-cycle and eliminating the waste of the structures at the end-of-life stage are required. To realize these goals, research efforts are committed to develop low-carbon and reusable composite systems for their applications in next-generation infrastructures.

The embodied carbon of steel-concrete composite beams is quantified by the CO₂ equivalent emissions generated at different stages in the life cycle including the material production, construction, operation and demolition at the end-of-life stage. To reduce the embodied carbon of structures, alternative and more advanced materials for fabricating low-carbon steel-concrete composite beams are required (Zhao et al. 2021). Besides, accurate design approaches that enable to reduce the design conservatism can also effectively reduce the material consumption associated with the design and subsequent embodied carbon of the composite beams (Uy, 2018; Fang et al. 2021; Chen et al. 2022). Compared with the conventional concrete used to form the composite beams, ultra-high performance concrete developed with much higher strength and improved durability can be applied to form lighter and more durable composite beams. The reduced weight of materials and structures can bring the benefits of reducing energy consumption for the transportation and construction (Uy, 2018; Fang et al. 2023; Liu et al. 2022a). Besides, the outstanding durability of UHPC required much

reduced maintenance compared with the structural components that are formed with conventional concrete and experience gradually structural deterioration (Suwaed & Karavasilis 2017). Thus, the structures formed with UHPC are proven to have lower life-cycle embodied-carbon compared with the conventional concrete counterparts (Dong 2018). Considering these advantages of UHPC for developing low-carbon structural elements, UHPC materials are investigated for its use to form steel-UHPC composite beams to reduce the life-cycle embodied carbon of the structures.

Comprehensive understanding of the structural performance of steel-UHPC composite beams is necessary in order to generate reliable and efficient design of the structures. The structural resistance and stiffness of a composite beam depends on the design of shear connections that connect the steel section with concrete slab and effectively transfer the longitudinal shear forces between the steel and concrete components. Conventional headed stud shear connections are welded permanently to the steel beams, hindering the dis-assembly of structural components for maintenance during the service-life or reuse at the end-of-life stage for sustainability (Suwaed & Karavasilis 2017; Rehman et al. 2016). Demountable shear connection development for steel-UHPC composite beams will maximize the sustainability of the structures and bring the opportunity to dismantle the beams and reuse the components for new infrastructures, facilitating the sustainable future and circular economy of the industry. Therefore, the structural behavior and design of demountable shear connection for steel-UHPC composite beams is the focus of this study.

High strength bolted shear connectors that enable to easily deconstruct the composite beams for sustainable rebuild (Ataei et al. 2019; Moynihan & Allwood 2014) and provides higher strength than stud connectors were investigated experimentally in this study. Experiments were conducted on steel-UHPC composite beam elements with HSS bolted shear connectors to test the behavior of the shear connectors. The ultimate strength, load-slip characteristics and failure modes of the specimens with different parameters related to shear connector arrangements were reported and discussed. Furthermore, the ultimate strengths were also compared with those estimated based on existing standards and the applicability of those methods for predicting the strengths of the HSS bolted shear connectors embedded in UHPC slabs was discussed to provide basis for engineers to implement the design of the structures.

2 EXPERIMENTS

2.1 *Specimens and material properties*

Eight steel-UHPC composite specimens designed with HSS bolted shear connectors were prepared for the experiments. The size and arrangements such as the spacing and height of bolted shear connectors are the main parameters considered in this study to investigate their effects on the behavior of the demountable shear connection embedded in UHPC slab components in order to identify the key parameters for design optimization. The specimens and their parameters are given in Table 1. In the table, the labels of the specimens describe the HSS bolt size, the vertical spacing of the bolt rows and the height of shear connection in the slab. For example, the specimen S1-16-100-h90 refers to the specimen with eight M16 bolts, the embedded height as 90mm in the UHPC slab and the vertical spacing of 100mm between two rows of bolts. The specimens with the 'R' in the label refer to the repeated test specimens to confirm the reliability of the experiments. The geometric properties of a typical specimen, S1-16-100, is shown in Figure 1. For the specimens, the HSS bolts in the grade of 8.8 were used while the 250UB37.3 steel beams were chosen for the specimens. For each specimen, two UHPC slabs with the width of 320mm and the thickness of 120mm and with the embedment of two layers of 12mm reinforcements were cast and connected with the steel beam section via pre-drilled holes by using eight single-nut embedded and pre-tensioned bolts, as shown in Figure 1. During the UHPC placement for the specimens, cylinder UHPC specimens with the standard size of 100×200mm were also prepared for measuring the properties of UHPC.

Table 1. Parameters of the specimens for the experimental investigations.

Specimen	Bolt size	Vertical spacing for bolt rows	Bolt height embedded in UHPC slab (mm)
S-16-100-h90	16	100	90
S-16-100-h90R	16	100	90
S-16-100-h70	16	100	70
S-16-100-h70R	16	100	70
S-16-150-h90	16	150	90
S-16-200-h90	16	200	90
S-20-100-h90	20	100	90
S-20-100-h90R	20	100	90

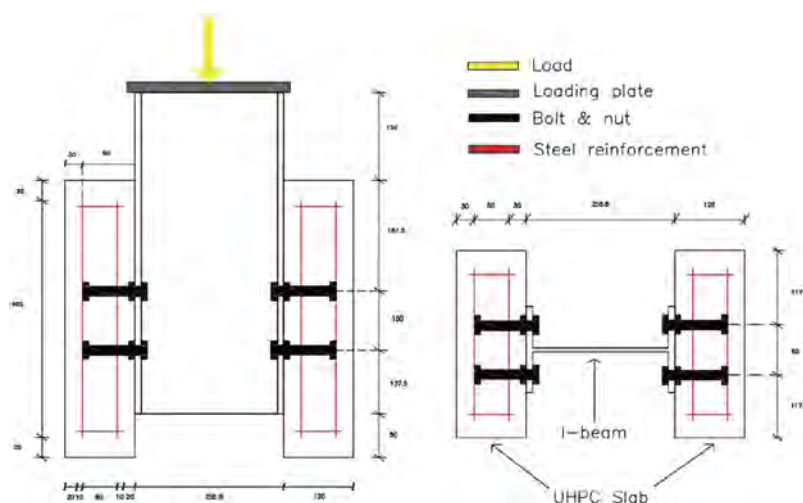


Figure 1. Dimensions in mm and details of the S-16-100-h90 specimen.

Material properties of the components forming the specimens were measured during the testing period for the steel-UHPC composite structural specimens. Tensile testing of the specimens extracted from the steel beam sections or fabricated from the 12mm reinforcements or HSS bolts were tested following the procedures applied in previous research for steel material property measurements (Liu et al. 2022b&c; Ke et al. 2023). The measurement results including the yield strength and ultimate strength were obtained, as shown in Table 2. The UHPC cylinder specimens were also tested during the days when the steel-UHPC specimens were tested after they were cured for more than 28 days. The resultant cylinder compressive strength (f_c) of the UHPC materials is 125MPa on average.

Table 2. Averaged material properties measurement results for the steel beam, reinforcements and HSS bolts.

Steel specimen	Components or size for each specimen	Yield strength (MPa)	Ultimate strength (MPa)
Steel beam section	flange	345	511
	web	374	519
12mm reinforcement	-	519	684
Grade 8.8 high-strength bolts	M16	790	932
	M20	754	886

2.2 Set-up and procedures of experiments

The steel-UHPC specimens with demountable HSS bolt shear connection were cured at ambient temperature for more than 28 days and subsequently tested using the set-up validated in previous studies (Pavlović and Veljković 2017; Zhang et al. 2019), as shown in Figure 2. The loading was applied to each specimen using a 5000kN loading cell via the displacement control. The displacement rate of 0.15mm/min was adopted to ensure the monotonic loading condition for the experiments and the capture of structural responses with the variation of the loading in the ascending and descending stages. Eight linear variable differential transformers (LVDTs) were located near the bolt connections to measure the slip between the steel and UHPC slabs, as shown in Figure 3.



Figure 2. The set-up of the testing on steel-UHPC composite structural specimen.



Figure 3. Locations of the LVDT placements on one side of the specimen for slip measurements.

2.3 Results of experiments

2.3.1 Failure mode

The failure mode observed for the specimens was the shear fracture failure of the bolts, as shown in Figures 4 and 5 for typical specimens with M16 and M20 bolts respectively. It can be observed in the figures that the fracture of the bolts occurred at the shear plane near the interface of the embedded nut and the steel beam flange, indicating the high stress concentration at the regions. Due to the very high strength of UHPC, minimal damage of the UHPC slab was observed, as shown in Figures 4 and 5.



Figure 4. Failure mode of S-16-150-h90 specimen.



Figure 5. Failure mode of S-20-100-h90 specimen.

2.3.2 Load-slip relationship and ultimate strength

The load versus slip relationship was also obtained from the experimental data and is plotted in Figures 6a and b for specimens with M16 and 20 bolts respectively. As can be seen in the figures, the pattern of the load-slip curves for different specimens is consistent. The variation of load with slip generally demonstrates four stages. At the initial stage, the load increases with quite limited increment of the slip due to the high friction generated at the interfaces of the steel beam and UHPC slab from pre-tensioning the HSS bolts. When the load becomes higher than the friction at the interface, in the second stage, the slip at the interface increases

obviously while the increment of loading is slower than that observed in the initial stage. The slip in the second stage is related to the clearance between the bolts and the pre-drilled holes in the steel beams. At the end of the second stage, the bolt shanks closely contacted the holes of the steel beams and the third stage of the load versus slip relationship started. The loads increased more significantly than that in the second stage since the steel beam and UHPC slab for each specimen transferred more load through the contact between the steel beam and bolted shear connection and that between the bolted shear connection and the UHPC slab. When the loading reached a relatively high level for a specimen, the slip increased gradually with very limited increment of the loading until the bolted shear connection experienced the fracture failure.

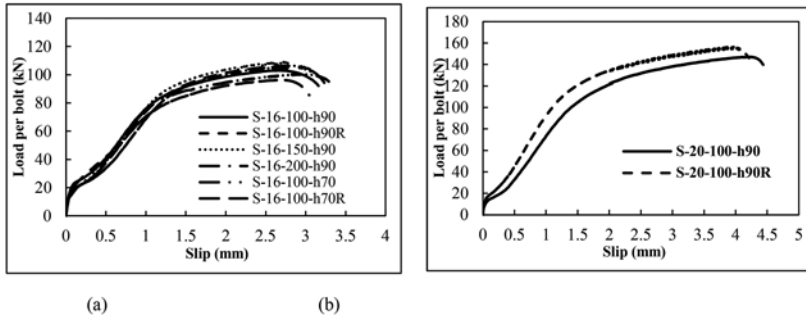


Figure 6. Load-slip curves for typical specimens prepared using (a) M16 bolts and (b) M 20 bolts.

From the load-slip curves, the ultimate strength of the specimens can be obtained and are reported in Table 3 as the resistance ($N_{u,exp}$) per bolt of each specimen. It can be observed in the table that the differences between the $N_{u,exp}$ measured for the specimens designed with the same parameters are minimal. By comparing the $N_{u,exp}$ for the S-16-100-h90 and S-16-100-h90R specimens with those for S-16-100-h70 and S-16-100-h70R, it is evident that the resistance of the high-strength bolted shear connection in UHPC slab is insensitive to the height embedded in the slab. Besides, the effect of vertical spacing between the rows of HSS bolts is also revealed from the results shown in Figure 6 and Table 3. The difference of the $N_{u,exp}$ for S-16-100-h90, S-16-100-h90R, S-16-150-h90 and S-16-200-h90 specimens with different vertical spacing between the rows of shear connection is less than 5%. Thus, the influence of vertical spacing is also limited. Furthermore, the performance of HSS bolt shear connection with larger sizes was also investigated. It is shown that increasing the size of the shear connection from M16 to M20 effectively leads to higher resistance and improved ductility, as observed in Figure 6 and Table 3. On average, the $N_{u,exp}$ for the specimens with M20 HSS bolts is about 46% higher than that for specimens with M16 HSS bolts.

Table 3. Ultimate strength from experiments and those predicted using design approaches.

Specimen	Resistance per bolt from experiments $N_{u,exp}$ (kN)	$N_{u,EC}$ (kN)	$N_{u,AS}$ (kN)
S-16-100-h90	102.9	99.98	119.35
S-16-100-h90R	105.4	99.98	119.35
S-16-100-h70	100.4	99.98	119.35
S-16-100-h70R	96.3	99.98	119.35
S-16-150-h90	108.9	99.98	119.35
S-16-200-h90	106.5	99.98	119.35
S-20-100-h90	147.2	148.4	177.14
S-20-100-h90R	156.4	148.4	177.14

3 EVALUATION OF EXISTING DESIGN APPROACHES

The experimental results for the resistance of HSS bolted shear connection are also used to evaluate the applicability of existing design approaches given for shear connections embedded in conventional concrete slabs. The accuracy of the design approaches in Eurocode 4 and Australian standard is described in the following sections.

3.1 Eurocode 4

Eurocode 4 primarily provides the specifications for estimating the resistance of headed stud shear connection for steel-concrete composite beams. The resistance for each shear connection ($N_{u,EC}$) can be taken as the lesser of the values estimated using Equations (1) and (2). In the equations, d is the diameter of the headed-stud shear connection, f_c is the compressive strength of the concrete slab, γ_v is the partial factor as 1.5 and E_{cm} is the elastic modulus of the concrete slab. In Equation (2), the parameter α is related to the height of shear connection (h_{sc}) embedded in the slab and can be calculated using Equation (3).

$$N_{u,EC} = 0.8 \times f_u \times \pi \times \frac{d^2}{4} / \gamma_v \quad (1)$$

$$N_{u,EC} = 0.29 \times \alpha \times d^2 \sqrt{f_c \times E_{cm}} / \gamma_v \quad (2)$$

$$\alpha = \begin{cases} 0.2 \left(\frac{h_{sc}}{d} + 1 \right) & \text{for } 3 \leq h_{sc}/d \leq 4 \\ 1 & \text{for } h_{sc}/d > 4 \end{cases} \quad (3)$$

These specifications were applied to estimate the resistance of HSS bolted shear connection with the strength predictions shown in Table 3. As can be seen in the table, the $N_{u,EC}$ estimated based on the Eurocode 4 are slightly lower than the $N_{u,exp}$ from experimental results. The mean value of $N_{u,exp}/N_{u,EC}$ ratios equals to 1.03 with the coefficient of variation (CoV) as 0.04, showing the close agreements between the $N_{u,EC}$ and $N_{u,exp}$.

3.2 Australian standard AS 2327

The Australian standard AS 2327 provides the approach for estimating the resistance ($N_{u,AS}$) of HSS bolted shear connection, as the lesser value calculated using Equation (4). The $N_{u,AS}$ estimated for the specimens tested in experiments are presented in Table 3. It can be seen in Table 3 that the resistance of the shear connection was overestimated based on AS 2327. On average, the $N_{u,AS}$ is higher than $N_{u,exp}$ by about 15% with the CoV of 0.04. Comparing the specifications from Eurocode 4 and AS 2327, the Eurocode 4 provides conservative strength predictions for the HSS bolted shear connection embedded in UHPC slab.

$$N_{u,AS} = \begin{cases} 0.5 \times d^2 \times f_u \\ 0.29 \times d^2 \sqrt{f_c \times E_{cm}} \end{cases} \quad (4)$$

4 CONCLUSIONS

The HSS bolted shear connection for steel-UHPC composite beams with demountability for reuse of the structural components were experimentally investigated in this study. Steel-UHPC beam components formed using HSS bolted shear connections with different dimensions, height in the UHPC slab and spacing between the rows of shear connection were prepared and tested in experiments. The experimental results show that the dimensions of the shear connection can significantly influence the resistance while the resistance of the HSS bolted shear connection is

insensitive to the height and spacing. The typical failure mode of the specimens is the shear connection fracture failure since the UHPC slab has quite high compressive strength and experiences ignorable damages. Based on the experimental results, the applicability of approaches in Eurocode 4 and AS 2327 standards for the design of shear connection in conventional steel-concrete composite beams to the HSS bolted shear connection in steel-UHPC composite beams was evaluated. The Eurocode 4 provides quite accurate and slightly conservative predictions for the resistance. However, AS 2327 standard provides unconservative strength predictions. Therefore, the specifications in Eurocode 4 can be considered and used in the design of steel-UHPC composite beams with HSS bolted shear connection.

REFERENCES

- AS/NZS 2327 2017. *Composite steel-concrete construction for buildings*, Standard Australia/New Zealand.
- Ataei, A., Zeynalian, M. & Yazdi Y. 2019. Cyclic behaviour of bolted shear connectors in steel-concrete composite beams. *Engineering Structures* 198: 109455.
- Chen, S.X., Fang, H., Liu, J.Z. & Chan, T.M. 2022. Design for local buckling behaviour of welded high strength steel I-sections under bending. *Thin-Walled Structures* 172: 108792.
- Dong 2018. Performance assessment and design of ultra-high performance concrete (UHPC) structures incorporating life-cycle cost and environmental impacts. *Construction and Building Materials*, 167, 414–425.
- EN1994-1-12004. *Eurocode 4: Design of Composite Steel and Concrete Structures-Part1-1: General Rules and Rules for Buildings*, European Committee for Standardization.
- Fang, H., Chan, T.M. & Young, B. 2021. Structural performance of concrete-filled cold-formed high-strength steel octagonal tubular stub columns. *Engineering Structures* 239: 112360.
- Fang, H., Li, Q.Y., Chan, T.M. & Young, B. 2023. Behaviour and design of high-strength octagonal CFST short columns subjected to combined compression and bending. *Journal of Constructional Steel Research* 200: 107679.
- Johnson, R.P. 2004. *Composite structures of steel and concrete: beams, slabs, columns, and frames for buildings*. Oxford, UK: Blackwell Publishing: p 41–45.
- Ke, K., Chen, Y.H., Zhou, X.H., Yam, M.C.H. & Hu, S.L. 2023. Experimental and numerical study of a brace-type hybrid damper with steel slit plates enhanced by friction mechanism. *Thin-Walled Structures* 182: 110249.
- Liu, J.Z., Fang, H. & Chan, T.M. 2022a. Experimental investigations on material properties and stub column behaviour of high strength steel irregular hexagonal hollow sections. *Journal of Constructional Steel Research* 196: 107343.
- Liu, J.Z., Fang, H. & Chan, T.M. 2022b. Investigations on material properties and residual stresses in cold-formed high strength steel irregular hexagonal hollow sections. *Thin-Walled Structures* 176: 109220.
- Liu, J.Z., Fang, H. & Chan, T.M. 2022c. Material properties and residual stresses of high strength steel hexagonal hollow sections. *Journal of Constructional Steel Research* 190: 107061.
- Moynihan, M.C. & Allwood, J.M. 2014. Viability and performance of demountable composite connectors. *Journal of Constructional Steel Research* 99: 47–56.
- Pavlović, M. & Veljković, M. 2017. FE validation of push-out tests using bolts as shear connectors. *Steel Construction* 10(2): 135–144.
- Rehman, N., Lam, D., Dai, X. & Ashour, A.F. 2016. Experimental study on demountable shear connectors in composite slabs with profiled decking. *Journal of Constructional Steel Research* 122: 178–189.
- Suwaed, A.S.H. & Karavasilis, T.L. 2017. Experimental evaluation of a novel demountable shear connector for accelerated repair or replacement of precast steel-concrete composite bridges. *Celpapers 1*: 4163–4172.
- Uy, B. 2018. Applications, behavior, and construction of high performance steels in steel-concrete composite structures. *Proceedings of 12th International Conference on advances in Steel-Concrete Composite Structures*, València, Spain, 91–97.
- Wang, J.J., Ke, K., Yam, M.C.H., Teng, M.H. & Wang, W. 2023. Improving structural robustness of steel frame buildings by enhancing floor deck connections. *Journal of Constructional Steel Research* 204: 107842.
- Zhang, Y.J., Chen, B.C., Liu, A.R., Pi, Y.L., Zhang, J.P., Wang, Y. & Zhong, L.C. 2019. Experimental study on shear behavior of high strength bolt connection in prefabricated steel-concrete composite beam. *Composites Part B* 159: 481–489.
- Zhao, M.H., Dong, Y. & Guo, H.Y. 2021. Comparative life cycle assessment of composite structures incorporating uncertainty and global sensitivity analysis. *Engineering Structures* 242: 112394.

MS2: Smart condition assessment of railway bridges
Organizers: T. Bittencourt, R. Calçada, D. Ribeiro,
H. Carvalho, M. Massao & P. Montenegro



Taylor & Francis

Taylor & Francis Group

<http://taylorandfrancis.com>

A monitoring based digital twin for the Filstal bridges

A. Lazoglu & H. Naraniecki
MKP GmbH, Hanover, Germany

I. Zaidman
DB Projekt Stuttgart-Ulm GmbH, Stuttgart, Germany

S. Marx
Technical University Dresden, Dresden, Germany

ABSTRACT: Ongoing advances in information technology enable improvements in both the quality and topicality of data-based condition information of physical structures. The digital twin, a sensor-based method to simulate a physical structure, is a promising approach to achieve a preventive and even partly predictive maintenance strategy in the future. This paper provides a digital twin concept for the Filstal railway bridges in Germany. Because of its importance for the transport network, its complex structural components and thus extensive condition monitoring, the Filstal bridges are well suited for the usage of a digital twin. The concept includes the integration, processing and aggregation of data from bridge inspections and analytical structural safety verifications as well as monitoring and diagnostic examinations to continuously display the bridge condition. Although the example at hand will be realized for a railway bridge, the core approach can be used for other bridge structures as well.

1 DIGITAL TWINS FOR FUTURE BRIDGE MAINTENANCE

In 2015, the United Nations unanimously adopted the 2030 Agenda including 17 sustainable development goals. These goals are global aspirations for a sustainable impact on social, economic and ecological developments. Goals number 9 and 13 relate to developments of sustainable, reliable and resource-efficient infrastructure by 2030, considering the Climate Change Program (United Nations 2022).

The German sustainability strategy for road and railway constructions incorporates the above-mentioned objectives and is characterized by the principle of “preservation before new construction” (BMVI 2021). Maintenance management for transport infrastructure in Germany, especially for bridges, is mainly carried out through regular visual inspections and analytical safety verifications. In addition, monitoring or diagnostic examinations of structures may become necessary. The heterogeneous data accumulated over the lifetime of a bridge is often available decentrally from different sources, both digital and analogue, and thus without contextualization.

Technical progress and digitalization are now able to support. High quality sensors, high computing power and complex algorithms for data analysis enable more detailed and higher quality condition acquisition and assessment. Furthermore, the improvement of collaborative work with digital data in BIM as well as the Internet of Things (IoT) offer an excellent basis for creating digital twins, which can positively influence the maintenance strategy of a structure and can therefore result in prolonged operational lifespan. Some initial realizations already show approaches and experience in the creation of digital bridge twins in practice, including (Hagen et. al. 2022), (Pregolato et. al. 2022) and (Wenner et. al. 2021). A comparison of these practical examples illustrates the heterogeneous approaches.

First guidelines such as the smart construction guideline (MEED 2021) or the Gemini principles (Bolton et al. 2018) have already been published internationally. In Germany, an initial guideline for digital twins in operation was developed by the Federal Ministry for Digital and Transport in 2022. With the Filstal bridges, a digital twin is being created for the first time for a railway bridge in Germany.

2 THE FILSTAL BRIDGES

The Filstal bridges are two parallel single-track railway overpasses in southwest Germany and are considered as prestigious due to their special construction method. The bridges went into operation in December 2022. Built as semi-integral structures, with continuous girders over six spans and structure lengths of 472 m and 485 m, the two bridges cross the valley of the Fils at a height of 75 m and are thus the third highest railway bridges in Germany (cf. Figure 1).



Figure 1. 3D scan of the right Filstal bridge.

The extraordinarily slender and deformable pillars are monolithically connected to the superstructure. Above the river, both structures are braced with two V-shaped pillars each, which have the function of frames. The superstructures are designed as longitudinally prestressed box girders. In (Zaidman et. al. 2022) the construction details and special features are discussed in more detail.

Due to exceptions from the common, normatively regulated design of railway bridges, calculation assumptions at neuralgic areas must be monitored and validated. For a better understanding, the most important neuralgic areas are briefly explained below.

- The longitudinal support of each bridge is designed as a special construction consisting of two crossing steel lamellas. The functionality of this longitudinal restraint bearings is relevant for the stability of the structures (cf. Figure 2 left).
- The guide bearings of the superstructures at the abutments limit the lateral displacement of the rail superstructure. The functionality of the bearings is therefore significant for traffic safety (cf. Figure 2 right).
- Large rail deformations can occur above the superstructure transitions. Joint constructions, rail extensions and special rail support points are installed at the transitions. The functionality of these constructions ensures traffic.
- The structures were shifted longitudinally after completion to initiate a compressive stress in the longitudinal restraint bearings. This longitudinal adjustment compensates the shortening of the structure from creepage and shrinkage. A renewed shift was predicted in 12 years after initial shift.
- In the case of superstructure deformation, high bending moments may be seen in the monolithic pillars. The design loads for tensile and compressive stresses of the superstructure may therefore not be exceeded.

One requirement for the operation of the bridge is a data plausibility check which is triggered once monitoring values exceed certain limits. In such a case, a warning message is sent to the person in charge.



Figure 2. Examples of neuralgic components - longitudinal restraint bearing (left) and guide bearing (right).

3 STRUCTURAL HEALTH MONITORING AND ALARM SYSTEM

For condition monitoring of the neuralgic areas of the Filstal bridges, an extensive monitoring system with 192 sensors was installed. Strain gauges on the longitudinal restraint bearings record local stresses and global forces for an evaluation of the functionality. Displacement sensors and inclinometers record relative displacements and relative rotations at the structural joints at the transition to the abutments, whereby bearing clearances can be evaluated. Furthermore, strain gauges and temperature sensors are applied on the reinforcement bars within the filigree pillars to record the pillar strains and compare them with permissible stresses. Temperature sensors at different cross-sections in the structure are used to extract the temperature-induced longitudinal displacements of the structure from the long-term total displacement and thus isolate the remaining creepage and shrinkage components. This is used to calculate the time of the subsequent longitudinal adjustment of the superstructures.

The measurement rate of the sensors is between 100 and 2500 Hz depending on the sensor type. All data are automatically transferred from the on-site measuring system to a cloud storage and form the basis for comprehensive multi-stage processing. The subsequent data processing procedures are modular. A module can contain general or structure-specific algorithms. Through a composition of several modules, an evaluation logic can be generated. Linked modules represent a workflow. The individual modules are technically implemented in the form of microservices. All workflows are managed and monitored by an orchestration framework. Every condition, every interim result and every processing step can be viewed and traced. Workflows can be started using event-based or time-controlled triggers. Figure 3 shows a simplified illustration of the data paths.

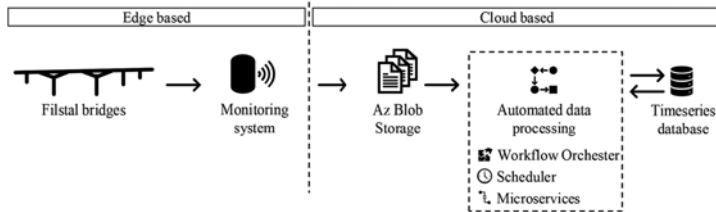


Figure 3. Data paths from acquisition to evaluation of the measurement data.

To achieve the highest possible data topicality, high frequency data transfer and data processing is required. This is why the processing steps were automated. The result of the data pre- and postprocessing steps gives quality-assured data as well as an evaluation of structural condition.

Calculations are carried out for the data from the neuralgic structures, which return the current conditions of the structure as a result. Raw data, calculated result data and conditions can be displayed, retrieved and analyzed via a created web platform (cf. Figure 4). The platform is available to those responsible for monitoring and checking the plausibility of the data.



Figure 4. Illustration of the Filstal bridges project in the web platform.

4 CONCEPT OF THE DIGITAL TWIN

4.1 *Connectivity and maturity of digital twins in bridge maintenance*

Depending on the industry sector and scope of the application, digital images of physical objects serve different purposes, leading to different definitions and characterizations (Grieves & Vickers 2017). In the context of bridge maintenance, the following summarizes definitions from the current state of the literature.

Digital twins are digital images of physical components (e.g. abutments), assets (e.g. bridges), systems (e.g. traffic routes), or processes (e.g. traffic management). A characteristic difference is the manual or automated data exchange between the physical object and the digital image. In (Kritzinger et. al. 2018), three degrees of connectivity are distinguished: The digital model (no automated data exchange), the digital shadow (unidirectional automated data exchange from the physical object to the digital images) and the digital twin (bidirectional automated data exchange). In (ARUP 2019), the metric “autonomy” is defined as the degree of independence from human interaction. In addition, the metrics “intelligence”, “learning” and “fidelity” are described. “Intelligence” describes the degree of replication of cognitive processes and fulfilment of tasks, “learning” is the degree of automatic learning for process optimization and “fidelity” is the degree of accuracy or closeness to reality of the available information. The metrics are assigned in five levels from 1-5. In (BuildingSMART 2022), five levels of maturity are also defined for the depth of information within the digital image. The first descriptive maturity level contains as-built data and is, for example, equivalent to a pure BIM model of the physical object. The second maturity level describes an informative representation and additionally uses sensor data, carries out analyses and aggregations and displays the gained information. The third maturity level enables predictivity by predicting future conditions. The prescriptive maturity level furthermore independently develops recommendations for action. In the last, fifth level of maturity, the digital representation acts autonomously. Research shows that realized digital twins in practice currently do not go beyond the third maturity level (ARUP 2019) (MEED 2021).

4.2 *Requirements for the digital twin of the Filstal bridges*

The uniqueness of structures and their varying importance in the traffic infrastructure result in different requirements for the digital image. For the Filstal bridges, one requirement was the automatic integration and aggregation of condition and structural safety information from monitoring data into condition indicators (CI). In addition, damages from regular visual inspections should be located with all the associated information. An existing BIM model is used as the basis for locating the information. Bridge relevant information are aggregated so that the condition and structural safety of the Filstal bridges can be seen based on only a few indicators. In addition, notifications from the alarm system should be integrated. The digital image is intended to provide support for the usual procedure of bridge maintenance.

The unidirectional automated data exchange between the physical and digital object corresponds to a digital shadow. The evaluation and aggregation of bridge data lead to a maturity level of at least 2 (informative representation). Condition predictions from the measurement

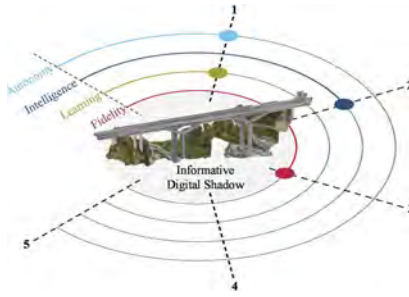


Figure 5. Characteristics of the digital image for the Filstal bridges.

data are calculated to some extent, yet sufficient data is not available. This matches analogously to an intelligence level of 2 according to (ARUP 2019). No algorithms for automatic learning (“learning” = level 1) are planned for the digital image, nor is autonomous action (“autonomy” = level 1). The information to be integrated is primarily maintenance-relevant information, which means that only a part of the total structure information is represented. The fidelity of this information can be understood as a reliable representation of some physical components to evaluate the current condition (“fidelity” = level 3). Figure 5 summarizes the different characteristics of the digital image of the Filstal bridges according to the definitions in chapter 4.1. To maintain consistency within this paper the term digital twin will be used.

4.3 3D model of the Filstal bridges

To precisely allocate the various data in the digital twin, a geometric model of the bridge is required. The detailed object information of the BIM model is used as a basis. The objects consist of geometries of different dimensions and associated semantic meta-information (attributes). In the existing BIM model, the bridges are modelled according to a defined bridge hierarchy and all sensors, damages and aggregated condition indicators from sensor data are allocated.

Due to the requirement of an automated, partially real-time, data exchange, the BIM model alone is inadequate. Only by processing and converting the BIM model it is possible to use the geometric model of the Filstal bridges with all semantic information of the components and the sensors as a basis for visualization and location.

4.4 Additional data base for the digital twin

For the automated integration of high-frequency data from the Filstal bridges, a database with a data model is set up in addition to the BIM model.

The designed ontology and the entities defined in it can be used to instantiate specific instance. The entirety of all instances represents the database of the digital twin. Instances can be, for example, bridge parts (e.g. pillar axis 10), damages, sensors or aggregated condition indicators. The transferred semantic information of the BIM model are basically static data that change less frequently over the life cycle. Appropriate technical interfaces and automated processes ensure that the static data of the database are updated immediately when the BIM model is updated.

Further mostly dynamic data is assigned to the individual instances of the digital twin in the database. For example, the condition information from the monitoring of the guide bearings during operation is continuously and automatically integrated into the database for the instance of the guide bearing. Updating is done in ascending order along the relationships of the ontology, so that parent objects always reflect the worst condition of their children.

A linked data approach makes it possible to assign or locate dynamic data in the geometric model in addition to the static data. With a corresponding update rate, current data can thus always be visualized.

4.5 Data aggregation

The intelligence of the digital bridge twin lies in its ability to analyze comprehensive and up-to-date data and convert them into useful information about the structure. Through the

analysis, a recommendation for action can be derived directly from the digital twin. The basis for this is the concept of information aggregation.

Current information about a bridge derives from different sources and is often available as heterogeneous data types, context-free and independent. A distinction must be made between information on assets, conditions and analytical structural safety verifications. The current condition of a bridge structure is recorded by bridge inspectors through regular, usually visual inspections. Damages are assessed about their influence on stability, traffic safety and durability for both road and railway bridges in Germany according to a rating system of grades from 1 to 4. The condition can change over the lifetime of a bridge and thus also the load-bearing capacity. Furthermore, the structural safety depends on the multitude of potential load scenarios and is evaluated by structural engineers within the framework of structural calculations and simulations. The results are analytically determined utilization level.

In the result, the main disciplines “bridge inspection” and “analytical verification” aim at evaluating the safety of the structure. An aggregation of the results is necessary for a comprehensive assessment, as they can influence each other or be mutually dependent. In the example of the Filstal bridges, the actual, variable stresses in the longitudinal restraint bearing are measured with the help of strain gauges and the structural safety is verified via calculated (theoretical) stress capacities and invariable stresses. The regular visual inspections of the bridge condition and the integration of inspection results into the simulations are indispensable, as they constantly update the calculated portion of the load-bearing capacity and indirectly, through the change in the load transfer properties, the calculated portion of the invariable stresses. Aggregation of the results of the disciplines also ensures a more comprehensive, mutual understanding between structural engineers and bridge inspectors.

An automated integration of the visual inspection results into the analytical (measurement-based) verification would currently involve a considerable amount of effort. On the one hand, damage and defects would have to be recorded and documented in sufficient detail. On the other hand, the effect of damage and defects on structural integrity would have to be predefined before integrating this into the computational simulations. For example, a reduction of the cross-sectional area in the case of corrosion damage or a reduction of the bending stiffness in the case of cracking. Because of this difficulty and the requirements for the digital twin of the Filstal bridges the aggregation between structural condition and safety assessment is not automated. Therefore, the condition information from the structural inspection and the structural safety information from the analytical verification are placed as separate information in the digital twin. The consideration of mutual influence is done manually. This concept represents an extension to the concept of the digital twin smartBRIDGE Hamburg in (Herbrand et. al. 2022), among others.

The aggregation of information takes place within the two clusters “bridge condition” and “structural safety”. “Monitoring” and “diagnostics” serve as support within the two clusters by generating additional information. The condition grade, as an indicator of the bridge condition from the visual inspection, and the ratio of the supported to the required track class as an indicator of structural safety are aggregated upwards via the bridge hierarchy.

5 VISUALIZATION AND USAGE OF THE DIGITAL TWIN

In this chapter, the current state of the visualization of the digital twin is shown and an outlook is given on the use cases in which advantages arise from the use of the digital twin.

Figure 6 shows the view for the longitudinal restraint bearing condition indicator within the platform condition control (CC). On the left hand-side the user has access to tabs for asset information, condition and structural safety information, sensor conditions and loading information. In addition, there is a notification tab, where all changes of conditions of all tabs are summarized.

The aggregated structure conditions as well as the structural safety and all other important condition information are summarized separately for each bridge in a structure summary in the top right-hand corner. For the condition and the structural safety calculated from measured data, a rating category is displayed in corresponding colors. In addition an exclamation mark can be assigned to both evaluations as an indicator for potential changes. Since sensor conditions and loading indicators are evaluated using anomaly detection, only exclamation marks can be displayed. The user can see the overall condition of the structures at any time and in any navigation level through the structure summary.

The navigation within the individual tabs takes place according to a defined bridge hierarchy via the selection of the individual bridge, the bridge part and with a final selection of the CI to be viewed. The linking of the CIs to bridge parts and their exact location in the model itself enable the bridge model in the background to be moved according to the navigation and the components and CIs to be highlighted in a user-friendly way. The interactivity between the bridge model and navigation makes the information easy to consume for the user. At the same time, by locating all important information, the digital twin enables a visual representation of neuralgic structure points and allows conclusions to be drawn about possible interactions, so that more detailed and qualitative assessments are possible.

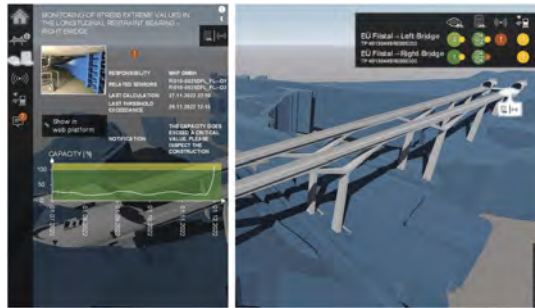


Figure 6. Visualization of the digital twin of the Filstal bridges in condition control.

As soon as a CI is selected by the user, the corresponding information is displayed in a panel (cf. Figure 6). In addition to the name of the CI, the categorization and an evaluation or possible notification, important additional information are displayed. The time diagram shows the result of the measurement-based detection of the last two weeks and compares it with the corresponding limit value. This gives the user a first sufficient insight into the CI's past. For further information on the complete history as well as on the measurement data of the sensors included in the detection, access is provided via the link to a web platform (cf. Figure 4).

The visualization and navigation concept developed together with structural inspectors allows the user a complete and simple overview of the structure's conditions. Information on damage, conditions and structural safety can be displayed and interpreted in parallel. Via the notification tab, the user can view all indicators that exceed limit value and subsequently initiate measures, which allows for a proactive response. The digital twin and the display in the selected form thus serve the bridge inspectors as an auxiliary tool for the operation of the Filstal bridges.

6 CONCLUSIONS

The Filstal bridges successfully went into operation in December 2022. The concept for the digital twin is currently being implemented. In the next steps, the missing components of the concept will be implemented until completion in June 2023, including optimization of the BIM model, setting up the database and development of the front end for visualization. The concept for digital twin was designed to be open and modular, so that further components can be easily connected. For example, it is possible to integrate the condition of mechanical parts on the structure. The contents of individual tabs in the visualization can also be expanded. Due to its modularity, the digital twin can be transferred to different structure types.

BIM was used in the concept as the basis for the visualization and instantiation of the digital twin. The geometric display in combination with the attribution of the structure makes it possible to address specific parts of the structure in the geometric model and accordingly in the visualization of the digital twin. In the future, further possible use cases of BIM in the implementation and operation of the digital twin must be investigated.

To make full use of the digital twin, the visual inspection procedure must be optimized. In perspective damage must be precisely located (geo-referenced). A transition must be made from time consuming manual maintenance documentation to automatic documentation and data processing, e.g. (Bast 2022).

According to the current state of art, the digital twin is only able to show the current state and the current structural safety. In the future, it should be possible to generate predictive conditions and structural safety with sufficient data, but there is still a need for research in this area. Approaches such as those in (Naraniecki et. al. 2022) allow, for example, the prediction of the bridge condition based on bridge and damage data, so that maintenance measures can be planned much more effectively.

The few practical realizations and the great need for optimization make it clear that clearly defined standards and definitions are necessary for establishing the digital twin in operation and maintenance. The digital twin of the Filstal bridges lays another cornerstone. It again demonstrates the added value of digital twins in the operational phase.

REFERENCES

- ARUP 2019. Digital Twin – Toward a meaningful framework. London, Published November 2019. Accessed December 14, 2022. <https://www.arup.com/perspectives/publications/research/section/digital-twin-towards-a-meaningful-framework>
- Bast 2022. Supporting bridge inspectors with interactive mixed reality visualizations of BIM process and geometry data. *Berichte der Bundesanstalt für Straßenwesen. Brücken- und Ingenieurbau Heft B 185*. <https://opus4.hbz-nrw.de/opus45-bast/frontdoor/index/index/docId/2725>
- BMVI 2020. Bundesministerium für Verkehr und digitale Infrastruktur. Bericht des BMVI zur Nachhaltigkeit 2020. Published May 2020. Accessed December 14, 2022. <https://bmdv.bund.de/SharedDocs/DE/Publikationen/G/ressortbericht-nachhaltigkeit.html>
- BMVI 2021. Bundesministerium für Verkehr und digitale Infrastruktur. Masterplan BIM Bundesfernstraßen. Published September 2021. Accessed December 14, 2022. <https://bmdv.bund.de/SharedDocs/DE/Anlage/StB/bim-rd-masterplan-bundesfernstrassen.html>
- BuildingSMART 2022. Take BIM Process to the next level with Digital Twins. Published 2022. <https://www.buildingsmart.org/take-bim-processes-to-the-next-level-with-digital-twins/>
- Bolton, A., Enzer, M., Schooling J. et al. 2018. The Gemini Principles: Guiding values for the national digital twin and information management framework. Centre for Digital Built Britain and Digital Framework Task Group. <https://www.cdcb.cam.ac.uk/system/files/documents/TheGeminiPrinciples.pdf>
- Deutsche Bahn AG 2022. BIM Strategie – Implementierung von Building Information Modeling (BIM) im Vorstandsressort Infrastruktur der Deutschen Bahn AG. https://www.deutschebahn.com/de/konzern/bahnwelt/bauen_bahn/Building-Information-Modeling-BIM-6876240
- Grieves, M. & Vickers, J. 2017. Digital Twin: Mitigating Unpredictable, Undesirable Emergent Behavior in Complex Systems - Transdisciplinary Perspectives on Complex Systems: New Findings and Approaches: 85–113. https://doi.org/10.1007/978-3-319-38756-7_4
- Kritzinger, W., Karner, M., Traar, G., Henjes, J. & Sihn, W. 2018. Digital Twin in manufacturing: A categorical literature review and classification. *IFAC-PapersOn-Line* 51 (11), pp. 1016–1022. <https://doi.org/10.1016/j.ifacol.2018.08.474>
- Hagen, A., Andersen, T. M., Reiso M. & Sletten K. 2022. Condition based monitoring and digital twins: Damage detection on a Norwegian bridge. *Bridge Safety, Maintenance, Management, Life-Cycle, Resilience and Sustainability. IABMAS 2022*. <https://doi.org/10.1201/9781003322641>
- Herbrand, M., Lazoglu, A., Ullerich, C., Marx, S. & Zehetmaier, G. 2022. Aggregation von Zustandsindikatoren aus Inspektions- und Monitoringdaten im Brückenbau. *Bautechnik*, 99: 95–103. <https://doi.org/10.1002/bate.202100095>
- MEED 2021. Middle East business intelligence. Digital Evolution - The critical impact of digital twins on Middle East construction. Published November 2021. Accessed December 14, 2022. <https://damassets.autodesk.net/content/dam/autodesk/www/campaigns/emea/docs/digital-evolution-report-final.pdf>
- Naraniecki, H., Hartung, R., Marx, S. & Klemt-Albert, K. 2022. Zustandsprognose von Ingenieurbauwerken auf Basis von digitalen Zwillingen und Bestandsdaten. *Bautechnik*, 99: 173–181. <https://doi.org/10.1002/bate.202100100>
- Pregolato M., Gunner S., Voyagaki E. et. al. 2022. Towards Civil Engineering 4.0: Concept, workflow and application of Digital Twins for existing infrastructure. *Automation in Construction*. Volume 141. <https://doi.org/10.1016/j.autcon.2022.104421>.
- United Nations 2022. The Sustainable Development Goals Report 2022. Published 2022. Accessed December 14, 2022. <https://unstats.un.org/sdgs/report/2022/>
- Wenner et. al. 2021. The Concept of Digital Twin to Revolutionise Infrastructure Maintenance: the Pilot Project smartBRIDGE Hamburg, 27th ITS World Congress, Hamburg, Germany
- Zaidman, I., Schumm, M., Kotz, P. and Steigerwald, T. 2022. Außergewöhnliche Eisenbahnbrücke über das Filstal – Entwurf, Planung und Ausführung des neuen Wahrzeichens von Baden-Württemberg. *Bautechnik*, 99: 262–271

An application of drive-by approach on a railway Warren bridge

L. Bernardini, A. Collina & C. Somaschini

Politecnico di Milano, Milan, Italy

K. Matsuoka

Railway Technical Research Institute, Tokyo, Japan

M. Carnevale

Università degli studi di Pavia, Pavia, Italy

ABSTRACT: The present paper illustrates a wavelet-based drive-by methodology to assess bridge health condition, identifying possible damage presence and position. The case study is represented by a single-track, medium span, Warren truss bridge, whose FE model was constructed referring to a real existing structure, and dynamically validated with experimental tests. Vertical bogie accelerations are processed by Continuous Wavelet Transform and the obtained scalogram is sectioned at a specific frequency, associated to the passage of the vehicle over each module of the truss structure. A damage index is then built up starting from the wavelet coefficients referred to this frequency. Therefore, the method exploits the structural conformation of the truss bridge as a tool for detecting damages occurred to its deck. The approach is tested using a 3D train-track-bridge dynamic interaction model: different speeds, track geometrical profiles and damage scenarios are explored to assess the effectiveness of the method and its robustness.

1 INTRODUCTION

Worldwide railway networks are exposed to increasing traffic demands, axle loads and train speeds (Hayward 2011) as well as ageing and deterioration (Fujiu et al. 2022). According to (Dinas et al. 2017), in 2017 it was estimated that in Europe the 75% of steel railway bridges were over 50 years old and almost 35% of them was older than a century. The author in (Lin 2018) reports that, in Japan, the 47% of bridges will be older than 50 years old in 2026. In Australia, considering a sample of 1122 railway bridges, it was reported that the 63% of them were older than 50 years old, while the 8% was older than 100 years old (Aflatooni et al. 2013). In India, in 2019, it was declared that 38,850 bridges were older than 100 years old, while (ASCE 2021) states that in USA the 7.5% of bridges are estimated to be structurally deficient, with the 42% of the total amount of bridges being at least 50 years old. In this context, a great challenge for worldwide infrastructure managers is to ensure operational safety while meeting increasing traffic demands and respecting budget constraints. Traditionally, monitoring of railway bridges is performed by means of visual inspections, that rely on operator skills and experience. Visual inspections, whose periodicity depends on bridge age and type, can be supported by a variety of NDT techniques (Helmerich et al. 2007). Visual inspections are generally featured by high costs, safety and accessibility problems and they are subject to operators' skills (Iacovino et al. 2022). Given these limitations, Structural Health Monitoring (SHM) comes into play to support visual inspections in a transition towards a more efficient condition-based maintenance (CBM) approach.

SHM divides into two main categories: direct approaches which are based on sensors directly deployed on the analyzed structure, and indirect approaches (even called drive-by), that rely instead on the instrumentation installed on vehicles that are used as exciters and mobile sensors (Malekjafarian et al. 2022). Direct approaches are widely spread and adopted (Das et al. 2016), but they have several limitations: costs associated to the measurement set-up and its maintenance,

low flexibility, given their tailored nature. To overcome these limitations and drawbacks, in recent years there has been growing interest in developing drive-by approaches (Malekjafarian et al. 2022). The latter are then divided into two main categories: modal and non-modal indirect approaches, depending on the index that is used as damage sensitive. Compared to conventional approaches (i.e., vibration-based direct technique), drive-by methods have advantages in terms of economy, transportability, and flexibility (Malekjafarian et al. 2022).

The present work proposes a non-modal continuous wavelet-based approach for damage identification and localization. Compared to existing literature which focuses on 2D simply supported beam models, this work deals with a 3D lattice structure, rarely adopted in past works. Moreover, the methodology exploits the modular structural conformation of the Warren truss bridge to identify possible damage occurrence: this new concept which may greatly improve drive-by SHM has not been deeply discussed in literature. The proposed damage index is verified in terms of its effectiveness and robustness inserting, between two consecutive runs, track geometrical irregularity profile and travelling speed modifications. The work is structured as follows: section 2 presents materials and models employed for simulations, and the signal processing technique adopted. Subsequently, section 3 illustrates and describes the obtained results, in terms of damage index effectiveness and robustness to exogenous factors other than the damage. Finally, conclusions are drawn.

2 MATERIALS AND MODELS

2.1 Bridge, track, train models

The bridge FE model presented in this work and shown in Figure 1 is derived from a real existing structure, corresponding to a steel Warren railway bridge, designed in 1946. The geometrical properties of the different elements composing the truss structure were computed by the available technical drawings. The Young Modulus of the adopted steel is assumed to be equal to $2.0 \cdot 10^5$ MPa. Material density is increased by 15% with respect to the nominal value of 7850 Kg/m^3 to take into account the elements of the joints, such as bolts and connecting plates. Moreover, non-structural elements such as track components (e.g., sleepers, steel plates) or handrails are modelled by means of concentrated masses. The ends constraints are assumed to be ideal, therefore, the bridge is considered as a simply supported structure, with a hinge at its entrance and sliding boundary at the exit, in the direction of train transit. Rayleigh damping is assumed: α and β are chosen to obtain a damping ratio in the range of 1% in correspondence of the first bending frequency. The bridge is fitted with a ballast-less track, where the connection between the rails and the girder in the model is represented through viscous-elastic elements, with the purpose to model timber sleepers and fastenings. Outside the bridge span, the track segments correspond to ballasted track.

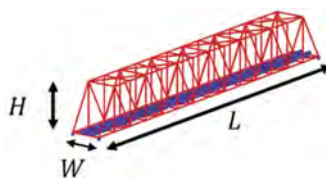


Figure 1. Railway bridge FE model. H: 7.7 m, L: 60.5 m and W: 5.25 m.

Track geometrical irregularity profiles (i.e., deviations from perfectly rectilinear rails) are obtained from a reference PSD function provided by (OREB176 1989). Two different profiles, plotted in Figure 2a (i.e., line 1 and 2) with their FFTs (see Figure 2b), were adopted in the performed set of simulations, to investigate the effect on method performances played by changes of track profile between consecutive runs. The difference in the two track profiles is limited to the shortest wavelengths, considering that it is associated with differential degradation of timber sleepers. The illustrated FE bridge model was validated from dynamic point of view, showing a maximum difference between first four frequencies all below the 5%, and

a good degree of similarity with experimental mode shapes (i.e., highest difference of 3%), as pointed out by the computation of MAC matrix (see Bernardini et al. 2022).

A three-dimensional multi-body rail vehicle model was used, with primary and secondary suspensions connecting carbody, bogie frames and wheelsets. The motion of each coach is described by 35 degrees of freedom, five for the carbody and each of the two bogies, as well as for each of the four wheelsets. The train adopted in this work is composed of 8 coaches. The end coaches of the convoy are 28% heavier and 5.3% longer, but they share the same bogie centre spacing (17.4 m) and wheelbase (2.85 m).

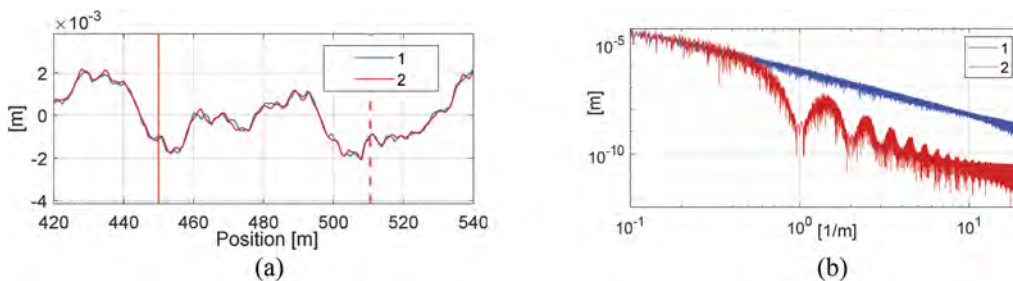


Figure 2. (a): Track geometrical irregularities. Red solid vertical line defines the entrance of the bridge, while the dashed one identifies bridge exit. (b): Track geometrical irregularities FFTs in double logarithmic scale.

Bridge structure and the rail vehicle represent two dynamical sub-systems coupled through contact forces and congruence at wheel-rail contact patches. Their equations of motion and the procedure for time domain integration are implemented in ADTreS, which is a non-commercial FE (for the structure) and multibody (for the train) simulation tool that has been developed, since three decades ago, by researchers of the Department of Mechanical Engineering of Politecnico di Milano (Bruni et al. 2004).

2.2 Damage scenarios and plan of simulations

In this paper three different damage scenarios were considered: the damage, modelled through a reduction of the 50% of the element elastic modulus, always interests deck cross-girder, in three different positions, as shown in Figure 3. In this way, it was possible to investigate the effect of damage position on the success of its detection by the proposed method.

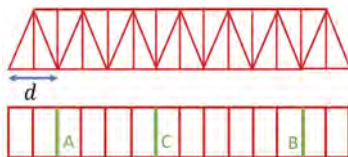


Figure 3. Damage location across bridge midspan in the three considered damage scenarios (A, B and C).

A group of 10 travelling speeds, ranging from 95 km/h to 104 km/h, was adopted in the simulations, to study the effect, on the performances of the methodology, caused by the deviations of vehicle speed from the reference one. Furthermore, the effect of changes of operational conditions between a run over healthy and damaged structure is of interest. It is important to introduce in the analysis damage hiding sources that can be encountered in real operating scenarios. For instance, assuming an actual implementation of the drive-by methodology, it is reasonable to assume that between one run over the studied structure and the subsequent, even if close in time, some operating conditions may slightly change, such as vehicle speed or track geometrical profile (see Figure 2). These changes consist in real-life noise covering factors, that may undermine the success of the methodology.

2.3 Local bridge deformability

As briefly mentioned before, when considering a diagnostic method relying on a comparison between two different runs, it is of interest to find an index which is as robust as possible to exogenous factors other than the defect. The latter is the target, but its identification can be undermined by a change of different operational factors. Some of them may depend on the vehicle, such as the case of different travelling speeds or coach weight in different runs. Other may depend on other factors, such as environmental agents (e.g., temperature effects) or track geometrical irregularity time evolution, as proposed by (Carnevale et al. 2019) and (Bernardini et al. 2021), but, according to authors best knowledge, generally neglected in literature.

In this work, the idea behind the chosen damage index, which is in the form of wavelet coefficients difference, is to capture structural changes occurred to any of the bridge modules. In fact, given the modular structure of the truss bridge subject of this study, it was noted that this structural configuration is reflected on vehicle response. Figure 4 illustrates the bogie vertical acceleration histories, referred to space, of the leading bogie of the first coach at different travelling speeds (Figure 4a) and their respective spectra (Figure 4b). From the latter it is possible to visualize a main harmonic component, which proportionally increases with speed (Figure 4b). This component is related to the periodicity of module length of the truss bridge, and thus the time necessary to cross it: from now on, the inverse of this time quantity will be referred to as $f_m(v/d)$, where the subscript stands for module. The signal component related to f_m is the starting point of the proposed diagnostic approach, since it may reflect any structural changes occurring to bridge module.

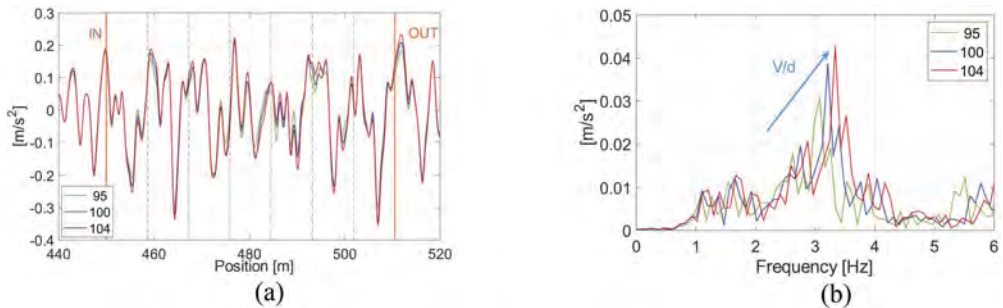


Figure 4. Bogie vertical acceleration at different speeds. (a): low pass filtered ($f_{cut} = 20 \text{ Hz}$) histories referred to space. (b): corresponding FFTs.

2.4 Signal processing and damage index

The proposed signal processing methodology relies on the observation and use of truss bridge local deformability. As shown in the previous section, the bogie vertical acceleration contains a strong harmonic component related to the passage of the bogie over each of the seventh bridge modules. This specific harmonic component may result useful for diagnostic purposes, since it can reflect any structural changes occurring to the module itself. In fact, as a damage occurs to a module of a bridge cross-girder, it is reasonable to expect a local variation of the energy associated to this target harmonic component (i.e., f_m). With the purpose to detect and identify this possible change, a Continuous Wavelet Transform (CWT) is used as a processing tool able to provide information both in time (thus space) and frequency. Equation 1 defines continuous wavelet transform operation:

$$C_{s,\tau} = \frac{1}{\sqrt{s}} \int_{-\infty}^{\infty} x(t) \cdot \psi_{s,\tau} \left(\frac{t-\tau}{s} \right) dt = \langle x, \psi_{s,\tau} \rangle \quad (1)$$

Where $C_{s,\tau}$ are the wavelet coefficients of the time signal $x(t)$, while $\psi_{s,\tau}$ is the wavelet employed (Morlet, in this case): moreover, s represents wavelet scale factor and τ represents the time shift. The adoption of the CWT, instead of the FFT, allows to acquire information that are not only related to frequency but also associated to spatial position across bridge span. While the CWT provides a picture of the energy content associated to each harmonic component of the signal for each time interval (thus position), the FFT provides instead a global overview, stationary in time. Therefore, assuming a damage occurring to one of the seven bridge modules, between healthy and damaged scenario, in correspondence of f_m we may still observe a change of the related FFT harmonic component, but this is reduced being averaged over the other six undamaged modules. It is reasonable to expect that the wavelet coefficients scalogram computed by performing the CWT will better point out the local stiffness variation associated to the damaged element, giving information that are both localized in time and frequency with a specific resolution. As mentioned above, we are specifically interested in the wavelet coefficients corresponding to f_m frequency. The signal processing necessary to the subsequent computation of damage index is shown and summarized in Figure 5.

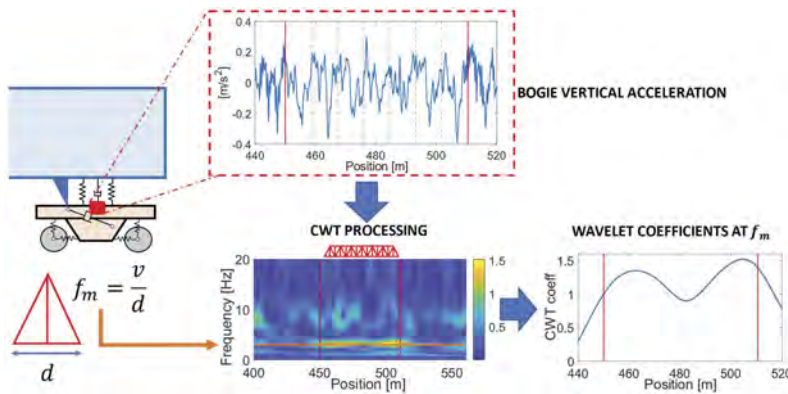


Figure 5. Signal processing procedure, starting from vertical bogie acceleration signal (at $v=100$ km/h) and ending with wavelet coefficients corresponding to the frequency f_m .

The wavelet coefficients associated with f_m are computed for each simulation run, then, the absolute value of their difference between damaged and healthy bridge scenarios is computed and assumed as the damage index (DI). When comparing different speeds, the DI is calculated with the frequency f_m related to each individual speed. The DI is expressed in Equation 2 as a function of f_m and position $\xi (= vt)$:

$$DI(f_m, \xi) = |C_d(f_m, \xi) - C_h(f_m, \xi)| \quad (2)$$

Damage position, if any, is then identified by the maximum value of the damage index DI:

$$\xi_{dam} = \max_{\xi} DI(f_m, \xi) \quad (3)$$

Finally, the positioning error of the damage is defined as follows:

$$e_{pos,d}\% = \frac{|\xi_{dam} - x_d|}{L_b} \cdot 100 \quad (4)$$

Where ξ_{dam} is the identified damage position, while x_d is the actual damage location and L_b is the bridge span length.

3 RESULTS

3.1 Damage index identification performances

Considering the case of a travelling speed of 100 km/h and vertical track irregularity N.1 in Figure 2a, with the assumption of no changes of these parameters between one run and the other, Figure 6 is obtained. In particular, the resulting wavelet coefficients at f_m (3.2 Hz) in case of healthy structure and three different damage locations (see Figure 3) are shown in Figure 6a. Moreover, Figure 6b illustrates the damage index DI as a function of position and damage scenarios: it can be observed the capability of the chosen damage index to identify the damage position, for all the locations considered. In fact, peaks in terms of DI (f_m) are observed in proximity of the defected cross-girder. This means that, in ideal conditions, the position of damage seems not to affect markedly the performances of the method, even if it must be observed that higher accuracy is obtained for scenarios A ($e_{pos,d} = 1.75\%$) and B ($e_{pos,d} = 2.41\%$) compared to scenario C ($e_{pos,d} = 6.41\%$). On the other hand, the latter scenario seems to cause larger discrepancy between damaged condition and the healthy case, leading to higher DI value. In Figure 6c it is possible to observe that in correspondence of damage position and its proximity, DI magnitude increases with higher travelling speed. The difference between DI curves at different speeds is higher at damage location, while far away from it, it generally decreases.

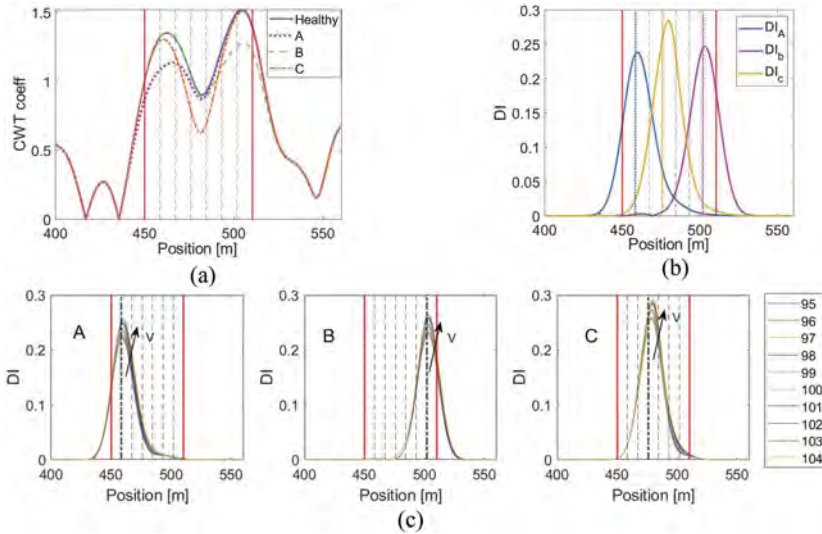


Figure 6. (a): CWT coefficients at f_m in different scenarios: healthy bridge and A, B and C damage locations (as reported in Figure 3). (b): DI as a function of damage location. Train speed 100 km/h, irregularity profile 1 (see Figure 2a). (c): DI as a function of travelling speed, irregularity profile 1 (see Figure 2a).

3.2 Damage index robustness

When dealing with a damage index based on a comparison among parameters computed in case of healthy and damaged structure, it is important to stress that between one train run and the other, several exogenous factors can be source of discrepancy, other than a structural damage. This discrepancy could lead to the identification of false alarms, or, even worse, they could lead to false negatives, since they could hide damage occurrence. That is why, in the present work, a sensitivity analysis is proposed to investigate the robustness of the presented damage index (see Equations 2 and 3) with respect to variations of track geometrical irregularity and travelling speed. As examples, in Figure 7 three distinct cases are presented: the first case regards the computation of DI considering two runs, with same irregularity but different speed (Figure 7a), while the second assumes same speed but different track irregularity (Figure 7b). Finally, the third case (Figure 7c) considers both different speeds and geometrical irregularity, between the two runs. In all the

presented scenarios, once the DI is computed, it is then windowed by means of a Tukey window to isolate and emphasize the region of interest only, in correspondence of the bridge structure.

Figure 7a concerns the robustness of the presented methodology to slight changes of train speed between consecutive runs: the DI peak follows damage position also in case of speed differences of 2 km/h between one run and the other. Better performances were obtained for damage scenarios A ($e_{pos,d}=1.75\%$) and B ($e_{pos,d}=3.41\%$), rather than scenario C ($e_{pos,d}=6.74\%$). It can be pointed out that better damage identification performances are achieved when the speed of the run over the damaged bridge is lower than the speed of the run on the healthy structure.

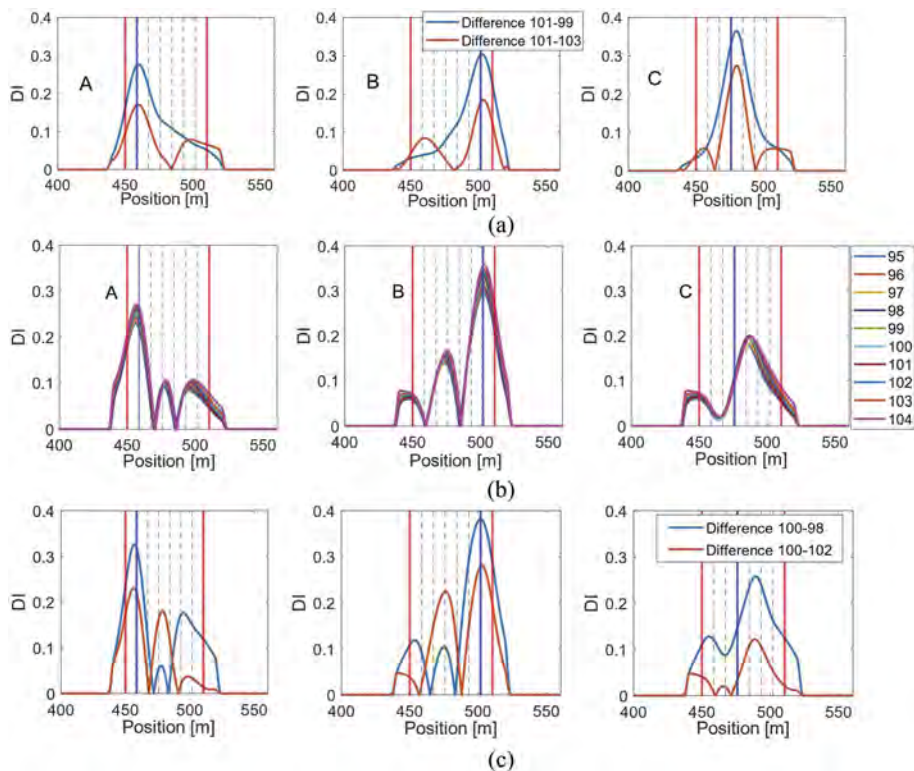


Figure 7. (a): Same track profile (i.e., irregularity 1 in Figure 2a) but different speed. (b): Same speed, but different track profile (1 and 2 in Figure 2a). (c): different speeds and different track profiles.

Moreover, it is possible to highlight that, despite maximum DI is always close to the damaged element, DI differs from zero also in the other regions across bridge span. This outcome is due to that, as shown in Figure 4b, different travelling speeds lead to different magnitudes of the frequency component associated to bridge module crossing on onboard signals.

Figure 7b shows the case in which a change of track irregularity profile (from N.1 to N.2) between the run on the healthy and the damaged bridge is assumed. Travelling speed is kept constant between damaged and healthy scenarios. Larger values in terms of DI peaks are observed for damage A and B, as well as better performances in terms of defect localization compared to scenario C, in which the peak of DI index is localized about one module after its actual position. The method appears to be less robust to a change of track geometrical profile compared to a change of speed between healthy and damaged scenario runs.

Finally, Figure 7c shows the DI when combining a change of train speed and track geometrical irregularity between runs over healthy and damaged bridge. For scenarios A ($e_{pos,d}=3.88\%$) and B ($e_{pos,d}=2.10\%$) the index is still able to identify damage presence with high accuracy, while for case C the identified defect position results to be about one module and half far from the actual location ($e_{pos,d}=21.95\%$). Figure 7c demonstrates that for damages occurring close to bridge ends

good identification performances and robustness to exogenous factors were achieved by the presented method. Conversely, the localization error significantly increases when dealing with a damage scenario closer to bridge midspan.

4 CONCLUSIONS

This paper presented a numerical investigation on the use of a wavelet-based approach for identifying presence and position of damages affecting cross-girders on a Warren Truss bridge deck. The described methodology exploits the local deformability of the structure to assess its health status. Wavelet coefficients associated to the so-called module passing frequency (expressed by the ratio $f_m = v/d$) are used as damage sensitive indexes, revealing good diagnostic performances. The approach has been tested by means of a 3D train-track-bridge dynamic interaction model, considering three different damage scenarios, consisting of a reduction of the 50% of the cross-girder Young modulus. The presented damage index consists of the absolute value of the difference between wavelet coefficients obtained from the run over damaged and healthy structures respectively: in particular, the coefficients of interest are the ones associated to the module crossing frequency (f_m). The adopted damage index shows good performances in terms of damage identification, and promising robustness to exogenous factors, other than the damage. Better damage localization performances were obtained for damages occurring close to the ends of the bridge than towards the midspan.

REFERENCES

- Aflatooni, M., Chan, T.H.T., Thambiratnam, D.P., Thilakarathna, I., 2013. Synthetic rating system for railway bridge management. *Journal of Civil Structural Health Monitoring*, 3(2), pp. 81–91.
- ASCE, 2021. Bridge Infrastructure Report Card.
- Bernardini, L., Carnevale, M. & Collina, A., 2021. Damage Identification in Warren Truss Bridges by Two Different Time-Frequency Algorithms. *Applied Sciences*, 11(22).
- Bernardini, L., Somaschini, C. & Collina, A., 2022. On Situ Vibration-Based Structural Health Monitoring Of A Railway Steel Truss Bridge: A Preliminary Numerical Study. (WCCM-XV) & (APCOM-VIII) Virtual Congress: 31 July – 5 August 2022, S. Koshizuka (Ed.)
- Bruni, S., Collina, A., Corradi, R. & Diana, G., 2004. Numerical simulation of train-track-bridge dynamic interaction. *Computational Mechanics: Proceedings of the Sixth World Congress on Computational Mechanics in Conjunction with the Second Asian-Pacific Congress on Computational Mechanics*, Beijing, 5-10 September 2004. Tsinghua University Press & Springer-Verlag.
- Carnevale, M., Collina, A. & Peirlinck, T., 2019. A feasibility study of the drive-by method for damage detection in railway bridges. *Applied Sciences*, 9(1).
- Das, S., Saha, P. & Patro, S., 2016. Vibration-based damage detection techniques used for health monitoring of structures: a review. *Journal of Civil Structural Health Monitoring*, 6(3), pp. 477–507.
- Dinas, A., Nikolaidis, T. N. & Baniotopoulos, C. C., 2017. Sustainable Restoration Criteria for a Historical Steel Railway Bridge. *Procedia Environmental Sciences*, Volume 38, pp. 578–585.
- Fujiu, M., Minami, T. & Takayama, J., 2022. Environmental Influences on Bridges Deterioration Based on Periodic Inspection Data from Ishikawa Prefecture, Japan. *Infrastructures*, 7(130).
- Hayward, A. C. G., 2011. Train loads on bridges 1825 to 2010. *International Journal for the History of Engineering and Technology*, 81(2), pp. 159–191.
- Helmerich, R., Bain, J. & Cruz, P., 2007. A guideline for railway bridge inspection and condition assessment including NDT toolbox. In: *Sustainable Bridges - Assessment for Future Traffic Demands and Longer Lives*. Bién J., Elfgrén L., Oloffson J., pp. 93–104.
- Iacovino, C., Turksezer, Z.I., Giordano, P.F. & Limongelli, M.P. 2022. Comparison of Bridge Inspection Policies in terms of Data Quality, *Journal of Bridge Engineering*, 27(3).
- Lin, W., 2018. Rehabilitation and Strengthening of Aged Steel Railway Bridges in Japan. *Journal of Civil & Environmental Engineering*, 8(2).
- Malekjafarian, A., Corbally, R. & Gong, W., 2022. A review of mobile sensing of bridges using moving vehicles: Progress to date, challenges and future trends. *Structures*, Volume 44, pp. 1466–1489.
- OREB176, 1989. Bogies with Steered or Steering Wheelsets. Report No. 1: Specifications and Preliminary Studies, Specification for a Bogie with Improved Curving Characteristics, Utrecht, The Netherlands: ORE.

Optimal design and application of 3D printed energy harvesting devices for railway bridges

J.C. Cámara-Molina, A. Romero & P. Galvín

Escuela Técnica Superior de Ingeniería, Universidad de Sevilla, Sevilla, Spain

E. Moliner & M.D. Martínez-Rodrigo

Department of Mechanical Engineering and Construction, Universitat Jaume I, Castellón, Spain

ABSTRACT: In this paper, the authors investigate energy harvesting on railway bridges. The tuning frequency for the optimal design of cantilever based 3D printed energy harvesters is studied. An analytical model to represent the electromechanical behaviour of the device is presented for the estimation of the energy harvested from train-induced bridge vibrations. A genetic algorithm constrained to geometry and structural integrity is used to solve the optimisation problem. Additive manufacturing by 3D printing of the substructure of the harvester is considered to maximise the design flexibility and energy performance. Optimal device prototypes with PAHT-CF15 substructure are designed for a real bridge in the Madrid-Sevilla High-Speed line. Finally, the performance of energy harvesting is evaluated from in situ experimental data measured by the authors. The results allow quantifying the energy harvested in a time window of three and a half hours and 19 train passages.

1 INTRODUCTION

One of the major limiting factors in the implementation of sensor networks in monitoring applications on railway structures is the lack of a long-term and low-maintenance power supply. Most existing systems require battery changes, and difficulties of access and infrequent maintenance operations can limit their practical implementation. In this sense, piezoelectric energy harvesting is becoming an alternative to the electrical supply of sensors and nodes in remote areas (Wei & Jing 2017, Yildirim et al. 2017). Within the context of this work, many research have focused on the development of energy harvesters based on the piezoelectric effect to transform railway-induced vibrations into electrical energy to be used in small power devices and sensors. The most common typology is that of a bimorph cantilever beam. These systems have the ability to generate energy from environmental vibrations in a frequency range of 3–100 Hz (Sarker et al. 2019). The predominant frequencies of vibrations caused by rail traffic in the infrastructure are within the above range, making it possible to supply low-power devices and sensors. An important problem of energy collection systems is associated with the fact that the performance of the energy production device is limited to a very narrow operating frequency band around its resonance frequency (Erturk & Inman 2011). If the excitation frequency deviates slightly from the resonance condition, the output power is drastically reduced. This unsatisfactory situation is mainly due to the fact that the generator resonant frequency is often not tuned to the vibration frequency. However, compared to some applications, the energy harvesting of railway bridges is less sensitive to frequency effects, because the dynamic behaviour of the structure is mainly determined by the fundamental mode shape (Museros & Alarcon 2005), which is relatively constant. One of the objectives of this work is the estimation of the natural frequency of a bridge and the tuning of harvesting systems in railway bridges.

2 APPROACH

The proposed approach considers that the energy harvester is attached to the bridge in a location defined by the coordinate x_b . This device is subjected to vertical vibration $z_b(x_b, t)$ induced by a train passage that travels at a speed V . The dynamic response of a bridge under the circulation of a rail convoy is complex and is affected by several factors. The most obvious and certain are the bridge properties, the geometric scheme of the train axles, and the speed of circulation V . Furthermore, there are other factors that are much more uncertain in determining the response of the bridge (Rocha et al. 2012), such as structural damping and various interaction mechanisms, the most relevant being vehicle-structure, track-structure, and soil-structure interaction effects. The dynamic response of a railway bridge due to train passage can be described by a stochastic process, assuming that the load has random amplitude described by a Poisson process (Zakęś & Śniady 2018).

The energy harvesting performance is closely related to the dynamic behaviour of the bridge during train passages (Romero et al. 2021), and maximum performance would be obtained when the harvester is tuned to the fundamental mode shape of the bridge. However, the performance of the energy harvester is limited to a narrow frequency bandwidth around the tuning frequency, and therefore the harvested energy is drastically reduced as a result of the detuning effect. Although the harvester device can be tuned to the natural frequency of the fundamental mode shape of the bridge, the uncertainties in the dynamic response affect not only the vibration levels but also the frequency content, making the choice of the tuning frequency more difficult.

In this work, due to the nature of the vibrations caused by rail traffic, the energy collected is processed statistically and represented by a stochastic process following a Gamma distribution $E \sim \Gamma(k, \theta)$ with mean $\mu_E = k\theta$ and variance $\sigma_E^2 = k\theta^2$, where k and θ are the shape and scale parameters, respectively. The mechanical energy is used as an estimate of the efficiency in the conversion of energy from the bridge vibration. A lumped mass model is used to represent the dynamic behaviour of the harvester. The properties of the system are given by the natural frequency ω , the mass m , and the damping coefficient c (Romero et al. 2021). The damping coefficient c is used to represent the energy transfer from the bridge vibration to the harvester system (Stephen 2006).

Then, the instantaneous power corresponds to the power absorbed by the harvester plus the kinetic energy and the mechanical energy in the system during the period T is a function of the velocity of the vibration:

$$E = c \int_0^T |\dot{y}(t)|^2 dt \quad (1)$$

where $y(t)$ denotes the vertical displacement of the lumped mass. The previous equation can be expressed in terms of the Fourier transform of the harvester velocity according to Parseval's theorem (Romero et al. 2021). Then, the displacement of the harvesting device is expressed in terms of the vertical displacement of the bridge and the frequency response function $H(\omega; \bar{\omega})$ of the harvester:

$$y(\bar{\omega}) = m\bar{\omega}^2 H(\omega; \bar{\omega}) z_b(x_b, \bar{\omega}) \quad (2)$$

Thus, the energy collected becomes:

$$E = c \int_{-\infty}^{\infty} |\dot{y}(\bar{\omega})|^2 d\bar{\omega} = c \int_{-\infty}^{\infty} |\iota \bar{\omega} m \bar{\omega}^2 H(\omega; \bar{\omega}) z_b(x_b, \bar{\omega})|^2 d\bar{\omega} \quad (3)$$

where, the imaginary unit number is denoted by the Greek letter ι to prevent confusion with the subscript i used in posterior derivations.

Therefore, the tuning frequency needs to be selected following a statistics procedure. In this work, a stochastic process is proposed to find the tuning frequency.

As an example, Figure 1 shows the frequency content of the acceleration in a railway bridge in three different circulations. The fundamental mode of this bridge corresponds to the first longitudinal bending mode shape with natural frequency $f_{b1} = 6.3$ Hz. More details about the structure can be found in (Galvin et al. 2020). The three circulations are: *i*) Renfe S102 travelling at $V = 290$ km/h (passage #2); *ii*) Renfe S012 at $V = 274$ km/h (passage #11); and *iii*) Renfe S100 at $V = 290$ km/h (passage #17). The passage numbers are in concordance with (Galvin et al. 2020). In all cases, the response presents peaks associated with the load (that is, the ratio of the train speed V to the bogie and axle distances and the corresponding harmonics) and to the lowest natural frequencies of the bridge. The peaks related to the fundamental mode shape were found in 5.16 Hz (passage #2), 5.6 Hz (passage #11) and 6.3 Hz (passage #17), that are in general lower than the natural frequency (marked by a vertical dashed line). Therefore, tuning the harvester is not trivial and the performance will be determined by the dynamic behaviour of the structure in forced vibration, in which the response associated with the fundamental mode shape can occur at frequencies lower than the natural frequency, as shown in Figure 1. A detuning higher than 1% can cause considerable power loss as shown in (Romero et al. 2021).

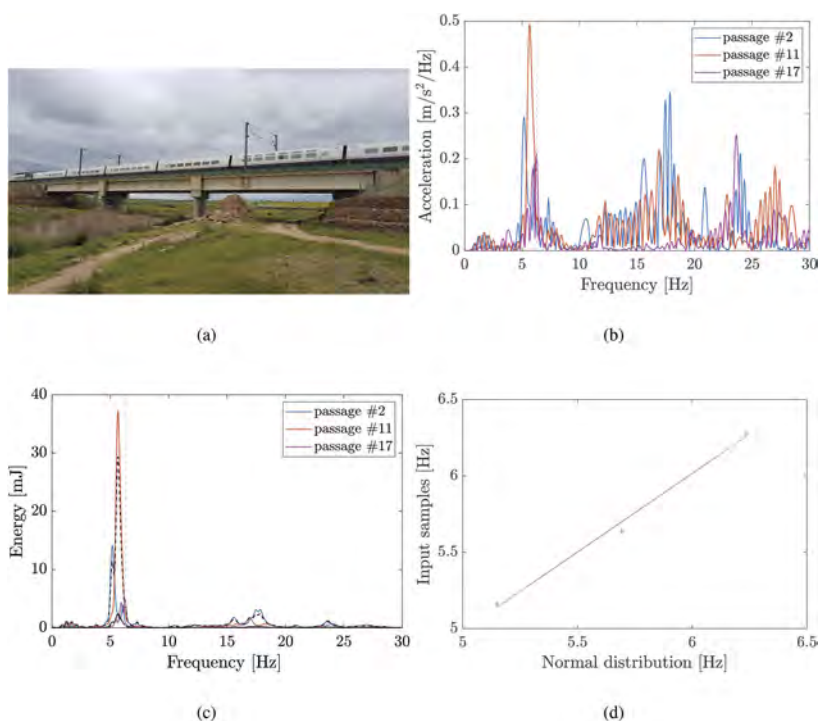


Figure 1. (a) General view of Jabalón HSL bridge. (b) Frequency content of the bridge acceleration at point A7 (see Galvin et al. 2020)) induced by different train circulations. The vertical line represents the first natural frequency of the bridge.

The proposed procedure considers the study of the scattering of the mechanical energy of different harvesters tuned from 1 Hz to 100 Hz to cover a wide range of frequencies, including the most fundamental frequencies of railway bridges. The mechanical energy is computed for each train passage using the experimental records of the bridge accelerations induced by 19 trains over the Tirteafuera bridge.

In order to verify the dispersion of the mechanical energy as a function of the excitation frequency to find the fundamental frequency of the bridge, a statistical analysis is carried out. The dynamic response of the device in the frequency domain is a complex random process in which the real and imaginary parts of the response follow a Gaussian distribution (Lombaert et al. 2014). Therefore, the modulus of the response is the absolute value of a circular bivariate

Gaussian random variable. The probability distribution of the latter follows the so-called Rayleigh distribution or, equivalently, the modulus of the dynamic response contribution, normalised by the squared standard deviation of the real and imaginary parts, follows a chi-square distribution with two degrees of freedom.

The proposed approach considers that the mechanical energy for each tuning frequency and excitation record follows a gamma distribution ($E(\omega_n \sim \Gamma(k, \theta))$), as the chi-square distribution with n degrees of freedom is a special case of the gamma distribution with the shape parameter $k = n/2$ and the scale parameter $\theta = 2$. The confidence intervals, standard deviation, and mean values of the mechanical energy can be derived from the cumulative distribution function, and the shape and scale parameters of the gamma distribution. The mean value of the mechanical energy for all train passages is computed as $\mu = k\theta$ and the standard deviation is $\sigma = \sqrt{k\theta^2}$.

Following, the results of an extensive experimental campaign are presented and the proposed tuning procedure is validated.

3 EXPERIMENTAL VALIDATION

An experimental campaign was carried out to assess the energy harvesting performance in a railway bridge in July-September 2022. The bridge under study belongs to the HSL Madrid-Sevilla. It is a single simply-supported span concrete bridge with three tracks. The deck is composed of a concrete slab of dimension 18m \times 20.6m (length \times width) resting on ten pre-stressed concrete I girders (see Figure 2). The slab carries two ballasted tracks with UIC gauge (1.435m) of high-speed lines separated from one ballasted track with Iberian gauge (1.668m) of a conventional line.



Figure 2. HSL bridge under study (38°43'33.06"N 4°5'20.05"W).

The main experimental campaign was carried out in September 2022 in order to characterise the dynamic properties of the structure along with the dynamic response of the bridge under railway traffic, the analysis of energy harvesting, and the validation of a harvester prototype in a relevant environment.

During the recordings, several RENFE trains (S100, S102, S103, S114, S130, R449, R599, Altaría and freight trains) crossed the bridges. Information that includes the axle schemes, coach distributions, the axle distances and axle loads, as well as more information in this regard, can be found in References (Galvin et al. 2020) and (Renfe).

3.1 Setup

A LAN-XI portable acquisition system from Brüel & Kjaer was used. Endevco model 86 piezoelectric accelerometers with a nominal sensitivity of 10 V/g and a lower frequency limit of approximately 0.1 Hz were used. An Ometron VH-1000-D laser vibrometer with nominal sensitivities 8.0064 V/m/s was used to measure the tip velocity of the harvester. The acquisition system fed the sensors (accelerometers). LAN-XI also performed the Analog/Digital conversion (A/D). The A/D was carried out at a high sampling frequency, which avoided aliasing effects. The acquisition equipment was connected to a laptop for data storage. The acquisition system was configured to avoid sensor overload. The recordings were decimated (to 256 Hz)

to perform data analysis in the frequency range of interest. The response was filtered applying a third-order Chebyshev filter with high-pass frequencies of 1 Hz.

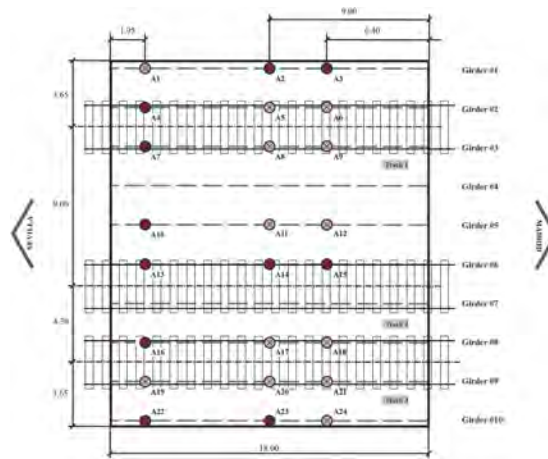


Figure 3. Scheme of the location of the sensors and experimental setup in HSL bridge over Tirteafuera River (38°43'33.06"N 4°5'20.05"W).

3.2 Tuning

In the first instance, vibration levels under operating conditions measured in July 2022 were used to estimate the tuning frequency. The measurement point *A14* located in the girder #4 was chosen. The laser vibrometer was used to avoid the installation of the scaffolding system at this stage. A total of 19 train circulations were recorded between 10.20 and 13.50h. Table 2 summarises the train passages including the type of train, track number according to Figure 3, traffic direction and travelling speed.

The mechanical energy was estimated for harvesters with a damping ratio of 1% tuned in the frequency range 1–30Hz. The confidence intervals, standard deviation, and mean values of the energy were estimated from the shape and scale parameters of the gamma distribution over the frequency range. Figure 4 shows the computed results. It can be observed a predominant frequency around 8 Hz where energy reaches its greatest values. There are also significant values of the energy around 9.3 Hz, which is interesting to note.

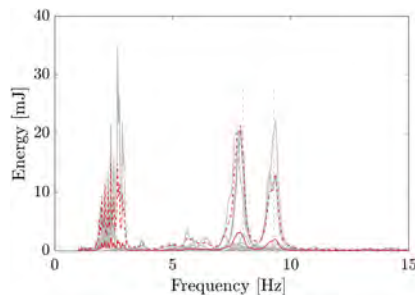


Figure 4. Mechanical energy for the bridge over the Tirteafuera River.

The tuning frequency was obtained from the maximum peaks for each circulation around the frequencies 8 Hz and 9.3 Hz. Figure 5 shows the quantile-quantile plot for the energy peak frequencies and a normal distribution with mean the tuning frequency. The results show a great agreement with the normal distribution. The tuning frequencies $f_{t1} = 7.8$ Hz and $f_{t2} = 9.28$ Hz are obtained from the mean value in both cases.

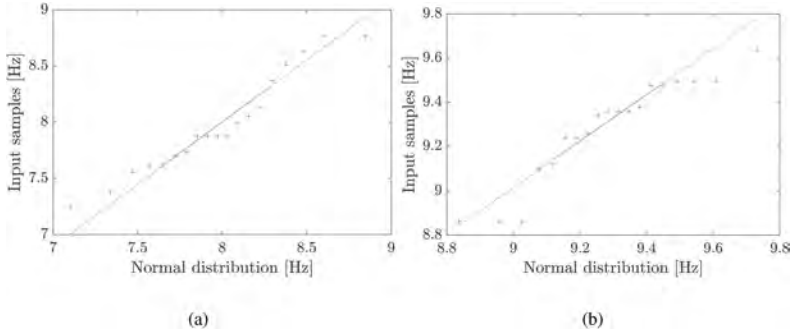


Figure 5. Quantile-quantile plot for tuning frequencies (a) $f_{i1} = 7.8$ Hz and (b) $f_{i2} = 9.28$ Hz.

3.3 Manufacture

An optimal tuning procedure has been performed to adjust the resonant frequency of the harvester to the tuning frequencies. Two energy harvesters tuned to the frequencies identified in the previous section have been manufactured with an optimal design. The piezoelectric patch selected for this application is the commercial DuraAct patch transducer P-876.A12 (Piceramic), composed of a piezoelectric layer covered by copper electrodes. The patch is embedded in a structure mechanically pre-stressed by a polymer surface, making it flexible. Patch dimensions are $L_p = 50$ mm, $b_p = 30$ mm, and $h_p = 0.2$ mm. Additive manufacturing using FDM 3D printing has been selected for the substructure. Among the variety of 3D printing materials, a high temperature polyamide carbon fiber reinforced material (PAHT CF15) is selected. PAHT CF15 is often used to replace metals in some applications due to its high strength.

The material properties of the substructure were experimentally estimated according to the ASTM D638-14 standard (ASTM, 2014). The material properties obtained were: mean Young's modulus $E_s = 7.40$ GPa with a standard deviation of $s_E = 0.33$ GPa; and tensile strength $\sigma_y = 94$ MPa with a standard deviation of $s_\sigma = 9.9$ MPa. A safety factor $\gamma_G = 1.33$ was used to assess structural integrity in the optimisation procedure to account for the standard deviation of the tensile strength.

The design parameters of the harvester are the result of a constrained optimisation problem where the maximum power dissipated by a harvester tuned to the fundamental frequency of the bridge is sought subject to the structural integrity of the system and the imposition of geometry constraints. The constrained optimisation problem is solved using a genetic algorithm and provides optimal values of the design parameters, length (L_s) and thickness (h_s) of the substructure, tip mass (M_t) and optimal load resistance (R_l). Harvesters with a damping ratio of 1% have been considered.

The optimal design parameters for each harvester are collected in Table 1

Table 1. Optimal design parameters for designed prototypes.

Device	L_s [mm]	h_s [mm]	M_t [kg]	R_l [k Ω]
Tirteafuera f_{i1}	106.7	0.94	0.09	664
Tirteafuera f_{i2}	90.9	0.73	0.076	552

3.4 Modal identification

The modal parameters of the bridge were identified from the ambient vibration data through an operational modal analysis using the Enhanced Frequency Domain Decomposition (EFDD) (Brincker et al. 2001). The EFDD technique is based on the decomposition of the power spectral density of the measured acceleration using singular value decomposition (SVD) (Tadeu et al. 2022). The natural frequencies of the structure are identified from the peaks of the singular

value curves of the accelerations of ambient vibrations (Figure 6). The fundamental mode corresponds to the first longitudinal bending mode with natural frequency $f_{b1} = 8.14$ Hz and modal damping $\zeta_{b1} = 1.72\%$. It is interesting to note that there is some decoupling between high-speed and conventional tracks due to the difference in mass of both areas, since the frequency of the fundamental mode is associated with the first bending mode of the bridge in the high-speed track area and there is another frequency associated with the first bending mode of the bridge in the conventional track area at $f_{b2} = 8.65$ Hz with $\zeta_{b2} = 1.42\%$. In addition, an important peak is observed at $f_{b3} = 9.54$ Hz corresponding to the first transverse bending mode with modal damping $\zeta_{b3} = 0.5\%$, and a peak at $f_{b4} = 11.51$ Hz of the first torsional mode with modal damping $\zeta_{b4} = 0.78\%$. These frequencies are higher than the tuning frequencies obtained previously due to effect of the crossing train in the dynamic response of the bridge.

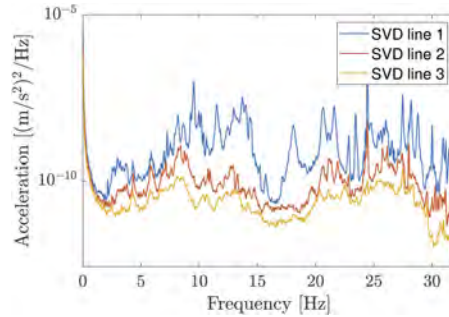


Figure 6. Singular Value Decomposition from ambient vibration.

Table 2 summarises the estimated energy collected with harvesters tuned to the tuning frequencies obtained with the proposed approach and harvesters tuned to the natural frequencies of the bridge. The results show that the energy generated in the case of harvesters tuned to the tuning frequency is much larger.

Table 2. Simulated Energy harvesting [mJ] in train passages recorded at Tirteafuera HSL Bridge (July 2022).

Passage	Train	Track	V [km/h]	E_{f1} [mJ]	E_{f2} [mJ]	$E_{f_{b1}}$ [mJ]	$E_{f_{b3}}$ [mJ]
1	S102	2	183.1	3.092	0.096	0.845	0.049
2	S102	3	200.6	0.317	0.012	0.328	0.008
3	S100	2	177.6	0.112	0.009	0.022	0.006
4	S114	2	221.0	0.003	0.018	0.006	0.011
5	S114	2	232.2	0.006	0.036	0.011	0.011
6	S103+S102-duplex	3-2	191.2	0.156	2.052	0.100	0.679
7	S114	3	197.7	0.228	0.005	0.080	0.003
8	S120	2	220.0	0.011	0.045	0.033	0.043
9	S120	3	220.0	0.006	0.033	0.010	0.022
10	S103	3	231.8	0.025	0.051	0.014	0.063
11	S100	2	168.6	0.004	0.127	0.005	0.186
12	R449	1	159.1	0.000	0.000	0.000	0.000
13	S114	3	198.0	0.131	0.010	0.032	0.015
14	S114	2	220.0	0.020	0.012	0.093	0.009
15	S100	3	176.8	0.012	0.015	0.005	0.022
16	S102	3	224.5	0.077	3.541	0.086	1.286
17	S102-duplex	2	176.4	1.911	0.191	0.570	0.191
18	S102	2	183.2	2.989	0.089	0.622	0.052
19	S100-duplex	2	184.4	0.071	0.040	0.065	0.020
		Total		9.173	6.380	2.927	2.676

4 CONCLUSIONS

The research presented here falls within the framework of the development of autonomous monitoring systems. A statistical procedure to estimate the tuning frequency of energy harvesters placed on railway bridges has been presented. A simplified lumped analytical model for the analysis of bimorph cantilever beams and an optimal tuning procedure have been followed. The analytical model allows us to study harvesters tuned to different frequencies with different lengths of substructure and PZT patches, which allows greater flexibility in the design. The performance of harvesters for a real bridge on the Madrid-Sevilla High-Speed line has been analysed. The energy collected by harvesters tuned to the frequencies obtained from the statistical process has been estimated, obtaining higher power levels than those tuned to the natural frequencies of the bridge.

ACKNOWLEDGEMENTS

The authors would like to acknowledge the financial support provided by the Spanish Ministry of Science, Innovation and Universities under the research project PID2019-109622RB; US-126491 funded by the FEDER Andalucía 2014–2020 Operational Program; and the Andalusian Scientific Computing Centre (CICA).

REFERENCES

- ASTM Designation: D638-14 Standard Test Method for Tensile Properties of Plastics. (2014).
- Brincker, R., Zhang, L. & Andersen, P., 2001, Modal identification of output-only systems using frequency domain decomposition, *Smart Materials and Structures*, 10 (3): 441–445.
- Erturk, A., & Inman, D.J., 2011, Broadband piezoelectric power generation on high-energy orbits of the bistable duffing oscillator with electromechanical coupling, *Journal of Sound and Vibration*, 330 (10): 2339–2353.
- Galvín, P., Romero, A., Moliner, E., De Roeck, G. & Martínez-Rodrigo, M.D., 2020, On the dynamic characterisation of railway bridges through experimental testing, *Engineering Structures* 226.
- Lombaert, G., Galvín, P., François, S. & Degrande, G., 2014, Quantification of uncertainty in the prediction of railway induced ground vibration due to the use of statistical track unevenness data, *Journal of Sound and Vibration*, 333, 18: 4232–4253.
- Museros, P., & Alarcón, E., 2005, Influence of the second bending mode on the response of high-speed bridges at resonance, *Journal of Structural Engineering*, 131 (3): 405–415.
- P-876 DuraAct Patch Transducer information, <https://www.piceramic.com/en/products/piezoceramic-actuators/patch-transducers/p-876-duraact-patch-transducer-101790/>.
- Renfe, Our trains. <https://www.renfe.com/es/en/renfe-group/renfe-group/fleet-oftrains>.
- Rocha, J. M., Henriques, A. A. & Calçada, R., 2012, Safety assessment of a short span railway bridge for high-speed traffic using simulation techniques, *Engineering Structures*, 40: 141–154.
- Romero, A., Cámara-Molina, J.C., Moliner, E., Galvín, P. & Martínez-Rodrigo, M.D., 2021, Energy harvesting analysis in railway bridges: An approach based on modal decomposition, *Mechanical Systems and Signal Processing*, 160.
- Sarker, M.R., Julai, S., Sabri, M.F.M., Said, S.M., Islam, M.M., & Tahir, M., 2019 Review of piezoelectric energy harvesting system and application of optimization techniques to enhance the performance of the harvesting system, *Sensors and Actuators, A: Physical*, 300.
- Stephen, N., 2006, On energy harvesting from ambient vibration, *Journal of Sound and Vibration* 293 (1): 409–425.
- Tadeu, A., Romero, A., Bandeira, F., Pedro, F., Dias, S., Serra, M., Brett, M. & Galvín, P., 2022, Theoretical and experimental analysis of the quasi-static and dynamic behaviour of the world's longest suspension footbridge in 2020 *Engineering Structures*, 253.
- Wei, C & Jing, X, 2017, A comprehensive review on vibration energy harvesting: Modelling and realization, *Renewable and Sustainable Energy Reviews*, 74: 1–18.
- Yildirim, T., Ghayesh, M.H., Li, W. & Alici, G., 2017 A review on performance enhancement techniques for ambient vibration energy harvesters, *Renewable and Sustainable Energy Reviews*, 71: 435–449.
- Zakeš, F. and Šniady, P., 2018, Vibrations of a multi-span beam subjected to a moving stochastic load, *Springer Proceedings in Mathematics and Statistics*, 248: 403–413.

Smart condition monitoring of a steel bascule railway bridge

J. Nyman, P. Rosengren & P. Kool

IoTBridge AB, Stockholm, Sweden

R. Karoumi & J. Leander

KTH Royal Institute of Technology, Stockholm, Sweden

H. Petursson

Swedish Transport Administration, Stockholm, Sweden

ABSTRACT: This paper presents a long-term monitoring campaign for safety assessment of an over 100 years old steel railway bridge in Vänersborg in the southwest of Sweden. Due to its age, the bridge is affected by severe corrosion, and cracks have been detected during inspection. In anticipation of a large-scale repair of the bridge, a comprehensive monitoring system has been installed. The monitoring system consists of 5 accelerometers, 16 strain gauges, 1 inclinometer and 3 weather measurement sensors (temperature, wind speed and wind direction). Data is collected continuously with high sampling frequency, transmitted to a structured IoT database in the cloud, and used for further processing and visualization. This paper describes the safety assessment processes, the underlying ideas behind them, the challenges encountered, and the developed monitoring dashboard for visualization of results. It also discusses the increased capabilities of the system after an entire year of monitoring.

1 INTRODUCTION

Today's modern transportation infrastructure relies, to a large extent, on structures that were built during the 20th century. A substantial number of bridges have reached their expected service life, and the number is rising. It is inevitable that some bridges will fail to comply with the safety requirements in the present regulations and should, formally, be strengthened or replaced. However, budget limitations will enforce a need to keep unfit bridges in service until remedial actions are possible.

A specific example is the railway bridge in Vänersborg in Sweden, shown in Figure 1. Since 1914, the bridge has carried commuter and freight trains over the Trollhätte channel. The bridge is opened several times per day to allow for boat traffic. The peculiar design of the counterweight mechanism causes bending of the truss members, and cracks have emerged in the riveted connections adjoining the concrete volume. Other parts are severely affected by corrosion, e.g., the upper chord of the leaf truss. Keeping the bridge's safety at an acceptable level requires recurrent inspections and maintenance actions.

Kühn et al. (2008) have suggested a stepwise assessment procedure for cases when standard measures fail to prove sufficient safety. The last phase (IV) in the approach includes intensified monitoring as a remedial action to reduce uncertainties in load effect estimations, combined with sophisticated assessment methods. A similar incremental assessment procedure is suggested by ISO (2010) with monitoring as a final intervention to provide sufficient safety.

Relating to the Vänersborg Bridge, a sensor system and a cloud-based data analysis framework were installed during autumn 2021 to facilitate continuous monitoring of the present state. This paper presents the bridge, the monitoring system and the analysis routines implemented. Some selected results from one year of monitoring are also presented.



Figure 1. A photo of the Vänernsberg Bridge.

2 THE VÄNERSBERG BRIDGE

The movable bridge can be attributed to a type described by y Koglin (2003) as a Single Leaf Heel Trunnion Bascule Bridge, sometimes called a Strauss Bascule Bridge. The design allows a low elevation above the water, without the need to build a watertight chamber for the counterweight.

It was constructed 1914-1916 and is built up by riveted steel members. As shown in Figure 1, the leaf is designed as a truss, acting as simply supported in its resting position. The single track has wooden sleepers attached directly to the open steel grid constituting the bridge deck. The axle loads are distributed through the system of sleepers – stringer beams – crossbeams to the main load-bearing truss. The lower and upper chords of the main truss and some of the diagonals have box-like sections. The other main members have I shaped cross-sections. Secondary bracings have typically L or T shaped sections.

The leaf is lifted by an operating link with rack attached to a trunnion at the upper joint of the main truss. The counterweight is attached by a link to the same joint assisting the lifting of the leaf. The counterweight is built up by its own truss but moves together with the leaf. The members consist of riveted plates and L profiles in box or I shape. The material in the members is steel classified as St37 with yield stress of 240MPa.

2.1 Instrumentation and data acquisition system

The data monitoring system consists of a HBM-Quantum data acquisition unit CX22B-W connected to one HBM-Quantum 16-channel measurement amplifier MX1615B (for strain gauges) and one 8 channel measurement amplifier MX840B (for accelerometers and inclinometer). The system is connected with a 4G-router for data transmittal to the cloud server. In addition, a Vaisala WXT530 weather station is installed to gather data on wind speed, wind direction and outside air temperature.

The selected logging procedure provides sampling of all sensors continuously at 200 Hz with a low pass filter at 50 Hz, with the exception of the weather data which is sampled at 4 Hz. At the end of each 10 minutes sampling period, the raw data for all sensors is stored in a file having a file name that identifies the date and time period when the data was recorded. The raw data files are backed up on-site on an external disk, and also continuously transmitted to the cloud server for real-time analyses and visualization in the dashboard (see Section 4).

The instrumentation is composed of:

- 16 strain gauges of type HBM weldable 350 ohms, LS31HT-6/350VE (Figure 2(a)).
- 5 piezoelectric accelerometers of type PCB type 393A03 with measurement range 0.5-2000 Hz and sensitivity 1 V/g (Figure 2(b)).
- 1 inclinometer of type Vigor Technology SST141 with measuring range $\pm 90^\circ$ (Figure 2(c)).
- 4G-router with antenna.

Figure 3 shows the sensor locations.

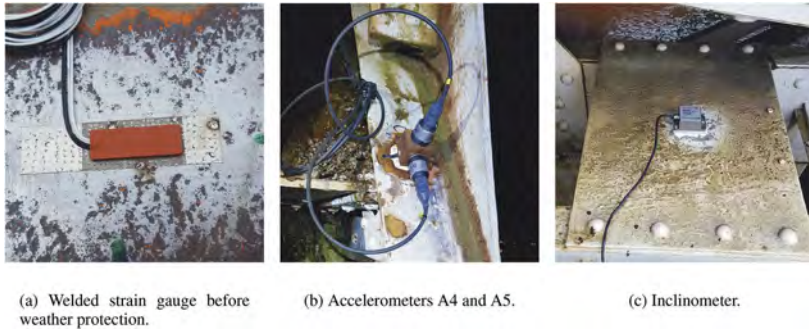


Figure 2. Photos of some of the sensors.

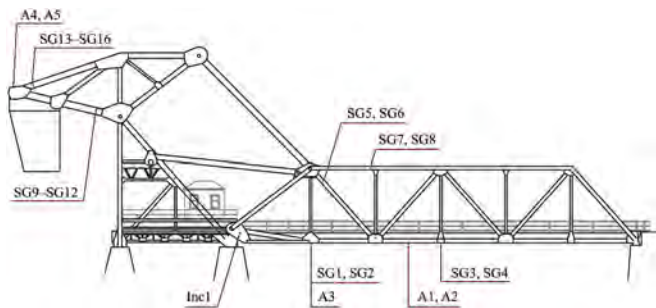


Figure 3. Sensor locations for the Vänersborg Bridge. A ~ accelerometer, SG ~ strain gauge, Inc ~ inclinometer.

3 DATA PROCESSING AND ANALYSES IN THE CLOUD

3.1 Data flow and processing

To enable a wide range of applications and to maximize the usability of the collected data, the raw measurement data files have to be transformed into a structured and interoperable data model. The data files are continuously sent from the edge gateway on the bridge to a backend cloud. There the files are parsed, filtered, cleaned and transformed for storage in a database. The database provides the basis for different decision support tools and is divided into two parts. One part is dedicated to handling the incoming IoT datastreams from the various sensors and supporting aggregation and visualization as well as exporting data to external data consumers such as smartphones and web browsers. The system implements the OGC SensorThings (OGC, 2021) standard for exchanging IoT data.

The second part of the database is dedicated to the analysis of data, for instance, to apply machine learning to detect a change in the behaviour of the bridge or extract sequences from the sensor data streams. PostgreSQL was selected as the storage engine because of its support for handling streamed IoT data as well as structured relational data. Figure 4 shows the overall software architecture and data flow of the bridge monitoring system.

3.2 Fatigue analysis

The strain gauges were placed to measure nominal strains, free from local stress concentrations caused by sharp geometry changes and rivets. The measurements provide time series for train passages and bridge openings. These are recalculated to stresses by Hooke's law and an elastic modulus of 210 GPa. By the standardized rainflow cycle counting routine (ASTM, 2017), stress range spectra are calculated for the loading events, describing the number of

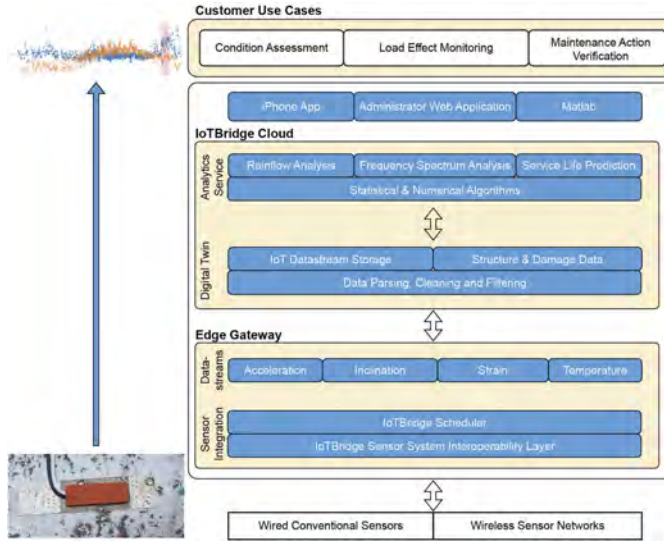


Figure 4. Software architecture and data flow in the bridge monitoring system.

cycles n in the associated stress range $\Delta\sigma$. By implementing the Palmgren-Miner rule (Palmgren, 1924; Miner, 1945), a fatigue limit state equation can be formulated as

$$G = D - \frac{(\gamma_{Mf}\gamma_{Ff})^3}{K_1} \sum_i n_i \Delta\sigma_i^3 - \frac{(\gamma_{Mf}\gamma_{Ff})^5}{K_2} \sum_j n_j \Delta\sigma_j^5 \quad (1)$$

where D is the limit value for the accumulated damage typically assigned to unity, γ_{Mf} and γ_{Ff} are partial safety factors. The indices i and j counts the stress ranges above and below the constant amplitude fatigue limit, respectively. The constants K_1 and K_2 represent the fatigue strength and are associated to the detail category $\Delta\sigma_c$ as

$$K_1 = 2 \cdot 10^6 \Delta\sigma_c^3, \quad K_2 = 5 \cdot 10^6 \Delta\sigma_D^5 \quad (2)$$

The variables $\Delta\sigma_c$ and $\Delta\sigma_D$ are defined in the Eurocode (CEN, 2008) together with the bilinear fatigue endurance curve implemented in (1). A limit state equal to or less than zero ($G \leq 0$) defines an exhausted service life.

For riveted bridge members, Kühn et al. (2008) suggest a detail category of $\Delta\sigma_c = 71$ MPa. The associated values are assigned to $\Delta\sigma_D = 52$ MPa and $\gamma_{Mf} \gamma_{Ff} = 1.35$. Moreover, a fatigue limit is considered with the value $\Delta\sigma_L = 29$ MPa which leads to exclusion of all stress ranges smaller than $\Delta\sigma_L/1.35 = 21$ MPa. The linear relation between the limit state and the number of cycles enables an estimation of the remaining service life by extrapolation.

3.3 Machine learning algorithms

The machine learning and damage detection process is composed of several sequential steps.

1. Event extraction. To compare the state of the bridge over time, some unit of comparison has to be selected. These are here denoted as events, where each event is a time series of measurements. Several different events are extracted and analyzed separately: trains of different type passing, the different phases of bridge openings and rest-sequences, i.e. sequences of measurements where there is little external influence occurring. The trains are divided into groups based

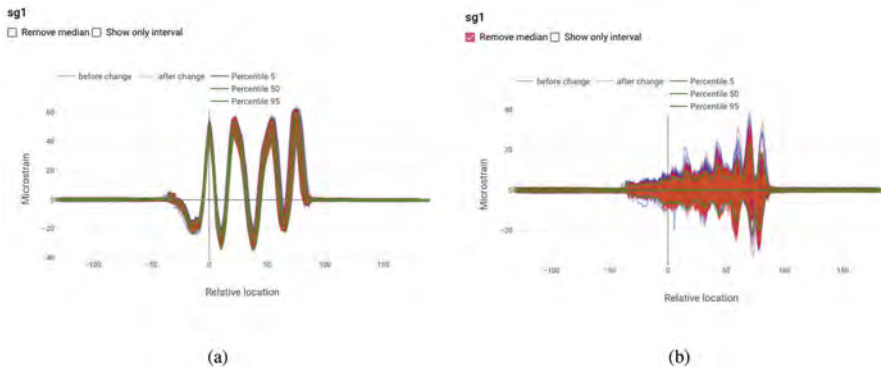


Figure 5. Comparing a number of events in the time domain for a strain gauge sensor before (in blue) and after (in red) a certain time point. In 5(a), the synchronized sensor measurements are shown. In 5(b), the same data is shown but with the trend subtracted. In this instance, there is no considerable change visible.

on the number of “peaks” found in the strain gauge measurements and the direction of the passing train. Each peak represents two adjacent bogies in two wagons or a bogie between two wagons.

2. Synchronization and preprocessing. The median is removed from all events. Thereafter, train passages are synchronized using the procedure presented in Lee et al. (2022) to put all trains on the same x-axis of “relative location”. It is calculated by first subtracting an absolute point (the first peak) from the time of each measurement to obtain a relative time for each measurement. Thereafter, the relative time is multiplied by velocity to obtain a location relative to the absolute point for each measurement. Bridge openings and rest-sequences are more easily synchronized using relative time. After the synchronization, a trend can be extracted from each event type independently by discretizing the x-axis and then calculating a mean for each point for a number of events. This trend can then be subtracted from each event to transform the time series to become more stationary. Subsequent steps process both sequences with and without trend. Examples of synchronized train passages, with and without trend, can be seen in Figure 5.
3. Feature extraction. After events have been categorized, synchronized and preprocessed, feature extraction can take place. Here time domain features, frequencies, cross-correlations and autoregressive model coefficients are extracted to be used as input for the next step.
4. Change detection. Finally, the features are fed into a change detection process to detect abnormal activity. Here only features of the same type of event are processed together and compared. The process uses Mahalanobis distance to fuse different subsets of features and then performs univariate change detection on the generated damage indices to detect changes. In most damage detection processes, changes are detected in single observations, but by using change detection, anomalies involving multiple points are instead detected. This can be advantageous in circumstances where outliers are common. Additionally, since subsets of features are used, the results become more interpretable. That is, if all features are involved in a found change, it is difficult to interpret what the change was caused by, but with few features it becomes easier.

4 MONITORING AND ANALYTICS DASHBOARD

To provide support for several different use cases such as condition assessment, load effect monitoring and maintenance action verification, a graphical dashboard has been implemented to assist bridge engineers and inspectors. The dashboard has multiple functions. One function is to provide a general overview of the bridge, e.g. are the sensors working, where are they located, how many train passages and bridge openings have there been, when did the last event occur, etc. An example of such information is shown in Figure 6.

The second function is to report analytical information relevant to maintenance planning or further theoretical analyses. Here, fatigue analysis is important, since it provides valuable information about the estimated accumulated damage and enables a prediction of remaining service life.



Figure 6. Dashboard overview.

Finally, the third function is a set of tools to analyze detected changes on the bridge to be able to make a decision if an inspection is necessary. To do this, features can be visualized, and synchronized events can be compared before and after the change in the time and frequency domain. An example of this functionality is shown in Figure 5 for a strain gauge sensor for a certain type of train passing with four peaks, where events before the change are colored in blue, and events after the change are colored in red. In Figure 5(a), the raw synchronized events are shown and in Figure 5(b) the same data is shown but with the trend subtracted. Subtracting the trend makes it easier to detect smaller deviations. In this case, there is no obvious difference before and after the change. There is also the option of clicking on individual discretized points in the time domain to visualize how they have changed over time.

5 RESULTS

From the start of December 2021 until December 2022, the bridge has been continuously monitored, with more than 25000 train passages and 2300 bridge openings having been registered. Examples of results from the monitoring and analyses are presented in the following sections.

5.1 Accumulated fatigue damage

An example of fatigue damage calculated for the measured strains in gauge SG9 is shown in Figure 7. The solid blue line is based on the recorded strains during the monitoring period. A forecast simulation for 365 days for the same sensor is shown as red lines starting in November 2022. The used forecast procedure has during the year been rudimentary, simply simulating similar traffic events and intensity, projecting past measurements into the future repeatedly for a number of iterations (in the figure 100). After a year or more of collected data, a more accurate model can be developed taking seasonal effects into account.

After about one year of collected data an accumulated fatigue damage of $D = 0.01$ is shown in Figure 7 for gauge SG9, which is the gauge giving the highest value so far. The forecast estimates the same amount of damage during the coming year. With this progress, the total service life can be estimated to be 100 years.

5.2 Sensor faults

Within the first few months of monitoring, four strain gauge sensors showed abnormal activity and a closer inspection revealed that it was caused by sensor faults. The current approach

for damage detection is more robust to these types of errors since it can still detect other changes from other subsets of features where sensor faults are not present. Furthermore, if a change is determined to be a sensor fault, a classifier can be generated using a simple threshold to eliminate these observations from the detection process.

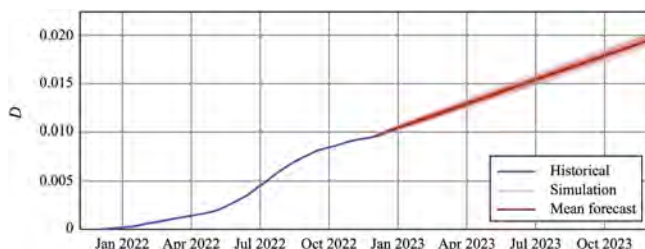


Figure 7. Accumulated fatigue damage and forecast simulation for strain gauge SG9.

5.3 Detected changes

As is generally known, it is often necessary to have collected the entire environmental cycle of variability before being able to more accurately anticipate and discriminate environmental change from structural change. Thus, this initial monitoring period can be seen as a more exploratory stage to oversee what kind of changes the bridge is subjected to. This is especially important in a country such as Sweden with diverse seasons and below-zero temperatures.

One of the more prominent patterns that was observed was the often non-linear changes that occurred during larger temperature changes when transitioning from spring to summer and from autumn to winter. One such example is shown in Figure 8 for a feature (blue), plotted together with temperature (orange) on a normalized y-scale. As can be seen, the change in trend for this feature across most of the year has a smaller impact than the variability between nearby observations. Yet, at the end of the year a large temperature change downwards caused an abrupt non-linear change. In Figure 9, the logged frequency spectrum is compared before (in blue) and after (in red) the change using the dashboard. As can be seen, the spectrum looks very different above 60 Hz before and after the time of change.

After a year has passed, it will be possible to control for environmental variability, and in particular temperature, more accurately.

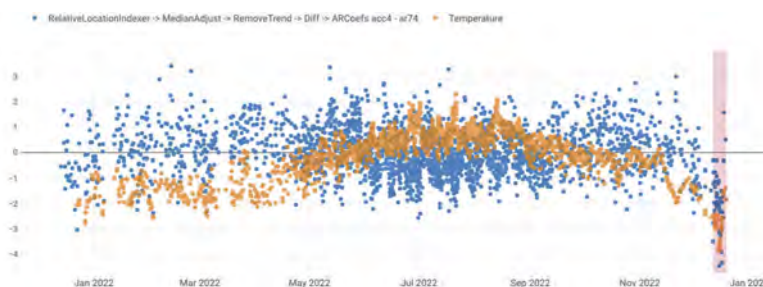


Figure 8. A detected change shown for a feature (blue) with temperature (orange) on a normalized y-scale. The detected change is shaded in red.

6 CONCLUSION

There are many challenges present in continuous real-world monitoring of bridges that are rarely taken into account in the academic sphere. Such as sensor faults, standardized procedures to simplify decision-making, system maintenance, etc. To handle these issues, practical and iterative improvements have been valuable to create a system that is more robust and effective. At the same time, observing and investigating within year data has been beneficial to understand the bridge and its behavior.

The most difficult issue, as discussed in section 5.3, is understanding what caused deviations to manifest in the data, and while tools for further visualization have been developed, it is still not always easy to make a decision. For this reason, in the future, incorporating more theoretical validation procedures, such as the finite element method, could be interesting to include another source of information into the system. Another option would be to include other sensors, such as cameras to connect data to tangible phenomena.

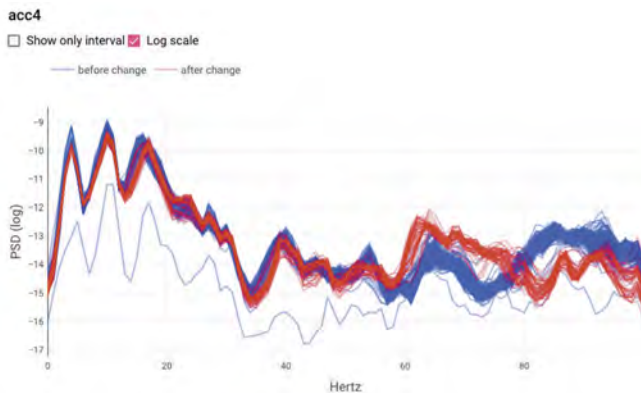


Figure 9. The logged frequency spectrum before (blue) and after (red) the timepoint of a change for a number of events. The change corresponds to the one shown in Figure 8.

Regarding the safety of the bridge, a yearly accumulated fatigue damage of about 0.01 is calculated for recordings at strain gauge SG9. This gives an estimation of the remaining fatigue life of 100 years which is about the same as the age of the bridge.

ACKNOWLEDGEMENTS

The assistance with the installation of the sensor network provided by Peab AB, and the funding provided by the Swedish Transport Administration (Trafikverket), are gratefully acknowledged.

REFERENCES

- ASTM (2017). *Standard Practices for Cycle Counting in Fatigue Analysis*. West Conshohocken, United States: ASTM International. ASTM E1049-85(2017).
- CEN (2008). *Eurocode 3: Design of steel structures – Part 1-9: Fatigue*. European committee for standardization (CEN). EN 1993- 1-9.
- ISO (2010). *Bases for design of structures – Assessment of existing structures*. International Organization for Standardization (ISO). SS-ISO 13822:2010.
- Koglin, T. L. (2003). *Movable Bridge Engineering*. Hoboken, New Jersey: John Wiley & Sons, Inc.
- Kühn, B., M. Lukic, A. Nussbaumer, H. Günther, R. Helmerich, S. Herion, M. Kolstein, S. Walbridge, B. Androic, O. Dijkstra, and O. Bucak (2008). *Assessment of Existing Steel Structures: Recommendations for Estimation of Remaining Fatigue Life*. Prepared under the JRC–ECCS cooperation agreement for the evolution of Eurocode 3.
- Lee, J., S. Jeong, J. Lee, S.-H. Sim, K.-C. Lee, and Y.-J. Lee (2022). Sensor data-based probabilistic monitoring of time-history deflections of railway bridges induced by high-speed trains. *Structural Health Monitoring* 21(6), 2518–2530.
- Miner, M. A. (1945). Cumulative damage in fatigue. *Journal of Applied Mechanics* 67, A159–A164.
- OGC (2021). *OGC SensorThings API Part 1: Sensing Version 1.1*. Open Geospatial Consortium (OGC). <https://docs.ogc.org/is/18-088/18-088.html>.
- Palmgren, A. (1924, april). Die Lebensdauer von Kugellagern. *VDI Zeitschrift* 68(14), 339–341.

A Bayesian bridge model update with complex uncertainty under high-speed train passages

K. Matsuoka

Railway Technical Research Institute, Tokyo, Japan

D. Mizutani

Tohoku University, Sendai, Japan

C. Somaschini, L. Bernardini & A. Collina

Politecnico di Milano, Milan, Italy

ABSTRACT: Bayesian structural model updating is an important technique to achieve digital twin with uncertainty. However, complexly distorted tails of the joint posterior probability density function (PDF) are not easy to estimate when a correlation exists between model parameters. Estimating the lower confidence bound of the joint posterior PDF requires several samples at the tails of the PDF. However, this task is difficult to achieve because the Markov chain Monte Carlo (MCMC) method concentrates on the samples near the expected value. Thus, to estimate the distorted tails of the joint posterior, the authors develop a new methodology called dual sampling, comprising two-step MCMCs. The second step sampling complements the samples around the tail of the joint posterior PDF, which are insufficient in the first step conventional MCMC method. The proposed method is applied to the maximum acceleration data of an Italian high-speed railway bridge.

1 INTRODUCTION

To manage a large number of structures, the development and practical application of structure monitoring methods have been promoted. Structural model update estimates the existing performance of a real structure by updating the parameters of the numerical model based on the measurement data obtained by monitoring. Especially since the pioneering work of Beck and Au (2002), a large body of research on Bayesian structural model updating has progressed (Simone et al. 2015).

Recently, attempts have been made to detect and evaluate damage by estimating structural models (parameters) that best fit measurement data and focusing on their uncertainty (Nishio et al. 2012; Kitahara et al. 2022). Additionally, a reliability design method for reinforcement considering uncertainties of updated model parameters has been developed (Matsuoka et al. 2020a).

Existing performance evaluations in Bayesian structural model updating often fail to assume independence between the estimated parameter uncertainties (Nishio et al. 2012). For example, in a bridge, multiple structural parameters (e.g., bending stiffness, support stiffness, and modal damping ratio) are estimated. However, the maximum displacement and acceleration at the mid-span, which are representative performance indicators, are due to a combination of these effects. In this case, each parameter cannot be evaluated independently because of the correlation of the uncertainties of each parameter (i.e., the spread of each parameter distribution). Therefore, evaluation of the tail space of the joint posterior probability density function (PDF), which considers the correlation between parameters, is required in the

uncertainty evaluation in the Bayesian structural model update. However, because samples around the tail of the joint posterior PDF are difficult to generate using the Markov chain Monte Carlo (MCMC) method (a typical Bayesian estimation method), another method for tail evaluation is required (Matsuoka et al. 2020b).

The authors in this study propose a new approach that uses a two-step MCMC method (Figure 1). Using the lower confidence bound (LCB) of the likelihood obtained using the MCMC method in the normal Bayesian structural model update, authors re-estimate the vicinity of the likelihood LCB, which represents the uncertainty, using another search method. Hence, the tail of the joint posterior PDF, which is complicatedly distorted, can be estimated. Figure 1 illustrates the case of two parameters as a conceptual diagram. However, as the number of parameters increases, the tail space to be estimated in the second step expands rapidly. The second step is spatial estimation instead of optimal value estimation. Therefore, the authors adopt the replica exchange MCMC (Lin et al. 2022), which is a numerical search method for objective functions with multiple peaks. This new approach is called the dual MCMC because it uses a two-step MCMC. After explaining the dual MCMC method, the proposed method is applied to the measured acceleration data of the Sesia bridge (Matsuoka et al. 2019).

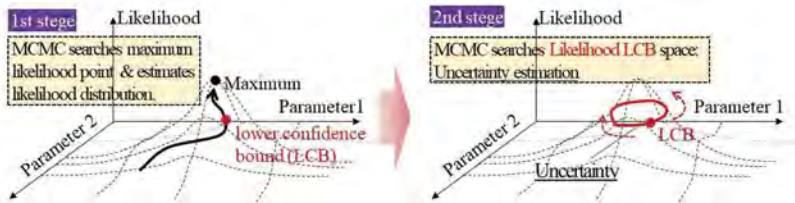


Figure 1. Concept of the dual MCMC, which is a method for estimating tails of joint posterior PDF when a correlation exists between parameters.

2 DUAL MCMC METHOD

2.1 Forward computation model

The target is a bridge where trains pass. For the forward calculation, the elastically supported beam at both ends and the moving load model presented in Figure 2 are used. In this study, the physical parameters (i.e., bending stiffness, support stiffness, and modal damping ratio) of the beam model illustrated in Figure 2(a) are updated using MCMC based on the maximum acceleration data of the bridge when trains pass. The unit length mass is assumed here to be known. The train was modeled as a moving load train with the same axle arrangement and axle load. Specifically, application to the more detailed finite element model presented by Matsuoka et al. (2019) is a future topic. The physical parameters of the bridge are updated using the MCMC method so that the maximum acceleration when a train passes by this model matches the measured value. Additionally, the tail of the joint posterior PDF, which represents the uncertainty that is lacking in the first step, is supplemented by the replica exchange MCMC in the second step.

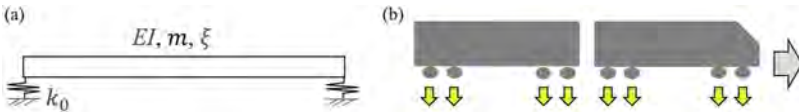


Figure 2. (a) Elastically supported beam at both ends and (b) moving load model.

2.2 First step: MCMC

The parameters of the beam model in Figure 2(a) are estimated using the MCMC method based on the bridge maximum acceleration. The response of the model shown in Figure 2 can be calculated from the theoretical solution of the equation of motion. Here the process of obtaining the maximum acceleration $a_M(v)$ at the bridge mid-span by giving the train speed v and other unknown parameters EI , k_0 , and ξ is expressed as a function F . Here, $\theta = [EI, k_0, \xi]$ is the unknown parameter vector.

$$a_M(v) = F(\theta, v) \quad (1)$$

Let $\mathbf{D} = (\tilde{y}_1, \tilde{y}_2, \dots, \tilde{y}_{S_n})$ be the measured data set of maximum acceleration when trains pass and $\mathbf{V} = (\tilde{v}_1, \tilde{v}_2, \dots, \tilde{v}_{S_n})$ be the train speed measured data. Note that S_n is the amount of data. From Bayes theorem, the occurrence probability of parameter vector θ given the measurement data set \mathbf{D} is given by Equation (2).

$$P(\theta|\mathbf{D}) \propto \mathcal{L}(\mathbf{D}|\theta)P(\theta), \quad (2)$$

where $\mathcal{L}(\mathbf{D}|\theta)$ is the likelihood function; $P(\theta)$ and $P(\theta|\mathbf{D})$ are the prior and posterior PDFs, respectively; \propto represents a proportional relation; and posterior PDF $P(\theta|\mathbf{D})$ is the distribution of parameter θ that represents the existing performance updated by the measured data set \mathbf{D} . Likelihood function $\mathcal{L}(\mathbf{D}|\theta)$ is defined as in Equation (3) in this paper. Furthermore, σ_1^2 is the variance of the normal distribution.

$$\mathcal{L}(\mathbf{D}|\theta) = \prod_{sn=1}^{S_n} N(\tilde{y}_{sn} - F(\theta, \tilde{v}_{sn}), \sigma_1^2) \quad (3)$$

Prior PDFs are set to be almost unconditional as in that of Mastuoka et al. (2020a). Equation (4), obtained by substituting the likelihood function and prior PDFs into Equation (2), is estimated using random walk Metropolis–Hastings (RW-MH), which is one of the MCMC methods.

$$P(\theta|\mathbf{D}) \propto P(k_0)P(EI)P(\xi) \prod_{sn=1}^{S_n} N(\tilde{y}_{sn} - F(\theta, \tilde{v}_{sn}), \sigma_1^2) \quad (4)$$

RW-MH is a method of obtaining samples from a PDF that cannot be sampled directly by generating random numbers. To obtain the p ($p = 2, \dots, \bar{p}$) sample $\theta^{(p)}$ of the model parameter θ using RW-MH, sample $\theta^{(p-1)}$ is added with a random number ϵ_p following a normal distribution with mean 0 and variance ν^2 to generate the p th sample candidate θ' .

$$\theta' = \theta^{(p-1)} + \epsilon_p, \quad \epsilon_p \sim N(0, \nu^2) \quad (5)$$

Because candidate θ' is generated according to a distribution different from the target distribution $P(\theta|\mathbf{D})$, it is corrected to match the distribution $P(\theta|\mathbf{D})$. In RW-MH, if the candidate follows the distribution $P(\theta|\mathbf{D})$, it is adopted, and if the probability of following is small, it is rejected with the probability. Specifically, the p th sample candidate is accepted with the probability expressed in Equation (6).

$$\alpha(\theta'|\theta^{(p-1)}) = \text{Min} \left[\frac{L(\mathbf{D}|\theta')}{L(\mathbf{D}|\theta^{(p-1)})}, 1 \right] \quad (6)$$

Practically, sampling is performed along with the Gibbs sampling method. With enough $p = \underline{p}$ iterations, $\theta^{(p)}$ converges to a random number generated from the distribution $P(\theta|\mathbf{D})$. The expected value and LCB of $P(\theta|\mathbf{D})$ can be calculated as statistics of $\theta = [\theta^{(\underline{p})}, \dots, \theta^{(\bar{p})}]$. However, the number of samples that correspond to the $P(\theta|\mathbf{D})$ tail is insufficient for evaluating

the uncertainty. Therefore, the likelihood \mathcal{L}_α that corresponds to the α LCB in the obtained $\mathcal{L}(\mathbf{D}|\boldsymbol{\theta})$ is used to estimate the tail space of the joint posterior PDF in the second step.

2.3 Second step: Replica exchange MCMC

The replica exchange MCMC is a type of extended ensemble method. It generates sample sequences using multiple MCMCs and exchanges the samples between sequences on the way. This exchange allows the movement between the peaks of the likelihood function via different sequences (Figure 3). Consequently, multimodal distributions and spatial estimations are possible.

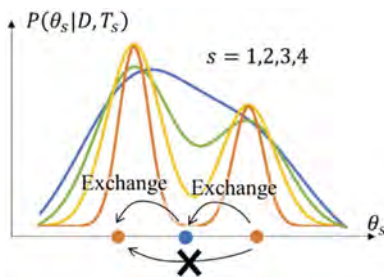


Figure 3. Mechanism of the movement between peaks by exchanging replica distributions.

Now, the generation probability of tail space Θ_α of the desired posterior PDF is defined as in Equation (7) by the joint distribution of S different replica distributions.

$$P(\Theta_\alpha) = P(\theta_1, \theta_2, \dots, \theta_S) = \prod_{s=1}^S P(\theta_s | \mathbf{D}, T_s) \quad (7)$$

However, because this is the estimation of the parameter space corresponding to α LCB (and not the estimation for best fitting to the data), the likelihood function is defined again. The new likelihood \mathcal{L}' in the second step spatial estimation problem is expressed as in Equation (8).

$$\mathcal{L}'(\mathbf{D}|\boldsymbol{\theta}_s, T_s) = N(\mathcal{L}(\mathbf{D}|\boldsymbol{\theta}_s) - \mathcal{L}_\alpha, \sigma^2) \quad (8)$$

Here, $N(\mathcal{L}(\mathbf{D}|\boldsymbol{\theta}_s) - \mathcal{L}_\alpha, \sigma^2)$ is the normal distribution with the expected value $\mathcal{L}(\mathbf{D}|\boldsymbol{\theta}_s) - \mathcal{L}_\alpha$ and variance σ^2 . Hence, $P(\theta_s | \mathbf{D}, T_s)$ is given by Equation (9).

$$P(\theta_s | \mathbf{D}, T_s) = \exp\left(\frac{-T_s \mathcal{L}'(\mathbf{D}|\boldsymbol{\theta}_s)}{Z(T_s)}\right) \quad (9)$$

Samples according to each replica distribution of Equation (9) are generated using the RW-MH, and the sample exchange between replica distributions is repeated with the exchange probability r according to Equation (10).

$$r = \exp[(T_{s+1} - T_s) \cdot (\mathcal{L}'(\mathbf{D}|\boldsymbol{\theta}_{s+1}) - \mathcal{L}'(\mathbf{D}|\boldsymbol{\theta}_s))] \quad (10)$$

Sample generation of each replica distribution in the replica exchange MCMC method can be calculated simultaneously through parallel computing. In this study, the method was implemented in Matlab.

3 APPLICATION TO SESIA VIADUCT

3.1 Test bridge and data

Dual MCMC presented in Chapter 2 is applied to the Sesia bridge (Matsuoka et al. 2019), an Italian high-speed railway bridge. The Sesia bridge is a steel–concrete composite bridge and has a span length of 45.2 m. Here, the maximum acceleration at the mid-span during the running of two types of trains (i.e., ETR500Y1 and ETR1000) obtained on the Sesia bridge (Figure 4) is used. As shown by Matsuoka et al. (2019), the maximum accelerations with 15 Hz LPF were used, where the primary bending mode of the bridge is dominant. Dual MCMC using a forward calculation model estimates the bridge bending stiffness, support stiffness, modal damping ratio, and their uncertainties. The numbers of target trains are six ETR500Y1 and 15 ETR1000. In MCMC at the first step, $\bar{p} = 1,000$ until burn-in, and $p = 20,000$ from burn-in to the end of the calculation. In the second step, replica exchange MCMC, the authors estimated the parameter space with a 5% LCB of the likelihood distribution obtained in the first step. The number of replica distributions is 4, and sampling was performed 20,000 times (a total of 80,000 samples) for each replica distribution.

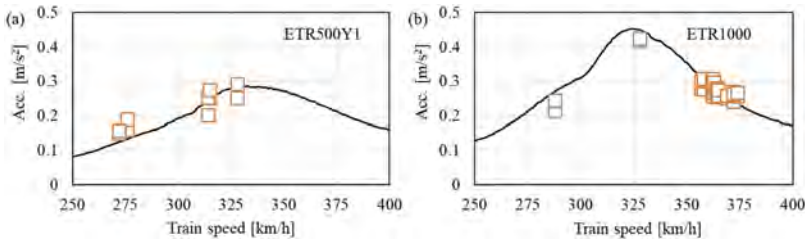


Figure 4. Measured values and calculation results of the expected value model of the posterior distribution obtained in the first step of MCMC.

3.2 Results of the first step MCMC method

Figure 5 shows each posterior distribution and joint posterior PDFs estimated using the MCMC method. Additionally, the black dots in the figure are the samples obtained in the second step of the replica exchange MCMC method, and the red line shows the 5% upper and lower confidential bands of the posterior distribution of each parameter. The estimated support stiffness is almost independent of other parameters. Meanwhile, a correlation exists in the joint posterior PDFs between the bending stiffness and modal damping ratio. Samples near the tail of the joint posterior PDF of the bending stiffness–modal damping ratio are outside the 5% LCB of each parameter because of this correlation. Therefore, the LCB parameter combination should be evaluated considering the correlation. Note that no problem exists in independently evaluating the expected value for each parameter. Figure 4 shows the evaluation results of the model with the expected values of the parameters obtained using the MCMC method in the first step. In the case of any train, it roughly agrees with the tendency of the sample.

3.3 Results of the second step MCMC

The tail space of the joint posterior PDF, which cannot be evaluated using the first step MCMC, was estimated using the replica exchange MCMC method. Figure 5 (black plots) illustrates the joint posterior PDF of the obtained sample. Evidently, the distorted tail space samples in the joint posterior PDF of the bending stiffness and modal damping ratio are heavily supplemented. Additionally, some correlation can be confirmed in the tail space of the joint posterior distribution of the support stiffness and bending stiffness. Figure 6 shows the

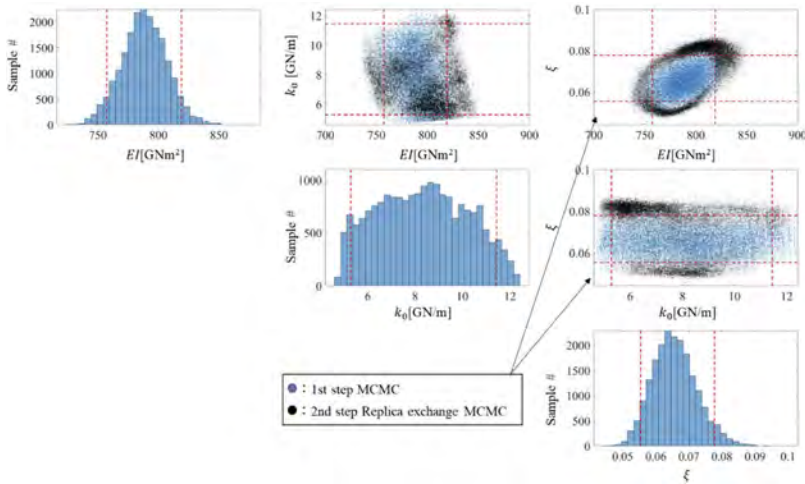


Figure 5. Posterior distributions of each parameter obtained using MCMC in the first step (black dots are the results of the second step).

estimated tail space (with a cylindrical shape) in the parameter space. These models represent the 5% LCB of the likelihood, and countless combinations of parameters exist that evaluate the maximum acceleration higher or lower than the measured data.

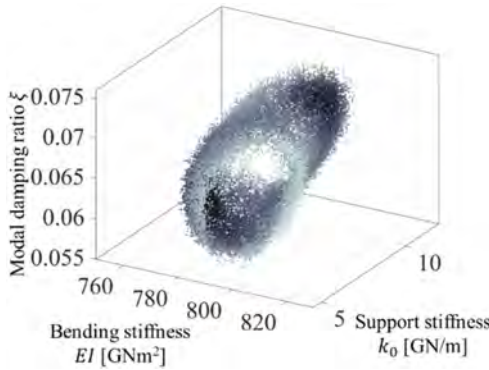


Figure 6. Tail space of the joint posterior distribution obtained using the replica exchange MCMC.

Therefore, selecting and using the most important model from the tail space are necessary. Generally, a model that evaluates values that are on the safe side is used. However, in the joint posterior distribution of the modal damping ratio and bending stiffness, a tail space with a lower limit of 5% outside the 5% LCB red line for each parameter exists. Therefore, the estimation of the tail space using the proposed method is clearly important for robust evaluation.

4 CONCLUSIONS

This study investigated the estimation of uncertainty when a correlation exists between parameters in the Bayesian structural model update. When a correlation exists between the parameters of the structural model, the tail of the joint posterior PDF is complexly distorted. Thus,

uncertainties cannot be evaluated by assuming that each parameter is independent. To estimate such a distorted tail space, the authors proposed a dual MCMC that uses two-step MCMCs. The expected value and likelihood distribution of each parameter were evaluated in the first step MCMC. Then, focusing on the LCB of the likelihood distribution obtained at the first step, the tail space of the joint posterior PDF, which cannot be evaluated using the first step because of insufficient samples, was largely compensated by the second step replica exchange MCMC.

The proposed method was applied to the maximum acceleration data of the Sesia bridge on the Italian high-speed railway. A correlation was found between the modal damping ratio and bending stiffness in the joint posterior PDF obtained using the MCMC method. Furthermore, the results of the second step replica exchange MCMC clarify that the tail space of the joint posterior PDF, which corresponds to 5% LCB of the likelihood, is a space with a cylindrical shape. Additionally, estimating the tail space considering the correlation is necessary because the model of 5% LCB when each distribution is assumed to be independent does not match the model considering the correlation.

ACKNOWLEDGMENTS

This work was supported by JSPS KAKENHI Grant Number JP22H01579.

REFERENCES

- Beck, J.L., & Au, S.K. 2002. Bayesian updating of structural models and reliability using Markov chain Monte Carlo simulation. *Journal of Engineering Mechanics* 128(4): 380–391.
- Kitahara, M., Bi, S., Broggi, M., & Beer, M. 2022. Distribution-free stochastic model updating of dynamic systems with parameter dependencies. *Structural Safety* 97: 102227.
- Lin, G., Wang, Y., & Zhang, Z. 2022. Multi-variance replica exchange SGCMC for inverse and forward problems via Bayesian PINN. *Journal of Computational Physics* 460: 111173.
- Matsuoka, K., Collina, A., Somaschini, C. & Sogabe, M. 2019. Influence of local deck vibrations on the evaluation of the maximum acceleration of a steel-concrete composite bridge for a high-speed railway. *Engineering Structures* 200: 109736.
- Matsuoka, K., Shinozaki, S. & Kaito, K. 2020a. Structural model update considering uncertainty and reliability assessment of strengthening effect: Application to additional supporting strengthening of a high-speed railway bridge. *Journal of Japan Society of Civil Engineers, Ser. AI* 76(3): 560–579.
- Matsuoka, K., Kaito, K. & Sogabe, M. 2020b. Bayesian time–frequency analysis of the vehicle–bridge dynamic interaction effect on simple-supported resonant railway bridges. *Mechanical Systems and Signal Processing* 135: 106373.
- Nishio, M., Marin, J., & Fujino, Y. 2012. Uncertainty quantification of the finite element model of existing bridges for dynamic analysis. *Journal of Civil Structural Health Monitoring* 2(3-4): 163–173.
- Simoen, E., De Roeck, G., & Lombaert, G. 2015. Dealing with uncertainty in model updating for damage assessment: A review. *Mechanical Systems and Signal Processing* 56-57: 123–149.

Computational analysis of a reinforced concrete railway bridge considering the soil-structure interaction

A.L. Gamino, R.R. Santos, T.N. Bittencourt & M.M. Futai
University of Sao Paulo (USP), Sao Paulo, SP, Brazil

H. Carvalho
Federal University of Minas Gerais (UFMG), Belo Horizonte, MG, Brazil

ABSTRACT: Bridges are a sensitive part of railway infrastructure and are subject to deterioration of their materials and support conditions during their life cycle. Regular use and the effects of time can affect the behavior of a structure. Therefore, the condition assessment of these assets is one of the most critical issues for infrastructure operators, aiding bridge integrity management. The present paper aims to study the dynamic structural responses and the soil-structure interaction of a reinforced concrete (RC) railway bridge. For this study, a six-span reinforced concrete bridge with 180 meters in total length, built in the 80s and rehabilitated in 2017, was employed as a case study. The bridge superstructure contains longitudinal beams with rectangular cross-sections, transverse beams, and a concrete deck with variable cross-sections. The infrastructure is composed of caissons supported by a rock layer. A numerical model was developed using the finite element method considering the soil-structure interaction process from Winkler springs calibrated adequately according to soil characteristics and foundation type. The springs, applied on the foundations and bearing devices, were positioned according to design and construction information, which provided physical and mechanical characteristics necessary to develop the computational modeling. Results regarding natural frequencies of vibration, deformations, displacements, accelerations, and velocities in the deck, beams, and pile caps of the railway bridge were analyzed and compared with monitoring results, assessing the bridge's structural response when subjected to dynamic loads. The numerical results adhered to those found in the monitoring campaign, thus validating the modeling methodology strategy employed in the bridge study. The results can be used to evaluate the structural condition and assess the bridge's behavior during its life cycle. Therefore, it can support the development of models to predict failures and even be incorporated into a digital twin that can be employed for bridge integrity management.

1 INTRODUCTION

Several studies have been directed toward improving damage detection and structural performance evaluation knowledge in recent years. These studies were motivated by the demands that emerged due to the increase in loading conditions, material deterioration, new conditions of use, or even exceptional events such as hurricanes, explosions, and earthquakes.

Inspection and monitoring strategies provide reliable data regarding the bridge condition and support activities of maintenance, strengthening, and retrofitting. In this sense, manual inspections are an essential source of information for structural integrity assessment. However, this activity can be time-consuming, laborious, expensive, unsafe, and highly subjective, depending on the inspector's experience (Spencer et al. 2019). Therefore, computer vision-based techniques are presented as innovative data resources to automate civil infrastructure

inspection, mainly when associated with Unmanned Aerial Vehicles (UAVs) for image acquisition (Yeum 2015, Catbas et al. 2018).

Parallel to the existing inspection activities for condition assessment, Structural Health Monitoring (SHM) stands out as a process to provide accurate and in-time information regarding bridge structural condition and performance. The strategy seeks to detect, locate, and quantify structural damages through data acquisition from field measurements. The obtained information can be used to plan and design maintenance activities, increase safety, verify design hypotheses, reduce uncertainties and, in general, increase our knowledge about the monitored structure (Glisic & Inaudi 2007). For example, using accelerometers and strain gauge sensors allows an analysis of the bridge's structural behavior, static and dynamic, under service conditions (Brownjohn 2007).

Integrating inspection and monitoring data to Finite Element Modeling (FEM) strategies enables the assessment of current deterioration or damage of a structural asset. Furthermore, it can assess future bridge behavior by adjusting the input parameters and load conditions in the numeric model. As stated by Brownjohn (2007), computational simulation via FEM exposes the integration between the structural elements, allowing a verification of the system's global behavior, whose validation is dependent on the values obtained in situ when using instrumentation techniques. Additionally, FEM models can help monitoring campaigns by identifying critical positions to assign the monitoring sensors.

Several studies have been carried out to investigate the influence of considering the soil-structure interaction (SSI) on the response of bridges to loads of a dynamic nature. SSI analysis evaluates the combined effects of soil, foundation, and structure bridge system structural responses, enabling a more complete computational representation of the asset condition. For example, Wu & Qiu (2020) studied the dynamic analyses of pile-supported bridges, including soil-structure interaction, under stochastic ice loads. For this case, nonlinear spring models were employed to represent the soil-foundation interface. The authors verified that structures supported by soft soils present higher displacements and lower natural frequencies than fixed supports.

Once implemented, numerical models must be calibrated appropriately. Thus, using experimental data collected from structural health monitoring systems is a common way to verify the efficiency of a model. For instance, Zangeneh et al. (2020) compared the modal characteristics of a high-speed railway bridge to its numerical models to propose a reliable simplified model adequate for design practices. In addition to finite element modeling, analytical formulations can provide essential insights into the influence of foundations on the overall stiffness of bridges, as done by Zangeneh et al. (2019). The authors proposed a simplified discrete model for calculating modal parameters of the fundamental vertical mode of a simply-supported beam on viscoelastic supports. It was observed that an important parameter to evaluate the soil-structure interaction relevance is the ratio between the superstructure stiffness and the soil-foundation system stiffness. A large value for this ratio implies a greater capacity of the soil to dissipate energy by radiation, making such a consideration beneficial for the system's structural performance.

In this context, including soil-structure interaction during the numerical modeling of bridges becomes essential for dynamic analysis, such as for evaluating the structure and foundation seismic performance (Raheem 2022). Studies in this regard have verified some of the following aspects: the influence of considering SSI and wave passage effects for the seismic vulnerability of continuous bridges (Ramadan et al. 2020); bridge failure probability estimation from uncertainties parameters on SSI modeling (Xie & Desroches 2019); quantification of the impact of considering soil-structure interaction for the development of bridge-specific fragility curves (Stefanidou & Kappos 2017); performance evaluation of a group of piles under seismic action considering soil-fluid-structure interaction (Zhan et al. 2020). Several other studies are being developed to expand the use and capabilities of SSI strategies.

The present work aims to apply the methodological aspects used in primary studies in the field of structural analysis for bridges considering soil-structure interaction to produce reliable computational results to evaluate the dynamic behavior of a reinforced concrete railway bridge. The developed numerical model, validated by monitoring campaigns, will provide subsidies to assess the structural condition and the bridge behavior during its life cycle.

2 RAILWAY BRIDGE CASE STUDY

2.1 Asset description

For this paper, a six-span reinforced concrete railway bridge with 180 meters in total length, built in the 80s and rehabilitated in 2017, was employed as a case study. The asset is in the northern region of Brazil. The bridge comprises two continuous sections: the first section includes two 25 meters spans, and the second has four 25 meters spans. Each section ends with abutments (Figure 1a), and there is a 5 cm joint between the two continuous sections at the intermediate supports. The bridge superstructure consists of two longitudinal beams with rectangular cross-sections, transverse beams, and a concrete deck with variable cross-sections. The superstructure is supported on the pile caps by neoprene bridge bearings. The infrastructure comprises pile caps and caissons supported by a rock layer (Figure 1b).



Figure 1. Case study railway bridge details: (a) abutment details, (b) detail of caissons and pile caps.

Due to an act of vandalism (Figure 2a), the continuous section with two spans of the bridge had to be recovered and reinforced in 2017 (Figure 2b). The longitudinal girders near one of the bridge abutments were repaired and strengthened, the transverse beams were



Figure 2. Bridge rehabilitation process: (a) damage caused by an act of vandalism in 2017, (b) process for bridge rehabilitation and strengthening.

reconstructed, and the damaged pile cap was repaired and reinforced. At the time, a comprehensive study had to be developed to define and design the retrofit activities. If a previous thorough condition assessment of the asset by inspection and/or monitoring campaigns and a validated computational model were available, the cost and time employed to determine the necessary interventions could have been minimized.

In order to create a 3D geometric model of the bridge, a parameterized model of the asset was developed using the environment Rhino/Grasshopper. The modeling strategy focused on obtaining a model with a reliable representation of the bridge geometry and the interaction between the parts. For the process, data from design and construction was employed, as well as “as-is” information provided by previous inspections. The railway bridge was modeled in two different arrangements: the bridge in its original configuration (before the vandalism act of 2017, Figure 3a) and the bridge configuration after the retrofit activities (Figure 3b).



Figure 3. Modeling arrangements: (a) bridge in its original configuration, (b) bridge after the rehabilitation and strengthening process (strengthening elements in dark gray).

2.2 Asset instrumentation

The asset was instrumented in 2020 to assess the condition of the strengthened region by a third-party company contracted by the bridge owner. The bridge modal parameters, such as natural frequencies, vibration modes, and damping ratio, were determined by ARTEMIS Modal Pro 6.1 software. The software uses two techniques for modal identification: one in the frequency domain (FDD – Frequency Domain Decomposition) and the other in the time domain (Stochastic Subspace Identification). In general, accelerations over time were converted to the frequency domain using mathematical and stochastic models. The final graph provided by the software presents the singular values obtained from the decomposition of the spectral density matrices. For each vibration mode, the natural frequency and its associated damping ratio can be obtained. Thus, from the monitoring responses, it is possible to locate the accelerometers according to the peaks provided in the graph and prepare the instrumentation plans to obtain the vibration modes in the field. Table 1 summarizes the natural frequencies for each vibration mode and their respective damping ratio.

The data obtained by the structural health monitoring campaign was employed to properly calibrate the computational models presented in this paper. A well-validated model can reduce model uncertainties and improve its accuracy in predicting the system’s structural responses.

Table 1. Experimental natural frequencies.

Mode	Frequency (Hz)	Damping ratio (%)
I	1.8	3.6
II	3.0	2.5
III	7.7	1.0
IV	9.6	0.2

2.3 Asset computational model

Springs were used along the caissons to simulate the soil-structure behavior. Details about the methodology employed can be found in Morrison (1993). It was decided to simulate the pipes in shell finite elements since the results found through discretization in bar elements proved to be incompatible with the instrumentation performed on the asset.

Using an adequately calibrated Winkler spring model to describe the behavior of a structure-foundation-soil system is one of the most commonly adopted methods to portray the combined effects of this type of system and its material properties. Thus, springs were employed along the caissons to simulate the soil-structure interaction behavior. The methodology adopted for this paper can be found in further detail in Morrison (1993). The bridge components were represented numerically by shell finite elements since this modeling approach provided more relevant results than a simplified modeling strategy with bar elements to describe the asset actual behavior verified on the field. In order to describe the soil-structure springs' stiffness, a soil Poisson's coefficient of 0.30 was adopted for the first 1.0 *m* layer of soil and 0.40 for the subsequent layers. Therefore, Table 2 displays the horizontal spring stiffness coefficients assumed according to the caisson's diameter (1.40 m) and the depth of the element.

Table 2. Soil-structure horizontal spring stiffness.

Depth (m)	Stiffness (<i>tflm</i>)
0.70	2352
7.00	11956

Springs with equivalent vertical stiffness were employed to represent the as-built steel support frames adopted for the bridge strengthening process, as detailed in Figure 2b. For this, a vertical spring stiffness of 170 *tflm* was assumed for the numerical model. The neoprene bearing pads were represented according to the technical procedures proposed by Guerreiro (2003). Table 3 presents the vertical spring stiffness adopted for the bridge bearing pads, considering a shear modulus of 1 *MPa* for the components.

Table 3. Neoprene bearing pads vertical stiffness.

Bridge axis	Stiffness (<i>tflm</i>)
E4	7.8
E5	3.3

Figure 4 illustrates the computational model with isoparametric shell elements with three nodes (linear interpolation) developed in CSiBridge 21 for the bridge after rehabilitation. The numerical model has about 52,000 nodes and 110,000 shell elements. The railway bridge foundations were assumed as fixed supports at the bedrock region.

The shell thickness element was calibrated in agreement with the asset modal frequencies obtained experimentally to evaluate the structural responses. The experimental damping rates have been used in the computational model according to modal patterns (Table 1).

A modal FEM free vibration analysis has been carried out using concrete strength and Young modulus applied in each asset region as established by Table 4. The experimental values for the damping ratio introduced in Table 1 were used to feed the computational model. The shell element thickness was calibrated in agreement with the modal frequencies obtained experimentally during the bridge condition assessment.

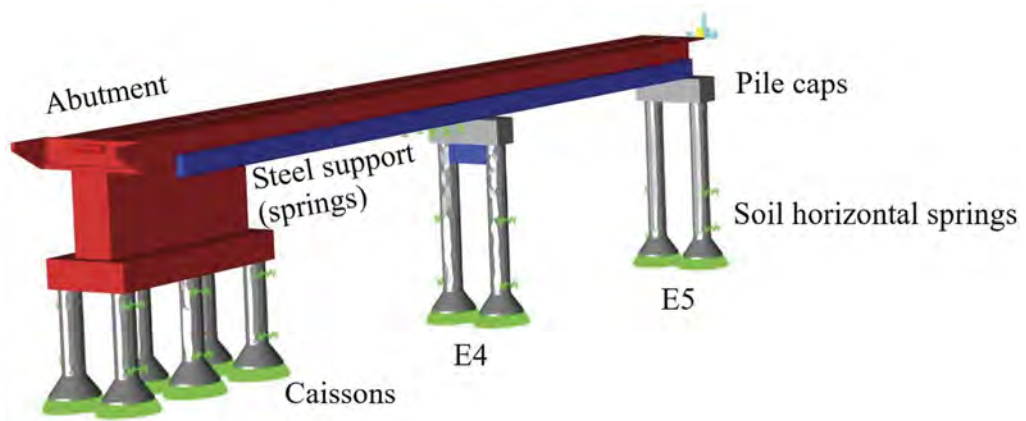


Figure 4. Bridge computational model and components description after strengthening.

Table 4. Concrete mechanical properties.

Bridge region	Concrete strength (<i>MPa</i>)	Young's modulus (<i>MPa</i>)
Superstructure	18	24091
Infrastructure	15	21797

3 COMPUTATIONAL RESULTS

The natural frequencies of the bridge after rehabilitation were compared with the bridge's original configuration to verify the increase in stiffness provided by the adopted strengthening strategies. Likewise, the natural frequencies rehabilitated bridge were compared with those extracted from the monitoring campaign performed by a third-party company in 2020 to validate the modeling approach developed in this paper. Figure 5 displays natural frequencies obtained by the modal analysis for Mode I and Mode II.

Table 5 presents a comparison between the natural frequencies obtained experimentally with the proposed computational model. A good convergence can be seen between the obtained results, which allows for validating the numerical model produced. It should also be noted that the modeling strategy adopted in this paper, which includes the soil-structure interaction, displayed better results when compared with the model produced by the third-party company. Thus, the use of a more detailed model, using shell elements instead of bar elements, in addition to the use of an SSI approach, provided satisfactory improvements to attain the bridge structural responses.

The deviation between the experimental results to the natural frequencies obtained by the numerical model proposed in this work was close to 5%. On the other hand, the computational model established by the third-party company displayed a 10% deviation from field measurements, demonstrating the improvements provided by the technique adopted for this paper.

The strengthening elements ensured a stiffness increase of 10% for the bridge compared to the original project when measured by the frequency in Mode I (longitudinal bending) and a stiffness increment of 11% for Mode II (torsion). Furthermore, the bridge strengthening caused an order of 10% approximately increase in stiffness for free vibration in Mode I and Mode II.

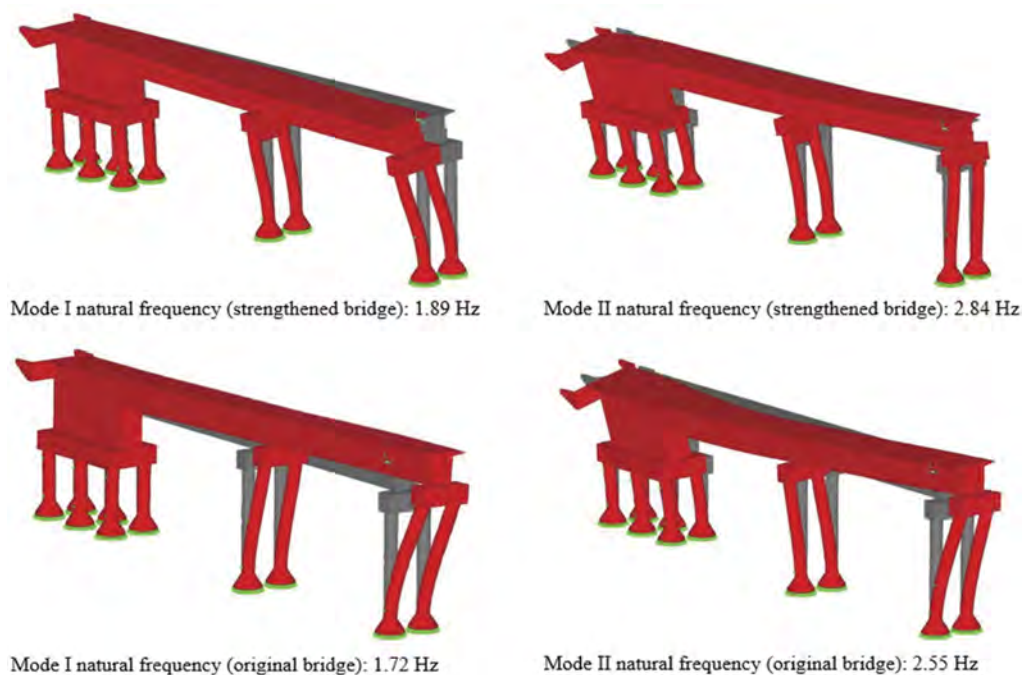


Figure 5. Modal analysis results.

Table 5. Comparison between computational and experimental natural frequencies.

Modal shape	Proposed Model	Third-party company model	Experimental
Mode I	1.89	2.00	1.80
Mode II	2.84	3.30	3.00

4 CONCLUSIONS

Based on the results obtained in this paper, it can be concluded that:

- SSI models provide satisfactory improvements in the numerical responses;
- The soil-structure model proposed by Morrison (1993) provided an adequate representation of the soil stiffness around the caissons;
- The approach described by Guerreiro (2003) proved to be compatible with the level of stiffness and damping in the neoprene bearing pads;
- The modeling strategy with shell elements proposed in this paper proved to be more efficient in representing the railway bridge actual behavior when compared to a modeling strategy considering beam finite elements;
- The strengthening process produces an increase of 10% in the bridge stiffness for bending and torsional behavior;
- The calibrated computational model represents the real-life asset, enabling the bridge condition assessment;
- A chain of analysis considering material degradation and different load case scenarios can be conducted using the validated model to predict the bridge behavior and support repair or strengthening measures for the structure;

- The validated modeling strategy will enable the performance assessment of the railway bridge throughout its life cycle and support the development of new research activities related to the management of this type of infrastructure.

ACKNOWLEDGEMENTS

The authors would like to acknowledge CNPq (The National Council for Scientific and Technology), FAPESP (grant #2020/02350-2, The São Paulo Research Foundation), and VALE Catedra Under Rail for providing financial support to develop this paper.

REFERENCES

- Brownjohn, J.M.W. 2007. Structural health monitoring of civil infrastructure. *Philosophical Transactions of the Royal Society A* 13: 589–622.
- Catbas, N., C. Z. Dong, C.Z., Celik, O., Khuc T. 2018. A vision for vision-based technologies for bridge health monitoring. In Maintenance, Safety, Risk, Manag. Life-Cycle Perform. Bridg. Proc. 9th Int. Conf. Bridg. Maintenance, Saf. Manag. IABMAS 2018, Melborn, 9-13 July 2018.
- CSiBridge 21. 2021. Bridge analysis design and rating. Version 21. Berkeley: Computers & Structures Inc.
- Glisic, B. & Inaudi, D. 2007. Fibre optic methods for structural health monitoring. Chichester: John Wiley & Sons.
- Guerreiro, L.A. 2003. *A borracha na concepção anti-sísmica. Faculdade de Engenharia da Universidade do Porto*. Porto: FEUP.
- Morrison, N. 1993. Interacción suelo-estructuras: semi-espacio de Winkler. *MSc. Dissertation; Universidad Politécnica de Cataluña*. Barcelona: UPC.
- Raheem, S. 2022. Soil-structure interaction for seismic analysis and design of bridges. In Alessio Pipinato (ed.), *Innovative Bridge Design Handbook (Second Edition)*. Oxford: Butterworth-Heinemann.
- Ramadan, O.M.O. et al. 2020. Assessment of seismic vulnerability of continuous bridges considering soil-structure interaction and wave passage effects. *Engineering Structures* 206(1): 110161.
- Spencer, B.F., Hoskere, V., Narazaki, Y. 2019. Advances in computer vision-based civil infrastructure inspection and monitoring. *Engineering* 5: 199–222.
- Stefanidou, S. & Kappos, A. 2017. Methodology for the development of bridge-specific fragility curves. *Earthquake Engineering & Structural Dynamics* 46(1): 73–93.
- Wu, T. & Qiu, W. 2020. Dynamic analyses of pile-supported bridges including soil-structure interaction under stochastic ice loads. *Soil Dynamics and Earthquake Engineering* 128: 105879.
- Xie, Y. & Desroches, R. 2019. Sensitivity of seismic demands and fragility estimates of a typical California highway bridge to uncertainties in its soil-structure interaction modeling. *Engineering Structures* 189: 605–617.
- Yeum, C.M. 2015. Vision-based automated crack detection for bridge inspection. *Computer-Aided Civil and Infrastructure Engineering* 30: 759–770.
- Zangeneh, A. et al. 2019. Fundamental modal properties of simply supported railway bridges considering soil-structure interaction effects. *Soil Dynamics and Earthquake Engineering* 121: 212–218.
- Zangeneh, A. et al. 2020. Dynamic soil-structure interaction in resonant railway bridges with integral abutments. *XI International Conference on Structural Dynamics*, Athens, 23-26 November 2020. Athens: Institute of Structural Analysis and Antiseismic Research.
- Zhan, L., Peng, C., Zhang, B., Wu, W. 2020. A SPH framework for dynamic interaction between soil and rigid body system with hybrid contact method. *Numerical and Analytical Methods in Geomechanics* 44: 1446–1471.

Drive-by damage detection methodology for high-speed railway bridges applying Mel-frequency cepstral coefficients

E.F. Souza

Federal University of Technology – Parana (UTFPR), Guarapuava, Brazil
University of São Paulo (USP), São Paulo, Brazil

T.N. Bittencourt & I. Ames

University of São Paulo (USP), São Paulo, Brazil

D. Ribeiro

School of Engineering, Polytechnic of Porto, Porto, Portugal

H. Carvalho

Federal University of Minas Gerais (UFMG), Belo Horizonte, Minas Gerais, Brazil

ABSTRACT: In this paper, a drive-by damage detection methodology for high-speed railway (HSR) bridges is addressed to appraise the application of Mel-frequency cepstral coefficients (MFCC) to extract the Damage Index (DI). A finite element 2D vehicle-track-bridge (VTBI) model that incorporates the train, ballasted track and bridge is presented. The formulation includes track irregularities and a damaged condition induced in a structure region. The feasibility of applying cepstrum analysis components to the indirect damage detection in HSR by on-board sensors is evaluated by numerical simulations. Different damage scenarios were simulated, as well as external excitations such as measurement noises and different levels of track irregularities. The results show that MFCC-based DI are highly sensitive regarding damage detection and robust to the noise. Bridge's stiffness can be recognized satisfactorily at high speeds and under different levels of track irregularities. Moreover, the magnitude of DI extract-ed from MFCC is related to the relative severity of the damage.

1 INTRODUCTION

With the continual development of new HSR lines around the world, bridges represent a significant component of these infrastructures; consequently, the demand for condition evaluation of such a vast number of bridges is rapidly rising (Wang *et al.*, 2021). Vibration-based Structural Health Monitoring (SHM) has been intensively researched as one of the most prevalent assessment techniques in the past few decades. In direct SHM, the dynamic responses of structures are often examined utilizing on-bridge sensors. However, deploying sensors and equipment for these sorts of monitoring is time-consuming and labor-intensive (Zhan *et al.*, 2021).

For this reason, indirect approaches for SHM of bridges have received significant interest. The most common method employed is a drive-by estimation of passing railway bridges based on the on-board measured data of a train in service traveling on the designated routes (Yang *et al.*, 2019). As a relevant application of the drive-by bridge inspection method (Micu *et al.*, 2022), the structural damage of the bridge under different conditions can be detected based on the identified modal parameters (OBrien, Malekjafarian and González, 2017).

Cepstrum-based operational modal analysis has been studied recently (Morgantini, Betti and Balsamo, 2021). Cepstrum analysis may detect slight spectrum variations from the vibration

signal as a function of quefreny. Initial cepstrum-based analytical studies show considerable potential for SHM applications (Randall, 2009). Despite the fact that this study topic has lately sparked interest in the SHM field, there are currently a limited number of works applying MFCC to indirect health monitoring for damage detection.

This study addresses a drive-by damage detection methodology for HSR bridges to evaluate the application of MFCC to extract bridge-damage-related features. The article’s organization is as follows: First, the train cars comprise four-axle vehicles, the track is treated as a beam resting on evenly distributed spring-mass systems, and the bridge deck of the high-speed rail has been described as a simply supported Bernoulli-Euler beam. The formulation covers track irregularities and induced damage circumstances in a particular structure section. Second, a demonstration of the suggested drive-by damage detection strategy and a discussion of the damage index extraction from the MFCC method are provided. After that, the feasibility of using cepstrum analysis components for indirect damage detection in HSR by on-board sensors is investigated using numerical simulations in which dynamic analyses are carried out using MATLAB® code. The final section summarizes the key results, and some prospects are highlighted.

2 METHODOLOGY

2.1 Vehicle-track-bridge dynamic interaction system

This section describes the 2-dimensional VTBI model used in the present study to numerically simulate a high-speed train response to a bridge crossing event. Plane VTBI systems can satisfactorily predict vertical dynamic response (Quirke *et al.*, 2017). As to ballasted railways tracks consisting of rails, pads, sleepers, ballast, and sub-ballast, it is possible to depict the track with varying degrees of complexity, which may be roughly categorized by the number of sprung layers taken into account (Cantero *et al.*, 2016).

2.1.1 Vehicle model

Figure 1a shows the multi-rigid-body vehicle model considered in this paper. The rigid bodies corresponding to the carbody and bogie frames have concentrated masses m_c and m_b , and rotational inertias J_c and J_b (about the transverse horizontal axes through its centers of gravity). The wheelsets were considered as lumped masses m_w coupled to the bogie frames by spring-dashpot sets constituting the primary suspension with spring stiffness k_{1y} , and damping coefficient c_{1y} . Spring-dashpot sets, constituting the secondary suspension system, couple bogie frames to the carbody (spring stiffness k_{2y} , and damping coefficient c_{2y}). Each car of the vehicle model contains ten independent degrees of freedom (DOFs): seven vertical displacements for the masses ($y_c, y_{b1}, y_{b2}, y_{w1}, y_{w2}, y_{w3}$, and y_{w4}) and three rigid bar pitching rotations (ϕ_c, ϕ_{b1} , and ϕ_{b2}). The train crosses the bridge at constant speed v with N_c independent vehicles.

2.1.2 Track model

Figure 1b depicts the track model as a beam laying on uniformly distributed spring-mass systems. Finite Element (FE) discretization models the rail as a 2D Euler–Bernoulli beam with four parameters: Young’s modulus E_r , sectional area A_r , moment of inertia about the transverse axis I_r , and mass per unit length m_r . The sleepers are represented as masses M_s within a regular spacing L_s and coupled to the rail by a spring-dashpot system (stiffness K_p and viscous damping C_p) representing the pad. A spring-dashpot layer with stiffness K_{ba} and damping coefficient C_{ba} connects the sleeper to the ballast bodies (lumped masses M_{ba}). The su-ballast’s dynamic qualities are considere as an extra spring-dashpot layer (stiffness K_{sb} and viscous damping C_{sb}). Random irregularity profile functions on the rail surface account for the x-coordinate rail irregularities $r(x)$, which are measured relative to the beam’s vertical static equilibrium locations (mean horizontal axle).

2.1.3 Bridge model

The HSR bridge deck is modeled as a simply supported Bernoulli-Euler beam (Figure 1c) utilizing FEM formulation with 2D beam elements, whose properties are mass per unit length of \bar{m}_b , Young’s modulus E_b , sectional area A_b , and moment of inertia I_b . In order to simulate the

structure's damage to be identified and localized indirectly by the passing vehicle, a beam region has its bending stiffness affected by a coefficient f_{sr} (reduction stiffness ratio).

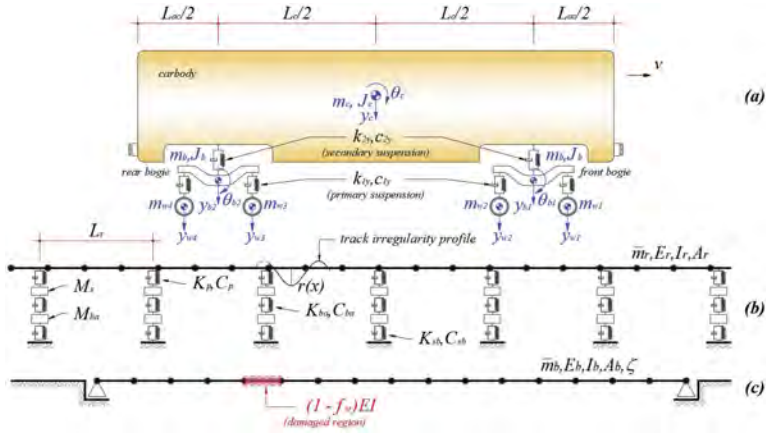


Figure 1. 2-D vehicle-track-bridge dynamic interaction system: (a) vehicle model, (b) track model, and (c) bridge model.

2.1.4 Equations of motion for the VTBI system

The subsystems aforementioned are integrated into a single VTBI model. A set of equations of motion describes each subsystem. These second-order differential equations can be represented in a general matrix form utilizing the time-dependent mass, damping, and stiffness global matrices \mathbf{M} , \mathbf{C} and \mathbf{K} , along with the vector of external forces \mathbf{F} , and solved for the vector \mathbf{X} of the global displacements (DOFs). The coupled equations of motion for the entire model can be represented as

$$\begin{bmatrix} \mathbf{M}_V & \mathbf{0} & \mathbf{0} \\ \mathbf{0} & \mathbf{M}_T & \mathbf{0} \\ \mathbf{0} & \mathbf{0} & \mathbf{M}_B \end{bmatrix} \begin{Bmatrix} \ddot{\mathbf{X}}_V \\ \ddot{\mathbf{X}}_T \\ \ddot{\mathbf{X}}_B \end{Bmatrix} + \begin{bmatrix} \mathbf{C}_V & \mathbf{C}_{VT} & \mathbf{0} \\ \mathbf{C}_{TV} & \mathbf{C}_T & \mathbf{C}_{TB} \\ \mathbf{0} & \mathbf{C}_{BT} & \mathbf{C}_B \end{bmatrix} \begin{Bmatrix} \dot{\mathbf{X}}_V \\ \dot{\mathbf{X}}_T \\ \dot{\mathbf{X}}_B \end{Bmatrix} + \begin{bmatrix} \mathbf{K}_V & \mathbf{K}_{VT} & \mathbf{0} \\ \mathbf{K}_{TV} & \mathbf{K}_T & \mathbf{K}_{TB} \\ \mathbf{0} & \mathbf{K}_{BT} & \mathbf{K}_B \end{bmatrix} \begin{Bmatrix} \mathbf{X}_V \\ \mathbf{X}_T \\ \mathbf{X}_B \end{Bmatrix} = \begin{Bmatrix} \mathbf{F}_V \\ \mathbf{F}_T \\ \mathbf{F}_B \end{Bmatrix} \quad (1)$$

where the subscripts V , T and B represent, respectively, the vehicle, track, and bridge subsystems.

The connectivity of the subsystems is theoretically defined by additional off-diagonal block matrices in equation (1). The beam element's form function and the mechanical parameters of the system determine these coupling terms.

2.2 MFCC-based drive-by damage detection

The primary objective of feature extraction is to transform the unprocessed input signal into a representation with minimal variables that contains the most discriminating information, which can effectively reduce the input's dimensionality and eliminate redundant or irrelevant information to generate a series of feature vectors. In this regard, cepstral analysis is widely employed to extract MFCC characteristics from raw data (Babajanian Bisheh *et al.*, 2021). The MFCC depicts the short-term power spectrum of a signal with a linear cosine transform of a log power spectrum on a nonlinear Mel frequency scale (Lee *et al.*, 2016). Figure 2 depicts a flowchart that summarizes the methodology developed in this paper for drive-by damage detection of HSR bridges using MFCC to extract features.

2.2.1 Vehicle's acceleration segmentation short-term spectra, adapted Mel-frequency scale and frequency warping

The Short-time Fourier Transform (STFT) analyzes the vehicle's acceleration signal's frequency content over time. Thus, sliding a window function over the vehicle's vertical acceleration time histories discretizes them into j segments. After segmentation and windowing, the STFT takes all segments' Discrete Fourier Transform (DFT) to calculate the vehicle's short-term spectra for each frame.

After the STFT has been evaluated, the frequency spectrum of each frame, in a procedure known as frequency warping, is undertaken to emphasize the signal's Mel-frequency characteristics. Considering that lower frequency of bridges is always more important, an adapted formula proposed by Mei *et al.* (2019) for the correspondence between Hertz f and Mel frequency m scales was applied and is as follows.

$$m = 5 \ln(1 + f/5) \quad (2)$$

The DFT values are weighed using a series of N triangular filters, known as a filter bank, to achieve frequency warping. This approach minimizes the amount of information that is corrupted in the spectrum (or Mel-spectra, or cepstrum) of the vehicle's reactions at frequencies higher than the bridge's relevant frequencies.

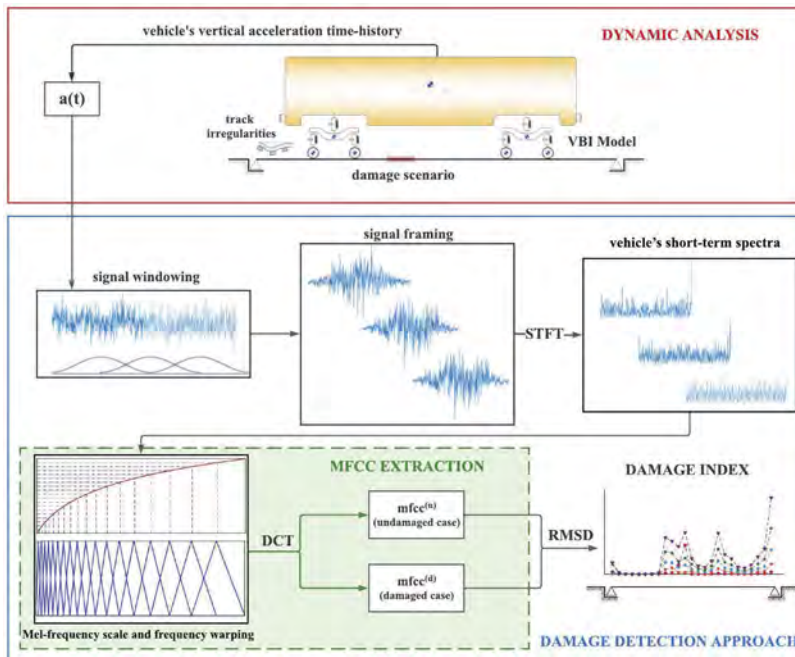


Figure 2. Flowchart of the drive-by damage detection approach using MFCC.

2.2.2 Mel-frequency cepstral coefficients (MFCC) and extracted Damage Index

The next step is obtaining the list of MFCC associated with the short-term spectra. The Inverse Discrete Cosine Transform (DCT) is employed, and then the \mathbf{mfcc}_j discrete vector related to the j th short-term cepstrum $X_j(f)$ becomes

$$\mathbf{mfcc}_j = \left\{ \mathbf{mfcc}_k^j \right\}^T, \quad k = 1, 2, \dots, N_f - 2 \quad (3)$$

with the k th component \mathbf{mfcc}_k given by

$$m fcc_k^j = \sum_{n=2}^{N_f-1} \text{Log}X_n \cos\left(\frac{\pi}{N-2}\left(n-\frac{3}{2}\right)k\right) \quad (4)$$

In Equations 3 and 4, N_f is the number of filters in the filter bank, and $\text{Log}X_n$ denotes the n th filter log-energy output, which can be written as

$$\text{Log}X_n = \log\left(\sum_{l=1}^{L_n} TF_n(f) \times |X_j(f)|^2\right) \quad (5)$$

in which TF_n is the n th triangular filter that is applied over the j th short-term power spectrum $|X_i(f)|^2$, in its $l = 1, 2, \dots, L$ samples.

In the last stage of the procedure, MFCC are used to calculate the damage indices (DI), from which the HSR bridge damage prognosis is performed. Thus, by comparing the aforementioned vectors \mathbf{mfcc}_i^u , extracted from the recorded vehicle's responses when it crosses the undamaged bridge, to the \mathbf{mfcc}_i^d ones, provided by the vehicle passing over the bridge under the presence of damage; the along bridge span DI are taken by the Root Mean Square Deviation described as

$$DI_j = \sqrt{\frac{\sum_{k=1}^{N-2} (m fcc_k^{j(u)} - m fcc_k^{j(d)})^2}{\sum_{k=1}^{N-2} (m fcc_k^{j(u)})^2}} \quad (6)$$

3 RESULTS AND DISCUSSION

The VBI model and the drive-by damage detection procedure have been implemented in MATLAB®, and the feasibility of using damage features extracted from MFCC in indirect SHM of HSR infrastructure is numerically evaluated in this section for two different levels of track disturbance: low disturbance (LD) and high disturbance (HD), in addition to the case where no irregularity is considered. To test the method's sensitivity to the severity of the damage, five damage scenarios were simulated in the bridge, assuming bending stiffness decreases of $f_{sr} = 5\%$, 10% , 15% , 20% and 25% in a portion of the Euler-Bernoulli beam with a length of 1.2m (the bridge span is $L=45$ m). In order to verify the sensitivity of MFCC-based DI to the position of the damage, these damage scenarios were investigated in different cases where these regions were located around the midspan cross-section and at $1/4$ of the span from the left support.

Table 1. Properties of the bridge model.

Properties		Notation	Value	Unit
Deck	Reinforced concrete density	ρ_c	2500	kg/m ³
	Reinforced concrete area	A_c	6.0191	m ²
Ballast (Zhai, 2020)	Ballast density	ρ_b	1750	kg/m ³
	Ballast area	A_b	3.6315	m ²
Sleeper (Zhai, 2020)	Sleeper mass (half)	m_s	170	kg
	Sleeper spacing (half)	l_s	0.60	m
Rail (Zhai, 2020)	Rail mass per unit length (per rail seat)	\bar{m}_r	60.64	kg/m
<i>Euler-Bernoulli beam:</i>				
Mass per unit length			13350	kg/m
Modulus of elasticity		E	39	GPa
Cross-section moment of inertia		I	2.60	m ⁴
Span length		L	45	m

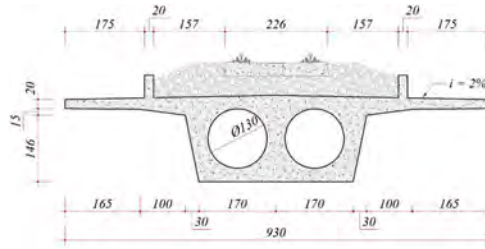


Figure 3. Idealized cross-section of the bridge numerical model.

Table 1 provides a summary of the bridge parameters, which were derived using an idealized cross-section with a reinforced concrete deck and ballasted track (Figure 3). A smooth rail profile was anticipated, and a 40-meter track length was considered before the bridge. The VTBI model was discretized with a bridge mesh size of 0.6 m and a rail mesh size of 0.2 m. The Rayleigh damping coefficients for the first and second bridge modes are adjusted to attain a damping ratio of 0.5%. Table 2 lists the assumed vehicle parameters for the ICE3 Velaro (Quirke *et al.*, 2017).

Table 2. Mechanical, geometrical, and suspension properties of the 2D vehicle model (ICE3 Velaro) (Quirke *et al.*, 2017).

Properties		Notation	Value	Unit
Concentrated masses	Carbody	m_c	47800	Kg
	Bogies	m_b	3500	Kg
	Wheelsets	m_w	1800	Kg
Rotary inertia	Carbody	J_c	1.96×10^6	kg.m ²
	Bogies	J_b	1715	kg.m ²
Stiffness coefficient	Primary suspension	k_{1y}	2.40×10^6	N/m
	Secondary suspension	c_{1y}	2.00×10^4	N.s/m
Damping coefficient	Primary suspension	k_{2y}	7.00×10^5	N/m
	Secondary suspension	c_{2y}	4.00×10^4	N.s/m
Distances				
Distance between bogie centers in one car		L_c	17.375	M
Distance between wheelset axles in one bogie		L_b	2.50	M
Distance between bogie centers from adjacent cars		L_{ac}	7.40	M

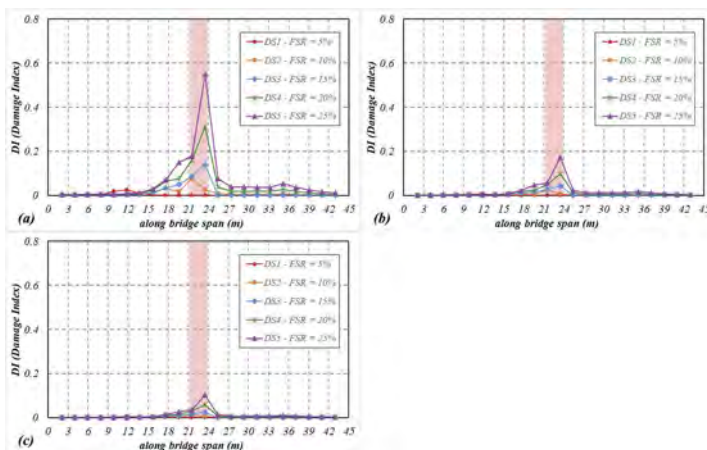


Figure 4. DI values under different damage conditions at the midspan, for the vehicle running at $v = 144$ km/h, and under different levels of track irregularities: (a) NC, (b) LD, and (c) HD.

3.1 Performance of the proposed drive-by damage detection using MFCC

The performance of MFCC in providing DI that can determine whether the system has structural damage is now under discussion. Figures 4 and 5 depict the DI values obtained for the train running speeds of $v = 144 \text{ km/h}$ $v = 288 \text{ km/h}$. The DI values obtained from MFCC gave robust information regarding the location of the damage. In addition, it can be observed that the sensitivity of the proposed DI to the degree of damage and its placement is unaffected. Figure 6 demonstrates that the DI values for scenarios with multiple damage.

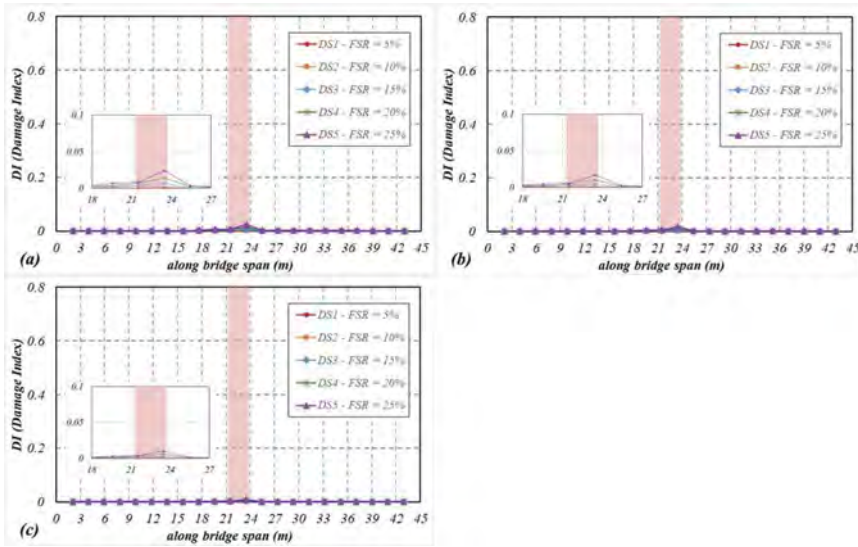


Figure 5. DI values under different damage conditions at the midspan, for the vehicle running at $v = 288 \text{ km/h}$, and under different levels of track irregularities: (a) NC, (b) LD, and (c) HD.

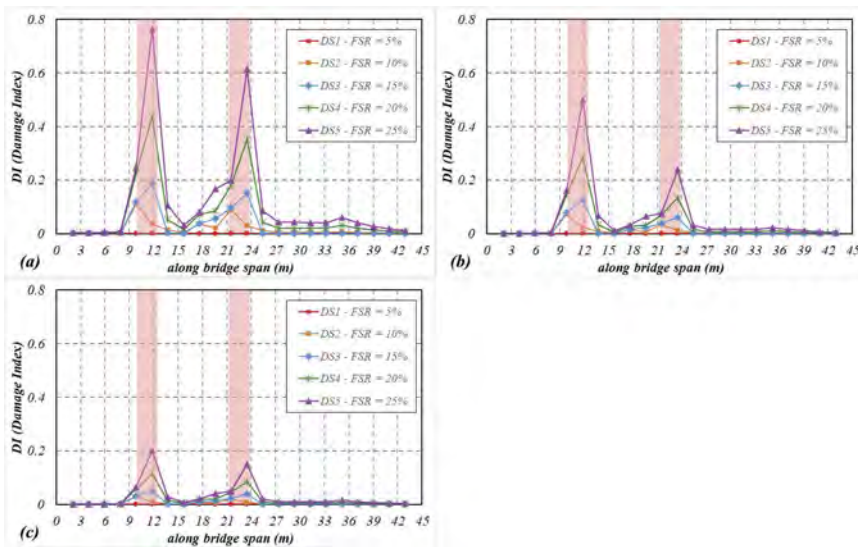


Figure 6. DI values under different damage conditions at the 1/4 of the span and at the midspan, for the vehicle running at $v = 144 \text{ km/h}$, and under different levels of track irregularities: (a) NC, (b) LD, and (c) HD.

4 CONCLUSIONS

This study evaluates the applicability of MFCC to a drive-by approach for HSR bridge deterioration detection. The proposed framework is implemented in MATLAB, and through numerical simulations, damage indices (DI) are extracted from the Root Mean Square Deviation of the MFCC calculated using the recorded vehicle responses when it crosses an undamaged bridge and those obtained when it passes over the structure under induced damage scenarios. Our investigation has led us to the following key findings:

- The MFCC-obtained DI values provided reliable information regarding the location of the damage. Under all conditions, the DI values could reliably indicate the location and severity of the damage.
- The magnitude of the feature generated from MFCC correlates with the speed of the vehicle over the bridge and the degree of track imperfections. The DI values are more sensitive to excitation sources resulting from track imperfections than to those resulting from damage.
- The results reveal that the distribution patterns of DI vary depending on the site of the damage, with a propensity to exhibit peaks close to the damaged zones.

REFERENCES

- Babajanian Bisheh, H., Ghodrati Amiri, G., Nekooei, M. and Darvishan, E. (2021). Damage detection of bridges based on combining efficient cepstral coefficients, *JVC/Journal of Vibration and Control*, SAGE Publications Inc., Vol. 27 No. 19–20, pp. 2279–2290.
- Cantero, D., Arvidsson, T., O'Brien, E. and Karoumi, R. (2016). Train–track–bridge modelling and review of parameters, *Structure and Infrastructure Engineering*, Taylor & Francis, Vol. 12 No. 9, pp. 1051–1064.
- Lee, J., Choi, H., Park, D., Chung, Y., Kim, H.-Y. and Yoon, S. (2016). Fault detection and diagnosis of railway point machines by sound analysis, *Sensors (Switzerland)*, MDPI AG, Vol. 16 No. 4.
- Mei, Q., Gül, M. and Boay, M. (2019). Indirect health monitoring of bridges using Mel-frequency cepstral coefficients and principal component analysis, *Mechanical Systems and Signal Processing*, Academic Press, Vol. 119, pp. 523–546.
- Micu, E.A., O'Brien, E.J., Bowe, C., Fitzgerald, P. and Pakrashi, V. (2022). Bridge Damage and Repair Detection Using an Instrumented Train, *Journal of Bridge Engineering*, American Society of Civil Engineers (ASCE), Vol. 27 No. 3.
- Morgantini, M., Betti, R. and Balsamo, L. (2021). Structural damage assessment through features in que-frency domain, *Mechanical Systems and Signal Processing*, Academic Press, Vol. 147.
- O'Brien, E.J., Malekjafarian, A. and González, A. (2017). Application of empirical mode decomposition to drive-by bridge damage detection, *European Journal of Mechanics, A/Solids*, Elsevier Ltd, Vol. 61, pp. 151–163.
- Quirke, P., Bowe, C., O'Brien, E.J., Cantero, D., Antolin, P. and Goicolea, J.M. (2017). Railway bridge damage detection using vehicle-based inertial measurements and apparent profile, *Engineering Structures*, Vol. 153, pp. 421–442.
- Randall, R.B. (2009). Cepstral Methods of Operational Modal Analysis, *Encyclopedia of Structural Health Monitoring*, John Wiley & Sons, Ltd, doi: <https://doi.org/10.1002/9780470061626.shm045>.
- Wang, Y., Wang, P., Tang, H., Liu, X., Xu, J., Xiao, J. and Wu, J. (2021). Assessment and prediction of high speed railway bridge long-term deformation based on track geometry inspection big data, *Mechanical Systems and Signal Processing*, Vol. 158, p. 107749.
- Yang, Y.B., Yang, J., Zhang, B. and Wu, Y. (2019). *Vehicle Scanning Method for Bridges*.
- Zhan, J., Wang, Z., Kong, X., Xia, H., Wang, C. and Xiang, H. (2021). A drive-by frequency identification method for simply supported railway bridges using dynamic responses of passing two-axle vehicles, *Journal of Bridge Engineering*, American Society of Civil Engineers (ASCE), Vol. 26 No. 11.

Evaluation of corroded reinforced concrete railway bridge subjected to concrete cracking under uncertainty

L.S. Moreira

Graduate Program in Civil Engineering (PPGEC), USP, São Paulo, Brazil
Federal University of Ceará (UFC) – Campus Crateús, Fortaleza, Brazil

T.N. Bittencourt & M.M. Futai

Department of Structural Engineering and Geotechnical (PEF), USP, São Paulo, Brazil

H. Carvalho

Department of Structural Engineering, Federal University of Minas Gerais (DEES),
UFMG, Minas Gerais, Brazil

ABSTRACT: The main mechanism of deterioration of reinforced concrete structures is the corrosion of steel reinforcement, and the maintenance and repair of corroded reinforced concrete structures costs billions of dollars per year. Several studies have been proposed with the aim of modeling the behavior of corroded reinforced concrete structures, highlighting the importance of evaluate the uncertainty of the corrosion phenomenon, and the corrosion initiation time and the corrosion rate have a significant impact on the reliability of these structures over time. Corrosion of reinforcements is usually expansive, subjecting the surrounding concrete to tensile stresses that can cause cracking and even spalling of the concrete. Although concrete cracking has an impact on both initiation and propagation of corrosion, few articles consider this effect in corrosion modeling. This article presents a reliability-based evaluation of corroded reinforced concrete structures. In the proposed model, analysis of concrete cracking due to reinforcement corrosion (expansion of steel bars) is carried out in order to update the corrosion propagation model. In the corrosion propagation phase, it is proposed different corrosion rates and compressive resistance of concrete cover, depending on the cracking state of the element. The proposed framework is illustrated on a reinforced concrete railway bridge.

1 INTRODUCTION

The rail network constitutes an important part of the transport infrastructure, and therefore the railway bridges must be maintained in order to guarantee the safety of their operation. The main mechanism of deterioration of reinforced concrete structures is the corrosion of steel reinforcement, and the maintenance and repair of corroded reinforced concrete structures costs billions of dollars per year.

The phenomenon of reinforcement corrosion in RC structures has several uncertainties, being intrinsic to the phenomenon, or contained in the measurement and quantification errors of factors that affect corrosion, as well as in the simulation of the structural behavior (Vatteri et al. 2016). In this way, probabilistic approaches are justified, since deterministic approach can lead to conservative structural responses in order to guarantee structural safety, but end up increasing maintenance costs (Pugliese & Sarno 2022). Furthermore, through probabilistic approach is possible to estimate the probability of failures mode, which is important in asset management.

Corrosion of reinforcements is usually expansive, subjecting the surrounding concrete to tensile stresses that can cause cracking and even spalling of the concrete. The corrosion rate is governed by the availability of water and oxygen at the steel surface (Vu & Stewart 2000) and

the phenomenon of concrete cracking can accelerate the entry of these components through the concrete cover. According to Zhang et al. (2019), the cracking of concrete cover can change the levels of corrosion in the reinforcements, which justifies the study and appropriate consideration of the corrosion rate after concrete cracking.

This article presents a reliability-based evaluation of corroded reinforced concrete structures. In the proposed model, analysis of concrete cracking due to reinforcement corrosion (expansion of steel bars) is carried out in order to update the corrosion propagation model. In the corrosion propagation phase, it is used accelerated corrosion rates and compressive resistance of concrete cover, depending on the cracking state of the element. The proposed framework is illustrated on a reinforced concrete railway bridge.

2 CORROSION MODELING

Corrosion is usually divided into two phases: initiation and propagation of corrosion. In some cases, as in this work, the concrete cracking period is also considered, due to the impact on the corrosion process.

The main effects considered in modeling structures under corrosion are: reduction of the steel area of the longitudinal bars and stirrups; changes in strength, stiffness and ductility of steel bars; changes in the strength and ductility of concrete under compression, due to cracking induced by the expansion of steel bars; deterioration of bond between steel bars and concrete; reduction of concrete confinement by stirrup corrosion.

This article presents the modelling of corroded RC structures through reduction of the steel area of the longitudinal bars, changes in the strength and ductility of concrete under compression, due to cracking induced by the expansion of steel bars, besides considering the acceleration of corrosion rate after concrete cracking.

2.1 Corrosion initiation

The main chemical protection against reinforcement corrosion is due to the high alkalinity of the concrete's interstitial water, due to the presence of calcium hydroxide ($\text{Ca}(\text{OH})_2$), released in cement hydration reactions. In this highly alkaline environment ($\text{pH} > 12.5$), a passivating film, consisting of a thin film of iron oxide (Fe_2O_3), is formed around the steel reinforcement, providing protection against corrosion. This protection is called passivation. The corrosion initiation corresponds to the period of time until the depassivation of the reinforcement.

The two main phenomena that can destabilize this protective film are concrete carbonation and chloride contamination. In this study, the bridge analyzed is located in a region where contamination by chlorides is not important, and the initiation mechanism being analyzed is the carbonation of the concrete.

In concrete carbonation, carbon dioxide presents in the atmosphere, when penetrating the concrete, reacts with hydrated cement compounds, transforming them into carbonates, thus reducing the alkalinity of the concrete.

Yang et al. (2014) presented a model to predict the depth of carbonation in concrete that is used in herein. The depth of carbonation progress (x) is given by:

$$x = \sqrt{\frac{2D_{\text{CO}_2}(t)\text{CO}_2}{a_{\text{CO}_2}} \cdot t} \quad (1)$$

where D_{CO_2} = diffusion coefficient (m^2/s); a_{CO_2} = amount of carbonatable constituents per volume of concrete; CO_2 = concentration of carbon dioxide in kg/m^3 .

The diffusion coefficient (D_{CO_2}) is:

$$D_{\text{CO}_2}(t) = \frac{136.6 \cdot 10^{-4}}{86400} \beta_s \beta_f \beta_h \left(\frac{a}{C}\right)^{0.1} [\varepsilon_p(t)]^2 \quad (2)$$

where β_s is a correction factor for SCMs, β_f is a coefficient related to the finishing materials; β_h is coefficient depending on relative humidity; $\varepsilon_p(t)$ = total porosity of cement; a = aggregate content in concrete (kg/m^3);

2.2 Concrete cracking initiation

Most corrosion products have a volume greater than intact steel reinforcement, that is, as corrosion occurs, due to expansion, the bars exert an internal pressure on the concrete cover, resulting in tensile stresses in the concrete, which can generate cracking of the concrete and even spalling of the concrete cover. In order to analyze the cracking limit state of concrete, and even modify the propagation of concrete after cracking, it is necessary to estimate the time between the onset of corrosion and cracking of the concrete.

El Maaddawy & Soudki (2006) developed a mathematical model in order to estimate the time from the corrosion initiation to concrete cracking, taking into account the internal pressure caused by the expansion of corrosion products. The concrete around corroded reinforcement is modeled as a thick-walled cylinder. The model is validated with experimental results available in the literature and is adopted herein. The expression to evaluate the time from corrosion initiation to concrete cracking (t_{cr}) is given:

$$t_{cr} = \left[\frac{7117.5(D + 2\delta_0)(1 + \nu + \psi)}{iE_{ef}} \right] \left[\frac{2Cf_{ct}}{D} + \frac{2\delta_0 E_{ef}}{(1 + \nu + \psi)(D + 2\delta_0)} \right] \quad (3)$$

where D = diameter of steel reinforcing bar (mm); δ_0 = thickness of porous zone; C = clear concrete cover (mm); ψ = factor depends on D , C and δ_0 ; f_{ct} = tensile strength of concrete; ν = Poisson's ratio of concrete (adopted 0.18); i = current density; E_{ef} = effective elastic modulus of concrete.

2.3 Corrosion propagation

It is possible to quantitatively assess the intensity of corrosion by measuring the flow of electrons or ions, that is, the density of the corrosion current, or just the corrosion current (i_{corr}). In this study, as carbonation corrosion is adopted, the corrosion considered will be uniform. For this purpose, based on the numerical corrosion propagation model proposed by Ghods et al. (2007), Ghods et al. (2008) developed a simplified model for determining the corrosion current that has more easily measurable input parameters, with experimental validation of the results obtained, that is adopted herein, which is given by the following expression:

$$i_{corr} = -3,7 \cdot 10^{-3} + \frac{5,06}{\rho} + \left(\frac{0,333}{\rho} - 3,83 \cdot 10^{-4} \right) \ln \left(\frac{D_{O_2} CsO_2}{c} \right) \quad (4)$$

where i_{corr} = corrosion current density (A/m^2), ρ is concrete resistivity ($\Omega.m$); c is the concrete cover (m); D_{O_2} is the oxygen diffusion coefficient (m^2/s); CsO_2 = dissolved oxygen concentration in pore water at the concrete surface (kg/m^3).

In order to estimate the resistivity of concrete (ρ), the mathematical model proposed by Zhang et al. (2021) is adopted herein

As the corrosion current varies after concrete cracking, the diameter of the steel bar $D(t)$, for the uniform corrosion model, is given (in mm), at time t , depending on the different time intervals as:

$$D(t) = \begin{cases} D_0 - 0,0232 \int_0^{t_{dep}+t} i_{corr}(t) dt, & \text{if } t_{dep} \leq t \leq t_{cr} \\ D_0 - 0,0232 \int_0^{t_{dep}} i_{corr}(t) dt - 0,0232 \int_{t_{dep}}^t k_{ac} i_{corr}(t) dt, & \text{if } t \geq t_{cr} \end{cases} \quad (5)$$

where D_0 is the initial diameter of the steel bar (mm); and i_{corr} is the current of corrosion ($\mu A/cm^2$), t_{dep} = time until depassivation or time to corrosion initiation, t_{cr} = time between corrosion initiation and concrete cracking; k_{ac} = acceleration corrosion coefficient after concrete cracking.

According to Ma et al. (2015), the corrosion rate increases as concrete cracking increases, however the quantification of the impact on corrosion is difficult, with epistemic uncertainty

in the acceleration coefficient (k_{ac}). Thus, the coefficient of acceleration is considered a random variable, with a normal distribution of mean 2.0 and coefficient of variation 0.25.

2.4 Effect of corrosion on concrete compressive strength

The concrete cracking or even the delamination of the concrete cover, in addition to facilitating the ingress of water and oxygen, which can accelerate the corrosion process of the reinforcements, can reduce the resistance of concrete cover, thus also reducing the resistance capacity of the structural element. In this study, this effect is considered through the model proposed by Coronelli & Gambarova (2004), who proposed the reduction of the cover concrete to compression, dependent on the magnitude of the average tensile strain in the transverse direction, based on modified compressive field theory of Vecchio & Collins (1986). The reduced concrete strength ($f_{c,red}$) proposed is adopted in this study and the equation is shown below:

$$f_{c,red} = \frac{f_c}{1 + K \frac{\varepsilon_1}{\varepsilon_{c0}}} \quad (6)$$

where K = coefficient related to bar roughness; ε_{c0} = strain at the peak compressive stress; f_c = concrete strength of intact concrete; ε_1 = average smeared tensile strain in the cracked concrete at right angles to the direction of the applied compression.

3 RELIABILITY ASSESSMENT

In structural reliability analysis, the safety and functionality of the structure can be evaluated by the probability of violation of ultimate and service limit states of a given structural element or of the entire structure, during its period of use. This type of analysis can be used for designing new structures or even for assessing the state of deterioration of existing structures.

3.1 Limits states

The limit states, or even the failure modes and loss of functionality of structures and structural elements can be quantified through equations called limit state equations. For each limit state of the structure, a limit state equation, $g(\mathbf{X})$, is written as a function of the random variables (\mathbf{X}):

$$g(\mathbf{X}) = g(\mathbf{X}_R, \mathbf{X}_S) = 0 \quad (7)$$

where \mathbf{X}_R and \mathbf{X}_S = vectors that describe the random variables associated with resistance and loading, respectively.

In this study, the functionality and safety of the bridge are analyzed by evaluating the main girder of the bridge. The service condition of the bridge is assessed in terms of cracking of the concrete and the safety condition is obtained from the flexural capacity of the beam, which is usually the critical limit state.

In determining the flexural capacity of the beam, the theory of Euler-Bernoulli is considered. The calculation of the resistant moment is obtained by continuously increasing the curvature of the section until crushing of the concrete or excessive deformation of the steel. The Fiber Method is adopted to compute the resulting forces across the section. The stress-strain ratio of the concrete used was that of the Brazilian standard NBR 6118 (2014), ignoring the contribution of concrete in tension. Steel was modeled as perfect elasto-plastic.

3.2 Monte Carlo simulation

The determination of the probability of failure and the reliability index can be obtained through simulation methods where the most used is the Monte Carlo simulation method, however its computational cost is high. In the Monte Carlo method, a finitely high number of simulations is performed, where in each simulation the model variables assume certain values, which are obtained using the probability distributions of the random variables.

In this study, the random variables are determined with Latin Hypercube Sampling. At each simulation, a set of random variables is obtained, which is then used to calculate each limit state. The time dependency is handled by discretizing the lifetime of the structure year by year.

3.3 Traffic loading

As the case study of this article refers to a railway bridge, and the structural element analyzed is the main beam of the bridge, a methodology for determining the maximum annual bending moment must be obtained. The monitoring of the train crossing over the bridge was carried out by measuring the wheel load, during different intervals over the course of a year.

Thus, from the data set obtained, statistics for wheel load were adjusted. From the wheel load statistics and the number of trains passes over a year, it was possible to numerically obtain the maximum annual bending moment and adjust a distribution of extreme values, which was then adopted in this study. The maximum annual bending moment due to train's passage was adjusted by a Gumbel distribution with $\mu_n = 2380$ kNm and $\beta = 1.02e-04$.

4 CASE STUDY

In order to apply the presented methodology, a railway bridge, designed in 1972, was used as a case study. The railway bridge has three simply supported spans of 18.67 m each, with a cross section of two beams. This bridge is mainly responsible for transporting iron ore.

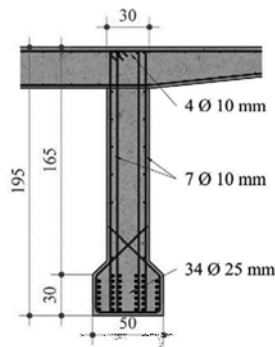


Figure 1. Geometry of girder transversal section, units in cm.

The following table presents the random variables and their respective adopted probability distributions. In order to determine the variables related to environmental conditions, data were obtained from the meteorological station near the bridge in question, available at INMET (2022).

The other statistics related to the geometry of the bridge and the materials used were obtained through the structural design of the bridge and recommendations available in the literature (Beck 2019, Santiago 2019, Morales 2017, Rocha et al. 2015, JCSS 2001).

Table 1. Distribution of random variables.

Variable	Distribution	Parameters
Concrete strength (f_c)	Normal	$\mu = 23.4$ MPa, $\sigma = 4.68$ MPa
Steel yield strength (f_y)	Normal	$\mu = 610$ MPa, $\sigma = 24.4$ MPa
Concrete specific mass	Normal	$\mu = 2500$ kg/m ³ , $\sigma = 125$ kg/m ³
Nominal cover (c)	Lognormal	$\mu = 3$ cm, $\sigma = 1$ cm
Relative humidity (RH)	Normal	$\mu = 72.64\%$, $\sigma = 4.68\%$
Temperature (T)	Normal	$\mu = 24.11$ °C, $\sigma = 0.81$ °C
CO ₂ concentration (CO ₂)	Normal	$\mu = 0.82$ g/m ³ , $\sigma = 0.1$ g/m ³
Resistance model error	Lognormal	$\mu = 1.2$, $\sigma = 0.18$
Load model error	Lognormal	$\mu = 1.0$, $\sigma = 0.1$

The number of simulations in Monte Carlo Simulation was adopted 200000. The high number of simulations was adopted due to the complexity of the analysis of the resistance to bending, in order to guarantee the adequate convergence of the method.

Figures 2 and 3 below show the histogram of the depassivation time and corrosion current, which directly impact the period of initiation and propagation of corrosion, respectively.

As for the depassivation time, it is possible to notice that the number of simulations grows gradually until the depassivation time is close to 30 years, after which it starts to fall. This information shows the importance of considering corrosion for evaluating the bridge in question.

Regarding the intensity of the corrosion current, it is noted that most of the simulations present values close to 1, however, higher values can be found, and this should contribute to the probability of failure. It is important to point out that these corrosion current values do not yet consider the possibility of corrosion acceleration over time, depending on the cracking of the concrete.

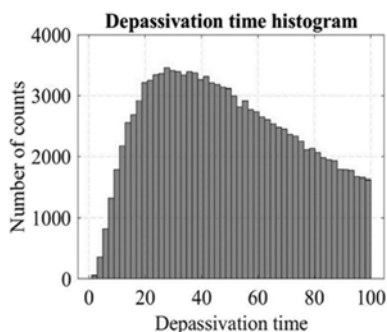


Figure 2. Depassivation time histogram (time in years).

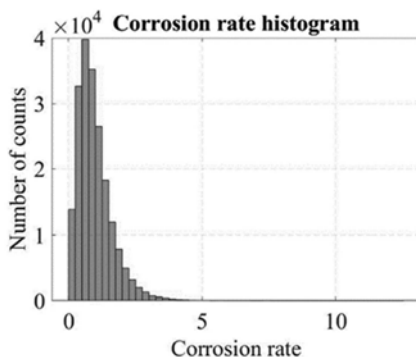


Figure 3. Corrosion rate histogram (corrosion current in $\mu\text{A}/\text{cm}^2$).

The following figure shows the reliability index over time for the service limit state of concrete cracking, due to expansion of the bars by corrosion. In analysis regarding the cracking service limit state of concrete, low reliability index results were obtained, being approximately equal to 2.0 in 10 years and equal to zero (failure probability equal to 50%), in less than 80 years. The explanation for the rapid deterioration of the concrete cover can be explained by the reduced cover used in the structural design.

It is also worth noting that although some authors consider only depassivation or concrete cracking as a limit state, the resistance capacity of structural elements, in general, is much higher than the service limit and the determination of the ultimate limit state can introduce relevant information to inspection, monitoring and intervention.

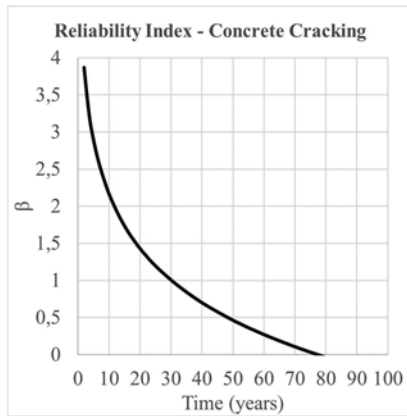


Figure 4. Reliability index for concrete cracking (service limit state).

Thus, Figure 5 presents the reliability index over time for the limit state related to the flexural capacity of the bridge's main girder.

In order to analyze the effect of cracking on the resistance capacity of the beam, due to the increase in corrosion and the reduction in the strength of the covering concrete after cracking, four models were built, with and without such effects. In model 1, the element strength was analyzed without increasing the corrosion rate and without loss of compressive strength of the cover concrete. In model 2, with an increase in the corrosion rate and without loss of compressive strength of the covering concrete. In model 3, without an increase in the corrosion rate and with loss of compressive strength of the covering concrete. Finally, in model 4, an increase in the corrosion rate and loss of compressive strength of the cover concrete was considered simultaneously.

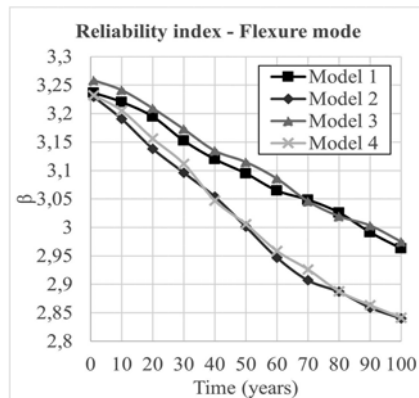


Figure 5. Reliability index for flexural capacity (safety limit state).

From the results of the reliability index related to bending, it is possible to analyze the impact of the effect of the acceleration of corrosion and reduction of the compressive strength of the cover after cracking.

In the analyzed example, the acceleration of corrosion had a significant impact, noting the different response in relation to models 1 and 2. However, the reduction of the compressive strength of the cover concrete did not present a significant difference, noting a small difference of response between models 1 and 3 and between models 2 and 4. This small difference can be explained by the slenderness of the cross-section (30x195 cm) and the small cover of the example in question, which corresponds to approximately only 1.5% of the total height. It can also be emphasized that this

difference is within the margin of error of the fiber method and the Monte Carlo method itself, which even with a relatively high number of simulations, still presented convergence difficulties.

5 CONCLUSIONS

The evaluation methodology of a reinforced concrete bridge subjected to reinforcement corrosion and concrete cracking was presented and applied in a real example, and can also be applied in other types of structures.

Concrete carbonation as a phenomenon of reinforcement depassivation was considered in the proposed methodology, although concrete cracking due to service loads was not considered, which could further accelerate the initiation process and consequently the deterioration of the structure by corrosion.

Through the analysis carried out, it was possible to notice that the impact of corrosion acceleration due to concrete cracking on the structural element's resistance capacity can be relevant and studies regarding the measurement of this acceleration coefficient are still quite scarce.

Although in the analyzed example the impact of reducing the compressive strength of the concrete cover was very small, it cannot be concluded that this effect can be neglected in all cases. Other examples, such as columns or beams with greater width, should be studied in order to understand the impact of this phenomenon on different corroded reinforced concrete structures.

REFERENCES

- ABNT, NBR 6118. 2014. Projeto de estruturas de concreto – procedimento. Rio de Janeiro.
- Ames, I., Moreira L.S., Bittencourt, T.N., Futai M.M., Beck, A.T. & Carvalho, H. 2022. Evaluation of deterioration modeling of corroded reinforced concrete railway bridges under uncertainty. *Bridge Safety, Maintenance, Management, Life-Cycle, Resilience and Sustainability*.
- Beck, A. T. (1st ed.) 2019. Confiabilidade e Segurança das Estruturas. Rio de Janeiro: Elsevier.
- Coronelli, D. & Gambarova, P. 2004. Structural Assessment of Corroded Reinforced Concrete Beams: Modeling Guidelines. *Journal of Structural Engineering* 130(8): 1214–1224.
- El Maaddawy, T & Soudki, K. 2006. A model for prediction of time from corrosion initiation to corrosion cracking. *Cement & Concrete Composites* 29, 168–175.
- Ghods, P., Isgor, O. B. & Pour-Ghaz, M. 2007. A practical method for calculating the corrosion rate of uniformly depassivated reinforcing bars in concrete. *Materials and Corrosion* 58(4): 265–272.
- Ghods, P., Isgor, O. B. & Pour-Ghaz, M. 2008. Experimental verification and application of a practical corrosion model for uniformly depassivated steel in concrete. *Materials and Structures* 41(7): 1211–1223.
- JCSS. 2006. Probabilistic Model Code. Joint Committee on Structural Safety.
- Ma, Y., Wang, L., Zhang, J., Xiang, Y., Peng, T. & Liu, Y. 2015 Hybrid Uncertainty Quantification for Probabilistic Corrosion Damage Prediction for Aging RC Bridges. *J. Mater. Civ. Eng.* 27(4): 04014152.
- Morales, F. M. L. 2017. Reliability-based classification of the load bearing capacity of existing bridges.
- Pugliese, F. & Di Sarno, L. 2022. Probabilistic structural performance of RC frames with corroded smooth bars subjected to near- and far-field ground motions. *Journal of Building Engineering* 49: 104008.
- Rocha, J. M., Henriques, A. A., Calçada, R. & Rönquist, A. 2015. Efficient methodology for the probabilistic safety assessment of high-speed railway bridges. *Engineering Structures* 101:138–49.
- Santiago, W.C. 2019. Calibração baseada em confiabilidade dos coeficientes parciais de segurança das principais normas brasileiras de projeto estrutural.
- Vecchio, F. & Collins, M. P. 1986. The modified compression field theory for reinforced concrete elements subjected to shear. *ACI Journal*, 83, 219–231.
- Vu, K. A. T. & Stewart, M. G. 2000. Structural reliability of concrete bridges including improved chloride-induced corrosion models. *Structural Safety* 22 (4), 313–333.
- Yang, K-H., Seo, E-A. & Tae, S-H. 2014. Carbonation and CO₂ uptake of concrete. *Environmental Impact Assessment Review* 46: 43–52.
- Zhang, M, Song, H., Lima, S, Akiyama, M & Frangopol, D. M. 2019. Reliability estimation of corroded RC structures based on spatial variability using experimental evidence, probabilistic analysis and finite element method. *Engineering Structures* 192: 30–52.
- Zhang, Q., Lun, P. Y. & Li, X. 2021. A simplified approach for prediction of concrete resistivity: experimental study and mathematic model. *Materials and Structures/Materiaux et Constructions* 54(4).

Structural reliability analysis of vehicle-bridge interaction based dynamic response for a high-speed railway bridge

I. Ames, T.N. Bittencourt, M.M. Futai & A.T. Beck

University of São Paulo (USP), São Paulo, Brazil

E.F. Souza

Federal University of Technology – Parana (UTFPR), Guarapuava, Paraná, Brazil

University of São Paulo (USP), São Paulo, Brazil

ABSTRACT: High-speed railways (HSR) are considered a reliable and efficient means of transportation which, combined with the capability of on-schedule attendance, emerges as a very competitive transportation system. These advantages have led to the rapid expansion of highway networks and the growing demand for higher operational speeds. In the design and operation context, HSR bridge dynamic analysis is thought to be a crucial element and, in most applications, the moving load method has been utilized for this purpose. However, for short and medium-span bridges, this method tends to be over-conservative, and the interaction between train and bridge considerably influences the accuracy of the bridge responses. Although several efforts have been dedicated to developing enhanced methodologies for the proper modeling of vehicle-bridge interaction (VBI), only a few studies have considered the uncertainties in material properties, geometry, and loading conditions. The acknowledgment of such uncertainties as an integrating part of the dynamic analysis may enhance the response prediction of the bridge, which enables the understanding of the probability of adverse outcomes due to excessive vertical accelerations of the deck. Loss of interlock among ballast grains, which degrades the rail stability, and the loss of wheel-rail contact, are examples of problematic performances of the bridge in such circumstances. In this study, the dynamic responses of a simply supported bridge are evaluated utilizing a 2-D VBI model, accounting for the influence of the passage of a high-speed train.

1 INTRODUCTION

High-speed railways (HSR) are considered a reliable and efficient means of transportation, which combined with the capability of on-schedule attendance, results in a very competitive transportation system. These advantages have led to the rapid expansion of highway networks and the growing demand for higher operational speeds (Rocha et al. 2014). Thus, as the construction of new high-speed lines and the retrofit of conventional ones for high-speed purposes have increased in recent years, the dynamic behavior of railway bridges has been subject of many research works (Johansson et al. 2014, Lu et al. 2012, Mellat et al. 2014, Moliner et al. 2012, Zeng et al., 2016).

In particular, the demand for bridges and viaducts along a high-speed railway is significantly greater relative to conventional railways, due to the inherent strict design criteria, resultant of large radii curves, and fully closed operation requisites. In France, the total bridge length of the lines of TGV Southeast Line from Paris to Lyon, TGV Northern Line from Paris to Lille, and TGV South-East Extension Line from Lyon to Valence hold the percentage of 6%, 21.5% and 32.2% of the railway extension, respectively (Guo et al. 2012).

In this context, the bridge's dynamic response is a design aspect that is not only related to the bridge's structural safety but overall railway line functionality. The moving loads

originated from the passing trains over the bridge induce a periodical excitation due to the regular axle spacing. Depending on the train velocity, the periodical load frequency may coincide with the structure's natural frequencies, causing a resonance phenomenon, with the amplification of the dynamic responses of the bridge. In this regard, the most critical configurations are the simply supported short-to-medium-span bridges (Moliner et al. 2012). In most design and operation applications, the moving load method has been utilized for assessing the HSR bridge dynamics. However, for short and medium-span bridges, this method tends to be over-conservative, and the interaction between train and bridge has a considerable influence on the accuracy of the bridge responses, thus justifying the recent efforts in the development of vehicle-bridge interaction (VBI) models (Rocha et al. 2014).

The amplification of the dynamic responses leads to high levels of deck's vertical acceleration which can cause adverse consequences concerning the train running safety and serviceability, such as ballast destabilization, loss of wheel-rail contact, increased fatigue-related damage, passenger discomfort, and higher risk of derailment due to the loss of the rail stability (Bebiano et al. 2017, Galvín et al. 2018, Rocha et al. 2012). The European Standard Eurocode (2003) limits the vertical acceleration of the deck at 3.5 m/s^2 for ballasted tracks and 5.0 m/s^2 for ballastless tracks. In the circumstances where the limit is reached, the deck must be stiffened or replaced.

Although the existence of uncertainties in the system is well acknowledged, most studies have conducted the dynamic analysis in a deterministic manner, disregarding all randomness involved with the parameters of both the structural system and vehicle. Nevertheless, uncertainties are intrinsic to the entire system, due to track irregularities, random material properties, and geometry in various manufacturing conditions, as well as load characteristics. Therefore, it is sensible to address the uncertainties of the parameters by employing a probabilistic approach (Liu et al. 2020, Mao et al. 2016, Rakoczy & Nowak 2014). Rocha et al. (2012), studied the safety of a filler beam railway bridge subjected to the passage of a deterministic TGV double high-speed train considering the uncertainties in the structure parameters. The variability of the bridge, track, and train was accounted for by Rocha et al. (2014), as well as track irregularities. Different methods for the safety assessment of railway bridges for high-speed trains were compared by Rocha et al. (2015), including the Monte Carlo Simulation and Latin Hypercube Sampling combined with a tail modeling method and an enhanced simulation procedure. In a similar context, laboratory tests were used by Matos et al. (2019) to update the structure model and compute the structural reliability. An application of robust design optimization of Tuned-Mass-Dampers and Multiple-Tuned-Mass-Dampers to vehicle-bridge coupled vibration problems was presented by Miguel et al. (2016). Parameters of bridge materials, environmental factors, and prestressing were considered by Liu et al. (2019). Both train and structure uncertainties were considered by Liu et al. (2020) and Mao et al. (2016) in a train-bridge coupled system analysis; and Gaussian random processes for the bridge and load characteristics were utilized by Wu and Law (2010).

This work aims to demonstrate the utilization of a VBI model in a structural reliability analysis of a simply supported bridge subjected to the passage of a Siemens ICE3 Velaro high-speed train, regarding the levels of vertical acceleration of the deck and considering uncertainties of both structure and vehicle.

2 VEHICLE-BRIDGE DYNAMIC INTERACTION SYSTEM

Vibrations caused by the passing trains can seriously impair the functionality of the track and bridge structures. In turn, the track and bridge's dynamic behaviors can influence the trains' dynamic performance. Therefore, in a comprehensive analysis, the train, track, and bridge must all be taken into account as a coupled system and analyzed simultaneously, thus enabling to identify the dynamic performance and service life of the train-track-bridge system (Zhai et al. 2019).

In general, in train-bridge dynamic interaction models, the bridge subsystem modeling utilizes Finite Element Method (FEM) or continuous beam theories, whereas the theory of multi-body system dynamics is adopted to establish the moving vehicle subsystem (Iwnicki et al. 2019, Zhai et al. 2013). This section describes the 2-dimensional VBI model used in the present

study to numerically simulate a high-speed train response to a bridge crossing event, which is regarded as an entire dynamic system in the derived dynamic governing equilibrium equations of motion. Despite the simplifications, plane VBI systems can satisfactorily predict the vertical dynamic response (Nguyen et al. 2014, Quirke et al. 2017), and the vehicle model presented as follows is widely used in the literature (Azimi 2011, Azimi et al. 2013, Ferrara 2013, Koç 2021, König et al. 2021, de Miguel et al. 2019, Youcef et al. 2013, Yu et al. 2018).

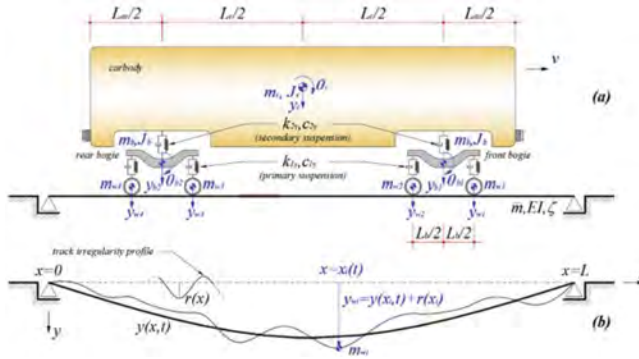


Figure 1. 2-D vehicle-bridge dynamic interaction system: (a) vehicle model and (b) bridge model.

2.1 Vehicle model

The multi-rigid-body vehicle model utilized for analysis is schematically described in Figure 1.a). It is considered a train constituted of N_c independent vehicles that crosses the bridge at a constant speed v . As the focus lies in evaluating the effect of resonance due to the periodical excitation induced by the train passage, each locomotive or wagon consists of a carbody, two bogies, four wheelsets, and the spring and damping connections between the components. The carbody and bogie frames were modeled as rigid bodies with concentrated masses given respectively by m_c and m_b , and rotary inertias J_c and J_b , taken about the transverse horizontal axis through its center of gravity. The wheelsets were represented as lumped masses m_w connected to the bogie frames by means of spring-dashpot sets representing the primary suspension with spring stiffness k_{1y} , and damping coefficient c_{1y} . Bogie frames are coupled to the carbody by spring-dashpot sets with spring stiffness k_{2y} , and damping coefficient c_{2y} , representing the secondary suspension system.

2.2 Bridge model

The bridge deck of the HSR has been modeled as a simply supported Bernoulli-Euler beam (Figure 1.b) with a mass per unit length of \bar{m} , Young's modulus E , moment of inertia I , and equivalent damping coefficient c . It was assumed that the downward deflection of the beam $y(x,t)$ is positive, as well as the rail irregularities $r(x)$ at the x -coordinate, taken into account by introducing random irregularity profile functions on the beam surface. Both deflection of the beam and track irregularities are measured relative to the beam's vertical static equilibrium locations (mean horizontal axle). The vertical deflection $y(x,t)$ of the beam is given by

$$y(x,t) = \sum_{i=1}^n A_i(t) \sin(i\pi x/L), \quad (1)$$

in which $A_i(t)$ is the amplitude of the i th shape mode at the instant t , i is the number of half-waves in which the beam is partitioned, n is the total number of modes, and L is the beam length.

2.3 Kinematic restrictions

Altogether, the vehicle model has 10 degrees of freedom (DOFs). However, it was imposed that each train's axle is kinematically constrained to the bridge deck to establish the dynamic

interaction on the VBI model (Lou & Zeng 2007) – the reaction forces of the structure are transmitted to the vehicle’s axles and vice versa (Quirke et al. 2017). Thus, the vehicle’s motion can be described by six independent DOFs (y_c , y_{b1} , y_{b2} , θ_c , θ_{b1} , and θ_{b2}), once the wheelset’s vertical displacements are constrained by the bridge displacements at the contact point between them (Figure 1.b) by the constraint equations

$$y_{wk}(x_k, t) = y(x_k, t) + r(x_k), \quad k = 1, \dots, 4. \quad (2)$$

For the numerical simulations, the vertical track profiles along the bridge’s length with random vertical irregularities were generated using a random function $r(x)$ of zero expectance and constant variance presented by Podworna (2015) and expressed by a trigonometry series as

$$r(x) = 2 \sum_{j=1}^N \sqrt{S(\Omega_j) \Delta\Omega} \cos(\Omega_j x + \phi_j), \quad (3)$$

where ϕ_j is a random phase with uniform distribution in $[0, 2\pi \text{ rad}]$, $S(\Omega_j)$ is the power spectral density (PSD) function evaluated in the j th spatial frequency Ω_j (rad/m) of the discrete domain $\Omega_j = \Omega_l + (j - 1/2)\Delta\Omega$, with $j = 1, 2, \dots, N$, and whose frequency band $\Delta\Omega = (\Omega_c - \Omega_r)/N$ is defined by the lower and upper limits spatial frequencies, respectively $\Omega_l = 2\pi L_{r,max}$ and $\Omega_u = 2\pi L_{r,min}$, and by the wavelength range $[L_{r,min}, L_{r,max}]$ in which the PSD function is included. The German PSD function has been used, which is written by

$$S_V(\Omega) = \frac{A_V \Omega_c^2}{(\Omega^2 + \Omega_r^2)(\Omega^2 + \Omega_c^2)}, \quad (4)$$

where $\Omega_c = 0.8246$ rad/m and $\Omega_r = 0.0206$ rad/m are the cut-off frequencies and A_V is the roughness constant (Zhai 2020).

2.4 Equations of motion for the VBI system

By using the Lagrange’s equation, the equations of motion for the VBI system have been derived and written in matrix form as

$$\mathbf{M}\ddot{\mathbf{u}} + \mathbf{C}\dot{\mathbf{u}} + \mathbf{K}\mathbf{u} = \mathbf{F}, \quad (5)$$

where \mathbf{M} , \mathbf{C} , and \mathbf{K} are the mass, damping, and stiffness time-dependent global matrices, and $\ddot{\mathbf{u}}$, $\dot{\mathbf{u}}$, \mathbf{u} , and \mathbf{F} are the acceleration, velocity, displacement, and load global vectors, respectively.

3 STRUCTURE RELIABILITY ANALYSIS

The probability of failure of a structure can be understood as the susceptibility of the violation of a limit state. On the other hand, the structural reliability expresses the level of confidence that the requisites concerning the performance of a structure will be kept, while the service life and design conditions are respected (Beck 2019). Usually, the structure behavior can be described by a limit state, which can be written as a function $g(\mathbf{X})$ of the random variables including the ones associated with the geometry and material properties, resistance, and actions:

$$g(\mathbf{X}) = g(X_1, X_2, \dots, X_n). \quad (6)$$

The equation $g(\mathbf{X}) = 0$ establishes the threshold between the failure domain $\Omega_f = \{\mathbf{x} | g(\mathbf{x}) \leq 0\}$ and the safety domain, and the failure probability can be expressed as

$$p_f = P[\{g(\mathbf{X}) \leq 0\}] = \Phi(-\beta) = \int_{\Omega_f} f_X(\mathbf{x}) d\mathbf{x}, \quad (7)$$

where $f_X(\mathbf{x})$ is the probability density function of the random variables in $g(\mathbf{X})$. The reliability index β is taken as a quantitative measure of the reliability of a structure (Šomodíková et al. 2016).

4 METHODOLOGY

The idealized structure under study is a ballasted prestressed voided slab bridge, constituted of a single simply supported span of 27m. The bridge characteristics are summarized in Table 1, as well as Figure 2. To elaborate the cross-section properties, the dimensions as in Aparicio (2009) were taken as reference.

Vehicle properties were assumed for the Siemens ICE3 Velaro High-Speed Train (Quirke et al. 2017) and are listed in Table 2, according to the uncertainties suggested by Salcher et al. (2016), except for the occupancy rate, adjusted to the statistics made available by the International Union of Rails (2020). The track irregularities with random roughness constant are considered in the path traveled by the train along the bridge's length.

Table 1. Variables for the bridge model.

Variable	Type	Distribution	Value/ parameters	Ref.
Cross-section area	Deterministic	-	5.5799 m ²	-
Inertia	Deterministic	-	2.2767 m ⁴	-
Concrete specific weight	Random	Gaussian	$\mu = 2625 \text{ kgf/m}^3$, $\sigma = 262.5 \text{ kgf/m}^3$	(Morales 2017)
Ballast specific weight	Random	Uniform	$a = 1500 \text{ kgf/m}^3$, $b = 2000 \text{ kgf/m}^3$	(Rocha et al. 2015)
Concrete compressive strength	Random	Gaussian	$\mu = 44.8 \text{ MPa}$, $\sigma = 4.48 \text{ MPa}$	(Santiago & Beck 2017)
Damping ratio	Random	Gaussian	$\mu = 2\%$, $\sigma = 0.3\%$	(Rocha et al. 2015)
Roughness constant	Random	Uniform	$a = 0.592 \times 10^{-6}$ rad m $b = 1.009 \times 10^{-6} \text{ rad m}$	(Salcher et al. 2016)

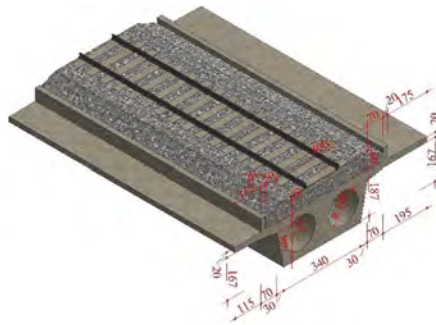


Figure 2. Typical cross-section dimensions for analysis.

Table 2. Vehicle properties.

Variable	Distribution	Value
Carbody mass	Gaussian	$\mu = 47800 \text{ kg}$, $\sigma = 478 \text{ kg}$
Bogie mass	Gaussian	$\mu = 3500 \text{ kg}$, $\sigma = 35 \text{ kg}$
Wheelset mass	Gaussian	$\mu = 1800 \text{ kg}$, $\sigma = 18 \text{ kg}$
Carbody rotary inertia	Gaussian	$\mu = 1.96 \times 10^6 \text{ kg m}^2$, $\sigma = 1.96 \times 10^4 \text{ kg m}^2$
Bogie rotary inertia	Gaussian	$\mu = 1715 \text{ kg m}^2$, $\sigma = 17.15 \text{ kg m}^2$
Primary suspension stiffness	Gaussian	$\mu = 2.40 \times 10^6 \text{ N/m}$, $\sigma = 2.40 \times 10^5 \text{ N/m}$
Secondary suspension stiffness	Gaussian	$\mu = 7.00 \times 10^5 \text{ N/m}$, $\sigma = 7.00 \times 10^4 \text{ N/m}$
Primary suspension damping	Gaussian	$\mu = 2.00 \times 10^4 \text{ N.s/m}$, $\sigma = 2.00 \times 10^3 \text{ N.s/m}$
Secondary suspension damping	Gaussian	$\mu = 4.00 \times 10^4 \text{ N.s/m}$, $\sigma = 4.00 \times 10^3 \text{ N.s/m}$
Occupancy rate	Beta	$\mu = 0.627$ $\sigma = 0.07$

The reliability analysis has been conducted through simulation using Latin Hypercube Sampling. The safety criterion adopted herein is controlled by the levels of vertical acceleration of the bridge's deck. Above the level of 7 m/s^2 the ballast layer may experience the loss of interlock between ballast grains, thus leading to the loss of lateral resistance of the sleepers, and thus characterizing the failure of the structure (Zacher & Baeßler 2009).

5 RESULTS

The adopted model proved suitable for simulations since the continuous beam model reduced the number of DOFs to be evaluated in each dynamic analysis, resulting in a significant reduction in overall computing time when compared to finite element models.

The histograms for the deck's vertical acceleration according to the train speed can be observed in Figure 3.a) for 290 km/h, 320 km/h, and 350 km/h.

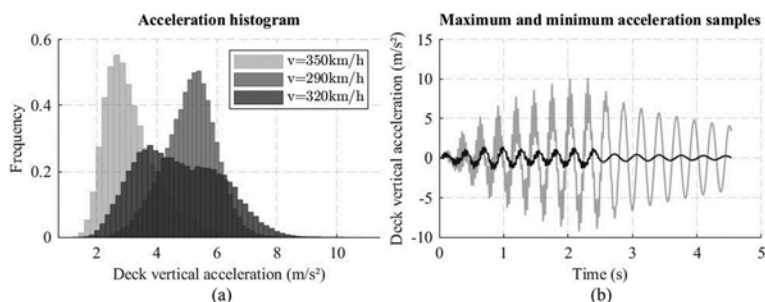


Figure 3. (a) Deck's vertical acceleration histograms; (b) Maximum (grey) and minimum (black) acceleration samples for the train speed of 320km/h.

Figure 3.b) compares two distinct samples for the vertical accelerations at deck's mid-span for a fixed train speed of 320 km/h. This result shows that the dynamic responses are susceptible to changes when the uncertainties are addressed and may deviate considerably from a deterministic analysis. The vertical accelerations of the deck proved to be equally sensitive to the train speed changes, once the train speed interval of 10 km/h induced visible impacts on the response values.

In Figure 4.a), the failure probabilities for all evaluated cases are described. The dynamic responses evaluated at the mean value of the random parameters are also presented in Figure 4.b) for comparative purposes. It is observed that the introduction of uncertainties in the dynamic analysis can cause a shift in the maximum resonant response, as for the proposed example the maximum response evaluated at mean values was registered for the speed of 300 km/h, which does not correspond to the train speed associated with the minimum reliability index (320 km/h).

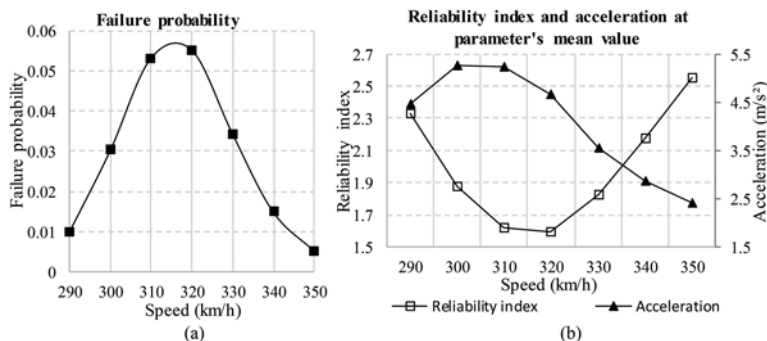


Figure 4. (a) Failure probabilities according to train speed; (b) Reliability index and acceleration at parameters' mean values according to train speed.

6 CONCLUSIONS

This paper aimed at evaluating the structural reliability of the dynamic response of a simply supported bridge subjected to the passage of a high-speed train. For this purpose, a VBI model along with simulation through Latin Hypercube Sampling was implemented.

The model proved to be efficient for the proposed evaluation, although with more refined evaluations and to smaller failure probabilities the number of required simulations may become computationally expensive.

The results showed that the dynamic responses are directly influenced by the presence of uncertainties, and that the failure probabilities can exhibit significant variation within the examined range of velocities. In addition, the inclusion of uncertainties in the analysis led to a change in the train speed at which the maximum resonant response occurred, when compared to the same dynamic evaluation performed at the mean values of the random variables.

REFERENCES

- Aparicio, A. (2009). Differences in designing high-speed railway bridges and highway bridges in Calçada, R., Delgado, R. and Matos, A.C. e (Eds.). *BRIDGES FOR HIGH-SPEED RAILWAYS*. Porto: Taylor & Francis.
- Azimi, H. (2011). Development of VBI Models with Vehicle Acceleration for Bridge-Vehicle Dynamic Response.
- Azimi, H., Galal, K. & Pekau, O.A. (2013). A numerical element for vehicle-bridge interaction analysis of vehicles experiencing sudden deceleration. *Engineering Structures* 49: 792–805.
- Bebiano, R., Calçada, R., Camotim, D. & Silvestre, N. (2017). Dynamic analysis of high-speed railway bridge decks using generalised beam theory. *Thin-Walled Structures* 114: 22–31.
- Beck, A.T. (2019). *Confiabilidade e Segurança Das Estruturas*, 1st ed. São Paulo: Elsevier Editora Ltda.
- EUROPEAN COMMITTEE FOR STANDARDIZATION (2003). *Eurocode 1: Actions of structures - Part 2: Traffic loads on bridges*.
- Ferrara, R. (2013). *A Numerical Model to Predict Train Induced Vibrations and Dynamic Overloads*.
- Galvín, P., Romero, A., Moliner, E. & Martínez-Rodrigo, M.D. (2018). Two FE models to analyse the dynamic response of short span simply-supported oblique high-speed railway bridges: Comparison and experimental validation. *Engineering Structures* 167: 48–64.
- Guo, W.W., Xia, H., De Roeck, G. & Liu, K. (2012). Integral model for train-track-bridge interaction on the Sesia viaduct: Dynamic simulation and critical assessment. *Computers and Structures* 112–113:205–216.
- International Union of Rails UIC (2020). Railisa: Rail Information System and Analyses.
- Iwnicki, S., Spiriyagin, M., Cole, C. & McSweeney, T. (Eds.). (2019), *Handbook of Railway Vehicle Dynamics*, 2nd ed., CRC Press.
- Jiang, L., Liu, X., Xiang, P. & Zhou, W. (2019). Train-bridge system dynamics analysis with uncertain parameters based on new point estimate method. *Engineering Structures* 199.
- Johansson, C., Nualláin, N.Á.N., Pacoste, C. & Andersson, A. (2014). A methodology for the preliminary assessment of existing railway bridges for high-speed traffic. *Engineering Structures* 58: 25–35.
- Koç, M.A. (2021). Finite element and numerical vibration analysis of a Timoshenko and Euler–Bernoulli beams traversed by a moving high-speed train. *Journal of the Brazilian Society of Mechanical Sciences and Engineering* 43(3).
- König, P., Salcher, P., Adam, C. & Hürzinger, B. (2021). Dynamic analysis of railway bridges exposed to high-speed trains considering the vehicle–track–bridge–soil interaction. *Acta Mechanica* 232(11): 4583–4608.
- Liu, X., Jiang, L., Lai, Z., Xiang, P. & Chen, Y. (2020). Sensitivity and dynamic analysis of train-bridge coupled system with multiple random factors. *Engineering Structures* 221.
- Lou, P. & Zeng, Q.-Y. (2007). Formulation of equations of motion for a simply supported bridge under a moving railway freight vehicle. *Shock and Vibration* 14(6): 429–446.
- Lu, Y., Mao, L. & Woodward, P. (2012). Frequency characteristics of railway bridge response to moving trains with consideration of train mass. *Engineering Structures* 42: 9–22.
- Mao, J., Yu, Z., Xiao, Y., Jin, C. & Bai, Y. (2016). Random dynamic analysis of a train-bridge coupled system involving random system parameters based on probability density evolution method. *Probabilistic Engineering Mechanics* 46: 48–61.

- Matos, J.C., Moreira, V.N., Valente, I.B., Cruz, P.J.S., Neves, L.C. & Galvão, N. (2019). Probabilistic-based assessment of existing steel-concrete composite bridges – Application to Sousa River Bridge. *Engineering Structures* 181: 95–110.
- Mellat, P., Andersson, A., Pettersson, L. & Karoumi, R. (2014). Dynamic behaviour of a short span soil-steel composite bridge for high-speed railways – Field measurements and FE-analysis. *Engineering Structures* 69: 49–61.
- de Miguel, A., Jacobsen, F., Lau, A. and Santos, I. (2019). Uncertainty analysis of track degradation at railway turnouts aided by a multi-body simulation software. *Journal of the Brazilian Society of Mechanical Sciences and Engineering* 41(12).
- Miguel, L.F.F., Lopez, R.H., Torii, A.J., Miguel, L.F.F., Beck, A.T. (2016). Robust design optimization of TMDs in vehicle-bridge coupled vibration problems. *Engineering Structures* 126: 703–711.
- Moliner, E., Museros, P. & Martínez-Rodrigo, M.D. (2012). Retrofit of existing railway bridges of short to medium spans for high-speed traffic using viscoelastic dampers. *Engineering Structures* 40: 519–528.
- Morales, F.M.L. (2017). *Reliability-Based Classification of the Load Bearing Capacity of Existing Bridges*.
- Nguyen, K., Goicolea, J.M. & Galbadón, F. (2014). Comparison of dynamic effects of high-speed traffic load on ballasted track using a simplified two-dimensional and full three-dimensional model. *Proceedings of the Institution of Mechanical Engineers, Part F: Journal of Rail and Rapid Transit* 228(2): 128–142.
- Podwórna, M. (2015). Modelling of random vertical irregularities of railway tracks. *International Journal of Applied Mechanics and Engineering* 20(3): 647–655.
- Quirke, P., Bowe, C., O'Brien, E.J., Cantero, D., Antolin, P. & Goicolea, J.M. (2017). Railway bridge damage detection using vehicle-based inertial measurements and apparent profile. *Engineering Structures* 153: 421–442.
- Rakoczy, A.M. & Nowak, A.S. (2014). Reliability-based strength limit state for steel railway bridges. *Structure and Infrastructure Engineering* 10 (9): 1248–1261.
- Rocha, J.M., Henriques, A.A. & Calçada, R. (2012). Safety assessment of a short span railway bridge for high-speed traffic using simulation techniques. *Engineering Structures* 40: 141–154.
- Rocha, J.M., Henriques, A.A. & Calçada, R. (2014). Probabilistic safety assessment of a short span high-speed railway bridge. *Engineering Structures* 71: 99–111.
- Rocha, J.M., Henriques, A.A., Calçada, R. & Rönquist, A. (2015). Efficient methodology for the probabilistic safety assessment of high-speed railway bridges. *Engineering Structures* 101: 138–149.
- Salcher, P., Pradlwarter, H. & Adam, C. (2016). Reliability assessment of railway bridges subjected to high-speed trains considering the effects of seasonal temperature changes. *Engineering Structures* 126: 712–724.
- Santiago, W.C. & Beck, A.T. (2017). A new study of Brazilian concrete strength conformance. *Revista Ibracon de Estruturas e Materiais* 10(4): 906–923.
- Šomodíková, M., Lehký, D., Doležel, J. & Novák, D. (2016). Modeling of degradation processes in concrete: Probabilistic lifetime and load-bearing capacity assessment of existing reinforced concrete bridges. *Engineering Structures* 119: 49–60.
- Wu, S.Q. & Law, S.S. (2010). Dynamic analysis of bridge-vehicle system with uncertainties based on the finite element model. *Probabilistic Engineering Mechanics* 25: 425–432.
- Youcef, K., Sabiha, T., El Mostafa, D., Ali, D. & Bachir, M. (2013). Dynamic analysis of train-bridge system and riding comfort of trains with rail irregularities. *Journal of Mechanical Science and Technology* 27(4): 951–962.
- Yu, C., Xiang, J., Mao, J., Gong, K. & He, S. (2018). Influence of slab arch imperfection of double-block ballastless track system on vibration response of high-speed train. *Journal of the Brazilian Society of Mechanical Sciences and Engineering* 40(2).
- Zacher, M. & Baeßler, M. (2009). Dynamic behaviour of ballast on railway bridges in Delgado, R., Calçada, R., Goicolea, J.M. & Gabaldón, F. (Eds.), *DYNAMICS OF HIGH-SPEED RAILWAY BRIDGES*, Taylor & Francis, Porto.
- Zeng, Q., Yang, Y.B. & Dimitrakopoulos, E.G. (2016). Dynamic response of high speed vehicles and sustaining curved bridges under conditions of resonance. *Engineering Structures* 114: 61–74.
- Zhai, W. (2020). *Vehicle-Track Coupled Dynamics: Theory and Applications*. Singapore. Science Press and Springer Nature Singapore Pte Ltd.
- Zhai, W., Han, Z., Chen, Z., Ling, L. & Zhu, S. (2019). Train-track-bridge dynamic interaction: a state-of-the-art review. *Vehicle System Dynamics* 57(7): 984–1027.
- Zhai, W., Xia, H., Cai, C., Gao, M., Li, X., Guo, X., Zhang, N., et al. (2013). High-speed train-track-bridge dynamic interactions – Part I: theoretical model and numerical simulation. *International Journal of Rail Transportation* 1(1–2): 3–24.



Taylor & Francis

Taylor & Francis Group

<http://taylorandfrancis.com>

*MS3: Integrating life-cycle engineering concepts into community
resilience and decision-support*
Organizers: J. van de Lindt, J. Padgett, A.R. Barbosa & N. Makhoul



Taylor & Francis

Taylor & Francis Group

<http://taylorandfrancis.com>

Resilience and the use of life-cycle cost analysis in civil engineering in the US

T. Neimeyer, B. Parsons & L. Champion

American Society of Civil Engineers, Reston, VA, USA

A. Kane

Institute for Sustainable Infrastructure, Washington, DC, USA

L. Orsenigo

ICMQ, Milan, Italy

ABSTRACT: This presentation will combine the efforts of the American Society of Civil Engineers (ASCE) and the Institute for Sustainable Infrastructure (ISI) to promote resilience and the use of life-cycle Cost Analysis in Civil Engineering in the US. ASCE's Committee on Sustainability (COS) is working on a US Standard (ASCE 73-xx) or Manual of Practice for sustainable infrastructure and the Standard or Manual has many references and ties to resilience and life-cycle cost analysis. Additionally, ASCE's Structural Engineering Institute has been working on sustainability through their SE 2050 initiative. ASCE's Grand Challenge for the Society is to reduce the life cycle cost of infrastructure projects by 50% by 2025 and steps taken to achieve this will be described.

ISI's Envision infrastructure rating tool has many ties to life-cycle cost analysis and resilience that would help a project achieve Verified, Silver, Gold, or Platinum awards. Three example projects in the US will be highlighted. Within the Envision tool, credit is given in several of its sections, and specifically, Credit LD3.3-Conduct a Life-Cycle Economic Evaluation as well as six (6) sections on resilience. ISI partnered with ICMQ to establish Envision in Italy and now has over 6 Envision awarded projects and over 300 people who have achieved ENV SP status in Italy. Two (2) example projects in Italy will be highlighted with a connection to resilience and life-cycle civil engineering.

1 INTRODUCTION

Two national societies based in the United States have taken on the challenge of pushing life cycle cost analysis, resiliency and sustainability for civil engineering infrastructure projects. They are the American Society of Civil Engineers (ASCE) and the Institute for Sustainable Infrastructure (ISI). This paper will describe their efforts and will give example projects that demonstrate resilience and sustainability. In addition, ISI has expanded its growth internationally and Italy will be hi-lighted for its efforts in using the Envision infrastructure rating tool.

2 ASCE

ASCE is the oldest of all American engineering societies having been founded in 1852. It has a robust membership of approximately 151,000 with locations all around the world. Within ASCE, there are nine technical Institutes, and we will be using the Structural Engineers Institute (SEI) to show what efforts are being made on Life Cycle Cost Analysis and sustainability as it relates to reduction of embodied carbon. Also, ASCE has many Committees that further their

efforts. Three committees specifically work on resiliency and sustainability. They are the Committee on Sustainability (COS), Infrastructure Resiliency Division (IRD) and the Committee on Adapting to Climate Change (CACC). To show ASCE's commitment to sustainability and resilience, you can look directly to their newly adopted code of ethics updated on October 26, 2020. Within the code of ethics, under the Natural and Built Environment, it is specifically stated that "Engineers adhere to the principles of sustainable development" as well as "Engineers mitigate adverse societal, environmental, and economic effects". These statements in the code of ethics demonstrate that ASCE is committed to sustainability and resilience.

In October of 2022, ASCE adopted a new strategic plan that will guide the Society's efforts over the next five (5) years. Within the Plan's strategic shifts section, it is clearly stated that "Innovate. Drive creative development and renewal of future-ready, safe, sustainable, equitable, robust, and resilient infrastructure". This guiding document empowers the Institutes and Committees of ASCE to develop sustainable and resilient infrastructure within their programs. The Committee on Sustainability has gone as far as proposing a performance-based Standard or Manual of Practice for Sustainable Infrastructure that is currently in the review and appeals process.

3 ASCE INDUSTRY LEADERS COUNCIL

ASCE has an advisory council to the ASCE Executive Director, and the Board of Direction known as the Industry Leaders Council (ILC). In July 2014, the ILC proposed that ASCE undertake a grand challenge of reducing the life cycle cost of infrastructure by 50% by 2025 and fostering the optimization of infrastructure investments for society. Within this grand challenge, there were four pillars of execution: 1. Life Cycle Cost Analysis, 2. Resilience, 3. Innovation and 4. Performance Based Standards for Design. The ASCE Board approved the grand challenge for incorporation throughout the Society. ASCE then commissioned the ENO Center for Transportation to publish a report on Maximizing the Value of Investments using Life Cycle Cost Analysis (LCCA). What the report noted was that the concept of life cycle cost analysis has many interpretations which make reporting and analyzing on LCCA progress from a national perspective almost impossible. Additionally, the report noted that while nearly all respondents to a survey on LCCA agreed that LCCA should be a part of the decision-making process, only 59% said they currently employ some form of it. Though the Grand Challenge held promise, the idea of measuring it on a national level did not. Nonetheless, the idea of increasing the use of LCCA began to take hold. One major infrastructure owner, the Port Authority of New York and New Jersey, requires LCCA to be used on most projects more than \$2.5 million in construction costs and has even developed a 12-page guide detailing how to apply LCCA while recognizing that its use was too costly on smaller projects. Other case studies in the ENO report included infrastructure owners from the US Army Corps of Engineers, the North Carolina and Pennsylvania Departments of Transportation, Denver's Regional Transit District, and the Metropolitan Transportation Commission for the San Francisco Bay Area.

While LCCA makes sense from a value viewpoint, many infrastructure owners have constrained budgets and are subject to four-year political election cycles. Though a project may have lower life cycle costs when including operations, maintenance and de-commissioning, the initial capital cost may be higher. If you only have limited budgets, you may make a less than optimal decision to take a lower up-front initial cost in order to do more projects. In doing so, you please the political stakeholders with more ribbon cuttings, while saddling future stakeholders with higher life cycle costs.

In 2015, ASCE engaged Lehigh University to undertake a survey of its membership entitled "Utilization of Life-Cycle Cost Analysis (LCCA) and Performance Based Design (PBD) for New and Existing Infrastructure". The conclusion stated "Overall, this report serves as baseline documentation describing the current use of LCCA and PBD strategies in the civil infrastructure sectors based upon the responses received from 67 survey participants. Several infrastructure sectors were polled in this study. Among the participants in the survey, most are focused on highways, buildings, and bridges; however, other infrastructure sectors such as the pipeline, fresh and wastewater systems, ports and waterways, transit, and rail industries are also represented among the responses. The most common professions polled were

professors, structural engineers, design engineers, project managers, and consultants. Accordingly, survey participants work for universities, engineering consultants, and government organizations. A majority of respondents work in the private sector and of those who work in the public sector, a majority indicated that their organization functions at the federal and state levels. Based on the survey results, it is concluded that life-cycle cost analysis is held in high regard and is of vital importance to most infrastructure sectors. A small percentage indicated that no official guidelines are employed, and that life-cycle analysis and management processes are only cost driven. More professionals use LCCA to evaluate different life-cycle management alternatives and design systems than those who do not, and among those who use LCCA methodologies, most indicated they use LCCA in the design and planning phase for new structures. Regarding the implementation of LCCA with respect to newly designed structures/systems, most said that there are no official guidelines (e.g., codes, standards, regulatory requirements) in their infrastructure sector. Furthermore, besides official guidelines, a majority of the time, engineering judgement is utilized to conduct LCCA regarding newly designed systems and O&M of existing systems.

Many survey participants believe that LCCA practices are neither consistent nor standardized. Additionally, there is a lack of versatile, accessible, and affordable software applications to help facilitate LCCA. In general, LCCA is not required in most sectors, and it is often not adopted because of the lack of a developed framework for analyzing all relevant costs. It is recommended that risk concepts be included within the life-cycle assessment of infrastructure systems. Additionally, the lack of awareness, standardization across infrastructure sectors, and political conflicts prevent the efficient implementation of LCCA. Many professionals agree that LCCA should be compulsory within their infrastructure sector and that publishing standards and/or guidance documents is the best way to promote the implementation of LCCA.”

One could conclude that this survey confirmed that most practitioners were familiar with LCCA and lauded its use, however the lack of standards/frameworks or official guidelines were an impediment to its use.

4 ASCE POLICIES

Within ASCE, there are over 200 policies that are approved by the Board of Direction. These policies are started at the Committee or Institute level and undergo reviews every three years. These policies guide ASCE as to positions on various issues from climate change to professional licensing. Several of these policies have relevancy to resilience and life cycle cost analysis as detailed below.

Perhaps the most relevant policy on resilience is Policy Statement 500-Resilient infrastructure initiatives adopted by the Board of Direction on July 11, 2020. The policy statement says, “The American Society of Civil Engineers (ASCE) supports initiatives that increase resilience of infrastructure against man-made and natural hazards through education, research, planning, design, construction, operation and maintenance. Development of performance criteria and uniform national standards that address interdependencies and establish minimum performance goals for infrastructure is imperative. Furthermore, an all-hazard, comprehensive risk assessment that considers event likelihood and consequence, encourages mitigation strategies, monitors outcomes, and addresses recovery and return to service should be routinely included in the planning/design process for infrastructure at all government levels.”

This policy statement was first approved in 2003 and has been revised and reapproved several times since.

ASCE’s Infrastructure Resilience Division (IRD) is a division/committee in the Committee on Technical Advancement established in 2014. The IRD’s purpose is to serve the civil engineering profession in advancing civil infrastructure and lifeline systems for local, regional, and national resilience against all hazards. Unified definitions for critical infrastructure and resilience can be found in ASCE’s Policy Statement 518. This Policy Statement defines critical infrastructure to include systems, facilities, and assets so vital that their destruction or incapacitation would have a debilitating impact on national security, the economy or public health, safety, and welfare. In this policy, resilience is the ability to plan, prepare for, mitigate, and

adapt to changing conditions from hazards to enable rapid recovery of physical, social, economic, and ecological infrastructure.

More relevant to Life-cycle cost analysis is ASCE Policy statement 451. In this policy statement, ASCE recommends the appropriate use of Life-Cycle Cost Analysis principles in planning and design processes to evaluate the total cost of projects. There can be no clearer statement on LCCA and ASCE's 2021 Report Card for America's infrastructure calls for smart investing by, among other methods, planning the cost of building, operating, and maintaining the infrastructure for its entire lifespan.

Other relevant ASCE policies include:

Policy 360-Climate Change

Policy 418-The role of the civil engineer in sustainable development

Policy 488-Greenhouse gases

Policy 517-United Nations sustainable development goals

Policy 556-Owners' commitment to sustainability

In Policy 418-The role of the civil engineer in sustainable development, it is clearly stated that ASCE supports performing Life Cycle Assessment on projects from planning to reuse. Lastly, in Policy 517-United Nations' Sustainable Development Goals, ASCE supports implementation of the civil engineering aspects of the UN Sustainable Development Goals (SDGs).

As can be seen by these Policy Statements, ASCE is very supportive of resilience and sustainability and the use of LCCA on civil engineering infrastructure projects.

5 ASCE STRUCTURAL ENGINEERS INSTITUTE (SEI) 2050

At ASCE, there are nine (9) Institutes. With 30,000 members, SEI is one of the largest and has a mission to advance and serve the structural engineering profession. ASCE's Structural Engineering Institute is at the forefront of a new program aimed at reducing embodied carbon in the structural engineering industry. The SEI Structural Engineers 2050 Commitment Program provides structural engineers with the tools and resources necessary to contribute and track projects toward the vision of net-zero embodied carbon structures by 2050. The program was developed in response to the SE 2050 Challenge, put forth by the Carbon Leadership Forum (CLF), that states "All structural engineers shall understand, reduce, and ultimately eliminate embodied carbon in their projects by 2050." In response to the CLF challenge, the SEI Sustainability Committee has been developing the first national program focused on structural engineering firm commitments to achieve net-zero embodied carbon structures by the year 2050. The SE 2050 Commitment Program is broken down into three strategies: plan, implement, and share. After a structural firm formally signs onto the commitment, it creates an embodied carbon action plan, centered on four main topics: an embodied carbon education plan, a reporting plan, reduction strategies, and advocacy. Firms will then implement their action plan with the support of educational resources and tools. Structural firms will input projects' embodied carbon measurements into the SE 2050 database. After an adequate amount of embodied carbon data has been collected for different regions and building types, embodied carbon benchmarks and reduction targets will be developed.

6 INSTITUTE FOR SUSTAINABLE INFRASTRUCTURE (ISI)

Based in Washington, DC, ISI is an education and research nonprofit (a 501c3) that was established in 2010 by the American Public Works Association (APWA), the American Society of Civil Engineers (ASCE), and the American Council of Engineering Companies (ACEC). ISI collaborated with the Zofnass Program for Sustainable Infrastructure at the Harvard University Graduate School of Design to develop Envision, an infrastructure rating tool for sustainability. Note how Envision has "isi" within its name.

The Envision rating system is utilized across the United States, Canada, and Italy. To date, over 135 projects have completed the third-party verification process representing over USD

\$130 billion in development. In addition, there are over 6,500 active credentialed professionals trained in the use of Envision—Envision Sustainability Professionals (ENV SPs).

Within the Envision framework there are several credits that address project life-cycle cost analysis (LCCA) and resilience. LCCA is directly addressed in credit LD3.3 Conduct a Life-Cycle Economic Evaluation. The levels of achievement within this credit begin with a standard LCCA of the proposed project. As they advance to higher levels of achievement Envision users then use LCCA to compare alternatives to inform better decision making. At the highest levels of performance Envision requires a sustainability cost-benefit analysis that monetizes the social, environmental, and financial costs and benefits of the project. This cost-benefit analysis must also demonstrate a net positive present value for the project.

Envision has six credits that work synergistically within its Resilience subcategory. These include CR.1 Avoid Unsuitable Development, CR 2.2 Assess Climate Change Vulnerability, CR 2.3 Evaluate Risk and Resilience, CR2.4 Establish Resilience Goals and Strategies, CR2.5 Resilience and CR2.6 Improve Infrastructure Integration. In order to be resilient, infrastructure must be informed, resourceful, robust, redundant, flexible, integrated, and inclusive. Resilience includes the ability to withstand short-term risks, such as flooding or fires, and the ability to adapt to changing long-term conditions, such as changes in weather patterns, sea-level rise, or changes in climate. Understanding the types of risks and probability of risks allows the project team to deliver an informed project design that anticipates and withstands these risks, minimizing its overall vulnerability. Maximizing resilience ensures a longer useful life and primes the project to more fully meet the future needs of the community.

These credits represent a mitigation hierarchy for resilience beginning with CR2.1 which encourages avoiding site-related risks whenever possible. In CR2.2 Envision users specifically identify vulnerabilities due to climate change and in CR2.2 they assess wider ranging risks to project performance (e.g., environmental hazards, changing demographics, and economic stressors). In CR2.4 project teams take the important step of embedding sustainability and resilience goals within the project delivery process in order to mitigate identified risks. CR2.5 requires project teams to implement monitoring and response systems to ensure resilience goals are met and maintained. In CR2.6 the project leverages other infrastructure systems to increase resilience through greater diversity, redundancy, or efficiency and to reduce the likelihood of systemic or cascading failures.

Throughout the Envision resilience credits higher levels of achievement are reached by expanding the scope of the resilience planning from the project level to the infrastructure network, and ultimately to the community. Below are two (2) case studies. In 2019 the Huntington Levee project received an Envision Bronze award. This 2,800-foot-long levee was designed to protect 160 homes in the floodplain from 100-year flood events. The community had previously been impacted three times by flooding since 2002. The project was completed in June 2019 and in July of 2019 a significant storm event brought waters close to the top of the new levee. The payback from this project was almost immediate in protecting the community.



Figure 1. Huntington Levee project in Fairfax County, Virginia.

In 2012 New York City was devastated by Superstorm Sandy. While the region suffered total damages of nearly \$50 billion, New York City alone experienced and estimated \$19 billion in damages. In 2022 the New York City East Side Coastal Resilience project received an Envision Gold award. The 2.4-mile-long \$1.45 billion USD flexible flood barrier protects over 110,000 residents from coastal flooding. In addition to providing flood protection the project improves open spaces, playgrounds, parks, and provides greater accessibility to coastal areas for the community.



Figure 2. The East Side Coastal Resiliency project uses a series of berms, flood walls, flood gates and raised parklands to create a continuous 2.4-mile barrier to protect 110,000 residents of the Lower East Side in Manhattan from future coastal and tidal flooding.

7 ISI IN ITALY

As ISI was increasing its presence in the US, an opportunity was presented in Italy. ISI partnered with ICMQ to establish Envision in Italy and now has 6 Envision awarded projects as well as three (3) in the pipeline and over 300 people who have achieved ENV SP status. Twenty-five (25) projects have done a preliminary assessment and three (3) guidelines have been published for the application of the Envision protocol to the Italian Railway Infrastructure, Transmission Electric Power Lines of Terna and Eolic Wind Farms. Below are two (2) case studies from Italy:

8 THE BOLOGNA BYPASS PROJECT

Serving as a vital transportation node for Italy and providing a strategic artery for a leading national manufacturer, the Bologna highway system is closely tied to the country’s economic prosperity.

The Bologna Bypass project is the first highway infrastructure project in Europe to receive the Platinum award — the highest attainable rating level with Envision®. At a cost of €1.5 billion, the bypass will strengthen the urban section of the A14 expressway linking Bologna, Bari, and Taranto with an extension of approximately 13 kilometers. While retaining connections with the A1 expressway linking Milan and Naples, and the A13 (Bologna-Padua) expressway, the bypass speeds up access to Bologna via the city’s ring road system. Vehicles will spend approximately 4.5 million fewer hours on the road per year as a result of the project. This will significantly enhance the quality of life in local communities and reduce CO2 emissions in metropolitan Bologna substantially (1,350 tons per year).

A significant feature of this project was that the design addressed not only the needs of vehicular traffic, but also the necessity of connecting the A14 highway with other

transportation modes, all informed by a strong network logic. The purpose was to integrate the bypass with key urban junctions and existing local infrastructure in a way that would generate socioeconomic value, maximize benefits and promote sustainability.

A public-private partnership (PPP) project, the Bologna bypass also benefited from the strong work of an interdisciplinary project team emphasizing transparency and broad stakeholder involvement throughout the design process. With this foundation, a transformative project took shape focusing on the environment, innovation, and mobility.

This project provided an historic opportunity to redevelop the bypass area on a regional scale while recognizing and protecting its environmental value; not least, by systematically reducing noise and air pollution.

The new system's interconnections are made of enclosures and protections, in contrast to the existing road network infrastructure — revolutionizing the traditional image of road facilities.

Specific consideration was given to how this new infrastructure would be integrated into the urban and landscape context. To cite one innovative example, the San Donnino sound tunnel adds significant green space and pedestrian urban spaces and includes the installation of photovoltaic panels capable of delivering 2.3 megawatts of power. Other examples include the use of overpasses and the design of acoustic barriers extending through the highway system for more than 20 km.

The bypass includes the establishment of a well-structured network of landscape-friendly infrastructure assets along the entire highway corridor. Some 20 kilometers of cycle-pedestrian paths will be constructed, urban underpasses will be improved, more than 130 hectares of “softscape” will be reclaimed, over 30,000 new trees will be planted, urban and rural parks will be reinforced and enlarged, and over 50 hectares of abandoned land will be returned to the region.

Aspects of the project that were selected for verification using the Envision framework included quality of life and economic impacts; the safeguarding of water resources and soil conservation; sustainable use of resources during construction; and climate resiliency. As well, the opportunity to strengthen the requirements governing contractors and the supply chain towards sustainability, in the invitations to tender, was identified by the project team. Finally, the importance of formulating policies for the correct identification and allocation of the resources needed to fulfill the project vision was also addressed through the Envision verification process.

The principles that guided the design for the Bologna Bypass, aligned with national and international directives, have truly changed the “design paradigm” for highway projects in Italy towards a holistic approach. That approach has also been adopted by Autostrade per l'ItaliaGroup, the company responsible for the project, as it pursues more effective design solutions supporting sustainability on future projects.

The new paradigm, at its core, is about the implementation of methodologies to realize an integrated design that makes it possible to monitor the full life-cycle of a project, and to advance projects in a collaborative environment with broad stakeholder involvement. This supports transparency around infrastructure project standards and outcomes that are geared towards sustainability.

9 PARCO EOLICO ALTO VASTESE

Two e2i Energie Speciali's Wind Farms, consisting of the full repowering of the previous plants located in Castiglione Messer Marino and Roccaspinalveti in the Abruzzo Region in Italy, have been recently awarded by Envision the Platinum certificate for sustainable infrastructure.

E2i Energie Speciali (E2i) is one of the leading companies in the Italian renewable energy market with a total installed capacity of approximately 724 MW, through 40 wind farms and 3 PV plants.

Castiglione Messer Marino e Roccaspinalveti wind farms' full repowering (i.e. a comprehensive entire reconstruction) are part of a Repowering plan which E2i, first in Italy, has been carrying out with the aim to increase its green energy production whilst minimizing

the impact on the territory by reducing the number of installed turbines and strengthening the relationship with local Communities.

In the Abruzzo Region, e2i installed 188 wind turbines in the early 2000s for a total capacity of 114 MW. A first phase of Repowering projects was concluded in 2019 resulting with an overall power output of 131 MW. A second phase involved the wind plants mentioned above which allowed to reach a new total power output of 145 MW.

In these repowering projects, the activities were focused in the Municipality of Castiglione Messer Marino, where 24 old wind turbine generators (WTGs) were replaced by 4 new VESTAS V114 wind turbines for a total installed capacity of 2MW and in the Municipality of Roccaspinaveti, where 23 old WTGs were replaced by 9 new VESTAS V114 wind turbines for a total installed capacity of 7 MW.

Compared to the previous plants now dismantled, such repowering project allowed to obtain the following positive environmental objectives: a 72% reduction of installed WTGs numerosity and approximately 1.5x increase of the power output, with a nearly 2.0x total energy production. The project layout considered the geological nature of the land, its altimetric profile as well as E2i's internal goal to re-utilize as much as possible existing roads and existing infrastructures, in order to minimize the environment impact. The expected annual energy production of these two new plants will be double the energy output of the previous plants at approx. 114 GWh/year, corresponding to the energy needs of approx. 42.000 residential customers in the Italian market and avoiding the emission of 32.000 tons of CO₂ equivalent. The recognition of the Platinum level confirms the high level of sustainability recognized to repowering projects which manage to take care of both social, environmental, and economic issues for local Communities and underlines how E2i pays significant attention to the entire life cycle of its plants, from the development and design phase to the construction, the operation, and the dismantling phases.

10 CONCLUSIONS

This document has outlined the importance and application of resilience, sustainability, and life cycle cost analysis in civil engineering projects. Many “forward thinking” infrastructure owners in the US use Life-Cycle Cost Analysis to help make decisions on their projects. But many do not. The same can be said for resilience and sustainability. Two US based Societies (ASCE and ISI) have made it an imperative that to do the “Right” project, you must consider resilience and sustainability and LCCA as a tool to be used to optimize decision making. Several surveys have shown that owners in the US may acknowledge the benefit of resilience and LCCA, however, they do not implement them on their projects. There needs to be considerably more progress and ASCE and ISI are helping to further this effort.

The Envision rating tool from ISI has many benefits. One of the better ones is having rating criteria that favor life cycle cost analysis and resilience. If implemented at the planning phase of a project, Envision will help the planner/engineer design a more resilient and sustainable project.

ASCE will continue to push its policies, Institutes, and committees to publish standards, and manuals on Engineering Practice to further the use of LCCA and designing resilience into projects. It is imperative that public and private sector infrastructure owners hear the “call” of both ASCE and ISI to make LCCA and resilience a part of larger infrastructure projects.

REFERENCES

- American Society of Civil Engineers Website(www.asce.org). 2022. Reston:Virginia.
- Eno Center for Transportation and American Society of Civil Engineers. 2014. *Maximizing the Value of Investments using Life Cycle Cost Analysis*. Reston: Virginia.
- Institute for Sustainable Infrastructure Website (www.sustainableinfrastructure.org). 2022. Washington: DC
- Lehigh University and American Society of Civil Engineers. 2015. *Utilization of Life-Cycle Cost Analysis (LCCA) and Performance Based Design (PBD) for New and Existing Infrastructure*. Reston: Virginia.

The value of multi-criteria decision analysis for asset management

J. Bödefeld

Federal Waterways Engineering and Research Institute, Karlsruhe, Germany

F. Marsili

Helmut Schmidt University/University of the Federal Armed Forces Hamburg, Germany

ABSTRACT: Ageing and neglected maintenance are the main reasons for an inadequate condition of waterway infrastructure in Germany. Available maintenance resources are limited, which is why prioritising maintenance measures is becoming increasingly important. In this paper, three different approaches to the maintenance prioritisation based on the Multi-Criteria Decision Analysis are presented for different constellations of infrastructure. First, the risk of neglecting the maintenance of ship locks is assessed with the help of the Multi-Attribute Utility Theory. Then, a concept based on the Simple Multi-Attribute Rating Technique is developed for the risk-based maintenance planning of a system of culverts. Lastly, an approach to vulnerability assessment of a levee system based on the Weighted Influence Non-linear Gauge System is formulated to derive weights for vulnerability indicators that also consider their interdependencies and permit the aggregation of the related information. The results show that the Multi-Criteria Decision Analysis supports the strategic prioritization of maintenance actions for waterways infrastructure and any infrastructure system with similar characteristics.

1 INTRODUCTION

Infrastructure is the backbone of a healthy economy and its management is a complex discipline that therefore plays an essential role in modern societies. Ageing of civil infrastructure adversely affects its performance. Due to limited resources in recent decades, an immense backlog of outstanding maintenance has built up (Ralph, 2015).

This is also true of the infrastructure of federal waterways in Germany. These waterways include more than 300 locks, 300 weirs and 240 culverts. All in all, there are around 2,000 engineering structures that require a corresponding amount of maintenance. The condition of locks detailed in Figure 1 is a direct consequence of this maintenance backlog. A quarter of the structures are in a non-sufficient condition and well over half of the structures that are currently in a sufficient condition will require action in the near future. As well as resolving the issue of infrastructures in a non-sufficient condition, proper maintenance management also needs to prevent structures that are in a sufficient condition from deteriorating into a non-sufficient condition.

In order to tackle the backlog with the limited resources available, the relevant maintenance measures must be prioritized. Prioritizing infrastructure management measures is a major challenge. Deciding which measures are suitable for each specific structure is a predominantly technical issue. Engineers have experience in identifying optimum solutions. However, a wider range of criteria must be taken into account when prioritizing measures for a large portfolio of assets. Finite resources will lead to assets and thus infrastructure being abandoned. This makes it all the more important to prioritize measures in an objective, transparent and fact-based way that balances interests. However, engineers have little experience in structuring decision-making processes that take decisions to another level.

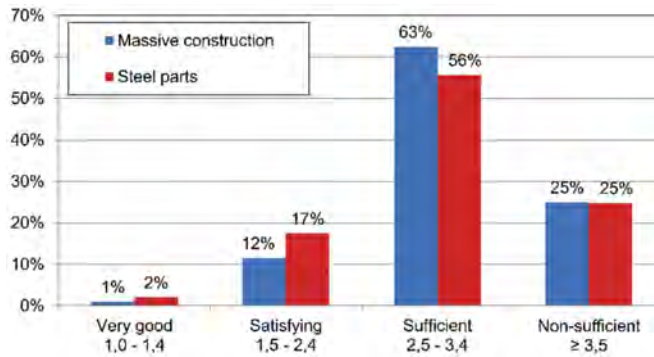


Figure 1. Condition of locks in Germany (BAW 2022).

In response to this challenge, risk-based maintenance strategies have been developed for identifying those system elements that are linked to higher probabilities of failure, and the magnitude of the consequences of failure, e. g. Arunraj & Maiti (2007). The risk arises in these cases from neglected maintenance. However, the problem of evaluating risk for infrastructure systems is not trivial.

Multi-criteria decision-making methods can be useful in solving this problem. These methods are introduced briefly in section 2. Section 3 considers use-cases for different waterway infrastructures and it demonstrates the possibilities of the method. The paper ends with a conclusion in section 4.

2 MULTI-CRITERIA DECISION ANALYSIS METHODS IN THE MAINTENANCE OF CIVIL INFRASTRUCTURE

It is possible to design a framework with stakeholder participation that can solve a given prioritization task using a combination of existing data and expert knowledge. In such a framework the discussion is steered away from the individual structure towards the target and the criteria, resulting in a transparent and comprehensible decision-making process.

The first step is to analyse the problem. Criteria such as the level of consideration (e.g. component, structure, network), the target (e.g. increasing availability or reliability) and the form of the result (e.g. classification, ranking) must be clarified. AI methods can promote understanding or reduce the dimension the given problem (Marsili & Bödefeld 2021b). Available and suitable attributes and their characteristics (e.g. qualitative, quantitative) must be set. Costly data collection can be avoided if it is possible to resort to existing data. The potential of secondary data, that is, data not explicitly collected for infrastructure management, should also be considered and exploited at this stage.

Then, a suitable method to combine the data with expert knowledge is selected. On the one hand, experts support the analysis of the problem and the definition of the target. On the other hand, they help to evaluate and weigh the importance of the various criteria and attributes. Finally, they evaluate the plausibility of the result.

As a rule, the criteria and the attributes describe the vulnerability or criticality of the alternatives, i.e. of the assets under consideration. A risk-oriented view results, even if risk has not been considered explicitly. The decision process identifies those structures for which a maintenance measure will have the greatest utility. These are the structures that are currently linked with the greatest risk of deferred maintenance.

3 USE-CASES FOR WATERWAY INFRASTRUCTURE

3.1 The Multi-Attribute Utility Theory (MAUT) for locks

In the first case study considered in this paper, the analysis focuses on a group of 18 locks located in a network of artificial canals and characterized by one, two or three chambers. The oldest lock chambers are about 100 years old, the youngest about 15 years. The locks have

very different characteristics. The construction of the chambers ranges from heavyweight walls to sheet piling to modern reinforced concrete. The type of lock gates varies e. g. from miter gates to sliding gates to lifting gates.

The aim of this approach is to increase the reliability, availability and maintainability of the locks. The locks that have a low reliability, availability or maintainability must therefore be identified because these are thus predestined for prioritized repair. Repair measures are planned at the level of the lock chambers, as these usually have to be closed for this purpose. Consequently, the approach described here also focuses on ranking the lock chambers according to the risk of a deferred maintenance; as there are 28 lock chambers with different designs, 28 different alternatives need to be evaluated. Prioritizing the repair of these objects is expected to significantly reduce the overall risk of the system. The attributes describing the alternatives have been aggregated with the Multi-Attribute Utility Theory (MAUT), in which preferences over attribute values are expressed by the definition of utility functions.

A strict, self-imposed constraint of the approach requires the use of existing data. The purpose of this was to avoid time-consuming data research so that results could be produced in a timely manner. All data were taken from existing databases explicitly developed for infrastructure management, and from databases which were not necessarily developed for this purpose (secondary database). The following six attributes were finally used for an evaluation of the alternatives; the first three attributes address the reliability of the lock, the second three attributes address the consequences of damage:

- the number of serious damages of the lock gates,
- the number of serious damages of the construction of the chamber,
- the number of unscheduled inspections,
- the number of unplanned service interruptions,
- the criticality of the lock service interruptions,
- the transport volume affected by the lock service interruption.

A major advantage of MAUT is that it enables quantitative and qualitative information to be combined. In particular, qualitative expert knowledge is integrated via the definition of the utility functions and the definition of the criteria or attributes weights. For the problem described, an exponential function was chosen to describe the utility, since all attributes show an increasing risk and thus an increasing benefit of a repair as the value increases.

The aim of the work was to demonstrate the potential of multi-criteria decision making in a civil-engineering world that is not used to its application. Although higher level approaches to identifying the utility function or determining the CE exist (Makhoul 2019), simple, pragmatic approaches were used to keep the structure of the analysis simple. Building on a basic acceptance of the procedure, corresponding improvements are conceivable for determining the parameters and for taking into account the individual assessment of the experts or stakeholders.

The choice of a parametric family for the utility function has the advantage that the definition of the parameters is based on the definition of a single quantity, called certainty equivalent (CE), which corresponds to a value of the utility of 0.5. The experts determine the CE, taking into account the minimum and maximum value of each attribute. Being increasing values of attributes linked to higher risk, the CE corresponds to the value of the attribute that is still acceptable for the experts. E.g. for the attribute “number of serious damages”, the experts have set a maximum permissible number of 1, and thus the value of the CE corresponds 1. This results in the utility function shown in Figure 2. Due to the increased benefit compared to a linear increase, a risk aversion of the experts becomes visible.

Thus, the benefit of a repair can be determined for each lock chamber depending on the characteristic of the attribute. In order to determine the total benefit, the attributes still have to be weighted. A direct rating method was chosen to find adequate weights: the experts were asked to determine them. These vary from 0.3 (criticality of lock service interruption) and 0.2 (unplanned service interruption and unscheduled inspection) to 0.15 (serious damages of the lock gate), 0.1 (serious damages of the construction) and 0.05 (transport volume). In the experts’ opinion the consequences of failures (service interruption and unscheduled inspection) contribute more to the risk than the probability of failure (serious damages) as they got higher weights.

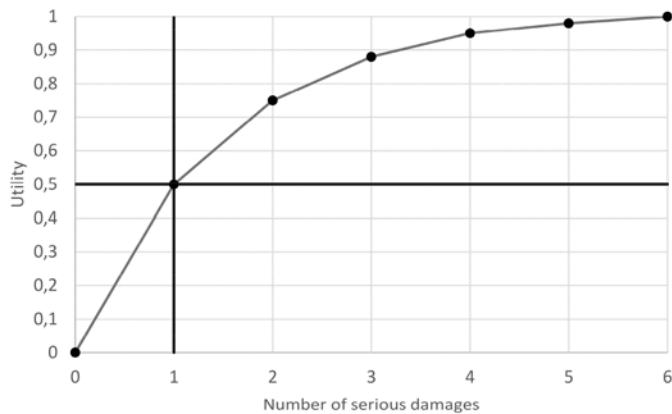


Figure 2. Utility function for the attribute “number of serious damages”.

Finally, a ranking for the repair of the lock chambers can be determined by identifying the aggregated utility. The result was visualized in a GIS map, with the benefit graded between 0 and 1 on a colour scale from green (0) to red (1), see Figure 3.

A detailed description of the approach is given in Marsili & Bödefeld (2021a). For the recording of individual expert opinions, reference is made to an extensive basic literature from the psychological field (Kahnemann 2012). Of course, other approaches are possible to elicit expert opinion. However, it is necessary to consider that multi-criteria analysis methods are still uncommon in the field of civil engineering. In choosing simple techniques, it is intended to promote a basic acceptance of the procedure, based on which the method can be further developed and more refined information elicitation techniques can be used.

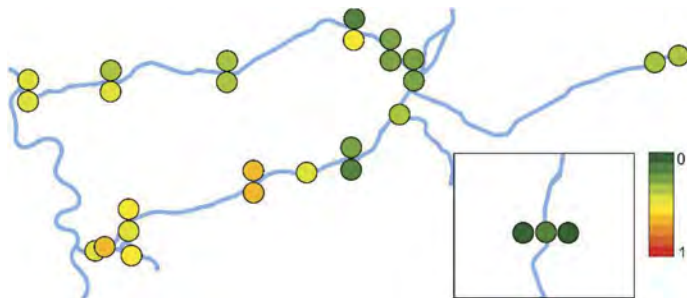


Figure 3. Aggregated utility (risk) for the 28 lock chambers.

3.2 The Simple Multi-Attribute Rating Technique (SMART) for a system of culverts

In the second case study, attention is put on an asset of 48 culverts characterized by different dimension, material, construction typology. The culverts encroach on a system of levees, built to retain water in an artificial canal system. Again, the goal is to identify those objects that are related to a higher risk of deferred maintenance, and therefore on which repair actions can have the greatest effect in terms of improving reliability and availability. Five attributes characterizing the culverts were extracted from an existing construction database:

- Encroachment on a levee (yes/no),
- Encroachment on a sealed canal (yes/no),
- Presence of a rake (yes/no),
- Presence of a sand trap (yes/no),
- Size of the drainage basin [m²].

Using a clustering approach based on k-medoids algorithm (Kaufmann & Rousseeuw 1990), the 48 alternatives were reduced to 15 representative objects corresponding to the cluster medoids. The optimal number of clusters was found using the silhouette approach by Rousseeuw (1987). In particular, the medoid is the point where the average dissimilarity between the medoid and all other cluster members is the lowest; it thus corresponds to the most central point in the cluster.

During a discussion among experts, four significant failure processes were identified: “collapse of the barrel/headwall”, “leakage out of the culvert”, “piping inside the culvert” and “afflux”. As the first three processes might lead to damage to the canal and further on to flooding due to levee breach, the last process may cause cross catchment flooding due to afflux of the culvert.

It can be seen that the influence of an attribute depends on the failure scenario. For example, a sand trap and a rake protect the culvert from structural damages, but can trigger the afflux scenario if not cleaned properly. Some attributes increase the probability of failure and the severity of the consequences. E.g. a big drainage basin might, on the one hand, transport debris and particles and thus increase the probability of failure. On the other hand, this results in greater cross catchment flooding.

The key steps of the Simple Multi-Attribute Rating Technique (SMARTS) are the definition of single-attribute utility functions and swing weighting. The definition of the single attribute utility functions is trivial for binary attributes as such attributes can only take two values corresponding to the maximum and minimum utility. For the single continuous attribute “drainage basin”, a linear function can be assumed, as it does not matter whether small improvements in the value of the attribute fall near the minimum, in the middle or near the maximum.

An intra failure scenario risk assessment is performed first by considering each failure scenario separately. The swing weights are determined in two steps. In the first step, the ranking of the weights is determined by ranking the attributes that contribute most to the risk. To do this, their values are varied from worst to best (swing). In the second step, the weights themselves are determined. Assuming that the swing from the worst to the best value of the first ranked attribute is worth a full 100 points, the deviation in the other attributes is evaluated in relation to this value by direct expert rating. The weights are then determined by dividing the assigned points by their total sum, as shown in Table 1.

Table 1. Swing weighting of the failure scenario “collapse of the barrel/headwalls”.

Attribute	Swing	Levee	Sealed Canal	Rake	Sand Trap	Drainage Basin	Rank	Score	Weight
Benchmark	No	No	No	Yes	Yes	0.04	0		
Levee	Yes	Yes	No	Yes	Yes	0.04	1	100	0.385
Sealed Canal	No	No	Yes	Yes	Yes	0.04	5	10	0.269
Rake	No	No	No	No	Yes	0.04	2	70	0.192
Sand Trap	No	No	No	Yes	No	0.04	3	50	0.115
Drainage Basin	No	No	No	Yes	Yes	72.70	4	30	0.038
							Total	260	1

The scenario-dependent utility can now be determined for each alternative. To determine the total utility of an alternative, the failure scenarios have to be weighted and the total benefit is summed up using the weighted sum method. This represents the inter failure scenario risk assessment. Three factors were considered to define the weights: the length of the cause-effect chain, the recognizability of the failure scenarios and the extent of the long-term consequences. The highest weight of 0.33 is given to the scenario “collapse of the barrel/headwalls”, followed by the scenarios “leakage out of the culvert” and “piping inside the culvert”, each with a weight of 0.25. The last scenario, “afflux”, receives a weight of 0.17.

The approach is aimed at promoting data-driven decisions, simplifying the structure of the decision problem and improving the interpretation of the results. The results show that 15

clusters are clearly identified within the set of 48 culverts. The prototypes can be considered as the alternatives of the decision problem. Four clusters containing 14 culverts can be recognized as dominant alternatives by means of the visual assessment of the attribute profiles characterizing each cluster.

Detailed notes on the approach can be taken from Marsili & Bödefeld (2021b).

3.3 *The Weighted Influence Non-linear Gauge System (WINGS) for dams*

Levees usually ensure a water level above the adjacent terrain. The dams presented in the study area are parts of artificial canals and therefore permanently exposed to water. Levee failure leads to serious damage, as the escaping water can cause devastating flooding of the surrounding area. Levee failure is often triggered by erosion, scouring and slippage, which subsequently cause part of the levee to collapse, visible through a loss of the levee crest or a hole in the levee.

When considering levees, the presence of penetrating structures implies special attention. On the one hand, encroaching structures imply a point of discontinuity in the levee body, which higher the vulnerability of the levee to the above-mentioned degradation processes. On the other hand, the condition of the levee influences the condition of a penetrating structure, e.g. instability of the levee provokes settlements to the penetrating structure. But the condition of the penetrating structure also influences the condition of the levee, e.g. in the case of leakage. A levee must therefore be considered as a system of systems (SoS) in which the interaction and interdependencies among subsystems is also taken into account. A new approach based on such consideration is proposed, according to which the Weighted Influence Non-linear Gauges System (WINGS) is applied to derive weights for vulnerability indicators that also consider their mutual casual interactions. Expert judgements are often fraught with uncertainty. To take this into account, the approach is combined with interval arithmetic. The final objectives are to identify the most important vulnerability factors and to develop an aggregated vulnerability index.

Two experts were recruited whose knowledge was discussed and visualized with the help of cognitive maps. The use of cognitive maps for the structured elicitation of expert opinions and stakeholder analyses has already been successfully applied in various contexts (Ferreri 2016). While one expert has a lot of experience in the study area, the experience of the second expert is derived from basic studies on levees. Additional information to support the analysis is derived from existing literature on canal levees and databases of historical earthen dam failures (TU Delft 2016).

In this way the binary vulnerability factors shown in Table 2 were identified. By simplifying, it is assumed that the factors take only two possible values: yes/no, fulfilled/not fulfilled, good/bad. These can be considered as binary parameters having two possible values, on/off, where “on” corresponds to “the vulnerability factor is enabled” and “off” corresponds to “the vulnerability factor is disabled”.

The experts indicate the strength of all vulnerability factors and the level of mutual influence using a direct rating system. It is thus possible to examine the structure of the relationships between the factors, to define the weight the factors according to their involvement in the system, and to classify them as “influencing” and “influenced”. In case of uncertainty, an interval evaluation is given. Following the WINGS methodology (Michnik 2013) and considering Alefeld et al. (2000) for interval arithmetic the bounds for the position and especially the total involvement value associated with each factor were obtained, from which the bounds for the vulnerability index will be derived.

It can be stated that

- the stability of the levee (St) and erosion (Er) have, as expected, the greatest influence;
- influencing factors with medium influence are culvert condition (CC), pipeline condition (PC) and vegetation (V);
- influenced factors with medium influence are internal seal (IS), seal (S), embankment walls (E) and drainage (D);
- all other factors are influenced to a small degree.

Table 2. Binary values assumed by the vulnerability factors.

Vulnerability factors	Disabled (off)	Enabled (on)
Pipeline encroachment (P)	No	Yes
Pipeline condition (PC)	Good	Bad
Culvert encroachment (C)	No	Yes
Culvert condition (CC)	Good	Bad
Other objects (O)	No	Yes
Stability of the levee (St)	Fulfilled	Not fulfilled
Soil erosion (Er)	Fulfilled	Not fulfilled
Burrowing animals (B)	No	Yes
Vegetation (V)	No	Yes
Change of the geometry (G)	No	Yes
Seal (S)	No	Yes
Internal seal (IS)	No	Yes
Drainage (D)	No	Yes
Embankment walls (E)	No	Yes
Inspection devices (I)	Yes	No
Levees water level (LH)	<3 m	≥3 m

To assess its vulnerability, the levee has to be divided into homogeneous segments, which are characterized by different lengths: from several hundred to a few meters (i.e. in case of object encroachment). For each segment, an interval vulnerability index is computed considering the upper and lower bound of the total involvement value which characterizes each vulnerability factor.



Figure 4. GIS maps showing a portion of the study area with the upper vulnerability index.

The visualization of the vulnerability assessment on GIS maps facilitates communication with third parties and other stakeholders affected by the vulnerability of the dams. The result can contribute to determining which objects should have priority for maintenance measures or at least require more in-depth consideration as a matter of priority. For further detailed information on the approach see Marsili et al. (2021c).

4 CONCLUSIONS

The task of infrastructure management requires tailored approaches to prioritizing the use of increasingly limited resources. The paper analysed three different elements of the waterway infrastructure with suitable applications of the multi-criteria decision-making method. An initial prioritization was made based on existing data.

AI methods, such as the cluster analysis used, are able to reduce the dimensionality of the problem and increase its understanding.

Although no explicit risk assessment was carried out, it was necessary to consider failure scenarios. The attributes considered in the MCDA can be assigned to vulnerability (probability of occurrence) and criticality (consequences). Thus, an implicit risk assessment was carried out for the lock chambers and culverts, and a vulnerability assessment was carried out for the dams without considering consequences.

The analysis already significantly promotes the understanding of the problem. All methods allow the combination of expert knowledge and existing data, which made it possible to achieve results quickly. Vagueness inherent in expert knowledge can be countered with interval arithmetic methods.

Suitable forms of visualization facilitate the presentation of the results and promote the necessary communication. The potential of the methods could thus be proven. Results may be improved by more detailed data, broader expert discussions and needs-oriented in-depth investigations.

ACKNOWLEDGMENT

This study has been developed within the research project PREVIEW, funded by the German Ministry of Education and Research, whose aim is to increase the resilience of German waterways infrastructures.

REFERENCES

- Arunraj, N. S.; Maiti, J. (2006): Risk-based maintenance-techniques and applications. *Journal of hazardous materials*, 142(3): 653–661. <https://doi.org/10.1016/j.jhazmat.2006.06.069>
- Ferretti, V. 2016. From stakeholders analysis to cognitive mapping and Multi-Attribute Value Theory: An integrated approach for policy support. *European Journal of Operational Research*. Elsevier. Vol. 253 (2). pages 524–541. <https://doi.org/10.1016/j.ejor.2016.02.054>
- Kahnemann, D. 2012. Schnelles Denken, Langsames Denken. Siedler Verlag München.
- Kaufman, L. & Rousseeuw, P. 1990. Finding Groups in Data: An introduction to cluster analysis. *Biometrics*. Vol. 47, No. 2 (Jun., 1991). p. 788 <https://doi.org/10.2307/2532178>
- Makhoul N. 2019. Seismic risk mitigation in buildings using a new method to encode a joint weighting function. Multi-attribute utility theory. *SN Applied Science 1*, 1103(2019) <https://doi.org/10.1007/s42452-019-1136-6>
- Marsili, F. & Bödefeld, J. 2021a. Identification of Waterways Maintenance Significant Units Using Secondary Data and Multi-Attribute Utility Theory. *Structure and Infrastructure Engineering*. <https://doi.org/10.1080/15732479.2021.1951771>
- Marsili, F. & Bödefeld, J. 2021b. Integrating Cluster Analysis into Multi-Criteria Decision Making for Maintenance Management of Aging Culverts. *Mathematics* 2021, 9, 2549. <https://doi.org/10.3390/math9202549>
- Marsili, F. & Bödefeld, J. & Weber, L. & Ghadami, M. 2021c. Vulnerability Assessment of Aging Levees with WINGS and Interval Arithmetic. 18th International Probabilistic Workshop. IPW 2021. Lecture Notes in Civil Engineering. vol 153. Springer, Cham. https://doi.org/10.1007/978-3-030-73616-3_65
- Marsili, F. & Bödefeld, J. 2022. PREVIEW - Resilienz kritischer Verkehrsinfrastrukturen am Beispiel der Wasserstraßen; Teilvorhaben: Kritikalität und risikobasierte Instandhaltungsstrategien am Beispiel der Verkehrswasserbauwerke am Westdeutschen Kanalnetz. FuE-Abschlussbericht. BAW Bundesanstalt für Wasserbau. <https://www.tib.eu/de/suchen/id/TIBKAT:1817181262/PREVIEW-Resilienz-kritischer-Verkehrsinfrastrukturen>
- Michnik, J. 2013. Weighted influence non-linear gauge system (WINGS)—An analysis method for the systems of interrelated components. *European Journal of Operational Research*. 228(3). 536–544. <https://doi.org/10.1016/j.ejor.2013.02.007>
- Ralph, P. 2015. Reliable maintenance planning, estimating and scheduling. Elsevier Science. <https://doi.org/10.1016/B978-0-12-397042-8.01001-9>
- Rousseeuw, P. 1987. Silhouettes: A graphical aid to the interpretation and validation of cluster analysis. *Journal of Computational and Applied Mathematics* 20. pp.53–65. [https://doi.org/10.1016/0377-0427\(87\)90125-7](https://doi.org/10.1016/0377-0427(87)90125-7)
- TU Delft. 2016. The International Levee Performance Database. 2016. Available online at: <http://leveefailures.tudelft.nl>

Toward enhancing community resilience: Life-cycle resilience of structural health monitoring systems

N. Makhoul

Politecnico di Milano, Milan, Italy

R. Kromanis

Universiteit Twente, Enschede, The Netherlands

ABSTRACT: Resilience is becoming a vital quality, particularly as our built environment faces increasing risks due to the aging of our infrastructure and climate change. Moreover, the built environment is relying largely on information technology and becoming digitalized. Consequently, it is crucial to ensure in addition to the resilience of structures and infrastructure, the resilience of the structural health monitoring SHM systems which provide information and help sustain and monitor the functionality of the built environment. The process involved in securing resilience throughout the life cycle of monitoring systems includes 1) planning and preparation before acute shock events and daily stressors, 2) absorption of shock events and 3) recovery and adaption afterward, as well as a continuous adaption for the daily stressors. Furthermore, enhancing the resilience of SHM systems contributes to, as well as improves, the resilience of structures and infrastructures. In this article, the life cycle resilience of SHM systems is discussed including community participation in SHM via crowdsensing. Comparisons between the resilience of SHM systems are presented. Results are discussed, and recommendations are offered.

1 INTRODUCTION

Hazards are becoming increasingly frequent, (i.e., due to increased urbanization, climate change, etc.) and infrastructure, societies, and the environment are suffering more severe consequences. Thus, it is vital to preserve the functionality of the critical infrastructure and community during and after hazard events, to minimize the losses and mitigate the risks of disasters. To mitigate the consequences of external chronic stresses and acute shocks, resilience-thinking is developed introduced lately for designing and assessing infrastructure as well as for urban planning. Resilience-based engineering aims to foresee and get ready and prepare for changing conditions (shocks and stresses), to adapt and recover rapidly from them, in addition to classical risk mitigation procedures (i.e., risk-based engineering). The focus of disaster mitigation strategies has shifted from disaster response to preparedness and prevention (Makhoul & Argyroudis 2018), (Makhoul & Argyroudis 2019), (Ayyub 2014), and (Ayyub 2015).

Resilience engineering is considered for all levels (i.e., materials, components, structures, networks, infrastructure, systems, the systems of systems, city levels, country, etc.), and aims to study multiple levels and hazard interdependencies. Community resilience includes all the above-mentioned and additionally encompasses social-technical-environmental interactions. The study aims to present accurately community resilience and to improve the decision-making procedure that it follows ((Folke et al. 2002),(Maguire & Hagan 2007), (Cutter et al. 2008)). Nevertheless, metrics and tools for the resilience quantification of socio-technical systems are still not soundly established, and procedures and standards are yet to arise (Lloyd's Register Foundation 2015). In (Koliou et al. 2020) a detailed state of the art of community resilience was offered and it was followed by the development of a community model (Roohi et al. 2021).

In the last decades, digitalization is playing a crucial role in everyday life and the built environment is relying predominantly on information technology and is becoming digitalized. The built environment is relying increasingly on structural health monitoring (SHM) and its data and information for

hazards, losses, and performance prediction modeling. Therefore, it is crucial to ensure the resilience of the SHM systems which provide information and help sustain and monitor the functionality of the built environment. Moreover, the community is gradually participating in the monitoring such as through crowdsourcing. However, until now, nothing was achieved on the topic of the resilience of the monitoring system and even less on the case of the involvement of society in monitoring. In (Makhoul et al. 2023a), a first study was done to address this issue by discussing the resilience of computer vision-based monitoring systems (CV-based systems) and their measurement. In (Makhoul et al. 2023b), adaptive pathways using emerging technologies (such as SHM systems, artificial intelligence (AI), and Machine Learning (ML)), the method was applied for critical transportation infrastructure and discussed as well resilience of CV-based systems, and AI and ML resilience and adaptation characteristics. Moreover, (Makhoul 2022), (Makhoul 2023b), and (Makhoul 2023a) discussed the data quality of SHM and related adequate decision-making processes.

In this article, we focus on the life cycle resilience of SHM systems. To this purpose, Section 1 discusses the resilience of SHM systems: Section 2.1 introduces resilience engineering and its methods and quantifications, Section 2.2 discusses the SHM systems and their types, then Section 2.3 presents the resilience of some examples of SHM systems. Section 3 offers the life cycle resilience of monitoring systems and life cycle costs. Finally, Section 4 concludes the main findings presented in this article.

2 RESILIENCE OF SHM SYSTEMS

2.1 *Resilience engineering*

The resilience importance takes source from the aptitudes of structures, assets, infrastructures, etc. to properly accommodate during its lifetime abrupt events and chronic stressors (e.g., earthquakes, hurricanes, storms, climate change, etc.). Those aptitudes or abilities are: 1) preparing and planning before an event/stressor, 2) absorbing the hazard (i.e., shocks and stresses) event consequences; 3) efficaciously responding to the hazard event disturbance by using the available resources efficiently (i.e., equipment, manpower, resources for operations, etc.); 4) recovering quickly and restoring the infrastructure/system functionality; 5) adapting to the changes of the situation and retaining improvement lessons for the future.

2.1.1 *Methods and quantifications*

Numerous resilience assessment procedures were suggested in the last decades (i.e., quantitative, qualitative assessment, deterministic and probabilistic techniques, 3) components, systems, networks, infrastructure, and system of systems levels) to face extreme and natural hazards. Among the several proposed methods, the attribute-based method (Fisher & Norman 2010) and (Pettit et al. 2010) analyze the system resilience properties (i.e., robustness, resourcefulness, adaptivity, and recoverability). It assesses the resilience semi-quantitatively or qualitatively by answering what makes it resilient and checking to what extent the properties are available). Performance-based approach quantifies the resilience of infrastructure, assets, systems, etc. (Bruneau et al. 2003), (Rose 2007), and (Alderson et al. 2015). It facilitates thus comparative analyses, cost-benefit, and planning analyses. The two procedures are complementary, and when combined provide the stakeholders with a comprehensive understanding of infrastructure resilience.

Moreover, numerous resilience assessment procedures are available such as the resilience-triangle method (Bruneau et al. 2003), the availability-based resilience approach (Ayyub 2014), and the simplified model (Ayyub 2015). This quantification increases in complexity conditional on needs and scales (i.e., single facility or system, systems, the system of systems, infrastructure networks, and community). Additionally, a variety of other resilience methods exist for instance the agent-based that considers complex systems, networks, users, control, and approximate reasoning comprising machine learning fuzzy logic. However, resilience assessment procedures need to be followed by adequate decision-making processes. Therefore, the adaptive pathways would be a suitable solution to consider the flexible aspect of the decision-making procedure and are very suitable for social and environmental applications and considerations such as the climate change adaptation process.

Several resilience metrics were offered such as in (Bruneau & Reinhorn 2007); (Reed et al. 2009); (Cimellaro et al. 2010); (Ouyang & Dueñas-Osorio 2014), (Nan & Sansavini 2017), (Capacci et al. 2020), and (Capacci & Biondini 2020).

The basic initial metric was formulated by the following Equation (1) for a single event:

$$R = \int_{t_0}^{t_h} Q(t) / (t_h - t_0) dt \quad (1)$$

where the functionality $Q(t)$ is a function ranging from 0% (i.e., loss of total performance) to 100% (i.e., no performance reduction).

The time t ranges from t_0 (i.e., the initial time of occurrence of the considered extreme event), t_i (i.e., the time of recovery work initiation), t_r (i.e., the recovery time from the event E), and t_h (i.e., the time of investigated horizon). T_{oh} , the total recovery time is formulated by $T_{oh} = t_h - t_0$.

The functionality of the system, infrastructure, structure, asset, etc. is subject to the losses induced by the disastrous event (E) occurring at t_0 . At E occurrence the functionality drops and is articulated by a loss function through fragility functions among others. The recovery function represents the functionality formulation in the aftermath of catastrophic event E and resulting losses. It is represented by a variety of shapes depending on the society's recovery capabilities and preparedness (Cimellaro et al. 2010) and (Bocchini et al. 2012). Figure 1 depicts the resilience metric and characteristics.

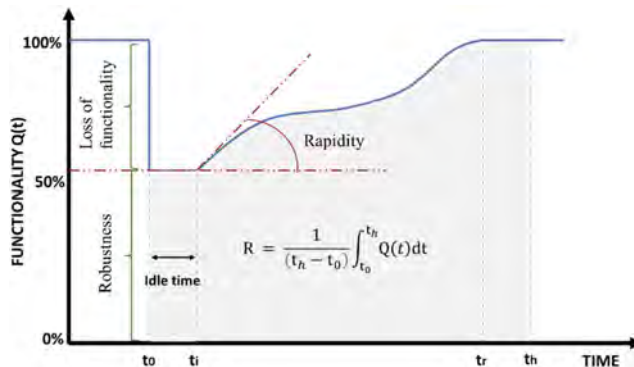


Figure 1. Resilience metric.

2.2 SHM SYSTEMS

With the advent of technologies, a wide range of SHM systems (sensors and sensing technologies) are commercially available. Sensors refer to physical devices that are designed specifically for collecting certain types of measurements. Sensing technologies can be attributed to approaches that are used to analyze data collected by devices that are not specifically designed for SHM purposes, for example, analyzing video-capturing bridge vibrations for the estimation of vibration parameters. SHM systems enable measuring physical (e.g., strain, displacement), environmental (e.g., temperature, humidity), and chemical (e.g., carbonation, corrosion) parameters. In this article types of SHM systems are defined by their intended use:

- 1) *Contact sensors* are either attached to the surface of a structure or inserted/integrated into elements of a structure (e.g., cast in concrete). Examples are (i) vibrating wire strain gauges installed on the surface of a concrete bridge (Barr et al. 2012), and (ii) wireless (strain gauge) sensor network for the instrumentation of prestressed concrete bridge (Hu et al. 2013).
- 2) *Non-contact (also remote) sensing* allows collecting measurements using either vision- or laser-based technologies without coming to a touching distance of the structure. Examples are (i) applications of modified GoPro action cameras for measuring vibration parameters of a suspension bridge (Kromanis & Elias 2023) and (ii) analysis of radar satellite data for the detection of unexpected bridge displacements (Cusson et al. 2021).

Table 1. Characteristics of the contact sensors, non-contact sensing, and crowdsensing.

Sensor or sensing technology	Type*	Pros	Cons	Failure	Repair	Time to repair
Vibrating wire strain gauge, sensor install on a steel bridge	C	High precision; high measurement collection frequency; reliable	Requires special attachment; usually, wired connection; expensive	Mechanical or electrical failure; detachment	replace or repair	days
Global position satellite, receivers installed on a bridge deck	C	Measures displacements in three axes;	Limited measurement resolution (approx. 1 cm); at least two receivers needed; expensive	Mechanical or electrical failure of a receiver; vandalism.	Replace or repair	days
Camera, a camera with a zoom lens installed away from the bridge	NC	No need to access the structure; low-costs; easy to use; distributed sensing	Limited measurement resolution (to the field of view and image processing algorithm); deluge of data	Mechanical or electronic; out of focus; vandalism	replace	In periodic monitoring (no failure), in continuously monitoring (hours/days)
Satellite imaging, Periodically collected and analyzed satellite images for bridge displacements	NC	Distributed measurement; no need to install sensors on the bridge	Satellite images are collected infrequently (days); images are expensive; difficult to analyze data	None expected	No repair needed	No failure expected
Smartphones, citizens provide smartphone sensor (accelerometer and gyroscope) data when crossing bridges	CS	No direct costs for sensors from asset owners; large volumes of data enable rather accurate estimates	Issues related to data privacy and ethics; limited measurement resolution; the need for a large amount of data	None	None	No failure

*C – contact, NC – non-contact, CS – crowdsensing

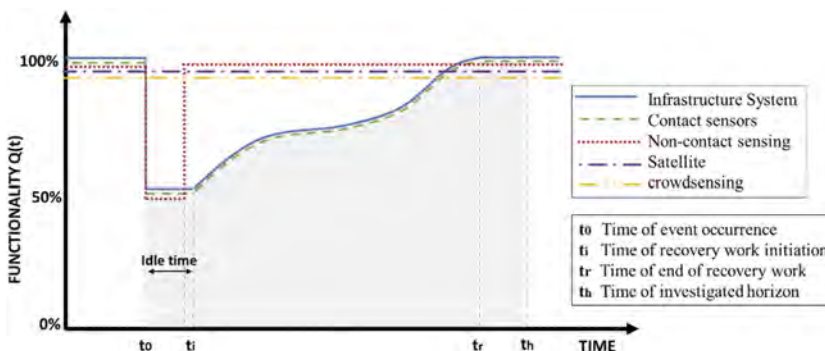


Figure 2. Functionality and resilience metric for infrastructure system and contact sensors, non-contact sensing, and crowdsensing.

3) *Crowdsensing* (also crowdsourcing) is a technique in which the deluge of data collected by citizens using smartphones is analyzed to assess the performance of a structure. Data can be collected from pedestrians and vehicle drivers ((Ozer & Feng 2017) and (Matarazzo et al. 2022)). This technique is very promising as it requires no investment in sensors and

sensing technologies. However, there are challenges related to data privacy that needs to be addressed before crowdsourcing become a ubiquitous sensing technology.

2.3 Examples of resilience of SHM systems

The recovery of functionality of infrastructure and monitoring systems depends on (i) the repair actions and their costs, (ii) the availability of manpower, their expertise, and costs, (iii) and the involvement of the society in the recovery work. In Table 1, some characteristics of the contact sensors, non-contact sensing, and crowdsensing are presented. The table details how these monitoring systems might fail and what needs repairing, the time needed to repair, and their limitations and advantages. Moreover, to ensure the redundancy of the monitoring systems in case of deterioration of contact monitoring systems, some non-contact monitoring systems (such as computer vision-based systems (e.g., cameras) and satellites imaging), as well as crowdsensing should be envisioned (even, today, though the accuracy of the latter is less than the former).

3 LIFE CYCLE RESILIENCE OF SHM SYSTEMS AND LIFE CYCLE COSTS

For ensuring the resilience of an infrastructure (or asset), it is necessary to consider the life cycle resilient assessment of the infrastructure system and the SHM system that it benefits from. Moreover, the life cycle maintenance costs for infrastructure systems and their relative SHM systems need to be considered. Figure 3 depicts the functionality, resilience metrics, and recovery of the considered infrastructure system lifetime and their related SHM systems (i.e., contact sensors, non-contact sensing, and crowdsensing). It shows two likely hazard events occurring at t_{01} and t_{02} , and their respective investigated time horizons t_{h1} and t_{h2} .

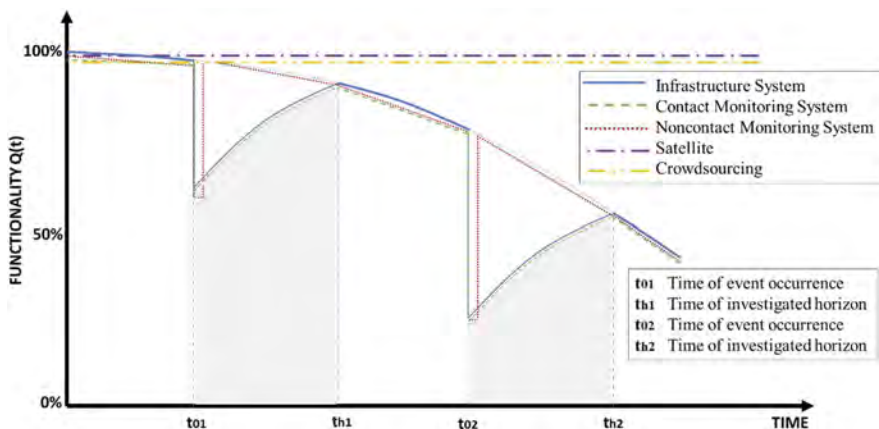


Figure 3. Functionality and resilience metric infrastructure system lifetime and the related contact sensors, non-contact sensing, and crowdsensing.

Life cycle maintenance costs were discussed by many researchers ((Messore et al. 2021), (Frangopol et al. 1997), (Liu & Frangopol 2005), and (Kong & Frangopol 2004)), where they introduced to compute the simple formulation of the present value of cumulative life-cycle maintenance cost (C_{PV}) due to all maintenance interventions. Maintenance interventions are allocated monetary expenses covering direct and indirect costs. The time effect is accounted for by a discount rate converting future cost into the value at the present time:

$$C_{PV} = \sum_{k=1}^N \frac{C_{t_k}}{(1 + \nu)^{t_k}} \quad (2)$$

where C_{t_k} is the cost of maintenance interventions applied at time t_k , and ν is the discount rate.

The cost in this article considers not only the cost of maintenance interventions for the infrastructure but as well the costs of the maintenance interventions for the SHM systems (contact sensors, non-contact sensing). Thus, the total cost of maintenance (C_{Total}) is given by Equation 3 along with the costs of the SHM systems in Equations 4 to 7.

$$C_{Total} = C_{Infrastructure} + C_{SHM\ System} \quad (3)$$

$$C_{SHM\ System} = C_{Contact} + C_{NonContact} \quad (4)$$

$$C_{Infrastructure} = \sum_{k=1}^n C_{0k} = \sum_{k=1}^n \frac{C_k}{(1 + \nu)^{t_k}} \quad (5)$$

$$C_{Contact} = \sum_{k_c=1}^n C_{0k_c} = \sum_{k_c=1}^n \frac{C_{k_c}}{(1 + \nu)^{t_{k_c}}} \quad (6)$$

$$C_{NonContact} = \sum_{k_{nc}=1}^n C_{0k_{nc}} = \sum_{k_{nc}=1}^n \frac{C_{k_{nc}}}{(1 + \nu)^{t_{k_{nc}}}} \quad (7)$$

where C_{tkc} and C_{tknc} are the cost of maintenance interventions applied at time t_{kc} and t_{knc} for the contact sensors, and non-contact sensing respectively. The cost of crowdsourcing is independent of the cost of the investment allocated to the infrastructure. Similarly, no additional cost is required for the usage of the satellite by the global position satellite receivers, while some costs are expected for satellite imaging. However, in both cases, no maintenance costs are expected. Finally, we note that Equations (2) to (7) can benefit from failure probabilities considerations such as in (Frangopol & Liu 2007), (Han et al. 2021), (Frangopol et al. 1997).

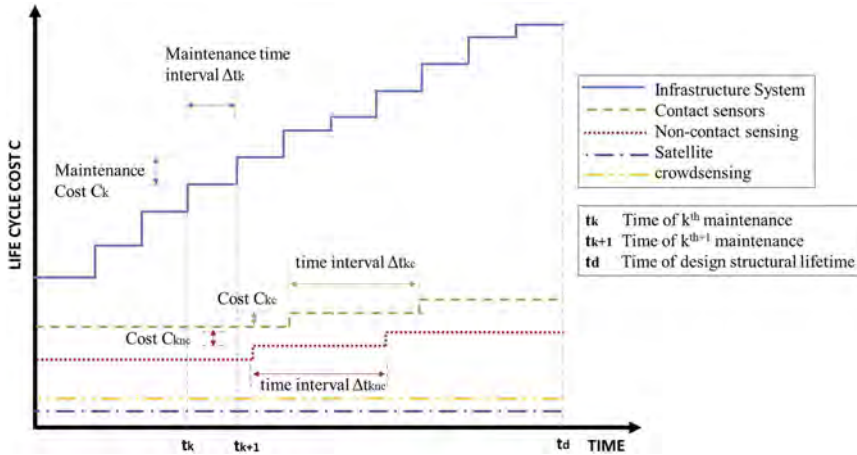


Figure 4. Life cycle costs for an infrastructure system and its SHM systems.

4 CONCLUSIONS

The built environment is relying largely on information technology and is becoming digitalized. In parallel resilience is a vital quality in this era. Therefore, in this article, the resilience of SHM systems and the effects on the life cycle infrastructure systems are discussed. Resilience engineering is briefly introduced and the types of SHM Systems and their characteristics are, mainly contact sensors, non-contact sensing, and crowdsensing. It is concluded that: 1) the loss functionality and recovery of contact sensors, in contrast to non-contact sensors, are tightly linked to the infrastructure system. Therefore, non-contact sensors can be replaced more easily than contact sensors. And their recovery time is minimal. 2) Non-contact sensors

and crowdsensing are more advantageous than contact sensors. They support and ensure the robustness and reliability of SHM systems and their measurements than contact sensors. 3) Satellite imaging can be used to enhance the resiliency of the measurements, as it is a source of backup for SHM with less probable disruptions.

ACKNOWLEDGEMENT

We thank Politecnico di Milano for funding this research through the Seal of Excellence project. The authors received financial support for this article from the Designing Systems for Informed Resilience Engineering (DeSIRE) Programme supported by the Centre for Resilience Engineering of the four universities of technology in the Netherlands (4TU).

REFERENCES

- Alderson, D.L., Brown, G.G. & Carlyle, W.M. 2015. Operational Models of Infrastructure Resilience. *Risk Analysis*, 35(4), 562–586. <https://doi.org/10.1111/risa.12333>
- Ayyub, B.M. 2014. Systems Resilience for Multihazard Environments: Definition, Metrics, and Valuation for Decision Making. *Risk Analysis*, 34(2), 340–355. <https://doi.org/10.1111/risa.12093>
- Ayyub, B.M. 2015. Practical Resilience Metrics for Planning, Design, and Decision Making. *ASCE-ASME Journal of Risk and Uncertainty in Engineering Systems, Part A: Civil Engineering*, 1(3). <https://doi.org/10.1061/AJRUA6.0000826>
- Barr, P.J., Petroff, S.M., Hodson, D.J., Thurgood, T.P. & Halling, M.W. 2012. Baseline testing and long-term monitoring of the Lambert Road Bridge for the long-term bridge performance program. *Journal of Civil Structural Health Monitoring*, 2(2), 123–135. <https://doi.org/10.1007/s13349-012-0023-2>
- Bocchini, P., Decò, A. & Frangopol, D. 2012. Probabilistic functionality recovery model for resilience analysis. In F. Biondini & D. M. Frangopol (Eds.), *Bridge maintenance, safety, management, resilience and sustainability. Proceedings of the Sixth International IABMAS Conference* (pp. 1920–1927).
- Bruneau, M., Chang, S.E., Eguchi, R.T., Lee, G.C., O'Rourke, T.D., Reinhorn, A.M., Shinozuka, M., Tierney, K., Wallace, W.A. & von Winterfeldt, D. 2003. A Framework to Quantitatively Assess and Enhance the Seismic Resilience of Communities. *Earthquake Spectra*, 19(4), 733–752. <https://doi.org/10.1193/1.1623497>
- Bruneau, M. & Reinhorn, A. 2007. Exploring the Concept of Seismic Resilience for Acute Care Facilities. *Earthquake Spectra*, 23(1), 41–62. <https://doi.org/10.1193/1.2431396>
- Capacci, L. & Biondini, F. 2020. Probabilistic life-cycle seismic resilience assessment of aging bridge networks considering infrastructure upgrading. *Structure and Infrastructure Engineering*, 16(4), 659–675. <https://doi.org/10.1080/15732479.2020.1716258>
- Capacci, L., Biondini, F. & Titi, A. 2020. Lifetime seismic resilience of aging bridges and road networks. *Structure and Infrastructure Engineering*, 16(2), 266–286. <https://doi.org/10.1080/15732479.2019.1653937>
- Cimellaro, G.P., Reinhorn, A. M. & Bruneau, M. 2010. Framework for analytical quantification of disaster resilience. *Engineering Structures*, 32(11), 3639–3649. <https://doi.org/10.1016/j.engstruct.2010.08.008>
- Cusson, D., Rossi, C. & Ozkan, I.F. 2021. Early warning system for the detection of unexpected bridge displacements from radar satellite data. *Journal of Civil Structural Health Monitoring*, 11(1), 189–204. <https://doi.org/10.1007/s13349-020-00446-9>
- Cutter, S.L., Barnes, L., Berry, M., Burton, C., Evans, E., Tate, E. & Webb, J. 2008. A place-based model for understanding community resilience to natural disasters. *Global Environmental Change*, 18(4), 598–606. <https://doi.org/10.1016/j.gloenvcha.2008.07.013>
- Fisher, R. & Norman, M. 2010. Developing measurement indices to enhance protection and resilience of critical infrastructure and key resources. *Journal of Business Continuity & Emergency Planning*, 4(3), 191–206.
- Folke, C., Carpenter, S., Elmqvist, T., Gunderson, L., Holling, C.S. & Walker, B. 2002. Resilience and Sustainable Development: Building Adaptive Capacity in a World of Transformations. *AMBIO: A Journal of the Human Environment*, 31(5), 437–440. <https://doi.org/10.1579/0044-7447-31.5.437>
- Frangopol, D.M., Lin, K.-Y. & Estes, A.C. 1997. Life-Cycle Cost Design of Deteriorating Structures. *Journal of Structural Engineering*, 123(10), 1390–1401. [https://doi.org/10.1061/\(ASCE\)0733-9445\(1997\)123:10\(1390\)](https://doi.org/10.1061/(ASCE)0733-9445(1997)123:10(1390))
- Frangopol, D.M. & Liu, M. 2007. Maintenance and management of civil infrastructure based on condition, safety, optimization, and life-cycle cost*. *Structure and Infrastructure Engineering*, 3(1), 29–41. <https://doi.org/10.1080/15732470500253164>

- Han, X., Yang, D. Y. & Frangopol, D. M. 2021. Optimum maintenance of deteriorated steel bridges using corrosion resistant steel based on system reliability and life-cycle cost. *Engineering Structures*, 243, 112633. <https://doi.org/10.1016/j.engstruct.2021.112633>
- Hu, X., Wang, B. & Ji, H. 2013. A Wireless Sensor Network-Based Structural Health Monitoring System for Highway Bridges. *Computer-Aided Civil and Infrastructure Engineering*, 28(3), 193–209. <https://doi.org/10.1111/j.1467-8667.2012.00781.x>
- Koliou, M., van de Lindt, J.W., McAllister, T.P., Ellingwood, B.R., Dillard, M. & Cutler, H. 2020. State of the research in community resilience: progress and challenges. *Sustainable and Resilient Infrastructure*, 5(3), 131–151. <https://doi.org/10.1080/23789689.2017.1418547>
- Kong, J.S. & Frangopol, D.M. 2004. Cost–Reliability Interaction in Life-Cycle Cost Optimization of Deteriorating Structures. *Journal of Structural Engineering*, 130(11), 1704–1712. [https://doi.org/10.1061/\(ASCE\)0733-9445\(2004\)130:11\(1704\)](https://doi.org/10.1061/(ASCE)0733-9445(2004)130:11(1704))
- Kromanis, R. & Elias, S. 2023. *Measuring Dynamic Response of the Wilford Suspension Bridge with a Vision-Based Measurement System: A Case Study* (pp. 280–289).
- Liu, M. & Frangopol, D.M. 2005. Multiobjective Maintenance Planning Optimization for Deteriorating Bridges Considering Condition, Safety, and Life-Cycle Cost. *Journal of Structural Engineering*, 131(5), 833–842. [https://doi.org/10.1061/\(ASCE\)0733-9445\(2005\)131:5\(833\)](https://doi.org/10.1061/(ASCE)0733-9445(2005)131:5(833))
- Lloyd's Register Foundation. 2015. *Foresight review of resilience engineering*.
- Maguire, B. & Hagan, P. 2007. Disasters and Communities: Understanding Social Resilience. *The Australian Journal of Emergency Management*, 22(2), 16–20. <https://doi.org/https://search.informit.org/doi/epdf/10.3316/informit.839750155412061>
- Makhoul, N. 2022. Review of data quality indicators and metrics, and suggestions for indicators and metrics for structural health monitoring. *Advances in Bridge Engineering*, 3(1), 17.
- Makhoul, N. 2023a. A new bayesian decision-making method to account for structural health monitoring data quality in bridge management. *Forthcoming*.
- Makhoul, N. 2023b. Bayesian Decision-Making Process Including Structural Health Monitoring Data Quality for Bridge Management. *KSCE Journal of Civil Engineering, Fortcoming*.
- Makhoul, N., Achillopoulou, D., Stamataki, N. & Kromanis, R. 2023a. The resilience of computer vision-based monitoring systems and their measurement. In C. R. M. Noori, M. Noori, C. Rainieri, M. Domaneschi, & V. Sarhosis (Eds.), *Data Driven Methods for Civil Structural Health Monitoring and Resilience: Latest Developments and Applications*. CRC Press/Taylor & Francis Publisher.
- Makhoul, N., Achillopoulou, D.V., Stamataki, N.K. & Kromanis, R. 2023b. Adaptive pathways using emerging technologies: Applications for Critical Transportation Infrastructure. *Forthcoming*.
- Makhoul, N. & Argyroudis, S. 2018. Loss estimation software: developments, limitations and future needs. *16ECEEE - 16th European Conference on Earthquake Engineering*.
- Makhoul, N. & Argyroudis, S. 2019. Tools for Resilience Assessment: Developments, Limitations and Future Needs. *ICONHIC2019 – 2nd International Conference on Natural Hazards & Infrastructure*.
- Matarazzo, T.J., Kondor, D., Milardo, S., Eshkevari, S.S., Santi, P., Pakzad, S.N., Buehler, M.J. & Ratti, C. 2022. Crowdsourcing bridge dynamic monitoring with smartphone vehicle trips. *Communications Engineering*, 1(1), 29. <https://doi.org/10.1038/s44172-022-00025-4>
- Messore, M.M., Capacci, L. & Biondini, F. 2021. Life-cycle cost-based risk assessment of aging bridge networks. *Structure and Infrastructure Engineering*, 17(4), 515–533.
- Nan, C. & Sansavini, G. 2017. A quantitative method for assessing resilience of interdependent infrastructures. *Reliability Engineering & System Safety*, 157, 35–53.
- Ouyang, M. & Dueñas-Osorio, L. 2014. Multi-dimensional hurricane resilience assessment of electric power systems. *Structural Safety*, 48, 15–24. <https://doi.org/10.1016/j.strusafe.2014.01.001>
- Ozer, E., & Feng, M. Q. (2017). Biomechanically influenced mobile and participatory pedestrian data for bridge monitoring. *International Journal of Distributed Sensor Networks*, 13(4), 155014771770524.
- Pettit, T.J., Fiksel, J. & Croxton, K.L. 2010. Ensuring supply chain resilience: development of a conceptual framework. *Journal of Business Logistics*, 31(1), 1–21. <https://doi.org/10.1002/j.2158-1592.2010.tb00125.x>
- Reed, D.A., Kapur, K.C. & Christie, R.D. 2009. Methodology for Assessing the Resilience of Networked Infrastructure. *IEEE Systems Journal*, 3(2), 174–180.
- Roohi, M., van de Lindt, J.W., Rosenheim, N., Hu, Y. & Cutler, H. 2021. Implication of building inventory accuracy on physical and socio-economic resilience metrics for informed decision-making in natural hazards. *Structure and Infrastructure Engineering*, 17(4), 534–554.
- Rose, A. 2007. Economic resilience to natural and man-made disasters: Multidisciplinary origins and contextual dimensions. *Environmental Hazards*, 7(4), 383–398.

The life-cycle of a community for physical-social interdependent resilience impacted by policy decisions following tornado hazards

W. Wang & J.W. van de Lindt

Department of Civil and Environmental Engineering, Colorado State University, Fort Collins, CO, USA

S. Hamideh

School of Marine and Atmospheric Sciences, Stony Brook University, Stony Brook, NY, USA

E. Sutley

Department of Civil, Environmental and Architectural Engineering, University of Kansas, Lawrence, KS, USA

ABSTRACT: Life-cycle concepts are used broadly in decision-making, such as the structural performance of buildings and lifeline systems and their management. However, life-cycle concepts are not yet explicitly incorporated into the community recovery modeling process, and nor do they typically consider socio-economics beyond a typical benefit-cost style analysis. This study incorporates life cycle concepts into community resilience analysis for physical-social interdependent networks following tornado hazards. More specifically, this study examines the preparedness, response, and recovery of buildings and households and explores the impacts of policy decisions on the life cycle phases across temporal and spatial domains using a fully interacting community resilience model. In order to achieve this goal, the methodology integrates a series of existing community resilience models across engineering and social science disciplines. This work can further expand and provide community decision-making support for physical-social interdependent networks impacted by more policy decisions and generic natural hazards.

1 INTRODUCTION

Life Cycle Assessment (LCA) has been traditionally considered a systematic procedure for compiling and examining the use of materials and energy and the associated environmental impacts resulting from the operation of a product or service system throughout its life cycle stages. The life cycle stages of a product or service system can last from the material extraction to the final disposal (ISO 14040). Over the last decade, life-cycle concepts have been broadly incorporated into structural engineering from various perspectives for decision-making and structure asset management. For example, Life Cycle Engineering (LCE) within civil engineering can assess a structure's long-term condition, safety, and serviceability, considering the effects of loading and environment as well as maintenance in conjunction with their economic impacts. The scope of the assessment is usually the whole life cycle of a structural system consisting of design, construction, use phase, and end of life (Dong 2016). In addition, life cycle concepts can help describe the entire process for an experimental study which included the construction, testing of buildings with retrofits (e.g., steel special moment frame, wood structural panels, viscous damping), collapse testing, and recycling and disposal (e.g. Bahmani et al. 2016).

However, life-cycle concepts are not yet explicitly incorporated into the community-level resilience modeling process, and nor do they typically consider socio-economics beyond a typical benefit-cost style analysis. In order to model a community as a life cycle problem, analysts and researchers should include true *interdisciplinarity* in community-level models and

can include *temporal* aspects of community recovery (van de Lindt 2021). From this perspective, this study incorporates life cycle concepts into community resilience analysis for physical-social interdependent networks following tornado hazards. More specifically, this study proposes a physical-social interdependent resilience methodology and examines the preparedness, response, and recovery of buildings and people and explores the impacts of policy decisions (e.g., mitigation retrofitting) on the life cycle phases across temporal and spatial domains using a fully interacting community resilience model.

2 PHYSICAL-SOCIAL INTERDEPENDENT RESILIENCE METHODOLOGY

Figure 1 shows the physical-social interdependent resilience methodology impacted by tornado hazards applied in this study. The methodology integrates a series of existing community resilience models across engineering and social science disciplines, including a household allocation model (Rosenheim et al. 2021), building damage model (Memari et al. 2018, Masoomi and van de Lindt 2016, Masoomi et al. 2018, Koliou et al. 2017), population dislocation model (Peacock et al. 2012, Rosenheim et al. 2021), residential building recovery model (Wang and van de Lindt 2021), and household housing recovery model (Sutley and Hamideh 2020).

The prerequisite step for the following physical-social resilience assessment is to assign building archetypes and their corresponding fragility functions to each building over the community and allocate housing unit information to a household level based on census-block socio-demographic data. The entire process starts with the building damage prediction. Subsequently, households may need to stay in emergency shelters/housing for approximately two weeks or more, temporarily moving out of their towns and dislocating. Over time following an event, residential buildings are repaired, new buildings are constructed, and ultimately households relocate to their permanent housing. Within each chained model mentioned earlier, Monte Carlo simulation (MCS) is widely applied to ensure uncertainty propagation.

This study uses a wind-induced residential building retrofit strategy as a typical policy decision to improve community resilience and examine how the policy decision impacts the preparedness, response, and recovery of buildings and people over the community, reflected in the physical-social interdependent resilience metrics. The typical resilience metrics for the physical-social interdependent networks following tornado hazards in this study include the number of non-functional buildings, the number of dislocated households, time needed for damaged residential buildings to be fully repaired, and the time needed for dislocated households to relocate to permanent housing.

3 ILLUSTRATIVE EXAMPLE USING JOPLIN MISSOURI TESTBED

Joplin is a typical small to medium size community and is located in Southwest Missouri in the United States. On May 22nd, 2011, an Enhanced Fujita 5 (EF5) tornado hit the city of Joplin, resulting in 161 fatalities and 1,150 injuries. The 2011 Joplin tornado is the costliest single tornado event in United States history, associated with a \$2.8 billion loss. Since then, the city of Joplin was increasingly selected by researchers as a testbed to perform multi-disciplinary community resilience assessments impacted by tornado hazards (e.g., Prevatt et al. 2012, Houston et al. 2017, Wang et al. 2021, Wang et al. 2022, Wang and van de Lindt 2022). In this illustrative example, a series of EF3 idealized tornado scenarios (Standohar-Alfano and van de Lindt 2015) created based on the historical events from 1973 to 2011 was developed as a stressor to strike the Joplin testbed at different locations. Figure 2 shows the overlay of the Joplin built environment and 30 horizontal EF3 idealized tornado scenarios, whose impacts will be averaged in this study.

Table 1 presents the original and retrofit designs for residential buildings applied to the community resilience assessment in this study. This illustrative example assumes the residential buildings were originally designed with the combination of wood shingles, wood sheathing panels nailed on center in 304.8 mm (12 inches) and at the edge in 152.4 mm (6 inches), and

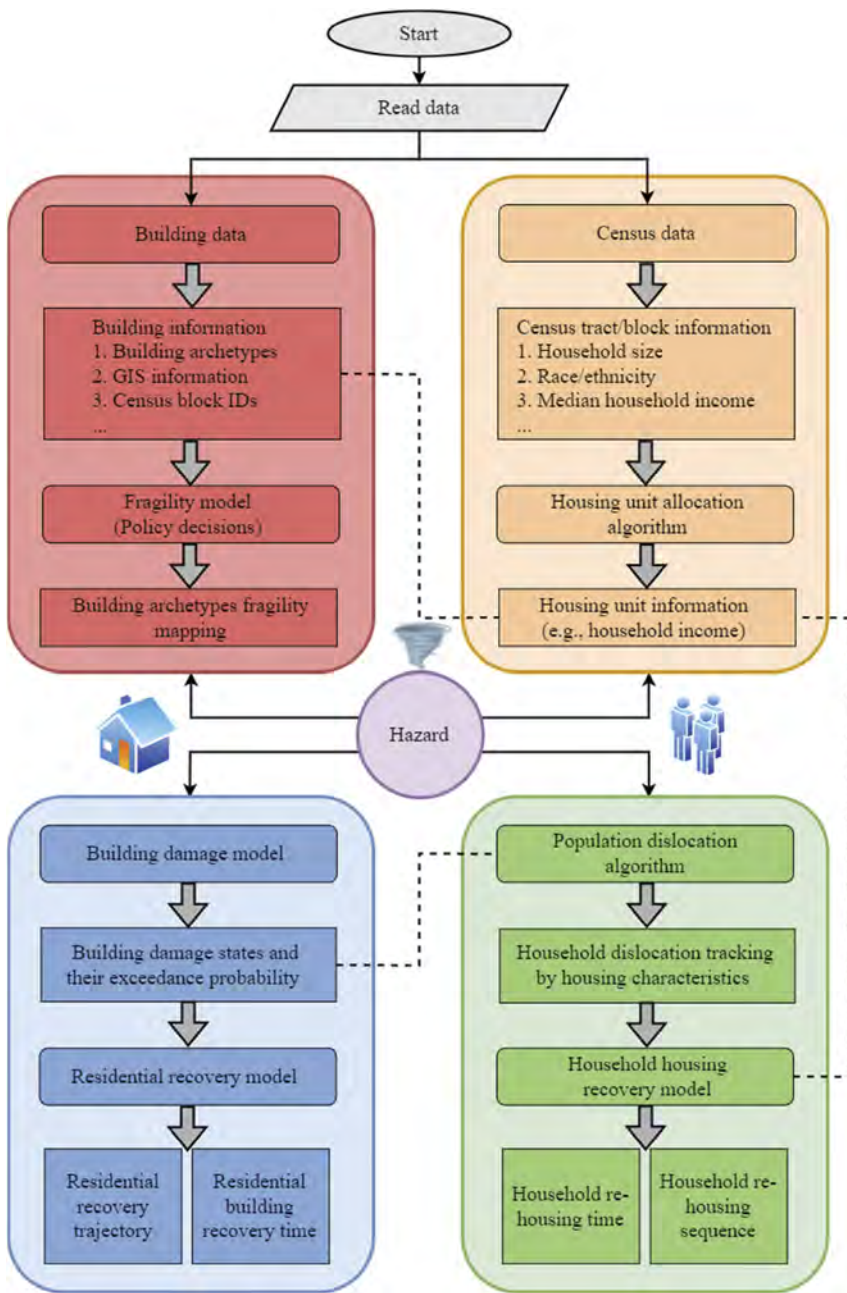


Figure 1. Physical-social interdependent resilience methodology flowchart.

two toenails for roof-to-wall connections. The retrofit designs for the residential buildings have improved asphalt shingles, wood sheathing panels nailed at all the locations in 152.4 mm (6 inches), and two hurricane clips for roof-to-wall connections. Please refer to the detailed fragility functions in different damage states in Wang et al. (2022) for original designs and retrofit designs of residential buildings. In general, this illustrative example assumes the buildings are non-functional when they are predicted with the probability of being in or exceeding moderate damage greater than 0.5 over the MCS realizations.

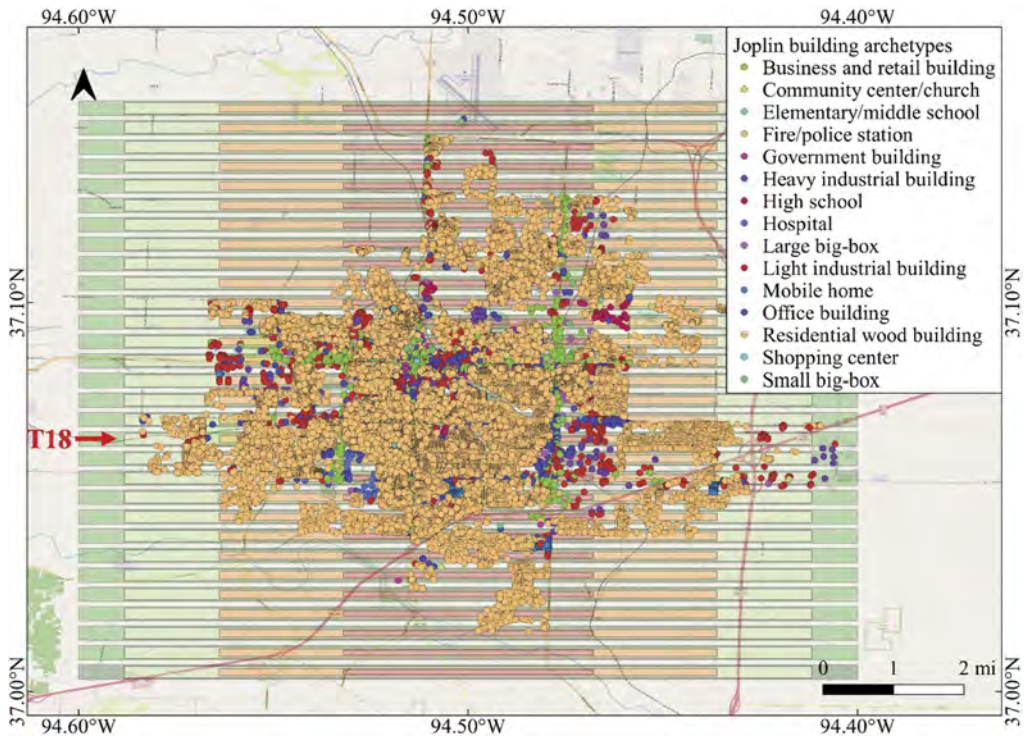


Figure 2. Joplin built environment and idealized tornado scenarios.

Table 1. Original designs and retrofit designs for residential buildings.

Structural elements	Selections	Original design	Retrofit design
Roof covering	Wood shingles	X	-
	Asphalt shingles	-	X
Roof sheathing nailing pattern	8d C6/12	X	-
	8d C6/6	-	X
Roof-to-wall connection type	Two 16d toenails	X	-
	Two H2.5 clips	-	X

If incorporating life-cycle concepts into the community resilience modeling, it is essential to use an interdisciplinary resilience assessment approach to model the community's life cycle phases, such as preparedness, response, and recovery, as mentioned earlier. In this illustrative example, the metrics of building damage and household dislocation, which are intended to represent maintaining of the physical service stability and population stability following tornado hazards, are used to describe the physical-social disruption response, as shown in Table 2. With the improvement of residential building performance, presumably increasing numbers of households would be able to stay at home and not dislocate; therefore, the physical-social network in the community is always interdependent. Table 2 presents the total number of buildings and households located within the tornado paths and the number of non-functional buildings and dislocated households with/without the improvement of retrofit designs impacted by a typical EF3 tornado scenarios and the average of all the simulated EF3 tornado scenarios. T18 is the tornado scenario striking the most buildings and households in the simulations. On average, when applying the retrofit designs to all the residential buildings within the tornado path, the percentage of non-functional buildings can be reduced from 84.8% to 57.4%, and the percentage of dislocated households can be reduced from 70.4% to 50.7%. The dislocated

households can be tracked by different household characteristics, such as tenure status, race/ethnicity, and household income, which are not elaborated herein for brevity.

Table 2. Building damage and household dislocation improved by retrofit designs of a typical MCS.

Tornado scenarios	Total number of buildings	Total number of households	Un-retrofitted		Retrofitted	
			Non-functional buildings	Dislocated households	Non-functional buildings	Dislocated households
T18	1,653 (100%)	2,027 (100%)	1,438 (87.0%)	1,404 (69.3%)	993 (60.1%)	988 (48.7%)
Mean	408 (100%)	570 (100%)	346 (84.8%)	401 (70.4%)	234 (57.4%)	289 (50.7%)
SD	473	659	404	463	275	330

Residential building recovery is essential for dislocated households to consider the relocation back to their pre-disaster community during the physical-social interdependent recovery process. The residential building recovery approach predicts the time required for residential buildings damaged in any damage state to fully recovered in this illustrative example (Wang and van de Lindt 2021). Figure 3 shows histograms of the recovery time of a typical residential building falling in the EF2 region of the T18 tornado scenario, where the recovery time of all residential buildings within a typical MCS realization fits a lognormal distribution. The average time for this residential building recovery before and after retrofits is 90.9 weeks and 54.9 weeks, respectively; meaning the recovery time can be shortened by 40%. Table 3 provides the percentage of residential buildings fully recovered in each time step within different (i.e., short-term, intermediate, long-term) recovery stages. The residential building recovery model applied in this illustrative example is a damage-driven recovery model considering the household capability to assess financial resources such as insurance, loans, and personal savings. The percentages of residential buildings fully recovered falling within the simulated tornado scenarios on average and those within the T18 tornado scenario have a slight difference due to different household characteristics at different census blocks. Without building retrofits, the percentages of residential buildings fully recovered in six months, one year, and two years are 9.2%, 23.1%, and 79.3%, on average for the 30 tornado scenarios. The percentages can be increased to 25.2%, 63.8%, and 93.1% for the same tornadoes when residential buildings were modeled as retrofitted.

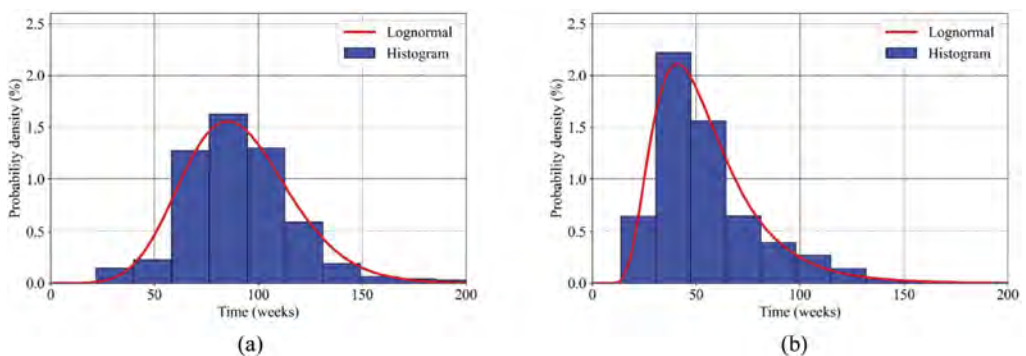


Figure 3. Histogram of a typical residential building recovery time in the EF2 region of the T18 tornado scenario: (a) without building retrofits; (2) with building retrofits.

The household housing recovery prediction in this illustrative example describes a complex long-term process for re-sheltering households after being disrupted by tornado hazards and consists of four stages: emergency shelter, temporary shelter, temporary housing, and permanent

housing (Bolin and Stanford 1998, Badeaux 2018). Sutley and Hamideh (2020) comprehensively detailed the four stages above to model household housing recovery as stages 1 to 4 and proposed a re-housing failure as a fifth possible stage. This illustrative example herein modified this model slightly and implemented it to predict the household housing recovery process. Figure 4 shows the household housing recovery sequence of a typical household residing in a residential building with and without retrofits where the residential building falls within the T18 tornado scenario. It is important to note that the household housing recovery model used herein is directly related to household social-vulnerability characteristics rather than residential building designs. However, improving residential building design can significantly reduce the severity of building damage and resulting household dislocation. Only dislocated households are predicted to have a household re-housing sequence, and non-dislocated households are assumed to stay in permanent housing. In reality, improving residential building design can also reduce the sequence’s duration and increase the number of households re-locate back to the community.

Table 3. The percentage of residential buildings fully recovered improved by retrofit designs (mean values).

Tornado scenarios	Residential buildings	Design hazard performance								
		Phase 1: Short-term			Phase 2: Intermediate			Phase 3: Long-term		
		Days			Weeks			Months		
		0	1-3	3-7	1-6	6-12	12-24	6-12	12-24	24+
T18 (an example)	Un-retrofitted	0%	0%	0%	0%	1.0%	7.7%	20.2%	78.1%	100%
	Retrofitted	0%	0%	0%	0%	2.8%	22.3%	61.0%	92.5%	100%
Average of all tornado scenarios	Un-retrofitted	0%	0%	0%	0%	1.3%	9.2%	23.1%	79.3%	100%
	Retrofitted	0%	0%	0%	0%	3.6%	25.2%	63.8%	93.1%	100%

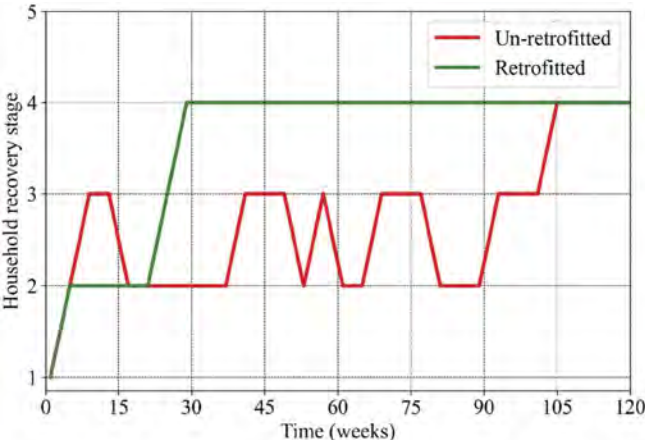


Figure 4. Household housing recovery sequence of a typical household residing in a residential building with/without retrofits.

Household housing recovery time is defined as whenever the household moves to permanent housing (Stage 4). Figure 5 illustrates the histograms of household housing recovery time of all households not experiencing household re-housing failure but residing in the residential buildings located in the T18 tornado scenario within a single MCS realization. Overall, the average recovery time for households moving back to permanent housing is reduced from 22.6 weeks to 19.8 weeks for all the tornado scenarios when applying mitigation retrofits to

their residential buildings. Note that the residential building recovery model is a physical model driven by building damage, and the household housing recovery model is a process-based model controlled by the household's social vulnerability. The integration and comparison between these two models need further investigation. However, it is clear from this initial analysis and comparison of these two models that households are likely to be ready for permanent housing before their previous residential building is fully repaired. This underscores the complexities of combining process-based and data-driven models in community resilience modeling, but it is noted here that it is still needed.

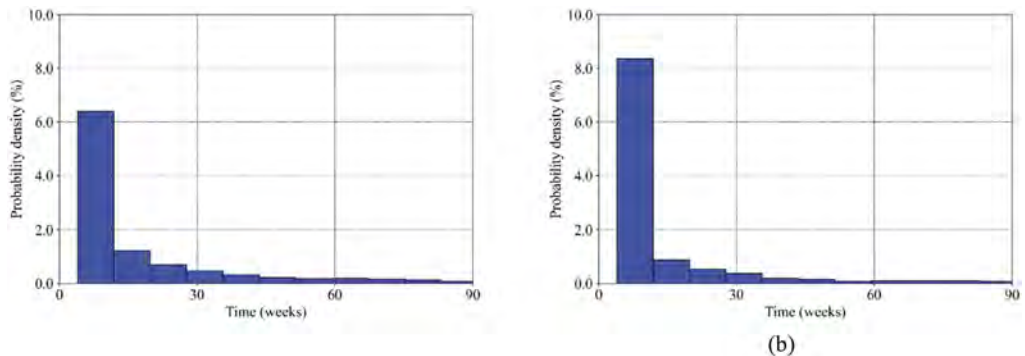


Figure 5. Histogram of household housing recovery time of most households residing in the residential buildings located in the T18 tornado scenario: (a) without building retrofits; (2) with building retrofits.

4 CONCLUSIONS

This study incorporates life cycle concepts into community resilience analysis, uses wind-induced residential building retrofit strategy as a typical policy decision to improve community resilience, and examines how the policy decision impacts the preparedness, response, and recovery of buildings and households within a community, reflected in the physical-social interdependent resilience metrics. On average, when applying residential building mitigation retrofitting subjected to EF3 tornado events, the percentage of non-functional buildings can be reduced from 85% to 57%, and dislocated households can be reduced from 70.4% to 50.7%. Considering the life cycle phases of physical-social interdependent networks on a temporal scale, the average residential building recovery time can be shortened by 40%. The household housing recovery model shows the average recovery time for households moving back to permanent housing is reduced from 22.6 weeks to 19.8 weeks with retrofitting of residential building, a less impactful result. The integration and comparison between residential building recovery and household housing recovery needs further exploration and, in particular, synthesizing the assumptions embedded in each model type. This work can further expand and provide community decision-making support for physical-social interdependent networks impacted by more policy decisions such as recovery financing and generic natural hazards such as earthquakes and floods.

ACKNOWLEDGEMENTS

The Center for Risk-Based Community Resilience Planning is a NIST-funded Center of Excellence; the Center is funded through a cooperative agreement between the U.S. National Institute of Standards and Technology and Colorado State University (NIST Financial Assistance Award Numbers: 70NANB15H044 and 70NANB20H008). The views expressed are those of the presenter and may not represent the official position of the National Institute of Standards and Technology or the U.S. Department of Commerce. The first author also acknowledges support granted by the 2021 ASCE O.H. Ammann Research Fellowship in Structural Engineering.

REFERENCES

- Arvanitoyannis, I.S., 2008. ISO 14040: life cycle assessment (LCA)–principles and guidelines. *Waste management for the food industries*, 97–132.
- Badeaux, L.L., 2018. *Measuring Sustainability and Resilience Qualities across Post-Disaster Temporary Housing* (Doctoral dissertation, University of Kansas).
- Bahmani, P., van de Lindt, J.W., Gershfeld, M., Mochizuki, G.L., Pryor, S.E. and Rammer, D., 2016. Experimental seismic behavior of a full-scale four-story soft-story wood-frame building with retrofits I: building design, retrofit methodology, and numerical validation. *Journal of Structural Engineering*, 142 (4): 1–14.
- Bolin, R. and Stanford, L., 1998. The Northridge earthquake: community-based approaches to unmet recovery needs. *Disasters*, 22(1), 21–38.
- Dong, Y., 2016. *Risk, Resilience, and Sustainability-Informed Assessment and Management of Aging Structural Systems*. Lehigh University.
- Koliou, M., Masoomi, H. and van de Lindt, J.W., 2017. Performance assessment of tilt-up big-box buildings subjected to extreme hazards: Tornadoes and earthquakes. *Journal of Performance of Constructed Facilities*, 31(5), 04017060.
- Houston, J.B., Spialek, M.L., First, J., Stevens, J. and First, N.L., 2017. Individual perceptions of community resilience following the 2011 Joplin tornado. *Journal of Contingencies and Crisis Management*, 25(4), 354–363.
- Masoomi, H., Ameri, M.R. and van de Lindt, J.W., 2018. Wind performance enhancement strategies for residential wood-frame buildings. *Journal of Performance of Constructed Facilities*, 32(3), 04018024.
- Masoomi, H. and van de Lindt, J.W., 2016. Tornado fragility and risk assessment of an archetype masonry school building. *Engineering Structures*, 128, 26–43.
- Memari, M., Attary, N., Masoomi, H., Mahmoud, H., van de Lindt, J.W., Pilkington, S.F. and Ameri, M.R., 2018. Minimal building fragility portfolio for damage assessment of communities subjected to tornadoes. *Journal of Structural Engineering*, 144(7), 04018072.
- Peacock, W.G., Gladwin, H. and Morrow, B.H., 2012. *Hurricane Andrew: Ethnicity, gender and the sociology of disasters*. Routledge.
- Rosenheim, N., Guidotti, R., Gardoni, P. and Peacock, W.G., 2021. Integration of detailed household and housing unit characteristic data with critical infrastructure for post-hazard resilience modeling. *Sustainable and Resilient Infrastructure*, 6(6), 385–401.
- Prevatt, D.O., Coulbourne, W., Graettinger, A.J., Pei, S., Gupta, R. and Grau, D., 2012, October. Joplin, Missouri, tornado of May 22, 2011: Structural damage survey and case for tornado-resilient building codes. American Society of Civil Engineers.
- Standohar-Alfano, C.D. and van de Lindt, J.W., 2015. Empirically based probabilistic tornado hazard analysis of the United States using 1973–2011 data. *Natural Hazards Review*, 16(1), 04014013.
- Sutley, E.J. and Hamideh, S., 2020. Postdisaster housing stages: a markov chain approach to model sequences and duration based on social vulnerability. *Risk Analysis*, 40(12), 2675–2695.
- van de Lindt, J.W., 2021. Understanding and modeling the resilience life cycle of communities: A multi-disciplinary endeavor. In *Life-Cycle Civil Engineering: Innovation, Theory and Practice* (58–66). CRC Press.
- Wang, W.L. and van de Lindt, J.W., 2021. Quantitative modeling of residential building disaster recovery and effects of pre-and post-event policies. *International Journal of Disaster Risk Reduction*, 59, 102259.
- Wang, W.L., van de Lindt, J.W., Hartman, B., Cutler, H., Kruse, J.L., McAllister, T.P. and Hamideh, S., 2022. Determination of individual building performance targets to achieve community-level social and economic resilience metrics. *Journal of Structural Engineering*, 148(5), 04022045.
- Wang, W., van de Lindt, J.W., Rosenheim, N., Cutler, H., Hartman, B., Sung Lee, J. and Calderon, D., 2021. Effect of residential building wind retrofits on social and economic community-level resilience metrics. *Journal of Infrastructure Systems*, 27(4), 04021034.
- Wang, W.L. and van de Lindt, J.W., 2022. Quantifying the effect of improved school and residential building codes for tornadoes in community resilience. *Resilient Cities and Structures*, 1(1), 65–79.

Impact of modeling uncertainty on seismic life-cycle cost analysis of RC building under mainshock-aftershock sequences

S.P. Rayjada, J. Ghosh & M. Raghunandan

Indian Institute of Technology Bombay, Mumbai, Maharashtra, India

ABSTRACT: Aftershocks can increase financial losses by causing further damage to buildings whose seismic capacity is already impaired in mainshock. To anticipate such losses, seismic life cycle cost analysis under mainshock-aftershock sequences is gaining interest from decision-makers in the past decade. Although, the state-of-the-art framework for aftershock loss assessment accounts for the uncertainty in state of the structure due to damage accumulation, time-dependent nature of seismic hazard and variability in the ground motion characteristics, one of the major uncertainties associated with variability in analytical building modeling parameters called “modeling” uncertainty is not accounted in the existing framework. Therefore, this study proposes a framework to assess the variability of expected seismic life cycle cost mainshock-aftershock sequences considering modeling uncertainty. Application of the framework is demonstrated using a case study example of four-story modern ductile reinforced concrete (RC) building and results reveal the criticality of considering the modeling uncertainty.

1 INTRODUCTION

Earthquake-induced losses place a significant financial burden on the stakeholders. Hence, modern construction practice must accurately evaluate such losses for efficient channeling of monetary resources. In this regard, seismic life cycle cost analysis (SLCCA) has proven to be a robust approach for decision-making that estimates the expected lifetime economic losses incurred due to seismic events in present-day value. SLCCA constitutes a probabilistic approach incorporating site-specific seismic hazard characteristics and vulnerability details of the structure of interest. Over the years, various methodologies have been developed and implemented for design optimization, retrofit prioritization and structural performance assessment, among others (Ellingwood & Wen 2005; Padgett et al. 2010; Wen & Kang 2001).

The traditional SLCCA framework deals with significant earthquake events with a long return period that provides sufficient time for the structure recovery. However, the major seismic event is often followed by a cluster of subsequent earthquakes within a short period, referred to as “aftershocks,” that pose additional risk to already damaged structures leading to a substantial additional financial burden to society. Hence, recent research efforts aim to account for the additional losses imparted due to aftershocks in the SLCCA framework (Shokrabadi & Burton 2018a; Yeo & Cornell 2009b). For instance, Yeo & Cornell (2009b) proposed the Markov process-based approach to estimate direct and indirect losses under mainshock-aftershock sequences. This approach is further extended by Shokrabadi & Burton (2018a) with reduced complexity and its application is demonstrated using a case study example. Furthermore, the study provided detailed insights into structural and non-structural losses in pre-mainshock and post-mainshock environments. Yin & Li (2011) and Song et al. (2016) utilized a sampling-based approach to estimate the lifetime loss under the mainshock-aftershock sequences for wood and steel building, respectively.

For the reliable implementation of these frameworks, it is essential to account for various sources of uncertainty during structural response assessment. Uncertainties may be considered to

stem from variability in ground motion characteristics termed “record-to-record” uncertainty (RTR) and uncertainty in analytical building modeling parameters called “modeling” uncertainty. Although studies in the past decade have highlighted the criticality of considering modeling uncertainty in seismic risk and life cycle assessment (Gokkaya et al. 2016; Liel et al. 2009; O’Reilly & Sullivan 2018), existing aftershock loss assessment frameworks do not incorporate the effect of modeling uncertainty. Therefore, this study proposes a framework to assess the impact of modeling uncertainty on seismic life cycle cost under mainshock-aftershock sequences.

At the onset, a brief overview of the SLCCA framework considering aftershocks is provided, followed by a framework to account for modeling uncertainty. In the proposed approach, the contribution of modeling uncertainty is derived from the mainshock analysis and aftershock fragility curves are adjusted accordingly. Thereafter, the application of the proposed framework is illustrated using a case study example of a four-story RC building. The paper ends with conclusions highlighting the key findings.

2 SEISMIC LIFE CYCLE COST CONSIDERING AFTERSHOCKS

The expected seismic life cycle cost during service life under a mainshock environment ($E[SLCC]_{MS}$) can be effectively calculated using analytical framework proposed by Ellingwood & Wen (2005) incorporating three essential components, namely site-specific hazard curve, seismic fragility and cost related to each damage state.

$$E[SLCC]_{MS} = \frac{1 - e^{-\alpha T}}{\alpha T} \sum_{i=1}^n [\ln(1 - P_{T,i}) - \ln(1 - P_{T,i+1})] C_{ds}^i \quad (1)$$

where, T is service life of the structure and α is an inflation-adjusted discount ratio. Consequently, n represents the total number of damage states while C_{ds}^i is the damage state-related cost. $P_{T,i}$ is T -year probability of exceeding damage state i that can be estimated as:

$$P_{T,i} = 1 - (1 - P_{Al,i})^T \quad (2)$$

In the above equation, $P_{Al,i}$ is an annual probability of exceeding each damage state determined by convolving site-specific hazard curve and seismic fragility.

$$P_{Al,i} = \int P_i[EDP > edp_i | IM] \left| \frac{dH(im)}{dim} \right| dim \quad (3)$$

where, $H(im)$ is seismic hazard curve representing an annual probability of exceeding the specified level of intensity measure $IM = im$. $P_i[EDP > edp_i | IM]$ is the probability of exceeding i^{th} damage state at a specified earthquake intensity $IM = im$ and can be obtained from a seismic fragility curve. EDP is an engineering demand parameter that characterizes the structural damage, and edp_i represents the threshold EDP for damage state i . The additional losses incurred due to aftershocks are calculated separately and added to the existing framework, as shown below.

$$E[SLCC]_{MSAS} = \frac{1 - e^{-\alpha T}}{\alpha T} \sum_{i=1}^n [\ln(1 - P_{T,i}) - \ln(1 - P_{T,i+1})] [C_{ds}^i + E[C_{AS}^i]] \quad (4)$$

where, $E[C_{AS}^i]$ represents the expected value of loss due to a series of aftershocks when the structure has already experienced damage state i under mainshock. This study utilizes the methodology proposed by Shokrabadi & Burton (2018a) to estimate $E[C_{AS}^i]$. It is important to note that the abovementioned SLCCA formulation under mainshock environment assumes that the structure will return to its pre-damaged state before next earthquake occurs. This assumption is valid for mainshock events as a time interval between successive major mainshock events is long enough to restore the building to its pre-mainshock state. However, a

series of aftershocks following a mainshock does not allow time to restore the building and the damage state of the building before each event is unknown. Hence, structural performance assessment under mainshock-aftershock sequences requires an explicit consideration of uncertainty in determining the state of the structure through Markov process-based formulation (Shokrabadi & Burton 2018a; Yeo & Cornell 2009b). Furthermore, it is computationally challenging to consider all possible events as multiple aftershock events likely follow the mainshock. To address this issue, Shokrabadi & Burton (2018a) proposed an efficient approach in which the time range of evaluation (time after mainshock during which aftershock is assumed to occur) is discretized into small unit-time intervals $[t_0, t_1]$ such that more than one earthquake cannot occur during the interval. For a given time interval, transition probability matrix representing uncertainty in the state of the structure can be estimated as:

$$\mathbf{P}(t_0, t_1) = \begin{bmatrix} P_{11}(t_0, t_1) & P_{12}(t_0, t_1) & \cdots & P_{1n}(t_0, t_1) \\ 0 & P_{22}(t_0, t_1) & \cdots & P_{2n}(t_0, t_1) \\ \vdots & \vdots & \ddots & \vdots \\ 0 & 0 & \cdots & 1 \end{bmatrix} \quad (5)$$

Here, $P_{ij}(t_0, t_1)$ terms represent the probability that the structure transitions to damage state j under the seismic event, given that it has already experienced damage state i under the previous event. $P_{ij}(t_0, t_1)$ can be calculated based on aftershock fragility curve as described below.

$$P_{ij}(t_0, t_1) = \mu(t_0, t_1) \int (P_{i,j}[EDP > edp_j | IM] - P_{i,j+1}[EDP > edp_{j+1} | IM]) f_{IM}(im) dim \quad (6)$$

where, $P_{i,j}[EDP > edp_j | IM]$ is the probability that a structure with an initial state i state exceeds the state j that can be obtained through aftershock fragility curves conditioned on initial state i . $f_{IM}(im)$ is the probability density function of intensity measure while $\mu(t_0, t_1)$ is aftershock occurrence rate for a given time interval. It is worthwhile to note that the rate of aftershock occurrence decay over time as the aftershocks are most likely immediately after mainshock and the temporal decay of aftershock rate is described by the nonhomogeneous Poisson process characterized by Omori's law (Yeo & Cornell 2009a). At time t_m after the mainshock (m time units), a transition probability matrix can be obtained as:

$$\mathbf{P}^m = \prod_{r=1}^m \mathbf{P}(t_{r-1}, t_r) \quad (7)$$

The aftershock loss at time t_m after mainshock is estimated using the transition probability matrix and structural damage loss matrix (\mathbf{E}_C) as shown in Equation (8). The elements of the damage loss matrix- E_{Cij} represent the difference of loss associated with two damage states i and j .

$$E[C_{AS}]^m = e^{-at_m} [\mathbf{P}^m \circ \mathbf{E}_C] \quad (8)$$

The aftershock losses corresponding to each damage state - $E[C_{AS}^i]$ (Equation (4)) are estimated by taking the sum of each row of $E[C_{AS}]^m$ matrix.

3 FRAMEWORK TO INCORPORATE MODELING UNCERTAINTY

While the previous section provides a brief introduction to SLCCA methodology considering aftershocks, this section aims to propose the framework to incorporate the effect of modeling uncertainty. Fundamentally, this study assesses the contribution of modeling uncertainty from mainshock analysis using a Monte Carlo simulation-based approach and aftershock fragility curves are adjusted accordingly. At the onset, the building is designed as per modern seismic design codes followed by numerical modeling in a finite element platform. The modeling uncertainty corresponds to the randomness associated with predicting finite element model

parameters. For example, if a building is modeled using lumped plasticity model by providing an inelastic spring at the ends of beam-column members as shown in Figure 1, uncertainty associated with predicting inelastic spring properties represents modeling uncertainty. As depicted in Figure 1, modeling uncertainty is captured by generating a sufficiently large number (N_{MC}) of nominally identical but statistically different building models. On the other hand, RTR uncertainty is incorporated by selecting a set of ground motions with varying attributes.

Incremental dynamic analysis (IDA) is performed by randomly pairing ground motion and building samples, followed by estimation of the median (med) and dispersion (β) of the fragility curve (Vamvatsikos & Cornell 2002). The fragility dispersion obtained for this case corresponds to the total uncertainty ($\beta = \beta_{TOT}$) that captures both the record-to-record variability and the modeling uncertainty. Thereafter, a building model developed with the mean estimate of model parameters termed as *Mean Model*, is subjected to a suite of ground motions for incremental dynamic analysis. In this case, corresponding fragility curve parameters represent only record-to-record uncertainty ($\beta = \beta_{RTR}$). As commonly adopted in literature, the modeling uncertainty contribution to the dispersion ($\beta = \beta_{MOD}$) can be conveniently extracted from the total uncertainty using square root of sum of squares (SRSS) technique for all damage states.

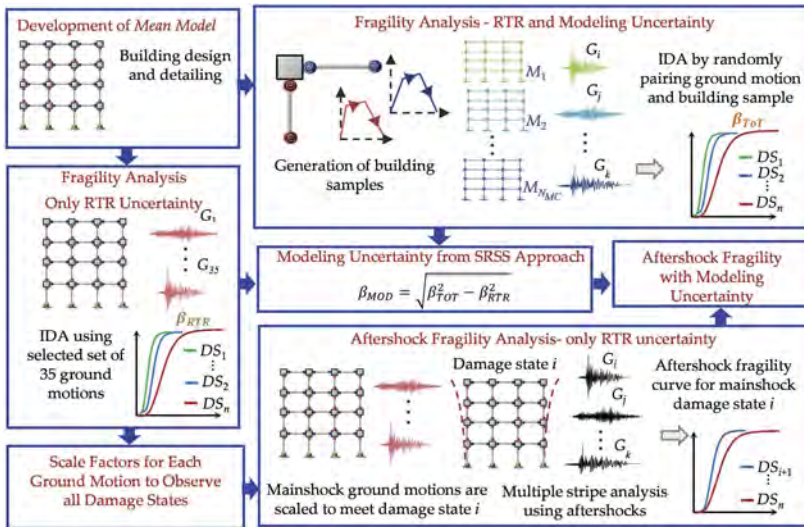


Figure 1. Framework to develop aftershock fragility curves considering modeling uncertainty.

For aftershock fragility assessment, *Mean Model* is first subjected to mainshocks scaled to a level that pushes the structure to a desired damage state i followed by multiple stripe analysis using aftershock ground motions as per the recommendation of Shokrabadi & Burton (2018b). This exercise is repeated for all mainshock damage states and corresponding aftershock fragility curves are obtained. The contribution of modeling uncertainty estimated earlier from mainshock analysis is added to the aftershock fragility curve parameters using SRSS approach.

4 CASE STUDY EXAMPLE

A four-story, three-bay commercial building in Los Angeles, USA is selected as a case study building to assess the impact of modeling uncertainty. The building is designed as a special moment resisting frame (SMRF) to withstand gravity and earthquake loads in accordance with modern seismic design standards in the USA (Raghunandan et al. 2015). The nonlinear finite element model of the building is developed as a 2-D moment resisting frame in the finite element platform OpenSEES (McKenna et al. 2012). The beams and columns are modeled as

lumped plasticity beam-column elements wherein the inelastic flexural springs are provided at the ends of elastic elements. These springs have nonlinear hysteretic properties that can capture complex structural behavior and the hysteresis model proposed by Ibarra et al. (2005) is used to characterize spring's cyclic behavior. The hysteresis model parameters include a monotonic backbone curve and a cyclic degradation parameter as depicted in Figure 2 determined based on Gaussian process regression (GPR) models recently proposed by Rayjada et al. (2023). These models are fitted to the experimental column test results with varying design and details and one potential advantage of GPR models lies in the pointwise estimates of prediction uncertainty based on the location of a data point within the sample space that leads to a more comprehensive estimation of modeling uncertainty (Rayjada et al. 2023).

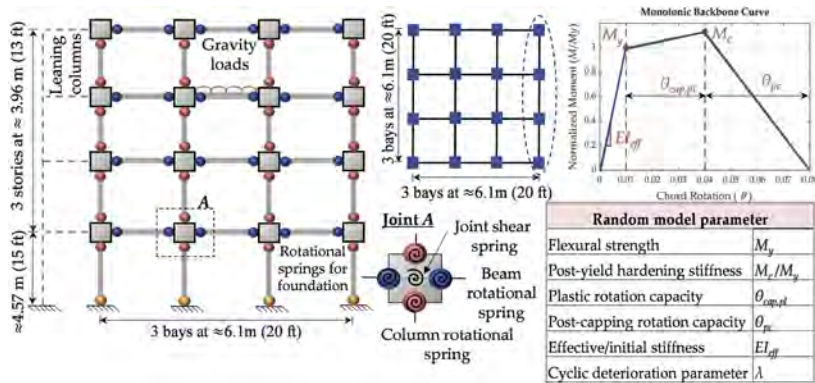


Figure 2. Graphical representation of analytical building model and random model parameters.

For the hysteresis model adopted here, six parameters, as depicted in Figure 2 are assumed to be random. A total of 3500 samples (N_{MC} in Figure 1) are generated to reflect modeling uncertainty based on GPR model. In this process, the correlation between parameters of the same element (beam or column) is considered as per Rayjada et al. (2023) while full correlation is assumed between parameters of beams (beam-to-beam) and columns (column-to-column). Furthermore, zero correlation is considered between beams and columns (beam-to-column).

4.1 Seismic fragility assessment

For developing fragility curves under mainshock environment, this study utilizes a set of 35 far-field crustal ground motions from FEMA P-695 (FEMA 2009) for IDA. To characterize ground motion intensity, elastic spectral acceleration for the fundamental time period of *Mean Model* - 0.75s ($Sa[T = 0.75 \text{ s}]$) at 5% damping is selected as *IM*. At the same time, maximum interstory drift ratio (ISD_{max}) is used as the *EDP* to describe the structural response. The damage states for fragility assessment are defined as per previous studies (Padgett & Li 2016) and presented in Table 1. As per the methodology proposed in Figure 1, IDA is performed for *Mean Model* and building samples to estimate fragility curve parameters as reported in Table 1. Furthermore, the contribution of modeling uncertainty to total uncertainty is calculated using SRSS approach and the reduction in median fragility is also estimated.

Aftershock fragility curves are developed for all mainshock damage levels as depicted in Figure 3 using multiple stripe analysis of the *Mean Model* (Shokrabadi & Burton 2018b). Here, the selected set of 35 ground motions is used as aftershocks for simplicity and structural performance assessment using recorded mainshock-aftershock sequences will be taken up in the future. Aftershock fragility curves are adjusted to account for modeling uncertainty by reducing the median as per Table 1 and increasing dispersion with β_{MOD} using SRSS approach. Aftershock fragility curves considering modeling uncertainty are presented in Figure 3 with dashed lines.

Table 1. Seismic fragility results.

Damage State	Description	Threshold ISD_{max}	Fragility Parameters RTR		Fragility Parameters TOT		Median Reduction	β_{MOD}
			med	β	med	β		
Slight	Light damage to structural components and finishes	1%	0.68	0.23	0.64	0.26	5%	0.12
Moderate	Moderate strength deterioration and unreparable damage	2%	1.31	0.33	1.23	0.33	6%	0.00
Extensive	Severe structural damage up to the point of incipient collapse	4%	2.14	0.39	1.95	0.40	9%	0.11
Complete	Collapse is imminent for a major portion	7.5%	3.01	0.45	2.60	0.48	14%	0.17

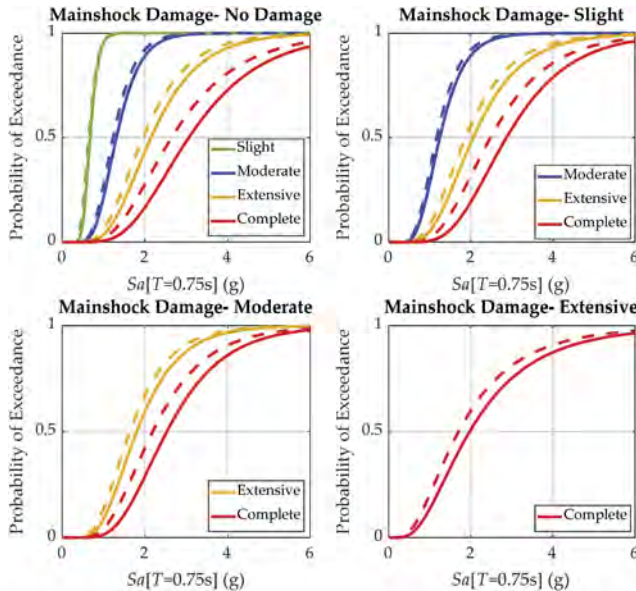


Figure 3. Aftershock fragility curves for all mainshock damage states. Fragility curves considering modeling uncertainty are presented with dashed lines.

4.2 Seismic hazard assessment and estimation of damage state transition probability

The seismic hazard curve for Los Angeles is obtained from Unified Hazard Tool developed by the United States Geological Survey (USGS 2014) for mainshock environment. To estimate the aftershock seismic hazard at a site, this study adopts the aftershock probabilistic seismic hazard analysis results by Yeo & Cornell (2009a). As per their simplified approach, aftershock seismic hazard curve is assumed to be 50 times the given mainshock hazard curve. Furthermore, Omori's law parameters proposed in previous literature for the California region are used to estimate the mean number of aftershocks $\mu(t_0, t_1)$ as mentioned in Equation (6) (Reasenbergs & Jones. 1989; Yeo & Cornell 2009a). It is assumed that the aftershocks can occur 30 days after a mainshock, and transition probability is evaluated (Equation (7)) with an increment of 0.01 days. The transition probability matrix at the end of 30 days is presented in Table 2. It is observed that the transition probability increases substantially by incorporating modeling uncertainty highlighting its criticality in SLCCA.

4.3 Damage state-related cost

Cost related to each damage state (C_{ds}^i in Equation (1)) typically includes various direct and indirect losses. However, only direct cost due to damage/repair is considered for simplicity in this study. Damage/repair costs corresponding to each damage state are represented as the percentage of replacement value, also referred to as the damage index. The damage index for slight, moderate, extensive, and complete damage states is assumed to be 5%, 20%, 40% and 100%, respectively as recommended by Ellingwood & Wen (2005). It is worthwhile to note that Ellingwood & Wen (2005) considered a 90% damage index for the complete damage state. However, the owner prefers to replace the building if damage/repair cost exceeds 60% of the replacement value (FEMA 2018). Therefore, 100% damage index is adopted for the complete damage. Replacement cost per sq. ft. (\$ 203) is obtained by converting FEMA-227 (FEMA 1992) estimates to present-day value. The damage loss matrix (\mathbf{E}_C in Equation (8)) is estimated for after-shock SLCCA based on the difference of cost associated with damage states.

Table 2. Damage state transition probability matrix at the end of 30 days.

	Without Modeling Uncertainty					With Modeling Uncertainty				
	Intact	Slight	Mod.	Ext.	Comp.	Intact	Slight	Mod.	Ext.	Comp.
Intact	0.8605	0.0931	0.0283	0.0101	0.0081	0.8459	0.1015	0.0296	0.0105	0.0125
Slight	0	0.9457	0.0337	0.0119	0.0087	0	0.9395	0.0344	0.0123	0.0138
Mod.*	0	0	0.9729	0.0148	0.0123	0	0	0.9662	0.0152	0.0186
Ext.*	0	0	0	0.9676	0.0324	0	0	0	0.9549	0.0451
Comp.*	0	0	0	0	1	0	0	0	0	1

* Mod. – Moderate, Ext.-Extensive, Comp. – Complete

4.4 Expected seismic life cycle cost

The expected seismic life cycle cost is estimated by incorporating modeling uncertainty for 50-year service life and 4% discount ratio according to the formulation illustrated earlier. The results for the mainshock environment and mainshock-aftershock sequences are depicted in Figure 4 (a). Overall, the expected seismic life cycle cost ($E[SLCC]$) has increased by 44% considering the effect of modeling uncertainty and mainshock-aftershock sequences revealing a severe underestimation of expected losses in the mainshock environment. Additionally, a 25% and 27% hike is observed after incorporating modeling uncertainty for mainshock environment and mainshock-aftershock sequences, respectively. Figure 4 (b) shows the effect of modeling uncertainty on aftershock losses related to each damage state - $E[C_{AS}^i]$ normalized with respect to replacement cost. Due to modeling uncertainty, an increase from 7.2% to 9.5% is observed in total aftershock losses. Furthermore, losses corresponding to intact and slight damage states are increased by 24% and 29%, respectively, while a 40% rise is observed for moderate and extensive damage states.

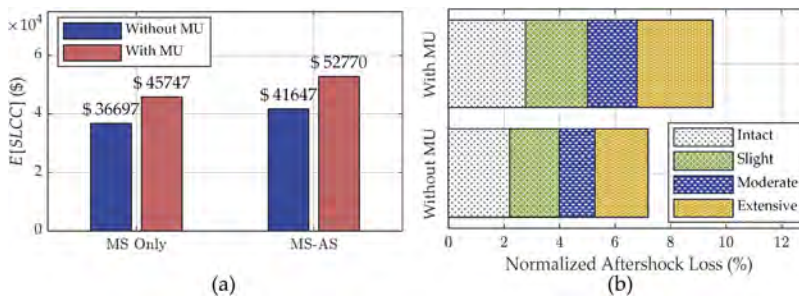


Figure 4. (a) Effect of modeling uncertainty (MU) on $E[SLCC]$ under mainshock environment (MS) and mainshock-aftershock (MS-AS) sequences (b) Aftershock losses related to each damage state $E[C_{AS}^i]$.

5 CONCLUSIONS

This study proposes a framework to incorporate the effect of modeling uncertainty for seismic life cycle cost assessment under mainshock-aftershock sequences and augments the existing literature that only accounts for naturally occurring ground motion variability. The framework includes a two-fold approach in which modeling uncertainty in beam-column parameters is characterized first using a novel Gaussian Process Regression approach. Subsequently, its impact on mainshock fragility curves is assessed by performing the incremental dynamic analysis of a large number of building samples. Based on the results, the aftershock fragility curves are adjusted to account for modeling uncertainty. The application of the framework is demonstrated using a case study example of a four-story commercial RC building. It is observed that the total aftershock losses increased by 32% and the expected seismic life cycle cost increased by 27 % after incorporating modeling uncertainty. As the characterization of detrimental effects of aftershocks is getting increasing attention from policymakers and stakeholders, this study recommends the adequate quantification and propagation of modeling uncertainty for reliable estimation of the expected seismic life cycle cost.

REFERENCES

- Ellingwood B.R., & Wen Y.K. 2005. Risk-benefit-based design decisions for low-probability/high consequence earthquake events in Mid-America. *Progress in Structural Engineering and Materials* 7 (2): 56–70.
- FEMA. 1992. A benefit-cost model for the seismic rehabilitation of buildings FEMA 227. Washington, DC.
- FEMA. 2009. Quantification of building seismic performance factors FEMA P 695. Redwood City, CA.
- FEMA. 2018. Seismic Performance Assessment of Buildings - Methodology, FEMA P58-1. Applied Technology Council (ATC), Redwood City, CA.
- Gokkaya B.U., Baker J.W., & Deierlein G.G. 2016. Quantifying the impacts of modeling uncertainties on the seismic drift demands and collapse risk of buildings with implications on seismic design checks. *Earthquake Engineering and Structural Dynamics* 45: 1661–1683.
- Ibarra L.F., Medina R.A., & Krawinkler H. 2005. Hysteretic models that incorporate strength and stiffness deterioration. *Earthquake Engineering and Structural Dynamics* 34 (12): 1489–1511.
- Liel A.B., Haselton C.B., Deierlein G.G., & Baker J.W. 2009. Incorporating modeling uncertainties in the assessment of seismic collapse risk of buildings. *Structural Safety* 31 (2): 197–211.
- McKenna F., Fenves G.L., & Scott M.H. 2012. Open system for earthquake engineering simulation (OpenSEES)
- O'Reilly G.J., & Sullivan T.J. 2018. Quantification of modelling uncertainty in existing Italian RC frames. *Earthquake Engineering and Structural Dynamics* 47 (4): 1054–1074.
- Padgett J.E., Dennemann K., & Ghosh J. 2010. Risk-based seismic life-cycle cost-benefit (LCC-B) analysis for bridge retrofit assessment. *Structural Safety* 32 (3): 165–173.
- Padgett J.E., & Li Y. 2016. Risk-Based Assessment of Sustainability and Hazard Resistance of Structural Design. *Journal of Performance of Constructed Facilities* 30 (2): 04014208.
- Raghunandan M., Liel A.B., & Luco N. 2015. Aftershock collapse vulnerability assessment of reinforced concrete frame structures. *Earthquake Engineering and Structural Dynamics* 44: 419–439.
- Rayjada S.P., Ghosh J., & Raghunandan M. 2023. Machine learning-based RC beam-column model parameter estimation and uncertainty quantification for seismic fragility assessment. *Engineering Structures* 278.
- Reasenber P., & Jones. L. 1989. Earthquake hazard after a mainshock in California. *Science* 243 (4895)
- Shokrabadi M., & Burton H. V. 2018a. Building service life economic loss assessment under sequential seismic events. *Earthquake Engineering and Structural Dynamics* 47 (9): 1864–1881.
- Shokrabadi M., & Burton H. V. 2018b. Risk-based assessment of aftershock and mainshock-aftershock seismic performance of reinforced concrete frames. *Structural Safety* 73: 64–74.
- Song R., Li Y., & Van De Lindt J.W. 2016. Loss estimation of steel buildings to earthquake mainshock-aftershock sequences. *Structural Safety* 61: 1–11.
- USGS. 2014. Unified Hazard Tool. *U.S. Geological Survey*
- Vamvatsikos D., & Cornell C.A. 2002. Incremental dynamic analysis. *Earthquake Engineering and Structural Dynamics* 31 (3): 491–514.
- Wen Y.K., & Kang Y.J. 2001. Minimum Building Life-Cycle Cost Design Criteria I : Methodology. *Journal of Structural Engineering* 127 (3): 330–337.
- Yeo G.L., & Cornell C.A. 2009a. A probabilistic framework for quantification of aftershock ground-motion hazard in California: Methodology and parametric study. *Earthquake Engineering and Structural Dynamics* 38 (1): 45–60.
- Yeo G.L., & Cornell C.A. 2009b. Building life-cycle cost analysis due to mainshock and aftershock occurrences. *Structural Safety* 31: 396–408.
- Yin Y.J., & Li Y. 2011. Loss estimation of light-frame wood construction subjected to mainshock-aftershock sequences. *Journal of Performance of Constructed Facilities* 25 (6): 504–513.

Sensitivity analysis on resilience components throughout the lifecycle of an asset

N.K. Stamataki

Laboratory of Reinforced Concrete & Seismic Design of Structures, Democritus University of Thrace, Xanthi, Greece

D.V. Achillopoulou

James Watt School of Engineering, University of Glasgow, Glasgow, UK

ABSTRACT: Sustainability of Critical Transport Infrastructures (CTIs) is split in three pillars economy, society and environment and can be estimated indirectly by quantifying resilience. The future provisions have led to the next generation of Eurocodes accounting for the climate change effects, severe increase of service loads, carbon emissions and invested capital. A novel methodology is introduced to quantify the resilience and sustainability level of CTIs, with a special focus on bridges. The different resilience components and distinct periods of the bridge's lifecycle are expressed by Key Performance and Performance Indicators. The components are factored through a Sensitivity Analysis to identify the crucial one. A case-study bridge is examined, exploiting data from its lifecycle to inform owners and stakeholders about the condition, functionality, and operation as well as the resilience and sustainability level. Based on the indicators, decision-making is assisted for a rapid and reliable data-driven asset's management and adaptation analysis.

1 INTRODUCTION

In the last decades, climate resilience and adaptation strategies for Critical Transport Infrastructures (CTIs), such as highway bridges, are of high strategic socioeconomic importance under the prism of sustainable design and maintenance solutions. CTIs have a crucial socioeconomic impact and are essential to withstand extreme hazard events caused by climate change and at the same time meeting the targeted levels of safety and functionality (Asian Development Bank 2021); (Capacci et al. 2022); (Panda & Ramos 2020). Especially, vulnerable high-way Reinforced Concrete (RC) bridges that are close to complete their lifecycle are facing long-term consequences, such as damages and/or disruption resulting in extensive losses. One third of the USA. bridges are characterized as structurally obsolete increasing the risk of losses. The investment to avoid losses of structurally deficient bridges, according to the American Road and Transportation Builders Association is over \$58 billion for their replacement or re-pair (Black 2022). What is more, according to the EU Joint Research Centre the annual expected damages caused to infrastructures are considered to reach €0.8 billion by the end of the century in Europe (Panda & Ramos 2020).

Recent climate projections underpin the increasing urgency of action by considering also global economic risks (Panda & Ramos 2020); (Drzik 2019); (Asian Development Bank 2021). In light of this, resilient and sustainable solutions, including adequate climate change mitigation and adaptation measures have a key role in the allocation of capital for CTIs. Resilience and sustainability are both drivers used to assist in the decision-making process of assets throughout their lifecycle expressed by various indicators (Frangopol et al. 2017); (Asian Development Bank 2021). The indicators that exceed thresholds can trigger pathways for

adjustment of the CTIs. The main objectives of this research are to introduce a novel methodology for the quantification of the resilience and sustainability levels of bridges and identify the criticality of the resilience components in each period. Through a Sensitivity Analysis (*SensAn*) the participation factors for the structural and functional components of resilience are weighted. The methodology is applied to the case-study bridge in the Netherlands and results in a reliable data-driven asset approach that correlates functional and structural performance to define the lifecycle analysis of the bridge.

2 METHODOLOGY

This proposed methodology of Achillopoulou et al. (2022) quantifies resilience and sustainability level of a bridge throughout its life cycle by using Resilience and Sustainability Indices (RIs and SIs), briefly illustrated in Figure 1. The estimation of the indices derives by considering: i) Key Performance Indicators (KPIs) that represent the distinct periods of the asset’s life-cycle (e.g. initial state, recovery period), each one of them contributes at a different level to the final estimation of SIs with the use of weight factors (Wf); ii) different components of resilience that express the structural integrity and the functionality level of the asset, each one also, contributes at a different level to the estimation of RIs by using participations factors (β_c) and iii) a number (n) of Performance Indicators (PIs) to define each one of the resilience components.

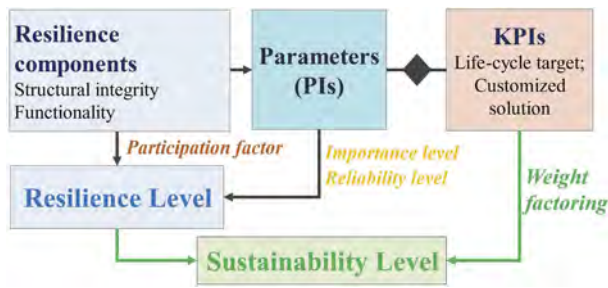


Figure 1. Schematic representation of the methodology.

Resilience quantification is a data-driven process based on the reliability (L_i) and importance (γ_i) level of the PIs as well as the criticality of the resilience components at the different periods of the bridge lifecycle as Equation 1 presents. The reliability level of each PI is taken into account with the use of a reducing factor (Achillopoulou et al. 2022); (Makhoul et al., in press). The factor’s value is crucial and depends on the damage type as well as the available monitoring or artificial data (Achillopoulou et al. 2020); (Argyroudis et al. 2022). The importance level for each PI ranges from 1 to 4, with 1 corresponding to a low importance level meaning that the parameter is not the most crucial to base upon decisions (Achillopoulou et al. 2022); (Makhoul et al., in press). Also, the participation factors of the components result from a Sensitivity Analysis (*SensAn*) based on the targeted resilience levels as described in the next section.

$$RI(t) = \beta_c(t) \cdot \frac{1}{n} \cdot \sum_i^c \gamma_i(t) \cdot L_i(t) \quad (1)$$

The sustainability’s pillars (society, environment, and economy) are considered indirectly in this methodology by the defined PIs that express the impact of an extreme event’s occurrence (e.g., extreme hazard due to climate change, traffic and/or population increase) on the asset’s structural integrity and functionality, the limitations of resources and the environmental legislation for the bridge mitigation measures. Sustainability level is defined by the SIs that scale from 1 to 4, with 4 corresponding to a high level of sustainability (Achillopoulou et al. 2022);

(Makhoul et al., in press). The SIs are estimated by utilizing the calculated RIs and the weighted KPIs using the metric in Equation 2.

$$SI(t) = \sum_1^m W_f(t) \cdot RI(t) \quad (2)$$

where m is the total number of the distinct periods of the asset's life cycle (KPIs).

3 CASE-STUDY

The oldest prestressed highway bridge of Flevopolder in the Netherlands, “Hollandse Bridge” is chosen as the case study due to the various mitigation measures taken over time as well as the fact that has been the main link between the Randstad and the province of Flevoland, including its two largest cities Almere and Lelystad. The bridge is operating since June of 1969 and from the very start, the traffic load increased radically resulting in functionality problems (Achillopollou et al. 2022). The development of the near town city, Almere, augmented the traffic flow further up to overloaded in the 1980s. During the 90s (from 1993 to 1999) various mitigation measures had been taken such as the widening of the bridge's deck. In 2007, the Dutch Organization for Applied Scientific Research decided that the bridge was unsafe to carry traffic loads over 12 tons and applied traffic restrictions. The decision led to tremendous economic losses for the county that busted the renovation of the bridge one year later (2008) and the installation of a Structural Health Monitoring (SHM) system. However, the continuous increase in the traffic load from 2011 to 2014 resulted in further actions that include the reconstruction of the existing bridge and the construction of a new one next to it. The bridge's timeline from 1699 to 2015 is illustrated in Figure 2.



Figure 2. Timeline of Hollandse bridge from 1969 to 2015.

4 SENSITIVITY ANALYSIS

Sensitivity analysis (*SensAn*) in linear programming is used to manage problems and answer hypothetical questions with precise estimates of the coefficients. The changes in the objective function's optimal solution are examined while coefficients varying within certain limits (Borogovo et al. 2018). In this study a *SensAn* is performed for the participation factors (β_c) of the resilience components to i) identify the criticality of the components per period and ii) evaluate the RIs of the case-study bridge based on the initial estimation (Achillopollou et al. 2022). The thresholds and the correlation of the RIs are defined based on the already calculated resilience curve as Table 1 concludes. Once the RIs thresholds are defined, the initial limits of the structural integrity (β_s) and functionality (β_f) participation factors are defined. The β_c are considered complementary and thus, only the initial values of the β_s are defined in Table 1.

Table 1. Resilience indices correlation and the initial limits of the participation factors components.

Period (m)	RI _m	RIs correlation	β_s initial limits
Initial state	RI _I	RI _I ≥ RI _E	$\beta_{s,I} \geq 0.30$
Absorption (exposure)	RI _E	RI _E ≥ RI _{ID1} & RI _E = RI _{cr}	$\beta_{s,E} \geq 0.20$
Idle-time 1 st	RI _{ID1}	RI _{ID1} ≤ RI _E & RI _{ID1} ≤ RI _{ID2/REC1}	$\beta_{s,ID1} \geq 0.30$
Idle-time 2 nd /Recovery 1 st	RI _{ID2/REC1}	RI _{ID2/REC1} ≥ RI _{ID1} & RI _{ID2/REC1} > RI _{cr}	$\beta_{s,ID2/REC1} \geq 0.16$
Recovery 2 nd	RI _{REC2}	RI _{REC2} ≥ RI _{ID2/REC1} & RI _{REC2} > RI _{cr}	$\beta_{s,REC2} \geq 0.16$
Recovery 3 rd	RI _{REC3}	RI _{REC3} ≥ RI _{REC2} & RI _{REC3} > RI _{cr}	$\beta_{s,REC3} \geq 0.45$
Adaptation 1 st	RI _{IAD1}	RI _{IAD1} ≥ RI _{REC3}	$\beta_{s,AD1} \geq 0.40$
Adaptation 2 nd	RI _{AD2}	RI _{AD2} ≥ RI _{IAD1}	$\beta_{s,AD2} \geq 0.40$

For example, the resilience index threshold at the initial state (RI_I) is presented in Figure 3a. The change of the RIs values while β_s ranges within the permissible limits (from 0 to 1) for the initial state and exposure are illustrated with the linear functions. The RI_{tot} values are higher for the initial state and lower for exposure as expected. In cases that RI_{tot} falls under the critical value equal to 40% of the initial index (RI_I), the structural component is less significant and there is a shift of the higher and lower values of the RI_{tot} between exposure and initial state. This practically means, that in order to realistically illustrate the resilience level of exposure lower than that of the initial state, the β_s factor should be at least 0.30.

To use further β_s for predicting the RIs in hypothetic scenarios, the distribution type and function of the factor are defined. This helps to reduce uncertainties and optimize the 1st estimation of the β_s which was based on experts' judgments. The histograms and Probability Density Functions (PDF) of the β_s have been used per period and the violin diagram of β_s has been plotted for the initial period as shown Figure 3b. The β_s distribution function followed is the t-distribution with n-1 degrees of freedom and the highest probability of β_s value is considered to be the median which is equal to 0.65. The distribution was divided in five percentiles (5%,35%,50%,75% and 95%) and the confidence interval taken into account was 95% present. With the defined values of the β_s factor, the resilience curve where redesigned.

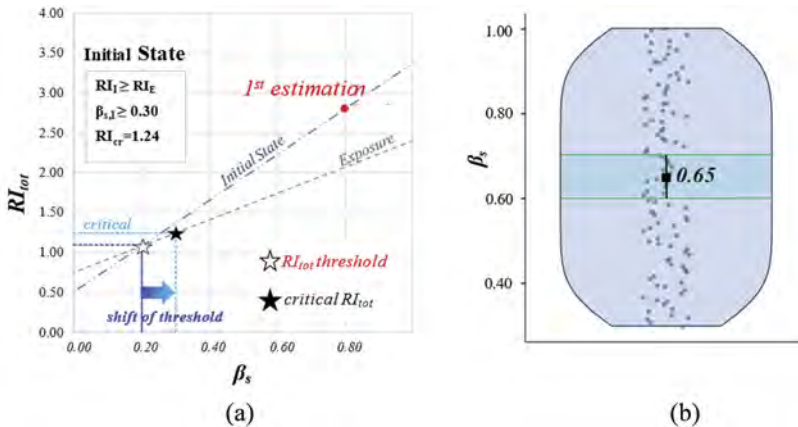


Figure 3. (a) Range of β_s values considering resilience thresholds in initial and exposure state and (b) β_s data distribution-violin diagram at initial state.

5 RESULTS

Table 2 lists β_s factor for each period of the asset. It includes also, the objective β_s prediction ($\beta_{s,mean}$), the range of the values between 25% and 95% percentiles as well as the bottom and upper limit of the confidence interval. The 1st estimation of the factor is proven to be among

the ranges except for the adaptation period in which the structural component's contribution is highly underestimated. Considering the goal values (95% confidence interval) for the adaptation period the error of the 1st estimation reaches up 46%. Whereas, for the recovery periods the 1st estimation of the structural component is most realistically considered, noting the smallest error. It is worth noticing that the highest error of the structural contribution to resilience derives for the exposure period. This means that it is underestimated and therefore higher losses are predicted.

Table 2. Predictions of structural resilience component factor (β_s) per period.

Period	Criteria KPIs	Objective $\beta_{s,mean}$	β_s limits			Goal (95% confidence interval)		1 st estimation $\beta_{s,1st\ estimation}$	1 st estimation error	
			$\beta_{s,min}$	$\beta_{s,max}$	$\beta_{s,min}$	$\beta_{s,max}$	$\beta_{s,min}$		$\beta_{s,max}$	<i>min</i>
Initial State	3.94	0.65	0.30	0.97	0.61	0.69	0.80	31%	16%	
Absorption (exposure)	3.26	0.60	0.30	0.96	0.55	0.66	0.30	-45%	-55%	
Idle time 1 st	2.38	0.65	0.35	0.95	0.55	0.75	0.50	-9%	-33%	
Idle-time 2 nd	2.76	0.57	0.20	0.94	0.48	0.66	0.50	4%	-24%	
Recovery 1 st										
Recovery 2 nd	2.79	0.53	0.11	0.96	0.44	0.62	0.50	14%	-19%	
Recovery 3 rd	2.95	0.72	0.48	0.96	0.66	0.79	0.70	6%	-11%	
Adaptation 1 st	3.78	0.84	0.76	0.93	0.61	0.93	0.50	-18%	-46%	
Adaptation 2 nd	3.81	0.90	0.81	0.99	0.88	0.93	0.50	-43%	-46%	

Based on the β_s predictions, the resilience curves are recalculated as illustrated in Figure 4a and are plotted versus the 1st estimation. The fundamental difference of the 1st estimation and the 95% confidence interval values (dark green shaded area) is that losses are considered higher and present abrupt decrease especially for the adaptation period. Whereas the predictions present a more balanced distribution of losses between the different periods. Figure 4b presents a Pearson correlation analysis of the KPIs considering the average importance values of all the PIs for each period of the asset towards the RIs derived for the predictions of β_s . This analysis advocates that the $RI_{tot,max95\%}$ is much better correlated with the importance level attribute to each PI per period. The reliability analysis confirms the methodology and the PIs adopted.

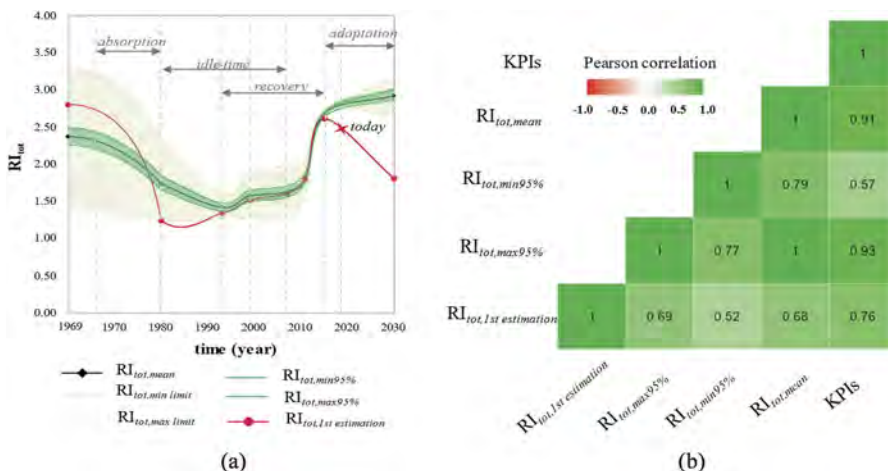


Figure 4. (a) Resilience based on predictions and (b) Pearson correlation of the KPIs and RI_{tot} .

6 CONCLUSIONS

The main conclusions of this study are outlined to the following:

- KPIs that are crucial for a balanced lifecycle of the asset is exposure and adaptation.
- Structural resilience component participation factor (β_s) is proven to follow a t-distribution with $n-1$ degrees of freedom for this case-study and the reliable values optimize the 1st estimation of the factor.
- The methodology is confirmed to be reliable for the importance level it gives to each one of the criteria and PIs chosen throughout the lifecycle of the asset.
- Further research is needed including other case-studies and make prediction of the s factor based on the bridge type.
- Future research aims in expanding the methodology including the investment capital component as well as unpredicted events.

REFERENCES

- Achillopoulou, D. V., Mitoulis, S. A., Argyroudis, S. A., & Wang, Y. 2020. Monitoring of transport infrastructure exposed to multiple hazards: A roadmap for building resilience. *Science of the total environment*, 746, 141001.
- Achillopoulou, D. V., Stamataki, N. K., Psathas, A., Iliadis, L., Karabinis, A. 2022. Resilience Quantification based on Monitoring & Prediction data Using Artificial Intelligence (AI). *IABSE Congress. Nanjing 2022-Bridges Structures. Connect. Integration and Harmonisation, Nanjing*, 21-23 September 2022.
- Argyroudis, S., Mitoulis, S., Chatzi, E., Baker, J., Brilakis, I., Gkoumas, K., & Linkov, I. 2022. Digital technologies can enhance climate resilience of critical infrastructure. *Climate Risk Management*, 35, p. 100387.
- Asian Development Bank-ADB & Global Center on Adaptation-GCA. 2021. A System-Wide Approach for Infrastructure Resilience: Technical Note. Available at: shorturl.at/GNPS8 (assessed 6 January 2023).
- Black, A. 2022. American Road & Transportation Builders Association: 2022 Bridge Report. Available at: <https://artbabridgereport.org/> (assessed 6 January 2023).
- Borgonovo, E., Buzzard, G. T., & Wendell, R. E. 2018. A global tolerance approach to sensitivity analysis in linear programming. *European Journal of Operational Research*, 267(1), 321–337.
- Capacci, L., Biondini, F., & Frangopol, D. M. 2022. Resilience of aging structures and infrastructure systems with emphasis on seismic resilience of bridges and road networks. *Resilient Cities and Structures*, 1(2), 23–41.
- Drzik, J. P. 2019. The World Economic Forum: Infrastructure around the world is failing. Here's how to make it more resilient. Available at: shorturl.at/EMZ23 (assessed 6 January 2023).
- Frangopol, D. M., Dong, Y. & Sabatino, S. 2017. Bridge life-cycle performance and cost: analysis, prediction, optimisation and decision-making. *Structure and Infrastructure Engineering*, 13(10), 1239–1257.
- Makhoul, N., Achillopoulou, D. V., Stamataki, N. K., & Kromanis, R. 2023 (in press). The resilience of computer vision-based monitoring systems and their measurement. *Data Driven Methods for Civil Structural Health Monitoring & Resilience: Latest Developments & Applications* (in press). Taylor & Francis.
- Panda, A. & Ramos, N. J. 2020. Making critical infrastructure resilient: Ensuring continuity of service-policy and regulations in Europe and Central Asia. Belgium: UN Office for Disaster Risk Reduction.

A Markovian framework to model life-cycle consequences of infrastructure systems in a multi-hazard environment

Kenneth Otárola

Scuola Universitaria Superiore (IUSS) Pavia, Pavia, Italy

Leandro Iannacone, Roberto Gentile & Carmine Galasso

University College London, London, UK

ABSTRACT: Existing frameworks for multi-hazard life-cycle consequence (LCCon) analysis typically disregard the interactions between multiple hazards and obtain the total LCCon as the sum of the consequences caused by the individual hazards modelled independently. This practice leads to inaccurate life-cycle consequence estimates and ineffective risk-informed decision-making for disaster-mitigation strategies and/or resilience-enhancing policies. In addition, most available LCCon formulations fail to accurately incorporate the damage-accumulation effects due to incomplete (or absent) repairs between different hazard events. To address these challenges, this paper introduces a Markovian framework for efficient multi-hazard LCCon analysis of deteriorating structural systems, appropriately accounting for complex interactions between hazards and their effects on a system's performance. The changes in the system's performance level (e.g., damage or functionality state) are quantified with transition probability matrices following the Markovian assumption and the expected LCCon estimates are obtained by combining the performance level distribution with suitable system-level consequence models, which can include direct asset losses as well as socio-economic consequences. To showcase the framework applicability, a simple road network with a single case-study ordinary reinforced concrete bridge subject to earthquake-induced ground motions and environmentally-induced corrosion deterioration is investigated, estimating consequences in terms of community welfare loss.

1 INTRODUCTION

Many existing risk modelling frameworks independently analyse and aggregate the expected consequences due to multiple hazards (e.g., Dong & Frangopol, 2016). However, it has been demonstrated that multiple, often interacting, hazards can lead to consequences greater than the sum of those related to individual hazards (e.g., De Angeli et al., 2022). As such, it is imperative to account for hazard interactions when quantifying the potential impacts of the events on the performance of critical assets and the communities they serve for risk-informed decision-making on future disaster-mitigation strategies and resilience-enhancing policies. The frameworks for multi-hazard life-cycle consequence (LCCon) analysis that have gained considerable attention over past years neglect such interactions. In addition, they assume that systems sustaining structural/non-structural damage are either instantaneously repaired or do not receive any repair actions after an event (e.g., Fereshtehnejad & Shafieezadeh, 2018). Hence, dynamic changes in the performance of the systems during their service life are not adequately tackled, preventing the accurate quantification of the associated LCCon estimates.

To enable the optimal life-cycle management of structural systems (e.g., buildings or bridges) subject to multiple (and often interacting) hazard events, and of the infrastructure systems that rely on them (e.g., road networks), this paper proposes a Markovian framework for multi-hazard LCCon analysis, which explicitly accounts for the interacting consequences of the hazard events. Using the Markovian assumption (e.g., Bonamente, 2017), the framework can adequately

model damage accumulation and, therefore, performance deterioration (i.e., reduction) while being computationally efficient (e.g., Iervolino et al., 2016). Markov processes have been extensively used for LCCon analysis of utility networks (e.g., Bocchini et al., 2013). They have also recently been used for life-cycle analysis of buildings, mainly in mainshock-aftershock-related applications (e.g., Shokrabadi & Burton, 2018). A comprehensive integration of the different types of hazard interactions is currently lacking in these formulations.

As such, the framework proposed in this paper advances the current knowledge by including the lifetime adverse impact of multiple hazard events and their interactions on the LCCon analysis of structural systems and associated infrastructure systems. It can also be integrated with suitable system-level consequence models to quantify the expected LCCon in terms of direct asset losses and socio-economic consequences. As an example, the proposed framework is applied to the LCCon analysis of a simplified transportation network with a single bridge subject to earthquake events and deterioration effects. Consequences are quantified in terms of welfare losses directly related to the increased travel time due to the actions taken on the bridge.

2 GENERAL FRAMEWORK

The proposed Markovian framework for multi-hazard LCCon analysis efficiently computes expected LCCon estimates of a structural system subject to multiple hazard events causing state changes. The performance of the system is modelled as a discrete-time, discrete-space Markovian process (i.e., treating the state of the process as a discrete variable; e.g., Iervolino et al., 2016). Namely, the system's performance domain is partitioned into mutually exclusive and collectively exhaustive performance states/levels. Such states should be represented using a single harmonised scale valid for different hazard types since specific hazards can cause different types of performance impairment to a system. Thus, for instance, a valid (hazard-agnostic) scale could be defined in terms of the system's functionality. For example, the adopted functionality states (FSs) for a bridge could be defined as: 1) no restrictions; 2) weight restrictions; 3) one lane open only; 4) emergency access only; 5) closure (e.g., Capacci et al., 2020). If the considered hazards can cause similar damage mechanisms to a system (i.e., a consistent damage scale can be used), the performance can also be defined directly in terms of damage states (DSs).

The transition probabilities between FSs (i.e., the probabilities that after one event, the system is in the m -th FS given that it was in the n -th FS before the event) are derived employing state-dependent functionality models (defining the probability of exceeding a FS given a hazard intensity and the FS achieved during a prior event; e.g., fragility relationships) and hazard models (defining the probability of exceeding a hazard intensity measure –IM– given the hazard characteristics; e.g., hazard curves). The transition matrices (i.e., the stochastic square matrices used to describe the FS transitions) are assembled by collecting each (n,m) transition probabilities between FSs, also characterising the system's performance deterioration. The resulting expected consequences are obtained from suitable system-level consequence models (i.e., linking the FSs to a consequence metric of interest).

In the following section, an analytical formulation is presented to compute the expected LCCon estimates. This formulation is based on classical hypotheses for performance-based engineering and is divided into two modelling stages (Zaghi et al., 2016). The first stage, hazard modelling, considers Level I interactions that are independent of the presence of a physical system (e.g., a landslide triggered by an earthquake event). The second stage, consequence modelling, considers Level II interactions resulting from the impact of hazards on a physical system, such as functional impairment due to the accumulation of damage during a seismic sequence.

For modelling purposes, the Level I interactions can be subclassified in (Iannacone et al., 2023): 1) *non-interacting*: hazards whose co-occurrence is purely coincidental (e.g., earthquakes and hurricanes); 2) *concurrent*: hazards that co-occur or have a significant joint probability of occurrence in a period of time (e.g., storm surge, sea waves, and strong wind that co-occur during a hurricane); 3) *successive*: hazards with a causal relationship. Two broad categories can be identified within successive hazards based on their causal relationship: *Type A* (i.e., when a secondary hazard is triggered by the occurrence of a primary hazard) and *Type B* (i.e., the rate of occurrence of a secondary hazard increases following the occurrence of a primary hazard).

Level II interactions are related exclusively to the impairment of a physical system's performance, described by damage or functionality states, given the occurrence of hazard events. In general, the system's performance deterioration can be caused by shock deterioration processes associated with hazard events occurring at a point in time (e.g., an earthquake-induced ground motion) or gradual deterioration processes associated with ageing and/or deteriorating mechanisms (e.g., steel rebars corrosion). System performance can also be recovered (i.e., improved) due to potential repair actions executed in between hazard events. However, such actions are typically intended to recover from shock deterioration processes rather than those due to gradual deterioration.

3 ANALYTICAL FORMULATION

The total expected LCC on estimates associated with a structural system subject to multiple hazard events can be obtained by summing the expected hazard-induced consequences during its service life, obtained as in Equation (1).

$$E[C] = \sum_{i=1}^{\infty} P(i, t_{LC}) \sum_{j=1}^i \mathbf{F}_{S_j} E[\mathbf{C}_{F_{S_j}}]^T \quad (1)$$

In Equation (1), \mathbf{F}_{S_j} is the $1 \times N_{F_S}$ probability mass function (PMF) of the system's FSs after the j -th hazard event, $E[\mathbf{C}_{F_{S_j}}]$ is the consequence model (i.e., a $1 \times N_{F_S}$ vector with the expected consequences associated with each FS), N_{F_S} is the total number of FSs, and $P(i, t_{LC})$ is the probability of having i hazard events during the service life (t_{LC}), obtained as in Equation (2).

$$P(i, t_{LC}) = \frac{(v_T t_{LC})^i e^{-(v_T t_{LC})}}{i!} \quad (2)$$

In Equation (2), v_T is the total rate of occurrence (in a selected time unit) of N_h hazards, regardless of their type and event characteristics. It is assumed that hazard events of the same type (h) occur according to a homogeneous Poisson process with a rate of occurrence equals v_h ($h = 1, \dots, N_h$). Therefore, v_T can be computed as in Equation (3).

$$v_T = \sum_{h=1}^{N_h} v_h \quad (3)$$

It is worth noting that $P(i, t_{LC})$ can also be obtained through a simulation-based approach (e.g., Iannacone et al., 2023). The PMF of the system's FSs after the j -th hazard event only depends on the current PMF of the system's FSs and can be estimated as in Equation (4).

$$\mathbf{F}_{S_j} = \mathbf{F}_{S_{j-1}} \mathbf{T}_{F_S} \quad (4)$$

In equation (4), $\mathbf{F}_{S_{j-1}}$ is the $1 \times N_{F_S}$ PMF of the system's FSs after the $(j-1)$ -th hazard event, and \mathbf{T}_{F_S} is the $N_{F_S} \times N_{F_S}$ transition matrix quantifying the probability of transitioning between the FSs given an event, obtained as in Equation (5).

$$\mathbf{T}_{F_S} = \sum_{t_j=0}^{t_{LC}} \sum_{t_{j-1}=0}^{t_j} f(t_{j-1}, t_j | i, t_{lc}) \mathbf{T}_S \mathbf{T}_{G, \Delta t_j} \mathbf{T}_{R, \Delta t_j} \quad (5)$$

In Equation (5), \mathbf{T}_{F_S} accounts for possible repair actions and gradual deterioration in the time between the occurrence of the $(j-1)$ -th hazard event and the j -th hazard event (i.e., interarrival-time), denoted as Δt_j . The quantity $f(t_{j-1}, t_j | i, t_{lc})$ is the PDF of two hazard events occurring at a time t_{j-1} and t_j , conditioned on the occurrence of i hazard events during the nominal lifetime of the system (details on how to obtain this PDF are shown in Fereshtehnejad & Shafieezadeh, 2018), \mathbf{T}_S is the

$N_{F_S} \times N_{F_S}$ transition matrix associated with a shock deterioration process accounting for the possible hazard events (e.g., earthquake- and flood-related events), $\mathbf{T}_{G,\Delta t_j}$ is the $N_{F_S} \times N_{F_S}$ transition matrix associated with a gradual deterioration process occurring in Δt_j (e.g., deteriorating mechanisms), and $\mathbf{T}_{R,\Delta t_j}$ is the $N_{F_S} \times N_{F_S}$ transition matrix associated with the repair actions occurring in Δt_j . The matrix \mathbf{T}_S can be obtained combining the $N_{F_S} \times N_{F_S}$ transition matrices for individual, non-interacting, hazard types \mathbf{T}_{S_h} , as in Equation (6).

$$\mathbf{T}_S = \sum_{h=1}^{N_h} \frac{v_h}{v_T} \mathbf{T}_{S_h} \quad (6)$$

A significant challenge in using Equation (1) is linked to the high computational cost of integrating all the possible outcomes for the occurrence of the hazard events and the total number of hazard events during the selected time horizon. Such a drawback is exacerbated by $\mathbf{T}_{G,\Delta t_j}$ and $\mathbf{T}_{R,\Delta t_j}$ being a function of Δt_j . Nonetheless, Equation (1) can be significantly simplified by modelling the expected LCCon estimates as the sum of the expected consequences in N_t fixed time intervals of length Δt , where $N_t = \lfloor t_{LC}/\Delta t \rfloor$. Selecting a sufficiently small Δt such that only one (primary) hazard event is likely within each interval, the expected LCCon estimates can be computed with Equation (7).

$$E[C] = \sum_{m=1}^{N_t} \mathbf{F}_{S_{t+m\Delta t}} E[\mathbf{C}_{F_S}]^T \quad (7)$$

In Equation (7), $\mathbf{F}_{S_{t+m\Delta t}}$ is the $1 \times N_{F_S}$ PMF of the system's FSs at time $t + m\Delta t$, computed as in Equation (8). \mathbf{F}_{S_t} is the $1 \times N_{F_S}$ PMF of the system's FSs at time t .

$$\mathbf{F}_{S_{t+m\Delta t}} = \mathbf{F}_{S_t} \prod_{i=1}^m [\nu_T \mathbf{T}_S \mathbf{T}_G + (1 - \nu_T) \mathbf{T}_R \mathbf{T}_G] \quad (8)$$

In equation (8), \mathbf{T}_S is the transition probability due to the gradual deterioration in the time interval Δt , \mathbf{T}_R is the transition probability due to the recovery actions in the time interval Δt , $\nu_T \mathbf{T}_S \mathbf{T}_G$ corresponds to the transition probability due to shock and gradual deterioration, multiplied by the probability of observing a shock-type hazard event in a selected Δt (equal to the rate ν_T under the small-interval assumption). $(1-\nu_T) \mathbf{T}_R \mathbf{T}_G$ corresponds to the transition probability due to repair actions and gradual deterioration, multiplied by the probability of not observing a shock-type hazard event in a selected Δt (equal to $1-\nu_T$ under the small-interval assumption). It is assumed that only a transition due to a hazard event or a repair action occurs in a unit of time since, commonly, repair actions will be interrupted after a significant event. Nonetheless, such an assumption can be relaxed. In this case, $\nu_T \mathbf{T}_S \mathbf{T}_G$ can be written as $\nu_T \mathbf{T}_S \mathbf{T}_R \mathbf{T}_G$. The following subsections describe the derivation of the described transition matrices.

3.1 Shock deterioration transition matrix

The shock-type deterioration transition matrix \mathbf{T}_S only has diagonal and upper-triangular entries corresponding to the probabilities of transitioning from a given FS to a higher FS (i.e., a transition between progressively worse FSs) or staying at the same FS after a hazard event. It is obtained from the transition matrix of the individual hazard types \mathbf{T}_{S_h} using Equation (6). Otáróla et al. (2023) detail how to assemble each \mathbf{T}_{S_h} accounting for Level I and II interactions in the four following cases: 1) hazard type h does not interact with other hazards; 2) hazard type h induces the simultaneous occurrence of other multiple concurrent hazards; 3) hazard type h is the primary hazard of a successive Type A interaction; 4) hazard type h is the primary hazard of a successive Type B interaction.

3.2 Gradual deterioration transition matrix

Before the gradual deterioration initiation time (t_i), there is no transition between FSs. Thus, the gradual-type deterioration transition matrix (i.e., \mathbf{T}_G) is numerically equal to the identity matrix ($\mathbf{T}_G = \mathbf{I}$). After t_i , the system starts transitioning from a given FS to a higher FS (i.e., a transition between progressively worse FSs) or staying at the same FS, and \mathbf{T}_G becomes an upper-triangular matrix whose entries correspond to the probability of transitioning in Δt , as in Equation (9) (which is valid for $t > t_i$). Several probabilistic models can be used to model the system's gradual deterioration (e.g., Duracrete, 2000, Iannacone & Gardoni 2019) and, thus, to obtain the (n,m) entry of the matrix \mathbf{T}_G . In the described procedure, gradual deterioration is treated for modelling purposes as the impact of non-monitored, yet frequent, small shocks.

$$\mathbf{T}_G(n, m) = \begin{cases} P(FS_m|FS_n, \Delta t) & \text{if } n < m \\ 1 - \sum_{i=1}^{N_{FS}} \mathbf{T}_G(n, i) & \text{if } n = m \\ 0 & \text{if } n > m \end{cases} \quad (9)$$

3.3 Repair actions transition matrix

The repair-type recovering transition matrix (i.e., \mathbf{T}_R) only has diagonal and lower-triangular entries relating to the probabilities of transitioning from a given FS to a lower FS (i.e., a transition between progressively better FSs) or staying in the same FS as the structural system recovers with time. The repair actions are modelled through a Poisson process. The daily rate of occurrence of an event where the system is recovered from a worse FS to a better FS is assumed as the inverse of the difference between the repair times of each FS ($T_{n,m}$). This time difference does not necessarily correspond to the repair times associated with each state-dependent FSs; however, this is the simplest approximation to a potential recovery path between the FSs. The values of $T_{n,m}$ are defined if $n > m$, and can be found in the literature (e.g., HAZUS, 2003). The (n,m) entry of the matrix \mathbf{T}_R is obtained as in Equation (10). The Δt should be expressed in the same units than $T_{n,m}$.

$$\mathbf{T}_R(n, m) = \begin{cases} \left(\frac{1}{T_{n,m}} \Delta t\right) e^{-\left(\frac{1}{T_{n,m}} \Delta t\right)} & \text{if } n > m \\ 1 - \sum_{i=1}^{N_{FS}} \mathbf{T}_R(n, i) & \text{if } n = m \\ 0 & \text{if } n < m \end{cases} \quad (10)$$

4 ILLUSTRATIVE APPLICATION

The proposed framework is demonstrated using a simplified case-study road network with a single symmetric double-span box-girder seat-type bridge (Figure 1a). Such a bridge represents a typical bridge vulnerability class in Southern California and is located in downtown Los Angeles (Lat: 34.052, Lon: -118.257). The bridge is characterised by: deck width: 23 m; number of spans: 2; span lengths: 45.7 m; number of columns: 2; columns radius: 0.85 m; columns height: 6.70 m. It comprises seat-type abutments (which include an arrangement of nonlinear springs for shear keys, elastomeric bearing pads, soil backfill, and abutment piles), column bents (which include nonlinear fibre sectional models for columns and column foundational springs), and an elastic superstructure representing the box-girder deck, designed and detailed according to Caltrans Seismic Design Criteria 2.0 (Caltrans, 2019). The bridge is assumed to undergo earthquake-induced ground motions while experiencing environmentally-induced corrosion deterioration in a marine splash exposure. DSs are used as performance states (so FS = DS in the previous equations) since a unique shock-type hazard is investigated, as in common performance-based engineering practice. The time- and state-dependent fragility relationships developed in Otárola et al. (2022) are used to assemble \mathbf{T}_S and HAZUS repair times are used to assemble \mathbf{T}_R (HAZUS, 2003). Table 1 to 3 presents the

transition matrices for the case-study bridge. In total, four DSs are adopted, corresponding to slight (DS1), moderate (DS2), extensive (DS3), and complete (DS4) structural damage. Although the entries for T_S and T_R are obtained from fragility and recovery models, respectively, values for T_G are ideal and are used for illustrative purposes, estimating its non-diagonal entries as those corresponding to T_S divided by 100 for $a\Delta t = 1$ month.

Table 1. T_S transition probability matrix.

DSs	DS0	DS1	DS2	DS3	DS4
DS0	0.9596	0.0297	0.0084	0.0009	0.0014
DS1	0	0.9893	0.0084	0.0009	0.0014
DS2	0	0	0.9969	0.0015	0.0016
DS3	0	0	0	0.9978	0.0022
DS4	0	0	0	0	1

Table 2. T_G transition probability matrix.

DSs	DS0	DS1	DS2	DS3	DS4
DS0	9.997e-1	2.471e-4	6.996e-5	7.517e-6	1.179e-5
DS1	0	9.999e-1	6.978e-5	7.343e-6	1.196e-5
DS2	0	0	9.999e-1	1.253e-5	1.340e-5
DS3	0	0	0	9.999e-1	1.833e-5
DS4	0	0	0	0	1

Table 3. T_R transition probability matrix.

DSs	DS0	DS1	DS2	DS3	DS4
DS0	1	0	0	0	0
DS1	0.3020	0.6980	0	0	0
DS2	0.1224	0.2180	0.6595	0	0
DS3	0.0746	0.1009	0.1927	0.6318	0
DS4	0.0858	0.0951	0.1156	0.1683	0.5351

The expected LCCon is estimated in terms of expected welfare loss ($E[\Delta W]$; i.e., a measure of the impact of road network disruption on the commuters' well-being, Silva-Lopez et al., 2022) and considering 80 years as the bridge's service life. A welfare-loss consequence model is developed, associating each DS to a restrictive action that causes an increase in the travel time of the members of the community, namely: 1) DS0: no restrictions; 2) DS1: speed restrictions; 3) DS2: one lane open only; 4) DS3: one lane open only and speed restrictions; 5) DS4: closure. The consequence estimates are obtained from analysing the road network performance given a restrictive action. The outcome of such analyses is the aggregated travel time of the commuters, T , from where the difference in the travel time is obtained as $\Delta T = T - T_0$, where T_0 is the travel time in the "no restrictions" case. To compute ΔT , a graph-based approach based on the shortest-path algorithm is implemented (Dijkstra, 2022). In this regard, the road network is idealised as a directed graph (the travels are assumed to be directed to a unique destination, i.e., node 4 in this application) where nodes represent the locations of interest and edges represent the links between these locations. A demand of 500, 500, and 1000 vehicles/h is assumed to originate from nodes 1, 2, and 3, respectively. The links are assumed to be at full capacity with no congestion in the "no restriction" case (i.e., vehicles move at the free flow speed); the free flow speed is assumed as 40, 80, 40, and 80 km/h for the two-lane links 1-2, 1-3, 2-4, and 3-4, respectively. A speed restriction is assumed to reduce the free flow speed to 75% of the original value. A lane closure is assumed to reduce the capacity of the link to the value C^* , causing a congestion and changing the aggregated travel time associated with the link to

$$T^* = \frac{C^*}{D} T_0 \quad (11)$$

In this case study, $C^* = C_0/2$ is assumed, where C_0 is the capacity of the link in the “no restriction” case. No reduction in the demand is assumed between cases.

The ΔT metric is then used to estimate the welfare loss (ΔW) as in Equation (12), using the same parameters presented in Silva-Lopez et al. (2022), where y is the commuter’s wage rate, assumed to be 17.8 USD/h. Thereby, the consequence model $E[C_{FS}] = [0, 52.26, 156.79, 261.32, 522.63]$ is proposed in utils/h units.

$$\Delta W = \frac{1}{2y^{0.26}} \Delta T \quad (12)$$

Figure 1b Shows the expected life-cycle welfare loss for the case-study road network for the bridge starting in pristine conditions ($F_{s_0} = [1, 0, 0, 0, 0]$) as obtained by employing the proposed framework. Additionally, the expected life-cycle welfare loss of a structural upgraded bridge at $t = 0$ years (yr) is presented. Such an upgrade is assumed to ideally increase the median fragility values by 20% (i.e., to increase the lateral-resisting system structural capacity). As expected, an enhancement in the bridge’s seismic lateral resisting system can significantly reduce its LCC estimates, as also observed in Figure 1b. Given the flexibility and efficiency of the proposed framework, such improvements can be analysed at any point in time and utilised to showcase the value and/or significance of risk management and adaptation pathways.

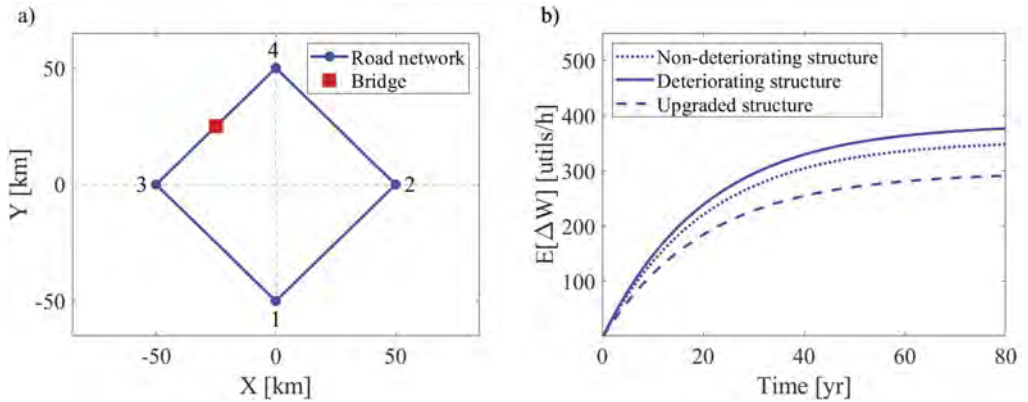


Figure 1. a) Case-study road network and b) expected life-cycle welfare loss.

5 CONCLUSIONS

The paper presented a Markovian framework for multi-hazard life-cycle consequence analysis of deteriorating structural systems. Transition matrices for shock deterioration, gradual deterioration, and repair actions were established to model the performance state change accounting for the possible interactions among hazards. Different unitary consequences (in terms of repair costs) were assigned to different performance states, allowing to obtain the expected Life Cycle Consequences of the system. The framework can be used to model the time- and state-dependent deterioration and recovery processes with significantly low computational demand. The proposed framework was applied for a simplified road network with a double-span box-girder seat-type bridge subject to earthquake-induced ground motions and corrosion-induced deterioration. The results showcase how the formulation can be implemented in actual risk modelling practice to adequately assess the life-cycle consequences of structural systems due to multiple hazards.

ACKNOWLEDGEMENTS

The authors acknowledge funding from UKRI GCRF under grant NE/S009000/1, Tomorrow's Cities Hub.

REFERENCES

- Bocchini, P., Saydam, D., & Frangopol, D. M. (2013). Efficient, accurate, and simple Markov chain model for the life-cycle analysis of bridge groups. *Structural Safety*, 40. <https://doi.org/10.1016/j.strusafe.2012.09.004>
- Bonamente, M. (2017). Statistics and Analysis of Scientific Data. In *Springer*.
- Caltrans. (2019). *Seismic Design Criteria. Version 2.0*. California Department of Transportation, Sacramento, CA.
- Capacci, L., Biondini, F., & Titi, A. (2020). Lifetime seismic resilience of aging bridges and road networks. *Structure and Infrastructure Engineering*, 16(2). <https://doi.org/10.1080/15732479.2019.1653937>
- De Angeli, S., Malamud, B. D., Rossi, L., Taylor, F. E., Trasforini, E., & Rudari, R. (2022). A multi-hazard framework for spatial-temporal impact analysis. *International Journal of Disaster Risk Reduction*, 73. <https://doi.org/10.1016/j.ijdrr.2022.102829>
- Dijkstra, E. W. (2022). A note on two problems in connexion with graphs. In *Edsger Wybe Dijkstra: His Life, Work, and Legacy* (pp. 287–290).
- Dong, Y., & Frangopol, D. M. (2016). Probabilistic Time-Dependent Multihazard Life-Cycle Assessment and Resilience of Bridges Considering Climate Change. *Journal of Performance of Constructed Facilities*, 30(5). [https://doi.org/10.1061/\(asce\)cf.1943-5509.0000883](https://doi.org/10.1061/(asce)cf.1943-5509.0000883)
- Duracrete. (2000). DuraCrete: Probabilistic Performance based Durability Design of Concrete Structures - Final Technical Report: General guidelines for durability design and redesign. In *Concrete*.
- FEMA. (2003). HAZUS-MH MR4 technical manual, multi-hazard loss estimation methodology earthquake model. In *National Institute of Building Sciences and Federal Emergency Management Agency (NIBS and FEMA)*. FEMA 366, Washington, DC.
- Fereshtehnejad, E., & Shafieezadeh, A. (2018). A multi-type multi-occurrence hazard lifecycle cost analysis framework for infrastructure management decision making. *Engineering Structures*, 167. <https://doi.org/10.1016/j.engstruct.2018.04.049>
- Iannacone, L., & Gardoni, P. (2019). Stochastic differential equations for the deterioration processes of engineering systems. In *The Proceedings of the 13th international conference on applications of statistics and probability in civil engineering (ICASP13)*, Seoul, South Korea.
- Iannacone, L., Gentile, R., & Galasso, C. (2023). Simulating interacting multiple natural-hazard events for lifecycle consequence analysis. *14th International Conference on Applications of Statistics and Probability in Civil Engineering, ICASP14*.
- Iervolino, I., Chioccarelli, E., & Suzuki, A. (2020). Seismic damage accumulation in multiple mainshock–aftershock sequences. *Earthquake Engineering and Structural Dynamics*, 49(10). <https://doi.org/10.1002/eqe.3275>
- Iervolino, I., Giorgio, M., & Chioccarelli, E. (2016). Markovian modeling of seismic damage accumulation. *Earthquake Engineering and Structural Dynamics*, 45(3). <https://doi.org/10.1002/eqe.2668>
- Lan, M., Gardoni, P., Luo, R., Zhu, J., & Lo, S. (2022). Risk-driven statistical modeling for hurricane-induced compound events: Design event implementation for industrial areas subjected to coastal floods and winds. *Ocean Engineering*, 251, 111159. <https://doi.org/https://doi.org/10.1016/j.oceaneng.2022.111159>
- Otárola, K., Fayaz, J., & Galasso, C. (2022). Fragility and vulnerability analysis of deteriorating ordinary bridges using simulated ground-motion sequences. *Earthquake Engineering and Structural Dynamics (in Press)*.
- Otárola, K., Iannacone, L., Gentile, R., & Galasso, C. (2023). A Markovian framework for multi-hazard life-cycle consequence analysis of deteriorating structural systems. *14th International Conference on Applications of Statistics and Probability in Civil Engineering, ICASP14*.
- Shokrabadi, M., & Burton, H. V. (2018). Building service life economic loss assessment under sequential seismic events. *Earthquake Engineering and Structural Dynamics*, 47(9). <https://doi.org/10.1002/eqe.3045>
- Silva-Lopez, R., Bhattacharjee, G., Poulos, A., & Baker, J. W. (2022). Commuter welfare-based probabilistic seismic risk assessment of regional road networks. *Reliability Engineering & System Safety*, 227, 108730. <https://doi.org/https://doi.org/10.1016/j.res.2022.108730>
- Zaghi, A. E., Padgett, J. E., Bruneau, M., Barbato, M., Li, Y., Mitrani-Reiser, J., & McBride, A. (2016). Establishing Common Nomenclature, Characterizing the Problem, and Identifying Future Opportunities in Multi-hazard Design. *Journal of Structural Engineering*, 142(12). [https://doi.org/10.1061/\(asce\)st.1943-541x.0001586](https://doi.org/10.1061/(asce)st.1943-541x.0001586)

Integrating life-cycle analysis into civil infrastructure resilience decision making: Illustrative application to seismic resilience modeling of US communities

Milad Roohi

University of Nebraska-Lincoln, Omaha, NE, USA

Jiate Li & John W. van de Lindt

Colorado State University, Fort Collins, CO, USA

ABSTRACT: This paper aims to integrate life-cycle analysis into civil infrastructure resilience modeling and decision-making in seismic-prone communities. To achieve this aim, the authors present a methodology for modeling seismic life-cycle resilience of interdependent buildings and lifeline systems and subsequently informing resilience decisions directly related to the maintenance and retrofit of interdependent infrastructure to enhance a community's physical, social, and economic systems. The methodology consists of 1) community data collection, 2) seismic hazard analysis, 3) physical damage analysis, and 4) system-level functionality and restoration analysis, 5) socio-economic impact analysis, 6) life-cycle optimization and retrofit decision-making. The methodology begins by developing geospatial datasets to characterize a community's interdependent civil infrastructure. Subsequently, ground motion prediction models are employed to simulate scenario earthquakes and obtain spatial intensity measures within the community. A fragility-based computational model of the networked infrastructure is then developed using graph theory to perform physical damage analysis using Monte Carlo simulations by accounting for structural aging and degradation. The damage estimates are used as input to an input-output model to perform functionality and restoration analysis by accounting for infrastructure networks' cascading failure and interdependency. An illustrative case study is presented to demonstrate the implication of the methodology to perform seismic life-cycle resilience in US communities, including Shelby County, TN. The methodology will assist engineers and urban planners in assessing the vulnerability of critical buildings and lifeline systems and developing life-cycle resilience-informed mitigation strategies to improve the seismic resilience of communities.

1 INTRODUCTION

Infrastructure systems are highly interconnected and interdependent, making them susceptible to disruptions caused by natural disasters and aging. The losses incurred due to these disruptions, the impact of climate change, and regulatory mandates have underscored the need for governments, private sectors, and communities worldwide to undertake a more thorough assessment of their portfolio exposure and risk. In the past decades, advanced catastrophe risk models have been developed to characterize the performance of the built environment and the direct and indirect impacts of natural hazards through data and analytics to develop risk management solutions and policies. More recently, extensive research has been conducted to develop advanced multiscale multidisciplinary community resilience modeling frameworks and computational tools to quantify multidisciplinary resilience metrics and compare alternative policies or strategies for mitigation and post-hazard recovery planning (Roohi et al. 2021, Deierlein et al. 2020, Cremen et al. 2023). These computational models adopt a system of

systems modeling approach to account for interdependency between networked infrastructure and socio-economic systems. Depending on data availability, the scale and hazard of interest, and computational resources, community resilience models can be developed with various levels of resolution and uncertainty. The community resilience models are computationally complex in which data availability, model assumptions, parameters, and inputs can play a crucial role in the accuracy and robustness of estimated resilience metrics. These resilience metrics are, by and large, primarily based on social science and economics; however, most civil engineering studies consider only damage and direct losses without the ability to accurately model indirect losses, e.g., those impacting the economic sectors that interact within a community.

Despite the advancements in resilience modeling and the capability of the models to distinguish the vulnerability of structures based on their characteristics (e.g., construction type, occupational type, seismic design code, and building height), other characteristics such as service age and environment of the structure are needed to be considered to improve the accuracy in evaluating the performance of the infrastructure. Several studies (Akiyama et al. 2011; Zheng et al. 2021) have demonstrated that deterioration and aging will significantly impact the service lifetime, seismic vulnerability, and seismic life-cycle performance of infrastructure systems. To account for these impacts, life-cycle analysis (LCA) is an essential tool that can be integrated into resilience modeling by assessing the performance of a structure throughout its lifespan to obtain a more comprehensive understanding of the impacts of the environment on infrastructure systems and how these systems can be made more sustainable and resilient. This analysis involves a detailed investigation of various elements of a system, including its design, construction, maintenance, and retrofitting. The analysis begins with a hazard assessment, which involves identifying potential damage due to a hazardous event. Engineers can determine the required design criteria for a structure based on this assessment. During the design phase, engineers use various design methods to ensure the structure can withstand the expected forces. The design process also involves selecting appropriate construction materials and techniques that can enhance the seismic resistance of the structure. Once the structure is constructed, it undergoes regular maintenance and inspection to identify any signs of damage or deterioration. If necessary, retrofitting measures can be implemented to improve the structure's performance. LCA can help owners and engineers to identify potential risks and to develop appropriate mitigation strategies. This analysis can also help to reduce the risk of structural damage and loss of life. This is particularly important as buildings built in the 1970s and earlier are still being utilized today, both in developing and developed regions of the world. However, these structures were not designed to adhere to the 1976 Uniform Building Code, which introduced design standards for ductile behavior during seismic activity (Bai et al. 2003). Consequently, these structures are vulnerable to damaging earthquakes, thereby presenting a potential danger. Thus, officials must provide various policy options to implement performance evaluation and retrofit plans for the most vulnerable (i.e., non-code and low-code compliant) and critical buildings.

The previous exposition highlights the need to develop integrated life cycle resilience modeling approaches capable of accounting for i) cascading impacts of the failure in components of infrastructure in the functionality of the networked system, ii) accounting for structural aging, strength degradation, and retrofit, which can significantly impact the seismic performance of infrastructure systems. This paper addresses this need by integrating LCA into civil infrastructure resilience modeling and decision-making in seismic-prone communities. To achieve this aim, the authors present a methodology for modeling seismic life-cycle resilience of interdependent buildings and lifeline systems and subsequently informing resilience decisions directly related to the maintenance and retrofit of interdependent infrastructure to enhance the community's physical, social, and economic systems. An illustrative case study is presented to demonstrate the implication of the methodology to perform seismic life-cycle resilience in US communities, including Shelby County, TN. The methodology will assist engineers and urban planners in assessing the vulnerability of critical buildings and lifeline systems and developing mitigation strategies to improve the seismic resilience of communities.

2 PROPOSED METHODOLOGY

The methodology consists of 1) community data collection, 2) seismic hazard analysis, 3) physical damage analysis, and 4) system-level functionality and restoration analysis, 5) socio-economic impact analysis, 6) life-cycle optimization and retrofit decision-making. The methodology begins by developing geospatial datasets to characterize a community's civil infrastructure and interdependency. Subsequently, ground motion prediction models are employed to simulate scenario earthquakes and obtain spatial intensity measures within the community. A fragility-based computational model of the networked infrastructure is then developed using graph theory to perform physical damage analysis using Monte Carlo simulations. The damage estimates are used as input to an input-output model to perform functionality and restoration analysis by accounting for infrastructure networks' cascading failure and interdependency.

2.1 Data and information of physical infrastructure

The initial phase of the process involves the creation of geospatial datasets (in the form of shapefiles) that describe the buildings and lifelines system of the community. This step also involves the development of an interdependency matrix for the physical infrastructure network. The interdependency is modeled by estimating the service areas of each network infrastructure and performing geospatial analysis to identify the buildings within each service area (refer to Linger and Wolioskx 2001 and Roohi et al. 2022 for further information). This information is critical to understanding the relationships between different infrastructure components and the potential cascading impact of a seismic event.

2.2 Spatial seismic hazard analysis

In the second step, a spatial multi-hazard analysis is conducted to generate a spatial distribution of hazard intensity measures to measure the effects of seismic wave propagation, liquefaction, and landslide as the main phenomena affecting the integrity of distributed networked infrastructure (see Farahani et al. for further details). The seismic event scenarios are generated using various ground motion prediction equations (GMPEs) developed for spatial hazard modeling. The GMPEs consider different characteristics, such as earthquake magnitude, the distance between source and site, local soil conditions, and fault mechanism. The intensity measures are selected based on the seismic vulnerability of the component or system of interest, including peak ground acceleration, spectral acceleration, peak ground velocity, or peak ground displacement.

2.3 Infrastructure systems model development

The third step in the process is to develop a fragility-based computational model of the networked infrastructure using the fundamental graph theory. This involves creating a directed graph model of the community, represented by an $n \times n$ adjacency matrix $M(\mathcal{G}) = [m_{ij}]$, and mapping fragility functions to individual components based on their structural attributes. These fragility functions relate a given hazard intensity measure to the conditional probability of exceeding a particular damage state, such as insignificant, moderate, extensive, or complete. Fragility functions are often described using a lognormal cumulative distribution function given by

$$F_R[IM = im] = \Phi \left[\frac{1}{\beta_k} \cdot \ln \left(\frac{im}{\lambda_k} \right) \right] \quad (1)$$

in which Φ is the standard cumulative probability function, λ_k median capacity and $\beta_k = \sigma(\ln R)$ or logarithmic standard deviation associate with d_{s_k} . In addition to the basic parameters of construction type, occupational type, and seismic design code, other parameters such as service age and environment of the structure are considered to better capture the life-cycle of the infrastructure. Structural aging and strength degradation can significantly impact the fragility parameters of

structures, particularly the median fragility, which is most affected. The loss of section caused by corrosion and deterioration can cause the median fragility to decrease, but the decrease may not be linearly related to the fragility, which takes into account the dynamic response and nonlinear behavior of the structural component. Therefore, a 20% loss in section may not correspond to a 20% decrease in median fragility. Due to uncertainties in the degradation mechanisms, aging also affects the variability and uncertainty (characterized by β). As a result of aging, these variabilities tend to increase. Structural fragility parameters can be modified to take aging into account, and this can be done using a Bayesian procedure to update the fragility models used in the risk assessment (Ellingwood and Song 1996). To illustrate the outcome of this update, Figure 1 presents the fragility curves of an arbitrary building structure under different service ages.

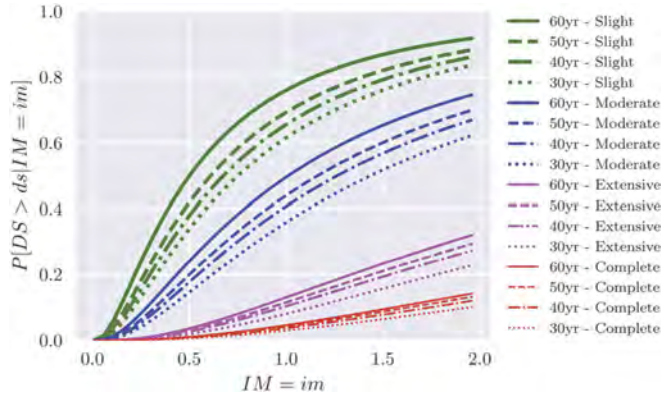


Figure 1. Illustrative fragility curves for an arbitrary building structure with different service age.

2.4 Physical damage and functionality analysis

The fourth step is to estimate each infrastructure component's damage and functionality states, given the hazard intensity measure. The damage estimate is obtained using the fragility functions given by Equation 2 to estimate potential damage to the physical infrastructure component. Given the fragility function F_R of an infrastructure component and hazard intensity measure IM , the conditional probability of damage measure is given by

$$P_f[DS \geq DS_k | IM = im] = \int_0^{im} \frac{1}{\sqrt{2\pi}\beta_k s} \exp\left[-\frac{1}{2} \left\{ \frac{\ln(s) - \lambda_k}{\beta_k} \right\}^2\right] ds \quad (2)$$

where $p_f(\cdot)$ denotes the probability of being at or exceeding a particular damage state, DS_k , for a given intensity measure, IM . Then, Monte Carlo simulations (MCS) are performed to estimate the physical damage to each infrastructure component. Subsequently, HAZUS restoration curves are used to estimate the functionality of each component immediately and days after a seismic event. Finally, the functionality estimates are used as input to an input-output (I-O) model to simulate the functionality of components by accounting for the interdependency between networked infrastructure. An I-O model uses a perturbation vector, given by u , to capture the inoperability of the components of a disrupted interconnected system due to cascading effects.

$$q = M(\mathcal{G})q + u \quad (3)$$

where $u = [u_1, u_2, \dots, u_n]^T$; $u_i \in [0, 1] \subset \mathbb{R}$ is the perturbation vector obtained from non-functionality of individual network components subject to seismic hazard and $q = [q_1, q_2, \dots, q_n]^T$; $q_i \in [0, \infty) \subset \mathbb{R}$ is the resulting non-functionality vector due to their

connections to the perturbed infrastructure components and their cascading failure. The non-functionally vector q can be calculated as follows:

$$q = \left(I - M(G)^T \right)^{-1} u \quad (4)$$

2.5 Life-cycle optimization and retrofit decision-making

Let R_i be the retrofit cost of a system of interest i ; T the (random) time of occurrence of the earthquake that may affect it, and L_i is the loss associated with earthquake loss for system i ; including damage and failure consequences, as well as repair and maintenance actions. L_i can be obtained by converting the DSs into monetary values. For buildings, repair costs are estimated by multiplying the square footage of each building type within that occupancy by the probability of that building type being in the given damage state and the repair costs per square foot for the given damage state (relative to the replacement cost). The structural loss for each structural system can be quantified as follows

$$L_i = CS_{occ} = BRC_{occ} \sum_{DV=IO}^c CS_{PL,i} = BRC_{occ} \sum_{DV=IO}^c p[DS = ds] RCS_{PL,occ} \quad (5)$$

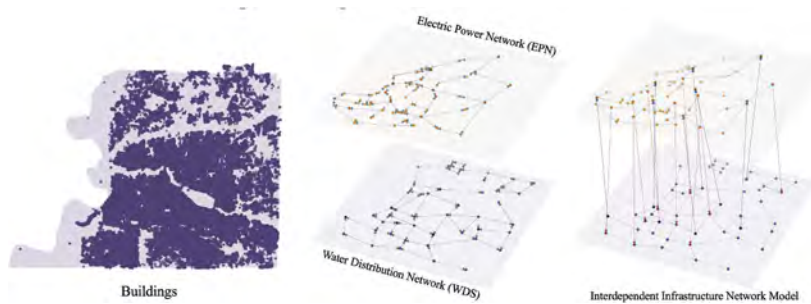


Figure 2. Buildings (left) and lifeline (right) systems of the MMSA. The figures show the directed graph for each networked lifeline system and their interdependent model.

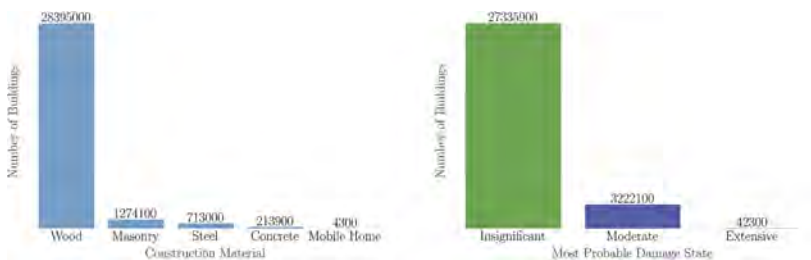


Figure 3. The number of buildings with various construction types (left) and most probable damage state subject to $M_w 7.1$ earthquake scenario (right).

where $CS_{PL,occ}$ is the cost of structural damage (repair costs) associated with damage state ds , and occupancy class occ , BRC_{occ} is the building replacement cost of occupancy class occ , as described in the HAZUS Inventory Technical Manual. $R_{CS_{PL,occ}}$ is the structural repair cost ratio (in % of building replacement cost) for occupancy class, i , in damage state, ds (refer to Table 112 of HAZUS Technical Manual). Then, the following objective function must be minimized to determine the optimal life-cycle-optimized community-level retrofit action:

$$U = \sum_{i=1}^N (R_i + E[L_i^{-qT}]) \quad (6)$$

where $E[\cdot]$ stands for expected value, and q is an adequate discount rate.

2.6 Case study: Memphis metropolitan statistical area (Mmsa), TN, US

This methodology is demonstrated through the case study of MMSA. The buildings, EPN, WDS, and boundary shapefiles were created using an extensive MMSA testbed database, including 306,003 buildings of various construction types and occupancy uses, collected by the Mid-America Earthquake Center. The community model was created with the Interdependent Networked Community Resilience Modeling Environment (IN-CORE), as shown in Figure 2. Fragility functions were assigned to each component based on their structural attributes. The Boore and Atkinson (2008) GMPE was used to generate two different scenario events with magnitudes $M_w 6.5$ and $M_w 7.1$ to study the effect of hazard intensity. Damage to all buildings and lifeline systems within the MMSA was evaluated using the mapped fragility curves and IMs. Component-level damage estimates were used to perform functionality and restoration analysis of buildings and networks, considering the interdependency between systems and the cascading failure of each network component using the I-O model.

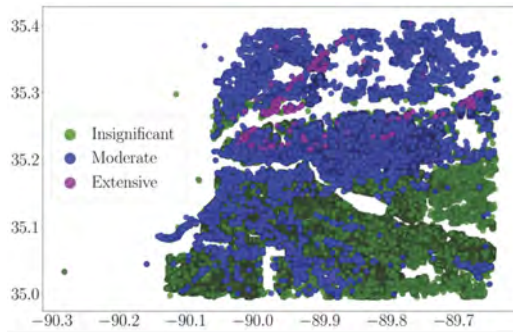


Figure 4. Most probable damage state subject to $M_w 7.1$ earthquake scenario.

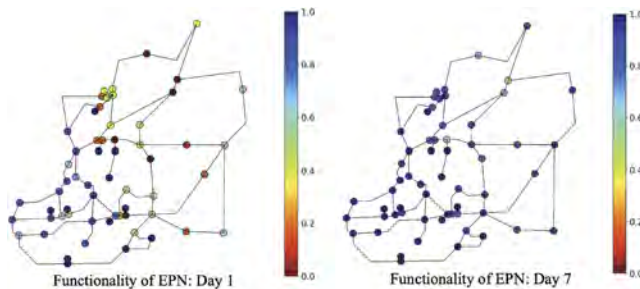


Figure 5. Functionality analysis of EPN substations by accounting for the interdependency between EPN and WDS subject to $M_w 7.1$ scenario earthquake.

2.7 Results and discussion

Figure 3 presents the number of buildings with various construction types. As can be seen, most of the buildings are wood construction. As a representative result, Figures 3 and 4 also present the statistics of the most probable damage state of buildings subject to $M_w 7.1$ scenario earthquake. Figure 4 presents example results obtained from functionality and restoration

Table 1. Building functionality estimates days following seismic events obtained by accounting for infrastructure interdependency.

Seismic Event	Functionality	1 day	3 days	7 days	30 days	90 days
M_w 6.5	Functional	30.2%	53.6%	98.6%	98.6%	98.6%
	Non-Functional	69.8%	46.5%	1.4%	1.4%	1.4%
M_w 7.1	Functional	16.8%	28.5%	86.5%	86.5%	86.5%
	Non-Functional	83.3%	71.5%	13.5%	13.5%	13.5%

analysis of EPN substations under M_w 7.1 scenario earthquake by considering the interdependency between EPN and WDS and the cascading failure of each network component using an I-O model (Haimes et al. 2005). Table 1 summarizes building functionality estimates by accounting for the interdependency between buildings, EPN, and WDS subject to M_w 6.5 and M_w 7.1 scenario earthquakes. Comparing the results for these two seismic events shows that high-intensity earthquake causes more significant impacts in terms of the number of buildings that do not operate normally to provide their regular and reliable pre-event services. The outcomes of the proposed methodology could be readily used as input to life-cycle optimization presented in the methodology section to investigate various community-level retrofit strategies and make informed decision-making. The results of this analysis can be used as input to social and economic models to quantify resilience metrics such as impacts of employment, household income, and population dislocation, as demonstrated in Roohi et al. 2021. This case study illustrates the capability of the proposed methodology to assist engineers and decision-makers in evaluating the vulnerability of critical buildings and lifeline systems and developing mitigation strategies to improve the seismic resilience of communities.

3 CONCLUSIONS

This paper presents a methodology for integrating life-cycle analysis into civil infrastructure resilience modeling and decision-making in seismic-prone communities. This integration allows assessing the performance of a structure throughout its lifespan to obtain a more comprehensive understanding of the impacts of the environment on infrastructure systems and how these systems can be made more sustainable and resilient. The proposed methodology is designed to model seismic life-cycle resilience of interdependent buildings and lifeline systems and inform resilience decisions directly related to the maintenance and retrofit of interdependent infrastructure to enhance community resilience. The methodology consists of community data collection, seismic hazard analysis, physical damage analysis, system-level functionality and restoration analysis, life-cycle optimization and retrofit decision-making. An illustrative case study is presented to demonstrate the implication of the methodology to perform seismic life-cycle resilience in US communities, including Shelby County, TN. The methodology will assist engineers and urban planners in assessing the vulnerability of critical buildings and lifeline systems and developing mitigation strategies to improve the seismic resilience of communities. The paper concludes by highlighting the need for integrated life cycle resilience modeling approaches capable of accounting for cascading impacts of the failure in components of infrastructure in the functionality of the networked system, accounting for structural aging, strength degradation, and retrofit, which can significantly impact the seismic performance of infrastructure systems.

REFERENCES

- Akiyama, M., Frangopol, D.M. and Matsuzaki, H., 2011. Life-cycle reliability of RC bridge piers under seismic and airborne chloride hazards. *Earthquake Eng. & Structural Dynamics*, 40(15),pp.1671–1687.
- Bai, J.W., Center, M.A.E. and Hueste, M.B., 2003. Seismic retrofit for reinforced concrete building structures. *Mid-America Earthquake Center, CM-4*

- Boore, D. M., and G. M. Atkinson. 2008. Ground-Motion Prediction Equations for the Average Horizontal Component of PGA, PGV, and 5%-Damped PSA at Spectral Periods between 0.01 s and 10.0 s. *Earthq. Spectra*, 24 (1): 99–138.
- Cremen, G., Galasso, C., McCloskey, J., Barcena, A., Creed, M., Filippi, M.E., Gentile, R., Jenkins, L.T., Kalaycioglu, M., Mentese, E.Y. and Muthusamy, M., 2023. A state-of-the-art decision-support environment for risk-sensitive and pro-poor urban planning and design in Tomorrow's cities. *International Journal of Disaster Risk Reduction*, 85, p.103400.
- Deierlein, G.G., McKenna, F., Zsarnóczay, A., Kijewski-Correa, T., Kareem, A., Elhaddad, W., Lowes, L., Schoettler, M.J. and Govindjee, S., 2020. A cloud-enabled application framework for simulating regional-scale impacts of natural hazards on the built environment. *Frontiers in Built Env.*, 6, p.558706.
- Ellingwood, B., and J. Song. 1996. *Impact of structural aging on seismic risk assessment of reinforced concrete structures in nuclear power plants*. Nuclear Regulatory Commission.
- Farahani, S., Shojaeian, A., Behnam, B. and Roohi, M., 2023. Probabilistic Seismic Multi-hazard Risk and Restoration Modeling for Resilience-informed Decision Making in Railway Networks. *Sustainable and Resilient Infrastructure*, pp.1–22.
- Haines, Y. Y., B. M. Horowitz, J. H. Lambert, J. R. Santos, C. Lian, and K. G. Crowther. 2005. "Inoperability Input-Output Model for Interdependent Infrastructure Sectors. I: Theory and Methodology." *J. Infrastruct. Syst.*, 11 (2): 67–79.
- Linger, S., Wolioskx, M. Los Alamos National Laboratory Report LA-UR-01-3361 ESRI Paper No. 889 Estimating Electrical Service Areas Using GIS and Cellular Automata. 2001.
- Roohi, M., J. W. van de Lindt, N. Rosenheim, Y. Hu, and H. Cutler. 2021. "Implication of building inventory accuracy on physical and socio-economic resilience metrics for informed decision-making in natural hazards." *Structural and Infrastructure Engineering*, 17 (4): 1–21.
- Roohi, M., Li, J., van de Lindt, J. 2022. Seismic functionality analysis of interdependent buildings and lifeline systems. 12th National Conference in Earthquake Engineering, Salt Lake City, UT.
- Linger, S., Wolioskx, M. Los Alamos National Laboratory Report LA-UR-01-3361 ESRI Paper No. 889 Estimating Electrical Service Areas Using GIS and Cellular Automata. 2001.
- Zheng, X.W., Li, H.N. and Gardoni, P., 2021. Life-cycle probabilistic seismic risk assessment of high-rise buildings considering carbonation induced deterioration. *Engineering Structures*, 231, p.111752.

Smart resilience: Capturing dynamic, uncertain and evolving lifecycle conditions

R. Rincon & J.E. Padgett

Rice University, Houston, TX, USA

ABSTRACT: Modern cities are becoming increasingly smart and interconnected, with the capacity to gather unprecedented amounts of information. However, available methods for resilience quantification lack agility to cope with the ever-changing conditions and data that underpin disaster resilience and lifecycle performance analysis. In this paper, we discuss the limitations in the models themselves, i.e. even though frameworks predict uncertain and temporally evolving system performance, they are unable to learn from new data. To address these limitations, we pose a ‘smart resilience modeling concept’ which presents the ability to update model estimations and to efficiently estimate the lifecycle resilience as new data emerges. Hypothetical examples on community infrastructure affected by deterioration effects and punctuated events are presented. This conceptualization is expected to lay a foundation for smart resilience models capable of capturing the dynamic, uncertain, and evolving characteristics of future environmental demands, societal characteristics, and infrastructure conditions.

1 INTRODUCTION

The exposure of the built infrastructure to disruptive events demands a comprehensive way to measure its resilience. The importance of its quantification lies in the need of communities to set a baseline, define resilience goals and actions, quantify progress, and to estimate the social benefits and losses of resilience-related decisions (Committee on Increasing National Resilience to Hazards and Disasters *et al.* 2012). Modeling techniques are needed to establish such measurement in a prospective way; we need to predict communities and systems’ capacity to withstand, adapt to and progressively recover after a disruption (Bruneau *et al.* 2003, Cimellaro *et al.* 2010). This requires interdisciplinary work and, although it has been a field of active research in the past decade, gaps and questions about measuring resilience still exist.

In the engineering community, there are difficulties in measuring resilience because of its multidimensional nature, the lack of evidentiary data and the uncertain and evolving conditions that underpin disaster resilience (National Academies of Sciences, Engineering, and Medicine 2019). Different efforts have been made to improve resilience estimation; for example, considering time-affected conditions of the engineering systems (Ghosh and Padgett 2010, Rokneddin *et al.* 2014, Jia and Gardoni 2019, Capacci *et al.* 2020); acknowledging the absorptive capacity of the system to accommodate or reduce the events’ impacts (Ouyang and Dueñas-Osorio 2012, Decò *et al.* 2013); take account of the availability of resources needed for recovery processes (González *et al.* 2016); the multi-hazards conditions and cascading effects (Hernandez-Fajardo and Dueñas-Osorio 2013); the varying demand-supply of infrastructure services after events (Ouyang and Dueñas-Osorio 2012, Blagojević *et al.* 2022), among others. However, existing resilience modeling paradigms are designed with constrained inputs and model settings, and therefore easily become outdated over time.

To solve this limitation, we pose the idea of a ‘smart resilience modeling approach’. We consider the infrastructure systems’ resilience as a dynamic and uncertain quantity that evolves as

data and new modeling approaches emerge. A ‘smart’ resilience model should be able to continuously learn from new data gathered, cope with shifts in environmental demands, consider variations in social needs and infrastructure uses, handle new monitoring parameters from emerging technologies, and others, adapting to the dynamic conditions of the systems. This paper presents the needs of such a framework using hypothetical examples. It is shown that lacking flexibility for coping with the emerging sources mentioned above may hinder the community spatial resilience, reduce their ability to identify and adaptively learn from varying threats and diminish the ability to understand the community progress towards resilience goals, with probable worse impacts within the most vulnerable populations.

2 LIFECYCLE RESILIENCE MODELING

Infrastructure lifecycle and resilience assessments are commonly separate analyses given the differences in their temporal scale. Lifecycle analyses typically evaluate the system time-dependent performance in which progressive and punctuated events can affect the infrastructure during decades of service (Sanchez-Silva *et al.* 2011). On the other hand, resilience assessments are usually related to the recovery phase after a punctuated disturbance occurred, often framed in a scale from days to years (see Figure 1). Recent emphasis has been given to the joint evaluation of lifecycle and resilience aiming to capture the increased vulnerability in aging infrastructure, shifts in user-demands over time and the adaptation of communities after shock-based events. However, lifecycle resilience modeling paradigms still lack flexibility to include these variations as new knowledge about the system becomes available at any point at time. This makes the lifecycle resilience modeling challenging to be repeatable, generalizable and, sometimes, impractical to be applied (National Academies of Sciences, Engineering, and Medicine 2019).

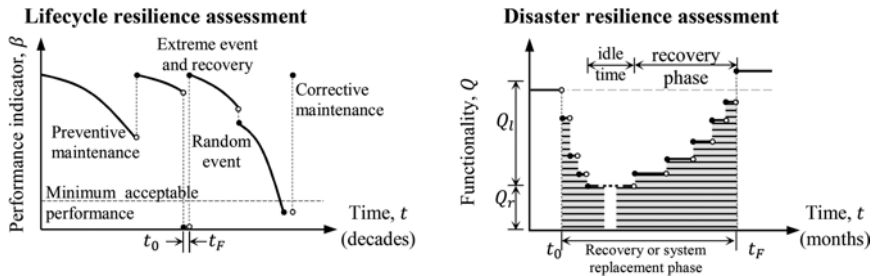


Figure 1. Lifecycle resilience analysis and resilience assessment time scales.

2.1 Smart resilience modeling

“Smart resilience” has appeared recently as a concept to depict the use of emerging technologies and intelligent practices (e.g. models, algorithms or tools) to enhance the system’s capacity to handle, absorb, react and recover from any disturbance (DesRoches and Taylor 2018, Kumar *et al.* 2019, Padgett *et al.* 2022). Different examples in the literature demonstrate these smart technologies has permeated the resilience lifecycle assessment, including real-time health monitoring, physical and social sensors, IoT, and digital twins (Li and Pozzi 2019, Fan *et al.* 2021, Panakkal and Padgett 2022, Yabe *et al.* 2022). Also the evaluation of the benefits obtained from introducing these smart technologies for infrastructure monitoring purposes and the adaptability gained by the possibility of on-time decision-making have seen a tremendous increase of interest from researchers (Rabiei and Modarres 2013, Malings and Pozzi 2016, Zuluaga and Sánchez-Silva 2020). However, most of the recent contributions tend to focus on specific and individual portions of the infrastructure resilience lifecycle, i.e. they concentrate on introducing data acquisition techniques for characterization of exposed inventory, definition of system parameters to be monitored, or estimation of system performance during the post-disaster response phase.

To address the measurement and estimation of infrastructure resilience we pose a ‘smart modeling paradigm’. We focus on the modeling paradigm itself to tackle the dynamic, uncertain and

evolving lifecycle conditions over time. Smart resilience modeling refers to algorithms able to infuse existing modeling techniques with the ever-changing conditions measured or observed on the systems' dynamics (social, environmental, physical, and others). Hence, these must be flexible algorithms able to evolve as new knowledge and innovative approaches arise in the infrastructure lifetime horizon (see Figure 2).

Figure 2 depicts, conceptually, the system resilience estimations influenced by potential sources of data such as periodic or continuous observations (red stars and lines, respectively). For example, with the vast advances in smart technologies, shifts in the functionality of the system could be suddenly observed. On the other hand, performance estimates of the system are predicted by means of existing algorithms, which may include the effect of degradation stressors (blue lines) or the estimation of recovery trajectories after a shock event (green line). One key goal of the smart resilience concept is to continuously fuse these different knowledge sources to inform future resilience models. The outcomes of such approaches result in mean estimates of the system performance with bounds that show the varying uncertainty and its relationship with data collection efforts (black solid and dashed lines). Such a modeling paradigm requires intelligent algorithms to estimate, efficiently and confidently, the actual resilience of the system as time evolves. Recursive Bayesian algorithms, active learning, and transfer learning techniques, among others, are envisioned for this purpose. Such methods can help to limit the resources required for computation and data gathering, overcome data limitations and introduce the heterogeneous gathered knowledge into the assessment of future systems' resilience.

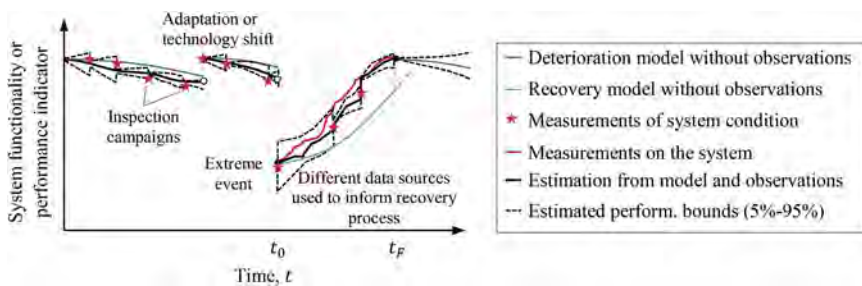


Figure 2. Resilience modeling of infrastructure performance over time and potential to leverage different data sources in a smart resilience framework.

3 ILLUSTRATIVE EXAMPLE

3.1 Problem definition

A rather simple transportation network is selected to explain the smart resilience approach (Figure 3). It consists of seven cities connected through 10 roads which condition depends on bridges' availability. Multi-span simply supported concrete bridges (assumed as representative of the bridges in the network) are affected by deterioration processes related to chloride ingress (Ghosh and Padgett 2010). The bridges' capacity to sustain service loads (i.e. live loads) and extreme loads (represented by seismic events) are affected. The live loads crossing the bridges are represented probabilistically by a three parameter Weibull distribution following Chowdhury *et al.* (2013), and seismic loads by a point of fault rupture that generates events whose magnitude follows a truncated Gutenberg-Richter model ($M_{w,min} = 5$, $M_{w,max} = 8$, $b = 1$). The loads and magnitude probability distributions are considered fixed in this study.

Bridges in this network are the only components considered susceptible to failure producing a complete road closure. Failure events related to live loads occur when a live load exceeds the bridge's moment capacity or the reliability index (β) reaches a value of $\beta = 2.6$ (Vishnu 2019). Besides, when a seismic event occurs leading to extensive damage is also considered as bridge failure (or if $\beta = 1.5$). It is assumed that a failure condition always requires a complete bridge closure for intervention purposes.

Inspection campaigns, information about failure events and data collected during repair activities are documented in Table 1. Bridge deterioration affected components are examined (using intrusive approaches) every 5 years. Deck or total bridge replacements are reported if the moment capacity has been exceeded on the bridge's deck or a seismic event damaged structures within the network. Finally, field observations of the progress and used times are collected during bridge interventions. These sources of information are used to update model inputs, model parameters or to infuse authoritative data within the predicted model estimations.

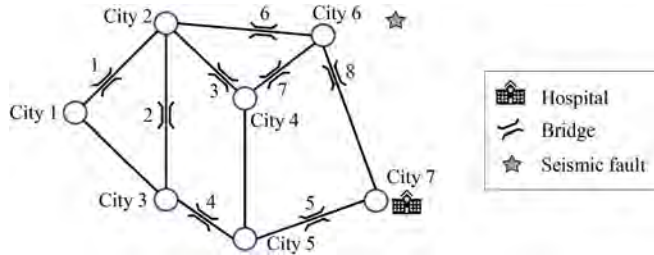


Figure 3. Hypothetical transportation network.

Table 1. Timeline of data collected and event occurrence.

Year	Event type	Data gathered	Unit
0	Exposed assets	Bridges ages: 45, 24, 26, 12, 47, 37, 19, 37	years
5	Bridge inspection	Deterioration affected parameters*	cm
15	Bridge inspection	Deterioration affected parameters*	cm
17	Seismic event, $M_w=5.7$	Damaged condition	0,0,0,0,1,0,1,0
25	Bridge inspection	Deterioration affected parameters*	cm
35	Bridge inspection	Deterioration affected parameters*	cm
36	Exceeded moment capacity on a bridge	Damaged condition	0,0,0,0,0,1,0,0
38	Seismic event, $M_w=7.8$	Damaged condition	0,1,0,1,0,1,0,1
40	Bridge inspection	Deterioration affected parameters*	cm

* Deterioration affected parameters correspond to rebars' diameter measured on columns, deck and elastomeric bearing dowels (data not shown here for brevity).

3.2 Lifetime reliability and resilience assessment

Given the small size of the network, the system failure evaluation is performed through matrix-based approaches (Kang *et al.* 2008). This method enumerates the m possible 'network states' into a matrix of system events \mathbf{C} ; i.e. the entire sample space of mutually exclusive and collectively exhausting (MECE) bridge states combinations or 'network states'. The probability of occurrence of each MECE events, arranged in vector $\mathbf{P}(\mathbf{t})$, is obtained using individual bridges' failure probabilities; these are time-dependent functions conditioned on seismic intensities im or live loads w , $p_S(im, t)$ and $p_L(w, t)$ respectively. Finally, the probability of disconnection $Pr(\mathbb{D}|t)$ of any source-terminal pair can be obtained using this method combined with network science algorithms (see details in Kang *et al.* 2008). In the present study, the probability of losing connection between any city and City 7 is defined as a network-level reliability metric of interest.

Additionally, the method has been extended to obtain the probability of network disconnection $N_{\mathbb{D}}$; a vector \mathbf{D} is created using the indicator function over the connectivity of the system for the MECE events (0 if the network is connected, and 1 otherwise). Then, $N_{\mathbb{D}}$ is computed as:

$$Pr(N_{\mathbb{D}}|t) = \mathbf{D}^T \mathbf{P}(\mathbf{t}) \quad (1)$$

For seismic events, the bridge's failure probability $p_S(im)$ is computed from the bridge fragility functions proposed by (Rokneddin *et al.* 2014) and the intensity measure obtained from the (Atkinson and Boore 1995) ground motion model. Hence, the network states probability vector \mathbf{P} is also conditioned on the magnitude of the event. The analysis of the unconditional failure probability of the system $P_{sys,s}$ requires the integration of the network failure events over the joint probability density function of the event magnitudes (Kang *et al.* 2008). In this study, $P_{sys,s}$ is computed for each time t of analysis obtaining a lifetime metric useful for decision making.

The system failure probability for extreme live loads depends on $p_L(w,t)$, which is obtained from the surrogate model presented by Vishnu (2019) for exceeding the allowable moment in a bridge deck. To consider the uncertainty on the bridge structural parameters and in live loads w (inputs required of the surrogate model), p_L is computed using 10,000 Monte Carlo (MC) simulations. Mean failure probability p_L for each year t is obtained by updating the deck reinforcement bar diameter on the MC analysis; then, p_L is used for the lifetime network reliability analysis.

In addition to reliability metrics, average network resilience is computed from the network states. Each network state, represented by one MECE event, indicates a unique network condition, thus MC analysis is used to simulate the bridge recovery processes. The recovery simulation of each damaged bridge follows the approach proposed by Decò *et al.* (2013) and simultaneous repairs are assumed to occur if the number of available crews (n_{crews}) is larger than one. The simulated repair schedule defines the time at which functionality at the road level is recovered, resulting in a stepwise network recovery profile. The 'network functionality' η is assumed to be equivalent to the 'global network efficiency' (weighted version) often used in network science (LiYing Cui *et al.* 2010). The time-dependent efficiency computed during the repair phase is normalized by the unperturbed network functionality η_0 , canceling out the normalization factor:

$$Q(t_r) = \frac{\eta(t_r)}{\eta(t_{r0})} = \frac{n(n-1) \sum_{j \neq i} \frac{1}{d_{ij}(t_r)}}{n(n-1) \sum_{j \neq i} \frac{1}{d_{ij}(t_{r0})}} \quad (2)$$

where $d_{ij}(t_r)$ refers to the distance between ij pairs considering all the available roads at recovery time t_r . The resilience metric is computed using Equation 3, with $Q(t)$ as the functionality metric, T_R assumed as the total time required to finish repair activities within the network, and a target functionality TQ, commonly assumed as 100% (Ouyang and Dueñas-Osorio 2012). This proposed metric depicts the evolution of the global system functionality (in terms of distance traveled by the users), between the nodes of the network, relative to the original system state.

$$R(t_r) = \frac{\int_0^{T_R} Q(t_r) dt_r}{\int_0^{T_R} TQ(t_r) dt_r} \quad (3)$$

The average network resilience obtained for each MECE event is arranged in vector \mathbf{U} . It is used to obtain the time-dependent mean network resilience N_R :

$$N_R(t) = \mathbf{U}^T \mathbf{P}(t) \quad (4)$$

4 RESULTS: SMART TIME-DEPENDENT RESILIENCE ASSESSMENT

New knowledge that emerges at a certain time t are denominated here as 'learning events'. If a certain learning event occurs during time t , the subsequent step should consider the knowledge acquired through a fusion process. For example, bridge mean failure probabilities for extreme live loads are initially predicted using a deterioration model without introducing any observation (see Figure 4a). These, translated into reliability indexes β , can help to define the expected year when bridge deck replacement must take place. Following a recursive Bayesian estimation approach, specifically the Kalman filter algorithm (Kalman 1960), lifetime predictions are updated by infusing the knowledge obtained from the inspection cycles defined in Table 1. The first inspection is clearly depicted by a large shift on the predicted values for β towards the "true performance" (i.e. when complete knowledge is available); beyond that point the recursive Bayesian approach improves the

model predictions, increasing its accuracy with every new observation. If after each updating process large computational efforts are needed, then smart algorithms can also be used to reduce the burden. For example, active learning reliability estimation methods, e.g. using gaussian process regression and MC analysis (Echard *et al.* 2011), are possible solutions for recomputing the large MC analysis. In addition to enhancing individual performance indicators, infusing the knowledge from observations clearly influences the computed mean network total restoration time T_R (i.e. the estimated performance) as depicted in Figure 4b. Annual expected T_R is relatively small considering that the failure associated to live loads, for this particular example, presents a low failure probability.

Observations about bridge deterioration on column and elastomeric bearing dowel rebars affect the expected seismic response of bridges. The model for parameterized seismic fragility functions (Rokneddin *et al.* 2014) is suitable for time-dependent analysis and it is easily updated as new information about the components' conditions is collected. However, although directly measured, data gathered is only representative of the real (yet uncertain) structural state. The probability of extensive damage predicted by the fragility functions is also updated indirectly as new information from the rebar condition is considered in the recursive Bayesian estimation. Figure 5a depicts the evolution of approximate seismic reliability index and the impact of new data introduced to the model. The implications of the observations on the bridge's conditions are propagated to the network reliability N_R as observed in Figure 5b. After some sequential observations the model greatly improves its guesses about the future resilience, reducing the error between the predicted and the 'true' system performance indicators.

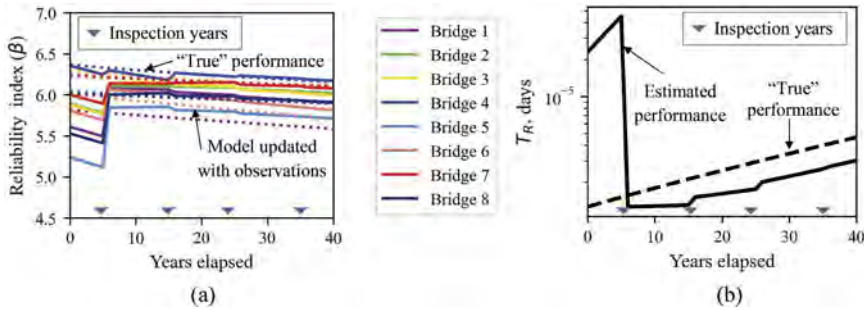


Figure 4. Model estimations and updated predictions for a) bridge-level reliability index and b) time-dependent mean network downtime for extreme live loads.

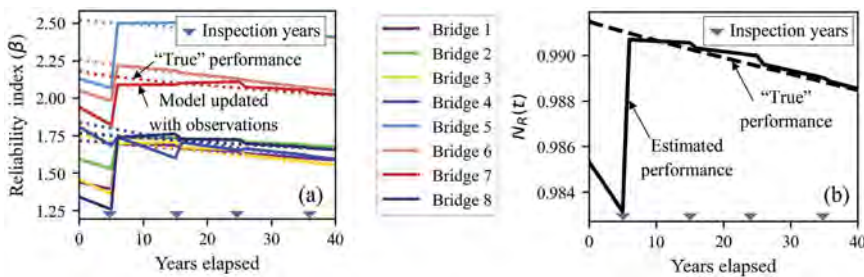


Figure 5. Model estimations and updated predictions for a) bridge-level reliability index for an event of Mw=6 and b) time-dependent mean network resilience for seismic events.

Finally, the occurrence of seismic events in years 17 and 38, and the failure of bridge N° 6 in year 36 require the total replacement of some bridges. Once these replacements are done, the recursive Bayesian estimation must be initiated again on those bridges using the information of the new conditions (e.g. new column rebar area). The introduction of renewed conditions is depicted as an abrupt positive modification on the mean network downtime and mean network resilience (see Figure 6). Note that this change influences both the 'true' and estimated performance; it occurs considering that the 'true' network vulnerability is also diminished with newer bridges. Repair

times measured during the intervention efforts could also be used to additionally improve the distributions of the model inputs (not included for brevity). This illustrative example shows that the model predictions sequentially updated with observations tend to represent more accurately the performance metrics at the component (bridge) and system (network) level.

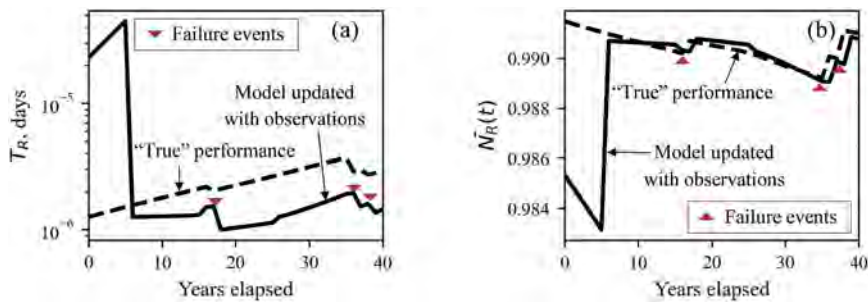


Figure 6. “True” and updated prediction of a) mean network downtime for live loads and b) mean network resilience for seismic demands, both including failure events occurred.

5 CONCLUSIONS

Models for resilience estimation commonly focus on instantaneous infrastructure resilience, lacking the ability to introduce data gathered throughout the system lifecycle. Also, existing models may not be able to improve the model parameters, not being able to cope with real ever-changing conditions. This paper attempts to review the challenges of such modeling frameworks and provides the ‘smart resilience’ concept as a practical solution. Smart resilience modeling refers to algorithms able to continuously learn from new data gathered, cope with shifts in environmental demands, consider variations in social needs and infrastructure uses, handle new monitoring parameters from emerging technologies, and others, adapting to the dynamic conditions of the systems. Hence, it is essential to use ‘smart’ algorithms such as active learning schemes to improve information gain, transfer learning techniques to cope with heterogenous and changing conditions, or recursive Bayesian approaches for continuous updating processes, among others. An illustrative example using a hypothetical transportation network is presented. Deteriorated conditions of aging-bridge parameters (specifically steel rebars) are assumed to be collected as well as the dates of bridge replacements (after failure occurs). The introduction of sequential data gathered to update existing model predictions were shown to improve the accuracy of metrics of interest, such as the bridge-level reliability index and network-level annual expected recovery times and annual mean resilience, demonstrating the importance of working toward smart resilience approaches.

ACKNOWLEDGMENTS

The authors would like to acknowledge the support provided by the National Science Foundation under Award Number CMMI-2227467. The first author would also like to acknowledge the grant support from the Fulbright-Minciencias scholarship program.

REFERENCES

- Atkinson, G.M. and Boore, D.M., 1995. Ground-motion relations for eastern North America. *Bulletin of the Seismological Society of America*, 85 (1): 17–30.
- Blagojević, N., Hefti, F., Henken, J., Didier, M., and Stojadinović, B., 2022. Quantifying disaster resilience of a community with interdependent civil infrastructure systems. *Str. and Infr. Engineering*, 0 (0): 1–15.
- Bruneau, M., Chang, S.E., Eguchi, R.T., Lee, G.C., O’Rourke, T.D., Reinhorn, A.M., Shinozuka, M., Tierney, K., Wallace, W.A., and von Winterfeldt, D., 2003. A Framework to Quantitatively Assess and Enhance the Seismic Resilience of Communities. *Earthquake Spectra*, 19 (4): 733–752.

- Capacci, L., Biondini, F., and Titi, A., 2020. Lifetime seismic resilience of aging bridges and road networks. *Structure and Infrastructure Engineering*, 16 (2): 266–286.
- Chowdhury, M., Putman, B., Pang, W., Dunning, A., Dey, K., Chen, L., and Clemson University. Dept. of Civil Eng., 2013. *Rate of deterioration of bridges and pavements as affected by trucks*. FHWA.
- Cimellaro, G.P., Reinhorn, A.M., and Bruneau, M., 2010. Framework for analytical quantification of disaster resilience. *Engineering Structures*, 32 (11): 3639–3649.
- Committee on Increasing National Resilience to Hazards and Disasters, Committee on Science, Engineering, and Public Policy, Policy and Global Affairs, and National Academies, 2012. *Disaster Resilience: A National Imperative*. Washington, D.C.: National Academies Press.
- Decò, A., Bocchini, P., and Frangopol, D.M., 2013. A probabilistic approach for the prediction of seismic resilience of bridges. *Earthquake Engineering & Structural Dynamics*, 42 (10): 1469–1487.
- DesRoches, R. and Taylor, J., 2018. The promise of smart and resilient cities. *The Bridge*, 48 (2).
- Echard, B., Gayton, N., and Lemaire, M., 2011. AK-MCS: An active learning reliability method combining Kriging and Monte Carlo Simulation. *Structural Safety*, 33 (2): 145–154.
- Fan, C., Zhang, C., Yahja, A., and Mostafavi, A., 2021. Disaster City Digital Twin: A vision for integrating artificial and human intelligence for disaster management. *Int. J. of Inf. Management*, 56, 102049.
- Ghosh, J. and Padgett, J.E., 2010. Aging Considerations in the Development of Time-Dependent Seismic Fragility Curves. *Journal of Structural Engineering*, 136 (12): 1497–1511.
- Ghosh, J. and Padgett, J.E., 2012. Impact of multiple component deterioration and exposure conditions on seismic vulnerability of concrete bridges. *Earthquakes and Structures*, 3 (5): 649–673.
- González, A.D., Dueñas-Osorio, L., Sánchez-Silva, M., and Medaglia, A.L., 2016. The Interdependent Network Design Problem for Optimal Infrastructure System Restoration: The interdependent network design problem for infrastructure restoration. *Computer-Aided Civil and Infr. Engineering*, 31 (5): 334–350.
- Hernandez-Fajardo, I. and Dueñas-Osorio, L., 2013. Probabilistic study of cascading failures in complex interdependent lifeline systems. *Reliability Engineering & System Safety*, 111: 260–272.
- Jia, G. and Gardoni, P., 2019. Stochastic life-cycle analysis: renewal-theory life-cycle analysis with state-dependent deterioration stochastic models. *Structure and Infrastructure Engineering*, 15 (8): 1001–1014.
- Kalman, R.E., 1960. A New Approach to Linear Filtering and Prediction Problems. *Journal of Basic Engineering*, 82 (1): 35–45.
- Kang, W.-H., Song, J., and Gardoni, P., 2008. Matrix-based system reliability method and applications to bridge networks. *Reliability Engineering & System Safety*, 93 (11): 1584–1593.
- Kumar, S.A.P., Bao, S., Singh, V., and Hallstrom, J., 2019. Flooding disaster resilience information framework for smart and connected communities. *Journal of Reliable Intelligent Environments*, 5 (1): 3–15.
- Li, S. and Pozzi, M., 2019. Predicting the Condition Evolution of Controlled Infrastructure Components Modeled by Markov Processes. *South Korea*, 8.
- LiYing Cui, Kumara, S., and Albert, R., 2010. Complex Networks: An Engineering View. *IEEE circuits and systems magazine (New York, N. Y. 2001)*, 10 (3): 10–25.
- Malings, C. and Pozzi, M., 2016. Value of information for spatially distributed systems: Application to sensor placement. *Reliability Engineering & System Safety*, 154, 219–233.
- National Academies of Sciences, Engineering, and Medicine, 2019. *Building and Measuring Comm. Resilience: Actions for Comm. and the Gulf Research Program*. Washington, D.C.: National Acad. Press.
- Ouyang, M. and Dueñas-Osorio, L., 2012. Time-dependent resilience assessment and improvement of urban infrastructure systems. *Chaos: An Interdisciplinary Journal of Nonlinear Science*, 22 (3), 033122.
- Padgett, J.E., Panakkal, P., and González, C., 2022. Chapter 12 – Infrast. impacts and vulnerability to coastal flood events. In: S. Brody, Y. Lee, and B.B. Kothuis, eds. *Coastal Flood Risk Red. Els.*, 151–165.
- Panakkal, P. and Padgett, J.E., 2022. OpenSafe Fusion [online]. *OpenSafe Fusion*. Available from: <https://www.opensafefusion.com/#> [Accessed 18 Apr 2022].
- Rabiei, M. and Modarres, M., 2013. A recursive Bayesian framework for structural health management using online monitoring and periodic inspections. *Reliability Eng. & System Safety*, 112: 154–164.
- Rokneddin, K., Ghosh, J., Dueñas-Osorio, L., and Padgett, J.E., 2014. Seismic Reliability Assess. of Aging Highway Bridge Networks with Field Instrum. Data and Correlated Failures, II: Application. *Earthquake Spectra*, 30 (2): 819–843.
- Sanchez-Silva, M., Klutke, G.-A., and Rosowsky, D.V., 2011. Life-cycle performance of structures subject to multiple deterioration mechanisms. *Structural Safety*, 33 (3): 206–217.
- Vishnu, N., 2019. Multi-threat Sust. Assessm. of Bridges and Bridge Networks. Rice University, Texas.
- Yabe, T., Rao, P.S.C., Ukkusuri, S.V., and Cutter, S.L., 2022. Toward data-driven, dynamical complex systems approaches to disaster resilience. *Proc. of the National Acad. of Sciences*, 119 (8), e2111997119.
- Zuluaga, S. and Sánchez-Silva, M., 2020. The value of flexibility and sequential decision-making in maintenance strategies of infrastructure systems. *Structural Safety*, 84: 101916.

*MS4: Vibration-based structural health monitoring, damage
identification and residual lifetime estimation*

Organizers: E. Reynders, G. Lombaert, E. Chatzi & C. Papadimitirou



Taylor & Francis

Taylor & Francis Group

<http://taylorandfrancis.com>

Structural damage estimation using short-time Fourier transform and improved convolution neural networks

C. Shi, Y. Aoues, R. Troian, D. Lemosse & H. Bai

Laboratoire de Mécanique de Normandie (LMN), Rouen, Normandie, France

ABSTRACT: Convolutional Neural Network (CNN) has demonstrated its excellent prospects in vibration-based structural damage detection due to its strong ability of feature learning and processing big data. However, most existing CNN-based damage detection methods can only allow damage pattern recognition, which may lead to the inability to identify and quantify unknown damage patterns. In this study, a new method called modified convolutional neural network based on Short-Time Fourier Transform (STFT) is developed for structural damage detection. The IASC-ASCE benchmark is used to evaluate the proposed method. Firstly, the vibration signals of different damage patterns of the benchmark structure are simulated based on its finite element model; secondly, STFT is performed to obtain their corresponding spectrograms; thirdly the spectrograms related to different damage patterns are fed into the CNN training; finally, a condition-based damage function is proposed to estimate the severity of any damage mode.

1 INTRODUCTION

Human beings in modern society are increasingly dependent on critical civil engineering facilities such as bridges, housing structures, water engineering, power generation systems, etc. Due to human and environmental factors, these infrastructures inevitably suffer structural degradation and deterioration during their service life. Structural damage will make the performance and reliability of the structure degrade. In some extreme cases, such as an earthquake or sudden overload, structural damage may even lead to catastrophic accidents, thus causing substantial economic losses and destructive social impacts. Therefore, driven by product life safety, human life safety, and economic impact, many large engineering structures and infrastructures urgently need effective means to assess their health conditions during service and to control or repair the possible damage. Structural health monitoring has become a new frontier research area in civil and structural engineering.

The study of damage identification methods has become essential in the health monitoring of large and complex structures. Damage to civil structures is diverse, ranging from simple structures (e.g., beam structures, shear structures) to complex structures (e.g., frame structures), all of which require damage quantification. There are various damage identification methods, they can be roughly divided into model-based and non-model-based methods (Shi 2012). Model-based methods are suitable for simple structures, which depend on a mathematical model and assume that the system is linear and time-invariant. Damage diagnosis is achieved by studying the variation of the dynamic parameters of the structure (stiffness, natural frequency, damage rate, etc.). In the non-model approach, sensors extract data from the structure for diagnosis instead of obtaining structural parameters. This approach is suitable for real-time damage detection of complex structures. Such techniques include flexibility-based model updating methods (Kodikara 2016), combined wavelet Hilbert transform (Mahato 2017), etc. Thanks to the increasing computational power and wide availability of low-cost sensors, data-driven

non-model based structural damage methods are more popular, and deep learning algorithms are increasingly used in vibration-based structural damage detection (Elshafey et al., 2010, Grande and Imbimbo 2012, Gu 2018). However, most existing CNN-based damage detection methods can only perform damage pattern recognition, which may lead to the inability to identify and quantify unknown damage patterns (Khodabandehlou 2019). In this study, we propose a new method, using a modified convolutional neural network based on short-time Fourier transform (STFT), for structural damage detection. The IASC-ASCE benchmark is adopted to evaluate the proposed method (Johnson 2004).

In the rest of the paper, the proposed method is described in Section 2. This section overviews four parts: the IASC-ASCE benchmark structure, the structural damage estimation pipeline, the Short Time Fourier Transform, and the proposed improved CNN by adding the “Probability of Damage” (PoD) function. Section 3 firstly introduces the basic damage patterns of benchmark structure used for CNN training and shows the corresponding damage values of the fundamental damage patterns; secondly, defined damage patterns are used for CNN testing, and the performance of the proposed approach is evaluated. Moreover, the structural damage estimation outputs expressed in terms of PoD scores and their correlations are discussed. Conclusions are given in Section 4.

2 DESCRIPTION OF THE PROPOSED METHOD

2.1 Benchmark description

The IASC-ASCE benchmark structure is a four-story, two-bay by two-bay steel-frame scale model structure built in the Earthquake Engineering Research Laboratory at the University of British Columbia, Canada (Johnson 2004). As shown in Figure 1, the footprint dimensions are 2.5 m × 2.5 m and the height of the frame is 3.6 m. Two parallel steel rods are installed diagonally at each bay to provide bracing. In this work, we have used the acceleration signal of 16 nodes of the structure, marked with green points. These measurements points are located at the middle of each side of the structure, two in the x and two in the y directions per floor (called $\ddot{y}_1, \ddot{y}_2, \dots, \ddot{y}_{16}$ in Figure 1).

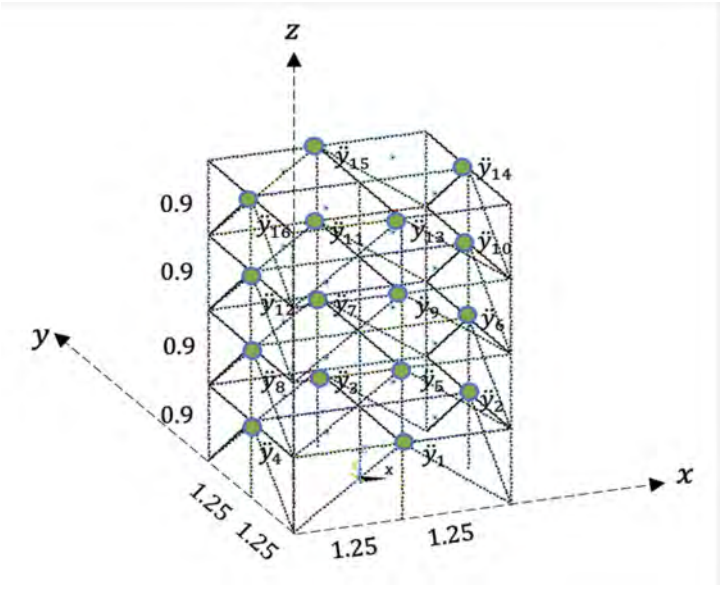


Figure 1. Model of the benchmark structure and location of 16 measured nodes, marked with green points.

2.2 Structural damage estimation procedure

A structural damage estimation pipeline is summarized in this section. The proposed pipeline can automatically learn the failure features and identify the health condition of the structure from the original vibration signals. The overall procedure of the proposed structural damage estimation pipeline is shown in Figure 2. The vibration signals for different damage modes are acquired at fixed measurement points on different finite element models of the IASC-ASCE benchmark structure. Afterward, the original vibration signal is truncated by a sliding window, which allows the generation of a set of sub-time series. The Short Time Fourier Transform of these generated sub-samples is then used as the input to the CNN. Since the main objective of this paper is to explore the efficacy and significance of the proposed PoD function, the damage quantization module is used. The CNN is trained with the known training set data of the underlying damage pattern, and then a test data set of the unknown damage pattern is used to verify the effectiveness of the proposed method for the detection of the unknown damage pattern.

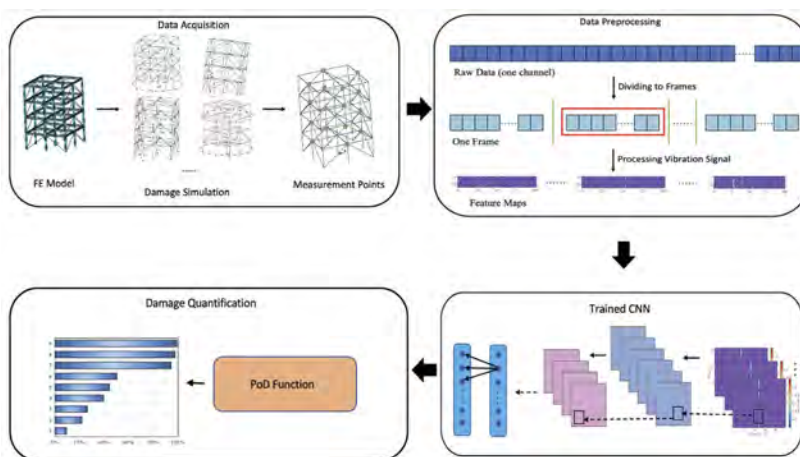


Figure 2. General pipeline of structure damage estimation.

2.3 Short-Time Fourier Transform (STFT)

The Short-Time Fourier Transform (STFT) is a popular method for analyzing nonstationary signals (Griffin and Lim 1984). The STFT obtains the frequency domain distribution of a waveform signal at a specific time through a time window function, and the time distribution of the frequency through the movement of the time window on the time axis, so that the STFT can obtain both the time and frequency domain characteristics of the signal. The visual representation in the time-frequency domain using STFT is called spectrogram. Spectrograms add time to the analysis of the Fast Fourier Transform (FFT) allowing the localization of both time and frequency. The Short-Time Fourier Transform is given by

$$S(\omega, \tau) = \int f(t)g^*(t - \tau)e^{-j\omega t} dt \quad (1)$$

where: “*” is the complex conjugate symbol; $g(t)$ is the time window function; $f(t)$ is the analyzed signal, and the STFT result $S(\omega, \tau)$ reflects the signal component of the analyzed signal at the frequency ω and the moment τ .

We assume that the experimental damage patterns from the paper (Dyke 2003) are used as the basic damage patterns $i(i = 0, 1, \dots, 8)$ of the structure and assign the corresponding damage indexes $Ds_i(i = 0, 1, \dots, 8)$ to them. The more severe the damage condition of the structure, the bigger the value of the damage index, Ds_0 means undamaged. For each damage

pattern, the number of channels of the sampled signal is 16, the sampling frequency is 1000Hz, and the sampling time is 4000s (i.e. 400,000 data points). As shown in the “Data Pre-processing” part of Figure 2, we divide the data for each channel into “Frames”, by defining the “Frame” length as $128 * 128$. For each data “Frame”, we perform the Short-Time Fourier Transform in order to get the spectrogram, the time-length of STFT is $128 * 128 / 1000 = 16.384s$, the frequency-length of STFT is 50Hz (discard useless information in high frequency). Figure 3 shows an example of the spectrograms obtained from the Short-Time Fourier Transform of the vibration signal on the undamaged IASC-ASCE benchmark structure, which contains the information of the damage features. When the structural damage varies, the spectrograms of the corresponding vibration signal also change. Therefore, for one channel of data (4000s), we can get $400,000 / (128 * 128) \approx 244$ spectrograms; for each damage pattern i , we have 16 channels, so we can get $16 * 244 = 3904$ spectrograms; for all damage patterns, we can get $9 * 16 * 244 = 3,5136$ spectrograms.

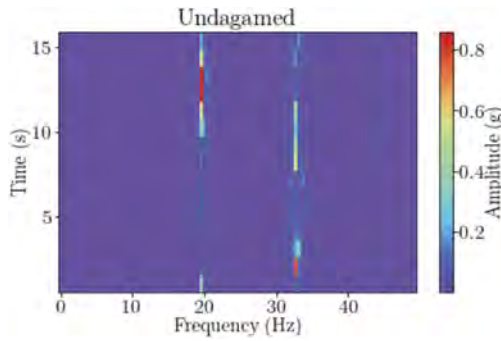


Figure 3. STFT spectrograms of vibration signal from undamaged IASC-ASCE structure.

2.4 Improved Convolutional Neural Network (CNN)

CNNs are feedforward artificial neural networks inspired by the visual cortex of animals. CNNs have been widely used in object detection in images, videos, and the classification of images (Li 2021). Each CNN consists of five kinds of layers: the input layer, the convolution layer, the pooling layer, the fully connected layer, and the output layer. The input layer is a passive layer that accepts the input image and passes the input to convolutional layers. The convolutional layers apply different filters to the input image to extract characteristic features. These filters are not fixed and are trained by a backpropagation algorithm. The subsampling (pooling) layers reduce the dimension of the convolutional layer output following each convolutional layer. The fully connected layers are similar to the hidden layers of a multilayer perceptron and together with the output layer, produce the output vector of the CNN. As shown in Equation 2, the essence of a convolutional neural network is to enable the original matrix (\mathbf{H}_0) to be transformed through multiple levels of data and mapped to a new mathematical model of feature representation (\mathbf{Y}):

$$\mathbf{Y}(i) = P(L = l_i | \mathbf{H}_0; (\mathbf{W}, \mathbf{b})) \quad (2)$$

where l_i denotes the i -th label category, \mathbf{W} represents the weight matrix, \mathbf{b} is the offset vector. In this study, the spectrograms obtained from the different damage patterns of the IASC-ASCE benchmark structure are used as input “images”. The training data fed into the CNN have a total of 3,5136 “images” corresponding to 9 damage patterns. For this purpose, a CNN with four convolutional layers (kernel size = 3), four max pooling layers (kernel size = 2), one fully connected layer (number of neurons = 9), and a softmax layer as the output layer is adopted. CNNs generally used for structural damage can only output the probabilities of trained damage pattern categories, but not the probabilities of arbitrary untrained damage

patterns. Therefore, we define a “Probability of Damage (Predicted)” (PoD), by decomposing the untrained structural damage patterns into known basic damage patterns as follows:

$$\bar{D} = \sum_{i=1}^n \psi_i D_{S_i} \quad (3)$$

where: \bar{D} is the predicted condition-based damage value, D_{S_i} represents the damage index of basic damage patterns, ψ_i is the probability or the weight that the damage seems to be on the basic damage pattern i ($\sum_{i=1}^n \psi_i = 1$), the output of the activation softmax function of the CNN.

3 RESULTS AND DISCUSSIONS

3.1 Basic damage patterns

A MATLAB-based finite element analysis code is developed by the IASC-ASCE SHM Task Group to generate the simulated structural response data (Johnson 2004). As shown in Table 1 and Figure 4, nine structural damage patterns are simulated on the benchmark frame with damaged elements marked by red. For each case, 16 acceleration signals are recorded by 16 accelerometers under shaker excitation. The structural damage is increased gradually from undamaged (Pattern 0) to very damaged (Pattern 8). The damage cases are introduced either

Table 1. Damage patterns of benchmark structure for CNN Training.

Patterns	Configuration
0	Undamaged
1	Removed braces on 1st floor in one bay on southeast corner
2	Removed braces on 1st and 4th floors in one bay on southeast corner
3	Removed braces on all floors in one bay on southeast corner
4	All east side braces removed
5	Removed braces on all floors on east face, and 2nd floor braces on north face
6	All braces removed on all faces
7	Configuration 7 + loosened bolts on floors 1 and 2 at both ends of beam on east face, north side
8	Configuration 7 + loosened bolts on all floors at both ends of beam on east face, north side

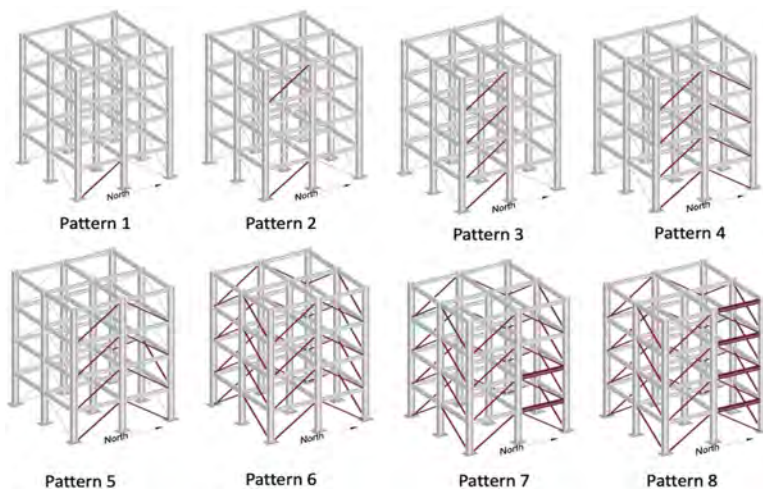


Figure 4. Damage patterns of benchmark structure for CNN Training, damaged elements marked by red.

by the removal of the diagonal braces at specific locations (Patterns 1–6) or by bolt loosening at several joint locations (Patterns 7 and 8).

Firstly, we collect the simulated damage data (16 channels of acceleration signals) generated by the reference structure under these 9 damage patterns; secondly, we slice these damage data and apply Short-Time Fourier Transform to them to obtain the spectrograms of the 9 damage patterns (as shown in Figure 5, Label i represent damage pattern i , here we only list the spectrograms of the first “Frame” of each damage pattern’s first channel); then we use these spectrograms as feature maps to input CNN for training; finally, we apply the PoD equation to output the damage degree under different damage patterns. As shown in Figure 6, we obtain the corresponding damage values for the nine basic damage patterns, ranging from no damage (DP0) to severe damage (DP8). From the bar chart on the right of Figure 6, we can see that the predicted corresponding damage values increase as the damage becomes severe. From the box plot on the left of Figure 6, the spacing of the red lines represents the degree of fluctuation of the values, we can see that the predicted damage values fluctuate more for DP6 and DP8. In this section, our training set and test set are both basic damage patterns, and the prediction results show that our CNN can output relatively accurate damage values.

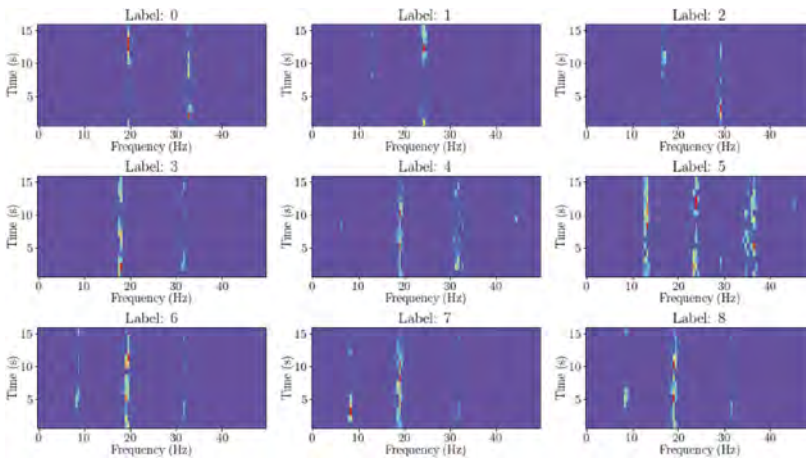


Figure 5. Short-Time Fourier Transform spectrograms of “Frame” 1 of Channel 1 for 9 damage patterns.

3.2 Structural damage estimation

In order to validate the effectiveness of the proposed STFT-based and improved CNN approach, which is not limited to already learned damage patterns but allows damage assessment of arbitrary damage patterns. Therefore eight additional new cases of structural damage are simulated on the baseline structure. For each case, the acceleration output is recorded by 16 accelerometers under shaker excitation. As shown in Table 2 and Figure 7, the structural damage gradually increases from undamaged (Pattern 0) to very damaged (Pattern 9) with damaged elements marked by red. The damage is caused by the reduction of stiffness at specific locations (Pattern 1), the removal of diagonal braces (Patterns 2-6), or the loosening of bolts at several connection locations (Patterns 7, 8).

Similarly, we first collect the simulated damage data (16 channels of acceleration signals) generated by the benchmark structure under these nine defined damage patterns and slice, and Short-Time Fourier transforms these damage data to obtain the spectrograms of the nine newly defined damage patterns, which are input to the CNN for testing. It is worth noting that the training set of the CNN is still the basic damage patterns at this point; however, the test set is newly generated with different damage patterns. Finally, we apply the PoD equation to output the degree of damage under the defined damage patterns. As shown in Figure 8, the orange bars represent the basic damage patterns, and the blue bars represent newly defined damage patterns, we obtained the corresponding damage values for the nine basic damage patterns and defined

Table 2. Defined damage patterns of benchmark structure for CNN Testing.

Patterns	Configuration
0	Undamaged
1'	2/3 stiffness in one bay on northeast corner on 1st floor
2'	Removed braces on 1st floor on east face, south side and 4th floor on north face, east side
3'	Removed braces on 1st, 2nd and 4th floors in one bay on southeast corner
4'	All east side braces and one bay on northeast corner on 1st floor removed
5'	Removed braces on all floors on east face, and 2nd floor brace on north face, west side
6'	Removed braces on floors 1, 2, 3 on all faces
7'	Configuration 7 + loosened bolts on floor 1 at the end of beam on east face, north side
8'	Configuration 7 + loosened bolts on floors 1, 2, 3 at both ends of beam on east face, north side

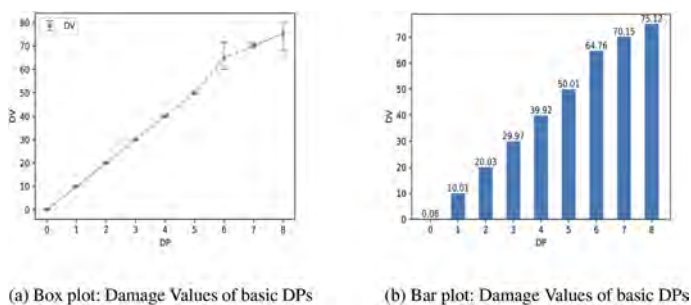


Figure 6. Damage values of basic DPs.

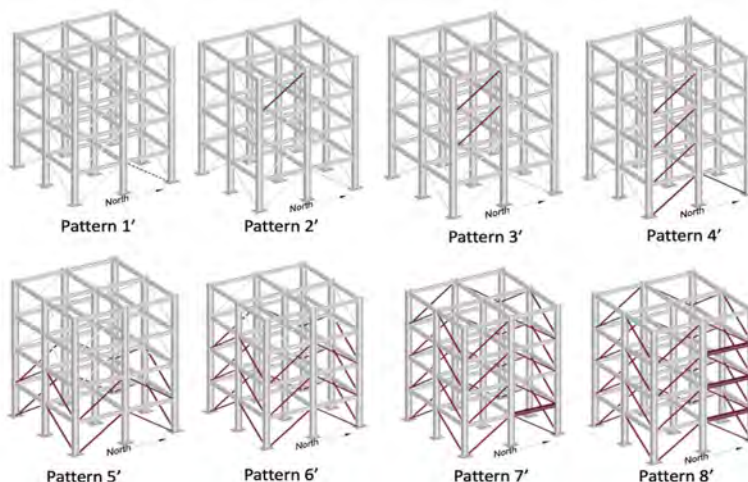


Figure 7. Defined Damage Patterns of benchmark for CNN Testing, damaged elements marked by red.

damage patterns, ranging from no damage (DP0) to severe damage (DP8). And we find that the newly defined damage cases are slightly lower than the basic damage category under each damage category, which basically corresponds to the actual defined structural damage cases.

4 CONCLUSIONS

CNNs have been proven to be an efficient vibration-based structural damage detection tool by many researchers. With the benchmark study data, the method simply processes the raw

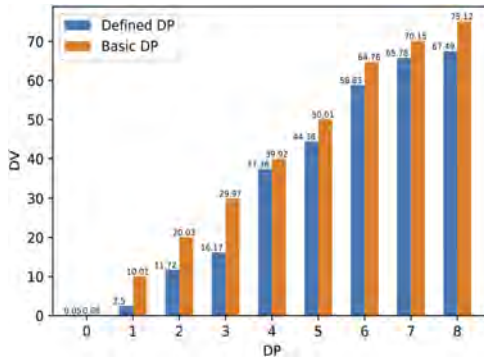


Figure 8. Comparison of Damage values for basic DPs and defined DPs.

acceleration data measured under shaker excitation and computes a single score that represents the actual damage state of the monitored structure. The results show that the proposed method is very successful in estimating the actual amount of structural damage for the nine damage scenarios of the benchmark study. In addition, with the introduction of the PoD equation, the proposed method goes beyond the traditional fixed damage pattern recognition and enables the evaluation of arbitrary damage patterns. Moreover, the CNN structure used in this paper is very simple, which means that it is easy to implement from a computational time perspective and does not require large hardware resources. However, the CNN-based approach proposed in this paper can only be utilized to examine the overall condition of the monitored structure. As a future research topic, the possibility of utilizing the structural dynamics analysis to identify the location of structural damage will be investigated.

REFERENCES

- Dyke, S. J. et al. 2003. Experimental phase II of the structural health monitoring benchmark problem. *Proceedings of the 16th ASCE engineering mechanics conference*.
- Elshafey, A.A. et al. 2010. Damage detection in offshore structures using neural networks. *Marine Structures* 23(1):131–145.
- Grande, E. & Imbimbo, M. 2012. A data-driven approach for damage detection: an application to the ASCE steel benchmark structure. *Journal of Civil Structural Health Monitoring* 2:73–85.
- Griffin, D. & Lim, J. 1984. Signal estimation from modified short-time Fourier transform. *IEEE Transactions on acoustics, speech, and signal processing* 32(2): 236–243.
- Gu, J. et al. 2018. Recent advances in convolutional neural networks. *Pattern recognition*, 77:354–377.
- Johnson, E.A. et al. 2004. Phase I IASC-ASCE structural health monitoring benchmark problem using simulated data. *Journal of engineering mechanics* 130(1): 3–15.
- Khodabandehlou, H. et al. 2019. Vibration-based structural condition assessment using convolution neural networks. *Structural Control and Health Monitoring* 26(2):e2308.
- Kodikara, K. et al. 2016. Model updating of real structures with ambient vibration data. *Journal of Civil Structural Health Monitoring* 6(3):329–341.
- Li, Z. et al. 2021. A survey of convolutional neural networks: analysis, applications, and prospects. *IEEE transactions on neural networks and learning systems*.
- Mahato, S. et al. 2017. Combined wavelet– Hilbert transform-based modal identification of road bridge using vehicular excitation. *Journal of Civil Structural Health Monitoring* 7(1):29–44.
- Shi, A & Yu, X.H. 2012. Structural damage detection using artificial neural networks and wavelet transform. *2012 IEEE International Conference on Computational Intelligence for Measurement Systems and Applications (CIMS) Proceedings* (pp. 7–11).

Dynamic characteristic study of a heritage structure in Tiruchirappalli city using operational modal analysis

S. Anjuna, N. Radhakrishnan & G. George

National Institute of Technology, Tiruchirappalli, Tamil Nadu, India

ABSTRACT: Majority of nations are spending a considerable part of their maintenance budget allocated for construction industry for retrofitting. This situation indicates there is an immediate need for establishment of an efficient health monitoring system. It is a well-known fact that the establishment of a health monitoring system is expensive in the installation stage, but economical in the long run from the perspective of preventive maintenance. Hence, the implementation of the health monitoring system on the bridge has adopted a systematic approach which includes optimization of sensors (triaxial accelerometers), establishment of a real time data acquisition and analysis by installing the LabVIEW based program for the same in the real time controller and validation of the results.

1 INTRODUCTION

Structural Health Monitoring (SHM) is applied as an effective methodology for preventive maintenance. There are numerous examples of its application in health monitoring of religious structures, heritage structures, innovative buildings, dams, bridges etc. However majority of application has been in the field of development of vibration based decision support system for bridge monitoring. There are 2.5 million number of operating bridges in the global road network. It has to be accepted that every bridge will be a prototype, and hence the strategy of decision making will vary for each of them. However the lessons learnt from each case study would be helpful for improving the existing methodologies. In this paper, Cauvery bridge which is also a heritage symbol of Tiruchirappalli city has been adopted for health monitoring. It was during a routine visual inspection by the experts, which lead to the observation that the leaning of rocker bearing creating excessive vibration to the bridge. Even though the fault was later rectified, it was suggested to establish a vibration-based health monitoring system for the structure. The core of the vibration based health monitoring lies in the modal identification, which can later be utilized for system identification. Thus, system identification and modal identification are inter-related objectives. The dynamic characterization of Golden Gate Bridge laid a new insight in to the field of vibration-based health monitoring. The reliability of the monitoring system depends upon the quality of data acquired. Hence, each stage of monitoring programme i.e selection of sensors, their number and location, installation, data acquisition and processing must be done with utmost care. With the availability of modern day sensors and efficient data acquisition systems, it can be desired to develop replace the conventional post processing of the data by a real time monitoring process, where the acquisition and processing are done simultaneously to know the real time behavior of the structure under consideration. This paper explains a systematic approach for health monitoring of a bridge structure, where each of the stages for real time data acquisition has been addressed. The methodology involves development of finite element model of the bridge in SAP 2000, optimization of sensors based on the analytical results, Installation of sensors, Real Time data Acquisition and Processing based on a LabVIEW program installed in a real time controller (NI cRIO 9040) and followed by validation of the results.

2 FINITE ELEMENT MODELLING

The finite element analysis of the bridge was done in SAP 2000 software. The total length of the bridge is 630 m, with 15 spans of 42m. The total width of the bridge deck is 10.5m. All the 15 spans of the bridge act individually as simply supported span. Thus, only single span is considered for analysis. The bridge is modelled as a reinforced concrete bridge with four T Girders of 1.8m depth and 130mm width at 2.5m spacing and eight number of cross diaphragm of depth 1.5m and 100 mm width. The bridge deck has a total thickness of 250 mm and is provided with 7.5m wide carriageway. The material properties were adopted as per the details given by the governing authority. Frame and Shell elements were used for modelling the superstructure and link elements for bearings. Figure 1 shows the model of the bridge in SAP 2000.

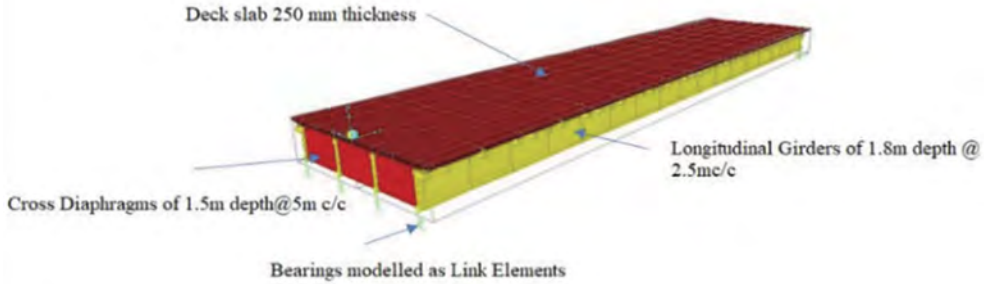


Figure 1. Model of the Bridge in SAP 2000.

3 OPTIMISATION OF TRIAXIAL ACCELEROMETERS

Proper planning of the vibration test is very crucial in extracting accurate modal properties. Hence, the most important task in modal analysis is placement of sensors. The Sensor placement strategy adopted in this study maximizes the determinant of Fischer Information Matrix (FIM) and there by maximizing the linear independency and signal strength. The objective of optimization of sensor is to ensure attainment of all the information required as well as avoiding sensor clustering. This methodology allows the vibration analysts to specify the location which they absolutely want to measure the vibration. However, the sensor location of the Analyst's choice can be as small as one and further be expanded. This methodology utilises the mode shapes obtained from FEM Model for pre-test planning.

Stage I: Approach for Modal Expansion

In structural dynamics, the displacement of a structure under dynamic loading is expressed as:

$$\mathbf{x}(t) = \sum_k^n \Phi_k q_k(t) = \Phi \mathbf{q}(t) \quad (1)$$

Where,

$\mathbf{x}(t)$ = Displacement response; $\mathbf{q}(t)$ = Modal Co-ordinates

Φ = Modal matrix corresponding to n selected mode shapes

N = Total Degrees Of Freedom in the FE Model

The vector $\mathbf{x}(t)$ is categorised in to $\mathbf{x}_m(t)$ and $\mathbf{x}_d(t)$ indicating measured and unmeasured part of the response vector $\mathbf{x}(t)$. Let $\mathbf{y}(t)$ denote the response measured and is given by:

$$\mathbf{y}(t) = \mathbf{x}_m(t) + \varepsilon(t) = \Phi_m \mathbf{q}(t) + \varepsilon(t) \quad (2)$$

where, $\varepsilon(t)$ denotes the error during measurement which is inevitable. Thus, it is important to minimise the residual $\varepsilon_y(t)$

$$\varepsilon_y(t) = y(t) - \Phi_m \hat{q}(t) \quad (3)$$

Assumption 1: i) $\varepsilon(t)$ = Gaussian, uncorrelated with zero mean
 ii) Number of sensors are greater than the number of mode shapes
 Thus, Homoscedasticity solution for Modal co-ordinates id expressed as

$$\hat{q}(t) = (\Phi_m^T \Phi_m)^{-1} \Phi_m^T y(t) = \Phi_m^\dagger y(t) \quad (4)$$

Assumption 2: There is equal confidence for all measurement points, then heteroscedasticity of $\hat{q}(t)$ must be consider.

$$\hat{q}(t) = (\Phi_m^T W \Phi_m)^{-1} \Phi_m^T W y(t) \quad (5)$$

W = weighing matrix (diagonal matrix)

$$W = \begin{bmatrix} \sigma_i^2 & \cdots & 0 \\ \vdots & \ddots & \vdots \\ 0 & \cdots & \sigma_m^2 \end{bmatrix}$$

σ_i^2 = Measurement variance for each sensor

Where, $\sum_q = (\Phi_m^T W \Phi_m)^{-1}$, \sum_q = Error covariance matrix

For the unmeasured degrees of freedom the estimation error variance for displacement estimate is expressed as:

$$\sum_{\hat{x}_d} = E[(\hat{x}_d - x_d)(\hat{x}_d - x_d)^T] = \Phi_d \sum_q \Phi_d^T \quad (6)$$

The objective for this stage is to minimize mean of trace of estimation error variance for the unmeasured DOFs $\frac{1}{d} tr(\Phi_d \sum_q \Phi_d^T)$

Stage II: Effective Independence and Redundancy Information

Even though minimisation of the error covariance of estimate of unmeasured displacement facilitates attaining reconstruction response of good quality. But, there might be chances of adjacent sensors sharing same information, thus the sensor redundancy must be minimized. Another matter of concern is sensor clustering, which arise due to uneven distribution of stiffness and mass in the structure. These issues are addressed by including triaxial effective independence and redundancy information in the optimisation steps.

As per assumption stated in stage I, the measurement noise can be considered as uncorrelated and equal at all location of sensor.

Thus, the error covariance matrix takes the following expression:

$$\sum_q = E[(q - \hat{q})(q - \hat{q})^T] = \sigma_0^2 (\Phi_m^T \Phi_m)^{-1} = \mathcal{Q}^{-1} \quad (7)$$

\mathcal{Q} representing the Fischer Information Matrix. In Effective Independence the objective is to maximise the FIM (trace or determinant). Thus, \mathcal{Q} can also be represented in terms of contribution from each sensor as:

$$\mathcal{Q} = \frac{1}{\sigma_0^2} \sum_{i=1}^m \Phi_m^{iT} \Phi_m^i = \frac{1}{\sigma_0^2} \sum_{i=1}^m \mathcal{Q}_i \quad (8)$$

m = number of sensor degree of freedoms
 i = i^{th} row of Φ

In the case of triaxial sensors, Equation 8 becomes

$$\mathbf{Q} = \frac{1}{\sigma_0^2} \sum_{i=1}^m \Phi_{3i}^T \Phi_{3i} = \frac{1}{\sigma_0^2} \sum_{i=1}^{m_n} \mathbf{Q}_{3i} \quad (9)$$

\mathbf{Q}_{3i} = elementary FIM at the i^{th} nodes

m_n = number of candidate sensor location, $\sigma_0^2 = 1$ (assumed)

To prevent clustering of sensors redundancy information criterion is used which measures the closeness between information coming from sensors at node i and node j , and is computed using the following equation:

$$R_{ij} = \frac{\|\mathbf{Q}_{3i} - \mathbf{Q}_{3j}\|}{\|\mathbf{Q}_{3i} + \mathbf{Q}_{3j}\|} \quad (10)$$

The R_{ij} value of 1 indicates sensors share no mutual information and a value of 0 indicating the sensors bring the same information. This criterion is considered as the constraint for optimisation here. Let \mathbf{Q}_0 represent the initial information matrix, having rank $u < n$, and the eigen vectors for \mathbf{Q}_0 be ψ_0 . These vectors will be spanning in u - n dimensional space. Thus, the orthogonal projector \mathbf{P} is represented as

$$\mathbf{P} = \psi_0 \psi_0^T \quad (11)$$

The information in the candidate sensor set can be obtained utilizing the projector \mathbf{P}

$\overline{\mathbf{Q}}_c = \mathbf{P} \mathbf{Q}_c \mathbf{P}^T$, where $\overline{\mathbf{Q}}_c$ represents information in the candidate set which is orthogonal to \mathbf{Q}_0 . The objective here is to determine and choose the sensor location which contribute the most to $\overline{\mathbf{Q}}_c$.

Thus, the triaxial effective independence $\overline{EfiT3}_i$ is utilized to measure the decrease in the information with removal of every i^{th} sensor from the candidate set.

$$\overline{EfiT3}_i = 1 - \det[\mathbf{I}_3 - \Phi_{3i} \overline{\mathbf{Q}}_c^\dagger \Phi_{3i}^T] \quad (12)$$

Implementation of Optimization

The methodology explained above was implemented as follows:

- 1) The location where the analysts absolutely wants the sensor to be fixed was chosen.
- 2) First Stage: Formation of Initial Sensor Set based on Sequential Sensor Placement and Tri-axial Effective Independence criterion.
- 3) For all the chosen sensor location (candidate set), \mathbf{Q}_{3i} is calculated and sorted based on the norm. The sensor location with largest norm is selected as first node.
- 4) Sensors in the candidate set are ranked based on the $\overline{EfiT3}_i$ value and the sensors with highest contribution are placed in the initial sensor set till the rank is full.
- 5) Second Stage: For the initial sensor set formed the is calculated and all the sensor nodes having R_{ij} less than the Threshold value R_0 is removed from the initial set. This method can be applied for large complicated finite element models with fine meshes and where tri-axial accelerometers are used for determining both twisting and bending modes. For the formulation of the FIM 12 modes obtained from the FEM Analysis were considered. As, nodes located inside the structure cannot be instrumented, the focus is on the nodes located on the outside surface of the bridge. The candidate sensor set considered for the optimization consisted of 162 sensor positions. The sensor position with largest norm (determinant of the FIM) obtained as 7.577×10^{27} was considered as the first sensor node. The remaining sensor positions were sorted according to the Effective Independence value and those sensors with a redundancy value ranging between 0.4 to 0.5 were considered as the optimal sensor positions.

Hence, from the methodology of optimization adopted it was found that 28 number of triaxial sensor position would be required for conducting a successful vibration study on the bridge, therefore out of 8 accelerometers, 4 of which are stationary accelerometers while rover accelerometers make up the balance 4. Figure 2 shows the adopted sensor layout as per optimization

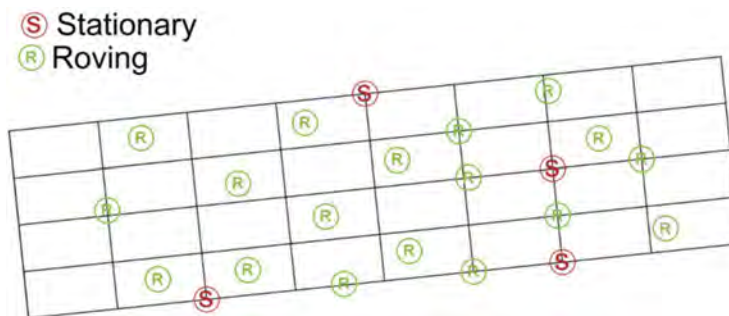


Figure 2. Adopted Sensor Layout.

4 BRIDGE MONITORING: INSTALLATION OF SENSORS, REAL TIME DATA ACQUISITION AND PROCESSING

An Ambient vibration test was conducted on the bridge to identify the modal properties. The sensors used for instrumentation consists of 8 triaxial accelerometers (5V/g, 0.02-200Hz), NI 9234 I/O Module, NI cRIO 9040 Real Time controller for data Acquisition, Signal Conditioning Module. The real time data acquisition and processing was programmed in LabVIEW. The accelerometers were attached to magnetic mount which was in turn placed on steel plate attached to the bridge structure. The steel plate was mounted to the underside of the bridge using 3M DP 420 adhesive. Figure 3 shows the instrumentation layout. Since cRIO-9040 is a real time controller, it is capable of data acquisition, processing and controlling in real time. The real challenge lies in programming the cRIO-9040 for data acquisition and processing in real time.

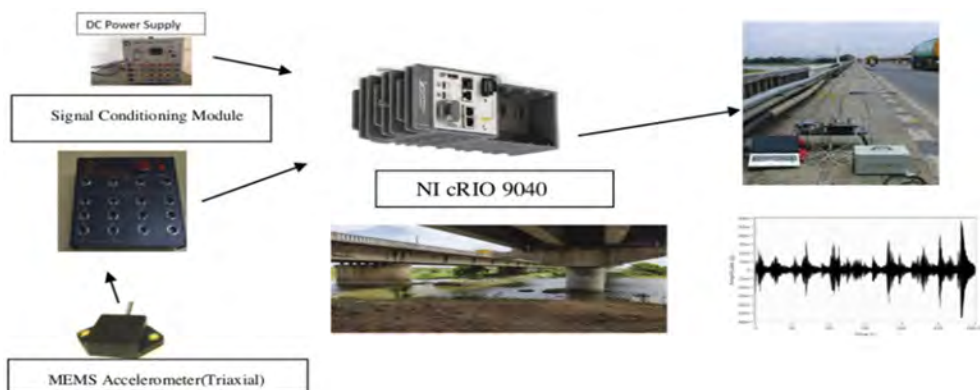


Figure 3. Layout of Instrumentation Adopted.

The LabVIEW programme for data acquisition and processing consists of two parts i) Acquisition of data in the cRIO controller and transferring the data to the computer ii) Displaying the data after receiving from the cRIO on the computer screen as shown in Figure 4

Step1: Using DAQmx Create Task.vi the data acquisition task was created. Once the channels are added, the channels which will be acquiring signals are specified using DAQmx Create Channel.vi. In this VI, the number of channels and the voltage range of sensors are provided. The

sampling rate is specified in DAQmx Sample clock .vi connected to DAQmx Create Channel.vi. Acquisition is started by DAQmx Start Task.vi and the data acquired is stored in a shared variable Data RT. To prevent losing data while sampling and for faster acquisition and transfer, both the programme are executed in stacked sequence. The acquisition is stopped after 45 minutes of data acquisition by a for loop and checking the loop count. The measurement is written in a TDMS file using Write to Measurement File.vi and saved in a file path. The file path is accessed as a constant in the data processing file and the analysis is done every 45 minute the data is taken.

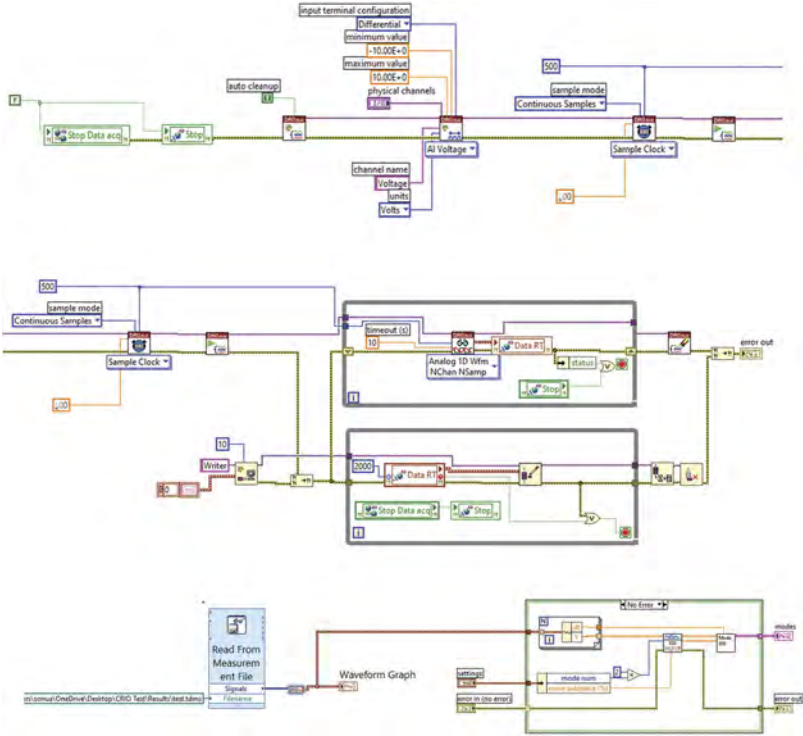


Figure 4. Data Acquisition, Processing and Analysis in Real Time.

5 RESULTS AND DISCUSSION

A comparison is done between the modal frequencies that are obtained from the Finite Element Analysis (FEA) in SAP 2000 and the modal frequencies determined from the Ambient Vibration Test. Good correlation is seen between the results of the first six modes obtained from the experiment and the results of the Finite Element Analysis. Table 1 presents the results from analytical and experimental methods.

Table 1. Modal frequencies obtained using FEM Analysis and OMA.

Mode	FEM Analysis			Modal VIEW			Frequency (Hz)			Damping ratio (ξ) %		
	Frequency (Hz)	Damping ratio(ξ) %		LSCE	FDD	Cov-SSI	LSCE	FDD	Cov-SSI	LSCE	FDD	Cov-SSI
1	2.53	1.06		2.62	2.63	2.62	1.08	1.02	1.04			
2	2.77	3.39		2.73	2.72	2.75	3.44	3.39	3.68			
3	3.75	3.92		3.37	3.44	3.54	3.88	3.90	3.94			
4	6.60	4.52		6.42	6.35	6.46	4.50	4.43	4.68			
5	8.38	4.29		8.90	8.76	8.79	4.20	4.33	4.29			
6	14.96	3.09		14.35	14.16	14.2	3.13	3.19	3.10			

The St-Id results are validated by a comparison that is made between the experimental modal estimates obtained from the three chosen OMA methods (LSCE, FDD, Cov-SSI). The widely used index, Modal Assurance criterion (MAC) is chosen for this study for determining the correlation between the mode shapes. The graphical representation of the MAC matrix obtained using the Cov-SSI method can be seen in Figure 5. From, the figure it is evident that the diagonal values fall in the range of 0.97 to 0.99 thereby showing that there is a good degree of consistency between the mode shapes. The results of the modal analysis conducted using the FEM model show that the range of the modal frequencies is 2.54 Hz-14.97 Hz, while the range of the damping ratio is 1.05%-4.5% as obtained from ModalVIEW. The damping ratios were compared with the results obtained from vibration data analysis in ModalVIEW, in order to test the accuracy of the data analysis code developed in LabVIEW. As good agreement is noted between both the numerical and experimental techniques, the structural model is validated. The modal parameters that are experimentally identified by the OMA methods of LSCE, FDD and Cov-SSI and the analytical results reveal that the range in the modal frequency is from 2.60Hz-14.34 Hz and the damping ratios tend to vary from 1.01% to 4.62 %. In the 3rd mode, the maximum error noted between numerical prediction and experiment in frequency is 11.97%. This error is attributed to uncertainty in modelling. Figure 6 shows the mode shapes obtained from FEM Analysis.

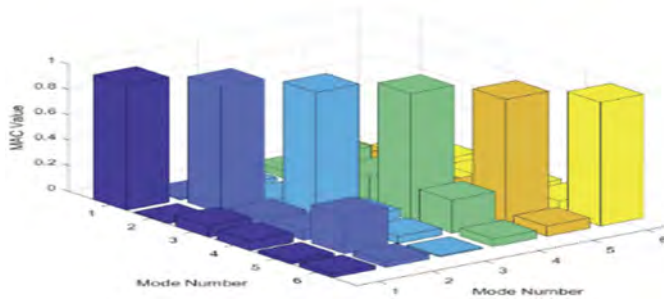


Figure 5. MAC matrix for the obtained mode shapes.

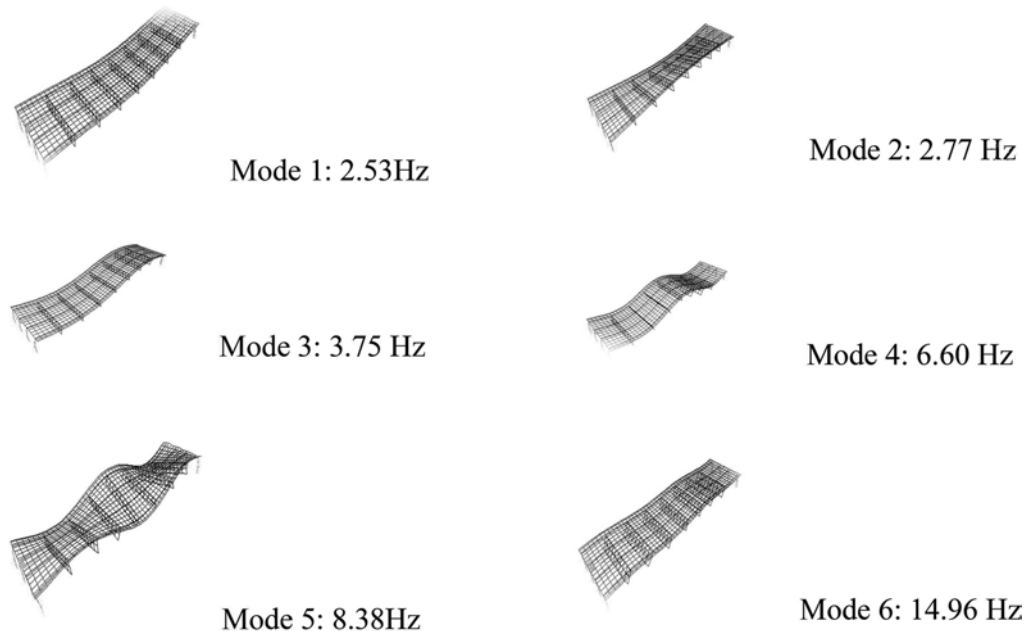


Figure 6. Mode Shapes from SAP 2000.

6 CONCLUSIONS

This research study systematically explains the methodology adopted for monitoring the structural health of bridges. The assessment of the bridge is done by optimal use of sensors and deploying advanced real-time controller on the structure. The conclusions derived from the study are presented as below:

1. The optimization methodology adopted in the study has helped to identify the first six modes of the structure, the inability to detect other modes may be due to insufficient external ambient excitation.
2. An attempt has been done to establish a real-time monitoring of the bridge using real-time controller, and LabVIEW programs installed in the controller were found to give reliable results.
3. Least Square Complex Exponential, Frequency Domain Decomposition, Covariance Driven-Stochastic Subspace Identification algorithms were applied for modal estimation. The acquisition of high-quality data is confirmed by the good agreement observed between the results of the analytical and experimental studies.
4. The programs developed for real time data acquisition and analysis provides a new insight in to the possibilities for establishing real time monitoring based on OMA, which can be successfully applied for other structures also.

REFERENCES

- Stephan, C 2012. Sensor placement for modal identification. *Mechanical Systems and Signal Processing* 27: 461–470
- Nieminen, V & Sapanen, J 2023. Optimal sensor placement for triaxial accelerometers for modal expansion. *Mechanical Systems and Signal Processing* 184

Optimal design of a vibration-based sensor network for bridge monitoring

M.F. Yilmaz

Ondokuz Mayıs University, Samsun, Turkey

K. Ozakgul & B.O. Caglayan

Istanbul Technical University, Istanbul, Turkey

ABSTRACT: Bridges are known to be the most fragile components in transportation systems. Furthermore, due to the fact that transportation networks were built many years ago, especially in developed countries, a significant portion of existing bridges have either reached the end of their lifespan or are approaching it. It would be impossible to demolish and replace all of these bridges due to the immense economic burden it would bring. As such, it is crucial to regularly monitor these bridges and create cost-effective maintenance, repair, and renewal plans in response to potential damage scenarios. In this context, long-term structural health monitoring applications appear to be an effective approach. The number of instruments used in these activities and the measurement intervals are essential to their applicability. While increasing the number of measurement points provides more comprehensive information about the structure, it also brings a great economic and operational burden in terms of both the installation cost and the evaluation of the data obtained after the measurement. Therefore, the number of instruments placed on the bridges should be kept to a minimum, while still allowing for accurate determination of the bridge's dynamic behavior. The objective of this study is to efficiently and inexpensively determine the number and placement of accelerometers to be utilized in long-term health monitoring activities. The study aims to investigate the most effective location for the instrumentation and minimize the number of sensors. Additionally, the obtained results were compared, and also the approach's efficiency was evaluated.

1 INTRODUCTION

Determining the dynamic parameters of structures is a current area of focus for civil engineers that is growing in importance. The need to determine these parameters provides crucial information, such as assessing whether newly constructed structures meet design conditions, analyzing existing structures, and identifying existing or potential damage. However, thanks to advancements in technology and scientific methods, it is now possible to determine the dynamic characteristics of structures using a variety of methods.

Furthermore, structural health monitoring systems make it possible for existing structures to be used cost-effectively and minimize structural risks. Additionally, the importance of building health monitoring methods has increased with the use of complex construction structures (Huang et al., 2017; Lin et al., 2017). The primary goal of vibration-based structural health monitoring systems is to determine parameters such as natural frequency, mode shape, and damping ratio, which constitute the structure's dynamic characteristics (Yi et al., 2016). Modal updating, damage detection, and warning systems can be created for structural safety with vibration measurements in structural health monitoring (Liu et al., 2014). However, real-time monitoring of complex structures and instant processing of the data obtained poses

challenging tasks that are difficult to implement and brings many problems to overcome (Cabboi et al., 2017). Therefore, many studies have been carried out in recent decades to perform the autonomous determination of dynamic parameters (Sun et al., 2017).

(Yang et al., 2019) investigated an automated model detection methodology using the Eigensystem Realization Algorithm (ERA) and Fuzzy C-Means (FCM) clustering to separate modes and find the stable ones. (Cabboi et al., 2017) proposed a methodology based on Stochastic Subspace and automated the analysis of mod shape and frequency. (Ubertini et al., 2013) developed a long-term structural health monitoring system with an automated analysis procedure to determine modal frequencies.

However, the high cost of sensors and installation has led researchers to conduct studies to enable vibration-based structural health monitoring using fewer sensors cost-effectively. In this context, different studies have been carried out to detect structural damage and determine the dynamic parameters of the structure by using the optimum number of sensors (Guo et al., 2004; Kim et al., 2000; Chang & Pakzad, 2015; Meo & Zumpano, 2005). Nevertheless, more studies are needed to eliminate the uncertainties arising from the proportionality feature of the mode shapes. Also, it is considered necessary to place each sensor in complex structures as it can contain information about the dynamic behavior of different structure regions. Determining the optimum sensor location is essential for both improving the measurements to be made with the help of sensors and minimizing the cost of structural health monitoring as a result of minimizing the number of sensors in structural health monitoring approaches. For this reason, many different studies are carried out, and different approaches and algorithms are developed to determine sensor locations, considering the cost analysis (Leyder et al., 2018; Papadimitriou & Lombaert, 2012).

Sadeghi Eshkevari et al. (2020) proposed a methodology using mobile sensors and calculating the bridge system's modal frequency by eliminating the vehicle frequency and getting information about the road's roughness and its effects on the measurement. The proposed methods successfully eliminated both vehicle vibration and roughness vibration.

Magalhães et al. (2007) considered a real cabled stayed bridge and obtained the dynamic parameters of this bridge separately using the methods: peak-picking (PP), frequency domain decomposition (FDD), covariance-driven stochastic subspace identification (SSI-COV), and data-driven stochastic subspace identification (SSI-DATA) and compared the modal frequency and damping ratio data in detail. In addition to all these studies, dynamic parameters, especially frequency content are significantly affected by many factors, such as temperature, wind, and climate conditions. For this reason, studies are conducted to determine the dynamic parameters of the structures by considering the environmental effects (Li et al., 2010).

The aim of this study is to determine the modal characteristics of a beam system, such as mode shape, modal frequency content, and damping ratio, using accelerometers placed on a simply supported beam system. In the measurements, the sensors will be handled separately, and the sensors that provide the most information about the dynamic behavior of the beam system will be identified. The goal is to accurately determine the beam system's dynamic parameters using fewer sensors.

2 SET UP AND EXPERIMENTAL MODEL

The experimental model was created using a steel box profile to form a simply supported structure. The box profile has a size of 50 mm x 50 mm and is 2 mm thick. 20 mm diameter steel bars are welded on both ends of the box profile and a roller is placed on one of these bars to create a movable support. The other end of the profile is fixed to the ground. The rod is free to rotate but prevented to translation to achieve an ideal condition and make it easier to predict the support conditions (see Figure 1).

Experimental measurements were obtained using two setups. In the first measurement, accelerometers were positioned at 0.25 m, 0.5 m, 0.75 m, and 1 m distances, as shown in red. In the second measurement, the accelerometer at 0.25 m was kept as a reference point and accelerometers were placed at distances of 1.25 m, 1.5 m, and 1.75 m (see Figure 1).



Figure 1. Sensor position of the experimental beam.

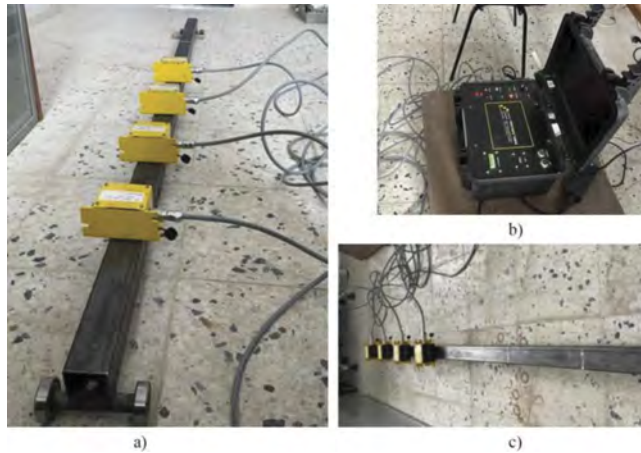


Figure 2. a) and c) Accelerometers on the experimental beam, b) Data acquisition system.

Experimental measurements were performed using the TESTLAB 2010 data acquisition system and field-type accelerometers (see Figure 2). To predict the dynamic behavior of the model, a mathematical model was created and the frequency values corresponding to the first six vertical modes were found to be 31.5 Hz, 125.44 Hz, 279.85 Hz, 490.68 Hz, 750.32 Hz, and 1044.92 Hz, respectively.

Two different sample sizes were used to measure the first three modes. The sample rates were 1000 Hz and 500 Hz, and the recording time was 180 seconds and 360 seconds, respectively. The measurements were made on the model under ambient vibrations, and the oscillation of the model was triggered by applying blows of specific periods and similar intensities to the ground. In the second case, the modal frequencies were more pronounced.

3 MEASUREMENTS

The measurements performed on the simple beam system were divided into two parts. In the first part of the measurements, half of the beam was measured. In the second part, the first accelerometer remained in its original position, while the other three accelerometers were moved to the second half of the beam, and the measurements were repeated. The records of the measurements obtained are shown in the figure below.

The measurements were recorded with a sample interval of 1 kHz for a total of 180 seconds. This duration was determined to be the maximum number of data that can be processed in Excel. In the recordings, small vibrations were applied to the ground to make the beam's modal behavior more discernible.

4 DATA ANALYSIS AND CALCULATION OF THE DYNAMIC PARAMETERS

The mode shapes of a beam were determined by using peak picking and frequency domain decomposition techniques. In peak picking, the natural frequencies of the beam were

identified by analyzing the frequency spectrum of the vibration data. The method used the peaks of the spectrum, which correspond to the natural frequencies of the system, to identify the different modes of vibration. Once the natural frequencies were identified, the corresponding mode shapes were determined by analyzing the vibration data at each frequency. The shape associated with that frequency is the mode shape.

Frequency domain decomposition is a technique that breaks down a frequency spectrum into its individual modes. It can be accomplished using different algorithms, such as Prony's method or the Matrix Pencil (MP) method. This approach takes advantage of the fact that different modes have distinct spectral components, which can be isolated and then reconstructed to obtain the mode shapes. By identifying the various spectral components, each mode can be extracted and the corresponding mode shape can be determined.

Both peak picking and frequency domain decomposition are effective methods for finding the mode shapes of a beam by analyzing its vibration data. These methods can be used individually or together, depending on the specific requirements of the analysis.

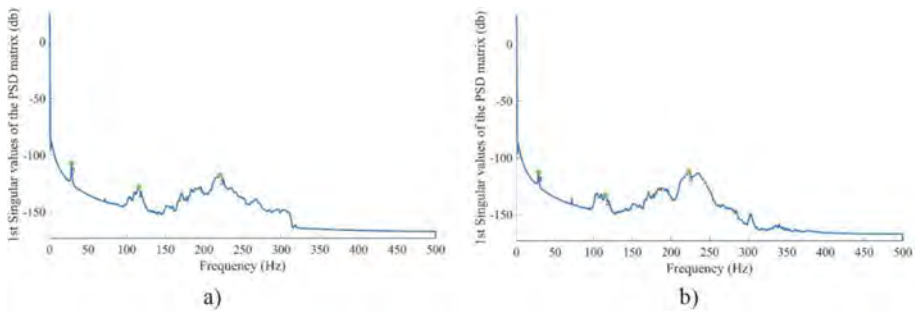


Figure 3. a) FFT of the first measurements, b) FFT of the second measurements.

The Matlab program was used to process the acceleration data obtained from the first measurement. First, the autocorrelation functions (ACFs) in Matlab were derived, and the frequency content was obtained. The obtained FFT data are shown in Figure 3. Based on these data, the frequency values of the first three modes of the beam can be determined. These values were found to be (28.81Hz, 115.7 Hz, 220.2 Hz) respectively.

The acceleration data obtained from the second half of the beam was used to repeat the analysis previously summarized in the section. The modal frequency values of the beam were obtained as (28.81Hz, 115.2Hz, and 235.4Hz), which matched the values obtained from the first measurements.

Filtering was applied separately for each frequency. The amplitudes in the regions where the accelerometers were located were determined for the ranges of these frequencies. These amplitudes were proportioned using the largest value as a reference, and the mode shape of the first measurements was obtained.

In the second measurement, filtering was applied to isolate the frequencies of the modes in the regions where they were located. Modal amplitudes were obtained for the locations of the accelerometers. The amplitude value of the first accelerometer, which was used as a reference, was the same as the amplitude value of the reference accelerometer in the same location in the second measurement. The modal amplitudes corresponding to the locations of the accelerometers were proportioned, and the mode shapes of the system were obtained (as shown in Figure 4).

The modal amplitudes corresponding to each accelerometer location were determined, and the mode shapes of the system were obtained by finding high-order polynomials that pass through the relevant points. The ideal case would be a symmetrical mode shape, but due to uncertainties in the support conditions, variations in the beam's material and cross-section, and the asymmetrical load caused by the accelerometers, a slight deviation from symmetry was observed. As the modal frequency values for this system were too high, the study focused on the data of the first three modes only.

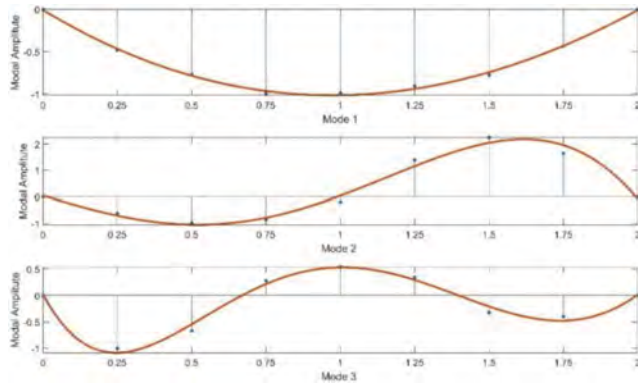


Figure 4. Mode shapes of the experimental beam.

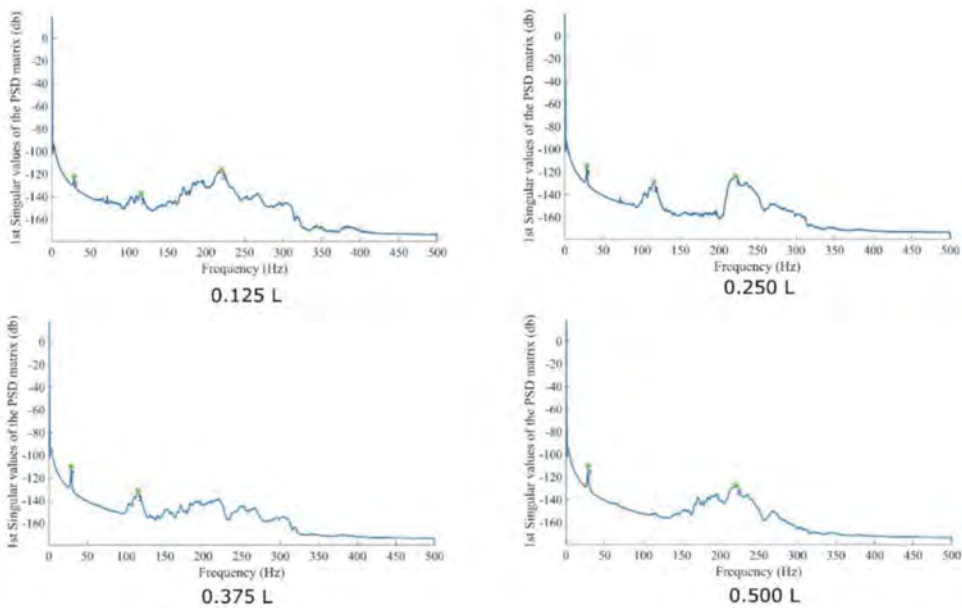


Figure 5. Individual FFT of the acceleration measurement.

The first three modes were identified in the graphics produced using data from an accelerometer located at a distance of $0.125L$ (see Figure 5). These modes are consistent with the modal frequencies obtained using data from seven accelerometers. When the modal frequencies obtained using data from accelerometers at $0.25L$ are considered, it is observed that the first three modes are still present, but with slightly different frequencies compared to the general case. When data from accelerometers at $0.375L$ and $0.5L$ is used, the frequency values of the first two modes and the first and third modes are obtained, respectively. By examining the modal frequencies obtained from each accelerometer in detail, it is found that the first three modes of the structure can be determined using data obtained from the first two accelerometers (see Figure 6).

Initially, all data was used to determine the mode shapes. The mode shapes obtained using data from the first two accelerometers were then compared with the mode shapes found in the initial case. For this system, it is necessary to use data from at least two accelerometers. One accelerometer data is used to determine the amplitude ratio of the relevant mode shape at that point, and the other accelerometer data is used to compare the amplitude values.

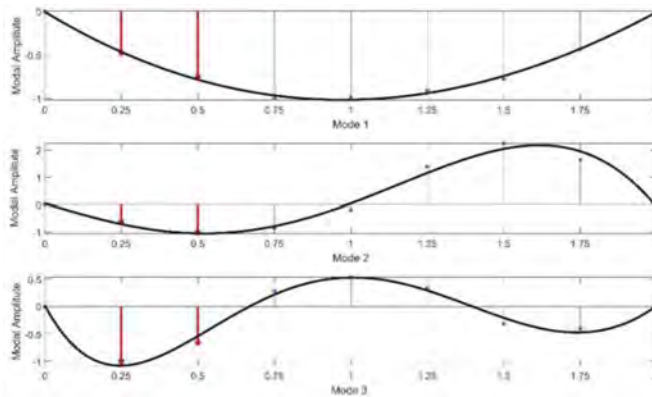


Figure 6. Comparison of the mode shape amplitude obtained using first two sensor measurements.

Using data from a single accelerometer, it is possible to determine the frequency values of the first three modes of the system with the help of accelerometers located at distances of $0.125L$ or $0.250L$. However, without multiple accelerometer data, it will not be possible to comment on the shape of the modes. When two accelerometers are used, if the accelerometers are placed at $0.125L$ and $0.250L$ distances, it allows for determination of both the modal frequencies and mode shape of the first three modes of the system. This provides the opportunity to compare the mode shape and identify any possible damage.

5 CONCLUSIONS

As a result of the study, the modal frequencies and mode shapes of a simply supported beam system were obtained by analyzing data from seven accelerometers. Additionally, the damping ratios of these mode shapes were determined. The initial modal frequency values were then reevaluated by using data from two accelerometers, and the compatibility of the mode shape with the initial mode shape was evaluated. It was found that it is possible to monitor a bridge using initial detailed measurements and a small number of accelerometers and measuring instruments in subsequent examinations, making it more cost-effective.

The use of two accelerometers shows that the mode shape and frequency values of the bridge can be accurately determined. Changes in the frequency values of the bridge provide important information about damages in the system. Additionally, differences in mode shapes can also indicate the location and extent of damage. This allows for more efficient and cost-effective structural examinations without the need for a large number of measuring devices for each examination.

The placement of the accelerometers is crucial for accurate frequency content and mode shape determinations with a minimum number of measurements. The study revealed that accelerometers placed at distances of $0.125L$ and $0.250L$ can be used to determine the frequency values and mode shapes of the first 3 modes. Conversely, accelerometers placed at distances of $0.375L$ and $0.5L$ only provided information about the frequency values of two modes, which were also different from each other. This indicates that the mode shape and frequency must be precisely targeted in advance and the accelerometer locations must be carefully selected.

REFERENCES

- Cabboi, A., Magalhaes, F., Gentile, C., & Cunha, A. 2017. Automated modal identification and tracking: Application to an iron arch bridge. *Structural Control and Health Monitoring* 24(1): e1854.

- Chang, M., & Pakzad, S. N. (2015). Optimal sensor configuration for flexible structures with multi-dimensional mode shapes. *Smart Materials and Structures*, 24 (5).
- Guo, H. Y., Zhang, L., Zhang, L. L., & Zhou, J. X. (2004). Optimal placement of sensors for structural health monitoring using improved genetic algorithms. *Smart Materials and Structures*, 13(3), 528–534.
- Huang, H.-B., Yi, T.-H., & Li, H.-N. (2017). Bayesian Combination of Weighted Principal-Component Analysis for Diagnosing Sensor Faults in Structural Monitoring Systems. *Journal of Engineering Mechanics*, 143(9)
- Kim, S. H., Yoon, C., & Kim, B. J. (2000). Structural Monitoring System Based on Sensitivity Analysis and a Neural Network. *Computer-Aided Civil and Infrastructure Engineering*, 15(4), 189–195.
- Leyder, C., Dertimanis, V., Frangi, A., Chatzi, E., & Lombaert, G. (2018). Optimal sensor placement methods and metrics—comparison and implementation on a timber frame structure. *Structure and Infrastructure Engineering*, 14(7), 997–1010.
- Li, H., Li, S., Ou, J., & Li, H. (2010). Modal identification of bridges under varying environmental conditions: Temperature and wind effects. *Structural Control and Health Monitoring*, 17(5), 495–512.
- Lin, S.-W., Yi, T.-H., Li, H.-N., & Ren, L. (2017). Damage Detection in the Cable Structures of a Bridge Using the Virtual Distortion Method. *Journal of Bridge Engineering*, 22(8).
- Liu, H., Song, G., Jiao, Y., Zhang, P., & Wang, X. (2014). Damage identification of bridge based on modal flexibility and neural network improved by particle swarm optimization. *Mathematical Problems in Engineering*, 2014.
- Magalhães, F., Caetano, E., & Cunha, Á. (2007). Challenges in the Application of Stochastic Modal Identification Methods to a Cable-Stayed Bridge. *Journal of Bridge Engineering*, 12, 746–754.
- Meo, M., & Zumpano, G. (2005). On the optimal sensor placement techniques for a bridge structure. *Engineering Structures*, 27(10), 1488–1497.
- Meo, M., & Zumpano, G. (2005). On the optimal sensor placement techniques for a bridge structure. *Engineering Structures*, 27(10), 1488–1497.
- Papadimitriou, C., & Lombaert, G. (2012). The effect of prediction error correlation on optimal sensor placement in structural dynamics. *Mechanical Systems and Signal Processing*, 28, 105–127.
- Sadeghi Eshkevari, S., Matarazzo, T. J., & Pakzad, S. N. (2020). Bridge modal identification using acceleration measurements within moving vehicles. *Mechanical Systems and Signal Processing*, 141.
- Sun, M., Mehrisadat, Alamdari, M., & Kalhori, H. (2017). Automated Operational Modal Analysis of a Cable-Stayed Bridge. *Journal of Bridge Engineering*, 22(12).
- Ubertini, F., Gentile, C., & Materazzi, A. L. (2013). Automated modal identification in operational conditions and its application to bridges. *Engineering Structures*, 46, 264–278.
- Yang, X.-M., Yi, T.-H., Qu, C.-X., Li, H.-N., & Liu, H. (2019). Automated Eigensystem Realization Algorithm for Operational Modal Identification of Bridge Structures. *Journal of Aerospace Engineering*, 32(2).
- Yi, T. H., Li, H. N., & Wang, C. W. (2016). Multi-axial sensor placement optimization in structural health monitoring using distributed Wolf algorithm. *Structural Control and Health Monitoring*, 23(4), 719–734.

Indirect bridge damage detection using frequencies identified from vibrations of a single two-axle vehicle

Z. Li, W. Lin & Y. Zhang

Department of Civil Engineering, Aalto University, Espoo, Finland

ABSTRACT: Bridge frequency identification using passing vehicles has been demonstrated as a promising approach in the last two decades. Compared to the traditional method that requires sensor systems installed on the bridge, the indirect method only needs a few sensors mounted on passing vehicles, making it potential to monitor a large number of bridges rapidly and economically. However, currently, most studies just checked the existence of the bridge's frequencies in the vehicle's vibrations and explored to identify its frequencies accurately. Few studies investigated the damage detection of bridges using indirectly extracted bridge frequencies. This paper presents an indirect bridge damage detection method using bridge frequencies identified from a passing two-axle vehicle's vibration data. Initially, the bridge's finite element model is carefully built, updated, and divided into several substructures. Damage factors of different substructures are utilized to represent their damage degrees. Then, the bridge's frequencies will be identified from the passing vehicle's vibrations. At this stage, contact-point responses of the vehicle are back-calculated from its accelerations, and the residual contact-point responses of the two axles are employed to eliminate the vehicle's frequencies and inverse effects of road roughness, making the bridge's frequencies highlighted in the frequency domain. Thirdly, an objective function based on numerical experiments is proposed to locate and quantify the damage. The proposed method is verified numerically by a half-car model and a simply supported bridge in this paper. The results indicate that both the locations and degrees of damage can be identified under different influence factors and show great potential in practical applications.

1 INTRODUCTION

The safety of bridge structures has been a concern in the last decades due to their deterioration and collapse (Barker 2022). Structural health monitoring (SHM) can provide essential techniques for bridge health condition assessment (Bao et al. 2019). Mature approaches have been developed by scholars using sensors installed directly on the bridge (the direct method). However, conventional methods typically need a large number of sensors mounted on the target bridge to form a sensing system, which is expensive and time-consuming.

To monitor the bridge indirectly, the drive-by method was proposed by Yang et al. (2004). The idea just requires several sensors adequately installed on the vehicle rather than the bridge (the indirect method), thus is economical and easy-to-operate. Since CP responses have nothing to do with the vehicle, no vehicle frequencies will appear in the frequency-domain spectrum, Yang et al. (2022) proposed to identify the bridge's frequencies using residual CP responses of a half-car model. Employing CP responses of the vehicle can improve the precision of identifying the bridge's frequencies. However, currently, few studies explored locating and quantifying the bridge's damage using the indirectly identified frequencies. The substructure isolation method is one of the effective methods to identify structural damage, in which the substructure is separated from the whole structure and thus can be analyzed individually (Hou et al. 2011, 2019, 2020a; Li et al. 2022). Combined with the indirect method, it has the potential to identify the bridge's damage indirectly.

This paper aims to locate and quantify the bridge's damage using indirectly identified bridge frequencies from the passing vehicle. Firstly, the equations for back-calculating CP responses using the half-car model with four Degrees of freedom (DOFs) are derived. Then, an objective function employing the identified frequencies is proposed. Thirdly, a numerical experiment is carefully designed to verify the proposed method. The remainder of this paper is structured as follows: Section 2 introduces the theoretical foundations for calculating CP responses and building objective functions. Section 3 provides the numerical simulation of a Vehicle Bridge Interaction (VBI) system and discusses several damage cases and influencing factors. Finally, this paper is concluded in Section 4.

2 THEORETICAL FOUNDATIONS

2.1 CP responses

2.1.1 VBI model

This section employs a half-car model with four DOFs, and the bridge is simulated by a simply supported beam, as illustrated in Figure 1. The finite element (FE) model for the VBI system is built in MATLAB.

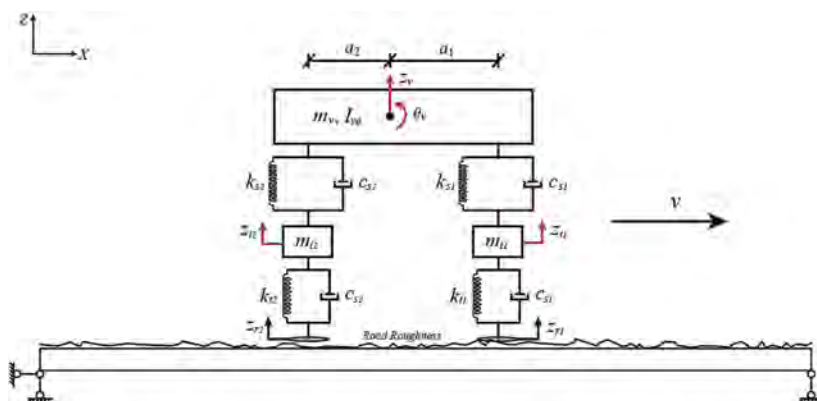


Figure 1. Half-car model and the simply supported beam.

In Figure 1, four DOFs of the vehicle are illustrated by red arrows. They are vehicle body bounce z_v , body pitching θ_v , and bounces of front and rear axles z_{t1} , z_{t2} . The displacements between the tire and road profile are represented by u_{c1} and u_{c2} . The mass of the vehicle body is m_v , and its pitching moment of inertia is $I_{v\theta}$. The masses for front and rear axles (including wheels) are m_{t1} and m_{t2} , respectively. The distances between the gravity center and front and rear axles are a_1 and a_2 . The stiffness and damping of the suspension system are represented by k_{s1} , k_{s2} , c_{s2} , c_{s2} , and for the tires, they are k_{t1} , k_{t2} , c_{t2} , c_{t2} respectively. The vehicle's speed is denoted by v . The vehicle's dynamic equilibrium equation is represented by Equation (1),

$$\mathbf{M}_v \ddot{\mathbf{z}}(t) + \mathbf{C}_v \dot{\mathbf{z}}(t) + \mathbf{K}_v \mathbf{z}(t) = \mathbf{p}_v \quad (1)$$

where \mathbf{M}_v , \mathbf{C}_v and \mathbf{K}_v are the vehicle's mass, damping, and stiffness matrices; $\ddot{\mathbf{z}}(t)$, $\dot{\mathbf{z}}(t)$ and $\mathbf{z}(t)$ are its acceleration, velocity, and displacement vectors, respectively; \mathbf{p}_v is the input excitation vector for the vehicle. These matrices are shown in Equations (2~5),

$$\mathbf{M}_v = \begin{bmatrix} m_v & 0 & 0 & 0 \\ 0 & I_{v\theta} & 0 & 0 \\ 0 & 0 & m_{t1} & 0 \\ 0 & 0 & 0 & m_{t2} \end{bmatrix} \quad (2)$$

$$\mathbf{C}_v = \begin{bmatrix} c_{s1} + c_{s2} & a_1 c_{s1} - a_2 c_{s2} & -c_{s1} & -c_{s2} \\ a_1 c_{s1} - a_2 c_{s2} & a_1^2 c_{s1} + a_2^2 c_{s2} & -a_1 c_{s1} & a_2 c_{s2} \\ -c_{s1} & -a_1 c_{s1} & c_{s1} + c_{t1} & 0 \\ -c_{s2} & a_2 c_{s2} & 0 & c_{s2} + c_{t2} \end{bmatrix} \quad (3)$$

$$\mathbf{K}_v = \begin{bmatrix} k_{s1} + k_{s2} & a_1 k_{s1} - a_2 k_{s2} & -k_{s1} & -k_{s2} \\ a_1 k_{s1} - a_2 k_{s2} & a_1^2 k_{s1} + a_2^2 k_{s2} & -a_1 k_{s1} & a_2 k_{s2} \\ -k_{s1} & -a_1 k_{s1} & k_{s1} + k_{t1} & 0 \\ -k_{s2} & a_2 k_{s2} & 0 & k_{s2} + k_{t2} \end{bmatrix} \quad (4)$$

$$\mathbf{p}_v = \begin{bmatrix} 0 \\ 0 \\ k_{t1} u_{c1} + c_{t1} \dot{u}_{c1} \\ k_{t2} u_{c2} + c_{t2} \dot{u}_{c2} \end{bmatrix}, \quad \mathbf{z} = \begin{bmatrix} z_v \\ \theta_v \\ z_{t1} \\ z_{t2} \end{bmatrix} \quad (5)$$

where $u_{ci} = u_{bi} + z_{ri}$, $\dot{u}_{ci} = \dot{u}_{bi} + \dot{z}_{ri}$, and u_{bi}, \dot{u}_{bi} are the bridge's deflection and velocity at the i -th contact point.

For the bridge, it is simply supported at each end, as shown in Figure 1. The beam can be divided into N_b Euler-Bernoulli elements and N_s substructures for damage locating purposes. Each node has two DOFs: vertical translation and rotation. The bridge's vibration equations can be denoted by Equation (6),

$$\mathbf{M}_b \ddot{\mathbf{z}}_b(t) + \mathbf{C}_b \dot{\mathbf{z}}_b(t) + \mathbf{K}_b \mathbf{z}_b(t) = \mathbf{p}_b^N \quad (6)$$

where \mathbf{M}_b , \mathbf{C}_b and \mathbf{K}_b are the bridge's mass, damping, and stiffness matrices. In this paper, the damping is simulated by the Rayleigh damping assumption, which can be obtained by $\mathbf{C}_b = \alpha \mathbf{M}_b + \beta \mathbf{K}_b$, where α and β can be obtained when the first two order damping ratios ζ_1, ζ_2 are set beforehand.

The interaction of the vehicle and the bridge is accomplished by the tires. When the tires of the vehicle are not on the bridge's nodes, the Hermitian cubic interpolation function is employed to distribute the CP force to its two adjacent nodes. This process can be finished by Equations (7~10),

$$\mathbf{p}_b^N = \mathbf{N}_c \mathbf{p}_b \quad (7)$$

$$\mathbf{p}_b = \begin{bmatrix} k_{t1}(z_{t1} - u_{c1}) + c_{t1}(\dot{z}_{t1} - \dot{u}_{c1}) - m_v g \cdot \frac{a_2}{a_1 + a_2} - m_{t1} g \\ k_{t2}(z_{t2} - u_{c2}) + c_{t2}(\dot{z}_{t2} - \dot{u}_{c2}) - m_v g \cdot \frac{a_1}{a_1 + a_2} - m_{t2} g \end{bmatrix} \quad (8)$$

$$\mathbf{N}_c = \begin{bmatrix} 0 & \cdots & 0 & \cdots & \boldsymbol{\Phi}_1 & \cdots & 0 \\ 0 & \cdots & \boldsymbol{\Phi}_2 & \cdots & 0 & \cdots & 0 \end{bmatrix}^T \quad (9)$$

$$\boldsymbol{\Phi}_i = \begin{bmatrix} 1 - 3d_i^2 + 2d_i^3 \\ d_i l_e (d_i - 1)^2 \\ 3d_i^2 - 2d_i^3 \\ d_i l_e (d_i^2 - d_i) \end{bmatrix}^T, \quad d_i = \frac{x_i(t) - (j-1)l_e}{l_e} \quad (10)$$

where $x_i(t)$, $i = 1, 2$ is the distance of the i -th contact points on the j -th element to the bridge's left end at t time, and l_e is the length of the bridge's element. By employing the Newmark- β method, we can get the bridge's deflections at nodes, namely \mathbf{z}_b . Then the deflection at contact points can be calculated using $\mathbf{u}_b = \mathbf{N}_c^T \mathbf{z}_b$, and the velocity can be obtained as $\dot{\mathbf{u}}_b = v(\mathbf{N}_c')^T \mathbf{z}_b + \mathbf{N}_c^T \dot{\mathbf{z}}_b$. Therefore, Equation (5) can be updated accordingly. After several iterations, the interaction between the vehicle and the bridge can converge at an acceptable precision.

2.1.2 Road roughness

In this paper, the road roughness is generated according to ISO 8608 (Technical Committee ISO/TC 1995). The procedure can be represented by Equations (11) and (12),

$$r(x) = \sum_{i=1}^N \sqrt{2G_d(n_i)\Delta n} \cos(2\pi n_i x + \theta_i) \quad (11)$$

$$G_d(n_i) = G_d(n_0) \left(\frac{n_i}{n_0}\right)^{-2} \quad (12)$$

where $r(x)$ is the generated road roughness. θ_i is uniformly distributed between 0 and 2π . Δn is selected as 0.01 cycle/m. n_0 is taken as 0.1 cycle/m, and n_i is set as numbers from 0.01 to 10 m^{-1} with an interval of 0.01 m^{-1} . $G_d(n_0)$ will be determined by the road class used in the simulation.

2.1.3 CP response calculation

By disassembling Equation (1), we can get the equilibrium equations related to the wheels as shown in Equations (13) and (14).

$$m_{t1}\ddot{z}_{t1} - c_{s1}(\dot{z}_v - \dot{z}_{t1} + a_1\dot{\theta}_v) - k_{s1}(z_v - z_{t1} + a_1\theta_v) + c_{t1}(\dot{z}_{t1} - \dot{u}_{c1}) + k_{t1}(z_{t1} - u_{c1}) = 0 \quad (13)$$

$$m_{t2}\ddot{z}_{t2} - c_{s2}(\dot{z}_v - \dot{z}_{t2} - a_2\dot{\theta}_v) - k_{s2}(z_v - z_{t2} - a_2\theta_v) + c_{t2}(\dot{z}_{t2} - \dot{u}_{c2}) + k_{t2}(z_{t2} - u_{c2}) = 0 \quad (14)$$

By taking the second order derivative of Equations (13) and (14), and rearranging items related to CP responses, we can get

$$\ddot{u}_{ci} + \frac{c_{ti}}{k_{ti}} \frac{d\ddot{u}_{ci}}{dt} = \Psi_i(t), i = 1, 2. \quad (15)$$

$$\Psi_2(t) = \frac{m_{t1}}{k_{t1}} \frac{d^2\ddot{z}_{t1}}{dt^2} - \frac{c_{s1}}{k_{t1}} \left(\frac{d\ddot{z}_v}{dt} - \frac{d\ddot{z}_{t1}}{dt} - a_1 \frac{d\ddot{\theta}_v}{dt} \right) - \frac{k_{s1}}{k_{t1}} (\ddot{z}_v - \ddot{z}_{t1} - a_1\ddot{\theta}_v) + \ddot{z}_{t1} + \frac{c_{t1}}{k_{t1}} \frac{d\ddot{z}_{t1}}{dt} \quad (16)$$

$$\Psi_2(t) = \frac{m_{t2}}{k_{t2}} \frac{d^2\ddot{z}_{t2}}{dt^2} - \frac{c_{s2}}{k_{t2}} \left(\frac{d\ddot{z}_v}{dt} - \frac{d\ddot{z}_{t2}}{dt} - a_2 \frac{d\ddot{\theta}_v}{dt} \right) - \frac{k_{s2}}{k_{t2}} (\ddot{z}_v - \ddot{z}_{t2} - a_2\ddot{\theta}_v) + \ddot{z}_{t2} + \frac{c_{t2}}{k_{t2}} \frac{d\ddot{z}_{t2}}{dt} \quad (17)$$

In Equations (15~17), m_{ti} , c_{ti} , k_{ti} and k_{si} can be measured in experiments. \ddot{z}_v , $\ddot{\theta}_v$ and \ddot{z}_{ti} are collected accelerations when the vehicle is passing the bridge. a_1 and a_2 are constants shown in Figure 1. For first- and second-order derivatives in Equations (16) and (17), they can be calculated by first-order finite difference formulas and second-order central formulas as shown in Equations (18) and (19).

$$\frac{d\ddot{z}_{ti}}{dt} = \frac{\ddot{z}_{ti}(s) - \ddot{z}_{ti}(s-1)}{\Delta t}, \frac{d\ddot{z}_v}{dt} = \frac{\ddot{z}_v(s) - \ddot{z}_v(s-1)}{\Delta t}, \frac{d\ddot{\theta}_v}{dt} = \frac{\ddot{\theta}_v(s) - \ddot{\theta}_v(s-1)}{\Delta t} \quad (18)$$

$$\frac{d^2\ddot{z}_{ti}}{dt^2} = \frac{\ddot{z}_{ti}(s+1) - 2\ddot{z}_{ti}(s) + \ddot{z}_{ti}(s-1)}{(\Delta t)^2} \quad (19)$$

We can see that Equation (15) is a first-order linear differential equation. Its solution can be represented by Equation (20), and due to the discrete data collection, it can be rewritten as Equation (21),

$$\ddot{u}_{ci}(t) = \begin{cases} \Psi_i(t), i = 1, 2, \text{ if } c_{ti} = 0 \\ \frac{k_{ti}}{c_{ti}} \exp\left(-\frac{k_{ti}}{c_{ti}} t\right) \left(\int_0^t \Psi_i(\tau) \exp\left(\frac{k_{ti}}{c_{ti}} \tau\right) d\tau \right), i = 1, 2., \text{ if } c_{ti} \neq 0 \end{cases} \quad (20)$$

$$\ddot{u}_{ci}(t) = \begin{cases} \Psi_i(t), i = 1, 2, \text{if } c_{ii} = 0 \\ \frac{k_{ii}}{c_{ii}} \left(\sum_{c_{ii}}^{t/\Delta t} \Psi_i|_s \exp\left(\frac{k_{ii}}{c_{ii}}(s\Delta t - t)\right) \Delta t \right), i = 1, 2; s = 1, 2, \dots \text{if } c_{ii} \neq 0 \end{cases} \quad (21)$$

where Δt is the sampling time interval, and s represents the s -th sampling point of the vehicle's accelerations.

2.2 Objective function

After the bridge's frequencies are extracted from the vehicle's vibrations, the next step is to identify the possible damage to the bridge. The proposed method requires a FE model of the undamaged bridge. As introduced in Equation (6), the mass, damping, and stiffness matrices of the undamaged bridge can be represented by \mathbf{M}_b , \mathbf{C}_b , and \mathbf{K}_b . The bridge is divided into N_s substructures, and its damage degree can be denoted by damage factors $\boldsymbol{\mu} = [\mu_1, \mu_2, \dots, \mu_{N_s}]^T$, in which μ_i represents the damage factor of the i -th substructure. If the damage factor $\mu_i < 1$, it means that the i -th substructure is damaged, and the damage degree is $1 - \mu_i$. If \mathbf{K}_{bi} is employed to represent the stiffness matrix of the i -th substructure in the global coordinates, the possibly damaged bridge's stiffness matrix can be calculated by Equation (22),

$$\mathbf{K}_b^d(\boldsymbol{\mu}) = \sum_{i=1}^{N_s} \mu_i \mathbf{K}_{bi} \quad (22)$$

where $\mathbf{K}_b^d(\boldsymbol{\mu})$ is the stiffness matrix of the possibly damaged bridge. The objective function using frequencies can be represented by Equation (23),

$$\Delta(\boldsymbol{\mu}) = \sum_k^K \left(\frac{\hat{\omega}_k(\boldsymbol{\mu}) - \omega_k}{\omega_k} \right)^2 + \lambda \|1 - \boldsymbol{\mu}\| \quad (23)$$

where $\hat{\omega}_k(\boldsymbol{\mu})$ is the natural frequencies calculated by the eigenvalue decomposition of \mathbf{M}_b and $\mathbf{K}_b^d(\boldsymbol{\mu})$. K means the first K order frequencies will be utilized for damage detection. ω_k is the k -th order natural frequency indirectly identified from the passing vehicle. The term $\lambda \|1 - \boldsymbol{\mu}\|$ is the l_1 -norm of $1 - \boldsymbol{\mu}$. Such a term is a typical approach that promotes the sparsity of identified damage (Hernandez 2014; Hou et al. 2020b). The damage factors of the damaged bridge can be obtained by optimizing $\boldsymbol{\mu}$ with an initial value.

3 NUMERICAL SIMULATIONS

3.1 Basic parameters of the VBI system

The basic parameters of the vehicle and the bridge are listed in Table 1, which is referred to the references (Li et al. 2020; He & Yang 2022).

For the vehicle, its speed is 5 m/s when passing the bridge and its frequencies are $f_{v1} \sim f_{v4}$ as shown in Table 1. The axle distance is 4.2 m. For the bridge, it is divided into ten substructures and each substructure includes two finite elements as shown in Figure 2. The bridge is simply supported at each end. The bridge's damping is temporarily set as zero and will be discussed in Section 3.3. The sampling frequency is set as 1 kHz.

For the road roughness, an A-class road with $G_d(n0) = 4e^{-6}$ is employed. Due to the tire contact with the road, the original road roughness is smoothed accordingly. The generated road roughness and its PSD are shown in Figures 3 and 4.

3.2 Bridge frequency identification

The vehicle's vibrations and responses in the frequency domain are shown in Figure 5. It can be seen from Figure 5 (b) that no bridge's frequencies can be identified using the vehicle's vibrations. The bridge's frequencies have been submerged in the road roughness spectrum and the vehicle's frequency-domain responses. It is hard to identify the bridge's frequency, and further damage detection is unachievable.

Table 1. Basic parameters of the vehicle and bridge.

VBI	Parameters (symbol)	Unit	Value
Vehicle	Body mass (m_v)	kg	17735
	Body moment of inertia $I_{v\theta}$	$kg \cdot m^2$	1.47×10^5
	Axle mass (m_{r1}, m_{r2})	kg	1500, 1000
	Suspension damping (c_{s1}, c_{s2})	$N \cdot s/m$	$3 \times 10^4, 4 \times 10^4$
	Tire damping (c_{t1}, c_{t2})	$N \cdot s/m$	0, 0
	Suspension stiffness (k_{s1}, k_{s2})	N/m	$2.47 \times 10^6, 4.23 \times 10^6$
	Tire stiffness (k_{t1}, k_{t2})	N/m	$3.74 \times 10^6, 4.6 \times 10^6$
	Axle distances (a_1, a_2)	m	2.18, 2.02
	Velocity (v)	m/s	5
	Vehicle frequencies ($f_{v1}, f_{v2}, f_{v3}, f_{v4}$)	Hz	1.61, 2.29, 10.35, 15.10
Bridge	Length (l_b)	m	30
	Flexural stiffness (EI)	N/m^2	1.375×10^{10}
	Mass per unit length (\bar{m})	kg/m	2000
	Bridge frequencies (f_{b1}, f_{b2}, f_{b3})	Hz	4.58, 18.31, 41.19

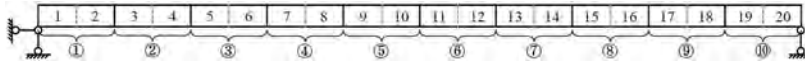


Figure 2. FE model of the bridge.

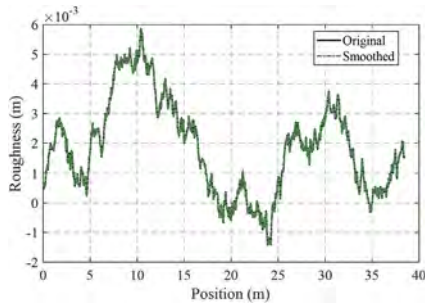


Figure 3. FE model of the bridge.

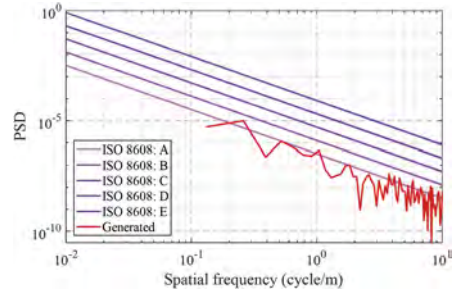
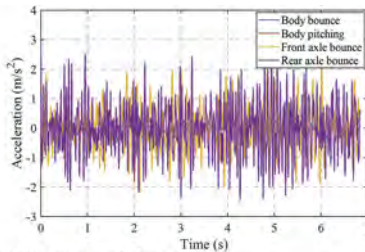
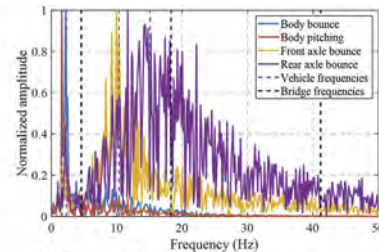


Figure 4. PSD of the road roughness.



(a) Vibrations of the vehicle



(b) FFT of the vehicle's vibrations

Figure 5. Vibrations and FFT spectrum of the vehicle.

To solve the problem, the residual CP responses of the vehicle's two wheels are utilized. After the vehicle's acceleration $\ddot{z}_v, \ddot{\theta}_v, \ddot{z}_{r1}, \ddot{z}_{r2}$ are recorded, CP responses of the front and rear wheels can be back-calculated using Equation (21). Then, to eliminate the inverse effects of road roughness, the residual CP responses of the front and rear tires are utilized. A specific calculation for residual CP responses can be found in reference (Yang et al. 2021). The bridge frequency identification results are shown in Figure 6.

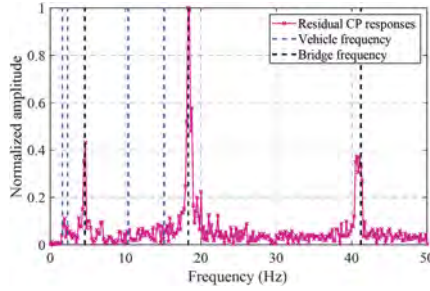


Figure 6. Bridge frequency identification results using residual CP responses.

It can be seen that when the residual CP responses are utilized, the bridge's frequencies are outstanding in the frequency spectrum. Also, for the third frequency, it can be noticed that it has been split into two parts: $f_{b3}^{id1} = f_{b3} - 3\pi v/l_b$ and $f_{b3}^{id2} = f_{b3} + 3\pi v/l_b$. Therefore, in the later damage identification process, the employed bridge's third frequency should be $f_{b3} = (f_{b3}^{id1} + f_{b3}^{id2})/2$.

3.3 Damage detection

As discussed in the last sections, it can be seen that when the residual CP responses are employed, the bridge's frequencies can be identified in the frequency domain. However, we can also notice that due to the influence of road roughness, errors in back-calculation of CP responses, and the separation of bridge's frequencies, etc., the accuracy of bridge frequencies cannot be obtained. This section will discuss identifying the bridge's damage using the indirectly identified frequencies. There are two scenarios for the damaged bridge:

- (1) Scenario 1: Minor damage, $\mu = [1, 1, 1, 1, 0.8, 1, 1, 1, 1, 1]$.
- (2) Scenario 2: Medium damage, $\mu = [1, 1, 1, 0.6, 1, 1, 1, 1, 1, 1]$.

The same FE model used in Section 3.2 is employed for damage detection. Initially, the bridge is assumed as healthy, namely, the initial damage factors are $\mu_0 = [1, 1, 1, 1, 1, 1, 1, 1, 1, 1]$. Then the damage factors are optimized using Equation (23). To verify the applicability of the proposed method, the damage identification results using true frequencies (ω_k') of the damaged bridge are also utilized compared with using the indirectly identified frequencies (ω_k) with or without bridge damping. The first three frequencies when the indirect method is employed are utilized for damage detection, namely $K=3$ in Equation (23).

When the bridge damping is not considered, the bridge's frequencies can be identified well (error $\leq 1.2\%$) as shown in Table 2, and the damage detection results are shown in Figure 7 (red bars). It can be seen from Figure 7 that even though there are some errors between the identified frequencies and the true ones, the bridge's damage can be identified with good precision, especially when the damage degree is low. When the damage degree increases, the damage detection accuracy goes down, and some substructures can be wrongly identified as damaged (e.g., substructure 9 in Figure 7 (b)).

Table 2. Frequencies used for damage detection.

Scenarios	Minor damage scenario			Medium damage scenario		
True frequencies of the damaged bridge ω_k'/Hz	4.469	18.252	40.464	4.429	17.279	40.083
Identified frequencies without bridge damping $\omega_{k,0}/Hz$ (error)	4.483 (0.31%)	18.276 (0.13%)	40.172 (0.72%)	4.483 (1.2%)	17.414 (0.78%)	40.000 (0.21%)
Identified frequencies with bridge damping $\omega_{k,d}/Hz$ (error)	4.310 (3.56%)	18.621 (2.02%)	40.517 (0.13%)	4.310 (2.69%)	17.069 (1.22%)	40.510 (1.07%)

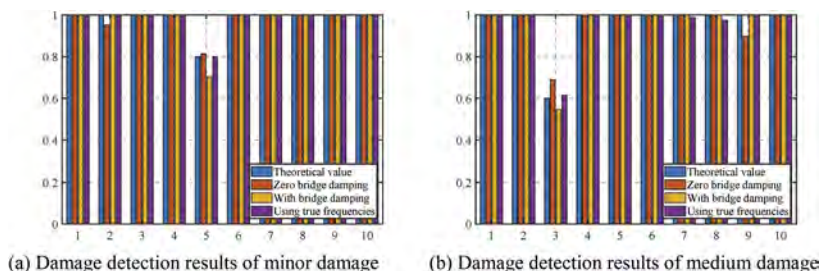


Figure 7. Damage detection results.

When the bridge's damping is assumed as $\zeta_1 = \zeta_2 = 0.01$. The bridge frequency identification errors increase (error $\leq 3.56\%$) as shown in Table 2. Figure 7 (yellow bars) confirms the effectiveness of the proposed objective function on damage detection. Both the position and degree of the bridge's damage can be detected when the damping is considered. But for the low damage scenario, the identification precision for damage degree decreases compared to the zero-bridge damping results.

4 CONCLUSIONS

In this paper, a damage detection strategy using indirectly identified frequencies of the bridge is proposed. A two-axle half-car model and a simply supported beam are utilized to verify the proposed method. The main concluding remarks are drawn below:

- (1) The vehicle's vibrations cannot be directly utilized to identify the bridge's frequencies when the road roughness is considered. By employing residual CP responses, both the vehicle's frequencies and the inverse effects of road roughness can be eliminated, making the bridge's frequencies outstanding and identifiable.
- (2) The bridge's damping plays a negative role in identifying the bridge's frequencies. The errors between true and indirectly identified frequencies will increase when the bridge damping is considered.
- (3) The proposed damage detection method can be used to locate and quantify the damage even though there are minor errors in indirectly identified bridge frequencies, which shows great potential in engineering applications.

Even though the bridge's damage can be detected with good precision, there are several factors that deserve further studies in engineering, such as multiple damage scenarios, high vehicle speed, engine effects, temperature effects, and ongoing traffics. The investigation of the above factors on damage detection will be included in our future studies before laboratory and field tests.

ACKNOWLEDGEMENTS

This research is fully financially sponsored by the Jane and Aatos Erkkö Foundation in Finland (Decision number: 210018). Y. Zhang is financially supported by the Academy of Finland (Decision number: 339493).

REFERENCES

- Bao Y., Chen Z., Wei S., Xu Y., Tang Z., & Li H. (2019) The State of the Art of Data Science and Engineering in Structural Health Monitoring. *Engineering* 5:234–242.
- Barker N. (2022) Norway to inspect timber bridges after 10-year-old glulam crossing collapses. <https://www.dezeen.com/2022/08/17/norway-timber-tretten-bridge-collapse/>. Accessed 24 Aug 2022

- He Y. & Yang J.P. (2022) Using acceleration residual spectrum from single two-axle vehicle at contact points to extract bridge frequencies. *Eng Struct* 266:114538.
- Hernandez E.M. (2014) Identification of isolated structural damage from incomplete spectrum information using l1-norm minimization. *Mech Syst Signal Process* 46:59–69.
- Hou J., Jankowski Ł., & Ou J. (2011) A substructure isolation method for local structural health monitoring. *Struct Control Heal Monit* 18:601–618.
- Hou J., Li Z., Jankowski Ł., & Wang S. (2020a) Estimation of virtual masses for structural damage identification. *Struct Control Heal Monit* 27:1–21.
- Hou J., Li Z., Zhang Q., Zhou R., & Jankowski Ł. (2019) Optimal placement of virtual masses for structural damage identification. *Sensors (Switzerland)* 19:1–18.
- Hou J., Li Z., Zhang Q., Jankowski Ł., & Zhang H. (2020b) Local mass addition and data fusion for structural damage identification using approximate models. *Int J Struct Stab Dyn* 20: 2050124.
- Technical Committee ISO/TC (1995) Mechanical Vibration–Road Surface Profiles–Reporting of Measured Data. International Organization for Standardization.
- Li J.T., Zhu X.Q., Law S.S., & Samali B. (2020) A Two-Step Drive-By Bridge Damage Detection Using Dual Kalman Filter. *Int J Struct Stab Dyn* 20: 2042006.
- Li Z., Hou J., & Jankowski Ł. (2022) Structural damage identification based on estimated additional virtual masses and Bayesian theory. *Struct Multidiscip Optim* 65:1–18.
- Yang Y.B., Lin C.W., & Yau J.D. (2004) Extracting bridge frequencies from the dynamic response of a passing vehicle. *J Sound Vib* 272:471–493.
- Yang Y.B., Mo X.Q., Shi K., Wang Z.L., Xu H., & Wu Y.T. (2021) Scanning torsional-flexural frequencies of thin-walled box girders with rough surface from vehicles' residual contact response: Theoretical study. *Thin-Walled Struct* 169:108332.
- Yang Y.B., Xu H., Wang Z.L., & Shi K. (2022) Using vehicle–bridge contact spectra and residue to scan bridge's modal properties with vehicle frequencies and road roughness eliminated. *Struct Control Heal Monit* 29: e2968.

Small-scale damage detection of bridges using machine learning techniques and drive-by inspection methods

Y. Lan, Z. Li, Y. Zhang & W. Lin

Aalto University, Espoo, Finland

ABSTRACT: The drive-by inspection approach for bridge health monitoring has received a lot of interest recently due to its advantages in mobility, economy and efficiency. The feasibility of it has been demonstrated by many studies via numerical simulations, laboratory experiments, and even field tests, when there is a noticeable damage. In terms of minor damages, however, the dynamic features (e.g., frequencies and mode shapes) of the damaged bridge are highly similar to those of the healthy one, for which traditional drive-by methods are likely to perform poorly. Machine learning techniques, which utilize the entire time-domain responses and are sensitive to tiny signal changes, have the potential to identify small-scale damages and achieve higher detection accuracy. This paper compares the performance of different machine learning methods on the indirect framework and proposes a strong classification algorithm for damage identification of bridges. Laboratory experiments were conducted to build the dataset by employing a steel beam and a scale truck model. It presents an early attempt to experimentally validate the feasibility of the drive-by inspection method to identify small structural changes in the bridge.

1 INTRODUCTION

In recent years, bridge maintenance and monitoring have become widespread concerns around the world (Malekjafarian et al. 2015). However, the direct methods for Structural Health Monitoring (SHM) have long been considered as expensive methods due to the enormous costs associated with sensor installation and maintenance (Abdulkarem et al. 2020). Moreover, because the instrumentation is permanently fixed on the bridge as a tailored SHM system, it can be challenging to transfer one monitoring framework to other bridges (Wang et al. 2022). These drawbacks restrain the broad application of direct SHM methods on bridges, and there is a need to develop an alternative strategy without instrumenting the bridge.

The drive-by bridge inspection method, an indirect SHM technique, has gained a lot of interest recently due to its benefits in mobility, economy, and efficiency (Malekjafarian et al. 2015). Studies have investigated the potential of the drive-by method in extracting bridge modal parameters, such as fundamental frequencies and mode shapes, via numerical simulations, laboratory experiments, and field tests (Yang et al. 2004; Lin & Yang 2005; Lan et al. 2022a, 2022b). Changes in modal parameters could indicate bridge deterioration, which is referred to as the modal parameter-based approach (Yang & Yang 2018).

However, most modal parameter-based methods fail to achieve satisfactory performance for small-scale damage detection due to several reasons. First, the bridge frequency, which is used in many studies as a damage indicator, lacks adequate information to indicate damage. They are easily impacted by environmental factors like temperatures (Spiridonakos et al. 2016). Second, mode shapes or their derivations are usually subject to measurement errors, disguising changes from small-scale damage (Zhang et al. 2019). Although there are some approaches based on indicators like displacement profile and moving force, similar problems have been discovered as well (O'Brien et al. 2014; O'Brien & Keenahan 2015; Lan 2021). Machine Learning (ML) methods can leverage the whole time-domain and frequency-domain responses rather than just peaks in the

spectrum (Liu et al. 2020); they are sensitive to small changes in the signal (Zhang et al. 2019). The combination of ML techniques and the drive-by method has the potential to identify small-scale damage and achieve higher detection accuracy.

Currently, compared with the application of ML technology on direct SHM, there have been few studies and implementations of ML techniques on indirect SHM (Wang et al. 2022). Based on Support Vector Machines (SVM), Cerda et al. (2014) successfully identified different bridge damage states with vehicle vibration data. In 2019, Artificial Neural Network (ANN) was first applied to indirect SHM problems by Malekjafarian et al. (2019), obtaining promising results for the damage detection of bridges. These studies verified the “potential” of ML methods in indirect SHM frameworks, but the ability of ML methods for small damage detection has not been fully exploited. On the other hand, since SVM and other normal classifiers may perform poorly for small-scale damages whose dynamic responses are highly similar to those of health, it is advantageous to build a strong classification algorithm that is sensitive to minor damage features.

A combined algorithm based on SVM and AdaBoost may provide a superior performance in this case. Studies show that SVM performs well on health state classification problems (Cerda et al. 2014), and combining it with a boosting algorithm may further improve its accuracy. AdaBoost can be used as a boosting strategy; it forces SVM to focus on misclassified samples from the minority class, preventing the minor damage features from being considered as noises (Kuncheva & Whitaker 2002). Linear and simple classifiers could better separate the high-dimensional spaces composed of vibration data in general, so linear-SVM is selected as the base learner in AdaBoost. However, the integration of linear SVM with AdaBoost is still difficult; it requires a suitable regularization parameter, C , to balance the “complexity” and “diversity” of SVM as the component classifier (Li et al. 2008). An optimization strategy for seeking the appropriate C value is therefore the key to building an efficient combination algorithm of AdaBoost-linear SVM.

This paper compares the performance of different ML methods on the indirect framework and proposes a strong classification algorithm, Optimized AdaBoost-linear SVM (OAB-linear SVM), for damage identification of bridges. Laboratory experiments were conducted to establish the dataset by employing a steel beam and a scale truck model. The paper presents an early attempt to experimentally validate the feasibility of the drive-by method to identify small damage in the bridge. ML models learn to identify bridge health states using raw vehicle acceleration signals as inputs. The model’s performance is evaluated by its accuracy in classifying the test sets of different health statuses. The experimental results from the vehicle are also compared with those acquired directly from the bridge model to show the feasibility of the indirect SHM framework.

2 METHODOLOGY

2.1 Background of different ML models and the proposed method

In this study, five different ML models will be chosen as the classifiers for structural health states, in addition to the proposed algorithm. They are Linear-SVM, RBF-SVM, Gaussian Process (GP), Artificial Neural Network (ANN), and Random Forest (RF). They are algorithms commonly used in structural health state classification problems, and their summaries are as follows:

Linear-SVM: One of the most robust and accurate models of well-known ML algorithms is SVM (Evgeniou & Pontil 2001). The goal of linear-SVM is to find separating hyperplanes that can separate the dataset as reliably as possible into distinct data classes. Ideally, when the data are completely linearly separable, the hyperplanes will be as far as possible from the nearest elements of the classes.

RBF-SVM: RBF-SVM, as one of the nonlinear SVMs, replaces hyperplanes with Gaussian manifolds, but the basic principle remains the same (Evgeniou & Pontil 2001). One can adapt SVM to be a nonlinear classifier, which allows SVM to separate nonlinearly separable support vectors.

GP: GP is a generalization of the Gaussian probability distribution and can be used for classification and regression (Rasmussen & Williams 2005). It is a type of kernel model, similar to SVM, but unlike SVM, it can predict highly calibrated class membership probabilities, although the choice and configuration of the kernel used at the heart of the method can be challenging.

ANN: ANN is based on a collection of connected units or nodes called artificial neurons, which loosely resemble the neurons in a biological brain (Goodfellow et al. 2016). Each connection, like the synapses in a biological brain, can transmit a signal to other neurons. Typically, neurons are aggregated into layers. Different layers may perform different transformations on their inputs. Signals travel from the first layer (the input layer) to the last layer (the output layer), possibly after traversing the layers multiple times.

RF: RF is an extension of the bagging method, which uses feature randomness in addition to bagging to produce an uncorrelated forest of decision trees (Ho 1995). For classification problems, the output of RF is the class selected by most trees. RF generally outperforms decision trees, but its performance can be affected by data characteristics.

OAB-linear SVM: the proposed algorithm employs SVM with a linear kernel as component classifiers in AdaBoost and seeks its best generalization performance in damage detection. SVM is a strong classifier, and there is a need to weaken its learning abilities to benefit from AdaBoost mechanisms. It consists of a training process and an optimizing process, as shown in Tables 1 and 2, respectively. The input data is divided into a training set and a validation set with a ratio of 9:1. In the training process, AdaBoost maintains a weight distribution over training samples, which is initially configured to be uniform. Linear SVM as the component classifier is called repeatedly in a series of cycles, T . Linear SVM trains a classifier, h_t , at each iteration, t , and the distribution, w^t , is updated in each iteration based on the prediction results on the training samples. Correctly classified samples are assigned smaller weights, while misclassified samples are given larger weights. In the optimizing process, a very small C value, C_{ini} , is initially set corresponding to a linear SVM with weak learning ability. Linear SVM with this C value is then trained by AdaBoost to return an accuracy on the validation set. After that, the C value is increased slightly by C_{step} , to improve the learning ability of linear SVM. This procedure is repeated until the final cycle, S , is completed. The classifier with the highest result accuracy is chosen as optimal for the given dataset. The values of C_{ini} , C_{step} , S , and T required for the algorithm are set as 0.01, 0.1, 1000, and 50, respectively.

Table 1. Training process.

Require: training samples with labels, $\{(x_1, y_1), \dots, (x_i, y_i), \dots, (x_N, y_N)\}$, where x_i represents the i -th vector in the training set; $y_i = \{-1, 1\}$ for damaged and healthy labels.

Require: the number of iterations at which boosting is terminated, T .

Initialize the weights of sub-training samples, $w_i^1 = 1/N$ ($i = 1, 2, 3, \dots, N$).

For iteration t in T :

- (1) Train a Linear SVM component classifier, h_t , on the weighted sub-training set.
- (2) Compute the training error of h_t : $\varepsilon_t = \sum_{i=1}^N w_i^t y_i \neq h_t(x_i)$.
- (3) Set the weight of the component classifier h_t : $\alpha_t = \frac{1}{2} \ln \left(\frac{1-\varepsilon_t}{\varepsilon_t} \right)$.
- (4) Update the weights of sub-training samples: $w_i^{t+1} = \frac{w_i^t \exp[-\alpha_t y_i h_t(x_i)]}{C}$, where $\sum_{i=1}^N w_i^{t+1} = 1$.

Output: $f(x) = \text{sign} \left(\sum_{t=1}^T \alpha_t h_t(x) \right)$.

Table 2. Optimizing process.

Require: validation samples with labels, $\{(x_1, y_1), \dots, (x_i, y_i), \dots, (x_M, y_M)\}$.

Require: AdaBoost-linear SVM, $f(x)$.

Require: the number of cycles in updating the regularization parameter, S .

Require: the initial regularization parameter, C_{ini} ; the step of regularization parameter, C_{step} .

For iteration s in S :

- (1) Calculate the accuracy on validation sets with $f(x)$: $\text{accuracy}[s] = \frac{TP+TN}{TP+TN+FP+FN}$, where TP, TN, FP, FN represent true positive, true negative, false positive and false negative predictions in samples.
- (2) Increase C value by C_{step} : $C = C_{step} \times s + C_{ini}$

Output: $F(x) = f_{s,max}(x)$ corresponding to the max accuracy[s].

2.2 Signal processing and diagnostic framework

Raw accelerations collected from the passing vehicle will be processed to build the dataset for ML models. Figure 1 shows the processing procedure for the vehicle accelerations. For each passage, the valid acceleration segment will be cut off after the acquisition of vehicle acceleration, where peaks can be found in the acceleration records of the front axle when the vehicle enters and exits the bridge due to expansion joints at both ends; they can be regarded as indicators for selecting the effective segments. Given the passage time of T , and the sampling frequency of F , there are totally $T \times F$ discrete points in the valid segment. To reduce the influence of noise, a sliding window-based method is used to process the selected data (window length = 10, stride = 1), after which the processed time-domain signals are utilized as inputs for ML models. In the study, the experiments were conducted in a normal laboratory environment, where white noise was the main source of noise. Thus, the Gaussian function is chosen as the window function. The database obtained from vehicle responses has a total of 1600 runs, and it is split into the training set and test set with a ratio of 85%:15%. ML models learn to identify bridge health states via the training set and their performance is evaluated by the accuracy in the test set.

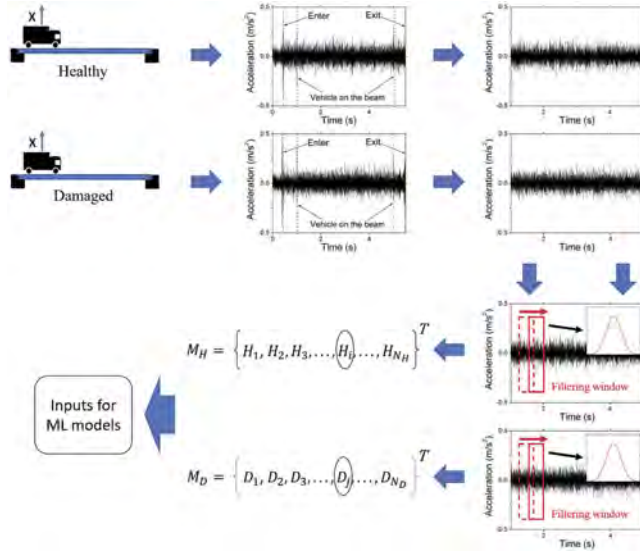


Figure 1. Signal processing procedure.

3 EXPERIMENTAL PROGRAM

Laboratory experiments were performed to validate the methodology using a steel beam and a scale truck model with an engine. Instead of inducing real structural damage, damaged states were simulated by adding masses to the beam to avoid permanent or irreversible destruction. It is a common practice in the laboratory that has been proven feasible by many studies, such as those conducted by Zhang et al. (2019), Liu et al. (2020), and Lan et al. (2023). The data acquisition system, which is PC-driven and has a sampling rate of 2 kHz, is the same for both the beam and the truck model; it is connected with sensors via wires. The sensors used in the study are made by Bruel & Kjaer (TYPE 4371), and relevant specifications are provided as follows: frequency range (0.1 – 12600 Hz), weight (11 gram), and sensitivity (1.0 pC/ms⁻²).

3.1 Bridge and vehicle models

Bridge model: Physical properties of the beam model (HEA400) are listed as follows: elastic modulus $E = 199$ GPa; density $\rho = 7.85 \times 10^3$ kg/m³; length $L = 4.4$ m; section area

$A = 15898 \text{ mm}^2$, and moment of inertia $I = 8.564 \times 10^7 \text{ mm}^4$. The setup and dimension details can be referred to in Figure 2. The setup includes an acceleration ramp, a deceleration ramp, and a guide rail (see Figure 3a) that is used to adjust the path of the vehicle so that it can pass straight through the beam. As artificial damage, masses were added to different locations of the beam (see Figure 3b); the details will be discussed later. For comparison purposes, three accelerometers were also instrumented at $0.1L$, $0.5L$, and $0.9L$ of the steel beam (see Figure 3c), respectively, to obtain the bridge vibrations during the vehicle's passage.

Vehicle model: Tamiya's Mercedes-Benz 1850L was employed as the vehicle model (see Figure 4a). Except for the weight, this engine-driven 1/14 scale model (568 mm \times 202 mm) realistically captures the configuration of a full-sized truck. The self-weight of the vehicle model is 4.05 kg, and a 6-kg mass is added inside the vehicle body; thus, the overall vehicle weight is 10.05 kg. Four accelerometers were mounted on the front of the car, the vehicle body, the rear axle, and the front axle, respectively, as described in Figure 4b, c. The maximum speed of the vehicle model is 0.9 m/s, and this speed is used in the test. Additionally, an acceleration ramp is employed to guarantee the maximum speed can be reached before the vehicle enters the bridge. The velocities maintain similar in each run.

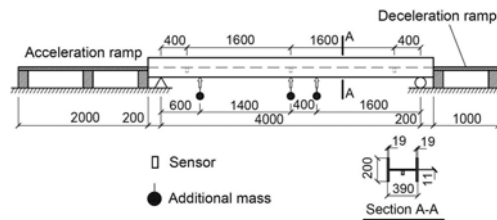


Figure 2. Details of the beam model (unit: mm).

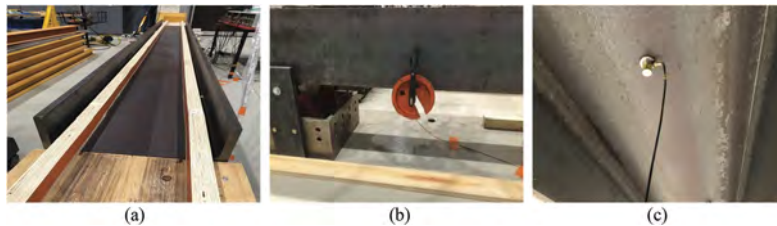


Figure 3. Setup for the beam model: (a) guide rail; (b) added mass; (c) accelerometer.

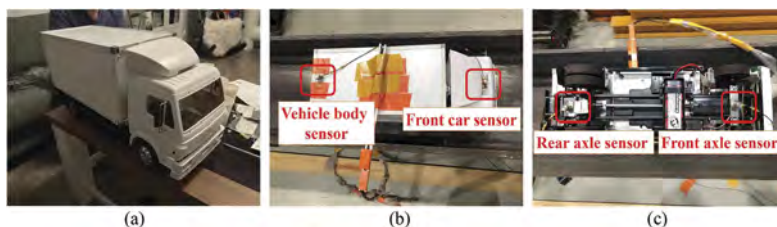


Figure 4. Setup for the vehicle model: (a) scale vehicle model; (b) sensor installation (top); (c) sensor installation (bottom).

3.2 Experimental dataset

For the diagnostic framework, data from both intact and damaged states of bridges are required. The vehicle was driven across the bridge repeatedly to acquire the dataset for

training and testing the ML models. There are totally 8 cases of health states including the healthy case used as baseline; these cases were collected from 3 damage locations and 5 damage severities, as described in Table 3. The placement of mass at different locations is used to validate the viability of the method; 0.5L (2 m) and 0.6L (2.4 m) stand for the damage locations at and near the mid-span of the bridge, and 0.15L (0.6 m) represents the damage location near the bridge support. Due to the larger vibration responses in the mid-span bridge, the detection performance of the mid-span is usually better than that near the support. 0.15L, as one of the most unfavorable location cases, is chosen to investigate the sensitivity of the method to the bridge damage by using various mass sizes. Each state contains 200 vehicle passages to establish the experimental dataset. Thus, there are 200 (runs) \times 8 (cases) \times 7 (sensors) = 11200 (signals), and each signal has 8000 discrete points corresponding to 4s of “valid segments”.

Table 3. Health state description.

Case No.	Location	Weight	Runs	Case No.	Location	Weight	Runs
0	0	0 (Healthy)	200	4	0.6 m	2 kg (0.4%)	200
1	0.6 m	20 kg (4%)	200	5	0.6 m	1 kg (0.2%)	200
2	0.6 m	10 kg (2%)	200	6	2 m	20 kg (4%)	200
3	0.6 m	5 kg (1%)	200	7	2.4 m	20 kg (4%)	200

4 RESULTS AND ANALYSIS

4.1 Damage indication performance

The main parameters of Linear-SVM, RBF-SVM, GP, ANN, and RF are determined by Grid Search (LaValle & Branicky 2004), as shown in Table 4. While the hyper-parameters of AB-linear SVM are tuned by the proposed optimizing method. The performance of each ML model is assessed via 5-fold cross-validation. The results from the rear axle sensor are illustrated herein, while results from sensors on other positions will be discussed later. Table 5 shows that the accuracy of ML algorithms decreases as the damage becomes less severe. The smallest damage of 1 kg (0.2%) used in the experiment can be successfully detected by ML models with accuracy ranging from 63.3% to 76.7%. The closer the accuracy is to 50% (random guess), the poorer the detection performance is, or the ML model is just not suitable for the SHM framework. Among these models, OAB-linear SVM outperforms other models by better classifying the damage states, which provides higher accuracy. It improves the accuracy by 6.2% on average when compared to the linear SVM, and by 5% to 16.6% compared to other algorithms. This is due to AdaBoost forces the linear SVM as a component classifier to concentrate on misclassified samples from the minority class, avoiding the minor damage features from being considered as noise. It is found that ML methods, especially the proposed algorithm, are of great significance for the identification of minor damages, which can expand the lower limit of detectable damage range.

Table 4. Major parameters of classification algorithms.

Algorithm	Configuration	Algorithm	Configuration
Linear-SVM	C=5	ANN	hidden_layer_sizes=(10, 4), alpha=1, max_iter=1000
RBF-SVM	gamma=0.01, C=5	RF	n_estimators=1000, max_features=20
GP	Kernel=10 * RBF(10)		

4.2 Performance comparison for sensor locations

The above results are acquired from the rear axle sensor, and the results from different sensor locations are presented in Table 6, where the results of the bridge sensor are used here to compare the direct and indirect methods. These results are based on OAB-linear SVM, as it has the highest accuracy, and similar results can be seen in other models. The data for the front-car

Table 5. Classification performance for ML models.

Cases	Details	OAB-linear SVM	Linear-SVM	RBF-SVM	GP	ANN	RF
Case1	0,15L, 20kg	88.3 %	83.3 %	73.3 %	75.0 %	81.7 %	78.3 %
Case2	0,15L, 10kg	85.0 %	78.3 %	70.0 %	71.7 %	78.3 %	75.0 %
Case3	0,15L, 5kg	81.7 %	75.0 %	68.3 %	70.0 %	75.0 %	71.7 %
Case4	0,15L, 2kg	78.3 %	73.3 %	65.0 %	66.7 %	73.3 %	68.3 %
Case5	0,15L, 1kg	76.7 %	70.0 %	63.3 %	65.0 %	71.7 %	66.7 %
Case6	0,5L, 20kg	93.3 %	86.7 %	76.7 %	81.7 %	85.0 %	83.3 %
Case7	0,6L, 20kg	91.7 %	85.0 %	76.7 %	78.3 %	85.0 %	85.0 %

sensor are not included in the table because the contact between the front car and the rail limits its free vibration. It can be observed that there is no significant difference in the accuracy of varied sensor locations, The similarity of results from the vehicle and bridge sensors implies that the indirect SHM framework is equally effective as the direct SHM system. Furthermore, the effectiveness of ML methods is not limited to a specific SHM framework or sensor location.

Table 6. Comparison performance for sensor locations.

Cases	Details	Car body	Rear axle	Front axle	Beam1	Beam2	Beam3
Case1	0,15L, 20kg	88.3 %	88.3 %	86.7 %	88.3 %	88.3 %	88.3 %
Case2	0,15L, 10kg	83.3 %	85.0 %	85.0 %	85.0 %	85.0 %	85.0 %
Case3	0,15L, 5kg	81.7 %	81.7 %	81.7 %	81.7 %	81.7 %	81.7 %
Case4	0,5L, 20kg	78.3 %	78.3 %	76.7 %	78.3 %	78.3 %	78.3 %
Case5	0,15L, 1kg	73.3 %	76.7 %	75.0 %	76.7 %	76.7 %	76.7 %
Case6	0,5L, 20kg	93.3 %	93.3 %	91.7 %	95.0 %	95.0 %	95.0 %
Case7	0,6L, 20kg	90.0 %	91.7 %	90.0 %	91.7 %	91.7 %	91.7 %

5 CONCLUSION

In this paper, the performance of different ML methods is compared, and a strong classification algorithm is proposed for the indirect SHM framework. Laboratory experiments using a steel beam and a scale truck model were performed to obtain the dataset. Additional weights on the beams as “artificial damage” are used to validate the effectiveness of different ML methods and the proposed algorithm in damage detection, especially small damages. Based on the experimental results, the following conclusions can be drawn:

- (1) ML methods are sensitive to damage. The ML methods used in this paper have accuracy ranging from 63.3% to 76.7% for small damage (0.2% severity), among which the proposed algorithm, OAB-linear SVM, shows the highest accuracy of 76.7%. They could expand the lower limit of the detectable damage range, which is of great benefit to the detection of minor damage.
- (2) OAB-linear SVM is demonstrated to outperform other ML models in the study, with improvements ranging from 5% to 16.6%. This could allow it to become a preferable option for damage detection problems.
- (3) The indirect SHM framework can be equally effective as the direct SHM system, and the effectiveness of ML methods is not limited to a specific SHM framework or sensor location.

A frontier of research is the integration of ML models with semi-supervised or unsupervised learning frameworks to build a new generation of smart bridges.

ACKNOWLEDGMENT

This research was fully sponsored by the Jane and Aatos Erkkö Foundation in Finland (Grant No. 210018). The first author was also financially supported by the Finnish Foundation for

Technology Promotion (TES) and Chinese Scholarship Council (CSC). The third author was funded by the Academy of Finland Postdoctoral Research Project (339493). Any findings, opinions, conclusions, and recommendations of this paper are those of the authors and do not necessarily reflect the views of the research sponsor.

REFERENCES

- Malekjafarian, A., McGetrick, P.J. & OBrien, E.J. 2015. A Review of Indirect Bridge Monitoring Using Passing Vehicles. *Shock and Vibration* 2015: 286139.
- Abdulkarem, M., Samsudin, K., Rokhani, F.Z. & A Rasid, M.F. 2020. Wireless sensor network for structural health monitoring: A contemporary review of technologies, challenges, and future direction. *Structural Health Monitoring* 19(3): 693–735.
- Wang, Z.L., Yang, J.P., Shi, K., Xu, H., Qiu, F.Q. & Yang, Y.B. 2022. Recent Advances in Researches on Vehicle Scanning Method for Bridges. *International Journal of Structural Stability and Dynamics*: 2230005.
- Yang, Y.B., Lin, C.W. & Yau, J.D. 2004. Extracting bridge frequencies from the dynamic response of a passing vehicle. *Journal of Sound and Vibration* 272(3): 471–493.
- Lin, C.W. & Yang, Y.B. 2005. Use of a passing vehicle to scan the fundamental bridge frequencies: An experimental verification. *Engineering Structures* 27 (13): 1865–1878.
- Lan, Y., Lin, W. & Zhang, Y. 2022a. Bridge frequency identification using vibration responses from sensors on a passing vehicle. *Bridge Safety, Maintenance, Management, Life-Cycle, Resilience and Sustainability*: 956–963.
- Lan, Y., Lin, W. & Zhang, Y. 2022b. Bridge Frequency Identification Using Multiple Sensor Responses of an Ordinary Vehicle. *International Journal of Structural Stability and Dynamics*: 2350056.
- Yang, Y.B. & Yang, J.P. 2018. State-of-the-Art Review on Modal Identification and Damage Detection of Bridges by Moving Test Vehicles. *International Journal of Structural Stability and Dynamics* 18(02): 1850025.
- Spiridonakos, M.D., Chatzi, E.N. & Sudret, B. 2016. Polynomial Chaos Expansion Models for the Monitoring of Structures under Operational Variability. *ASCE-ASME Journal of Risk and Uncertainty in Engineering Systems, Part A: Civil Engineering* 2(3): B4016003.
- Zhang, Y., Miyamori, Y., Mikami, S. & Saito, T. 2019. Vibration-based structural state identification by a 1-dimensional convolutional neural network. *Computer-Aided Civil and Infrastructure Engineering* 34(9): 822–839.
- OBrien, E.J., McGetrick, P.J. & González, A. 2014. A drive-by inspection system via vehicle moving force identification. *Smart Structures and Systems* 13(5): 821–848.
- OBrien, E.J. & Keenahan, J. 2015. Drive-by damage detection in bridges using the apparent profile. *Structural Control and Health Monitoring* 22(5): 813–825.
- Lan, Y. 2021. Improving the Drive-by Bridge Inspection Performance by Vehicle Parameter Optimization. *8th Asia Pacific Workshop on Structural Health Monitoring (SAMWSHM)*: 195–202.
- Liu, J., Chen, S., Bergés, M., Bielak, J., Garrett, J.H., Kovačević, J. & Noh, H.Y. 2020. Diagnosis algorithms for indirect structural health monitoring of a bridge model via dimensionality reduction. *Mechanical Systems and Signal Processing* 136: 106454.
- Cerda, F., Chen, S., Bielak, J., Garrett, J.H., Rizzo, P. & Kovacevic, J. 2014. Indirect structural health monitoring of a simplified laboratory-scale bridge model. *Smart Structures and Systems* 13(5): 849–868.
- Malekjafarian, A., Golpayegani, F., Moloney, C. & Clarke, S. 2019. A Machine Learning Approach to Bridge-Damage Detection Using Responses Measured on a Passing Vehicle. *Sensors* 19(18): 4035.
- Kuncheva, L.I. & Whitaker, C.J. 2002. Using Diversity with Three Variants of Boosting: Aggressive, Conservative, and Inverse. *Multiple Classifier Systems*: 81–90.
- Li, X., Wang, L. & Sung, E. 2008. AdaBoost with SVM-based component classifiers. *Engineering Applications of Artificial Intelligence* 21(5): 785–795.
- Evgeniou, T. & Pontil, M. 2001. *Support Vector Machines: Theory and Applications*. *Machine Learning and Its Applications*: 249–257.
- Rasmussen, C.E. & Williams, C.K.I. 2005. *Gaussian Processes for Machine Learning*. Cambridge: MIT Press.
- Goodfellow, I., Bengio, Y. & Courville, A. 2016. *Deep Learning*. Cambridge: MIT Press.
- Ho, T.K. 1995. Random decision forests. *Proceedings of 3rd International Conference on Document Analysis and Recognition*: 278–282.
- Lan, Y., Zhang, Y. & Lin, W. 2023. Diagnosis algorithms for indirect bridge health monitoring via an optimized AdaBoost-linear SVM. *Engineering Structures* 275: 115239.
- LaValle, S.M., Branicky, M.S. & Lindemann S.R. 2004. On the Relationship between Classical Grid Search and Probabilistic Roadmaps. *The International Journal of Robotics* 23(7–8): 673–692.

Structural health monitoring of the KW51 bridge based on detailed strain mode shapes: Environmental influences versus simulated damage

D. Anastasopoulos, K. Maes, G. De Roeck, G. Lombaert & E.P.B. Reynders
Department of Civil Engineering, KU Leuven, Leuven, Belgium

ABSTRACT: Strain mode shapes are attractive features for vibration-based monitoring as their sensitivity to local damage is known to be high. However, the assessment of their performance in situ has remained an open problem. This work presents the continuous dynamic strain monitoring of a steel railway bridge with FBGs for one year. The natural frequencies and strain mode shapes of ten modes are automatically identified from operational strain time histories, on an hourly basis. The influence of temperature on these modal characteristics is quantified and then investigated with a FE model of the bridge. A clear influence of temperature on the natural frequency of most modes is identified, especially during frost periods, contrary to the strain mode shapes, which are mostly insensitive to temperature changes, as confirmed also by the FE model. The FE model is employed to investigate also the influence of simulated local damage on the modal characteristics.

1 INTRODUCTION

Vibration-Based Monitoring (VBM) (Fan & Qiao (2010)) aims to identify structural damage by identifying damage-related changes in modal characteristics of a structure. Natural frequencies are the most widely used modal characteristics in VBM. They are mainly sensitive to global stiffness changes and thus, the influence of small-scale damage can be quite limited ((Fan & Qiao (2010)), while their temperature sensitivity can be high enough to hide the presence of damage. Displacement mode shapes are also used in VBM. They are more sensitive to local damage and less sensitive to temperature than natural frequencies but the disadvantage is that a dense grid of accelerometers is required to achieve damage localization ((Fan & Qiao (2010)), which is costly.

Strain mode shapes are an alternative to displacement mode shapes that offer several advantages (Anastasopoulos et al. (2019)). Strain-based features are much more sensitive to local damage than modal displacements and dense grids of strain sensors can be easily achieved when fiber-Bragg gratings (FBG) are employed, due to their multiplexing option. Laboratory experiments on concrete beams have illustrated that strain mode shapes are highly sensitive to local damage, while they are insensitive to temperature changes (Anastasopoulos et al. (2019)). In recent experiments, the strain mode shapes of a railway bridge were monitored with a dense grid of FBGs and were also found to be insensitive to temperatures higher than 0°C (Anastasopoulos et al. (2021)).

The second year of monitoring of this bridge, known as KW51, is presented here. During this period, the bridge was subjected to frost, which did not occur during the first year. The influence of frost on the bridge's strain mode shapes is studied first. Second, the physical interpretation of the influence of temperature on the modal characteristics of the bridge is given. This is achieved through a detailed finite element (FE) model of the bridge. Third, the influence of local stiffness changes on the bridge's modal characteristics is investigated. These changes are simulated in the FE model and the obtained influence is quantified and implemented on the experimentally obtained strain mode shapes. A sensitive *damage index*, which combines information from several modes, is used to detect the induced changes. The present paper is an abbreviated version of a more detailed study to be found in Anastasopoulos et al. (2022).

2 THE KW51 BRIDGE

The KW51 is a 117m steel tied-arch railway bridge (Figure 1) that crosses the Leuven-Dijle Canal in Leuven, Belgium. The deck consists of two main girders and thirty-three transverse beams. The bridge is supported on four neoprene bearings, which directly sit on two concrete abutments.



Figure 1. The KW51 bridge, as seen from its north side.

3 VIBRATION-BASED MONITORING

Two independent monitoring systems have been installed on the bridge. The first one was installed in 2018 to monitor accelerations with uniaxial accelerometers and strains with strain gauges (Maes et al. (2022)) and the second in 2019 to monitor the dynamic long-gauge strains of the main girders of the bridge with FBG sensors in a dense grid (Anastasopoulos et al. (2021)).

3.1 *Dynamic strain sensing system with fiber-Bragg gratings*

Dynamic strains of the bridge have been monitored with 79 FBGs, inscribed in four optical fibers. The FBGs are located at the top surface of the bottom flange of the girders (Figure 2). The fibers are attached to the flanges via a custom clamping system, to measure axial strains. The FBGs measure the average strain between two clamping blocks over a gauge-length of 2.5 m. The strain acquisition is conducted with a FAZ Technologies I4G interrogator. The monitoring begun in February 2019 and ended in March 2021. The findings of the first year of monitoring were presented in Anastasopoulos et al. (2021), next to the detailed description of the monitoring system. In February 2021, negative temperatures occurred that resulted in freezing of the ballast. The influence of frost on the strain mode shapes is investigated here.

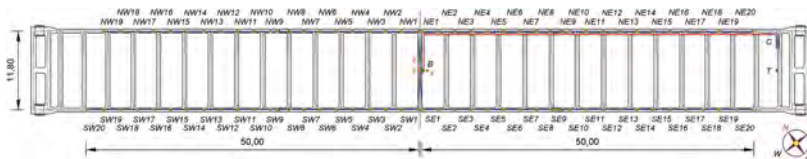


Figure 2. Strain monitoring system of the KW51 bridge (top view of the deck). Orange cubes: clamping blocks; blue rectangles: FBGs; C: cabinet with acquisition system; T: temperature sensor. The FBGs are labeled as; NE: northeast, NW: northwest, SE: southeast, SW: southwest.

4 STRAIN-BASED OPERATIONAL MODAL ANALYSIS

Every hour, the monitoring system captures 900 s of ambient and operational dynamic strains at a sampling rate of 1,000 Hz. Each dataset is used for Operational Modal Analysis (OMA), to identify the modal characteristics of the bridge at the corresponding time. More than 10,000 OMAs were conducted during the monitoring period that is being reported here (09/2019 to 03/2021).

The data processing and system identification are conducted with the Matlab toolbox MACEC (Reynders et al. (2021)). The data-driven stochastic subspace identification (SSI-data) method is employed for system identification (Peeters & De Roeck (1999)). The process of mode selection is

automated with the use of hierarchical clustering, as explained in detail in Anastasopoulos et al (2021). Thirteen modes are identified in the frequency range 0-7 Hz, which are classified as deck or arch modes, depending on which part of the bridge is predominantly deformed. The natural frequency, damping ratio and strain mode shape of three of these modes are given in Figure 3.

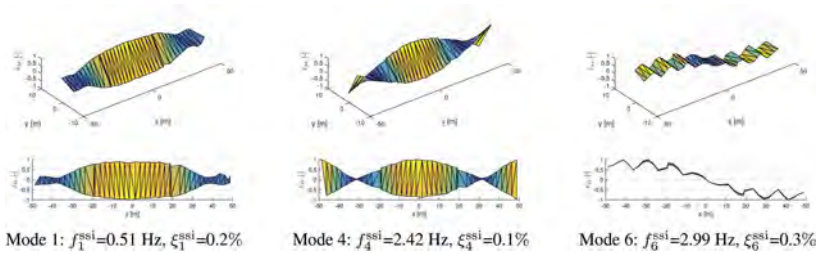


Figure 3. Strain mode shape, natural frequency and damping ratio of three modes of the KW51 bridge, as identified from a strain-based OMA. Mode 1: 1st lateral bending (arch); Mode 4: 3rd lateral bending (arch); Mode 6: 2nd vertical bending (deck). Top subplots: 3D view; bottom subplots: front (x - z) view.

4.1 Influence of temperature on the identified modal characteristics

The natural frequencies of modes 1, 4 and 6 are plotted as a function of temperature in Figure 4. A bilinear relation between natural frequency and temperature is observed, with a knee point around 0°C. The linear regression between temperature (T) and natural frequency (f) is computed for each mode, both for $T > 0^\circ\text{C}$ and $T < 0^\circ\text{C}$. The relative change of natural frequency for each mode Δf_j [%], for a temperature change of $\Delta T = +5^\circ\text{C}$ is also given.

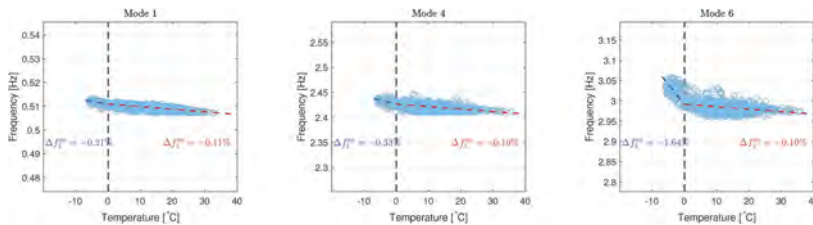


Figure 4. Natural frequencies of the continuously identified modes 1, 4 and 6 of the KW51 bridge as a function of temperature, as identified from strain-based OMAs using SSI-data (f_j^{SSI}). The dashed lines denote the linear regression of the data $f(T)$ for $T > 0^\circ\text{C}$ (red) and $T < 0^\circ\text{C}$ (blue).

The measured temperature correlates well with the identified natural frequencies. The natural frequencies decrease with increasing temperature, both for positive and negative temperatures. An increase of $\Delta T = 5^\circ\text{C}$ in temperature, when $T > 0^\circ\text{C}$, results in a relative decrease of about $\Delta f_5 = 0.1 - 0.2\%$ for the natural frequencies. However, this behaviour is much stronger for negative temperatures, where a reduction of more than 1% is observed for mode 6 between $T = -6^\circ\text{C}$ and $T = 0^\circ\text{C}$. This significant increase of the natural frequencies for negative temperatures is most probably due to frost of the ballast layer and the formation of ice (Maes et al. (2022)).

The influence of temperature on the strain mode shapes is investigated using the process of Anastasopoulos et al. (2021), for the first year of monitoring. The identified strain mode shapes are clustered into non-overlapping temperature groups k with a range of 3°C , based on the temperature that was recorded during each test. The sample mean $\mu[\psi_j]$ of all strain mode shapes in a group is computed, as well as the sample standard deviation $\sigma[\psi_j]$ and the related $\pm 2\sigma$ confidence interval $\text{CI}[\psi_j]$, which boils down to a 95%CI for normally distributed samples.

The results indicate that the 95% CI of the different temperature groups overlap completely, and they have nearly the same width. This confirms that there is no statistically significant influence of temperature on the strain mode shapes, a conclusion that was also drawn in Anastasopoulos et al. (2021) and thus, these results are not reproduced here. Since strain mode shapes are not influenced by temperature, the statistical uncertainty that is observed on them is probably related to identification errors and it can be further reduced by averaging. Hence, the standard deviation of the sample mean of the entire set of N_k strain mode shapes of a temperature group k is calculated, which is related to the standard deviation of the set as $\sigma[\mu[\psi_j]] = \sigma[\psi_j]/\sqrt{N_k}$.

The narrow confidence intervals of the sample mean of the different temperature groups overlap and they all have nearly the same width for most modes, which strengthens the conclusion that there is no statistically significant influence of the temperature on most strain mode shapes. However, for the higher arch and deck modes, i.e., mode 4 (3rd lateral mode of the arch) a relatively small and uniform influence of frost on the strain mode shapes is observed (Figure 5). The influence is minor but nevertheless statistically significant (Figure 5). The 95% CI of the sample mean of the negative temperature groups is not fully overlapping with these of the positive temperature groups, indicating a uniform influence of negative temperatures on strain mode shapes of mode 4.

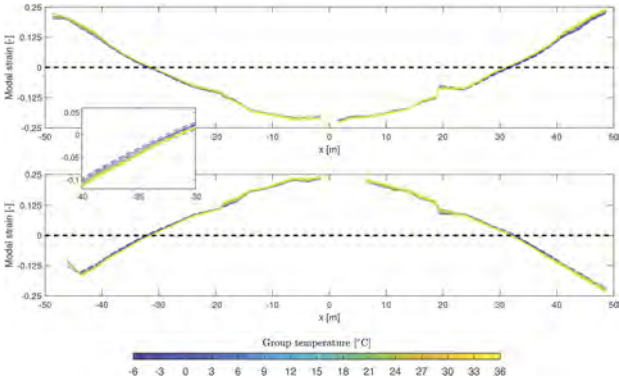


Figure 5. Sample mean $\mu[\psi_4^{ssi,(k)}]$ (continuous lines) and 95% CI $[\mu[\psi_4^{ssi,(k)}]]$ (dashed lines) of the sample mean, of the strain mode shapes that have been identified in each temperature group k for mode 4. The top and bottom subplots contain the strain mode shapes at the north and south sides of the bridge, respectively. A more detailed view of the zone from -40m to -30m is also given for the south-west strain mode shapes.

5 FINITE ELEMENT MODEL OF THE BRIDGE

A detailed FE model of the KW51 bridge (Figure 6a) was built in Maes et al. (2022), using the MATLAB toolbox Stabil (François et al. (2021)). The Young’s modulus of the steel is taken as $E_s=200$ GPa, while of the ballast layer as $E_b=550$ MPa. The model was calibrated using a set of modal characteristics identified from a detailed acceleration-based OMA.

A linear reduction of about 1% of the natural frequency for an increase of temperature from 0°C to 40°C is observed in Figure 4. To investigate this behaviour with the FE model, E_s is reduced by 3%, from 206 GPa at -10°C to 200 GPa at 40°C (Figure 6b), a realistic reduction for a temperature increase of C. The frost of the ballast results in a significant increase of the natural frequencies for $T < 0^\circ\text{C}$ (Figure 4). In the FE model, $E_b = 550$ MPa, for $T > 0^\circ\text{C}$, while for $T < 0^\circ\text{C}$ its value is linearly increased to 1750MPa, which was obtained from calibrating the FE model with modal characteristics obtained from the acceleration monitoring system during a frost period.

The frost of the ballast does not occur uniformly or instantaneously, due to its thermal inertia and the uneven exposure to the sun. In practice, E_b increases gradually in time and space from 550 MPa to 1750 MPa, as the frost of the ballast progresses, but this process is difficult to model in detail. Instead, this relationship is considered to be linear with $E_b(0^\circ\text{C} = 550$ MPa and

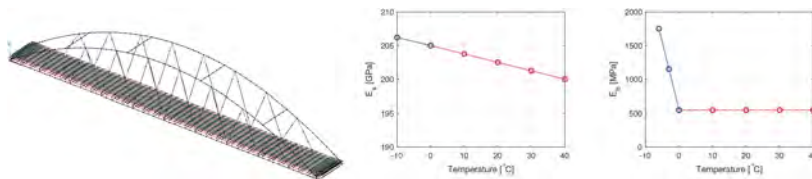


Figure 6. 3D view (left) of the FE model of the KW51 bridge (Maes et al. (2022)). Temperature versus the Young's modulus of the steel E_s (center) and the ballast E_b (right) as incorporated in the FE model.

$E_b(-6^\circ\text{C})=1750$ MPa (Figure 6c), a simplification that appears to capture the behaviour of the bridge. In order to evaluate the model with the results of the dynamic strain monitoring, the modal characteristics of the bridge are calculated from the FE model assuming five temperatures cases: CT1 ($T = -6^\circ\text{C}$), CT2 ($T = -3^\circ\text{C}$), CT3 ($T = -0^\circ\text{C}$), CT4 ($T = 20^\circ\text{C}$) and CT5 ($T = 40^\circ\text{C}$).

5.1 Influence of temperature on the modal characteristics

The calculated natural frequencies of modes 1, 4 and 6 versus temperature for the five temperature cases are plotted in Figure 7. The experimental natural frequencies versus the corresponding temperature at which they were identified are also included. Overall, the natural frequency-temperature relation is well-captured by the validated FE model. The numerical and the experimental slope of the linear regression are in good agreement, confirming the accuracy of the model, which is used to investigate also the influence of temperature on strain mode shapes.

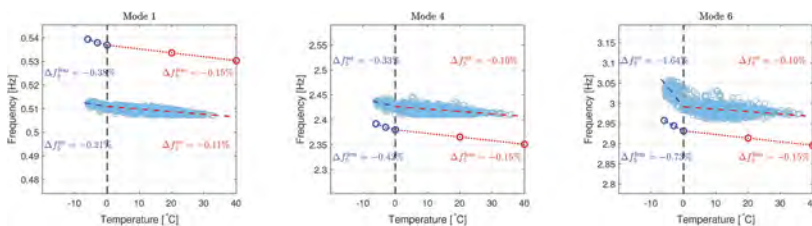


Figure 7. Natural frequencies of the continuously identified modes 1, 4 and 6 of the KW51 bridge as a function of temperature, as identified from SSI-data (f_j^{SSI}) and calculated from the FE model (f_j^{FE}). The dashed and the dotted lines denote the linear regression of the data $f(T)$ for $T > 0^\circ\text{C}$ (red) and $T < 0^\circ\text{C}$ (blue) for both the experimental (dashed lines) and the numerical (dotted lines) natural frequencies.

In Figure 8, the numerical strain mode shapes of mode 4 are illustrated, as obtained for the five temperature cases. For this mode, a uniform influence of negative temperatures was identified from the experimental results (Figure 5). The FE model confirms that for this higher order mode, a relatively small but uniform influence of negative temperatures on its strain mode shapes exists, i.e., when the ballast freezes. Similar behaviour is observed for other higher order modes and thus, they are not reproduced here. The model confirms also the temperature insensitivity of the low order modes, as for these only minimal changes are observed (if any) on their strain mode shape.

Positive temperatures have no effect on the strain mode shapes of any of the modes as the ballast stiffness no longer (drastically) changes in this temperature range. For the three temperature cases that are simulated, where temperatures of 0°C , 20°C and 40°C are considered, the calculated strain mode shapes completely overlap (Figure 8). This behaviour confirms the temperature insensitivity that is observed in the experimental strain mode shapes, when $T > 0^\circ\text{C}$ (Figure 5).

5.2 Influence of local stiffness changes on the modal characteristics

Since only the main girders of the KW51 are instrumented, it is expected that mainly local mass and stiffness changes in the girders can be detected from the strain mode shapes. The FE model

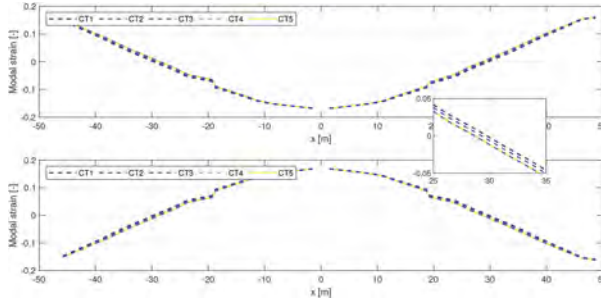


Figure 8. Strain mode shapes $\psi_{4,CTk}^{fem}$ of mode 4 that have been obtained for the four temperature cases. The top and bottom subplots contain the strain mode shapes at the north and south sides of the bridge, respectively. A detailed view of the zone 25m to 35m is given for the south-east strain mode shapes.

is used to investigate the influence that local stiffness changes on the main girders have on modal characteristics. Such changes can be caused by, e.g., corrosion, and result in a reduced cross-section and thus, stiffness. The stiffness of a beam element of the north girder is modified in the model by reducing its E_s by 10%, 20% and 30% for three stiffness cases (SC_i), respectively.

The numerical strain mode shapes of mode 6 for the three cases and the undamaged bridge are given in Figure 9. A clear and local change of the modal strain amplitude is observed at the

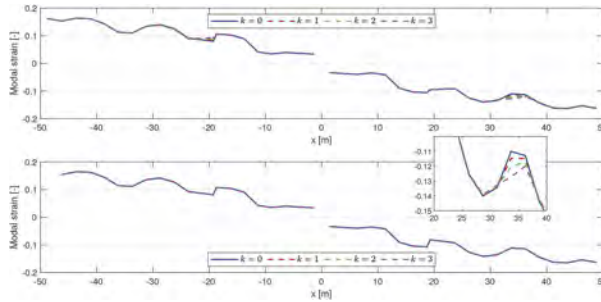


Figure 9. Strain mode shapes $\psi_{FE,i}^{(k)}$ of mode 6 that have been obtained for the four stiffness cases. The top and bottom subplots contain the strain mode shapes at the north and south sides of the bridge, respectively. A detailed view of the zone from 20m to 40m for the north-east strain mode shapes is given.

location of reduced stiffness ($x \approx 35$ m, top subplot), which becomes more pronounced for lower values of elastic modulus. Similar changes are observed on the remaining strain mode shapes.

However, when the original modal strain amplitude is close to zero, no changes can be observed, while in reality, strain mode shapes are subjected to identification uncertainty. This underlines the importance of combining information from several modes in order to increase the chance of identifying local stiffness changes. The following process is adopted, which accounts also for the identification uncertainty of the strain mode shapes that are obtained from the measurements (Figure 5). The modes that are combined are the ones that enjoy the highest identification accuracy and the minimum influence of temperature, even during frost, i.e, modes 1, 2, 3 and 6.

First, a six-month period (03/2020 to 08/2020) is taken as the *reference* period where no stiffness changes occur on the structure. The relative difference is computed between the modal strain i of mode j as identified from the modal test number t , $\psi_{j,i}(t)$, and a reference value $\psi_{j,i}^{ref}$:

$$\Delta\psi_{j,i}(t) [\%] = \frac{\psi_{j,i}(t) - \psi_{j,i}^{ref}}{\psi_{j,i}^{ref}} 100\%, \quad t < t_{dam} \quad (1)$$

where the considered undamaged period stretches from $t = 1$ until $t = t_{dam} - 1$. Possible choices for $\psi_{j,i}^{ref}$ include the modal strains identified during the first test, or an average value over a period during which the structure is known to be in undamaged condition. In what follows, the second option is followed such that $\psi_{j,i}^{ref} = \frac{1}{t_{dam}-1} \sum_{t=1}^{t_{dam}-1} \psi_{j,i}(t)$. The relative amplitude change of the modal strain at $x \approx 35$ m of the north-east strain mode shapes, where the stiffness change is implemented in the FE model is calculated for all tests within the undamaged period and for modes 1, 2, 3 and 6. The mean and the 95% CI over the same period are also calculated.

Second, a six-month *damage* period is considered (09/2020 to 03/2021) during which, the modal strain amplitude of each identified mode is modified according to the observed amplitude changes in the FE model for the different stiffness cases. The relative change is obtained as:

$$\Delta\psi_{j,i}^{(k)}(t) [\%] = \frac{\lambda_{j,i}^{(k)} \psi_{j,i}(t) - \psi_{j,i}^{ref}}{\psi_{j,i}^{ref}} 100\%, \quad t \geq t_{dam}, \quad \text{and} \quad \lambda_{j,i}^{(k)} = \frac{\psi_{FE,j,i}^{(k)}}{\psi_{FE,j,i}^{(0)}} \quad (2)$$

Third, a 24-hour rolling average is introduced to reduce the uncertainty in the data. Therefore, $\psi_{j,i}(t)$ is replaced by a rolling 24-hour average $\hat{\psi}_{j,i}(t)$ in Eqs. 1 and 2. In Figure 10, the relative change of the modal strain amplitude before and after the introduction of the stiffness changes is given, as calculated for a rolling 24-hour average over the considered periods for mode 6. The reduced uncertainty results in narrow 95% CI, which allow for detecting all damage cases. Similar behaviour is observed for modes 1 and 2, while mode 3 is not influenced by the stiffness changes, as the modal strain at $x \approx 35$ coincides with a nodal point for mode 3.

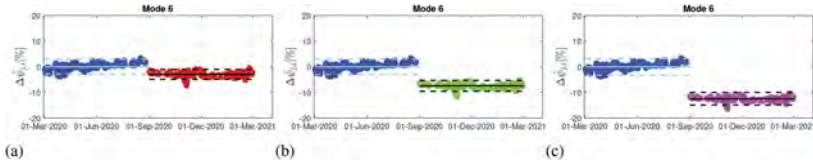


Figure 10. Relative change of the modal strain amplitude with respect to the reference value during the undamaged period (blue) and during the period with simulated damage cases SC_k ; (a) $k = 1$ (red), (b) $k = 2$ (green) and (c) $k = 3$ (magenta). The graphs are obtained for the 24-hour rolling average modal strain at $x \approx 35$ m of the north-east strain mode shapes. The continuous lines and the dashed lines denote the mean and the 95% CI of the relative modal strain amplitude change of each mode and period.

Finally, the information of the various modes is combined in a *damage index* (DI). The average of the relative changes of a modal strain i over all modes j is taken in order to yield the aggregate DI for each damage case k :

$$\widehat{DI}_i^{(k)} [\%] = \frac{\sum_{j=1}^{n_m} |\Delta\hat{\psi}_{j,i}^{(k)}|}{n_m} \quad (3)$$

The DI, as obtained at the location of the damage for the three damage cases is given in Figure 11. It can be observed that the DI changes shortly after the start of the damage period and is sensitive in all induced damage cases. The change in the DI exceeds the identification uncertainty for all cases and thus, damage can be identified with high confidence.

Last, the influence of the reduced stiffness on the natural frequencies is investigated. Natural frequencies are slightly reduced, even for the 30% reduction case, where the relative changes of natural frequencies, range from $\approx 0.01\%$ to 0.03% . The low sensitivity of natural frequencies to local stiffness changes, when compared to their sensitivity to temperature, underlines the difficulty to identify these changes without introducing data normalization techniques (Maes et al. (2022)).

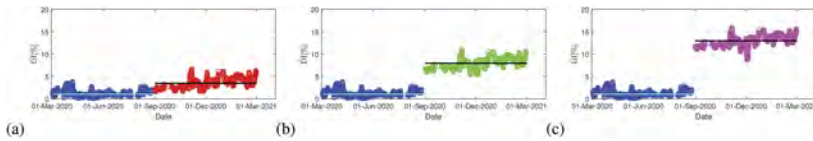


Figure 11. Damage Index (DI) as obtained during the undamaged period (blue) and during the period with simulated damage cases SCk ; (a) $k = 1$ (red), (b) $k = 2$ (green) and (c) $k = 3$ (magenta). The DI is obtained for the 24-hour rolling average modal strain at $x \approx 35$ m of the north-east strain mode shapes. The continuous lines denote the mean DI of each period.

6 CONCLUSIONS

The dynamic strains of the KW51 bridge were monitored with long-gauge FBG sensors for a two-years period. During the second year, the bridge was subjected to frost.

The influence of frost is found to be significant on natural frequencies, causing amplitude changes up to 1.7% for a temperature drop from 0°C to -5°C . This change is much higher than the one caused by a positive temperature change from 0°C to $+5^{\circ}\text{C}$, which is up to 0.15% for the same modes. This behaviour is found to be a result of the frost of the ballast layer.

The strain mode shapes of the lower order deck and arch modes were found to be insensitive to temperature, even during frost periods. For higher order modes, a small and uniform influence is observed during frost periods, as a result of the frost of the ballast. For $T > 0^{\circ}\text{C}$ though, no influence is observed in the temperature range $0^{\circ}\text{C} - 36^{\circ}\text{C}$ as the ballast stiffness no longer (drastically) changes in this range. This behaviour is confirmed also by the FE model.

The sensitivity of strain mode shapes to local damage is also studied. For this reason, the stiffness of a girder is locally reduced in a FE model. This reduction causes local amplitude changes in the strain mode shapes, which can be clearly detected even when the identification uncertainty is accounted for, thanks to a damage index that combines information from all modes.

ACKNOWLEDGEMENTS

This research was performed in the framework of the project *Robust vibration-based damage identification with a novel high-accuracy strain measurement system* (G099014N), funded by the Research Foundation Flanders (Belgium) and the project *Monitoring of structures and systems with fiber optic sensors* (HBC.2019.2505), funded by Flanders Innovation & Entrepreneurship (Belgium). K. Maes is a postdoctoral fellow (12Q9218N) of the Research Foundation Flanders.

REFERENCES

- Anastasopoulos, D., De Roeck, G. & Reynders, E. 2019. *Influence of damage versus temperature on modal strains and neutral axis positions of beam-like structures*. Mech Syst Signal Proc 134, 106311.
- Anastasopoulos, D., De Roeck, G. & Reynders, E. 2021. *One-year operational modal analysis of a steel bridge from high-resolution macrostrain monitoring: influence of temperature vs. retrofitting*. Mech Syst Signal Proc 161, 107951.
- Anastasopoulos, D., Maes, K., De Roeck, G., Lombaert, G. & Reynders, E. 2019. *Influence of frost and local stiffness variations on the strain mode shapes of a steel arch bridge*. Eng Struct 273, 115097.
- Fan, W. & Qiao, P. 2010. *Vibration-based damage identification methods: a review and comparative study*. Struct Health Monit 10(1), 83–111.
- François, S., Schevenels, M., Dooms, D., Jansen, J., Wambacq, J., Lombaert, G., Degrande, G. & De Roeck, G. 2021. *Stabil: an educational Matlab toolbox for static and dynamic structural analysis*. Computer Appl Eng Educ, 1–18.
- Maes, K., Van Meerbeeck, L., Reynders, E. & Lombaert, G. 2022. *Validation of vibration-based structural health monitoring on retrofitted railway bridge KW51*. Mech Syst Signal Proc 165, 108380.
- Peeters, B. & De Roeck, G. 1999. *Reference-based stochastic subspace identification for output-only modal analysis*. Mech Syst Signal Proc 13(6), 855–878.
- Reynders, E., Schevenels, M. & De Roeck, G. 2021. *MACEC 3.4: The Matlab toolbox for experimental and operational modal analysis*. Report BWM-2021-04, Dept Civil Engineering, KU Leuven.

Dissipated hysteretic energy reconstruction for high-resolution seismic monitoring of instrumented buildings

Milad Roohi

University of Nebraska-Lincoln, Omaha, NE, USA

Eric M. Hernandez

University of Vermont, Burlington, VT, USA

David V. Rosowsky

Kansas State University, Manhattan, KS, USA

ABSTRACT: This paper proposes a high-resolution seismic monitoring framework that employs dissipated energy as a feature for damage detection and localization in instrumented building structures. The methodology consists of (1) implementing a nonlinear state observer to reconstruct the dynamic response at all degrees of freedom (DoF) of a structural model, (2) employing the reconstructed response to estimate element-by-element forces and displacements, and (3) using estimated displacement, forces, and constitutive laws to estimate element-level dissipated energy. The main advantages of the proposed energy-based approach are that i) the proposed feature is physically meaningful and correlates well with the level of cyclic damage experienced during strong earthquakes, ii) dissipated energy can be reconstructed from element-level stress-strain fields that can be estimated from global acceleration measurements, and (iii) dissipated energy can be calibrated using experimental data. The effectiveness of the proposed energy-based seismic monitoring framework is investigated using data from the Van Nuys hotel tested, a seven-story reinforced concrete (RC) building instrumented by the California Strong Motion Instrumentation (CSMIP) Program (Station 24386). The Van Nuys building experienced insignificant structural and mostly nonstructural damage during the 1992 Big Bear earthquake. Two years later, the building was severely damaged during the 1994 Northridge earthquake, in which localized damage occurred in five of the nine columns on the fourth story (between floors four and five) of the south longitudinal frame.

1 INTRODUCTION

Vibration measurements from structures can be used for various purposes, including but not limited to model calibration, code verification, structural health monitoring, and vibration control. Researchers and engineers have recognized the importance of seismic instrumentation in the past two decades for quantitative and rapid performance assessment of buildings during and immediately following earthquakes (Porter et al. 2004; Celebi et al. 2004; Roohi and Hernandez 2020; Cheraghzade and Roohi 2022; Yazdanpanah et al. 2023). Despite the immediate appeal, technical, logistical, and economic challenges are associated with seismic instrumentation and performance assessment in the case of instrumented buildings. Building instrumentation and its maintenance can be expensive, and budget constraints may not allow for exhaustive floor-by-floor or component-level instrumentation. These buildings exhibit a high degree of nonlinear behavior even during moderate ground motions, which makes it challenging to interpret the measured seismic response and provide a quantitative measure of the estimated level of damage caused by an earthquake.

To address the challenges highlighted, this paper presents a nonlinear model-based state observer (NMBO) to enhance a high-fidelity nonlinear finite element model of the building

with a limited number of response measurements during the seismic event and reconstruct the complete dynamic response of the building. This approach deviates from model-driven approaches that update the model parameters. Instead, it performs nonlinear FE model-data fusion by feeding the sensor measurements as corrective forces applied to a modified FE model of the building. This enhanced model provides estimates of all relevant response quantities, such as inter-story drift and element forces, with their corresponding uncertainty. The performance of NMBO for nonlinear state estimation has been validated using case studies of real-world instrumented steel, reinforced concrete, and woodframe buildings (Hernandez et al. 2018; Roohi and Hernandez 2020; Roohi et al. 2021b; Hernandez et al. 2019)

The NMBO is employed to propose a methodology for reconstructing element-by-element dissipated energy and seismic damage indices in minimally instrumented buildings to perform high-resolution seismic monitoring. The methodology first employs the NMBO to estimate the complete seismic response of an instrumented building. The estimated response is then used as input to mechanics-based damage models to quantify element-level damage indices and perform seismic damage diagnosis and prognosis of a building. The proposed framework is validated using real measured data from the Van Nuys hotel tested, a seven-story reinforced concrete (RC) building instrumented by the California Strong Motion Instrumentation (CSMIP) Program (Station 24386). The Van Nuys building experienced insignificant structural and mostly nonstructural damage during the 1992 Big Bear earthquake. Two years later, the building was severely damaged during the 1994 Northridge earthquake, in which localized damage occurred in five of the nine columns on the fourth story (between floors four and five) of the south longitudinal frame.

2 SYSTEM OF INTEREST AND MEASUREMENT MODEL

This paper focuses on typical building structures in which floor diaphragms can be assumed to be rigid for in-plane deformations. For this type of structures, the response to seismically induced ground acceleration can be accurately modeled by the following simultaneous set of nonlinear differential equations

$$\mathbf{M}\ddot{q}(t) + \mathbf{C}_D\dot{q}(t) + F_r(q(t)) = -\mathbf{M}\mathbf{b}_1\ddot{u}_g(t) + \mathbf{b}_2\omega(t) \quad (1)$$

The vector $q(t) \in \mathbb{R}^n$ represents the relative displacement (with respect to the ground) of all stories. For most buildings of interest, this results in three independent components per floor (two lateral displacements and a rotation about the vertical axis). The number of degrees of freedom is denoted as n , $\mathbf{M} = \mathbf{M}^T \in \mathbb{R}^{n \times n}$ is the mass matrix, $\mathbf{C}_D = \mathbf{C}_D^T \in \mathbb{R}^{n \times n}$ is the damping matrix, $F_r(\cdot)$ is the resultant global restoring force vector which is obtained from the contribution of individual shear wall restoring forces to the global diaphragm coordinates. The matrix $\mathbf{b}_1 \in \mathbb{R}^{n \times r}$ is the influence matrix of the r ground acceleration time histories defined by the vector $\ddot{u}_g(t) \in \mathbb{R}^r$. The matrix $\mathbf{b}_2 \in \mathbb{R}^{n \times p}$ defines the spatial distribution of the vector $\omega(t) \in \mathbb{R}^p$, which in the context of this paper represents the process noise generated by unmeasured excitations and/or modeling errors.

This paper assumes that measurements $y(t)$ of the dynamic response of the structure consist of horizontal accelerations measured in three independent and non-intersecting directions. Vertical accelerations are typically also measured; however, this paper focuses only on horizontal acceleration measurements. The vector of m acceleration measurements $y(t)$ is modeled as

$$y(t) = -\mathbf{c}_2\mathbf{M}^{-1}[\mathbf{C}_D\dot{q}(t) + F_r(q(t)) - \mathbf{b}_2\omega(t)] + v(t) \quad (2)$$

where $\mathbf{c}_2 \in \mathbb{R}^{m \times n}$ is a Boolean matrix that maps the DoFs to the measurements, and $v(t) \in \mathbb{R}^{m \times 1}$ is the measurement noise.

3 NONLINEAR MODEL-BASED STATE OBSERVER (NMBO)

A nonlinear state observer for state estimation in nonlinear systems can be written in a state-space form as

$$\dot{\hat{x}}(t) = \mathbf{f}(\hat{x}(t)) + \mathbf{G}(y(t) - \mathbf{C}\hat{x}(t)) \quad (3)$$

where $\hat{x}(t)$ denotes mean state estimate, \mathbf{G} is a feedback gain, \mathbf{C} is the measurement matrix and is the measurement. We expand nonlinear function $\mathbf{f}(\cdot)$ using a Taylor series around the current estimate of the state vector and obtain a first-order approximation by dropping higher-order terms of power series as follows

$$\dot{\hat{x}}(t) = \mathbf{A}_{\hat{x}(t)}\hat{x}(t) + \mathbf{G}[y(t) - \mathbf{C}\hat{x}(t)] = (\mathbf{A}_{\hat{x}(t)} - \mathbf{GC})\hat{x}(t) + \mathbf{G}y(t) \quad (4)$$

We assume that velocity estimates are equal to the derivative of the estimates of displacement and choose the upper partition of feedback gain to be zero. The lower partition to be $\mathbf{M}^{-1}\mathbf{c}_2^T\mathbf{E}$, where matrix \mathbf{E} is a matrix free to be selected in order to minimize the trace of the state error covariance and maps the DoFs to the measurements. This choice of \mathbf{G} makes the observer realizable as a modified finite element model of the system with added grounded dampers and excited by corrective forces obtained from velocity measurements scaled by added damper values. In second-order form, the proposed nonlinear model-based state observer (NMBO) estimate of displacement response is given by

$$\mathbf{M}\ddot{\hat{q}}(t) + (\mathbf{C}_D + \mathbf{c}_2^T\mathbf{E}\mathbf{c}_2)\dot{\hat{q}}(t) + \mathbf{F}_r(\hat{q}(t)) = \mathbf{c}_2^T\mathbf{E}y(t) \quad (5)$$

where $\hat{q}(t)$ is the time history of the estimated response at all DoFs of the model, and $y(t)$ is noise-contaminated velocity measurements obtained from acceleration measurements. The main advantage of the NMBO is that the nonlinear state observer can be implemented in advanced structural simulation software packages. This allows the state observer to be computationally efficient in the propagation of the state estimate through the nonlinear dynamics of a system.

To determine the feedback gain matrix \mathbf{E} , the objective function to be minimized is the trace of the estimation error covariance matrix. Since for a general nonlinear multi-variable case, a closed-form solution for the optimal matrix \mathbf{E} has not been found, a numerical optimization algorithm is used. To derive the objective optimization function, Equation 5 is linearized as follows

$$\mathbf{M}\ddot{\hat{q}}(t) + (\mathbf{C}_D + \mathbf{c}_2^T\mathbf{E}\mathbf{c}_2)\dot{\hat{q}}(t) + \mathbf{K}_0\hat{q}(t) = \mathbf{c}_2^T\mathbf{E}y(t) \quad (6)$$

where the elements of the stiffness matrix \mathbf{K}_0 are given by

$$\mathbf{K}_{0_{ij}} = \left. \frac{\partial \mathbf{F}_{r,i}}{\partial q_j} \right|_{q_j} = 0 \quad (7)$$

By defining the state error as $e = q - \hat{q}$, the expression for the state estimation error is given by

$$\mathbf{M}\ddot{e}(t) + (\mathbf{C}_D + \mathbf{c}_2^T\mathbf{E}\mathbf{c}_2)\dot{e}(t) + \mathbf{K}_0e(t) = b_2u(t) - \mathbf{c}_2^T\mathbf{E}v(t) \quad (8)$$

To derive an expression for the state error covariance, we take Fourier transforms of both sides of Equation 8 and obtain the following

$$(\mathbf{M}\omega^2 + (\mathbf{C}_D + \mathbf{c}_2^T\mathbf{E}\mathbf{c}_2)i\omega + \mathbf{K}_0)e(\omega) = b_2u(\omega) - \mathbf{c}_2^T\mathbf{E}v(\omega) \quad (9)$$

with \mathbf{H}_o defined as

$$\mathbf{H}_o = (-\mathbf{M}\omega^2 + (\mathbf{C}_D + \mathbf{c}_2^T\mathbf{E}\mathbf{c}_2)i\omega + \mathbf{K}_0)^{-1} \quad (10)$$

From Equation 9, the expression for the state error estimate in the frequency domain is

$$e(\omega) = \mathbf{H}_o(b_2u(\omega) - \mathbf{c}_2^T\mathbf{E}v(\omega)) \quad (11)$$

and the error spectral density matrix Φ_{ee} is given by

$$\Phi_{ee}(\omega) = \mathbf{H}_o \mathbf{b}_2 S_{ww}(\omega) \mathbf{b}_2^T \mathbf{H}_o^* + \mathbf{H}_o \mathbf{c}_2^T \mathbf{E} S_{vv}(\omega) \mathbf{E}^T \mathbf{c}_2 \mathbf{H}_o^* \quad (12)$$

where the matrices $\Phi_{ww}(\omega)$ and $\Phi_{vv}(\omega)$ are the power spectral density of the uncertain excitation on the system and measurement noise, respectively. To select the \mathbf{E} matrix, the following optimization problem must be solved

$$\begin{aligned} & \underset{\mathbf{E}}{\text{minimize}} && J = \text{tr}(\mathbf{P}) \\ & \text{subject to} && \mathbf{E} \in \mathbb{R}^+ \end{aligned} \quad (13)$$

where \mathbf{P} is the displacement estimation error covariance matrix given by

$$\mathbf{P} = \mathbb{E} \left[(q(t) - \hat{q}(t)) - (q(t) - \hat{q}(t))^T \right] = \int_{-\infty}^{+\infty} \Phi_{ee}(\omega) d\omega \quad (14)$$

With this selection of the feedback matrix \mathbf{E} , the NMBO becomes a modified nonlinear model of the system with added grounded dampers obtained from a linearized model of the system in the measurement locations and excited by forces that are linear combinations of the measurements proportional to the added dampers. The performance of NMBO has been previously studied compared to the Unscented Kalman Filter (UKF), demonstrating that NMBO outperforms other existing state-of-the-art nonlinear state observers in reconstructing the dynamical response of large-scale instrumented structures (Roohi et al. 2021).

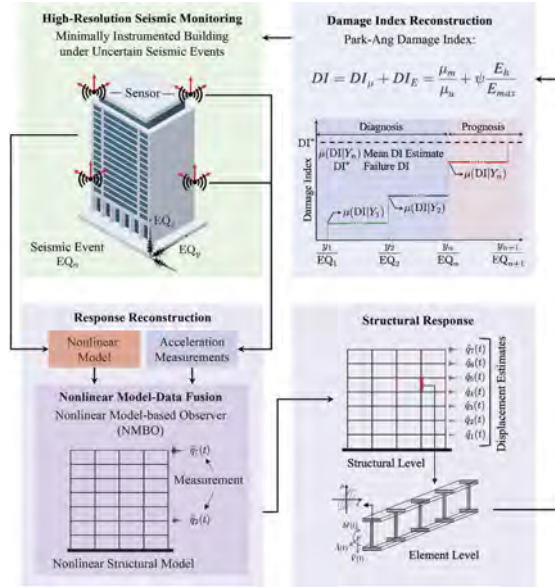


Figure 1. Summary of the proposed methodology for high-resolution seismic monitoring.

4 METHOD OF APPROACH

The methodology consists of (1) implementing a nonlinear state observer to reconstruct the dynamic response at all degrees of freedom (DoF) of a structural model, (2) employing the reconstructed response to estimate element-by-element forces and displacements, and (3) using estimated displacement, forces, and constitutive laws to estimate element-level dissipated energy. The main advantages of the proposed energy-based approach are that i) the proposed feature is physically meaningful and correlates well with the level of cyclic damage experienced during strong earthquakes, ii) dissipated energy can be estimated from element-level stress-strain fields reconstructed from global acceleration measurements, and (iii) dissipated energy can be calibrated

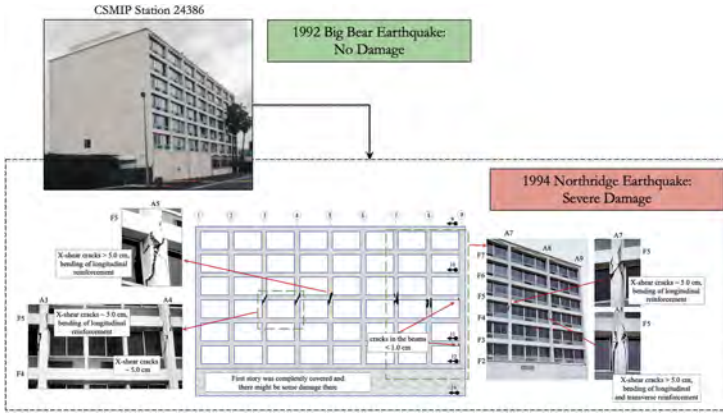


Figure 2. Schematic representation and photo records of seismic damage following 1992 Big Bear and 1994 Northridge earthquakes.

using experimental data. To implement the methodology, the NMBO uses response measurements of an instrumented building, typically in the form of accelerations, to reconstruct the complete dynamic response of the structure. From the reconstructed response, the seismic damage index (DI) for every structural element is estimated using a mechanics-based low-cycle fatigue damage model. The reconstructed response is then used for high-resolution seismic monitoring by performing damage detection, localization, and quantification. This paper employs the Park and Ang (1985) damage model for the estimation of element-level damage indices given by

$$DI = DI_{\mu} + DI_E = \frac{\mu_m}{\mu_u} + \psi \frac{E_h}{E_{max}} \quad (15)$$

where DI_{μ} and DI_E = damage due to excessive deformation and dissipated hysteretic energy, respectively; μ_m = maximum ductility experienced during the earthquake; μ_u = ultimate ductility capacity under monotonic loading; ψ = calibration parameter; E_{max} = maximum hysteretic energy dissipation capacity for all relevant failure modes; and E_h is the dissipated hysteretic energy, which can be calculated using element-level stress-strain or force-displacement demand estimates of NMBO by integrating the area under hysteresis loops as follows:

$$E_h = \frac{1}{2} \int \epsilon^T \sigma dV \quad (16)$$

where σ and ϵ = stress and strain demands, respectively, and V = total volume of an element. In distributed plasticity beam-column elements, where energy dissipation occurs primarily due to flexure, the dissipated hysteretic energy (E_h) can be calculated by integrating the moment-curvature response along the element, as follows:

$$E_h = \int_0^L M \phi dx = \sum_{j=1}^{N_p} (M \phi|_{x=\xi_j}) \omega_j \quad (17)$$

where M and ϕ = moment and curvature response of elements, respectively; N_p = number of integration points along the element; and ξ_j and ω_j = locations and associated weights of integration points, respectively. Although this paper restricts our attention to flexure-related damage, other energy dissipation mechanisms, such as those, due to shear and axial deformation, can also be readily included if needed.

5 CASE STUDY: VAN NUYS HOTEL TESTBED

This section illustrates the proposed framework using seismic response measurements from Van Nuy's hotel. The CSMIP instrumented this building as Station 24386, and the recorded

data of this building are available from several earthquakes, including the 1971 San Fernando, 1987 Whittier Narrows, 1992 Big Bear, and 1994 Northridge earthquakes. From these data, measurements during the 1992 Big Bear and 1994 Northridge earthquakes are used in this study to demonstrate the proposed framework. The history of damage to the Van Nuys building is well-documented due to its instrumentation and inspection following earthquakes. The documents reveal that the building underwent minimal structural and mostly nonstructural damage before the 1994 Northridge earthquake. However, this earthquake caused extensive damage to the building, particularly in the south longitudinal frame. Five of nine columns on the fourth story suffered significant damage due to inadequate transverse reinforcements. Shear cracks of five centimeters or more and bending of the longitudinal reinforcement were easily visible. The building was red-tagged following the post-earthquake inspection. Figure 2 depicts the seismic damage in the south frame caused by the Northridge earthquake and shows the location of sensors at the ground, 1st, 2nd, 5th, and 7th floors. (Trifunac and Ivanovic 2003).

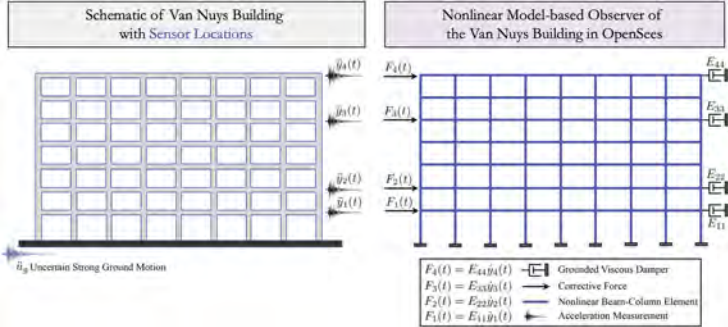


Figure 3. Schematic of Van Nuys hotel tested with sensor locations (left); and NMBO with corresponding added viscous dampers and corrective forces in measurement locations (right).

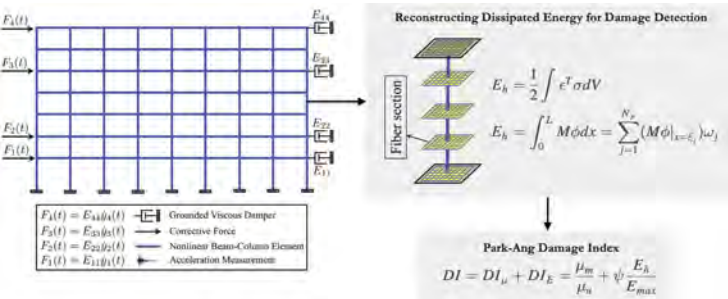


Figure 4. Implementation of the proposed methodology for reconstructing element-level dissipated energy and damage indices for high-resolution monitoring of the Van Nuys Hotel tested.

A two-dimensional fixed-base model was utilized in the OpenSEES environment to implement the nonlinear FE model of the building. This model represents one of the longitudinal frames of the building. The modeling approach employed beams and columns using the distributed plasticity modeling method. Force-based beam-column elements were used to accurately determine yielding and plastic deformations along the element's integration points. The nonlinear response of force-based elements was evaluated using the Gauss-Lobatto integration method. Each beam and column element was discretized using four integration points, and the cross-section of each element was subdivided into fibers. The uniaxial Concrete01 material was used to construct a Kent-Scott-Park object with a degraded linear unloading and reloading stiffness and zero tensile strength. The longitudinal reinforcing steel was modeled using the uniaxial Steel01 material as

a bilinear model with kinematic hardening, with elasticity modulus and strain hardening parameters assumed to be 200GPa and 0.01, respectively. An unconfined concrete model was defined to model concrete due to insufficient transverse reinforcement in the beams and columns.

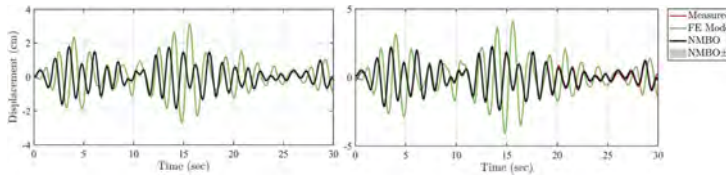


Figure 5. Comparison of displacement estimates using NMBO and open-loop FE analysis with measurements in non-instrumented fourth (left) and instrumented seventh (right) stories during Big Bear earthquake.

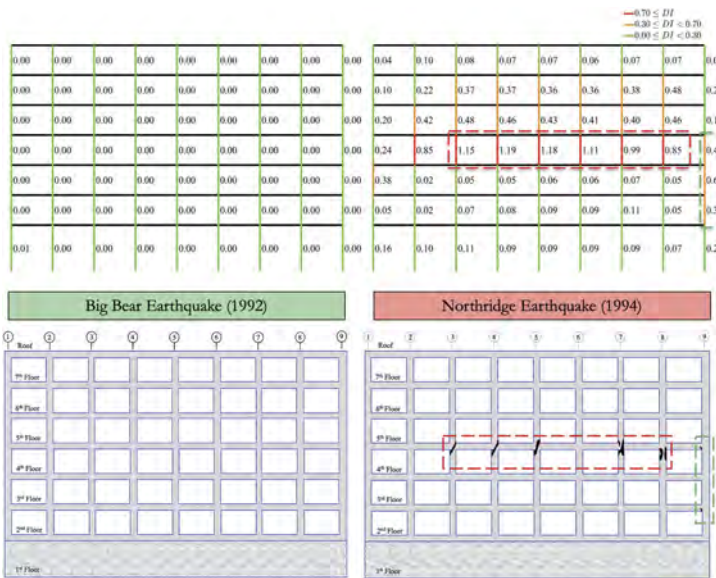


Figure 6. Reconstructed element-by-element damage indices using the measured response during the 1992 Big Bear earthquake (left) and 1994 Northridge earthquake (right).

To implement the NMBO in OpenSEES, the Van Nuys building was modeled using a nonlinear FE model and response measurements. The formulation of the NMBO is presented in the following subsections, detailing the step-by-step process. In order to estimate the complete seismic response, dynamic analysis was performed on the modified OpenSEES nonlinear FE model, which had grounded dampers added at measurement locations and was subjected to corrective forces. Figure 3 shows the schematic of the Van Nuys hotel testbed, including the location of accelerometers and the NMBO, which includes added viscous dampers and corrective forces at measurement locations.

The NMBO model was used to implement the proposed methodology schematically summarized in Figure 4. Figure 5 compares displacement estimates using NMBO with estimates obtained from open-loop FE analysis and actual measurements in instrumented 7th and non-instrumented fourth stories during the Big Bear earthquake. Measured represents the measured response, FE Model represents the open-loop FE analysis of the OpenSEES model under measured ground motion, and NMBO represents the estimated response using the OpenSEES NMBO with sensor measurements from measured locations along with 1σ estimation uncertainty bound. As can be seen, the NMBO accurately reconstructs the response at both instrumented and non-instrumented floors. Upon further examination of the entire time

frame for both earthquakes, it is apparent that the NMBO estimations and their variance from the true value fall within the confidence interval. Subsequently, the reconstructed response was input to the Park-Ang damage model to reconstruct element-level damage indices and use them for damage detection, localization, and quantification. Figure 6 schematically depicts the seismic damage suffered during the Northridge earthquake to compare the reconstructed DIs with the building's actual performance. The shear cracks with width ≥ 5 cm are highlighted with a red dash box, and the shear cracks ($0.5 \text{ cm} \leq \text{width} \leq 1 \text{ cm}$) are highlighted with a green dashed box. As can be seen, the element-by-element comparison of estimated DIs with post-earthquake inspection results confirms the accuracy of the damage localization using the proposed mechanistic approach.

6 CONCLUSIONS

This paper presents the development of a high-resolution seismic monitoring framework that employs dissipated energy as a feature for damage assessment in instrumented buildings. A nonlinear model-based observer (NMBO) is derived from combining a nonlinear structural model of a minimally instrumented building and its response measurements to reconstruct the complete dynamic response of the system. The reconstructed response is then input to a mechanics-based low-cycle fatigue damage model to estimate element-by-element damage indices and perform high-resolution seismic monitoring. The proposed approach was validated using data from the Van Nuys Hotel testbed. The proposed framework correctly estimated the linear behavior and no damage during the Big Bear earthquake and identified the major damage locations in the beam/column joints on the south frame's fourth floor during the Northridge earthquake. To the authors' best knowledge, the results presented in this paper constitute the most accurate and highest resolution damage estimates obtained for the Van Nuys hotel tested.

REFERENCES

- Celebi, M., Sanli, A., Sinclair, M., Gallant, S. and Radulescu, D., 2004. Real-time seismic monitoring needs of a building owner—and the solution: a cooperative effort. *Earthquake Spectra*, 20(2),333–346.
- Cheraghzade, M. and Roohi, M., 2022. Deep learning for seismic structural monitoring by accounting for mechanics-based model uncertainty. *Journal of Building Engineering*, 57, p.104837.
- Hernandez, Eric, Milad Roohi, and David Rosowsky. "Estimation of element-by-element demand-to-capacity ratios in instrumented SMRF buildings using measured seismic response." *Earthquake Engineering & Structural Dynamics* 47, no. 12 (2018): 2561–2578.
- Park, Y.J., Ang, A.H.S. and Wen, Y.K., 1985. Seismic damage analysis of reinforced concrete buildings. *Journal of Structural Engineering*, 111(4),pp.740–757.
- Porter, K., Mitrani-Reiser, J. and Beck, J.L., 2006. Near-real-time loss estimation for instrumented buildings. *The Structural Design of Tall and Special Buildings*, 15(1),pp.3–20.
- Roohi, Milad, Hernandez, E.M., and Rosowsky, D., 2019. "Nonlinear seismic response reconstruction and performance assessment of instrumented wood-frame buildings—Validation using NEESWood Capstone full-scale tests." *Structural Control and Health Monitoring* 26, no. 9: e2373.
- Roohi, M. and Hernandez, E.M., 2020. Performance-based post-earthquake decision making for instrumented buildings. *Journal of Civil Structural Health Monitoring*, 10, pp.775–792.
- Roohi, M., Erazo, K., Rosowsky, D. and Hernandez, E.M., 2021a. An extended model-based observer for state estimation in nonlinear hysteretic structural systems. *Mechanical Systems and Signal Processing*, 146, p.107015.
- Roohi, M., Hernandez, E.M. and Rosowsky, D., 2021b. Reconstructing element-by-element dissipated hysteretic energy in instrumented buildings: application to the Van Nuys Hotel testbed. *Journal of Engineering Mechanics*, 147(1), p.04020141.
- Trifunac, M., and Ivanovic, S., 2003. Analysis of drifts in a seven-story reinforced concrete structure. Rep. No. CE 03-10. Los Angeles: Univ. of Southern California.
- Yazdanpanah, Omid, Kiarash M. Dolatshahi, and Omid Moammer. "Rapid seismic fragility curves assessment of eccentrically braced frames through an output-only nonmodel-based procedure and machine learning techniques." *Engineering Structures* 278 (2023): 115290.

Follow-up assessment of a prestressed concrete road bridge based on dynamic bridge behaviour – analysis of structural integrity and evaluation of maintenance condition

T. Reimoser & R. Veit-Egerer

VCE Vienna Consulting Engineers ZT GmbH, Vienna, Austria

A. Schmitt

BBV Systems GmbH, Bobenheim-Roxheim, Germany

Y. Benitz

Stadt Pforzheim Grünflächen- und Tiefbauamt, Pforzheim, Germany

ABSTRACT: This contribution is devoted to a prestressed concrete road bridge structure in Pforzheim, Germany, which has been in operation since 1953. Due to the limited accessibility of certain prestressed concrete members, a reliable assessment based on periodic visual inspections only is not ensured. Therefore, an in-depth full scale vibrational analysis was performed according to DIN 1076 (1999) in order to assess the structural integrity and maintenance condition of the superstructure. A follow-up assessment in 2020 is compared with a baseline investigation from 2003, having been conducted by the same organisations in a similar manner.

1 INTRODUCTION

1.1 *Scope of investigation*

The scope of this investigation is based on a long-term track record of assessment projects from VCE, e.g. described in Wenzel (2005, 2009) or Veit-Egerer et al. (2008, 2018, 2019, 2022):

- A non-destructive dynamic measurement of the bridge deck using a dense grid of accelerometers to determine the mechanical behaviour of the load-bearing prestressed concrete structure under unrestricted traffic.
- Analysis of structural degradation, evaluation of structural integrity based on the collected data. In particular, the focus lies on the buried tension/compression members in the abutment area.
- Additionally, Finite Element models of the bridge were developed in order to determine reference parameters by means of modal analysis. The models were used both to compare the results of the follow-up measurement 2020 to the respective numerical values and to quantify the expected changes in modal parameters due to a retrofitting measure in 2006.
- The investigation is concluded by the means of an overall assessment comparing the measured reference data from 2003 with the measurement 2020 to display the progression of structural maintenance condition of the bridge over time.
- Subsequently, the findings from the performed bridge analysis are transferred into recommendations for short- and midterm measures in terms of bridge maintenance, retrofit or reconstruction.

1.2 *Bridge description*

The investigated prestressed concrete road bridge is located in Pforzheim, Germany and has been in operation since 1953. A key feature of this frame bridge is the design of the side spans,

consisting of frame legs constructed as separated tension and compression members (Figure 1). These prestressed concrete members are buried in the ground and therefore not accessible for conventional periodic visual inspections according to DIN 1076 (1999).

The main span has a length of 37.1 m, the side spans are 4.3 m long. The bridge consists of two separated superstructures (total width 14 m), which are both made of a double T-beam (Figure 2).

The bridge deck has been retrofitted by the means of an additional layer of reinforced concrete in 2006.

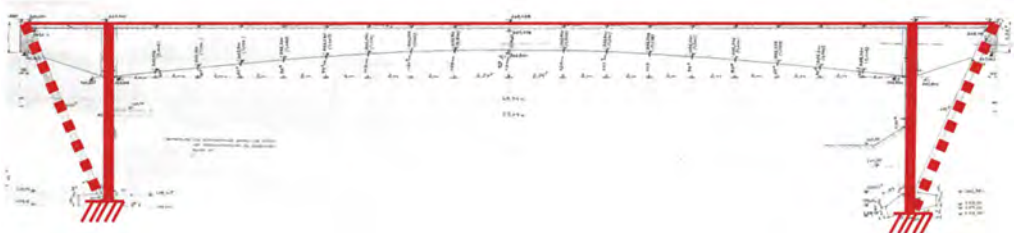


Figure 1. Longitudinal bridge section with emphasis on certain structural properties (dashed line: tension members, solid line: compression members).

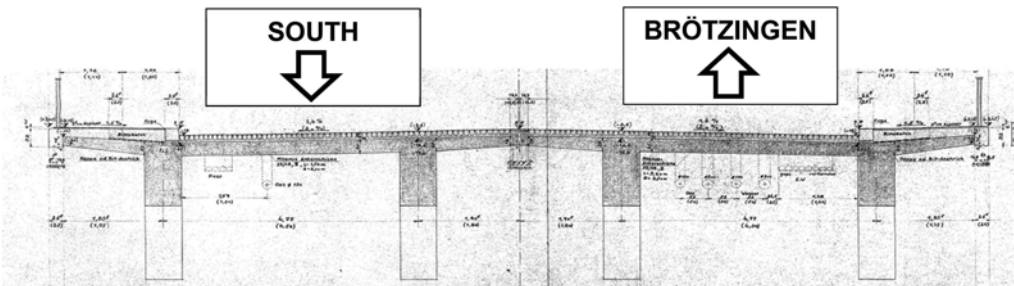


Figure 2. Cross-section of the superstructure.

2 DESCRIPTION OF MEASUREMENT

The follow-up dynamic measurement of the bridge deck was performed in November 2020, using a dense grid of accelerometers along both sidewalks (Figure 3). The measurement was conducted under unrestricted road traffic, for approximately half a day. Both the sensor layout and the meteorological conditions were comparable to the baseline investigation carried out in 2003 (VCE & BBV, 2004).

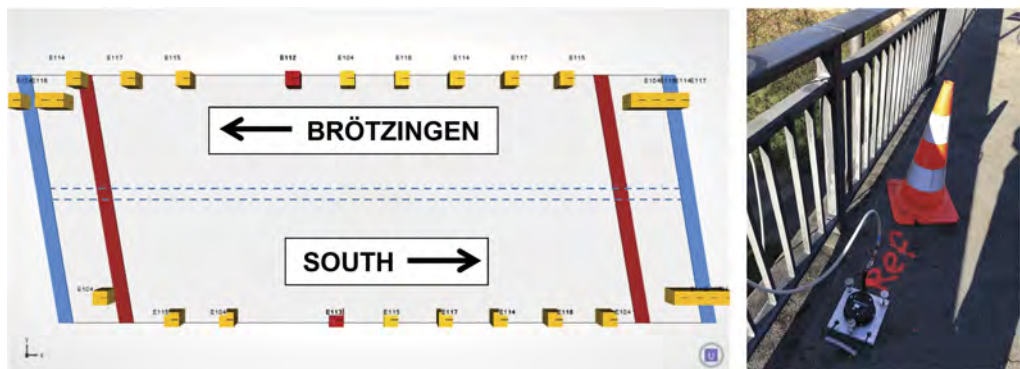


Figure 3. Monitoring sensor layout.

3 DYNAMIC BEHAVIOUR

3.1 General

The assessment of structural integrity and maintenance condition of this bridge was based on the following indicators:

- Eigenfrequencies
- Mode shapes
- Energy dissipation (damping)
- Evaluation of structural integrity (spectrograms)
- Vibration intensity analysis

Additionally, numerical models of the superstructure were developed to provide reference values for the bridge structure.

The following sections will focus only on the decisive parameters in the assessment of this bridge. A more in-depth analysis of all indicators can be found in the full report (VCE & BBV, 2021a).

3.2 Frequency analysis & dynamic system identification 2020

The frequency spectra obtained from the measurement data 2020 (Figure 4) show a distinct dynamic characteristic for both structures. The dominant eigenfrequencies are already clearly visible from the raw spectra in all three analysed directions.

In addition, two other sources contributing to the bridges' dynamic characteristics can be seen from the spectra:

- Even though the two superstructures are statically independent, they share the pavement and thus there is interaction between both superstructures.
- Urban traffic management leading to frequent traffic jams on the bridge.

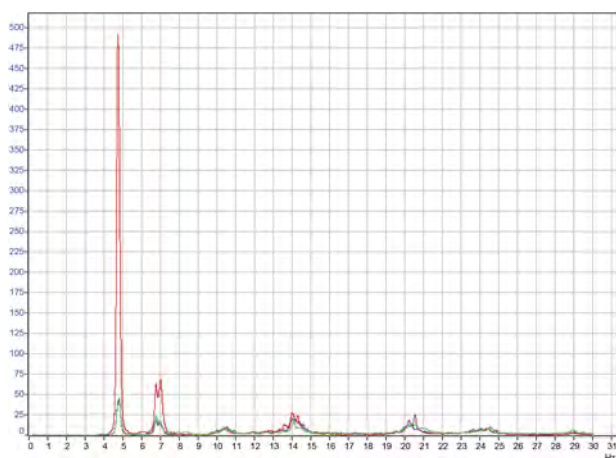


Figure 4. ANPSD vertical, 0.2-30 Hz (direction Brötzingen).

Table 1 summarises the decisive eigenfrequencies and describes the respective type of dynamic response, which is referring to an analysis of the corresponding mode shapes derived from the measurement.

The comparison of the eigenfrequencies direction Brötzingen and direction south shows a high level of conformity between both superstructures. This indicates a comparable structural maintenance condition.

Table 1. Dynamic system identification 2020 (one measurement for each of the separate superstructures).

No.	Type of loading	measured eigenfrequency 2020 direction Brötzingen [Hz]	measured eigenfrequency 2020 direction south [Hz]	specification on on type of dynamic response
1	1 st bending mode	4.74	4.70	1BT
2	1 st torsional mode	6.76	6.72	1TL
3	2 nd bending mode	10.73	11.39	2BT
4	2 nd torsional mode	14.08	14.11	2TL
5	3 rd bending mode	20.55	20.25	3BT

3.3 FEM modelling

Two reference FEM models were prepared in order to determine modal parameters by numerical simulation. These models reflect the undamaged condition of the bridge 2020 and 2003 (after and before the retrofitting measure).

For simplification, only one of the two identical superstructures was modelled – according to drawings provided by the bridge owner (Figure 5). Initially, the models were reduced to the primary load-bearing structure: edge beams and pavement were only included as modal masses and thus not contributing to the bridge’s stiffness. The models focus on the main span of the bridge, the rigid connection to the prestressed side spans is implemented as fixed support.

This idealisation represents the limit state of non-deteriorated frame with fully intact prestressed tension members in the abutment area.

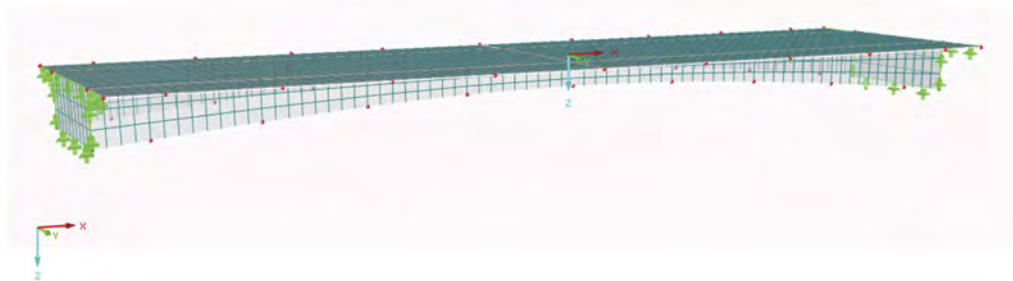


Figure 5. FEM model of the main span.

The results of the computational analysis are shown in Table 2. The comparison of both models provides an expected average increase for the considered decisive eigenfrequencies in the range of 5% due to the retrofitting of the bridge deck with an additional reinforced concrete layer.

Table 2. Eigenfrequencies obtained from numerical modelling (both directions).

No.	FEM model 2020 [Hz]	FEM model 2023 [Hz]	DELTA [%] 2020 vs. 2003	specification on on type of dynamic response
1	4.24	4.09	3.7	1BT
2	5.24	4.94	6.0	1TL
3	9.54	9.11	4.7	2BT
4	11.10	10.42	6.6	2TL
5	16.06	15.41	4.2	3BT
		Mean:	5.0	

3.4 Comparison of the follow-up measurement 2020 with the baseline measurement 2003

3.3.1 Eigenfrequencies

Table 3 compares the eigenfrequencies derived from the follow-up measurement in 2020 to the baseline measurement in 2003. Both bridge decks show an average increase of eigenfrequencies of 4.5%, which is in good accordance with the models' output of 5.0%. This confirms that the additional concrete layer fulfils the purpose of providing additional stiffness to the structure.

Table 3. Measured Eigenfrequencies (both directions).

No.	direction Bröt- zingen 2020 [Hz]	direction Bröt- zingen 2003 [Hz]	DELTA [%] 2020 vs. 2003	direction south 2020 [Hz]	direction south 2003 [Hz]	DELTA [%] 2020 vs. 2003
1	4.74	4.49	5.6	4.70	4.55	3.2
2	6.76	6.33	6.8	6.72	6.34	6.0
3	10.73	10.86	-1.2	11.39	10.88	4.6
4	14.08	13.36	5.4	14.11	13.38	5.4
5	20.55	19.62	4.7	20.25	19.40	4.4
		Mean: 4.3			Mean: 4.7	

3.4.2 Evaluation of structural integrity

So-called trend spectrograms are an essential evaluation tool for full-scale measurements on bridge structures. They visualise the signal either in a frequency-time or a frequency-bridge-length waterfall plot; the colour scaling represents the energy content of the oscillation and therefore the respective intensity. In the present case, trend spectrograms over time were chosen to evaluate the stability of the decisive eigenfrequencies within the follow-up measurement on one hand. On the other hand, by including both data from the baseline measurement and the follow-up measurement in one plot (Figure 6) it is possible to assess the progression of structural integrity over time.

Distinctive stable eigenfrequencies over time indicate a regular load-bearing behaviour under the prevailing load regime. For the baseline assessment in 2003, this was the case under the given operational circumstances (see Section 3.2). The follow-up assessment produces even more stable trends and a lift of all decisive eigenfrequencies of approximately 5% can be seen. Thus, the retrofitting measure has an effective and positive impact both in terms of overall stiffness as well as in terms of the system's ability to cope with the given dynamic loading.

3.4.3 Vibration intensity analysis

Intensive dynamic loading causes fatigue failure of structures. The vibration intensity represents the energy impact into the structure. The intensity for the investigated bridge object is determined at all sensor positions and is included into a diagram, which represents the corresponding risk level. According to the classification by Beards (1996), the vibration intensity is subdivided into four regions, ranging from low probability of damage due to dynamic stress (Region I) up to very high probability of damage (Region IV).

In 2003, the bridge structure responded more sensitive to traffic impact loading than in 2020, with structural response in vertical direction showing vibration intensity close to Region II. (Figure 7 – left). Region II indicates impact conditions, where damage might be caused by continuous dynamic stress. However, in 2020 the vibration intensities have lowered, which is attributed to the positive impact of the retrofitting measure (Figure 7 – right).

3.5 Comparison of the measurement with the numerical model

Table 4 and 5 summarise the results of the measurements 2020 and 2003 and the respective FEM models. A mean difference between measurement and modelling of approximately 22% for both the baseline and the follow-up measurement could be identified. This indicates an unchanged maintenance condition of the primary load-bearing structure. Moreover, no signs of effective mechanical degradation since the baseline measurement have been detected.

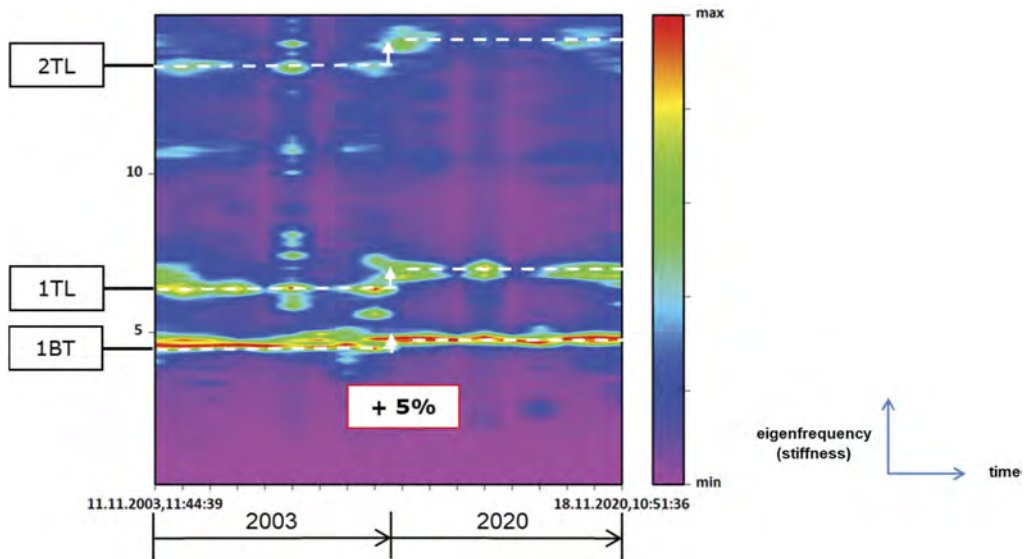


Figure 6. Trend spectrogram vertical, 0.2-15 Hz (direction Brötzingen).

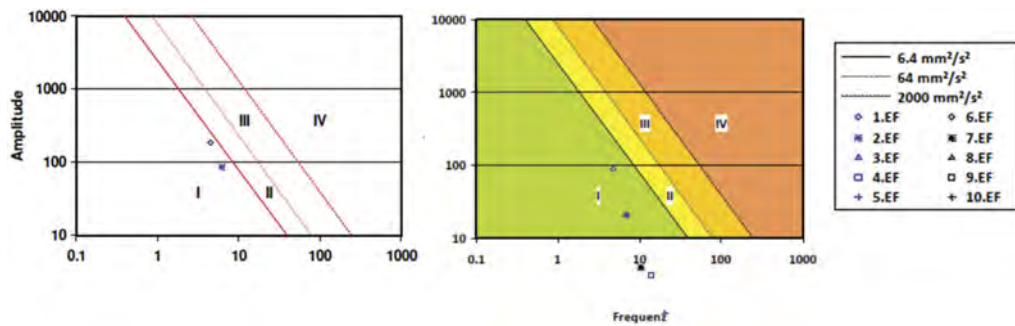


Figure 7. Measured vibration intensity 2003 (left) and 2020 (right) (direction Brötzingen).

In general, a delta of +22% in measured frequencies compared to a vital FEM model states a very good mechanical condition of the prestressed concrete structure.

Table 4. Comparison: numerical model vs. measurement 2020.

FEM model No.	FEM model 2020 [Hz]	Measurement Brötzingen 2020 [Hz]	DELTA [%] FEM vs. measurement	Measurement south 2020 [Hz]	DELTA [%] FEM vs. measurement
1	4.24	4.74	11.8	4.70	10.8
2	5.24	6.76	29.1	6.72	28.3
3	9.54	10.73	12.5	11.39	19.4
4	11.10	14.08	26.8	14.11	27.0
5	16.06	20.55	27.9	20.25	26.1
		Mean:	21.6	Mean:	22.3

However, there are certain limits to this comparison due to simplifications in the FEM modelling. To complete this assessment, the reasons and the composition within the obtained difference of 22% between measurements and modelling have been investigated:

Table 5. Comparison: numerical model vs. measurement 2003.

No.	FEM model 2003 [Hz]	Measurement Brötzingen 2003 [Hz]	DELTA [%] FEM vs. measurement	Measurement south 2003 [Hz]	DELTA [%] FEM vs. measurement
1	4.09	4.49	9.8	4.55	11.2
2	4.94	6.33	28.2	6.34	28.4
3	9.11	10.86	19.3	10.88	19.5
4	10.42	13.36	28.2	13.38	28.4
5	15.41	19.62	27.3	19.40	25.9
			Mean: 22.5		Mean: 22.7

- First of all, neither the bridges' pavement nor the edge beams were included in the models, only their modal masses were considered. This is estimated to add a maximum of 3% (pavement) and 5% (edge beams) to the bridges' stiffness in terms of frequency if modelled more precisely.
- Furthermore, modelling the bridge as a monolithic concrete cross-section whereas in reality it is a composite cross-section, containing both normal reinforcement and prestressing steel, results in lower frequencies in the model (5%).
- Past assessment projects, e.g. VCE & BBV (2021b) have shown that the increase of modulus of elasticity in uncracked concrete over time can have a positive hidden impact on the evaluation of structural integrity of existing prestressed concrete bridge structures. Eurocode 2 (DIN EN 1992-1-1 (2011)) provides a possibility to quantify this increase in concrete strength over time; for the investigated bridge the authors derived an effect of at least 6% on the eigenfrequencies.

In total, these identified and validated contributions to the delta between measurement and FEM model sum up to 19% (from the given initial deviation of 22%). The remaining difference between measurement and FEM model (+3%) is within the expected modelling uncertainty.

4 CONCLUSIONS

The non-destructive dynamic measurement of Brötzingen Brücke provides insight on the following matters:

- The full functionality of the buried tension/compression members in the abutment area is confirmed by comparing the measurement results with a numerical model in terms of an idealised, non-deteriorated frame with intact prestressed tension members in the abutment area.
- The effectiveness of the retrofitting measure in 2006 can be seen by the increase of eigenfrequencies between baseline and follow-up measurement of 5%. This increase matches the reference value obtained from numerical modelling and the positive effect is confirmed both by trend spectrograms and vibration intensity analyses.
- The eigenfrequencies derived from the measurement are on average 22% higher than the eigenfrequencies obtained from the intact FEM model.
- Both the follow-up and the baseline measurement show the same deviation (+22% in frequencies) when compared to the respective FEM model. This means that the structural maintenance condition has not changed over time.
- The reasons and the composition within the obtained difference between measurements and modelling have been investigated in a conservative manner and confirmed the extent of 22%.
- Even when remaining modelling uncertainties are taken into account, this result states a very good mechanical condition of the prestressed concrete bridge.

It can be concluded that the conducted full-scale vibrational analysis as an additional in-depth assessment according to DIN 1076 (1999) provides an added value to the regular periodic visual inspection by addressing the mechanical evaluation of structural resistance and its possible change over time.

REFERENCES

- Beards, C. F. 1996. *Structural Vibration-Analysis and Damping*. Arnold (A Member of the Hodder Headline Group). London, Great Britain.
- DIN 1076:1999-11 Engineering structures in connection with roads - inspection and test, DIN Deutsches Institut für Normung e.V., Berlin, Germany.
- DIN EN 1992-1-1:2011 Eurocode 2: Design of concrete structures - Part 1-1: General rules and rules for buildings; German version EN 1992-1-1:2004 + AC:2010, DIN Deutsches Institut für Normung e.V., Berlin, Germany.
- VCE & BBV 2004. Brötzinger Brücke – Dynamische Charakteristik des Brückentragwerks. Messungen, Vergleichsrechnungen und Interpretation der Ergebnisse. Vienna, Austria.
- VCE & BBV 2021a. Brötzinger Brücke – Zustandsbeurteilung mit BRIMOS® Structural Health Monitoring. Sonderprüfung des Brückendecks im Sinne der DIN 1076. Vienna, Austria.
- VCE & BBV 2021b. Kallhardtbrücke - Stadt Pforzheim: Zustandsbeurteilung mit BRIMOS® Structural Health Monitoring. Sonderprüfung des Brückendecks im Sinne der DIN 1076. Vienna, Austria.
- Veit-Egerer, R. & Hubka, M. 2008. Silniční most přes trať ČD za obcí Komořany - Dynamické chování vzhledem k provoznímu stavu a zatížitelnosti metodou BRIMOS® - Determination of Structural Integrity and Explicit Load Capacity of a Prestressed Concrete Bridge by means of Dynamic Monitoring (written & presented in Czech language) in Proceedings of the 13th International Symposium BRIDGES. Sekurkon. Brno, Czech Republic.
- Veit-Egerer, R., Bursa, J. & Synek, J. 2018. Follow-up assessment on an old concrete road bridge based on operational dynamic bridge behaviour – analysis of structural integrity and determination of loading capacity. In: Caspele, R., Taerwe, L., & Frangopol, D. (Eds.). *Life Cycle Analysis and Assessment in Civil Engineering: Towards an Integrated Vision: Proceedings of the Sixth International Symposium on Life Cycle Civil Engineering (IALCCE 2018), 28–31 October 2018*, Ghent, Belgium (1st ed.). CRC Press.
- Veit-Egerer, R., Valkova, T., Černík, F. & Koutník, J. 2019. Untersuchung der Belastbarkeit einer bestehenden Massivbrücke mittels dynamischer Sonderprüfung in *16. D-A-CH Tagung Erdbebeningenieurwesen & Baudynamik (D-A-CH 2019)*. Innsbruck, Austria.
- Veit-Egerer, R., Bursa, J. & Synek, J. 2022. Periodic assessment of an old concrete road bridge based on operational dynamic bridge behaviour with regard to structural integrity and the remaining load bearing capacity. In *IABSE Symposium Prague 2022 (ePDF) – Challenges for Existing and Oncoming Structures, 25–27 May 2022*, Prague, Czech Republic
- Wenzel H. 2009. *Health Monitoring of Bridges*. J. Wiley and Sons Ltd, Chichester, England.
- Wenzel H., Pichler D. 2005. *Ambient Vibration Monitoring*. J. Wiley and Sons Ltd, Chichester, England.

Laboratory validation of an Arduino based accelerometer designed for SHM applications

S. Komarizadehasl, E. Delgado, G. Ramos & Jose Turmo

Department of Civil and Environment Engineering, Universitat Politècnica de Catalunya, BarcelonaTech

J. A. Lozano-Galant

Department of Civil Engineering, Universidad de Castilla-La Mancha

ABSTRACT: Nowadays, low-cost sensors based on low-cost microcontrollers and microprocessors are gaining a lot of attention from researchers. This increasing interest is due to the fact that the implementation of low-cost solutions may make Structural Health Monitoring (SHM) applicable and affordable to structures with a low budget for their SHM. However, many of the present solutions do not have comparable accuracy and resolution with those of the traditional commercial accelerometers. Also, the noise density of these newly developed prototypes has not been checked through laboratory experiments. In fact, the characteristics of the designed and created accelerometer are simply copied from the datasheet of the chipset used to develop the solution. Moreover, the sampling frequency of the majority of the available low-cost solutions usually is lower than 100 Hz. This paper presents a consistent work with the development of a low-cost wireless accelerometer with a sampling frequency of 333 Hz and noise density of $51\mu\text{g}/\sqrt{\text{Hz}}$. This accelerometer's accuracy, noise density, and reliability are evaluated through a series of laboratory experiments. It is essential to mention that this accelerometer does not need any additional data acquisition equipment and is self-sufficient.

1 INTRODUCTION

Civil infrastructures and structures might be considered the leading basis of modern society; consequently, their health state is of the highest importance (J. Lei, Xu, & Turmo, 2018). Evaluating structures along with their health-state assessment is needed to reduce reparation costs, maintenance, and, eventually, for certifying infrastructure/structure safety (Peng, Nogal, Casas, & Turmo, 2021b). Structural Health Monitoring (SHM) applications issue statistics on structures' functioning states and their structural responses (Peng, Nogal, Casas, & Turmo, 2021a) (X. Lei, Xia, Komarizadehasl, & Sun, 2022).

For measuring the structural responses (such as deflections, strains, rotation, temperature, humidity, and accelerations) over time, sensors are widely used in SHM systems (Komarizadehasl, Komary, et al., 2022). The recorded information of the sensors is then used for structural performance estimations (Komarizadehasl, Lozano, Lozano-Galant, Ramos, & Turmo, 2022). In fact, natural phenomena can be categorized as static or quasi-static and dynamic (Atencio, Komarizadehasl, Lozano-Galant, & Aguilera, 2022). On the one hand, some environmental elements (such as temperature or humidity) change very slowly, so they can be considered to perform either as quasi-static or static (Farré-Checa, Komarizadehasl, Ma, Lozano-Galant, & Turmo, 2022). On the contrary, some events (such as traffic-induced vibrations, ambient activities, and waves from seismic activities) are considered dynamic because their changing rate is significantly affected by the time (Mobaraki et al., 2022).

According to the literature (see, e.g., (Komary et al., 2023)), most civil structures' significant natural frequencies vary between 0.2 and 100.0 Hz. It should also be noted that most of the ambient vibrations in civil structures are characterized by low amplitudes (Tran-Ngoc et al., 2018). In fact, the acceleration amplitude of these structures can be as low as 0.04 g. This characteristic shows the necessity of using accelerometers with low noise density and high sensitivity for SHM of bridges (Tran-Ngoc et al., 2018). The commercial MEMS accelerometers have a bandwidth of a few kHz. However, their design for higher frequencies has a lower noise density (Lee & Eun, 2022). Finally, it should be highlighted that the sensitivity of an accelerometer has an indirect ratio with the squared value of the resonant frequency. For that reason, the higher the accelerometer's sampling frequency, the lower its sensitivity (Farrar, Park, Allen, & Todd, 2006). For that, many researchers tried to develop low-cost MEMS accelerometers with limited sampling frequency and vibration amplitude range for civil SHM (Shi, Zhang, Jiao, Zhao, & Cao, 2021)

The literature review shows a lack of consistent work, including all the following points in single inception for a low-cost accelerometer: (1) access to the time through Internet, for accurate sensor synchronization, (2) wireless control, (3) scheduling for a synchronized data acquisition experiment, and, finally, (4) measuring the ND and data resolution after the system was wired and (5) performing experimental eigenfrequency analyses on actual infrastructures.

Recently a Cost Hyper Efficient Arduino Product (CHEAP) was introduced by Komarizadehasl et al. (Komarizadehasl, Mobaraki, Ma, Lozano-Galant, & Turmo, 2021). Different laboratory tests were performed to validate CHEAP's performance, and the results of CHEAP were compared with those of two commercial seismic accelerometers (PCB 393A03 and PCB 356B18).

This paper aims to adapt CHEAP to solve all the detected problems and to develop a new Low-cost Adaptable Reliable Accelerometer (LARA). A laboratory test campaign was designed to validate LARA's performance against its older version. In this set of experiments, frequencies ranging from 0.1 Hz to 32 Hz and acceleration amplitudes in the range of [0.001–9.806 m/s^2] were tested. Furthermore, another field test is performed on a short-span foot-bridge in Barcelona. In this experiment, the eigenfrequencies of LARA are compared with a commercial dynamic sensor (HI-INC) (Komarizadehasl, Lozano, et al., 2022). HI-INC is a dynamic inclinometer with a sampling frequency of 250 Hz.

2 TRIAXLE WIRELESS LOW-COST ADAPTABLE RELIABLE ACCELEROMETER (LA-RA) WITH POST-SYNCHRONIZATION CAPABILITY

Recently a Cost Hyper Efficient Arduino Product (CHEAP) was introduced by Komarizadehasl et al. (Komarizadehasl et al., 2021). LARA is an upgraded version of CHEAP that has a frequency sampling of 333 Hz, an acceleration range of ± 2.0 g, and effective bandwidth of 165 Hz. LARA is built into two parts: (1) A sensing part: this contains the aligned accelerometers and the multiplexor, which is shown in Figure 1. It should be noted that LARA consists of five aligned low-cost MEMS accelerometers. It is since when the results of a few accelerometers with unique inherent dynamic noises are averaged, the signal under study remains invariable. And (2) an acquisition part: consisting of an Arduino and a Raspberry Pi.

LARA has the following more features that CHEAP did not have: (1) higher bandwidth: achieving a faster sampling frequency (333 Hz) by efficiently rewriting all the library codes, (2) independency: this accelerometer is not dependent on any connected computer for data acquisition. LARA has an attached low-cost microprocessor that allows the acquired data to be saved on an SD card or any portable flash or hard drive, (3) triaxial data acquisition: having all the accelerometers of LARA in x , y , and z direction aligned makes the final product suitable for triaxial data acquisition—besides, if needed, it can work as a uniaxial, biaxial accelerometer, (4) low Noise Density, (5) Internet timestamp and synchronization: the Network Time Protocol (NTP) of LARA is activated, (6) Experimental analysis: in this paper, a short span was instrumented, and the eigenvalue analyses of LARA are compared with those of

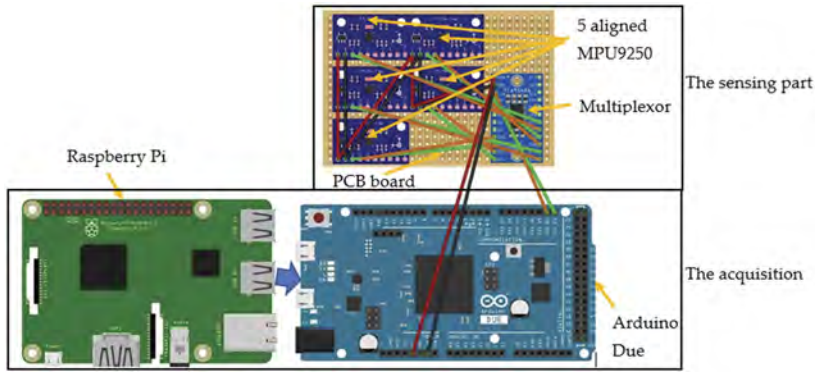


Figure 1. The sensing and acquisition part of LARA.

certified vibration sensing devices, and (7) wireless accessibility: the user can have access to the saved data wirelessly through the Internet. Therefore, LARA can be controlled, get upgraded through online commands and data can be recorded.

3 LABORATORY TESTS AND RESULTS

3.1 Sensitivity, ND, and resolution evaluation

This section compares the sensitivity, ND, and resolution of a single MPU9250 accelerometer with CHEAP and LARA.

The accelerometers' sensitivity can be defined as the ratio of the input (induced vibrations of the shaking table) to the output (the information reported by the accelerometer). The ADC formula for calculating the LSB is shown in Equation (1) (Elhatab, Uddin, & OBrien, 2019).

$$LSB = \frac{Input\ voltage}{2^{(number\ of\ bits)}} \quad (1)$$

In Equation (1), with an input voltage of 2.5 and an ADC scale of 16, each unit of LSB is equivalent to 0.03814 mv. In this way, with 16,384 LSB/g for acceleration amplitude range of ± 2.0 g, the comparable sensitivity of MPU9250, CHEAP, and LARA is calculated as 625 mV/g.

To calculate ND and resolution of the devices, a long-term test was performed. The ND results of the different accelerometers are calculated using Equation (2) (Kwong, 2017).

$$ND = \sqrt{\frac{\sum_1^N (x_i - \mu)^2}{N * f}} \quad (2)$$

In Equation (2), the x_i is the reported values of the accelerometers in the time-domain, μ is the average of all x_i values, N is the number of used samples, and f is the sampling frequency of the accelerometer.

The calculated ND of MPU9250, CHEAP, and LARA for the z -directions are 390, 162, and 81 $\mu\text{g}/\sqrt{\text{Hz}}$, respectively. In addition, the ND of LARA for both x and y directions is 51 $\mu\text{g}/\sqrt{\text{Hz}}$.

Since the evaluation of the accelerometer's resolution depends on the number of samples ("Data Acquisition Handbook," n.d.), for a fair comparison between devices with various sampling frequencies, the same number of the acquired samples were used in the test. For

illustrating the resolution of the accelerometers, their reported data have been transformed from time-domain to frequency-domain by a Fast Fourier Transform (FFT). The results for different sensors are reported in Figure 2.

Analysing the frequency domain diagrams of acquired data of LARA for all the axes, it was obtained that the resolution of LARA for x and y axes is 0.00005 m/s^2 . The resolution for x and y -directions is 44% better than the z -axis because of the absence of gravitational acceleration of the earth in those directions. As a result, the resolution of this accelerometer is evaluated as 0.00005 m/s^2 .

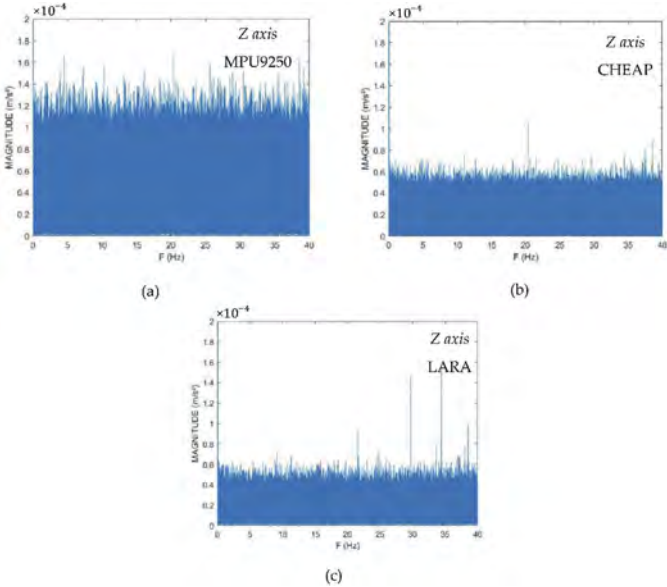


Figure 2. Frequency domain diagrams for z axis of: (a) MPU9250, (b) CHEAP, and (c) LARA.

3.2 Frequency validation

An experiment to validate the frequency report of LARA is presented in this section. A jack that could induce displacements with a known frequency was used. Although the jack is very accurate in reproducing a specific frequency, its performance is limited in movement. Therefore, for every experiment, the jack presents a report. This report is the time-domain information of the activities of its lower jaw.

The vibration platform used in this paper (INSTRON 8803) was programmed using Wave-Matrix2 Dynamic Software. This jack can create various waveform types with the frequency range of 0.1 to 100 Hz and its resonant frequency is 134 Hz. The movement direction of the vibration platform was in z -direction.

For validating the accelerometers' accuracy, 11 tests with various frequency ranges (from 0.1 Hz to 32 Hz) were performed. For finding the frequency report of the accelerometers, the accelerometers' time-domain raw data were converted to the frequency domain by an FFT program written in the MATLAB software.

The accelerometer's frequency error is estimated by calculating the percentage error of the plot value from the reference value of the excitation device. Table 1 compares the frequency errors of LARA, CHEAP, and MPU9250 with the jack's reference values.

Analysis of Table 1 shows that a single MPU9250 is reporting the same frequency error as the CHEAP from 2 Hz on. Since this MPU9250 is one of the CHEAP accelerometers, its frequency report is synchronized with CHEAP. It can also be deduced from this table that a single MPU9250 has not enough resolution for frequencies smaller than 2 Hz. Further analysis of Table 1 shows that CHEAP cannot visualize signals with a frequency smaller than 0.4

Table 1. Frequency validation of the accelerometers.

Frequency (Hz)	LARA's error (%)	CHEAP'S error (%)	MPU9250'S error (%)
0.1	0.450		
0.2	0.295		
0.3	0.260		
0.4	0.050	0.470	
0.5	0.006	0.011	
2	0.005	0.025	0.025
4	0.000	0.000	0.000
8	0.003	0.003	0.003
10	0.004	0.004	0.004
16	0.001	0.001	0.001
32	0.003	0.003	0.003

Hz either. In fact, LARA has a broader range of frequency than MPU9250 and CHEAP and can locate signals up to 0.1 Hz with 0.5% of error. In fact, the frequency range of LARA, based on the presented information, is between 0.1 Hz and its bandwidth (165 Hz).

3.3 Acceleration amplitude validation

An experiment was carried out with the jack to compare the acceleration acquisition of MPU925, CHEAP, and LARA. The jack was calibrated to move with a frequency of 4 Hz and a displacement range of 0.1 mm from its null axis. During each test, the jack reported its time-domain information with a sampling frequency of 500.

For validating the accelerometers' accuracy, their acceleration amplitude report of the sensors was converted to displacements. Then, high-pass and low-pass filters removed signals with frequencies smaller than 0.1 Hz and bigger than 1/10 of the accelerometer's bandwidth. These filters are MATLAB functions that can filter the signals out of the interest range. Finally, the FFT analysis was carried out.

The results of the FTT Analysis shows that even though all accelerometers are reporting the same frequency, they measure the induced signal's magnitude inconsistently. MPU9250, CHEAP, and LARA have measured the jack's displacement as 0.098913, 0.10023, and 0.10068 mm. Further analysis shows that CHEAP and LARA's magnitude report has less than 0.5% error from each other. In fact, CHEAP and LARA have measured the jack's displacements with 1.55% and 1.2% errors from the introduced displacement measurement of the jack.

4 REAL STRUCTURE TEST AND RESULTS

This section presents a field test carried out on a short-span bridge for comparing the measured eigenfrequencies of LARA with those of a high-precision sensor. The footbridge is shown in Figure 3. As shown, it is connected to an elevator box and from the other side, it is located on an abutment.

After mounting the sensors to the bridge, they were connected to the rest of the monitoring components (power bank, USB 4G dongle, Arduino, and Raspberry Pi) manually. It is important to highlight that to enable its communication throughout the Internet, the Raspberry Pi was previously configured with a WiFi hotspot. In fact, after its assemblage on site the Raspberry Pi was used to initiate the data acquisition process remotely, using the Virtual Network Computing (VNC) software (Atencio et al., 2022). The acquired data was first collected on the memory card of the Raspberry Pi. Then, when the data acquisition process finished, the obtained data were moved to a computer using the VNC software. The location of the commercial dynamic sensor (HI-INC) and LARA on the mid-span of the bridge.



Figure 3. A picture of the pass way bridge.

Table 2 presents results of the eigenfrequency analysis of LARA and the used high-precision inclinometer dynamic (HI-INC).

Table 2. Comparison of the first three mode steps frequencies of LARA with HI-INC.

Mode Number	HI-INC	LARA	Difference
1	3.90 Hz	3.85 Hz	1.28%
2	7.91 Hz	7.91 Hz	0.20%
3	9.94 Hz	9.93 Hz	0.88%
4	26.25 Hz	26.01 Hz	0.91%
5	42.81 Hz	41.70 Hz	0.27%

Comparing the measured eigenfrequencies of LARA with those of HI-INC shows a maximum error of 1.28%.

5 CONCLUSION

Developing low-cost sensors is essential for Structural Health Monitoring (SHM) of structures with a low budget for their SHM assessments. These sensors can allow engineers to leave the equipment on the structure for monitoring. In previous works, a Cost Hyper Efficient Arduino Product (CHEAP) was introduced, and its performance was validated in laboratory experiments. By upgrading both hardware and software of the CHEAP, a new triaxial Low-cost Adaptable Reliable Accelerometer (LARA) is introduced. The advantages of LARA with respect to CHEAP are:

- (1) By rewriting codes, LARA achieved a faster sampling frequency.
- (2) Having a connected Raspberry Pi to the Internet made LARA independent of any attached computer for data sampling.
- (3) Having aligned correctly, its accelerometers made LARA triaxial.
- (4) Having a better and more efficient connection reduced LARA's ND.
- (5) Having the time of the Internet for future data synchronization.
- (6) Being completely wireless excluded the need for an engineer's presence on the site for data acquisition.

To evaluate the LARA performance, resolution, and ND, a set of laboratory experiments was performed. These obtained results show that LARA has less ND ratio than MPU9250 and CHEAP for the same number of acquired data. Furthermore, comparing the effects of MPU9250, CHEAP, and LARA with the reports of the shaking table show that LARA is more accurate in reporting both frequency and acceleration amplitude than MPU9250 and CHEAP in a laboratory experiment with the same time duration.

A field test on a footbridge in Barcelona with a span length of 14 m has been carried out using LARA accelerometer. The generated frequencies of the eigenfrequency analysis from LARA have been validated with a commercial high-precision sensor (HI-INC).

REFERENCES

- Atencio, E., Komarizadehasl, S., Lozano-Galant, J. A., & Aguilera, M. (2022). Using RPA for Performance Monitoring of Dynamic SHM Applications. *Buildings* 2022, Vol. 12, Page 1140, 12(8), 1140. <https://doi.org/10.3390/BUILDINGS12081140>
- Data Acquisition Handbook. (n.d.). Retrieved March 6, 2021, from <https://www.mccdaq.com/support/Data-Acquisition-Handbook>
- Elhattab, A., Uddin, N., & O'Brien, E. (2019). Extraction of Bridge Fundamental Frequencies Utilizing a Smartphone MEMS Accelerometer. *Sensors*, 19(14), 3143–3163. <https://doi.org/10.3390/s19143143>
- Farrar, C. R., Park, G., Allen, D. W., & Todd, M. D. (2006). Sensor network paradigms for structural health monitoring. *Structural Control and Health Monitoring*, 13(1), 210–225. <https://doi.org/10.1002/STC.125>
- Farré-Checa, J., Komarizadehasl, S., Ma, H., Lozano-Galant, J. A., & Turmo, J. (2022). Direct simulation of the tensioning process of cable-stayed bridge cantilever construction. *Automation in Construction*, 137, 104197. <https://doi.org/10.1016/J.AUTCON.2022.104197>
- Komarizadehasl, S., Komary, M., Alahmad, A., Lozano-Galant, J. A., Ramos, G., & Turmo, J. (2022). A Novel Wireless Low-Cost Inclinometer Made from Combining the Measurements of Multiple MEMS Gyroscopes and Accelerometers. *Sensors* 2022, Vol. 22, Page 5605, 22(15), 5605. <https://doi.org/10.3390/S22155605>
- Komarizadehasl, S., Lozano, F., Lozano-Galant, J. A., Ramos, G., & Turmo, J. (2022). Low-Cost Wireless Structural Health Monitoring of Bridges. *Sensors* 2022, Vol. 22, Page 5725, 22(15), 5725. <https://doi.org/10.3390/S22155725>
- Komarizadehasl, S., Mobaraki, B., Ma, H., Lozano-Galant, J.-A., & Turmo, J. (2021). Development of a Low-Cost System for the Accurate Measurement of Structural Vibrations. *Sensors*, 21(18), 6191–6213. <https://doi.org/10.3390/S21186191>
- Komary, M., Komarizadehasl, S., Tošić, N., Segura Pérez, I. S., Lozano-Galant, J. A., & Turmo, J. (2023). Low-Cost Technologies Used in Corrosion Monitoring. *Sensors* 2023, Vol. 23, Page 1309, 23(3), 1309. <https://doi.org/10.3390/S23031309>
- Kwong, K. (2017). *MEMS Accelerometer Specifications and Their Impact in Inertial Applications*. 95. Retrieved from http://www.eecg.utoronto.ca/~johns/nobots/theses/pdf/2017_keiming_kwong_masc.pdf
- Lee, E.-T., & Eun, H.-C. (2022). An Optimal Sensor Layout Using the Frequency Response Function Data within a Wide Range of Frequencies. *Sensors* 2022, Vol. 22, Page 3778, 22(10), 3778. <https://doi.org/10.3390/S22103778>
- Lei, J., Xu, D., & Turmo, J. (2018). Static structural system identification for beam-like structures using compatibility conditions. *Structural Control and Health Monitoring*, 25(1), 1–15. <https://doi.org/10.1002/STC.2062/ABSTRACT>
- Lei, X., Xia, Y., Komarizadehasl, S., & Sun, L. (2022). Condition level deteriorations modeling of RC beam bridges with U-Net convolutional neural networks. *Structures*, 42, 333–342. <https://doi.org/10.1016/J.ISTRUC.2022.06.013>
- Mobaraki, B., Komarizadehasl, S., Javier, F., Pascual, C., Lozano-Galant, A., & Soriano, R. P. (2022). A Novel Data Acquisition System for Obtaining Thermal Parameters of Building Envelopes. *Buildings* 2022, Vol. 12, Page 670, 12(5), 670. <https://doi.org/10.3390/BUILDINGS12050670>
- Peng, T., Nogal, M., Casas, J. R., & Turmo, J. (2021a). Planning low-error SHM strategy by constrained observability method. *Automation in Construction*, 127, 103707. <https://doi.org/10.1016/j.autcon.2021.103707>
- Peng, T., Nogal, M., Casas, J. R., & Turmo, J. (2021b). Role of sensors in error propagation with the dynamic constrained observability method. *Sensors*, 21(9), 2918. <https://doi.org/10.3390/s21092918>
- Shi, Y., Zhang, J., Jiao, J., Zhao, R., & Cao, H. (2021). Calibration Analysis of High-G MEMS Accelerometer Sensor Based on Wavelet and Wavelet Packet Denoising. *Sensors* 2021, Vol. 21, Page 1231, 21(4), 1231. <https://doi.org/10.3390/S21041231>
- Tran-Ngoc, H., Khatir, S., De Roeck, G., Bui-Tien, T., Nguyen-Ngoc, L., & Abdel Wahab, M. (2018). Model Updating for Nam O Bridge Using Particle Swarm Optimization Algorithm and Genetic Algorithm. *Sensors* 2018, Vol. 18, Page 4131, 18(12), 4131. <https://doi.org/10.3390/S18124131>

Pre-posterior effectiveness of modal extraction techniques for vibrational tests design

A. Lotti, D. Tonelli, S. Zorzi & D. Zonta

University of Trento, Trento, Italy

E. Tubaldi

University of Strathclyde, Glasgow, UK

ABSTRACT: When designing forced vibration tests, engineers must choose the performances of structural health monitoring (SHM) systems, such as sampling frequency and duration of the acquisition, which influence the accuracy of the modal parameters extracted from SHM data. However, this choice must be taken a priori before installing sensors and having any measurements available. In this paper, we propose an approach for forced vibration tests design that provides the expected uncertainty of modal parameters to be extracted from SHM data before performing the test (i.e., a pre-posteriori). Then, we present an experimental campaign of forced vibration tests on a small-scale structure monitored by an SHM system. We repeated the tests by changing the performances of the SHM system to investigate the sensitivity of the modal parameters' accuracy to SHM system performances. The results suggest that the pre-posterior approach provides the expected uncertainties of modal parameters which are in line with those extracted experimentally.

1 INTRODUCTION

Several bridge failures have characterized the last decade, some of which caused great concern in the public community (Calvi et al., 2019). Effective and rapid actions are required to extensively check the condition state of bridges and perform maintenance work on the most degraded ones (Giordano et al., 2022). Structural health monitoring (SHM) can provide helpful information to rapidly identify damage initiation and propagation and assess the reliability of the monitored structures (Bado & Casas, 2021; Tonelli et al., 2022). In particular, vibration-based SHM is one of the most used techniques for identifying variations in structural responses, e.g., resulting from natural degradation and structural damages. When designing forced vibration tests, engineers must choose the performances of SHM systems, such a sampling frequency (f_s), duration of the acquisition (T), signal-to-noise ratio (SNR), and bit resolution (n_{bit}). These performances influence the accuracy of the modal parameters extracted a posteriori from SHM measurements (Chang & Kim, 2016; Giordano et al., 2021; Maia, 1998). However, operators must choose the performances before installing the sensors and having any measurements available (i.e., a priori). Therefore, it is necessary to define a procedure that estimates the expected uncertainty of modal parameters before performing the test (i.e., a pre-posteriori) (Caspani et al., 2022). This paper addresses this need and presents the pre-posterior approach that has been adopted by the Italian Technical Committee UNI/CT 021/GL 08 'Structural Monitoring Group' and will be integrated into the new version of the Italian Standard UNI 10985: Vibrations on bridges and viaducts (UNI Ente Italiano di Normazione, 2002). Then, we present an experimental campaign of forced vibration tests carried out on a small-scale structure with two degrees of freedom, aiming to validate this pre-posterior approach. The campaign consists of artificial impulse excitation tests performed through an instrumented hammer. Finally, we discuss the results and draw conclusions.

2 PRE-POSTERIOR APPROACH FOR MODAL EXTRACTION

This section presents the approach for estimating the pre-posterior uncertainty of modal parameters extracted from artificial impulse excitation tests. In general, the a posteriori uncertainty of the extracted parameters depends on the extraction method used, which in this case is the curve fitting method of the frequency response function (FRF). The formulation presented in this section consists of practical guidelines and assumes as known the uncertainty in the amplitude of the FRF σ_H and the frequency resolution Δf_H .

2.1 Pre-posterior uncertainty of the frequency response function

The amplitude of the experimental FRF extracted from a vibration test is always characterized by an uncertainty σ_H , which depends on the duration of the test and the uncertainty in the acceleration measurements. To evaluate the effectiveness of the vibration test during its design phase – when we do not have measurements yet – we must estimate an expected value of σ_H . There is not a commonly recognised method to do that. Therefore, we developed an algorithm that estimates σ_H by comparing (i) the analytic FRF resulting from a predictive model based on the geometrical and mechanical properties of the structure, with (ii) the experimental FRF we expect will result from a vibration test, characterized by an uncertainty that propagates from measurements.

(i) We define a predictive model of the structure at hand based on measured geometrical and mechanical properties. This model is defined by a mass matrix and stiffness matrix. We solve the eigenvalue problem and obtain the modal properties (e.g., natural frequencies f_k and mode shapes $\phi^{(k)}$). We assume the value of damping ratio ζ_k based on the structural type and materials. Then, we calculate the analytic FRF of the structure, defined as the ratio between the output acceleration A_r at storey r and the input force at storey e , F_e , both expressed in the frequency domain:

$$H_{re}(if) = \frac{A_r(if)}{F_e(if)} = \left[\sum_{k=1}^N \frac{\phi_r^{(k)} \phi_e^{(k)}}{(f_k^2 + 2if\zeta_k f_k - f^2)} \right] \cdot f^2 \quad (1)$$

(ii) We generate a set of M FRFs, each obtained by adding to the FRF calculated in (i) a Gaussian noise with a coefficient of variation V_H – it depends on the sensors' performances. Then, we discretise the FRFs for a fixed value of resolution Δf_H (Figure 1.a), which depends on the duration of the test. Now, the M discretised FRFs represent the variability we expect to have in the experimental FRF due to the measurement uncertainty. We fit the FRFs (Figure 1. b), we considered the resonance condition ($f = f_k$) and calculate the FRFs amplitude.

For each fitted FRF, we calculated the difference in the amplitude between the fitted FRF and the analytic FRF (Figure 1.c): we obtained M residuals. The pre-posterior uncertainty σ_H is the standard deviation of the distribution of the M residuals.

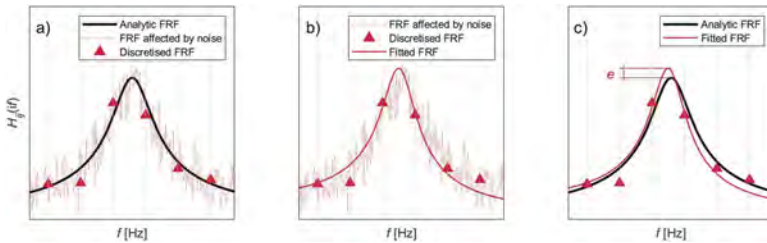


Figure 1. Algorithm for the estimation of σ_H : (1.a) adding noise to FRF model and discretising with resolution Δf_H , (1.b) fitting of the discretised FRF, (1.c) calculating the residual e .

2.2 Forced testing with artificial impulse excitation

Our pre-posterior approach assumes that the expected uncertainty in the estimation of the natural frequencies σ_f is of the same order of magnitude as the frequency resolution of the FRF:

$$\sigma_f \cong \Delta f_H = 1/T_{\text{eff}} \quad (2)$$

where T_{eff} is the effective acquisition time, defined as the minimum between the (i) time of acquisition and (ii) the time required for damping the free oscillations, i.e., the oscillations become smaller than the measurement noise σ_N . The following formula gives the amplitude of the free oscillations (in displacement):

$$|x(t, f)| = |x_{\text{max}} e^{-\zeta 2\pi f t} \sin(2\pi f t)| = |x_{\text{max}}| e^{-\zeta 2\pi f t} \quad (3)$$

where x_{max} denotes the maximum amplitude of the response (in displacement); ζ is the damping ratio; f is the natural frequency. We impose the condition (ii) for the calculation of T_{eff} (f):

$$|x(t, f)| = \sigma_N \quad (4)$$

From which we obtain:

$$T_{\text{eff}}(f) = \frac{1}{\zeta 2\pi f} \ln\left(\frac{x_{\text{max}}}{\sigma_N}\right) \quad (5)$$

By combining Equation 2 and Equation 5, we can express the uncertainty σ_f as:

$$\sigma_f \cong \frac{1}{T_{\text{eff}}(f)} = \frac{\zeta 2\pi f}{\ln\left(\frac{x_{\text{max}}}{\sigma_N}\right)} \quad (6)$$

The expected uncertainty in the estimation of the damping ratios σ_{ζ_k} can be calculated as a first approximation through error propagation. Let us focus on the resonance condition for the k -th mode ($f = f_k$). Therefore, the FRF H_{re} as inertance (i.e., accelerance) becomes:

$$H_{re}(f = f_k) = \frac{\phi_r^{(k)} \phi_e^{(k)}}{2\zeta_k} \quad (7)$$

where e corresponds to the degree of freedom (DoF) *excited* and r to the DoF where the *response* is monitored.

If we propagate the uncertainty of the damping ratio ζ_k through Equation 7 by neglecting the variability of the mode shapes (i.e., assuming to perform the curve fitting around the resonance point $f = f_k$ by changing only ζ_k), we obtain the relationship between the uncertainties σ_H and σ_{ζ_k} :

$$\sigma_H = \frac{\partial H_{re}(f = f_k)}{\partial \zeta_k} \sigma_{\zeta_k} \rightarrow \sigma_{\zeta_k} = \left(\frac{\partial H_{re}(f = f_k)}{\partial \zeta_k}\right)^{-1} \sigma_H \quad (8)$$

The sensitivity $\partial H_{re}(f = f_k)/\partial \zeta_k$ is given by the following expression:

$$\frac{\partial H_{re}(f = f_k)}{\partial \zeta_k} = \frac{\phi_r^{(k)} \phi_e^{(k)}}{2} \left(-\frac{1}{\zeta_k^2}\right) \quad (9)$$

By neglecting the sign, we obtain:

$$\sigma_{\zeta_k} = \frac{2\zeta_k^2}{\phi_r^{(k)} \phi_e^{(k)}} \sigma_H = \zeta_k \frac{2\zeta_k}{\phi_r^{(k)} \phi_e^{(k)}} \sigma_H = \zeta_k \frac{\sigma_H}{H_{re}(f = f_k)} \quad (10)$$

Also, the expected uncertainty in the estimation of the mode shapes can be approximated through error propagation. Let us condense the mode shapes into a single factor $A_{re}^{(k)}$:

$$A_{re}^{(k)} = \phi_r^{(k)} \phi_e^{(k)} \quad (11)$$

Again, let us focus on the resonance condition for the k -th mode ($f = f_k$). In this case, if we propagate the uncertainty of the mode shapes through Equation 7 by neglecting the variability of the damping ratio (i.e., assuming to perform the curve fitting around the resonance point $f = f_k$ by changing only $A_{re}^{(k)}$), we obtain the relationship between the uncertainties σ_H and $\sigma_{A_{re}^{(k)}}$:

$$\sigma_H = \frac{\partial H_{re}(f = f_k)}{\partial A_{re}^{(k)}} \sigma_{A_{re}^{(k)}} \quad (12)$$

The sensitivity $\partial H_{re}(f = f_k)/\partial A_{re}^{(k)}$ is given by the following expression:

$$\frac{\partial H_{re}(f = f_k)}{\partial A_{re}^{(k)}} = \frac{1}{2\zeta_k} \quad (13)$$

By substituting Equation 13 into Equation 12, we obtain the following expression:

$$\sigma_{A_{re}^{(k)}} = 2\zeta_k \sigma_H \quad (14)$$

We can identify two cases at this stage:

$r = e$, the estimation of the modal component at the point where the excitation is applied, with $A_{rr}^{(k)} = (\phi_r^{(k)})^2$.

$r \neq e$, the estimation of the modal component at a different point from where the excitation is applied, with $A_{re}^{(k)} = \phi_r^{(k)} \phi_e^{(k)}$.

In the first case, the modal component $\phi_r^{(k)}$ can be determined by Equation 15. Through error propagation, we obtain $\sigma_{\phi_r^{(k)}}$ from Equation 16:

$$\phi_r^{(k)} = \sqrt{A_{rr}^{(k)}} \quad (15)$$

$$\sigma_{\phi_r^{(k)}} = \frac{\partial \phi_r^{(k)}}{\partial A_{rr}^{(k)}} \sigma_{A_{rr}^{(k)}} = \frac{1}{2\sqrt{A_{rr}^{(k)}}} \sigma_{A_{rr}^{(k)}} = \frac{1}{2} \phi_r^{(k)} \frac{\sigma_{A_{rr}^{(k)}}}{A_{rr}^{(k)}} \quad (16)$$

In the second case, the modal component $\phi_e^{(k)}$ can be determined by Equation 17. Through error propagation, we obtain $\sigma_{\phi_e^{(k)}}$ from Equation 18:

$$\phi_e^{(k)} = \frac{A_{re}^{(k)}}{\phi_r^{(k)}} \quad (17)$$

$$\sigma_{\phi_e^{(k)}}^2 = \left(\frac{\partial \phi_e^{(k)}}{\partial A_{re}^{(k)}} \right)^2 \sigma_{A_{re}^{(k)}}^2 + \left(\frac{\partial \phi_e^{(k)}}{\partial \phi_r^{(k)}} \right)^2 \sigma_{\phi_r^{(k)}}^2 \quad (18)$$

Finally, by combining Equation 18 and Equation 16 and under the hypotheses $\sigma_{A_{re}^{(k)}} = \sigma_{A_{rr}^{(k)}}$, and $\phi_e^{(k)} = c \phi_r^{(k)}$, we obtain:

$$\sigma_{\phi_e^{(k)}} = \frac{\sigma_{A_{re}^{(k)}}}{\phi_r^{(k)}} \sqrt{1 + \left(\frac{\phi_e^{(k)}}{2\phi_r^{(k)}} \right)^2} \quad (19)$$

3 ESTIMATION OF PRE-POSTERIOR AND POSTERIOR UNCERTAINTIES

Modal extraction can be performed in both time and frequency domains. A summary of these methods can be found in (Ewins, 2000). In this paper, we focus only on a frequency domain extraction technique based on the estimation of the experimental FRF. To validate the pre-posterior approach, we carried out an experimental campaign of artificial impulse vibration tests on a two Degrees of Freedom (DoF) shear-type steel frame (Figure 2). We performed the tests under controlled conditions in the laboratory of the Department of Civil and Environmental Engineering of the University of Strathclyde. Table 1 reports the datasheets of the instrumentation used: PCB 393B04 piezoelectric accelerometers, NI 9234 data acquisition module with chassis c-DAQ NI 9189, instrumented hammer PCB 086C03, and a shaking table series LO.F.H.I.S. ND1301.

3.1 Pre-posterior estimation of modal parameters

With Equations 6-10-16-19 introduced in Section 2, we estimated the expected uncertainty (i.e., the uncertainty a pre-posteriori) of the modal parameters by using only the prior knowledge of the structure. We studied the eigenvalue problem of the structural model based on the stiffness and mass matrixes defined a priori and determined the mean values a priori of the

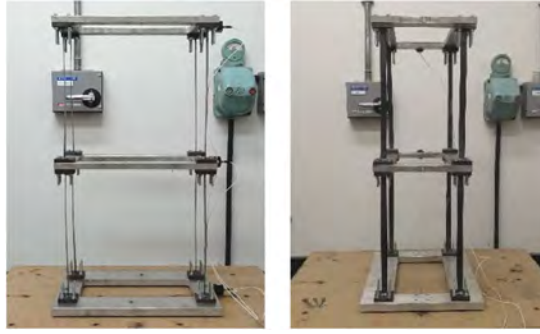


Figure 2. Steel shear-frame with 2 DoFs used for the vibration tests.

Table 1. Datasheet of the used instrumentation.

Accelerometer PCB 393B04		Shaking-table LO.F.H.I.S. ND1301	
Sensitivity ($\pm 10\%$)	102 mV/(m/s ²)	Moving plate working area	600 mm x 800 mm
Measurement Range	± 49 m/s ² pk	Moving plate thickness	57 mm
Frequency Range ($\pm 5\%$)	0.06 to 450 Hz	Moving plate material	Aluminium
Frequency Range ($\pm 10\%$)	0.05 to 750 Hz	Maximum load	100 kg
Frequency Range (± 3 dB)	0.02 to 1700 Hz	Maximum peak force	2000 N
Resonance Frequency	≥ 2500 Hz	Maximum continuous force	900 N
Wideband Resolution	0.000003 g RMS	Maximum velocity	2.5 m/s kg
Linearity	$\leq 1\%$	Usable frequency range	0-100 Hz
Transverse Sensitivity	$\leq 5\%$		
Hammer PCB 086C03		Acquisition module NI9234	
Sensitivity ($\pm 15\%$)	2.25 mV/(N)	Signal ranges	± 5 V
Measurement Range	± 2224 N pk	Channels	4
Resonance Frequency	≥ 22 kHz	Sample rate	51.2 kS/s/ch
Wideband Resolution	0.000003 g RMS	Input configurations	0.05 to 750 Hz
Linearity	$\leq 1\%$	Noise at max sampling rate	0.02 to 1700 Hz
		Isolation continuous	0.000003 g RMS

natural frequencies and the mode shapes. Furthermore, we adopted the mean values of damping ratios equal to $\zeta_1 = \zeta_2 = 0.2\%$. For the estimation of σ_H , we used the algorithm explained in Section 2.1 and assumed the coefficient of variation of the FRF equal to $V_H = 2\%$. Then, we assumed the maximum expected amplitude of the response (in displacement) equal to $x_{\max} = 0.01$ m (Equation 6).

Given that we performed the tests in the laboratory under controlled conditions, we neglected the contributions due to mechanical background noise and temperature variation. Therefore, we calculated the background noise by considering only the contribution related to the electrical noise of the accelerometer and acquisition module:

$$\sigma_N = (\sigma_{N,NI9234}^2 + \sigma_{N,PCB393B04}^2)^{1/2} = 3.92 \cdot 10^{-5} \text{m/s}^2$$

The expected uncertainty of the modal parameters extracted with the pre-posterior approach is given in Table 2.

3.2 Posterior estimation of model parameters

We performed each test five times to take into account the variability of the test itself (e.g., reproducibility of the laboratory conditions and the operator activity). Moreover, we simulated different vibrational SHM systems with different performances to study the sensitivity of

Table 2. Pre-posterior uncertainty of the modal parameters.

T	Δf_H	σ_{f_1}	σ_{f_2}	σ_{ζ_1}	σ_{ζ_2}	$\sigma_{\phi_1}^{(1)}$	$\sigma_{\phi_2}^{(1)}$	$\sigma_{\phi_1}^{(2)}$	$\sigma_{\phi_2}^{(2)}$
[s]	[Hz]	[Hz]	[Hz]	[%]	[%]	[m ^{-1/2}]	[m ^{-1/2}]	[m ^{-1/2}]	[m ^{-1/2}]
10	0.1000	0.0039	0.0097	0.0807	0.0170	0.0562	0.1426	0.0761	0.1059
20	0.0500	0.0039	0.0097	0.0219	0.0090	0.0281	0.0713	0.0380	0.0529
30	0.0333	0.0039	0.0097	0.0134	0.0079	0.0187	0.0475	0.0254	0.0353
45	0.0222	0.0039	0.0097	0.0094	0.0074	0.0125	0.0317	0.0169	0.0235
60	0.0111	0.0039	0.0097	0.0084	0.0072	0.0094	0.0238	0.0127	0.0176
90	0.0100	0.0039	0.0097	0.0077	0.0071	0.0062	0.0158	0.0085	0.0118
120	0.0083	0.0039	0.0097	0.0073	0.0071	0.0047	0.0119	0.0063	0.0088

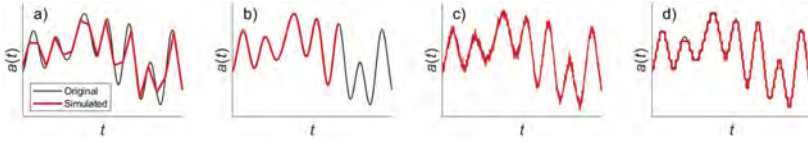


Figure 3. Simulation of different f_s (2.a), T (2.b), SNR (2.c), n_{bit} (2.d) for the same signal.

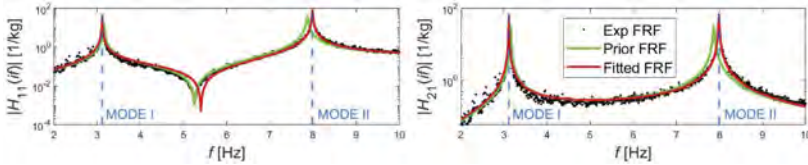


Figure 4. Fitting of the experimental FRFs H_{11} and H_{21} for the impulse excitation test.

modal parameters extracted from data. In particular, we simulated the changes in the SHM systems' performances by varying sampling frequency (f_s), duration of the test (T), signal-to-noise ratio (SNR) and bit resolution (n_{bit}) during the data processing directly on the signal acquired. Figure 3 schematise these changes.

We extracted the modal parameters by performing a non-linear regression on the experimental FRF of the 2 DoF system (Figure 4). The fitting was performed on by using the model described by Equation 1. Posterior uncertainties of modal parameters extracted from the experimental tests through non linear regression are shown in Section 4 in Figures 5 – 7, along with the pre-posterior uncertainties.

4 COMPARISON, DISCUSSION, AND VALIDATION

This chapter discusses the most significant comparisons between the modal parameters' uncertainties extracted with the pre-posterior and posterior approaches described in Section 3. The comparison was made for different SHM system's performances: sampling frequency (f_s), duration of the test (T), signal-to-noise ratio (SNR) and bit resolution (n_{bit}). Here we discuss the effect of T , SNR , and n_{bit} on artificial impulse excitation tests.

In Figure 5, the posterior standard deviations σ_{f_1} and σ_{f_2} of the steel frame's natural frequencies f_1 and f_2 are shown as a function of T and SNR . Figure 5 also shows the pre-posterior uncertainties estimated according to Equation 6, which are independent of T and SNR . We observe that the posterior standard deviations are highly affected by the performances of the SHM system: as SNR decreases ($SNR < 3$ dB), the difference between posterior and pre-posterior uncertainties σ_{f_1} and σ_{f_2} becomes increasingly prominent. On the other hand, by increasing the duration of the test ($T > 40$ s), the posterior standard deviations tend

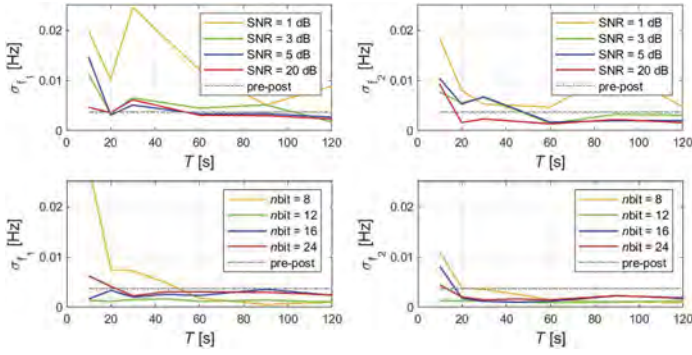


Figure 5. Standard deviation a posteriori (coloured lines) and pre-posteriori (dashed lines, label pre-post) of natural frequencies f_1 , and f_2 as a function of (T, SNR) and (T, n_{bit}) for fixed $f_s = 5128$ Hz.

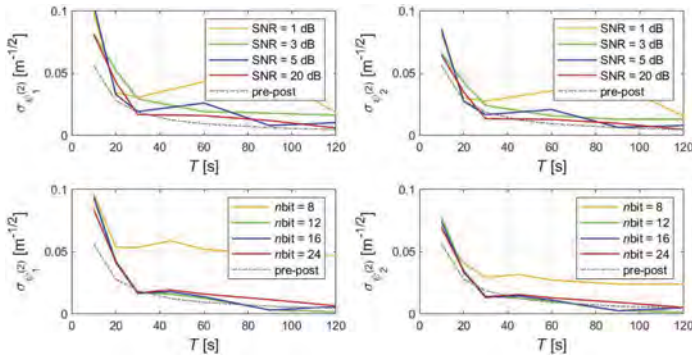


Figure 6. Standard deviation a posteriori (coloured lines) and pre-posteriori (dashed lines, label pre-post) of mode shape $\phi^{(2)}$ as a function of (T, SNR) and (T, n_{bit}) for fixed $f_s = 5128$ Hz.

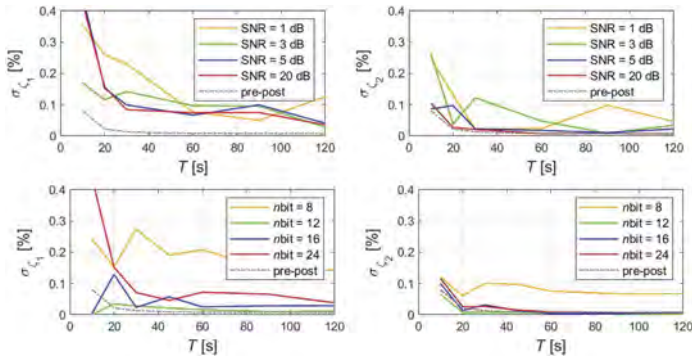


Figure 7. Standard deviation a posteriori (coloured lines) and pre-posteriori (dashed lines, label pre-post) of damping ratios ζ_1 , and ζ_2 as a function of (T, SNR) and (T, n_{bit}) for fixed $f_s = 5128$ Hz.

to their pre-posterior values. The same trend can be observed in the case of mode shapes (Figure 6): for high values of duration of the test ($T > 60$ s), signal-to-noise ratio ($SNR > 20$ dB), and bit resolution ($n_{bit} > 8$), the standard deviations estimated a posteriori are more similar to the pre-posterior value. As another example, Figure 7 shows the standard deviations related to the damping ratios as a function of SNR and T , and of n_{bit} and T .

5 CONCLUSIONS

This paper proposes an approach aiming at quantifying the pre-posterior uncertainty of modal parameters extracted through vibrational tests and verifies its effectiveness through a campaign of laboratory tests. The approach was applied to a two-degrees-of-freedom shear-type steel frame. The structure was studied under controlled conditions by using dynamic tests, in particular forced impulse excitation tests. The modal extraction technique was applied by varying the performances of the monitoring system, including sampling rate, duration of the test, signal-to-noise ratio, and bit resolution. The posterior standard deviation was calculated from the experimental results and compared to the estimated pre-posterior uncertainties.

We observed that the pre-posterior approach accurately predicts the posterior uncertainty of the modal parameters (same order of magnitude), at least in this case of a small structure under laboratory conditions. Moreover, we observed that the difference between these posterior and pre-posterior uncertainties is mainly affected by the duration of the test. For short duration of the test ($T < 40$ s), the influence of signal-to-noise ratio and bit resolution becomes more significant. In future experimentation, we will repeat the activity described in this paper for vibrational test design for real-scale structures.

REFERENCES

- Bado, M. F., & Casas, J. R. (2021). A Review of Recent Distributed Optical Fiber Sensors Applications for Civil Engineering Structural Health Monitoring. *Sensors*, 21 (5), Art. 5. <https://doi.org/10.3390/s21051818>
- Calvi, G. M., Moratti, M., O'Reilly, G. J., Scattarreggia, N., Monteiro, R., Malomo, D., Calvi, P. M., & Pinho, R. (2019). Once upon a Time in Italy: The Tale of the Morandi Bridge. *Structural Engineering International*, 29(2), 198–217. <https://doi.org/10.1080/10168664.2018.1558033>
- Caspani, V. F., Tonelli, D., Poli, F., & Zonta, D. (2022). Designing a Structural Health Monitoring System Accounting for Temperature Compensation. *Infrastructures*, 7 (1), Art. 1. <https://doi.org/10.3390/infrastructures7010005>
- Chang, K.-C., & Kim, C.-W. (2016). Modal-parameter identification and vibration-based damage detection of a damaged steel truss bridge. *Engineering Structures*, 122, 156–173. <https://doi.org/10.1016/j.engstruct.2016.04.057>
- Ewins, D. J. (2000). *Modal testing: Theory, practice and application* (2. ed). Research Studies Press.
- Giordano, P. F., Iacovino, C., Quqa, S., & Limongelli, M. P. (2022). The value of seismic structural health monitoring for post-earthquake building evacuation. *Bulletin of Earthquake Engineering*, 20(9), 4367–4393. <https://doi.org/10.1007/s10518-022-01375-2>
- Giordano, P. F., Quqa, S., & Limongelli, M. P. (2021). Statistical Approach for Vibration-Based Damage Localization in Civil Infrastructures Using Smart Sensor Networks. *Infrastructures*, 6 (2), Art. 2. <https://doi.org/10.3390/infrastructures6020022>
- Maia, N. M. M. (A c. Di). (1998). *Theoretical and experimental modal analysis* (Repr). Research Studies Press [u.a.].
- Tonelli, D., Rossi, F., Brighenti, F., Verzobio, A., Bonelli, A., & Zonta, D. (2022). Prestressed concrete bridge tested to failure: The Alveo Vecchio viaduct case study. *Journal of Civil Structural Health Monitoring*. <https://doi.org/10.1007/s13349-022-00633-w>
- UNI Ente Italiano di Normazione. (2002). *UNI 10985:2002—Vibrazioni su ponti e viadotti*. <https://store.uni.com/uni-10985-2002>



Taylor & Francis

Taylor & Francis Group

<http://taylorandfrancis.com>

MS5: Life-cycle performance assessment of civil engineering systems
Organizers: M. Akiyama, D.M. Frangopol & H. Matsuzaki



Taylor & Francis

Taylor & Francis Group

<http://taylorandfrancis.com>

Structural reliability assessment of RC shield tunnels with nonuniform steel corrosion

Z. He & C. He

MOE Key Laboratory of Transportation Tunnel Engineering, Southwest Jiaotong University, Chengdu, China

ABSTRACT: Steel corrosion is a dominant source for the deterioration of reinforced concrete (RC) structures, which is always spatially nonuniform and discretely distributed in the RC components. Owing to the statically indeterminate features of tunnel structures, both the mechanical responses (e.g., bending moment and axial force) and the ultimate bearing capacity of segmental linings will be affected substantially with the increase in steel corrosion. In this paper, a probabilistic model for simulating the spatial variation of steel corrosion is proposed in conjunction with a random field and the effect of sustained load. An approach for estimating the residual $M-N$ capacity (i.e., residual bending moment and corresponding axial force) of corroded segment section is introduced. Monte Carlo simulation (MCS) incorporated with finite difference method (FDM) is performed to investigate the failure probability of corroded RC shield tunnels. Dangerous segmental lining sections of shield tunnels with the evolution of steel corrosion deterioration are revealed based on an illustrative example.

1 INTRODUCTION

For a reinforced concrete (RC) shield tunnel in an aggressive environment, premature steel corrosion and serious concrete cracking of tunnel linings have been extensively observed. Because of the effect of spatially distributed corrosion damages, reduction of strength and stiffness of the segmental linings will inevitably happen at some local areas, which shall substantially affect the long-term safety of a RC shield tunnel. To provide rational decisions on the timing of repair and intervention plans for a deteriorated tunnel structure, it is important to have an accurate investigation on the mechanical response and estimation on the reliability along the sections of segmental lining by incorporating the spatial variability of steel corrosion.

Kudo and Guo (1994) and Sun (2011) have initiatively studied the durability of RC shield tunnels based on an underwater tunnel in Japan and China, respectively. Next, significant attentions have been given to the evolution of steel corrosion in RC segment under chloride attacks or stray current (Li et al., 2018; Yu et al., 2020), the estimation on ultimate bearing capacity and failure mechanism of RC tunnel linings (Zhang et al., 2022), and the reliability-based performance assessment of deteriorated shield tunnels (He et al., 2020; Zhang et al., 2021). However, these studies are far from the requirements to accurately evaluate the structural performance of a corrosion-affected RC tunnels due to the assumption of uniform steel corrosion in tunnel lining.

In this paper, a probabilistic approach for evaluating the structural performance of deteriorated RC shield tunnels is introduced. A random field integrated with lognormal distribution is established to simulate the nonuniform steel corrosion in a bearing segment. A random field-based numerical model for the corrosion-affected RC segmental lining and an analytical model to evaluate the load-bearing capacity of a corroded RC segment are developed. Finally,

Monte Carlo simulation (MCS) incorporated with finite difference method (FDM) is performed to investigate the failure probability of corroded RC shield tunnel. The effects of corrosion degree and nonuniformity of the external steel reinforcements on structural performance of a RC shield tunnel are revealed in an illustrative example.

2 STOCHASTIC MODEL FOR NONUNIFORM STEEL CORROSION IN SEGMENT UNDER SUSTAINED LOAD

2.1 Non-Gaussian random field

A random field can be described as a set of indexed random variables describing the random nature of a system in space and time (Vanmarcke, 1983), which can be characterized by the main statistical information of the variables of interest (e.g., mean, variance, probability distribution, and correlation function, etc.). Due to its simplicity and accuracy, CMD is adopted herein to generate the random variables associated with the spatial distribution of steel corrosion. According to Srivaranun et al. (2022), a log-normal random field S with n location in space is adopted herein to describe the nonuniform steel corrosion, which can be produced as follow:

$$\mathbf{S} = \exp(\mu_{\ln s} \cdot \mathbf{T} + \sigma_{\ln s} \cdot \mathbf{L} \times \mathbf{U}) \quad (1)$$

$$\mu_{\ln s} = \ln \mu_s - \frac{1}{2} \sigma_{\ln s}^2 \quad (2)$$

$$\sigma_{\ln s} = \sqrt{\ln \left[1 + (\sigma_s / \mu_s)^2 \right]} \quad (3)$$

where μ_s and σ_s represent the mean and the standard deviation of non-normalized corrosion property, respectively; \mathbf{T} is a unit vector with dimensions of $n \times 1$; \mathbf{U} is a standard Gaussian vector with n independent random variables (i.e., $n \times 1$ dimension); \mathbf{L} is a decomposition matrix for the correlation matrix \mathbf{R} of a normalized random variable among all locations (i.e., $n \times n$ dimension), which satisfies $\mathbf{L}\mathbf{L}^T = \mathbf{R}$ and is typically realized using Cholesky decomposition (Agarwal et al., 2014).

2.2 Correlation matrix associated with the corrosion of circumferential steel reinforcements in tunnel lining

The correlation coefficient ρ (i.e., the elements in the correlation matrix \mathbf{R}) represents the spatial correlation between the variables (e.g., steel corrosion levels A_{loss}) at two locations (i.e., the center of field elements), which can be calculated with a prescribed autocorrelation function (Li et al., 2018). Generally, the correlation coefficient increases to unity as the correlated elements become closer. Regarding the spatial-variant steel corrosion in a circumferential tunnel lining, ρ is approximated in this study based on an assumed 1D exponential correlation function:

$$\rho = \begin{cases} \exp \left[-\sqrt{\left(\frac{|\theta_2 - \theta_1| r_c}{L_c} \right)^2} \right], & |\theta_2 - \theta_1| \leq \pi \\ \exp \left[-\sqrt{\left(\frac{(2\pi - |\theta_2 - \theta_1|) r_c}{L_c} \right)^2} \right], & |\theta_2 - \theta_1| > \pi \end{cases} \quad (4)$$

where θ_1 and θ_2 are the radian from the right waist of tunnel to the center of steel elements; r_c is the radius associated with the location of corroded rebar in a circular segmental lining; L_c represents the correlation length of the steel corrosion level in the longitudinal direction of a rebar. In term of the non-Gaussian random field, Nataf transformation for the correlation matrix is required (Li et al., 2011).

For a bearing RC segment, the spatial correlation of A_{loss} along the length of rebars (i.e., correlation length L_c) has been empirically derived and discussed based on Equation 4 based on the experimental results (see He et al. (2022) for more details); L_c ranges from 58 mm to 142 mm by the regression analysis, with respect to the RC segmental specimen corroded under different load levels. Since the RC segmental linings works under complex mechanical conditions and the internal force always varies with the location of tunnel segments, L_c was set as 100 mm for the correlation coefficient ρ for the bearing RC segments in this study.

3 APPROACH FOR ESTIMATING STRUCTURAL PERFORMANCE OF RC SHIELD TUNNEL WITH NONUNIFORM STEEL CORROSION

3.1 Numerical model of spatial-variant corrosion damaged RC segment

For a corrosion-affected RC shield tunnel, spatial-variant damages of RC segments occur due to the nonuniform steel corrosion. A simplified method reducing the integral rigidity and strength of RC segmental linings shall be difficult to reveal the structural behaviors accurately. To have a rational estimation on structural performance of the deteriorated RC shield tunnel, structural numerical analysis has to be performed by incorporating the stochastic modeling of the spatial variability of corrosion damages in RC segments.

Figure 1 shows a three-dimensional (3D) numerical model of the corrosion-affected RC segments in FLAC3D v5.0. One tunnel segment ring was modeled to illustrate the nonlinear response of tunnel structures. Six deteriorated RC segments were assembled using the longitudinal joints. Segment concrete was modeled by eight-node brick element; two-node beam element was used to model the circumferential reinforcements in the extrados and the intrados of segment. Stirrup and steel-concrete interface were not considered due to the model simplification. To simulate the joint effect of shield tunnel, three-node interface element was adopted to model the longitudinal joints between the adjacent segments.

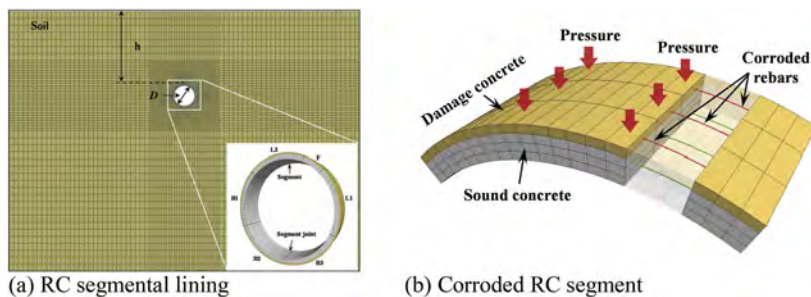


Figure 1. Modeling of spatial-variant damaged RC shield tunnel due to steel corrosion.

Input material parameters are associated with the properties of segment concrete, steel reinforcements and segment joints. According to the samples of spatial steel corrosion distributions, reduced cross-sectional area of reinforcements was modeled in each corroded steel element. To characterize the local effect of steel corrosion on the deterioration of segment concrete, the corrosion-affected concrete was represented as the concrete elements linked with these corroded rebars; reduced compressive strength was assigned to the corrosion-affected concrete elements based on the corrosion level of nearest steel elements. The modeling details and material parameters for a deteriorated RC tunnel structure are same with that in He et al. (2022).

3.2 Ultimate load-bearing capacity of corroded RC segment

For a RC shield tunnel, the segmental linings suffer from the combined actions of axial compression forces and flexural bending moments. The estimation on ultimate bearing capacity of

corroded RC segments shall be performed by considering the eccentricity of internal forces and the degree of corrosion damages, which always vary with the locations of the cross-section of segmental lining. In this study, normal cross-section analysis was performed to establish the analytical model for estimating ultimate bearing capacity along the sections of corroded RC segment in conjunction with the average corrosion ratio-based approach. The basic hypotheses of normal cross-section analysis based on the damage features of corrosion-affected RC segments are given as follows: (1) the strains vary linearly over the depth of cross section of segment (i.e., plain section assumption); (2) the corrosion deterioration of reinforcements is characterized only by reducing steel cross-section area (i.e., no strength loss); (3) the concrete cover in compressive zone is ignored when compressive steel bars are corroded; (4) the effects of loss/degradation of steel-concrete bond and the corrosion of stirrups are not taken into account.

Based on the approach associated with the conventional section analysis of a non-corroded RC component, the analytical model for a corrosion-affected RC segment was developed for three loading cases, including large eccentricity compression, small eccentricity compression and axial compression. The detailed procedure for the section analysis using force and moment equilibrium has been presented in He et al. (2022). Herein, an example $M-N$ curves for a deteriorated RC segment are given in Figure 2 illustrating the effect of steel reinforcement corrosion in tensile or compressive side.

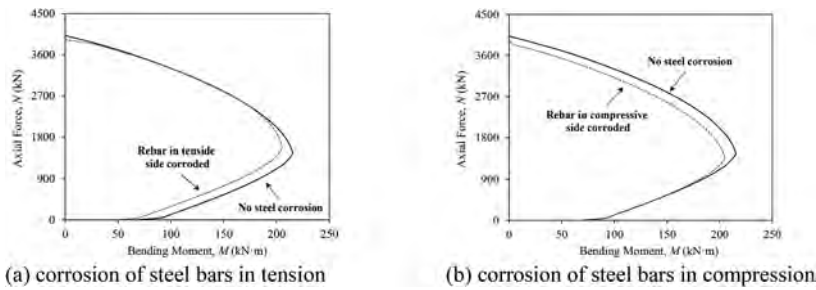


Figure 2. Interaction diagrams for $M-N$ of a corroded RC segment.

3.3 Structural reliability of corrosion-affected RC shield tunnel

Because of natural randomness (e.g., soil properties) and a series of possible corrosion distributions of steel reinforcements, it is necessary to estimate the performance of a corrosion-affected shield tunnel based on reliability analysis. Considering the failure of tunnel structure is always determined as the ultimate limit state that the combined internal forces of axial compression N and flexural bending M exceed the ultimate bearing capacity (i.e., N_u-M_u envelope) at any normal sections of segments (Gong et al. 2014). A performance function for the reliability estimation at each section of the corrosion-affected RC shield tunnel is applied through the axial compression force $N(\theta, A_{loss})$. The structural failure probability $P(\theta, A_{loss})$ is defined as:

$$P(\theta, A_{loss}) = P[Z(\theta, A_{loss}) = N_u(\theta, A_{loss}, e) - N(\theta, A_{loss}) \leq 0] \quad (5)$$

where P is the failure probability at each section in the circumferential direction of segmental lining; A_{loss} is the steel cross-section area loss at a specified location along the length of nonuniform corroded reinforcements; θ is the location of section in the counterclockwise direction from the right waist of tunnel; e is the eccentricity, determined as $e = M(\theta, A_{loss})/N(\theta, A_{loss})$.

4 ILLUSTRATIVE EXAMPLE

The shield tunnel studied here is assumed to be located at Shenzhen. The depth of the shield tunnel is assumed to be 20 m; the structure is in a homogeneous layer of mud rock; the diameter

of segmental lining is 6.7 m. Monte Carlo simulation (MCS) incorporating numerical method was conducted to investigate the structural performance of a deteriorated RC shield tunnel. The parameters of the random variables representing the uncertainties of geotechnical condition are given in Table 1, including the density (ρ_m), ground stiffness (E_m), cohesion force (c_m) and friction angle (ϕ_m) of mud rock. For the corroded RC segmental lining, the spatial variability of steel cross-section loss was modeled as a stationary random field with a log-normal distribution ($\mu = mA_{loss}$ and $\sigma = 0.2$) and a correlation length of 0.1m. Both uniform and nonuniform corrosion with the average steel cross-section area losses (mA_{loss}) of 0%, 15% and 30% have been considered for the steel reinforcements at the extrados of the segmental lining. A sample size of 1000 has been performed in the MC analysis.

Table 1. Statistical information of the uncertain geotechnical parameters.

Geotechnical parameter	Distribution	Mean	Standard Deviation
Density, ρ_m (kg/m ³)	Lognormal	1730	501.7
Elasticity modulus, E_m (GPa)	Lognormal	0.6	0.3
Cohesive force, c_m (kPa)	Lognormal	75	2.475
Friction angle, ϕ_m (°)	Lognormal	22	2.2

Figure 3 demonstrates that the failure probabilities along the sections of the segmental lining in RC shield tunnel due to the corrosion of external reinforcements. As show in Figure 3a, the segment joints around 45°, 135°, 200° and 350° always withstand a high failure risk due to the large and increasing failure probability; tunnel crown and waists exhibit to be safe as a result of the small failure probabilities at these sections. Note that the highest failure probabilities generally happen at the vicinity of segment joints around 45° and 135° as the increase in the degree of steel corrosion. Regarding the influence of the uniform or spatial-variant corrosions of external reinforcements, a similar failure probability distribution along the sections is revealed in Figure 3b, while the assumption of uniform corrosion can lead to an overestimation on the failure probability of segmental lining. Therefore, a consideration on the spatial variability of steel corrosion can substantially help in improving the accuracy of the reliability estimation of a corrosion-affected RC shield tunnel.

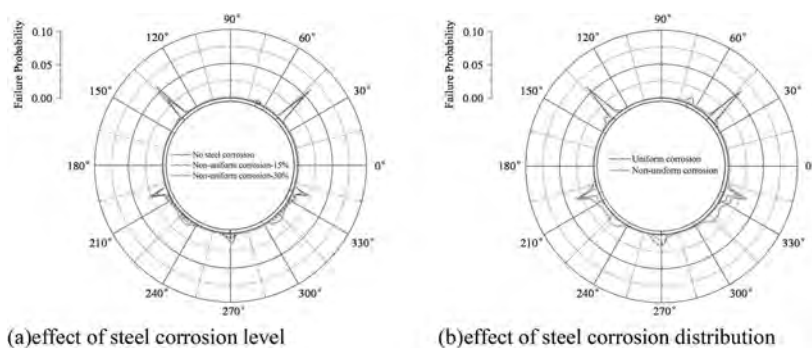


Figure 3. Failure probability along the sections of RC segment lining.

5 CONCLUSIONS

A random field-based approach was implemented to model the spatial variability of steel corrosion in RC segment under the sustained loading. Lognormal distribution was adopted to characteristic the statistical characteristic of steel corrosion in the bearing RC segment. In structural reliability assessment, the segment joints are exposed to be a high hazard in a corrosion-affected RC shield tunnel; these locations exhibit a growth in the failure probabilities

with the increase of steel corrosion. Because ignoring the nonuniformity of steel corrosion shall result in an overestimation on the local failure probabilities of RC segmental lining, it is important to estimate the structural performance of a deteriorated RC shield tunnel incorporating the spatial variability of steel corrosion.

REFERENCES

- Agarwal, M. & Mehra, R. 2014. Review of Matrix Decomposition Techniques for Signal Processing Applications. *International Journal of Engineering Research and Applications* 4(1): 90–93
- GB 50010-2010. 2015. *Code for design of concrete structures 2015th ed.* Beijing: Ministry of Housing and Urban-Rural Development of the People's Republic of China.
- Gong, W., Wang, L., Juang, C. H., Zhang, J. & Huang, H. 2014. Robust geotechnical design of shield-driven tunnels. *Computers and Geotechnics* 56: 191–201.
- He, Z., Srivaranun, S., Akiyama, M. & Frangopol, D.M. 2020. Life-cycle reliability-based design and reliability updating of reinforced concrete shield tunnels in coastal regions. *Structure and Infrastructure Engineering* 16 (4): 726–737.
- He, Z., He, C., Ma, G., Wang, S. & Huang, X. 2022. Experimental investigation on the deterioration process and spatial variation of corrosion damage of RC segment specimens under sustained load. *Construction and Building Materials* 349: 128731.
- He, Z., Ma, G., He, C., Yang, W. & Xu, G. 2022. Performance assessment of deteriorated RC shield tunnels integrated with stochastic field-based modeling for nonuniform steel corrosion. *Engineering Failure Analysis* (Under review).
- Kudo, I. & Guo, S. 1994. Study on durability and anti-corrosion: Trans-Tokyo bay highway shield tunnel. *Collection of Translations on Tunnelling (Modern Tunnelling Technology)* 10: 20–28.
- Li, D., Chen, Y., Lu, W. & Zhou, C. 2011. Stochastic response surface method for reliability analysis of rock slopes involving correlated non-normal variables. *Computers and Geotechnics* 38: 58–68
- Li, Q. & Ye, X. 2018. Surface deterioration analysis for probabilistic durability design of RC structures in marine environment. *Structural Safety* 75: 13–23.
- Srivaranun, S., Akiyama, M., Masuda, K., Frangopol, D.M. & Maruyama, O. 2022. Random field-based reliability updating framework for existing RC structures incorporating the effect of spatial steel corrosion distribution. *Structure and infrastructure engineering* 18(7): 967–982.
- Sun, J. 2011. Durability problems of lining structures for Xiamen Xiang'an subsea tunnel in China. *Journal of Rock Mechanics and Geotechnical Engineering* 3(4): 289–301.
- Vanmarcke, E. 1983. *Random Fields: Analysis and Synthesis*. MIT Press.
- Yu, S., Jin, H. & Bi, X. 2020. Effect of geometry form of load crack on rust layer distribution of outside steel in segment. *Engineering Mechanics* 37: 118–128.
- Zhang, D. & Chen, C. 2021. Time-dependent Reliability Analysis of Shield Tunnel Structure under Corrosion Conditions of Segment Rebars and Bolts. *Modern Tunnelling Technology* 58: 111–120.
- Zhang, W., Qiu, J. & Zhao, C. 2022. Structural behavior degradation of corroded metro tunnel lining segment. *Structure and Infrastructure Engineering* (online).

Life-cycle analysis of aging structures based on reliability approach

S. Joshi, A. Thorat, H. Dehadray & M. Tundalwar

UBMS Research Group (URG), Mumbai, India

ABSTRACT: Bridge management plays an important role to ensure the sustainability of bridge infrastructure. Life cycle analysis [LCCA] of such ageing bridge structures has to be based on dynamic, robust, and real-time information. The performance of the ageing bridge structure under live loading needs to be monitored. Performance data will need to be used for triggering interventions. GABM enables deterioration model based on dynamic, real-time monitoring data under live load conditions. Monitoring is periodic and for short time durations. Monitoring results in time series data revealing the possible decrements in the performance of the bridge structure. Decrements in performance are linked to increments in distress occurring in the bridge. Deterioration models based on such evaluated increments in distress results in more realistic prediction about the future behavior of the bridge. Sustainability yields maximize the Economic, Social, and Environment benefits.

1 INTRODUCTION

Bridges are a significant part of infrastructure development. The performance of in-service bridges is of great concern to asset owners and civil engineers in this era with rapid growth in public awareness of infrastructure safety. (Ignacia 2022) The structures start to deteriorate from the time of completion of construction and continue as time passes, prominently due to environmental and physical factors such as corrosion, carbonation, impact, fatigue, etc. According to Irina Stipanovic, structural infrastructure failures are happening because of catastrophic events and these events are a result of climate change. However, only this factor is not responsible for failure. A large number of infrastructures all over the world are over 50 years old and suffer from extensive deterioration that affects their serviceability. The high costs associated with preserving the ageing structures in conjunction with the limited funds allocated for their maintenance pose significant technical and financial challenges, which require systematic approaches for risk-informed condition assessment.

This scenario calls for decision-making to be based on reliable accurate information regarding the progression of distress which is the basis of the deterioration process. Most Bridge Management protocols are dependent upon the judgement of engineers inspecting the bridge (Joshi 2022). The data collected by the engineering staff will need to be supplemented with factual data related to the performance of bridge elements showing distress (Michael 2014). It is an established fact that an increment in distress results in decrement in performance. By using Structural health monitoring (SHM), it is possible to monitor the bridge periodically. It is possible to monitor the response of the bridge structure which reveals changes to the material and geometric properties. SHM is important for maintenance planning to find a cost-effective solution to reduce costs and extend the life of critical assets like bridges. SHM for bridge structures is generally referred to, for the damage detection or characterization strategy for real-time assessment of structural condition. Structural Health Monitoring of distressed bridges elements over short durations will yield the required factual information about the

elements. Periodic records of such short-term monitoring will result in creating time series of data.

The challenge is to correlate this decrement in performance to increments of distress. The correlation will allow changing the Cause matrix to Performance-based cause matrix. Cause matrix enables formation of Deterioration model which forms the basis for risk estimates and further optimization of fund allocations. Increment in distress generates a scenario where in we can modify the Cause matrix generated by the prognosis of the bridge inspection engineer/team. From acceptance of judgmental prognosis, we have a solution wherein the Cause matrix is modified by actual observation of performance of the bridge and its elements. Integration of SHM within the analytics of GABM [Global Analytics for Bridge Management] steers the decision-making process away from person dependent judgement to factual observation and performance based decision-making procedure.

Life Cycle Cost Analysis (LCCA) is a useful tool for selecting the most reasonable scheme from an economic standpoint. The challenge is to use the LCCA within Bridge Management. SHM integration helps to get a more realistic view of LCCA. The paper presents a methodology of using LCCA within Bridge Management. LCCA, is used to choose the best economic design for both structural integrity and durability. Comparison of alternative design approaches, strategies, identification of cost-effective improvement, Project's budget, cum economic viability assessment, and long-term financial planning all are possible within LCCA. LCCA is a process of evaluating the total costs over the life of a bridge. Total costs include initial costs and project future costs such as maintenance, repair, rehabilitation, and reconstruction (discounted to today's money value). LCCA and total cost incurred from construction to the end of service life evaluation are the basis for decision-making for project selection among various alternatives. LCCA is also used to evaluate different design features of a bridge for selecting the best option among alternatives.

2 STRUCTURAL HEALTH MONITORING INTEGRATION IN GABM

Structural Health Monitoring [SHM] have been in use for investigating the behaviour of the structures since decades. What initially started with steel structures soon encompassed the concrete structures also. SHM is today possible either by close contact or remotely. Various techniques are available to analyse the data generated by SHM. This analysis makes it possible to identify the performance of the structure (Joshi 2022, Markov 2014).

This performance to be used in Bridge Management needs to be converted to known parameters for which data has been collected over the past many years. SHM historically was never linked to identifying the various causes that lead to the deterioration of structures. Again, past research in this has provided various techniques that make it possible to identify the location, extent, and severity of distress.

The challenge was to correlate this performance or identified distress to the three cause processes of deterioration. Such correlation could make it possible to generate the Cause matrix. The cause matrix is the starting point of any further applications of analytics in Bridge management. The three principal processes identified by EN1504 are the Physical process, the Mechanical process, and the Chemical process (Michael 2014). Further, these principal processes are subdivided into 11 sub-processes. The rating assigned to these 11 sub-processes forms the Cause matrix. Three main reasons are identified and listed out for the need to identify the location of the damage is critical to the structural evaluation and the deterioration process (Joshi 2022, Cao 2018, Hugh 2003).

Different modes of failure are location dependant and assume criticality based on their location along the length of the element. The strength of the element as evaluated using the deteriorated cross section affects the load capacity of the member along the length of the element. None of the existing BMS including GABM can provide accurate digitized data relating to

the location of the damage or distress (Joshi 2022, Markov 2014). GABM allows for using the cause matrix as the base for the evaluation of the deterioration process.

These shortcomings within BMS are required to be overcome by using all available new innovative technologies. Integration of technologies, which can provide data regarding the correct geospatial location of distress would be the first phase in the refinement. Moreover, the next phase is to be identifying the critically distressed elements and evaluate the performance of such severe distress elements under live loading using Structural health monitoring [SHM] for short durations only. Using this data as base data, we shall need to repeat SHM observations over time to create a time series data that is used to compare with base data collected initially.

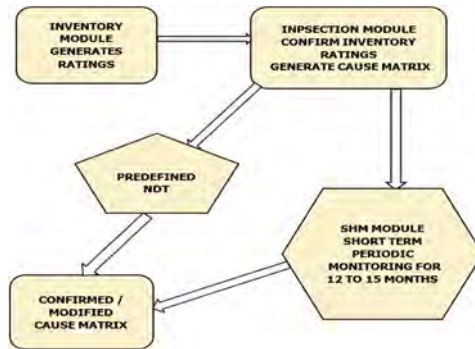


Figure 1. Process of data utilization within GABM.

The solution of partial Integration of SHM with GABM provides to utilize the performance to evaluate the deterioration process in bridges or any other infrastructure (Joshi 2022). This solution is able to develop a deterioration model based on performance monitoring. The results should yield sufficient information regarding the present status and types of distress and severity of distress resulting from causes. SHM will provide confirmation of the type of distress, its extent and its severity. Based on this SHM, will confirm the prognosis and resultant cause matrix is updated to be used for all further analytics within GABM

Presently this is done by Non-Destructive testing. SHM will replace NDT. SHM conducted on distressing elements for the periodic short term will yield time series data relating to changes in the performance of the bridge element on which SHM is conducted. This change in performance can assist in the application of modification to the cause matrix. A modified cause matrix will result in more realistic and factual deterioration modelling.

2.1 Application of deterioration models to LCCA

Because of the rising interest in predicting the future condition of infrastructure assets. The focus is mainly on the importance of safety, construction materials used and structural functionality. The deterioration model is a link between a structural condition that assesses the extent and severity of damages, and the factors affecting structural deterioration such as age, material properties, environmental conditions, etc. The deterioration model is intended to describe the process and mechanisms by which assets deteriorate and even fail through their service life.

Based on the assigned ratings primary cause of distress can be identified. All other contributory causes are called secondary causes. These observations conclude the inspection process.

Moreover, it involves confirmation of the prognosis. To date, this confirmation was done by Non-destructive testing techniques. The confirmed Cause Matrix is used as the first of the important data. The system starts with the help of data collated during the Bridge Information System [BIS] namely Inventory, Inspection and Testing process helps to confirm the prognosis of the Deterioration process.

Small-duration SHM monitoring under live loads will result in the identification of such changes over time. The first such monitoring should be implemented based on identified distress and cause matrix-generated post-Inspection. In GABM, to ensure the optimization of funds, the assignment of available budgetary allocations for rehabilitation intervention is allotted to bridges which qualify for such allocation. Other bridges are stored in the list of Bridges under Observation and Monitoring [BUOM] Bridges in this BUOM are subjected to short-term SHM over 12 to 15 months.

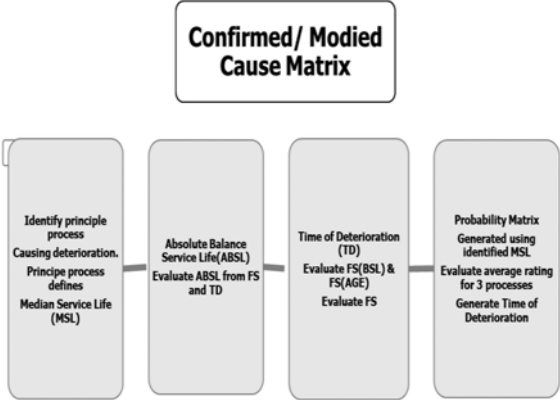


Figure 2. Analytics flow chart Cause matrix to Deterioration model.

After this initial monitoring, repetitive short-duration monitoring is applied. The time lapse between two sets of monitoring can be defined by the severity of distress observed in the first set of the Inspection cycle. Such time series data will yield a decrement in performance, which is related to increments in distress zone and severity.

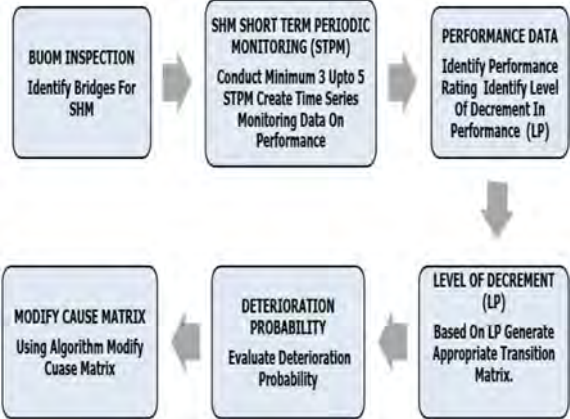


Figure 3. Flow chart of partial integration of SHM and GABM.

2.2 Two types of SHM to achieve the objective are as follows

Remote or No contact SHM: System wherein the parameters essential like Vibration, acceleration, frequency, strain, and displacement is captured by technology without being in contact with the bridge or bridge elements.

Close Contact SHM: System wherein major strain, stress, linear displacement, inclination, vibration, frequency, acceleration, and corrosion potential is measured by sensors [Strain Gauges, Linear Variable Differential Transformer (LVDT), Tilt Meter, Inclinator Sensors, Acoustic Emission Sensors (AE), Fibre Optic Sensors, Corrosion Sensors, Accelerometer] in close contact with various desired components/ elements of bridges.

Both the “No contact” and “Close Contact” systems will yield results that identify typical changes in performance parameters to determine the correlation between the decrease in performance parameters and an increase in distress zone and severity.

Research in the application of computing algorithms to SHM to evaluate the performance of the structure under live loads has resulted in over 15 known and tested techniques to evaluate performance and link it to the extent and severity of distress. SHM-based parameter observes the performance between Initial Scenario and Operational Scenario which shows the “Presence of Distress situation” of structure.

GABM provides a solution for partial integration of SHM with Bridge management analytics. The resultant deterioration model prepared is more realistic and based on factual performance data. Further analytics applications will yield more reliable results.

3 LIFE CYCLE COST ANALYSIS (LCCA) FOR USING RESULTS DERIVED FROM SHM

Structural Health Monitoring (SHM) provides operational performance, early warning data, future prediction, and analysis. It is widely used in many bridge infrastructures, which helps the behavior of the structure and access the real-time monitoring of the structure using different technologies and sensors. The idea to utilize the results from various SHM elements of the bridge structure will help to better analyze the results that are generated from the LCCA to determine and calculate the economic design from various alternatives prepared to maintain the structural integrity, and restore the durability of the structure.

3.1 Necessity of LCCA for bridges

LCCA is a cost-centric approach for determining the most cost-effective alternative. The life-span of various bridge components is determined by their rate of deterioration. The pier and foundation are more vulnerable to deterioration because of environmental or collision impacts. The environmental exposure of steel components influences quickly the steel corrodes. A bridge is a long-term, multi-year investment, and the cost to an agency for a bridge is never a one-time expense. Bridge components require preservation and maintenance actions to counter the effects of deterioration throughout their Service Life. Each design alternative must first show it reliably achieves project requirements such as service life, structural stability, and desired level of maintenance (Irina 2020, Wiie 2011, Satish 2015).

Conventional LCCA results in an evaluation of Internal Rate of Return [IRR] which is mostly dependent on direct costs and benefits. Bridge structure connects two area which otherwise are not connected. Such unconnected areas could be residential, commercial or island zones. This connection adds value and intangible benefits to the area which it connects. This results in generation of employment opportunity for population of the residential area. Such increased employment potential results in a general increase of turnover of the organizations operating in the commercial zones. Island zones get better availability of consumer goods at cheaper cost resulting in saving due to the connections that the bridge provides. The Bridge also results in increased emission of gases and degradation of forest cover due to increase in traffic in the area brought under influence of the bridge. This is intangible cost arising due to bridge in the area. Evaluation of all such intangible or indirect costs and

benefits yield the realistic IRR. Such IRR can be termed as the IRR including Intangible impact. Application of LCCA to evaluate both tangible and intangible impact of the bridge on the area is applied within GABM.

Evaluation of the best-suited bridge to be allocated funds for rehabilitation interventions can now be altered based on the Sustainability Index [SI] evaluated from the LCCA which calculated IRR including Intangible impact. Every bridge on the list of BOUM is subjected to LCCA which yields SI for the bridge. Every bridge on the list of BOUM is subjected to LCCA which yields SI for the bridge.

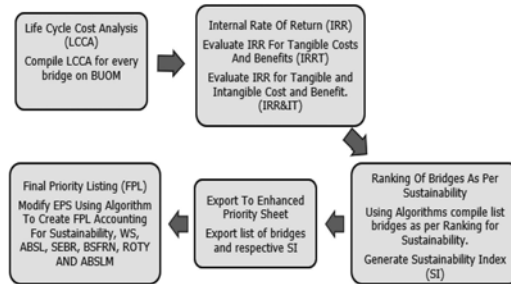


Figure 4. Flow chart of LCCA in GABM.

This SI matrix is then exported to Economic Priority sheet [EPS]. Application of algorithm results in Final Priority Listing [FPL] which is accounts for Sustainability, Sum of Critical weightage and Influence weightage, type of road, Absolute Balance service life [ABSL] of the bridge, Structural, Functional and Socio-Economic ratings of the bridge.

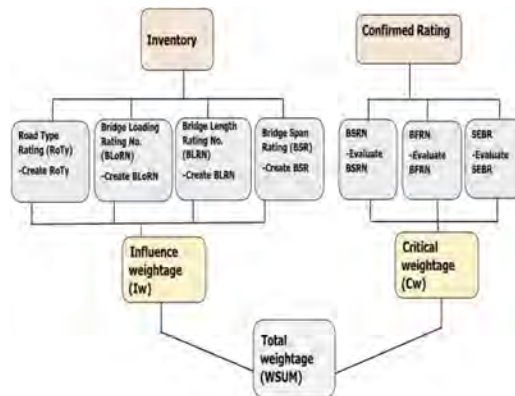


Figure 5. Flow chart of GABM Priority and Ranking.

Bridges selected for rehabilitation interventions based on FPL ensure that the optimization of fund allocation not only follows technical and commercial principles of allocation but also ensure that rehabilitated bridges will enhance the Sustainability of the network.

4 RESULTANT SUSTAINABILITY

Sustainability is defined as the preservation of the present environmental, economic and social structure of the society for the present generation and also ensuring that the same is maintained for the future generation (Mohammaderza 2014) . The decision-making within any Bridge

Management system should ensure Sustainability (Mmm group 2015) . GABM empowers the application of Sustainability within the management of the life cycle of the bridge.

LCCA is a decision-making tool particularly useful from the conceptualization of the bridge to its decommissioning. It ensures to evaluation rate of return for the design of Bridges as it predicts lifetime expenses and supports the inspections management and the maintenance activities. Bridges or any other infrastructure should be seen as a key part of the economic activity and well-being of a given community (Joshi 2022).

Currently, the use of sustainable materials in the construction of bridges is increasing ensuring a positive impact on the environment, economic and social parameters. LCCA which ensure this can be applied as a tool for calculating and comparing the life cycle cost of a projects (Hugh 2003, Goh 2009).

While a structure is designed from economic, technical and safety perspectives, the environmental performance was often not considered in the decision-making process. GABM enables maintenance, strengthening, repair, and rehabilitation of bridges if interventions are applied timely. This ensures maximizing the life span of bridges without the need for replacement. Such interventions ensure to reduce the cost of the life cycle and reduce the impact on the environment by reducing the usage of raw materials. These interventions enhance the environmental and economic management in the entire life cycle by maximizing the benefits for the given costs. The timely provision of interventions ensures economic benefits by managing the cost-effectiveness in the design of such interventions, by ensuring to reduce the detour travel time, congestions, and traffic jams delay resulting in avoidance of productivity loss and its impact on the reduction of GDP of the area of influence of the bridge. Such intervention also ensures to enhance a social benefit by reduction or avoidance of failure/ collapse and increased reliability of network which impacts the safety during travel, life loss, timely delivery of goods and raw materials which are crucial to maintaining the productivity which ensures stable GDP. Environmental goals of minimizing the carbon emissions are ensured by avoidance of traffic jams, and longer journey time due to detours in case of closure of the bridge for a longer period when collapse occurs.

Sustainability ensures to delivery of the optimal level of service safely to existing and future bridge users in the most cost-effective way. LCCA enables us to prioritize investments on the assets that need it most. This optimization is ensured by a risk-based analysis to identify cost-effective investments during conceptualization, designing, construction, and during the entire operational life of the bridge.

5 CONCLUSIONS

Several infrastructure networks are currently facing issues, such as increasing annual maintenance costs, ageing infrastructure, as well as climate change impacts. The main purpose of the reliability-based life cycle analysis of the ageing structures model presented is to satisfy the required performance. This needs to also consider and ensure the economic, social, and environmental impacts of different maintenance and safety strategies.

Management needs reliable data, which is collated during Inventory and Inspection process. In the inspection process, the inspectors record certain information regarding distress structure and based on observations, the inspector comes to conclusion. The accuracy of the result depends on the experience and judgement of the engineer. Most of the infrastructure management systems rely on this judgement. Mostly majority of the networks are faced with ageing problems. Bridge structures constructed before or during the last five decades face aging scenario. This necessitates the need to have realistic management systems. Within GABM the functionalities of deterioration modelling, risk analysis and fund allocation were till date based on theoretical evaluation and observation of increments of distress in the bridge. GABM system has evolved over time to provide solutions to users. GABM management procedures include the impact of Sustainability of infrastructure, Life Cycle Cost Analysis (LCCA), and Structural Health Monitoring (SHM). The main forte of the approach is to identify the cause of distress structure and then apply short duration real-time monitoring to determine the changes in behaviour of the ageing bridge under live loads. This helps engineers to record performance and

the changes. Application of developed algorithms correlates current deterioration of the structures to the decision-making process. This approach enhances the observation and judgement based conclusions of engineers to realistic performance based approach.

The Bridge Management Analytics include the use of accurate and realistic data for the generation of deterioration models, the inclusion of socio-economic parameters to assess the benefits [direct and indirect] that accrue to the area of influence under the bridge. Finally, LCCA tool is utilized to assess the life cycle costs impacts that are used in the decision-making during the entire life cycle. Data from various several Socio-Economic parameters collated under GABM protocol enables to ensure that the evaluation of intangible advantages or costs that result from a bridge structure are applied to access the economic impact. Using enhanced LCCA technique, ensures the decision-making process is based on realistic approach. Through this approach, sustainability goals are also guaranteed, ensuring that a structure fulfils present requirements without endangering the ability of future generations to satisfy their own. A sustainable course of action should preserve the harmony of the three key factors of social, economic, and environmental issues. Sustainable bridges support the environmental, social, and economic systems that we depend on. Life cycle analysis of ageing structures based on reliability approach ensures Sustainability and Economic growth.

REFERENCES

- Cao Wang et al., Estimating the Resistance of Aging Service-Proven Bridges with A Gamma Process-Based Deterioration Model, *School of Civil Engineering, The University of Sydney, Sydney, NSW, Australia – December 12, 2018.*
- Goh K.C et al., Developing A Lifecycle Costing Analysis Model for Sustainability Enhancement in Road Infrastructure Design; *Proceedings of The Second Infrastructure Theme Postgraduate Conference: Rethinking Sustainable Development—Planning, Infrastructure Engineering, Design and Managing Urban Infrastructure, Brisbane, Queensland – March 26, 2009.*
- Hugh Hawk, National Cooperative Highway Research Program NCHRP Report 483, *Bridge Life-Cycle Cost Analysis 2003.*
- Ignacio J. Navarro et al., Role of The Social Dimension in The Sustainability-Oriented Maintenance Optimization of Bridges in Coastal Environments, *Wit Transactions on The Built Environment, Vol 196-2020.*
- Irina Stipanovic et al., Reliability-Based Life Cycle Management of Bridge Subjected to Fatigue Damage, *A Section of The Journal Frontiers in Built Environment, Submitted to Bridge Engineering – December 04, 2020.*
- Joshi S, et al., Enhancement in Indian Bridge Management System recently, *Scientific Paper Structural Engineering International, Submitted on: May 27, 2022*
- Joshi S et al., Towards Performance-Based Dynamic & Real Time Bridge Management, *ConstroFacilitator – August - 2022.*
- Joshi S, et al., Paradigm Shift – Performance Driven Bridge Management, *Constrofacilitator – August - 2022.*
- Joshi S, et al., Bridge Management Analytics for Sustainability and Economy, *Constrofacilitator, September – 2022.*
- Markov et. al, NCHRP Synthesis 397: Bridge Management Systems for Transportation Agency Decision Making, *Transportation Research Board (TRB) – May 28, 2014.*
- Michael RaupachTill Büttner et al., Concrete Repair to EN 1504-Diagnosis, Design, Principles and Practice, *CRC PressTaylor & Francis Group, March 23, 2014.*
- Mmm Group, Primer on The Sustainability Considerations for Bridges, *Transportation Association of Canada (Tac) - October 2015.*
- Mohammadreza Y, et al., A Multi-Criteria Analysis for Bridge Sustainability Assessment: A Case Study of Penang Second Bridge, Malaysia. *Life-Cycle Des. Perform - December 2014.*
- Paul D. Thompson et al., National Cooperative Highway Research Program, NCHRP Report 713 Estimating Life Expectancies of Highway Assets, *Volume 1 - March 2012.*
- Rizal Taufiq Fauzi et al., Exploring the Current Challenges and Opportunities of Life Cycle Sustainability Assessment. *Sustainability – January – 2019.*
- Satish Chandra et al., Bridge Life Cycle Cost Analysis, *Jetir 2020, Volume 7, Issue 5 - May 2020. Bertha Maria Batista Santos, Simplified Model of Road-User Costs for Portuguese Highways – October 07, 2015.*
- Wije Ariyaratne et al., Sustainable Bridges: The Thread of Society, *Building and Maintaining Bridges to Be Sustainable, Roads and Traffic Authority of NSW, Australia – October 2011.*

Baseline digital twin models for key performance management of prefabricated bridges

C.S. Shim, G.T. Roh, M.U. Kang & Y.H. Lee
Chung-Ang University, Seoul, Korea

ABSTRACT: Prefabricated bridge members requires more strict quality management for easier assembly. Design for manufacturing and assembly(DfMA) has been started to be adopted for bridge structures. In this paper, digital engineering models are developed to consider these new requirements. Rule-based modeling is used to create the 3D geometry models which has automatic model update by geometry inspection data at the stage of fabrication, erection and completion of the assembly. Prestress and connections are essentially included in the prefabricated bridge. Designed values should be updated through quality inspection process. For preassembly check, data templates for prefabricated members are proposed and a pilot application is performed for a prestressed concrete bridge. Camber, lateral deformation, stress conditions are selected as key performance indices of the prestressed concrete girder. A simple sensing system is applied to the girder from the beginning of fabrication to the end of assembly. When the bridge is completed, the owner can have a baseline digital twin model of the bridge. Data and digital engineering models are delivered to the maintenance system.

1 INTRODUCTION

1.1 *DfMA&M for a prefabricated bridge*

OSC is an innovative technology that the construction industry is most actively attempting. Prefabricated members are eco-friendlier than their precast counterparts because of generation of minimal waste and energy efficiency. DfMA (Design for Manufacture and Assembly) allows parts of construction projects to take place off-site, which can reduce project length, cost, material use, and worker injuries. To enable DfMA, designers require more systematic information considering whole life-cycle of a structure. Prefabricated structures have various connections. The final assembly of the structure is done on-site. As in the manufacturing industry, the performance of the prefabricated structures needs to be assessed continuously from the completion of the construction. Therefore, DfMA&M (Design for Manufacture, Assembly and Maintenance) is a concept for the prefabrication in construction industry.

Definition of maturity levels of DTs for construction was proposed from 0 to 5 (Evans et al. 2019). They provide different principles and their usage according to the levels. However, more specific definition for the maintenance is required. Zhang et al., (2022) proposes a framework to utilize digital twins for construction site management. One of the technical difficulties is in accumulating knowledge from design to construction in improving the process and decision making. Another challenge in the nontechnical side is that human participation is essential for decision making despite low-level operations done autonomously.

Digital models of precast concrete members are generated from design calculations considering design codes and specifications. The models are utilized to assist preassembly checks and instructions to control geometry errors of each member (Shim et al. 2018, Nguyen et al. 2022). To realize a fully prefabricated bridge, predefined digital models for each member and required data for the assembly are essential. Nguyen et al. (2022) suggested digital engineering

models for DfMA of the prefabricated bridges. The digital models are continuously updated by inspected geometry changes during fabrication, time-depended deformation, and assembly. Through this process, the as-built models are submitted to a bridge owner for the maintenance. Mixed reality using the digital twin models (DTMs) for improving semantic information visualization of bridge maintenance system was utilized (Nguyen et al. 2022). These data during the project delivery are required to build a baseline digital twin model by combining with measured sensing data for key performance of the prefabricated bridge.

1.2 Key performance indicators for a prestressed concrete girder

For the maintenance of a prestressed concrete bridge, the main parameters are long-term properties of concrete, remained prestressing force, and corrosion of prestressing steels. There are multiple stages such as fabrication, prestressing, dead load by bridge decks, composite section, and second dead load by the pavement and the barrier. Long-term behavior of the prestressed concrete girder such as deflection, stress change by creep, shrinkage, and relaxation needs to be monitored by collecting data at each stage. When the data are accumulated for a prefabricated member, design can be much improved for more reliable prediction of life-cycle performance.

In this paper, a baseline digital twin model for full-prefabricated bridge superstructure is suggested. Data templates for collecting information are created from design calculation to the completion of a bridge. Digitalized inspections of geometry and an efficient sensing system are included in the process of the model update.

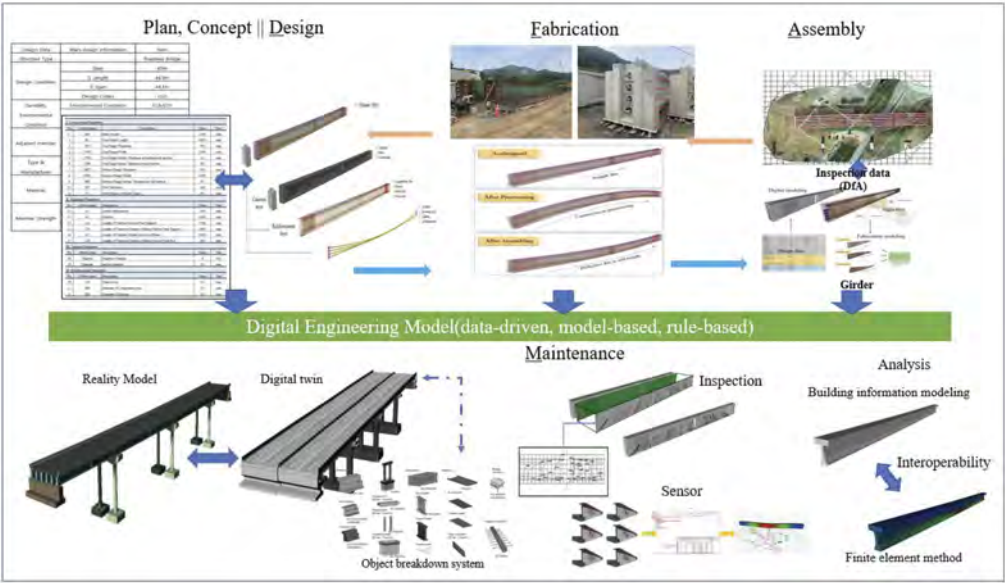


Figure 1. Digital model and its data-frame during its life-cycle based on DfMA & M.

2 DEFINITION OF DIGITAL TWIN MODEL

2.1 Digital geometry model

The first level of DTM is to define exact geometry of the structural members. A structure is a deformable object by loadings and time-depended properties such as creep. Current BIM (building information modeling) models should be revised by the change of geometry. A prefabricated bridge consists of individual structural members and connections. Due to the change of geometry, predefined constraints between parameters are essential for DfMA. For example, full-depth prefabricated bridge decks are assembled with multiple prestressed concrete (PSC) girders as shown in Figure 2. Parameters for the preassembly of the members

are location of the shear pockets in the precast deck and location of shear connectors on the top flange of the girders. During the fabrication stage, two sets of the data are collected by a scanning device such as a LIDAR. Digitalized inspection provides the predefined coordinates for the assembly check.

Due to prestressing of the girders and time-dependent behavior, the PSC girders have deformation resulting in the change of locations of the connectors. After the erection of the girders, these deformations should be captured by a UAV-scanning. A length-adjustable lateral beam can be designed to accommodate the unexpected lateral deformation by prestressing. Before assembly between the decks and the girders, assembly instructions are generated by the preassembly simulation. The data for the geometry control of the prefabricated bridge is important to build a digital twin model at the construction stage. Unknown design parameters such as the elastic modulus of concrete and the effective prestressing forces after jacking can be obtained.

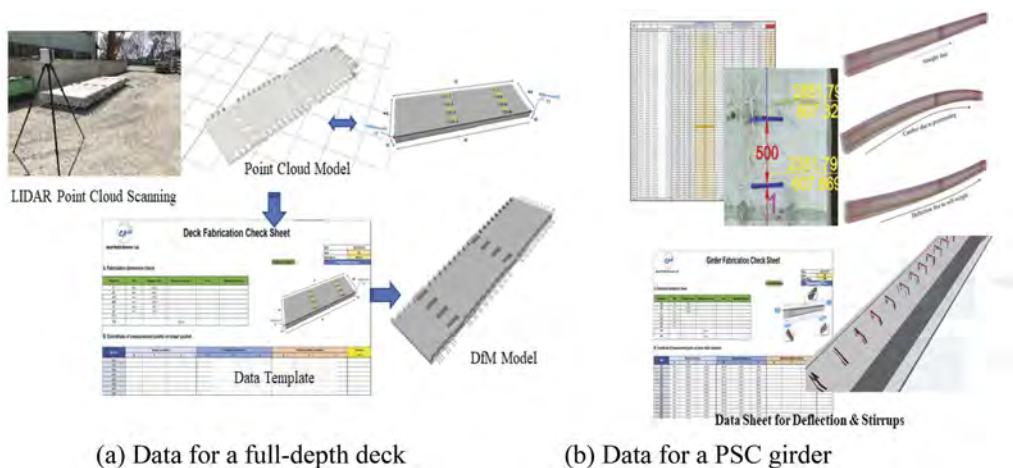


Figure 2. Data for DfMA application of a prefabricated bridge.

2.2 Analysis model

The second level of DTM is to enable the simulation of structural behavior of a structure. Two-way interoperable data exchange is required to realize the second level. From the digital geometry model with meta-data including the material properties and the effective prestressing force, a simulation model is generated. In this paper, the OpenSeesPY is selected for the analysis. The girder is modeled by *dispBeamColumn* element. Data for the generation of the analysis model are extracted from the geometry model, which is one-way data transfer. Analyzed results such as deformation and stress contour are imported to the DTM for the visualization of the structural behavior. For the baseline model, data from material tests and inspection tasks should replace the initial design data. For multiple girder bridges, it is required to select an indicating member to represent the time-dependent behavior of the whole girders.

At the time of prestressing, the prestressing forces (elongation data) and resulting camber values are obtained by a fabricator. The measured flexural stiffness of each girder can update the analysis models, and the data are stored in the digital twin models of the girders. Time-dependent deformation and deformation by additional loadings are monitored by a sensing system for the indicating member. Through this process, the baseline digital twin model at the bridge completion stage can be obtained for O&M tasks.

2.3 Model update by sensing data

The third level of DTM is to enable the prediction of future performance of a structure by accumulating data through sensing and analysis. A structural health monitoring system is not commonly used for girder bridges. A sensing system for updating of the digital twin model is

suggested and developed. Embedded sensors and a temperature sensor are monitored by a sensing system with an E-paper that requires very low power to visualize the sensor data. Before concrete casting, the sensors are installed and the sensing system is connected at the time of prestressing.

Figure 3 presents the data delivery from design to completion of the bridge construction. The initial data are assumed values. The 3D geometry of the member generates the analysis model with concrete and prestressing tendons. During fabrication, the initial model is updated by the prestressing force and the relevant camber. Then, sensor data monitored at a predefined period update the analysis model and geometry of the DTM. The DTM is continuously updated at the stage of assembly, composite action, 1st dead load, and 2nd dead load. As-built digital twin model is the baseline model for the maintenance of the bridge.

During the operation period, the most important issue of the prestressed concrete girder bridge is corrosion of the internal tendons. The internal corrosion cannot be visually observed and has a huge impact on the safety and service life of a bridge. Once the baseline DTM is established at the completion time of the bridge construction, the key performance indicator is the section loss of the internal tendons by the corrosion. The twin model can be used in the periodical inspection and assessment for prediction as well as structural evaluation of the bridge.

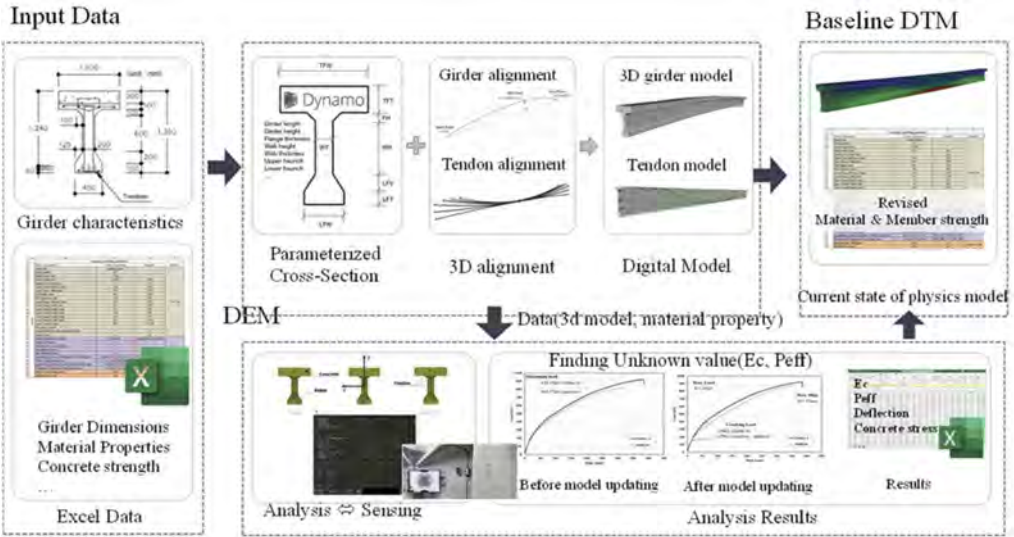


Figure 3. Flow chart for digital interoperability between BIM & Analysis.

3 IMPLEMENTATION TO A PREFABRICATED BRIDGE

3.1 A prestressed concrete girder bridge

A national research program on smart construction is in progress in Korea. The proposed digital twin concept and the developed technologies are being implemented to a expressway bridge. The bridge consists of prestressed concrete girders with span length of 35m and 50m. Figure 4 shows the bridge layout and the assembly stage. Steel lateral beams and full-depth precast decks are assembled with the PSC girders. The required data for the update of the DTM are obtained by an official inspection process to control geometry quality.

3.2 Implementation

A national research program on smart construction is in progress in Korea. The proposed digital twin models and the information delivery at each stage are being applied to the bridge.

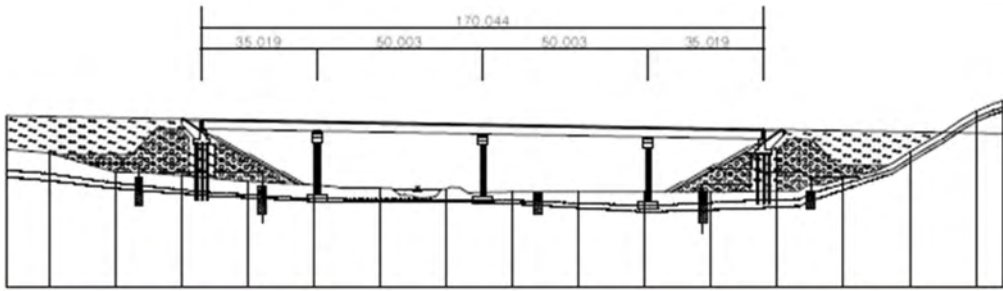


Figure 4. A PSC bridge for implementation.

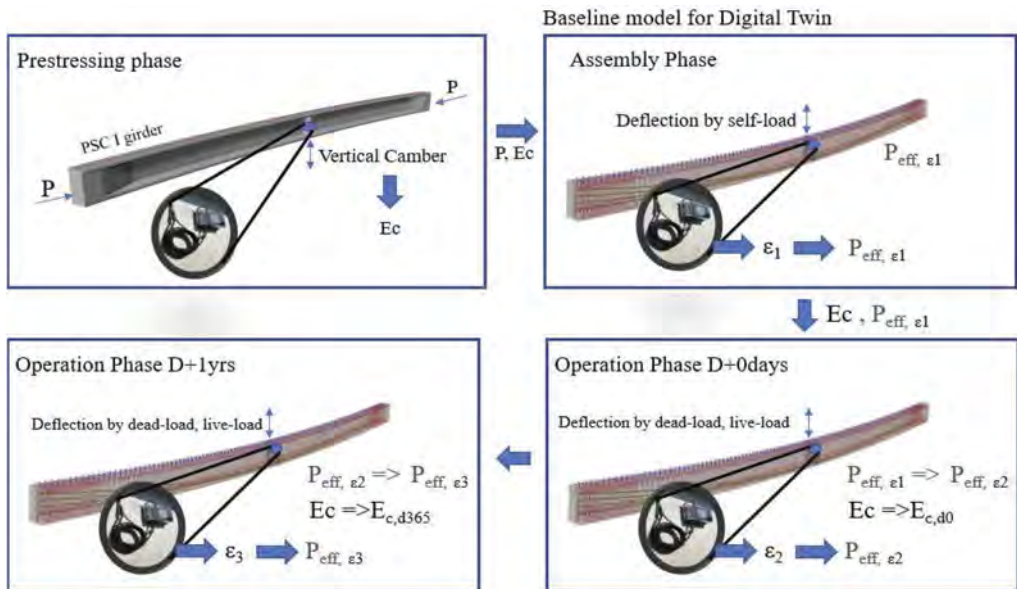


Figure 5. Baseline digital twin model and its update process.

An external girder near an abutment was selected as the indicating member. From the design calculation, the expected response in terms of deflection and strain values at several locations is collected. Figure 5 presents the process of the model update by the captured data during the fabrication and the assembly. Key parameters are the elastic modulus of concrete, remained prestressing forces, and section loss by the possible internal damage of the tendons. The sensing system has a target operation period of 10 years after the completion. There is a linked R&D program to build a digital twin model for existing bridges that have service life longer than 30 years. The internal corrosion of the tendon is the main interest for the assessment of the existing PSC girder (Jeon et al. 2021).

4 CONCLUSIONS

Prefabricated structures must provide productized specifications and performance. We proposed a digital twin model that can evaluate this long-term performance even though the concrete prefabricated structures have uncertainties in material properties and long-term behavior. Interoperability between 3D digital geometry modeling and the finite element analysis through the open platform, which can actively reflect geometry changes at each construction stage, was secured through data exchange. A procedure for updating the digital twin model using data acquired during the manufacturing and assembly process was presented. A low-power sensing system was used to monitor the initial performance of the structures and to update and verify the digital twin model. At the completion of the construction, the bridge's owner can have an efficient and reliable baseline digital twin model for maintenance.

ACKNOWLEDGEMENT

This research was conducted with the support of the “National R&D Project for Smart Construction Technology (RS-2020-KA156007)” funded by the Korea Agency for Infrastructure Technology Advancement under the Ministry of Land, Infrastructure and Transport, and managed by the Korea Expressway Corporation.

REFERENCES

- Evans, S. & Savian, C. & Burns, A. & Cooper, C. 2019. Digital twins for the built environment, The Institution of Engineering and Technology
- Jeon, C.H. & Sim, C. & Shim, C.S. 2021. The effect of wire rupture on flexural behavior of 45-year-old post-tensioned concrete bridge girders. *Engineering Structures* 245: 112842
- Nguyen, D.C. & Park, S.J. & Shim, C.S. 2022. Digital engineering models for prefabricated bridge piers. *Smart structures and systems* 30(1): 35–47.
- Nguyen, D.C. & Shim, C.S. 2022. Design for Manufacturing and Assembly-Oriented Parametric Modeling of Prefabricated Bridges, *Proceedings of IABSE Symposium: Challenges for Existing and Oncoming Structures*, Prague, Czech Republic, 25–27.
- Nguyen, D. C. & Nguyen, T. Q. & Jin, R. & Jeon, C. H., & Shim, C. S. 2022. BIM-based mixed-reality application for bridge inspection and maintenance. *Construction Innovation* 22(3): 487–503.
- Shim, C.S. & Dang, S.N. & Park, S.J. 2018. Three-dimensional information delivery for design and construction of prefabricated bridge piers, *Struct. Eng. Int.* 28(1): 6–12.
- Zhang, J. & Cheng, J.C.P. & Chen, W. & Chen, K. 2022. Digital Twins for Construction Sites: Concepts, LoD Definition, and Applications. *Journal of Management in Engineering*, 38(2).

Analysing the impact of local factors on the life-cycle of metallic bridge girders

G. Calvert & M. Hamer

Advanced Analytics, Technical Authority, Network Rail

L. Neves & J. Andrews

Resilience Engineering Research Group, University of Nottingham

ABSTRACT: A fundamental component of a life cycle analysis of a bridge is the modelling of asset condition post-construction. To enhance the accuracy of bridge deterioration models, several studies have calibrated models based on cohorts that incorporate structural characteristics and local factors. However, it is common that these characteristics are independently modelled to avoid sparse cohorts. In this study, a bridge element deterioration model is developed that can simultaneously incorporate multiple structural and local characteristics. The incorporation of multiple co-variates is made possible by an approach that exploits the multiple defect deterioration model proposed by Calvert et al. (2021). The model is tested on a cohort of 36,075 metallic bridge girders from bridges on the British railway network. The modelling approach is shown to provide statistically significant improvements in the prediction accuracy of deterioration. Moreover, a life cycle analysis outlines the significant cost and condition differences between benign and aggressive cohorts.

1 INTRODUCTION

The asset management of civil infrastructure is a critical task for transportation organisations, with maintenance, rehabilitation, and replacement activities requiring huge amounts of resources. To forecast resource requirements and maximise the impact of allocated resources, infrastructure asset managers use strategic lifecycle costing models to support decision making. To evaluate the lifecycle of civil infrastructure post-construction one needs the means to evaluate how the asset deteriorates and a means to evaluate the effectiveness of asset interventions. The accurate evaluation of the entire lifecycle is contingent on the deterioration modelling being accurate.

There are a plethora of methodologies to model structural deterioration of bridges (Frangopol, Dong & Sabatino 2017), however, for strategic network level modelling Markov modelling calibrated using condition data from visual inspections is the most common. The use of condition data to calibrate deterioration models does have its limitations given the somewhat arbitrary condition scales used and the subjectivity of the examiners when recording the assessments. Despite the limitations of the condition data, the use of such is data is widespread amongst asset managers due to the relative abundance of data compared to more empirical measurements.

There are different hierarchical modelling frameworks for the strategic modelling of bridges (Hamer, Calvert & Neves 2022), ranging from the highest level of network level evaluations for a portfolio of bridges to the lowest level of modelling at component level. An evaluation of a whole structure can be performed by assuming that the components form some configuration of a series-parallel system. Most transportation agencies assign and predict a single condition score for each component. However, the assessment of components using a single condition score is somewhat arbitrary and does not adequately describe the diverse physical process of deterioration.

In previous studies, it has been shown that it is possible to strategically model bridge components using a methodology that enables the evaluation of multiple degradation modes simultaneously (Calvert, et al. 2020, Calvert, et al. 2021). Moreover, in previous studies it has been shown that the calibration of deterioration models using condition data should be

conducted such that co-variables such as geographical location, bridge loading and structural positioning should be used to form cohorts. In this paper, a cohort analysis will be performed such that the deterioration of bridge components with multiple defect mechanisms and multiple co-variables can be evaluated simultaneously.

2 MULTIPLE DEFECT DETERIORATION MODELLING

In previous studies a Dynamic Bayesian Network (DBN) model has been used to evaluate the progression of multiple deterioration mechanisms on metallic bridge components (Calvert, et al. 2021). The defects evaluated in the modelled components included, the deterioration of paintwork/coating, corrosion and a mechanism named Structural Component Failure (SCF) which incorporated instances of buckling permanent distortion/displacement and tearing/fracture. A visualisation of the multiple defect deterioration DBN model is shown in Figure 1.

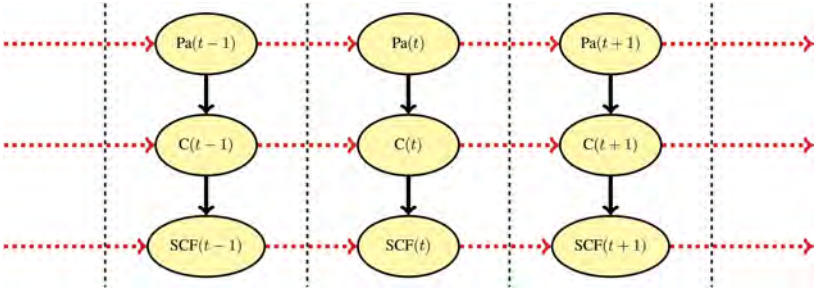


Figure 1. Dynamic Bayesian Network deterioration model.

Bridges represent a diverse asset class, with each bridge having its own distinct composition of structural elements. To facilitate intervention co-ordination and strategy development, bridges are commonly described by a hierarchical decomposition of elements. For example, at Network Rail the hierarchy for structural assets is defined by asset groups (e.g. underbridge), asset sub-groups (e.g. construction material), major elements (e.g. deck) and minor elements (e.g. inner main girder). When aggregating minor elements to determine an overall score for a bridge, particular minor elements have a designation of being a principal loading bearing element, which are used to attribute a greater weighting for elements that are structurally integral to the loading capability of a bridge.

A railway underbridge has the railway line going over the deck of the bridge. Conversely, a railway overbridge has the railway line going under the deck of the bridge. It is generally expected that an underbridge will deteriorate at a faster rate than the overbridge given that the underbridge has the loading of the railway on its deck. The MGE and MGI classifications are used to denote the exposed and inner main girders, respectively. The term of main girder is used to describe a longitudinal main girder or beam that spans between the abutments, piers or columns. The outer two beams on any deck are classified as MGE with the remaining main girders classified as MGI. For this study, main girders will be used as the component type to be analysed.

Model calibration cohorts that divide exam records by an element belonging to an underbridge or overbridge, and whether an element is an inner or exposed have been shown by previous studies to be statistically significant (Yianni, et al. 2016). For this study, such model calibration cohorts were found to be statistically significant for the multiple defect DBN model when compared to a generic cohort for main girders. This analysis was assessed by using a likelihood ratio test, the Akaike Information Criterion (AIC) and the Bayesian Information Criterion (BIC).

The DBN model parameters were calibrated using a method of maximum likelihood on Network Rail bridge condition data from visual inspections. The condition data is recorded using a condition scale known as Severity Extent (SevEx) and it can be used to note the absence or presence of each defect and the extensiveness of each defect if present. The calibrated parameters for inner and exposed main girders are shown in the table below.

Table 1. DBN Parameter values – transition rates stated in $years^{-1}$.

	(Pa1 → Pa2)	(Pa2 → Pa3)	(Pa3 → Pa4)	
MGI-BU	0.1952	0.1606	0.0284	
MGE-BU	0.1769	0.1529	0.0332	
	(C1 → C2) Pa1	(C1 → C2) Pa2	(C1 → C2) Pa3	(C1 → C2) Pa4
MGI-BU	0.005	0.1969	0.3523	0.9526
MGE-BU	0.005	0.1753	0.4274	0.7014
	(C2 → C3) Pa1	(C2 → C3) Pa2	(C2 → C3) Pa3	(C2 → C3) Pa4
MGI-BU	0.0957	0.0957	0.1172	0.1172
MGE-BU	0.0453	0.0453	0.1545	0.1545
	(C3 → C4) Pa1	(C3 → C4) Pa2	(C3 → C4) Pa3	(C3 → C4) Pa4
MGI-BU	0.0219	0.0219	0.0247	0.0247
MGE-BU	0.0341	0.0341	0.0367	0.0367
	(F1 → F2) C1	(F1 → F2) C2	(F1 → F2) C3	((F1 → F2) C4
MGI-BU	0.0038	0.0054	0.0060	0.01030
MGE-BU	0.013	0.0035	0.0094	0.0157

3 ADDITIONAL DETERIORATION FACTORS

The deterioration models in this study are calibrated using inspection records rather than experimental data, although it is still critical that the aforementioned properties that alter deterioration behaviour are considered in the model calibration. Previous studies have analysed additional properties that can influence deterioration such as traffic volumes, asset age, coastal proximity, structure type amongst others (Huang, Mao & Lee 2010, Morcoux, Rivard & Hanna 2002, Yianni, et al. 2016) and shown that their consideration is statistically significant to calibrated deterioration models. However, the early studies were often limited to analysing properties independently, which is problematic for scenarios when more than one property has been identified as influencing deterioration, as an asset manager wants to incorporate all of the properties simultaneously.

3.1 Coastal proximity

Bridges situated in close proximity to the coast are exposed to high atmospheric salinity and prevailing winds, which can accelerate the deterioration of structural components. To determine the proximity of a bridge to the coast, the co-ordinates of the bridge were evaluated against 51,043 reference co-ordinates of the coastline from the Global Self-consistent, Hierarchical, High-resolution Geography Database (GSHHG). Upon determining the proximity to the coast for all bridges, the bridges were split into two cohorts: CP1 – Less than or equal to 10 km from the coast and CP2 – More than 10 km from the coast.

3.2 Material

Across a network of bridges and even a bridge, metallic bridge elements can be constructed out of different metal materials. These different metals will corrode at different rates. For example, Agrawal, Kawaguchi & Chen (2010) analysed highway bridges in New York state, where from approximately 1968, metal bridges were constructed using weathering steel, which was a different steel composition than was typically used before 1968, called ‘steel’. In the Weibull-based analysis, weathering steel was found to deteriorate at a slower rate than the steel after 20 years.

The Network Rail portfolio contains metal bridges constructed out of cast iron, wrought iron, early steel, weathering steel and steel. ‘Early Steel’ is steel that was manufactured prior to 1956 and ‘Steel’ denotes steel manufactured from 1956 onwards. For the purposes of this study, three cohorts were formed based on material type: M1 – Wrought Iron, M2 – Early

Steel and M3 – Steel. Cast iron was omitted from the study due to discrepancies in the recording of condition for this material at Network Rail.

3.3 Track category

For road bridges, it is common to consider the traffic volume and road system when determining cohorts for model calibration (Scherer & Glagola 1994). Road traffic volume is commonly measured using Annual Average Daily Traffic (AADT). The road system indicates the type of road system a bridge is situated on e.g. interstate/motorway, primary or secondary. Moreover, Zhang & Cai (2012) shown that increased vehicle speed has a negative effect on fatigue reliability of bridge components.

Track categorisation considers annual tonnage for a section of track and the designated line speed for trains on that section of track. The categories are used to specify requirements relating to design, maintenance, renewal and inspection of track. For railway underbridges, track category can be used as an indicator of traffic loading and route type. Tonnage is measured using Equivalent Million Gross Tonnes Per Annum (EMGTPA), which accounts for the variations caused by different rolling stock. The calculation that Network Rail uses for EMGTPA is similar to the calculation for “theoretical traffic load” specified by the International Union of Railways (UIC 2019). Line speed is measured in miles per hour and track sections with a greater permitted line speed are typically located on strategically important routes e.g. mainline services. At Network Rail there are seven track categories, Cat 1, 1A, 2, 3, 4, 5 and 6. For this study, there are two track category cohorts considered: TC1 – (Cat 1, 1A and 2) and TC2 – (Cat 3, 4, 5 and 6).

The boundary between the track category definitions is a line speed of 91 mph between 0 and 7.2 EMGTPA. For annual tonnage greater than 7.2 EMGTPA, the line speed is defined as $-55 \cdot \log(w) + 200$, where w is the annual tonnage in EMGTPA of the track section. The boundaries for categories are based on historical and experimental data.

4 INCORPORATING MULTIPLE FACTORS INTO MULTIPLE DEFECT MODEL

For this study, the condition records of 36,075 main girders are considered. When additional properties are incorporated into the model, the records used in model calibration are split into smaller cohorts. The inclusion of coastal proximity, material type, track category and being an inner or exposed girder in a more detailed model will increasingly limit the size of the available data for specific instances of model calibration.

If distinct rates or a scaling factor permutation were calibrated that did not maintain the monotonic increase, the model could output the perverse scenario that the more degraded an influencing defect is, the slower the corresponding defect degradation rate is. For example, if the rate for $(C1 \rightarrow C2)|Pa3$ is 0.675 and the rate for $(C1 \rightarrow C2)|Pa4$ is 0.55, the model would be returning a lowering rate of corrosion as the paintwork condition degrades. This scenario would ultimately disincentivise paintwork maintenance interventions when performing a life cycle analysis, which goes against engineering judgement. To include multiple properties simultaneously, they could be strategically input into the model on a per defect basis.

The multiple defect model shown in Figure 1 incorporates the underbridge/overbridge and exposed/inner status of the component for all of the defects in the deterioration model. However, each of the additional properties that influence deterioration is then input to the existing model for a particular defect type. The paintwork scaling factors are specific to the proximity of the bridge component to the coast. The corrosion scaling factors are specific to the material type that the bridge component is constructed out of. The SCF scaling factors are specific to the component’s bridge track category.

The relationship between the local, structural and material properties is shown in Figure 2. This particular model configuration ensures that there are minimal additional parameters being added to the model to avoid the over parameterisation of the condition data. However, if a girder being close to the coast results in increased paintwork degradation, corrosion will occur at a greater rate due to the worse paintwork condition. Similarly, if a particular material

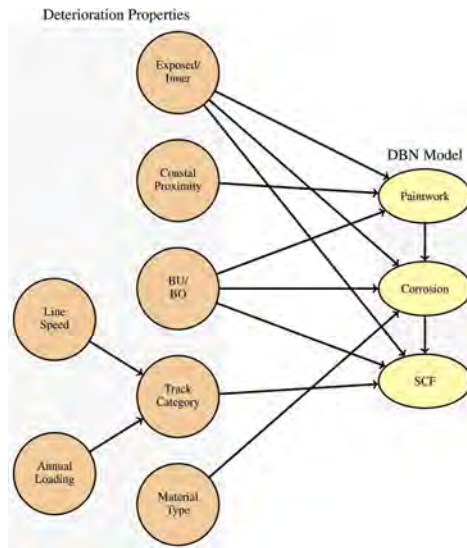


Figure 2. Influencing properties for defect deterioration model.

type corrodes at a faster rate, the instances of SCF occurring will increase due to the causal influence between those defects.

As a case study, the enhanced multiple defect deterioration model from the previous section was calibrated using the Network Rail condition records for railway underbridges. The scaling factors that maximised the log-likelihood function for the condition records used in calibration are shown in Table 2 for paintwork, corrosion and SCF.

Table 2. Scaling factors for DBN model based on additional characteristics.

	Pa Scaling Factors		C Scaling Factors			SCF Scaling Factors	
	CP1	CP2	M1	M2	M3	TC1	TC2
MGI	1.3580	0.9096	1.4048	1.2562	0.8108	1.6822	0.7235
MGE	1.2223	0.9210	1.4031	1.2966	0.7621	1.1430	0.9354

It can be observed that for each of the scaling factors, components with the more aggressive properties, i.e. CP1, M1, M2 and TC1, have a value greater than one and the components with the less aggressive properties, i.e. CP2, M3 and TC2, have a factor value less than one. This enables the components with aggressive properties to deteriorate at a faster rate than the baseline rate and conversely, the components with less aggressive properties can deteriorate at a slower rate than the baseline rates. Consequently, each component would have a contextualised deterioration rates for its composition of local, structural and material properties.

Engineering expertise would suggest that the closer a bridge is to the coast, the greater the rate of deterioration, similarly, wrought iron and early steel would deteriorate faster than steel and finally that the greater the bridge loading or line speed is, the greater the rate of deterioration. This is observed in the deterioration factor values and the values obtained in the initial case study adhere to the following inequalities,

$$\gamma_{Pa}^{CP1} \geq \gamma_{Pa}^{CP2}, \quad (1)$$

$$\gamma_C^{M1} \geq \gamma_C^{M2}, \quad (2)$$

$$\gamma_C^{M2} \geq \gamma_C^{M3}, \quad (3)$$

$$\gamma_{SCF}^{TC1} \geq \gamma_{SCF}^{TC2}, \quad (4)$$

where γ is a scaling factor and the subscript indicates the defect and the superscript denotes the relevant deterioration factor cohort.

4.1 Model selection

For the initial case study for underbridges there are two models, Model A with 28 Parameters (Baseline transition rates) and Model B with 42 Parameters (28 Baseline parameters, 7 scaling factors for MGI and 7 scaling factors for MGE). The likelihood ratio test statistic is 875.5, which gives a p-value that is infinitesimal ($<10^{-5}$) and suggests that the difference between Model A and B is statistically significant. This is again supported by Model B having the lowest value for AIC and BIC, making it the preferred candidate model despite its increased parameters.

4.2 Life cycle analysis

To evaluate the implications of main girders being modelling with additional characteristics, a life cycle analysis was performed to evaluate the effects of the different deterioration properties under different maintenance strategies. The following cohorts of deterioration properties were considered:

- Cohort 1 - MGI-BU Baseline
- Cohort 2 - MGI-BU, M1, CP1, TC1 (aggressive properties)
- Cohort 3 - MGI-BU, M3, CP2, TC2 (benign properties)
- Cohort 4 - MGE-BU Baseline
- Cohort 5 - MGE-BU, M1, CP1, TC1 (aggressive properties)
- Cohort 6 - MGE-BU, M3, CP2, TC2 (benign properties)

The different cohorts will be assessed using three different maintenance strategies, Strategy A - Fixed renewal of paintwork every five years, Strategy B - Fixed renewal of paintwork every ten years and Strategy C - No paintwork-only interventions. A life cycle analysis was performed using a Petri model which simulated the deterioration of a component, inspection regime and application of each maintenance strategy. The Petri net model is described in (Calvert, et al. 2021).

To compare between the different cohorts and strategies, there are two Key Performance Indicators (KPI) considered for the 35-year simulation period: Average total Time in Poor Condition (ATPC) and Average Total Costs. The study KPIs are presented in Figure 3 as a scatter plot, where it can be observed that there are three clusters formed from different cohorts and maintenance strategies. The red ellipse includes the KPIs for Cohorts 2 and 5 under strategies A, B and C; these cohorts represented the most aggressive scaling factors, with wrought iron, a coastal proximity of within 10km of the coast and belonging to a track category with the greatest loading/highest line speeds. Conversely, the green ellipse includes the cohorts from the least aggressive scaling factors. The yellow ellipse includes the KPI results for the baseline parameters for inner and exposed main girders.

From Figure 3 it is observable that both the scaling factors and the maintenance strategy have a great impact on the resultant KPIs. The traditional breakdown of inner and exposed main girders returns a smaller difference in KPIs when compared to the differences between KPIs between the same element type and different deterioration properties. For any of the simulated results, for any given strategy, the following expressions hold true,

$$Cost_1 - Cost_3 < Cost_2 - Cost_1, \quad (5)$$

$$Cost_4 - Cost_6 < Cost_5 - Cost_4, \quad (6)$$

$$ATPC_1 - ATPC_3 < ATPC_2 - ATPC_1, \quad (7)$$

$$ATPC_4 - ATPC_6 < ATPC_5 - ATPC_4, \quad (8)$$

where the numeric subscript denotes the cohort identifier. From (5) and (6), it can be stated that the savings in total cost for the least aggressive cohort compared to the baseline is less than the added expense of the most aggressive cohort compared to the baseline. Similarly, from (7) and (8), the reduction in ATPC for the least aggressive cohort to the baseline is less than the increase in ATPC for the most aggressive cohort compared to the baseline. Such observations have huge importance when allocating resources in a constrained budget scenario. The difference in cost and ATPC between the least aggressive and baseline cohorts, and the difference between the most aggressive and baseline cohorts were expected not to be equal. Moreover, there are more components that feature in the less aggressive cohort than the most aggressive cohort. Consequently, it would make sense that the values obtained by the least aggressive cohort are closer to the baseline values, as the baseline cohort is ultimately an average result based on the composition of all cohorts, so will be skewed to larger cohorts.

For each cohort there is a general trend that the ATPC increases from Strategy A to B to C. However, the reduced ATPC comes at a cost, with a trend that Strategy A is the most expensive and Strategy C is the least expensive. These observed trends correspond with what engineering expertise would predict as Strategy A dictates a more regular preventative maintenance schedule.

It can be stated that the cohorts (Cohorts 2 and 5) with the most aggressive properties, i.e. CP1, M1 and TC1, return the upper limit for total cost and ATPC. Conversely, the cohorts (Cohorts 3 and 6) with the least aggressive properties, i.e. CP2, M3 and TC2, returns the lower limit for total cost and ATPC. It was expected that the least aggressive and most aggressive cohorts would act as bounds for cost and ATPC indicators. Moreover, the baseline cohorts (Cohorts 1 and 4) return values for total cost and ATPC between the two limits, which conforms with the expectation that the baseline cohorts serve as an average based on the asset composition of the calibration data.

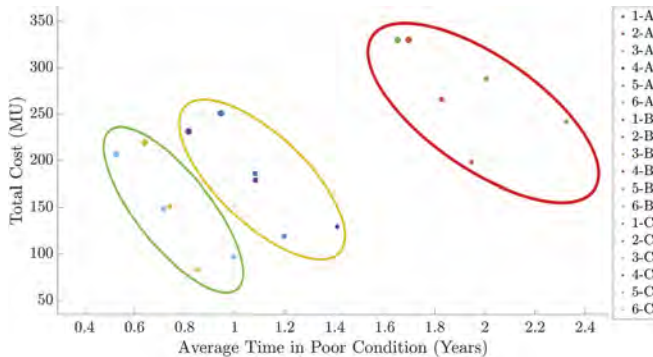


Figure 3. Scatter plot of cost and condition KPIs, where $i-j$ denotes the Cohort ID and Strategy ID respectively.

5 CONCLUSION

The study in this paper analysed deterioration rates for main girders from metallic bridges. An initial set of deterioration rates were calibrated for the traditional cohort breakdown of underbridges/overbridges and inner/exposed main girders using condition records from the bridge inspection regime on the British railway. Statistical analysis confirmed that the inclusion of these structural properties increases the accuracy of the multiple defect deterioration model without over fitting the model due to the additional parameters.

Existing literature has shown that there are additional properties aside from the aforementioned structural properties that alter the deterioration rates of bridge components. In this study the deterioration factors of coastal proximity, component material type, bridge loading and railway line speed were considered. Commonly, properties that alter deterioration rates are identified by calibrating models by data cohort splitting, however, this typically results in the inability of including multiple factors due to data sparsity. This paper presented a novel approach to incorporate multiple deterioration factors by including the factors on a per defect basis with the defects also having causal influences. The incorporation of the deterioration factors was shown to provide a statistically significant improvement in model accuracy.

Finally, the enhanced deterioration model with the multiple deterioration factors integrated into a wider asset management Petri Net model to perform a life cycle analysis. The life cycle analysis revealed that the different deterioration factors returned quite diverse values for the considered KPIs of average total time in poor condition and average total cost. Moreover, the incorporation of the deterioration factors in the life cycle analysis enables increased decision support capabilities for asset managers by facilitating targeted intervention strategy development particularly for constrained budget scenarios and developing equitable resource allocation for different administrative regions. In future work and in the advent of additional data, additional deterioration properties may be identified and included in the metallic bridge component deterioration model. Moreover, properties may be identified for additional material types.

ACKNOWLEDGEMENTS

Gareth Calvert completed his PhD research at the University of Nottingham. This work was supported by the Engineering and Physical Sciences Research Council [EP/N50970X/1]. Additional support was received from Network Rail.

REFERENCES

- Agrawal, A.K., A. Kawaguchi, & Z. Chen. 2010. Deterioration Rates of Typical Bridge Elements in New York. *Journal of Bridge Engineering* 15 (4): 419–429.
- Calvert, G., L. Neves, J. Andrews, & M. Hamer. 2020. Multi-defect modelling of bridge deterioration using truncated inspection records. *Reliability Engineering & System Safety* 200: 106962.
- Calvert, G., L. Neves, J. Andrews, & M. Hamer. 2021. Incorporating defect specific condition indicators in a bridge life cycle. *Engineering Structures* 246: 113033.
- Frangopol, D.M., Y. Dong, & S. Sabatino. 2017. Bridge life-cycle performance and cost: analysis, prediction, optimisation and decision-making. *Structure and Infrastructure Engineering* 13 (10): 1239–1257.
- Hamer, M.J., G.S. Calvert, & L.A.C. Neves. 2022. An overview of strategic bridge life cycle modelling on the British Railway. *Proceedings of the Eleventh International Conference on Bridge Maintenance, Safety and Management (IABMAS 2022)* Barcelona: CRC Press.
- Huang, R.Y., I.S. Mao, & H.K. Lee. 2010. Exploring the deterioration factors of RC bridge decks: a rough set approach. *Computer-Aided Civil and Infrastructure Engineering* 25 (7): 517–529.
- Morcous, G., H. Rivard, & A.M. Hanna. 2002. Case-based reasoning system for modelling infrastructure deterioration. *Journal of Computing in Civil Engineering* 16 (2): 104–114.
- Scherer, W.T. & D.M. Glagola (1994). Markovian Models for Bridge Maintenance Management. *Journal of Transport Engineering* 120 (1): 37–51.
- UIC. 2009. Classification of lines for the purpose of track maintenance. Technical Report Leaflet 714, Union Internationale des Chemins de Fer.
- Yianni, P.C., L.C. Neves, D. Rama, J.D. Andrews, & R. Dean. 2016. Incorporating local environmental factors into railway bridge asset management. *Engineering Structures* 128 (1): 362–373.
- Zhang, W., & C.S. Cai. 2012. Fatigue reliability assessment for existing bridges considering vehicle speed and road surface conditions. *Journal of Bridge Engineering* 17 (3): 443–453.

Quantifying the effects of long duration ground motions on the lifetime seismic losses of aging highway bridges

S. Shekhar

Indian Institute of Technology Mandi, Mandi, India

B. Panchireddi

Gallagher Re, Mumbai, India

J. Ghosh

Indian Institute of Technology Bombay, Mumbai, India

ABSTRACT: Despite the propensity of long duration earthquakes in subduction zones, little attention has been paid on life-time seismic loss assessment of highway bridges that are simultaneously undergoing prolonged corrosion deterioration. Consequently, this paper investigates the combined effect of ground motion duration and corrosion deterioration on lifetime seismic vulnerability and loss assessment of highway bridges. A representative case-study multi-span simply supported bridge located in Seattle is considered, where long duration earthquakes are more likely to occur. Two sets of spectrally equivalent long and short duration ground motions are considered to perform nonlinear dynamic analyses of the three-dimensional bridge analytical model. It is observed that the consideration of the effects of long duration ground motion significantly increases the failure probability of the bridge components in comparison to the short duration record set. Additionally, lifetime corrosion deterioration is found to aggravate the influence of long duration earthquakes on the seismic vulnerability of the case-study highway bridge. The seismic life-cycle cost analysis considering regional seismic hazard curve and probabilistic repair strategies reveal significantly higher seismic losses from long duration earthquakes in comparison with short duration earthquakes.

1 INTRODUCTION

Large subduction zone earthquakes in the recent past, such as those from Sumatra, Indonesia (M_w 9.1, 2004); Wenchuan, China, (M_w 8.0, 2008); Maule, Chile (M_w 8.8, 2010); Iquique, Chile (M_w 8.2, 2014), and Tohoku, Japan (M_w 9.0, 2011); have underlined the potential for substantial financial losses, as well as human casualties. Ground motion time-history records from subduction earthquakes are typically observed to be longer in duration than those from shallow crustal earthquakes and therefore could aggravate damage to infrastructure systems, such as highway bridges. Recognizing the damaging effects of long duration ground motions, in the recent past several researchers have investigated the influence of ground motion duration on the seismic vulnerability of building typologies (Raghunandan and Liel 2013; Chandramohan et al. 2016; Barbosa et al. 2017; Belejo et al. 2017). Pertaining to highway bridges, Ou et al. (2014) and Lopez et al. (2020) has demonstrated the influence of ground motion duration on the hysteretic response, displacement capacity, and failure modes of reinforced concrete bridge columns. Recently, Kabir et al. (2019) has numerically demonstrated that highway bridge component and system-level failure probabilities are more dominated by long duration records than near-fault and far-field ground motions. Despite these observations, there has been a historic lack of consideration of ground motion duration aspects towards seismic life-cycle cost analysis of highway bridge structures.

In addition to susceptibility to intermittent earthquake hazards, highway bridges may also be continuously exposed to harsh environmental conditions resulting in aging and deterioration of critical load-resisting components. Recent studies identify chloride-induced corrosion as the most common cause of environmental degradation for highway bridges. This deterioration mechanism causes significant strength degradation of critical bridge components such as columns, bearings, and bridge decks, among others, and if not properly monitored and managed, can result in a significant reduction in structural functionality and losses, particularly during extreme events such as earthquakes. Consequently, in the past decade, several studies have focused on lifetime seismic loss assessment of highway bridges under joint aging and seismic threats (Alipour et al. 2011; Ghosh and Padgett 2011; Dong et al. 2013; Dong and Frangopol 2016; Shekhar et al. 2018). While these investigations focus on the simultaneous effect of aging and earthquake loads on the lifetime seismic losses, the impact of long duration ground motions that may be critical for the structural safety of deteriorating highway bridges remains unaccounted. For deteriorating bridges, only recently, Panchireddi et al. (2021) has examined the influence of ground motion duration from subduction sources on bridge fragility, and a methodical evaluation towards seismic life-cycle cost analysis still remains unaddressed.

Addressing the gaps, this study focuses on understanding and quantifying the differences in lifetime seismic losses of aging highway bridges when subjected to long or short duration earthquake ground motions. For this purpose, a case-study multi-span simply supported highway bridge in marine splash exposure condition located in subduction earthquake zone within Seattle, U.S. is selected. Next, suites of spectrally equivalent short and long duration ground motions are adopted, followed by an incremental dynamic analysis-based framework for seismic fragility assessment of the bridge structure as it continues to age along the service life. The seismic fragility curves for the as-built and aging structure are then convolved with the regional hazard information to compute lifetime seismic losses.

2 REPRESENTATIVE CASE-STUDY AGING BRIDGE: DETERIORATION MECHANISMS AND FINITE ELEMENT MODEL

To demonstrate the influence of ground motion duration on lifetime seismic loss assessment of aging highway bridges, this study considers Seattle, Washington as the case-study region. Located within the Pacific Northwest Cascadia region, past historical events reveal that Seattle is prone to both short duration (crustal) and long duration (subduction) earthquakes. Additionally, highway bridges in the case-study Seattle region are also prone to aging and corrosion deterioration due to continuous exposure to chlorides from the Pacific Ocean. This study considers a multi-span simply supported (MSSS) concrete girder bridge for the case-study example (Panchireddi et al. 2021). This bridge type is prevalent in Washington state and accounts for more than 21% of all highway bridges in this region (FHWA 2019).

While multiple bridge components experience continuous corrosion deterioration during their design life, corrosion deterioration of reinforced concrete (RC) bridge columns significantly impact the seismic response (Andisheh et al. 2016) and hence considered in this study. Corrosion deterioration in RC bridge columns initiates after a time-gap referred to as corrosion initiation time. During this period, chloride ions progressively ingress into the concrete cover and depassivates the reinforcing steel initiating corrosion. This study utilizes the widely adopted probabilistic model proposed by Duracrete (2000) to predict corrosion initiation time that depends on concrete cover depth, chloride diffusion coefficient, equilibrium chloride concentration, and critical chloride concentration, among others. Based on the probabilistic analysis considering the uncertainty of the above-mentioned parameters from Duracrete (2000), the mean corrosion initiation time of case-study bridge columns is estimated as 10 years. Following corrosion initiation, in the propagation phase, corrosion deterioration primarily leads to reduction in the cross-sectional area of the embedded reinforcing steel along with other secondary effects such as reduction in mechanical properties of steel and concrete. The time-dependent corrosion rate for the marine-splash environmental exposure condition is adopted from the work of Vu and Stewart (2000). Figure 1 depicts the mean time-dependent degradation of the steel rebar area along

with the lower and upper limits of the uncertainty band representing 5th and 95th percentile confidence bounds. At the end of 75 years of service life, 11.3% mean reduction in reinforcing steel area is observed. Although not shown here, at the end of service life, the deteriorated RC columns also undergo 5.7%, 58.1%, 6.4%, and 76.9% mean reduction in the steel strength, ultimate strain, concrete core strength, and cover concrete strength, respectively – signifying the need to consider these secondary effects in the lifetime performance assessment of highway bridges.

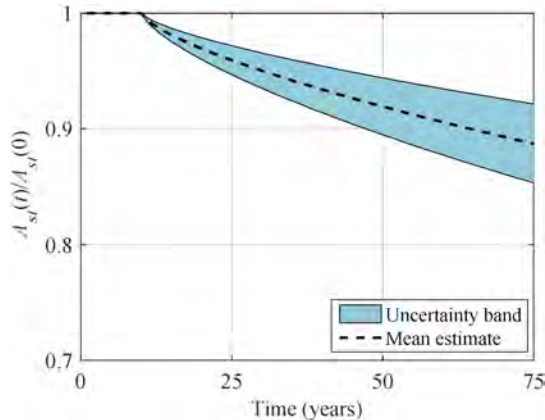


Figure 1. Variation of mean reinforcing steel area with time along with the lower and upper limits of the uncertainty band representing 5th and 95th percentile confidence bounds.

A three-dimensional detailed finite element model of the case-study bridge is developed using the finite element package OpenSees (McKenna et al. 2000) incorporating corrosion deterioration effects. More details on finite element model of the case-study bridge can be found in Panchireddi et al. (2021). Note that for the deteriorated bridge, the consequences of chloride-induced corrosion, such as area loss of steel and secondary effects such as reduction mechanical properties of steel and concrete are incorporated by altering the properties of column fiber defined cross-section.

3 SUITE OF SHORT AND LONG DURATION GROUND MOTION RECORDS

To study the impact of duration on aging bridge vulnerability and loss assessment, this study adopts the short and long duration ground motion suites from Chandramohan et al. (2016). The short duration ground motion set consists of 22 orthogonal pairs of shallow crustal earthquake records from the FEMA P695 far-field accelerograms (FEMA 2009). All the 44 (22 × 2) individual ground motions are found to be relatively short with *significant duration* ($D_{S_{5-75}}$) lesser than 25 s and hence are referred as short duration ground motions (Barbosa et al. 2017; Belejo et al. 2017). Note the *significant duration* is described by the time interval over a specific range of the Arias Intensity (5–75% or 5–95% of peak value (Trifunac and Brady 1975), and has been widely regarded as an appropriate indicator to investigate the effects of ground motion duration in the past studies (Raghunandan and Liel 2013; Chandramohan et al. 2016).

For each short duration ground motion, a corresponding long duration record with $D_{S_{5-75}}$ more than 25 s and closely matched response spectra is chosen. From the past subduction earthquakes across the globe including recent Wenchuan (China, 2008), Maule (Chile, 2010), and Tohoku (Japan, 2011), among others, a total of 44 long duration ground motions are selected that are spectrally equivalent with the 44 (22 × 2) short duration ground motions. The spectral equivalent long duration ground motions are obtained based on algorithm proposed by Chandramohan et al. (2016). Figure 2(a) shows the comparison of mean response spectra of short and long duration earthquake ground motion set. It is observed that the mean response spectra of both ground motion set closely matches underlining the spectral

equivalence. It is worthwhile to note that the differences in seismic response of structures when subjected to spectrally equivalent short and long duration ground motion pair can be primarily attributed to the duration aspect alone. Figure 2 (b) shows the significant duration of two ground motion set. The $D_{S_{5-75}}$ values of chosen long duration ground motions are larger than 25 s with overall geometric mean of $D_{S_{5-75}}$ value as 63.15 s. The geometric mean of $D_{S_{5-75}}$ value of short duration ground motions is 5.32 s.

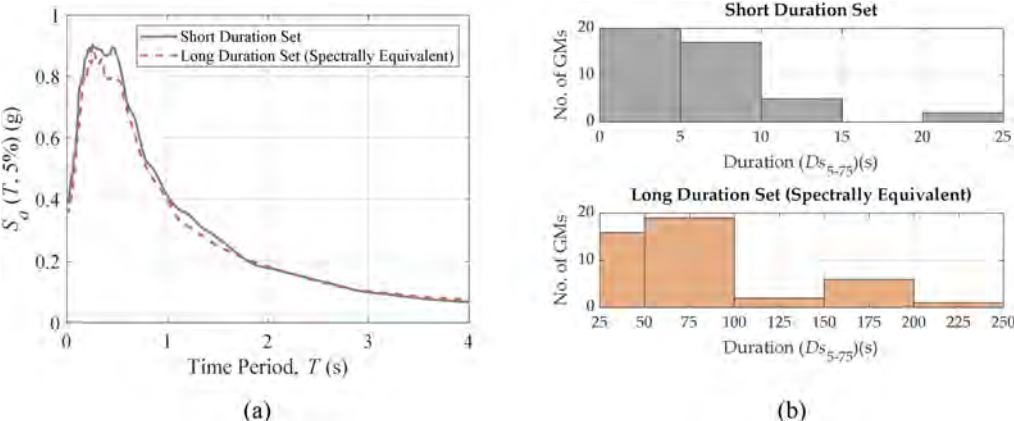


Figure 2. (a) Comparison of mean response spectra of short and long duration earthquake record sets, and (b) Histograms of the 5–75 % significant duration ($D_{S_{5-75}}$) of the ground motions in the spectrally equivalent long and short duration record sets.

4 SEISMIC FRAGILITY ANALYSIS CONSIDERING GROUND MOTION DURATION AND AGING EFFECTS

Seismic fragility curves constitute important precursors to life-cycle cost assessment of highway bridges. For both short and long duration ground motion sets, seismic fragility curves are developed at 0 years (Pristine), 25 years, 50 years, and 75 years. The bridge component fragility curve at any intermediate year (required for life-cycle analysis) are approximated using interpolation. The incremental dynamic analysis (IDA) is used to quantify seismic demand of highway bridge components. For both short and spectrally equivalent long duration ground motion sets a series of non-linear time-history analysis is performed at various scaled intensity levels and bridge components response are measured using engineering demand parameters (*EDPs*). The Park and Ang damage index (Park et al. 1985) is used as an *EDP* for bridge columns that measures seismic damage as a combination of maximal ductility demand and dissipated hysteretic energy. For bearings and abutments, maximum shear strain and maximum passive displacement, respectively are used as *EDP*. The corresponding limit states for various damage states of bridge components are adopted from past literature and reported in Panchireddi et al. (2021).

Utilizing the IDA results and limit state capacity of various damage states, the seismic fragility curves are developed for different bridge components considering short and long duration record sets. Figure 3 (a) shows the moderate damage state component fragility curves of the MSSS concrete bridge in as-built condition for short and long duration ground motion record sets. As the figure reveals, bearings are the most vulnerable component in both record sets followed by columns and abutments. In comparison to the short duration ground motion set, the long duration ground motion set results in higher vulnerability across all components. This is expected since the components will be subjected to a greater number of load reversals and energy demands for long duration records resulting in increase in damage and failure likelihood. The median fragility estimates (*PGA* corresponding to 50% failure probability denoted

as median PGA here) of moderate damage state for long duration record set are 21%, 9%, and 12% lower than that obtained from short duration record set for columns, elastomeric bearings, and abutments, respectively. Figure 3 (b) shows the combined influence of corrosion deterioration and ground motion duration on the seismic fragility curves of bridge columns for extensive damage state. As the figure reveals, both duration and aging have significant impact on the seismic vulnerability of bridge columns. The corrosion of bridge columns results in a reduction of strength and stiffness, and consequently, longer duration ground motions due to higher number of inelastic cycles cause more damage accumulation in bridge columns resulting in the increase in seismic demand and failure probability.

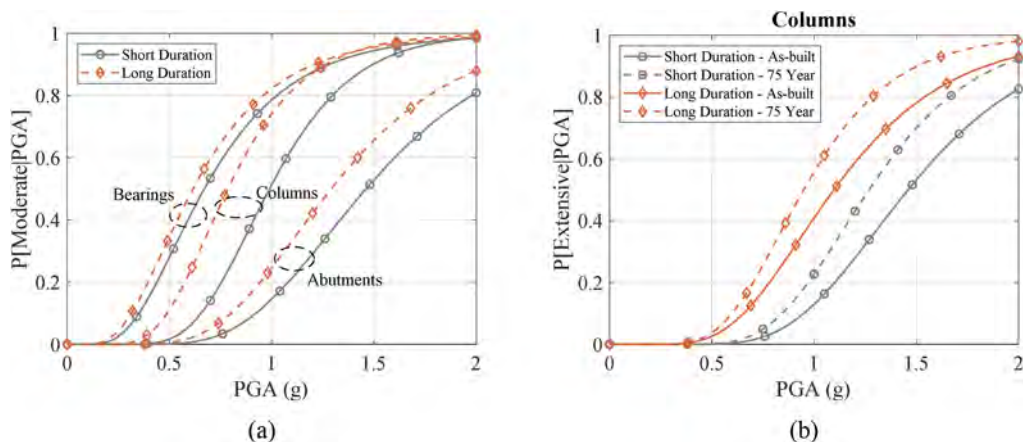


Figure 3. (a) Impact of ground motion duration on seismic fragility of as-built case-study bridge components, and (b) Joint impact of ground motion duration and corrosion deterioration on seismic fragility of as-built and 75-year-old corroded bridge columns.

5 SEISMIC LIFE-CYCLE COST ANALYSIS

Seismic life-cycle cost ($SLCC$) analysis of highway bridges requires information related to the regional hazard curves, seismic fragility of bridge structures across different damage states and associated repair cost information. The following sections first describes the seismic life-cycle cost procedure, followed by discussion on seismic hazard, adopted component repair strategies and associated cost. Finally, expected seismic life-cycle cost considering duration and aging effects is presented for the case-study bridge located in Seattle, Washington.

5.1 Seismic life-cycle cost formulation

The present study adopts a probabilistic approach introduced in Ghosh and Padgett (2011) and later improved by Sebastiani (2016) for seismic life-cycle cost estimation of aging highway bridges. This framework accounts for time-varying seismic fragility curves of bridge components, regional hazard information, uncertainty in component repair techniques and associated repair costs, and the contribution of multiple correlated bridge components to arrive at bridge system level life-cycle costs. Utilizing this methodology, for particular bridge component m the expected seismic life-cycle cost from repairs over a period of time T is computed as:

$$E[SLCC_{m,H}] = \sum_{t=1}^T \sum_{ds=1}^{DS} \sum_{j=1}^J \left[\lambda_{m,ds,H}(t) e^{-\sum_{\tau=1}^{t-1} \lambda_{m,ds,H}(\tau)} \times \frac{P(C_{m,ds,j}) C_{m,ds,j}}{(1 + \alpha)^t} \right] \quad (1)$$

where, $\lambda_{m,ds,H}(t)$ is the time-varying mean annual rate of failure for damage state ds only for hazard H (short duration crustal earthquakes, or long duration subduction earthquakes), DS is the total number of damage states for the m^{th} bridge component under consideration, $P(C_{m,ds,j})$ is the probability of choosing the j^{th} repair strategies with an associated cost $C_{m,ds,j}$, J being the total number of viable repair strategies for the bridge component for that particular damage state and α is the discount ratio to convert future costs into present values. This study considers a design service life (T) of 75 years and after-inflation risk-free discount ratio (α) of 3% to bring future costs to present values. More detail on the adopted repair strategies for different bridge components and the associated probabilities is elaborated in the subsequent section.

For rare hazard events, such as earthquakes, the mean annual rate of failure can be approximated by the annual probability of failure due to damage state ds only as:

$$\lambda_{m,ds,H}(t) = P_{m,ds,H}^{Annual}(t) - P_{m,ds+1,H}^{Annual}(t) \quad (2)$$

The annual failure probability for bridge component m in damage state ds , $P_{m,ds,H}^{Annual}(t)$ is typically calculated as a convolution between the seismic fragility and hazard curve as:

$$P_{m,ds,H}^{Annual}(t) = \int_a \left[Fragility_{m,ds,H}(t) | PGA = a \right] \left| \frac{dH(a)}{d(a)} \right| d(a) \quad (3)$$

where, $Fragility_{m,ds,H}(t) = a$ represents the probability of damage state exceedance at time t for short duration or long duration earthquakes, given the earthquake intensity $PGA = a$, and $H(a)$ is obtained from the seismic hazard information. The expected life-cycle cost of the overall bridge system is calculated as the sum of cost of individual bridge components.

5.2 Seismic hazard, component repair strategy and associated costs

The seismic hazard at a site is represented by the seismic hazard curve that quantifies the annual probability of exceedance of ground motion intensities. The seismic hazard curve of Seattle, Washington is obtained from USGS (2015) considering earthquakes from crustal and subduction sources. Note that this study considers total lumped hazard curve to obtain mean annual rate of failure and lifetime losses, for accurate seismic loss assessment future work will consider deaggregated seismic hazard curves from crustal and subduction sources. Multiple repair strategies may exist for the same level of damage to a particular bridge component following seismic events and adoption of one repair strategy over another depends on the discretion of the engineer or availability of materials, among other factors. This study considers such uncertainties in repair procedure and probability of adopting one repair strategy over another ($[P(C_{m,ds,j})]$ in Equation 1) are adopted from the web based survey conducted by Padgett and DesRoches (2007) for different critical bridge components such as columns, bearings, abutments, among others.

5.3 Expected seismic life-cycle cost

The duration-dependent time-varying seismic fragility curves for different bridge components obtained in Section 4 are used in conjunction with regional seismic hazard information and probable repair strategies and associated costs to estimate the expected seismic life-cycle cost of the aging case-study bridge. Figure 4 shows the total system-level seismic life-cycle costs of the case-study MSSS bridge for short and long duration record sets. The seismic life-cycle cost obtained from long duration record set are 62% higher than those obtained from short duration record set. A higher system-level seismic losses is expected from the long duration record sets, as case-study bridge components are more vulnerable to long duration ground motions as shown earlier in Figure 3. The figure also demonstrates the contribution of different bridge components to system-level seismic life-cycle costs, indicated by the total length of the colored bar chart. For both short and long duration ground motions record sets, elastomeric bearings

contribute most towards total losses followed by columns and abutments. These findings are consistent with the observed component-level seismic fragility curves (shown earlier in Figure 3 (a)), wherein elastomeric bearings emerge as the most vulnerable components, thereby contributing highest to the system losses. Additionally, elastomeric bearing failure potentially leads to deck unseating, resulting in substantial repair costs. The percentage contribution from columns, elastomeric bearings, and abutments towards system-level losses considering short duration ground motions record set are 10%, 88%, and 2%, respectively. These percentage contributions are 26%, 72%, and 2%, respectively, for long duration ground motions record set. It is also worthwhile to note that for both record sets, the complete damage state-induced repairs dominate the overall loss with 44% contribution towards total losses for short duration record set and 54% for the long duration record set. Additionally, for long duration record set, non-consideration of aging and deterioration in seismic life-cycle cost analysis leads to 16% and 8% underestimation in seismic losses of columns and bridge system.

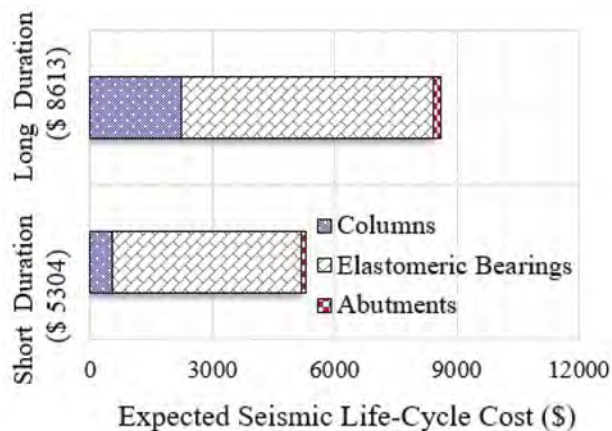


Figure 4. Contribution of different bridge components to system-level losses for short and long duration ground motions record sets.

6 CONCLUSIONS

This study investigates the combined influence of ground motion duration and corrosion deterioration on seismic life-cycle costs for highway bridges. In this regard, a multi-span simply supported concrete girder bridge located in Seattle, Washington, is chosen as the representative case-study structure. Two different sets of time-varying fragility functions for short and long duration ground motions record sets are derived using the incremental dynamic analyses. The duration-dependent time-evolving seismic fragility curves of critical bridge components are convolved with regional seismic hazard information, and bridge components probable repair techniques to compute component and system-level expected seismic life-cycle costs. Results reveal a significant increase in the vulnerability and lifetime economic losses of bridge components and system under the joint consideration of long duration earthquake shock and corrosion deterioration.

The component-level seismic fragility curves indicate that long duration ground motions affect the bridge components more than short duration records. The long duration record set cause 50% probability of extensive damage for as-built columns at 24.8% lower *PGA* compared to short duration record set. For bridge columns, the combined effect of corrosion deterioration and duration significantly influences the failure probability. The percentage change in median *PGA* of extensive damage state due to the joint influence of duration and aging are 27%, 30%, and 35%, respectively, for 25, 50, and 75-year-old corroded bridge columns. Seismic life-cycle cost analysis of the case-study MSSS bridge reveals higher seismic losses from long duration earthquakes. The

system-level losses considering long duration ground motions are 62% higher than corresponding losses obtained from short duration record set. Additionally, for bridges located in subduction zones, non-consideration of long duration earthquake shock and corrosion deterioration leads to underestimation of seismic losses by 69%. Based on the above findings, for highway bridges located in subduction zones and prone to harsh environmental exposure, this study recommends the consideration of duration and aging aspects for the seismic design.

REFERENCES

- Alipour, A., Shafei, B., & Shinozuka, M. 2011. Performance evaluation of deteriorating highway bridges located in high seismic areas. *Journal of Bridge Engineering*, 16(5): 597–611.
- Andisheh, K., Scott, A., & Palermo, A. 2016. Seismic behavior of corroded RC bridges: Review and research gaps. *International Journal of Corrosion*, Hindawi Publishing Corporation: 1–22.
- Barbosa, A. R., Ribeiro, F. L., & Neves, L. A. 2017. Influence of earthquake ground-motion duration on damage estimation: application to steel moment resisting frames. *Earthquake Engineering & Structural Dynamics*, 46(1): 27–49.
- Belejo, A., Barbosa, A. R., & Bento, R. 2017. Influence of ground motion duration on damage index-based fragility assessment of a plan-asymmetric non-ductile reinforced concrete building. *Engineering Structures*, 151: 682–703.
- Chandramohan, R., Baker, J. W., & Deierlein, G. G. 2016. Quantifying the influence of ground motion duration on structural collapse capacity using spectrally equivalent records. *Earthquake Spectra*, 32(2): 927–950.
- Dong, Y., & Frangopol, D. M. 2016. Probabilistic time-dependent multihazard life-cycle assessment and resilience of bridges considering climate change. *Journal of Performance of Constructed Facilities*, 30(5): 04016034.
- Dong, Y., Frangopol, D. M., & Saydam, D. 2013. Time-variant sustainability assessment of seismically vulnerable bridges subjected to multiple hazards. *Earthquake Engineering & Structural Dynamics*, 42(10): 1451–1467.
- Duracrete. 2000. *Probabilistic Performance Based Durability Design of Concrete Structures: Final Technical Report*. The European Union – Brite EuRam III.
- FEMA. 2009. *Quantification of Building Seismic Performance Factors*. Technical report FEMA P695, Federal Emergency Management Agency, Washington, D.C.
- FHWA. 2019. *National bridge inventory data*. Federal Highway Administration, Washington D.C.
- Ghosh, J., & Padgett, J. E. 2011. Probabilistic seismic loss assessment of aging bridges using a component-level cost estimation approach. *Earthquake Engineering & Structural Dynamics*, 40(15): 1743–1761.
- Kabir, M. R., Billah, A. M., & Alam, M. S. 2019. Seismic fragility assessment of a multi-span RC bridge in Bangladesh considering near-fault, far-field and long duration ground motions. *Structures*, 19: 333–348.
- Lopez, A., Dusicka, P., & Bazaez, R. 2020. Performance of seismically standard bridge reinforced concrete columns subjected to subduction and crustal earthquakes. *Engineering Structures*, 207: 110216.
- McKenna, F., Fenves, G., & Scott, M. 2000. *Open system for earthquake engineering simulation*. University of California, Berkeley, CA.
- Ou, Y. C., Song, J., Wang, P. H., Adidharma, L., Chang, K. C., & Lee, G. C. 2014. Ground motion duration effects on hysteretic behavior of reinforced concrete bridge columns. *Journal of Structural Engineering*, 140(3): 04013065.
- Padgett, J. E., & DesRoches, R. 2007. Bridge functionality relationships for improved seismic risk assessment of transportation networks. *Earthquake Spectra*, 23(1): 115–130.
- Panchireddi, B., Shekhar, S., & Ghosh, J. 2021. Influence of ground motion duration on the seismic vulnerability of aging highway bridges. *Structure and Infrastructure Engineering*, 1–23.
- Raghunandan, M., & Liel, A. B. 2013. Effect of ground motion duration on earthquake-induced structural collapse. *Structural Safety*, 41: 119–133.
- Sebastiani, P. E. 2016. Performance-based seismic assessment for life-cycle cost analysis of existing bridges retrofitted with seismic isolation. Ph.D. Thesis, Sapienza University of Rome, Italy.
- Shekhar, S., Ghosh, J., & Padgett, J. E. 2018. Seismic life-cycle cost analysis of ageing highway bridges under chloride exposure conditions: modelling and recommendations. *Structure and Infrastructure Engineering*, 14(7): 941–966.
- Trifunac, M. D., & Brady, A. G. 1975. A study on the duration of strong earthquake ground motion. *Bulletin of the Seismological Society of America*, 65(3): 581–626.
- USGS. 2015. “Hazards: Seismic Hazard Maps and Data.” <<http://earthquake.usgs.gov/hazards/>> (Nov. 14, 2011).
- Vu, K. A. T., and Stewart, M. G. 2000. Structural reliability of concrete bridges including improved chloride-induced corrosion models. *Structural Safety*, 22(4): 313–333.

Seismic demand hazard assessment for RC bridges considering cumulative damage over time

D. Herrera & D. Tolentino

Departamento de materiales, Universidad Autónoma Metropolitana (UAM), CDMX, México

ABSTRACT: Natural disasters may significantly affect the functionality of highway transportation systems causing unacceptable socioeconomic losses. With the aim to estimate the instant at which a given damage threshold is exceeded, an approach to calculate numerical exceedance demand rates that considers the cumulative damage due to earthquakes over time is presented. The uncertainties related to mechanical and geometric properties as well as the occurrence of seismic loads are considered. The approach is illustrated on two continuous reinforced concrete bridges designed to comply with a drift threshold equal to 0.002. The systems are located in Acapulco, Guerrero, Mexico. Fragility and exceedance demand rates are estimated for different times of interest. The contribution of cumulative damage in the estimation of both fragility curves and exceedance demand rates over time is discussed.

1 INTRODUCTION

Many Mexican cities are located in earthquake-prone regions such as Mexico City and Acapulco City, making them vulnerable to infrastructure damage and devastation in terms of human lives and economic losses. Communities take years to recover from economic and social destruction caused by earthquakes. Therefore, earthquake mitigation is paramount in reducing loss of life and structural damage. To facilitate the recovery period that follows a seismic event, it is essential to estimate the damage condition from a probabilistic point of view to calculate the expected structural damage to local infrastructures. In case of reinforced concrete road bridges, it is essential to keep them at acceptable safety levels during their lifespan because they contribute to the economic growth of cities by promoting tourism, improving the response to needs or requests from communities, fostering the movement of merchandise, emergency equipment, passengers as well as the increase in surplus value in the area. In Mexico, more than 96% of all passengers are transported through the highways and 80% of the merchandise is mobilized in the country through these. The above generates about 2.5 million jobs and a contribution of 4.8% to the National Gross Domestic Product (GDP) (INEGI, 2021; INEGI, 2022).

Reinforced concrete bridges are subjected to different kind of environmental loads over time, researchers have proposed different approaches to estimate the structural performance of bridges under seismic loads using experimental and analytical techniques (Lehman et al. 2004, Yadav et al. 2017). In addition to deterministic response evaluation, probabilistic performance measures by considering uncertainty in hazard, material parameters, modeling variables and deterioration parameters have gained popularity in recent past such as seismic fragility assessment (Shinozuka et al., 2000, Nielson & DesRoches, 2007, Choe et al. 2008, 2009, Ghosh & Padgett, 2010, Pan et al. 2010). Severe damage to bridges and other vulnerable system components can cause economic losses associated with essential maintenance and repair interventions and economic consequences due to lack of network connectivity and downtime (Zhou et al. 2010; Decò et al. 2013). Bocchini and Frangopol (2011, 2012) developed a stochastic computational approach for fragility analysis and cost-based prioritization of interventions on spatially distributed bridges in transportation networks under disruptive

events. Recently, the seismic resilience of the life cycle and the vulnerability of the transportation bridge network have been studied under multiple hazards (Capacci & Biondini, 2020, Capacci et al., 2020). On the other hand, different methodologies have been proposed to consider the effect of cumulative damage over time due to seismic sequences (Cui et al. 2019; Panchireddi and Ghosh, 2019; Tolentino et al. 2020).

The probabilistic estimation of demand exceedance rates is a useful tool for decision-making and risk mitigation in structural systems, since it allows to determine the return period at which a given threshold of damage is exceeded. Various researchers have proposed different methodologies to obtain demand exceedance rates such as Mackie and Stojadinović (2001) that present an analysis of seismic demand on reinforced concrete bridges located in California. Demand exceedance rates are also estimated for reinforced concrete buildings (Liu et al. 2016). A methodology has been proposed to obtain demand hazard curves in gravity dams (Gavabar & Alembagheri, 2018). Demand exceedance rates are estimated in structural steel buildings (Maleki et al. 2019; Deylami and Mahdavi-pour, 2016; Afsar Dizaj et al. 2018).

The main objective of this article is to estimate numerical demand exceedance rates considering the effect of cumulative damage due to earthquakes over time. As observed in the cited works, demand exceedance rates are usually obtained through closed-form mathematical expressions and the possible damage caused by seismic sequences over time is not considered. Demand exceedance rates are obtained on two reinforced concrete bridges designed to comply with a drift threshold equal to 0.002.

2 DEMAND EXCEEDANCE RATES OVER TIME

The mean value of the exceedance demand rate, $v_D(d)$, proposed by Cornell et al. (2002) is extended to consider the possible cumulative damage at the instant t as follows:

$$v_D(d, t) = \int_0^t \int_0^\infty \int_0^\infty |v(\dot{y})| P(D_{seismic} \geq d|y, t) f_{D_{seismic}}(d|t) dy dddt \tag{1}$$

where $v(\dot{y})$ represents the first derivative of the mean annual failure; $P(D_{seismic} \geq d|y, t)$ is the structural fragility due to earthquakes at instant t and $f_{D_{seismic}}(d|t)$ is the probability density function of demand at the instant, t .

3 UNCERTAINTIES, SEISMIC EVENTS AND WAITING TIMES

The uncertainties related to materials construction and manufacturing processes help account for potential bias that needs to be considered when using nominal properties. Uncertainties have a significant influence on increasing or decreasing the structural response. When the structural response is expressed in terms of a reliability indicator, the system can exhibit desirable or undesirable reliability levels due to consideration of uncertainties. Table 1 shows the mechanical uncertainties of the materials. The geometric uncertainties of the structural sections are shown in Table 2. The uncertainties associated with the structural and non-structural elements are shown in Table 3.

Table 1. Mechanical uncertainties of materials.

Material	Nominal resistance (MPa)	Mean (MPa)	C.V.	Reference
Concrete	27.60	34.22	0.15	(Nowak et al. 2011)
	31.00	37.21	0.14	
	41.40	47.61	0.125	
Steel reinforcement	412	448.85	0.0369	(Rodríguez & Botero, 1995)

Table 2. Geometric uncertainties of structural elements (Ellinwood et al. 1980).

	Bias factor	C.V.
Slab elements	+7.62E-04	6.60E-03
Beams height	-5.334E-03	6.35E-03
Beam width	+2.54E-03	3.81E-03
Columns dimensions	+1.524E-03	6.35E-03
Cover	+8.128E-03	4.318E-03

Table 3. Uncertainties for structural and nonstructural elements (Nowak & Szerszen, 1998).

	Bias factor	C.V.	Distribution function
Factory items	1.03	0.08	Normal
Site elements	1.05	0.10	Normal
Asphalt	0.075*	0.25	Normal
Non-structural elements	1.03-1.05	0.08-0.01	Normal

The ground motion data set used as input for the seismic estimation has been used from two seismographic stations close to the study case (Tolentino & Carrillo-Bueno, 2018). The data set complies with 46 ground motions recorded during the past several decades. The mean epicentral distance is equal to 170.58 km and the dominant period of the soil site is around 0.51 s. The simulation of intensities of each seismic movement was carried out based on the seismic hazard curve, SHC, of the site for the fundamental period of the structure. The SHC indicates the number of times that that a certain level of intensity is exceeding per unit of time. It is assumed that the SHC of each structure is known. The simulation of intensities is carried out based on the cumulative distribution function, CDF, of the SHC as shown in the following equation:

$$F(y) = 1 - \frac{(y/y_0)^{-r}(y_{\max} - y/y_{\max} - y_0)^\varepsilon}{v_0} \quad (2)$$

where y_0 is the seismic intensity necessary to produce damage to structure; y_{\max} represents the maximum spectral acceleration in the SHC; r and ε are fitting constants of the SHC. With the aim to simulate waiting times between seismic events, it is assumed that these follow a stochastic Poisson process then, the events follow an exponential distribution (Melchers & Beck, 2017). Performing some mathematical steps on the CFD of the exponential distribution, the waiting times between seismic occurrences, T_i , are obtained as shown in the following equation:

$$T_i = - \left| \frac{\ln(u)}{v_0} \right| \quad (3)$$

4 NONLINEAR MODELLING AND CUMULATIVE DAMAGE

Structures are exposed to different environmental loads over time. If the occurrence of environmental load or solicitation is similar to the solicitation that governed the design, there is a high probability that the structure presents certain damage. The structural damage can be estimated by means of concentrated plasticity considering that plastic hinges occur at a distance close to the ends of the elements. The structure under study is modeled by using Ruaumoko 3D program (Carr, 2003). It is assumed that columns and cap beams elements provide the lateral stiffness of the system. Furthermore, the bridge deck only transmits dead loads. The modified Takeda hysteresis rule is used to estimate the plastic hinges. On the other hand, if no maintenance actions are performed after the occurrence of an intense seismic load,

the system could accumulate damage and if this process is repeated, it is probable that the system would present undesirable reliability levels in a short period of time. To identify the possible cumulative damage, the following steps show the damage accumulation process.

1. n simulated bridges are generated with simulated properties.
2. Simulation of intensities associated with n simulated models are generated.
3. $i = 1$
4. The i – th simulated intensity is associated with the n – th structural model related with an instant of interest, t . Then, the i -th simulated intensity and the $(i+1)$ – th simulated intensity are scaled by a factor $\beta_m = i_{sim}/i_T$, which is the result of the ratio between the simulated intensity and the spectral acceleration associated with the dominant period of the structure, T . The structural response is obtained by extracting the maximum drift, $D_{i,y,t}$, at the bridge deck.
5. A seismic record, $S_{k,i}$, is randomly selected and is multiplied by a scale factor, ψ_e , that produces the drift value, $D_{i,y,t}$, obtained in step 4.
6. $i = i + 1$
7. A seismic record, r_{i-1} , is associated with the $(i+2)$ – th simulated intensity and it is scaled by the factor β_m . Then, the system is subjected to two seismic loads, $S_{k,i}$ plus r_{i-1} and the maximum drift, $D_{(i-1),y,t}$, is obtained.
8. The process is repeated from step 5 to 7.

5 APPLICATION EXAMPLE

Demand exceedance rates are obtained based on two reinforced concrete bridges. The first case, referred to as case A that consists of four lanes, a height of 9 m and a total length of 175 m. Case study B is a RC bridge that consists of 4 spans with a total length of 130 m and 8 m of height clearance. Table 4 shows the dimensions and reinforcement of columns and cap beams sections of both study cases. Each system has a compressive strength, f'_c , equal to 30 MPa for columns and cap beams while a value of 45 MPa is considered for AASHTO beams. The structures are designed to comply with a drift level equal to 0.002 and these are located in Acapulco, Mexico. Case A and B reports a fundamental period equal to 0.34 and 0.28 s, respectively. It is important to mention that both case studies have five circular columns, nine AASHTO type VI beams, and a total width equal to 18.06 m.

Table 4. Geometry and design of structural elements.

Case study	Structural element	Geometry (m)	Rebar (m)	Cover thickness (m)
A	Columns	$\phi = 2$	38- ϕ 0.03175	0.05
	Cap beams	$b = 2; h = 1.4$	16- ϕ 0.0254	0.05
B	Columns	$\phi = 1.85$	34- ϕ 0.0254	0.05
	Cap beams	$b = 2; h = 1.5$	16- ϕ 0.0254	0.05

5.1 Structural demand over time

The structural demand over time is obtained by means of nonlinear dynamic analysis. Fifty bridges with simulated properties are considered for each case study. The cumulative damage is estimated using the procedure described in section 4. Different instants of time such as 0, 50, 75, 100 and 125 years are considered. Figure 1a and b show the median value of demand for different time instants for case A and B, respectively. In Figure 1a is observed that the initial ordinates of the demand increase as time progresses ($y/g = 0.10$). These initial ordinates present values of 0.00087, 0.00165, 0.00242, 0.00312 and 0.00385. This implies that for intensities equal to 0.10 y/g , the seismic demand increases by 90.51%, 178.83%, 258.67% and 342.86% for the instants of 0, 50, 75, 100 and 125 years. The above suggest that the structure experimented damage over time. For the case of the instant of 50 years at 0.20 y/g , it is

obtained a value of $\bar{D}_{|y,t}$ equal to 0.0032 thus, the pre-establish design drift threshold of 0.002 has been reached at 50 years. Besides, it is observed an increment of 184.96% from 0 to 125 years for intensities equal to 0.20 Sa/g. On the other hand, it can be observed that the collapse condition is reached when seismic intensities present values higher than 0.70 y/g. Figure 1b shows the structural demand over time obtained for study case B. Figure 1b provides the following data: a) the median demand value at 0.10 y/g is equal to 0.00088 for the case of no damage; for the subsequent time instants, an initial ordinate due to cumulative damage is noted and b) the median of the demand is equal to 0.00115, 0.00161, 0.00207 and 0.0028 for the instants of 50, 75, 100 and 125 years. This implies that the demand caused by earthquakes increases of around 31.04%, 82.66%, 134.28% and 216.95%.

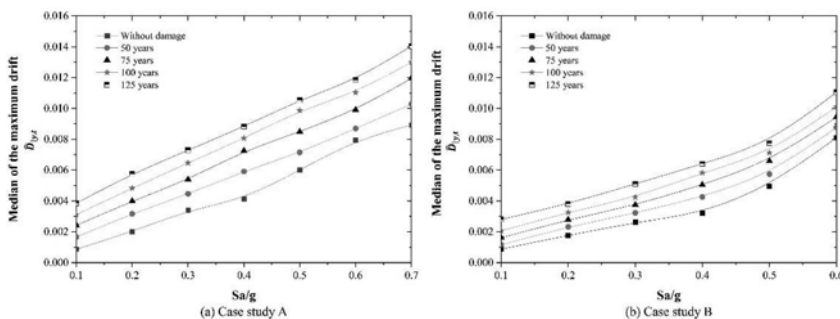


Figure 1. Median of the demand for: a) case A and b) case B.

5.2 Structural demand over time

Fragility curve over time indicates the probability of exceeding a certain level of demand at the instant t . This reliability indicator is estimated as follows (Tolentino et al. 2020):

$$P(D_{seismic} \geq d|y, t) = 1 - \Phi\left(\frac{\ln(d) - \ln(\bar{D}_{|y,t})}{\sigma_{\ln D_{|y,t}}}\right) \quad (4)$$

where $\bar{D}_{|y,t}$ is the median of the demand related to a particular damage due to earthquakes for a given intensity y at a time instant t ; d is a predefined demand threshold; $\sigma_{\ln D_{|y,t}}$ is the standard deviation of the natural logarithm of demand for an intensity y at time t . Figure 2 shows the fragility curves obtained for the case study A and B considering time instants of 0, 50, 75, 100 and 125 years associated to different drift thresholds such as 0.002, 0.004, 0.006 and 0.012. Figure 2a-d shows the fragility curves obtained for the study case A. Figure 2a shows that the probability of exceeding 0.002 is close to zero for intensities smaller than 0.10 y/g for 0 and 50 years. Besides, it is observed that for intensities greater than 0.50 y/g, the probability close to one is reached. It is important to observe that there are different initial ordinates associated with intensities of 0.10 y/g, this is due to the consideration of cumulative damage due to earthquakes over time. Figure 2b illustrates that the probability of exceeding 0.004 is reached for intensities greater than 0.65 y/g and there are probabilities close to zero for the cases of 0 and 50 years for intensities not greater than 0.20 y/g. On the other hand, Figure 2c shows that the probability of exceeding the drift threshold of 0.006 is reached after 0.70 y/g for all instants. Probabilities of exceedance close to zero are reached before 0.25 y/g for the instants of 0 and 50 years. Figure 2d shows that the probability of exceeding the drift threshold of 0.012 at any point in time is close to one. On the other hand, Figure 2e-h shows the fragility curves obtained for the study case B. Figure 4e shows that the probability of exceeding 0.002 is near to zero for y/g values minor than 0.20 at the instant equal to zero. In contrast, the probability of exceeding 0.002 is near to one for values greater than 0.55 y/g for all cases. Figure 2f shows that 0.004 is exceeded when values greater than 0.60 y/g are presented and the

probability is close to zero for the instants of 0 and 50 years for intensities not greater than 0.25 y/g. Figure 2g shows that values greater than 0.60 y/g exceedance the drift threshold of 0.006 for times of 75, 100 and 125 years. The probability of exceedance 0.006 is near to zero for values lower than 0.30 y/g for instants of 0 and 50 years. For 75 years, the probability is close to zero for y/g values less than 0.20. The greatest probability of exceeding the value of 0.012 is equal to 0.38 (see Figure 2h), this implies that there is a certain probability that the structure collapse at 0.7 y/g at any time. Based on the above, it is noticed that the case of study A is more vulnerable than the case study B, this is mainly due to differences in geometry and steel reinforcement between both cases.

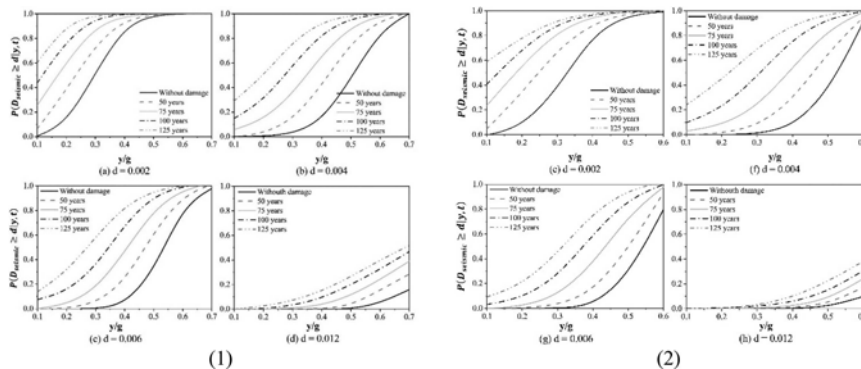


Figure 2. Fragility curves over time: (1) case study A and (2) case study B.

5.3 Mean annual demand exceedance rate over time

Demand exceedance rates indicate the frequency that a drift level is exceeded at a certain instant, t . It is essential to mention that the inverse of a demand exceedance rate is the return period, which provides information about the exceedance of a certain damage threshold in terms of time. Figure 3a and b show the exceedance rates for periods 0, 50, 75, 100 and 125 years for both cases A and B, respectively. Figure 3a illustrates the subsequent details: a) the design level (0.002) has exceedance rates equal to 0.0159, 0.0182, 0.0214, 0.0263 and 0.0314 for times of 0, 50, 75, 100 and 125 years, respectively, b) the mean annual exceedance rate increases as cumulative damage is increased over time with a mean percentage of 18.44%, c) differences of 13.97% between 0 and 50 years for 0.002 are presented. d) at the instant of 75 years, it is obtained an exceedance rate equal to 0.0214 associated with a return period equal to 46.76 years. Figure 3b shows the following information: a) the drift threshold of 0.002 present increments of 11.03%, 29.49%, 55.57%, and 83.85% for time instants of 0, 50, 75, 100, and 125 years, respectively, b) at $t = 75$ years the mean exceedance rate is equal to 0.0167 which is associated with a return period of 59.53 years, c) the mean exceedance rate of the design threshold increases up to 20.14% and 40.11% for the instants of 100 and 125 years, compared to the instant of 75 years. d) for the instant $t = 0$ years (without damage), it is observed that the exceedance rate of the drift threshold of 0.012 is equal to 0.00026 associated with a return period of 3838.78 years, which implies that the structure will not collapse under this limit state condition.

6 CONCLUSIONS

An approach to obtain numerical exceedance demand rates that consider cumulative damage caused by seismic sequences was proposed. Uncertainties associated with mechanical and geometrical properties were considered. The approach was illustrated in two continuous bridges designed to comply with a value of drift equal to 0.002. Different instants were considered to estimate the possible damage due to earthquakes over time. Fragility curves were obtained considering different time instants such as 0, 50, 75, 100 and 125 years associated to the drifts

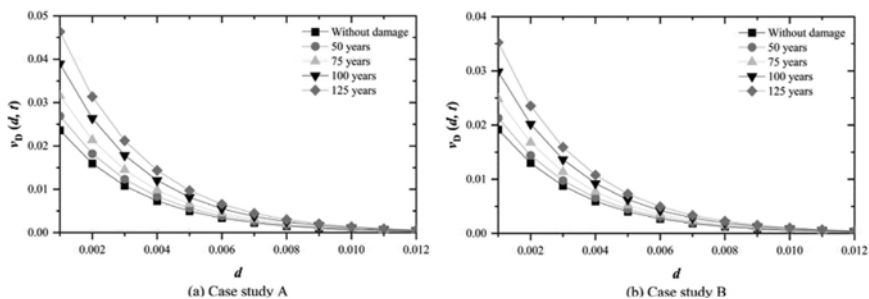


Figure 3. Demand exceedance rates over time for: a) case A and b) case B.

of 0.002, 0.004, 0.006, and 0.012. The effect of cumulative damage due to earthquakes leads the structures to present high probabilities of exceeding all drift thresholds for the intensities under study. Demand exceedance rates were determined for different instants considering drift thresholds between 0.001 and 0.012. In accordance with the recommendations of AASHTO regulations (AASHTO, 2012), the lifespan of the bridges must be guaranteed for a period of 75 years; with this, the demand seismic hazard at 75 years indicates that the design drift threshold is exceeding after 46.76 and 59.53 years for the study case A and B, respectively. The above implies that the structures have a high probability of exceeding the design drift threshold before reaching the lifespan. These does not imply that the structures will be at risk of collapse, but there is a high probability that they could present certain damage. The proposed approach allows evaluating future conditions considering the effect of cumulative damage caused by seismic loads.

The information provided by such evaluation is helpful in the decision-making process during the design of new structures. Moreover, the exceedance demand rate associated to a certain limit state indicates the reserves of structural strength that the system has in a certain instant of time. The approach can be taken as the basis for maintenance and inspection plans with the aim of preserving the structure with adequate reliability levels.

ACKNOWLEDGEMENTS

The first author thanks CONACyT and UAM for the economic support to develop his PhD research. The second author thanks the support given by Consejo Nacional de Ciencia y Tecnología through the Ciencia Básica Project CB 2017-2018 A1-S-8700 and Universidad Autónoma Metropolitana.

REFERENCES

- AASHTO 2012. *Standard specifications for highway bridges*. American Association of State Highway and Transportation Officials. Washington, DC, USA.
- Afsar Dizaj, E., Fanaie, N., & Zarifpour, A., 2018. Probabilistic seismic demand assessment of steel frames braced with reduced yielding segment buckling restrained braces. *Advances in Structural Engineering*, 21 (7): 1002–1020.
- Bocchini, P. & Frangopol, D.M., 2011. A stochastic computational framework for the joint transportation network fragility analysis and traffic flow distribution under extreme events. *Probabilistic Engineering Mechanics*, 26 (2): 182–193.
- Bocchini, P. & Frangopol, D.M., 2012. Optimal Resilience- and Cost-Based Postdisaster Intervention Prioritization for Bridges along a Highway Segment. *Journal of Bridge Engineering*, 17 (1): 117–129.
- Capacci, L. & Biondini, F., 2020. Probabilistic life-cycle seismic resilience assessment of aging bridge networks considering infrastructure upgrading. *Structure and Infrastructure Engineering*, 16 (4): 659–675.
- Capacci, L., Biondini, F., & Titi, A., 2020. Lifetime seismic resilience of aging bridges and road networks. *Structure and Infrastructure Engineering*, 16 (2): 266–286.
- Carr, A.J., 2003. RUAUMOKO 3D Volume 3: User manual for the 3-Dimensional version. *Christchurch, University of Canterbury, New Zealand*.

- Choe, D., Gardoni, P., Rosowsky, D., & Haukaas, T., 2008. Probabilistic capacity models and seismic fragility estimates for RC columns subject to corrosion. *Reliability Engineering and System Safety*, 93 383–393.
- Choe, D.E., Gardoni, P., Rosowsky, D., & Haukaas, T., 2009. Seismic fragility estimates for reinforced concrete bridges subject to corrosion. *Structural Safety*, 31 (4): 275–283.
- Cornell, C.A., Jalayer, F., Hamburger, R.O., & Foutch, D.A., 2002. Probabilistic Basis for 2000 SAC Federal Emergency Management Agency Steel Moment Frame Guidelines. *Journal of Structural Engineering*, 128 (4): 526–533.
- Cui, S., Guo, C., Su, J., Cui, E., & Liu, P., 2019. Seismic fragility and risk assessment of high-speed railway continuous-girder bridge under track constraint effect. *Bulletin of Earthquake Engineering*, 17 (3): 1639–1665.
- Decò, A., Bocchini, P., & Frangopol, D.M., 2013. A probabilistic approach for the prediction of seismic resilience of bridges. *Earthquake Engineering and Structural Dynamics*, 42 (10): 1469–1487.
- Deylami, A. & Mahdavi-pour, M.A., 2016. Probabilistic seismic demand assessment of residual drift for Buckling-Restrained Braced Frames as a dual system. *Structural Safety*, 58 31–39.
- Ellinwood, Bruce R.; Galambos, T. V.; McGregor, J. G.; Cornell, C.A., 1980. *NBS SPECIAL PUBLICATION 577 Development of a Probability Based Load Criterion for American National Standard A58 Building Code Requirements for Minimum Design Loads in Buildings and Other Structures*.
- Gavabar, S.G. & Alembagheri, M., 2018. Structural demand hazard analysis of jointed gravity dam in view of earthquake uncertainty. *KSCE Journal of Civil Engineering*, 22 (10): 3972–3979.
- Ghosh, J. & Padgett, J.E., 2010. Aging Considerations in the Development of Time-Dependent Seismic Fragility Curves. *Journal of Structural Engineering*, 136 (12): 1497–1511.
- Instituto Nacional de Estadística y Geografía (INEGI) 2021. *Producto Interno Bruto de México*. <https://www.inegi.org.mx/temas/pib/>.
- Instituto Nacional de Estadística y Geografía (INEGI) 2022. *Transportes*. Available from: <https://www.inegi.org.mx/temas/transportes/>.
- Lehman, D., Moehle, J., Mahin, S., Calderone, A., & Henry, L., 2004. Experimental Evaluation of the Seismic Performance of Reinforced Concrete Bridge Columns. *Journal of Structural Engineering*, 130 (6): 869–879.
- Liu, X.X., Wu, Z.Y., & Liang, F., 2016. Multidimensional performance limit state for probabilistic seismic demand analysis. *Bulletin of Earthquake Engineering*, 14 (12): 3389–3408.
- Mackie, K. & Stojadinović, B., 2001. Probabilistic seismic demand model for California highway bridges. *Journal of Bridge Engineering*, 6 (6): 468–481.
- Maleki, M., Ahmady Jazany, R., & Ghobadi, M.S., 2019. Probabilistic seismic assessment of SMFs with drilled flange connections subjected to near-field ground motions. *International Journal of Steel Structures*, 19 (1): 224–240.
- Melchers, R.E. & Beck, A.T., 2017. *Structural Reliability Analysis and Prediction*. Structural Reliability Analysis and Prediction. Chichester, UK: John Wiley & Sons Ltd.
- Nielson, B.G. & DesRoches, R., 2007. Analytical Seismic Fragility Curves for Typical Bridges in the Central and Southeastern United States. *Earthquake Spectra*, 23 (3): 615–633.
- Nowak, A., Rakoczy, A., & Szeliga, E.K., 2011. Revised statistical resistance models for R/C structural components. *American Concrete Institute, ACI Special Publication*, 284 61–76.
- Nowak, A.S. & Szerszen, M.M., 1998. Bridge load and resistance models. *Engineering Structures*, 20 (11): 985–990.
- Pan, Y., Agrawal, A.K., Ghosn, M., & Alampalli, S., 2010. Seismic Fragility of Multispan Simply Supported Steel Highway Bridges in New York State. I: Bridge Modeling, Parametric Analysis, and Retrofit Design. *Journal of Bridge Engineering*, 15 (5): 448–461.
- Panchireddi, B. & Ghosh, J., 2019. Cumulative vulnerability assessment of highway bridges considering corrosion deterioration and repeated earthquake events. *Bulletin of Earthquake Engineering*, 17 (3): 1603–1638.
- Rodríguez, M. & Botero, J., 1995. Comportamiento sísmico de estructuras considerando propiedades mecánicas de aceros de refuerzo mexicanos. *Revista de Ingeniería Sísmica*, 1 (49): 39–50.
- Shinozuka, M., Feng, M.Q., Kim, H.-K., & Kim, S.-H., 2000. Nonlinear Static Procedure for Fragility Curve Development. *Journal of Engineering Mechanics*, 126 (12): 1287–1295.
- Tolentino, D. & Carrillo-Bueno, C.A., 2018. Evaluation of Structural Reliability for Reinforced Concrete Buildings Considering the Effect of Corrosion. *KSCE Journal of Civil Engineering*, 22 (4): 1344–1353.
- Tolentino, D., Márquez-Domínguez, S., & Gaxiola-Camacho, J.R., 2020. Fragility assessment of bridges considering cumulative damage caused by seismic loading. *KSCE Journal of Civil Engineering*, 24 (2): 551–560.
- Yadav, R., Chen, B., Yuan, H., & Lian, Z., 2017. Experimental Investigation of CFST-RC Bridge Piers under Cyclic Loading. *Procedia Engineering*, 173 1723–1730.
- Zhou, Y., Banerjee, S., & Shinozuka, M., 2010. Socio-economic effect of seismic retrofit of bridges for highway transportation networks: A pilot study. *Structure and Infrastructure Engineering*, 6 (1–2): 145–157.

Development of maintenance systems for bridge members

K. Kwon, Y. Choi & J.S. Kong

School of Civil, Environmental and Architectural Engineering, Korea University, Seoul, Korea

ABSTRACT: Recently, the number and total length of Korean bridges are increasing aged 30 years after completion of construction. In particular, 46% of bridges are more than 20 years old, and the ratio of old bridges will surge after 10 years. In fact, the collapse of the “Seongsu Bridge” occurred in 1994, and the cause of the collapse is a failure of proper maintenance, and there is a need for an active bridge maintenance scenario. So, there is a growing social interest in bridges and infrastructure that has deteriorated. Also, studies on performance prediction and maintenance decision making of structures are underway. Therefore, the trend of increase in maintenance costs can be expected, thus more rational bridge maintenance is needed. Therefore, in this study, the condition of the bridge is predicted by using a deterioration model using bridge maintenance data in Korea so that a limited maintenance budget can be effectively utilized. And through the degradation model, a cost optimization technique is used. Therefore, it is possible to reduce the maintenance budget and support realistic maintenance decision-making model compared to the existing maintenance scenarios.

1 INSTRUCTIONS

1.1 *Background*

Currently, the number of infrastructure facilities for bridges in Korea is steadily increasing as shown in Figure 1. In addition, the proportion of aging facilities that have been used for 30 years is increasing. Therefore, social interest in the maintenance and management of bridges is currently increasing. Therefore, in the case of the Republic of Korea, it has been changed from post-preventive maintenance, which is taken in case of an accident on a bridge, to proactive maintenance, which is taken before an accident occurs. For proactive purposes, research is being actively conducted to plan maintenance in advance by collecting maintenance data and predicting the status and performance of the bridge through data analysis. However, despite the research on bridge maintenance and social interest, the SOC field budget is decreasing as shown in Figure 1. Therefore, the budget is insufficient due to the increase in maintenance costs.

In fact, a period of rapid increase in aging infrastructure is expected, and due to a lack of budget and careless management of facilities, large-scale accidents actually occurred. Representative examples in Korea include the collapse of Seongsu Bridge (1994), the collapse of the Morandi Bridge in Janova, Italy (2018), and the collapse of the arch bridge in Taiwan (2019). Therefore, in order to prevent such a large-scale accident, it is necessary to efficiently use the bridge maintenance budget in a limited budget. In this study, an optimal maintenance scenario is proposed for performing preliminary maintenance of bridges.

Using the results of the bridge performance prediction to propose an optimal maintenance scenario, a maintenance scenario was derived to derive the optimal maintenance/reinforcement time and cost converted to the present value by applying the concept of a halving rate during the target life.

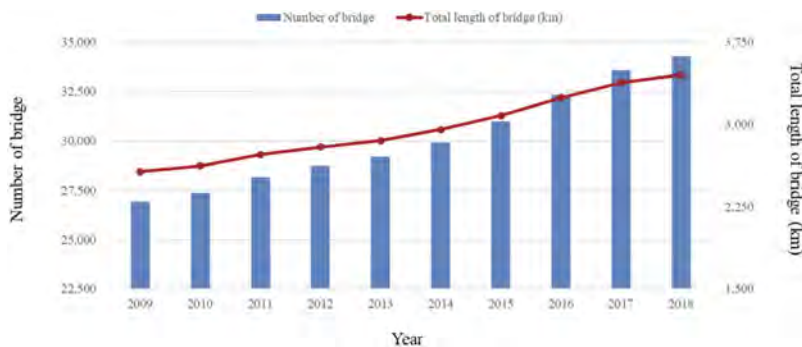


Figure 1. Bridge statistics in South Korea.

The currently developed bridge optimal maintenance scenario study is as follows. (Liu, M, 2005) applied a multi-purpose optimization technique based on genetic algorithms to create maintenance plans for old bridges. (Eslam Mohammed, 2022). established bridge maintenance plans at the project level and network level through Chaotic-based optimization model. (N Erdogan, 2021) prioritized optimal maintenance plans using optimization algorithms. And recently, a study on the condition of bridges using machine learning models is being conducted. For example, (Assad, 2020) classified the state of the deck using the k-neighbor (KNN) method and the artificial neural network (ANN) method classified according to distance. Also, (Choi, 2020) uses the LSTM method to predict the performance of the concrete deck to consider the time-series characteristics of the bridge deck members.

1.2 Objectives

For the development of the optimal maintenance system for this study, the steps are composed of 4 steps and are as follows: First, we collected bridge data and inspection history information through the Korean Bridge Integrated Management System (BMS), and established a model for condition pre-diction. Second, a model was used to quantitatively evaluate the cost and effectiveness of bridge maintenance through BMS repair and reinforcement data and expert surveys. Third, to derive the optimal system-level maintenance scenario, the maintenance combination was selected by analyzing the de-pendent relationship analysis and damage correction effects of replacement with members. Finally, we propose an optimal bridge maintenance scenario using the state prediction model and the LCC model of the bridge using genetic algorithms. And we checked the efficiency compared to the existing member level evaluation.

2 BRIDGE STATUS PREDICITON MODEL

2.1 Data set

In order to perform optimal maintenance of road bridges, a bridge condition prediction model is required. Most of the recent bridge condition prediction models predict the condition with bridge inspection history data, which is a performance-based bridge maintenance method, which is mainly analyzed by the change in the performance index of the constituent members of the bridge according to the usage time. Here, the performance index means the defect index obtained by converting the condition grade obtained through inspection and diagnosis into points. The definition of the defect index is as follows and summarized in Table 1.

In addition, the bridge condition inspections evaluated by the Korean BMS are largely divided into regular inspections, precise safety inspections, and emergency inspections. The bridge inspection data used in this study predicted the condition of the bridge using precision diagnosis data.

Table 1. Definition of the defect index of bridges.

Condition state	A	B	C	D	E
Defect Index	0.1	0.2	0.4	0.7	1
Range of defects	$0 \leq X < 0.13$	$0 \leq X < 0.13$	$0.26 \leq X < 0.49$	$0.49 \leq X < 0.79$	$0.79 \leq X < 1$
Condition index	0.9	0.8	0.6	0.3	0

2.2 Prediction model of bridge member status rate

In the case of the status grade data of Korean bridges, it is widely distributed in rate B, and when all data are simply regression analyzed, there is a problem that the degradation tendency of the bridge cannot be grasped. Therefore, in this study, the result of calculating the deterioration slope over time by classifying the bridge member and span without using the state grade of the entire bridge was used. In addition, the deterioration equation was used to derive the optimal scenario for bridge maintenance.

In order to develop a model for predicting the state of the bridge used, the dependent variable of the bridge maintenance data was set as the defect index, and the independent variable was designated as the common year, and the maintenance data for each bridge member was subjected to a single variable regression analysis. At this time, the degradation rate for each member of the bridge was calculated. Regression analysis was conducted by designating the dependent variable as the degradation rate of the individual bridges of the short variable regression analysis using the calculated member-specific degradation rate, and the independent variable as the maximum span, ADTT, average humidity, and surface chloride. The multivariate regression equation used a quadratic polynomial in the univariate regression analysis, and as a result of comparing and analyzing the Cross Term effects of the variable tubes, the effects of each other are insufficient, so it is expressed as Equation 1

$$\beta_0 + \beta_1 x_1 + \beta_2 x_2 + \beta_3 x_3 + \beta_4 x_4 + \beta_5^2 x_1^2 + \beta_6^2 x_2^2 + \beta_7^2 x_3^2 + \beta_8^2 x_4^2 \quad (1)$$

where x_1 = maximum span length; x_2 = average daily truck traffic(ADTT); x_3 = average humidity; and x_4 = amount of surface chloride

2.3 Cost and evaluation model for repair reinforcement

For optimal maintenance of a bridge, a model that can quantitatively predict and evaluate the maintenance costs and effects required during the life cycle of the structure is required. Therefore, in this study, a quantified model for the cost and effect of repair and reinforcement was presented. In order to calculate the expected cost according to the status index of each member, the representative repair and reinforcement method for each member was selected by referring to the BMS "Guidelines for Writing Bridge&Tunnel Survey" in Korea. In addition, using this data, a DB on the cost and effect of repair reinforcement was established through a survey by the managing director of the inspection diagnosis service and repair reinforcement report analysis. In addition, the expected cost according to the status index of each member evaluated in this study was expressed as shown in Equation 2-4 below based on the DB.

$$E(U_{ele}(c.i)) = \sum_1^n (U_{ele}^{RAM}(c.i) \times Q_{ele}^{RAM}(c.i) \times F_{ele}^{RAM}(c.i)) \quad (2)$$

where $E(U_{ele}(c.i))$ = Expected cost of unit price by condition index (c.i) of element (ele); $U_{ele}^{RAM}(c.i)$ = Unit price of representative Application Method; $Q_{ele}^{RAM}(c.i)$ = rate of representative Application Method; $F_{ele}^{RAM}(c.i)$ = Frequency of representative Application Method and n = Number of representative Application Method

$$C_{ele}(c.i) = E(C_{ele}(c.i)) \times M_{ele} \quad (3)$$

where $C_{ele}(c.i)$ = Repair and reinforcement costs; and M_{ele} = Total member quantity.

$$E(B_{ele}(c.i)) = \sum_1^n (B_{ele}^{RAM}(c.i) \times F_{ele}^{RAM}(c.i)) \quad (4)$$

where $E(B_{ele}(c.i))$ = Expected value of the state improvement index by state index (c.i) of the element (ele); and $B_{ele}^{RAM}(c.i)$ = State improvement index of Representative application method(RAM);

The expected cost of repair and reinforcement costs according to the status grade of the member can be expressed as the product of the unit price of the representative repair and reinforcement method and the frequency of application of the method to the total quantity. In the case of the total quantity applied, the difference in the status index before and after the repair and reinforcement measures was assumed, and in the case of the frequency of application of the representative method, it was calculated based on the number of applications of the public law for damage by state grade.

3 OPTIMAL MAINTENANCE SCENARIO

In order to establish an efficient bridge maintenance strategy, it is necessary to estimate the optimal bridge maintenance cost by considering the life cycle performance and cost model. Figure 2-3 is the concept of a bridge maintenance scenario using the developed degradation model. Figure 2 shows that in existing maintenance scenario, it is difficult for bridge inspectors to consider the correlation and degradation rate of each member for repair and reinforcement during the life of the structure, so it is difficult to estimate efficient maintenance costs. However, as show in Figure 3, this study analyzed the dependency of replacement by each member and the tendency of degradation acceleration due to the damage transition effect by providing a system level maintenance scenario, and selected a maintenance combination to suggest an optimal system level maintenance scenario.

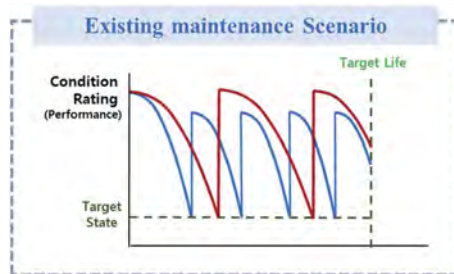


Figure 2. Concept graph of existing maintenance scenario.

The existing maintenance scenario is a method of replacement or repair when repair reinforcement reaches a specific state during the target life of the structures. However, in the system-level maintenance scenario, it is necessary to consider the maintenance combination of various members rather than separately considering the maintenance of each opening member. This is because members in the upper structure of the bridge are replaced by slabs and floor plates when replacing walls, and overlapping costs such as replacing floor plates when replacing girder, and replacing bridge packaging when replacing floor plates. However, the use of system-level maintenance scenarios can be expected to eliminate duplicate costs by adjusting the timing of absent action.

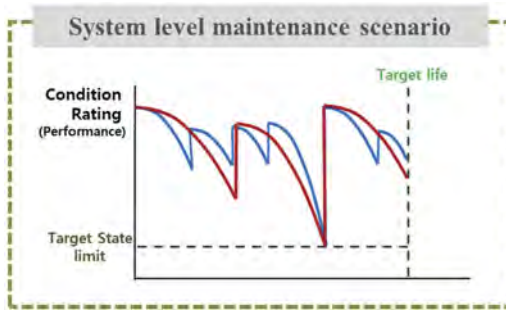


Figure 3. Concept graph of System level maintenance scenario.

3.1 Development of optimal maintenance scenario

The purpose of this study is to find the repair and reinforcement time and cost to minimize the system-level life cycle cost considering the replacement fault system and damage transition effect of the members while maintaining the optimal maintenance level during the target function for optimal maintenance is as Equation 5–7.

$$RRC = \sum_{K=1}^n \frac{1}{(1+q)^{tk}} c_{ele}(c.i_k) \quad (5)$$

where $C_{ele}(c.i_k)$ = Repair and reinforcement cost function at condition index in bridge element; and q = Discount rate.

$$EC = \sum_{K=1}^T \frac{1}{(1+q)^t} c^{rins}(t) + c^{pins}(t) + c^{psdia}(t) \quad (6)$$

where $c^{rins}(t)$ = Regular inspection cost at time t ; $c^{pins}(t)$ = Precise inspection cost at time t ; and $c^{psdia}(t)$ = Precise safety diagnosis cost at time t .

$$LCC_{ele}(C.I) = \sum_{K=1}^n \frac{1}{(1+q)^{tk}} c_{ele}(c.i_k) + \sum_{K=1}^T \frac{1}{(1+q)^t} c^{rins}(t) + c^{pins}(t) + c^{psdia}(t) \quad (7)$$

where $LCC_{ele}(C.I)$ = Maintenance costs for the target lifetime.

Using the optimization method, the optimal maintenance concept is shown in Figure 4. Figure 4 shows the optimal maintenance scenario flow chart and constraints using the GA method.

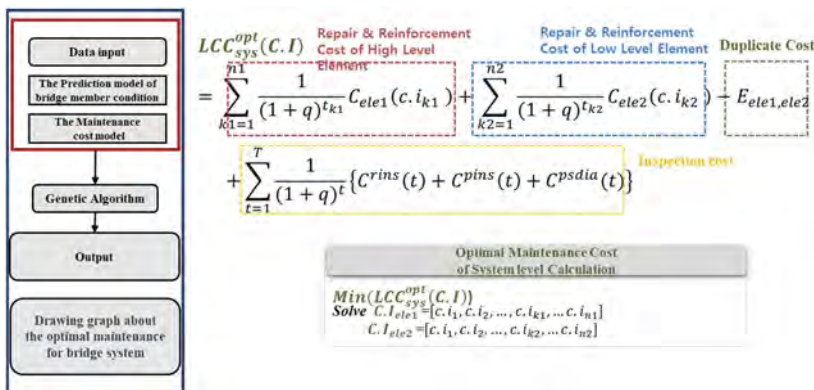


Figure 4. Optimal algorithm for bridge maintenance about time point and cost using G.A.

4 APPLICATION OF GENETIC ALGORITHM

This section describes the optimization method that is applied to the planning problem of maintenance measures based on cost minimization and quality maximization. In this study, GA optimization be adopted for the combination problem due to the large number of combinations. And Ga is maintains a population of candidate solutions for the problem at hand, and makes it evolve by iteratively applying a set of stochastic operators. In addition, as illustrated global minimum (or maximum) can be achieved well because it does not use gradient methods unlike other existing optimizations. As show in Figure 5 is GA Basic structure.

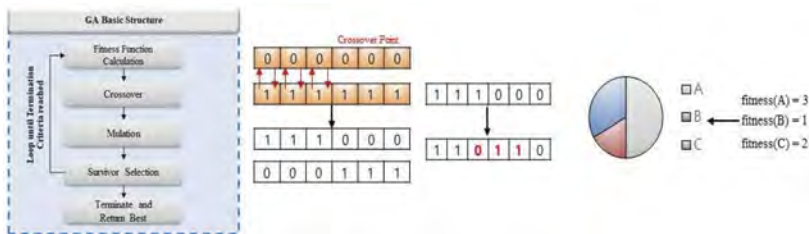


Figure 5. Genetic Algorithm of basics structure & Concepts.

5 VERIFICIATION OF OPTIPMAL MAINTENANCE COST

This chart Compare the existing maintenance costs with the optimal maintenance costs at the single element level. The life cycle costs are the sum of the repair & reinforcement cost, inspection cost and so on, but the study will only perform an analysis of t he repair and reinforcement costs. Existing maintenance costs were calculated by assuming that improvement action were carried out on specific conditions. The optimal maintenance costs were calculated the condition index at the point of repair and reinforcement that minimizes the life cycle cost.

In this study target bridge is Samseong Bridge. The bridge is a steel box girder bridge, and total span length is 53 meters and width 24 meters, location is Deoksan-myeon, Yesan-gun, Chungcheongnam-do, Republic of Korea and Traffic passage is National Road (Opening: 2007. 12.21). Input values for concrete deck and Asphalt Pavement include deterioration rate, cost model and total volume.

6 PROPOSAL OF MAINTENANCE SCENARIO AND VERIFICATION OF OPTIMAL MAINTENANCE COST

6.1 *Optimal maintenance cost (Concrete deck)*

Compare Existing Maintenance Scenario costs and Optimal Maintenance Scenario Costs. Figure 6 shows the different maintenance systems about Concrete Deck. blue line is the existing management maintenance scenario for the concrete deck. It is assumed that current maintenance is carried out in the status grade (C), It is assumed that current maintenance is carried out in the status grade (C). a target life is 100 years and a discount rate of 2%. because The discount rate was set to 1.01 % by reflecting the actual discount rate for a decade by Economic Statistics System (ECOS) in the bank of Korea. In conclusion, using the LCC Cost Model, we calculated the total cost. Existing Maintenance Cost is 260,312,000 KRW, and Optimal Maintenance Cost of Element Level is 196,771,157 KRW and The optimal scenario is that when the condition index(B) is reached, the reinforcement, occurs approximately 50 years after the replacement occurs. Finally, Cost Efficiency of Optimal Maintenance Cost (Element Level) is 24%. so it is possible to predict 24% cost savings through optimal preventive maintenance at element level

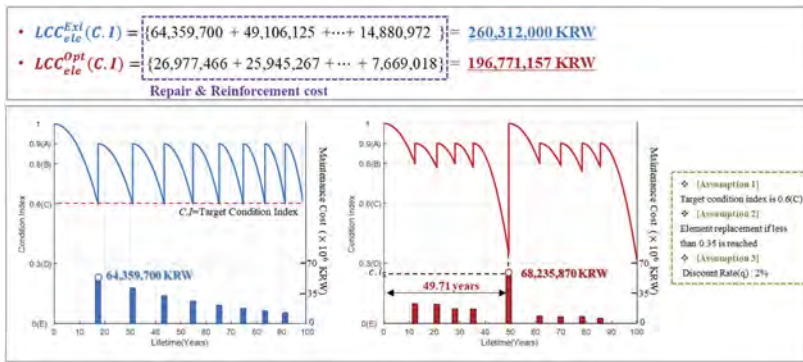


Figure 6. Compare existing maintenance cost and optimal maintenance cost (Concrete deck).

6.2 Optimal maintenance cost (Pavement)

Compare Existing Maintenance Scenario costs and Optimal Maintenance Scenario Costs about Asphalt Pavement. Figure 7 shows the different maintenance systems about Concrete Deck. as well as blue line is the existing management maintenance scenario for the concrete deck. Also, it is assumed that current maintenance is carried out in the status grade (D), It is assumed that current maintenance is carried out in the status grade (D), Element replacement if less than 0.35 is reached, a target life is 100 years and a discount rate of 2%. ratio of deterioration rate(α) is 20%. Finally, Compare the two scenarios, the Existing Replacement were performed 11-year cycle and the optimal Replacement 15.4year cycle except for the last cycle. And existing maintenance cost is 195,688,000 KRW and Optimal Maintenance Cost of Element Level is 176,255,000 KRW therefore, Cost Efficiency of Optimal Maintenance Cost of Element Level is 10%. So, it is possible to predict 1cost savings through optimal preventive maintenance at element level.

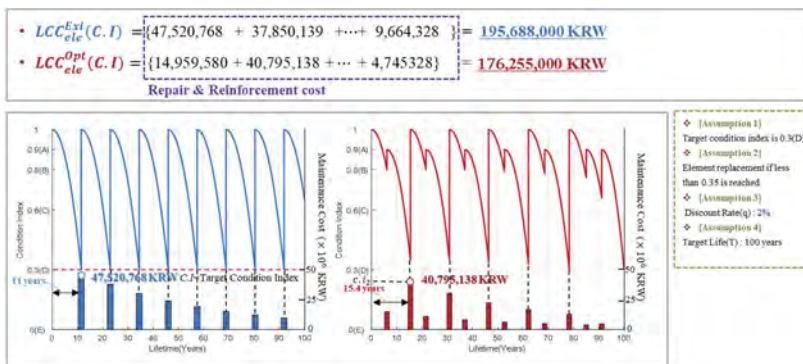


Figure 7. Compare existing maintenance cost and optimal maintenance cost (pavement).

7 CONCLUSIONS

In this study, a maintenance scenario was proposed using optimization methods. In this study result is expected to reduce the repair and reinforcement costs caused by non-optimized maintenance plans. For examples, Using the GA algorithm, we confirm that the optimal maintenance scenario cost is 18.81% less than the existing maintenance scenario cost of concrete deck & asphalts pavements. So, it was found that the optimization method using optimal algorithm is effective. And if updating deterioration model of the optimal maintenance scenario with the Rating profile obtained from the actual inspection is expected to be a more reliable algorithm.

ACKNOWLEDGEMENTS

This work is supported by the Korea Agency for Infrastructure Technology Advancement(KAIA) grant funded by the Ministry of Land, Infrastructure and Transport (Grant RS-2022-00142566).

REFERENCES

- Abdelkader, E.M., Moselhi, O., Marzouk, M. and Zayed, T., 2022. An exponential chaotic differential evolution algorithm for optimizing bridge maintenance plans. *Automation in Construction*, 134, p.104107.
- Assaad, R., & El-adaway, I. H. (2020). Bridge infrastructure asset management system: Comparative computational machine learning approach for evaluating and predicting deck deterioration conditions. *Journal of Infrastructure Systems*, 26(3), 04020032.
- Choi, Y., Lee, J., & Kong, J. (2020). Performance degradation model for concrete deck of bridge using pseudo-LSTM. *Sustainability*, 12(9), 3848.
- Erdogan, N., Pamucar, D., Kucuksari, S. and Deveci, M., 2021. An integrated multi-objective optimization and multi-criteria decision-making model for optimal planning of workplace charging stations. *Applied Energy*, 304, p.117866.
- Liu, M. and Frangopol, D.M., 2005. Multiobjective maintenance planning optimization for deteriorating bridges considering condition, safety, and life-cycle cost. *Journal of Structural Engineering*, 131(5), pp.833–842.

Durability analysis and optimization of a prestressed concrete bridge strengthened by a fiber reinforced concrete layer

S. Schoen, P. Edler & G. Meschke

Institute for Structural Mechanics, Ruhr University Bochum, Germany

S. Freitag

Institute for Structural Analysis, Karlsruhe Institute of Technology, Germany

ABSTRACT: The durability of reinforced concrete (RC) structures is influenced by uncertain service loads and material properties, which must be taken into account in service life-oriented structural design. The consideration of aleatory and epistemic uncertainties allows probabilistic service life predictions in the context of service life design, replacing the classical safety factors.

In the context of this article, the service life of a prestressed concrete bridge strengthened with a fiber reinforced concrete (FRC) layer is to be maximized. The L3378 bridge near Fulda-Lehnerz in Germany will be used as a reference structure. The bridge consists of four prefabricated prestressed RC girders with T-girder cross-section, supplemented by an RC layer and an additional FRC layer. The FRC layer is made of ultra-high-performance fiber reinforced concrete (UHPFRC) and is intended to increase the load-bearing capacity while also serving as a waterproofing layer.

For the optimization, finite element simulations are performed to determine the most sensitive parameters. The fiber orientation of the UHPFRC layer, the prestressing force and position, the bond between concrete and steel, and the material properties are investigated, and then the most sensitive parameters are applied as uncertain parameters for the maximization of the service life, while the cost of material is to be minimized. Although the reference structure is build new, the presented design approach is also applicable to the strengthening of existing structures to extend their service life. For this reason, the original design is finally compared with a conventional design without FRC layer in terms of failure probability considering stochastic live loads and polymorphic uncertainties.

1 INTRODUCTION

Reinforced and prestressed concrete bridges are designed for a long service life, but often have to be repaired at an early stage due to excessive cracks. One way to minimize these cracks, is the use of alternative materials such as fiber-reinforced concrete (FRC). FRC combines conventional concrete with randomly oriented fibers added during the mixing process. These fibers improve the concrete ductility after cracking, which is traditionally remedied with reinforcement. FRC can be specifically customized to meet particular requirements due to different fiber materials including steel, glass and carbon fibers, different fiber geometries such as microfibers or macrofibers with different anchorage, different fiber content, and a variety of concrete mixture (Holschemacher et al. 2017). One example is the bridge L3378 near Fulda-Lehnerz in Germany, which is strengthened by an additional thin ultra-high-performance fiber reinforced concrete (UHPFRC) layer, while the rest of the cross-section consists of reinforced normal weight concrete (RC). This UHPFRC layer consists of an ultra-high strength concrete with steel micro fibers (Pelke et al. 2018). Difficulties arise in the design of bridges with FRC, because there are currently no adequate design codes for the design of bridges with FRC structures. For this reason, within the scope of this paper, a reliability design optimization approach considering polymorphic uncertainties (Edler et al. 2019) is applied to reduce the required steel reinforcement. Aleatory uncertainties are characterized by a known variability given by a large number of data, and therefore, are modeled by stochastic

distributions. However, if only a few data is available, i.e. a lack of knowledge (e.g. the fiber orientation), it is called epistemic uncertainty and modeled by intervals or fuzzy numbers (Möller & Beer 2008). In the context of this paper, aleatory and epistemic uncertainties are intended to replace classical safety factors. For the optimization, a multilevel model is utilized for the analysis of FRC structures, whereby the influence on the structural response can be directly evaluated based on a selected fiber type, content and orientation (Zhan & Meschke 2016). The post-cracking behavior of plain concrete (PC), RC, and FRC structures using finite element (FE) analysis is described by a discrete crack approach using interface elements (Ortiz & Pandolfi 1999). The post-cracking behavior is derived from the tensile separation law for the particular material.

2 MATERIAL MODEL FOR REINFORCED CONCRETE AND FIBER REINFORCED CONCRETE

A discrete crack finite element model (Ortiz & Pandolfi 1999) is utilized to model the cracking behavior of concrete under tension. This model is characterized by cohesive interface elements, which are inserted between linear-elastic triangular finite elements (i.e. bulk elements). The fracture behavior of plain and fiber reinforced concrete is modeled by the sum of two separate nonlinear traction-separation laws $t = t^{\text{concrete}} + t^{\text{fibers}}$ within the integration point of each of the interface element.

2.1 Material model for plain concrete

Considering the behavior of plain concrete with exponential softening first, we obtain the following traction-separation relationship

$$t^{\text{concrete}}(\omega) = f_{ct} \exp\left(-\frac{\omega f_{ct}}{G_f}\right), \quad (1)$$

where ω is the effective crack separation (Gudzucic & Meschke 2021), f_{ct} the tensile strength and G_f the fracture energy.

2.2 Extension for fiber reinforced concrete

Once cracks initiate in FRC, fibers provide a bridging traction acting on the crack faces to keep the crack width small. This is considered via the traction-separation relationship $t^{\text{fibers}}(\omega)$, which takes also the fiber orientation and the fiber geometry into account. This traction-separation relationship is determined by integrating the pullout force-displacement relations $F(\omega, \theta, \tilde{x})$ of all crack-bridging fibers, taking into account their inclination to the crack surface θ and the embedding lengths \tilde{x} . This results, according to Wang et al. (1989), in a function of the smeared fiber pull-out forces

$$t^{\text{fibers}}(\omega) = \frac{c_f}{A_f} \cdot \int_0^{L_f/2} \left[\int_0^{\arccos(2\tilde{x}/L_f)} F(\omega, \theta, \tilde{x}) p(\theta) d\theta \right] p(\tilde{x}) d\tilde{x}, \quad (2)$$

where c_f describes the volume fraction A_f and L_f the fiber cross section and the fiber length, respectively, and $p(\theta)$ the probability density of the fiber orientation. The spatial orientation of the fibers depends on the dimensions of the structural component and the casting direction. In order to take these factors into account, a method to calculate the probability density $p(\theta)$, based on a given fiber orientation profile $\lambda_{\text{cast}} = [a, b, c]$ was developed in Zhan & Meschke (2016). Here, an ellipsoid represents the spatial preference of fibers in the global coordinate system (Figure 1, center). It should be noted that an isotropic fiber orientation is described graphically by a sphere with the fiber orientation profile $\lambda_{\text{cast}} = [0.33, 0.33, 0.33]$. Considering a homogeneous fiber distribution, within the structural component, $p(\tilde{x})$ is equal to $\frac{L_f}{2}$ (Wang et al. 1989). Since obtaining the traction-separation relationship of the fiber-reinforced

concrete can only be evaluated numerically, it is replaced within the FE model by an analytical, parameterized surrogate function

$$t^{\text{fibers}}(\omega) = t_1 \left(\omega_u - \frac{\omega}{\omega_u} \right) + t_2 \omega \exp(c_1 - c_2 \omega). \quad (3)$$

The coefficients t_1, t_2, c_1, c_2 are determined by fitting the surrogate function to the numerical evaluation of Eq. 2 and ω_u represents the ultimate crack opening.

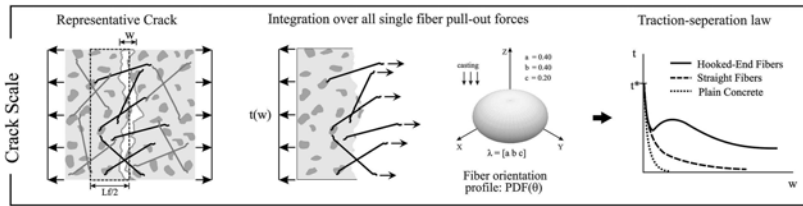


Figure 1. Multi-level modelling of FRC. Integration of the pull-out response of all fibers crossing a representative crack and considering their orientation to calculate the traction-separation law.

2.3 Embedded rebar model

The reinforcement is considered by a discretization-independent embedded rebar model with geometrically linear truss elements. The properties of steel are taken into account with an elastoplastic material behavior using the v . Mises yield criterion with linear hardening. The interaction between reinforcing steel and concrete is considered with a bond-slip law using the *fib* Model Code 1990. The internal force contribution of the reinforcement slip with respect to the bulk matrix is penalized to enforce a displacement constraint between the rebar and the concrete (Gall et al. 2018).

3 BRIDGE WITH ULTRA-HIGH-PERFORMANCE CONCRETE LAYER

The bridge L3378 has a standard RQ 11 cross-section with two lanes and a width of 8.0 m. The structure replaces a two-span, flat-founded reinforced concrete slab girder from 1967, whose condition rating had dropped to 3.5 in the last structural inspections. A repair was not economical due to the continued increase in traffic load. The new design includes the two-span prestressed concrete deck with span widths of 17.10 m and 20.41 m and a total static height of 1.05 m. The cross-section contains three different horizontal components. The base consists of 2 single-span girders, each consisting of four T-shaped precast prestressed concrete girders of strength class C45/55 with a height of 0.85m (see Figure 2a). The precast concrete is supplemented by a 0.13m thick in-situ concrete of strength class C35/45. The cross-section is finished horizontally at the top with a 0.07m thick reinforced ultra-high-performance reinforced concrete (UHPRC) layer strengthened with steel microfibers (Pelke et al. 2018). The final bridge is presented in Figure 2b and the material properties are listed in Tables 1 and 2.

3.1 Sensitivity analysis

Since usually a large number of realizations is needed for probabilistic service life prediction, the bridge is reduced to a 2D model with a constant line load of $q = 100$ kN/m. The microfibers in the top layer are used to limit the cracks at the middle support, but this is only possible if the fibers are aligned longitudinally to the beam. The fiber orientation is considered by a spherical distribution of the probability density function $p(\theta)$ (see Eq. 2), with the orientation profile $\lambda_{cast} = \left[\lambda_f, \frac{1-\lambda_f}{2}, \frac{1-\lambda_f}{2} \right]$. The semi-major axis λ_f is modeled as an interval $\lambda_f = [0.30, 0.45]$. This interval bandwidth is based on the experimental results of Tiberti et al. (2018), where 140 equally sized bending beams with two different casting processes were examined with respect to their fiber orientation within the cross section. The measured inclination between 53.1° and 34.9° corresponds to the fiber orientation parameter λ_f in the range of 0.30 to 0.45.

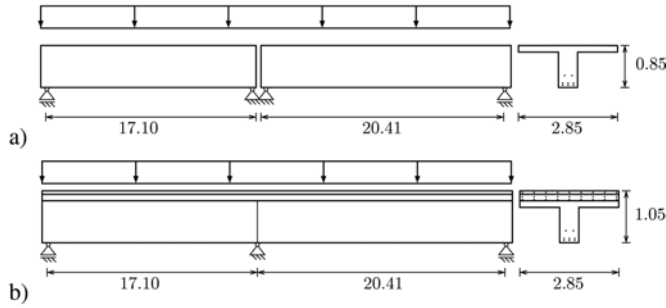


Figure 2. Schematic representation of the bridge a) in the first state of construction and b) in the final state of construction.

Table 1. Material properties of concrete.

Property		C45/55	C35/45	UHPC	HPC	Unit
Young's modulus	E	36,000	34,000	50,000	40,000	[N/mm ²]
Poisson's ratio	ν	0.2	0.2	0.2	0.2	[-]
Tensile strength	f_{ct}	3.8	3.2	11	7	[N/mm ²]
Compressive strength	f_{cm}	53	43	167.5	80	[N/mm ²]
Fracture energy	G_f	0.148	0.143	0.181	0.15	[N/mm]
Volume fraction	c_f	-	-	150	60	[kg/m ²]

Table 2. Material properties of steel.

Property		St1570/1770	B500	Unit
Young's modulus	E	195,000	200,000	[N/mm ²]
Yield stress	σ_{ys}	1770	500	[N/mm ²]

In Figure 3a), the maximum crack width w_{max} at the top edge of the cross-section is plotted as a function of the applied load q for different cases of fiber orientation within the UHPRC layer. Contrary to expectations, the fiber orientation has an influence on the initiation of the cracks at the top edge. This is due to the fact that the in-situ concrete layer has a significantly lower tensile strength than the fiber-reinforced concrete layer, and thus, the in-situ concrete layer starts to crack first (see Figure 4b)). Consequently, the crack starts in the middle of the cross-section and grows towards the top. Especially with horizontal fiber orientation ($\lambda_f = 0.45$), this crack propagation is limited through the fibers. However, as soon as the crack reaches the upper edge, the fibers can hardly limit the crack width, since even with horizontal fiber orientation ($\lambda_f = 0.45$), the crack width increases rapidly. Nevertheless, the maximum allowable crack width of $w_{crit} = 0.2$ mm according to Eurocode 2 is maintained for all three cases at the design load of $q = 100$ kN/m.

Beside the fiber orientation, the crack width may be influenced by other effects, e.g. an increase in the design load or a decrease in the prestressing force. Both scenarios are likely to happen in reality. For example, due to creep and shrinkage of the concrete, the prestressing force is time-variant, i.e., not equal to the initially applied prestressing force. This loss depends on various factors such as the age of the concrete, temperature and humidity during prestressing. For simplicity, according to the design guidelines (Eurocode 2) for this structure, a prestressing loss of 15% may be considered. To illustrate the influence of the prestressing loss, the maximum crack width w_{max} is plotted as a function of the applied load q for $\lambda_f = 0.45$ and $P_{loss} = 15\%$ in Figure 3 a), as well. Here, even for a horizontal fiber orientation ($\lambda_f = 0.45$) at the design load of $q = 100$ kN/m the maximum crack width $w_{cr} = 0.27$ mm is clearly above the maximum allowable crack width of $w_{crit} = 0.2$ mm (Eurocode 2).

In the following, an alternative design (variant B) will be investigated. In order to better emphasize the positive effects of fiber-reinforced concrete, the upper two layers are combined,

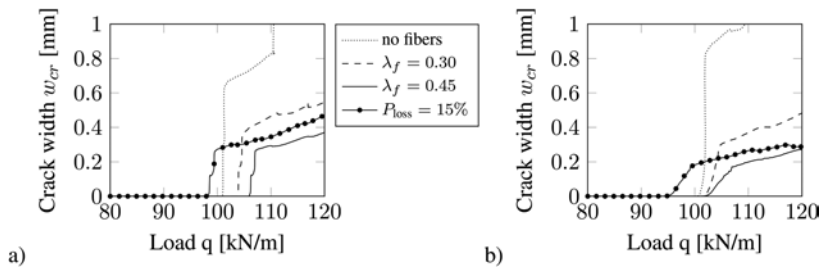


Figure 3. Crack width depending on the load for different fiber orientation and different prestressing force for a) variant A and b) variant B.

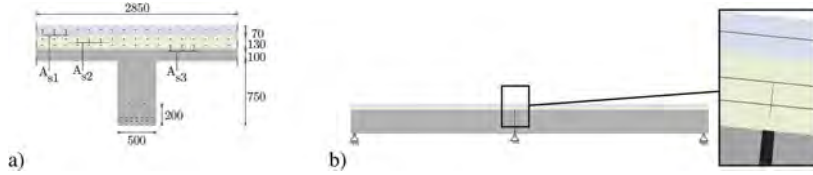


Figure 4. Illustration of crack initiation of variant A.

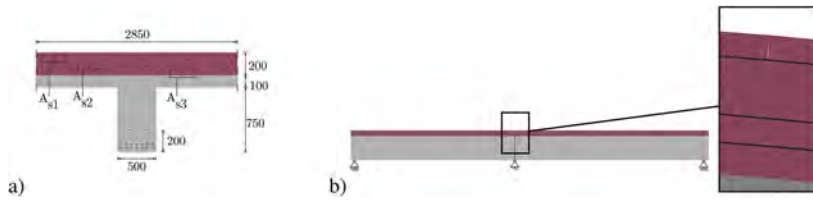


Figure 5. Illustration of crack initiation of variant B.

meaning the bridge consists of the prestressed precast beam and a 0.2 m thick fiber-reinforced HPC layer (see Figure 5a). The material properties are summarized in Table 1. Since fibers with hook end are able to limit the crack width even better than normal fibers or microfibers, for variant B steel fibers of type DRAMIX 60 are utilized. The use of such steel fibers in HPC has already been validated in Gudzulic et al. (2020). In Figure 3b), the maximum crack width w_{max} is plotted as a function of the applied load q for the same scenarios as for the original design (variant A). In variant B due to the significantly lower tensile strength compared to variant A, cracking begins at a lower applied load q . However, especially in case of fibers with horizontal orientation ($\lambda_f = 0.45$), the crack width is limited even at a higher loads. Moreover, with horizontal fiber orientation ($\lambda_f = 0.45$) and a prestressing loss of $P_{loss} = 15\%$, the maximum crack width ($w_{cr} = 0.18$ mm) is beneath the maximum allowable crack width of $w_{crit} = 0.2$ mm at the design load of $q = 100$ kN/m.

3.2 Reliability design optimization

In the following, a reliability design optimization is performed for variant A and variant B considering uncertainties in loading, prestressing loss and fiber orientation. In addition, a reliability design optimization for a third variant (variant B0), which investigates the influence of fibers on the objective function, is performed. For this purpose, variant B was modeled without fibers. In other words, for variant B0 all material properties and layer thicknesses correspond to those of variant B and only the top layer is high performance concrete (HPC), instead of a high performance fiber reinforced concrete (HPFRC). Due to more steel fibers in variant B compared to variant A and variant B0, the aim is to reduce the steel reinforcement, to save costs, by still maintaining the serviceability. The objective is to minimize the total steel reinforcement A_s at the

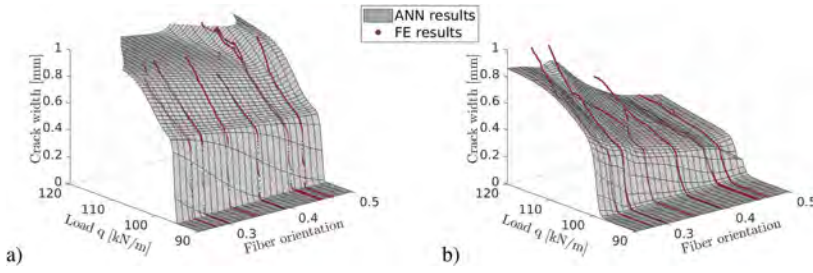


Figure 6. Crack width depends on the load and the fiber orientation for a fixed prestressing loss of $P_{loss} = 10\%$ and amount of reinforcement of $A_{s1} = 18\text{Ø}16\text{mm}$, $A_{s2} = 14\text{Ø}14\text{mm}$ and $A_{s3} = 0$ for a) variant A and b) variant B.

middle support by constraining the failure probability, which is based on a maximal acceptable crack width of $w_{cr} = 0.2\text{mm}$. This can be formulated for variant A and B as

$$\begin{aligned} \min : \quad & \hat{Z}(A_s) = A_s \\ \text{s.t. :} \quad & c(A_s, q, \lambda_f, P_{loss}) = P_f(\omega_{cr}(A_s, q, \lambda_f, P_{loss}) \leq 0.2) - P_{f,acc} \leq 0, \end{aligned} \quad (4)$$

and for variant B0 as

$$\begin{aligned} \min : \quad & \hat{Z}(A_s) = A_s \\ \text{s.t. :} \quad & c(A_s, q, P_{loss}) = P_f(\omega_{cr}(A_s, q, P_{loss}) \leq 0.2) - P_{f,acc} \leq 0. \end{aligned} \quad (5)$$

In Eq.4 and 5, the accepted probability of failure is described by $P_{f,acc} = \Phi(-\beta)$, where Φ is the cumulative distribution function of the standard normal distribution and β is the reliability index, which is set to be $\beta = 1.5$ in case of serviceability, according to DIN EN 1990. The load q and the prestressing loss P_{loss} are described as a priori, random variables, using Gaussian distributions with different mean values $\mu(q)$ kN/m and variance $\sigma(q) = 1$ kN/m for the load and a mean value $\mu(P_{loss}) = 10\%$ and variance $\sigma(P_{loss}) = 1\%$ for the prestressing loss. One optimization was performed for each of the various mean values of the load to investigate the influence of the load on the optimal amount of reinforcement. The fiber orientation parameter is considered as an interval $\lambda_f = [0.30; 0.45]$ for variant A and B. The total steel reinforcement is the sum of the support reinforcement $A_s = A_{s1} + A_{s2} + A_{s3}$ (see Figure 4 a) and Figure 5a)), where A_{s1} is kept constant as a minimum of $A_{s,min} = A_{s1} = 18\text{Ø}16\text{mm}$ is needed according to the design guidelines, while A_{s2} and A_{s3} are within the interval $[4\text{Ø}8\text{mm}; 18\text{Ø}16\text{mm}]$. This range was chosen since, considering the existing cross-section width of 2.85 m, it is not reasonable to place less than four rebars in one row and $18\text{Ø}16\text{mm}$ per row is the existing amount of reinforcement of Variant A. For the optimization, the Particle Swarm Optimization (PSO) (Kennedy & Eberhart 1995) is applied with an extension to consider aleatory and epistemic uncertainties (Edler et al. 2019).

For the optimization, the FE simulations performed for each variant, is replaced by artificial neural networks (ANN) with feed forward architecture to speed up the computation time (Freitag et al. 2020). For all three variants, the same 150 models are generated, using Latin hypercube sampling (LHS) of prestress loss and amount of support reinforcement. In addition, for variant A and B the fiber orientation has been sampled as well. For variant A and B, an ANN with four input parameters (λ_f , P_{loss} , A_s and q), two layers with 10 and 5 hidden neurons and one output neuron w_{cr} (4-10-5-1) is sufficient to approximate the FE simulations with an accuracy of $R = 0.992$ for variant A and $R = 0.989$ for variant B, respectively. For variant B0, an ANN with three input parameters (P_{loss} , A_s and q), two layers with 8 and 4 hidden neurons and one output neuron w_{cr} (3-8-4-1) is adequate to approximate the FE simulations with an accuracy of $R = 0.908$. At this point, it should be noted that it is ensured that all ANN provide sufficiently accurate results especially in the range $w_{cr} \leq 0.2\text{mm}$, for subsequent optimization.

Figure 6 presents the results obtained by the ANN and the FE simulations for crack width versus fiber orientation and load for variant A (a) and B (b). It may be observed that the fiber orientation influences the crack width in variant B significantly more than for variant A, while the crack width increases for variant A at smaller load than for variant B independent of the fiber orientation.

3.3 Results

For a better illustration, the total amount of steel (sum of steel reinforcement and steel fibers) is presented in Figure 7 as the steel weight m rather than the area of steel A_s . In Figure 7a), the minimum required weight of steel reinforcement m_{rebar} , for which the constraint is fulfilled ($w_{\text{cr}}(A_s, q, \lambda_f, P_{\text{loss}}) \leq 0.2 \text{ mm}$), is given as a function of the mean value of the load, for variant A (black) and variant B (purple) for $\lambda_f = 0.30$ (dashed line) and 0.45 (solid line), for each variant and also for variant B0 (dotted line). The maximum load, at which the constraint is still fulfilled, is marked with a circle.

For variant A, the amount of reinforcement barely depends on the fiber orientation and much more one the mean value of the load. Only the minimum reinforcement is required, up to a mean value of the load of $\mu(q) = 93.2 \text{ kN/m}$ for $\lambda_f = 0.30$ and $\mu(q) = 93.5 \text{ kN/m}$ for $\lambda_f = 0.45$. With further increase in the load, the required amount of reinforcement increases, the maximum amount of reinforcement is required for $\lambda_f = 0.30$ at $\mu(q) = 98.0 \text{ kN/m}$ and for $\lambda_f = 0.45$ at $\mu(q) = 99.2 \text{ kN/m}$. At higher mean value of the load, the constraint ($w_{\text{cr}}(A_s, q, \lambda_f, P_{\text{loss}}) \leq 0.2 \text{ mm}$) is not fulfilled anymore. This means that, even with optimal fiber orientation, the serviceability limit state is not met at the design load of $q = 100 \text{ kN/m}$, if uncertain loads and prestressing losses are taken into account.

For variant B, the minimum required amount of reinforcement is influenced by the fiber orientation and the mean value of the load. Only the minimum reinforcement is required, up to a load of $\mu(q) = 96.2 \text{ kN/m}$ for $\lambda_f = 0.30$ and $\mu(q) = 99.3 \text{ kN/m}$ for $\lambda_f = 0.45$. With further increasing mean value of the load, variant B requires rapidly more reinforcement for fiber orientation of $\lambda_f = 0.30$ as the the maximum amount of reinforcement is required at $\mu(q) = 99.4 \text{ kN/m}$, while for $\lambda_f = 0.45$ the maximum amount of reinforcement is not required until $\mu(q) = 103.5 \text{ kN/m}$. Consequently, the serviceability limit state is met for variant B, with consideration of uncertainties, for the design load as well as for higher mean value of the load but only for a good fiber orientation of $\lambda_f = 0.45$. Finally, comparing variant B and variant B0 (without fibers), it can be observed that, especially with a small amount of reinforcement, the fibers contribute significantly to the crack width reduction for any fiber orientation. If more reinforcement is required due to the load, the function of variant B rises just as quickly as one with fiber orientation $\lambda_f = 0.30$.

In Figure 7b), the minimum required total weight of steel ($m_{\text{tot}} = m_{\text{fibers}} + m_{\text{rebar}}$, where $m_{\text{fibers,A}} = 1.06 \text{ t}$, $m_{\text{fibers,B}} = 1.21 \text{ t}$ and $m_{\text{rebar}} = m_{\text{As,1}} + m_{\text{As,2}} + m_{\text{As,3}}$) is given as a function of the mean value of the load. Here, it can be seen that variant B is the most economical choice for a mean value of the load higher than $\mu(q) = 94 \text{ kN/m}$, if it can be ensured that $\lambda_f = 0.41$. Meaning, if a horizontal fiber orientation can be ensured, due to the casting process, and thus the interval range of the fiber orientation can be reduced to $\lambda_f = [0.41; 0.45]$, variant B is to be preferred.

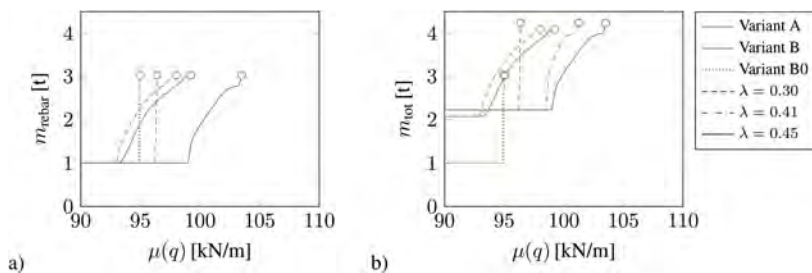


Figure 7. Optimization results for a) Weight of required reinforcement for different mean value of the load and b) Total weight of steel for different mean value of the load.

4 CONCLUSION

In this contribution, a prestressed bridge strengthened with fiber-reinforced concrete was investigated with respect to its maximum crack widths. It was observed that due to different types of concrete, cracks occur within the cross-section already at loads smaller than the design load. For this reason, an alternative cross-section of only two instead of three different concrete types has been presented (variant B). Variant B consists of a thicker fiber concrete layer with fewer but larger fibers, which significantly reduces the crack widths. In addition, less steel reinforcement is needed for the same load, and thus reducing the total amount of steel. In the next step, in addition to the cracks above the support, the cracks in the field should also be investigated, as well as the load-bearing capacity of both variants. Moreover, it would also be possible to add the concrete layer thickness as additional design variable in order to also optimize the required concrete material volume.

ACKNOWLEDGMENT

The authors gratefully acknowledge the financial support of the German Research Foundation (DFG) within Subproject 6 (Project number 312921814) of the Priority Programme “Polymorphic uncertainty modelling for the numerical design of structures - SPP 1886”.

REFERENCES

- Edler, P., S. Freitag, K. Kremer, & G. Meschke (2019). Optimization approaches for the numerical design of structures under consideration of polymorphic uncertain data. *ASCEASME Journal of Risk and Uncertainty in Engineering Systems Part B: Mechanical Engineering* 5(4), 041013 (12 pages).
- European Committee for Standardisation (2005). *EN 1992 - Eurocode 2: Design of concrete structures. European Committee for Standardisation*
- Freitag, S., P. Edler, K. Kremer, & G. Meschke (2020). Multilevel surrogate modeling approach for optimization problems with polymorphic uncertain parameters. *International Journal of Approximate Reasoning* 119, 81–91. Special issue on Computing with confidence.
- Gall, V. E., S. Butt, G. Neu, & G. Meschke (2018). An embedded rebar model for computational analysis of reinforced concrete structures with applications to longitudinal joints in precast tunnel lining segments. In G. Meschke, B. Pichler, and J. G. Rots (Eds.), *Computational Modelling of Concrete Structures (EURO-C 2018)*, pp. 705–714. CRC press.
- Gudzulic, V. & G. Meschke (2021). Multi-level approach for modelling the post-cracking response of steel fibre reinforced concrete under monotonic and cyclic loading. *Proceedings in Applied Mathematics and Mechanics*.
- Gudzulic, V., G. Neu, G. Gebuhr, S. Anders, & G. Meschke (2020). Numerisches Mehrebenen-Modell für Stahlfaserbeton: Von der Faser- zur Strukturebene. *Beton und Stahlbetonbau* 115, 146–157.
- Holschemacher, K., F. Dehn, T. Müller, & F. Lobisch (2017). *Betonkalender 2017*, Chapter Faserbeton. Ernst und Sohn.
- Kennedy, J. & R. C. Eberhart (1995, November-December). Particle swarm optimization. In *Proceedings of the IEEE International Conference on Neural Networks*, Piscataway, NJ, USA, pp. 1942–1948. IEEE Press.
- Möller, B. & M. Beer (2008). Engineering computation under uncertainty – Capabilities of non-traditional models. *Computers and Structures* 86, 1024–1041.
- Ortiz, M. & A. Pandolfi (1999). Finite-deformation irreversible cohesive elements for three-dimensional crack-propagation analysis. *International Journal for Numerical Methods in Engineering* 44(9), 1267–1282.
- Pelke, E., A. Jaborek, D. Berger, & E. Brühwiler (2018). Überführungsbauwerk der L3378 bei Fulda-Lehnerz – Erster Einsatz von UHFB in Deutschland im Straßenbrückenbau, Teil 1: Projektentwicklung und Baudurchführung. *Beton- und Stahlbetonbau* 113(11), 831–841.
- Tiberti, G., F. Germano, A. Mudadu, & G. Plizzari (2018). An overview of the flexural postcracking behavior of steel fiber reinforced concrete. *Structural Concrete* 19, 695–718.
- Wang, Y., S. Backer, & V. Li (1989). A statistical tensile model of fibre reinforced cementitious composites. *Composites* 20(3), 265–274.
- Zhan, Y. & G. Meschke (2016). Multilevel computational model for failure analysis of steel fiber reinforced concrete structures. *Journal of Engineering Mechanics (ASCE)* 142 (11), 04016090 (1–14).

Multivariate inspection of German steel civil infrastructure using autonomous UAS

D. Thomas & M. Gündel

Lehrstuhl für Stahlbau und Stahlwasserbau, Helmut Schmidt University/University of the Federal Armed Forces Hamburg, Germany

A. Wickers, M. Alpen & J. Horn

Professur für Regelungstechnik, Helmut Schmidt University/University of the Federal Armed Forces Hamburg, Germany

ABSTRACT: Aging civil infrastructure and increasing traffic loads lead to deteriorating assets and the need for regular manual inspections, which generally entail at least partial closure of the asset and operational downtime. These costly inspections can be overcome by employing autonomous unmanned aircraft systems (UAS) to carry out the required inspections. Utilizing a variety of sensor configurations, AI-based analysis, and data fusion through a web-based interface, more objective comparisons between infrastructure assets can be obtained quickly. Within the dtcc.bw-MISDRO project the Norderehbbrücke of the German Autobahn, Freihafenelbbrücke of the Hamburg Port Authority, a railway bridge over the river Oste from Deutsche Bahn and a barrage over the river Weser from the German Federal Waterways and Shipping Authority are to be inspected via UAS with visual cameras, lidar, hyperspectral imaging and further sensors to detect typical steel defects. In this paper the planned non-destructive testing methods for automatic defect detection, the automatic path planning, and the design of the UAS are presented.

1 INTRODUCTION

Germany's federal infrastructure network contains approximately 52,000 motorway bridges, 26,000 railway bridges and 2,300 hydraulic structures. Every three years, these structures are subjected alternately to a major inspection and a minor inspection to check for damage and defects in the structure and ensure that they are safe for traffic. The result is a condition score between 1.0 and 4.0; a score of 1.0 corresponds to a very good structural condition and a score of 4.0 corresponding to an unsatisfactory condition with an immediate need for action. Many structures are in poor condition due to their age and the sharp increase in heavy goods traffic. Currently, the condition rating for 17 % of federal motorway bridges, 35 % of railway bridges and 75 % of hydraulic structures is 3 or worse (Bundesanstalt für Straßenwesen, 2021; Bundesanstalt für Wasserbau, 2018; DB Netz AG, 2022). The inspection of the structures is carried out by specially trained civil engineers, using inspection equipment, elevated work platforms, pier access equipment and road-rail vehicles for support. This process requires a section-by-section closure of the structure, leading to increased traffic delays, worker danger, and significant economic losses. Each infrastructure operator in Germany has their own inspection guidelines and building management system. DIN 1076 is the standard norm for inspection of infrastructure and influences the guidelines for train bridges and hydraulic structures (DIN, Normenausschuss Bauwesen, 1999). Unmanned aircraft system (UAS)-based inspection techniques offer the potential to drastically reduce the economic impact of the inspections, as aerial inspection can be performed without interfering in the operation of the asset and the technology can inspect significantly larger areas per unit of time

than a human inspector. In addition, the subsequent algorithm-based analysis makes the evaluation more objective and independent of the individual inspector. In the dtcc.bw project MISDRO, a joint-research project by the Helmut-Schmidt-University/University of the Federal Armed Forces and the companies “BuP. Boll Beraten und Planen”, “Emqopter”, “Synergeticon” and “Wölfel Engineering”, four steel infrastructure structures belonging to the associated partners Autobahn GmbH, DB Netz AG, Hamburg Port Authority and the Federal Waterways and Shipping Administration will be examined by UAS.

In this paper, we present a review of relevant inspection guidelines and the research work in this field in Germany. In addition, we present our unmanned aircraft system, the algorithmic flight planning and the proposed non-destructive testing methods for steel structures.

2 STATE OF THE ART OF UAS-BASED INSPECTION IN GERMANY

Automation of structural inspection by UAS is an active field of research. A review by Feroz and Dabous emphasizes the lack of standardizations, changes in weather conditions, limited battery capacity, and legal frameworks as limiting factors for general use. The focus of the research was on RGB imaging and analysis of concrete damage (Feroz and Abu Dabous, 2021). The article “Review of Robotic Infrastructure Inspection Systems” emphasizes changing environmental disturbances and GPS-denied scenarios as future challenges for UAVs and furthermore localization and control methods for sensor data. Cracking and corrosion are well detectable, while it is much more difficult to detect mechanical deformations (Lattanzi and Miller, 2017). In German-speaking countries, research on UAS-based bridge inspection is being pursued in several projects. Blankenbach from the Geodetic Institute of RWTH Aachen University researches it in the projects TwinGen, RiverCloud, and BIMxD structure inspector XR. At Bauhaus University Weimar, Morgenthal conducted research in the project “Assessment of Aging Infrastructure Structures with Digital Technologies (AISTEC)” to detect small cracks in concrete using high-resolution RGB cameras on UAS. Predecessor projects were “Unmanned Aerial Systems for Condition Assessment of Structures” from June 2013 to April 2015 and the continuation of the project from January 2017 to June 2018. The final report on the first project confirmed the basic practicality of UAS for inspections in support of human inspectors. Data acquisition time can be significantly shortened and qualitatively increased with the use of UAS. Additionally, this study proved that cracks and spalling could be reliably detected by the UAS (Morgenthal et al., 2015). The follow-up project investigated the fusion of the RGB image data with thermal images and the integration of the data into existing BIM software tools. Here, the size of the data sets and the heterogeneity of the data were noted. Additional research is required specifically in the areas of data analysis and data modeling (Hallermann et al., 2019). In 2022, the current status on the integration of inspection data into a BIM model was published (Taraben et al., 2022). In Austria, the project “RISK-MON - Plant Inspection and RISK MONitoring with High Performance Drones and Sensors” was running until the end of 2019. Important results from this study were the systematic analysis of the applicability of cameras, laser scanners, thermography, multispectral analysis and georadar for UAS and the determination of the best operating conditions for the drone. In this regard, images of concrete were also taken under laboratory conditions using a hyperspectral camera in the wavelength range from 900 to 1700 nm (Bergmeister et al., 2022). The research institutions of several infrastructure operators in Germany are currently researching drone-based inspections (Makiello, 2022; Morgenthal et al., 2021). Deutsche Bahn is investigating drone-based inspections for environmental and nature protection in the project “Digital Remote Sensing and Route Inspection using Unmanned Aerial Systems (Drones)”. Meanwhile, UAS-based inspection systems with RGB cameras and laser scanners are also being used commercially by companies such as “STRUCINSPECT”, “TopSeven”, and “Guido Morgenthal Technologies in Civil Engineering”. Previous work and applications of UAS-based inspection systems have focused predominantly on reinforced concrete structures, using primarily RGB cameras, with additional information also being provided by various combinations of thermal imaging cameras and laser scanners. Common to all projects is the

use of RGB cameras and laser scanners being adopted as the primary sensor technology. To the best of the authors' knowledge, the use of UAS-based inspection systems for the condition assessment of steel structures has received only small research attention.

3 METHODS FOR UAS-BASED INSPECTION OF CIVIL STEEL STRUCTURES

3.1 *Typical defects of steel infrastructure*

Analysing the German inspection guidelines and inspection reports of the Norderelbbrücke, Freihafenelbbrücke in Hamburg, the barrage Dörverden over the river Weser, and a railway bridge over the river Oste, the typical defects and their cause and consequence on steel infrastructure are categorized into corrosion, fractures, biota, moisture and deformation. The objective of the inspection is to detect these types of defects with high accuracy and assess their impact on the load-bearing capabilities of the structures, such that any repair work can be identified as early as possible. Another categorization scheme for the main defects of steel structures was developed in the Duratinet project and comprises the categories contamination, deformation, deterioration, discontinuity, displacement and loss of material. In our classification scheme, the categories displacement and loss of material are enveloped into the category deformation, while for deterioration and contamination are replaced by the categories of corrosion and coating, and biota. This scheme is a more sensor-orientated than a defect type orientated scheme (Correia et al., 2012).

Corrosion and protection coating defects on German motorway bridges are evaluated according to the German guideline "Richtlinien für die Erhaltung des Korrosionsschutzes von Stahlbauten", where color changes, e.g. from dirt, vegetation, salt on the corrosion protection system, should be noted. The thickness of the protection layer should be according to the minimum designed layer thickness and at least more than 200 µm if the planned thickness is not known. Occasional cracks of the protection layer or more occurrences should be noted. Visible corrosion should also be detected. In addition cracking and delamination of the coating system should be noted if they are detectable by 10x magnification. For fractures e.g., from fatigue, every fracture or suspected fracture in the steel structure should be noted and observed for changes. Biota defects should be understood as a general defect, containing flora, fauna and funga, i.e. bird droppings, algae, clams, fungi, dirt and further biological components which typically do not belong on a steel structure. Every instance of biota detected should be noted. Moisture and water content on steel structure occurs due to defects of the drainage or design flaws and leads to increased corrosion of the structure and should be analysed. Every steel deformation, e.g. dents, should be noted. There is no limit on the minimum detectable deformation. This also includes other changes in the geometry, for example, missing or loose rivets and screws. In summary, we use corrosion, coating, fractures, biota, moisture and deformation as inspection categories.

3.2 *UAS-based non-destructive testing methods for steel structures*

To detect defects via UAS, factors limiting the selection of the suitable sensor arrays are the sensors' size, weight, observation distance and image resolution. Within this project, a measurement distance of 3 to 10 m to the structure is considered as feasible. Drones with a take-off weight of 10 kg can typically carry a payload of 3 kg. This payload contains a gimbal to suppress vibration and orientate the sensor to the area of interest and should be bottom- and top-mountable to inspect floor beams. The first iteration of the drone setup used in the project has a maximum payload of 1,7 kg excluding the gimbal. In Germany, the inspector must be within reach of the structure to perform a visual inspection. Additional tools such as a hammer, a crack-width card or magnifying glasses are often used for inspecting areas of particular interest. For the analysis of steel structures, other common non-destructive testing (NDT) methods are, for example, endoscopy, ultrasound, thermography, magnetic particle inspection, eddy-current testing, hardness test and dye penetrant inspection. However, the majority of these methods are either contact-based NDT methods or contact-less methods that should be conducted as close as possible to the structure. As a result, most of these conventional methods are not suitable for drone-based inspections. There is ongoing research focused on developing contact-based methods for UAS, however, they come with the disadvantage

of a much lower inspection rate (inspected surface per hour) when compared to contact-less methods. For this reason, only electromagnetic (EM)-based detection methods appear to be suitable. The usable spectral range of EM-based methods is restricted by scattering, absorption and hazard characteristics of the radiation. Microwave-based methods (e.g. radar) are applicable but neglected in this work, as they use larger antennas and their precision is lower than using visual inspection methods (e.g. lidar). Bathymetric lidar is not considered in this project, as sensors for UAS weigh about 5 kg. In summary, the visual spectral range (380-780 nm), near-infrared (NIR, 780-1400 nm), short wavelength infrared (SWIR, 1400-3000 nm) and thermal infrared (3000-15000 nm) are applicable for UAS-based inspection. Imaging techniques using this spectral range are: RGB-, panchromatic-, multispectral-, hyperspectral-, thermographic-cameras and lidar.

3.3 *Illumination*

The radiation can be measured by the imaging techniques passively during daylight, but for specific tasks, additional illumination is beneficial. The emission spectrum, light direction, pulse time, coherence and polarisation of the additional light source are configurable. Coherence and polarisation are important for interferometry or polarisation microscopy, but not applicable on vibrating drones. Different orientations of the light source are used for Shape-from-Shading (SfS), highlighting differences in surface height. The pulse time is used in time of flight measurement methods (ToF) like lidar. For drone-based lidar, accuracies of about 1 cm are reported, but dent deformation are typically in the millimeter range (Bergmeister et al., 2022). Another method of illumination, which can be used for this range is structured light. Here, accuracies of 5 mm at a distance of 3 m for low-cost sensors up to 0.03 mm are reported (Cao et al., 2021). When using structured light, reflections can cause difficulties for reconstruction. Thus, illumination is only used if necessary in shadowed areas and for SfS, ToF and Structured light measurements at the steel structures. Because LED lamps, energy saving lamps, and lasers have an irregular emission spectrum, thermal light bulbs or halogen lamps should be used when a more continuous illumination spectrum is necessary for multispectral or hyperspectral imaging.

3.4 *Hyperspectral imaging*

The advantage of multispectral and hyperspectral imaging (HSI) is the ability to acquire a spectrum for comparison with the spectral fingerprint of specific materials, e.g. vegetation, water, and corrosion. HSI is commonly used in remote sensing of the earth atmosphere and many different spectral indices have been developed to detect specific materials. One example is the identification of vegetation by using the (hyperspectral) Normalized Difference Vegetation Index (NDVI).

Depending on the sensor, multispectral and hyperspectral cameras are sensitive to the NIR and SWIR range. Currently, there is no general recommendation which spectral range is preferable for inspection. It has been shown that the SWIR range is applicable for corrosion detection (Zahiri et al., 2022), but a drawback of SWIR cameras is their absence of the visual range, which is important for the calculation of more common spectral indices in remote sensing, like vegetation indices. Disadvantages of HSI setups are their cost, lower resolution and more complex white balance adjustment. For white balance with RGB cameras the intensity of the three colour bands must be adjusted, for which automatic algorithms exist. For HSI, more than one hundred spectral bands must be adjusted with a reflectance target. After the balance adjustment, changing levels of illumination, which can be caused by changing weather conditions or shading of the structure, result in necessary readjustments. Furthermore, the probability of over-saturating one of the many spectral bands increases.

3.5 *Applied UAS-based NDT methods within the MISDRO project*

The selected NDT methods in the MISDRO-project, their typical spectral range and main application area are presented in Table 1. As the cost, image size, and the inspection rate differs between sensors, the RGB camera is used as a first tool for acquiring an overview of the structure.

After around 30 minutes of flight time of a UAS, a battery change is necessary. On this change, the recorded data disk is transferred to a gateway computer, which further analyses the data and determines areas of interest which possibly contain defects or their indicators and recommends the next sensor configuration.

For the evaluation of the different sensors, test specimens are developed and a database is created from images of different structures. The database is used for training and testing machine learning methods for image segmentation of typical steel defects. Finally, the final inspection results are projected onto a BIM model of the structures.

Table 1. Deployed NDT methods within the MISDRO project.

NDT method	Spectral range (nm)	Main Application area
RGB camera	380 - 780 nm	Corrosion, Coating, Fractures,
Biota, Deformation		
- Shape-from-Shading		Coating, Fractures
- Structured Light		Deformation
Panchromatic camera	380 - 780 nm	Fractures
NIR-Hyperspectral camera	350 - 1000 nm	Corrosion, Coating, Biota, Moisture
Thermography camera	7.5 - 13.5 μ m	Fractures, Moisture
Lidar	typ. 900 nm	Deformation

4 SPECIFICATION OF THE UNMANNED AIRCRAFT SYSTEM

4.1 Hardware of the UAS

For the MISDRO project a UAS is developed and customized by *Emqopter* from Würzburg, Germany. To ensure a maximum of flexibility there is a switchable mounting system for the gimbal holding the sensors used for inspection. Moreover, in order to allow an inspection from all directions, it is possible to attach the gimbal both to the top and the bottom of the flight platform. The UAS itself is designed in a X-configuration with eight rotors in total, two for each arm. For the positioning, computation and communication the following parts are most important. Parts marked with a * are not finally selected for now. The basic hardware components and how they are connected is presented in Figure 1.

Computation units

- Flightcontroller *Pixhawk 6X*
- *Gigabyte BRIX* Onboard PC (*Intel i7 10710*)
- Microcontroller unit for datafusion

Positioning sensors

- *Here2-* and *Here3-* GPS system
- *Poszyx Creator One* positioning system
- *Holybro* telemetry module 433 MHz
- Lidar sensor*
- Ultrasonic sensor*

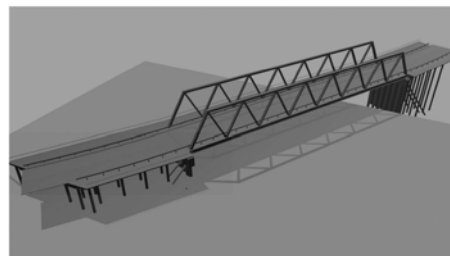
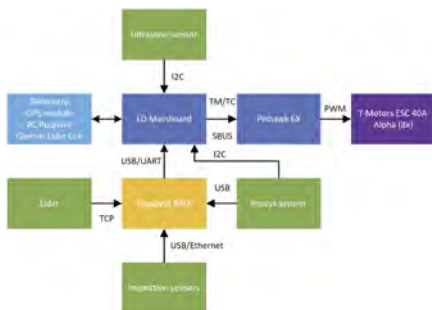


Figure 1. Basic concept of the used hardware setup on the UAS.

Figure 2. Simulation environment in Gazebo with a model of the Travehafenbrücke and a UAS.

4.2 Process of inspection

The inspection can be split up in two major steps. In the first step (Pre-computation), a flight mission based on an already existing BIM model of the inspected infrastructure is created. The second part (Live-computation) receives and executes this mission, maintaining a live map of the environment and a simple collision avoidance for the UAS. The concept is structured as follows.

4.2.1 Pre-computation

Creating a model of the desired infrastructure: To ensure that all relevant information is captured in a model of an infrastructure, mainly two different representations are created for the infrastructures stated above: A BIM model representing the civil engineering aspects and a pointcloud model of the whole environment, which is used for the calculation of a path along the desired inspection points. As an example, a basic BIM model of the Travehafenbrücke is shown in Figure 3a. The model has been created with the help of existing building plans. Moreover, a pointcloud model of the same infrastructure is shown in the top left of Figure 3b. For this case it is just a sampled version of the BIM model, but it can also be recorded on the actual building with a lidar.

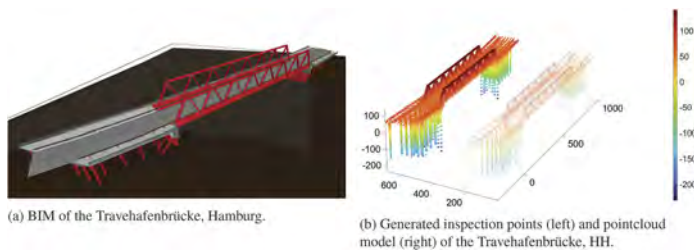


Figure 3. Different model types of the Travehafenbrücke located in Hamburg.

Computation of a Voxelmap: Since the pointcloud consists of a huge amount of data which is not necessarily needed for a path planning algorithm, it is filtered for redundant points and represented in a Voxelmap with a constant spacing. This process is repeated for different spacings, so different resolutions of the object can be taken into account. For the current state of the project this is a sufficient approach. However, literature shows that equidistant spacing ends up with a significantly worse performance in terms of calculation time compared to approaches that only use small spacing around obstacles. For example, cell division as presented in (Yuan et al., 2022) or other tools and methods can be implemented to improve the algorithm in terms of calculation time and the amount of produced data.

Offline mission planning: The mission planning algorithm takes a Voxelmap and a starting point of the UAS as an input. To define a subspace that can be reached by the drone, a Voxelmap with a sufficient grid spacing depending on the size of the UAS is taken as an input for a wavefront-algorithm (Nam et al., 2016). Any voxel that can be reached by the wavefront outgoing at the starting point is marked. The remaining voxels are obviously surrounded or cut off by obstacles and therefore not members of the reachable subspace. Based on this representation of the environment the occupied voxels are used to create inspection points based on parameters depending on a defined safety distance, the size of the drone and the method of the inspection. The algorithm is forced to create the inspection points at a defined distance and in a 90° angle to the surface of the obstacle. Therefore, the plane normal vector is taken into account. Points can only be created at unoccupied voxels which are members of the reachable subspace. In the bottom right of Figure 3b all inspection points associated to the pointcloud model are presented. The inspection points created are saved and then sorted to obtain an optimal route along all inspection points. Currently, the route is determined using the basic routing algorithm of the Google OR Toolbox (Perron and Furnon, 2023). The optimization problem solved by this algorithm is called “travelling salesman problem” in the literature. The costfunction of this optimization is based on the euclidean distance of the waypoints and an additional penalty for movements up- or downwards, representing the increased energy consumption of the drone during those flight maneuvers. Future adjustments of this approach will aim at a capacity which is “picked up” in every step between waypoints in order

to create several routes with a maximal length. Thereby, the maximum lifetime of the battery packs can be taken into account. Based on the created sequence a basic gridbased path planning algorithm (Hart et al., 1968) is used to create a way between the inspection points. Literature shows many different approaches for this kind of problems, both gridbased and non-gridbased (Han, 2019). Further tests for this part of the algorithm are planned.

4.2.2 Live-computation

The mission created by the pre-computation is fundamental for the live mission of the UAS. At this stage of the project the missions have only been tested on simulations. Figure 2 shows a picture of an UAS during the simulative flight along the model of the Travehafenbrücke. A deployment on the real infrastructure is planned for the year 2023, where the following tasks have to be solved by the flight controller and the sensors of the UAS.

Reference system and SLAM: To perform a real and autonomous flight along the desired points, which are passed to the flightcontroller after the pre-computation, an adjustment has to be made in terms of the coordinates of the waypoints. The UAS sensors create a live map of the environment, yet the infrastructure and its pre-computation model have to match in terms of a reference coordinate system, so that the Voxelmap can be transferred into the real world. Therefore, the UAS uses the ultrasonic reference system and the lidar - both mentioned in section 4.1 - to create a live map. A SLAM (Simultaneous Localization and Mapping) algorithm then matches the infrastructure model of the pre-computation to the live map to allow a conversion from the computational grid into the real worlds coordinate system.

Live controller: As mentioned in section 4.1 the *Pixhawk 6X* is implemented on the UAS. The implemented flight controller uses a cascaded structure of PID-controllers to perform the flightmission. Further, different control approaches are currently tested to increase the performance compared to the code provided by the *PX4* software. The literature shows that many different types have been tested to perform a UAS mission, however, the results of a model predictive approach and an energy-based trajectory controller are taken into account for now (Fritsch, 2014; Tzoumanikas et al., 2020). Since this process is not finished yet, no final decisions can be presented here. The results will be presented in a future paper.

Additional features: In addition to the flight controller, future work will also focus on additional features and safety options. Therefore, different sensors will be tested to implement a collision avoidance ensuring the safety of the UAS. At the current state of the project only a simple collision “detect and avoid” system is implemented on the UAS basically stopping the drone if an obstacle is detected. For a more optimized solution dynamic path adjustments are a goal to reach, so that the autonomy of the system can be guaranteed.

5 CONCLUSION

After reviewing NDT methods for steel structures, the implemented sensors for UAS-based inspections within the MISDRO project are RGB-, panchromatic-, thermal-, NIR-hyperspectral cameras and lidar to detect the typical defects corrosion, fatigue, deformation, moisture and biota. Regarding the UAV flight missions have been tested on a simulation successfully. Future work will therefore focus on the implementation of the SLAM and reference system, so that information provided by the pre-computation can be optimally used by the UAS. The main difficulty for this will be the implementation of a system, which can operate under the absence of a GPS signal, which sometimes occurs during flights below a bridge or in areas with bad signal strength. In terms of the control algorithm used by the flight controller a final decision will be made in the near future. Also different performance enhancements and features will be added to the pre-computation and the UAS. In the next steps, they are applied on the Norderelbbrücke and Freihafenelbbrücke in Hamburg, the train bridge over the river Oste and the weir Dörverden to collect data for training and evaluating different machine learning algorithms. Furthermore, the creation of an image dataset of typical structural steel damage with visual and hyperspectral images is planned in order to train and validate ML models. The dataset will be used to test different spectral indices to determine the optimal spectral bands for moisture, corrosion and different biota detection. Challenging are

the light conditions at the structure, as they can change during an aerial survey. With the help of the 3D models, different lighting situations and damage cases can be simulated. The detected damages are finally stored in a central database and visualized with a web interface, including 3D display, so that those responsible for the building can immediately see the current condition and do a quick assessment and initiation of further measures is possible.

REFERENCES

- Bergmeister, K., A. Strauss, and M. Hoffmann (2022). *Digitale Zustandserfassung von Gebäuden, Infrastrukturbawerken und Naturgefahren*, Chapter VIII, pp. 533–606. John Wiley & Sons, Ltd.
- Bundesanstalt für Straßenwesen (2021, November). BAST - Homepage - Zustand- snoten der Brücken (Excel). <https://www.bast.de/DE/Statistik/Bruecken/Zustandsnoten-excel.xlsx>. Accessed: 2023 01 09.
- Bundesanstalt für Wasserbau (2018). BAWMerkblatt Schadensklassifizierung an Verkehrswasser- bauwerken (MSV). *BAW-Merkblätter, -Empfehlungen und -Richtlinien*
- Cao, H., F. Gu, P. Xie, and Z. Song (2021). Accuracy Analysis of ToF and Structured Light with Different Baseline Lengths in the Mobile Smart Terminals. In *Proceedings of the 2020 4th International Conference on Vision, Image and Signal Processing, ICVISP 2020*, New York, NY, USA. Association for Computing Machinery.
- Correia, M., H. Pernet, M. Salta, L. Gaillet, H. Patricio, and F. Schoefs (2012). *Duratinet: Maintenance and Repair of Transport Infrastructure*. LNEC Publisher.
- DB Netz AG (2022). Deutschlands Eisenbahnbrücken — DB Netze Brückenportal. <https://bruecken.deutschebahn.com/>. Accessed: 2023 01 09.
- DIN, Normenausschuss Bauwesen (1999). DIN 1076: Ingenieurbauwerke im Zuge von Straßen und Wegen, Überwachung und Prüfung, Ausgabe 11/1999.
- Feroz, S. and S. Abu Dabous (2021). UAV-Based Remote Sensing Applications for Bridge Condition Assessment. *Remote Sensing* 13(9).
- Fritsch, O. (2014). *Energiebasierte Lage-und Positionsfolgeregelung für einen Quadrocopter*. Ph. D. thesis, Technische Universität München.
- Hallermann, N., P. Debus, J. Taraben, A. Benz, G. Morgenthal, V. Rodehorst, C. Völker, T. Abbas, T. Gebhardt, and S. Daubert (2019). Unbemannte Fluggeräte zur Zustandsermittlung von Bauwerken - Fortsetzungsantrag. Abschlussbericht. In *Forschungsinitiative Zukunft Bau, Band F 3157*, pp. 1–61. Fraunhofer IRB Verlag.
- Han, J. (2019). An efficient approach to 3D path planning. *Information Sciences* 478, 318–330.
- Hart, P. E., N. J. Nilsson, and B. Raphael (1968). A Formal Basis for the Heuristic Determination of Minimum Cost Paths. *IEEE Transactions on Systems Science and Cybernetics* 4(2), 100–107.
- Lattanzi, D. and G. Miller (2017). Review of robotic infrastructure inspection systems. *Journal of Infrastructure Systems* 23(3), 04017004.
- Makiello, L. (2022). Multi-Sensor Fusion for a UAV/USV Tandem System for Spatial Data Collection of Waterways. In *Proceedings of 33. Forum Bauinformatik*.
- Morgenthal, G., N. Hallermann, and M. Achtelik (2015). Unbemannte Fluggeräte zur Zustand- sermittlung von Bauwerken. Abschlussbericht. In *Forschungsinitiative Zukunft Bau, Band F 2971*, pp. 1–135. Fraunhofer IRB Verlag.
- Morgenthal, G., V. Rodehorst, N. Hallermann, P. Debus, and C. Benz (2021). *Bauwerksprüfung gemäß DIN 1076 – Unterstützung durch (halb-)automatisierte Bildauswertung durch UAV (Unmanned Aerial Vehicles – Unbemannte Fluggeräte)*.
- Nam, L. H., L. Huang, X. J. Li, and J. F. Xu (2016). An approach for coverage path planning for UAVs. In *2016 IEEE 14th International Workshop on Advanced Motion Control (AMC)*, pp. 411–416.
- Perron, L. and V. Furnon (2023). Google OR-Tools. v9.4. <https://developers.google.com/optimization/>. Accessed: 2023 01 09.
- Taraben, J., M. Helmrich, and G. Morgenthal (2022). Datenmodelle für digitale Zwillinge von Brücken und bildbasierte Zustandsaufnahmen. *Bautechnik* 99(2), 134–142.
- Tzoumanikas, D., Q. Yan, and S. Leutenegger (2020). Nonlinear MPC with Motor Failure Identification and Recovery for Safe and Aggressive Multicopter Flight. In *2020 IEEE International Conference on Robotics and Automation (ICRA)*, pp. 8538–8544.
- Yuan, M.-s., T.-l. Zhou, and M. Chen (2022). Improved lazy theta* algorithm based on octree map for path planning of UAV. *Defence Technology*.
- Zahiri, Z., A. Lamberti, J. Wielant, and P. Scheunders (2022). Characterization Of Corrosion Products On Carbon Steel Using Hyperspectral Imaging In Short-Wave Infrared (SWIR). In *2022 12th Workshop on Hyperspectral Imaging and Signal Processing: Evolution in Remote Sensing (WHISPERS)*, pp. 1–4.

A lifecycle analysis approach to the impact of green roofs on the structural and thermal performances of buildings

S. Kalantari

Sapienza University of Rome, Italy

M.R. Rashedi & R. Ehsani

Amirkabir University of Technology, Tehran, Islamic Republic of Iran

F.M. Tehrani

California State University, Fresno, California

ABSTRACT: Buildings account for more than 40% of global energy consumption and up to a third of global greenhouse gas emissions in developed and developing countries. Electricity is currently the primary energy used for cooling buildings and appliances, but most countries use fossil fuels for heating. Both energy sources cause significant CO₂ emissions. Plants and vegetation improve air quality and reduce greenhouse gas emissions directly by absorbing greenhouse gases such as carbon dioxide from the atmosphere or indirectly by reducing energy use. Further, plants reduce the roof temperature by providing shade on roof surfaces. Large-scale implementation of rooftop gardens substantially reduces energy consumption and ultimately lowers energy costs but impact the overall weight of the building and require additional construction cost. Therefore, the impact of green roofs on various structural and thermal performances of buildings varies for extensive intensive or semi-intensive systems. These interacting impacts warrant a lifecycle analysis to optimize the extent of green roof applications concerning sustainability performance measures, including energy, emissions, water, and waste. This paper addresses the lifecycle analyses of green roofs in the hot summer Mediterranean climate like Rome in Italy or similar cities in the region. The target climate is essential to indicate the value of green roofs in warming climates around the globe. Moreover, results translate energy consumption to releasing greenhouse gas emissions and measures of water and waste related to structural or thermal operations. Conclusions enable building professionals to assess the challenges and opportunities of green roof applications on new and existing buildings.

1 INTRODUCTION

The concentrations of carbon dioxide (CO₂), methane (CH₄), nitrous oxide (N₂O), and other halocarbons are rising in the atmosphere due to human activity, according to observations from global monitoring stations (MacCracken 2001). Because of their ability to warm the climate, these gases are collectively known as greenhouse gases (MacCracken 2001). Carbon dioxide comes first and foremost on the list of all the greenhouse gases produced by human activities. The primary cause of the production of this gas is the excessive combustion of fossil fuels like coal and oil (Shahzad 2015). Cement production also releases carbon dioxide into the atmosphere (Shahzad 2015). Due to the continual raises in the earth's temperature for greenhouse gases, these gases are contributing negatively to global warming's devastation (Shahzad 2015). Buildings now account for more than 40% of the energy consumed worldwide and up to a third of the greenhouse gas emissions (Huovila et al. 2009). Additionally, the buildings and construction sector is a substantial source of non-CO₂ GHG emissions due to halocarbons, CFCs, HCFCs, and hydrofluorocarbons (HFCs) as insulation materials, cooling agents, and refrigerants

(Huovila et al. 2009). In six American cities, the peak urban electric consumption increased from 2% to 4% for every one °C increase in the daily maximum temperature above the threshold of 15 to 20 °C (Bianchini & Hewage 2012).

Buildings consume energy primarily in two ways: first, to maximize heating, ventilation, and air conditioning to maintain the interior as comfortable as possible; and second, to produce electricity to operate the necessary domestic applications, both of which result in a rise in global CO₂ emissions (Hughes et al. 2011). Currently, electricity is the primary energy source used for heating and appliances in buildings, while most nations use fossil fuels for cooling, which are significant contributors to carbon emissions (Chalmers 2014). Elective policies can result in energy-efficient and climate-resilient structures, hence reducing the increase of greenhouse gas (GHG) emissions (Chalmers 2014). The most severe result of global warming is increased sea levels because melting glaciers and ice sheets would result in higher water levels in the seas, rivers, and lakes, which may cause massive flooding (Shahzad 2015).

A practical solution to sustain the future development of resilient infrastructure relies on quantitative measures of energy, waste, water, and greenhouse gas emissions aligned with social equity and justice (Iskandar et al. 2022; Nelson & Tehrani 2018; Tehrani 2019; Tehrani 2022; Tehrani & Nelson 2022). These measures typically represent a bottom-up estimate of infrastructure development tasks throughout the lifecycle of engineered systems (Tehrani et al. 2013; Tehrani & Dadkhah 2018; Tehrani et al. 2019). Further, the objective approach to infrastructure resilience in response to future disasters requires an assessment of climate change consequences in various climate zones (Kalantari et al. 2023). This paper utilizes similar techniques to address a gap in applying green roofs for sustainable and resilient development.

2 LITERATURE REVIEW

2.1 *Benefit of vegetation*

Integrating plants and other wildlife can benefit cities (Dastan Diznab & Tehrani 2022). For example, plants can provide shade for buildings and pavements and cool buildings, thereby reducing energy use and slowing the deterioration of pavements, lowering the cost of maintaining them (Alhashimi et al. 2018). By absorbing greenhouse gases like carbon dioxide from the atmosphere, plants, and vegetation can also improve air quality and reduce greenhouse gas emissions, or they can do so indirectly due to the decreased energy use (Alhashimi et al. 2018).

2.2 *Effect of vegetation on buildings*

In every climate, green roofs are the best option for lowering the temperature of the exterior roof surface (Barreca 2016). Although green roofs are possible for pollution management and lowering indoor temperatures, it is vital to consider several variables, such as initial high construction costs, high maintenance expenses, and roof leakage issues (Dauda & Alibaba 2020). The major drawback of green roofs is their high cost, which is significantly more than the cost of regular roofs due to their unique design, which includes many more layers than the standard roof, as well as the fact that they are built of expensive, imported materials (Drozd 2019). The weight of a green roof is another drawback (Hemati et al. 2021). It is significantly taller than a typical roof. Because of this, the structure's load capacity must be raised, adding to the structure's weight (Drozd 2019). The dark surfaces (concrete and asphalt) and the lack of vegetation raise the warmth in metropolitan areas (Bianchini & Hewage 2012).

2.3 *Benefits of green roofs*

The life cycle evaluation is significantly impacted by the energy advantages that the various types of green roofs offer, and when energy demands are low and roof replacement cycles are short, the materials used to build the roof are crucial (Kosareo & Ries 2007). By offering a one-time tax abatement, the City of New York made it easier to build green roofs. If the green roof accounts for at least 50% of the total roof area, the building owner can receive a tax break of \$48/m² (Bianchini & Hewage 2012). Green roofs may also contribute to food security in various communities (Tehrani & Zamani-Alaei 2020).

2.4 Roof gardens and different types

A roof garden is an excellent approach to improving city buildings through landscape design, which may turn unused space into a helpful area that offers ecological and economic services (Jafari et al. 2015).

Benefits of longevity While conventional roofs only last roughly 20 years, green roofs are predicted to last between 40 and 55 years (Bianchini & Hewage 2012).

There are three different kinds of green roofs, according to the International Green Roof Association (2013); Extensive green roofs, semi-intensive green roofs, and intensive green roofs. Extensive green roofs are appropriate for less demanding and slow-growing plant communities since they contain little nutrients and are not particularly deep. Semi-Intensive Green Roofs have more options because of the characteristics of having a deeper ground level, different grasses, herbaceous perennials, and shrubs like lavender can be planted, but tall-growing bushes and trees are still absent. Lawns, perennials, shrubs, and trees, as well as other garden-related items, may all be planted, and extra amenities, walkways, seats, playgrounds, and even ponds can be built on the intensive green roofs because designing is not limited to these roofs (Jafari et al. 2015). Figure 1 shows different types of green roofs and their characteristics.

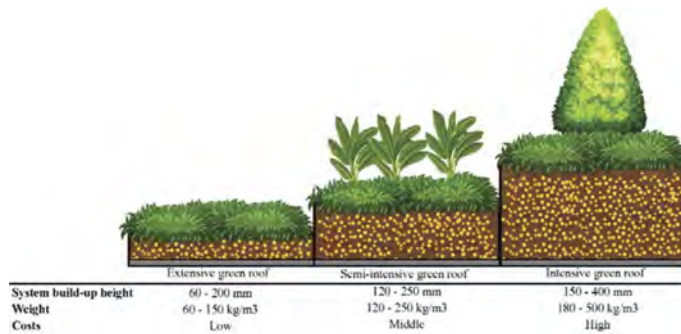


Figure 1. Different types of green roofs and their characteristics (Raji et al. 2015).

3 METHODOLOGY

As one of the most sophisticated building energy simulation tools that include a green roof model, EnergyPlus was chosen as the simulation platform for investigating the influence of green roofs on the thermal performance of buildings (Tehrani et al. 2018; Silva 2014). A building's hourly energy consumption may be modeled using the EnergyPlus simulation model under user-specified construction, internal loads, schedules, and weather (Sailor 2008). Based on interior and outdoor environmental conditions, EnergyPlus simulates energy flows for heating, cooling, lighting, ventilation, and other functions (Silva 2014). EnergyPlus has several advantages as the simulation platform for using the green roof model, including the advancement, updates, and widespread application for buildings (Sailor 2008). Two input files are needed to run a simulation; a building input data file (IDF) containing all the study case's features and a weather data file containing information about the location's climate.

This study examines the studies of green roofs in Rome, Italy, or other cities with a Mediterranean climate (Köppen climate classification: Csa), which has moderate winters and warm to hot summers. The research's hypothesis states that the rooftop garden building experienced much lower internal temperatures due to natural shading. Additionally, the rooftop garden would minimize heat flow through the roof, slowing the release of heat and lowering the demand for cooling or heating by the experiment of building a model house with a rooftop garden.

Many studies looked at the impact of growth media characteristics, including moisture content, relative density, and growing medium thickness, on the thermal efficiency of green roofs (Raji et al. 2015). Permpituck and Namprakai (2012) compared two sets of green roofs with

soil thicknesses of 10 cm and 20 cm to a bare roof, and their findings demonstrate a considerable decrease in energy consumption (31% and 37%) and heat transmission (59% and 96%) for soil depths of 10 cm and 20 cm as compared to a bare roof (Raji et al. 2015).

3.1 Building model

Choosing material was based on the templates of open studio software for the 3C climate zone. The building model used for this paper had three floors with two units in each building; each unit's area is considered 110 m² (the average apartment area in Italy). In the building, 24 windows have been placed, 8 of which are 1.3 meters in 1.3 meters, and the other 16 are 1.3 meters in 2 meters. The 1.3 by 1.3 windows affect an area of 77 square meters, and the 1.3 by 2 affect 16.5 square meters of each house.

EnergyPlus software has two specific inputs; IDF (building model + windows information + material) and weather file. Chart 1 shows the monthly average temperature of Rome in the year 2021 taken from EnergyPlus.

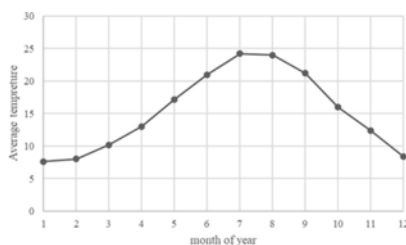


Chart 1. Monthly average temperature of Rome.

The heating, ventilation, and air conditioning (HVAC) system was chosen to be “PTAC” based on residential buildings and the 3C climate zone (Goel et al. 2017). A packaged terminal air conditioner or PTAC is a ductless, through-the-wall heating and cooling system. For heating, it is considered that gas is used, and for cooling, it is considered that electricity is used. The air-conditioning system works with a setpoint temperature of 21°C in the summer and 28°C in the winter.

3.2 Green roof model

For green roofs, there is a mixture of soil and lightweight expanded clay aggregate, which expanded clay acts as insulation and drainage (Tehrani 1998; Gerami et al. 2007). Expanded clay serves as the filter and drainage layer in this study. Invigoration of Roots and Soil Improvement might be noted as an advantage of applying expanded clay (Boudaghpour & Hashemi 2008). The soil layer was defined for green roofs in the Energyplus model based on the 30% expanded clay mixture matrix to 70% soil. The mechanical properties of this mixture are conductivity: 0.272 - density:866 - specific heat: 1140. Also, in this study, a 45-year life span was assigned to the green roof options (Kosareo & Ries 2007). In Table 1, the input is given to the software. Table 2 shows the input for different layers of green roofs in the software, and Table 3 shows the thickness input for different green roofs. It should be noted that although the EGR has a life expectancy of more than 40 years, it is challenging to do a meaningful feasibility analysis over such a lengthy time frame (Giama 2021). The conventional roof has a thermal installation equal to 0.07 meters and a waterproof membrane with a thickness of 0.005 meters.

3.3 Embodied energy and CO₂ emissions used for building a roof garden

In Table 4, the data for CO₂ sequestration is available. These data reflect calculations of emissions using environmental product declarations and other energy conversion coefficients for various materials and construction equipment. Production and fuel consumption rates follow standard construction practice guidelines.

Table 1. Input for different green roofs.

Green roof type	Leaf area index	Height of plant (m)	Soil thickness (m)
Extensive	1	0.05	0.1
Semi-intensive	2.5	0.5	0.35
Intensive	5	1	0.7

Table 2. Input for different layers of green roof in the software.

Material	Description	Energy (kW.h/kg)	CO ₂ emissions (kg CO ₂ /kg)	Density (kg/m ³)
Installation	Polystyrene foam	24.58	6.12	33.7
Waterproof Membrane	Bituminous membranes	0.5605	0.64	1100
Roof Barrier	Polyethylene	23.571	3.27	920
Protection layer	Polypropylene	20.932	3.64	905
Substrate	63% crushed brick -7% compost-30% LECA	1.01039	0.294	858.7

(Koroxenidis & Theodosiou 2021)

Table 3. Thickness input for different green roofs (m).

Material	Extensive	Semi-intensive	Intensive
Installation	0.049	0.049	0.049
Waterproof Membrane	0.004	0.005	0.006
Roof Barrier	0.0005	0.0008	0.001
Protection layer	0.002	0.004	0.008
Substrate	0.1	0.35	0.7

(Koroxenidis & Theodosiou 2021)

Table 4. CO₂ sequestration.

Green roof type	Annual CO ₂ Reduction (kg CO ₂ .m ⁻² .yr ⁻¹)
Extensive	0.5547
Semi-intensive	1.3868
Intensive	2.7736

(Kuronuma et al. 2018)

4 RESULTS

4.1 Energy consumption

This paper has studied four different cases: a building without a green roof, an extensive green roof, a semi-intensive green roof, and an intensive green roof. Also, in the reviewed model, it is assumed that only electricity is used for cooling in the hot season, and natural gas is used for heating in the cold season. Chart 2 shows the total energy used in building with different roofs. The chart shows that the most energy used in the building is when a conventional roof is used, and the minor energy usage goes to intensive green roofs. However, differences can be seen when the energies are divided into those used in heating and cooling systems. It is seen that extensive roofs use more electricity than conventional roofs. Analyses show that insulation plays a much more critical role in cooling systems than the type of green roof. This theory is based on defined thicknesses for components similar to conventional roofs, insulation, and waterproofing in types of green roofs. The thickness of the insulation and waterproofing membrane in the modeled conventional roof is more than the extensive roof and is near the semi-intensive roof but less than the intensive roof. This difference is seen in chart 2. Table 5 indicates the energy percentage saved using green roofs. Based on this table, it can be concluded that the effect of semi-intensive green roofs on saving electricity is insignificant compared to conventional roofs and that extensive roofs do not save electricity. In general, Intensive green roofs save more energy than others. Also, it is seen that green roofs have a much more noticeable impact in saving the energy of the heating system.

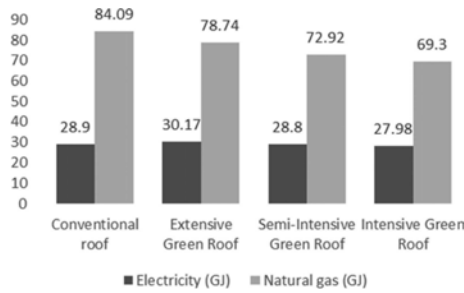


Chart 2. Total HVAC Energy Consumption.

Table 5. Energy percentage saved while using green roofs.

Green roof type	Cooling System (%)	Heating System (%)
Extensive	-4.394	6.362
Semi-intensive	0.346	13.283
Intensive	3.183	17.588

As mentioned, a 45-year life span was assigned to the green roof options. Assuming that we consider the amount of impact on energy for all types of green roofs constant throughout their lifespan, the amount of energy saved during their lifetime can be calculated. This energy is then compared with embodied energy. The energy saved in extensive and semi-intensive green roofs is more than the energy needed to produce these structures. It is also notable that although intensive roofs saved more annual energy than other types, the embodied energy was more than the energy saved in all their life.

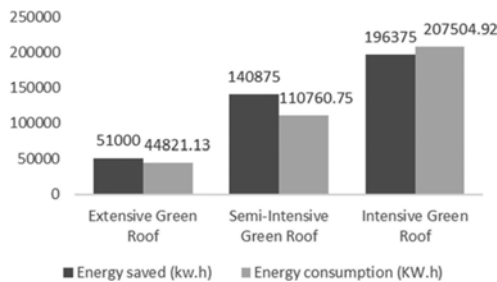


Chart 3. Energy saved and energy consumption in different roof gardens (kW.h).

4.2 CO₂ emission saving comparison of different roof gardens

This study used a life cycle assessment to calculate the CO₂ emissions from the production process and maintenance practices of different green roofs. We assessed the CO₂ payoff for modular green roofs by calculating their CO₂ payback time. CO₂ payback is the time it takes for a green roof system's CO₂ reduction to offset the CO₂ emitted during production and maintenance. The CO₂ payback consists of two major parts; The reduction owing to sequestration, which is the process of capturing and storing atmospheric carbon dioxide done by vegetation, and the CO₂ reduction owing to energy saving. The sequestration is calculated based on previous studies and for each roof garden based on the leaf area index (LAI).

On the other hand, the energy saving in this study is the energy saved in electricity and natural gases, which have different CO₂ emission rates. Chart 4 indicates the total CO₂ payback during 45 years of each type of roof garden. Also, Chart 4 shows the embodied CO₂ needed and the CO₂ payback and saving for each type of roof garden. Based on this diagram, it can be concluded that all roof guards offset the effect of carbon dioxide during their lifetime.

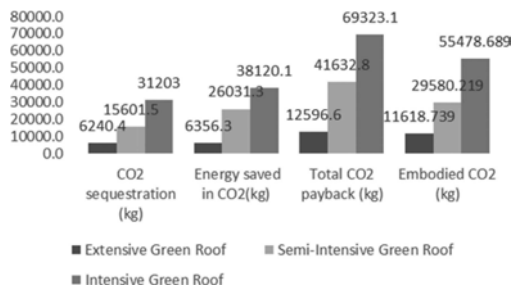


Chart 4. Total CO₂ payback during 45 years of the existence of each type of roof garden.

5 CONCLUSION

This study quantified the CO₂ emitted during the production and maintenance of a hypothetical modular green roof and estimated the CO₂ reduction from energy savings and CO₂ sequestration. The study results show that CO₂ emissions are offset through CO₂ sequestration and energy savings during the lifespan and even less than the life span, which indicates that green roofs contribute to atmospheric CO₂ reduction and global warming mitigation within their lifespan.

The studies of this paper showed that intensive green roofs do not offset their embedded energy. Also, in this study, we concluded that extensive and semi-intensive green roofs compensate for their construction and maintenance energy during their lifetime. Based on this conclusion and examining energy inflation in Italy, we can conclude which is more optimal from a financial point of view.

The amount of time required to retrieve the CO₂ emitted from the construction phase for extensive, semi-intensive and intensive green roofs are 41.5, 32, and 36 years and the time required to retrieve the energy consumed from the construction phase for extensive, semi-intensive and intensive green roofs are 39.5, 35.4 and 47.5 years.

In this study, many parameters were not investigated, such as the type of plants and the amount of energy required for maintenance and different CO₂ sequestrations. These are parameters in need of further studies.

REFERENCES

- Alhashimi, L., Aljawi, L., Gashgari, R. and Almoudi, A., 2018, August. The effect of rooftop garden on reducing the internal temperature of the rooms in buildings. In *Proc. 4th World Congr. Mech., Chem., and Mater. Eng.*, Madrid, Spain, 16–18.
- Barreca, F., 2016. Rooftop gardening. A solution for energy saving and landscape enhancement in Mediterranean urban areas. *Procedia-Social and Behavioral Sci.*, 223, 720–725.
- Boudaghpour, S. and Hashemi, S., 2008. A study on light expanded clay aggregate (LECA) in a Geotechnical view and its application on greenhouse and greenroof cultivation. *Int. J. Geol.*, 4, pp.59–63.
- Chalmers, P., 2014. Climate change: Implications for buildings. Key findings from the intergovernmental panel on climate change fifth assessment report.
- Dastan Diznab, M. A., and Tehrani, F. M. 2022. Mapping Standards and Rating Measures of Structural Green Roofs for Socio-Environmental Life Cycle Assessments. In: Bloom, M. F., and Reddy, K. R. (eds.), *Proc. ASCE Int. Conf. on Sustainable Infrastructure 2021*, Houston, Texas, Dec. 6-10, 2021, pp. 82–90. Doi: 10.1061/9780784483879.008
- Dauda, I.S.A.I.A.H. and Alibaba, H.Z., 2020. Green roof benefits, opportunities and challenges. *Int. J. Civ. Struct. Eng. Res*, 7, 106–112.
- Del Barrio, E.P., 1998. Analysis of the green roofs cooling potential in buildings. *Energy and buildings*, 27 (2), 179–193.
- Drozd, W., 2019. Problems and benefits of using green roofs in Poland. In *IOP Conf. Series: Earth and Environ. Sci.* 214(1), 012076.
- Gerami, M. A., Tehrani, F. M., and Esfahani, A. N. 2007. The Complete Guide to Lightweight Expanded Clay Aggregate in Agriculture and Landscaping. in Persian, LECA, Tehran, Iran.
- Giama, E., Papageorgiou, C., Theodoridou, I. and Papadopoulos, A.M., 2021. Life Cycle Analysis and Life Cycle Cost Analysis of green roofs in the Mediterranean climatic conditions. *Energy Sources, Part A: Recovery, Utilization, and Environ. Effects*, 1–14.

- Goel, S., Rosenberg, M.I. and Eley, C., 2017. ANSI/ASHRAE/IES Standard 90.1-2016 performance rating method reference manual (No. PNNL-26917). Pacific Northwest National Lab. (PNNL), Richland, WA.
- Hemati, M., Dastan Diznab, M. A., and Tehrani, F. M. 2021. Seismic Assessment for Resilience of Steel Moment Frames with Green Roof Using Endurance Time Method. *EMI Int. Conf.*, Mar. 22-24, 2021, Durham University, UK.
- Hughes, B.R., Chaudhry, H.N. and Ghani, S.A., 2011. A review of sustainable cooling technologies in buildings. *Renewable and Sustainable Energy Reviews*, 15(6), 3112–3120.
- Huovila, P., Ala-Juusela, M., Melchert, L., Pouffary, S., Cheng, C.C., Ürge-Vorsatz, D., Koepfel, S., Svenningsen, N. and Graham, P., 2009. Buildings and climate change: Summary for decision-makers. Environment in Developing Communities. *CivilEng*, 3(2), 427–440. Doi: 10.3390/civileng3020025
- Jafari, N., Utaberta, N., Yunos, M.Y.M., Ismail, N.A., Ismail, S., Ariffin, N.F.M., Jafari, N. and Valikhani, M., 2015. Benefits of roof garden in order to usage of urban agriculture at roof garden in high-rise building in Malaysia. *Advances in Environ. Biology*, 9(24), 86–92.
- Kalantari, S., Ehsani, R., and Tehrani, F.M., 2023. A worldwide survey of concrete service life in various climate zones. In: Pacheco-Torgal, F. and Granqvist, C-G. (eds.), *Adapting the Built Environment for Climate Change*, Chapter 9, Cambridge, MA: Elsevier, 183–200.
- Koroxenidis, E. and Theodosiou, T., 2021. Comparative environmental and economic evaluation of green roofs under Mediterranean climate conditions—Extensive green roofs a potentially preferable solution. *J. Cleaner Production*, 311, 127563.
- Kosareo, L. and Ries, R., 2007. Comparative environmental life cycle assessment of green roofs. *Building and Environ.*, 42(7), pp.2606–2613.
- Kuronuma, T., Watanabe, H., Ishihara, T., Kou, D., Touda, K., Ando, M. and Shindo, S., 2018. CO₂ payoff of extensive green roofs with different vegetation species. *Sustainability*, 10(7), 2256.
- MacCracken, M.C., 2001. Global warming: a science overview. In *Global Warming and Energy Policy*. Springer, Boston, MA.
- Nelson, D. and Tehrani, F.M., 2018. Is Resilience . . . Sustainable? *APWA Reporter*, 85(8), 53–56.
- Permpituck, S. and Namprakai, P., 2012. The energy consumption performance of roof lawn gardens in Thailand. *Renewable energy*, 40(1), 98–103.
- Raji, B., Tenpierik, M.J. and Van Den Dobbelen, A., 2015. The impact of greening systems on building energy performance: A literature review. *Renewable and Sustainable Energy Reviews*, 45, 610–623.
- Sailor, D.J., 2008. A green roof model for building energy simulation programs. *Energy and buildings*, 40 (8), 1466–1478.
- Shahzad, U., 2015. Global warming: Causes, effects and solutions. *Durreesamin J.*, 1(4), pp.1–7.
- Silva, M., 2014. Green roofs energy performance simulation. MSc. Thesis, U. de Lisboa, Lisbon, Portugal.
- Tehrani, F.M., 1998. The Comprehensive Guide to LECA, in Persian. Mehrashna, Tehran, Iran.
- Tehrani, F.M., 2019. Deploying and Rating Sustainable Practices for Resilient Bridge Infrastructure. Keynote Lecture, *Proc. Fifth Int. Conf. Bridges*, Tehran, Iran: Amirkabir University of Technology. Dec. 17-18, 2019, MS05.
- Tehrani, F.M., 2022. Deployment of Sustainable Practices using Lightweight Aggregates for Bridge Infrastructures. In: Davis, C. A., Yu, K., and Tacioglu, E. (eds.), *Proc. ASCE Lifelines 2022*, Los Angeles, CA: University of California, Los Angeles. Feb. 7-11, 2022, 187–197. Doi: 10.1061/9780784484432.018
- Tehrani, F.M., Alexandrou, A., Mahoney, M., Adhikari, D., and Raymond, M., 2014. Energy inputs and carbon dioxide emissions from construction equipment during construction of a golf course. *Int. J. Eng. Research and Innovation*. 6(2), 78–86.
- Tehrani, F.M., and Dadkhah, M., 2018. A Case Study on the Analysis of Energy and Emissions for Sustainability Rating. *Int. J. Climate Change*. 1(3), 13–23. Doi: 10.18848/1835-7156/CGP/v1i03/13-23
- Tehrani, F.M., and Nelson, D., 2022. From Sustainability to Resilience: A Practical Guide to ENVISION, In: Ettouney, M. (ed.) *Objective Resilience*, ASCE, Reston, VA. doi: 10.1061/9780784415894.ch3
- Tehrani, F.M., and Zamani-Alaei, M. 2020. Sustainable Engineering for Resilient Food Security. *39th Annual Agribusiness Management Conf.*, Oct. 28- Nov. 19, 2020, Fresno, CA.
- Tehrani, F.M., Farshidpour, F., Pouramini, M., Mousavi, M., and Esfahani, A. N. 2018. Sustainability rating of lightweight expanded clay aggregates using energy inputs and carbon dioxide emissions in lifecycle analysis. *Proc Sixth Int. Symposium on Life Cycle Civ. Eng.*, IALCCE, Ghent, Belgium. Oct. 2018, 2989–2993.
- Tehrani, F.M., Pouramini, M., and Mohammadiyaghini, E., 2019. Sustainability Assessment and ENVISION Rating of Lightweight Masonry Walls in Conventional Buildings. *Proc. Int. Conf. Sustainable Infrastructure 2019*, Los Angeles, CA, ASCE. Nov. 6-9, 2019, 502–507. Doi: 10.1061/9780784482650.054

Deep learning-based life-cycle system reliability assessment of asphalt pavement

Jiyu Xin & Dan M. Frangopol
Lehigh University, Bethlehem, USA

Mitsuyoshi Akiyama
Waseda University, Tokyo, Japan

ABSTRACT: Asphalt pavement should be represented as a series system of limit state functions associated with the international roughness index, rut depth, alligator cracking, and transverse cracking. Traditional regression-based prediction models are too simplified to account for the relationship between pavement performance and the operating conditions associated with climate, traffic, pavement structure and property parameters. In this study, a deep learning model based on bidirectional long short-term memory neural networks is trained using the long-term pavement performance database to learn the nonlinear and complex relationship between four performance indicators and their associated parameters. Based on multiple time-variant limit-state functions incorporating the uncertainties associated with these parameters, deep learning model prediction, and international roughness index measurement, Monte Carlo simulation is conducted to estimate the system reliability of the asphalt pavement. In an illustrative example, the effects of different parameters on the life-cycle system reliability are investigated based on two pavement sections.

1 INTRODUCTION

As an integral part of roadway networks, asphalt pavements may start to deteriorate from the day they enter into service due to a multitude of stressors such as increasing traffic loads, various climatic conditions, and the associated material deterioration of asphalt mixture (Xin 2021). If they are not managed timely and effectively, a significant decrease or even failure in structural functionality and safety of asphalt pavements could occur. This jeopardizes the mobility of freight and commodities for economic vitality and access to a range of users for societal benefits. According to the 2021 Report Card for America's Infrastructure (ASCE 2021), over four million miles of public roadways are carrying people and goods to their destinations every day; however, more than 40% of these vital lifelines are now in poor or mediocre condition. Reliability-based performance indicators and single- and multi-objective optimal methodologies under uncertainty are gaining increased attention as effective tools for finding rational maintenance and rehabilitation strategies during the life-cycle management of infrastructure systems (Frangopol 1985; Frangopol 1995; Frangopol and Das 1999; Yang et al. 2004; Frangopol 2011; Ghosn et al. 2016; Frangopol et al. 2017; Garcia-Segura et al. 2017; Akiyama et al. 2020). Therefore, it is essential to accurately estimate the life-cycle asphalt pavement performance with the aid of deterioration modeling methodologies that consider various uncertainties.

Traditionally, prediction models used for life-cycle assessment of asphalt pavement performance include purely mechanistic, mechanistic-empirical (M-E), regression-based, and subjective (Haas & Hudson 2015). These models are either with low prediction accuracy (e.g., regression-based) or too complicated (e.g., M-E). Xin et al. (2021a, 2021b, 2022) first adopted artificial neural networks (ANN) and long short-term memory (LSTM) networks to predict the performance indicator of the international roughness index (*IRI*) for new and in-service asphalt pavement. The obtained prediction accuracy is larger than that of regression equations used in the mechanistic-empirical pavement design guide (MEPDG) by the American Association of State Highway and Transportation Officials (AASHTO, 2020). This demonstrates the ability of machine learning models in the automatic and efficient understanding of the complex relationship between pavement performance and the associated operating conditions including climate, traffic, and pavement structure and property parameters. However, the above research only considered one performance indicator (i.e., *IRI*) and several associated parameters. In fact, asphalt pavement is a series system characterized by multiple failure modes associated with *IRI*, rut depth (*RUT*), alligator cracking (*AC*), and transverse cracking (*TC*), and considered failed if any one of the indicators exceeds the corresponding threshold (AASHTO, 2020).

In this paper, a more sophisticated deep learning (DL) model based on bidirectional long short-term memory (BiLSTM) neural networks is constructed, trained, and applied to learn the relationship between the performance indicators and the associated parameters using the long-term pavement performance (LTPP) database. The DL model with BiLSTM neural networks not only can learn the long-term dependencies between input sequence data (compared with ANN) but also process the input sequence data both ways (chronologically and anti-chronologically), which could catch patterns that may be overlooked by a unidirectional long-short term memory neural network (Greff et al. 2017; Chollet 2021). Based on the accurate predictions of the performance indicators by the DL model, while incorporating the uncertainties associated with climate, traffic, and pavement structure and property parameters, DL model prediction, and *IRI* measurement, Monte Carlo simulation (MCS) is conducted to calculate the system reliability of the asphalt pavement. The effects of fourteen parameters on the life-cycle system reliability are investigated based on two LTPP pavement sections in the United States.

2 DEEP LEARNING-BASED SYSTEM RELIABILITY

2.1 General procedure

Figure 1 presents the flowchart of the system reliability estimation methodology of asphalt pavement based on the deep learning model with BiLSTM memory networks. This flowchart consists of two main parts:

- (1) Training database collected from the LTPP program and prediction of performance indicators using the trained BiLSTM-based deep learning model.
- (2) System reliability analysis of asphalt pavement considering the uncertainties associated with several input parameters, DL model prediction, and *IRI* measurement.

2.2 Database for model training

The LTPP program is the largest and most comprehensive pavement performance database worldwide (LTPP 2022). The LTPP database published in August 2022 (Standard Data Release 36) is collected for training the DL model. Specifically, 4880 sets of data are collected from 63 pavement sections in the General Pavement Studies (GPS) program, including GPS-1, GPS-2, and GPS-6, and the Specific Pavement Studies (SPS) program, including SPS-1, SPS-3, SPS-5, and SPS-8 test sections, respectively.

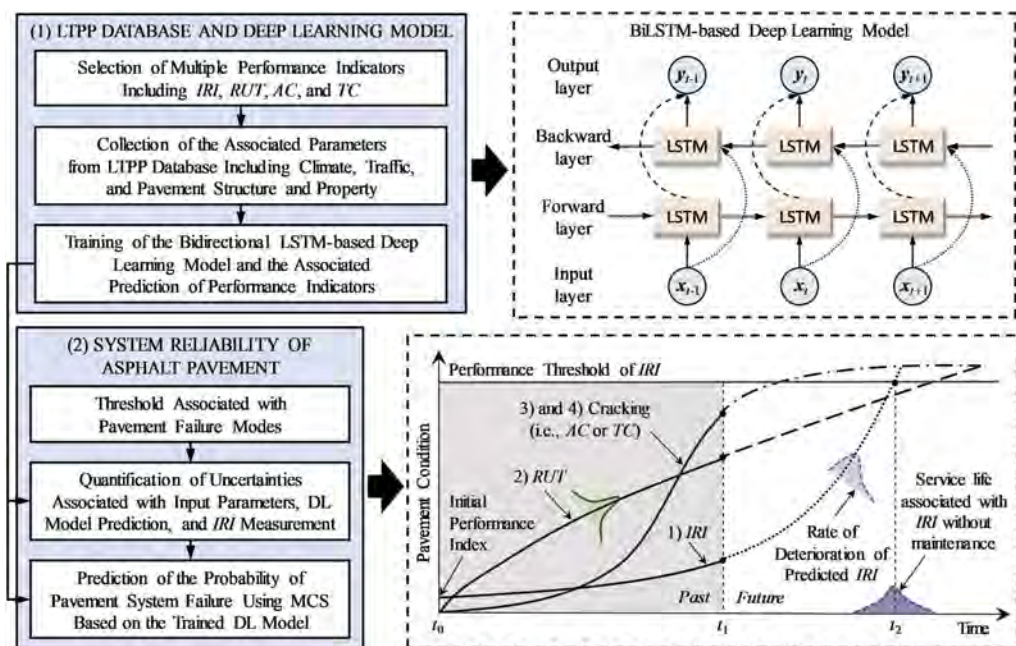


Figure 1. Flowchart of system reliability estimation of asphalt pavement using deep learning model.

Four performance indicators used for evaluating the functional adequacy and structural condition of asphalt pavement, including *IRI*, *RUT*, *AC*, and *TC*, are selected as the output of the DL model. For the input, the selected fourteen parameters are as follows (FHWA 2017):

- Climate parameters including (a) Hum_{max} and Hum_{min} : average of daily maximum and minimum relative humidity for the month, respectively (%); (b) *Precip*: total monthly precipitation (mm); (c) *Snow*: monthly total snowfall (mm); (d) *Temp*: average of daily mean air temperatures for the month (degree Celsius); (e) *FI*: monthly freezing index; (f) *FT*: monthly freeze thaw (days); and (g) *Wind*: average of daily mean wind speed for the month (m/s);
- Traffic parameters including (a) *kESAL* and (b) *AADT*: annual equivalent single axle loads in thousands and average daily number of trucks in the LTPP lane, respectively;
- Pavement property parameters including (a) *Age*: time since the initial construction (years) and (b) *DFL*: deflection response of pavement to a load of known magnitude (μm); and
- Pavement structural parameters including (a) H_{asp} and (b) H_{base} : thickness of asphalt layer and base & subbase layers, respectively (cm).

2.3 Deep learning model

Deep learning is able to deal with large datasets by automatically and efficiently figuring out the complex relationship between inputs and outputs (Chollet 2021). The deep learning model consisting of BiLSTM neural networks was constructed, as shown in Figure 2, to predict the performance indicators of asphalt pavement based on the associated operating conditions (i.e., climate, traffic, and pavement property and structure). Specifically, the model contains an input sequence layer, two BiLSTM layers, three fully connected layers, two dropout layers, and a regression output layer. In total $N = 4880$ datasets, 70% and 30% are used as training and test data, respectively. Figure 3 shows the comparison between the predicted and measured performance indicators for training and test data, respectively. The coefficient of determination (R^2) values for all indicators are larger than those of distress prediction equations presented in the MEPDG (AASHTO 2020).

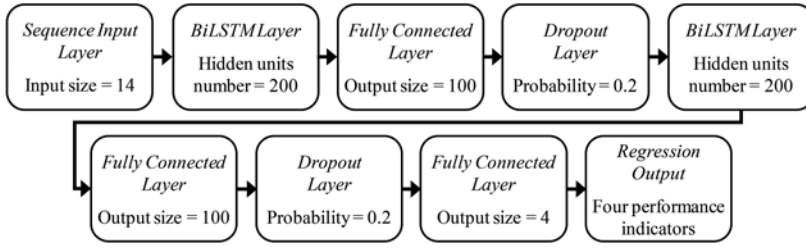


Figure 2. The structure diagram of the DL model based on BiLSTM.

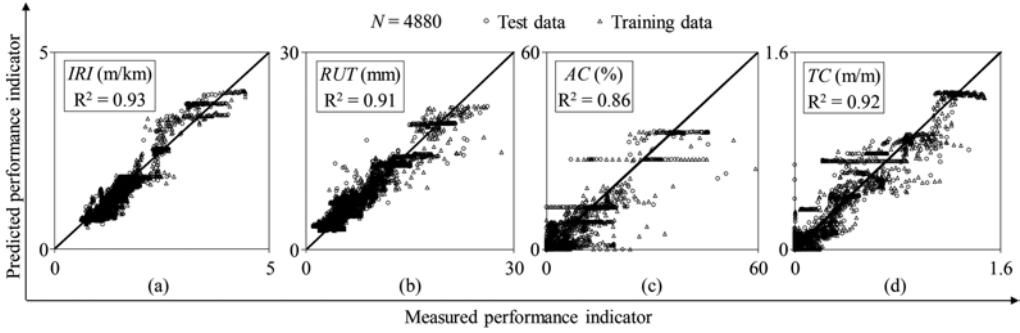


Figure 3. Training results of (a) *IRI*, (b) *RUT*, (c) *AC*, and (d) *TC* using the DL model.

2.4 System reliability analysis using DL model

MCS is adopted to compute the system reliability, as:

$$Pr_{r, sys}(t) = E \left\{ I \left[\min_i g_i(X_i) \right] \right\} = \frac{\sum_{j=1}^{N_{simu}} I \left[\min_i g_i(X_{ij}) \right]}{N_{simu}} \quad (1)$$

in which

$$g_1(X_1) = Thres_1 - [DL_1(X_{input}) + \varepsilon_{DL,1} + \varepsilon_{meas}(IRI)], i = 1 \quad (2)$$

$$g_i(X_i) = Thres_i - [DL_i(X_{input}) + \varepsilon_{DL,i}], i = 2, 3, \text{ and } 4 \quad (3)$$

where $E\{\cdot\}$ = expected value, $I[\Delta]$ = indicator function of Δ defined as $I[\Delta] = 1$ at $\Delta > 0$ and $I[\Delta] = 0$ at $\Delta \leq 0$, \min = finding the minimum elements of an array, $i = 1$ to 4 denote the four failure modes associated with the *IRI*, *RUT*, *AC*, and *TC*, respectively, g_i = individual limit state functions (LSF) of i , vector $X_{ij} = j$ -th sample value of vector X_i in the total number of simulations N_{simu} , $Thres_i$ = threshold of indicator i , DL_i = indicator i predicted by the DL model, $X_{input} = (X_1, X_2, \dots, X_{14})^T$ = variable vector as illustrated in Section 2.2, $\varepsilon_{DL,i}$ = DL model error associated with the prediction of indicator i , and $\varepsilon_{meas}(IRI)$ = *IRI* measurement error.

3 CASE STUDY

3.1 Input parameters for DL model

The proposed system reliability estimation methodology is applied to two existing LTPP asphalt pavement sections ID 42-B340 in Pennsylvania and ID 12-0112 in Florida, respectively. The

parameters (i.e., mean and standard deviation (SD)) associated with the variables for the DL model prediction and system reliability calculation are those indicated in Xin (2021).

3.2 Time-variant system reliability using DL model

Figure 4 shows the calculated system reliability for pavement section (a) ID 42-B340 in Pennsylvania and (b) ID 12-0112 in Florida versus time using Equation 1. The threshold associated with the system reliability is 75%. It can be seen that the system reliability of pavement sections ID 42-B340 and ID 12-0112 reaches the threshold at approximately 8.3 and 7.3 years, respectively, indicating that appropriate preventive maintenance actions should be scheduled in advance to postpone the rehabilitation or reconstruction of the corresponding pavement.

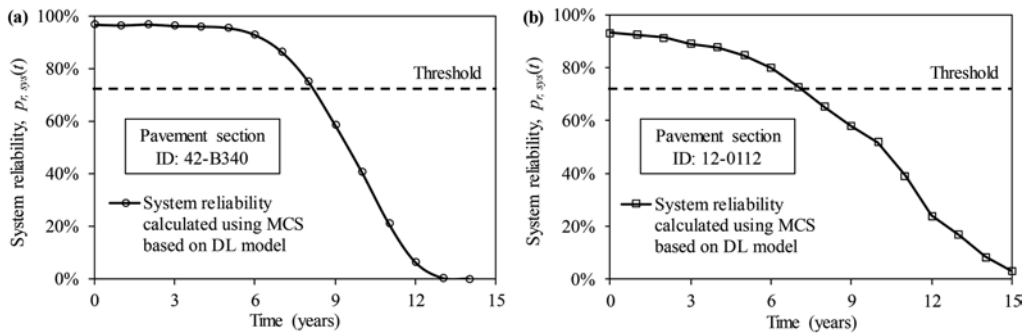


Figure 4. Time-variant system reliability of asphalt pavement section (a) ID 42-B340 and (b) ID 12-0112.

4 CONCLUSIONS

A novel deep learning model is proposed in this paper to realize the proper predictions associated with asphalt pavement performance indicators. The model is built based on the bidirectional long short-term memory neural networks and is trained with high predictive accuracy using the collected LTPP database.

Based on the trained model, the life-cycle system reliability analysis method is presented considering the four correlated failure modes, the associated operating conditions, DL model error, and measurement uncertainty of the asphalt pavement using MCS.

Traffic, climate, and pavement structure and property have significant effects on the life-cycle performance of the asphalt pavement, which should be taken into account for the decision-making on optimum M&R strategies.

REFERENCES

- Akiyama, M., Frangopol, D.M., & Ishibashi, H. 2020. Toward life-cycle reliability-, risk-and resilience-based design and assessment of bridges and bridge networks under independent and interacting hazards: emphasis on earthquake, tsunami and corrosion. *Structure and Infrastructure Engineering*, 16(1), 26–50.
- American Association of State Highway and Transportation Officials (AASHTO). 2020. *Mechanistic-empirical pavement design guide* (3rd ed.). Washington, DC: AASHTO.
- American Society of Civil Engineers (ASCE). 2021. *2021 Report Card for America's Infrastructure*. Reston, VA.
- Chollet, F. 2021. *Deep learning with Python*. Simon and Schuster.

- Federal Highway Administration (FHWA)—Office of Research, Development, and Technology: Infrastructure R&D. 2017. *The long-term pavement performance program* (FHWA-HRT-15-049). McLean, VA: FHWA.
- Frangopol, D.M. 1985. Sensitivity of reliability-based optimum design. *Journal of Structural Engineering*, 111(8), 1703–1721.
- Frangopol, D.M. 1995. Reliability-based optimum structural design. Chapter 16 in *Probabilistic Structural Mechanics Handbook*, C. Sundararajan, ed., Chapman & Hall, New York, 352–387.
- Frangopol, D.M. 2011. Life-cycle performance, management, and optimisation of structural systems under uncertainty: accomplishments and challenges. *Structure and Infrastructure Engineering*, 7(6), 389–413.
- Frangopol, D.M., & Das, P.C. 1999. Management of bridge stocks based on future reliability and maintenance costs. *Current and Future Trends in Bridge Design, Construction, and Maintenance*, P.C. Das, D.M. Frangopol, & A.S. Nowak, eds., The Institution of Civil Engineers, Thomas Telford, London, 45–58.
- Frangopol, D.M., Dong, Y., & Sabatino, S. 2017. Bridge life-cycle performance and cost: analysis, prediction, optimisation and decision-making. *Structure and Infrastructure Engineering*, 13(10), 1239–1257.
- Garcia-Segura, T., Yepes, V., & Frangopol, D.M. 2017. Multi-objective design of post-tensioned concrete road bridges using artificial neural networks. *Structural and Multidisciplinary Optimization*, Springer, 56(1), 139–150.
- Ghosn, M., Frangopol, D.M., McAllister, T.P., Shah, M., Diniz, S., Ellingwood, B.R., Manuel, L., Biondini, F., Catbas, N., Strauss, A., & Zhao, Z.L. 2016. Reliability-based structural performance indicators for structural members. *Journal of Structural Engineering*, 142(9): F4016002.
- Greff, K., Srivastava, R.K., Koutník, J., Steunebrink, B.R., & Schmidhuber, J. 2016. LSTM: A search space odyssey. *IEEE transactions on neural networks and learning systems*, 28(10), 2222–2232.
- Haas, R., Hudson, W.R., & Falls, L. C. 2015. *Pavement asset management*. Hoboken, NJ: John Wiley & Sons.
- Long-Term Pavement Performance (LTPP). 2022. *Data from: LTPP DataPave online* [Dataset]. Retrieved from <https://infopave.fhwa.dot.gov/Data/DataSelection>
- Xin, J. 2021. *Probabilistic life-cycle design and maintenance of asphalt pavement using neural networks and deep learning* (Doctoral dissertation). Waseda University, Tokyo, Japan. Retrieved from <http://hdl.handle.net/2065/00081581>
- Xin, J., Akiyama, M., Frangopol, D.M., Zhang, M., Pei, J., & Zhang, J. 2021a. Reliability-based life-cycle cost design of asphalt pavement using artificial neural networks. *Structure and Infrastructure Engineering*, 17(6), 872–886.
- Xin, J., Zhang, M., Akiyama, M., Frangopol, D.M., & Pei, J. 2021b. Life-cycle reliability estimation of asphalt pavement based on machine learning approach. *Life-Cycle Civil Engineering: Innovation, Theory and Practice*, A. Chen, X. Ruan, and D.M. Frangopol, eds., CRC Press/Balkema, Taylor & Francis Group plc, London, 246–251.
- Xin, J., Akiyama, M., Frangopol, D.M., & Zhang, M. 2022. Multi-objective optimisation of in-service asphalt pavement maintenance schedule considering system reliability estimated via LSTM neural networks. *Structure and Infrastructure Engineering*, 18(7), 1002–1019.
- Yang, S.-I., Frangopol, D.M., & Neves, L.C. 2004. Service life prediction of structural systems using life-time functions with emphasis on bridges. *Reliability Engineering & System Safety*, 86(1), 39–51.

Climate change impact on the integrity of structures and infrastructure in mountainous or hilly areas

Y. Tsompanakis & N. Makrakis

Technical University of Crete, Chania, Greece

P.N. Psarropoulos

National Technical University, Athens, Greece

D.M. Frangopol

Lehigh University, Pennsylvania, USA

ABSTRACT: Climate Change (CC) includes both global warming driven by human-induced emissions of greenhouse gases and the resulting large-scale shifts in weather patterns. Although there have been previous periods of CC, since the mid-20th century humans have had an unprecedented impact on Earth's climate system and have caused changes on a global scale. One of the most important issues of the complex phenomenon of CC is the fact that the higher temperatures are increasing the rates of evaporation, causing more weather-related extreme incidents, such as intense storms and heavy rainfalls. Since the frequency, duration and intensity of the rainfalls are related to the instability and/or the erosion of a natural or an artificial soil slope, it becomes evident that the integrity of any structure or infrastructure located on a mountainous or a hilly region may be directly or indirectly affected by the CC during its lifetime. Under this perspective, the current paper focuses on the potential impact of CC on the instability and/or the erosion of natural and artificial soil slopes at mountainous or hilly areas, and subsequently on the integrity of the structures and infrastructure in these areas. The results illustrate that in these specific problems of geotechnical engineering (i.e., slope instability and erosion) the impact of CC may be either detrimental or beneficial, depending on the prevailing circumstances and local site conditions. Accordingly, geo-scientists and especially geotechnical engineers should collect all the required data (i.e., topographical, geological, hydro-geological, geotechnical, and seismological), assess their potential variation over time, and examine each potentially unstable area on a case-by-case basis.

1 INTRODUCTION

The over-increasing need for sufficient and uninterrupted energy production and transmission has led to the further development (i.e., design, construction and operation) of Critical Energy Structures (CESs) and Infrastructure (CEI), worldwide. The term “Critical Energy Structures” describes structures, such as onshore or offshore wind turbines and offshore fixed platforms, which have rather limited dimensions. On the other hand, “Critical Energy Infrastructure” is mainly the large-scale high-pressure gas or -in the near future- hydrogen pipelines, as well as the power transmission cables, which extend for hundreds to thousands of kilometers onshore and/or offshore. Such structures and infrastructure are extremely expensive engineering projects of paramount importance, directly as a capital asset and indirectly as an essential element, that contribute to a productive economy and ensure energy production, transmission and security. Nevertheless, CESs and CEI often face various challenges that depend on the ground/seabed characteristics and the potential geohazards of the area under consideration.

The instability of natural slopes (i.e., landslides) can be considered as one of the most unpredictable and destructive onshore and offshore geohazards with significant consequences on the structural performance of adjacent or crossing structures and lifelines, on the regional and national/

international economy, as well as on human losses (Cruden and Varnes, 1996). A landslide constitutes a natural geological activity triggered by seismic and other dynamic loads (if any), groundwater table fluctuation, soil erosion and/or other factors. It is highlighted that in mountainous and hilly areas, landslides triggered by rainfalls are the most usual type of geohazard, leading to an annual average of approximately 1000 fatalities, as reported from the “EM-DAT” Database (Guha-Sapir et al., 2022).

Landslides can cause sudden or progressive displacements at the ground surface or at the seafloor and may result in failure of structures and infrastructure due to imposed External Loads (ELs), Permanent Ground Displacements (PGDs) and/or a combination of these actions. It is noted that the complete avoidance of potentially unstable slopes is sometimes technically and economically unfeasible. Indicatively, the European Gas Pipeline Incident Data Group (EGIG, 2015) has reported that the 85% of gas pipelines accidents due to geological reasons across Europe from 2004 to 2013 were related to landslides. Additionally, in the mountainous areas of Andes, almost 50% of CEI failures have been caused by landslides (Esford et al., 2004). Under this perspective, the realistic assessment of the potential geohazard of slope instability in conjunction with the resulting structural distress of Critical Energy Structures and Infrastructure constitutes an essential process during their design phase.

Although there have been previous periods of CC, the unprecedented impact of humans on Earth’s climate system in recent decades has caused a climate crisis, which has created an urgent and dangerous situation, capable of imposing a tremendous (direct or indirect) impact on the structural integrity of such Critical Energy Structures and Infrastructure worldwide. In general, CC involves both global warming driven by human-induced emissions of greenhouse gases, as well as the resulting large-scale and long-term shifts in weather patterns. More specifically, CC causes long-term shifts in the frequency, duration and intensity of rainfalls, a fact that is directly related to the groundwater table fluctuation and the soil erosion phenomena, and consequently, to the geohazard of slope instability. It has been reported that the intensity of precipitation extremes, such as heavy rainfalls, have been increased in the past 50 years, even for areas with a decrease in average precipitation levels, such as central Europe and the Mediterranean Region. However, according to Masson-Delmotte et al. (2021) heavy precipitation events are expected to occur more frequent as a direct consequence of CC.

It should be stressed that the European Commission underlines the emerged threat of CC on the structural performance of CESs and CEI, as a very crucial topic. In particular, considering that: (i) approximately 5% of the total population lives in areas susceptible to landslides, (ii) heavier precipitation due to CC could indirectly affect CESs and CEI that have been designed in the past and cross or are placed close to potentially unstable slopes, (iii) CESs and CEI are indirectly related to other social, economic and environmental factors, exacerbating risks to individual and household well-being and quality of life, and (iv) there are important knowledge and regulation gaps that need to be addressed for both national and cross-border uninterrupted energy production and supply, it becomes evident that the impact of CC on the structural behavior of CESs and CEI is of paramount important and it will undoubtedly have a substantial social, environmental and financial impact worldwide. Along these lines, the current paper aims to assess -utilizing simplified analytical methodologies- the impact of the anticipated CC on the geohazard of slope instability and the consequent threat on the integrity of (existing or future) Critical Energy Structures and Infrastructure.

2 PROBLEM DESCRIPTION

Slope instability constitutes a complex geohazard that mainly depends on physical processes and is usually assessed by means of the Factor of Safety (FS). The latter can be defined as the ratio of the resisting forces to the driving forces, under static or dynamic conditions. FS lower than one indicates an unstable slope and in this case the evaluation of ELs, PGDs and/or a combination of these actions is also required for the Soil Structure Interaction (SSI) or the Soil Infrastructure Interaction (SII) (Kramer, 1996). Several methods have gradually been developed for calculating the FS of a soil slope, such as limit equilibrium methods, infinite slope approach, numerical methodologies, and the more-computationally-efficient Artificial Intelligence methodologies. The most important parameters that dominate the resulting FS are related to: (a) the slope inclination and

the geomorphological characteristics of the area of interest, (b) the mechanical properties of the soil material(s) (i.e., soil cohesion and internal friction angle), as their values determine the shear strength and (c) the seismic and other dynamic loads (if any), as they can either reduce the shear strength or increase the shear stresses.

However, it is worth noting that potential groundwater flow plays a key role in the stability of soil slopes. An increase of the level of groundwater table, usually attributed to rainfalls, is the most common reason for slope failure, since it reduces the effective stresses of the soil slope and consequently, the corresponding FS. Figure 1 depicts that the frequency, duration and intensity of the rainfalls determine the ratio between: (a) evaporation - transpiration, (b) runoff, (c) infiltration – percolation and (d) root water uptake. The latter, in conjunction with the soil properties, determine the level of the groundwater table. The increased levels of precipitation may have triggered a slope failure 4 miles east of Oso, Washington, DC, USA, which occurred in 2014 and resulted in 43 fatalities (Henn et al., 2015). Precipitation could also trigger landslides destabilized by a previous event, e.g., an earthquake, as observed in the landslides triggered by a rainstorm after the Wenchuan earthquake (Tang et al., 2011).

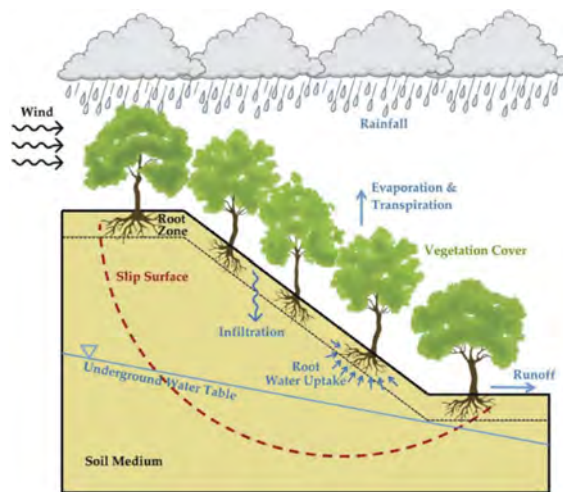


Figure 1. The hydrological cycle and the main consequences of rainfall on soil slopes (adopted from Emadi-Tafti and Ataie-Ashtiani (2019)).

CC has various impacts on the weather and consequently on the aforementioned hydrological cycle. Several researchers have investigated the anticipated impacts of CC on hydrological processes (Green et al., 2011) and changes in the annual precipitation patterns (Kaźmierczak and Kotowski, 2014). Specifically, one of the most important issues of CC is the fact that the higher temperatures and greater wind velocities are increasing the rates of evaporation, causing more frequent and intense storms and heavy rainfalls, even in countries where such phenomena were very rare in recent history. In parallel, the high volume of rainfalls affects the hydraulic conductivity and moisture of the soil, and consequently, the water infiltration. Additionally, high temperatures constitute a direct threat for the vegetation and forestry, which are directly related to root water uptake. Finally, the resulting runoff constitutes the remaining rainfall volume. Hence, it is evident that the CC affects the hydrological cycle.

However, apart from the weather conditions (i.e., frequency, duration and intensity of rainfall and wind), the characteristics of the slope (i.e., slope inclination, soil properties, and vegetation cover and forestry) also play an important role on the ratio between the evaporation - transpiration, runoff and infiltration – percolation and they can be affected from the consequences of CC. Evidently, the runoff is directly related to the potential erosion parallel to the slope surface and the potential flooding phenomena downstream that will also cause a transversal erosion at the slope toe. Soil erosion phenomena may alter the geometric characteristics of the slope and affect

its stability. The infiltration - percolation is related to the level and the shape of the groundwater table, and subsequently to the slope instability.

According to Figure 2, the FS of a soil slope is strongly affected and gradually decreases with respect to time due to various factors, such as the weathering and the heavy rainfall, whereas the impact of the erosion at the slope toe is detrimental (Popescu, 2002). Due to CC, slope instabilities and landslides are expected to occur more frequently (Psarropoulos et al., 2022), as the frequency, duration and intensity of the rainfalls are undoubtedly related to the instability and/or the erosion of a natural soil slope. Hence, it becomes evident that the realistic quantification of CC effects on the average annual precipitation is a critical issue for slope stability. However, in order to investigate such complex phenomena, hydrological models combined with the aforementioned slope stability analysis methods have been developed to calculate the FS of a slope under such conditions (Crosta and Frattini, 2008).

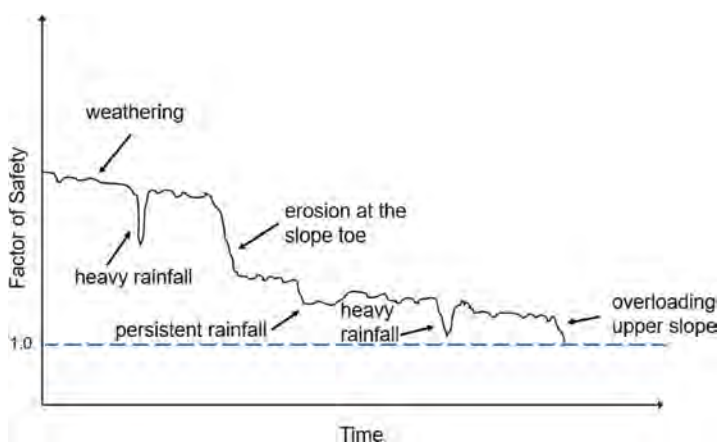


Figure 2. Changes in the Factor of Safety with respect to time (modified from Popescu (2002)).

As it has already been described, the phenomenon of slope instability constitutes a severe threat for CESs and CEI due to the high frequency of landslide occurrence, combined with the fact that especially large-scale energy infrastructure will unavoidably cross several potentially unstable slopes. The excessive PGDs that could be generated due to a slope failure are considered the most critical type of loading for CEI, sine the resulting deformation, in terms of stresses/strains, could lead to failure due to tension or buckling, resulting in significant leaks, major environmental impacts and long periods of service disruption (Vasseghi et al., 2021). Figure 3a presents slope instabilities close to the routing of Trans Adriatic Pipeline (TAP) in central Albania, while Figure 3b displays soil erosion phenomena along the routing of TAP close to the Greek-Albanian borders.



Figure 3. (a) Slope instability phenomena and (b) soil erosion phenomena close to the routing of TAP (photos taken by P.N. Psarropoulos).

3 ANALYTICAL ASSESSMENT

Herein, a simplified approach considering a plane translational slide has been examined, aiming to facilitate the understanding of the impact of the groundwater table on the resulting FS of a soil slope. In general, during a typically infinite translational slide, the upper mass of soil or sediments moves along a planar surface parallel to the ground surface or seabed. The soil mass movement may be represented in a simplified manner by a rigid block of height z , sliding on an inclined planar surface of angle θ . In order to demonstrate the effect of the aforementioned parameters on the FS, a parametric study has been conducted considering two different cases: (a) soil slope without groundwater table, and (b) soil slope with an inclined groundwater table. The resulting Factors of Safety have been evaluated considering three cases regarding clay under drained and undrained conditions, respectively, and sand. The angle of friction, ϕ , has been chosen equal to 30° , whereas soil cohesion under drained and undrained conditions, c and c_u , respectively, have been set equal to 20 kPa. In all cases the unit weight, γ , has been set equal to 17 kN/m^3 , while two cases of z have been taken into account ($z = 5 \text{ m}$ and $z = 15 \text{ m}$).

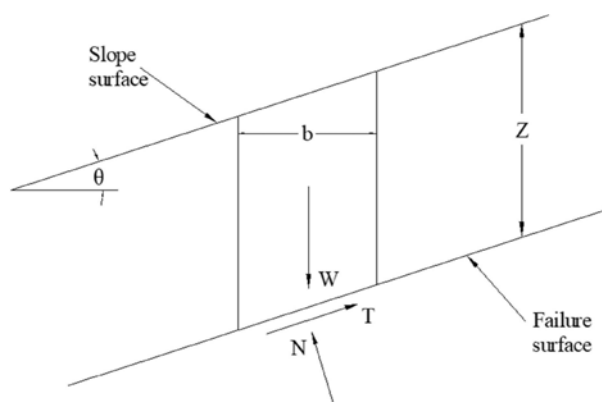


Figure 4. Sketch of a planar translational slide without the presence of groundwater table.

Figure 4 depicts the infinite translational slide without the presence of groundwater table, whereas the associated FS is expressed by:

$$FS = \frac{c}{\cos^2 \theta} + \frac{z \cdot \gamma \cdot \tan \phi}{z \cdot \gamma \cdot \tan \theta} \quad (1)$$

Accordingly, Figure 5 displays the resulting FS by means of the slope inclination angle, θ , and slope height, z , for the three aforementioned cases. More specifically, results from Figure 5a reveal that FS is quite high for small values of slope inclination (i.e., $\theta < 10^\circ$), and subsequently it gradually decreases with the increase of the inclination. It is worth noticing that z has a marginal impact on FS. As shown in Figure 5b, cohesionless soil material has exhibited a different behavior, compared to the other two cases, since the corresponding FS has been remained unaffected from the change of z . Moreover, it can be clearly observed that FS reaches 1 (i.e., the critical FS) when slope inclination is equal to angle of internal friction (i.e., $\phi = \theta$). Figure 5c, where $\phi = 0^\circ$, demonstrates that FS depends on both the slope inclination, θ , and height, z . Particularly, the resulting FS is relatively low, compared Figures 5a and b, especially when z is high, even at low values of slope inclination. In general, it can be clearly seen the soil mechanical properties and slope inclination may have a detrimental impact on FS, since reducing c and/or ϕ or increasing the value of slope inclination can produce lower values of FS.

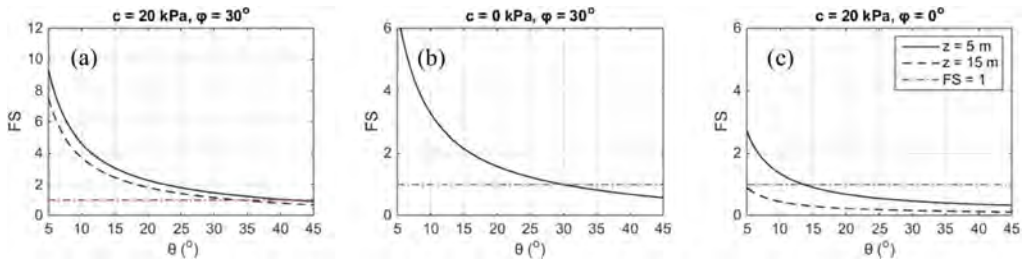


Figure 5. Variation of FS with respect to slope inclination, θ , without groundwater table for the three examined soil types.

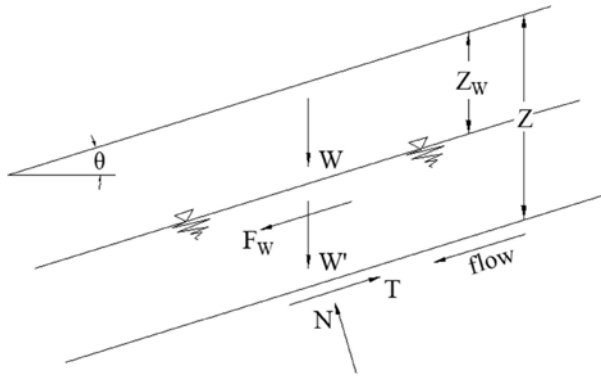


Figure 6. Sketch of a planar translational slide with the presence of groundwater table.

Figure 6 presents an infinite planar translational slide with inclined groundwater table. Assuming that the unit weights of the soil above and below the groundwater table (bulk and saturated unit weights) are equal to γ , the weight W' of a submerged segment is:

$$W' = \gamma' \cdot \alpha \cdot z \quad (2)$$

where γ' is the effective unit weight, derived by subtracting the unit weight of water γ_w from γ ; φ = angle of internal friction; γ = unit weight. The resulting FS' is calculated in this case as follows:

$$FS' = \frac{\frac{c}{\cos^2 \theta} + (z \cdot \gamma' + z_w \cdot \gamma_w) \cdot \tan \varphi}{z \cdot \gamma \cdot \tan \theta} \quad (3)$$

A parametric study has been conducted for the same three characteristic cases, taking into account the existence of groundwater table up to the middle (i.e., $z_w = z/2$) and up to the top of the layer (i.e., $z_w = 0$), as well. Hence, Figure 7 depicts the variation of the FS by means of slope inclination, for two different values of z . More specifically, Figures 7a to c correspond to the special case where $z_w = z/2$ and it can be clearly seen that an increase of the slope inclination has yielded a substantial decrease of FS', while an unfavourable impact of the increase of slope height on FS' has been revealed. Comparing Figures 7a and b (corresponding to $z_w = z/2$) with Figures 7d and 8e (corresponding to $z_w = 0$), it is obvious that an increase of the level of groundwater table has a detrimental impact on FS', as it was expected.

It is worth noticing that in clayey materials under drained conditions and in sandy soil materials $FS' = 1$ occurs when θ is much lower than φ , compared to dry conditions. Nonetheless, it is highlighted that increasing the level of groundwater table has not affected the case of

clay under undrained conditions. It can be generally observed that the FS of a soil slope is considerably affected by the soil mechanical properties and slope inclination, regardless of the presence of groundwater table, since reducing c and/or ϕ or increasing the value of slope inclination can produce lower values of FS or FS'. Nonetheless, increasing the level of groundwater table results in lower values of FS'. Moreover, by comparing a clayey soil material under drained conditions with and without the presence of groundwater table, it can be noticed that the presence of water leads to a substantial decrease of the FS. Analogous behaviour can be observed for the case of cohesionless soil material, with the exception that the height z of sliding mass has no impact on FS.

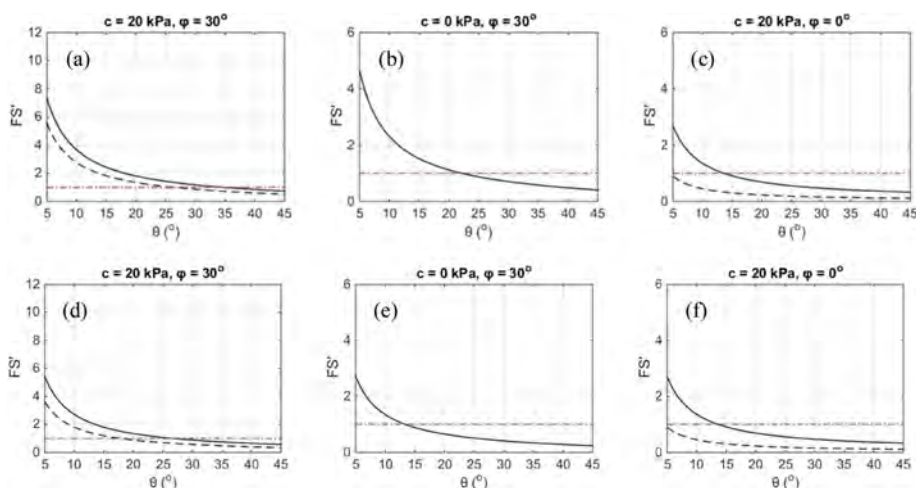


Figure 7. Variation of FS' with respect to slope inclination, θ , with inclined groundwater table for the three examined soil types. Cases (a), (b), and (c) are associated with $z_w = z/2$, while cases (d), (e) and (f) are associated with $z_w = 0$.

4 CONCLUSIONS

The current study focuses on the potential impact of CC on the structural performance of CESs and CEI that are located in or crossing mountainous or hilly areas and are exposed to the geohazard of slope instability. Despite that CC is generally considered as a major threat (since it is usually related to destructive phenomena), the current study shows that in these specific problems of geotechnical engineering (i.e., slope instability and soil erosion) the impact of CC on CESs and CEI may be either detrimental or beneficial depending on the local site conditions and the prevailing circumstances.

Undoubtedly, CC leads to more intense (i.e., heavier), but shorter in duration and less frequent, rainfalls. Hence, on the one hand, runoff is increased and consequently floods downstream and transversal erosion at the slope toe are increased (reduced slope stability – detrimental to CESs and CEI). In addition, the increased runoff may lead to increased erosion along the slope, which can be beneficial or detrimental, since the erosion may decrease or increase the slope inclination, respectively, depending on the circumstances. On the other hand, CC leads to a lower level of groundwater table due to the relatively decreased infiltration (higher slope stability – beneficial to CESs and CEI). Therefore, geo-scientists and especially geotechnical engineers should collect all the required input data (i.e., topographical, geological, hydro-geological, geotechnical and seismological) in order to examine the impact of CC on each potentially unstable area and subsequently on the integrity of CESs and CEI on a case-by-case basis.

REFERENCES

- Crosta, G.B., Frattini, P., 2008. Rainfall-induced landslides and debris flows. *Hydrol. Process.* 22, 473–477.
- Cruden, D.M., Varnes, D.J., 1996. Landslide types and processes, Special Report - National Research Council, Transportation Research Board.
- Emadi-Tafti, M., Ataie-Ashtiani, B., 2019. A Modeling Platform for Landslide Stability: A Hydrological Approach. *Water (Switzerland)* 11, 2146.
- Esford, F., Porter, M., Savigny, K.W., Muhlbauer, W.K., Dunlop, C., 2004. A risk assessment model for pipelines exposed to geohazards. In: *Proceedings of the Biennial International Pipeline Conference, IPC, October 4-8, 2004. Calgary, Alberta, Canada.*
- European Gas Pipeline Incident Data Group (EGIG), 2015. Gas Pipeline Incidents: 9th Report of the European Gas Pipeline Incident Data Group (period 1970-2013). Doc. Number EGIG 14.R.0403. Groningen, the Netherlands.
- Green, T.R., Taniguchi, M., Kooi, H., Gurdak, J.J., Allen, D.M., Hiscock, K.M., Treidel, H., Aureli, A., 2011. Beneath the surface of global change: Impacts of climate change on groundwater. *J. Hydrol.* 405, 532–560.
- Guha-Sapir, D., Below, R., Hoyois, P., 2022. EM-DAT: The CRED/OFDA International Disaster Database – www.emdat.be – Université Catholique de Louvain – Brussels – Belgium [WWW Document]. URL <https://www.emdat.be/> (accessed 2.9.2022).
- Henn, B., Cao, Q., Lettenmaier, D.P., Magirl, C.S., Mass, C., Brent Bower, J., Laurent, M. St., Mao, Y., Perica, S., 2015. Hydroclimatic conditions preceding the March 2014 Oso Landslide. *J. Hydrometeorol.* 16, 1243–1249.
- Kaźmierczak, B., Kotowski, A., 2014. The influence of precipitation intensity growth on the urban drainage systems designing. *Theor. Appl. Climatol.* 118, 285–296.
- Kramer, L.S., 1996. Geotechnical earthquake engineering. Prentice Hall.
- Masson-Delmotte, V., Zhai, P., Pirani, A., Connors, S.L., Péan, C., Berger, S., Caud, N., Chen, Y., Goldfarb, L., Gomis, M.I., Huang, M., Leitzell, K., Lonnoy, E., Matthews, J.B.R., Maycock, T.K., Waterfield, T., Yelekçi, O., Yu, R., Zhou, B., 2021. IPCC, 2021: Climate Change 2021: The Physical Science Basis. Contribution of Working Group I to the Sixth Assessment Report of the Intergovernmental Panel on Climate Change. Cambridge, United Kingdom and New York, NY, USA.
- Popescu, M.E., 2002. Landslide causal factors and landslide remedial options. In: *3rd International Conference on Landslides, Slope Stability and Safety of Infra-Structures, Singapore.* pp. 61–81.
- Psarropoulos, P.N., Makrakis, N., Tsompanakis, Y., 2022. Impact of climate change on the integrity of onshore gas pipelines crossing mountainous or hilly areas. In: *17th Pipeline Technology Conference, 7-10 March 2022, Berlin.*
- Tang, C., Zhu, J., Qi, X., Ding, J., 2011. Landslides induced by the Wenchuan earthquake and the subsequent strong rainfall event: A case study in the Beichuan area of China. *Eng. Geol.* 122, 22–33.
- Vasseghi, A., Haghshenas, E., Soroushian, A., Rakhshandeh, M., 2021. Failure analysis of a natural gas pipeline subjected to landslide. *Eng. Fail. Anal.* 119, 105009.

Assessing life-cycle seismic fragility of corroding reinforced concrete bridges through dynamic Bayesian networks

F. Molaioni & Z. Rinaldi

Department of Civil Engineering and Computer Science Engineering, University of Rome Tor Vergata, Rome, Italy

C.P. Andriotis

Faculty of Architecture and the Built Environment, Delft University of Technology, Delft, The Netherlands

ABSTRACT: Bridge structures are exposed to several chronic and abrupt stressors, among which the combined effects of corrosion and earthquakes pose a major threat to their long-term safety. Probabilistic risk assessment frameworks that quantify and propagate uncertainties inherent to these phenomena are necessary to mitigate this threat. This paper proposes a dynamic Bayesian network for state-dependent seismic fragility functions, capturing corrosion and seismic effects over time. Markovian transitions among deterioration states for different bridge components are developed, combining chloride diffusion and corrosion propagation models with non-stationary Gamma processes. State-dependent fragility curves are derived based on non-linear dynamic time-history analyses given possible degradation configurations of the structure, accounting for uncertainties in material, geometry, and deterioration parameters. Record-to-record variability is captured using synthetic ground motions. Results on a 4-span Gerber bridge showcase the suitability of the framework for describing life-cycle fragility, and its capacity for embedding in advanced algorithmic decision-making workflows is discussed.

1 INTRODUCTION

Bridges are infrastructure constituents of key socioeconomic importance, supporting vital road, rail, and pedestrian transportation systems. During their life-time, these structures must endure several continuous and sudden exogenous stressors.

Depending on the construction materials and environmental exposure, deterioration phenomena, such as corrosion, can have severe safety-reducing effects that increase over time (Vu & Stewart 1998). These become particularly critical when combined with extreme event hazards, such as those manifested in seismic-prone regions (Choe et al. 2008, Cui et al. 2018, Ghosh & Padgett 2010, Shekhar & Ghosh 2021).

Over the past century, the bridge construction sector has greatly focused on reinforced concrete designs due to material availability, cost-effectiveness, and structural performance considerations. A major deterioration factor for these structures, many of which are currently approaching or have well exceeded their design life, is corrosion of steel rebars (Bertolini et al. 2005), which exacerbates typical structural weaknesses against seismic loads. Besides strength and ductility reduction for the main concrete members due to rebar mass losses, corrosion also affects the performance of smaller, yet critical, bridge compartments, such as steel bearings, e.g. through plate thickness reduction, interlocking of sliding surfaces, and bolt failures (Mander et al. 1996). As such, bridges are heterogeneous time-dependent systems, where local component dynamics interact to eventually define global systemic behaviors and risks over the entire life-cycle. Numerous studies have dealt with the quantification of seismic safety losses deteriorating reinforced concrete bridges (Choe et al. 2008, Cui et al. 2018), also explicitly considering their multi-component character (Ghosh & Padgett 2010, Shekhar & Ghosh 2021).

Properly assessing structural safety losses is prerequisite for our ability to efficiently maintain the massive stock of aging concrete bridges, which is, in turn, paramount both for

minimizing the use of concrete in construction, thus curbing its major environmental impact, and for streamlining the immense economic needs of structural interventions. In that sense, managing structural integrity of existing bridges, requires not only at modeling of the aforementioned mechanical deterioration phenomena and their uncertainties, but also making these integrable with decision analysis frameworks.

In past years, the field of decision-making under uncertainties for existing structures has focused on coupling stochastic deterioration models, Bayesian decision principles, and advanced algorithmic procedures. Given the complexity of inspection and maintenance planning, featuring numerous possible actions in highly probabilistic environments, the problem has been shown to be efficiently defined within the global optimization framework of partially observable Markov decision processes (Andriotis & Papakonstantinou 2019, Morato et al. 2022). At the core of this formulation is expressing the deteriorating environment as a Dynamic Bayesian Network (DBN), which allows for efficient uncertainty propagation and inference over multiple time steps.

To address this need, this paper proposes a DBN approach allowing for updatable state-dependent seismic fragility functions, capturing long-term corrosion and seismic effects over time. The framework is applied to a case study bridge, modeled as a multi-component system, whose components are columns (COL), high type fixed bearings (HTFB), high type expansion bearings (HTEB), and low type fixed bearings (LTFB). In Section 2, the entire approach is described. First, the DBN structure is presented as well as the states which characterize it, namely the Corrosion Deterioration States (CDSs) and Seismic Damage States (SDSs). Then, the methodologies for determining both the conditional probabilities for Markovian transition among different corrosion damage states and the state-dependent seismic fragility curves are described. Section 3 is devoted to the case study bridge description to which the approach is applied. Then, in Section 4, the chloride corrosion probabilities over the lifetime of the structure are quantified and presented, as well as the state-dependent fragility curves, and the longitudinal effects of corrosion on the seismic fragility of column components. Finally, in Section 5, the main findings are summarized, underlining the suitability of the framework for capturing life-cycle fragility, as well as for being integrated with algorithmic decision-making workflows towards enhanced structural safety.

2 METHODOLOGY

2.1 DBN for life-cycle seismic fragility of deteriorating bridges

Seismic fragility functions represent the probability of a structure exceeding a seismic damage state (SDS), which quantifies structural damage in a discrete space in terms of an Engineering Demand Parameter (EDP), given an intensity measure (IM) of seismic action. As discussed in the previous section, seismic fragility is expected to increase over time due to structural deterioration for aging bridges. Therefore, encoding the corrosion intensity in a discrete space through the vector of corrosion deterioration state (CDS) of the system components, and the structural damage of those through the vector of seismic damage state (SDS), this probability can be expressed as:

$$P_{SDS,t} = P(SDS_t \geq s | IM_{0:t}, CDS_{0:t}, SDS_{0:t-1}) \quad (1)$$

where, without loss of generality, IM can also refer to vectors.

In this study, as an IM, the Peak Ground Acceleration (PGA) of the ground motion is used. For CDSs, rebars/bolts mass loss, M_{loss} [%], steel plates thickness reduction, PTR [mm], and the additive coefficient of friction k_{corr} [-], accounting for the interlocking effects due corrosion for expansion bearings, are used. The discretization and value ranges of these quantities are given in Table 1 for each component type, i.e. the columns component (CDS_{COL}), and the bearings component (CDS_{BEA}). SDSs for each component are defined through lognormal distribution of EDPs according to (Ghosh & Padgett 2010), with respective thresholds shown in Table 2, for each component type. The inference of Eq. (1) requires, in general, the use of a large number of analyses, that must combine the effects of corrosion and seismic action over the structural lifetime. To solve this problem, a Dynamic Bayesian Network (DBN) for quantifying the risk of aging bridges over their life-cycle is here developed and shown in Figure 1. A DBN is a directed acyclic graphical model that is particularly suitable for modeling

temporal patterns affected by uncertainties and can be used to easily solve inference problems. In such a model, variables are introduced through nodes, while conditional probabilities between these are represented by directed links. This way, it is possible to decompose the entire problem into smaller, easier-to-compute components by evaluating each probabilistic dependency with independent analyses.

The time-dependent nature of the seismic risk for aging structures is dynamically described through time-slices connected by conditional probabilities among CDS nodes, for which the Markovian assumption is considered. This way, CDS at time step $t+1$ depends only on the CDS in slice t :

$$P_{CDS,t} = P(CDS_0) \prod_0^{t-1} P(CDS_{\tau+1}|CDS_{\tau}) \quad (2)$$

To complete the description of the probabilistic graphical model, the following transitions between variables are introduced: the Markovian transition that describes the probability of having a corrosion state $CDS=j$ at time $t+1$, given the corrosion state $CDS=i$ at the previous time step t ; and the state-dependent and time-invariant fragility functions, describing the probability of the bridge reaching a seismic damage state SDS, given the IM and the corrosion deterioration state CDS. It is worth noting that, as CDSs are discrete and the corrosion phenomenon is time-dependent, Markovian transitions are described by non-stationary matrices, while fragilities are continuous functions since the IM variable is not subject to discretization. In addition, Markovian transitions between SDS nodes over time may be introduced to consider that the resulting structural damage carries over to the next time step if no repair action is not taken.

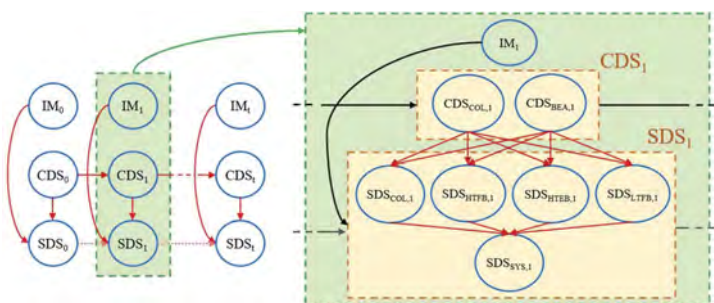


Figure 1. DBN for life-cycle seismic fragility of deteriorating bridges in this study. Overall model including nodes and transitions (left); Interactions of components and system states within the single time step (right).

Table 1. Corrosion Deterioration States.

CDS		0	1	2	3
Component	Parameter	LB-UB	LB-UB	LB-UB	LB-UB
Columns	M_{loss} [%]	0-0	0-15	15-30	30-45
Bearings	M_{loss} [%]	0-0	0-15	15-30	30-45
Bearings	PTR [mm]	0-0	0-3.5	3.5-5.1	5.1-6.5
Bearings	k_{corr} [-]	0-0	0-0.35	0.35-0.64	0.64-0.92

* M_{loss} = rebars/bolts mass lost, PTR = plates thickness reduction, k_{corr} = additive coefficient of friction for expansion bearings.

2.2 Non-stationary transition for corrosion initiation and propagation

Non-stationary transitions among CDSs are calculated through a probabilistic analytical assessment of the rebars/bolts mass loss, M_{loss} [%], over the life-time of the structure. The other corrosion parameters, i.e., PTR [mm] and k_{corr} , are assumed to follow the same transitions in accordance with the CDSs defined in Table 1. In addition, the transition for corrosion initiation and propagation are calculated separately to account for the two-phase nature of

Table 2. Probabilistic seismic damage states thresholds.

Component	EDP	Slight		Moderate		Extensive		Complete	
		M	D	M	D	M	D	M	D
COL	Curvature ductility [-]	1.29	0.59	2.1	0.51	3.52	0.64	5.24	0.65
HTEB-L	Displacement [mm]	37.4	0.6	104.2	0.55	136.1	0.59	187	0.65
HTEB-T, HTEB, LTFB	Displacement [mm]	6	0.25	20	0.25	40	0.47	187	0.65

* M = median of the lognormal distribution, D = Dispersion of the lognormal distribution, L = Longitudinal direction, T = Transverse direction.

the phenomenon. Chloride corrosion occurs when the chloride content at the depth of the bars, C , exceeds the critical threshold, C_{cr} , and thus destroys the protective film of the reinforcing bars, exposing them to aggressive agents. Chloride penetration into the concrete volume is captured by Fick's second law, under the assumption of constant chloride content at the outer surface (Choe et al. 2008, Cui et al. 2018, Ghosh and Padgett 2010, Shekhar & Ghosh 2021), C_s , and considering the diffusion coefficient, D_c , through the model proposed in (fib 2006). The time to corrosion initiation, T_{corr} [years], which defines the transition from CDS=0 to CDS=1, is thus determined by discretizing the structure life-time in yearly time-slices and determining the first slice when $C(x,t) > C_{cr}$.

Corrosion propagation over time is a phenomenon governed by environmental and concrete parameters and is strongly characterized by aleatoric uncertainties. To capture its randomness, the phenomenon is modeled through a Gamma process, in which the mean annual increase in uniform bar penetration is calculated with the model proposed by (Vu & Stewart 1998) and considering a CoV of 0.5 (fib 2006). To calculate the mass loss for steel rebars/bolts, which defines the CDS, a corrosion morphology model must be introduced. In this study, the model proposed by (Val & Melchers 1997), which relates the maximum penetration in the rebar with the mass lost through the pitting factor R (i.e., ratio between maximum and uniform penetration) is adopted. Furthermore, the pitting factor is considered as a random variable to account for the randomness of the corrosion morphology, following the probability distribution suggested in (Stewart & Al-Harthy 2008). The corrosion initiation time, T_{corr} [years], is also required in the propagation model, thus, the statistics obtained through the initiation model are used to consider its variability. Therefore, changes in CDSs are evaluated for each time step, t , by calculating the annual increase in rebar/bolt mass losses.

Non-stationary transitions for both the initiation and propagation phases represents the conditional probability of having CDS= j at time $t+1$, given that CDS= i at time-slice t . This probability is estimated as:

$$P(\text{CDS}_{t+1} = j | \text{CDS}_t = i) = \frac{\#(\text{CDS}_{t+1} = j \cap \text{CDS}_t = i)}{\#(\text{CDS}_t = i)} \quad (3)$$

For this study a sample size of 10^6 Monte Carlo simulations has been observed to be sufficient. More details on statistical properties adopted in this study for the random variables are given in Section 3.

2.3 State-dependent fragility curves

The state-dependent and time-invariant fragility functions are estimated by comparing probabilistic demand parameters and capacity limit states for structural components. Demand parameters for structural components, are determined using nonlinear dynamic analysis, and a suite of synthetic ground motions to account for the record-to-record variability (Vlachos et al. 2018). To account for uncertainties in materials, construction details, model, and seismic demand, 25 nominally identical but statistically different Finite Element (FE) models of bridges were considered, for which 250 synthetic ground motions were applied, resulting in a sample size of 6250 demand parameters. Three-dimensional FE models were set up using OpenSees (McKenna 2011). The non-linear behavior of structural components is taken into

account for those considered as most vulnerable with respect to seismic and deterioration phenomena, i.e., COL, HTFB, HTEB, LTFB. For each structural component, 50 capacity values were sampled as per Table 2, and compared with the 6250 demand parameters, resulting in a total of 312500 SDS labels for component as a function of the IM.

This dataset was used for multinomial logistic regression, thus allowing the prediction of the probability of belonging to a given SDS as a function of IM through the softmax function (Andriotis et al. 2018). Therefore, the fragility for a limit state $SDS=i$ is obtained through sum of the softmax functions related to the SDSs $\geq i$:

$$P(SDS_i \geq i | IM, CDS) = \frac{\sum_{j=i}^J e^{\beta_{0,j} + \beta_{1,j} \ln(IM)}}{\sum_{j=0}^J e^{\beta_{0,j} + \beta_{1,j} \ln(IM)}} \quad (4)$$

where J is the number of SDSs defined in Table 2, plus one, to consider the possibility of not activating any damage state. For the choice of multinomial logistic regression compared to other methodologies to define fragility functions the interested reader is referred to (Yi et al. 2022).

2.4 Corrosion modeling of structural components

The non-linear behavior of columns due to steel reinforcement corrosion has been considered by reducing as a function of M_{loss} the (i) reinforcement strength; (ii) concrete cover strength and stiffness; and (iii) concrete core confinement. Steel rebar and bolt yielding strengths have been reduced according to the degradation law for uniform and pitting corroded rebars proposed in (Imperatore et al. 2017). Note that the morphological nature of the corrosion is taken into account by considering uniform corrosion law if pitting factor R is lower than 4, and pitting corrosion law if R is higher than 4, thus identifying the type of corrosion as suggested in (Bertolini et al. 2005).

Concrete cover cracking following the expansion of the oxides produced by the corrosion process is accounted as proposed in (Coronelli & Gambarova 2004), and evaluating the average crack opening due to corrosion oxides expansion with the model proposed by (Vidal et al. 2004). In (Coronelli & Gambarova 2004), it is also suggested to consider the concrete cover stiffness reduction, which is accounted in this work in a simplified but safety-aware way, by neglecting the presence of the concrete cover upon exceedance of an average crack width of 1mm. Confinement losses of the concrete core, evaluated as proposed in (Mander et al. 1988), are accounted reducing the yielding strength of the stirrups. Bearings modeling approaches are based on the extensive study by (Mander et al. 1996), in which the experimental behavior of several types of steel bearings is compared with analytical methods, and in which valuable suggestions for the finite element modeling are reported. Following this approach, the mechanical behavior of these components is studied and modeled separately, with regard to the longitudinal and transverse direction of the bridge. For these components, the failure modes considered, as well as the analytical approaches for estimating the ultimate strength, even in the presence of corrosion, are referred to (Mander et al. 1996, Shekhar & Ghosh 2021).

3 CASE STUDY BRIDGE

The methodology described in the previous section is applied to an archetype 4-span bridge, representative of a wide range of seismic-vulnerable and deterioration-sensitive existing reinforced concrete bridges, present in infrastructure networks. The main geometrical features and finite element modeling choices are summarized in Figure 2. The deck has six prestressed I-beams, 1.5 m high, and presents two Gerber spans between half-joints. The column piers have a double circular cross-section of 1.3m diameter. Seismically vulnerable features of the bridge include the poor detailing of the columns as longitudinal reinforcement ratio equals 1% and circular stirrup spacing of 250mm, without any additional confinement in the dissipative zone.

For columns, nonlinear beam-column elements are used with appropriate (un)confined concrete and steel properties in OpenSees. The structural component is discretized along the height into three distinct elements. This way, since wide value ranges for CDSs are considered,

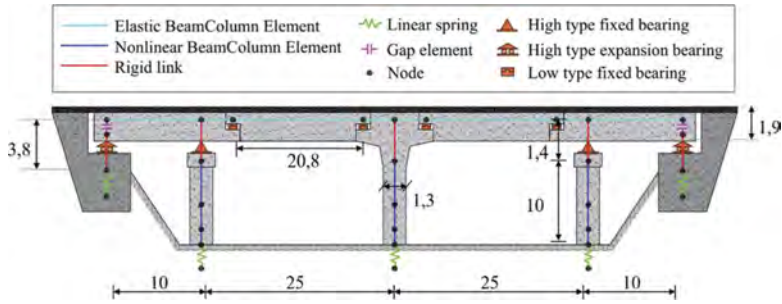


Figure 2. The studied 4-span Gerber bridge with respective geometrical and FE modeling features.

as shown in Table 1, the chance to have different corrosion intensity (M_{loss}) within the same CDS along the height of the column is accounted, thus the possibility of plastic hinges in zones away from the column base due to corrosion is captured (Yuan et al. 2017). The behavior of the bearings is modeled through friction and hysteretic links in the direction where displacements are constrained, and friction links only in the longitudinal direction for HTEB. Pile foundations are modeled using soil-foundation springs with linear behavior, abutments are modeled with linear translational springs, considering both passive and active stiffnesses. Abutment-deck gaps are modeled through gap elements.

Following the definitions of (Duracrete 2000), environmental effects of both “splash” zone, representative of the use of de-icing salts, and “atmospheric zone” were compared. Moreover, “humid” exposure is considered. For the evaluation of CDSs transitions, the following random variables are assumed for components’ materials and geometry: a lognormal distribution with mean 30 mm and CoV of 20% for the concrete cover depth; a discrete uniform distribution between [0.4,0.45,0.50] for the water-cement ratio; a normal distribution with mean 293° K and CoV of 2% for the actual temperature; and a Gumbel distribution with characteristics defined in (Stewart & Al-Harthy 2008) for the pitting factor. In addition, the other random variables in the chloride propagation model are assumed according to the values suggested in (Duracrete 2000, fib 2006, Choe et al. 2008). For the bridge FE model, the following random variables are considered for material properties: a normal distribution with a mean 43 MPa and CoV of 20% for the concrete mean cylindrical compressive strength; a lognormal distribution with mean 520 MPa and CoV of 10% for the steel yielding strength. The other material properties such as ultimate strain for (un)confined concrete, and steel stiffnesses, are adopted as suggested in (Cui et al. 2018). Regarding values for random variables related to others modeling parameters, reference is made to (Nielson & DesRoches 2007).

4 RESULTS

In this section, the built model is applied for assessing the state-dependent fragility of the studied bridge. In Figure 3, the CDS probabilities, P_{CDS} , for structural components over the structural lifetime, relatively to both “splash” and “atmospheric” zones, are shown; these are generated by multiplying the observed non-stationary transitions by Eq (2). As expected, a higher probability of corrosion activation and propagation for the “splash” zone is found, as it is representative of a more chloride-aggressive environment. Environmental effects resulted in the following CDS probabilities after 100 years for the “splash” zone: $P_{CDS=0} = 0.0289$, $P_{CDS=1} = 0.2342$, $P_{CDS=2} = 0.2374$, $P_{CDS=3} = 0.4995$; and on the other hand, for the “atmospheric” zone, the following CDS probabilities, P_{CDS} , after 100 years are found: $P_{CDS=0} = 0.9726$, $P_{CDS=1} = 0.0124$, $P_{CDS=2} = 0.0064$, $P_{CDS=3} = 0.0085$. The results of seismic nonlinear dynamic analyses for column components are presented with respect to 4 corrosion scenarios, i.e., $DCS_{COL} = 0$ & $DCS_{BEA} = 0$, $DCS_{COL} = 1$ & $DCS_{BEA} = 0$, $DCS_{COL} = 2$ & $DCS_{BEA} = 0$, $DCS_{COL} = 3$ & $DCS_{BEA} = 0$. In Figure 4 the respective state-dependent fragility curves for column components are reported, thus showing the corrosion effects on their seismic safety.

The longitudinal effects of columns corrosion for their fragility for both “splash” and “atmospheric” are shown in Figure 5; these are obtained by combining the above results on non-stationary

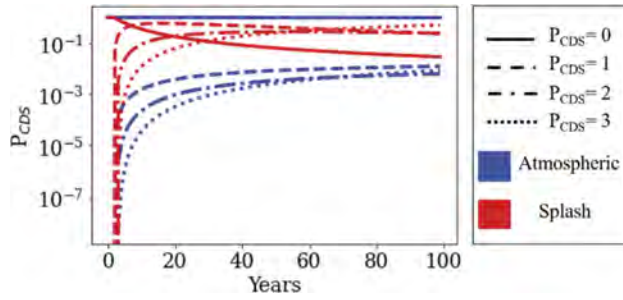


Figure 3. Probability for corrosion deterioration states (P_{CDS}) of structural components over their lifetime.

CDS probability and state-dependent fragilities through the weighted sum of the logistic functions based on P_{CDS} . This way, the suitability of the method for predicting time-varying fragility effects due to exposure to chloride-aggressive environments over the structural life is highlighted.

5 CONCLUSIONS

In this paper, a dynamic Bayesian network for life-cycle seismic fragility assessment of aging bridges is developed. The methodology is applied to a 4-span Gerber bridge case study, modeled as a multi-component structural system, with components referring to different columns and bearing types, to properly define seismic damage state characteristics under corrosion. Non-stationary Markovian transitions among deterioration states of the structural components are estimated through Monte Carlo simulation, and based on available probabilistic models for corrosion initiation and propagation. The seismic fragility with respect to five states of seismic damage is learned through multinomial logistic regression based on the results of nonlinear dynamic analyses, in which uncertainties in materials, geometry, modeling, seismic action and corrosion process are accounted. The results confirm the sensitivity of seismic responses to corrosion effects, and display how different aggressive environments can change the seismic safety of the bridge

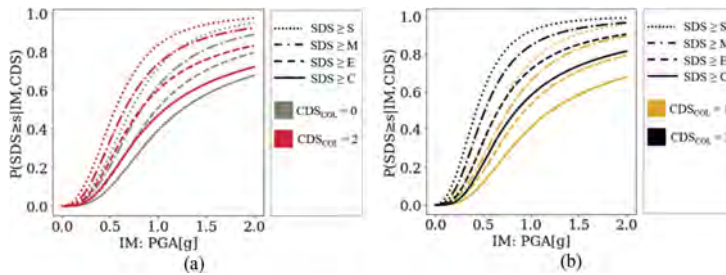


Figure 4. State-dependent fragility curves for the 4-span bridge columns. a) Comparison between scenarios $CDS_{COL} = 0$ and $CDS_{COL} = 2$; b) Comparison between scenarios $CDS_{COL} = 1$ and $CDS_{COL} = 3$.

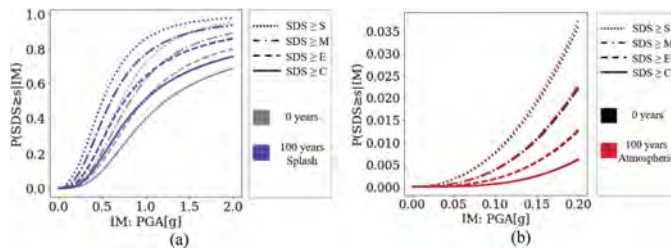


Figure 5. Time-varying effects on columns fragility for several chloride-aggressive environments. a) Effects after 100 years and “splash” zone; b) Effects after 100 years and “atmospheric” zone.

components over time. The proposed approach is an important step towards effective and flexible assessment and management of aging bridges structures. The DBN structure makes it possible to add new variables in the probabilistic graph without affecting those presented here, as well as to lend itself to advanced decision-support systems relying on Markov processes which can be consistently to the derived transition probabilities. Along these lines, possible extensions include, among others, consideration of residual structural capacity in the damage state definition, coupling of component limit states with non-seismic loads, and incorporation of action and observation variables for fragility updates based on inspection and maintenance outcomes.

REFERENCES

- Andriotis, C. P., & Papakonstantinou, K. G. (2018). Extended and generalized fragility functions. *Journal of Engineering Mechanics*, *144*(9), 04018087.
- Andriotis, C. P., & Papakonstantinou, K. G. (2019). Managing engineering systems with large state and action spaces through deep reinforcement learning. *Reliability Engineering & System Safety*, *191*, 106483.
- Bertolini, L., Elsener, B., Pedferri, P., & Polder, R. (2005). Corrosion of Steel in Concrete: Prevention, Diagnosis, Repair.
- Choe, D. E., Gardoni, P., Rosowsky, D., & Haukaas, T. (2008). Probabilistic capacity models and seismic fragility estimates for RC columns subject to corrosion. *Reliability Engineering and System Safety*, *93*(3), 383–393.
- Coronelli, D., & Gambarova, P. (2004). Structural assessment of corroded reinforced concrete beams: Modeling guidelines. *Journal of Structural Engineering*, *130*(8), 1214–1224.
- Cui, F., Zhang, H., Ghosh, M., & Xu, Y. (2018). Seismic fragility analysis of deteriorating RC bridge substructures subject to marine chloride-induced corrosion. *Engineering Structures*, *155*, 61–72.
- Duracrete. 2000. Probabilistic performance based durability design of concrete structures. Final Technical Rep. (Document BE95-1347/R17). Lyngby, Denmark: European Union—Brite EuRam III
- Ghosh, J., & Padgett, J. E. (2010). Aging considerations in the development of time-dependent seismic fragility curves. *Journal of Structural Engineering*, *136*(12), 1497–1511.
- Imperatore, S., Rinaldi, Z., & Drago, C. (2017). Degradation relationships for the mechanical properties of corroded steel rebars. *Construction and Building Materials*, *148*, 219–230.
- fib, F. I. B. (2006). Model code for service life design. Model code.
- Mander, J. B., Priestley, M. J., & Park, R. (1988). Theoretical stress-strain model for confined concrete. *Journal of structural engineering*, *114*(8), 1804-1826.
- Mander, J. B., Kim, D.-K., Chen, S. S., & Premus, G. J. (1996). Response of Steel Bridge Bearings to Reversed Cyclic Loading.
- McKenna, F. (2011). OpenSees: A framework for earthquake engineering simulation. *Computing in Science and Engineering*, *13*(4), 58–66.
- Morato, P. G., Andriotis, C. P., Papakonstantinou, K. G., & Rigo, P. (2022). Inference and dynamic decision-making for deteriorating systems with probabilistic dependencies through Bayesian networks and deep reinforcement learning.
- Nielson, B. G., & DesRoches, R. (2007). Seismic fragility methodology for highway bridges using a component level approach. *Earthquake Engineering and Structural Dynamics*, *36*(6), 823–839.
- Shekhar, S., & Ghosh, J. (2021). Improved Component-Level Deterioration Modeling and Capacity Estimation for Seismic Fragility Assessment of Highway Bridges. *ASCE-ASME Journal of Risk and Uncertainty in Engineering Systems, Part A: Civil Engineering*, *7*(4).
- Stewart, M. G., & Al-Harthy, A. (2008). Pitting corrosion and structural reliability of corroding RC structures: Experimental data and probabilistic analysis. *Reliability Engineering and System Safety*, *93*(3), 373–382.
- Val, D.V. and Melchers, R. E. (1997). Reliability of Deteriorating RC Slab Bridges. *Journal of Structural Engineering*, 1638–1644.
- Vidal, T., Castel, A., & François, R. (2004). Analyzing crack width to predict corrosion in reinforced concrete. *Cement and Concrete Research*, *34*(1), 165–174.
- Vlachos, C., Papakonstantinou, K. G., & Deodatis, G. (2018). Predictive model for site specific simulation of ground motions based on earthquake scenarios. *Earthquake Engineering and Structural Dynamics*, *47*(1), 195–218.
- Vu, K. A. T., & Stewart, M. G. (2000). Structural reliability of concrete bridges including improved chloride-induced corrosion models. *Structural Safety*.
- Yi, S., Papakonstantinou, K. G., Andriotis, C. P., & Song, J. (2022). Appraisal and mathematical properties of fragility analysis methods. In *Proceedings of the 13th International Conference on Structural Safety and Reliability (ICOSSAR)*.
- Yuan, W., Guo, A., & Li, H. (2017). Seismic failure mode of coastal bridge piers considering the effects of corrosion-induced damage. *Soil Dynamics and Earthquake Engineering*.

MS6: Smart maintenance and AI applications
Organizers: H. Furuta, N. Catbas & Y. Nomura



Taylor & Francis

Taylor & Francis Group

<http://taylorandfrancis.com>

Bolt axial force detection using deep learning based on vision methods

Y. Chen, J. Lai, G. Hayashi & T. Yamaguchi
Osaka Metropolitan University, Osaka, Japan

ABSTRACT: Previous studies have found that high-strength bolt axial force of many in-service bridges decreased by 10%–20% from the design bolt axial force. One of the reasons is that the bolts cannot be tensioned to the design axial force owing to various difficult construction conditions and errors. Appropriate control of the axial force while fastening the bolts is important. Contact methods using ultrasonic testing and eddy currents have been employed to detect bolt axial force. This paper proposes a non-contact vision-based bolt axial force detection method using deep learning. We focus on the relative deformation feature of the bolt head inscriptions and train the neural network via regression method. The training results indicate that even when the image size is reduced to 448 pixels, it was able to obtain correct results for axial force detection for the type of bolt that was used to train the model.

1 INTRODUCTION

High-strength friction bolted joints (hereafter referred to as friction joints) are often used in the field joints of steel bridges (AASHTO, 2020; Eurocode3, 2005; Japan Road Association (JRA), 2017). A prior study (Iida et al., 2021) investigated the residual axial force of high-strength bolts after friction joints have been in service for several years. The results showed that the residual axial force of many bolts was 10%–20% lower than the design axial force, irrespective of the service life of the friction joints and erection conditions of the steel bridges. This disparity was attributed to variations in the torque coefficients of bolts in situ joints and difficulties in controlling the construction quality (Iida et al., 2021, 2022).

Given that the residual bolt axial force may be lower than the designed axial force owing to limited control of the axial force during fastening, it is crucial to ensure the appropriate bolt axial force in the initial stage.

Among the contact methods to detect the bolt axial force, a novel method to measure axial force by using the vibration of bolts has been reported (Toh et al., 2019). An axial force evaluation method using eddy current has also been proposed (Akutsu et al., 2022). Further, (Hirao et al., 2022) proposed an ultrasonic bolt axial force evaluation method using machine learning based on characteristic signals to detect the bolt axial force. However, considering the construction conditions in situ, determining the axial force using an axial force meter (ultrasonic or load cell type) or percussion test on-site would be difficult (e.g., in case of on-site construction in aerial work platforms). Considering the current aging population and decreasing number of engineers, developing a non-contact method to control bolt axial forces is necessary.

Convolutional neural network (CNN)-based methods using bolt head photographs have been explored for non-contact axial force control since 2012. (Huynh et al., 2019; Ramana et al., 2019) proposed CNN-based methods for determining whether a bolt is tight based on the bolt diameter and exposed shaft length. (Zhao et al., 2019) studied the effects of aspects such as angle and exposure associated with the bolt head photographs, which are used as



Figure 1. Experimental setup to measure actual bolt axial force and record the picture of bolt head.

training data for a CNN, on the recognition rate. The results of the aforementioned studies have high potential applicability in controlling bolt tension by using photographs of the bolt heads; thus, CNNs may be used to realize the management of bolt axial forces in situ.

Bolt recognition generally employs the shape of the bolt as a feature for classification analysis; there are no rigorous requirements concerning the accuracy of the image. In this study, we developed a method to extract the relative deformation of bolt head inscriptions to detect bolt axial force by training the neural network with regression. Because of the need to observe even small deformations, it demands relatively large image sizes. We investigated the possibility of managing bolt axial forces based on photographs of bolt heads by using CNNs and high-strength hexagonal bolts. Additionally, we investigated the practicality of the method by fully adapting the specifications, such as the brightness, resolution, and focal length, of the photographs to an in-situ construction environment.

2 EXPERIMENT

2.1 Set up

Figure 1 shows that a 500 kN hydraulic jack (hand pump) was used to apply the bolt axial force, while a load cell and data logger (TDS-630) were used to measure the true bolt axial force, which was recorded in the computer. Simultaneously, the bolt head picture was taken by a digital single-lens reflex camera (Sony $\alpha 1$). Both the camera and data logger were set to record (take pictures) data at 2 s. Table 1 shows the detailed settings of the device.

Table 1. Device and parameter settings.

Name	Parameter
Data Logger	TDS-630
Measurement interval	2 s
Load speed	2 kN/1 s
Camera	Sony $\alpha 1$
Lens	FE 24-70 mm F2.8 GM II
F-stop	f/2.8
Exposure time	1/80 s
ISO	200
Focal length	70 mm
Resolution	350 DPI

2.2 Dataset and case

Considering the different surface properties of each bolt, 12 bolts were prepared for this study. We took 200 pictures of each bolt and augmented them to 1,000. A picture was taken at 5 kN intervals, and when the load reached approximately 106 kN, the bolts were unloaded to 10 kN.

Owing to the different traits of the bolt head surface, two series of cases were established in this study to discuss the qualities needed to detect the bolt axial forces. To discuss the effects of the input image size on the training accuracy, the image size was set as a parameter as shown in Table 2.

The valid dataset has a similar experiment environment as the training data and uses similar bolt series, while the test dataset uses completely different bolts and experiments at the real bolted joint.

Table 2. Discussion case and its parameters.

Series	Total number of bolt	Inputs size	Number of input picture		
			Train	Valid	Test
One-bolt	1	1120 × 1120 672 × 672	1600	400	400
Multi-bolt	12	448 × 448 224 × 224	8000	2000	2000

2.3 Hardware and software configurations

Training deep learning networks (especially using high-resolution images) requires ample computing power. A Dell 7910 workstation was used for training the model. The workstation featured an Nvidia RTX A4000 (16 GB GDDR6 GPU memory) and 256 GB of RAM. The model training was based on PyTorch, CUDA, and cuDNN.

3 CONVOLUTIONAL NEURAL NETWORK

Evidently, the deeper the neural network, the harder it is to train. Deeper networks can cause vanishing and exploding gradient problems. To avoid such problems, we used ResNet-50 in this study (He et al., 2016) as the base framework for the network architecture. This framework introduces a residual block that could skip some layers to connect the activations of one layer to other layers as expressed in $y = \mathcal{F}(x, \{W_i\}) + x$. As shown in Figure 2, the output of the network used logistic regression analysis, wherein the output class was 1 for the speculative axial force of the bolt. The loss function (MSE loss) and sigmoid function were used in the output regression layer. Stochastic gradient descent (SGD) was used in the optimizer. The hyperparameters of the optimizer and dropout layer are shown in Table 3.

When high-strength bolts are subjected to axial force, the bolt heads deform to a concave shape, and the relative positions of bolt head inscriptions change. The input images were converted from 24-bit color to 8-bit grayscale format. This grayscale value matrix was read, and a convolution layer was used to extract the features. A convolution kernel (filter) was used as a bias (W_i). The extracted data was processed by a pooling layer to perform maximum or average processing as shown in Figure 3. The training was then completed by iteratively computing the feature values to obtain the best bias.

4 DATA PREPROCESSING

4.1 Data augmentation

The original input images were randomly augmented nine times using one of the following augmentation algorithms: additive Gaussian noise, add (adds a value to all pixels in an image),

Table 3. Hyperparameters of training.

Hyperparameters	Value
Optimizer	SGD
Learning rate	0.001
Momentum	0.9
Dropout	0, 0.25, 0.5, 0.8
Loss Function	MSELoss
Full Connection Layer	1, 2, 3
Epoch	500

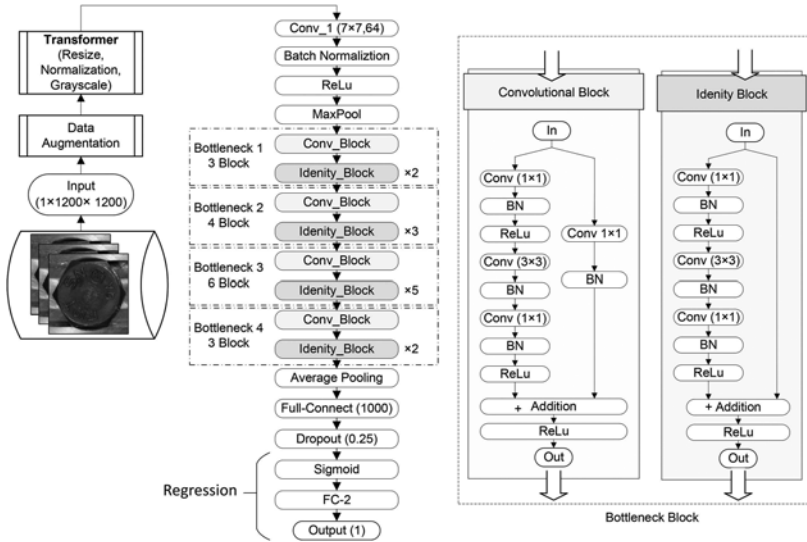


Figure 2. CNN architecture based on resNet50, and the residual block.

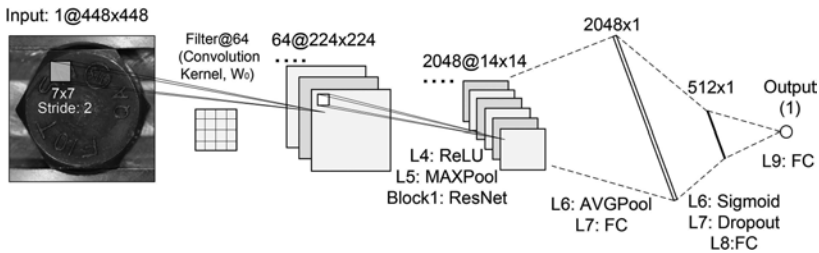


Figure 3. Extraction of bolt head features and setting of bias.

multiply (multiplies all pixels in an image using a specific value), edge detection (detects all edges in an image), contrast normalization, and sharpen. Figure 4 shows the original input image and that augmented using the additive Gaussian noise and sharpen algorithms.

4.2 Transformer

All the images were treated using grayscale processing, so the input layer of the network was set to 1. To study the effect of the image size on the prediction accuracy, the input images were resized to 1,120 (0.0029 mm/pixel), 672 (0.048 mm/pixel), 448 (0.073 mm/pixel), and 224 (0.15 mm/pixel) pixels.

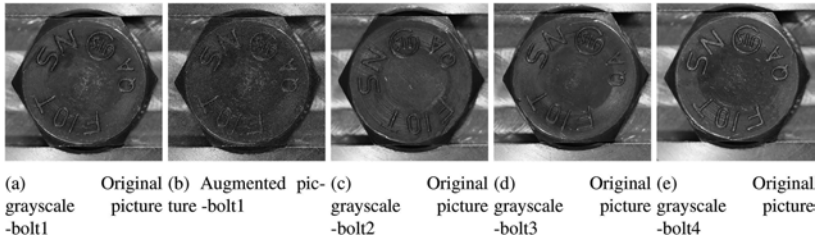


Figure 4. Input picture (Augmented using additive Gaussian noise, sharpening).

5 RESULTS

5.1 Performance measures

In this study, we used the mean squared error (MSE), root mean squared logarithmic error (RMSE), mean absolute error (MAE), and coefficient of determination (R^2) to evaluate the regression model.

The MSE represents the average of the squared difference between the original and predicted values in the data set. It is used to measure the variance of the residuals.

$$\text{MSE} = \frac{1}{N} \sum_{i=1}^N (y_i - \hat{y}_i)^2 \quad (1)$$

RMSE is the square root of the MSE. It is used to measure the standard deviation of the residuals.

$$\text{RMSE} = \sqrt{\frac{1}{N} \sum_{i=1}^N (y_i - \hat{y}_i)^2} \quad (2)$$

The MAE represents the average of the absolute difference between the actual and predicted values in the result. It is used to measure the average of the residuals in the result.

$$\text{MAE} = \frac{1}{N} \sum_{i=1}^N |y_i - \hat{y}_i| \quad (3)$$

R^2 represents the proportion of the variance in the dependent variables, which is explained by the regression model:

$$R^2 = 1 - \frac{\sum_{i=1}^N (y_i - \hat{y}_i)^2}{\sum_{i=1}^N (y_i - \bar{y})^2} \quad (4)$$

Where y_i is the actual value and \hat{y}_i the predicted value. \bar{y} is the mean value of the actual dataset.

5.2 Impact of input image size on accuracy

Figure 5 shows the R-squared test result of the one-bolt and multi-bolt series. For the one-bolt series, the size of the input image does not greatly influence the verification result. However, when the training data has 10 different bolts and the input image is reduced to 224 (0.15 mm/pixel), the R-squared (accuracy) of the validation results drops dramatically to around 0.5. This is so because when there are multiple bolts, the amount of features to be extracted is more than that of a single bolt.

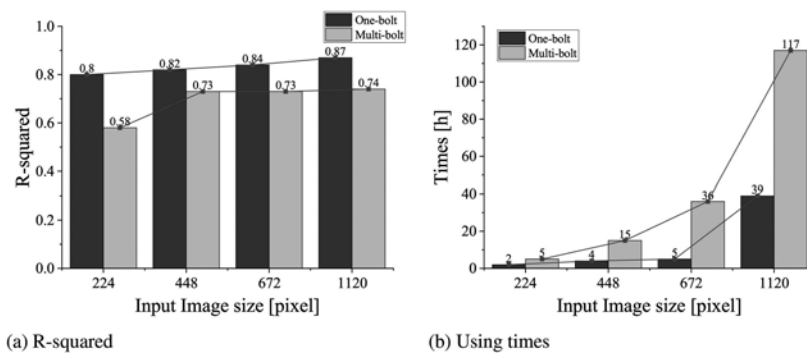


Figure 5. The R-squared and time test result of one-bolt series and multi-bolt series.

Additionally, the time required for each series of calculations is shown in the figure. When the training data reaches 8,000 images (multiple bolts), it takes 117 hours to train a set of high-resolution images (size 1,120, 0.029 *mm/pixel*) and 15 hours to train images of size 448 (0.073 *mm/pixel*) that have a small R-squared (accuracy) difference. Considering the computational cost and feasibility of the application for real-time bolt axial force detection, sizes 448 or 672 are the recommended image sizes. The image size here is the image that contains exactly the entire bolt head.

5.3 Validation results

The relationship between the prediction and label data of the one-bolt and multi-bolt series is shown in Figure 6. Regarding the validation dataset, most of the predictions were accurate. In case of valid multiple bolts, the detected bolt axial force has a large variate. It is assumed that because each bolt head has a different shape, the network detects the bolt head features incorrectly.

Table 4 shows the total validation result of the one-bolt and multi-bolt series. Dropout is a regularization technique used to reduce overfitting in neural networks by randomly setting a fraction of the input units to 0 during training. The greater the dropout parameter, the better would be the obtained results. Even when the parameter was 0.8, the training results indicate remarkable performance. The amount of features needed to train a network using the bolt heads is not as large as expected, and this task does not require particularly high-pixel images.

On the test dataset, an R^2 value of only 0.48 is attained, indicating that this network could not detect bolt axial force in diverse environments with different bolts. The surface traits of each bolt head varied and the relative positions of the head inscriptions were inconsistent, thereby resulting in the inability of the network to obtain the required amount of features. Since the training data had been greatly augmented, the input images were grayscale, and the images were cropped to include only the bolt head during training, it can be concluded that environmental factors hardly affect the model performance.

5.4 Training loss

Figure 7 shows the relationship between total loss and epoch (a is case 5 and b is case 10). Most cases converge to 0 loss at approximately 250 epochs. The training was suspended after reaching approximately 500 epochs. Although the validation loss fluctuated slightly between 250 and 500 epochs, no overfitting occurred.

6 CONCLUSIONS

This study used a modified ResNet-based neural network to detect the bolt axial force using bolt head images. When the bolt was subjected to an axial force, the head of the bolt deformed into a concave shape, and the axial force of the bolt was detected by determining the relative

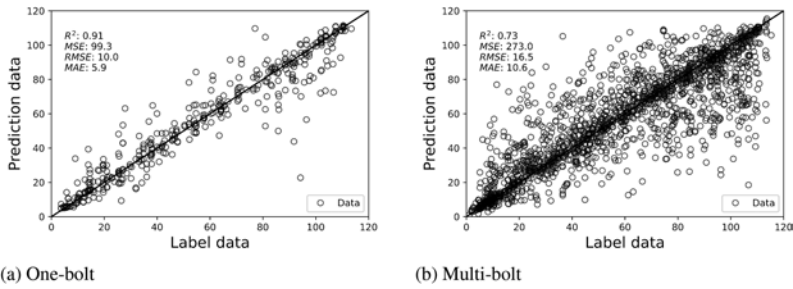


Figure 6. Relationship between prediction and label data.

Table 4. Total validation result.

case	Series	Input size	FC layer	Droupout	MSE	RMSE	MAE	R ²
1	one	224	1	0	221.89	14.89	9.9	0.8
2	one	448	1	0	214.98	14.31	8.94	0.82
3	one	672	1	0	208	14.4	8.9	0.84
4	one	1120	1	0	146.34	12.1	6.92	0.87
5	one	448	1	0.8	134.74	11.6	7.13	0.88
6	one	448	3	0	135	11.8	7.86	0.87
7	one	448	3	0.25	131	11.4	7.06	0.88
8	one	448	3	0.5	124.6	11.4	7.06	0.89
9	one	448	3	0.8	99.2	9.96	5.88	0.91
10	Multi	224	3	0.8	352.31	26.23	14.2	0.58
11	Multi	448	3	0.8	273.01	16.52	10.57	0.73
12	Multi	672	3	0.8	251.15	15.34	10.25	0.73
13	Multi	1120	3	0.8	246.2	15.1	9.83	0.74
14	Test-multi	448	3	0.8	614.55	25.75	18.32	0.48

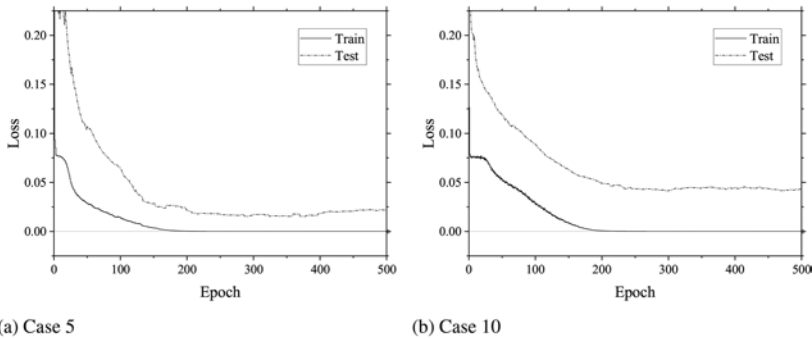


Figure 7. Total loss under different cases.

change in the features of the bolt head. The network included a dropout layer to prevent overfitting and a modified output full connection layer; further, the activated function changed network to the regression method.

- When the input image size was reduced from 1120×1120 (0.029 mm/pixel) to 448×448 pixels (0.073 mm/pixel), the validation results converged and did not change considerably. Even when the image size was reduced to 448 pixels, the proposed model was able to obtain correct results for axial force detection, with an R-squared value of 0.91 and a mean absolute error of 5.8 kN. Considering the computational cost and feasibility of the application

of this method for real-time bolt axial force detection, 448 or 672 pixels are the recommended image sizes. The images used in this study were of the entire bolt heads.

- The dropout layer plays an important role in optimizing the training results; even when the dropout parameter was set to 0.8, the model obtained good training results. The number of features needed to train the network using the bolt head images was not as large as expected.
- Although good results on the validation set were obtained using this model, the network did not perform suitably on the test set. Further research must be conducted to overcome the variations in the number of features corresponding to the different types of bolts.

ACKNOWLEDGEMENT

This work was supported by the SPRING program of the Japan Science and Technology Agency (JST SPRING, Grant No. JPMJSP2139).

REFERENCES

- AASHTO (2020). *AASHTO LRFD Bridge Design Specifications* (9th ed.). Washington, DC: American Association of State Highway and Transportation Officials.
- Akutsu, A., E. Sasaki, M. Tai, and T. Shimozato (2022). Advancement of Eddy Current Based Evaluation of Axial Force of High-Strength Bolts. In *IABSE Symposium Prague 2022*, pp. 1148–1155.
- Eurocode3 (2005). EN 1993-1-8: *Eurocode 3: design of steel structures - Part 1-8: Design of joints*. London: European Committee for Standardization.
- He, K., X. Zhang, S. Ren, and J. Sun (2016, 6). Deep Residual Learning for Image Recognition. In *2016 IEEE Conference on Computer Vision and Pattern Recognition (CVPR)*, pp. 770–778. IEEE.
- Hirao, K., E. Sasaki, Y. Ito, K. Takeya, K. Suzuki, and K. Morita (2022). Proposal of ultrasonic bolt axial force evaluation method using machine learning and signal processing. In *IABSE Symposium Prague 2022*, pp. 1140–1147.
- Huynh, T. C., J. H. Park, H. J. Jung, and J. T. Kim (2019, 9). Quasi-autonomous bolt-loosening detection method using vision-based deep learning and image processing. *Automation in Construction* 105, 102844.
- Iida, T., K. Sugiura, T. Yamaguchi, Y. Kitane, and H. Oda (2021). A basic study on the residual axial force of the high-strength hexagon bolt friction joints in the steel road plate girder bridges serviced for 34 years. *Steel Construction Engineering (In Japanese)* 28(112), 63–74.
- Iida, T., K. Sugiura, T. Yamaguchi, Y. Kitane, and H. Oda (2022). Basic research on the evaluation of residual axial force of actual bridge high -strength bolts of different bridge types, bolt types, and joint surface treatments. *Journal of Structural Engineering, A (In Japanese)* 68A, 441–457.
- Japan Road Association (JRA) (2017). Japan road association, Specifications For Highway Bridges Part II steel bridges.
- Ramana, L., W. Choi, and Y.-J. Cha (2019, 3). Fully automated vision-based loosened bolt detection using the Viola–Jones algorithm. *Structural Health Monitoring* 18(2), 422–434.
- Toh, G., J. Gwon, and J. Park (2019). Determination of clamping force using bolt vibration responses during the tightening process. *Applied Sciences (Switzerland)* 9(24), 5379.
- Zhao, X., Y. Zhang, and N. Wang (2019, 1). Bolt loosening angle detection technology using deep learning. *Structural Control and Health Monitoring* 26(1), e2292.

Proposal of deep learning ensemble method for phased array ultrasonic testing for tube-to-tubesheet weld of heat exchange

H. Hattori & J. Murakami

Nichizotech Incorporation, Osaka, Japan

N. Shinmura

Nichizotech Incorporation, Kumamoto, Japan

K. Shinoda, M. Abe & T. Katayama

Hitachi Zosen Corporation, Kumamoto, Japan

R. Ioka & T. Wada

Hitachi Zosen Corporation, Osaka, Japan

ABSTRACT: We have developed a system that inspects the entire circumference of tube-to-tube sheet welds using phased array ultrasonic testing for manufacturing of heat exchangers. Therefore, a huge number of images were generated during the inspection. In the past, inspectors made visual judgments based on these images, but due to the long inspection period, it was difficult to inspect all of them. As a solution to this problem, we have developed a system that automatically detects flaws in weld. In constructing the flaw detection system, image processing, AE (Autoencoder), and CNN (Convolutional Neural Network) were examined, but individual judgment accuracy was not sufficient. Therefore, an ensemble method was applied. In the proposed method, the reliability of each discriminator was calculated for each image to be evaluated, and the presence or absence of flaws was finally determined according to the reliability. It was confirmed that the accuracy was improved by applying this flaw detection system.

1 INTRODUCTION

As an inspection method for tube-to-tubesheet weld in multitube heat exchangers, phased array ultrasonic testing (PAUT) is used to detect flaws, such as welding defects and cracks, and measure the weld metal height and to verify integrity and conformity to design dimensions (Abe et al. 2017, Shinoda et al. 2019). Flaw detection data were used to generate 360 flaw detection images per tube, and then a system was put into practical use that judges the presence/absence of flaws by using deep learning AI technology (Abe et al. 2022). In this paper, we describe the improvement of the reliability calculation method for classifiers.

2 PHASED ARRAY ULTRASONIC TESTING SYSTEM

An instrument equipped with an array probe is inserted into a tube and propagates ultrasonic waves from the tube inside to inspect all 360 degrees of the tube's circumference at the tube-to-tubesheet weld, at 1-degree intervals. Using multiple array probes based on the tube diameter, linear and sector scans are performed by electronic scanning, improving the flaw detection accuracy. As a guide, the inspection time is 1 minute or less per tube, with some additional time for repositioning the PAUT device.

3 FLAW DETECTION IMAGE

Figure 1 shows the flaw detection image data of the tube sheet welding specimen. The specimen has an artificial hole with a diameter of 1 mm (flat-bottomed hole, FBH) in a direction parallel to the tubesheet surface and perpendicular to the tube axis. The top center image shows the linear scan results, and the top left and right images show the sector scan results from the tube end and root sides of the array, respectively. The bottom image shows the whole circumference, called the C-scope, obtained by turning the array probe 360 degrees, and the detection data for the FBH is displayed in the band indicating the weld joint. As shown in the segment circled in red in Figure 1, the FBH is clearly detected. A similar flaw detection result was obtained for another test specimen with an artificial hole in a direction oblique to the tubesheet surface and parallel to the tube axis. If the weld height is insufficient, the band indicating the weld is narrower. If there is a defect in the weld, a reflection echo will appear. And so, the integrity of the weld can be clearly confirmed.

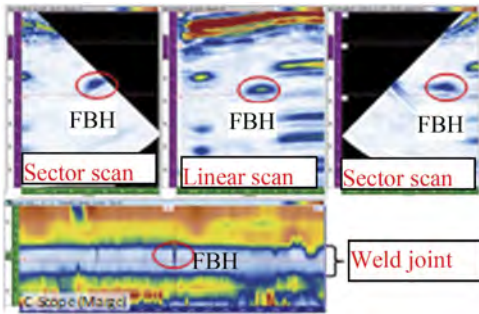


Figure 1. Screen displaying scan results for FBH.

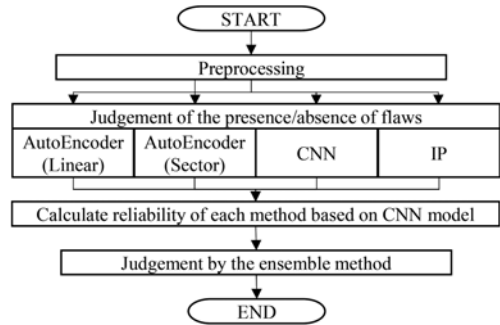


Figure 2. Judgement flow for PAUT of tube-to-tubesheet weld joint.

4 FLAW DETECTION SYSTEM

The flaw positions, weld metal heights, shapes and sizes of reflection echoes, and other parameters may vary in complicated ways in flaw detection images depending on the welding conditions of the tube-to-tubesheet weld, contact conditions of the array probe, and other factors, even if the thicknesses and diameters of tubes are the same. The proposed decision support system provides an integrated optimal solution to each problem by combining multiple judgment methods in order to improve the accuracy in judging the presence/absence of flaws while taking these variations into account.

4.1 Judgement system

Figure 2 shows the judgement flow for the present system. YOLO, Convolutional Neural Network (CNN), and Auto Encoder (AE), which are all classified as deep learning approaches, were adopted (Hinton et al. 2006, Krizhevsky et al. 2012, Rendon et al. 2016, Wen et al. 2016, Zhao et al. 2017). In this system, the detection images were preprocessed to use as input data for the judgement system. At first, the flaw detection area was extracted by YOLO. The presence/absence of flaws was judged by using image processing (IP), image classification using CNN, and image restoration using AE on the preprocessed flaw detection images. The probability of being correct was calculated for each judgment method with the reliability level by CNN. Finally, an ensemble judgment was made based on the judgment results and reliability for each method, and the final judgment result was output. Each system is described in detail below.

4.2 Preprocessing: Extraction of the judgment area by YOLO

In order to judge only the tube-to-tubesheet weld in the flaw detection image, the judgment area was extracted using the YOLO object detection method. The extracted area is surrounded by

a black dashed line and contains the tube-to-tubesheet weld, targeting (1) to (4) in Figure 3(a), which are echoes reflected from the periphery (tube surfaces at the tube end and root sides) of the tube-to-tubesheet weld (bottom echoes). The above area was annotated to learn the coordinate information as training data, and the area detection model shown in Figure 3(b) was created.



Figure 3. Detection area and extraction result by YOLO.

4.3 Judgment by IP

IP is a method of distinguishing pixel values of images based on a pre-set threshold. In the case of judging the presence/absence of flaws in flaw detection images by IP, the detection area was first extracted using YOLO, and a flaw was then judged to be present if there was more than a certain number of pixel values with levels greater than the threshold among all the pixels in the area, excluding bottom echoes.

4.4 Judgment by image classification using CNN

CNN is highly accurate as a method of image classification, and it extracts and classifies image feature values. In the case of judging the presence/absence of flaws in flaw detection images by CNN, the detection area was first extracted using YOLO, and then the images were classified into 2 groups (with flaws and without flaws) based on the results of learning images with flaws and images without flaws.

4.5 Judgment by image restoration using AE

AE is an unsupervised learning technique, and it has the advantage of being able to learn with only normal data. In the case of judging the presence/absence of flaws in flaw detection images by AE, the detection area was first extracted using YOLO, and then the difference in pixel value at the flaw position was used as the judgment index. It was judged that there was a flaw if the difference in the pixel value was greater than a certain value and that there was not a flaw if the value was less than a certain value.

4.6 Judgment results by each judgment method

Table 1 shows the results of judging 16,920 test images, including 762 images with flaws, using the IP, CNN, and AE methods (Shinoda et al. 2022). The test images were randomly extracted from flaw detection data of actual equipment. Accuracy represents the probability of correctly classifying the presence/absence of flaws in all the images. Precision represents the probability of including the actual images with flaws in the results predicted to include flaws. Recall represents the probability of correctly judging the images with flaws and it's an indicator of the oversight. Finally, specificity represents the probability of correctly judging the images without flaws and it's an indicator of the over-detection.

Because of the focus on increasing Recall accuracy to reduce the number of flaw images that were not detected, Precision accuracy was also proportionally reduced. In addition, some of the images that were classified correctly or incorrectly differed depending on the method. For example, images incorrectly judged by CNN, which had the highest recall among the individual methods, were sometimes judged correctly by IP and AE. Therefore, the reliability and ensemble judgments were adopted.

Table 1. Judgment results by each method.

Method	Accuracy (%)	Precision (%)	Recall (%)	Specificity (%)
IP	98.4	74.0	98.4	98.4
CNN	94.0	42.6	99.6	93.7
AE	98.3	73.8	97.2	98.4

4.7 Reliability judgment

To determine the reliability of each method, we prepared data of correct and incorrect images judged by each method. These images were used as training data of a newly constructed CNN model. The output value from the model was then defined as the reliability of each method. Specifically, its output value is given a numerical value between 0 and 1 as the probability that each method is correct. The reliability of each image was calculated for each judgment method as input the images of flaws from which the judgment area was extracted by YOLO. If the image is similar to an image that was previously correct, the reliability is given a value close to 1. If the image is similar to an image that was previously incorrect, the reliability is given a value close to 0.

It takes time to calculate the weight for each image, but it is possible to make more precise judgments because it is determined based on past results.

4.8 Ensemble judgment

Ensemble judgments were made based on the sum (y) of the products of the judgment results (x_i) and reliability (r_i) for each judgment method, as shown in the equation below. The ensemble judgment result was deemed to be the final judgment result: $y > 0$ for images with flaws; $y < 0$ for images without flaws; $y = 0$ for not determinable. It represents a comprehensive judgment result that appropriately takes into consideration the judgment results of each method according to their reliability based on the flaw detection image.

$$y = \sum x_i r_i \quad (1)$$

where x_i is the judgment result for each method (with a flaw, 1; without a flaw, -1) and r_i is the reliability for each method (real number from 0 to 1).

Table 2 shows the results of an ensemble judgment for the 16,920 test images used in Section 4.6. Although there was 1 undetected image among the 762 images with flaws, the judgement accuracy was improved for every index compared with the results for each of the individual judgment methods, and it was possible to reduce not only the undetected images with flaws but also the erroneously detected images without flaws.

Table 2. Judgment results by ensemble system.

Method	Accuracy (%)	Precision (%)	Recall (%)	Specificity (%)
Ensemble	99.4	88.6	99.9	99.4

5 VERIFICATION ON THE ACTUAL EQUIPMENT

5.1 Verification on the actual equipment

Table 3 shows the results of judging 36,723 test images, including 11,896 images with flaws. Those data were different from the data of the previous chapter. In this case, the size of tube is bigger than previous one and another condition is also different. Thus, AE for judgement and CNN for reliability was learned the data form this equipment. Since this tube-to-tubeseet was in service, the inner surface has some corrosion. From this thing, the obtain data has some noise. Then, the accuracy was lower than the result of the previous one.

Table 3. Judgment results by each method and ensemble system.

Method	Accuracy (%)	Precision (%)	Recall (%)	Specificity (%)
IP	60.9	59.2	92.0	23.0
AE(Linear)	77.1	89.6	66.0	90.7
AE(Sector)	52.3	56.5	56.6	47.1
Ensemble	76.3	76.2	82.6	68.7

From this result, it's confirmed the accuracy of ensemble system lower than accuracy of the AE used linear image. So, the reliability of each test data was confirmed. Tables 4, 5 and 6 show the relationship of the correct/incorrect and the reliability for each image. In those table, the reliability was divided two categories, less than 0.5 or more.

Table 4. The relationship of the correct/incorrect and the reliability for IP.

Status	Reliability < 0.5	Reliability >= 0.5	Accuracy (%)
Incorrect	10,606	3,764	73.8
Correct	6,853	15,500	69.3

Table 5. The relationship of the correct/incorrect and the reliability for AE used linear image.

Status	Reliability < 0.5	Reliability >= 0.5	Accuracy (%)
Incorrect	6,587	1,807	78.5
Correct	9,930	18,399	64.9

Table 6. The relationship of the correct/incorrect and the reliability for AE used sector image.

Status	Reliability < 0.5	Reliability >= 0.5	Accuracy (%)
Incorrect	9,626	7,880	55.0
Correct	6,557	12,660	65.9

From those results, it was confirmed the accuracy of reliability is less than 80%, especially, the accuracy for AE used sector image are less than 70%. It means correlation between correctness and reliability was low.

5.2 Improve the reliability calculation method

In this section, the image to calculate the reliability was changed to composite image. Composite image was made from linear and sector images. The value of each pixel of composite image is max value of those three images. By using composite image, it is expected the accuracy of reliability is improved.

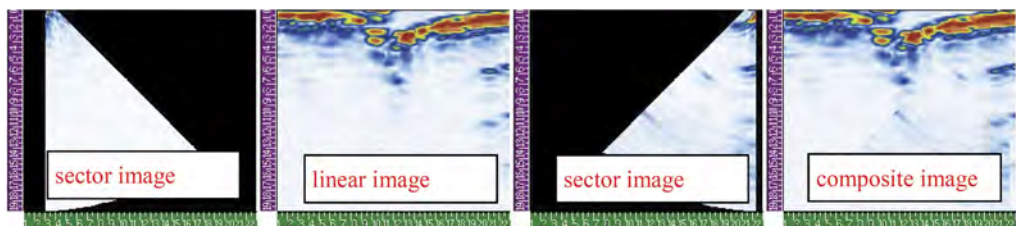


Figure 4. Composite image.

Tables 7, 8 and 9 show the relationship of the correct/incorrect and the reliability for each image when use the composite image using same data with Section 5.1.

Table 7. The relationship of the correct/incorrect and the reliability for IP.

Status	Reliability < 0.5	Reliability >= 0.5	Accuracy (%)
Incorrect	12,240	2,130	85.2
Correct	4,128	18,225	81.5

Table 8. The relationship of the correct/incorrect and the reliability for AE used linear image.

Status	Reliability < 0.5	Reliability >= 0.5	Accuracy (%)
Incorrect	7,605	789	90.6
Correct	5,837	22,492	79.4

Table 9. The relationship of the correct/incorrect and the reliability for AE used sector image.

Status	Reliability < 0.5	Reliability >= 0.5	Accuracy (%)
Incorrect	13,767	3,739	78.6
Correct	4,394	14,823	77.1

From those results, it was confirmed the accuracy was of reliability was improved to more than 77%.

Table 10 shows the results of same data with section 5.1.

Table 10. Judgment results by improved ensemble system.

Method	Accuracy (%)	Precision (%)	Recall (%)	Specificity (%)
Ensemble	85.8	85.8	88.9	82.0

From Table 10, it is confirmed the accuracy of ensemble system and other parameter were improved more than 10% compare with the result of section 5.1. Thus, it is concluded the ensemble method that using composite image is efficient.

6 CONCLUSION

A PAUT testing device for the tube-to-tubesheet weld in multi-tube heat exchangers and a flaw detection system that automatically judges acquired flaw detection data for the presence/absence of flaws were previously developed. By improving the reliability calculation method, the system represents a highly accurate judgement method, as it reduces the undetected images with flaws and erroneously detected images without flaws in flaw detection images. A method to prevent unacceptable welds from being missed was established, this reduced the judgment time by at least 75%, compared with judging all flaw detection images visually, and enabled practical use as a total number inspection for tube-to tubesheet weld.

REFERENCES

Abe, M., Murakami, J. & Shinmura, N. 2017. Ultrasonic Testing and Photographic Imaging System for Tube to Tubesheet Weld of Heat Exchanger. ASME PVP2017-65569, 1–8
 Abe, M., Shinoda, K. & Wada, T. 2022. Application of AI Judgment in Phased Array Ultrasonic Testing for Tube to Tubesheet Weld, Journal of the Japan Welding Society Vol.91 No.2, 29-34 (in Japanese)

- Hinton G. E. & Salakhutdinov, R. R. 2006. Reducing the Dimensionality of Data with Neural Networks, *Science*, 313, 5786, 504–507
- Redon, J., Divvala, S. & Girshick, R. et al. 2016. You Only Look Once: Unified, Real-Time Object Detection, *IEEE Conference on Computer Vision and Pattern Recognition*, 779–788.
- Shinoda, K., Abe, M. & Murakami. 2019. Phased Array Ultrasonic Testing for Tube-to-Tubesheet Welding in Tubular Heat Exchanger, *JWS, Proceedings of the Welding Structure Symposium'2019*, 38s–43s (in Japanese)
- Shinoda, K., Abe, M., Katayama, T., Ioka, R. Wada, T. Shinmura, N., Murakami, J. and Hattori, H. 2022. Reducing Application of Phased Array Ultrasonic Testing for Tube-to-Tubesheet Weld of Head Exchanger using Deep Learning, *Proceeding of IIW 2022 International Conference on Welding and Joining*, 180–183.
- Wen, Y., Zhang, K. & Li, Z. et al. 2016. A Discriminative Feature Learning Approach for Deep Face Recognition, *European Conference on Computer Vision (ECCV), Part VII, Lecture Notes in Computer Science book series (LNCS)*, 9911, 499–515
- Zhao, H., Shi, J. & Qi, X. et al. 2017. Pyramid Scene Parsing Network, *IEEE Conference on Computer Vision and Pattern Recognition (CVPR)*, 2881–2890

Innovative methods for the inspection of hydraulic structures

A. Seiffert & J. Bödefeld

Federal Waterways Engineering and Research Institute, Karlsruhe, Germany

ABSTRACT: For many years, inspections of hydraulic structures have been carried out in the same way using analogue methods. However, the challenges associated with such inspections are increasing. Making greater use of digital technologies during inspections could help to manage these challenges. The Federal Waterways Engineering and Research Institute therefore conducted a systematic study to determine to what extent innovative methods, such as UAS, laser scanning and multibeam sonar can support hydraulic structure inspections.

1 INTRODUCTION

Regular inspections of the hydraulic structures on Germany's federal waterways are indispensable to ensure the safe, economical and sustainable operation of the infrastructure. Inspections of hydraulic structures are carried out at least every six years. The associated expenses are not negligible as each inspection requires that the structure is drained of water. An ageing infrastructure, the often large dimensions of hydraulic structures and the multitude of damage mechanisms place higher requirements on inspection staff. As it is not always possible to bypass hydraulic structures in the network of waterways, it would be desirable to shorten inspection times while ensuring at least the same level of inspection quality. Advances in digitisation with high-resolution sensors, powerful storage media and intelligent machine learning algorithms could provide opportunities for increasing efficiency. While innovative structural inspection methods have already been tested successfully in pilot projects, a systematic overview of the potential offered by such methods in the inspection of hydraulic structures in particular is still lacking.

With this background in mind, the Federal Waterways Engineering and Research Institute carried out the research project 'Innovative methods for structural condition assessment' in cooperation with the Geodetic Institute of RWTH Aachen University. The starting point for the project was a systematic documentation of the inspection process to identify optimisation opportunities. This documentation was used to select innovative methods that could potentially support the inspection of hydraulic structures. The methods were tested on a drained and on a flooded navigation lock. The tests comprised carrier platforms (unmanned aerial system and remotely operated underwater vehicle); measuring instruments (laser scanner, hand-held scanner, thermal imaging camera and multibeam sonar) and evaluation methods (photogrammetry and machine learning). All these methods were systematically assessed for their user-friendliness and the quality of data provided. Based on the results, a recommendation for the use of innovative methods for the inspection of hydraulic structures was prepared.

2 CONVENTIONAL INSPECTION OF HYDRAULIC STRUCTURES

The research project began by analysing current approaches to inspections of hydraulic structures, i.e. the conventional methods applied. This analysis served as the starting point for

identifying suitable innovative inspection methods and consisted of two parts: an analysis of existing regulations for structural inspections, and participation in two inspections. Administrative Regulation VV-WSV 2101 of the German Federal Waterways and Shipping Administration (WSV) on the inspection of structures (Federal Ministry for Digital and Transport 2022) is the basic regulation governing the inspection of structures falling within the competence of the WSV. According to this regulation, the ‘condition at the time of inspection has to be assessed and documented, and on this basis the necessary action has to be taken without delay’. To this end, assets with a particularly high potential risk and level of complexity, e.g. weirs and navigation locks, must be drained of water and inspected at least every six years.

Participation during the research project in the inspections of a weir and a navigation lock resulted in the identification of two distinct groups of inspection aids. On the one hand, smaller aids such as digital cameras, notepads, spray paint, torches, crack templates and hammers were used to determine and document damage. On the other hand, larger aids and tools were employed to facilitate access to the structures, e.g. ladders, cherry pickers, lifting platforms, work baskets and platforms and various types of scaffolding. Additional measuring instruments such as rebar detectors were used to examine damage in specific cases, but not routinely. The digital camera was therefore the only digital method used as a standard procedure in the inspections attended. The inspection process observed for the structures was documented to evaluate which innovative methods can be integrated into this process. Four process steps were identified as essential to meeting the inspection objectives. In chronological order these are: identifying anomalies e.g. deviations from the target condition; detecting damage; assessment of damage and damage documentation. Each step is characterised by different data collection requirements. Identifying deviations from the target condition is essential for the subsequent steps and thus the focus of the following field tests.

3 SELECTION OF INNOVATIVE METHODS

A literature review was conducted to select suitable innovative methods for the inspection of hydraulic structures. This review resulted in a list of innovative methods that are suitable for purpose. Given the fixed project period, only a limited number of methods could be evaluated. The selection criteria were, first, the assumed direct benefit of the method for the inspection work and, second, the assumed expense for testing the method. The methods selected for the drained lock were unmanned aircraft (drone), terrestrial laser, thermography, hand-held triangulation scanner, photogrammetry and damage detection using machine learning. The drone and terrestrial laser were selected because, according to the literature, both systems are capable of capturing high-resolution images of areas above water level in a relatively short period of time. The combination of an aerial system with the photogrammetric method has the advantage of providing a textured model (Nooralishahi et al. (2021), Hubbard and Hubbard (2020), Holst et al. (2016)) while the strength of the terrestrial laser lies in the accuracy of size determination (Truong-Hong & Laefer (2014), Anil et al. (2013), Mischo et al. (2019)). Thermography was considered to be a useful supplement as, in contrast to these two methods, it holds greater potential for the detection of cavities and voids (Mold et al. (2020), Rocha et al. (2018)). The main advantage of the hand-held triangulation scanner is probably its ability to make three-dimensional measurements of damages or structural components (Kus et al. (2009), Fuentes et al. (2007)). Image-based detection of damages using machine learning was selected for the project as it seems a suitable method for the efficient evaluation of large data volumes in particular (Morgenthal et al. (2021), Dais et al. (2021), Blut et al. (2021)).

The remotely operated vehicle (ROV), imaging sonar and echo sounder were tested on the flooded structure. The remotely operated underwater vehicle can prove an efficient solution for visual inspections of individual areas (Sugimoto et al. (2017), António Neves Lousada et al. (2021)). In addition, it can be equipped with an imaging sonar so that this method can also be tested without significant additional cost. In contrast, the use of an echo sounder appeared to be a suitable method for the efficient surveying of large areas and subsequent modelling. It was therefore considered a useful addition to the ROV (Moisan et al. (2018), Holste et al. (2019), Müller-Braune (2022)).

4 FIELD TESTS

The north chamber of the Sülfeld navigation lock was used as a test object for the tests carried out both underwater and above water. This particular test object was chosen because it is possible to drain the lock, the scheduled time of drainage aligned well with the project schedule, and there are various types of damage in the lock. The lock is located on the Mittelland Canal near the German city of Wolfsburg. Of its two chambers, the north chamber was used for the field tests because it is older and in poorer condition. The chamber was built in 1938 using concrete gravity walls with a suspended floor. An assessment in May 2021, prior to the construction inspections, rated the lock's condition at the poorest level of 4. The field tests comprised only the lock chamber and the gates of the facility, as these are decisive for its functioning. Four chamber blocks, each 12 m long, were selected for the manual mapping of damages. This was done in a conventional way, e.g. by marking and measuring the damaged areas followed by photo documentation. The comparative data thus collected are used to evaluate the detection capability of the innovative methods.

Table 1. Tested methods.

Method	Model	Area	Result
Unmanned aerial system (UAS)	Matrice M300, Sony Alpha 7 RII, Sony RX0II	Chamber	Images, 3D surface model
	Elios, 1/2,3" CMOS, Lepton 3.5 FLIR	Culvert	
Terrestrial laser	Leica-P30	Chamber	Point cloud
Hand-held triangulation scanner	Artec MHT	Specific damages	Point cloud
Thermal imaging camera	FLIR T660	Specific damages	Thermal images
Remotely operated vehicle (ROV)	Blueprint Oculus Multibeam Sonars - M1200D	Chamber Specific damages	Videos, sonar images
Multibeam sonar	Multibeam Teledyne SeaBat T50-P	Chamber	Point cloud

Table 1 shows the tested methods. Drone-based inspection and recording of the lock chamber's condition was carried out with the unmanned aircraft system (UAS) Matrice M300. The UAS was manually piloted without pre-programmed flight routes. It recorded the condition of the entire lock chamber including the gates. The chamber walls and the gates were surveyed from a distance of around 3 m while a shorter distance of around 1.5 m was used for the four chamber blocks where damages were documented. An image overlap of 60–70% was used so that the images could be put together by means of photogrammetry to obtain a textured 3D surface model of the lock chamber. In addition, the images were used to evaluate the capability of detecting damage automatically using machine learning methods. A UAS specifically designed for indoor inspections – the Elios model from Flyability – was used to survey the culvert at the upper lock head. This UAS is protected by a cage and is therefore collision tolerant. Similarly to outdoor applications, data are collected as raster images with an overlap of 60–70% and at a distance from the wall of around 50 cm. In this way, the ceiling and the walls of the culvert were mapped. The Leica-P30 panorama scanner was used as the model for terrestrial laser scanning. The entire lock chamber was surveyed from several locations at 10 m distance with an approximate effective ground resolution of 1 cm. The four chamber blocks in which damages were mapped were surveyed at a higher resolution of around 0.5 mm, which corresponds to the UAS's resolution. A FLIR T660 thermal imaging camera was used to test the potential of thermography for identifying cavities and delaminations. As

the literature reviewed contained a reference to the potential suitability of thermography, thermal imaging was carried out on the chamber wall approximately one hour after direct solar radiation. A suspected cavity was checked by tapping the potentially damaged area. The Artec MHT hand-held triangulation scanner was tested by performing three-dimensional scanning of specific damages, such as cracks and spalling in the chamber walls. The tests mainly focused on user experience for the inspection staff, which is why the responsible staff conducted the tests.

The unmanned underwater vehicle and the multibeam sonar were deployed in the flooded lock. The remotely operated vehicle (ROV) was used to detect specific areas of damage. Its equipment comprised an RGB camera and an imaging sonar. The multibeam sonar, on the other hand, was used to survey the entire lock chamber and generate a 3D surface model. The ROV used was the DeepTrekker Revolution with an integrated Blueprint Oculus M1200D multibeam imaging sonar. The south chamber blocks 3 and 12 were inspected because damages had been mapped there and were greater in number than in the north blocks. First, the ROV was positioned at different depths, in each case at 2 m distance from the chamber wall, and the sonar collected images from various angles. Subsequently, the wall section was surveyed horizontally at different depths and at a distance of around 1/2 m to produce video recordings. An underwater surveying system comprising a boat, a Teledyne SeaBat T50-P multibeam sonar and a tachymeter was used to obtain a complete survey of the chamber. This enabled the entire lock chamber, i.e. the walls, the floor and the gates, to be surveyed.

5 RESULTS OF THE FIELD TESTS

To evaluate the diagnostic capability of the innovative methods for damage detection, the generated images were compared with the results of manual damage mapping. Cracks were the prominent damage pattern found in the chamber blocks and were therefore used as the criterion for assessing detection capability. The evaluation revealed that around 80% of the cracks identified by manual damage mapping could be detected on the laser scanning images. The images generated by the UAS had the second-best recognition rate with around 70% of the cracks being detected on them. By contrast, automatic damage detection applied to the UAS images was unsatisfactory with a recognition rate of only around 10%. Underwater methods as well only yielded unsatisfactory results regarding crack detection. Around 10% of the cracks were visible on the ROV images, whereas the images derived from echo sounding showed no cracks at all. Further investigations are required for both methods to enable an appropriate assessment of their reliability. Using thermography to detect cavities showed the potential of this method which should also be investigated in a more detailed study.

The hand-held triangulation scanner was the only method that proved to be of little practical use, especially in comparison to its benefit. The results were therefore not analysed in detail. The experience gathered in the project has been documented in a decision matrix to support potential users of innovative methods in the selection of a suitable method. Table 2 shows the resulting matrix: it contains an estimate of the maximum resolution and 3D accuracy attained in the project, the time needed for data collection and the cost of the methods. It should be noted that these data reflect the experience gathered in the project; they show trends but do not provide a sufficient basis for generally applicable statements. This applies in particular to the resolution and accuracy indicated, which depend on the sensor used, the working distance and other factors such as the georeferencing accuracy. As a result, the values indicated in the table are qualitative, with + representing a low, and +++ representing a high value. As is evident from the project findings, the highest resolution can be attained with the hand-held triangulation scanner. Next in the ranking are the UAS and the terrestrial laser scanner, both of which were also able to detect damage in the sub-millimetre range in the project.

In contrast, active thermography and multibeam echo sounding only detected damages at a scale of several centimetres. No reliable information on the resolution obtained with the ROV is available from the project. The 3D accuracy that can be achieved is only indicated in the matrix for those methods that are capable of generating a 3D model, i.e. UAS with

Table 2. Decision matrix.

Method	Max. resolution	3D accuracy	Time for data collection	Cost	Use cases								
					1	2	3	4	5	6	7	8	
Unmanned aerial system (UAS)	++	+	1 day for 6 chamber blocks*	++	x	x	x	x					
Indoor-UAS	++		½ day for 1 culvert*	++		x	x						
Terrestrial laser	++	++	2 days for 1 chamber block*	++	x	x			x	x			
Thermal imaging camera	+		½ day for 1 chamber block*	++								x	
Hand-held triangulation scanner	+++	+++	10 min for 1 m ² *	++				x		x			
Multibeam sonar	+	+	½ day for chamber block*	+	x						x	x	
Remotely operated vehicle (ROV)	n. s.		2 hours for chamber block*	++			x	x					x

* Reference: Sülfeld lock; chamber: 6,000 m²; chamber block: 160 m²; culvert: 150 m².

Use cases:

- 1: 3D model
- 2: Detection of damage
- 3: Visual identification of damage
- 4: Measurement of damage
- 5: Detection and measurement of spalling
- 6: Deformation measurement
- 7: Detection of voids
- 8: Identification of baffles

orthophotography, terrestrial laser scanner, hand-held triangulation scanner and multibeam sonar. Again, the best results in the sub-millimetre range were obtained with the hand-held scanner; the accuracy of other surveying methods was in the centimetre range. The time needed to collect data indicated in the matrix relates to the dimensions of the test object, i.e. the north chamber of the Sülfeld ship lock. In this case, thermography and multibeam sonar are the fastest methods while the survey with the hand-held triangulation scanner was most time-consuming. In view of the multitude of available sensors and system providers, the cost of each method is also stated in qualitative terms: + represents a minor and +++ a major cost advantage. The project showed that the multibeam sonar has a minor cost advantage while the UAS and hand-held triangulation scanner were associated with a major cost advantage.

6 CONCLUSIONS

There are many opportunities for continuing the research work. For example, the object studied could be altered, additional methods investigated and the findings transferred for practical use. Altering the object would include in particular changing the damage features (limited to cracks in this research project), and the type of object studied (a navigation lock in this project). Moreover, the project focused on recording the current condition of the structure. However, it can be assumed that, because of their standardised recording technology, digital methods are most effective when they are used more frequently, i.e. for recurrent inspections of structures. This would help to obtain more detailed knowledge about damage development, which would be useful for its assessment. The terrestrial laser scanner with a camera is another innovative method that should be taken into consideration as it can generate highly accurate textured images. Including this method in the scope of further research would therefore be highly interesting, in particular because the terrestrial laser scanner was used with positive results in the navigation lock. The additional use of a laser line scanner for underwater

investigations might be promising as it would probably provide a higher resolution than the multibeam sonar. Last but not least, it is important to remain focused on transferring the lessons learned into practice. It should be specified, for example, how innovative methods can be integrated in structural inspection processes, not only in respect of data collection but also for the evaluation and assessment of data.

REFERENCES

- Anil, Engin Burak; Akinci, Burcu; Garrett, James H.; Kurc, Ozgur 2013. Characterization of Laser Scanners for Detecting Cracks for Post-Earthquake Damage Inspection. In Ferri Hassani, Osama Moselhi and Carl Haas (ed.): *Proceedings of the 30th International Symposium on Automation and Robotics in Construction and Mining (ISARC 2013): Building the Future in Automation and Robotics. 30th International Symposium on Automation and Robotics in Construction and Mining; Held in conjunction with the 23rd World Mining Congress*. Montreal, Canada, 8/11/2013-8/15/2013: International Association for Automation and Robotics in Construction (IAARC) (Proceedings of the International Symposium on Automation and Robotics in Construction (IAARC)).
- António Neves Lousada, Sérgio; Freitas Camacho, Rafael; Suárez Palacios, Josué 2021. Under-water Technical Inspections Using ROV Applied to Maritime and Coastal Engineering: The Study Case of Canary Islands. In Sérgio António Neves Lousada (Ed.): *Underwater Work*.
- Blut, Christoph; Büttner, Till; Becker, Ralf; Wollenberg, Raymond; Özcan, Baris; Stahl, Heiner; Blankenbach, Jörg 2021. DigiPark - Digitalisierung in der Bauwerksinstandsetzung. In *kevb 7 (1)*: 91–100.
- Dais, Dimitris; Bal, İhsan Engin; Smyrou, Eleni; Sarhosis, Vasilis 2021. Automatic crack classification and segmentation on masonry surfaces using convolutional neural networks and transfer learning. In *Automation in Construction*: 125, 103606. DOI: 10.1016/j.autcon.2021.103606.
- Federal Ministry of Digital Affairs and Transport (ed.) 2022. Bauwerksinspektion VV-WSV 2101 (Verwaltungsvorschrift der Wasserstraßen- und Schifffahrtsverwaltung des Bundes).
- Fuentes, L. M.; Finat, Javier; Fernández-Martin, J. J.; Martínez, J.; SanJose, J. I. 2007. Some Experiences in 3D Laser Scanning for Assisting Restoration and Evaluating Damage in Cultural Heritage. In Johann Nimmrichter, Wolfgang Kautek und Manfred Schreiner (Ed.): *Lasers in the conservation of artworks. LACONA VI proceedings, Vienna, Austria, Sept. 21-25, 2005*, Bd. 116. Berlin, Heidelberg, New York: Springer (Springer proceedings in physics, 116): 543–551.
- Holst, Ralph; Sperber, Martin; Gößmann, Rainer 2016. Bauwerksprüfung unterstützt durch neue Besichtigungstechniken – Erste Erfahrungen. In *Bautechnik* 93 (10): 742–746.
- Holste, Karsten; Hesse, Christian; Neumann, Ingo; Bassen, Sebastian (2019): 3D HydroMapper – digitale Inspektion von Bauwerken über und unter Wasser. In *Bautechnik* 96 (12): 951–953. DOI: 10.1002/bate.201900097.
- Hubbard, Bryan; Hubbard, Sarah 2020. Unmanned Aircraft Systems (UAS) for Bridge Inspection Safety. In *Drones* 4 (3): 40. DOI: 10.3390/drones4030040.
- Kus, A.; Unver, E.; Taylor, A. 2009. A comparative study of 3D scanning in engineering, product and transport design and fashion design education. In *Comput. Appl. Eng. Educ.* 17 (3): 263–271. DOI: 10.1002/cae.20213.
- Mischo, Hendrik; Seifried, Jörg; Thiele, Klaus; Schanzenbach, Stephan; Grassl, Martin 2019. Vom 3-D-Laserscan zum BIM-Modell. In *Bautechnik* 96 (7): 564–571. DOI: 10.1002/bate.201900031.
- Moisan, Emmanuel; Charbonnier, Pierre; Foucher, Philippe; Grussenmeyer, Pierre; Guillemin, Samuel 2018. Evaluating a Static Multibeam Sonar Scanner for 3D Surveys in Confined Underwater Environments. In *Remote Sensing* 10 (9): 1395. DOI: 10.3390/rs10091395.
- Mold, Lisa; Auer, Mathias; Strauss, Alfred; Hoffmann, Markus; Täubling, Benjamin (2020): Thermografie zur Erfassung von Schäden an Brückenbauwerken. In *Bautechnik* 97 (11): 789–801.
- Morgenthal, Guido; Rodehorst, Volker; Hallermann, Norman; Debus, Paul; Benz, Christian 2021. Bauwerksprüfung gemäß DIN 1076 – Unterstützung durch (halb-)automatisierte Bildauswertung durch UAV (Unmanned Aerial Vehicles – Unbemannte Fluggeräte). Inspections of structures in accordance with DIN 1076 – support by (semi-)automated image analysis with UAV (unmanned aerial vehicles).
- Müller-Braune, Frederic 2022. Damm- und Staubeckenuntersuchung mit Multibeam- und Laserscan: Talsperre Cranzahl - Ein Fallbeispiel von Sitowise in Zusammenarbeit mit der LTV Sachsen. XII. Mittweidaer Talsperrentag. In Hochschule Mittweida, University of Applied Science (Ed.): *Messtechnische Überwachung von Stauanlagen. XII. Mittweidaer Talsperrentag*.

- Nooralishahi, Parham; Ibarra-Castanedo, Clemente; Deane, Shakeb; López, Fernando; Pant, Shashank; Genest, Marc et al. 2021. Drone-Based Non-Destructive Inspection of Industrial Sites. A Review and Case Studies. In *Drones* 5 (4): 106. DOI: 10.3390/drones5040106.
- Rocha, J.H.A.; Santos, C. F.; Póvoas, Y. V. (2018): Evaluation of the infrared thermography technique for capillarity moisture detection in buildings. In *Procedia Structural Integrity* 11: 107–113. DOI: 10.1016/j.prostr.2018.11.015.
- Sugimoto, Hideki; Moriya, Yoichi; Ogasawara, Tetsuya 2017. Underwater survey system of dam embankment by remotely operated vehicle. In 2017 IEEE Underwater Technology (IEEE OES International Symposium on Underwater Technology 2017 Busan). UT 2017 Busan, February 21-24, 2017, Novotel Ambassador Hotel on Haeundae, Busan, South Korea. 2017 IEEE Underwater Technology (UT). Busan, South Korea, 2/21/2017-2/24/2017. Oceanic Engineering Society; Institute of Electrical and Electronics Engineers. Piscataway, NJ: IEEE: 1–6.
- Truong-Hong, Linh; Laefer, Debra F. 2014. Application of Terrestrial Laser Scanner In Bridge Inspection: Review and an Opportunity. In *IABSE Symposium, Madrid 2014: Engineering for Progress, Nature and People*. IABSE Symposium, Madrid 2014: Engineering for Progress, Nature and People. Madrid, Spain, 9/3/2014-9/5/2014: International Association for Bridge and Structural Engineering (IABSE) Zurich, Switzerland (IABSE Reports): 2713–2720.

Behaviour of corroded bridge bearing and full-bridge modeling

A. Hiraoka, G. Hayashi & T. Yamaguchi

Osaka Metropolitan University, Osaka, Japan

ABSTRACT: Corrosion of bridge bearings can cause fatigue cracking from welds at the edge of the bottom plate. It is important that assessment of the condition of the bridge bearing for determining the soundness and load-bearing capacity of the bridge. In this study, the relationship between corrosion level and bearing function is clarified by FE analysis using a detailed bearing model. The behavior of bearing is applied to the full-bridge model as spring properties to study the differences in bridge response due to bearing corrosion. The analysis is targeted at corrosion on the contact surface of the spherical bearing (BP-A), which is in the largest number of steel bearings in service. Analysis of the corroded bearing showed that if the friction coefficients of the contact surfaces were increased, the bearing could not follow the displacement of the girder and rotated in the opposite direction to that of the intact bearing. The increased friction coefficient may cause fatigue cracks due to the increased compressive stress at the sole plate edge. Furthermore, this paper presents a cost-effective modelling of the bearing behaviour by representing it with two-directional and rotational springs and proposing spring constants and mounting positions according to the degree of corrosion.

1 INTRODUCTION

Bearings are installed at the contact point between a superstructure and substructure. Bearings are necessary to transmit the loads acting on the superstructure to the substructure and to follow the horizontal and rotational displacements of the superstructure smoothly (Japan Road Association, 2019:). However, bearings are installed in narrow spaces, such as those between the bridge girder ends and abutments, and leakage occurs from the upper expansion joints. This results in several reports of corrosion damage to steel bearings and anchor bolts (Brinckerhoff, 1992:), which may cause fatigue cracks near the sole plate at the girder ends owing to the decrease in bearing function. Consequently, several studies have been conducted on the effects of corrosion damage on the functions of steel bearings. (Fan, 2015; Kamaitis, 2001:)

Studies on the decrease in bearing function due to corrosion have focused on the BP-A bearing, which is the most used steel bearing in Japan. The BP-A bearing consists of a bearing plate (BP) with vertical force support, horizontal movement, and rotation functions (Japan Road Association, 2019:). There is a sliding motion of the horizontal contact surface between the upper shoe and BP, which performs the horizontal deformation function, whereas the spherical contact surface between the BP and lower shoe performs the rotational function. However, corrosion of the contact surfaces of BP-A bearings has been reported in several cases. Because of this corrosion, BP-A bearings cannot follow the displacements of the superstructure, resulting in horizontal forces that were not considered in the design (Niwa, 2018:). This leads to a concentration of compressive stress at the weld at the end of the sole plate in the lower flange, which causes fatigue cracks (Yamamura, 2010:). 6. These studies were conducted on after-service BP-A bearings. Few studies have focused



Figure 1. Examples of damage in hinge bearings.

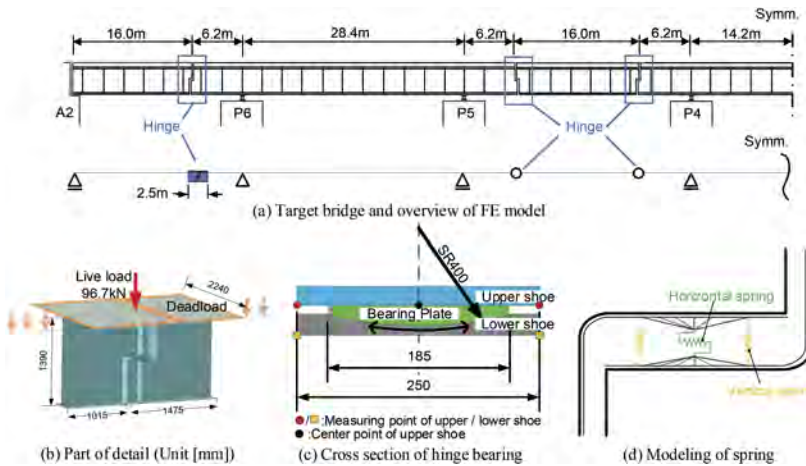


Figure 2. Actual target bridge and analysis model.

Table 1. Material properties.

	Elastic Moduli [GPa]	Poisson ratio	The moment of inertia of beam[mm ²]
Slab	30	0.2	3.37×10^{10}
Girders, Upper and lower shoe	200	0.3	
Bearing plate	100	0.3	–

on the in-service corrosion levels, and the effect of the resulting changes in behaviour on the horizontal forces should be investigated.

A bridge type with BP-A bearings and a high likelihood of bridge collapse owing to fatigue cracks is the cantilever-suspended girder bridge. These bridges have continuous girders with intermediate hinges to increase the span length. However, corrosion at the intermediate hinge bearing (hereafter, hinge) is often reported because of leakage from the expansion joint installed above. As a consequence, fatigue cracks in the girders are often reported around the hinge (Figure-1). However, the relationship between bearing corrosion and fatigue crack initiation is unclear.

In addition, few studies have examined the effects on the entire bridge depending on the degree of corrosion of the bearings. In the overall bridge model, the corroded bearings are mostly modelled with either simple springs or perfect adherence. There has been no investigation into whether this model reproduces the corroded bearing behaviour.

In this study, the relationship between the hinge corrosion level and fatigue cracks in the surrounding members was clarified. In addition, a model using springs that can reproduce the behaviour of a corroded hinge was investigated.

2 ANALYSIS MODEL

The actual target bridge, which was completed in 1959, is a cantilever–suspended non-synthetic girder bridge with seven spans, including suspended-span and cantilever-girder lengths of 16.0 m and 40.8 m (6.2 m + 28.4 m + 6.2 m), respectively. Because the target bridge is symmetrical, its general drawing is presented from the A2 abutment to its centre, as illustrated in Figure-2. In the analysis model, a symmetry condition was provided in the centre, and a 1/2 model was created. In this study, only one main girder was modelled because the focus was on the effect of corrosion at the hinge on the local response. To focus on the hinge of the end-suspension girder, only the area surrounding the hinge was modelled in detail, as shown in Figure-2(a) and (b).

Table 2. Vertical and horizontal spring constant.

Case		Case-0.05		Case-0.4	
Measuring point		Left	Right	Left	Right
Sum of contact pressure [N]		22373.7		21499.5	
Vertical disp.[mm]	Upper	-7.41	-7.48	-7.26	-7.26
	Lower	-7.61	-7.23	-7.46	-7.15
	Difference	0.20	-0.25	0.19	-0.11
Vertical spring constant [N/mm]		109578.3	90311.2	110770.8	187441.2
Horizontal relative displacement [mm]		0.514		0.037	
Horizontal spring constant [N/mm]		2178.3		229474.9	

To clarify the behaviour of the hinge during corrosion, the bearing was modelled in detail, and an FE analysis was performed with the friction coefficient of the contact surface as a parameter. Using the results of this study, a model of the corroded bearing using spring elements was investigated, and a model is proposed that gives similar results to the detailed model. The general-purpose FEM software Abaqus/Standard 2022 was used for analysis. The detailed model, spring model, and loading conditions are described below:

2.1 Detailed model

In the detailed model, the hinge was modelled using an eight-node solid element. A cross-sectional view of the hinge is shown in Figure-2(c). Because detailed drawings of the hinge were not available, the radius of curvature was set to ensure a contact area that satisfied the allowable bearing stress required in the design.

The webs and flanges around the hinge were modelled using four-node reduced-integral shell elements, whereas the girders outside the shell element parts were modelled with two-node beam elements. The area to be modelled with shell elements was between the vertical stiffeners. This is the area where stress fluctuations are eliminated, which was determined in a preliminary analysis. The coupling condition between the girder of the beam elements and the shell element is a rigid coupling with a multi-point restraint. The element sizes were set to 5 mm × 5 mm for the hinge, 30 mm × 30 mm for the girder of the shell, and 100 mm × 100 mm for the girder of the beam. Table-1 presents the properties of the materials used in this study. In this analysis, the corrosion level at the bearing contact surface was determined by varying the friction coefficient. Three corrosion levels were considered. The friction coefficients were set to 0.05 for the intact condition and 0.4 for a corroded surface in service. The case of shared nodes of the contact surface was also investigated, assuming a complete fixing.

2.2 Spring model

A model with springs that can reproduce the behaviour of corroded bearings was obtained using the detailed bearing model studied above. The bearings exhibited rotational behaviour

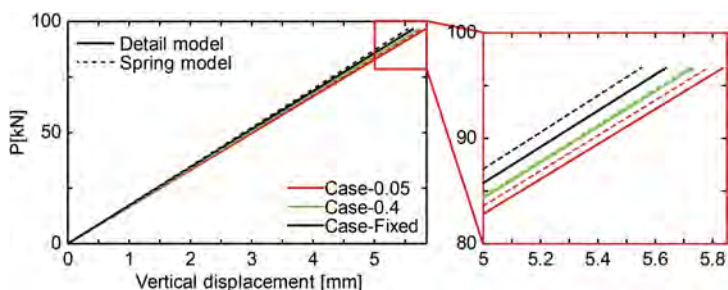


Figure 3. Vertical displacement at the underside of the lower flange just below the hinge centre point.

perpendicular to the bridge axis, horizontal displacement in the direction of the bridge axis, and vertical displacement. Thus, three springs were installed in two directions, and their spring constants were varied to represent the behaviour of different degrees of corrosion. The spring installation method is illustrated in Figure-2(d). In this model, the reference points were set at the top surface of the upper flange in the main cantilever span and the bottom surface of the lower flange in the suspended span of the notch. These sets were joined to two nodes placed in the middle of the upper and lower notch surfaces. A horizontal spring was introduced between the two nodes. Here, the range of the flange to the connection is the same as the contact surface between the flange and the upper or lower shoes in the detailed model.

Vertical springs were introduced between the two nodes located on the boundary line with shoes in the flanges. The nodes were joined to the boundary line. The calculation of the vertical and horizontal spring constants was based on the results of the study of different friction coefficients in the detailed bearing model. The calculation method is described as follows:

2.2.1 Vertical and horizontal spring constant

To calculate the spring constant, the frictional force on the spherical contact surface that resists the behaviour was calculated. The frictional force was calculated as the total contact pressure on the contact surface multiplied by the friction coefficient. This frictional force, divided by the vertical and horizontal displacement of the hinge, was used as the spring constants.

The vertical displacement of the hinge required to calculate the vertical spring was determined by subtract the vertical displacement of the measuring point of the lower shoe from that of the upper shoe. This value was calculated for each edge of the point.

The horizontal displacement required for the calculation of the horizontal spring constant was defined as the relative displacement between the centre point of the BP and the lower shoe on the contact surface. Table-2 lists the values used in the calculations and the obtained vertical and horizontal spring constants.

2.3 Loading method

Subsequently, the loading conditions are discussed. The dead loads were introduced as distributed loads on the entire top surface of the slab in the detailed section and on the beam elements in the beam element section. To calculate the live load, a preliminary analysis was carried out assuming that a carriage with a wheel load (front axle weight: 12.5 t, rear axle weight: 12.5 t) equivalent to the design live load specified in the Specification for Highway Bridges was running in the centre of one side of the two-lane road. From the results, the load on a main girder, where most of the loads are distributed, is placed as a concentrated load (96.7 kN) directly above the hinge. The loading steps were as follows: dead loads were introduced in Step 1 and live loads were loaded in Step 2.

3 ANALYSIS RESULTS OF DETAILED MODEL

3.1 Vertical displacement

The vertical displacement at the underside of the lower flange just below the hinge centre point is indicated by the solid line in Figure-3. The vertical deflections at the final loading

stage are 5.84 mm for Case-0.05, 5.73 mm for Case-0.4, and 5.64 mm for Case-Fixed. This indicates that the deflection tends to decrease as the degree of corrosion increases. However, the differences between the cases are very small, with an error between Case-0.05 and Case-Fixed of only 3.5%. This indicates that the corrosion occurring at the hinge had a small effect on the overall bridge response.

3.2 Principal stress distributions

We focus on the principal stress distribution around the hinge in the final loading phase. The maximum principal stress distribution on web is shown in Figure-4(a). As can be observed, a tensile stress of approximately 70 N/mm² occurs at the notch on the cantilever-girder, which is considered the starting point for fatigue cracks. However, the stress levels at this location did not differ between the cases and remained constant. This is attributed to the web on the cantilever-girder side, which restrains the downward vertical displacement of the flange at the hinge. Because the vertical displacements described in Section 3-1 exhibit small differences between the cases, the stress levels are also expected to have small differences. The direction of the principal stresses was found to be 45° to the bridge axis at the notch on the cantilever-girder. This indicates that the direction of the principal stress is in the direction of the fatigue crack extension in the notch. In conclusion, the tensile stresses occurring in the notches are dependent on their shape, and the influence of corrosion is considered to be small.

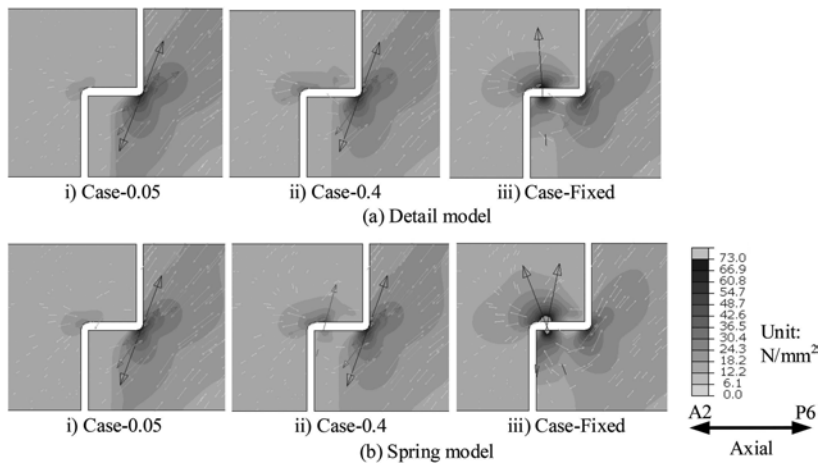


Figure 4. Maximum principal stress in the web.

The minimum principal stress distribution in the web is shown in Figure-5(a). High compressive stresses of approximately 70 and 130 N/mm² occur in Case-0.04 and Case-Fixed, but they are of approximately 30 N/mm² in Case-0.05, near the edge of lower shoe on cantilever-girder. From the vertical displacement of the hinge shown in Figure-6, it is considered that in Case-0.4 and Case-Fixed, the bearing cannot follow the displacement of the girder owing to the large friction coefficient at the contact surface, and the bearing rotates around the end of the cantilever-girder side. The results indicate that fatigue cracks may extend from the flange at the bearing end to the web as the degree of corrosion increases.

4 ANALYSIS RESULTS OF SPRING MODEL

The analytical results of the spring model were compared with the results of the detailed model, and the reproducibility of the spring model was discussed.

4.1 Vertical displacement

The vertical displacement at the lowest point of the web, just below the hinge centre point, is indicated by the dotted line in Figure-2. The vertical deflection at the final load stage is 5.78 mm for Case-0.05, 5.72 mm for Case-0.4, and 5.55 mm for Case-Fixed, which is smaller than that in the detailed model. However, the errors are small, at approximately 1%, 0.2%, and 1.6%, respectively, and the error between Case-0.05 and Case-Fixed is 4.1%, which is approximately equal to the 3.5% error in the detailed model. Thus, it is considered that the spring model reproduces the vertical displacement of the bridge during corrosion.

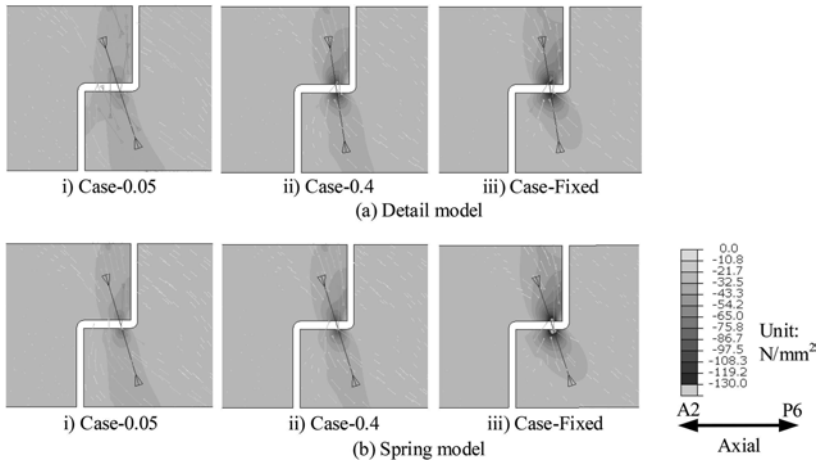


Figure 5. Minimum principal stress in the web.



Figure 6. Vertical displacement of the hinge.

4.2 Principal stress distributions

We focus on the principal stress distribution around the hinge in the final loading phase. The maximum principal stress distribution in the web is shown in Figure-4(b). The maximum principal stress distribution in the notch on the side of the cantilever girder was similar to that of the detailed model in terms of the stress degree, area, and principal stress direction. The tensile stress at the upper shoe end of the web on the suspension girder side is approximately 120 N/mm², that is, 1.6 times higher than that in the detailed model. This occurs because of the large vertical spring constant, which significantly influences the stress level in this area. The hinge is displaced in the vertical direction owing to elastic deformation even when the contact surface is fixed; however, the spring model does not take this effect into account.

Next, focusing on the minimum principal stress distribution in the web shown in Figure-5(b), it can be observed that the large minimum principal stresses occurring the edge of lower shoe on cantilever-girder are larger than those in the detailed model. In Case-0.05 and Case-Fixed, the compressive stress was approximately twice as high. In the detailed model, the flange is gently deformed as the bearing is elastically deformed, whereas in the spring model, the flange is rigidly coupled to the spring introduction node. Thus, the flange deformation is greater in the spring introduction and non-spring introduction areas. This is thought to increase the compressive stress generated.

5 CONCLUSIONS

In this study, an FE analysis was used to determine the effect of changes in the coefficient of friction, which simulates the effects of the corrosion level of the hinge bearing in the form of a BP-A bearing on the vertical deflection, which is one of the overall bridge responses, and on the principal stresses in the surrounding members. In addition, we developed a modelling method using springs to reproduce those effects. The following conclusions were drawn:

- Although the vertical deflection decreased as the degree of corrosion on the hinge contact surface increased, the error between Case-0.05 and Case-Fixed was small (3.5%), indicating that the influence of corrosion was small.
- On the web of the cantilever-girder, a maximum principal stress of approximately 70 N/mm² occurred at the notch, which was the starting point for fatigue cracks. However, the stress level did not vary with the degree of corrosion. This is attributed to the web on the cantilever-girder side restraining the downward vertical displacement of the flange at the hinge.
- In Case-0.4 and Case-Fixed under corrosion, the compressive stresses at the web of the cantilever-girder were found to be 3.5 and 5 times higher than those in Case-0.05, respectively. This is due to the fact that the bearing rotates around the end of the cantilever-girder side because the friction coefficient at the contact surface is too large to follow the displacement of the girder.
- In the spring model, the vertical deflection had a maximum error of 1.6% compared to that in the detailed model, which can be considered highly reproducible.
- In the spring model, focusing on the maximum principal stresses occurring in the notch of the cantilever-girder's web, it was found that the principal stress degree and its directions at the notch, where fatigue cracks start, could be reproduced almost as well as in the detailed model.
- In the spring model, the maximum principal stress distribution at the upper shoe end of the suspension girder's web of Case-Fixed was found to be approximately 1.6 times higher than that in the detailed model. This is because the vertical spring constant in the spring model does not consider the elastic deformation of the hinge.

ACKNOWLEDGEMENT

This work was supported by Grants-in-Aid for Ueda Memorial Foundation.

REFERENCES

- Japan Road Association. 2019. *Road Bridge Bearing Handbook*.: Maruzen Publishing Co.,Ltd.: 100–100
- Parsons Brinckerhoff. 1992. *Bridge inspection and rehabilitation. A practical guide*.: John Wiley & Sons: 280
- Xiaohu Fan & Jason P. McCormick. 2015. Characterisation of the behaviour of steel bridge bearings under cyclic load reversal. *Structure and Infrastructure Engineering* (Volume11 Issue6): 744–760
- Z. Kamaitis. 2001. Behaviour and design of rocker bearings in bridge structures. *Statyba*. (Volume7 Issue3): 207–212
- Yuichiro Niwa, Kentaro Matsumoto, Shuji Yajima & Yusuke Kobayashi. 2018. Reinforcement for fatigue damage of welded joints of sole plate in steel railway composite girder. *Journal of structural engineering* (64A): 421–434
- Koichi Yamamura, Hideaki Deto & Shoji Iwasaki. 2010. About the Influence degree that the Decrease of the Support Function causes for the Stress in the Existing Steel Composite I Girder Bridge. *Journal of structural engineering* (56A):701–709

Damage identification of corroded arch bridge using vibration characteristics and rotational angle

K. Akahoshi, G. Hayashi, Y. Chen & T. Yamaguchi

Department of Civil Engineering, Osaka Metropolitan University, Osaka, Japan

ABSTRACT: Identifying the number and location of damage is an important issue in the vibration health monitoring of bridges. This study aimed to improve the accuracy of damage detection using the natural frequencies utilized in conventional monitoring and the rotational angle of the bridge in the transverse direction. An analytical model was constructed based on a reduced arch model developed by the laboratory group. Damage in the hanger members, stiffening girders, and cross girders of the analytical model was investigated with reference to the corrosion reported for real arch bridges. Two selections were obtained from this damage, and the damage was modeled. Eigenvalue and static analyses were then carried out to investigate the accuracy of damage type and damage location detection based on the natural frequency and rotation displacement changes caused by each damage pattern. The results showed that the natural frequencies of damage at the location where the mode shape is predominant change significantly, and that the natural frequencies that change for each damaged member are different. It was also found that the damage that could not be identified by natural frequencies alone could be detected using the angle of rotation. These results indicate the possibility of classifying damage locations and types when there is more than one type of damage.

1 INTRODUCTION

In Japan, the number of bridges significantly increased during the periods of high economic growth. Consequently, the number of bridges that are 50 or more years is increasing rapidly. Therefore, it is important that these bridges be inspected and repaired. The current inspection methods are mainly visual inspections that require engineers to visit the site. This method is inefficient, and the inspection results are subjective. Therefore, structural health monitoring has attracted attention as an alternative to visual inspection. In particular, vibration-based structural health monitoring (VSHM) is being utilized because the damage and deterioration that are difficult to observe are more likely to appear in vibration characteristics. Once a damage detection method for vibration health monitoring is established, the damage can be detected simply by installing sensors on-site and analyzing the data obtained. Therefore, many studies are being undertaken from various perspectives to improve the accuracy of vibration health monitoring.

Numerous parameters are currently being considered for damage detection. For example, (Morichika et al., 2021) studied the displacement as a bridge response, whereas (Zhou et al., 2022) used mode shapes and natural frequencies to determine the amount of change in values when a real bridge is damaged. (Mustafa et al., 2018) proposed a damping-based damage detection method. (Moughty and Casas, 2017) compared the most detectable energy-based parameters. More recently, parameter identification procedures have been black-boxed and anomaly detection based on acceleration waveforms has also been performed (Shang et al., 2022). Although all the parameters have the potential to detect damage, the relationship between the parameters and damage has not been clarified. In this study, the goal was to detect multiple damages. (Lee et al., 2014) stated that by placing sensors at the damage location, it is possible to detect multiple damages without prior data. However, the possibility of detection depends on the location of the sensor. Therefore, in this study, a single measurement position was selected, and the effect of

damage on the overall response of the bridge was investigated. Based on the above, the parameters that have the potential for multiple damage detection were selected after confirming the effect of each damage on the parameters, and the possibility of detecting them was shown.

The studied bridges were arch bridges. Examples of arch bridge accidents include the Nanfangao Straddling Port Bridge collapse in Taiwan in 2019, and the Rokujutani Water Environment collapse in Japan in 2021. Both were caused by corrosion and rupture of the hangers. Although many studies have been conducted on arch bridges (Wang and Su, 2021), (Maes et al., 2022), the effects of damage at each position of each member have not been clarified. Therefore, this study clarified the effects of damage on the parameters based on the FEM analysis of a steel arch bridge model and showed the possibility of multiple damage detection.

2 FEM ANALYSIS

2.1 Subject bridge

Figure 1 shows the overall view of the bridge model and the number of the damage to be considered (member name + 'a' or 'b' side + damage number). The damage is described in detail in Section 2.5. The model is a 1/15 scale model of a 750 m long Langer arch bridge. The model bridge is a steel arch bridge with a total length of 5000 mm, width of 567 mm, and height of 893 mm. The bridge is composed of arch ribs, stiffening girders, cross girders, hangers, and gusset plates. The steel used was SS400 (JIS G 3101). SS400 has a tensile strength of 400-510 N/mm² and a yield point of 245 N/mm² or more up to a thickness of 16mm. Hangers and arch ribs were connected to the stiffening girders with M10 bolts via gusset plates. The cross-sectional shapes of the members are presented in Table 1.

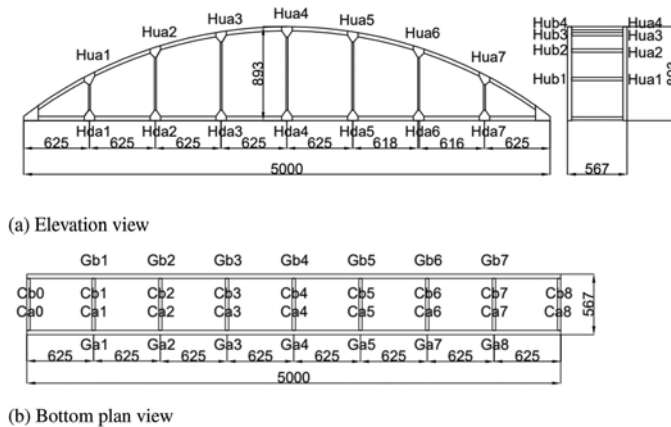


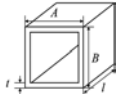

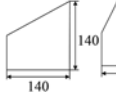
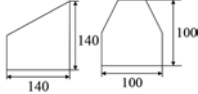
Figure 1. Overall view.

2.2 Analysis model

In this study, to perform damage detection using a simplified model, the entire arch bridge was modeled as a beam element. Figure 2 shows a general view of the analytical model. Each number corresponds to the damage number in Damage Figure 1. The finite analysis software Abaqus/Standard 2022 was used. The overall stiffness was 200000 N/mm², Poisson's ratio was 0.3, density was 77 kN/m³, and total weight was 65 kg. The gusset plates of hangers were represented by increasing the cross section of the beam elements in that area. The stiffness was modified such that the gussets connecting the stiffening girders and arch ribs were taken into account. The gusseted girders were rigidly connected to each other by gusset welds; therefore, the entire bridge was considered to be a single member in the analytical model. In this model, the arch ribs and stiffening girders were divided into 250 sections, the transverse girders into

30 sections, the suspension members into 20 to 40 sections depending on their length, and the damaged sections into 3 sections. The boundary conditions were roller supports at two of the four corners and pin supports at the remaining corners. In Figure 2, the boundary condition is shown only at a point in the foreground.

Table 1. Analysis model.

Element	Size ($A \times B \times t \times l$) (mm)	Cross section
Stiffening girder	$40 \times 40 \times 1.6 \times 5000$	l : Length of damage
Arch rib	$40 \times 40 \times 2.0 \times 5000$	
Cross girder	$30 \times 30 \times 1.6 \times 487$	
Hanger	$16(A) \times 4.5(t)$	
Gusset	$t = 3$	

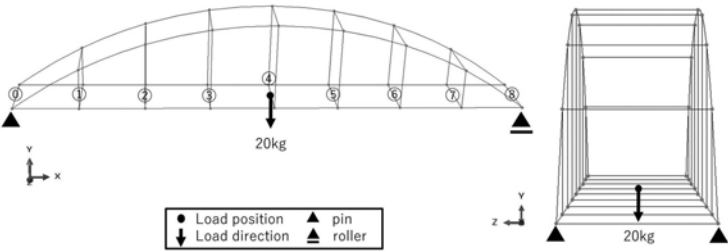


Figure 2. Analysis model.

2.3 Analysis outline

Eigenvalue and static analyses were performed. Eigenvalue analysis was performed at the maximum frequency of 100 Hz. For static analysis, a concentrated load of 20 kg was applied. The positions and directions are shown in Figure 2.

2.4 Parameters

The rotational angle (rotational displacement in the analysis) and natural frequencies, which can be measured with a quartz triaxial accelerometer, were selected as those that can be easily measured on an actual bridge. The measurement points in the analysis were the loading positions shown in Figure 2. As shown in Figure 2, there are rotational displacements in the x-, y-, and z-directions, clockwise about the axes. The natural frequencies of the modes could be measured up to the third bending mode.

2.5 Damages

The damage was assumed to be localized corrosion of the hanger and internal corrosion at each point of the cross girder and stiffening girder. In these places, the damage is difficult to

confirm, in accordance with the report on the falling-arch bridge accident mentioned earlier and the periodic inspection guidelines for road bridges. Figure 1 shows the damage locations and numbers. Each damage was modeled by making the cross section of the damaged section deficient. Damage levels consisting of 25%, 50%, and 75% reductions in the plate thickness were assumed. The analysis cases are listed in Table 2. First, three analyses were conducted for each of the three damage levels, as shown in Figure 1, for a single damage location. Next, 10 locations were selected such that each member had three or four damage levels, and two damage levels were selected from the 10 locations. The degree of damage was set to nine levels such that each member had three levels of damage.

Table 2. Analysis case.

	Damage type	combination	degree	case
Singledamage	60	60	3	180
Double damage	10	78	Damage1:3 Damage2:3 3×3=9	708

3 ANALYSIS RESULTS

To determine the effect of each damage on the parameters, we first considered the case of a single damage.

3.1 Natural frequency

Figure 3 shows the horizontal and bending mode shapes obtained from this analysis. Although the mode shapes were not used as parameters, a comparison of the natural frequencies showed that they are based on mode shapes. We obtained the first and second horizontal modes, first and second torsional modes, and first, second, and third bending modes, with the third bending mode as the maximum frequency. Next, considering the change in natural frequencies when each type of damage occurs, it was found that for each member, there was a natural frequency that tended to change when the member was damaged. Cross girders had first and second horizontal modes, and the hangers had first and second bending modes. No independent natural frequencies were observed for the stiffening girders; however, the bending mode showed a greater change than that in the other members.

Figure 4 shows the change in natural frequencies of the (a) first horizontal mode, (b) second horizontal mode, (c) first bending mode, (d) second bending mode, and (e) third bending mode when each damage occurred. The horizontal axis represents the damage number shown in Figure 1 and 2, which indicates the location of the damage. The plot line is different for each damaged member, and the shape of each member is shown in the legend. The vertical axis represents the difference in vibration frequencies between the healthy and damaged members. First, as shown in (a), we can see that the change is larger when the cross-girder is damaged. Damage numbers 0 and 8 are particularly significant, and the mode shape is that of the girder with 0 and 8 as nodes, indicating that the oscillation in this mode depends significantly on the stiffness of the girder. The mode shapes of the girders at other damage numbers also changed more than those of the other members. Overall, the contribution of transverse girders to this mode was high. Similarly, as shown in (b), the dominant position is different from that of the first mode, and the damage numbers 1, 2, 6, and 7 are dominant. In the second bending mode shown in (c), the hanger mode is dominant in both the upper and lower modes. Damage number 4 is dominant, but the mode shape shows that the node is located at the center of the span. This mode is highly dependent on the stiffness of the suspension. As shown in (d), the change in the mode shape is also significant when the hanger is damaged, but the effect of the damage to the stiffening girder is slight. As shown in (e), the change in both the stiffening girder and hanger is significant, but the mode shape oscillates when the dominant part is a node.

From the above, it can be said that each member has a dominant mode and the change is the greatest at the nodal point. In addition, because there are two dominant frequencies for the cross girder and hanger, and because the dominant feature values are opposite, the two frequencies can be used together to facilitate classification. In terms of damage detection, it is possible to determine the damaged member; however, considering the symmetry and the fact that the values are the same on the a and b sides, other indices are necessary.

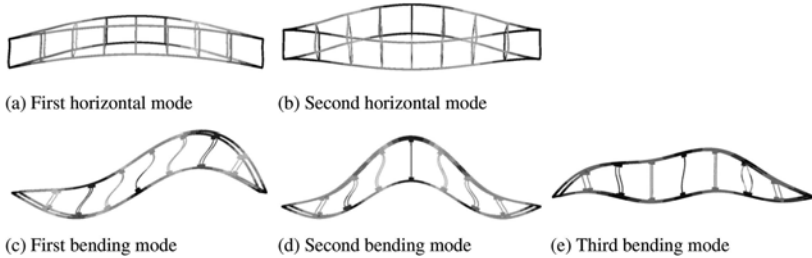


Figure 3. Mode shapes.

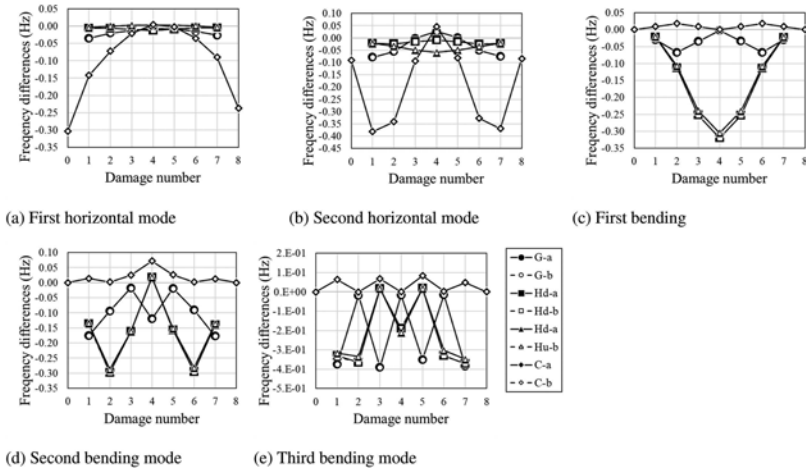


Figure 4. Relationship between damaged areas and natural frequencies.

3.2 Rotational displacement

Similarly, Figure 5 shows a comparison of the rotational displacement values along the vertical axes. The x-, y-, and z-axes are used as the centers of rotation in (a), (b), and (c), respectively. As shown in (a), the difference between the a and b sides, which did not appear in the other parameters, is evident. This is because the center rotates in the direction of the damage. The rotation angle in the x-direction coincides with the change in displacement, indicating that the rotation angle also increases as the load-bearing capacity decreases. As depicted in (b), the differences between the left and right sides and between the a and b sides are significant. The reason for the large difference between the left and right sides of the stiffening girders is considered to be the roller support provided to stiffening girder number 8, which reduces the damage effect. The large influence of the hanger, which rotates in the opposite direction of the corrosion, is shown in (c). The z-axis can be used to distinguish between the left and right sides. The above results indicate that the rotational displacement is used to determine whether the damage is in the degree position, because it is tilted toward the direction of the damage. Rotational displacement can be used as an indicator to determine the position of the damage level.

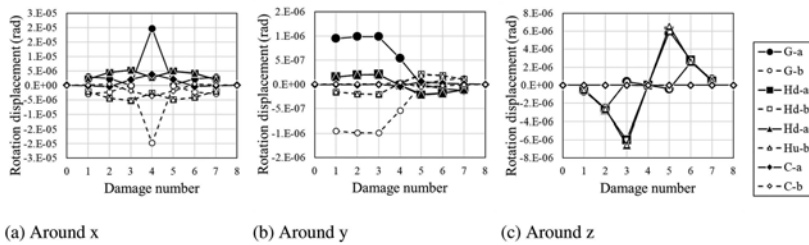


Figure 5. Relationship between damaged areas and rotational displacement.

3.3 Difference by damage level

Figure 6 shows a three-dimensional space in which the dominant mode for each material is selected. The origin indicates the healthy state. Part (a) in of the figure shows the natural frequency parameters, which are the most likely to detect damage, for three different degrees of damage. Only the damage from 1 to 4 on the a side is considered. Because there is little difference between the top and bottom of the suspension, only damage on the bottom side is represented. The values for different damage levels are plotted as ●-25%, + -50%, and ◊-75%, and a straight line connecting the 75% damage level and the healthy level is also drawn. The change in the degree of damage appears almost on a straight line.

However, a closer look reveals that this change appears on a curve that is very close to a straight line.

Part (b) shows the difference when the damage degree of Ha3, which varies greatly, is finely changed. The change in value appears in the form of a certain curve. The numbers next to the plot indicate the plate thickness. Considering the equation of motion, the natural frequency can be expressed as the square root of stiffness and mass. When the damaged stiffness changes in stages, the natural frequency can be expressed as a function of stiffness. Therefore, the change in the damage phase can be considered to be quadratic.

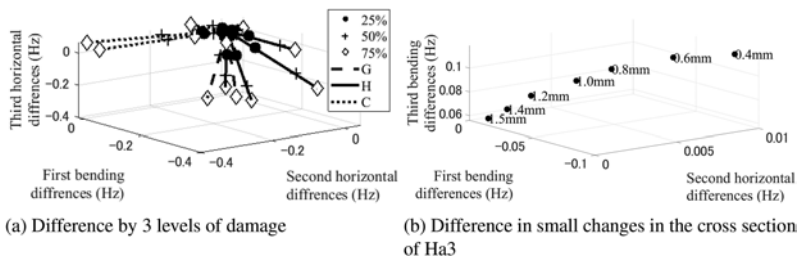


Figure 6. Difference in natural frequencies of the three modes at varying degrees of damage.

3.4 Multiple damage

The change in the values in the case of multiple damages was considered. The dominant frequencies in each member are considered to be the second horizontal mode, the first bending mode, and the third bending mode. As shown in Figure 7 (a), the horizontal axis is the second horizontal mode and the vertical axis is the second bending mode; as depicted in (b), the horizontal axis is the first bending mode and the vertical axis is the third bending mode; and, as shown in (c), the horizontal axis is the second bending mode and the vertical axis is the third bending mode. The shape of each plot depends on the combination of members, as shown in the legend. Among the analyzed cases, only the cases related to suspension members are shown. For example, the triangles represent damage to the hangers and stiffening girder, which indicates that the damage can be plotted as a single overlaid damage, and that there is cohesiveness among the damaged components. Damage that is difficult to classify in (a) can be classified to a certain extent in (b) and (c). However, as shown in Figure 4, it is difficult to distinguish stiffening girders from hangers.

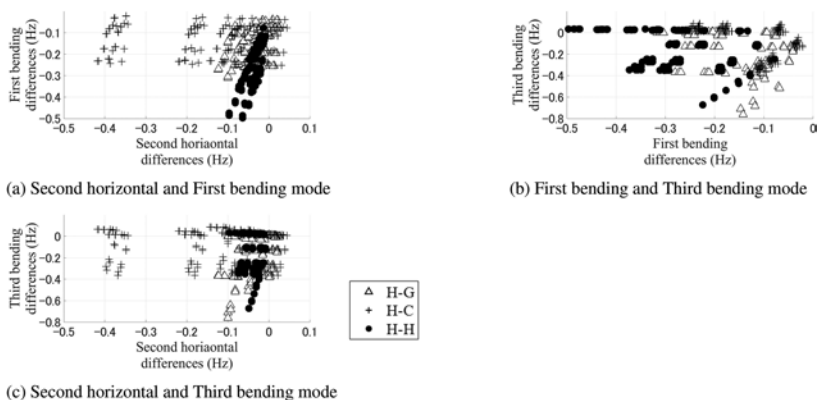


Figure 7. Multiple damage using two natural frequencies.

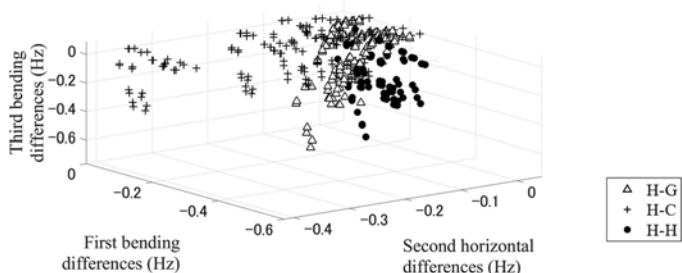


Figure 8. Multiple damage using three natural frequencies.

Based on the above, multiple damage values are plotted in a three-dimensional space with three modes along the axes (Figure 8), where the x-axis represents the second horizontal mode, the y-axis represents the first bending mode, and the z-axis represents the third bending mode. The shapes of the plots are different for each combination of members, as shown in Figure 7. This figure shows that the damage is grouped by shape, and that it is possible to distinguish the damaged components. In addition, for each damage combination, a plane appears on which the curves described in Section 3.3 are added, and the different damage stages are indicated on the plane. By looking at the plotted locations, it is possible to understand the damaged member and location of the damage to some extent.

By examining these planes and plotted locations, the damaged member and location of the damage can be determined to some extent. Furthermore, the location of the damage within the same member can be determined more accurately by comparing the values of the two dominant frequencies for each member, as described in Section 3.1. Furthermore, as described in Section 3.2, the rotational displacement can be used to identify damage on the left or right side, or on the a or b side. The combination of rotational displacement and natural frequency can be used for more accurate damage detection for stiffening girders and damage locations that are difficult to detect on only one side of the girder, and it is also possible to determine whether the damage is single or multiple. For example, if the eigenvalues are calculated in advance using an analytical model, the location of the damaged member can be plotted in space, as shown in Figure 8, and the detailed location can be found by examining the two frequencies and rotational displacements at which the damaged member is dominant.

4 CONCLUSION

In this study, we confirmed how the damaged member and its location affect the parameters for damage detection and then examined how the parameters should be appropriately used for multiple damage detection. The conclusions are as follows.

- The influence of each damage on rotation angle and natural frequency is based on its shape, and the nodal point is dominant in taking that shape. Thus, there is a dominant mode in the natural frequency for each member.
- As certain curves appear when the degree of damage is varied, it is possible to predict the values for other degrees of damage if some values are obtained in advance.
- The damaged member can be identified based on the significant change in natural frequency, and its location can be determined from the natural frequency and rotation angle that prevail when the member is damaged. Using this method, there is a possibility of multiple damage detection.

Additional issues include determining the actual number of damages that can be detected using machine learning, and to what extent the trends in this study will be apparent when the actual values are measured. In addition, damage detection requires the prediction of the values in advance, and the model must be effectively updated to predict the values with good accuracy.

ACKNOWLEDGEMENT

This research was supported by the JFE 21st Century Foundation Technical Research Grant Steel Technology Research.

REFERENCES

- Lee, S. G., G. J. Yun, and S. Shang (2014). Reference-free damage detection for truss bridge structures by continuous relative wavelet entropy method. *Structural Health Monitoring* 13(3), 307–320.
- Maes, K., L. Van Meerbeek, E. Reynders, and G. Lombaert (2022). Validation of vibration-based structural health monitoring on retrofitted railway bridge kw51. *Mechanical Systems and Signal Processing* 165, 108380.
- Morichika, S., H. Sekiya, Y. Zhu, S. Hirano, and O. Maruyama (2021). Estimation of displacement response in steel plate girder bridge using a single mems accelerometer. *IEEE Sensors Journal* 21(6), 8204–8208.
- Moughty, J. J. and J. R. Casas (2017). Performance assessment of vibration parameters as damage indicators for bridge structures under ambient excitation. *Procedia Engineering* 199, 1970–1975. X International Conference on Structural Dynamics, EUROLYN 2017.
- Mustafa, S., Y. Matsumoto, and H. Yamaguchi (2018). Vibration-based health monitoring of an existing truss bridge using energy-based damping evaluation. *Journal of Bridge Engineering* 23(1), 04017114.
- Shang, Z., G. Xin, Y. Xia, and L. Sun (2022). A multi-label classification method for anomaly detection of bridge structural health monitoring data. pp. 1280–1287.
- Wang, W. and M. Su (2021). Damage identification in hangers of through-arch bridges using static deflection difference at the anchorage point. *Applied Sciences* 11(22).
- Zhou, X., C.-W. Kim, F.-L. Zhang, and K.-C. Chang (2022). Vibration-based bayesian model updating of an actual steel truss bridge subjected to incremental damage. *Engineering Structures* 260, 114226.

Identification of spalling in concrete structures by a hammering test using autoencoder

Hisao Emoto & Nobuki Fukui

Social Systems and Civil Engineering, Tottori University, Tottori-City, Japan

Yuto Iitaka

Industrial Technology and Systems Engineering, Fukushima College, Iwaki-City, Japan

Shin-ichi Kanazawa

Civil Engineering Program, Faculty of Engineering, Niigata University, Niigata-City, Japan

ABSTRACT: Visual inspection of bridges is important to maintain the sustainability of civil infrastructure. A hammering test is one of the non-destructive and verified methods used for this purpose, by which an expert inspector identifies spalling inside a concrete structure. The reliability of this method depends on the technique of the inspector. However, Japan society faces the problem of a scarcity of labor across all fields. Because of this, there are few training opportunities for new inspectors to learn the technique. This study aims to identify spalling concrete by using an autoencoder, instead of professional inspectors. First, a spalled concrete specimen was used to record the hammering sounds. The experimental method and a comparison of frequency spectra at each level of damage were described. Next, the autoencoder was applied to identify spalling concrete, and a comparison of the identification precision at each damage level was conducted. The results of the analysis show that spalling concrete can be identified by autoencoder to a concrete thickness of less than 30 mm.

1 INTRODUCTION

In Japan, civil infrastructure works, such as bridges, are needed for a sustainable society. To maintain vital bridge infrastructure, visual inspection is typically needed every 5 years per Japanese government policy. A hammering test is one of the most reliable, non-destructive methods used by expert inspectors to identify spalling inside of concrete. A weakness of this method, however, is that it relies on the technical expertise of inspectors. Exacerbating this, Japan faces a social problem of scarce labor across all fields due to a low birthrate and a retired labor demographic. Added to this are Japanese social goals of changing working culture to balance work and life. To resolve these problems, the Japanese government aims to realize a Society 5.0 era in which cyberspace and physical space are highly integrated. For example, the Ministry of Land, Infrastructure, Transport and Tourism plans to change working life and improve production efficiency through i-Construction.

Towards these efforts, this study aims to identify spalling concrete by using an autoencoder instead of professional inspectors. For this work, an autoencoder was developed using a neural network for the reconstruction of input data by compressing dimensional algorithms. For the experimental portion of the study, a spalling concrete specimen was first produced for the hammering test. The size of this specimen was $1500 \times 1200 \times 600$ (mm). The test was run by hammering the center point of each 50 mm mesh about 10 times, while collecting the frequency spectra of each damage area. Next, an autoencoder was used to identify spalling concrete for damaged or non-damaged specimens. Input and output data represented the damage level feature of each frequency spectrum between 10 Hz until 10,000 Hz. The autoencoder output data was reconstructed using the input data. When the correct model was used, the input value should be the

same as the output data. If the output value is different from the input value, this indicates spalling concrete (a damage condition). This different value is quantified as the reconstruction error (the mean squared error). A real bridge world does not provide the damaged concrete condition for autoencoder model learning, because when a damaged concrete condition is found, the bridge manager needs to repair it. Because of this, non-damaged data is used for autoencoder model learning. A comparison of the precision of identification of each damage level is described. The damage level is fundamentally based on the thickness of the covering concrete and the size of the spalling material. Finally, this study found the optimal parameters to identify spalling concrete by autoencoder as a thickness of covering concrete of less than 30 mm.

2 OUTLINE OF A HAMMERING TEST

A hammering test is a concrete bridge inspection method that detects the presence or absence of a damage condition from differences in the hammering sound (MLIT 2016). Types of damage conditions include spalling due to the cracks and corrosion of reinforcing bars in the concrete and poor adhesion of cement. In the hammering test shown in Figure 1, a hammering sound is used by an expert inspector to judge the concrete damage level. If the hammering sound is clear and dry, spalling is not indicated, and if the sound is dull, spalling is indicated. Spalling concrete needs to be repaired immediately when detected by the hammering sound. In addition, deterioration aging and leaking rainwater may cause internal abnormalities that cannot be seen. These areas of damage must also be removed because they affect the safety of the structure and the aesthetic appearance of the outer wall.

The hammering test is also a standard inspection method in the road bridge inspection guidelines for detecting the spalling of concrete, loose bolts, damage to repair/reinforcing materials, and abnormalities in anchorages (MLIT 2019).

However, a hammering test is based on the subjective senses (hearing) of the inspector to detect the presence or absence of a damage from the different hammering sounds. Therefore, the inspector's experience and skill are required, and the inspection results may differ depending on the inspector. Furthermore, there are cases in which even an expert engineer cannot clearly judge the damaged conditions by hearing. Finally, with this method there is no objective assignment of value for the level of damaged and undamaged conditions. Because the data is subjective and qualitative based on the hearing of the inspector, it is impossible to continuously store bridge damage assessment data and evaluation.

Recently, the Japanese government recommended changing society's working style in an initiative called Society 5.0. To meet this goal and increase production efficiency, infrastructure damage inspection should become more automated by robots. To automate the bridge inspections, the hammering test first needs to be quantified.

3 TEST SPECIMENS AND EXPERIMENTAL METHODS

3.1 *Design of the damaged test specimens*

This study aims to clarify how to identify real-world hammering sounds by autoencoder. For this, we used a spalling concrete specimen with known characteristics, such as the thickness of concrete cover, and damage condition, such as the length, thickness, and location of spalling.



Figure 1. Example of a hammering test at spalling concrete in a damaged specimen.

The spalling concrete specimen's properties are shown in Figure 2 and Table 1. The size of the spalling concrete specimen is $1500 \times 600 \times 1200$ mm with locations of spalling damage shown in Figure 3. The damage locations were determined by the air gap located inside existing spalling concrete, referred to as the spalling material. The air gap was represented by NR sponge rubber. The specimen was set up with concrete spalling on each side of the specimen. A wide specimen was utilized (600 mm) so that locations of damage did not affect the hammering sound or vibration on each side. Table 1 shows the material specimen, where the spalling material used was NR sponge rubber. The planar shape of the spalling material was a square, with sides of 100 mm, 150 mm, and 200 mm. The thickness of the spalling concrete material was 5 mm, 10 mm, and 20 mm. The thickness of the covering concrete was 30 mm, 60 mm, 90 mm, and 150 mm.

The main factor which ordinarily causes spalling in concrete is the expansion due to rebar corrosion in concrete. In this study, the thickness of covering concrete was determined by the minimum thickness based on road bridge specifications (Japan Road Association 2019). A thickness of 30 mm was set from the minimum cover of reinforcing bars in the beam. A thickness of 60 mm was set from the minimum cover to prevent corrosion of steel materials in areas affected by chloride induced deterioration damage (countermeasure categories II and III). Similarly, a thickness of 90 mm was set from the minimum cover to prevent corrosion of steel materials in areas where the effects of chloride induced deterioration are severe (countermeasure category S). In addition, a thickness of 150 mm was set for cases where the spalling concrete occurs along the main rebar.

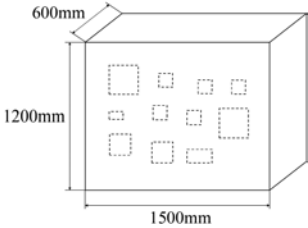
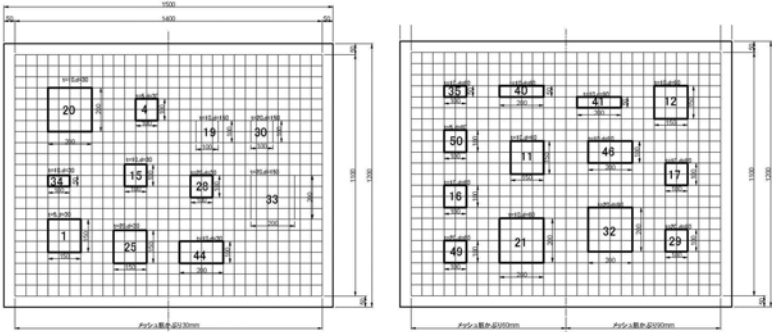


Figure 2. Dimensions and locations of spalling damage in a concrete specimen.

Table 1. Properties of the damaged concrete specimen.

Property	Value
Dimension	$1500 \times 600 \times 1200$ mm
Type of concrete	Ordinary concrete
Design reference strength	24 N/mm^2
Main rebar	SD-345 D16
Distributing rebar	SD345 D13
Thickness of covering concrete	150 mm



(a) Thickness of covering concrete at 30 mm (b) Thickness of covering concrete at 60 mm and 90 mm (bold rectangle) and at 150 mm

Figure 3. Location of damaged areas (spalling concrete).

3.2 Experimental method and conditions

In this study, a hammering sound was recorded through an audio interface using a condenser microphone. The hammering point was the center of a 50 mm square mesh in each spalling concrete specimen. The method of evaluating the hammering sound data used the average spectrum of ten hammering sounds per mesh.

The main part of the hammering sound was processed by a computer program from the input time-sound pressure signal. Device details and specification are provided in Figure 4 and Table 2. The recording conditions are presented in Table 3. Recording time was 100 msec, which includes 3 msec before the peak amplitude and 97 msec after the peak. A time of 97 msec was enough to converge amplitude waves, as shown in Figure 5. Sampling frequency was 44,100 Hz, based on the audible frequency band. Generally, the audible frequency band of a healthy young person is between 20 Hz to 20,000 Hz (MOE 2019). In addition, in order to record and quantify sound waves, which are continuous signals, it is necessary to collect (sampling and quantizing) discrete signals by measuring the sound waves at regular intervals.

At this time, sound waves with a frequency higher than the Nyquist frequency (a frequency equivalent to 1/2 of the sampling frequency) cause a phenomenon of aliasing when sampling, and are not faithfully reproduced as the original signal during playback (sampling theorem). Therefore, in order to record sound waves up to 20,000 Hz, which is the limit of human hearing, it is necessary to record at a sampling frequency of 40,000 Hz or higher, which is twice the Nyquist frequency. From this, we recorded the hammering sound at 44.1 kHz, which is more than 40,000 Hz, is widely used for general application, and is compatible with the audio interface used in this research. The sound pressure of the hammering sound input from the microphone varies greatly depending on the strength of the hammering, the distance between the hammering position and the microphone, and the input sensitivity of the audio interface. Because the hammering test is performed manually, it is not always possible to hammer with the same strength. Additionally, this research assumes that the hammering sound is input by holding a condenser microphone in the hand opposite to the hand holding the hammer, so the distance between the hammering position and the microphone is not constant. Therefore, to reduce the differences in sound pressure caused by these factors, all hammering sound data were divided by the maximum amplitude of each hammering sound data, with the maximum amplitude of “1” used for normalization.



Figure 4. Setup of the sound recording devices.

Table 2. Sound recording device details.

Device name	Type	Detail	
Unidirectional microphone	SYNCO Mic-D2	Frequency Response	20 Hz – 20 kHz
		Sensitivity	-32 dB ± 3 dB
		Max. Input SPL	130 dB
		Signal to Noise Ratio	80 dB
		Dynamic Range	117 dB
Audio interface	behringer U-PHORIA UMC202HD	Frequency response	10 Hz – 60 kHz
		Impedance	3kΩ
		Max. input level	-4 dBu
		Supported sample rates	44.1/48/88.2/96/176.4/192 kHz

Table 3. Parameter condition.

Type	Value
Number of Chanel	1 (mono recoding)
Length of recoding	100 msec
Sampling rate	44,100 Hz
Bit	16 bits

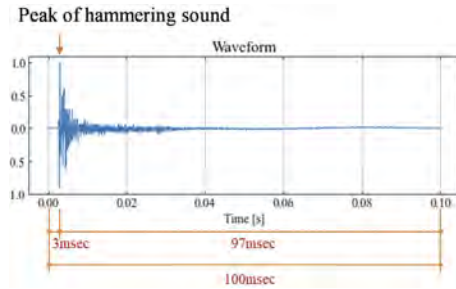


Figure 5. Graph of hammering sound amplitude and length of the recording data.

3.3 Comparison of spectra for each damage level

To confirm only the effect of the “thickness of covering concrete” on the frequency spectrum of the hammering sound for spalling concrete, we compared spalling conditions that had the same shape and thickness of spalling material. Figure 6 shows the frequency spectrum of the non-damaged part of the specimen and the frequency spectrum used for the study of the “thickness of covering concrete” of the spalling. The spalling conditions filled in with the same color in the “No.” column have the same spalling shape and thickness. In Figure 6, the frequency spectrum of the defective part of the specimen shows a different outline than the frequency spectrum of the sound part of the specimen when the thickness of covering concrete was shallower (the length of one side of the spalling was larger). In particular, there was a noticeable difference between the spectra No. 20 and No. 21. Spectra No. 11, No. 12, No. 28, No. 49 and No. 29 were similar to the frequency spectrum of the healthy part of the specimen, as the thickness of covering concrete was larger. The above results show that identification of spalling concrete is easier with a thinner thickness of covering concrete.

We further examined the effect of the size of the spalling concrete. By comparing the difference in the frequency spectrum depending on the condition of the spalling material, it was found that the effect of the thickness of the spalling material on the frequency spectrum was less pronounced.

The “thickness of covering concrete” and “size of the spalling material” represent most of the differences in the frequency spectrum. This is likely due to the fact that only the spalling concrete vibrates with hammering, and the impact force is not transmitted beyond a certain thickness depth.

Therefore, the examination of the applicability of the autoencoder to the hammering test in this study was conducted for the “thickness of covering concrete” and “size of the spalling material”.

4 APPLICATION OF AUTOENCODER FOR DETECTING SPALLING CONCRETE

4.1 Outline of an autoencoder

An autoencoder (Geoffrey E. 2006) is a type of neural network for the reconstruction of input data by compressing dimensional algorithms. This model is shown in Figure 7.

In neural networks, the expressive power of the network is usually enhanced by setting more neurons in the hidden layer than in the input and output layers. On the other hand, an autoencoder constructs a neural network by reducing the number of neurons in the hidden layer relative to the input and output layers. When it is learning in this state, the input data were compressed between the input layer and the hidden layer, and restored between the hidden layer and the output layer. This compression process is called encoding, and the reconstruction process is called decoding. By training the input layer and the output layer with the same data, a generative model that can reconstruct the input data in the output layer can be decoded. If the input value is equal to the output value, it can be determined that the data compressed by the middle (hidden) layer represents the features of the data. This type of autoencoder algorithm is called dimensionality reduction.

4.2 Application of an autoencoder for detecting spalling concrete

Anomaly detection through dimensionality reduction is based on the premise that it is possible to transfer the dimensionality-reduced feature values to a space in which normal data and abnormal data are distributed in separate regions (Chandola 2009).

In this study, the hammering sound data have values in each frequency band, with generally hundreds to thousands of feature values. However, bridge inspection engineers can identify anomalies despite hearing thousands of feature values. In other words, the sound can be classified as normal and abnormal values based on reducing the data to a low-dimensional vector, removing thousands of redundant feature values. Therefore, in this research, we attempted anomaly detection by dimensionality reduction using an autoencoder.

When the autoencoder is trained only on normal data, the trained model becomes a generative model that reproduces normal data from the input data. When abnormal data are input to this model, the autoencoder performs fragile reconstruction because it has not learned the abnormal data, and outputs features close to normal data. Here, the mean squared error (MSE) of the input and the output is the error of reconstruction. MSE is a minimum value if input data are normal. This means the input and output data are roughly equal. On the other hand, MSE is a maximum value if input data are abnormal. This means the input and output data are quite different values. In this study, the autoencoder can identify hammering sound differences due to setting a threshold value for the MSE (reconstruction error).

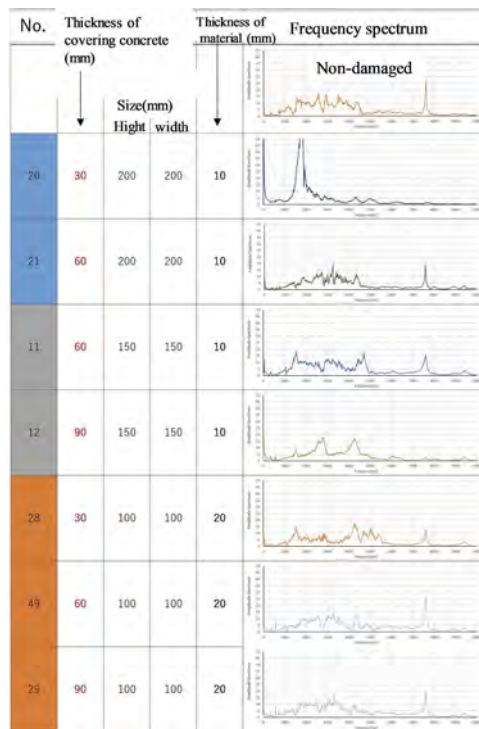


Figure 6. List of frequency spectrum for spalling concrete damage areas by the “thickness of covering concrete” and size of spalling condition.

4.3 Results of identifying spalling concrete using damaged specimens

Hammering sound data were recording from a point at each 50 mm mesh in the damaged specimen, as shown in Figure 3. In this figure, “d” is thickness of the covering concrete and “t” is the thickness of the spalling material. The center of each mesh was hammered 10 times. The

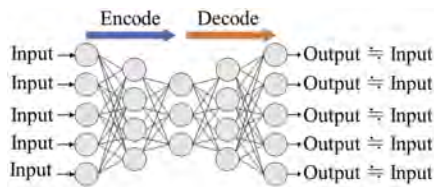


Figure 7. Model of an autoencoder.

parameters of the hammering sound data are shown in Table 4. The parameters of the autoencoder for identifying the hammering sound are shown in Table 5.

The results of identifying spalling concrete by autoencoder are shown in Figure 8 (the training data set is sample1). The identification results in Figure 8 are represented by the MSE value (reconstruction error) for each mesh as detected by the autoencoder. A threshold value of reconstruction error for identifying normal and abnormal was set to “10”. The areas marked in red in Figure 8 are the areas identified as abnormal.

As a result, spalling concrete could be identified with any learning data set (sample 1 to sample 3). The spalling concrete was identified with thicknesses of covering concrete less than 30 mm and length of a spalling material more than 150 mm.

However, the autoencoder couldn't identify spalling concrete at thicknesses of covering concrete of more than 60 mm. This is because the frequency spectrum of hammering becomes similar with a deeper thickness of covering concrete or a smaller area of spalling, which results in a reconstruction error value too small for detection through the autoencoder method in this study.

The above results determine that the applicable range of hammering sound identification by autoencoder for these trials is at thicknesses of covering concrete of less than 30 mm and a spalling size of more than 150 mm × 150 mm.

Table 4. Outline of the hammering sound data for inspection of the damaged specimen.

Number of learning data	normal (non-damaged) hammering sound 10 times by repeating (3 patterns: sample 1, sample 2, sample 3)
Number of test data	1040 (normal 864, abnormal 176)
Range of frequency	0-10,000 Hz
Resolution of frequency	10 Hz
Number of features	1000

Table 5. Parameters of the autoencoder used to identify the hammering sound.

Number of units	Input layer	1000
	Hidden layer 1	16
	Hidden layer 2	4
	Hidden layer 3	16
	Output layer	1000
Activation function	Hidden layer	ReLU function
	Output layer	Identity function
Loss function		Mean squared error
Optimal algorithms		Adam
Learning rate		0.001
Learning rate decay		0.001
Batch size		1
Number of epochs		200
Adding noise rate at input layer		0.1

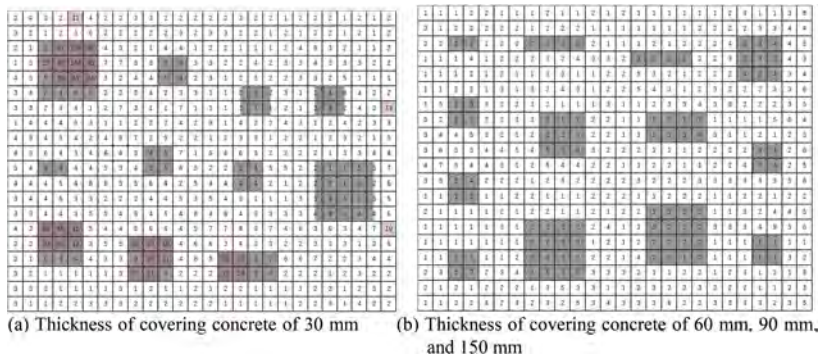


Figure 8. Results of identifying spalling concrete by autoencoder (training data: sample 1).

5 CONCLUSIONS

In this paper, we attempted to identify spalling concrete by autoencoder. A spalling concrete specimen was made $1500 \times 600 \times 1200$ mm in size, and hammering sound data were recorded as training datasets. Recorded sound data were converted to frequency spectra for each sample point. Then, the data features for each damage level were described by a comparison of frequency spectra. Autoencoder learned by using non-damaged hammering sound data. If output data were different from input data, spalling concrete could be detected due to reconstruction error value (the mean squared error), with a threshold value for identifying damage condition set to a reconstruction error of 10. In this research, the autoencoder could identify damage conditions for a thickness of covering concrete less than 30 mm and a spalling size of more than $150 \text{ mm} \times 150 \text{ mm}$. In the future, methods are needed to identify damage at deeper thicknesses of covering concrete.

ACKNOWLEDGEMENTS

This paper would not have been possible without the contributions of many Fukushima college students and civil engineers. We would like to thank the FUJI P.S CORPORATION for making the specimen. We also summarized a part of Mr. Yasutaka BABA's advanced course thesis at Fukushima college in this paper.

REFERENCES

- MLIT (Ministry of Land, Infrastructure, Transport and Tourism) (2016), Third party damage preventive measures for bridges, <https://www.pwri.go.jp/caesar/manual/pdf/daisansya_youryou_2016.pdf>, (accessed 2022.11.30)
- MLIT (Ministry of Land, Infrastructure, Transport and Tourism) (2019), Road bridge inspection guidelines, <https://www.mlit.go.jp/road/sisaku/yobohozen/tenken/yobo4_1.pdf>, (accessed 2022.11.30)
- MOE (Ministry of the Environment) (2019), About a mechanism of low frequency sound, <<https://www.env.go.jp/air/teishuuhaon1zenntai.pdf>>, (accessed 2022.11.30)
- Japan Road Association (2019), Specifications and commentary for Road Bridges (IV substructure), Maruzen Publishing Co., Ltd., p. 71, 86.
- Geoffrey E. Hinton; R. R. Salakhutdinov (2006), "Reducing the Dimensionality of Data with Neural Networks", Science, Vol. 313, pp. 504–507.
- Chandola, V., Banerjee, A. and Kumar, V. (2009), Anomaly Detection: A Survey, ACM Computing Surveys, Vol. 41, Issue3, Article 15, 2009.7

Corrosion progress detection in steel bridge from vehicle-mounted camera images based on deep learning

S. Ozaki & Y. Nomura

Ritsumeikan University, Kusatsu, Japan

H. Furuta

Osaka Metropolitan University, Osaka, Japan

H. Yamazaki & Y. Yamato

Kanko Co., Ltd., Osaka, Japan

ABSTRACT: In recent years, the structural integrity of social infrastructures has become a concern as they age, and how to efficiently and accurately assess their structural integrity is important in developing maintenance management plans. In this study, we aim to save time and labor by automating the evaluation of corrosion progress using machine learning. Specifically, we will investigate whether it is possible to detect corrosion based on deep learning using images of monorail bridges taken from an on-board camera, and then evaluate the progress of corrosion using images taken at the different inspection time.

1 INTRODUCTION

In recent years, the structural integrity of aging and unsafe social infrastructure has become a major concern, and how to assess structural integrity effectively and accurately has become an essential part of maintenance planning. 2015 saw the revision of Japan's Road Act, which requires that bridges with a span of 2.0 m or more be visually inspected in close quarters once every 5 years. The new law requires a close visual inspection once every 5 years for bridges with a span of 2m or more. Currently, these bridges are visually inspected by specialized engineers. However, in anticipation of a future shortage of engineers due to a declining population, it is important to establish a labor-saving system for inspections while assuring the accuracy of inspections by skilled engineers.

In a previous study by Nakamura et al. 2021, a learning model for a corrosion detector of steel bridges using CNN as a machine learning method was constructed using photos of the condition of road bridge inspection results conducted by Fukushima Prefecture as training data. The learning model was constructed using the cross-validation method and the results of a field survey of actual bridges in the Kitakata area as test data to evaluate generalization performance. However, no progress evaluation was conducted, and we believe that the model is not suitable for judging the priority of repair locations. In this study, we aim to save time and labor by automating the evaluation of corrosion progress using machine learning. Specifically, we will investigate whether it is possible to detect corrosion based on deep learning using images of monorail bridges taken from an on-board camera, and then evaluate the progress of corrosion using images taken before and after the progress of corrosion.

2 SYSTEM FLOWCHART

Figure 1 shows the two-stage evaluation system flow including object detection (YOLOv5) and additive mixture of color method in this study. First, YOLOv5, which was trained using teacher data, is used to detect corroded areas in the 2021 image, and a rectangle is displayed in the corroded area. The images with corroded areas are narrowed down to those with a uniform angle of view between the images captured in 2020 and 2021. After that, the additive mixture of color method is applied to evaluate whether the corrosion has progressed.

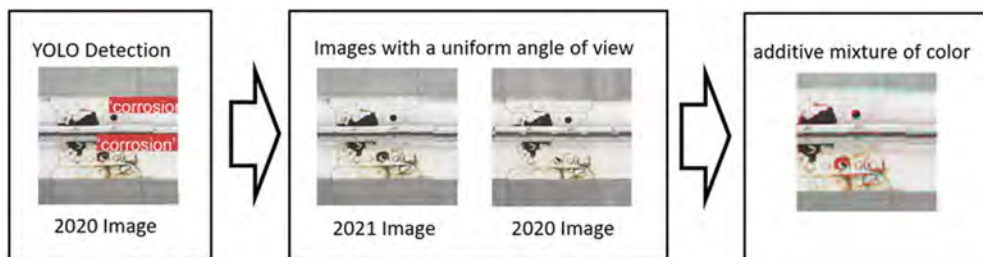


Figure 1. System overview.

2.1 YOLOv5

The structural surface damage screening technology in this study is based on general object detection using deep learning, and YOLO is used as the detection method. The most important feature of YOLO in object detection is that it extracts candidate regions of the target object and simultaneously calculates the class probability of those candidate regions in a single guess. This allows for very fast and real-time object detection, even for video images. YOLO is one of the fastest general object detection systems proposed so far, but YOLOv2 and YOLOv5 have also been more accurate detection tools. These, like YOLO, are offered as part of Darknet. In this study, the fastest detection method, YOLOv5, is used; the inference flow of the YOLO system is shown below. The network structure of YOLOv5 used in this study is shown in Figure 4, and is roughly divided into three parts: Backbone, Neck, and Head. Backbone creates feature maps for each image through convolutional operations. In Figure 2, CBL refers to Conv2D, BatchNormal, and LeakyRELU. CSPNet (Cross Stage Partial Network, Wang et al. 2020) is used for feature extraction by performing convolution on a portion of the feature map and concatenating the remaining portions. By adjusting the width and depth of the BottleneckCSP, there are four weights of the learned model in YOLOv5: s , m , l , and x . The weights of the learned model are then used as the weights of the SSP (Spatial Space Profiler). Then, in the SPP (Spatial Pyramid Pooling, He et al. 2014) layer, the extracted features are changed into fixed-length feature vectors for each candidate region. Next, Neck is a layer that combines the feature maps generated by Backbone, where PANet (Path Aggregation Network, Liu et al. 2018) and FPN (Feathre Pyramid Network, Lin et al. 2017) based on Mask R-CNN proposed by He et al. 2017 are used. A bottom-up feature pyramid structure based on PANet (Path Aggregation Network) and FPN (Feathre Pyramid Network) is employed. This enables recognition of objects of different scales. Finally, the Head uses the feature map generated by the Neck to make predictions about the coordinates and class of the box. In YOLOv5, the confidence for the candidate region is calculated as follows.

$$GloU = \frac{|A \cap B|}{|A \cup B|} - \frac{\left| \frac{C}{(A \cup B)} \right|}{|C|} \quad (1)$$

$$LGIoU = 1 - GIoU \quad (2)$$

GIoU Loss (Generalized IoU Loss, Rezatofighi et al. 2019) is employed as the loss function; GIoU makes it possible to quantify how far apart the two regions are when the two bounding boxes do not overlap at all. The GIoU is calculated as follows using the product and sum of the two regions plus the smallest and identically shaped region surrounding the two regions. Note that GIoU Loss is calculated by subtracting GIoU from 1.

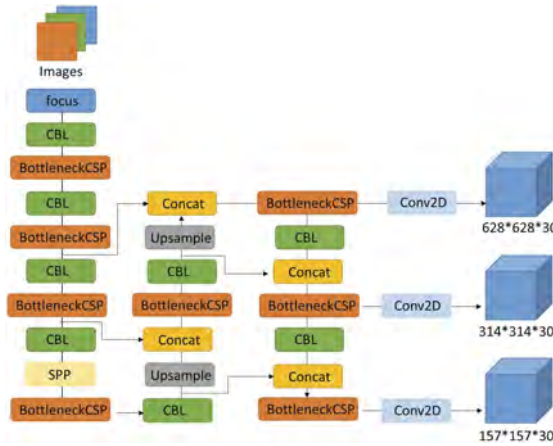


Figure 2. The architecture of YOLOv5.

2.2 Additive mixture of color method

Figures 3 and 4 illustrate the concept of additive mixture of color and the specific additive mixture of color process used in this study. The values in both images represent the RGB value of each pixel. Additive mixture of color is a method of adding colors using the three primary colors of light (Figure 3). The three primary colors of light are red, green, and blue, and various colors can be created from these three colors. As shown in Figure 4, mixing red and cyan produces a whitish color. In this case, the image before corrosion is converted to a red scale without the green and blue information, and the image after corrosion is converted to a cyan scale without the red information. In other words, by adding both images together, changes before and after corrosion can be indicated by colors such as white, black, red, and cyan. As a specific example, as shown in the first line of Figure 4, the RGB values before and after corrosion progress are both black (0, 0, 0), so the color of the areas with no change before and after corrosion progress is close to black (0, 0, 0) in the additive color mixture result. In addition, the area where the bridge was stained in the previous year and the stain disappeared this year is cyan (0,255,255), as shown in the second line from the top in Figure 4. Similarly, areas where there was no corrosion but corrosion has progressed are closer to red (255,0,0), as shown in the third line from the top in Figure 4. Finally, if there is no change before and after corrosion, as in the case of black, the color is closer to white (255,255,255) in the result of additive mixing, as in the fourth line from the top of Figure 4. In other words, areas that remain unchanged before and after the corrosion process return to their original color, while areas that have changed are displayed in cyan or red. Based on the above, as shown in the lower part of Figure 4, the additive mixture of color method can be used to identify only the areas where corrosion has progressed. However, it is assumed that the angle of view is the same for both images. In Figure 4, assuming no development, the same image is converted to red and cyan scales and then subjected to additive mixture of color.



Figure 3. The three primary colors of light.

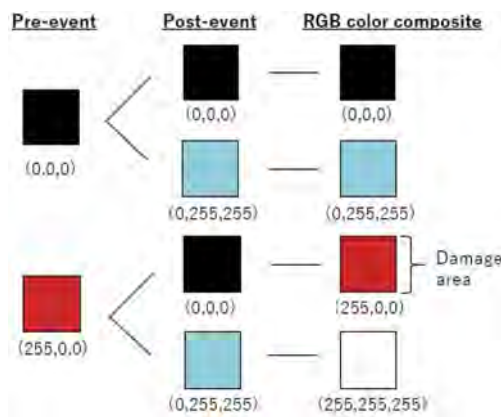


Figure 4. Additive mixture of color method.

3 CORROSION DETECTION BY YOLOV5

In order to perform object detection, it is necessary to learn information about corrosion in images. This requires the creation of an image and metadata associated with the image. This process is called annotation. In this study, since the corrosion in the image is the detection area, the coordinates are used as metadata. Labelling, an annotation tool, is used to annotate the detection images used as training data. The image of the corroded area is generated as metadata for the training data. The data utilized in the demonstration experiment consisted of 2,282 images taken by engineers. In this study, we limited the annotation to images with corroded areas out of the images taken in 2020. This study adapts the general object detection technique YOLOv5. In this study, we used YOLOv5m, which is a heavy processing and has good accuracy. From the above data, YOLO was used on 376 pieces of training data and 36 pieces of validation data to train and detect corroded areas. The batch size was set to 8 and the number of epochs to 1000. In this study, the probability of detecting corrosion was calculated using the confidence level, which is one of the indices for object detection. The threshold of detection probability was set at 0.40.

Figure 5 shows the training loss, precision and recall when trained. Each figure are stopped in the middle because the early stopping function, which stops overlearning, is activated in each case. Overlearning is a phenomenon in which excessive adaptation occurs only to the training data. The loss shows that learning is progressing well, since it is getting smaller as the number of epochs increases. Finally, the loss is 0.0427, the fit is 0.709, and the recall is 0.545.

Corrosion was detected in 107 images from 570 images captured in 2020, and in all 32 images that were judged to be corroded by the technicians. The average confidence level was about 0.6, and there were no false positives. The example of detection results is shown in Figure 6.

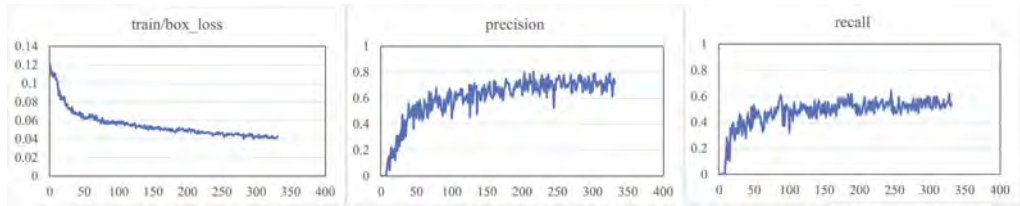


Figure 5. Training procedure.

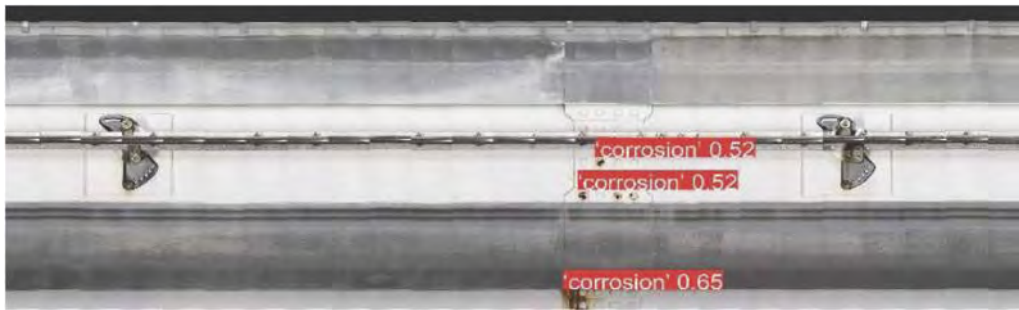


Figure 6. Example of corrosion detection results.

4 CORROSION PROPAGATION DETECTION BY ADDITIVE MIXTURE OF COLOR MEDHOD

Of the 107 images in which corrosion was detected, 32 images showed progressive corrosion, and a comparison of the images in 2020 and the images in 2021 shows that the corrosion has spread. The examples of corrosion propagation results by Additive mixture of color method is

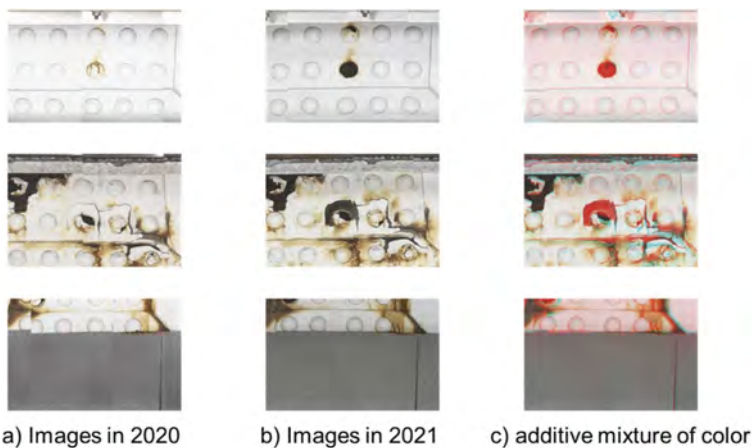


Figure 7. Examples of corrosion propagation results.

indicated in Figure 7. As shown in this figure, it is found that the corrosion progression area was detected correctly.

However, as shown in the black box on the right side of Figure 8, false positives were observed in some areas. It is considered to be due to the misalignment of the camera mounted on the inspection vehicle caused by the vibration of the bridge during the shooting.

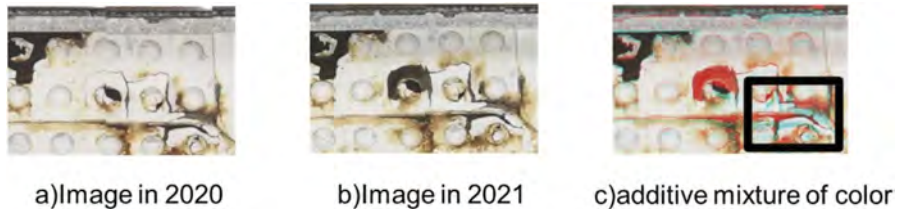


Figure 8. Example of false detection for corrosion results.

5 CONCLUSIONS

The purpose of this study was to develop a system that can detect structural surface damage with high accuracy and speed using visual damage inspection results, and a system to evaluate the progress of damage using the additive mixture of color method. In addition to the detection technique using YOLO, which is capable of high-speed processing of large-area and large-volume images, the three primary colors of light We aimed to improve the accuracy of damage detection and progress evaluation by adapting additive mixture of color using. At YOLO, the lack of the detection of corrosion is close to zero, which is the standard, and we were able to achieve this with the data currently in our possession. At additive mixture of color, we confirmed that the corrosion progresses could be detected only when the angle of view is uniform. In the future, we plan to research methods to unify the angle of view, which is a condition for applying additive mixture of color.

REFERENCES

- He, K., Zhang, X., Ren, S., & Sun, J. 2014. Spatial Pyramid Pooling in Deep Convolutional Networks for Visual Recognition, European Conference on Computer Vision (ECCV 2014), Vol.8691, 346–361.
- He, K., Gkioxari, G., Dollár, P. & Girshick, R. 2017. Mask RCNN, 2017 IEEE International Conference on Computer Vision (ICCV), 2980–2988.
- Lin, T., Dollár, P., Girshick, R., He, K., Hariharan, B., & Belongie, S. 2017. Feature Pyramid Networks for Object Detection, 2017 IEEE Conference on Computer Vision and Pattern Recognition (CVPR), 936–944.
- Liu, S., Qi, L., Qin, H., Shi, J., & Jia, J. 2018. Path Aggregation Network for Instance Segmentation, Proceedings of the IEEE Conference on Computer Vision and Pattern Recognition (CVPR), Vol. 1, 8759–8768.
- Nakamura, K., Izumi, Y. & Koda, Y. 2020. Detection of Corrosion Locations on Steel Bridges Using Convolutional Neural Network, *Journal of AI and Data Science*, Vol. 1, No. J1, 373–381. (in Japanese)
- Wang, C., Mark Liao, J., Wu, Y., Chen, P., Hsieh, J. & Yeh, I. 2020. CSPNet: A New Backbone that can Enhance Learning Capability of CNN, 2020 IEEE/CVF Conference on Computer Vision and Pattern Recognition Workshops (CVPRW), 1571–1580.

Development of a cable inspection robot for cable-stayed bridges

K. Kawamura & W. Zheng

Yamaguchi University, Ube, Yamaguchi, Japan

M. Shiozaki

Sumitomo Mitsui Construction, Chuo-ku, Tokyo, Japan

ABSTRACT: The authors have developed a cable inspection robot for the cable-stayed bridges (CSBs). The robot is possible to photograph the entire circumference of the CSB cable surface with several cameras while moving up and down along the cable, and then creating an image development diagram of the CSB cable surface from the video. By utilizing an image development diagram, it is possible to confirm the position and the shape of damage to the cable, which can be difficult to grasp using video only.

1 INTRODUCTION

The number of the cable-stayed bridges (CSBs) in Japan is 319 as of March 2021 (MLIT 2021) and the need for maintenance is increasing. The cable inspection of CSBs is either conducted visually on aerial work platforms or carried out by inspectors with special altitude technology. However, these inspection methods are problematic in that there is a limit to the inspection height, and there is a problem that the work must be carried out at the height which is dangerous for the inspector. Consequently, the study on developing CSB cable inspection robot is being done in Japan. In terms of existing studies, the cable inspection robots have been developed by Chodai Corporation (Chodai co., Ltd. 2017) and Nishimatsu Construction Corporation (Nishimatsu Construction co., Ltd. 2022) in addition to the robot used in this study (Kawamura et al. 2016, 2017, 2021).

The authors have developed a cable inspection robot for the CSBs. The robot is possible to photograph the entire circumference of the CSB cable surface with several cameras while moving up and down along the cable, and then creating an image development diagram of the CSB cable surface from the video. By utilizing an image development diagram, it is possible to confirm the position and the shape of damage to the cable, which can be difficult to grasp using video only.

The robot is able to automatically synchronize the start time of each mounted camera to avoid timing errors in order to make an image development diagram. Specifically, by making a majority of red LEDs set in the inspection robot flash synchronously in time with each camera, the flicker can be confirmed to be within the processing range of the image development diagram of the inspection robot. In addition, the initial illumination of the red LED is automatically detected within the photographic image, and the photographic image synchronization of each camera is executed. However, due to the existence of pixels similar in red color to that of the LEDs, it is possible to perform a false identification, leading to unwanted synchronizations. Therefore, a method was proposed to install the red LEDs on green base plates in order to perform the detection with fewer similar color pixels in the shooting area. In addition, Yolov5 (Glenn, 2020), a deep learning model used for object detection, was used in the automatic detection. The paper outlines a method to make an image development diagram in the following chapters.

2 INSPECTION METHOD OF CSB INSPECTION ROBOT

2.1 Introduction

This chapter describes the CSB cable inspection robot developed by the authors. The robot is to photograph the cable surface with the robot and make the image development diagram of the cable surface from the produced video. Figures 1 and 2 show a diagram of the CSB and a photo of the robot installed on a cable. At point A in Figure 1, video photography is started manually. After the robot rises to point B, the red LEDs in the robot flashes and returns to point A. The image development diagram is made using the video taken during the descent from location B to A.

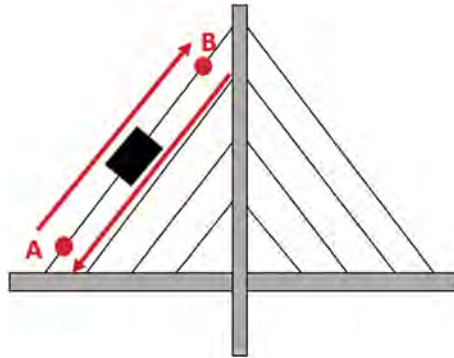


Figure 1. Schematic image of a bridge by the cable-stayed bridge cable inspection robot.

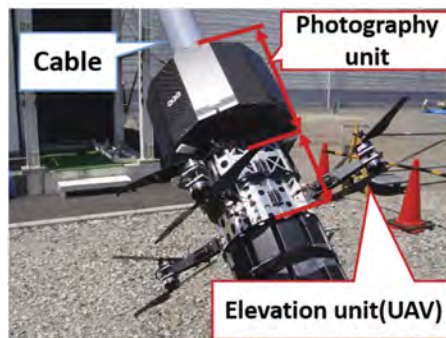


Figure 2. Photograph of cable-stayed bridge cable inspection robot.

2.2 Component of the cable-stayed bridge cable inspection robot

As shown in Figure 2, the robot is composed of three units: a photography unit, an elevation unit (UAV), and the image development diagram software. The elevation unit is used to raise the photography unit, detaching from the photography unit after reaching the destination so as not to interfere with photography. Inside the photography unit, six cameras are mounted so that the entire surface of a cable can be photographed at a single elevation. In addition, the descent speed mechanism keeps the descent speed of the photography unit stable, while a separate device records the distance (mm) in which the photography unit has moved in relation to the cable as well as the angle of rotation. The amount of movement recorded by this measuring device is then used when creating an image development diagram.

2.3 Image deployment diagram production

The processing of image development diagram software can be divided into the following seven steps.

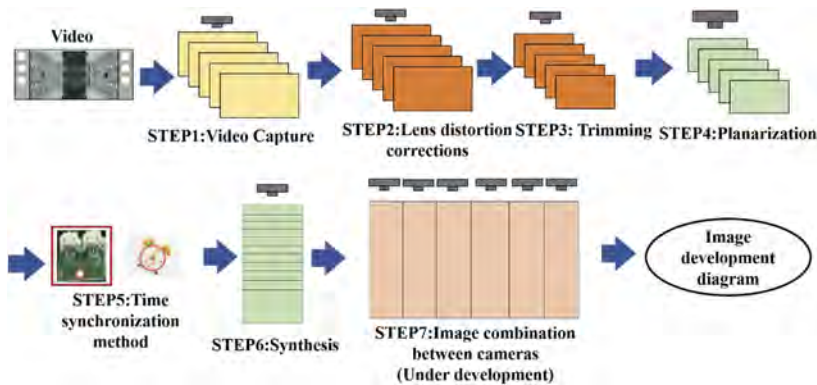


Figure 3. Flow of image deployment diagram production.

STEP 1: Video Capture. PNG files are generated for each video frame from the video taken by the photography unit.

STEP 2: Lens distortion correction. Lens distortion correction is then performed on all captured images generated in STEP 1.

STEP 3: Trimming. After lens distortion correction, the area where the cable is projected is cropped off. The crop range is specified using the first captured image and applied uniformly to the remaining images.

STEP 4: Planarization. This step makes a planarized image for the surface of the cable.

STEP 5: Time synchronization method. It is necessary to synchronize the start time of the image development diagram making process for each of the six cameras mounted on the robot. Therefore, a number of green bases equipped with red LEDs are installed inside the robot. The configuration condition is that all cameras can detect any kind of red LEDs, which are set to light up at the same time as the start of the image development diagram. Thus, in order to grasp the start time of the image development diagram process, it is necessary to correctly obtain the frame number for when the red LEDs begin flashing. The next chapter describes the LED detection process.

STEP 6: Synthesis. Using the movement data recorded during photography, the images made in STEP 4 are then combined into a single synthesized image of the cable surface.

STEP 7: Image combination between cameras. Since STEPS 1~5 occur for all six cameras on the photography unit, a detailed image of the entire circumference of the cable surface can be generated by further combining all of the continuous images made during STEP 5.

3 TIME SYNCHRONIZATION METHOD

3.1 Introduction

This chapter describes the time synchronization method for making an image development diagram. Specifically, a method for automatically detecting the flash of the red LEDs from captured video was adopted in order to synchronize six cameras installed on the robot.

3.2 Necessity of LED detection

During STEP 5 of the image development process mentioned in 2.4, it is necessary to synchronize the start time of the image development diagram making process for each of the six

cameras mounted on the robot. Therefore, a number of green bases equipped with red LEDs are installed inside the robot. Figures 3 and 4 respectively show photos taken inside the robot and the enlarged area of the green bases equipped with red LEDs. The configuration condition is that all cameras can detect any kind of red LEDs, which are set to light up at the same time as the start of the image development diagram. Thus, in order to grasp the start time of the image development diagram process, it is necessary to correctly obtain the frame number for when the red LEDs begin flashing.

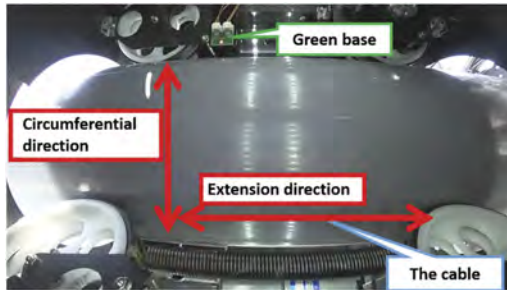


Figure 4. Interior of cable-stayed bridge cable inspection robot.

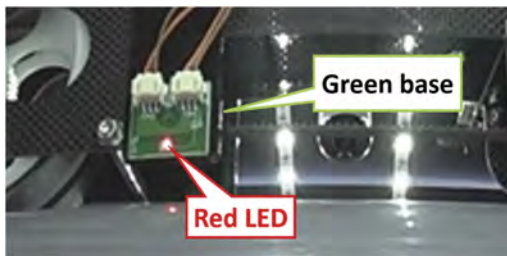


Figure 5. Enlarged image of a green base.

3.3 Method of LEDs detection

The robot unifies the start time of image development by detecting whether the red LEDs on the green bases are lit at the same time. The goal is to automatically detect the lighting of red LED from the video taken by the cameras mounted on the robot; the illumination of the red LEDs is detected only after the green base with fewer similar pixels is detected in the captured image, thereby reducing the possibility of false detection. In addition, the CSB cable inspection robot will experience vibration during lifting and lowering, resulting in the position of green bases and red LEDs on an image not being set correctly. For this reason, yolov5 (Glenn, et al. 2020) that deep learning object detection algorithm proposed in 2020 was employed to accurately track the detection of green bases in video. The specific detection methods of green bases and red LEDs will be described in the next section.

3.4 LED detection process

Processing of the red LEDs lighting detection algorithm that is performed on every camera is divided into the following four steps. Figure 6 shows the flow of the detection algorithm and summarizes the details of each step.

STEP 1: The video is read frame by frame.

STEP 2: Use Yolov5 to get information about the range of the exploration rectangle containing the green base and judge whether the base exists. The information of exploration rectangle contains the xy coordinates of the center corner of the rectangle, as well as its length and width.

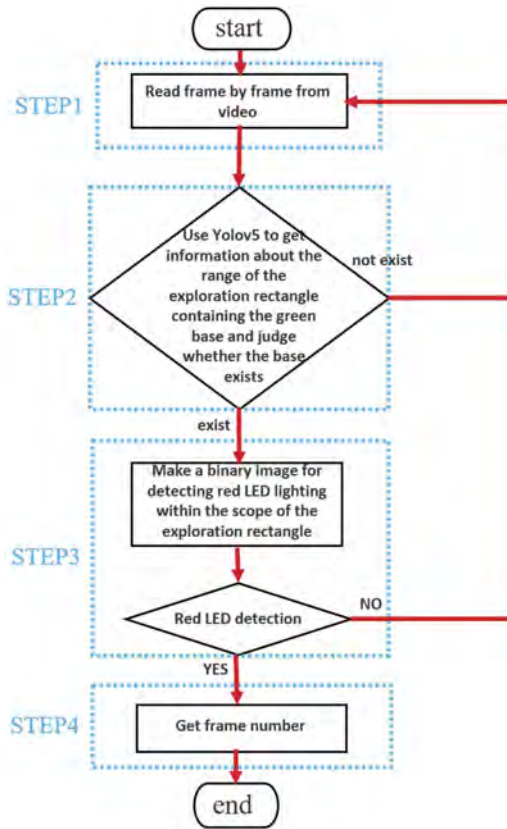


Figure 6. LED Detection Algorithm Flow Chart.

STEP 3: This step involves detecting the illumination of red LEDs within the search rectangle obtained in STEP 2, and the color representation of the image pixels value is converted from RGB format to HSV (Hue, Saturation, Value) format (Hideaki, S. & Takashi, O. 2017), also referred to as Hexcone Model. The color parameters in this model are hue, saturation and brightness respectively. RGB format is typically used for pixel values, but because it is difficult to specify the range of specific colors with RGB, this study used HSV format instead to intuitively show the brightness, hue, and saturation of visualized images. First, the pixel value (HSV) of the rectangular frame's xy coordinates are binarized according to the following Equation 1:

$$I(x, y) = \begin{cases} 255, & (0, 43, 46) \leq h(x, y) \leq (10, 255, 255) \\ 0, & \text{otherwise} \end{cases} \quad (1)$$

A threshold for separating red LED light from other pixel values within a predetermined HSV range is set, with pixels falling within this range designated as 255 (white) and those outside the range as 0 (black). In this way, targeted sections of the image are converted into 255 pixels by Formula 1 and identified as red. The range of red HSV values used in Formula was determined in advance by the authors through image analysis of the red LED lights. If the sum of pixel values in the exploration rectangular for the binary image is more than 1, it is assumed that the red LEDs are lit and the algorithm proceeds to STEP 4. When a pixel is determined as red by Formula 1 its pixel value will be 255, and the sum of pixel values in the search rectangular box is 255. In other words, if there is even one red pixel in the exploration rectangular, it treats the red LEDs as lit.



Figure 7. On-site verification of the cable inspection robot.



Figure 8. Appearance of Bridge M1 inspected by the cable inspection robot.

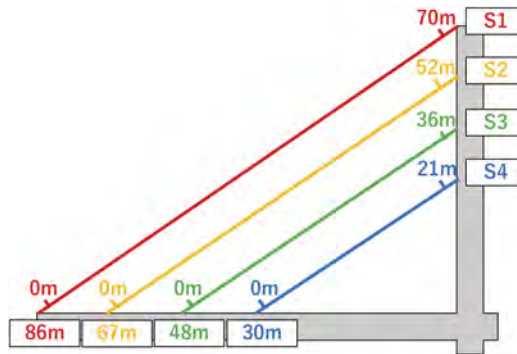


Figure 9. The shooting distance of the cable inspection robot on the cable.

On the other hand, if the sum of pixel values in the exploration rectangle is 0, it is judged that the red LEDs are not lit and will return to STEP 1.

STEP 4: In the event STEP 3 determines that the red LEDs are lit, the frame number of the image is obtained and the algorithm terminates.

4 APPLICATION OF THE INSPECTION ROBOT TO AN EXISTING BRIDGE

The robot was applied to the existing bridge (Bridge A1) in order to verify the ability of the shooting and the accuracy of the image development diagram. Figures 7 and 8 are the scene of

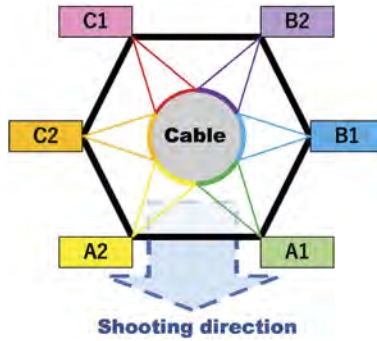


Figure 10. Camera placement in the robot.

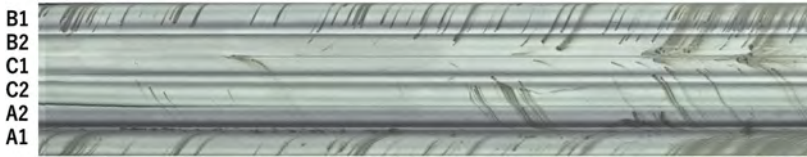


Figure 11. Image development diagram at 67~70m of the cable S1.

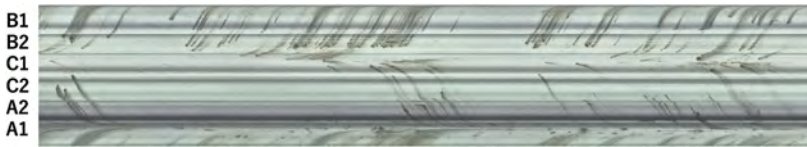


Figure 12. Image development diagram at 64~67m of the cable S1.



Figure 13. Image development diagram at 61~64m of the cable S1.

on-site verification. Figure 7 is a scene where the robot is attached to the cable. Figure 8 shows the appearance of Bridge M1. As shown in Figure 9, there are 4 cables on one side of the bridge, which shows the shooting distance of the cable inspection robot on each cable. S1, S2, S3 and S4 are ID of each cable. The total lengths are 86m, 67m, 48m, 30m. The shooting distance are 70m, 52m, 36m, 21m, respectively. Then, Figure 10 illustrates the camera placement in the robot and the shooting direction. A1,A2,B1,B2,C1 and C1 are ID of each camera.

Figures 11 to 13 are the part of the image development diagram of cable S1 as an example to illustrate the accuracy of the image development diagram. The A1 to C2 in Figures 11 to 13 are correspond the camera ID in Figure 10. As shown in Figures 11 to 13, within the range of 64~70m of the cable S1, the images taken by each camera were well combined. However, the region in the red box in Figure 13 is slightly misaligned due to that there was unevenness at the joint of the cable.

5 CONCLUSIONS

This study describes the cable inspection robot for CBSs developed by the authors and explains in detail the entire process of making the image deployment diagram and the operation process of time synchronization method. Then, the robot is verified for an existing bridge. As a result, the robot is suitable for practical application.

REFERENCES

- MLIT(Ministry of Land, Infrastructure, Transport and Tourism). 2021. Annual report of road statistics and present state of bridges in 2021. Retrieved from Ministry of land, infrastructure and transport website: <https://www.mlit.go.jp/road/ir/ir-data/tokei-nen/2021/nenpo03.html>.
- Chodai co., Ltd. 2017. The Cable-Stayed bridge cable inspection robot VESPINAE. Retrieved from VESPINAE website: <https://www.chodai.co.jp/news/2017/03/012664.html>.
- Nishimatsu Construction co., Ltd. 2022. the cable protection pipe inspection robot of the Cable-Stayed bridge coroner checker. Retrieved from coroner checker website: <https://www.nishimatsu.co.jp/solution/assets/pdf/00073.pdf>.
- Kawamura, K. & Hasegawa, T. & Shiozaki, M. 2016. Basic study of an inspection record system for cable-stayed bridge cable inspection robot, *Journal of Japan Society of Civil Engineers*, Ser. F3 (Civil Engineering Informatics), Vol.72, No.2: I_83-I_92.
- Kawamura, K. & Hasegawa, E. & Shiozaki, M. 2017. Development of inspection record system mounted on a cable inspection robot for cable-stayed bridges, *Journal of Japan Society of Civil Engineers*, Ser. F3 (Civil Engineering Informatics) 2017 Vol.73 Issue 2: I_201-I_210.
- Kawamura, K. & Hasegawa, E. & Shiozaki, M. & Nakamura, T. 2021. A geometric transformation method of a cable surface image for cable-stayed bridge inspection, *Journal of Japan Society of Civil Engineers*, Ser. F3 (Civil Engineering Informatics) 2021 Vol.77 Issue 2: I_51-I_57.
- Glenn, J. 2020. Retrieved from github website: <https://github.com/ultralytics/yolov5>.

Application of cluster analysis and Markov chain model for network-level highway infrastructure management

A. Amir & M. Henry

Shibaura Institute of Technology, Kotou-ku, Tokyo, Japan

ABSTRACT: Khyber Pakhtunkhwa province, Pakistan's third-largest provincial economy, is totally dependent on road transport. To upkeep the highway infrastructure in good condition, an effective, efficient, economical, and sustainable management technique needs to be devised. The pavement deterioration prediction is a vital element for an efficient pavement management system that can help the road authorities in determining the appropriate maintenance technique. The research aimed to develop the pavement deterioration prediction model at the network-level using Markov Chain. However, at the network-level, the road characteristics are not uniform due to which it is difficult to classify the road sections into families for applying Markov Chain. Thus, first Agglomerative Cluster Analysis was applied to define pavement families with similar characteristics. Then, the deterioration prediction models were developed for pavement families using Markov Chain. The combination of AHC with Markov Chain found was found an effective technique for pavement deterioration models at the network-level.

1 INTRODUCTION

The deterioration of road pavement results from the damaging effect of traffic loading, environmental conditions, age, and other associated factors greatly affects safety, serviceability, and riding quality. The maintenance management of deteriorated pavements poses a great challenge to engineers due to the random nature of the deterioration process and the complex relationship between pavement characteristics or variables (Surendrakumar et. al., 2013). Due to the uncertainty in the pavement deterioration process, the Pavement Maintenance Management System (PMMS) is becoming increasingly more complex. The PMMS is separated into two general levels: network level and project level (Smith et. al., 2001). The network level management system deals with the entire pavement network and involves high-level decisions related to network-wide planning for budget optimization, whereas the project level deals with smaller sections within the network and is generally involved with the decisions relating to condition, Maintenance Rehabilitation, and Reconstruction (MR&R) assignment and unit cost. According to the AASHTO guideline for the pavement management system, the approaches for the pavement management system can either be top-down by dealing with the network level first or can be bottom-up by dealing with the project level decision first depending upon data amount (Coree et. al., 1990).

The provincial highways road network of Khyber Pakhtunkhwa province of Pakistan consists of 3000 km of asphaltic pavements but, according to a report published by Asian Development Bank (ADB), only 27.7% of provincial highways are in fair to good condition while the rest are in poor conditions (ADB, 2018). The main element which contributes to the maintenance backlog is the absence of an effective maintenance plan to correlate the data for the development of the maintenance plan (Amir et. al., 2022). The research aimed to utilize the existing provincial highway network data of Khyber Pakhtunkhwa for network-level planning. Budget planning at the network level is complex due to the irregular behavior of pavement deterioration. However, the prediction for future repair demands of the road infrastructure at

the network level can be helpful for budget planning. The estimation of the repair demands, and life cycle cost is normally determined by deterioration models (Jiang et. al., 2000). These models can be deterministic or probabilistic (stochastic). The prediction models developed by deterministic and stochastic approaches differ in concept, formulation, and output format (Li. N et. al., 1996). There are many deterministic models developed for regional or local Pavement Management Systems, such as traffic-related models, time-related models, interactive-time-related models, and generalized models (Md. Sohail, 2015). However, by using the deterministic approaches, the developed model cannot explain some problems, such as in quantifying the parameters that are the main reason for pavement deterioration, the unpredictability of traffic loading and environmental conditions, and especially the bias when performing the subjective evaluations of pavement condition (Li et al.,1997). In recent years, pavement engineers and researchers have paid considerable attention to stochastic models. A stochastic model was developed for pavement deterioration represented by the Markov transition process (Li. et al., 1997). Dynamic programming combined with the Markov process produces optimal budget requirements for the given analysis period (Butt et al., 1994). Wang et al. developed the Markov transition probability model by using the pavement historical data for the categorized highway for the Arizona Department of Transportation (Wang et al., 1995). Butt et al. presented the approach for budget optimization based on the pavement deterioration model by utilizing the Markov process for the airport pavement network. The pavement sections were classified into families based on surface type, traffic, maximum deflection, etc., and then the Markov prediction model for each family was developed (Butt et al., 1994).

In this research, first, Agglomerative Hierarchical Cluster Analysis was carried out on the provincial road network data to identify different families of pavement sections with similar characteristics. Then, the Markov prediction model was developed for each pavement family to find the deterioration progress for the next ten years.

2 METHODOLOGY

The overall flow chart of the research study is shown in Figure 1. The pavement characteristics data of the provincial highway network of Khyber Pakhtunkhwa, which were collected from the Communication and Works (C&W) Department, Peshawar, Pakistan, were used in the research. The data comprised 18 characteristics of bituminous pavements with various ages of pavements ranging from 1-6 years old road.

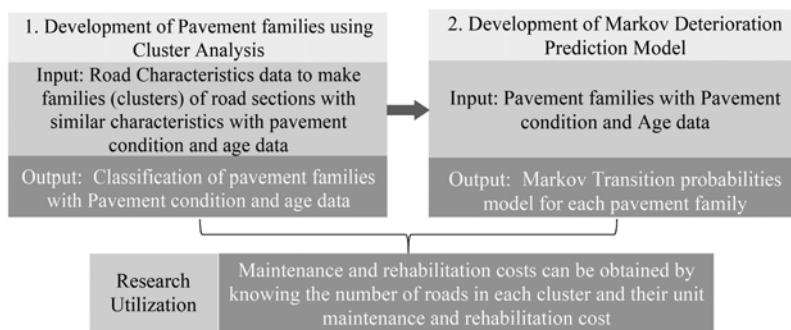


Figure 1. Methodology flow chart.

2.1 Cluster analysis

The first step of the research was to group the road sections having similar characteristics. Therefore, the Agglomerative Hierarchical Cluster Analysis was done to make the clusters or families of road sections that have similar characteristics.

Agglomerative Hierarchical Cluster Analysis, the most common type of hierarchical clustering, is an unsupervised machine-learning technique that sequentially groups objects into clusters based on similarities between the characteristics of objects (Murtagh et al., 2012). This technique was used in this research because it is a bottom-up approach that starts from the smaller clusters and is then combined to form the bigger clusters based on similarities. The analysis was carried out in an open-source statistical analysis software R (R Core Team, 2022) following the guidelines provided by Kassambara (2017).

In this research, the features for the cluster analysis were the road characteristics, such as traffic loading, cross and longitudinal drainage condition, the importance of the road, and pavement terrain (the full list of variables is shown in the results). All the features were converted into nominal data for performing cluster analysis. Different hierarchical trees, or dendrograms, were constructed with different distance methods. The dendrogram with Generalize Distance Measures (GDM) and the Mcquitty linkage function was selected because the numbers of data in the clusters were sufficient for the calculation of the probability matrix for the Markov model. However, the correlation coefficients between the generalized distance matrices and their respective cophenetic distance matrices were only the second highest among the linkage functions tested.

2.2 Development of Markov prediction model

The next step of the research was to develop a Markov Chain prediction model for each group of road section families. Markov's property is satisfied by stochastic processes where future states are determined by their present state instead of their past state. Hence, it means that the present state is the cumulative result of all past states (Surendrakumar et. al., 2013). So, the Markov transition matrix is the stationary stochastic matrix, and the matrix describing the initial condition of the system is the initial probability distribution matrix. The combination of both matrices is used for defining the deterioration processes. Hence the entire process consists of two steps: first, to develop the defined size of the transitional matrix, and second, the initial transition matrix and current conditions are multiplied to get the future conditions.

In deterioration modeling, the model elements change randomly with the progression of time. Hence, in the case of pavement deterioration, it is assumed that the pavement starts its life in nearly good condition and then undergoes a series of duty cycles that deteriorate its condition. In this research, the pavement states are expressed in terms of three pavement conditions - good, fair, and bad as defined in data obtained by the department as shown in Table 1. Thus, three 3x3 transition probability matrices were developed.

Table 1. Description of pavement condition.

Pavement Condition	IRI	Speed (kph)	Area Damaged (%)
Bad	7-10	25-40	10-25
Fair	4-6	40-60	5-10
Good	0-4	Over 60	-

2.3 Transition probability matrix

The first step of the Markov chain is to predict the transition probabilities in different states. For this purpose, the historical condition data were analyzed to get the transition matrix for each family. The initial data consisted of the pavement condition data in the year 2021 and the year of last rehabilitation or the year of construction, from which the age of the pavement was calculated for every road section. It was assumed that the road condition was good in the year of rehabilitation or construction, and no major maintenance treatment was performed during the pavement life. From this data, the pavement conditions in transition years were established, and subsequently, the probability and percentage in each condition were calculated. A sampling of the three pavement condition states data for Cluster 1 are shown in Table 2, which were used for the calculation of the initial transition matrix for Markov Chain prediction for future years.

2.4 Markov chain prediction

The Markov chain's initial step is to determine transition probability. If $\{X_n, n=0,1,2,\dots\}$ is the Markov chain, and $X_n=i_n$ represents that the procedure is cited in pavement condition (i) and at year n, then the conditional probability $P_{ij}(n,n+1)$ is called one-step transition probability from any specific pavement condition state (i) to a one-step lower pavement condition state (j) at the year n:

$$P_{ij}(n, n + 1) = P[X_{n+1} = j | X_n = i_n], n = 0, 1 \dots \quad (1)$$

Thus, according to the Markov chain process, the probability of transition from any specific pavement condition (i) to an immediate future pavement condition (j), given all previous pavement conditions and the current condition (j), is distinct from the previous conditions (states) and dependent only on the current condition (j) (Ahmed et. al., 2019) It means that the transition probabilities are assumed to be stationary or unchanged over the time period of interest and independent of how the current state was reached. The probability P_{ij} symbolizes the likelihood that the procedure will create a change to status (i), given that presently the method is status (j) as represented by the equation below:

$$P_{ij} \geq 0, \sum_{i=0}^n P_{ij} = 1, j = 0, 1, \dots \dots \quad (2)$$

Similarly for the transition matrix having P_{ij} , then the probabilities will be:

$$P = \begin{pmatrix} P_{00} & P_{10} & \dots \\ P_{01} & P_{11} & \dots \\ \cdot & \cdot & \dots \end{pmatrix} \quad (3)$$

However, the transition probabilities are represented as:

$$P_{00} = 1 - \alpha, P_{10} = \alpha, P_{11} = 1 - \beta \text{ and } P_{01} = \beta \quad (4)$$

Then after a single time interval, the probability transition matrix is specified by:

$$P = \begin{pmatrix} 1 - \alpha & \beta \\ \alpha & 1 - \beta \end{pmatrix} \quad (5)$$

Where α and β are possible values of probability.

The transition probability P_{ij} was determined for each of the three pavement states, from Equation 2 where n_{ij} represents the transition number as of state i (initial state) towards state j (next level deterioration state) in a specific time and n_i signifies the overall component number in state i before transition.

Table 2. Sampling of condition data for Cluster 1.

Roads Section	Years						
	2015	2016	2017	2018	2019	2020	2021
1	3	3	2	1	1	1	1
2	3	3	2	1	1	1	1
3	.	.	.	3	3	2	1
4	.	3	3	2	1	1	1
.
.15	3	2

3 RESULTS AND DISCUSSIONS

3.1 Classification of the road families

The result of the cluster analysis is shown in Figure 2. The cutting of the tree was done at a specific height so that each cluster should contain the maximum number of road sections with similar characteristics or features. Hence, five clusters were obtained in total, but only three clusters were selected for building the deterioration model with Markov chain because they contained a sufficient number of pavement age data necessary for developing the model.

Table 3 shows the in-cluster mean values of the road characteristics for each of the three clusters, or road families. It was observed that Cluster 1 consisted of a family of roads that are in hilly areas and leading to tourism destinations, having in-cluster mean values of 0 and 1 for these features, respectively. Furthermore, in this family, traffic load conditions were generally medium, cross and longitudinal drainage conditions were good, and the roads were less important and not leading to the industrial or mines and minerals areas. Cluster 2 represents the family of highly important roads with high traffic load in the plain areas, as the mean values for high traffic load and pavement terrain was 1, and the mean value for road importance was 0.94. Other factors such as cross and drainage conditions were found to be good, and the roads were not leading to tourism areas nor were they industrial traffic roads. Similarly, Cluster 3 as found to be a family of road sections leading to mines and mineral areas, with an in-cluster mean value of 1, while drainage condition of the roads was fair, the roads were less important, had medium traffic, and were not leading to tourism or industrial areas.

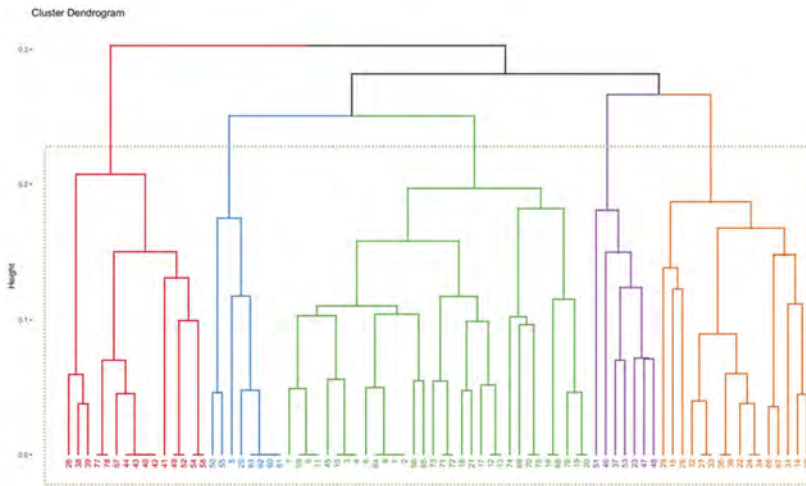


Figure 2. Dendrogram of road sections by road characteristics and distribution by clusters.

3.2 Markov deterioration prediction model

Next, the Markov deterioration prediction model was developed for each of the three families selected from the cluster analysis. The 3x3 transition probability matrices obtained for three road families are shown in Table 4. Using the transition probabilities and assuming the road sections in each road family begin in good condition, the predicted condition distributions for the 10-year time period for each road family are shown in Figures 3, 4, and 5.

From the deterioration model, it was observed that the rate of deterioration of the family of roads in hilly areas with medium traffic load (Cluster 1) is more than the plain areas (Cluster 2) with high traffic load. In Khyber Pakhtunkhwa province of Pakistan, the extreme climatic impact may be the cause of the early deterioration of pavements in hilly areas. There is a snowy season for four (4) months in northern areas of Pakistan. The erosion may be the factor responsible for the early deterioration of pavement surface in mountainous regions. In winter, when water fills

Table 3. In-cluster mean values for each road characteristic.

Variables	Description of variables	Cluster 1 n=16	Cluster 2 n=18	Cluster 3 n=33
Pavement Terrain	Hilly=0, Plain=1	0.00	1.00	0.25
High Traffic load	Yes=1, No=0	0.13	1.00	0.12
Medium Traffic load	Yes=1, No=0	0.80	0.00	0.75
Low Traffic load	Yes=1, No=0	0.06	0.00	0.12
Strategic importance	Yes=1, No=0	0.19	0.20	0.21
Road importance	Yes=1, No=0	0.46	0.94	0.50
Good culvert condition	Yes=1, No=0	0.96	0.94	0.00
Fair culvert condition	Yes=1, No=0	0.04	0.03	1.00
Bad culvert condition	Yes=1, No=0	0.00	0.03	0.00
Good drainage condition	Yes=1, No=0	0.80	0.50	0.00
Fair drainage condition	Yes=1, No=0	0.00	0.15	1.00
Bad drainage condition	Yes=1, No=0	0.20	0.21	0.00
Tourism roads	Yes=1, No=0	1.00	0.00	0.31
Industrial roads	Yes=1, No=0	0.00	0.31	0.12
Mines and minerals roads	Yes=1, No=0	0.06	0.46	1.00
n=numbers of count in each cluster				

small cracks in the pavement’s surface and it gets frozen, the expansion in volume can cause internal pressure, damage the pavement, and lead to erosion of roads. Salt used for deicing is another cause of pavement deterioration in snowy areas (Amir et. al., 2022). When salt mixes with water, it increases freeze-thaw damage and road scaling problem (Althoey et. al., 2021). On the other hand, the lower rate of deterioration for the roads of the plain area with high traffic (Cluster 2) may be because the roads are appropriately designed for the high traffic volume.

The rate of deterioration for the family of road sections that lead to mines and minerals (Cluster 3) is very high as compared to the other two families. If there is no maintenance, it is predicted that the roads will deteriorate completely within four years. This may be due to uncontrolled overloaded vehicles frequently using these roads because overloading had been an issue for the provincial highway network in Khyber Pakhtunkhwa province due to its quarrying, logging, and mining industries and related traffic, especially in the marble-producing areas. These pavements are designed following AASHTO specification with a single axle load of 18000lb but, according to a report published by Asian Development Bank (ADB), trucks in Khyber Pakhtunkhwa are overloaded up to 95% above the permissible load limits (ADB, 2018). Due to overloading, the design life of pavement reduces and results in pavement deterioration (Amir et. al., 2022). The provincial road authority needs to give more attention to mines and minerals areas roads. The implementation of routine and periodic maintenance may aid to slow the rate of deterioration, if practiced properly, and may help in increasing the life of the pavement.

Table 4. Deterioration Transition Matrix for Cluster 1, Cluster 2, and Cluster 3

States	Good	Fair	Bad	States	Good	Fair	Bad	States	Good	Fair	Bad
Good	0.79	0.21	0	Good	0.88	0.11	0	Good	0.39	0.61	0
Fair	0	0.80	0.20	Fair	0	0	1.00	Fair	0	0.15	0.85
Bad	0	0	1.00	Bad	0	0	1.00	Bad	0	0	1.00
Cluster 1: Hilly areas, tourism roads, medium traffic, good drainage cond.				Cluster 2: Plain areas, high traffic, good drainage condition.				Cluster 3: Mines and minerals roads, medium traffic, fair drainage cond.			

4 CONCLUSIONS

The research aimed to develop the pavement deterioration prediction model based on the existing data of the provincial road network at the network level that can be utilized for budget

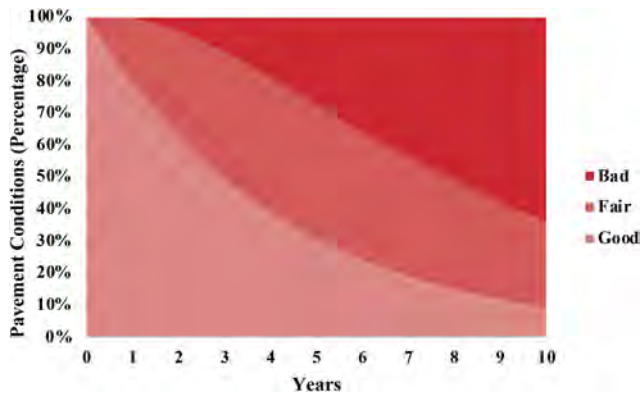


Figure 3. Pavement deterioration model w.r.t age for Cluster 1 (Hilly areas, tourism roads, medium traffic, good drainage condition).

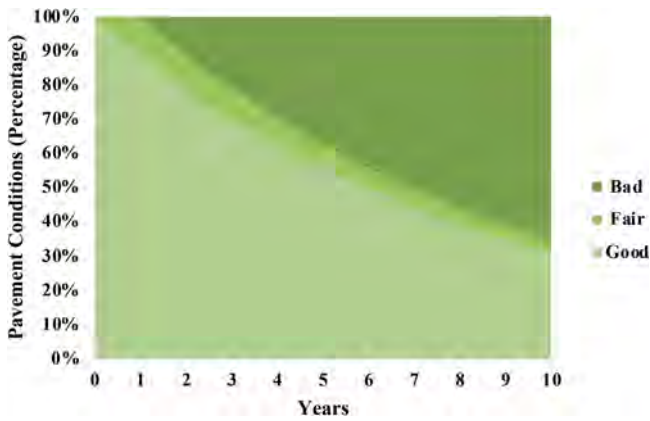


Figure 4. Pavement deterioration model w.r.t age for Cluster 2 (Plain areas, high traffic, good drainage condition).

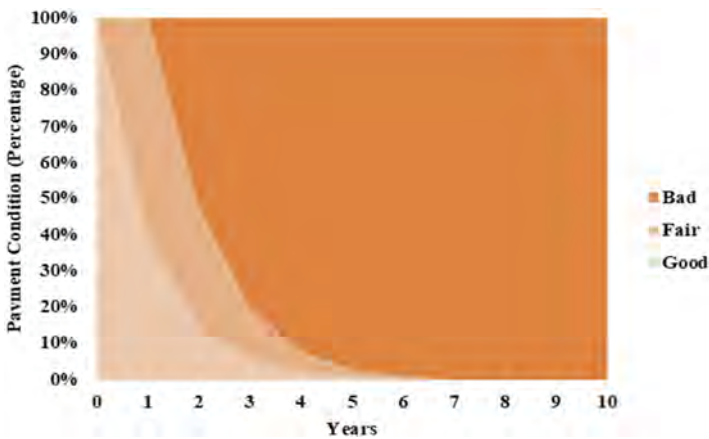


Figure 5. Pavement deterioration model w.r.t age for Cluster 3 (Mines and minerals roads, medium traffic, fair drainage condition).

optimization. At the network level, the pavement condition data with time is sometimes difficult to collect for the entire pavement network. The study intended to develop the approach for predicting pavement deterioration based on the existing data available with the road department by classifying the road network into different families using Cluster Analysis before applying Markov Chain Analysis. The Agglomerative Hierarchical Cluster Analysis assisted to classify the road sections into families having similar characteristics with the identifications of dominant road variables for each family. The technique of using AHC was found effective for network-level analysis where the road characteristics are not uniform, and it is difficult to classify the road sections with similar characteristics into groups before applying the Markov Chain approach. The Markov chain model can then be easily developed for each family for determining pavement deterioration with time for network-level management. By knowing the per unit cost of maintenance for different types of pavement conditions, the highways authority can formulate the maintenance management plan for the network level for future years.

ACKNOWLEDGEMENT

The authors would like to express their gratitude to the Japan International Cooperation Agency (JICA) for their support through the Road Asset Management Platform, to Shibaura Institute of Technology (SIT), Tokyo for providing the environment for the research, and to Pakhtunkhwa Highway Authority, Communication and Works Department, Peshawar, for sharing the data and requisite information.

REFERENCES

- ADB - Asian Development Bank. Board of Directors. 2018. Report and Recommendation of the President to the Board of Directors: Proposed Loans for the Additional Financing Islamic Republic of Pakistan: Khyber Pakhtunkhwa Provincial Roads Improvement Project. Asian Development Bank.
- Amin, M., & Reza, S. 2015. The pavement performance modeling: deterministic vs. stochastic approaches. In *Numerical methods for reliability and safety assessment*: 179–196. Springer, Cham.
- Attoh-Okine, N.O. 1999. Analysis of learning rate and momentum term in backpropagation neural network algorithm trained to predict pavement performance. *Advances in engineering software* 30(4): 291–302.
- Amir, A., & Henry, M. 2022. Factors Affecting the Deterioration of Bituminous Pavements in Khyber Pakhtunkhwa Province, Pakistan. In *the 17th East Asia-Pacific Conference on Structural Engineering & Construction (EASEC 17)*, Singapore-Towards a resilient and sustainable city.
- Butt, A. A., Shahin, M. Y., Carpenter, S. H., & Carnahan, J. V. 1994, May. Application of Markov process to pavement management systems at the network level. In *3rd international conference on managing pavements 2*: 159–172. Washington, DC: National Research Council, Transportation Research Board.
- Coree, B. J., & White, T. D. 1990. *AASHTO flexible pavement design method: fact or fiction?* (No. 1286).
- Ellis, H., Jiang, M., & Corotis, R. B. 1995. Inspection, maintenance, and repair with partial observability. *Journal of Infrastructure Systems*: 1(2): 92–99.
- Guignier, F. and Madanat, S. 1999. “Optimization of infrastructure systems maintenance and improvement policies.” *Journal of Infrastructure Systems*: 5 (4): 124–134.
- Li, N., Xie, W.C. and Haas, R. 1996. Reliability-based processing of Markov chains for modeling pavement network deterioration. *Transportation research record*, 1524(1): 203–213.
- Murtagh, F. and Contreras, P., 2012. Algorithms for hierarchical clustering: an overview. *Wiley Interdisciplinary Reviews: Data Mining and Knowledge Discovery*, 2(1): 86–97.
- Opon, J. and Henry, M. 2019. An indicator framework for quantifying the sustainability of concrete materials from the perspectives of global sustainable development. *Journal of Cleaner Production* 218: 718–737.
- Smith, R. E., Zulyaminayn, M., Pilson, C. C., Dossey, T., McCullough, B. F., & Mukherjee, B. 2001. *Integration of Network and Project-Level Performance Models for TxDOT PMIS* (No. FHWA/TX-01/1727-2). Texas Transportation Institute.
- Surendrakumar, K., Prashant, N., & Mayuresh, P. 2013. Application of Markovian probabilistic process to develop a decision support system for pavement maintenance management. *International Journal of Scientific & Technology Research*, 2(8): 295–303.
- Kassambara, A., 2017. *Practical guide to cluster analysis in R: Unsupervised machine learning* (Vol. 1). Sthda.
- Wang, K.C. and Zaniewski, J.P., 1995. Optimization techniques for pavement management. In *Road Engineering Association of Asia and Australasia (REAAA)*, Conference, 8th, 1995, Taipei, Taiwan (1).

Digital twin-oriented maintenance: A hybrid finite element and surrogate model approach for predicting the excavation-induced tunnel displacement

Y. Gu, L. Zhang & Q. Ai

Shanghai Jiao Tong University, Shanghai, China

X. Jiang

Dalian University of Technology, Dalian, China

Y. Yuan

Tongji University, Shanghai, China

ABSTRACT: The excavation-induced tunnel displacement is an increasing problem with the intensive utilization of urban underground space. To rapidly and accurately predict the deformations in different scenarios, this study proposed a practical framework to build a digital twin of the tunnel–soil–foundation pit by a hybrid finite element (FE) and surrogate model approach. First, a parametric FE model is constructed, with 13 parameters as inputs and tunnel deformations at 5 positions as outputs. Then, a uniform design is adopted to generate the parameter sampling space of the FE examples, which reduces the number of samples for machine learning (ML) and computational cost. Finally, a surrogate model based on back propagation neural network (BPNN) is established, and the FE computation results and measured data from a real project are employed for verification. The results show that the accuracy of the validation set is more than 91.38%, the accuracy of the test set is more than 80%, and the error with the measured data is less than 1.5 mm. The BPNN-based surrogate model is high-efficient with a computational time of milliseconds. The established surrogate method could replace the expensive physics-based FE model for faster computation. The contribution is valuable in constructing digital twins of the tunnel during operation, especially suitable for safety assessment of existing tunnel in the scenario of adjacent engineering activities.

1 INTRODUCTION

Intensive utilization of underground space in urban areas has resulted in an increased number of excavations. A certain number of foundation pit projects must be located close to existing tunnels. However, it has been reported that the excavation of adjacent foundation pit threatens the structural safety and service life of the existing tunnel (Ai, et al., 2023). Therefore, rapid and accurate prediction of the deformation of existing tunnel in different scenarios is necessary to mitigate the risks involved during operation.

Analytical solution and FE simulation are the traditional methods for studying the response of existing tunnels during the excavation of adjacent foundation pits. Owing to the requirements of real-time response and computational accuracy, it is difficult to apply these two methods for rapid prediction and accurate evaluation of the excavation-induced deformation of an existing tunnel.

In recent years, artificial intelligence (AI)-based surrogate models have been introduced to solve forecasting problems during tunnel construction and operation. Their applications focus on the prediction of surface settlement or building damage caused by tunneling or excavation

(Zhang et al., 2020c; Ou, Teng, & Li, 2020). Furthermore, some studies have focused on AI-supported optimization of construction parameters, such as shield steering, grouting pressure, and face pressure (Zhao et al., 2019; Freitag et al., 2018; Cao et al., 2020; Ninić, Freitag, & Meschke, 2017). However, the application of an AI-based surrogate model to predict the response of existing tunnels during excavation of adjacent foundation pit is limited (Zhang et al., 2020a). It is challenging to predict the response of existing tunnels during excavation of adjacent foundation pit in different scenarios.

With advances in digital technology, digital twins have emerged as promising tools for risk management of urban infrastructure operations and maintenance (Liu et al., 2022). Owing to the complex modeling process and high computational cost of FE numerical simulation, a surrogate model can be introduced to simulate complicated and time-consuming numerical calculations. Therefore, with the ultimate purpose of constructing a digital twin of a tunnel–soil–foundation pit system, this study proposes a hybrid FE simulation and surrogate model approach for predicting excavation-induced deformation of an existing tunnel in various scenarios.

2 FRAMEWORK OF THE PROPOSED METHOD

Surrogate model refers to the method of establishing an approximate mathematical model to simulate complicated and time-consuming numerical calculations through limited samples and their responses, where the samples are often selected by experimental design (Meng et al., 2021; Kapusuzoglu et al., 2022). The proposed method performs FE simulations for physics-based interpretation of tunnel deformation, adopts an optimized experimental design to reduce the number of samples for ML, and employs a BPNN to build a surrogate model. The framework of the proposed method is shown in Figure 1.

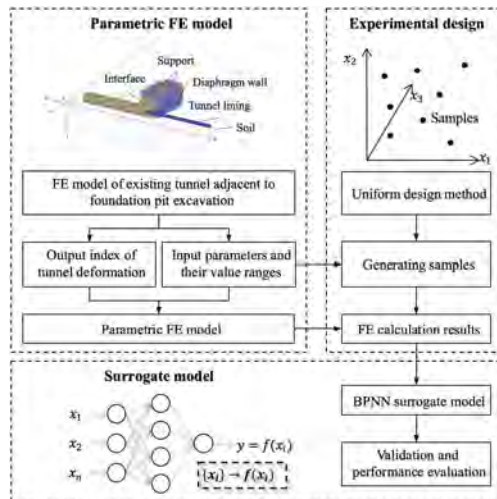


Figure 1. Framework of the proposed method.

3 PARAMETRIC FE MODEL

3.1 Scenarios in parametric FE model

To realize flexible modeling under a large number of parametric combinations, Python scripting API embedded in PLAXIS 3D was used in this study. The relative positions of the tunnel and foundation pit include three scenarios: tunnel is located below the foundation pit; tunnel is located parallel to the lateral side of the foundation pit; and tunnel intersects the foundation pit diagonally as shown in Figure 2.

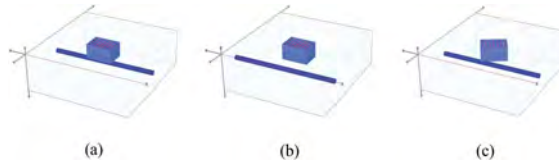


Figure 2. Scenarios of relative position of tunnel and foundation pit: (a) tunnel is located directly below the foundation pit, (b) tunnel is located on the paralleled lateral side of the foundation pit, and (c) tunnel intersects the foundation pit diagonally.

3.2 Model simplification and parameterization

The problem of excavation-induced tunnel deformation is influenced by several parameters. The parameters can be divided into soil, geometric, relative position, material, retaining structures of the foundation pit, and construction stages.

The geometric parameters of the tunnel and foundation pit include the outer diameter of tunnel D , buried depth of tunnel T_d , length of the foundation pit F_l , width of the foundation pit F_w , and depth of the foundation pit F_d .

The relative position parameters of the tunnel and foundation pit include the distance from the foundation pit to tunnel D_t and angle between the tunnel and foundation pit θ .

The retaining structures of the foundation pit are complicated; therefore, they are simplified into diaphragm walls and inner supports. We have assumed that the diaphragm wall is isotropic and continuous and all inner supports are of the same material and dimensions. The main parameters of the plate and beam elements are thickness, unit weight, and Young's modulus.

Among the abovementioned parameters, some with a small range of variation are set as constants. A total of 13 input variables are defined for the parametric model: soil unit weight γ , Young's modulus of soil E , effective cohesive force c' , effective internal friction angle ϕ' , buried depth of tunnel T_d , length of foundation pit F_l , width of foundation pit F_w , depth of foundation pit F_d , distance from the center of the foundation pit to tunnel axis D_t , angle between the tunnel axis and longer edge of foundation pit θ , thickness of diaphragm wall t_w , Young's modulus of diaphragm wall E_w , and horizontal spacing of support D_b . The outputs of parametric model are horizontal displacement u_{y_i} and vertical displacement u_{z_i} ($i = 1, 2, 3, 4, 5$) of five positions on the tunnel that act as evaluation indices of tunnel deformation.

4 EXPERIMENTAL DESIGN FOR GENERATING FE SIMULATIONS

4.1 Overview of uniform design

This study adopted a uniform design for generating samples for FE simulations. Uniform design is an experimental design method in which samples are distributed uniformly throughout the test space through a set of carefully designed tables (Fang et al., 2000). It is particularly suitable for multilevel tests because the number of tests is equal to the number of levels. The samples were selected using a uniform design table and corresponding use table. The uniform design table is represented by $U_n(q^m)$ or $U_n^*(q^m)$, indicating that the table is applicable to n tests, q levels, and m variables at most.

4.2 Experimental design of this study

In this study, we used 13 variables at 130 levels; that is, 130 FE simulations. The samples were designed using the $U_{130}^*(130^{130})$ table. The range of values of each variable determined by the literature research (Ye, Zhao, & Wang, 2021; Zhang, Xie, & Zhang, 2018; Zheng, & Wei, 2008), relevant specifications (JCSS, 2001), and measured data are listed in Table 1, and the value of each level is determined accordingly. After the FE numerical calculation, samples that are unfeasible on the relative position of the tunnel and foundation pit or whose calculation

results are not convergent owing to large deformation during construction are not considered. Ultimately, 77 groups of effective samples and their responses were obtained.

Table 1. Range of values of variables.

Variables/unit	Value range
Soil unit weight γ / ($\text{kN}\cdot\text{m}^{-3}$)	[16, 22]
Young's modulus of soil E / kPa	[4000, 16000]
Effective cohesive force c' / kPa	[1, 21]
Effective internal friction angle φ' / °	[14, 30]
Buried depth of tunnel T_d / m	[6, 24]
Length of foundation pit F_l / m	[10, 100]
Width of foundation pit F_w / m	[10, 80]
Depth of foundation pit F_d / m	[6, 24]
Ratio of distance from the center of the foundation pit to tunnel axis to length of foundation pit D_t / F_l	[0, 2]
Angle between tunnel axis and longer edge of foundation pit θ / °	[0, 90]
Thickness of diaphragm wall t_w / m	[0.6, 1.2]
Young's modulus of diaphragm wall E_w / kPa	$[2 \times 10^7, 3.3 \times 10^7]$
Horizontal spacing of support D_b / m	[3, 7]

5 SURROGATE MODEL BASED ON BPNN

5.1 Structure of the BPNN-based surrogate model

A BPNN-based surrogate model was adopted in this study. BPNN is popular and powerful for complex nonlinear function fitting or sample recognition and classification, and it has been adopted in many studies in the tunneling field (Zhang et al., 2020b).

As mentioned in Section 4, the inputs of 77 samples are used to generate uniform design and their outputs, and their outputs are calculated using the parametric FE model established in Section 3. The outputs of each sample are the horizontal displacement u_{yi} and vertical displacement u_{zi} ($i = 1, 2, 3, 4, 5$) at five positions on the tunnel. The relative location L of the five positions was taken as the input of BPNN, and the horizontal displacement u_{yi} or vertical displacement were the outputs. Thus, two BPNNs with 14 input dimensions, one output dimension, and 385 training data (77 samples \times 5 positions) were established. The two BPNNs had the same network structure, including two hidden layers containing 14 and 4 neurons, as shown in Figure 3.

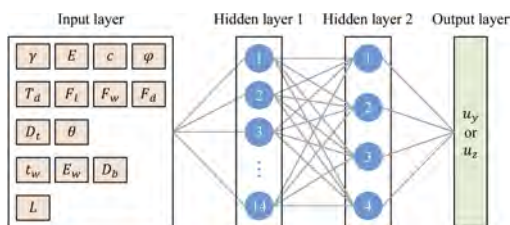


Figure 3. Structure of BPNN.

5.2 Training of the surrogate model

In this study, the horizontal displacement is defined as positive when the tunnel moves toward the foundation pit, and the vertical displacement is positive when the tunnel rises. Considering that unavoidable errors exist in actual measurements, if the error between the predicted value and actual measurement is less than ± 1 mm, the prediction will be considered accurate.

Therefore, the accuracy rate (*ACC*) is defined as the proportion of accurate predictions as shown in Equation (1),

$$ACC = \frac{1}{N} \sum_{i=1}^N I(|f(x_i) - f^*(x_i)| \leq 1) \tag{1}$$

where $f(x)$ is the actual value, $f^*(x)$ is the predicted value, N is the number of data points and $I(\cdot)$ is the indicator function, which is equal to one if the condition in the bracket is satisfied and zero otherwise.

The predictions of BPNN-based surrogate model are shown in Figure 4. In addition, Table 2 shows the accuracy rates of the horizontal and vertical displacement predictions, which are calculated using Equation (1). To predict the horizontal displacement, the accuracy rates for the training and validation sets were 97.40% and 96.55 %, respectively. For predicting the vertical displacement, the accuracy rates were 94.05% and 91.38% for the training and validation sets, respectively.

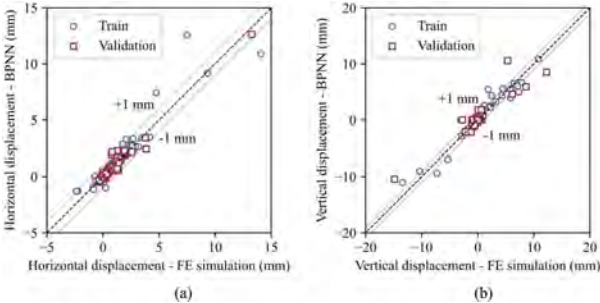


Figure 4. Accuracy of the BPNN-based surrogate model on training and validation sets: (a) BPNN vs FE simulation by horizontal displacement and (b) BPNN vs FE simulation by vertical displacement.

Table 2. Accuracy rate of the BPNN-based surrogate model.

Data set	Accuracy rate	
	Horizontal displacement	Vertical displacement cm
Training set	97.40%	94.05%
Validation set	96.55%	91.38%

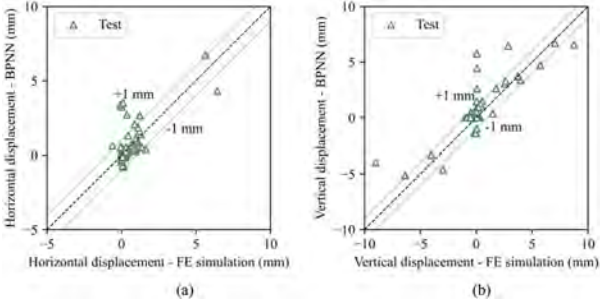


Figure 5. Accuracy of BPNN on test set: (a) BPNN vs FE simulation by horizontal displacement and (b) BPNN vs FE simulation by vertical displacement.

5.3 Validation by FE simulation

Additional 16 samples were randomly generated based on the parametric FE model as the test set. The displacements predicted by the BPNN-based surrogate model and original results calculated by parametric FE simulation are plotted in Figure 5. The accuracy rates for the test set of horizontal and vertical displacements are 85.00 and 80.00%, respectively. The computational time ranges from microseconds to milliseconds and decreases with the computed number of scenarios, so that the surrogate model is capable of real-time response and large amounts of calculation.

6 ILLUSTRATIVE EXAMPLES

6.1 Information of the investigated project

The measured data of a real project in Shanghai were used to verify the performance of the BPNN-based surrogate model. The project block is divided into nine sections for foundation pit excavation. The north side of the excavation (foundation pit 1a) is adjacent to a metro line, and the nearest distance between the existing metro tunnel and foundation pit is only 9.2 m.

The foundation pit 1a is rectangular in shape and its area is approximately 4133 m². The excavation depth of the foundation pit is 22.1 m with five layers of concrete support. The buried depth of the existing adjacent metro tunnel is approximately 10 m. The profiles of the foundation pit excavation and existing tunnels are shown in Figure 6.

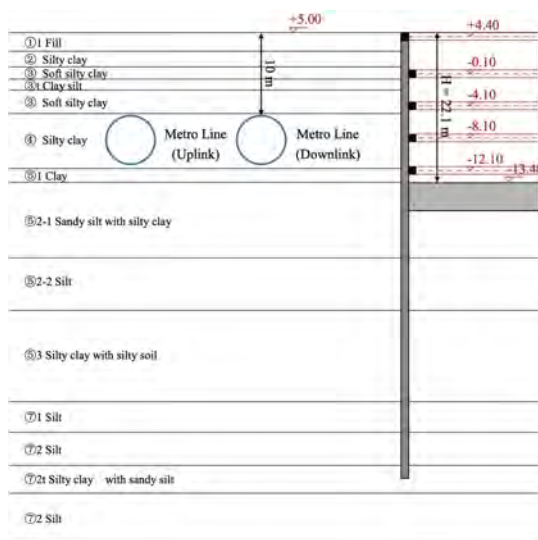


Figure 6. Profiles of the foundation pit excavation and existing tunnels.

6.2 Parameters as the inputs of surrogate model

To adapt to the parametric FE model established previously, the foundation pit was simplified as a rectangular structure with a length of 71.5 m and width of 57.8 m. The angle between the tunnel and foundation pit was approximately 13°, and the distance between the center of foundation pit and axis of the tunnel was approximately 63 m. The parameters are listed in Table 3.

6.3 Results and discussions

The values predicted by the BPNN-based surrogate model and measured values are compared in Figure 7, where the midpoint of tunnel *M* corresponds to the measuring point position of zero. The predicted and measured values are of the same order and trend with an error of less

Table 3. Model parameters drawn from the investigated project.

Parameters / unit	Value
Soil unit weight γ / ($\text{kN}\cdot\text{m}^{-3}$)	16.81
Young's modulus of soil E /kPa	8149
Effective cohesive force c /kPa	4
Effective internal friction angle φ° / °	24.7
Buried depth of tunnel T_d / m	10
Length of foundation pit F_l / m	71.5
Width of foundation pit F_w / m	57.8
Depth of foundation pit F_d / m	22.1
Distance from the center of the foundation pit to tunnel axis D_t / m	63
Angle between tunnel axis and longer edge of foundation pit θ / °	13
Thickness of diaphragm wall t_w / m	0.8
Young's modulus of diaphragm wall E_w / kPa	2.87×10^7
Horizontal spacing of support D_b / m	9.1

than 1.5 mm indicating that the surrogate model is reliable. The predicted values, measured values, and error between them are listed in Table 4.

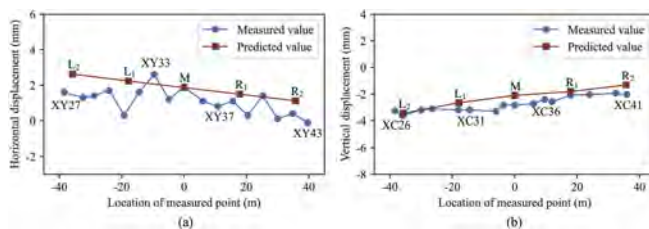


Figure 7. Validation of measured data from a real project: (a) horizontal displacement and (b) vertical displacement.

Table 4. Validation of measured data.

Location	Horizontal displacement/mm			Vertical displacement/mm		
	Measured	Predicted	Error	Measured	Predicted	Error
L_2	1.43	2.62	1.19	-3.77	-3.45	0.32
L_1	0.76	2.23	1.47	-3.20	-2.66	0.54
M	1.90	1.86	-0.04	-2.83	-2.11	0.72
R_1	0.78	1.49	0.71	-2.12	-1.82	0.31
R_2	0.38	1.11	0.74	-2.01	-1.32	0.69

The BPNN-based surrogate model for predicting tunnel deformation caused by excavation is more efficient and user-friendly than the FE simulation. Moreover, the computational time of the surrogate model is as fast as microseconds to milliseconds. Simultaneously, accuracy of the surrogate model can predict tunnel deformation with an error of less than 1.5 mm from the measured data of the actual project.

7 CONCLUSION

In this study, we proposed a hybrid FE and surrogate model approach to predict excavation-induced deformation of existing tunnels, with the ultimate purpose of constructing a digital twin of a tunnel–soil–foundation pit system. The following conclusions were drawn:

- (1) A parametric FE model of a shield tunnel during excavation of adjacent foundation pit was established with the ability to simulate different scenarios, such as relative position of the tunnel and foundation pit, soil parameters, geometric parameters, material parameters, retaining structures of the foundation pit, and construction stages. Parametric FE is the data source and foundation due to which surrogate model is physically interpretable.
- (2) The uniform design method shows advantages when faced with complex numerical problems with high dimensions and multiple levels by proposing a surrogate model with high accuracy and low computational cost.
- (3) The BPNN-based surrogate model showed good prediction performance. Considering ± 1 mm error as the accuracy evaluation standard, the accuracy of validation set was $> 91.38\%$, accuracy of the test set was $> 80\%$, error with the measured data from a real project was < 1.5 mm; and the calculation time was milliseconds.
- (4) Even though there is scope for further improvement, the verification results showed that the approach has the potential for generalization and application.

REFERENCES

- Ai, Q., Gu, Y., Yuan, Y., Jiang, X., Wang, H., Yu, H., Huang Y., 2023. Integrated waterproofing evaluation method for longitudinal joints of shield tunnel subjected to extreme surcharge: Numerical analysis and experimental validation. *Tunn. Undergr. Space Technol.* 131, 104834.
- Cao, B. T., Obel, M., Freitag, S., Mark, P., Meschke, G., 2020. Artificial neural network surrogate modelling for real-time predictions and control of building damage during mechanised tunnelling. *Adv. Eng. Softw.* 149, 102869.
- Fang, K. T., Lin, D. K., Winker, P., Zhang, Y., 2000. Uniform design: theory and application. *Technometrics* 42(3), 237–248.
- Freitag, S., Cao, B. T., Ninić, J., Meschke, G., 2018. Recurrent neural networks and proper orthogonal decomposition with interval data for real-time predictions of mechanised tunnelling processes. *Comput. Struct.* 207, 258–273.
- JCSS, 2001. *PROBABILISTIC MODEL CODE*. ISBN 978-3-909386-79-6. URL: <https://www.jcss-lc.org/jcss-probabilistic-model-code/> (Accessed December 26, 2022)
- Kapusuzoglu, B., Mahadevan, S., Matsumoto, S., Miyagi, Y., Watanabe, D., 2022. Multi-Level Bayesian Calibration of a Multi-Component Dynamic System Model. *J. Comput. Inf. Sci. Eng.* 23(1), 011006.
- Liu, X., Wang, Y., Koo, R. C., Kwan, J. S., 2022. Development of a slope digital twin for predicting temporal variation of rainfall-induced slope instability using past slope performance records and monitoring data. *Eng. Geol.* 308, 106825.
- Meng, D., Li, Y., He, C., Guo, J., Lv, Z., Wu, P., 2021. Multidisciplinary design for structural integrity using a collaborative optimization method based on adaptive surrogate modelling. *Mater. Des.* 206, 109789.
- Ninić, J., Freitag, S., Meschke, G., 2017. A hybrid finite element and surrogate modelling approach for simulation and monitoring supported TBM steering. *Tunn. Undergr. Space Technol.* 63, 12–28.
- Ou, C. Y., Teng, F., Li, C. W., 2020. A simplified estimation of excavation-induced ground movements for adjacent building damage potential assessment. *Tunn. Undergr. Space Technol.* 106, 103561.
- Ye, S., Zhao, Z., Wang, D., 2021. Deformation analysis and safety assessment of existing metro tunnels affected by excavation of a foundation pit. *Undergr. Space* 6(4), 421–431.
- Zhang, D. M., Xie, X. C., Li, Z. L., Zhang, J., 2020a. Simplified analysis method for predicting the influence of deep excavation on existing tunnels. *Comput. Geotech.* 121, 103477.
- Zhang, J., Xie, R., Zhang, H., 2018. Mechanical response analysis of the buried pipeline due to adjacent foundation pit excavation. *Tunn. Undergr. Space Technol.* 78, 135–145.
- Zhang, P., Wu, H. N., Chen, R. P., Chan, T. H., 2020b. Hybrid meta-heuristic and machine learning algorithms for tunneling-induced settlement prediction: A comparative study. *Tunn. Undergr. Space Technol.* 99, 103383.
- Zhang, P., Wu, H. N., Chen, R. P., Dai, T., Meng, F. Y., Wang, H. B., 2020c. A critical evaluation of machine learning and deep learning in shield-ground interaction prediction. *Tunn. Undergr. Space Technol.* 106, 103593.
- Zhao, C., Hölter, R., König, M., Alimardani Lavasan, A., 2019. A hybrid model for estimation of ground movements due to mechanized tunnel excavation. *Comput.-Aided Civil Infrastruct. Eng.* 34(7), 586–601.
- Zheng, G., Wei, S. W., 2008. Numerical analyses of influence of overlying pit excavation on existing tunnels. *J. Cent. South Univ. Technol.* 15(2), 69–75.

Development of simple fatigue crack propagation monitoring using IoT

T. Ishikawa

Kansai University, Suita-shi, Osaka, Japan

N. Matsumoto

Kansai University Graduate School of Science and Engineering, Suita-shi, Osaka, Japan

K. Komon

Asco Co., Ltd., Tottori-shi, Japan

ABSTRACT: In this study, the authors investigate the strain caused by the release of residual stress introduced by welding when fatigue cracks initiate and propagate. The change in the strain under the unloading condition due to fatigue crack initiation and propagation is verified via fatigue tests performed on an out-of-plane gusset joint. Subsequently, to measure and transfer the strain under the unloading condition in actual bridges, the authors create a data logger device using a single-board computer equipped with an Internet-of-Things system. The abovementioned fatigue tests are performed using the developed logger device. The measured strains are transferred via a low-power wide-area network and monitored on an Internet platform. Using the proposed system, the strains can be monitored periodically to capture fatigue crack initiation and propagation via the Internet platform.

1 INTRODUCTION

The initiation and propagation of fatigue cracks are typically encountered on steel bridges. Currently, the number of fatigue cracks in orthotropic steel decks in urban highway bridges is increasing in Japan. Some fatigue cracks in steel bridges have been monitored for crack propagation instead of for crack repair because of the slow growth of fatigue cracks. However, periodic monitoring of fatigue cracks is costly and labor intensive. Therefore, low-cost monitoring systems for fatigue-crack propagation are required.

In fatigue tests, the initiation of a fatigue crack is detected by a decrease in the strain range (or stress range) measured using strain gauges near the welding. This is because fatigue cracks prevent stress transfer at the welded joint. However, this method cannot be applied to actual bridges carrying random-weight vehicles. Meanwhile, researchers reported that different strains were measured under unloading conditions in fatigue tests owing to the initiation and propagation of fatigue cracks (Ishikawa et al. 2022). This is because the residual stress generated near the welded joint was released by fatigue crack initiation. By focusing on the change in residual stress near the weld toe, a method to detect fatigue cracks by measuring the residual stress using X-rays has been proposed (Ishikawa et al. 2017).

In this study, the change in strain under the unloading condition via fatigue crack initiation and propagation was verified based on fatigue tests performed on an out-of-plane gusset joint. Additionally, to measure and transfer the strain under the unloading condition in actual bridges, the authors created a data logger device using a single-board computer equipped with an Internet-of-Things (IoT) system. Fatigue tests under stress ratio $R = -1$ were performed on the out-of-plane gusset joint, and the strain was measured under the unloading condition

using the developed logger device. The measured strains were transferred via low-power wide-area (LPWA) network and monitored on an Internet platform.

2 CONFIGURATION OF STRAIN DATA LOGGER

The main components of the strain logger and data communication system used in this study are shown in Figure 1. The Arduino Uno R3 was used as a single-board computer. A two-channel strain amplifier shield (AD8426) was used for strain measurement. This equipment can measure -2000 to 2000 microstrains. In this study, two strain amplifier shields were used in a cascade configuration to measure four sets of strain data. In addition, a strain gauge bridge was constructed using 120 Ω metal film resistors with a tolerance of +0.1% to connect the strain gauges with the 120 Ω resistors. Power was supplied to the developed logger from a laptop computer. Notably, in field measurements, a strain gauge with a resistance of 350 Ω is preferable for reducing battery consumption.

A Sigfox shield for Arduino (UnaShield V2S) was used to transmit the measurement data for the LPWA. Additionally, Soracom Air for Sigfox (Soracom IoT platform) was used as the web platform to monitor the measurement data, as shown in Figure 1.



Figure 1. Main component of strain data logger and Soracom IoT platform.

3 FATIGUE TEST

3.1 Specimens

The out-of-plane gusset weld joint tested in this study is shown in Figure 2. The material properties and chemical compositions of the specimens are presented in Table 1. The out-of-plane gusset weld joint specimen used in this study comprised a 12-mm-thick, 200-mm-wide main plate, and a 12-mm-thick, 100-mm-high gusset plate. The gusset plate was fillet welded to the main plate via semi-automated CO₂ gas-shielded arc welding. The material used to create the specimen was JIS-SM490Y, whose yield and tensile stresses are 365 and 490 MPa, respectively.

In this study, a plate bending fatigue test machine (Yamada et al. 2007) was used for the fatigue tests, as shown in Figure 3. This plate bending tester has been used in many studies (Baik et al. 2011, Fu et al. 2018, Ishikawa et al. 2017, 2022, Yuanzhou et al. 2016). For the plate bending fatigue tests of the out-of-plane gusset welded joints, the nominal stress range was defined as the average strain range measured by strain gauges B and C (see Figure 2) multiplied by the Young's modulus of steel.

Table 1. Material properties and chemical compositions.

Steel type	Yield stress (MPa)	Tensile strength (MPa)	Elongation (%)	Chemical compositions (%)				
				C	Si	Mn	P	S
SM490Y	431	549	25	0.16	0.28	1.32	0.009	0.004

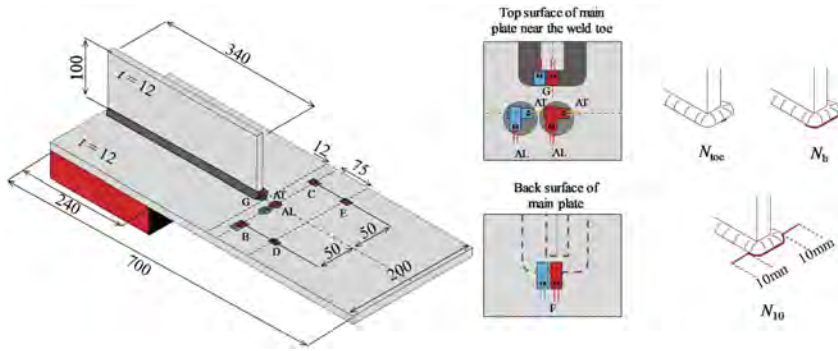


Figure 2. Out-of-plane gusset specimen, and definition of fatigue crack sizes.

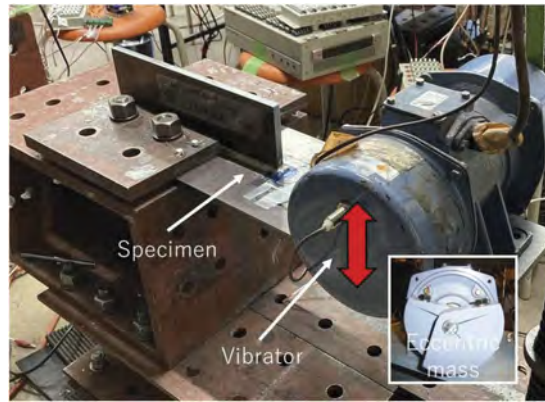


Figure 3. Plate bending fatigue test.

Fatigue tests were performed at a stress ratio of $R = -1$, and the nominal stresses were set at 70, 95, 110, and 150 MPa; the specimens subjected to these stresses were labeled as AW70, AW95, AW110, and AW150, respectively. To monitor the fatigue crack initiation and propagation, shielded copper wires with a diameter of 0.05 mm were adhered onto the weld bead and the surface of the main plate; subsequently, the fatigue lives corresponding to the crack sizes were obtained, as shown in Figure 2. N_{toe} , N_b , and N_{10} were used to denote the crack sizes when a crack initiates at the weld toe, when the crack propagates off the fillet weld toe, and when the crack propagates to 10 mm long, respectively.

3.2 Strain measurement

In this study, uniaxial and biaxial strain gauges with a gauge length of 1 mm (three-wire temperature compensated) were used. The locations of strain gauges A to G are shown in Figure 2. For the strain gauge at CH-A placed near the weld toe, two-directional gauges were used to measure the strain perpendicular and parallel to the fatigue crack. The longitudinal and transverse direction gauges at CH-A was designated as CH-AL and CH-AT, respectively.

To compare the strain measured by the dynamic strainmeter and the developed strain data logger, two strain gauges were adhered to CH-A, -B, -F, and -G at each specified location in the specimen. However, the strain gauges fixed to the dynamic strainmeter and the developed data logger were separated by approximately 5 mm in the transverse direction of the specimen. Every 10–15 min, 4096 data points (approximately 2 s) were recorded at 2000 Hz using the dynamic strainmeter. The strain measured by the developed data logger via the LPWA network was similar to that measured by the dynamic strainmeter, with the maximum and minimum strains measured once every 10 to 15 min.

4 FATIGUE TEST RESULTS AND DISCUSSION

4.1 Fatigue strength

Figure 4 shows the relationship between stress range and the number of cycles for the fatigue life N_{10} obtained from the fatigue tests performed in this study. The figure also includes the reference data (JSSC, 2020). Based on the figure, the fatigue strength of the specimens used in this study was consistent with the fatigue test results.

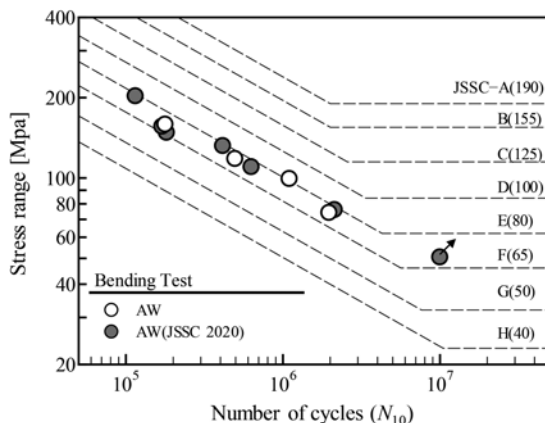


Figure 4. Fatigue strength N_{10} of out-of-plane gusset specimens.

4.2 Change in strain range

The relationship between the strain range measured by the dynamic strainmeter at each location in Specimen AW95 and the number of cycles is shown in Figure 5. The mean strain at each measurement location is plotted in this figure. Because the fatigue test was conducted at a stress ratio of $R = -1$, the mean strain became the strain under the unloading condition. Additionally, the figures show the fatigue lives of N_{10c} , N_b , and N_{10} .

The strain range measured by CH-AL near the weld toe decreased gradually owing to fatigue crack development, whereas the strain ranges at CH-B and C increased (see Figure 5). This increase was due to the stress concentration at the crack tip approaching the strains at CH-B and C. The strain range at CH-F, which was located at the back side of the main plate, changed owing to fatigue crack development as well. At all locations, the changes in the mean strain were more significant than those in the strain range. This is because the residual stress released by the fatigue crack almost yielded the stress in the tension-introduced area.

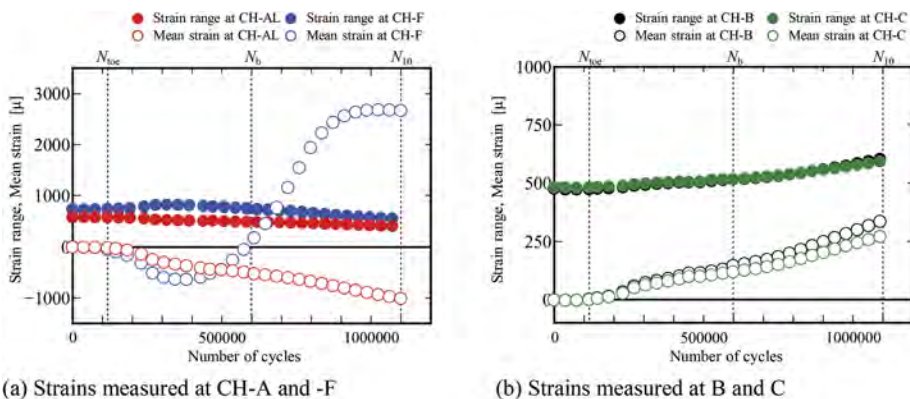


Figure 5. Relationships between strain range and each of mean strain and number of cycles ($\Delta\sigma=95$ MPa).

4.3 Change in mean strain

The relationships between the change in the mean strain obtained from gauges CH-AL, -B, -F, and G in the axial direction of the specimen and the number of cycles based on the fatigue tests are shown in Figure 6. In these figures, the mean strains measured by the dynamic strainmeter and developed data logger are shown. The results for specimens AW150 and AW95 are shown at positions CH-AL, -B, and -F, whereas those for specimens AW110 and AW70 are shown at positions CH-AL, -B, and -G. The fatigue life for each crack length is shown in the figures. As shown in Figure 6, the mean strain at CH-AL, which is in the tensile residual stress region, approached the compressive side, whereas the mean strain at CH-B, which is in the compressive residual stress region, approached the tensile side. The mean strain at CH-F on the back surface of the main plate approached the compressive side and then the tensile side. The mean strain at CH-G at the weld bead decreased at lower cycle numbers compared with that at the other measurement points and then increased. Changes in the mean stress depended on the residual stress condition and crack propagation path. The strain in the tensile residual stress area evolved to compressive strain via crack initiation and propagation, whereas the strain in the compression residual stress area evolved to tensile strain via the crack. Additionally, the strain measured at CH-F and -G near the crack propagation path changed owing to crack propagation and residual stress release.

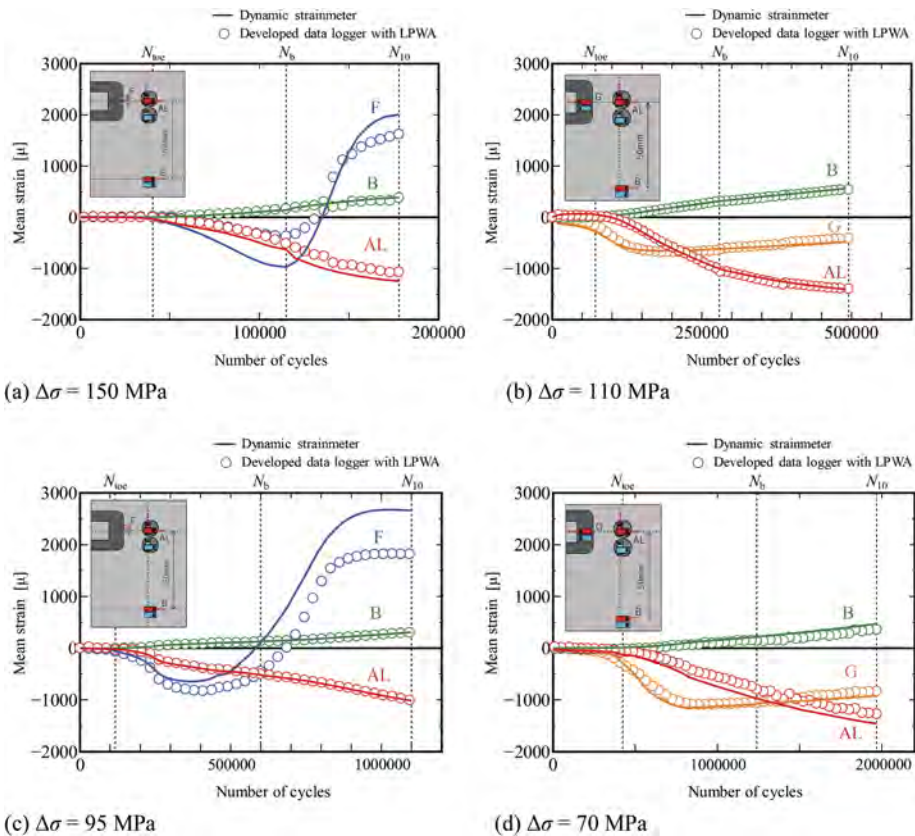


Figure 6. Relationships between mean strains recorded at CH-AL, -B, and -F and number of cycles.

As shown in Figure 6, the mean strain measured by the developed data logger and the dynamic strainmeter show a similar tendency. However, their measurement values differed slightly owing to the difference in the location of the strain gauges. Therefore, the initiation and propagation of fatigue cracks can be evaluated based on the change in the mean strain of the gauges at locations CH-AL, -B, -F, and -G in the axial direction of the specimen.

Figure 7 shows the relationship between the mean strain and number of cycles obtained from biaxial strain gauges CH-AL and -AT near the weld toe in the axial and transverse directions, respectively. The results shows that the mean strain measured by gauges CH-AL and CH-AT decreased and increased, respectively. This occurred because the strain direction of CH-AL was in the tensile residual stress region, whereas that of CH-AT was in the compressive residual stress region.

The measurements in the axial and transverse directions might be distinguishable under the effect of temperature change even at the measurement positions of gauges AL and AT because the decrease/increase in the mean strain can be confirmed.

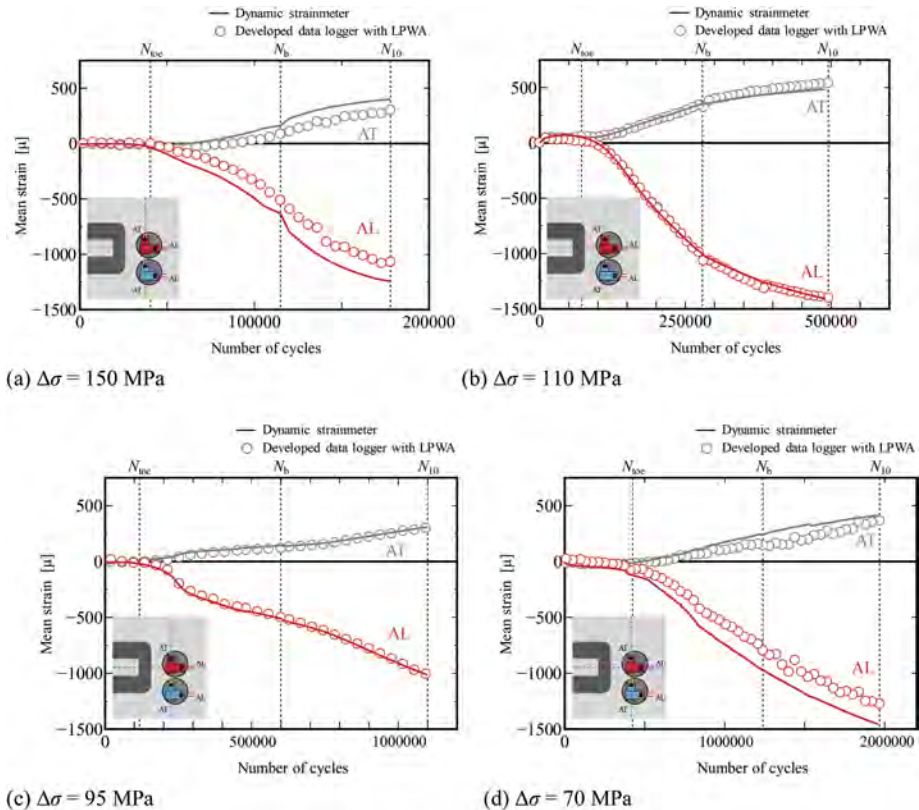


Figure 7. Relationships between mean strain at CH-AL and AT and number of cycles.

5 CONCLUSIONS

In this study, an IoT strain data logger transmission system using a single-board computer equipped with an LPWA network was developed. Subsequently, the feasibility of using the system to monitor fatigue crack initiation and propagation for out-of-plane gusseted welded joints subjected to plate-bending fatigue tests was clarified. The main conclusions obtained were as follows:

- 1) In the out-of-plane gusset specimen, the fatigue crack initiation and propagation can be evaluated by measuring the strain under the unloading condition (mean strain in this study) near the weld joint using a strain data logger.
- 2) The measurements performed in the tensile and compressive residual stress regions near the welding joint and the strain under the unloading condition in the axial and transverse directions of the specimen can be distinguished under the effect of temperature change.
- 3) The change in strain by the releasing of residual stress is considered to be a suitable index for fatigue crack propagation monitoring using LPWA.

REFERENCES

- Baik, B., Yamada, K. and Ishikawa, T. (2008) "Fatigue strength of fillet welded joint subjected to plate bending," *International Journal of Steel Structures*, 8(3), pp. 163–169.
- Fu, Z.Q., Ji, B.H., Zhang, C. and Li, D. (2018) "Experimental study on the fatigue performance of roof and U-rib welds of orthotropic steel bridge decks", *KSCE Journal of Civil Engineering*, Vol. 22, pp. 270–278.
- Ishikawa, T., Tamura, T., Okumura, T., Matsumura, T., Uchiyama, M. and Fujii, M. (2017) "Research on fatigue crack detection technique by residual stress measurement," *Journal of Structural Engineering, A*, Vol. 63, pp. 517–526.
- Ishikawa, T. and Matsumoto, N. (2022) "Evaluation of strain change under unloading conditions by initiation and propagation of fatigue crack" *Journal of Structural Engineering, A*, Vol. 68, pp. 554–563.
- Japan Society of Steel Construction, JSSC (2020) "Technical data on fatigue countermeasures for toughening and extending the service life of steel bridges," *JSSC Technical Report*, No. 12.
- Yamada, K. Osonoe, T. and Ojio, T. (2007) "Bending fatigue test on welded joint between vertical stiffener and deck plate," *Steel Construction Engineering*, Vol. 14, No. 55, pp. 1–8. (in Japanese).
- Yuanzhou, Z.Y., Ji, B.H., Fu, Z.Q. and Ge, H.B. (2016) "Fatigue performance of cracked rib-deck welded joint retrofitted by ICR technique," *International Journal of Steel Structures*, Vol. 16, No. 3, pp. 735–742.

Detection of debonding of CFRP bonded steel members using the AE method

M. Mizutani & T. Ishikawa

Kansai University, Suita-shi, Osaka, Japan

Y. Fujii

Kanazawa Institute of Technology, Nonoichi-shi, Japan

ABSTRACT: In the CFRP bonded repair of steel members, the stress in the steel members is transmitted to the CFRP by the adhesive layer. The debonding of the CFRP should be prevented to sustain the repair effect. Therefore, early detection of CFRP debonding is necessary for the CFRP bonded repair of steel members. This study conducted debonding tests on CFRP bonded steel plates using strain gauges and installed AE sensors. Consequently, elastic waves were detected by the AE sensor at an earlier stage than debonding detection by strain gauges. The position of elastic wave generation during debonding was determined by the AE, and the debonding propagation behavior was compared with that given by the energy release rate. The results indicated that the two trends were almost identical.

1 INTRODUCTION

In Japan, many steel bridges have suffered from corrosion damage. Corrosion countermeasures include repainting for minor corrosion of steel members and bolting the patch plates for corrosion with sectional loss of steel members. Carbon fiber reinforced polymer (CFRP) bonded repair is also a repair method for corrosion-damaged steel members. CFRP is a composite material with excellent material properties such as light weight, high strength, and corrosion resistance. CFRP bonding repair has advantages in terms of workability and corrosion resistance compared with steel patch repair by welding or high-strength bolts.

In CFRP bonded repairs, the stress in the steel members is transmitted to the CFRP by the adhesive layer. Stresses in the adhesive are concentrated at the CFRP end, where the cross section changes. Therefore, when the applied load increases, the CFRP may be debonded. Guidelines for CFRP bonding repairs prescribe the prevention of delamination of CFRP under the design load (Cadei et al. 2004 and JSCE 2018). The guidelines prescribe the maximum principal stress and energy release rate as indices to evaluate CFRP debonding. Currently, CFRP bonding repairs are widely performed on steel members of bridges worldwide (Hollaway and Cadei 2002, Miller et al. 2001 and Sugiura et al. 2009). However, the possibility of debonding of CFRP in in-service still remains for CFRP bonding repair. Therefore, techniques for the early detection of CFRP debonding are necessary to ensure the safety of steel bridges.

Strain gauges are often used to detect debonding in the specimens of CFRP bonded steel members in laboratory tests. Debonding at the location of the strain gauge is determined by the change in the relationship between the applied load and the strain. For the fatigue tests of CFRP bonded steel members, a method of determining the debonding of CFRP and stopping the test at an arbitrary debonding position by electrically detecting the breakage of a thin enameled wire placed on the side of the specimen has also been attempted (Thay et al. 2018). Because these debonding detection methods can only detect debonding at the sensor location, multiple sensors

must be installed to evaluate the progress of debonding. In contrast, the acoustic emission (AE) method is a method to detect delamination from a distant location (Matta et al. 2006 and Zhou et al. 2004). The AE method analyzes brittle fracture phenomena such as adhesive debonding as elastic waves. Elastic waves are transmitted through steel members when adhesives are damaged, and AE sensors can be attached to steel members. In this study, the authors focused on the AE method as a technique for monitoring the debonding of CFRP bonding repairs and conducted debonding tests using strain gauges and AE sensors installed on the specimens.

2 DEBONDING TEST OF CFRP BONDED STEEL PLATES

In this study, two cantilever bending tests were conducted using CFRP at different bonding positions. The test types are shown in Figure 1. The specimens are described in the following section.

2.1 Tests to evaluate initial delamination

The test specimen and setup are shown in Figure 1(a). In the test shown in Figure 1(a), debonding propagates instantaneously. This is because debonding of the CFRP propagates in the direction in which the applied bending moment increases. This test simulates the debonding of the CFRP ends under severe conditions. In this study, the test shown in Figure 1(a) was called the ID test.

The material properties of the steel plates, CFRP, and adhesives used for the specimens in the ID test are listed in Tables 1-3. A CFRP with the fiber direction in the longitudinal direction was used. The steel plate was 50 mm wide and 9 mm thick, and the CFRP was bonded 150 mm from the steel plate end. The CFRP was bonded along the fiber direction of the CFRP, corresponding to the axial direction of the specimen. A two-component epoxy resin was used as an adhesive. After CFRP bonding, the specimens were cured in a room at 20°C for at least 24 h before loading tests were conducted. For the ID tests, half of the CFRP was fixed and the specimen was loaded with a manual jack at 275 mm from the fixed end, as shown in Figure 1(a).

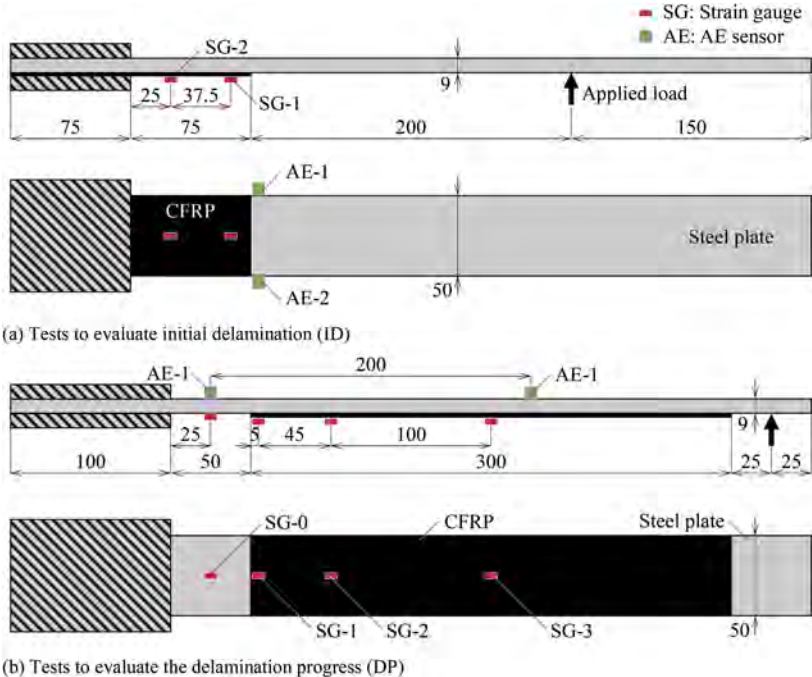


Figure 1. Dimension of specimen and test setup (unit: mm).

Table 1. Mechanical properties of steel plates.

Type	Steel	Thickness [mm]	Yield stress [N/mm ²]	Tensile strength [N/mm ²]	Elongation [%]
ID	SM490Y	9	420	550	25
DP	SM490Y	9	427	553	25

Table 2. Mechanical properties of CFRP.

Thickness [mm]	Tensile strength [N/mm ²]	Young's modulus [kN/mm ²]
2	2,400	167

Table 3. Mechanical properties of adhesive.

Compressive elastic modulus [N/mm ²]	Poisson's ratio	Tensile shear strength [N/mm ²]
2,000	0.38	more than 9.8

Strain gauges and AE sensors were placed on the specimen at the positions shown in Figure 1(a). Two AE sensors were mounted on the side of the specimen at the CFRP end of a CFRP bonded steel plate. The AE sensors had a resonant response at 300 kHz and a good frequency response in the range of 125-750 kHz. The AE sensors had a threshold value of 45 dB and acquired elastic waves at a sampling frequency of 1 MHz.

2.2 Tests to evaluate delamination progress

In the test shown in Figure 1(b), called the DP test, the debonding of the CFRP propagates in the direction where the applied bending moment decreases. Therefore, debonding progresses gradually from the CFRP end toward the center of the specimen. Hence, the propagation of debonding by AE as well as the energy release ratio can be confirmed by the DP test. The materials used for the specimens in the DP test are listed in Tables 1-3. A 300 mm long CFRP was bonded 50 mm from the fixed side. The curing procedure for the specimens in the DP test was the same as that used in the ID test. In this test, the load was applied 375 mm from the fixed end using a universal testing machine with displacement control at a speed of 1 mm/min.

Strain gauges and AE sensors were placed on the specimen at the positions shown in Figure 1 (b). Two AE sensors were mounted on the top surface of the specimen, 200 mm apart, as shown in Figure 1(b). The AE sensor used in this test was the same as that used in the ID test. However, the AE sensor was set to a threshold value of 40 dB and sampling frequency of 5 MHz.

3 TEST RESULTS

3.1 Initial delamination specimens

Figure 2 shows the relationship between the applied load and the strain for the ID test. The vertical axis represents applied load P , and the horizontal axis represents strain ε of SG-1 and SG-2 in the CFRP. The relationships between the applied load and the strain of the CFRP show a linear relationship up to the sudden drop in the strain around applied load $P = 1.0$ kN. This is because the stress is no longer transmitted to the CFRP owing to the debonding. The sudden drop in the strains in SG-1 and SG-2 indicates that debonding of the CFRP

developed simultaneously. Figure 2 shows that the debonding applied load of ID-1 was 1.01 kN and that of ID-2 was 1.02 kN.

Figures 3 and 4 show the AE results for test specimens ID-1 and ID-2, respectively. Figure 3 shows the cumulative counts with respect to the elapsed time and applied load. Figure 4 shows the energies with respect to the elapsed time and applied load. In each figure, the time when the CFRP debonding occurred is indicated by a dashed line.

As shown in Figure 3, the cumulative counts increased when debonding occurred. In addition, the accumulated counts increased before debonding (for example, around 270 s in Figure 3(a)). As shown in Figure 4, more than 30 V·s of energy was generated at the time of debonding. As shown in Figure 4, the energy of approximately 10 V·s was detected at the time when the cumulative counts increased before debonding, as shown in Figure 3. The detection of this small energy suggested that micro-damage occurred to the adhesive prior to debonding.

3.2 Delamination progress specimens

Figure 5 shows the applied load–strain relationship obtained from the DP tests. The filled circles within the experimental values are measured per second. The theory shown in Figure 5 is based on the shear lag theory (Ishikawa et al. 2012) derived by considering the force transfer of the adhesive that was derived for a similar condition in the DP test. As shown in Figure 5, the experimental and theoretical values were in good agreement with each other in the lower applied load range, where the experimental results showed linearity. However, strain gauge SG-1 in DP-1, as shown in Figure 5(a), showed a small response. As shown in Figure 5, as the applied load increased, the values of the strain gauges SG-1 through SG-3 on the CFRP side reached zero. The applied loads when the strain was zero were defined as the debonding loads at each strain location. The debonding loads are listed in Table 4. Figure 5 and Table 4 show

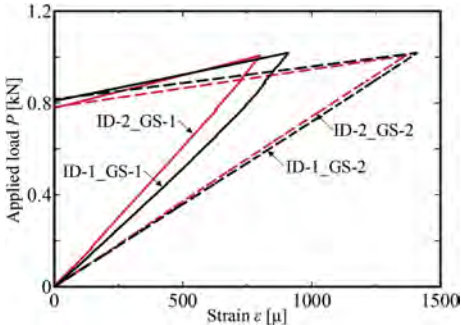


Figure 2. Relationship between the applied load and strains for the ID test.

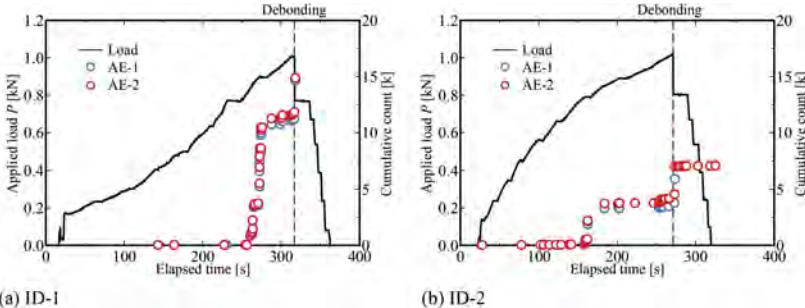


Figure 3. Counts with respect to the elapsed time and applied load for specimen ID.

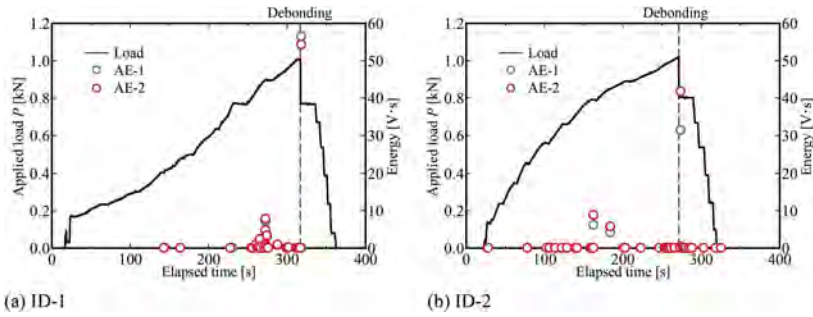


Figure 4. Energies with respect to the elapsed time and applied load for specimen ID.

that debonding of the CFRP gradually propagated from the CFRP end on the fixed side toward the center of the specimen as the test load increased. This was because the closer the debonding propagated toward the applied load position, the smaller was the bending moment generated at the debonding tip in relation to the applied load. This was also because the energy release rate per unit load at the debonding tip decreased as the debonding progressed, and the remaining adhesive length of the CFRP became shorter (Ishikawa et al. 2012). In the case of SG-3, where the measured strain gradually decreased after reaching a maximum value, the lag in force transmission owing to the movement of the bonded edge caused by the debonding process might be affected. Compared with DP-1 (Figure 5(a)), the debonding load of DP-2 (Figure 5(b)) was generally lower and the bond strength was weaker.

Figure 6 shows the cumulative counts with respect to the elapsed time and applied load. The drawn AE result is the only event used in the analysis of the source of the elastic wave with the two AE sensors described below. The time of debonding at zero strain at each location is indicated by dashed lines in Figure 6. Notably, the cumulative count of AE increased with the time of debonding at SG-1 to debonding at SG-3. However, as shown in Figure 6(a), for DP-1, the accumulated counts increased even before debonding of SG-1. As aforementioned, the small change in strain in DP-1_SG-1 might indicate that debonding at SG-1 was not accurately estimated. The slope of the cumulative counts for specimen DP-2 (Figure 6(b))

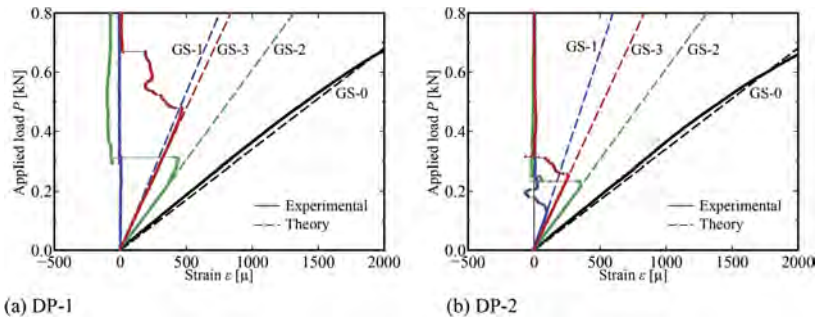


Figure 5. Relationship between the applied load and the strain for the DP test.

Table 4. Debonding load of specimen DP [N].

	Reference strain gauges		
	SG-1	SG-2	SG-3
DP-1	311	311	752
DP-2	178	232	312

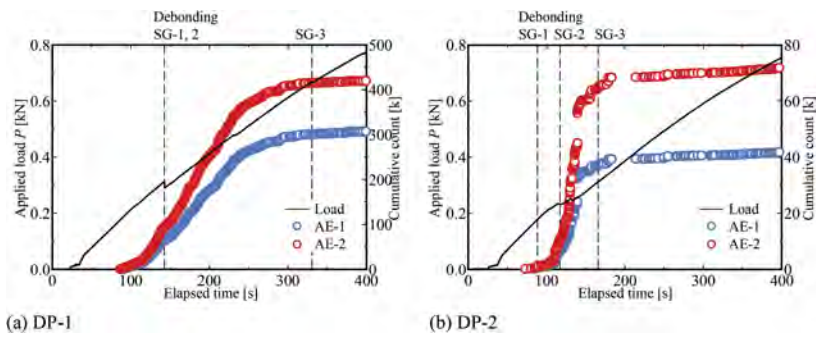


Figure 6. Counts with respect to the elapsed time and applied load for specimen DP.

was larger than that for specimen DP-1 (Figure 6(a)). This indicated that debonding propagation was faster for specimen DP-2 than for specimen DP-1.

3.3 Analysis of the debonding evolution of specimen DP

Figure 7 shows the results of the applied load and position of elastic wave generation. The position of the generated elastic wave was linearly evaluated using the time difference between the events when the generated elastic wave arrived at the two AE sensors. The velocity of sound propagating through the steel was assumed to be 5,900 m/s. To reduce the noise in location determination, a filter was applied to modify the threshold value to 50 dB. The solid line in Figure 7 shows the relationship between the debonding load and the debonding length from the CFRP end that is determined by the energy release rate described below.

As shown in Figure 7, as the load increased, the debonding tip location moved from the fixed side to the center of the specimen. Therefore, in conclusion, the debonding propagation behavior was captured by the AE sensors. However, elastic waves were also observed at points where the CFRP was not adhered ($x = -25$ to 0 mm). Therefore, the measurement method must be improved to capture only the elastic waves caused by debonding and evaluate the AE parameters. In addition, it should be noted that only two AE sensors were used in this study; therefore, evaluation in the width direction was not possible. In particular, specimen DP-1 might not debond uniformly in the width direction owing to the relationship between the applied load and the strain and the variation in the results of the AE method.

As shown in Figure 8, considering debonding with a length of l_{cr} from the CFRP end on the fixed side, the energy release rate associated with the progress of debonding is given by the equations below (Mizutani et al. 2022).

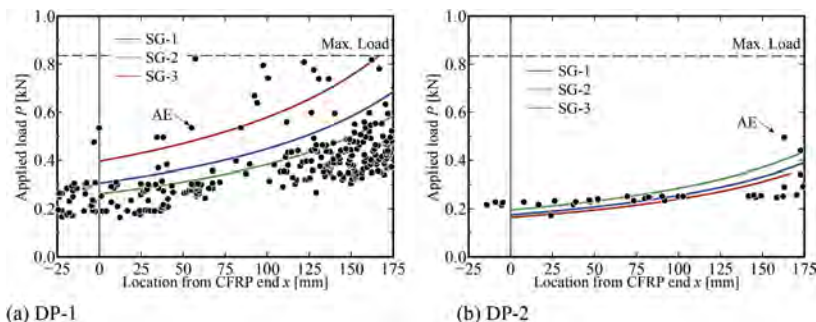


Figure 7. Counts with respect to the elapsed time and applied load for specimen DP.

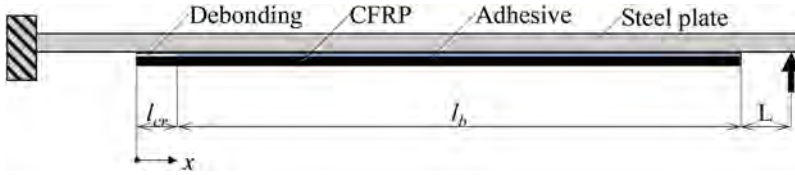


Figure 8. Modeling of debonding for the energy release rate.

Table 5. Energy release rate for specimen DP (unit: N/mm).

	Reference strain gauges		
	SG-1	SG-2	SG-3
DP-1	0.085	0.062	0.143
DP-2	0.028	0.035	0.025

$$G = \frac{h}{2G_e} \tau_{cr}^2 \quad (1)$$

$$\tau_{cr} = -\frac{cK}{ab_c} \left\{ \frac{L + l_b}{\tanh(cl_b)} - \frac{L}{\sinh(cl_b)} + \frac{1}{c} \right\} P \quad (2)$$

where $c = \sqrt{b_c G_e a^2 / (h E_s I_s K Z_1)}$; $K = 1 / (1 + Z_1 Z_2 r_s^2 / a^2)$; $r_s = \sqrt{I_s / A_s}$; $a = t_s / 2 + h + t_c / 2$; $Z_1 = 1 + I_c / (n I_s)$; $Z_2 = 1 + n A_s / A_c$; $n = E_s / E_c$; G = energy release rate at the debonding tip; τ = shear stress at the debonding tip; l_b = remaining bond length; E_s = Young's modulus of the steel plate; E_c = Young's modulus of CFRP; G_e = shear modulus of elasticity of adhesive; I_s = sectional secondary moments of the steel plate; I_c = sectional secondary moments of CFRP; A_s = cross-sectional area of the steel plate; A_c = cross-sectional area of CFRP; t_s = thickness of the steel plate; t_c = thickness of CFRP; h = thickness of adhesive; b_c = width of CFRP.

The energy release rate is a debonding index used in the Japan Society of Civil Engineers (JSCE) guidelines (JSCE, 2018). Shear stress τ (Equation (2)) was derived based on the shear lag theory. Table 5 lists the energy release rates calculated from the debonding loads at each strain gauge listed in Table 4. The $P - x$ relationships, which were calculated by applying the relationship between debonding length and applied load from Equation (1) by applying the values in Table 5 as the critical energy release rates, are shown in Figure 7. This figure indicates that the evaluation of debonding propagation by the energy release rate has a tendency similar to the results of debonding propagation given by the AE. In particular, the debonding evaluation using the SG-2 results showed good agreement with the AE results.

4 CONCLUSIONS

In this study, to evaluate the debonding of CFRP, debonding tests were conducted on CFRP bonded steel members using strain gauges and installed AE sensors. The cumulative counts and energies associated with debonding of the CFRP were identified from the ID test that evaluated the initial debonding. Consequently, elastic waves were detected by the AE sensor at an earlier stage than the detection of debonding by strain gauges.

The source of the elastic waves could be estimated using two AE sensors from the DP test that evaluated the evolution of the debonding propagation. As the applied load increased, the location of the elastic waves moved from the CFRP end on the fixed side to the center of the specimen. The energy release rate was used to evaluate the debonding propagation, and the results were almost identical to the AE results.

REFERENCES

- Cadei, J.M.C., Strafford, T.J., Hollaway, L.C. & Duckett, W.G. 2004. Strengthening metallic structures using externally bonded fibre-reinforced polymers, *CIRIA*, C595, 514–522. London: CIRIA
- Hollaway, L.C. and Cadei, J. 2002. Progress in the technique of upgrading metallic structures with advanced polymer composites, *Progress in Structural Engineering and Materials*, Volume 4, Issue 2, 131–148.
- Ishikawa, T., Shimizu, M., Hattori, A. & Kawano, H. 2012. Effect of loading conditions on adhesive stresses of steel members strengthened by bonding CFRP plates, *Journal of Japan Society of Civil Engineers, Ser. A2 (Applied Mechanics (AM))*, Volume 68, Issue 2, I_715-I_726. (In Japanese)
- Japan Society of Civil Engineers (JSCE) 2018. Guidelines for Repair and Strengthening of Structures Using Externally Bonded FRP. Tokyo: Maruzen Publishing Co., Ltd. (In Japanese)
- Matta, F., Rizzo, P., Karbhari, V.M. & Scalea, F.L. 2006. Acoustic emission damage assessment of steel/CFRP bonds for rehabilitation, *Journal of Composites for Construction*, Volume 10, Issue 3, 265–274.
- Miller, T.C., Chajes, M.J., Mertz, D.R. & Hastings, J.N. 2001. Strengthening of a steel bridge girder using CFRP plates, *Journal of Bridge Engineering*, Volume 6, Issue 6, 514.
- Mizutani, M., Ishikawa, T. & Fujii, Y. 2022. Evaluation of debonding damage in CFRP bonded steel plates by acoustic emission method, *Proceedings of Constructional Steel*, Volume 30, 159–164. (In Japanese)
- Sugiura, H., Kobayashi, A., Inaba, N., Homma, A., Ohgaki, K. & Nagai, M. 2009. A proposal of design and construction method of repair for corroded steel members by carbon fiber sheets, *Doboku Gakkai Ronbunshuu F*, Volume 65, Issue 1, 106–118. (In Japanese)
- Thay, V., Nakamura, H., Lin, F. & Horii, H. 2018. Evaluation of fatigue strength of adhesively bonded joints between steel plates and patch plates using epoxy resin adhesive, *Journal of Japan Society of Civil Engineers, Ser. A1 (Structural Engineering & Earthquake Engineering (SE/EE))*, Volume 74, Issue 5, II_56-II_66. (In Japanese)
- Zhou, W., Liu, R., Lv, Z., Chen, W. & Li, X. 2015. Acoustic emission behaviors and damage mechanisms of adhesively bonded single-lap composite joints with adhesive defects, *Journal of Reinforced Plastics and Composites*, Volume 34, Issue 1, 84–92.

Condition-based maintenance of fatigue-sensitive structures using model predictive control

S. Kong, R. Cao, J. Cheng & Y. Liu

Huazhong University of Science and Technology, Wuhan, China

ABSTRACT: Structural damage such as fatigue cracks can cause the deterioration of structural performance during service life. Condition-based maintenance (CBM) methods are developing rapidly in life-cycle management to address the decision-making of fatigue structural maintenance. In this paper, a new CBM method for deriving the optimal maintenance policy is proposed using Model Predictive Control (MPC). MPC is an optimization-based control method for constrained systems. The control actions are decided by solving a nonlinear programming problem with constraints. A fatigue detail of an offshore wind turbine (OWT) structure is applied to demonstrate the proposed method. The results show that the MPC-based method is feasible to obtain low-cost CBM policies for life-cycle maintenance. Furthermore, the performance of MPC-based method is compared with policies obtained by the time-based cyclic repair approach. The comparison study shows that the MPC policies result in lower life-cycle costs in general.

1 INTRODUCTION

OWT is generally subjected to continuous deterioration during its service life. Structural damage such as fatigue cracking can lead to serious safety issues (Liu & Frangopol, 2019). To maintain an adequate reliability level, repairs should be planned at appropriate times during the lifetime (Cheng et al., 2022). Total life-cycle costs should be considered to decide on an optimal maintenance policy (Frangopol, 2011). Operating and maintenance (O&M) cost accounts for a large portion of the total life-cycle costs of OWT (Turan et al., 2009). Compared to operating costs, maintenance costs are more important in controlling the life-cycle costs of OWT (Ren et al., 2021). Maintenance has a strong influence on downtime duration over the lifetime of an offshore wind turbine and consequently contributes considerably to the total life-cycle costs. Though the performance of OWT degrades over time, reasonable and efficient maintenance strategies and procedures can reduce the downtime caused by aging equipment (Ren et al., 2021). Condition-based maintenance is an advanced maintenance strategy that attracts increased attention in solving maintenance problems. This paper proposes a new framework for deriving the optimal CBM maintenance policy.

Maintenance strategies are typically categorized as corrective (reactive) maintenance, proactive maintenance, and opportunistic maintenance according to when maintenance is conducted (Ren et al., 2021). Nielsen & Sørensen (2011) compared the costs of two distinct maintenance strategies for OWT, namely with and without the inclusion of periodic imperfect inspections. Dao et al. (2021) proposed an integrated maintenance strategy of corrective maintenance, imperfect time-based preventive maintenance and condition-based maintenance for OWT and compared with other traditional maintenance strategies. They evaluated the influence of different important parameters, such as failure rate, reliability of inspections, inspection interval, and the decision rule for repairs.

MPC is an optimization-based control method for constrained systems. Su et al. (2015) used MPC to extend a control system framework for optimal planning of railway maintenance operations. The merit of the MPC-based methodology is that the objective function explicitly captures

the trade-off between maintenance costs and the health condition of the OWT. This is crucial to facilitate the decision-making process. Moreover, other factors concerning the management of OWT like downtime due to maintenance, can also be conveniently added to the MPC optimization problem. MPC provides a promise method to derive the optimal CBM policy.

In this paper, an adaptable MPC-based framework for optimal life-cycle management planning of OWT is proposed. This framework is flexible and can be adapted dynamically considering the measured wind and wave data representative for the location of the OWT. The control actions are decided by solving a finite horizon optimal control problem in real time. A case study on an OWT is applied to demonstrate the proposed framework. This paper compares the maintenance costs using MPC with different horizons. A simple cyclic repair approach with the same objective function is also implemented and optimized for comparison.

2 MODEL DESCRIPTION

2.1 Fatigue degradation progress model

A widely used model for fatigue degradation progress adapted from fracture mechanics is the Paris Law (Paris & Erdogan, 1963). It has been adopted in wind turbine degradation modeling (Zhu et al., 2013). In this research, the OWT component degrades gradually, and its health state is represented by a continuous degradation indicator, D . It is shown in Equation 1.

$$\frac{dD}{dN} = C(\Delta K)^m \quad (1)$$

Where dD is the degradation growth, N is the number of load cycles, Δk is the stress intensity factor depending on the load applied on the component, C and m are material parameters representing material properties of the component.

Generally, the number of operating cycles per unit time is given. The number of cycles per hour is assumed to be constant $dN/dt = 360/h$. The equivalent fatigue degradation growth depending on time is presented as in Equation 2.

$$\frac{dD}{dt} = \frac{dN}{dt} C(\Delta K)^m \quad (2)$$

The continuous degradation indicator D is assumed to be calibrated on a relative scale from 0 to 1 for all components. The degradation $D = 0$ means a healthy component, while $D = 1$ represents a component with a bad state. The initial degradation size $D(0) = D_0$. The D is higher with the more severe degradation of the component. Maintenance makes D lower, which depends on the types of maintenance activity and its effectiveness.

Δk depends on the current damage size D (Nielsen & Sørensen, 2011), and is given by

$$\Delta K = \beta \cdot \Delta s \cdot \sqrt{\pi D} \quad (3)$$

$$\Delta s = H_t \cdot x_s \quad (4)$$

Where β is the geometry factor, and x_s is the proportionality factor of estimating Δs . H_t is the mean significant wave height. The wave height and the wind speed are strongly correlated (Braam & Eecen, 2005). In this paper, the main focus is to model different maintenance activities and to illustrate the benefits of CBM policies derived from MPC. Therefore, the wind speed is assumed as follow.

$$v_t = \alpha H_t \quad (5)$$

The accumulated degradation of the OWT component is updated by Equation 6.

$$D_{t+1} = D_t + \frac{dD}{dt} \Delta t \quad (6)$$

Then the time-dependent degradation D_t is obtained. However, some parameters mentioned before are associated with large uncertainty. For example, the degradation level after replacement depends on how well the replacement has been performed. In this paper, it is assumed to be a stochastic variable D_0 , which is also the initial degradation size. The mean significant wave height is also uncertain. These parameters are assumed to follow the distributions shown in Section 4. Considering the uncertainties, we can obtain the failure rate $P_f(t)$ depending on the current degradation growth D_t .

$$P_f(t) = \frac{N(D_t > 1)}{N_0} \tag{7}$$

Where N_0 is the number of cycles, and $N(D_t > 1)$ is the number of failures in N_0 .

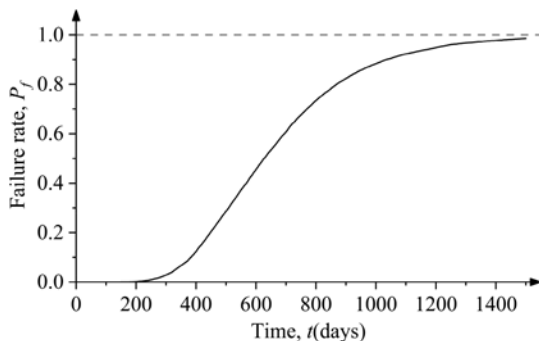


Figure 1. Failure rate curve.

2.2 Maintenance activities and impacts

This paper evaluates three possible maintenance options: (1) to do nothing, (2) repair, and (3) replacement. To do nothing has no effect on the OWT component. A short description of the repair and replacement is given as follow.

- *Repair*: Repair can maintain the degradation level for a constant period T_0 . After this period, the failure rate will develop as before the repair.
- *Replacement*: Replacement is carried out when the condition has worsened, and the failure rate is fairly high. It requires much cost and time, but it can renew the component, which leads to a healthy status for a longer period.

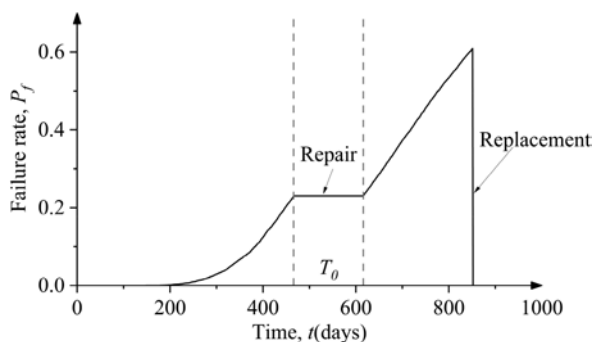


Figure 2. Maintenance activities and impacts.

MPC-based method can be used to observe the probability of failure. It can combine the cost and performance in fixed horizons with the reliability of OWT components to decide what maintenance policies would be adopted at certain points.

3 MPC FOR MAINTENANCE OPERATION PLANNING

3.1 State space model

The failure rate $P_f(t)$ depending on time is shown in Equation 7. The failure rate at real time-step k is denoted by $x(k)$, and the failure rate at degradation time-step i is denoted by $P_f(i)$. Considering an auxiliary variable $\mathbf{P}(i)$ and the input $\mathbf{u}(k)$.

$$\mathbf{P}(i) = [P_f(i+1) \quad P_f(i) \quad 0] \quad (8)$$

$$\mathbf{u}(k) = [u_1(k) \quad u_2(k) \quad u_3(k)]^T \quad (9)$$

The state space model of failure rate at real time-step k is shown as follow.

$$\begin{cases} x(k+1) = \mathbf{P}(i)\mathbf{u}(k) \\ x(k+2) = [\mathbf{P}(i+1)\mathbf{u}(k+1) \quad P_f(i) \quad 0]\mathbf{u}(k) \\ x(k+3) = [[\mathbf{P}(i+2)\mathbf{u}(k+2) \quad P_f(i+1) \quad 0]\mathbf{u}(k+1) \quad P_f(i) \quad 0]\mathbf{u}(k) \\ \vdots \end{cases} \quad (10)$$

With the constraint:

$$M_1 \leq x(k) \leq M_2 \quad (11)$$

The M_1 is the lower bound of the failure rate, and the upper bound is the M_2 .

The input $\mathbf{u}(k)$ is a discrete input representing the three maintenance strategies: to do nothing, repair, replacement. The three control actions are associated with three binary variables $u_1(k)$, $u_2(k)$ and $u_3(k)$. Obviously, $u_1(k) = 1$ means to do nothing, thus $i = i + 1$. $u_2(k) = 1$ represents to adopt repair, and means that degradation time-step i will remain unchanged for a constant period T_0 . Furthermore, replacement would be applied if $u_3(k) = 1$, causing $i=0$. Considering only one of them would be adopted at time-step k , we can add the constraint:

$$u_1(k) + u_2(k) + u_3(k) = 1 \quad (12)$$

3.2 Objective function formulation

The goal of maintenance operations planning is to prevent failure of OWT components and minimize the possible maintenance cost as well as the accumulated energy not supplied.

C_{rpm} is the individual cost per replacement activity, and C_{rpr} is the cost per repair activity. The accumulated energy not supplied can be estimated by maintenance downtime. T_{rpm} is maintenance downtime per replacement activity, and the maintenance downtime per repair action is symbolized by T_{rpr} . The power output of a normal OWT, $P(k)$, is shown as follow (Dao et al., 2021).

$$P(k) = \begin{cases} \frac{1}{2} C_\rho A_r v_k^3 & \text{if } v_{cut-in} \leq v_k < v_{rated} \\ P_{rated} & \text{if } v_{rated} \leq v_k \leq v_{cut-out} \\ 0 & \text{otherwise} \end{cases} \quad (13)$$

Where ρ is the air density; C_ρ is the power coefficient; A_r is the rotor swept area; v_k is the wind speed at time-step k ; P_{rated} is the OWT rated power; v_{cut-in} is the cut-in wind speed; v_{rated} is the rated wind speed; $v_{cut-out}$ is the cut-out wind speed.

Considering the power price b , the cost function $J(k)$ at time-step k as follows.

$$J(k) = \lambda (0 \quad C_{rpr} + bP(k)T_{rpr} \quad C_{rpm} + bP(k)T_{rpm}) \begin{pmatrix} \hat{u}_1(k) \\ \hat{u}_2(k) \\ \hat{u}_3(k) \end{pmatrix} + [\hat{x}(k+1|k)]^2 \quad (14)$$

Where $\hat{u}_1(k)$, $\hat{u}_2(k)$ and $\hat{u}_3(k)$ are the estimated maintenance strategies at time-step k . The weighting parameter λ balances the two conflicting objectives. Denote the estimated state x at

sample step $k + j$ with information available at sample step k by $\hat{x}(k + j|k)$. Let N_p be the prediction horizon, and define:

$$\tilde{J}(k) = J(k) + J(k + 1) + \dots + J(k + N_p - 1) \quad (15)$$

as the objective function at real time-step k .

3.3 MPC controller

This problem is accordingly transformed to be a minimization problem with the objective function $\tilde{J}(k)$ which is shown in Equation 15. And this problem is subject to Equation 8-14.

The modified MPC-based approach is shown as follows.

Initialization: Given the initial state $x(0) = x_0$ and the degradation time-step $i = 0$.

- **Step 1:** Solve Equation 8-15 to obtain the optimal solution $\hat{\mathbf{u}}(k) \hat{\mathbf{u}}(k + 1) \dots \hat{\mathbf{u}}(k + N_p + 1)$.
- **Step 2:** The MPC controller $\mathbf{u}(k) = \hat{\mathbf{u}}(k)$ is applied at the maintenance instant k . The remains of the optimal solution $\hat{\mathbf{u}}(k + 1) \dots \hat{\mathbf{u}}(k + N_p + 1)$ are discarded. The predicted state $x(k + 1)$ can be obtained by applying $\mathbf{u}(k)$ to Equation 10. The actual system state over the next sampling period is updated by $x(k + 1)$.
- **Step 3:** Let $x(k + 1)$ be the initial state for the next predictive horizon $k = k + 1$, and go back to the **Step 1**.

The above MPC algorithm will go over the sustainability period to obtain the optimal control strategy.

4 CASE STUDY

In this section, a case study for an OWT is presented for illustrative purpose. It is a 10-MW OWT with characteristics from (Bak et al., 2013), which is shown in Table 1. The damage parameters in the example are assumed to follow the values and distributions as shown in Table 2. The scale parameter α is assumed to be 5. The lower bound of the failure rate M_1 is assumed to be 0, and the upper bound M_2 is supposed to be 1. Moreover, the mean significant wave height H_1 is assumed to follow Weibull distribution, whose scale parameters is 1.38, and shape parameters is 1.60 (Braam & Eecen, 2005). The cost and time data are presented in Table 3. The constant period of repair T_0 is assumed to be 150 days. The power price b is supposed to be 0.035 £/kWh (Nielsen & Sørensen, 2011).

The MPC controller mentioned before is implemented in Python with the Gurobi Optimizer 9.5.2. The initial condition $x(0) = M_1$, and the sampling time is 10 days. The ratio of C_{rpm} to C_{rpr} is assumed to be 10. We present the simulation results with three different prediction horizons N_p , and three different weights λ .

To be a comparison, a cyclic repair strategy with the same objective function is also optimized. The period for repair T_1 and the period for replacement T_2 should be decided (Su et al. 2015). And the latter is fixed as $T_2 = nT_1 + (n - 1)T_0/step$. All possible combinations of T_1 and n is adopted to obtain the best maintenance plan.

Table 1. Wind turbine characteristics (adopted from Bak et al. (2013)).

Parameter	value
Power rating	10 MW
Rotor diameter	178.3 m
Cut-in wind speed	4 m/s
Rated wind speed	11.4 m/s
Cut-out wind speed	25 m/s
Power factor	0.44

Table 2. Distribution types for damage parameters (Nielsen & Sørensen, 2011).

Symbol	mean	COV	Distribution
m	2	-	Deterministic
β	1	-	Deterministic
C	9.26×10^{-10}	0.2	Lognormal
x_s	11.5	0.1	Lognormal
D_0	0.02	0.02	Exponential

Table 3. The cost and time data (adopted from Dao et al. (2021)).

Symbol	value
C_{rpr}	4.5 (£1000)
C_{rpm}	45 (£1000)
T_{rpr}	11.55 (h)
T_{rpm}	115.5 (h)

The results of the MPC approach are shown in Figure 3-5 and Figure 6 represents the results from the cyclic approach. The results in Figure 3-6 show that a larger weight λ results in higher overall failure rate level. This is because a larger weight λ represents the cost has greater proportion in the objective function. Thus the optimizer tends to decrease cost instead of failure rate level. Figure 4-6 show that the larger weight λ causes later replacement.

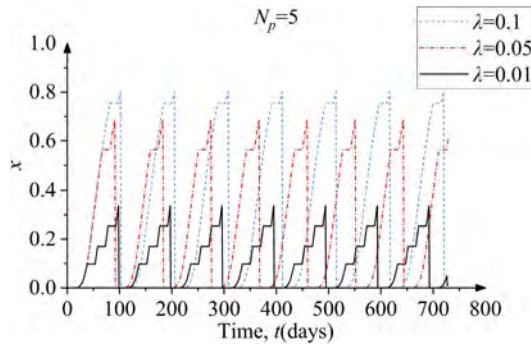


Figure 3. Predicted state x for different weights $\lambda = 0.01, 0.05, 0.1$ and a short prediction horizon $N_p = 5$.

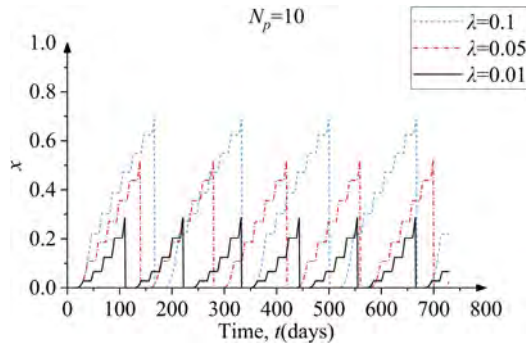


Figure 4. Predicted state x for weights $\lambda=0.01, 0.05, 0.1$ and a medium prediction horizon $N_p = 10$.

In Figure 3-5, it is shown that a longer prediction horizon causes a more cautious maintenance plan, which means lower overall degradation level. Because the optimizer will be long-sighted to prevent failure with the increasing of prediction horizon. Furthermore, the effect of increasing prediction horizon is the reverse of increasing weight. In Figure 3-6, The cyclic policy tends to adopt more replacement than MPC-based method with the same weight.

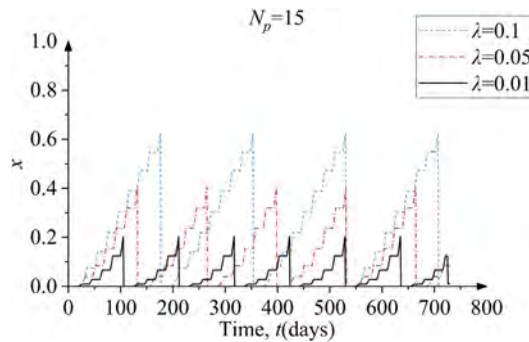


Figure 5. Predicted state x for weights $\lambda=0.01, 0.05, 0.1$ and a long prediction horizon $N_p = 15$.

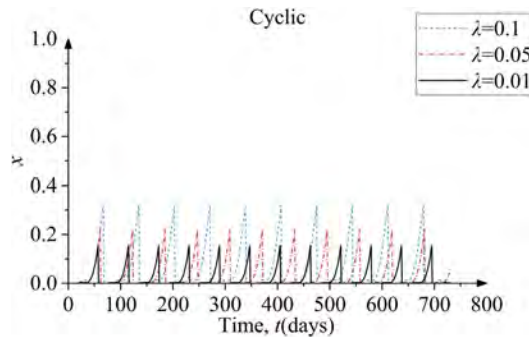


Figure 6. The effect of the cyclic approach with different weights $\lambda=0.01, 0.05, 0.1$.

The comparison of the MPC method and simple cyclic preventive maintenance approach is given in Table 4, where J is the objective function. In Cases 1-3, 5-7, and 9-11, there is a lower objective function with a longer prediction horizon and the same weight. However, In

Table 4. Comparison of the two optimal approaches.

Case	$N_p N$	λ	number of Repair	number of replacement	Cost (£1000)	J
1	5	0.01	21	7	470.135	6.429
2	10	0.01	26	6	444.303	5.325
3	15	0.01	28	6	454.636	4.942
4	Cyclic	0.01	13	12	687.120	8.170
5	5	0.05	8	7	402.973	66.728
6	10	0.05	25	5	387.474	23.113
7	15	0.05	27	5	397.806	21.692
8	Cyclic	0.05	12	11	630.291	34.393
9	5	0.1	7	7	397.806	119.380
10	10	0.1	25	4	335.811	41.412
11	15	0.1	28	4	351.310	40.119
12	Cyclic	0.1	11	10	573.461	64.650

Cases 2-3, 6-7, and 8-9, we can see the longer prediction horizon doesn't result in lower cost. This is because the optimizer considers not only the cost but also the performance. The objective function is lower although the cost is higher in Cases 2-3, 6-7, and 8-9. Moreover, in Cases 1-4, 5-8, and 9-12, it can be seen that with a long enough prediction horizon, the maintenance plan obtained by MPC always performs better than the plan obtained by the cyclic approach. The cost and objective function of the former are lower than those of the latter.

5 CONCLUSIONS

This paper presents a new MPC-based method for deriving the optimal CBM policy. It can decide on replacement or repair that would be adopted at certain points by considering the cost and performance in fixed predicted horizons. A fatigue detail of an OWT structure is applied to demonstrate this proposed method. The simulation results with different predictive horizons and weights are presented. It is shown that the MPC-based method can balance the cost and performance well. There will be lower cost and objective function by applying the MPC approach with a long enough predicted horizon. The results indeed demonstrate the merits of MPC as an optimization-based approach to aid decision-making in the maintenance of OWT structures. For further research, the ratio of the cost of the two maintenance strategies can be discussed. Furthermore, the cost of inspections can be included in a more comprehensive study.

ACKNOWLEDGEMENTS

This research is supported by the Fundamental Research Funds for the Central Universities (HUST: No. 2020kfyXJJS047).

REFERENCES

- Bak, C., Zahle, F., Bitsche, R., Kim, T., Yde, A., Henriksen, L. C., Henriksen, et al. 2013. The DTU 10-MW reference wind turbine. In *Danish wind power research 2013*.
- Braam, H., & Eecen, P. J. 2005. *Assessment of wind and wave data measured at IJmuiden Munitiestortplaats*. Petten: ECN.
- Cheng, J., Liu, Y., Cheng, M., Li, W., & Li, T. 2022. Optimum condition-based maintenance policy with dynamic inspections based on reinforcement learning. *Ocean Engineering*, 261, 112058.
- Dao, C. D., Kazemtabrizi, B., Crabtree, C. J., & Tavner, P. J. 2021. Integrated condition-based maintenance modelling and optimisation for offshore wind turbines. *Wind Energy*, 24(11),1180–1198.
- Frangopol, D. M. 2011. Life-cycle performance, management, and optimisation of structural systems under uncertainty: accomplishments and challenges 1. *Structure and Infrastructure Engineering*, 7(6),389–413.
- Liu, Y., & Frangopol, D. M. 2019. Utility and information analysis for optimum inspection of fatigue-sensitive structures. *Journal of Structural Engineering*, 145(2), 04018251.
- Nielsen, J. J., & Sørensen, J. D. 2011. On risk-based operation and maintenance of offshore wind turbine components. *Reliability engineering & system safety*, 96(1),218–229.
- Paris, P., & Erdogan, F. 1963. A critical analysis of crack propagation laws. *Journal of Basic Engineering*, 85, 528–533.
- Ren, Z., Verma, A. S., Li, Y., Teuwen, J. J., & Jiang, Z. 2021. Offshore wind turbine operations and maintenance: A state-of-the-art review. *Renewable and Sustainable Energy Reviews*, 144, 110886.
- Su, Z., Núñez, A., Jamshidi, A., Baldi, S., Li, Z., Dollevoet, R., & Schutter, B. D. 2015. Model predictive control for maintenance operations planning of railway infrastructures. *International Conference on Computational Logistics* (pp. 673–688). Springer, Cham.
- Turan, O., Ölçer, A. İ., Lazakis, I., Rigo, P., & Caprace, J. D. 2009. Maintenance/repair and production-oriented life cycle cost/earning model for ship structural optimisation during conceptual design stage. *Ships and Offshore Structures*, 4(2),107–125.
- Zhu, W., Fouladirad, M., & Bérenguer, C. 2013. A predictive maintenance policy based on the blade of offshore wind turbine. *2013] Proceedings Annual Reliability and Maintainability Symposium (RAMS)* (pp. 1–6). IEEE.

A deep learning-based corrosion prediction model for paint-coated steel with defects

F. Jiang & M. Hirohata

Graduate School of Engineering, Osaka University, Suita, Osaka, Japan

ABSTRACT: In recent years, numerical analysis of corrosion characteristics to accurately predict corrosion progress has received increasing attention from researchers. In actual construction, steel is mostly treated with coating for corrosion prevention. This study used steel SS400 with two kinds of coating, they were taken from the actual steel bridges. Defects were created artificially on the coating to simulate the corrosion progress when the coating is defective. Corrosion tests were carried out in two corrosive environments. Corrosion data of steel plate surfaces at different stages were used as data sets. In this study, a generative adversarial network (GAN) was used to build a prediction model of the corroded surface. The prediction model could simulate the damage of paint-coating around the defect at various stages and predict the corrosion of the steel plate in the final removal of the coating. Based on comparative results, this corrosion prediction model showed outstanding performance.

1 INTRODUCTION

Steel structures play an important role in modern buildings and facilities, and about 30% of buildings in Japan (in terms of total floor area) are steel-framed structures (Tsuji, M. & Kanno, R., 2016). Among bridges, many are constructed with steel as a major part of the structure. In the United States, more than 30% of bridges are built with steel as the only or major component (ESC Group, 2021). To this day, there are still many pre-1930s steel structures in use around the world (Farhey et al., 1997). As a result, more and more researchers are becoming concerned about the deterioration of steel bridges (Rashidi, M. et al., 2017). Corrosion is one of these important issues. Corrosion poses many hazards to steel structures, it can weaken the structural integrity, increasing the risk of collapse or failure. This can be particularly dangerous in the case of bridges, buildings, and other critical infrastructure, as the collapse of such structures can result in injury or death. It can also reduce the load-bearing capacity of steel structures (Bonopera, M. et al., 2018), making them less able to support the weight and stresses placed upon them. This can lead to the failure of structural components, such as beams, columns, and foundations.

The importance of monitoring and controlling corrosion on steel structures cannot be overstated, as it is essential to preserving the integrity and functionality of these structures. Regular inspection and maintenance of steel structures can help to identify corrosion early on, allowing for timely repairs and preventative measures to be taken. This can help to extend the lifespan of steel structures, reduce the risk of failure, and save money on costly repairs or replacements. Effective corrosion monitoring and control also requires the use of corrosion-resistant materials and coatings, as well as proper design and construction techniques. By considering these factors from the outset, it is possible to mitigate the risk of corrosion and ensure the long-term performance and reliability of steel structures. Therefore, it is important for practical maintenance work if fast and accurate corrosion simulation and prediction models can be developed mathematically. For example, it is possible to assess whether the corrosion

conditions observed during periodic inspections of steel bridges are likely to lead to serious damage before the next inspection. In addition, it is difficult to obtain detailed information on the distribution of corroded surface profiles during normal inspections, but through numerical analysis, the spatial variation of corroded surface profiles can be predicted, making it possible to assess the load-bearing capacity of a structure using methods such as finite element analysis to obtain more accurate information. Therefore, with the development of numerical simulation techniques, more effective corrosion prediction has attracted more and more attention. These new techniques can predict the corroded surfaces of steel structures to save monitoring time and enable early warning of steel repairs.

In recent years, deep learning has shown great potential in many fields. With the development of machine learning and deep learning techniques, they have been widely used in modeling and prediction tasks. Several studies have used SVM (support vector machine) for quantitative assessment of pipe corrosion (Yan, B. et al., 2014). Corrosion of steel structures using weathering steel was studied, and these bridges often suffer severe surface corrosion damage, leading to structural performance degradation. Traditional visual monitoring and classification methods are time-consuming and subjective, and do not provide a valid quantitative evaluation. In a previous study, a deep learning-based method to predict the corroded surface condition of uncoated steel was proposed (Jiang, F. & Hirohata, M., 2022). This method showed excellent performance for corrosion prediction of uniformly corroded uncoated steel. However, these previous studies needed to remove rust from its surface before modeling in order to investigate the actual condition of the corroded surface, which undoubtedly increased the difficulty of practical application. In addition, in actual steel structures, steel is mostly treated with coatings for corrosion protection. Therefore, this study used the corroded surface without rust removal to predict the next stage of corroded surface, and the study was conducted for paint-coated steel, which is commonly used in steel structures. Corrosion of paint-coated steel is a process in which the coating on the surface of the steel breaks down and the steel beneath is exposed to the environment, leading to corrosion. The rate and severity of corrosion can vary depending on a number of factors, including the type of coating, the environment in which the steel is used, and the care and maintenance of the coating. In general, coated steel is less susceptible to corrosion than uncoated steel because the coating provides a barrier between the steel and the environment. However, coated steel is not immune to corrosion, and coatings can break down over time due to a variety of factors.

In this study, adversarial learning was used to simulate future stages of corroded surfaces, with data sets collected from actual paint-coated steel specimens (taken from two actual bridges). Two corrosion tests were conducted, accelerated corrosion test ISO 16539 method B (Jiang, F. et al., 2022), and atmospheric exposure test conducted in Choshi, Japan. Because the purpose of this study is to predict the next stage of corrosion based on the current corrosion and to determine the current corrosion state, generative adversarial network (GAN) was chosen as the model for predicting corrosion. To expand the variety of datasets, Gaussian noise and GAN were used to enhance the datasets, which can improve the accuracy of the prediction model. Together with UNet (Ronneberger, O. et al., 2015), ViT (Dosovitskiy, A. et al., 2020), and Mobilenetv2 (Sandler, M. et al., 2018), the model can be used to predict the next stage of corrosion based on the current corrosion condition. In addition, the model can be used to determine the type of steel coating and to determine the stage of its corrosion. Based on experimental results compared with other models, it was confirmed that the model has good accuracy in predicting the corrosion surface of paint-coated steel. The main contribution of this study is to propose a GAN-based corrosion prediction model, which can predict and simulate the next stage of corrosion based on the current corrosion state of paint-coated steel; the model can predict not only the distribution of corroded surfaces containing rust, but also the actual corrosion (corroded surfaces with rust removal). Compared with traditional methods, the method proposed in this study can predict the corrosion progress faster and more accurately, and this prediction method can save a lot of cost and time for corrosion assessment and maintenance of steel structures using coated steel.

2 EXPERIMENT

2.1 Specimen

Two types of painted SS400 steel were used as specimens. They were designated C1 and C2, respectively, and they were both taken from real bridges. The paint-coated steel C1 was taken from the girders of a highway bridge in Osaka, which served from 1969 to 2002. Paint-coated steel C2 was used for the girders of a railroad bridge in Shimane near the seaside, which served from 1966 to 2019 (Liu, J. et al., 2022). As shown in Figure 1, these specimens were cut into 150 mm × 70 mm × 9 mm steel plates. There were 6 specimens for each type of coating, and a total of 12 specimens were used for corrosion tests. The coated surfaces of the specimens were machined to introduce initial defects of 2 mm in width (brown area in Figure 1), simulating the corrosion of the coated steel surface after damage in a real environment. The back and sides of the specimen were protected with anti-corrosion tape, and the uncorroded part of the edge was used as a reference surface after the corrosion tests (black area in Figure 1). After each stage of the corrosion test, a laser focus measurement system was used to measure the corrosion depth data of the corroded surface in the measurement area (red area in Figure 1). It has a resolution of 0.2 μm and a measurement interval of 0.1 mm.



Figure 1. Dimension and measurement area of the specimen.

2.2 Corrosive environments

In this study, in order to develop a corrosion prediction model for different paint-coated steels under different corrosive environments, corrosion tests were conducted on two kinds of paint-coated steel, C1 and C2, under two corrosive environments. These two environments were the accelerated corrosion test ISO 16539 Method B, and the atmospheric exposure test conducted at Choshi, Japan. There were three specimens for C1 and C2 in each of the two test environments.

ISO 16539 Method B is a new accelerated corrosion test used for steel structures such as bridges, Figure 2 shows its procedure (Jiang, F. et al., 2022). Synthetic seawater with a saturation of 3.5% was sprayed on the surface. The increase in specimen weight after spraying was measured to achieve a target salt content of $28.0 \pm 2.8 \text{ g/m}^2$ per specimen. The drying and wetting process was repeated every 3 hours, with a 1-hour transition process. A cycle of 8 hours consisted of drying, transition and wetting. This cycle was performed 8 times and then the surface of the specimen was cleaned with water. Then synthetic seawater was sprayed on the surface of the steel plates and the drying and wetting process lasted 11 times. Specimens in this corrosive environment were measured by the laser focus measurement system at 0 (initial state without corrosion), 1, 3, and 6 months to obtain corroded surface data including rust. In addition, at 6 months, the rust was removed from the surface of the specimen, and the actual corrosion surface data (without rust) was measured. Therefore, each specimen in this corrosive environment was measured 5 times.

The atmospheric exposure test conducted at Choshi is a corrosion test conducted in a real environment. The location of this test is the Choshi Atmospheric Exposure Center, located at 35°43' N, 140°45' E. The distance from the nearest seashore is 4 km and the height from sea level is 54 m. This site has a general corrosive environment (Kamimura, T. et al., 2006). Because corrosion

progresses more slowly in the atmospheric exposure environment than in the accelerated corrosion test environment, the corrosion test in the atmospheric exposure environment was conducted over a longer period of time. Therefore, specimens in this corrosive environment were measured by the laser focus measurement system at 0 (initial state without corrosion), 3, 6, and 12 months to obtain corroded surface data including rust. In addition, at 12 months, the rust was removed from the surface of the specimen, and the actual corrosion surface data (without rust) was measured. Again, each specimen in this corrosive environment was measured 5 times.

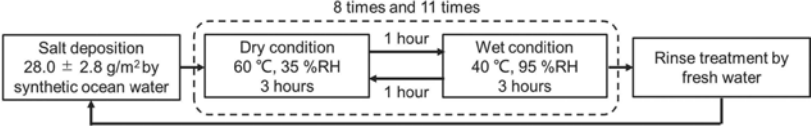


Figure 2. Procedure of accelerated corrosion test ISO 16539 Method B.

3 DATA SET SETTINGS

Table 1 shows the use of 12 specimens for this study. As mentioned in Section 2, the experimental data of each specimen contains corroded surface data for four periods in the status before rust removal and one corroded surface data in the final period with rust removed. Among them, the specimen data numbered 1, 2, 4, 5, 7, 8, 10, and 11 were used as the training set. The specimen data numbered, 3, 6, 9, and 12 were used as the test set. The corrosion prediction model in this study used the corroded surface data from the first three stages as input to predict and generate the corroded surfaces before and after rust removal for the last stage. The prediction results were compared with the real experimental data to obtain the accuracy of the model.

Table 1. Data set settings.

Type	No.	ISO 16539 Method B (month)					No.	Exposure test at Choshi (month)				
		0	1	3	6	6 A*		0	3	6	12	12 A*
C1	1	Train	Train	Train	Train	Train	4	Train	Train	Train	Train	Train
C1	2	Train	Train	Train	Train	Train	5	Train	Train	Train	Train	Train
C1	3	Test	Test	Test	Test	Test	6	Test	Test	Test	Test	Test
C2	7	Train	Train	Train	Train	Train	10	Train	Train	Train	Train	Train
C2	8	Train	Train	Train	Train	Train	11	Train	Train	Train	Train	Train
C2	9	Test	Test	Test	Test	Test	12	Test	Test	Test	Test	Test

* “A” represents the specimen after rust removal.

4 METHODOLOGY

4.1 Model structure

In this study, Gaussian noise and GAN were used to enrich the dataset. UNet + ViT were used as the generator and Mobilenetv2 was used as the discriminator. The generator was mainly used to simulate the next stage of regression of the input data. The role of the discriminator was to determine whether the input data was the data generated by the generator. In addition, the discriminator trained in this model could also be used to determine the type of steel coating and the current stage of the corroded surface. In this model, the adam optimizer was used as the optimizer. Figure 3 illustrates the structure and the procedure of this corrosion prediction model.

4.2 Generative Adversarial Network (GAN)

As a class of deep learning frameworks, generative adversarial network (GAN) can learn from datasets and generate new data with similar statistics. GAN is often used for data augmentation,

especially when the dataset is limited. In this study, because of the long period of corrosion tests, there was very limited data available as the original dataset. Therefore, GAN was used to enrich the dataset and generate new training samples based on the corroded surface data collected from the corrosion tests. GAN and its two variants, Information maximizing GAN (InfoGAN) (Chen, X. et al., 2016) and Conditional GAN (CGAN) (Mirza, M. & Osindero, S., 2014), were used as comparison models for the corrosion prediction model proposed in this study.

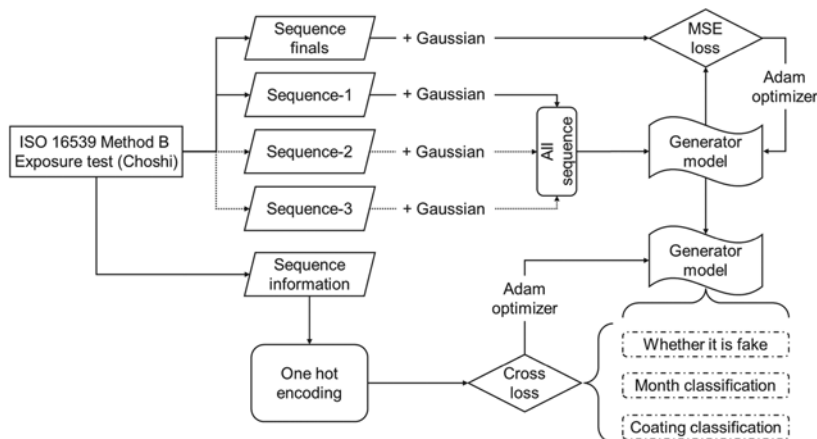


Figure 3. Model structure.

4.3 Generator and discriminator

The corrosion prediction model proposed in this study consists of UNet + ViT as the generator and Mobilenetv2 as the discriminator. UNet was originally designed for biomedical image segmentation. The architecture has two paths. One is a systolic path (or encoder), which is a traditional stack of convolutional and max-pool layers that captures the background in the image. The other path is the symmetric extension path (or decoder), which allows precise localization using transposed convolution. It can handle images of any size, and it is a fully convolutional network (Ronneberger, O. et al., 2015). ViT model, which introduces transformer structure to computer vision. ViT has more similarity between features obtained from shallow and deep layers. Also, it can achieve better performance than CNN on image classification tasks (Dosovitskiy, A. et al., 2020). Mobilenetv2 is an effective model for feature extraction, object detection and segmentation. It is a mobile architecture based on an inverted residual structure that uses deeply separable convolution as an effective building block (Sandler, M. et al., 2018). The model allows the decoupling of the input/output domain from the expressivity of the transform, which provides a convenient framework for further analysis. Its performance has been validated in many missions, such as image classification and object detection. To be more suitable for the discriminator in this study, an additional sigmoid activation function has been added in Mobilenetv2, where 0 is false and 1 is real.

4.4 Model training

The size of the original corrosion depth data of each specimen was 201×581 , and it was scaled to 256×1024 by feeding it in 0 s. A learning rate of 0.0001 and the adam optimizer were used to train the GAN model. $\text{Sigma} = \text{variance}^2$ was used as the sigma activation function. The leaky rate was 0.2. Adam beta values were [0.5, 0.99]. Gaussian noise and the corrosion depth data from the previous stage were used as input to UNet-ViT, and the corrosion depth data from the next stage were used as the target. Mobilenetv2 was used as the discriminator to determine whether the input image was generated by UNet-ViT or the real image, and each step was based on the GAN model for training. At the end of each Epoch, only the UNet-ViT was trained (fine-tuning the difference between the generated and real data).

5 RESULT

5.1 Comparative results

In this study, the accuracy of the different models and their prediction accuracy for corroded surfaces were compared separately for the results. The accuracy of different models is shown in Table 2, the RMSE (Root Mean Square Error) was used as the indicator of the goodness of the model, with lower indicating better accuracy. The results show that the model proposed in this study outperforms other models in all indicators. On the other hand, the prediction accuracy of different models for corroded surfaces is shown in Table 3, because it is to compare whether the predicted corroded surface is close to the real experimental results, not the regression of the model, therefore, the MAE (Mean Absolute Error) was used as the indicator to compare the results, the lower means that the model predicts the corroded surface results closer to the experimental results. The results show that the model proposed in this study has only one specimen whose predicted results are not as good as the other models. In general, the corrosion prediction model proposed in this study was outstanding in predicting the corroded surface of paint-coated steel with defects in the next stage based on former stages.

Table 2. Comparative results of the accuracy (RMSE) of different models.

Model	Discriminator	Prediction	Stage	Coating	Best Epoch
GAN	18.48	8.18	0.69	1.24	20
InfoGAN	3.37	3.37	1.31	1.15	80
CGAN	3.85	3.69	1.01	1.01	40
UNet + ViT	1.63	2.07	0.48	0.83	80

Table 3. Comparative results of the prediction accuracy (MAE) of different models for corroded surfaces before and after rust removal (B represents before rust removal, A represents after rust removal).

Model	No.3 B	No.3 A	No.6 B	No.6 A	No.9 B	No.9 A	No.12 B	No.12 A
GAN	8.43	12.23	7.09	13.78	16.32	16.49	5.34	20.23
InfoGAN	2.29	2.36	1.67	2.19	1.69	1.69	1.60	1.36
CGAN	1.32	1.65	1.41	1.02	1.67	2.18	2.03	2.29
UNet + ViT	0.90	1.17	1.22	1.27	1.38	1.52	1.30	1.30

5.2 Example of corrosion prediction

Figure 4 shows an example of predicting the corroded surface of paint-coated steel by this model. Corroded surface data for 0, 1, and 3 months from specimen No. 3 were used to predict and generate the 6-month corroded surface before rust removal and the 6-month corroded surface after rust removal. (a) and (b) are the predicted 6-month corroded surface before rust removal and 6-month corroded surface after rust removal, respectively. (c) and (d) are the actual 6-month corroded surface before rust removal and 6-month corroded surface after rust removal, respectively. (e) and (f) are the specimen photographs of the actual 6-month corroded surface before rust removal and 6-month corroded surface after rust removal, respectively. The results show that the prediction results are very similar to the experimental results, confirming the validity of the model.

6 CONCLUSION

In steel structures such as steel bridges, paint-coated steel is widely used. Establishing a reliable corrosion prediction method for paint-coated steel is of great importance for maintenance in real facilities. In this study, the corrosion of paint-coated steel with defects was investigated for the case of damage that occurred on the actual coating. An effective corrosion

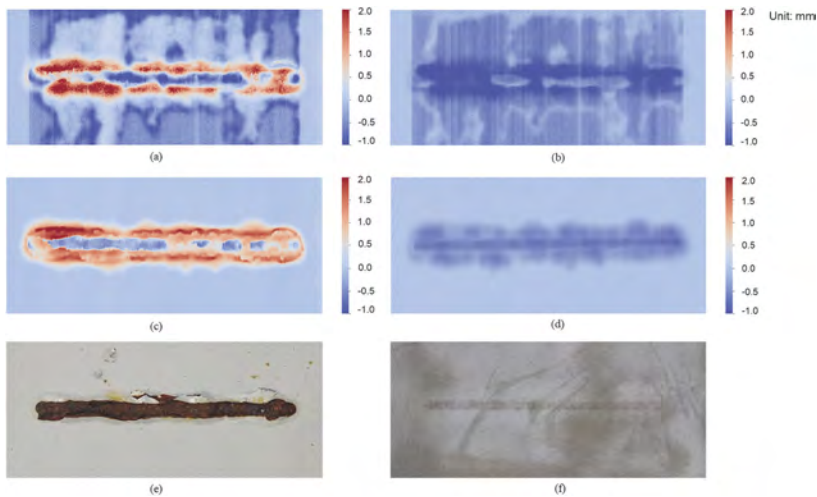


Figure 4. Comparative results of the predicted and experimental corroded surfaces of specimen No. 3. (a) Predicted 6-month corroded surface before rust removal; (b) Predicted 6-month corroded surface after rust removal; (c) Actual 6-month corroded surface before rust removal; (d) Actual 6-month corroded surface after rust removal; (e) Specimen photograph of actual 6-month corroded surface before rust removal; (f) Specimen photograph of actual 6-month corroded surface after rust removal.

prediction model was developed using a GAN-based model trained on the corroded surface data of steel plates obtained from corrosion tests of two paint-coated steels under two different corrosive environments. The model could predict the corroded surface of the next stage based on the previous corroded surface, and also determined the coating type of the steel plate and the current corrosion stage. By comparison, the prediction accuracy of the model proposed in this study was better than other baseline models. This study contributes to simplifying the determination of the corrosion level of paint-coated steel structures and saves time and cost for actual maintenance. In future work, more corrosion cases will be considered. For example, the distinction between the shape of coating defects will be added. The actual paint-coated steel surface is coated with a variety of damaged shapes, it is necessary to investigate how the different shapes of defects affect the corrosion progress.

REFERENCES

- Bonopera, M., Chang, K.C., Chen, C.C., Lin, T.K. and Tullini, N., 2018. Compressive column load identification in steel space frames using second-order deflection-based methods. *International Journal of Structural Stability and Dynamics*, 18(07), p.1850092.
- Chen, X., Duan, Y., Houthoofd, R., Schulman, J., Sutskever, I. and Abbeel, P., 2016. Infogan: Interpretable representation learning by information maximizing generative adversarial nets. *Advances in neural information processing systems*, 29.
- Dosovitskiy, A., Beyer, L., Kolesnikov, A., Weissenborn, D., Zhai, X., Unterthiner, T., Dehghani, M., Minderer, M., Heigold, G., Gelly, S. and Uszkoreit, J., 2020. An image is worth 16x16 words: Transformers for image recognition at scale. *arXiv preprint arXiv:2010.11929*.
- ESC Group, 1997. Application of Structural Steel in Bridges. <https://www.escsteel.co.id/post/application-of-structural-steel-in-bridges>.
- Farhey, D.N., Thakur, A.M., Buchanan, R.C., Aktan, A.E. and Jayaraman, N., 2021. Structural deterioration assessment for steel bridges. *Journal of Bridge Engineering*, 2(3), pp.116–124.
- Jiang, F. and Hirohata, M., 2022. A GAN-Augmented Corrosion Prediction Model for Uncoated Steel Plates. *Applied Sciences*, 12(9), p.4706
- Jiang, F., Hirohata, M., Liu, J. and Ojima, K., 2022. Application of accelerated cyclic test with synthetic ocean water salt-deposition process to the evaluation on corrosion characteristics of weathering steel. *Corrosion Engineering, Science and Technology*, 57(3), pp.280–289.

- Kamimura, T., Hara, S., Miyuki, H., Yamashita, M. and Uchida, H., 2006. Composition and protective ability of rust layer formed on weathering steel exposed to various environments. *Corrosion Science*, 48(9), pp.2799–2812.
- Liu, J., Ojima, K., Jiang, F., Hirohata, M., Nakayama, T. and Sakamoto, T., 2022, September. Corrosion Acceleration Test on Weathering Steel and Paint-coated Steel for Bridge Structural Members. In *IOP Conference Series: Materials Science and Engineering* (Vol. 1252, No. 1, p. 012042). IOP Publishing.
- Mirza, M. and Osindero, S., 2014. Conditional generative adversarial nets. *arXiv preprint arXiv:1411.1784*.
- Rashidi, M., Ghodrat, M., Samali, B., Kendall, B. and Zhang, C., 2017. Remedial modelling of steel bridges through application of analytical hierarchy process (AHP). *Applied Sciences*, 7(2), p.168.
- Ronneberger, O., Fischer, P. and Brox, T., 2015, October. U-net: Convolutional networks for biomedical image segmentation. In *International Conference on Medical image computing and computer-assisted intervention* (pp. 234–241). Springer, Cham.
- Sandler, M., Howard, A., Zhu, M., Zhmoginov, A. and Chen, L.C., 2018. Mobilenetv2: Inverted residuals and linear bottlenecks. In *Proceedings of the IEEE conference on computer vision and pattern recognition* (pp. 4510–4520).
- Tsuji, M. and Kanno, R., 2016. Advances in steel structures and steel materials in Japan. *Nippon Steel & Sumitomo Metal Technical Report*, (113), pp.3–12.
- Yan, B., Goto, S., Miyamoto, A. and Zhao, H., 2014. Imaging-based rating for corrosion states of weathering steel using wavelet transform and PSO-SVM techniques. *Journal of Computing in Civil Engineering*, 28(3), p.04014008.

*MS7: Non-deterministic model updating for structural
health monitoring of existing structures*
Organizers: M. Kitahara, M. Broggi, M. Beer & T. Kitahara



Taylor & Francis

Taylor & Francis Group

<http://taylorandfrancis.com>

System identification and damage assessment of benchmark model H

G.S. Wang & C.W. Lo

Chaoyang University of Technology, Taichung, Taiwan

F.K. Huang

Department of Water resources and Environmental Engineering, Tamkang University, New Taipei City, Taiwan

ABSTRACT: Most of the existing buildings available for damage assessment are slightly or severely damaged, and these data may not be sufficient to establish damage indicators. To solve this problem, the experimental method is used to simulate different damage states, followed by identifying the parameters of the associated damaged structure. Consequently, damage indices that describe the degree of damage can be computed using the identified parameters, and then the threshold values of different damage states can be reached afterward. In this paper, the system identification method, called the hybrid genetic algorithm, is used to analyze the measurement from the shaking table test of a series of 3-story steel frame structures, called the benchmark model H constructed in the NCREE. This series of tests tries to simulate different damage states. In fact, structural models are a series of structures simulating various damage states by varying the numbers of diagonal bracings on both sides of x direction. The dimension of the structure is 3m in the longitudinal direction and 2m in the transverse direction. The shaking table test is carried out in the sequence from Full Bracing (FB) in the x direction to the bare frame. From Case1 to Case3, the vertical diagonal bracings of the outer side are removed one by one from the first floor to the third floor in the x direction. In this way, eccentric structures with varying degrees of damage can be simulated. Finally, all diagonal bracings in the x direction are removed, leading to a Bare Frame (BF). With the change in the dynamic parameters of the elastic system under earthquake, the damage assessment method is applied to determine the degree of damage and the location or floor of damage.

1 INTRODUCTION

System identification was first applied to aerospace engineering and mechanical engineering, and later was applied to civil engineering. It is a technique to model the system by analyzing the input and output measurements produced by the system. Most identification methods are calculus-based search methods. A good initial guess of the parameter and the gradient or higher-order derivatives of the objective function are generally required. There is always the possibility of falling to a local minimum. On the other hand, genetic algorithms (GAs) are optimization procedures inspired by natural evolution. They model natural evolutionary processes, such as selection, recombination, and mutation, and work on populations of individuals rather than a single solution. Consequently, algorithms are parallel and global search for techniques that search multiple points and are more likely to obtain a global solution. Many GA applications have been performed on a variety of optimization problems in the engineering area. However, relatively few applications have been made on structural identification. Koh et al. (2003) proposed a hybrid

strategy for exploiting the merits of GA and a local search operator. Two local search methods were studied: an existing SW method and a proposed method called the MV method. The numerical study showed that the hybrid strategy performs better than GA alone. The author (Wang 2005) applied the real-coded GA to structural identification problems. The validity and efficiency of the proposed GA strategy were explored for the cases of systems with simulated input/output measurements. Furthermore, the strategy was also applied to the existing structure. Genetic algorithms (GAs) are global search techniques for optimization. However, GAs are inherently slow and are not good at hill-climbing. In order to accelerate the convergence to the optimal solutions, a hybrid GA identification strategy that employs the Gauss-Newton method as the local search technique, was also proposed and verified by the author (Wang 2009).

In addition to predicting the responses of structures, system identification techniques can also monitor changes in system parameters or characteristics, and can even determine the subsequent step to take, such as repair or retrofit, based on the damage state of the structure. In the past two decades, many scholars have been engaged in research of structural health monitoring. So-called structural health monitoring is the process of comparing the current state of the structure with the undamaged state or the baseline state to determine whether the structure is damaged under the attack of earthquakes or other types of external forces, so as to determine the location and degree of damage.

Buildings are damaged by strong earthquakes, resulting in changes in dynamic parameters. To avoid identifying the nonlinear model of the damage structure, we can analyze the system parameters using the measurements collected from low intensity that occurred before and after the damaged earthquake. According to changes before and after an attack of the strong earthquake, it is possible to carry out the damage assessment. In recent years, many scholars have been engaged in the research of damage indices. The selected damage index must be a physical quantity sufficient to show the degree of damage of the structure. The relationship between the physical quantity and the available structural parameters must be derived. Buildings available for damage assessment have minor or major damage, so the damage indices evaluated accordingly may not be adequate. To solve this problem, the experimental method can be used to simulate various damage states, followed by identifying the parameters of the associated damaged structure. Then, the damage indices that describe the degree of damage can be computed using the identified parameters, and the threshold value of different damage states can be attained.

In this paper, the system identification method, called the hybrid genetic algorithm, will be used to analyze the measurements from the shaking table test of a series of three-story steel frame structures simulating different damage states. The Benchmark Model H was constructed in the NCREE, which is a series of structures that simulate different numbers of diagonal bracings on both sides of the x direction. With the change in the dynamic parameters of the elastic system under earthquake attacks, the damage assessment method will be used to determine the degree of damage and the location or floor of damage.

2 HYBRID GENETIC ALGORITHM AND DAMAGE INDICES

Genetic algorithms are different from traditional optimization methods. It searches for the optimal solution simultaneously by randomly selecting multiple initial points (Holland 1962). Each individual in the population is equivalent to a search point. After generations of evolution, each point moves towards the optimal solution. Due to this characteristic of the genetic algorithm, the chance of reaching the extremum is greatly enhanced compared to other methods. GAs are inherently slow and poor at hill climbing. To compensate for the computational inefficiency in hill-climbing when the solution yielded by GA approaches the optimal value, a local search operator, the Gauss-Newton method is merged with the GA strategy (Wang 2009).

2.1 Genetic algorithm

The genetic algorithm models natural evolutionary processes, such as selection, recombination, and mutation. The algorithms work on populations of individuals instead of a single solution. In

this way, the search is performed in a parallel manner. However, better results can be obtained by introducing multiple subpopulations. Every subpopulation evolves over a few isolated generations (like the single population GA) before one or more individuals are exchanged between subpopulations using the mechanisms of migration and competition. The multi-population GA models the evolution of a species in a way more similar to nature than a single population.

2.2 Gauss-Newton method

The purpose of using the local search method is not for the best solution, but for a better solution in a local area. The global search capability of the local search method is not required to be very efficient. Since the Gauss-Newton method has been demonstrated to be an efficient method in nonlinear least square problems, it is appropriate to use it in the optimization problem of the prediction error in system identification problems. Therefore, the local search method used in this paper is the Gauss-Newton method. For the problem of system identification, an objective function minimized is a sum of square errors as

$$E(\tilde{x}) = \frac{1}{2} \sum_{i=1}^N [f_i(\tilde{x})]^2 = \frac{1}{2} \sum_{i=1}^N [y_i - v_i(\tilde{x})]^2 \quad (1)$$

where \tilde{x} is the vector of the parameters which will yield the least square error between the measured response y_i and the predicted response $v_i(\tilde{x})$, and N is the number of measurement sequences. According to the Gauss-Newton method, a new iterated parameter \tilde{x}_{m+1} can be evaluated in terms of the current parameter vector \tilde{x}_m as

$$\tilde{x}_{m+1} = \tilde{x}_m - [J^T(\tilde{x}_m)J(\tilde{x}_m)]^{-1} J^T(\tilde{x}_m)[f_i(\tilde{x}_m)] \quad (2)$$

where denoting $J(\tilde{x})$ as the Jacobian matrix of $E(\tilde{x})$.

2.3 Hybrid genetic algorithm

The Gauss-Newton method is performed after completing the evolution process of every 10 generations. Accordingly, a new hybridization of a GA with the Gauss-Newton method is formed. Figure 1 shows the structure of this hybrid GA.

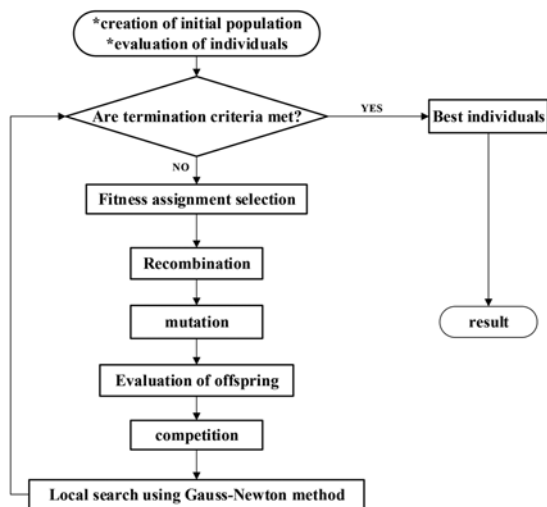


Figure 1. Structure of hybrid GA.

2.4 Damage indices

Damage assessment is a process of determining the location, nature, and severity associated with the target structure. Damage to the structure alters its dynamic characteristics. This change can be characterized by changes in the modal parameter, i.e., modal frequencies, modal damping value, and mode shape associated with each mode. Various damage indices have been proposed to quantify structural damage in structures subjected to seismic excitation. Some of them are reviewed as follows:

Dipasquale & Cakmak (1990) defined the maximum softening index for the one-dimensional case, where only the fundamental modal frequency is considered. The index is given by where T_{und} is the undamaged natural period and T_m is the maximum natural period during the excitation duration. The maximum softening index demonstrates a measure of a combination of both the stiffness degradation and the plasticity effect.

MAC indicates the correlation between two measured mode shapes from two different states (Dipasquale & Cakmak 1989). Let ϕ_A and ϕ_B be the undamaged and damaged mode shapes, respectively, MAC is then defined for modes j and k as follows:

$$MAC(j, k) = \frac{[\sum_{i=1}^N (\phi_A)_{ij}(\phi_B)_{ik}]^2}{[\sum_{i=1}^N (\phi_A)_{ij}^2 \sum_{i=1}^N (\phi_B)_{ik}^2]} \quad (3)$$

where N is the number of coordinates included, and i is the coordinate of column vector associated with the specific mode shape. In other words, $(\phi_A)_{ij}$ denotes the i^{th} coordinate of the j^{th} column (mode) of ϕ_A and $(\phi_B)_{ik}$ the i^{th} coordinate of the k^{th} column (mode) of ϕ_B . MAC values range from 0 to 1, that is, 0 for no correlation and 1 for full correlation (no damage). If the mode shapes ϕ_A and ϕ_B are identical, then the MAC will be 1, indicating full correlation. Therefore, MAC can be used to detect the existence of damage by identifying these values altered from their original values for individual modes, that is, $j = k$.

3 SHAKING TABLE TESTS OF BENCHMARK MODEL H

In December 2005, the National Earthquake Engineering Research Center built three-story Benchmark Models A, B, C, and D for a series of shaking table tests (Lin 2006). Then on 17 September 2008, a series of shaking table tests of the benchmark model H as shown in Figure 1 were carried out. The dimensions of the benchmark structure are 3m in the longitudinal direction (x-axis), 2m in the transverse direction (y-axis), and 3m in the story height, and the total height of the structure is 9m. Two sets of accelerometers are installed in the X and Y directions on the top of the three stories of the benchmark structure as shown in Figure 2 (a). The responses measured by the two parallel sets of sensors are averaged. Two sets of accelerometers in the X direction and Y direction are also installed on the shaking table to measure the input ground motions. Relative acceleration responses can be computed by subtracting the ground motion from the measured absolute response.

This series of tests aims to mimic the damaged state of the structure using the failure of the vertical diagonal bracings. Structure models are a series of structures with different numbers of vertical bracings on both sides of the x direction. The series of shaking table tests starts from the Full Bracing (FB) model with diagonal bracing on both sides of the X direction to the Bare Frame (BF) model with no diagonal bracing on both sides of the X direction. Cases 1 to 3 represent the models in which the vertical diagonal bracings on the rear side are removed one by one from the first floor to the third floor to simulate eccentric structures with different degrees of damage. The final model is the Bare Frame with all the diagonal bracings removed on both sides. Figure 2 (b)~(f) illustrate the undamaged state (FB) and the four damaged states from Case 1 to Bare Frame.

The excitation records are a set of wide-band random noise records and three sets of earthquake records, including the N-S component of the El Centro earthquake in 1940, the N-S components of the TCU076 station and TCU082 station of the Chi-Chi earthquake in 1999.

The above four records are scaled into records with maximum ground acceleration (PGA) equal to 100gal and 200gal, respectively, and these records act on the benchmark structure first in the X direction. In this paper, only the response subject to excitation of the N-S component of the El Centro scaled to PGA equal to 100gal and 200gal in the X-direction will be used for analysis.

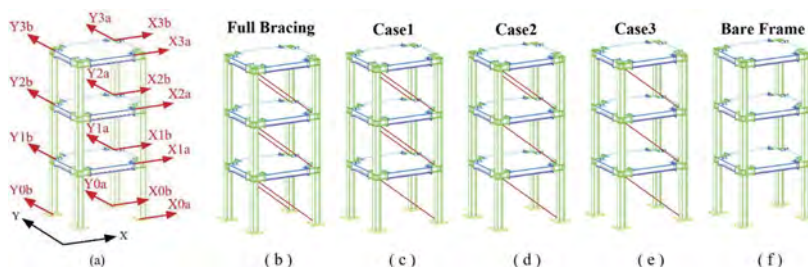


Figure 2. (a) Sensor layout of benchmark model H; (b) Full Bracing; (c) Case 1; (d) Case 2; (e) Case 3; (f) Bare Frame (redraw of Lin 2006).

4 IDENTIFICATION AND DAMAGE ASSESSMENT OF BENCHMARK MODEL H

4.1 Identification model

The motion equation of an MDOF system subjected to a single excitation can be transformed into a modal equation through modal superposition, as

$$\ddot{u}_{sm} + 2\xi_m \omega_m \dot{u}_{sm} + \omega_m^2 u_{sm} = -P_{sm} \ddot{u}_g, \quad s = 1, 2, \dots, n \quad (4)$$

where u_{sm} is the modal displacement in mode m at the s^{th} DOF, and P_{sm} the effective participation factor in mode m at the s^{th} DOF associated with the ground motion \ddot{u}_g . The measurement equation at the s^{th} DOF can be represented as

$$y = \ddot{u}_s = \sum_{m=1}^N \ddot{u}_{sm} = \sum_{m=1}^N P_{sm} \ddot{u}_g - 2\xi_m \omega_m \dot{u}_{sm} - \omega_m^2 u_{sm} \quad (5)$$

where \ddot{u}_s is the relative acceleration at the s^{th} DOF, and N is the total number of modes. $2\xi_m \omega_m$, ω_m^2 , and P_{sm} are the modal parameters to be identified in this case. To assess the accuracy of the proposed identification technique, the error index $E.I.$ is defined as the average of the K measurements as

$$E.I. = \left[\frac{1}{K} \sum_{j=1}^K \frac{\sum_{i=1}^{N_s} (y(i,j) - v(i,j))^2}{\sum_{i=1}^N y(i,j)^2} \right]^{1/2} \quad (6)$$

where N_s is the number of measurement sequences, $y(i,j)$ is the measured relative acceleration response of j^{th} measurement at the i^{th} sampling time, and $v(i,j)$ is the associated estimated acceleration response.

4.2 Results of identification

The hybrid Genetic algorithm is employed to identify the parameters of the benchmark model H under excitations of the N-S component of the El Centro scaled to PGA equal to 100gal and 200gal in the X-direction. The first three modes are identified using excitation and response.

Figure 3 shows the comparison between the estimated response and the measured response on the top floor of the Bare frame under excitations from the El Centro earthquake of PGA equal to 100gal. The error index associated with this floor is 8.64% and this result shows that the searchability of the hybrid genetic algorithm is superior. The hybrid Genetic algorithm can be applied to the parametric identification of the other four cases including Full Bracing (FB), Case 1, Case 2, and Case 3 when subject to excitation with PGA equal to 100 gals. It can also be applied to the parametric identification of the five cases when subject to excitation with PGA scaled to 200 gals. Figure 4 shows the comparison of the parameters identified for all cases with PGA equal to 100 gals and 200 gals. From this figure, it can be concluded that the values of the first modal frequencies will decrease with the removal of more bracing.

Figure 5 shows the comparison of the first effective participation factors of each floor in all cases for the PGA equal to 100 gals and 200 gals. The damaged states of the floors are related to the change of story drifts, while the effective participation factors are related to the mode shapes. Consequently, the damaged state of the floor or the story drift can be observed from the change in the mode shapes of two adjacent floors. From the comparison of the effective participation factors on the first floor, it can be found that the story drift of the first floor of Case 1 is much larger than the story drift of the FB case, indicating that the first floor of Case 1 was damaged. Furthermore, the story drifts on the second and third floors for Case 1 are almost 0 compared to the values of the FB case, indicating that the second and third floors for Case 1 were undamaged. For Case 2, the story drift of the second floor is relatively large, while that of the third floor is almost zero, indicating that the second floor is damaged, but the third floor is not damaged. The drift of the third floor of Case 3 is larger than that of Case 2 and Case 1, implying that the third floor was damaged. In the last case of BF, it can be found that the story drift of each floor increases, so the damage is more severe.

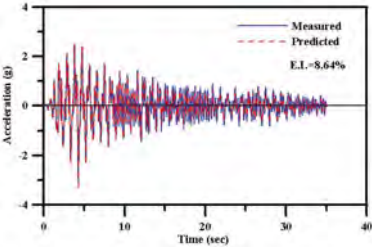


Figure 3. Comparison of measured response with identified response on the top floor of the Bare frame.

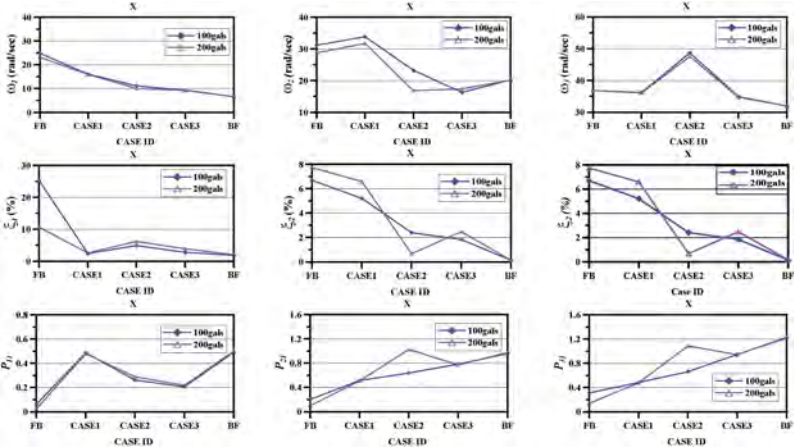


Figure 4. Identified modal frequencies, modal damping ratios, and first modal participation factors.

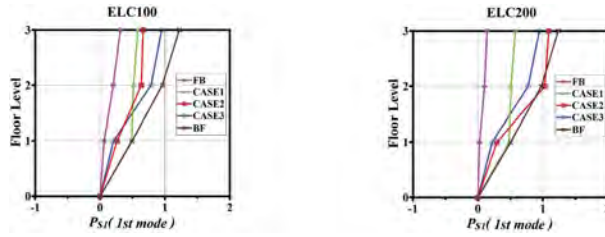


Figure 5. Comparison of the first modal participation factors with PGA equal to 100gal and 200gal.

4.3 Damage assessment

The results of the maximum damage index in the X direction of each case under the El Centro earthquake scaled to PGA equal to 100gal and 200gal are plotted in Figure 6. The period converted from the first modal frequency of the FB case is used as the undamaged or baseline period. From the first subfigure of Figure 6, it is found that the maximum softening index increases first to 35.243% in Case 1. In Case 2 and Case 3, the indices further increase to 55.266% and 62.712%, respectively. In the last case of BF, the index increases to 73.426%. The damage is getting worse as the braces are removed. From the second subfigure, it can be seen that the maximum softening indices of Case 1 to the BF cases are 59.671%, 56.725%, 31.203%, and 71.661%, respectively, which generally conform to the trend, but the index of Case3 is too low.

By substituting the identified effective modal participation factors into the formula of the MAC index, the results of the first mode can be yielded. Figure 7 shows the results of MAC (1,1) of the five cases under the attacks of the El Centro earthquake scaled to 100 gals and 200 gals. The first modal participation factor identified in the FB case also referred to a baseline value. It can be observed from the two subfigures that the values of MAC(1,1) of the first mode associated with Case 1 dropped to about 0.8. However, the values of Case 2, Case 3, and BF case are larger than that of Case 1 and are all close to 1. In summary, it can be concluded that the MAC index calculated by the effective participation factor of the first mode cannot reflect the actual damage state.

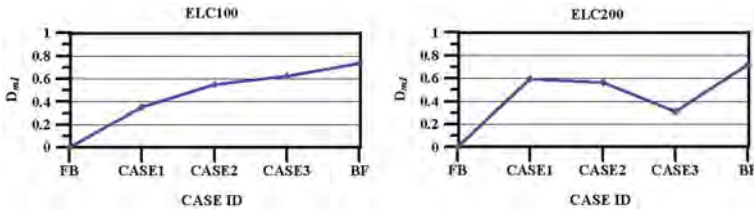


Figure 6. Comparison of the maximum softening indices of the first mode with PGA equal to 100 gal and 200 gal.

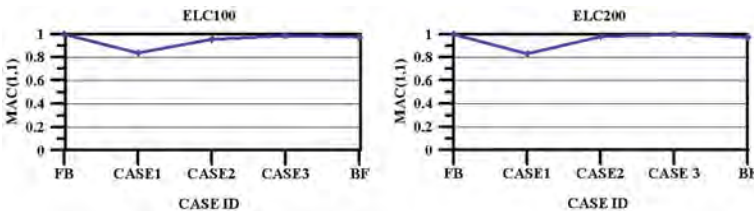


Figure 7. Comparison of the MAC indices of the first mode with PGA equal to 100 gal and 200 gal.

5 CONCLUSIONS

In this paper, system identification and damage assessment of the benchmark model H were carried out. The Benchmark Model H was constructed in the NCREE, which is a series of structures simulating different numbers of diagonal bracings on both sides of x direction. The modal parameters were identified by the hybrid genetic algorithm. Then the maximum softening damage indices of the first mode and the MAC indices of the first mode based on the identified modal parameters were used for damage assessment. Therefore, this study draws the following important conclusions:

1. From the comparison of the effective participation factors on the first floor, it can be found that the story drift of the first floor of Case 1 is much larger than the story drift of the FB case, indicating that the first floor of Case 1 was damaged. The story drift of the second floor of Case 2 is relatively large, while that of the third floor is almost zero, indicating that the second floor is damaged. The story drift of the third floor of Case 3 is larger than that of Case 2 and Case 1, implying that the third floor was damaged. In the last case of BF, it can be found that the drift of the story of each floor becomes larger compared to the other cases, so the damage to the entire structure is getting more severe.
2. The results of the maximum softening indices show that the damage is getting worse as more bracings are removed. According to the case study of this benchmark structure, the range of the maximum softening index of the first mode for the slight damage state can be set as 0.2 to 0.4, the range for the moderate damage state can be set as 0.4 to 0.65, and the range for the severe damage state can be set as 0.65 or more.
3. From the results of the MAC indices of the first mode, the value decreased for Case 1 with one bracing removed, but increased instead for Case 2 with two bracings removed and Case 3 with three bracings removed. These results indicate that this index cannot reflect the actual state of damage.

ACKNOWLEDGEMENT

The authors would like to express their gratitude to Prof. C.C. Lin of National Chung-Shin University and Dr. Lin of National Center for Research on Earthquake Engineering, Taiwan for their effort to collect the accelerograms of a 3-story benchmark building structure.

REFERENCES

- Dipasquale, E. & Cakmak, A.S. 1989. On the relation between local and global damage indices. *Report No. NCEER/89-0034, State University of New York at Buffalo.*
- Dipasquale, E. & Cakmak, A.S. 1990. Seismic damage assessment using linear models. *Soil Dynamics and Earthquake Engineering* 9(4): 194–215.
- Holland, J.H. 1962. Outline for a logical theory of adaptive systems. *Journal of the Association for Computing Machinery* 3: 297–314.
- Koh, C.G. Chen, Y.F. and Liaw, C.Y., 2003. A hybrid computational strategy for the identification of structural parameters. *Computers and Structures*, 81, 107–117.
- Lin, P. & et al. 2006. Shaking table test of the benchmark building structure, *Report No. NCREE-06-020, National Center for Research on Earthquake Engineering, Taipei, Taiwan.*
- Wang, G. S. & Lin, H.H. 2005. Application of genetic algorithm to structural dynamic parameter identification. *Journal of the Chinese Institute of Civil Engineering and Hydraulic Engineering* 17(2): 281–291.
- Wang, G.S. 2009. Application of hybrid genetic algorithm to system identification. *Structural Control and Health Monitoring* 16(2): 125–153.

Updating simplified jack-up model using basin test data

J.X. Cao & S.T. Quek

National University of Singapore, Singapore, Singapore

S.L. Zhang, C. Zhang & M.B. Cai

Technology Centre for Offshore and Marine, Singapore (TCOMS), Singapore

M. Si

National University of Singapore, Singapore, Singapore

Technology Centre for Offshore and Marine, Singapore (TCOMS), Singapore

ABSTRACT: The development of an accurate and reliable jack-up model is essential for understanding the hydrodynamic performance of structure, as well as ensuring the structural safety. As part of development of a digital twin, a simplified jack-up numerical model was created based on basin model test. Critical components are the fixity of leg-to-hull connection and spudcan fixity where spring elements were employed. Model updating technique was applied to the measured data to identify the parameters of these fixities. These data, including the hull displacement, leg-to-hull and spudcan moments, were incorporated into the cost function where the difference between model prediction and measured structural responses were minimized. Using the updated model, the predicted responses were consistent with the measured data indicating that the boundary fixities were reasonably estimated. The updated jack-up model can serve as a reliable platform for monitoring and predicting the overall performance of the actual structure.

1 INTRODUCTION

Jack-up structure is a type of mobile platform used for oil and gas exploration and production. It usually consists of a buoyant hull and several movable truss legs. The legs and hull are connected through a rack-chock system, and the bottom of each leg rests on a spudcan footing. These facilitates the operation mode as a fixed platform as well as transit mode as a floating platform. The fixity systems of the leg-to-hull connection and spudcan make the jack-up quite sensitive in terms of dynamic response (Bienen and Cassidy 2009). The basic configuration of a jack-up is a large hull near the top, supported by slender truss legs founded on spudcans, which complicates the structure-wave interaction modelling with respect to hydrodynamic loads. To fully assess a jack-up structure, understanding its dynamic characteristics under different structural configurations and varying load conditions is important and necessary for safe design and maintaining performance (Mirzadeh et al. 2016).

Researchers have focused on analyzing the measurement data in time and/or frequency domain to make quantitative assessments of structural nonlinearity, hydrodynamic characteristics and spudcan fixity. Liu et al. (1991) analyzed laboratory measured data of jack-ups in irregular waves and revealed the influence of nonlinear properties on structural dynamics. The dynamic response of a jack-up moored on the dock under various sea states was also presented (Liu et al. 2015). Such basin models are often based on similarity laws and may not represent of the actual structures accurately. For this reason, in-situ measurement of actual jack-ups has been employed to study the wave kinematics, hydrodynamic loads, global structural response, structural natural period, damping properties and effect of soil-structure interaction (Temperton et al. 1991; Yin et al. 2020). The in-situ measurement under complex environmental conditions provided realistic information for structural health monitoring and gave insight into acceptance criteria of standards.

Numerical analysis of jack-ups serves as a complementary tool to explore the internal forces under different limit states and predict the dynamic response under wave loading. Pisanò et al. (2019) proposed a full continuum nonlinear finite element (FE) modelling framework for jack-up-spudcan soil system to investigate soil-structure interaction effect on response. Although a fully detailed model can simulate the internal force of each member accurately and provide reliable structural analysis, it is quite time-consuming.

In cases where detailed responses or forces are not needed and the prediction of global structural responses is sufficient, simplified jack-up models provide the most efficient tool. Various simplified models, including equivalent 3-leg stick (Liu et al.1991) and sub-structural models (Wang et al. 2014), have been developed. They can be used for overturning checks and reliability analysis. However, such type of model requires calibration due to the highly simplified assumptions, including the fixity of the boundary conditions. This paper presents the development of a simplified model based on the basin test of jack-up modelled at a scale of 1:30, with focus on the fixity of leg-to-hull connection and spudcan fixity. The boundary fixity properties were estimated using model updating technique where the updated results based on power spectral density (PSD) were presented. The calibrated jack-up model can subsequently be used to examine the overturning resistance and assess the dynamic performance under potential future loads.

2 BASIN TEST OF JACK-UP AND STRUCTURAL MODEL

2.1 Basin test

To develop a structural digital twin framework, a generic jack-up model at 1:30 scale was designed and fabricated to comprehend its hydrodynamic performance and gather high quality datasets through basin tests. A sequence of tests based on various wave conditions and operating modes was executed, where a detailed description can be found in Chen et al. (2022). In this paper, the jack-up in its elevated mode was investigated and analyzed.

Figure 1a Shows the time history of hull displacement. The hull displacement was derived from the accelerometers on the hull by double integration. The PSD of the hull displacement is presented in Figure 1b. The first peak is about 0.40 Hz, representing the dominant component of wave load. The second peak coincides at approximately 0.83 Hz, corresponding to the fundamental frequency of the jack-up model.

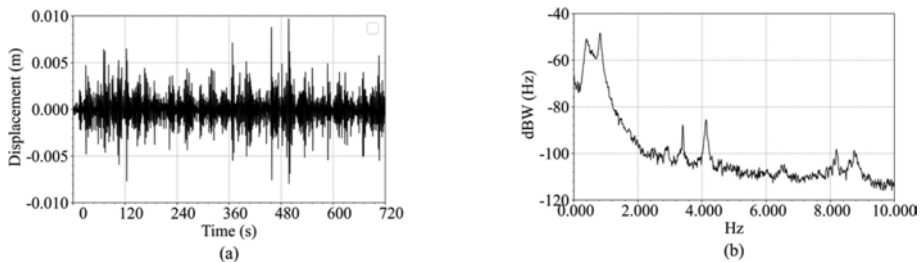


Figure 1. Comparison of hull displacements: (a) time history, (b) power spectral density (PSD).

The moment at the forward leg-to-hull connection, measured using load cell, is shown in Figure 2. The amplitude of moment ranges from -76 N·m to 92 N·m. From the PSD of the moments shown in Figure 2b, the first and second peaks are at 0.41 Hz and 0.82 Hz, respectively. The frequencies obtained from the moments at the leg-to-hull connection are consistent with those from the hull displacements.

To evaluate the spudcan fixity, the moments at the spudcan were measured using load cells and plotted in Figure 3, where “Fwd”, “Stb” and “Pt” denote the forward, starboard and port legs, respectively. All of the recorded moments have approximately the same amplitude. To quantify the influence of the spudcan moment, Table 1 compares statistics from the time history of the moment at each leg. The moment amplitude of the forward leg is slightly larger than those of the

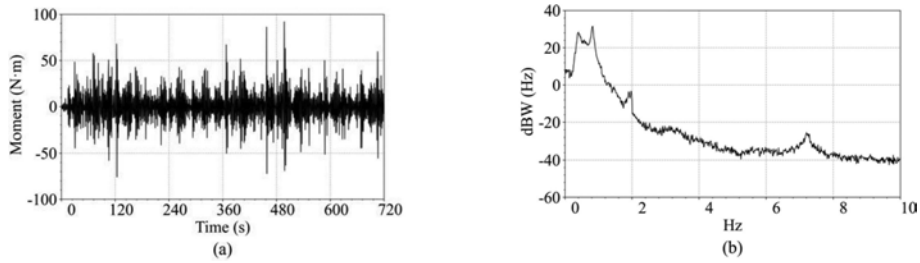


Figure 2. Comparison of leg-to-hull moment: (a) time history, (b) PSD.

other legs. Given the mean values are close to zero, the positive and negative moment amplitudes would be approximately the same (also indicated by the very low skewness coefficients). Since the spudcan provides some moments, non-zero spudcan moments will lead to a redistribution of the leg bending moments and hence spring elements should be used for the spudcan footing.

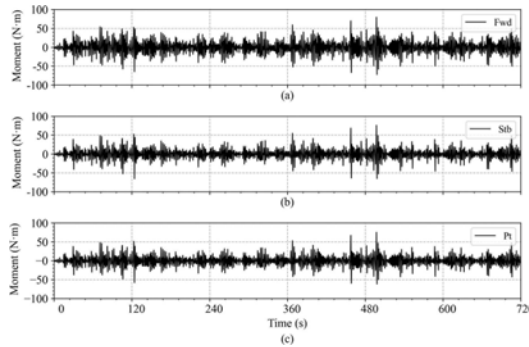


Figure 3. Comparison of spudcan moments: (a) forward leg, (b) starboard leg, (c) port leg.

Figure 4 Presents the PSD of the moments at the spudcans, and the first and second peaks of the PSD for all three legs are listed in Table 2. The first PSD peak of the three legs is determined to be at about 0.41 Hz, while the second one is around 0.82 Hz, consistent with those obtained from the hull displacements and the leg-to-hull moments, confirming the wave and fundamental structural frequencies.

Table 1. Statistics from time history of moments at spudcan.

Case	Leg	Maximum	Minimum	Mean	std. devn.
A	Forward	79.64	-72.50	0.066	15.64
	Starboard	76.15	-65.76	-0.188	12.35
	Port	75.42	-62.04	-0.008	12.25

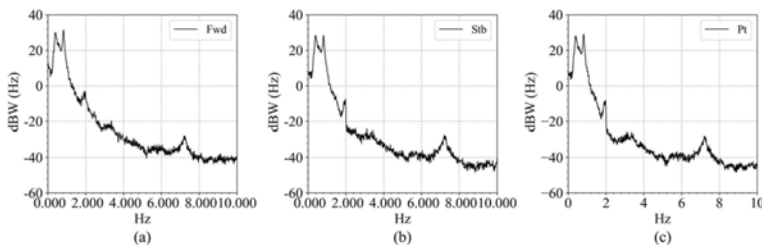


Figure 4. Comparison of moment PSD at legs of spudcan: (a) forward, (b) starboard, (c) port.

Table 2. First two peaks in PSD of spudcan moment (Hz).

Peak	Forward	Starboard	Port
First peak	0.42	0.41	0.41
Second peak	0.81	0.83	0.82

2.2 Structural model

A numerical model of the jack-up based on the basin test results was created as shown in Figure 5. The truss structure of each leg was simplified as an equivalent beam positioned at the geometric center of the leg. The hull was taken a rigid body, modelled with some nodes connected by weightless rigid elements. As the flexibility between the leg and the hull influences the distribution of the leg bending moment and the transfer of the shear force, spring elements were used to model the leg-to-hull connections, as shown in Figure 5b. The spudcan fixity has significant influence on the dynamic characteristic of jack-up. For instance, increased spudcan fixity may increase the natural frequency of the global structure whereas the assumption of zero fixity (i.e. pinned footing) would be very conservative. To estimate the spudcan fixity accurately, it is modelled using spring elements, as shown in Figure 5c.

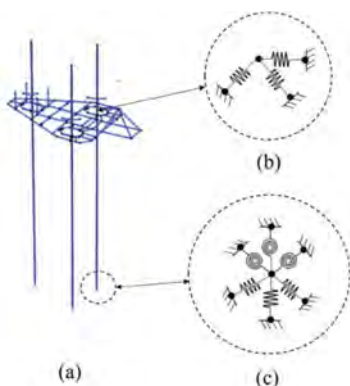


Figure 5. Schematic diagram of (a) simplified stick model, (b) springs for leg-to-hull connections, (c) springs for spudcan fixity.

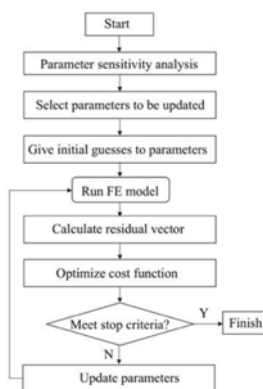


Figure 6. Procedure of model updating.

Rayleigh damping was introduced to simulate structural damping, whose coefficients α and β were determined from two specific modes. For the calculation of wave loading, Morison's equation was employed. It is normally sufficient for dynamic analysis because the horizontal dimension of the leg is significantly smaller than the wavelength.

The aforementioned description is some key features associated with updating the model. An extensive modelling process was presented by Zhang et al. (2022). The equivalent simplified model can efficiently calculate dynamic responses at the expense of model precision, since for each leg, the detailed truss structure replaced by an equivalent beam. Importantly, calculating the fixity of the leg-to-hull connection and spudcan is still a challenging task as the fixity is related to the working condition. Model updating technique serves as an effective tool to calibrate the unknown parameters based measured data.

3 MODEL UPDATING PROCEDURE

The constructed jack-up model can analyze the hydrodynamic performance and response prediction under various load conditions if properly calibrated. In general, the structural response predicted by the FE model may differ from measurement data for reasons such as the fixity of boundary conditions, and variability in material properties. To obtain a good representative

FE model, the measured data are used to update the selected model parameters in the FE model. In essence, FE model updating is an optimization problem to narrow the gap between model prediction and measurement data, which is formulated as

$$\theta^* = \arg \min_{\theta} F(\hat{y}(\theta), y) = \arg \min_{\theta} F(\theta), \quad (1)$$

where θ is a vector of the selected parameters to be updated, $\hat{y}(\theta)$ is the predicted response related to the model parameters θ , y is the measured data, and $F(\cdot)$ denotes the cost function.

There are a variety of alternative formulations for the cost function. One of the simplest indices is the natural frequency, and the other popular index is the mode shape (Guo et al. 2018). However, both indices utilize limited response information, which may not be sensitive to the updated parameters. In this paper, the PSD is taken as a cost indicator, expressed as

$$F(\theta) = \|r(\theta)\|_2^2 = [r(\theta)]^T r(\theta) = \sum_{i=1}^{N_t} r_i^2(\theta), \quad (2)$$

where $r = y - \hat{y}(\theta)$ is the residual vector, N_t is the total number of data points, $\|\cdot\|_2$ denotes the 2-norm of a vector.

In the basin test, various types of data were collected from a heterogeneous set of sensors. For example, the spudcan and leg-to-hull moments were recorded using load cells, and the hull displacement was obtained by integrating the acceleration twice. To accommodate the largest possible amount of measured data, different kinds of measured data were incorporated into a single cost function with different weights. Since different types of measurement data had different magnitudes, ill-conditioning may arise if they were considered in a single cost function. For this reason, data measured from heterogeneous sensors were normalized and the cost function was reformulated as

$$F(\theta) = \sum_{j=1}^{N_s} \sum_{i=1}^{N_t} w_j \bar{r}_{ij}^2(\theta) = \sum_{j=1}^{N_s} \sum_{i=1}^{N_t} w_j (y_{ij} - \hat{y}_{ij}(\theta)), \quad (3)$$

where \bar{r}_{ij} is the normalized residual vector in the i -th row and j -th column, y_{ij} and \hat{y}_{ij} corresponds to measured data from sensors and prediction response from FE models, respectively. Each column j represents data from a sensor at all time, with N_s denoting the total number of sensors. Each row represents a point in time, with N_t as the total number of time steps. The weight factor w_j is generally interpreted as the “confidence” in the j -th sensor data.

According to equations (1) and (3), the optimization problem for model updating can be constructed as

$$\theta^* = \arg \min_{\theta} F(\hat{y}(\theta), y) = \arg \min_{\theta} \sum_{j=1}^{N_s} \sum_{i=1}^{N_t} w_j (y_{ij} - \hat{y}_{ij}(\theta)), \quad (4)$$

Since most of the selected parameters have physical meaning, the solution θ^* should be bounded. For example, Yong’s modulus or stiffness are often nonnegative. Thus, a constraint optimization function for updating model is expressed as

$$\theta^* = \arg \min_{\theta} \sum_{j=1}^{N_s} \sum_{i=1}^{N_t} w_j (y_{ij} - \hat{y}_{ij}(\theta)), \quad (5a)$$

$$\text{subject to } L_{\theta} \leq \theta \leq U_{\theta}, \quad (5b)$$

where L_{θ} and U_{θ} represent the lower and upper limit of the selected parameters.

To solve the optimization problem in equation (5), the `fmincon` solver in MATLAB optimization toolbox is used, where the solver specializes in finding the minimum values of constrained nonlinear problem. Once the update process reaches the functional tolerance or the maximum number of iterations, the parameter values obtained are taken as optimal. Figure 6 summarizes the procedure of model updating. It starts with selecting parameters, where an experienced engineer generally supplies many potential parameters for selection. The sensitivity analysis method is introduced to determine which parameters are to be calibrated. Having selected the parameters to be updated, initial guesses and constraint conditions are assigned to them. The parameters are then fed into the FE model to generate the structural response. By comparing the predicted response against the measured data, the residual vector can be calculated and used to estimate the cost function with the different weights. The optimization

solver is then employed to produce a new set of parameters. The generated parameters are used in the FE model and the procedure is repeated until the stopping criteria is met.

4 MODEL UPDATING OF JACK UP

4.1 Parameter selection for updating

The selected parameters to be updated significantly influence the accuracy and convergence of the model updating. Conceptually, if all physical parameters are selected for tuning, the FE model can model the actual structure fairly well. However, having too many updating parameters may produce an overfitted model, resulting in an unreliable updated model. Choosing an appropriate number of parameters to be updated is crucial.

In the modelling process, an equivalent beam replaced the detailed truss structure of each leg. This means that the representative area (A) and shear stiffness coefficient (ζ) of the section require updating. The equivalent diameter of each leg also affects the hydrodynamic coefficients, while the wave forces are difficult to measure accurately in the basin test. The hydrodynamic coefficients including the drag coefficient (C_d) and inertial coefficient (C_m) were chosen to be updated. Rayleigh damping was assumed for the structure, with coefficients α and β chosen for updating. The two kinds of boundary conditions in the FE model to be updated were the leg-to-hull connections and the spudcan connection as their fixity are difficult to determine. The parameters to be updated are listed in Table 3.

Table 3. Parameters selected for updating.

Parameter label	Description	Notation
P1	Section area of each leg.	A
P2	Shear stiffness coefficient of an equivalent section.	ζ
P3	Spudcan stiffness of forward leg in the x direction.	K_{sfx}
P4	Spudcan stiffness of starboard leg in the x direction.	K_{ssx}
P5	Spudcan stiffness of port leg in the x direction.	K_{spx}
P6	Spudcan stiffness of forward leg in the y direction.	K_{sfy}
P7	Spudcan stiffness of starboard leg in the y direction.	K_{ssy}
P8	Spudcan stiffness of port leg in the y direction.	K_{spsy}
P9	Spudcan stiffness of all the three legs in the z direction.	K_{sz}
P10	Stiffness of leg-to-hull connection for a forward leg.	K_{hf}
P11	Stiffness of leg-to-hull connection for port and starboard legs.	K_{hps}
P12	Hydrodynamic coefficient (drag coefficient).	C_d
P13	Hydrodynamic coefficient (inertial coefficient).	C_m
P14	Rayleigh damping coefficient.	α
P15	Rayleigh damping coefficient.	β

The parameters in Table 3 can be classified into three categories: the first concerns structural properties (A , ζ , and β), the second is the fixity of connections (K_{sfx} , K_{ssx} , K_{spx} , K_{sfy} , K_{ssy} , K_{spsy} , K_{sz} , K_{hf} and K_{hps}), and the third corresponds to hydrodynamic characteristics (C_d and C_m). These parameters in the three categories have coupled effects on the structural response which complicates the model updating process. For example, part of the first category (A and ζ) and the entire second category influence the stiffness matrix; the damping matrix is calculated from structural damping (α and β) and water added damping (C_m).

4.2 Model updating results

Nominal values (if absent, values based on engineering experience) of the parameters were used to start the model updating procedure. Given that the unknown parameters had different amplitudes, they were normalized to unity. Their lower and upper bounds were set to 0.1 and 4, that is within an order of magnitude from the initial values. As mentioned earlier, the `fmincon` solver in MATLAB optimization toolbox was employed and the stopping criteria were set to a tolerance of $1e-5$, limited by the maximum number of iterations of 1500.

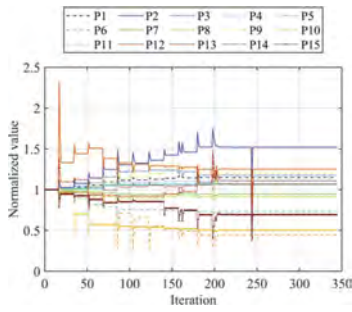


Figure 7. Values of normalized parameters with iteration.

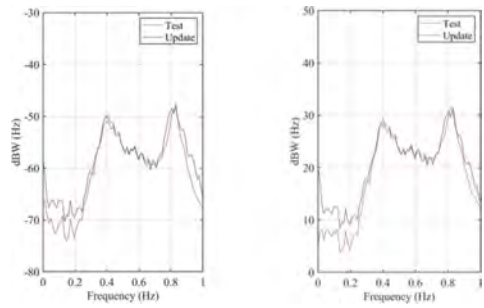


Figure 8. Comparison of PSD of structural response: (a) displacement, (b) leg-to-hull moment.

The values of updated parameters with iteration steps are shown in Figure 7, where all parameters converged within 343 iterations. P12 and P14 showed a large jump at the 17th and 244th iterations, respectively. Figures 8 and 9 compare the PSD of the updated results against the test data, which matched fairly well especially at the two peaks. The updated parameters were then used as inputs in the FE model to generate the structural responses. The hull displacements are compared with the measured displacements in Figure 10 showing good match in the overall trend. It showed that the displacement generated at the point level was consistent with the test data. Figures 11 also illustrate the similar agreement for the leg-to-hull moment.

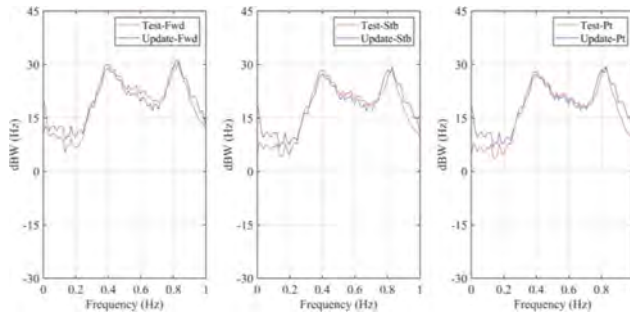


Figure 9. Comparison of PSD of spudcan moment in three legs.

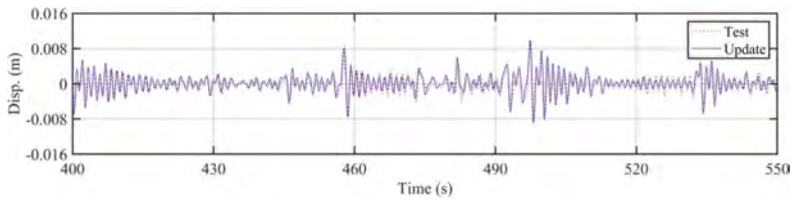


Figure 10. Comparison of hull displacement from 400 to 550 s.

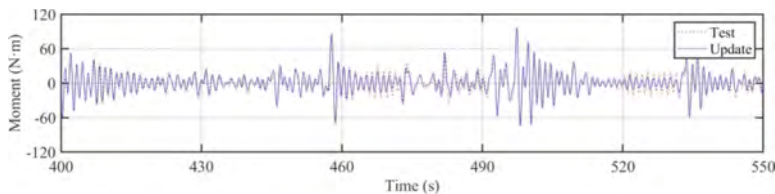


Figure 11. Comparison of leg-to-hull moment from 400 to 550 s.

5 CONCLUSIONS

This work presented the finite element model updating of a jack-up structure based on basin test data. The measured hull displacement, leg-to-hull, and spudcan moments were analyzed in time and frequency domains. The identified fundamental frequency of the jack-up structure was 0.82 Hz while the dominant frequency of the irregular wave was around 0.42 Hz. A simplified jack-up model was created based on the basin test, which considered the fixity of leg-to-hull connection and spudcan fixity amongst other structural and hydrodynamic parameters to be identified. The simplified model with fifteen selected parameters was calibrated by minimizing the cost function represented by the power spectral density of measurement data and the corresponding FE predicted response. Due to the simplicity of the model, noise in the measured data and variability in the loadings, large uncertainties exist in the estimated shear stiffness coefficient, spudcan stiffness in the z direction for all 3 legs, stiffness of the leg-to-hull connections, hydrodynamic drag coefficient and the structural damping coefficients.

ACKNOWLEDGEMENTS

The authors would like to thank the invaluable assistance provided by the TCOMS Ocean Basin Support Team during the ocean basin experiments. This work is funded by the Enhancing Offshore System Productivity, Integrity and Survivability in Extreme Environments (ENSURE) programme. The fund supported by A*STAR under its RIE 2020 Industry Alignment Fund (Grant No: A19F1a0104) is also appreciated.

REFERENCES

- Bienen, B., & Cassidy, M. J. (2009). Three-dimensional numerical analysis of centrifuge experiments on a model jack-up drilling rig on sand. *Canadian Geotechnical Journal*, 46(2), 208–224.
- Chen, W. K., Zhang, S., Cai, M., Zhang, C., Yu, M., ... & Si, M., (2022), Model tests of a stiffness-similar jack-up. Part 1: model design, fabrication and structural pre-tests (internal report, TCOMS Pte Ltd).
- Guo, N., Yang, Z., Wang, L., Ouyang, Y., & Zhang, X. (2018). Dynamic model updating based on strain mode shape and natural frequency using hybrid pattern search technique. *Journal of Sound and Vibration*, 422, 112–130.
- Liu, P., Massie, W. W., Wolters, J. G., & Blaauwendraad, J. (1991, May). Response of jackup models to irregular waves. In *Offshore Technology Conference*. OnePetro.
- Liu, P., Massie, W. W., Wolters, J. G., & Blaauwendraad, J. (1993). Nonlinear simulation of jackup platform models. *SPE drilling & completion*, 8(02), 118–124.
- Liu, L., Yuan, H., Yang, J., Tian, X., Li, C., & Lu, H. (2015, June). A Wave Basin Model Test Study for a Jackup Moored on the Dock. In *The Twenty-fifth International Ocean and Polar Engineering Conference*. OnePetro.
- Mirzadeh, J., Kimiaei, M., & Cassidy, M. J. (2016). Effects of irregular nonlinear ocean waves on the dynamic performance of an example jack-up structure during an extreme event. *Marine Structures*, 49, 148–162.
- Pisanò, F., Schipper, R., & Schreppers, G. J. (2019). Input of fully 3D FE soil-structure modelling to the operational analysis of jack-up structures. *Marine Structures*, 63, 269–288.
- Temperton, I., Stonor, R. W. P., & Springett, C. N. (1999). Measured spudcan fixity: analysis of instrumentation data from three North Sea jack-up units and correlation to site assessment procedures. *Marine structures*, 12(4-5), 277–309.
- Wang, X. M., Koh, C. G., & Zhang, J. (2014). Substructural identification of jack-up platform in time and frequency domains. *Applied Ocean Research*, 44, 53–62.
- Yin, Q., Yang, J., Xu, G., Xie, R., Tyagi, M., Li, L., ... & Pang, D. (2020). Field experimental investigation of punch-through for different operational conditions during the jack-up rig spudcan penetration in sand overlying clay. *Journal of Petroleum Science and Engineering*, 195, 107823.
- Zhang, C., Zhang, S., Cai, M., Yu, M., Santo, H. & Si, M., (2022). Combining reduced-order stick model with full-order finite element model for efficient analysis of self-elevating units, *Journal of Marine Science and Engineering*, 2021 (under review).

Application of unscented transformation for Bayesian updating

T. Shuku

Okayama University, Okayama City, Okayama, Japan

T. Kitahara

Kanto Gakuin University, Kanagawa, Japan

ABSTRACT: Bayesian updating has been widely used in civil engineering for many different purposes such as parameter identification, model updating, reliability analysis. Bayesian updating usually requires high computation cost, and some methodologies are available to reduce the computational costs. One of the methodologies that has been commonly used for system identification/control in time-series problem includes unscented transformation (UT). In UT, the prior and posterior probability density functions (PDFs) are approximately estimated with $2n + 1$ data points (n is the number of parameters of interest): it means that only $2n + 1$ times simulations are required for Bayesian inference. However, UT assumes that prior and posterior PDFs follow Gaussian PDFs and has limitations for some practical applications. This paper investigates the performance and limitations of UT in Bayesian updating in terms of estimation accuracy of posterior PDFs through synthetic examples. Comparison of UT with Monte Carlo filter (MCF) is also made.

1 INTRODUCTION

Bayesian updating has been widely used in civil engineering for many different purposes such as parameter identification, model updating, reliability analysis. There are many algorithms for implementing Bayesian updating, and Markov Chain Monte Carlo (MCMC, Metropolis et al. 1953) method has been commonly used in civil engineering because of its easy implementation and versatility (e.g., Beck and Au 2002).

In MCMC, samples are directly drawn from the posterior in a sequential way, so one sample after the other, after a burn-in period. The samples are correlated, often 100% when the new sample is not accepted, making them very insufficient in some applications, e.g., the improved performance might not be worth the additional computational costs.

To reduce the computational costs in Bayesian updating, some methodologies are available. One of the methodologies that has been commonly used for system identification/control in time-series problem includes unscented transformation (UT, e.g., Julier and Uhlmann 2004). In UT, the prior and posterior probability density functions (PDFs) are approximately estimated with $2n + 1$ data points (n is the number of parameters of interest): it means that only $2n + 1$ times simulations are required for Bayesian inference. However, UT assumes that prior and posterior PDFs follow Gaussian PDFs and has limitations for some practical applications.

This paper investigates the performance and limitations of UT in Bayesian updating in terms of estimation accuracy of posterior PDFs through synthetic examples. Comparison of UT with Monte Carlo filter (MCF) or particle filter (PF) (Gordon et al. 1993; Kitagawa 1996) is also made.

2 UNSCENTED KALMAN FILTER

An algorithm for Bayesian updating based on UT is called unscented Kalman filter (UKF), and it uses UT to pick a minimal set of sample points (called sigma points) around the mean. The sigma points are then propagated through the nonlinear functions, from which a new mean and covariance estimate are then formed. The resulting filter depends on how the transformed statistics of the UT are calculated and which set of sigma points are used. It should be remarked that it is always possible to construct new UKFs in a consistent way.

For certain systems, the resulting UKF more accurately estimates the true mean and covariance. This can be verified with Monte Carlo sampling or Taylor series expansion of the posterior statistics. In addition, this technique removes the requirement to explicitly calculate Jacobians, which for complex functions can be a difficult task in itself (i.e., requiring complicated derivatives if done analytically or being computationally costly if done numerically), if not impossible (if those functions are not differentiable).

The following subsections briefly describes sigma points and UKF.

2.1 Sigma points

In UKF, n -dimensional random variable \mathbf{x} with mean $\bar{\mathbf{x}}$ and covariance $\mathbf{P}_{\mathbf{xx}}$ is approximated by $2n + 1$ weighted points, which are called *sigma points*, given by:

$$\begin{aligned}\mathcal{X}_0 &= \bar{\mathbf{x}} \\ \mathcal{X}_i &= \bar{\mathbf{x}} + \left(\sqrt{(n + \kappa)\mathbf{P}_{\mathbf{xx}}} \right)_i \\ \mathcal{X}_{i+n} &= \bar{\mathbf{x}} - \left(\sqrt{(n + \kappa)\mathbf{P}_{\mathbf{xx}}} \right)_i\end{aligned}\quad (1)$$

$$\begin{aligned}W_0 &= \kappa / (n + \kappa) \\ W_i &= 1 / (2n + 2\kappa) \\ W_{i+n} &= 1 / (2n + 2\kappa)\end{aligned}\quad (2)$$

where κ is a hyperparameter that controls the location of sigma points, $\left(\sqrt{(n + \kappa)\mathbf{P}_{\mathbf{xx}}} \right)_i$ is the i^{th} column of the matrix square root of $(n + \kappa)\mathbf{P}_{\mathbf{xx}}$ and W_i is the weight which associated with the i^{th} point.

2.2 Unscented filter

The algorithm of the Bayesian updating (filtering) based on UT can be summarized as follows:

1. Define initial mean vector \mathbf{x}_0 and initial covariance matrix \mathbf{P}_0 .
2. Observation update:
 - a) Create a set of sigma points using Equations (1) and (2).
 - b) Transform sigma points via model f .

$$\mathbf{y}_i = f(\mathcal{X}_i), \quad i = 0, 1, \dots, 2n$$

- c) Compute the predicted mean

$$\bar{\mathbf{y}} = \sum_{i=0}^{2n} W_i \mathbf{y}_i$$

- d) Compute the covariance matrices \mathbf{V} and \mathbf{U} .

$$\mathbf{V} = \sum_{i=0}^{2n} W_i (\bar{\mathbf{y}} - \mathbf{y}_i)(\bar{\mathbf{y}} - \mathbf{y}_i)^{\text{T}} + \mathbf{R}$$

$$\mathbf{U} = \sum_{i=0}^{2n} W_i (\bar{\mathbf{x}} - \mathcal{X}_i)(\bar{\mathbf{y}} - \mathbf{y}_i)^T$$

e) Compute Kalman gain \mathbf{K} . and filtered estimate \mathbf{x}

$$\mathbf{K} = \mathbf{U}\mathbf{V}^{-1}$$

$$\mathbf{x} = \mathbf{x} + \mathbf{K}(\mathbf{y} - \bar{\mathbf{y}})$$

3 NUMERICAL EXAMPLE

The performance of UKF to estimate posterior distributions was investigated through a simple numerical test. The following 3rd order polynomial was used as a model f :

$$y = f(x_1, x_2) = 0.02x_1^3 - 0.02x_2^3 \quad (3)$$

where x_1 and x_2 are the model parameters which are assumed to be unknown. The posterior distribution of $\mathbf{x} = [x_1, x_2]^T$ is given by:

$$p(\mathbf{x}|\bar{\mathbf{y}}) \propto p\{\bar{\mathbf{y}}|f(\mathbf{x})\}p(\mathbf{x}) \quad (4)$$

where $\bar{\mathbf{y}}$ is observation. We assumed that $p(\mathbf{x})$ follows the Gaussian distribution defined by

$$N(\mu, \mathbf{C}), \mu = \mathbf{0} = \begin{bmatrix} 0 \\ 0 \end{bmatrix}, \mathbf{C} = \begin{bmatrix} 1.0 & 0.0 \\ 0.0 & 1.0 \end{bmatrix} \quad (5)$$

Figure 1 shows the prior distribution of \mathbf{x} approximated with 10,000 Monte Carlo samples.

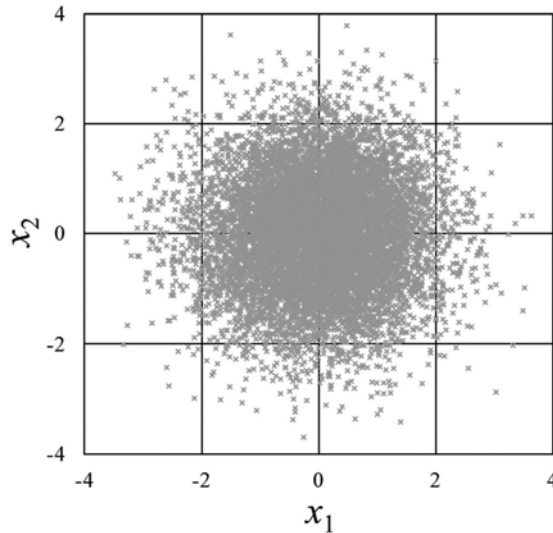


Figure 1. Prior PDF of x_1 and x_2 .

Two types of observation data, $\bar{y} = 0.2$ and $\bar{y} = 0.6$, are considered, and they intuitively correspond to nonlinear and strong nonlinear problems respectively. The observation noise is assumed to follow the Gaussian distribution with $\mu = 0.0$ and $\sigma = 0.1$.

The posterior distributions of x and y were estimated using UKF with different hyperparameters to investigate the effects of the hyperparameters on the estimation. Three different parameter values, which are $\kappa = 0.1, 1.0,$ and $2.0,$ were considered in UKF. Since the target problem is nonlinear, the analytical solution of the posterior distribution is not available. We estimated the posterior distributions using PF with 10,000 samples and assumed the results by PF as “true” or “analytical” solutions to discuss the performance of the UKF.

Figure 2 shows a comparison of posterior PDFs between UKF and PF for $\bar{y} = 0.2$. Although UKF gives analytical form of posterior distributions, the results of UKF are shown as Monte Carlo samples ($N = 10,000$). The result of UKF with $\kappa = 0.1$ is similar to the prior PDF, and the hyperparameter seems to be too small to capture the distribution. The result of UKF with $\kappa = 1.0$ well captures the posterior distribution, and UT can be used in Bayesian updating to reduce the computation cost.

Figure 3 shows a comparison of posterior PDFs between UKF and PF for $\bar{y} = 0.6$. The true posterior distribution is very complex seems difficult to capture UKF. The UKF seems to difficult to capture the complex posterior distribution with high accuracy, but the error between estimated and true distributions by properly tuning the hyperparameter. This study does not discuss the method of hyperparameter tuning, but some authorized methods which are commonly used in machine learning such as cross-validation can be applied in this problem.

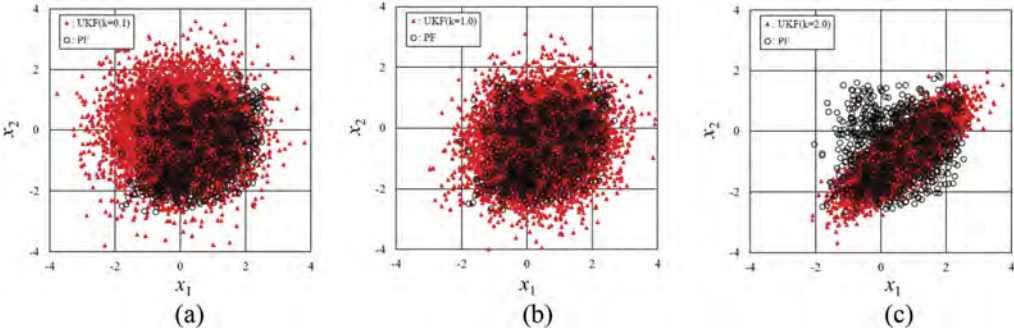


Figure 2. Posterior PDF of x_1 and x_2 ($\bar{y} = 0.2$).

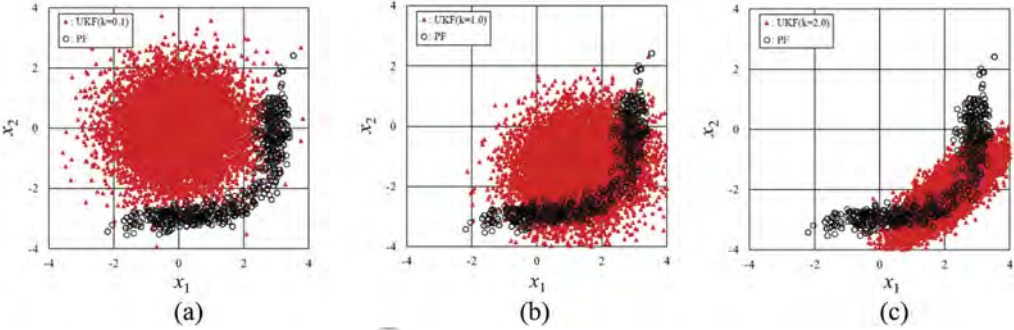


Figure 3. Posterior PDF of x_1 and x_2 ($\bar{y} = 0.6$).

Figure 4 shows the comparison of cumulative distribution function (CDF) for y between PF and UKF. When $\bar{y} = 0.2$, the CDF estimated by UKF is similar to true CDF. When $\bar{y} = 0.6$, the CDF estimated by UKF is very different from the true CDF, and it seems difficult to estimate the shape of posterior distribution of y by UKF. These results indicate that UKF can work in weakly nonlinear problems, but not the case in strongly nonlinear problems.

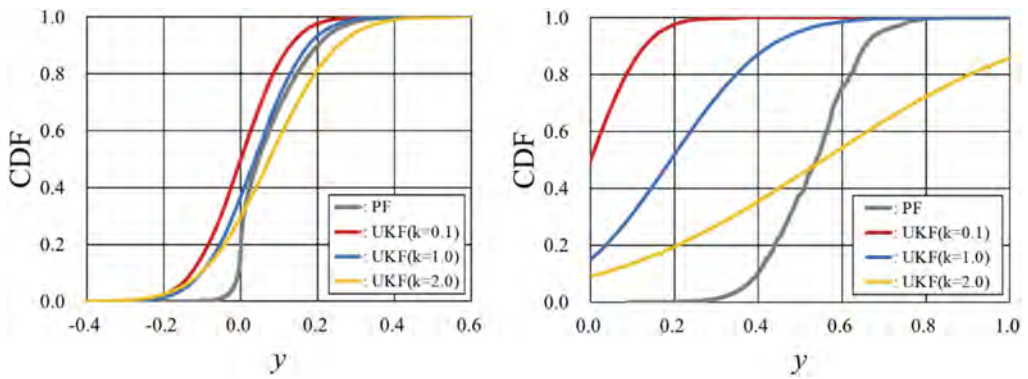


Figure 4. Posterior CDF of y : a) $\bar{y} = 0.2$; b) $\bar{y} = 0.6$.

4 CONCLUSIONS

This study investigated the performance of UT and UKF for Bayesian updating or estimation for posterior distributions through a simple numerical example. When the problem is weakly nonlinear, UT or UKF can reasonably estimate the posterior distributions with low computation cost. However, the problem is strongly nonlinear, it is difficult to capture the shape of the posterior distribution using UKF. In addition, hyperparameter tuning strongly impacts on the estimation, and UKF cannot work when appropriate parameters are not used. How to tune the hyperparameter is left for the future research.

REFERENCES

- Beck, J. L. and Au, S. K. 2002. Bayesian updating of structural models and reliability using Markov chain Monte Carlo simulation. *J. Eng. Mech.* 128(4): 380–391.
- Gordon, N. J., Salmond, D. J. and Smith, A. F. M. 1993. Novel approach to nonlinear/non-Gaussian Bayesian state estimation. *IEEE Proceedings-F* 140(2): 107–113.
- Kitagawa, G. 1996. Monte Carlo filter and smoother for non-Gaussian nonlinear state space models. *Journal of Computational Graphical Statistics* 5: 1–25.
- Julier, S. J. and Uhlmann, J. K. 2004. Unscented filtering and nonlinear estimation, *Proceedings of the IEEE* 92(3): 401–422.
- Metropolis, N., Rosenbluth, A.W., Rosenbluth, M.N., Teller, A.H. and Teller, E. 1953. Equation of state by fast computing machines. *J. Chemical Physics* 21: 1087–1092.

Environmental influence on structural health monitoring systems

J.-H. Bartels

Institute of Concrete Structures, TU Dresden, Dresden, Germany

M. Kitahara

Department of Civil Engineering, The University of Tokyo, Tokyo, Japan

S. Marx

Institute of Concrete Structures, TU Dresden, Dresden, Germany

M. Beer

Institute for Risk and Reliability, Leibniz University Hannover, Hannover, Germany

Institute for Risk and Uncertainty, University of Liverpool, Liverpool, UK

ABSTRACT: Monitoring is becoming increasingly important for the condition assessment of structures, as it allows continuous assessment. The aim is to identify changes in the condition of the structure that cannot be detected by purely visual inspection. In this paper, a typical measurement system used in practice is investigated under laboratory conditions with regard to its temperature dependence. A method for temperature compensation of laser distance measurements is presented and a Bayesian model updating is applied, with which a temperature compensation function over time can be determined semi-automatically. It is shown that the temperature-dependent transfer function should first be generated at the structure in order to perform a reliable temperature compensation. Furthermore, the application of Bayesian Model Updating shows a reliable fit of the temperature-dependent transfer function over time, so that the engineer is provided with a helpful tool for semi-automated temperature compensation in the case of time-variant behavior.

1 INTRODUCTION

For condition monitoring of structures, Structural Health Monitoring (SHM) is becoming increasingly important, as it allows continuous condition assessment of the structure and usefully supplements on-site inspections (Farrar and Worden 2007; Wedel and Marx 2022). The aim of monitoring is to identify changes in the condition of the structure that can only be inadequately detected by the purely visual inspection (Worden et al. 2007), whereby the goal of monitoring can only be achieved by comparing at least two different states: the reference state with the current state (Worden and Tomlinson 2019). For large infrastructures (e.g. wind turbines or bridges), however, the change in condition due to aging is very small (Hübler et al. 2022), so that precise measurements are required to be able to make reliable comparisons. The problem is that not only the behavior of the structure, but also other influences such as temperature affect the measurement signal. The question arises how such influences can be quantified and compensated.

This paper aims to make a contribution to this by investigating a measurement system typically used in practice under laboratory conditions with regard to its temperature dependence and its time-dependent behavior. For this, a method for temperature compensation is presented and Bayesian Model Updating (BMU) is applied, with which a temperature compensation function can be determined semi-automatically. This paper consists of five chapters. In

chapter 2, the measurement principle of the investigated Laser Triangulation Sensor (LTS) is explained and the principle of BMU is described. In chapter 3 the experimental setup with the measurement system used and the exposures are explained. On this basis, the temperature dependence of the measurement signal is analyzed. With the help of time-variant investigations, BMU is applied in chapter 4 and it is shown that a reliable updating of the temperature dependence over time is possible. Chapter 5 concludes with a summary and an outlook.

2 THEORIES AND METHODOLOGIES

2.1 Laser triangulation sensor – measurement principle

In this paper, LTS is used because it enables to investigate a simple measurement principle and it can be used in Offshore Wind Turbine (OWT) or bridge monitoring. The LTS measures the distance to an object surface by calculating the angle and provides a non-contact method of position measurement (Murakami 1994).

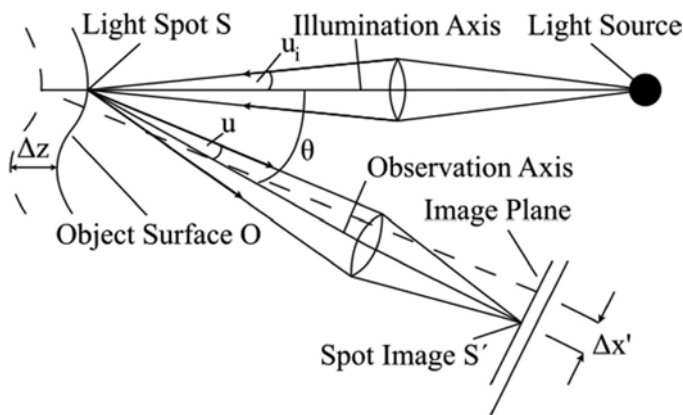


Figure 1. Measurement principle of LTS.

A laser beam is projected on the object surface O and a light spot S can be observed on it. The light spot is imaged through a lens with a numerical aperture $\sin(u_i)$ (Dorsch et al. 1994; Berns et al. 2019). The position of the spot image S' is determined with a position sensitive detector called photodiode array (PDA). The PDA is based on the CCD principle (charge-coupled device) and contains light sensitive electronic components using the internal photoelectric effect. From the position of the light spot on the image plane, the position of the measuring object is calculated (Löffler-Mang 2012). For a detailed description of the measurement principle, the reader is referred to Bartels et al. 2023.

2.2 Bayesian model updating – Transitional Markov Chain Monte Carlo (TMCMC)

For engineering problems, mathematical models are typically used to simulate and evaluate the behavior of structures under load conditions. This virtual behavior corresponds only poorly to the real physical structure. To solve this problem, model updating techniques can be applied to update physical input parameters. The parameters then describe e. g. material properties of a structure (Worden and Tomlinson 2019). These parameters are measured on the real structure and are integrated into the mathematical model of the virtual system to be updated, so that the difference between the mathematical model and the real physical behavior of the system is minimized.

The physical behavior of a system is described by a mathematical function $M(x; \vartheta)$, where x defines the vector of unchangeable model parameters and ϑ the vector of changeable model parameters to be updated. The mathematical relationship between the requested quantity

\mathbf{D} (e. g., the output of the measured distance by the LTS) and the mathematical prediction model $M(x; \vartheta)$ is defined by

$$\mathbf{D} = M(x; \vartheta) + \epsilon, \quad (1)$$

where ϵ describes the model or measurement error. The uncertainty in the model parameters ϑ can be accounted for using a probability density function (PDF). These problems are called forward problems because they can be solved analytically or with simple Monte Carlo simulations (Li and Caracoglia 2019). Monte Carlo simulation is used to generate the requested data \mathbf{D} for a known common PDF. The problem in reality is that the best-fit joint PDF is not known, which links the model parameters ϑ to the requested quantity \mathbf{D} . This is called the inverse problem (Lye et al. 2021). The advantage of implementing Bayesian inference in BMU process is that prior information about the requested model parameters ϑ can be combined with the observed data \mathbf{D} . Hence, the stochastic character of the quantity \mathbf{D} to be inferred can be generated. So, if a set of n independent and identically distributed observations ($D_1; D_2; \dots; D_n$) is made, then the pre-information is updated using Bayes' theorem (Mares et al. 2006). This leads to a posterior distribution of the requested model parameters ϑ under the condition of the observations made \mathbf{D}

$$P(\vartheta|\mathbf{D}) = \frac{P(\mathbf{D}|\vartheta) \cdot P(\vartheta)}{P(\mathbf{D})}, \quad (2)$$

where \mathbf{D} represents the observation vector, $P(\vartheta)$ the statistical distribution of the prior, $P(\mathbf{D}|\vartheta)$ the likelihood function, $P(\mathbf{D})$ the evidence, and $P(\vartheta|\mathbf{D})$ the posterior distribution. Instead of the analytical solution, the Monte Carlo method, which is easy to apply, is usually used. To apply the method, samples must be generated, which are performed using the iterative TMCMC sampler. For more detailed information on the TMCMC algorithm, please refer to Ching and Chen 2007.

3 EXPERIMENTAL SETUP AND TRANSFER FUNCTION

For the investigation of the temperature influence on laser measurements, a total of six LTSs within a measuring system is exposed to different temperatures within a climate chamber and analyzed whether and in which way the measurement signal changes.

3.1 Sensors, measurement system and environmental influence

The experimental setup is shown in Figure 2.

The entire measuring system consists of LTS, cable and measuring amplifier. As can be seen in Figure 2, the LTSs are fixed on a base plate with upstand and measure the horizontal distance to the upstand. The special feature: the base plate and the upstand are made of the material Alloy 36, an iron-nickel alloy with a small coefficient of thermal expansion of $\alpha_{T, \text{Alloy36}} = 0.50 \cdot 10^{-6} \text{ 1/K}$. Compared to this material, construction steel ($\alpha_{T, \text{Stahl}} = 13.00 \cdot 10^{-6} \text{ 1/K}$) has a coefficient of thermal expansion more than 20 times higher. With this design, it is possible to attribute changes in the measurement signal to the measurement system, since the influence of base plate strain due to temperature change is negligible. LTSs with a measuring range of 10 mm are tested, which measure within the measuring distances 16 mm to 26 mm. To examine the entire measurement range of the LTS, three initial distances d_{sel} between the sensor and the upstand are selected ($d_{\text{sel}} \approx [17 \text{ mm}; 21 \text{ mm}; 25 \text{ mm}]$).

3.2 Temperature-dependent transfer function

In the climate chamber, temperatures are varied between -10 °C and +50 °C in 10 K steps. The planned temperature curve can be seen in Figure 3.

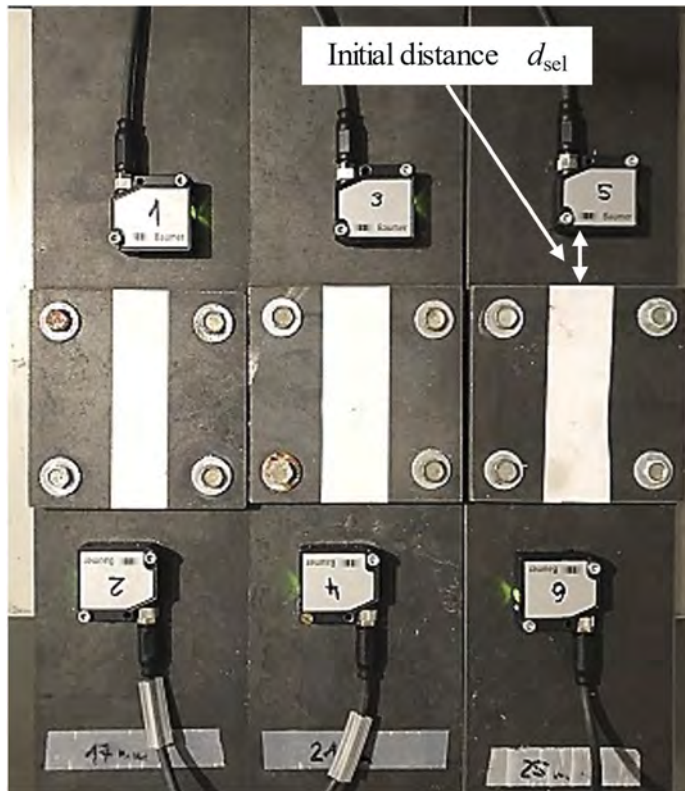


Figure 2. Experimental setup for the LTS investigation of temperature and time dependence.

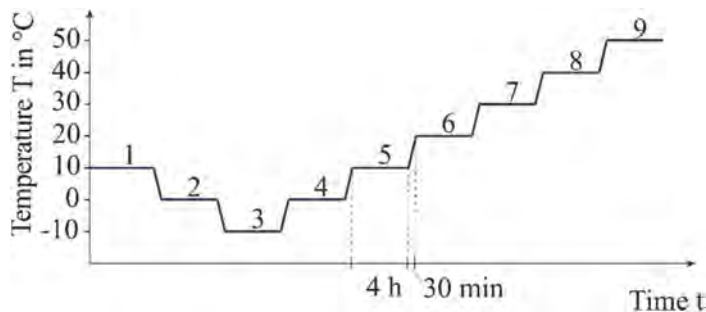


Figure 3. Intended temperature regulation for the determination of the temperature-dependent transfer function.

By varying the temperature, a reproducible test of the LTS with respect to the temperature dependence is possible. Each temperature level is kept constant for 4 h and the respective temperature change by 10 K is achieved within 30 min. Keeping the temperature constant for 4 h has two objectives: on the one hand, the temperature inertia of the experimental setup is overcome, so that the temperature can be assumed for the measuring system, the base plate and the ambient temperature. On the other hand, a representative amount of data can be generated over this period. With a sampling rate of 1 Hz, 14,400 measured values are generated over 4 hours. Only the constant temperature and measurement distance ranges are cut and the arithmetic mean is calculated as the expected value.

This procedure is carried out for all temperature levels, so that a total of seven expected values are calculated from -10 °C to $+50\text{ °C}$ in 10 K steps. The values are related to the measured

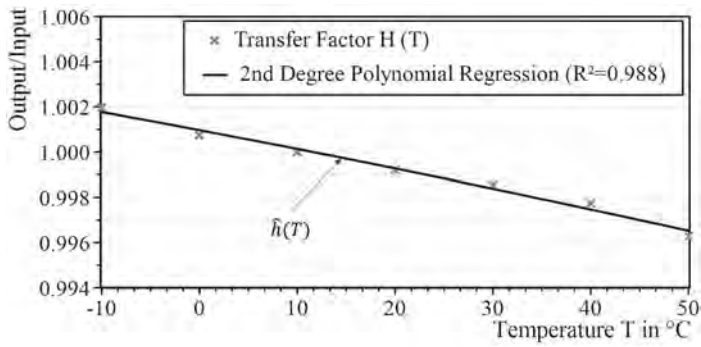


Figure 4. Temperature dependent transfer function for one LTS.

distance at 10 °C (reference value). This quotient between the measurement distance at a given temperature and the measurement distance at 10 °C is referred to as the transfer factor $H(T)$. The individual transfer factors are approximated by a 2nd degree regression polynomial to the so-called temperature-dependent transfer function (see Figure 4). The detailed description of the procedure for calculating the temperature-dependent transfer function is given in Bartels et al. 2022.

3.3 Time-dependence of the transfer function

With the knowledge of the temperature dependence of the LTS, the time dependence of the transfer function is to be analyzed in the next step. For this, the measurement system is subjected to a modified temperature and humidity curve (see Figure 5) using the same experimental setup as shown in Figure 2.

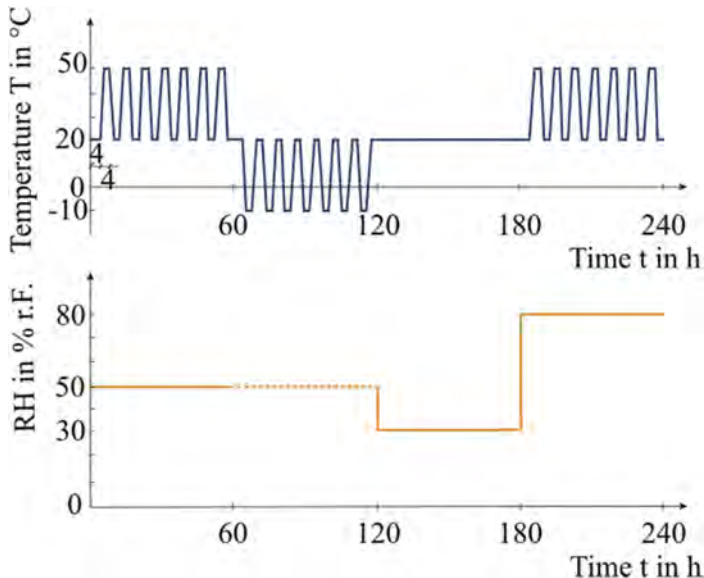


Figure 5. Intended temperature and humidity regulation for the aging tests.

The temperature and humidity can be divided into four phases, with each phase starting and ending at a temperature of 20 °C. This has the advantage that the measurement signal can be compared with the output signal (also at 20 °C) after each aging phase. In order to be able to record the time variance of the transfer function, the test for determining the temperature-dependent transfer

function according to chapter 3.2 is carried out after each 240-hour aging test and compared with the transfer function from Figure 4. The result is shown in Figure 6.

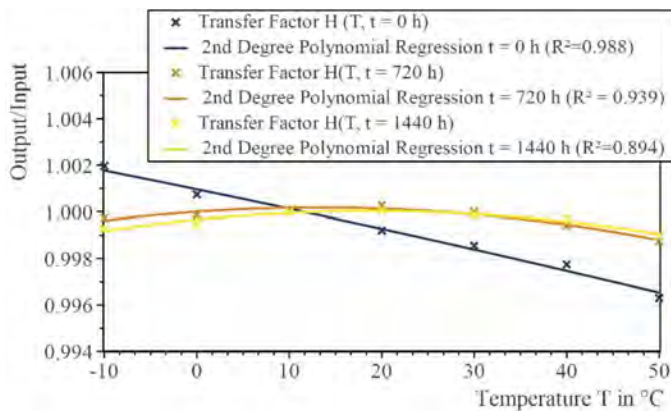


Figure 6. Investigation of the time variance of the temperature-dependent transfer function.

To enable the humidity to be controlled as well, the experimental setup had to be installed in a different climate chamber that can vary both the temperature and the humidity. At time $t = 0$ h the experimental setup is in the “old” climate chamber, at time $t = 720$ h the experimental setup is in the “new” climate chamber.

It can be clearly seen that the reconstruction of the measuring system has led to a change in the temperature-dependent transfer function. This circumstance means that this transfer function should only be determined in practice after successful installation of the measurement system on the structure when the system is no longer moved. A determination in the laboratory would lead to unreliable and non-reproducible results. After reconstruction the temperature-dependent transfer function does not change much over the considered test period of 1440 h, so that a time-invariant temperature-dependent transfer function can be assumed.

4 BAYESIAN MODEL UPDATING OF TRANSFER FUNCTION

The question arises whether the results from sections 3.2 and 3.3 can also be approximated with BMU. This would mean a partial automation of the measurement data evaluation and accordingly support the interpreting engineer in the quasi-real-time evaluation of the monitoring data. For this, the transfer function from the manual approximation is compared with the one generated by BMU. The result of the BMU is shown in Figure 7.

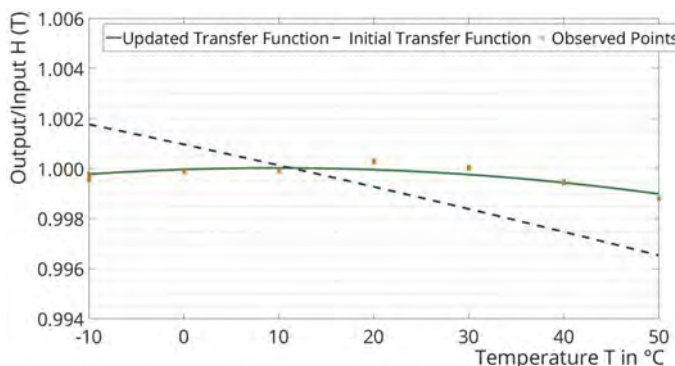


Figure 7. Transfer function calculated with BMU.

The initial transfer function at time point $t = 0$ h is updated for time point $t = 720$ h. The visual comparison between Figure 6 and Figure 7 shows a good agreement of the transfer functions at time point $t = 720$ h. This finding is quantified in the next step. For this, the mathematical model of the transfer function is important, which includes the parameters ϑ_i to be updated. With equation (3)

$$\hat{h}(T, \vartheta_i) = 1.00096 \cdot \vartheta_1 + (-8.18380 \cdot 10^{-5}) \cdot T \cdot \vartheta_2 + (-1.37294 \cdot 10^{-7}) \cdot T \cdot \vartheta_3 \quad (3)$$

the transfer function for updating is defined at time $t = 0$ h, where T describes the temperature. In the manual approximation of the transfer function at time $t = 720$ h, the parameters of the 2nd degree regression polynomial are determined so that they can be compared with the parameters of the transfer function at time $t = 0$ h. The quotient of the respective parameters results in the fitting factor ϑ_i . For the validation of BMU, the change of the transfer function is considered once between the time points $t = 0$ h to $t = 720$ h and between $t = 960$ h to $t = 1200$ h. The results are listed in Table 1.

Table 1. Comparison of manual approximation vs. BMU (TMCMC).

		ϑ_1	ϑ_2	ϑ_3
t = 0 h to 720 h	2 nd degree polynomial	0.99903	-0.33468	7.52741
	BMU (TMCMC)	0.99901	-0.35000	7.90000
	Error	0.002 %	4.576 %	4.950 %
t = 960 h to 1200 h	2 nd degree polynomial	1.00034	0.60755	0.68738
	BMU (TMCMC)	1.00025	0.65980	0.68000
	Error	0.008 %	8.600 %	1.074 %

It becomes clear that the error between manual approximation and BMU is small. Both in the updating process between strongly varying transfer functions ($t = 0$ h to 720 h) and in the case of similar transfer functions ($t = 960$ h to 1200 h), the procedure is accurate. Nevertheless, the fitting factors in the BMU process are determined with an uncertainty, since an expected value is calculated on the basis of a large number of samples, which is calculated with a standard deviation. In future experiments, it will be investigated how large the standard deviation of the individual parameters can be so that the smallest changes in the transfer functions can be reliably determined and are not lost in the standard deviation of the fitting factors ϑ_i .

5 CONCLUSION AND OUTLOOK

In this paper, a measurement system typically used in practice was tested under laboratory conditions with respect to its temperature dependence and its time-dependence. A method for the temperature compensation of LTSs was presented and furthermore a BMU was applied, with which a temperature compensation function can run semi-automatically over time.

It is shown that the generation of the temperature-dependent transfer function must first be applied on the structure to be monitored in order to perform reliable temperature compensation.

Furthermore, the application of a BMU with TMCMC algorithm shows a reliable fitting of the temperature-dependent transfer function over time. Thus, this procedure providing the interpreting engineer with a helpful tool for semi-automated temperature compensation in the presence of time-variant behavior of the measurement system.

Future studies will address the time variance of the measurement system in more detail. In addition, the uncertainty of the BMU must be taken into account when calculating the transfer function so that marginal change in the measurement system and at the structure can be reliably captured. This is the only way to reliably assess structures using monitoring systems over several years.

ACKNOWLEDGEMENT

This research was funded by the German Research Foundation (DFG), as part of the Collaborative Research Centre 1463 (SFB 1463) “Integrated Design and Operation Methodology for Offshore Megastructures” (subproject C01, project number 434502799).

REFERENCES

- Bartels, J.-H., Gebauer, D., & Marx, S. 2023. Einflüsse auf die Messunsicherheit von SHM-Systemen und deren Kompensation am Beispiel von Laser-Distanzmessungen. *Bautechnik*. Advance online publication. <https://doi.org/10.1002/bate.202200102>
- Berns, K.; Köpper, A.; Schürmann, B. 2019. Technische Grundlagen Eingebetteter Systeme. Elektronik, Systemtheorie, Komponenten und Analyse. Wiesbaden: Heidelberg.
- Ching, J. & Chen, Y.-C. 2007. Transitional Markov chain Monte Carlo method for Bayesian model updating, model class selection, and model averaging. In *Journal of Engineering Mechanics* (7), pp. 816–832.
- Dorsch, Rainer G.; Häusler, Gerd; Herrmann, Jürgen M. 1994. Laser triangulation: fundamental uncertainty in distance measurement. In *Appl. Opt.* (33), pp. 1306–1314.
- Farrar, C. R.; Worden, K. 2007. An introduction to structural health monitoring. In *Phil. Trans. R. Soc. A.* (365), pp. 303–315.
- Hübler, C.; Hofmeister, B.; Wernitz, S.; Rolfes, R. 2022. Validierung von daten- und modellbasierten Methoden zur Schadenslokalisierung. In *Bautechnik* (99), pp. 433–440.
- Li, S.; Caracoglia, L. 2019. Surrogate Model Monte Carlo simulation for stochastic flutter analysis of wind turbine blades. In *Journal of Wind Engineering and Industrial Aerodynamics* (188), pp. 43–60.
- Löffler-Mang, M. 2012. Triangulation. In *Optische Sensorik*. Vieweg + Teubner Verlag.
- Lye, A.; Cicirello, A.; Patelli, E. 2021. Sampling methods for solving Bayesian model updating problems: A tutorial. In *Mechanical Systems and Signal Processing* (159), pp. 1–43.
- Mares, C.; Dratz, B.; Mottershead, J. E.; Friswell, M. I. 2006. Model updating using Bayesian estimation. In *International Conference on Noise and Vibration Engineering, Katholieke Universiteit Leuven*, pp. 18–20.
- Murakami, F. 1994. Accuracy assessment of a laser triangulation sensor. In *Conference Proceedings. 10th Anniversary. IMTC/94. Advanced Technologies in I & M. 1994 IEEE Instrumentation and Measurement Technology Conference*, pp. 802–805.
- Wedel, F.; Marx, S. 2022. Application of Machine Learning Methods on Real Bridge Monitoring Data. In *Engineering Structures* (250), pp. 1–47.
- Worden, K.; Tomlinson, G. R. 2019. *Nonlinearity in Structural Dynamics*: CRC Press.
- Worden, K.; Farrar, C. R.; Manson, G.; Park, G. 2007. The fundamental axioms of structural health monitoring. In *Proc. R. Soc. A.* (463), pp. 1639–1664.

Distribution-free stochastic model updating with staircase density functions

M. Kitahara

The University of Tokyo, Tokyo, Japan

T. Kitahara

Kanto Gakuin University, Yokohama, Japan

S. Bi

University of Strathclyde, Glasgow, UK

M. Broggi & M. Beer

Leibniz University Hannover, Hannover, Germany

ABSTRACT: In stochastic model updating, hybrid uncertainties are typically characterized by the distributional p-box. It assigns a certain probability distribution to model parameters and assumes its hyper-parameters as interval values. Thus, regardless of the updating method employed, the distribution family needs to be known a priori to parameterize the distribution. Meanwhile, a novel class of the random variable, called staircase random variable, can discretely approximate a wide range of distributions by solving moment-matching optimization problem. The first author and his co-workers have recently developed a distribution-free stochastic updating framework, in which model parameters are considered as staircase random variables and their hyper-parameters are inferred in a Bayesian fashion. This framework can explore an optimal distribution from a broad range of potential distributions according to the available data. This study aims to further demonstrate the capability of this framework through a simple numerical example with a parameter following various types of distributions.

1 INTRODUCTION

Model updating has been widely accepted as a fascinating technique to mitigate the discrepancy between model outputs and measurements (Mottershead and Friswell, 1993). The conventional deterministic model updating aims to calibrate model parameters to find their optimal values from a single set of the measurement data. It has been successfully employed in a wide range of practical applications, including the correction of complex finite element models. However, this approach considers the model and measurement data as deterministic, ignoring uncertainties in both modeling and measuring processes.

In contrast, the stochastic model updating aims to calibrate not parameters themselves but their probability distributions, so that corresponding model outputs reproduce the uncertainty characteristics of the multiple sets of the measurement data (Mares et al., 2006). This can be achieved by finding the optimal values of the distribution hyper-parameters that minimize a stochastic distance between model outputs and measurement datasets. Bi et al. (2019) employed the Bhattacharyya distance and developed a Bayesian updating framework that utilizes a distance-based approximate likelihood. The capability of this framework has been demonstrated upon complex applications, e.g., the first edition of NASA UQ problem (Crespo et al., 2014).

More recently, the latest edition of NASA UQ problem (Crespo and Kenny, 2021) has posed a challenge in the stochastic model updating to calibrate the parameter distributions without prior information about their distribution families. Motivated by this, the first author and his co-workers have developed a distribution-free stochastic updating framework, where the parameter distributions

are approximated by staircase density functions (SDFs) (Kitahara et al., 2022a; Kitahara et al., 2022b). SDF is a discrete probability density function (PDF) defined for the staircase random variable (SRV) which has a bounded support set and prescribed values for the first four moments (Crespo et al., 2018). It has no analytical solution but enables to discretely approximate a broad range of distributions by solving moment-matching optimization problem. This distribution-free stochastic updating framework has been demonstrated that it enables to calibrate the parameter distributions with no constraining hypothesis on the distribution formats. However, its capability to estimate various types of distributions has not been thoroughly investigated. Hence, this study aims at further demonstrating the feasibility of this framework through a simple numerical example with a parameter following various types of distributions, including heavy-tailed and multi-modal distributions.

2 OVERVIEW OF DISTRIBUTION-FREE STOCHASTIC UPDATING FRAMEWORK

2.1 *Bhattacharyya distance*

In the stochastic model updating, the stochastic discrepancy between model outputs and measurement datasets needs to be quantified and minimized. Let $\mathbf{Y}_D = \{\mathbf{y}^{(i)}; i = 1, \dots, N_D\}$ be N_D sets of the measurement data $\mathbf{y} \in \mathbb{R}^m$. Let also $\mathbf{Y}_S = \{\mathcal{M}(\mathbf{x}^{(i)}); i = 1, \dots, N_S\}$ be the corresponding N_S model outputs parameterized through a model parameter vector $\mathbf{x} \in \mathbb{R}^n$. In this study, the stochastic discrepancy between \mathbf{Y}_S and \mathbf{Y}_D is quantified as the Bhattacharyya distance, and its theoretical definition is given as:

$$d_B(\mathbf{Y}_S, \mathbf{Y}_D) = -\log \left[\int_{\mathbf{y}} \sqrt{f_{\mathbf{Y}_S}(\mathbf{y})f_{\mathbf{Y}_D}(\mathbf{y})} d\mathbf{y} \right] \quad (1)$$

where $f_{(\cdot)}(\mathbf{y})$ represents the PDF of \mathbf{y} ; \mathbf{y} denotes the support domain \mathbf{y} which comprises the m -dimensional space. Equation (1) indicates that the Bhattacharyya distance measures the degree of overlap between two different distributions. However, the direct evaluation of Equation (1) is generally impractical because the PDF of \mathbf{Y}_D often cannot be precisely estimated due to the very limited number of available measurement datasets. Hence, Bi et al. (2019) proposed the so-called binning algorithm to discretely evaluate the Bhattacharyya distance as:

$$d_B(\mathbf{Y}_S, \mathbf{Y}_D) = -\log \left\{ \sum_{i=1}^{N_{bin}} \sqrt{P_{\mathbf{Y}_S, i} P_{\mathbf{Y}_D, i}} \right\} \quad (2)$$

where N_{bin} indicates the total number of bins; $P_{(\cdot), i}$ represents the probability mass function of \mathbf{y} at the i th bin. N_{bin} is set as $N_{bin} = 10^n$ in this study.

2.2 *Staircase density functions*

Let the model parameters \mathbf{x} be independent random variables having the support set $[\underline{\mathbf{x}}, \bar{\mathbf{x}}]$ and prescribed values for the hyper-parameters $\boldsymbol{\theta}_x = [\boldsymbol{\mu}, \mathbf{m}_2, \mathbf{m}_3, \mathbf{m}_4]$ that consists of the mean vector $\boldsymbol{\mu} \in \mathbb{R}^n$, variance vector $\mathbf{m}_2 \in \mathbb{R}^n$, third-order central moment vector $\mathbf{m}_3 \in \mathbb{R}^n$, and fourth-order central moment vector $\mathbf{m}_4 \in \mathbb{R}^n$. Note that, in practice, the third- and fourth-order central moments are normalized by the variance as the skewness $\tilde{\mathbf{m}}_3$ and kurtosis $\tilde{\mathbf{m}}_4$, respectively, in the updating procedure. Any such variables must satisfy the feasibility conditions $g(\boldsymbol{\theta}_x) \leq 0$ given in Crespo et al. (2018). The realizations of $\boldsymbol{\theta}_x$ that satisfies these conditions constitute the feasible domain $\Theta = \{\boldsymbol{\theta}_x : g(\boldsymbol{\theta}_x) \leq 0\}$.

Let also the support set $[\underline{\mathbf{x}}, \bar{\mathbf{x}}]$ partitioned into n_b sub-intervals with the equal length of $\boldsymbol{\kappa} = (\bar{\mathbf{x}} - \underline{\mathbf{x}})/n_b$, \mathbf{x} can be then considered as SRVs the PDF of which is expressed as:

$$f_X(\mathbf{x}) = \begin{cases} p^j & \forall \mathbf{x} \in (\mathbf{x}^j, \mathbf{x}^{j+1}], \forall j = 1, 2, \dots, n_b \\ 0 & \text{otherwise} \end{cases} \quad (3)$$

where $l^j (= \prod_{i=1}^n l_i^j)$ is the PDF value at the j th bin; $\mathbf{x}^j = \mathbf{x} + (j-1)\boldsymbol{\kappa}$. $n_b = 25$ is utilized in this study, The marginal staircase densities are obtained by solving the optimization problem:

$$\underset{l_i}{\operatorname{argmin}}\{J(l_i) : \mathbf{A}(\boldsymbol{\theta}_{x_i}, n_b)\mathbf{l} = \mathbf{b}(\boldsymbol{\theta}_{x_i}), \boldsymbol{\theta}_x \in \Theta\} \quad (4)$$

where J denotes the cost function; $\mathbf{A}\mathbf{l} = \mathbf{b}$ are moment matching constraints. This optimization problem is convex when the cost function is a convex function. In this study, the cost function is defined as follows based on the principle of maximum entropy:

$$J(l_i) = \kappa_i \log l_i^T \mathbf{l}_i \quad (5)$$

2.3 Approximate Bayesian computation

In the proposed stochastic model updating framework, approximate Bayesian computation (ABC) (Beaumont, 2019) is employed. ABC is based on the well-known Bayes' theorem:

$$P(\boldsymbol{\theta}_x | \mathbf{Y}_D) = \frac{\tilde{\mathcal{L}}(\mathbf{Y}_D | \boldsymbol{\theta}_x) P(\boldsymbol{\theta}_x)}{P(\mathbf{Y}_D)} \quad (6)$$

where $P(\boldsymbol{\theta}_x)$ denotes the prior distribution of the hyper-parameters $\boldsymbol{\theta}_x$ that reflects one's initial beliefs on $\boldsymbol{\theta}_x$; $P(\boldsymbol{\theta}_x | \mathbf{Y}_D)$ is the posterior distribution of $\boldsymbol{\theta}_x$ that represents the posterior state of knowledge on $\boldsymbol{\theta}_x$; $\tilde{\mathcal{L}}(\mathbf{Y}_D | \boldsymbol{\theta}_x)$; is the so-called approximate likelihood function that serves as the connection between the measurement datasets \mathbf{Y}_D and $\boldsymbol{\theta}_x$; $P(\mathbf{Y}_D)$ means the evidence ensuring that the integral of the posterior distribution equal to one.

Given the support set $[\underline{\mathbf{x}}, \bar{\mathbf{x}}]$, the support set of $\boldsymbol{\theta}_x$ can be obtained based on the feasibility conditions as:

$$\Omega = [\underline{\boldsymbol{\theta}}_x, \bar{\boldsymbol{\theta}}_x] = \begin{bmatrix} \underline{\boldsymbol{\mu}}, \bar{\boldsymbol{\mu}} \\ \underline{\mathbf{m}}_2, \bar{\mathbf{m}}_2 \\ \underline{\mathbf{m}}_3, \bar{\mathbf{m}}_3 \\ \underline{\mathbf{m}}_4, \bar{\mathbf{m}}_4 \end{bmatrix} = \begin{bmatrix} \underline{\mathbf{x}}, \bar{\mathbf{x}} \\ \mathbf{0}, \frac{(\bar{\mathbf{x}} - \underline{\mathbf{x}})^2}{4} \\ -\frac{(\bar{\mathbf{x}} - \underline{\mathbf{x}})^3}{6\sqrt{3}}, \frac{(\bar{\mathbf{x}} - \underline{\mathbf{x}})^3}{6\sqrt{3}} \\ \mathbf{0}, \frac{(\bar{\mathbf{x}} - \underline{\mathbf{x}})^4}{12} \end{bmatrix} \quad (7)$$

In this study, the hyper-parameters $\boldsymbol{\theta}_x$ are assumed to be independent each other and the prior distribution is expressed as:

$$P(\boldsymbol{\theta}_x) = U_{4n}(\Omega) I_{\Theta}(\boldsymbol{\theta}_x) \quad (8)$$

where $U_{4n}(\Omega)$ denotes the PDF of $4n$ independent multivariate uniform distribution on Ω ; I_{Θ} denotes the indicator function that equals to one if $\boldsymbol{\theta}_x \in \Theta$ and otherwise equals to zero.

The approximate likelihood function is defined using an arbitrary kernel. The principle behind it is that it should return a high value when the stochastic discrepancy between the model outputs and measurement datasets is small and, conversely it penalizes $\boldsymbol{\theta}_x$ that leads to a large stochastic discrepancy. In this study, the Gaussian kernel is utilized and the stochastic discrepancy is measured by the Bhattacharyya distance. Thus, the approximate likelihood function is defined as:

$$\tilde{\mathcal{L}}(\mathbf{Y}_D | \boldsymbol{\theta}_x) = \frac{1}{\varepsilon \sqrt{2\pi}} \exp \left\{ -\frac{d_B(\mathbf{Y}_S, \mathbf{Y}_D)^2}{2\varepsilon^2} \right\} \quad (9)$$

where ε indicates the scaling parameter which controls the centralization degree of the posterior distribution. A smaller ε provides a more peaked posterior distribution, which is more likely to converge to the true values, but needs more computation burden for convergence. In this study, it is set as $\varepsilon = 0.02$.

The posterior distribution in Equation (6) generally has no analytical solution and thus needs to be estimated using advanced sampling techniques. In this study, the transitional Markov chain Monte Carlo (TMCMC) sampler (Ching and Chen, 2007) is employed. TMCMC is a sequential

approach sampling from a series of intermediate distributions which will progressively converge to the true posterior distribution. The j th intermediate distribution is expressed as:

$$P_j(\theta_x) \propto \tilde{\mathcal{L}}(\mathbf{Y}_D|\theta_x)^{\beta_j} P(\theta_x) \quad (10)$$

where β_j indicates the so-called reduction coefficient. Its value starts from $\beta_j = 0$ in the initial step and gradually increases until $\beta_m = 1$ in the final step. β_j is adaptively computed from the samples of the previous step. Markov chains then propagate new samples starting from the ones in the previous step with higher likelihood values. The reader can refer to Ching and Chen (2007) for details of the TMCMC sampler.

3 NUMERICAL EXAMPLES

3.1 Problem descriptions

The proposed stochastic model updating framework is demonstrated upon a simple three degree-of-freedom (DOF) spring-mass system shown in Figure 1. The stiffness coefficients k_1 , k_2 , and k_3 are supposed to be uncertain with the uncertainty characteristics summarized in Table 1. k_1 and k_2 follow Gaussian distributions, whose hyper-parameters, i.e., means and standard deviations, are not fully determined but fall within given intervals as listed in the third column of Table 1. On the contrary, the distribution family of k_3 is unknown before model updating and only the support set is given as $[5.0, 7.0]$. Hence, it is assumed to be characterized as a SRV and its hyper-parameters are fall within the intervals computed as Equation (7). As a consequence, in total eight hyper-parameters are treated as interval-valued parameters and updated through the proposed procedure. Besides these uncertain parameters, the remaining parameters (i.e., stiffness coefficients k_4 to k_6 and masses m_1 to m_3) are set to be constants with determined values: $k_i = 5.0$ N/m ($i = 4, 5, 6$), $m_1 = 0.7$ kg, $m_2 = 0.5$ kg, and $m_3 = 0.3$ kg.

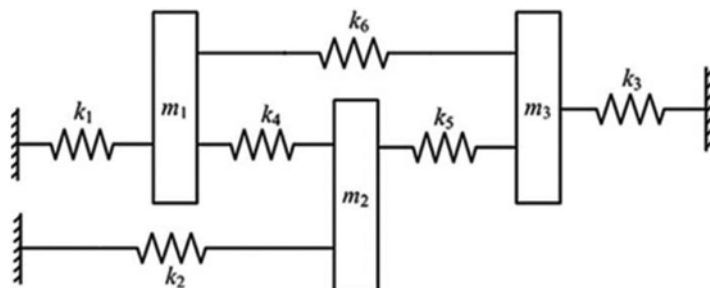


Figure 1. 3-DOF spring-mass system.

Table 1. Uncertainty characteristics of the model parameters.

Parameter	Uncertainty characteristics		Target values of hyper-parameters
	Distribution family	Support set/ hyper-parameters	
k_1	Gaussian	$\mu_1 \in [3.0, 7.0], \sigma_1 \in [0.0, 0.5]$	$\mu_1 = 4.0, \sigma_1 = 0.3$
k_2	Gaussian	$\mu_2 \in [3.0, 7.0], \sigma_2 \in [0.0, 0.5]$	$\mu_2 = 5.0, \sigma_2 = 0.1$
k_3	Unknown	$k_3 \in [5.0, 7.0]$	Given in Table 2
k_4-k_6, m_1-m_3	Deterministic	–	–

In addition to the prior information on the uncertainty characteristics, target values of the hyper-parameters in k_1 and k_2 are shown in the last column of Table 1. On the other hand, to investigate the capability of the proposed approach calibrating a wide range of distributions without the prior knowledge about their distribution families, five different distributions presented in Figure 2 are

considered as the target distribution of k_3 . Properties of these distributions are also provided in Table 2. The first distribution is a (truncated) Gaussian distribution of which hyper-parameters $\theta_1 = [\mu_{11}, m_{21}, \tilde{m}_{31}, \tilde{m}_{41}]$ are given in Table 2. While the distribution is truncated because the support set of k_3 is a closed interval, its mean and variance are determined such that the support set covers more than the 99.99 % confidence interval of the original Gaussian distribution. The remaining distributions are given by SDFs with the hyper-parameters, $\theta_i = [\mu_{1i}, m_{2i}, \tilde{m}_{3i}, \tilde{m}_{4i}]$, $i = 2, \dots, 4$. The second distribution is a (left) skewed one having a positive skewness. The third distribution is a flat one having a larger variance and smaller kurtosis compared to the Gaussian distribution. The fourth distribution is a heavy-tailed distribution having a larger kurtosis. Finally, the fifth distribution is a bi-modal distribution.

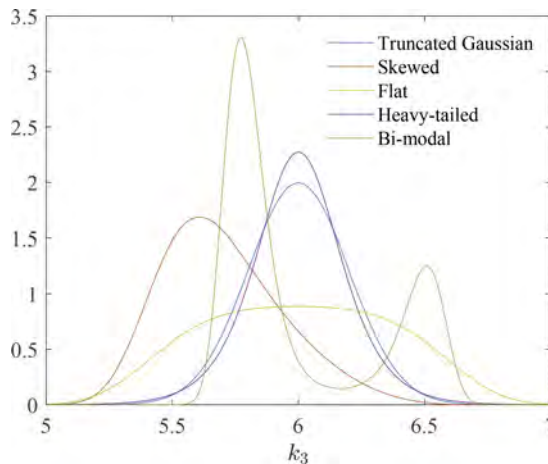


Figure 2. PDF for the target distributions of k_3 .

Table 2. Target distributions of k_3 .

Distribution format	Hyper-parameters
Truncated Gaussian	$\mu_{11} = 6.0, m_{21} = 0.04, \tilde{m}_{31} = 0.0, \tilde{m}_{41} = 3.0$
Skewed	$\mu_{12} = 5.7, m_{22} = 0.06, \tilde{m}_{32} = 0.5, \tilde{m}_{42} = 3.0$
Flat	$\mu_{13} = 6.0, m_{23} = 0.14, \tilde{m}_{33} = 0.0, \tilde{m}_{43} = 2.25$
Heavy-tailed	$\mu_{14} = 6.0, m_{24} = 0.04, \tilde{m}_{34} = 0.0, \tilde{m}_{44} = 4.2$
Bi-modal	$\mu_{15} = 6.0, m_{25} = 0.10, \tilde{m}_{35} = 0.8, \tilde{m}_{45} = 2.0$

The outputs of the system are the three eigen-frequencies f_1, f_2 and f_3 . The measurement datasets consisting of these eigen-frequencies are generated through multiple model evaluations with multiple sets of the model parameters sampled from their target distributions. In this study, the number of datasets are set as $N_D = 1000$. Figure 3 depicts the measurement datasets in the plane of the first and third frequencies for the case where the truncated Gaussian distribution is employed as the target distribution of k_3 . The reference range in the figure means the 95 % confidence interval of the sample distribution. Moreover, 1000 samples of the model parameters are generated by assigning a set of randomly selected initial values of the hyper-parameters, and subsequently 1000 initial model outputs are obtained through the model evaluations. These outputs are also presented in Figure 3. As can be seen, the scatters of the initial outputs are clearly apart from the measurement datasets; thus, model updating is necessary to obtain the model outputs as close as the measurement datasets.

3.2 Model updating results

For the case where the target distribution of k_3 is the truncated Gaussian distribution, totally 17 TCMC iterations are executed to reach convergence. Figure 4 illustrates histograms of

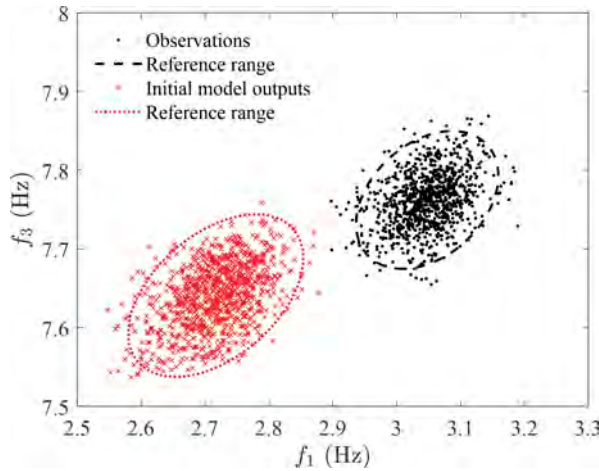


Figure 3. Target relative position of the measurement datasets and initial model outputs.

1000 posterior samples of the eight hyper-parameters, i.e., μ_i and σ_i ($i = 1,2$) as well as θ_1 . The ranges of the horizontal axes are identical to the intervals of the prior uniform distribution. It can be observed that all the hyper-parameters are significantly updated from the prior distribution. The means of the posterior samples are obtained as the posterior estimates of the hyper-parameters and presented in Table 3. The posterior estimates show good agreement with the target values. It should be noted that a relatively large error in m_{21} can be caused due to its very small target value. The updated distribution of k_3 is then obtained as a SDF with the posterior estimates of the hyper-parameters θ_1 . Figure 5 illustrates the updated distribution as the histogram of samples generated from the SDF. As can be observed from the figure, the updated distribution coincides well with the target. Uncastruncated Gaussian distribution.

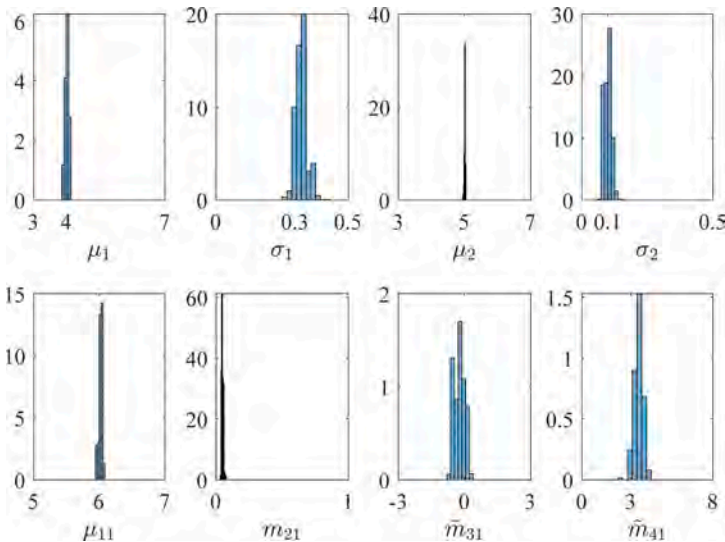


Figure 4. Posterior distribution of the hyper-parameters in histograms.

Figure 6 shows a relative position of the measurement datasets and updated model outputs. The updated outputs are obtained through the model evaluations with 1000 sets of the model parameters sampled from their updated distributions. Compared to the initial model outputs presented in Figure 3, the updated model outputs fit well with the measurement datasets,

Table 3. Posterior estimates of the hyper-parameters.

Hyper-parameters	Target values	Posterior estimates ^a
μ_1	4.0	4.01/4.00/3.98/4.01/4.04 (1.0) ^b
σ_1	0.3	0.322/0.328/0.329/0.327/0.346 (15.3) ^b
μ_2	5.0	5.01/4.99/5.00/5.00/4.99 (0.2) ^b
σ_2	0.1	0.100/0.098/0.094/0.098/0.088 (12.0) ^b
$\mu_{11}/m_{21}/\tilde{m}_{31}/\tilde{m}_{41}$	6.0/0.04/0.0/3.0	6.02 (0.3)/0.046 (15.0)/0.05/2.94 (2.0)
$\mu_{12}/m_{22}/\tilde{m}_{32}/\tilde{m}_{42}$	5.7/0.06/0.5/3.0	5.69 (0.2)/0.064 (6.7)/0.402 (19.6)/3.36 (12.0)
$\mu_{13}/m_{23}/\tilde{m}_{33}/\tilde{m}_{43}$	6.0/0.14/0.0/2.25	5.99 (0.2)/0.155 (10.7)/-0.006/2.30 (2.2)
$\mu_{14}/m_{24}/\tilde{m}_{34}/\tilde{m}_{44}$	6.0/0.04/0.0/4.2	6.00 (0.0)/0.045 (12.5)/0.174/4.05 (3.6)
$\mu_{15}/m_{25}/\tilde{m}_{35}/\tilde{m}_{45}$	6.0/0.1/0.8/2.0	6.01 (0.2)/0.106 (6.0)/0.740 (7.5)/2.01 (0.5)

^a Percentage errors compared to the target values in parentheses.

^b Posterior estimates for all the five cases in a row and their maximum percentage errors in parentheses.

which demonstrates that the proposed updating procedure enables to calibrate the model so that its outputs represent wholly the uncertainty characteristics of the measurement datasets.

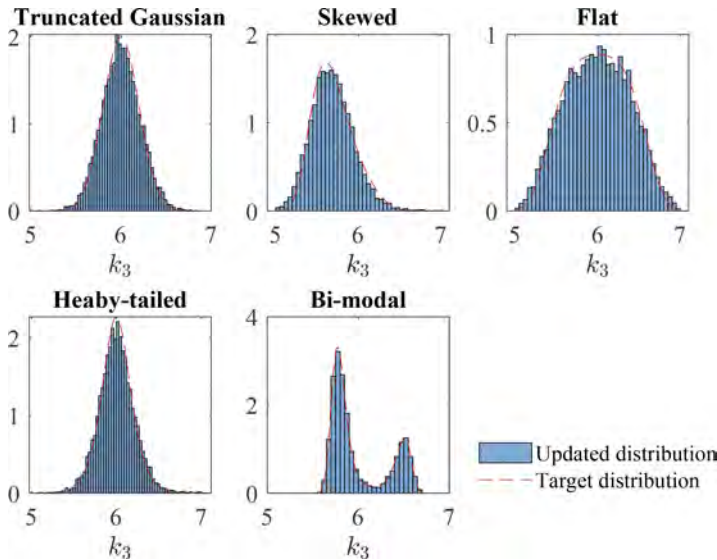


Figure 5. Updated distributions of k_3 .

Similarly, the proposed updating procedure is also performed for the remaining cases with the different target distributions of k_3 . For all the cases, the obtained posterior estimates of the hyper-parameters are summarized in Table 3. All the posterior estimates of the hyper-parameters show good agreement with the target values, including the higher-order moments such as the skewness and kurtosis in the SDFs, and the maximum percentage error compared to the target values is less than 20 %. The updated distributions of k_3 , which assign the posterior estimates of the hyper-parameters are also illustrated in Figure 5 for these cases. It can be seen that the updated distributions coincide well with the target distributions, indicating that the proposed updating procedure can quantify the parameter uncertainty as an appropriate probability distribution including heavy-tailed and multi-modal distributions. Finally, the updated model outputs are obtained through the model evaluations with the updated parameter distributions and compared with the measurement datasets. While relative positions of the updated model outputs and measurement datasets are not further provided for the sake of brevity, it is confirmed that the updated model outputs are properly tuned for all the cases and fit well with the measurement datasets.

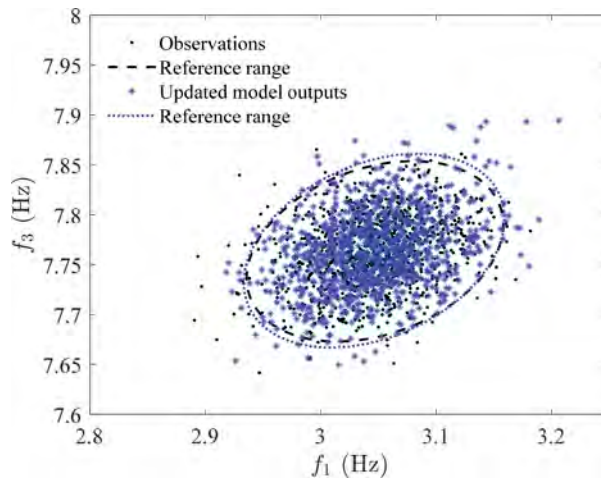


Figure 6. Target relative position of the measurement datasets and updated model outputs.

4 CONCLUSIONS

In this study, we present a distribution-free stochastic model updating framework to quantify the parameter uncertainty that forms a broad range of probability distributions, including heavy-tailed and multi-modal distributions, without the prior knowledge about their distribution families. The unknown parameter distribution is characterized by SDF, and it is assumed that only its support set is known a priori. Its hyper-parameters, i.e., the first four moments, are then inferred through the ABC procedure aiming at minimizing the Bhattacharyya distance between the model outputs and measurement datasets. The proposed updating framework is demonstrated on a simple 3-DOF spring-mass system, in which five different distributions are assumed as the target distribution of a model parameter. The results demonstrate that the proposed procedure has a potential to calibrate the arbitrarily parameter distribution as appropriate so that the model outputs recreate wholly the uncertainty characteristics of the measurement datasets.

REFERENCES

- Baumont, M.A. 2019. Approximate Bayesian Computation, *Annual Review of Statistics and Its Application* 6: 379–403.
- Bi, S. & Broggi, M. & Beer, M. 2019. The role of the Bhattacharyya distance in stochastic model updating. *Mechanical Systems and Signal Processing* 117:437–452.
- Ching, J. & Chen, Y.C. 2007. Transitional Markov Chain Monte Carlo Method for Bayesian Model Updating, Model Class Selection, and Model Averaging. *Journal of Engineering Mechanics* 133(7): 816–832.
- Crespo, L.G. & Kenny, S.P. & Giesy, D.P. 2014. The NASA Langley multidisciplinary uncertainty quantification challenge. In *Proc. 16th AIAA Non-Deterministic Approaches Conf.*, Maryland.
- Crespo, L.G. & Kenny, S.P. & Giesy, D.P. & Stanford, B.K. 2018. Random variables with moment-matching staircase density functions. *Applied Mathematical Modelling*, 64: 196–213.
- Crespo, L.G. & Kenny, S.P. 2021. The NASA Langley multidisciplinary uncertainty quantification challenge. *Mechanical Systems and Signal Processing* 152: 107405.
- Kitahara, M. & Bi, S. & Broggi, M. & Beer, M. 2022. Nonparametric Bayesian stochastic model updating with hybrid uncertainties. *Mechanical Systems and Signal Processing* 163: 108195.
- Kitahara, M. & Bi, S. & Broggi, M. & Beer, M. 2022. Distribution-free stochastic model updating of dynamic systems with parameter dependencies. *Structural Safety* 163: 108195.
- Mares, C. & Mottershead, J.E. & Friswell, M.I. 2006. Stochastic model updating: Part 1-theory and simulated example, *Mechanical Systems and Signal Processing* 20(7): 1674–1695.
- Mottershead, J.E. & Friswell, M.I. 1993. Model Updating In Structural Dynamics: A Survey. *Journal of Sound and Vibration* 167(2): 347–375.

Efficient posterior estimation for stochastic SHM using transport maps

J. Grashorn

Institute for Risk and Reliability, Leibniz University Hannover, Germany; International Research Training Group (IRTG) 2657, Leibniz University Hannover, Germany

M. Broggi

Institute for Risk and Reliability, Leibniz University Hannover, Germany

L. Chamoin

Laboratoire de Mécanique Paris-Saclay (LMPS), Université Paris-Saclay, CentraleSupélec, ENS Paris-Saclay, CNRS, France

M. Beer

Institute for Risk and Reliability, Leibniz University Hannover, Germany; Institute for Risk and Uncertainty, University of Liverpool; Shanghai Institute for Disaster Prevention and Relief, Tongji University

ABSTRACT: Accurate parameter estimation is a challenging task that demands realistic models and algorithms to obtain the parameter's probability distributions. The Bayesian theorem in conjunction with sampling methods proved to be invaluable here since it allows for the formulation of the problem in a probabilistic framework. This opens up the possibilities of using prior information and knowledge about parameter distributions as well as the natural incorporation of aleatory and epistemic uncertainties. Traditionally, Markov Chain Monte Carlo (MCMC) methods are used to approximate the posterior distribution of samples given some data. However, these methods usually need a large amount of samples and therefore a large amount of model evaluations. Recent advances in transport theory and its application in the context of Bayesian model updating (BMU) make it possible to approximate the posterior distribution analytically and hence eliminate the need for sampling methods. This paves the way for the usage in real-time applications and for fast parameter estimation. We investigate here the application of transport maps to a simple analytical model as well as a structural dynamics model. The performance is compared to an MCMC approach to assess the accuracy and efficiency of transport maps. A discussion about requirements for the implementation of transport maps as well as details on the implementation are also given.

1 INTRODUCTION

Model parameter estimation is a daily task in many engineering disciplines. In SHM it proved to be very useful to track the changes in a system during its lifetime, thus making it possible to evaluate occurring damage or degradation of components in the system. In applications with uncertainties and stochastic parameters the model updating is usually done by using the Bayesian theorem; however depending on the system at hand the posterior density can not be calculated analytically. For the exploration of the posterior distribution then algorithms based on Markov Chain Monte Carlo (MCMC) are used, since these approaches do not require knowledge about the posterior topology. However, a downside of MCMC is that the convergence can not easily be assessed and sometimes many samples are needed in order to fully reach an adequate result. Some MCMC

algorithms also suffer from burn-in. Recently there have been advances in optimal transport theory (Villani 2009) which were applied in the Bayesian updating context (Parno and Marzouk 2018; Spantini et al. 2018). This opens up the possibility of circumventing some of the issues of MCMC methods, since transport maps provide a means of formulating an analytical relationship between some chosen, easy to evaluate reference distribution and the posterior distribution. Integrals can thus be evaluated on the reference distribution and then be transported to the posterior. In addition, sampling from the posterior becomes a simple evaluation of the map. The problem of finding this map is solved by optimization. Previous works have implemented transport map (TM) approximation in various use-cases, using synergies of this approach with model order reduction techniques to speed up the process (Rubio et al. 2019a,b).

In the following chapters the advantages and disadvantages of the TM approach when compared to an MCMC estimation are investigated. For this purpose we use two academic examples, one exponential function with two parameters and one structural model with three degrees of freedom.

2 PARAMETER ESTIMATION

2.1 Bayesian model updating

Let $\theta \in \mathbb{R}^d$ be a d -dimensional random variable with probability $p(\theta)$ describing uncertain parameters of a model $\mathcal{M}(\theta)$. Given measured data \mathbb{D} the probability of observing θ in $\mathcal{M}(\theta)$ under the condition of can \mathbb{D} be calculated using Bayes' theorem (Beck et al. 1998)

$$p(\theta|\mathbb{D}) = \frac{p(\mathbb{D}|\theta)p(\theta)}{p(\mathbb{D})} \quad (1)$$

where the likelihood $p(\mathbb{D}|\theta)$ describes the probability of observing the data under the assumption of θ and is usually modeled as a stochastic distance between $\mathcal{M}(\theta)$ and \mathbb{D} . One key difficulty in Bayesian model updating (BMU) is the irregular and unknown shape of $p(\theta|\mathbb{D})$ and the fact that it can only be evaluated point-wise. Therefore, MCMC methods are employed to explore the probability space (Beck and Au 2002). The obtained posterior distribution $p(\theta|\mathbb{D})$ is an expression for the updated probability for θ constrained by the observation of \mathbb{D} . $p(\mathbb{D})$ is constant for any given set of model and data so Eq. (1) is also used in the non-normalized form

$$p(\theta|\mathbb{D}) \propto p(\mathbb{D}|\theta)p(\theta). \quad (2)$$

This poses no issue for MCMC methods since the posterior's shape is not affected.

The MCMC algorithm used in this paper is the Transitional MCMC (TMCMC) method (Ching and Chen 2007). The main idea is to introduce an exponent $\alpha_j \in [0, 1]$ to the likelihood

$$p(\theta|\mathbb{D}) \propto p(\mathbb{D}|\theta)^{\alpha_j} p(\theta) \quad (3)$$

and increasing α_j with each level j starting from $\alpha_1 = 0$, which is equal to sampling from the prior density. For $\alpha_j = 1$ Eq. (3) becomes Eq. (2). Values for α_j for the intermediate levels are chosen based on the variance of the drawn samples. After drawing samples from the prior density, the Adaptive Metropolis-Hastings algorithm is used to draw samples for the next level until $\alpha_j = 1$ is reached. The main motivation behind TMCMC is to avoid the problem of sampling from difficult target PDFs but sampling from a series of PDFs that converge to the target PDF and that are easier to sample (Ching and Chen 2007).

2.2 Transport maps

A transport map M is a deterministic coupling between a reference density ρ and the target density π

$$\int f(y)\pi(y)dy = \int (M(x))\rho(x)dx \quad \text{with } Y = M(X) \quad (4)$$

where the target density in the case of BMU is the posterior distribution. The reference density can be chosen freely by the analyst. Common choices are standard normal or standard uniform distributions (Spantini et al. 2018). Any integrals on the target density can thus be calculated on the reference density by use of the map M . Moreover, samples from the target density Y can be drawn by drawing samples X from the reference density and then evaluating the map M . This makes it possible to find an analytical formulation for the posterior density in BMU, which is usually difficult or impossible. The task now becomes to find the map M . A map can be any invertible function $M : \mathbb{R}^d \rightarrow \mathbb{R}^d$, e.g. polynomials or even neural networks (Parno and Marzouk 2018). Using the notation $M_{\#}$ for the push-forward operation the mismatch of the approximation $\pi \approx M_{\#}\rho$ can be expressed with the Kullback-Leibler (KL) divergence

$$\mathcal{D}_{\text{KL}}(M_{\#}\rho|\pi) = \mathcal{D}_{\text{KL}}(\rho|M_{\#}^{-1}\pi) \quad (5)$$

$$= \mathbb{E}_{\rho} \left[\log \frac{\rho}{M_{\#}^{-1}\pi} \right] \quad (6)$$

where the invertibility of the map is used in Eq. (5). With \mathbf{a} as map parameters Eq. (6) becomes

$$\mathcal{D}_{\text{KL}}(M_{\#}\rho|\pi) = \int_X [\log \rho(x) - \log \pi(M(\mathbf{a}, x)) - \log [|\det \nabla M(\mathbf{a}, x)|]] \rho(x) dx \quad (7)$$

Due to optimality and uniqueness properties, maps M were proposed to be monotonic, lower-triangular and constructed from components

$$M^k(\theta_{1,\dots,k}, \mathbf{a}) = f(\theta_1, \dots, \theta_{k-1}, \mathbf{0}, \mathbf{a}) + \int_0^{\theta_k} g(\partial_k f(\theta_1, \dots, \theta_{k-1}, \bar{\theta}, \mathbf{a})) d\bar{\theta} \quad (8)$$

where $f: \mathbb{R}^d \rightarrow \mathbb{R}$ and $g: \mathbb{R}^d \rightarrow \mathbb{R}_+$ so that the resulting map has the structure

$$M(\boldsymbol{\theta}) = \begin{bmatrix} M^1(\theta_1) \\ \dots \\ M^d(\theta_1, \dots, \theta_d) \end{bmatrix} \quad (9)$$

A good approximation of the posterior density results in a small KL divergence, so that Eq. (7) can be transformed into a minimization problem. Note that $\rho(x)$ does not depend on the map parameters and instead of the full posterior $\pi = p(\boldsymbol{\theta}|\mathbb{D})$ the non-normalized form

$$\tilde{\pi} = p(\mathbb{D}|\boldsymbol{\theta})\rho(\boldsymbol{\theta}) \quad (10)$$

can be used. Furthermore, since M consists of analytical functions, the involved integrals can easily be computed by suitable quadrature rules (i.e. Gauss, Monte Carlo etc.). The final minimization problem to obtain the needed map parameters \mathbf{a} is then

$$\min_{\mathbf{a}} \sum_i w_{q,i} [-\log(\tilde{\pi}(M(\mathbf{a}, \boldsymbol{\theta}_{q,i}))) - \log(|\det \nabla M(\mathbf{a}, \boldsymbol{\theta}_{q,i})|)] \quad (11)$$

where $w_{q,i}$ and $\boldsymbol{\theta}_{q,i}$ are weights and integration points for the quadrature rule.

For computations, the framework MParT was used (MParT Development Team 2022). As a basis for the functions f in (8) Hermite polynomials with a selectable degree were chosen. Higher order maps usually are better able to approximate the target function, however since more parameters need to be optimized their computation is also more costly. The maximum map order n can be chosen adaptively, since maps can be combined in the form

$$\mathcal{M}(\boldsymbol{\theta}) = M_n \circ M_{n-1} \circ \dots \circ M_1(\boldsymbol{\theta}) \quad (12)$$

where the subscript denotes the map order and each M_i is of the form (9). If the accuracy of \mathcal{M} after calculation of the i -th component is deemed too low, another component of order $i+1$ can be computed.

2.2.1 Laplace approximation

As a first approximation a map to a Gaussian with mean $\boldsymbol{\theta}_0$ and covariance Σ_0 can be calculated by use of Laplace approximation. $\boldsymbol{\theta}_0$ and Σ_0 are found by solving the optimization problem

$$\boldsymbol{\theta}_0 = \arg \min_{\boldsymbol{\theta}} -\log \tilde{\pi}(\boldsymbol{\theta}) \quad (13)$$

which corresponds to finding the mode of the posterior. Σ_0 corresponds to finding the Hessian \mathcal{H} at $\boldsymbol{\theta}_0$, the final Laplace map thus becomes (Rubio et al. 2019a)

$$L(\boldsymbol{\theta}) = \boldsymbol{\theta}_0 - \mathcal{H}^{-\frac{1}{2}}\boldsymbol{\theta} \quad (14)$$

The Laplace approximation can be used to regularize the problem when combined with (12) to give the final form of \mathcal{M}

$$\mathcal{M}(\boldsymbol{\theta}) = M_n \circ M_{n-1} \circ \dots \circ M_1 \circ L(\boldsymbol{\theta}) \quad (15)$$

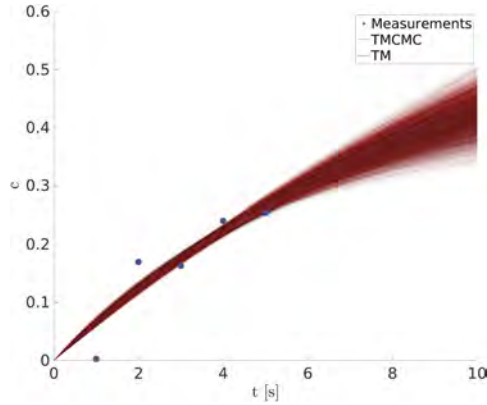


Figure 1. Plot of c over t for the analytical exponential model. Blue dots are noisy measurements, red and black lines are outputs of samples taken from TM and TCMC approaches respectively.

Table 1. Number of model, gradient and hessian evaluations for TCMC and both cases of TM approximations.

		Model evaluations
TCMC		45000
TM	1st order	12636
	2nd order	20900
	3rd order	12500
	Total	46036

3 EXAMPLES

3.1 Analytical exponential model

As a simple example we show the application of transport maps to an analytical problem of the form

$$c = A(1 - e^{Bt}) + \zeta \quad (16)$$

with prior distributions $A, B \sim N(0, 1)$, $\zeta \sim \mathcal{N}(0, \sigma_M^2)$, where ζ is a zero-mean Gaussian noise with variance σ_M^2 . The model was taken from (Parno and Marzouk 2018). The parameters to estimate are thus A and B . Data is taken from evaluating Eq. (16) at times $t = \{1, 2, 3, 4, 5\}$ with parameters $A = 0.4$ and $B = 0.2$. Letting c_M be the vector of measurements, $\theta = [A, B]^T$ and $\sigma_M = 0.1$ the problem to solve for obtaining the log-posterior becomes

$$\begin{aligned} \log p(\theta|c_M) &= \log[p(c_M|\theta) \cdot p(\theta)] \\ &= -\frac{1}{\sigma_M^2} \sum_{i=1}^5 (c_{M,i} - [\theta_1(1 - e^{\theta_2 t_i})])^2 - \frac{1}{2} \theta^2 \end{aligned} \quad (17)$$

Note that for the optimization procedure in Eq. (11) the gradient $\nabla_a \mathcal{D}_{\text{KL}}$ is needed, which by applying the chain rule ultimately also needs $\nabla_{\theta} \mathcal{M}(\theta)$. Since this problem is analytical the derivatives are readily available, however special care needs to be taken in situations where this is not the case.

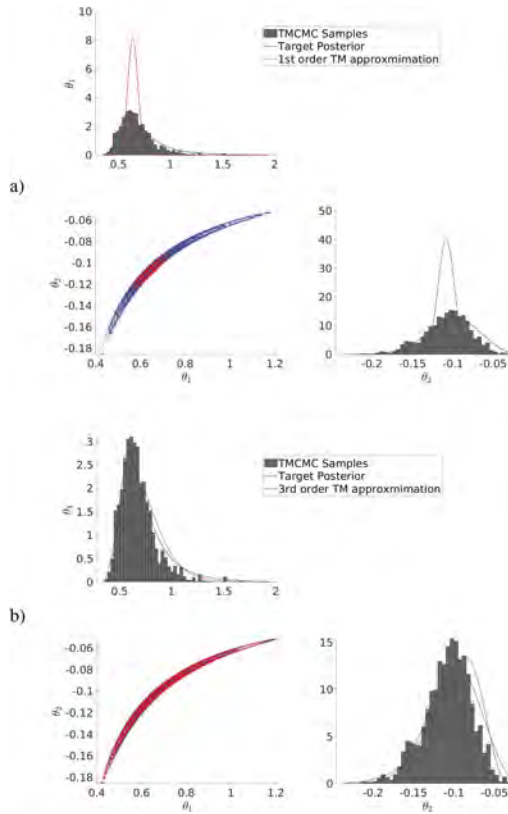


Figure 2. Marginal posteriors for updating results of TMCMC and TM approximations for the analytical exponential system. Figure a) shows a first order map approximation, b) shows a subsequent approximation with a third order map.

Figure 1 shows a result plot with indicated measurements and results taken from samples from transport maps and TMCMC. For TMCMC 5000 samples were taken per level, for the TM approach a MC-integration with 100 samples was used to calculate parameters of subsequent maps up to order 3. The results of the posterior approximation with first, second and third order TM are shown in Figure 2, together with samples taken from TMCMC and the true posterior function. In addition, Table 1 shows the number of model calls for TMCMC and for the calculation of each order of TM, together with the total amount of model calls for all three calculated maps. These results show that the first order map is only able to capture the mean of the posterior and some of its correlation structure, whereas second and third order map are able to make a better approximation. Since a first order map defines a linear relationship between the reference Gaussian and the target density the result can also only be a Gaussian. The computational cost of TM and TMCMC is comparable, however no care was taken to optimize the numerical integration scheme in the TM approach. The results show however some bias in the TMCMC samples which is a common occurrence since the convergence of MCMC methods can not be assessed easily.

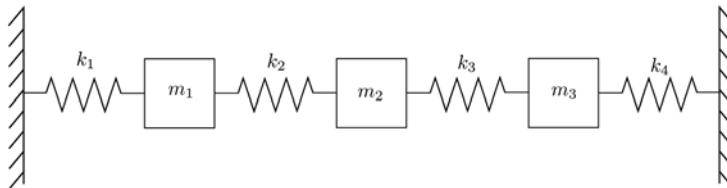


Figure 3. 3-DOF system with three masses m_1 , m_2 and m_3 connected by four springs.

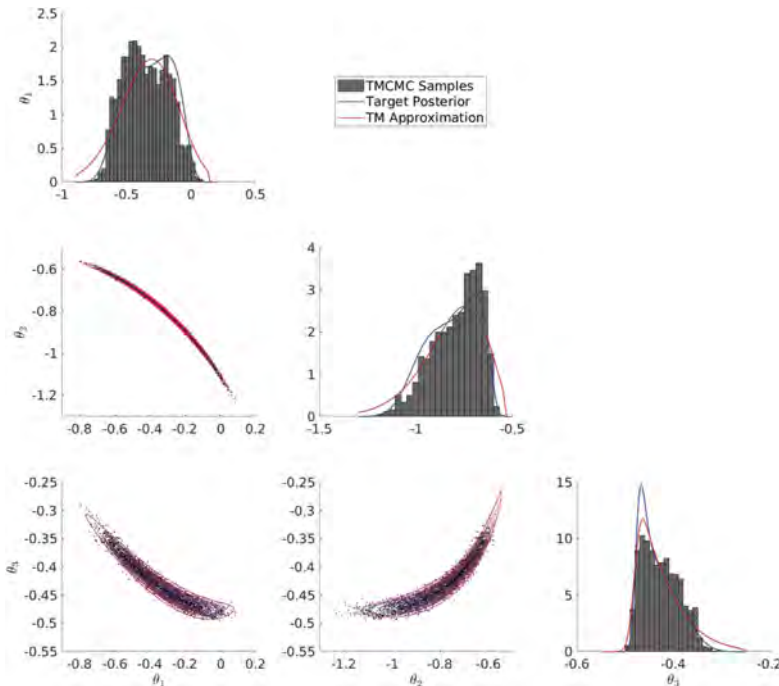


Figure 4. Marginal posterior results for posterior estimation of 3-DOF-system with TMCMC and 5th order TM approach.

Note that after calculation of the map coefficients, a fully analytical expression is obtained which allows for cheap drawing of new samples if needed. Doing the same with MCMC methods would require further model evaluations.

3.2 3-DOF-SYSTEM

For the second example we chose a three degree of freedom system with four springs (see Figure 3) with $m_1 = 100$ kg, $m_2 = 200$ kg and $m_3 = 300$ kg. k_1 , k_2 , and k_3 are uncertain with a prior distribution of $k_{1,2,3} \sim U(100, 3500) \frac{\text{N}}{\text{m}}$. As data we chose the three natural frequencies that can handily be calculated from the system's equations with parameters $k_1 = 1500 \frac{\text{N}}{\text{m}}$, $k_2 = 750 \frac{\text{N}}{\text{m}}$, and $k_4 = 1000 \frac{\text{N}}{\text{m}}$. For regularization purposes $k_1 - k_3$ are transformed to standard normal space using the inverse CDF method (Devroye 1986)

$$k_i(\theta_i) = 100 + (3500 - 100) \Phi(\theta_i), \quad i \in \{1, 2, 3\} \quad (18)$$

where θ_i are the random variables to be updated and Φ is the CDF of the standard normal distribution. With ω_m as the vector of measured natural frequencies the posterior becomes

$$\log p(\boldsymbol{\theta}|\omega_m) = \frac{1}{\sigma_M^2} (\omega_m - \mathcal{M}(\boldsymbol{\theta}))^2 - \frac{1}{2} \boldsymbol{\theta}^2 \quad (19)$$

where $\mathcal{M}(\boldsymbol{\theta})$ is the model to calculate the natural frequencies ω from the system's matrices.

Note that for the optimization the expression $\partial \mathcal{M}(\boldsymbol{\theta}) / \partial \boldsymbol{\theta}$ is needed and the system matrices depend on \mathbf{k} , such that

$$\frac{\partial \mathcal{M}(\boldsymbol{\theta})}{\partial \boldsymbol{\theta}_i} = \frac{\partial \mathcal{M}(\boldsymbol{\theta})}{\partial k_i} \frac{\partial k_i}{\partial \boldsymbol{\theta}_i} = (3500 - 100) \phi(\theta_i) \frac{\partial \mathcal{M}(\boldsymbol{\theta})}{\partial k_i}. \quad (20)$$

where $\phi(\theta)$ is the PDF of the standard normal distribution.

Results of the updating procedures can be seen in Figure 4. For the TM approach a Gauss-Hermite integration of order five was chosen this time and the maximum order of the map was also five. For TMCMC again 5000 samples were used per level.

The target posterior in this example is more complex and shows almost a bi-modal distribution which is more difficult for the TM approach to approximate since higher order maps are needed. The mean and general covariance structure however are nicely approximated. Because of the more complicated shape of the posterior it was found that the TM approximation needed more model evaluations than the TMCMC approach. However the TMCMC samples also again show some bias.

4 CONCLUSION

In this contribution the transport map approach for estimation of the posterior in Bayesian parameter estimation was compared to standard MCMC. Both methods were used on noisy data from an analytical exponential model and a model of natural frequencies of a 3-DOF dynamical system. The TM estimation shows great promise in circumventing some of the problems arising in MCMC sampling, however the implementation and tuning of the parameters in the TM approach require more care. Especially the need to use optimization methods for finding the maps is prohibitive of their use if the problem at hand is too complex and not analytical. While the latter is not generally the case in engineering applications there exist a wide variety of model order reduction methods to replace the original system with a surrogate model that uses analytical functions. In these cases transport maps show great promise since the model becomes differentiable. The result of the transport map approximation is a fully analytic expression of the posterior distribution, allowing for integration and resampling in an efficient way, which is one of the main advantages over MCMC-based

methods. Furthermore, since the KL-divergence is used to optimize the map parameters the convergence between approximation and true posterior is directly evaluated. In MCMC methods the mismatch between approximation and posterior is not quantified which can lead to bias in the drawn samples. Moreover, sequential updating which was not covered here, is naturally possible in the transport map approach by combining multiple maps. Issues with optimization convergence that arise due to the complicated shape of the posterior distribution could be reduced this way, since the change in the approximated posteriors is smaller in the sequential setting when compared to using all data points at once. The usage of transport maps for sequential updating is also interesting for on-line parameter estimation when combined with model-order reduction methods.

ACKNOWLEDGMENTS

Funding by the Deutsche Forschungsgemeinschaft (DFG, German Research Foundation) for the GRK2657 (grant reference number 433082294) is greatly appreciated.

REFERENCES

- Beck, J. L. & S.-K. Au (2002). Bayesian updating of structural models and reliability using markov chain monte carlo simulation. *Journal of engineering mechanics* 128(4), 380–391.
- Beck, J. L., L. S. Katafygiotis, et al. (1998). Updating models and their uncertainties. i: Bayesian statistical framework. *Journal of Engineering Mechanics-Proceedings of the ASCE* 124(4), 455–462.
- Ching, J. & Y.-C. Chen (2007). Transitional markov chain monte carlo method for bayesian model updating, model class selection, and model averaging. *Journal of engineering mechanics* (7), 816–832.
- Devroye, L. (1986). *Non-Uniform Random Variate Generation*. Springer New York, NY.
- MParT Development Team (2022). Monotone Parameterization Toolkit (MParT). Version 1.2.0.
- Parno, M. D. & Y. M. Marzouk (2018). Transport map accelerated markov chain monte carlo. *SIAM/ASA Journal on Uncertainty Quantification* 6(2), 645–682.
- Rubio, P.-B., L. Chamoin, & F. Louf (2019b). Real-time bayesian data assimilation with data selection, correction of model bias, and on-the-fly uncertainty propagation. *Comptes Rendus Mécanique* 347(11), 762–779.
- Rubio, P.-B., F. Louf, & L. Chamoin (2019a). Transport map sampling with pgd model reduction for fast dynamical bayesian data assimilation. *International Journal for Numerical Methods in Engineering* 120(4), 447–472.
- Spantini, A., D. Bigoni, & Y. Marzouk (2018). Inference via low-dimensional couplings. *The Journal of Machine Learning Research* 19(1), 2639–2709.
- Villani, C. (2009). *Optimal transport: old and new*, Volume 338. Springer.

Evaluating the minimum cross-section thickness of a conveyor support structure member

Y. Yang, D. Ogawa & T. Nagayama

Department of Civil Engineering, the University of Tokyo, Tokyo, Japan

S. Kato, K. Hisazumi & T. Tominaga

Nippon Steel Corporation, Tokyo, Japan

ABSTRACT: Conveyor support structures are often under a corrosive environment with the accumulation of dust from the conveyor. The corrosive damage may cause severe safety problems. Specifically, the minimum cross-section thickness of each bottom chord member, which determines the ultimate tensile capacity, is important in the safety assessment of the structure. This study develops a strategy for evaluating the minimum cross-section thickness of the member based on the cross-sectional modes (CSMs). Firstly, the member is divided into 10 sections and the average thickness of each section is estimated using a Bayesian model updating method; subsequently, a regression model presenting the relationship between the average cross-section thickness and the minimum cross-section thickness is approximated using real members' thickness distributions; finally, the minimum cross-section thickness is evaluated based on the estimated average thickness and the regression model. The proposed strategy is validated through hammer tests on a real damaged specimen.

1 INTRODUCTION

A conveyor support structure is often exposed to a very corrosive environment because of the dust accumulation on the lower chord members from the conveyor mechanical part above. Traditionally, the health conditions of the members are checked by visual or hands-on inspection. However, these approaches may encounter difficulties in practice, e.g., it is unreliable to visually check the members' conditions from a remote place, and while the risk of entanglement accidents is high when an inspector approaches the structures too close. Therefore, a contactless inspection method is necessary.

In previous research, Rana et al. (2019) showed that the CSMs of the lower chord members which have L-shape cross-sections are localized and the sensitivities of the CSMs to the local damages are high. In addition, the approaches of contactless measurements of CSMs were investigated, and their practical applicability was demonstrated by acoustic excitation experiments (Kato et al. 2018) and operational vibration data (Yang et al. 2021). However, the quantitative evaluations of the damages are still challenging. The lower chord members of a conveyor support structure are of significant focus here because they are highly susceptible to corrosive environments, and their tensile load-carrying capacities are determined by the minimum cross-section thickness.

In the research, a strategy is developed for evaluating the minimum cross-section thickness of the member. The strategy contains three steps: 1) the member is divided into 10 sections and the average thickness of each section is estimated based on the CSM information using a Bayesian model updating method; 2) using real corrosive members' thickness distributions, a regression model which presents the relationship between the average cross-section thickness and the minimum cross-section thickness is approximated; 3) using the estimated average

thickness from step 1), the minimum cross-section thickness of the member is evaluated based on the regression model obtained in step 2). In particular, two approaches to consider the error variances for the Bayesian model updating are investigated in step 1). In the following, the proposed strategy is explained in section 2. In section 3, the strategy is validated through hammer tests on a real damaged specimen. Finally, conclusions are given in section 4.

2 THE METHODOLOGIES OF THE STRATEGY

2.1 Bayesian model updating based on the CSMs

In the study, the Bayesian model updating method is applied. According to Bayes's theorem, the posterior distribution of parameter θ is computed as

$$p(\theta|\mathbf{D}) = \frac{p(\mathbf{D}|\theta)p(\theta)}{p(\mathbf{D})} \quad (1)$$

In equation (1), \mathbf{D} represents the modal information, e.g., modal frequencies and modal shapes; $p(\theta)$ and $p(\mathbf{D}|\theta)$ are the prior distribution and the likelihood function of the parameters respectively; $p(\mathbf{D})$ is the so-called evidence which is a normalization constant. The evidence value does not influence the shape of the posterior distribution, but its evaluation is useful in Bayesian model selection.

When considering the modal information as the available data for Bayesian model updating, it is assumed that the \mathbf{D} consists of N sets of modal information data, i.e., $\mathbf{D} = \{\mathbf{D}_1 \mathbf{D}_2 \cdots \mathbf{D}_N\}$, and each data set includes n extracted modal frequencies $f_{i,j}^m$ and the corresponding incomplete modal shape vector $\Phi_{i,j}^m$ ($i=1\sim N, j=1\sim n$). In practice, the N data sets of modal information can be obtained by processing different measured data sets and using different modal analysis methods.

In the process of the model updating, the corresponding eigen-frequency $f_j^e(\theta)$ and the partial eigen-vector $\Phi_j^e(\theta)$ are calculated from the updated FE model defined by θ . Based on these values, the likelihood functions for the modal frequency $f_{i,j}^m$ and modal shape $\Phi_{i,j}^m$ are written as

$$p(f_{i,j}^m|\theta) = c_{f,j} \exp \left[-\frac{1}{2} \left(\frac{1 - f_{i,j}^m/f_j^e(\theta)}{\varepsilon_{f,j}} \right)^2 \right] \quad (2)$$

$$p(\Phi_{i,j}^m|\theta) = c_{\Phi,j} \exp \left[-\frac{1}{2\varepsilon_{\Phi,j}^2} \left\| \frac{\Phi_{i,j}^m}{\|\Phi_{i,j}^m\|} - \Phi_j^e(\theta) \frac{\Phi_j^e(\theta)^T (\Phi_{i,j}^m/\|\Phi_{i,j}^m\|)}{\Phi_j^e(\theta)^T \Phi_j^e(\theta)} \right\|^2 \right] \quad (3)$$

in which the $c_{f,j}$ and $c_{\Phi,j}$ are the normalization constants of the two likelihood functions respectively, they need to be determined by integrating the corresponding exponential terms; $\varepsilon_{f,j}$ and $\varepsilon_{\Phi,j}$ are the error variances of the modal frequency and shape respectively. The detailed derivations of these equations can be found in Vanik (1997). Assuming that the probabilities of the measured modal information are independent of different orders of modes and the data sets, the overall likelihood function is the product of all the components of modal frequencies and modal shapes as

$$p(\mathbf{D}|\theta) = \prod_{i=1}^N \prod_{j=1}^n p(f_{i,j}^m|\theta) p(\Phi_{i,j}^m|\theta) \quad (4)$$

If the likelihood function and the prior distribution are available, the parameters can be identified by sampling the un-normalized posterior distributions of equation (1). Several sampling approaches can be employed, e.g., MCMC, HMC, and TMCMC. In the study, the prior distribution $p(\theta)$ is assumed as a uniform distribution for each parameter.

2.2 Determination of the weighting of the error variances

In the modal information-based model updating, the relative weighting between the error variances of the modal frequency $\varepsilon_{f,j}$ and the modal shapes $\varepsilon_{\Phi,j}$ should be selected carefully (Goller et al. 2012). In the study, the target member of a conveyor support structure is divided into 10 sections, and the average thickness of each section is to be identified based on the CSM information. Compared with a real damage scenario that is continuous, this simplified model will certainly present some errors in terms of the eigen-frequencies and eigen-vectors. In the study, two approaches are investigated for determining the weightings of the error variances.

In the first approach, the modeling errors are investigated numerically. Specifically, a FE model of the member with continuous thickness reduction is first built using shell elements; correspondingly, a 10-section model with the same dimension is built, in which the thickness of each section is the average value of the same region in the original model; a number of pairs of the models are created in such manner, and the errors of the eigen-frequencies and eigen-vectors between the original and the simplified models are calculated as

$$\tilde{\varepsilon}_{f,j} = \sqrt{\left(\frac{f_j^{orig} - f_j^{simp}}{f_j^{simp}}\right)^2} \quad \tilde{\varepsilon}_{\Phi,j} = \sqrt{\left\| \frac{\Phi_j^{orig}}{\|\Phi_j^{orig}\|} - \Phi_j^{simp} \frac{(\Phi_j^{simp})^T (\Phi_j^{orig} / \|\Phi_j^{orig}\|)}{(\Phi_j^{simp})^T \Phi_j^{simp}} \right\|^2} \quad (5)$$

where the superscript ‘simp’ and ‘orig’ represent the simplified model and the original model respectively; the subscript ‘j’ stands for the j -th mode. Figure 1 presents the thickness contours of a pair of the original and simplified models.

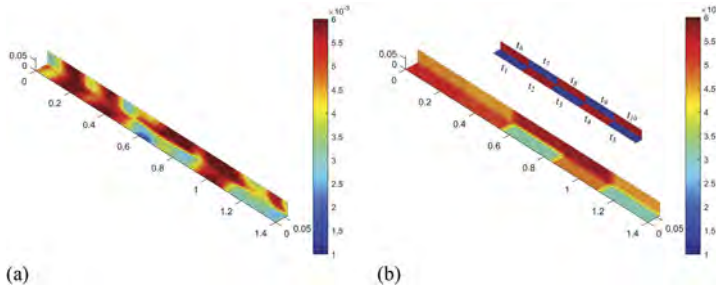


Figure 1. The thickness contour of (a) the original model; (b) the simplified model.

The original model is created randomly, and the thickness distribution of the elements on either flange or web follows a Gaussian process with an exponential quadratic kernel

$$t(x) \sim GP\left(\mu, \sigma_t^2 \exp\left(-\frac{(x_i - x_j)^T (x_i - x_j)}{2\sigma_l^2}\right)\right) \quad (6)$$

in which x represents the coordinate vector of the central point of one element, μ is the mean value and is set as 5 mm; σ_t and σ_l are variance amplitude and correlation length parameters respectively, and they are set as 1.5 mm and 0.06 m. These values are determined based on a real member that has an intact thickness of 6 mm, length of 1.4 m, and flange (web) length of 0.065 m. The FE model of the member is shown in Figure 1.

A total of 3000 pairs of original models and simplified models are created, the eigen-frequency and eigen-vector errors of them are calculated, and they are presented as scattering points in Figure 2.

From the figures, it is observed that: 1) the errors of the three CSMs’ frequencies do not show evident correlations between each other; 2) the correlation between the 1st CSM’s frequencies and modal shapes shows a rough linear tendency, and the errors of the modal shapes

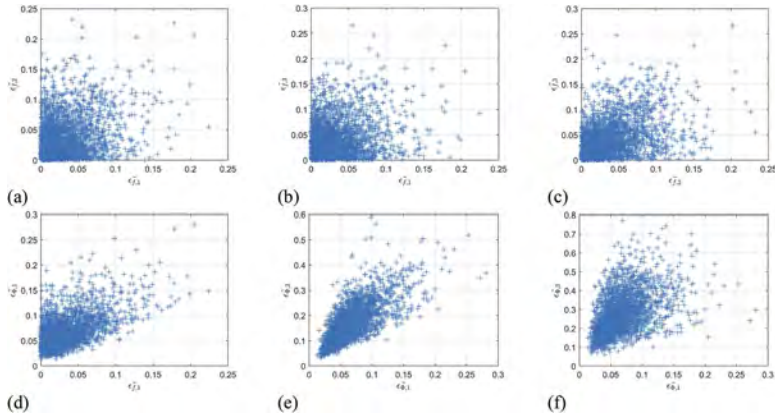


Figure 2. Scattering points of errors of (a) the 1st and the 2nd CSM frequencies; (b) the 1st and the 3rd CSM frequencies; (c) the 2nd and the 3rd CSM frequencies; (d) the 1st CSM's frequency and modal shape; (e) the 1st and the 2nd CSM modal shapes; (f) the 1st and the 3rd CSM modal shapes.

could be much larger than zero even though the frequency errors are about zero; 3) the linear correlations between the 1st CSM modal shapes and the other two kinds of modal shapes are more clear than Figure 2(d), but the dispersions become larger as the errors increase. Based on the numerical results, the relationships between the errors are approximated as

$$\tilde{\varepsilon}_{f,1} = \tilde{\varepsilon}_{f,2} = \tilde{\varepsilon}_{f,3} \quad \tilde{\varepsilon}_{\phi,1} = 0.045 + 0.62\tilde{\varepsilon}_{f,1} \quad \tilde{\varepsilon}_{\phi,2} = 2.35\tilde{\varepsilon}_{\phi,1} \quad \tilde{\varepsilon}_{\phi,3} = 3.63\tilde{\varepsilon}_{\phi,1} \quad (7)$$

In terms of the second approach, following the evidence-based method proposed by Goller et al. (2012), a ratio α between the error variances of the modal shapes and the modal frequencies is assumed, i.e.,

$$\alpha = \varepsilon_{\phi,j} / \varepsilon_{f,j} \quad (8)$$

Based on the α value, the Bayesian model updating is conducted, and the model evidence $p(\mathbf{D})$ is calculated. By implementing the analyses for a series of α values, the model with the largest evidence value is selected as the optimal one.

In the following, the two approaches are employed for identifying the thickness values t_k ($k=1\sim 10$) of the simplified model as well as the modal frequency errors. Based on the results in Figure 2, one error parameter ε_f for the modal frequencies is assumed, and the error parameters for the modal shapes $\varepsilon_{\phi,j}$ can be calculated according to equation (7) or equation (8). Thus, there are 11 parameters to be identified for the model.

2.3 The evaluation of the minimum cross-section thickness

In the previous section, the approach for estimating the average thickness of each section of the member is explained. By using the estimated thickness, a minimum cross-section thickness in the longitudinal direction can be calculated, i.e., $0.5\min(t_1+t_6, t_2+t_7, t_3+t_8, t_4+t_9, t_5+t_{10})$. However, because the estimated thickness is an averaged value, directly using these values will underestimate the true maximum thickness reduction, and further, overestimate the ultimate tensile capacity.

To find the relationship between the average cross-section thickness and the minimum cross-section thickness, the thickness distributions of three real corrosive members are analyzed. They are members A, B, and C in Figure 3. In the figure, the thickness values and lengths of the different members are normalized with respect to 100% and 1 for the conveniences of analyses. The blue, orange, and green lines represent the thickness of the cross-sections, the flange's central lines ($t_1\sim t_5$ direction), and the web's central lines ($t_6\sim t_{10}$ direction) respectively. The blue lines, i.e.,

the cross-section thickness, are calculated as the average values of thickness in one cross-section location, and this data will be used in the following.

First, a 1/5-length region of the member, i.e., section t_1 and t_6 , is selected; by shifting the region from one end to the other in the longitudinal direction, the average cross-section thickness and the minimum cross-section thickness within the region are calculated; for each of the three members, 100 pairs of the data are obtained. Finally, a linear regression model is approximated and shown in Figure 4(a).

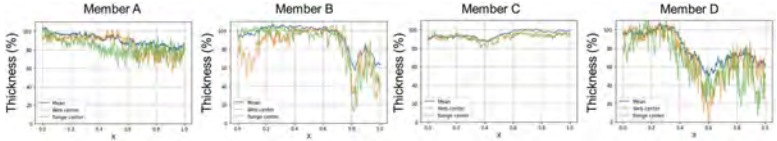


Figure 3. The thickness distributions of real corrosive members.

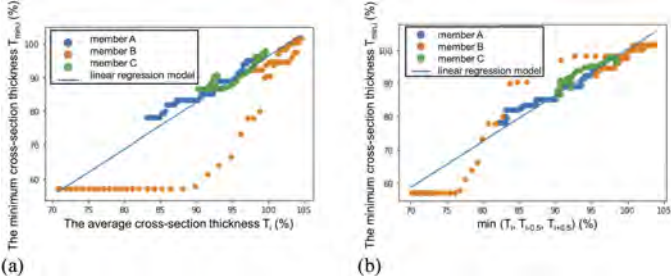


Figure 4. The relationship between the average cross section thickness and the minimum cross-section thickness.

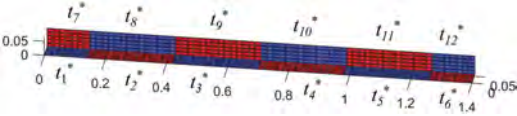


Figure 5. The 12-section model.

It is shown that the linear regression model can reproduce the relationship for members A and C well with an error below 10%. However, the error for member B could be larger than 20%. The outliers are due to the cases where the minimum cross-section thickness exists at the boundaries of the calculation region. Based on the facts, it is considered that by including the thickness values of the adjacent regions, the accuracy of the model can be improved. Figure 4(b) shows the modified regression model where the x -axis is replaced by $\min(T_i, T_{i-0.5}, T_{i+0.5})$. T_i , $T_{i-0.5}$, and $T_{i+0.5}$ denote the average cross-section thickness of the calculation region and those of the regions shifted 1/10-length left and right respectively. Compared with the previous one, the maximum error of the model is reduced to 10%. The formula of the regression model is written in equation (9).

$$\hat{T}_{\min,i} = 1.39 \min[T_i, T_{i-0.5}, T_{i+0.5}] - 38.4 \tag{9}$$

In order to evaluate the minimum cross-section thickness based on equation (9), in addition to the 10-section model in Figure 1(b), the thickness of a 12-section model shown in Figure 5 should also be estimated.

3 EXPERIMENTAL VALIDATIONS

In this section, the thickness of a specimen with real corrosion is estimated using the Bayesian model updating method. In fact, the specimen is member D in Figure 3, of which the real object and the true thickness distribution are shown in Figure 6. The FE model to be estimated is shown in Figure 1(b) and Figure 5 for the 10-section model and the 12-section model respectively. This model is built with 4-node shell elements, which has 700 elements and 4554 DOFs in total. Some of the fundamental information of the model is listed in Table 1.

The hammer tests were conducted with two Laser Doppler Velocimeters (LDVs), i.e., one is set as the reference station and the other is the moving measurement station. The velocity responses of 27 points were measured in 26 cases. The 27 measurement points contain 9 equally spaced points at the corner line and 9 equally spaced points at each outer edge line of the flange and web. They are shown as the ‘b-line’, ‘a-line’, and ‘c-line’ in Figure 6(b). The first three CSMs of the specimen are extracted from the signals; the modal frequencies are 97.5 Hz, 163.8 Hz, and 273.5 Hz respectively. The detailed experiment configuration and the CSM shapes are presented in Figure 7.

Table 1. The fundamental information of the FE model to be estimated.

Length	Flange (web) length	Density	Young’s modulus	Poisson’s ratio
1.4 m	0.065 m	7850 kg/m ³	210 GPa	0.25

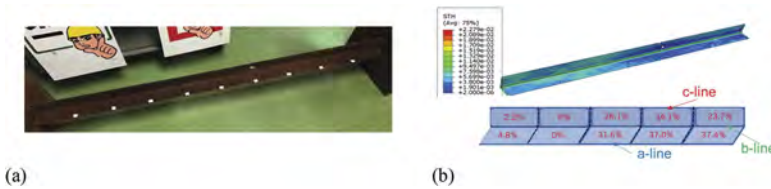


Figure 6. (a) The real specimen to be estimated; (b) the true thickness distribution of the specimen.

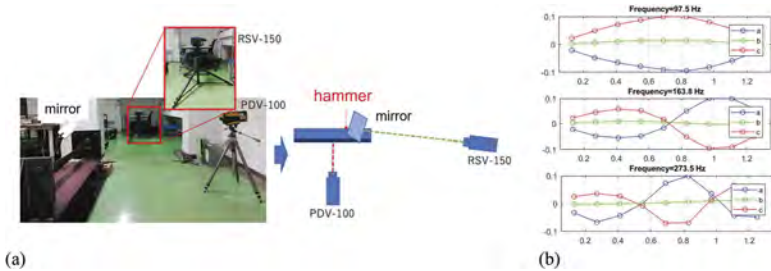


Figure 7. (a) The experiment configuration; (b) the identified first three CSMs.

The model updating is implemented using the TCMCMC algorithm. The prior distribution of a thickness t_k is defined uniformly between 1 mm and 6 mm, and the range of ε_f is [0.01, 0.1]. The modal information is the first three CSMs’ frequencies and shapes. The data set is one, but it is assumed that 10 data sets with the same results are used in the analysis.

The posterior parameter distributions obtained using approach 1 for the 10-section model are shown in Figure 8. The errors of the parameters are listed in Table 2. In the table, the thickness errors are calculated based on the median values of the sampled parameters. The true value is the average thickness of each section of the real member. The c.s.i stands for the cross-section consisting of t_i and t_{i+5} , and its error is calculated based on the average of the two thickness values. Using approach 1, the log value of the evidence $p(\mathbf{D})$ is 28.3.

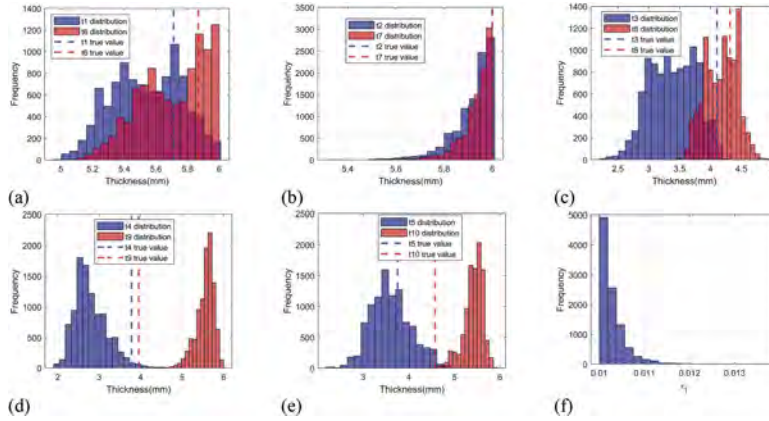


Figure 8. The posterior distributions of parameters based on approach 1: (a) t_1 and t_6 ; (b) t_2 and t_7 ; (c) t_3 and t_8 ; (d) t_4 and t_5 ; (e) t_5 and t_{10} ; (f) ϵ_f .

Table 2. The identification errors of the thickness and cross-sections based on approach 1(2).

t_6	t_7	t_8	t_9	t_{10}
2.4% (1.5%)	0.8% (2.7%)	2.6% (3.2%)	41.9% (45.8%)	19.0% (2.2%)
t_1	t_2	t_3	t_4	t_5
3.0% (1.2%)	0.9% (2.9%)	17.6% (34.6%)	28.1% (33.2%)	5.1% (20.4%)
c.s.1	c.s.2	c.s.3	c.s.4	c.s.5
2.7% (0.2%)	0.8% (2.8%)	9.9% (15.2%)	7.7% (7.2%)	8.2% (10.4%)

When applying approach 2, the FE model is updated based on a series of α values. In this case, the α values of 1.0, 2.0, 5.0, 10.0, 20.0, 30.0, 40.0, 50.0, and 100.0 are calculated. The log values of the evidence are shown in Figure 9. It is found that the maximum evidence value, i.e., 36.5, is obtained when $\alpha=30$. Besides, in Figure 9, the log evidence value using approach 1 is also plotted, and this value is equivalent to $\alpha=15$ or 50 in approach 2. The errors in the case are shown in the parentheses in Table 2.

Based on the results, it is found that the estimation error of the average thickness of one section could be as large as about 40%, however, the error is reduced to about 15% when the average cross-section thickness is considered, i.e., the average thickness value of two sections in the same cross-section. The two approaches give similar accuracies while approach 1 slightly outperforms approach 2. It is noted that the log evidence value of approach 1 is smaller than that of approach 2. This phenomenon is probably due to the relatively large inaccuracy of the system model, and it should be investigated in the future.

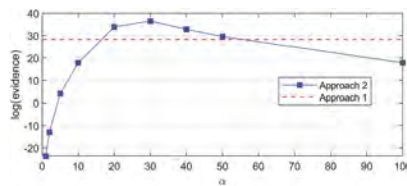


Figure 9. The log values of evidence based on a series of α values using approach 2.

In terms of the estimations of the 12-section model, the same procedures are implemented. Their results will not be presented here due to the limitation of the space. The minimum thickness of each cross-section and the results of the two approaches are presented in Figure 10 and Table 3,

in which the normalized values are presented. The results of the two approaches are close to each other, and both approaches show that the minimum cross-section thickness occurs at c.s.3 or c.s.4 with about 41% thickness ratio. Compared with the true value, the estimations overestimate the reduction ratio by about 10% which is on the safe side from the engineering's point of view.

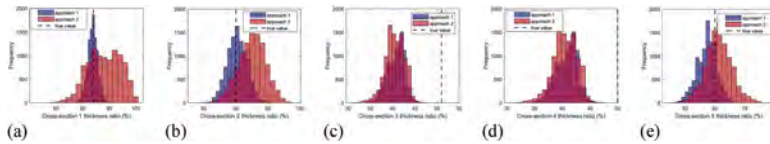


Figure 10. The estimations of the minimum cross-section thickness based on approach 1 and 2: (a) c. s.1; (b) c.s.2; (c) c.s.3; (d) c.s.4; (e) c.s.5.

Table 3. The estimated minimum cross-section thickness.

	c.s.1	c.s.2	c.s.3	c.s.4	c.s.5
Approach 1	91.9%	90.2%	41.0%	41.0%	57.5%
Approach 2	94.1%	92.6%	40.6%	40.6%	61.2%
True value	92.0%	90.0%	51.0%	50.0%	60.0%

4 CONCLUSIONS

In this paper, a strategy is proposed to evaluate the minimum cross-section thickness of a lower chord member of a conveyor support structure. The strategy includes estimating the average thickness of the member's sections using a Bayesian model updating method and the CSMs; constructing a regression model for evaluating the minimum cross-section thickness from the average cross-section thickness based on real members' thickness datasets; evaluating the minimum cross-section thickness using the estimated thickness from step 1) and the regression model from step 2). Particularly, in step 1), two approaches to consider the error variances for the Bayesian model updating are investigated.

The method is validated through hammer tests on a real corrosive specimen. The estimation results based on the two approaches are similar. The results show that even though the estimation error of the average thickness of one section could be as large as about 40%, the estimation error of the average cross-section thickness is reduced to 15%. For the tested specimen, the minimum cross-section thickness is underestimated by about 10%, which is on the safe side from the perspective of practical engineering.

REFERENCES

- Goller, B., Beck, J. L., & Schueller, G. I. 2012. Evidence-based identification of weighting factors in Bayesian model updating using modal data. *Journal of Engineering Mechanics* 138(5): 430–440
- Kato, S., Nagayama, T., Su, D., Hisazumi, K., & Tominaga, T. 2018. Identification of a cross-sectional vibration mode of a belt conveyor support structure using acoustic loading (in Japanese). *Journal of Structural Engineering* 064A: 354–363.
- Rana, S., Nagayama, T., Hisazumi, K., & Tominaga, T. 2019. Damage identification of a belt conveyor support structure based on cross-sectional vibration characteristics. *Structure Control and Health Monitoring* 26(6): e2349.
- Vanik, M. W. 1997. *A Bayesian probabilistic approach to structural health monitoring*. California Institute of Technology.
- Yang, Y., Nagayama, T., Kato, S., Hisazumi, K., & Tominaga, T. 2021. Sensitivity analysis and identification of cross-sectional modes of a belt-conveyor structure using operational vibration. *Proceedings of the 76th annual conference of Japan Society of Civil Engineers*: I–134.

Scenario-oriented analysis of bridges subjected to non-deterministic combined seismic actions based on finite element modeling

S. Yamamoto & G. Shoji

University of Tsukuba, Ibaraki, Japan

M. Ohsumi

Public Works Research Institute, Ibaraki, Japan

ABSTRACT: In this study, we proposed the concept of resilience design for seismic damage to infrastructure and lifeline structures by extending the framework of the seismic damage estimation system for infrastructure and lifeline structures proposed in previous studies. Based on the resilience design system, a scenario-oriented analysis was conducted to estimate damage scenarios for road bridges damaged by the 2016 Kumamoto earthquake using three-dimensional finite element analysis. As input actions, surface fault displacement and strong ground motions were used, and damage scenarios were estimated for each seismic action and resilience design for these damage scenarios was examined.

1 INTRODUCTION

Many infrastructure and lifeline structures in a highly seismic hazardous country have been severely damaged by subduction zone earthquakes and inland crustal earthquakes. Seismic damage to infrastructure and lifeline structures in response to anticipated earthquakes is diverse, complex and uncertain because of complex seismic effects such as strong ground motions, surface fault displacement, liquefaction and slope failure. However, from the perspective of infrastructure management and decision-making, road bridge administrators are responsible for identifying probabilistic risks and all possible failure scenarios of road bridges exposed to uncertain seismic actions and for providing earthquake countermeasures that satisfy the needs of road bridge users. Therefore, accurate seismic damage estimation for infrastructures and lifeline structures is required. This seismic damage estimation can contribute to the resilience (Bruneau et al. 2003) and anti-catastrophic capability (Honda 2018) of infrastructures and lifeline structures.

For example, Ichimura et al. (2011), Hori (2018) and Hori et al. (2018) proposed an integrated earthquake simulation using high-performance computing and an automatic construction method of analytical models for urban structures. They have estimated the seismic hazard and damage risk for a hypothetical earthquake by analysing seismic ground motion and the seismic response of urban areas. Decò et al. (2013) proposed a framework to quantify the resilience of bridge structures subject to an extreme seismic ground motion from the perspectives of non-deterministic evaluation. Ohsumi et al. (2021) proposed a scenario design method that considers road-bridge collapse, focussing on the rapid functional recovery of road bridges even if they lose their functionalities because of excess seismic ground motion. Minakawa & Shoji (2022) proposed a framework for a digital twin-based seismic damage estimation system consisting of three subsystems: a seismic action input system, a damage estimation system and an estimation data output system.

By extending the framework of the seismic damage estimation method given by Ref. (Minakawa & Shoji 2022), this study proposes the concept of resilience design for seismic damage to infrastructure and lifeline structures. Additionally, the proposed system evaluates the behaviour of infrastructure and lifeline structures in response to non-deterministic combined seismic actions through multiple trials. Representative examples of the implementation of scenario-oriented analysis for road bridges and specific countermeasures for resilience design are also presented.

2 FRAMEWORK FOR RESILIENCE DESIGN SYSTEM

Figure 1 shows the flowcharts of the resilience design system in seismic disasters. The system considers the interrelationship between physical space and virtual space and consists of three subsystems in each space: a seismic action input system, a damage estimation system and an estimation data output system.

The seismic action input system acquires earthquake-induced actions such as seismic ground motion, liquefaction, slope failure, surface fault displacement and tsunami, which are input to the infrastructure and lifeline structures to be targeted for damage estimation. For example, seismic action data are derived from real-time sensor data and time series data based on observations in physical space. In the virtual space, seismic actions expected to cause damage to the target infrastructures and lifeline structures are determined by numerical simulations. The validity of the estimated seismic action data is ensured by utilising the interrelationship between physical space and virtual space.

The first stage in the damage estimation system is to identify weak points of network properties in the infrastructures and lifeline structures that are exposed to seismic action in each space. This approach is known as 'damage screening'. Using aerial images and visual interpretation, for example, sites at high risk of damage can be retrieved from the physical space. A network model is constructed in the virtual space, seismic actions are input and weak points are extracted by evaluating vulnerability based on the damage function. The second stage involves identifying more specific time series damage scenarios and modes. This approach is known as 'damage focussing'. In the physical space, for example, damage modes are estimated using drones for proximity monitoring. In the virtual space, infrastructures and lifeline structures assumed to be at high risk of damage through damage screening are modeled using a three-dimensional (3D) finite element (FE) method, and by inputting the seismic action data estimated by the seismic action input system, more detailed damage modes of the target structures are estimated.

The estimation data output system provides data collected by drones and images taken by a camera in the physical space, as well as damage information estimated by damage screening and a visualisation of a structure by damage focussing in the virtual space. These outputs are emailed to administrators and users of infrastructure and lifeline structures to mitigate and prevent disasters in an appropriate digital format.

Damage scenarios and damage modes for target structures can be estimated by linking physical and virtual spaces through the system process. A design to improve the resilience of infrastructures and lifeline structures consists of three elements: [1] hardware and software earthquake countermeasures, [2] crisis management immediately after a disaster and [3] emergency recovery after a disaster. In this study, this process is defined as a resilience design. Using road bridges as an example, examples of elements [1] in resilience design include seismic reinforcement of bridge piers, the installation of vibration control dampers in bearings, flexible joints of auxiliary conduits that accommodate power lines and revision of standards for seismic design. In the case of element [2], administrators may include damage information, such as identifying damaged infrastructure and lifeline structures and the presence of secondary disasters, in traffic control. In the case of element [3], restorative materials are warehoused. The restorative materials include temporary vents for emergency restoration work, repair materials to fill cracks in piers, steel support materials to replace broken bearings and sandbags to fill the gap between joints.

In the proposed system, a series of seismic action input system—damage estimation system—and estimation data output system operations are executed in multiple physical and virtual space trials. For example, the physical parameters used in estimating seismic ground motion are changed for each trial in the seismic action input system. From the above multiple trials, it is possible to calculate the simultaneous multi-dimensional probability density of the response of the structure when combined non-deterministic seismic actions are considered. Examples of probability random variables are the displacement of the maximum response and its direction. This probability distribution enables the evaluation of the variability and expected behaviour of damage scenarios. We can select resilience design elements with high accuracy and valid variation, and provide them to administrators and users of infrastructure and lifeline structures, thereby contributing to developing more sophisticated and accurate disaster prevention and mitigation countermeasures.

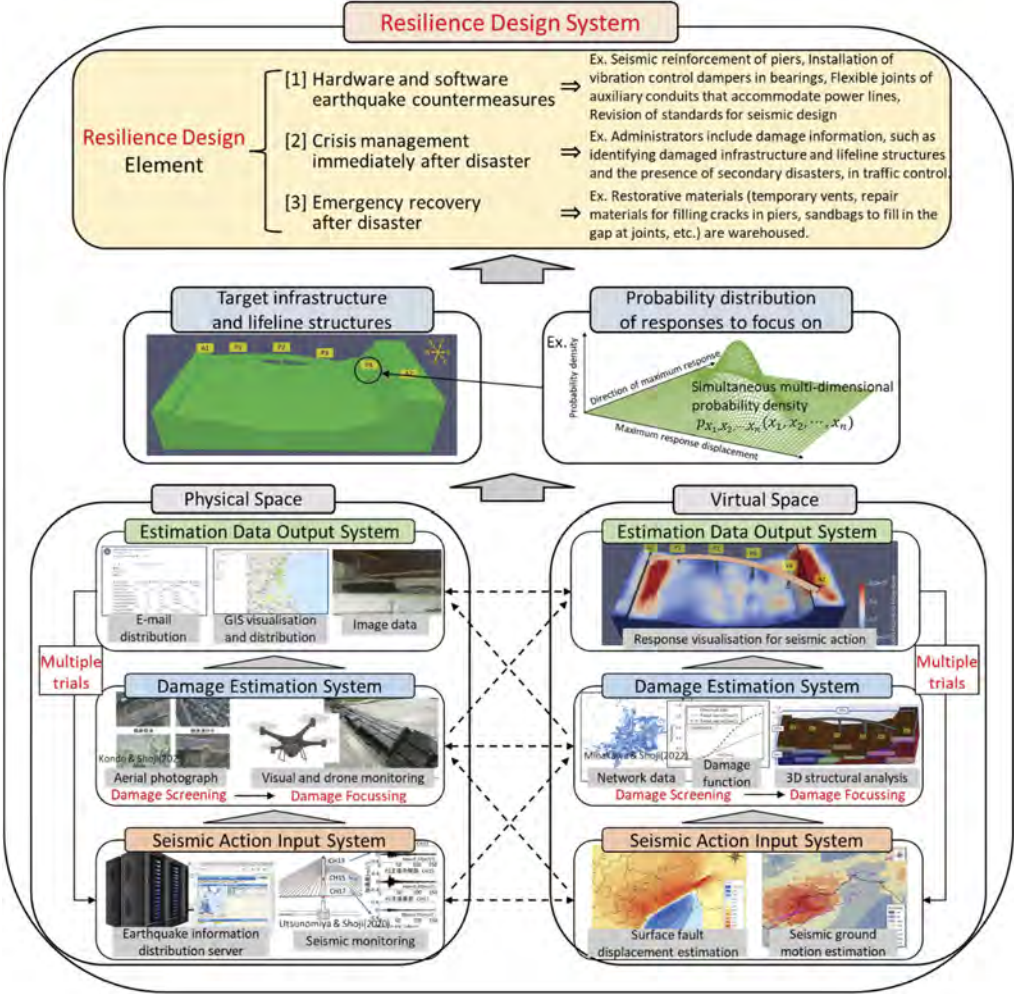


Figure 1. Flowcharts of the resilience design system in seismic disasters.

3 CASE STUDY OF SCENARIO-ORIENTED ANALYSIS

Based on the damage estimation system in the virtual space shown in Figure 1, a scenario-oriented analysis was conducted to estimate damage scenarios by 3D FE analysis for a typical road bridge damaged by the 2016 Kumamoto earthquake. Although the above results are based

on a case study of a damaged bridge, they serve as an example of preliminary damage estimation in virtual space for infrastructure and lifeline structures exposed to seismic hazards.

3.1 Analysis model

Figure 2 shows a 3D FE model of the bridge structure-underground interconnected system that is considered in this study. This model can be constructed in advance in a virtual space based on the design drawings provided by the road bridge administrator. In the target structures, abutments A1 and A2 have reinforced concrete (RC) abutments, and piers P1, P2, P3 and P4 have overhanging RC piers. Laminated rubber bearings are used as bearings. The 3D FE model uses tetrahedral first-order elements to model the abutments, piers and underground. Pentahedral and hexahedral first-order elements are used to model the slabs and laminated rubber bearings. Triangular and quadrilateral first-order shell elements are used to model the girders and auxiliary conduits. The case studies for surface fault displacement and strong ground motions use this model in Figure 2.

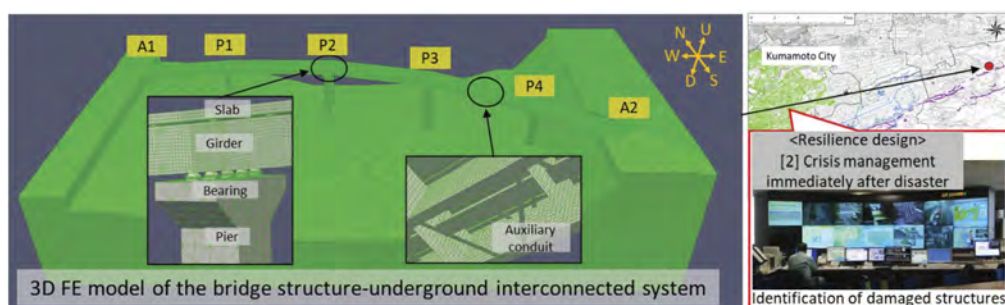


Figure 2. 3D FE model of the bridge structure-underground interconnected system.

3.2 Case study for surface fault displacement

The surface fault displacement in the 3D FE model was estimated from the Okada (1985) equation. The boundary conditions were based on those of Habu et al. (2017), where the displacement in the normal direction of the ground side was constrained, and the rest of the boundaries were free boundaries. Linear static analysis was conducted by inputting the amount of surface fault displacement as forced displacement in five incremental steps at intervals of 50 m mesh to the ground bottom. To consider uncertainty in the direction of surface fault displacement, the surface fault displacement estimated from the Okada equation was rotated by 30 degrees for each 50 m mesh on the EW-NS plane, for a total of 12 cases of analysis. When the angle is counterclockwise on the EW-NS plane with the east direction as 0 degrees, the surface fault displacement estimated from the Okada equation is 73 to 84 degrees, which we call Case 1. The conjugate gradient (CG) method was used as the linear solver; in these cases, the symmetric successive over-relaxation (SSOR) method was used as the pre-processing method, and the threshold for determining convergence iteratively was set at 1.0×10^{-6} .

Figure 3 shows the response scenarios to surface fault displacement in Case 1 and the related resilience design. The overall response of the abutments and piers is dominated by the settlement and northeast directions, and joint failure at abutments A1 and A2 is estimated. The response of piers P2 and P3 increases, and significant shear deformation or rupture of the laminated rubber bearings on these piers is anticipated. Therefore, from the viewpoint of element [3] in resilience design, advanced preparation of restoration personnel and materials is necessary. Furthermore, there is a significant differential in displacement between piers P1 and P2, which may induce cracks in the slab and buckling of the bridge girders. Additionally, because the breakage of the auxiliary conduits of the power line attached to the bridge girders is anticipated, countermeasures to make the conduit joint flexible can be considered from the viewpoint

of element [1] in resilience design. Figure 3 also shows histograms of the absolute response displacement and direction of response displacement at pier and abutment tops on the EW-NS plane as variables. For piers P1 and P2, there is variation in absolute response displacement even in almost the same direction of response displacement. Therefore, from the viewpoint of element [1] in resilience design, for piers P1 and P2 in particular, countermeasures such as installing a device to control displacement in the direction where the displacement variation becomes large can be considered.

3.3 Case study for strong ground motions

The strong ground motions input to the 3D FE model were the site-specific waveforms at the location of the target structure, which were estimated using the finite difference method (Yamamoto et al. 2022). Linear dynamic analysis was conducted by inputting these site-specific waveforms as an inertia force to the 3D FE model. Damage focussing, which estimates the detailed damage scenario in Figure 1 in a time-series, necessitates high accuracy and rapid analysis time. In this case, the implicit method was used to solve the equation of motion, the CG method was used as the linear solver, SSOR was used as the pre-processing method and the threshold for determining the convergence iteratively was set to 1.0×10^{-6} .

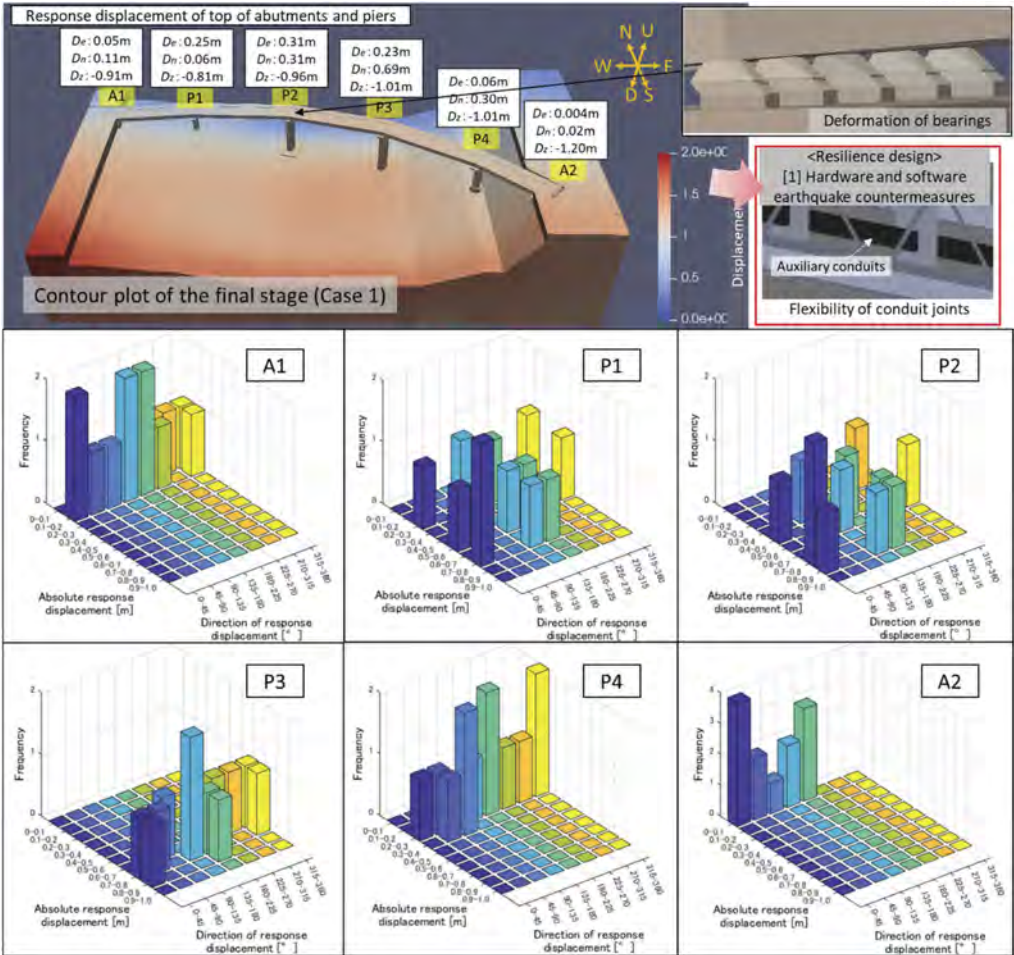


Figure 3. Case study for surface fault displacement.

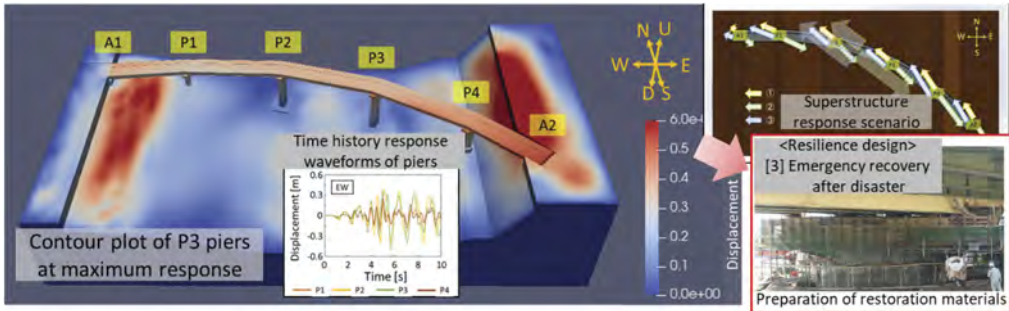


Figure 4. Case study for strong ground motions.

Figure 4 shows the response scenario to strong ground motions and the associated resilience design. Because of the complex behaviour of the superstructure, rupture of the bridge fall prevention cables and failure of the joints are assumed. Additionally, it is assumed that the response of the superstructure causes a rupture region in the laminated rubber bearings on all abutments and piers and that the rupture timing differs as follows: P3B, P4B, P2B, A2B, P1B and A1B (for example, A1B is the rubber bearing on the abutment A1). The response displacement at the top of each pier exceeded 1%, showing that the piers may reach the plastic zone where cracking occurs. Based on the above damage scenarios, it is required to plan to install detour routes and prepare restoration personnel and materials from the viewpoint of element [3] in resilience design.

4 CONCLUSIONS

In this study, we proposed a framework for a resilience design system for seismic damage to infrastructure and lifeline structures. As a representative example of the damage estimation system for resilience design to a road bridge, a scenario-oriented analysis was conducted to estimate damage scenarios for the road bridge damaged in the 2016 Kumamoto earthquake using 3D FE analysis. Strong ground motions and surface fault displacement input actions were used to estimate damage scenarios for each seismic action, and countermeasures for resilience design against the damage scenarios were presented. By repeating the above cases, for example, 1000 times while changing the seismic actions to consider the uncertainty, it is possible to evaluate the variability and expected behaviour of the damage scenarios and carry out a fair resilience design in a non-deterministic approach.

ACKNOWLEDGMENTS

Kumamoto Reconstruction Project Office provided invaluable information on the structural characteristics of the target road bridge and the geotechnical properties of the underground. Assistant Professor Naoki Morita at the University of Tsukuba and other members of the FrontISTR Commons for their many helpful suggestions on FEM analysis. We express our deepest gratitude to everyone involved. The support received via JSPS KAKENHI Grant Number JP 22H01569 is gratefully acknowledged. The authors would like to thank MARUZEN-YUSHODO Co., Ltd.(<https://kw.maruzen.co.jp/kousei-honyaku/>) for English language editing.

REFERENCES

Bruneau, M. Chang, S.E. Eguchi, R.T. Lee, G.C. O'Rourke, T.D. Reinhorn, A.M. Shinozuka, M. Tierney, K. Wallace, W.A. & Winterfeldt, D.V. 2003. A framework to quantitatively assess and enhance the seismic resilience of communities. *Earthquake Spectra* 19(4): 733–752.

- Decò, A. Bocchini, P. & Frangopol, D.M. 2013. A probabilistic approach for the prediction of seismic resilience of bridges. *Earthquake Engineering & Structural Dynamics* 42(10): 1469–1487.
- Haba, K. Sonobe, H. Sawada, M. & Hori, M. 2017. Study on application of high performance computing to fault displacement simulation. *Journal of Japan Society of Civil Engineers A2* 73(2): 821–830.
- Honda, R. 2018. Study for implementation of anti-catastrophe-oriented seismic design. *Journal of Japan Society of Civil Engineers A1* 74(4): 1078–1086.
- Hori, M. 2018. *Introduction to Computational Earthquake Engineering*. Japan: World Scientific Pub Co Inc.
- Hori, M. Ichimura, T. Wijerathne, L. Ohtani, H. Chen, J. Fujita, K. & Motoyama, H. 2018. Application of high performance computing to earthquake hazard and disaster estimation in urban area. *Frontiers Built Environment* 4:1. doi: 10.3389/fbuil.2018.00001.
- Ichimura, T. Hori, M. Quinay, P.E. Wijerathne, M.L.L. Suzuki, T. & Noguchi, S. 2011. Comprehensive numerical analysis of fault-structure systems - Computation of the large-scale seismic structural response to a given earthquake scenario -. *Earthquake Engineering & Structural Dynamics* 41(4): 795–811.
- Minakawa, T. & Shoji, G. 2022. Digital twin concept of infrastructure earthquake damage estimation system based on cyber-physics space. *Proceedings of the Eleventh Symposium on Disaster Mitigation and Resilience of Infrastructures and Lifeline Systems*. JSCE: 1–5.
- Ohsumi, M. Nakao, H. Ishizaki, S. & Shoji, G. 2021. Proposal of design method for collapse scenario design of road bridge by controlling failure likelihood. *Journal of Japan Society of Civil Engineers A1* 77(4): 360–372.
- Okada, Y. 1985. Surface deformation due to shear and tensile faults in a half-space. *Bulletin of the Seismological Society of America* 75(4): 1135–1154.
- Yamamoto, S. Shoji, G. & Ohsumi, M. 2022. Clarification of the damage mechanism of the long-period bridge system damaged by the 2016 Kumamoto earthquake. *15th World Congress on Computational Mechanics (WCCM-XV) & 8th Asian Pacific Congress on Computational Mechanics (APCOM-VIII)*: Paper No. 3403.

Probabilistic-based model updating on a prestressed concrete box girder

X. Zhou, D. Chen & C.-W. Kim

Department of Civil and Earth Resources Engineering, Kyoto University, Kyoto, Japan

ABSTRACT: The prestressed concrete (PC) bridge is one of the most widely-used bridges. In recent years, their maintenance has become a significant problem in civil engineering. This study aims to investigate the applicability of a probabilistic-based model updating method to the structural health monitoring (SHM) of a PC box girder. The static loading test and vibration measurement were conducted on a PC box girder. A finite element (FE) model was established to reproduce the experiment process. Although the tendency between simulation results and measured data was similar, the discrepancies between them were also observed. To this end, a probabilistic-based model updating method using structural modal properties was used to consider the uncertainties in the system to improve the performance of the simulation. The transitional Markov Chain Monte Carlo (TMCMC) algorithm is taken as a sampler to estimate the distribution of model parameters. The results showed that the discrepancy in the modal properties decreased after updating. The updated FE model was also applied in the simulation of the static loading test, and better fitness in the linear state was observed. However, responses in a nonlinear state did not match well.

1 INTRODUCTION

In Japan, since many bridges were constructed more than 50 years ago during rapid economic growth, the reports of their deterioration and aging were increasing. Therefore, the maintenance and management of such bridges become urgent. Current evaluation methods are largely based on human sensory inspections, such as seeing and touching. However, these approaches are often subjective and need many professional engineers. For example, after the Sasago Tunnel ceiling panel fall accident in 2012 in Japan, local governments in Japan have been required to visually inspect road bridges with a span length of more than 2 m once every five years since July 2014. However, in approximately 20% of local governments, only a limited number of bridges are effectively managed due to a lack or absence of qualified engineers engaged in bridge maintenance work. Therefore, it is necessary to develop a quantitative, simple, and objective non-destructive technology to rationally maintain and manage bridges.

Several technologies have been developed, for instance, using image technology combined with drones to measure the extent of cracks and using infrared and electromagnetic waves to inspect and diagnose the surface and internal condition. The approach based on dynamic properties, such as natural frequencies, and mode shapes, is also widely applied. Dynamic properties can well reflect the change in mass and stiffness of structures and are therefore effective in evaluating structural performance. Moreover, vibration experiments are easy to implement, and particularly acceleration data are easy to acquire (Kim et al. 2016).

In structural engineering, FE models are widely used for structural analysis. Compared with field experiments, FE analysis can save time and costs. However, due to the limited available information and simplification in modeling, uncertainties, such as material properties, geometric properties, boundary conditions, and load conditions, invariably exist in the

system. Model updating methods would calibrate these uncertain parameters in the FE model based on the measurement data.

The Bayesian model updating (Jaynes 2003, Patelli et al. 2017, Zhou et al. 2022) is one of the most popular probabilistic-based approaches. Uncertain parameters are assumed to follow a certain probability distribution based on experimentally obtained data. Beck and Katafygiotis (Beck & Katafygiotis 1998) and Katafygiotis and Beck (Katafygiotis & Beck 1998) comprehensively improved the framework of Bayesian model updating, including model classes for structures and probability models for system errors. The model classes and probability models in the Bayesian model updating are furtherly investigated in many studies (Beck & Yuen 2004, Muto & Beck 2008, Goller et al. 2012). The Bayesian model updating approaches have been conducted for reliability analysis and damage detection on many linear or nonlinear structures in laboratory and actual conditions (Jang & Smyth 2017, Lam et al. 2018, Song et al. 2018, Moravej et al. 2019, Zhou et al. 2022).

Predicting the actual responses by the updated model might be an effective approach for SHM. However, the vibration data is often amplitude-dependent and easily affected by the surrounding environment. Moreover, it is not fully investigated that the accuracy of the simulation of the static loading process by the FE model is updated by vibration data. To acknowledge these challenges, one must investigate the feasibility of SHM by vibration-based Bayesian model updating.

In this study, loading and vibration experiments were conducted on a PC box girder. This process was also reproduced by FE analysis. Then, a probabilistic-based model update using identified dynamic properties was conducted to minimize the discrepancy between the simulation and experiment. The TMCMC (Ching & Chen 2007) method is taken as the sampling method to generate a sample sequence from the posterior distribution. After updating based on the frequency domain, the static loading process simulation is also conducted on the updated model.

2 METHODOLOGY

2.1 Bayesian model updating method

The formulation of the posterior PDF of uncertain parameter vector θ ($\theta \in \mathbf{R}^{N_\theta}$, N_θ is the number of uncertain parameters), under the condition system response D , is given as follows.

$$P(\theta|D) = \frac{P(D|\theta)P(\theta)}{P(D)} \quad (1)$$

where $P(D)$ is the evidence of system response D , and $P(D) = \int P(D|\theta)P(\theta)d\theta$; $P(\theta)$ is the prior PDF; $P(D|\theta)$ is the likelihood function, which donates the conditional probability of D given θ . In the vibration-based model updating process, the likelihood function is given as:

$$P(D|\theta) = c_l e^{-J(\theta)/2\sigma^2} \quad (2)$$

where $J(\theta) = \sum_{i=1}^{N_m} \left(\left(1 - \langle \varphi_i(\theta), \hat{\varphi}_i \rangle \right)^2 + \left(1 - f_i(\theta)/\hat{f}_i \right)^2 \right)$; $f_i(\theta)$ and $\varphi_i(\theta)$ are the i th natural frequency and normalized mode shape vector under the given uncertain parameter vector θ obtained from the FE model while \hat{f}_i and $\hat{\varphi}_i$ are the measured values from the experiments or monitoring; N_m is the total number of modes; c_l is the normalized constant.

2.2 Transitional Markov chain Monte Carlo

Although the Bayesian model updating method can provide a posterior distribution, the complexity of its PDF makes it difficult to generate samples directly from the posterior distribution. Therefore, an efficient sampler is necessary. In this study, TMCMC (Ching & Chen 2007) is used to generate samples efficiently. The essence of TMCMC is to use a series of asymptotic intermediate

distributions, $(P_j(\theta|D), j = 0, 1 \dots m, \theta \in \mathbf{R}^{N_\theta})$, to approach the final distribution. The importance sampling method is used to transfer between the intermediate distributions. With the value of j increasing, the $P_j(\theta|D)$ becomes more closed to the target distribution $P(\theta|D)$.

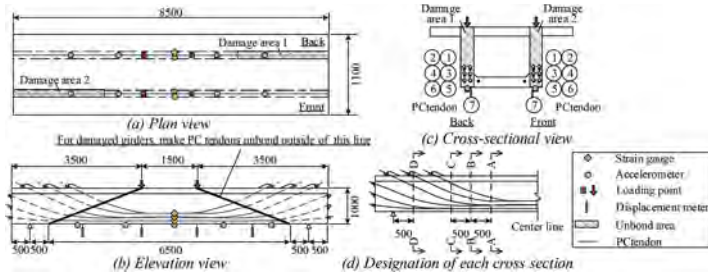


Figure 1. Specimen drawing.

Table 1. Material properties of specimen.

Compressive strength of concrete	52.7 MPa
Young's modulus of concrete	32.31 GPa
Poisson's ratio of concrete	0.207
Longitude reinforcement ratio	0.3% (web), 0.2% (upper slab), 0.5% (lower slab)
Stirrup reinforcement ratio	0.2%
Prestress	About 1000 MPa
Yield strength of Reinforcing bar	354 MPa
Young's modulus of Reinforcing bar	192 GPa
Yield strength of PC tendon	1600 MPa
Young's modulus of PC tendon	200 GPa

For the asymptotic intermediate distribution $P_j(\theta|D)$, the values of their variances $(\sigma_j, j = 1 \dots m)$ are different, and $P_j(\theta|D)$ is shown as:

$$P_j(\theta|D) = c_j e^{-J(\theta)/2\sigma_j^2} \quad (3)$$

Especially, assuming $P_0(\theta|D) = c_0$ follows a uniform distribution. The adjacent intermediate distributions are connected by importance sampling such as TMCMC. The process that generates sample sequence of $\theta_{j+1,l}$ following the distribution of $P_{j+1}(\theta|D)$ can be described as:

$$\theta_{j+1,l} = \theta_{j,k} \text{ with probability } w_{j,k}^n, \quad k = 1, 2, \dots, N_j, \quad l = 1, 2, \dots, N_{j+1} \quad (4)$$

Therein, weighting $w_{j,k}^n$ is given as:

$$w_{j,k}^n = \frac{e_k}{\sum_{t=1}^{N_j} e_t} \quad (5)$$

where $e_k = \exp\left(-\frac{J(\theta_{j,k})}{2}\left(\frac{1}{\sigma_{j+1}^2} - \frac{1}{\sigma_j^2}\right)\right)$, N_j indicates the number of samples in j th step.

3 EXPERIMENT

3.1 PC box girder test specimen

The test specimen is a 1/2 scale sound PC box girder and more details can be found in Figure 1 and Table 1.

3.2 Static and dynamic experiments

The static loading and vibration experiments are conducted on the test specimen to investigate the static and dynamic responses of the PC box girder. In the static loading experiment, sixteen displacement gauges (SDP, CDP: Tokyo Measuring Instruments Lab) are installed on the lower slab of the PC box girder. The test specimen is subjected to four-point loading by a 30 MN large structural universal testing machine (12 MN for positive bend during testing), as shown in Figure 2. Static loading was applied four times, as Load 1, Load 2, Load 3, and Load 4. Load 1 is 10% higher than the initial cracking load, Load 2 is the shear cracking load, Load 3 is the stirrup yield load (the load when yielding occurs at a certain point among all stirrups), and Load 4 is the ultimate load (crushing of the upper slab). The loading process is shown in Figure 3.

In the vibration experiment, ten accelerometers (NP-2120: Ono Sokki, sampling frequency 2000Hz) were placed on the lower slab of the PC box girder as shown in Figure 1. The impact hammer (8208-Modal, Brüel & Kjær company) was applied on the upper surface of the upper slab right above each acceleration sensor after the unloading of the static test. The same excitation was performed 10 times at each hit point. According to the different steps, they were called St.1, St.2, and St.3.

3.3 Experimental results

3.3.1 Static test

The yield load (F_y) was 1020 kN, and the ultimate load was 2033 kN. In the loading and unloading process, residual deformation can be observed in Figure 4. The load-displacement curve demonstrates that the main girder does not reach the ultimate failure state until the last loading step.



Figure 2. Photo of experiment.

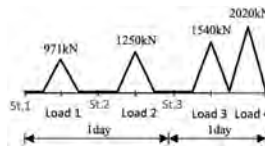


Figure 3. Process of static and dynamic experiments.

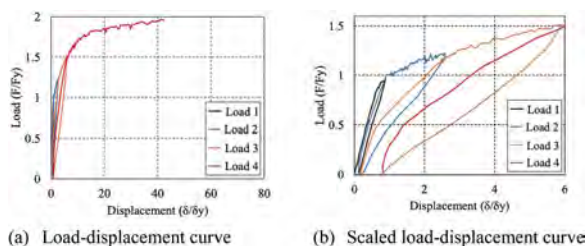


Figure 4. Static loading.

Table 2. Dynamic properties of the FE model with design values and with results of experimentation.

		1 st bending mode	2 nd bending mode
Experiment	Freq. (Hz)	29.27	67.32
	Freq. (Hz)	33.78	81.75
Simulation	Difference of Freq. (%)	15.41	21.43
	MAC	0.99	0.64

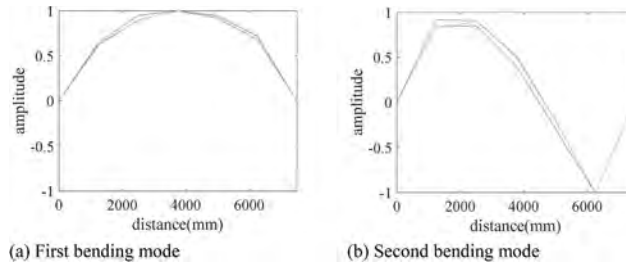


Figure 5. Mode shapes.

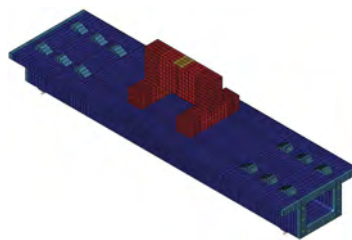


Figure 6. FE model.

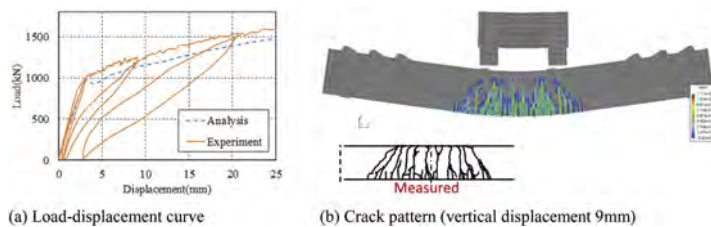


Figure 7. Simulation for static loading test.

3.3.2 Dynamic test

A total of two modes, the first and second bending modes, can be identified. Table 2 and Figure 5 indicate the natural frequencies and the corresponding mode shapes.

4 MODEL UPDATING

4.1 FE model

The FE model is established by DIANA 10.4, as shown in Figure 6, and the main girder is modeled with solid elements. The horizontal and vertical springs are applied to the support points to qualify the uncertainties in the boundary conditions. The dynamic properties of the

FE model under design values (the same as in Table 1) are shown in Table 2. Compared with the results identified from experiments, the differences in the natural frequencies of both the first and second bending modes are significant, and the difference in mode shapes of the second bending mode is also observed. The static loading process is also applied to the model. Figure 8(a) indicates the load-displacement curve in the midspan, and Figure 8 (b) presents the development of the cracks from FE analysis with a sketch of cracks observed from the experiment for comparison. It is clear that there are differences in the load-displacement curves after the yield point between the simulation and experiment.

4.2 Sensitivity analysis

Before the model updating, a sensitivity analysis was conducted to investigate the effect of each parameter in the dynamic analysis. It was observed that Young's modulus of steel almost has no impact on the eigenvalue analysis. The clear changes in natural frequencies were observed with the fluctuation in concrete density and Young's modulus. The natural frequencies change significantly under both vertical and horizontal springs. Therefore, four types of parameters, including the mass and Young's modulus of concrete, and vertical and horizontal springs, will be considered in the updating process. Some results are shown in Figure 8.

4.3 Model updating process and results

The proposed model updating algorithm is applied to the target structure to improve the performance of the simulation. The results are summarized in Figure 9, Table 3, and Table 4. Figure 9 presents the marginal distribution of each model parameter. Table 4 illustrates the most probable value (MPV) of model parameters. Table 4 indicates the dynamic parameters under MPV of model parameters in Table 3. Comparing Table 4 with Table 2, a significant improvement in the natural frequencies of both the first and second bending modes can be observed. The discrepancy in mode shapes of the second bending mode is also decreased, and the MAC value becomes close to 1. It was confirmed that the updated model is consistent with the experimental data on vibration properties. However, the specific gravity and Young's modulus of concrete exceed the acceptable range in terms of material properties.

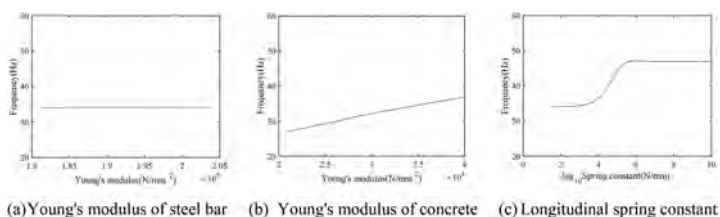


Figure 8. Results of sensitivity analysis.

Table 3. MPV of updated model parameters.

	Concrete density (t/m^3)	Concrete Young's modulus (GPa)	Horizontal spring (kN/mm)	Vertical spring (left) (kN/mm)	Vertical spring (right) (kN/mm)
Initial	2.28	34.00	0	∞	∞
Updated	2.50	23.21	$10^{7.36}$	$10^{4.94}$	$10^{4.34}$

4.4 Static simulation by updated model

It is necessary to confirm the performance of the updated model in the static process since the values of the updated Young's modulus of the concrete were far from the design values. This

Table 4. MPV of the updated frequencies and MAC.

		1st bending mode	2nd bending mode
Experiment	Freq. (Hz)	29.27	67.32
	Freq. (Hz)	30.47	63.89
Simulation	Difference of Freq. (%)	4.10	-5.09
	MAC	0.95	0.81

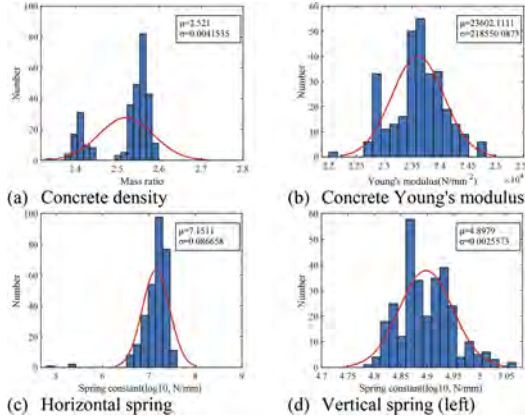


Figure 9. Marginal distribution of updated model parameters.

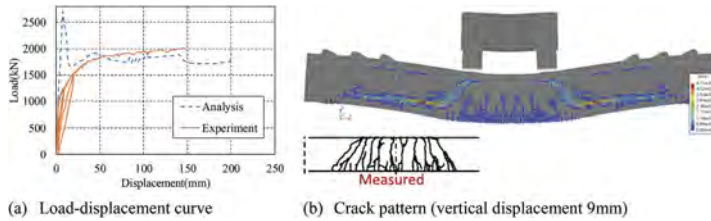


Figure 10. Simulation for static loading test.

section will discuss the simulation of the static loading process to examine the changes in bridge performance.

Figure 10 (a) shows the load-displacement curve in the midspan from the simulation under updated model parameters, and Figure 10 (b) presents the development of the cracks from FE analysis with an updated FE model with a sketch of cracks observed from the experiment for comparison. In the linear state up to around 1000kN, Figure 10 (a) shows a better fitness than Figure 8(a). However, a significant discrepancy can also be observed in the nonlinear state around displacement of 9mm. Major differences may be rooted in lower Young's modulus identified through the FE model update and the consideration of the longitude spring in support of the updated FE model. Therefore, bending cracks hardly occur in concrete while shearing cracks easily. Considering spring elements at supports is very useful in modal parameter-based FE model updates as the boundary condition is quite sensitive to the frequencies as can be seen in Figure 8 (c). However, for the PC girder, the large horizontal spring could increase prestress effect and may affect the structural behavior of the PC girder. Therefore, as the next step for this study, the following two items will be investigated: one is changing the design of the model parameters in updating process; another is establishing a new objective function, which includes both dynamic and static properties from experiments, for model updating.

5 CONCLUSIONS

This study aims to investigate the applicability of a probabilistic-based model updating method to the structural health monitoring (SHM) of a PC box girder. In the initial model, clear discrepancies in both static loading and vibration processes can be observed. After updating with the dynamic properties, the performance in the vibration and static loading (in the linear state) process is largely improved. The FE model updated by dynamic properties can successfully reproduce the static loading process (in a linear state). It is confirmed that the model updating can improve the accuracy of simulation in both static loading and vibration processes, and is effective for SHM.

However, the distribution of identified model parameters is not in the normal range, and the system responses in a nonlinear state do not match very well. Therefore, the gap between simulation and experiment still exists in a nonlinear state, which means the application of this approach is still limited. Further research considering the nonlinear state is necessary.

ACKNOWLEDGMENTS

This study is partly sponsored by a Japanese Society for Promotion of Science (JSPS) Grant-in-Aid for Scientific Research (B) under Project No.22H01576, which is greatly acknowledged.

REFERENCES

- Abdel Wahab, M.M. & De Roeck, G. 1998. Dynamic testing of prestressed concrete bridges and numerical verification. *J of Bridge Engineering* 3(4): 159–169.
- Beck, J.L. & Katafygiotis, L.S. 1998. Updating models and their uncertainties. i: Bayesian statistical framework. *J of Engineering Mechanics* 124(4): 455–461.
- Beck, J.L. & Yuen, K.V. 2004. Model selection using response measurements: Bayesian probabilistic approach. *Journal of Engineering Mechanics* 130(2): 192–203.
- Ching, J. & Chen, Y.C. 2007. Transitional Markov chain Monte Carlo method for Bayesian model updating, model class selection, and model averaging. *J of Engineering Mechanics* 133(7): 816–832.
- Goller, B., Beck, J.L. & Schueller, G.I. 2012. Evidence-based identification of weighting factors in Bayesian model updating using modal data. *J of Engineering Mechanics* 138(5): 430–440.
- Jang J. & Smyth A. 2017. Bayesian model updating of a full-scale finite element model with sensitivity-based clustering. *Structural Control and Health Monitoring* 24(11): e2004.
- Jaynes, E.T. 2003. Probability theory: The logic of science. Cambridge: Cambridge University Press.
- Katafygiotis, L.S. & Beck, J.L. 1998. Updating models and their uncertainties. ii: model identifiability. *J of Engineering Mechanics* 124(4): 463–467.
- Kim, C.W., Chang, K.C., Kitauchi, S. & McGetrick, P.J. 2016. A field experiment on a steel Gerber-truss bridge for damage detection utilizing vehicle-induced vibrations. *Structural Health Monitoring* 15(2): 174–192.
- Lam, H.F., Yang, J.H., & Au, S.K. 2018. Markov chain Monte Carlo-based Bayesian method for structural model updating and damage detection. *Structural Control and Health Monitoring* 25(4): e2140.
- Moravej, H., Chan, T.H., Nguyen, K.D., & Jesus, A. 2019. Vibration-based Bayesian model updating of civil engineering structures applying Gaussian process metamodel. *Advances in Structural Engineering* 22(16): 3487–3502.
- Muto, M. & Beck, J.L. 2008. Bayesian updating and model class selection for hysteretic structural models using stochastic simulation. *J of Vibration and Control* 14(1-2): 7–34.
- Patelli, E., Govers, Y., Broggi, M., Gomes, H.M., Link, M., & Mottershead, J.E. 2017. Sensitivity or Bayesian model updating: a comparison of techniques using the DLR AIRMOD test data. *Archive of Applied Mechanics* 87(5): 905–925.
- Song, M., Yousefianmoghadam, S., Mohammadi, M.E., Moaveni, B., Stavridis, A. & Wood, R.L. 2018. An application of finite element model updating for damage assessment of a two-story reinforced concrete building and comparison with lidar. *Structural Health Monitoring* 17(5): 1129–1150.
- Zhou, X. Kim, C.W. Zhang, F. & Chang, K.C. 2022. Vibration-based Bayesian model updating of an actual steel truss bridge subjected to incremental damage. *Engineering Structures* 260: 114226.

Applicable schemes for the Vehicle-Bridge Interaction System Identification method

K. Yamamoto & R. Shin
University of Tsukuba, Japan

ABSTRACT: The VBISI (Vehicle-Bridge Interaction System Identification) method is a drive-by monitoring method that estimates the vehicle's and bridge's parameters and road unevenness simultaneously only from vehicle vibration and position data. The estimation process randomly assumes the mechanical parameters of vehicle and bridge, and solves two processes, namely the IEP (Input Estimation Problem) of the vehicle and the DRS (Dynamic Response Simulation) of the bridge to estimate the road unevenness. It is realized by updating the mechanical parameters by minimizing the residual of the estimated road unevenness. This paper introduces and compares the potential schemes: PSO (Particle Swarm Optimization), NM (Nelder-Mead) method and MCMC (Monte Carlo Markov Chain). The differences between these schemes are also examined numerically in this study. PSO is very efficient but needs large calculation resources, NM is very efficient and shows high accuracy, MCMC is very costly but gives the reliable.

1 INTRODUCTION

1.1 *Research background of this study*

As more bridges are constructed in many countries, the maintenance cost is also expected to be higher. Thus, many researchers in this field are intensively developing technologies for easy bridge inspections. One possible option is DBM (Drive-by Bridge Monitoring).

At the beginning of the development of DBM technologies, Y.B. Yang's Indirect Approach (2004) has inspired many proposed methods. This method uses vibration sensors installed on the traveling vehicle and extracts the bridge natural frequencies only from the measured vertical acceleration vibrations of the traveling vehicle. Yang et al. have verified the applicability of their method analytically (Yang, 2004), numerically (Yang & Chang, 2009) and experimentally (Ling & Yang, 2005). According to the existing studies (Yang & Chang, 2009), the estimation accuracy of the first natural frequency has been improved, but the technical issues remain in the estimation of the second and higher natural frequencies that are expected to be sensitive to bridge damages.

On the other hand, this study focuses on and extends Nagayama's method (Zhao et. al, 2019); (Xue, 2020): Nagayama's method estimates road roughness only from vehicle vibration data. First, they randomly assume the mechanical parameters of the vehicle and compose the Kalman Filter for the equation of motion of the vehicle. The Kalman Filter applied to the vehicle vibration data can estimate the road profiles as the inputs of the front and rear wheels. Spatial-synchronization of the estimated road profiles is expected to return two same road roughness under the condition that the randomly-assumed mechanical parameters match the correct values. The residual between the synchronized road roughness of the front and rear wheels can be used as the objective function to find the correct vehicle mechanical parameters. The combination of the mechanical parameters that gives the smallest residual can be that of the correct values of the vehicle. According to the previous study, the residual can be evaluated in the frequency domain, and the estimation accuracy for road roughness is not bad.

The advantages of Nagayama's method are as follows: 1) the mechanical parameters of the vehicle can be estimated. The inspectors do not need to calibrate the vehicle system in advance. 2) The inputs of the vehicle can be estimated. Even if bridges are on the route, the estimated inputs should include the bridge vibration components. The mechanical parameters of the bridge can be estimated as well as those of the vehicle.

The authors have already proposed the method (Yamamoto et al., 2022), called the VBISI (Vehicle-Bridge Interaction System Identification) method, for estimating all mechanical parameters of a traveling vehicle and a monitored bridge and road roughness by extending Nagayama's method (Xue, 2020). This method is composed of two procedures: 1) IEP (Input Estimation Problem) of the vehicle, and 2) DRS (Dynamic Response Simulation) of the bridge. First, the proposed method randomly assumes the mechanical parameters of the vehicle-and-bridge system. Next, substituting the assumed parameters and measured data of the vehicle acceleration vibrations into IEP and DRS, the road profiles of the front and rear wheels are estimated. Then, the residual between the spatially-synchronized estimated road profiles can be calculated. Repeating these processes from randomly assuming the parameters, the mechanical parameters are expected to converge.

However, examining the optimization methods is still a technical issue in this study. The easiest scheme is the MCMC (Monte Carlo Markov Chain) method (Yamamoto et al., 2022). This method is an idea that assumes many particles at once in the solution space, of which each axis indicates a mechanical parameter, and changes their position slightly to lower residual. The particles would randomly travel in the multidimensional solution space to search for the lowest residual. The MCMC method can consume computation resources.

The second option is the PSO (Particle Swarm Optimization) method (Kennedy, 1995); (Mat-sushita, 2010). This method is also a Monte Carlo-based method, in which the particles travel towards the global and local best points with inertia velocities. The convergence ratio of this method is expected to be much faster than MCMC, but it is necessary to set the hyperparameters.

The third option is the NM (Nelder-Mead) method (Nelder & Mead, 1995); (Gao, 2012). This algorithm is known as a fast and accurate optimization scheme. The particles geometrically search the minimum residual point in a large solution space.

1.2 The purpose and methodology of this study

This paper compares the MCMC, PSO and NM methods and discusses the applicability of these algorithms to the VBISI method. The numerical simulation is also done to obtain the vehicle vibration data as the measured data.

2 BASIC THEORY

2.1 Vehicle-Bridge Interaction system

Consider a vehicle system shown in Figure 1. The vehicle body is modeled as a rigid body with mass m_s and inertia I_s . The suspensions of the front ($i=1$) and rear ($i=2$) axles are respectively composed by springs k_{si} and dashpot c_{si} . The i -th unsprung-mass m_{ui} is connected with the sprung rigid body (m_s, I_s) by the i -th suspension (k_{si}, c_{si}) and with the road pavement by the i -th wheel modeled by spring k_{wi} . Let $x_i(t)$ and $x_G(t)$ be the positions of the front wheel ($i=1$), the rear wheel ($i=2$), and the Gravity center G of the vehicle body, respectively. They are time function but the distance is constant. Letting d_i be the distance from G to axel i , the equation of motion of the vehicle can be expressed as:

$$\mathbf{M}_v \ddot{\mathbf{w}}_v(t) + \mathbf{C}_v \dot{\mathbf{w}}_v(t) + \mathbf{K}_v \mathbf{w}_v(t) = \mathbf{f}_v \quad (1)$$

where

$$\mathbf{M}_v = \begin{bmatrix} \frac{m_{s1}}{d_1+d_2} & \frac{m_{s2}}{d_1+d_2} & \mathbf{0} \\ \mathbf{0} & m_{u1} & 0 \\ 0 & 0 & m_{u2} \end{bmatrix}, \quad (2)$$

$$\mathbf{C}_v = \begin{bmatrix} c_{s1} & c_{s2} & -c_{s1} & -c_{s2} \\ d_1 c_{s1} & -d_2 c_{s2} & -d_1 c_{s1} & d_2 c_{s2} \\ -c_{s1} & 0 & c_{s1} & 0 \\ 0 & -c_{s2} & 0 & c_{s2} \end{bmatrix}, \quad (3)$$

$$\mathbf{K}_v = \begin{bmatrix} k_{s1} & k_{s2} & -k_{s1} & -k_{s2} \\ d_1 k_{s1} & -d_2 k_{s2} & -d_1 k_{s1} & d_2 k_{s2} \\ -k_{s1} & 0 & k_{s1} + k_{u1} & 0 \\ 0 & -k_{s2} & 0 & k_{s2} + k_{u2} \end{bmatrix}, \quad (4)$$

$$\mathbf{w}_v(t) = \begin{Bmatrix} w_{s1}(t) \\ w_{s2}(t) \\ w_{u1}(t) \\ w_{u2}(t) \end{Bmatrix}, \quad (5)$$

and

$$\mathbf{w}_v(t) = \begin{Bmatrix} w_{s1}(t) \\ w_{s2}(t) \\ w_{u1}(t) \\ w_{u2}(t) \end{Bmatrix}. \quad (6)$$

The mass components m_{s1} and m_{s2} are

$$m_{s1} = \frac{d_2 m_s}{d_1 + d_2}, \quad (7)$$

and

$$m_{s2} = \frac{d_1 m_s}{d_1 + d_2}. \quad (8)$$

The loads acting on this vehicle system are produced by the input profile:

$$\mathbf{f}_v = \begin{Bmatrix} 0 \\ 0 \\ k_{u1} u_1(t) \\ k_{u2} u_2(t) \end{Bmatrix}. \quad (9)$$

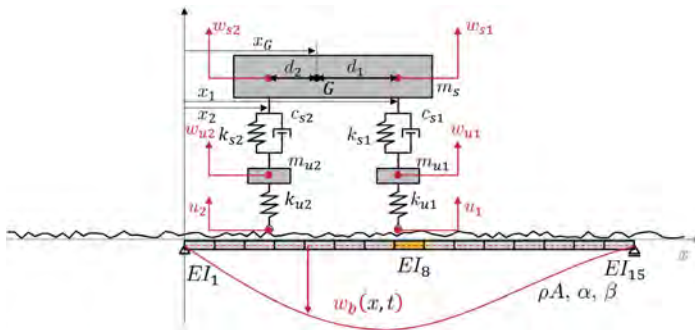


Figure 1. Vehicle and Bridge model.

On the other hand, as shown in Figure 1, the bridge girder is modeled as an Euler-Bernoulli beam, of which mass per unit length is $\rho A(x)$ and flexural rigidity is $EI(x)$. The following equation can express the equation of motion of a bridge:

$$\rho A \ddot{w}_b(x, t) + \frac{\partial^2}{\partial x^2} \left(EI \frac{\partial^2 w_b}{\partial x^2} \right) = \sum_{k=1}^n \delta(x - x_k) P_k(t) \quad (10)$$

where $w_b(x, t)$ represents deflection of the bridge. In Figure 1, the downward deflection of the bridge is drawn as positive, but note that all mathematical expressions in this paper are written assuming that the upward deflection is positive. $P_k(t)$ is an external force acting on the bridge at $x = x_k$. In this formula, $\delta(x)$ is the Dirac's delta function. Applying FEM (Finite Element Method) to this formula, Equation 2 becomes:

$$\mathbf{M}_b \ddot{\mathbf{w}}_b(t) + \mathbf{C}_b \dot{\mathbf{w}}_b(t) + \mathbf{K}_b \mathbf{w}_b(t) = \mathbf{f}_b \quad (11)$$

where \mathbf{M}_b , \mathbf{C}_b and \mathbf{K}_b represent the mass, damping and stiffness matrices of the bridge, respectively. $\mathbf{w}_b(t)$ is the deflection vector, and $\mathbf{f}_b(t)$ is the external force vector. \mathbf{C}_b is Rayleigh damping ($\mathbf{C}_b = \alpha \mathbf{M}_b + \beta \mathbf{K}_b$). The stiffness of k -th element is given by EI_k . This paper assumes that ρA is constant. In this process, introducing the basis function vector $N(x)$, the bridge deflection can be approximated by $w_b(x, t) = N(x) \cdot \mathbf{w}_b(t)$. Thus, applying the Galerkin method, the Finite Element matrices can be given by:

$$\mathbf{M}_b = \int_0^L N N^T dx, \quad (12)$$

and

$$\mathbf{K}_b = \int_0^L \frac{\partial^2 N}{\partial x^2} \frac{\partial^2 N^T}{\partial x^2} dx. \quad (13)$$

In the VBI system considered in this study, the external forces are only the traffic loads, and the reaction forces acting at the supports. The traffic loads can be given by the following formula:

$$\mathbf{f}_b(t) = \mathbf{L}(t) \mathbf{p}(t) \quad (14)$$

where

$$p_i(t) = k_{ui}(w_{ui} - u_i) = -m_{si}(\ddot{w}_{si} + g) - m_{ui}(\ddot{w}_{ui} + g), \quad (15)$$

$$\mathbf{L}(t) = [N(x_1(t)) \ N(x_2(t))]. \quad (16)$$

The following equation can give the input profiles of the traveling vehicle:

$$\mathbf{u}(t) = \mathbf{r}(t) + \mathbf{L}^T(t) \mathbf{w}_b(t), \quad (17)$$

where $\mathbf{r}(t)$ and $\mathbf{L}^T(t) \mathbf{w}_b(t)$ denote the road profile and bridge profile, respectively. The bridge profile indicates the bridge deflection under the wheels. As the vehicle position changes, the component of the bridge displacement under the wheel $w_b(x_i(t), t)$ is a time function and FEM makes it $\mathbf{L}^T(t) \mathbf{w}_b(t)$. The road profile satisfies that $r_i(t) = R(x_i(t))$, where $R(x)$ is the road roughness as a spatial function.

By solving Equation 1, the dynamic responses of the vehicle and the bridge can be simulated.

2.2 The VBISI method

This study proposes the VBISI method that identifies all mechanical parameters of VBI system: m_s , c_{si} , k_{si} , m_{ui} , k_{ui} , x_i , ρA , EI_k , α , β and estimate the road roughness $R(x)$. The VBISI method solves the vehicle's IEP and the bridge's DRS to estimate road profiles $\mathbf{r}(x)$. The vehicle's IEP can be solved by introducing Kalman Filter, while the bridge's DRS can be solved by the Newmark- β method. Assuming that the mechanical parameters \mathbf{X} can be expressed as:

$$\mathbf{X} = [c_{s1}, k_{s1}, c_{s2}, k_{s2}, m_{u1}, m_{u2}, k_{u1}, k_{u2}, d_1, \rho A, EI_1, EI_2, \dots, EI_{15}, \alpha, \beta], \quad (18)$$

where $d_1 = x_1 - x_G$. Each value of \mathbf{X} indicates each axis of the solution space. The objective function is:

$$J(\mathbf{X}) = \int_0^L (R_1(x) - R_2(x))^2 dx \quad (19)$$

where $R_i(x)$ is the spatial synchronized estimate from $r_i(t)$:

$$R_i(x_i(t)) = r_i(t) \quad (20)$$

As optimization algorithm to change \mathbf{X} to minimize the value of $J(\mathbf{X})$, the MCMC, PSO, and Nelder Mead methods are compared.

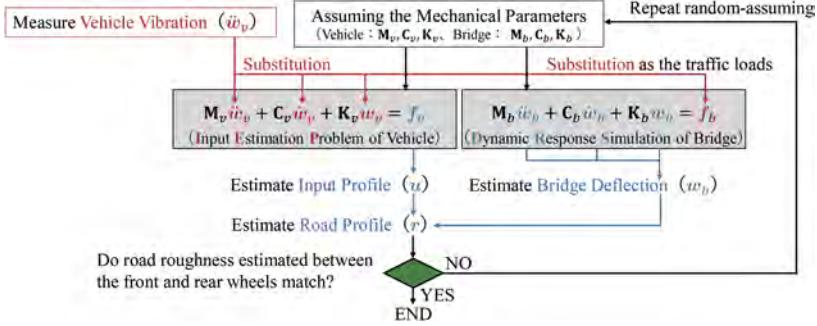


Figure 2. The algorithm of the VBISI method.

2.3 The MCMC method

The MCMC (Monte Carlo Markov Chain) model is called the Random Walk problem. Each particle is put in the space of $(\mathbf{X}^{(i)}, J^{(i)})$ and randomly tries to change the position $\mathbf{X}^{(i)}$. If the next position $\mathbf{X}^{(i)} + \Delta\mathbf{X}$ has a lower height $J(\mathbf{X}^{(i)} + \Delta\mathbf{X}) < J(\mathbf{X}^{(i)})$, the particle $\mathbf{X}^{(i)}$ must move to the next position $\mathbf{X}^{(i)} + \Delta\mathbf{X}$. On the other hand, if the next height is higher than the current height ($J(\mathbf{X}^{(i)} + \Delta\mathbf{X}) \geq J(\mathbf{X}^{(i)})$), it is probabilistically decided whether the particle moves or not. As the number of variables to be identified is large, particles in the latter case never move (Yamamoto et. al, 2022) to converge the process quickly.

2.4 The PSO method

The PSO (Particle Swarm Optimization) method is inspired by the movement of flocks of birds. This method is very similar to the MCMC method, but the position increment $\Delta\mathbf{X}$ is not randomly decided. Each particle $\mathbf{X}^{(i)}$ is set randomly first and moves in the solution space, remembering the best position the particle passes and referring to the best position among all particles. The former and the latter are called “Local Best” $\mathbf{L}^{(i)}$ and “Global Best” \mathbf{G} , respectively. The increment at the k -th step is given by the following formula:

$$\Delta\mathbf{X}_k^{(i)} = \alpha\Delta\mathbf{X}_{k-1}^{(i)} + \beta(\mathbf{L}_k^{(i)} - \mathbf{X}_k^{(i)}) + \gamma(\mathbf{G}_k^{(i)} - \mathbf{X}_k^{(i)}) \quad (21)$$

2.5 The NM method

The NM (Nelder-Mead) method (Nelder & Mead, 1995); (Gao, 2012) is also a kind of Monte Carlo simulation, but the most likely point is searched geometrically. First, several particles are randomly set in the solution space. Next, the NM method evaluates J of the geometric points calculated from the generated particles. The geometric points indicate centroids and internal/external points on the line connecting the tentative optimal point and the next point.

3 NUMERICAL EXPERIMENT

3.1 Vehicle-bridge interaction system model for numerical simulation

The mechanical parameters of the vehicle and bridge models are shown in Table 1. The dynamic simulation of the VBI system with these values is implemented by adopting the Newmark- β method. The road roughness $R(x)$ introduced in this simulation is shown in Figure 3.

Table 1. The mechanical Parameters of the Vehicle and Bridge models for numerical simulation.

Body	Mass	m_s	8310 [kg]	Front Tire	Mass	m_{u1}	469 [kg]
	Front from G	d_1	1.215 [m]		Stiffness	k_{u1}	4,790,000 [kg/s ²]
	Rear from G	d_2	2.175 [m]		Rear Tire	Mass	m_{u2}
Front Suspension	Damping	c_{s1}	24,200 [kg/s]	Mass per unit length	Stiffness	k_{u2}	4,310,000 [kg/s ²]
	Stiffness	k_{s1}	456,000 [kg/s ²]		Flexural Rigidity	ρA	4400 [kg/m]
Rear Suspension	Damping	c_{s2}	29,000 [kg/s]	Rayleigh Damping	EI_i	1.56×10^{11} [Nm ²]	
	Stiffness	k_{s2}	431,000 [kg/s ²]		α	0.7024	
					β	0.0052	

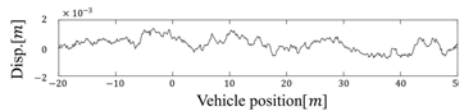


Figure 3. Road roughness.

3.2 Simulated responses

The simulated vibrations of the VBI system are obtained as shown in Figure 4. This study takes the simulated acceleration vibrations of the vehicle, which are shown in Figure 4 (a), as the measured data. By applying the VBISI method to these vehicle vibration data, we can estimate the road roughness and the mechanical parameters of the vehicle and bridge simultaneously.

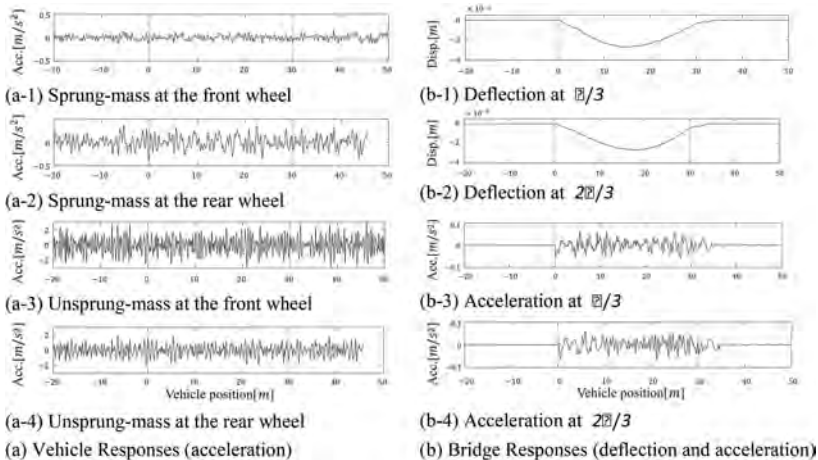


Figure 4. Simulated vibrations.

4 RESULTS AND DISCUSSION

4.1 Application of the MCMC method

The MCMC method for the VBISI method is easy to code but is less computationally efficient and less accurate. This method prepares many particles and lets them search for the optimal combination of the mechanical parameters randomly in the solution space. As the solution space has a large dimensionality, the probability of reaching the optimal solution is expected to be low.

By applying the MCMC method to the measured vehicle vibration data, the result shown in Table 2 is obtained. As the estimated values are normalized by the correct values, 1.0 indicates the correct value. The accuracy of the prior information is 20%, 0.8 and 1.2 indicate that the corresponding parameter cannot be estimated. According to this table, the accuracy of vehicle body mass m_{s1} and m_{s2} is reasonable, while others are not accurate.

Table 2. The estimation accuracy of the VBISI method powered by the MCMC method.

	mean	std		mean	std		mean	std
m_{s1}	0.989	0.025	EI_1	0.998	0.151	EI_{11}	1.010	0.128
m_{s2}	0.973	0.088	EI_2	0.961	0.125	EI_{12}	0.978	0.149
c_{s1}	1.059	0.208	EI_3	1.026	0.170	EI_{13}	1.033	0.150
c_{s2}	1.086	0.265	EI_4	1.021	0.123	EI_{14}	0.950	0.137
k_{s1}	1.103	0.237	EI_5	1.018	0.123	EI_{15}	0.999	0.138
k_{s2}	0.900	0.275	EI_6	1.060	0.146	ρA	0.980	0.132
m_{u1}	1.154	0.225	EI_7	1.018	0.127	α	0.981	0.324
m_{u2}	1.078	0.220	EI_8	0.983	0.136	β	1.063	0.331
k_{u1}	1.188	0.192	EI_9	1.014	0.132			
k_{u2}	1.155	0.265	EI_{10}	1.044	0.111			

4.2 Application of the PSO method

The PSO method is also based on the Monte Carlo algorithm, which is less computationally efficient. The estimation accuracy is expected to depend on the initial particle position; if one particle is generated near the optimal solution in the initial step, the particles can efficiently search for the optimal solution.

The result of the PSO method is shown in Table 3. According to this table, the standard deviation of each parameter decreases from that obtained from the MCMC method. The mean of each parameter is also closer to the correct value. This means that the PSO method can improve the efficiency of the VBISI method.

Table 3. The estimation accuracy of the VBISI method powered by the PSO method.

	mean	std		mean	std		mean	std
m_{s1}	0.989	0.009	EI_1	1.003	0.042	EI_{11}	1.006	0.047
m_{s2}	1.024	0.030	EI_2	1.002	0.056	EI_{12}	1.012	0.041
c_{s1}	1.001	0.085	EI_3	0.987	0.035	EI_{13}	1.007	0.039
c_{s2}	1.009	0.107	EI_4	1.009	0.041	EI_{14}	1.005	0.047
k_{s1}	1.053	0.100	EI_5	0.995	0.053	EI_{15}	0.996	0.046
k_{s2}	0.974	0.084	EI_6	0.998	0.056	ρA	0.995	0.027
m_{u1}	1.040	0.088	EI_7	0.996	0.046	α	0.980	0.135
m_{u2}	0.993	0.089	EI_8	1.007	0.042	β	1.012	0.123
k_{u1}	1.055	0.086	EI_9	1.002	0.046			
k_{u2}	1.020	0.097	EI_{10}	0.998	0.046			

4.3 Application of the NM method

The results of the NM method are also shown in Table 4. The results show that the estimation accuracy for all parameters is superior to the other schemes. The accuracy of the stiffness at both ends of the bridge decreased slightly. This can be due to the small amplitude at the bridge ends.

Table 4. The estimation accuracy of the VBISI method powered by the Nelder Mead method.

	mean	std		mean	std		mean	std
m_{s1}	0.997	0.007	EI_1	1.001	0.100	EI_{11}	0.999	0.008
m_{s2}	0.985	0.020	EI_2	1.001	0.080	EI_{12}	0.991	0.012
c_{s1}	0.984	0.088	EI_3	1.046	0.053	EI_{13}	1.005	0.018
c_{s2}	1.036	0.060	EI_4	0.966	0.035	EI_{14}	1.011	0.033
k_{s1}	1.033	0.093	EI_5	1.005	0.010	EI_{15}	0.962	0.097
k_{s2}	1.021	0.057	EI_6	1.012	0.014	ρA	1.005	0.005
m_{u1}	1.029	0.092	EI_7	0.998	0.006	α	1.084	0.229
m_{u2}	1.047	0.060	EI_8	0.996	0.008	β	0.967	0.070
k_{u1}	1.035	0.093	EI_9	0.995	0.010			
k_{u2}	1.069	0.062	EI_{10}	1.011	0.007			

5 CONCLUSION

This paper applies three different algorithms to the optimization process of the VBISI method: The MCMC method, the PSO method, and the NM method. The best efficient and accurate method is the NM method. The MCMC method is less efficient and less accurate. The accuracy of the PSO method depends on the initial positions of particles. The result of this study indicates that the NM method is the most promising option, but it should be improved.

The VBISI method is an extension of Nagayama’s method for road surface estimation so that it can also identify bridge parameters. The novelty and originality of the VBISI method lie in the ability to inspect the bridge. However, the estimation accuracy of the NM method for bridge parameters is not enough for inspection. An obstacle to improving accuracy is a lack of computational power. If more computational resources are invested, it can be expected that the final result will be more accurate. However, considering that the analysis of big data obtained from many vehicles and bridges is expected in the future, it is unrealistic to increase the number of computational resources to be used without limit. Thus, a quick algorithm, like a non-Monte Carlo optimization algorithm, must be developed.

REFERENCES

- Gao, F. & Han, L., 2012. Implementing the Nelder-Mead simplex algorithm with adaptive parameters. *Computational Optimization and Applications*, 51(1),259–277.
- Kennedy, J. & Eberhart, R.C., 1995. Particle swarm optimization, *Proc. of IEEE International Conference on Neural Networks*, 1942–1948.
- Ling, C.W. & Yang, Y.B., 2005. Use of a passing vehicle to scan the fundamental bridge frequencies: An experimental verification. *Engineering Structures*, 27, 1865–1878.
- Matsushita, H., Nishio, Y. & Saito, T., 2010. Particle swarm optimization with novel concept of complex network, *Proc. of International Symposium on Nonlinear Theory and its Applications, Krakow*, 5-8 September 2010. Poland.
- Nelder, J.A. & Mead, R., 1965. A simplex method for function minimization. *The computer journal*, 7 (4),308–313.
- Yamamoto, K., Fujiwara, S., Tsukada, K., Shin R. & Okada, Y., 2022. Numerical Studies on Bridge Inspection using Data obtained from sensors on vehicle, *Proc. of 13th International Workshop on Structural Health Monitoring, Stanford University*, 7-9 December 2021. CA: USA.
- Yang, Y.B., Lin, C.W. & Yau, J.D., 2004. Extracting bridge frequency from the dynamic response of a passing vehicle. *Journal of Sound and Vibration*, 272, 471–493.
- Yang, Y.B. & Chang, K.C., 2009. Extracting the bridge frequencies indirectly from a passing vehicle, Parametric study. *Engineering Structures*, 31, 2448–2459.
- Xue, K., Nagayama, T. & Zhao, B., 2020. Road profile estimation and half-car model identification through the automated processing of smartphone data, *Mechanical Systems and Signal Processing*, 142, 106722.
- Zhao, B., Nagayama, T. & Xue, K., 2019. Road profile estimation and its numerical and experimental validation by smartphone measurement of the dynamic responses of an ordinary vehicle, *Journal of Sound and Vibration*, 457, 92–117.

Risk-based resilience assessment framework for thermal power plants after a catastrophic seismic event

A. Yuyama

Central Research Institute of Electric Power Industry, Abiko, Chiba, Japan

G. Shoji

University of Tsukuba, Tsukuba, Ibaraki, Japan

Y. Kajitani

Kagawa University, Takamatsu, Kagawa, Japan

ABSTRACT: This paper presents a framework to assess the seismic resilience of thermal power plants, which can be applied for power shortage risk analysis during earthquakes and the subsequent recovery process. The key issue of the proposed framework is that in addition to seismic damage and recovery assessment of power plants, we consider operational risk that could cause unscheduled outage of plants. In a situation where multiple power plants are shut down after a catastrophic seismic event, we need to ensure power generation capacity by operating the remaining power plants efficiently and unexpected shut down of plants due to equipment failures could cause power shortage immediately. The effectiveness of the proposed framework is validated throughout the application to an anticipated earthquake scenario.

1 INTRODUCTION

In recent years, due to the increasing complexity of power system and exacerbation of natural disasters, power outage risks have been evolving on an unprecedented scale (Panteli & Mancarella 2015, Bie et al. 2017). In particular, though power plants are generally well-designed against seismic hazards, the shutdown of them due to earthquakes can have a serious impact on the stable supply of electric power because once they suffer from the severe seismic damage, it takes a longer time to resume operations (Karagliannis et al. 2017, Nicolas et al. 2019). Recently, the typical examples have occurred in rapid succession in Japan, namely the 2011 off the Pacific coast of Tohoku earthquake (M_w 9.0), the 2018 Hokkaido Eastern Iburi earthquake (M_w 6.6) and the 2022 Fukushima-oki earthquake (M_w 7.3). These cases gave us some important insights into natural disaster risk of power supply system such as 1) the diversity of both physical damage and recovery process of facilities caused by simultaneous damages over a wide area, 2) the potentiality of cascading failures across the whole power system triggered by some facility damages, and 3) the possibility of compound risks due to superimposition of natural disasters and component failures. In order to understand the complicated impact of such large-scale disasters on power grid and discuss effective countermeasures, it is necessary to develop an integrated risk assessment framework for the entire power system, including both supply (generation, transmission, transformation and distribution facilities) and demand system. Numerous studies have been devoted for this issue as reviewed in Wang et al. (2016) and Bhusal et al. (2020). In this paper, as a contribution to such systemic analysis, we propose a framework for supply capacity evaluation of thermal power plants after a catastrophic seismic event.

Thermal power plants are a stable power source whose importance in ensuring the reliability of the power supply system has been reaffirmed in recent years. This is because they have still maintained their position as the main power source in worldwide (IEA 2021) and are expected to play

a role as a flexible regulator to cope with fluctuations in the output of renewable energy generation, which has increased rapidly in these days (Kubik et al. 2012, Eser et al. 2016). However, while various approaches have been taken to clarify the seismic vulnerability and performance of components and buildings composed of thermal power plant such as field surveys (e.g. Stevenson 1995, Koizumi et al. 2014), experimental tests (e.g. Chiba & Fujita 2004) and response analysis (e.g. Wang et al. 2018), their general resilience as power generation function after a seismic event is not well understood. The one reason for this is that thermal power plants are complex systems consisting of a wide variety of facilities across the fields of civil engineering, architecture, and machinery, therefore, it is difficult to define the fragility of all constitutive components and model the internal logic between the performance of individual components and their power generation functions. For example, Rahman & Edwards (2015) proposed a method for probabilistically predicting the recovery duration of coal-fired power plant after earthquakes by modeling plant system as a network with individual component as nodes and the flow of goods and services among components as links, and then defining fragility and recovery curves for each facility. Hamed et al. (2022) developed a hybrid simulation framework to assess the post-earthquake production capacity of a thermal power plant using system dynamics to assess the production capacity under a certain damage condition of components and agent-based model to evaluate the allocation of resources and recovery process. All of these studies take a so-called “bottom-up approach”, allowing cost-benefit analysis of differences in system configurations and restoration strategies, but on the other hand, they have not been verified using actual earthquake experience data.

In assessing power generation capacity after a seismic event, the primary procedure is to estimate the physical damage and their repair time of individual power plant caused by the earthquake as focused on the previous studies. In addition, in the situation where multiple power plants shutdown simultaneously, power supply and demand balance can become tight and it results in high burden concentration on available power plants, such as those of unaffected or those have been restored earlier. It is pointed out that these heavy reliance on the certain power plants can increase the risk of “unscheduled outage”, which means the unexpected shutdown or output suppression due to component malfunction or emergency repair. Therefore, in order to evaluate the total power generating capacity during the recovery process from immediately after a large-scale earthquake, we need to re-defined the whole process as “compound disaster” where the burden on the “power generation system” consisting of the multiple thermal power plants will increase in a chain reaction triggered by the physical damage caused by the

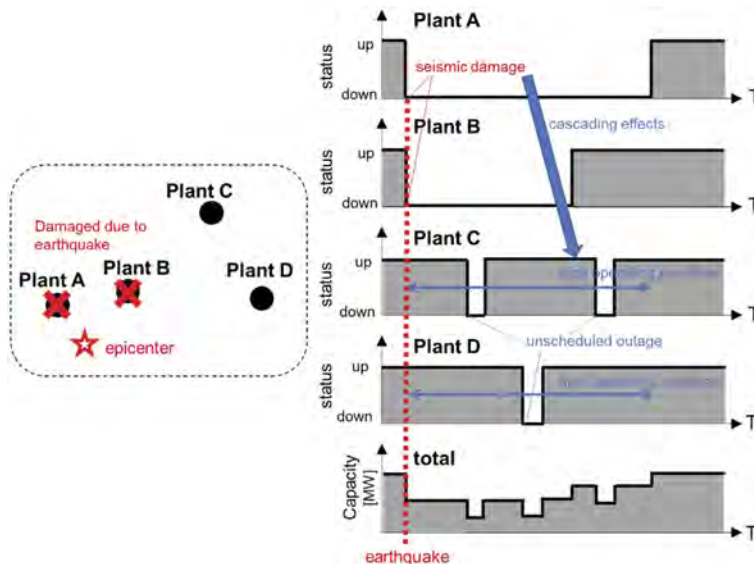


Figure 1. Post-earthquake power generation capacity and the concept of “compound disaster”.

earthquake (Figure 1). In this study, we propose a framework to assess the total power generation capacity of thermal power plants after a seismic event considering both the direct damage and recovery of power plants due to an earthquake and unscheduled outage risk based on the analysis of the actual operational data after the 2011 off the Pacific coast of Tohoku earthquake.

2 FRAMEWORK

“Resilience triangle” is a concept theorized by Bruneau et al. (2003) to express the quality of infrastructure during and after an earthquake. When we employ the concept to the resilience of thermal power plants, it can be interpreted as the loss and subsequent recovery process of the total power generation capacity of geographically distributed multiple power plants. Figure 2 shows the actual data after the aforementioned 3 recent earthquakes in Japan. The purpose of this study is to develop the framework to estimate those curves under a scenario earthquake, defining as “total power generation capacity curve”. Specifically, as shown in Figure 3, we assume that each thermal power unit can simply take 3 different states: “up (operable)”, “down (shutdown due to an earthquake damage)” and “down (shutdown due to failure)”. The state transitions are ruled by using seismic damage and recovery model (red arrows in Figure 3) and the unscheduled outage model (blue arrows in Figure 3) that the authors developed based on the actual data of thermal power plants.

In the following, we present the models to estimate seismic damage and recovery duration of thermal power plants and the probability of unscheduled outage occurrence in 3.1 and 3.2 respectively. In 3.3, the integrated flow to evaluate the total power generation capacity curve is proposed and it is applied to an anticipated earthquake scenario and the results is summarized in section 4.

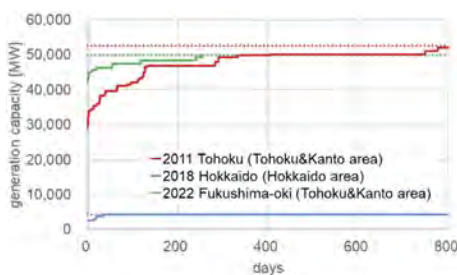


Figure 2. Total thermal power generation capacity curves of the recent major earthquakes in Japan.

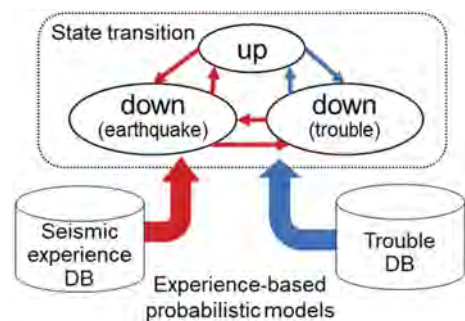


Figure 3. State transitions of thermal power units.

3 MODEL DEVELOPMENT

3.1 Seismic damage and recovery model

The 2 steps probabilistic models developed based on the statistical analysis of experience data from 29 thermal power plants affected by the 2011 off the Pacific coast of Tohoku earthquake by the authors (Yuyama & Kajitani 2014) is used to estimate the recovery time of thermal power plants due to an earthquake.

The first model is the “fragility functions” of each of typical plant sub-system. Fragility curves of each 3 damage rank (severe/ moderate/ minor) were estimated for 9 sub-systems (e.g. boiler, turbine & generator, fuel facilities), respectively. Using these functions, the probability that the damage rank of the s th plant sub-system is k at a certain ground motion level a can be calculated (Equation 1).

$$P_{i,k}(a) = \Phi\left(\frac{\ln a - \mu_{s,k}}{\sigma_s}\right) \quad (1)$$

where $P_{i,k}$ = probability that the damage rank of the i th plant sub-system is greater than or equal to k ; a = peak ground acceleration (PGA) [gal]; $\mu_{s,k}$, σ_s = parameters of fragility functions (Table 1).

The second model is “recovery function” that evaluates the probability that the recovery duration of a thermal power plant whose damage pattern of plant sub-systems is X exceeds the arbitrary value t (Equation 2).

$$G(t|X) = \Pr(T_{rcov}^{EQ} \leq t|X) = \Phi\left(\frac{\ln t - \beta X}{\sigma}\right) \quad (2)$$

where T_{rcov}^{EQ} = recovery duration from seismic damage [day]; X = damage pattern of plant sub-systems (Equation 3); σ , β = parameters of recovery functions (Equation 4).

$$X^T = \{x_{s,k}\} = \{x_{1,C}, x_{2,C}, x_{3,B}, x_{4,C}, x_{5,A}\} \quad (3)$$

where $x_{s,k}$ = binary variable that denotes if the damage rank of the s th sub-system is greater than or equal to k (1) or not (0).

$$\sigma = 0.54 \quad (4a)$$

$$\beta = [1.12 \ 1.22 \ 1.41 \ 1.30 \ 1.74] \quad (4b)$$

The most appropriate combination of sub-system and damage rank was selected using AIC as an indicator through regression analysis of the actual data on the sub-system damage patterns and the required recovery periods.

Using the presented models, this study estimates the recovery duration of a certain thermal power plant after an earthquake as below:

- (1) obtain the ground motion intensity (PGA) at the target power plant location,
- (2) estimates the damage pattern of plant sub-system using the fragility functions,
- (3) evaluates the recovery duration using the recovery function.

Table 1. Parameters of fragility functions.

Sub-system s	1. Water inlet/outlet facilities	2. Power receiving facilities	3. Boiler facilities	4. Flu gas treatment facilities	5. Service buildings
$\mu_{s,A}$	—	—	—	—	—
$\mu_{s,B}$	5.89	5.94	5.39	6.26	—
$\mu_{s,C}$	5.50	5.59	4.87	6.02	—
σ_s	0.65	0.34	0.58	0.20	—

* “—” indicates that parameter estimation did not occur due to the lack of observations.

3.2 *Unscheduled outage model*

In order to evaluate the probability of unscheduled outage of thermal power plants, we employ the experience-based models developed by the authors. The models we use in this paper are updated from the original ones (Yuyama et al. 2018) by using some additional operational data of thermal power generating units during 2011 and 2012 summer in Japan. In the paper, four models were constructed according to the type of power generation method (Conventional (abbreviated as Conv)/ Combined Cycle (CC)) and the experience of unscheduled outages during the season (First accident during the season (abbreviated as 1)/ Two or more accidents during the season (2)). The relationship between the operating period and the

probability of unscheduled outages was modeled based on the theory of survival analysis. Suppose the operational time to failure of a thermal power generation unit is D^{Acc} , the probability that a target unit has not experienced failure at the arbitrary time t is defined as Equation 5.

$$S(t) = \Pr(D^{Acc} > t) = 1 - F(t) \quad (5)$$

where $S(t)$ = a survival function; $F(t)$ = a cumulative distribution function of the failure time.

The probability that an unscheduled outage occurs at t after surviving by t is as below:

$$h(t) = \frac{f(t)}{S(t)} \quad (6)$$

where $h(t)$ = a hazard function; $f(t)$ = a probability density function of the failure time.

In addition, a proportional hazard model (Equation 7) is introduced to consider the characteristics of each unit such as age, power generation capacity and fuel type.

$$h(t) = h_0(t) \cdot r(y, \beta) \quad (7)$$

where $r(y, \beta)$ = a function of explanatory variables y and parameters β .

In the paper, $F(t)$ is assumed to be either Weibull, lognormal, gaussian, logistic or exponential distribution. Weibull distribution (Equation 8) is selected as appropriate model for Conv1, lognormal distribution (Equation 9) for Conv2, CC2 and exponential distribution (Equation 10) for CC1 using AIC.

$$F(t|\beta) = 1 - \exp\left(-\left(\frac{t}{\varphi}\right)^\gamma\right) \quad (8a)$$

$$\varphi = \exp(y'\beta) \quad (8b)$$

$$F(t|\beta) = \Phi\left(-\frac{(\ln t - y'\beta)^2}{2\sigma^2}\right) \quad (9)$$

$$F(t|\beta) = 1 - e^{-\lambda t} \quad (10a)$$

$$\lambda = \frac{1}{\exp(y'\beta)} \quad (10b)$$

The maximum likelihood estimation is adopted to determine the parameters and the results are shown in Table2.

Table 2. Parameters of unscheduled outage models.

variables x	explanations	β			
		Conv1	Conv2	CC1	CC2
Intercept		8.009	3.540	7.057	14.428
Year	2011(0)/2012(1)	-0.436	-	-	-
PWR		-0.016	0.018	-	-
LN(PWR)	generation capacity [MW]	-	-	-1.125	-4.042
Age		-0.024	-	-	-
LN(Age)	age	-	-	0.587	1.323
Oil	fuel dummy for oil	-0.909	-	-	-
Oil_LNG	fuel dummy for combination of oil & LNG	-	-	-	-
LNG	fuel dummy for LNG	-	-	2.109	4.055
Gas	fuel dummy for gas	14.637	-	19.272	-
LN(σ)		-	0.741	-	0.458
LN($1/\gamma$)		0.288	-	-	-

As for the simulation of the recovery time after the failures, a non-parametric resampling approach is adopted and the actual recovery time records in the same database collected for the estimation of unscheduled outage probability is used. More details are described in Yuyama et al. (2018).

Using the models and simulation method presented above, the occurrence and recovery of a certain thermal power generating unit after an earthquake is simulated as below:

- (1) obtain the characteristics of the target power generating unit,
- (2) estimates the operational time to failure using the unscheduled outage model,
- (3) evaluates the recovery duration based on the resampling of the actual recovery time records from the database.

3.3 Simulation of total power generation capacity

Figure 4 shows the flowchart to simulate the power generation capacity of a target thermal power plant unit under a scenario earthquake, combining the model described in section 3.1 and 3.2. The “total power generation capacity curve $C(t)$ ” of multiple thermal power plants (units) is calculated by the summation of the power generation capacity of all units whose status is “up” at time t .

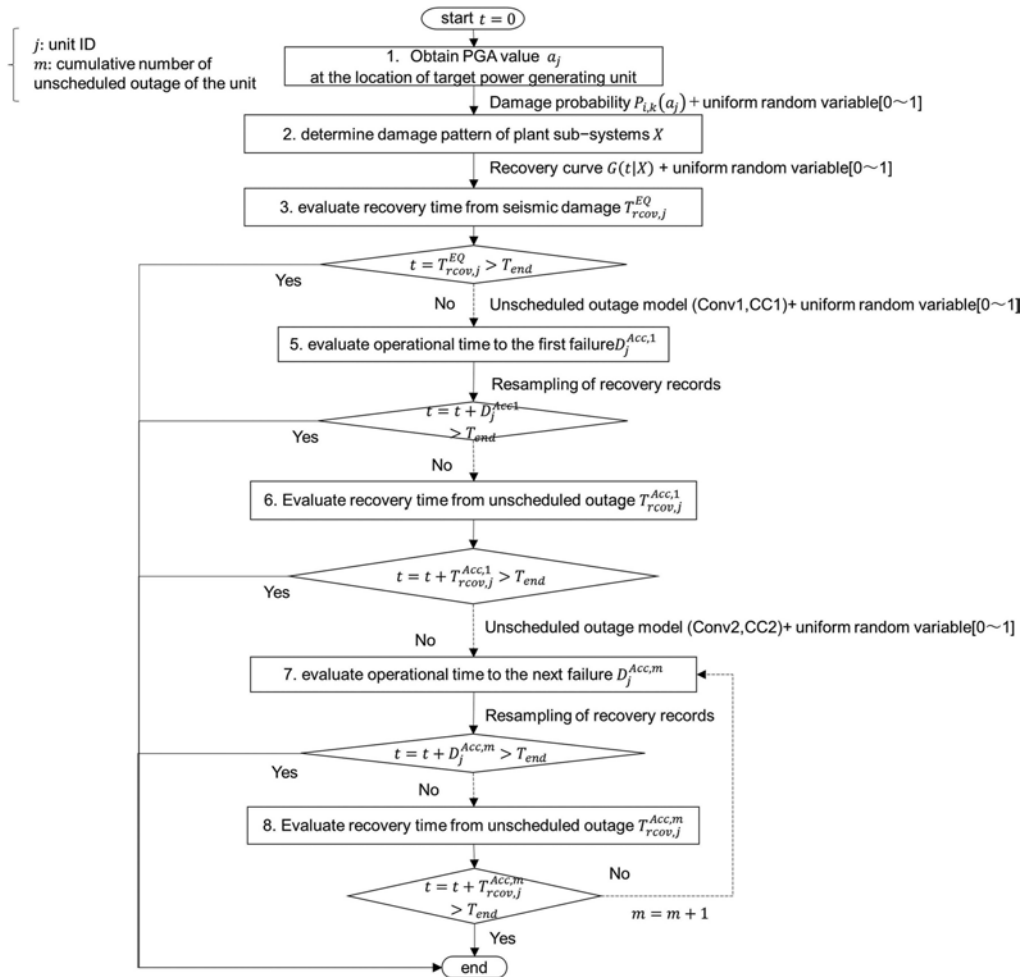


Figure 4. Flowchart to simulate generation capacity of a thermal power unit after a seismic event.

4 CASE STUDY

In this section, we simulate the total power generation capacity curve of thermal power plants after an anticipated earthquake scenario, anticipated Tokyo Metropolitan earthquakes. Figure 5 shows the distribution of seismic ground motion and the location of thermal power plants. 17 plants 92 units (total 44,330MW) located in Kanto area are included in this case study. Figure 6 shows the simulated average, maximum and minimum potential power generation curves (1,000 simulations) of the cases where only seismic damage is considered (EQ) and both the seismic damage and unscheduled outages are included (EQ+Acc). In the case considering only earthquake damage, the supply capacity immediately after the earthquake dropped to about 9,700 MW (Δ 78%) on average and it takes 77 days to secure 50% of the initial capacity (22,152MW) and 185 days for 80% . Figure 7 shows the results of evaluating the maximum difference in supply capacity for each simulation case when only earthquake damage is considered and when both seismic damage and unscheduled outages are included. In this simulation, the maximum loss of supply when multiple units experience unscheduled outages simultaneously is approximately 17% (7645MW) of the total capacity of the power plants. This suggests that the occurrence of unscheduled outages may pose an additional risk in the operation of power plants during the recovery process after an earthquake.

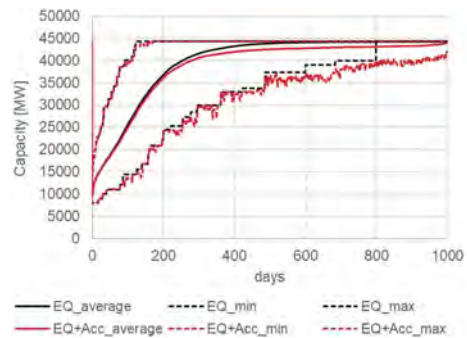
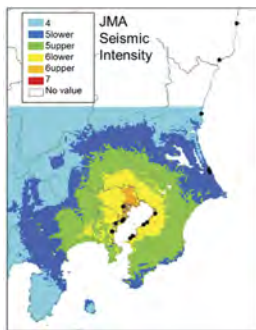


Figure 5. Distribution of ground motion intensity and the location of thermal power plants. Figure 6. Simulated power generation curves.

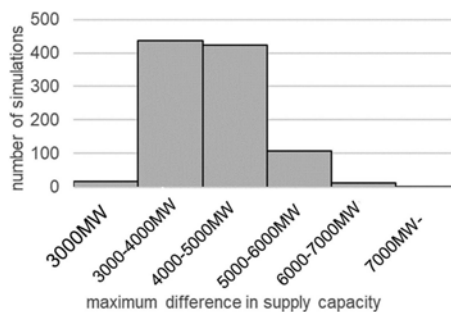


Figure 7. Maximum differences in supply capacity in each simulation.

5 CONCLUSIONS

In order to evaluate the resilience of thermal power plants to a large-scale complex disaster, this study developed a framework to simulate the potential supply capacity of thermal power plants after a scenario earthquake by integrating various models such as 1) seismic fragility

curves to predict physical damage of constitutive components in plants and 2) seismic recovery function to estimate recovery time based on the information of component damage patterns and 3) unscheduled outage model to estimate operational time to unscheduled outage, which are developed based on the damage and restoration data of thermal power plants caused by 2011 off the pacific coast of Tohoku earthquake and the operational records of thermal power plants during the subsequent high demand seasons. The application of this framework enables to evaluate various damage and restoration patterns of thermal power plant and their frequency of occurrence.

REFERENCES

- Bie, Z., Lin, Y., Li, G. & Li, F. 2017. Battling the Extreme: A Study on the Power System Resilience. Proceedings of the IEEE 105(7): 1253–1266.
- Bhusal, N., Abdelmalak, M., Kamuzaman, M. & Benidris, A.M. 2020. Power System Resilience: Current Practices, Challenges, and Future Directions. *IEEE Access* 8: 18064–18086.
- Bruneau, M., Chang, S.E., Eguchi, R.T., Lee, G.C., O'Rourke, T.D., Reinhorn, A.M., Shinozuka, M., Tierney K., Wallace, W.A. & Winterfeldt, D. 2003. A framework to quantitatively assess and enhance the seismic resilience of communities. *Earthquake Spectra* 19(4): 733–752.
- Chiba, T. & Fujita, S. 2004. Seismic proving test of equipment and structures in thermal conventional power plant. *Journal of Japan Association for Earthquake Engineering* 4(3): 457–464.
- Eser, P., Singh, A., Chokani, N. & Abhari, R.S. 2016. Effect of increased renewables generation on operation of thermal power plants. *Applied Energy* 164: 723–732.
- Hamed, M.D., Ghafory-Ashtiani, M. & Hosseini, M. 2022. Hybrid simulation modeling framework for evaluation of Thermal Power Plants seismic resilience in terms of power generation. *International Journal of Disaster Risk Reduction* 78: 103120.
- International Energy Agency. 2021. *Key World Energy Statistics 2021*. Paris: IEA Publications.
- Karagiannis, G.M., Chondrogiannis, S., Krausmann, E. & Turksezer, Z.I. 2017. *Power grid recovery after natural hazard impact*. Luxembourg: European Commission.
- Koizumi, Y., Okawa, T., Asano, H., Nakagaki, T., Inumaru, J., Inada, F. & Ozawa, M. 2014. Chapter 7 Damages to Energy Infrastructures. *Report of JSME Research Committee on the Great East Japan Earthquake Disaster*. Tokyo: The Japan Society of Mechanical Engineers.
- Kubik, M.L., Coker, P.J. & Hunt, C. 2012. The role of conventional generation in managing variability. *Energy Policy* 50: 253–261.
- Nicolas, C., Rentschler, J., Albertine, P.L., Oguah, S., Schweikert, A., Deinert, M., Koks, E., Arderne, C., Cubas, D., Li, J. & Ichikawa, E. 2019. *Stronger Power: Improving Power Sector Resilience to Natural Hazards*. Washington, DC: World Bank.
- Panteli, M. & Mancarella, P. 2015. Influence of extreme weather and climate change on the resilience of power systems: Impacts and possible mitigation strategies. *Electric Power Systems Research* 127: 259–270.
- Rahman, M. & Edwards, M. 2015. A component level approach to the earthquake vulnerability of critical infrastructure facilities. *Proc. the Tenth Pacific Conference on Earthquake Engineering Building an Earthquake-Resilient Pacific, Sydney, 6-8 November 2015*. Sydney: Australian Earthquake Engineering Society.
- Stevenson, J.D. 1995. Survey of strong motion earthquake effects on thermal power plants in California with emphasis on piping systems. Volume 1, Main report.
- Wang, J., Dai, K., Yin, Y. & Tsefamariam, S. 2018. Seismic performance-based design and risk analysis of thermal power plant building with consideration of vertical and mass irregularities. *Engineering Structures* 164: 141–154.
- Wang, Y., Chen, C., Wang, J. & Baldick, R. 2016. Research on Resilience of Power Systems Under Natural Disasters—A Review. *IEEE Transactions on Power Systems*. 31(2): 1604–1612.
- Yuyama, A. & Kajitani, Y. 2014. Estimation of damage and recovery function of thermal power plants based on the data of the 2011Tohoku Earthquake and Tsunami. *Journal of Japan Society of Civil Engineers A1* 70: 664–677. (In Japanese)
- Yuyama, A., Kajitani, Y. & Shoji, G. 2018. Simulation of operational reliability of thermal power plants during a power crisis: Are we underestimating power shortage risk?. *Applied Energy*. 231:901–913.

Non-deterministic seismic damage detection of road infrastructure analysing image training database

R. Kondo & G. Shoji

University of Tsukuba, Ibaraki, Japan

ABSTRACT: In this paper, we visually deciphered the damage to road structures in 25 aerial photographs which were taken after the 2016 Kumamoto earthquake and detected these damage modes according to the image training database of seven damage modes: road surface cave-in, road surface liquefaction, road surface cracks, road surface collapse, road surface steps, falling rocks and landslides and building debris on road surface. Specifically, texture analysis produced a histogram of six feature values: contrast, variance, skewness, kurtosis, energy and entropy, and a threshold were set to detect damage. The results presented that the coefficients of variation of kurtosis and entropy were small and effective for damage detection.

1 INTRODUCTION

The Kumamoto earthquake, which struck on April 14 and 16, 2016, severely damaged road structures. In order to prompt lifesaving and restoration activities, technology is required in identifying widespread earthquake damage for infrastructure quickly. In the detection of earthquake hazards, such as slope failure and liquefaction, Midorikawa and Miura (2010) extracted the areas of slope damage caused by the 2008 Iwate-Miyagi Nairiku earthquake from high-resolution synthetic aperture radar (SAR) images, and Rathje et al. (2017) measured the horizontal displacement owing to the liquefaction which was caused by the 2011 Canterbury earthquake from satellite images. The displacement was measured from satellite images taken before and after the earthquake using light detection and ranging (LiDAR) and optical image correlation. In terms of detecting surface faults, Gori et al. (2018) conducted field mapping from images taken by LiDAR and unmanned aerial vehicles (UAVs) during the 2016 earthquake in central Italy.

In terms of detecting damage to buildings and civil engineering structures as a result of slope failure, liquefaction, and surface fault displacement, which include seismic motion, Matsuoka and Yamazaki (2004) focused on the backscattering characteristics of the affected area in the 1995 Hyogo-ken Nambu earthquake and evaluated damage to buildings by using European Remote-Sensing Satellite (ERS) images before and after the earthquake. In terms of detecting damage to buildings, Miura et al. (2016) conducted a texture analysis by using high-resolution SAR images taken during the 2010 Haiti earthquake. A linear discriminant function based on the difference and correlation coefficient was calculated from the images taken before and after the earthquake in detecting collapsed buildings. As an example of a study focusing on earthquake damage to road surfaces, Maruyama et al. (2006) identified damage to expressways from aerial photographs taken during the 2004 Mid Niigata prefecture earthquake. Sezaki et al. (2017) attempted to automatically detect road damage from images taken by a vehicle-mounted camera during the 2016 Kumamoto earthquake. Yoshinari and Shoji (2020) identified damage to road structures from satellite images taken after the 2018 Hokkaido Iburi eastern earthquake. Kondo and Shoji (2022) attempted to identify damage to road surfaces according to the texture analysis by using aerial photographs taken during the 2016 Kumamoto earthquake.

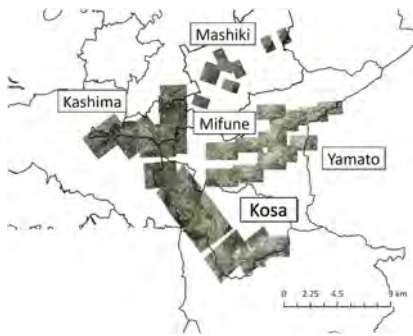


Figure 1. The spatial distribution of the aerial photographs.



Figure 2. Definition of damage modes of road surfaces.

There are various modes of seismic damage to road surfaces, and even image analysis using aerial photographs, which is more accurate, can be difficult sometimes even though many studies on the application of image analysis to earthquake damage to buildings have been conducted recently. Therefore, in this study, we examined the damage caused by the 2016 Kumamoto earthquake, attempted to detect various modes of seismic damage to road surfaces on a set of high-quality aerial photographs and discussed the accuracy of the detection.

2 AERIAL PHOTOGRAPHS AND DAMAGE MODES FOR ANALYSIS

2.1 The aerial photographs

Twenty-five aerial photographs which were taken by the Geospatial Information Authority of Japan (GSI) were used for the survey of Mashiki Town, Kashima Town, Mifune Town and Kosa Town in Kamimashiki County, Kumamoto Prefecture, which were particularly damaged by the Kumamoto earthquake. Aerial photographs were taken on April 15, 16, 20, 29 and 22 July 2016, using Ultra Cam X, Ultra Cam Xp and Digital Mapping Camera equipment. Aerial photography was taken at altitudes ranging from 1,396 to 3,366 m. The images have a resolution of 1,200 dpi and a scale of 1/10,000; thus, the length of one pixel on the ground is about 20 cm.

Figure 1 shows the spatial distribution of the aerial photographs to be analysed. There are eight aerial photographs of Mashiki Town, five of Kashima Town, two of Mifune Town and ten of Kosa Town. They have been system-corrected and ortho-rectified following the acquisition of these photographs. These corrections are made to compensate for distortions caused by the coordinates measured at the time of acquisition, distortions caused by the sensor structure, and distortions caused by height differences in topography, buildings, and other factors.

The 25 aerial photographs were used in performing a visual interpretation of road surface damage modes. Seven damage modes were defined as follows: road surface cave-in, road surface liquefaction, road surface cracks, road surface collapse, road surface steps, falling rocks and landslides, and building debris, based on the analyses of Shoji and Sakurai (2011) and Kondo and Shoji (2022). Figure 2 shows the damage modes. Cave-in is a partial collapse of the road surface that occurs primarily at the shoulder. Liquefaction is a condition in which the entire road surface sinks which results in sand and water fountains. Cracks are relatively large fractures in the road surface that can be identified from the aforementioned 1 pixel 20 cm equivalent aerial photographs. Collapse is a condition in which, in addition to road surface damage, the shoulder or slope has collapsed beyond the width of the road. Steps vary in height by 10 cm or more at expansion joints between the road and bridge girders at the abutment of bridges. Rockfall and landslide is a situation in which a road is completely or partially blocked by falling rocks or soil. Building debris is a situation in which buildings facing the road are damaged to the extent that they are completely or partially destroyed, and debris is scattered to the extent that road traffic is obstructed.

The total number of damaged locations in the 25 aerial photographs is 171. Liquefaction was the predominant damage mode at 77 locations, followed by cracks at 33 locations, steps at 26 locations, collapses at 19 locations, building debris at 10 locations, cave ins at 3 locations and rockfall and landslides at 3 locations. Figure 3 shows the visual readings of the damaged areas for CKU-2016-27_C9-6.tif, CKU-2016-27_C7-9.tif and CKU-2016-27_C5-37.tif. In a town-by-town comparison, Mashiki Town, which is closest to the epicentre, suffered the most damage. Liquefaction was the most common cause of damage for road surfaces in urban areas, while rockfall and landslides were relatively common in mountainous areas.

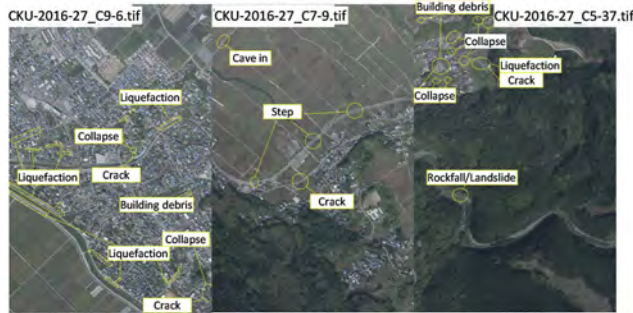


Figure 3. Visual detection for damage modes of road surfaces.

3 TEXTURE ANALYSIS

3.1 Process of construct data

The process of generating data for image analysis from aerial photographs is shown as (1) affine transformation is used in correcting the geometry; (2) rubber sheet is used to correct the positions of the aerial photograph and road edge data; (3) raster transformation is used to correct the slope of the image; (4) the aerial photograph is converted into polygons; (5) the polygons are divided into meshes that correspond to the number of pixels in the aerial photograph. From the viewpoint of the aforementioned 1-pixel accuracy, the sizes of the polygons are approximately 20 cm square. (6) By using the road edge data, the polygons of the aerial photograph are cut and divided into the road and non-road portions to obtain polygon data for the road portion only. (7) The meshes created in (5) and the polygons created in (6) are overlaid to obtain the meshed polygon data of only the road section. (8) By using the damage database created in the previous section, polygons of the damaged area are created. (9) By superimposing the road mesh created in (7) on the polygons of the damaged area created in

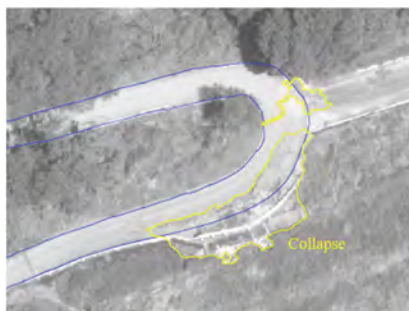


Figure 4. Monochromatized image for road surface collapse.

(8), meshed polygon data of the damaged area is created. The mesh data created in (7) and (9) are used to extract pixel data from aerial photographs for analysis.

3.2 Method of texture analysis

The monochromatized images shown in Figure 4 are considered more accurate in the detection of the various damage modes on the road surface shown in Figure 2 although the aerial photographs are RGB colour images.

$$I = 0.3R + 0.59G + 0.11B \quad (1)$$

where I is the luminance value in 256 levels as a measure of brightness, and R , G and B are the pixel value in the Red, Green and Blue channels, respectively. In order to extract damaged areas of road surfaces with high accuracy, six characteristic values, contrast (CNT), variance (VAR), skewness (SKW), kurtosis (KRT), energy (EGY) and entropy (EPY), were selected based on the findings of Yoshinari and Shoji (2020) and Haralick et al. (1973), as shown in the following equations.

$$CNT = \sum_0^{255} l^2 \cdot P(l) \quad (2a)$$

$$VAR = \sum_0^{255} (l - MEN)^2 \cdot P(l) \quad (2b)$$

$$SKW = \frac{1}{VAR^2} \sum_0^{255} (l - MEN)^3 \cdot P(l) \quad (2c)$$

$$KRT = \frac{1}{VAR^3} \sum_0^{255} (l - MEN)^4 \cdot P(l) \quad (2d)$$

$$EGY = \sum_0^{255} P^2(l) \quad (2e)$$

$$EPY = - \sum_0^{255} P(l) \cdot \log_N P(l) \quad (2f)$$

An approximation of the probability density of luminance values, $P(l)$, is used in calculating the characteristic values. $P(l)$ is represented by the histogram $H(l)$ of luminance values ($l=0\sim255$) for each pixel divided by N , the total number of pixels in the window, where MEN denotes the mean value of l . In this study, a window of height and width of 27 pixels * 27 pixels is used, so N is 729. Figure 5 shows the analysis results for the aerial photograph CKU-2016-27_C6-21.tif. The left figure shows the spatial distribution of each feature in the road area, and the right figure shows the histogram of each feature in the road area.

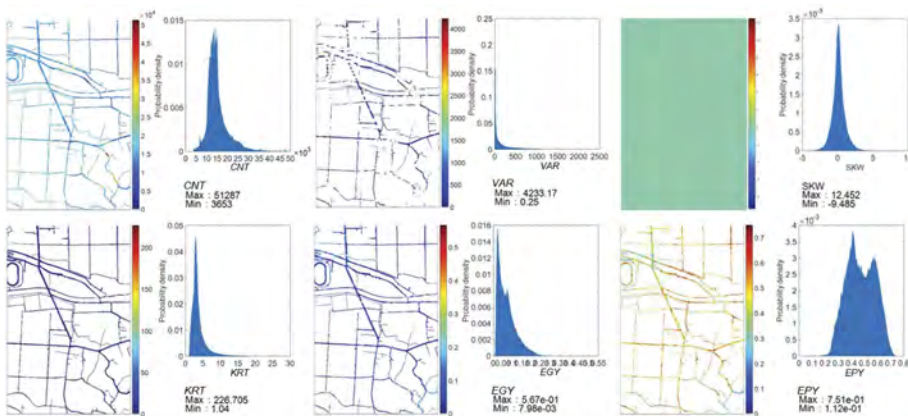


Figure 5. Spatial distribution and histogram of each characteristic value for the aerial photograph CKU-2016-27_C6-21.tif.

CNT is a quadratic moment around the origin and is considered to be effective in distinguishing damage in cases where the luminance values are low in comparison to the surrounding road areas, such as cracks and cave-ins. *SKW* represents the distortion of the distribution; however, it is unlikely to be an effective feature, and it is presented here for comparison with other characteristic values because the distortion of the histogram is not large in this analysis. *KRT* is the fourth-order moment around the mean, which represents the sharpness of the probability density function and takes a large value when the distribution is concentrated near the mean. Although *EPY* shows the opposite tendency to *EGY*, it can distinguish liquefaction damage from the same viewpoint as *EGY*.

4 CALCULATION OF THRESHOLD AND DAMAGE DETECTION

4.1 Calculation of threshold

Threshold values are calculated according to the least-squares method from the characteristic values in the damaged area of aerial photographs as follows.

$$d_i = c_t - c_i \quad (3a)$$

$$D = \sum_{i=1}^N d_i^2 \quad (3b)$$

A provisional threshold c_t is determined by using Equation (3a), and for every 1~Nth damaged road pixel in the damaged area, the difference d_i between the provisional threshold and the characteristic values c_i is calculated. The threshold value is the feature value which is obtained when the sum of the squares of the differences D is the smallest for all damaged road pixels. For each characteristic value, 25 aerial photographs were used in calculating the threshold value, and the threshold value with guaranteed accuracy was adopted. Table 1 shows the mean, standard deviation (SD), and coefficient of variation (COV) of the threshold value for each feature. Table 1 shows that the coefficients of variation of *KRT* and *EPY* are 0.1838 and 0.1148, respectively, which are smaller than the coefficients of variation of 20% of other features, which indicate that these features are effective in distinguishing damage.

Table 1. Mean, standard deviation (SD) and coefficient of variation (COV) of the thresholds.

	<i>CNT</i>	<i>VAR</i>	<i>SKW</i>	<i>KRT</i>	<i>EGY</i>	<i>EPY</i>
Mean	13280	504.2	0.233	3.89	0.0381	0.572
SD	4783	341.4	0.475	0.715	0.0180	0.066
COV	0.3602	0.6772	2.0427	0.1838	0.4723	0.1148

4.2 Method of damage detection

We discuss the valid features and ranges of damage detection by using the average values of the thresholds shown in Table 1. Damage detection is performed by identifying pixels within the range of the damaged area in the following four cases assuming a coefficient of variation of 0.05 and 0.1: (1) 10% positive and negative, (2) 10% positive, (3) 10% negative, and (4) 5% positive and negative.

4.3 Consideration for result

Damage detection was performed on 25 aerial photographs, and the accuracy was checked visually. In cases (2) 10% positive and (4) 5% positive and negative, 22 of the 25 images produced

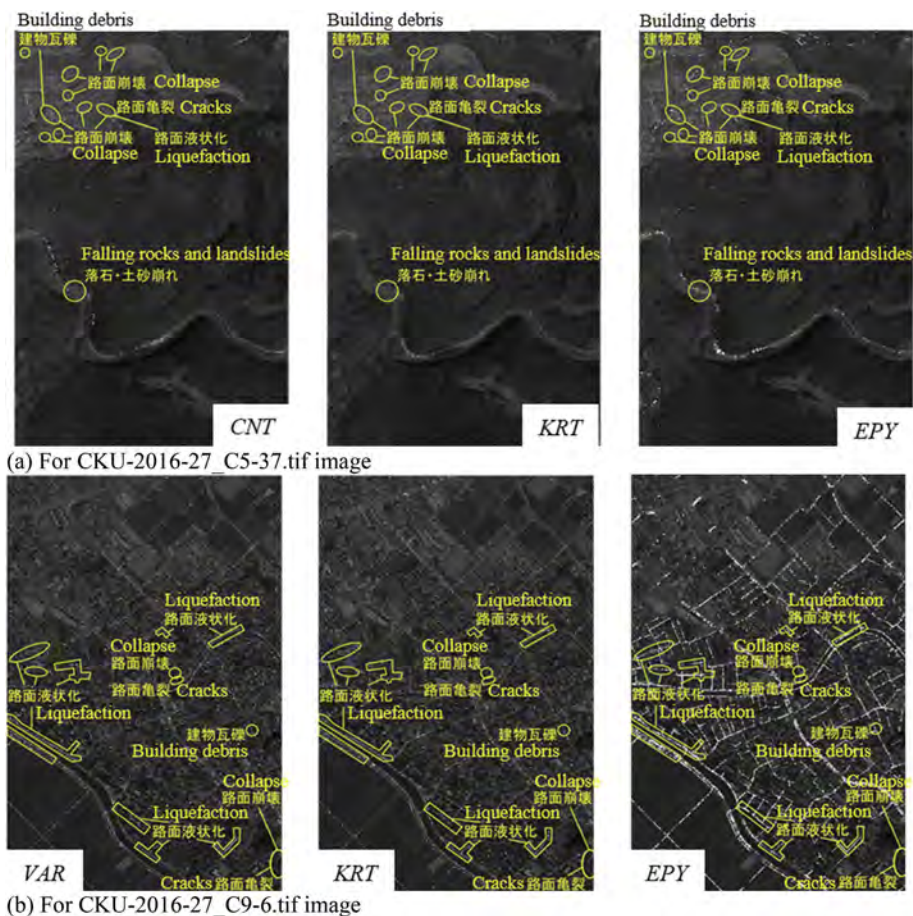


Figure 6. Damage detection result for each characteristic value.

good results with few false positives. Among them, the damage detection results for CKU-2016-27_C5-37.tif and CKU-2016-27_C9-6.tif are shown in Figure 6, and the histogram of features and damage detection range for each image are shown in Figure 7.

The damage caused by liquefaction was detected by *VAR*, *EGY* and *EPY* as shown in Figure 6(a); damage caused by cracking was detected by *KRT* and *EGY*; damage caused by collapse was detected by *VAR*, *KRT*, and *EPY*; damages caused by rockfall and landslide were detected by *KRT* and *EPY*; damage caused by building debris was detected by *CNT* and *EPY*.

KRT and *EPY* were the most common features in the extraction of these damage modes, and *KRT*, a fourth-order moment around the mean, may have discriminated well by emphasising variation in the brightness of the damaged area. The *EPY* showed better detection results for damage caused by liquefaction. This is because road liquefaction results in sand and water fountains, which darken the damaged area, so *EPY*, which shows larger values with smaller pixel luminance, is considered effective. However, in the case of road surface cracks, *EPY* was not a suitable feature because false positives were frequently observed for the area of damage. In the case of road surface collapse, *EPY* was a suitable feature because it was effective in detecting areas which appeared darker in relation to the road surface, as was the case with the road liquefaction described above.

In Figure 6(b), the damage caused by road liquefaction was detected by *CNT*, *VAR* and *KRT*; damage caused by road surface collapse was detected by *VAR* and *EGY*; damage caused by building debris was detected by *CNT* and *KRT*; however, there were no good

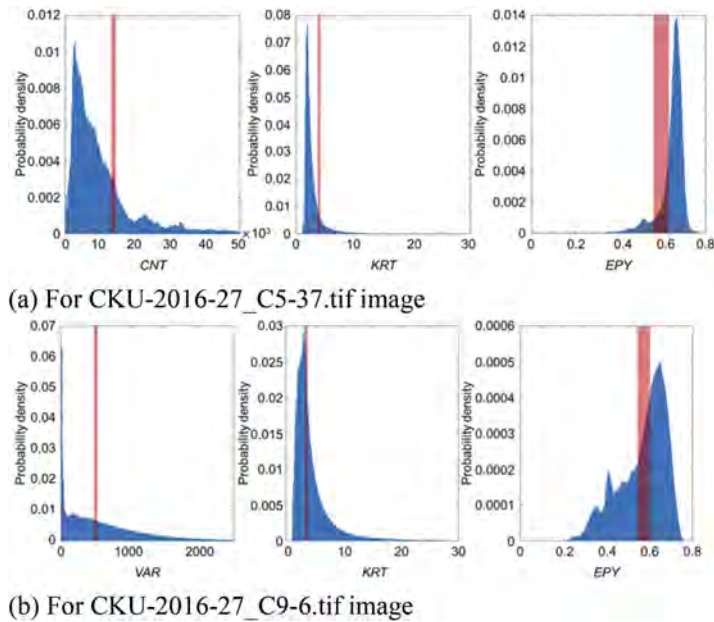


Figure 7. Histogram of each characteristic value and damage detection range.

indicators for detecting damage caused by road surface crack. In Figure 6(a), *KRT* and *EPY* were dominant, whereas in Figure 6(b), *KRT* was dominant. The reason is that road liquefaction was the outstanding damage mode in terms of both the number of damaged areas and the area of damaged regions. In addition, *VAR* showed good detection results for all damage modes, including road liquefaction and road collapse. There are many false positives in *EPY* for all damage modes as shown in Figure 6(b). This could be because, in urban areas, shadows of buildings and vehicles are reflected on the road, and the brightness values are not uniform even on undamaged road areas, resulting in false detection of damaged areas.

VAR was the common feature in the two images for road liquefaction. In contrast, *KRT*, which was not a good feature in Figure 6(a), showed good results for road surface liquefaction. This could be because *KRT*, which more strongly reflects differences in luminance, showed better results due to the large variation in luminance values in the road area described above. *KRT* was effective for detecting road surface cracks in Figure 6(a), but it could not detect them in Figure 6(b). Comparing the damaged areas of both road surface cracks, the damaged area in Figure 6(a) appears darker, which could be because the area in Figure 6(b) is outside the range of the damage detection threshold. In Figure 6(b), the road surface collapse was detected by *VAR* and *EPY*, whereas in Figure 6(a), it was detected by *VAR*, *KRT* and *EPY*. *VAR* was detectable in both images. The reason why *KRT* was unsuitable for detecting road surface collapse in Figure 6(b) is that the threshold value of CKU-2016-27_C9-6.tif is about 26% larger than the average value, and the area of the road surface collapse is not as large as the area of the road. The road surface collapse area was considered to be outside the range of the threshold value for damage detection because of the large difference in brightness between the road area and the collapse. In contrast, the reason why *EPY* was a suitable feature for detecting road surface collapse in Figure 6(b) is that it has a complementary relationship with the *EPY* index, which could have resulted in more areas being detected as false positives, but in Figure 6(b), suitable results were obtained, and the reason for this is a subject for future study.

5 CONCLUSION

Seismic damage modes of road surfaces were extracted in terms of six characteristic values according to the texture analysis of 25 aerial photographs which were taken after the 2016 Kumamoto earthquake. The coefficients of variation of kurtosis (*KRT*) and entropy (*EPY*) were smaller than those of other features, and they were found to be effective features for damage detection in terms of the threshold values. In terms of the damage discrimination range, 10% of the positive and 5% of the positive and negative values from the threshold showed good results, which had a relatively small area of false positives. Variance (*VAR*) and *KRT* were relatively common features that are suitable for detecting each damage mode, particularly for road liquefaction. *KRT* was also effective for detecting road surface crack damage, but it may not be possible to distinguish between it and other features which depends on the quality of the aerial photograph. *KRT* and *EPY* were the most effective features for detecting rockfall and landslides, and *VAR* was the most effective feature for detecting road surface collapse.

ACKNOWLEDGEMENTS

The support received via JSPS KAKENHI Grant Number JP 22K18303 is gratefully acknowledged. The authors would like to thank MARUZEN-YUSHODO Co., Ltd.(<https://kw.maruzen.co.jp/kousei-honyaku/>) for English language editing.

REFERENCES

- Gori, S., Falcucci, E., Galadini, F., Zimmaro, P., Pizzi, A., Kayen, R. E., Lingwall, B. N., Moro, M., Saroli, M., Fubelli, G., Di Domenica, A., Stewart, J. P. 2018. Surface faulting caused by the 2016 Central Italy seismic sequence: field mapping and LiDAR/UAV imaging. *Earthquake Spectra* 34(4): 1585–1610.
- Haralick, R. M., Shanmugam, K., and Dinstein, I. 1973. Textual features for image classification. *IEEE Trans, Systems, Man and Cybernetics* SMC-3 (6): 610–621.
- Kondo, R. & Shoji, G. 2022. Seismic damage detection of road structures by image analysis using aerial photograph. *Japan Society of Civil Engineers 2022 Annual Meeting*. CS10–73. In Japanese.
- Maruyama, Y., Yamazaki, F., Yogai, H., Tsuchiya, Y. 2016. Image processing of aerial photographs to detect the damaged sections of expressways. *The 12th Japan Earthquake Engineering Symposium*: 1262–1265. In Japanese.
- Matsuoka, M. & Yamazaki, F. 2004. Use of satellite SAR intensity imagery for detecting building areas damaged due to earthquakes. *Earthquake Spectra* 20(3): 975–994.
- Midorikawa, S. & Miura, H. 2010. Extraction of landslide areas due to the 2008 Iwate-Miyagi-Nairiku, Japan earthquake from high-resolution SAR image. *Journal of JAEE* 10 (3): 25–32. In Japanese.
- Ministry of Land, Infrastructure, Transport and Tourism. Geographical Survey Institute. Maps & Geospatial Information. <https://www.gsi.go.jp/kibanjoho/kibanjoho40027.html>
- Ministry of Land, Infrastructure, Transport and Tourism. Geographical Survey Institute. Maps & Geospatial Information. <https://www.gsi.go.jp/tizu-kutyu.html>
- Miura, H., Midorikawa, S., Matsuoka, M. 2016. Building damage assessment using high-resolution satellite SAR images of the 2010 Haiti earthquake. *Earthquake Spectra* 32(1): 591–610.
- Rathje, E.M., Secara, S. S., Martin, J. G., van Ballegooy, S., Russell, J. 2017. Liquefaction-induced horizontal displacements from the Canterbury earthquake sequence in New Zealand measured from remote sensing techniques. *Earthquake Spectra* 33(4): 1475–1494.
- Sezaki, R., Maruyama, Y., Nagata, S. 2017. Extraction of road damage after an earthquake using images captured by a car-mounted camera. *Proceedings of the Annual Conference of the Institute of Social Safety Science* 41: 53–56. In Japanese.
- Sakurai, T., Shoji, G., Takahashi, K., Nakamura, T. 2012. Damage assessment on road structures due to slope failures in the 2011 off the Pacific coast of Tohoku earthquake. *Proceedings of the International Symposium on Engineering Lessons Learned from the 2011 Great East Japan Earthquake*, Tokyo, 1-4 March 2012: 961–972.
- Yoshinari, K. & Shoji, G. 2020. Image analysis for road structure damage due to the 2018 Hokkaido Iburi Tobu earthquake. *Proc. 17WCEE* Paper No. C001678.

*MS8: Resilience and sustainability of steel based hybrid
building structures in the life-cycle environment
Organizers: D. Dubina, F. Dimu & V. Ungureanu*



Taylor & Francis

Taylor & Francis Group

<http://taylorandfrancis.com>

Life-cycle assessment of cold formed steel buildings: Main influential materials and parameters

O. Iuorio

University of Leeds, Leeds, UK
Politecnico di Milano, Milan, Italy

A. Gigante

University of Sannio, Italy

ABSTRACT: Reducing the carbon footprint of the built environment is a duty to achieve the target of the 2030 Urban agenda. The built environment is, indeed, responsible for about 42% of the EU total energy consumption and about 35% of the greenhouse gases emissions. One of the challenges in reducing the impact of building on the environment is in quantifying them, with a good degree of accuracy. To this end, over the last decades, life cycle methodologies and metrics have been developed for the assessment of green-house gases impacts of material, products, and components, that can be applied by academics and professionals. However, the quality of the assessment relies on the quality of data related to the amount of materials used for the studied building or component, and the corresponding adopted embodied carbon coefficients. This paper aims to shed light on this two key aspects investigating the cradle – to – gate life cycle impacts of a cold formed steel building, for which high accuracy is provided in terms of amount of materials and for some of the embodied carbon coefficients. The results will provide a useful benchmark for the wider academic community in terms of environmental impacts of cold formed steel structures, which is still a under-investigated field, and shed lights on the uncertainties generated by the selection of embodied carbon coefficients.

1 INTRODUCTION

Prefab systems, also known as offsite constructions, are today at the forefront for the development of low carbon construction systems. Prefab systems includes a large family of systems that according to the level of prefabrications can be defined as stick-built (when single components are produced in factory and then assembled on site with mechanical fasteners), panelized (when full walls or floor panels are realized in controlled environment and connected together on site, and volumetric (when fully tridimensional pods, or rooms are realized in factory and brought to site to be vertically and horizontally connected). Prefab systems, after having historical mix fortune, are today widely spreading for the realization of high standards long-terms construction systems. They are indeed very often associated to new energy-efficient buildings (Gervasio et al 2018, Iuorio et al 2019). Among prefab system, cold-formed steel (CFS) construction systems are becoming popular systems for the speed of production, the quality of final products and the structural efficiency.

1.1 *The contributions of the work*

This paper aims to investigate the environmental impacts of a cold-formed steel building, discuss the main contributing components and to critically analyze how the adoption of a variety

of databases for the calculation of the embodied carbon (EC) can provide significant differences in the obtained results.

2 CASE STUDY

This research examines a CFS school built in Italy in 2009. The school comprises 6 joint one storey stick-built CFS buildings of about 4 m height. The school has been designed for a grade 2 seismic zone according to the Italian classification OPCM 2006 and was designed and built to achieve the best energy class. All walls and roofs comprises CFS components and are designed according to sheathing braced methodologies, which accounts for the collaborations between steel profiles and sheathing panels, to achieve the required racking capacity (Iuorio, 2009). All steel components (i.e. wall studs, tracks, and rafters, as well as roof joists, tracks and blockings) are made of steel grade S320, which are zinc coated and dip – hot galvanized, and have thicknesses ranging between 1.5mm to 3.0mm. The structural sheathing panels are made by 9mm thick type 3 Oriented Strand Boards (OSB). The definition of the functional “packets” and technological choices visible in Figure 1c aimed to the eco-efficiency of the building in its life-cycle, and included wood wool panels (CELENIT) and hemp fiber as thermal insulation material for walls and roof, and gypsum based panels for fire resistance. All the sections of walls and floors are discussed in detail in Iuorio et al 2023.



Figure 1. British Force School (BFS): a. general view; b. typical wall; c. external wall stratification.

3 METHODOLOGY

One of the most complete and accurate methodology for the environmental assessment of the environmental impacts of a construction system is the life cycle analysis, which can be carried out in accordance to the ISO 14040/44 standard. In this paper, a cradle-to-gate LCA methodology of the BFS school is analysed, to understand the impacts of the structural and non-structural components of a CFS building, for which the bill of material is defined with high accuracy, because retrieved by official design and construction documents. Later in section 5, the results of the LCA study for the main structural components will be compared to those attainable from a simplified approach.

3.1 LCA of the BFS building

In his study the LCA boundaries include only the production stage (A1–A2–A3). Modules A1, A2 and A3 are indicated as a single aggregated module which includes all the steps from the cradle-to-gate (raw material supply, transport impacts and manufacturing) of the building components adopted for the case study construction. The total GHG emissions deriving from phases A1 to A3 represent the embodied emissions of the building. The life cycle analysis is developed with the use of One Click LCA automated life cycle assessment software (One Click), according to the requirement of the (EN 15978) standard, which is in line with the (ISO 14040/44) standard. As reported in Table 1, six standard impact categories are considered in this study.

Table 1. Impact categories considered.

Impact Category	Abbreviation	Unit
Global warming potential	GWP	kgCO ₂ -eq
Acidification potential	AP	kgSO ₂ -eq
Eutrophication potential	EP	kgPO ₄ -eq
Ozone depletion potential	ODP	kgCFC ₁₁ -eq
Formation of ozone of lower atmosphere	POCP	kgC ₂ H ₄ -eq
Total use of primary energy	TUPE	MJ

According to the LCA methodology, the bill of materials has been calculated for each examined building component, and then for each material the corresponding cradle-to-gate impacts have been evaluated on the basis of the corresponding EPD, retrieved in the One Click databases.

3.2 Life cycle inventory

In order to analyse the environmental impact of the case study, the following Table 2 show the quantities of materials used for the walls (both load-bearing and non load-bearing walls) and roof of the BFS School, making the distinction between materials for structural and non-structural components.

Table 2. Bill of materials.

	Construction Material	Quantity (Density)	Struct./ Non-Struct.
Foundation	Concrete (12/15 MPa)	199 m ³ (2400 kg/m ³)	Non-Struct.
	Concrete (30/37 MPa)	424 m ³ (2200 kg/m ³)	Struct.
	Rebar	18.3 ton (7850 kg/m ³)	Struct.
	Cold Formed steel (CFS)	44.6 ton (7850 kg/m ³)	Struct.
	OSB panels	52.6 m ³ (617 kg/m ³)	Struct.
	Wood wool panels—CELENIT N 25	28 m ³ (460 kg/m ³)	Non-Struct.
Load-Bearing Wall	Wood wool panels—CELENIT N 50	56 m ³ (360 kg/m ³)	Non-Struct.
	Fibre-cement panels	8.9 m ³ (1850 kg/m ³)	Non-Struct.
	Gypsum fibreboard—Knauf Vidifire	106 m ³ (1180 kg/m ³)	Non-Struct.
	Hemp Fibre insulation	300 m ³ (35 kg/m ³)	Non-Struct.
Non-load Bearing Wall	Cold Formed steel (CFS)	6.4 ton (7850 kg/m ³)	Non-Struct.
	Mineral fibre insulation	46 m ³ (56 kg/m ³)	Non-Struct.
	Gypsum fibreboard—Knauf Vidifire	46 m ³ (1180 kg/m ³)	Non-Struct.
	Cold Formed steel (CFS)	50.9 ton (7850 kg/m ³)	Struct.
	OSB panels	45 m ³ (617 kg/m ³)	Struct.
	Wood wool panels—CELENIT N 25	126 m ³ (460 kg/m ³)	Non-Struct.
Roof	Hemp Fibre insulation	252 m ³ (35 kg/m ³)	Non-Struct.
	Corrugated galvanized steel	2524 m ² (13.95 kg/m ²)	Non-Struct.

4 RESULTS

Table 3 indicates the overall GHG impacts of the BFS school according to the six impact categories. The results shows that the EC of the building amounts to approximately 606 tons of

CO₂e. As shown in Figure 2, about 70% of these GHG emissions are due to the materials and quantities used in walls (load-bearing and not-load-bearing walls) and roof, while 24.1% is due to the foundations. Among the other analysed impact categories, the contribution of the materials included in the wall mainly covers the impacts quantified in EP, ODP and TUPE with percentages equal to 62%, 54% and 44%, respectively. The roof components are primarily responsible for the observed AP and POCP impacts, with percentages incidence of 47% and 51%, respectively. The foundation are primarily responsible for 24.1% of GWP and for 20% of the AP, plus about 14% on average for the remaining impact categories.

Table 3. Global LCIA results.

	GWP tonCO ₂ -eq	AP tonSO ₂ -eq	EP kgPO ₄ -eq	ODP kgCFC11-eq	POCP kgC ₂ H ₄ -eq	TUPE MJ
Total	606	1.8	370	40 × 10 ⁻³	152	8'090'092

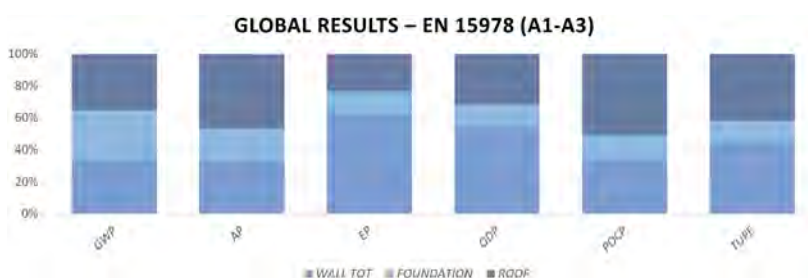


Figure 2. LCIA results: incidence percentages in each impact category.

In terms of percentage incidence of the individual materials within each building component, Table 4 and Figures 3 report the LCIA results for the foundations. The main responsible of the quantified impacts for foundations is the concrete C30/37. In terms of GWP, this material accounts for 70.5%, with about 130 tons of CO₂e. The steel reinforcement for concrete (C 30/37) has the greatest impact in terms of POCP (about 31.9%) while it has a very low impact in terms of GWP and AP, with incidence percentages of 5.5% and 3.5% respectively. The Lean concrete (C 12/15) has lower impact the C 30/37 both because it is present in a smaller quantity and because it has a lower carbon factor (ECC). In particular, from the EPDs, concrete C30/37 and concrete C12/15 have emission factors of 294 kgCO₂e/m³ and 217 kgCO₂e/m³, respectively.

Table 5 and Figure 4 show the LCA results for the CFS structural walls. The structural components (CFS and OSB panels) are responsible for 9.44×10^4 tonCO₂-eq that correspond to 51.5% of the total GWP of the load-bearing walls. In particular, CFS profiles show a predominant EC (80%) with respect to OSB panels (20%). The non-structural building materials cause an overall EC of about 8.9×10^4 tonCO₂-eq. Among them, the three thermal insulation panels cause about 18.1% of the GWP of the walls. Natural hemp fiber insulation is present in greater quantities but is much more sustainable than wood wool insulation panels. Instead, the fibre-gypsum board and the fibre cement panel are responsible for 14.5% and the 16% of EC, respectively. As for the other considered impact categories, the structural CFS is the most impacting building material in terms of AP (31%), followed by the fibre-gypsum board (26.8%). In addition, the fibre-gypsum board involves 67% of the EP of the walls. In terms of ODP, OSB panels and fibre-gypsum board are the most impacting materials, with percentages of 43.8% and 30.1%, respectively. Furthermore, the insulating panels in wood wool (CELENIT N 50 and CELENIT N 25) are responsible for 30.1% of the photochemical ozone creation potential of the structural walls. At the same time, structural materials (structural CFS and OSB) account for about 43.7% (28.7% and 15%, respectively) in the POCP

indicator. The materials that involve the greatest total use of primary energy are the structural CFS and the fibre-gypsum boards, respectively, with percentages of 32.9% and 25.7%. In this case, the percentage of incidence of non-structural materials is approximately 58.3%.

Table 6 and Figure 5 show LCA results for non-load-bearing walls. It is observed that, in all analysed impact categories, the least sustainable material is the fibre-gypsum board (responsible for 44.8% of the total GWP), followed by the non-structural CFS (responsible for 41.9% of the total GWP). The mineral fibre insulation panel is the most sustainable material.

Table 4. LCIA results: Foundation.

Material	GWP kgCO ₂ -eq	AP kgSO ₂ -eq	EP kgPO ₄ -eq	ODP kgCFC11-eq	POCP kgC ₂ H ₄ -eq	TUPE MJ
Structural	1.41×10^5	2.70×10^2	4.12×10	4.28×10^{-3}	1.78×10	8.6×10^5
Non-structural	4.45×10^4	9.38×10	1.23×10	1.30×10^{-3}	3.98×10	2.50×10^5
Total	1.85×10^5	3.64×10^2	5.35×10	5.58×10^{-3}	2.18×10	1.11×10^6

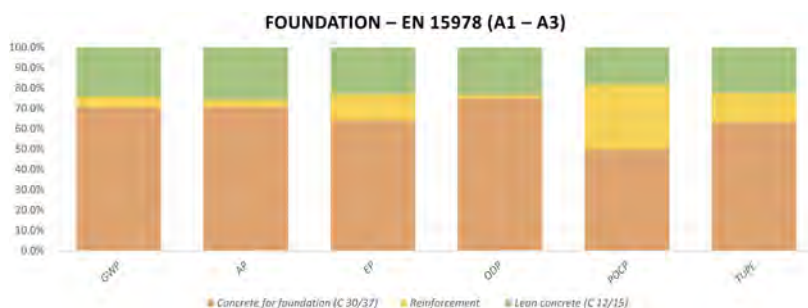


Figure 3. Percentage incidence of building materials in LCIA results: Foundation.

Table 5. LCIA results: Load-bearing Walls.

Material	GWP kgCO ₂ -eq	AP kgSO ₂ -eq	EP kgPO ₄ -eq	ODP kgCFC11-eq	POCP kgC ₂ H ₄ -eq	TUPE MJ
Structural	9.44×10^4	1.66×10^2	2.14×10	8.42×10^{-3}	2.10×10	1.29×10^6
Non-structural	8.86×10^4	3.53×10^2	1.55×10^2	1.08×10^{-2}	2.69×10	1.80×10^6
Total	1.83×10^5	5.19×10^2	1.76×10^2	1.92×10^{-2}	4.79×10	3.09×10^6

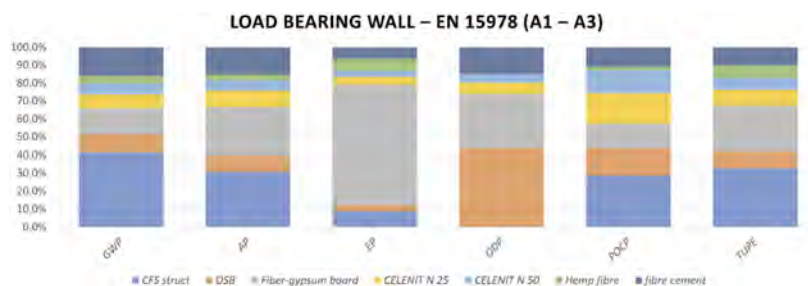


Figure 4. Percentage incidence of building materials in LCIA results: load-bearing walls.

Table 6. LCIA results: Non Load-bearing Walls.

	GWP kgCO ₂ -eq	AP kgSO ₂ -eq	EP kgPO ₄ -eq	ODP kgCFC11-eq	POCP kgC ₂ H ₄ -eq	TUPE MJ
Total	2.60×10^4	9.89×10	5.65×10	2.85×10^{-3}	5.36	5.64×10^5



Figure 5. Percentage incidence of building materials in LCIA results: Non Load-bearing Walls.

Finally, Figure 6 shows the results for the roof. In this case, the structural components are responsible for 10.25×10^4 kgCO₂-eq (Table 7) and cover 47.8% of total GWP. The materials that most affect the embodied carbon are the CFS (40.2%), CELENIT N 25 (29.9%) and corrugated galvanized metal sheets (19.3%). As in the case of the walls, the hemp fiber insulation has lower impact than CELENIT N, involving just 3% of the GWP. Regarding AP, the percentages are equal to 45.1%, 26.8% and 21.8% for the corrugated galvanized metal sheets, CELENIT N 25 and CFS, respectively. In terms of TUPE, the CFS and the OSB account for 34.2% and 6.9%, respectively. Among the non-structural materials, CELENIT N 25 show a greatest impact (34.7%).

Table 7. LCIA results: Roof.

Material	GWP kgCO ₂ -eq	AP kgSO ₂ -eq	EP kgPO ₄ -eq	ODP kgCFC ₁₁ -eq	POCP kgC ₂ H ₄ -eq	TUPE MJ
Structural	10.25×10^4	2.23×10^2	2.26×10	7.31×10^{-3}	2.19×10	1.40×10^6
Non-structural	11.25×10^4	6.22×10^2	6.42×10	5.39×10^{-3}	5.59×10	1.99×10^6
Total	2.15×10^5	8.45×10^2	8.68×10	1.27×10^{-2}	7.78×10	3.39×10^6

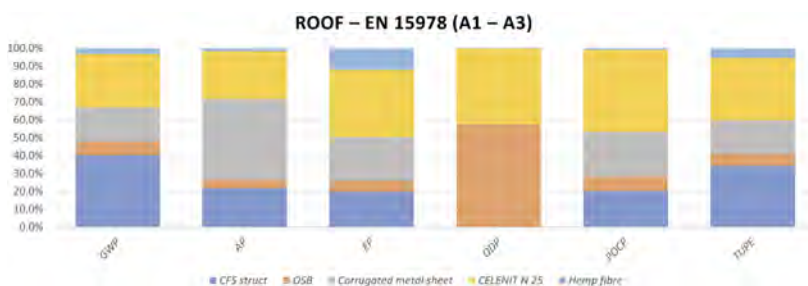


Figure 6. Percentage incidence of building materials in LCIA results: Roof.

5 COMPARISON BETWEEN DIFFERENT LCA DATABASES

As discussed the GWP is key environmental impact to evaluate the EC of a building/construction. The key variables that drive the definition of EC are the amount of material per unit of the building and the Embodied Carbon coefficient (ECC) in terms of kgCO₂e per kg of material. While, as seen, the first variable is closely dependent on the analyzed project, instead the evaluation of ECC is certainly more complex, since, the environmental profiles of the materials used in constructions are rarely available. To understand how much the definition/selection of ECC can influence the total EC results, here a simplified methodology (De Wolf et al 2014) is applied for the evaluation of the EC of the main structural components/materials and for the evaluation of the ECCs, two databases, namely ICE (Hammond & Jones 2010) and AMECO were considered. In particular, the ICE has been published by the University of Bath, and presents ‘cradle-to-gate’ data for carbon and energy impacts of primary building materials, mainly focused on the UK market. However, since in many cases the production of energy to manufacture a process is the dominant carbon impact and therefore this data can be extrapolated to different markets with different energy sources. The database presents some of the background for the data sources enabling the user to infer data quality. The AMECO Software calculates environmental impacts of buildings and bridges made of steel and concrete. Table 8 shows the obtained results. Please note that the quantities of concrete and CFS refer only to the structural components. The quantities of OSB and rebar are the total quantities calculated for the BFS. The ECCs from the two external databases are higher in all cases, with the exception of steel. In the case of concrete, the values are highly comparable while both in the case of OSB and steel reinforcement the ICE and AMECO coefficients are more than double those from One Click LCA. Clearly these differences are reflected in the calculation of the GWP. However, the total values calculated for the structural materials considered are comparable and equal to about 328 tons of CO₂e and 333 tons of CO₂e respectively with the ECCs coming from One Click LCA and those provided by the two external databases. As can be seen in Figure 7, the use of ECCs from different databases leads to a different percentage incidence of structural materials compared to the total GWP they generate. In fact, according to the LCA conducted using One Click LCA (Figure 7a), steel represents the most impactful structural material in terms of GWP (51.5%), while in the second case (Figure 7b) concrete accounts for 40.3 % of the total GWP of structural materials and steel accounts for 36.1%.

Table 8. BFS: Global Warming evaluation with different databases.

Material	kg	EC (ICE/AMECO) [kgCO ₂ e/kg]	GWP (ICE/ AMECO) [kgCO ₂ e]	EC (One Click LCA) [kgCO ₂ e/kg]	GWP (One Click LCA) [kgCO ₂ e]
Steel	95500	1.24 ²	118420	1.77	169035
OSB	60219	0.99 ¹	59617	0.45	27099
Concrete	1017600	0.13 ¹	132288	0.12	122112
Rebar	18317	1.24 ²	22713	0.55	10074

1 Coefficients evaluated on the basis of ICE (ICE 2010)

2 Coefficients evaluated on the basis of AMECO

6 CONCLUSION

This study analyses the LC impacts of a CFS building built in Italy. The LCA is developed according to a cradle-to-gate approach, investigating the impacts of both structural and non structural components. The study demonstrates, when the building is a single story building, as for the investigated case, the GWP is nearly equally shared between walls, roof and

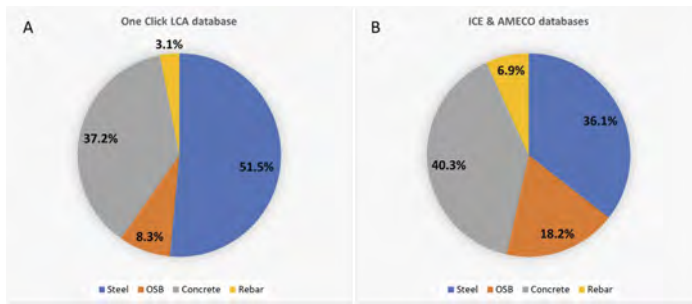


Figure 7. Percentage incidence on total structural materials GWP: a) ECCs from One Click LCA; ECCs from ICE & AMECO.

foundation (see Figure 2). But when the materials are analysed, it is clear the strong incidence provided by the CFS structural members, followed by OSB panels (for a total combined incidence of 80% of structural walls GWP). Among the insulations, the hemp fibre is that with lower incidence. While for the foundation, the impacts are primarily driven by the C30/37 concrete. Therefore, these results restate the utmost importance and necessity to optimize the structural system, and that future code allowing the dissipative design of CFS system could have a significant impact also on the environmental profile of this prefab system. Finally, section 5, shows how EC results are strongly dependent on the ECCs considered, with the simple example showing how the percentage incidence can be flipped by considering a different variety of ECC database. Therefore, the continue development of EPDs for current and future building materials will be the most appropriate approach to develop reliable assessments.

REFERENCES

- AMECO: <http://amsections.arcelormittal.com>. Accessed on July 2021.
- De Wolf, C., Iuorio, O., and Ochsendorf, J., 2014. Structural Material Quantities And Embodied Carbon Coefficients: Challenges And Opportunities. In *5th Annual School of Architecture Symposium*. Portland USA, 309–328.
- European Committee for Standardization, EN 15978: sustainability of construction works. Assessment of environmental performance of buildings. Calculation method, Brussels, Belgium, 2011.
- Gervasio, H, Dimova S, Pinto A. 2018. Benchmarking the Life-Cycle Environmental Performance of Buildings, *Sustainability*, 10(5).
- Hammond, G. & Jones C. Inventory Of Carbon & Energy (ICE 2010) version 2.0, A BSRIA guide, Ed. Fiona and Peter Tse, 2010.
- ISO 14040; Environmental Management-Life Cycle Assessment—Principles and Framework. International Organization for Standardization: Geneva, Switzerland, 2006.
- Iuorio, O. 2007. Cold-formed steel housing. *Pollack Periodica*. 97-108 2.3.
- Iuorio, O, Wallace A, Simpson K. 2019. Prefabs in the North of England: Technological, Environmental and Social Innovations. *Sustainability*. 11.14.
- Iuorio, O., Gigante, A., De Masi, R. 2023 Life Cycle Analysis of Innovative Technologies: Cold Formed Steel System and Cross Laminated Timber, *Energies*, 16.
- One Click LCA Software. Available online: <https://www.oneclicklca.com> (accessed on 20 December 2022).

The new construction products regulation: Opportunity or barrier for reused constructional steel?

P. Hradil, L. Fülöp & M. Wahlström

VTT Technical Research Centre of Finland Ltd., Espoo, Finland

C. del Castillo

European Convention for Constructional Steelwork, Brussels, Belgium

ABSTRACT: This paper discusses the implication of the new provisions of the proposed Construction Products Regulation on the constructional steel reuse. The regulation extends its scope to products either previously placed on the EU market or installed in the EU, but at the same time provides guidance how to treat used, remanufactured or surplus products and a possibility to derogate from the full Declaration of Performance rules for products that have been previously assessed. The requirements include stable material properties, safety, durability and exclusion of overloaded components assessed by de-installer or pre-deconstruction auditor. The technical guidance and protocols for structural steel reuse are developed as Annex to EN 1090-2 in the CEN/TC 135. In our study, we provide an example of such process applied on the components recovered from a single-storey industrial hall that are offered for reuse in another building project.

1 INTRODUCTION

Constructional steel components are the best suitable building elements for reuse. In most cases already designed with bolted connections, their deconstruction is usually reversed assembly process with some minor modifications. This approach can significantly improve sustainability of the constructional steelwork (Ungureanu et al. 2019), but at the same time, the reliability and resilience of steel and steel-based structures should not be compromised. For instance, the elements recovered from aged structures, demolition or post disaster recovery are significantly more challenging to reuse than relatively new components maintained in a good condition. Despite these challenges, there are some successful examples of reusing elements from such buildings. To date, the primary motivation for reusing structural steel has been economic benefits of the specific project (Balcar, 2005, Kuhnhenne, 2018). However, it is important to note that successful reuse cases in Europe are also limited due to various legislative barriers.

The upcoming environmental regulations, e.g.; the EU Taxonomy (EU 2020), Environmental Performance of Buildings Directive, EPBD (EU 2021), and the different national regulations, will set stringent embodied carbon thresholds. Compared to primary steel, reused steel production carbon emissions are significantly lower. The first Environmental Product Declaration, EPD, available for reused section claims Global Warming Potential values for the production stage of reusable steel under 50 kgCO₂e/t (EPD International 2022). Reused steel can therefore become a cost-effective near zero emissions construction material. In addition, the consideration of reuse as the End-of-Life option for primary steel elements provides environmental benefits beyond the current lifecycle. Hence, steel reuse will become a more common practice in the future.

Our survey (Hradil et al. 2014) identified missing legislation and standardization as one of the greatest obstacles to the structural components reuse already in 2014. The situation has

changed since then and new regulations, technical specifications, industry guides and standards were released in support of circular economy of building products, many of them specifically for constructional steel.

The constructional steel products covered by the European harmonization are so-called constituent products (e.g. sections, sheets or bars) and assemblies or specific structural elements fabricated from those constituents (called structural steelwork). The harmonized European Standard EN 1090-2 (CEN 2018) provides requirements for execution of structural steelwork, and since 2018 it allows use of constituent products that are not covered by the relevant harmonized standards if their properties are specified (clause 5.1 of EN 1090-2). This can be interpreted as the possibility to reuse non-CE marked steel products and then provide CE marking of the steelwork according to this standard (Widenoja et al. 2018, Wahlström et al. 2019). The amendment to the new version of EN 1090-2 is being drafted by CEN/TC135 with the rules for quality assessment of used steel sections and fabricated structural components. This will allow manufacturers and reuse operators to declare consistently performance of such products. The testing methodology is based on the testing protocol from PROGRESS project (Pimentel et al. 2020) and on the Swedish guidance for structural steel reuse (MVR 2021).

A new annex to EN 15804 (CEN 2019) was released in 2019 with the rules for calculation of environmental impacts of materials beyond the system boundary when more than one recycling route is used. This is important especially for steel as the part of end-of-life material not suitable for reuse will be always recycled. The methodology is consistent with PEF rules (Eurometaux 2019) and our findings from PROGRESS project (Ungureanu et al. 2019). The complementary rules specific for steel structures were published in 2021 as prEN 17662 (CEN 2021) by CEN/TC 135/WG 17. Declaration of environmental impacts is becoming very important as many European countries are adapting requirements and limits for such impacts in the new construction projects (Kuittinen 2019).

Finally, the designers will receive guidance on the calculation of structural resistance, stability and serviceability of existing load-bearing structures and components in the new generation of the Eurocodes. The technical committee CEN/TC 250/WG 2 published technical specification TS 17440 (CEN, 2020b) with general principles of assessment and retrofitting of existing structures and is currently preparing rules specific for steel structures (CEN 2020a).

2 CONSTRUCTION PRODUCTS REGULATION

The European market of constructional products is regulated since the release of the Construction Products Directive (EU 1989). The purpose of the Directive was to remove technical barriers to trade in construction products between different Member States. It established a system of harmonized technical specifications, attestation of conformity, a framework of notified bodies, CE marking of construction products and list of six essential requirements to be satisfied in order to place the product on the market. The Directive was replaced by the Construction Products Regulation (CPR) in 2011 (EU 2011) which came into full force on 1st July 2013 for the supply of structural steel products. The CPR provides further clarification of the established rules and responsibilities of the actors, introduces the need to issue declaration of performance (DoP) as a basis of CE marking and lists seven essential basic requirements for construction works (BRCWs) based on the essential requirements from the Directive. The new BRCW no. 7 “Sustainable use of natural resources” states that the construction works must be designed, built and demolished to ensure the reuse or recyclability of the construction works, their materials and parts after demolition. Unfortunately, the CPR does not contain any guidance how to declare performance of reused building products in order to place them on the European Union market.

This issue has been addressed in the proposal for a new Construction Product Regulation (EU 2022a) adapted in 2022. The proposal widens the scope of the CPR to reused and 3D-printed products and pre-fabricated single family houses as well as to products not only put on the market, but also those installed in the European Union. Both changes are important for the circular economy of steel products because the products are often reused without placing on EU market (e.g. as a result of direct contract between the parties or internally within

different facilities owned by the same company). The number of BRCWs is extended to eight with hazardous emissions separated from BRCW no. 3 as BRCW no.7 and the sustainable use of natural resources moved to the last position.

2.1 Modified declaration of performance for used, remanufactured and surplus products

The Article 12 of the CPR proposal (EU 2022) lays down conditions for simplified procedure to declare performance of recovered building products from construction, demolition or renovation works if they were previously assessed (and their original DoP is available) or they are going to be used for decoration purposes. Such solution might be attractive in near future when the owners of buildings constructed after 2013 (when CE marking of steel products became compulsory) will strive to reuse steel sections as constituent products or the whole steelwork.

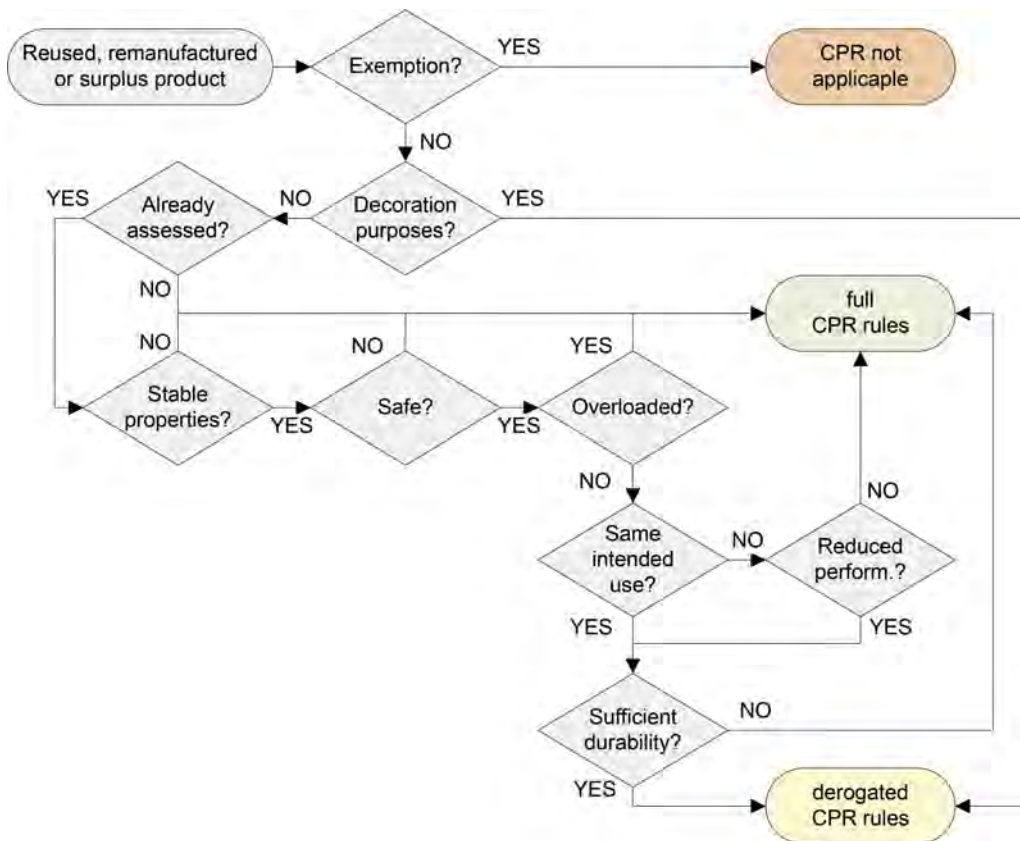


Figure 1. Procedure to reach derogated CPR rules according to the article 12.

To satisfy the requirements for the simplified CPR assessment, the product (constituent product or steelwork) shall fulfill the following criteria (see Figure 2):

- (1) It has been already assessed and its properties are known. The authorities may also require Digital Product Passport according to the Ecodesign Directive (EU 2022b) including appropriate labeling and traceability system (Hradil et al. 2023).
- (2) It has stable properties for the intended new use and is not affected by degradation. In the case of steel, a proper inspection of the coating and corrosion damage should be performed during the pre-deconstruction audit.

- (3) It is safe to use. This means the toxicity of the coatings and integrity of the connections should be checked during the audit. However, the CPR does not specifically allocate the responsibilities on the stability of chemicals and mechanical properties for the new intended use and neither the health and safety considerations that seem to be responsibility for the later user or owner. Moreover, there is not any existing recommendation for weld inspections of reclaimed structural elements.
- (4) It is not overloaded and no plastic deformation is registered. This requirement is in line with the proposed annex to EN 1090-2 (CEN 2018). In particular, the CPR allocates member states the responsibility to define stresses that render the product unsuitable and to demonstrate that the product has not been subjected to such stresses according to the protocol established by the de-installer in accordance with Article 29 and the documentation on the conditions of a certain building, so-called “building log-book” (Hradil et al. 2023).
- (5) It has the same intended use or different use with reduced performance. In our interpretation it means that it is covered by the same harmonized standard as the existing DoP and it is either used in the same building design (including wind, snow and seismic loads) or the reduced performance is confirmed by the corresponding structural calculation according to the Eurocode 3 (CEN 2005).
- (6) It has sufficient durability. Durability is declared in design according to the Eurocode 0 (CEN 2002) and the service life is typically 50 years for buildings. Therefore, the product can be reused with the original design up until the remaining service life or its service life extension has to be supported by the relevant structural checks with possibly modified safety factors and/or additional reinforcement.

2.2 Harmonization of rules for execution of steel structures from reused elements

The reuse of structural steel from existing buildings is currently possible due to clause 5.1 of EN 1090-2. Despite no protocols are defined in the current EN 1090-2 versions, different industry standards are available and the recommendations and testing methodologies from PROGRESS project (Pimentel et al. 2020) and on the Swedish guidance for structural steel reuse (MVR 2021) can be currently followed. Some member states are also working on the development of national standards on steel reuse. However, there is a need for developing a family of harmonized standards at EU level.

CEN/TC 135 has received the mandate to develop a technical standard on the “Reuse of Steel”. The mandate includes Execution Classes 1, 2 and 3. The first version of the standard is expected to be published as an EN 1090-2 Annex and will be likely released during 2024. Based on both PROGRESS project and the MVR 2021 recommendations, the new CEN/TC 135 Technical Standard on steel re-use will for the first time set protocols for the re-qualification of steel within an EN normative

The Technical Standard will provide specific testing protocols for constituent products depending on the date of production and the documentation available. These protocols include a specific protocol for steel manufactured after 1970’s when certificates are available. The protocol is simple and accurate and will likely meet the CPR requirements for the lower execution classes in new buildings. So, member states should adopt this standard and its future developments as reference to define the stresses that render the products unsuitable and how to certify that reclaimed products has not been subjected to stresses that makes it unsuitable for the new intended use.

In addition, this protocol and other included in the TS will provide the necessary tools to enable the re-use of reclaimed steel when DoP are not available.

The first version of the Technical Standard will be limited in scope and will not cover all the stresses that make a reclaimed product unsuitable for the new intended use, but it is expected that future work will extend the different testing protocols in the standard to cover weld inspections, fatigue design or seismic loads covering EXC1, EXC2 and EXC3 fabricated and constituent products.

3 REUSE OF CONSTRUCTIONAL STEEL FROM SINGLE STOREY HALL

The demolition of the year prize in Finland was awarded in 2022 for deconstruction of the steel hall which was fully documented and its structural members were included in the electronic traceability system with RFID tags and cloud-based information database (Hradil et al. 2023) developed and demonstrated in EU ICEBERG project. The demolition area in Lämminpää district of Tampere, Finland contained in total 15 buildings constructed between 1928 and 2016, four of them deconstructed for future reuse (see Figure 2) by the demolition contractor and partner in the project, Purkupiha Group Oy. Purkupiha arranged the standard pre-demolition inspection, developed deconstruction plan and executed the disassembly of the steelwork (see Figure 3), VTT and other partners from ICEBERG project then assisted with additional inspection work such as 3D scanning and installation of RFID tags for the cloud-based traceability system (Hradil et al. 2023).

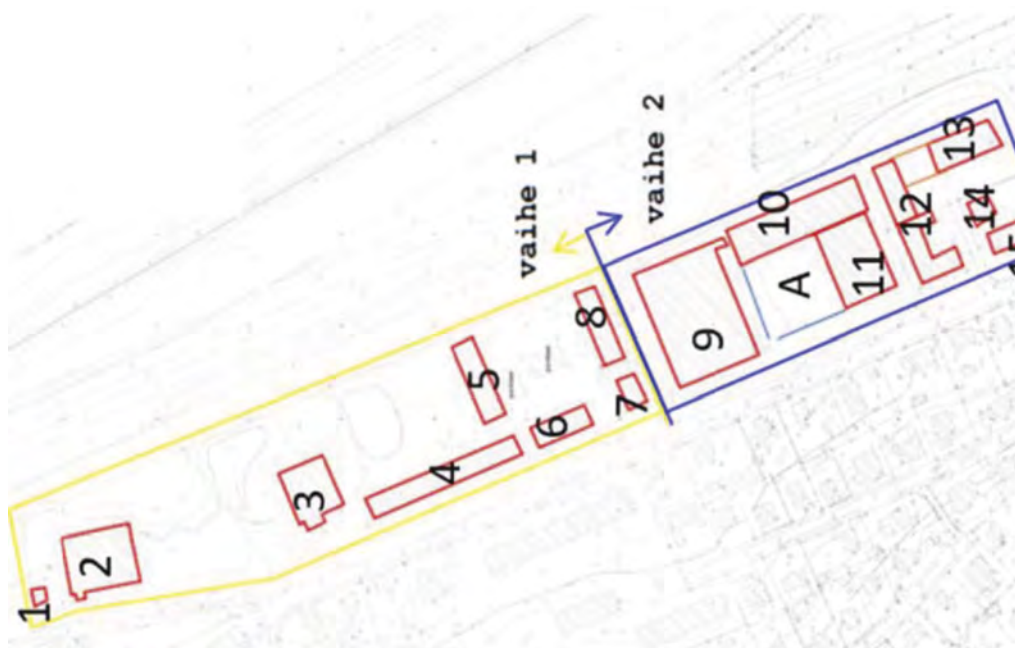


Figure 2. Buildings in the area of Tampere, Lämminpää demolished and deconstructed in two stages (vaihe 1 and 2) in 2022.

The contractor is then arranging a direct sale between the previous and new owner of the building elements. Some of them can be also sold on the company's own online sales platform (Purkupiha Group Oy 2022). We will use this example as a background for several hypothetical case studies to compare current requirements of the existing CPR (EU 2011) and EN 1090-2 (CEN 2018) to the possible future scenarios with the proposed CPR (EU 2022) and annex to EN 1090-2 for reuse of steel sections. The comparative study includes two different steel halls:

- **A:** Old building (typically constructed before 2013 with no CE-marking) without any existing documentation and CE marking,
- **B:** New building (constructed after 2013) with existing design documentation and CE-marking of the individual steel sections according to EN 10025-1 (CEN 2004) and the whole steelwork according to EN 1090-2 (CEN 2018).



Figure 3. Steel hall in Lämminpää district, Tampere, Finland (left) and its deconstruction (right).

The following most common business models in steel reuse (Ungureanu et al. 2020, Sansom et al. 2020) are considered in the study:

- Direct reuse of the whole steelwork when the owner of the building remains the same (typical case of building relocation) or agrees with the new owner directly without putting the deconstructed steelwork on the market,
- Sale of the steelwork when the building is deconstructed and offered for sale for instance on online market such as Purkupiha Group Oy (2022),
- Sale of sections deconstructed and separated from end-plates and other welded attachments for instance following the business model of Cleveland Steel & Tubes Ltd (2022).

The requirements for CE marking and material testing are summarized in Table 1.

Table 1. Comparison of the scenarios with deconstructed old steel hall (A) and new steel hall (B).

Case	Direct reuse		Sale of steelwork		Sale of sections	
	A	B	A	B	A	B
<i>Current requirements (CPR from 2011, EN 1090-2:2018)</i>						
New CE marking of sections	no ¹⁾	no ¹⁾	no ¹⁾	no ¹⁾	no ¹⁾	no ¹⁾
New CE marking of steelwork	no ²⁾	no ²⁾	yes ³⁾	yes ³⁾	-	-
Testing of reclaimed material	not clear ⁴⁾	no	yes ⁵⁾	no	yes ⁵⁾	no
<i>Future requirements (proposed CPR from 2022, EN 1090-2:2018 + annex about reuse)</i>						
New CE marking of sections ¹⁾	Yes ⁶⁾	no ⁷⁾	Yes ⁶⁾	no ⁷⁾	not clear ⁸⁾	no ⁷⁾
New CE marking of steelwork	Yes ⁶⁾	no ⁷⁾	Yes ⁶⁾	no ⁷⁾	-	-
Testing of reclaimed material	yes	no	yes	no	yes	no

- 1) Reused sections are not covered by any harmonized standard
- 2) Products not placed on Union market are not in the scope of the current CPR
- 3) Clause 5.1 of EN 1090-2 allows use of constituents not covered by harmonized standards
- 4) Testing is not required by standards or regulations, but may be required by building authority
- 5) Clause 5.1 of EN 1090-2 requires specification of material properties
- 6) The new CPR covers also products installed in the European Union
- 7) CE marking may be based on the original DoP according to Article 12 of the proposed CPR
- 8) It is not clear if EN 10025-1 will be considered as relevant harmonized standard for reclaimed sections when the testing rules from the proposed annex to EN 1090-2 will come into force

In our study, we identified two situations when the current and planned regulation is not clear about the required procedure:

- (1) The requirements for testing of materials reused directly without CE marking are not specified in any EU regulation or standard, and therefore may be subjected to the decision of

the local building authority. For instance, the building control in Finland may require testing of materials of unknown origin according to the recommendation from the Finnish Ministry of the Environment.

- (2) At the moment the interpretation of the scope of harmonized standard EN 10025-1 (CEN 2004) is that it does not cover reclaimed steel sections (Widenoja et al. 2018, Wahlström et al. 2019) because it does not provide any relevant testing protocol. However, the testing protocol will be described in the annex of EN 1090-2 (CEN 2018), and therefore the future interpretation might be different. In such case, the Clause 5.1 of EN 1090-2 will be irrelevant. It should be noted that the knowledge of material properties is required in any case, and therefore material testing cannot be avoided.

4 SUMMARY AND CONCLUSIONS

The proposed CPR brings additional administrative burden for materials and structures reused directly without putting them on EU market. They will require corresponding DoP according to the harmonized standards. The derogated CPR procedure according to the Article 12 is only relevant to the products with existing assessment (produced after 2013), design documentation and functional product passport with traceability system. Most of the buildings constructed up to date might not qualify for this procedure. However, the implementation of the proposed CPR may not in general cause additional costs for testing of materials.

We acknowledge that the proposed CPR clarifies the certification process of reclaimed structural steel products and lays down rules for improved harmonized standards, but its implementation for the current building stock will be difficult and may create additional barriers for the circular economy before the digital product passports will be in use and the buildings already assessed by the current CPR will come to age and will be subjected to deconstruction and possible reuse.

We recommend that the building authorities in EU Member States adapt rules for building products traceability as soon as possible to be able to approve the conformity of the new declared certification to the corresponding products at the time of their future deconstruction. This will remove the most severe barriers of the proposed CPR to the structural steel (and possibly other materials) reuse.

ACKNOWLEDGEMENTS

The research presented in this paper was supported by the EU project ICEBERG. This project has received funding from the European Union's Horizon 2020 research and innovation programme under grant agreement No 869336.

REFERENCES

- Balcar A. 2005, *Ing. Arnošt Balcar - montované haly*, interview published at the company webpage, accessed online at <http://www.haly-sklady.cz/> 1.6.2018.
- CEN 2002. *EN 1990: 2002, Eurocode - Basis of structural design*, Brussels: European Committee for Standardization.
- CEN 2004. *EN 10025-1:2004, Hot rolled products of structural steels - Part 1: General technical delivery conditions*, Brussels: European Committee for Standardization.
- CEN 2005. *EN 1993-1-1:2005, Eurocode 3: Design of steel structures - Part 1-1: General rules and rules for buildings*, Brussels: European Committee for Standardization.
- CEN 2018. *EN 1090-2:2018, Execution of steel structures and aluminium structures - Part 2: Technical requirements for steel structures*, Brussels: European Committee for Standardization.
- CEN 2019. *EN 15804:2012+A2:2019 Sustainability of construction works - Environmental product declarations - Core rules for the product category of construction products*, Brussels: European Committee for Standardization.

- CEN 2020a. *CEN/TC 250 Business Plan Version 9*, Brussels: European Committee for Standardization.
- CEN 2020b. *TS 17440:2020 Assessment and retrofitting of existing structures*, Brussels: European Committee for Standardization.
- CEN 2021. *prEN 17662:2021 Execution of steel structures and aluminium structures - Environmental Product Declarations - Product category rules complementary to EN 15804 for Steel, Iron and Aluminium structural products for use in construction works*, Brussels: European Committee for Standardization.
- Cleveland Steel & Tube Ltd 2022. *Company webpage*, accessed online at <https://cleveland-steel.com/>, 1.12.2022.
- EPD International, 2022. *Reusable steel Environmental Product Declaration in accordance with ISO 14025 and EN 15804:2012+A2:2019*, Warrington: European Metal Recycling.
- EU 1989. *Council Directive 89/106/EEC of 21 December 1988 on the approximation of laws, regulations and administrative provisions of the Member States relating to construction products*, Brussels: European Union.
- EU 2011. *Regulation (EU) No 305/2011 of the European Parliament and of the Council of 9 March 2011 laying down harmonised conditions for the marketing of construction products and repealing Council Directive 89/106/EEC (Text with EEA relevance)*, Brussels: European Union.
- EU 2020. *Regulation (EU) 2020/852 of the European Parliament and of the Council of 18 June 2020 on the establishment of a framework to facilitate sustainable investment, and amending Regulation (EU) 2019/2088 (Text with EEA relevance)*, Brussels: European Union.
- EU 2021. *Proposal for a Directive of the European Parliament and of the Council on the energy performance of buildings (Text with EEA relevance)*, Brussels: European Union.
- EU 2022a. *Proposal for a Regulation laying down harmonised conditions for the marketing of construction products, amending Regulation (EU) 2019/1020 and repealing Regulation (EU) 305/2011*, Brussels: European Union.
- EU 2022b. *Proposal for a Regulation of the European Parliament and of the Council establishing a framework for setting ecodesign requirements for sustainable products and repealing Directive 2009/125/EC*, Brussels: European Union.
- Eurometaux 2019. *Product Environmental Footprint Category Rules (PEFCR) for Metal Sheets for Various Applications version 28/06/2019*, Woluwe-Saint-Pierre: Association Européenne des Métaux.
- Hradil, P., Talja, A., Wahlström, M., Huuhka, S., Lahdensivu, J. & Pikkuvirta, J. 2014, *Re-use of structural Elements: Environmentally efficient recovery of building components*, VTT Technology 200, Espoo: VTT Technical Research Centre of Finland.
- Hradil, P., Jaakkola, K. & Tuominen, K. 2023. *RFID-based traceability system for constructional steel reuse. In Proc. of the Eighth International Symposium on Life-Cycle Civil Engineering (IALCCE 2023), Milan, 2-6 July 2023.* (submitted manuscript) Milan: Balkema.
- Kuhnhenne, M., Pyschny, D., Hradil, P., Sansom, M., Kesti, J., Dubina, D. & Ungureanu, V. 2018. *Report on the reuse potential of single-storey steel buildings*, Deliverable D1.2 of PROGRESS project, Aachen: RWTH.
- Kuittinen, M. (Ed.) 2019. *Method for the whole life carbon assessment of buildings*, Publications of the Ministry of the Environment 2019:23, Helsinki: Ympäristöministeriö.
- MVR 2021. *Återbruk av stål i bärande konstruktioner Krav- & Processbeskrivning*, MVR BS04:2021, Stockholm: Mekaniska Verkstädernas Riksförbund.
- Pimentel, R., Girão-Coelho, A., Sansom, M., Hradil, P., Fülöp, L., Ungureanu, V. & Kesti, J. 2020. *Quality verification protocol including test results*, Deliverable D2.3 of PROGRESS project, Ascot: Steel Construction Institute.
- Purkupiha Group Oy 2022. *Free online market of deconstructed building products*, accessed online at <http://www.purkutori.fi>, 1.12.2022.
- Sansom, M., Hradil, P. & Kamrath, P. 2020. *Circular economy business models*, Deliverable D5.3 of PROGRESS project, Ascot: Steel Construction Institute.
- Ungureanu, V., Greca, D., Hradil, P., Vares, S., Sansom, M. & Pyschny, D. 2019. *Report on the methodology to declare environmental benefits of reused elements*, Deliverable D5.1 of PROGRESS project, Timișoara: Universitatea Politehnica Timișoara.
- Ungureanu, V., Fechete, H. & Dubina, D. 2020. *Factsheets on review of existing deconstruction cases*, Deliverable D1.1 of PROGRESS project, Timișoara: Universitatea Politehnica Timișoara.
- Wahlström, M., Hradil, P. & Sansom, M. 2019. *Legal barriers and opportunities in structural steel reuse*, Deliverable D1.3 of PROGRESS project, Espoo: VTT Technical Research Centre of Finland.
- Widenoja, E., Myrhe, K. & Kilvær, L. 2018. *DIP15 Ombruk av konstruksjonsstål og tilhørende byggmaterialel*, Oslo: Norsk Stålförbund.

A comparative life-cycle assessment of structural composite steel-concrete floor systems – A case study

I. Lukačević & A. Rajić

Faculty of Civil Engineering, University of Zagreb, Zagreb, Croatia

V. Ungureanu

Politehnica University of Timisoara, Timisoara, Romania

Romanian Academy, Timisoara Branch, Timisoara, Romania

R. Buzatu

Politehnica University of Timisoara, Timisoara, Romania

ABSTRACT: Upon recognition of the advantages of composite steel-concrete structures, solutions that integrate built-up cold-formed steel sections have become more prevalent in the last few decades. Some of the reasons for the increased interest in composite steel-concrete structures are that components of such systems are easy to manipulate, transport, and erect due to reduced weight. These advantages can be even more significant if the system is designed for demountability, reflecting the environmental impacts at the end-of-life of the system. This paper deals with a cold-formed steel-concrete composite floor system as part of the LWT-FLOOR project at the Faculty of Civil Engineering, University of Zagreb, Croatia. Cold-formed steel elements are built-up beams with back-to-back profiles such as flanges and corrugated webs. Cold-formed steel elements are connected by fast and productive spot-welding technology, while composite action between steel and concrete is realised through innovative demountable shear connections with structural bolts. The LWT-FLOOR system has numerous potential benefits, which will be investigated through experimental, numerical research with the support of probabilistic methods and, of course, life cycle analyses. This paper presents a practical application of integrating environmental impacts associated with the mentioned LWT-FLOOR system and the traditional composite structural floor system with hot-rolled steel beams. A comparative Life Cycle Assessment (LCA) of structural composite steel-concrete floor systems along with a Life Cycle Cost (LCC) are given. Impact analyses at different levels such as production and end-of-life were performed. This research reflects what makes a sustainable design with an example of a cold-formed steel-concrete composite system, which addresses the need for improved awareness of materials.

1 INTRODUCTION

The interaction between steel and concrete has been widely used in structural engineering due to the multiple benefits that result from combining the desirable mechanical properties of each material. The advantages of structural steel are high tensile strength and ductility, while concrete ones are high stiffness and high compressive strength (Androić et al. 2012). In recent years, different solutions with cold-formed steel elements and lightweight concrete were investigated to find better behaviour over traditional solutions with hot-rolled steel elements and concrete slabs (Lukačević et al. 2022).

Based on built-up cold-formed steel beams with corrugated web, which show excellent behaviour throughout experimental (Benzar et al. 2015; Ungureanu et al. 2018b, 2018a) and numerical research (Ungureanu et al. 2021, 2019b, 2019a), it was possible to develop a new composite floor

system with the integration of concrete slab over built-up steel elements. LWT-FLOOR system represents innovation that maximises the values of each building component and used materials. This system has been investigated within the research project LWT-FLOOR at the University of Zagreb, Faculty of Civil Engineering, Croatia (Lukačević et al. 2022).

The proposed structural system is formed of built-up cold-formed steel beams and cast-in-place concrete slabs that are interconnected using an innovative type of shear connection.

The LWT-FLOOR project integrates fast and productive spot welding technology and innovative cold-formed steel-concrete composite solutions proposing a new construction method as a combination of built-up cold-formed steel members and cast-in-place concrete slab. This potentially cost-effective and sustainable floor system could offer vital benefits in a high degree of prefabrication, reusability, and suitability for larger spans. The LWT-FLOOR system has numerous potential benefits, which will be investigated through experimental, numerical research with the support of probabilistic methods and of life cycle analyses.

This paper presents a practical application of integrating environmental impacts associated with the LWT-FLOOR system mentioned and the traditional composite structural flooring system with hot-rolled steel beams. A comparative Life Cycle Assessment (LCA) of the structural composite steel-concrete floor system and traditional beam systems along with a Life Cycle Cost (LCC) was performed. The environmental impact analyses were carried out for different levels, such as production and end-of-life stages. This research reflects what makes a sustainable design with an example of a cold-formed steel-concrete composite system, which addresses the need for improved awareness of materials.

2 COMPARISON OF LWT-FLOOR SYSTEM WITH TRADITIONAL SYSTEMS

2.1 General

Considering the benefits of applying cold-formed steel (CFS) profiles in structures, the comparison of LWT-FLOOR steel cross-sections and traditional hot-rolled cross-sections is shown. LWT-FLOOR steel cross-section is formed of four C profiles connected in one unit with a corrugated web, and the beam is reinforced at the ends with shear plates. To make an appropriate comparison with the traditional system with hot-rolled sections, several criteria are observed:

- steel beam height, h ,
- cross-sectional area, A ,
- moment of inertia, I_y ,
- steel beam mass, m .

Based on the mentioned criteria, the profiles with the same or similar characteristics were searched among hot-rolled sections.

Analysed LWT-FLOOR steel cross-section has an overall height of 400 mm, and the length of the beam is 6 m. The steel beam is built-up of four C profiles whose height is 120 mm and the thickness is 2.5 mm. The mass of each profile is 4.61 kg/m, and the cross-sectional area is 600 mm² for each profile. All four cold-formed C120/2.5 profiles have a mass of 110.64 kg and a cross-sectional area of 2400 mm².

Considering that the corrugated web is not extended from end-to-end of the beam, its length is 5622 mm (unfold length is 6783 mm). The thickness of the analysed corrugated web is 1.0 mm, and the height is 400 mm. All mentioned leads to the corrugated web mass of 21.3 kg.

Four shear plates that reinforced the LWT-FLOOR steel beam are 400 mm high and 870 mm long. The thickness of shear plates is 1.0 mm. The mass of all four shear plates is 10.9 kg.

Based on mentioned geometry and arrangement of steel elements in the cross-section, the moment of inertia for the LWT-FLOOR steel beam is calculated with a value of 5063.7×10⁴ mm⁴. Based on this value, the hot-rolled profile will be searched for the same/similar moment of inertia criterion. Considering that cold-formed steel profiles are usually class 3 or 4, effective W_y values will be used to calculate the beam's bending resistance. In the following sections, a comparison based on mentioned criteria is shown. All steel elements are steel grade S350 GD.

2.2 Steel beam height and cross-sectional area

The height of the LWT-FLOOR steel beam is 400 mm. The same height has a hot-rolled steel profile IPE 400. The sectional area of IPE 400 is 1643 mm^2 , and the mass is 66.3 kg/m . This means that the steel beam IPE 400, with a length of 6 m, has a mass of 397.8 kg . The moment of inertia of IPE 400 is $23130 \times 10^4 \text{ mm}^4$.

In Figure 1a), the comparison between the LWT-FLOOR steel beam and IPE 400 is shown based on the same steel beam height. Based on shown values in Figure 1a), it is possible to see that the LWT-FLOOR steel beam has approximately four times reduced mass, cross-sectional area and moment of inertia.

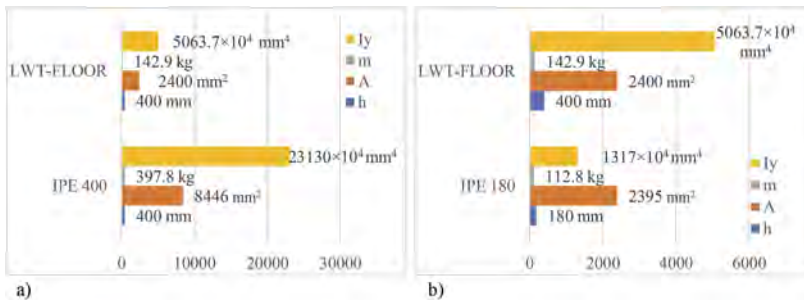


Figure 1. Comparison of beams a) with same steel beam height and b) with a similar cross-sectional area.

Considering the cross-sectional area of the LWT-FLOOR steel beam, the hot-rolled profile, IPE 180, which has a similar value of the cross-sectional area as the LWT-FLOOR steel beam, is chosen. The cross-sectional area of the LWT-FLOOR steel beam is 2400 mm^2 , while that of IPE 180 is 2395 mm^2 . The difference is negligible. The total mass of the IPE 180 beam is 112.8 kg , while the moment of inertia is $1317 \times 10^4 \text{ mm}^4$.

In Figure 1b), the comparison between the LWT-FLOOR steel beam and IPE 180 is shown based on a similar cross-sectional area. In Figure 1b), it is shown how beams with a similar cross-sectional area can have a height difference of up to 50%. Also, it is possible to see how a beam with a similar cross-sectional area can significantly differ in the moment of inertia.

2.3 Moment of inertia and steel beam mass

Considering the criterion of the moment of inertia, the LWT-FLOOR steel beam is compared with two hot-rolled profiles: IPE 240 and IPE 270. Mentioned profiles are chosen because the value of the moment of inertia of the LWT-FLOOR steel beam is in the range of moments of inertia of IPE 240 and IPE 270. The values and comparison of all other criteria for mentioned profiles are shown in Figure 2a).

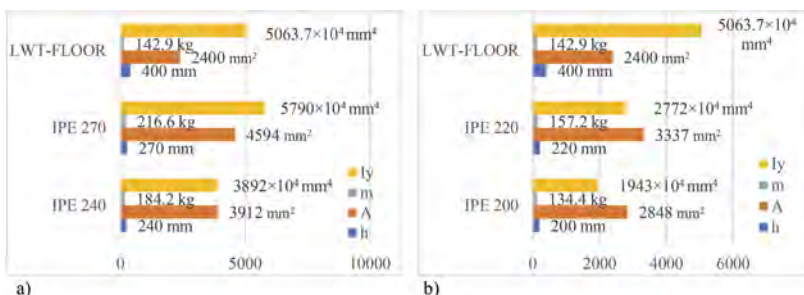


Figure 2. Comparison of beams a) with a similar moment of inertia and b) with a similar mass.

In Figure 2a), it is shown how beams, despite the similarity in a moment of inertia, have different cross-sectional areas. Also, the LWT-FLOOR beam has reduced mass compared to IPE 240 and IPE 270. On the other side, the height of the LWT-FLOOR beam is greater than it is for chosen hot-rolled profiles.

Based on the mass similarity, the profiles compared with the LWT-FLOOR beam are IPE 200 and IPE 220. These two profiles are compared because the value of the mass of the LWT-FLOOR beam is between the masses of IPE 200 and IPE 220. The comparison is shown in Figure 2b).

Figure 2b) shows a comparison of the LWT-FLOOR beam with two other steel beams composed of hot-rolled sections with the same mass. It is possible to see how steel beam height can be doubled for a similar value of mass and have a greater moment of inertia which will be important for the bending resistance of the beam. Furthermore, the LWT-FLOOR steel beam has a greater height, but a lower cross-sectional area compared to sections IPE 200 and IPE 220.

2.4 Bending resistances of analysed beams

In order to improve the application of the LWT-FLOOR beam, the bending resistance between different composite steel-concrete beams is compared. In previous paragraphs, the comparison between steel beams is shown. Now, the metal deck and concrete slab are positioned on each mentioned beam. For establishing the shear connection, bolts M12 with a height of 85 mm and quality 8.8 are used. The overall height of the concrete slab is 120 mm, and the used concrete class is C25/30. The height of the metal deck rib is 60 mm. The axial distance of metal sheet ribs in the longitudinal direction is 240 mm. The effective width of the concrete slab is 1500 mm. The LWT-FLOOR beam is designed as simply supported.

After creating composite beams, the calculation of bending resistances for full shear connection and in the case when shear connectors are positioned in pairs is shown. It is necessary to emphasise that for calculating the bending resistance of the composite LWT-FLOOR beam, the effective moment resistance, $W_{y,eff}$ is used because of the slender cross sections.

Figure 3 shows the comparison of bending resistances for full shear connection and when shear connectors are positioned in pairs.

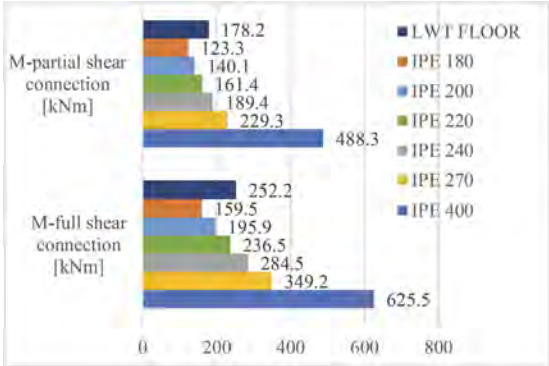


Figure 3. Bending resistance for composite steel-concrete beams.

It is very important to say that a full shear connection is not possible to achieve by arranging the shear connectors because the ribs of the metal deck determine the arrangement of shear connectors. Full shear connection is possible only by tie constraint in the numerical model, which will eliminate the slip between steel and concrete elements. For that reason, only the case when shear connectors are arranged in pairs will be discussed. Also, the longitudinal distance between bolts is defined by the axial distance of metal deck ribs and amounts to 240 mm. At the analysed shear length, nine bolt pairs are positioned, and an equal number of bolt pairs are positioned on every analysed beam.

Considering that position of the neutral axis for composite beam IPE 400 is in the steel part of the composite section, the bending resistance for the mentioned beam is calculated with W_y ,

while for other composite beams made of hot-rolled steel profiles $W_{y,pl}$ is used because the neutral axis is in the concrete slab. The bending resistance for the LWT-FLOOR beam is calculated as it is explained in the paper (Lukačević et al. 2022). Based on the results shown in Figure 3, it is concluded that the LWT-FLOOR beam has very good bending resistance among all analysed composite beams. IPE 400 beam has the greatest bending resistance, as expected. LWT-FLOOR composite beam has a bending resistance similar to IPE 240. Another beam with higher resistance than the LWT-FLOOR beam is IPE 270. Taking into account the cross-sectional area and weight of beams that have greater bending resistance than the LWT-FLOOR beam, it is concluded that mentioned beams have greater cross-sectional area than the LWT-FLOOR beam, which also leads to greater mass. Considering all mentioned, the LWT-FLOOR beam can be considered as a potentially good candidate for buildings of business or residential purposes. The next section will provide the LCA analysis results, which will show the environmental impact of the proposed LWT-FLOOR system compared to the traditional steel-concrete composite floor systems previously analysed in this paper.

3 LIFE CYCLE ASSESSMENT

The LCA carried out presents the environmental impact of each composite floor system discussed earlier in the paper, from cradle-to-gate with modules C and D. In the analysis was considered the Production stage phases (A1, A2, A3) and End-of-life (C1, C2, C3, C4), in conjunction with Potential environmental loads and benefits (D), under EN 15643-1:2012 and EN 15804:2012+A2:2019, using GaBi database and LCA software (Sphera Solutions GmbH 2021). The declared unit in the analysis is one composite floor system with a length of 6000 mm.

In the production stage (modules A1-A3) it was considered the extraction and processing of raw materials, as well as energy consumption, the transportation of the raw materials to the manufacturers or to the ready-mix plant (the model includes road transportation of each raw material using Euro 5 articulated lorries transport (16 t payload capacity), the manufacture of products, packaging, the energy consumption and the waste generated at the production plants, the water during the concrete manufacturing process.

In a normal-use scenario, we assumed that no maintenance (B2), repair (B3), replacement (B4), nor refurbishment (B5) is needed. Therefore, the assessment does not specify values for module B.

In this assessment, the end-of-life scenario for each one of the seven composite floor systems studied involved an instance of “demolition and recycling”. Module C1 includes the use of diesel fuel used by work machines during the demolition process, and module C2 includes the transport to waste processing (a conservative assumption of 50 km by lorry 16t payload capacity was used). For modules C3 and C4, the scenarios included are representative of one of the most probable alternatives: 90% of steel is transformed into secondary material in a recycling plant (based on the European average), and 10% of the steel is assumed to be landfilled while the concrete is 50% recycled and 50% landfilled.

Module D reflects the avoided burdens considering the potential recycling of the construction materials after the end-of-life stage of the composite floor systems. The scrap content in the steel components (steel profiles, corrugated steel sheet, bolts) has been acknowledged. Only the mass of primary steel in the components was considered to provide a benefit to avoid double counting. For the concrete, the avoided product is considered crushed aggregate.

4 RESULTS OF LCA AND ECONOMIC IMPACT

This paper presents a practical application of integrating environmental impacts associated with the LWT-FLOOR system mentioned and the traditional composite structural flooring system with hot-rolled steel beams. The research reflects the benefits of a sustainable design with an example of a cold-formed steel-concrete composite system, which addresses the need for improved awareness of materials.

Tables 1, 2, and 3 outline the greenhouse gas (GHG) emissions for each case scenario. As the results show (see Table 1), in the production stage (A1-A3), the emissions reflected by the Global

Warming Potential-total (GWP-total) indicator are up to 34% smaller when LWT-FLOOR is used in comparison with the traditional steel-concrete composite floor systems based on the IPE 220 - IPE 400 steel beams. Only the steel-concrete composite floor systems based on beams with a similar cross-sectional area (IPE 180) and on beams with a similar moment of inertia (IPE 200) record smaller emissions in the GWP-total, in the production stage, than the LWT-FLOOR.

Table 1. LCA results for the Production stage.

Environmental impacts	Production stage – Modules A1-A3							
	Unit	LWT-Floor	IPE 400	IPE 270	IPE 240	IPE 220	IPE 200	IPE 180
GWP-total	kg CO2 eq	7,29E+02	1,11E+03	8,30E+02	7,80E+02	7,38E+02	7,03E+02	6,69E+02
GWP-fossil	kg CO2 eq	7,27E+02	1,11E+03	8,29E+02	7,78E+02	7,37E+02	7,01E+02	6,68E+02
GWP-biogenic	kg CO2 eq	4,90E-01	7,13E-01	5,13E-01	4,77E-01	4,47E-01	4,22E-01	3,98E-01
GWP-luluc	kg CO2 eq	6,88E-01	8,82E-01	7,12E-01	6,81E-01	6,56E-01	6,35E-01	6,14E-01
Ozone depletion potential	kg CFC-11 eq	3,53E-05	1,99E-05	1,99E-05	1,99E-05	1,99E-05	1,99E-05	1,99E-05
Acidification pot.	mol H+ eq	2,80E+00	3,30E+00	2,53E+00	2,39E+00	2,28E+00	2,18E+00	2,09E+00
EP-freshwater	kg P eq	1,78E-01	8,38E-02	8,36E-02	8,36E-02	8,35E-02	8,35E-02	8,35E-02
EP-marine	kg N eq	5,31E-01	6,10E-01	4,44E-01	4,15E-01	3,90E-01	3,69E-01	3,49E-01
POCP (“smog”)	kg NMVOC eq	2,52E+00	2,71E+00	2,10E+00	1,99E+00	1,90E+00	1,82E+00	1,75E+00
ADP-minerals & metals	kg Sb eq	7,31E-03	4,12E-03	4,50E-03	4,56E-03	4,62E-03	4,67E-03	4,71E-03
ADP-fossil resources	MJ	5,98E+03	1,00E+04	6,98E+03	6,44E+03	5,98E+03	5,60E+03	5,24E+03
Water use	m3 eq	2,88E+02	1,78E+02	1,79E+02	1,79E+02	1,79E+02	1,79E+02	1,79E+02

Table 2. LCA results for the End-of-life stage.

Environmental impacts	End-of-life stage – Modules C1-C4							
	Unit	LWT-Floor	IPE 400	IPE 270	IPE 240	IPE 220	IPE 200	IPE 180
GWP-total	kg CO2 eq	3,25E+01	3,59E+01	2,97E+01	2,86E+01	2,77E+01	2,69E+01	2,62E+01
GWP-fossil	kg CO2 eq	3,25E+01	3,64E+01	3,00E+01	2,88E+01	2,79E+01	2,71E+01	2,63E+01
GWP-biogenic	kg CO2 eq	1,68E-02	-5,01E-01	-2,60E-01	-2,16E-01	-1,80E-01	-1,50E-01	-1,21E-01
GWP-luluc	kg CO2 eq	2,56E-02	3,56E-02	3,02E-02	2,92E-02	2,84E-02	2,77E-02	2,71E-02
Ozone depletion potential	kg CFC-11 eq	9,52E-06	9,73E-06	8,63E-06	8,43E-06	8,26E-06	8,13E-06	7,99E-06
Acidification pot.	mol H+ eq	3,66E-01	4,15E-01	3,49E-01	3,38E-01	3,28E-01	3,20E-01	3,12E-01
EP-freshwater	kg P eq	5,62E-03	5,91E-03	5,60E-03	5,55E-03	5,50E-03	5,46E-03	5,43E-03
EP-marine	kg N eq	4,69E-02	4,34E-02	2,65E-02	2,35E-02	2,10E-02	1,88E-02	1,68E-02
EP-terrestrial	mol N eq	1,43E+00	1,41E+00	1,22E+00	1,18E+00	1,15E+00	1,13E+00	1,11E+00
POCP (“smog”)	kg NMVOC eq	4,09E-01	4,02E-01	3,49E-01	3,40E-01	3,32E-01	3,25E-01	3,19E-01
ADP-minerals & metals	kg Sb eq	8,61E-05	6,68E-04	3,91E-04	3,41E-04	3,00E-04	2,65E-04	2,32E-04
ADP-fossil resources	MJ	7,67E+02	8,24E+02	7,33E+02	7,17E+02	7,03E+02	6,91E+02	6,81E+02
Water use	m3 eq	1,35E+01	1,51E+01	1,41E+01	1,39E+01	1,37E+01	1,36E+01	1,35E+01

For the end-of-life stage (C1-C3), the results show (see Table 2) that the emissions in the GWP-total are all smaller with 9-19% for the traditional steel-concrete composite floor systems based on hot-rolled steel profiles than the LWT-FLOOR, except for the steel-concrete composite floor system based on the IPE400 steel beam, which indicated 10.46% more emissions in the GWP-total than the LWT-FLOOR.

Table 3 shows the potential benefits and loads beyond the system boundaries reflected by each type of composite floor system analysed through the considered recycle scenario of the LCA. The LCA potential savings are reflected as negative values, while positive values define potential burdens of material utilisation.

For the GWP-total indicator, the results show that beyond the system boundary, in the scenario where LWT-FLOOR is used, the potential savings are 83%-141% higher than in the scenarios where traditional steel-concrete composite floor systems were considered. Figure 4a) shows the total LCA results of the scenarios in terms of GWP - total, including loads and benefits beyond the system boundary.

Table 3. LCA results for the potential environmental benefits of the assumed scenarios.

Environmental impacts	Loads and benefits beyond the system limits - Module D							
	Unit	LWT-Floor	IPE 400	IPE 270	IPE 240	IPE 220	IPE 200	IPE 180
GWP-total	kg CO2 eq	-2,61E+02	-1,42E+02	-1,20E+02	-1,16E+02	-1,13E+02	-1,10E+02	-1,08E+02
GWP-fossil	kg CO2 eq	-2,61E+02	-1,42E+02	-1,20E+02	-1,16E+02	-1,13E+02	-1,10E+02	-1,08E+02
GWP-biogenic	kg CO2 eq	-2,61E-01	1,96E-01	3,43E-02	5,43E-03	-1,86E-02	-3,89E-02	-5,81E-02
GWP-luluc	kg CO2 eq	-2,07E-01	-7,92E-02	-7,98E-02	-7,99E-02	-8,00E-02	-8,01E-02	-8,02E-02
Ozone depletion potential	kg CFC-11 eq	-1,35E-05	-7,18E-06	-6,60E-06	-6,50E-06	-6,41E-06	-6,34E-06	-6,27E-06
Acidification pot.	mol H+ eq	-1,19E+00	-6,67E-01	-5,83E-01	-5,68E-01	-5,56E-01	-5,45E-01	-5,35E-01
EP-freshwater	kg P eq	-1,15E-01	-4,14E-02	-4,06E-02	-4,04E-02	-4,03E-02	-4,02E-02	-4,01E-02
EP-marine	kg N eq	-2,37E-01	-1,16E-01	-9,97E-02	-9,67E-02	-9,43E-02	-9,22E-02	-9,03E-02
EP-terrestrial	mol N eq	-2,66E+00	-1,56E+00	-1,39E+00	-1,36E+00	-1,33E+00	-1,31E+00	-1,29E+00
POCP ("smog")	kg NMVOC eq	-1,17E+00	-6,98E-01	-5,84E-01	-5,64E-01	-5,47E-01	-5,33E-01	-5,19E-01
ADP-minerals & metals	kg Sb eq	-2,93E-03	-1,11E-03	-1,09E-03	-1,09E-03	-1,08E-03	-1,08E-03	-1,08E-03
ADP-fossil	MJ	-2,76E+03	-1,36E+03	-1,20E+03	-1,17E+03	-1,15E+03	-1,13E+03	-1,11E+03
Water use	m3 eq	-1,19E+02	-4,50E+01	-4,19E+01	-4,14E+01	-4,09E+01	-4,05E+01	-4,01E+01

For the economic impact of the assessed steel-concrete composite floor systems, it was considered the financial cost of the analysed scenarios associated with the Production stage. The prices considered in the analysis represent the prices of construction materials listed on the Romanian market in December 2022 and do not include VAT. Figure 4b) shows the total production cost of each scenario, in terms of euro+VAT/steel-concrete composite floor considered in the analysis previously presented in the paper.

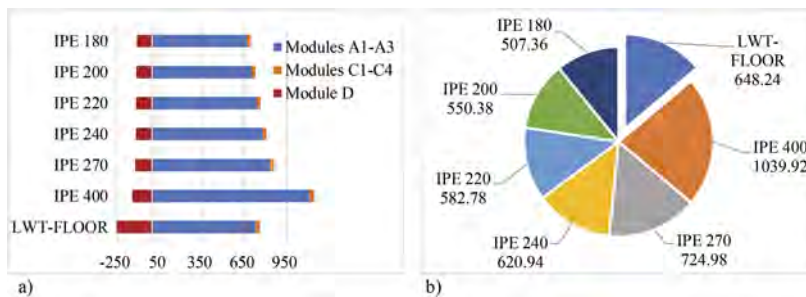


Figure 4. Total LCA results and production costs of the steel-concrete composite floor systems a) environmental impact: GWP - Total [kg CO2 e] and b) production cost [Euro + VAT].

As the results of the economic impact show, in the production stage (A1-A3), the costs of the LWT-FLOOR are above the costs of the production of the traditional steel-concrete composite floor systems based on the IPE 180 - IPE 240 steel beams, but with 37.6% smaller than the solution based on IPE 400 steel beam.

5 CONCLUSIONS

The present assessment considered different case studies of steel-concrete composite floor systems based on hot-rolled beams and the LWT-FLOOR system, an innovative

demountable composite floor system developed at the University of Zagreb, Faculty of Civil Engineering, Croatia.

The system is based on cold-formed steel elements, which are built-up beams with back-to-back channel profiles and corrugated web, connected by spot-welding technology and cast-in-place concrete slabs that are interconnected using an innovative type of shear connection.

In the first part of the paper, by comparing the geometrical characteristics of different composite beam configurations, it is concluded that the LWT-FLOOR beam has good bending resistance with low material consumption.

The LCA and LCC assessment in the second part of the paper focused on the structural feasibility, environmental benefits, and economic savings of the LWT-FLOOR system set side by side with the traditional steel-concrete composite floor systems. The results showed that in the production stage, the environmental impact (reflected by the GWP-total indicator) is up to 34% smaller when LWT-FLOOR is used in comparison with the traditional steel-concrete composite floor systems based on the IPE 220 - IPE 400 steel beams, while the costs of it are smaller with 10-37% compared to steel-concrete composite floor systems based on the IPE 270 - IPE 400.

On the other hand, in terms of environmental impact, the GWP-total indicator shows that the potential savings by recycling the materials at the end-of-life of the composite floor systems are 83%-141% higher in the scenario where LWT-FLOOR is used than in the scenarios where traditional steel-concrete composite floor systems were studied.

ACKNOWLEDGEMENTS

This research was partially funded by the Croatian Science Foundation, grant number UIP-2020-02-2964 (LWT-FLOOR project - Innovative lightweight cold-formed steel-concrete composite floor system), project leader: Ivan Lukačević and by a grant of the Romanian Ministry of Research and Innovation, CCCDI-UEFISCDI, project number PN-III-P2-2.1-PTE-2021-0237-Wellformed-Frames.

REFERENCES

- Androić, B., Dujmović, D. & Lukačević, I. 2012. Design of Composite Structures According to Eurocode 4. *IA Projektiranje*, Zagreb, Croatia.
- Benzar, S., Ungureanu, V., Dubina, D. & Burca, M. 2015. Built-Up Cold-Formed Steel Beams with Corrugated Webs Connected with Spot Welding. *Adv. Mater. Res.* 1111, 157–162.
- EN 15643-1:2012. *Sustainability of construction works. Sustainability assessment of buildings. Part 1: General framework*. CEN, Brussels, Belgium.
- EN 15804:2012+A2:2019. *Sustainability of construction works - Environmental product declarations - Core rules for the product category of construction products*. CEN, Brussels, Belgium.
- Lukačević, I., Čurković, I., Rajić, A. & Bartolac, M. 2022. Lightweight Composite Floor System - Cold-Formed Steel and Concrete - LWT-FLOOR Project. *Buildings* 12, 209.
- Sphera Solutions GmbH 2021. *GaBi: Product Sustainability Software*. (10.6).
- Ungureanu, V., Both, I., Burca, M., Grosan, M., Neagu, C. & Dubina, D. 2018a. Built-up cold-formed steel beams using resistance spot welding: experimental investigations. *The Eighth International Conference on Thin-Walled Structures (ICTWS 2018)*. Lisbon, Portugal, Portugal, e-Proceedings.
- Ungureanu, V., Both, I., Burca, M., Tunea, D., Grosan, M., Neagu, C. & Dubina, D. 2018b. Welding technologies for built-up cold-formed steel beams: experimental investigations. *The Ninth International Conference on Advances in Steel Structures (ICASS'2018)*. Hong Kong, China, e-Proceedings.
- Ungureanu, V., Lukačević, I., Both, I. & Burca, M. 2019a. Numerical investigation of built-up cold-formed steel beams connected by spot welding. *The Evolving Metropolis, 2019 IABSE Congress*. New York USA, e-Proceedings.
- Ungureanu, V., Lukačević, I., Both, I., Burca, M. & Dubina, D. 2019b. Built-Up Cold-Formed Steel Beams with Corrugated Webs Connected by Spot Welding - Numerical Investigations. *The International Colloquia on Stability and Ductility of Steel Structures (SDSS 2019)*. Prague, Czech Republic, e-Proceedings.
- Ungureanu, V., Both, I., Burca, M., Radu, B., Neagu, C. & Dubina, D. 2021. Experimental and numerical investigations on built-up cold-formed steel beams using resistance spot welding. *Thin-Walled Structures* 161, 107456.

Sustainability and seismic resilience of hybrid lightweight residential buildings

D. Dubina & V. Ungureanu

Politehnica University of Timisoara, Timisoara, Romania
Romanian Academy, Timisoara Branch, Timisoara, Romania

M. Mutiu

Politehnica University of Timisoara, Timisoara, Romania

ABSTRACT: In the first part of the paper, three examples of sustainable mixed building technologies are presented, which, for the main frame, combine cold-formed with hot-rolled steel sections, using timber for floor joists and cladding studs. In the second part of the paper, two examples of single-family houses made of cold-formed steel wall studs sheathed with OSB are detailed. The buildings are located in moderate seismic regions. The paper presents aspects related to design and detailing, including aspects of structural features. For structural design, a prescriptive method was applied, based on the test results on full-scale shear wall panels made of cold-formed steel profiles and OSB panels, under monotonic and cyclic loads. The results of life-cycle analyses of these constructions, compared with various traditional solutions, are also presented.

1 INTRODUCTION

In recent years, users, architects, and engineers have all been searching for the most economical building systems for dwellings. In this context, steel-framed houses have become a choice in many European countries, including Romania. The mechanical properties and lightweight of cold-formed steel profiles make them suitable for use in areas with low and moderate seismic risk. That is the reason why the new European Design Code for Seismic Resistant Buildings - Eurocode 8, still in the inquiry phase, has explicitly included design provisions for such structures (Landolfo et al. 2022). Light steel frame (LSF) structures of thin-walled cold-formed steel (TWCFS) wall studs and joisted floors are gaining growing popularity in modern construction practise worldwide, both in new developments and as a cost-effective and low-carbon solution for the vertical extension of existing buildings. The ease of off-site manufacturing using LSF structures offers many benefits compared to traditional methods, including: (a) improved quality and productivity, reduced material use, less waste, and savings of 30-50% in total construction time and associated costs; (b) flexibility for more customised design solutions complying with the Design for Manufacture and Assembly approach; and (c) scalability of automation technologies in the construction industry.

However, the current use of LSF structural systems is limited due to critical drawbacks such as the low local buckling resistance of TWCFS elements, the low lateral stiffness, and robustness of typical LSF systems and the limitations of current design and optimisation approaches to exploit their full capacity. Mixed technologies, also called hybrid construction, combine thin-walled cold-formed steel profiles with thicker hot-rolled steel profiles and/or with timber, to increase the stiffness and resistance, in the end improving the robustness and durability of building structures (Mortazavi et al. 2018). Lightweight cold-formed composite steel-concrete structural systems have continuously been increasing within the field of structural engineering due to efficient material usage, particularly noticeable when using cold-formed built-up sections and the innovative types of shear connections (Lukačević et al. 2022).

Compared with ordinary steel moment resisting frames or with cold-formed steel wall stud systems, the economic assessment demonstrates that hybrid framed structures can save up to

23% in framing costs. On the other hand, hybrid framed structures can lead to less environmental impact than previous two systems (Usefi et al. 2021). These buildings have great potential for prefabrication, making hybrid framed structures a better option with respect to many social compact indicators such as noise, air, vibration and dust pollution and traffic.

2 EXAMPLES OF RESIDENTIAL BUILDING HYBRID STRUCTURES

2.1 *Urban villa*

The structure is a block of flats built in 2007 in Timisoara, a moderate seismic zone, with a temperate continental climate, in Romania (Ungureanu et al. 2011a). The keys to this kind of structure are built-in flexibility and energy efficiency. The main structure is made of steel profiles with light floors. Column-free and free floor slabs were the optimum answer to allow users to optimally reconfigure internal areas and this generally means long-span solutions. Some innovative design solutions have been used in this project, i.e. thermo-energetic cladding system, gas-electric energy supply system etc. Several types of cladding systems have been analysed, and for the chosen solution, data related to the performance of the cladding system have been collected during the 2008/2009 autumn/winter season. Figure 1 presents architectural views, the structure during erection, and the final view of the building.



Figure 1. Urban Villa. Hybrid structure: hot-rolled steel main frame, cold-formed steel wall-studs, cladding and OSB shear panels, light concrete composite floor slabs.

An intensive study has been carried out to choose the correct cladding solution (Mutiu 2011). Given the wide variations in seasonal temperature levels, as described above, and the cumulative effects of (1) overheating of the south and west facades in summer and (2) heat loss due to the effect of the wind chill on the north/northwest sides of the facade in winter, special attention was paid first of all to passive energy savings measures. Consequently, the envelope design was directed to achieve three main objectives: (1) to minimize heat loss through the envelope; (2) to ensure high levels of physical wellbeing; (3) to equip the building with an energy saving heating system.

2.2 *Traditional family house*

This is a single-family private house built in 2006 in Timisoara, Romania. The main structure is made of steel profiles, while the floor and roof are made of timber elements. The building combines modern and traditional materials and techniques (see Figure 2) to obtain a typical Transylvanian village house (Mutiu 2011).



Figure 2. Traditional family house. Hybrid structure: hot-rolled steel for the main steel skeleton, timber rafters, supporting floor and roof, and timber wall stud claddings.

2.3 Modern family house

This single-family private house, with courageous architecture, was built in 2010 in Resita, South-West of Romania, in a low seismic but quite windy zone. Architectural and structure views during construction are presented in Figure 3 (Mutiu 2011). In terms of flexibility in layout, the use of hot-rolled steel framing presents several advantages, such as longer spans and large wall openings.

In addition, architectural expression can be pushed to the limit through cantilevers and roof overhangs. To support an envelope, a secondary structural system (wall structure) is required. Such structures are usually made of lightweight studs and constitute the frame on which the successive envelope layers are fastened. Extended use of OSBs on the upper floors provides stiffness and high shear strength, allowing them to behave as rigid boxes (see Figure 3).



Figure 3. Modern family house. Hybrid structure: hot-rolled steel for the main frame, OSB-sheathed cold-formed steel wall studs, composite light concrete and cold-formed steel trapezoidal sheeting.

3 CASE STUDY

3.1 Sustainable detached family house

The first case study presents an innovative structure-envelope solution, enabling flexible floor plan and modular construction, faster fabrication and erection times and high solution diversity for flooring and envelope (Dubina et al. 2010). The architectural concept is based on the development of a rectangular footprint of 5.60 m × 13.40 m, which gives a first module of 75 m², for a one-level unit. The dwelling is a two-storey building, with a terrace roof, with a gross built area of 150 m² and a usable area of 124.41 m². Figure 4 presents the 3D view of the house. A further development of the house is possible by adding a new module by horizontal addition, extending in this way the living area.

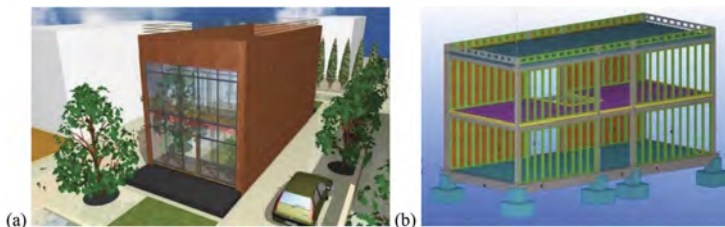


Figure 4. 3D view of the house: (a) architectural layout; (b) structural layout.

The proposed construction system, as shown in Figure 4, consists of: (1) hot-rolled steel framed structure; (2) secondary structure is composed of cold-formed steel studs (or wood studs); (3) various envelope systems; (4) floor structure - light concrete topping on trapezoidal steel deck; (5) double-glazed loggias with PVC or aluminium frames; (6) foundations and slab/cast in place reinforced concrete; (7) terrace roof or pitched roof. The achievement of thermo-energetic efficiency was another goal set by the design team. Several factors were considered: (1) indoor temperature and air quality; (2) thermal insulation; (3) moisture protection; (3) different heating and cooling systems; (4) passive ventilation and shading; (5) glazed terraces act as a buffer zone; (6) skylights will be used to improve cross ventilation for the one-level house.

The main steel structure is a two-storey portal frame structure in the transverse direction, while longitudinal shear walls are used to resist horizontal forces from the wind and earthquake. The columns are made of hot-rolled steel profiles and are rigid at the base in the transverse direction and pinned in the longitudinal direction. The transversal girders are made of hot-rolled steel profiles with semi-rigid beam-to-column connections, while the longitudinal girders are pin-ended. To take over horizontal longitudinal loads, shear walls made of cold-formed steel studs sheathed with 10 mm OSB on both sides are used.

The structure is designed considering the climatic and seismic conditions of the city of Timisoara, Romania. The loads used for the design of the structure are taken according to Romanian codes, aligned with the relevant Eurocodes. To control floor vibrations, a deflection of $L/350$ was considered reasonable for a family house. In terms of seismic response, the performance of the shear walls is crucial. The results of the full-scale wall panels test, made with a cold-formed wall-stud skeleton and different cladding arrangements, commonly used in residential buildings, tested at the Politehnica University of Timisoara (Dubina et al. 2010), have been used as reference values to check the available shear strength of walls.

The shear resistance of cold-formed steel wall stud panel specimens sheathed with 10 mm OSB under cyclic loads was found to be 69844 N, as shown in Figure 5 (Dubina et al. 2010). For a panel length of 3.6 m, this leads to a value of 19.40 kN/m.

Based on experimental results, a very simple method can be applied to calculate the efficiency of shear wall panels. Due to the fact that the structure is very regular, with planes of symmetry on both axes and distinct load path, the analysis can be divided following the two principal directions, i.e. transversal and longitudinal ones. In the transverse direction, the seismic action is resisted by the portal frames, while longitudinally by the shear walls. Finally, the lengths of walls necessary to provide the shear capacity were calculated.

The design approach also included information about the environmental impact of the building (Dubina et al. 2010). For this purpose, the next step in design is a comparative life-cycle analysis of the house described above for various solutions.

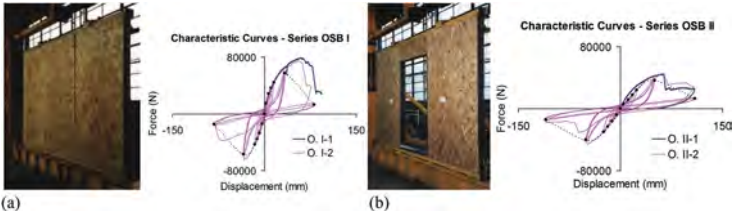


Figure 5. Design assisted by testing. Experimental curves for wall panels sheathed with OSB.

For this purpose, the building was designed in four different solutions, each of them having its own structural system, as follows: (1) hot-rolled steel framing, the innovative structure; (2) cold-formed steel framing; (3) wood framing and (4) masonry. *Hot-rolled steel frames*: moment resisting frames in transversal directions, while in longitudinal direction the structure is stiffened by cold-formed shear walls sheathed with OSB. The floor structure is made of light concrete topping on a trapezoidal steel deck. The infrastructure is made up of an isolated foundation connected to the foundation beams. *Cold-formed steel framing structure*. In this case, the construction system consisted of: (1) isolated foundations under columns linked by foundation beams and a concrete floor slab; (2) cold-formed steel profiles for the framed skeleton structure (C150 cold-formed sections); (3) secondary structure made of cold-formed steel studs (C150 profiles spaced at 600 mm) on which OSB is laid interior and exterior, in order to stiffen the steel framing for lateral loads, including wind and seismic loads; (4) floor structure made of OSB on trapezoidal steel deck; (5) envelope system and double-glazed loggias with aluminium frames; (6) flat roof (thermal and hydro-insulations) laid on trapezoidal steel sheeting. *Wood framing structure*, which is carried out on the same principle as the cold-formed system. In this case, the wood skeleton extends to the roof. The secondary structure and envelope are built on the same principle as in the case of the cold-formed house. *Masonry structure*. This is the classic

Romanian solution of dwelling, with 25 cm thick hollow brick walls and thermal insulation of polystyrene. The infrastructure system is ensured by continuous foundations under the walls and a solid concrete slab. The flooring and roof are also a 13 cm reinforced concrete slab.

Besides the life-cycle analysis at the level of structural skeletons, studies regarding the cladding solution, versatility and adaptability on the four structural skeletons are integrated. Several aspects are presented in turn, in order to underline the impact for different stages during the life-cycle: (a) construction stage only; (b) construction stage and final disposal of materials; (c) construction stage, disposal and maintenance. Figure 6 presents the scoring of all stages of the life-cycle of buildings (single score) as a direct sum of the construction stage, the maintenance of the building for a 50-year service life period of and the disposal at the end-of-life for the constitutive materials.

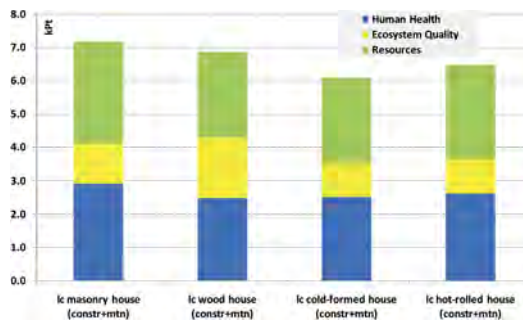


Figure 6. LC comparison on environmental impact for construction, including maintenance and end-of-life.

In a single score analysis and considering the boundary conditions, i.e. all identical components are left out of the comparison (see Dubina et al. 2010), the steel houses (6096 and 6481 eco-points, respectively) present an important advantage in front of masonry house (7192 eco-points), while the score for the wood house is about the average value corresponding to the impact of the other three solutions. Of course, many parameters (such as national or regional peculiarities, climatic zones, or distance from the material distributors) can affect these results. From this point of view, one has to observe the trends and not the values given by the analyses.

In addition to this, the following advantages of this structural system can be underlined: (1) functional and aesthetic architecture; (2) modularity and adaptability; (3) improved structural performance, particularly for seismic action; (4) cost-effective.

The analyses performed show the following aspects: (1) steel framing solutions (both hot-rolled and cold-formed framings) represent a good alternative to the classic masonry house, both from safety and sustainability points of view; (2) all framing solutions present a better environmental impact for construction stage and life-cycle analyses on building materials compared to the classic masonry house; (3) the maintenance process of steel and wood solutions is more complex than that of a masonry house. Furthermore, it could be easily observed that maintenance plays a major role in terms of environmental impact.

3.2 *TWCFS shear wall studs OSB-sheathed family house*

The structure for this single-family house was built in 2005 in Ploiesti (Ungureanu et al. 2011b), in a zone of higher seismic risk ($a_g = 0.35g$). There are two main characteristics of the built house, namely the lightweight-steel framing and the architectural solution constrained by the shape of the site (see Figure 7). From an architectural point of view, the main challenge of the project was to fit this private house on an irregularly shaped lot of only 168 m². The resulting cube-shaped building was measured at the end of 84 m² of built area on each of the two floors.

Due to the proximity of the buildings on adjacent properties, the next difficulty consisted of finding the balance between the right amounts of views, natural light, and privacy. Because the building seats in the property limit, it was impossible to provide window openings on that side. This was also one of the reasons for the roof to have a single slope, the height of the building ranging from 9 to 10.5 m. Each floor has approximately 2.75 m height with a roof slope of 30°. Two skylights located above the staircase and the hallway were placed to provide a light shaft to enhance the centre.



Figure 7. (a) 3D view of the house; (b) steel skeleton; (c) skeleton with structural OSB sheathing.

The structural skeleton is made of light-gauge C-shaped profiles (C150/1.5) spaced at intervals of 600 mm, with a thickness of 1.5 mm, fixed with self-drilling screws of 4.8 mm diameter (see Figure 7b). The height of the cross-section of profiles is 150 mm, which governed the thickness of the walls. To withstand horizontal actions and to provide stiffness and strength, the walls were stiffened with 12 mm thick OSB provided on both sides of the structural walls (see Figure 7c).

The load bearing beams in the slab are C200/1.5 profiles disposed at 600 mm intervals, this distribution resulting from the condition of controlling the vibrations of the floor rather than from strength conditions. Roof purlins were obtained as Z150/1.5 profiles spaced at 1200 mm intervals.

The floor diaphragms were designed to be based on the same principle of covering with OSB. No concrete was used on the slab. The isolated foundations under the columns were connected by foundation beams. The floor at ground level (a 10 cm concrete slab) was carried out over a dense soil bed and a layer of compacted gravel.

In terms of seismic response, the methodology presented in Section 3.1 was applied, in which full-scale shear wall panels made with a cold-formed wall stud skeleton and different cladding arrangements were tested (Ungureanu et al. 2011b). On the basis of experimental results, the methodology presented above can be applied to calculate the efficiency of shear wall panels, the structure being divided in two principal directions, i.e. transversal and longitudinal ones. Finally, the length of walls necessary to provide the shear capacity were calculated.

For 3D analysis, the rigidity induced by the sheathing has been replaced by equivalent cross bracings and considering the frame to be pinned. Rigidity criteria and test results on wall specimens have been used to calibrate the area of equivalent braces. The structure is subjected to torsion during an earthquake because some walls are fully sheathed, while others accommodate all the openings. The maximum shear force in this wall was 43 kN (12.8 kN/1m).

The total length of the shear wall panels that compose the analysed TWCFS structure, for the ground and first floors, both in the transverse (TV) and longitudinal (LG) direction are: (1) for the transverse direction, ground floor 21.55 m and first floor 17.12 m; (2) for the longitudinal direction, ground floor 17.22 m and first floor 12.42 m.

The masses were calculated from the earthquake combinations ($1 \times$ self weight + $0.4 \times$ live load + $0.4 \times$ snow load) according to Romanian standards. The first three vibration modes of the structure have been simulated using FE analysis, and the corresponding periods of vibration are the following: $T_1 = 0.38$ s, $T_2 = 0.35$ s and $T_3 = 0.26$ s.

In a first step, the total mass of the structure is evaluated, at the level of the first floor and at the roof level, taking into account the loads and safety coefficients considered for the special combination of seismic action:

$$\sum_{j=1}^n G_{k,j} + \gamma_I A_{E,k} + \sum_{i=2}^m \psi_{2,i} Q_{k,i} \quad (1)$$

where: $A_{E,k}$ – characteristic value of seismic action; $\psi_{0,i}$ – factor for combination value of the variable action i ; Q_i – 0.4 for snow load and live load.

It results: (i) the total mass at the floor level $M_{\text{floor}} = 23.07$ t and (ii) the total mass at the roof level $M_{\text{roof}} = 11.71$ t. Accordingly, the total seismic force applied to the structure is:

$$S_e(T) = \gamma_I \cdot a_g \cdot \beta(T) \cdot g \cdot M = 1 \cdot 0.28 \cdot 2.75 \cdot 9.81 \cdot (23.07 + 11.71) = 262.72\text{kN} \quad (2)$$

Considering that the deformation is linear in terms of height, the horizontal load is distributed to both levels as follows:

$$S_1 = S_r \cdot \frac{z_1 \cdot G_1}{\sum (z_j \cdot G_j)} = 262.72 \cdot \frac{3 \cdot 23.07}{(3 \cdot 23.07 + 7 \cdot 11.71)} = 120.27\text{kN}$$

$$S_2 = S_r \cdot \frac{z_2 \cdot G_2}{\sum (z_j \cdot G_j)} = 262.72 \cdot \frac{7 \cdot 11.71}{(3 \cdot 23.07 + 7 \cdot 11.71)} = 142.45\text{kN} \quad (3)$$

The total seismic force corresponding to both levels are:

$$T_{ground\ floor} = S_1 + S_2 = 262.72\text{kN} \text{ and } T_{first\ floor} = S_2 = 142.45\text{kN} \quad (4)$$

Based on experimental work, for the analysed shear wall panels, the shear capacity under cyclic loadings was found to be 69844 N (Ungureanu et al. 2011b), which means for a length of 3.6 m of the tested panels an experimental reference capacity of 19.40 kN/m.

Finally, the length of walls necessary to provide the shear capacity results as:

$$L_{ground\ floor} = \frac{T_{ground\ floor}}{P_{calc}} = \frac{262.72}{19.40} = 13.54\text{m} < 21.55\text{m(TV)}; < 17.22\text{m(LG)} \quad (5)$$

$$L_{first\ floor} = \frac{T_{first\ floor}}{P_{calc}} = \frac{142.45}{19.40} = 7.34\text{m} < 17.12\text{m(TV)}; < 12.42\text{m(LG)}$$

Examples of shear walls in the transversal and longitudinal directions are presented in Figure 8.

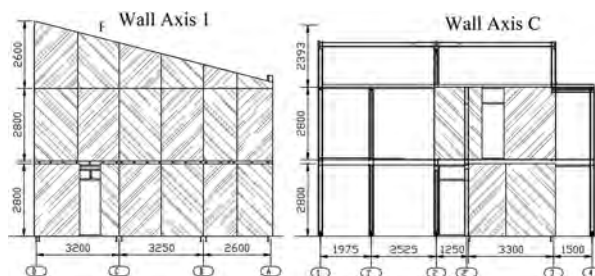


Figure 8. Examples of shear walls on transversal and longitudinal directions (Ungureanu et al. 2011b).

To have a complete study, the integration of environmental impact was performed in the design of the buildings. The case study compares the environmental impact of a single-family house, designed in two different situations: the existing thin-walled cold-formed house and the same house designed in masonry solution, the so-called traditional house. Impact analyses were performed at different levels: (i) construction, (ii) construction and end-of-life, (iii) life cycle including maintenance and, (iv) life cycle including maintenance and consumable goods (Ungureanu et al. 2011b). The structural system of the masonry house was made up of 25 cm masonry walls, a concrete floor, continuous foundations and a wooden roof structure. Due to the different thicknesses of the walls used in the two solutions, the main preoccupation was to obtain the same interior volume for all rooms. The design considers the same location of the building and the same imposed and climatic loadings. The details of the environmental impact comparison were presented in detail by Ungureanu et al. (2011b). Both solutions were designed for a service life of 50 years.

In a single score representation (see Figure 9), and considering the boundary conditions (all identical components are left out of the comparison, i.e. windows, doors etc.), the metallic house (2750 eco-points) presents an important advantage in front of the traditional home (4220 eco-points). Of course, many parameters (such as national or regional peculiarities, climatic zones, or distance from the material distributors) can affect these results.

The main conclusion of the study highlights that steel dwellings with cold-formed structural elements represent a good alternative to masonry houses, not only with respect to structural requirements but also considering the environmental impact assessment.

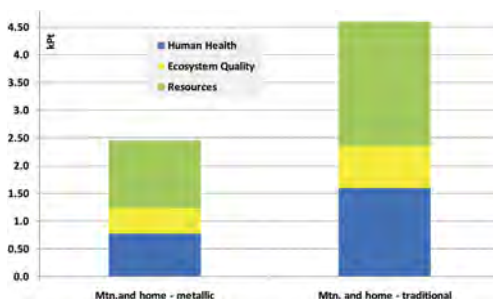


Figure 9. Life-cycle comparison on environmental impact for the metallic and traditional house (single score) for construction, including maintenance and end-of-life.

4 CONCLUDING REMARKS

The five examples summarised in the actual paper represent a complete sustainable technology of high-performance thermos-energetic materials for cladding and finishing and use productive and qualitative technologies both for fabrication and erection. It enables one to obtain flexible partitions and allows for further upgrade, easy modifications and/or development.

All buildings are located in moderate-to-high seismic regions. Compared to traditional housing technologies, steel frame houses, in addition to their technical advantages and improved quality of both structure and finishing, are also cost-effective. The hybrid structures of the mainframes of these buildings have proven their advantages compared to the traditional solutions.

Another important aspect to be highlighted for this type of structures is the end-of-life of construction products that plays an important role, considering the circular economy, as buildings have a long intended life span and require a significant amount of material resources. To maintain circularity, these resources must be kept in use through modularity, reuse, reclaim, or recycling. The end-of-life credentials of structural materials vary due to their inherent properties. Therefore, the reuse of steel is a viable solution to meet the criteria of the circular economy and reduce energy demand.

REFERENCES

- Dubina, D., Ungureanu, V., Ciutina, A., Tuca, I. & Mutiu, M. 2010. Sustainable detached family house - case study. *Journal of Steel Construction. Design and Research* (3):154–162.
- Landolfo R., Shakeel, S. & Fiorino, L. 2022. Lightweight steel systems: Proposal and validation of seismic design rules for second generation of Eurocode 8. *Thin-Walled Structures* 172:108826.
- Lukačević, I., Čurković, I., Rajić, A. & Bartolac, M. 2022. Lightweight Composite Floor System-Cold-Formed Steel and Concrete - LWT-FLOOR Project. *Buildings* 12(2):209.
- Mortazavi, M. Sharafi, P., Ronagh, H., Samali, B. & Kildashti, K. 2018. Lateral behaviour of hybrid cold-formed and hot-rolled steel wall systems: Experimental investigation. *J. Const. Steel Res.* 147:422–432.
- Mutiu, M. 2011. Design, Building Solutions and Performances for Steel Framed Houses, *PhD Thesis*, Politehnica University of Timisoara, Romania, No.78, Series 5, Civil Engineering.
- Ungureanu V., Ciutina, A. & Dubina, D. 2011a. Analyses of sustainability and environmental impacts of steel framed buildings – example from practice in Romania. *Proceedings of the 9th Nordic Symposium on Building Physics*. Tampere, Finland, Volume 3, 1347–1354.
- Ungureanu, V., Ciutina, A., Tuca, I., Dubina, D., Grecea, D., Fülöp, L. 2011b. Structural and Environmental Performance of Steel Framed Houses: A Case Study. *Summary report of the Cooperative Activities. Cost Action C25. Volume 1: Integrated approach towards sustainable constructions*, 395–428.
- Usedfi, N., Sharafi, P., Mortazavi, M., Ronagh, H. & Samali, B. 2021. Structural performance and sustainability assessment of hybrid-cold formed modular steel frame. *J. of Building Engineering* 34:101895.

Influence of fastening systems on the ultimate capacity of steel-faced sandwich wall panels under transverse loads

F. Dinu, C. Neagu & S. Lindiri

Politehnica University Timisoara, Romania

M. Senila

Technical University of Cluj-Napoca, Cluj-Napoca, Romania

ABSTRACT: Light weight sandwich wall panels are largely used for different kind of commercial or industrial buildings. They are typically designed from the weather/climate related conditions of the site (wind action, thermal comfort). Despite their low weight, they have adequate load carrying capacities under transverse (out of plane) loads, e.g., wind loads. However, under extreme loading conditions, like external explosions, such walls can be heavily damaged or destroyed, either under positive or negative pressure phases. The study presented in the paper describes the results obtained on wall sandwich panel elements tested for transverse loading until complete failure. The panels are arranged as single span systems supported on side rails and loaded at the mid-span using a quasi-static monotonic loading protocol. After an initial quasi-linear response, the maximum bending strength is reached. Then, due to a local buckling of the top face at mid-span, a sudden drop in load capacity is recorded, followed by a second increase in capacity due to development of catenary forces. If the end fasteners have adequate resistance, the ultimate capacity in the catenary stage can be significantly higher than the peak flexural capacity, which is generally used in the design. For small edge distance, the failure takes place due to the pull over of the fastener head through the top face of the sandwich panel and tearing of the bottom face around the fasteners. For large edge distances, the failure is due to the excessive deformations of the supporting rails. The increase in the ultimate panel capacity by means of adequate fastening and supporting enhances the robustness and reduces the risk for the occupants, all at a small increase in costs.

1 INTRODUCTION

Sandwich panels are largely used for modern wall systems in building constructions, particularly in commercial and industrial buildings. They are composed of two faces connected by a low-density material core. Such an example is the PUR steel sandwich panel, which is composed of two thin steel faces connected by a low-density polyurethane foam layer. The two faces may be also made from composite materials, e.g., glass fiber reinforced plastic, GFRP. For wall applications, the two walls are generally flat or lightly profiled (Davies 1993). Walls made from sandwich panels are light, low-weight systems, typically designed from the weather/climate related conditions of the site (wind action, thermal comfort), with or without limited in-plane axial loads. The determination of the load-bearing capacity required for the design of sandwich panels is based to a large degree on test results (ECCS 127 2009), (Georgescu & Ungureanu 2014, Georgescu et al. 2014). In case of extreme loading conditions, like the ones generated by external explosions, the pressure exerted on the wall elements significantly exceeds the wind pressures used in the initial design of the walls and can heavily damage or destroy the closing walls (UFC 3-340-02, 2014). As a result, the shock wave or fragments that are projected at high speed can injure the building occupants or cause further structural damage at the interior (WBDG 2019), (FRAMEBLAST 2018). For such extreme cases, it can become uneconomical to adopt the traditional design based on flexural capacity, because, combined with the small mass of the wall, a significant strengthening may be required. In such cases, the ultimate capacity may be increased by allowing the development of catenary forces in the panels using appropriate end

restraints, i.e., connections with the support structure. Even several test programs on the response of wall sandwich panels under transverse (out of plane) loading were developed, they were mostly used to determine the flexural strength and deformation, which is mainly governed by the local buckling (wrinkling) of the panel face in compression (ECCS 127 2009), (Pokharel & Mahendran 2005), (EN 1993-1-3 2006), (Pokharel & Mahendran 2003). The local buckling (wrinkling), and consequently the flexural strength and stiffness, is also influenced substantially by the core density, i.e., soft cores make the panel more vulnerable to localized effects under concentrated loads, and inwards wrinkling of the compression face (Sharaf et al. 2010). A test program on sandwich panels was done by Chong and Hartsock (Chong & Hartsock 1993). They evaluated the ultimate flexural buckling failure of foam-filled sandwich panels with light gauge cold formed metal faces.

Five types of panels with three face configurations and four kinds of rigid urethane foam were subjected to center point loading, and the results were compared with mathematical derived solutions. An experimental program devoted to the evaluation of the mechanical characteristics and load (Kuhnhenne et al. 2020) bearing capacity of sandwich panels used for roofs and walls was conducted by Vayas et al. (Vayas et al. 2010). The four-point bending tests on three simply supported panels showed a similar response, with a quasi-linear behavior up to the attainment of the maximum load, followed by a fast drop in capacity. The test program was limited to the evaluation of the flexural peak capacity, without any consideration of the post-flexural response. The results indicated that, after the peak ultimate flexural capacity is reached, the resistance is steadily decreasing. In a recent experimental program conducted by Kuhnhenne et al. (Kuhnhenne et al. 2020), used sandwich panels, which were in service for over 14 years, were tested to check if they still comply with the actual strength and stiffness requirements. Four types of tests were performed, including bending tests. The research also investigated the effect of perforations due to end fasteners and the feasibility of a new clamping system to provide the fixation of the sandwich panel on the building substructure without any penetration.

The study presented in the paper investigates the ultimate capacity and failure mode of PUR sandwich panels with steel faces under quasi-static transverse loading. Eight double hinged specimens were tested, four with the span of 1.9 m and four with the span of 2.5 m. For reference, two additional bending tests were performed on simply supported specimens, one of 1.9 m span and one on of 2.5 m span, respectively. These two tests aimed to evaluate the response in the absence of any in-plane axial restraint (flexural response only). The panels were supported by cold formed lipped channels. Such sections are commonly used in practice as side rails for sandwich panel walls. The experimental tests were performed within SAFE-WALL project (*SAFE-WALL* 2020), which included similar tests on liner trays (Dinu et al. 2022), but also near field blast tests on a full-scale steel frame building with walls from same sandwich panels (Dinu et al. 2022) and liner trays, but the results are not reported here.

2 DESCRIPTION OF THE EXPERIMENTAL PROGRAM

The panels investigated in the test program are polyurethane foam sandwich panels with 0.4 mm thick steel faces and $t_p = 100$ mm thick core (noted PUR 100/0.4). The panels are 1000 mm wide and are supported by cold formed lipped channel side rails (section C150/2 mm) spanning $L_{SR} = 4.5$ m. The geometric and material characteristics of the panels and side rails are presented in Table 1.

Table 1. Geometric and material characteristics of panels and side rails.

Element	Steel grade	Yield strength f_y	Tensile strength f_u
		N/mm ²	N/mm ²
Side rail C150/2	S350GD-275Z	350*	420*
PUR/0.4	S250GD	303	330

*Values presented in the table are nominal values

The experimental program included ten tests, see Table 2. Eighth specimens were tested for double hinge condition, while two reference specimens were tested for simply supported

condition. The test set-up is shown in Figure 1 and Figure 2. The double-hinged panels were connected to the side rails using six self-drilling screws 5.5/6.3 at each end, while the side rails are connected to the support structure using UPN65 stubs and three bolts M12x35 mm, class 8.8, see Figure 2c. Note that the two reference specimens tested for bending had fasteners at one end, only. To prevent the loss of capacity of side rails by out-of-plane bending and lateral-torsional buckling, lateral restraints were provided as follows (Figure 1a):

- On the areas outside the width of the sandwich panel, the rails were supported at the top flange using 3 studs made from cold formed lipped channels on each side.
- On the areas inside the width of the sandwich panel, the rails were supported at the level of the web using two pairs of round steel rods.

It should be mentioned that in a real structure, the wall panels act as lateral restraints to the side rails for inward deflections, but the level of restraining is only verified for flexural stage (or small deformations). The parameters considered in the experimental program are the panel span, the type of the fastener washer, and the edge distance of the fasteners. For the panel span, two distances were used, i.e., 1.9 m and 2.5 m, respectively. It is expected that the increase of the panel span to thickness ratio, L_p/t_p , will favor the development of the catenary response due to higher flexibility. For reference, additional bending tests were performed on simply supported specimens to evaluate the flexural response in the absence of any in-plane axial restraint. As for the washers, excepting a single 1.9 m span specimen, for which self-drilling screws with standard EPDM washers were used, for the rest of the specimens, additional steel washers with a diameter of 27 mm and a thickness of 2 mm were added. The additional washers (see Figure 2b) increase the contact area with the sandwich panel and reduce/prevent the pull-over effect through the top (external) steel face. This is generally required when higher load bearing capacity of panel fastenings is required. As for the edge distance of the fasteners, e_1 (Figure 1b), it was 50 mm and 125 mm, respectively. Note that the minimum edge distance is typically defined by the panel manufacturer (EN 1993-1-3 2006). Also, if the edge distance is smaller than 45 mm, the pull-over resistance derived from the test results must be reduced (ECCS 127 2009). It is therefore expected that the increase of the edge distance of the fasteners will lead to larger catenary forces and higher ultimate capacity.

The load was applied at the middle of the panel, using a transversal steel beam to distribute the load force along the panel width. The test was quasi-static, with the load incremented up to the failure of the specimen using displacement control. Because the stroke of the hydraulic jack was not sufficiently long, several stops were made to allow the addition of some spacers. During these stops, the force was reduced to zero. However, the unloading and reloading intermediate phases were removed from the force-displacement curves.

Table 2. Description of the specimens.

Specimen	Span L_p m	Edge distance e_1 mm	Washers
SP-1.9 -50	1.9	50	EPDM
SP-1.9 -50-W/1	1.9	50	EPDM + W*
SP-1.9 -50-W/2	1.9	50	EPDM + W*
SP-1.9 -125-W	1.9	125	EPDM + W*
SP-2.5 -50-W/1	2.5	50	EPDM + W*
SP-2.5 -50-W/2	2.5	50	EPDM + W*
SP-2.5 -125-W/1	2.5	125	EPDM + W*
SP-2.5 -125-W/2	2.5	125	EPDM + W*
SP-1.9-bending**	1.9	125	EPDM
SP-2.5-bending**	2.5	125	EPDM

*EPDM - ethylene propylene diene monomer (EPDM) washers

W - steel washer with 27 mm diameter and 2 mm thickness

**For bending tests, end fasteners were used for one end only, and the other end was free to slide

Linear variable differential transformers (LVDT) were used to measure the displacements at several locations in the panel and side rails, see Figure 1b. Digital image correlation system

VIC-3D was used to measure the longitudinal strains at several locations in the top and bottom steel faces. The VIC-3D system was positioned near one of the panel supports, where bending moment is negligible, thus indicating the possible development of the catenary force in the panel during post-flexural deformation stage (Figure 1b).

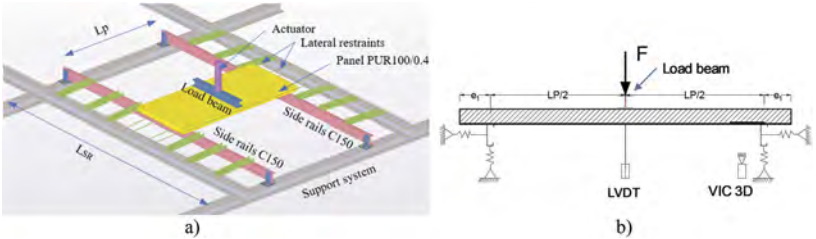


Figure 1. Test set-up and instrumentation: a) isometric view; b) longitudinal view.

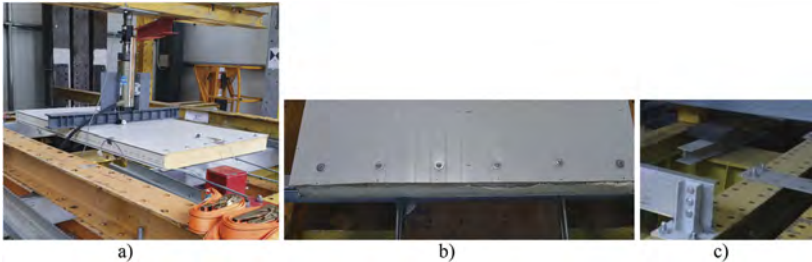


Figure 2. View with test setup: a) overview of the experimental setup and a panel ready for testing; b) end fasteners with additional steel washers connecting the panel to the side rail; d) side rail connections to the support structure.

3 EXPERIMENTAL RESULTS

Figure 3a and b show the force-displacement curves for the 1.9 m and 2.5 m span specimens, respectively, while Figure 4 shows the global view of a specimen after test and the detailed view of the typical plastic mechanism at the midspan. The vertical forces corresponding to the maximum flexural capacity (F_f) and to the ultimate stage (F_u) and the associated displacements (D_f and D_u) are presented in Table 3. Note that the vertical displacement contains only the displacement of the panel, without considering the contribution from the side rails. As seen from Figure 3, the behavior of the panels tested for double hinge conditions is characterized by three distinct zones. First, there is a quasi-linear elastic behavior up to the attainment of the maximum flexural capacity - point A on the curves. After point A, the panels have a sudden drop in capacity, associated with a local dynamic instability of the top face in compression – point B on the curves. After point B, a second increase in capacity is observed, and, for all specimens, the force corresponding to the ultimate capacity, F_u (point C on the curves), is higher than F_f , excepting the specimen SP-1.9-50-W/2, where the test was stopped before reaching the ultimate capacity due to technical issues (see Table 3).

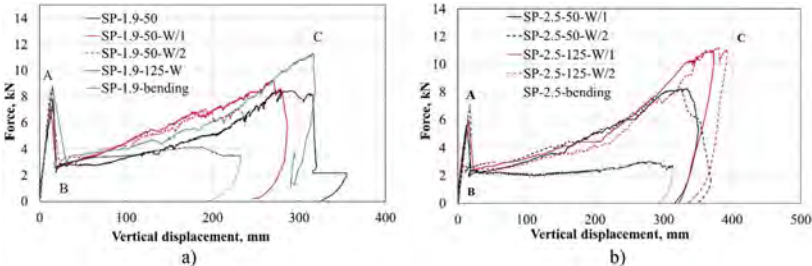


Figure 3. Force vs. vertical displacement curves: a) 1.9 m span specimens; b) 2.5 m span specimens.



Figure 4. Specimen after test: a) global view; b) detailed side view with the plastic mechanism at midspan.

Table 3. Maximum forces with corresponding vertical displacements, and failure mode for all specimens.

Specimen	F_f kN	D_f mm	$F_{f,r}$ kN	F_u kN	D_u mm	Failure mode
SP-1.9-50	7.7	29	2.3	8.3	350	Mode 1
SP-1.9 -50-W/1	7	11	2.6	9.3	270	Mode 2
SP-1.9 -50-W/2	8.2	13.7	2.7	7.1	231	Mode 2
SP-1.9 -125-W	8.6	14.4	2.9	11.4	317	Mode 3
SP-1.9-bending	9.0	17.3	3.1*	3.1	-	-
SP-2.5 -50-W/1	5.5	13	2.0	8.2	328	Mode 2
SP-2.5 -50-W/2	5.9	13.8	2.5	8.1	326	Mode 2
SP-2.5 -125-W/1	5.8	15.9	2.4	11.0	372	Mode 3
SP-2.5 -125-W/2	5.8	15.8	2.2	11.3	380	Mode 3
SP-2.5-bending	5.9	19.3	2.5*	2.5	-	-

*The residual flexural capacity for simply supported specimens was considered constant till failure

For the specimens tested for simple supported conditions, after the attainment of the maximum flexural capacity, the panel have a similar drop in capacity due to the local dynamic instability of the top face in compression and remains almost constant until the end of the test. Note that, for each span, the „residual “flexural capacity, $F_{f,r}$, of simply supported specimen and double hinge specimens is very close. Based on the observations made during each test, three failure modes were identified, see Table 3. They are influenced by the type of washer and edge distance, but also by the flexural capacity (in plane and out of plane) of the side rails supporting the panels. Thus, Mode 1 is characterized by a pullover of the fasteners through the top steel face combined with the tearing and buckling (folding) of the bottom steel face (see Figure 5). This failure mode takes place only for specimen SP-1.9-50, where the fasteners have standard EPDM washers only. Once additional larger steel washers are used, the pull-over of the fasteners through the top steel face is prevented, and failure takes place due to the tearing and buckling (folding) of the bottom steel face, which is identified as Mode 2 (see Figure 6). The angle between the two rupture lines is approximately 30° (see Figure 5c). One may note that similar failure mode may be also seen in spot welding of thin steel plates (Dubina et al. 2012). Mode 3 represents the failure of the side rails due to a combination of in plane and out of plane bending, but without the failure of the end connections (in Mode 1 or Mode 2) (see Figure 7a, b). The larger the edge distance, the larger the



Figure 5. Mode 1 of failure, with pull-over of fasteners through the top steel face (a), bottom steel face teared and buckled (folded) (b), and close-up view of the rupture lines (c).



Figure 6. Mode 2 of failure, with pull-over of fasteners through the top steel face prevented (a) and bottom steel face teared and buckled (folded) (b).

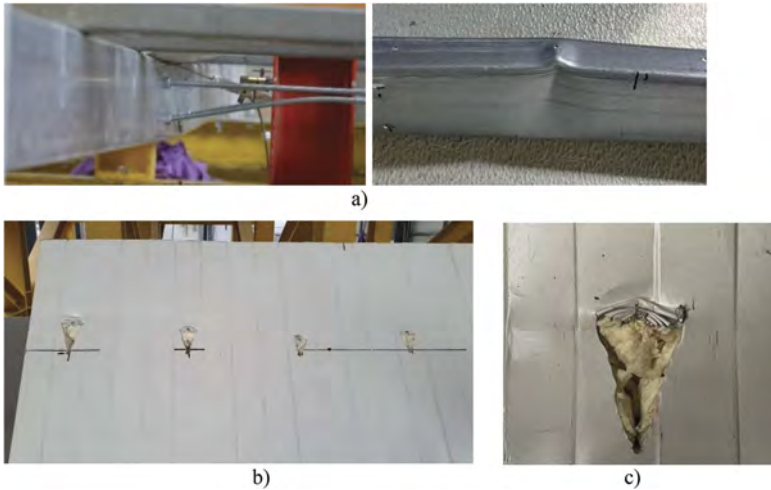


Figure 7. Mode 3 of failure, with failure of the side rail (a), bottom steel face teared and buckled (folded) (b), and close-up view of the rupture lines and folding area (c).

folding zone (see Figure 7c) and, consequently, the ultimate resistance is not given by the fasteners but by the supporting rails. Note that side rails were designed to resist the design loads applied on the panels at the Ultimate Limit State.

Figure 8 shows the contribution of catenary action to total load resistance for two specimens, i.e., SP-1.9 -125-W and SP-2.5-125-W/1, respectively. Note that the catenary action was obtained by subtracting the bending resistance (quasi-constant after point B) from the total resisted load. As may be seen from Table 3, except for the specimen SP-1.9 -50-W/2 (in whose case, the test was stopped before reaching the ultimate capacity due to technical issues) and the specimen SP-1.9-50 (standard

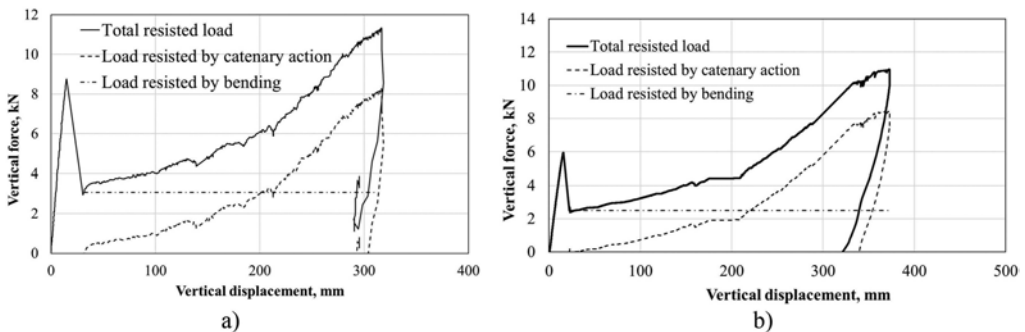


Figure 8. Contribution of catenary action to total load resistance: a) specimen SP-1.9 -125-W; b) specimen SP-2.5 -125-W/1.

EPDM washers only), for all the other specimens, the catenary action that developed during large deflection stage increased the load capacity significantly. It is also important to note that, even the flexural capacities are larger for shorter spans, the ultimate loads at failure are very similar.

To evaluate the development of the catenary force in the panels and the contribution of the two steel panel faces, the longitudinal strains measured with VIC-3D system were employed. As seen from Figure 9, up to point B, the strain measurements at the bottom face indicate a small variation with the increase of the applied force. Then, because the supports restrain the horizontal displacements of the panel end, catenary action develops in the panel. This development is indicated by the continuous increase of the strains (elongations) up to the attainment of the ultimate capacity (point C). From Figure 9, it may also be seen that the elongations, and therefore the tensile forces, are not constant along the panel width, but decrease from the longitudinal edge (extensometer E0) to the middle of the panel (extensometer E10). This also suggests that the contribution of fasteners in resisting the catenary forces and, ultimately, the contribution to the ultimate capacity, F_u , varies along the panel width. Also, because the end fasteners are flexible when loaded by in plane axial force, the catenary force is transferred almost entirely through the bottom face. This may be seen from the very small deformations of the top steel face around the screw head at the end of the test, see Figure 10, with no visible elongations.

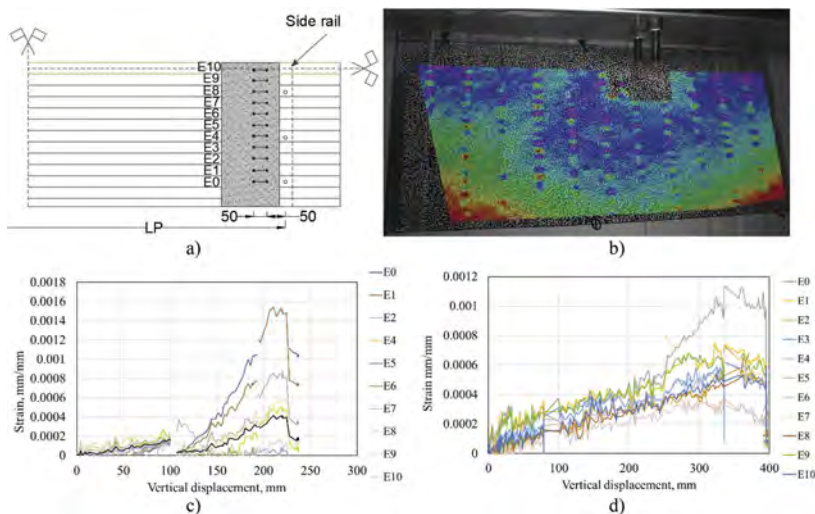


Figure 9. Strains measurements in the bottom steel face using VIC 3D system: a) position of the virtual extensometers; b) strain distribution for SP-1.9-125-W at ultimate force; c) positive strains increase for SP-1.9-125-W; d) positive strains increase with the increase of vertical displacement for SP-2.5-125-W/2.



Figure 10. Top steel face after the test (exemplified for SP-2.5-50-W/1, left, and SP-1.9-50-W/1).

4 CONCLUSIONS

Sandwich wall panels are largely used for different kind of commercial and industrial buildings. Despite their low weight, sandwich panels have high load carrying capacity under transverse loads. However, under extreme loading conditions, like near field explosions, the panels can be destroyed

or severely damaged, either under positive or negative pressure phase. The traditional design based on flexural capacity becomes uneconomical and may prohibit the use of sandwich panels when resistance against such high pressures is intended. The ultimate capacity can however benefit from the development of the catenary response, which is significantly higher than the flexural response if appropriate end fastenings (number of screws, edge distance, larger washers) and supporting restraints are provided. The increase in the ultimate panel capacity by means of adequate fastening and supporting enhances the robustness and reduces the risk for the occupants, all at a small increase in costs. Even if the in-plane forces in the fasteners at ultimate stage are not evenly distributed along the panel width, the ultimate capacity increases proportionally with the number of fasteners. When end distance increases from 50 mm to 125 mm, the ultimate capacity increases, in average, by more than 30% for 1.9 m span panels, and by more than 90% for 2.5 m span panels. This increase is conditioned by the use of additional larger washers to prevent the pull-over failure (noted as Mode 1). The ultimate capacity of the panels can be also increased by strengthening the side rails, as catenary forces can induce significant in-plane and out-of-plane bending moments. The ongoing research focuses on optimizing the number of fasteners and improving the local detailing to enhance the catenary response of the wall panels. Near field blast tests on a full-scale steel frame building with sandwich wall panels and improved fastenings and local detailing are also in progress.

REFERENCES

- Blast Safety of the Building Envelope | WBDG - Whole Building Design Guide*. 2019. Available from: <https://www.wbdg.org/resources/blast-safety-building-envelope#desc>.
- Chong, KP & Hartsock, JA. 1993. Structural analysis and design of sandwich panels with cold-formed steel facings. *Thin-Walled Structures*. 16(1):199–218.
- Davies, J. 1993. Sandwich panels. *Thin-Walled Structures*. 16(1–4):179–198.
- Dinu, F, Neagu, C, Marginean, I, Jakab, D, Ungureanu, V, Dubina, D & Abrudan, O. 2022. Experimental evaluation of the ultimate capacity of wall sandwich panels. In: *Steel Constructions*. V. 1. Bucharest. 39–48.
- Dinu, F, Neagu, C, Marginean, I, Laszlo, R, Ghiciei, E, Senila, M, Heghes, B & Constantinescu, M. 2022. Experimental blast tests on light non-load bearing external walls. In: *Steel Constructions*. V. 1. Bucharest. 125–132.
- Dubina, D, Ungureanu, V, & Landolfo, R. 2012. *Design of Cold-formed Steel Structures: Eurocode 3: Design of Steel Structures. Part 1-3 Design of Cold-formed Steel Structures*, A Wiley Company.
- ECCS 127. 2009. *Preliminary European Recommendations for the Testing and Design of Fastenings for Sandwich Panels*. ECCS – European Convention for Constructional Steelwork.
- EN 1993-1-3. 2006. *Eurocode 3: Design of steel structures - Part 1-3: General rules - Supplementary rules for cold-formed members and sheeting*. Brussels: CEN.
- Experimental validation of the response of a full-scale frame building subjected to blast load FRAME-BLAST*. 2018. Executive Agency for Higher Education, Research, Development and Innovation Funding: UEFISCDI.
- Georgescu, M & Ungureanu, V. 2014. Stabilisation of continuous Z-purlins by sandwich panels: Full scale experimental approach. *Thin-Walled Structures*. 81:242–249.
- Georgescu, M, Ungureanu, V & Dubina, D. 2014. Full scale experimental approach of sandwich panel roofing diaphragm action. *Proceedings of the 7th International Conference on Thin-Walled Structures - ICTWS2014*. 28 September – 2 October, Busan, Korea.
- Kuhnhenne, M, Pyschny, D & Janczyk, K. 2020. Reuse of steel sandwich panels. In: *Life-Cycle Civil Engineering: Innovation, Theory and Practice*. CRC Press.
- Pokharel, N & Mahendran, M. 2003. Experimental investigation and design of sandwich panels subject to local buckling effects. *Journal of Constructional Steel Research*. 59(12):1533–1552.
- Pokharel, N & Mahendran, M. 2005. An investigation of lightly profiled sandwich panels subject to local buckling and flexural wrinkling effects. *J Constr Steel Res*. 61(7):984–1006.
- Safety of buildings walls and claddings against accidental explosions SAFE-WALL*. 2020. Executive Agency for Higher Education, Research, Development, and Innovation, UEFISCDI.
- Sharaf, T, Shawkat, W & Fam, A. 2010. Structural Performance of Sandwich Wall Panels with Different Foam Core Densities in One-way Bending. *Journal of Composite Materials*. 44(19):2249–2263.
- UFC 3-340-02 2014. *Structures to resist the effects of accidental explosions*. DoD.
- Vayas, I, Dasiou, M-E & Lignos, XA. 2010. Experimental and numerical investigation of polyurethane sandwich panels. In: *SDSS'Rio 2010*. V. 1. Rio de Janeiro. 921–928.

Simplified assessment of the cyclic performance of steel constructions in aggressive environments

A. Milone & R. Landolfo

University of Naples “Federico II”, Naples, Italy

ABSTRACT: Owing to their peculiar destination of use, steel constructions such as bridges or offshore constructions are often placed in aggressive environments. In such cases, the combined action of cyclic loadings and material degradation can lead to sudden corrosion fatigue (CF) collapse if structures are not properly protected. In the present work, a simplified technique to assess the cyclic performance of steel constructions located in aggressive environments is introduced. The presented methodology relies on the concept of “critical corrosion degree” η^*_{Rd} , i.e. the minimum rate of corrosion which induces fatigue collapse for a given target service life t^* . Accordingly, CF checks can be hence expressed in a “demand vs. capacity” form more in line with principles of performance-based engineering. An existing railway riveted bridge located in Italy is hence selected as a case-study to provide a first application of the presented procedure with regards to a full-scale existing structure. Finally, parametrical analyses are presented in order to highlight the sensitivity of predicted cyclic performance to physical and mechanical variables governing corrosion fatigue phenomenology.

1 INTRODUCTION

After the second half of XXth century, fatigue performance of new and existing steel structures became a relevant civil engineering topic due to major fatigue-related failures (Anderson, 2017).

When dealing with existing steel structures, fatigue damage can be coupled with another relevant source of damage, i.e. material degradation, mainly in the form of metallic corrosion (Milone et al., 2022). Corrosion involves a progressive material loss due to electrochemical processes which are extremely sensitive to local environmental conditions (i.e., humidity, salinity, temperature). Hence, both time- and space-depending evolution of corrosion can sensibly vary during service life, leading to phenomena such as pitting (i.e. localized) corrosion or sudden changes in rate of corrosion in time.

When corrosive processes occur in conjunction with cyclic loads, corrosion damage is not merely summed to fatigue damage; namely, the two processes influence each other due to multiple factors (Milone et al., 2022):

- On one hand, fatigue cracking creates preferable spots for corrosion development, as the cracks can penetrate through protective layers (i.e. zinc coatings, ducts. . .), if present;
- On the other hand, corrosion induces a reduction of the resisting cross-section, resulting in stress amplifications which accelerate fatigue cracking.

In light of the above, it is clear that phenomenology of corrosion fatigue in steel structures is a complex topic to be addressed and it is still an open field of research at the present time (Cascini et al., 2008).

The present work attempts at providing a unified and simplified methodological approach for the fatigue assessment of steel structures in aggressive environments. This purpose is

addressed by introducing a “critical corrosion degree” η^*_{Rd} associated to an assigned fatigue life t^* , which allows carrying out fatigue checks in an explicit “demand vs. capacity” form.

This paper is mainly divided in three parts. In the first part, each step of the procedure is presented. In the second section, an application of the presented methodology is reported for a corroded riveted bridge located in Italy. Finally, parametrical analyses are performed in the third part with regard to most critical members.

2 OUTLINE OF THE PRESENTED PROCEDURE

The proposed methodology for the simplified corrosion fatigue assessment of steel structures in aggressive environments is based on the well-known Miner’s rule for damage cumulation, which is already codified in EN1993:1–9 (CEN, 2005) within the framework of the Damage Tolerant (DT) approach.

Nevertheless, in this work, fatigue checks will be presented in a more direct “capacity vs. demand” approach in line with performance-based engineering. This aspect is addressed by introducing the concept of “critical corrosion degree” η^*_{Rd} for an assumed target fatigue life t^* .

2.1 Step 1: Definition of corrosion trend

As highlighted previously, corrosive phenomena are highly sensitive to local boundary conditions. In general, in years immediately after the construction time, corrosion is limited due to the presence of preventive measures. Once the protection layer is worn, the corrosion process sharply accelerates. Finally, after significant superficial corrosion products have already formed, the corrosive process usually slows down, approaching a stabilized rate (Figure 1, dashed curve).

Compliantly, and according to ISO 9224 (ISO, 2012) recommendations, in the presented approach the corrosion development is approximated by a polyline with two branches (Figure 1, solid polyline). The slopes ratio among the two branches is equal to C: 1, with $C = 1 \div 5$ depending on the corrosivity category as defined in (ISO, 2012).

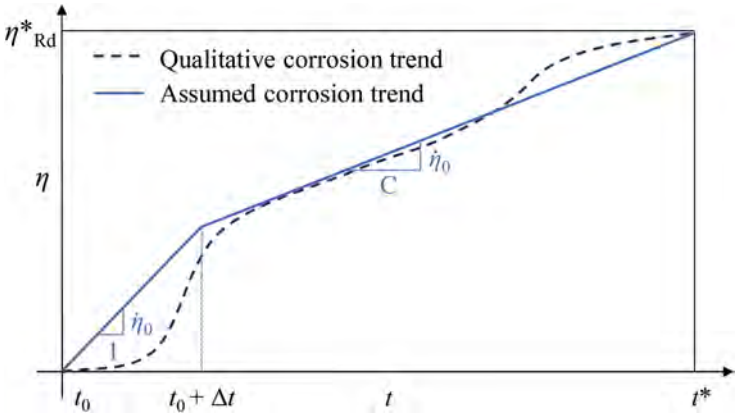


Figure 1. Qualitative (black dashed curve) and assumed (red solid polyline) trends for corrosion development for the proposed methodological approach.

The knee point of the bi-linear curve is assumed to occur $\Delta t = 10$ years after construction time. The corrosion degree η is assumed null for $t = t_0$. Conversely, for $t = t^*$ (target fatigue life) a “critical corrosion degree” η^*_{Rd} is introduced, i.e., the minimum corrosion degree which induces corrosion fatigue collapse for $t = t^*$.

The selection of a proper value for t^* has to be intended as a designer’s choice, which depends on the expected influence of fatigue and material degradation on structural performance. The corrosion degree at a given time $\eta(t)$ is hence expressed by Equation 1a-b:

$$\eta(t) = \begin{cases} \dot{\eta}_0(t - t_0) & t \leq t_0 + \Delta t \\ \frac{\dot{\eta}_0}{c}(t - t_0) + \Delta t \dot{\eta}_0 \left(1 - \frac{1}{c}\right) & t_0 + \Delta t < t \leq t^* \end{cases} \quad (1a)$$

$$\dot{\eta}_0 = \frac{\eta_{Rd}^*}{\Delta t \left(1 - \frac{1}{c}\right) + \frac{t^*}{c}} \quad (1b)$$

in which η_0 represents the corrosion rate assumed for the first branch of the polyline. Equation 1a-b holds true for an arbitrary value of η_{Rd}^* , the actual value of which will be derived in Step 4.

2.2 Step 2: “Unaltered” structural analysis

According to (ISO, 2012), the expected amount of material loss due to corrosion do not exceed few $\text{mg}/(\text{year} \cdot \text{m}^2)$ even in the case of extremely aggressive environments. Hence, global stiffness reduction due to corrosion can be initially neglected, performing structural analysis on the “unaltered” structure.

In this way, extreme values of the stress characteristics ($S_{0,\min}$; $S_{0,\max}$) can be determined only once. Influence of corrosion will be later accounted in terms of local stresses amplifications.

2.3 Step 3: Evaluation of “real” load spectrums

After estimating “unaltered” stress characteristics $S_{0,\min}/\Delta S_0$, “unaltered” local stresses $\sigma_{0,\min}/\Delta \sigma_0$ can be determined using expressions from the theory of elasticity. Hence, introducing appropriate stress magnification factors (SMFs), “real” corrosion-depending stresses $\sigma_{\eta,\min}/\Delta \sigma_{\eta}$ can be evaluated.

At least two sources of amplification have to be accounted for, i.e., local erosion of the resisting cross-section and the presence of mean tensile stresses $\sigma_{0,m} > 0$ (Goodman, 1899). Corrosion-induced amplification can be modelled by means of an SMF (SMF_{η}), which is a function of (i) cross-section properties in pristine conditions X_0 ; (ii) cross-section properties reduction ΔX_{η} ; and (iii) the type of corrosive process (CP). In the simplest case (uniform corrosion), SMF_{η} can be expressed as follows (Equation 2):

$$SMF_{\eta,uniform} = \left(1 - \frac{\Delta X_{\eta}}{X_0}\right)^{-1} \approx \frac{1}{1 - \eta} \quad (2)$$

Non uniform corrosion (“pitting”) can be modelled by scaling $SMF_{\eta,uniform}$ by means of a non-dimensional function $f(t, CP)$ defined case-by-case. Indeed, when relevant, pitting can be modelled by means of equivalent notches inducing local stress amplifications (Berto et al., 2014). To this end, multiple expressions for $f(t, CP)$ functions can be found in Peterson et al. (1997).

“Real” corrosion-depending stresses $\sigma_{\eta,\min}/\Delta \sigma_{\eta}$ are hence derived as follows (Equation 3a-b):

$$\sigma_{\eta,min} = SMF_{\eta} \sigma_{0,min} \quad (3a)$$

$$\Delta \sigma_{\eta} = SMF_{\eta} \Delta \sigma_0 \quad (3b)$$

In case of complex stress histories, “real” stress histories are expressed by means of “real” oscillograms, in which each point $\sigma_{\eta}(t)$ is derived by magnifying SMF_{η} times the related “unaltered” stress $\sigma_0(t)$.

Hence, cycle counting is performed considering only the fluctuating part of amplified stresses (e.g. with Rainflow method – CEN, 2005). Cycle counting yields an approximated “real” load spectrum ($\Delta \sigma_{\eta,i}$; n_i). The equivalent fatigue demand accounting for mean stress effect $\Delta \sigma_{eq,i}$ is hence estimated (Equation 4):

$$\Delta\sigma_{eq,i}(t) = \Delta\sigma_{\eta,i}(t) \cdot SMF_{Eq}(t) \quad (4)$$

where SMF_{Eq} is an equivalent magnification factor accounting for the mean stress effect. According to consolidated practice, Goodman (1899) model is selected to deal with pulsating stress histories. It should be remarked that SMF_{Eq} implicitly depends on $\Delta\sigma_{\eta,i}$, as Equation 5a-b holds:

$$SMF_{Eq}(t) = \frac{1}{1 - \frac{\sigma_{m,i}(t)}{f_u}} \geq 1 \quad (5a)$$

$$\sigma_{m,\eta,i}(t) = \sigma_{\eta,min,i}(t) + \frac{\Delta\sigma_{\eta,i}(t)}{2} \quad (5b)$$

with f_u being the ultimate tensile strength (UTS) of structural steel. The evaluation of $\Delta\sigma_{eq,i}$ is performed for each stage of the structural service life, thus obtaining $(t^* - t_0)$ “equivalent” load spectrums, which represent the overall fatigue demand on the analyzed structure (Figure 2).

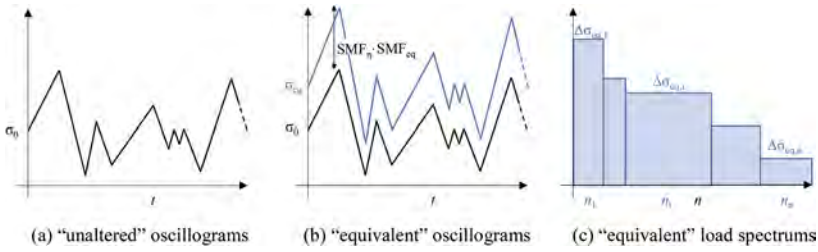


Figure 2. Estimation of “real” load spectrum from aperiodic stress histories.

2.4 Step 4: Estimation of critical corrosion degree

Using Miner’s rule for damage accumulation, the actual value of the critical corrosion degree η^*_{Rd} can be estimated by imposing that total damage D_{TOT} reaches unity for $t = t^*$ (Equation 6):

$$f(\eta^*_{Rd}, t^*) = 1 - D_{TOT}(\eta^*_{Rd}, t^*) = 1 - \sum_{t=t_0}^{t^*} \frac{n_i}{N_i(\Delta\sigma_{eq,i}(\eta^*_{Rd}))} - 1 = 0 \quad (6)$$

Evaluation of the number of stress cycles up to failure N_i has to be performed using a S-N- η fatigue strength domain to account for fatigue strength reduction due to material degradation (Equation 7a-b – Adasooriya et al., 2020):

$$\log \frac{5 \times 10^6}{N_i} = m_{1,\eta} \log \left(\frac{\Delta\sigma_{D,\eta}}{\Delta\sigma_{Eq,i}} \right) \quad (7a)$$

$$\log \frac{N_i}{5 \times 10^6} = m_{2,\eta} \log \left(\frac{\Delta\sigma_{Eq,i}}{\Delta\sigma_{D,\eta}} \right) \quad (7b)$$

with $\Delta\sigma_{D,\eta}$ being the modified constant amplitude fatigue limit (CAFL, $N = 5 \times 10^6$) for the selected element, accounting for the effect of corrosion, and $m_{1,\eta}/m_{2,\eta}$ being the corrosion-depending inverse slopes of LCF/HCF branch of the S-N curve, respectively.

According to Adasooriya et al. (2020), modified CAFL can be derived assuming that the stress range $\Delta\sigma_{10000}$ inducing collapse for $N = 10^4$ does not depend on η . Thus, $\Delta\sigma_{D,\eta}$ can be calculated starting from the “pristine” detail class ($\Delta\sigma_c$, $N = 2 \times 10^6$ – Equation 8a-b):

$$\Delta\sigma_{D,\eta} = \frac{\Delta\sigma_{10000}}{(5 \times 10^2)^{\frac{1}{m_{1,\eta}}}} \quad (8a)$$

$$\sigma_{D,10000} = (2 \times 10^2)^{\frac{1}{m_{1,0}}} \cdot \Delta\sigma_C \quad (8b)$$

with $m_{1,0}$ being the inverse slope of the LCF branch according to EN1993:1-9 (CEN, 2005) in pristine conditions.

Consistently with Adasooriya et al. (2020), the inverse slopes are assumed to linearly reduce as η increases (Equation 9a-b):

$$m_{1,\eta} = m_{1,0} - \frac{\eta}{\eta_{ref}} \Delta m_{1,\eta} \quad (9a)$$

$$m_{2,\eta} = m_{2,0} - \frac{\eta}{\eta_{ref}} \Delta m_{2,\eta} \quad (9b)$$

in which $m_{1,0}/m_{2,0}$ are the inverse slopes of the S-N curve in pristine conditions, respectively; $m_{1,\eta}/m_{2,\eta}$ are the corrosion-affected inverse slopes and $\eta_{ref}/\Delta m_{1,\eta}/\Delta m_{2,\eta}$ are experimental parameters expressing the influence of corrosion on fatigue behavior.

In this work, $\eta_{ref} = 0.2$, $\Delta m_{1,\eta} = 0.375 m_{1,0}$, and $\Delta m_{2,\eta} = 0.375 m_{2,0}$ are assumed compliantly with experimental results reported in Adasooriya et al. (2020).

Conservatively no endurance limit is assumed (that is, $m < \infty$ independently from the assumed stress range). The resulting shape of S-N- η domains is depicted in Figure 3 for increasing values of corrosion degree η .

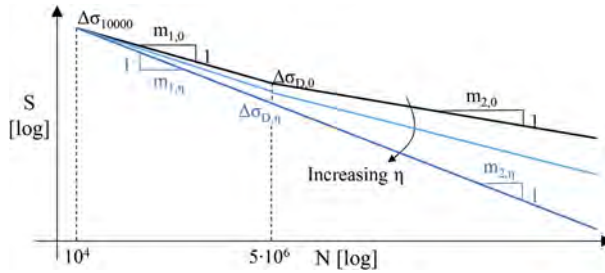


Figure 3. Assumed shape of S-M- η domains for corrosion fatigue analyses.

2.5 Step 5: Corrosion fatigue checks

Once η_{Rd}^* is known, corrosion fatigue checks can be performed by controlling that “corrosion demand” at a given time $\eta_{Ed}(\bar{t})$ does not exceed the “corrosion capacity” $\eta_{Rd}(\bar{t})$ for the same \bar{t} (Equation 10):

$$\eta_{Ed}(\bar{t}) \leq \eta_{Rd}(\bar{t}) = \eta_{Rd}^* - \frac{\eta_{Rd}^*}{\Delta t(C-1) + t^*} (t^* - \bar{t}) \quad (10)$$

Based on Equation 10, three different structural damage stages can be identified, namely:

1. For $0 < \eta_{Ed}(\bar{t}) < \eta_{Rd}(\bar{t})$, the structure can be safe with regard to corrosion fatigue failure;
2. For $\eta_{Rd}(\bar{t}) < \eta_{Ed}(\bar{t}) < \eta_{Rd}^*$, the necessity of maintenance measures emerges as values of $\eta > \eta_{Rd}^*$ are expected to be attained for $t < t^*$;
3. For $\eta_{Ed}(\bar{t}) > \eta_{Rd}^*$, the structure quickly requires safety measures against corrosion fatigue collapse, which is indeed predicted to occur.

3 CASE STUDY

The presented procedure is hence applied with reference to an existing riveted railway bridge located in Italy (bridge over “Gesso” torrent, Montecalvo Irpino, Italy). The structure was erected during 1960s to replace a former masonry bridge damaged by 1962 Irpinia earthquake.

Four existing masonry piles were preserved, while the deck was rebuilt by means of three identical 29 m long 3D truss steel bays (see Figure 4a).

Steel members were realized by coupling hot-rolled and/or welded profiles by means of riveted battens. 22 mm hot-driven rivets were also implemented for connecting members via gusset plates. Namely, chords have an inverted Π section made of battened angles and plates.

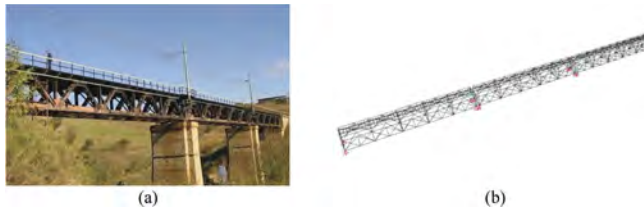


Figure 4. (a) View and (b) modelling of the selected case study (railway bridge over “Gesso” torrent).

H-shaped welded profiles were used for vertical struts, while diagonals were made by battening two C profiles. Due to Italian Railway Network Management (RFI) provisions (RFI, 2011), no zinc coating was applied to protect members and connections from ongoing corrosion.

“Unaltered” global analysis accounting for “real” train loads as defined in RFI (2011) was performed using SAP2000 v.23 (CSI, 2021) (Figure 4b). All members were modelled by means of equivalent mono-dimensional frame elements. According to the original design report (Landolfo et al., 2010), an Fe 50.2 steel grade ($f_u = 500 \text{ N/mm}^2$) was assumed for all elements. The number of passages per year was assumed based on data provided by RFI (Table 1).

Table 1. Train loads for the selected case study according to RFI indications.

Train Type [-]	Total Load [kN]	Total Length [m]	Velocity [km/h]	Passages/Day [1/d]
3	9400	385.5	250	7
4	5100	237.6	250	6
8	10350	212.5	100	1
9	2960	134.8	120	1

In order to reproduce the actual phenomenology of corrosion, a progressive thickness reduction for elements on the bottom was assumed. Indeed, due to stagnation of meteoric waters, degradation phenomena are highly promoted in the inferior portion of the 3D truss. Moreover, owing to the structural scheme, lower steel members were considered as more prone to fatigue damage due to significant mean tensile stresses.

For the sake of brevity, only corrosion fatigue analyses for most critical elements are reported, i.e. *i*) the mid-span segment of lower chords, *ii*) tension diagonals closest to supports and *iii*) vertical struts located at mid-span. Figure 5a shows geometrical features and “unaltered” load spectrums for the considered members.

Critical corrosion degree was estimated considering a C3 exposition class ($C = 2.5 - \text{ISO}, 2012$) for all the elements (Figure 5b-c). According to Italian Ministry of Transportations (MIT) provisions for bridges (MIT, 2018), $t^* = 100$ years was set as target fatigue life, while a detail class $\Delta\sigma_C = 71 \text{ N/mm}^2$ for connections was selected compliantly with EN1993:1-9 (CEN, 2005).

It can be noticed that estimated values of η^*_{Rd} are rather variable for investigated members ($\eta^*_{Rd} = 50.7\%, 80.1\%$ and 27.5% for the lower chord, the diagonal and the vertical strut,

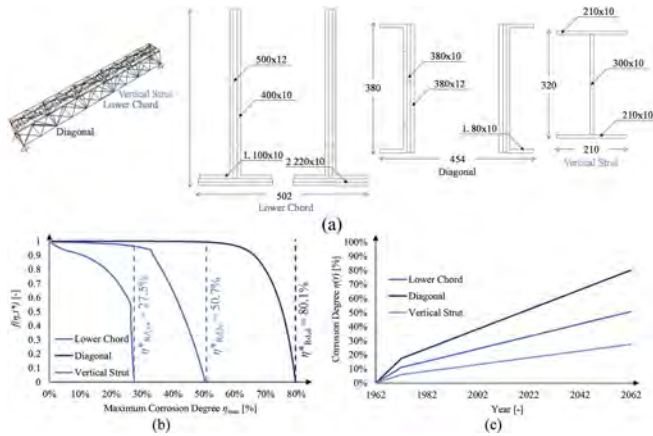


Figure 5. (a) Main geometrical features, (b) damage functions $f(\eta, t^*)$ and (c) critical corrosion trends for each considered critical element, e.g., lower chords, diagonals and vertical struts.

respectively). Indeed, while a significantly high critical corrosion is derived for both lower chords and diagonals, in case of vertical struts the effect of corrosion is more pronounced.

This outcome depends on the small cross-section of struts, which lead to high stress ranges even for low values of corrosion degree η . Appreciable damage arise also in lower chords for $\eta \geq 30\%$. Conversely, diagonals always show a significant range of safety against corrosion fatigue failure.

3.1 Parametrical analyses

In order to investigate the influence of physical/mechanical variables on the corrosion fatigue performance of structural members, parametrical analyses were conducted varying the

Table 2. Assumed values of parameters for parametrical analyses.

Parameter	Reference Value	Range of Variation
CX [-]	C3	C1 ÷ C5
f_u [N/mm ²]	500	340 ÷ 600
t^* [years]	100	50 ÷ 150
R [-]	0.3 (Lower Chord), 0.4 (Diagonal), 0.0 (Vertical Strut)	0.0 ÷ 0.5

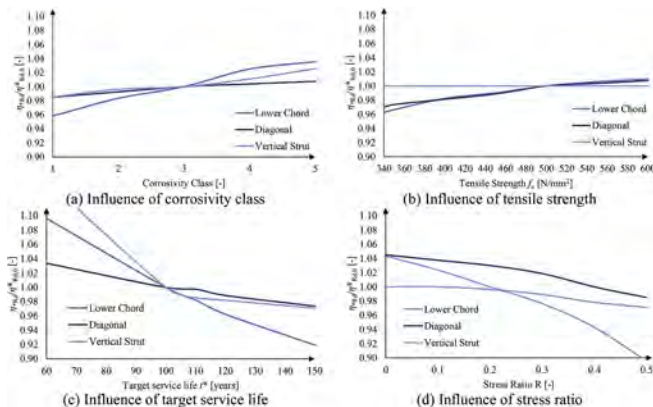


Figure 6. Results of parametrical analyses on investigated elements.

following parameters, namely: *i*) corrosivity class CX , *ii*) tensile strength f_u , *iii*) target service life t^* and *iv*) stress ratio R (Table 2).

Results of parametrical analyses are reported in Figure 6. One can notice that, as expected, the diagonal is less sensitive ($\pm 4\%$) to boundary conditions variations due to the negligible impact of corrosion fatigue on its service life. Conversely, lower chord displays a more significant sensitivity with respect to varied parameters.

Namely, increasing t^* or R a significant increment of damage is predicted, with a variation $\Delta\eta^*_{Rd} \approx -10\%$ with respect to the reference value in both cases (Figure 6c-d, dark blue plots). Finally, vertical strut is highly sensitive to t^* ($\Delta\eta^*_{Rd} = -15\%$ for $t^* = 60$ years), while other parameters do not appreciably affect the value of η^*_{Rd} . It should be noted that, as compressive mean stress arises in such element due to permanent loads, f_u has no effect on η^*_{Rd} .

4 CONCLUSIONS

A simplified methodology for the corrosion fatigue assessment of steel structures in aggressive environments was presented. The proposed method was hence applied with reference to an existing riveted bridge located in Italy. In light of the results, the following conclusions can be drawn:

- The proposed method for the corrosion fatigue analysis of steel structures is based on the concept of “critical” corrosion degree η^*_{Rd} , which is derived for a selected target fatigue life t^* ;
- The selected case study has a good performance against corrosion fatigue failure (i.e., $\eta^*_{Rd} = 50.7\%$, 80.1% and 27.5% for the lower chord, the diagonal and the vertical strut, respectively).
- Vertical struts are the most exposed elements due to their reduced pristine cross-section;
- Parametrical analyses showed how target fatigue life t^* and stress ratio R are the most influent parameters for the corrosion fatigue performance of the selected case study;
- Further studies on different full-scale steel structures located in aggressive environments will be conducted to prove the reliability of the presented simplified procedure.

REFERENCES

- Adasooriya, N.D., Pavlou, D., Hemmingsen, T. 2020. Fatigue strength degradation of corroded structural details: A formula for S-N curve, *Fatigue Fract. Eng. Mater. Struct.*, 43, 721–733.
- Anderson, T.L. 2017. Fracture Mechanics - Fundamentals and Applications, 4th Ed., Boca Raton, FL, USA; Taylor & Francis Group: Boca Raton, FL, USA.
- Berto, F., Lazzarin, P. 2014. Recent developments in brittle and quasi-brittle failure assessment of engineering materials by means of local approaches, *Mater. Sci. Eng. R Rep.*, 75, 1–48.
- Cascini, L., Landolfo, R., Portioli, F. 2008. An integrated approach to durability design of steel structures against atmospheric corrosion, *Key Eng. Mat.*, 385-387, 657–660.
- CEN (European Committee for Normalization) 2005. EN1993:1–9Eurocode 3: Design of Steel Structures—Part 1–9: Fatigue; CEN: Brussels, Belgium.
- Computer and Structures Inc. 2021. SAP2000 – User’s Manual Version v.23.
- Goodman, J. 1899. Mechanics Applied to Engineering, Green & Company: London, UK.
- ISO (International Organization for Standardisation) 2012. ISO 9224: Guiding Values for the Corrosivity Categories, ISO: Geneva, Switzerland.
- Landolfo, R., Cascini, L., D’Aniello, M., Portioli, F. 2010. Gli effetti del degrado da fatica e corrosione sui ponti ferroviari in carpenteria metallica: Un approccio integrato per la valutazione della vita residua, *Costr. Met.*, 6, 37–46 [In Italian].
- Milone, A., Landolfo, R., Berto, F. 2022. Methodologies for the Fatigue Assessment of Corroded Wire Ropes: A State of the Art Review, *Structures*, 37, 787–794.
- MIT (Italian Ministry of Infrastructures & Transportations) 2018. D.M. 17/ 01/2018:Aggiornamento delle «Norme Tecniche per le Costruzioni», MIT: Rome, Italy.
- Peterson R.E., Pilkey W.D. 1997. Peterson’s Stress Concentration Factors – Second Edition, John Wiley & Sons: New York, NY, USA.
- RFI (Italian Railway Network) 2011. RFI DTC INC PO SP IFS 003 A: Specifica per la verifica a fatica dei ponti ferroviari, RFI: Rome, Italy [In Italian].

Multi-hazard robustness assessment of seismic resistant multi-story steel frame buildings

D. Dubina, F. Dinu & J. Dominiq

Politehnica University Timisoara, Romania

Romanian Academy, Timisoara Branch, Romania

ABSTRACT: Buildings designed and constructed in accordance with the today code provisions are expected to withstand frequent hazards without structural damage and to prevent collapse under rare events (e.g., strong earthquakes). However, there are also situations where multiple or cascading hazards can occur, e.g., earthquake aftershocks or fire after earthquake. In such cases, even if the structure survives the first event with minimal damages that do not affect the global stability, the subsequent events can severely damage critical members and potentially cause extensive damages or even failures. The study presented in the paper investigates the response of a typical steel frame structure under cascading scenarios that involve damage to both lateral and gravity load resisting systems. The parameters considered in the study are the initial design conditions (level of overstrength in members), load scenarios (single/multi hazard events), and residual capacity after first event. Numerical models were calibrated against relevant test data. Results indicated appropriate resistance for single and multi-hazard loading scenarios. Even the structure showed adequate progressive collapse resistance, the internal column loss scenarios drawn attention, as they led to extensive damage in the perimeter moment resisting frames, which were still undamaged after the earthquake. It is expected that the multi-hazard design can be used to obtain more robust building structures against extreme loading events and improve the life-cycle performance of built infrastructure.

1 INTRODUCTION

Structural robustness and prevention of progressive collapse of building structures are specific safety conditions required by modern codes and standards, including Eurocodes (EN 1990 2002). The successful application in practice of this policy requires special attention not only from construction industry specialists (structural engineers, architects, builders) but also from authorities and insurance companies. The importance of design for robustness became evident following tragic events, such as the collapse of the Twin Towers in New York following the September 11, 2001, attacks, which led to the need for more elaborate design provisions (Demonceau et al. 2021). The design for robustness of building structures can be done considering either the direct effects of an extreme action or a certain extension of the damage following an unknown/unforeseen event using the Alternate Path method ((DoD 2009) (EN 1991-1-7 2006)). The methods in the first category require clear identification and definition of the accidental action. Typical examples are fire, gas explosion, or impact. In some cases, the development of local damage may be allowed, but not to a disproportionate extent to the original cause ((Demonceau et al. 2021), (EN 1991-1-7 2006)). However, in certain circumstances, accidental actions may exceed the conditions considered in the codes, or cannot be defined with sufficient accuracy, for example in cascading load scenarios, e.g., earthquake after earthquake, fire after earthquake or fire after explosion. One such example is the Christchurch (New Zealand) earthquake series of 2010-2011. First, it was not the strongest motion, i.e., 2010 event with magnitude 7.1, to cause the most losses (economic costs, fatalities) but the smaller 2011

aftershock (magnitude 6.3), which was responsible for 185 fatalities and more than 40 billion US \$. So, the new earthquake models should probably include the cascading effect of earthquake aftershock sequences (Bruneau & MacRae 2017). Second, the post-earthquake reconstruction process, which brought to surface the urban resilience as a main goal. So, even the concept was not necessarily new (Bruneau et al. 2003), it was probably the first time it was considered on such a large scale. The reconstruction favored the use of several innovative and emerging structural systems to make the new buildings of Christchurch more seismically resilient, e.g., low damage/replaceable technology construction. The advantages of such approaches have been also documented in (Dubina et al.2008; DUAREM 2015; Dubina et al. 2020, 2021; Jakab et al. 2022). Thus, it is becoming more widely accepted that preventing loss of life and reducing the damages due to single strong hazards (which are the main aims today) are simply not sufficient for a good modern structure and a resilient environment, but we need also to consider that:

- At smaller scale, buildings should be better prepared for unforeseen hazards - robust systems.
- At larger scale, built infrastructure should be less vulnerable and easier to repair to large scale single or multi hazard events – more resilient systems.

So, to be resilient, a structural system needs the capacity to resist the hazard, or robustness, and the ability to recover from the hazard in a timely and cost-effective manner. But these two components are very much dependent on the design concept and structural requirements for single and multi-hazard loading scenarios. During the past decade, a significant number of research projects related to the structural response of steel and composite buildings under various exceptional loading situations (impact, fire, explosion, ...) have been carried out (*ADBLAST* 2015; *CODEC* 2016; *FRAMEBLAST* 2018). Outcomes of these recent scientific actions included new design approaches to mitigate progressive collapse accounting for the full potential of materials used in steel or steel-concrete composite structures. Of particular importance is the *FAILNOMORE* project entitled “Mitigation of the risk of progressive collapse in steel and composite building frames (Demonceau et al. 2021). The project aimed at consolidating the existing knowledge and transform it into practical recommendations and guidelines. The output included design guidelines for steel and composite structures subjected to identified and unidentified threats, such as impacts, explosions, fires, and earthquakes, but also detailed worked examples. The examples give information about the design of steel and composite steel-concrete structures considering single hazards (e.g., explosion) or multi-hazard events (e.g., column loss following strong earthquake). In what concerns the column loss events for bare steel frame structures, results indicated that, even the seismic resistant systems perform better than non-seismic ones, they remain vulnerable to columns loss scenarios affecting parts designed for gravity loads only. Thus, when the column loss affects the internal structure with pinned beam ends, the damage propagates, and the progressive collapse develops on the entire affected area. The pinned connections cannot resist the large axial force demands resulted from the column loss. To limit the damage and prevent the progressive collapse, the alternatives to the pinned connection strengthening (which may be difficult to attain) are the use of moment resisting connections instead of pinned connections (redesign), or use of composite action of the beam with the concrete slab (Demonceau et al. 2021). The case-study building presented in the paper was initially designed for the ultimate limit state (ULS) and serviceability limit state (SLS), with additional requirements for damage limitation state (DL) in case of seismic action. Then the structure was tested for cascading hazard scenarios that involve a strong ground motion, followed by the loss of a column. In the first step, the structure is subjected to a design earthquake and the response is calculated using push-over analyses and the N2 method (EN 1998-1 2004). In the second step, the structure already tested for design earthquake is investigated for column loss scenarios using the alternative load path (ALP) method and nonlinear dynamic procedure (NDP), in accordance with the UFC 4-023-03 guidelines (DoD 2009). Several locations are considered for column loss

scenarios, which are assumed to be lost one at a time. They include only columns that are part of the seismic load resisting system.

2 DESIGN OF THE STRUCTURE

The isometric view of the structure is shown in Figure 1a. The main structural system consists of a dual system made of an internal V-braced cores and perimeter moment resisting frames (MRFs). The beam grid with main and secondary beams are designed to resist gravity loads (Figure 1b).

The structure has 6 stories of 4.0 m high each, 6 bays of 8.0 m in the longitudinal direction, 3 bays of 12.0 m in the transversal direction – internal, and 6 bays of 6.0 m in the transversal direction – perimeter. The design used S355 steel for all members, excepting non-dissipative beams in the braced frames, which were made of S460 steel grade. H sections were used for all steel elements. The joints were designed according to the EN 1993-1-8 provisions (EN 1993-1-8 2011), with additional requirements for seismic resistant systems in terms of minimum capacity (EN 1998-1 2004). The actions that were used in the design of each structural typology are:

- Dead load: $g_k = 5 \text{ kN/m}^2$ on floors, and $g_k = 4 \text{ kN/m}^2$ on the façade
- Live load for office buildings: $q_k = 3 \text{ kN/m}^2$
- Wind pressure: $q_b = 0.4 \text{ kN/m}^2$
- Snow load: $s_k = 1.5 \text{ kN/m}^2$
- Seismic action: Type 1 response spectrum, ground type B, $a_g = 0.25g$, $q = 4.8$ (EN 1998-1 2004).

Combination of actions for ULS and SLS were considered in compliance with EN 1990. Additionally, according to EN 1998, DL requirements were considered. The structural analysis was carried out using 3D models and linear elastic analyses. The calculations were performed using the SAP2000 software. For the seismic design, a modal response spectrum analysis was conducted. Also, the plastic mechanism and seismic response by means of non-linear static analysis procedure (push-over analysis) was evaluated using the N2 method. The output of the design is presented in Table 1. More details about design are given in (Demonceau et al. 2021).

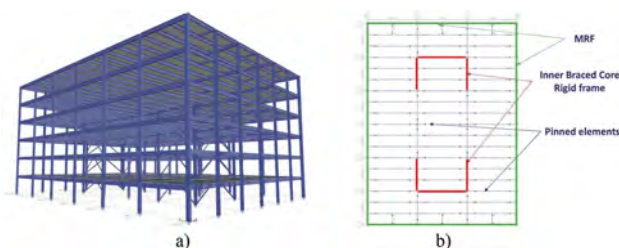


Figure 1. Geometry of the structural system: a) isometric view; b) plan view with spans and bays and position of lateral load resisting system (MRF + CBF) (Demonceau et al. 2021).

3 DEFINITION OF HAZARD SCENARIOS AND ANALYSIS PROCEDURES

The main objective of the study is to evaluate the robustness of the structure following two extreme events that can affect the structure one upon another. The two cascading hazards refer to a strong earthquake that can damage the main lateral load resisting system, followed by a column loss, either due to the indirect effects of the seismic action or due to other causes (e.g., localized fire).

In the first step, the seismic response of the structure is analysed using the N2 method (EN 1998-1 2004). This method combines the nonlinear static (pushover) analysis of a multi-degree of freedom model with the response spectrum of a single degree of freedom system. The distribution of the lateral loads along the height followed two patterns, i.e., one uniform (uniform response acceleration) and one as an inverted triangle (similar to the first mode shape). However, only the first distribution is presented, as it brings higher demands. Two performance levels (or limit states) were used in the analysis, i.e., DL and ULS.

Table 1. Sections for beams, columns and braces (Demonceau et al. 2021).

Element	Direction	Story	Section
Perimeter beams	X	1-6	IPE550
	Y	1-6	IPE600
Interior beams	X	1-6	IPE550
	Y	1-6	IPE550
Inner core beams	X	1-3	H800*
		4-5	HEM800
		6	HEM700
	Y	1-3	HEM500
		4-6	HEB500
		1-6	HE550B
Corner columns		1-6	HE550B
Perimeter columns		1-6	HE500B
Inner core columns		1-6	HD400X463
Brace	X	1-3	HEA320
		4	HEA260
		5	HEA220
		6	HEA200
		1-3	HEA320
		4-5	HEA260
	Y	6	HEA220

* H800 is a built-up section with $h = 814\text{mm}$, $b = 380\text{mm}$, $t_f = 50\text{ mm}$, and $t_w = 30\text{ mm}$

In the second step, the structure, damaged due to earthquake, is investigated for column loss scenarios using the alternative load path (ALP) method and nonlinear dynamic procedure (NDP), in accordance with the UFC 4-023-03 guidelines (DoD 2009). Several critical locations are considered for column loss, which are assumed to be removed one at a time, see Figure 2. Note that the removal scenarios include only columns that are part of lateral load resisting system. Also, if a column has vertical braces attached, they are also removed. As reported in (Demonceau et al. 2021), the loss of columns from gravity load resisting area may be also of interest, because the beams attached to the columns are generally connected using simple connections. The ALP method ascertains the capacity of a structure to resist the loss of a critical load-bearing element without causing disproportionate collapse. In the NDP, first, the gravity load is calculated with Equation (1) and applied on the structure using a static analysis:

$$G = [DL + 0.5LL] \quad (1)$$

where G is the increased gravity load on floors, DL is the dead load and LL is the live load.

Then, in the second stage the column is removed almost instantaneously (i.e., 0.001 seconds) to account for the dynamic effects.

Both the nonlinear static analysis and column loss analysis were done using the plastic hinge concept. Columns were modeled using discrete plastic hinges, located at both ends, of axial-moment interaction, type P-M2-M3, defined according to ASCE/SEI 41-13 provisions (“ASCE/SEI 41-13” 2014). For beams however, plastic hinges were modeled using flexural moment hinge type (M3-type), defined also according to (“ASCE/SEI 41-13” 2014) but calibrated against relevant test data obtained within the framework of the “Structural conception and collapse control performance based design of multi-story structures under accidental actions CODEC” research project (CODEC 2016), (Dinu et al. 2016). The test setup is illustrated in Figure 3a, while Figure 3b shows the detailed numerical model developed with the SAP2000 software. In the test, the vertical load was applied quasi-statically at the top of the central column using a displacement control protocol and

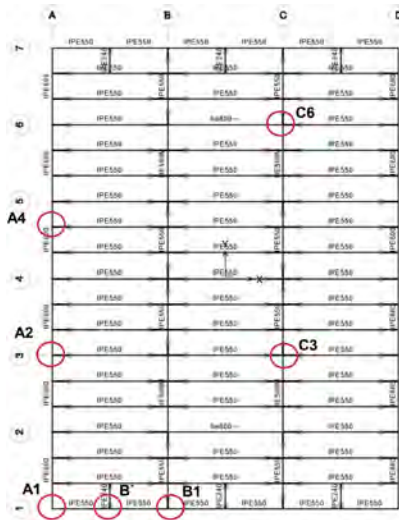


Figure 2. The column removal locations.

was gradually increased until the failure of the specimen. The ultimate vertical load capacity of the numerical model was obtained by carrying out a displacement controlled dynamic pushdown analysis, but with a low speed, similar with the experimental one. The numerical model consists in beam elements with nominal specimen geometry, material properties based on the material tests, and P-M2-M3 hinge types, assigned at both ends of the main beams and columns (Marginean et al. 2019). Figure 4 shows the vertical force versus vertical displacement curves at the central column. The numerical results show a very good correlation with the experimental ones.

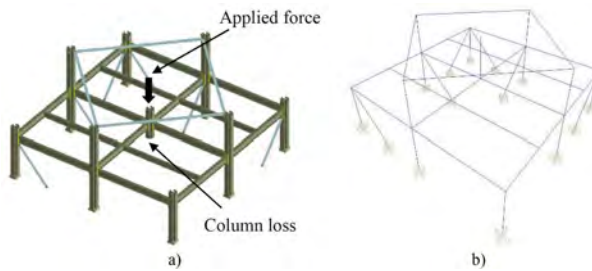


Figure 3. Geometry of test specimen (a) and SAP2000 numerical model (b).

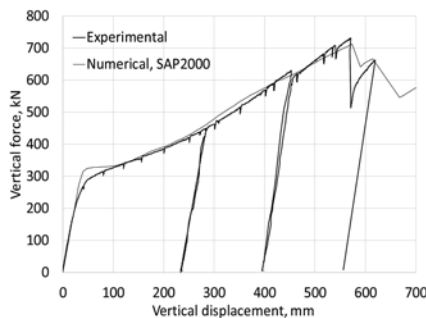


Figure 4. Force-displacement curves, experimental vs. numerical.

4 RESULTS

To evaluate the seismic demands at ULS, the structure is pushed sideway to its top target displacement D_t using a monotonically increasing uniform pattern of lateral forces.

Figure 5 shows the capacity curves for transversal and longitudinal directions and the target points for ULS and DL. Figure 6 shows the plastic mechanisms for transversal and longitudinal directions corresponding to target displacement D_t at the ULS. No plastic hinges develop in perimeter moment resisting frames in neither X nor Y direction at ULS, but only in the braced frames.

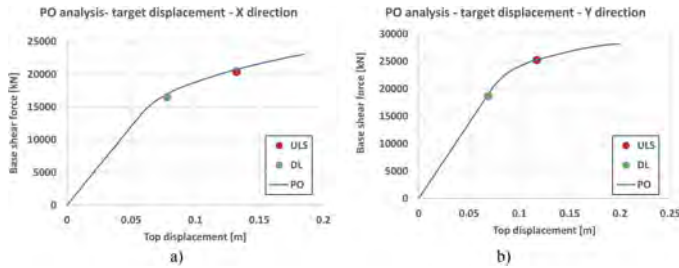


Figure 5. Seismic analysis: a) push-over curve with the position of the target point, X direction; b) push-over curve with the position of the target point, Y direction.

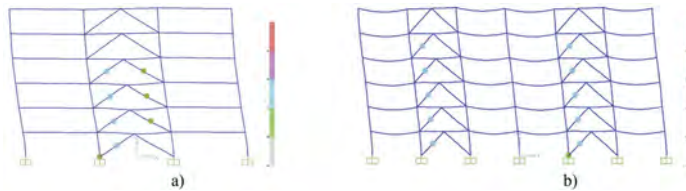


Figure 6. Seismic analysis: a) plastic mechanism corresponding to target displacement D_t at ULS, interior transversal frame; b) plastic mechanism corresponding to target displacement D_t at ULS, interior longitudinal frame.

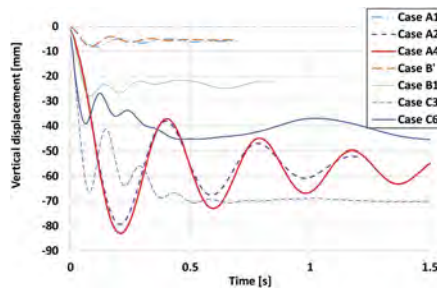


Figure 7. Vertical displacement in time for the considered removal scenarios.

After the damage state following an earthquake is evaluated, alternate load path method is applied for all removal scenarios, all located at the ground floor. The scenarios involve columns on the short and long sides of the façade but also interior columns from the braced spans. Figure 7 shows the history of vertical displacement above the removed column for the column removal scenarios, and indicates the progressive collapse is prevented in all cases. The plastic mechanisms presented in Figure 8 show that, for each scenario, the level of damage is moderate. For interior column removal scenarios affecting the braced spans (cases C3 and C6), the results indicate a possible hazardous situation. Thus, if we use a detailed view of the structure and separate the internal structure from the perimeter frames (see Figure 9), it may be seen that plastic deformations spread also in the perimeter MRFs, with plastic hinges both

in beams and columns. Note that after the seismic action ends, there are no residual deformations in the perimeter MRFs, and plastic hinges are only the results of column removal in the braced spans. This is explained by the smaller tributary area for gravity loads, but also by the large level of flexural overstrength in beams resulted when the contribution of the perimeter MRFs is checked, i.e., the duality should be checked by verifying that the MRFs carry at least 25% of the seismic force.

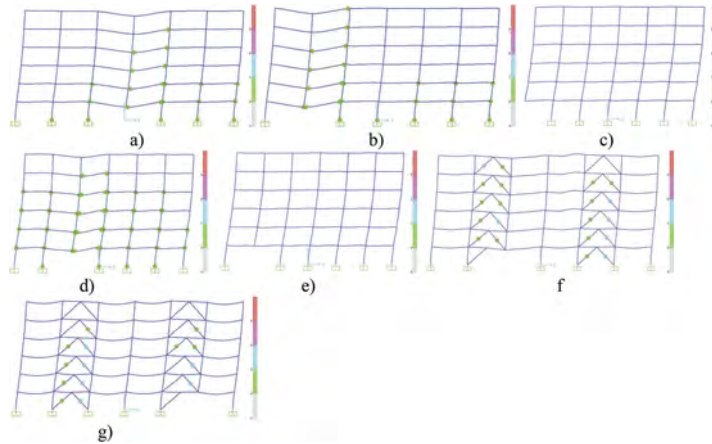


Figure 8. Plastic mechanism after column loss for the considered scenarios: a) case A4; b) case A2; c) case A1; d) case B1; e) case B'; f) case C3; g) case C6.

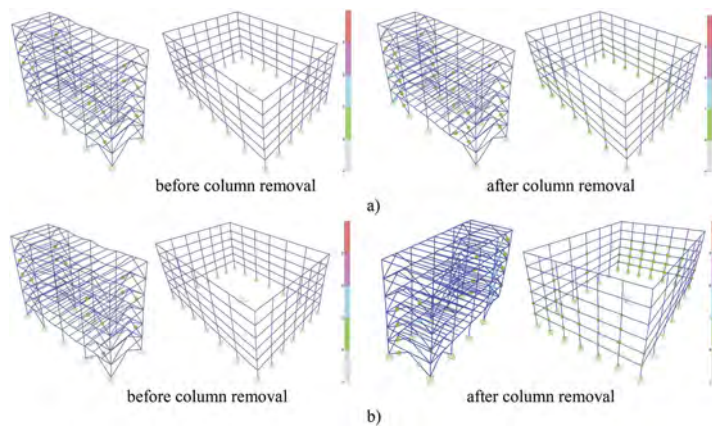


Figure 9. Plastic mechanisms following seismic event, before and after interior column loss: a) scenario C3; b) scenario C6.

5 CONCLUSIONS

Earthquake engineering and seismic design and practice have seen significant developments in the last decades. However, with all these developments, the potential for losses and extensive disruption of social and economic life due to seismic events remain high. One reason is the effect of multiple hazards occurrence, e.g., earthquake aftershocks, fire after earthquake, or fire after explosion. In such cases, even the structure survives the first event with damages that do not affect the global stability, the subsequent events can severely damage critical members and potentially cause extensive damages or even failures. The case study structure was initially

designed for the ULS and SLS requirements, with additional requirements for DL in case of seismic action. The response in case of column loss following an earthquake was investigated using the APM and nonlinear dynamic procedure. Even the structure showed adequate progressive collapse resistance, the internal column loss scenarios drawn attention, as they led to extensive damage in the perimeter moment resisting frames, which were still undamaged after the earthquake. It is expected that the results of the study can be used to design more robust building structural systems against extreme loading events and improve the life-cycle performance of built infrastructure.

REFERENCES

- Advanced design methods for BLAST loaded steel structures (ADBLAST): final report*. 2015. Luxembourg: Publications Office.
- “American Society of Civil Engineers ASCE. Seismic Rehabilitation of Existing Buildings ASCE/SEI 41-13”. 2014.
- Bruneau, M & MacRae, G. 2017. *Reconstructing Christchurch: A Seismic Shift in Building Structural Systems*. The Quake Centre, University of Canterbury.
- Bruneau, M, Chang, SE, Eguchi, RT, Lee, GC, O’Rourke, TD, Reinhorn, AM, Shinozuka, M, Tierney, K, et al. 2003. A Framework to Quantitatively Assess and Enhance the Seismic Resilience of Communities. *Earthquake Spectra*. 19(4):733–752. 10.1193/1.1623497.
- CODEC, *Structural conception and collapse control performance based design of multi-story structures under accidental actions*. 2016. Executive Agency for Higher Education, Research, Development and Innovation Funding: UEFISCDI.
- Demonceau, J-F, Golea, T, JASPART, J, Elghazouli, AY, Khalil, Z, Santiago, A, Santos, AF, Silva, L, et al. 2021. *Design Recommendations against Progressive Collapse in Steel and Steel-Concrete Buildings [FAILNOMORE]*.
- Dinu, F, Marginean, I, Dubina, D & Petran, I. 2016. Experimental testing and numerical analysis of 3D steel frame system under column loss. *Engineering Structures*. 113:59–70. 10.1016/j.engstruct.2016.01.022.
- DoD. 2009. *UFC 04-023-03: Unified facilities criteria: Design of buildings to resist progressive collapse*. (UFC 04-023-03). Washington (DC), US: United States Department of Defense.
- DUAREM. 2015. 10.2788/539418.
- Dubina, D, Stratan, A & Dinu, F. 2008. Dual high-strength steel eccentrically braced frames with removable links. *Earthquake Engineering & Structural Dynamics*. 37(15):1703–1720. 10.1002/eqe.828.
- Dubina, D, Dinu, F & Stratan, A. 2020. High-strength steel and dissipative fuse solutions for seismic-resistant building structures. *Steel Construction-Design and Research*. 13(3):154–164. 10.1002/stco.202000028.
- Dubina, D, Dinu, F & Stratan, A. 2021. Resilience of dual steel-dual frame buildings in seismic areas. *Steel Construction-Design and Research*. 14(3):150–166. 10.1002/stco.202100016.
- EN 1990. 2002. *Eurocode 0: Basis of Design*. (CEN). Brussels: European Committee for Standardisation.
- EN 1991-1-7. 2006. *Eurocode 1 - Actions on structures - Part 1-7: General actions - Accidental actions*. Brussels: European Committee for Standardisation.
- EN 1993-1-8. 2011. *Eurocode 3: Design of steel structures - Part 1-8: Design of joints*. Brussels: European Committee for Standardisation.
- EN 1998-1. 2004. *Eurocode 8 - Design of structures for earthquake resistance - Part 1: General Rules, seismic actions and rules for buildings*. European Committee for Standardization.
- Experimental validation of the response of a full-scale frame building subjected to blast load FRAMEBLAST*. 2018. Executive Agency for Higher Education, Research, Development and Innovation Funding: UEFISCDI.
- Jakab, D, Dinu, F, Stratan, A, Marginean, I & Dubina, D. 2022. Multi-hazard Robustness Assessment of Seismic Resistant Dual Frame Concentrically Braced Frames. In: *Proceedings of the 10th International Conference on Behaviour of Steel Structures in Seismic Areas*. F.M. Mazzolani, D. Dubina, & A. Stratan, Eds. Cham: Springer International Publishing. 405–413.
- Marginean, I, Dinu, F, Șlancarová, J & Mach, R. 2019. Influence of modeling criteria on the response of steel frame structures to column removal. *Romanian Journal of Technical Sciences. Series: Applied Mechanics*. 64(2):11–122.

Laser scanning technology for the evaluation of damage in complex building envelopes after extreme load events

P.C. Zdrenghia, F. Dinu, S. Herban & C. Neagu
Politehnica University Timisoara, Romania

ABSTRACT: Deformations and displacement measurements of structural/non-structural components of a building are often required during its design life, and several instruments and technologies are available (e.g., displacement transducers, total stations). However, this task can become very challenging for complex environments and/or when large deformations or displacements are expected, e.g., large building facades or large deformations under extreme loading. For such applications, terrestrial laser scanning (TLS), or Topographic LiDAR (Light Detection and Ranging), can be employed. Such systems provide high accuracy and high resolution measurements, and therefore can be used for complex loading environments, which can be otherwise difficult to perform using traditional methods. The paper presents the application of a terrestrial LiDAR system for deformation measurements of a lightweight façade made from wall liner trays, installed on a full-scale steel frame building model. The tests involve the detonation of several high energy explosive charges in the proximity of the building. The surface approximation is captured by TLS precise solutions, transformed into colored point clouds and then to 3D models. The results can be further used to calibrate advanced numerical models or to make rapid damage assessments and optimization of the recovery activities.

1 INTRODUCTION

For a community to be resilient, it requires robust infrastructure that can withstand hazards (single/multiple-exceptional threats) and demonstrate sufficient residual capacity, and rapid recovery after disruptive events (Figure 1). Developing appropriate tools and intervention procedures and optimizing allocation of resources help creating more disaster resilient communities. The loss of functionality due to insufficient robustness and or insufficient residual capacity can be alleviated if preventive rehabilitation strategies are employed. On the other hand, the rapid loss and damage evaluation, taking into consideration the evolution in time, can significantly shorten the recovery time. It is therefore necessary to increase the emergency preparedness and response capacity to effectively respond to a disaster.

Post-event information gathered through monitoring, sensing, and other field measurements helps the rapid damage assessment and the recovery activities. Aerial and digital technologies can also be used for damage assessment following major disasters, e.g., unmanned aerial vehicles (UAV) for post-disaster assessment and response; remote sensing techniques, such as interferometric synthetic aperture radar; improved location intelligence, early warning and relief response via social media and crowdsourcing.

Generally, damage assessment is focused on the information required to restore the facility to its pre-disaster condition. The inaccurate damage assessment (underestimated, overestimated) may lead to wrong decisions. Rapid (local) and comprehensive damage assessments are therefore critical. First, local damage assessment is used to determine if the damages resulting from the hazard can be addressed by existing resources. Then, comprehensive damage assessment activities focus on the damage assessment for buildings and infrastructure to establish the causes/levels of damage and to provide the most cost-effective solution/recommendation (repairing/strengthening/demolition).

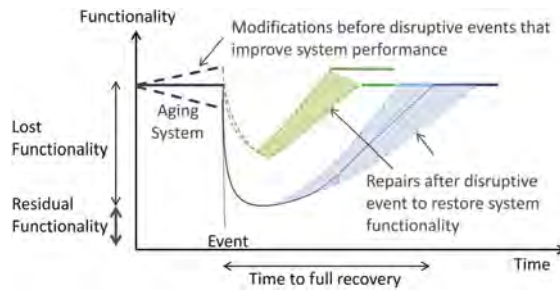


Figure 1. Resilience concept, adapted from (Bruneau et al. 2003) and (McDaniels et al. 2008).

According to EN 1991-1-7 (EN 1991-1-7 2006), structural robustness is the ability of a structure to withstand extreme events like fire, explosions, impact or the consequences of human error, without being damaged to an extent disproportionate to the original cause. Generally, buildings are not designed for loading conditions generated by explosions, excepting the facilities designed to resist such actions (e.g., blast resistant buildings) or buildings where gas is burned or regulated EN 1990 (EN 1990 2002). Thus, when buildings are subjected to such extreme loads, they may sustain extensive damages (Demonceau et al. 2021).

The paper presents the application of a terrestrial LiDAR system for deformation measurements of a lightweight façade made from wall liner trays installed on a full-scale steel frame building model. The tests involve the detonation of several high energy explosive charges in the proximity of the building. The surface approximation was captured by TLS precise solutions, transformed into colored point clouds, and then to 3D CAD models. The results were further used for the calibration of numerical models. Damage levels based on maximum mid-span deformations were also proposed. Such results can be employed in damage assessment and recovery activities. The results were obtained in the framework of SAFE-WALL research project “Safety of building walls and claddings against accidental explosions” (SAFE-WALL 2020).

2 TEST SET-UP AND INSTRUMENTATION

The object under investigation is a full-scale 3D steel frame building structure. The steel frame structure has two spans of 4.5 m each, two bays of 3.0 m each, and two stories of 2.5 m each (Figure 2a). More details may be found in (FRAMEBLAST 2018). The structure is designed for persistent and seismic design situations (EN 1990 2002).

On one side, the building has a façade made from steel-based wall panels. The panels were assembled in two configurations, i.e., right hand side span with standard wall layers – system S1 (inner metal liner, thermal insulation, outer weather cladding), and left hand side with inner metal liner only – system S2, see Figure 2b. The liner trays are MBS KS100/600 type panels with 0.88 mm thickness, S320 GD steel (see (EN 10326 2013) for Technical delivery conditions). Liner trays are placed horizontally and fixed to the supporting steel columns using six 5.5 mm S-MD55Z self-drilling screws at each panel end.

The model was tested under increasing blast loads until complete failure of the wall panels. The blast charges were placed at a height of 1.5 m from the ground and 1.5 m from the wall, first at right midspan, then at left midspan. The charges were positioned normal to the 3rd liner tray (from the ground). The laser measurements were done on the initial undeformed walls, then for the following tests:

- Test RT1: right span, charge weight of 1.144 kg
- Test RT2: right span, charge weight of 2.288 kg
- Test LT1: left span, charge weight of 0.572 kg
- Test LT2: left span, charge weight of 1.144 kg

The tests were done at the INSEMEX blast testing facility in Petroșani, Romania, and used different instrumentation, i.e., high-speed cameras, pressure sensors, strain gauges, displacement transducers, and Z+F IMAGER 5010C type terrestrial laser scanner (see Figure 3).

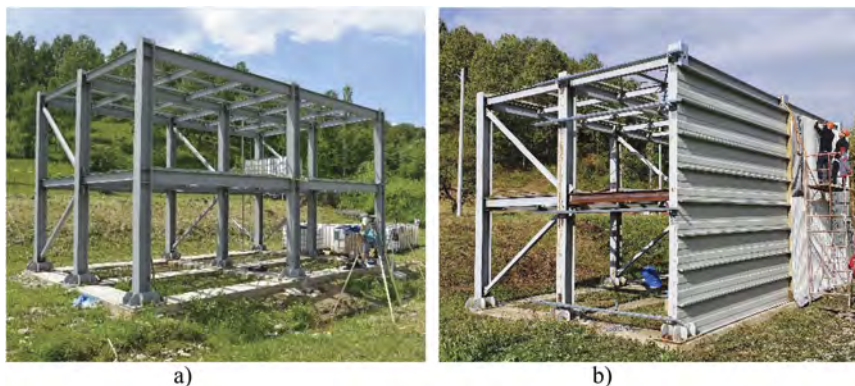


Figure 2. General view of the building structure (a) and steel based faced during construction (b).

Surveying methods based on laser scanning are very effective to obtain accurate data about the response of the structural and non-structural elements, including the residual panel deformations and displacements. The Z+F IMAGER 5010C (M.S. Quintero et al. 2008) is a static ground scanner mounted on a rigid tripod and has a fixed position during the data acquisition process. It also belongs to the category of active scanners, which emit controlled radiation in the form of a laser wave and determinate the position of the laser point on the scanned object using the built-in camera. The scanner has an integrated HDR (High Dynamic Range) camera, with a resolution of 60 megapixels, and it is appropriate for capturing high-resolution, high-quality images. This type of scanner has also a dynamic compensation, which is designed to provide the position correction so that the instrument does not suffer any offset during successive measurements (Figure 4). The position has been constantly corrected, so that the maximum offsets did not exceed $\pm 2^\circ$, thus resulting in very high accuracy holds.



Figure 3. General view of the building, with the LIDAR system installed on position.

To determine the coordinates of the points, the scanner uses the time-shift principle, making it ideal for lens scanning due to the speed of the scan and the higher resolution compared to the scanners based on the time-of-flight method. The time-shift method is often used in wave measurements. This method is used in both total stations using the laser function for distance measurements and in active laser scans. It involves the measurement of a phase difference between transmitted and received waves.

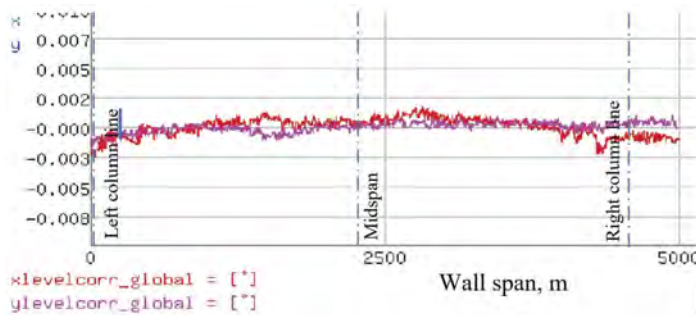


Figure 4. Detected tilting changes between two low encoder positions ($< 0.007^\circ$).

The maximum data acquisition of the device could reach 1.016.000 points per second, but the actual measurements were made at lower rates. Furthermore, due to the relatively large number of people involved in the site testing (and implicitly during the scanning process), the use of this type of laser was found more appropriate as it has a wavelength of $1.5 \mu\text{m}$ (laser class 1, (EN 60825-1 2014)) and the laser beam is rated harmless.

Paper targets were used as landmarks and were placed at different locations around the building. These paper targets are made of two black triangles attached to the center of the paper, which is the reference point in the post-processing stage. Considering the particularity of the blast test conditions, i.e., the pressure propagates at large distance from the source, the location of the paper targets has been carefully considered. They have a critical role in aligning the point clouds and coordinate systems in consecutive scans (before and after the explosion). The minimum requirement is that there are at least three common targets between scanning stations (i.e., before and after the test). If the targets are located too far, the accuracy is low, while if they are too close to the blast, they could be destroyed or they can change the position, which means the measurements are compromised.

Each scan series consisted of two separate scans, i.e., an initial scan to capture the initial shape of the wall panels, and a second one performed after the test to determine the deformations caused by explosion (Figure 5). Seven paper targets were used in average and were placed at distances ranging between 10 and 70 meters from the scanning stations. Although the paper targets were placed at a relatively large distance from the center of the explosion, three targets were affected by the pressure wave, as they were moved from the initial position. Also, one target proved to be too far to provide satisfactory accuracy.

To determine the optimal position of a scan station, it is important to consider the range of the scanner, the maximum distance to which the scanner ensures maximum accuracy, and coverage. To optimize the number of scan stations, the distance between them was adjusted to reduce the points overlapping (the same points seen on several stations). It is also necessary to determine the positions that are providing the largest coverage area of interest, without any obstruction on the laser beam path. Therefore, the scanner position was chosen such that the emitted laser beam intersected the scanned surface as much as possible in a perpendicular direction.

To process the results and obtain the point clouds of the façade system, test data were first exported using the Z+F Laser control program. The accuracy obtained in the alignment of the point clouds was very high and showed an average error of only 1.7 millimeters.

Initially, the point cloud is in grayscale (Figure 6), but during the post-processing phase each point is colored by using panoramic images which are taken by the camera incorporated in the laser scanner (see Figure 7). The larger the point cloud, so is the computational demands. Therefore, some points were considered redundant and removed from the point cloud, because they referred to objects that are not of interest (e.g., trees, terrain). The cleaning process was done with the CloudCompare program (see Figure 8).

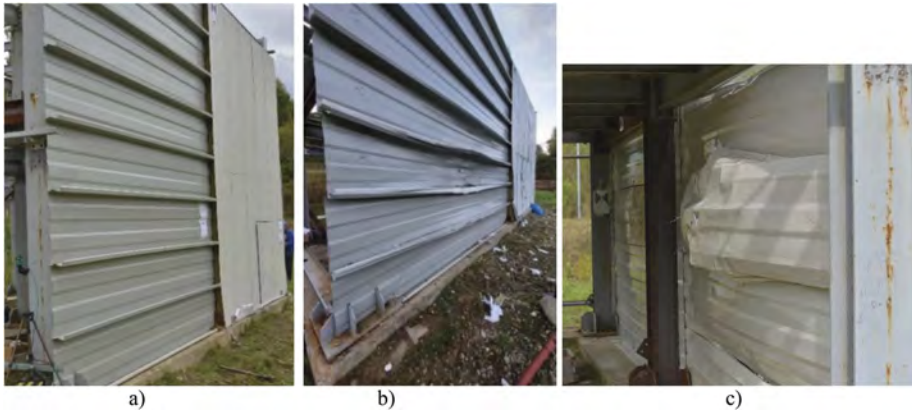


Figure 5. View with undeformed wall panels (a), view from exterior with wall panels damaged due to blast (b), and view from interior at the end of the tests (c).



Figure 6. The initial point cloud is in grayscale.



Figure 7. Uncleaned point cloud of the facade before the explosion (a) and after the explosion (b).

3 RESULTS AND DISCUSSIONS

To obtain accurate results, the scans taken before and after the explosion had to have the same coordinate system. Therefore, the coordinates of the paper targets used in the first scan (initial shape) were used as baseline for the second scan (final shape). Post-processing done using CloudCompare software reduced the number of points from an initial 2.7 million to 300.000 points. This step allowed us to reduce the thickness of the point cloud and to obtain the deformed shapes of the panels with accuracy.



Figure 8. Cleaned point cloud of the facade before the explosion a) and after the explosion b).

The deformations could be seen directly from the CloudCompare software (Figure 9), which presents the residual deformations after the tests RT1 (on S1) and LT2 (on S2). It may be seen for a charge of 1.144 kg, the deformations of S1 panels are moderate compared with S2, which has one panel completely failed. However, due to the limitations of the software in handling the results, they were exported in a more general CAD format (i.e., DXF) (see Figure 10).



Figure 9. Top view of the cleaned point cloud of the deformed shape after the tests RT1 (on S1) and LT2 (on S2).

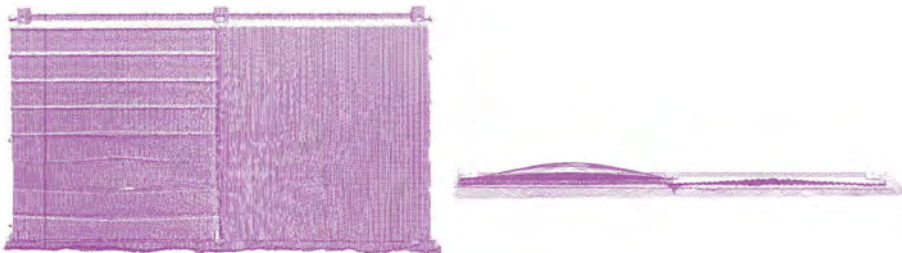


Figure 10. Final point cloud of the deformed shape in DXF format: a) front view; b) top view.

Figure 11 presents the residual deformations for the two wall systems, S1 and S2. Due to some technical issues, for S2 system only the scan after LT2 test provided accurate result. The deformation reported here for LT1 has been measured only at the midspan using a ruler. For S1, there were two valid scans, one for RT1 and one for RT2. As may be seen, for the same blast parameters in RT1 and LT2, i.e., 1.144 kg TNT and stand-off distance $R = 1.5$ m, panels in S2 attains the ultimate capacity and fails, while panels in S1 suffer extensive deformations but the failure is prevented. S1 system steel demonstrate some residual capacity even at a much powerful blast, i.e., 2.288 kg TNT (same stand-off distance $R = 1.5$ m).

Damage levels of wall components under blast loads can be defined by reference to a range of ductility, μ , and support rotation values, θ (Hoffmeister et al. 2015). Some guidance on response limits for structural components of steel-based walls can be found in (DoD 2020) and (DoD 2008). Table 1 shows typical values for cold formed corrugated thin wall members (DoD 2020) and experimental values for the two wall systems presented in Figure 11. For ease of use, Figure 11 presents the panel chord rotation, in degrees, but also the deformation-to-span ratios,

which are more common in the design practice. Note that, the maximum transient deflection limit used in steel-based liner tray design against wind is $L/150$. This limit is associated with elastic design, without any residual deformations of the panels.

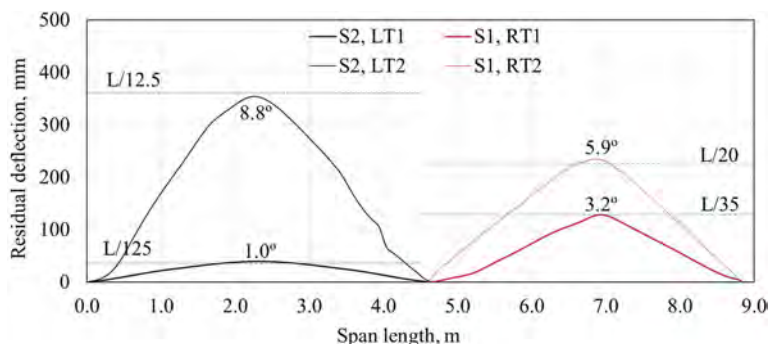


Figure 11. Residual deformations in the 3rd panel from the ground row, comparison between the two façade systems, S1 and S2.

Table 1. Response limits for cold formed structural steel members in terms of chord rotation, θ (DoD 2020).

Element	Damage level:	Moderate	Heavy	Hazardous
			Moderate-to-Heavy	Heavy-to-Hazardous
<i>Corrugated panel</i>	Full tensile membrane capacity	3°	6°	12°
	<i>Some tensile membrane capacity</i>	1°	4°	8°
	No tensile membrane capacity	1.3°	2°	4°
Liner tray, system S1		3.2°		5.9°
Liner tray, system S2		1.0°		8.8°

As seen in Table 1, for system S1, the panel behaviour is dominated by flexural response with some tensile membrane capacity, and the two damage levels can be associated with moderate-to-heavy and heavy-to-hazardous responses, respectively. For system S2, which is made of inner metal liner trays only, rotation for LT1 indicates a moderate damage, while the maximum chord rotation is larger than the hazardous response limit ($\theta > 8^\circ$).

For both systems, higher response limits can be achieved (i.e., full tension membrane) if the premature failure of the end connections in shear is prevented. Also, even the unprotected liner trays in system S2 demonstrate a larger deformation capacity than S1, the panels fail at smaller blast pressures due to a lack of interaction between adjacent panels (they work more like 2D systems) and more concentrated blast pressure around midspan.

4 CONCLUSIONS

Terrestrial Laser Scanning can be effectively used for gathering valuable information in the aftermath of an extreme event, e.g., strong earthquakes, extreme weather events, or accidental explosion. They can be installed at certain range from the objective, with minimum on site

demands. The results can help providing a rapid damage assessment and optimize the recovery activities. They are particularly efficient for complex environments, e.g., building facades, where other more traditional techniques may be difficult to apply and with less accurate results.

The results presented in the paper showed the application of laser scanning technique to assess the residual deflections in wall panels mounted on a 3D steel frame building. To reduce the size of the point cloud, results were filtered, without a significant impact on the accuracy. The complex deflected shape of the panels were represented with high accuracy and will be used to calibrate numerical models which under development. The results were also used to propose preliminary damage assessment criteria using predefined chord rotation values, suggesting terrestrial laser scanning represents an effective method that can be used to make a rapid damage assessment and optimizes the recovery activities.

ACKNOWLEDGEMENTS

This work was partly supported by grant of the Romanian National Authority for Scientific Research and Innovation, CNCS/CCCDI - UEFISCDI, project number PN-III-P2-2.1-PED-2019-1765, within PNCDI III: "Safety of buildings walls and claddings against accidental explosions" SAFE-WALL.

REFERENCES

- Bruneau, M, Chang, SE, Eguchi, RT, Lee, GC, O'Rourke, TD, Reinhorn, AM, Shinozuka, M, Tierney, K, et al. 2003. A Framework to Quantitatively Assess and Enhance the Seismic Resilience of Communities. *Earthquake Spectra*. 19(4):733–752. 10.1193/1.1623497.
- Demonceau, J-F, Golea, T, Jaspert, J, Elghazouli, AY, Khalil, Z, Santiago, A, Santos, AF, Silva, L, et al. 2021. *Design Recommendations against Progressive Collapse in Steel and Steel-Concrete Buildings [FAILNOMORE]*.
- DoD. 2020. *UFC 4-010-01: DoD minimum antiterrorism standards for buildings, with change 1*. (UFC 4-010-01). United States Department of Defense.
- EN 1990. 2002. *Eurocode 0: Basis of Design*. (CEN). Brussels: European Committee for Standardisation.
- EN 1991-1-7. 2006. *Eurocode 1 - Actions on structures - Part 1-7: General actions - Accidental actions*. Brussels: European Committee for Standardisation.
- EN 10326. 2013. *Continuously hot-dip coated strip and sheet of structural steels - technical delivery conditions*. (CEN). Brussels: European Committee for Standardisation.
- EN 60825-1:2014/A11:2021 - *Safety of laser products - Part 1: Equipment classification and requirements*. 2014. Available from: <https://standards.iteh.ai/catalog/standards/clc/ec219835-bd1b-4edb-8ce8-967fce69f499/en-60825-1-2014-a11-2021> [Accessed 31 January 2023].
- Experimental validation of the response of a full-scale frame building subjected to blast load FRAMEBLAST*. 2018. Executive Agency for Higher Education, Research, Development, and Innovation Funding: UEFISCDI.
- Hoffmeister, B, Schillo, N, Colomer, C, Elghazouli, A, Nardini, L, Salvatore, W, Lecompte, D, Reyman, B, et al. 2015. *Advanced design methods for BLAST loaded steel structures (ADBLAST): final report*. Luxembourg: Publications Office.
- McDaniels, T, Chang, S, Cole, D, Mikawoz, J & Longstaff, H. 2008. Fostering resilience to extreme events within infrastructure systems: Characterizing decision contexts for mitigation and adaptation. *Global Environmental Change*. 18(2):310–318. 10.1016/j.gloenvcha.2008.03.001.
- M.S. Quintero, M. De Bruyne, R. Poleman, M. Hankar, S. Hankar, B. H. Caner, P. Craven, L. Budei, et al. 2008. Theory and practice on Terrestrial Laser Scanning. *Flemish Agency of the European Leonardo DaVinci programme*.
- Safety of buildings walls and claddings against accidental explosions SAFE-WALL*. 2020. Executive Agency for Higher Education, Research, Development and Innovation Funding: UEFISCDI.
- Single degree of freedom structural response limits for antiterrorism design PDC TR-06-08*. 2008. Protective Design Center, Army Corps of Engineers, USA.

Design strategies for reusable structural components in the built environment

F. Kavoura & M. Veljkovic

Delft University of Technology, The Netherlands

ABSTRACT: The technical solutions for deconstruction are reviewed and investigated in the building sector as this is an expected trend under the sustainability requirements set in the EU Commission's "Green Deal" towards net zero greenhouse gas emissions by 2050. Two of the main research areas for efficient deconstruction strategies are; i) the behavior of multi-material structural components (hybrid structures) that combine the advantages of mechanical properties and architectural appearance of different construction materials, and ii) the techniques and mechanical properties of connections between structural components which allow deconstruction and reuse. However, there is a very limited number of studies and methods into specific demountable and hybrid structural systems, and even fewer focus on their practicability and feasibility. Since these systems have the potential to reduce construction waste, encourage resource efficiency and reduce embodied carbon impacts, it is expected that they will contribute immensely to a sustainable built environment. This paper focuses on technical solutions of the design strategies that currently have been developed for hybrid and steel reusable structural systems, and proposes an approach on implementing structural floor systems designed with the linear approach to a circular building environment.

1 INTRODUCTION

1.1 *Re-use of steel structural components*

In response to the sustainability requirements set in the EU Commission's "Green Deal" (European Commission, 2018) towards reduction of the greenhouse gas emissions, it is estimated that the structural design for deconstruction (leading to structural components' reuse) is going to contribute considerably to the sustainable development of the built environment (Brambilla et al., 2019). The construction sector is responsible for a big percentage of the annual resource consumption, of construction and demolition waste, and of total energy consumption. The preferred strategy in order to achieve a sustainably built environment is to design for demounting, and reuse of the structural components before thinking about repair, remanufacturing, or recycling following Cramer's (Cramer, 2015) scheme on how a circular economy can be incorporated for sustainable construction. Demountability and reuse are the main focus areas in the construction sector since they allow for value retention of the structural members, the potential for cost reduction in extended life cycles, a smaller environmental impact and consequently enhancing sustainable construction.

The idea of reusing steel structural elements is developing through the years. Even if it is still in primitive application in practice, it is highly supported by approaches addressing nowadays the reusability of buildings like "Donorskelet" (Terwel & Korthagen 2021), bridges like the "Nationale Bruggenbank" (2023) or platforms that create digital databases on reclaimed steel structural elements like the "Circulair Bouwen in 2023" (2023). Also, recommendations for the reuse of steel structures have been made stating that any sign of plastic deformation is a reason for rejection and presenting a strategy to support reuse (SCI 2019, Progress 2020). Even if broad concepts on the reusability of structures have been discussed and developed in the aforementioned concepts, very few have presented extended processes to successfully implement the concept in real-life structures. An overview of the reusability of steel and steel-concrete hybrid floor systems is discussed in the next Sections.

1.2 Steel-dominated hybrid demountable structures

Current developments of the steel and steel-dominating hybrid structures underline their advantages with respect to their speed of construction, optimum material use, and consequently decrease in floor weight and the self-weight of the structure while achieving larger floor span when compared with other types of structural systems (e.g. reinforced concrete, timber) (Ahmed et al, 2019). The skeleton of these steel-dominating hybrid structures is made mainly of steel structural components where nearly one hundred percent of the steel is recycled or reused while they can be easily mounted, demounted, and reused with the use of bolted connections. So, as the demand for new structures and the need for reusing existing ones are increasing due to the growing pace of urbanization, there is no doubt that the selection of steel-dominating hybrid structures can have an immense contribution to the sustainable development of the built environment.

Hybrid structures as defined in this paper, consist of floor systems with hybrid beams (steel structural components and multi-material floor and deck systems) that exhibit excellent structural characteristics, in terms of their stiffness and strength, when compared with steel or reinforced concrete beams. The reason is that they combine the advantages of mechanical properties of different construction materials (e.g. concrete in compression and steel in tension). When it comes to the connections of their floor systems with the steel beams, the demountable shear connectors have shown that they can play a significant role in the deconstructability of these systems (Pavlovic et al. 2013, Nijgh et al. 2018).

So, through the transition from a linear economy to a circular one for steel-dominated hybrid structures, a few proposed solutions are summarized in Figure 1. Specifically, through research developments of the last few years the conventional constructional method of the steel-concrete composite floor systems, the steel beams are connected with welded headed studs which are encased within the concrete slab in order to achieve the necessary shear connection. Through developments, this construction method can be transformed into a demountable structure which could lead to a sustainable built environment. This could be achieved through the use of “green” concrete materials [e.g. geopolymers (Liu et al. 2015, Ataei et al. 2016)] the reuse of the structures’ components through the use of demountable connectors (Pavlovic et al. 2013, Nijgh et al. 2018, Odenbreit et al. 2019), and the optimum material use through the use of tapered and high strength steel beams (Nijgh et al. 2018) and composite slabs (Gritsenko et al. 2019).

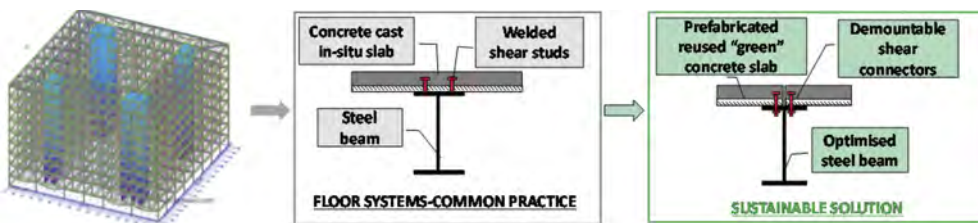


Figure 1. Development of a sustainable solution for a hybrid floor system through research developments focusing on optimum material utilization and floor system deconstruction and reuse (though demountable connectors).

2 REUSE OF STEEL-DOMINATED HYBRID STRUCTURES

2.1 Reuse of steel structural systems

Design for deconstruction of one-story steel buildings has been presented in detail in the RFCS project Progress (2020) where the in-situ and relocated reuse scenarios are examined thoroughly. The overall same approach for the reusability of reclaimed steel structural components is also adopted by SCI (2019). Accordingly, the process for the reuse of reclaimed steel structural elements is described in Figure 2. The three main phases for the reuse of a structural component and its implementation in the circular building environment include a) the pre-deconstruction audit and assessment for reuse, b) sampling and testing, and c) design for reuse.

The first phase of the pre-deconstruction audit and assessment for reuse includes the preliminary assessment for the evaluation of the feasibility of reclaiming and reusing the existing steelwork. A preliminary overall visual inspection (e.g. identifying problems such as excessive corrosion, excessive/plastic deformation of the structural elements, etc.) and quantitative/empirical evaluation and reporting (e.g. dimensions of joints and their connectors, etc.) of the existing steelwork are undertaken within this phase. The second phase of sampling and testing includes techniques that quantify the material properties and verify the structure. The testing programs include a range of destructive (DT) and non-destructive (NDT) tests. Non-destructive tests (NDT) do not damage the structure and can be useful to locate and/or measure the size of the defects. Some examples are hardness tests, positive metal identification (using X-ray Fluorescence and optical emission spectrometry), and small punch testing. Destructive testing (DT) techniques require extracting (by cutting or drilling) small samples from the existing structure following the EN 10025 (2004) standards. Destructive testing (DT) techniques include tensile testing, chemical composition analysis, Charpy impact test, and metallography. Last, the design for reuse phase includes the design considerations for achieving a reliable structure with reclaimed steel elements and the structural analysis principles according to EN 1993 provisions.

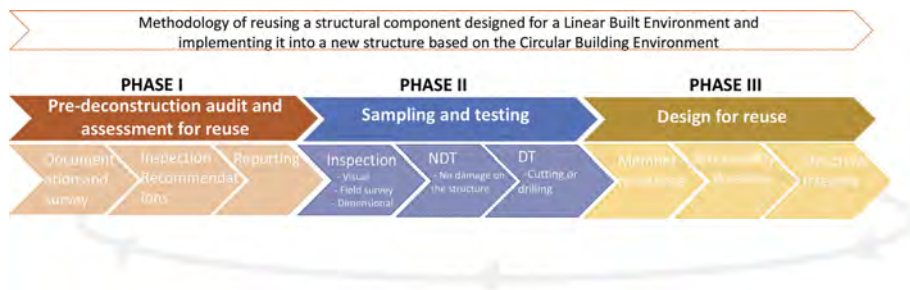


Figure 2. Methodology of reusing a structural component designed for a linear built environment and implementing it into a new structure based on the circular building environment according to the RFCS project Progress (2020).

2.2 Case studies

The idea of reusing steel structural elements is highly supported by approaches addressing nowadays the reusability of buildings like “Donorskelet” (Terwel et al. 2021) (see Figure 3), bridges like the “Nationale Bruggenbank” (2023), or platforms that create digital databases on reclaimed steel structural elements like the “Circular Bouwen in 2023” (2023). Additionally, projects worldwide have proved that reuse of the old steel structure was more feasible than designing and erecting a new steel structure with the same dimensions and functionality (Wakefield 2017, Snyder 2022). Several case studies are presented in detail in the RFCS project Progress (2020) and illustrate the use of reclaimed steel structures in various EU countries and some of the technical issues that were overcome. It is underlined that the case studies and consultations with the supply chain, confirm the technical viability of the reuse of steel reclaimed elements. The additional time/program and cost of using reclaimed steel have been identified as significant barriers across the supply chain. However, the structural design using reclaimed steel elements has shown environmental and economic benefits. These benefits are discussed in Section 3.1.

Case studies using reclaimed steel elements taken from stocks and digital databases on truss bridges (van Lookeren Champagne 2022) and frame structures (Rademaker 2022) have been studied recently. These studies support the design by considering that not all profiles, lengths, and dimensions are available at all times when having such databases (Gorgolewski 2008, Bukauskas 2020). Also, reclaimed elements often lack information about material properties and the used standards when being manufactured. For this reason, the need for a standardized process for the reuse of steel elements is underlined. Countries like the Netherlands, are in the process to standardize the procedure to guarantee the material properties by



Figure 3. Construction of Biopartner 5, whereby steel elements are used from the neighboring Gorlaeus-building (Terwel et al. 2021).

NEN-EN 1993-1-1 for new structural steel for reclaimed steel profiles. The goal is then that the required information about the reclaimed steel element will be included in a material passport, which will be presented in the digital database.

3 DEMOUNTABLE STRUCTURES AND CONNECTORS

3.1 *Demountable and reused floor systems – environmental impact assessment*

The sustainability potential of demountable-reused structures has been assessed by several studies through a Life Cycle Assessment (LCA). The LCA is an internationally used technique that aims at the analysis and evaluation of the environmental aspects and impacts of a product from the procurement of raw materials to the end-of-life stage which can consist of reuse, recycling, or disposal (International Organization for Standardization, 2006). Then different types of emissions are unified into several environmental impact categories which all together determine the total impact. The total impact may be expressed in the functional unit €, which describes the cost society is willing to pay for measures to achieve each emission target. In the Netherlands, this value is called MKI-value or shadow cost. The information obtained from the LCA results concludes a more comprehensive decision process, including quantitative information about the total environmental impact of the structure (International Organization for Standardization, 2006).

Through LCA it has been evaluated that a demountable steel-dominated hybrid structure could reduce considerably the amount of environmental footprint (Brambilla et al. 2019, Bohlen 2021, van Maastrigt 2019). The demountability and consequently the reusability of these systems are supported by the use of demountable shear connectors which allow for the assembly and disassembly of the systems. A detailed list and discussion about types and the structural performance of demountable connectors through the years are given in Section 3.2.

3.2 *Demountable connectors*

The key structural component for achieving a demountable and reusable structure is the type of shear connectors used for the connection between the steel beam and the floor system (for cast-in-situ and prefabricated slabs) (Kavoura et al. 2022a). One of the first types of demountable connectors introduced in the literature is the friction-grip bolt (see Figure 4a). These pre-loaded bolts have been tested in the late 1960s, through push-out and beam tests (Dallam 1968) in order to evaluate if full interaction occurs between the concrete slab and the steel beam within the serviceability limit states. It was reported that friction-grip bolts are demonstrating higher fatigue strength than conventional welded shear studs.

Another type of demountable connection that has been investigated experimentally and analytically in the literature is the bolted shear connectors with embedded nuts (see Figure 4b) (Kwon et al. 2010, Pavlovic et al. 2013). Push-out experiments and detailed FE models have been investigated on prefabricated concrete slabs with single-nut bolt shear connectors (Pavlovic et al. 2013).

They have demonstrated a reduced stiffness of 50% at service loads when compared with headed studs but they could achieve approximately 95% shear resistance (Pavlovic et al. 2013). Post-installed double-nut bolt connectors were used in an investigation of the strengthening of existing bridge girders (Kwon et al. 2010). Static experiments on post-installed double nut bolt connectors showed that they have lower shear strength and ductility when compared with post-installed friction-grip bolted shear connectors but they exhibit high stiffness in the elastic range.

The behavior of bolted shear connectors with a coupler system (see Figure 4b) has been recently studied experimentally on push-out and beam tests (Kozma et al. 2019, Nijgh et al. 2018, Nijgh et al. 2019, Gritsenko et al. 2019). This connector consists of a coupler welded on a steel L-shaped profile on top of the steel beam in which two bolts are connected. One bolt is embedded in the slab and a second removable bolt is placed from below the steel beam flange. In this concept of shear connectors, the coupler has higher strength than the bolts, so damage related to the overloading of the shear connector accumulates in the external bolt, rather than in the embedded coupler. In this way, in a subsequent life cycle, the external bolt can be replaced and the concrete deck is fit for use (Nijgh et al. 2019).

In subsequent studies, injected bolted shear connectors with a coupler system (see Figures 4 c and d) were tested in push out and beam tests on prefabricated slabs (Nijgh et al. 2018, Nijgh et al. 2019) and composite slabs with profiled steel sheeting (Gritsenko et al. 2019). After the injection and curing, the epoxy resin acts as a load-bearing element, and its resistance is substantially higher than its uniaxial compression strength due to the natural confinement provided by the bolt hole (Nijgh 2021). The injected bolted shear connectors allow for oversized holes which can account for the fabrication and execution tolerances and consequently improve the execution efficiency. Even if the increased bolt-to-hole clearance causes a decrease in the effective shear connector's stiffness (Yang et al. 2018), injecting the remaining bolt-to-hole clearance with an epoxy resin has the potential to mitigate this decrease in stiffness (Nijgh 2021). Last, these injected demountable connectors with a novel injected steel-reinforced resin have demonstrated high stiffness when compared to the conventional injectant bolted connections under different deck applications (e.g. concrete and FRP) and consequently confinement conditions (Kavoura et al. 2022b).

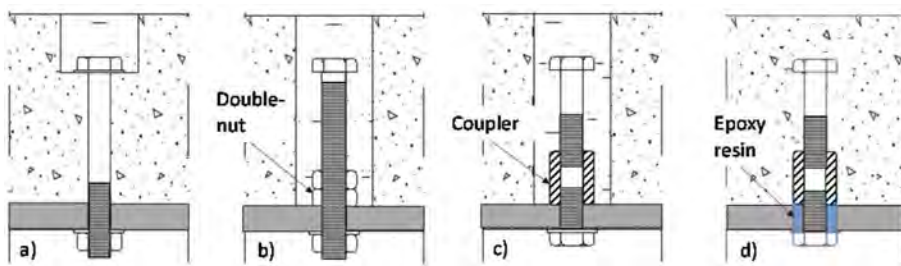


Figure 4. Types of demountable bolted connectors a) friction grip bolts, b) double-nut, c) coupler system connectors, d) injected bolted shear connectors with a coupler system.

3.3 Demountable and reused floor systems – structural behavior

In this paper, the developments on the reuse of steel reclaimed elements and the technical solutions for reusing a steel-nominated hybrid floor system are discussed. Several research has been conducted on these two thematic areas but up to now there is a research gap on how these could be combined. In the general theoretical framework of reusing a structural component designed for a linear built environment and implementing it into a new structure based on the circular building environment, the reuse of steel structural components is well-investigated and implementations are attempted through standardization processes (Progress, 2020). However, when it comes to the reuse of hybrid floor systems research and real-life applications still need to be developed.

A first attempt at the analysis of floor systems designed with the linear approach is realized in this paper through a case study. A conventional floor system with continuous beams and a corresponding

demountable solution are analyzed in the program Midas (2011) for comparing their structural performances. The two structural systems are explained in Figure 5 along with their dimensions.

The main concept of this short case study is to evaluate modeling techniques and results by implementing demountable connections between composite beams and slabs created with the linear built approach. These connections are modeled as spring elements between the two structural components with the shear and tensile mechanical characteristics of a bolt connected at the locations of zero bending moments of the continuous beam. The vertical displacement and bending moment contour maps are shown in Figures 6 and Figure 7 respectively. It is observed that in the case of the demountable floor system, the maximum deformations occur close to the end supports. This behavior is caused by the semi-rigid connection between the hybrid beam and the concrete slab implemented as spring elements. The alternation of the bolted demountable connector which is commonly used as a shear connector in hybrid beams (presented in Section 3.2) to another type of connector more suitable for these applications or the implementation of more rigid connectors, could result in a slab behavior closer to the conventional one. Even if technical solutions for connecting hybrid beams with a slab have not yet been developed, this is a research area with great potential and contribution to the sustainable building environment.

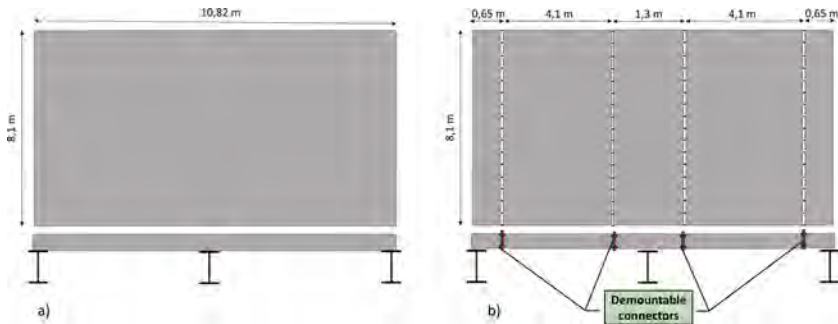


Figure 5. a) Conventional and b) demountable steel-concrete hybrid floor systems (not in scale).

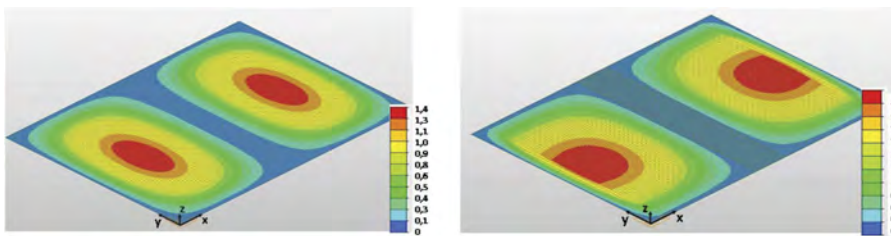


Figure 6. Vertical displacements in mm of a) conventional and b) demountable steel-concrete hybrid floor systems.

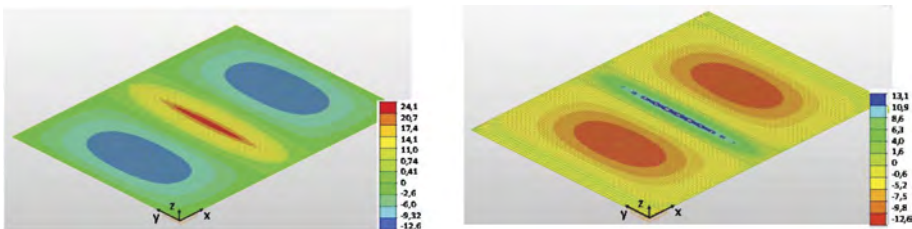


Figure 7. Moment around y-axis in $kN \cdot m/m$ for a) conventional and b) demountable steel-concrete hybrid floor systems.

4 CONCLUSIONS

This paper presents an overview of the most recent developments regarding the efficient strategies for the reuse of reclaimed steel elements and multi-material structural components (hybrid structures), and the types and properties of connections between structural components which allow deconstruction and reuse. The main conclusions of this paper are summarized below:

- The idea of reusing composite structural elements has been developing through the years. Even if it is still at the initial stage of application in practice, it is highly supported by guidelines and recommendations in addressing the reusability of buildings.
- The three main phases for the reuse of a structural component and its implementation in the circular building environment include a) the pre-deconstruction audit and assessment for re-use, b) sampling (in terms of grouping) and certification of structural components, and c) design for reuse as instructed by well-developed guidelines (SCI 2019, Progress 2020).
- Through LCA it has been evaluated that a demountable steel-dominated hybrid structure could considerably reduce the amount of environmental footprint.
- The reuse of hybrid floor systems and their implementation into a circular building environment, even if they were created with the linear execution approach, has not been developed and needs further investigation. A first attempt at implementing the connection between the hybrid beams and the concrete slabs shows that maximum deformations occur close to the end supports rather than at the midspan of the slab. This behavior will eventually require more sophisticated modeling and implementation of connections between the two systems, in order to capture the real behavior of the system in the vertical and horizontal directions.

REFERENCES

- Ahmed, I.M., Tsavdaridis, K.D. 2019. The evolution of composite flooring systems: applications, testing, modelling and Eurocode design approaches. *Journal of Constructional Steel Research*. 155: 286–300.
- Ataei A., Bradford M.A., Liu X. 2016. Experimental study of composite beams having a precast geopolymer concrete slab and deconstructable bolted shear connectors. *Engineering Structures*. 114.
- Brambilla, G., Lavagna, M., Vasdravellis, G., Castiglioni, C.A. 2019. Environmental benefits arising from demountable steel-concrete composite floor systems in buildings. *Resources, Conservation and Recycling*. 141: 133–142.
- Bukauskas, A. 2020. Inventory-constrained structural design (Doctoral dissertation). University of Bath.
- Cramer J. 2015. Circulaire economie: van visie naar realisatie, Utrecht Sustainability Institute.
- Dallam L. N. 1968. High-strength bolt shear connectors - Pushout tests. *Journal of the American Concrete Institute*. 65: 767–769.
- EN 10025-1 2004. Hot rolled products of structural steels. General technical delivery conditions. *BSI*.
- European Commission 2018. Proposal for a regulation of the European Parliament and of the Council establishing the framework for achieving climate neutrality and amending Regulation EU 2018/1999 (European Climate Law).
- Gritsenko A., Nijgh M.P., and Veljkovic M. 2019. Towards a demountable composite slab floor system. *Proceedings of Nordic Steel 2019*.
- Gorgolewski, M. 2008. Designing with reused building components: Some challenges. *Building Research & Information*. 36: 175–188.
- International Organization for Standardization. 2006. ISO 14040:2006(en) environmental management — life cycle assessment — principles and framework. Retrieved January, 2023, from <https://www.iso.org/obp/ui/#iso:std:iso:14040:ed-2:v1:en>
- Kavoura F., and Veljkovic M. 2022a. Technical Practices Of Re-Usable Steel-Concrete Composite Structural Systems. *3rd Coordinating Engineering for Sustainability And Resilience CESARE 2022*. Jordan University of Science and Technology.

*MS9: Recent development IoT- and ICT-based
infrastructure inspection and management
Organizers: C. Kim, V. Sarhosis, M. Noori & Y. Zhang*



Taylor & Francis

Taylor & Francis Group

<http://taylorandfrancis.com>

A computer vision-based identification of natural frequency of a pole structure and damage detection

D. Kawabe

Graduate School of Global Environment Studies, Kyoto University, Kyoto, Japan

C.-W. Kim

Department of Civil and Earth Resources Engineering, Kyoto University, Kyoto, Japan

ABSTRACT: This study aims to investigate a way of estimating natural frequencies and detecting damage of a full-scale pole structure by means of video footage as a preliminary investigation. The accuracy of estimated frequency from a processed video are compared with the identified results by accelerometers installed on the structure. Furthermore, loosening states of the anchor bolt as a damaged scenario are also recorded for the assessment of damage detection. A phase-based motion magnification method is used for visualizing the mode shapes of the target pole. Then, its vibration is extracted using the Kanade-Lucas-Tomasi Tracker that is one of the optical flow method to track the featured points from the processed video. Changes in estimated natural frequencies at all damaged data were observed, which shows the possibility of the proposed approach for damage detection of the target pole although the accuracy of estimated natural frequencies needs improvement.

1 INTRODUCTION

There are many pole structures such as lighting poles and traffic sign poles, along the road. Periodic inspection is crucially important to prevent them from being collapsed. Since it is time-consuming and labor-intensive to conduct the visual inspection of pole structures due to a large number of such structures, infrastructure asset owners are looking to develop a quick and cost-effective anomaly detection method.

One innovative idea is in utilizing sensing equipment installed inside the inspection vehicle and obtaining the information on the road, which is called the drive-by inspection method. For example, the identification of road roughness and bridge damage from the accelerometer installed on the car has been studied as a cost-efficient method (Gonzalez et al. 2008, Harris et al. 2010). Focusing on the information from in-vehicle footage, detecting corrosions or concrete cracks of the target structures by means of artificial intelligence (AI) has been studied following the improvement of image processing technology nowadays (Petricca et al. 2016, Kim et al. 2017).

The causes of the collapse of the pole structure are basically inside corrosion at the basement of the main poles, fatigue cracks at the base welding location because of the maximum bending moment, or anchor bolts' loosening in the basement. As they are located in the basement of the structure, it is difficult to detect such damage visually from the inspection car. As an alternative way to the visual inspection, vibration-based structural health monitoring focusing on changes in frequency, damping ratio and mode shapes is an effective method for damage detection (Doebling et al. 1996). For example, the changes in natural frequency due to fatigue cracks of a truss bridge are correlated to the reduced stiffness of the structure (Chang & Kim 2016).

The aim of this study is, therefore, to obtain the modal information on the target pole structure from video footage and detect the severity of the damage before collapse among the large

volume of pole structures. This study attempts to extract the modal information of the target pole structure from the video footage at a fixed point. Since information except the target pole structure exists in the recorded video, it is necessary to identify the area of the specific pole from the entire angle of the view. Digital image correlation (Chu et al. 1985) is one of the basic methods to obtain the modal information from the video, but the drawback is the necessity of installing the marks beforehand. In this study, we investigate the application of the phase-based motion magnification method (Wu et al. 2012, Wadhwa et al. 2013), which magnifies slight movements in the video footage. The phase-based motion magnification method first processes the whole angle of view so as to emphasize the target vibration mode of the structure by magnifying the featured bandwidth in the recorded video footage. The tracks of displacement of the target pole structure are extracted using processed video and natural frequencies are estimated. Furthermore, this study measures the video when one anchor bolt is completely loosened as a damaged scenario and investigates the changes in estimated frequencies.

A laboratory experiment for a full-scale pole structure is carried out. Five tri-axial accelerometers were installed for the purpose of identifying true modal parameters such as frequencies and mode shapes. Next, the vibration of the pole is recorded by a commercially available digital camera but high framerate setting. The phase-based motion magnification is applied to the video footage, and wave patterns of the pole are extracted using the Kanade-Lucas-Tomasi Tracker (hereafter “KLT Tracker”) (Lucas & Kanade 1981) that is one of the optical flow methods to track the featured points in the processed video.

2 MODAL CHARACTERISTICS OF THE TARGET POLE

2.1 Laboratory experiment

The steel hollow pole structure for a full-scale laboratory experiment is shown in Figure 1, whose height and diameter of the pole are 5.9 m, and 190.7 mm respectively, and the length of the beam is 2.9 m. The beam and the pole are fixed with four bolts as shown in Figure 1. The baseplate is welded at the basement of the main pole and is reinforced with six triangular ribs (Figure 1). The pole is connected to floor through a base concrete block fixed by four anchor bolts (Figure 2).

For the purpose of identifying natural frequencies and mode shapes of the target structure, Figure 1 also shows the locations of tri-axial accelerometers (shown as solid red circles), five of which are installed in the pole to clarify mode shapes, while one of which is on top of the base

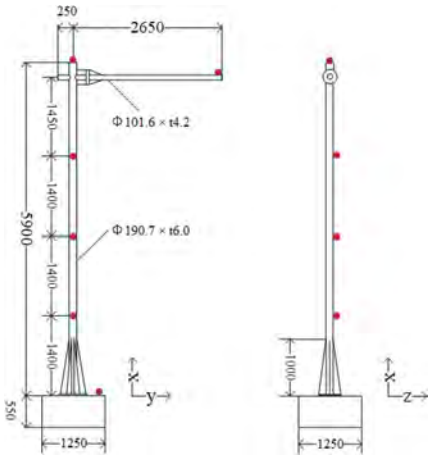


Figure 1. The target full-scale pole structure and the locations of the tri-axial accelerometer. Therein solid red circles denote the location of the accelerometers.

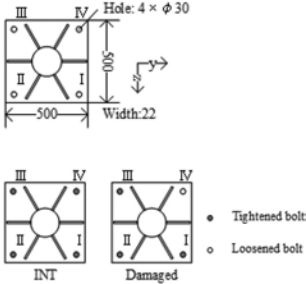


Figure 2. The size of the baseplate of the pole and the states of the anchor bolts at INT and Damaged scenarios.

concrete block to check the movement of the base concrete block. This experiment measures its vibration when the human-induced impact is conducted at a meter height from the baseplate. Twenty impact vibrations, performed at 30-second intervals in each scenario, were acquired, and the average value was used as the true value of the structure. The sampling frequency was 200 Hz.

This study also discusses the feasibility of detecting anomalies caused by anchor bolt loosening. Healthy condition (hereafter called INT) measures its vibration when all anchor bolts are tightened, while a damaged scenario (hereafter called Damaged) denotes the state of one anchor bolt being completely loosened. Figure 2 shows the size of the baseplate and the location where the anchor bolt loosens.

2.2 Modal parameter identification

Natural frequencies and mode shapes of the pole were identified by means of stochastic subspace identification (VanOverschee & DeMoor 2012). Identified frequencies and mode shapes of the pole are summarized in Figure 3. Since this study intends to use the video footage recorded in a driving vehicle, the 1st bending mode of the pole in the Y axis (Figure 3a) is selected for further consideration.

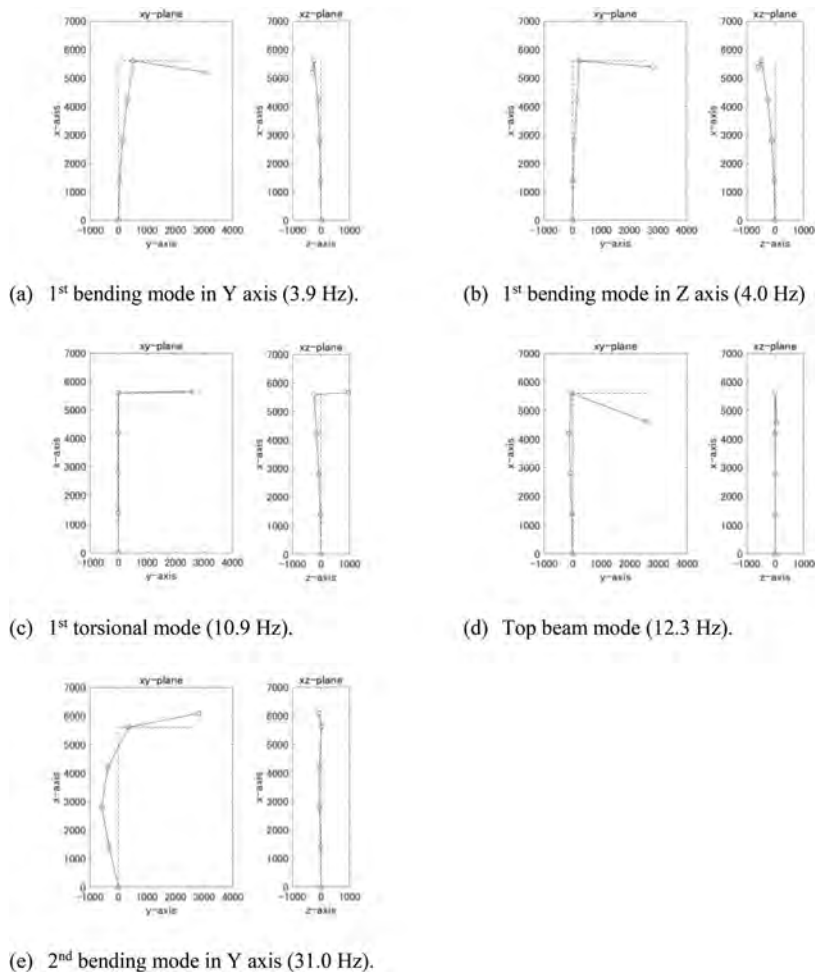


Figure 3. Identified natural frequencies and mode shapes of the pole.

Table 1 shows the identified frequencies in INT and Damaged scenarios. The change in natural frequency due to one anchor bolt loosening was 0.4 Hz which was an 11% reduction from the INT state and was the largest ratio of other modes. It implies that the 1st bending mode of the pole structure can be most easily affected by the changes in boundary conditions at the basement.

3 VIDEO PROCESSING FOR EXTRACTING MODAL PARAMETERS

3.1 Phase-based motion magnification

Wu et al. (2012) demonstrated how imperceptible movements in videos can be revealed using Eulerian video magnification. The Eulerian video magnification is an algorithm for the amplification of small motions in videos. Since videos are made of a series of images and thus have two domains - the spatial domain and time domain - the basic principle behind this algorithm is to take a video and decompose it in the spatial domain by filtering into amplitude and phase signals, followed by time-frequency bandpass filtering. The filtered signal is amplified and reconstructed back into a video where the apparent motion of objects in a video is larger than in the real-time video, occurring at a temporal frequency selected by the user. As a result, small motions in video footage that were difficult to see can be magnified to become obvious to the viewer.

This study uses phase-based video motion processing (Wadhwa et al. 2013) which updates the Eulerian video magnification to be significantly less sensitive to noise. The key approach in the phase-based method is to use complex-valued steerable pyramids at the spatial decomposition process. If f stands for the image intensity at position and time, one can express the observed intensities with respect to a displacement function $f(x + \delta(t))$ in which $\delta(t)$ indicates a displacement function. Since the goal of motion magnification is to synthesize the signal for some amplification factor α , the intensities are modified to $f(x + (1 + \alpha)\delta(t))$. Using the Fourier series decomposition, the displaced image profile can be written in Eq. (1) as a sum of complex sinusoids.

$$f(x + \delta(t)) = \sum_{\omega=-\infty}^{\infty} A_{\omega} e^{i\omega(x+\delta(t))} \quad (1)$$

where ω represents a single frequency at each band. From Eq. (1), to express the motion of the targets, the phase differences between the base frame and a frame at a certain time are calculated.

A complex sinusoid of the band for frequency ω is defined as Eq. (2).

$$S_{\omega}(x, t) = A_{\omega} e^{i\omega(x+\delta(t))} \quad (2)$$

Since S_{ω} in the phase part contains image motion information, changes in motion can be manipulated by changing in phases. To isolate the motion at temporal frequencies, the phase $\omega(x + \delta(t))$ is applied to a DC balanced filter. The result is written in Eq. (3).

$$B_{\omega}(x, t) = \omega\delta(t) \quad (3)$$

The phase B_{ω} is, then, multiplied by the sub-band phase S_{ω} and the complex sinusoid of temporal frequencies ω whose motion is magnified can be written as Eq. (4).

$$\hat{S}_{\omega}(x, t) := S_{\omega}(x, t) e^{i\alpha B_{\omega}} = A_{\omega} e^{i\omega(x+(1+\alpha)\delta(t))} \quad (4)$$

Table 1. Identified frequencies at INT and Damaged scenarios.

	INT	Damaged
1 st bending mode of the pole in y-axis	3.9 Hz	3.5 Hz

Sinusoid $\hat{S}_\omega(x, t)$ is the complex sinusoid that has motions $1+\alpha$ times the input. By reconstructing decomposed images, the magnified video of temporal frequencies ω is built.

3.2 Video setting

This study uses a mirrorless camera that is commercially available. The camera was positioned 9 m away to fit in the angle of the view. Considering the Nyquist frequency, the framerate and resolution were set to 120 fps, and 1920×1080 , respectively. Although the recording time for each dataset is 10 seconds, frames from 301 to 600 were used for the analysis. INT and Damage scenarios were recorded twice and three times, respectively.

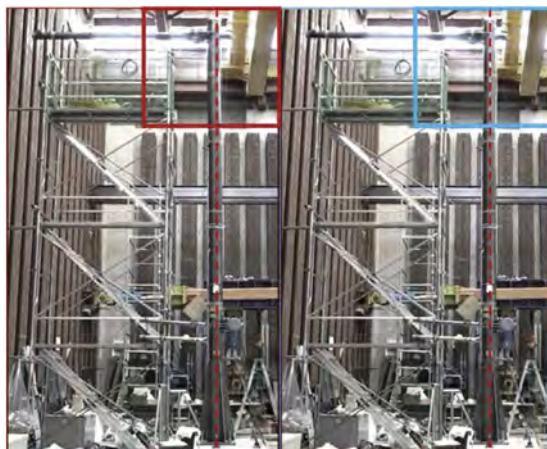


Figure 4. Full-scale pole structure and the locations of the tri-axial accelerometer.



(a) Magnified video (an enlarged view in Figure 4).



(b) Original video.

Figure 5. Comparison of frames at the top of the main pole in the magnified video with those in the original video.

3.3 Results in applying phase-based motion magnification

The result of applying the phase-based motion magnification is shown in Figure 4, where the lower and upper bandpass was set to 3Hz and 3.5Hz so as to include the target frequency of the 1st bending mode in the Y axis of the pole (see Table 1). The amplification factor α was set to 100 in this study. Figure 4 represents the frame images when the main pole is most amplified in the front-back Y direction. The vertical red dashed lines draw from the center position of the pole at the basement. For clear visualization, Figure 5a shows an enlarged view of the enclosure around the top of the main pole in Figure 4. For comparison, Figure 5b shows the original video frame at the same location in Figure 5a. It is clear that the processed video visualizes the amplification of vibrations of the pole.

3.4 Magnified wave extraction by use of KLT tracker

Modal characteristics of the target pole are identified from the processed video. This study focused on two regions around the tip of the beam and the top of the main pole (see red marks in Figure 6) where the amplitude of the 1st bending mode in the Y direction is relatively large. Both regions coincide with the accelerometer positions. The ID numbers of the accelerometers are called sensors 60, and 61, respectively. Then, the featured points inside the regions are detected and tracked. We use minimum eigenvalues of the gradient matrix as featured points (Shi 1994). For example, extracted featured points at the tip of the beam under INT condition are shown in Figure 7, where eight featured points were extracted. It can be seen that the featured points are well extracted from the edge of the beam. The KLT Tracker which is one of the Optical Flow methods is used for tracking the featured points. In this study, the average of the sub-pixel values of the point cloud in each region in each frame image is calculated and considered as the displacement waveform at the location where the sensor was featured.

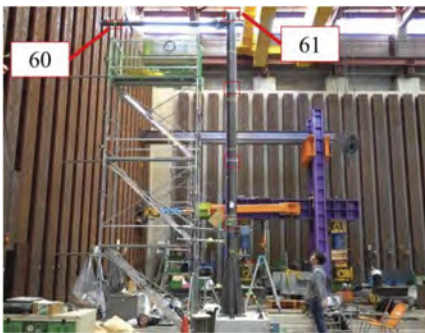


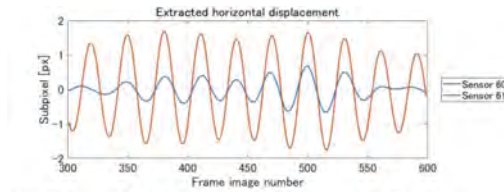
Figure 6. Regions of extracting featured points. The number indicates the ID number of the accelerometers.



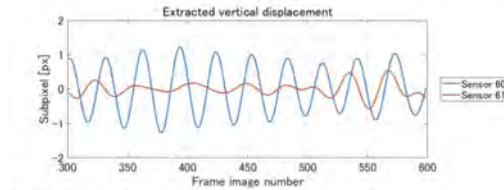
Figure 7. An example of detecting featured points at the region of the tip of the beam shown as white cross symbols.

The extracted displacement wave of the INT condition is shown in Figure 8. Figures 8a and 8b indicate horizontal and vertical directions, respectively. According to Figure 8a, the horizontal displacement near sensor 61 (top of the pole) was larger than that near sensor 60, while the vertical displacement showed the opposite trend. From the result, it can be said that the vibration waveforms can be extracted from the video in which 1st bending mode in the Y direction is magnified using the method for detecting and tracking featured points at each frame.

The displacement waveform in INT and Damaged conditions are compared as shown in Figure 9. Blue and red lines indicate the extracted results from the 1st recording in the INT condition and from the 1st recording in the Damaged condition, respectively. It is clear that the wave frequency in the Damaged condition is decreased because the period of the Damaged condition is longer than that of the INT condition.



(a) Extracted horizontal displacement waveform.



(b) Extracted vertical displacement waveform.

Figure 8. Extracting displacement waveform from magnified video in INT condition.

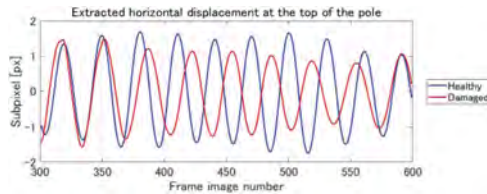


Figure 9. Comparison of displacement waveform from INT scenario with that from Damaged scenario.

Table 2. Identified frequencies at INT and Damaged scenarios.

	1 st recording	2 nd recording	3 rd recording	Identified by accelerometers
INT	4.0 Hz	4.0 Hz		3.9 Hz
Damaged	3.6 Hz	3.6 Hz	3.6 Hz	3.5 Hz

Furthermore, this study conducts Fast Fourier Transform to obtain the peak in the frequency domain of the waveform as the estimated natural frequency of the 1st bending mode in the Y direction. Horizontal displacement at the region on sensor 61 and vertical displacement at that on sensor 60 is used. Table 2 shows the estimated natural frequencies from the video footage of the INT scenario and the Damaged scenario. The natural frequencies estimated from the processed video, both in the INT and Damaged condition, were estimated to be 0.1Hz higher than those from the accelerometers. One reason might be the resolution of the identified frequency from the short time history. Although the accuracy of identifying frequency still needs improvement, it can be seen that the identified frequencies in the Damaged scenario were decreased. Therefore, there is a possibility of detecting structural anomalies in the pole structure by estimating natural frequencies from the magnified video although the amount of sampling should be added for clarification of the estimated variables.

4 CONCLUSIONS

This study conducts a damage-induced experiment on a full-scale pole structure to extract the frequency from the video footage and discusses the feasibility of anomaly detection. To clarify

the accuracy of estimated modal information obtained from videos, modal parameters identified from accelerometers installed on the pole are assumed as ground truth.

Phase-based motion magnification method is used to extract the vibration information from the video footage. This study focused on the 1st bending mode in the direction parallel to the top beam. Featured points using minimum eigenvalues of gradient matrix were detected from the processed video near a region of the tip of the beam and that of the top of the pole where their amplitudes were relatively large, and tracked using the KLT Tracker. Observations showed that displacement waveforms mostly consistent with the 1st bending mode were obtainable. In order to clarify the natural frequency, tracked displacement waveforms were transformed to the frequency domain using the fast Fourier transform, and the dominant frequencies were picked up. Both in the INT and Damaged conditions, 0.1Hz higher frequencies than those from the accelerometers were observed. One reason might be the resolution of the identified frequency from the short time history. Although the accuracy of identifying frequency still needs improvement, the decreasing tendency of the frequency due to the loosened bolt was observed. It encourages us to identify frequencies from the magnified video for detecting structural anomalies in the pole structure.

ACKNOWLEDGMENTS

This work was supported by JSPS KAKENHI Grant Number JP21K20448, and JST-Mirai Program Grant Number JPMJMI21I3, Japan.

REFERENCES

- Chang, K.C. & Kim, C.W. 2016. Modal-parameter identification and vibration-based damage detection of a steel truss bridge, *Engineering Structures*, 122: 156–173.
- Chu, T.C., Ranson, W.F. & Sutton, M.A. 1985. Applications of digital-image-correlation techniques to experimental mechanics, *Experimental Mechanics*, 25(3): 232–244.
- Doebling, S.W., Farrar, C.R., Prime, M.B. Shevitz, D.W. 1996. *Damage identification and health monitoring of structural and mechanical systems from changes in their vibration characteristics: a literature review*. Los Alamos National Lab., NM.
- Gonzalez, A., O'Brien, E.J., Li, Y.Y. & Cashell, K. 2008. The use of vehicle acceleration measurements to estimate roughness, *Vehicle System Dynamics*, 6: 483–499.
- Harris, N.K., Gonzalez, A., O'Brien, E.J. & McGetricck, P. 2010. Characterization of pavement profile heights using accelerometer readings and a combinational optimization technique, *Journal of Sound and Vibration*, 329(5): 497–508.
- Kim, C.W., Chang, K.C., Sasaki, Y. & Suzuki, Y. 2017. A feasibility study on crack identification utilizing images taken from camera mounted on a mobile robot, *Procedia Engineering*, 188: 48–55.
- Lucas, B.D. & Kanade, T. 1981. An iterative image registration technique with an application to stereo vision, *Proceedings of the 7th International Joint Conference on Artificial Intelligence, April 1981*. Vancouver.
- Petricca, L., Moss, T., Figueroa, G. & Broen, S. 2016. Corrosion detection using AI: a comparison of standard computer vision techniques and deep learning model, *Proceedings of the 6th International Conference on Computer Science, Engineering and Information Technology*: 91–99.
- Shi, J. 1994. Good features to track, *Proceedings of IEEE Conference on Computer Vision and Pattern Recognition*: 593–600.
- VanOverschee, P. & DeMoor, B.L. 2012. *Subspace identification for linear systems: theory-implementation-applications*, Springer Science & Business Media.
- Wadhwa, N., Rubinstein, M., Durand, F. & Freeman, W.T. 2013. Phase-based video processing, *ACM Transactions on Graphics*, 32(4):1–10.
- Wu, H.Y., Rubinstein, M., Shih, E., Guttag, J., Durand, F. & Freeman, W. 2012. Eulerian video magnification for revealing subtle changes in the world, *ACM Transactions on Graphics*, 31(4):1–8.

A framework for digital twinning of masonry arch bridges

I.B. Muhit

School of Civil Engineering, University of Leeds, Leeds, UK

School of Computing, Engineering & Digital Technologies, Teesside University, Middlesbrough, UK

D. Kawabe

Department of Civil and Earth Resources Engineering, Kyoto University, Kyoto, Japan

D. Loverdos & B. Liu

School of Civil Engineering, University of Leeds, Leeds, UK

Y. Yukihiro & C-W. Kim

Department of Civil and Earth Resources Engineering, Kyoto University, Kyoto, Japan

V. Sarhosis

School of Civil Engineering, University of Leeds, Leeds, UK

ABSTRACT: As the significant number of European bridge stock comprises more than 100 years old masonry arch bridges, restrictions to the operation of these bridges or their closure due to increased traffic load can result in network disruptions with subsequent economic losses. Apparently, most of these bridges are carrying loads above those envisaged by their original designs. This paper presents the development of a framework for the digital twinning of masonry arch bridges to enhance their management and provide informed decisions for their repair and maintenance schemes. As a case study, a full-scale masonry arch bridge with a 3.0m span is considered here. The framework starts with the development of a 3D geometry using an innovative photogrammetry approach, which accurately captured the overall geometry and local irregularities of the masonry bridge. Afterwards, dynamic characteristics i.e., natural frequency and modal shape of the masonry arch bridge can be obtained from ambient vibration tests by instrumenting the bridge with accelerometers. A Bayesian approach is then implemented to identify structural modal properties under different time windows as a comparison for further assessments. Data from the developed 3D geometry (via photogrammetry) and modal properties are combined to develop a high-fidelity numerical model for structural analysis. This numerical model can be continuously calibrated using monitoring data from the testing of the masonry arch bridges under service loadings. The framework presented in this study has the potential to conduct an autonomous condition-based assessment of ageing masonry arch bridges, characterised by advanced real-time monitoring, and data-informed decisions to understand damage accumulation.

1 INTRODUCTION

Although the introduction of new and modern construction materials such as steel, reinforced and prestressed concrete has reduced the further development of masonry arch bridge construction, there are still thousands remaining stone and brick masonry arch bridges around Europe, most of which were built between the second half of the 19th century and the first decades of the 20th century. For instance, only in the UK, there are about 40,000 masonry arch bridges in daily use on highways, railways and canals, representing an estimated 40–50% of the total bridge stock (Page 1993). Most of these bridges are still in service despite the current traffic loads are much higher than those assumed in the original design, which was carried out on the base of empirical criteria or simple design rules (Brencich & Morbiducci 2007). Moreover, masonry arch bridges are deteriorating over time after being subjected to a prolonged exposure to traffic loads, large vibrations, foundation settlements, environmental conditions and extreme natural events.

The management and assessment of ageing masonry structures constitute a major challenge across the public infrastructure. Network Rail (UK) acknowledged that the assessment methods currently used by the industry are antiquated and/or over-simplistic (Network Rail 2011). For example, for the assessment of masonry arch bridges, the Military Engineering Experimental Establishment (MEXE) method is still in use; which dates back to the 1940s, has a very limited predictive capability, and offers little scope for future enhancement (Sarhosis et al. 2016).

Over the last three decades, significant efforts have been devoted to the development of numerical models to represent the complex geometry and non-linearity behaviour of masonry bridges subjected to external loads and extreme events e.g. floodings, subsidence and earthquakes. Such models range from considering masonry as a continuum (macro-models) to the more detailed ones that consider masonry as an assemblage of units separated by mortar joints (meso-models). The precise quantification of the masonry structure is further complicated by the higher degree of spatial variability of the masonry material properties compared to other construction materials, such as steel or concrete. Variations of material properties can be incorporated into the finite element analysis (FEA) combined with Monte-Carlo simulation (Muhit et al. 2022, Sarhosis et al. 2020).

Furthermore, a vital aspect when modelling masonry structures based on the meso-scale modelling approach is the accuracy in which the geometry of the masonry structure is transferred in the numerical model. So far, the geometry of masonry bridges is captured with traditional techniques (e.g. visual inspection and manual surveying methods) which are labour intensive and error prone. In the last ten years, advances in laser scanning and photogrammetry have started to drastically change the building industry since such techniques are able to capture rapidly and remotely digital records of objects and features in a point cloud format. In particular, there are cost-effective works in transitioning from point clouds obtained from images and/or terrestrial laser scanning to structural analysis models (Loverdos & Sarhosis 2022, 2023a, 2023b).

On the other hand, considerable research efforts have also been devoted to replacing traditional maintenance plans based on periodic visual inspections with more efficient structural health monitoring (SHM) plans. In general, SHM relates the implementation of long-term monitoring systems and damage identification algorithms to conduct condition-based maintenance. Damage identification is organised on a scale of increasing complexity, including (i) Detection, (ii) Localization, (iii) Classification, (iv) Extension, and (v) Prognosis. In this context, damage identification algorithms are generally classified as unsupervised or supervised techniques (Giglioni et al. 2021). The implementation of unsupervised techniques is relatively simple, since damage inference is conducted by simply processing monitoring data. Nevertheless, their ability to achieve damage identification levels beyond detection (Level I) is considerably limited. Conversely, supervised learning techniques exploit both monitoring data and engineering knowledge through structural simulation models. While the implementation of such techniques is challenging due to the epistemic uncertainties typically involved in any structural model, their ability to relate the structural performance to the intrinsic health condition makes it possible to detect, localise, quantify and predict the evolution of damage. It is thus essential to count on reliable structural models to effectively develop condition-based maintenance plans.

Therefore, it is evident that the traditional way of assessing masonry arch bridges becomes obsolete with the rapid changes in traffic loading and natural material degradation; hence, management practices will have to evolve to reduce the impact of novel threats. This paper presents the development of a framework for the digital twinning of masonry arch bridges to enhance their management and provide informed decisions for their repair and maintenance schemes.

2 MASONRY ARCH BRIDGE DIGITAL TWIN FRAMEWORK

The principal motivation of the proposed framework is to develop and establish a methodology for autonomous condition-based assessment of ageing masonry arch bridges, characterised by advanced photogrammetry and/or laser-scanning, real-time monitoring, probabilistic damage identification and data-informed decisions for repair and maintenance schemes. The first step of the workflow is to develop an initial geometric digital twin of masonry

arch bridges from digital images followed by the development of high-fidelity numerical models capable of reproducing the main damage mechanisms and accounting for the inherent variability of the material properties. Then, automated Operational Modal Analysis (OMA) using ambient vibration data can be accomplished in order to develop a computational digital twin model through surrogate modelling. Continuous model calibration using Bayesian model selection and parameter inference methods are necessary to localise and quantify the damage of the masonry arch bridge. As a case study, a full-scale masonry arch bridge constructed in the George Earle testing laboratory of the University of Leeds is considered here. The bridge has been constructed as part of the EPSRC project, Exploiting the resilience of masonry arch bridge infrastructure: a 3D multi-level modelling framework (EP/T001348/1).

2.1 *Advanced photogrammetry/ laser-scanning*

The workflow of documentation, inspection, and assessment of existing structures can be improved by the use of modern technologies such as laser-scanning and photogrammetry. Terrestrial laser-scanning (TLS) uses specialised equipment which able to emit multiple laser-beams to measure the distance of random points in space and acquire their XYZ coordinates, and possibly colour. The recorded points form a point cloud (Point Cloud Data, PCD), that provides an accurate representation of an object or space. Multiple records can be combined to extend the coverage to regions not visible from a single capture point. Photogrammetry, on the other hand, refers to the process followed to obtain realistic information about an object or area from image data (i.e. distance, colour, etc.). It can be used to produce similar results to TLS by following a different approach. A sequence of images is used to generate a PCD of the captured object and can be achieved by identifying the location of a common point between multiple images through triangulation. Due to the nature of photogrammetry, it is more approachable, than laser-scanning, since it does not require specialised equipment.

Regarding structural assessment, the PCD can also be used to generate numerical models for structural analysis (Kassotakis & Sarhosis 2021). Other applications of photogrammetry/laser-scanning include the generation of orthorectified imagery of structures. Ortho-images may be used for reliable measurements on a single plane (i.e. XY, XZ, YZ). Combined with recent advances in computer vision can offer a further understanding of the asset. Applications of image processing allow the automatic feature detection of masonry elements. Especially when combined with artificial intelligence to provide more reliable results (Loverdos & Sarhosis 2022). That even makes the generation of discrete models of masonry structures viable (Loverdos et al. 2021), albeit limited to 2D-plane. The integration of detected features, to the PCD or reality mesh directly, is also possible (Kalfarisi et al. 2020) which assists with the aspect of visualisation and can be a powerful tool for automation of the visual inspection of existing masonry structures. Lastly, a combination of the methods and technologies mentioned above is the precursor of future developments regarding the generation of digital-twin models, of existing masonry structures from visual-data. Those techniques can be utilised to generate semi-automatically a complete digital replica of a structure, visualise changes to the structural form, assess the current state, and evaluate the future behaviour of the structure.

The case study considered here is a 3.0 m span masonry arch bridge constructed in the laboratory and using sophisticated photogrammetry techniques a 3D model of the structure was generated. Initially, 1218 pictures of the structure were captured, with a minimum of 50% overlap. Sample images used to generate the PCD are shown in Figure 1. These images were recorded using a smartphone with a 64-megapixel camera and a maximum resolution of 9248 x 6944 (POCO F2 Pro). The images were captured from the surrounding of the structure, at different heights and distances (Figure 2). Photogrammetry software such as the Context-Capture from Bentley was used to generate the dense point-cloud and reality-mesh. Four control points were assigned manually, to improve the alignment and scale the structure to the real dimensions. The control points were assigned to multiple images, at the 4 main corners of the structure near the bottom (upper side of the concrete floor). The control points were necessary to connect the multiple alignments produced. Finally, the reality mesh was coloured, textured, and smoothed (Figure 3).



Figure 1. Sample images for the generation of the sparse point-cloud.

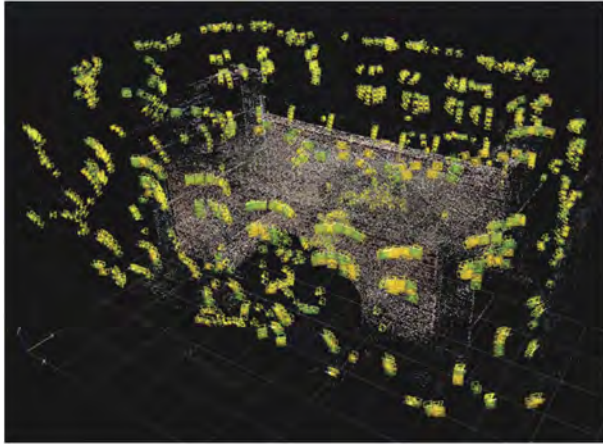


Figure 2. Camera locations and sparse point-cloud (tie-points).



Figure 3. Textured reality-mesh of the dense point-cloud.

2.2 Stochastic computational model and numerical analysis

The imported 3-D geometry can be used to develop a high-fidelity stochastic numerical model of the masonry arch bridge. This numerical model can be a finite element model (FEM) or discrete element model (DEM) depending on the requirements. Stochastic spatial numerical modelling, which considers the variability of material properties within a given structural system, often better represents the real scenario; nevertheless, it involves different levels of complexity in terms of model development, probabilistic information of crucial material

parameters, computational cost, etc. For a simplistic case a deterministic model can be considered, where various material properties are each assumed to have a single de-fined value (mean value) throughout the structure. However, since inconsistency in the quality of workmanship, curing processes, and masonry materials may result in spatial variability even in the same structure, it is vital to consider the spatial and temporal variability of material strengths to estimate the capacity of the masonry arch bridge. In this way, the mesoscale modelling approach can be combined with the Monte-Carlo simulation (MCS) technique. The rationale for this choice is that not only does mesoscale allows separate descriptions of masonry units and mortar joints, but also it permits the consideration of the unit-to-unit variability in the spatial stochastic analyses. In this case, it is necessary to quantify and restrict the number of random variables to only those parameters on which the masonry arch bridge response under service loading is sensitive. Random variables or uncertainty parameters can be categorised as statistically independent, spatially variable, and/or spatially dependent.

2.3 *Operational modal analysis and digital twin*

The computational model developed in the previous stage (initial numerical model) may involve considerable sources of uncertainty that should be minimised before constructing the digital twin. Hence certain parameters of the numerical model should be calibrated using structural health monitoring data. One way could be utilising the modal properties determined by an initial ambient vibration test (AVT). Vibration-based structural health monitoring technique originated in the 1990s and is now being used extensively. Its fundamental principle is to assess the state of a structure by detecting changes in its dynamic properties, such as natural frequencies, mode shapes, and modal damping ratios, before and after damage occurs. More specifically, the natural frequency (or the natural period of vibration) of a structure is regarded to be only associated with the mass and stiffness of the structure. For a large-scale structure, i.e., a bridge, the damage-induced loss in the mass of the structure is negligible. However, these damages, including the local buckling and cracks, can result in stiffness reduction, which can further lead to changes in the natural frequencies of the structure (Huynh et al. 2005).

The process of AVT consists of two main steps. The first is the detection of the vibration response of the structure. In principle, structural vibration should be excited by external loads and captured by, i.e. accelerometers. In the laboratory condition, the vibration of model structures could be excited by impact-load or other forced vibration excitation techniques. For the real large-scale structure, the usage of forced vibration excitation techniques (e.g. shakers) as excitation is usually impractical. In these cases, measuring structural response triggered by environmental excitations or ground microtremors (i.e. traffic loads, wind, etc.) could be an option. The number of sensors and the location of each sensor should be designed based on the geometry, dynamic response characteristics, and boundary conditions of the structure. So far, several methodologies have been proposed for optimising the placement of sensors (Gao et al. 2005). After the dynamic response is captured, extraction of the dynamic properties from the measurements and identification of damage indicators is the second step. It is worth noting that pre-processing of the raw data may be required to attenuate the influence of environmental noise on the detected signal, such as baseline correlation and low-pass filtering.

The masonry arch bridge considered in this paper as a case study was instrumented with four tri-axial accelerometers on top of the two spandrel walls of the full-scale masonry arch bridge model as shown in Figure 4. Three of the accelerometers were mounted on the south-face of the spandrel wall above the quarter span, crown and three-quarters of the arch barrel, and one on the middle of the north wall, allowing the torsional mode of the bridge to be determined. It's worth noting that the setup of these accelerometers is not definitive and can be arranged in different patterns, if needed. AVTs were conducted before and during each phase of loading applications to capture frequency variations of the masonry arch bridge which facilitated the identification of the damage to the bridge resulting from load applications. For each vibration test, impact loads were applied manually using a rubber hammer as the excitation. Ten impacts were carried out with an interval of 5 seconds between each impact.

Therefore, each measurement took around 1 minute. In addition, the sampling frequency was set to be equal to 200 Hz in order to accurately capture the dynamic response of the bridge.

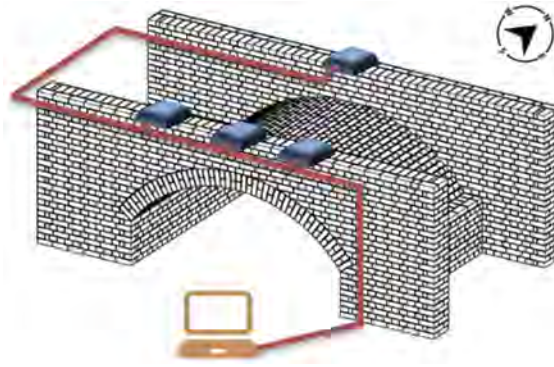


Figure 4. Accelerometer instrumentation for ambient vibration test on the masonry arch bridge (note: backfill is not shown here for simplicity).

The modal features of the structure can be identified through operational modal analysis (OMA), and the uncertainties in the numerical modelling shall be reduced through model updating, minimising the differences between the experimental and the numerical modal signatures. On this basis, potential damage scenarios and failure patterns of the masonry arch bridge can be simulated from this stochastic computational model followed by sensitivity analysis for parametrisation. The simulated damage mechanisms then be used to train a set of computationally efficient surrogate models, which will act as black-box functions mapping the considered damage-sensitive parameters and the modal features of the structure (Garcia-Macias & Ubertini, 2022). In particular, the surrogate modelling approach can combine adaptive sparse polynomial chaos expansion (PCE) and Kriging meta-modelling to provide local/global modelling capabilities with maximum flexibility. These surrogate models will act as Digital Twins of the structure under investigation, being possible to conduct quasi-real-time damage identification. To do so, automated OMA techniques can be developed to continuously extract the modal features of the bridge from periodically recorded ambient vibrations.

2.4 Bayesian model update and damage identification

Damage identification is organised in a scale of increasing complexity, including Level I - Detection, Level II - Localization, Level III - Classification, Level IV - Extension, and Level V - Prognosis. The time series of modal signatures can be processed through statistical pattern recognition and in case an anomaly is detected (Level I), the damage identification algorithm should be activated. This algorithm can involve a Bayesian model selection approach, through Transitional Markov Chains (TMC) to identify which damage mechanism has been activated. A major limitation of traditional Bayesian model updating regards the difficulties related to the presence of ill-conditioning in the inverse model calibration. Although the definition of prior probability distribution functions to certain parameters may limit this aspect, ill-conditioning can be hardly eliminated, and the appearance of misidentifications may arise. This may compromise the efficiency of the subsequent detailed inspection or rehabilitation intervention. To alleviate this issue, an innovative approach, post-event photogrammetry (captured from laboratory tests after the damage occurred) can be used to constrain the optimisation problem, thus minimising the ill-conditioning in the calibration. To achieve so, simple local metrics based on image processing are under development to constrain (0 – unconstrained, 1- fully constrained) certain model parameters that do not clearly experience damage, while imposing no constraints on model parameters that may have experienced

damage. Once the Bayesian model selection completes, the probability distributions of the model parameters will be used to localise and quantify the damage. The general workflow of the digital twin development based on photogrammetry, MCS and SHM techniques are sketched in Figure 5.

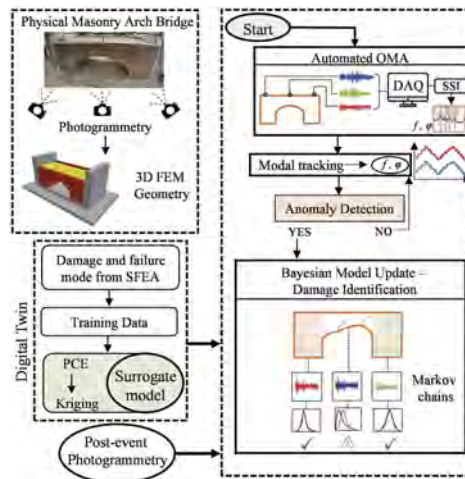


Figure 5. Workflow of masonry arch bridge digital twin development.

3 CONCLUSIONS

This paper presents an overview and workflow of the framework for digital twinning of masonry arch bridges which will automate the SHM of masonry arch bridges from a physical bridge to the prediction of damage by digital twin. This concept is well-positioned to promote world-class state-of-the-art research and a significant academic and scientific impact is envisaged through the utilisation of innovative algorithms, high-quality monitoring techniques and novel numerical methods.

This proposed framework involves the systematic development of the 3D geometry of the masonry arch bridge from digital images, i.e. using photogrammetry. Unit block and mortar joint recognition can be achieved by using an image processing algorithm based on an improvement of the marked controlled watershed algorithm. The result will be an automatically segmented point cloud with each individual masonry unit isolated and in a format suitable to be inputted into structural analysis models, if necessary. The geometrical accuracy of the algorithm can be assessed based on its ability to map geometric irregularities by verification against measurements from total stations.

The processed 3D computational modelling geometry can then be used to develop a high-fidelity stochastic numerical modelling of masonry arch bridges. A suitable FEM or DEM can be considered where spatial variability of material strengths are considered and the modelling approach is combined with the Monte-Carlo simulation technique to evaluate the probabilistic response of the bridge.

To improve the computational model and minimise the sources of uncertainty, the developed model should be calibrated using the modal properties determined by an ambient vibration test. The modal features of the structure could be identified through operational modal analysis, and the uncertainties in the FEM/DEM can be reduced through model updating, minimising the differences between the experimental and the numerical modal signatures. Then a digital twin can be developed from surrogate modelling which combines adaptive sparse polynomial chaos expansion and Kriging meta-modelling to provide local/global

modelling capabilities. These digital twins can be further calibrated or enhanced through Bayesian model updates when any anomaly is detected from the automated operational modal analysis.

This concept is still in its infancy and several components of it need further studies to enhance clarity and obtain reliable information. The framework proposed and the work reported in this paper is part of a broader project, which is in progress. The developed framework would inform dynamic characteristics such as parametric resonance, eigenfrequencies, dynamic amplification factor, and periodic motions attributed to the interaction between vehicle and masonry arch bridge. The fundamental idea is to establish a relationship and form a ‘bridge’ between existing knowledge/practice and advanced automation techniques.

REFERENCES

- Brench, A. & Morbiducci, R. 2007. Masonry arches: Historical rules and modern mechanics. *International Journal of Architectural Heritage* 1: 165–189.
- Gao, Q., Cui, K., Li, J., Guo, B. & Liu, Y. 2020. Optimal layout of sensors in large-span cable-stayed bridges subjected to moving vehicular loads. *International Journal of Distributed Sensor Networks* 16 (1).
- García-Macias, E. & Ubertini, F. 2022. Real-time Bayesian damage identification enabled by sparse PCE-Kriging meta-modelling for continuous SHM of large-scale civil engineering structures. *Journal of Building Engineering* 59: 105004.
- Gigliani, V., García-Macias, E., Venanzi, I., Ierimonti, L. & Ubertini, F. 2021. The use of receiver operating characteristic curves and precision-versus-recall curves as performance metrics in unsupervised structural damage classification under changing environment. *Engineering Structures* 246, 113029.
- Huynh, D., He, J. & Tran, D. 2005. Damage location vector: A non-destructive structural damage detection technique. *Computers & Structures* 83(28-30): 2353–2367.
- Kalfarisi, R., Wu, Z.Y. & Soh, K. 2020. Crack Detection and Segmentation Using Deep Learning with 3D Reality Mesh Model for Quantitative Assessment and Integrated Visualization. *Journal of Computing in Civil Engineering* 34(3): 04020010.
- Kassotakis, N. & Sarhosis, V. 2021. Employing non-contact sensing techniques for improving efficiency and automation in numerical modelling of existing masonry structures: A critical literature review. *Structures* 32: 1777–1797.
- Loverdos, D. & Sarhosis, V. 2022. Automatic image-based brick segmentation and crack detection of masonry walls using machine learning. *Automation in Construction* 140: 104389.
- Loverdos, D. & Sarhosis, V. 2023a. Automation in Documentation of Ageing Masonry Infrastructure Through Image-Based Techniques and Machine Learning. In: Rizzo, P., Milazzo, A. (eds) *European Workshop on Structural Health Monitoring. EWASHM 2022, Lecture Notes in Civil Engineering* 270: 727–735.
- Loverdos, D. & Sarhosis, V. 2023b. Geometrical digital twins of masonry structures for documentation and structural assessment using machine learning. *Engineering Structures* 275(A): 115256.
- Loverdos, D., Sarhosis, V., Adamopoulos, E. & Drougkas, A. 2021. An innovative image processing-based framework for the numerical modelling of cracked masonry structures. *Automation in Construction* 125: 103633.
- Muhit, I.B., Masia, M.J., Stewart, M.G. & Isfeld, A.C. 2022. Spatial Variability and Stochastic Finite Element Model of Unreinforced Masonry Veneer Wall System Under Out-of-plane Loading. *Engineering Structures* 267: 114674.
- Network Rail. 2011. *Letter to the Office of Rail and Road*. London, UK.
- Page, J. 1993. *Masonry arch bridge, state of art review*. London: HMSO, Department of Transport, Transport Research Laboratory.
- Sarhosis, V., De Santis, S. & de Felice, G. 2016. A review of experimental investigations and assessment methods for masonry arch bridges. *Structure and Infrastructure Engineering* 12 (11): 1439–1464.
- Sarhosis, V., Forgacs, T. & Lemos, J. 2020. Stochastic Strength Prediction of Masonry Structures: A Methodological Approach or a Way Forward?. *RILEM Technical Letters* 4: 122–129.

Quality analyses of crowdsourced smartphone trips for bridge dynamic monitoring

T.J. Matarazzo

United States Military Academy, New York, USA
Massachusetts Institute of Technology, Massachusetts, USA

I. Dabbaghchian, L. Cronin & S.N. Pakzad

Lehigh University, Pennsylvania, USA

S.S. Eshkevari

Uber Technologies Inc., California, USA
Massachusetts Institute of Technology, Massachusetts, USA

H. Yin & R. Lassman

Cornell Tech, New York, USA

P. Santi & C. Ratti

Massachusetts Institute of Technology, Massachusetts, USA

ABSTRACT: Recent studies have demonstrated that important bridge dynamic properties can be extracted from crowdsourced smartphone data collected during vehicle trips. The key benefit of crowdsourced smartphone vehicle trip (SVT) data is the potential ease in producing large volumes of useful data at very low costs compared to modern SHM networks. Crowdsourcing inherently involves trade-offs in data quality for data scale; however, the extent to which data quality varies with respect to trip metadata, such as vehicle speed or smartphone model, etc., are not well understood. This paper evaluates the sensitivities of bridge dynamic property estimates with respect to individual trips or groups of trips, i.e., subsets, based on about 700 SVT datasets collected on a real bridge. Overall, this paper demonstrates an application of classification models in identifying “low quality” datasets, i.e., those that corresponded to less accurate mode shape estimates. This tool shows potential to quickly flag low-quality datasets during preprocessing which could help optimize the accuracy of the SHM information produced.

1 INTRODUCTION

Structural Health Monitoring (SHM) and Structural Modal Identification (SID) aim to assess the condition and performance of structures through the measurement and analysis of their dynamic behavior. In practice, SHM and SID are subject to challenges that can inhibit regular implementation. The setup and maintenance of SHM systems can require significant financial resources, investments in hardware, software development, and human resources. Traditional monitoring methods are based on a distributed sensor network that is installed directly on the structure (Brownjohn et al., 1992; Smyth et al., 2003; Lynch and Loh, 2006). Over the past two decades, indirect modal identification methods for bridges have been developed to determine bridge modal properties by analyzing measurements from sensors that are not installed on the structure, instead, the sensors may be within a moving vehicle (Yang et al., 2004; Lin and Yang, 2005). These methods aim to mitigate issues related to data acquisition, data management, system cost, and system maintenance.

Indirect methods have the advantage of being non-intrusive, low-cost, simple, and comparatively easy to implement; but as these tools are relatively new, their accuracy and reliability have primarily been demonstrated in controlled experimental tests or using synthetic data that not necessarily represent real-world conditions (Yang and Chang, 2009; McGetrick et al., 2015; Yang et al., 2020; Gonzalez et al., 2012; Eshkevari et al., 2019, 2020, 2022; Gkoumas et al., 2023; Malekjafarian et al., 2022). Simultaneously, the efficiencies of a mobile sensor network and the ability to incorporate cheap, ubiquitous sensors such as smartphones are appealing. Smartphones have gained unprecedented penetration rates and have been broadly utilized across research fields such as epidemiology Massaro et al. 2019, mapping Li et al. 2017, human mobility Miranda et al. 2021, Schlapfer et al. 2021, driver behavior Vlahogianni and Barmponakis 2017, road surface analysis Mednis et al. 2011, and others. While smartphones contain less accurate sensors overall, studies have established how they can successfully be applied in SHM and some limitations trips Feng et al., 2015, Sitton et al., 2020. Recent studies of indirect methods using smartphone sensors in real-world applications in real-world settings that consider operational traffic loading and typical bridge trips McGetrick et al., 2017, Matarazzo et al., 2018. Specifically, it has been shown that accurate bridge modal frequency estimates can be extracted from data crowdsourced from smartphone-vehicle trips (SVT) (Matarazzo et al., 2022).

Crowdsourcing smartphone measurements inherently involves trade-offs in data quality for data scale. Crowdsourced SVT data fall into one of three classes based on the analysts' ability to oversee and influence data collection: controlled, partially-controlled, and uncontrolled (Matarazzo et al., 2022). The extent to which SVT data quality varies with respect to trip metadata, such as vehicle speed or smartphone model, etc., are not well understood. In some cases, the crowdsourced SVT metadata might indicate that the quality of an individual dataset is poor, and its inclusion would negatively affect SHM quantities of interest. In other words, the aggregate estimates considering all collected data may not be the most accurate. These considerations become especially important when data volumes become orders of magnitude larger, i.e., tens of thousands of datasets. For instance, crowdsensing platforms with monthly data streams on the order of thousands would greatly benefit from pre-processing tools that can discard datasets that may be noisy or less likely to positively impact SHM features of interest. This study investigates the evaluation of the quality of individual datasets with respect to the population (all data) and their classification, which can help develop tools used to produce accurate estimation results.

2 CROWDSOURCED DATA COLLECTED ON A REAL BRIDGE

The smartphone-vehicle trip (SVT) data used in this study were collected by smartphones within moving vehicles as they traveled over a 272-m long, steel arch bridge in northern Italy as part of the *Good Vibrations* project (Lab, 2023). The data was collected as part of a collaboration with Anas Sp.A. The data are best described by the partially-controlled data class as the analysts provided guidelines to those collected data, but did not enforce them or oversee data collection. In total 677 SVT datasets were collected using smartphones in the organization's maintenance trucks.

The accelerometer and GPS sensors within the smartphone were utilized to record physical response measurements during each trip. The data logged for each trip included the trip start time, GPS (latitude, longitude) sampled at a rate of 1 Hz, as well as phone orientation and triaxial accelerometer measurements (X, Y, and Z-directions) sampled at 100 Hz. In addition, a standard fixed sensor network was installed on the bridge to document structural modal properties. Existing methods can be implemented to extract bridge dynamic properties from the aggregated SVT data (Matarazzo et al., 2022; Cronin et al., 2022). This paper focuses on the estimation of the absolute value of the mode shape (AMS) of the first vertical vibration mode. Cronin et al., 2022 describes the modal properties of this bridge and presents the method used to compute the AMS in detail.

3 MEASURING DATASET QUALITY

The quality of a dataset is a relative property. Metrics used to assess quality are constructed with respect to specific quantities of interest. In this study, the estimated structural modal properties are of interest; specifically, the absolute value of the mode shape (AMS) of the first vertical vibration mode. The methodology used to extract the AMS based on the SVT data is described in Cronin et al., 2022. Overall, the methodology provides one aggregated AMS estimate, $|\phi_{total}|$, considering all 677 datasets.

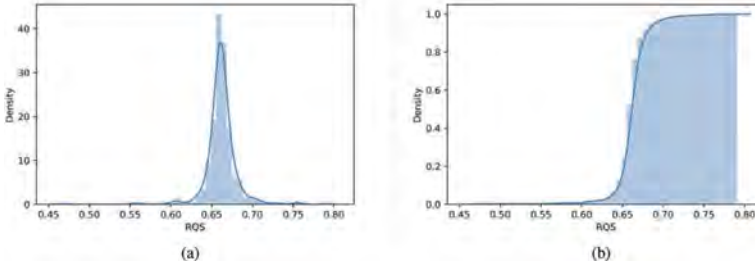


Figure 1. A) Probability Density Function (PDF) and b) Cumulative Distribution Function (CDF) of the quality score metric (QS).

The goal is to evaluate an individual dataset's contribution to the overall AMS. It is important to note the methodology for estimating AMS requires a group of datasets; therefore, it is not possible to obtain an AMS estimate using only one dataset. A Monte Carlo Sampling technique is used to group an individual dataset i , with $N - 1$ other datasets at random (group size is N). The Monte Carlo sampling technique is repeated R times for each dataset, for all 677 datasets. To quantify the quality of an individual dataset i , the mode shapes are compared using the MAC value. MAC values are computed between all R AMS and the aggregated AMS, $|\phi_{total}|$, and the Quality Score (QS) for dataset i is defined as the average of these MAC values.

$$QS_i = \frac{1}{R} \sum_{j=1}^R MAC(|\phi_{i,j}|, |\phi_{total}|)$$

Like the MAC value, the QS metric ranges between 0 and 1, where 1 indicates the highest consistency with the AMS considering all 677 datasets. Note QS is affected by the group size N and the total number of iterations R . Overall, if the group size N is too large, the quality scores will not vary much between individual datasets because the computed AMS estimates will be very similar to the aggregate AMS. In this study, $N = 25$, which is approximately 4% the size of the total number of samples, and $R = 200$.

The probability density function (PDF) and cumulative distribution function (CDF) for the QS values are shown in Figures 1a and 1b. The PDF shows a distribution with one primary peak, and small peaks on either side. The large peak has a mode near $QS = 0.66$, the small peak on the left has a mode near $QS = 0.61$, and the small peak on the right has a mode near $QS = 0.75$. Overall, these plots suggest that it may be a subset of datasets that correspond to lower QS values. This study will consider a classification problem in which two classes of datasets are defined based on a QS threshold: (i) good quality data and (ii) poor quality data. At first glance, it appears a QS threshold near $QS = 0.65$ or above may result in a useful data split.

4 DATASET FEATURES

Each SVT dataset contains over a dozen measurement channels such as acceleration in three directions, vehicle speed, GPS, GPS accuracy, etc. The goal is to use these channels to discover or identify features that will ultimately have some predictive power with respect to the QS

metric, which, in the context of this problem, would suggest a strong influence on dataset quality. There are nearly endless possibilities for features as they can be based on raw channel data, transformed data, combinations/interactions of the data, and more. Simultaneously, dimensionality reduction techniques such as principal component analysis (PCA), autoencoders, T-distributed Stochastic Neighbor Embedding (t-SNE) Van der Maaten and Hinton 2008, or uniform manifold approximation (UMAP) McInnes et al. 2018 are useful when selecting features. Nonetheless, relatively basic features were chosen at first to help maintain model interpretability and to consider recent findings in the indirect bridge monitoring and vehicle-bridge-road interaction literature, e.g., higher vehicle speeds can result in datasets with low signal-to-noise ratios (SNR) (McGetrick et al., 2015; Eshkevari and Pakzad, 2019; Yang et al., 2020).

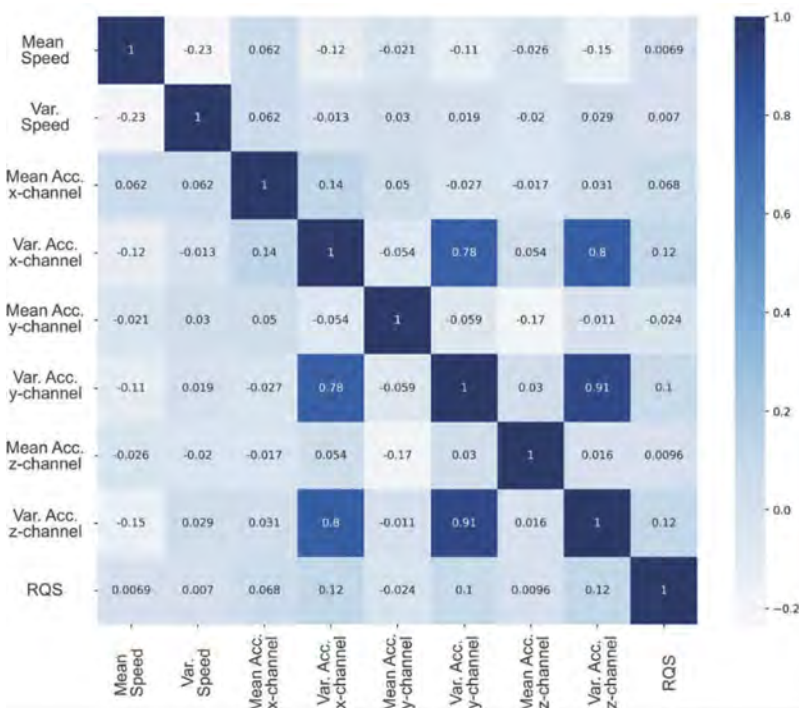


Figure 2. Correlation matrix of selected data features, “RQS” corresponds to the QS metric.

To start, eight features were considered in this study: 1-2) mean and variance of the vehicle speed, and the 3-8) mean and variance of the acceleration in all three directions. Figure 2 shows a matrix of the Pearson cross-correlation coefficients of all nine features and the QS. Overall, there are some notable cross-correlations among the features, e.g., variances of different accelerations. Most of these features have a low correlation with QS. The variance of the acceleration in the x-direction and z-direction features had the highest correlation with QS, although they were still relatively low. This indicates that individually, these specific features may not be strong predictors if considering isolated linear models. Although, it is not possible to fully evaluate each feature’s predictive potential for QS without further analysis, which may include some preliminary model fitting.

5 CLASSIFICATION PROBLEM SETUP AND ANALYSES

Each dataset was assigned a label as either “high-quality” (HQ) or “low-quality” (LQ). This classification is determined based on the CDF of the QS metric. The data are split at the 75th

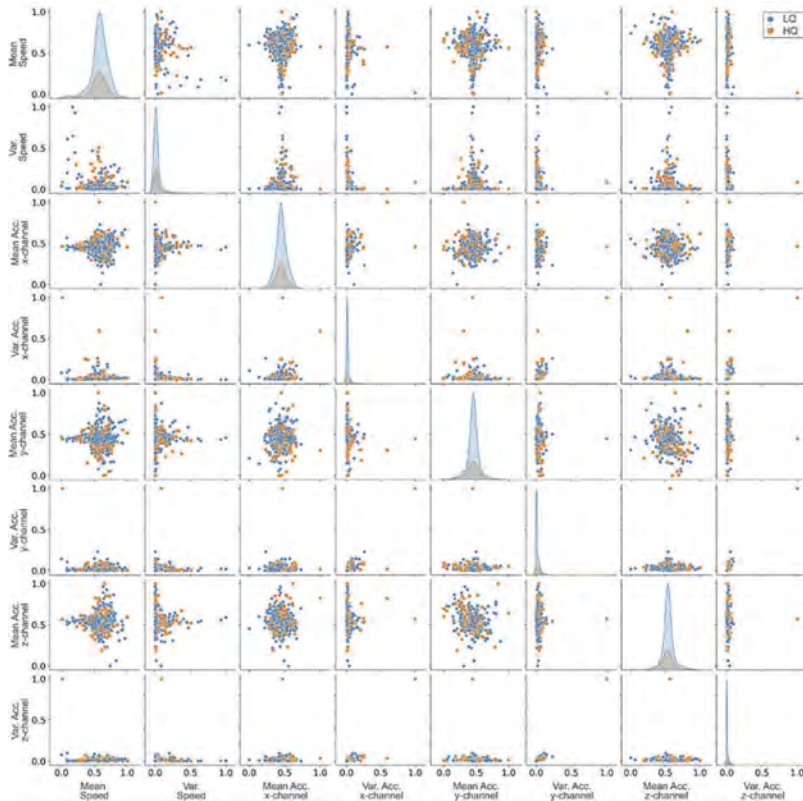


Figure 3. Pairs plot of the scaled features and dispersion of classes. Blue dots correspond to low-quality (LQ) labels and orange dots correspond to high-quality (HQ) labels.

percentile, which corresponds to a RQ threshold of 0.67 and results in 508 “poor” datasets and 169 “good” datasets. Figure 3 shows scatter plots of the eight features considered and specifies which datasets were labeled as HQ or LQ. These sorts of scatter plots can be useful for several reasons. They may help uncover potential multicollinearity problems. They can also help the analyst get a picture of whether the classes are completely mixed or if there are some clear separations. Overall, the features do not appear to have strong linear relationships with each other and there were no cases that yielded a “clean” separation between the two classes (HQ and LQ).

Once the features are selected and the datasets are labeled, classification models can be considered. An array of machine learning (ML) models were considered such as Logistic Regression, Support Vector Machines, Decision Trees, Naive Bayes, and others. Notice that the class sizes are imbalanced: there are 508 low-quality datasets and 169 high-quality datasets. Some of the ML models considered achieved a relatively high accuracy (about 75%) with the trivial solution of simply classifying all datasets as LQ. Of course, that is not a desirable model and there are formal methods for treating the class balance problem; however, for the context of this study, suitable models were found using basic ML methods.

6 RESULTS AND DISCUSSION

Three ML models were found to provide a reliable performance and were considered further: (1) support vector machines (SVM) with rbf kernels, (2) Logistic regression (LR), and (3) eXtreme gradient boosting (XGB). All models used the default hyperparameters specified in

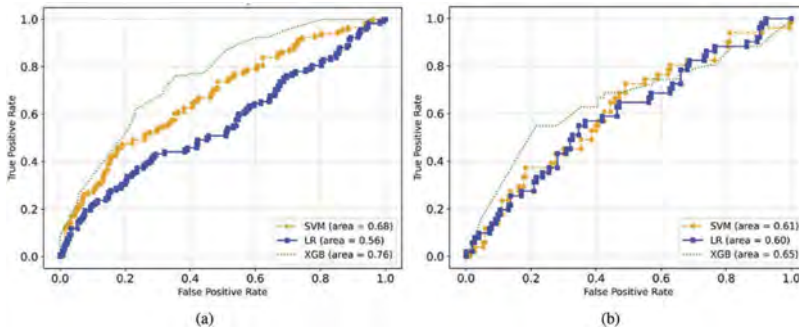


Figure 4. The output of ML models, ROC curves for a) training datasets, b) testing datasets.

the scikit-learn Python library. These models were selected based on the receiver operating characteristic (ROC) curve area under the curve (AUC). To better evaluate these models, the data were split into training and testing portions (70% training, 30% testing).

Figures 4a and 4b show the ROC for the three models based on training data and testing data. Overall, the testing ROC AUC values were 0.60 and above which indicates a satisfactory prediction performance. The XGB model appears to have the best performance out of the models considered; however, it is important to note the potential for a high false positive rate. In the context of this problem, false positives would suggest the removal of HQ datasets, which is undesirable. It may be beneficial to have a reduced true positive rate in order to maintain very few false positives. This trade-off can be accounted for in the cost function of an ML model or via the operating point in the ROC.

The models determined are a good start in establishing a basic capability for predicting whether the inclusion of certain datasets will negatively affect a quantity of interest, i.e., the absolute value of the mode shape. This preliminary study was limited in scope and considered basic features that were directly related to the measured channels in an effort to maintain basic model interpretability. Furthermore, this study did not consider advanced feature selection methods. That is, it is possible to find more accurate classification methods (perhaps those with lower false positive rates) using the same source data.

7 CONCLUSIONS

When considering a large number of noisy datasets, there could be tradeoffs in quantity and quality. This study analyzed 677 smartphone datasets collected during vehicle trips, i.e., smartphone-vehicle trips (SVT), over a bridge in Italy. Depending on the SHM analysis and the quantities of interest, the omission of some datasets can result in more accurate estimates of dynamic properties. That is, some of the collected datasets negatively contribute to the aggregate result. This paper focused on determining which SVT datasets should be selected when estimating the absolute value of the mode shape (AMS) for the first vertical mode.

Eight features within the SVT data were considered, which were based on basic statistics of the vehicle speed and triaxial acceleration measurements. A quality score (QS) metric was defined to quantify the contributions an individual dataset has on the AMS estimate. A QS threshold was implemented to assign each dataset with a “low quality” label or a “high quality” label. A suite of machine learning (ML) models were applied to the classification problem. The models (SVM, XGB, and LR) with the best overall performance (as measured by ROC AUC) were kept for further analysis. When using a 70-30 train-test split, all three models produced AUC values above 0.60 for the testing data, which is satisfactory.

This study established a basic capability for predicting whether the inclusion of certain datasets will negatively affect a quantity of interest. Nonetheless, it is important to note

limitations. High false positive rates could have potentially negative consequences: by removing higher quality datasets from the analysis, the expected advantages of this type of data filtering system could be negated. The exploration of ML models that penalize false positives in the cost function could resolve this issue. Simultaneously, this study considered relatively basic features; more advanced feature engineering, feature selection, and dimensionality reduction through the use of autoencoders or uniform manifold approximation (UMAP), could yield models with superior performances.

One potential outcome from research on the quality of SVT data is the identification of trip metadata or features that are indicative of a positive contribution to the data set as a whole. These types of results can help develop tools to quickly flag low-quality datasets during pre-processing, a consideration which becomes especially important when data volumes become orders of magnitude larger, i.e., tens of thousands of datasets. For instance, crowdsensing platforms with monthly data streams on the order of millions would greatly benefit from pre-processing methods that can discard datasets that may be excessively noisy or otherwise negatively impact the determination of SHM features of interest.

ACKNOWLEDGEMENTS

The authors would like to thank Anas S.p.A., Allianz, Brose, Cisco, Dover Corporation, Ford, the Amsterdam Institute for Advanced Metropolitan Solutions, the Fraunhofer Institute, the Kuwait-MIT Center for Natural Resources and the Environment, Lab Campus, RATP, Singapore-MIT Alliance for Research and Technology (SMART), SNCF Gares & Connexions, UBER, the U.S. Department of Defense High-Performance Computing Modernization Program, the U.S. Army Program Executive Office Aviation, and all the members of the MIT Senseable City Lab Consortium for supporting this research.

REFERENCES

- Brownjohn, J., A. Dumanoglu, and R. Severn 1992. Ambient vibration survey of the fatih sultan mehmet (second bosphorus) suspension bridge. *Earthquake engineering structural dynamics*: 21(10), 907–924.
- Cronin, L., S. S. Eshkevari, T. J. Matarazzo, S. Milardo, I. Dabbaghchian, P. Santi, S. N. Pakzad, and C. Ratti 2022. Identifying damage-sensitive spatial vibration characteristics of bridges from wide-spread smartphone data. *arXiv Preprint*.
- Eshkevari, S. S., L. Cronin, T. J. Matarazzo, and S. N. Pakzad 2022. Bridge modal property identification based on asynchronous mobile sensing data. *Structural Health Monitoring*: 0(0), 14759217221109014.
- Eshkevari, S. S., T. J. Matarazzo, and S. N. Pakzad 2020. Bridge modal identification using acceleration measurements within moving vehicles. *Mechanical Systems and Signal Processing*: 141, 106733.
- Eshkevari, S. S. and S. Pakzad 2019. Bridge structural identification using moving vehicle acceleration measurements. *Dynamics of Civil Structures*: Volume 2, pp. 251–261. Springer.
- Eshkevari, S. S., S. N. Pakzad, M. Takac, and T. J. Matarazzo 2019. Modal Identification of Bridges Using Mobile Sensors with Sparse Vibration Data. *Journal of engineering mechanics*: 146(4), 04020011
- Feng, M., Y. Fukuda, M. Mizuta, and E. Ozer 2015. Citizen sensors for shm: Use of accelerometer data from smartphones. *Sensors*: 15(2), 2980–2998.
- Gkoumas, K., M. C. Galassi, D. Allaix, A. Anthoine, S. Argyroudis, G. Baldini, L. Benedetti, F. Bono, J. Brownjohn, E. Caetano, et al. 2023. Indirect structural health monitoring (ishm) of transport infrastructure in the digital age. Technical report, Luxembourg: Publications Office of the European Union.
- Gonzalez, A., E. J. O'Brien, and P. McGetrick 2012. Identification of damping in a bridge using a moving instrumented vehicle. *Journal of Sound and Vibration*: 331(18), 4115–4131.
- Lab, S. C. 2023. Mit senseable city lab good vibrations project website. https://senseable.mit.edu/good_vibrations/. Accessed: 2023-01-03.
- Li, X., C. Ratti, and I. Seiferling 2017. Mapping urban landscapes along streets using google street view. *International cartographic conference*: pp. 341–356. Springer.
- Lin, C. and Y. Yang 2005. Use of a passing vehicle to scan the fundamental bridge frequencies: An experimental verification. *Engineering Structures*: 27(13), 1865–1878.

- Lynch, J. P. and K. J. Loh 2006. A summary review of wireless sensors and sensor networks for structural health monitoring. *Shock and vibration digest*: 38(2), 91–130.
- Malekjafarian, A., R. Corbally, and W. Gong 2022. A review of mobile sensing of bridges using moving vehicles: Progress to date, challenges and future trends. *Structures*: 44, 1466–1489.
- Massaro, E., D. Kondor, and C. Ratti 2019. Assessing the interplay between human mobility and mosquito borne diseases in urban environments. *Scientific reports*: 9(1), 1–13.
- Matarazzo, T. J., D. Kondor, S. Milardo, S. S. Eshkevari, P. Santi, S. N. Pakzad, M. J. Buehler, and C. Ratti 2022. Crowdsourcing bridge dynamic monitoring with smartphone vehicle trips. *Communications engineering*: 1(1), 29.
- Matarazzo, T. J., P. Santi, S. N. Pakzad, K. Carter, C. Ratti, B. Moaveni, C. Osgood, and N. Jacob 2018. Crowdsensing framework for monitoring bridge vibrations using moving smartphones. *Proceedings of the IEEE*: 106(4), 577–593.
- McGetrick, P., D. Hester, and S. Taylor 2017. Implementation of a drive-by monitoring system for transport infrastructure utilising smartphone technology and gnss. *Journal of Civil Structural Health Monitoring*: 7(2), 175–189.
- McGetrick, P. J., C.-W. Kim, A. Gonzalez, and E. J. Brien 2015. Experimental validation of a drive-by stiffness identification method for bridge monitoring. *Structural Health Monitoring*: 14(4), 317–331.
- McInnes, L., J. Healy, and J. Melville 2018. Umap: Uniform manifold approximation and projection for dimension reduction. *arXiv preprint*: arXiv:1802.03426.
- Mednis, A., G. Strazdins, R. Zviedris, G. Kanonirs, and L. Selavo 2011. Real time pothole detection using android smartphones with accelerometers. *2011 International conference on distributed computing in sensor systems and workshops (DCOSS)*: pp. 1–6. IEEE.
- Miranda, A. S., Z. Fan, F. Duarte, and C. Ratti 2021. Desirable streets: Using deviations in pedestrian trajectories to measure the value of the built environment. *Computers, Environment and Urban Systems*: 86, 101563.
- Schlapfer, M., L. Dong, K. O’Keeffe, P. Santi, M. Szell, H. Salat, S. Anklesaria, M. Vazifeh, C. Ratti, and G. B. West 2021. The universal visitation law of human mobility. *Nature*: 593(7860), 522–527.
- Sitton, J. D., D. Rajan, and B. A. Story 2020. Bridge frequency estimation strategies using smartphones. *Journal of Civil Structural Health Monitoring*: 1–14.
- Smyth, A. W., J. S. Pei, and S. F. Masri 2003. System identification of the vincent thomas suspension bridge using earthquake records. *Earthquake Engineering Structural Dynamics* 32(3), 339–367.
- Van der Maaten, L. and G. Hinton 2008. Visualizing data using t-sne. *Journal of machine learning research*: 9(11).
- Vlahogianni, E. I. and E. N. Barmponakis 2017. Driving analytics using smartphones: Algorithms, comparisons and challenges. *Transportation Research Part C: Emerging Technologies*: 79, 196–206.
- Yang, Y. and K. Chang 2009. Extracting the bridge frequencies indirectly from a passing vehicle: Parametric study. *Engineering Structures*: 31(10), 2448–2459.
- Yang, Y.-B., C. Lin, and J. Yau 2004. Extracting bridge frequencies from the dynamic response of a passing vehicle. *Journal of Sound and Vibration*: 272(3-5), 471–493.
- Yang, Y.-B., J. P. Yang, B. Zhang, and Y. Wu 2020. *Vehicle Scanning Method for Bridges*. Wiley Online Library.

Remote ambient vibration-based scour monitoring system

S. Kitagawa & H. Yano

Fuji Electric, Co. Ltd, Tokyo, Japan

C.-W. Kim & D. Kawabe

Department of Civil and Earth Resources Engineering, Kyoto University, Kyoto, Japan

ABSTRACT: This study proposes a remote scour monitoring system especially focusing on ambient vibration monitoring as an alternative method for the conventional impact test. The remote scour monitoring system consists of an edge computing system, wireless communication and cloud computing. The ambient vibration signals are processed and the target frequency is identified in the edge computing system. The identified frequencies are sent to a cloud computing system via mobile telecommunications. In the cloud computing, possibility of scour is estimated and warnings are sent out. A stochastic warning index is proposed for alarming the scour event because of relatively poor signal to noise of the ambient vibration signals comparing to that from the impact test.

1 INTRODUCTION

Many Japanese railway companies adopt an impact test on the railway bridge pier as a promising scour detection method focusing on changes in frequencies. However, the impact test is a labor-intensive and time-consuming method and is inapplicable for real-time monitoring during heavy rains. Real-time scour monitoring using bridge vibrations thus has been considered an alternative method to the conventional impact test (Kim et al. 2017). Since changes in the stability of the pier foundation link to changes in natural frequencies for the rocking motion of the pier, identification of modal frequency is the first step for vibration-based scour detection.

This study aims to propose a remote scour monitoring system which comprises an edge computing system, a remote data-delivering function, and a cloud system for scour alarming. To estimate the natural frequency of the target bridge, accelerometers were installed on the top of the bridge pier and the bridge girders for the impact test, and two sensors on the pier top were left for the ambient vibration-based scour monitoring. A fast Bayesian FFT (Au 2011) is adopted for the modal identification from microtremor measurement, which provides higher identification accuracy and statistical information about the identification.

The estimated posterior distribution of the target frequency is used for real-time scour detection. Two approaches are investigated. One is the method utilizing an index from the ratio of newly identified frequency to that of a healthy state. The possibility of the scour is estimated by comparing the index with a scour assessment scale specified in the Japanese guideline (Ministry of Land, Infrastructure, Transport and Tourism, Railway Bureau 2007). The other is the method utilizing probability distributions of the identified frequency during the normal river water period (hereafter “normal period”) and swollen river water period (hereafter “swollen period”).

2 REMOTE MONITORING SYSTEM

The remote monitoring system comprises triaxial accelerometers, an edge computing system, data delivering module, and a stochastic scour assessment system. Using this system, there is no need to dispatch engineers to the bridge during flood events, while changes in the target frequency of the observation piers are remotely monitored for scour detection. Instead of a conventional impact test that detects changes in frequency from the free vibration, the remote monitoring system examines the ambient vibration. The monitored ambient vibration signals are processed and the target frequency is identified in the edge computing system, and the identified frequencies are sent to a cloud computing system via a mobile phone network (see Figure 1). In cloud computing, the possibility of scour is estimated, and send out warnings as needed. In another implementation, it is also possible to identify the target frequency on a cloud server without installing an edge computer. Furthermore, by adding a water level sensor to the system, it is possible to analyze the relationship between water level and identified frequency.

3 SCOUR MONITORING

The monitoring bridge is a steel plate girder railway bridge with a span length of 22.5 m, a pier height of 9 m, and a width of 3 m, designed for a single railway track. The photo of the target pier is shown in Figure 2. 13 triaxial sensors were installed on the top of the pier and connecting girders during the impact test, while all sensors except two sensors installed upstream and downstream of the pier top were removed after the impact test. Figure 3 shows the sensor deploying map. Two sensors left on the pier top (sensors ①-① and ①-③) are used for long-term ambient vibration monitoring. The sampling frequency of the measurement is 200Hz.

Modal parameters of the monitoring pier such as frequency, damping ratio, and mode vector were first identified from the vibration data during the impact test. The dominant frequency for the rocking mode was identified as 9.2 Hz. The scour assessment needs vibration data not only from the normal period but also from the swollen period. Figure 4 shows examples of ambient vibration observed during the normal period whose amplitude was less than 0.1 gal. During the swollen period, it was around 1 gal caused by rising water and increasing speed of river flow. The fast Bayesian FFT is used to identify the posterior probability of modal parameters from ambient vibrations.

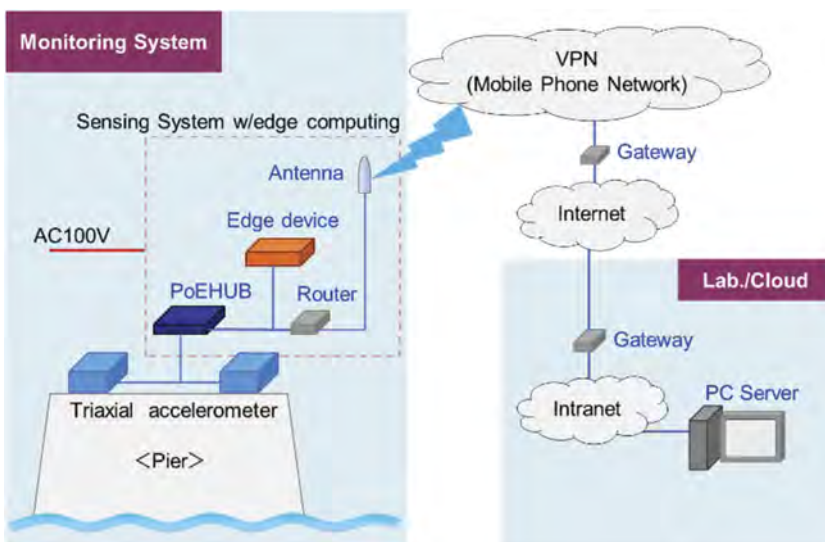


Figure 1. Remote scour monitoring system.

This study examines the ambient vibrations monitored on 30th September 2018 and 1st October 2018 as data during the swollen period. Figure 5a) shows the change in water level per five minutes from noon on September 30 to noon on October 1. The “water level” represents the distance between the water surface and the lower flange of the bridge girder. The “swollen condition” is defined as the period the water level is lower than 6m and the other period is defined as the “normal condition”. Figure 5b) shows the identified target frequency by means of the fast Bayesian FFT in which the horizontal axis shows the observation time.

Table 1. Soundness index of scour.

Soundness Index	Category	Assessment
$\kappa \leq 0.70$	A1	Scour
$0.70 < \kappa \leq 0.85$	A2	Scour progressing
$0.85 < \kappa \leq 1.00$	B	Low possibility
$1.00 < \kappa$	S	Healthy



Figure 2. Monitoring bridge.

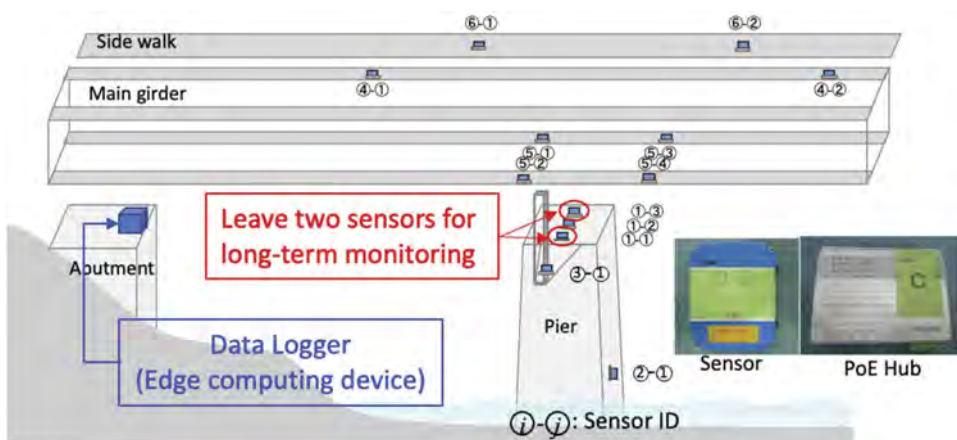
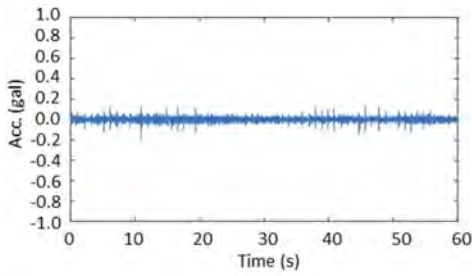
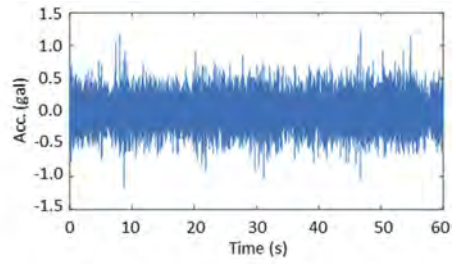


Figure 3. Sensor deploying map.



a) during normal river water period.



b) during swollen river water period.

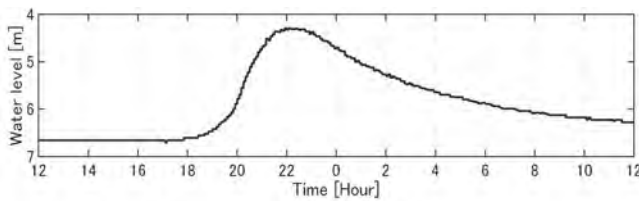
Figure 4. Measured microtremors.

Table 2. Parameter of stable distribution.

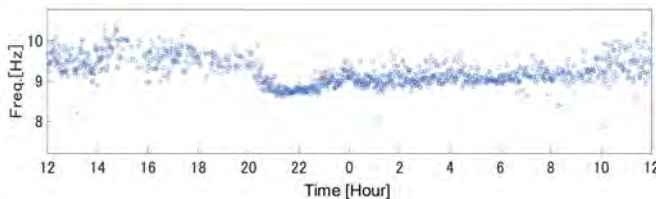
Parameter	Range	Remarks
α	$0 < \alpha \leq 2$	Characteristic exponent
β	$-1 \leq \beta \leq 1$	Skewness parameter
γ	$0 < \gamma < \infty$	Scale parameter
d	$-\infty < d < \infty$	Location parameter

Table 3. Relationship between soundness index and stochastic warning index.

Freq.	Soundness Index	Category	SWI (Ψ_c)
$X \leq 6.4\text{Hz}$	$\kappa \leq 0.70$	A1	$\Psi_c \leq 0.0016$
$6.4\text{Hz} < X \leq 7.8\text{Hz}$	$0.70\text{Hz} < \kappa \leq 0.85\text{Hz}$	A2	$0.0016 < \Psi_c \leq 0.0053$
$7.8\text{Hz} < X \leq 9.1\text{Hz}$	$0.85 < \kappa \leq 1.00$	B	$0.0053 < \Psi_c \leq 0.46$
$9.1\text{Hz} < X$	$1.00 < \kappa$	S	$0.46 < \Psi_c$



a) water level per five minutes.



b) identification frequency.

Figure 5. Observed water level and identified frequency from noon September 30 to noon October 1.

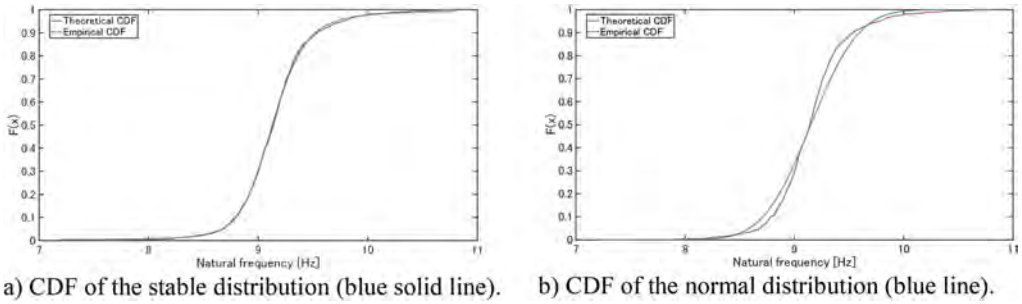


Figure 6. CDF of the observed frequency in normal river water period (red line).

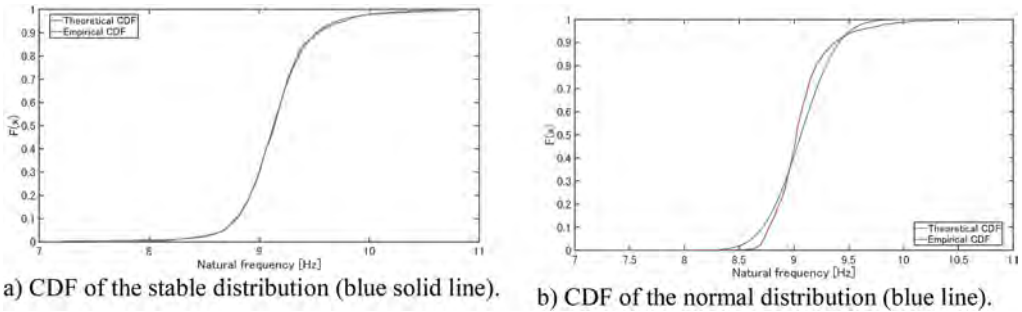


Figure 7. CDF of the observed frequency in swollen river water period (red line).

4 REAL-TIME SCOUR ASSESSMENT

The PDF of the Levy flight distribution of the frequency during the normal period is estimated, and the parameters of the PDF of the Levy flight distribution are identified by the maximum likelihood estimation (MLE). The characteristic function of the Levy-flight distribution is given by Equation 1.

$$\Psi(t, \alpha, \beta, \gamma, d) = E(e^{-itZ}) \quad (1)$$

where the characteristic exponent α determines the rate of decay, *i.e.*, if it becomes smaller the tails get fatter. While the parameter β is an indication of the skewness of the distribution, with $\beta = 0$ corresponding to the symmetric case. The parameters γ and d simply translate and scale the distribution but have no effect on its shape. The location parameter d equals the median of the PDF. Z is the random variable and t denotes the parameter for the characteristic function (Adler et al. 1996). The parameters used in the Levy flight distribution are summarized in Table 2.

The PDF of the Levy flight distribution is represented as $S_N(\alpha_N, \beta_N, \gamma_N, d_N, Z)$ which is the inverse transformation of the characteristic function shown in Equation 1. The parameters of PDF of the Levy flight distribution under normal conditions (S_N) were estimated by means of the MLE. Identified parameters were $\alpha_N = 1.59$, $\beta_N = 0.32$, $\gamma_N = 0.18$ and $d_N = 9.11$.

The CDF of S_N is shown in the blue line of Figure 6a) while the red line shows the CDF of the observed frequency in the normal period. For comparison, the CDF following a normal distribution is shown in Figure 6b). From Figure 6a), it is obvious that the CDF curve of the Levy flight distribution matches well, especially at tails, with that of the observed CDF. On the other hand, Figure 6b) demonstrates that the tails in the normal distribution do not match well with the observed one and as a result lead to a poorer accuracy in scour assessment.

Since the number of data samples of the observed frequency during the swollen period is small, it was quite difficult to grasp the whole picture of the PDF. Therefore, measured ambient

vibration was overlapped in order to increase the number of data samples for system identification, and 50% of the data block was overlapped. Then the PDF of the observed frequency from the overlapped data samples, $S_F(\alpha_F, \beta_F, \gamma_F, d_F, Z)$, was estimated in the same manner to the normal period. Identified parameters were $\alpha_F = 1.62$, $\beta_F = 0.94$, $\gamma_F = 0.14$ and $d_F = 8.99$.

The CDF of S_F is shown in the blue line of Figure 7a). For comparison, the CDF assumed to follow normal distribution is shown in Figure 7b). Similar to the normal period, it is obvious that the CDF curve of the Levy flight distribution matches well with that of the observed CDF while the tails in the normal distribution do not match well with the observed one. Assuming the PDF of the estimated reference frequency of the pier during the normal period is given by $S_N(\alpha_N, \beta_N, \gamma_N, d_N, X)$, the stochastic warning index (SWI), Ψ_c is estimated as follows.

$$\Psi_c = \Psi(\alpha_N, \beta_N, \gamma_N, d_N, Z_m) \quad (2)$$

where, $\Psi(\alpha_N, \beta_N, \gamma_N, d_N, Z_m)$ is the CDF of S_N and Z_m denotes the mean natural frequency during the swollen period. The SWI estimated using Equation 2 is called *Method-A* in this study.

Here, a concept of marginal indicator of stochastic warning index (MISWI), Ψ_s , is proposed to assess scour occurrence. If SWI during the swollen period reaches the MISWI, it indicates a possible occurrence of scour. The MISWI can be defined considering relationships with the soundness index in Table 1. The soundness indices 0.70, 0.85, and 1.00 correspond to frequencies of 6.4Hz, 7.7Hz, and 9.1Hz respectively if the frequency in healthy condition is 9.1Hz.

The relationship between the soundness index κ and the SWI, Ψ_c is summarized in Table 3. When the soundness index κ is 0.70, the corresponding frequency $Z_m = 6.4$ Hz and the corresponding SWI is $\Psi_c = 0.0016$. Indeed, category A1 shows extremely low probability as SWI = 0.0016, and the stochastic approach can link to risk analysis.

In order to obtain the higher probability of the Type I error (occurrence of scour is determined even under health condition) and lower probability of the Type II error (scour is occurred while health condition is determined), the MISWI is set to be $\Psi_s = 0.05$ as an example, which is larger than the threshold value ($\Psi_c = 0.0053$). It is noted that how to decide MISWI depends on the risk sensitivity of bridge authorities.

Assuming that the PDF for the target frequency during the swollen period can be represented by S_F , the SWI during the swollen period is estimated utilizing Equation 3 which is called *Method-B* in this study.

$$\Psi_c = \int_{-\infty}^{\infty} S_F \int_{-\infty}^X S_N dZ dX \quad (3)$$

Although the scour assessment taking into account of the uncertainty of the frequency during the swollen period was discussed, one needs to wait until the water level return to the normal period to identify the PDF characteristic of the target frequency using Equations 2 and 3 during the swollen period. Thus, considering the time series on the identified frequency of the target pier during the swollen period, three different methods for calculating the real-time stochastic warning index (RWI) are proposed.

Assuming that the empirical PDF parameters of α_F , and γ_F are given beforehand from the past observations, and the frequency, X_t , during the current swollen period is observed, the likelihood function during the swollen period is given as Equation 4.

$$L_F(X) = S_F(\alpha_F, \beta_F, \gamma_F, X_t, X) \quad (4)$$

where X_t is the identified frequency from a data sample measured at a time span, e.g. identified frequency from every 1-minute data sample.

Replace $S_F(\alpha_F, \beta_F, \gamma_F, X_t, X)$ in Equation 3 to the likelihood function $L_F(X)$ in Equation 4, the RWI is given as Equation 5 that is called *Method-C*.

$$\Psi_c(t) = \int_{-\infty}^{\infty} L_F(X) \int_{-\infty}^X S_N dZ dX \quad (5)$$

In real-time scour detection, it is crucially important to reduce computation time. Therefore, instead of applying Equation 5, as a simplified method the time series of frequency, Z_t , during the swollen period is considered in estimating RWI using Equation 6 which is called *Method-D*.

$$\Psi_c(t) = \Psi(\alpha_N, \beta_N, \gamma_N, d_N, Z_t) \quad (6)$$

Considering each frequency of swollen river water period as a normal distribution by using the identified frequency and standard deviation obtained from the fast Bayesian FFT, RWI can be given as Equation 7 that is called *Method-E*.

$$\Psi_c(t) = \int_{-\infty}^{\infty} N(X_t, \sigma_t) \int_{-\infty}^X S_N dZ dX \quad (7)$$

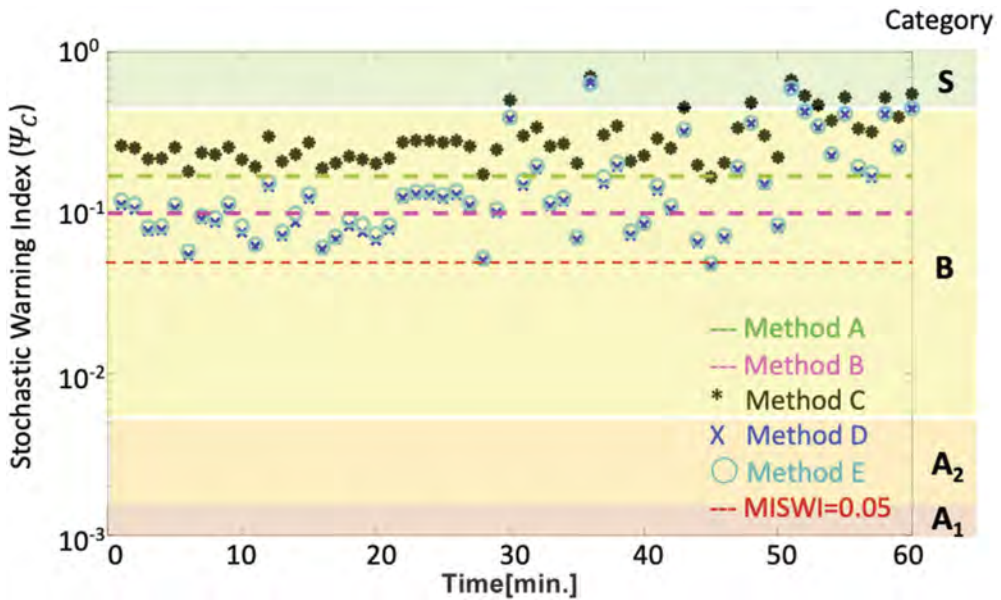


Figure 8. Stochastic warning index according to different methods.

where, X_t and σ_t denote the mean and standard deviation of the identified frequency during the swollen river water period, which is obtained by means of the fast Bayesian FFT.

Ambient vibration data from 22:00 to 23:00 on 30th September 30 in 2018 is again considered an example the ambient vibration data. Assume every identified frequency at a time as real-time data X_t and estimate the RWI at each time, time series of the RWI during the swollen river water period is shown in Figure 8, where the vertical axis indicates the RWI and the horizontal axis indicates the monitoring time. The horizontal red dotted line denotes the assumed MISWI, $\Psi_S = 0.05 = 5\%$. It can be seen that a warning is not announced during the swollen river water period.

Figure 8 shows that SWI is in the range of $0.0053 < \Psi_c \leq 0.46$ which corresponds with category B, which means that there is a low possibility of scour during the target period. It can also be seen that *Method-D*, which estimates the RWI using the CDF of the normal period and

time series of frequency during the swollen period, resulted in a decision on the safe side among three methods, *Method-C* to *Method-E*. In other words, *Method-C*, which considers the probability distribution of frequencies both from the normal period and the swollen period, resulted in the most economic decision on the scour occurrence.

5 CONCLUSIONS

This study proposes a remote scour monitoring system using ambient vibration monitoring of the bridge pier during swollen river water period. The natural frequency of the bridge pier was identified with high accuracy from the ambient vibration during the swollen river water period.

Reliability-based scour assessment, parameters of the PDF of the Levy flight distribution are identified by means of the maximum likelihood method using the frequency of the pier during normal and swollen river water periods, and the stochastic warning index is proposed and data collected from real swollen river water period is used as a case study. A real-time reliability-based scour assessment is also investigated.

This study demonstrated the effectiveness of the proposed remote scour monitoring system. It is possible to assess probabilistic scour occurrence by using the ambient vibration data during swollen river water period. Moreover, the feasibility of the real-time stochastic scour assessment was observed.

ACKNOWLEDGMENTS

This work is supported by the Grant-in-Aid for JSPS (Grant No: 22H01576) in part. The financial support is greatly acknowledged. It is also greatly acknowledged that Dr. T. Sato, emeritus professor at Kyoto University, provided intensive discussions on the stable distribution and warning index.

REFERENCES

- Adler, R., Feldman, R & Taqqu, M.S. 1996. A Practical guide to heavy tails. *Statistical Techniques and Applications*, 313–314.
- Au, S.K. 2011. Fast Bayesian FFT method for ambient modal identification with separated modes. *J Eng Mech ASCE* 137(3),214–226.
- Kim, C.W., Kawabe, D., Kitagawa, S. Shinoda, M., Nakamura, T. & Yao, H. 2017. Remote vibration monitoring for scouring detection of a railway bridge. In *Proc. of SMAR 2017*.
- Ministry of Land, Infrastructure, Transport and Tourism, Railway Bureau. 2007. Railway structures maintenance management standard and commentary (structural edition), pp.169–170. (in Japanese)

The ratio of stress amplitudes between two directions around welded part of trough rib in orthotropic decks with fatigue cracks

Ryo Saita & Mone Ueno

Graduate School of Arts and Science, Iwate University, Morioka, Japan

Yuma Sugimoto & Hiroshi Onishi

Faculty of Science and Engineering, Iwate University, Morioka, Iwate, Japan

ABSTRACT: Usually, an inspection for fatigue cracks in steel structures is often executed with visual inspection, penetrant testing and magnetic particle testing as necessary. However, the visual inspection depends on inspectors' knowledge and skills, so overlook of cracks can occur. Non-destructive inspection such as penetrant testing and magnetic particle inspection cannot detect fatigue cracks inside steel plates. Therefore, the authors proposed cracks detection method focusing on the ratio of stress amplitudes between two directions near the weld as an auxiliary mean of an inspection of steel structures. In this study, we verified whether cracks can be detected quantitatively by comparing and examining the results of vibration fatigue test and FEM analysis for the welding lines of trough rib in orthotropic decks. As a result, fluctuations in the ratio of stress amplitudes are confirmed due to the occurrence and progress of cracks. This method isn't dependent on inspectors' knowledge and skills, may be able to detect damage inside the structure, so it can be an auxiliary mean of the existing inspection method.

1 INTRODUCTION

Orthotropic steel decks are widely used because they are lighter than concrete decks and the rapid execution of orthotropic steel decks is possible in recent years. On the other hand, fatigue cracks in steel orthotropic decks due to repetitive loading have become a serious problem in the maintenance of bridges. Many fatigue cracks occur in places near welding lines and they progress. Among them, cracks that progress in the direction penetrating the deck plate may cause the road surface to collapse if the cracks progress to the deck plate. It must be careful because it may cause damage to use. Usually, an inspection of fatigue damage is often executed with visual inspection, penetrant testing and magnetic particle testing as necessary. However, visual inspection is dependent on the inspector's knowledge and skills. Magnetic particle testing and penetrant testing are also unable to detect cracks if they are not on or near the surface. These inspections cannot deal with cracks and defects inside the structures. To solve these problems, this study investigates a method that can detect cracks even by inexperienced inspectors as an auxiliary tool to visual inspection and nondestructive testing.

In a previous study conducted by Horiai at Iwate University, they carried out vibration fatigue test using specimens that simulate the welding lines of trough rib in orthotropic steel decks (Horiai et al. 2017.). It shows that the presence or absence of cracks can be judged by checking the stress ratio (Y/X) in the longitudinal direction (X -axis) and the right-angle direction (Y -axis). When considering the presence or absence of cracks, it is difficult to judge by stress in one direction only. Because it must be judged including the load (external force) applied to the candidate structure at that time. Therefore, in the study conducted by Horiai et al., the stress in each axial direction is nondimensionalized by taking the ratio of the stress, which makes it possible to judge the presence

or absence of cracks more easily. On the other hand, fatigue problems are usually organized using stress amplitude rather than actual stress value.

Therefore, in this study, based on the data from previous study, we examined whether it is possible to detect cracks quantitatively by confirming the ratio of stress amplitudes in two directions around fatigue cracks (hereinafter, this is called “stress amplitude ratio”). In addition, we studied the effectiveness of this method in confirming the stress amplitude ratio centered on the fatigue crack, by comparing the vibration fatigue test data with the results of the FEM analysis.

2 VIBRATION FATIGUE TEST ON TROUGH RIB

This chapter presents an overview of the vibration fatigue tests on the welded part of trough rib in orthotropic decks, which was a previous study conducted at Iwate University.

2.1 Test overview

Figure 1 and Figure 2 show an overview of the vibration fatigue tester used in the previous study and a photo of the test situation (Yamada et al., 2008.). In this study, the specimen was set up so that the ribs were facing upward, referring to the test conducted by Yamada (Yamada & Samol. 2008.). In the previous study, a coil spring was installed at the tip of the specimen, and the specimen was pushed down by this coil spring. The fatigue test was carried out with the stress ratio applied to the specimen being pulsated ($R > 0$).

2.2 Test specimens

Figure 3 shows the specimen used in this study. The material of the specimens is SM400A, and a rib corresponding to a plate thickness of 6 mm of trough rib is welded at an angle of 78° to a base material of 12 mm thickness, 300 mm width and 700 mm length simulating orthotropic steel deck plate. Usually, the standard is that the penetration amount in the welding lines of U-rib is 75 % or more of the plate thickness. In this study, as shown in Figure 4, by making from end parts of the rib about 75 mm into a range where the amount of penetration was large, by making the rib center about 50 mm into a range where the amount of penetration was small. We attempted to generate cracks starting point in the center of the width of the specimen. A hole with a diameter of 24 mm is for installation in a vibration fatigue testing machine, and a hole with a diameter of 14 mm is for installing an eccentric motor.

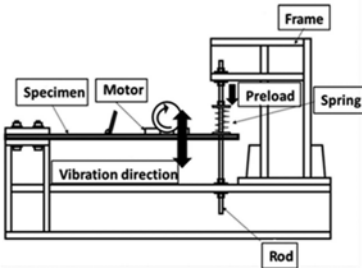


Figure 1. Overview of vibration fatigue test.



Figure 2. Vibration fatigue test of simulated the welding lines of trough ribs.

2.3 Attached gauge situation

Figure 5 shows the state of the strain gauge attached to the specimen. To measure the stress including the effect of stress concentration, the gauge was attached to a position 5 mm away from the weld toe in the longitudinal direction (X-axis) and 50 mm away from

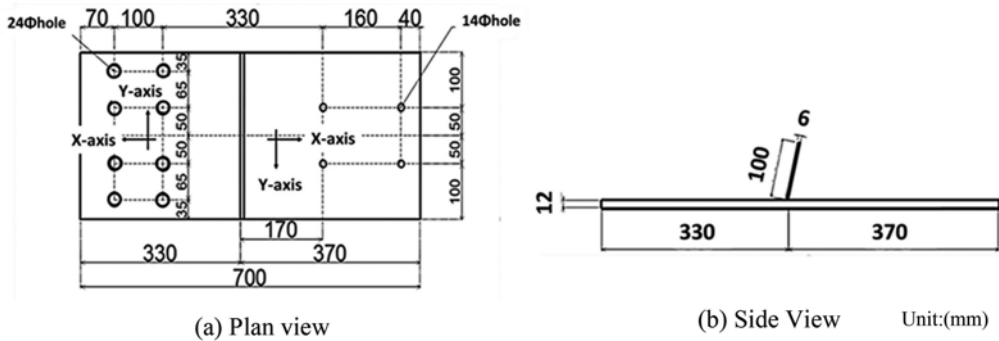


Figure 3. Test specimens.

the right-angle direction (Y-axis), referring to bridge measurements (Notional institute for land and infrastructure management ministry of land, 2008.) and wheel load running tests (Yoshinami et al. 2012). G1' gauge is 70 mm away from G4 in the longitudinal direction (X-axis), G2' gauge is further 75 mm away from G1' in the right-angle direction (Y-axis), and G3' gauge is away from G4 in the right-angle direction (Y-axis). We used the results of strain measured with the G1', G2', and G3' gauges, the nominal stress range was determined from the proportional relationship (Kinoshita and Arakawa 2012; Kinoshita and Arakawa 2013; Sakano and Arai 2004). G1 to G4 triaxial gauges were FRA-1-11, and G1' to G3' uniaxial gauges were FLA-1-11.

2.4 Experimental conditions

Table 1 shows the nominal stress of each of specimens at the start of the test and the number of cycles at the end of the test. The test end condition is that when the stress in the right-angle direction (Y-axis) is larger than the stress in the longitudinal direction (X-axis) or the fatigue cracks occurring from the weld toe reached this position and the enameled wire which was attached to the plane side without a rib until the cracks generated from the vicinity of the weld progressed in the thickness direction and penetrated broke.

3 TEST RESULT

3.1 How to calculate stress amplitude and stress amplitude ratio

In this consideration, strains measured by triaxial strain gauges are used to calculate the stress amplitude. The first axis of the triaxial gauge is the longitudinal direction (X-axis) and the second axis is the right-angle direction (Y-axis). From the strains in each of these two directions, the stress amplitude in the longitudinal direction (X-axis) and the right-angle direction (Y-axis) were calculated, respectively, using following equation (1).

$$\Delta\sigma = \frac{(\varepsilon_{\max} - \varepsilon_{\min}) \times E}{2} \quad (1)$$

Where $\Delta\sigma$ = Stress amplitude (MPa); ε_{\max} = Maximum Strain (μ),
 ε_{\min} = Minimum Strain (μ); E = Young's modulus ($2.1 \times 10^5 \text{ N/mm}^2$).

The stress amplitude ratio was calculated by referring to the method used by Horiai et al. In this study, since the principal stress were oriented is the longitudinal direction (X-axis), the stress amplitude ratio was calculated using the following equation (2).

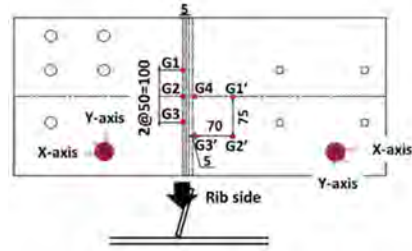
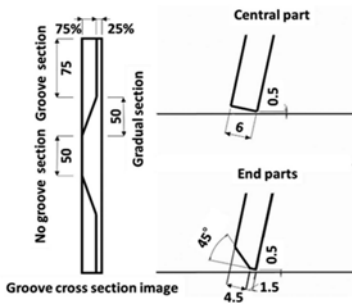


Figure 4. Cross section of the specimen groove.

Figure 5. Attached gauge position (Rib side).

Table 1. Nominal stress range and Number of cycles.

Specimen	Nominal stress range (MPa)	Number of cycles
No.1	99.7	1,941,900
No.2	99.8	2,001,900

$$\text{Stress amplitude ratio} = \Delta\sigma_Y / \Delta\sigma_X \quad (2)$$

Where $\Delta\sigma_X$: Stress amplitude (MPa) in longitudinal direction (X-axis);
 $\Delta\sigma_Y$: Stress amplitude (MPa) in the right-angle direction (Y-axis).

3.2 Fluctuation of stress amplitude ratio around cracks

Figure 6 shows the variation of the stress amplitude ratio of each gauge for specimens No. 1 and No. 2 in the vibration fatigue test. The stress amplitude ratio of all specimens tended to increase as the cracks progressed. For each specimen, the fluctuation of the stress amplitude ratio at the G4 gauge was the largest. This is because G4 is closest to the crack and was greatly affected by crack growth.

Because the trough rib is a closed cross section, it is difficult to take measurements on the inside of the rib, such as at the G4 gauge position, which is close to where the deck plate penetration crack would be expected to occur. Stress amplitude ratio variations similar to those of the inner ribs were observed in the outer ribs such as G1 to G3.

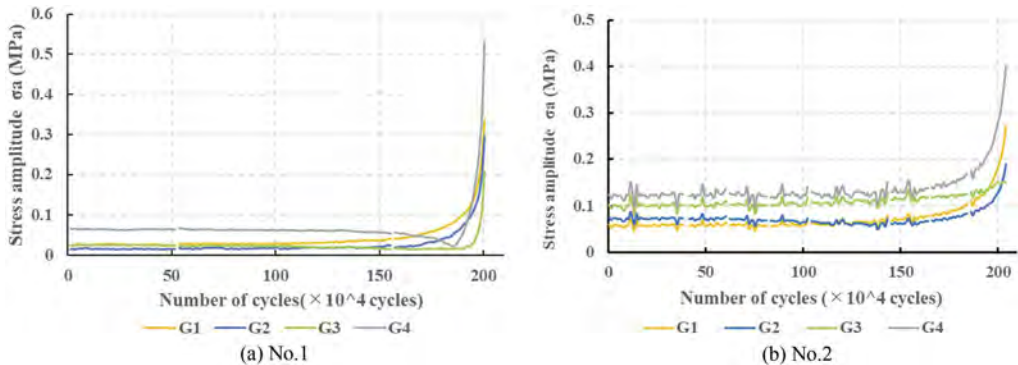


Figure 6. Fluctuation of stress amplitude ratio.

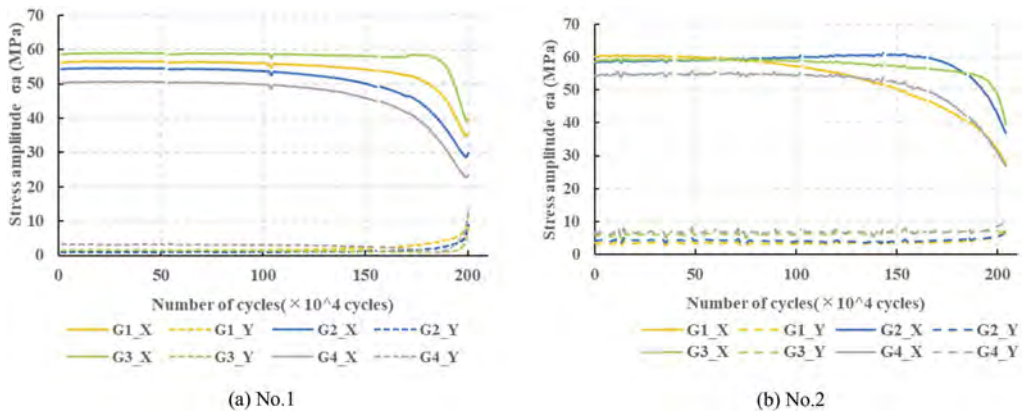


Figure 7. Fluctuation of stress amplitude.

3.3 Fluctuation of stress amplitude around cracks

Figure 7 shows the fluctuation of stress amplitude in the longitudinal direction(X-axis) and right-angle direction(Y-axis) at each gauge position for specimens No.1 and No.2. Figure 7 shows that the stress amplitude in the x-axis direction decreases significantly until the end of the test. On the other hand, the stress amplitude in the y-axis direction increased slightly toward the end of the test, but this was not a significant change compared to the stress amplitude in the x-axis direction. The reason for this fluctuation may be as follows. If fatigue cracks occur near the position where the strain gauge is attached, the amount of stress transfer in that area decreased. Therefore, the stress amplitude in the longitudinal direction(X-axis) at the attachment position decreases. When the cracks occur, the direction of the principal stress is to avoid the cracks. Therefore, the stress amplitude on Y-axis tended to increase with the cracks progress.

4 FEM ANALYSIS

4.1 FEM analysis overview

Based on the result of the vibration fatigue test, the analysis model was examined. The analysis was performed using three-dimensional FEM general-purpose analysis software (Sofistik). The material properties of the analysis model were set to be the same as those of the test specimen, with Young's modulus of steel $E = 2.1 \times 10^5 \text{ N/mm}^2$ and Poisson's ratio $\nu = 0.3$.

4.2 Analysis model

The analysis model is a model of a part of the fatigue test specimen as shown in Figure 8, and was rigidly bounded with constrained XYZ displacement and rotation on the side fixed to the vibration fatigue testing machine. Based on the test results, the crack was assumed to be a deck plate penetration crack that propagated from the weld root of the trough rib. The point of crack occurrence is assumed to be at the center of the specimen. A total of 10 models with crack lengths ranging from 0 mm to 36 mm were analyzed. The crack pattern and study area are shown in Figure 9. In this figure, cracks are indicated by red lines and welds by gray filled areas. The area outside the trough ribs, where strain gages can be attached on the bridge, is considered to be the study area in this study. The area is bounded by the black line. Since the crack depth was not measured during the vibration fatigue test, the crack depth was assumed to be about (crack depth/crack length = 1/2~1/3). We checked the stress status around the cracks in each model. The mesh size of the area around the weld to be verified is 1 mm.

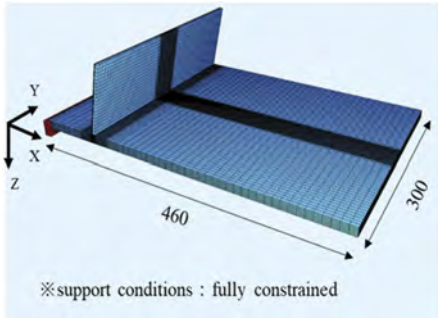


Figure 8. FE model overview.

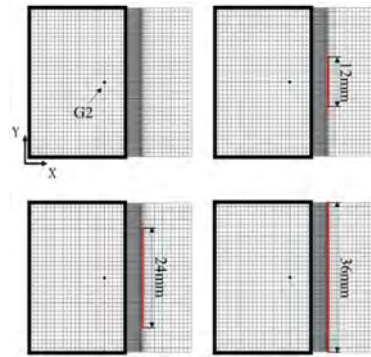


Figure 9. Crack length pattern and study area.

4.3 Analysis result

Fluctuation of the stress amplitude and stress amplitude ratio at G2 and G4 position is shown in Figure 10. Similar to the test results, the stress amplitude in the X-axis direction decreased significantly with crack initiation and propagation at each gauge positions; the stress amplitude in the Y-axis direction showed a slight decrease but no clear fluctuation. Therefore, with crack propagation, a trend toward an increase in the stress amplitude ratio was confirmed. The increase in the stress amplitude ratio is larger at the G4 gage position closer to the crack and smaller at the G2 gage position farther from the crack.

Contour diagram of stress amplitude ratio for each crack length is shown in Figure 11. The study area is shown in Figure 9. In the case of no crack, stress amplitude ratio of less than 0.3 were confirmed for all elements in the study area. For crack length (b) 4 mm, 0.30–0.35 in stress amplitude ratio was confirmed at 2 mm from the weld toe, indicating that the crack occurrence was affected by the crack. (hereinafter, the area of stress amplitude ratio above 0.30 is called “influence area”).

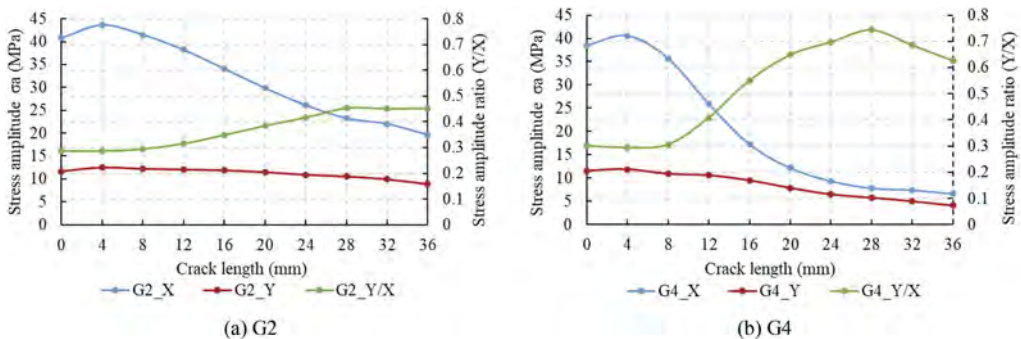


Figure 10. Fluctuation of stress amplitude ratio (FEM analysis).

In the case of crack length (c) 8 mm, the influence area was confirmed to be 4 mm from the weld toe, and in the case of crack length (d) 12 mm, the influence area was confirmed to be 9 mm from the weld toe. Thereafter, it was confirmed that the influence area of the stress amplitude ratio expanded as the crack propagated. It is considered possible to judge the presence or absence of cracks by attaching strain gauges within the influence area where the fluctuation of the stress amplitude ratio is confirmed. In the vibration fatigue test, a strain gauge was attached at a distance of 5 mm from the weld end for measurement. This method is considered to be effective for cracks longer than 12 mm, when a strain gauge is attached 5 mm from the weld toe to detect cracks.

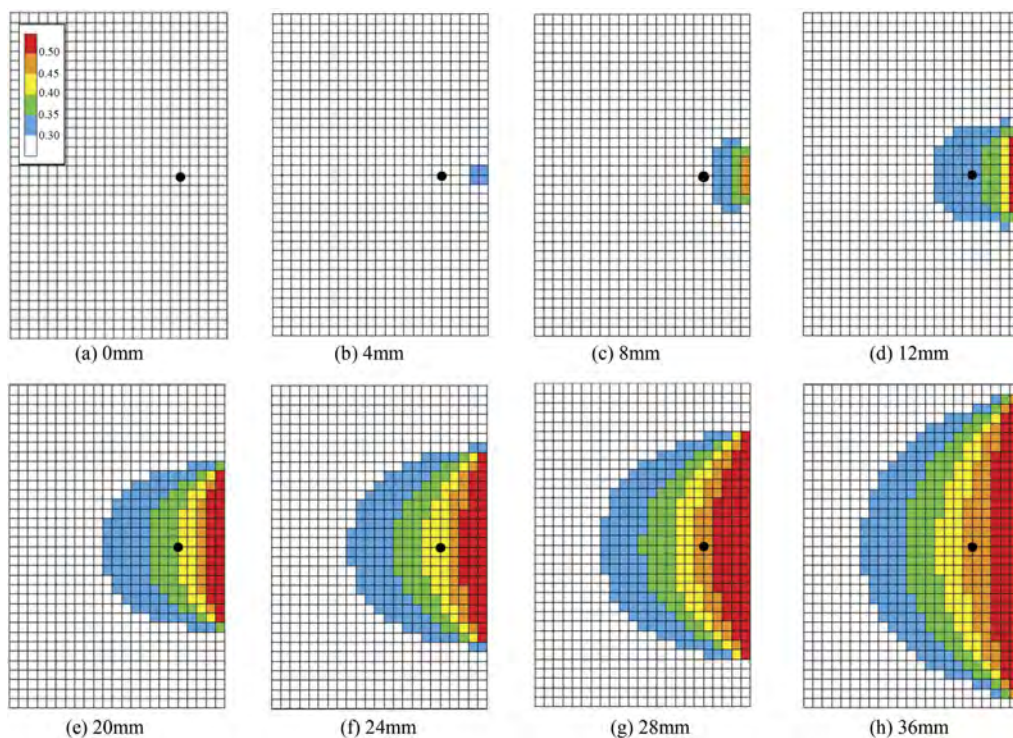


Figure.11. Contour diagram of stress amplitude ratio.

5 CONCLUSION

In this study, in the fatigue damage of steel structures, we focused on cracks in welded part of trough rib in orthotropic decks. We examined whether the presence or absence of cracks could be determined by confirming the stress amplitude ratio around the cracks. The findings of this paper are shown below.

- (1) The stress amplitude ratio increases with crack propagation because the decrease in the stress amplitude in the longitudinal direction(X-axis) is larger than the fluctuation of the stress amplitude in right-angle direction(Y-axis).
- (2) Regarding the deck plate penetration crack, it is clarified that the cracks can be judged by examining the ratio of stress amplitudes between two directions near the welded part outside the rib.
- (3) In the FEM analysis, it is confirmed that the area where the stress amplitude ratio increased with crack propagation was expanded.

For the purpose of detecting deck plate penetration cracks for welded part of trough rib in orthotropic decks, strain gauges are attached at a distance of 5 mm from the weld toe in the direction perpendicular to the bridge axis. From fatigue test and analysis results, it is considered possible to detect a crack by confirming the fluctuation of the stress amplitude ratio.

REFERENCES

- A. Horiai, Y. Kuwabara, M. Miura, T. Shingin and H. Onishi. 2017. "Variations of principal stress brought by the fatigue occurrence", *Japan society of materials science*, Reliability symposium.
- Japan Road Association. 2017. Road Bridge Specification /Explanation, II Steel bridge/steel member edition, pp.595.

- K. Kinoshita and S. Arakawa. 2012. "A simulation analysis of fatigue crack propagation path of out-of-plane gusset joints under out-of-plane bending by XFEM", *Proceedings structural engineering*, Vol.58A, pp.824–833.
- K. Kinoshita and S. Arakawa. 2013. "Fatigue crack propagation analysis considering crack aspect ratio for out-of-plane gusset joints under bending", *Journal of the Japan society of civil engineers A1 (structural engineering and earthquake engineering)*, Vol.69, No.1, pp.20–25.
- K. Yamada, T. Ojio, A. Torii, Biehn Baik, Y. Sasaki and S. Yamada. 2008. "Influence of shot blasting on fatigue strength of out-of-plane gusseted specimens under bending", *Proceeding structural engineering*, Vol.54A, pp522–529.
- K. Yamada and Ya Samol. 2008. "Plate bending fatigue tests for root crack of trough rib of orthotropic steel deck", *Proceedings of Structural Engineering, Japan Society of Civil Engineers*, Vol.54A, pp.675–684.
- M. Sakano and M. Arai. 2004. "Effect of thickness on fatigue strength of out-of-plane gusset welded joints", *Journal of the Japan society of civil engineers*, No.766.
- Notional institute for land and infrastructure management ministry of land. 2008. infrastructure, transport and tourism, Japan association of steel bridge construction, "Cooperative research on durability of the steel members on bridges -Survey on the inspection of the orthotropic steel decks-", *Technical note of national institute for land and infra-structure management*, No.471.
- S. Yamada, N. Watanabe, K. Yamada and T. Ojio. 2008. "Development and application examination of simple vibration fatigue testing machine", *Topy tekko technical report*, No.24, pp.15–22.
- T. Yoshinami. 2012. "Detection method of cracks at the root of welding portions of U-shaped rib to deck plate in orthotropic steel deck by frictional strain gauge", *Osaka university graduate school master's thesis*.

Ambient-vibration-based operational modal analysis and cable tension estimation in the long-term SHM of a cable-stayed bridge

W.J. Jiang & C.-W. Kim
Kyoto University, Kyoto, Japan

K. Ono
Eight-Japan Engineering Consultants, Kobe, Japan

ABSTRACT: This paper presented a study of operational modal analysis and cable tension estimation using ambient vibration in long-term bridge SHM. Bayesian operational modal analysis under ambient vibration was conducted in a cable-stayed bridge by the means of a Bayesian FFT and the coupling effect of cable-deck vibration is discussed. A Bayesian cable tension estimation method is proposed with the identification uncertainty in the estimates of cable tension. Further, the effect of EOVs in long-term SHM of cable tension was investigated with an integration of identification uncertainty using a probabilistic predictive model. The result indicated the effect of EOVs in the longest cable is much more dominant compared to the shortest cable at bridge deck end. Finally, a Gaussian mixture model (GMM) based anomaly detection method in the long-term SHM of stay cable was proposed and investigated with the likelihood as a damage sensitive feature (DSF) and the damage effect according to a simulated analysis. The result showed that this method can provide a meaningful indication of damage under a certain premise.

1 INTRODUCTION

The cable-stayed bridge has been widely constructed around the world. As a crucial component in this structure, the stay cable is always faced with long-term deterioration caused by corrosion, fatigue, etc. For the management and maintenance of cable-stayed bridges, it is of great meaning to conduct real-time long-term structural health monitoring (SHM) of the stayed cables, among which the dynamic characteristics and cable tension are acknowledged as two informative features reflecting the condition of cables and bridge.

The ambient-vibration-based long-term SHM, which does not require artificial excitation, offers a promising way for realizing remote and economical monitoring of bridges. There have been many types of research such as frequency domain decomposition (FDD), stochastic subspace identification (SSI), a series of Bayesian operational modal analysis (OMA) methods (e.g., Fast Bayesian FFT), etc., which make the ambient-vibration-based modal analysis efficient and flexible. Further, cable tension, as a more intuitional physical feature, has also been investigated in the relation to the dynamics of cables (Shimada 1994, Zui et al. 1996, Yamagiwa et al. 1999).

By examining the estimated cable tension in long-term bridge SHM, it is believed that potential damage effects in cables can be traced timely. However, there are still many issues remaining in the ambient-vibration-based long-term bridge SHM. One is the low signal-to-noise ratio (SNR) with weak excitation which makes the identification uncertainty (IU) prominent. Another one is the effect of environmental and operational variations (EOVs), which raises the variability of long-term records in SHM. Therefore, to make a deep perception of these issues, this study investigates ambient-vibration-based cable tension estimation and the

identification uncertainty and EOVs-induced variability in the long-term monitoring of cable tensions with Bayesian approaches.

2 METHODOLOGY

2.1 Fast Bayesian FFT

As one of the ambient-vibration-based operational modal analysis methods, a fast Bayesian FFT approach (Au et al. 2013, Au 2017) is introduced here. By associating Bayesian inference with the FFTs of vibration response, Bayesian FFT gives a basic form as follows.

$$p(\boldsymbol{\theta}|\hat{\mathcal{F}}_k) = p(\hat{\mathcal{F}}_k)^{-1}p(\hat{\mathcal{F}}_k|\boldsymbol{\theta})p(\boldsymbol{\theta}) \quad (1)$$

where $\boldsymbol{\theta}$ denotes the system parameters of the structure to be identified, and $\hat{\mathcal{F}}_k$ are the estimated FFTs data at different frequencies f_k .

Assuming that the power spectral density (PSD) is complex Gaussian distribution and independent at different frequencies, the posterior distribution in Equation 1 has a linear relationship with the likelihood function as follows.

$$p(\boldsymbol{\theta}|\hat{\mathcal{F}}_k) \propto p(\hat{\mathcal{F}}_k|\boldsymbol{\theta}) = \frac{\pi^{-nN_f}}{\prod_k |E_k(\boldsymbol{\theta})|} \exp\left[-\sum_k \hat{\mathcal{F}}_k^* E_k(\boldsymbol{\theta})^{-1} \hat{\mathcal{F}}_k\right] = e^{-L(\boldsymbol{\theta})} \quad (2)$$

The theoretical PSD matrix of data at the k^{th} FFT for given $\boldsymbol{\theta}$ is shown in Equation 3.

$$E_k(\boldsymbol{\theta}) = E\left(\hat{\mathcal{F}}_k \hat{\mathcal{F}}_k^* | \boldsymbol{\theta}\right) + E[\varepsilon_k \varepsilon_k^* | \boldsymbol{\theta}] = \sum_{i=1}^m \sum_{j=1}^m h_{ik} h_{jk}^* S_{ijk} \boldsymbol{\phi}_i \boldsymbol{\phi}_j^T + S_e \mathbf{I}_n \quad (3)$$

The negative log-likelihood function (NLLF) of Equation 2 can be written as Equation 4. The most probable value (MPV) of $\boldsymbol{\theta}$ can be estimated as, $\hat{\boldsymbol{\theta}} = \arg \min_{\boldsymbol{\theta}} L(\boldsymbol{\theta})$.

$$L(\boldsymbol{\theta}) = nN_f \ln \pi + \sum_k \ln |E_k(\boldsymbol{\theta})| + \sum_k \hat{\mathcal{F}}_k^* E_k(\boldsymbol{\theta})^{-1} \hat{\mathcal{F}}_k \quad (4)$$

where, the system parameter $\boldsymbol{\theta}$ comprises modal frequencies $f_{i=1}^r$ and modal damping ratios $\zeta_{i=1}^r$ denoted in transfer functions h_{ik}^r corresponding to each mode, partial mode shapes $\boldsymbol{\phi}_{i=1}^r$, PSD matrix of modal forces $S = [S_{ij}]_{r \times r}$, and the PSD matrix of prediction errors $S_e \mathbf{I}_n$. In addition, r represents the number of dominant modes in a specified frequency band where the estimation is conducted. n is the number of sensors to collect the ambient vibration response. N_f is the number of FFT points in the specified frequency band.

2.2 Bayesian cable tension estimation

The relation between modal frequency of cable and cable tension can be derived from the free vibration differential equation of cable as follows.

$$m \frac{\partial^2 v(x, t)}{\partial t^2} + EI \frac{\partial^4 v(x, t)}{\partial x^4} - T \frac{\partial^2 v(x, t)}{\partial x^2} - h(t) \frac{\partial^2 v(x, t)}{\partial x^2} = 0 \quad (5)$$

where $v(x, t)$ denotes the vertical vibration deflection, x is the longitudinal coordinate of the cable and t denotes time. The symbol m is the mass of the cable per unit length, EI denotes the flexural rigidity of the cable and T is the cable tension force. $h(t)$ denotes the dynamic tension.

According to relative research (Shimada 1994, Zui et al. 1996, Yamagiwa et al. 1999), the influence of ambient vibration-induced dynamic cable tension $h(t)$ and the cable sag is generally small and ignorable for simplicity. Assuming that the boundary condition is simply supported, the solution of Equation 5 can be presented as follows.

$$\left(\frac{f_i}{i}\right)^2 = \frac{\pi^2 i^2}{4ml^4} EI + \frac{1}{4ml^2} T \quad (6)$$

where i is mode order and f_i denotes the i^{th} modal frequency of the cable; l is the length of cable.

With identified modal frequencies of the cable, the estimation of cable tension from Equations 6 can be treated as a regression problem. A basic form of the Bayesian linear regression (BLR) model can be written as follows.

$$y = X\beta + \varepsilon, \quad \varepsilon \sim N(0, \sigma^2) \quad (7)$$

where y is an $n \times 1$ vector of response variable; X is an $n \times d$ matrix of predictor variables; β is a $d \times 1$ vector of coefficients; ε denotes the *iid* error term which obeys a normal distribution with zero mean and variance σ^2 for each observation; n is the number of observations, and d is the number of predictor variables. The Bayesian inference can then be used to obtain the posterior distribution of (β, σ^2) as follows.

$$p(\beta, \sigma^2 | y, X) = p(y|X)^{-1} \cdot p(y|X, \beta, \sigma^2) \cdot p(\beta, \sigma^2) \quad (8)$$

Further, the marginal posterior of β can be given as,

$$p(\beta | y, X) = \int p(\beta, \sigma^2 | y, X) d\sigma^2 \quad (9)$$

When the Jeffreys non-informative prior is given as Equation 10,

$$p(\beta, \sigma^2) \propto \frac{1}{\sigma^2} \quad (10)$$

the marginal posterior of β is analytically tractable and follows a d dimensional *t-location-scale* distribution shown in Equation 11.

$$p(\beta | y, X) \sim t_d \left(\hat{\beta}, \frac{(y - X\hat{\beta})'(y - X\hat{\beta})}{n - d} (X'X)^{-1}, n - d \right) \quad (11)$$

where the three parts in the right hand are the location parameter, scale parameter, degree of freedom, in sequence. $(\cdot)'$ represents a transposition of (\cdot) . The notations (y, X, β, n, d) are the same as Equation 7, while $\hat{\beta}$ is the least-squares estimate of β with a form as follows.

$$\hat{\beta} = (X'X)^{-1} X'y \quad (12)$$

Without loss of generality, substituting Equation 6 into Equation 7, the Bayesian cable tension estimation framework can be established as shown in Equation 13.

$$y = \left\{ \left(\frac{f_i}{i} \right)^2 \right\}_{n \times 1}, \quad X = \left[\frac{\pi^2 i^2}{4ml^4} \quad \frac{1}{4ml^2} \right]_{n \times 2}, \quad \beta = \left\{ \begin{matrix} EI \\ T \end{matrix} \right\}_{2 \times 1} \quad (13)$$

The posterior distribution of β contributes to a simultaneous estimation of cable tension and flexural rigidity, along with the estimation uncertainty.

2.3 Gaussian mixture model and conditional likelihood

It is rational to model the temperature effect as a way of data normalization which aims to improve the damage sensitivity while reducing the interference of EOVs (Jiang et al. 2022). Intuitively, regression may be a simple way to model the relationship between temperature and cable tension. However, there are other complex and unknown environmental factors (latent variables) in a real system of EOVs also, which can make it difficult to represent the correlation between temperature and cable tension in a regressive manner. Alternatively, modeling the joint distribution of temperature and cable tension offers a probabilistic way to consider the temperature effect and uncertainty. The conditional likelihood of cable tension estimate over temperature plays a role like data normalization of the temperature effect. In practice, the joint distribution of temperature and cable tension may be complicated due to the effect of latent variables. The Gaussian mixture model (GMM), as a flexible way to model almost arbitrary distribution, is introduced in this study to model the temperature effect in cable tension estimates in long-term bridge SHM.

A basic form of a multivariate GMM can be given as,

$$p(x) = \sum_{k=1}^K \pi_k N(x|\mu_k, \Sigma_k) \quad (14)$$

which is a linear superposition of K Gaussian components with mixing coefficients denoted as π_k , and the sum of π_k is equal to 1. $p(z_k = 1) = \pi_k$ denotes the mixing proportion of the k^{th} Gaussian component.

It has been proved the Expectation-Maximization (EM) algorithm can be used to estimate the parameters of GMM $\theta = \{\pi_k, (\mu_k, \Sigma_k)\}_{k=1}^K$ with a closed form of iteration. The major steps of using EM for parameter estimation can be summarized below (Bishop 2006).

Step 1. Initialization of the parameters $\theta = \{\pi_k, (\mu_k, \Sigma_k)\}_{k=1}^K$ and calculate the log-likelihood of data.

Step 2. **E step.** Calculate the responsibilities (posterior probabilities of component memberships) with the parameters from the previous step as follows.

$$\gamma(z_{nk}) = p(z_k = 1|x_n) = \frac{\pi_k N(x_n|\mu_k, \Sigma_k)}{\sum_{j=1}^K \pi_j N(x_n|\mu_j, \Sigma_j)} \quad (15)$$

Step 3. **M step.** Update the parameters with the calculated responsibilities as follows.

$$\mu_k^{\text{new}} = \frac{1}{N_k} \sum_{n=1}^N \gamma(z_{nk}) x_n \quad (16a)$$

$$\Sigma_k^{\text{new}} = \frac{1}{N_k} \sum_{n=1}^N \gamma(z_{nk}) (x_n - \mu_k^{\text{new}})(x_n - \mu_k^{\text{new}})^T \quad (16b)$$

$$\pi_k^{\text{new}} = \frac{N_k}{N} \quad (16c)$$

$$N_k = \sum_{n=1}^N \gamma(z_{nk}) \quad (17)$$

Equation 17 can be interpreted as the effective number of observations assigned to the k^{th} Gaussian component.

Step 4. Evaluate the log-likelihood with the updated parameters as,

$$\ln p(X|\mu, \Sigma, \pi) = \sum_{n=1}^N \ln \left\{ \sum_{k=1}^K \pi_k N(x_n|\mu_k, \Sigma_k) \right\} \quad (18)$$

and check the convergence of either the parameters or the log-likelihood. If not converged, return to Step 2.

With the excellent properties of Gaussian distribution (the marginal and conditional distributions are still Gaussians), it can be proved that the conditional distribution of the multivariate GMM is still a GMM. Here, we take T as a notation of the cable tension, and H as a notation of temperature. Then, we can get the conditional likelihood as Equation 19, which is still a GMM and leads to an analytical form of conditional likelihood.

$$p(T|H) = \frac{p(T, H)}{p(H)} = \sum_{k=1}^K \frac{\pi_k N(H|\mu_k^H, \Sigma_k^H)}{\sum_{j=1}^K \pi_j N(H|\mu_j^H, \Sigma_j^H)} N(T|\mu_k^{T|H}, \Sigma_k^{T|H}) \quad (19)$$

Table 1. OMA of three typical cables by fast Bayesian FFT.

Cable	Item	Order				
		1	2	3	4	5
C1	f_i (σ)(Hz)	1.07(0.0010)	2.11(0.0012)	3.18(0.0009)	4.24(0.0020)	5.31(0.0013)
C5	f_i (Hz)	2.07(0.0013)	4.14(0.0014)	6.26(0.0031)	8.45(0.0058)	10.63(0.0035)
C8	f_i (Hz)	1.64(0.0026)	3.32(0.0088)	4.96(0.0040)	6.65(0.0057)	8.14(0.0033)



Figure 1. A side view of the cable-stayed bridge. Figure 2. Layout and sensor map for bridge SHM.

3 LONG-TERM SHM OF A CABLE-STAYED BRIDGE

3.1 Background

The monitored bridge is a single-tower cable-stayed bridge shown in Figure 1. The major span length of the bridge is about 124 m and the height of the pylon is about 48 m. A short-term ambient vibration test was carried out in November 2020. The corresponding sensor setup and structural layout are shown in Figure 2. Ambient-vibration signals from cables at the anchor, cables at the bridge deck, bridge deck, and the pylon were collected during the short-term test. Further, the long-term SHM of two cables, the longest one denoted as C1 and the shortest one denoted as C5 in Figure 2 at the bridge deck, was conducted from December 2020 to January 2022. During the long-term SHM, the ambient vibrations were recorded remotely.

3.2 OMA and cable tension estimation

To get the dynamic characteristics of the bridge and cables, the fast Bayesian FFT was first applied for operational modal analysis of the bridge and cables. In this paper, three typical cables (C1, C5, and C8 cables as marked in Figure 2) are selected to simplify the discussion even though all the cables were measured during the short-term bridge SHM.

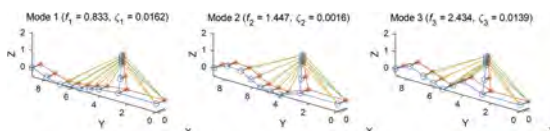


Figure 3. OMA of the whole bridge (first three mean bending modal properties).

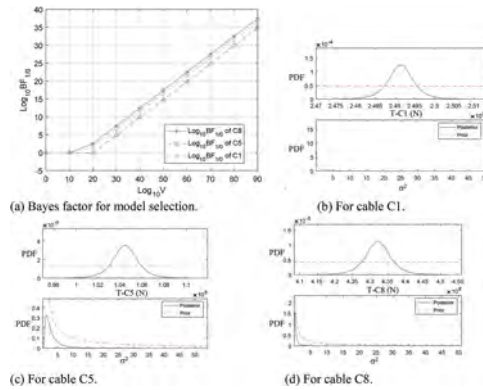


Figure 4. (a) Bayes factor along with increasing uncertainty in prior distribution of cable tension; (b)(c) (d) Prior and posterior estimates of cable tension T and error variance σ^2 .

Figure 3 showed the OMA results of the whole bridge. The first three modal frequencies are quite low as the cable-stayed bridge is a very flexible structure. Meanwhile, it should be noted that for the cables at the bridge deck end, the cable vibration is affected by the bridge vibration seriously, which calls for more attention to the OMA of the cables at the bridge deck end. Table 1 presented the OMA results of three typical cables. It shows that the identification uncertainty in the OMA results of the cables is not significant.

The proposed Bayesian cable tension estimation is applied to identify cable tensions from ambient vibrations. A model selection between Equation 6 for the simply supported beam theory and Equation 7 for the string theory was carried out by the means of Bayes factor $B_{1/0}$ which is the ratio of two model evidence with two hypotheses H_0 and H_1 . Therein, H_0 denotes the null hypothesis meaning that identified modal frequencies support Equation 6 more, i.e., the effect of the flexural rigidity on cable tension identification cannot be ignored, while H_1 denotes the alternative hypothesis meaning that the data support Equation 7 more, i.e., the effect of flexural rigidity can be ignored. The Bayes factor along with increasing uncertainty in the prior distribution is presented in Figure 4(a), where V stands for a hyper-parameter of Gaussian-Inverse-Gamma conjugate prior which controls the uncertainty in the prior of parameters (EI , T). It indicates that with less prior information about cable tension, the identified modal frequencies support the string theory more, i.e., the effect of flexural rigidity can be ignored in the subsequent procedure of the Bayesian cable tension estimation. The estimated cable tension using the Bayesian linear regression is shown in Figures 4(b-d). It is noted that the identification uncertainty in the three cables was different; i.e., the lowest identification uncertainty was observed at the longest cable at the bridge deck (C1 cable).

3.3 Long-term SHM with GMM and conditional likelihood

Long-term ambient vibration monitoring was also conducted for the longest and the shortest cables at the bridge deck, i.e., C1 and C5 cables. The long-term sequence of Bayesian cable tension estimates is shown in Figure 5. Observing the sequence of cable tension estimates, it is noted that the identification uncertainty and the effect of EOVs in two cables occupied different extents. Further, by using the predictive probabilistic model introduced in the study (Zhang & Au 2016), the predictive distribution for an unknown future time point is given in Figure 6 with a depiction of ensemble variability. From Figure 6, it is clear that the effect of EOVs is dominant in the longest cable at the bridge deck, while for the shortest cable, the identification uncertainty contributes more to the ensemble variability. This observation may offer some guidance for the research of seasonal effects in long-term SHM of cable tensions.

The effect of IU and EOVs in the long-term monitoring of cable tensions previously discussed may decrease the sensitivity to damage occurrence. As a way to consider the temperature effect

(one of the major EOVs), a multivariate GMM is used to model the joint distribution of the temperature and cable tensions monitored for almost one year. As shown in Figure 7, the fitted GMM and trace of conditional means indicated complex but different correlations between cable tension and temperature in cables, with the interference of other latent environmental variables.

In this study, the conditional likelihood of cable tension over temperature is introduced as a damage-sensitive feature (DSF) which eliminated the temperature effect in the cable tension. To get a comparison with the damage state, a finite element model (FEM) is established using ANSYS and updated by the particle swarm optimization (PSO) algorithm, as shown in Figure 8. The relative changes of cable tension caused by the damage in the effective area of target cables are checked using the updated FEM, of which results are summarized in Table 2. Then, based on the fitted GMM, the conditional negative log-likelihood function (NLLF) is investigated for anomaly detection in long-term bridge SHM while removing the temperature effect in cable tension. As shown in Figure 9, the result indicates the conditional NLLF based on the fitted multivariate GMM performed well as a DSF which removed the temperature effect and is sensitive to the damage extent of 10% and even 5% of cable section area.

Table 2. Damage effect obtained by simulation in FEM.

	5% damage	10% damage
Relative changes in T-C1 (%)	3.1	6.33
Relative changes in T-C5 (%)	2.47	5.08

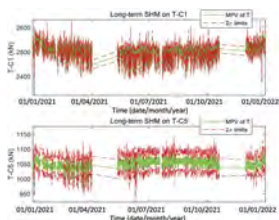


Figure 5. Bayesian cable tension estimates (upper plot for C1; lower plot for C5).

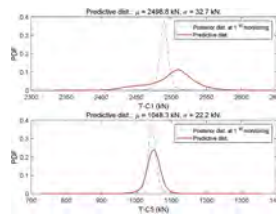


Figure 6. Ensemble variability involving the identification uncertainty and EOVs (upper plot for C1, lower plot for C5).

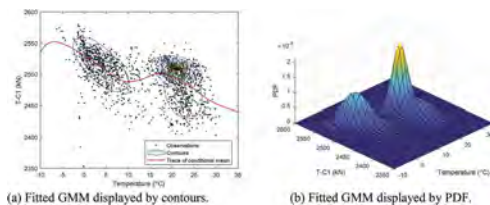


Figure 7. Fitted GMM on the one-year observations of cable tension T-C1 and temperature.

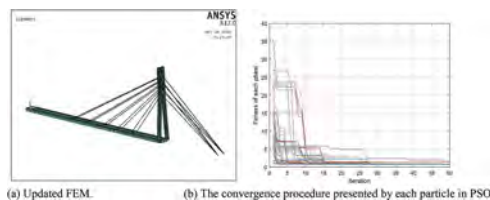


Figure 8. Updated FEM based on PSO.

4 CONCLUSIONS

This study investigates the ambient-vibration-based OMA and cable tension estimation in a cable-stayed bridge with Bayesian approaches. The identification uncertainty and effect of EOVs in cable tensions are discussed with a long-term SHM campaign in two typical cables C1 and C5. Finally, a GMM and conditional NLLF-based approach is proposed to eliminate the temperature effect in cable tension and operate as a DSF in anomaly detection in long-term bridge SHM.

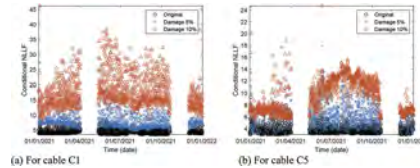


Figure 9. Conditional NLLF of cable tension over the temperature in long-term SHM.

The feasibility of fast Bayesian FFT for OMA and Bayesian cable tension estimation using environmental vibrations was verified to reveal the identification uncertainty. It should be noted that the cable vibration at the bridge deck end is seriously affected by the bridge vibration under ambient excitations, which calls for more attention compared to those cables at the bridge anchor end in the identification process.

Observations from identification uncertainty and the effect of EOVs in cable tensions demonstrated that the effect of EOVs is more prominent in the longest cable than the shortest one, which indicated the longer cables in the cable-stayed bridge may be more sensitive to the EOVs and it may be worthwhile to conduct data normalization in these cables.

The correlation between cable tension and temperature is proved to be complicated and different in two cables C1 and C5, with the interference of other latent environmental variables. The GMM and conditional NLLF-based approach is therefore used to remove the temperature effect like a data normalization process. Further, the use of conditional NLLF as a DSF is proved to be an effective monitoring index for anomaly detection in long-term SHM of cables.

ACKNOWLEDGMENTS

This study is supported by Research Committee on Technological Development for Infrastructure and the Japanese Society for the Promotion of Science (JSPS) Grant-in-Aid for Scientific Research (B) under project No.22H01576. Those technical and financial supports are gratefully acknowledged.

REFERENCES

- Au, S.K., Zhang, F.L. & Ni, Y.C. 2013. Bayesian operational modal analysis: theory, computation, practice. *Computers and Structures* 126: 3–14.
- Au, S.K. 2017. *Operational Modal Analysis: Modeling, Bayesian Inference, Uncertainty Laws*. Singapore: Springer.
- Bishop, M.C. 2006. *Pattern Recognition and Machine Learning*. New York: Springer.
- Jiang, W-J., Kim, C.W., Goi, Y. & Zhang, F. 2022. Data normalization and anomaly detection in a steel plate-girder bridge using LSTM. *ASCE-ASME J of Risk and Reliability in Engineering Systems, Part A: Civil Engineering* 8(1): 04021082–1–18.
- Shimada, T. 1994. Estimating method of cable tension from natural frequency of high mode. *Proc., JSCE*. 501(1–29), 163–171.
- Yamagiwa, I., Utsuno, H., Sugii, K. & Honda, Y. 1999. Simultaneous identification of tension and flexural rigidity of cables. *Kobe Steel Engineering Reports* 49(2).
- Zhang, F.L. & Au, S.K. 2016. Probabilistic model for modal properties based on operational modal analysis. *ASCE-ASME J of Risk and Uncertainty in Engineering Systems, Part A: Civil Engineering* 2 (3): B4015005–B4015005.
- Zui, H., Shinke, T. & Namita, Y. 1996. Practical formulas for estimation of cable tension by vibration method. *J. Struct. Eng.* 122(6) 651–656.

Uncertainty quantification of modal properties using half year monitoring data of a plate girder bridge

Y. Goi & C.-W. Kim

Department of Civil & Earth Resources Engineering, Kyoto University, Kyoto, Japan

ABSTRACT: In short to medium span bridges, traffic induced vibration enables vibration monitoring of bridges without interrupting the traffic. Changes in modal properties possibly indicates stiffness loss caused by damages on the bridges. In actual bridges, however, the noisy condition caused by the traffic loadings interrupts modal estimation. Also, the seasonal fluctuation of temperature alters modal properties of bridges. To deal with the uncertainty involved in noisy condition, authors previously proposed Bayesian inference method to quantify uncertainty of modal properties. In the proposed method, the uncertainty involved in modal properties are quantified as posterior distribution using unsupervised machine learning. This study investigates the efficacy of the proposed method under the temperature fluctuation. A half-year monitoring data on a plate girder bridge is adopted for the investigation. On the plate girder bridge, 10 uniaxial accelerometers equipped on the lower flange continuously measure acceleration. Firstly, to clarify that the proposed method detects changes in modal properties caused by temperature change, the proposed method is applied to the datasets separately measured from different seasons. Secondly, to verify the feasibility of the proposed uncertainty quantification for the varying temperature, the samples monitored from different seasons are mixed with each other. The posterior distribution of the modal properties are compared to their temperature fluctuation.

1 INTRODUCTION

Vibration based structural health monitoring provides a research field for nondestructive evaluation based on physical measurements and computer analyses to complement existing visual inspection methods. Changes in modal properties possibly indicates stiffness loss caused by damages on the structures. Especially for short to medium span bridges, the traffic excites the bridges continuously, and thus vibration monitoring is available without interrupting the traffic. In actual bridges, however, the noisy condition caused by the traffic loadings is one of the difficulties involved in the operational modal identification. That is because the noisy condition induces spurious estimators of modal properties. To cope with the problem, the authors have proposed an efficient time-domain modal identification method for bridges by uncertainty quantification using unsupervised machine learning (Goi and Kim 2021). This study applies the proposed uncertainty quantification to half year monitoring data of a plate girder bridge (Goi and Kim, 2018) and verifies the proposed method.

Aiming at practical use, the authors have intended to avoid complicate model as possible. So far, the proposed method is based on steady dynamical model and no temperature fluctuation is taken in account. This study investigates scope of the previously proposed model in advance of developing further expansion of the model for machine learning. In the proposed method, the vector autoregressive (VAR) model is adopted as the stochastic model representing the bridge vibration. Bayesian inference method is applied to obtain the posterior distribution of the regressive coefficients of the VAR model. Following the well-known modal

analysis theory, the regressive coefficients are transformed to the estimators of modal properties. The uncertainty of the modal properties are quantified through the transformation.

Although the proposed method enables to evaluate uncertainty involved in steady VAR process, it have been not validated for non-steady process with varying temperature. Therefore, this study investigates the efficacy of the proposed method under the temperature fluctuation. Firstly, the proposed method is applied to the datasets separately measured from different seasons, namely on September and on February, and the posterior distributions of the modal frequencies are compared with each other. Secondly, the samples monitored from the two seasons are mixed with each other. The posterior distribution from mixed sample are observed to verify the feasibility of the proposed uncertainty quantification for the varying temperature.

2 METHODOLOGY

2.1 Bayesian inference

Here, the previously proposed Bayesian inference method is described. For further discussion, see also (Goi and Kim 2021). We assume that a synchronized discrete time series of the acceleration measured at m measurement locations on a bridge, and assume that the time series includes n data points. A zero-mean time series is produced by subtracting the mean value from the measured acceleration. Letting $\mathbf{y}_k \in \mathbb{R}^{m \times 1}$ ($k = 1 \dots n$) denote a column vector at the k -th time step of the time series with components corresponding to the measurement locations, and letting $\boldsymbol{\phi}_k = [\mathbf{y}_{k-1}; \dots; \mathbf{y}_{k-p}]$, then the following VAR model with sufficient model order p is known to approximate the time series obtained from a linear structural system excited by white noise (He and De Roeck 1997).

$$\mathbf{y}_k = \mathbf{W}\boldsymbol{\phi}_k + \mathbf{e}_k \quad (1)$$

Here, $\mathbf{W} \in \mathbb{R}^{m \times m}$ denotes the AR coefficient matrix and $\mathbf{e}_k \in \mathbb{R}^{m \times 1}$ denotes a zero-mean Gaussian white noise vector. Letting $\boldsymbol{\Sigma}$ denote the covariance matrix of \mathbf{e}_k , \mathbf{y}_k follows the following Gaussian distribution.

$$p(\mathbf{y}_k | \boldsymbol{\phi}_k, \mathbf{W}, \boldsymbol{\Sigma}) = \mathcal{N}(\mathbf{y}_k | \mathbf{W}\boldsymbol{\phi}_k, \boldsymbol{\Sigma}) \quad (2)$$

where $\mathcal{N}(\cdot | \mathbf{W}\boldsymbol{\phi}_k, \boldsymbol{\Sigma})$ denotes the PDF following the multivariate Gaussian distribution with expectation $\mathbf{W}\boldsymbol{\phi}_k$ and covariance matrix $\boldsymbol{\Sigma}$. This study presumes that the time series are measured l times. Let \mathbf{y}_k^i ($i = 1 \dots l$) denote the measured acceleration at k -th time step in i -th time series and n_i denote its data length. Let $\mathbf{Y}_i = [\mathbf{y}_{p+1}^i, \dots, \mathbf{y}_{n_i}^i]$ and $\boldsymbol{\Phi}_i = [\boldsymbol{\phi}_{p+1}^i, \dots, \boldsymbol{\phi}_{n_i}^i]$. Because the noise term \mathbf{e}_k is white noise, the following PDF is obtained.

$$p(\mathbf{Y}_i | \boldsymbol{\Phi}_i, \mathbf{W}, \boldsymbol{\Sigma}) = \prod_{k=p+1}^{n_i} \mathcal{N}(\mathbf{y}_k^i | \mathbf{W}\boldsymbol{\phi}_k^i, \boldsymbol{\Sigma}) \quad (3)$$

The PDF in Equation 3 is the likelihood function for parameters \mathbf{W} and $\boldsymbol{\Sigma}$. The Bayesian theorem provides the following relationship.

$$p(\mathbf{W}, \boldsymbol{\Sigma} | \mathbf{Y}_1, \dots, \mathbf{Y}_l) \propto \prod_{i=1}^l p(\mathbf{Y}_i | \boldsymbol{\Phi}_i, \mathbf{W}, \boldsymbol{\Sigma}) p(\mathbf{W}, \boldsymbol{\Sigma}) \quad (4)$$

For simplicity, this study adopts uniform prior distribution, i.e. $p(\mathbf{W}, \boldsymbol{\Sigma}) \propto \text{Const.}$, to represent non-informative prior. Accordingly, Equation 4 produces following distribution.

$$p(\mathbf{W}, \boldsymbol{\Sigma} | \mathbf{Y}_1, \dots, \mathbf{Y}_l) = \mathcal{M}\mathcal{N}(\mathbf{W} | \mathbf{M}, \boldsymbol{\Sigma}, \mathbf{L}^{-1}) \mathcal{I}\mathcal{W}(\boldsymbol{\Sigma} | \boldsymbol{\Psi}, \nu) \quad (5)$$

where

$$\mathbf{L} = \sum_{i=1}^l \Phi_i \Phi_i^T \quad (6)$$

$$\mathbf{M} = (\sum_{i=1}^l \mathbf{Y}_i \Phi_i^T) \mathbf{L}^{-1} \quad (7)$$

$$\nu = -(mp + m + 1) + \sum_{i=1}^l (n_i - p) \quad (8)$$

$$\Psi = \sum_{i=1}^l \mathbf{Y}_i \mathbf{Y}_i^T - \mathbf{M} \mathbf{L} \mathbf{M}^T \quad (9)$$

In that equation, $\mathcal{MN}(\mathbf{W}|\mathbf{M}, \Sigma, \mathbf{L}^{-1})$ and $\mathcal{IW}(\Sigma|\Psi, \nu)$ respectively stand for the following matrix-normal and inverse-Wishart distributions (Dzunic et. al. 2017) as

$$\mathcal{MN}(\mathbf{W}|\mathbf{M}, \Sigma, \mathbf{L}^{-1}) = (2\pi)^{-\frac{mp \times m}{2}} |\mathbf{L}^{-1}|^{-\frac{m}{2}} |\Sigma|^{-\frac{mp}{2}} \times \exp\left\{-\frac{1}{2} \text{tr}\left[\mathbf{L}(\mathbf{W} - \mathbf{M})^T \Sigma^{-1} (\mathbf{W} - \mathbf{M})\right]\right\} \quad (10)$$

$$\mathcal{IW}(\Sigma|\Psi, \nu) = 2^{-\nu m/2} \Gamma_m\left(\frac{\nu}{2}\right) |\Psi|^{\frac{\nu}{2}} |\Sigma|^{-\frac{(\nu+m+1)}{2}} \times \exp\left\{-\frac{1}{2} \text{tr}[\Psi \Sigma^{-1}]\right\} \quad (11)$$

where $\Gamma_m(\cdot)$ is the multivariate gamma function.

To find optimal model order p , this study adopts following Bayesian information criterion (BIC) (Schwarz 1978).

$$BIC = N \left(m \ln 2\pi + \ln |\hat{\Sigma}| + m \right) + M \ln N \quad (12)$$

where $\hat{\Sigma}$ represents most likelihood estimator of Σ , M denotes the number of parameter, and N denotes total data length.

2.2 Uncertainty quantification

The uncertainty of the each identified mode is derived from Equation 5 as follows. First, this study assumes Σ is fixed to the most likelihood estimator for simplicity, instead of the inverse-Wishart distribution. Therefore, the posterior distribution of \mathbf{W} is given as follows instead of Equation 10.

$$p(\mathbf{W}|\mathbf{Y}_1, \dots, \mathbf{Y}_l) = \mathcal{MN}(\mathbf{W}|\mathbf{M}, \hat{\Sigma}, \mathbf{L}^{-1}) \quad (13)$$

It is known that the VAR model in Equation 1 is reproduced to the following state space model (Heylen et. al. 1997).

$$\phi_{k+1} = \mathbf{A} \phi_k + \begin{bmatrix} \mathbf{I}_m \\ \mathbf{O} \end{bmatrix} e_k \quad (14)$$

$$\mathbf{y}_k = [\mathbf{I}_m \quad \mathbf{O}] \phi_{k+1} \quad (15)$$

where \mathbf{I}_m denotes the eigenmatrix of size m , \mathbf{O} denotes the zero matrix with the appropriate size, and $\mathbf{A} \in \mathbb{R}^{mp \times mp}$ represents the following matrix.

$$\mathbf{A} = \begin{bmatrix} \mathbf{W} \\ \mathbf{I}_{m(p-1)} \quad \mathbf{O} \end{bmatrix} \quad (16)$$

The eigenvalue decomposition of the matrix \mathbf{A} is given as follows.

$$\mathbf{A} = \mathbf{P} \Lambda \mathbf{P}^{-1} \quad (17)$$

where $\mathbf{\Lambda}$ denotes diagonal matrix composed of the eigenvalues of matrix \mathbf{A} , and \mathbf{P} denotes a matrix composed of the corresponding eigenvectors. It is well known that the eigenvalues represent the poles of the transfer function of the dynamic model given in Equations 14–15. That is, letting ω_i and ζ_i respectively represent the i -th eigen-angular frequency and damping ratio, and λ_i denote the i -th eigenvalue of the matrix \mathbf{A} , the following relation is given.

$$\lambda_i = \exp \left[\left(-\zeta_i \omega_i + j \sqrt{1 - \zeta_i^2} \omega_i \right) \Delta t \right] \quad (18)$$

where Δt represents the sampling interval and j represents the imaginary unit. Accordingly, the i -th eigen frequency f_i is given as

$$f_i = \frac{1}{2\pi\Delta t} |\ln \lambda_i| \quad (19)$$

This study adopts standard deviation (std) of the eigen frequencies to quantify the uncertainty of modal estimation. The std is defined as

$$\text{std}(f_i) = \sqrt{E[(f_i - E[f_i])^2]} = \frac{1}{2\pi\Delta t} \sqrt{E[(|\ln \lambda_i| - E[|\ln \lambda_i|])^2]} \quad (20)$$

where $E[\cdot]$ denotes the expectation of a random variable. Because the matrix \mathbf{W} in Equation 13 is composed of random variables, the random distribution of \mathbf{W} is transformed into the random distribution of λ_i .

For efficacy, this study produces approximated closed form solution of $\text{std}(f_i)$ as follows. First, according to Equations 13 and 16, the expectation of matrix \mathbf{A} is given as

$$\bar{\mathbf{A}} = \begin{bmatrix} \mathbf{M} \\ \mathbf{I}_{m(p-1)} & \mathbf{O} \end{bmatrix}. \quad (21)$$

Let the eigenvalue decomposition of $\bar{\mathbf{A}}$ represent with the following equation.

$$\bar{\mathbf{A}} = \bar{\mathbf{P}} \bar{\mathbf{\Lambda}} \bar{\mathbf{P}}^{-1} \quad (22)$$

And let the deviation of matrices \mathbf{A} and $\bar{\mathbf{A}}$ respectively represent as $\tilde{\mathbf{A}} = \mathbf{A} - \bar{\mathbf{A}}$ and $\tilde{\mathbf{\Lambda}} = \mathbf{\Lambda} - \bar{\mathbf{\Lambda}}$. Ignoring the squared deviations, the eigenvalues are approximated as follows.

$$\text{diag}(\tilde{\mathbf{\Lambda}}) = \text{diag}(\bar{\mathbf{P}}^{-1} \tilde{\mathbf{A}} \bar{\mathbf{P}}) \quad (23)$$

where $\text{diag}(\tilde{\mathbf{\Lambda}})$ represents a vector composed from the diagonal elements of matrix $\tilde{\mathbf{\Lambda}}$. Equations 16 and 21 ensures that matrix $\tilde{\mathbf{A}}$ is given as

$$\tilde{\mathbf{A}} = \begin{bmatrix} \mathbf{W} - \mathbf{M} \\ \mathbf{O} \end{bmatrix}. \quad (24)$$

Letting $\tilde{\mathbf{W}} = \mathbf{W} - \mathbf{M}$ and $\mathbf{V} = \left(\left\{ \bar{\mathbf{P}}^{-1} \right\}_{[:,1:m]} \right)^T$, where $\{\cdot\}_{[:,1:m]}$ denotes a submatrix consisting of the first m columns, Equation 23 is transformed as

$$\text{diag}(\tilde{\mathbf{\Lambda}}) = \text{diag}(\mathbf{V}^T \tilde{\mathbf{W}} \bar{\mathbf{P}}). \quad (25)$$

Therefore, the i -th diagonal member $\tilde{\lambda}_i$ is given as $\tilde{\lambda}_i = \mathbf{v}_i^T \tilde{\mathbf{W}} \mathbf{p}_i$ where \mathbf{v}_i and \mathbf{p}_i are respectively represent the i -th column of matrices \mathbf{V} and \mathbf{P} . It is known that mode shapes are estimated as real value of \mathbf{v}_i . Using Taylor expansion, $\ln \lambda_i$ in Equation 20 is approximated as

$$\ln \lambda_i \cong \ln \bar{\lambda}_i + \frac{1}{\bar{\lambda}_i} \tilde{\lambda}_i. \quad (26)$$

Therefore, the std is approximated as

$$\begin{aligned} \text{std}(f_i) &= \frac{1}{2\pi\Delta t} \sqrt{\text{E} \left[\left(|\ln \lambda_i| - \text{E}[|\ln \lambda_i|] \right)^2 \right]} \cong \frac{1}{2\pi\Delta t} \sqrt{\text{E} \left[\left(|\ln \lambda_i| - |\ln \bar{\lambda}_i| \right)^2 \right]} \\ &\leq \frac{1}{2\pi\Delta t |\bar{\lambda}_i|} \sqrt{\text{E} \left[\left(|\tilde{\lambda}_i| \right)^2 \right]} = \frac{1}{2\pi\Delta t |\bar{\lambda}_i|} \sqrt{\mathbf{p}_i^T \mathbf{L}^{-1} \mathbf{p}_i^* \mathbf{v}_i^T \hat{\Sigma} \mathbf{v}_i^*} \end{aligned} \quad (27)$$

3 FIELD MEASUREMENT

The field experiment was conducted on a single span composite steel plate girder bridge shown in Figure 1. The span length is around 40m. On the bridge deck, accelerometers and strain gauges were installed as shown in Figure 1b. Each of the accelerometers and the strain gauges monitors dynamic response of the bridge at sampling rate 200 Hz. Each of the accelerations are measured in vertical direction, the strain gauges settled on the middle of the span measured longitudinal strain on the bottom of the lower flange. The traffic-induced vibration is monitored from September 2016 to March 2017. Further detail of the field experiment is discussed in (Goi and Kim 2018).

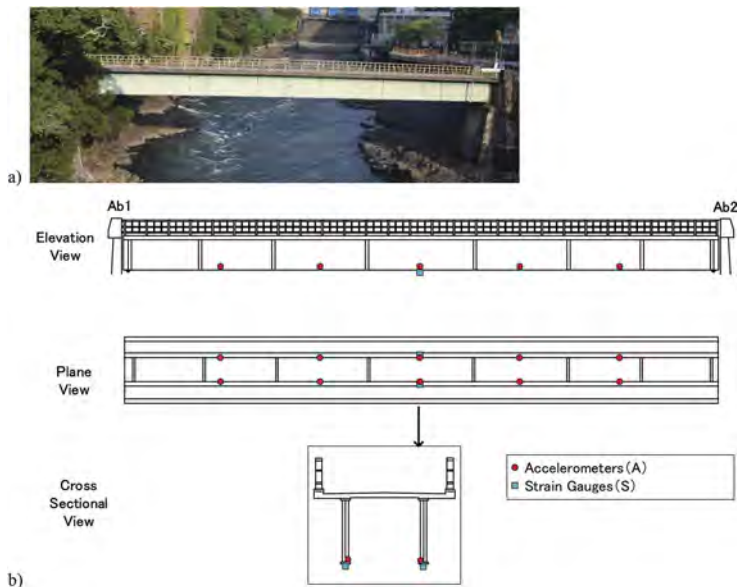


Figure 1. The target bridge: a) photograph; b) sensor deployment.

To crop the time series for Bayesian inference, this study utilizes strain gauges equipped on the lower flange at the middle of the span. For instance, Figure 2 shows 5 minutes time series measured by the strain gauges and the accelerometer. Therein, the time series of the strain are smoothed with low-pass filter of 1 Hz and averaged together for clarity. The peaks appear in the time series of the strain, which is marked as circles in Figure 2a as the vehicles pass on the

bridge. Those peaks and their widths are detected by means of peak picking analysis. Accordingly, the moment at the entrance and exit of the vehicle can be roughly estimated from the peak width. This study experimentally obtains time series data by following rules:

- The vehicle-induced vibrations between the vehicle entrance and 5 seconds after the vehicle exit are extracted from long term monitoring data.
- If the extracted areas coincide with each other, those time series are discarded.
- The extracted time series are normalized by dividing root mean square of the all data contained in the time series.

The vertical lines depicted in Figure 3 represent extraction window in the time series for instance. Figure 2b describes that the vehicle-induced vibrations are correctively extracted from the raw time series data.

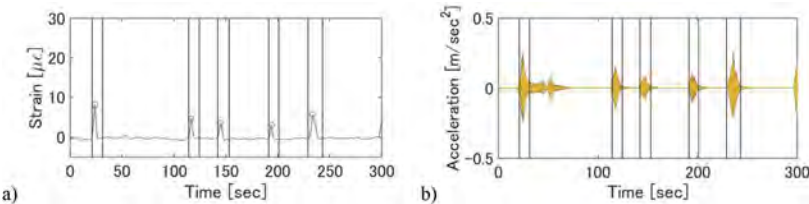


Figure 2. Time series before the pre-processing: a) Averaged strain; b) Acceleration.

4 RESULTS

This study provide datasets which derive from the summer and winter. This study adopts time series measured on 2nd-3rd September as the datasets from summer; time series measured on 1st-2nd February as the datasets from winter. The datasets contain 24-hour time series in each day. For fair comparison, the time duration for Bayesian inference is fixed as two days. As mentioned in the introduction, the proposed method is applied to the datasets separately measured from the different seasons. Also, the samples from the two seasons are mixed with each other. Accordingly, this study examine the three cases provided in Table 1. Case 1 and 2 are datasets respectively measured in the summer and winter, and Case 3 is the mixed dataset.

Table 1. Test cases for the hypothesis testing.

Case	Duration	Description
Case1	2nd Sep. and 3rd Sep.	Measured in summer
Case2	1st Feb. and 2nd Feb.	Measured in winter
Case3	2nd Sep. and 1st Feb.	Mixed dataset

Table 2. Expectation and std of the estimated modal frequencies (Hz).

Mode	Expectation (Hz)			Standard Deviation (Hz)			Mode shape
	Case1	Case2	Case3	Case1	Case2	Case3	
Mode1	3.1417	3.1160	3.0977	0.0018	0.0020	0.0020	1st Bending
Mode2	3.7007	3.7383	3.7237	0.0013	0.0011	0.0011	1st Torsional
Mode3	4.9857	4.9414	4.9574	0.0011	0.0010	0.0011	1st Torsional
Mode4	8.4821	8.4318	8.4435	0.0015	0.0014	0.0018	Not clear
Mode5	9.3394	9.4725	9.3848	0.0013	0.0013	0.0023	2nd Bending
Mode6	11.0347	11.1178	11.0756	0.0012	0.0010	0.0012	2nd Torsional
Mode7	15.4165	15.5730	15.4735	0.0016	0.0014	0.0021	Not clear
Mode8	17.8136	17.9514	17.8581	0.0015	0.0015	0.0015	3rd Torsional

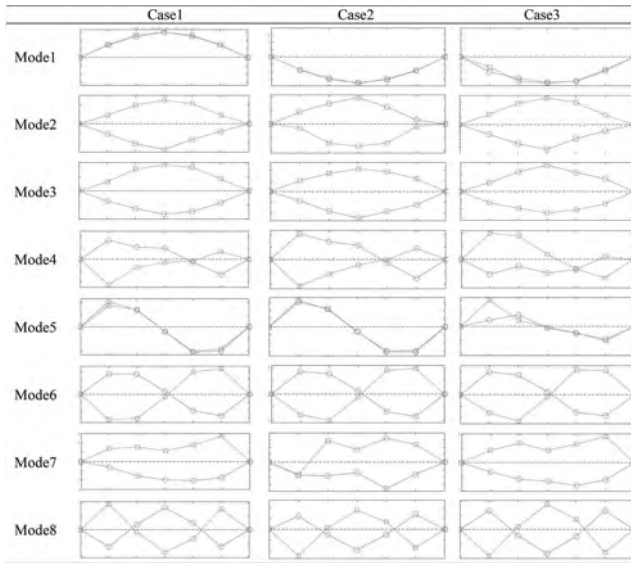


Figure 3. Estimated mode shapes.q.

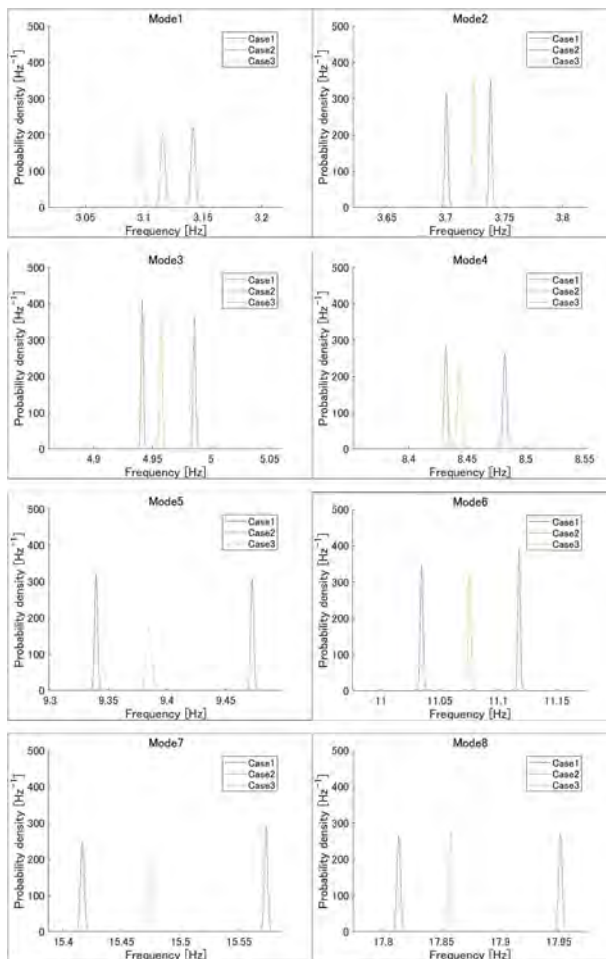


Figure 4. Probability density functions of posterior distribution.

The proposed method is applied for each of the dataset and the posterior distribution of the modal frequencies is produced. Table 2 summarize the expectation and std of the modal frequencies. Figure 3 shows estimated mode shapes corresponding to each of the estimated frequencies. These modal properties are automatically extracted by sorting the std of modal frequencies in ascending order (Goi and Kim 2021). The results in Table 2 are also summarized in probability density functions shown in Figure 4.

It is observed that the posterior distribution of the modal frequencies slightly altered between the two season. Except Model1, the posterior distribution obtained from Case3, the mixed dataset, locate between the Case1 and Case2. That result indicate that the most probable value of the modal frequencies except Model1 estimated from the mixed dataset is located between the two seasons. However, it seems the posterior distribution of Case3 underestimate the uncertainty caused by temperature changes, i.e. its deviation are much less than frequency changes between Case1 and Case2. That is possibly because the VAR process merely assumes steady dynamic system and changes in modal properties caused by temperature is not taken into account. Further investigation

5 CONCLUSION

This study validate uncertainty quantification using Bayesian inference steady vector autoregressive (VAR) model. Posterior distribution of the modal frequencies is approximately formulated from the posterior distribution of regressive coefficients. A half-year monitoring data on a plate girder bridge is adopted for the investigation. The proposed method is applied to the datasets separately measured from summer and winter. Also, the samples monitored from different seasons are mixed with each other for comparison.

The quantified uncertainty enables prompt modal identification from long term monitoring data. Most of the expectations estimated from mixed dataset locate between the ones estimated from the two seasons. However, the posterior distribution tends to underestimate uncertainty caused by seasonal fluctuation. Their deviation were much less than the changes in frequency between the two seasons. That is possibly because the VAR model does not take the seasonal fluctuation into account. The results indicate room for improvement in the proposed method. Aiming at practical health monitoring, the proposed method is to be expanded to multi-class unsupervised machine learning or hierarchical Bayesian models.

ACKNOWLEDGMENTS

This study was partly sponsored by a Japanese Society for Promotion of Science (JSPS) Grant-in-Aid for Scientific Research (B) under project No.22H01576 and for Early-Career Scientists under Project No. 19K15072. That financial support is grate-fully acknowledged.

REFERENCES

- Dzunic, Z., Chen, J.G., Mobahi, H., Büyüköztürk, O., and Fisher, J.W., A Bayesian state-space approach for damage detection and classification, *Mech. Syst. Signal Process.*, 96, 239–259, 2017.
- Goi, Y. and Kim, C.W., Investigation of Bayesian damage detection method for long-term bridge health monitoring. In *Proc. of 6th Int. Symp. on Life-Cycle Civil Eng.* Ghent, Belgium, 2018.
- Goi, Y. and Kim, C.W., Time-domain modal identification of bridges based on uncertainty quantification, In *Proc. of 10th International Conference on Bridge Maintenance, Safety and Management*, Online, 2021.
- He, X. and De Roeck, G., Reference-based stochastic subspace identification for output-only modal analysis. *Mech. Syst. Signal Process.* 13(6): 855–878, 1999.
- Heylen, W., Lammens, S. and Sas, P., *Modal Analysis Theory and Testing*. Leuven: KU Leuven.
- Schwarz, G., Estimating the dimension of a model. *Ann. Stat.* 6(2): 461–464, 1978.

Study on estimation of reaction force based on vibration measurement of girders

I. Kim*, S. Watanabe, Y. Goi, Y. Kitane & K. Sugiura

Kyoto University, Department of Civil & Earth Resources Engineering, Kyoto, Japan

N. Okubo

Takada Kiko Co., Ltd., Engineering Division, Osaka, Japan

ABSTRACT: In this research, a method for estimating reaction forces using the vibration characteristics of steel plates is examined. In general, it is known that the natural frequencies of steel plates decrease as compressive forces on them increase. Applying compressive forces to the steel plates experimentally, the vibration characteristics of the steel plates are obtained, and the changes in natural frequencies of the steel plates as the load increases are understood. The change in natural frequencies when compressive forces act on steel plates is theoretically and analytically determined, and the reaction forces acting on the steel plates are inversely estimated by comparing the change of natural frequencies determined theoretically and analytically with those determined experimentally.

1 INTRODUCTION

It is important to understand the dead load distribution of each bearing to ensure the safety of the bridge design in bridge construction and maintenance. However, it is currently not possible to determine the dead load distribution. After bridges put into service, localized corrosion which is likely to occur in the bearings due to the fact that bearings tend to be installed in narrow spaces and other factors such as age-related deterioration, natural disasters such as earthquakes and heavy rainfall, and movement of the superstructure and substructure due to active loads such as vehicle traffic and wind loads may cause uneven dead load distribution. In general, a slight non-uniformity of dead load on bridges does not immediately cause functional failure, such as crushing of the bearings due to exceeding the design load. If the dead load distribution can be determined, it is desirable to equalize the dead load distribution by reinforcing the structure when unexpected non-uniformities occur. Currently, inspection methods for bearings rely on subjective judgment, such as close-up inspection. A rubber bearing with a built-in sensor that acts as a load cell to measure the load has been developed, but this method can only be applied to newly constructed bridges or when the bearing is replaced. Therefore, it is an urgent issue to develop a nondestructive inspection method to measure the dead load contribution.

This study aims to develop a methodology for estimating the reaction forces acting on structural members using the vibration characteristics of steel. Researches show that the vibration characteristics are used for estimating column force acting on spherical tank, and cable tension. As a fundamental study, steel plate specimens are prepared and subjected to a compressive force to determine those vibration characteristics. The vibration characteristics obtained by experiments are compared with those obtained by analysis and theory, and the compressive force acting on the steel plate is estimated from the vibration characteristics.

*Corresponding author

2 NATURAL VIBRATION OF A FLAT PLATE

2.1 Theory of bending vibration of a plate

The H-steel specimen, which is loaded from the top and bottom, is assumed to be a double-end fixed beam subjected to compressive forces. The vibration equation for deflection v of a beam with compressive load can be expressed as follows,

$$\rho A \frac{\partial^2 v}{\partial x^2} + EI \frac{\partial^4 v}{\partial x^4} + P \frac{\partial^2 v}{\partial x^2} = 0 \quad (1)$$

where ρ is the density of the plate, E is Young's modulus, I is the moment of inertia, A is the area of the cross-section, x is the coordinates of the bridge axial direction, and P is the compressive load.

Assume the special solution is $v = X(x)e^{int}$, where n is the angular frequency, Equation (1) becomes an ordinary differential equation.

$$EI \frac{d^4 X}{dx^4} + P \frac{d^2 X}{dx^2} - \rho A n^2 X = 0 \quad (2)$$

Put $X(x) = X_0 e^{\lambda x}$ as a solution for the equation, then let λ as shown below.

$$\lambda = \begin{cases} \pm i\lambda_1 \\ \pm \lambda_2 \end{cases}, \left(\lambda_1 = \sqrt{\frac{\sqrt{P^2 + 4\rho A E I n^2} + P}{2EI}}, \lambda_2 = \sqrt{\frac{\sqrt{P^2 + 4\rho A E I n^2} - P}{2EI}} \right) \quad (3)$$

Therefore, the solution of Equation (2) is

$$X(x) = A \sin \lambda_1 x + B \cos \lambda_1 x + C \sinh \lambda_2 x + D \cosh \lambda_2 x \quad (4)$$

Since the displacement and deflection angle at the fixed end is 0,

$$\begin{cases} X(0) = 0, & \left. \frac{dX}{dx} \right|_{x=0} = 0 \\ X(l) = 0, & \left. \frac{dX}{dx} \right|_{x=l} = 0 \end{cases} \quad (5)$$

where l is the bridge span.

Substituting the boundary condition (5) into Equation (4), the following equation is obtained.

$$2\lambda_1 \lambda_2 + (\lambda_2^2 - \lambda_1^2) \sin \lambda_1 l \sinh \lambda_2 l - 2\lambda_1 \lambda_2 \cos \lambda_1 l \cosh \lambda_2 l = 0 \quad (6)$$

Then Equation (6) is

$$2\sqrt{\frac{\rho A}{EI}} n (1 - \cos \lambda_1 l \cosh \lambda_2 l) - \frac{P}{EI} \sin \lambda_1 l \sinh \lambda_2 l = 0 \quad (7)$$

When $P = 0$, put $\lambda = \lambda_0$, $n = n_0$, then Equation (7) is as follows.

$$1 - \cos \lambda_0 l \cosh \lambda_0 l = 0 \quad (8)$$

By solving Equation (8), λ_0 , n_0 is obtained as follows.

$$\lambda_0 = \sqrt[4]{\frac{\rho A n_0^2}{EI}}, \quad n_0 = \frac{1}{l^2} \sqrt{\frac{EI}{\rho A}} (\lambda_0 l)^2 \quad (9)$$

Define α as follows where P_{cr} is the buckling load of the fixed beam at the both end.

$$\alpha \equiv \frac{1}{2} \frac{1}{\lambda_0^2} \frac{P}{EI} = 2 \left(\frac{\pi}{\lambda_0 l} \right)^2 \frac{P}{P_{cr}} \left(\because P_{cr} = \frac{4\pi^2 EI}{l^2} \right) \quad (10)$$

Then Equation (7) can be rewritten as follows.

$$\begin{aligned} \frac{n}{n_0}(1 - \cos\lambda_1 l \cosh\lambda_2 l) - a \sin\lambda_1 l \sinh\lambda_2 l &= 0 \\ \rightarrow n &= \frac{a \sin\lambda_1 l \sinh\lambda_2 l}{1 - \cos\lambda_1 l \cosh\lambda_2 l} n_0 \end{aligned} \quad (11)$$

where λ_1, λ_2 are as follows.

$$\lambda_1 = \lambda_0 \sqrt{\sqrt{\frac{n^2}{n_0^2} + \alpha^2} + \alpha}, \quad \lambda_2 = \lambda_0 \sqrt{\sqrt{\frac{n^2}{n_0^2} + \alpha^2} - \alpha} \quad (12)$$

By solving Equation (11) using Equation (12) and the dimensions of the H-steel specimen of Figure 4, the following graph can be obtained.

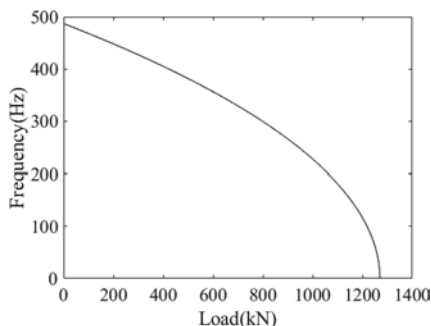


Figure 1. Theoretical load-frequency relation.

2.2 Analytical approach to H-steel specimen

Finite element analysis is performed using the analysis software ABAQUS. The dimensions of the specimen are shown in Figure 4, and fillets are omitted for simplicity. The analysis is performed using solid elements, which are first-order reduced integral elements with eight contacts. Unit volume mass is $7850 \text{ (kg/m}^3\text{)}$, Poisson's ratio is 0.3, and Young's modulus is 206 (GPa) . The mesh of the specimen is a 5 mm regular hexahedron shown in Figure 2. However, only in the direction of the web thickness, a mesh of 0.1 mm is used for the analysis shown in Figure 3. The bottom flange is completely fixed, while the top flange is free to displace only in the loading direction, restraining the displacement of the sides of the top flange in two directions perpendicular to the load. Surface forces were applied to the upper flange to determine the natural frequencies of the specimen.

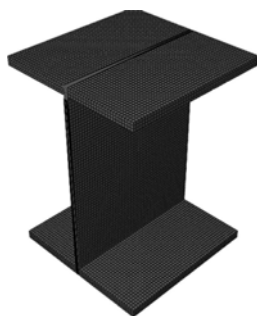


Figure 2. Specimen overview.

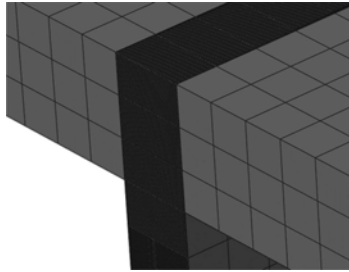


Figure 3. Enlarged mesh view of the web.

3 COMPRESSION TEST OF A PLATE

3.1 Specimen dimensions and test method

3.1.1 Specimen dimensions

Specimen dimensions and the location of accelerometers and uniaxial strain gauges are shown below. The accelerometers are placed about 10 mm above the uniaxial strain gauges so that they do not overlap. Uniaxial strain gauges are installed on both front and back sides. The names are set as shown in the Figure 4. The specimen is made of SS400. Uniaxial strain gauges are used to ensure that eccentric loading does not occur.

3.1.2 Test method

Compression forces are applied vertically by hydraulic system universal testing machine. The load is increased by 10 kN up to 240 kN. Under each loading condition, acceleration data are collected while striking the specimen 50 times by a hammer. The strike point is at the center of the specimen, about 20 mm to the left of the uniaxial strain gauge so as not to strike the uniaxial strain gauge and the striking plane is the opposite plane on which the accelerometers are placed. The accelerometers used are NP2110 (Ono Sokki Co.,Ltd.), NP-2110 (Ono Sokki Co., Ltd.), and PV-87 (Rion Co.,Ltd.) from left to right in the figure above. The sampling frequency is 50 kHz.

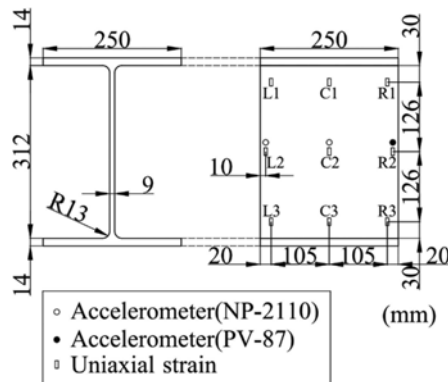


Figure 4. Dimensions of a H-steel specimen.

3.2 Target mode frequency

Frequency analysis is performed using the accelerometer of PV-87 because it is more accurate at lower frequency. Figure 3 shows the graph obtained by the Welch's power spectral density estimation method (Pwelch) when 100kN is applied on the plate. The window length is 2^{15} , a Hamming window is used for each segment, and the overlap ratio is 50%.

Next, the superimposed results of the Pwelch for each loading condition are shown in Figure 4. As an example, the results for 50 kN, 100 kN, 150 kN, and 200 kN loading conditions are superimposed.

Referring to Figure 5, Figure 6 is enlarged to focus on the area around 450 Hz where the power is maximum. Theoretical calculations show that the frequency is 400-500 Hz in the 0-250 kN loading range. Therefore, the peak near 450 Hz is presumed to be the target vibration mode, and the mode shape of the target mode is expressed as shown in Figure 7.

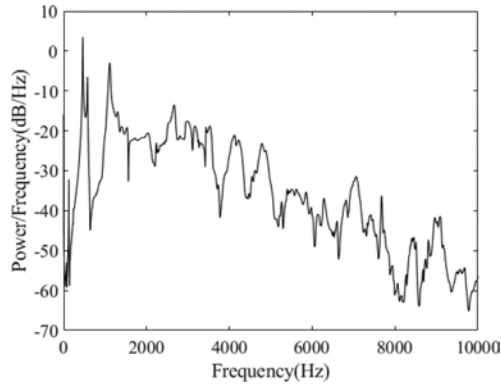


Figure 5. Example of Pwelch.

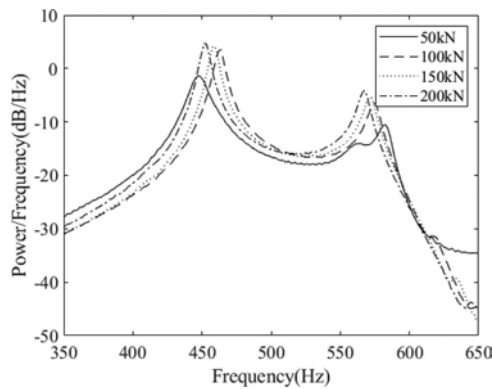


Figure 6. Superimposed Pwelch result.



Figure 7. Target vibration mode.

3.3 Comparison of frequency transition by theory, analysis and experiment

Peaks near 450 Hz are picked up for each loading condition and compared with the frequency transition identified in Chapter 2. Figure 8 shows an overlay of Pwelch for all loading conditions. As can be seen in Figure 8, the peak around 450 Hz is prominent under each loading conditions, and analytical and numerical results show that the target mode remains near 450 Hz. Therefore, the target mode is considered to be consistent between the experimental results and the analytical and numerical results. The natural frequencies of the target mode under each loading condition are obtained by peak picking from the graph. Figure 9 shows that the frequencies of the target mode obtained by the experiment tends to increase from 0 to 100 kN loading and to decrease from 100 to 240 kN loading. The peaks for the 0 and 10 kN loadings are not obtained because the peaks are crushed or does not appear.

One possible cause of the increased frequency in the small load region is a lack of support condition settings. Compressive load is applied using a compression plate of $\phi 180mm$. Two $380 \times 380 \times 25mm$ plates are placed on top of the specimen to prevent the stress from concentrating only directly under the compression plate. However, stress transmission is insufficient, so rotation is possible at the upper end of the specimen and support conditions of fixed at the bottom end and simply supported at the upper end are established in the range of small loads. As the load increases, the support condition approaches asymptotically to fixed at both ends, and the frequency decreases after 100 kN loading.

Analysis is performed every 30 kN by ABAQUS. The relative errors between the theoretical and analytical values are less than 2.0% at all loading. The natural frequency transitions lower than the theoretical value. It is because the mesh is coarse. Bending deformation is dominant in thin plates. Therefore, it is thought that the analytical values can be brought closer to the theoretical values by refining the mesh or using shell elements.

After 100 kN loading, when the natural frequency starts to decrease, the relative errors between the theoretical and experimental values are less than 1.3%. Therefore, after 100 kN loading, the compressive force acting on the specimen can be estimated from the experimental vibration characteristics.

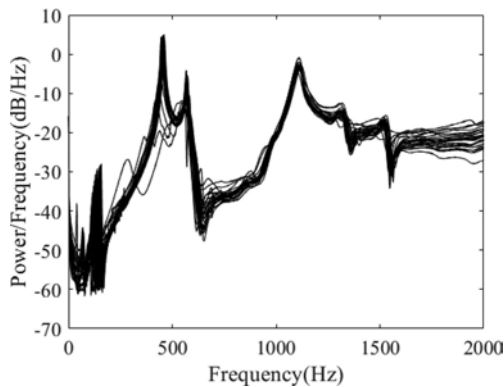


Figure 8. Superimposed figure of Pwelch for all loading condition.

4 CONCLUSION

In this paper, the compression bending test is conducted on SS400 steel plate specimen to confirm the relationship between compressive force and the natural frequency. The results are compared with theoretical and analytical values to confirm the validity of the results.

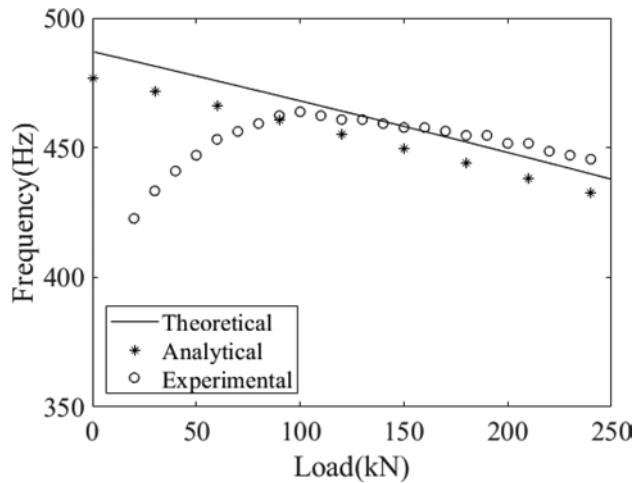


Figure 9. Comparison of theoretical, analytical and experimental frequency.

The relative errors between the theoretical and analytical values are less than 2.0%, therefore the validity of the analysis is confirmed.

The frequencies of the target mode obtained by the experiment tends to increase from 0 to 100 kN loading and to decrease from 100 to 240 kN loading, and after 100 kN loading, when the natural frequency starts to decrease, the relative errors between the theoretical and experimental values are less than 1.3%, therefore the compressive force acting on the specimen can be estimated from the experimental vibration characteristics.

REFERENCES

- Hideyo S, Naoaki T, Takeshi N, A Method for Estimating Column Force Distribution of a Spherical Tank, *High Pressure Institute of Japan*, Vol. 17, No.2, 1979
- Pang-jo C, Development of Sensored Rubber Bearing and its Application for Bridge Health Monitoring, *Annual journal of engineering, Ehime University*, 2012, Vol. 11, pp 184–190
- Peter D. Welch, The Use of Fourier Transform for the Estimation of Power Spectra: A Method Based on Time Averaging Over Short, Modified Periodograms, *IEEE TRANSACTIONS ON AUDIO AND ELECTROACOUSTICS*, VOL. AU-15, NO.2, JUNE 1967
- Shinya K, Theory of Vibration for Civil Engineering, *Morikita Publishing Co., Ltd.*, 2006
- Tohru S, Kunihiro H, Hiroshi Z, Haruhisa N, Practical Formulas for Estimation of Cable Tension by Vibration Method, *Proceedings of the Japan Society of Civil Engineers*, 1980, Volume 1980, Issue 294, Pages 25–32

Change in vibration characteristics of steel poled structure with damage

M. Kato, Y. Goi & Y. Kitane

Department of Civil and Earth Resources Engineering, Kyoto University, Kyoto, Japan

K. Sugiura

Department of Urban Managenet, Kyoto University, Kyoto, Japan

Y. Adachi

Hanshin Expressway Research Institute for Advanced Technology, Osaka, Japan

ABSTRACT: This study aims to investigate change in vibration characteristics of full-scale poled structure made of steel by vibration test. Due to the cyclic loading, the poled structures are susceptible to failure resulting from the damages such as cracks or loosened bolts. As the fundamental study for the development of SHM technique, cyclic vibration test using exciter was conducted on the structure and relationship conditions and identified vibration characteristics were discussed. Additionally, data with loosening anchor bolts were also collected to simulate the damage on the base. The experimental result shows that natural frequency decreases with increasing the degree of damage. Besides, it was found that two vibration modes with close natural frequencies were identified as one when the structure was intact, but were separated into two modes when the support conditions changed.

1 INTRODUCTION

In Japan, proportion of the bridges which are 50 years old is 34%. Inspection, monitoring and maintenance has become increasingly important take early actions against defects and deterioration. For more effective structural management, SHM have been focused for many years. The target structure was a sign support structure, which is cantilevered with a single pole. Sign support structures mount signages and Variable Message Sign (VMS) to guide motorist to their destination or show them various information. These structures are constantly exposed to wind loading, and for those structures mounted on bridges, to bridge vibrations induced by passing vehicles (Kacin et al. (2010)). As they have long span length and relatively small cross-sectional area and mass, these sign structures are flexible, resulting in low natural frequencies and damping; they are prone to having large-amplitude vibration and fatigue cracking under wind loading or vibration of bridges. Due to the cyclic loading, the structures are susceptible to failure resulting from the damages such as cracks or loosened bolts (Li et al. (2005)). SHM techniques have large possibility in monitoring such structure to prevent failure. In this study, we were focusing the damage at the base. As the fundamental study of the damage detection technique using sensor, change in vibration characteristics with two types of damages at the base were investigated; one was conducted with loosening anchor bolts, and another was with cracks through cyclic loading test.

2 EXPERIMENTAL APPROACH

A post structure that the cantilevered support structure is supported by a single vertical pole, was fabricated specifically for the laboratory testing. Figure 1 gives its general view. The post

specimen was attached to the concrete foundation using four anchor bolts. At the middle of the post, an exciter was equipped to excite vibration mode of the structure. Information on the specimen are presented in Figure 1 and Figure 2. Vibration characteristics were estimated with two types of damages: loosening anchor bolts and cracks. The vibration was recorded through total 6 triaxial accelerometers with a sampling frequency of 200 Hz and vibration characteristics were estimated.



Figure 1. General view of target structure.

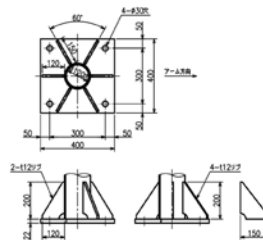


Figure 2. Base plate detail.

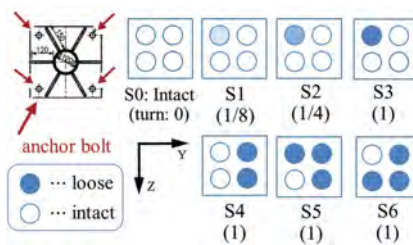


Figure 3. Anchor bolts loosening scenarios.

For the loosening anchor bolt case, total 7 cases for loosening anchor bolts and one intact case were examined (see Figure 3). S0 is an intact case. From S1 to S3, one bolt was loosened with 1/8, 1/4, and 1 turns, i.e., 45°, 90°, and 360°, respectively. Two or three bolts are turned once in S4 to S6. Sensors were installed as shown in Figure 4.

For the crack case, the structure were under cyclic loading to generate fatigue crack. Since a fatigue crack occurred in the weld of the mast arm after 600,000 cycles, the arm was removed for safety (Figure 5). Hence, for the crack case, we are focusing on the structural behavior after removing the arm. No other crack was observed just after

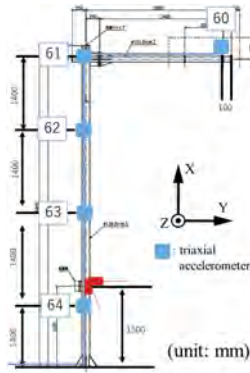


Figure 4. Test setup for bolt loosening case.

removing the mast arm. As show in Figure 6 and Figure 4, total 5 triaxial accelerometers and an exciter (URAS VIBRATOR KEE3-6C) were installed. The exciter, which can excite the vibration in various frequency by vibrating in the arm (Y) direction, was mounted 1.5 m from the base for cyclic loading test. Besides, to capture the stress response, two uniaxial strain gauges were mounted as shown in Figure 7 and 8. Cyclic loading test using an exciter was conducted. Crack lengths were examined by magnetic particle testing after every 10,000 loadings. Once a structure developed an crack connecting to a next crack, loading test was finished.

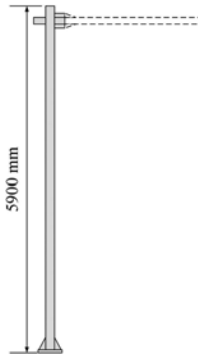


Figure 5. Schematic of target structure after removing the arm.

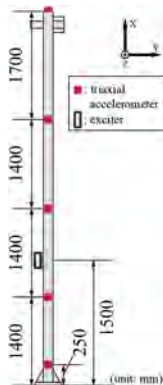


Figure 6. Test setup for crack case.

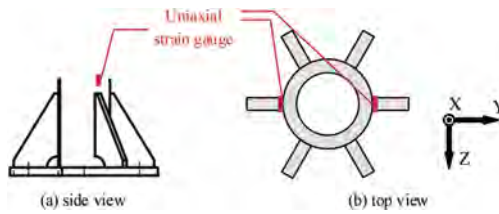


Figure 7. Strain gauge setup.

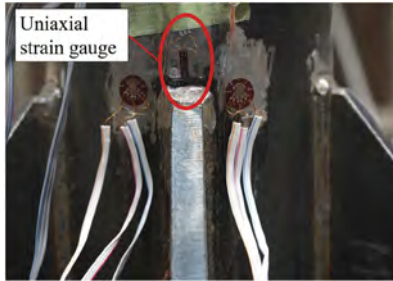


Figure 8. Close-up of strain gauge.

In order to identify the vibration characteristics, the structure was excited by pushing with hands in two directions: y-axis direction, the arm direction, and z-axis direction, perpendicular to the arm. The structure was pushed once every 1 minute for 11 minutes; it was excited 10 times in one test. For the crack case, the number of samples varied for each loading stage. Therefore the mean values of frequencies obtained for each cycle was taken as representative of the frequency for that cycle.

As an modal analysis method, stochastic subspace identification (SSI) (Van Overschee and De Moor (1996) & De Cock et al. (2003)), a time-domain system identification method which estimates state space model from output-only measurement, was used to identify structure's natural frequencies and mode shapes.

3 RESULTS AND DISCUSSION

3.1 Anchor bolt loosening case

Here, the vibration modes of first two smallest frequencies, 1st bending mode and 1st torsional mode, were focused. Mode shapes (Figure 9-10) and natural frequencies were identified. The rate of change in frequencies with respect to the frequency for S0, the intact state, were calculated as represented in Figure 12 and Figure 13. It should be noted that for the 1st bending mode, three directions of vibration were observed (Figure 11). The C-direction mode was separated into two directions A and B as loosening the anchor bolts. It could be thought that the structure originally has two adjacent modes, A-direction mode and B-direction mode, which can be seen as one mode, C-direction mode, in the intact condition because these two modes are too close.

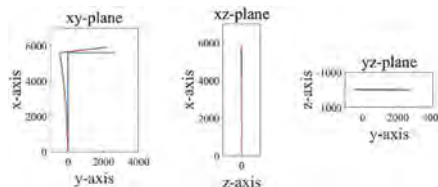


Figure 9. Mode shape for the 1st bending mode in bolt loosening test.

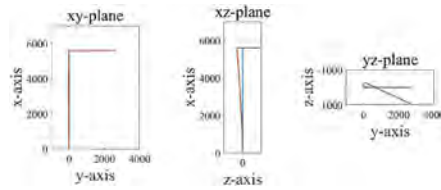


Figure 10. Mode shape for the 1st torsional mode in bolt loosening test.

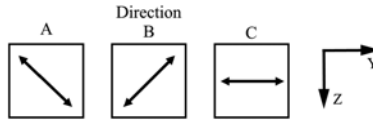


Figure 11. Swing directions of the 1st bending mode in bolt loosening test.

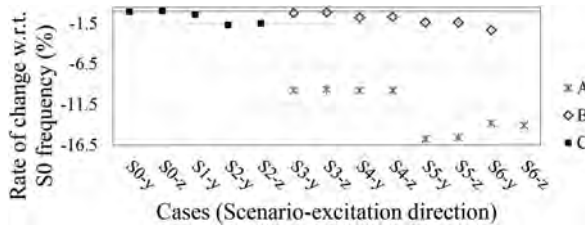


Figure 12. Rate of change in frequencies for the 1st bending mode with respect to S0 frequency.

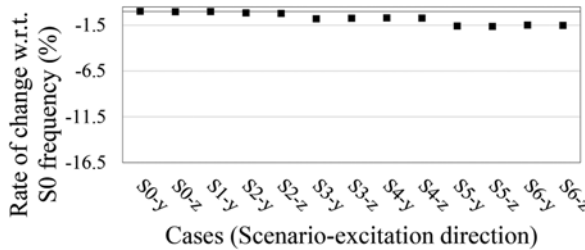


Figure 13. Rate of change in frequencies for the 1st torsional mode with respect to S0 frequency.

3.2 Crack case

For the crack case, after 723,000 cycles, cracks were found for the first time. The crack propagated with cyclic loading. All cracks initiated at a weld toe adjacent to the pole shaft, then propagated circumferentially from either side of the initiation point (see example in Figure 14). The record of crack propagation are described in Figure 15. The rate of section loss were calculated as given in Table 1. Here, the section loss is calculated as ratio of total length of crack to the original circumference. It can be seen that the crack growth is active in one direction (A-direction in Figure 11), and is gentle in another direction (B-direction in Figure 11).

From the output acceleration data, natural frequencies and mode shapes of this structure were identified with SSI method. The first four vibration modes were focused. Let the name of vibration mode be Mode 1, Mode 2, and so on, from the lowest natural frequency.

Typical mode shapes for each mode are listed in Figures 16a-16d. The value of the frequencies are for after 600,000 cycles of loading, the intact state. In these four modes, 1st and 2nd

bending mode in two directions were observed: direction A and B in Figure 11. Mode 1 and Mode 2 are the 1st bending mode with A and B-direction of swing, respectively. Mode 3 and Mode 4 are the 2nd bending mode with A and B-direction of swing, respectively.

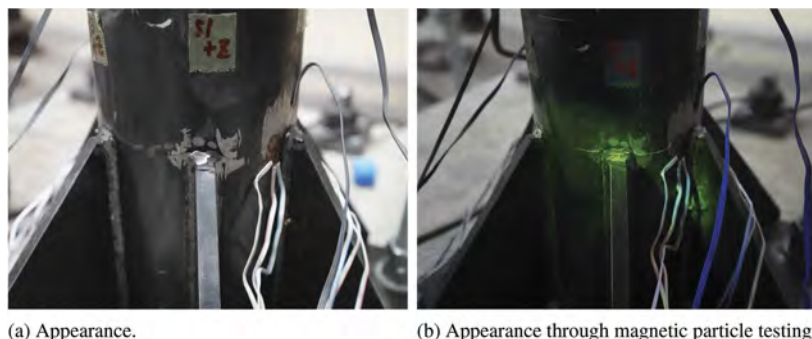


Figure 14. Example of crack.

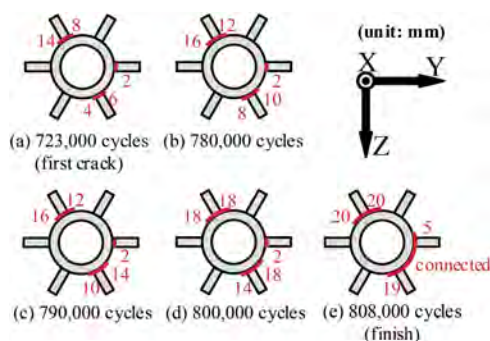


Figure 15. Crack length and location at each cycle.

Table 1. Section loss due to crack.

Cycles	Total crack length (mm)	Rate of section loss (%)
723,000	34	7.741
780,000	48	10.93
790,000	54	12.30
800,000	70	15.94
808,000	137	31.24

For each mode, natural frequencies were estimated and the rate of change in frequencies with respect to the frequency at 600,000 cycles, the intact state, were calculated. As can be seen in Figure 17a and 17c, it appeared that natural frequency of the vibration modes in which their swings are in direction-A tends to decrease as increasing cycles. For Mode 2 and Mode 4 however, relatively insensitive trend was observed compared to direction-A vibration modes' frequency changes. As in Figure 15, the crack propagation was not uniform in circumference. Hence, only the vibration mode in the direction where crack is propagating was sensitive to the increasing in crack length. According to these results, the selection of target vibration mode of focus is important in crack detection using the frequency change.

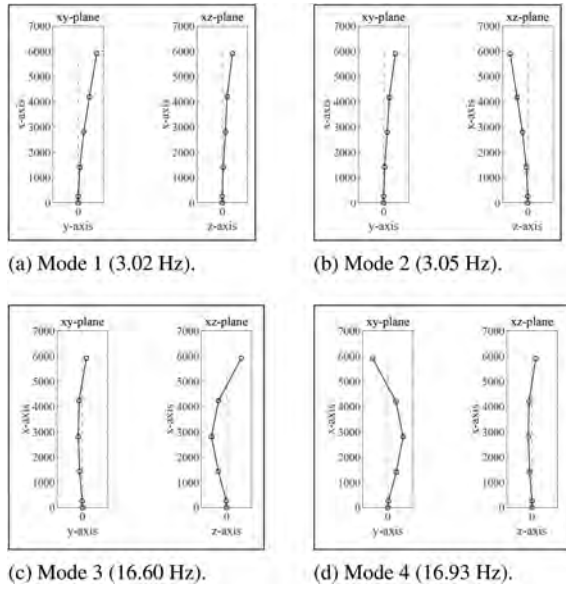


Figure 16. Typical mode shape for each mode.

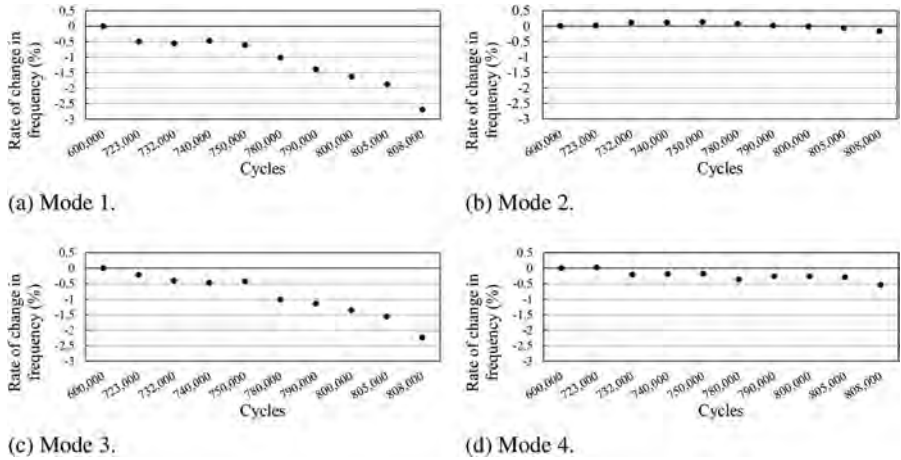


Figure 17. Rate of change in frequencies with respect to the 600,000 cycles' frequency.

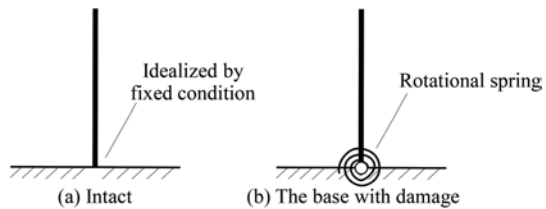


Figure 18. Structure model for intact and with damage at the base.

The structure can be modeled as depicted in Figure 18. Model (a) is describing the intact case. For model (b), it can be said that the spring constant, which indicates how much the rotation at the base is restricted, is decreased as loosening anchor bolts. Suppose this model,

model (a) can be regarded as model (b) of which spring constant is increased, and the spring constant decreases as the crack grows. Therefore, it can be inferred that propagation of crack leads to decrease in natural frequency.

4 CONCLUSIONS

This article discusses the change in vibration characteristics with damage at the base. Two types of damage were simulated: loosening anchor bolts artificially and producing fatigue under cyclic loading test. Natural frequencies and corresponding mode shapes were estimated in each damage stages.

For both two types of damages, loosening anchor bolts and increasing crack length leads to decrease in natural frequencies. It was interpreted as the stiffness at the base was decreased due to these damages. Besides, as the natural frequencies changed, two modes with close natural frequencies were identified as one when intact state, but were separated into two modes when the support conditions changed. In the crack case, it was observed that the sensitivity of frequency changes to the crack propagation depends on crack locations and target vibration modes. Hence, if anomaly detection is attempted through changes in vibration characteristics, the selection of vibration mode is considered to be important. Moreover, this experiment was conducted indoors, with no traffic and no whether change. In order to apply in the real world, further investigation with external factors such as traffic loading or temperature changes should be conducted.

REFERENCES

- De Cock, K., B. De Moor, and K. Leuven (2003). Subspace identification methods. Contribution to section 5, 933–979.
- Kacin, J., P. Rizzo, and M. Tajari (2010). Fatigue analysis of overhead sign support structures. *Engineering Structures* 32(6), 1659–1670.
- Li, X., T. Whalen, and M. Bowman (2005, 01). Fatigue strength and evaluation of double-mast arm cantilevered sign structures. *Transportation Research Record* 1928, 64–72.
- Van Overschee, P. and B. De Moor (1996). *Stochastic Identification*, pp. 57–93. Boston, MA: Springer US.



Taylor & Francis

Taylor & Francis Group

<http://taylorandfrancis.com>

MS10: Advances in life-cycle earthquake engineering
Organizers: L. Capacci, M. Akiyama, F. Biondini & D.M. Frangopol



Taylor & Francis

Taylor & Francis Group

<http://taylorandfrancis.com>

Review of advances in life-cycle seismic risk and resilience of bridges and bridge networks

L. Capacci & F. Biondini

Politecnico di Milano, Milan, Italy

D.M. Frangopol

Lehigh University, Bethlehem, PA, USA

ABSTRACT: Risk assessment and mitigation programs have been carried out over the last decades in the attempt to reduce transportation infrastructure downtime and post-disaster recovery costs after seismic events. Mathematical frameworks have also been proposed to provide a basis for development of predictive models for functionality and resilience of structures and infrastructure networks, particularly regarding bridges and transportation systems. In risk and resilience frameworks, the effects of aging and environmental aggressiveness should be explicitly considered, affecting the structural performance and functionality of civil infrastructure systems. This review paper discusses principles, methodologies, open issues, and current developments in the field of life-cycle seismic risk and resilience of aging bridges and bridge networks.

1 INTRODUCTION

The quality of life of modern communities relies on the ability of infrastructure networks to cope with hazards, absorbing their impact and restoring as soon as possible the pre-event conditions (Bruneau et al. 2003). Designing lifelines and infrastructure components to meet modern safety standards and planning proper management policies are key tasks to satisfy the primary needs of communities not only under operational conditions, but also in a state of emergency (Frangopol 2011). For this reason, transportation networks play a key role guaranteeing connectivity in the aftermath of extreme events, such as earthquakes, to ensure deployment of emergency aids and to promptly repair the built environment. Bridges are crucial elements designed to bypass obstacles otherwise not easily detoured (Capacci et al. 2022a).

The economic impact of aging and deterioration processes on existing structures and infrastructure systems is exceptionally high, particularly for bridges and transportation networks (ASCE 2021). Vulnerability assessment is traditionally carried out by neglecting any deterioration mechanism that may adversely affect the performance of structural systems, implicitly assuming that structures are optimally maintained during their lifetime. The detrimental effects of aggressive chemical attacks and other physical damage mechanisms can exacerbate losses over time in structural performance under both service loadings and extreme events, such as earthquakes (Biondini and Frangopol 2016). Despite the advances in civil and structural engineering, there has not been enough progress in developing methodologies and best practices for life-cycle design, assessment, maintenance, and management of bridges under seismic and other independent and interdependent hazards (Akiyama and Frangopol 2018, Biondini and Frangopol 2018, 2019).

This review paper focuses on concepts, methods, issues, and accomplishments in the field of life-cycle seismic risk and resilience of structures and infrastructure systems, with specific focus on bridges and bridge networks. Special attention is paid to: principles and dimensions of infrastructure risk assessment; established methodologies and open issues regarding regional seismic

hazard and fragility of spatially-distributed bridges; definitions and frameworks of infrastructure resilience; network functionality and bridge recovery for seismic resilience assessment; life-cycle probabilistic concepts affecting lifelines seismic resilience of under environmental stressors.

2 LIFE-CYCLE RESILIENCE-BASED SEISMIC RISK OF AGING BRIDGE NETWORKS

2.1 *Seismic hazard of spatially-distributed vulnerable assets*

Classical approaches to Probabilistic Seismic Hazard Analysis (PSHA) rely on the assumption that earthquakes are mutually independent following a stationary Poisson process fully described by their mean annual rate of occurrence (Cornell 1968). In the context of PSHA, seismic Intensity Measures (IMs) are synthetic parameters the ground motion at a reference site severity at the location of the investigated structure (Riddell 2007). Selecting the most appropriate metric is a fundamental task to define reliable estimates of structural demand (Luco and Cornell 2007). Attenuation laws or Ground Motion Prediction Equations are predictive models calibrated by multivariate regression analysis based on historical datasets adopted to statistically estimate IM likelihood based on seismogenic source features and causative rupture scenarios (Douglas 2003).

The spatial correlation of ground motion is critical for seismic hazard assessment of infrastructure networks with spatially distributed vulnerable elements. Statistical models of seismic hazard allow simulating seismic intensities maps at the relevant sites of vulnerable components (Stergiou and Kiremidjian 2010). Lognormal random fields are typically adopted to statistically model seismic IMs in the investigated region, with dispersion associated to within-event and between event variability (Crowley and Bommer 2006, Jayaram and Baker 2010). Regarding seismic sequences in the aftermath of major events, aftershocks tend to occur in time with decaying frequency and average magnitude lower than the mainshock (Iervolino et al. 2018). Refined frameworks can be applied to quantify consequences and uncertainties in seismic vulnerability and risk assessment (Dong and Frangopol 2015).

2.2 *Seismic fragility of vulnerable bridges*

The failure probability of vulnerable bridges is addressed based on the concept of fragility curves, which is the conditional probability of occurrence of a prescribed failure event given the seismic hazard IM (Shinozuka et al. 2000). Methodologies for seismic fragility assessment involve research efforts in the field of seismic engineering and structural reliability (Billah and Alam 2015). Analytical fragility curves establish the seismic response based on structural analyses and they are typically obtained by non-linear time-history analyses. Alternatives to analytical frameworks are provided by empirical fragility curves, correlating IMs with damage datasets obtained via in-field reconnaissance reports from past earthquakes (Basoz and Kiremidjian 1998). Depending on the available data related to earthquake-induced damage, statistical procedures have been developed to calibrate the related fragility curves (Porter et al. 2007, Baker 2015, Lallemand et al. 2015).

Uncertainties involved in seismic fragility assessment are mostly related to aleatory models in the investigated structure and to record-to-record variability of input ground motion. Model uncertainties on mechanical properties can be incorporated in seismic response analysis methods with simulation-based techniques (Franchin et al. 2018). Adopting a sufficiently large dataset of representative seismic signals is a key issue that should be carried out with appropriate procedures (Katsanos et al. 2010). Recently, the number of recorded accelerograms has increased considerably owing to strong events in countries with well-instrumented record networks, boosting the development of automated procedures of natural ground motion selection and scaling for seismic response analysis (Baker and Lee 2018). Physics-based numerical simulations of earthquake ground motion can complement the recorded data providing signals based on local source and site configurations (Paolucci et al. 2021).

Seismic reliability assessment of infrastructure networks can be carried out based on analytical methods relying on numerical simulation techniques (Kilantis and Sextos 2019). Assessing

the vulnerability of large-scale networks is challenging due to computational costs as well as incomplete information on bridge vulnerability and their statistical dependency (Der Kiureghian and Song 2008). Refined simulation frameworks can foster computational efforts and estimate accuracy (Capacci and Biondini 2022, 2023).

3 PROBABILISTIC LIFE-CYCLE INFRASTRUCTURE RESILIENCE

3.1 *Qualitative definitions and quantitative metrics of infrastructure resilience*

Resilience can be regarded as the ability of structures and infrastructure systems to: resist an extreme event, limiting operational outages and irreversible damage; absorb its impact, mitigating losses induced by disruptions and downtime; recover as rapidly as possible adequate operability conditions (Bruneau et al. 2003). Resilience indicators typically rely on the definition of a functionality metric Q comprehensively describing the system performance from the time of event occurrence t_0 up to a prescribed horizon time t_h . To compare the effect of different hazard scenarios and recovery strategies, resilience R is often quantified as the integral mean of the functionality profile over the interval from occurrence time to horizon time, respectively t_0 and t_h (Bruneau and Reinhorn 2007, Bocchini and Frangopol 2012a, Capacci et al. 2020):

$$R = \frac{1}{t_h - t_0} \cdot \int_{t_0}^{t_h} Q(t) dt \quad (1)$$

In the field of seismic risk mitigation, several frameworks have been developed to provide a basis to measure the functionality and resilience at various scales, including communities and societies (Chang and Shinozuka 2004, Rose 2004, Cimellaro et al. 2016) as well as lifeline components and systems such as transportation networks (Bocchini and Frangopol 2012a,b, Decò and Frangopol 2013, Dong and Frangopol 2015, Capacci et al. 2020). Significant reviews oriented to the definition of resilience indicators of critical infrastructure systems are available, mostly regarding different dimensions (Cantelmi et al. 2022), taxonomy (Poulin and Kane 2022), computational tools (Shadabfar et al. 2022). Among all hazards and critical infrastructure, particular efforts have been devoted to seismic risk assessment (Freddi et al. 2022, Yin et al. 2022) of transportation systems (Faturechi and Miller-Hooks 2015, Sun et al. 2020), with specific focus on bridge networks (Gidaris et al. 2017, Banerjee et al. 2019, Capacci and Biondini 2020).

3.2 *Functionality and recovery of infrastructure road networks*

Connectivity of transportation networks is critical in disaster response of hazard-prone communities, in which infrastructure managers are called to guarantee the users' safety by imposing regulatory restrictions to traffic (Mackie and Stojadinovic 2006). Sociological aspects exacerbate complexities in the seismic assessment of transportation lifelines since the state of emergency influence drivers' habits, such as adapting routes and travel modes and destinations depending on the traffic conditions (Erath et al. 2009), impairing economically valuable activities such as working or shopping (Cho et al. 2001), and exacerbating irrational behaviors under emergency when traffic information is limited (Feng et al. 2020). Besides direct costs of infrastructure repair, temporary limitations to traffic capacity due to traffic limitations over bridges damaged by seismic events induces significant indirect losses associated to ongoing maintenance activities (Liu and Frangopol 2006) and damage occurrence due to multiple hazards (Yang and Frangopol 2020a).

Functionality metrics of transportation networks can be classified into topological, relying on graph theory to rank vulnerable components by indicators of roads connectivity and nodes accessibility (Cimellaro et al. 2021), and flow-based metrics, comprehensive functionality measures of assigned traffic flows and travel times (Bocchini and Frangopol 2011a). Flow-based metrics require the solution of mathematical optimization problems, such as simplified

shortest path analysis or more complex congestion-based frameworks, which account for the actual traffic capacity (Bocchini and Frangopol 2011b).

The formulation of recovery models is an essential component in resilience assessment. Several analytical models have been proposed to capture the recovery pattern from seismic damage based on engineering judgment and statistical analysis from empirical data (Padgett and DesRoches 2007, Bocchini and Frangopol 2012b, Decò et al. 2013, Biondini et al. 2015, Karamlou and Bocchini 2016, Sharma et al. 2018, Misra et al. 2020, Mitoulis et al. 2021).

3.3 *Life-cycle seismic resilience under uncertainties*

Depending on the environmental conditions to which structures are exposed, chemical attacks and physical damage may dramatically reduce the mechanical properties of key structural members (Enright and Frangopol 2001, Biondini et al. 2004, Ellingwood 2005, Malerba 2014). Traditional design methodologies need to be revised to account for the evolution over time of structural performance over the service life and classical time-invariant indicators should be revisited (Frangopol and Das 1999, Yang et al. 2004, Saydam and Frangopol 2011, Zhu and Frangopol 2012, Biondini and Frangopol 2016, 2019, Ghosn et al. 2016a). Life-cycle structural and infrastructure performance assessment aims at investigating time-variant indicators, such as reliability (Akiyama et al. 2010, Bocchini and Frangopol 2011c, Ghosn et al. 2016b, Frangopol and Kim 2022), robustness (Ghosn et al. 2010, Biondini and Frangopol 2014, Lu et al. 2022), redundancy (Okasha and Frangopol 2010, Biondini and Frangopol 2017, Capacci et al. 2022b), risk (Saydam and Frangopol 2013, Yang and Frangopol 2020b, Messori et al. 2021), and sustainability (Dong et al. 2013, Bocchini et al. 2014).

The time-variant seismic performance of structures and infrastructure systems should be evaluated in probabilistic terms, accounting for uncertainties propagating over their lifetime and regarding seismic demand and capacity of structural systems (Decò and Frangopol 2011, Akiyama and Frangopol 2014, Dong and Frangopol 2017) and critical infrastructure networks (Akiyama et al. 2020, Argyroudis et al. 2019, 2020, Capacci et al. 2020). Deterioration processes exacerbate the impact of model uncertainties in time-variant seismic reliability (Akiyama et al. 2011, Ghosh et al. 2015, Yanweerasak et al. 2018), cost estimate (Kumar et al. 2009, Shekhar et al. 2018), and seismic performance assessment (Biondini et al. 2014, Titi and Biondini 2014). Research efforts are also focused on the calibration of time-variant fragility curves (Ghosh and Padgett 2010, Zhong et al. 2012, Rao et al. 2017, Silva et al. 2019, Su et al. 2019).

Infrastructure resilience should not be intended as a static property of the system since deterioration mechanisms exacerbate the impact of interdependent events on vulnerable lifeline components and systems (Capacci and Biondini 2020, Yang and Frangopol 2020a, Ishibashi et al. 2021). Therefore, life-cycle resilience frameworks under seismic and other interacting hazards should account for the effects of aging and deterioration processes (Biondini et al. 2015, Capacci and Biondini 2020, Capacci et al. 2020) and maintenance and repair interventions under uncertainty (Frangopol et al. 2017). Emphasis is currently devoted to addressing the impact of time-variant environmental stressors under non-stationary climate conditions to vulnerability and resilience assessment of structures and infrastructure systems (Dong and Frangopol 2016, Yang and Frangopol 2019, 2020b, Liu et al. 2020, Capacci and Biondini 2021).

4 CONCLUSIONS

Public authorities, owners, and political systems are called to ensure suitable resilience levels of critical infrastructure systems for optimal life-cycle management of aging structures and transportation networks, especially in earthquake-prone regions. This paper discussed recent advances and efforts made to establish probabilistic frameworks for life-cycle seismic risk and resilience assessment of aging structures and infrastructure systems, with emphasis on bridges and bridge networks. The presented review focused on concepts, methodologies and tools to be incorporated into practical policies to inform the decision-making process for ex-ante

preventive retrofit interventions and ex-post effective recovery actions of key lifeline components under seismic and other hazards.

REFERENCES

- Akiyama, M., Frangopol, D.M., Yoshida, I. 2010. Time-dependent reliability analysis of existing RC structures in a marine environment using hazard associated with airborne chlorides. *Engineering Structures* 32(11): 3768–3779.
- Akiyama, M., Frangopol, D.M., Matsuzaki, H. 2011. Life-cycle reliability of RC bridge piers under seismic and airborne chloride hazards. *Earthquake Engineering & Structural Dynamics* 40(15): 1671–1687.
- Akiyama, M. & Frangopol, D.M. 2014. Long-term seismic performance of RC structures in an aggressive environment: Emphasis on bridge piers. *Structure and Infrastructure Engineering* 10(7): 865–879.
- Akiyama, M. & Frangopol 2018. Life-cycle reliability of bridges under independent and interacting hazards. *Maintenance, Safety, Risk, Management and Life-Cycle Performance of Bridges*, CRC Press/Balkema, Taylor & Francis Group plc, London, 16–35.
- Akiyama, M., Frangopol, D.M., Ishibashi, H. 2020. Toward life-cycle reliability-, risk-, and resilience-based design and assessment of bridges and bridge networks under independent and interacting hazards: Emphasis on earthquake, tsunami and corrosion. *Structure and Infrastructure Engineering* 16(1): 26–50.
- Argyroudis, S.A., Mitoulis, S.A., Winter, M.G., Kaynia, A.M. 2019. Fragility of transport assets exposed to multiple hazards: State-of-the-art review toward infrastructural resilience. *Reliability Engineering & System Safety* 191: 106567.
- Argyroudis, S.A., Mitoulis, S.A., Hofer, L., Zanini, M.A., Tubaldi, E., Frangopol, D.M. 2020. Resilience assessment framework for critical infrastructure in a multi-hazard environment: Case study on transport assets. *The Science of the Total Environment* 714: 136854.
- ASCE, 2021. *Report card for America's infrastructure*. American Society of Civil Engineers.
- Baker, J.W. 2015. Efficient analytical fragility function fitting using dynamic structural analysis. *Earthquake Spectra* 31(1): 579–599.
- Baker, J.W. & Lee, C. 2018. An improved algorithm for selecting ground motions to match a conditional spectrum. *Journal of Earthquake Engineering* 22(4): 708–723.
- Banerjee, S., Vishwanath, B., Devendiran, D. 2019. Multi-hazard resilience of highway bridges and bridge networks: A review. *Structure and Infrastructure Engineering* 15(12): 1694–1714.
- Basoz, N. & Kiremidjian, A.S. 1998. *Evaluation of bridge damage data from the Loma Prieta and Northridge, California earthquakes*. Technical Report, MCEER-98-0004.
- Billah, A.H.M.M. Alam, M.S. 2015. Seismic fragility assessment of highway bridges: a state-of-the-art review. *Structure and Infrastructure Engineering* 11(6): 804–832.
- Biondini F., Bontempi F., Frangopol D.M., Malerba, P.G. 2004. Cellular automata approach to durability analysis of concrete structures in aggressive environments. *Journal of Structural Engineering*, 130 (11): 1724–1737.
- Biondini, F., & Frangopol, D.M. 2014. Time-variant robustness of aging structures. Chapter 6. In D. M. Frangopol & Y. Tsompanakis (Eds.), *Maintenance and safety of aging infrastructure*. London: CRC Press, Taylor & Francis Group, 163-200.
- Biondini, F. & Frangopol, D.M. 2016. Life-cycle performance of deteriorating structural systems under uncertainty: Review. *Journal of Structural Engineering* 142(9): F4016001.
- Biondini, F., & Frangopol, D.M. 2017. Time-variant redundancy and failure times of deteriorating concrete structures considering multiple limit states. *Structure and Infrastructure Engineering* 13(1): 94–106.
- Biondini, F. & Frangopol, D.M. 2018. Life-cycle performance of civil structure and infrastructure systems: Survey. *Journal of Structural Engineering* 144(1): 06017008.
- Biondini, F. & Frangopol, D.M. (eds.) 2019. *Life-cycle design, assessment and maintenance of structures and infrastructure systems*. Reston, VA: ASCE.
- Biondini, F., Camnasio, E., Palermo, A. 2014. Lifetime seismic performance of concrete bridges exposed to corrosion. *Structure and Infrastructure Engineering* 10(7): 880–900.
- Biondini, F., Camnasio, E., Titi, A. 2015. Seismic resilience of concrete structures under corrosion. *Earthquake Engineering & Structural Dynamics* 44(14): 2445–2466.
- Bocchini, P. & Frangopol, D.M. 2011a. A stochastic computational framework for the joint transportation network fragility analysis and traffic flow distribution under extreme events. *Probabilistic Engineering Mechanics* 26(2): 182–193.

- Bocchini, P. & Frangopol, D.M. 2011b. A probabilistic computational framework for bridge network optimal maintenance scheduling. *Reliability Engineering & System Safety* 96(2): 332–349.
- Bocchini, P. & Frangopol, D.M. 2011c. Generalized bridge network performance analysis with correlation and time-variant reliability. *Structural Safety* 33(2): 155–164.
- Bocchini, P. & Frangopol, D.M. 2012a. Optimal resilience- and cost-based postdisaster intervention prioritization for bridges along a highway segment. *Journal of Bridge Engineering* 17(1): 117–129.
- Bocchini, P. & Frangopol, D.M. 2012b. Restoration of bridge networks after an earthquake: multicriteria intervention optimization. *Earthquake Spectra* 28(2): 426–455.
- Bocchini, P., Frangopol, D.M., Ummenhofer, T., Zinke, T. 2014. Resilience and sustainability of civil infrastructure: toward a unified approach. *Journal of Infrastructure Systems* 20(2): 04014004.
- Bruneau, M. & Reinhorn, A.M. 2007. Exploring the concept of seismic resilience for acute care facilities. *Earthquake Spectra* 23(1): 41–62.
- Bruneau, M., Chang, S.E., Eguchi, R.T., Lee, G.C., O'Rourke, T.D., Reinhorn, A.M., Shinozuka, M., Tierney, K., Wallace, W.A., Winterfeldt, D.V. 2003. A framework to quantitatively assess and enhance the seismic resilience of communities. *Earthquake Spectra* 19(4): 733–752.
- Cantelmi, R., Di Gravio, G., Patriarca, R. 2021. Reviewing qualitative research approaches in the context of critical infrastructure resilience. *Environment Systems and Decisions* 41(3),341–376.
- Capacci, L. & Biondini, F. 2020. Probabilistic life-cycle seismic resilience assessment of aging bridge networks considering infrastructure upgrading. *Structure and Infrastructure Engineering* 16(4): 659–675.
- Capacci, L. & Biondini, F. 2021. Resilience-based seismic risk assessment of aging bridge networks under climate change. *10th International Conference on Bridge Maintenance, Safety and Management (IABMAS 2020)*, Sapporo, Japan, April 11-15, 2021.
- Capacci, L. & Biondini, F. 2022. Efficient sampling techniques for simulation-based life-cycle structural reliability and seismic fragility assessment. *13th International Conference on Structural Safety and Reliability (ICOSSAR 2021)*, September 13-17, 2022, Shanghai, China.
- Capacci, L. & Biondini, F. 2023. Cross-Entropy-based Stationary Proposal Importance Sampling for life-cycle structural reliability and seismic risk assessment. *14th International Conference on Applications of Statistics and Probability in Civil Engineering (ICASP14)*, Dublin, Ireland, July 9-13, 2023.
- Capacci, L., Biondini, F., Titi, A. 2020. Lifetime seismic resilience of aging bridges and road networks. *Structure and Infrastructure Engineering* 16(2): 266–286.
- Capacci, L., Biondini, F., Frangopol, D.M. 2022a. Resilience of aging structures and infrastructure systems with emphasis on seismic resilience of bridges and road networks. *Resilient Cities and Structures* 1(2): 23–41.
- Capacci, L., Biondini, F., Frangopol, D.M. 2022b. Failure times of deteriorating RC bridges under uncertainty. *11th International Conference on Bridge Maintenance, Safety, and Management (IABMAS 2022)*, Barcelona, Spain, July 11-15, 2022.
- Carturan, F., Pellegrino, C., Rossi, R., Gastaldi, M., Modena, C. 2013. An integrated procedure for management of bridge networks in seismic areas. *Bulletin of Earthquake Engineering* 11(2): 543–559.
- Chang, S.E. & Shinozuka, M. 2004. Measuring improvements in the disaster resilience of communities. *Earthquake Spectra* 20(3): 739–755.
- Chang, L., Peng, F., Ouyang, Y., Elnashai, A.S., Spencer, B.F. 2012. Bridge seismic retrofit program planning to maximize postearthquake transportation network capacity. *Journal of Infrastructure Systems* 18(2): 75–88.
- Cimellaro, G.P., Renschler, C., Reinhorn, A.M., Arendt, L. 2016. PEOPLES: A framework for evaluating resilience. *Journal of Structural Engineering* 142(10): 04016063.
- Cimellaro, G.P., Arcidiacono, V., Reinhorn, A.M. 2021. Disaster resilience assessment of building and transportation system. *Journal of Earthquake Engineering* 25(4): 703–729.
- Cornell, C.A. 1968. Engineering seismic risk analysis. *Bulletin of the Seismological Society of America* 58 (5): 1583–1606.
- Crowley H. & Bommer J.J. 2006. Modelling seismic hazard in earthquake loss models with spatially distributed exposure. *Bulletin of Earthquake Engineering* 4(3): 249–73.
- Decò, A. & Frangopol, D.M. 2011. Risk assessment of highway bridges under multiple hazards. *Journal of Risk Research* 14(9): 1057–1089.
- Decò, A. & Frangopol, D.M. 2013. Life-cycle risk assessment of spatially distributed aging bridges under seismic and traffic hazards. *Earthquake Spectra* 29(1): 127–153.
- Decò, A., Bocchini, P., Frangopol, D.M. 2013. A probabilistic approach for the prediction of seismic resilience of bridges. *Earthquake Engineering & Structural Dynamics* 42(10): 1469–1487.
- Dong, Y. & Frangopol, D.M. 2015. Risk and resilience assessment of bridges under mainshock and aftershocks incorporating uncertainties. *Engineering Structures* 83: 198–208.

- Dong, Y. & Frangopol, D.M. 2016. Probabilistic time-dependent multi-hazard life-cycle and resilience assessment of bridges considering climate change. *Journal of Performance of Constructed Facilities* 30 (5): 04016034.
- Dong, Y., Frangopol, D.M., Saydam, D. 2013. Time-variant sustainability assessment of seismically vulnerable bridges subjected to multiple hazards. *Earthquake Engineering & Structural Dynamics* 42(10): 1451–1467.
- Der Kiureghian, A. & Song, J. 2008. Multi-scale reliability analysis and updating of complex systems by use of linear programming. *Reliability Engineering & System Safety* 93(2): 288–297.
- Dong, Y. & Frangopol, D.M. 2017. Probabilistic assessment of an interdependent healthcare–bridge network system under seismic hazard. *Structure and Infrastructure Engineering*, 13(1):160–170.
- Douglas, J. 2003. Earthquake ground motion estimation using strong-motion records: a review of equations for the estimation of peak ground acceleration and response spectral ordinates. *Earth-Science Reviews* 61(1-2): 43–104.
- Ellingwood, B.R. 2005. Risk-informed condition assessment of civil infrastructure: state of practice and research issues. *Structure and Infrastructure Engineering* 1(1): 7–18.
- Enright, M.P. & Frangopol, D.M. 1999. Condition prediction of deteriorating concrete bridges using Bayesian updating. *Journal of Structural Engineering* 125(10): 1118–1124.
- Erath, A., Birdsall, J., Axhausen, K.W, Hajdin, R. 2009. Vulnerability assessment methodology for Swiss road network. *Journal of the Transportation Research Board* 2137: 118–126.
- Faturechi, R. & Miller-Hooks, E. 2015. Measuring the performance of transportation infrastructure systems in disasters: A comprehensive review. *Journal of infrastructure systems* 21(1): 04014025.
- Franchin, P., Ragni, L., Rota, M., Zona, A. 2018. Modelling uncertainties of Italian code-conforming structures for the purpose of seismic response analysis. *Journal of Earthquake Engineering* 22(sup2): 1964–1989.
- Frangopol, D.M. 2011. Life-cycle performance, management, and optimisation of structural systems under uncertainty: Accomplishments and challenges. *Structure and Infrastructure Engineering* 7(6): 389–413.
- Frangopol, D.M. & Bocchini, P. 2012. Bridge network performance, maintenance and optimization under uncertainty: Accomplishments and challenges. *Structure and Infrastructure Engineering* 8(4): 341–356.
- Frangopol, D.M. & Das, P.C. 1999. Management of bridge stocks based on future reliability and maintenance costs. *Current and Future Trends in Bridge Design, Construction, and Maintenance*, The Institution of Civil Engineers, Thomas Telford, London, 45–58.
- Frangopol, D.M. & Kim, S. 2022. *Bridge Safety, Maintenance and Management in a Life-Cycle Context*, CRC Press, A Science Publishers Book, Boca Raton.
- Frangopol, D.M., Dong, Y., Sabatino, S. 2017. Bridge life-cycle performance and cost: Analysis, prediction, optimization, and decision-making. *Structure and Infrastructure Engineering* 13(10): 1239–1257.
- Freddi, F., Galasso, C., Cremen, G., Dall’Asta, A., Di Sarno, L., Giaralis, A., Gutiérrez-Urzúa, F., Málaga-Chuquitaype, C., Mitoulis, S.A., Petrone, C., Sextos, A., Sousa, L., Tarbali, K., Tubaldi, E., Wardman, J., Woo, G. 2021. Innovations in earthquake risk reduction for resilience: Recent advances and challenges. *International Journal of Disaster Risk Reduction* 60: 102267.
- Ghosh, J. & Padgett, J.E. 2010. Aging considerations in the development of time-dependent seismic fragility curves. *Journal of Structural Engineering* 136(12): 1497–1511.
- Ghosn, M., Moses, F., Frangopol, D.M. 2010. Redundancy and robustness of highway bridge superstructures and substructures. *Structure and Infrastructure Engineering*, 6(1-2): 257–278.
- Ghosn, M., Dueñas-Osorio, L., Frangopol, D.M., McAllister, T.P., Bocchini, P., Manuel L., Ellingwood, B.R., Arangio, S., Bontempi, F., Shah, M., Akiyama, M., Biondini, F., Hernandez, S., Tsiatas, G. 2016a. Performance indicators for structural systems and infrastructure networks. *Journal of Structural Engineering* 142(9): F4016003.
- Ghosn, M., Frangopol, D.M., McAllister, T.P., Shah, M., Diniz, S., Ellingwood, B.R., Manuel, L., Biondini, F., Catbas, N., Strauss, A., Zhao, Z.L. 2016b. Reliability-based structural performance indicators for structural members. *Journal of Structural Engineering* 142(9): F4016002.
- Gidaris, I., Padgett, J.E., Barbosa, A.R., Chen, S., Cox, D., Webb, B., Cerato, A. 2017. Multiple-hazard fragility and restoration models of highway bridges for regional risk and resilience assessment in the United States: state-of-the-art review. *Journal of structural engineering* 143(3): 04016188.
- Iervolino, I., Chioccarelli, E., Giorgio, M. 2018. Aftershocks’ effect on structural design actions in Italy. *Bulletin of the Seismological Society of America* 108(4): 2209–2220.
- Ishibashi, H., Akiyama, M., Frangopol, D.M., Koshimura, S., Kojima, T., Nanami, K. 2021. Framework for estimating the risk and resilience of road networks with bridges and embankments under both seismic and tsunami hazards. *Structure and Infrastructure Engineering* 17(4): 494–514.

- Jayaram, N. & Baker, J.W. 2010. Efficient sampling and data reduction techniques for probabilistic seismic lifeline risk assessment. *Earthquake Engineering & Structural Dynamics* 39(10): 1109–1131.
- Karamlou, A. & Bocchini, P. 2016. From component damage to system-level probabilistic restoration functions for a damaged bridge. *Journal of Infrastructure Systems* 23(3): 04016042.
- Katsanos, E.I., Sextos, A.G., Manolis, G.D. 2010. Selection of earthquake ground motion records: A state-of-the-art review from a structural engineering perspective. *Soil Dynamics & Earthquake Engineering* 30(4): 57–169.
- Kilantis, I. & Sextos, A. 2019. Integrated seismic risk and resilience assessment of roadway networks in earthquake prone areas. *Bulletin of Earthquake Engineering* 17(1): 181–210.
- Kumar, R., Gardoni, P., Sanchez-Silva, M. 2009. Effect of cumulative seismic damage and corrosion on the life-cycle cost of reinforced concrete bridges. *Earthquake Engineering & Structural Dynamics* 38(7): 887–905.
- Lallemant, D., Kiremidjian, A., Burton, H. 2015. Statistical procedures for developing earthquake damage fragility curves. *Earthquake Engineering & Structural Dynamics* 44(9): 1373–1389.
- Liu, M. & Frangopol, D.M. 2006. Optimizing bridge network maintenance management under uncertainty with conflicting criteria: Life-cycle maintenance, failure, and user costs. *Journal of Structural Engineering* 132(11): 1835–1845.
- Liu, L., Yang, D. Y., Frangopol, D.M. 2020. Network-level risk-based framework for optimal bridge adaptation management considering scour and climate change. *Journal of Infrastructure Systems* 26(1): 04019037.
- Lu, T., Capacci, L., Anghileri, M., Bianchi, S., Biondini, F., Dong, L. 2022. Simulation-based seismic risk and robustness assessment of aging bridge networks. *International Journal of Civil Engineering* (In Press). DOI: 10.1504/IJCIS.2024.10048368.
- Luco, N. & Cornell, C.A. 2007. Structure-specific scalar intensity measures for near source and ordinary earthquake ground motions. *Earthquake Spectra* 23(2): 357–392.
- Mackie, K.R. & Stojadinović, B. 2006. Post-earthquake functionality of highway overpass bridges. *Earthquake Engineering & Structural Dynamics* 35(1): 77–93.
- Malerba, P.G. 2014. Inspecting and repairing old bridges: Experiences and lessons. *Structure and Infrastructure Engineering* 10(4): 443–470.
- Messore, M.M., Capacci, L., Biondini, F. 2021. Life-cycle cost-based risk assessment of aging bridge networks. *Structure and Infrastructure Engineering* 17(4): 515–533.
- Misra, S., Padgett, J.E., Barbosa, A.R., Webb, B.M. 2020. An expert opinion survey on post-hazard restoration of roadways and bridges: Data and key insights. *Earthquake Spectra* 36(2): 983–1004.
- Mitoulis, S.A., Argyroudis, S.A., Loli, M., Imam, B. 2021. Restoration models for quantifying flood resilience of bridges. *Engineering Structures* 238: 112180.
- Okasha, N.M. & Frangopol, D.M. 2010. Time-variant redundancy of structural systems. *Structure and Infrastructure Engineering* 6(1-2): 279–301.
- Padgett, J.E. & DesRoches, R. 2007. Bridge functionality relationships for improved seismic risk assessment of transportation networks. *Earthquake Spectra* 23(1): 115–130.
- Paolucci, R., Smerzini, C., Vanini, M. 2021. BB-SPEEDset: A validated dataset of broadband near-source earthquake ground motions from 3D physics-based numerical simulations. *Bulletin of the Seismological Society of America* 111(5): 2527–2545.
- Porter, K., Kennedy, R., Bachman, R. 2007. Creating fragility functions for performance-based earthquake engineering. *Earthquake Spectra* 23(2): 471–489.
- Poulin, C. & Kane, M.B. 2021. Infrastructure resilience curves: Performance measures and summary metrics. *Reliability Engineering & System Safety* 216: 107926.
- Rao, A. S., Lepech, M.D., Kiremidjian, A.S. 2017. Development of time-dependent fragility functions for deteriorating reinforced concrete bridge piers. *Structure and Infrastructure Engineering* 13(1): 67–83.
- Riddell, R. 2007. On ground motion intensity indices. *Earthquake Spectra* 23(1): 147–173
- Rose, A. 2004. Defining and measuring economic resilience to disasters. *Disaster Prevention and Management* 13(4): 307–314.
- Saydam, D. & Frangopol, D.M. 2011. Time-dependent performance indicators of damaged bridge superstructures. *Engineering Structures* 33(9): 2458–2471.
- Saydam, D., Bocchini, P., Frangopol, D.M. 2013. Time-dependent risk associated with highway bridge networks. *Engineering Structures* 54: 221–233.
- Shadabfar, M., Mahsuli, M., Zhang, Y., Xue, Y. 2022. Resilience-based design of infrastructure: Review of models, methodologies, and computational tools. *Journal of Risk and Uncertainty in Engineering Systems, Part A: Civil Engineering* 8(1): 03121004.

- Sharma, N., Tabandeh, A., Gardoni, P. 2018. Resilience analysis: A mathematical formulation to model resilience of engineering systems. *Sustainable and Resilient Infrastructure* 3(2): 49–67.
- Shekhar, S., Ghosh, J., Padgett, J.E. 2018. Seismic life-cycle cost analysis of ageing highway bridges under chloride exposure conditions: Modelling and recommendations. *Structure and Infrastructure Engineering* 14(7): 941–966.
- Shinozuka, M., Feng, M. Q., Lee, J., Naganuma, T. 2000. Statistical analysis of fragility curves. *Journal of Engineering Mechanics* 126(12): 1224–1231.
- Silva, V., Akkar, S., Baker, J., Bazzurro, P., Castro, J. M., Crowley, H., Dolsek, M., Galasso, C., Lagomarsino, S., Monteiro, R., Perrone, D., Pitilakis, K., Vamvatsikos, D. 2019. Current challenges and future trends in analytical fragility and vulnerability modeling. *Earthquake Spectra* 35(4): 1927–1952.
- Stergiou, E.C. & Kiremidjian, A.S. 2010. Risk assessment of transportation systems with network functionality losses. *Structure and Infrastructure Engineering* 6(1-2): 111–125.
- Su, L., Wan, H-P., Dong, Y., Frangopol, D.M., Ling, X-Z. 2019. Seismic fragility assessment of large-scale pile-supported wharf structures considering soil-pile interaction. *Engineering Structures* 186: 270–281.
- Sun, W., Bocchini, P., Davison, B.D. 2020. Resilience metrics and measurement methods for transportation infrastructure: The state of the art. *Sustainable and Resilient Infrastructure* 5(3): 168–199.
- Titi, A. & Biondini F. 2014. Probabilistic seismic assessment of multistory precast concrete frames exposed to corrosion. *Bulletin of Earthquake Engineering* 12(6): 2665–2681.
- Yang, D.Y. & Frangopol, D.M. 2019. Societal risk assessment of transportation networks under uncertainties due to climate change and population growth. *Structural Safety* 78: 33–47.
- Yang, D.Y. & Frangopol, D.M. 2020a. Life-cycle management of deteriorating bridge networks with network-level risk bounds and system reliability analysis. *Structural Safety* 83: 101911.
- Yang, D.Y. & Frangopol, D.M. 2020b. Risk-based portfolio management of civil infrastructure assets under deep uncertainties associated with climate change: A robust optimization approach. *Structure and Infrastructure Engineering* 16(4): 531–546.
- Yang, S-I., Frangopol, D.M., Neves, L.C. 2004. Service life prediction of structural systems using lifetime functions with emphasis on bridges. *Reliability Engineering & System Safety* 86(1): 39–51.
- Yanweerasak, T., Withit, P., Akiyama, M., Frangopol, D.M. 2018. Life-cycle reliability assessment of reinforced concrete bridge structures under multiple hazards. *Structure and Infrastructure Engineering* 14(7): 1011–1024.
- Yin, H.C., Kassem, M.M., Nazri, F.M. 2022. Comprehensive review of community seismic resilience: concept, frameworks, and case studies. *Advances in Civil Engineering* 7668214.
- Zhong, J., Gardoni, P., Rosowsky, D. 2012. Seismic fragility estimates for corroding reinforced concrete bridges. *Structure and Infrastructure Engineering* 8(1): 55–69.
- Zhu, B., Frangopol, D.M. 2012. Reliability, redundancy and risk as performance indicators of structural systems during their life-cycle. *Engineering Structures*. 41: 34–49.

Agile analysis of life-cycle damage cost of concrete frame structures under earthquake

J.M. Bairán & M. García

Universitat Politècnica de Catalunya (UPC - BarcelonaTech)

Department of Civil and Environmental Engineering, Barcelona, Spain

ABSTRACT: Seismic events can produce damage and collapse of constructions, impacting the expected life-cycle cost and out-of-service time. Past seismic events showed that socioeconomic consequences at community scale are dramatic, even with non-collapsed structures, resulting in low resilience. To improve this, understanding the probable condition along service life of current structures and new designs is crucial for prioritizing the needs for structural upgrade, and support decision making. This process must consider the effects of different damage scenarios, from light to collapse. Nevertheless, this process is costly and time consuming, making difficult its application at a large scale or in non-special designs. In this paper, a methodology for agile LCC produce by earthquake damage is applied to a case-study consisting of multi-storey moment-resisting concrete frame. Its low computational cost makes it adequate for supporting resilience decision making related to a suite of structures or the assessment of new designs.

1 INTRODUCTION

Seismic events can produce damage and collapse of constructions. As the expected resistance demands under large earthquakes are typically much larger than the ones under normal situations, design practice focuses on collapse prevention in order to guarantee life safety of the users at a reasonable initial cost. Therefore, severe damage is considered admissible. This is consistent with the consideration of earthquakes as accidental events. Nevertheless, the damage produced in the infrastructures of a given location causes a serious consequence to the community, in the socioeconomic point of view, due to the repair and demolition costs, and inoperative time or reduced functionality of the damaged structures during recovery time, Capacci et al (2022).

Events like the earthquake in Haiti 2009, showed the catastrophic consequences of extensive collapse in a community, which can extend during more than a decade under lack of preparedness. On the other hand, locations with generalized applications of seismic design regulations succeeded in preventing extensive collapse, such as Christchurch 2009, Pampanin (2012). However, the large extension of damaged structures required demolition and repair of most of the financial district, resulting in reduced functionality during several years, lack resilience, with dramatic socioeconomic consequences.

To improve this situation, understanding the probable condition along service life of current structures and new designs is crucial for identifying needs for structural upgrade and support decision making. This process should consider the effects different damage scenarios, from light to collapse. In addition, cost and probability of occurrence are then assessed in order to support informed decisions. However, this is usually costly and time consuming, which limits its applicability at a large scale for ordinary designs. Nevertheless, to achieve

realistic benefits in the community scale, agile and cost-effective methods that can be applied in broad scale are needed.

In this paper, a seismic damage assessment method which can be applied at an agile computation time is used to quantify the probability of exceedance of economic cost during the service life of a concrete frame structure. Through a rational basis, the method estimates the evolution of the damage intensity and distribution of structures along the push-over curve. It avoids iterative process to find the performance points at different seismic intensities for each increment of displacement. The seismic intensities are further associated to the annual probability of occurrence through a hazard model. The damage distribution and fragility curves are estimated in less computing time than required using detailed multiple time-history simulations, while providing an estimation of the probability of exceedance of the damage state. For each damage scenario, the repair cost is assessed considering suitable repair activities for simulated local damage intensity, characterized by means of plastic deformation, and a construction costs database. The methodology is applied to a case-study consisting of multi-story moment-resisting concrete frame. Because of the rational approach and low computation cost, the approach is adequate for supporting resilience decision taking related to a suite of structures or the assessment of new designs.

2 DAMAGE ESTIMATION METHOD

In order to estimate the repair cost of the structure under seismic events, the damage distribution should be assessed. A general approach to estimate structural damage produced by earthquakes in a structure requires the non-linear dynamic analysis of the structure under a given seismic event. To consider the uncertainties of future seismic events, it is necessary to analyse a number of seismic records that are representative of the location seismicity. On the other hand, the uncertainties on the structural performance, resulting from material variability, geometry imperfections, among others, can be assessed by considering these parameters as random variables. Nevertheless, it is generally accepted that the variability of the earthquake demand exceeds that of the structural characteristics, Yamin (2015), so a plausible estimation can be made considering only the earthquake variability.

The previously described approaches provide a good estimation of the damage; however, they require significant computation effort and time. Therefore, an agile methodology will estimate the damage by means of a static non-linear push-over analysis curve of the structure. Based on the characteristics of the push-over curve, damage thresholds are defined which are associated to specific repair operations. In this paper, the four damage thresholds described in Equations (1)–(4), as proposed by Lagomarsino et al (2003), will be used.

$$Sd_1 = 0.7D_y \quad (1)$$

$$Sd_2 = D_y \quad (2)$$

$$Sd_3 = D_y + 0.25(D_u - D_y) \quad (3)$$

$$Sd_4 = D_u \quad (4)$$

Where Sd_1 , Sd_2 , Sd_3 , and Sd_4 represent the spectral displacement at 0.5 probability of initiation of the damage limit states light (*LS1*), moderate (*LS2*), severe (*LS3*), and complete (*LS4*), respectively. D_y and D_u are the spectral displacement at yielding and ultimate conditions, in an energy equivalent bilinear representation of the push-over curve.

The previous thresholds can be used as an agile estimation of the fragility curve of each limit state. By accepting that the probability of not-exceeding a certain damage limit state, when the spectral displacement takes a value S_d , follows a log-normal distribution, the fragility curve of the limit state can be computed as in Equation (5). Where Sd_i is the displacement threshold, and β_i is the coefficient of variation of the natural logarithm of the spectral

displacement, which are taken as $\beta_1=0.28$, $\beta_2=0.29$, $\beta_3=0.34$, and $\beta_4=0.45$ for buildings, see Moreno and Bairán (2012, 2015).

$$P(DS \geq DS_i) = \Phi \left[\frac{1}{\beta_i} \cdot \ln \left(\frac{S_d}{S_{d_i}} \right) \right] \quad (5)$$

As mentioned above, the uncertainties structural characteristics can be considered small compared to that of the earthquake demand. In this case, the annual probability of not exceeding a specific spectral displacement S_d can be associated the probability of not exceeding the seismic intensity that produces that displacement in the structure. A seismic hazard function of the form of Equation (6) is used to relate the peak ground acceleration (PGA) intensity with the return period. The annual probability of not exceedance is computed in terms of the return period considering it as a Poisson process. To relate the spectral displacement (S_d) is determined as the performance point in the push-over curve given response spectrum with a PGA value (a).

$$a = a_{ref} \left(\frac{T_{ref}}{T} \right)^{\frac{1}{k}} \quad (6)$$

3 LIFE CYCLE COST

Each displacement in the performance point is associated to a probability of not-exceedance and a probability of developing a specific damage state, computed as described in the previous section. The expected life cycle repair cost of earthquake damage is computed by means of Equation (7). Here, P_{DS_i} is the probability of exhibiting a damage state j in one year, assuming that each seismic event probability is independent. RC is the reference repair cost of the damage state, associated to a repair technique in each damaged region. The distribution of damaged regions is taken according to the distribution and damage states in each plastic hinge. $PV(t)$ is the present value factor for a cost expended in time t . Finally, s is the discount rate that accounts for inflation and opportunity cost.

$$E(RC_j) = \sum_{t_i}^{t_{life}} \sum_j PV(t_i) P_{DS_i} RC_j \quad (7)$$

$$PV(t) = (1 + s)^{-t} \quad (8)$$

4 EXAMPLE

Consider the reinforced-concrete frame structure shown in Figure 1, representative of a square plan building, with identical frames in the two directions. The dead and live loads acting on each frame are 15 kN/m and 6 kN/m, respectively. The structure is built with concrete class C30/37 and steel reinforcement class 400C, according to Eurocode 2. The structure is considered located in a soil class C, with a reference PGA of 0.502 g for a return period 475 years. The seismic hazard is described by Equation (6), taking $k=3.71$.

Figure 2 show the push-over of the structure, where the displacements of each damage limit state thresholds have been highlighted. The resulting fragility curve, computed using Equation (5), is shown in Figure 3. Each curve represents the probability of not exceeding the corresponding limit state when the spectral displacement takes the value S_d . Therefore, the vertical distance between curves indicates the probability of exhibiting the damage in the limit state corresponding to the curve below.

The repair cost associated to each damage state the damage distribution under each displacement distribution are shown in Figure 4. Both the distribution, quantity and damage state in each hinge are analysed. A specific repair technique is applied to each concrete region depending the damage state that exhibits. Namely, crack injection is applied to light damage,

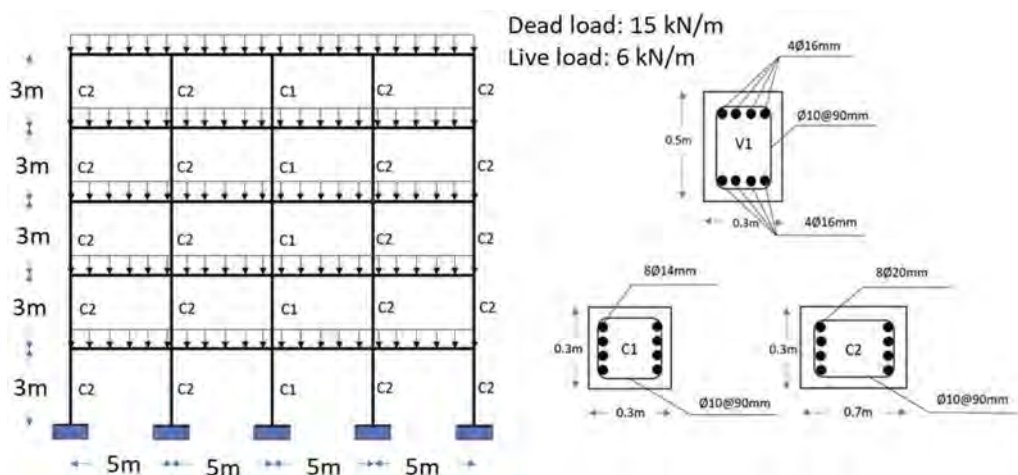


Figure 1. Reinforced concrete frame.

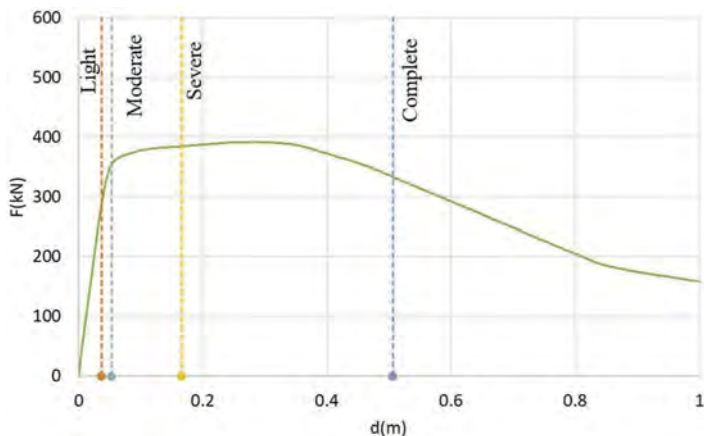


Figure 2. Push-over curve showing the displacement thresholds for the four limit states considered.

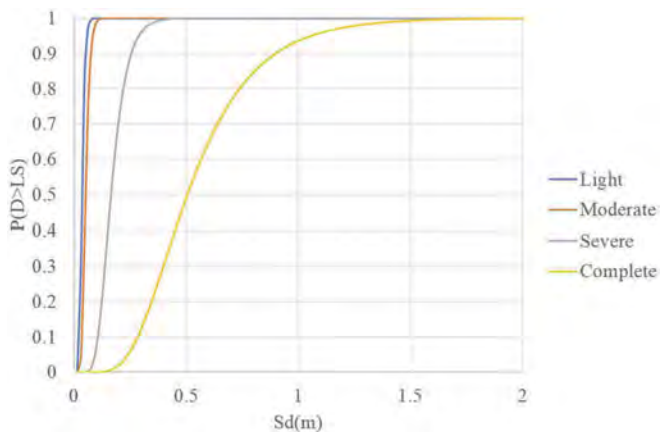


Figure 3. Fragility curves for each damage limit state.

concrete cover restitution is applied to moderate damage. Major repairs with reinforcement replacement restoring of concrete layer is associated to severe damage. Finally, in the case of complete damage, complete demolition and substitution is considered. The costs of the damage region have been estimated using a construction the construction database, CYPE (2022). The resulting unit costs per damaged region and limit state are summarized in Table 1.

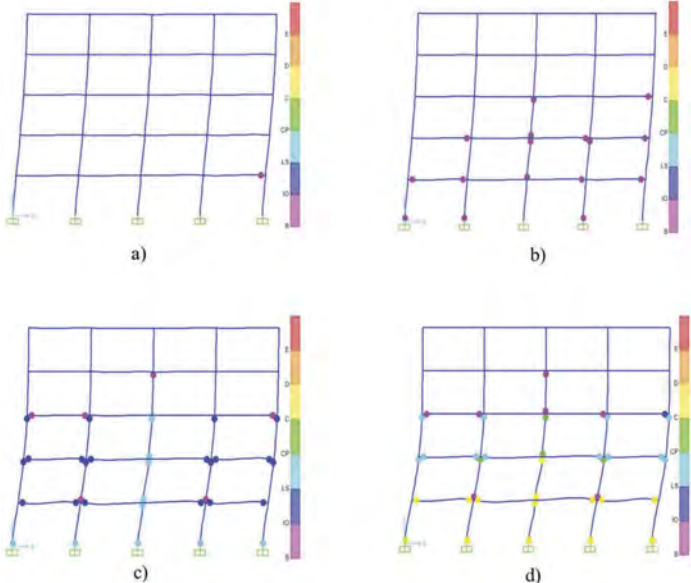


Figure 4. Damage distribution in each plastic hinge in the limit states a) light, b) moderate, c) severe, d) complete.

Table 1. Repair costs per damaged region.

Element type	Id.	Unit	Repair cost in each limit state			
			LS1	LS2	LS3	LS4
Column	C2	€/m	430.66	423.91	374.73	3,237.60
Column	C1	€/m	212.41	254.35	282.95	2,781.50
Beam	V1	€/m	302.05	275.54	297.80	611.70
Slab	L1	€/m ²	64.95	186.15	143.90	639.56

The repair cost in the threshold displacement of the damage state is computed based on the unit repair costs and the damage distribution. Furthermore, a repair cost function in terms of the spectral displacement is constructed, see Figure 5a, by multiplying the repair cost for each damage limit state by the probability of exhibiting each particular damage state, determined from the fragility function. This cost is accumulated during a reference service life period, taken as 50 years, by means of Equation (7). The annual probability of exceeding each spectral displacement is shown in Figure 5b. To obtain this distribution, the ground acceleration that produces a performance point in the displacement d was determined. Secondly, the probability of each seismic scenario is computed by means of the hazard function of the location. It can be inferred that displacements associated to complete and high damage, show very small probability of occurrence; while other damage intensities have larger contributions.

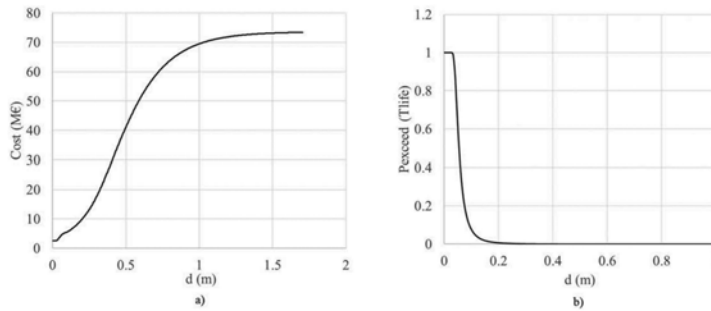


Figure 5. Variation of the expected repair cost with the spectral displacement (a) and annual probability of exceedance of the spectral displacement (b).

By combining the two curves of Figure 5, the probability distribution of exceeding a repair cost during the life of the structure is computed, as described in Figure 6, for the complete building. This cost accounts for the contribution of all possible damage states, from light to complete. As evidenced, there is a probability of 0.5 of exceeding a repair cost 4.1 M€ during the life of the structure, while there is a probability of 0.1 of exceeding a repair cost of 5.5 M€.

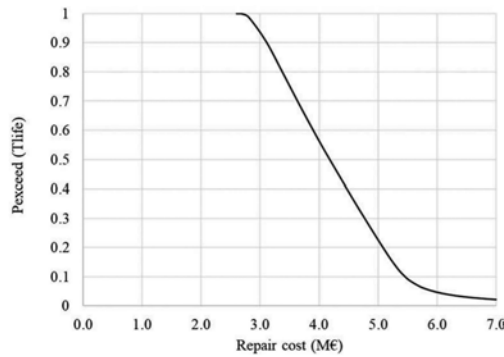


Figure 6. Probability of exceeding a repair cost (M€) during the reference service life of 50 years.

5 CONCLUSIONS

A simplified methodology for the agile or fast assessing of repair costs associated to seismic damage along the service life of a structure was presented, based on rational simplifications. The method was applied to reinforced concrete frames.

The approach requires significant less computation time than explicit non-linear time history analyses for the estimation of damage scenarios. In addition, it avoids iteration processes for finding performance points in the push-over, allowing for a fast estimation of the different seismic intensities along all points of the push-over curve. This makes the method suitable for estimation of the damage scenarios at increasing seismic intensities return periods in individual or system of buildings.

A case study consisting of a typical reinforced concrete ductile frame structure, design as per modern design standards, was investigated. The analysis showed that the costs related to light and moderate damage have a significant contribution to the expected repair cost to seismic damage along the service life. This can be attributed to the higher probability of occurrence of moderate earthquakes that are capable of triggering such damage distribution, without creating a risk of collapse. Considering independent events and one event per year, the probability distribution of expected repair damage along the service life showed a 0.5 probability of exceedance 4.1 M€, and a 0.1 probability of exceedance a repair cost of 5.5 M€.

The procedure can be used for fast analysis of the impacts of individual design alternatives and potential socioeconomical consequences of a system of infrastructures. Future extensions of the method will be dedicated to the assessment of time to recover functionality and of reliability indexes of isolated and a combination of structures in a location. Furthermore, as the method relies on the push-over estimation, it is sensitive to the structure irregularities and force distribution pattern. Current research is being carried out to assess the influence of the load patten in the predicted response.

It should be pointed out that the current application, the uncertainties of the structural parameters were considered negligible compared to that of the earthquake action, this hypothesis is supported on previous research that were more focused on extensive damage and collapse. Additional research will also investigate the influence of structural uncertainties on the light and moderate damage. Similarly, the impact of non-structural damage and components in the cost, functionality loss and time to recover may be also incorporated in the assessment approach by means of adequate engineering parameters that represent the non-structural damage events that can further be considered in the cost analysis.

ACKNOWLEDGEMENTS

This study was developed in the scope of research projects PID2021-123701OB-C21, funded by MCIN/ AEI/10.13039/501100011033 and European Regional Development Funds (ERDF) “A way to make Europe”, and TED2021-130272B-C21 funded by MCIN/ AEI/ 10.13039/501100011033 “European Union NextGenerationEU/PRTR”.

REFERENCES

- Capacci, L, Biondini, F., Frangopol, D.M. (2022), “Resilience of aging structures and infrastructures systems with emphasis on seismic resilience of bridges and road networks: Review”, *Resilient Cities and Structures*, 1, 23–41.
- CYPE Ing. (2022), “Generador de precios de la construcción”, url: <http://www.generadordeprecios.info/#gsc.tab=0>, accessed May 18, 2022.
- Lagomarsino, S.; Penna, A. (2003), “Guidelines for the implementation of the II level vulnerability methodology. WP4: Vulnerability assessment of current buildings”. Technical presentation RISK-UE project: An advanced approach to earthquake risk scenarios with app. to different European towns. 2003.
- Moreno-González, R. Bairán, J.M. (2012), “Seismic damage assessment of waffled slabs reinforced concrete buildings in Barcelona”, *Int. Journal of Arch. Heritage*, Vol. 7.
- Moreno-González, R. Bairán, J.M. (2015), “Performance of existing modernist buildings in Barcelona”, *ASCE-Journal of Performance of Constructed Facilities*, Vol. 29, 4.
- Pampanin, S. (2012), “Reality-check and renewed challenges in earthquake engineering: Implementing low-damage”, 15th World Conference of Earthquake Engineering, Lisboa.
- Youssef, N.F., Tunick, D., Naeim, F., Lew, M., Carpenter, L., Rojas, F., Saragoni, R., Schachter, M. (2011). “Performance of the Torre Bosquemar and Olas buildings in San Pedro de la Paz and the Pedro de Valdivia building in Concepción in the 27 February 2010 offshore Maule, Chile earthquake”, *Structural Design of Tall and Special Buildings*, 20, 65–82.
- Yamin-Lacouture, L.E. (2015), “Riesgo sísmico de edificaciones en términos de pérdidas económicas mediante integración de costos de reparación de componentes”, Ph.D. Dissertation, Universitat Politècnica de Catalunya, Barcelona, Spain.

Methodology for determining optimal countermeasure for bridges under seismic and tsunami hazards

H. Ishibashi

Nihon University, Koriyama, Japan

M. Akiyama

Waseda University, Tokyo, Japan

S. Koshimura

Tohoku University, Sendai, Japan

ABSTRACT: A methodology for determining the optimal countermeasure for bridges subjected to ground motion and tsunami is proposed. Seismic and tsunami fragility curves of a bridge pier and bearing are developed considering the effects of seismic damage prior to tsunami action. The structural vulnerabilities against horizontal and vertical forces are investigated separately in this paper. Seismic and tsunami hazard curves are obtained assuming the occurrence of an earthquake. Uncertainties associated with fault movement, hazard intensity and structural vulnerability are considered based on Monte Carlo simulation. The expected recovery time of bridges (i.e. risk) is estimated based on the failure probabilities of bridge piers and bearings, and used to determine the optimal countermeasure for bridges. As an illustrative example, the proposed methodology is applied to bridges which would be affected by the anticipated Nankai Trough earthquake.

1 INTRODUCTION

In the 2011 Great East Japan earthquake, many bridge superstructures, despite being retrofitted to protect the superstructure from excessive displacement due to seismic actions, were washed away by hydrodynamic forces. The failure mode of a bridge subjected to both ground motion and tsunami is determined by the vulnerability of structural components, such as pier and bearing, and the hazard intensities. Moreover, the recovery time required for bridge reconstruction after an earthquake depends on the failure mode. For example, in case the bridge superstructure is washed away due to tsunami, the reconstruction work would take a very long time. It is considered that the pre-disaster preparation for achieving rapid reconstruction of bridge is needed in coastal regions potentially threatened by giant tsunami, whereas conventional seismic retrofitting is appropriate for the bridges located in inland regions. The appropriate countermeasures for bridges should be taken before an earthquake considering the recovery time.

Risk is expressed in the consequence and probability of the events (CIB 2001) and can be used as a performance indicator to determine the optimal countermeasures for undesired events. Ishibashi et al. (2021) proposed a methodology for determining the retrofitting prioritization of road structures under multiple hazards based on the risk. Decò & Frangopol (2011) presented a framework for assessing the time-dependent total risk of bridges considering the life-cycle performance. Risk-based approach is important to manage the bridges in earthquake-prone areas.

In addition to seismic retrofitting, the technologies for the rapid construction of temporary bridges are needed considering the possibility that bridge superstructures near the coastline would be washed away due to tsunami. Mineyama et al. (2020) proposed the bridge girder with double end plate connection using high strength bolts to reduce the on-site bridge construction time. Ishibashi et al. (2022) presented the precast reinforced concrete blocks for the bridge superstructure which can be assembled in a short time without using heavy machinery. These technologies on temporary bridges are useful in the severe situation after tsunami events and can contribute to enhancing the disaster resilience. It is important to develop a methodology for determining whether seismic retrofitting of piers or preparation of temporary bridges is more appropriate for bridges expected to be damaged by future earthquakes.

This paper presents a methodology for determining optimal countermeasures for bridges under seismic and tsunami hazards based on the risk of post-disaster recovery time. Seismic and tsunami fragility curves of a bridge pier and bearing and hazard curves are estimated by performing Monte Carlo simulation (MCS)-based analyses. Structural vulnerabilities of the pier against horizontal seismic force and the bearing against horizontal and vertical tsunami forces are estimated in the fragility assessment. Risk is defined as the recovery time of damaged bridges. The optimal countermeasure for bridges is determined by comparing the risk reduction due to seismic retrofitting of the pier and due to pre-disaster preparation of temporary bridge girders which can be used after washout of superstructures during the tsunami event. In an illustrative example, the proposed methodology is applied to the bridges located in a city affected by the anticipated Nankai Trough earthquake. The optimal countermeasures for individual bridges are discussed based on the risk.

2 PROCEDURE FOR DETERMINING OPTIMAL COUNTERMEASURE FOR BRIDGES UNDER SEISMIC AND TSUNAMI HAZARDS

2.1 Hazard assessment

Figure 1 shows the procedure for determining the optimal countermeasure for bridges under seismic and tsunami hazards. In this paper, probabilistic seismic and tsunami hazard analyses are performed based on the MCS given the occurrence of an earthquake. The average stress drops of the seismic and tsunami fault models, which are the critical parameters used to

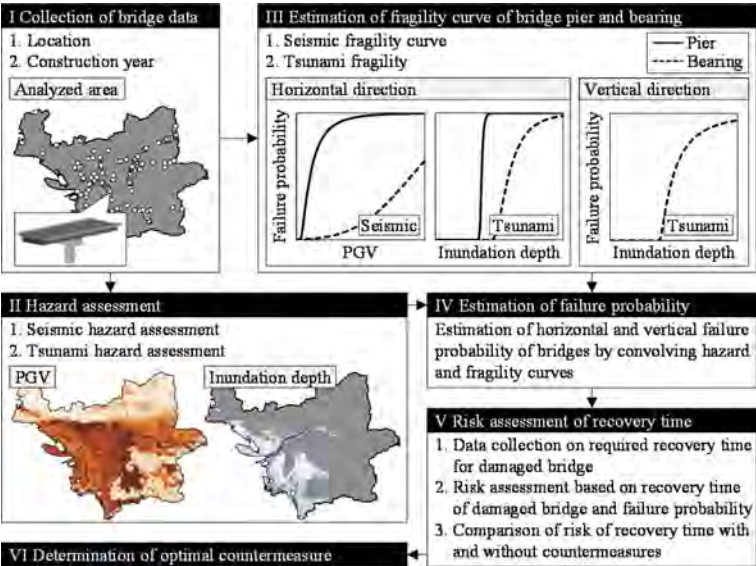


Figure 1. Procedure for determining optimal countermeasure for bridges under seismic and tsunami hazards.

calculate the dislocation and moment magnitude of an analyzed earthquake (HERP 2017), are considered random variable in the MCS. To estimate the seismic hazard curve at the location of analyzed bridges, the maximum velocity on the engineering bedrock is obtained using the attenuation relationship provided by Si & Midorikawa (1999) as follows:

$$\log V_b = 0.58M_w + 0.0031D_f - \log X_{eq} - 0.002X_{eq} - 1.19 + \varepsilon \quad (1)$$

where V_b is the maximum velocity on the engineering bedrock, M_w is the moment magnitude, D_f is the fault depth, X_{eq} is the equivalent hypocentral distance provided by Ohno et al. (1993), and ε is the associated model uncertainty.

Peak ground velocity (PGV) is then estimated by multiplying the maximum velocity on the engineering bedrock by the amplification factor calculated using the formula developed by Fujimoto & Midorikawa (2006).

Inundation depth is used as a tsunami intensity measure. The initial tsunami water level due to fault movement is computed using formulas developed by Okada (1985) considering the uncertainty associated with average stress drop. MCS-based horizontal 2D tsunami propagation simulations based on nonlinear longwave theory (Goto et al. 1997) are performed using the initial water level as the initial condition to estimate the inundation depth at the location of individual bridges. The cumulative distribution functions associated with the relationship between PGV and inundation depth are approximated by lognormal distributions based on the results of MCS.

2.2 Fragility curve

Seismic and tsunami fragility curves of a bridge pier and bearing are developed considering the horizontal and vertical failure directions. Sequential nonlinear seismic response analysis and tsunami pushover analysis are performed to consider the effects of seismic damage on the reduction in tsunami capacity. Horizontal force due to ground motion and tsunami and vertical tsunami force are used to estimate the horizontal and vertical structural vulnerabilities, respectively.

When estimating the fragility curves of a pier, the damage state for horizontal seismic force is determined based on the maximum displacement, shear force and residual displacement of the pier. For a bearing, both horizontal and vertical forces are considered in the vulnerability assessment. The damage states are determined according to the recovery time required after an earthquake and divided into three levels: none (= DS_1), moderate (= DS_2) and complete (= DS_3).

Many seismic waves observed during past earthquakes in Japan are used in the MCS-based nonlinear seismic response analyses. Horizontal and vertical tsunami forces are computed using empirical formulas provided by the Subcommittee on Analysis of Damaged Bridge due to the Great East Japan Earthquake (2015). The uncertainties associated with material properties, structural vulnerabilities and empirical formulas are considered in the MCS. Fragility curves are estimated by fitting the following equation based on a log-normal cumulative distribution function:

$$P_{fi}(DS_i|\gamma) = \int_0^\gamma \frac{1}{\sqrt{2\pi}\sigma_i(x-l_i)} \exp\left[-\frac{\{\ln(x-l_i) - \mu_i\}^2}{2\sigma_i^2}\right] dx \quad (2)$$

where DS_i is damage state, $P_{fi}(DS_i|\gamma)$ is conditional failure probability that damage state becomes greater than or equal to DS_i given the hazard intensity = γ , and μ_i , σ_i and l_i are parameters. The natural logarithm of $X-l_i$ is normally distributed with mean μ_i and variance σ_i^2 . Although l is commonly zero when estimating fragility curves, it is considered to improve the fitting of the estimated curves to the results of MCS.

2.3 Risk assessment

Horizontal and vertical failure probabilities are estimated using the fragility curves for horizontal and vertical failure directions, respectively, and hazard curves obtained at the locations of bridges. The recovery time of bridges is determined based on the data obtained in past disasters. The risk as the expected post-disaster recovery time of bridges is defined by the following equation:

$$T_r = \sum_{i=1}^3 P_{fp,h}(DS_i) \cdot T_{p,h}(DS_i) + \sum_{i=1}^3 P_{fb,h}(DS_i) \cdot T_{b,h}(DS_i) + \sum_{i=1}^3 P_{fb,v}(DS_i) \cdot T_{b,v}(DS_i) \quad (3)$$

where T_r is risk of post-disaster recovery time of a bridge, $P_{fp,h}(DS_i)$ and $T_{p,h}(DS_i)$ are failure probability and recovery time of piers given DS_i in the horizontal direction, respectively, $P_{fb,h}(DS_i)$ and $T_{b,h}(DS_i)$ are failure probability and recovery time of bearings given DS_i in the horizontal direction, respectively, and $P_{fb,v}(DS_i)$ and $T_{b,v}(DS_i)$ are failure probability and recovery time of bearings given DS_i in the vertical direction, respectively. In this study, since the failure events of pier and bearing are assumed to be independent, the expected recovery time due to the damage to bridge pier or bearing is assessed separately in Equation (3). The effects of countermeasures for damages to piers and bearings are assessed separately based on the risk reduction due to the countermeasure.

3 ILLUSTRATIVE EXAMPLE

3.1 Analyzed area

A megathrust earthquake along the Nankai Trough (i.e. the Nankai Trough earthquake) is predicted to occur in the near future and cause strong ground motion and tsunami in the Pacific coastal region of Japan (HERP 2013). The countermeasures for bridges in Wakayama City, which is located in the coastal region expected to be affected by the Nankai Trough earthquake, are discussed in the illustrative example. The data on location and construction year of bridges provided by MLIT (2022) are used in this study.

3.2 Hazard assessment

In the seismic hazard assessment, average stress drop is modeled as a truncated lognormal distribution with a mean of 2.1 MPa and a standard deviation of 1.1 MPa based on the data provided by the Cabinet Office, Government of Japan (2012). When estimating tsunami hazard curves, a truncated lognormal distribution with a mean of 1.9 MPa and a standard deviation of 1.9 MPa is used to generate average stress drops in the MCS (Murotani et al., 2013). In addition, two seismic and eleven tsunami fault models provided by the Cabinet Office, Government of Japan (2012) are used, respectively, considering the uncertainty associated with the locations of large-slip areas. Figure 2 shows the contours associated with mean PGV and inundation depth in Wakayama City.

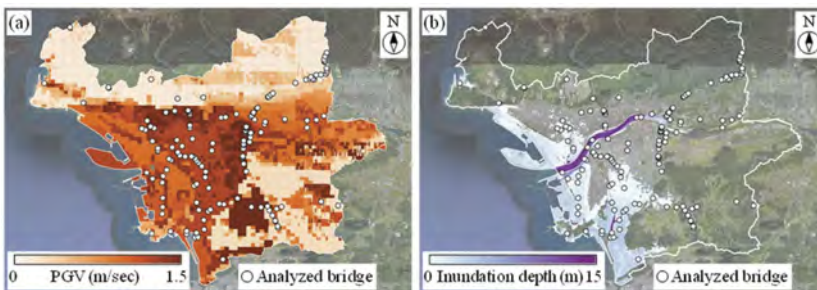


Figure 2. Contours associated with (a) mean PGV and (b) inundation depth in Wakayama City.

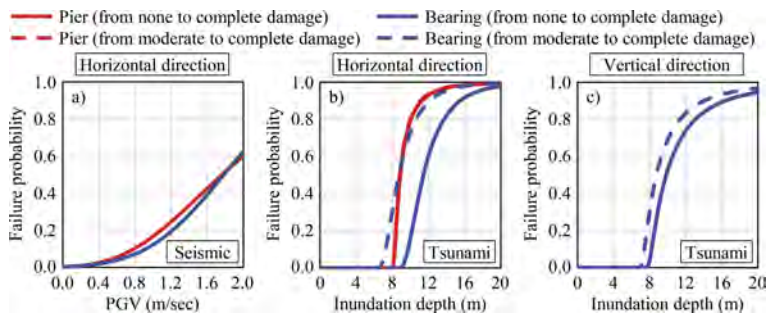


Figure 3. Fragility curves: (a) seismic fragility curves of 1996 pier, (b) tsunami fragility curves of bearing (horizontal direction) and (c) tsunami fragility curves of bearing (vertical direction).

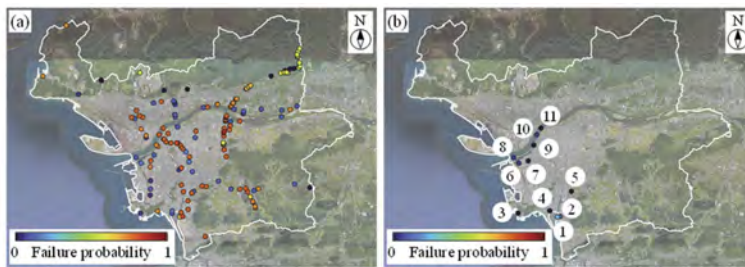


Figure 4. (a) horizontal failure probability of piers and (b) vertical failure probability of bearings.

Table 1. Recovery times of piers and bearings with moderate and complete damages.

Direction	Bridge component	Damage state	
		Moderate	Complete
Horizontal	Pier	30 days	90 days
	Bearing	3 days	5 days
Vertical		3days	120 days (without preparation of temporary bridge)
			30 days (with preparation of temporary bridge)

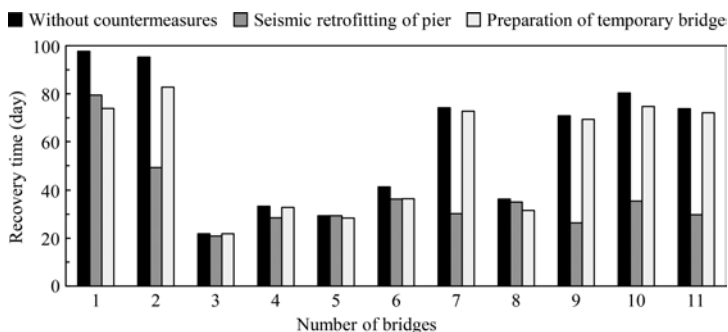


Figure 5. Estimated risk as the expected recovery time.

3.3 Fragility curves

Four types of piers designed in accordance with the Japanese seismic specifications published in 1964, 1980, 1990 and 1996 are modeled based on Karim & Yamazaki (2003) and applied to the

analyzed bridges considering the differences in seismic performance by the construction year. Herein, each pier is referred as 1964, 1980, 1990 and 1996 piers, respectively. 1996 pier has seismic performance equivalent to the current Japanese seismic design code. The pier height is assumed to be 6 m. Hence, vertical tsunami forces act on the bearings when the inundation depth is greater than 6 m. The bearing is designed based on Abe et al. (2004) and Hashimoto et al. (2005). The seismic and tsunami fragility curves of 1996 pier and the bearing are shown in Figure 3.

3.4 Determination of optimal countermeasure based on risk

Figure 4 shows the horizontal failure probability of piers and vertical failure probability of bearings of analyzed bridges. Eleven bridges can be completely damaged due to vertical tsunami force caused by the anticipated Nankai Trough earthquake as shown in Figure 4 (b). In this paper, seismic retrofitting of piers and pre-disaster preparation of temporary bridge girders for vertical damage to bearings are considered countermeasures. The recovery times of piers and bearings listed in Table 1 are set based on Shoji et al. (1997) and the report provided by the Subcommittee on the Survey on Emergency Temporary Bridges for Emergency Construction During Disaster (2020). The fragility curves of 1996 pier are applied when estimating the risk assuming seismic retrofitting of piers. Pre-disaster preparation of temporary bridge girders is considered to achieve rapid reconstruction of bridges as listed in Table 1. In the risk assessment using Equation (3), the failure probability of piers $P_{fp,h}$ and recovery time of bearings damaged vertically $T_{b,v}$ can be reduced by seismic retrofitting and pre-disaster preparation of temporary bridge girders, respectively.

The estimated risk as the expected recovery time is shown in Figure 5. Bridge 5 has sufficient seismic capacity even without retrofitting of the pier since bridge 5 was designed according to the seismic specification published in 1996. Seismic retrofitting of bridge piers can reduce the failure probability and associated risk calculated using Equation (3). However, the optimal countermeasure for bridge 1 is the pre-disaster preparation of temporary bridge girders because bridge 1 has high vertical failure probability due to tsunami as shown in Figure 4(b). This result demonstrates that optimal countermeasures for reducing the risk depends on the structural vulnerabilities of bridge components and hazard intensities.

4 CONCLUSIONS

A risk-based methodology for determining the optimal countermeasure for bridges under both seismic and tsunami hazards is proposed. Fragility curves of a pier and bearing are developed considering the damage in the horizontal and vertical directions since post-disaster recovery time of bridges depends on the failure mode. Hazard curves are also obtained based on MCS considering the uncertainty associated with fault movement. In the illustrative example, the risk of recovery time of bridges affected by the Nankai Trough earthquake is estimated. The optimal countermeasures for bridges should be determined based on the risk to achieve rapid reconstruction.

In this study, the risk as the expected recovery time is assessed without considering the correlation between the failures of piers and bearings. In addition, the differences in recovery time of bridges should be considered since the time associated with the recovery activities depends on various factors, such as bridge type, length and location. Further research is needed to improve the proposed framework to determine more appropriate countermeasures for bridges subjected to ground motion and tsunami.

ACKNOWLEDGMENT

This work was supported by JSPS KAKENHI Grant Number JP21K14235 and the joint research grant in 2022 from Co-creation Center for Disaster Resilience, International Research Institute of Disaster Science (IRIDeS) at Tohoku University.

REFERENCES

- Abe, M., Yoshida, J., Fujino, Y., Morishige, Y., Uno, S. & Usami, S. 2004. Experimental investigation of ultimate behavior of metal bridge bearings under seismic loading. *Journal of Japan Society of Civil Engineers*, 773(1-69): 63–78 (in Japanese).
- Cabinet Office, Government of Japan. 2012. Investigative commission on the modeling of giant earthquake caused by Nankai Trough earthquake: Modeling of seismic fault (in Japanese).
- CIB (International Council for Research and Innovation in Building and Construction). 2001. Risk assessment and risk communication in civil engineering. TG 32 Report 259, Rotterdam: Council for Research and Innovation in Building and Construction.
- Decò, A. & Frangopol, D.M. 2011. Risk assessment of highway bridges under multiple hazards. *Journal of Risk Research* 14(9): 1027–1089.
- Fujimoto, K. & Midorikawa, S. 2006. Relationship between average shear-wave velocity and site amplification inferred from strong motion records at nearby station pairs. *Journal of Japan Association for Earthquake Engineering* 6(1): 11–22 (in Japanese).
- Goto, C., Ogawa, Y., Shuto, N. & Imamura, F. 1997. Numerical method of tsunami simulation with the leap-frog scheme. IUGG/IOC Time Project.
- Hashimoto, S., Abe, M. & Fujino, Y. 2005. Damage analysis of Hanshin Expressway viaducts during 1995 Kobe earthquake. III: Three-span continuous girder bridges. *Journal of Bridge Engineering* 10(1): 61–68.
- HERP (Headquarters for Earthquake Research Promotion). 2017. Strong Ground Motion Prediction Method for Earthquakes with Specified Source Faults (“Recipe”). https://www.jishin.go.jp/main/chousa/17_yosokuchizu/recipe.pdf (in Japanese)
- HERP (Headquarters for Earthquake Research Promotion). 2013. Long-term evaluation of Nankai Trough earthquakes. https://www.jishin.go.jp/regional_seismicity/rs_kaiko/k_nankai/ (in Japanese)
- Ishibashi, H., Akiyama, M., Frangopol, D.M., Koshimura, S., Kojima, T. & Nanami, K. 2021. Framework for estimating the risk and resilience of road networks with bridges and embankments under both seismic and tsunami hazards. *Structure and Infrastructure Engineering* 17(4): 494–514.
- Ishibashi, H., Akiyama, M., Fujiwara, M., Uno, Y. & Hiromitsu, T. 2022. Precast RC blocks with connections composed of steel shear keys and CFRP sheets for the superstructure of temporary bridges in a postdisaster situation. *Journal of Bridge Engineering* 27(8): 04022061.
- Mineyama, Y., Sugimoto, Y., Sugita, K. & Yamaguchi, T. 2020. Development of an emergency bridge with the double end plate connection using high strength bolt. *Proc. 16th East Asian-Pacific Conf. Struct. Eng. Constr.* 101: 385–394.
- MLIT (Ministry of Land, Infrastructure, Transport and Tourism). 2022. National road facility inspection database. <https://road-structures-map.mlit.go.jp/> (in Japanese)
- Murotani, S., Satake, K. & Fujii, Y. 2013. Scaling relations of seismic moment, rupture area, average slip, and asperity size for M~9 subduction-zone earthquakes. *Geophysical Research Letters* 40(19): 5070–5074.
- Ohno, S., Ohta, T., Ikeura, T. & Takemura, M. 1993. Revision of attenuation formula considering the effect of fault size to evaluate strong motion spectra in near field. *Tectonophysics* 218(1–3): 69–81.
- Okada, Y. 1985. Surface deformation due to shear and tensile faults in a half-space. *Bulletin of the Seismological Society of America* 75(4): 1135–1154.
- Shoji, G., Fujino, Y. & Abe, M. 1997. Optimal allocation of earthquake-induced damage for elevated highway bridges. *Journal of Japan Society of Civil Engineer*, 569(563): 79–94 (in Japanese).
- Si, H. & Midorikawa, S. 1999. New attenuation relationships for peak ground acceleration and velocity considering effects of fault type and site condition. *Journal of Structural and Construction Engineering* 64(523): 63–70 (in Japanese).
- Subcommittee on Analysis of Damaged Bridge due to the Great East Japan Earthquake, Japan Society of Civil Engineers. 2015. Final report. Part II: Damage analysis due to tsunami. 1-391 (in Japanese).
- Subcommittee on Survey on Emergency Temporary Bridges for Emergency Construction During Disaster, Japan Society of Civil Engineers. 2020. Activity report. 1–46 (in Japanese).
- Karim, K.R. & Yamazaki, F. 2003. A simplified method of constructing fragility curves for highway bridges. *Earthquake Engineering & Structural Dynamics* 32(10): 1603–1626.

Seismic damage control of bridges with deteriorated seismic isolation bearings by rupture of anchor bolts

H. Matsuzaki

National Defense Academy of Japan, Yokosuka, Japan

ABSTRACT: When accessibility to repair damage to bridge columns is a problem, as in the case of multi-span continuous bridges over rivers, it is necessary to avoid the ultimate failure of the bridge columns as well as the seismic isolation bearings. In this study, improving the reparability of seismically isolated multi-span continuous girder bridges by the rupture of the anchor bolts of the deteriorated isolation bearings was investigated by incremental dynamic analysis and fragility analysis. As a result, it was shown that the ultimate failure of rubber layers of the seismic isolation bearings and the columns can be sufficiently avoided under extreme ground motions by the rupture of the anchor bolts, even if the ageing deterioration of bearings is considered.

1 INTRODUCTION

Seismic isolation bearings are widely used to improve the seismic performance of bridges. However, rupture of laminated rubber bearings and large cracks in lead rubber bearings occurred at several bridges during the 2011 Tohoku earthquake and the 2016 Kumamoto earthquake (Akiyama et al., 2020; Takahashi & Hoshikuma, 2013). It is necessary to avoid the rupture of seismic isolation bearings to maintain the functionality of seismically isolated bridges after seismic events. Matsuzaki (2022) showed that the seismic safety of isolated bridges can be significantly improved by setting an adequate capacity hierarchy between the seismic isolation bearings and the bridge column, as it can prevent the rupture of the seismic isolation bearings under extreme ground motions even if the ageing deterioration of the bearings is considered.

When accessibility to repair damage to bridge columns is a problem, as in the case of multi-span continuous bridges over rivers, it is necessary to avoid the ultimate failure of the bridge columns as well as the seismic isolation bearings. For such bridges, it is expected that seismic damage control of bridges by the rupture of the anchor bolts of the bearings under extreme ground motions can be used to interrupt load transmission to columns, thereby preventing rupture of the rubber layers of the bearings and a large nonlinear response displacement development at the column, which needs a long repair time and significant costs. It is also noted that the rupture of anchor bolts can be used because multi-span continuous girder bridges can also prevent unseating of the deck after the rupture of the anchor bolts. Another factor that enhances restoration is that the rupture of the anchor bolts provides space corresponding to the height of the bearings so that the superstructure can be easily jacked up during restoration.

In this study, improving the reparability of seismically isolated multi-span continuous girder bridges by the rupture of the anchor bolts of the deteriorated isolation bearings will be investigated by incremental dynamic analysis (IDA) proposed by Vamvatsikos & Cornell (2002) and fragility analysis.

Table 1. Configurations of the target seismically isolated bridges.

Bridge	Bridge column		Seismic isolation bearing (lead rubber bearing)			
	Size (m)	Height (m)	Mass (ton)	Effective size (mm)	Total thickness of rubber layer (mm)	Anchor bolts
15- ϕ 48	3.4 \times 2.7	15	451	520 \times 520	68	4 \times ϕ 48
15- ϕ 32	3.4 \times 2.7	15	451	520 \times 520	68	4 \times ϕ 32
15- ϕ 30	3.4 \times 2.7	15	451	520 \times 520	68	4 \times ϕ 30
8- ϕ 46	2.7 \times 2.0	8	194	520 \times 520	68	4 \times ϕ 46
8- ϕ 30	2.7 \times 2.0	8	194	520 \times 520	68	4 \times ϕ 30
8- ϕ 28	2.7 \times 2.0	8	194	520 \times 520	68	4 \times ϕ 28

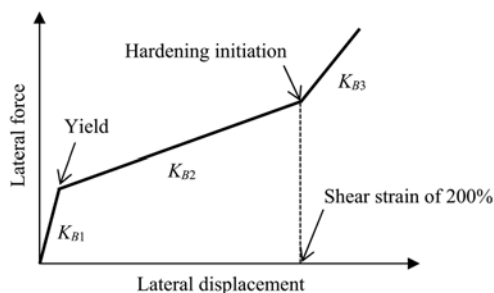


Figure 1. Skeleton of the lateral force–lateral displacement relationship of lead rubber bearings.

2 TARGET BRIDGES AND ANALYTICAL CONDITIONS

2.1 Target bridges

The target bridges are seismically isolated multi-span continuous steel girder highway bridges on the stiff soil in Kumamoto City, as shown in Table 1. Lead rubber bearings were adopted as seismic isolation bearings and the mass of superstructure was 600 ton. As the effects of the column height on the seismic behavior of isolated bridges is significant (Matsuzaki, 2022), columns with two different column heights were considered. Bridges 15- ϕ 48 and 8- ϕ 46 were designed according to the Design Specifications for Highway Bridges (Japan Road Association, 2017) and the Bearing Handbook for Highway Bridges (Japan Road Association, 2018). To investigate the effects of rupture of the anchor bolts under extreme ground motions, bridges with rupture of the anchor bolts are also considered by reducing the diameter of the anchor bolts.

2.2 Analytical modelling of seismically isolated bridges

Lead rubber bearings were idealized based on a tri-linear model considering strain hardening of rubber, as shown in Figure 1. In Figure 1, the ratio of K_{B1} to K_{B2} was set as 6.5:1 based on the Japan Road Association (2018) and the ratio of K_{B3} to K_{B2} was set based on Naito et al. (2017). The skeleton and hysteresis of reinforced concrete columns were idealized based on bi-linear model and Takeda degrading stiffness model by Takeda et al. (1970), respectively. Dynamic response analysis was conducted in the longitudinal direction by idealizing a reinforced concrete column with bearings as a two-degree-of-freedom model. Rayleigh damping was assumed, in which the damping ratios of the column and the isolation bearing were 2% and 0%, respectively.

2.3 Long-term ageing deterioration estimation of seismic isolation bearings

To investigate the effects of the ageing deterioration, time after construction $t=30$ years was considered. Long-term ageing deterioration characteristics of lead rubber bearings

Table 2. Input ground motions.

Earthquake	Recording station (Component)
1995 Kobe	JMA Kobe (NS, EW), KEPCO Shin-Kobe (NS, EW) and Kobe University (NS)
2004 Niigata-ken Chuetsu	K-NET Ojiya (NS, EW), KiK-net Kawanishi (EW) and K-NET Tokamachi (NS)
2007 Noto	K-NET Togi (EW)
2008 Iwate-Miyagi Nairiku	KiK-net Higashi-Naruse (NS, EW), KiK-net Ichinoseki-Nishi (NS, EW), K-NET Naruko (NS) and KiK-net Ichinoseki-Higashi (NS)
2011 Nagano-ken Hokubu	K-NET Hakuba (NS)
2016 Kumamoto	KiK-net Kikuchi (NS), K-NET Ichinomiya (NS, EW) and K-NET Ohzu (NS, EW)
2018 Hokkaido Iburi-Tobu	K-NET Oiwake (NS, EW) and K-NET Mombetsu (EW)

Table 3. Uncertain factors.

Uncertain factor	Distribution	Characteristic value	Coefficient		
			Mean	C.O.V.	
Superstructure Mass	Normal	600 ton	1.05 ¹⁾	0.05 ¹⁾	
Isolation bearing	Yield strength	Calculated based on the Japan Road Association (2018)	1.13 ¹⁾	0.18 ¹⁾	
	Shear stiffness	Calculated based on the Japan Road Association (2018)	1.04 ²⁾	0.04 ²⁾	
	K_{B3}/K_{B2}	Normal	-	3.1 ³⁾	0.09 ³⁾
	Rupture strain	Normal	250%	1.34 ¹⁾	0.11 ¹⁾
	Shear strength of anchor bolts	Normal	469 N/mm ²	0.75 ⁴⁾	0.014 ⁴⁾
Bridge column	Compressive strength of concrete	Normal	23.5 N/mm ²	1.20 ¹⁾	0.10 ¹⁾
	Section area of steel bar	Normal	Nominal value	0.97 ¹⁾	0.01 ¹⁾
	Yield strength of steel bar	Normal	345 N/mm ²	1.20 ¹⁾	0.07 ¹⁾
	Young's modulus of steel bar	Normal	2.06×10^5 N/mm ²	0.97 ¹⁾	0.01 ¹⁾
	Mass	Normal	Listed in Table 1	1.05 ¹⁾	0.05 ¹⁾
	Ultimate displacement δ_{t3}	Normal	Calculated based on Public Works Research Institute (2013)	1.062 ⁵⁾	0.181 ⁵⁾

1) Adachi, 2002

2) Japan Road Association, 2018

3) Naito et al., 2017

4) Public Works Research Institute, 2022

5) Public Works Research Institute, 2013

were modelled based on accelerated thermal oxidation tests by Itoh et al. (2006) and Itoh & Gu (2009). It was assumed that lead core is kept sound during the service period of the target bridges. The average yearly temperature to evaluate the ageing process of the bearings was set as 17.2 °C based on observation data by the Japan Meteorological Agency from 1991 to 2020.

It has been reported that the decrease ratio of rupture strain and the increase ratio of shear stiffness are nearly the same based on the loading tests of isolation bearings used for actual bridges by Hayashi et al. (2014) and Shinohara & Hoshikuma (2015). Thus, it was assumed that the decrease ratio of rupture strain is same as the increase ratio of shear stiffness in this study.

2.4 Input ground motions

A total of 25 horizontal components of observed ground motions with a peak ground velocity (*PGV*) of 0.50 m/s or higher recorded at stiff soil in Japan were selected and used in this study, as shown in Table 2. In the incremental dynamic analysis and fragility analysis, ground motions that were adjusted to the required *PGV* by varying amplitude properties were used.

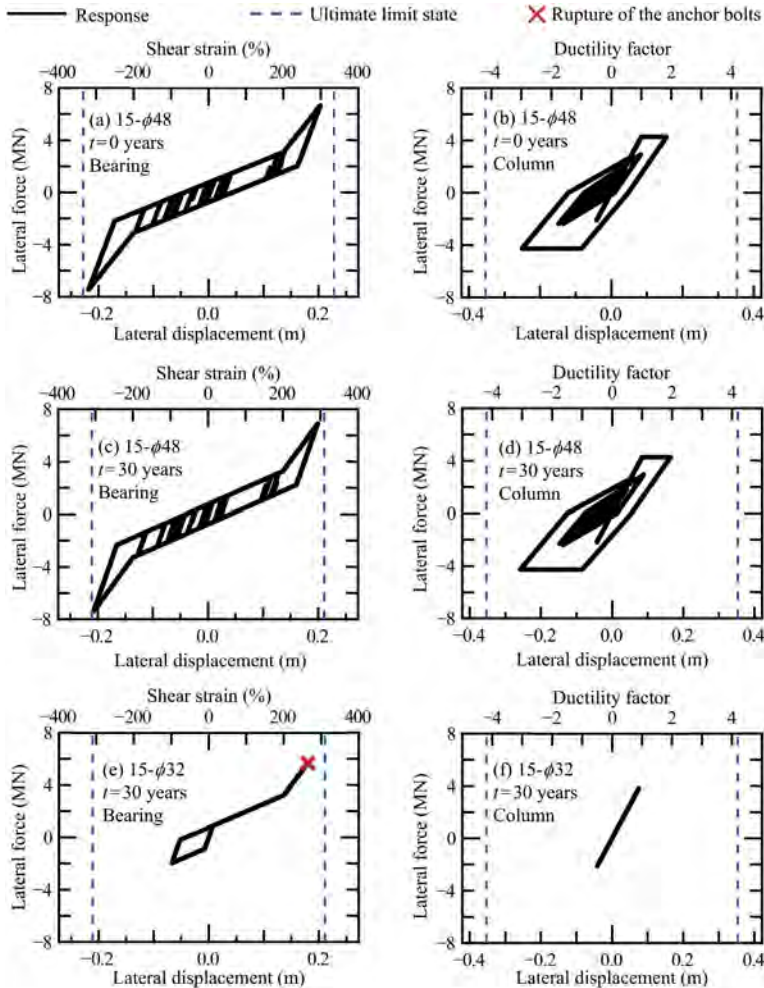


Figure 2. Lateral force–lateral displacement relationship of the isolation bearings and the 15 m high columns subjected to NS component of KiK-net Kikuchi record adjusted to *PGV* of 0.9 m/s.

2.5 Ultimate limit states of seismically isolated bridges

In the incremental dynamic analysis and fragility analysis, shear strength of the anchor bolts, rupture strain of the rubber layer of the bearings and the ultimate displacement of the column δ_{ls3} (Public Works Research Institute, 2013) were considered as the ultimate limit states. As the load transfer between the bearing and the column after the rupture of the rubber layer or the anchor bolts of the bearing is sufficiently small, the post-behaviour after reaching these ultimate limit states does not need to be considered.

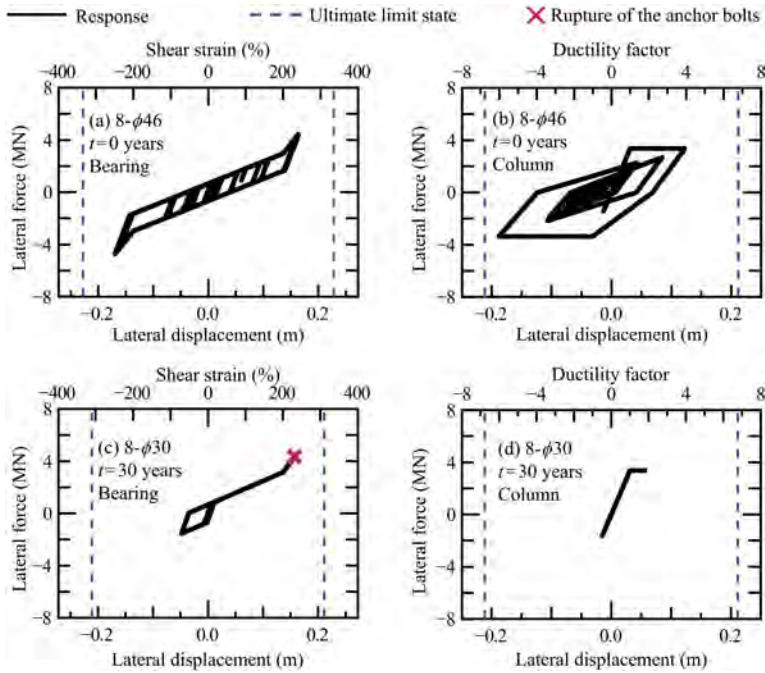


Figure 3. Lateral force–lateral displacement relationship of the isolation bearings and the 8 m high columns subjected to NS component of KiK-net Kikuchi record adjusted to PGV of 0.9 m/s.

2.6 Uncertain factors

Uncertain factors in evaluating the material and mechanical properties of seismically isolated bridges were considered, as shown in Table 3. Statistics on shear stiffness of bearings, shear stiffness ratio K_{B3}/K_{B2} , shear strength of anchor bolts, the ultimate displacement of the column $\delta_{l,3}$, and others were obtained from the Japan Road Association (2018), Naito et al. (2017), Public Works Research Institute (2022), Public Works Research Institute (2013) and Adachi (2002), respectively. In the incremental dynamic analysis and fragility analysis, Monte Carlo simulations were conducted with 25,000 trials for each peak ground velocity, and the discrete conditional probabilities of failure were approximated by a lognormal cumulative distribution function.

3 EFFECTS OF THE RUPTURE OF THE ANCHOR BOLTS ON THE BEHAVIOUR OF BRIDGES WITH DETERIORATED SEISMIC ISOLATION BEARINGS

3.1 Lateral force–lateral displacement relationships of the bearings and the columns

Figures 2 and 3 display the lateral force–lateral displacement relationships of the isolation bearings and the columns subjected to NS component of KiK-net Kikuchi record adjusted to PGV of 0.9 m/s using the mean values shown in Table 3. PGV of the design ground motion level corresponds to 0.67 m/s considering the regional modification factor, thus PGV of 0.9 m/s is higher than that of the design ground motion. Even immediately after the bridge is in service, the peak shear strain of the seismic isolation bearing is close to the rupture strain in case the column height is 15 m, as shown in Figure 2(a). However, it is confirmed that the progress of ageing deterioration reduces the rupture strain, resulting in a further reduction in the safety margin of the isolation bearing, as shown in Figure 2(c). Even at the same 30 years after construction, the response of the column is within the range of elastic response because the peak

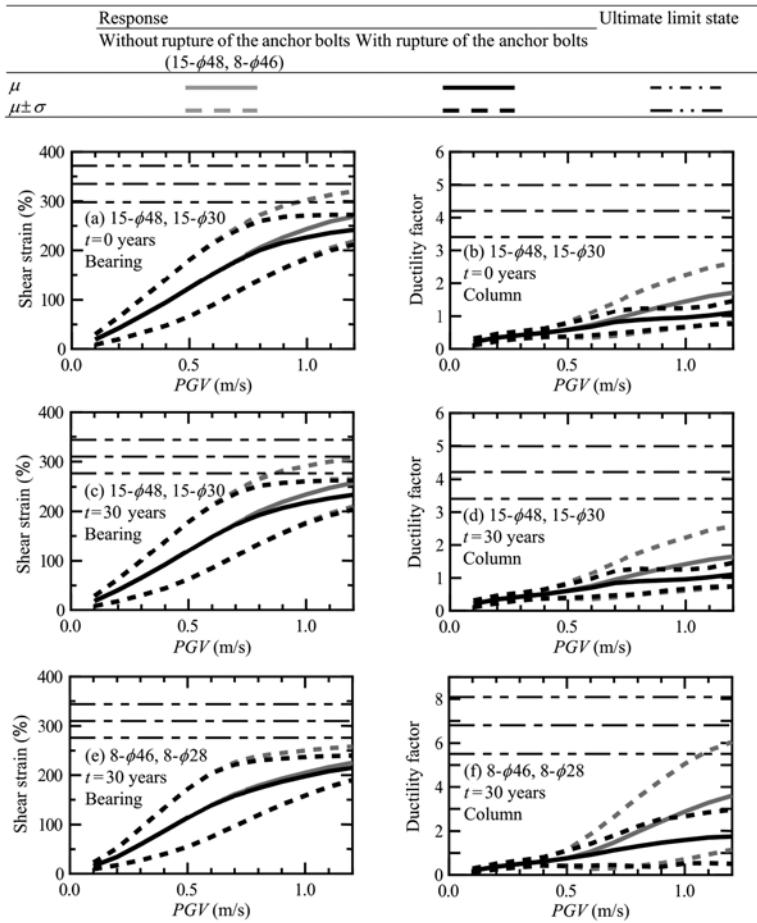


Figure 4. IDA curves with and without the rupture of the anchor bolts.

response shear strain of the seismic isolation bearing is reduced by the rupture of the anchor bolts, and the peak transmitted load from the isolation bearing to the column is also reduced, as shown in Figures 2(e) and (f).

In the case of 8 m high column as shown in Figure 3(a), while the safety margin of the seismic isolation bearing is large, the column exhibits seismic response displacement close to the ultimate displacement. The large response displacement of the column considering ageing deterioration for 30 years after construction can also be reduced to relatively small displacement by the rupture of the anchor bolts, as shown in Figure 3(d).

3.2 IDA curves

Figure 4 displays the mean and plus/minus the standard deviation of the response of the isolation bearings and columns. The responses of the seismic isolation bearing of Bridge 15- ϕ 48 shown in Figure 4(a) and the column of Bridge 8- ϕ 46 shown in Figure 4(f) indicate that the response exceed the ultimate limit states, respectively. Thus, if the anchor bolts are not ruptured under extreme ground motions, bridges with higher column heights are more likely to cause the rupture of the rubber layer of seismic isolation bearings, while bridges with lower column heights are more likely to cause the columns to reach their ultimate displacement, consistent with the results of Matsuzaki (2022). Furthermore, the possibility of rupture of the rubber layer increases as the isolation bearing is deteriorated, as shown in Figure 4(c).

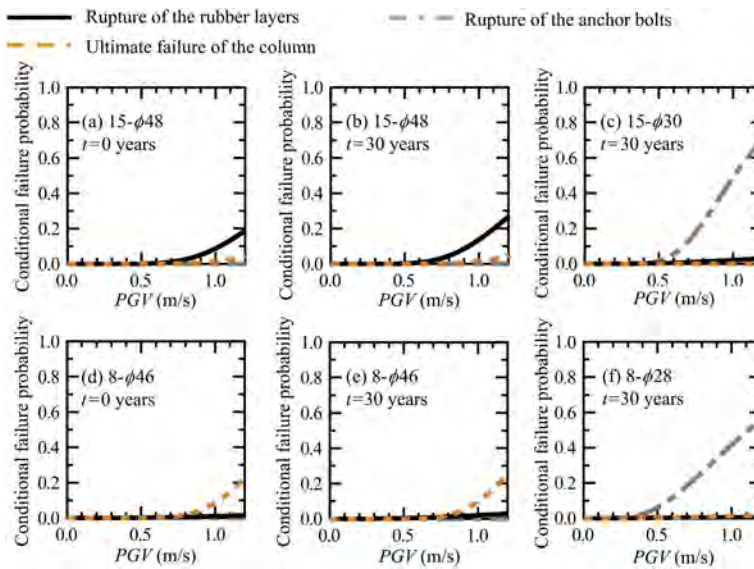


Figure 5. Fragility curves of the target seismically isolated bridges.

It has been shown that damage control by the rupture of the anchor bolts not only suppresses the peak response shear strain of seismic isolation bearings, but also reduces the seismic response of columns, especially under extreme ground motion that exceeds the design ground motion. In the case column height is low, the seismic response of the columns tends to be large, and the effect of reducing the response of the seismic isolation bearing is relatively small, but the effect of reducing the nonlinear response of the columns with large variations is significant.

3.3 Fragility curves

Figure 5 displays the fragility curves of the target seismically isolated bridges. As is clear from the IDA curves shown in Figure 4, even if the seismic isolation bearings are not deteriorated, they are likely to rupture at the rubber layers of the isolation bearings when the column height is 15 m, and the response of the columns is likely to reach the ultimate displacement when the column height is 8 m. Furthermore, it can be confirmed that the possibility of damage is more likely to increase as the seismic isolation bearings deteriorate over time. On the other hand, as shown in Figures 5(c) and (f), it is shown that the ultimate failure of rubber layers of the seismic isolation bearings and the columns can be sufficiently avoided under extreme ground motions by the rupture of the anchor bolts, even if the ageing deterioration of bearings is considered.

4 CONCLUSIONS

In this study, improving the reparability of seismically isolated multi-span continuous girder bridges by the rupture of the anchor bolts of the deteriorated isolation bearings was investigated by incremental dynamic analysis and fragility analysis. The following conclusions can be drawn:

- 1) The damage control by the rupture of the anchor bolts not only suppresses the peak response shear strain of seismic isolation bearings, but also reduces the seismic response of columns, especially under extreme ground motion that exceeds the design ground motion. In the case column height is low, the effect of reducing the nonlinear response displacement of the columns is significant.

- 2) Fragility curves show that the ultimate failure of rubber layers of the seismic isolation bearings and the columns can be sufficiently avoided under extreme ground motions by the rupture of the anchor bolts, even if the ageing deterioration of bearings is considered.

ACKNOWLEDGEMENTS

This study was supported by JSPS KAKENHI Grant Number JP19K04568. It is appreciated that strong ground motions were provided by K-NET and KiK-net of National Research Institute for Earth Science and Disaster Resilience, Japan Meteorological Agency, Japan Association for Earthquake Engineering and NGA databases of Pacific Earthquake Engineering Research Center.

REFERENCES

- Adachi, Y. 2002. Reliability assessment and limit state design method for isolated bridge structures under extreme ground motions. Doctoral thesis, Kyoto University, Japan.
- Akiyama, M., Frangopol, D.M. and Ishibashi, H. 2020. Toward life-cycle reliability-, risk- and resilience-based design and assessment of bridges and bridge networks under independent and interacting hazards: emphasis on earthquake, tsunami and corrosion. *Structure and Infrastructure Engineering*, 16(1): 26–50.
- Hayashi, K., Adachi, Y., Komoto, K., Yatsumoto, H., Igarashi, A., Dang, J. and Higashide, T. 2014. Experimental verification for remaining performance of lead rubber bearings with aging deterioration. *Journal of Japan Society of Civil Engineers*, Ser. A1, 70(4):I_1032–I_1042.
- Itoh, Y., Satoh, K., Gu, H. and Yamamoto, Y. 2006. Study on the deterioration characteristics of natural rubber bearings. *Doboku Gakkai Ronbunshuu A*, 62(2): 255–266.
- Itoh, Y. and Gu, H.S. 2009. Prediction of aging characteristics in natural rubber bearings used in bridges. *Journal of Bridge Engineering*, 14(2): 122–128.
- Japan Road Association. 2017. *Design Specifications for Highway Bridges V Seismic Design*. Tokyo: Maruzen.
- Japan Road Association. 2018. *Bearing Handbook for Highway Bridges*. Tokyo: Maruzen.
- Matsuzaki, H. 2022. Time-dependent seismic reliability of isolated bridges considering ageing deterioration of lead rubber bearings. *Structure and Infrastructure Engineering*, 18(10-11): 1526–1541.
- Naito, N., Mazda, T., Uno, H. and Kawakami, M. 2017. Seismic performance evaluation of LRB considering Mullins effect and hardening. *Journal of Japan Society of Civil Engineers*, Ser. A1, 73 (4): I_499–I_510.
- Public Works Research Institute. 2013. *Technical Note of PWRI*, 4262.
- Public Works Research Institute. 2022. *Technical Note of PWRI*, 4422.
- Shinohara, M. and Hoshikuma, J. 2015. Experimental evaluation of property of lead rubber bearing damaged due to earthquake. *Journal of Japan Society of Civil Engineers*, Ser. A1, 71 (4):I_587–I_599.
- Takahashi, Y. and Hoshikuma, J. 2013. Damage to road bridges induced by ground motion in the 2011 Great East Japan Earthquake. *Journal of JSCE*, 1(1): 398–410.
- Takeda, T., Sozen, M.A. and Nielsen, N.N. 1970. Reinforced concrete response to simulated earthquakes. *Journal of the Structural Division*, 96(12): 2557–2573.
- Vamvatsikos, D. and Cornell, C.A. 2002. Incremental dynamic analysis. *Earthquake Engineering & Structural Dynamics* 31(3): 491–514.

Probabilistic resilience assessment of aging bridge networks based on damage disaggregation and stationary proposal importance sampling

L. Capacci & F. Biondini
Politecnico di Milano, Milan, Italy

A.S. Kiremidjian
Stanford University, Stanford, CA, USA

ABSTRACT: This paper presents a mathematical framework to investigate the relative importance of seismic damage scenarios to the probability of failing to meet target performance measures for spatially-distributed aging bridge networks. The proposed framework relies on a statistical approach adapted from disaggregation procedures typical of probabilistic seismic hazard analysis. The estimate accuracy is enhanced using a novel simulation-based methodology proposed in previous works based on Importance Sampling with Stationary Proposal distributions (SP-IS). The basic random variables involved in risk assessment are efficiently sampled from a near-optimal simulation density based on the minimization of the Kullback–Leibler cross-entropy. A simple road network is investigated to highlight the benefits to computational effort of the proposed SP-IS numerical method and to explore the potentialities of the concept of damage disaggregation in communicating to infrastructure managers and policy makers the large-scale consequences of natural hazards and aid the optimal management and prioritization of essential maintenance interventions.

1 INTRODUCTION

Life-cycle seismic risk assessment is critical for the optimal management of lifelines and for the emergency response of communities affected by natural hazards, such as earthquakes. In transportation systems and road networks, the damage induced by sudden extreme events and the consequences on the post-event performance of infrastructure systems with spatially distributed vulnerable elements can be evaluated with site-specific analysis (Stergiou and Kiremidjian 2010). In this context, the concept of resilience has been gaining increasing importance of performance-based assessment of infrastructure system, particularly for bridges and transportation networks exposed to natural and man-made hazards (Capacci et al. 2022a). Resilient infrastructure systems are able not only to resist the impact of extreme events, but also to absorb their consequences and promptly recover the pre-event functionality (Bruneau et al. 2003). Bridges are particularly vulnerable assets due to the interaction of seismic hazards with environmental aggressiveness inducing mechanical deterioration (Biondini et al. 2015, Rao et al. 2017).

Most probabilistic methodologies for seismic loss assessment that have been formulated based on the PEER's framework have the advantage of aggregating into a single comprehensive measure of seismic risk all the sources of uncertainty associated to regional hazards, element fragility and system exposure. The concept of disaggregation aims at evaluating the relative contributions of specific detrimental events representative of the risk components. For example, disaggregation is a well-established procedure to address the relative contribution of different sources and shaking characteristics of the

expected ground motion at a site (Bazzurro and Cornell 1999). In the context of seismic loss assessment, this concept can also be adopted to investigate the impact of different damage scenarios and structural components to risk metrics in terms of economic direct costs (Aslani 2004) as well as performance-based measures (Capacci et al. 2021).

The paper proposes a mathematical framework and a numerical procedure to assess the exceedance rate of target values of a life-cycle resilience-based risk measure and to disaggregate such metric into the time-variant relative contributions of relevant damage scenarios. The following sections summarize the constitutive components of seismic risk analysis of infrastructure systems, proposing a comprehensive analytical framework encompassing probabilistic seismic hazard of spatially distributed assets, life-cycle seismic fragility of aging structures and resilience-based exposure of infrastructure systems. The annual failure rate of occurrence of prescribed failure events is numerically quantified by means of Importance Sampling with a Stationary Proposal distribution (SP-IS) optimally selected from a chosen family of parametric distributions based on the minimization of the Kullback–Leibler Cross–Entropy (KL-CE). A simple network with three aging bridges is investigated to highlight the ability of damage disaggregation to identify the relevance of vulnerable network components, its evolution in time due to the interdependencies between seismic and environmental hazards, and the significance of the identification of dominant damage scenarios to inform retrofit prioritization strategies.

2 RESILIENCE-BASED SEISMIC RISK AND DAMAGE DISAGGREGATION

2.1 Seismic risk metrics based on failure recurrence rate

Probabilistic Seismic Hazard Analysis (PSHA) aims at describing the occurrence rate of severe seismic events under uncertainties. At the infrastructure level, seismic hazard is assessed at multiple sites accounting for the spatial distribution of vulnerable assets. Earthquake recurrence is described based on historical data and the characteristics of active faults and area sources, which can be conveniently collected in a vector with n_h seismic hazard parameters \mathbf{H}_h informative of possible rupture scenarios in the region. The multivariate lognormal random variable \mathbf{I} collectively describes the seismic scenario based on the intensity measure i_b of the ground shaking at the site of the n_b vulnerable infrastructure elements, such as bridges in a road network. Ground motion prediction models define the probabilistic relationship of intensity measures \mathbf{I} conditional on the hazard parameters \mathbf{H}_h . According to the total probability theorem (Ang and Tang 2007), the Probability Density Function (PDF) of seismic scenario \mathbf{I} is defined as:

$$f_{\mathbf{I}}(\mathbf{i}) = \int_{\mathbb{R}^{n_h}} f_{\mathbf{I}|\mathbf{\eta}_h}(\mathbf{i}|\mathbf{\eta}_h) \cdot f_{\mathbf{H}_h}(\mathbf{\eta}_h) \cdot d\mathbf{\eta}_h \quad (1)$$

where vectors \mathbf{i} and $\mathbf{\eta}_h$ represent outcomes of the intensity and hazard variates, respectively.

The recurrence of seismic events from the k -th seismogenic source in a prescribed region is commonly represented by Poisson processes with annual rate of earthquake occurrence ν_k . Based on the total probability theorem, the annual rate of occurrence of a failure event E can be described by its occurrence probability conditional on the seismic intensity scenario \mathbf{i} :

$$\nu_E = \int_{\mathbb{R}^{n_b}} P[E|\mathbf{i}] \cdot |d\lambda(\mathbf{i})| \quad (2)$$

where $|d\lambda(\mathbf{i})|$ is the differential annual rate of exceedance of a given seismic intensity scenario \mathbf{i} :

$$|d\lambda(\mathbf{i})| = \left(\sum_{k=1}^{n_f} \nu_k \right) \cdot f_{\mathbf{I}}(\mathbf{i}) \cdot d\mathbf{i} \quad (3)$$

and n_f is the total number of faults and area sources in the region.

2.2 Time-variant fragility curves and network damage rate

Given the seismic hazard scenario, the second step in seismic risk assessment of bridge networks deals with the probability that network components suffer damage in the aftermath of severe ground motions. Also, the life-cycle seismic capacity of vulnerable bridges can be affected in time by damage processes related to long-term environmental aging and short-term shock events.

Time-variant fragility curves represent the exceedance probability of a prescribed damage state s_b conditional to seismic intensity i_b at the b -th site of deteriorating bridges:

$$P_{s_b}^E(i_b, t) = P[S_b(t) \geq s_b | i_b] \quad (4)$$

where $S_b(t)$ is the discrete univariate stochastic process representing the time-variant bridge damage state. Fragility curves can also be analytically described by the Cumulative Distribution Function (CDF) of the bridge seismic capacity. Fragility curves can be fitted based on empirical data and physics-based models via suitable statistical procedures (Lallemant et al. 2015).

Damage state combinations among the set of bridges composing the infrastructure network can be represented by collecting into vector \mathbf{s} the damage states s_b of the b -th bridge. Given the seismic intensity scenario \mathbf{i} , the occurrence probability of a damage state combination \mathbf{s} corresponds to the conditional probability of the intersection of events representing the occurrence of a damage state to each bridge:

$$P[\mathbf{S}(t) = \mathbf{s} | \mathbf{i}] = P\left[\bigcap_{b=1}^{n_b} [S_b(t) = s_b | i_b]\right] \quad (5)$$

where $\mathbf{S}(t)$ is the discrete multivariate stochastic process representing in vectorial form the time-variant bridge damage combination. The damage combination probabilities depend on several factors affecting the bridge seismic capacities, such as their mutual correlation (Capacci and Biondini 2018).

2.3 Resilience and failure rate

When bridges suffer damage in the aftermath of a seismic event occurring at time t_0 , the operation of road networks can be severely impaired due to traffic restrictions imposed by infrastructure owners to ensure the users' safety in the emergency management. The network performance can be quantified based on a comprehensive measure of network functionality $Q = Q(\mathbf{d}) \in [0, 1]$ depending on the combination \mathbf{d} of traffic limitations d_b imposed along the n_b bridges in the network. For example, the functionality can be defined as the ratio between the Total Travel Time TTT of all road users in unrestricted conditions (i.e., $\mathbf{d} = \mathbf{0}$) and the TTT given the bridge damage combination:

$$Q(\mathbf{d}) = \frac{TTT(\mathbf{0})}{TTT(\mathbf{d})} \quad (6)$$

Then, the progressive repair activities carried out to recover the load-bearing capacity of damaged bridges allow releasing in time the traffic restrictions and, in turn, restore the network functionality. Given the initial damage combination \mathbf{s} and the repair interventions on each bridge in the network, resilience can be quantified based on the integral mean of the functionality profile $Q(t)$ from the time of seismic event occurrence t_0 up to a fixed horizon time t_h :

$$R(\mathbf{s}) = \frac{1}{\Delta t_h} \int_{t_0}^{t_h} Q(\mathbf{s}, t) dt \quad (7)$$

In the context of seismic risk analysis, this resilience measure can be adopted as an overall metric of exposure. Therefore, the failure probability to meet a prescribed resilience target

r given the seismic scenario \mathbf{i} can be defined based on the total probability theorem accounting for all possible damage combinations n_s over the bridge network:

$$F_{R(t)|\mathbf{i}}(r|\mathbf{i}) = \sum_s F_{R|\mathbf{s}}(r|\mathbf{s}) \cdot P[\mathbf{S}(t) = \mathbf{s}|\mathbf{i}] \quad (8)$$

where F_R is the CDF of the resilience measure, $F_{R|\mathbf{s}}$ is the same CDF conditional on the occurrence of a given damage combination \mathbf{s} . Finally, the annual failure rate in meeting a prescribed resilience target r is expressed as in Equation 2 considering as failure event $E = \{R \leq r\}$:

$$\nu_{R \leq r}(r, t) = \int_{\mathfrak{R}_+^b} F_{R(t)|\mathbf{i}}(r(t)|\mathbf{i}) \cdot |d\lambda(\mathbf{i})| \quad (9)$$

2.4 Damage disaggregation and predominant events

Damage disaggregation allows detecting which damage states suffered by the bridges in the network are more likely to cause unsatisfactory resilience levels based on their probability of occurrence. In analytical terms, the conditional occurrence probability of a generic event E_1 given the occurrence of event E_2 can be determined based on the Bayes' theorem (Ang and Tang 2007):

$$P[E_1|E_2] = \frac{P[E_2|E_1] \cdot \nu_{E_1}}{\nu_{E_2}} \quad (10)$$

In the present paper, events E_1 and E_2 are respectively associated to the occurrence of a seismic event that leads to an insufficient level of network resilience and the occurrence of a prescribed set of damage combinations. Therefore, the probability that resilience is lower than a threshold target r due to the occurrence of the bridge damage combination \mathbf{s} is defined as follows:

$$P_{s|r}(\mathbf{s}, r; t) = P[\mathbf{S}(t) = \mathbf{s}|r] = \frac{F_{R|\mathbf{s}}(r|\mathbf{s}) \cdot \nu_s(t)}{\nu_{R \leq r}(r, t)} \quad (11)$$

Given a target performance level in terms of network resilience, the predominant damage combination identifies which bridge or set of bridges in the network would provide the most relevant contribution to the seismic risk metric. This information can foster the prioritization of ex-ante retrofit activities as well as ex-post repair strategies, which would respectively benefit the seismic capacity of single bridges and the emergency response of the infrastructure system. Accounting for aging processes, the relevance of each damage combination would also evolve in time providing further insight on the optimal ex-ante preventive maintenance actions aimed at counteracting the detrimental effect of environmental deterioration.

3 EFFICIENT SIMULATION TECHNIQUE

3.1 Stationary Proposal Importance Sampling (SP-IS)

In life-cycle structural reliability and seismic risk assessment, uncertainties in bridge structural capacity vary in time due to stochastic deterioration processes. Simulation-based techniques numerically estimate the probability of event occurrence based on the multidimensional integral:

$$P_f(t) = \int_{\mathbf{x}} I(\mathbf{x}) \cdot f_{\mathbf{X}(t)}(\mathbf{x}) d\mathbf{x} \quad (12)$$

where $f_{\mathbf{X}(t)}$ is the time-variant joint PDF of the set of basic random variables $\mathbf{X}(t)$ and the indicator function $I(\mathbf{X}) = I\{g(\mathbf{X}) \leq 0\}$ is a Heaviside step function equal to 1 in the failure domain bounded by the limit state function $g(\mathbf{X})$ and 0 in the safe domain.

In life-cycle risk assessment of aging systems, traditional simulation strategies may be numerically inefficient in accurately estimating failure probabilities related to multiple reliability problems. Advanced simulation techniques rely on alternative formulations of the failure

probability integral to reduce the variance of the reliability estimator. In Importance Sampling (IS), the integral is reformulated in terms of the proposal simulation density $\psi(\mathbf{x})$:

$$P_f(t) = \int_{\mathbf{x}} I(\mathbf{x}) \cdot f_{\mathbf{X}(t)}(\mathbf{x}|t) \cdot \frac{\psi(\mathbf{x})}{\psi(\mathbf{x})} d\mathbf{x} \quad (13)$$

Such formulation relies on the definition of the IS weighting coefficients W as the ratio between the actual time-variant PDF $f_{\mathbf{X}(t)}$ and the sampling stationary PDF ψ (Capacci and Biondini 2021)

$$W(\mathbf{x}, t) = \frac{f_{\mathbf{X}(t)}(\mathbf{x})}{\psi(\mathbf{x})} \quad (14)$$

The IS failure probability estimator with sample size N is the mean of the indicator function I_i for the i -th simulated set of random variables \mathbf{x}_i weighted at time t by the coefficients $w_i(t) = W(\mathbf{x}_i|t)$:

$$p_{IS}(t) = \frac{1}{N} \sum_{i=1}^N I_i \cdot w_i(t) \quad (15)$$

In traditional Monte Carlo simulation methods, samples are generated from a distribution progressively evolving over the system lifetime, requiring one simulation per observation time t for a prescribed deterioration model. On the other hand, SP-IS requires a single simulation to estimate probabilities at different times t and aging model by suitably weighting each failed sample.

3.2 Cross-Entropy-based optimal Stationary Proposal sampling density (CE-SP-IS)

The choice of the sampling density ψ is a key issue to ensure accuracy and efficiency of the SP-IS framework. Minimizing the IS estimate variance effectively improves the simulation performance. The aim of the cross-entropy-based methodology is to formulate a near-optimal simulation density from a chosen family of parametric distributions that minimizes the Kullback–Leibler (KL) cross-entropy (CE), which is a measure of discrepancy between a prescribed distribution and the absolute best sampling density (Rubinstein 1981). The KL-CE between the best possible density p^* and a prescribed proposal PDF ψ with parameters \mathbf{v} is expressed as:

$$D_{KL} = \int_{\mathbf{x}} p^*(\mathbf{x}) \cdot \ln p^*(\mathbf{x}) d\mathbf{x} - \int_{\mathbf{x}} p^*(\mathbf{x}) \cdot \ln \psi(\mathbf{x}, \mathbf{v}) d\mathbf{x} \quad (16)$$

The formulation of the best density p^* accounting for the n_c reliability problems for all investigated combinations of time instants t , limit states s and parametric scenarios p is defined as follows (Capacci and Biondini 2023):

$$p^*(\mathbf{x}) = \frac{1}{n_c} \left[\sum_{c=1}^{n_c} \frac{I(\mathbf{x}|s) \cdot f_{\mathbf{X}(t)}(\mathbf{x}|t, p)}{P_f(t, s, p)} \right] \quad (17)$$

where the combinations $c = \{t, p, s\}$ encompass the n_c possible combinations. The basic random variables distribution $f_{\mathbf{X}}$ can change over time t given the parametric scenario p , whilst the limit states s affect the definition of the indicator function I . The density p^* is formally unknown, since it requires the knowledge of the target failure probabilities P_f of the n_c reliability problems.

The proposal parameters minimizing the cross-entropy are obtained by formulating an optimization problem that maximizes the second term in D_{KL} . Closed-form updating rules to iteratively solve the optimization problem are available for exponential distributions (Rubinstein and Kroese 2004). Proposal distributions characterized by Gaussian Mixtures (GMs) can be adopted to efficiently map the most significant regions in the failure domain based on K joint-normal variates with relative probability π_k , mean vectors $\boldsymbol{\mu}_k$, and covariance matrices $\boldsymbol{\Sigma}_k$ (Kurtz and Song 2013). The CE optimization problem is also equivalent to a Maximum Likelihood Estimate of the mixture parameters and expectation-maximization algorithms can

further refine the estimates of the statistical parameters $\{\pi, \mu, \Sigma\}_k$ of each Gaussian density (Geyer et al. 2019). When random variables are characterized by non-normal distributions, they can be simulated in the standard normal space \mathbf{u} , where also weighting coefficients w_i can be retrieved, whilst indicator functions I_i are sampled based on a suitable transformation into their actual space \mathbf{x}_i (Capacci and Biondini 2023).

4 APPLICATION

4.1 Seismic hazard scenario, lifetime bridge fragility and road network topology

The investigated infrastructure system is sketched in Figure 1. The road network is composed by three main cities interconnected by highways with a vulnerable bridge. Major seismic events are equally likely to occur with annual earthquake occurrence rate $\nu_m=0.05$ over the square seismogenic area sources with normal prevalent faulting mechanism. Moment magnitudes M_w are governed by a truncated Gutenberg-Richter distribution:

$$F_{M_w}(m) = \frac{1 - 10^{-b(m-m_{\min})}}{1 - 10^{-b(m_{\max}-m_{\min})}} \quad (20)$$

Uncertainties in the ground motion intensity at the bridge sites are incorporated by the ground motion prediction model derived from the Italian strong motion database in Bindi et al. (2011) with Peak Ground Acceleration as seismic intensity measure.

The life-cycle seismic capacity $\bar{I}_b(t)$ of the three spatially-distributed vulnerable aging bridges in the network is described by statistically independent lognormal fragility curves. The standard deviation of the logarithm of the seismic capacity is $\zeta=0.60$ for all bridges. The median seismic capacity $\bar{i}_{b,m}$ deteriorates in time due to environmental aging with the following degradation law:

$$\bar{i}_{b,m}(t) = \bar{i}_{b,m0} - k_b \cdot t^2 \quad (21)$$

Daily users' traffic flows f_{OD} from Origin O to Destination D are modeled as statistically independent symmetric triangular distributions over the range $f_{OD}^{mode} \pm 1500$ cars/hour. Traffic demands are also perfectly correlated within the same OD pair (e.g., f_{12} and f_{21}). Travel times t_{OD} are then assigned by shortest path analysis based on the network topology. Secondary roads of length $l_{detour}=30$ km also guarantee the connectivity between city pairs when the related bridge along the main highway is closed. Uniform random variables between 230 and 330 characterize the probabilistic model for the recovery times $T_{r,b}$ for each bridge. Traffic flow modes f_{OD}^{mode} , speed limits ν_{\max} and roadway lengths l_{OD} are all collected in Figure 1.

Additional information regarding seismic hazard, time-variant fragility model and network resilience assessment can be found in Capacci et al. (2020), Capacci and Biondini (2021).

4.2 Resilience-based life-cycle seismic risk mitigation by bridge retrofit

Figure 2a shows the time-variant mean annual rate of non-meeting $n_s=2$ resilience targets $r=60\%$ and 70% considering the retrofit of a single bridge at 30 years of lifetime. Figure 2b shows the time-variant risk measure considering the retrofit at 30 years of two bridges. For the sake of simplicity, each retrofit intervention is assumed to reset to pristine conditions both median seismic fragility model and deterioration rate. Risk is assessed at $n_r=26$ time instants from pristine conditions to 50 years (every 2 years) with $n_p=7$ deterioration scenarios: (1) no retrofit actions, (2-4) retrofit of a single bridge and (5-7) retrofit of bridge pairs. The risk estimates are obtained by calibrating with the CE-SP-IS methodology a near-optimal Gaussian mixture model composed by $n_k=3$ densities to solve $n_c=n_s \cdot n_r \cdot n_p=364$ reliability problems with a single simulation of sample size $N=10^6$.

The results discussed are consistent with the considerations on damage disaggregation discussed in the next Section. Although the retrofit of only bridge B1 is inducing the lowest risk

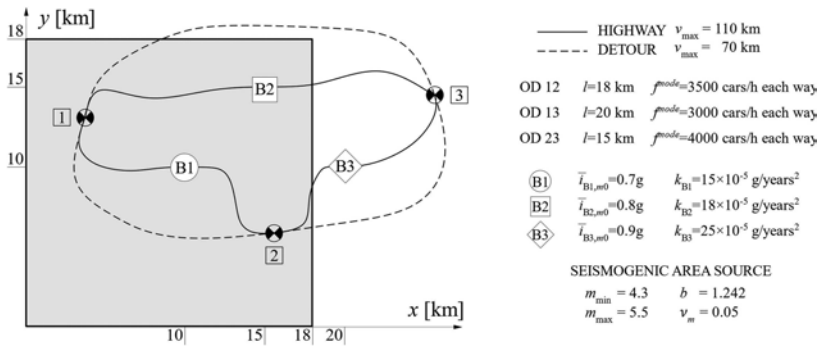


Figure 1. Seismic hazard scenario and road network topology of spatially-distributed aging bridge network.

at 30 years with resilience target 70%, the same intervention on only bridge B3 is more beneficial long-term due to its larger network exposure and faster capacity decay rate. For resilience target $r=60\%$, it is critical to prioritize the retrofit of the most relevant bridge B3.

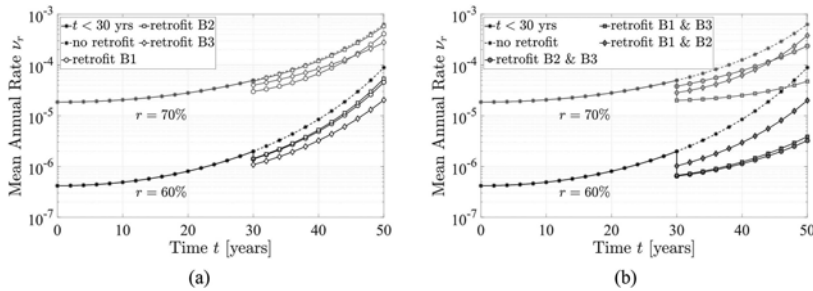


Figure 2. Time-variant annual failure rate of target resilience $r=60\%$ and 70% with retrofit at $t=30$ years of (a) one bridge and (b) bridge pairs.

4.3 Damage disaggregation for resilience-based life-cycle seismic risk mitigation by retrofit

The sensitivity of the road network to the damage suffered by one or more of its vulnerable elements depends on the proportion of the risk metrics ascribed to the occurrence of such damage. The features in terms of hazard, fragility, deterioration, and exposure of each bridge are defined in such a way that it is not intuitive to capture which bridge damage scenario would be more relevant to the seismic risk measure. Since the median seismic intensity in the ground motion prediction model is inversely proportional to the source-to-site distance, the most prone bridge to seismic hazard is B1. This is due to the fact that the site of B1 is close to the geometrical centroid of the area source and it is more likely that the earthquake epicenter is close compared to bridges B2 (located at a peripheral zone of the seismicogenic area) and B3 (located outside the area source). Concerning the initial seismic fragility based on the medians $\bar{I}_{b,m0}$ collected in Figure 1, B1 and B3 are respectively characterized by the least and most capacity in pristine conditions. On the other hand, B1 and B3 respectively experience the least and most severe deterioration of seismic capacity given the decay rates k_b . Finally, the impact of bridge closure to the resilience metrics depends on network topology and traffic demand. Thus, bridge B3 is the most vulnerable since its closure induces the largest detour affecting on average the largest traffic flow.

Figure 3 represents the time-variant probability that a specific bridge is damaged when the resilience target is not met considering $r=60\%$ and 70% . This graph allows addressing which bridge failure is more likely to induce unsatisfactory system performance given all uncertainties in seismic hazard, time-variant fragility and network exposure. For more restrictive target

of seismic resilience (Figure 3a), the most critical bridge is B3 (i.e., the most exposed bridge in the network). For less restrictive target of seismic resilience (Figure 3b), the most relevant bridge is initially B1 (i.e., the most hazard-prone and fragile in pristine conditions). Nonetheless, the fast degradation rate of the most exposed bridge B3 progressively increases its relevance in time, overcoming the conditional probability associated to B1 after about 45 years. It is worth noting that the conditional probabilities in Figure 3 represent collectively exhaustive events since the resilience target may not be met only if at least one bridge is damaged (i.e., $\min_b\{s_b\}=1$), but they are not mutually exclusive since more than one bridge may be damaged by the earthquake.

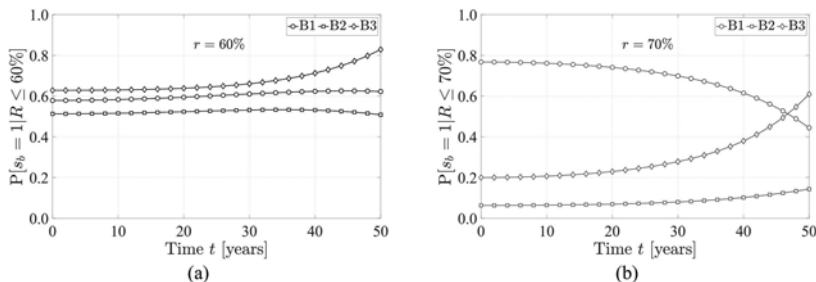


Figure 3. Disaggregation of bridge damage occurrence for target resilience (a) 60% and (b) 70%.

Figure 4 shows the disaggregation with respect to the number of bridges damaged in the network for the same resilience targets. It is evident that $s_n=2$ damaged bridges is the most likely amount of collapsed elements inducing failure in meeting a resilience target of 60% (Figure 4b). For target $r=70\%$, the collapse of only one bridge (i.e., $s_n=1$) is the most relevant event. The probability of widespread damage (i.e., large s_n) increases in time due to deterioration. Since these probabilities are conditional to mutually exclusive and collectively exhaustive events, their sum at a given time t is unitary based on the total probability theorem.

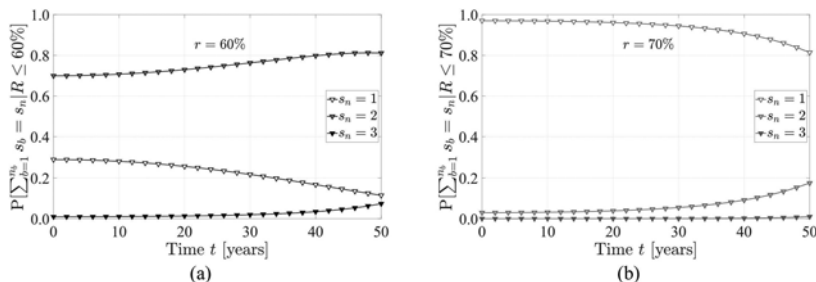


Figure 4. Disaggregation of network damage occurrence for target resilience (a) 60% and (b) 70%.

5 CONCLUSIONS

The prioritization of essential interventions on vulnerable infrastructure components is critical in life-cycle management of lifeline systems, such as road networks with spatially-distributed aging bridges. The analytical framework proposed in the paper aims at quantifying the relative importance of relevant damage scenarios based on probability disaggregation of resilience-based seismic risk metrics. Investigating a simple road network with three bridges characterized by different features regarding seismic hazard, time-variant fragility and system exposure allowed demonstrating the capability of the proposed methodology in prioritizing retrofit strategies. The lifetime seismic risk estimates have been assessed with the aid of a novel advanced technique inspired by Importance Sampling that selects the optimal density

for the numerical simulation of seismic damage and network resilience. Further research should be devoted to investigating potentialities and issues of upscaling analytical and numerical approaches to life-cycle structural reliability of critical structures with complex deterioration patterns (Capacci et al. 2022b).

REFERENCES

- Ang, A.H.S., Tang W.H. 2007. *Probability concepts in engineering: Emphasis on applications to civil and environmental engineering* (vol. I, 2nd ed.), Hoboken, NJ: Wiley.
- Aslani H. 2004. *Probabilistic earthquake loss estimation and loss disaggregation in buildings*. Doctoral Thesis, Stanford University, Stanford, CA, USA.
- Bazzurro P., Cornell C.A. 1999. Disaggregation of seismic hazard. *Bulletin of the Seismological Society of America*, 89(2),501–520.
- Bindi D., Pacor F., Luzi L., Puglia R., Massa M., Ameri G., Paolucci R. 2011. Ground motion prediction equations derived from the Italian strong motion database. *Bulletin of Earthquake Engineering*, 9(6),1899–1920.
- Biondini F., Camnasio E., Titi A. 2015. Seismic resilience of concrete structures under corrosion. *Earthquake Engineering and Structural Dynamics*, 44(14),2445–2466.
- Bruneau M., Chang S.E., Eguchi R.T., Lee G.C., O'Rourke T.D., Reinhorn A.M., Shinozuka M., Tierney K., Wallace W.A., von Winterfeldt D. 2003. A framework to quantitatively assess and enhance the seismic resilience of communities. *Earthquake Spectra*, 19(4),733–752.
- Capacci, L., Biondini, F. 2018. Life-cycle seismic resilience of aging bridges and road networks considering bridge capacity correlation. *9th International Conference on Bridge Maintenance, Safety and Management (IABMAS 2018)*, Melbourne, Australia, July 9–13, 2018.
- Capacci, L., Biondini, F. 2021. Importance sampling in life-cycle seismic fragility and risk assessment of aging bridge networks. *1st Conference of the European Association on Quality Control of Bridges and Structures (EUROSTRUCT 2021)*, Padova, Italy, 29 August–1 September 2021.
- Capacci, L., Biondini, F. 2023. Cross-Entropy-based Stationary Proposal Importance Sampling for life-cycle structural reliability and seismic risk assessment. *14th International Conference on Applications of Statistics and Probability in Civil Engineering (ICASP14)*, Dublin, Ireland, July 9-13, 2023.
- Capacci, L., Biondini, F., Titi, A. 2020. Lifetime seismic resilience of aging bridges and road networks. *Structure and Infrastructure Engineering*, 16(2),266–286.
- Capacci, L., Biondini, F., Kiremidjian, A.S. 2021. Damage disaggregation for seismic resilience assessment of aging bridge networks. In *17th World Conference on Earthquake Engineering (17WCEE)*, Sendai, Japan, September 27–October 2, 2021.
- Capacci, L., Biondini, F., Frangopol, D.M. 2022a. Resilience of aging structures and infrastructure systems with emphasis on seismic resilience of bridges and road networks: Review. *Resilient Cities and Structures*, 1(2),23–41.
- Capacci, L., Biondini, F., Frangopol, D.M. 2022b. Failure times of deteriorating RC bridges under uncertainty. *Proceedings of the Eleventh International Conference on Bridge Maintenance, Safety and Management (IABMAS 2022)*. Barcelona, Spain, July 11–15, 2022.
- Geyer, S., Papaioannou, I., Straub, D. 2019. Cross entropy-based importance sampling using Gaussian densities revisited. *Structural Safety*, 76, 15–27.
- Kurtz, N., Song, J. 2013. Cross-entropy-based adaptive importance sampling using Gaussian mixture. *Structural Safety*, 42, 35–44.
- Lallemant D., Kiremidjian A.S., Burton H. 2015. Statistical procedures for developing earthquake damage fragility curves. *Earthquake Engineering & Structural Dynamics*, 44, 1373–1389.
- Rao A.S., Lepech M.D., Kiremidjian A.S., 2017. Development of time-dependent fragility functions for deteriorating reinforced concrete bridge piers. *Structure and Infrastructure Engineering*, 13(1),67–83.
- Rubinstein R. 1981. *Simulation and the Monte Carlo methods*. Hoboken (NJ): John Wiley and Sons, Inc.
- Rubinstein R., Kroese D. 2004. *The cross-entropy method: a unified approach to combinatorial optimization, Monte-Carlo Simulation, and machine learning*. New York (NY): Springer, Inc.
- Stergiou E.C., Kiremidjian, A.S. 2010. Risk assessment of transportation systems with network functionality losses. *Structure and Infrastructure Engineering*, 6(1-2), 111–125.

Dynamic characteristic of geodesic domes with different location of mass

D. Bysiec, T. Maleska & A. Janda

Faculty of Civil Engineering and Architecture, Opole University of Technology, Opole, Poland

ABSTRACT: The paper presents the numerical analysis of geodesic domes in which different location of mass was taken into account. In addition, the dynamic excitation was used and the seismic record from US (El Centro from 1941) was applied in the numerical models. The geodesic domes subjected to the dynamic analysis were created based on two different methods of subdividing spherical triangles (the original octahedron face). These structures are often used for the strategic reference point in the city. Sometimes, these structures are used in typical buildings. The analysed structures were made of steel, which is recommended for the lightweight structures with large spans. It should be emphasized, that the designing of steel domes is currently a challenge for structural engineering, as well as architects, who take into account their aesthetic considerations. In current research the finite element method in conjunction with numerical program was used. A non-linear analysis of the behavior of steel domes as a result of a given seismic excitation was performed. This paper presents the results of displacements and accelerations in time domain. The results of this analysis show the impact of the method of shaping the topology of the structure grid under seismic excitation on the response of geodesic domes. The obtained results will be helpful for these structures located on the seismic areas during designing and service. These results can also be helpful during the life-cycle of structure, where various types of equipment (additional masses) for domes are used at different stages of the structure's exploitation, which can change the nature of the work of the dome structure.

1 INTRODUCTION

Geodesic domes are light structures with a unique structure and are often a reference point for the place where they are built. These structures are called lightweight structures, which are characterized by a low use of structural material (usually made of steel) in relation to the span. As a result, they arouse the admiration of even outsiders. Apart from the aesthetic aspect, these constructions are part of the idea of sustainable development, through the appropriate use of construction material (Figure 1). On the other hand, sustainable development plays an increasingly important role in everyday life of every human being. As a result, lightweight structures become even lighter, and their load-bearing sections are stretched to the limit (Pilarska 2020, Bysiec 2023).

Lightweight structures have been analyzed for years in various optimization aspects. Most often, various types of algorithms and optimization methods are used as part of the optimization, the purpose of which is to reduce their weight. For example, Saka (2007a) as well as Carbas & Saka (2012) used the harmony search algorithm to present the optimal solution to the structure geometry. Another algorithm, that is the coupled genetic algorithm was presented also by Saka (2007b). To obtain the optimal cross-section of elements of domes, the enhanced colliding bodies optimization (ECBO) method was used in the paper by Kaveh & Rezaei (2015) or the charged system search (CSS) method in the paper by Kaveh & Talatahari (2011). Other algorithms used to optimize the structure include, for example SHADE algorithm used by Kaveh et al. (2022), the Jaya algorithm used by Dede et al. (2020), the Rao's algorithms used by Dede et al. (2022). Taking into account geometric nonlinear behavior of the domes, Gholizadeh & Barati (2014) considered the optimization process. Optimization of domes was also presented by Ye & Lu (2018), as well as by Grzywinski et al. (2019). The presented papers include activities that may translate into reduced environmental impact through lower consumption of construction material (steel). As part of these analyses, the effect of static load on the construction of geodesic domes, roofs, towers, etc. was investigated.

However, the influence of the method of shaping the topology of geodesic dome structures on the consumption of the construction material (steel) has been rarely investigated. Such actions were taken in the papers of Pilarska (2018a,b, 2020), where the focus was on the grid topology of single-layer geodesic domes. Two methods of creating the mesh topology of the tested domes were used in these papers. Based on these studies, it was noticed that the use of a different mesh shaping method has a more positive effect on weight reduction (by about 17%) than the use of an optimization algorithm. As a rule, such algorithms were able to reduce the weight of the supporting structure only by about 2% (Dede et al. 2022) or about 2 - 9% (Kaveh et al. 2022).

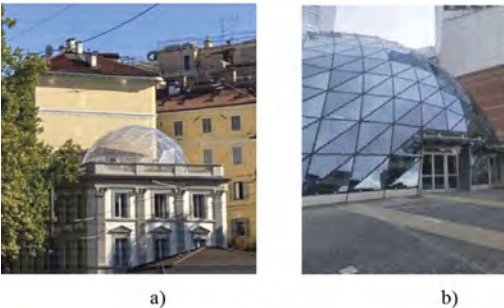


Figure 1. Example of geodesic domes of: a) residential house in Milan (Italy), b) dome of the Warsaw shopping center (Poland).

This approach was also tested for dynamic effects on the mentioned structures. In the paper of Pilarska & Maleska (2021), these domes were subjected to seismic excitation, and it was considered that as a result of seismic loading, the geodesic domes behaved differently than during static tests. It turned out that dome structures made according to method 2 better suppress seismic excitation.

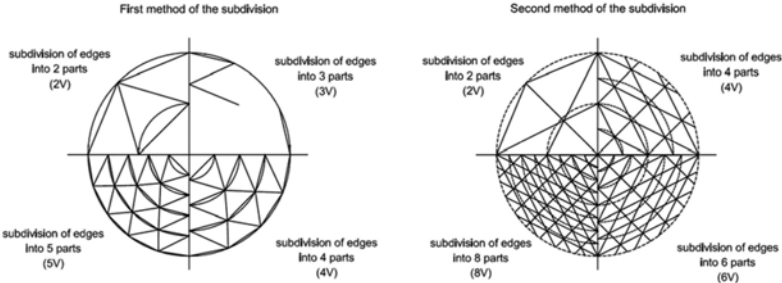


Figure 2. Methods of subdividing of geodesic dome from numerical research.

However, the question arises what will happen when the ideal structure of the geodesic dome is disturbed or additionally loaded asymmetrically. Additionally, what happens if such a structure is subjected to strong seismic excitation. It should be added that the use of additional mass in the structure may affect the life-cycle of structure, and in some cases even destroy the structure due to the addition of too much mass (structure equipment, additional devices). In this paper, the authors will try to answer this question by locating the mass in different places of the domes. In addition, these domes will be loaded by the strong El Centro record. The paper analyzes the displacements and accelerations for the tested domes, which are analysed during life-cycle of structure.

2 DESCRIPTION OF GEODESIC DOMES

2.1 General remarks

Geodesic domes were made based on earlier research by Pilarska (2012, 2018a, b, 2020), as well as Pilarska & Maleska (2021). Selected structures were built based on two methods of

creating their mesh topology. These methods differ in the method of connecting the points formed by dividing the edges of the initial octahedron, which is the basis for creating the geodesic domes analyzed in this article. The methods are presented in detail in the papers by Bysiec (2008, 2009a, b). Figure 2 presents graphically the differences between the two methods of creating geodesic dome structures used in this paper. The tested domes has 2888 struts (method 1) and 2904 struts (method 2).

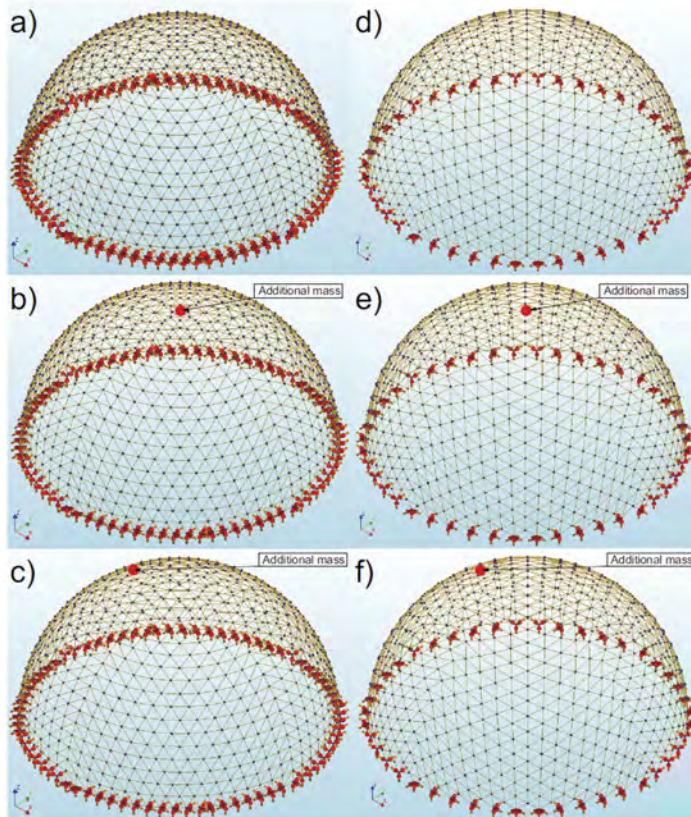


Figure 3. Models of geodesic domes from DIANA FEA: a) I¹, b) II¹, c) III¹, d) I², e) II², f) III².

These domes were the basis for numerical research (model I¹ and model I²), in which the impact of the mass located in two different places, i.e. in the middle of the dome span (model II¹ and model II²) and located about 10 meters from the centre of the dome (model III¹ and model III²) was tested. The mass suspended in these places had a weight of two tons and was suspended in a node. The individual models are shown in Figure 3. The suspended mass was designed to simulate the suspension of various types of equipment that is mounted to the lightweight construction. In addition, the central mass suspension does not interfere with the ideal and symmetrical construction of the geodesic dome. However, this arrangement may be disturbed by a mass located in a different place than the centre of the dome's span, which was done in models III¹ and III².

2.2 Material properties

In this research the geodesic domes were domes made of steel struts (round pipes) of S235 standard steel. The properties of this steel grade are: (i) Poisson's ratio (ν) 0.3, (ii) Kirchhoff module (G) 80.76 GPa, (iii) Young's modulus (E) 210 GPa, (iv) thermal expansion coefficient (α) 1.2×10^{-5} , (v) volumetric weight (γ) 7850 kg/m³, and (vi) partial safety factor (γ_M) 1.0. The steel elements were modelled as a linearly elastic isotropic material (according to Eurocode 3 (2005), Pilarska & Maleska (2021)).

3 RESULTS OF NUMERICAL ANALYSIS

3.1 General remarks

In order to determine the impact of a seismic excitations on geodesic domes, the numerical program DIANA FEA was used for two methods of shaping the topology of the structure. This program is based on the finite element method. In this program, a non-linear analysis of the behavior of steel domes as a result of the given El Centro seismic excitation was performed. The behavior of the domes over time was analyzed using the Time History method. This method is commonly used to determine the response to seismic excitation of various engineering structures (Maleska & Beben 2023, 2022, Maleska et al. 2021, Maleska et al. 2019, Bonkowski et al. 2018). Thanks to the obtained results, typical values for seismic analysis, i.e. displacement and acceleration, were analyzed (Table 1). In total, 6 numerical models were analyzed, in which two different methods of shaping the structure topology were analysed. Thus, in model I¹ and I², no additional mass was suspended, in models II¹ and II², the mass (2 tons) was suspended in the middle of the dome span, and in models III¹ and III², the mass (2 tons) was displaced from the centre by about 10 m, as shown in Figure 3c, f.

Table 1. Results of numerical analysis from DIANA FEA.

	Model I (without mass)		Model II (with central mass)		Model III (with lateral mass)	
	Method 1	Method 2	Method 1	Method 2	Method 1	Method 2
Displacements [cm]						
Dx	8.84	6.58	12.48	6.94	11.95	7.33
Dy	6.05	9.04	10.84	8.64	10.59	8.47
Dz	4.27	7.60	6.13	6.12	6.42	8.0
Accelerations [m/s ²]						
Ax	19.12	3.81	25.72	5.09	31.58	5.40
Ay	14.65	3.99	35.59	4.05	31.88	4.35
Az	14.99	5.15	29.88	4.78	32.11	4.17

3.2 Displacements

Based on the numerical analysis, the highest displacement values were obtained for horizontal directions (Dx, Dy). The highest displacement (12.48 cm - Dx) was observed for the model III¹, i.e. for the dome shaped according to the method 1 used to create the mesh topology, in which the additional mass was suspended in the middle of the span of the structure. Analyzing the displacement values obtained for models III¹ and III², in which the additional mass was suspended at a distance of 10 m from the centre of the span of the structure, it can be seen that they were similar to the displacement values of the models with the centrally suspended mass II¹ and II². Only in vertical displacements (Dz – Figure 4) a slight increase of 5-31% was recorded, respectively in models III¹ (6.42 cm) and III² (8.0 cm) compared to the values from models II¹ (6.13 cm) and II² (6.12 cm).

Comparing the displacement values for the initial model for method 1 (model I¹ - without additional mass), it can be seen that the addition of additional mass in the dome structure increased the maximum displacements in all directions (Dx, Dy and Dz). In the case of the model where the mass was shifted by 10 m relative to the centre of the span, the displacement values were lower in the horizontal directions (by 2-4% compared to models with the mass located in the centre of the span). For the vertical direction, a slight increase in displacements (by approx. 5%) was noted for the III¹ model with the mass located 10 m from the span centre, compared to the II¹ model.

In the case of method 2 of creating the dome structure, it can be seen that the use of additional mass in the structure does not significantly affect the displacement results. In general, it can be stated that the displacement results were very similar. The maximum difference in the case of horizontal displacements (model III²) was 6% in relation to the model I², and in the case of vertical displacements the difference was 20% also in relation to the model I².

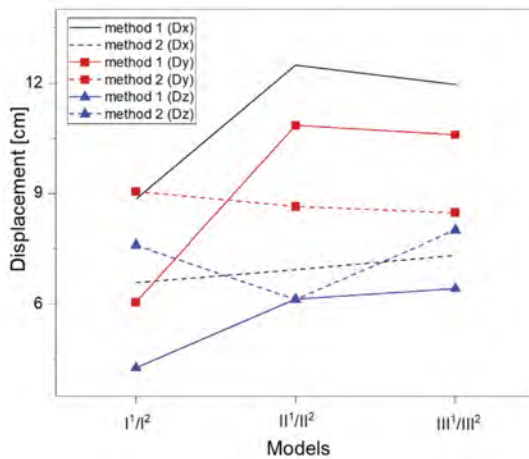


Figure 4. Maximal displacements in numerical models.

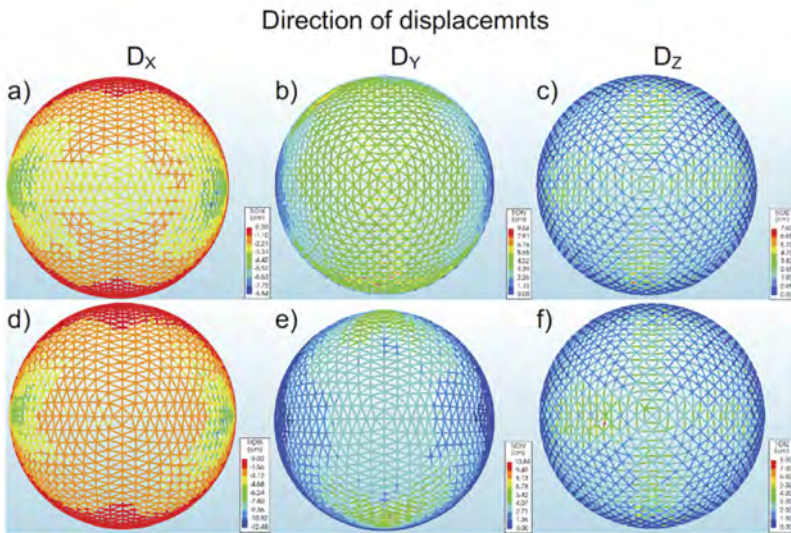


Figure 5. View of maximal displacements of model: a) I¹, b) I², c) I², d) II¹, e) II¹, f) III².

In addition, it should be added that the place of maximum displacement values was observed in the side sectors of the domes. This trend was visible for models I and II (Figure 5a-e). In contrast, in models III (III¹ and III²), the highest values were observed in the places where the additional mass was suspended (Figure 5f).

3.3 Accelerations

The highest acceleration (Figure 6) values were obtained for structures created according to method 1 of shaping their topology. The maximum value was recorded in model II¹, and its value was 35.59 m/s² (Figure 7e). This value was obtained in the horizontal direction when the additional mass was located in the middle of the dome's span. Thus, based on the acceleration results, a significant effect of the additional mass located in the dome structure can be seen in both horizontal and vertical directions.

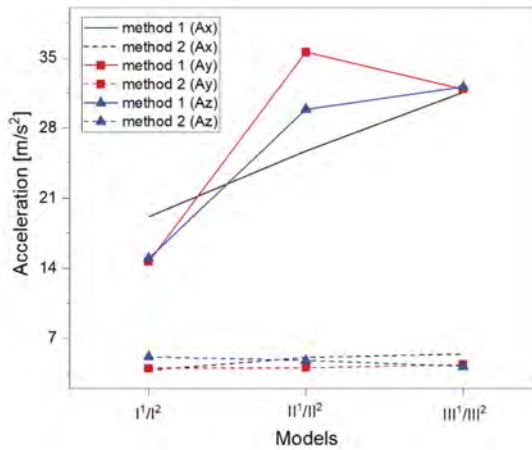


Figure 6. Maximal accelerations in numerical models.

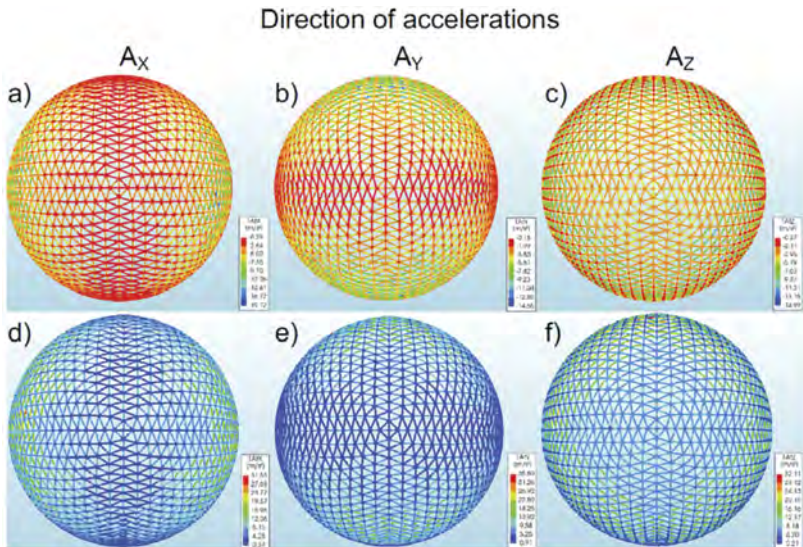


Figure 7. View of maximal accelerations of model: a) I¹, b) I¹, c) I¹, d) III¹, e) II¹, f) III¹.

It can also be seen that the use of an additional mass with a displacement (model III¹) in relation to the model where the mass was located in the middle of the span resulted in a slight reduction of accelerations in horizontal directions, i.e. by about 10%. On the other hand, in the vertical direction (model III¹) there was a slight increase (by 8%) compared to model II¹.

In the case of the second method of creating the structure of the domes, it can be seen that the use of additional mass in the construction of the domes does not significantly affect the obtained values. The acceleration values were much lower than for method 1 of creating a dome sphere. The maximum value for method 2 was 5.40 m/s² (model III²) and was lower in compare to method 1 by 85% (model II¹).

In turn, the maximum acceleration values were observed around 1/4 and 1/2 of the height of the dome (Figure 7). This tendency is noticeable in all the analyzed models, which is a different tendency than in the case of displacements, where the location of the maximum values was influenced by the asymmetrically suspended mass.

4 CONCLUSIONS

After the numerical analysis of the impact of seismic excitation on geodesic domes, it can be concluded that the obtained values are affected by the additional mass suspended in the dome structure. In all analyzed cases, there was an increase in the maximum values. In addition, it can be seen that geodesic domes made according to the second method of shaping the topology of the dome structure better suppress seismic excitations than domes made according to the first method. Moreover, it can be stated that:

- the location of the maximum displacements depends on the location of the additional mass, which is the opposite tendency as in the case of accelerations, in which the maximum values appeared in a specific area of the domes (regardless of the location of the additional mass),
- maximum displacements and accelerations occurred in the domes created according to the first method, in model II, where the additional mass was located in the middle of the span of the domes,
- the highest values were recorded in horizontal directions, both for displacements and accelerations,
- suspending additional mass (additional equipment or devices) in an existing structure may change its response to dynamic excitation and therefore may affect the life-cycle of structure.

As the conducted analysis showed, it is not possible to clearly determine the impact of the additional suspended mass in the dome structure. Therefore, further research is needed in this area to know the exact response of domes located in seismic areas and impact of life-cycle of geodesic dome structure. The conducted research will be helpful for designers dealing with dome structures and lightweight structures.

REFERENCES

- Bonkowski, P., Zembaty, Z. & Minch, M.Y. 2018. Time history response analysis of a slender tower under translational-rocking seismic excitations. *Engineering Structures* (155): 387–393. <https://doi.org/10.1016/j.engstruct.2017.11.042>.
- Bysiec, D. 2008. A group of spherical tessellations based on regular octahedron. *Biuletyn Polskiego Towarzystwa Geometrii i Grafiki Inżynierskiej* (18): 58–68.
- Bysiec, D. 2009. Topology and geometry usage of regular octahedron-based polyhedra for chosen family spherical structures analysis. *INTERTECH 2009, II International Interdisciplinary Technical Conference of Young Scientists. Poznan*. 250–254.
- Bysiec, D. 2009. A group of spherical tessellations based on second family regular octahedron-based polyhedra. *Biuletyn Polskiego Towarzystwa Geometrii i Grafiki Inżynierskiej* (19): 49–59.
- Bysiec, D. 2023. Sustainable Shaping of Lightweight Structures Created According to Different Methods. *Sustainability* 15(4), 3236. <https://doi.org/10.3390/su15043236>.
- Carbas, S. & Saka, M.P. 2012. Optimum topology design of various geometrically nonlinear lattice domes using improved harmony search method. *Struct. Multidiscipl. Optim.* 45: 377–399. <https://doi.org/10.1007/s00158-011-0675-2>.
- Dede, T., Grzywinski, M. & Selejdak, J. 2020. Continuous size optimization of large-scale dome structures with dynamic constraints. *Structural Engineering and Mechanics*. 73(4): 397–405. <https://doi.org/10.12989/sem.2020.73.4.397>.
- Dede, T., Atmaca, B., Grzywinski, M. & Rao, R.V. 2022. Optimal design of dome structures with recently developed algorithm: Rao series. *Structures*. 42: 65–79. <https://doi.org/10.1016/j.istruc.2022.06.010>.
- EN 1993. 2005. Eurocode 3: Design of steel structures. *European Committee for Standardization*. Brussels, Belgium.
- Gholizadeh, S. & Barati, H. 2014. Topology Optimization of nonlinear single layer domes by a new metaheuristic. *Steel Compos. Struct.* 16(6): 681–701. <https://doi.org/10.12989/scs.2014.16.6.681>.
- Grzywinski, M., Dede, T. & Ozdemir, Y.I. 2019. Optimization of the braced dome structures by using Jaya algorithm with frequency constraints. *Steel Compos. Struct.* 30(1): 47–55. <https://doi.org/10.12989/scs.2019.30.1.047>.
- Kaveh, A. & Talatahari, S. 2011. Geometry and topology optimization of geodesic domes using charged system search. *Struct. Multidiscipl. Optim.* 43: 215–229. <https://doi.org/10.1007/s00158-010-0566-y>.

- Kaveh, A. & Rezaei, M. 2015. Optimum topology design of geometrically nonlinear suspended domes using ECBO. *Struct. Eng. Mech.* 65(4): 667–694. <https://doi.org/10.12989/sem.2015.56.4.667>.
- Kaveh, A., Hamedani, K. B. & Hamedani, B. B. 2022. Optimal Design of Large-scale Dome Truss Structures with Multiple Frequency Constraints Using Success-history Based Adaptive Differential Evolution Algorithm. *Periodica Polytechnica Civil Engineering*. <https://doi.org/10.3311/PPci.21147>.
- Maleska, T., Nowacka, J. & Beben, D. 2019. Application of EPS Geof foam to a Soil–Steel Bridge to Reduce Seismic Excitations. *Geosciences* 9(448). <https://doi.org/10.3390/geosciences9100448>.
- Maleska, T., Beben, D. & Nowacka, J. 2021. Seismic vulnerability of a soil-steel composite tunnel – Norway Tolpinrud Railway Tunnel Case Study. *Tunnelling and Underground Space Technology* 110 (103808). <https://doi.org/10.1016/j.tust.2020.103808>.
- Maleska, T. & Beben, D. 2022. Behaviour of soil-steel composite bridge with various cover depths under seismic excitation. *Steel and Composite Structures* 42(6): 747–764. <https://doi.org/10.12989/SCS.2022.42.6.747>.
- Maleska, T. & Beben, D. 2023. Behaviour of Soil–Steel Composite Bridges under Strong Seismic Excitation with Various Boundary Conditions. *Materials* 16(2), 650. <https://doi.org/10.3390/ma16020650>.
- Pilarska, D. 2012. Comparative static analysis of two families two-layered octahedron-based geodesic domes, *XVIII Lightweight Structures in Civil Engineering*. 149–154.
- Pilarska, D. 2018. Octahedron - based spatial bar structures–the form of large areas covers. *Proceedings of the Third Scientific Conference Environmental Challenges in Civil Engineering. Opole*.
- Pilarska, D. 2018. Comparative analysis of various design solutions of octahedron - based spatial bastructures. *Proceedings of the XXIV Conference of Lightweight Structures in Civil Engineering. Lodz*.
- Pilarska, D. 2020. Two subdivision methods based on the regular octahedron for single- and double-layer spherical geodesic domes. *International Journal of Space Structures* (4): 160-173. doi:10.1177/0956059920956944.
- Pilarska, D. & Maleska, T. 2021. Numerical Analysis of Steel Geodesic Dome under Seismic Excitations. *Materials* 14(4493). <https://doi.org/10.3390/ma14164493>.
- Saka, M.P. 2007. Optimum geometry design of geodesic domes using harmony search algorithm. *Adv. Struct.* 10(6): 595–606. <https://doi.org/10.1260/136943307783571445>.
- Saka, M.P. 2007. Optimum topological design of geometrically nonlinear single layer latticed domes using coupled genetic algorithm. *Comput. Struct.* 85: 1635–1646. <https://doi.org/10.1016/j.compstruc.2007.02.023>.
- Ye, J. & Lu, M. 2018. Optimizations of domes against instability. *Steel Compos. Struct.* 28(4): 427–438. <https://doi.org/10.12989/scs.2018.28.4.427>.

Life-cycle benefits of seismic protection using a novel active mass damper

C. Fontana

University School for Advanced Studies (IUSS), Pavia, Italy

M. Caruso & R. Pinho

University of Pavia, Pavia, Italy

F. Menardo, G. Rebecchi & A. Bussini

ISAAC srl, Milan, Italy

ABSTRACT: There is an ever-growing societal pressure for the development and implementation of earthquake risk mitigation solutions that not only minimize economic, environmental, and social losses due to seismic hazard during the building operational phase, but which also limit the environmental impact associated to the construction and other life cycle stages of the seismic protection product itself. Innovative active mass damper (AMD) devices are ideally placed to meet such societal demands, given their limited quantity of material use and low-maintenance needs, replaceability and recyclability of components. In addition, AMDs also present the added advantage of being particularly non-invasive, thus reducing architectural impact, and of being quickly installable, hence limiting disruption to the use of the building. This study, therefore, discusses life cycle economic, environmental, and social impact evaluations for a case-study building equipped with a novel AMD device, with a view to highlight the advantages, also in comparison with other seismic retrofitting techniques, of such a seismic protection solution under a life cycle perspective.

1 INTRODUCTION

Acknowledgement, amongst the structural engineering community, of the relevance of Life Cycle design considerations and approaches continues to increase, given current global concerns on:

- climate change;
- vulnerability of the built environment to natural hazards;
- scarcity of natural resources.

Given that the building sector is undoubtedly intertwined with all the above issues, in the recent years the combined targets of reducing carbon emissions, while improving the resistance to natural hazards and reducing the use of natural resources, have been set as a “strategic priority” by the European Union (EU) and consequentially by national governments. Significant funding has been allocated to the renovation of existing buildings, which is recognised as the key action to achieve the above combined targets. To foster such an integrated approach to buildings renovation, in 2019 the EU Parliament entrusted the Joint Research Centre (JRC) with the REEBUILD project, which had the scope of “producing knowledge, guidelines and policy recommendations for the implementation of integrated techniques for the seismic strengthening and energy efficiency improvement of existing buildings”. Among the project products, the reports on current national policies (Butenweg et al, 2022) provide a valuable image of the progress across the member countries towards these EU objectives.

The building engineering research community has thus now recognised that a “discipline-gap” exists in this field: current methods and practice tend to treat separately and with different levels of analysis and expected performances the various aspects (e.g. structural performance, energy efficiency, reusability) of the whole building, often preventing the achievement of retrofitting solutions that are the “best possible” given the above combined targets. This increased awareness has led to the recent conceptualisation, formalisation, testing and proposal of frameworks (e.g. Caruso et al., 2021, 2023; Clemett et al., 2022a; Passoni et al., 2021), that can include state-of-the-art assessment procedures and retrofit options from different disciplines (seismic/structural, energy, environmental, etc.), and provide measures of the combined targets fulfilment in terms of single or multiple parameters. The proposed assessment frameworks are essential elements of the effort towards the achievement of the combined targets; the scientific consensus on the use of such frameworks would allow the adoption, as a reference standard, of integrated life cycle approaches in the current practice of buildings renovation. In this context, two aspects are emerging as relevant and valuable for focus, even though, strictly speaking, external to the frameworks, i.e. the wide range of the retrofit options offer and their level of invasiveness.

The existing literature on seismic retrofit techniques is very extensive, and a state-of-art review is beyond the scope of this study. A typical taxonomy segmentation is given by the structural scheme: for reinforced concrete (RC) frames, steel frames and unreinforced masonry (URM) wall structures, several retrofitting techniques have been developed for both local and global interventions (e.g. Triantafyllou et al., 2022). The wide set of retrofit options available in practice to be used as input in an evaluation framework by a practitioner is however severely narrowed by two main “excluding factors”: the personal experience/familiarity of the design team with a given technique and the reluctance of the owner/tenant to consent interruption to the building’s use.

The impact of such “excluding factors” is deemed very high by the authors; their effect can range from an exiguous and sub-optimal initial set of retrofit options to the definitive renouncing to undertake a seismic retrofit. This hypothesis is well supported by the situation in Italy, where the strongest EU policies were in force, until current revision, through the “Superbonus 110%” scheme, instituted by the Italian law 77/2020 (Italian Parliament, 2020). The Superbonus created, in principle, an almost ideal context for the proliferation of seismic retrofit interventions; the tax discount was over 100%, covering the entire cost of retrofitting, and it was transferable to third parties, potentially reducing to zero the owner’s investment. Technical requirements were also limited thanks to the absence of minimal thresholds for the performance improvement indexes. Nevertheless, the most recent data (ENEA, 2019) on buildings renovation in Italy show that only 2% of the energy retrofitting interventions on multi-owner buildings has been integrated with seismic retrofit in the pre-Superbonus incentives context. Reliable statistics on the effects of the Superbonus scheme are instead still missing on the seismic side; a local survey conducted by the authors on practitioners working in high-hazard regions provides a rough estimate of 10%, almost entirely referring to local interventions from the outside (i.e., RC joints strengthening).

The scenario outlined above highlights the importance of focusing research efforts in the investigation of innovative and non-invasive seismic retrofitting techniques that, if properly disseminated in the current practice, would contribute to (i) reducing the retrofitting “excluding factors” in current practice, (ii) improving the effectiveness of EU policies on integrated renovation of buildings, and (iii) enhance the proposed integrated life-cycle assessment frameworks with a broader range of intervention options.

A recent and promising proposal in the family of innovative intervention techniques is the employment of Active Mass Dampers (AMDs), which, with respect to the more traditional Tuned Mass Dampers (TMDs), feature real-time active mass control, and are characterised by an engineered plug-and-play packaged arrangement that features a level of non-invasiveness that is superior to all other alternatives in the current panorama of structural retrofitting solutions.

This study, therefore, focuses on life cycle economic, environmental, and social impact evaluations of AMD devices, through their application to a case-study building discussed in another recent work (Caruso et al., 2023).

2 ACTIVE MASS DAMPERS

2.1 Description of AMD devices

The AMD systems considered in this work are developed by ISAAC Antisismica and rely on the concept of a single-degree-of-freedom sliding mass, to which a controlled force is applied. The reaction to the applied force generated by the sliding mass inertia is transmitted to the device supports and therefore it enters in the structure at the installation floor. The sliding mass can be also seen as a surrogate of a fixed point, not available in the structure, to which the reaction of the structure to the forcing action is applied.

The complete system is composed of four main elements: 1) the machine, which is the hardware package containing the mass, the actuator system, the local control logic and the sensors for the real time tracking of the machine's response parameters; 2) the power supply unit, for the energy storage and release to the machine during the working cycles; 3) the building's sensor network, which is an array of sensors distributed in the building for the real time transmission of the dynamic parameters required as input by the control algorithm; and 4) the central computer, where the control algorithm is stored and executed according to the input-output signals to the other components.

The first AMD device developed by ISAAC, named I-PRO 1 (Figure 1), featured an electro-hydraulic actuator, inertial mass of 2.4 tons, total mass of 4 tons, dimensions 1.25 x 4.2 m, and available mass stroke of ± 0.5 m (Rosti et al, 2022). The inertial mass motion could reach a maximum velocity of 5 m/s and an acceleration of 9 g, capable of generating on the installation floor a stabilizing force of up to 220 kN. The control algorithm was a velocity-based one, known as "sky-hook" in the literature. Its inputs are real-time velocities at the ground and at the machine installation floor (typically the top one); the target force calculated by the algorithm is the delta velocity times a gain parameter (G), expressed in kN·s/m or ton/s. The operational parameters are then calculated and transferred to the machine, which forces the mass to have the target reaction force at each time.



Figure 1. Left: I-PRO 1 machine during full scale test in EUCENTRE (from Rebecchi et al, 2021). Right: typical installation layout on the top floor of an RC frame existing building.

An important point about the "sky hook" algorithm implemented by ISAAC in AMD devices is the dynamic equivalence with a dashpot, confirmed by test-bench and full-scale tests (Rebecchi & Bussini, 2021). In brief, a comparative analysis between the full-scale test and nonlinear time-history analysis (NTHA) simulation on a numerical model, in which the machine was modelled as a linear dashpot connected to a top floor structural node and to an added external node subjected to the same acceleration time histories assigned to the base nodes, showed a near perfect coincidence in the force history. Based on this result, it was possible to explore the system capabilities in various application scenarios with a good confidence in simulation accuracy (Casto et al, 2022).

In 2022, ISAAC presented a second-generation AMD system, named Electro-Pro 20x (Figure 2). The design was greatly simplified by substituting the electro-hydraulic actuator with a 15-kW synchronous linear motor, thus eliminating the limitations related to the stroke of the hydraulic components. The system, in the basic single-machine configuration, has a reduced maximum force limit (i.e. 20.8 kN vs 220 kN of the I-PRO 1 prototype) and is intended for a multi-machine layout with an increased flexibility of the system to meet the required design performance and with a much simpler installation in any building. Rebecchi et al (2022) investigated the performance of an 8-machines system through numerical simulations of the

application to a 14-storey building in region with a low level of seismic hazard. In this work, this second-generation AMD system will be considered as first scenario, termed AMD-1.

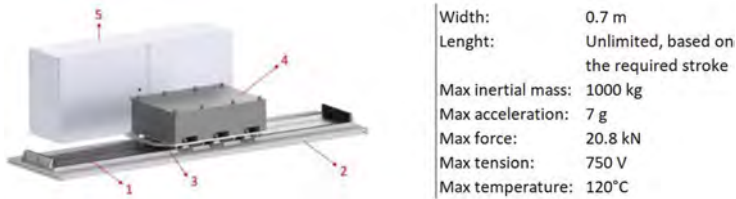


Figure 2. Electro-Pro 20x machine and main technical data (adapted from Rebecchi et al, 2022). 1) permanent magnets, 2) basement for the anchor to sub-structure, 3) linear forcer, 4) mobile mass; 5) machine box including drivers, power system and other electrical components.

2.2 Environmental impact assessment of AMD devices

The Life Cycle Assessment (LCA) for the AMD Electro-Pro 20x requires some assumptions to address the analysis according to EN 15978 (CEN, 2011), which is the current reference standard for buildings LCA in the Europe. The reference to this standard is necessary since the AMD system is completely defined only after installation in the building and its use and end-of-life phases follow that of the building itself. AMD is therefore assimilated to a “technical building system”, somehow extending the definition 3.35 in EN 15978, which is currently limited to systems traditionally installed in buildings (heating, lighting, etc.).

The functional equivalent is a single Electro-Pro 20x in a building. System boundaries are analysed according to the “modularity principle” of EN 15978; in this first attempt the Product Stage (modules A1 to A3) is investigated. The Transportation Stage (A4) and the Construction/Installation Stage (A5) are not considered, due to variability of the former related to the installation location and, to the neglectable contribution of the latter since installation is realised by human work with no further impact. The stage B (Use) is also not considered, due to the peculiar characteristics of the system, i.e. the inherently negligible active time (up to minutes) if compared with the whole building service life. Stages C (end-of-life) and D (reuse-recovery-recycle) will be instead investigated in future research, given that a refined analysis is needed to properly assess the input flows, especially to stage D, due to the highly diversified nature of the system components.

The Life Cycle Inventory (LCI) for the Product Stage (A1 to A3), following what is typically referred to as “cradle-to-gate” LCA, was carried out based on the Bill of Materials (BOM) of the considered system. The BOM was divided in three main component categories: (i) raw and semi-finished components (e.g. steel plates, aluminium profiles etc.), analysed with the ICE database (Hammond & Jones, 2008); (ii) electrical power components (such as linear motor, power cables, batteries etc.), analysed with available Environments Declarations of Performance (EDPs) on similar components and LCA literature and (iii) electronic components, analysed with the available LCA literature.

The cradle-to-gate LCA resulted in 2.5 ton of equivalent carbon dioxide (eCO₂) for a single Electro-Pro 20x machine. This value is a first estimate, suitable for the scope of this study but to be refined in future research. The estimate of AMD carbon footprint is expected to be significantly reduced by considering the foreseen high percentage of components that will enter in phase D, producing a negative contribution to the LCA summation.

2.3 Economic and social impact evaluations of AMD devices

The current cost per AMD machine is in the 50-80 k€ range, depending on the number of machines to be installed and on the related economies of scale. Since the considered solution is still at an early stage of its commercial life, an “R&D quota” related to development costs is included. The cost also includes an “Engineering quota” related to the technical services provided by ISAAC before and after the supply and installation. The combined incidence of the

quotas is estimated to be around 10% and it can be neglected in a comparative analysis with other retrofitting options, whose costs are estimated from a market price-list summation.

For what concerns the social impact, which is typically associated to the reduction of earthquake-induced casualties/injuries, whilst the I-PRO 1 device features already a high potential for improvement with respect to the as-built configuration, its second generation counterpart is still in requirement of further technological developments before it may be capable of providing a similar benefit, as will be shown in the subsequent Section.

3 CASE-STUDY APPLICATION

3.1 Case-study building description

The case study building is a 6-storey residential building located in Sanremo, in the North-West of Italy (illustrated in Figure 3). The site is characterised by a medium level of seismic hazard, with a peak ground acceleration (PGA) on rock soil of 0.146 g for a return period of 475 years, corresponding to the code-defined life safety limit state (LSLS). The building, described in more detail in Caruso et al (2023), was built in the 70s with a RC structure composed of frames in the X (East-West) direction. The interstorey height of 3 m determines a total height of 18 m, the total floor surface is 2800 m² and the total mass is about 2350 tons.

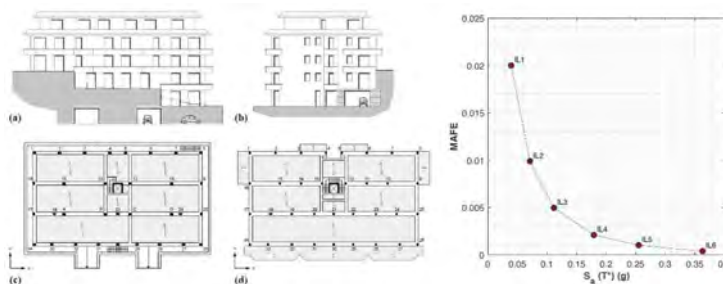


Figure 3. Left: building configuration (a) South and (b) East elevations, (c) first and (d) typical floor plans. Right: site hazard curve for six Intensity Levels with return periods of 50 (DLLS), 101, 201, 475 (LSLS), 975 (CPLS) and 2475 years. Both figures adapted from (Caruso et al., 2023).

In the as-built configuration, a nonlinear distributed inelasticity model was developed with the software SeismoStruct (Seismosoft, 2022), with slabs modelled as rigid diaphragms, and stairs and infills simulated by equivalent loads on the beams.

3.2 As-built earthquake loss assessment

The earthquake loss assessment was performed through the FEMA P-58 procedure, as implemented in the PACT tool (FEMA, 2018). The engineering demand parameters (EDPs) needed for the loss assessment were calculated through a Multiple Stripe Analysis (MSA), with 20 horizontal pairs of ground motion recordings for the six intensity levels (ILs) shown in Figure 3. A total roof displacement of 0.15 m was assumed as the collapse criterion and a complete performance model was built in PACT, with detailed inventory of structural and non-structural damageable elements divided in 8 categories in both directions. All the fragility functions considered were drift-based, thus the interstorey drift ratio (IDR) was the driving EDP for the entire assessment process. The main as-built loss assessment results were: (i) economic Expected Annual Loss (EAL) equal to 9,600 €, i.e. 0,26% of the building replacement cost (ReC); (ii) environmental Expected Annual Emissions (EAE) equal to 4.2 ton eCO₂, i.e. 0.27% of the building replacement environmental impact (ReI); (iii) social Expected Annual Loss of Life (EALL) equal to 0.008 casualties per year.

3.3 Application of the AMD device on the case-study building

In the first retrofit scenario (AMD-1), the as-built structural model was updated with the introduction of AMD Electro-Pro 20x devices. These were modelled through a “dashpot equivalence”, using a linear dashpot in series with a bilinear link element that simulates the force saturation at 20 kN. In such first configuration, 16 machines were applied on the 5th floor of the building, namely, 8 in X direction and 8 in the Y direction, respectively. The main machine parameters are the moving mass of 1 ton and the Gain parameter, set at 150 kN·s/m. Compared with the total mass of the structure, and considering that each machine has as upper force limit of 20 kN, a synthetic index can be defined as the ratio between the structure weight and the max damping force that the AMDs can apply to the installation floor. This ratio, named AMD_{WR} , is equal to 0.7% in both directions, and it can be used to evaluate the AMDs effectiveness at different levels of base shear and for comparison between different scenarios and case studies. A second retrofit scenario (AMD-2) was explored as well, removing the force limit of AMD-1 and doubling the Gain parameter to 300 kN·s/m, with a view to investigate the damping forces generated by such a retrofit solution that is not constrained by current-state technology (it is noted that this level of retrofitting performance can be readily achieved by the first generation devices). Finally, an AMD-3 scenario was also investigated, further increasing the Gain parameter, which was set at 600 kN·s/m, with the objective to study if and how the building interacts with a higher level of damping forces, in terms of members capacity and vibrational regime.

The MSA results of the building in all retrofitted scenarios are summarized in Figures 4 and 5 in X and Y direction, respectively, for three significant ILs: i) at IL1 all AMD scenarios are comparable, and their effectiveness is driven by the Gain parameter increase; ii) at IL4 AMD-1 is prone to saturation in the stiffer X direction, maintaining its effectiveness in Y, while AMD-2 and AMD-3 are able to extensively keep the IDR profiles within 0.5% (code-specified DLLS); iii) at IL5, the AMD-3 scenario shows the negative effects of the interaction between the high damping forces and the building local capacity to transmit them, at the 5th floor in both directions.

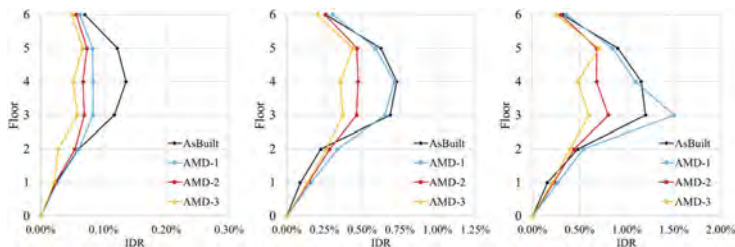


Figure 4. MSA results; IDR profiles in X direction for most significant ILs. From left: IL1-50y (DLLS); IL4-475y (LSLS); IL5-975y (CPLS).

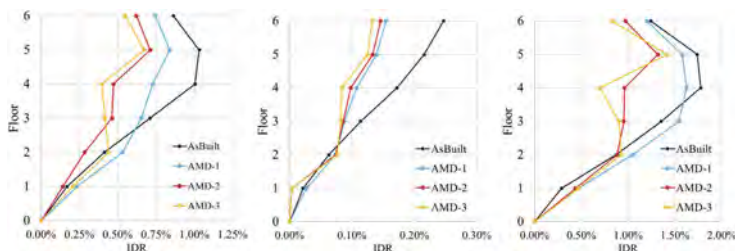


Figure 5. MSA results; IDR profiles in Y direction for most significant intensity levels (IL). From left: IL1-50y (DLLS); IL4-475y (LSLS); IL5-975y (CPLS).

For each scenario, the IDR values at 3rd, 4th and 5th floors in both directions were averaged to obtain a more synthetic index, termed IDR₃₄₅, that facilitates the evaluation of the global effect of the retrofit in the building's portion that is more prone to damage (Figure 6). These results clearly show the high potential of AMD devices, as their technological/performance capabilities evolves, to reduce the IDR response values, in this specific application up to 0.5% in absolute terms (as shown for IL5 in Figure 6, left) and keeping the relative reduction in the 30-40% range (as visible from IL1 (DCLS) up to IL5 (CPLS) in Figure 6, right). These results can be achieved by AMD systems with AMD_{WR} ratio in the 3-4% range.

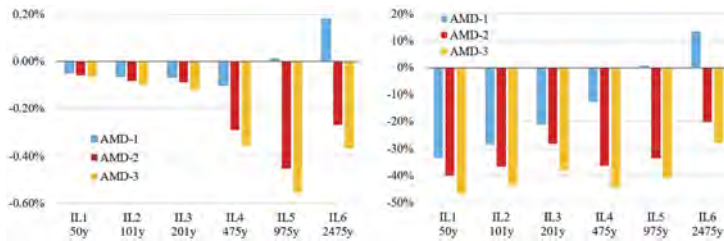


Figure 6. IDR₃₄₅ variation after the retrofit scenarios; the baseline is the as-built scenario. Left: absolute variation; Right: relative variation.

3.4 Comparison with other retrofitting measures adopted

The EDPs obtained from the MSA analysis were introduced in PACT to carry out the performance-based loss assessment for all the AMD scenarios herein considered, and compared with the results of both the as-built and the base-isolation retrofitting solution considered in Caruso et al (2023). The preliminary results of the loss analysis are reported in Table 1, which, it is noted, does not show or highlight the extremely significant (low-)invasiveness advantage of the AMD solution with respect to the base-isolation. In other words, whilst the base-isolation retrofitting strategy does manage to achieve a higher degree of reduction of the socio-economic-environmental impact of earthquakes on this specific building, it also imposes a very significant level of disruption, given that the building will not only have to be vacated for a lengthy period, but will also then require important post-seismic retrofit restoration works of non-structural elements and contents. Such type of disruption, inexistent with the AMD solutions, would in most cases render the base-isolation retrofitting strategy effectively unapplicable.

Table 1. PACT loss results. As-built and base isolation from Caruso et al (2023).

Loss results	As-built reference	Base isolation retrofit	AMD-1 retrofit	AMD-2 retrofit	AMD-3 retrofit
EAL (£/yr)	9,557	1,097	6,640	3,314	4,178
EAL (% ReC)	0.26	0.03	0.18	0.09	0.11
EAE (kg eCO ₂ /yr)	4,240	506	3,178	1,799	2,090
EAE (% ReI)	0.27	0.03	0.20	0.12	0.13
EALL (casualties/yr)	0.0082	0.0009	0.0060	0.0019	0.0042

Another interesting observation from the results shown in Table 1 is the confirmation that there is an optimum upper limit to the level of damping forces that one might wish to introduce with AMD devices; when the level of “restrain” introduced at the top of a building becomes too high, it might start having a counterproductive effect (due to the large local forces that are introduced at the top floors, and the ensuing damage), as the comparison between the results obtained with the AMD-3 configuration with respect to the AMD-2 one clearly shows.

4 CONCLUSIONS

This study is a first attempt to investigate the effectiveness of a novel AMD retrofit system considering environmental, economic, and social performance parameters in a multi-scenario analysis that considers both current technology and potential evolutions. The system was tested in a case study building from existing literature. The environmental evaluation was performed via a simplified LCA, limited to the embodied equivalent carbon emission.

The set of results obtained thus far are very encouraging; they show that, with the evolution of the AMD technology (see AMD-2 scenario considered above) and the natural decrease in the production cost of these devices, a significant reduction of life-cycle impact from earthquakes can be obtained with an essentially negligible level of invasiveness. The latter, it is reemphasised, is instead extremely high for traditional retrofitting solutions, which often discourages seismic retrofitting, with an ensuing high cost for society and the planet.

REFERENCES

- Butenweg, C., Gervasio, H., Gkatzogias, K., Manfredi, V., Masi, A., Pohoryles, D. A., Tsionis, G. and Zaharieva, R., Policy measures for seismic and energy upgrading of buildings in EU Member States – *REEBUILD: Integrated techniques for the seismic strengthening and energy efficiency of existing buildings*, Publications Office of the European Union, Luxembourg, 2022, doi:10.2760/518982, JRC130039
- Caruso, M., Pinho, R., Bianchi, F., Cavalieri, F., Lemmo, M.T. (2021). Integrated economic and environmental building classification and optimal seismic vulnerability/energy efficiency retrofitting. *Bulletin of Earthquake Engineering*, Vol. 19, 3627–3670.
- Caruso M, Pinho R, Bianchi F, Cavalieri F, Lemmo MT. Multi-criteria decision-making approach for optimal seismic/energy retrofitting of existing buildings. *Earthquake Spectra*. 2023;39(1):191–217.
- Casto M, Menardo F, Rosti M, Perrone D, Mesiano G, Nascimbene R, Aiello M. (2022). Seismic retrofit of a RC school building with traditional and innovative techniques. 3rd European Conference on Earthquake Engineering & Seismology. Bucharest, Romania, 2022
- Clemett, N., Gallo, W. W. C., O’Reilly, G. J., Gabbianelli, G., Monteiro, R. (2022a). Optimal seismic retrofitting of existing buildings considering environmental impact, *Engineering Structures*, Vol. 250
- CEN (2011). 15978:2011 Sustainability of Construction Works—Assessment of Environmental Performance of Buildings—Calculation Method; European Committee Standardization, Brussels, Belgium.
- FEMA (Federal Emergency Management Agency). 2018. Seismic performance assessment of buildings, volume 3: Supporting electronic materials and background documentation. 3rd ed. Washington, DC
- Hammond, G.P., Jones, C.I., 2008. Embodied energy and carbon in construction materials. *Proceedings of the Institution of Civil Engineers-Energy*, 161(2), 87–98.
- Italian Parliament, 2020. Legge 17 luglio 2020, n.77. *Gazzetta Ufficiale della Repubblica Italiana* n.180
- National Agency for new technologies, energy, and sustainable economic development (ENEA) (2019), Le detrazioni fiscali per l’efficienza energetica e l’utilizzo delle fonti rinnovabili di energia negli edifici esistenti, Rapporto annuale 2019
- Passoni, C., Marini, A., Belleri, A., Menna, C. (2021). Redefining the concept of sustainable renovation of buildings: State of the art and an LCT-based design framework, *Sustainable Cities and Society*, Vol. 64.
- Rebecchi G., Bussini A. 2021. La protezione sismica attiva: prove sperimentali, simulazioni numeriche e strumenti per la progettazione, *Progettazione sismica*. Vol. 13, N. 6. <https://doi.org/10.7414/PS.13.1.6>.
- Rebecchi G, Menardo F, Bussini A, Diamanti P, Rosti M, Del Viva F, Masiello G, Sguazzo S, (2022). An innovative active control system for the seismic retrofit of a precast R.C. wall-bearing building. XIX ANIDIS Conference, Seismic Engineering in Italy
- Rosti M, Cii S, Bussini A, Calvi PM, Ripamonti F, (2022). Design and Validation of a Hardware-In-the-Loop Test Bench for Evaluating the Performance of an Active Mass Damper. *Journal of Vibration and Control*.
- Seismosoft (2022) “SeismoStruct 2022 – A computer program for static and dynamic nonlinear analysis of framed structures,” available from <https://seismosoft.com/>.
- Triantafyllou, T. C., Bournas, D. A. and Gkournelos, P., Novel technologies for the seismic upgrading of existing European buildings, Publications Office of the European Union, Luxembourg, 2022.

Decision-making procedures for optimal seismic-energy integrated retrofitting of buildings

M. Caruso & R. Pinho

Department of Civil Engineering and Architecture, University of Pavia, Pavia, Italy

R. Monteiro

University School for Advanced Studies (IUSS), Pavia, Italy

Faculty of Engineering, University of Porto, Porto, Portugal

R. Couto

University School for Advanced Studies (IUSS), Pavia, Italy

ABSTRACT: Given the current climate emergency, it is already well-known that retrofitting interventions on existing buildings should be aimed not only at reducing their operational energy consumption, but also at improving their seismic performance. Indeed, the environmental impact of repair and retrofitting activities after strong earthquakes, or other hazardous events, cannot be overlooked, especially in regions with high seismic hazard. Several multi-criteria decision-making (MCDM) approaches are available in the literature for the identification of optimal retrofitting solutions for buildings. Such methods typically consider a range of economic, social, and technical aspects that are assumed to be of interest to decision-makers (e.g. duration of works, architectural impact, need for specialised workers, etc.), however, the importance of including environmental indicators among the relevant decisional variables has been only recently explored. The present study shows the application to a case-study building of two alternative MCDM approaches (i.e. those recently developed by Caruso et al., 2021, and Clemett et al., 2023) for identification of optimal retrofitting strategies, accounting for energy efficiency and related environmental impacts. The main differences between the approaches are highlighted and discussed, in terms of considered decision-making parameters and corresponding weights, rankings of retrofitting options and identification of optimal retrofitting strategies.

1 INTRODUCTION

The recently adopted Paris Agreement on Climate represents the international commitment to mitigate the impacts of climate change by keeping the rise in the global average temperature ideally below 1.5°C above pre-industrial levels. Such ambitious target is expected to be achieved by at least halving global carbon emissions by 2030 and by reaching climate neutrality by 2050.

As it is already well known, the building sector is one the main contributors to global greenhouse gas (GHG) emissions, raw material depletion and waste production. In addition, repair and retrofitting activities after strong seismic or other hazardous events, can affect the environmental impact of buildings' operational life. In Italy, a large portion of the building stock was built after the second world war and prior to the introduction of modern seismic design codes. Such buildings, mostly reinforced concrete (RC) moment-resisting frames with unreinforced masonry infills, are extremely vulnerable to seismic events, and, at the same time, they have poor energy performance. For these reasons, retrofitting interventions on existing buildings should be aimed at reducing their operational energy consumption as well as at improving their seismic performance.

During the last years, the scientific community has made significant efforts to quantify earthquake-induced environmental impacts, typically not included in standard life cycle assessment (LCA) procedures, demonstrating their relevance, especially in regions with a high level of seismic hazard

(e.g. Belleri and Marini, 2016). In tandem, researchers have also recently been focusing on the development of combined/integrated energy and structural retrofitting solutions, acknowledging the importance of improving both performances towards increased sustainability and the advantage of shared construction activities (e.g. Marini et al., 2017; Menna et al., 2021; ReLUI5 WP5, 2019-2021).

In this ongoing research and development context, several multi-criteria decision-making (MCDM) approaches have been proposed in recent literature for the identification of optimal seismic and/or energy retrofitting solutions for buildings. Such methods, which usually do not consider seismic and energy retrofitting in an integrated manner, mostly consider economic, social, and technical criteria that are typically of interest to decision-makers (e.g. duration of works, architectural impact, need for specialised workers, etc.). Only recently, environmental indicators have been included among the relevant decisional variables in some MCDM methods.

The present study illustrates the application of two different MCDM approaches (i.e. those recently developed by Caruso et al., 2021, and Clemett et al., 2023) to a case-study school building in Central Italy, highlighting and discussing their advantages and disadvantages.

2 MULTI-CRITERIA DECISION-MAKING APPROACHES

The multi-criteria decision-making approach proposed by Clemett et al. (2023) provides a framework for considering the performance of alternative retrofitting strategies across a broad range of decision variables and uses a weighted average method to select the optimal solution. The decision maker is first asked to identify a set of relevant parameters, on which the performance of each retrofitting alternative will be evaluated. Each variable is then assigned a weighting factor based on how important it is to the decision maker (i.e. a larger weight factor indicates that a variable is assumed to be more important to the decision maker than one with a smaller weight). Weights can be determined using rigorous methods, such as the analytical hierarchy procedure (AHP) (Saaty, 1980) or based on engineering judgement. The ideal and least ideal solutions based on each decision variable are then identified (i.e., the best and worst performing retrofitting option for each decision variable) and compared with each retrofitting option considered (by calculating the n-space Euclidean distance between the decision matrix values for a design alternative and the ideal and least ideal alternatives). Lastly, once the relative closeness of each alternative to the least ideal solution is calculated, the option with the highest relative closeness (i.e., the farthest from the least ideal) is identified as the preferred solution. The decision variables proposed in Clemett et al. (2023), and corresponding weights, are: C1 – installation cost of the retrofit intervention (0.15); C2 – expected annual costs, including expected seismic losses, maintenance cost of retrofit components, and annual energy costs (0.19); C3 – life cycle environmental impacts, including contributions of retrofitting intervention (both installation and end of life), expected seismic losses, maintenance, and energy consumption (0.18); C4 – annual probability of failure (0.14); C5 – duration of works (0.13); C6 – architectural impact (0.06); C7 – need for specialised labour/design knowledge (0.05); and C8 – required interventions at the foundations (0.1). The considered weight vector was determined using AHP and the professional judgment of the authors (Clemett et al., 2023).

The MCDM for the identification of optimal seismic/energy retrofitting strategies for buildings proposed instead by Caruso et al. (2021), and further extended in Caruso et al. (2023), is based on four relevant decision-making parameters, namely, post-retrofit economic and environmental life cycle impacts (including both earthquake-induced losses and energy consumption, similar to decision variable C3 proposed in Clemett et al., 2023), payback period of the retrofit investment and expected life losses due to seismic hazard. Life cycle costs and carbon emissions are evaluated throughout the post-retrofit building's life cycle by summing up the contributions of retrofitting intervention (both installation and end of life), earthquake-induced losses, and operational energy consumption, all normalised by the total floor area of the building and its expected post-retrofit life. The payback period (PB) of the retrofit investment quantifies the number of years needed to recover the initial investment through the savings due to the retrofitting option adopted (e.g. reduction of seismic expected losses achieved through a seismic strengthening intervention). Lastly, the expected annual life losses (EALL) can be estimated through a chosen casualty model (e.g. ATC, 2018). Based on the above four parameters, the optimal retrofitting option for a given building can

be visually determined through the use of radar plots by checking the one with the smallest ensuing area, i.e. the one that concurrently minimizes all the considered variables. It is noted that the PB is normalised by the expected post-retrofit life of the given building, whilst the other three parameters are normalised by the as-built corresponding values.

3 CASE-STUDY APPLICATION

3.1 Case-study building: As-built seismic and energy performance assessment

The case-study school building is located in Isola del Gran Sasso d'Italia, Abruzzo, Italy, featuring one-way RC moment resisting frames with unreinforced masonry (URM) infills. The school consists of two aboveground stories and a small partial basement at the east end. The first and second floors each have an area of approximately 630 m² and interstorey heights of 3.75 and 4.25 m, respectively. The structure was built between the 1960s and 1970s, thus representing an example of typical Italian construction prior to the introduction of modern seismic design codes. A more detailed description of the building, along with architectural plans and elevations, can be found in Prota et al. (2020).

A numerical model of the case-study building for the seismic performance assessment was developed using OpenSees (McKenna et al., 2010), as presented in Figure 1. The model consists of flexural elements (i.e., beams and columns), beam-column joints (BCJs), a staircase, and URM infills. More information about the modelling of structural and non-structural elements of the case-study building can be found in the studies of Carofilis et al. (2020, 2021). A preliminary seismic assessment, carried out through pushover analyses (as further described in Clemett et al., 2023), identified the moment capacity of the BCJs at which tensile cracking occurs and the shear capacity of the short columns adjacent to the URM infills as the most critical structural weaknesses of the building. Following the preliminary assessment, a detailed seismic loss assessment was performed using multiple-stripe analysis (MSA) through the PEER performance assessment and calculation tool (PACT) (ATC, 2018).

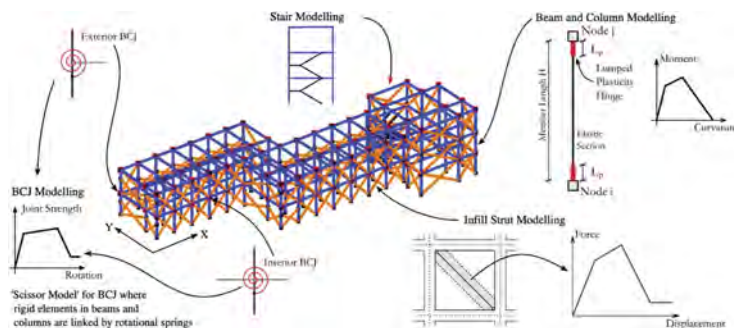


Figure 1. Three-dimensional representation of the numerical model developed in OpenSees (taken from Clemett et al., 2023).

The energy performance of the case-study building was assessed using the EDILCLIMA software (EDILCLIMA, 2021). Most of the modelling parameters were defined by local design codes based on the building's occupancy typology. Four different thermal zones representing the basement, ground floor, first floor, and the stairwell were included in the model. All thermal zones were assumed to be heated, with heating set-point temperature of 20°C. Ventilation of the building was assumed to be provided naturally (i.e., no mechanical ventilation plant). The thermal properties of the envelope elements were determined by defining the stratigraphy of each component's constituent materials, and the ensuing total thermal transmittances (U-values) are summarized in Clemett et al. (2023). Thermal bridges were included to correct the two-dimensional heat flow that occurs at the intersections of different building elements (i.e. external wall elements, external and internal wall elements, external walls and RC columns, external walls and roof/

interstorey floors/ground floor, and external walls and windows). The heating energy was assumed to be supplied by a traditional natural gas boiler system. Domestic hot water was assumed to be provided by the same heating system used for space heating.

3.2 Seismic/energy retrofitting options

Following the preliminary seismic assessment, which identified the structural deficiencies of the building, four different seismic retrofit measures (SRMs) were designed and analysed. A description of each SRM is provided in Figure 2. For all SRMs, URM infills were separated from the RC frames by the provision of a seismic gap to eliminate column–infill interaction and reduce the shear forces acting on the columns. The design procedure for each SRMs and any associated assumptions are reported in previous studies (Carofilis et al., 2020; Clemett et al., 2022).

Regarding the improvement of the energy performance of the building, three different combinations of energy retrofit measures (ERMs) were considered. A summary of the ERMs adopted for each energy retrofit intervention is presented in Figure 2. Each intervention aims, simultaneously, at reducing heat losses to the external environment and at increasing the energy efficiency of systems operating within the given building. The invasiveness of each intervention increases from E1 to E3 to meet the performance requirements described in the Italian Ministerial Decree (Il Ministro Dello Sviluppo Economico, 2015).

Finally, the four seismic interventions were coupled with each energy intervention, leading to twelve possible retrofit alternatives, as illustrated in Figure 2. Each coupled intervention is designated by S_iE_j , where S_i and E_j correspond, respectively, to the reference number of the considered seismic and energy retrofit schemes.

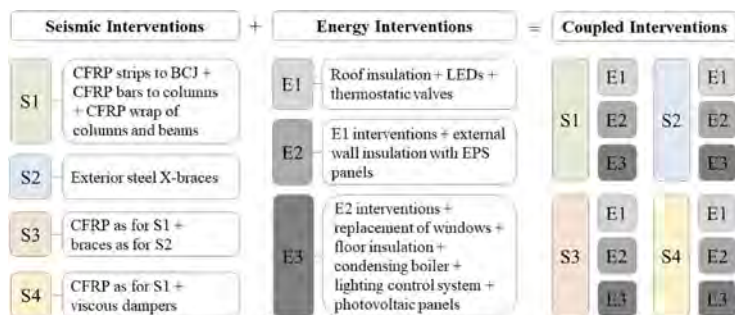


Figure 2. Summary of seismic (S_i), energy (E_i), and coupled interventions (S_iE_j).

3.3 Integrated assessment of the coupled retrofitting strategies

The seismic and energy performance of the twelve possible retrofit alternatives was herein assessed, with the following assumptions:

- SRMs were assumed not to be relevant for the energy assessment of the retrofitted building (for instance, S_1E_1 , S_2E_1 , S_3E_1 , S_4E_1 have the same energy performance);
- the influence of the ERMs on the structural response of the building was neglected, given that these types of measures mostly involve non-structural components (e.g. windows, lighting systems, etc.) not influencing the structural behaviour of the structure.

The impact of the SRMs on the seismic performance of the case-study structure was, at first, assessed through the employment of the N2 method and later through a comprehensive performance-based seismic assessment and loss analysis. The results of the preliminary assessment through pushover analysis have shown an increase of the base shear capacity of the structure at the life safety limit state for all SRMs, with the largest improvements given by S3 and S4, and an increase of the interstorey drifts due to the separation of the URM infills from the RC frames (still compliant with code-specified limits). The performance-based seismic assessment was then conducted through MSA, and, as a result, S4 showed the best improvement, with a noticeable reduction of peak floor accelerations (PFAs) and peak story drifts (PSDs) if compared to those of the as-built structure.

The energy performance of the building for each energy-retrofitted configuration was assessed using EDILCLIMA and the main results, consisting of the primary energy performance (PEC), equivalent CO₂ emissions, annual energy costs (AECs), and Italian energy class ratings, are summarized in Table 1. PEC represents the total energy consumption of the building and it is used to determine the corresponding energy class rating. Classes are represented by a 10-letter scale (A4-G) and are assigned based on the performance of the building compared to that of a reference building with the same geometry and occupational class but with code-defined energy efficiency minimum requirements. By comparing the results obtained for the as-built configuration with the ones from each energy retrofitting option, the improvements of the energy performance are noticeable, progressively increasing from E₁ to E₃, in line with the severity of the intervention.

Table 1. Energy performance assessment summary results for each energy retrofitting option.

Option	PEC (kWh/m ²)	Eq. CO ₂ (kgCO ₂ e)	AEC (€)	Energy Class
As-built	309	76,651	12,718	E
E ₁	221.76	52,476	8,765	D
E ₂	166.63	40,716	7,121	C
E ₃	64.92	14,982	3,109	A2

Finally, a detailed seismic loss assessment was performed through the PACT calculation tool (ATC, 2018) for each combination of seismic and energy retrofit interventions. The presence of ERMs was accounted for in the seismic loss assessment in terms of additional repair consequences to specific non-structural components and in an increased building value (as seen in Table 2). Both parameters increase with the severity of the intervention (from E₁ to E₃). The influence of ERMs on the loss assessment was also considered as described in Clemett et al. (2023).

Table 2. Replacement cost and environmental impacts (EIs) for the as-built and retrofitted structures.

Option	Replacement cost (€)	Replacement EI (kgCO ₂ e)
As-built	2,652,242	1,830,000
S _i E ₁	2,700,684	1,867,485
S _i E ₂	2,792,918	1,888,749
S _i E ₃	2,858,340	1,982,159

The main results of the seismic loss assessment are presented in Table 3 in terms of expected annual loss (EAL), expected annual environmental impacts (EAEI), annual probability of failure (APF), and expected annual loss of life (EALL), which will be then used to apply the MCDM methods described previously.

Table 3. Loss assessment summary results for each combined intervention.

Option	EAL (€/yr)	EAEI (kgCO ₂ e/yr)	APF (10 ⁻² yr ⁻¹)	EALL (p/yr)
As-built	34,151	23,344	1.002	0.2665
S ₁ E ₁	6,775	4,240	0.166	0.0832
S ₁ E ₂	7,320	4,634	0.187	0.0832
S ₁ E ₃	7,478	4,755	0.181	0.0832
S ₂ E ₁	15,897	10,099	0.455	0.1851
S ₂ E ₂	15,982	10,279	0.470	0.1851
S ₂ E ₃	16,065	10,340	0.437	0.1851
S ₃ E ₁	10,115	6,051	0.246	0.1321
S ₃ E ₂	10,657	6,452	0.266	0.1321
S ₃ E ₃	11,464	6,996	0.274	0.1321
S ₄ E ₁	3,452	2,045	0.079	0.0346
S ₄ E ₂	3,585	2,138	0.074	0.0346
S ₄ E ₃	3,593	2,134	0.068	0.0346

4 OPTIMAL INTEGRATED RETROFITTING STRATEGIES

4.1 Decision variables

Table 4 summarises the decision variable values used in the Clemett et al. (2023) methodology, as well as the resulting ranking (R). The option ranked as 1 (i.e. S₄E₃) is the optimal solution, while the option ranked as 12 is the worst one. In turn, Table 5 summarises the decision variable values used in the Caruso et al. (2021) methodology as the ranking of each alternative, while Figure 3 shows the radar plots for three coupled retrofitting intervention (i.e. S₁E₁, S₃E₃, S₄E₃), those representing the best and the worst solutions, and an intermediate one. The red dashed lines indicate the as-built configuration, for which the normalised parameters are equal to 1 (except for the PB, where the unit value refers to the expected post-retrofit life, which here is assumed as 20 years). Option S₄E₃ resulted to be the optimal solution, based on its ensuing area in radar plots.

Table 4. Decision variable values to be implemented in Clemett et al. methodology.

Option	C ₁ (€)	C ₂ (€/yr m ²)	C ₃ (kgCO ₂ e/ yr m ²)	C ₄ (10 ⁻² yr ⁻¹)	C ₅ (days)	C ₆ (-)	C ₇ (-)	C ₈ (-)	R
S ₄ E ₃	817,230	14.22	16.99	0.068	48	0.1617	0.1511	4.77	1
S ₄ E ₂	645,245	16.43	34.27	0.074	44	0.1617	0.1511	4.77	2
S ₄ E ₁	584,415	17.05	42.12	0.079	44	0.1617	0.1511	4.77	3
S ₃ E ₃	529,907	16.10	19.67	0.274	46	0.0934	0.0844	16.61	4
S ₃ E ₂	357,922	17.74	36.56	0.266	42	0.0934	0.0844	16.61	5
S ₂ E ₃	416,678	16.68	21.52	0.437	29	0.0555	0.0135	16.54	6
S ₃ E ₁	297,092	18.07	44.19	0.246	42	0.0934	0.0844	16.61	7
S ₂ E ₂	244,694	18.83	38.83	0.470	24	0.0555	0.0135	16.54	8
S ₂ E ₁	183,863	19.48	46.57	0.455	22	0.0555	0.0135	16.54	9
S ₁ E ₃	1,462,370	14.45	23.49	0.181	65	0.0227	0.0844	5.71	10
S ₁ E ₁	1,229,555	16.87	48.28	0.166	61	0.0227	0.0844	5.71	11
S ₁ E ₂	1,290,386	16.55	40.72	0.187	61	0.0227	0.0844	5.71	12

4.2 Comparison of results obtained with the two MCDM approaches

From both methods, the optimal solution is S₄E₃, which couples the global energy retrofitting intervention (roof, floors and walls insulation + LEDs + thermostatic valves + new windows + condensing boiler + lighting control system + photovoltaic panels) and the structural intervention with CFRP and viscous dampers. However, some differences can be found in the above-presented rankings.

Table 5. Decision variable values to be implemented in Caruso et al. methodology.

Option	Life cycle costs (€/yr m ²)	Life cycle emissions (kgCO ₂ e/yr m ²)	PB (years)	EALL (p/yr)	R
S ₄ E ₃	36.03	28.48	23	0.0346	1
S ₄ E ₂	31.95	42.86	20	0.0346	2
S ₃ E ₁	23.73	49.51	11	0.1321	3
S ₄ E ₁	30.57	49.24	19	0.0346	4
S ₃ E ₂	25.38	43.35	13	0.1321	5
S ₂ E ₁	23.08	50.55	9	0.1851	6
S ₃ E ₃	29.98	29.36	18	0.1321	7
S ₂ E ₂	24.43	44.23	11	0.1851	8
S ₂ E ₃	28.56	29.90	16	0.1851	9
S ₁ E ₃	63.56	47.21	52	0.0832	10
S ₁ E ₂	59.38	61.50	51	0.0832	11
S ₁ E ₁	57.73	67.67	50	0.0832	12

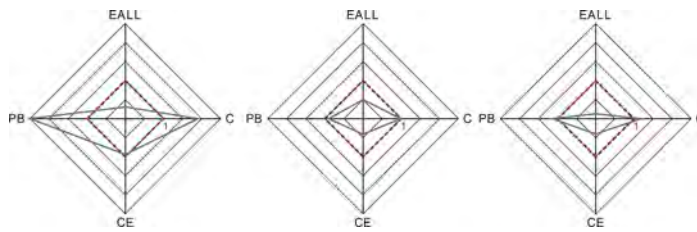


Figure 3. Examples of radar plots: normalized post-retrofit costs (C), carbon emissions (CE), payback period (PB) and expected loss of life (EALL) of three retrofitting configurations (i.e. S_1E_1 , S_3E_3 , S_4E_3).

The ranking of alternatives obtained by applying the Clemett et al. (2023) methodology shows that, from the seismic viewpoint, S_4 performs always better than S_3 , S_3 better than S_2 , and S_2 better than S_1 . Regarding the energy performances, instead, E_3 is preferred over both E_1 and E_2 . The surpassing of S_2E_3 over S_3E_1 on the ranking list demonstrates the higher benefits of the energy performance improvement of E_3 over the improved structural performance of S_3E_1 . Among the eight decision variables, S_4E_3 was observed to be the best solution based on four of them, namely: expected annual costs (C2), life cycle environmental impacts (C3), annual probability of failure (C4) and required intervention at the foundations (C8).

When applying the Caruso et al. (2021) methodology, from the structural viewpoint, S_1 is always the worst option, but the other solutions led to different results. S_2 and S_3 perform well in terms of life cycle costs and payback periods, moderately in terms of life cycle emissions, and inadequately in terms of EALL when compared to other solutions. S_4 , instead, has yielded the lowest EALL values, and performed moderately on all the other variables. From the energy point of view, E_3 is not always the best solution, since it has very high costs (thus a high PB) and environmental impacts due to installation. Moreover, E_3 solutions foresee seismic economic losses that are more relevant than costs of energy consumption, whereas the opposite occurs in terms of environmental impacts. Among the four considered decision variables, S_4E_3 was observed to be the best solution based on two of them, i.e. life cycle carbon emissions and expected annual loss of life.

The application of both methods has highlighted some relevant differences, not only in the results, but also in the approach. Concerning costs, it is noted that in the methodology of Clemett et al. (2023) the costs of installation (C1) and other costs (C2) are not considered as a single decision-making variable (as the life-cycle costs in Caruso et al. (2021)), whereas C3 refers to the total life-cycle EI (similar to life-cycle carbon emissions in Caruso et al. (2021)). In addition, in Caruso et al. (2021) the post-retrofit life is assumed to be 20 years, whereas in Clemett et al. (2023) the code-based nominal building life is considered (i.e. 75 years). Lastly, in the methodology of Caruso et al. (2021) costs and environmental impacts due to maintenance of retrofitting components are not included.

Concerning the decision variables used, one last observation is related to the weights assigned to each variable and the ensuing results. In the Caruso et al. (2021) method, all four variables are assumed as equally important, thus a 25% weight is assigned to each of them. On the other hand, economic parameters in Clemett et al. (2023) (i.e. C1+C2) have a total weight of 34%, whereas life-cycle environmental impacts have a weight of 18% and the annual probability of collapse of 10%. The overall similarity between the results from the two methods may be related to the fact that the highest weights are assigned to similar (economic, environmental and social) parameters.

Lastly, in the Clemett et al. (2023) approach a relative comparison is made between the options, i.e. the optimal solution is identified based on the relative closeness to an ideal solution that is the best in the considered range. On the contrary, in the Caruso et al. (2021) approach, every retrofitting option is compared to the as-built configuration (through the normalisation of variables).

5 CONCLUSIONS

Several multi-criteria decision-making (MCDM) approaches have been recently proposed in the literature for the identification of optimal retrofitting strategies for existing buildings. The present study demonstrates the application to a case-study building of two alternative MCDM approaches (i.e. those recently developed by Caruso et al., 2021, 2023, and Clemett et al., 2023), which account

for economic, environmental, and social aspects that are assumed to be of interest to decision-makers (e.g. running costs and environmental impacts, duration of works, architectural impact, need for specialised workers, etc.). An existing school building, located in Central Italy, representative of typical Italian construction prior to the introduction of modern seismic design codes was analysed with twelve integrated retrofitting options, and the two MCDM approaches were used to identify the optimal retrofitting solution. The optimal solution given by the application of both methodologies was observed to be S_4E_3 , which couples the global energy retrofitting intervention (roof, floors and walls insulation + LEDs + thermostatic valves + new windows + condensing boiler + lighting control system + photovoltaic panels) and the structural intervention with CFRP and viscous dampers. Despite this global agreement, some differences between the approaches were found, mostly in terms of the type of decision variables considered, the definition of economic decision variables and expected post-retrofit building life, the weights assigned to each decision variable of interest, and the methodology with which the alternative retrofitting options are compared.

ACKNOWLEDGEMENTS

This research was funded by the Italian Civil Protection Department (Dipartimento della Protezione Civile), within the framework of the ReLUIS-DPC 2022–2024 research project, more specifically its WP5 activities (focused on the development and verification of integrated seismic and energy retrofitting solutions) and by the Portuguese Foundation for Science and Technology, through the project SERENE - 2022.08138.PTDC.

REFERENCES

- Applied Technology Council (ATC) 2018. Seismic performance assessment of buildings, Volume 1-Methodology. Rep. No. FEMA P-58-1. <https://femap58.atcouncil.org/reports>.
- Belleri, A., Marini, A. 2016. Does seismic risk affect the environmental impact of existing buildings? *Energy and Buildings* 110: 149–158.
- Carofilis, W., Perrone, D., O'Reilly, G. J., Monteiro, R., Filiatrault, A. 2020. Seismic retrofit of existing school buildings in Italy: Performance evaluation and loss estimation. *Engineering Structures* 225: 111243.
- Carofilis, W., Gabbianelli, G., Monteiro, R. 2021. Assessment of multi-criteria evaluation procedures for identification of optimal seismic retrofitting strategies for existing RC buildings. *Journal of Earthquake Engineering* 26(11): 5539–5572.
- Caruso, M., Pinho, R., Bianchi, F., Cavalieri, F., Lemmo, M.T. 2021. Integrated economic and environmental building classification and optimal seismic vulnerability/energy efficiency retrofitting. *Bulletin of Earthquake Engineering* 19: 3627–3670.
- Caruso, M., Pinho, R., Bianchi, F., Cavalieri, F., Lemmo, M. (2023). Multi-criteria decision-making approach for optimal seismic/energy retrofitting of existing buildings. *Earthquake Spectra* 39(1): 191–217.
- Clemett, N., Carofilis, W., O'Reilly, G. J., Gabbianelli, G., Monteiro, R. 2022. Optimal seismic retrofitting of existing buildings considering environmental impact. *Engineering Structures* 250: 113391.
- Clemett, N., Carofilis, W., Gabbianelli, G., O'Reilly, G. J., Monteiro, R. 2023. Optimal Combined Seismic and Energy Efficiency Retrofitting for Existing Buildings in Italy. *Journal of Structural Engineering* 149(1): 04022207.
- EDILCLIMA (EDILCLIMA Software and Engineering) 2021. EC700 Calcolo Prestazioni Energetiche Degli Edifici—Versione 11. Borgomanero, Italy. EDILCLIMA Software and Engineering.
- Il Ministro Dello Sviluppo Economico 2015. D. Interm. 26/06/2015, Applicazione delle metodologie di calcolo delle prestazioni energetiche e definizione delle prescrizioni e dei requisiti minimi degli edifici.
- Marini, A., Passoni, C., Belleri, A., Feroldi, F., Preti, M., Metelli, G., Giuriani, E., Riva, P., Plizzari, G. 2017. Combining seismic retrofit with energy refurbishment for the sustainable renovation of RC buildings: A proof of concept. *European Journal of Environmental and Civil Engineering* 26(7): 1–21.
- Menna, C., Del Vecchio, C., Di Ludovico, M., Mauro, G. M., Ascione, F., Prota, A. 2021. Conceptual design of integrated seismic and energy retrofit interventions. *Journal of building engineering* 38: 102190.
- McKenna, F., M. H. Scott, and G. L. Fenves. 2010. Nonlinear finite-element analysis software architecture using object composition. *Journal of Computing in Civil Engineering* 24(1): 95–107.
- Prota, A., Di Ludovico, M., Del Vecchio, C., Menna, C. 2020. Progetto DPC-ReLUIS 2019-2021 WP5: Interventi di rapida esecuzione a basso impatto ed integrati, 72.
- ReLUIS - DPC 2019–21 project, WP5 - Low-impact integrated and fast-assembled interventions.
- Saaty, T. L. 1980. The analytic hierarchy process. New York. McGraw-Hill.

*MS11: Life-cycle asset management and the complexity
of socio-environmental-technical transitions*
Organizers: A. Hartmann, M. Hertogh, J. Bakker & H. Roebbers



Taylor & Francis

Taylor & Francis Group

<http://taylorandfrancis.com>

Multi-stakeholder service life design for rail level crossings

Y. Shang, R. Binnekamp & A.R.M. Wolfert

*Department Materials, Mechanics, Management Design, Faculty of Civil Engineering & Geosciences,
Delft University of Technology, Delft, The Netherlands*

ABSTRACT: Improvement in rail asset safety, comfortability and serviceability is gaining importance. This requires effective service life management by incorporating multi-stakeholder desires in the early design stage. Typical stakeholders are asset owners, train users and maintenance service providers. To allow for this change, the traditional single-sided engineering mechanics track design approach requires a shift towards an integrative design approach that best fits for common purpose while assuring continuous rail asset performance. Within the current paper, a multi-objective simulation-based optimization methodology that combines finite element modeling with preference function modeling is proposed to integrate multi-stakeholder preferences into the service life design. The applicability of the methodology is demonstrated in a design case for level crossings. It is shown that integrating specific stakeholders' preferences will substantially influence the optimal track design configuration, allowing the level crossing design to be managed focusing on best fit for common purpose rather than on mechanical behavior only.

1 INTRODUCTION

Transition zones in a railway network occur at changes in track form and or substructure properties. Examples can be found where a track transits from the open track (normally of the ballast type) to a slab track section to cross a roadway or waterway through supporting structures such as bridges and level crossings. The variation in track form causes a sudden change in track support stiffness, which gives rise to additional dynamic forces when vehicles pass by, associated with a change in elevation of the wheels. This, over a number of loading cycles, leads to the development of differential settlement between the (settlement-free) supporting structures and connecting track, which further increases loads and accelerates track degradation through successive deterioration of track geometry and components (Le Pen et al., 2014).

A typical design guiding principle for mitigating the transition problems is to reduce the dynamic amplification by smoothing stiffness variations along the track. This can be achieved by modifying railpad stiffness, varying sleeper sizes, and installing under sleeper pads at transitions (Indraratna et al., 2019). Amongst these measures, incorporating elastic elements (e.g., the railpads) with different properties can be considered an efficient means to vary track vertical stiffness and dampen vibrations and noise (Sol-Sánchez et al., 2015). Besides, sleepers act as supporting elements to distribute vehicle loads on the track. The design parameters such as spacing and size are also relevant to the local track dynamic behavior. For instance, a reduction in sleeper distances causes an increase in track (vertical) support stiffness, which however also implies more construction costs. As Ortega et al. (2021) reported, the separation of 1 m per spacing results in a 40% cost reduction per km compared to the standard sleeper spacing (0.6 m).

Parametric variations can effectively provide a design solution that allows for a homogeneous distribution of stiffness throughout the track, reducing the dynamic impact in the vehicle-track system and improving long-term track performance. This further reduces the associated maintenance efforts/costs, relevant to the management goals of maintenance service providers. Besides, as

system dynamics are interactive between the vehicles and track, the level of track dynamic amplification also influences the vehicle system responses, e.g., carbody accelerations, which relate closely to the driving comfort of passengers and hence the level of service.

The above impact of variations in track design reflects multi-stakeholder desires. It demonstrates that the railway track design requires an integrative approach incorporating both rail asset feasibility (technics) and stakeholder desirability (e.g., affordability, serviceability). However, the traditional ways of designing the transitions (or the railway track in general) mainly focused on meeting one single technical objective. The mitigation measures for the transitions are mainly developed based on mechanical responses such as wheel-rail contact forces without considering related social needs.

The current study proposes a novel way of integrating hard engineering and soft social aspects to model design problems for railway track structures. Since stakeholder objectives might be conflicting (where no single design solution exists that simultaneously satisfy all), integrating multi-perspectives to evaluate track design alternatives requires optimization techniques to balance stakeholders' preferences and actual rail structural performance. For this purpose, a preference-based optimization tool is combined with a finite element (FE)-based model to capture a wider variety of design aspects. The former translates vague societal needs into crisp engineering design variable values. The FE model characterizes the track dynamic behavior under moving vehicles and serves as a basis for parametric optimization.

2 METHODOLOGY

2.1 Overview - problem definition

The relationship between track input parameters and dynamic responses can be defined by

$$\mathbf{y} = g(\mathbf{x}) \quad (1)$$

where $\mathbf{x} = (x_1, x_2, \dots, x_n)$ is a vector containing a list of track parameters defined in n -dimensional space, e.g., railpad stiffness, sleeper spacing. $\mathbf{y} = (y_1, y_2, \dots, y_k)$ is the vector collecting k responses of interest. Eq. (1) is defined by a FE model, which is introduced in Section 2.2.

Three stakeholder groups are of high relevance in railway service life management, i.e., asset owners, train users, and maintenance service providers. Their interests can be reflected in investment cost, riding comfort, and long-term track performance, respectively (see Table 1).

Table 1. Objectives and performance measures.

Objectives	Performance measures	Unit
Minimize initial investment	C_{cap} - investment cost	€
Maximize riding comfort	A_{max} - max-to-min of carbody acceleration	m/s ²
Minimize expected long-term degradation	E_{max} - max. differential energy dissipation	N·m

Specifically, 1) the sleeper spacing and number of strengthened sleepers in a transition can influence the investment cost. 2) The riding comfort is quantified by *max-to-min difference of carbody accelerations* induced when a vehicle passes through a transition. The lower the carbody accelerations, the higher level of service is expected. 3) The long-term degradation mainly concerns the damage to the ballast layer, as it is the main driver causing track geometry degradation in the transitions. This can be directly related to the mechanical energy dissipated in the ballast layer. The *maximum differential energy dissipation* between adjacent sleepers is selected here as an indicator to assess the sensitivity of a track design to the expected damage (Sadri et al., 2019). The higher the energy dissipated into the ballast layer, the stronger the degradation can be expected. Therefore, reducing the amount of dissipated energy represents an important aim for damage reduction in overall track geometry condition and savings in maintenance efforts/costs.

The objective C_{cap} is evaluated through an explicit function, which is elaborated in Section 3. A_{max} and E_{max} are quantities generated from numerical simulations, where an FE-based model is developed (Section 2.2) to model the coupling dynamics between the vehicle and track.

2.2 Modeling of vehicle-track dynamics

A numerical model is developed to simulate vertical dynamic interaction between the railway track and moving vehicle, which is parametric for optimization purposes. As shown in Figure 1, the vehicle is represented by a multi-body system consisting of a carbody, a bogie, and a wheel, which are connected through suspension systems. The vehicle travels at a constant speed on a ballast-slab transition. The load from the vehicle is assumed to be symmetrically distributed, and consequently, half of the track is studied in this work.

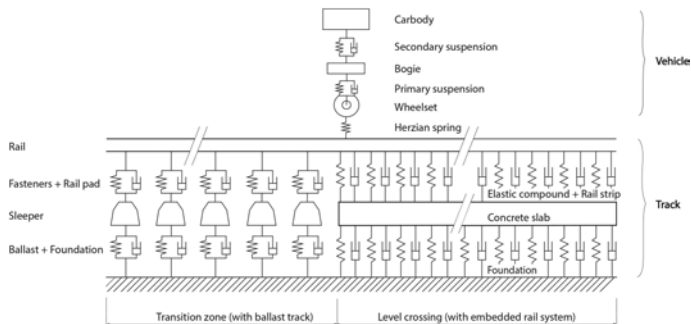


Figure 1. Schematics for a vehicle and a ballast-slab transition.

The track structure is formulated by FEM: the ballast track (left) is represented by a two-layer discretely supported model, and the slab track (right) is continuously supported according to system features of the embedded rail system (ERS). Various design options are available for slab track structures. We consider ERS in this work as it is an innovative track design solution and has been increasingly employed in discrete railway assets such as bridges and level crossings. For details of the ERS features, the reader is referred to Yang et al. (2021).

In the model, the rail and concrete slab are meshed with Euler-Bernoulli beam elements. The supporting components in the ballast track consist of railpads represented by Kelvin-Voight (KV) elements, sleepers as masses, and underlying ballast and foundation layer modelled collectively as the KV elements. Similar to the railpads in the ballast track, elastic compound and rail strip in ERS are placed underneath the rail to provide track elasticity and constrain the vertical rail deflection, which is also modelled by the KV elements, as proposed in Yang et al. (2021).

The vehicle-track interaction problem is solved by integrating the two subsystems into a global system, where the individual system matrices are coupled to formulate global ones, and the global equations of motion (EOM) can be expressed as

$$\mathbf{M}_g \ddot{\mathbf{U}}_g + \mathbf{C}_g \dot{\mathbf{U}}_g + \mathbf{K}_g \mathbf{U}_g = \mathbf{F}_g \quad (2)$$

where \mathbf{M}_g , \mathbf{C}_g and \mathbf{K}_g denote, respectively, the mass, damping, and stiffness matrices of the global system. \mathbf{U}_g , $\dot{\mathbf{U}}_g$ and $\ddot{\mathbf{U}}_g$ are the displacement, velocity, and acceleration vectors of the global system, respectively. \mathbf{F}_g is the global force vector.

The track model is developed in COMSOL, where the system matrices are formulated and exported to MATLAB. The vehicle system matrices are established in MATLAB, which are then coupled with the exported track matrices to formulate the global ones, as written in Eq. (2). The global EOM is solved in the time domain using the Newmark integration method, which is implemented in MATLAB. This co-simulation methodology of connecting COMSOL and MATLAB to solve vehicle-structure dynamics was first developed and validated with a beam case by Shang

et al. (2022) and extended to a railway structure by Shang et al. (2023). The reader is referred to these works for extensive descriptions of the coupling method.

2.3 Preference based design optimization

Multi-objective design optimization (MODO) applies to decisions that need to be taken in the presence of trade-offs between several objectives. This applies to all types of design scenarios, including the railway track design. Various methods have been devised to solve MODO problems, which can be categorized depending on how the designer articulates the preferences, i.e., a priori and a posteriori articulation of preferences. *A priori* articulation indicates that the relative importance of the objective functions is specified before running the optimization. In cases where no a priori information is available, it is adequate to map all potential solutions and allow the designer to make a decision afterward. Such methods are referred to as *a posteriori* methods.

A priori methods are reflected by parameters such as weights and aggregation scores (Zhilyaev et al., 2022; van Heukelum et al., 2022). The weighted min-max (or goal attainment) approach is a common solution technique in *a priori* methods. The basic idea is that the designer specifies a target value (i.e., the goal) for each objective, and the ‘min-max’ seeks to find a solution that minimizes the maximum deviation between the target values for the objectives and values of a candidate solution. When it is applied in the preference-based decision-making domain, all the solutions are mapped by preference scores on a 0-100 scale, and the value of 100 implies the goal. This solution mapping essentially translates the stakeholder preference into deviation from the goal in relative terms, and the minimization of the largest deviation can be formalized as

$$\underset{\mathbf{x}}{\text{minimize}} \quad U = \max_i \{w_i \times [100 - P_i(g_i(\mathbf{x}))]\} \quad (3)$$

where $g_i(\mathbf{x})$ represents the value of i^{th} ($i = 1, 2, 3$) objective (see Table 1) given a specific design configuration \mathbf{x} . $P_i(\cdot)$ is the preference function corresponding to i^{th} objective. It translates $g_i(\mathbf{x})$ to a preference measurement, where stakeholder preference information is encoded in the function and used to rank design solutions. w_i is the weight associated to i^{th} objective.

In each single run, the ‘min-max’ approach produces a single best solution, representing the best compromise among stakeholders. To provide more flexibility in the decision making process, a posteriori articulation is integrated as an alternative in the proposed methodology to solve the MODO problem. Techniques based on genetic algorithms (GA) seem suitable for solving MODO as they can simultaneously handle a set of potential solutions (or a population). This allows the designer to find several members of the Pareto set in a single run of the algorithm (Chang, 2014). The GA-based approaches have extensive applications in railway mechanics, such as the design of vehicle suspensions (Alkhatib et al., 2004), switches and crossings (Pålsson & Nielsen, 2012), and a ballast-slab transition (Aggestam & Nielsen, 2019).

One of the most popular GA-based approaches for MODO is the Nondominated Sorting Genetic Algorithm II (NSGA-II) developed by Deb et al. (2002). The process includes the creation of the initial population and design iterations. Initial individuals are randomly created, and function evaluations are performed for each individual, which is then sorted based on two attributes: non-domination rank and crowding distance. The non-domination rank of an individual is assigned by comparing its function value with the rest. The lower rank (higher fitness) is preferred between two solutions with different ranks. Further, the crowding distances apply when the solutions are in the same rank, and the solution in a less crowded area is preferred. The computation of the two entities guides the selection process at each iteration toward a uniformly spread-out Pareto front (Chang, 2014). Further details of the sorting process are referred to Deb et al. (2002).

2.4 The Kriging metamodel

Applying optimization algorithms in railway mechanics is in general a computationally demanding task. Simulating railway mechanics often requires advanced computational methods, e.g., FEM and discrete element method. The evaluation of these models can be time-consuming and

even more challenging when vehicle-track interaction is considered (as is the general case in transition-related works). To keep the computational cost affordable, metamodeling techniques are integrated into the current methodology, which can provide accurate approximations to the responses of the FE model (see Section 2.2) at reduced computational time.

Metamodeling (also known as surrogate modeling) is frequently used across engineering disciplines in combination with physical experiments or expensive simulation models. Due to the computational efficiency (than the original model), it often supports engineering tasks that require the design space exploration, such as design optimization, model calibration and reliability analysis.

The effectiveness of using metamodels is interconnected with the problem types and modeling conditions (e.g., dimensionality, (non)linearity, sample size). Kianifar & Campean (2020) systematically compared the performance of several metamodeling options in relation to the well-defined problem categories, where the Kriging model with Matérn 5/2 correlation function shows competing performance among the candidates in terms of accuracy and robustness. Therefore, we choose the Kriging model in this work to approximate Eq. (1), which can be expressed as

$$\hat{g}(\mathbf{x}) = \mathbf{f}^T(\mathbf{x}) \boldsymbol{\beta} + Z(\mathbf{x}) \quad (4)$$

where $\hat{g}(\mathbf{x})$ is the approximation of $g(\mathbf{x})$ predicted by the Kriging. $\mathbf{f}^T(\mathbf{x}) \boldsymbol{\beta}$ is the mean value of $\hat{g}(\mathbf{x})$, including q arbitrary functions $\{f_j; j = 1, \dots, q\}$ and the corresponding coefficients $\{\beta_j; j = 1, \dots, q\}$. It represents the global characteristics (the trend) of the model. $Z(\mathbf{x})$ captures the local deviations by a Gaussian process with expectation being zero and variance being σ^2 .

For a single objective, when training samples $\mathbf{x} = \{\mathbf{x}_1, \mathbf{x}_2, \dots, \mathbf{x}_m\}^T$ are determined, the corresponding output $\mathbf{y} = \{y_1, y_2, \dots, y_m\}^T$ can be obtained by querying the FE model at \mathbf{X} . This forms a training set $\Phi = \{(\mathbf{x}_i, y_i) | i = 1, \dots, m\}$, and the covariance of $Z(\mathbf{x})$ can be given by

$$\text{cov}[Z(\mathbf{x}_i), Z(\mathbf{x}_j)] = \sigma^2 R(\mathbf{x}_i, \mathbf{x}_j) \quad (5)$$

where $R(\mathbf{X}_i, \mathbf{X}_j)$ is the correlation function for any pair of $(\mathbf{X}_i, \mathbf{X}_j)$. The Matérn 5/2 correlation function is used given its accuracy and robustness as evaluated by Kianifar & Campean (2020).

3 ILLUSTRATIVE EXAMPLE: A RAIL LEVEL CROSSING

3.1 Optimization problem formulation

A level crossing design case is selected to demonstrate the application of the proposed methodology. A ballast-slab transition is often presented in a level crossing, where the ERS design (with concrete slabs installed to replace the ballast layer) is applied for crossing traffic. This poses an abrupt variation in track support stiffness since the connecting section is of the ballast type. The current optimization problem is therefore formulated to achieve a smooth stiffness transition between the connecting ballast track and ERS-based level crossing.

The design variables are listed in Table 2, which are collected in a design vector \mathbf{X} ($\mathbf{X} = [x_s, x_r, x_{r1}, x_{r2}, x_{r3}, x_l]$). The variable x_l is specific to ERS design, while the others are related to the ballast track. The rail strips in ERS are elastic components underneath the rails, similar to the railpads in the ballast track. Two types of rail strips with predefined stiffness properties have been developed for ERS. The current practice in the Netherlands utilizes type I strip, and the effect of applying (softer) type II strip on the mechanical behavior of level crossings is under investigation. It is also worth mentioning that the variables x_s and x_l are treated as discrete values to align the optimization setting with the FE discretization. The value implies the number of 0.05m-long finite elements. The lower bound of x_s means 0.5 m, and the upper bound is 0.7 m. This range is considered reasonable and can maintain structural integrity, according to Ortega et al. (2021). x_l has a lower bound of 0 and upper bound of 6 m, implying that a 6-m level crossing is considered in the example.

The track parameters in the FE model are defined according to a typical Dutch level crossing design. The vehicle parameters refer to VIRM trains, which are double-deck trains operated by Dutch Railways. For details of the parameter setting, the reader is referred to Shang et al. (2023).

Table 2. Definition of design variables.

Variables	Unit	Range of definition	Related objectives
Sleeper spacing (x_s)	-	$x_s \in \mathbb{Z} : x_s \in [10, 14]$	$A_{max}, C_{cap}, E_{max}$
Number of strengthened sleepers (x_n)	-	$x_n \in \mathbb{Z} : x_n \in [0, 15]$	$A_{max}, C_{cap}, E_{max}$
Railpad stiffness ($x_{r_i}, i = 1, 2, 3$)	MN/m	$x_{r_i} \in \mathbb{R} : x_{r_i} \in [50, 1000], i = 1 \dots 3$	A_{max}, E_{max}
Length of type II rail strip (x_l)	-	$x_l \in \mathbb{Z} : x_l \in [0, 120]$	A_{max}, E_{max}

Three objectives (see Table 1 and 2) are considered in the optimization. Two Kriging meta-models are established to approximate E_{max} and A_{max} , respectively. Initially, 2000 points of \mathbf{x} are generated based on Latin Hypercube sampling. The FE model is queried at these input locations to generate the quantities of E_{max} and A_{max} . The input-output formulates a dataset further split into training, validation, and test sets. The Kriging parameters are tuned based on the leave-one-out (LOO) cross-validation (CV) approach using the training and validation data. The model performance is evaluated on the test set using relative training error, which yields 2% and 1% for the metamodels of predicting E_{max} and A_{max} , respectively.

The objective C_{cap} is calculated depending on x_s and x_n . 1) x_s is varied within a 5-m section adjacent to the level crossing. Ortega et al. (2021) analyzed the effect of sleeper spacing (x_s) on construction cost savings. A brief resume of cost reduction in spacing alternatives was reported compared with the standard spacing (0.6 m). This work utilizes this cost relation, where the total cost of placing sleepers with the standard spacing is assumed as €3000, and the costs for other spacing alternatives are calculated based on the cost ratio provided by Ortega et al. (2021). 2) x_n concerns the number of strengthened sleepers in the transition. It is assumed that the cost ratio between the strengthened and normal type is 1.5 and the unit cost of using the normal sleeper in the transition region is €400.

3.2 Results and discussion

Single-objective optimization problems are firstly solved, and the results are presented in Table 3. The optimum produced from Alt. 1-3 represents the preferred track design solution for maintenance service providers, train users, and asset owners, respectively. The maximization problems in Alt. 4-6 are solved to gather extremes for each objective and facilitate the association of a preference function to each objective in the following multi-objective problem formulation.

Table 3. Design solutions and corresponding objective values from single-objective optimization. Optimal values are highlighted for each problem.

Design alternatives	Design solutions	Objective values		
	$\mathbf{x}=[x_s, x_n, x_{r1}, x_{r2}, x_{r3}, x_l]$	$E_{max}(N)$	$A_{max}(m/s^2)$	$C_{cap}(€)$
Alt. 1: E_{max} minimization	$\mathbf{x}=[13,6,139,179,50,30]$	0.1107	0.2300	9967.7
Alt. 2: A_{max} minimization	$\mathbf{x}=[10,3,74,50,50,0]$	0.1814	0.2148	10013
Alt. 3: C_{cap} minimization	$\mathbf{x}=[14,0,78,78,0]$	0.2836	0.2529	8562.2
Alt. 4: E_{max} maximization	$\mathbf{x}=[14,0,885,50,1000,41]$	1.3880	0.2332	8562.2
Alt. 5: A_{max} maximization	$\mathbf{x}=[14,4,50,593,792,84]$	0.6909	0.2570	9362.2
Alt. 6: C_{cap} maximization	$\mathbf{x}=[10,15,78,78,78,0]$	0.2160	0.2136	12413

The optimization of C_{cap} depends on variable x_s and x_n only (as highlighted in Design solutions to Alt. 3&6), and the remaining variables are fixed as default values. It can be observed that C_{cap} is conflicting with the other objectives: the design with larger sleeper spacing and ‘zero’ use of strengthened sleepers is preferable from a cost perspective; however, it does not help reduce expected damage in the ballast (E_{max}) and maintain the level of train service (A_{max}).

By comparing the solutions from Alt. 1-2 and Alt. 4-5, the first observation is that softer railpads ($x_{r_i}, i = 1, 2, 3$) are recommended to reduce the dynamic impact in the vehicle-track system. In Alt. 1, the optimum of x_{r3} is far less than those for x_{r1} and x_{r2} . x_{r3} refers to the stiffness of the

railpad adjacent to the crossing, and the optimum is linked to x_l . $x_l = 30$ means a 1.5m-long type II (softer) strip is recommended in connection with a soft railpad (x_{r3}) in the ballast track. This allows for a homogeneous distribution of track support stiffness. Hence, a lower effect of load transmitted to the ballast layer can be expected (i.e., reduced E_{max}). It also explains the optimal solution in Alt. 4, where a contradicting outcome is produced. Compared to Alt. 1, Alt. 2 suggests not using the softer strip in ERS in order to minimize A_{max} . The reason could be that E_{max} focuses on the dynamics in track underlayers while A_{max} relates to the upper vehicle dynamics.

The objective values in Table 3 show that by minimizing C_{cap} (Alt. 3), E_{max} and A_{max} will deviate from their minimum; however, E_{max} can be minimized without degrading A_{max} too much (Alt. 1). This can be explained by the interactive dynamics between the vehicle and track structure, i.e., the objectives E_{max} and A_{max} are correlated. It is also worth mentioning that the objectives considered depend on different design variables: C_{cap} is influenced by x_s and x_n only, while the others depend on the entire variable set. Therefore, the competing nature of these objectives can be observed but optimizing one does not necessarily lead to the opposite extremes of the others. Still, the MODO formulation is required as trade-offs are presented between the objectives.

In the MODO, a linear preference function is assigned for each objective. The max and min of each objective are used to construct a reasonable range for associating a preference function to an objective. For example, as shown in Figure 2 (a), for maintenance service provides, the preference for E_{max} of 0.1 equals 100, representing the desired level, and the preference for E_{max} of 1.4 equals 0, which is the worst scenario that should be avoided.

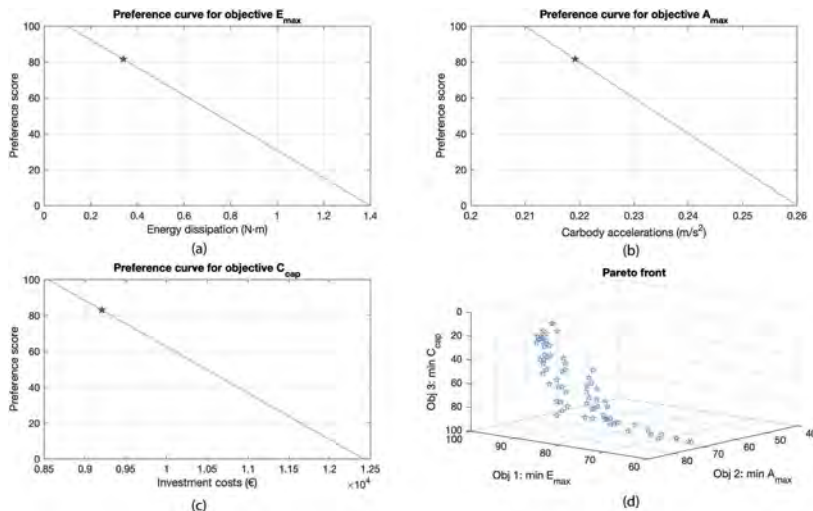


Figure 2. MODO outcomes: preference curve for objective (a) E_{max} , (b) A_{max} , and (c) C_{cap} including the optimum obtained from a priori min-max method; (d) Pareto front for three objectives from a posteriori GA-based approach.

The optimal objective values from the minmax method are also marked on the preference curves in Figure 2 (a)-(c), where equal weights are assigned. The objective scores are almost equal (~82), with $E_{max} = 0.3398$, $A_{max} = 0.21982$, and $C_{cap} = 9207$. Compared with the outcomes from single-objective problems (Table 3), it illustrates the rationale behind the goal attainment paradigm: the method seeks to find a balanced solution among the stakeholders. Besides, the solution is $\mathbf{X} = \{11, 0, 89, 50, 50, 53\}$, showing that the soft railpads and strips (x_{ri} , x_{ji} , $i = 1, 2, 3$) are recommended from both the single-objective and MODO problems at the junction between the level crossing and transition. However, compared with the single-objective problems, MODO formulation that integrates the stakeholders' preferences substantially influences the solution to sleeper parameters (x_s and x_n), since the variables have an actual influence on the objective C_{cap} and it is conflicting with the others.

The Pareto front generated from NSGA-II is presented in Figure 2 (d). It shows that none of the objective functions can be improved in value without degrading some of the other objective

values. The solutions mapped on the front are equally good, allowing the designer to make a decision afterward.

4 CONCLUSIONS

Effective service life management of railway assets requires multi-stakeholder desires to be incorporated into the early design stage. This necessitates an integrative design approach that incorporates both rail asset feasibility and stakeholder desirability. For this purpose, the current work presents a novel way of integrating hard engineering and soft social aspects to model design problems for railway track structures. Three representative stakeholder groups and respective interests are defined in terms of railway mechanics, affordability, and serviceability. The perspectives are translated to preference measures, which are further used to formulate design optimization problems. Three techniques, namely, FEM, metamodeling, and preference-based modeling, are integrated into the optimization framework, which seeks to find optimal design configurations that balance stakeholder preferences and actual track performance in a reasonable computational effort. A level crossing design case is provided, where the obtained design solutions demonstrate relevance to stakeholder preferences and long-term track performance. It shows that the proposed methodology allows the track design to be managed focusing on best fit for common purpose rather than on mechanical behavior only. The case study is for demonstration purposes, and the design methodology is applicable to other railway asset types.

REFERENCES

- Alkhatib, R., Jazar, G.N. & Golnaraghi, M.F. 2004. *Optimal design of passive linear suspension using genetic algorithm*. Journal of Sound and vibration, 275(3-5), pp.665–691.
- Aggestam, E. & Nielsen, J.C. 2019. *Multi-objective optimisation of transition zones between slab track and ballasted track using a genetic algorithm*. Journal of Sound and Vibration, 446, pp.91–112.
- Chang, K.H. 2014. *Design theory and methods using CAD/CAE: The computer aided engineering design series*. Academic Press.
- Deb, K., Pratap, A., Agarwal, S. & Meyarivan, T.A.M.T. 2002. *A fast and elitist multiobjective genetic algorithm: NSGA-II*. IEEE transactions on evolutionary computation, 6(2), pp.182–197.
- Indraratna, B., Sajjad, M.B., Ngo, T., Correia, A.G. & Kelly, R. 2019. *Improved performance of ballasted tracks at transition zones: A review of experimental and modelling approaches*. Transportation Geotechnics, 21, p.100260.
- Kianifar, M.R. & Campean, F. 2020. *Performance evaluation of metamodelling methods for engineering problems: towards a practitioner guide*. Structural and Multidisciplinary Optimization, 61(1), pp.159–186.
- Le Pen, L., Watson, G., Powrie, W., Yeo, G., Weston, P. & Roberts, C. 2014. *The behaviour of railway level crossings: Insights through field monitoring*. Transportation Geotechnics, 1(4), pp.201–213.
- Ortega, R.S., Pombo, J., Ricci, S. & Miranda, M. 2021. *The importance of sleepers spacing in railways*. Construction and Building Materials, 300, p.124326.
- Pålsson, B.A. & Nielsen, J.C. 2012. *Track gauge optimisation of railway switches using a genetic algorithm*. Vehicle system dynamics, 50(sup1), pp.365–387.
- Sadri, M., Lu, T. & Steenbergen, M. 2019. *Railway track degradation: The contribution of a spatially variant support stiffness-Local variation*. Journal of Sound and Vibration, 455, pp.203–220.
- Shang, Y., Nogal, M. & Wolfert, A.R.M. 2022. *A co-simulation solution for vehicle-track interaction dynamics problems*, in: The Fifth International Conference on Railway Technology: Research, Development and Maintenance, Elsevier, Montpellier, France.
- Shang, Y., Nogal, M., Teixeira, R. & Wolfert, A.R.M. 2023. *Optimal design of rail level crossings and associated transition zones using adaptive surrogate-assisted optimization*. Engineering Structures, 282, p.115740.
- Sol-Sánchez, M., Moreno-Navarro, F. & Rubio-Gámez, M.C. 2015. *The use of elastic elements in railway tracks: A state of the art review*. Construction and building materials, 75, pp.293–305.
- van Heukelum, H.J., Binnekamp, R. & Wolfert, A.R.M. 2022. *Human preference and asset performance systems design integration*. Submitted to Structure and Infrastructure Engineering, under review.
- Yang, Z., Zhang, P. & Wang, L. 2021. *Wheel-rail impact at an insulated rail joint in an embedded rail system*. Engineering Structures, 246, p.113026.
- Zhilyaev, D., Binnekamp, R. & Wolfert, A.R.M. 2022. *Best Fit for Common Purpose: A Multi-Stakeholder Design Optimization Methodology for Construction Management*. Buildings 2022, 12, 527.

Preference-based service life design of floating wind structures

H.J. van Heukelum & A.C. Steenbrink

Royal Boskalis, Papendrecht, The Netherlands

O. Colomés

Department Hydraulic Engineering, Faculty of Civil Engineering & Geosciences, Delft University of Technology, Delft, The Netherlands

R. Binnekamp

Department Materials, Mechanics, Management & Design, Faculty of Civil Engineering & Geosciences, Delft University of Technology, Delft, The Netherlands

A.R.M. Wolfert

Department of Engineering Structures, Faculty of Civil Engineering & Geosciences, Delft University of Technology, Delft, The Netherlands

ABSTRACT: Floating wind farms are a promising solution for offshore wind energy production in deep waters. However, the design optimisation process of these farms is difficult due to their complex and multidisciplinary nature. Furthermore, current optimisation methods: 1) ignore and/or provide no insight into the dynamic interplay between the preference-dominated management domain and the object-performance-dominated engineering domain; 2) are limited to evaluating potentially sub-optimal design alternatives; 3) contain fundamental aggregation modelling errors; 4) do not return a single optimal design point. This paper presents an optimisation framework that overcomes these shortcomings and enables truly integrative multi-objective design optimisation. It includes a surrogate model that interacts with the wind turbine simulation tool OpenFAST to enable preliminary design of the structure's mooring system. Applied to a demonstration project and validated against real projects in a maritime contractor environment, the workflow shows improvements in tender performance and added value over single-sided cost optimisations.

1 INTRODUCTION

A promising solution for wind energy production in deep waters is the development of Off-shore Floating Wind Farms (OFWF), as areas with deeper water tend to have higher wind energy densities, but do not allow the economic installation of bottom-founded structures (Spring 2020). The complexity introduced by e.g. high quality requirements, the novelty of the technology and the number of (external) stakeholders (see also Van Gunsteren (2011)), together with the multidisciplinary nature of these developments, create an environment in which modelling and optimising of the (iterative) design process is of great added value, but also challenging and complicated.

In addition, classical design optimisation methods have inherent problems because they are single-sided and ignore and/or provide no insight into the dynamic interplay between the preference-dominated management domain and the object-performance-dominated engineering domain (Van Heukelum et al. 2022). Furthermore, design optimisation is often limited to a posteriori evaluation of (manually) generated design alternatives, with no guarantee that the optimal design alternative is considered because the number of feasible design alternatives is too large to evaluate them all.

Moreover, to enable proper multi-objective design optimisation (MODO), all objectives must be translated into a common domain, for which the affordability domain is commonly chosen in the offshore industry. However, according to classical utility theory, decisions are made based on value or preference and not based on money, as money is not a (fixed) property of objects (Barzilai

2010). Moreover, classical MODO methods contain fundamental (aggregation) modelling errors because mathematical operations are applied without being defined (Barzilai 2006, 2022).

Finally, ignoring preferences is also a major shortcoming of the commonly used Pareto front (Lee et al. 2011, Kim et al. 2022). Searching for the most fit for common purpose design solution involves finding the most preferred solution, not a set of equally preferred solutions from which decision-makers still have to choose through negotiation.

To overcome all the aforementioned problems, this paper presents an optimisation method for the service-life design of OFWFs that integrates preference function modelling and engineering performance, allowing the unification of the managerial domain (subject desirability) with the engineering domain (object feasibility). To this end, an optimisation framework is created within the so-called Preferendus, a software tool that is part of the Odesys design methodology and uses the IMAP optimisation method (Van Heukelum et al. 2022). This paper demonstrates this framework through a demonstration project and gives insight into the applicability of the framework, which has been validated at the Dutch marine contractor Boskalis.

1.1 Data availability statement

The optimisation framework, including the input file of the demonstration projects with all the modelling information, can be found on the GitHub repository of the Preferendus: <https://github.com/TUDELFT-Odesys/Preferendus>.

2 THE OFWF SERVICE-LIFE DESIGN DEMONSTRATOR

The optimisation framework is modelled based on the Odesys mathematical statement introduced by Van Heukelum et al. (2022), see Figure 1. Two stakeholders are considered: 1) an energy service provider (the client) and 2) the marine contractor Boskalis. They are interested in the design of the mooring system and the installation schedule, which creates an optimisation problem where feasibility plays an important role in finding the optimal solution based on the desires of the stakeholders.

Four objectives are considered: project duration, installation costs, fleet utilisation and CO₂ emissions. For the client, a shorter project duration means that the OFWF will start generating revenues sooner. In addition, reducing CO₂ emissions benefits the client’s carbon footprint and the social acceptance of the project. For the contractor, the focus will be on reducing costs to make it more competitive. Secondly, its fleet management department will be interested in the opportunity to improve fleet utilisation through the project.

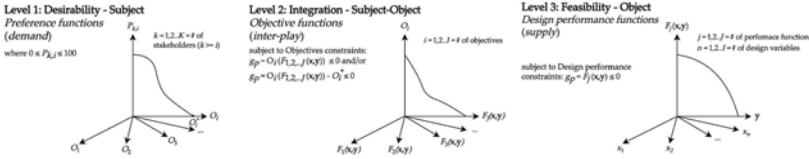


Figure 1. Conceptual threefold framework, where desirability-subject (preference functions, level 1) and the feasibility-object (design performance functions, level 3) are integrated subject-object (objective functions, level 2). Source: Van Heukelum et al. 2022.

3 LEVEL 3 – DESIGN PERFORMANCE FUNCTIONS

This section introduces the relevant design performance functions and design variables in two parts: installation scheduling and mooring system design. This mooring design is restricted to Drag Embedded Anchors (DEA), Suction Piles (SP) and Anchor Piles (AP).

3.1 Installation schedule

The installation schedule depends on two components: the number of available vessels (and their characteristics), and the time it takes these vessels to perform a task. The available vessels are

listed in Table 1. Whether a vessel can perform a task ($x_i = 1$) or not ($x_i = 0$) is expressed by boolean design variables (x_1 to x_{21}) for all tasks except hook-up. For the hook-up, only one vessel is used (see subsection 3.1.1), and the integer design variable x_{22} expresses which vessel. All vessels have different properties (e.g. deck space for anchors) that affect their performance, which can be found in the input file of the framework (see subsection 1.1).

In addition, each task is decomposed into building blocks that describe the time required to complete a sub-activity. During optimisation, the workable months are determined based on environmental data (see subsection 3.2.1) and the overall schedule is constructed from these building blocks, which can be found in the input file of the framework.

To correctly model the installation schedule, three design performance constraints are added to ensure that: 1) the number of installation vessels is ≥ 0 , since the definition of the design variables x_1 to x_{21} allows a total number of installation vessels equal to zero; 2) an equal number of vessels are present when both anchors and mooring lines (ML) are installed simultaneously; 3) a vessel does not perform overlapping tasks.

Table 1. Available vessels and the associated design variables.

Vessel	SP install	AP install	DEA install	Taut ML install	Catenary ML install	Stev-tensioning*	Hook-up
Winchester	x_1	x_5					
Atlas	x_2		x_7	x_{10}	x_{15}	x_{18}	$x_{22} = 0$
Edinburgh	x_3			x_{11}			$x_{22} = 1$
Symphony			x_8	x_{12}	x_{16}	x_{19}	$x_{22} = 2$
Legacy			x_9	x_{13}	x_{17}	x_{20}	$x_{22} = 3$
Scout	x_4	x_6		x_{14}		x_{21}	

* method to achieve higher proof-loads by vertical lifting instead of horizontal pulling (Vryhof 2017).

3.1.1 Assumptions

Some assumptions are made in the modelling: 1) if the design force on the DEA is greater than the bollard pull of the installation vessel, stev-tensioning will be required. If this is carried out using the Scout (a heavy lift vessel), an additional anchor handling tug will be required for the same period at a day rate of €50,000; 2) the hook-up is limited by the delivery time of new Floating Wind Turbines (FWTs), which is assumed to be one FWT every six days. As this rate is lower than the hook-up period, the number of hook-up vessels is set to one. In addition, the hook-up requires one large and one medium tug for towing and station keeping, which have a fixed day rate of €54,000 and €24,000 respectively; 3) for an AP, the ML is always installed at the same time as the anchor, as is the case for a DEA. For an SP, the ML can be installed simultaneously or separately. Stev-tensioning is always done separately.

3.2 Mooring system design

Most of the design variables for an OFWF mooring system are uncontrollable and result from factors like soil and environmental conditions and local marine policy. Of the controllable design variables, the following are considered in the optimisation:

- Anchor type, x_{23} : DEA, SP, or AP.
- Mooring type, x_{24} : Taut or catenary. Catenary moorings consist only of chain ($d=0.333\text{m}$; $M=685\text{ kg/m}^3$; $EA=3.27\text{E}9\text{N}$), taut moorings have a lower and an upper chain with polyester rope ($d=0.211\text{m}$; $M=23\text{ kg/m}^3$; $EA=3.89\text{E}9\text{N}$ (BEXCO n.d.)) in between.
- Shared anchors, x_{25} : an AP or SP can connect two or three MLs, reducing the total number of anchors to be installed.
- Anchor diameter/width, x_{26} : the diameter (for AP or SP) or width (for DEA) of the anchors.
- Anchor length, x_{27} : the length of the anchor.
- Anchor radius, x_{28} : the radius of the anchors with respect to the FWT.
- Unstretched length, x_{29} : the unstretched length of the ML.

To check that the mooring design is sufficient, a design performance constraint is added to the model, stating that the so-called utilisation factor u should be less than 1:

$$u = \frac{\text{design force on the anchor}}{\text{design resistance of the anchor}} = \frac{F_d}{R_d} = \frac{\gamma_f F_a}{\gamma_M R_a} < 1 \quad (1)$$

Where γ_f is a safety factor for the anchor load; γ_M is a safety factor for the anchor resistance; F_a is the anchor load; R_a is the anchor resistance. For determining this force F_a , the open-source wind turbine simulation tool OpenFAST (NREL n.d.[a]) is used, together with the IEA 15MW reference turbine (Gaertner et al. 2020) and its semi-submersible platform (Allen et al. 2020).

3.2.1 Environmental conditions

TurbSim (NREL n.d.[b]) is used to simulate the wind field for the OpenFAST simulations. This software generates fully stochastic wind fields that allow the effect of turbulence on the dynamics of an FWT to be considered. The reference wind speed for the simulation is determined by statistical analysis of hourly data obtained via Hershbach et al. (2018).

The (irregular) wave field is generated by HydroDyn (Jonkman et al. 2014), where the wave spectrum is determined using the JONSWAP spectral equation (Katopodes 2018). This is a function of both the significant wave height H_S and the peak wave period ω_m , which can be determined by statistical analysis of the hourly data obtained via Hershbach et al. (2018). Sea currents are also simulated in the HydroDyn module, using the power law (Jonkman et al. 2014). This is a function of the velocity of the sea current at the still water level U_0 and the water depth d . U_0 is obtained either from local databases (e.g. EMODnet (n.d.)) or from scientific papers.

Two Design Load Cases (DLC) are considered in the optimisation: DLC1.6 and the Survival Load Case (SLC) (DNV 2021c). During DLC1.6, the turbine operates at the rated wind speed in waves with a 1/50-year H_S . During the SLC, both the 1/100-year wind speed and the 1/100-year H_S occur and the turbine is idling. The environmental conditions are simulated co-aligned (i.e. with the same heading) for a heading of 0° , 30° , and 60° relative to the FWT, where 60° is the heading parallel to a mooring line. A yaw-misalignment of $\pm 8^\circ$ is also included in the simulations.

3.2.2 Integration of OpenFAST in the optimisation

Due to the long runtime of OpenFAST simulations, the integration into the optimisation framework is currently done via a surrogate model. This integration consists of five steps divided into two phases: the offline phase (steps 1 to 3), which is performed separately and prior to optimisation, and the online phase, which is an integral part of the framework.

Step 1 – offline phase: determine mooring configurations

The reference mooring design (Allen et al. 2020) is scaled to different water depths (120-150 metres) and taut configurations, based on a comparison between the behaviour of the new design and the reference design under different (static) loads (via Hall et al. (2021)). For this scaling, the design variables have been limited to the anchor radius (x_{28}) and the unstretched length of the mooring line (x_{29}), which consequently become indirect design variables.

Step 2 – offline phase: run OpenFAST

OpenFAST is being run with six 700-second simulations per design scenario, each being a combination of two design load cases (DLC1.6 & SLC), three propagation directions (0° , 30° , 60°), two mooring types (taut & catenary) and three yaw misalignments (-8° , 0° , 8°), resulting in 216 runs per water depth. The result of a simulation is a binary file containing, among other things, the time series of forces on all three anchors of the FWT.

Step 3 – offline phase: analyse the OpenFAST results

The results of the OpenFAST simulations are processed in a script, which for each design scenario: 1) eliminates the initialisation phase of the catenary mooring systems; 2) generates 60-minute time series for three FWTs by (quasi-randomly) combining the six 700-second runs; 3) calculates the net force on the shared anchors using the time series of three FWTs; 4) finds the forces F_a for one, two and three connected MLs per design scenario. All these forces are then multiplied by a safety factor (DLC1.6: $\gamma_f = 1.35$; SLC: $\gamma_f = 1.1$ (DNV 2021c)) to give the design forces F'_d . At the same time, a script is run to determine the angles of the taut MLs with respect to the mudline.

Step 4 – online phase: determine governing forces

The final design forces F_d are determined for both catenary and taut moorings, and for both shared and non-shared anchors, by taking the maximum of the design forces F'_d from the relevant design scenarios. Note: for shared anchors, F_d is the highest of either two or three connected MLs.

Step 5 – online phase: determine anchor dimensions

For all three types of anchors, the point where the chain attaches to the anchor (i.e. the padeye) is below the mudline. Because of friction with the soil, the chain will form a (so-called) inverse catenary shape below the mudline. Neubecker & Randolph (1995) describe a system of equations to determine the tension T_d and angle θ_a of the ML at the padeye, based on the design force F_d and angle θ_m at the mudline and the ML and soil characteristics. In addition, the position of the padeye is required, which for APs and SPs is set to 1/2 the anchor length below the mudline for clay and 2/3 the anchor length for sand. For DEAs, the optimum angle θ_a is determined by the manufacturer and set as a constant in the calculation for T_d . Here $\theta_{a,DEA} = 41^\circ$ for clay and $\theta_{a,DEA} = 31^\circ$ for sand (Vryhof 2018). The anchor resistance R_d and the utilisation factor u can then be calculated, applying the safety factors γ_M according to the DNV-OS-C101 design code (DNV 2021a):

- Drag embedded anchors: the design is limited to Vryhoff's Stevin MK3, Stevpris MK5 and Stevpris MK6 anchors. ABS (2013) describes design formulae that can be used to obtain the required mass $M_{required}$ of a DEA for a given force T_d . In addition, based on the information provided by Vryhof (2018), it is possible to determine the DEA that best matches the values for the anchor length (x_{27}) and width (x_{26}). Knowing the mass of this DEA (M_{DEA}), it is possible to calculate the utilisation factor:

$$u = \frac{F_d}{R_d} = \frac{M_{required}}{0.77 \cdot M_{DEA}} \leq 1 \quad (2)$$

- Suction anchors: for SPs, first the maximum suction-assisted penetration length must be determined (Houlsby & Byrne 2005a,b), in order to calculate the horizontal (H_{ult}) and vertical (V_{ult}) capacity of the anchor (Equation 42 to 49 of Arany & Bhattacharya (2018)). Finally, T_d must be decomposed into a horizontal (H_d) and vertical (V_d) component in order to calculate the utilisation factor (Randolph & Gourvenec 2017):

$$u = \frac{F_d}{R_d} = \frac{M_{required}}{0.77 \cdot M_{DEA}} \leq 1 \quad (3)$$

- Anchor piles: for APs, the horizontal and vertical failure mechanisms are considered separately. For the horizontal failure mechanism, the 'short' pile failure mechanism can be used as described by Randolph & Gourvenec (2017), since 1) the padeye is at a significant depth below the mudline and 2) the lengths of the APs are limited compared to e.g. deepwater moorings of oil & gas platforms. Plastic hinging is therefore unlikely and only soil failure needs to be considered. The vertical failure mechanism of an AP is mainly determined by the weight of the anchor and the soil-pile friction. Therefore, the same design formulae can be used as for an SP. The utilisation factor can be calculated as:

$$u = \frac{F_d}{R_d} = \frac{M_{required}}{0.77 \cdot M_{DEA}} \leq 1 \quad (4)$$

In addition to Equation 1, the mooring system has two other design performance constraints. The first is that a DEA cannot be used for taut and shared anchor systems as it is not designed for vertical and multidirectional loads. The second restricts the L/D and D/t ratios of the APs and SPs. See ABS (2013) for reference values.

3.2.3 Assumptions

In the current development phase of the optimisation framework, only a preliminary design is considered, as the improvement in optimisation results that a more detailed design will entail does not currently outweigh the additional complexity of developing the necessary design

calculations. For this preliminary design, some assumptions are made: 1) all MLs can be stretched indefinitely, and the minimum breaking load (MBL) is not currently considered; 2) the effect of cyclic loading on the anchors and associated fatigue is neglected, only the ultimate limit state is considered; 3) the soil is assumed to be uniform.

The current approach to determine the force F_d for shared anchors is likely to result in the over-dimensioning of anchors with three MLs, as the net force for two MLs is often greater than the net force for three MLs. Therefore the design force F_d of anchors with three MLs will be too high. This should be addressed in further development, although the current approach overcomes problems with the reliability of shared anchors in the event of ML failure (DNV 2021b).

4 LEVEL 2 – OBJECTIVE FUNCTIONS

The optimisation framework considers four objectives that form the link between the design performance (level 3) and the preference functions (level 1):

1. Project duration (PD): the project duration is determined by a proprietary Discrete Event Simulation (DES) combining the design variables with the task durations.
2. Installation cost (IC): installation costs are primarily based on the day rates of the vessels multiplied by the time they work on the project. In addition, a daily surcharge is added for anchor installation vessels, depending on the type of anchor (x_{23}).
3. Fleet utilisation (FU): fleet utilisation is represented by normalising the number of days a vessel is booked over the next 12 months (i.e. the vessel with the lowest number of days booked has a score of 0 and the vessel with the highest number of days has a score of 1).
4. CO₂ emission (CE): the CO₂ emission of a project depends on the fuel consumption of the vessels, related to the activity of the vessel (e.g. idling, sailing, towing), multiplied by a conversion rate (per tonne MGO, 3.206 tonne CO₂ is emitted).

5 LEVEL 1 - PREFERENCE FUNCTIONS

To quantify stakeholder desirability, preference functions are constructed that describe the relationship between an individual stakeholder's preference P and a particular objective O . In addition to these functions, the weights associated with the different preference functions have to be determined, both in close cooperation with the different stakeholders. Furthermore, they can change during the design process when stakeholders better understand the impact of their preference functions and associated weights on the process (Arkesteijn 2019). Both the demonstration project and the validation described in this paper, use preference functions and weights determined based on input from floating wind project experts within Boskalis.

6 DEMONSTRATION PROJECT

To demonstrate the application of the framework, a demonstration project has been set up where 45 FWTs are installed (see the data availability statement for the input file containing further project specifics). Three optimisations have been compared: Single-Objective Design Optimisation (SODO) of the installation costs, and MODO with the IMAP and min-max method (Van Heukelem et al. 2022). The final ranking and outcomes for the objectives are shown in Table 2. All designs favour (shared) SPs, MODO min-max with a taut mooring and others with a catenary mooring. The MODO IMAP achieves the best design configuration by balancing the four objectives to best reflect stakeholder preferences. Three other observations are made:

- 1) Due to the conflict between installation cost and fleet utilisation objectives, employing less expensive vessels will reduce the fleet utilisation factor. Rather than choosing one over the other, the min-max method finds a compromise that does not benefit the overall design configuration, revealing a significant drawback of this method.
- 2) The lowest cost is achieved by installing anchors and MLs separately, reducing the time one vessel has to wait for another to complete an installation task. However, this significantly

increases the duration of the project, as the hook-up will start a year later. It could be argued that this design configuration would never be considered because the project duration is unrealistically long. The fact that the actual design configuration would be similar to the configuration obtained by MODO IMAP confirms that this model is a welcome addition to design optimisation in the offshore industry.

- 3) The demonstration project shows the added value of integrated design optimisation. Traditionally, the anchor design is determined by the client and the contractor has to build their schedule around it (waterfall design process). However, this can lead to inefficient use of vessels and delayed project delivery. Here, the design is an integral part of the optimisation, allowing for an overall better design, even if this would deviate from a purely engineering perspective. This is particularly interesting for shared anchors, which are unfavourable from an engineering viewpoint but favourable from a schedule and cost perspective.

Table 2. Table with the results of the objectives and their ranking.

Optimisation	PD [days] <i>weight = 0.25</i>	IC [€1E6] <i>weight = 0.50</i>	FU [-] <i>weight = 0.20</i>	CE [kt] <i>weight = 0.05</i>	Final Ranking
MODO IMAP	619 (<i>P = 96.5</i>)	56.81 (<i>P = 98.5</i>)	0.83 (<i>P = 74.4</i>)	21.9 (<i>P = 94.6</i>)	1. (<i>P = 100</i>)
SODO Costs	985 (<i>P = 41.5</i>)	54.71 (<i>P = 99.2</i>)	0.83 (<i>P = 74.4</i>)	21.6 (<i>P = 94.8</i>)	2. (<i>P = 41</i>)
MODO min-max	619 (<i>P = 96.5</i>)	61.13 (<i>P = 96.8</i>)	0.98 (<i>P = 97.6</i>)	19.7 (<i>P = 96.1</i>)	3. (<i>P = 0</i>)

7 VALIDATION OF THE OPTIMISATION FRAMEWORK

The optimisation framework has been validated during a meeting with offshore floating wind experts within Boskalis and demonstrated that it can be of great value to a tender team. A tender team always has a bias and especially when the design process consists of evaluating design alternatives, this bias can lead to eliminating alternatives based on intuition, when in fact they are competitive. The optimisation framework removes this bias from the design process, which is in line with what Kahneman (2011) suggests when he distinguishes between thinking fast (decision-making based on intuition) and thinking slow (decision-making using e.g. mathematical decision support tools). Moreover, the framework delivers initial results within an hour (if the surrogate model contains sufficient data), compared to one or more days in the current situation. This is a significant improvement and offers opportunities beyond the development of OFWF.

8 STEPS FOR FURTHER DEVELOPMENT

Based on the assumptions made, the following steps have been identified for further development. To improve the integration of the surrogate model, two steps for further development are identified: 1) consideration of the MBL of the MLs; 2) inclusion of fatigue loading in the design of the anchors. The first will address a shortcoming of the current model and resolves a problem with the script that calculates the taut mooring designs, which currently results in excessive tensions in the polyester rope. The second will add an important element to the design of the anchors, as dynamic loads have a significant effect on the anchor resistance R_a . It would also be interesting to extend the surrogate model to include platforms other than the current semi-submersible platform.

In addition, the following development steps are identified based on the validation in the tender team: 1) take the delivery of the first FWT as $t = 0$ for the schedule; 2) improve the DES with a focus on the calculation of the number of anchors and MLs on board vessels and the start of ML installation if it is done separately from the anchor installation; 3) improve the calculation of installation costs by including procurement and fuel costs; 4) improve the calculation of CO₂ emissions by including emissions from anchor fabrication and onshore activities.

9 CONCLUSIONS

This paper presents an optimisation framework that enables the unification of the engineering domain (object feasibility) with the management domain (subject desirability) and a truly integrative MODO method that can accommodate conflicting objectives of multiple stakeholders whilst simultaneously considering different engineering object variables and design constraints. The applicability of the optimisation framework is shown for a demonstration project, demonstrating its added value over a compromise solution and single-sided cost optimisation, and the efficiency of integrative design. Finally, validation of the framework shows it brings significant improvement in tender performance, both in terms of removing bias from design and improving process speed. Steps for further development include improving the surrogate model and DES and extending the installation cost and CO₂ emission calculations.

REFERENCES

- ABS. 2013. *Offshore Anchor Data for Preliminary Design of Anchors of Floating Offshore Wind Turbines* (Tech. Rep.). American Bureau of Shipping.
- Allen, C. et al. 2020. *Definition of the UMaine VoltturnUS-S Reference Platform Developed for the IEA Wind 15-Megawatt Offshore Reference Wind Turbine* (Tech. Rep. NREL/TP-76773). IEA
- Arany, L. & Bhattacharya, S. 2018. Simplified Load Estimation and Sizing of Suction Anchors for Spar Buoy Type Floating Offshore Wind Turbines. *Ocean Engineering* 159: 348–57.
- Arkesteijn, M. 2019. *Corporate Real Estate Alignment: A Preference-Based Design and Decision Approach* [Doctoral dissertation, Delft University of Technology]. <https://doi.org/10.7480/abe.2019.12>.
- Barzilai, J. 2006. Preference Modeling in Engineering Design. In Lewis, K. E. et al. (Eds.), *Decision Making in Engineering Design*. ASME Press.
- Barzilai, J. 2010. Preference Function Modelling: The Mathematical Foundations of Decision Theory. In M. Ehrgott et al. (eds.), *Trends in Multiple Criteria Decision Analysis*. Springer.
- Barzilai, J. 2022. *Pure Economics*. FriesenPress.
- BEXCO. n.d. *Deeprope Polyester [Eur]* (Tech. Rep.).
- DNV. 2021a. *Design of Offshore Steel Structures, General - LRFD Method* (Tech. Rep. DNV-OS-C101).
- DNV. 2021b. *Floating Wind Turbine Structures* (Tech. Rep. DNV-ST-0119).
- DNV. 2021c. *Loads and Site Conditions for Wind Turbines* (Tech. Rep. DNV-ST-0437).
- EMODnet. n.d. *EMODnet Physics*. <https://map.emodnet-physics.eu>.
- Gaertner, E. et al. 2020. *Definition of the IEA Wind 15-Megawatt Offshore Reference Wind Turbine* (Tech. Rep.). Golden (Colorado). www.nrel.gov/publications.
- Hall, M. et al. 2021. *MoorPy: Quasi-Static Mooring Analysis in Python*. NREL.
- Hersbach, H. et al. 2018. *ERA5 Hourly Data on Single Levels from 1959 to Present*. Copernicus Climate Change Service (C3S).
- Houlsby, G. T., & B. W. Byrne. 2005a. Design Procedures for Installation of Suction Caissons in Clay and Other Materials. *Proceedings of the Institution of Civil Engineers-Geotechnical Engineering* 158 (2): 75–82.
- Houlsby, G. T., & B. W. Byrne. 2005b. Design Procedures for Installation of Suction Caissons in Sand. *Proceedings of the Institution of Civil Engineers-Geotechnical Engineering* 158 (3): 135–44.
- Jonkman, J. M. et al. 2014. *HydroDyn User's Guide and Theory Manual* (Tech. Rep.). NREL.
- Kahneman, D. 2011. *Thinking, Fast and Slow*. Macmillan.
- Katopodes, N. D. 2018. *Free-Surface Flow: Shallow Water Dynamics*. Butterworth-Heinemann.
- Kim, S. et al. 2022. Probabilistic Multi-Objective Optimum Combined Inspection and Monitoring Planning and Decision Making with Updating. *Structure and Infrastructure Engineering* 18 (10-11): 1487–1505.
- Lee, S. et al. 2011. Preference-Based Maintenance Planning for Deteriorating Bridges Under Multi-Objective Optimisation Framework. *Structure and Infrastructure Engineering* 7 (7-8): 633–44.
- Neubecker, S. R., & Randolph, M. F. 1995. Performance of Embedded Anchor Chains and Consequences for Anchor Design. *Proceedings Annual Offshore Technology Conference*. OnePetro.
- NREL. n.d. *OpenFAST*. <https://www.nrel.gov/wind/nwtc/openfast.html>.
- NREL. n.d. *TurbSim*. <https://www.nrel.gov/wind/nwtc/turbsim.html>.
- Randolph, M., & Gourvenec, S. 2017. *Offshore Geotechnical Engineering*. CRC press.
- Spring, M. J. J. 2020. Global Expansion of Offshore Wind Power Depends on Overcoming Significant Challenges Facing Floating Wind Turbines. *Offshore Technology Conference*. OnePetro.
- Van Gunsteren, L. A. 2011. *Stakeholder-Oriented Project Management: Tools and Concepts*. Vol. 6. IOS Press.
- Van Heukelum, H. J. et al. 2022. Human Preference and Asset Performance Systems Design Integration [Manuscript Submitted for Publication].
- Vryhof. 2017. *Stevensioner: Enabling installations* (Tech. Rep.).
- Vryhof. 2018. *Anchor Manual 2018: The Guide to Anchoring* (Tech. Rep.).

A life-cycle assessment framework for pavement management considering uncertainties

A. Vargas-Farias, J. Santos & A. Hartmann
University of Twente, Enschede, The Netherlands

F. Van der Pijl
Rijkswaterstaat, Utrecht, The Netherlands

ABSTRACT: Life cycle assessment (LCA) is a methodology widely endorsed by the pavement community and increasingly adopted by transportation agencies worldwide to account for the environmental impacts of pavements throughout their entire life cycle. LCA studies in this context are prone to the effects of uncertainties due to (1) the long analysis periods that stretch across numerous maintenance and rehabilitation (M&R) cycles, (2) the need of different types and sources of data and additional models and (3) multiple methodological decisions to be made by the analyst. Nevertheless, LCA studies are often done deterministically and omit important phases and phenomena from the systems boundaries, thereby reducing the reliability and representativity of the results. To overcome this challenge and to foster the integration of LCA models with existing pavement management systems, this paper presents the development and application of a LCA framework that evaluates the environmental performance of pavement M&R treatments. Further, it incorporates the effects of pavement-vehicle interaction into the analysis and accounts for multiple types of uncertainties, namely those associated with the value of parameters, methodological choices and data quality. Probability distributions and value scenarios are used to characterize the uncertainties which are propagated into the results using Latin hypercube sampling and scenario analysis. A sensitivity analysis using tree-ensemble methods is adopted to unveil the most influential parameters on the variance of the outputs. The outcomes of this research work aim to advance the applicability of LCA in the context of pavement management, and to improve the understanding of the effects of uncertainties in the outcomes of the analysis.

1 INTRODUCTION

Road pavements are long-lived infrastructures that undergo periodic maintenance and rehabilitation (M&R) treatments over their lifetime. The application of such treatments ensures that pavement condition remains above desirable levels, but it also results in significant cumulative environmental impacts due to the vast consumption of natural resources and energy it entails. In light of the rising environmental awareness, assessing the environmental impacts of road pavements is an important step towards the achievement of sustainability goals.

Life cycle assessment (LCA) is an approach that evaluates the environmental impacts of road pavements over the course of their service life that has gained significant recognition in the field of pavement management (PM) and has become instrumental in the context of sustainability transition (Miliutenko *et al.*, 2014; Rangelov *et al.*, 2020; Santero *et al.*, 2011; Santos *et al.*, 2015). However, the validity of LCA in this setting is often called into question, as most pavement LCA studies tend to exclude important phases from the system boundaries of the analysis, particularly the use phase (Xu *et al.*, 2019), and ignore the effects of uncertainty on the results.

LCA offers the option to calculate the impacts of pavement materials production, construction, use, M&R, and end-of-life (EOL) (Santero *et al.*, 2011). Conventionally, the focus of the assessment has been placed in the production, construction and EOL phases (Xu *et al.*, 2019). However, as the environmental impacts of the use phase may represent a large share of total life cycle impacts (Harvey *et al.*, 2016; Santos *et al.*, 2022), recent LCA studies have begun to account for the effects of pavement-vehicle interaction (PVI), a use phase mechanism, in their assessments (Akbarian *et al.*, 2012; Gregory *et al.*, 2016; Noshadravan *et al.*, 2013; Santos *et al.*, 2022). PVI is the relationship between pavement characteristics and vehicle fuel efficiency, determined by pavement rolling resistance (RR). As RR increases, so do the fuel consumption and the emissions generated by the vehicles moving across the road (Bryce *et al.*, 2014; Van Dam *et al.*, 2015). Although in a comprehensive analysis it is essential to take into account every phase of the pavements' life cycle to ensure representativity and accuracy, the absence of the use phase is not the only omission often found in multiple pavement LCA studies.

Uncertainty is unavoidable in LCA studies, and despite the fact that it directly affects the reliability of the results, conventional LCA analyses often consider single input values. The need for the consideration of uncertainties in LCA has been recognized in the past (Huijbregts, 1998; Santero *et al.*, 2011), but limited attention has been given to developing and including uncertainty analysis approaches in LCA studies (Lo Piano and Benini, 2022), let alone in the pavement domain.

The first step of a un uncertainty analysis in LCA consists of identifying and selecting the main types and sources of uncertainty (Igos *et al.*, 2019). This includes distinguishing between parameter and scenario uncertainty. Parameter uncertainty is primarily caused by inaccuracies in input data used to model processes and flows caused by data quality and variability. LCA studies in the pavement domain place attention on several specific sources of parameter uncertainty related to the different pavement life cycle phases (Azarijafari *et al.*, 2018; Gregory *et al.*, 2016; Noshadravan *et al.*, 2013; Santos *et al.*, 2022), including PVI and the models used to predict the pavement condition over time (Gregory *et al.*, 2016; Noshadravan *et al.*, 2013; Santos *et al.*, 2022; Ziyadi *et al.*, 2017). Among other sources, scenario uncertainty arises from methodological and normative choices made during the goal and scope definition, such as LCA software and LCI database selection (Santos *et al.*, 2017), system boundary choices (Gregory *et al.*, 2016), allocation methods (Azarijafari *et al.*, 2018), etc.

After identifying sources and types of uncertainty, the next step is to characterize them. Characterization can be done qualitatively or quantitatively. In qualitative characterizations, it is common practice to estimate data quality levels and to construct alternative scenarios based on different methodological choices (Igos *et al.*, 2019). The pedigree matrix approach implemented in the ecoinvent database (Weidema *et al.*, 2013) has been employed in the pavement LCA field to account for the uncertainty due to data quality, rendering its further quantitative characterization possible (Azarijafari *et al.*, 2018; Gregory *et al.*, 2016; Noshadravan *et al.*, 2013). Quantitatively, uncertainties can be characterized by defining minimum and maximum parameter values and/or probability density functions (PDFs) (Igos *et al.*, 2019). Data variability can be represented with PDFs when the sample size is large (Yu *et al.*, 2018), or by minimum and maximum values for smaller sample sizes (Gregory *et al.*, 2016). When only single values are available, predetermined uncertainty values retrieved from the ecoinvent database can be used (Azarijafari *et al.*, 2018; Gregory *et al.*, 2016; Noshadravan *et al.*, 2013). In turn, scenarios can be represented by discrete choices with equal likelihood or with alternative value scenarios (e.g., minimum and maximum values) (Azarijafari *et al.*, 2018; Gregory *et al.*, 2016).

Once uncertainties have been characterized, they are propagated to the results. Two common methods used in pavement LCA literature are Monte Carlo sampling (MCS) and scenario analysis (Azarijafari *et al.*, 2018; Gregory *et al.*, 2016; Noshadravan *et al.*, 2013; Santos *et al.*, 2022; Yu *et al.*, 2018). MCS is a commonly used method to propagate parameter uncertainties (Igos *et al.*, 2019). However, it requires large sample sizes and can be computationally expensive. To reduce the computational time, Latin hypercube sampling (LHS) can be used. It is an efficient modification of MCS that divides the input distribution into equal intervals from which a sample point is selected randomly (Groen *et al.*, 2014; Igos *et al.*, 2019). It guarantees that all intervals are sampled equally, and that no area is over- or under-sampled. Therefore, it is particularly useful for contexts where the sample size must be kept as small as possible. Scenario analysis entails the single or

simultaneous variation of parameters, methodological choices and model formulations to analyze uncertainties in LCA (Igos *et al.*, 2019). Sampling and scenario analysis can be used together to combine parameter and scenario uncertainties (Azarijafari *et al.*, 2018; Gregory *et al.*, 2016).

Moreover, a comprehensive uncertainty analysis in LCA should include a sensitivity analysis to investigate how changes in parameters and methodological choices affect the results (Harvey *et al.*, 2016) and to identify which elements have the largest contributions to the overall uncertainty (Igos *et al.*, 2019). In the pavement field, one-at-a-time analyses (Godoi Bizarro *et al.*, 2020) and Spearman's rank correlation coefficients (Gregory *et al.*, 2016) have been used to identify the most influential parameters and scenarios. In other fields, the calculations of Sobol indices (Igos *et al.*, 2019; Jaxa-Rozen *et al.*, 2021a), a well-known global sensitivity analysis (GSA) technique, has been adopted to quantify the relationship and importance of each input in the variance of the LCA outputs. However, this method comes at a high computational cost. In turn, Extra Trees is a computational efficient method that can handle large number of parameters and produce reliable results at smaller sample sizes, while offering results comparable to those of Sobol indices (Jaxa-Rozen and Kwakkel, 2018). In LCA, Extra Trees has been used as a preliminary screening step to identify the most influential parameters on the uncertainty (Jaxa-Rozen *et al.*, 2021a), but to the authors' best knowledge it has never been applied in the pavement LCA field.

In view of the considerations and limitations mentioned above, this study aims to further expand the development and applicability of LCA in the context of sustainable pavement management by creating a framework tailored to road pavement M&R that accounts for the effects of PVI and includes a comprehensive uncertainty analysis methodology.

2 METHODS

2.1 LCA framework

The proposed LCA framework described in this paper focuses on the LCA of individual pavement M&R cycles that involve the application of asphalt overlays, although it can be expanded to include any other type of M&R treatments. LCA studies in the context of M&R often cover long analysis periods spanning multiple M&R cycles. In the current setting the analysis period is constrained to the time between the application of a treatment and the subsequent need for a new one. In addition to the analysis period, the definition of the functional unit considers the characteristics of the pavement system being treated, including its structure (surface, binder, and/or base layers and subgrade), geometrical and functional characteristics, materials and the traffic it is expected to carry (Harvey *et al.*, 2016).

Moreover, the LCA framework is consistent with Dutch reference documents, specifically the asphalt product category rules (NL-PCR) (Van der Kruk *et al.*, 2022) and the Determination Method (Nationale Milieudatabase, 2020). The system boundaries for the analysis encompass all relevant life cycle processes and flows, including the production (material extraction, acquisition, transportation, and processing into asphalt mixtures), construction (on-site paving activities and equipment use), use (processes that impact the environment during the service life, with an emphasis on PVI) and end-of-life (EOL) phases (i.e. removal, recycling and transportation of waste materials) as outlined by Santero *et al.*, (2011).

2.2 Uncertainty analysis

The uncertainty analysis starts with the identification of the different foreground-related uncertain parameters and methodological choices that potentially can influence the environmental impact calculations. Although accounting for uncertainty related to the background is to some extent feasible and would result in a more robust analysis, its actual realization would imply an extreme increase of the number of uncertain parameters and the level of complexity the analysis.

Data variability can be represented with PDFs derived from empirical data when available, or with the predefined values provided by theecoinvent method in the absence of empirical data

(Weidema *et al.*, 2013). These values are then aggregated with data quality uncertainty according to the criteria established by the ecoinvent method, with data quality being described using log-normal distributions. The procedure provided by Muller *et al.*, (2016) is adopted to facilitate the numerical integration with data quality uncertainty values when data variability is represented using distributions other than log-normal. Scenarios are developed based on different value options, such as different machinery production rates, recycled asphalt pavement (RAP) content in the composition of the mixture, and the type of bitumen added.

In the proposed LCA framework the propagation of uncertainties to the results involves the application of a combination of LHS and scenario analysis. LHS is employed to reduce computational time in the evaluation of parameter uncertainty. Scenario analysis, in turn, is used to evaluate the effect of changing scenarios. According to Jaxa-Rozen *et al.*, (2021), 12,000 simulations are sufficient for the LHS analysis when the sensitivity analysis method is adequate for a relatively small number of samples. As such, the Extra Trees method is adopted to identify the most influential parameters in the uncertainty of the outcomes for different scenarios following the configuration recommended by Jaxa-Rozen and Kwakkel, (2018). It is important to note that LHS should be performed for each scenario considered in the analysis, allowing for its subsequent sensitivity analysis. Figure 1 summarizes the uncertainty methodology proposed in the framework.

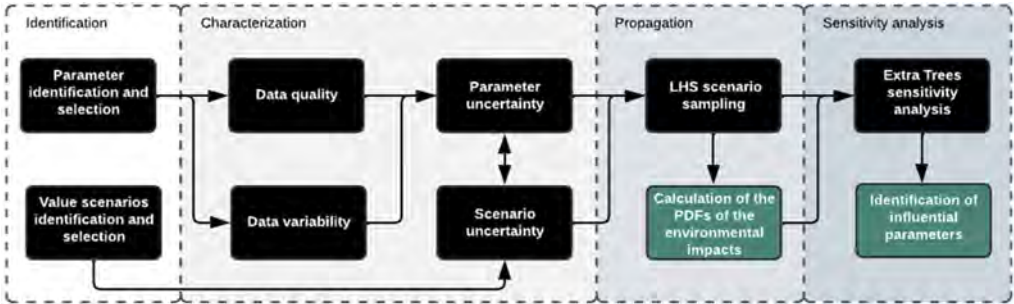


Figure 1. Uncertainty analysis methodology. Black boxes represent the application steps of the methodology, whereas the green ones depict the handling of the outcomes of the methodology.

3 CASE STUDY

The applicability of the proposed framework is illustrated by using the case study of a mill-and-fill M&R treatment for the main road pavement network in the Netherlands. The chosen treatment, selected from a collection of over 75 potential hot mix asphalt overlay options, involves the application of a 50mm-thick layer of Durable ZOAB (DZOAB), which is a porous asphalt mixture with enhanced durability commonly used in the Netherlands.

The functional unit for the analysis is defined as a straight and plan 1km-long carriageway road pavement segment section with 3 lanes, each 3.5km-wide. Traffic data, including average daily intensity values for passenger cars, heavy duty trucks (HDV), and HDV + trailers, were sourced from the INWEVA geographical information system and datasets (Rijswaterstaat, 2022) and are presented in Table 1. The traffic growth rate, set at 1.9%, was determined based on information from the National Statistics Office of the Netherlands (CBS, 2022). The analysis period, corresponding to the average lifespan of a DZOAB surface, is 14 years.

Table 1. Traffic intensity in number of vehicles: statistics.

Vehicle type	Mean	Std	Min	Max
Passenger car	26064	17513	2276	101325
HDV	1744	1035	219	7292
HDV + trailer	2061	1477	140	8872

The system boundaries were adapted from the NL-PCR to align them with the context of M&R (Figure 2), with the exception of leaching, which was excluded from the use phase due to the absence of primary data (Van der Kruk et al., 2022). A construction rate of 1000 ton/day was used in the analysis. Additionally, the environmental benefits of recycling RAP into new pavement materials outside the system boundaries were not considered as RAP enters the system free-of-burden in mixtures with RAP content. Input data for each life cycle phase, except PVI, were obtained from the NL-PCR and the Ecoinvent 3.3 database.

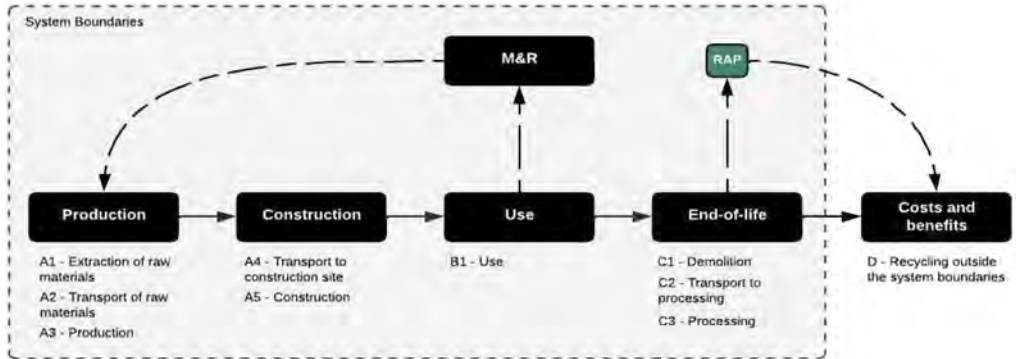


Figure 2. System boundaries of the case study.

The environmental impacts of PVI were calculated using the MIRIAM model (Hammarström *et al.*, 2012). Moreover, linear models were developed for predicting the evolution of roughness and macrotexture over time, respectively represented by the International Roughness Index (IRI) and Mean Profile Depth (MPD), using real IRI and MPD measurements of the Dutch main road network provided by the Dutch Ministry of Infrastructure ‘Rijkswaterstaat’ (RWS). The values of the parameters of the performance models using pavement age as predictor are presented in Table 2. The results are assumed to follow a normal distribution with a mean corresponding to the predicted IRI and MPD values and a standard deviation (std) equivalent to the mean absolute error (MAE) of the model. Vehicle speeds were determined based on Dutch speed limits (Rijksoverheid, 2022) and were assumed to follow a normal distribution with a mean corresponding to the speed limits and a coefficient of variation of 0.1. For facilitating the calculation and to match the size of the traffic intensity sample of the Dutch road pavement network, approximately 4000 MCS runs were completed to estimate the total additional fuel consumption due to RR over the analysis period. The results follow a normal distribution, and the values of the parameters are presented Table 3. The environmental impacts were then calculated and incorporated into the LCA model using the method described by Santos *et al.* (2022), which uses the fuel efficiency and environmental impacts of transportation services (excluding the upstream impacts attributed to infrastructure) to model PVI effects.

Table 2. IRI and MPD linear pavement performance models parameters and statistics.

Pavement performance model	Year 0	Annual increase	MAE
IRI (m/km)	0.9993	0.0296	0.0325
MPD (mm)	1.1063	0.0209	0.1207

Table 3. Total extra fuel consumption due to RR in the analysis period (l/km).

Vehicle type	Mean	Std
Passenger car	68967.84	46675.05
HDV	17729.00	10516.89
HDV + trailer	58536.78	41941.30

The uncertainty analysis was conducted using two scenarios for RAP content: (1) a mixture with 0% RAP and (2) a mixture with 30% RAP. The NL-PCR was used to determine the input values for mixture composition and energy expenditure for asphalt mixtures production, as well as diesel consumption for construction and removal processes, based on the amount of RAP in the mixture (Van der Kruk et al., 2022). All foreground input value parameters assigned to each scenario, including materials, transport, additional vehicle fuel consumption, and energy consumption for production, construction and EOL were considered in the analysis. Data quality uncertainty was calculated using the ecoinvent method (Weidema *et al.*, 2013), as well as the variability of the parameters, with the exception of PVI, whose variability values were computed in the earlier step.

Each scenario was sampled 12,000 times with LHS and environmental impacts of each sample were calculated using the OpenLCA software with a Python interface adapted from the one developed by Jaxa-Rozen et al. (2021b). To identify the most uncertain parameters, an ExtraTrees regression was applied using the scikit-learn Python library (Pedregosa *et al.*, 2012). Finally, given that the environmental impacts of the use phase are expected to be predominant and highly uncertain, two additional scenarios in which one excluded the effects of PVI in module B (use phase) were considered to provide more meaningful insights on the influence of the several parameters on the uncertainty of the outcomes.

4 RESULTS AND DISCUSSION

The environmental impact results for the scenarios including and excluding the use phase are illustrated with the global warming impact category and are presented in Figure 3(a) and (b), respectively. From the analysis of the Figures, it can be seen the use of RAP allows the reduction of the environmental impacts, although this result is almost imperceptible when the use phase is considered. This is due to the overwhelming contribution of the environmental impacts associated with PVI, which outweigh the influence of the remaining phases.

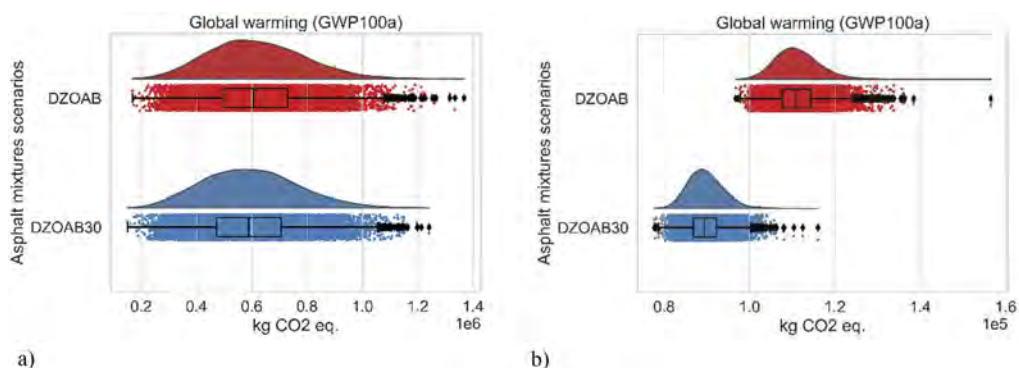


Figure 3. Environmental impact for scenarios (a) including PVI effects and (b) excluding PVI effects.

The results of the sensitivity analysis indicate that in scenarios that include the use phase, fuel consumption has the greatest influence on the uncertainty of the outcomes. This can be attributed to the large variability and predominant contribution of extra fuel consumption to the environmental impacts. In contrast, the contribution of other parameters in the scenarios thereof is relatively similar and mostly below the order of 1%. In scenarios that exclude the use phase, there is greater variation in the contributions of different parameters to uncertainty. Notably, transport has a significant effect on uncertainty, particularly the transportation of raw materials via transoceanic ships in module A1, and freight transport to and from the construction site in modules A4 and C2. This can likely be credited to the large uncertainty values assigned to transport exchanges by the ecoinvent method. When taking a closer look at individual life cycle phases, activities related to EOL in module C1, encompassing milling, sweeping and cleaning, and the consumption of natural gas for mixture heating in module A3, are

the major contributors to total uncertainty after transport. Finally, when examining the contribution of raw asphalt materials processes in module A1 to total uncertainty, bitumen and large size aggregates present the greatest contributions from this phase.

5 CONCLUSION AND FUTURE RESEARCH WORK

In this study, an LCA framework is proposed for evaluating the environmental impacts of M&R treatments under uncertainty. The key features of this framework include the consideration of PVI in the analysis, the incorporation of parameter and scenario uncertainties in the assessment, and the application of a tree-based ensemble method for sensitivity analysis to determine the most influential parameters in the uncertainty of the outcomes.

The environmental impact results of the case study indicate that when the use phase is considered, the reduction of impacts occurring in other phases becomes imperceptible, even when PVI impact values are relatively low. This substantiates the importance of including the use phase in the analysis, and ensuring that the pavement remain in good condition during the analysis period to reduce extra fuel consumption due to increased RR.

The sensitivity analysis conducted in this study revealed that in scenarios that include the use phase, the contribution of PVI to the uncertainty in the results is overwhelming. In order to gain a deeper understanding of the influence of the various parameters on the uncertainty, further sensitivity analyses were conducted using scenarios that exclude the use phase. The results showed that transportation processes have a significant impact on the uncertainty of the outcomes.

In conclusion, the outcomes of this research work helped to advance the applicability of LCA in the context of pavement M&R, and to improve the understanding of the effects of uncertainties on the outcomes. Further, it offers the possibility of identifying areas with the highest potential for environmental performance improvements by determining the extent to which impacts can be reduced.

Additional research work in this domain will be performed by incorporating other M&R measures beyond asphalt overlays. Additionally, the incorporation of advanced GSA techniques, such as variance-based and distribution-based methods (e.g. Sobol and PAWN), as well as the development of empirical uncertainty factors to account for process variability will be pursued.

REFERENCES

- Akbarian, M., Moeini-Ardakani, S.S., Ulm, F., Akbarian, M., Sina Moeini-Ardakani, S., Ulm, F.-J. and Nazzal, M. (2012), "Mechanistic Approach to Pavement-Vehicle Interaction and Its Impact on Life-Cycle Assessment", *Transportation Research Record: Journal of the Transportation Research*, Vol. 2306, pp. 171–179, doi: 10.3141/2306-20.
- Azarjafari, H., Yahia, A. and Amor, B. (2018), "Assessing the individual and combined effects of uncertainty and variability sources in comparative LCA of pavements", *Int J Life Cycle Assess*, Vol. 23, pp. 1888–1902, doi: 10.1007/s11367-017-1400-1.
- CBS. (2022), "Hoe ontwikkelt het aantal wegvoertuigen zich?", available at: <https://www.cbs.nl/nl-nl/visualisaties/verkeer-en-vervoer/vervoermiddelen-en-infrastructuur/wegvoertuigen> (accessed 22 November 2022).
- Godoi Bizarro, D., Keijzer, E., Abed, A., Parry, T. and Canhoto Neves, L. (2020), *Pavement LCM Sustainability Data Analysis. Deliverable D3.1*.
- Gregory, J.R., Noshadravan, A., Olivetti, E.A. and Kirchain, R.E. (2016), "A Methodology for Robust Comparative Life Cycle Assessments Incorporating Uncertainty", *Environmental Science and Technology*, Vol. 50 No. 12, pp. 6397–6405, doi: 10.1021/acs.est.5b04969.
- Groen, E.A., Heijungs, R., Bokkers, E.A.M. and de Boer, I.J.M. (2014), "Methods for uncertainty propagation in life cycle assessment", *Environmental Modelling and Software*, Elsevier Ltd, Vol. 62, pp. 316–325, doi: 10.1016/j.envsoft.2014.10.006.
- Hammarström, U., Eriksson, J., Karlsson, R. and Yahya, M.-R. (2012), *Rolling Resistance Model, Fuel Consumption Model and the Traffic Energy Saving Potential from Changed Road Surface Conditions VTI Rapport 748A*.
- Harvey, J.T., Meijer, J., Ozer, H., Al-Qadi, I.L., Saboori, A. and Kendall, A. (2016), *Pavement Life Cycle Assessment Framework*.
- Huijbregts, M.A.J. (1998), "Application of uncertainty and variability in LCA", *The International Journal of Life Cycle Assessment*, Vol. 3 No. 5, p. 273, doi: 10.1007/BF02979835.

- Igos, E., Benetto, E., Meyer, R., Baustert, P. and Othoniel, B. (2019), “How to treat uncertainties in life cycle assessment studies?”, *International Journal of Life Cycle Assessment*, The International Journal of Life Cycle Assessment, Vol. 24 No. 4, pp. 794–807, doi: 10.1007/s11367-018-1477-1.
- Jaxa-Rozen, M. and Kwakkel, J. (2018), “Tree-based ensemble methods for sensitivity analysis of environmental models: A performance comparison with Sobol and Morris techniques”, *Environmental Modelling & Software*, Vol. 107, pp. 245–266, doi: 10.1016/j.envsoft.2018.06.011.
- Jaxa-Rozen, M., Pratiwi, A.S. and Trutnevyte, E. (2021a), “Variance-based global sensitivity analysis and beyond in life cycle assessment: an application to geothermal heating networks”, *The International Journal of Life Cycle Assessment*, Vol. 26 No. 5, pp. 1008–1026, doi: 10.1007/s11367-021-01921-1.
- Jaxa-Rozen, M., Pratiwi, A.S. and Trutnevyte, E. (2021b), “Analysis workflow for sensitivity analysis and scenario discovery”, doi: 10.5281/ZENODO.4560195.
- Van der Kruk, T., Overmars, L. and Keijzer, E. (2022), “Product Category Rules voor bitumineuze materialen in verkeersdragers en waterwerken in Nederland (‘PCR Asphalt v2.0’)”, p. 75.
- Miliutenko, S., Kluts, I., Lundberg, K., Toller, S., Brattebø, H., Birgisdóttir, H. and Potting, J. (2014), “Consideration of life cycle energy use and greenhouse gas emissions in road infrastructure planning processes: Examples of Sweden, Norway, Denmark and The Netherlands”, *Journal of Environmental Assessment Policy and Management*, Vol. 16 No. 4, p. 1450038, doi: 10.1142/S1464333214500380.
- Muller, S., Lesage, P. and Samson, R. (2016), “Giving a scientific basis for uncertainty factors used in global life cycle inventory databases: an algorithm to update factors using new information”, *The International Journal of Life Cycle Assessment*, Vol. 21 No. 8, pp. 1185–1196, doi: 10.1007/s11367-016-1098-5.
- Nationale Milieudatabase. (2020), *Bepalingsmethode Milieuprestatie Bouwwerken VI*, Vol. 0.
- Noshadravan, A., Wildnauer, M., Gregory, J. and Kirchain, R. (2013), “Comparative pavement life cycle assessment with parameter uncertainty”, *Transportation Research Part D: Transport and Environment*, Vol. 25, pp. 131–138, doi: 10.1016/j.trd.2013.10.002.
- Pedregosa, F., Varoquaux, G., Gramfort, A., Michel, V., Thirion, B., Grisel, O., Blondel, M., et al. (2012), “Scikit-learn: Machine Learning in Python”, *Journal of Machine Learning Research*, Vol. 12, pp. 2825–2830.
- Lo Piano, S. and Benini, L. (2022), “A critical perspective on uncertainty appraisal and sensitivity analysis in life cycle assessment”, *Journal of Industrial Ecology*, John Wiley & Sons, Ltd, Vol. 26 No. 3, pp. 763–781, doi: 10.1111/JIEC.13237.
- Rangelov, M., Dylla, H., Davies, J. and Sivaneswaran, N. (2020), “Integration of life cycle assessment into planning and project delivery for pavements in the USA”, *The International Journal of Life Cycle Assessment*, The International Journal of Life Cycle Assessment, doi: 10.1007/s11367-020-01777-x.
- Rijksoverheid. (2022), “Wat is de maximumsnelheid voor auto’s op de snelweg? | Rijksoverheid.nl”, available at: <https://www.rijksoverheid.nl/onderwerpen/verkeersregels/vraag-en-antwoord/wat-is-de-maximumsnelheid-voor-auto-s-op-de-snelweg> (accessed 22 November 2022).
- Rijswaterstaat. (2022), “INWEVA Webviewer”, available at: <https://maps.rijswaterstaat.nl/gwproj55/index.html?viewer=Inweva.Webviewer> (accessed 22 November 2022).
- Santero, N.J., Masanet, E. and Horvath, A. (2011), “Life-cycle assessment of pavements. Part I: Critical review”, *Resources, Conservation and Recycling*, Elsevier B.V., Vol. 55 No. 9–10, pp. 801–809, doi: 10.1016/j.resconrec.2011.03.010.
- Santos, J., Ferreira, A. and Flintsch, G. (2015), “A life cycle assessment model for pavement management: methodology and computational framework”, *International Journal of Pavement Engineering*, Vol. 16 No. 3, pp. 268–286, doi: 10.1080/10298436.2014.942861.
- Santos, J., Miller, S. and Cerezo, V. (2022), “Pavement vehicle interaction (PVI): the elephant in the pavement life cycle assessment (LCA) room”.
- Santos, J., Thyagarajan, S., Keijzer, E., Flores, R.F. and Flintsch, G. (2017), “Comparison of Life-Cycle Assessment Tools for Road Pavement Infrastructure”, *Transportation Research Record: Journal of the Transportation Research Board*, Vol. 2646 No. 1, pp. 28–38, doi: 10.3141/2646-04.
- Weidema, B.P., Bauer, C., Hischer, R., Mutel, C., Nemecek, T., Reinhard, J., Vadenbo, C.O., et al. (2013), *Overview and Methodology. Data Quality Guideline for the Ecoinvent Database Version 3. Ecoinvent Report 1 (V3)*.
- Xu, X., Akbarian, M., Gregory, J. and Kirchain, R. (2019), “Role of the use phase and pavement-vehicle interaction in comparative pavement life cycle assessment as a function of context”, *Journal of Cleaner Production*, Elsevier Ltd, Vol. 230, pp. 1156–1164, doi: 10.1016/J.JCLEPRO.2019.05.009.
- Yu, B., Liu, Q. and Gu, X. (2018), “Data quality and uncertainty assessment methodology for pavement LCA”, *International Journal of Pavement Engineering*, Vol. 19 No. 6, pp. 519–525, doi: 10.1080/10298436.2016.1176166.
- Ziyadi, M., Ozer, H. and Al-Qadi, I.L. (2017), “Functional unit choice for comparative pavement LCA involving use-stage with pavement roughness uncertainty quantification (UQ)”, *Pavement Life-Cycle Assessment - Proceedings of the Pavement Life-Cycle Assessment Symposium*, 2017, pp. 133–144, doi: 10.1201/9781315159324-15.

To replace or not to replace: A model for future functional performance of bridges

S.C.A. Mooren, A. Hartmann & S. Asgarpour

University of Twente, Enschede, The Netherlands

ABSTRACT: In The Netherlands most bridges reach their end-of-life for functional reasons. Bridges need to be replaced because the adjacent network is widened or the traffic load has increased. Socio-technical developments lead to changes in the functional requirements of bridges and, thus, the decision to replace them. However, determining the functional end-of-life of bridges remains challenging, since it requires insights into future socio-technical trends and their impact on infrastructure networks. In this paper we present a model for the assessment of the future functional performance level of bridges under four future scenarios. The model covers three functional performance criteria: traffic flow, safety and environmental impact and uses a number of performance indicators: intensity/capacity ratio (traffic flow), automatic incident detection and lighting (safety), and noise (environment). It has been developed on the python-based platform MoViCI, which stands for and is used for modelling and visualizing critical infrastructure. The model estimates future traffic intensities of the national road network in the Randstad area in The Netherlands based on which the functional performance is computed per bridge, per indicator, per year. The model output shows that numerous bridges are expected to reach their functional end-of-life before the technical end-of-life. This can empower asset managers in their life cycle performance assessment and, as a result, in scheduling interventions and allocating budgets more effectively.

1 INTRODUCTION

Road transportation plays a central role in fulfilling mobility needs of goods and people. In academic literature a consensus exists that investment in road infrastructure yields economic growth and an increase in productivity, albeit limited by saturation (Arvin et al., 2015; Bougheas et al., 2000; Crescenzi et al., 2016; Fernald, 1999). The main mode of transport in The Netherlands is the car (Hilbers et al., 2020). Hence, road network infrastructure plays a significant role in the movement of people and economic growth. Meanwhile, major challenges lie ahead in the preservation of infrastructure. The usage of assets constructed at mass in the 1960s, has changed to an extent that was unforeseen at the time of designing it; traffic has increased 8-fold (Rijkswaterstaat, 2021). Statistical research shows that bridges and viaducts in The Netherlands, on average, have a lifespan of 80 years (Nooij, 2016). Rijkswaterstaat (RWS), the road agency managing the main road network in The Netherlands, faces a large number of assets reaching the end of their lifetime in the coming years (Klatter, 2019). As a result, expenditures for infrastructure renewal are expected to increase drastically (du Nouska, 2021; Bleijenberg, 2021).

A large challenge for road agencies is to get a clear picture of when assets reach their end-of-life. How assets reach their end-of-life varies (Mellal, 2020). Infrastructure obsolescence has often been studied from a structural perspective. Much less so has functional obsolescence been studied, or modelled. Nevertheless, at least in The Netherlands the majority of bridges have been replaced for functional reasons. Research conducted at the behest of RWS shows that demolition for 88.9% of 216 bridges took place because of functional obsolescence. (Nooij, 2016). Thus, for asset managers it is crucial to know how functional performance

develops over time. It is namely used to schedule maintenance activities, renovations, and renewals. Without these insights, asset managers are limited in their integral decision making.

Bridges require special attention as they are critical structures with a vital connectivity role in road infrastructure. Bridges are costly to construct and maintain, and are subject to unique loads that they must be able to withstand to ensure safety. Thus, the scope has been limited to bridges and viaducts. The following twofold research question has been formulated: *How does functional performance of bridges and viaducts as part of a network develop over time (1), and how can these insights contribute to infrastructure asset management decision making (2)?*

Bechtel et al. (2016) characterize functional obsolescence using congestion performance measures at bridges from probe-vehicle data. The study offers detailed insights into congestion performance. However, the methodology operates on past (or at best live) data. In contrast, this paper aims to aid asset managers with a model that provides insights into the possible future functional performance of bridges.

2 RESEARCH DESIGN

A design science research (DSR) approach has been adopted (van Aken et al., 2016) in order to answer the research question, where the model plays a central role. To develop the model, the process as displayed in the flowchart in Figure 3 has been followed. The ovals represent the starting point. The squares stand for activities that have been carried out. The parallelograms serve as a representations for input/output. The shapes with a curved bottom represent documents. Finally, the arrows show links between flowchart entities, where solid means uni-directional and dotted means bidirectional.

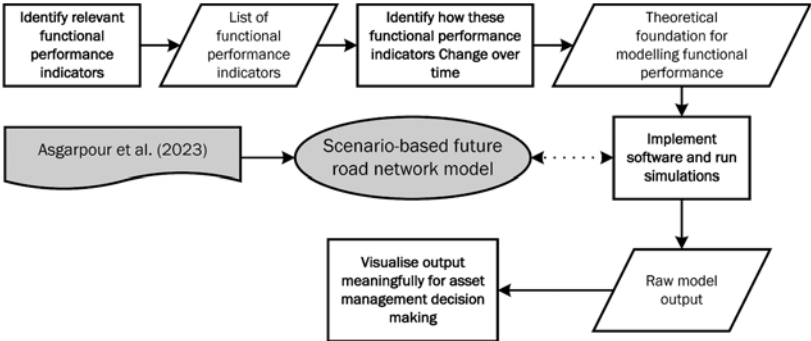


Figure 1. The research process.

The first step is to identify the functional performance indicators that are to be included in the model. First an extensive list of candidate indicators has been composed by reviewing studies previously conducted at RWS (Cuendias González, 2018; van Iddekinge, 2020; Xie, 2017) and scientific literature. All candidate indicators received a score [0-2] on three criteria: relevance, feasibility to model, and time dynamism. Relevance relates to the degree of functional nature of the indicator. In other words: does the indicator relate to functional requirements, and does an insufficient performance level induce interventions? Feasibility to model refers to whether the indicator can realistically be captured in a traffic model. The time dynamism score depends on whether the FPI’s value can reasonably be expected to change over time. Scores were initially assigned by the authors and discussed in interviews with employees at RWS, specialised in the end-of-life of bridges. Summing each candidate FPI over all three criteria gives us the total score: $s_i = p_i + t_i + m_i$. A shortlist has been created for every FPI where $s_i \geq 5$. Certain indicators from the shortlist could be combined, before reaching the final selection of FPI’s.

For the selected FPI’s a theoretical foundation has been built to allow for implementation in the model representing reality. Reviews of scientific literature, internal documents at RWS, and

legal documentation has been combined with interviews with experts at RWS (Table 1) for increased validity. Consequently, the modelling approach has been determined through investigation of the available datasets and the base model inherited from Asgarpour et al. (2023).

Table 1. Expert interviews.

Alias	Expertise	Date	Duration (min)
Expert 1	Assets end-of-life	8-3-22	60
Expert 2	Noise emission roads	30-3-22	60
Expert 3	Life cycle management	29-4-22	50
Expert 4	Traffic safety & road design	3-5-22	60
Expert 5	Safety indicator database	9-5-22	50
Expert 6	Noise emission roads	26-7-22	35

In previous research a traffic model has been developed “to propose an integrated, scenario-based, and transparent model for freight, passenger, emission, and energy demand estimation of the road network” (Asgarpour et al., 2023). The traffic model serves as the base model for this study. The base model contains road traffic prognoses from 2019 to 2050. The study area is confined to the Randstad in the West of The Netherlands, which accounts for the majority of the national economic activity and about half of the population. The main highways and national roads are represented in the network. The base model presents in annual time steps, among other indicators, the traffic flow throughout the network. 4 unique future scenarios have been simulated to account for uncertainty. The scenarios have been adopted from a Delphi study by Neef et al. (2020):

- **Green Revolution:** Green Revolution portrays the most environmentally friendly future possible, wherein emission and the use of fossil energy are drastically reduced. Energy transition investment and societal acceptance for a greener lifestyle are ample. Henceforth, remote working is ingrained.
- **Infraconomy:** The obvious wordplay and contraction on infrastructure and economy paints a world where the driving force is economic interest. Limited efforts will be made to tackle climate change. Meanwhile globalisation continues at a high pace in an upward trend. The economy is characterized by strong product-based developments, where a dependence of fossil fuel remains.
- **Missed-Boat:** The missed-boat scenarios is epitomized by challenges regarding governance, politics, society and the environment, which yields shortcomings with regard to a sustainable society. Fossil energy will remain a source of energy at large, whereas environmental friendly technologies will be adopted to a limited level.
- **Safety Revolution:** Safety Revolution depicts a world where well-being is the summum bonum, at the expense of economic growth. Work weeks are shorter, virtual meetings are on the rise, environmentally friendly means of transport experience an increase and population will grow disproportionately fast in rural areas. As a result of a more conscious lifestyle, slowbalization sets through. This expresses itself in more local consumption.

Following the modelling approach, the next step was software implementation, before finally running the simulations. After running the simulations, the final step was to visualise the model’s output to support the asset management decision process.

3 MODEL DEVELOPMENT

3.1 Indicator selection

An initial list of 89 candidate FPI’s has been composed based on previous literature reviews on the functional performance of bridges (Cuendias González, 2018; van Iddekinge, 2020; Xie, 2017). After assigning the scores and checking them with employees at RWS, 20 FPI’s

with an $s_i \geq 5$ remained. Certain FPI's have been combined, since they represent similar requirements. In the end, 3 FPI's remained:

- Traffic flow;
- Noise;
- Safety to users.

3.2 Modelling variables

The FPI's require a theoretical foundation, in order to implement them into the model. Traffic flow has thoroughly been studied since the popularisation of cars. Greenshields (1934) first described when the traffic flow approaches the maximum flow, density increases, and cars are forced to reduce speed. Subsequently, a considerable amount of research to formulate the speed-density relationship (de Dios Ortúzar and Willumsen, 2011; Ni, 2016), with variations in degree of fitness and parsimony. Akçelik and Rouphail (1993) showed that a reduction in speed gets increasingly sharper as the proportion between traffic volume and capacity approaches and exceeds 1.0 as a result of *overflow*. Ever since, the relationship between traffic volume and capacity is often referred to as volume/capacity ratio or intensity/capacity ratio (I/C ratio). In this paper, the latter definition will be used from now on. Geometry comes into the picture when the I/C ratio is too high and capacity enhancing measures are proposed.

RWS is legally obligated to comply with noise regulations. For 60,000 (fictitious) reference points along the highways in The Netherlands, an individual noise production ceiling has been stipulated. The stipulated noise production ceiling minus the computed noise level is called noise space. RWS annually reports the remaining noise space of all reference points to the ministry in a compliance report. All reference points with noise space less than 0.5 dB, or a negative value even, require clarification from RWS. At reference points where the (impeding) exceedance is not of temporary nature, RWS has a number of possible interventions at their disposal such as applying a new service level to the highway produces less noise. In case that is insufficient other measures such as noise barriers will be explored.

Safety is a precondition for a road network. Nevertheless, traffic safety has seldom been an immediate cause for replacement or renovation of bridges. Expert 4 indicated that generally safety starts playing a role once it has been ascertained that an asset has reached its end-of-life, and replacement and renovation is initiated. Nevertheless, other interventions such as the installation of lampposts may be required. Traffic safety can be described both quantitatively and qualitatively. To express traffic safety quantitatively, safety performance functions (SPFs), also known as accident prediction models, have been developed (American Association of State Highway and Transportation Officials, 2010; Intini et al., 2021; Lord and Mannering, 2010; Persaud et al., 2002). However, SPF's are more suitable for stretches of road, rather than on a bridge level. Instead, RWS has adopted a more proactive and pragmatic method to manage traffic safety: VIND (VeiligheidsINDicator; Safety indicator). In essence, VIND is a geographic database where road stretches' shortcomings are stored. Road stretches of 100 meter long are uniformly rated on a three point scale (green, orange, red) for 12 characteristics. Green means the situation meets the guidelines; there is no increased risk. Red depicts a highly undesirable situation. Orange means the situation is potentially unsafe, depending on compensating measures. It is up to the local road manager to make a judgement call on whether or not the risk is acceptable. The list of characteristics in VIND are as follows, where an asterisk (*) indicates a dynamic characteristic:

- Road surface roughness
- Shoulder right side
- Shoulder left side/middle
- Horizontal curve
- Traffic jam tail protection*
- Cant
- Transverse gradient
- Emergency lane presence

- Illumination*
- Driving speed
- Starting point guide rail right side
- Starting point guide rail left side/middle

The dynamic characteristics' values changes over time as a result of changes in the environment, contrary to the other characteristics where their values only change as a result of deterioration or interventions by the road agency. Thus, the 2 dynamic indicators have been incorporated into the model as FPI's for traffic safety, each according to their own evaluation process. Traffic jam tail protection receives the score 'Green' only if the I/C ratio is greater than 0.8 and automatic incident detection is present. Otherwise it is labelled 'Orange'. Lighting as an FPI receives the score 'Green' if lighting is present and/or when the traffic flow is smaller then 3000 pcu-e. Otherwise it is labelled 'Red'.

Multiple road segments with varying scores may be connected to a single bridge. To discover where interventions are required, the model has been programmed to find most critical value through minimum aggregation on the following list [Red, Orange, Green, N/A].

3.3 *Modelling approach*

To evaluate the future functional performance levels, the bridges should be connected to the road segments. RWS has all their bridges stored in a database. The database contains bridge properties such as ID, name, description, type, status, latitude, and longitude among others.

Several filters have been applied to the database to obtain the desired selection of bridges. First of all, all bridges outside the study area were filtered out. Secondly, all bridges out of service have been excluded. Finally, the remaining bridge records within the study area that were not part of the main road network were deleted. After the operations 1183 bridges remained.

The connection between the road segments and bridges depends on the topological reality. We distinguish 3 types of connections between the base model and the bridges from the database: bridges *in*, *over*, or *in and over* the road segment(s) from the base model. A bridge *over* the road segment(s) means that the national road is located under the bridge. On the upper side of the viaduct can be another road, bicycle path, foot path or railway that may be managed by another infrastructure agency such as a province, municipality or railway agency. A bridge *in* the road segment(s) means that the national road is on the upper deck. On the lower side may be a body of water, another road, a railway, or a valley. In the case of a bridge *in and over* the road segments, 2 national roads intersect at the location of the bridge. For all bridges two empty fields were created to store information on the connected to road segments, both on the upper deck and on the lower side. It can be deducted that in any case every record must contain a value for at least one of the fields. A large share of bridges could be linked semi-automatically to the road segments using QGIS' join attributes by nearest based on the (manually) entered number of nearest road segments. The database contained information on whether the bridge was in or over the national road. Thus, it was known whether to publish the road segments ID(s) to the upper deck or lower side columns. For bridges at the intersection of national roads a connection has been established by manually entering the road segments' IDs.

Out of the 1183 bridges 191 instance have road segments linked to both the upper deck and lower side; bridges at the intersection of national roads. In 197 cases road segments are only linked to the lower side; bridges over the national road. In the remaining 795 cases, the road segments are exclusively linked to the upper deck; bridges in a national road.

3.4 *Model output*

After software implementation took place and the simulations have been run, the model yields values for every bridge, per year, per indicator, per scenario. From this data 4-dimensional data cubes can be created (Gray et al., 1997). Asset managers can access any value or array of values through different queries such as roll-up, drill down, slice (and dice), and pivoting (Gray et al., 1997; Han et al., 2012; Neha, 2020).

For enhanced human interpretation, the model’s output can be displayed in multiple different visualisations (Sternadt and Tavares, 2010). Three types will be discussed, from macro to micro. Because the bridges contain spatial properties, the values can be displayed on a map. The platform MoViCI has the built-in functionality to present the results as displayed in Figure 2. Users can move the slider at the bottom to scroll through the years. Users can also hover over a bridge to see the exact values of each indicator of a bridge.

Alternatively, asset managers can select a series of bridges. These bridges can be sorted in ascending order on expected year of technical end-of-life. From the model output it can be derived for each scenario whether, and when, a critical value will be reached. In an example in Figure 3 bridges have been selected through a query on highway name A28. In this case it has been forecasted that 9 bridges reach a critical I/C ratio in at least one future scenarios before the bridge reaches its technical end-of-life. Analysis of all bridges in the model shows that 773 out of 1183 bridges (65%) will reach a critical I/C ratio of 0.8 in at least one scenario.



Figure 2. A screenshot of the model output where the selected scenario is infraconomy and the current year is 2030. The visualised indicator is the I/C ratio.

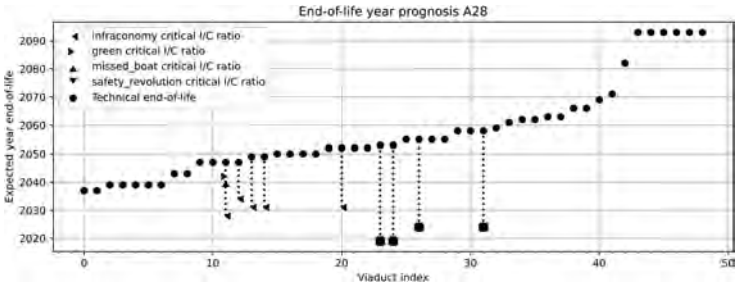


Figure 3. Bridges part of highway A28 from left to right in ascending order of expected technical end-of-life, with the first year they reach a critical I/C ratio value of 0.8 under the 4 scenarios.

On a micro level, asset managers may be interested in individual bridges, and how their indicator values progress over time. For this purpose, a python script has been created where users can enter a bridge number, and select indicator. In the example in Figure 4, the I/C ratio of bridge 173 can be inspected throughout the years for the 4 scenarios. In contrast with the previous figure, this visualisation gives more information on the duration of the critical value, as well as the magnitude.

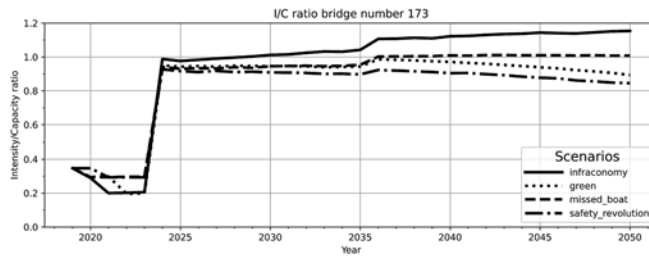


Figure 4. An example plot displaying the progression of the I/C ratio throughout the years for bridge number 173. The change in functional performance between 2023 and 2024 is associated with planned investments to enhance capacity downstream that will be finished in 2024. This makes the highway segment of the viaduct more attractive, leading to higher traffic intensity. All the while the capacity of bridge 173 remains constant.

4 DISCUSSION

Asset managers seek to maximise value for the objects that they manage. Functional performance has been underexposed, as previous scholars have often focused on the technical intricacies of bridges. The model developed in this study adds a new dimension to assessing bridges' life cycle performance by considering the functional performance level of bridges over a longer period of time. Interventions can be scheduled differently as a result of the insights in the functional performance. Particularly when it is forecasted that the functional performance drops below the functional requirements before the technical end-of-life is reached.

The different scenarios offer insights into potential impact on the bridges. In the infraconomy scenario traffic intensities continue to grow throughout the network. This proves to be detrimental for bridges' service life. For all bridges where a critical I/C ratio (at 0.8) will be reached before 2050, infraconomy is always the scenario where this occurs first, if not exclusively, according to the model's output. Nevertheless, reaching an I/C ratio of 0.8 does not by definition necessitate replacement or renovation.

The model has a number of shortcomings that need to be taken into account for the interpretation of the output. The base model, where traffic intensity prognosis takes place, sets the intensity to 0 where there is a parallel road segment. Thus, the I/C ratio is also skewed, since the parallel road segment receives much more traffic than what can be reasonably expected in reality. Another shortcoming is that for the majority of bridges the road segments are only linked to the upper deck or lower side exclusively. On the opposite side of the bridge there might be a road that is managed by another agency. This model does not take into account when those segments' performance becomes insufficient, which jeopardizes the bridge's remaining life time.

5 CONCLUSIONS

The purpose of this research was to develop a model that aids asset managers in their decision making by providing more insight into how functional performance develops over time. The developed model shows that bridges' functional end-of-life is expected to be reached before their technical end-of-life in numerous cases. Through 3 different types of visualisations, the model informs asset managers about the future functional performance of bridges, based on 4 indicators: I/C ratio, traffic jam tail protection, lighting, and noise. As a result, asset managers are empowered in scheduling their interventions and allocating budgets more effectively. The current model compares 4 distinct possible future scenarios. However, from the model in its current form it cannot be derived how likely each scenario is to occur. For future research it is recommended to consider a range of scenarios, so that uncertainty can be quantified better. A Monte Carlo method could be used to sample from a probability distribution of input parameters. Additionally, alternative indicators could be considered and implemented.

REFERENCES

- Akçelik, R. and Roupail, N. M. (1993). Estimation of delays at traffic signals for variable demand conditions. *Transportation Research Part B: Methodological*, 27(2):109–131.
- American Association of State Highway and Transportation Officials (2010). *Highway safety manual*. 1st edition.
- Arvin, M. B., Pradhan, R. P., and Norman, N. R. (2015). Transportation intensity, urbanization, economic growth, and CO2 emissions in the G-20 countries. *Utilities Policy*, 35:50–66.
- Asgarpour, S., Hartmann, A., Gkiotsalitis, K., and Neef, R. (2023). Scenario-Based Strategic Modeling of Road Transport Demand and Performance. *Transportation Research Record: Journal of the Transportation Research Board*, 0.
- Bechtel, A. J., Brennan, T. M. J., and Mesquita de Araujo, J. (2016). Characterizing Bridge Functional Obsolescence Using Congestion Performance Measures Determined from Anonymous Probe-Vehicle Data. *Journal of Performance of Constructed Facilities*, 30(2).
- Bleijenberg, A. N. (2021). Instandhouding civiele infrastructuur. Proeve van landelijk prognoserapport vervanging en renovatie.
- Bougheas, S., Demetriades, P. O., and Mamuneas, T. P. (2000). Infrastructure, specialization, and economic growth. *Canadian Journal of Economics*, 33(2):506–522.
- Crescenzi, R., Cataldo, M. D., and Rodríguez-Pose, A. (2016). Government Quality and the Economic Returns of Transport Infrastructure Investment in European Regions. *Journal of Regional Science*, 56(4):555–582.
- Cuendias González, S. (2018). Implementation of performance age principle in the decision-making process at Rijkswaterstaat.
- de Dios Ortúzar, J. and Willumsen, L. G. (2011). *Modelling transport*. 4th editio edition.
- du Nouska, S. (2021). Minister Visser slaat alarm: miljarden extra tekort voor infra en onderhoud.
- Fernald, J. G. (1999). Roads to Prosperity? Assessing the Link Between Public Capital and Productivity. *The American Economic Review*, 89(3):619–638.
- Gray, J., Chaudhuri, S., Bosworth, A., Layman, A., Reichart, D., Venkatrao, M., Pellow, F., and Pirahesh, H. (1997). Data Cube: A Relational Aggregation Operator. *Data Mining and Knowledge Discovery*, 1(1):29–53.
- Greenshields, B. (1934). A study of traffic capacity. *Proc. Highway Res. Board 14*, pages 448–477.
- Han, J., Kamber, M., and Pei, J. (2012). *Data Cube Technology*.
- Hilbers, H., van Meerkerk, J., Snellen, D., Euwals, R., Hendrich, T., van Ruijven, K., and Verstraten, P. (2020). Ontwikkeling Mobiliteit. PBL/CPB-notitie ten behoeve van de werkgroep toekomstbestendige mobiliteit van de brede maatschappelijke heroverwegingen 2020.
- Intini, P., Berloco, N., Cavalluzzi, G., Lord, D., Ranieri, V., and Colonna, P. (2021). The variability of urban safety performance functions for different road elements: an Italian case study. *European Transport Research Review*, 13(1).
- Klatzer, L. (2019). Prognoserapport 2019, vervanging en renovatie, prognose voor de periode 2020 tot en met 2050.
- Lord, D. and Mannering, F. (2010). The statistical analysis of crash-frequency data: A review and assessment of methodological alternatives. *Transportation Research Part A: Policy and Practice*, 44(5):291–305.
- Mellal, M. A. (2020). Obsolescence – A review of the literature. *Technology in Society*, 63.
- Neef, R., Verweij, S., Busscher, T., and Arts, J. (2020). A common ground? Constructing and exploring scenarios for infrastructure network-of-networks. *Futures*, 124(August): 102649.
- Neha, T. (2020). Data Cube.
- Ni, D. (2016). Equilibrium Traffic Flow Models.
- Nooij, S. (2016). Sloopoorzaken bruggen en viaducten in en over rijkswegen.
- Persaud, B., Lord, D., and Palmisano, J. (2002). Calibration and Transferability of Accident Prediction Models for Urban Intersections. *Transportation Research Record*, 1784(1):57–64.
- Rijkswaterstaat (2021). Instandhouding infrastructuur vraagt komende jaren forse investeringen.
- Sternadt, D. A. and Tavares, J. M. R. S. (2010). Introduction of Human Perception in Visualization Computational modeling of radiobiological effects View project Motion Tracking & Analysis View project Introduction of Human Perception in Visualization. Technical report.
- van Aken, J., Chandrasekaran, A., and Halman, J. (2016). Conducting and publishing design science research: Inaugural essay of the design science department of the Journal of Operations Management. *Journal of Operations Management*, 47:48:1–8.
- van Iddekinge, R. (2020). Linking asset management and GIS: developing a spatial performance of viaducts and roads for replacment decisions at Rijkswaterstaat.
- Xie, Y. (2017). Quantifying the performance age of highway bridges.

The end-of-life of bridges: Integrating functional, technical and economic perspective

A. Hartmann

University of Twente, Enschede, The Netherlands

J.D. Bakker

Rijkswaterstaat, Utrecht, The Netherlands

ABSTRACT: Bridges are typically designed for 80-100 years. However, within this long period the performance requirements can change due to socio-economic and socio-technical developments. This can mean the bridge becomes functionally obsolete, since, for example, its dimensions do not allow certain vehicles to pass or it cannot offer the required traffic capacity. The residual life of a bridge is often a matter of whether the bridge and its components can still cope with changing performance requirements, whether there are technical solutions available to maintain the bridge, and whether it is economically attractive to keep the bridge in place. We propose an integrative approach for determining the residual life of bridges by bringing together the functional, technical and economic perspective on bridge performance.

1 INTRODUCTION

Bridges are essential infrastructure objects of transportation networks and as such their functioning at desired performance levels contribute to the economic prosperity and social welfare of nations. However, sustaining safe and reliable performance levels of bridges has become a challenging tasks for infrastructure agencies and the challenge will persist in the coming years. This is mainly because the majority of existing bridges in many countries was built in the period between 1950 and 1970. Since the typical design service life of bridges is between 80 and 100 years, many bridges are expected to reach the end of their lifetime within the next decades. To plan their renewal and replacement in a managerially and financially feasible manner, infrastructure agencies need to get a better grip on the residual life of their bridge stock. Often this is done from a technical perspective with the physical failure of structures defining the end of life (Chang and Garvin, 2008). Main emphasis is put on understanding the deterioration of bridges and detecting deficiencies such as concrete cracks, structural deflections, erosion, or fatigue that indicate physical failure (COST, 2014).

However, during the long lifetime of bridges the functional requirements can change due to social, technological and environmental developments that particularly lead to higher traffic intensities and loads than originally anticipated. Bridges can become functionally obsolete before the end of their designed life. This can mean, for example, bridge dimensions do not allow larger vehicles to pass or bridges cannot offer the required traffic capacity. Previous studies have shown that bridges are often renewed or replaced because of functional rather than technical deficiencies (Rijkswaterstaat, 2016). Of course, the interaction of functional and technical reasons finally determines the performance of bridges. For example, the increase in traffic loads has changed the functional requirement of many bridges. Although this changed requirement can be already seen as a reason for the obsolescence of bridges, the load bearing capacity or actual performance of bridges is often large enough to deal with increased

loads due to safety margins in the bridge design. However, increased traffic loads can lead to a faster deterioration of the bridge structure through which the performance level will drop. Maintenance and rehabilitation measures can counteract the deterioration process, but require the availability of technical solutions to cope with the structural deficiencies and sufficient resources to implement these solutions. Particularly the costs of keeping an aged and fast deteriorating bridge in place then become another decisive factor for setting the end-of-life of a bridge.

Whether it should be invested in a bridge or not, is a decision of the infrastructure agency. This also means, whether a bridge has reached its end-of-life is a decision to be made by the agency. The decision not only has to deal with the economic feasibility of bridge interventions, but also with the risk acceptance level of the agency. In the context of our example, the agency may conclude that the performance a bridge was designed for is not sufficient for the increased traffic load and decide that the bridge has reached the end of its life. The residual life of a bridge is then always a matter of whether an agency considers the current performance level of a bridge as sufficient to cope with changing requirements, sees possibilities to bring a bridge to an acceptable performance level, and considers sustaining an acceptable performance level as economically feasible. In this paper, we propose an integrative approach for determining the residual life of bridges by bringing together the functional, technical and economic perspective on bridge performance.

2 END-OF-LIFE OF BRIDGES

2.1 *Bridge performance*

Bridges are built to deliver mobility services to different communities (e.g., car drivers, transport companies, pedestrians) but also have undesired impacts such as noise or environmental pollution. The performance of a bridge then describes whether the bridge is able to provide the intended services and to prevent the unintended impacts over an extended time and at specified levels with the available resources. For example, a bridge of a certain load category can effectively provide mobility services for vehicles that fall within this load category as long as the bridge structure does not show serious deficiencies and, in case of deficiencies, resources are available to remove them. With this it becomes clear that the performance of a bridge hinges on its structural characteristics and material properties, here the load bearing capacity. It becomes also clear that bridge performance depends on a number of different functional characteristics of the entire bridge structure and its components, such as the load category the bridge belongs to. The performance level of a bridge then can change in two ways. First, the actual performance (e.g., load bearing capacity) can decline over time due to the degradation of structural characteristics and material properties until it approaches the minimum acceptable performance level. Second, the minimum acceptable performance level (e.g., load category) increases over time or at certain moments in time because of changing expectations and requirements. In both cases, the actual performance level can fall below the required performance level and in both cases an infrastructure agency can decide to implement intervention measures to increase the actual performance level. However, the agency can also decide that the bridge or its components have reached the end of their life.

2.2 *Functional end-of-life*

The functional end-of-life describes the point in time when a bridge no longer meets current or expected performance requirements, even though its technical deficiencies are marginal. The performance level of the bridge has not decreased because of a deteriorated structure. What has changed, is the required performance level the bridge needs to provide. These changed requirements typically stem from socio-technical and socio-economic developments and include technological changes (e.g., new types of vessels require higher bridges), regulatory changes (e.g., assessing structural safety of existing structures), economic changes (e.g., more heavy traffic due to local business park), and behavioral changes (e.g., less traffic due to more

homeworking) (Lemer, 1996). Although it is almost for sure that expectations and requirements will change, it is much more uncertain how fast they change and in which direction. The functional end-of-life implicates the replacement of the bridge, because it does not meet the minimal performance requirements accepted by the agency and it is not possible to technically adapt the bridge to the new requirements.

2.3 *Technical end-of-life*

The technical end-of-life often comes with two connotations. The first one corresponds with the design life of bridges and describes the period of time for which bridge performance should stay above a minimum acceptable level. Typically, bridge performance is decreasing over time as a result of technical deficiencies. The reasons for these deficiencies can be manifold and include deterioration and aging of bridge structure, environmental circumstances, material quality or execution of construction and maintenance works (COST, 2014). When serious technical deficiencies occur, the performance of a bridge and its components can reach a minimum acceptable level and, thus, their technical end-of-life. However, in most cases the bridge lifetime can be extended by applying maintenance and rehabilitation measures. The second connotation then refers to a situation in which a bridge or its components are unrepairable and the performance cannot be brought back above the minimum acceptable level. A reason might be outdated technology or the unavailability of spare parts. Since currently available technologies, techniques and materials can deal with most technical deficiencies, only a small number of bridges will be completely renewed or replaced due to technical reasons (Bakker, Roebers, & Knoops, 2016). The decision rather becomes an economical one.

2.4 *Economic end-of-life*

Considering that almost any bridge can be maintained or rehabilitated, costs finally dominates decisions. This not only includes the costs for individual interventions, but also the expected cumulated costs over the lifecycle of a bridge to keep it on a desired performance level. Since technical deficiencies can increase in number and frequency with older structures and components, the maintenance and rehabilitation costs will increase as well. At a certain point in time, it might no longer financially viable to keep the bridge or its components in place and replacing it becomes the economically more attractive alternative (Bakker, Roebers, & Knoops, 2016). The bridge has reached its economic end-of-life. However, deciding on whether replacement is economically more favorable compared to maintenance requires to set an expected replacement year until which the bridge needs to be maintained. This makes it challenging to estimate the residual life time of bridges. In the following an integrative approach is proposed that brings together technical, economical and functional perspective on performance and the end-of-life of bridges.

3 INTEGRATED APPROACH FOR DETERMING THE RESIDUAL LIFE OF BRIDGES

3.1 *Overview*

The approach consists of four main steps:

1. In a first step, the relevant performance aspects and indicators for the evaluation of bridges are identified and the assessment scale is established.
2. The second step is the evaluation of the bridge performance from a functional perspective which includes assessing the performance of the bridge in the light of current and future socio-economic and socio-technical developments and estimating the functional end-of-life.
3. In a third step the performance is assessed from a technical perspective and the technical possibilities to keep or attain an acceptable performance level until the end of the functional life are identified.

4. The fourth step is the assessment of whether it is economically viable to maintain the bridge until the end of its functional life or to replace it immediately.

3.2 Identifying performance aspects

Bridge performance is multidimensional and typically includes a number of aspects of the mobility service delivery. Typical performance aspects are shown in Table 1.

These performance aspects need further decomposition to become measurable. Here, different performance indicators need to be identified. A (not comprehensive) overview of potential indicators is given in Table 2.

Table 1. Bridge performance aspects.

Performance aspect	Definition
<i>Safety</i>	refers to the effect of bridges on the risk of user to get involved in an accident.
<i>Availability</i>	refers to the effect of bridges on the time duration in which they can be used when needed and as intended.
<i>Accessibility</i>	refers to the effect of bridges on the possibilities of users to cross over and under the bridges.
<i>Reliability</i>	refers to the effect of bridges on the time duration in which they can be used without any disruptions.
<i>Environment</i>	refers to the effect of bridges on their direct physical and natural surroundings.
<i>Resource efficiency</i>	refers to the effect of bridges on the absorption of material, energy, labor for constructing, maintaining and operating the bridges. It can be also regarded as the required life-cycle costs to have a functioning bridge in place.

Table 2. Bridge performance indicators.

Performance aspect	Potential indicators
<i>Safety</i>	Annual number of death people by traffic accidents on/ under the bridge Annual number of hospitalized people by traffic accidents on/ under the bridge Annual number of accidents with material damage on/under the bridge
<i>Availability</i>	Traffic flow on/under the bridge The average increase of time in minutes of detouring the traffic through an alternative route if the bridge is closed The average increase of time in minutes of using an alternative transportation if the bridge is closed
<i>Accessibility</i>	User delay costs derived from traffic congestion caused by the bridge Load class of the bridge Height under the bridge Width on/under the bridge
<i>Reliability</i>	Roughness index of the bridge surface Age of the bridge Failure probability of bridge components
<i>Environment</i>	CO2 emissions produced during the bridge lifecycle Noise emissions produced by the bridge Whether the bridge has been built with reusable or recyclable materials that could ease the bridge dismantling Whether the bridge construction materials contain polluting materials
<i>Resource efficiency</i>	Maintenance costs Operating costs Renewal costs

The selection of indicators should be driven by their representation of the performance aspect and the bridge context from the perspective of the infrastructure agency, their relevance for the agency, and the availability of data.

3.3 Functional assessment

The purpose of the functional assessment is to determine the current and future bridge performance as the result of changes in the bridge context and whether or when a bridge has reached its functional end-of-life and needs to be replaced. This requires in a first step to set up the measurement scale for performance indicators and defining the performance level that still meets the expectations and, thus, can be accepted. Infrastructure agencies often use qualitative scales to express bridge performance and acceptance level. For example, this might be a 4-point scale ranging from 1 (perfect performance) to 4 (poor performance). The quantification of the performance levels helps in assessing bridge performance but requires the availability of performance data. In Table 3 possible measurement scales for the two indicators user delay costs and bridge heights are shown.

Table 3. Performance indicator scale.

	Level 1 (Perfect)	Level 2 (Good)	Level 3 (Fair)	Level 4 (Poor)
<i>User delay cost (€/km)</i>	0 - 2.000	2.000 - 36.000	36.000 - 347.000	> 347.000
<i>Bridge height (m)</i>	$H \geq 4,45$	$4,05 \leq H < 4,45$	$3,85 \leq H < 4,05$	$H < 3,85$

The acceptable minimum performance level highly depends on the nature of the performance indicators, the context of the bridge, and the risk attitude of the agency. The minimum level can relate to specific regulations (e.g., for the load class), can be the result of policy constraints (e.g., maintenance costs), or can emerge from the user behavior (e.g., traffic flow). For example, it can be decided that the scoring of performance indicators at Level 4 is not acceptable and that Level 3 represents the minimum score to be achieved. After setting the minimum performance level, the current performance of a bridge is evaluated. The evaluation may reveal that one or more indicators score below the defined performance threshold. This would mean, the bridge has reached its functional end-of-life. However, this does not necessarily mean that the bridge needs to be immediately replaced. The bridge may still continue performing at this level if the agency is willing to temporarily accept the higher risks associated with it. This might be particularly the case if performance levels include larger safety margins (Chang and Garvin, 2008). There might be also possibilities for interventions to increase the performance level of the bridge. For example, a bridge that scores poor on user delay costs may have extra space on the bridge deck for adding an additional lane. In both cases, the bridge should be technically assessed to decide on its functional life.

The bridge could also score sufficiently on all relevant performance aspects. Then, the future performance development should be modelled to estimate the remaining functional life of the bridge. In other words, through simulating different future scenarios of the socio-economic bridge environment the moment in time can be identified when bridge performance falls below the acceptable performance level. Here, transport demand is the main factor linking socio-economic developments and bridge performance. For example, an increase in global trade will lead to higher transport demand which in turn can lower bridge performance in terms of availability and environment. Socio-economic developments that influence transport demand include economic development (e.g., world trade), transportation energy mix (e.g., fuel price), and mobility behavior (e.g., remote working) (Asgarpour et al., 2023). Other factors that can be expected to influence bridge performance as well are investments in innovations and environment protection commitment. Both factors affect energy demand and amount of emission. Besides socio-economic developments, climate change impacts also may increase the performance requirements of bridges. For example, regular heavy rainfalls may

set higher requirements in terms of availability and accessibility, because a bridge and adjacent roads are more often flooded.

An example of modelling the future infrastructure performance is the scenario-based strategic model proposed by Asgarpour et al. (2023). This model determines changes in the performance of road transport infrastructure under future scenarios. It estimates freight and passenger transport demand based on several socio-economic demand drivers, and capacity utilization, emission and energy consumption as performance indicators resulting from transport demand. By applying the model to the main road network in three Dutch provinces, it could be shown that if the road network stays at the current capacity level, it will experience noticeable capacity problems and delays until the year 2050 under an economic growth scenario. The model is further developed for the functional assessment of bridges for three performance indicators: traffic flow, noise, user safety (Mooren et al., 2023). There are two possible outcomes of this assessment: (i) the bridge is already at the end of its functional life or (ii) the expected remaining time before the bridge will reach its functional end-of-life.

3.4 *Technical assessment*

The purpose of the technical assessment is twofold: (i) it determines the current and future bridge performance as the result of a deteriorating bridge structure, and (ii) it identifies possible interventions to maintain or increase bridge performance to a desired level. While the functional assessment is interested in changes of performance requirements, the technical assessment concerns changes in the structural characteristics and material properties of a bridge through which performance requirements cannot be met. For example, reinforced concrete beams of a bridge can show degradation of structural stiffness and load bearing capacity leading to damages (Liu et al., 2018) and, thus, lower accessibility (e.g., load restriction) and resource efficiency (e.g., maintenance costs). Then, the technical end-of-life is reached when degradation processes reduce the performance level of a bridge to an extent that is no longer acceptable by the infrastructure agency. Here, the relationship with the functional end-of-life comes to the fore. The acceptable performance level reflects the expectations of stakeholders on bridge performance and the structural degradation reduces the capability of a bridge to meet these expectations. This means, one of the two outcomes of the functional assessment becomes the starting point for the technical assessment of a bridge.

In case the bridge is already at the end of its functional life, the technical assessment should determine whether an immediate replacement of the bridge is needed or to which extent and over which period of time reduced but still acceptable structural safety margins allow to fulfill the expected performance requirements. A bridge may experience more heavy traffic loads that extend the design loads of the bridge. The bridge has reached the end of its functional life, but due to safety margins in the bridge design the bridge is still able to accommodate the higher traffic load. For the agency this basically means a trade-off between reliability and accessibility. The agency lowers the requirements for reliability to allow higher accessibility requirements. Here, assessing the capability of the bridge to carry the higher traffic load asks for advanced probabilistic approaches that model significant deterioration mechanisms and load time dependency. However, these approaches involve intense working procedures, require larger amount of data and are usually costly. They seem only reasonable for bridges showing significant structural deterioration and for which a further reduction of safety margins can be expected (Viana da Rocha et al., 2016). An important part of the technical assessment then becomes the inspection of the bridge structure and the monitoring of the bridge behavior. Particularly the latter can help in providing information about the actual structural response of a bridge to increased loads and real structural changes, which allow for the prediction and identification of damages (de Raat et al., 2023). Based on the insights in the structural degradation of a bridge, the consequences for bridge performance, and the risk acceptance of the agency, the agency can decide on possible interventions to reduce or eliminated the deterioration over a certain period of time.

In case of a bridge with an expected remaining period of time before the bridge reaches its functional end-of-life, the technical assessment should show to which extent the structural characteristics and material properties of bridge are changing within the remaining functional life and whether these changes lead to the technical end-of-life. For example, the load class of a bridge might be sufficient for the current traffic loads but future scenarios in terms of truck platooning may reveal that within 10 to 15 years the loads will be above the bridge design level (Ling et al, 2022). The deterioration of the bridge within this period may lead to a drop in the performance level as well. The bridge may reach its technical end-of-life. However, maintenance and rehabilitation interventions can increase the performance level, so that the bridge can be kept in place until the end of the estimated end of the functional life.

3.5 *Economical assessment*

The purpose of the economical assessment is to estimate and compare the costs of different intervention options for dealing with bridge performance that are under a minimum acceptable level. This means, the economical assessment is done for the two cases described under technical assessment. For the first case, when a bridge has reached its functional end-of-life and for which the agency could identify measure to maintain the bridge at a higher performance level, the assessment should show for which period of time the maintenance costs outweigh the costs of a direct replacement of the bridge. At the end of this estimated period the bridge is at the economic end-of-life provided that the agency is willing to accept the functioning of the bridge at a performance level that is below the acceptable level but within safety margins. For the second case, when a bridge has a remaining functional life, the assessment should compare the life-cycle costs for two options: (i) maintaining the bridge and replacing it at the end of its functional life, and (ii) direct replacement of the bridge and subsequent maintenance. If the direct replacement is the economically more attractive option, the bridge is at its economic end-of-life.

4 CONCLUSION

When should a bridge be replaced or how long will a bridge perform at desired levels? Deciding on the residual life of a bridge is a challenging tasks for infrastructure agencies, since it cannot be reduced to technical deficiencies. The replacement of a bridge is a matter of functional, technical, and economical reasons. In this paper, we proposed an integrative approach for the assessment of bridge performance from a functional, technical and economical perspective and we showed how these three perspectives interact in determining the end-of-life of bridges. We believe that adopting such an integrative approach by infrastructure agencies can lead to more informed and underpinned decisions on the replacement of bridges and a more balanced planning of the replacement tasks many infrastructure agencies are confronted with.

REFERENCES

- Asgarpour, S., Hartmann, A., Gkiotsalitis, K., & Neef, R. 2023. Scenario-Based Strategic Modeling of Road Transport Demand and Performance. *Transportation Research Record*, 03611981221143377.
- Bakker, J., Roebers, J. H., & Knoops, J. 2016. Economic end of life indicator (EELI). In J. Bakker, D. M. Frangopol, K. van Breugel (eds), *Life-Cycle of Engineering Systems*, CRC Press: 1788–1795.
- Chang, J., & Garvin, M. J. (2008). A new model for infrastructure service life with applications to bridge assessment and management. *Public Works Management & Policy*, 12(3): 515–532.
- COST. 2014. COST Action TU1406: Quality specifications for roadway bridges, standardization at a European level. Brussels.
- Da Rocha, T. V., Stipanovic, I., & Hartmann, A. 2016. A risk-based model for maintenance decision support of civil structures using RAMS. In J. Bakker, D.M. Frangopol, K. van Breugel (eds), *Life-Cycle of Engineering Systems*, CRC Press: 1758–1765.

- Mooren, S., Hartmann, A. & Asgarpour, S. 2023. To replace or not to replace: a model for future functional performance of bridges. To be published in *Proceedings of the Eighth International Symposium on Life-Cycle Civil Engineering*, Milano, Italy.
- Ling, T., Deng, L., He, W., Wu, H., & Deng, J. 2022. Load Effect of Automated Truck Platooning on Highway Bridges and Loading Strategy. *Sensors*, 22(20): 7704.
- Liu, F., Zhou, J., & Yan, L. 2018. Study of stiffness and bearing capacity degradation of reinforced concrete beams under constant-amplitude fatigue. *Plos one*, 13(3): e0192797.
- Raat, de G.A., Bakker, J.D., Luiten, G.T., Paulissen, J.H., Vogel, de, B.Q., Scholten, H., & Graaf, de, S. 2023 Predictive twin for steel bridge in the Netherlands. To be published in *Proceedings of the Eighth International Symposium on Life-Cycle Civil Engineering*, Milano, Italy.
- Rijkswaterstaat. 2016. *Sloopoorzaken Bruggen en Viaducten in en over Rijkswegen* (Demolition of Bridges and Viaducts in and over National Roads). Utrecht.

How to estimate costs of replacement for an aging infrastructure, a Dutch case study

G.A. De Raat

Rijkswaterstaat, Utrecht, The Netherlands

ABSTRACT: In the Netherlands many objects in the national infrastructure are reaching or have reached the end of their designed lifespan. To ensure sufficient budget for replacement or renovation, an estimation of costs for the next 30 years is needed. This requires an estimate of the year of end-of-service life and an estimate of replacement costs. As Rijkswaterstaat is responsible for 64.000 structures, in addition to roads and waterways, an in depth investigation of each object is not feasible. Therefore, we use a combination of three methods. To estimate the costs of replacing or renovating an object we make use of the key figures that are derived from building new objects. However a replacement or renovation comes with different challenges. Furthermore there are some unknown cost variables. The paper also describes how the 2022 estimation process differs from the previous years.

1 INTRODUCTION

Rijkswaterstaat is the executive agency of the Ministry of Infrastructure and Water Management in The Netherlands. It manages and develops the main road network and waterway network plus the main water systems. Our objectives are to ensure that The Netherlands is protected against flooding, that there is sufficient green space and an adequate supply of clean water, and that people can travel quickly and safely from A to B.

To reach these objectives Rijkswaterstaat manages 64.000 structures, in addition to roads and waterways. These contain ca. 7000 km roads and 800 km dykes and dams, which contain 4000 larger fixed object like viaducts and the majority of bridges, and 500 objects with movable parts like sluices, movable bridges and storm surge barriers.

The majority of these objects will reach their designed lifespan in the current and upcoming decades and need to be replaced or renovated in the upcoming decades. In order to manage this wave of replacements and renovations a program was started to research ways of defining the end-of-service life and to determine the amount of funding (expenditure) needed to replace or renovate the infrastructure of Rijkswaterstaat. In this program we work together with engineering companies, other asset managers and knowledge institutes. Ultimately the goal of the program is to incorporate the developed methods into the day-to-day processes so that the program itself can be discontinued.

This paper describes how we have estimated the expenditure for these replacements or renovations over time in 2022 (Klatter 2022). This is the basis for government funding for these measures and is estimated per decade. Due to results of an audit on the previous way of estimating, in 2022 we changed our approach in a number of ways. Parallel to this change in approach there is an ongoing improvement in the estimation by collecting more and better data on our assets and the state they are in, by adding more types of assets, by more sharply defining the scope and by improving the costs models. This is a continuous effort for the whole of Rijkswaterstaat as e.g. the data and definitions are used for other purposes as well. The paper also discusses a number of the consequences of this way of working.

The paper describes the scope of the estimate (measures and assets), followed by the way the end-of-service life and the costs were determined. It then compares this estimate with the previous version and ends with conclusions and outlook.

2 SCOPE OF THE ESTIMATE

2.1 *Scope of measures*

Asset management activities at Rijkswaterstaat are funded out of three different sources. Firstly, investments in expansion of our infrastructure like adding new assets or new functionalities, secondly, maintenance during the lifespan of an asset and thirdly investments in renovation and replacement when an object has arrived at its end-of-service life due to economical (maintenance is getting more expensive) or technical (no longer able to function properly) reasons. These investments also include IT upgrades. The last source of funding is the subject of this paper.

In practice it is not always clear which source to use for a specific asset management activity. For example, the question can be asked when something is a large maintenance project or a renovation, or whether supporting heavier traffic is a new function that asks for an investment or merely a cause for faster deterioration and therefore a reason for replacement. This is an ongoing process, that over time will change the estimate of expenditure in more and more incremental ways.

2.2 *Scope of assets*

For the estimation in previous years the scope of the asset portfolio was partly determined by gathering asset overviews from our different regions. In 2022 the main corporate asset register was used. This led to a clearer and more orderly scope. However, not all objects are taken into account for the estimate:

As we are still refining the estimation process some types of assets are yet to be taken into account. These consists of large groups of smaller objects and about a dozen of larger ones. For example, Rijkswaterstaat owns one mechanical siphon, which has not been added yet. The first estimation is that these will add 4% to the total costs for replacement and renovation.

Secondly, some type of objects are managed just by maintenance measures, like river beds and dunes.

A third category of excluded objects are those that were under construction on March 1st 2022 and therefore already had funding. As soon as these objects are operational, the costs for renovation and replacement have to be added to the financial reserves for asset management, including maintenance. The same goes for objects that change owner. This category constitutes a small number of objects.

The final category consists of the objects with lacking data, like year of construction or measurements, or lacking a cost model. For those it was not possible to make a reliable estimate. This is still a significant quantity of small objects. It is expected that this leads to a small under-estimation of the needed funding, about 1%.

We therefore roughly estimate that the estimation covers 95% of the costs.

3 DETERMINING END-OF-SERVICE LIFE

As the scope states this paper describes the way we estimated the costs for replacement and renovation, which for this estimate are projected to take place at the end-of-service life. Due to construction planning in reality these can differ some.

The methods described below were used to determine the end-of-service life. Note that for the estimation process costs are accumulated per decade. The methods are applied in the

described order and each method excludes the objects that were subject of the previous method(s). A schematic overview of the methods in time is given in Figure 1. This shows that the further we move through time, the estimation relies more on statistical analysis. For the near future we are able to look at individual objects or smaller groups.

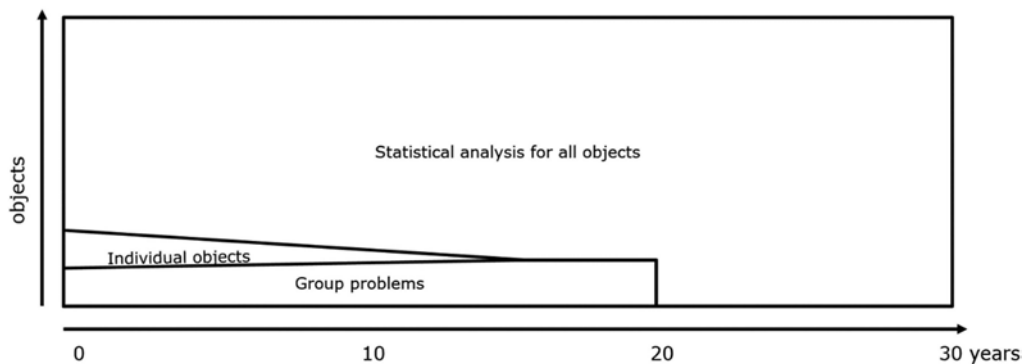


Figure 1. Schematic representation on how the assets are divided over the different methods over time.

3.1 Statistics

We start with a statistical analysis for all objects. Based on past experiences and design criteria a statistical lifetime for each type of structure has been determined. For example, for a sluice the statistical lifetime is 108 years. This lifetime is added to the year of construction, which results in the expected statistical end of life for each structure. The group and individual approach, see below, then overrule the statistical analysis. However, as shown in Figure 1, the major part of the objects have an estimated end-of-service life based on statistics.

3.2 Group approach

A group approach is used in the case that there are known problems for similar objects. These problems can arise from the same developments that are described under method 1: new insights and changings loads. Based on expert opinion a certain percentage of one type of assets was attributed to a decade. For example, 10 percent of a specific type of bridges is expected to fail between 2031 and 2040. It is at this point unknown to which exact structures this pertains. For the purpose of the cost estimate this method suffices. This method was limited to the current and the next decade. The approach per individual object can overrule the group approach. This has only occurred in a few occasions.

3.3 Per individual object

At the time of construction of an infrastructural object design calculations are made that take into account the degradation of the used material and the loads to withstand. One uses the available technical codes that describe the ways to execute these calculations and what safety factors to use. However, all of these can change over time. New insights in material degradation, calculation methods and safety factors arise, and loads can change in different ways than predicted at the inception of an object. For instance, bridges carry more and heavier traffic than their original design loads. All these factors can influence the end-of-service life. Therefore, we have recalculated the design of a number of bridges with help of finite element models. It is planned to do this for more bridges and other types of structures. However, these calculations can take up to two years to execute, including collecting data and sampling of material. In 2022 this was only done for a handful of objects.

As we try to make these calculations only for objects that are probably very near the end of their life, the resulting predictions of end-of-service life are mostly in the near future.

Besides calculations Rijkswaterstaat experts with a long service record estimated end-of-service life. Since we only give an estimation per decade, this is accurate enough for our purpose.

3.4 *Renovation regime for complex objects*

The determined end-of-service life of an object as described above is assumed for the object as a whole. The movable parts and operating systems in 500 more complex objects, like sluices and tunnels, that are to be replaced or upgraded during the service lifespan of the object are taken part of the estimation of the expenditure for renovation and renewal. To determine these moments of renovation we use standard intervals, e.g. 20 years for a small upgrade and for a big overhaul a standard interval of 50 years is used. The latter occurs theoretically only once, since the end-of-service life for most complex objects is about a 100 years. These renovations and replacement are shown in Figure 2.

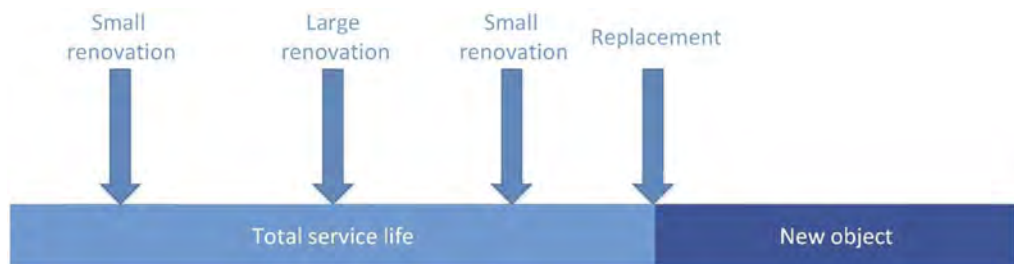


Figure 2. Schematic representation of the renovation and replacement regime of a complex object.

4 DETERMINING COSTS

Parallel to determining the end-of-service life, the costs for replacement and renovation were determined. We distinguish three categories that are described in the next paragraphs: The baseline: costs that we can substantiate with data, uncertainty in costs that we can only estimate, costs depending on future trends.

4.1 *Baseline*

For the baseline first the direct costs (man-hours for construction, material and equipment) are determined to which percentages are added for indirect costs like engineering and taxes. The latter are a percentage of the direct costs, varying per type of structure. The key figures for the direct and indirect costs are based on years of experience of commissioning new infrastructure. The uncertainty that this causes is addressed in the next paragraph. We then proceeded to parametrize these costs of the same type of objects over the surface area (e.g. m² surface of a small concrete bridge) or length (e.g. per running meter for sheet piles).

We set the price level of the direct costs at January 2022. Of course prices have increased significantly due to the war in Ukraine, for example for steel and it is uncertain how prices will develop over time. However by choosing a fixed date, costs can be adjusted when prices stabilize over time by comparing these to the ones at the fixed date.

For the projection of the costs over time it is assumed that the costs occur instantaneous at the end-of-service life. Rijkswaterstaat does not use depreciation of value over time. Furthermore, even though costs like design and preparation costs are made before the moment of replacement the costs are projected at one specific year.

Finally agreed upon extra costs by the asset owner were added. For durability like the use of sustainable materials etc. 2% is added to the total amount. For diverting traffic while executing measures at our main road network 7% is added to the total estimated costs for renovating or replacing parts of the main roadwork. As there is no agreement on costs for traffic while working on waterway network, no cost were taken into account for this. This all results in a baseline as is shown in Figure 3.

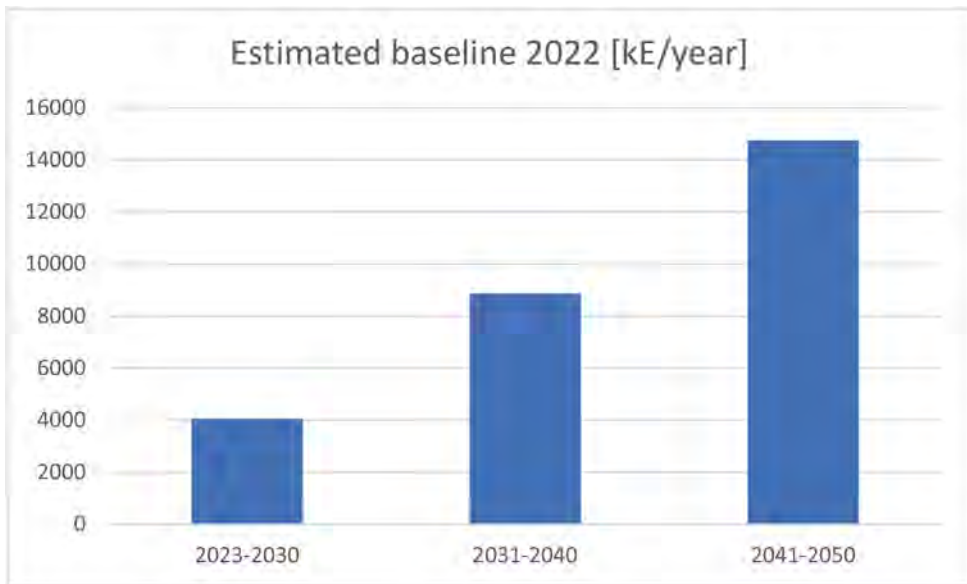


Figure 3. The estimated baseline fur funding.

4.2 Uncertainties

Experience with renovation of replacement projects is still limited and key figures have yet to be derived. It is acknowledged however that costs can differ. For example, having to work within an existing infrastructure constraints an optimal design. Next to these there are developments that will take place in the foreseeable future, like more use of IT, bundling construction of several objects in one portfolio and incorporating resilience to climate change. Also, due to new regulations, new objects like bridges should be rebuild wider than they were, with additional costs for the adjacent road infrastructure. For these expenses Rijkswaterstaat experts estimated percentages to add on to or subtract from the baseline. However, since they are less predictable and depend on future decisions they were not added to the baseline itself. Depending on the type of assets the percentages add up to 70%. To manage expectations, innovations are only taken into account as proven technology, at which point they are incorporated into the baseline.

There are two other significant uncertainties that influence the total expenditure. For both these uncertainties scenario analyses where done. The first significant uncertainty is renovation instead of replacement at the end-of-service life or a whole object. This choice depends on many factors which are only partly under the control of Rijkswaterstaat. A scenario analysis for bridges shows a decrease in needed funding of 100 to 550 million euros per decade.

The second significant uncertainty are those objects that have to fulfil a new demand. These demands can occur before the end-of-service life or when end-of-service life is reached. Historically, 88 percent of the replaced bridges were replaced as part of an investment in infrastructure improvement, like road widening (Rijkswaterstaat 2026), and therefore financed through a different source of funding. Whether this will continue in the future is unknown. There are

limiting factors for new functions, like saturation of the demands on the infrastructure and the current nitrogen crisis. Either way, these measures are funded from a different source and impact the estimation for replacement and renovation. A scenario analyses for fixed objects shows a decrease of the total estimate up to 15%.

In the report on the estimation we did not add up these uncertainties. To estimate the total costs of investments we only take the uncertainties into account that enlarge the estimate. The decisions to renovate or replace and the decisions to add new demands are made outside of Rijkswaterstaat and therefore we can only partly influence these decisions.

4.3 *Future trends*

The last category are uncertainties that we are not yet able to express in costs, like climate-adaptation, truck platooning or other developments that are awaiting policy changes from the government. These costs were not taken into account in the estimate.

5 COMPARISON TO PREVIOUS ESTIMATE

As stated in 2022 a big step was made to make the process reproducible. Before 2022 a bandwidth of 50 % was used to take uncertainties into account. In 2022 this bandwidth was broken down into the different components some which were added to the baseline, like the percentages for durability and diverting traffic. Many of the other component we described in paragraph 4.2. Also some objects that have missing data were left out altogether in the 2022 version. This makes a comparison between the estimate of 2022 and earlier estimates difficult or even impossible.

6 CONCLUSIONS

The estimation process to determine the needed funding for renovations and replacements is still developing and has come a long way. In 2022 the process was adjusted to be more reproducible which led to a different approach than before and makes a comparison to previous estimates difficult.

To further improve the estimation, steps can be taken to collect more data on the objects and incorporate all objects that are in need of renovation or replacement in the next 25 to 30 years. Also key figures for determining the costs need to be based on renovations and replacements instead of new constructions. It can take several years of experience with renovations and replacements to build a costs database to extract key figures from.. Furthermore, more methods to determine the end-of-service life need to be developed. Not only funding, but also staff is needed at Rijkswaterstaat and our contractors to execute the necessary measures. As there is a shortage of staff, this will limit to ability to execute the needed measures and therefore influence the needed budget.

How to translate the estimate and the remaining uncertainties into government funding is yet to be established in conjunction with the policy department of the Ministry of Infrastructure and Water Management.

REFERENCES

- Klatter, L. 2022. Prognoserapport 2022 Vervanging en Renovatie (in Dutch)
Rijkswaterstaat. 2016. Sloopoorzaken Bruggen en Viaducten in en over Rijkswegen (Demolition of Bridges and Viaducts in and over National Roads) Utrecht.

Plannability of maintenance in life-cycle decision making for infrastructure

J.D. Bakker & R. Treiture

Rijkswaterstaat, Utrecht, The Netherlands

ABSTRACT: Most infrastructure management systems include maintenance planning. Traditionally these maintenance plans are generated based on condition based inspection procedures. In the past decades, infrastructure management organizations like Rijkswaterstaat have moved towards a more tactical maintenance planning, where maintenance and replacement measures are planned at forehand based on known object behavior, and inspections are used to verify and to adjust the maintenance plan based on observations. Practice shows however, that not all maintenance can be planned at forehand. For the long term planning, it is important to have some idea of the plannability of maintenance. This is also relevant for estimation of the expected performance. This paper describes how Rijkswaterstaat has come to estimates of the ratio between regular, plannable periodic maintenance and more incident driven maintenance, and how this can be used in performance management, maintenance planning and end of life evaluations.

1 INTRODUCTION

1.1 *General*

This paper deals with plannability of maintenance. Plannability is a very important aspect for maintenance managers working with life-cycle maintenance plans. A considerable part of the maintenance is initiated by random events, in time and place. This issue is seldomly explicitly dealt with. Sometimes the expected effect of unplanned maintenance is neglected in maintenance plans, or modelled as planned maintenance, both leading to an unreliable maintenance plan. This paper deals with this issue, from the experience of Rijkswaterstaat. Rijkswaterstaat uses life-cycle maintenance plans since a few decades. In the recent years the awareness of the plannability issue grows. This paper deals with the recent insights on how to look at plannability issues, and describes the first steps Rijkswaterstaat is making on this issue. After a brief introduction on Rijkswaterstaat in chapter 1, chapter 2 will explain the different aspects on (un)plannability of maintenance from the experience of Rijkswaterstaat. Chapter 3 describes the use of life-cycle maintenance plans at Rijkswaterstaat, and explains where plannability is an issue and how Rijkswaterstaat takes a first step in dealing with this. Chapter 4 deals with the conclusions and the way forward.

1.2 *Rijkswaterstaat*

Rijkswaterstaat is a government agency within the Dutch Ministry of Infrastructure. Rijkswaterstaat maintains and operates 3 national networks: the Main Water System (transport of water to the sea, and along the sea-shore), the Main Waterway System (transport over water, ships) and the Main Road Network (road traffic). These transport networks need supporting infrastructure to be able to deliver performance: All these infrastructure are assets, owned by the government but maintained by Rijkswaterstaat.

1.2.1 *Responsibilities and finance structure*

Rijkswaterstaat is financed separately for new construction, large scale maintenance and replacement projects, and the regular maintenance works. Both the new construction and the large scale reconstruction and replacement works are financed project wise (Klanker et al., 2016). To finance the regular maintenance works (all those activities needed to maintain the required performance levels) Rijkswaterstaat agrees every 4 years with the ministry on a Service Level Agreement (SLA) that defines the performance to be delivered for an agreed maintenance budget (van der Velde et Al, 2012). This SLA-period will increase to 8 years in the near future. This SLA requires a solid financial justification methodology.

1.2.2 *Service level agreements for asset management*

The SLA contains a set of Performance Indicators for a delivered outcome, and both a long term and a short term cost estimate of the needed budget to deliver this performance. The justification for this cost estimate is based on Object Maintenance Regimes (OBR) for the long term, and explicit maintenance plans for the short term. The OBR describes life-cycle maintenance strategies for different asset types. Based on these OBR's an estimate of long term budget need is made based on unit prizes (P) per type of asset * the quantity (Q) of these assets.

Short term budget needs (1-6 years) are based on actual life cycle maintenance plans for individual structures. Even though the assumptions for short term maintenance needs are based on the same OBR's, the individual maintenance plans may differ from the long term average. Typical reasons are:

- On object level the distribution of cost in time is not even. Maintenance needs may vary considerably from one year to the other;
- Maintenance backlog may cause additional cost in the short term planning;
- Inspection leads to a more precise planning than the long term average expectations;
- The short term planning consists of actual planned projects rather than individual long term average maintenance activities.

1.2.3 *Plannability of maintenance activities*

Until recently, both the OBR's and the life-cycle maintenance plans presumed predictable behavior in time. The assumption was, that based on the construction type and the used materials a maintenance prognosis could be generated, predicting all the needed maintenance activities in time. Inspection would predominantly be needed to justify the exact moment of maintenance.

Practice shows however, that inspections also lead to new maintenance activities, that were not predicted before in the OBR's or in the life-cycle maintenance plans (Bakker & Klatter, 2012). Neglecting this more or less “unplanned maintenance” can lead to an under-estimation of the necessary budgets on the long term and to an unstable maintenance programming, because the “new facts” that emerge from the inspection often lead to both constant replanning and budget shortfalls. Therefore the realization came that some sort of budget reservation was needed both in the OBR's and in the short term maintenance planning to deal with these uncertainties. Until recently, the only reservations taken into account were those for calamities that need immediate repair.

First efforts at Rijkswaterstaat to quantify the financial impact of unplanned maintenance have led to (conservative) reservations in the OBR's and in the life-cycle maintenance planning. But more detailed studies still need to be done to actually quantify the financial impact more precise. First step will be to describe the logic and philosophy on dealing with planned and unplanned maintenance. This paper does so. Chapter 2 describes this logics, based on the findings at Rijkswaterstaat. Chapter 3 will give a state of the art on how Rijkswaterstaat deals with the plannability of maintenance at this moment. Chapter 4 deals with the evaluation and conclusion.

2 THE CONCEPT OF PLANNABILITY EXPLAINED

2.1 *Life-cycle maintenance plans*

2.1.1 *General*

Traditionally maintenance managers rely on inspections exclusively for their maintenance planning. In recent decades the use of life-cycle maintenance plans increases in popularity. A life-cycle maintenance plan is a plan that shows all the expected maintenance activities in time. Such plan can be based on general expectations on ageing of elements in structures over time, and usually has some form of justification, for instance general reference maintenance strategies and cost justification. More complex maintenance plans have explicit LCC-optimization tooling and explicit simulation capability on expected performance effects of maintenance scenario's. Life-cycle maintenance plans can be updated based on inspections.

2.1.2 *Structures*

If periodic inspection are the exclusive source for maintenance prognosis, maintenance will be reactive, with a limited capability to look forward in time. This is why maintenance managers nowadays try to combine maintenance activities of different assets as effective as possible, and therefore an insight of the expected maintenance needs for at least 6 years ahead or longer is needed.

For civil structures the use of condition based maintenance is still quite common, because:

- Probability of detection is generally high: In most cases risks are well detectable, if inspection is done with the right focus. A good risk inventory before inspection is generally sufficient to focus inspection at such way that a reliable prognoses of future activities can be made up to 4 years ahead, and rough estimates up to 10 years ahead.
- The time between the first detection of a damage indicator and the latest moment of repair is generally long; For instance, concrete reinforcement corrosion often takes decades to develop from the first damage detection to actual failure (providing the indicator can be detected);
- Failure seldom happens suddenly. In most cases structures give clear warning sighs like deformation or cracks long before actual failure occurs.

Nevertheless, for civil structures the need for life cycle maintenance planning rather than purely condition based maintenance prognosis increases, because:

- Purely condition based maintenance tends to be reactive, and often lacks a life cycle optimal maintenance strategy.
- Large scale maintenance projects sometimes take 5 to 10 year preparation time. Maintenance managers try to combine as much as possible maintenance in one project. This is hard to do without at least some form of a lifecycle plan;
- Condition based data only is an insufficient base for long term maintenance agreements. For instance: Service Level Agreements between Asset Owners (like ministries) and Asset Managers (like government agencies);
- Only condition based information is insufficient to make a reliable cost estimate for long term maintenance contracts (for instance Design, Build, Finance and Maintain contracts)
- Only condition based information is insufficient to make lifecycle comparison between replacement scenario's and maintenance scenario's;
- Only condition based information provides information on maintenance need, but does not provide a good basis to define a maintenance backlog, because a reference is missing (maintenance backlog starts from the moment that a structure is not maintained at the economical most optimal moment, not when the condition is already bad).

2.1.3 *Electrical and mechanical components*

There is a big cultural difference between a typical “electrical and mechanical maintenance engineer” and a typical “civil maintenance engineer”. Many electrical and mechanical maintenance engineers work in the process industry, where “time is money”. The electrical and mechanical components are performance killers, leading to downtime if one component

suddenly fails, or if machines need to be taken out of production for maintenance. Not surprisingly the process industry has been upfront in their aim to optimize maintenance and maximize productivity. Condition based maintenance is less common for electrical and mechanical components. There are some good reasons why:

- The probability of detection is not high: It takes high inspection intervals or intense monitoring to detect failing components timely;
- Inspection induces an additional risk of failure: If components need to be taken apart in order to do a good inspection, there's always an additional risk of failure during inspection and right after inspection;
- The time between detection of a failure indicator and the time to repair is often too short to plan maintenance efficiently with a minimal downtime;
- If a component shows unplanned failure, this often directly leads to functional failure.

Not surprisingly life-cycle maintenance plans are common practice in the electrical and mechanical engineering. So called “planned maintenance” is a leading strategy for these types of components. Replacement is often done time-based or usage-based, (long) before actual failure is expected. Maintenance can be planned years ahead, based on general schedules, doing as much as possible in a minimal downtime. Usually not all components are replaced time-based or usage-based. Those elements that are non-critical (for instance in case of redundancy) are replaced correctively, after failure. The choice between corrective and preventive maintenance, and the optimization of life-cycle maintenance plans with a minimal downtime is a typical job for the maintenance engineer.

2.2 *Statistical predictability versus plannability*

2.2.1 *General*

Life-cycle maintenance plans show their value for those maintenance activities that are “plannable”: Those activities that can be predicted in time and cost. In this chapter we will focus on plannability over time, and discuss how to deal with those maintenance activities that can statistically be predicted, but cannot be planned in time in life-cycle maintenance plans.

2.2.2 *Maintenance strategies for plannable maintenance events*

Most life-cycle maintenance plans and maintenance optimization models on the market are dealing primarily with plannable maintenance events and corrective maintenance events. The assumption is that there are no random events, and all maintenance decisions are initiated by aging processes with a predictable maintenance need in time. Aging can be either chemical or mechanical, or a combination of both. Either based on statistical data or based on theoretical modeling of the aging effect, it is possible to make maintenance strategies that can be planned in a life-cycle maintenance plan. Depending on the accepted risks and the options to quantify the aging (inspection, monitoring, prediction modeling) the maintenance measure can be taken either

- 1) long before failure (time- or use dependent preventive maintenance);
- 2) at an optimized intervention level (condition based or predictive) or
- 3) after failure (corrective maintenance).

Preventive maintenance is perfectly plannable in a life-cycle maintenance plan based on fixed maintenance intervals. Condition based or predictive maintenance is plannable too, based on expected maintenance intervals (from theory and practical experience), but the planning needs to be adjusted based on inspection. Corrective maintenance usually presumes direct replacement after failure. Therefore, failure induced maintenance cannot be planned. An age-dependent financial reservation can be made tough.

In many cases failure of a component does not directly cause failure of the complete functionality. For instance, if 3 road lanterns have failed, spread out over a row of 25 lanterns, the total road-lightning may still be sufficient. In this case the failure of 3 lanterns is not considered to be corrective maintenance. “3 failed lanterns” can be an intervention level for condition based maintenance, and can be considered as plannable, since the lightning system has not failed yet.

Life cycle maintenance plans need to be explicit on the related maintenance strategy, because the interpretation in the planning differs: A preventive replacement 10 years from now can be planned accurately, but a corrective replacement 10 years from now is merely a financial reservation: in practice the actual replacement may be earlier or later, directly after failure.

2.2.3 Random maintenance events: An example

Some maintenance and repair activities cannot be planned in advance. For instance, if a viaduct is damaged in a collision with a vehicle. If this happens, repair will be needed. If the probability is 1 to 50 each year for a viaduct to be involved in some sort of collision, this does not result in a plannable maintenance activity every 50 years. The cost of this repair may vary from €1.000,- to €1.000.000,-. Still yet, for each bridge it's possible to make a statistical prediction of the probability of collapse per year and the expected cost. If a bridge stock includes several thousand of viaducts, this statistical prediction can be used to make a yearly reservation for collision risk. But this does not lead to a plannable maintenance action, up until an individual bridge is involved in a collision. Cost of collision are statistically predictable, but the maintenance is not plannable.

2.2.4 Randomness of sudden external events

Collision is a sudden random event. Sudden random events are not plannable. Only after an event has occurred, the needed counter measure can be planned. Sometimes the probability of a random event is time dependent. In case of traffic collision: If traffic grows, and the amount of special transports and high vehicles grows, the probability of collision grows. Likewise, risks of damage due to overloading increases as the traffic becomes heavier.

Many sudden random external events have some sort of time dependent probability. Therefore, it is likely for structures that the risks on random events increase while the structure ages, for instance because of changing surroundings.

Some random external events only effect aged structures. For instance, an old open asphalt pavement is very sensitive for frost. The probability of needed repair and the amount of repair depends strongly on the age of the pavement. Still yet, repair of the pavement is only needed if it freezes.

2.2.5 Randomness in maintenance and repair needs due to human errors in design, construction and maintenance

Most building codes are based on probabilistic assumptions. Usually, these building codes assume an uncertainty in material strength and an uncertainty in stresses due to loads. These calculations do not quantify the effect of human error, because it is challenging to predict what this will be. The examples are numerous, even for our most common materials:

- Some typical examples for concrete structures: badly placed reinforcement bars, forgotten shear reinforcement, gravel nests, insufficient concrete cover, badly injected post-tensioning ducts etc.
- Some typical examples for steel structures: improper welding (too hot, too thin, damage of surrounding coating), galvanic corrosion, local peak stresses in orthotropic structures, etc.
- Electrical and mechanical components: effects of leaking water (causing a short circuit), bad electric contacts, insufficient cooling, oil leaks, eccentric mechanical power transfer, etc.

These random flaws in design, construction and maintenance can have a variety of possible effects, on both functionality and maintenance cost. As long as these flaws are hidden, it is not possible to plan maintenance actions in time to deal with the effects. Similar to the external events, the only way to take these effects into account is to make a financial reservation, based on statistic information on probability of occurrence and the spread in possible cost effects.

Time dependency can be the case: Some effects will typically show in the first years after design. Other effects will reduce the technical life. A typical example are common problems in orthotropic bridge decks. The fatigue life is shortened drastically due to local high steel stresses in the orthotropic plates.

Structures are usually constructed in such way that warning signs can be seen long before failure. If a structure reaches the so-called "Usability Limit State (ULS)", usually clear

deformations can visually be detected. A sudden failure without any warning signs is very uncommon for structures. For electrical and mechanical components random sudden failure is much more common.

Random flaws in design, execution and maintenance are either detected timely in condition based monitoring or repaired after failure as corrective maintenance.

2.3 *Creating Life Cycle Maintenance plans combining plannability and statistical predictability*

Generally speaking, there are three options for cost estimates in a maintenance plan:

1. A planned activity with a cost estimate at a certain point in time: Both the year the maintenance activity is needed and the cost are known.
2. An expected activity with cost estimate, with an uncertainty on the exact needed moment: Based on the expectation a budget reservation can be made at a certain point in time, but the activity cannot be planned.
3. A random activity with a probability per year.

The plannability can be different for the short term planning than for the long term. The table below proposes a categorization for plannability of maintenance in short and long term maintenance plans:

Table 1. Categorization of plannability of maintenance.

Nr	Initiator	Example	Maintenance strategy	Plan-ability	Short-term planning	Long-term planning
1	Regular ageing	Electrical components	Preventive (planned) maintenance	++	Cost planned in maintenance plan in the planned year	Cost planned in maintenance plan in the planned year
2	Regular ageing	Coating on steel	Condition based Maintenance	+	Cost planned in maintenance plan based on condition data	Cost expectation and estimated year in maintenance plan based on averages
3	Regular ageing	Redundant battery	Corrective maintenance	-	Financial reservation in expected year of failure	Cost expectation and estimated year in maintenance plan
4	Random events (timely Warning)	Reinforcement corrosion	Condition based maintenance	0	Age dependent financial reservation	Age dependent. financial reservation.
5	Random events (time dependent, sudden)	Frost damage on aged pavement	Corrective maintenance	-	Age dependent financial reservation	Age dependent financial reservation
6	Random events (sudden)	Vehicle collision; Shortcut in electrical Component	Corrective maintenance	-	Financial yearly reservation	Financial yearly reservation

2.4 *Life cycle planning considering random events*

Looking at the table above, it becomes clear that a life cycle planning should account explicitly for all these types of cost expectations, both for the short term as for the long term. Not everything is plannable in a sense that it is known what activity will be done in what year. But the unplanned part can still be estimated explicitly. Clear distinction should be made between the plannable activities and the expected activities, both in financial reservation and in maintenance planning and contracting.

3 CASE RIJKSWATERSTAAT: FIRST STEPS IN DEALING WITH PLANNABILITY FOR STRUCTURES

3.1 *Initiation of the discussion on plannability*

In 2020-2022 there has been an internal and an external audit at Rijkswaterstaat to look at the reliability of the financial justification of short term and long-term budgets. This has led to major improvements in the complete justification system. But one of the tough to answer questions from the auditors was about uncertainties in the planning. The auditor raised questions on the budgetary impact of incidental maintenance activities. So far there was no research done to quantify this. Not for all types of assets there was structured data to answer this question, but for structures there was a good dataset available.

3.2 *Identifying plannability in the maintenance information systems*

Rijkswaterstaat has different software systems for different asset types. The system for structures (like bridges, viaducts, locks, weirs etc.) is called DISK. DISK contains the decomposition of all these structures in Building Objects, Elements and Building parts. The life-cycle maintenance plan contains maintenance strategies on element level (Bakker & Klatter, 2012). Examples of elements are the bridge deck, the pavement, the supports, the joints etc. For each of these elements there are standardized maintenance strategies. These are used to build up the maintenance plan.

A standard maintenance measure has a name, an interval, a unit and a price per unit. To make a maintenance measure in the life-cycle maintenance plan the amount of unit is added, and the latest year. For instance: Bridge deck - Concrete repair under bridge – every 30 years – 17€/m² Amount: 360 m², last year of previous execution: 2010; expected new year: 2040. During inspection an inspector will advise if both cost and expected year are still correct. But he can also find something unexpected. Then he will make an extra maintenance measure. For instance: the concrete is damaged due to collision with a vehicle. Then the inspector will make a ‘one-time maintenance measure’, containing a description, a cost estimate, and an advised and latest year of execution. For instance: bridge deck - repair of collision damage - €10.000,-, - 2023-2024. In this way the standard maintenance measures can be distinguished from the incidental ones: The incidental maintenance measures have no interval. All data from DISK is periodically exported to the planning system (RUPS)

3.2.1 *Research methodology*

Imperfect data had to be analyzed to quantify the (minimal justifiable) needed reservations for the unplanned maintenance. The planning system was used as historical data source. Only those maintenance measures identified as “obviously unplanned” would be taken into account.

A representative dataset was analyzed by 2 specialist independently. All maintenance measures with an interval were considered as “planned”, so the focus was on those measures with no interval. The 2 specialists, and each independently, identified the “obviously unplanned maintenance”, that was beyond doubt not covered in some way by our standard maintenance scenario’s. After rating the maintenance activities independently, the 2 specialists compared the results, and discussed the differences to come to a shared result.

Based on this analyses the conclusion was that at least 20% of all maintenance was clearly unplanned, compared to the maintenance strategies that are covered in the OBR. The real number was likely to be much higher, but could not be proven based on the available data.

3.2.2 *Taking account of the unplanned maintenance*

Based on the analysis result, Rijkswaterstaat raised the long-term cost estimates for structures by 20% to cover the uncertainty related to the unplanned maintenance. This figure was incorporated in the OBR. For the short-term planning also a reservation for unplanned maintenance was made in the programming. As explained in paragraph 2, most unplanned maintenance activities don’t need to be performed directly once the first indicators are observed. However, the uncertainty decreases in time, as inspection data detects the first signs of unplanned events. Therefore, it is presumed that the uncertainty is time dependant: for t+1: 5% for t+2: 10%, for t+3: 15%, and for t+4: 20%.

3.2.3 Further indicators

This 20% figure is a very conservative figure, because it had to be justifiable in an audit. In practice this figure is probably much higher. The table below shows another indicator. In DISK inspectors are asked to classify the damage to a root cause. The table below shows a limited dataset from DISK from one region. It can be seen that inspectors rate only about 35% of the encountered damages to regular aging. Clearly human error plays a major role in maintenance in practice.

Table 2. Causes of defects.

Damage initiator	Number of registrations
Normal aging	1750
Unknown/don't know	874
Flaw in design	300
Flaw in maintenance	122
Flaw in execution work during construction	402
Flaw in execution work during maintenance	1331
Excessive loads or usage	145
Total	4924

The big difference between the 20% uncertainty in maintenance cost and the $(100\%-35\%)=65\%$ of the damages related to other things than regular ageing, can have different reasons:

- Not all damages have the same cost effect. Those related to regular aging may have a relatively large cost effect;
- The 20% is known to be conservative.
- Some maintenance is considered to be plannable but is actually an estimate for random events. Take the example of concrete maintenance discussed above: Concrete is designed to last 100 years without damage initiation. Therefore an experience figure of maintenance every 30 years cannot be correct. Practically this figure represents the effect of all sorts of different unplanned maintenance events.

4 EVALUATION AND CONCLUSIONS

Life-cycle maintenance planning becomes more common nowadays. In these plans maintenance is often considered to be plannable, with normal aging as leading. However, one should question how well this assumption fits practice for instance with civil structures. This paper shows the importance of that discussion. Wrong assumptions lead to unreliable long term maintenance prognoses and unstable short term maintenance planning. From scientific perspective much more research should be done on this topic. Most research nowadays focusses on predictive, time dependent behavior leading to plannable maintenance. Based on the findings in this paper, focused research is recommended on plannability of maintenance. A possible research item might be the applicability of models used by insurance companies to deal with uncertainties related to unplanned maintenance, for instance models for health insurance.

REFERENCES

- Bakker, J.D. & Klatter H.E. 2012. Risk Based Inspection (RBI) at Rijkswaterstaat. *Proceedings of 6th international conference on bridge maintenance, safety and management, Stresa, Italy.*
- Klanker, G., Klatter, L., Bakker, J. 2016. Issue approach for medium term renovation and replacement planning, *Proceedings of 8th international conference on bridge maintenance, safety and management, Foz Iguacu, Brazil.*
- Van der Velde, J., Klatter, H.E. and Bakker, J.D. 2012, A holistic approach to asset management in the Netherlands, *Structure and Infrastructure Engineering*, Taylor & Francis.

Predictive twin for steel bridge in The Netherlands

G.A. de Raat & J.D. Bakker

Rijkswaterstaat, Utrecht, The Netherlands

G.T. Luiten & J.H. Paulissen

TNO, Delft, The Netherlands

B.Q. de Vogel, H. Scholten & S. de Graaf

Geodan, Amsterdam, The Netherlands

ABSTRACT: Predictive digital twins can support asset managers in assessing the end-of-service life phase of infrastructure. This paper reports on the development of a standardized Digital Twin System Architecture integrating various system layers, which can help asset managers in effectively and efficiently deploying (new) digital technologies to manage their asset networks. A Field-Lab in the Moerdijk bridge region allowed to perform the experiments, research and development of relevant building blocks towards the implementation of this digital twin architecture for steel bridges. This includes the chain from sensor-data, data-management, data-processing towards 3D visualization in a geospatial environment.

1 INTRODUCTION

1.1 *The Renovation & Replacement research program*

Rijkswaterstaat is the executive agency of the Ministry of Infrastructure and Water Management in The Netherlands that manages and develops the main road and waterway network plus the main water systems. These networks include 178 steel bridges amongst many other structures, roads and waterways. The majority of these objects have reached their designed lifespan and need to be replaced or renovated in the upcoming decades. It is important that these measures are timed well: too late and the network cannot be used due to safety concerns, too early and unnecessary destruction of capital will occur. As the wave of upcoming replacements will require a great effort of Rijkswaterstaat and other involved parties (e.g. engineering firms, contractors), an optimal order of measures is required. Since the degradation of an object may have been different than expected (e.g. due to higher traffic loads), it is not justifiable to simply use the initially established end-of-life. For that reason, a research program was started. One of the avenues to explore is how data and digitization can be used to more efficiently predict the end-of-service life. A complete re-calculation of a bridge takes time and effort. Therefore, the process for steel bridges is threefold. At this moment expert-judgement and quick scans are used to determine the order of the re-calculations. By using sensors and predictive digital twin techniques we aim to accelerate the calculations and make them more accurate. Throughout the infrastructure sector (and other sectors) many definitions of digital twinning are used. In the framework of the long term end goal of this research a predictive digital twin of a bridge is defined as a digital replica of the physical bridge that contains, connects and carries various types of relevant data and simulation tools over the whole life cycle of the bridge. The digital twin is connected to the physical bridge through data, e.g. inspection data and/or (near real-time) monitoring data about the current state of the bridge, and contains models to transfer these data into predictions regarding structural safety and technical end-of-life. The digital twin also contains a visualization tool to

retrieve information and insights in a user-friendly way. This definition is based on the work of Cambridge Centre for Smart Infrastructure and Alan Turing Institute (Ye et al 2019).

2 TOWARDS DIGITAL TWINS FOR END-OF-SERVICE LIFE PHASE

2.1 *Vision on application of digital twins*

Over the last decades, academia, engineering companies and asset managers have started to adopt a variety of digital technologies (e.g. models, sensors, data-analysis methods) to address end-of-service life questions for infrastructural objects like steel bridges. For example, there are detailed finite element models (FEM) to calculate the stress levels in bridge components. Another example are advanced fatigue crack growth models that can be updated by inspection and sensor data to monitor real-time loads and stresses on bridges. Until a few years ago, most of these methods were predominantly based on expert knowledge. During the last years, however, the availability of data, data-driven methods, computational power and visualization technology has increased rapidly. This raises the question how these digital technologies can be effectively and efficiently applied for the end-of-service life challenges of asset-managers.

Digital twinning is one of the upcoming data-driven approaches that is receiving increasingly more interest. A digital twin bridges the gap between the physical and the digital by bringing real world data and models in a virtual environment. Such a virtual replica of the physical world can facilitate data-driven working and lead to more efficient decision-making and asset management in an ever digitizing society.

In the built environment, digital twins are starting to receive more interest, being mainly useful for inspection purposes (Pan & Zhang 2021) and predictive maintenance, especially when combined with sensor data and model results (Khajavi et al 2019). Building information models (BIM) can play an important role in digital twins, as these models hold detailed information on the properties of all components of a construction on an architectural level (Lu et al. 2019, Menassa 2021).

The aforementioned examples feature digital twins of a single physical system. A next step is to develop comprehensive digital twins that bring together data from multiple physical systems. An example of this upscaling are Digital Twins for the Physical Living Environment (DTFL), which integrate geospatial data of physical and geographic objects on a regional scale along with data of the dynamic processes (e.g. through sensor data) that are taking place.

The incorporation of BIM models in the wider context of a DTFL remains relatively unexplored. Importing a BIM model into a DTFL is challenging as it requires accurate geospatial positioning of the BIM model. This is complicated as BIM models are often stand-alone models that lack georeferencing. Bringing a BIM model into a DTFL can have great added value for a construction or infrastructure object. For example, the interaction can be established between the model and factors like subsurface, weather or real-time traffic flow. Also, it can facilitate assessing the impact of planned construction work on the external living environment.

2.2 *Standardization of architecture*

A standardized Digital Twin System Architecture (Figure 1) is essential to efficiently develop and apply current and future digital technologies. Creating object specific DT's from a standardized architecture/framework will prevent the need to start from scratch with each new digital twin and it allows to create digital twins for specific types of assets and problems in a flexible and repeatable way. It also contributes to standardization and interoperability amongst the many stakeholders involved in life cycle of the asset. The system architecture consists of various building blocks like data, models and visualization. Decoupling of system layers and standardization of the interfaces will prevent vendor lock-in. This way, digital twins of assets can become a an instrument to better retain information and insights throughout the (remaining) life cycle.

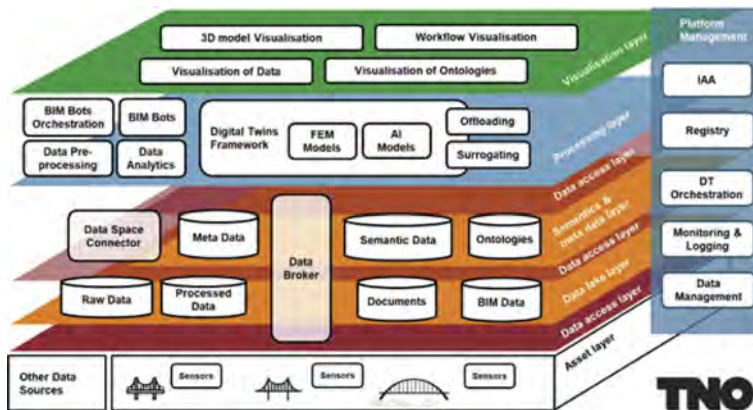


Figure 1. Standardized Digital Twin System Architecture.

3 USE CASE END-OF-SERVICE LIFE PHASE STEEL BRIDGES

3.1 Use case Field-Lab Moerdijk bridge

Rijkswaterstaat and TNO started a Field-Lab in the Moerdijk bridge region to facilitate collaborative experiments, research and development towards the implementation of Digital Twins for the end-of-service life phase of steel bridges. For this stage in the life cycle structural safety and fatigue (crack growth at specific hotspots in the steel structure due to cyclic loads) are important risks. The current practice at Rijkswaterstaat is to manage these risks with various types of inspections, structural assessments and continuous monitoring (Paulissen et al, 2018). The data and models involved in in this Field-Lab have been used as input for the experiments within the Digital Twin System Architecture and building blocks for steel bridges.

This chapter of the paper summarizes the progress so far. The focus was mainly on the modelling and visualization of data. A DTFM portal was developed to visualize both the data and models results of the bridge within a geospatial context (see 3.5). Furthermore we have prototyped two data management solutions (3.2) and applied three distinct analytical approaches to model stresses on the bridge (3.3).

3.2 Building blocks

On the **Asset layer**, a monitoring system was used that continuously records the dynamic strains resulting from trucks. The sample rate of the recordings is 100 Hz to capture the effect of individual truck wheels. Besides these continuous monitoring, a controlled load experiment was done to record the effect of a known load on the bridge. This type of monitoring can be used to calibrate the structural analysis models. The calibration is done by comparing the recorded load effects to assumptions from assessment standards. In the context of the Digital Twin development, the data were used as input for the Data -and Processing layer.

3.3 Data management

On the **Data layer**, two data management solutions were investigated and prototyped. The first focuses on robust and efficient storage and handling of large-scale time series datasets. This was done using Microsoft Azure Cloud storage and TimescaleDB, which is a database based on PostgreSQL. Once uploaded to the database, the data can be handled, queried and visualized much quicker than traditional CSV-files. TimescaleDB also allowed for easy interfacing with analytical tools and dashboarding software. The second solution holds a more broad oriented data management system that focuses on registering and organizing

various types of datasets along with the relevant metadata in a single portal. The prototype is based on the open-source data management system CKAN. The prototype includes links to geometric datasets and models (i.e. point clouds & BIM), inspection data, time series data and a structural analysis models. Both data management solutions aim to make data available in a Findable, Accessible, Interoperable and Reusable way. This is important for being able to make more efficient use of the available data for the life cycle asset-management. It also contributes to innovation once datasets become more easily accessible to organizations doing R&D.

3.4 *Data processing*

On the **Processing layer**, three data-analysis tools were investigated.

Bridge Weight in Motion (Rodenburg et al, 2022), is an analysis tool that extracts truck load parameters (e.g. axle configurations, axle loads and gross vehicle weights) from the monitoring system as described before. This is important information to determine the loads that need to be assessed to determine the structural safety and fatigue life of the bridge. In current practice, this is done based on generic load models from European and National standards (e.g. Eurocodes including National Annexes). This results in uncertainties and possibly over-/underestimations of the loads that are used for the assessment of the bridge. Integration of this tool in a Digital Twin environment contributes to effectively determining bridge specific traffic loads, which can be used for the structural assessment and efficient long term monitoring of traffic loads on the bridge.

The second analysis tool is **ProbEye**, an open-source parameter estimation tool developed by TNO and the German knowledge institute Bundesanstalt für Materialforschung und -prüfung. The tool combines a model, prior knowledge about its input parameters and measurements to obtain the probability density function of model parameters (Vereecken et al, 2022). It explicitly accounts for model uncertainties and measurement inaccuracies. As such, models can be made more accurate by making use of measurement data. In the case of the Moerdijk bridge, the tool was used to calibrate structural assessment model constructed in FEA software DIANA. This models calculates the deformations, forces and stresses in the bridge structure. Because the method requires many model evaluations, computation time is a specific challenge. This is was overcome by surrogate modelling and parallel computing in the cloud. The latter was done in close collaboration with DIANA. Integration of this tool in the Digital Twin results in more accurate structural analysis models .

The third tool is **continuous automated analysis** and converts continuous monitoring data into interpretable parameters for assessing the structural safety and fatigue life of the bridge. This involves filtering, data cleaning, temperature correction and conversion of measured quantities (strains) into relevant quantities for structural assessment. The tool is directly interfaced with the Timescale database such that the analysis is automatically done when new data are uploaded in the database. This is valuable for continuous (trend) monitoring of traffic load effects during the life cycle of bridges.

3.5 *Visualisation of a DTFL*

For the **Visualisation layer**, we have focused on implementing the steel bridge in a comprehensive DTFL. A DTFL requires a 3D environment that integrates data in a geospatially accurate way. The open-source software library CesiumJS is a state-of-the-art tool that is becoming increasingly popular to visualize DTFLs. The CesiumJS software allows for displaying geospatial data in a full 3D environment in a web browser. As part of this study, we developed a generic Cesium-based application and interface that can be reused for different purposes.

Within a Cesium-based viewer, data can be displayed both as 2D map layers (e.g. WMS services) or 3D physical objects. For running in a web browser, the application is easily accessible for a wide public. At the same time, visualizing a 3D digital twin in a browser while maintaining a satisfying performance level is challenging when dealing with large quantities of data. Browser

cache and performance can easily be overloaded. An important way to prevent this is through 3D tiling, which is a technique to subdivide 3D objects in a set of numerous tiles.

3D Tiles is an open standard of the Open Geospatial Consortium (OGC) and designed for streaming large 3D geospatial datasets. By using 3D tilesets, only the data that are close to the user's viewpoint are requested and visualized in the web application. In that way, the user only retrieves the necessary data, optimizing the performance of the application.

The conversion of data for display in the digital twin requires two main processing steps. First, the data is processed to 3D objects through a mesh tessellation or triangulation and set to the specific geodetic system for Cesium (EPSG: 4978). Secondly, the 3D objects are converted into a 3D tileset. This processing pipeline is not yet standardized and can vary substantially between different data types like point clouds, BIM models or other custom 3D objects. Especially for BIM, there is a large variety of file formats, which complicates the establishment of a uniform data processing protocol.

The digital twin environment that we developed includes a number of nation-wide data sets for the Netherlands. Within the Netherlands, a wide variety of data is openly available in a number of key registries. We processed a set of these data sets into the viewer, including all buildings and trees. Furthermore, a nation-wide digital elevation model (DEM) is available and can be loaded into the Cesium environment as a tiled mesh to visualize the terrain in 3D. Any map layers are then draped over the 3D terrain.

The visualization platform provides a custom user interface, which allows users to intuitively switch between different map layers, data sets and model results. The so-created digital twin infrastructure can be used for variable applications in the field of the physical living environment.

For the Moerdijk bridge, we used the Cesium-based web application to visualize the results from FEM. The Moerdijk bridge itself is visualized in the viewer as a BIM model, which was available in Revit file format (.rvt) (Figure 2). The elements of the BIM model were first converted into 3D geometries using FME while retaining the BIM attributes and then stored in a PostgreSQL database. Subsequently, a 3D tileset of the BIM model was generated using the tool pg2b3dm and stored in a cloud-based service. A separate 3D tileset was generated for nine different structural elements of the bridge to enable visualization of distinct parts of the construction. The subdivision consisted of the vertical web, inclined web, top flange, bottom flange, overlay, diaphragms, cantilever beams, cantilever beam sidewalls and top stiffeners.

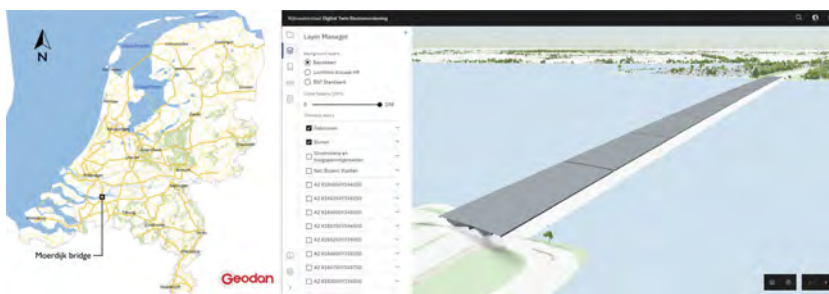


Figure 2. Location of the Moerdijk bridge in the southwest of the Netherlands (left) and the BIM of the bridge positioned in the digital twin environment (right). A user interface allows for selecting which data are being visualized.

Model results from the FEM were projected directly on this detailed representation of the bridge from the BIM model (Figure 3). Multiple FEM model results can be attached to a single element so that it is possible to dynamically switch between them. The precise model outcomes for each component of the BIM model can also be retrieved by clicking on a specific structural element to get the corresponding object information.

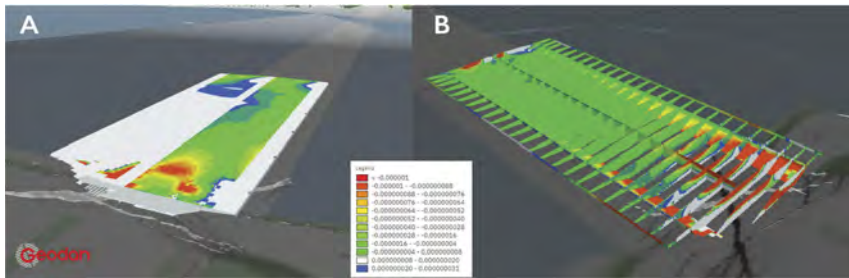


Figure 3. Results of the FEM for a truck passing over the Moerdijk bridge are visualized in the digital twin for one bridge section. A. FEM results for the overlay displayed within the entire BIM. B. FEM results displayed on only the vertical web, inclined web, diaphragms, cantilever beams and sidewalls. The other bridge elements are hidden to have a clear view of the internal structure of the bridge.

In addition to the model results, inspection photos of the bridge can be retrieved from the digital twin. The locations where photos are taken are indicated by an arrow symbol, whose orientation corresponds to the direction in which the photo was taken. The corresponding image file can be retrieved by clicking on the arrow symbol. The entire set of inspection photos comprises more than 19.000 files. Visualization and retrieval of photos from the digital twin helps to maintain a clear overview of the available images.

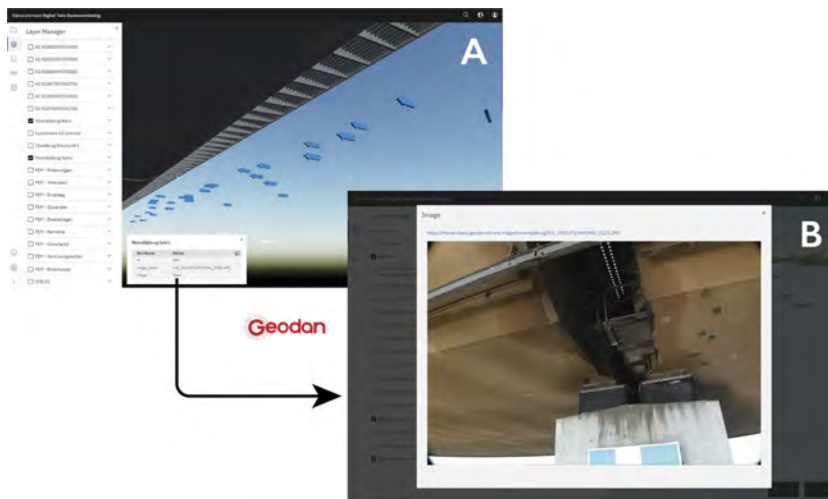


Figure 4. The BIM of the Moerdijk bridge viewed from below. The arrows indicate the position and direction of photos taken during inspections. The photos can be retrieved by clicking on the corresponding arrows.

4 CONCLUSIONS

The digital twin of the Moerdijk bridge presents a first step towards developing a virtual environment for managing the end-of service-life phase of the bridge. At the moment, the prototype offers the BIM integration along with two data sources: a set of FEM results and georeferenced inspection photos. Visualization of the FEM in the digital twin environment can facilitate the monitoring and prediction of the structural safety and fatigue life of the structure through time.

The developed digital twin offers a platform to incorporate a wide variety of other additional data types that may be of interest for monitoring purposes. For instance, 3D meshes

obtained through laser scanning or photogrammetry techniques may have added value for the detection of fractures and deformations. Another important aspect for bridge monitoring would be the time component. Real-time information from sensors (e.g. strain monitoring) and results of data-analysis (e.g. fatigue spectra, traffic loads) can be incorporated into the digital twin through API implementation, while time sliders can add a 4D component to the viewer to gain insight into changes in the bridge through time. Displaying a high-performance digital twin in a browser was long considered impossible, but is now becoming achievable thanks to state-of-the-art software libraries like CesiumJS.

By bringing together relevant data from multiple sources, the digital twin can provide a comprehensive overview of the current state and potential risks. This can lead to better decision-making and cost reductions regarding the maintenance of infrastructure objects.

So far we have adopted a wide approach, to be able to test a broad spectrum of techniques. In due time cost-effectiveness analyses will be made so the best tools can be selected. We will also take the possibilities of implementing the necessary processes into account. For example a technique to determine parameters for re-calculations that cannot be widely used by engineering companies in their assessment of an object is less likely to be used in the long term.

The next goal is that the digital twin platform for the Moerdijk bridge can be easily reused for other infrastructure objects. The use of a standardized Digital Twin System Architecture can contribute to the effectiveness and efficiency of further developing and applying this potential.

So far we have learnt that the main challenges to achieve this mainly revolve around standardization and interfacing. Much of the data processing has to be automated to expand the implementation of the digital twin infrastructure. For example, the transfer of FEM results into the viewer is still manual work at the moment. Ideally, however, FEM results are directly coupled to the digital twin. This automatization would facilitate model results to easily be reflected in the viewer. Furthermore, as more data become available, model results may be updated through machine learning algorithms. Such model updates must also be able to be fed back easily into the viewer (top layer in the suggested system architecture from Figure 1).

Altogether, the entire spatial data infrastructure has to mature, from data storage to data management, supported data types, data processing and user interfaces. Only then it can effectively be deployed in the working processes of the bridge managers. Nevertheless, the developed prototype shows the potential of a geospatial digital twin portal for bridge managing purposes.

Another lesson is that it might be better to gather different companies and stakeholders at the start of building a digital twin. With our current DT each stakeholder started in their own area of expertise and these data sources had to be merged together in a later phase.

In a later phase we aim to use the digital twin for the maintenance during the total life span.

Furthermore, while the initial development was focused on technical users (structural engineers, technical advisors), the imaginable uses of digital twins are broader. In future, it may be extended to other users (decision makers, modelers, etc.).

REFERENCES

- Khajavi, S. H., Motlagh, N. H., Jaribion, A., Werner, L. C., & Holmström, J. 2019. Digital twin: vision, benefits, boundaries, and creation for buildings. *IEEE access*, 7, 147406–147419.
- Lu, Q., Xie, X., Heaton, J., Parlikad, A. K., & Schooling, J. 2019. From BIM towards digital twin: strategy and future development for smart asset management. *International Workshop on Service Orientation in Holonic and Multi-Agent Manufacturing* (pp. 392–404). Springer, Cham.
- Menassa, C. C. 2021. From BIM to digital twins: A systematic review of the evolution of intelligent building representations in the AEC-FM industry. *Journal of Information Technology in Construction (ITcon)*, 26(5), 58–83.
- Pan, Y. & Zhang, L. 2021. A BIM-data mining integrated digital twin framework for advanced project management. *Automation in Construction*, 124, 103564.

- Paulissen, J.H. & van Es, S.H.J. & Peelen, W.H.A. & Klatter H.E. 2018. Information requirements for effective management of an aging transport network. *IALCCE 2018; The Sixth International Symposium on Life-Cycle Civil Engineering*, Ghent 28-31 October 2018.
- Rodenburg, J.D. & van Es, S.H.J. & Paulissen, J.H. & de Bakker, M.P. & Hengeveld, S.T. 2022. Application of a modular bridge weigh-in-motion system on an orthotropic bridge deck. *IABMAS 2022; 11th International Conference on Bridge Maintenance, Safety and Management, Barcelona July 2022*.
- Vereecken, E. & Slobbe, A. & Rózás, Á. & Botte, W. & Lombaert, G. & Caspeele, R. 2022. Efficient Bayesian model selection and calibration using field data for a reinforced concrete slab bridge. *Structure and Infrastructure Engineering; Maintenance, management, Life-Cycle Design and Performance. October 2022*. DOI: 10.1080/15732479.2022.2131847
- Ye C. & Butler L, et al. 2019. A Digital Twin of Bridges for Structural Health Monitoring. *Proceedings of the 12th International Workshop on Structural Health Monitoring* <https://github.com/Geodan/pg2b3dm>

*MS12: Advanced strengthening and retrofitting solutions
for existing concrete structures
Organizers: N. Randl & E. Rossi*



Taylor & Francis

Taylor & Francis Group

<http://taylorandfrancis.com>

Numerical investigation of the effects of graphene on the mechanical properties of fibre reinforced cementitious matrix composite

X.M. Zhu, M.N. Su & Y.C. Wang

School of Engineering, The University of Manchester, UK

ABSTRACT: In this study, graphene is introduced to the cementitious matrix to improve not only the mechanical properties of the matrix but also the bonding properties. This study proposes a finite element model for graphene modified FRCM composite and validates the model by comparison against experimental results. Results showed that the increase of the mortar stiffness due to the introduction of graphene would lead to the increase of the elastic stiffness but the decrease of the strain of the composite. The stronger interfacial bonding brought by graphene would result in less strain developed at the cracking development stage. Graphene also led to more in-depth penetration of matrix into fibre bundles, which increases the ultimate strain of the composite. In addition, the constitutive models generated from parametric study were also used to assess two existing analytical models.

1 INTRODUCTION

Fibre reinforced cementitious matrix (FRCM) composite have been proved a successful alternative solution of fibre reinforced polymer (FRP) in structural strengthening field recently (Zhu et al., 2018; Su et al., 2019a, b). FRCM composite is composed by one or more fibre reinforcement layers embedded in cementitious matrix. The use of organic resin matrix for FRP is replaced by inorganic cementitious matrix in FRCM to improve the compatibility between fibre and matrix (Feng et al. 2020a). Although FRCM composite is capable of improving the confinement, shear and flexural capacity of structural members, the issue of weak bonding at the fibre-matrix interface is still a concern (Feng et al. 2020b; Zhu et al. 2021). The typical failure of FRCM composite is a combination of slippage between fibres as well as partial fracture of fibres. This is due to the partially penetration of cementitious matrix into carbon fibre bundles; only the fibres directly bonded matrix (i.e. external fibres) would fracture while the internal fibres are pulled out. The penetration of matrix determines the proportion of external part of carbon fibres and largely determines the ultimate strengths of the FRCM composite.

Great efforts have been made by adding graphene nanoparticles into the cementitious matrix to enhance the matrix properties (Yang et al. 2017; Li et al. 2017). This idea is now applied to FRCM composite. Compared to the traditional FRCM composites, the introduction of graphene into the FRCM composite (Gr-FRCM) is expected to (a) enhance the mechanical properties of the cementitious matrix, (b) improve the fibre-matrix interfacial bonding and (c) increase the penetration of cementitious matrix into fibre yarns. This study aims to understand the effects of graphene on the tensile behaviour of FRCM composite plates. Thus, the study will firstly develop a finite element model on FRCM composite plates and validated against test results; secondly, the validated model will be used to carry out a parametric study to examine the effects of key parameters; finally, the newly generated results will be compared to analytical models.

2 FINITE ELEMENT MODELLING

2.1 Model development and validation

The geometry of a typical Gr-FRCM composite sample under tension is shown in Figure 1(a). The composite is comprised of one layer of carbon fibre mesh embedded in graphene modified cementitious matrix. The sample is designed with a gauge length of 220 mm and clamping length of

140 mm at each end. The thickness of matrix layer is 5 mm. Geometries of the carbon fibre mesh is presented in Figure 1(b), which is made in form of bidirectional grid with a uniform bundle width of 3 mm, and the gap between two adjacent fibre bundles is 7 mm and 6 mm in warp and weft directions, respectively. The thickness of the fibre mesh is 0.154 mm. The total width of the Gr-FRCM sample is 50 mm and each specimen contains five longitudinal fibre bundles.



Figure 1. Geometry of Gr-FRCM sample and fibre mesh.

The main material properties used in the finite element models are summarized in Table 1, which were corresponded to matrix with 0% (G0), 0.035% (G1) and 0.07% (G2) graphene (percentage of cement weight). The properties include the Young's modulus E_m and the tensile strength f_{mc} of matrix, the Young's modulus E_f and the tensile strength f_{fu} of carbon fibre mesh, as well as the shear stress-slip stiffness k_s , the shear strength τ_s and the fracture energy G_s of fibre-mortar interface. A simplified bilinear response of interface traction separation relationship is defined to simulate the mechanical interaction between the mortar and fibre. The damage initiation is defined using the maximum nominal stress criteria, and the damage propagation is captured via fracture energy with linear softening.

Table 1. Material properties for the Gr-FRCM composite model.

	E_m (MPa)	f_{mc} (MPa)	E_f (MPa)	f_{fu} (MPa)	k_s (N/mm ³)	τ_s (MPa)	G_s (N/mm)
G0	47900	4.19	79770	1931	14.23	2.35	1.62
G1	55800	4.38	79770	1931	19.99	2.59	1.72
G2	59752	4.67	79770	1931	20.72	2.95	1.80

The boundary conditions are set by restraining horizontal and vertical movement and rotation of all external nodes at the bottom surface of mortar. A vertical displacement load is applied on the upper surface of the matrix. Meanwhile, in order to simulate the clevis gripping test setup, only elastic properties are applied to mortar and fibre mesh at both ends, to allow the damage of the composite occurring within the gauge length. The mortar and fibre mesh parts are both built using 3D linear brick elements with eight nodes (C3D8R), in order to reduce integration and hourglass control. The mesh sizes of 5 mm and 3 mm are employed for mortar and fibre mesh, respectively. Thus, a total of 1000 solid elements and 2222 nodes are formed within mortar part, meanwhile, a total of 968 elements and 2896 nodes are generated within the fibre mesh.

Typical force-deformation curves of Gr-FRCM composite obtained from finite element modelling are compared with experimental results for specimens G0, G1 and G2, as shown in Figure 2 and Table 2. The comparison shows that the two results are in good agreement, and the numerical model is able to capture the full tensile behaviour of Gr-FRCM composite from mortar cracking to the ultimate.

3 PARAMETRIC STUDY

Compared with the conventional FRCM composite, graphene could enhance FRCM composite by improving the mechanical properties of the cementitious matrix, the fibre-matrix interfacial bonding and the penetration of cementitious matrix into fibre yarns, which will enhance the utilization efficiency of fibre at ultimate of the composite. Therefore, the parametric study would

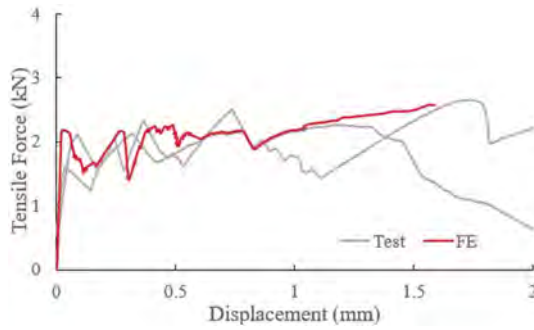


Figure 2. Comparison of experimental and numerical force-displacement curves of Gr-FRCM composite (for matrix with 0.035% graphene).

Table 2. Comparison between test and FE modelling results.

Samples	Elastic modulus (MPa)		Cracking force (kN)		Cracking deformation (mm)		Ultimate load (kN)		Ultimate displacement (mm)	
	Test	FE	Test	FE	Test	FE	Test	FE	Test	FE
G0	95	93	2.45	2.18	0.023	0.021	2.81	2.98	1.51	1.45
G1	100	109	2.67	2.29	0.022	0.019	2.92	3.11	1.54	1.55
G2	104	110	2.75	2.31	0.019	0.020	3.21	3.19	1.54	1.56

focus on the key parameters influenced by the introduction of graphene, including the tensile strength f_{mc} and modulus E_m of matrix, the shear stress-slip stiffness k_s , the shear strength τ_s and the fracture energy G_s of fibre-mortar interface, as well as the thickness of external fibre layer t_f .

Based on current theories (Filippou & Chrysostomou 2020, Larrinaga et al. 2013), the stress-strain curves of FRCM composite can be simplified into an analytical model with three phases, as shown in Figure 3. Phase I of the curve represents the elastic behaviour when fibre and matrix work together to resist external loads, ending up with the initial cracking (section OC). Phase II refers to a period of crack development from initial cracking to the maximum number of cracks on matrix, during which the fibres experience a certain level of interfacial debonding and/or slip-page (section CT). Phase III is the post-cracking stage from the completion of multi cracking to the ultimate failure, at which the resistance was mainly provided by carbon fibres (section TU).

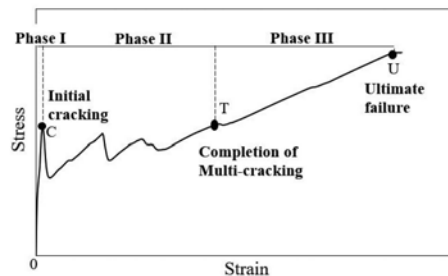


Figure 3. Typical stress-strain relationships of FRCM composite under tension.

3.1 Effects of matrix properties

Figure 4 shows a comparison between tensile stress-strain curves of FRCM composites with three different types of matrix; the properties of specimens are listed in Table 3. The stress is derived by dividing the total force by cross-section area of the fibre mesh, and the strain is

calculated based on the deformation within the gauge length. It indicates that the modulus E_m and tensile strength f_{mc} of matrix mainly influences the first two phases. The greater value of E_m (i.e. a rise of 46% from M1 to M3) results in the increase of the elastic stiffness (35%) of the composite at Phase I and slightly improved stiffness (9%) of the composite at Phase III, but the decrease of the strain (41%) developed at Phase II (see Figure 5). In addition, when the tensile strength f_{mc} is enhanced, the stress of FRCM developed at the ultimate failure is increased; for instance, from M1 to M3, the ultimate failure stress is increased by around 22% (see Figure 4).

Table 3. Material properties for three types of mortar.

Mortar Type	E_m (MPa)	f_{mc} (MPa)
M1	40482	4.19
M2	46828	4.29
M3	75754	5.95

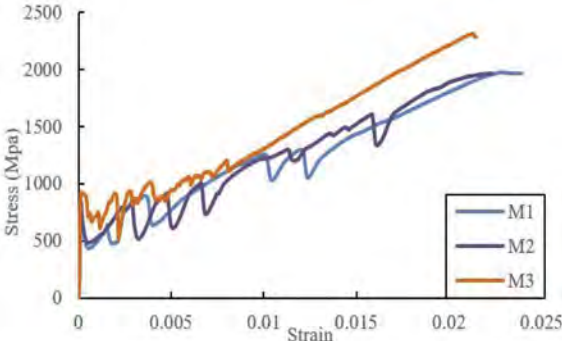


Figure 4. Stress-strain curves of FRCM composite with different mortar properties.

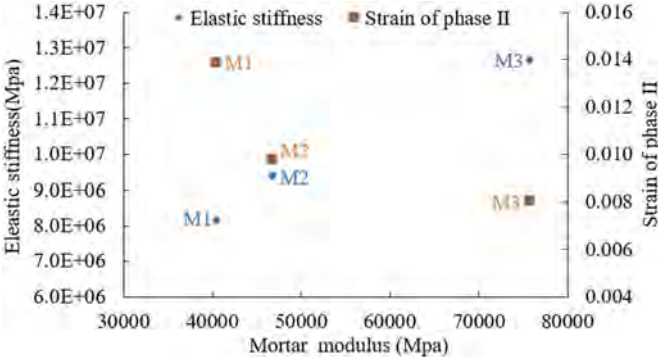


Figure 5. Effects of mortar modulus on the elastic stiffness and strain of Phase II.

3.2 Effects of fibre-mortar interfacial properties

Since different graphene dosage will result in different interfacial bonding strength between mortar and fibre, three key parameters relating to interfacial bonding (i.e. the shear stress-slip stiffness k_s , the shear strength τ_s and the fracture energy G_s) are examined, as listed in Table 4. The interfacial properties were carefully chosen herein to cover both weak and strong interface cases.

Table 4. Parametric study on different fibre-mortar interfacial properties.

Sample label	k_s (N/mm ³)	τ_s (Mpa)	G_s (N/mm)
Int01	1.42	0.24	0.16
Int05	7.12	1.18	0.81
Int08	11.38	1.88	1.30
Int1	14.23	2.35	1.62
Int2	28.46	4.70	3.24
Int3	42.69	7.06	4.86
Int5	71.15	11.76	8.11
Int10	142.30	23.52	16.21

The stress-strain curves of FRCM composite with relatively weak and strong interface are presented in Figure 6(a) and (b), respectively. To better present the effects of interfacial properties, the relationships between the strain developed at Phase II and the shear stress-slip stiffness k_s of each sample are plotted in Figure 7. It can be seen that the FRCM composites with weak interface experience a longer period of curve fluctuation (Phase II) generally, which is caused by more fibre mesh slippage after cracks occurs at the surrounded matrix. For example, with an 60% increase in shear stress-slip stiffness from Int08 to Int2, the strain of Phase II decrease 13%. FRCM composite sample Int01 failed much earlier than other samples, because the very weak interfacial bonding makes the embedded fibre slip severely after mortar initially crack and fibres unable to further resist external loads after the failure of matrix. On the other hand, the FRCM composites with strong interface limit the strain development of Phase II. With the further increase of interfacial properties, the strain developed at Phase II were almost the same at 0.0075 (see Figure 7). With strong interfacial properties, the strain developed at Phase II is due to the mortar cracking alone without the fibre slipping according to the numerical model results. The prohibition of fibre slippage makes the stress more efficiently transfer between mortar and fibre till the number of mortar cracks becomes stable.

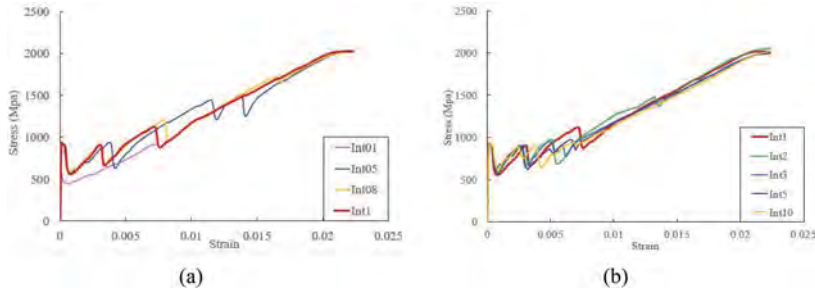


Figure 6. Stress-strain curves of FRCM composite with different interfacial bonding.

3.3 Effects of amount of external fibres

As mentioned earlier, introduction of graphene could accelerate the hydration reaction and promote the generation of hydration products inside of carbon fibre bundles. Thus, four different thickness of external fibre layers t_f are considered in this parametric study, as shown in Table 5. Figure 8 presents the comparison results among stress-strain curves of these samples. Values of the cracking stress f_c , the strain developed at Phase II ε_T and Phase III ε_U are extracted and summarized in Figure 9. It is concluded that the number of external fibres affects (a) the cracking stress of the FRCM composite at the end of Phase I, (b) the strain developed at Phase II and (c) the strain at ultimate at Phase III. Specifically, when the thickness of external fibre triples from 0.167 mm to 0.502 mm in the models, the composite cracking stress is decreased by 69% from 927MPa to 269MPa (see Figure 9(a)), the strain of Phase

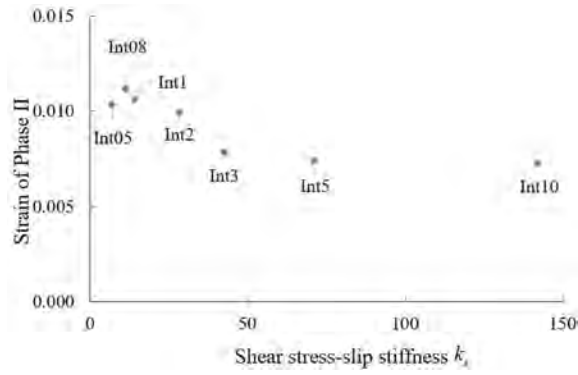


Figure 7. Effects of interfacial properties on the strain developed at Phase II.

II is decreased by 54% (from 0.0106 to 0.0048), while the ultimate strain is increased by 17% from 0.019 to 0.023 (see Figure 9(b)).

Table 5. Details of fibre thickness and fibre-mortar interfacial properties used in parametric study.

Sample label	t_f (mm)	k_s (N/mm ³)	τ_s (Mpa)	G_s (N/mm)
T1Int05	0.084	7.12	1.18	0.81
T1Int1	0.084	14.23	2.35	1.62
T2Int05	0.167	7.12	1.18	0.81
T2Int1	0.167	14.23	2.35	1.62
T3Int05	0.335	7.12	1.18	0.81
T3Int1	0.335	14.23	2.35	1.62
T4Int05	0.502	7.12	1.18	0.81
T4Int1	0.502	14.23	2.35	1.62

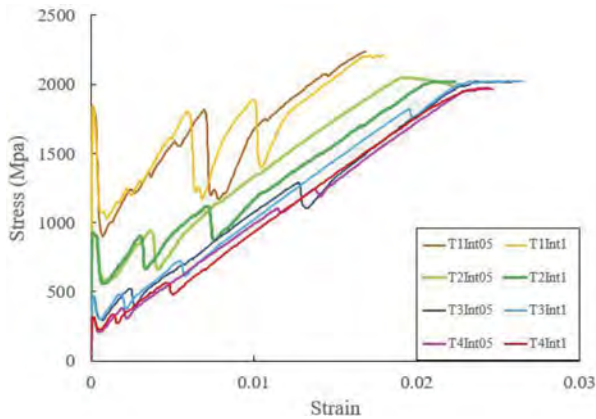


Figure 8. Stress-strain curves of FRCM composite with different thickness of external fibre.

4 ANALYTICAL MODELS

The comparison between modelling results and theoretical calculation results by the classical ACK model (Aveston 1973) and a model based on cracking theory in EC2 (Larrinaga et al.

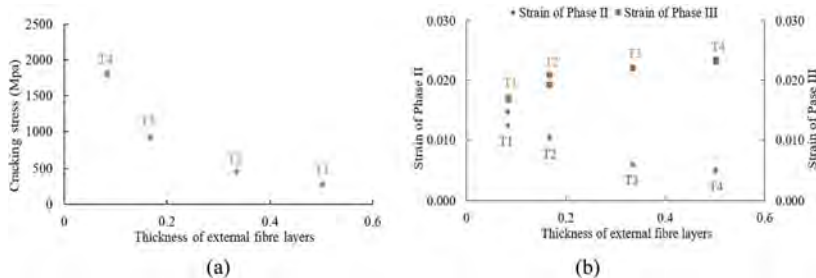


Figure 9. Effects of thickness of external fibre layers on the (a) cracking stress and (b) strain.

2013) is carried out. A typical numerical curve (Sample Int08) presented in Section 3.2 is used to for comparison, as shown in Figure 10.

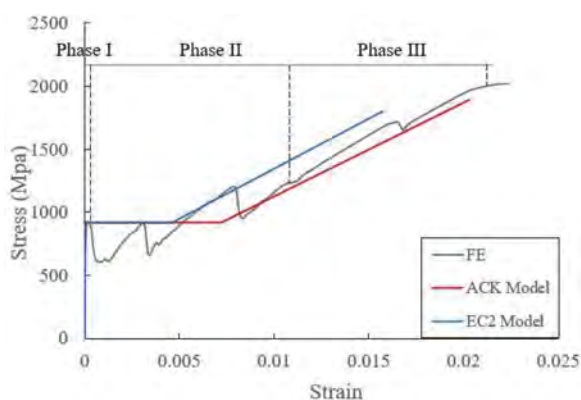


Figure 10. Comparison on stress-strain curves obtained from FE modelling and two analytical models.

It is shown that both analytical models can predict the elastic stiffness and the cracking stress of Phase I, but fail to accurately predict the strain and stress developed at Phase II and Phase III. To be specific, the strain developed at Phase II is around 0.011, while the ACK model and EC2 model underestimate it as 0.007 and 0.004, respectively. The stress developed at Phase II gets increased compared with the cracking stress, but both models overlook the stress growth at Phase II. For the ultimate point, which is around 0.021 for strain and 2004 MPa for stress in the FE curve, the ACK model is 5% underestimation of strain and 6% underestimation of stress, but the EC2 model significantly underestimate the strain and the stress by 29% and 12% respectively. For ACK model, the underestimation may come from its assumption of a constant shear bonding strength between the fibre and mortar during the damage interaction phase, while this bond strength increases due to fibre slippage as shown in numerical curves. The EC2 model was developed based on the cracking pattern of reinforced concrete, which could be different for the cases for FRCM composite plate as the bonding mechanism of cement/reinforcement is apart from that of cement/fibres.

5 CONCLUSIONS

This study investigates the tensile behaviour of graphene enhanced fibre reinforced cementitious matrix (FRCM) composite plate by numerical study. A finite element model was built and validated based on the experimental results of graphene modified FRCM composites. Upon validation, a parametric study is performed focusing on the key parameters related to the mechanical properties brought by the introduction of graphene, including the tensile strength and modulus of mortar, the shear stress-slip stiffness, shear strength and fracture

energy of fibre-mortar interface, as well as the amount of external fibre layer directly bonded with matrix. The effects of these parameter on the constitutive model of FRCC composite were investigated. Results showed that:

- The increase of the mortar stiffness (+46%) would lead to the increase of the elastic stiffness (+35%) but the decrease of the strain (-41%) of the composite, while the tensile strength of mortar was beneficial for the deformation of the FRCC composite.
- The interfacial property had a significant impact on curve profile of Phase II: stronger interfacial bonding in general would result in less strain developed at Phase II.
- When the number of external fibres directly bonded with matrix became triple, the cracking stress and the strain developed at Phase II were found to decrease approximately 70% and 54% respectively, but the ultimate strain of the composite was increased by more than 15%.
- In addition, the curves generated from the numerical model were also compared with two existing analytical models (i.e. the ACK model and the EC2 model). Both models underestimated the ultimate strain and stress of the composite. In order to improve the accuracy of analytical models, parameters corresponding to interfacial properties and external fibres are suggested to be included in the analytical model.

ACKNOWLEDGEMENT

The authors would like to acknowledge the financial support from the Engineering and Physical Sciences Research Council (EPSRC) Fund (EP/T021748/1) for the completion of this research work.

REFERENCES

- Aveston, J., Cooper, G.A., Kelly, A. 1971. The properties of fibre composites. *Conference 4th November 1971*. IPC Science & Technology Press Ltd. London 15–24.
- Aveston, J., & Kelly, A. 1973. Theory of multiple fracture of fibrous composites. *Journal of Materials Science*, 8(3):352–362.
- AC434-0616-R1. 2016. Acceptance Criteria for Masonry and Concrete Strengthening using Fabric-Reinforced Cementitious Matrix (FRCC) and Steel Reinforced Grout (SRG) Composite Systems. American Concrete Institute, Farmington Hills.
- Feng, R., Liu, Y., Zhu, J. H., et al 2020a. Flexural behaviour of C-FRCC strengthened corroded RC continuous beams. *Composite Structures*, 245:112200.
- Feng, R., Zhang, J.Z., Zhu, J. H., Feng, X. 2020b. Experimental study on interface bonding fatigue behavior of C-FRCC composites in ICCP. *Construction and Building Materials*, 259: 119660.
- Filippou, C.A. & Chrysostomou, C. Z. 2020. Analytical model for textile reinforced mortar under monotonic loading. *Construction & Building Materials*, 258: 120178.
- Grande, E., Milani, G., & Imbimbo, M. 2020. Theoretical model for the study of the tensile behavior of FRCC reinforcements. *Construction & Building Materials*, 236: 117617.
- Larrinaga, C.C., San-José, J.T., & Garmendia, L. 2013. Non-linear analytical model of composites based on basalt textile reinforced mortar under uniaxial tension. *Composites. Part B, Engineering*, 55: 518–527.
- Li, W., Li, X., Chen, S. J., Liu, Y. M., et al. 2017. Effects of graphene oxide on early-age hydration and electrical resistivity of Portland cement paste. *Construction and Building Materials*, 136: 506–514.
- Su, M.N., Wei, L.L., Zhu, J.H., Ueda, T., et al. 2019a. Combined Impressed Current Cathodic Protection and FRCC Strengthening for Corrosion-Prone Concrete Structures. *Journal of Composites for Construction*, ASCE 23 (4).
- Su, M.N., Zeng, C.Q., Li, W.Q., Zhu, J. H., et al. 2019b. Flexural performance of corroded continuous RC beams rehabilitated by ICCP-SS. *Composite Structures*, 232:111556.
- Yang, H., Monasterio, M., Cui, H., Han, N. 2017. Experimental study of the effects of graphene oxide on microstructure and properties of cement paste composite. *Composites. Part A, Applied Science and Manufacturing*, 102: 263–272.
- Zhu, J.H., Su, M.N., Huang, J., Ueda, T., et al. 2018. The ICCP-SS Technique for Retrofitting Reinforced Concrete Compressive Members subjected to Corrosion. *Construction and Building Materials*, 167: 669–79.
- Zhu, M.C., Zhu, J. H., Ueda, T., Matsumoto, K., et al. 2021. Bond behavior of carbon fabric reinforced cementitious matrix (FRCC) composites considering matrix impregnation. *Composite Structures*, 262: 113350.

Experimental behavior of FRCM-confined concrete under high temperature

F. Faleschini & C. Pellegrino
University of Padova, Padova, Italy

K. Toska
CY Cergy Paris Université, Neuville-sur-Oise, France

ABSTRACT: The paper investigates the behavior of concrete confined through FRCM (Fiber Reinforced Cementitious Matrix) composites subjected to high temperatures. Small scale cylindrical specimens (150x300 mm) were confined using two types of carbon fiber (dry and resin impregnated). For the sake of comparison two layers of FRCM were applied to all confined specimens. After curing, cylinders were exposed to four ranges of increasing temperatures being 20°C (ambient), 80°C, 100°C and 250°C and then tested under cyclic loading. The experimental results show that thermal stress significantly influences the confinement effectiveness of FRCM composites. Exposure to high temperatures reduces the ultimate confined strength and strain. For specimens confined with resin impregnated fibers, the observed stress-strain trend of confined elements tested after high temperatures exposure significantly differs from specimens tested under standard ambient conditions.

1 INTRODUCTION

Composite materials have been widely used in structural engineering to strengthen and upgrade existing concrete or masonry structures. Among others, fabric reinforced cementitious composites are gradually substituting the use of fiber reinforced polymers (FRPs) in the construction industry. This is mainly due to a better performance of FRCM composites in terms of durability and a higher compatibility with concrete and masonry substrates, because they replace the use of polymeric resins as a binding phase in favor of cementitious matrices, suitably added with substances aimed at improving their interaction with the resistant phase and support (Papanicolaou et al. 2008, Harajli et al. 2010). The cement-based matrix of the composites offers some advantages in comparison with the epoxy-based matrix of FRPs such as: easier application, especially onto rough and irregular surfaces like in old masonry (Mazzotti et al. 2015) or concrete construction, better bond behavior at high temperatures (Tetta & Bournas 2016, Raoof & Bournas 2017) and higher physical and chemical compatibility with the concrete or masonry substrate (Donnini & Corinaldesi 2017).

The beneficial effects from these features compensate the lower effectiveness of cementitious composites than FRPs (Donnini et al. 2019). Confinement of axially loaded concrete columns through FRCM jacketing is one of the main applications of the composite. Bournas et al. (2007) compared the confinement effectiveness of FRP and FRCM composites on small scale concrete specimens. Toska & Faleschini (2021) experimentally investigated the effect of cyclic loading and of different bonding conditions on the confinement effectiveness of FRCM composites (Toska et al. 2023). The ability to enhance seismic performance of FRCM jacketing was also experimentally investigated for undamaged and damaged reinforced concrete columns subject to cyclic horizontal loading (Bournas et al. 2009, Toska et al. 2022).

However, cementitious composites are relatively recent and further research is still needed to understand their behavior. One of the still little studied aspects concerns the effect of high temperatures on the behavior of composites and the effectiveness of the interventions in which these materials are applied when exposed to high thermal stresses. Some researchers have compared the loss of strength of FRCM or TRM cementitious composites with those of FRP ones by means of tensile tests on specimens conditioned to thermal stress (Donnini et al. 2017, Messori et al. 2019). As expected, the results show a clear better resistance to high temperatures for the FRCM composites although, after a certain temperature, a decreasing trend in the tensile strength of the tested specimens is observed as the temperature increases. Recently, Kapsalis et al. (2021) published an extensive review on experimental investigations dealing with the behavior of textile reinforced concrete subjected to high temperatures. The same authors later on investigated the performance of textile-reinforced concrete after fire exposure (Kapsalis et al. 2022). TRC specimens with various reinforcement (carbon or glass fibers, uncoated or coated textiles) were casted and subjected to temperatures up to 700°C. The residual tensile capacity of the exposed specimens is analyzed and the results showed that the use of uncoated carbon fibers is the most promising solution to maintain a high residual capacity after fire exposure.

Regarding the behavior con FRCM-confined concrete under high temperature, Trapko (2013) investigated the effectiveness of confinement using FRCM composites in comparison to those confined through FRPs when subject to high temperatures. However, the investigated temperature range varies only from 40 °C to 80 °C. Ombres et al. (2021) investigated confinement through PBO-FRCM composites subject to temperatures ranging between 20 °C and 200 °C. The test results evidenced that the thermal conditioning affected both the mechanical properties of the FRCM materials and the effectiveness of the concrete confinement.

In this context, the present study investigates the performance of FRCM confined concrete subject to temperatures varying from ambient to 250 °C. Cylindrical specimens were confined with two types of FRCM jackets that differ from the carbon fabric applied: dry and epoxy resin coated.

2 EXPERIMENTAL PROTOCOL

2.1 *Materials and specimens*

In the presented experimental campaign, small scale specimens with $b \times h$ dimensions 150 x 300 mm were casted using the same concrete batch. For the FRCM composite, the reinforcement consists in two types of carbon fabric: one in dry condition and the other coated using an epoxy-resin solution. The inorganic matrix consists in a premixed fiber reinforced cementitious mortar with a compressive strength of 25 MPa and flexural strength of 4.8 MPa. All materials were provided by the same manufacturer. The properties of the carbon fiber are shown in Table 1. For the sake of comparison and based on the previous experience of the authors, all specimens were confined using two FRCM layers.

Confinement was applied following always the same protocol. First the concrete specimen was damped with water to avoid water absorption from the FRCM composite, a first layer of mortar (3-4 mm thick) was applied around the cylinder and above it the carbon fabric was wrapped gently pushing it into the matrix. Then a second layer of mortar and then fabric was applied repeating the same procedure. The last layer was covered with the last mortar application. Carbon fabric was applied continuously with a final overlapping length of 200 mm.

Table 1. Properties of carbon fibers.

Fiber type	t_f (mm)	E_f (GPa)	f_f (MPa)	ε_f (%)
Carbon	0.047/0.061	240	4900	1.80



Figure 1. Application of the confining FRCM jacketing on the cylindrical specimens.

After FRCM jacketing application specimens were left curing for at least 90 days and then, before axial compression testing, they were exposed to increasing temperature levels being: 20 °C (ambient), 80 °C, 100 °C, 250 °C. Only specimens confined with coated carbon fibers were exposed to the 80 °C temperature. This aimed to investigate if the epoxy coating would undergo any degradation even for temperatures lower than 100 °C, given the poor behavior of organic matrixes at high temperatures. Specimens features are summarized in Table 2.

Table 2. Specimens' features.

Specimen	D (mm)	l_b (mm)	t_f (mm)	Fabric	T (°C)	Layers
REF	150	-	-	-	20	-
C2_Amb_1	150	200	0.047	Dry	20	2
C2_100_1	150	200	0.047	Dry	100	2
C2_250_1	150	200	0.047	Dry	250	2
2CR_Amb_1	150	200	0.061	Coated (Epoxy Resin)	20	2
2CR_80_1	150	200	0.061	Coated (Epoxy Resin)	80	2
2CR_100_1	150	200	0.061	Coated (Epoxy Resin)	100	2
2CR_250_1	150	200	0.061	Coated (Epoxy Resin)	250	2

2.2 Test setup and loading protocol

After the temperature exposure, specimens were axially loaded adopting a cyclic loading protocol. The tests were carried out using a universal loading machine under displacement control mode. Single compressive cycles were performed using a displacement rate of 0.6 mm/min was used for both loading and unloading paths. To avoid the complete unloading of the specimens and undesired movement of the specimens itself or of the instrumentation a small axial load of about 0.5 MPa was maintained during the unloading cycles. Before loading, both the upper face of the specimens was capped with high-strength mortar to ensure a proper distribution of the axial loading.

The axial load was acquired continuously during the test, using the 600 kN load cell of the universal testing machine. Axial strains were monitored using three linear voltage displacement transducers (LVDTs), that acquired the displacement between the top and bottom plates. LVDTs were installed equally spaced at 120°. Figure 2 shows a reference specimen and the instrumentation disposition during the testing.



Figure 2. Test setup.

3 RESULTS

3.1 Failure modes

Specimens confined with dry and coated carbon fabric showed different crack pattern and failure modes while no significant differences were observed in the crack pattern of the confined specimens when exposed to different temperatures. First, small vertical cracks were observed in the confinement jacket when the axial load was near the initial unconfined strength for all tested specimens. After an initial homogeneous crack distribution, a main crack, generally near the overlapping end, propagates until failure is reached. For specimens confined with epoxy resin coated carbon fabric, the failure was more abrupt and is characterized by wider crack openings and also spalling of the external mortar layer.

3.2 Axial stress-strain behavior: Dry vs resin impregnated carbon fiber

All specimens were tested under a cyclic compression loading protocol, however, for the sake of simplicity, only the envelope curves will be considered in this section. The initial concrete strength was evaluated on two specimens and the unconfined axial stress-strain curves together with the failed specimens after testing are shown in Figure 4. The unconfined compressive strength is 20.6 MPa while the axial strain at peak stress was about 0.36%. At ambient temperature, specimens confined with dry carbon fabric displayed a similar behavior to what previously observed by some of the authors in a previous work (Toska & Faleschini, 2021). The first peak, reached at strain values close to those observed for unconfined concrete, is followed by a slight strength decrease which in turn is followed by a new stress increase or by an almost constant strength until failure. On the other hand, for specimens confined with coated carbon fibers the softening phase was not observed and the stress-strain curves were characterized by a hardening trend until failure. Carbon fabric coated in epoxy-resin performed better both in terms of axial strength and axial strain capacity. For normal ambient temperature this



Figure 3. Final crack pattern for a) C_20_2C, b) C_250_2C, c) C_20_2CR and d) C_250_2CR.

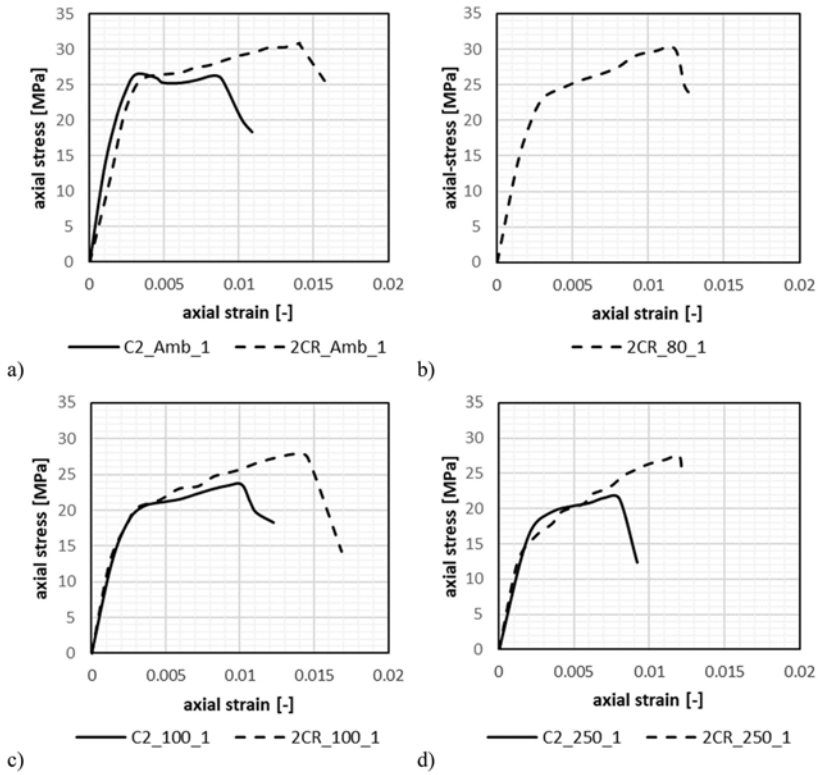


Figure 4. Axial stress-strain curves for specimens confined with dry and pre-impregnated fabrics at different temperature steps: a) ambient, b) 80 °C, c) 100 °C and d) 250 °C.

is in line with what previously observed by some of the authors in (Toska et al. 2023). The better behavior of coated carbon FRCM jacketing, in terms of confined peak strength and strain, surprisingly, was maintained also for the higher temperature steps. Strength enhancement, results about 19%, 17% and 27% more effective for coated cases respectively for ambient, 100 °C and 250 °C. Since specimens are tested after cooling down, investigating their residual capacity, the better performance of jackets with coated fabrics is believed to be due to melting and re-hardening of the polymeric coating of the fabric that results in a better fiber-matrix bond. Similar behavior was observed also on pullout test by de Andrade Silva et al. (2014) for temperatures up to 200 °C.

3.3 Influence of high temperature

Figure 5 Compares axial stress-strain curves for confined concrete through FRCM composite with dry carbon fabric. Both curves, for specimens exposed at 100 °C and 250 °C, result significantly different from the one for ambient temperature. The effect of high temperature is significant already at 100 °C. Strength enhancement at the first peak (at axial strain near to that of unconfined concrete), that is very clear and significant for specimens at ambient temperature, is not present after high temperature exposure. Confined strength results 26.4 MPa for ambient temperature specimens, 23.5 MPa after 100 °C exposure and 21.4 MPa after 250 °C exposure. Ultimate axial strain at 100 °C is about 1%, resulting slightly higher than at ambient temperature (about 0.9%) and at 250 °C (about 0.8%).

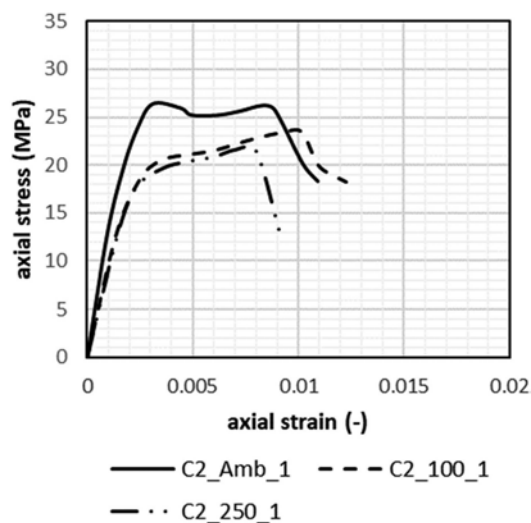


Figure 5. Axial stress-strain curves for specimens confined with dry carbon fabric.

Specimens confined with coated carbon fabric also experienced a significant performance reduction when exposed to high temperatures. Confined peak strength decreased from 30.7 MPa at ambient temperature to 27.5 MPa after 250 °C exposure. At 80 °C, strength remained similar to the unconditioned one (about 30 MPa), while at 100 °C peak strength was almost the same as the one recorded at 250 °C (about 28 MPa). The ultimate axial strain capacity remained relatively high, varying between 1.2% and 1.4%. Even though peak strength degradation was low (about 10%), axial stress-strain curves (Figure 6) differ significantly for the different temperature steps. As observed for the dry-fabric cases, strength enhancement at the first peak (following the first branch of the stress-strain curve) is gradually reduced as temperature gets higher, moving the inflection point of the hardening branch lower for each step.

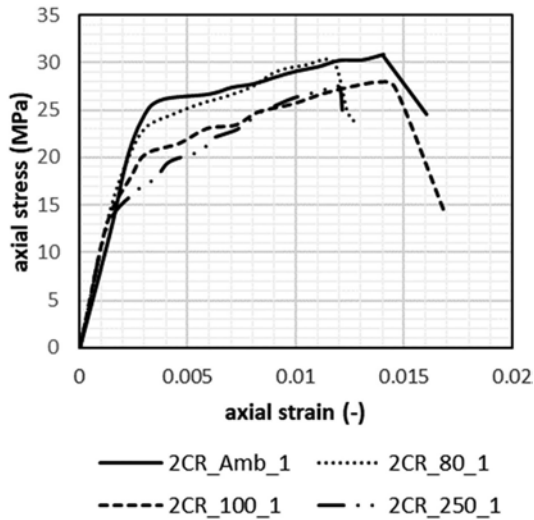


Figure 6. Axial stress-strain curves for specimens confined with coated carbon fabric.

4 CONCLUSIONS

The present work investigates the behavior of FRCM confined concrete when exposed to high temperatures. Small scale cylindrical concrete specimens were casted and confined using two types of carbon FRCM composites, that differ on the initial treatment of the fabric: dry and epoxy resin coated were tested. After 90 days of curing from the jacketing application, specimens were exposed to increasing temperature steps: 20 °C (ambient), 80 °C, 100 °C and 250 °C. After cooling down, the specimens were tested under compressive cyclic behavior to investigate their residual strength and strain capacity. Results show a significant change in the axial stress-strain behavior after high temperature exposure. Epoxy coated FRCM jackets performed better than dry ones at all temperature steps, both in terms of strength enhancement and axial strain capacity. Between ambient and maximum considered temperature (i.e. 250 °C), 19% strength reduction was observed for dry carbon FRCM while only 10% for coated ones.

REFERENCES

- Bournas, D. A., Lontou, P. V., Papanicolaou, C. G., & Triantafillou, T. C. (2007). Textile-reinforced mortar versus fiber-reinforced polymer confinement in reinforced concrete columns. *ACI Structural Journal*, 104(6), 740.
- Bournas, D. A., Triantafillou, T. C., Zygouris, K., & Stavropoulos, F. (2009). Textile-reinforced mortar (TRM) versus FRP jacketing in seismic retrofitting of RC columns with continuous or lap-spliced deformed bars. *J. Compos. Constr.*, 13(5), 360–371.
- de Andrade Silva, F., Butler, M., Hempel, S., Toledo Filho, R. D., & Mechtcherine, V. (2014). Effects of elevated temperatures on the interface properties of carbon textile-reinforced concrete. *Cement and Concrete Composites*, 48, 26–34.
- Donnini, J., y Basalo, F. D. C., Corinaldesi, V., Lancioni, G., & Nanni, A. (2017). Fabric-reinforced cementitious matrix behavior at high-temperature: Experimental and numerical results. *Composites Part B: Engineering*, 108, 108–121.
- Donnini J, Corinaldesi V. (2017) Mechanical characterization of different FRCM systems for structural reinforcement. *Constr Build Mater*;145:565–75.
- Donnini, J., Spagnuolo, S., & Corinaldesi, V. (2019). A comparison between the use of FRP, FRCM and HPM for concrete confinement. *Composites Part B: Engineering*, 160, 586–594.
- Harajli M., ElKhatib H., San-Jose J.T. (2010) Static and cyclic out-of-plane response of masonry walls strengthened using textile-mortar system. *Journal of Materials in Civil Engineering*, 22(11), pp. 1171–1180.

- Kapsalis, P., Triantafillou, T., Korda, E., Van Hemelrijck, D., & Tysmans, T. (2022). Tensile Performance of Textile-Reinforced Concrete after Fire Exposure: Experimental Investigation and Analytical Approach. *Journal of Composites for Construction*, 26(1), 04021067.
- Kapsalis, P., Tysmans, T., Van Hemelrijck, D., & Triantafillou, T. (2021). State-of-the-Art Review on Experimental Investigations of Textile-Reinforced Concrete Exposed to High Temperatures. *Journal of Composites Science*, 5(11), 290.
- Mazzotti C, Ferracuti B, Bellini A. (2015) Experimental bond tests on masonry panels strengthened by FRP. *Compos B Eng*;80:223–37.
- Messori, M., Nobili, A., Signorini, C., & Sola, A. (2019). Effect of high temperature exposure on epoxy-coated glass textile reinforced mortar (GTRM) composites. *Construction and Building Materials*, 212, 765–774.
- Ombres, L., Mazza, P., & Verre, S. (2021). Effects of Thermal Conditioning at High Temperatures on the Response of Concrete Elements Confined with a PBO-FRCM Composite System. *Journal of Materials in Civil Engineering*, 34(1), 04021413.
- Papanicolaou C.G., Triantafillou T.C., Papathanasiou M., Karlos K. (2008) Textile reinforced mortar (TRM) versus FRP as strengthening material of URM walls: Out-of-plane cyclic loading. *Materials and Structures*, 41(1), pp. 143–157.
- Raof SM, Bournas DA. (2017) Bond between TRM versus FRP composites and concrete at high temperatures. *Compos B Eng*;127:150–65.
- Tetta ZC, Bournas DA. (2016) TRM vs FRP jacketing in shear strengthening of concrete members subjected to high temperatures. *Compos B Eng*;106:190–205.
- Toska, K., & Faleschini, F. (2021). FRCM-confined concrete: monotonic vs. cyclic axial loading. *Composite Structures*, 268, 113931.
- Toska, K., Faleschini, F., Zanini, M. A., (2023). Confinement of concrete with FRCM: influence of bond aspects and cyclic loading. *Construction and Building Materials*, (accepted).
- Toska, K., Hofer, L., Faleschini, F., Zanini, M. A., & Pellegrino, C. (2022). Seismic behavior of damaged RC columns repaired with FRCM composites. *Engineering Structures*, 262, 114339.
- Trapko, T. (2013). The effect of high temperature on the performance of CFRP and FRCM confined concrete elements. *Composites Part B: Engineering*, 54, 138–145.

Retrofit of RC bridge half-joints: Applications and remarks with emphasis on post-tension techniques

G. Santarsiero, V. Picciano, A. Masi & G. Ventura
School of Engineering – University of Basilicata, Potenza, Italy

ABSTRACT: Due to their advantages, many reinforced concrete road bridges were built according to the Gerber scheme in which the so-called half-joints represent a key structural component. Besides their advantages, some drawbacks can be found in this type of bridge, mainly related to the deterioration process of the half-joints that leads to reinforcement corrosion and consequent concrete cracking and spalling. Therefore, many bridges may need over time specific retrofit interventions to guarantee the required level of safety. This paper first describes the retrofit techniques currently available in the literature. Numerical simulations are then carried out to investigate the effectiveness of a specific technique based on post-tensioning. Refined nonlinear finite element models were used to characterize the post-tension effects on the load-bearing capacity of a case study half-joint also in presence of simulated chloride-induced corrosion, and to outline the optimal prestress level to be used to obtain the wanted performance improvements.

1 INTRODUCTION

In the past, the Gerber scheme was widely used for the construction of reinforced concrete road bridges due to its advantages in terms of both stress distribution and the related statically determinate conditions. According to this scheme, the cantilever and the simply supported spans are connected to each other through the so-called half-joints, which represent a key component of these bridges (Kun et al. 2015).

Despite the advantages, a frequent problem related to this kind of bridge is the malfunctioning of drains, which causes seepage across expansion joints (Lee 1994). In particular environmental conditions, the presence of chloride ions may enhance the degradation phenomena leading to reinforcement corrosion and consequent cracking and spalling of concrete (Gjørøv 2009), especially in the cantilever part (Figure 1).

Another issue is related to the very narrow space in correspondence with the joints' position, which causes difficulties in inspections leading to incorrect quantification of degradation (Desnerck et al. 2018). In the literature, two cases of bridges' collapse are related to the half-joint failure. The first is the de la Concorde overpass collapse in 2006, a bridge situated in Laval (Canada). The other case is related to the Gerber bridge overpass in Annone Brianza (Italy), which collapsed in 2016 following the passage of a 108-ton truck. In both cases, the deterioration of the half-joints and damage already present on the bridge coupled with some design and construction flaws were responsible for the collapse (Mitchell et al. 2011, Di Prisco et al. 2018).

For this reason, the assessment of these structural components, also accounting for degradation modelling, coupled with rehabilitation, through careful planning and design of the interventions by the bridge owners and practitioners, are crucial, in order to increase their structural performance and therefore to extend the lifespan of bridges.

To this end, this paper first reports a brief review of the currently available intervention techniques for bridge half-joints, accounting for both previous experimental studies in the literature and interventions carried out on existing bridges. Through the analysis of each technique's main advantages and disadvantages, it is possible to identify the one which results the

least disruptive and expensive and the most easily applicable. This is the post-tension technique, based on the use of external high-strength post-tensioned rods, which are restrained on the top and the bottom of half-joint's surfaces through steel plates.

Therefore, the paper presents an application of this technique to half-joints of a case study bridge, the Musmeci bridge in Italy (e.g. Marmo et al. 2019), in which, through nonlinear numerical simulations, the performance improvements at both serviceability and ultimate limit state have been evaluated, accounting for the variation of the prestress applied and also considering the presence of different chloride-induced corrosion scenarios.



Figure 1. Degradation of an RC bridge's half-joint: a) view from the intrados and b) bridge scheme and viewpoint.

2 REVIEW OF THE AVAILABLE RETROFIT OPTIONS FOR HALF-JOINTS

When it comes to bridge half-joints, there can be several reasons for which repair or strengthening interventions are needed: increased traffic loads compared to the time of design and consequent increase in strength demands; decrease in concrete and reinforcement's strength due to the accumulation of decay; the presence of widespread cracks which may cause a loss of serviceability or, in extreme cases, the collapse of the structure. As a result, researchers have developed and studied different techniques to account for all these aspects.

In the literature, there are techniques developed and tested on the half-joints properly belonging to bridge structures, and techniques more suitable for dapped-end beams often used on the roofs of industrial buildings or in the floor systems of buildings used for parking or otherwise prefabricated. In addition, the various techniques differ from each other in the particular materials used, in the different performance objectives, or even in the different installation configurations taking into account the geometry of the structural element at hand.

Among the available retrofitting techniques, a rather invasive intervention consists of joining the cantilever and suspended span in such a way as to completely change the bridge's statically determined scheme to one of a continuous bridge. This intervention has been developed and patented by Fukuoka (1999) and the connection is made through the use of horizontal high-strength steel bars restrained to the existing concrete of the half-joints. In addition to being very invasive, the intervention is also very costly since new bearings must be placed on the piers to allow the absorption of thermal expansions.

On the other hand, a non-invasive and easy technique consists of the use of high-strength post-tensioned bars installed along the undapped part of the half-joints in a vertical or inclined direction, in order to increase the load-bearing capacity of the half-joint. The only installation operation consists of drilling holes on the side of the joints, through the curb or transverse beam, if present, for the positioning of the bars (Figure 2). Such an intervention was carried out on the existing Scafa bridge located in Fiumicino (Italy) (Alessandrini & Burba 1994) and the PRC Gerber bridge on the Po River near the town of Pieve Porto Morone (Italy) (Di Prisco 2019).

The main objective of this technique is to provide an increase in the load-bearing capacity of the half-joint and, in addition, the prestressing action also favours the limitation of cracks during service conditions. In order to quantify the performance gains offered by the technique, Atta & Taman (2016) carried out an experimental tests campaign on Gerber beams in which the post-tensioned bars were installed in different configurations and positions. In particular, they

showed that the three configurations illustrated in Figure 2 exhibited improved behaviour by providing strength gains of 81%, 65%, and 83%, respectively, with respect to the beam without intervention.

A technique able to intervene on the deteriorated concrete of the half-joint, provide an increase in strength and, at the same time, provide protection against long-term degrading agents consists in the realisation of a steel jacketing system bonded to the lateral surfaces of the half-joint through the use of transversal bars. Such an intervention was carried out on the Generale Franco Romano viaduct in the Piedmont region (Italy) (Lafranconi et al. 2018). The increase in load-bearing capacity can be provided by the installation of post-tensioned vertical bars restrained above and below the saddle, as shown in Figure 3a. The only disadvantage of the technique is that the intervention is mainly carried out along the lateral surfaces of the half-joints, which are not always accessible due to the presence of a connection curb or the transverse beam connecting the deck's girders.

Finally, there are techniques in the literature based on the use of composite materials in the form of plates, laminates or fabrics bonded externally to the surfaces of the half-joints (Figure 3b). The most commonly used solutions are carbon fibre-reinforced polymer (CFRP) or fibre-reinforced polymer (FRP). The advantage of these materials lies primarily in their ability to provide strength improvements while occupying very small volumes, which makes them suitable for Gerber saddles. Some authors have tested the performance of these materials by carrying out experimental campaigns on dapped-end beams used in precast buildings. In particular, Taher (2005) analysed the performance of different configurations of CFRP laminates, differing in the inclination of the laminates with respect to the beam axis or in the installation position, obtaining an increase in strength in the range of 17-42%. Nagy-György et al. (2012) performed experimental tests using FRP plates or fibres in different configurations, obtaining that the highest performance was provided using a combination of vertical and inclined fibres. The disadvantage of using composite materials is mainly related to their excessive cost. Furthermore, the application of materials on the side surfaces of the half-joints is not always permitted due to the structural constraints mentioned above.

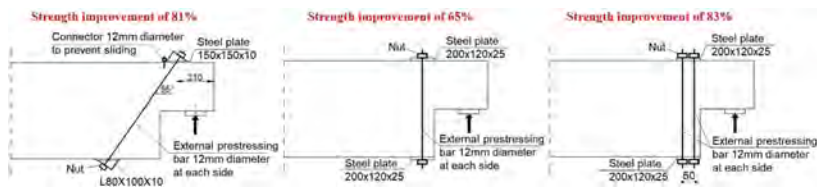


Figure 2. The most performed post-tensioned solutions tested by Atta & Taman (2016).

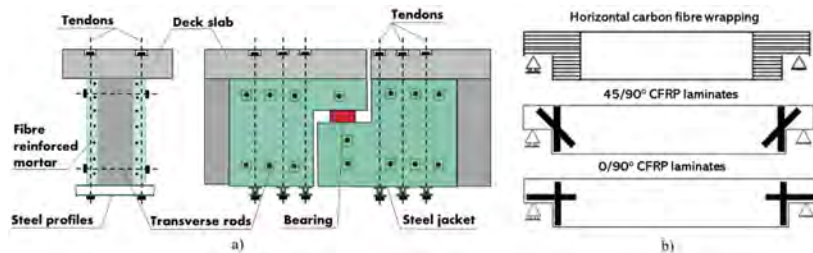


Figure 3. a) Schematic view of the jacketing system, adapted from Lafranconi et al. (2018) and b) different configurations of externally bonded composites (Taher 2005, Nagy-György et al. 2012).

2.1 Remarks on the choice of the optimal intervention

If we want to compare the techniques described above, in addition to the advantages and disadvantages of each one, we have to analyse further aspects related mainly to the construction in place. In particular, Santarsiero et al. (2023) compared the techniques taking into account

several aspects: the construction costs; the disruption caused to the bridge and road traffic; the need to lift the suspended span; the need to carry out repair work before the actual intervention; and, finally, also considering the performance improvement by comparing the half-joints' failure modes before and after the intervention.

What emerges is that the techniques which require the lifting of the suspended span (i.e. jacketing and application of composites) are the most expensive and disruptive. In contrast, the post-tensioning technique is the least invasive, the most economical and adaptable to the different geometric configurations present in existing bridges.

In fact, in the majority of cases, the deck of a Gerber bridge is in the configuration illustrated in Figure 4, in which the girders are connected by a transverse beam and/or a curb at the dapped-ends. This configuration impedes the realisation of all those techniques which work on the lateral surfaces of the beams. Therefore, it is very important to assess the feasibility of an intervention, i.e. its applicability in reality, when one is called upon to choose between different types.

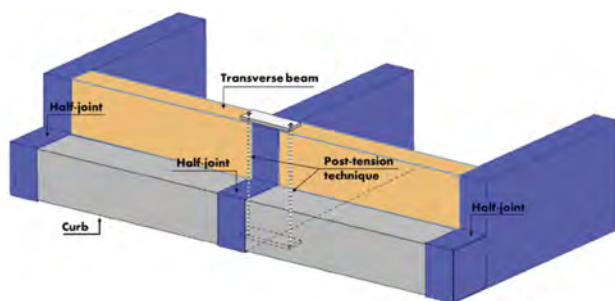


Figure 4. Typical Gerber bridge deck configuration and applicability of the post-tension intervention technique.

3 POST-TENSION TECHNIQUE: NUMERICAL SIMULATION

In order to deepen and quantitatively evaluate the performance improvements provided by the post-tension technique, this section describes a numerical simulation carried out by nonlinear finite element analyses. The intervention is applied on a half-joint belonging to the bridge on the Basento river in Potenza (Italy), carefully described in previous articles (Santarsiero et al. 2021, Marmo et al. 2019), designed by Sergio Musmeci matching older codes (Circolare n. 384 del 1962). It is worth reminding that the bridge's RC box deck is 16 m wide and supported by the vault every 17.30 m for a total length of 300 m. Moreover, the deck is provided with suspended spans (10.38 m long) connected by half-joints which are shown in detail in Figure 5a.

Numerical simulations were carried out using the finite element software ATENA (Červenka et al. 2021), which is able to accurately reproduce the reinforced concrete structures' behaviour according to the nonlinear fracture mechanics theory (Bazant & Oh 1983). In particular, it is possible to simulate the nonlinear behaviour of concrete both in compression (crushing) and in tension (cracking). Further details on the constitutive models used are provided in a previous article by Santarsiero et al. (2021). The main results of the numerical simulations are here briefly summarized as they are widely described in Santarsiero & Picciano (2023).

Figure 5b shows the FEM model of the studied half-joint in the presence of intervention. Within the analyses, the presence of degraded conditions due to chloride-induced corrosion was also simulated. In fact, the software makes it possible to simulate the chloride ions ingress into the concrete and the initiation and propagation of reinforcement corrosion through a refined mechano-chemical model (Červenka et al. 2017), which takes into account the acceleration of the phenomenon induced by the presence of concrete cracks caused by the loads acting on the half-joint.

In particular, the model is based on the 1D chlorides diffusion process within the concrete, modelled through Fick's second law (Zhang et al. 2010) accounting for three fundamental

parameters: the surface chlorides concentration C_s (as % of cement mass), the chloride diffusion coefficient D_{ref} (m^2/s) and the critical chloride content C_{crit} (as % of cement mass).

In the previous study by Santarsiero et al. (2021), the significance of the three parameters was investigated in detail and, in particular, analyses were carried out with different combinations of their values in order to identify the one which produces the worst effects in terms of corrosion and loss of bearing capacity.

Therefore, in this study, in order to analyse the ability of the post-tension-based intervention to improve the condition of a severely degraded half-joint, a triad of values was deterministically selected based on literature data (Angst 2019, Bertolini et al. 2004, Hájková et al. 2018, Van der Wegen et al. 2012) relating to aggressive environmental conditions concerning road bridges in harsh climates exposed to de-icing salts.

Evaluating the nonlinear concrete and steel behaviour, the design strength values calculated according to the Italian Guidelines (Ministry of Infrastructure, CSLP 2020) were used. The design strength of the analysed concrete structure is $f_{cd} = -17.24$ MPa (Santarsiero & Picciano 2023). As a function of the latter value, the other material properties required for the numerical simulations were calculated. In particular, $f_{ctd} = 1.59$ MPa, $E = 29,253.88$ MPa and $GF = 1.31E-4$ MN/m (Fib, Fédération Internationale du Béton 2010).

Similarly, the reinforcement properties were calculated: the design yielding stress is the same as the characteristic one $f_{yd} = f_{yk} = 375$ MPa, as the former can be obtained by the ratio between the latter and the maximum value of confidence factor, $CF = 1$, depending on the achieved knowledge level (Ministry of Infrastructure 2018); the failure stress is equal to $f_{td} = 460$ MPa and the failure strain ε_t is set to 18%.

As for the intervention, this is carried out according to configuration No. 2 tested by Atta & Taman (2016) (illustrated in the central scheme of Figure 2), through the use of two external 26.5 mm diameter high-strength Dywidag-type steel bars, equipped with corrosion protection system, with yielding stress $f_y = 950$ MPa and failure stress $f_t = 1050$ MPa. The bars were restrained at the top and bottom (Figure 5b) through two S275JR ordinary steel plates (EN 1993-1-1 2005, Ministry of Infrastructure 2018) 500 mm wide, 150 mm long and 100 mm thick.

11 analyses were performed taking into account the variability of two parameters in particular: the corrosion period (t_{corr}) and the prestress value applied to the external bars (σ_p). With regard to the first parameter, a corrosion period of 45 years was considered, which would correspond to the current state of the bridge taking into account that it was completed just 45 years ago; and a period of 95 years, in order to assess the effect of the intervention following a further 50 years of corrosion. Concerning the second analysis parameter, the prestress value was varied in terms of percentages with respect to the yield strength of the external bars, considering the following four cases: $0.05f_y$, $0.15f_y$, $0.30f_y$, $0.40f_y$.

Ultimately, the following analysis intervals can be distinguished in each of the performed analyses: a first interval, identical to all the analyses, in which the half-joint is loaded by the vertical reaction, at the intermediate point of the nib, equal to 270 kN (relative to the permanent structural and non-structural loads transferred by the suspended span); a second interval in which the chlorides ingress, which is a function of the cracks generated in the previous interval, and the effects in terms of corrosion and consequent load-bearing capacity reduction are simulated, accounting for the two selected periods; a third interval in which the post-tension intervention is made active by applying the selected prestress values in the external bars; and, finally, a last interval in which, through a displacement control analysis, the half-joint is brought to failure to assess the ultimate capacity P_u .

4 ANALYSIS OF RESULTS

This section describes the main results of the performed numerical analyses, referring to the recent work by Santarsiero & Picciano (2023) for a more in-depth discussion. In particular, the performance of the post-tension intervention was analysed at both the serviceability (SLS) and ultimate limit state (ULS) as a function of the applied prestressing.

Concerning the performance improvements at SLS, the cracking load P_c was monitored for each of the analyses. The latter represents the load at which a limit crack width of 0.20 mm is

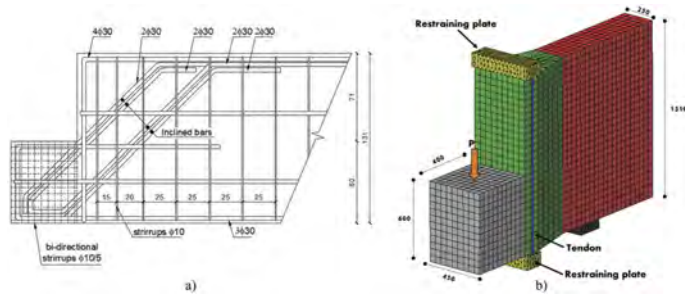


Figure 5. a) Musmeci bridge's half-joints (dimension in cm) and b) FEM model (dimension in mm).

reached as reported within the current codes (Ministry of Infrastructure 2018, EN 1992-1-1 2004) depending on the aggressiveness of the environment and the corrosion sensitivity of the reinforcement bars. As shown in Figure 6a, the cracking load of retrofitted models increases, with respect to the as-built corroded ones, with an almost linear trend as the prestress in the bars increases. In particular, there is a significant enhancement for prestressing values of $0.15f_y$ or more. Furthermore, ΔP_c values are greater for analyses with 95 years of corrosion than for those considering 45 years, especially for high post-tension values. Ultimately, the half-joint's conditions at the serviceability limit state improve due to the intervention, which reduces the cracks' width and, thus, also limits the ingress of degrading agents.

Figure 6b shows the variation of the ultimate load P_u as a function of the applied post-tension. As can be seen, the load-bearing capacity of the half-joint is not greatly affected by the tendons' prestress, showing a significant improvement even for low post-tension values. Furthermore, a greater increase in P_u is obtained after 45 years of corrosion, with an average ΔP_u equal to 25%, compared to the average increase of 18% in the case of 95 years of corrosion. In fact, in the latter case, the reinforcement is more corroded, limiting the increase in load-bearing capacity offered by the intervention.

Thus, the post-tensioning intervention makes it possible to recover the share of load-bearing capacity lost due to reinforcement corrosion as a result of 95 years of chloride pollution. In fact, the ultimate capacity assumes the same value as the as-built condition, as can be also seen from the load-deflection curves of the retrofitted (coloured-dashed lines) and as-built (black continuous line) models in Figure 7b. In the case of a 45-year corrosion simulation, it provides an increase in performance, which is also higher than that of the as-built condition (Figure 7a).

In order to generalize the results here obtained, the effects of the reinforcement layout were investigated in Santarsiero & Picciano (2023), in which the same analyses were performed considering the absence of the inclined bars depicted in Figure 5a. It has been observed that post-tension interventions are able to provide an even more significant performance enhancement when inclined bars are absent, in terms of both cracking load and ultimate load improvement.

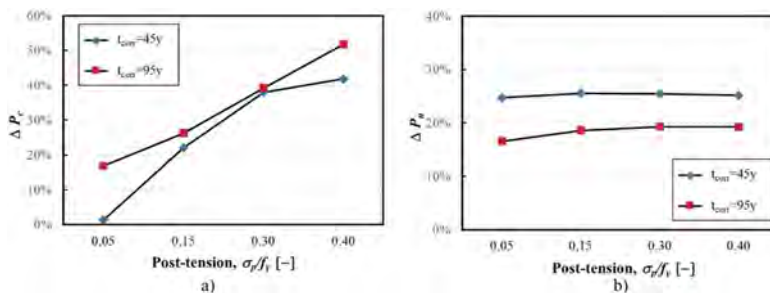


Figure 6. Cracking load (a) and ultimate load (b) improvements for retrofitted models with respect to as-built corroded conditions after 45 and 95 years, as a function of the applied prestress values.

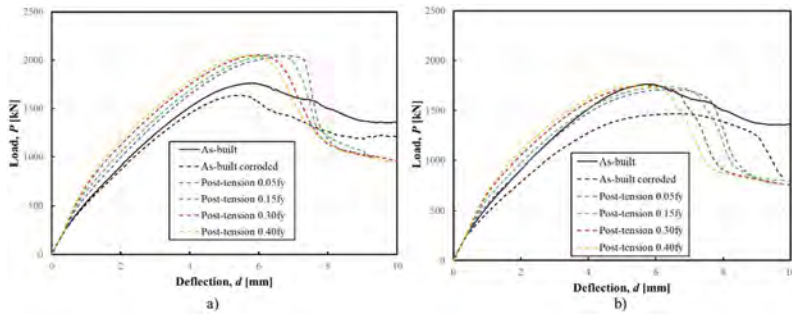


Figure 7. Load-deflection curves of the performed analyses after (a) 45 and (b) 95 years of corrosion.

5 CONCLUSIONS

This paper firstly reports a review of the currently available retrofitting techniques for half-joint bridges, with a specific focus on post-tension techniques, which have a higher ease of application when curb and transverse beams are present close to the bridge half-joints. Hence, post-tension is the most suitable technique to improve the load-bearing capacity of reinforced concrete half-joints. Subsequently, the results of a numerical investigation carried out on an existing bridge half-joint have been described. Results point out the effect of the installation of post-tension rods to improve the serviceability and ultimate capacity, also considering the effect of corrosion due to chlorides. The analyses demonstrated that cracking load values are almost linearly dependent on the prestress values imposed on the rods with a great benefit to durability enhancement due to the smaller crack width in the post-intervention condition. As for the ultimate load capacity, the prestress value shows a lower influence. In fact, also small prestressing values provide a significant increase in the load-bearing capacity. Finally, it has been found that, if the intervention is carried out after 45 years of simulated corrosion, evident advantages in terms of capacity improvement can be obtained, contrarily to what is found intervening after 95 years, when the heavier degradation effects, occurred on steel reinforcement, limit the recovery of load-bearing capacity.

ACKNOWLEDGMENTS

This study was partially developed under the financial support of the Italian Department of Civil Protection, within the ReLUIS-DPC 2022–2024 project (WP5, Task 5.4 “Upgrading and retrofitting interventions of existing bridges”). This support is gratefully acknowledged.

REFERENCES

- Alessandrini, F., & Burba, P. (1994). Il degrado strutturale degli appoggi. *Rassegna tecnica del Friuli-Venezia-Giulia*, *N.4/1994*, Anno XLIV (in Italian).
- Angst, U. M. (2019). Predicting the time to corrosion initiation in reinforced concrete structures exposed to chlorides. *Cement and Concrete Research*, *115*, 559–567.
- Atta, A., & Taman, M. (2016). Innovative method for strengthening dapped-end beams using an external prestressing technique. *Materials and Structures*, *49(8)*, 3005–3019.
- Bazant, Z. P., & Oh, B. H. (1983). Crack Band Theory for Fracture of Concrete. *Materials and Structures*, *16(3)*, 155–177.
- Bertolini, L., Elsener, B., Pedferri, P., Polder, R. B., & Polder, R. (2004). *Corrosion of Steel in Concrete: Prevention, Diagnosis, Repair*. John Wiley & Sons.
- Červenka, J., Hajkova, K., Jendele, L., Sajdlova, T., & Smilauer, V. (2017). Durability assessment of reinforced concrete structures assisted by numerical simulation. *Proceedings of the 71st RILEM Annual Week & ICACMS*.
- Červenka, V., Jendele, L., & Jan Červenka, J. (2021). *ATENA Program Documentation, Part 1, ATENA Theory Manual, 2000-2021*.

- Circolare n. 384 del 1962 del Ministero LL.PP. “Norme relative ai carichi per il calcolo dei ponti stradali” (Ministero dei Lavori Pubblici). (in Italian).
- Desnerck, P., Lees, J. M., Valerio, P., Loudon, N., & Morley, C. T. (2018). Inspection of RC half-joint bridges in England: analysis of current practice. In *Proceedings of the Institution of Civil Engineers-Bridge Engineering* (Vol. 171, No. 4, pp. 290–302). Thomas Telford Ltd.
- Di Prisco, M. (2019). Critical infrastructures in Italy: State of the art, case studies, rational approaches to select the intervention priorities. In *fib Symposium 2019: Concrete-Innovations in Materials, Design and Structures* (pp. 49–58). International Federation for Structural Concrete.
- Di Prisco, M., Colombo, M., Martinelli, P., & Coronelli, D. (2018). The technical causes of the collapse of Annone overpass on SS. 36. In *Italian Concrete Days 2018* (pp. 1–16). ITA.
- EN 1992-1-1 (2004) (English): Eurocode 2: *Design of concrete structures - Part 1-1: General rules and rules for buildings*. Authority: The European Union Per Regulation 305/2011, Directive 98/34/EC, Directive 2004/18/EC].
- EN 1993-1-1 (2005) (English): Eurocode 3: *Design of steel structures - Part 1-1: General rules and rules for buildings* [Authority: The European Union Per Regulation 305/2011, Directive 98/34/EC, Directive 2004/18/EC]
- Fib, Fédération Internationale du Béton. (2010). *Model Code 2010 First Complete Draft*; Fib Bulletin n. 55; Lausanne, Switzerland; Volume 1.
- Fukuoka, K. (1999). *Reinforcing Structure For Henge Section Of Gerber Bridge* (Patent Number: 5,893,187). Unites States patent, Date of Patent: Apr. 13, 1999.
- Gjørv, O. E. (2009). *Durability Design of Concrete Structures in Severe Environments*. Taylor & Francis: London, UK; New York, NY, USA.
- Hájková, K., Šmilauer, V., Jendele, L., & Červenka, J. (2018). Prediction of reinforcement corrosion due to chloride ingress and its effects on serviceability. *Engineering Structures*, 174, 768–777.
- Kun, S., Vogt, R., & Leuenberger, O. (2015). Rehabilitation of reinforced concrete Gerber bridges. *Proceedings of the Third Conference on Smart Monitoring, Assessment and Rehabilitation of Civil Structures, SMAR 2015, Antalya, 7–9 September 2015, Turkey*.
- Lafranconi, L., Massone, G., & Pasqualato, G. (2018). Analysis and rehabilitation of the Generale Franco Romano viaduct. *Italian Concrete Days 2018*, CTE Conference Milano/Lecco 13–16 Giugno 2018.
- Lee, D.J. (1994). *Bridge Bearings and Expansion Joints*. Second edition, G. Maunsell & Partners, Kent UK, 1994.
- Marmo F, Demartino C, Candela G, Sulpizio C, Briseghella B, Spagnuolo R, Xiao Y, Vanzì I, Rosati L. (2019). On the form of the Musmeci’s bridge over the Basento river. *Engineering Structures*, 191, 658–673.
- Ministry of Infrastructure, CSLP. (2020). *Guidelines on Risk Classification and Management, Safety Assessment and Monitoring of Existing Bridges*. Ministry of Infrastructure: Rome, Italy, 2020 (in Italian).
- Ministry of Infrastructure. (2018). *Aggiornamento delle Norme tecniche per le costruzioni*. Ministry of Infrastructure, DM 17 gennaio 2018, Suppl. or. n.30 alla G.U. n.29 del 4/2/2008. (in Italian).
- Mitchell, D., Marchand, J., Croteau, P., & Cook, W. D. (2011). Concorde overpass collapse: structural aspects. *Journal of performance of constructed facilities*, 25(6), 545–553.
- Nagy-György, T., Sas, G., Dăescu, A. C., Barros, J. A., & Stoian, V. (2012). Experimental and numerical assessment of the effectiveness of FRP-based strengthening configurations for dapped-end RC beams. *Engineering structures*, 44, 291–303.
- Santarsiero, G., & Picciano, V. (2023). Durability enhancement of half-joints in RC bridges through external prestressed tendons: The Musmeci Bridge’s case study. *Case Studies in Construction Materials*, 18, e01813.
- Santarsiero, G., Masi, A., & Picciano, V. (2021). Durability of Gerber saddles in RC bridges: Analyses and applications (Musmeci Bridge, Italy). *Infrastructures*, 6(2), 25.
- Santarsiero, G., Picciano, V., Masi, A. (2023). Structural rehabilitation of half-joints in RC bridges: a state-of-the-art review. Submitted to *Structure and Infrastructure Engineering*.
- Taher, S. D. (2005). Strengthening of critically designed girders with dapped ends. *Proceedings of the Institution of Civil Engineers-Structures and Buildings*, 158(2), 141–152.
- Van der Wegen, G., Polder, R. B., & van Breugel, K. (2012). Guideline for service life design of structural concrete—a performance based approach with regard to chloride induced corrosion. *Heron*, 57(3), 153–168.
- Zhang, J., Wang, J., & Kong, D. (2010). Chloride diffusivity analysis of existing concrete based on Fick’s second law. *Journal of Wuhan University of Technology-Mater. Sci. Ed.*, 25(1), 142–146.

Enhancing Textile Reinforced Concrete materials by admixing short dispersed fibres

E. Rossi & N. Randl

Carinthia University of Applied Sciences, Spittal, Austria

ABSTRACT: Textile Reinforced Concrete (TRC) is a material consisting of a high-performance fabric embedded in a cementitious matrix. It has been widely studied for new thin-walled structures and strengthening and retrofit applications. The low tensile strength of the cementitious matrix often limits the full utilization of the material. The splitting forces generated by the loaded fabric often result in spalling of the cementitious matrix with consequent loss of functionality of the material. This problem can be overcome by admixing short dispersed fibres in the cementitious matrix. The resulting material is named Fibre/Textile Reinforced Concrete (F/TRC). An overview of the state of the art on experimental tests that highlight the difference in performance between F/TRC and TRC materials is presented. It can be seen that short dispersed fibres play a fundamental role in achieving higher performances. The results highlight how they influence the failure mode, the crack pattern, and the stress transfer.

1 INTRODUCTION

Textile Reinforced Concrete (TRC) is a relatively new layered concrete composite material consisting of high performance fabrics, generally made of carbon, AR-glass, basalt, or synthetic fibres, embedded in a fine-grained cementitious matrix. This material is often addressed also as Textile Reinforced Mortar (TRM) or Fabric Reinforced Cementitious Matrix (FRCM). It has been used to produce thin walled elements both for structural and non-structural use (Hegger & Voss 2008, Botelho Goliath et al 2021), and for structural strengthening applications (Nobili & Falope, 2017, Koutas et al. 2019, Adam et al. 2020). The success of TRC as a strengthening material has to be sought in its high compatibility with concrete and masonry substrates, and to the capability of overcoming some of the limitations of more traditional FRP applications, such as poor behaviour on wet surfaces and at high temperatures.

The relatively brittle nature of the matrix used to produce TRC can however result in premature failure, thus preventing a full utilization of the high-strength fabrics. This phenomenon is particularly evident in the case of splitting or splitting-related failure of TRC elements. It is a consequence of the stress transfer between the fabric's rovings and the surrounding cementitious matrix and is enhanced by the variable geometry of the rovings themselves and the reduced concrete cover (Preinstorfer & Kollegger 2020, Preinstorfer & Kromoser 2020, Tekle et al. 2021, Beßling & Orlowsky 2022). The same phenomenon, i.e. splitting of concrete, is a limiting factor for the full utilization of the anchored material's strength whenever the end anchorage of a reinforcing bar, cast-in (García-Taengua et al. 2014) or post-installed (Randl & Kunz 2014), has to be designed for small concrete covers. An effective way to overcome such limitation in TRC applications consists in the introduction of short dispersed fibres in the cementitious matrix, thus increasing its tensile properties. The resulting material, named Fibre/Textile Reinforced Concrete (F/TRC) (Rossi et al. 2021b), is able to exhibit strongly improved performances both at the material level and structural level (Barhum & Mechtcherine 2013; Dong et al. 2020, 2021, Dinh et al. 2021). The present article summarises some of the results of the CON_FIT

project and discusses the enhanced properties of F/TRC against more traditional TRC, both at the material level, through experimental testing of small TRC and F/TRC specimens, and at structural level, when these materials are used for strengthening purposes. The focus will be on two main aspects: change in the failure mode, which generally results in a better utilization of the high performance fabrics and change in the crack pattern, which can significantly orient design choices at Serviceability Limit States (SLS).

2 CHANGE IN FAILURE MODE

The most noticeable effect of the introduction of short dispersed fibres in the cementitious matrix of TRC is the change in failure mode. The increased tensile properties of the matrix are able to absorb the tensile stresses generated by the splitting forces, ultimately leading to a change in the failure mode and, consequently, higher performances of the material. At the material level, this was observed on tensile tests performed on lap-spliced textiles (Rossi et al., 2021c). The tested specimens consisted of Ultra High Performance Concrete (UHPC) internally reinforced with fully epoxy-impregnated carbon textiles. The textile was arranged in order to have a connection between the top and bottom parts of the plates through the overlap of two rovings. Furthermore, a notch was cut in the plate, around the lap-spliced connection, to force the first crack to appear in that specific region. While several different geometries were tested, the comparison between TRC and F/TRC was performed on asymmetric configurations with an overlapping length of 100 mm. The F/TRC was produced admixing 2 vol% of steel fibres having a length of 5 mm and a diameter of 0.15 mm (aspect ratio: 33.3). As can be seen in Figure 1, the splitting failure of the TRC specimen caused the loss of the concrete cover over the overlapped textile. The F/TRC specimen, instead, failed by textile pull-out. This, in turn, resulted in a higher load carrying capacity of the F/TRC specimens which failed,



Figure 1. Comparison of TRC and F/TRC failure modes in lap splice tests.

on average, at a load of 21.7 kN, compared to the TRC specimens, which failed on average at 14.4 kN.

A similar behaviour was also observed when TRC and F/TRC solutions were used to strengthen Reinforced Concrete (RC) beams in bending (Rossi et al. 2021b) and in shear (Rossi et al., 2022). In the case of strengthening in bending, RC beams having a cross section of 220x450 mm and a length of 2.5 m were strengthened in the tensile zone using a carbon textile fabric embedded in different cementitious matrices and using different typologies and arrangements of mechanical anchoring solutions. The direct comparison of TRC and F/TRC consisted of a single textile layer embedded in a UHPC matrix and without the use of mechanical anchorage devices. The F/TRC was made admixing 2.5 vol% of the same steel fibres mentioned in the previous case. In this case, both specimens failed due to rupture of the textile, thus achieving similar performances. Nevertheless, the F/TRC-strengthened element showed a slightly higher maximum load carrying capacity (370.5 kN) than its TRC-strengthened counterpart (362.1 kN). Also the failure mode was somehow different; while the F/TRC strengthened specimen showed rupture of the textile in a single longitudinal position, the TRC counterpart exhibited rupture of the rovings in different locations accompanied by a substantial loss of the UHPC cover in a rather diffuse area (Figure 2 left).

In the case of shear strengthening, the effect of short dispersed fibres is even more evident. In that context, one should note that apart from the other mentioned effects of adding fibers, they also contribute strongly to the shear resistance of a high strength concrete materials (Randl et al. 2018), which applies also to layers of new concrete subsequently attached to the web. The specimen consisted of 6.3 m long RC T-beams with a 220x450 mm web and a flange of 600x150 mm. The shear reinforcement, in the form of closed Ø10 stirrups spaced at 100 mm along the whole length of the beam in the flange. The same diameter and spacing was adopted also in the web but the shear failure zones were cast without stirrups. The shear span was 1.3 m long resulting in a span-to-effective-depth ratio of 3.47. The specimens were strengthened with carbon textile arranged in different configuration and embedded in a pre-mixed HPC matrix. The F/TRC strengthening elements were prepared as in the case of the bending beams i.e., 2.5 vol% of short steel fibres. The comparison of the TRC and F/TRC strengthening solutions was performed on a 2-layer side bonded setup. The TRC strengthening solution failed due to interlaminar shearing i.e., formation of a planar crack along the plane of the textile, at a load of 397.9 kN, while the F/TRC solution failed due to debonding at a load of 518.7 kN. The two different failure modes are visible in Figure 2 right.



Figure 2. Comparison of TRC and F/TRC strengthening solutions failure modes in flexural (left) and shear (right) beam tests.

3 CRACK PATTERN

The presence of short dispersed fibres in F/TRC materials and F/TRC-strengthened elements plays also a role in the resulting crack pattern. Mészöly et al. (2020) performed a study on the behaviour of TRC and F/TRC plates in bending. The plates were prepared using a UHPC matrix reinforced either with AR-glass or carbon. The F/TRC was produced using 2 vol% of steel fibres having a length of 15 mm and a diameter of 0.2 mm. The results of the tests showed the superior performances of F/TRC which exhibited a higher cracking load, as well as reduced crack opening combined with a more diffuse crack pattern (Figure 3).

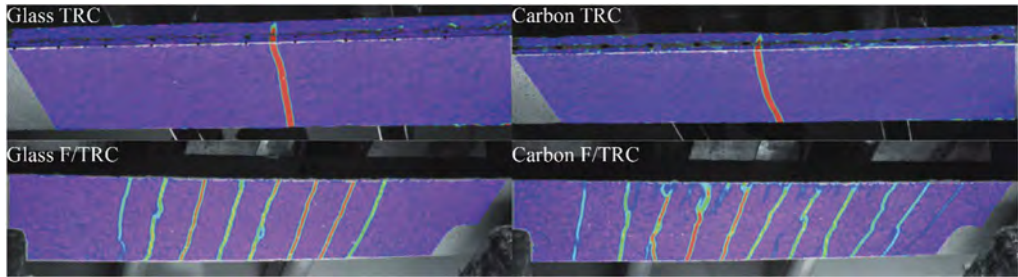


Figure 3. Comparison of the crack patterns of TRC and F/TRC at 1 mm crack opening (modified from Mészöly, Ofner and Randl, 2020).

When this kind of materials are used as strengthening elements, instead, an opposite behaviour can be observed. In a follow-up study on the effect of TRC and F/TRC strengthening elements upon flexural RC beams (Rossi et al 2021a) focused on the evolution of the crack pattern, it was observed that F/TRC strengthening, compared to TRC, would result in an increase in the cracking load for smaller cracks (0.1 – 0.2 mm) but not for larger cracks. Furthermore, before yielding of the longitudinal reinforcement, it would result in an overall reduced number of smaller cracks, while the larger ones tended to be less affected. After reaching the yielding load, instead, the crack opening rate of the TRC-strengthened specimen would strongly increase, while, with F/TRC, it seemed substantially unaffected. The average and maximum crack opening did not show significant differences. Analogous behaviours were observed also when strengthening RC beams in shear and RC column stubs in compression.

In the case of shear strengthening of RC beams (Rossi et al. 2022), the TRC strengthening element exhibited, at the maximum load, a rather diffuse crack pattern characterized by a strong concentration of diagonal cracks spanning from the support to approximately 1/3 of the shear span. Furthermore, subvertical cracks were visible at a regular spacing along the rest of the strengthening layer. The F/TRC strengthened element, instead, showed only limited cracking. Few diagonal cracks were located at approximately 1/3 of the shear span towards the support, and subvertical cracks were barely observable (Figure 4). Thus a more efficient crack control can be achieved compared to other shear strengthening methods (Randl & Harsányi 2018).

Similar results were also observed when TRC and F/TRC were used to strengthen RC columns (Mattarollo et al. 2022). The test specimens consisted of short circular column stubs externally confined with carbon or basalt TRC or F/TRC. The RC column stubs were 675 mm high and had a diameter of 200 mm. The strengthening solutions consisted of a continuous textile sheet, either of carbon or basalt, wrapped around the specimen in a 2-layer configuration and embedded in a HPC matrix. The steel fibres used to produce F/TRC were 5 mm long with a diameter of 0.15 mm and admixed in a 2.5 vol% ratio.

The specimens confined with TRC failed at an average load of 1145 kN and 1177 kN for basalt and carbon, respectively. The crack pattern of these specimens was characterized by the presence of many cracks, most of which were running along the whole height of the specimens. The F/TRC strengthened specimens, instead, failed at an average load of 1353 kN and 1368 kN for basalt and carbon, respectively. In this case the crack pattern featured a reduced

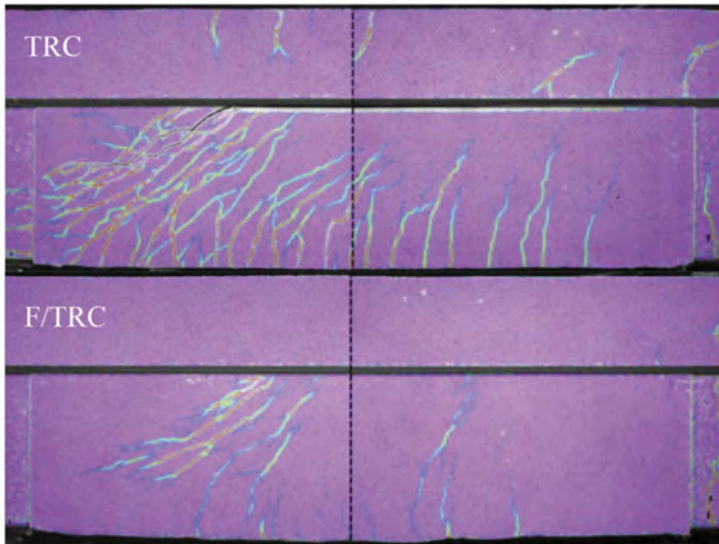


Figure 4. Comparison of the crack patterns of TRC and F/TRC shear strengthening at maximum load (modified from Rossi *et al.*, 2022).

number of cracks, which mostly were running from either the top or bottom of the specimens till approximately the middle. (Figure 5).



Figure 5. Comparison of the crack patterns of carbon TRC and F/TRC used to confine RC columns.

4 CONCLUSIONS

Fibre/Textile Reinforced Concrete (F/TRC) can overcome the limitations of traditional TRC related to its brittle matrix. The admixture of short dispersed fibres improves the tensile behaviour of the cementitious material, thus preventing or strongly limiting undesired phenomena such as premature splitting and interlaminar shearing. This, in turn, affects the failure mode and, consequently the overall performance of these materials enabling a higher utilization of the high-performance reinforcement. Within the CON_FIT project, F/TRC elements were

casted using short steel fibres admixed in High- and Ultra-High- Performance Concretes, and different type of fabrics. Compared to TRC, F/TRC exhibited better performance both as a material and when used to strengthen RC elements. It showed its capability of effectively preventing splitting phenomena, which resulted in more favorable failure modes and, consequently, in higher maximum loads. Furthermore, it had a strong influence on the crack pattern. At the material level it tended to reduce the maximum crack opening and increase the total number of cracks. When used as a strengthening solution, instead, it showed a tendency to reduce the overall number of cracks and increase the cracking load.

ACKNOWLEDGMENTS

This work was supported by the Austrian Research Promotion Agency (FFG) in the framework of the CON_FIT project [grant number 866881]; likewise, the Authors would like to thank the companies solidian GmbH, PAGEL Spezial-Beton GmbH & Co. KG, w&p Beton Holding GmbH, Hitexbau GmbH - Albani Group GmbH & Co. KG, and Kimia S.p.a. for the supply of material equipment.

REFERENCES

- Adam, V., Bielak, J., Dommes, C., Will, N. and Hegger, J. 2020. Flexural and Shear Tests on Reinforced Concrete Bridge Deck Slab Segments with a Textile-Reinforced Concrete Strengthening Layer, *Materials*, 13 (18), p. 4210. Available at: <https://doi.org/10.3390/ma13184210>.
- Barhum, R. & Mechtcherine, V. 2013. Influence of short dispersed and short integral glass fibres on the mechanical behaviour of textile-reinforced concrete, *Materials and Structures*, 46(4),pp. 557–572. Available at: <https://doi.org/10.1617/s11527-012-9913-3>.
- Befling, M. & Orlovsky, J. 2022. Quantification of the Influence of Concrete Width per Fiber Strand on the Splitting Crack Failure of Textile Reinforced Concrete (TRC), *Polymers*, 14(3),p. 489. Available at: <https://doi.org/10.3390/polym14030489>.
- Botelho Goliath, K., Cardoso, D. and de A. Silva, F. 2021. Flexural behavior of carbon-textile-reinforced concrete I-section beams, *Composite Structures*, 260, p. 113540. Available at: <https://doi.org/10.1016/j.compstruct.2021.113540>.
- Dinh, N.H., Park, S.-H. and Choi, K.-K. 2021. Effect of dispersed micro-fibers on tensile behavior of uncoated carbon textile-reinforced cementitious mortar after high-temperature exposure, *Cement and Concrete Composites*, 118, p. 103949. Available at: <https://doi.org/10.1016/j.cemconcomp.2021.103949>.
- Dong, Z., Deng, M., Zhang, C., Zhang, Y., and Sun, H. 2020. Tensile behavior of glass textile reinforced mortar (TRM) added with short PVA fibers, *Construction and Building Materials*, 260, p. 119897. Available at: <https://doi.org/10.1016/j.conbuildmat.2020.119897>.
- Dong, Z., Deng, M., Dai, J., and Song, S. 2021. Flexural strengthening of RC slabs using textile reinforced mortar improved with short PVA fibers, *Construction and Building Materials*, 304, p. 124613. Available at: <https://doi.org/10.1016/j.conbuildmat.2021.124613>.
- García-Taengua, E., Martí-Vargas, J.R. and Serna, P. 2014. Splitting of concrete cover in steel fiber reinforced concrete: Semi-empirical modeling and minimum confinement requirements, *Construction and Building Materials*, 66, pp. 743–751. Available at: <https://doi.org/10.1016/j.conbuildmat.2014.06.020>.
- Hegger, J. and Voss, S. 2008. Investigations on the bearing behaviour and application potential of textile reinforced concrete, *Engineering Structures*, 30(7),pp. 2050–2056. Available at: <https://doi.org/10.1016/j.engstruct.2008.01.006>.
- Koutas, L. N., Tetta, Z., Bournas, D. A., and Triantafyllou, T. C. 2019. Strengthening of Concrete Structures with Textile Reinforced Mortars: State-of-the-Art Review, *Journal of Composites for Construction*, 23 (1), p. 03118001. Available at: [https://doi.org/10.1061/\(ASCE\)CC.1943-5614.0000882](https://doi.org/10.1061/(ASCE)CC.1943-5614.0000882).
- Mattarollo, G., Randl, N., Pauletta, M., and Rossi, E. 2022. CONFINEMENT OF COLUMNS WITH TEXTILE REINFORCED CONCRETE: AN EXPERIMENTAL COMPARISON BETWEEN BASALT AND CARBON TEXTILE REINFORCED CONCRETE, in *Proceedings for the 6th fib International Congress 2022. Concrete Innovations for Sustainability*, Oslo, Norway, pp. 2286–2295.
- Mészöly, T., Ofner, S. and Randl, N. 2020. Effect of Combining Fiber and Textile Reinforcement on the Flexural Behavior of UHPC Plates, *Advances in Materials Science and Engineering*, 2020, pp. 1–8. Available at: <https://doi.org/10.1155/2020/9891619>.

- Nobili, A. and Falope, F.O. 2017. Impregnated carbon fabric-reinforced cementitious matrix composite for rehabilitation of the Finale Emilia hospital roofs: case study, *Journal of Composites for Construction*, 21 (4). Available at: [https://doi.org/10.1061/\(ASCE\)CC.1943-5614.0000780](https://doi.org/10.1061/(ASCE)CC.1943-5614.0000780).
- Preinstorfer, P. and Kollegger, J. 2020. New insights into the splitting failure of textile-reinforced concrete, *Composite Structures*, 243, p. 112203. Available at: <https://doi.org/10.1016/j.compstruct.2020.112203>.
- Preinstorfer, P. and Kromoser, B. 2020. Influence of geometrical parameters on the splitting forces in textile-reinforced concrete, *Materials and Structures*, 53(6), p. 152. Available at: <https://doi.org/10.1617/s11527-020-01590-w>.
- Randl, N. and Harsányi, P. 2018. Developing optimized strengthening systems for shear-deficient concrete members, *Structural Concrete*, 19(1), pp. 116–128. Available at: <https://doi.org/10.1002/suco.201600187>.
- Randl, N. and Kunz, J. 2014. Post-installed reinforcement connections at ultimate and serviceability limit states, *Structural Concrete*, 15(4), pp. 563–574. Available at: <https://doi.org/10.1002/suco.201300094>.
- Randl, N., Mészöly, T. and Harsányi, P. 2018. Shear Behaviour of UHPC Beams with Varying Degrees of Fibre and Shear Reinforcement, in D.A. Hordijk and M. Luković (eds) *High Tech Concrete: Where Technology and Engineering Meet*. Cham: Springer International Publishing, pp. 500–507. Available at: https://doi.org/10.1007/978-3-319-59471-2_60.
- Rossi, E., Randl, N., Mészöly, T. and Harsányi, P. 2021a. Effect of TRC and F/TRC Strengthening on the Cracking Behaviour of RC Beams in Bending, *Materials*, 14(17), p. 4863. Available at: <https://doi.org/10.3390/ma14174863>.
- Rossi, E., Randl, N., Mészöly, T. and Harsányi, P. 2021b. Flexural Strengthening with Fiber-/Textile-Reinforced Concrete, *ACI Structural Journal*, 118(4). Available at: <https://doi.org/10.14359/51732647>.
- Rossi, E., Randl, N., Harsányi, P. and Mészöly, T. 2021c. Overlapped joints in Textile Reinforced Concrete with UHPC matrix: An experimental investigation, *Materials and Structures*, 54(4), p. 152. Available at: <https://doi.org/10.1617/s11527-021-01739-1>.
- Rossi, E., Randl, N., Harsányi, P. and Mészöly, T. 2022. Experimental study of fibre-reinforced TRC shear strengthening applications on non-stirrup reinforced concrete T-beams, *Engineering Structures*, 256, p. 113923. Available at: <https://doi.org/10.1016/j.engstruct.2022.113923>.
- Tekle, B.H., Messerer, D. and Holschemacher, K. 2021. Bond induced concrete splitting failure in textile-reinforced fine-grained concrete, *Construction and Building Materials*, 303, p. 124503. Available at: <https://doi.org/10.1016/j.conbuildmat.2021.124503>.

Shear strengthening with F/TRC: Experimental investigation on real scale RC beams

E. Rossi & N. Randl

Carinthia University of Applied Sciences, Villach, Austria

ABSTRACT: Shear strengthening of existing structures is a key activity in ensuring adequate safety. Shear deficient Reinforced Concrete (RC) elements exhibit rather brittle failures which can lead to disastrous consequences. Furthermore, even elements which are not prone to shear failure might require installation of shear strengthening solutions, for example after a bending capacity enhancement intervention. Among the different shear strengthening methods available today, the use of Textile Reinforced Concrete (TRC) was given particular attention by both scholars and practitioners due to its compatibility with the substrate material and the overcoming of the intrinsic limitations of Fiber Reinforced Polymer (FRP) solutions. An enhanced version of TRC, named Fibre/Textile Reinforced Concrete (F/TRC) and consisting in the admixture of short dispersed fibres in the cementitious matrix of TRC material, was recently developed and showed high potential as a strengthening material. The use of F/TRC as shear strengthening method was tested in the structural laboratory of Carinthia University of Applied Sciences on real scale RC beams. The effect of these strengthening solutions was evaluated in detail using a Digital Image Correlation (DIC) system. The present article describes the strengthening potential of these solutions and provides insights on the progression of the different observed failure modes, including debonding and interlaminar shearing.

1 INTRODUCTION

Structural strengthening is a key activity in the modern construction sector. The continuously aging structures, the increase in loads such as traffic, and the increased frequency of extreme events related to climate change are the main drivers of this activity. Particularly important, in this context, is shear strengthening due to the brittle nature of shear failure. Furthermore, even structural elements which are not prone to shear failure might need to be strengthened in shear in order to avoid vulnerability shifts consequent to other strengthening operations such as flexural strengthening. Different strengthening solutions against shear have been studied in the recent past, including post-installed reinforcing elements (Randl & Kunz 2009, 2014), Fibre Reinforced Plastics (FRP) and innovative anchor solutions (Randl & Harsányi 2018), and especially Textile Reinforced Concrete (TRC) (Brückner et al. 2006; Escrig et al. 2015; Tetta et al. 2016; Adam et al. 2020; Pohoryles et al. 2021; Rossi et al. 2022). This material, also known as Textile Reinforced Mortar (TRM) or Fabric Reinforced Cementitious Matrix (FRCM), is a high performance cementitious composite consisting of one or multiple layers of high strength fabrics, generally made of carbon, AR-glass, or basalt fibres, embedded in a cementitious matrix. Fibre/Textile Reinforced Concrete (F/TRC) is, instead, an enhanced version of TRC materials which is able to overcome the limitations related to the low tensile performances of the cementitious matrix by admixing to it short dispersed fibres, thus preventing undesired failure modes such as splitting and interlaminar shearing (Rossi et al. 2021a, b, Rossi et al. 2022). These materials have been used to produce thin-walled structural elements (Hegger & Voss 2008; Botelho Goliath et al. 2021) as well as strengthening solutions for

existing structures (Nobili & Falope 2017; Koutas et al. 2019; Furtado et al. 2020; Li et al. 2021). It is also well known that short dispersed fibres can contribute strongly to the shear resistance of a high strength or ultra-high performance concrete (Randl et al. 2018), which applies also to layers of new concrete subsequently attached to the web.

The present work focuses on experimental tests of TRC and F/TRC shear strengthening solutions applied on real-scale Reinforced Concrete (RC) T-beams. The different behaviour of the two materials will be analysed in terms of increase in the load carrying capacity and change in failure mode. Through the use of the results obtained from the Digital Image correlation (DIC) monitoring system, an analysis of the debonding and interlaminar shearing phenomena is performed. In particular, the results shown hereafter will complement a previous research campaign (Rossi et al. 2022) by enabling important considerations on the efficiency of the strengthening solutions and highlighting the differences between the observed failure modes.

2 MATERIALS AND METHODS

The specimens consisted in 6.3 m long T-beams having two shear deficient zones, one at each end of the beam. The width of the cross section was 220 mm in the web and 600 mm in the flange. The total height of the beam was 450 mm, 150 of which in the flange. Each beam had 2 shear deficient zones. In the presented cases, the shear deficient zones had no stirrups in the web. The rest of the beam was reinforced with Ø10 stirrups spaced at 100 mm. The longitudinal reinforcement consisted of 8 Ø10 rebars in the flange and 6 Ø30 rebars in the tensile zone of the web, arranged in two layers. The beam was designed to be tested in a three point bending configuration with a total span of 3.9 m and a shear span of 1.3 m, resulting in a shear span to effective depth ratio of approximately 3.5. A schematic representation of the beams can be seen in Figure 1.

The concrete used to cast the beam was a C40/50 with a mean cube compressive strength of 60.7 MPa. The steel for the longitudinal and transversal reinforcement was a B 550B.

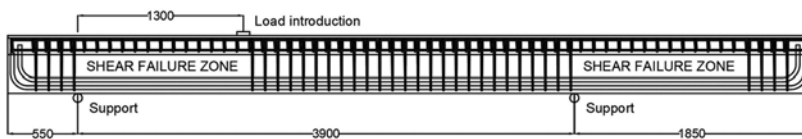


Figure 1. Geometry of the beam specimens (modified from Rossi et al. 2022).

Several strengthening solutions were tested during the experimental campaign. They were all designed in a way to prevent or delay the formation and propagation of typically observed shear cracks in such type of T-beams (Stoerzel et al. 2015). The present work focuses on 4 different side-bonded solutions: S1 – a single layer TRC strengthening; S2 – a double layer TRC strengthening; FR-S1 – a single layer F/TRC strengthening; FR-S2 – a double layer F/TRC strengthening. Each strengthening solution employed a high performance cementitious matrix, admixed with 2.5 vol% of short dispersed steel fibres in the case of F/TRC solutions, and a fully impregnated carbon fabric. The cementitious matrices had a cube compressive strength of 90.6 MPa and 90.3 MPa, tested on 100x100x100 mm specimens, and a flexural tensile strength of 7.1 MPa and 18.8 MPa, tested on 40x40x160 mm prisms, for TRC and F/TRC respectively. The carbon fabric was characterized by rovings having a cross-sectional area of 3.62 mm² and a spacing of 25 mm from their axis. The tensile strength of then longitudinal and transversal rovings was 3100 MPa and 3300 MPa, respectively ('solidian GRID Q142/142-CCE-25 Technical Data Sheet').

The tests were performed in displacement control with a speed of 0.5 mm/min. The testing and measurement equipment consisted of a 2.1 MN hydraulic cylinder with a resolution of 0.01 kN, a two-system stereo DIC photogrammetric equipment and an LVDT used to monitor the deflection of the beam.

3 RESULTS AND DISCUSSION

All the specimens failed in shear, signaled by the presence of one or more diagonal cracks running from the support to the load introduction. The results of the tests, in the form of Force-Deflection curves can be seen in Figure 2. The reference beam started to fail at approximately 250 kN, when the web was fully cracked. At this stage, however, the shear cracks did not yet propagate to the flange. The beam was thus able to carry additional load, reaching a maximum of 291.7 kN when the diagonal crack propagated in the flange towards the load introduction. Specimen S1 failed at 358.5 kN, recording a maximum load increase of 22.9%, due to interlaminar shearing i.e., formation of a crack in the plane of the textile which separated the textile fabric from the rest of the structure. Specimen S2 exhibited a similar behaviour, failing due to interlaminar shearing at a load of 397.8 kN (36.4% increase in maximum load). This specimen, however, exhibited a rather horizontal branch of the force deflection curve, characterized by the presence of several drops in load. This was attributed to the capability of the 2-layer configuration to redistribute some of the stresses between the two layers. Specimen FR-S1 recorded a maximum load increase of 46.5%, corresponding to a maximum load of 427.3 kN. This specimen exhibited a mixed failure mode. On the side where the DIC measurement was taking place, extensive debonding in the central strengthened region could be observed. On the other side, instead, a clear shear crack was visible and, upon further inspection, pull-out of the textile fabric was observed. Specimen FR-S2 failed due to debonding of the strengthening layers at a load of 518.7 kN, corresponding to a maximum load increase of 77.8%. A summary of the test results can be found in Table 1. Focusing on the effect that 2-layers configurations (S2 and FR-S2) have on the overall capacity increase and comparing them with 1-layer configurations (S1 and FR-S1), an interesting behaviour arises. S1 strength increase accounts for 66.8 kN while S2 accounts for 106.1 kN. The ratio between the two is 1.59, showing a less than linear contribution of the additional layer. Similarly FR-S1 provided a strength increase of 135.6 kN while FR-S2 of 227.0 kN, corresponding to a ratio of 1.67. While these four tests alone are not enough to define a law correlating the strength increase to the number of layers, the relative low difference observed in the two cases hints to the fact that the contribution of the additional layer is strongly reduced, at least in side-bonded configurations, and might account for approximately 60%.

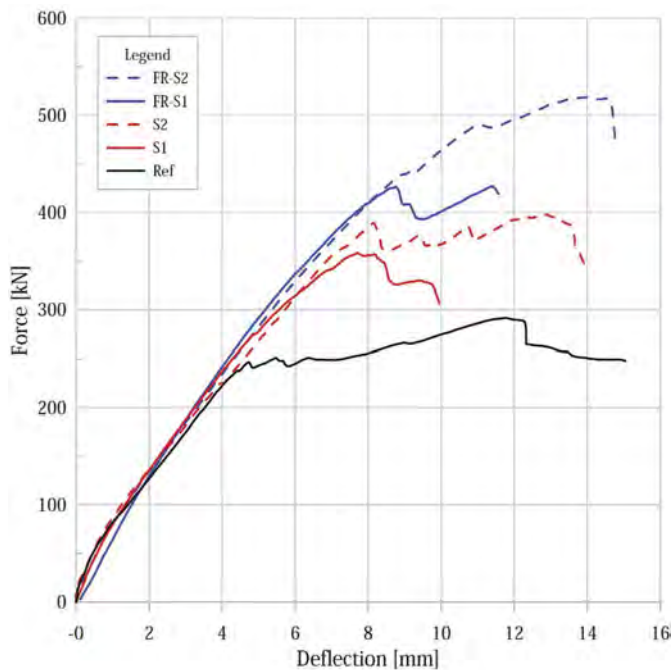


Figure 2. Force-deflection curves of specimens (data partly from Rossi et al. 2022).

Table 1. Overview of testing program and results.

Specimen	Strengthening material	N° of layers	Maximum force [kN]	Deflection at maximum force [mm]	Performance increase [%]
Reference	-	-	291.7	11.8	-
S1	TRC	1	358.5	7.7	22.9
S2	TRC	2	397.8	12.9	36.4
FR-S1	F/TRC	1	427.3	11.4	46.5
FR-S2	F/TRC	2	518.7	14.0	77.8

To better analyse the failure modes that were observed during testing, with special reference to interlaminar shearing and debonding, the out-of-plane displacement (OOP) was measured with the aid of the DIC measurement. Such results can be seen in Figure 3. The plotted results refer to a post-failure condition of the beams, corresponding to a load decrease of approximately 10% of the maximum load. As it can be seen, specimens S1 and FR-S1 showed a very similar pattern of OOP. In both cases OOP was located in the same region i.e., bottom central part of the strengthened region progressing upwards towards the flange. In the case of specimen S1, the OOP shows high values around the shear crack which tend to concentrate in the bottom part and diminish further away from the crack itself. Specimen FR-S1, while exhibiting a similar pattern, is characterized by a more diffused distribution of high OOP which tends to diminish in a longer distance from the maximum. This difference, combined with the force-deflection results, shows that F/TRC is able to retain its strengthening capability even when part of the layers are debonded from the existing structure. This interpretation is confirmed by the results of specimens S2 and FR-S2. In this case, the maximum OOP was located in different points for the two beams. In the case of S2, the OOP is concentrated in the top left area of the strengthening layer (near the support) and, once again, around a shear crack. In the case of FR-S2, instead, the OOP is the highest in the bottom right corner (under the load introduction) and propagates along nearly the whole length of the strengthening layer. Specimen FR-S2, however, despite having a significant portion of the F/TRC layer debonded from the substrate, was able to contribute to a performance increase more than three times than what was obtained with specimen S2.

Focusing on the specific patterns of OOP that the different solutions exhibit, some interesting considerations can be formulated. Comparing S1 and S2, it can be seen that, in both cases, the OOP tends to concentrate around the main diagonal shear crack, which however shifted towards the left side in specimen S2. The addition of the second textile layer, however, resulted in a more diffuse propagation of the interlaminar shearing phenomenon, probably due to internal stress redistribution. Comparing FR-S1 and FR-S2, instead, a significant change in behaviour is observable. As already mentioned, FR-S1 showed a concentration of OOP around the main shear cracks, albeit more diffused than S1. FR-S2, contrarily, showed that OOP was concentrated at edges of the strengthening layer. This difference hints at the fact that, most probably, the combined effect of the 2-layer configuration, together with the increased performance of F/TRC, can effectively bridge across the main shear crack, shifting the main vulnerability to other stress concentration areas, such as the corners of the strengthening layer.

4 CONCLUSIONS

An experimental campaign was performed at the structural laboratory of Carinthia University of Applied Sciences testing different TRC of F/TRC shear strengthening solutions. The tests highlighted how the different materials and configurations contribute to increasing the load carrying capacity of the strengthened element. Different failure modes were observed, including interlaminar shearing and debonding. In the case of side-bonded strengthening solutions, TRC elements always failed due to interlaminar shearing. The use of F/TRC materials could effectively prevent this failure mode. This resulted in a higher load carrying capacity. The

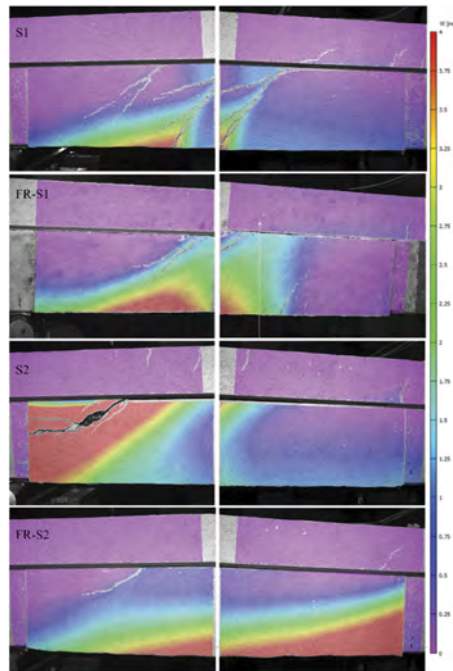


Figure 3. Out-of-plane displacement of the strengthening solutions.

presence of an additional textile layer, independently of the employed material (TRC or F/TRC) showed a less than linear increase in the additional load carrying capacity. Furthermore, with the aid of DIC measurement, it was possible to observe that TRC interlaminar shearing failure was located in the surroundings of shear cracks and led to failure of the specimen when the phenomenon interested a relatively contained part of the element. Contrarily, F/TRC side bonded solutions show a good stress redistribution capability, enabling the specimen to still be able to carry loads even when significant parts of it were debonded from the substrate. Such phenomenon even led to a vulnerability shift for the 2-layer F/TRC strengthening solution, where the debonding was concentrated in the corner of the strengthening solution instead of being around the main shear crack.

ACKNOWLEDGMENTS

This work was supported by the Austrian Research Promotion Agency (FFG) in the framework of the CON_FIT project [grant number 866881]; likewise, the Authors would like to thank the companies solidian GmbH and PAGEL Spezial-Beton GmbH & Co. KG for the supply of material equipment.

REFERENCES

- Adam, V., Bielak, J., Dommes, C., Will, N. & Hegger, J. 2020. Flexural and Shear Tests on Reinforced Concrete Bridge Deck Slab Segments with a Textile-Reinforced Concrete Strengthening Layer, *Materials*, 13(18), p. 4210. Available at: <https://doi.org/10.3390/ma13184210>.
- Botelho Goliath, K., Cardoso, D. & Silva, F. 2021. Flexural behavior of carbon-textile-reinforced concrete I-section beams, *Composite Structures*, 260, p. 113540. Available at: <https://doi.org/10.1016/j.compstruct.2021.113540>.

- Brückner, A., Ortlepp, R. & Curbach, M. 2006. Textile reinforced concrete for strengthening in bending and shear'. *Materials and Structures*, 39(8), pp. 741–748. Available at: <https://doi.org/10.1617/s11527-005-9027-2>.
- Escrig, C., Gil, L., Bernat-Maso, E. & Puigvert, F. 2015. Experimental and analytical study of reinforced concrete beams shear strengthened with different types of textile-reinforced mortar, *Construction and Building Materials*, 83, pp. 248–260. Available at: <https://doi.org/10.1016/j.conbuildmat.2015.03.013>.
- Furtado, A., Rodrigues, H., Arêde, A. & Varum, H. 2020. Experimental tests on strengthening strategies for masonry infill walls: A literature review, *Construction and Building Materials*, 263, p. 120520. Available at: <https://doi.org/10.1016/j.conbuildmat.2020.120520>.
- Hegger, J. & Voss, S. 2008. Investigations on the bearing behaviour and application potential of textile reinforced concrete, *Engineering Structures*, 30(7), pp. 2050–2056. Available at: <https://doi.org/10.1016/j.engstruct.2008.01.006>.
- Koutas, L.N., Tetta, Z., Bournas, D. & Triantafyllou, T. 2019. Strengthening of Concrete Structures with Textile Reinforced Mortars: State-of-the-Art Review, *Journal of Composites for Construction*, 23(1), p. 03118001. Available at: [https://doi.org/10.1061/\(ASCE\)CC.1943-5614.0000882](https://doi.org/10.1061/(ASCE)CC.1943-5614.0000882).
- Li, T., Deng, M., Jin, M., Dong, Z. & Zhang, Y. 2021. Performance of axially loaded masonry columns confined using textile reinforced concrete (TRC) added with short fibers, *Construction and Building Materials*, 279, p. 122413. Available at: <https://doi.org/10.1016/j.conbuildmat.2021.122413>.
- Nobili, A. & Falope, F.O. 2017. Impregnated carbon fabric-reinforced cementitious matrix composite for rehabilitation of the Finale Emilia hospital roofs: case study, *Journal of Composites for Construction*, 21 (4). Available at: [https://doi.org/10.1061/\(ASCE\)CC.1943-5614.0000780](https://doi.org/10.1061/(ASCE)CC.1943-5614.0000780).
- Pohoryles, D.A., Melo, J. & Rossetto, T. 2021. Combined Flexural and Shear Strengthening of RC T-Beams with FRP and TRM: Experimental Study and Parametric Finite Element Analyses, *Buildings*, 11 (11),p. 520. Available at: <https://doi.org/10.3390/buildings11110520>.
- Randl, N. & Harsányi, P. 2018. Developing optimized strengthening systems for shear-deficient concrete members, *Structural Concrete*, 19(1), pp. 116–128. Available at: <https://doi.org/10.1002/suco.201600187>.
- Randl, N. & Kunz, J. 2009. Biegeschubversuche an Stahlbetonbalken mit nachträglich eingemörtelter Querkraftbewehrung, *Beton- und Stahlbetonbau*, 104(11), pp. 728–736. Available at: <https://doi.org/10.1002/best.200900042>.
- Randl, N. & Kunz, J. 2014. Post-installed reinforcement connections at ultimate and serviceability limit states, *Structural Concrete*, 15 (4), pp. 563–574. Available at: <https://doi.org/10.1002/suco.201300094>.
- Randl, N., Mészöly, T. & Harsányi, P. 2018. Shear Behaviour of UHPC Beams with Varying Degrees of Fibre and Shear Reinforcement, in D.A. Hordijk and M. Luković (eds) *High Tech Concrete: Where Technology and Engineering Meet*. Cham: Springer International Publishing, pp. 500–507. Available at: https://doi.org/10.1007/978-3-319-59471-2_60.
- Rossi, E., Randl, N., Mészöly, T. & Harsányi, P. 2021a. Flexural Strengthening with Fiber-/Textile-Reinforced Concrete, *ACI Structural Journal*, 118 (4). Available at: <https://doi.org/10.14359/51732647>.
- Rossi, E., Randl, N., Harsányi, P. & Mészöly, T. 2021b. Overlapped joints in Textile Reinforced Concrete with UHPC matrix: An experimental investigation, *Materials and Structures*, 54(4), p. 152. Available at: <https://doi.org/10.1617/s11527-021-01739-1>.
- Rossi, E., Randl, N., Harsányi, P. & Mészöly, T. 2022. Experimental study of fibre-reinforced TRC shear strengthening applications on non-stirrup reinforced concrete T-beams, *Engineering Structures*, 256, p. 113923. Available at: <https://doi.org/10.1016/j.engstruct.2022.113923>.
- solidian GRID Q142/142-CCE-25 Technical Data Sheet.
- Stoerzel, J., Randl, N. & Strauss, A. 2015. Monitoring shear-induced degradation of reinforced and pre-tensioned concrete members, in *Providing Solutions to Global Challenges. IABSE conference*, Geneva, Switzerland, pp. 1148–1157. Available at: <https://doi.org/10.2749/222137815818358394>.
- Tetta, Z.C., Koutas, L.N. & Bournas, D.A. 2016. Shear strengthening of full-scale RC T-beams using textile-reinforced mortar and textile-based anchors, *Composites Part B: Engineering*, 95, pp. 225–239. Available at: <https://doi.org/10.1016/j.compositesb.2016.03.076>

State of the art in flexural prestressing of RC members with SMA materials

J. Rogowski & R. Kotynia

Department of Concrete Structures, Lodz University of Technology, Lodz, Poland

ABSTRACT: Prestressing concrete is a great technique to improve the serviceability state of RC members subjected flexure. Relatively new materials such as iron-based shape memory alloys (FeSMA) can be a great alternative for conventional prestressing system. Using the shape memory effect, concrete members can be prestressed without the need of hydraulic jacks, ducts or anchor heads. The flexurally strengthened members exhibit higher cracking load, initial stiffness and reduced deflections with simultaneous ductile behaviour up to failure that is usually due to concrete crushing. In the paper, a brief description of FeSMA including utilization of shape memory effect for prestressing and tensile behaviour of materials is presented. The existing prestressing systems for flexural strengthening of RC members are described. Previous studies based on flexural strengthening using prestressed memory steel are revised, summarized and discussed. Selected real-life implementation is described to confirm the practicality and feasibility of the strengthening using FeSMA systems.

1 INTRODUCTION

The number of existing reinforced concrete structures that need to be strengthened is constantly increasing. The need for retrofitting may be caused by the deterioration of structures, changes in usage, increasing design requirements or design errors. Traditional methods of strengthening include, for instance, additional concrete layer in the compression zone or externally added steel reinforcement. These methods, known as passive strengthening, mainly improve the load-bearing capacity and do not affect significantly the serviceability limit state. One of the most effective methods to reduce deformations and crack widths of RC members is prestressing of concrete. However, existing strengthening techniques with prestressed carbon composites require complex mechanical anchorage and additional special devices such as hydraulic jacks that increases significantly the overall costs of strengthening. Prestressing CFRP systems are in most cases bonded to the concrete surface using epoxy and their ultimate load is limited due to the bond strength. Additionally, a sudden failure due to delamination is a common failure mode (Kotynia 2019). Hence, new methods of active strengthening are still in demand and developed.

Prestressing using shape memory alloys (SMA) should be considered a promising alternative for the existing prestressing methods of existing concrete members. These metallic alloys have unique abilities that allow them to return to their initial shape after having been permanently deformed. The ability to recover inelastic deformations occurring automatically by unloading is called superelasticity. If the return to the predefined shape has to be activated, e.g. upon heating, the phenomenon is called the shape memory effect (SME). Some mechanical stress appears in the material if the deformation recovery is restrained. The stress obtained after heating the material to a certain temperature and cooling it down is called recovery stress and can be used for prestressing some concrete members.

The superelasticity is characteristic of the most popular nickel-titanium based alloys (NiTiSMA). Their applications have been limited in the civil engineering industry due to their

high material costs, however, they have already confirmed their potential for retrofitting concrete members and can be used as dampers, actuators or self-centering elements (Mohd Jani et al. 2014). An iron-based shape memory alloys (FeSMA) seems to be a more suitable material for structural retrofitting not only due to a reasonable production cost but also higher Young modulus and relatively low temperature of activation (Leinenbach et al. 2012). SME can be used for flexural strengthening of RC beams or slabs, shear strengthening or active confinement of RC columns. Overall state of the art in the topic of strengthening and self-centering of concrete structures was summarized in a review by (Raza et al. 2022).

This paper is focused on the topic of flexural strengthening of RC structures with prestressed FeSMA materials and provides a background for future research. The key parameters of memory steel and prestressing systems are briefly described. The previous experimental studies with flexurally strengthened RC members using FeSMA are summarized, important results from the research are discussed and recommendations for future research are highlighted.

2 DESCRIPTION OF IRON-BASED SHAPE MEMORY ALLOYS

2.1 *Prestressing systems*

The method of prestressing concrete structures using FeSMA reinforcements is quite similar for all technique of strengthening. This method of prestressing is characterized by ease of applications and does not require hydraulic jacks, anchor heads or ducts. A bar, strip or wire made of memory steel is initially prestrained (permanently elongated) at room temperature. The prestrained reinforcing material is then applied to the concrete surface or embedded in concrete. The FeSMA reinforcement has to be fixed to the concrete member to restrain the deformation. The reinforcement is then heated to activate the shape memory effect. Various heating systems may be used to provide heat supply: gas torch, infrared heating, electrical resistive heating. Since the deformations of FeSMA materials are restrained, the recovery stress develops in the memory steel. The force is transferred to a concrete member through anchorage system or bonding between FeSMA and surrounding materials and prestress occurs in the concrete. The prestressing force depends on the recovery stress of the alloy that for different Fe-Mn-Si alloys are in the range of 130–580 MPa (Cladera et al. 2014). The recovery stress highly depends on composition of the alloy, thermomechanical training, level of initial prestraining, and temperature of activation. (Michels et al. 2018b) indicated that increasing the maximal temperature during activation provides higher recovery stress. However, the high temperature inside the concrete or cementitious grout may lead to deteriorating its mechanical properties, so the recommended temperature is in range 160 – 350°C. Based on the previous research studies the optimal level of prestraining is in range 2 – 4 % (Michels et al. 2018b, Shahverdi et al. 2018). In general, the recovery stress is much lower than the initial prestress in the CFRP reinforcement and the prestressing force for FeSMA system would be from two to four times lower than for the CFRP prestressing (assuming a similar cross-section area of reinforcements for both systems) (Rogowski & Kotynia 2022).

The following prestressing systems should be highlighted (Schranz et al. 2019):

- externally applied reinforcements (EAR). The most common is prestressing using unbonded FeSMA strips that are fixed to a concrete member with anchoring device (Strieder et al. 2019) or using direct fastening system (Michels et al. 2018a). The latter method is based on fixing the strip to concrete by installation the nails in the pre-drilled holes using powder-activated tools. The strip is not in contact with concrete between the end anchorages and acts as an external unbonded tendon during loading the structure.
- near-surface mounted (NSM) reinforcements. The FeSMA strips or bars are inserted into the concrete grooves which are filled with cementitious mortar (Shahverdi et al. 2016b, Schranz et al. 2021). The reinforcement may be additionally fixed using end-anchorages (Rojab & El-Hacha 2017a).
- bars embedded in the shotcrete layer (Shahverdi et al. 2016a).
- bars as longitudinal tensile reinforcements mounted before casting of concrete member (Yeon et al. 2022).

2.2 Tensile behaviour

Stress-strain behaviour of memory steel is similar to a conventional steel. The behavior of SMA during unloading is nonlinear. FeSMA exhibit ultimate strength of 680–1000 MPa with ultimate tensile strain equal to 16–50% (Shahverdi et al. 2018). In contrast to composites, they are fully isotropic materials. The initial Young modulus of FeSMA is about 170 GPa and is lower than steel and the high modulus CFRP. It should be emphasized that elastic modulus depends on actual state of alloy. It is about 25 – 50% lower after activation than in elastic state (Shahverdi et al. 2018, Yang et al. 2021). Moreover, stress relaxation occurs in the FeSMA materials. A decrease of 10% in recovery stress was observed after 1000 h by (Michels et al. 2018b). During the life cycle of the structure, the total relaxation losses are estimated at 15 – 20%. Re-heating of FeSMA to the activation temperature and cooling to the ambient temperature (multiple activation) can retrieve a significant part of the prestressing losses (Hosseini et al. 2018).

3 LITERATURE REVIEW

Experimental research studies dedicated to flexural strengthening using iron-based shape memory alloys are summarized in Table 1. It contains information about steel reinforcement ratio, ρ_s , FeSMA reinforcement ratio, ρ_{SMA} , ductility index, I_D , and cracking load increment, ΔP_{cr} , that are calculated as follows:

$$\rho_s = \frac{A_{s,t}}{A_c} * 100\% \quad (1)$$

where $A_{s,t}$ = area of tensile steel reinforcement; A_c = cross-section area.

$$\rho_{SMA} = \frac{A_{SMA}}{A_c} * 100\% \quad (2)$$

where A_{SMA} = area of FeSMA reinforcement; A_c = cross-section area.

$$I_D = \frac{d_{ult}}{d_y} \quad (3)$$

where d_{ult} = deflection at ultimate load; d_y = deflection at yielding load.

$$\Delta P_{cr} = \frac{P_{cr,str} - P_{cr,ref}}{P_{cr,ref}} * 100\% \quad (4)$$

where $P_{cr,str}$ = cracking load of strengthened beam; $P_{cr,ref}$ = cracking load of reference beam.

Table 1. Experimental tests of flexurally strengthened RC members using FeSMA materials.

Reference	Strengthening technique	ρ_s %	ρ_{SMA} %	Load type**	Failure mode*	I_D	ΔP_{cr} %
(Shahverdi et al. 2016a)	FeSMA bars embedded in a shotcrete layer	0.25	0.25 or 0.5	4PBT	CC	N/A	235 – 360
(Shahverdi et al. 2016b)	FeSMA strips as NSM reinforcement	0.27	0.18	4PBT	CC or SR	N/A	110 – 135
(Rojob & El-Hacha 2017a)	FeSMA bar as NSM reinforcement with end-anchorage	0.88	0.35	4PBT	CC	4.5 – 4.8	111 – 142
(Rojob & El-Hacha 2017b)	FeSMA bar bent 90° angle at both ends as NSM reinforcement	0.88	0.35	4PBT	CC	8.27	20
(Rojob & El-Hacha 2018a)	FeSMA bar as NSM reinforcement with end-anchorage	0.88	0.35	FAT+ 4PBT	CC	22.7	26

(Continued)

Table 1. (Continued)

Reference	Strengthening technique	ρ_s %	ρ_{SMA} %	Load type**	Failure mode*	I_D	ΔP_{cr} %
(Rojob & El-Hacha 2018b)	FeSMA bar as NSM reinforcement with end-anchorage	0.88	0.35	4PBT	CC	8 – 14.4	36 – 48
(Michels et al. 2018a)	End-anchored externally applied FeSMA strips to the bottom surface	0.31	0.2	4PBT	CC	2.69 – 3.21	240 – 460
(Hong et al. 2018)	FeSMA strips as NSM reinforcement	0.39	0.05, 0.1 or 0.15	4PBT	CC	N/A	26 – 89
(El-Hacha & Rojob 2018)	FeSMA strips as NSM reinforcement with end-anchorage	0.75	0.15 or 0.21	4PBT	CC	5.3 – 7.1	25 – 59
(Strieder et al. 2019)	End-anchored externally applied FeSMA strips to the bottom surface	0.62	0.22	4PBT	N/A	N/A	321
(Shahverdi & Czaderski 2019)	FeSMA strips as NSM reinforcement	0.27	0.18	4PBT	N/A	N/A	N/A
(Schranz et al. 2021)	FeSMA bars as NSM reinforcement	2.45	0.23	CAN	CC	6.93 – 7.49	232 – 265
(Hong et al. 2022)	FeSMA rods as longitudinal tensile reinforcement with end-anchorage	-	0.2, 0.3, 0.4 or 0.5	4PBT	CC	N/A	47.6 – 112.8
(Yeon et al. 2022)	FeSMA rods as longitudinal tensile reinforcement with end-anchorage	-	0.2, 0.3, 0.4 or 0.5	4PBT	CC	N/A	40.2 – 101.6

* CC means concrete crushing, SR steel rupture

** 4PBT means 4 point bending test, CAN tests with force on the slab cantilever, FAT is a fatigue test
N/A means that data were not available

RC beams strengthened with FeSMA strips as NSM reinforcements were investigated by (Shahverdi et al. 2016b). The FeSMA strips were prestrained up to 2% and glued with cement-based mortar in grooves (without end anchorages). The strips were activated by resistive heating for 3 beams, while they remained inactivated in one beam. Bonding strength between glued with cement-based mortar FeSMA strips and concrete was sufficient to transfer the prestressing force. The prestressed beams exhibited a higher cracking load by 80% compared to the non-prestressed beam and lower mid-span deflections (up to a load of ~12 kN)). As could be expected, prestressing did not increase the ultimate load in comparison to the nonactivated beam. Two of the activated beams failed due to strip rupture, however they experienced significant deflections of more than 1/40 of the span length. The long-term behaviour of similar beams (activated and nonactivated) was studied by (Shahverdi & Czaderski 2019). The beams were loaded (until more than their cracking load) using a concrete block in May 2015 and their mid-span deflection and crack propagation have been monitored for about 4 years. The mid-span deflection has increased from 4.3mm to 10.2mm in the activated beam and from 7.3mm to 13.2mm. Since both beams presented similar behaviour, the study noted that the stress relaxation (reduction in prestressing force) is not significant.

The application of FeSMA bars embedded in a shotcrete layer for flexural strengthening of RC beams was investigated by (Shahverdi et al. 2016a). The bars were initially prestrained to 4%, then fixed by mechanical hooks to the roughened bottom side of the beams and activated by resistive heating at 160°C. The beam with 2 FeSMA bars exhibited about 240 and 80% higher cracking load compared to the reference beam and a beam strengthened with 2 steel bars, respectively. However, the cracking load (determined using digital image correlation measurements) was lower for the beam with 4 FeSMA bars compared to the one with only 2 bars. It could be caused by shrinkage cracks of the shotcrete layer prior to the loading and should be further investigated to develop this technique. Nevertheless, load at midspan deflection of 4mm (corresponding to the serviceability limit state) increased by 63 and 165% compared to the reference beam for the beams with 2 and 4 bars, respectively.

Ribbed FeSMA bars were used for strengthening of two-field RC slab subjected to flexure with one part acting as a cantilever. Two system of strengthening were used. In the first (denoted as CR), the bars were placed in a roughened surface of beam and anchored at their ends over a length of half meter with grout. For other slabs (denoted as NSM), the bars were mounted as NSM reinforcement with the anchorage zone of 600mm performed by filling the grooves with cementitious mortar. After activation at 200°C using a resistive heating device, the remaining length between the anchorages was filled with the grout or mortar. The effectiveness of prestressing was confirmed by an increase in the cracking load (76 – 94% and 232 – 265% compared to the reference slab and non-activated slab with NSM bars, respectively) and a decrease in the length of the cracked zone between the outermost bending cracks in comparison with non-prestressed beams. Longitudinal cracks developed in the concrete cover during loading, but their width was negligible compared to the transverse bending cracks. The bond strength of FeSMA bars and surrounding materials was sufficient to avoid premature bonding failure – the slabs exhibited high ductile behavior up to fail due to the crushing of concrete.

Series of studies with FeSMA smooth bars as NSM reinforcements were conducted by Rojob & El-Hacha. The bars were initially prestrained to 6%, grooved into the tension side of the beams, end-anchored with steel plates, and heated up to 300 – 350°C using heating tapes or a rosebud torch. Finally, the grooves were grouted after cooling the bars to room temperature to create a bond between the concrete and bars. (Rojob & El-Hacha 2017a) indicated that in comparison with the reference beam, the cracking load increased by 111 and 142% for beams with FeSMA bar without and with additional thermomechanical training, respectively. (Rojob & El-Hacha 2017b) tested different anchorage systems where the bar was bent 90° angle at both ends, and the ends were inserted into pre-drilled holes that were then filled with epoxy. Compared to the previous anchorage solutions, a drop in the strain was clearly noticeable which could lead to a reduction of prestressing force transferred to the beam. Hence, only a 20% increase in cracking load was achieved. In both studies, the anchorage setting during the loading tests was observed (resulting in a relaxation of bars) and the debonding between the FeSMA bar and grouting material was noticed at higher loads (about the yielding load). The fatigue behaviour of RC beams with prestressed FeSMA bars was studied by (Rojob & El-Hacha 2018a). At low levels of fatigue load, corresponding to stress levels in the tensile steel reinforcement (of reference beam) equal to 0.29 and 0.53 of yield strength, the strengthened beams exhibited better performance than the reference beam. At higher levels of fatigue load, the deterioration in the bond between the FeSMA bar and surrounding grouting material resulted in the loss of strain in the bar started occurring. In consequence, the continued degradation led to the rupture of bars at the anchorage zone after 5.5 million load cycles. The performance of RC beams exposed to freeze-thaw cycles and sustained load (50% of ultimate capacity of the unstrengthened beam) was investigated by (Rojob & El-Hacha 2018b) and compared to the non-exposed beams. After the application of freeze-thaw cycles, the grout was completely spalled, hence FeSMA bar acted as an unbonded prestressed tendon. Reduction of 19 and 12% in the yielding and ultimate load due to the deterioration in the stiffness was noticed for the prestressed beam exposed to freeze-thaw cycles. The exposure did not affect the ductile behavior of the beams until failure. In all presented studies, the smoothness of the bars resulted in a lower bond strength of the bar and surrounding grout.

FeSMA strips were used as NSM reinforcements for flexural strengthening of RC beams in a study conducted by (Hong et al. 2018). The strips were prestrained to 2 or 4%, inserted in grooves cut in the concrete cover that was then filled with the rapid hardening cement mortar (90% of the length of strips was embedded). Activation of the strips was performed using resistive heating to the temperature of 160°C. The recovery stress resulted in the upward displacement of beams that was greater for the higher value of initial prestraining. Activation of FeSMA strips increased the cracking load of prestressed beams by 16 and 35% compared to the beam with non-activated strips and improved flexural rigidity. However, the behaviour of beams was still ductile up to fail due to the crushing of concrete. (El-Hacha & Rojob 2018) investigated large-scale RC beams strengthened with NSM FeSMA strips that were prestrained to 3% and activated at 150°C using heating tapes. The strips were end-anchored and the grooves were filled with adhesive after cooling the strips down to room temperature. The

beam with 7 activated strips showed 59% increase in the cracking load compared to the reference beam. The cracking loads of beams with 5 activated and non-activated strips were close (the difference of less than 3% was not explained by the authors) but the prestressed beam exhibited higher stiffness up to the yielding load. Finally, the prestressed beams were compared with beams strengthened using NSM CFRP – the FeSMA beams exhibited only slightly lower strength but significantly higher ductility.

Externally applied and unbonded FeSMA strips were used for active strengthening of RC beams by (Michels et al. 2018a). The FeSMA strips were prestrained to 2%, mechanically anchored to the concrete beam with the direct fastening method and activated by resistive heating at 160°C. The beams prestressed with FeSMA strips exhibited higher cracking load and enhanced stiffness compared to an unstrengthened beam and a beam passively strengthened with CFRP strip. Moreover, the FeSMA beams retained ductile behavior and failed due to the concrete crushing after steel yielding. A slightly lower ultimate concrete compressive strain value equal to 2.5‰ was measured that is in line with knowledge for unbonded external prestressing tendon, as a result of more concentrated beam rotation occurring within the maximal bending moment zone (Michels et al. 2018a). FeSMA strips were also used for the flexural strengthening of RC beams (Strieder et al. 2019). The strips were end-anchored to the beam with a special clamping device and thermally activated at 200°C by sequentially infrared heating. Sequential activation of strips does not influence the failure mode of the beam but has an impact on the level of prestress (usually higher temperature of activation could be required). The cracking load and initial stiffness of the prestressed beams were significantly higher compared to the reference beam and a beam strengthened with a passive steel strip. One of the beams was then loaded to 30kN, unloaded and reactivated at 350°C before loading up to failure to simulate behaviour of a damaged beam strengthened with FeSMA. The structural behavior of this beam remained ductile up to failure

(Hong et al. 2022) and (Yeon et al. 2022) used FeSMA rods as tensile reinforcement of concrete beams and slabs, respectively. The effect of FeSMA area, activation and additional end-anchorage were investigated. The rods were prestrained to 4% and activated at 160°C by resistive heating. Both beams and slabs exhibited ductile behavior up to failure due to concrete crushing after yielding of FeSMA reinforcements. Activation of rods significantly increased cracking loads but the ultimate loads remained at the same level. The greater number of rods, the higher prestress of specimens (was observed as the greater camber of beam or slab during the activation process) that resulted in higher cracking load increment compared to the non-activated specimens with the same reinforcements. The beam with activated rods without anchoring devices exhibited similar behaviour (including initial camber, cracking load and ultimate load) indicating that the bonding strength between concrete and FeSMA reinforcements was sufficient to prevent prestress loss due to slippage.

4 PRACTICAL IMPLEMENTATION

The first practical implementation of flexural strengthening with prestressed FeSMA strips took place in 2017 in Villigen, Switzerland (Michels et al. 2018a). The change of the static system caused by the removal of load-bearing wall resulted in the need of additional reinforcement. The combination of three strengthening methods was used to ensure minimal loss of room height and guarantee a satisfying behavior at the serviceability and ultimate limit state. The slab was strengthened by a steel girder installed between two supporting walls. The lack of lower flexural steel reinforcement above the removed wall was covered by applications of 12 CFRP strips. 14 FeSMA strips was applied in the perpendicular directions to the girder to deliver the prestressing in the slab and cover serviceability requirements. The FeSMA strips were fixed with nails using a direct fastening system and activated by resistive heating at 160°C.

5 CONCLUSIONS

In the paper, the state of the art in the topic of flexural strengthening using prestressed FeSMA materials is presented. The literature review shows that prestressing with FeSMA can be an

interesting alternative to conventional prestressing systems. The shape memory effect exhibited by FeSMA can be used to prestress RC slabs and beams. The effectiveness of flexural strengthening was confirmed both in experimental tests and practical implementation. FeSMA materials for flexural strengthening can be used as: externally applied or near-surface mounted reinforcement, embedded in a shotcrete layer or a tensile longitudinal reinforcement. All techniques of strengthening are much easier to perform in comparison with prestressing using CFRP materials.

The activation process is carried out by heating to the temperature in the range of 160 – 350°C. It can be performed using various methods including: heating using a gas burner, infrared heating or electrical resistive heating. The heating method may affect the prestressing level that is also highly dependent on composition of the alloy, initial prestraining and activation temperature. In general, the recovery stress are in the range of 130–450 MPa that resulted in 2 – 4 times lower prestressing forces in comparison to prestressing with CFRP materials.

The activation of SMA improves the structural performance of RC members especially in serviceability states. The prestressed beams and slabs exhibited greater cracking and yielding load, higher initial stiffness of the beams and reduced deflections. However, the behaviour of members prestressed with FeSMA is ductile up to failure that is caused in most cases by crushing of concrete after steel yielding. The ductility index for beams strengthened with FeSMA remains high and is similar to under reinforced concrete beams. Strengthening with FeSMA materials can be combined with other strengthening techniques e.g. with non-prestressed CFRP strips to provide maximum gains in both serviceability and ultimate limit states.

The elasticity modulus of FeSMA is dependent on the actual state of the alloy and the initial value is 30 – 50% higher than the value after activation –the latter value should be used for design purposes. The FeSMA is also affected by stress relaxation. The prestress loss due to relaxation is estimated to be about 15 – 20% in the life cycle of structure. Multiple activation allows to retrieve part of this loss.

The following recommendations should be considered in future research to develop the knowledge of prestressing RC members using FeSMA:

- effects of various heating methods and multiple activations on the prestressing level of FeSMA;
- prestress losses (including loss due to the slippage at anchorages) and long-term behavior of FeSMA used for prestressing of RC structures;
- development of more accurate methods of determining recovery stress after application of FeSMA materials to RC structure;
- combination of strengthening using prestressed FeSMA and non-prestressed CFRP materials.

REFERENCES

- Cladera, A., Weber, B., Leinenbach, C., Czaderski, C., Shahverdi, M., & Motavalli, M. 2014. Iron-based shape memory alloys for civil engineering structures: An overview. *Construction and Building Materials*, 63, 281–293. <https://doi.org/10.1016/j.conbuildmat.2014.04.032>
- El-Hacha, R., & Rojob, H. 2018. Flexural Strengthening of Large-Scale Reinforced Concrete Beams Using Near-Surface-Mounted Self-Prestressed Iron-Based Shape-Memory Alloy Strips. *Pci Journal*, 63, 55–65. <https://doi.org/10.15554/pcij63.6-03>
- Hong, K. N., Lee, S., Yeon, Y., & Jung, K. 2018. Flexural Response of Reinforced Concrete Beams Strengthened with Near-Surface-Mounted Fe-Based Shape-Memory Alloy Strips. *International Journal of Concrete Structures and Materials*, 12(1), 1–13. <https://doi.org/10.1186/S40069-018-0279-Y/FIGURES/13>
- Hong, K. N., Yeon, Y. M., Ji, S. W., & Lee, S. 2022. Flexural Behavior of RC Beams Using Fe-Based Shape Memory Alloy Rebars as Tensile Reinforcement. *Buildings*, 12(2). <https://doi.org/10.3390/BUILDINGS12020190>
- Hosseini, E., Ghafoori, E., Leinenbach, C., Motavalli, M., & Holdsworth, S. 2018. Stress recovery and cyclic behaviour of an Fe-Mn-Si shape memory alloy after multiple thermal activation. *Smart Materials and Structures*, 27, 25009. <https://doi.org/10.1088/1361-665X/aaa2c9>
- Kotynia, R. (2019). FRP composites for flexural strengthening of concrete structures theory, testing, design. <https://doi.org/10.34658/9788372839961>

- Leinenbach, C., Kramer, H., Bernhard, C., & Eifler, D. 2012. Thermo-Mechanical Properties of an Fe–Mn–Si–Cr–Ni–VC Shape Memory Alloy with Low Transformation Temperature. *Advanced Engineering Materials*, 14(1–2), 62–67. <https://doi.org/10.1002/ADEM.201100129>
- Michels, J., Shahverdi, M., & Czaderski, C. 2018a. Flexural strengthening of structural concrete with iron-based shape memory alloy strips. *Structural Concrete*, 19(3), 876–891. <https://doi.org/10.1002/suco.201700120>
- Michels, J., Shahverdi, M., Czaderski, C., & El-Hacha, R. 2018b. Mechanical performance of iron-based shape-memory alloy ribbed bars for concrete prestressing. *ACI Materials Journal*, 115(6), 877–886. <https://doi.org/10.14359/51710959>
- Mohd Jani, J., Leary, M., Subic, A., & Gibson, M. A. 2014. A review of shape memory alloy research, applications and opportunities. *Materials & Design (1980-2015)*, 56, 1078–1113. <https://doi.org/10.1016/J.MATDES.2013.11.084>
- Raza, S., Shafei, B., Saiid Saiidi, M., Motavalli, M., & Shahverdi, M. 2022. Shape memory alloy reinforcement for strengthening and self-centering of concrete structures—State of the art. *Construction and Building Materials*, 324, 126628. <https://doi.org/https://doi.org/10.1016/j.conbuildmat.2022.126628>
- Rogowski, J., & Kotynia, R. 2022. Comparison of Prestressing Methods with CFRP and SMA Materials in Flexurally Strengthened RC Members. *Materials 2022, Vol. 15, Page 1231, 15(3)*, 1231. <https://doi.org/10.3390/MA15031231>
- Rojob, H., & El-Hacha, R. 2017a. Self-prestressing using iron-based shape memory alloy for flexural strengthening of reinforced concrete beams. *ACI Materials Journal*, 114(2), 523–532. <https://doi.org/10.14359/51689455>
- Rojob, H., & El-Hacha, R. 2017b. New anchorage mechanism for smooth Fe-SMA bar used for flexural strengthening of RC beams using NSM technique. *SMAR 2017: Fourth International Conference on Smart Monitoring, Assessment and Rehabilitation of Civil Structures*.
- Rojob, H., & El-Hacha, R. 2018a. Fatigue performance of RC beams strengthened with self-prestressed iron-based shape memory alloys. *Engineering Structures*, 168, 35–43. <https://doi.org/10.1016/j.engstruct.2018.04.042>
- Rojob, H., & El-Hacha, R. 2018b. Performance of RC beams strengthened with self-prestressed Fe-SMA bars exposed to freeze-thaw cycles and sustained load. *Engineering Structures*, 169, 107–118. <https://doi.org/10.1016/J.ENGSTRUCT.2018.04.009>
- Schranz, B., Michels, J., Czaderski, C., Motavalli, M., Vogel, T., & Shahverdi, M. 2021. Strengthening and prestressing of bridge decks with ribbed iron-based shape memory alloy bars. *Engineering Structures*, 241, 112467. <https://doi.org/10.1016/J.ENGSTRUCT.2021.112467>
- Schranz, B., Michels, J., Czaderski, C., & Shahverdi, M. 2019. Strengthening of concrete structures with iron-based shape memory alloy elements: Case studies. *SMAR 2019: Fifth Conference on Smart Monitoring, Assessment and Rehabilitation of Civil Structures*.
- Shahverdi, M., Czaderski, C., Annen, P., & Motavalli, M. 2016a. Strengthening of RC beams by iron-based shape memory alloy bars embedded in a shotcrete layer. *Engineering Structures*, 117, 263–273. <https://doi.org/10.1016/J.ENGSTRUCT.2016.03.023>
- Shahverdi, M., Czaderski, C., & Motavalli, M. 2016b. Iron-based shape memory alloys for prestressed near-surface mounted strengthening of reinforced concrete beams. *Construction and Building Materials*, 112, 28–38. <https://doi.org/10.1016/J.CONBUILDMAT.2016.02.174>
- Shahverdi, M., Michels, J., Czaderski, C., & Motavalli, M. 2018. Iron-based shape memory alloy strips for strengthening RC members: Material behavior and characterization. *Construction and Building Materials*, 173, 586–599. <https://doi.org/10.1016/j.conbuildmat.2018.04.057>
- Shahverdi, M., & Czaderski, C. 2019. Long-term behavior of reinforced concrete beams strengthened by iron-based shape memory alloy strips. *SMAR 2019: Fifth International Conference on Smart Monitoring, Assessment and Rehabilitation of Civil Structures*.
- Strieder, E., Aigner, C., Petautschnig, G., Horn, S., Marcon, M., Schwenn, M., Zeman, O., Castillo Ruano, P., Wan-Wendner, R., & Bergmeister, K. 2019. Strengthening of Reinforced Concrete Beams with Externally Mounted Sequentially Activated Iron-Based Shape Memory Alloys. *Materials*, 12, 345. <https://doi.org/10.3390/ma12030345>
- Yang, Y., Breveglieri, M., & Shahverdi, M. 2021. Effect of Phase Changes on the Axial Modulus of an FeMnSi-Shape Memory Alloy. *Materials 2021, Vol. 14, Page 4815, 14(17)*, 4815. <https://doi.org/10.3390/MA14174815>
- Yeon, Y. M., Hong, K. N., & Ji, S. W. 2022. Flexural Behavior of Self-Prestressed RC Slabs with Fe-Based Shape Memory Alloy Rebar. *Applied Sciences (Switzerland)*, 12(3). <https://doi.org/10.3390/APP12031640>

FRP shear dowels - Experimental investigation

Đ. Čairović, M. Zlámal, J. Venclovský & P. Štěpánek
Brno University of Technology, Brno, Czech Republic

ABSTRACT: Main aim of this paper is to present extensive experimental investigation and define different load-bearing mechanisms, in cases when FRP shear dowels were provided as the reinforcement crossing the interface. More precisely, research was focused on use of non-corrosive GFRP (Glass-Fibre Reinforced Polymer) rebars as durable alternative to commonly used steel dowels, with a potential to significantly reduce life-cycle costs connected with maintenance of the structures.

1 INTRODUCTION

The need for strengthening of existing concrete structures has become more pronounced over the last decade, since a great number of buildings and engineering structures across Europe is reaching their design life span. Demolition and replacement of those structures with newly built is mainly cost inefficient and has higher negative impact on environmental and social aspects of the civil engineering sector. Therefore, strengthening of those structures is usually recommended, since it can extend their life, while at the same time ensuring the serviceability requirements and the safety of all users.

In cases of structural repairs, placing an additional concrete layer over existing structures is one of the most common types of structural strengthening. But whenever new concrete is cast against existing hardened concrete layer, concrete-to-concrete load transfer becomes relevant, since monolithic behaviour of composite structure needs to be ensured.

Strength of the interface is generally governed by the properties of adhesive bond or amount of the reinforcement crossing the interface. If adequate surface preparation cannot be realized, or adhesion is insufficient, shear dowels must be provided.

In order to fully utilize shear reinforcement, it has to be assumed that adhesive bond is lost, and that crack will appear along the interface. Especially in the cases of vertical interfaces, those cracks can be main cause of many durability issues like corrosion of the reinforcement. For that reason, performance of FRP (Fibre Reinforced Polymers) shear dowels was investigated, representing durable alternative to commonly used steel dowels (Čairović *et al.*, 2021).

2 EXPERIMENTAL INVESTIGATION

As described above, behaviour of the reinforced concrete-t-concrete interfaces is rather complex problem, and its resulting strength is governed by different, mutually affected load-bearing mechanisms. For that reason, experimental investigation was divided into 3 dedicated tasks:

- To obtain shear strength of GFRP reinforcement,
- To assess strength of the interface with GFRP reinforcement and
- To assess strength of the interface with typical steel reinforcement, to serve as reference.

2.1 Shear strength of GFRP rebars

Shear strength of commonly used steel reinforcement can be estimated by for example von Mises failure hypothesis (Randl, 2013), where the magnitude of the shear yield stress is $\sqrt{3}$ -times lower than the tensile yield stress in the case of simple tension. For reinforcement grade B500 B, corresponding shear strength will be approximately 320 MPa. Somewhat higher value of 420 MPa was obtained experimentally but still, it can be stated that abovementioned approximation provides reasonable results.

This cannot be applied for FRP reinforcement, due to its un-isotropic character. Also, somewhat lower values of shear strength can be expected, since best properties of the FRP rebars can be obtained in longitudinal direction i.e., direction of load-bearing fibres. Transverse shear strength of FRP rebars can be evaluated by standardized test methods, using double shear test machine (ACI 440.3R, 2004; ISO 10406-1, 2015), presented in Figure 1. Specimen is sheared on two planes by two blades converging along the faces perpendicular to its axial direction. Typical failure of specimens is presented in Figure 2.



Figure 1. Transverse shear test: experimental test setup (right).



Figure 2. Transverse shear test: failure of GFRP specimen (left) and B500 B steel specimen (right).

Experimentally obtained values of transverse shear strength and basic mechanical properties of the rebars used in this experimental investigation are summarized in Table 1. below.

Even thou tensile strength of used GFRP was much higher, oppose to steel reinforcement, ultimate shear strength of 180 MPa was obtained. This value is even lower, comparing to the steel reinforcement, since as it was already stated, loading direction in case of transverse shear is perpendicular to the direction of the fibres and this mechanical property is mainly governed by the properties of matrix. For that reason, steel rebars 8 mm in diameter were substituted with 10 mm GFRP bar, leading to similar shear resistance.

Table 1. Mechanical properties of FRP and steel reinforcing bars.

	Yielding strength f_y [MPa]	Ultimate tensile strength f_u [MPa]	Ultimate shear strength τ_s [MPa]	Modulus of elasticity E [GPa]
Steel B500 B	548	645	420	200
GFRP	-	1080	180	52

2.2 Interface shear strength

To evaluate performance of GFRP (Glass Fibre Reinforced Polymers) rebars as a shear reinforcement for concrete-to-concrete interfaces, push-off tests were performed (Ćairović *et al.*, 2021). This test configuration is mainly used to characterize the shear strength of reinforced interfaces. In fact, test configurations in this category uniquely allow the use of shear reinforcement that crosses the interface, either perpendicularly or inclined.

Dimensions of the specimen were $400 \times 400 \times 300$ mm, while both concrete layers had the same thickness of 150 mm. Specimens were performed in 3 stages: casting of the substrate layer, post-installation of the shear dowels and casting of the overlay, as presented in Figure 3.

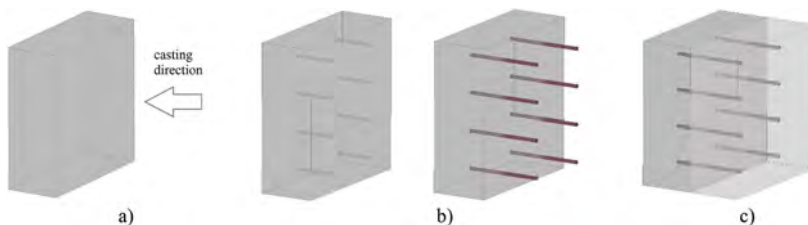


Figure 3. Stages of specimen preparation: a) casting of the substrate layer; b) post-installation of the shear dowels; c) casting of the overlay.

In cases when shear dowels were provided, either GFRP 10 mm in diameter or steel reinforcement B500 B 8 mm in diameter was used. Based on reinforcement provided, 4 different series can be defined: with 2, 4, 8 and 16 rebars. Orientation of the reinforcement is shown in Figure 4. Each series also included one referential specimen, without any reinforcement crossing the interface.

In all the cases, distance of the bar from the edge was at least 50 mm. This distance, larger than 5 diameters, should ensure that splitting of the concrete cover will not likely occur

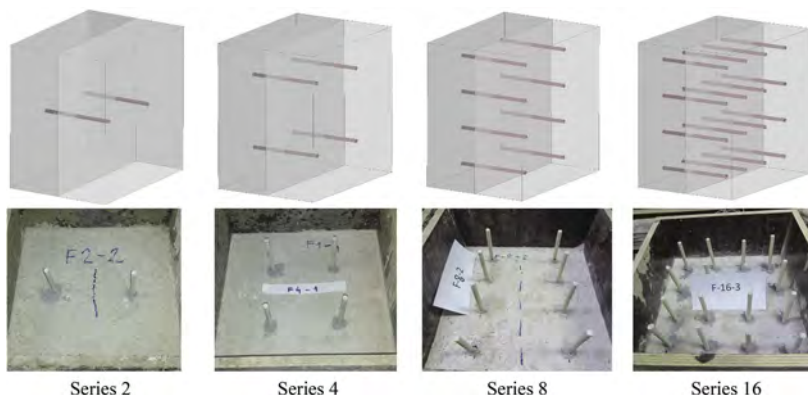


Figure 4. Orientation of the reinforcement for different series.

(for more information see for ex. (Vintzēleou and Tassios, 1986)). Anchorage length of 100 mm was chosen, and being larger than 10 bar diameters it should be sufficient, since according to (Randl, 2013) no influence on the magnitude of the shear resistance have been observed for anchorage depths of $6 \varnothing$ or more.

Seven days after casting of the substrate layer, 14 mm and 16 mm diameter holes were drilled for steel and FRP reinforcement, respectively. Afterwards, shear dowels were bonded using commercial epoxy adhesive, following by placing of the overlay concrete.

Concrete mixtures for both concrete layers have been adjusted, to realistically reflect possible in-situ applications. For that reason, mechanical properties of substrate layer are significantly lower, comparing to the overlay. It corresponds to the situation when old concrete structure is strengthened by additional concrete layer.

In addition to reinforcement properties summarized in Table 2, mechanical properties of hardened concrete were also experimentally obtained.

Table 2. Mechanical properties of the concrete.

	Mean cubic compressive strength $f_{cm,cube}$ [MPa]	Mean splitting tensile strength f_{ctm} [MPa]
Substrate concrete	23.5	2.1
Overlay concrete	77.6	3.6

Testing presented in Figure 3, occurred 28 days after overlay was cast. Supporting and loading beams were carefully aligned and placed approximately 5 mm from the interface plane. Specimen was also anchored to the column, 100 mm below top surface.

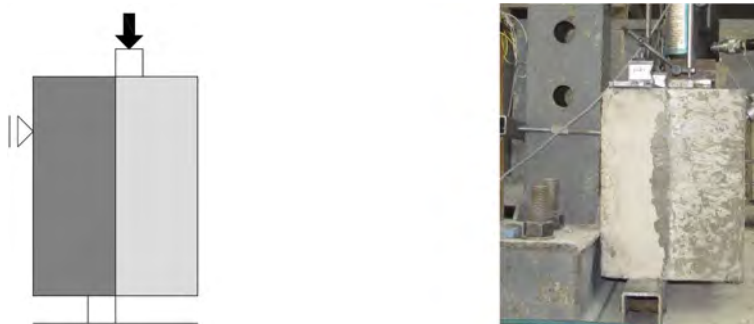


Figure 5. Push-Off Test setup: scheme (left) and experimental test setup (right).

Experimentally obtained values of ultimate applied loads and corresponding interface slips are summarized in Table 3, below (see Section 4 for definitions of ultimate forces). Labelling of series corresponds to material of the reinforcement and number of provided rebars (for example F2: FRP reinforcement, 2 rebars).

Based on obtained results and its mutual comparison presented in Figure 6, it can be stated that, even though somewhat higher values of shear slips were observed if FRP reinforcement was used, it represents good alternative to traditionally used steel reinforcement.

3 RESULTS AND DISCUSSION

In (fib, 2013) two bond-slip behaviours have been distinguished, corresponding to ultimate strength of the interface and its main contributors. In accordance with presented behaviour, three ultimate resisting forces have been presented in Figure 6, and defined as follows:

Table 3. Push-Off Test Results.

Series	Reinf.	Ø [mm]	No. of bars [-]	ρ [%]	F _{MAX,0} [kN]	w ₀ [mm]	F _{MAX,I} [kN]	w _I [mm]	F _{MAX,II} [kN]	w _{II} [mm]
REF	-	-	-	0.0%	117.6	-	-	-	-	-
S2	B500 B	8	2	0.6%	198.9	0.021	-	-	70.4	5.358
S4	B500 B	8	4	1.3%	118.4	0.031	113.4	0.387	135.3	14.331
S8	B500 B	8	8	2.5%	211.4	0.038	280.6	0.153	229.6	8.532
S16	B500 B	8	16	5.0%	226.2	0.059	384.8	0.413	329.3	7.022
F2	GFRP	10	2	1.0%	229.5	0.075	-	-	-	-
F4	GFRP	10	4	2.0%	144.8	0.015	154.4	2.561	-	-
F8	GFRP	10	8	3.9%	210.6	0.100	292.6	1.647	-	-
F16	GFRP	10	16	7.9%	211.1	0.035	399.7	2.418	-	-

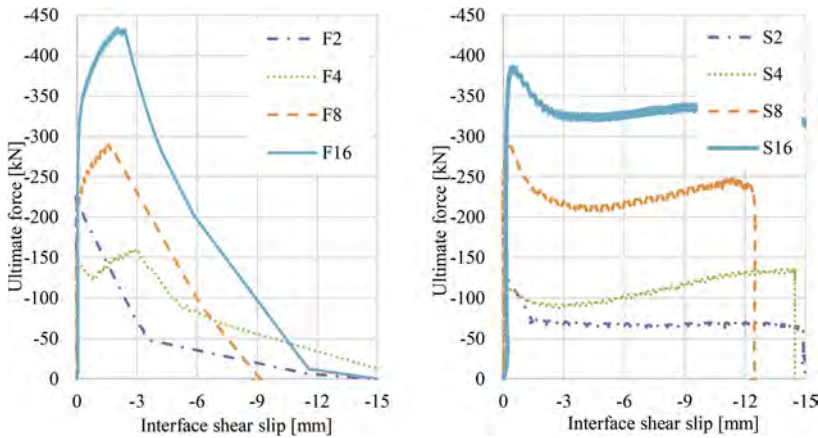


Figure 6. Typical Force-Slip diagrams for interfaces with FRP (left) and steel (right) reinforcement.

- $F_{max,0}$ corresponding to brittle failure mode typical for interfaces without shear reinforcement,
- $F_{max,I}$ represent ductile failure mode and contribution of reinforcement, friction and mechanical interlocking and
- $F_{max,II}$ observed during kinking of the reinforcement.

For the purposes of this experimental study, force $F_{max,II}$ can be neglected, since kinking effect occurs together with extensive deformations of the interface, therefore it is not relevant for design purposes. Opposite to $F_{max,II}$, force $F_{max,0}$ occurs at relatively low slips and describes brittle interface failure. Even though it is relevant for the design of concrete-to-concrete interfaces in general, behaviour of the interfaces without shear reinforcement is out of the scope of this paper.

According to (fib, 2013), strength of the interfaces intersected by steel dowels τ_{Rdi} can be estimated as follows:

$$\tau_{Rdi} = c_r \cdot f_{ck}^{1/3} + \mu \cdot \sigma_n + \kappa_1 \cdot \rho \cdot f_{yd} (\mu \cdot \sin \alpha + \cos \alpha) + \kappa_2 \cdot \rho \cdot \sqrt{f_{yd} \cdot f_{cd}} \leq \beta_c \cdot \nu \cdot f_{cd}. \quad (1)$$

where c_r = the coefficient for aggregate interlock effects at rough interfaces; f_{ck} = characteristic value of cylinder compressive strength of concrete; μ = coefficient of friction; σ_n = the (lowest expected) compressive stress resulting from an eventual normal force acting on the interface; κ_1 = the interaction coefficient for tensile force activated in the reinforcement or the dowels; ρ = the reinforcement ratio of the reinforcing steel crossing the interface; f_{yd} = design yield strength of reinforcing steel in tension; α = the inclination of the reinforcement crossing the interface; κ_2 = the

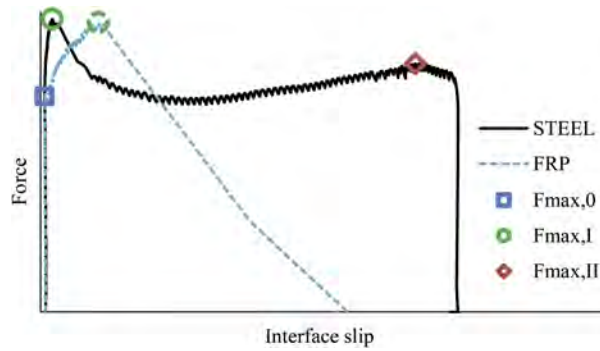


Figure 7. Typical force-slip behaviour of reinforced interfaces.

interaction coefficient for flexural resistance; f_{cd} = design value of cylinder compressive strength of concrete; β_c = the coefficient for the strength of the compression strut and ν = reduction.

First part of the equation corresponds to aggregate interlock at rough interfaces. As recommended, value of the coefficient c_r for smooth interfaces is assumed to be zero.

Second part describes the dry friction, caused by normal stress acting perpendicular to the interface plane and could be neglected for the purposes of this investigation. Regardless, it is assumed that recommendations listed in (fib, 2013; Randl, 2013) are applicable. Based on previous observations and recommendations available in the literature (Čairović *et al.*, 2016, 2019; Čairović, 2021), it could be stated, that even though recommended value of coefficient of friction μ is 0.6, somewhat higher values are usually obtained.

Third part represents friction caused by clamping forces and it depends on interaction coefficient κ_1 , yielding strength of the steel and the reinforcement ratio. Since yielding of the bars will not occur if FRP reinforcement was used, last part of the equation corresponding to flexural resistance of the reinforcement can be omitted i.e., value of interaction coefficient for flexural resistance κ_2 can be set as zero. Correspondingly, value of κ_1 can be adjusted and instead of 0.5, recommended for interfaces other than very smooth, 1.0 can be used since no interaction is expected and full contribution of dowel action can be assumed.

Hence, if FRP rebars were used as shear dowels, following modified design equation can be used for estimation of interface strength:

$$\tau_{Rd,FRP} = c_r \cdot f_{ck}^{1/3} + \mu \cdot \sigma_n + \rho \cdot \tau_s(1 + \mu) \leq \beta_c \cdot \nu \cdot f_{cd} \quad (2)$$

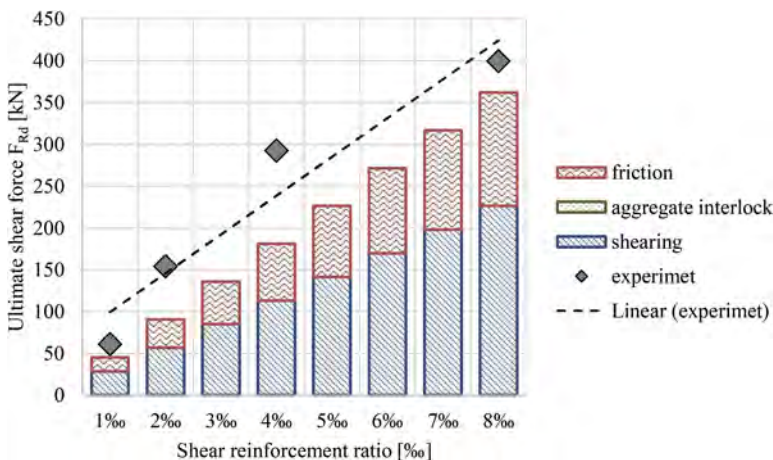


Figure 8. Dependence between interface strength and reinforcement ratio.

In general, good correlation between experimentally obtained results and the resulting interface strength determined using abovementioned Equation (2) was obtained, as presented in Figure 7. Presented analytical approach slightly underestimates interface strength. One of the main reasons is, as stated above, that a somewhat higher contribution of friction was usually observed.

It has to be stated, that experimentally obtained dependence between interface strength and reinforcement ratio shows non-linear character. For that reason, it is not recommended to use the proposed equation for the estimation of strength for the interfaces with reinforcement ratio outside of the scope of this experimental investigation.

4 CONCLUSIONS

Based on extensive experimental study presented above, following conclusion could be drawn:

- Performance of the concrete-to-concrete interfaces reinforced with GFRP rebars has been experimentally validated and in general shows good behaviour, comparable to the interfaces with traditional steel reinforcement;
- Analytical approach has been presented, allowing the design of the interfaces reinforced with FRP rebars and extension of the application fields of this durable and environmentally friendly material;
- Further research, including different types of reinforcement, concrete classes and/or surface preparation methods is necessary to confirm presented results and allow structural applications of FRP dowels and use of presented analytical design approach in everyday practice.

Extensive numerical analysis, aiming to detailly investigate load-bearing mechanisms and strength of the interfaces intersected by FRP and steel dowels, has been carried out at present and it will be presented in future contributions.

ACKNOWLEDGEMENTS

This work was supported by the Technology Agency of the Czech Republic (TACR), project No. TH04020431 “Extension of the application area of FRP reinforcement in concrete structures” and project No. FW01010520 “Development of bent composite reinforcement for environmentally exposed concrete constructions”. This support is gratefully acknowledged.

REFERENCES

- ACI 440.3R (2004) *Guide Test Methods for Fiber-Reinforced Polymers (FRPs) for Reinforcing or Strengthening Concrete Structures*, American Concrete Institute.
- Čairović, Đ. *et al.* (2016) ‘Comparison and Review of Concrete-to-Concrete Interface Shear Resistance According to Major Design Codes’, *Solid State Phenomena*. Trans Tech Publications, Ltd., 249, pp. 166–172. doi: 10.4028/www.scientific.net/ssp.249.166.
- Čairović, Đ. *et al.* (2019) ‘Frp shear dowels as alternative reinforcement of concrete-to-concrete interface’, in *fib Symposium*. Krakow, pp. 1275–1282.
- Čairović, Đ. (2021) *PhD Thesis: Behavior of the concrete-to-concrete interface without shear reinforcement*. Brno: Brno University of Technology.
- Čairović, Đ. *et al.* (2021) ‘Suitability of different tests for characterization of the dimpled concrete-to-concrete interface’, *Structural Concrete*, 22(2), pp. 757–774. doi: 10.1002/suco.201900513.
- fib (2013) *fib Model Code for Concrete Structures 2010*. Weinheim, Germany: Wiley-VCH Verlag GmbH & Co. KGaA. doi: 10.1002/9783433604090.
- ISO 10406-1:2015 (2015) *Fibre-reinforced polymer (FRP) reinforcement of concrete — Test methods — Part 1: FRP bars and grids*. 2nd edn. Available at: <https://www.iso.org/standard/63657.html> (Accessed: 25 August 2022).
- Randl, N. (2013) ‘Design recommendations for interface shear transfer infibModel Code 2010’, *Structural Concrete*. Wiley, 14(3), pp. 230–241. doi: 10.1002/suco.201300003.
- Vintzēleou, E. N. and Tassios, T. P. (1986) ‘Mathematical models for dowel action under monotonic and cyclic conditions’, *Magazine of Concrete Research*, 38(134), pp. 13–22. doi: 10.1680/mac.1986.38.134.13

Bond behavior of CFRP-concrete systems using toughened epoxies

D.V. Achillopoulou

James Watt School of Engineering, University of Glasgow, Glasgow, UK

A. Kosta

Laboratory of Reinforced Concrete and Seismic Design of Structures, Democritus University Of Thrace, Xanthi, Greece

A. Montalbano

Sika Services AG, Zurich, Switzerland

F. Choffat

Sika Technology AG, Zurich, Switzerland

ABSTRACT: In the current research the interface response of Carbon Fiber Reinforced Polymers (CFRP) adhesively bonded on concrete substrates is investigated considering two scenarios with and without corroded reinforcement. The investigation includes Near Surface Mounted (NSM) CFRP strengthening schemes embedded to concrete using two-component epoxy adhesive layers, a conventional and a toughened one. The bond-slip behavior of the interfaces between the concrete and FRPs was investigated with a modified double shear test configuration. The experimental results indicate a different effect of the toughened adhesive on the response of the interface as the interface is not affected by corrosion. The crack propagation of the interface is depicted by two different distinct branches, a fully elastic up to the peak shear stress-strain, and a quasi-stable branch up to final pull out of the composite. The reduced stiffness and high energy absorbing capacity toughened adhesive epoxies are proven to be optimal retrofitting solutions for concrete applications.

1 INTRODUCTION

Structures often suffer from exposure to extreme corrosive environments leading to a decrease in their structural performance and safety. Therefore, retrofitting solutions using bonded composites such as Fiber Reinforced Polymers has attracted a lot of interest resulting in a technological advancement of structural refurbishment. The efficiency of the retrofitting measures depends mainly on the response of the interface between the concrete substrate and the composite (Mehta, & Monteiro. 2014); (Siddika et al. 2019).

The FRPs are applied on an adhesive layer, mainly epoxy adhesives for structural applications. This kind of strengthening enhances the deformability of the strengthened structure without increasing the stiffness of the member or changing the geometry of the elements (Heiza et al. 2014); (Siddika et al. 2019). The integrity of the concrete substrate and the type of epoxy adhesive used influence the bonding of the strengthening measure and the level of integration into concrete. Standard epoxy adhesives normally show high tensile modulus and result in brittle fracture of the matrix. Lately, toughened epoxy adhesives are developed having lower stiffness and higher fracture energy due to rubber-like nanoparticles of their matrix. These adhesives are mainly designed for dynamic loads (Kasper 2019); (Achillopoulou et al. 2021); (Achillopoulou et al. 2022).

The objective of this research paper is to explore the application of such adhesives to FRP measures for concrete solutions. To address this objective, the interfacial response of FRP and

concrete substrate is investigated experimentally. Due to the brittle behavior of concrete, there was a focus on the examination of the limitation of the substrate's crack propagation by comparing conventional and toughened retrofitting systems. Cracking schemes created to the interface due to the initial stage of corrosion are also examined. The interaction of the concrete substrate with the epoxy adhesive layer is studied by conducting double-lap shear tests. The toughened adhesives are expected to absorb more energy before debonding while having a lower modulus of elasticity (Kasper 2019); (Achillopoulou et al. 2021); (Achillopoulou et al. 2022).

2 EXPERIMENTAL INVESTIGATION

The current study was supported through an experimental campaign. The campaign has two phases: a) laboratory accelerated corrosion simulation and b) shear testing. The wider experimental campaign includes commercialized FRP systems (Near Surface Mounted bars-NSM) applied in concrete substrates containing health or corroded reinforcement using three different adhesive layers, one of which is toughened (Sikadur®-370), while the rest two are compatible.

2.1 *Materials*

Nine concrete blocks with dimensions 150x150x250mm were prepared according to (ACI 1991); (EN1008 1995); (Su et al. 2001) with 28-day compressive strength of 37.5MPa corresponding to a tensile strength of 3MPa. All blocks contained steel rebar ($f_{sy}=500\text{MPa}$) of 18mm diameter in the middle of the cross-section placed longitudinally to the concrete block. CFRP NSM (Sika® CarboDur® S: density $\rho=1.6\text{kg/L}$, tensile strength $\sigma_u=3100\text{MPa}$, modulus of elasticity $E_{0.05-0.25\%}=170\text{GPa}$, tensile strain $\epsilon_{EAB}=1.8\%$) were bonded symmetrically on opposite sides of the concrete blocks at a bond length equal to 200mm.

The NSMs are embedded on the concrete cover in a groove opened using a diamond cutting wheel. The groove's depth was equal to 3.3mm. The systems were applied with a dry layup process and according to the technical specification of the manufacturer. The interfaces were treated properly to have a laitance contaminant-free, open-textured surface and were cleaned with air pressure to remove loose material, dust and rust. The two components' epoxy adhesives were mixed according to the manufacturer's recommended ratio and time (3:1 for Sikadur®-30, 4:1 for Sikadur®-330 and 100:74 for Sikadur®-370). Before the application of the FRPs to the groove, the specimens were cleaned with a grease-free, solvent-based cleaning agent (Sika® Colma Cleaner). The composites were left to cure at ambient conditions (20°C, 50% relative humidity-RH) for at least a week before testing.

2.2 *Accelerated corrosion*

The concrete prisms were exposed to cycles of wet and dry conditions. They were submerged in a tank containing a NaCl-water solution of 3.5-5% weight concentration (Figure 1a), which covered one third of the cross-section size of the concrete blocks (van Zijl & Paul 2018); (Batuwitige et al. 2017). A continuous power supply ($\approx 1\text{mA}$) (Batuwitige et al. 2017) wired in the steel rebars for about three weeks was used to create a low ratio of corrosion equal to 6% of the steel rebar cross-section. After three weeks, the prisms were cured to dry conditions in the lab.

2.3 *Experimental configuration*

Various experimental setups of double lap tests exist in the international literature (Mukhtar & Faysal 2018). These configurations permit the direct examination of the shear stresses of the interface and the bonding capacity of the materials. This study uses the double lap shear test (Figure 1b) modified by Achillopoulou (2021). In this setup, the FRPs are gripped using steel plates that are supported to a rigid steel frame from which the concrete block is hanged. The hollow support permits relative slips between the concrete block and the FRPs if a compression load is applied to the concrete block. The steel plates were further altered to fit the cross-section shape of the FRPs and also to reduce their potential slip during the test by formulating a wedge

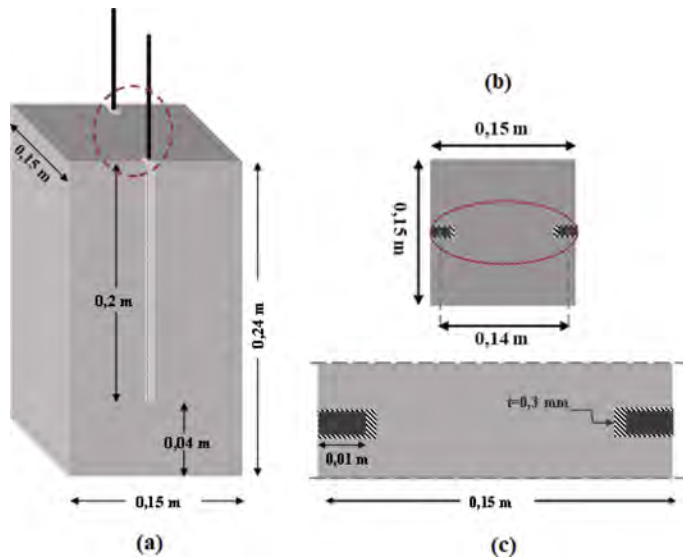


Figure 1. Concrete prism (a) embedment length of NSM bar, (b) detail, (c) cross-section plan view.

Table 1. Mechanical properties of epoxy adhesive layers and FRPs.

Type	ρ^* [kg/L]	σ_u^* [MPa]	E^* [GPa]	ε^* [%]
Sikadur [®] -30	2	26	9500	0.3
Sikadur [®] -330	1.4	29	4000	1
Sikadur [®] -370	1.7	30	5000	2.5
Sika [®] CarboDur [®] -S	1.6	3100	170	1.8

* Where ρ is density, σ_u is tensile strength, E is the modulus of elasticity within values 0.05-0.25% and ε is tensile strain (EAB).

(Figure 3a, b, c). For the case of NSM, the experimental setup practically simulates the pull-out tests aimed to characterize bonding. The tests were performed on a compression machine at a speed of 1mm/min at room temperature (20°C). The measurements of the deformation of the central part of the CFRP were recorded using a high accuracy laser sensor. Also, two Linear Displacement Transducers (LDVT) with a maximum capacity of 100mm, were used to measure the displacement of the upper level of the concrete block and the grips.

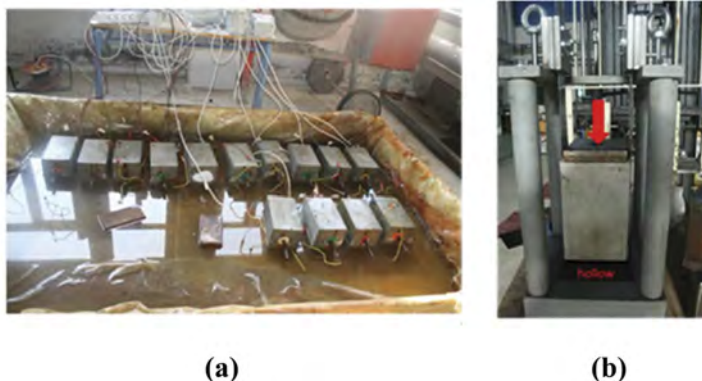


Figure 2. Experimental campaign: (a) accelerated corrosion, (b) double lap (DL) setup.

3 RESULTS

3.1 Experimental results

The bond level is measured up to the stress level needed so the NSM bars are pull-out. The results are presented in shear stress-shear deformation diagrams for the three different adhesives used for the healthy and corroded substrate. Table 2 below contains the characteristic values of the experimental results, the mean values and errors. All tests presented a similar response. An initial branch with small stiffness variations up to the maximum point is noted for all adhesive layers used (Figure 4), followed by an abrupt reduction and subsequently a remaining load. The peak point is related to the ultimate strain limit of the adhesives. At those instants the curve reaches the peak and then becomes non-linear. The extensive slip is denoted by a practically stable load level due to the mechanical interlock of the materials.

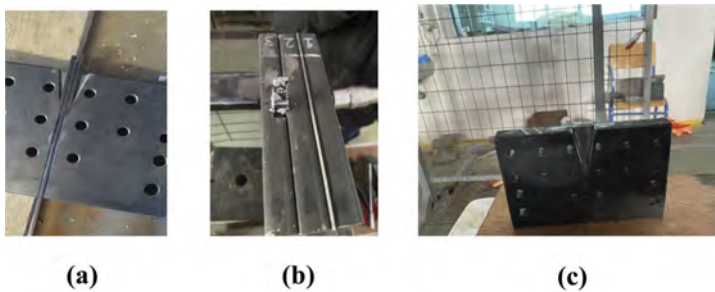


Figure 3. Altered gripping steel plates: (a) gripping profile, (b) gripping end, (c) wedge shape.

According to test results for the healthy concrete substrate (Figure 4a, b, c), all adhesives presented the same levels of stresses without any significant variations (5-12%). The strain levels were similar for the conventional Sikadur®-30 and the toughened Sikadur®370 adhesive. Even though, the modulus of elasticity of the toughened epoxy is almost half of that of the conventional adhesive, its high deformability is dominant in shear stress distribution along the interface. If compared with Sikadur®-330, which has an intermediate level of mechanical properties, the performance of the toughened layer is also enhanced, in terms again of strain levels before the final pull-out. The transition point is presented in early strain levels for Sikadur®-370. The epoxy is activated earlier and bears the strains before bonding is completely lost and interlocking of materials is only acting. This means that in all cases, the toughened epoxy absorbs the highest percentage of energy before failure. Compared to Sikadur®-330, the toughened epoxy absorbs almost 70% higher energy, whereas, the energy closes to Sikadur®-30 epoxy. The remaining stress level is similar in all cases.

The second series of tests examined the effect of corrosion in early stages on the bonding of the NSMs. The compatible adhesives Sikadur®-30 and Sikadur®-330 presented a slightly different response compared to the healthy specimens. For this scheme (Figure 4d, e), both adhesives presented a reduced (5%) initial stiffness, different though stress-strain field. For the case of Sikadur®-30 stresses are 15-25% lower when the substrate is corroded, noted 15-45% lower levels of strains. The intermediate adhesive layer Sikadur®-330 presents similar stresses in both substrate schemes, though the peak point occurred in lower strains some of them even 70% lower. Regarding the toughened adhesive Sikadur® -370, the response was slightly different and practically there is no significant influence of the corrosion products on the bonding capacity of this category. In fact, the curve is also less steep after the peak point (Figure 4f) denoting a different scheme in crack propagation on the substrate before pull-out. In terms of energy, the NSM embedded using the toughened epoxy Sikadur®-370 presented higher energy than all.

3.2 Failure modes

At end of the tests, differences were also reported regarding the failure modes between the compatible and toughened adhesives used to embed the NSMs. Those differences are related

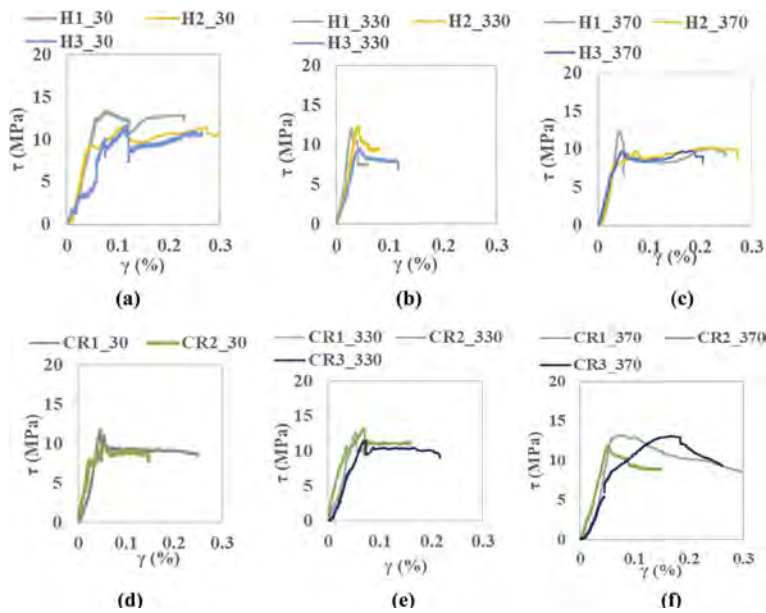


Figure 4. Shear stress-strain curves for healthy substrate (a) Sikadur® 30, (b) Sikadur® 330, (c) Sikadur® 370 and for corroded substrate (d) Sikadur® 30, (e) Sikadur® 330, (f) Sikadur® 370.

Table 2. Experimental results.

Healthy substrate								Corroded substrate							
	τ^{trans}	τ^{peak}	τ^u	γ^{trans}	γ^{peak}	γ^u	E		τ^{trans}	τ^{peak}	τ^u	γ^{trans}	γ^{peak}	γ^u	E
	(MPa)								(MPa)						
	%								%						
	(MJ/m ³)								(MJ/m ³)						
H130_1	12.10	13.80	12.05	0.06	0.08	0.21	1.85	Cr30_1	12.32	10.48	9.25	0.06	0.07	0.25	1.96
H130_2	9.23	11.34	10.91	0.05	0.11	0.27	2.64	Cr30_2	7.99	10.05	8.47	0.04	0.06	0.15	0.94
H130_3	10.07	11.60	10.02	0.08	0.12	0.26	2.04								
mean 30	10.47	12.25	10.99	0.06	0.10	0.25	2.18	mean 30	10.15	10.27	8.86	0.05	0.07	0.20	1.45
H1330_1	12.36	9.44	9.29	0.04	0.06	0.08	0.70	Cr330_1	10.38	13.35	10.10	0.05	0.07	0.16	1.36
H1330_2	13.10	10.1	9.80	0.05	0.07	0.09	0.62	Cr330_3	10.15	13.85	10.25	0.04	0.09	0.17	1.38
H1330_3	9.28	8.23	7.76	0.05	0.06	0.11	0.57	Cr330_3	6.85	10.35	10.10	0.06	0.09	0.21	1.61
mean 330	11.58	9.26	8.95	0.05	0.06	0.09	0.63	mean 330	9.13	12.52	10.15	0.05	0.08	0.18	1.45
H1370_1	12.34	9.06	9.20	0.04	0.06	0.25	1.92	Cr370_1	13.13	12.46	9.38	0.07	0.11	0.25	1.99
H1370_2	8.06	9.63	9.83	0.03	0.08	0.27	2.12	Cr370_2	11.22	9.37	8.91	0.06	0.10	0.15	1.05
H1370_3	6.69	9.56	9.05	0.03	0.07	0.20	1.41	Cr370_3	7.29	13.03	9.86	0.06	0.18	0.27	1.94
mean 370	9.03	9.42	9.36	0.03	0.07	0.24	1.81	mean 370	10.55	11.62	9.38	0.06	0.13	0.22	1.66

* Where τ^{trans} is shear stress on transition point, τ^{peak} is the peak shear stress, τ^u is shear stress on ultimate point, γ^{trans} is shear deformation on transition point, γ^{peak} is the shear deformation corresponding to the peak shear stress, γ^u is shear deformation on ultimate point and E is the energy absorbed.

to the microstructure of the adhesives. The stress and strain profiles are not constant along the NSM- concrete interface, presenting stress concentration at the extremities. After the loss of bonding depicted with the abrupt loss of shear stress, the progressive detachment corresponds to the post-linear stage shown in the shear stress-strain curves (Figure 4). In that stage, the NSM and concrete continue to interact due to interlocking and friction. The compatible adhesives Sikadur®-30 and Sikadur®-330, exhibited a rather mixed failure that is adhesive-

concrete interface failure. The loss of bonding was accompanied by measurable slip at the NSM strip (Figure 5b). For the case of Sikadur®-370, the failure differs. At the end of the tests, the failure observed was associated with the concrete local plastification (Figure 5c). An adhesive to concrete interface failure was noted, since a concrete cone breakout was detached at the loading end together with the NSM strip followed by slip. This variation is related to the structure and technology of the epoxy itself. The initial design of this adhesive includes rubber-like nano-particles that permit the adhesive to absorb more energy and let the propagation to occur in a larger area. In the case of the toughened epoxy, the cone size is comparatively larger (Figure 6c, d). The cone is formatted at an angle of 45 degrees and its depth is almost 20% of the bonded length of the bar. Compared to the compatible epoxies, the cone is more than the double in volume. The case of toughened epoxy used, resembles to the anchor-bolt failure when embedded in concrete (EN1992-4 2017). This interaction between concrete and NSM can be beneficial to the overall performance of the element.

In the case of the corroded steel reinforcement, the fracture is related to the cone breakout size. The corrosion simulated in the lab corresponds to mild rates which means that the cracking pattern in the mass of the concrete is limited ($w \approx 0.3\text{mm}$) reaches yet the surface and the pit in which the NSM is placed (Figure 6d). For the toughened epoxy, the cone created is much larger than the compatible ones, the corrosion cracking didn't affect the overall response. On the contrary, after the peak point, the load was distributed in the cracked concrete mass and the response was quite stable.

4 CONCLUSIONS

- The modified double-lap testing configuration is suitable also for testing NSM bonding solutions. The wedge modification at the grip plates restrains the slip of the composites, increasing accuracy in shear measurements.
- The bond behavior of NSM is characterized by linear elastic branch up to the peak point followed by a softening transition branch. The softening stage occurs gradually by crack opening propagating from the epoxy layer up to the limit slip point and final pull out of the mounted NSM.

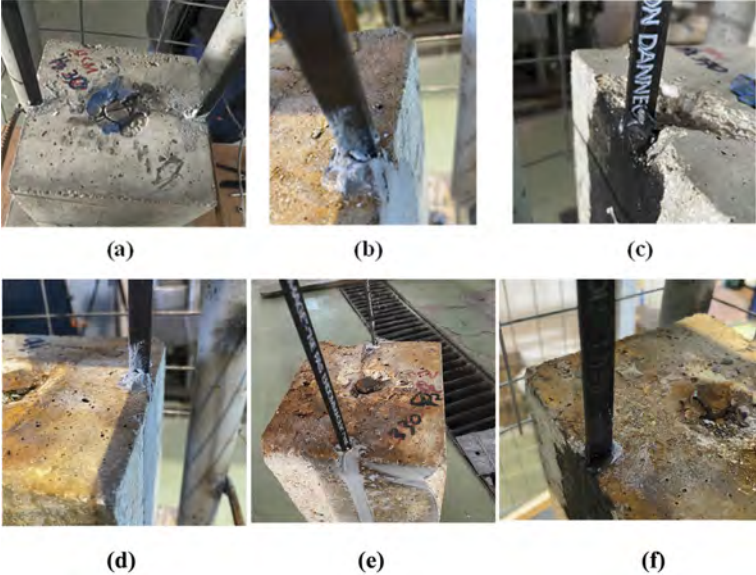


Figure 5. Failure modes (a), (b), (d), (e) for compatible adhesives, (c), (f) for toughened adhesives.

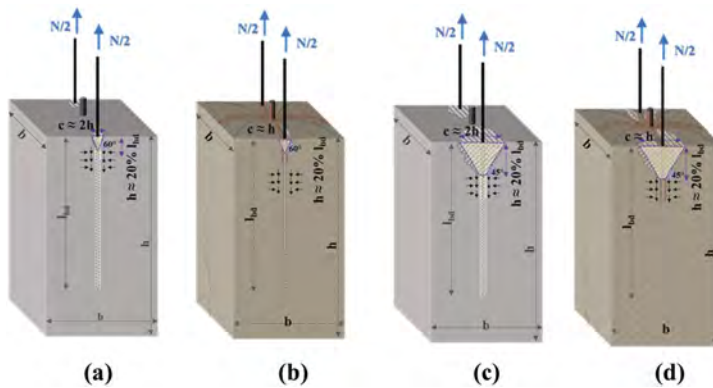


Figure 6. Failure modes: breakout cone (a), (b) for compatible adhesives, (c), (d) for toughened adhesives.

- The corrosion of the substrates affected mainly the conventional epoxies schemes that is Sikadur[®]-30 and Sikadur[®]-330. These adhesives are characterized by lower strain capacity and mainly high Elastic modulus, especially Sikadur[®]-30 having the highest Elastic modulus. The influence of the toughened epoxy Sikadur[®]-370 was practically negligible.
- In the analysis of the failure modes clear differences on the breakout cones denote that the toughened epoxy Sikadur[®]-370 depict a significantly better distribution of the pull load along a larger bonding depth. The breakout cone's volume is more than the double for this epoxy.
- NSM mounted using the toughened epoxy Sikadur[®]-370 absorbs the similar or higher energy ratio if compared with the other two compatible ones. The adhesive is being designed mainly to bear dynamic stresses and to be applied on steel substrates. The application on concrete substrate for structural strengthening especially for NSM systems seems to be effective, especially for structures with high corrosion risk (e.g. bridges decks). The fact that the substrate's corrosion does not affect the system which still deforms and continues to absorb energy can be beneficial to structural applications.

ACKNOWLEDGEMENTS

This study has received funding from the European Union H2020-Marie Skłodowska-Curie Research Grants Scheme MSCA-IF-2018 (grant agreement no 845549: BRIFACE-Novel assessment of bridge retrofitting measures through Interface Efficiency Indices (InterFeis) using a Guided Wave-based monitoring method). Sika AG, as one of the industrial partners of the project, has essentially contributed to the realization of the experimental program. Special thanks to the Democritus University of Thrace and the laboratory of Reinforced Concrete and Seismic Design of Structures for collaborating on the experimental campaign.

REFERENCES

- Achillopoulou, D. V. 2021. Investigation of the bond behaviour of interfaces of CFRP sheet strengthening schemes enhances with toughened epoxy adhesive layers in corroded concrete substrates. *8th International Conference on Computational Methods in Structural Dynamics & Earthquake Engineering COMPDYN 2021*, 27-30 June, Streamed from Athens, Greece.
- Achillopoulou, D. V., Montalbano, A. & Choffat, F. 2022. Interface Response of CFRP Fabrics for Concrete Substrates Enhanced with Toughened Epoxy Adhesive Layers. In *10th International Conference on FRP Composites in Civil Engineering: Proceedings of CICE 2020/2021* 10 (pp. 1632–1644). Springer International Publishing.
- ACI Committee 211. 1991. Standard practice for selecting proportions for normal, heavy-weight, and mass concrete, ACI 211.1–91.

- Attard, T. L. 2020. Toughened carbon-fiber reinforced epoxy via isophorone diisocyanate amine surface modification. *Polymer*, 191, 122268.
- Batuwitage, C., Fawzia, S., Thambiratnam, D. & Al-Mahaidi, R. 2017. Durability of CFRP strengthened steel plate double-strap joints in accelerated corrosion environments. *Comp. Struct.*, 160, 1287-1298.
- Carloni, C., D'Antino, T., Sneed, L. H. & Pellegrino, C. 2018. Three-dimensional numerical modeling of single-lap direct shear tests of FRCM-concrete joints using a cohesive damaged contact approach. *Journal of Comp. for Construction*, 22(1), 04017048.
- EN 1008. 1995. Mixing Water for Concrete Specification for Sampling, Testing & Assessing the Suitability of Water, Including Water Recovered from Processes in the Concrete Industry, as Mixing Water for Concrete, Brussels: CEN, European Commission for Standardization.
- EN1504-4. 2004. Products & systems for the protection & repair of concrete structures: Definitions, requirements, quality control & evaluation of conformity-Part 4: Structural bonding, European Commission. for Standardization.
- EN1992-4. 2017. 'Eurocode 2-Design of concrete structures-Part 4: Design of fastenings for use in concrete', CEN/TC 250.
- Heiza, K., Meleka, A. N., Nabil, A. & Tayel, M. 2014. State-of-the art review: Strengthening of reinforced concrete structures–different strengthening techniques. *In Sixth International Conference on Nano-Technology in Construction*, 6, pp. 22–24.
- Kasper, Y., Albiez, M., Ummenhofer, T., Mayer, C., Meier, T., Choffat, F., Ciupack, Y. & Pasternak, H. 2021. Application of toughened epoxy-adhesives for strengthening of fatigue-damaged steel structures, *Construction & Building Materials*, 275.
- Mehta, P. K. & Monteiro, P. J. 2014. Concrete: microstructure, properties, and materials. *McGraw-Hill Education*.
- Mukhtar F. M. & Faysal, R. M. 2018. A review of test methods for studying the FRP-concrete interfacial bond behavior, *Construction & Building Materials*, 169, 877–887.
- Siddika, A., Al Manum, M. A., Alyousef, R. & Amran, Y. M. 2019. Strengthening of reinforced concrete beams by using fiber-reinforced polymer composites: A review. *Journal of Building Engineering*, 25, 1000798.
- Shi, J.W. & Cao, W.H. & Wu, Z.S. 2019. Effect of adhesive properties on the bond behaviour of externally bonded FRP-to-concrete joints. *Composites Part B: Engineering*, 177.
- Su, N., Hsu, K. C. & Chai, H. W. 2001. A simple mix design method for self-compacting concrete, *Cement & concrete research*, 31(12), 1799–1807.
- van Zijl, G. P. & Paul, S. C. 2018. A novel link of the time scale in accelerated chloride-induced corrosion test in reinforced SHCC, *Construction & Building Materials*, 167, 15–19.

The effect of fatigue loading on the behavior of externally bonded CFRP-to-concrete joints using the grooving method

M. Khorasani

Department of Civil and Environmental Engineering, Politecnico di Milano, Milan, Italy
Department of Civil Engineering, Isfahan University of Technology, Isfahan, Iran

G. Muciaccia

Department of Civil and Environmental Engineering, Politecnico di Milano, Milan, Italy

D. Mostofinejad

Department of Civil Engineering, Isfahan University of Technology, Isfahan, Iran

ABSTRACT: Grooving methods (GM) have remarkably shown higher efficiency than externally bonded reinforcement (EBR) in anchoring the fiber-reinforced polymers (FRP) used for retrofitting concrete structures. The behavior of the EBR and GM installation methods were evaluated in many studies, however the behavior of grooving methods under fatigue loading has not been assessed yet, and the present study is the first attempt to achieve the above aim. Accordingly, three concrete slabs with the dimension of $650 \times 650 \times 200$ mm³ were strengthened using carbon FRP (CFRP) sheets bonded via the EBR and grooving methods and then tested by a single lap-shear setup. Furthermore, the bond behavior of CFRP strips-to-concrete substrate was investigated in this research in terms of the load capacity, slip, and debonding mechanism. The results showed that the grooving method improved the bond properties of CFRP-to-concrete joints under fatigue loading. By using this alternative technique, the number of cycles until failure (fatigue life) increases incredibly under the same fatigue cycle loading and the service life of strengthened members could be improved under fatigue loading.

1 INTRODUCTION

In recent years, fiber-reinforced polymers (FRPs) have emerged as a trustworthy option for the repair and rehabilitation of concrete structures. The attentions of researchers have been attracted because of their advantageous properties such as low weight, high tensile strength, ease of transport, easier application in confined spaces, minimizing disruption of occupancy, and high durability under harsh environmental conditions (ACI440.2R, 2017, Fib-Bulletin-90, 2019). Despite all the advantages, FRP materials also have some disadvantages. Debonding of FRP composites from concrete substrate is a major concern in retrofitting of reinforced concrete structures. In fact, the efficiency of the retrofitting system relies on the perfect bond between FRP and substrate, and thus, loss of bond would diminish the full capacity of FRP reinforcement system (Smith and Teng, 2002). In order to postpone FRP debonding and instead of using the conventionally externally bonded reinforcement (EBR) method or near surface mounted method (NSM), Mostofinejad and Mahmoudabadi studied externally bonded reinforcement on groove (EBROG) technique (Figure 1) in 2010 (Mostofinejad & Mahmoudabadi, 2010). The promising results of their research paved the road for further studies and developing the method comprehensively. EBROG technique is based on cutting grooves in concrete cover, filling them with proper adhesive, and attaching FRP composites on the surface, without any other surface preparation prior to FRP installation (Mostofinejad and Mahmoudabadi, 2010). So far, several studies implemented grooving method (Sanginabadi et al., 2022b, Sanginabadi et al., 2022a, Mohammadi Ghahsareh & Mostofinejad, 2021). CFRP-to-concrete bonded joints in CFRP

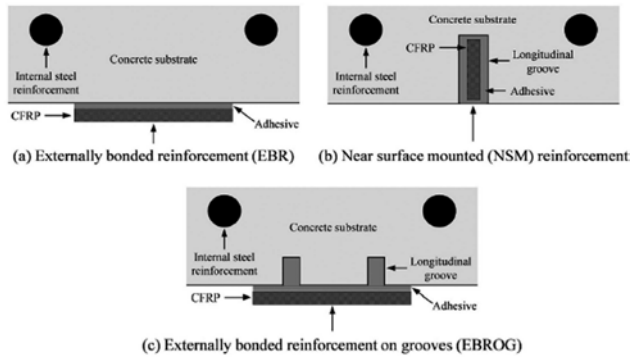


Figure 1. Schematic drawing of different bonding techniques (Moshiri et al., 2020).

strengthened structures may also be subjected to fatigue cyclic loading. Potential performance degradation of the bonded joints due to fatigue cyclic loading may affect the performance of the structure. Research has shown that bond degradation due to fatigue cyclic loading could redistribute stresses to the internal reinforcement resulting a lower fatigue life of the structure (Quatlebaum et al., 2005) and reduce their ductility (Harries et al., 2006).

Therefore, it is important to develop a sound understanding of the behavior of CFRP-to-concrete bonded joints under fatigue cyclic loading. Fatigue response of FRP-strengthened members depends on the maximum applied load in a load cycle (Kim and Heffernan, 2008). If the maximum load in a load cycle, P_{max} is less than 50% of the quasi-static failure load, the test is said to be performed under high-cycle fatigue conditions. On the other hand, if the maximum load P_{max} is greater than 50% of the quasi-static failure load, the test is said to be performed under low-cycle fatigue conditions (Carloni et al., 2012). Against this background, this research presents an experimental study investigating the behavior of CFRP-to-concrete bonded joints using EBROG method under fatigue cyclic loading that has not been studied before.

2 EXPERIMENTAL PROGRAM

2.1 Specimens details

Three concrete slabs with dimensions of $650 \times 650 \times 200$ mm³ (width \times length \times thickness) were cast. According to the width of the specimen, it is possible to install four FRP strips on each face. Also, choosing such dimensions makes the samples more similar to each other.

2.2 Strengthening techniques

The EBR and EBROG methods were used to bond the CFRP strip to the concrete surface. In the EBR, conventional surface preparation was conducted by grinding the surface to remove the weak outer layer of concrete and to expose the aggregates (Figure 2a). In the EBROG method, three longitudinal grooves (Figure 2b), each having cross-section of 5×5 mm² (width \times depth) and a clear spacing of 10 mm were cut in the concrete. The grooves were cleaned with compressed air and filled with epoxy resin, and the CFRP strip was attached to the grooves by applying a thin layer of epoxy resin.

2.3 Material properties

The average compressive strength of concrete cubes at the time of testing was 35.7 MPa. Unidirectional CFRP strips of type Sika wrap-300C (Sika, 2017) a width and thickness of 50 and 0.17 mm, respectively. The elastic modulus of the strips was 230 GPa. The CFRP ultimate tensile strength and ultimate tensile strain were 4000 MPa and 1.7%, respectively. A two-component epoxy adhesive labeled as Sikadur 330 (Sika, 2019) with an elastic modulus of 4.5 GPa, an ultimate tensile strength of 30 MPa, and an ultimate tensile strain of 0.9% was used.

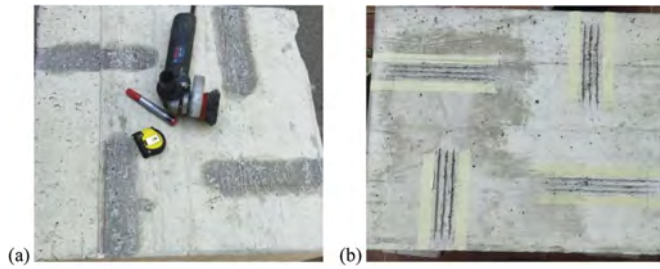


Figure 2. Surface preparation; (a) EBR method, (b) EBROG method.

2.4 Test layout

The test layout is presented in Table 1. Two slabs were strengthened with CFRP strips using EBR method, two specimens were retrofitted with CFRP strips by EBROG method. Labels are arranged like EBR-M or F-n and EBROG- $b_g \times h_g$ -M or F-n. Herein, symbols b_g and h_g denote the groove width and depth, respectively. The capital letters “M” and “F” indicate loading scheme with monotonic procedure and fatigue cyclic procedure, respectively. Icon n represents order of repetitive similar tests (1, 2 or 3).

Table 1. Test layout.

No.	Specimen label	f_{cu} (MPa)	CFRP strip width, (mm)	CFRP bond length (mm)	Strengthen- ing method	Loading scheme	Groove dimensions	
							Width, b_g (mm)	Depth, h_g (mm)
1	EBR-M-1	35.7	50	200	EBR	Monotonic	-	-
2	EBR-M-2							
3	EBR-F-1	35.7	50	200	EBR	Fatigue	-	-
4	EBR-F-2					Cyclic		
5	EBR-F-3							
6	EBROG-5×5-M-1	35.7	50	200	EBROG	Monotonic	5	5
7	EBROG-5×5-M-2							
8	EBROG-5×5-F-1	35.7	50	200	EBROG	Fatigue	5	5
9	EBROG-5×5-F-2					Cyclic		
10	EBROG-5×5-F-3							

2.5 Loading procedure

The testing procedure is carried out in several steps (Figure 3). First, the loading is applied monotonically at a rate of 0.05 mm/min to a predetermined force value. Subsequently, unloading is carried out till a force value equal to the mean one of the foreseen. Finally, cyclic loading is applied at a rate of 4 Hz until failure. While applying the cyclic loading, the displacement of FRP strip at the loaded end is monitored by two LVDT's. The tested sample is also visually checked for any possible fracture during the fatigue cyclic loading.

2.6 Test setup

An apparatus specifically designed for the assessment bond behavior of CFRP-to-concrete joints was used to carry out single lap-shear tests, equipped with a 100 kN hydraulic jack. A load cell was used to accurately measure the tensile force applied to the specimen. An illustration of the test setup is shown in Figure 4.

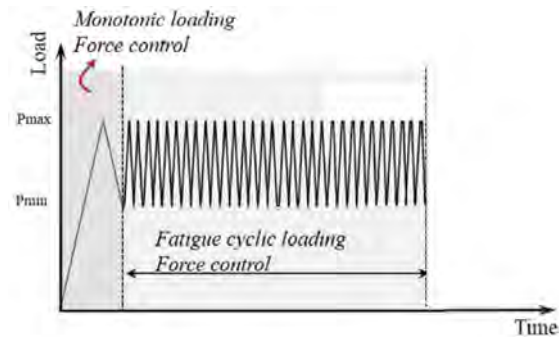


Figure 3. Loading scheme (Zhou et al., 2021).



Figure 4. Test setup.

3 EXPERIMENTAL RESULTS AND DISCUSSIONS

3.1 Failure mode

As shown in Figure 5, by applying monotonic load, the EBR tested specimens failed due to debonding of FRP sheets off the concrete substrate (Figure 5a). On the other hand, for EBROG specimens, the failure mode involved deep debonding of FRP strips with a layer of concrete under static loading scheme (Figure 5b). In fatigue cyclic tests, all specimens (EBR and EBROG) failed by debonding of FRP strips off the substrate concrete. It is worth noticing that a concrete cone zone was accidentally observed at the end of FRP strip in EBROG specimens under fatigue loading (Figure 5d).

3.2 Static bond strengths of EBR and EBROG specimens

The results showed that the EBROG method improved the bond resistance of FRP-to-concrete joints. EBROG specimens achieved an average load of 28 kN and 100% higher than EBR specimens.

3.3 Fatigue life of EBR and EBROG specimens

Result showed the number of cycles until failure (the fatigue life) increased in EBROG joints under the same cycle amplitude as EBR joints. The maximum fatigue life achieved 2,416,750 and 109,947 cycles for EBROG and EBR specimens, respectively. A summary of fatigue life of specimens are presented in Table 3. It is worth noticing that under fatigue load, the strain distribution along the FRP strip consists mainly of three lengths, namely, the early rapid development length (the first length near loaded end, I-region) that FRP is separated from concrete surface in this region and expanded over time. In fact, debonding propagated towards from the loaded end to far end. The second length (II-region) is development length that moves to end of

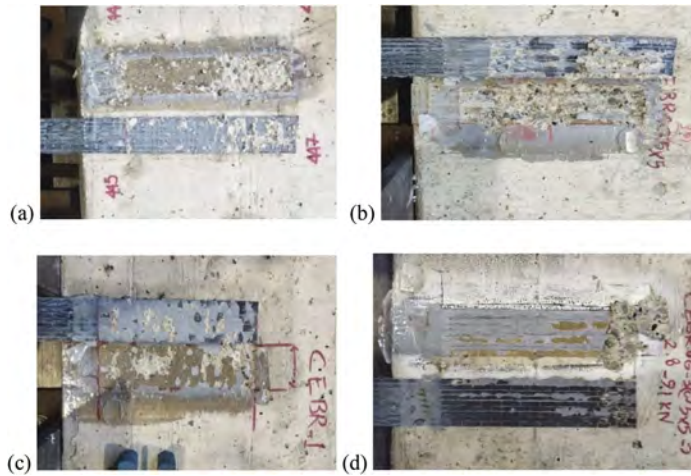


Figure 5. Failure modes, (a) EBR-M, (b) EBROG-M, (c) EBR-F, (d) EBROG-F.

Table 2. Bond strength of specimens at monotonic loading.

No.	Specimen label	f'_c (MPa)	Peak load (kN)	P_m (kN)	CFRP bond length (mm)
1	EBR-M-1	35.7	13.9	14	200
2	EBR-M-2		14.2		
6	EBROG-5×5-M-1	35.7	26.7	28	200
7	EBROG-5×5-M-2		29.4		

FRP strip over time and last region is undeveloped length (III-region) that decreases its length over time until suddenly, end of FRP strip delaminated with concrete cone (Figure 6).

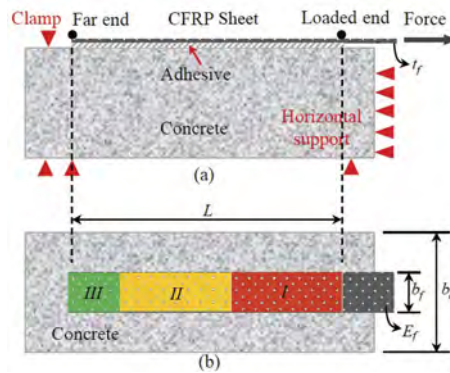


Figure 6. Schematic drawing of the different development lengths under fatigue loading: (a) the elevation view, (b) the top view.

4 THEORETICAL ANALYSIS

4.1 Evaluation of bond strength of EBR and EBROG in static conditions

A wide array of empirical and numerical models has been developed for predicting the bond strength of EBR installation method. Among these, the well-known bond strength model due to Chen and Teng (Chen & Teng, 2001) according to Equation (1) described here was used for comparisons to evaluate the bond strength in the present study.

Table 3. Fatigue life of specimens at cyclic loading.

No.	Specimen label	Fatigue upper limit, P_{\min} (kN)	Fatigue lower limit, P_{\max} (kN)	Fatigue life, N_f (cycles)	Time until failure, t_f (hours)
3	EBR-F-1	2.8	9.1	109947	7.6
4	EBR-F-2			55382	3.8
5	EBR-F-3			88124	6.1
8	EBROG-5×5-F-1	2.8	9.1	1259104	87.4
9	EBROG-5×5-F-2			2416750	167.8
10	EBROG-5×5-F-3			2129335	147.9

$$P_{Cheng\&Teng} = 0.427 \beta_p \beta_L b_f L_e \sqrt{f_c} \quad (1)$$

where L_e = effective bond length presented by Equation (2); and β_L =reduction factor to predict the bond strength of FRP–concrete joint calculated by Equation (3). The coefficient β_p in Equation (4) considers the width ratio of the bonded FRP sheets to the concrete member b_f/b_c . It is worth mentioning that ACI 440.2R (ACI 2017) is based on the model proposed in Chen and Teng (2001).

$$L_e = \sqrt{\frac{E_f t_f}{\sqrt{f_c}}} \quad (2)$$

$$\beta_L = \begin{cases} 1 & \text{if } L \geq L_e \\ \sin \frac{\pi L}{2L_e} & \text{if } L < L_e \end{cases} \quad (3)$$

$$\beta_p = \sqrt{\frac{2 - b_f/b_c}{1 + b_f/b_c}} \quad (4)$$

In Equation (4), b_f and b_c are the width of the bonded FRP strip to the concrete member width, respectively. For predicting maximum load of EBROG joints, Mostofinejad and Moghaddas (Moghaddas & Mostofinejad, 2019) proposed a novel equation as a modified version of Equation (1) which a novel term called groove coefficient (β_g) had been introduced. The modified model may be expressed in the form of Equations (5) and (6):

$$P_{M\&M} = \beta_g P_{Chen\&Teng} \quad (5)$$

$$\beta_g = f'_{t_c}{}^{-0.33} (E_f t_f)^{-0.08} (8.1 - 0.006 h_g^2 + 0.1 h_g + 0.04 b_g) \quad (6)$$

where b_g and h_g are groove width and depth, respectively. Zamani and Mostofinejad (Zamani Ghaleh & Mostofinejad, 2022) proposed a relation for the failure strain of externally bonded reinforcement on groove (EBROG) joints derived through regression analysis according to Equations (7) and (8):

$$P_{Z\&M} = E_f t_f b_f \varepsilon_{eff} \quad (7)$$

$$\varepsilon_{eff} = 1.474 (f'_c)^{0.162} (b_f)^{-0.2885} (E_f t_f)^{-0.5} \times (b_g)^{0.16} (d_g)^{0.0755} \quad (8)$$

Table 4. Bond strength prediction of specimens at monotonic loading.

No.	Specimen label	P_{exp} (kN)	$P_{exp,avg}$ (kN)	$P_{Cheng\&Teng}$ (kN)	$P_{M\&M}$ (kN)	$P_{Z\&M}$ (kN)
1	EBR-M-1	13.9	14	12.5	-	-
2	EBR-M-2	14.2				
6	EBROG-5×5-M-1	26.7	28	-	21	23.5
7	EBROG-5×5-M-2	29.4				

In general, results show that the relation proposed by Zamani and Mostofinejad (2022) outperforms the model proposed in Moghaddas and Mostofinejad (2019) in terms of estimating EBROG joint bond capacity.

4.2 Evaluation of fatigue life of specimens

Demers (Demers, 1998) studied the tensile fatigue behavior of several glass fiber and carbon composite reinforcements. According to his research, Equation (9) was proposed corresponds to the lifetime of CFRP. Zhu et al. (Zhu et al., 2016) studied the fatigue behavior of CFRP-concrete interfaces on beam specimens. The experimental campaign allowed them to develop a model (Equation (10)) in which the fatigue life of the interface depends mainly on the loading amplitude (T) and concrete compressive strength (f_c). Additionally, new relationship was presented by Chalot et al. (Chalot et al., 2019) that uses Wohler curve to predict the fatigue life according to Equation (11).

$$\text{Log}(N) = \frac{1}{0.0519} (0.8227 - \frac{P_{\max}}{P_u}) \quad (9)$$

$$\ln(N) = -31.646(T - 0.8386)(0.0021f_c' + 0.8724), \quad T = \frac{P_{\max} - P_{\min}}{P_u} \quad (10)$$

$$\text{Log}(N) = \frac{1}{0.051} (0.925 - \frac{P_{\max}}{P_u}) \quad (11)$$

Table 5 compares the fatigue life of different methods. As it can be seen in Table 5, the differences among different methods are high and needs a new approach to calculate fatigue life of CFRP-to-concrete bonded joints especially for EBROG installation methods.

Table 5. Fatigue life prediction of CFRP bonded joints at cyclic loading.

No.	Specimen label	N _{f,exp} (cycles)	N _{f,Demers} (cycles)	N _{f,Zhu} (cycles)	N _{f,Chalot} (cycles)
3	EBR-F-1	109947	2138	undefined	245471
4	EBR-F-2	55382			
5	EBR-F-3	88124			
8	EBROG-5×5-F-1	1259104	undefined	undefined	undefined
9	EBROG-5×5-F-2	2416750			
10	EBROG-5×5-F-3	2129335			

5 CONCLUSIONS

The innovative aspect of the current study consists in an evaluation of number of cycles until failure for EBR and EBROG specimens under fatigue loading. For the purposes of such study, 10 single lap-shear tests were designed and conducted to compare the EBR and EBROG bond strengths on the basis of different loading scheme such as monotonic loading and fatigue cyclic loading. The following conclusions may be drawn from the obtained results.

1. All EBR specimens under static loading underwent FRP debonding failure through the adhesive layer, while the failure mode of the EBROG joints were debonding of the FRP strips through the concrete layer. For fatigue cyclic loading, the FRP debonding with end concrete cone was observed in EBROG loading. However, for EBR specimen under fatigue cyclic loading, just FRP debonding was observed until end of loading.
2. Compared with the conventional surface preparation (EBR method), three grooves with dimension of 5x5 mm² cut beneath the FRP sheet was observed to increase bond strength by an average of 100%.
3. The Chen and Teng bond strength model is found to underestimate the specimens' failure load strengthened using the EBROG method. Furthermore, by using the models of Moghaddas and Mostofinejad or Zamani and Mostofinejad, the goodness of fit was confirmed.

4. EBROG method could significantly increase the number of cycles of CFRP-to-concrete joints comparing to EBR method at same loading range. In fact, the service life of FRP strengthened members under fatigue loading could be improved by EBROG method.

ACKNOWLEDGEMENTS

The tests were carried out at Material Testing Laboratory of Milan Polytechnic, which is thanked for the financial support. Authors would like to express their gratitude to Daniele Spinelli for his support in carrying-out the experimental activities. During the visiting research period of the first author at Polytechnic of Milan, financial support was offered by the Iranian Ministry of Science, Research and Technology (MSRT), which is admirably acknowledged.

REFERENCES

- ACI440.2R (2017) Guide for the design and construction of externally bonded FRP Systems. Michigan, American Concrete Institute Farmington Hills.
- Carloni, C., Subramaniam, K. V., Savoia, M. & Mazzotti, C. (2012) Experimental determination of FRP-concrete cohesive interface properties under fatigue loading. *Composite Structures*, 94, 1288–1296.
- Chalot, A., Michel, L. & Ferrier, E. (2019) Experimental study of external bonded CFRP-concrete interface under low cycle fatigue loading. *Composites Part B: Engineering*, 177, 107255.
- Chen, J. F. & Teng, J. (2001) Anchorage strength models for FRP and steel plates bonded to concrete. *Journal of structural engineering*, 127, 784–791.
- Demers, C. E. (1998) Fatigue strength degradation of E-glass FRP composites and carbon FRP composites. *Construction and building materials*, 12, 311–318.
- FIB-BULLETIN-90 (2019) Externally bonded FRP reinforcement for RC structures. Lausanne, Switzerland, fib Task Group 5.1.
- Harries, K. A., Aidoo, J., Zorn, A. & Quattlebaum, J. (2006) Deterioration of FRP-to-concrete bond under failure loading. *Advances in Structural Engineering*, 9, 779–789.
- Kim, Y. J. & Heffernan, P. J. (2008) Fatigue behavior of externally strengthened concrete beams with fiber-reinforced polymers: State of the art. *Journal of Composites for Construction*, 12, 246–256.
- Moghaddas, A. & Mostofinejad, D. (2019) Empirical FRP-concrete bond strength model for externally bonded reinforcement on grooves. *Journal of Composites for Construction*, 23, 04018080.
- Mohammadi Ghahsareh, F. & Mostofinejad, D. (2021) Groove classification in EBROG FRP-to-concrete joints. *Construction and Building Materials*, 275, 122169.
- Moshiri, N., Czaderski, C., Mostofinejad, D., Hosseini, A., Sanginabadi, K., Breveglieri, M. & Motavalli, M. (2020) Flexural strengthening of RC slabs with nonprestressed and prestressed CFRP strips using EBROG method. *Composites Part B: Engineering*, 201, 108359.
- Mostofinejad, D. & Mahmoudabadi, E. (2010) Grooving as alternative method of surface preparation to postpone debonding of FRP laminates in concrete beams. *Journal of Composites for Construction*, 14, 804–811.
- Quattlebaum, J. B., Harries, K. A. & Petrou, M. F. (2005) Comparison of three flexural retrofit systems under monotonic and fatigue loads. *Journal of Bridge Engineering*, 10, 731–740.
- Sanginabadi, K., Yazdani, A., Mostofinejad, D. & Czaderski, C. (2022a) Bond behavior of FRP composites attached to concrete using EBROG method: A state-of-the-art review. *Composite Structures*, 116060.
- Sanginabadi, K., Yazdani, A., Mostofinejad, D. & Czaderski, C. (2022b) RC members externally strengthened with FRP composites by grooving methods including EBROG and EBRIG: A state-of-the-art review. *Construction and Building Materials*, 324, 126662.
- Sika, G. (2017) Product data sheet, SikaWrap-300C, Woven carbon fiber fabric for structural strengthening.
- Sika, G. (2019) Technical data sheet, Sikadur-330, 2-part thixotropic epoxy adhesive.
- Smith, S. T. & Teng, J. (2002) FRP-strengthened RC beams. II: Assessment of debonding strength models. *Engineering structures*, 24, 397–417.
- Zamani Ghaleh, R. & Mostofinejad, D. (2022) Empirical Expression for Failure Strain in EBROG-Bonded FRP-Concrete Joints. *Journal of Composites for Construction*, 26, 04022036.
- Zhou, H., Fernando, D. & Dai, J.-G. (2021) The bond behaviour of CFRP-to-concrete bonded joints under fatigue cyclic loading: An experimental study. *Construction and Building Materials*, 273, 121674.
- Zhu, J.-T., Wang, X.-L., Kang, X.-D. & Li, K. (2016) Analysis of interfacial bonding characteristics of CFRP-concrete under fatigue loading. *Construction and Building Materials*, 126, 823–833.

Externally applied textile reinforced systems on RC members: Innovative and sustainable materials and techniques

F. Bencardino & R. Curto

Department of Civil Engineering, University of Calabria, Rende, Cosenza, Italy

ABSTRACT: To hinder overbuilding and find sustainable solutions in the construction sector, recent scientific researches consider the strengthening and repair of existing reinforced concrete (RC) structures using innovative materials and techniques. The Textile Reinforced (TR) system applied according to the traditional Externally Bonded (EB) technique is considered a suitable strengthening method due to the use of inorganic matrix. Using a matrix with sustainable environmental aspects, a mortar added with fibres from waste materials, that is also a corrosion inhibitor of the steel rebars, the EB technique can be replaced by the Inhibiting-Repairing-Strengthening (IRS) technique. The IRS technique is an eco-friendly strengthening method because it reduces the number of manufacturing steps and amount of chemical products used; this means less time and environmental pollution. This work shows the experimental behaviour of RC beams strengthened by IRS technique compared with the EB technique and discusses about the intermediate/end debonding strain helpful to design.

1 INTRODUCTION

Safeguarding and recovering existing building stock is becoming a major issue for several countries around the world. The common and recurring problems related to the durability of the existing reinforced concrete (RC) structures concern the corrosion of the steel rebars and the cracking of the concrete until the achievement of the spalling (expulsion of the concrete cover). In fact, these problems greatly reduce the geometric and mechanical properties of RC elements with negative effects that can affect only a part or even the entire structure. The RC degradation phenomena can have several causes: physical, chemical, mechanical, structural and biological.

In the past, different solutions have been proposed in order to solve the problems of existing RC structures. Among the effective and innovative strengthening and repair interventions of recent years is the Textile Reinforced (TR) system (Rossi et al., 2022). This method is now the most common recovery tool in engineering practice and it is considered a suitable strengthening method thanks to the use of an inorganic matrix (reinforced with dry or coated fibres in the form of an open mesh textile) that exhibits significant heat resistance, allows vapour permeability, and can be applied at low temperatures or on wet surfaces. In addition, this system has other advantages such as: lightness and handle, long-term durability, ease and speed of installation, high resistance against sulphates, and can be removed without harming the original structure. For these reasons, this system can be considered as an evolution of the previous Fibre Reinforced Polymer (FRP) system.

The TR system is known in the literature with different names, based on the types of matrix, fibres and substrate to be strengthened. The most common names are: Fabric-Reinforced Cementitious Matrix (FRCM); Textile Reinforced Mortar (TRM); Fibre Reinforced Mortar (FRM); Mineral Based Composites (MBC); Textile Reinforced Concrete (TRC), though the latter is usually used in new constructions.

The mechanical effectiveness of TR system is strongly influenced by: a) tensile properties of the cementitious matrix; b) capacity of the cementitious matrix to impregnate the roving of the textile;

c) effective fibre/matrix interface bond properties; and d) bond between the cementitious matrix and the concrete substrate.

The most suitable fibres used to make textiles for strengthening and repair of RC structures are Carbon, PBO (Poly-p-phenylene BenzobisOxazole), and Steel. If the textile is made of steel strands (stainless steel or UHTSS – Ultra High Tensile Strength Steel) the system is also called SRG (Steel Reinforced Grout).

Despite the advantages listed above, the traditional technique of application of TR systems use polluting products and materials. For example, the use of corrosion inhibitors necessary for the treatment of existing rebars has a significant environmental impact. It is known that reinforcement corrosion causes cracking in the concrete surface of RC beams, decreasing their load-bearing capacity (Srivaranun et al., 2023).

Therefore, two problems must be addressed in parallel: the need to strengthening/repair existing structures using effective and structurally valid methods and the need to use innovative and sustainable solutions, materials and techniques. In this direction, the paper shows that the use of an inorganic matrix with passivating properties coupled with stainless steel (or UHTSS) strips provide a TR system that can be applied according to an innovative and most sustainable technique, the Inhibiting-Repairing-Strengthening (IRS) technique, with a satisfactory structural performance. Moreover, some relationships for the evaluation of intermediate/end debonding strain, helpful for the design of the strengthening system, are also discussed.

2 EB, NSM AND IRS TECHNIQUES

Currently, many existing RC structures and infrastructures that need to be strengthened are also deteriorated. The most popular degradations, such as aggregate expansion or corrosion of internal reinforcing bars, cause chemical reactions in concrete leading to expansive damaging phenomena. These phenomena, created by alkali-silica reaction or corrosion of steel, may induce mechanical stresses that can cause the formation of cracks. Furthermore, if the bars were poorly installed and are located close to the concrete surface in contact with the air spalling can easily occur and flat fragments of concrete are detached from the concrete mass. This process may be accelerated by carbonation that decreases alkalinity, which is essential for corrosion prevention of the internal steel bars. The deterioration of cover concrete may engender an iterative process which leads to the reduction of the resistant section (steel bars and concrete) and consequently to a loss of structural strength. The causes of the internal steel bars corrosion should be addressed and the corrosion-related deterioration should be repaired before the installation of any strengthening system.

Therefore, for strengthening of deteriorated RC members, three different procedures could be used: traditional Externally Bonded reinforcement (EB) technique, Near Surface Mounted (NSM) technique or Inhibiting-Repairing-Strengthening (IRS) technique.

The traditional EB technique shown in Figure 1 is based on steel, carbon or PBO TR systems. Typically, this technique is used for strengthening of RC elements subjected mainly to flexure and shear. To make and apply the TR system using the traditional EB reinforcement technique, it is necessary to perform specific operations listed below (*fib* Bulletin 103, 2022): remove deteriorated concrete from all damaged areas; clean and protect corroded steel bars (application of corrosion inhibitors); restore the concrete using shrinkage-free cement grouts (reconstruction of original section shape); roughen and wet the concrete surface. Then proceed with the application of a first layer (upper layer) of mortar (matrix) with a suitable average thickness and of the fabric on the first layer of wet matrix; finally apply the second layer (bottom layer) of mortar (matrix) making sure that the textile is perfectly embedded into the matrix by pressing it with a spreader or steel roller.

In the Near Surface Mounted (NSM) technique, shown in Figure 2, the TR system is made using steel fibres (UHTSS and stainless steel). This technique is based on the bonding of the TR system in pre-cut grooves in the concrete cover, in the case of undamaged concrete structures. Instead, for deteriorated structures, the TR system must be glued to the surface obtained by removing the entire damaged concrete cover.

This technique consists in the application of the following operations (*fib* Bulletin 103, 2022): removal of deteriorated concrete from all damaged areas and removal of unsound

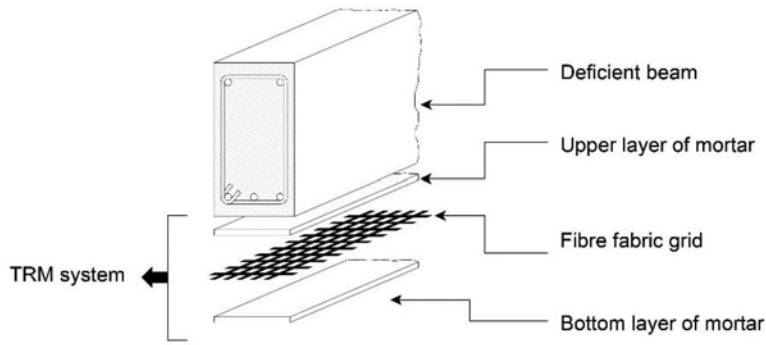


Figure 1. EB Technique.

concrete; cleaning and protection of corroded steel bars (application of corrosion inhibitors); application of a first layer (upper layer) of mortar (matrix) with a suitable average thickness depending on the amount of damaged concrete cover; application of steel fibre sheet reinforcement over the first layer of wet matrix; application of the second layer (bottom layer) of mortar (matrix) making sure that the textile is perfectly embedded into the matrix by pressing it with a spreader or steel roller.

Inhibiting-Repairing-Strengthening (IRS) technique shown in Figure 2, consists in the installation of UHTSS or a stainless steel strip in the cover concrete, restoring this latter with an alkali-activated matrix/geopolymers which also acts as a corrosion inhibitor/protection. The steps to perform this technique are as follows: removal (variable thickness) of the cover concrete damaged due to physical, chemical, and mechanical deterioration; assessment of the internal steel bars and brushing/sandblasting of corroded bars; application of the first layer (upper layer) of inorganic matrix, which also acts as a corrosion inhibitor/protection. The thickness (10-20-30 mm) depends upon the depth of the removed deteriorated concrete (degraded, weakened and no cohesive concrete); application of UHTSS or stainless steel reinforcement over the first layer wet matrix; application of the second layer (bottom layer) of inorganic matrix (thickness 5-10 mm) making sure that the reinforcement is perfectly embedded into the matrix by pressing it with a spreader or steel roller, and also checking that it comes out between the cords to ensure optimum adhesion between the first and second layer of matrix.

The TR system, made with stainless steel strip or UHTSS sheet and inorganic matrix with passivation property, applied according to the novel IRS technique contains sustainable aspects in terms of materials and execution works. Specifically, the inorganic matrix contains slag and/or fly ash (mineral additives) and provides corrosion protection. It is not necessary to use further chemical products/compounds to the treatment of the internal steel bars. The new and sustainable application technique of the external reinforcement allows to carry out three steps in one step, reducing the costs and times of carrying out the intervention.

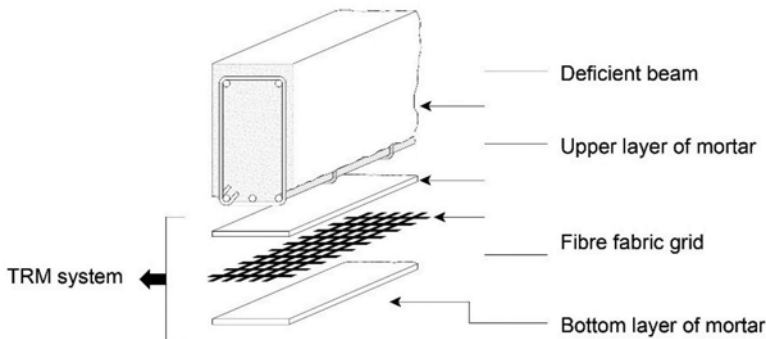


Figure 2. NSM or IRS Technique.

3 EXPERIMENTAL PERFORMANCE: EB/IRS TECHNIQUE

3.1 Experimental tests

In order to test the structural effectiveness of the IRS technique, an experimental programme was defined and developed.

Three groups (A, B, and C) of strengthened RC beams were tested under monotonic load. Each group includes three RC beams: one beam strengthened with IRS technique, one beam strengthened with EB technique and another un-strengthened control beam. The strengthening system consisted of a unidirectional stainless steel strip with an elastic modulus equal to 177.6 GPa and a characteristic tensile strength of 1238 N/mm² (ST4-0622) embedded into an alkali-activated mortar with a compressive strength ≥ 50 MPa and an adhesion to concrete ≥ 2 MPa (ST11-1022).

Geometric parameters and strengthening arrangements of the tested beams are shown in Figures 3, 4 and 5, and the details are given in Table 1. For each group are summarised: number of the tested specimens; length (L), width (b), and height (h) of the beams; shear span (a); length to height ratio (L/h); shear span to depth ratio (a/d), area of the tension (A_s) and compression (A'_s) longitudinal steel reinforcements; reinforcement ratio ($\rho_s = A_s/(bd)$).

To simulate a wide range of existing RC structures built during the '60s and '70s, the specimens were cast using low concrete strength, and both smooth (12 mm diameter bars) and ribbed steel bars (8 mm and 16 mm diameters). The mechanical properties of the materials are given in Table 2 (f_{cm} : concrete compressive strength; f_{cm} : concrete tensile strength; E_{cm} : Young Modulus; f_{ym} : yield strength of steel bars).

The smooth steel bars were found/taken in a disused building/demolition site.

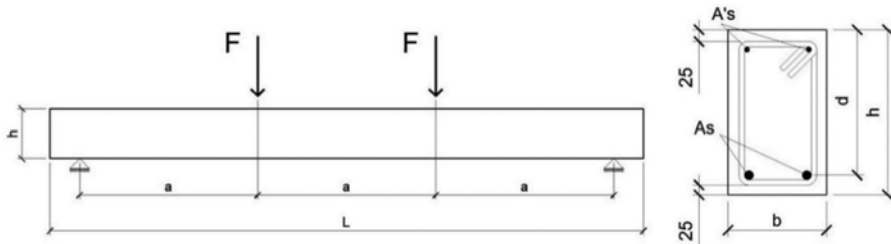


Figure 3. Geometry of the tested beams: RC un-strengthened beam.

The beams were internally and externally instrumented and tested under four-points bending. Two vertical loads were applied symmetrically to the midspan of the beams with a constant bending moment region and a constant shear span. All the beams were simply supported and tested with a shear span to depth ratio of $a/d=4.1$. Test setup is shown in Figure 6.

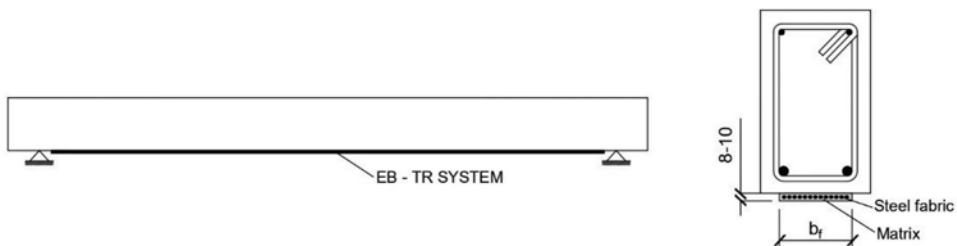


Figure 4. Geometry of the tested beams: RC beam strengthened with EB-TR system.

3.2 EB/IRS strengthened RC beams: Structural behaviour

The load-midspan deflection curves and deflections under maximum load are shown in Figures 7, 8, and 9 for the beams of groups A, B and C, respectively. Both EB-TR and IRS-TR strengthening

Table 1. Geometric properties of the RC beams.

Group	Number of Specimens	L [mm]	b [mm]	h [mm]	L/h	a [mm]	a/d	A_s	ρ_s [%]	A'_s	Stirrups
A	3	3000	150	250	12	900	4.1	2Φ12	0.69	2Φ8	Φ8/150mm
B	3	4800		400		1500		2Φ16	0.73		
C	3	3000		250		900		2Φ12	0.69		

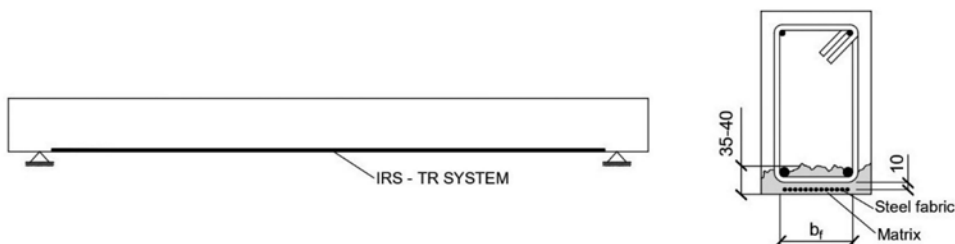


Figure 5. Geometry of the tested beams: RC beam strengthened with IRS-TR system.

Table 2. Mechanical properties of concrete and internal steel bars (MPa).

Group	Concrete			Internal steel bars
	f_{cm}	f_{ctm}	E_{cm}	f_{ym}
A	16.8	1.7	26093	367.1
B	16.8	1.7	26093	492.0
C	6.5	0.9	-	585.6



Figure 6. Test setup.

systems improved the load carrying capacity and decreased the ultimate deflections, and then the ultimate rotations, of the corresponding RC control beam. Furthermore, the structural behaviour of the beams A-IRS and B-IRS was better, in terms of ultimate load and deflections, compared to the corresponding RC beams strengthened with traditional EB technique (A-EB, B-EB).

As regards the failure mode, all un-strengthened beams failed in conventional ductile mode with crushing of compressive concrete after yielding of internal steel bars. With reference to EB technique, the strengthened beams A-EB and B-EB failed by sudden end debonding without warnings. This phenomenon was probably due to the surface treatment. Indeed, the beam C-EB that was subject to a deeper moist sandblasting and hydraulic scouring failed by concrete crushing, without delamination. It should also be highlighted that the concrete strength was very low for the beams of group C respect to the beams of the groups A and B. With reference to IRS technique, the beam A-IRS failed by delamination at stainless steel-matrix interface, after extensive cracking, and the beams B-IRS and C-IRS failed by concrete crushing.

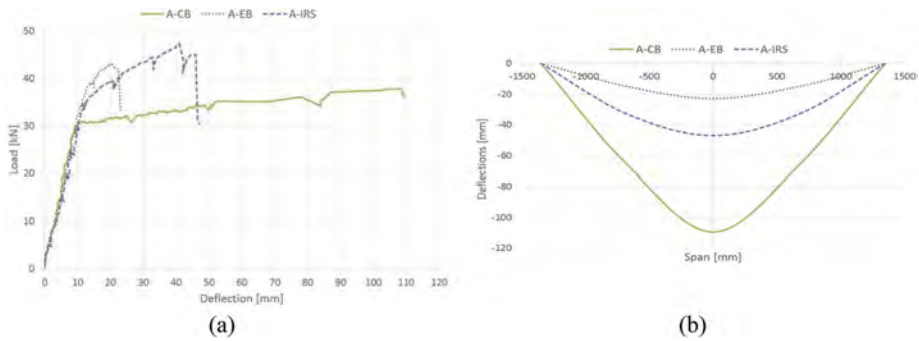


Figure 7. Group A: (a) load-midspan deflection curves; (b) deflections under maximum load.

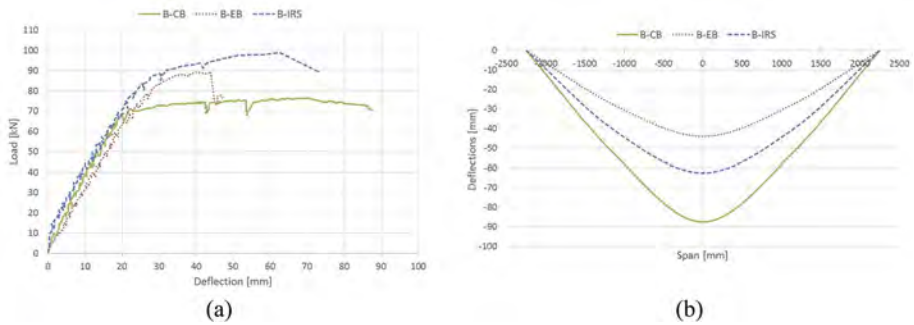


Figure 8. Group B: (a) load-midspan deflection curves; (b) deflections under maximum load.

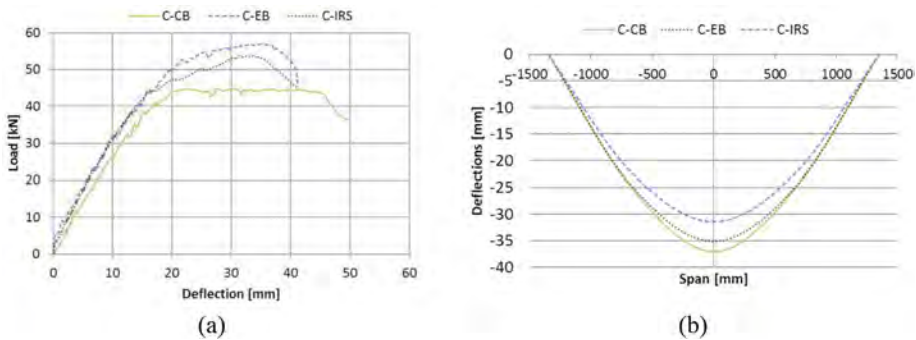


Figure 9. Group C: (a) load-midspan deflection curves; (b) deflections under maximum load.

The experimental results highlight the effectiveness of IRS solution that provided comparable or better structural performance to traditional EB technique.

Figures 10 and 11 show the cracking pattern and failure mode of the beams strengthened with EB-TR and IRS-TR systems, respectively. It should be noted (Figures 10a and b) that for the beams strengthened with EB technique delamination at concrete-TR interface without damage at concrete substrate occurred. Instead, for the beams strengthened with IRS technique (Figures 11a and b) debonding at fibre-matrix interface (group A) and concrete crushing in the midspan section (group B) was observed.

4 INTERMEDIATE/END DEBONDING STRAIN IN TR SYSTEM

According to CNR-DT 215/2018 Guidelines, the strain limit in TR system can be evaluated with reference to the conventional strain limit ($\epsilon_{lim,con}$) and the corresponding conventional

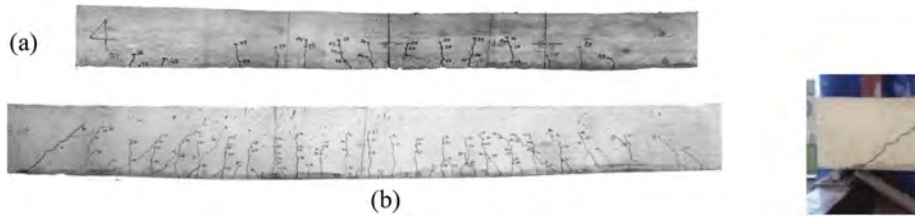


Figure 10. Cracking pattern and failure mode of EB-strengthened beams: (a) beam of group A (length 3000 mm); (b) beam of group B (length 4800 mm).

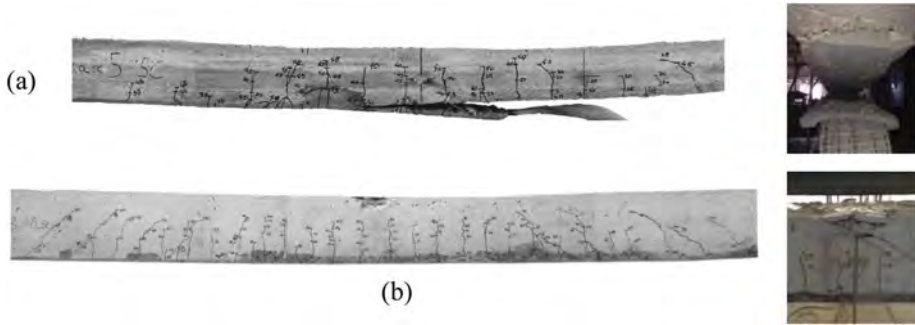


Figure 11. Cracking pattern and failure mode of IRS-strengthened beams: (a) beam of group A (length 3000 mm); (b) beam of group B (length 4800 mm).

stress limit ($\sigma_{lim,con}$). The $\varepsilon_{lim,con}$ corresponding to the end-debonding of the TR system is determined by the following formula:

$$\varepsilon_{lim,con} = \frac{\sigma_{lim,con}}{E_f}. \quad (1)$$

For the mechanical characterisation of the dry strip fibres, Direct Tensile tests were carried out. From the ultimate stress (σ_u) and the corresponding ultimate strain (ε_u), the elastic modulus of the fibre (E_f) is determined as follows:

$$E_f = \frac{\sigma_u}{\varepsilon_u}. \quad (2)$$

Instead, Direct Single-Lap Shear tests allow to determine the value of the maximum force (F_{max}), which together with the known value of the area of the fibres in the strip, allows to calculate the value of the conventional stress limit according to the formula:

$$\sigma_{lim,con} = \frac{F_{max}}{A_f}. \quad (3)$$

Note the $\varepsilon_{lim,con}$, the conventional strain limit of intermediate debonding ($\varepsilon_{lim,con}^{(a)}$) can be obtained by applying the following formula:

$$\varepsilon_{lim,con}^{(a)} = \alpha \varepsilon_{lim,con}. \quad (4)$$

The amplification coefficient α can be taken as equal to 1.5 for all the TR strengthening systems. However, there is in the literature a simpler method for determining intermediate debonding. It is possible to give the debonding predictive as a simple formula (Bencardino et al., 2018) as follows:

$$\varepsilon_{f,deb} = \alpha(n_f E_f t_f)^{-\beta}. \quad (5)$$

Where α and β are the coefficients that take into account the different mechanical characteristics of TR systems (fibres and matrix). In order to evaluate the average value of intermediate strain debonding the suitable coefficients should be: $\alpha = 2.25$ and $\beta = 0.55$.

5 CONCLUSIONS

The IRS innovative technique has proved more sustainable and effective than the traditional EB technique. Compared to the un-strengthened control beam, the data show an increase in terms of failure load of strengthened beams of 16% for the EB technique and 27% for the IRS technique in Group A; an increase of 15% for the EB and 30% for the IRS in Group B; only for the Group C the results show an inverse trend with a greater increase for the EB with 28% compared to IRS with 22%. Therefore, both techniques improved the load carrying capacity and decreased the ultimate deflections, and then the ultimate rotations, of the corresponding RC control beam. However, the behaviour of the strengthened beams with the IRS technique is interesting and effective from several points of view. By combining these important structural behaviour features with the sustainable aspects inherent the implementation of this technique, it can be concluded that the IRS technique is a viable solution to the problem of existing structures and meets the objectives of acting with more effective, sustainable and rapid methods.

The intermediate/end debonding strain, useful in designing a TR strengthening system, can be calculated according to the CNR-DT 215/2018 procedure or using the proposed simple formula. In both cases the obtained values are comparable.

ACKNOWLEDGMENTS

The activities developed in this scientific work were carried out during the PhD course XXXVII cycle (R. Curto), PON R&I 2014-2020 and University of Calabria, Azione IV.5 “Green”.

REFERENCES

- Bencardino, F., Carloni, C., Condello, A., Focacci, F., Napoli, A., Realfonzo, R. 2018. Flexural behaviour of RC members strengthened with FRCM: State-of-the-art and predictive formulas, *Composites Part B: Engineering*, 2018, 148, pp. 132–148.
- CNR-DT 215/2018. Guide for the Design and Construction of Externally Bonded Fibre Reinforced Inorganic Matrix Systems for Strengthening Existing Structures. *CNR*, 2019. Rome, Italy.
- fib* Bulletin 103, 2022. Guide for Strengthening of Concrete Structures. Guide to good practice, Task Group 8.1, Chapter 6, pp. 120–161. <https://doi.org/10.35789/fib.BULL.0103>, May 2022.
- Rossi, E., Randl, N., Harsányi, P., Meszöly, T. 2022. Experimental study of fibre-reinforced TRC shear strengthening applications on non-stirrup reinforced concrete T-beams, *Engineering Structures*, Elsevier, <https://doi.org/10.1016/j.engstruct.2022.113923>
- Srivarannun, S., Akiyama, M., Yamada, T., Frangopol, D. M., Xin, J. 2023. A novel combined experimental-machine learning approach to estimate the probabilistic capacity of RC beams with spatially correlated rebar corrosion in transverse and longitudinal directions, *Engineering Structures*, Elsevier, <https://doi.org/10.1016/j.engstruct.2023.115588>
- ST4-0622 Kimisteel INOX 800. Stainless steel unidirectional reinforcing fabric with high resistance, used in structural reinforcing system.
- ST11-1022 Betonfix MONOLITE N. Thixotropic high-resistance, normal curing mortar, for structural and non-structural repair of reinforced concrete structures.

Experimental investigation on strengthening of RC members with HSC overlays

N. Randl & M. Steiner

Carinthia University of Applied Sciences, Spittal/Drau, Austria

ABSTRACT: High performance concretes (HPC) with higher compressive strength are particularly suitable for subsequently generating reinforcing overlays on existing structures. The aim of the herein presented research was to experimentally demonstrate the suitability of such approach and verify an improved bond at the interface between HPC overlay and normal strength concrete (NSC) as substrate. For this purpose, small and large scale tests with different specimen geometries and setups were performed, investigating the interface shear transfer between high strength overlay and normal strength substrate. In general, the small scale tests provided consistent results with rather low scatter for same test-setups and roughness categories. The bond strength values with HPC were significantly higher than observed with normal strength overlay. While the NSC overlays showed, based on visualization of the crack pattern via digital image correlation, some slight signs of delamination in the member tests, the HPC overlays lead to a monolithic behavior of the tested composite slabs.

1 INTRODUCTION

Adding new concrete layers to an existing structure can be an effective and sustainable way for retrofitting reinforced concrete (RC) members and increasing their performance. Concretes with higher strength are particularly suitable for this purpose due to their advantageous mechanical properties such as better resistance or higher durability (Pelke et al. 2018, Orgass et al. 2018). While interface shear forces are preferably transferred via bond mechanisms between new and old concrete, perpendicular tensile forces have to be covered by adequate connectors (Randl et al. 2005) or post-installed reinforcing bars (Randl & Kunz 2014).

In the case of the herein considered concrete overlays, the focus is laid on toppings where the adhesive bond between the old and the new concrete is the key mechanism. Applications to the tensile side of an RC member would usually require connectors and depend on an adequate tensile reinforcement of the overlay, like textile fabrics which are increasingly researched in that context (Rossi et al. 2021a, b).

The aim of the research project was to experimentally demonstrate suitability and verify improved bond with HSC overlay concrete in comparison to common NSC overlay concrete. Studies such as those by Lenz (2012) at the Technical University of Munich or Júlio et al. (2006) show that rheology and specific concrete properties, as usually present in high-strength concretes in particular, can be decisive for achieving very good bond properties. Julio et al. (2006) as well as Randl et al. (2016) could show in their previous studies that higher overlay strength leads to potentially better bond. The same applies also for highest strength, i.e. ultra-high performance concrete, overlays where numerous recent studies proved the achievable excellent adhesive bonding (Javidmehr & Empelmann 2021, Ju et al. 2020, Semendary & Svecova 2020, Valikhani et al. 2020, Zhang et al. 2020).

The present research project deals with the application of HSC overlay concrete on NSC base material. The adhesive bond along such joints was investigated and characterized experimentally

in various setups. A key factor in this context was the accurate execution, description and recording of the substrate's surface roughening.

2 EXPERIMENTAL CAMPAIGN

2.1 General remarks

Several series of different small-scale bond and interface shear tests have been performed to investigate the adhesive bond resistance between NSC and subsequently applied HSC. The small-scale tests were typical specimen for the investigation of the interface shear capacity (Reinecke (2004), Randl (2013), Zanotti & Randl (2019)). For the determination of the shear strength along the interface, two different test setups were used: Shear specimens with vertical ("Push-Out") and with inclined joint ("Slant Shear").

Large scale tests involved 10 base slabs with the dimensions 3600 x 1000 x 240 mm, where a 60 mm thick layer of overlay concrete was applied. The dimensions and the layout of the reinforcement were designed on the basis of Eurocode 2 in such a way that a shear force failure with the highest possible shear stress at the interface was to be expected, while a premature flexural failure was prevented.

2.2 Materials and surface characteristics

The substrate was made of NSC - normal strength concrete C 45/55, the high-strength overlay concrete (HSC) corresponded to strength classes C 70/85 to C 80/95. For comparison purposes, also C 45/55 was also applied as overlay concrete on three slabs. The exact mean 28-day compressive cube strength values are given in Table 1. For the C 80/95 (2nd series) crushed aggregates (size 8/16 mm) were used instead of the round ones from the C70/85 (1st series).

The hardened concrete properties were determined on cubes with dimensions 150x150x150 mm, the modulus of elasticity was derived from prisms 120x120x360 mm. Furthermore, the splitting tensile strength was determined on cylindrical specimens 100x200 mm.

Table 1. Fresh and hardened concrete properties.

concrete type	slump flow [mm]	28d – compression strength [N/mm ²]	splitting tensile strength [N/mm ²]	E-Modulus [N/mm ²]
C 45/55(1 st series)	420	61,2	3,6	26400
C 45/55(2 nd series)	480	59,0	4,9	25500
C 70/85(1 st series)	460	87,9	6,5	33200
C 80/95(2 nd series)	500	101,9	6,2	36500

Before placing the HSC layer, the hardened substrate concrete was roughened with high pressure water jetting at approximately 2000 bar. The test specimens were produced and categorized with intended roughness depths of $R_t < 1.5$ mm ("smooth"), $1.5 \text{ mm} \leq R_t < 3$ mm ("rough"), and $R_t \geq 3.0$ mm ("very rough"). The surface roughness was measured directly after the surface treatment (Figure 1) by means of the sand patch method (fib (2012)).



Figure 1. Roughness measurement on HPW-jettted slab surface.

2.3 Test setup and test execution

2.3.1 Small scale tests

2.3.1.1 Push-out tests

The specimens for the Push-Out tests are shown in Figure 2. The load was introduced vertically into the mid segment very close to the interface in order to avoid significant eccentricities and in consequence load deviations. Nevertheless, due to the small eccentricity of 10 mm between load introduction and bearings, some limited bending moment transferred via the interface cannot be avoided, causing minor tensile stresses perpendicular to the interface.



Figure 2. Dimensions and front view of Push-Out Tests (units: mm).

2.3.1.2 Slant Shear tests

Slant shear tests (specimen geometry see Figure 3) represent a typical setup for the determination of the adhesive bond strength in shear along an interface. The ratio between shear force and normal force depends on the inclination of the interface (65° , 70° and 75°). By varying the joint inclination, the relationship between adhesive bond and generated frictional resistance resulting from normal stresses can be roughly identified.

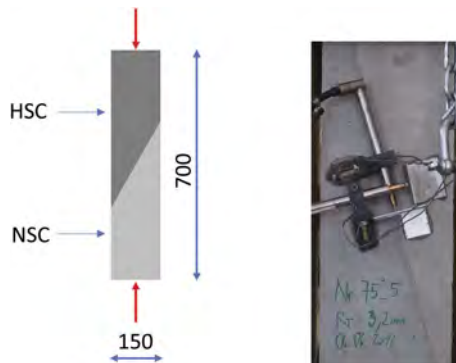


Figure 3. Dimensions and front view of Slant Shear Test (units: mm).

To prevent the introduction of lateral forces, plain steel plates with lubricant in between were placed on top between specimens and actuator and a spherical bearing was used at the bottom (see also Randl et al. (2020)).

2.3.1.3 Large scale tests

The test program includes 10 large scale tests with different overlay and roughness configurations, as listed in Table 2. The 100 mm wide and 240 mm thick base slabs were provided with a strong longitudinal bending reinforcement (10 \varnothing 26 mm) to avoid premature bending failure in

the four-point bending test. The aim was to achieve finally a shear failure and thus produce maximum shear stresses along the joint. The flexural capacity of the slabs was designed to be about a factor of 2 higher than the shear resistance. All test specimens were designed without shear reinforcement. An important boundary condition, especially when determining the exact geometry, was to maintain a shear slenderness $a/d \geq 3$ (a = distance load introduction - support, d = effective depth) in order to avoid direct load transfer via inclined compression struts into the supports. The detailed geometry and the overall setup are displayed in Figure 4 (see also Randl & Steiner (2020)).

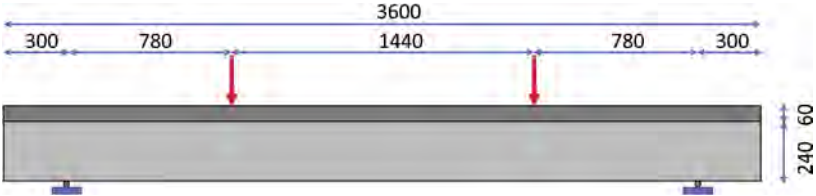


Figure 4. Geometry and setup of slab specimen.

Displacement transducers were applied to record the deflection as well as potential openings or lateral displacements at the interface. Strain gauges were applied to the bending tensile reinforcement and on various locations at the top surface of the concrete overlay. Such measurements allow for back-calculating the local shear stresses along the interface. The formation of the crack pattern and the development of crack widths were recorded by a photogrammetric system.

Two slabs were subjected to some cyclic loading during the overlay concrete placement and the overlay hardening phase in order to simulate vibrations caused by traffic on a parallel lane.

3 TEST RESULTS

3.1 Small scale tests

3.1.1 Push-out tests

All Push-out tests ended up with a clear rupture along one or sometimes both interfaces, i.e. adhesive bond failure along the interface. The main shear load was superimposed by a small moment due to the eccentricities between interface axis and load introductions/supports. Bond failure took always place very abruptly at only small displacements below 0.10 mm. Figure 5 shows the overall test results from the 1st and 2nd series graphically. The reason for the comparatively higher adhesive bond τ_{bond} in the 2nd series can be found in the modified concrete mix design: The crushed aggregates and the higher concrete strength favor the shear bond and also the interlocking between the substrate and the overlay compared to, for example, the use of round gravel. Furthermore, the increase of the adhesive bond strength can be attributed to the lower viscosity, larger

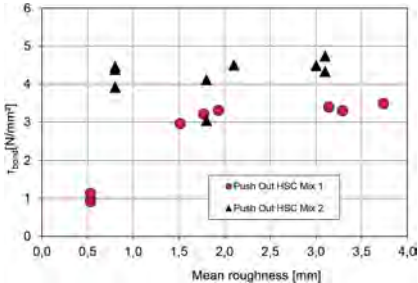


Figure 5. Results of Push-Out tests.

slump flow and better workability of the 2nd mix. As can be seen in Figure 5, no further increase of the bond strength was observed at a mean roughness larger than about 2 mm.

3.1.2 Slant shear tests

The Slant Shear tests ended up with a brittle failure, depicting different failure modes: A larger proportion (61%) of the tests failed along the interface as foreseen, with the fracture surface partially propagating into the lower strength concrete. Some tests showed a mixed kind of failure, i.e. the fracture surface followed partly the interface, ending up however with compression failure in the substrate concrete. Pure compression failure of the substrate concrete was partly observed especially with high roughness and more evident in the 2nd series where higher bond strength was measured. The results of the test series are in general consistent, with no pronounced outliers upwards or downwards.

As the shear force is superimposed by a normal force perpendicular to the interface, the identification of the pure adhesive bond strength τ_{bond} requires the definition of a failure criterion. A simple but still sufficiently accurate and widely used approach to describe the shear resistance along an interface provided by bond and frictional forces is the Mohr Coulomb hypothesis (Randl 2013). Based on this failure criterion, taking into account the measured failure loads and the dimensions of the specimens, the adhesive bond-strength values τ_{bond} of the joints can be calculated. Thereby, representative values for the friction coefficient can be chosen on the basis of the mean values presented in Randl (2013): 1.2 for $R_t < 1.5$ mm (“smooth”), 1.4 for $1.5 \text{ mm} \leq R_t < 3 \text{ mm}$ (“rough”), and 1.5 for $R_t \geq 3.0$ mm (“very rough”). Figure 6 shows the calculated adhesive bond values τ_{bond} , resulting on the basis of the before mentioned coefficients of friction. These coefficients were also checked by means of regression analyses and turned out as the best fitting approach for the relevant roughness category. Similar to the Push-Out tests, also in the Slant Shear tests no further increase in bond strength was recorded for higher roughness values. Even some single lower values were observed at high roughness, which is partly attributed to premature compression failure, but such test results still provide meaningful lower bound values.

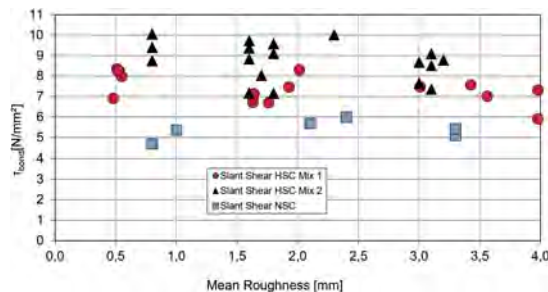


Figure 6. Results of slant shear tests.

3.2 Large scale tests

All test slabs failed primarily in shear. With the exception of slab 6, a further load increase and the formation of a 2nd load maximum (“LM”) was observed after a 1st LM with an associated load drop; in 3 cases, even a 3rd LM was formed under increasingly large deflections. The frequently observed multiple load peaks can be attributed to the fact that after formation of the 1st shear crack, due to the strong bending tensile reinforcement, there was usually no total collapse, but together with further opening of the first shear crack and increasing deflection a shear crack formation on the other side of the slab could be observed until the final collapse.

For the evaluation of the load-bearing behavior, the results of the 1st LM are of main importance (see Table 2). These were consistent throughout and no outliers were observed. A comparison of the ultimate loads achieved (1st LM in each case) showed a certain influence of the applied overlay concrete: The mean values of the 1st LM were 919.7 kN with NSC overlay, 952.4 kN with HSC overlay (thus 3.6% higher), and lowest with HSC overlay under cyclic preloading at 898.6

kN. The highest loads at the first maximum were measured in all three overlay concrete configurations (NSC, HSC, and HSC cyclically preloaded) at the lowest interface roughness of 0.8-0.9 mm in each case. Since in all cases primarily a shear failure of the slabs and not a failure of the interface was decisive, it cannot be concluded that a lower roughness depth leads to better bond effects; however, the trend from the small scale tests (no significant increase of the bond strengths at higher surface roughness) is also reflected in the large scale tests.

Table 2. Failure loads (1st LM) observed in slab tests.

Slab No.	roughness R_t [mm] ²⁾ S / R / VR	overlay concrete NSC / HSC	1 st LM [kN]	interface damage
1	1,6	NSC	902,4	Yes
2	3,0	HSC	951,3	No
3	3,0	NSC	914,1	Yes
4	0,8	NSC	942,6	Yes
5	1,5	HSC	951,9	No
6	1,7	HSC	896,7	No
7	0,8	HSC	1014,9	Yes
8	0,8	HSC	947,2	No
9 ¹⁾	0,9	HSC	860,9	Yes
10 ¹⁾	1,5	HSC	936,2	Yes

1) Slabs vibrated during overlay casting

2) S...smooth, R...rough, VR...very rough

The influence of the type of overlay concrete on the achieved failure loads (Figure 7; 1st LM) was however less significant than in the small scale tests, which is to be expected because local bond damage in slabs can be better compensated by load redistributions (Randl et al. (2008)).

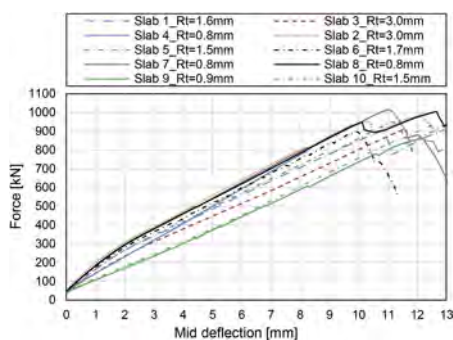


Figure 7. Load deflection curves of the slab tests.

4 DISCUSSION OF THE TEST RESULTS

4.1 Small scale tests

The results of the bond strength tests show an increase of the values with increasing overlay concrete quality (HSC), at the same substrate quality, in the order of about 35% on average compared to NSC in the Slant shear tests. Thus, overall, a decisive influence of the concrete parameters and concrete quality on the bond strength could be verified. In general, a very rough interface ($R_t \geq 3$ mm) produced no significant increase in shear bond strength compared to a rough interface (in the tests: $R_t \approx 2$ mm).

It also became apparent that the different test setups do not provide the same adhesive bond strength: in the Push-Out test, the values for rough interface were approx. 3 N/mm² in the 1st series (4 N/mm² in the 2nd series), whereas the values of the adhesive bond strengths were significantly

higher in the Slant Shear test with approx. 7-8 N/mm² in the 1st series (8-9 N/mm² in the 2nd series). Thus, even if the frictional component is eliminated via the Mohr-Coulomb failure hypothesis, the Slant Shear test setup has a clear favorable effect on the recorded bond strength due to the compressive stress state in comparison to pure interface shear loading with the Push-Out setup.

4.2 Large scale tests

The shear cracks developed, as expected, between the support and the load introduction. By means of the photogrammetric DIC (Digital Image Correlation) measuring system, the initiation and development of the cracks and the crack pattern were precisely recorded at each load level. After evaluation of all 10 test slabs, three different failure patterns reflecting the influence of the interface bond quality could be identified (see also Table 2): All tests with NSC overlay (slabs no. 1, 3 and 4) showed local damage in the interface zone: In two cases (slabs no. 1 and 3) the shear crack followed partly the interface. In the case of slab 4, local small area detachments of the overlay in the edge area were detected during the subsequent inspection of the fracture surfaces. In the case of the slabs with HSC overlays (slabs no. 2, 5, 6, 7 and 8), the shear crack crossed the interface diagonally without any signs of deviation due to the crossing interface (see Figure 8). Only in the case of slab 7, the slab with the highest first load maximum, a crack offset near the load application zone and a localized detachment of a small overlay concrete fragment in the edge area were observed. The bond in slabs 9 and 10, on the other hand, was obviously significantly weakened due to the cyclic preloading during the pouring of the concrete; as a result, the shear crack followed partly the interface over a longer distance. In these areas, clear delamination of the overlay also occurred in the further course of failure.

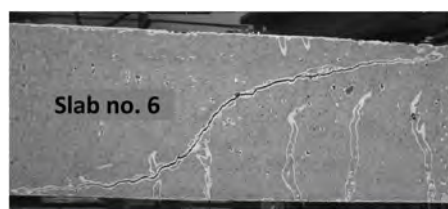


Figure 8. Crack pattern of slab no. 6 at 1st load maximum.

The back-calculated interface shear stresses were partly in the range of the interface bond strength recorded in the Push-Out tests. In the case of slab 7 with the highest bond stress (3,8 MPa) where some slight cracking along the interface was observed, the bond stress was at the level of the strength measured in the Push-Out tests (Figure 5).

5 CONCLUSION

The bond strength between HSC overlay and NSC substrate was studied in small scale and large scale tests. It was clearly shown that significantly higher bond strengths were observed with HSC concretes than achievable with NSC.

The combination of small scale and large scale tests provided a full picture of the load bearing behavior and the adhesive bond mechanism. The influence of the investigated parameters such as variation of roughness depth emerges more pronounced in the small scale tests. The numerical analysis of the large scale tests is backed up by calibrating the interface parameters from the small scale tests. Based on the presented tests, with HSC overlays bond values are about 20-30% higher than usually achieved with NSC overlays. Taking this into account in the design, the degree of roughening could be reduced e.g. from the category “very rough” to “rough” (fib (2012)), still providing the same interface shear resistance like with NSC concrete. In addition to the good bonding properties, HSC also offers other advantages, such as higher resistance to mechanical abrasion or better durability.

ACKNOWLEDGMENTS

The research project was funded by the Austrian Research Promotion Agency FFG and co-financed by the ÖBV member companies ASFiNAG, ÖBB-Infrastruktur, PORR, STRABAG and RTB ROHRDORFER Transportbeton, for which the authors would like to express their sincere thanks to all of them.

REFERENCES

- Cervenka, J. & Papanikolaou, V. K. 2008. Three dimensional combined fracture-plastic material model for concrete. *International Journal of Plasticity* 24: 2192–2220
- Fib (Fédération internationale du béton) 2012. *Fib Model Code for Concrete Structures 2010*, Lausanne.
- Javidmehr, S., Empelmann, M. 2021. Shear Bond between Ultra-High Performance Fibre Reinforced Concrete Overlays and Normal Strength Concrete Substrates, *Sustainability* 13 (15): 8229
- Ju, Y., Shen, T., Wang, D. 2020. Bonding behavior between reactive powder concrete and normal strength concrete, *Construction and Building Materials* 242
- Júlio, E., Branco F., Silva, V., Lourenco, J. 2006. Influence of added concrete compressive strength on adhesion to an existing concrete substrate, *Building and Environment* 41: 1934–1939.
- Lenz, P. 2012: *Beton-Beton-Verbund Potenziale für Schubfugen*. Doctoral Thesis, Technische Universität München
- Orgass, M., Klitsch, B., Wißler, M., Tauscher, F., Dehn, F. 2018. Überführungsbauwerk der L 3378 bei Fulda-Lehnerz. Erster Einsatz von UHFB in Deutschland im Straßenbrückenbau, Teil 2: Betontechnologie und Qualitätssicherung, *Beton- und Stahlbetonbau* 113 (12): 821–830
- ÖNORM EN 1992-1-1: Eurocode 2, Bemessung und Konstruktion von Stahlbeton- und Spannbetontragwerken – Teil 1-1, Austrian Standards Institute 2009
- Pelke, E., Jaborek, A., Berger, D., Brühwiler, E. 2018. Überführungsbauwerk der L 3378 bei Fulda-Lehnerz. Erster Einsatz von UHFB in Deutschland im Straßenbrückenbau, Teil 1: Projektentwicklung und Baudurchführung, *Beton- und Stahlbetonbau* 113 (11): 831–841
- Randl, N., Münger, F., Wicke, M. 2005. Verstärkung von Brückentragwerken durch Aufbeton, *Bauingenieur* 80 (4): 207–214
- Randl, N., Zilch, K., Müller, A. 2008. Bemessung nachträglich ergänzter Betonbauteile mit längsschubbeanspruchter Fuge, *Beton- und Stahlbetonbau* 103 (7): 482–497
- Randl, N. 2013. Design recommendations for interface shear transfer in fib Model Code2010, *Structural Concrete* 14 (3): 230–241
- Randl, N. & Kunz, J. 2014. Post-installed reinforcement connections at ultimate and serviceability limit states. *Structural Concrete* 15(4): 563–574.
- Randl N., Steiner M., Peyerl M. 2016. Sustainable strengthening of RC members with High Performance Concrete overlays, *IABMAS 2016*:1308–1315.
- Randl N., Steiner M., Peyerl M. 2020. Hochfester Aufbeton zur Tragwerksverstärkung - Teil 1: Kleinkörperversuche, *Beton- und Stahlbetonbau* 115/2: 106–116
- Randl, N. & Steiner, M. 2020. Hochfester Aufbeton zur Tragwerksverstärkung - Teil 2: Bauteilversuche, *Beton- und Stahlbetonbau* 115/5: 375–384
- Reinecke, R.: *Haftverbund und Rissverzahnung in unbewehrten Betonschubfugen*. Dissertation, Lehrstuhl für Massivbau, Technische Universität München, 2004
- Rossi, E., Randl, N., Mészöly, T., Harsanyi, P. 2021a. Effect of TRC and F/TRC Strengthening on the Cracking Behaviour of RC Beams in Bending, *Materials*, 14(17), 4863
- Rossi, E., Randl, N., Mészöly, T., Harsanyi, P. 2021b. Flexural Strengthening with Fiber-/Textile-Reinforced Concrete, *ACI Structural Journal* 118(4): 97–107
- Semendary, A., Svecova, D. 2020. *Factors affecting bond between precast concrete and cast in place ultra high performance concrete (UHPC)*, *Engineering Structures* 216 (2020)
- Valikhani, A., Jahromi, A.J., Mantawy, I.M., Azizinamini, A. 2020. Experimental evaluation of concrete-to-UHPC bond strength with correlation to surface roughness for repair application, *Construction and Building Materials* 238
- Zanotti, C., Randl, N. 2019. Are concrete-concrete bond tests comparable?, *Cement and Concrete Composites*, Volume 99: 80–88
- Zhang, Y., Zhu, P., Wang, X., Wu, J. 2020. Shear properties of the interface between ultra-high performance concrete and normal strength concrete, *Construction and Building Materials* 248, 118455

Innovative shear strengthening with post-installed undercut anchors

N. Randl & P. Harsányi

Carinthia University of Applied Sciences, Spittal/Drau, Austria

J. Kunz

Hilti Corporation, Schaan, Liechtenstein

ABSTRACT: Shear strengthening of existing structures is a rather difficult task with respect to the short available anchorage length in the structural member and the target of reasonable activation of the strengthening element before the rather brittle shear failure takes place. In order to overcome such technical requirements, an innovative undercut anchor was developed. The anchors are set into predrilled holes from the soffit of a structure and, via application of a torque moment, slightly pre-tensioned. The undercut solution provides a very short and effective anchorage inside the concrete, and applying a torque moment already activates the system during installation. Large-scale tests on 5.4 m long T-beams designed for shear failure have been performed to verify the functioning of such strengthening solution. All tests ended up in shear failure, with nearly full utilization of the post-installed anchors and load gains around 40% with four and 90% with seven rods.

1 INTRODUCTION

1.1 *General*

The task of retrofitting existing buildings and infrastructure is strongly gaining importance with respect to ever-increasing traffic loads and the target to reduce the environmental impact by increasing the lifespan of a structure instead of demolishing and rebuilding it. Strengthening in shear may be not just a stand-alone task, but become an additional necessity when such structure is undergoing global strengthening and rehabilitation measures. This is also due to the fact that new, refined prediction formulae for shear resistance of RC members are meanwhile available, which increasingly enter codes of practice.

Local strengthening in shear requires usually a very efficient anchorage of the strengthening solution, in order to introduce tensile forces over short distances into the strengthening elements. Otherwise, it would be very difficult to activate the subsequently applied strengthening elements and make use of their tensile properties. This is due to the rather brittle shear failure mode and its specific typology and failure pattern (Störzel et al. 2015).

Another frequent requirement is coming from the infrastructure operators, who request to avoid significant interruptions of the traffic flow during the strengthening process. Unfortunately, shear strengthening techniques require quite often also construction works on the top side of a structure.

1.2 *Traditional methods*

Traditional methods of shear strengthening are based on the following basic principles (Figure 1):

- a) Attaching or, if possible, wrapping around CFRP/textile/steel sheets or straps
- b) Clamping with steel rods/tendons passing aside or crossing the member in a vertical direction
- c) Applying reinforced shotcrete or cast additional concrete layers (Randl et al. 2005)

If the CFRP sheets cannot be fully wrapped around, which is usually the case, appropriate end anchorages are required in order to prevent premature delamination of the sheets from the concrete substrate (Kalfat et al. 2013). Such anchorage should be designed to transfer the tensile load directly to the RC member's compressive zone (Täljsten 2003, Randl & Harsanyi 2018). In general, high-bond two-component adhesives are used to glue the sheets to the clean and preferably slightly roughened existing concrete surface. Steel rods passing through the cross-section in a vertical direction are quite easy to handle and install, however, require construction works also on the top side of the structure (Breveglieri et al. 2014).

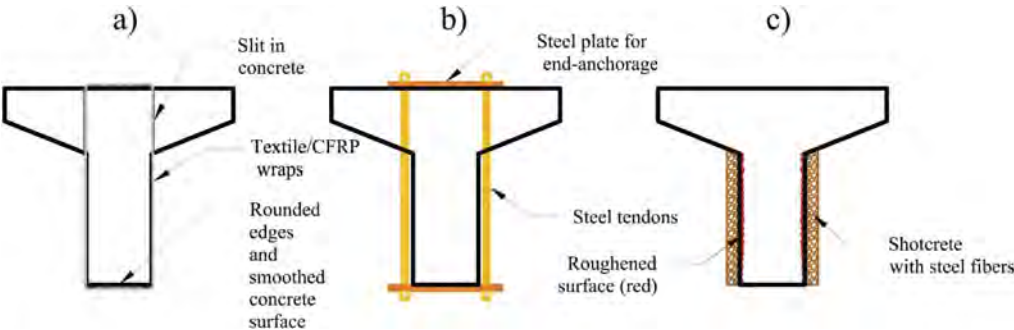


Figure 1. Overview of some traditional shear strengthening techniques.

1.3 *Post-installed reinforcement*

Post-installed reinforcement is used successfully in various situations of structural applications. A core purpose of the technique is to connect new and old parts of reinforced concrete structures, ensuring the full transfer of forces. The post-installed reinforcing bars are inserted into pre-drilled holes and glued in with an appropriate high-bond mortar. A key requirement in that context is the assurance of sufficient anchorage to the old concrete. While the basic anchorage length is in-line with according specifications in codes of practice for the anchorage of cast-in reinforcement, sophisticated approaches allow for reduced embedment depths (Randl & Kunz 2014).

Such types of post-installed reinforcing bars can also be successfully used for structural strengthening of a RC member. Former tests performed by Randl & Kunz (2009) and Kunz et al. (2013) show that the subsequent insertion of inclined reinforcing bars is an effective method to enhance the shear resistance of existing concrete members significantly. The results of these investigations have been translated into a design concept based on fib Model Code 2010 (Muttoni & Fernandez 2013). With respect to the required bond length, an inclination of the bars of preferably 45° is recommended to achieve sufficient end anchorage in the concrete compression zone (Figure 2).



Figure 2. Setup of post-installed reinforcement for strengthening in shear.

Marti et al. (2016) have investigated shear strengthening with vertical post installed shear reinforcement and provided recommendations to the Swiss Federal Roads Office (Bundesamt für Strassen 2016).

2 STRUCTURAL TESTS WITH INNOVATIVE UNDERCUT SLEEVE ANCHORS

2.1 Method and anchor installation

While standard shear reinforcement with stirrups or double headed studs have clearly defined, local anchorage zones, post-installed straight bonded bars have the drawback that their anchorage zone extends over a certain bond stretch. Figure 3 shows the principal stresses activated in the concrete by the two types of anchorage.

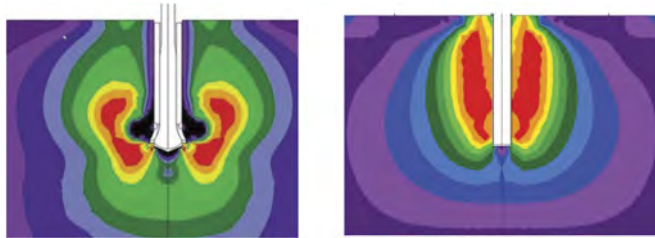


Figure 3. Principal stress from headed anchorage (left) and bonded anchor (right).

In close cooperation with the Hilti Corp., an innovative anchor element has been developed which allows for quick installation and immediate activation due to pre-tensioning via an applied torque moment. The steel anchor consists of a rod with a cone-shaped undercut at the end, providing a clearly defined local anchorage, and is embedded in a tubular sleeve. Before installation, a hole has to be drilled to provide sufficient embedment depth. After injection with an appropriate high-bond mortar, the anchor is set into the hole. Due to the undercut element at the end of the rod and the free length within the steel sleeve, it can be immediately torqued. After hardening of the mortar, higher loads can be applied as the bond between the sleeve and the borehole allows for additional utilization of the tensile resistance of the steel sleeve (see Figure 4).

Such anchors for strengthening in shear provide various advantages compared to other traditional methods:

- Allowance for installation from the soffit, thus avoiding/minimizing traffic interruptions
- Activation already at serviceability load level, i.e. when the installation torque is applied

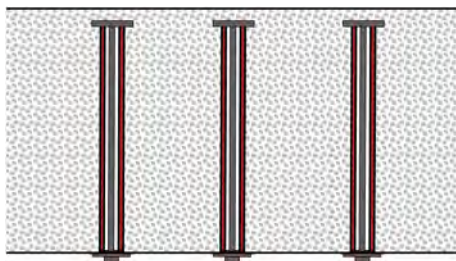


Figure 4. Working principle of undercut sleeve anchors.

2.2 Testing program

A number of six 5.4 m long T-beams was designed in a way that shear failure was to be expected, even in the case of an enhanced shear load-bearing capacity due to applied strengthening. For that purpose, a strong longitudinal reinforcement consisting of four 30 mm and two 25 mm diameter bars as longitudinal tensile reinforcement situated at the bottom of the beam were foreseen. As top reinforcement, only four 14 mm diameter bars and two 10 mm diameter bars were placed in order to create a stable reinforcement cage.

The T-cross section had a height of 600 mm and an overall flange width of 700 mm, while the width of the web was 200 mm. Such a shape should simulate a typical representative cross-section with practical relevance. Considering the distance of 1.585 m between load introduction and support in the chosen 3-point load setup, the shear span-to-depth ratio a/d was 3.24 (with an effective depth d of 489 mm).

No stirrup reinforcement was provided in the beam sections between load introduction and closest support where the subsequent strengthening was to be applied.

Figure 5 displays the test setup. While the reference test had no stirrup reinforcement at all, the other beams were designed with stirrups outside the strengthening zone to avoid premature shear failure in the non-strengthened zones. Apart from those sections, along the remaining length 12 mm diameter stirrups at a 190 mm spacing were cast-in to enforce shear failure at the critical shear span and avoid premature failure in bending.

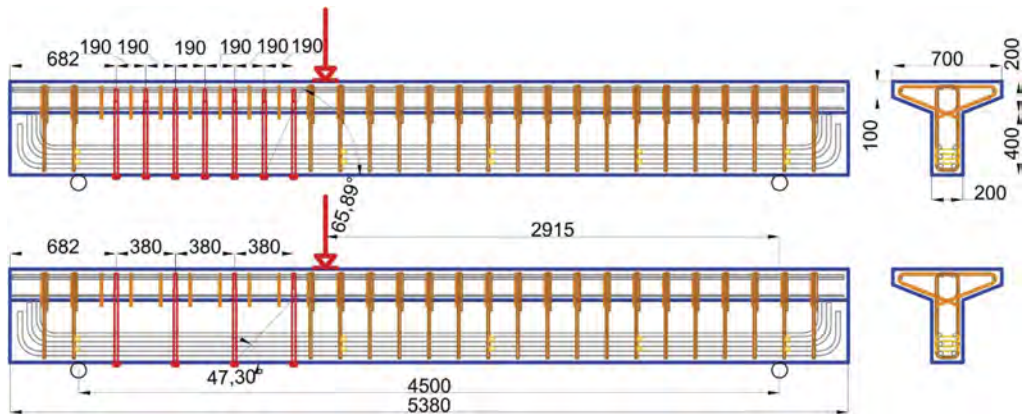


Figure 5. Test setup with reinforcement layout and strengthening variants (units in mm).

The number of installed anchors varied between 4 and 7, with a spacing of 380 mm with 4 and 190 mm with 7 anchors. In order to simulate a practical approach, the anchors were installed in the lab from underneath the beams, which were placed on supports at a height of about 1 m. The overall testing program is summarized in Table 1. Here, the abbreviation PUAnc stands for Post-installed Undercut Anchors, followed by the number of subsequently installed anchors and the test number.

Table 1. Overview of testing program and results.

Test	No. of elements	Spacing [mm]	F_{\max} [kN]	V_{\max} [kN]	$F_{\max}/F_{\max,ref}$
Reference	0	-	370.9	240.3	1.00
PUAnc_4_1	4	380	612.0	396.4	1.65
PUAnc_4_2	4	380	515.0	333.0	1.39
PUAnc_4_3	4	380	499.4	323.5	1.35
PUAnc_7_1	7	190	681.7	441.6	1.84
PUAnc_7_2	7	190	714.5	462.8	1.93

2.3 Material data

The beam specimens were made of normal-strength concrete C30/37. The mean concrete strength measured on 150 mm cubes on the day of testing was 43.5 N/mm².

The longitudinal reinforcing bars provided at the bottom of the beams consisted of high-grade steel S670/800, in order to ensure maximum flexural resistance with a still reasonable reinforcement degree. The nominal yield strength was 670 N/mm² with an average value of 725 N/mm². All other types of used reinforcement, i.e. longitudinal top bars and stirrups, were

made of Austrian standard steel B550 B with a nominal yield strength of 550 N/mm² and an average yield strength close to 600 N/mm².

Concerning the anchor element itself, the internal threaded rod had a steel strength grade 8.8 according to EN ISO 898-1, with a metric screw thread size M12. In combination with the steel sleeve, the outer diameter of the whole strengthening element was around 17 mm, with a free anchorage length of around 500 mm. The strengthening elements were installed in diameter 22mm hammer-drilled holes.

3 FATIGUE TESTING OF UNDERCUT ANCHOR SOLUTIONS

In order to test the load-bearing behavior of the prototypes under fatigue loading, single cyclic tests with three beams and varying load amplitude were carried out. The load was applied in a force-controlled manner using a hydraulic cylinder with a maximum dynamic capacity of 500 kN at frequencies between 3 Hz and 4 Hz. The performed tests aimed at identifying possible weak points for further development and improvement of the prototypes at a later stage. An overview of the test program and its results (maximum number of endured cycles) can be found in Table 2.

Table 2. Setup and results of shear tests subject to cyclic loading.

Test	Spacing [mm]	Min force [kN]	Max force [kN]	Max shear force [kN]	ΔV_{cyclic} [kN]	No. of cycles
PUAnc_7_3	380	32.5	305	236,6	204,02	34.460
PUAnc_7_4	380	27.1	235	184,8	161,12	590.000 ^{1}
PUAnc_7_5	380	27.1	280	218,1	189,96	38.670

{1} First anchor failure; as even after 1.5 million load cycles the beam did not fail, the test was stopped

4 TEST RESULTS

4.1 Failure modes

All tested beams showed a typical shear failure mode: The first single and slightly inclined shear cracks with an inclination of roughly 60°-70° to the horizontal axis appeared at the reference beam at a load level of about 130 to 140 kN, and at the strengthened beams such cracks showed up consistently at a significantly higher load level of around 200 to 250 kN in between the strengthening elements.

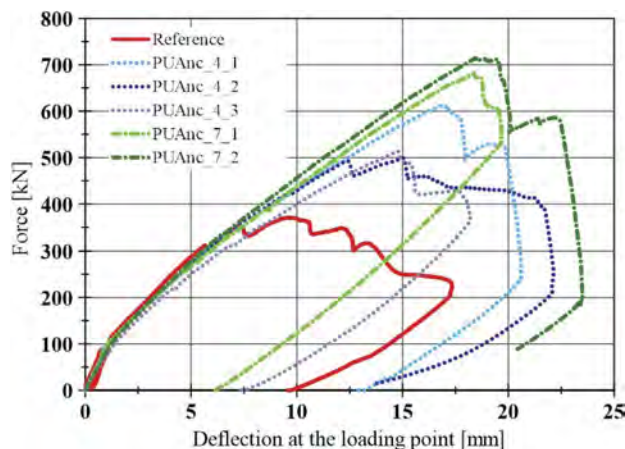


Figure 6. Force deflection curves of the tested beams.

At a load level of 300 to 350 kN, i.e. close to the failure load of the unreinforced reference beam (see load-deflection curves in Figure 6), the inclination of the propagating shear cracks started to decline to an angle between 30° and 45° to the horizontal axis. At the reference beam this was followed quickly by the formation of a continuous critical shear crack and, having passed through the flanged section, soon led to final failure. At the same load level, the strengthened beams showed no significant loss in stiffness as the strengthening elements were increasingly activated at that stage: pronounced shear cracks started to form in between the elements and the formation of a typical truss mechanism was initiated.

The load transfer via the truss mechanism was more and more identifiable and clearly developed above a load level of about 400 to 450 kN. Before the total failure of the beams, an increasing number of less inclined cracks appeared (around 25° to the horizontal axis), partly unifying and crossing the strengthening elements while showing an increasing crack width. Finally, one or two main cracks started to propagate through the whole cross-section (see Figure 7).

The failure took then place in such a way that a first inner rod of an undercut anchor broke and in most cases fell out of the sleeve. However, this first rupture of one single rod never led to a total loss: after a sudden limited drop in the load, again some recovery of the load was observed until another rod broke. Such behavior can be attributed to a redistribution of the load to other, still fully working anchors. Final failure was usually reached with the rupture of the second or even another third rod. The bonded sleeves remained intact in the structure, thereby preventing a sudden total breakthrough of the concrete beam. Additional information on observed failure modes is provided in Randl & Harsanyi (2018).



Figure 7. Photograph of representative failure mode after ultimate failure (strengthened with 7 anchors).

4.2 Achieved load gain

All strengthened beam specimens exhibited a significant load increase due to the applied strengthening elements. Despite the rather small cross-section of each rod, impressive loads were achieved with the strengthened beams. In comparison to the reference beam, the shear capacity was nearly doubled (enhancement factor 1.88) with the application of seven post-installed anchors, while a number of four rods still led to an average increasing factor of 1.46. Obviously, the increase in the number of anchors from 4 to 7, corresponding to a reduction of the spacing from 380 to 190 mm, did not lead to a proportional increase in the shear load-bearing capacity. This is due to the fact that with respect to the kinematics of the shear failure mode and the mechanical properties of the used steel not all anchor rods can be fully activated at the same time.

Apart from the mere absolute values of the achieved load enhancements, another meaningful approach to judge the efficiency is based on a very simple model used also by other researchers (see e.g. Belarbi et al. 2012): The maximum tensile strength $A_{si} \cdot f_{um}$ of all strengthening elements crossed by the assumed inclined shear crack is summed up and related to the ultimate shear load observed in the test: $k = \sum A_{si} \cdot f_{um} / V_{ult}$. Thereby, with 4 undercut anchors, an efficiency factor k of more than 80% turns out, which can be rated as very high. Note that this consideration is only a rough approach as additional effects providing a contribution to shear resistance, such as dowel action of the longitudinal reinforcement or exact kinematics of shear crack formation, are not taken into account.

4.3 Fatigue test results

All three beam specimens failed in a similar manner (see Table 3). Depending on the applied load amplitude, a different number of cycles was achieved. PUAnc_7_3 with a maximum applied cyclic shear force of 236.6 kN failed after 34.460 cycles due to a fatigue failure of the inner undercut anchor along the threaded rod. Despite the comparatively high force-controlled load application, the remaining steel sleeve was able to ensure ductile failure over another 30 load cycles. With a maximum shear force of 184.8 kN, it was possible to achieve a number of 590.000 cycles in the case of PUAnc_7_4 until the first inner threaded rod failed in a similar manner. Nevertheless and in contrast to the previous test, it was possible to maintain a sufficient loadbearing capacity due to the still intact sleeve tube, however at increased deformation and crack opening, and proceed with the fatigue test. The test was finally terminated after 1.5 million load cycles as there was no indication of any forthcoming total failure of the beam. In the third cyclic test PUAnc_7_5, a maximum shear force of 218.1 kN was applied. The beam showed the same failure behavior as PUAnc_7_3 and PUAnc_7_4 before and a first anchor, i.e. the inner threaded rod, failed after 38670 cycles. Hereafter, the beam underwent another 2000 additional cycles until it finally collapsed.

Table 3. Overview of the fatigue failure modes.

Test	Description of failure mode
PUAnc_7_3	Rupture of the second anchor (from support) after 34.460 cycles, followed by beam collapse after an additional 30 cycles
PUAnc_7_4	Failure of the third anchor (from support) after 590.000 cycles, followed by increasing deflections, test was aborted after 1.5 million cycles
PUAnc_7_5	Failure of the second anchor (from support) after 38.670 cycles, followed by beam collapse after an additional 2.000 cycles

Compared to the static load tests, the behavior differed on one side due to the load-controlled test procedure. On the other side, it could be observed that the failure due to fatigue loading was not identical to the static failure mode. After the failure of the first inner threaded rod, the deformation of the beams increased significantly. This led in consequence to a pronounced and progressive crack propagation parallel to the compressive struts, entering the compressed flanges of the T-shaped cross section. Finally extensive spalling of the concrete in the bending tensile zone was observed in the surroundings of failed anchors (Figure 8).



Figure 8. Photograph of fatigue failure of tested beam.

5 CONCLUSIONS

Strengthening in shear by means of newly developed sleeved undercut anchors is an effective way to achieve significant load enhancements without the requirement of large interventions in the existing structure. As such kind of anchorage can be set from the bottom side of an RC member, the traffic flow is not affected by the construction works. Due to the concentrated

load introduction at the anchor's head, this type of sleeved undercut anchor can be set in the vertical direction.

In the different shear tests performed with a varying number of anchors, a load increase between around 40% with 4 anchors and 90% with 7 anchors was achieved.

The undercut anchors succeed with their concentrated load introduction which enables prompt loading and in addition some pre-stressing effect when applying the torque moment. This allows for immediate activation and is helpful also for serviceability limit state considerations (e.g. crack control).

The cyclic load tests performed, allowed the identification of a possible optimization potential of the prototypes and showed that significant force transmission via the bonded steel sleeve is possible, even in case of failure of the inner threaded rod. By adapting the prototype, it should also be possible to optimize the intended reinforcement method for dynamic load scenarios.

Even though in the present tests an injection mortar was used, the undercut anchors would also work without the bond between the sleeve and the surface of the borehole (however, the contribution of the sleeve would in that case have to be canceled).

ACKNOWLEDGEMENT

The project was funded by the Austrian FFG (Grant no. 840549), together with the Austrian Infrastructure Operators for Motorways (ASFINAG) and Railways (ÖBB) which is greatly acknowledged.

REFERENCES

- A. Belarbi, A., Bae, S.-W., & Brancaccio, A. 2012. Behavior of full-scale RC T-beams strengthened in shear with externally bonded FRP sheets. *Constr. Build. Mater.* 32: 27–40.
- Breviglieri, M., Aprile, A., Barros, J.A.O. 2014. Shear strengthening of reinforced concrete beams strengthened using embedded through section steel bars. *Eng Struct.* 81:76–87.
- Bundesamt für Strassen, 2016. Querkraftverstärkung einseitig zugänglicher Stahlbetonplatten mit eingemörtelten Bewehrungsstäben. *Forschungsprojekt AGB 2009/003 auf Antrag der Arbeitsgruppe Brückenforschung (AGB)*
- Kalfat, R., Al-Mahaidi, R. & Smith, S.T. 2013. Anchorage devices used to improve the performance of reinforced concrete beams retrofitted with FRP composites: state-of-the-art review. *J Compos Constr.* 17(1):14–33.
- Kunz, J., Fernández-Ruiz, M., Muttoni, A. 2013: Enhanced Safety with Post-Installed Shear Reinforcement. *fib-Symposium "Engineering a Concrete Future", Tel Aviv, 22 to 24 April 2013.*
- Marti, P., Seefeld-Ebert, B., & Beck, A. 2016. Querkraftverstärkung einseitig zugänglicher Stahlbetonplatten mit eingemörtelten Bewehrungsstäben. *Eidgenössisches Departement für Umwelt, Verkehr, Energie und Kommunikation UVEK, Bundesamt für Strassen, 678.*
- Muttoni, A., Fernandez Ruiz M. 2013: Design Method for Post-Installed Shear Reinforcement with Hilti Tension Anchors HZA. *MFIC ingénieurs conseils, Report 11-A01-R1. 2013.*
- Randl, N., Münger, F., Wicke, M. 2005. Verstärkung von Brückentragwerken durch Aufbeton, *Bauingenieur* 80 (4): 207–214
- Randl, N. & Harsányi, P. 2018. Developing optimized strengthening systems for shear-deficient concrete members. *Structural Concrete* 19(1): 116–128.
- Randl, N. & Kunz, J. 2009. Biegeschubversuche an Stahlbetonbalken mit nachträglich eingemörtelter Querkraftbewehrung. *Beton- und Stahlbetonbau* 104 (11): 728–736.
- Randl, N. & Kunz, J. 2014. Post-installed reinforcement connections at ultimate and serviceability limit states. *Structural Concrete* 15(4): 563–574.
- Störzel, J., Randl, N. & Strauss, A. 2015. Monitoring shear-induced degradation of reinforced and pre-tensioned concrete members. *In IABSE Conference, Geneva 2015: Structural Engineering: Providing Solutions to Global Challenges; Report, Geneva, 23-25 September 2015: 1148–1157.*
- Täljsten, B. 2003. Strengthening concrete beams for shear with CFRP sheets. *Construction and Building Materials* 17(1): 15–26.

MS13: Safety and durability of high-performance structures
Organizers: X. Gu & Q. Yu



Taylor & Francis

Taylor & Francis Group

<http://taylorandfrancis.com>

Evolution of seismic fragility of reinforced concrete columns subjected to corrosion

Y. Liu, W.P. Zhang & X.L. Gu

Department Structural Engineering, College of Civil Engineering, Tongji University, Shanghai, PR China

Y. An

Department Civil Engineering, Guanxi University, Nanning, PR China

ABSTRACT: This paper presents a stochastic methodology to investigate the evolution of seismic fragility for reinforced concrete (RC) columns subjected to corrosion. On account of the increasing variability of mechanical properties of corroded reinforcement, a finite element (FE) model is proposed by incorporating a stochastic constitutive model of corroded rebars. The developed fiber-based FE model is calibrated using a set of experimental data and then extended to conduct pushover analyses and nonlinear time history analyses of RC columns with different corrosion degrees. The results of damage limit states (DLSs) determined by stochastic pushover curves indicate that DLSs for deteriorating columns are corrosion-dependent and follow lognormal distributions. Based on incremental dynamic analyses (IDAs), the fragility analyses results show that reinforcement corrosion has adverse effects on life-cycle seismic performance of RC columns. Comparisons are made between the proposed methodology and traditional approaches to developing seismic fragility curves for corroded RC columns. Considerable underestimations of seismic fragility across different DLSs were found using the traditional approach compared to the stochastic methodology.

1 INTRODUCTION

In the past few decades, reinforcement corrosion in RC structures has gradually received extensive attention. RC columns or piers located in environmentally aggressive areas such as chloride-laden environments inevitably suffer from the effect of chloride-induced corrosion during their lifetime. Corrosion leads to the reduction of the load-carrying capacity of reinforcement (Zhang et al. 2014a) and cracking or spalling of concrete cover (Chen et al. 2020). Many coastal regions are tectonically active areas, and deterioration of the seismic performance of marine structures will generally increase the risk of economic loss and casualties caused by earthquake events (Sharma et al. 2016). As a consequence, it is of great significance to investigate the evolution of life-cycle performance of RC structures subjected to seismic hazard.

More recently, several experimental studies have focused on the effect of corrosion on the structural performance of RC columns under cyclic loading (Meda et al. 2014, Zhang et al. 2023). The outcomes of these studies show that the load-carrying capacity, stiffness, and ductility of the columns gradually deteriorate with the increase of corrosion degree. Meanwhile, as an important part of performance-based seismic design, seismic fragility has become a research hotspot in the field of earthquake engineering. Results in previous studies pointed out that with the increase in service time, the seismic fragility of the corroded structure increases, resulting in an increase in the failure probability of the structures (Xu et al. 2021). However, in most current studies, the damage limit states implemented in the development of fragility curves for corroded RC structures were those recommended for pristine structures, ignoring the time-dependence of the damage limit state. As a matter of fact, the corrosion-independent damage limit states might lead to an unrealistic estimation of the failure probability for corroded structures. Recent studies (Dizaj et al. 2018) have confirmed that damage limit states used for fragility assessment of deteriorated structures should be considered as corrosion-dependent parameters. Nevertheless, the limitation in current

literature lies in the perspective of deterministic analysis without accounting for the increasing variability in mechanical properties of corroded rebars. Few previous researchers (Ghosh & Sood 2016) have proposed probability distributions for corrosion-dependent damage limit states by incorporating a stochastic process model of corroded rebars. Hence, an important missing link for evaluating the life-cycle seismic fragility of deteriorating RC columns consists of putting forward a stochastic method that contains the randomness in reinforcement corrosion.

In this study, a fiber-based FE model including the impact of corrosion on reinforcement and concrete is proposed. The corrosion-dependent damage limit states distributions of corroded RC columns are obtained via a huge number of pushover analyses. An approach to developing seismic fragility curves for uncorroded and corroded RC columns considering stochastic evolution of mechanical properties of corroded rebars is presented.

2 PROBABILISTIC CORROSION DETERIORATION MODELING

2.1 Stochastic constitutive model for corroded rebars

One of the major concerns in practical engineering is the residual capacity and service life of aging RC structures. Due to the variability of the environmental action and the non-uniformity of concrete materials, concrete carbonization, chloride penetration, and reinforcement corrosion are all stochastic processes. Accordingly, the variability of mechanical properties of rebars varies with the initiation and propagation of corrosion. That is, the degradation of mechanical properties of corroded rebars is also a stochastic process (Zhang et al. 2021). It is obvious that a deterministic analysis method may result in extremely conservative structural reliability assessment, causing potential structural safety problems. Tensile tests (Zhang et al. 2012) of corroded rebars indicated that the nominal yield strength, the nominal ultimate strength, and the ultimate strain decreased, and the yield plateau shortened and even disappeared with the propagation of corrosion. Based on tests results, a deterministic model of stress-strain relationship was proposed by Zhang et al. (2014b) as shown in Figure 1 and Equations 1–2.

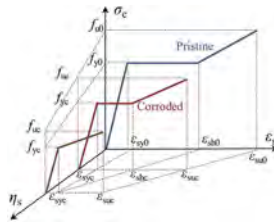


Figure 1. Stress-strain curves of corroded rebars.

$$\sigma_{sc} = \begin{cases} E_{sc}(\eta_s)\varepsilon_{sc}, & \varepsilon_{sc} \leq f_{yc}(\eta_s)/E_{sc}(\eta_s) \\ f_{yc}(\eta_s), & \varepsilon_{shc}(\eta_s) \geq \varepsilon_{sc} > f_{yc}(\eta_s)/E_{sc}(\eta_s) \\ f_{yc}(\eta_s) + E_{shc}[\varepsilon_{sc} - \varepsilon_{shc}(\eta_s)], & \varepsilon_{suc}(\eta_s) \geq \varepsilon_{sc} > \varepsilon_{shc}(\eta_s) \end{cases} \quad (1)$$

$$f_{yc} = \frac{\alpha_{yc}}{1 - \eta_s} f_{y0} \quad ; \quad f_{uc} = \frac{\alpha_{uc}}{1 - \eta_s} f_{u0} \quad (2)$$

where η_s is corrosion degree based on the average loss of cross-sectional area; σ_{sc} and ε_{sc} is nominal stress and strain of corroded rebars, respectively; f_{yc} and f_{uc} are the nominal yield and ultimate strengths of corroded rebars, respectively; ε_{yc} , ε_{shc} and ε_{suc} are the yield strain, hardening strain and ultimate strain, respectively; E_{sc} and E_{shc} are the elastic modulus and hardening modulus, respectively; f_{y0} and f_{u0} are the yield and ultimate strengths of uncorroded rebars, respectively; α_{yc} and α_{uc} are the yield and ultimate load ratios, respectively. More details about the definition of the model parameters are available in Zhang et al. (2014b). It is noted that mechanical properties of both uncorroded and corroded rebars are normally distributed, while the coefficient of variation

risers with the increase of corrosion degree. Consequently, the probability distribution models of mechanical properties for uncorroded steel bars and the stochastic process models for mechanical properties of corroded rebars were established by Zhang et al. (2014b):

$$f(x) = \frac{1}{\sqrt{2\pi}\delta\mu} \cdot \exp\left[-\frac{(x-\mu)^2}{2(\delta\mu)^2}\right] \quad (3)$$

$$f[x(\eta_s)] = \frac{1}{\sqrt{2\pi}\delta(\eta_s) \cdot \mu(\eta_s)} \cdot \exp\left[-\frac{[x(\eta_s) - \mu(\eta_s)]^2}{2[\delta(\eta_s) \cdot \mu(\eta_s)]^2}\right] \quad (4)$$

where x and $x(\eta_s)$ are the elastic modulus, yield load ratios, ultimate load ratios and ultimate strain for uncorroded and corroded rebars, respectively; μ and δ are corresponding mean and coefficient of variation. The relationships between $\mu(\eta_s)/\delta(\eta_s)$ and η_s are summarized in Table 1.

Table 1. Relationships between $\mu(\eta_s)/\delta(\eta_s)$ and η_s .

Stochastic process	$\mu(\eta_s)$	$\delta(\eta_s)$
E_{sc}	2.047	$\delta(\eta_s) = 0.303\eta_s + 0.079$
α_{yc}	$\mu(\eta_s) = -1.092\eta_s + 1$	$\delta(\eta_s) = 0.479\eta_s + 0.034$
α_{uc}	$\mu(\eta_s) = -1.152\eta_s + 1$	$\delta(\eta_s) = 0.559\eta_s + 0.028$
ε_{suc}	$\mu(\eta_s) = -1.092\eta_s + 1$	$\delta(\eta_s) = 0.677\eta_s + 0.216$

2.2 Impact of reinforcement corrosion on contribution of concrete

The impact of corrosion is not limited to steel bars only. The volumetric expansion actions of corrosion products induce internal tensile stresses in the concrete around the rebar, which leads to unexpected concrete cracking and spalling along the longitudinal direction of the rebar (Chen et al. 2020). In order to account for the effects of reinforcement corrosion on the contribution of concrete cover, the simplified equivalent method proposed by Coronelli (2004) is adopted:

$$\lambda = \frac{1}{1 + K\varepsilon_1/\varepsilon_{c0}} \quad (5)$$

where λ is a reduction factor for compressive strength of concrete cover; K is the steel bar roughness and diameter which can be taken as 0.1; ε_{c0} is concrete strain corresponding to the peak compressive stress; and ε_1 is average tensile strain in cracked concrete. More details about the parameters are available in Coronelli (2004). However, the stirrups corrosion inevitably causes reduction in both cross-sectional areas and mechanical properties, decreasing the confinement effects and strength improvement of core concrete, which can be considered by the reduction of the stirrup ratio and yield strength of the corroded stirrups. According to the Kent-Scott-Park model (Scott et al. 1982), compressive strength of core concrete and its corresponding strain are increased by factor of K_c , which is calculated as follows:

$$K_c = 1 + \frac{\rho_s f_{yh}}{f_c} \quad (6)$$

where f_{yh} is yield strength of stirrups; ρ_s is the stirrups ratio; f_c is the compressive strength of the sound concrete. As stirrup corrosion increases, the value of K_c inevitably decreases.

3 FINITE ELEMENT MODEL OF RC COLUMNS

3.1 FE model using non-linear fiber beam-column element

In this section, a fiber-based finite element model via *OpenSees* is presented. As shown in Figure 2, the whole length of the column incorporated with the fiber section is divided into six displacement-based elements with three Gauss integration points. The fiber section includes three

parts: longitudinal reinforcement fiber, core concrete fiber and cover concrete fiber. The fiber of each part is given the aforementioned constitutive model in Section 2, in which the concrete and reinforcement adopt *Concrete02* material model and *Hysteretic* material model, respectively. A set of uncorroded and corroded RC columns were designed according to Chinese code. The cross-sectional details of the proposed columns are shown in Figure 3. Each column was reinforced with 12 longitudinal rebars and stirrups with a spacing of 100 mm. Deformed rebars with a diameter of 16 mm were used as longitudinal rebars, and plain rebars with a diameter of 8 mm were used as stirrups. The cubic compressive strength of sound concrete was 30 MPa.

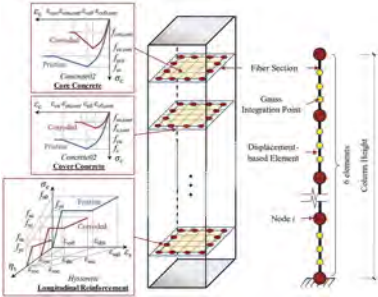


Figure 2. Overview of proposed FE model.

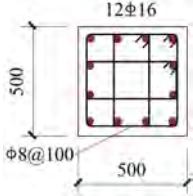


Figure 3. Column cross section.

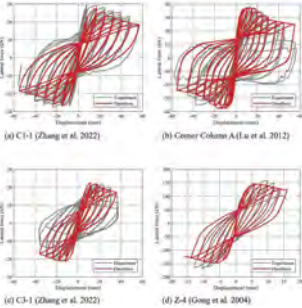


Figure 4. Validation of proposed FE model.

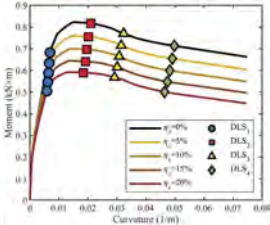


Figure 5. Deterministic pushover analyses.

3.2 Model validation

The cyclic loading tests of uncorroded and corroded RC columns in the literature (Zhang et al. 2022; Lu et al. 2012; Gong et al. 2004) were compared with the calculation results of the proposed FE model. Column C1-1 in Zhang et al. (2022) and Corner Column A in Lu et al. (2012) were selected to validate for uncorroded specimens, while Column C3-1 with the corrosion degree of 0.166 in Zhang et al. (2022) and Z-4 with the corrosion degree of 0.09 in Gong et al. (2004) were selected for corroded one. As shown in Figure 4, the calculation results are basically consistent with the test results, which indicates that the model can be used to simulate the response of RC columns under earthquakes.

4 STOCHASTIC PUSHOVER ANALYSIS

4.1 Influence of corrosion on damage limit states

The purpose of pushover analysis is to determine the damage limit states (DLS) of components or structures. In the process of determination, according to FEMA (2003), the curvature ductility ratio (Equation 7) of the column is selected as the engineering demand parameter for pushover analysis.

$$\mu_\phi = \frac{\phi}{\phi_y} \quad (7)$$

where μ_ϕ is the curvature ductility ratio (CDR) for a curvature ϕ experienced by the RC column during the pushover analysis; ϕ_y is the idealized yield curvature.

Four different DLSs are defined by the value of critical cross-sectional curvature, including slight damage (DLS₁), moderate damage (DLS₂), severe damage (DLS₃) and complete damage (DLS₄). As the outermost tensile reinforcement yields with the onset of visible concrete cracking, the column is considered to be in the slight damage state (DLS₁) with the curvature $\phi_S = \phi_y$. Thus, for the DLS₁, the curvature ductility ratio following Equation (7) equals 1. For the curvature ϕ_M , when the concrete strain at the critical cross-section reaches a value of 0.002, the column is assumed to be in the moderate damage state (DLS₂). The curvature ϕ_C is recommended as the complete damage state (DLS₄) when the compressive strain in the extreme concrete fiber attains a value of ε_{cu} at which stirrups start to fracture. This fracture strain can be calculated as:

$$\varepsilon_{cu} = 0.004 + 1.4 \frac{\rho_s f_{yh} \varepsilon_{uh}}{f_{cc}} \quad (8)$$

where ε_{uh} is the tensile strain of stirrups corresponding to the ultimate stress and f_{cc} is the compressive strength of core concrete. Referring to Ghosh & Sood (2016), this study takes geometric mean of the DLS₂ and DLS₄ as the curvature for severe damage state (DLS₃).

In order to investigate the impact of reinforcement corrosion on damage limit states (DLS), different degrees of corrosion ($\eta_s = 0, 0.05, 0.1, 0.15, 0.2$) are considered and a series of non-linear pushover analyses are conducted. Figure 5 illustrates the results of deterministic pushover analyses. Corrosion-dependent damage limit states for RC columns are obtained and summarized in Table 2. It is shown that with the increase of corrosion degree, the load-carrying capacity gradually degrades, and each damage limit state decreases in varying degrees.

Table 2. Corrosion-dependent DLS.

η_s	0	0.05	0.10	0.15	0.20
DLS ₁	1.00	1.00	1.00	1.00	1.00
DLS ₂	3.04	2.91	2.83	2.77	2.67
DLS ₃	4.68	4.56	4.46	4.36	4.22
DLS ₄	7.21	7.10	6.98	6.86	6.72

4.2 Stochastic pushover curves and distributions of corrosion-dependent DLSs

Before stochastic pushover analysis, it is essential to sample four of the parameters based on the abovementioned stochastic constitutive model of corroded rebars in Section 2. Latin hypercube sampling method was used to conduct 100-time sampling campaign for four parameters (E_{sc} , α_{yc} , α_{uc} , and ε_{suc}) under four corrosion degrees (0.05, 0.1, 0.15 and 0.2). For all the reinforcements in the same column obtained by Latin hypercube sampling, the same constitutive relationship was adopted, while the constitutive relationship between different columns is different. Pushover analysis was carried out on 400 random RC columns under four corrosion degrees, and the stochastic pushover curves were obtained as depicted in Figure 6. It is found that the dispersion of pushover curve gradually increases with the increase of corrosion degree.

The distribution characteristics of each DLS were obtained by statistical analysis of stochastic pushover curves. A complete list of fitted distribution types for the DLSs are presented in Table 3. Consistent with previous studies on corroded columns (Ghosh & Sood 2016), the DLSs are found to follow lognormal distributions. It is noted that following Equation 7, the mean value corresponding to the slight damage state always equal to 1, and the logarithmic standard deviation is 0.035 based on the consideration of epistemic uncertainty. As shown in Table 3, the mean value of the DLS decreases with the increase of the corrosion degree of the RC column. However, the standard deviation is increasing, which indicates that the corrosion of the reinforcement increases the dispersion of the DLS. Additionally, when the corrosion degree is constant, the standard deviation increases with the increase of the damage degree.

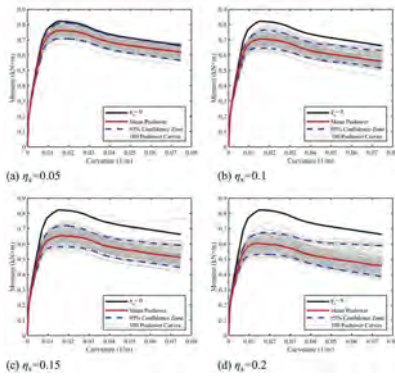


Figure 6. Stochastic pushover curves.

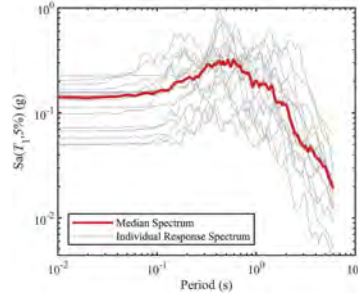


Figure 7. Acceleration Spectra of selected ground motions.

Table 3. Distributions of corrosion-dependent DLS.

η_s	0.05	0.10	0.15	0.20
$DLS_1(\mu, \sigma)$	$LN(1.00, 0.035)$	$LN(1.00, 0.035)$	$LN(1.00, 0.035)$	$LN(1.00, 0.035)$
$DLS_2(\mu, \sigma)$	$LN(1.34, 0.089)$	$LN(1.27, 0.142)$	$LN(1.21, 0.156)$	$LN(1.15, 0.176)$
$DLS_3(\mu, \sigma)$	$LN(1.78, 0.092)$	$LN(1.72, 0.145)$	$LN(1.65, 0.161)$	$LN(1.59, 0.183)$
$DLS_4(\mu, \sigma)$	$LN(2.22, 0.095)$	$LN(2.16, 0.150)$	$LN(2.09, 0.168)$	$LN(2.03, 0.190)$

5 SEISMIC FRAGILITY ANALYSIS BASED ON IDA

5.1 Ground motion selection

The IDA depends on nonlinear time history analyses of scaled ground motion records. Specifically, a ground motion record is applied to the structure and scaled up and down until reaching the imminent collapse. Usually, 8-to-12 scaling points should be enough to reach the desired performance and prevent excessive scaling which could affect ground motion features. In this study, a suite of 16 ground motion records are selected from Ground Motion Database of the Pacific Earthquake Engineering Research Center (PEER 2003). Figure 7 illustrates the elastic response spectra with damping equal to 5% of all un-scaled ground motions.

5.2 Deterministic and stochastic IDA results

First, a deterministic incremental dynamic analysis is performed. In this study, the peak ground acceleration (PGA) was adopted as intensity measure (IM) parameter. The IDA curve under a single ground motion was obtained by connecting the structural response points corresponding to the PGA of each record subjected to 20-time amplitude modulations, as shown in Figure 8a~e. The IDA curve cluster was obtained by summarizing 16 IDA curves, and then the median value of each IDA curve can be calculated. Finally, summarize the median value of IDA curve under each degree of corrosion to Figure 8f. It is found that with the increase of corrosion degree, the response of the RC columns increases gradually when the PGA keeps unchanged.

Afterwards, the stochastic IDA is conducted based on the Latin hypercube sampling. Under each amplitude modulated PGA, nonlinear time history analysis of 16 records is completed for 100 randomly generated corroded columns. In other words, $20 \times 16 \times 100 = 32000$ times of nonlinear time history analysis is required for a corrosion degree. The maximum curvature of each dynamic time history analysis and the corresponding PGA points are summarized to obtain the distribution of IDA as shown in Figure 9. It is demonstrated that with the gradual increase of the PGA, the dispersion of the maximum curvature gradually increases. In addition, With the increase of corrosion degree, the dispersion of maximum curvature increases gradually.

5.3 Seismic fragility curves

Seismic fragility curves are classical tools to evaluate the seismic vulnerability of structures. Fragility is defined as the probability that demand exceeds capacity conditional on a specified hazard intensity. To plot the fragility curves, first using IDA results, the corresponding curvature ductility ratio (CDR) of a given IM are calculated for different ground motion records. Then, using the following fragility function the probability of exceeding a given DLS is calculated:

$$P_f[\text{CDR} \geq \text{DLS}_i | IM = x] = 1 - \Phi\left(\frac{\ln(\text{DLS}_i) - \mu_{\ln}}{\sigma_{\ln}}\right) \quad (9)$$

where P_f is the probability that CDR exceeds i th DLS given that $IM = x$; Φ is the normal distribution function with a logarithmic mean of μ_{\ln} and logarithmic standard deviation of σ_{\ln} .

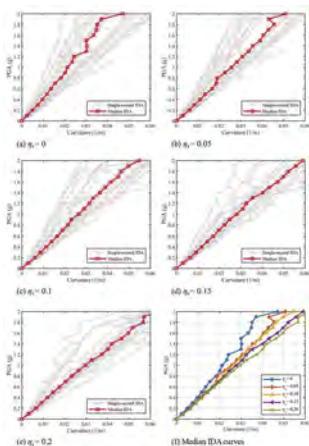


Figure 8. Deterministic IDA curves.

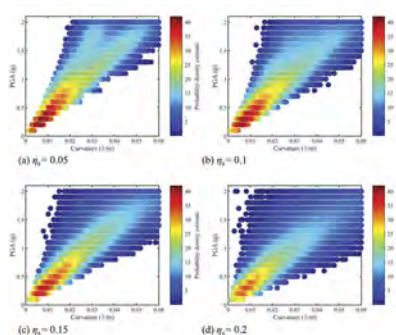


Figure 9. Distribution of stochastic IDA.

Similarly, based on the results of the maximum curvature obtained from the aforementioned stochastic IDA, the seismic fragility curve considering the variability of mechanical properties for reinforcement is calculated and displayed in Figure 10. It can be derived from Figure 10 that the consideration of the variability of mechanical properties for reinforcement defensibly increases the seismic fragility of RC columns, which may later lead to a raise in failure probability of structures under earthquake action. The causes of this phenomenon would be analyzed from the perspective of statistics. The increase of the randomness of the mechanical properties of the structure leads to the increase of the randomness of the seismic response. As a consequence, the standard deviation in the fragility function will increase, which causes the seismic fragility curve to move up. The comparison between fragility curves using the traditional deterministic approach and the

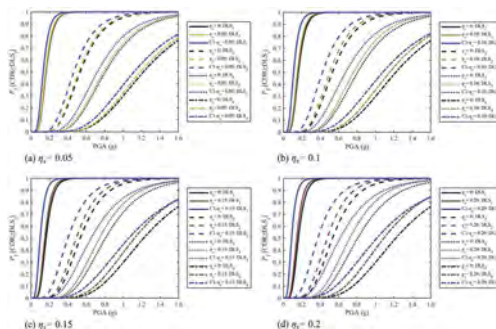


Figure 10. Seismic fragility curve considering stochastics.

proposed stochastic method illustrates that an obvious underestimation is drawn without the consideration of the increasing variability of mechanical properties for corroded rebar.

6 CONCLUSIONS

This paper provides a novel stochastic method to evaluate the seismic performance of corroded RC columns. The distribution of corrosion-dependent DLS and the seismic fragility curves obtained using deterministic and stochastic approaches is obtained through a number of push-over analyses and IDAs. The following conclusions were drawn:

- The corrosion-dependent DLSs all follow lognormal distributions. The mean value of damage limit state decreases and the standard deviation increases with the increase of corrosion degree.
- The traditional deterministic analysis method has the problem of underestimating the failure probability of deteriorated RC columns. The seismic fragility analysis method proposed in this paper can be closer to the actual circumstances.
- The limitation of the proposed method is the corrosion-dependence of DLS. The distribution of corrosion-dependent DLS will be developed into the distribution of time-dependent DLS in the further investigation.

REFERENCES

- Chen, J.Y., Zhang, W., Tang, Z., & Huang, Q. 2020. Experimental and numerical investigation of chloride-induced reinforcement corrosion and mortar cover cracking. *Cement and Concrete Composites* 111: 103620.
- Coronelli, D. & Gambarova, P. 2004. Structural Assessment of Corroded Reinforced Concrete Beams: Modeling Guidelines. *Journal of Structural Engineering* 130(8): 1117–1279.
- Dizaj, E.A., Madandoust, R., & Kashani, M. 2018. Exploring the impact of chloride-induced corrosion on seismic damage limit states and residual capacity of reinforced concrete structures. *Structure and Infrastructure Engineering* 14(6): 714–729.
- FEMA. 2003. HAZUS Earthquake model technical manual. Washington DC: Federal Emergency Management Agency.
- Ghosh, J. & Sood, P. 2016. Consideration of time-evolving capacity distributions and improved degradation models for seismic fragility assessment of aging highway bridges. *Reliability Engineering & System Safety* 154: 197–218.
- Gong, J.X., Zhong, W., & Zhao, G. 2004. Experimental study on low-cycle behavior of corroded reinforced concrete member under eccentric compression. *Journal of Building Structures* 05: 92-97+104. ((in Chinese))
- Lu, X.Z., Ye, L., Pan, P., & Qian, J. 2012. Pseudo-static collapse experiments and numerical prediction competition of RC frame structure II: key elements experiment. *Building Structures* 42(11): 23–26+2. ((in Chinese))
- Meda, A., Mostosi, S., Rinaldi, Z., & Riva, P. 2014. Experimental evaluation of the corrosion influence on the cyclic behaviour of RC columns. *Engineering Structures* 76: 112–123.
- PEER (Pacific Earthquake Engineering Research Center). 2013. PEER Ground Motion Database.
- Scott, B.D., Park, R., & Priestley, M. 1982. Stress-strain behavior of concrete confined by overlapping hoops at low and high strain rates. *Journal of the American Concrete Institute* 79(1): 13–27.
- Sharma, K., Deng, L., & Noguez, C. 2016. Field investigation on the performance of building structures during the April 25, 2015 Gorkha earthquake in Nepal. *Engineering Structures* 121: 61–74.
- Xu, J.G., Cai, Z., & Feng, D. 2021. Life-cycle seismic performance assessment of aging RC bridges considering multi-failure modes of bridge columns. *Engineering Structures* 244: 112818.
- Zhang, W.P., Chen, J., & Yu Q., Gu X. 2021. Corrosion evolution of steel bars in RC structures based on Markov chain modeling. *Structural Safety* 88: 102037.
- Zhang, W.P., Liu, Y., Hu, F., & Gu, X. 2023. Experimental and numerical investigation on seismic performance of corroded RC columns of low-strength concrete. *Bulletin of Earthquake Engineering* 21: 2103–2140.
- Zhang, W.P., Shang, D., & Gu, X. 2014b. Stochastic model of constitutive relationship for corroded steel bars. *Journal of Building Materials* 17(5): 920–926. ((in Chinese))
- Zhang, W.P., Song, X., Gu, X., & Li, S. 2012. Tensile and fatigue behavior of corroded rebars. *Construction and Building Materials* 34: 409–417.
- Zhang, W.P., Zhou, B., Gu, X., & Dai, H. 2014a. Probability distribution model for cross-sectional area of corroded reinforcing steel bars. *Journal of Materials in Civil Engineering* 26(5): 822–832.

Experimental study on water absorption in unsaturated concrete

J. Fang, C. Jiang & X.L. Gu

Key Laboratory of Performance Evolution and Control of Engineering Structures (Ministry of Education), Tongji University, Shanghai, P.R. China

ABSTRACT: The water absorption behavior plays an important role in assessing the durability performance of concrete structures. The oven drying at high temperature is a common pretreatment for concrete to reach dry state before absorption tests, whereas the concrete of existing structures remain at saturated or partially saturated states. This paper studies the effects of initial water content on the water absorption behavior of concrete. And the different water contents were achieved by drying concrete under atmospheric environment with different relative humidity at 23 °C. The result shows that the absorption rate increases with the initial water content of concrete decreasing. Finally, a transport model is established to predict the water absorption amount of concrete with different initial contents.

1 INTRODUCTION

The deterioration processes of concrete structures, including aggressive ions penetration and carbonation, are all influenced by the water transport in concrete. Aggressive ions need liquid water as carrier to penetrate into concrete, while the carbonation reaction process of concrete also takes place in the water. Therefore, it is essential to study water transport performance in concrete for durability assessment of concrete structures.

Water absorption capacity is one of the important indexes to evaluate the water transport performance of concrete. There are numerous studies that have been conducted to investigate the effects of different factors on the water absorption into concrete. These affecting factors include water to cement ratio (Zhang et al., 2020), admixture (Zhao et al., 2021), static loads (Wang and Li, 2014) and frost damage (Alyousif et al., 2016). However, the oven drying at high temperature is a common pretreatment for concrete to reach dry state before absorption tests in previous studies while the concrete of existing concrete structures remain at saturated or partially saturated states.

In this paper, the effect of initial water content of concrete on water absorption was studied using the experimental method. Moreover, a predictive model based on Lucas–Washburn equation was established to calculate the mass of water absorption.

2 EXPERIMENTS

2.1 *Materials and mix proportion*

The mixture proportion of concrete is listed in the Table 1. Ordinary Portland cement (PO 42.5) and deionized water were used to make the mixture. The ISO standard sand and crushed stone with the size of 5-16 mm were used as fine aggregates and coarse aggregates, respectively. After casting, the specimen was cured at 20 ± 2 °C, with the relative humidity set at 95% for 150 days.

Table 1. Mix proportion of concrete.

	Water	Cement	Sand	Coarse aggregate
W/C	(kg/m ³)	(kg/m ³)	(kg/m ³)	(kg/m ³)
0.53	190	359	717	1076

2.2 Sample preparation

One prism concrete specimen with water-cement ratio of 0.53 was casted in this study, and the dimensions were 300 mm × 100 mm × 100 mm. Four pieces (100 mm × 100 mm × 50 mm) used for absorption test were cut from the middle part of cured specimen, as illustrated in Figure 1. All sides of the test pieces were sealed with epoxy resin, leaving two surfaces with dimensions of 100 mm × 100 mm exposed. Then all the pieces were immersed in the deionized water for 35 days to reach the saturated states. To reach unsaturated states with different initial water content, three saturated pieces (C-1~3) were stored in 3 sealed containers with constant relative humidity. According to the previous research (Zhang et al., 2016), the maximum and minimum month-average relative humidity of the sites on the west coast of the Yellow Sea were 86.1% and 62.5%, respectively. Refer to above records, the relative humidity controlled by saturated salt in container were set as 86% (KCl), 79% (NaCl) and 67% (NaBr), respectively. The another one (C-4) was oven-dried at 50 °C to reach a dry state. All the pieces were took out of container or oven until reaching a constant weight (relative change < 0.1%/7 d).

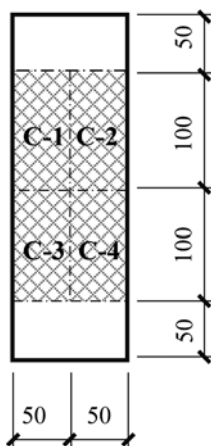


Figure 1. The cutting method for concrete specimen C-1~C-4 (Unit: mm).

2.3 Water absorption test

Four unsaturated specimens with different initial water content (initial internal relative humidity) were used to study capillary water absorption behavior of concrete. The non-cutting surface was immersed into liquid deionized water of 3-5 mm, and the top cutting surface was covered with a loose plastic sheet. The specimens were weighed on a balance with accuracy of 0.01 g and a damped towel was used to blot off surface water as the specimen was removed from the water. The mass of specimens was measured at 5 min, 15 min, 30 min, 1 h, 2 h, 4 h and 6 h, respectively.

3 RESULTS AND DISCUSSION

3.1 Water absorption results

The water absorption I is calculated as:

$$I = \frac{m_t}{\rho_w A} \quad (1)$$

where I = the water absorption per unit area (mm); m_t = the cumulative water absorption mass (g); ρ_w =liquid water density (g/mm³); A = the exposed area of specimen (mm²).

The relationship between water absorption I and time square root $t^{1/2}$ are shown in Figure 2. Consistent with the other previous studies (Hall, 1989), the water absorption of concrete with different initial water content increase linearly with time square root during the absorption process, which can be expressed as:

$$I = St^{1/2} \quad (2)$$

where S = the sorptivity of concrete (Hall, 1989) .

And it is obvious that the water absorption rate increases with the initial water content degree (initial internal relative humidity) decreasing, e.g., the sorptivity of oven-dried concrete is 8.5, 5.9 and 4.8 times that of concrete dried in atmospheric environment with relative humidity of 86%, 79% and 67%, respectively. The external water spreads into pore in concrete induced by the capillary force. As the internal relative humidity decrease, the condensed water in the pores with large radius gradually evaporates (Jiang et al., 2019), which means there are more empty pore for concrete with lower internal relative humidity to absorb water and induce a large sorpsivity.

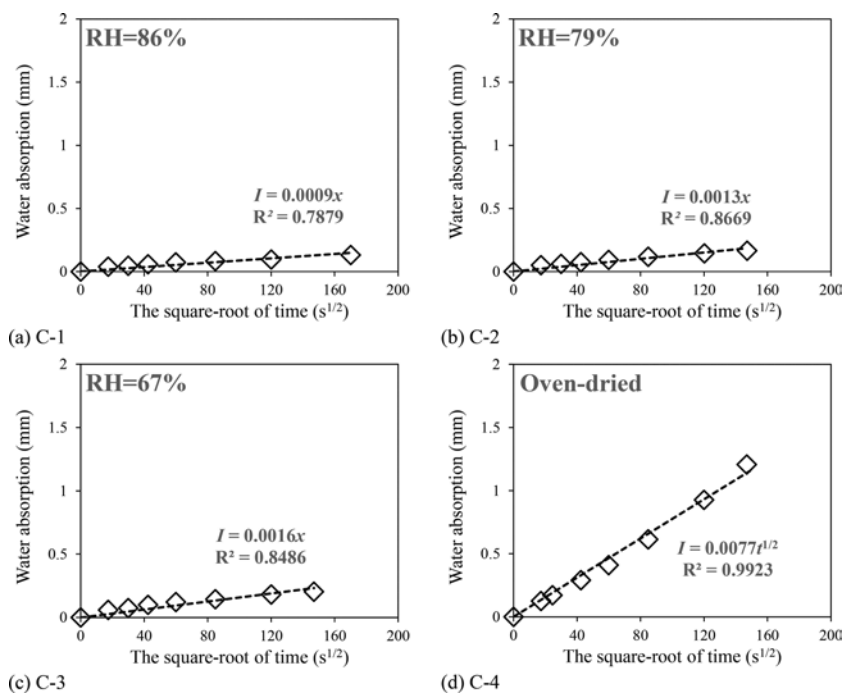


Figure 2. Cumulative water absorption of concrete with different initial water content.

3.2 Predictive model of water absorption

The process water absorption into concrete is controlled by the gravity and the surface tension of the liquid water. Because of the low water absorption height during the tests, the gravity can be neglected and then the Lucas–Washburn equation can be used to evaluate the capillary water absorption process in a cylindrical pore (Zhang et al., 2020):

$$h = \sqrt{\frac{r\gamma\cos\theta}{2\mu}t} \quad (3)$$

where h =height of water absorption (m); r = the radius of the cylindrical pore (m); γ =surface tension of liquid water (N/m), which is related to the absolute temperature T (Ishida et al., 2007):

$$\gamma = 2.66 \times 10^{-4}T^2 + 3.17 \times 10^{-3}T + 94.6 \quad (4)$$

θ =contact angle between the water and pore wall, which can be set as 0 for cementitious materials; μ = viscosity of liquid water (Pa·S) and also depend on the temperature (Ishida et al., 2007):

$$\mu = 3.88 \times 10^{-8}T^4 - 4.63 \times 10^{-5}T^3 + 2.37 \times 10^{-2}T^2 + 5.45T + 470 \quad (5)$$

Assuming that the pores in concrete are cylindrical tubes with different radius and well connected, the water absorption for concrete can be calculated based on Lucas–Washburn and pore size distribution, which is expressed as:

$$I(t) = \frac{1}{\rho_w A} \int_{r_c}^{r_{max}} \varphi \pi r^2 \rho_w \sqrt{\frac{r\gamma\cos\theta}{2\mu}} t p_d(r) dr \quad (6)$$

where φ =the porosity of concrete, which can be determined by:

$$\varphi = \varphi_{cp}(1 - V_a) \quad (7)$$

where φ_{cp} =the porosity of hardened cement paste, which can be obtain by (Zheng and Zhou, 2008):

$$\varphi_{cp} = \frac{\frac{w}{c} - 0.17\alpha}{\frac{w}{c} + 0.32} \quad (8)$$

where α =hydration degree, which is calculated by:

$$\alpha = 0.217 \ln\left(\frac{w}{c}\right) + 0.06 \ln(t_c) + 0.618 \quad (9)$$

where t_c =curing age in days; and $p_d(r)$ = probability density function of the pores, which can be determined by BJH method based on the water vapor sorption isotherms (WVSI) (Xi et al., 1994):

$$W(\text{RH}) = \frac{CkV_m\text{RH}}{(1 - k\text{RH})[1 + (C - 1)k\text{RH}]} \quad (10)$$

where RH=the relative humidity; C , k , V_m =parameter related to material types, and the method to determine these parameter can refer to the reference (Xi et al., 1994); r = radius of pores (m); r_{max} = the maximum radius of empty pore for absorption in concrete (m); r_c = the

critical radius, the evaporation of liquid water would take place when the radius of pore is larger than critical radius (m), which can be expressed as:

$$r_c = -\frac{2\gamma M}{\rho_w RT \ln(\text{RH})} + t_a \quad (11)$$

where M =the mass of water molecular (kg/mol); R = the gas constant (J/K/mol); RH =the relative humidity; t_a =the thickness of adsorbed water (Jiang et al., 2019):

$$t_a = t_0 \ln\left(\frac{-E_{ad} C^{1/3}}{RT \ln(\text{RH})}\right) \text{ (nm)} \quad (12)$$

where $t_0 = 0.191$ nm; E_{ad} = activation energy for adsorption ($E_{ad}=5900$ J/mol); R = gas constant (J/K/mol); T = the absolute temperature (K).

The pores corresponding to the equation (3) are assumed as cylindrical and straight, while the real pores in concrete are tortuous. The tortuosity factor of hardened cement paste can be set as $\pi^2/4$ (Huang et al., 2015). The transport performance of aggregate is much lower than that of cement paste, thus the existing of aggregate in concrete increases the path length of water transport and thus slows down the water absorption rate. The tortuosity factor induced by aggregate is linked to the volume of aggregate, which is proposed as (Shafikhani and Chidiac, 2020):

$$\tau_{\text{agg}} = \frac{3 - V_a}{3(1 - V_a)} \quad (13)$$

where V_a = the total volume fraction of aggregates.

Considering the total tortuosity of concrete, equation (6) is modified as:

$$I(t) = \frac{1}{\rho_w A} \int_{r_{\min}}^{r_{\max}} \frac{\pi r^2 \rho_w}{\tau} \sqrt{\frac{r\gamma \cos\theta}{2\mu}} t p_d(r) dr \quad (14)$$

where $\tau = \tau_{\text{cp}} \cdot \tau_{\text{agg}}$

Furthermore, the connectivity of pores in concrete is complex, e.g., the pore with larger radius may connect to the smaller pores. And the liquid water in large pores in concrete would be entrapped by the connected pores with smaller radius even the relative humidity of concrete decreases to the critical value for evaporation of liquid water in large pore, which is known as the ink bottle effect. The volume fraction of empty pore for water absorption may reduce due to the ink bottle effect, and the probability for large pore occupied by entrapped liquid water can be obtained as (Maekawa, 2008):

$$f_d(r) = \frac{\int_{r_{\min}}^{r_c} p_d(r) dr}{\int_{r_{\min}}^r p_d(r) dr} \quad (15)$$

where r_{\min} =the minimum radius of empty pore for absorption in concrete (m).

Considering the entrapped liquid water in large pore, equation (14) is modified as:

$$I(t) = \frac{1}{\rho_w A} \int_{r_{\min}}^{r_{\max}} [1 - f_d(r)] \frac{\pi r^2 \rho_w}{\tau} \sqrt{\frac{r\gamma \cos\theta}{2\mu}} t p_d(r) dr \quad (16)$$

The comparisons of the mass of water absorption test and calculated method are plotted in Figure 3. It can be found that the predicted water absorption is higher than experimental one with the initial relative humidity of 67%, which might be induced by the randomness of

concrete. But overall, the predicted mass absorption for concrete with different initial water content are close to the experimental results, demonstrating the acceptable accuracy of model predictions.

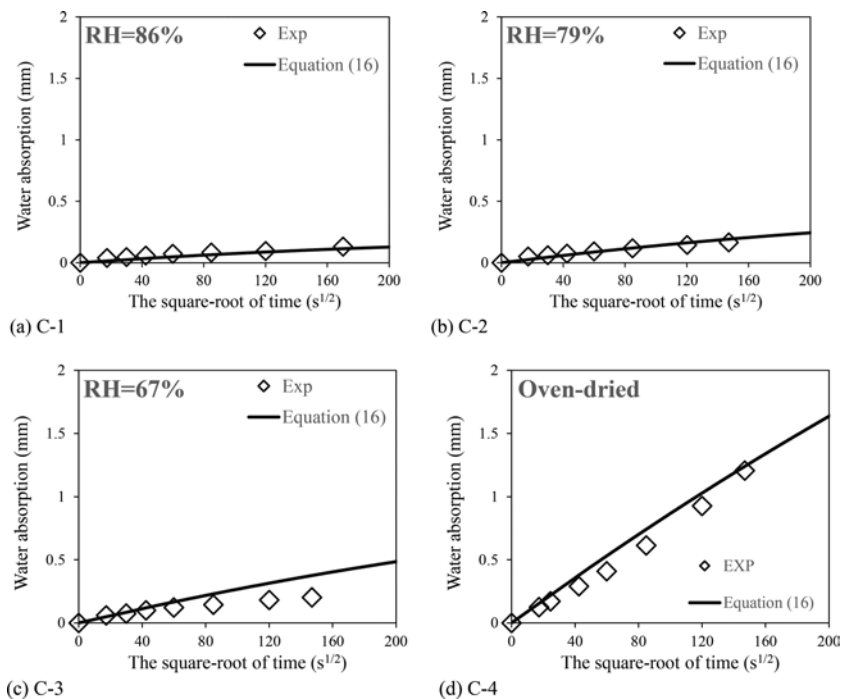


Figure 3. Comparison between calculated and experimental results of water absorption.

4 CONCLUSIONS

In this paper, the effects of initial water contents (initial internal relative humidity) on the water absorption behavior of concrete were studied experimentally and a transport model was established to predict the mass of water absorption. The main conclusions are as following:

The rate of water absorption increases with the initial water content (initial internal relative humidity) decrease. And the sorptivity of oven-dried concrete is 8.5, 5.9 and 4.8 times that of concrete dried in atmospheric environment with relative humidity of 86%, 79% and 67%, respectively.

The predictive model for water absorption was established based on Lucas–Washburn equation, which also considered the tortuosity and ink bottle effect of pores. The tortuosity factor of concrete was defined based on porosity and volume fraction of aggregate, while the ink bottle effect was determined from pore size distribution. And it was found that the predicted absorption masses were in acceptable agreement with experimental results.

REFERENCES

- Alyousif, A., Lachemi, M., Yildirim, G., Aras, G. H. & Sahmaran, M. (2016) Influence of Cyclic Frost Deterioration on Water Sorptivity of Microcracked Cementitious Composites. *Journal of Materials in Civil Engineering*, 28.
- Hall, C. (1989) Water sorptivity of mortars and concretes: a review. *Magazine of Concrete Research*, 41, 51–61.

- Huang, Q.-h., Jiang, Z.-l., Gu, X.-l., Zhang, W.-p. & Guo, B.-h. (2015) Numerical simulation of moisture transport in concrete based on a pore size distribution model. *Cement and Concrete Research*, 67, 31–43.
- Ishida, T., Maekawa, K. & Kishi, T. (2007) Enhanced modeling of moisture equilibrium and transport in cementitious materials under arbitrary temperature and relative humidity history. *Cement and Concrete Research*, 37, 565–578.
- Jiang, Z. L., Xi, Y. p., Gu, X. l., Huang, Q. h. & Zhang, W. p. (2019) Modelling of water vapour sorption hysteresis of cement-based materials based on pore size distribution. *Cement and Concrete Research*, 115, 8–19.
- Maekawa, K. (2008) *Multi-scale modeling of structural concrete*, Crc Press.
- Shafikhani, M. & Chidiac, S. E. (2020) A holistic model for cement paste and concrete chloride diffusion coefficient. *Cement and Concrete Research*, 133, 106049.
- Wang, L.-c. & Li, S.-h. (2014) Capillary absorption of concrete after mechanical loading. *Magazine of Concrete Research*, 66, 420–431.
- Xi, Y. P., Bazant, Z. P. & Jennings, H. M. (1994) Moisture Diffusion in Cementitious Materials - Adsorption-Isotherms. *Advanced Cement Based Materials*, 1, 248–257.
- Zhang, H.-f., Zhang, W.-p., Gu, X.-l., Jin, X.-y. & Jin, N.-g. (2016) Chloride penetration in concrete under marine atmospheric environment – analysis of the influencing factors. *Structure and Infrastructure Engineering*, 12, 1428–1438.
- Zhang, J.-c., Lin, C., Dong, B.-q., Tang, L.-p. & Hong, S.-x. (2020) Inverse modeling deduction of pore distribution in cement materials from capillary absorption features. *Cement and Concrete Composites*, 109.
- Zhao, H.-t., Wu, X., Huang, Y.-y., Zhang, P., Tian, Q. & Liu, J.-p. (2021) Investigation of moisture transport in cement-based materials using low-field nuclear magnetic resonance imaging. *Magazine of Concrete Research*, 73, 252–270.
- Zheng, J.-j. & Zhou, X.-z. (2008) Analytical Solution for the Chloride Diffusivity of Hardened Cement Paste. *Journal of Materials in Civil Engineering*, 20, 384–391

Monitoring electrochemical chloride extraction process by testing chloride ion contents in electrolyte

C. Song, C. Jiang & X.L. Gu

Key Laboratory of Performance Evolution and Control for Engineering Structures (Ministry of Education), Tongji University, Shanghai, PR China

ABSTRACT: The monitoring of Electrochemical Chloride Extraction (ECE) of RC structures is crucial for both theoretical study and engineering practice, but the detection process is usually difficult to achieve. In this study, the ECE test was carried out and a method of synchronous monitoring ECE was explored. During the tests, the electrolyte of the ECE system was collected every day for daily chloride extraction monitoring. The outcomes show that the daily extraction content of chloride was high at the beginning (0 – 3 days) but declined and tended to be stable toward the end (after 3 days). The accumulated contents of chloride ions found in the electrolyte are compatible with the differences of total chloride ion contents measured before and after ECE (with a deviation of less than 4.7%), which proved the feasibility of the present method.

1 INSTRUCTION

The popularity of reinforced concrete (RC) constructions has expanded along with the growth of the construction industry. At the same time, long-term service of RC structures will be facing an important issue of durability degradation. When the performance of a structure starts to degrade, it will take the cost of maintenance and repair leading to significant financial losses (Zhang et al. 2018, Zhou et al. 2018). Hence, it is crucial to take action to stop RC structures from corroding and degrading.

An existing RC structures in marine atmospheric environment has a high risk of corrosion and durability degradation caused by chloride ion invasion (Chen et al. 2018, Gu et al. 2020). In order to alleviate the corrosion of steel bars, Electrochemical Chloride Extraction (ECE), which imposes electric fields in concrete cover and hence can effectively discharge chloride ions out of concrete, is a potential strategy to postpone the corrosion initiation.

In ECE process, understanding the chloride extracting progress is crucial for both theoretical study and engineering practice. In a theoretical study, monitoring the ECE progress can help to validate the model and solve the daily chloride discharge (Toumi et al. 2008). In engineering practice, an excessively lengthy power supply will increase the financial cost while an insufficiently short power supply will not remove the chloride completely as intended. In order to balance the rewards of time and cost, the chloride extraction process is suggested to be closely monitored (Song et al. 2022, Castellote et al. 2000).

However, due to the destructive nature of concrete chloride ion testing, it is often not possible to obtain real-time progress of chloride extraction by testing concrete. In this paper, a method for tracking ECE processes is proposed based on monitoring the content of chloride ions in the electrolyte, and the feasibility of the method is verified through experiments.

2 EXPERIMENT

2.1 Materials

The testing objects were cut from concrete blocks exposed to the actual marine atmospheric environment for 9 years in a coastal site in Qingdao of China (36°3' N, 120°25' E) (Zhang et al. 2016). The mix design of concrete is listed in Table 1. Ordinary Portland cement and deionized water were used and water-cement ratio was set as 0.53. ISO standard sand was used as fine aggregates. Figure 1 shows the exposure site and its location. Three concrete blocks (numbered Q32, Q36 and Q50) were selected from the concrete frame as test objects. In order to diversify the distribution of chloride ions in the tests, three blocks with different exposure positions were selected (Q32 – 2nd story with one-sided exposure, Q36 – 2nd story with three-sided exposure, Q50 – 3rd story with three-sided exposure).

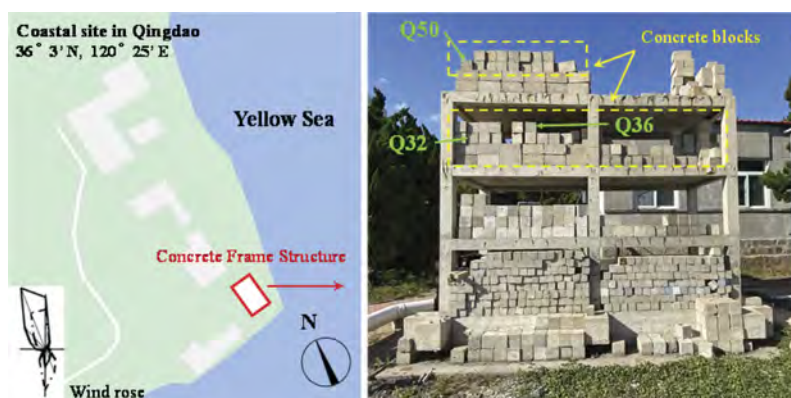


Figure 1. Exposure site of a natural marine atmospheric environment in Qingdao of China.

Table 1. Concrete mix proportion.

Cement type	W/C	Cement	Water	Coarse Aggregates	Fine Aggregate
		kg/m ³	kg/m ³	kg/m ³	kg/m ³
P.O 42.5	0.53	368	195	1103	735

The concrete processing method is shown in Figure 2. Only the central area of the windward side (the cube surrounded by red dashed lines) was used for the ECE test. It is considered that the chloride ion in this area (the depth is 50 mm) is a one-dimensional transmission, i.e., the chloride ion content in the same depth is consistent across different points at the windward side.

2.2 ECE process

Figure 3 shows the diagram of electrolytic cell. The specimen is sealed in a plastic pipe to isolate the cathode and anode solution. To achieve complete separation of the cathode and anode electrolyte, epoxy resin was used to fill the space between the pipe and the specimen. Titanium mesh is used as a cathode and anode plate. The system is angled at a 25-degree to the horizontal to avoid ion accumulation in the local area and influence boundary conditions. The sodium hydroxide solution of 0.10 mol/L was used as an electrolyte. A current regulator with a range of 30 V and an accuracy of 0.001 A was utilized to supply a constant current density of 1 A/m² (area of cathode surface).

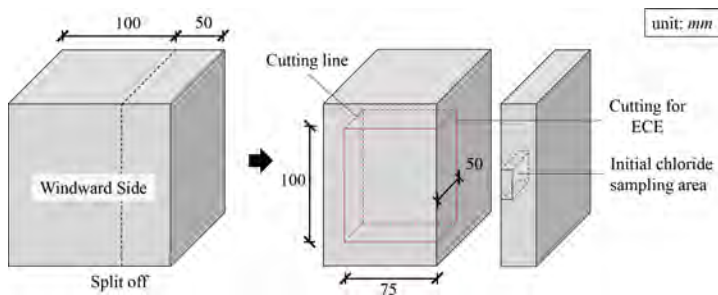


Figure 2. Concrete processing method.

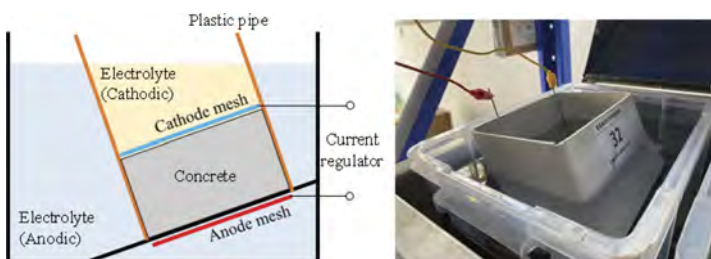


Figure 3. Electrochemical Chloride Extraction system.

For chloride content monitoring, the electrolytes (both anode and cathode) were renewed every day and the volume of the cathode/anode solution remained constant during daily replacement. When renewing the solution, the electricity was disconnected temporarily. Then, the solution was well stirred with a stirring rod and 100 ml of the solution was taken as a sample. After sampling, replace the previous electrolyte with the new solution and turn on the power once more. The daily discharge of chloride ions from the collected samples will be measured by potentiometric titration.

According to the daily collected chloride ion content samples, the electrochemical chloride extraction process can be terminated at the specified time according to the test intent.

2.3 Chloride profiling

The initial and the after ECE chloride contents inside concrete, as well as the chloride ion contents of the electrolyte samples, were tested by the potentiometric titration method. ZDJ-4B Potentiometric Titrator was used for measurement.

For profiling the chloride distribution of concrete, concrete powder samples were first collected using a milling machine. The mass of the powder at each interval was guaranteed to be at least 25.0 g. Following sampling, the amounts of free and total chlorides in all sources were extracted by water-soluble (distilled water) and acid-soluble (1 mol/L HNO_3) methods, respectively. The chloride ion content was given as a percentage of the mass of the concrete.

The electrolyte samples were directly titrated after acidification treatment, and all chloride titration processes presented in this work followed the guidelines of JGJ/T 322-2013 in China.

3 RESULTS AND DISCUSSION

The daily extracted chloride content of the entire ECE process is shown in Figure 4

The figure shows that even while the specimen's water-cement ratio is constant, under the same current density, the chloride ion extraction rate varies due to different locations on the frame structure. The three samples all displayed a tendency for high discharge rates during the early stages (0 – 3 days), and gradually declining rates during the latter stages (after 3 days).

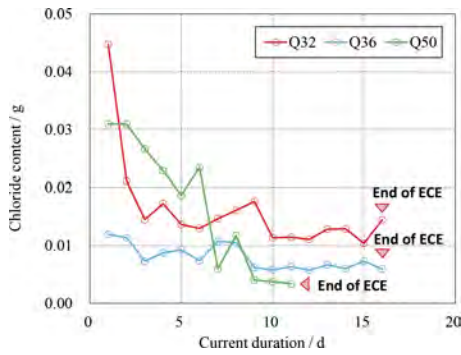


Figure 4. Daily chloride extraction content (electrolyte).

For model validation, the three ECE processes were all stopped when chloride was not entirely removed. When the daily chloride extracted content was observed to have a significant decrease (After 10 days), the current was cut off. Specimen Q50 was ended after 11 days of power on, specimens Q32 and Q36 were terminated after 16 days of power on.

Figure 5 shows the chloride ion distribution of the three specimens before and after ECE process. Following the ECE process, the free and total chloride ion contents of the three specimens decreased, while the peak of a chloride ion distribution curve showed no visible change. Based on the daily tracking of electrolytes, the goal of monitoring the ECE process has been achieved. Effective monitoring of ECE process can avoid energy waste caused by the prolonged power supply.

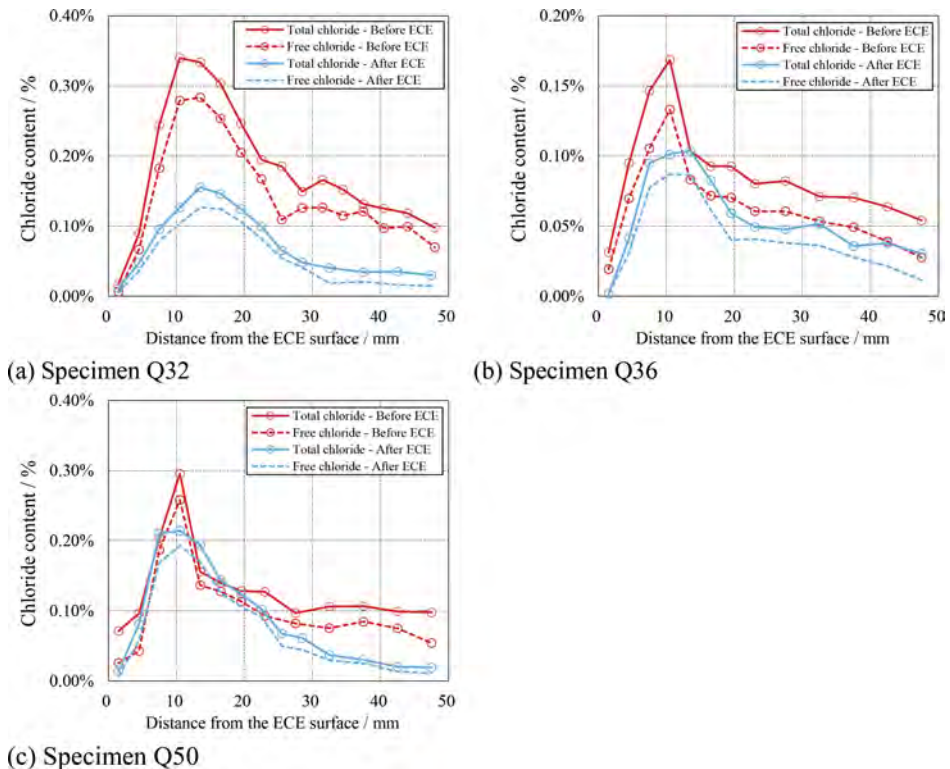


Figure 5. Chloride distribution in concrete before and after ECE.

Figure 6 illustrates the comparison of the chloride remaining content after the ECE process with chloride titrated in the electrolyte. The total chloride ion contents in the electrolyte of the three specimens were closer to the sum of total chloride ion discharge, with deviations of 4.0%, 4.7%, and -1.0%, respectively. Compared with free chloride ions, the discrepancies were -15.5%, -15.6%, and -22.8%, respectively. Overall, the electrolyte's accumulated chloride ion content and the reduction content of total chloride ion in concrete have good consistency. The electrolyte monitoring method can effectively estimate the residual total chloride ion content in concrete.

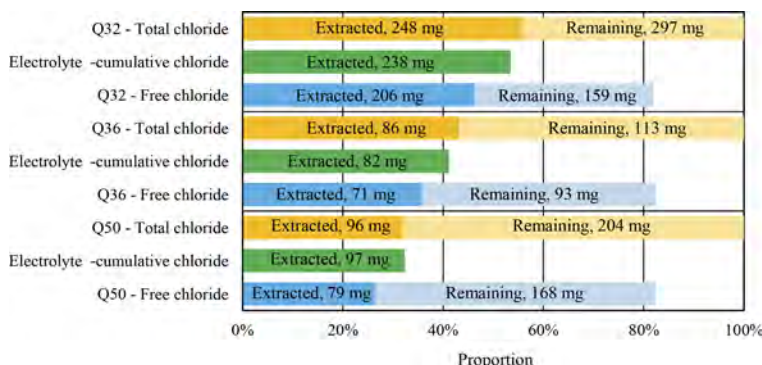


Figure 6. Comparison of chloride extracted in concrete and electrolyte.

4 CONCLUSIONS

In the ECE process of concrete with natural chloride ion intrusion, the daily extraction amount of chloride ions is at its highest during the first 3 days and it decreases after those 3 days.

The error between the total amount of chloride ions extracted from the electrolyte and the actual total amount of chloride ions extracted from the concrete is less than 4.7%, demonstrating that the ECE process tracking method by monitoring the electrolyte works is good.

REFERENCES

- Castellote, M. et al. 2000. Electrochemical removal of chlorides - modelling of the extraction, resulting profiles and determination of the efficient time of treatment. *Cement and Concrete Research* 30(4): 615–621.
- Chen, J.Y. et al. 2019. Modeling time-dependent circumferential non-uniform corrosion of steel bars in concrete considering corrosion-induced cracking effects. *Engineering Structures* 201: 109766.
- Gu, X.L. et al. 2020. Corrosion of Stirrups under Different Relative Humidity Conditions in Concrete Exposed to Chloride Environment. *Journal of Materials in Civil Engineering* 32(1): 04019329.
- Song, C. et al. 2022. Calibration analysis of chloride binding capacity for cement-based materials under various exposure conditions. *Construction and Building Materials* 314: 125588.
- Toumi, A. et al. 2007. Experimental and numerical study of electrochemical chloride removal from brick and concrete specimens. *Cement and Concrete Research* 37: 54–62.
- Zhang, H.F. et al. 2016. Chloride penetration in concrete under marine atmospheric environment – analysis of the influencing factors. *Structure and Infrastructure Engineering* 12(11): 1428–1438.
- Zhang, W.P. et al. 2018. Structural behavior of corroded reinforced concrete beams under sustained loading. *Construction and Building Materials* 174: 675–683.
- Zhou, B.B. et al. 2018. Polarization behavior of activated reinforcing steel bars in concrete under chloride environments. *Construction and Building Materials* 164: 877–887.

Experimental study on stress recovery behavior of Fe-SMA subjected to multi-activation

Q.Q. Yu, Z.Y. Chen, X.L. Gu, X.W. Xiao & W.P. Zhang

*Key Laboratory of Performance Evolution and Control for Engineering Structures (Tongji University),
Ministry of Education, Shanghai, China
Tongji University, Shanghai, China*

Y.H. An

Guangxi University, Guangxi, China

ABSTRACT: Shape memory alloy (SMA) has shown great promise in retrofitting of aged infrastructure because it could be employed to conveniently apply prestress. However, the stress recovery behavior of iron-based SMA (Fe-SMA) has not been fully understood. This study presents an experimental study on Fe-SMA subjected to multi-activation. Eight specimens were prepared and loaded by two million cyclic loading simultaneously with thermal scenarios. Afterward, they were re-activated up to four times. Lost recovery stress due to fatigue was pronouncedly retrieved by reactivation. In addition, the Fe-SMA samples after fatigue loading could be reused to provide prestress for other applications but the count for reusability was limited. This study explores functional-fatigue behavior of the material and provides some useful suggestions for the strengthening technique.

1 INTRODUCTION

Shape memory alloy (SMA) is an alloy that can be deformed when cold but returns to its pre-deformed (“remembered”) shape when heated, which is called shape memory effect (SME). In addition, it is also recognized as superelastic, which means an alloy can return to its initial state after unloading even if the deformation is very large. Initially widely explored and adopted in aerospace engineering (Hartl & Lagoudas 2007, Barbarino et al. 2014) and medical devices (Song 2010, Morgan 2004), SMA materials nowadays are attracting more attention in the community of civil engineering. They are employed in fields of self-centering and energy dissipation as well as prestress strengthening (Jani et al. 2014, Huang et al. 2020, Czaderski et al. 2014, Rojob & El-Hacha 2018, Izadi et al. 2018). They could be employed to conveniently apply prestress and the recovery stress indicates the stress generated in SMA after the activation process. In comparison with nickel-titanium (NiTi-SMA), iron-based SMA (Fe-SMA) is relatively new and less understood. It has a lower price and wider temperature hysteresis (Cladera et al. 2014).

Lee et al. (2013) conducted a series of fatigue tests on Fe-SMA samples and found that major decline in recovery stress was witnessed in the first cycle. When subjected to cyclic loading with a strain range of 0.070%, the initial 2×10^2 cycles resulted in 11% reduction in the recovery stress, nevertheless only 5% further decrease was witnessed in the followed 2×10^4 cycles (Hosseini et al. 2018, Ghafoori et al. 2017). Loss of the recovery stress due to fatigue was retrieved by a second activation (Hosseini et al. 2018). In addition to fatigue loading, it was demonstrated that thermal loading also showed detrimental effect on the recovery stress. The recovery stress was dramatically declined from 350 to 156 MPa when temperature was increased from -20 to 60 °C in Lee et al. (2013).

This paper presents an experimental study on the stress recovery behavior of Fe-SMA subjected to multi-activation. Fe-SMA samples were under fatigue (strain ranges of 0.035% and 0.070%, two million cycles) and thermal loading (room temperature (RT), $-20\text{ }^{\circ}\text{C}$, $60\text{ }^{\circ}\text{C}$, -20 to $60\text{ }^{\circ}\text{C}$) followed by multi-activation up to four times. Eventually, the strips were monotonically loaded to failure to monitor variation in the machinal properties.

2 EXPERIMENTAL PROGRAM

Eight dog-bone shaped specimens were prepared and tested under fatigue followed by multi-activation. The experimental work was conducted at the Key Laboratory of Performance Evolution and Control for Engineering Structures (Tongji University).

2.1 Materials and specimens

The Fe-SMA strips were provided in rolls by the refer-AG in Switzerland. Tensile coupon test samples were prepared according to AS 1391 (2007) and are illustrated in Figure 1. Two holes were made at both ends of the specimen for connection to the actuator with the extension rods in the environmental chamber.

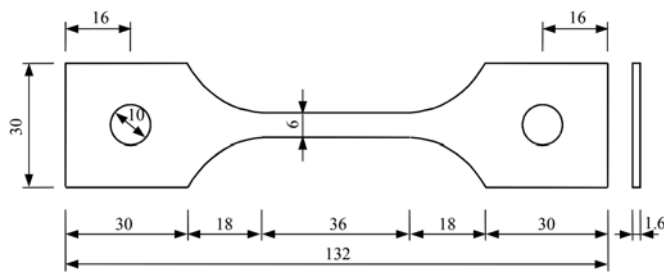


Figure 1. Specimen geometry and dimensions (unit in mm, not to dimension).

2.2 Test set-up

The SMA samples were first activated according to the strategy explored by the authors in the preliminary study (Gu et al. 2021), i.e., pre-strain of 8%, activation temperature of $350\text{ }^{\circ}\text{C}$ and preload of 50 MPa. The corresponding recovery stress ranged from 413 to 436 MPa. Afterward, fatigue and thermal loading were first applied to the SMA samples before multi-activation. The tests were conducted using a servo-hydraulic uniaxial testing machine (maximum loading capacity of 100 kN). Additionally, a Mechanical Testing & Simulation (MTS) furnace (Figure 2a) was employed to carry out the test at $60\text{ }^{\circ}\text{C}$, and an MTS environment chamber (Figure 2b) was selected to perform the test at $-20\text{ }^{\circ}\text{C}$ and cyclic temperature (-20 to $60\text{ }^{\circ}\text{C}$).

All the specimens after cyclic loading were reactivated by multiple times to explore the functional fatigue of the Fe-SMA and consequently potential reuse of the material. It has been reported that the prestress generated by Fe-SMAs declines as a result of creep/relaxation under fatigue (Hosseini et al. 2018, Ghafoori et al. 2017). Therefore, the second activation (the first activation referred to the original one before fatigue) was conducted in the present study to investigate retrievability of the lost prestress. In addition, considering the sustainable development, it is worthwhile to investigate whether the Fe-SMA could be recycled and reused, i.e., the functional fatigue of the material (Eggeler et al. 2004). Hence, after the second activation, the specimens were unloaded and then pre-tensioned again for the following activations. Preliminary tests with an initial preload of 50 MPa were conducted and the stress declined continuously to 0 MPa during the heating process and increased to ~ 50 MPa in the cooling

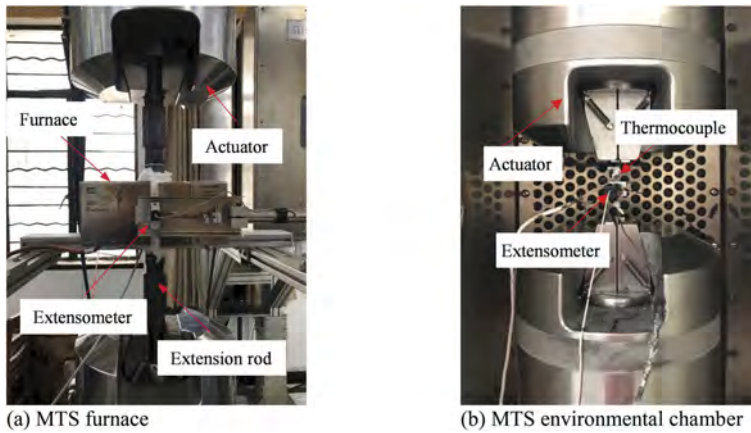


Figure 2. Test set-up.

process, indicating no SME but only thermal expansion and contraction (Gu et al. 2021). In order to promote SME of the Fe-SMA, a higher level of preload of 150 MPa was adopted. When the stress declined to 0 MPa, the test was halted to avoid compression in the test apparatus. With a larger preload, a higher heating temperature could be reached, which may activate SME. This step was repeated several times to find the upper limit of the reusing times. If the increased stress after heating and cooling was lower than 50 MPa, the re-activation test was stopped.

After the multiple activation tests, the specimens were monotonically loaded to failure at 1 mm/min. The initial elastic modulus, 0.2% yield strength, ultimate strength, and elongation at break were recorded.

3 RESULTS AND DISCUSSION

3.1 Multi-activation of the Fe-SMA

Table 1 summarizes the program and results of multiple activation tests. The specimen nomenclature is as follows: 0.035 and 0.070 represent two cyclic strain ranges (0.035% and 0.070%) adopted in the experimental program; the final letters R, L, H and C denote the four scenarios of thermal loading, i.e., room temperature, low temperature of $-20\text{ }^{\circ}\text{C}$, high temperature of $60\text{ }^{\circ}\text{C}$, cyclic temperature from -20 to $60\text{ }^{\circ}\text{C}$.

The cyclic strain ranges are commonly used in fatigue tests of retrofitted steel structures (Hosseini et al. 2017, Yu et al. 2013, Aljabar et al. 2017). Because the maximum frequency of strain-control fatigue for the test equipment could only reach 2 Hz, which was much lower than the expected test frequency (20 Hz), equivalent stress-control fatigue loading was applied to each specimen for two million cycles. The stress ranges corresponding to strain ranges of 0.035% and 0.070% were 57 MPa and 114 MPa, respectively, according to the initial elastic modulus of 162 GPa of the SMA strip. In the cases with constant temperatures, the loading frequency was set as 20 Hz. In the case with cyclic temperature, a loading frequency of 12 Hz was adopted to match the temperature variation (Chen et al. 2023).

In Table 1, the 1st activation indicates the original one before fatigue. The 2nd to 4th activations were adopted to investigate the recoverability of the lost prestress due to fatigue. By comparing the recovery stress after the 1st activation and the initial preload before the 2nd activation, it was found the recovery stress slightly decreased after fatigue and thermal loading, with the reduction percentage ranging from 1.4 to 27.8%. The higher fatigue loading histories exhibited a more detrimental effect.

Table 1. Program and results of multiple activation tests.

Specimen	Fatigue loading range (MPa)	Test temperature (°C)	The 1 st activation			The 2 nd activation			The 3 rd activation			The 4 th activation		
			Initial preload (MPa)	Maximum heating temperature (°C)	Recovery stress (MPa)	Initial preload (MPa)	Maximum heating temperature (°C)	Final stress (MPa)	Initial preload (MPa)	Maximum heating temperature (°C)	Final stress (MPa)	Initial preload (MPa)	Maximum heating temperature (°C)	Final stress (MPa)
F-0.035-R	57	RT	56	362	413	365	388	393	150	143	220	151	103	149
F-0.035-L	57	-20	54	353	423	470	463	470	148	150	252	151	93	170
F-0.035-H	57	60	51	356	436	341	381	402	150	174	247	150	114	168
F-0.035-C	57	-20 ~ 60	53	353	421	368	439	452	150	153	259	150	102	185
F-0.070-R	114	RT	54	353	417	327	413	414	150	144	233	149	103	168
F-0.070-L	114	-20	51	353	427	421	466	473	150	159	249	150	106	157
F-0.070-H	114	60	53	352	428	309	288	352	150	117	200	149	112	194
F-0.070-C	114	-20 ~ 60	53	354	427	329	421	438	149	155	238	151	97	164

During the 2nd activation, the stress first declined remarkably with the increase of temperature due to thermal expansion. As temperature increased, ϵ -martensite was gradually transformed to γ -austenite, leading to the SME effect. When the stress decreased to 10 MPa, the heating process was halted in case of compression. The corresponding temperature was recorded as the maximum heating temperature (Table 1). When the temperature returned to RT, the stress gradually increased regardless of the loading histories. The recovery stress lost due to creep/relaxation was noticeably retrieved. Four specimens were witnessed a higher recovery stress in comparison with that after the original activation, among which the specimen F-0.070-L displayed a maximum improvement of 11%. However, a second recovery stress of 352 MPa, which was 17% lower than its original level, was achieved in the specimen F-0.07-H.

More activation procedures were tried to explore the functional fatigue and potential reuse of the Fe-SMA. Figure 3 plots the stress recovery behavior during the 3rd and 4th activation procedures. In Figures 3a and 3b, the curves first declined and then became less steep due to SME. However, in Figures 3c and 3d, the decreased rates of all the curves seemed to be stable. When the temperature cooled to RT, stress of the specimens reached to 200–260 MPa in the 3rd activation (Table 1) while that in the 4th activation attained 150–200 MPa (Table 1). It was, therefore, believed that slight SME existed in the 4th activation. Based on the limited test results, the functional fatigue of Fe-SMA investigated in the present study was restricted to three times.

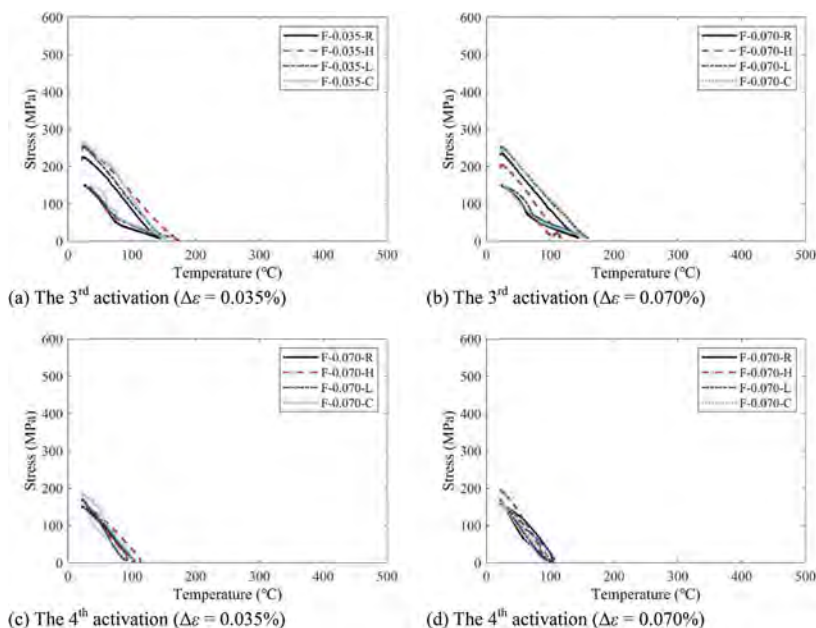


Figure 3. Stress recovery behavior after multiple activation.

3.2 Tensile behavior after multi-activation

After fatigue and thermal loading, as well as multi-activation, tensile behavior of the samples was tested and is compared with that of the as-received Fe-SMA in Figure 4. Regardless of temperature variation and fatigue strain ranges, all the specimens with loading histories exhibited similar mechanical properties (i.e., initial elastic modulus, 0.2% yield strength and ultimate strength). At the elastic stage, all the curves seemed to follow the same path. When reaching into the plastic phase, the specimens after fatigue and multi-activation presented a higher stress level than the as-received Fe-SMA. The averaged 0.2% yield strength and ultimate strength of the specimens after fatigue and multi-activation are 522 MPa and 961 MPa, which are both 6.3% higher than the corresponding values tested at RT, respectively.

The slight enhanced mechanical property may be relevant to the 4th activation, where no SME was observed, and therefore more stress-induced ϵ -martensite existed in the samples. In comparison with γ -austenite, ϵ -martensite led to a more pronounced strain hardening and higher tensile strength (Frommeyer et al. 2003). Therefore, the stronger mechanical properties were witnessed in the samples after fatigue and multi-activation. In terms of the elongation at break, the average value of the specimens after fatigue and multi-activation was 36.8%, slightly higher than that tested at RT. Hoessini et al. (2018) also tested the mechanical property of Fe-SMA after multi-activation, where the Fe-SMA experienced first activation, first cyclic loading, second activation and second cyclic loading. The ultimate tensile strength and elongation were similar to the as-received specimen and therefore, indicating no damage induced to the Fe-SMA in the activation or cyclic loading. However, in the present study, a higher mechanical property was witnessed in the specimens after multi-activation. The different findings may be resulted from the times of activation. Since no SME existed in the 4th activation, larger amount of stress-induced ϵ -martensite left in the sample and led to better mechanical properties.

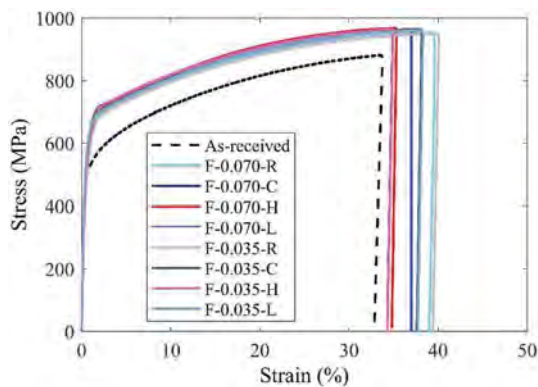


Figure 4. Tensile behavior of as-received Fe-SMA and those after fatigue and multi-activation.

4 CONCLUSIONS

This study presents an experimental study on Fe-SMA subjected to multi-activation. Fatigue and thermal loading applied to Fe-SMA samples led to reduction in recovery stress of 1.4 – 27.8%. Loss in the recovery stress was pronouncedly retrieved by reactivation, which demonstrated promise in life-cycle maintenance of infrastructure. The Fe-SMA samples after service loading could be reused to provide prestress for other applications but the count for reusability was limited. The machinal properties of the Fe-SMA after fatigue and thermal loading, as well as multi-activation remained approximately the same.

ACKNOWLEDGEMENTS

This study was supported by the National Natural Science Foundation of China (Project No. 52222803). We also thank re-fer AG in Switzerland for providing Fe-SMA materials.

REFERENCES

- Aljabar, N.J., Zhao, X.L., Al-Mahaidi, R., Ghafoori, E., Motavalli, M. & Koay, Y.C. 2017. Fatigue tests on UHM-CFRP strengthened steel plates with central inclined cracks under different damage levels. *Composite Structures* 160: 995–1006.
- AS13912007. *Methods for Tensile Testing of Metals*. Australia: Sydney.

- Barbarino, S., Saavedra Flores, E.I., Ajaj, R.M., Dayyani, I. & Friswell, M.I. 2014. A review on shape memory alloys with applications to morphing aircraft. *Smart Materials and Structures* 23(6): 63001.
- Chen, Z.Y., Gu, X.L., Vollmer, M., Niendorf, T., Ghafoori, E. & Yu, Q.Q. 2023. Recovery stress behavior of Fe-SMA under fatigue and thermal loading. Submitted to *Thin-Walled Structures*.
- Cladera, A., Weber, B., Leinenbach, C., Czaderski, C., Shahverdi, M. & Motavalli, M. 2014. Iron-based shape memory alloys for civil engineering structures: An overview. *Construction and Building Materials* 63: 281–293.
- Czaderski, C., Shahverdi, M., Brönnimann, R., Leinenbach, C. & Motavalli, M. 2014. Feasibility of iron-based shape memory alloy strips for prestressed strengthening of concrete structures. *Construction and Building Materials* 56: 94–105.
- Eggeler, G., Hornbogen, E., Yawny, A., Heckmann, A. & Wagner, M. 2004. Structural and functional fatigue of NiTi shape memory alloys. *Materials Science and Engineering A-Structural Materials. Properties Microstructure and Processing* 378(1): 24–33.
- Frommeyer, G., Udo, B. & Peter, N. 2003. Supra-ductile and high-strength manganese-TRIP/TWIP steels for high energy absorption purposes. *ISIJ International* 43(3): 438–446.
- Ghafoori, E., Hosseini, E., Leinenbach, C., Michels, J. & Motavalli, M. 2017. Fatigue behavior of a Fe-Mn-Si shape memory alloy used for prestressed strengthening. *Materials & Design* 133: 349–362.
- Gu, X.L., Chen, Z.Y., Yu, Q.Q. & Ghafoori, E. 2021. Stress recovery behavior of an Fe-Mn-Si shape memory alloy. *Engineering Structures* 243: 112710.
- Hartl, D.J. & Lagoudas, D.C. 2007. Aerospace applications of shape memory alloys. *Proceedings of the Institution of Mechanical Engineers, Part G: Journal of Aerospace Engineering* 221(4): 535–552.
- Hosseini, E., Ghafoori, E., Leinenbach, C., Motavalli, M. & Holdsworth, S.R. 2018. Stress recovery and cyclic behaviour of an Fe–Mn–Si shape memory alloy after multiple thermal activation. *Smart Materials and Structures* 27(2): 25009.
- Hosseini, A., Ghafoori, E., Motavalli, M., Nussbaumer, A. & Zhao, X.L. 2017. Mode I fatigue crack arrest in tensile steel members using prestressed CFRP plates. *Composite Structures* 178: 119–134.
- Huang, H., Khalid, M.M. & Chang, W.S. 2020. Adaptive tuned mass damper with shape memory alloy for seismic application. *Engineering Structures* 223: 111171.
- Izadi, M.R., Ghafoori, E., Motavalli, M. & Maalek, S. 2018. Iron-based shape memory alloy for the fatigue strengthening of cracked steel plates: Effects of re-activations and loading frequencies. *Engineering Structures* 176: 953–967.
- Jani, J.M., Leary, M., Subic, A. & Gibson, M.A. 2014. A review of shape memory alloy research, applications and opportunities. *Materials & Design* 56(56): 1078–1113.
- Lee, W.J., Weber, B., Feltrin, G., Czaderski, C., Motavalli, M. & Leinenbach, C. 2013. Stress recovery behaviour of an Fe-Mn-Si-Cr-Ni-VC shape memory alloy used for prestressing. *Smart Materials and Structures* 22(12): 125037.
- Morgan, N.B. 2004. Medical shape memory alloy applications-the market and its products. *Materials Science and Engineering A-Structural Materials Properties Microstructure and Processing* 378(1): 16–23.
- Rojab, H. & El-Hacha, R. 2018. Fatigue performance of RC beams strengthened with self-prestressed iron-based shape memory alloys. *Engineering Structures* 168: 35–43.
- Song, C.L. 2010. History and current situation of shape memory alloys devices for minimally invasive surgery. *The Open Medical Devices Journal* 2(1): 24–31.
- Yu, Q.Q., Chen, T., Gu, X.L., Zhao, X.L. & Xiao, Z.G. 2013. Fatigue behaviour of CFRP strengthened steel plates with different degrees of damage. *Thin-Walled Structures* 69: 10–17.

SMFL-based probability distribution of minimum cross-sectional areas of corroded steel bars

J.L. Qiu, W.P. Zhang & Q.Q. Yu
Tongji University, Shanghai, China

Z.P. Chen
Guangxi University, Nanning, China

ABSTRACT: In this study, a non-destructive quantitative characterization method for the probability distribution of minimum cross-sectional areas of corroded steel bars was proposed based on the dynamic linkage mechanism of the induced magnetic and self-magnetic flux leakage fields variation of steel bars. The experiment data of 28 corroded steel bars were employed to verify this method. The results indicate that the quantitative self-magnetic flux leakage variation ratio dH had a linear correlation with the cross-sectional area unevenness degree dS_n with a ratio of about 1. Based on the index dS_n and cross-sectional area ratio K that obey the Weibull distribution and Gamma distribution, respectively, the probability distribution of minimum cross-sectional area S_{\min} in a certain segment of corroded steel bars can be confirmed.

1 INTRODUCTION

Suffering from an aggressive environment, the steel bars of reinforced concrete (RC) structures inevitably corroded, resulting in a substantial reliability reduction (Bojórquez, Ponce, Ruiz, et al, 2021). Some structural reliability assessment method of corroded RC structures is well-established, such as the out-crossing rate method (Veneziano, Cornell, & Grigoriu, 1977), the first-order reliability method (Frangopol, Lin, & Estes, 1997), the time-series method (Kaminski, 2013), the probability density function method (Akiyama, Frangopol, & Ishibashi, 2020; Li, & Chen, 2009), and the equivalent limit performance function-based method (Guo, Dong, Gardoni, & Gu, 2021). However, these reliability assessment methods still have difficulties in establishing and solving mathematical models.

To avoid complex math problems, the Monte Carlo simulation (MCS) method is widely employed (Stewart, & Al-Harthy, 2008; Zhang, Song, Lim, Akiyama, & Frangopol, 2019). The calculation accuracy of the MCS method relies on the accurate probability distributions of the corroded rebar's cross-sectional area, which can be characterized by the cross-sectional area spatial heterogeneity factor R well (Bojórquez, Ponce, Ruiz, Bojórquez, Reyes-Salazar, Barraza, ... & Baca, 2021; Zhang, Zhou, Gu, & Dai, 2014; Gu, Guo, Zhou, Zhang, & Jiang 2018). However, factor R may not be suitable for a specific in-service RC structure. Corrosion of steel bars will cause self-magnetic flux leakage (SMFL) field variation that is linearly related to the corrosion degree, which is an effective method to characterize the exact corrosion characteristics of steel bars non-destructively (Zhang, Li, Zhou, Tong, & Xia, 2023; Huang, Dong, Fu, Qiu, Liu, Li, & Che, 2022; Qiu, Zhang, Zhou, & Zhang, 2021). Furthermore, the SMFL-based steel corrosion assessment is independent of stochastic corrosion processes (Qiu, Zhou, Zhao, Zhang, & Liao, 2020), and thus the enormous statistical work for the probability distributions of R could be avoided.

In this study, the linear correlation between the corrosion unevenness degree and the SMFL field variation ratio of the corroded rebars was revealed. Then, the SMFL-based probability distribution of minimum cross-sectional areas of corroded steel bars was established.

2 THEORETICAL BASIS

The corrosion-induced SMFL field variation can be theoretically analyzed based on the magnetic dipole theory (Shi & Zheng, 2016; Dutta, Ghorbel, & Stanley, 2009). In general, steel bars are uniformly magnetized in the longitudinal direction (X-direction), that is, $M_x = \text{constant}$, $M_y = 0$, and $M_z = 0$ (Qiu, Zhang, Zhou, & Zhang, 2021), as shown in Figure 1. Based on the minimum magnetic free energy principle, the longitudinally magnetized steel bar with a V-shaped corrosion defect has magnetic charges uniformly distributed on the circular ridge-lines, as shown in Figure 1. The linear distribution densities of magnetic charges are:

$$\rho_{s1'} = \frac{r}{2} M_x, \quad \rho_{s2'} = -\frac{d}{2} M_x, \quad \rho_{s3'} = \frac{d}{2} M_x, \quad \rho_{s4'} = -\frac{r}{2} M_x \quad (1)$$

According to Coulomb's law of magnetism and Figure 1, the x , y , and z components of SMFL field \mathbf{H}_S and induced magnetic field \mathbf{H}_I could be obtained. For example, the x component of \mathbf{H}_S and \mathbf{H}_I are:

$$\begin{cases} H_{Sx} = \frac{dM_x}{8\pi\mu_0} f_1(x, y, z, w, r) \\ H_{Ix} = \frac{M_x}{8\pi\mu_0} f_2(x, y, z, l, r) \end{cases} \quad (2)$$

where $f_1(x, y, z, w, r)$ is a function of x, y, z, w, r , and $f_2(x, y, z, l, r)$ is a function of x, y, z, l, r .

Based on the H_{Sx} and H_{Ix} components, a quantitative index I for the cross-sectional corrosion degree that is not affected by M_x can be constructed:

$$I = \frac{T_1(H_{Sx})}{T_2(H_{Ix})} = d \frac{T_1[f_1(x, y, z, w, r)]}{T_2[f_2(x, y, z, l, r)]} = d \cdot f_3(x, y, z, w, l, r) \quad (3)$$

where $T_1(-)$ and $T_2(-)$ are two primary factors extracted from the H_{Sx} and H_{Ix} curves, and $f_3(x, y, z, w, l, r)$ is a function of x, y, z, w, l, r .

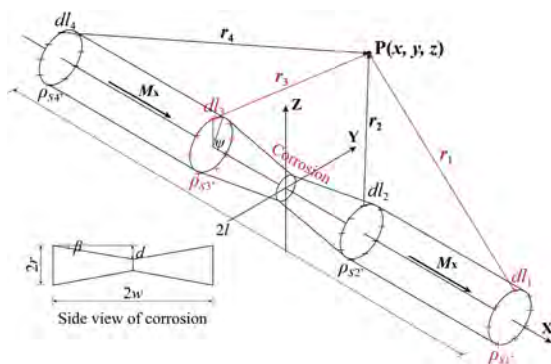


Figure 1. Magnetic dipole calculation model of longitudinally magnetized steel bars with steady state magnetic charge distributions.

3 THE EXPERIMENT DETAILS

3.1 The corroded steel bar specimens

As shown in Figure 2(a), the corroded rebar specimens were taken from a longitudinal girder of a wharf bridge that naturally corroded in the marine environment for 26 years. The marine-atmosphere zone steel bars at the top of the girder are barely corroded, while the tidal zone steel bars at the bottom of the girder are severely corroded. Both the top and bottom longitudinal steel bars of the girder were taken out and cut into 1000 mm long short specimens. The

original naturally corroded steel bar specimens were numbered S-NC-1 - S-NC-22, and the loose corrosion products on their surface were cleaned with a plastic brush and clean water. The middle 750 mm regions of 6 original uncorroded steel bar specimens numbered S-AC-1 - S-AC-6 were corroded by the applied-current method (Li, Dong, He, Fu, & Jin, 2022) with random corrosion duration to obtain uneven corrosion morphologies.

3.2 The 3D structural light scanning of the corrosion morphology

As shown in Figure 2(b), the accurate corrosion morphologies of all specimens were obtained using 3D structured light scanning with an accuracy as high as 0.02 mm. First, the structured light projector continuously projects several specific blue fringe patterns onto the corroded steel bar, which are distorted by the uneven corrosion morphology and then captured by the camera. According to the camera geometry model and the triangulation principle, the partial surface point cloud of the steel bar containing some mark points can be obtained based on these distorted blue fringe patterns. Finally, by identifying the mark points, the multiple surface region point clouds can be accurately merged into a complete surface point cloud, based on which the surface and solid models of the corroded steel bar can be obtained.

3.3 The SMFL field scanning

As shown in Figure 2(c), the TSC-7M-16 micro-magnetic scanner with an accuracy of 0.1 A/m was used to scan the SMFL field of all specimens. The scanning trolley equipped with a displacement pedometer moves along the longitudinal scanning path directly above the corroded steel bar, while the micro-magnetic sensors on the trolley detect the SMFL field variation. With a displacement interval of 1 mm, the displacement and the corresponding SMFL field data were recorded by the host. The vertical distance between the micro-magnetic sensors and the upper surface of the corroded steel bar is defined as the lift-off height (LFH). The value of LFH was taken as 5, 10, 30, 50, and 100 mm in this study, where 30 mm equals the concrete cover thickness of the common RC structure.

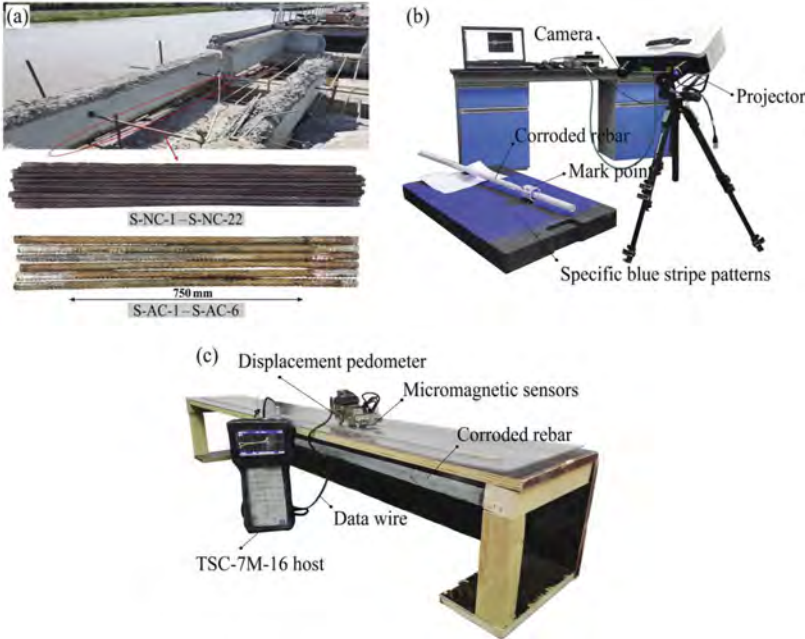


Figure 2. (a) The naturally corroded specimens S-NC-1 – S-NC-22 and the applied-current corroded specimens S-AC-1 – S-AC-6, (b) the 3D structural light scanning of the steel bars’ corrosion morphology, and (c) the SMFL field variation scanning of the corroded steel bar.

4 RESULTS AND DISCUSSION

4.1 The cross-sectional area and SMFL field variation of the corroded rebars

The experimental results of the cross-sectional area S and SMFL field components H_x and H_z of a typical naturally corroded specimen S-NC-8 are shown in Figure 3(a). The sharp peaks and fluctuations of the S curve indicate the position of the stirrups and the uneven corrosion morphology, respectively. The fluctuations of the H_x and H_z curves indicate the SMFL field variation induced by the uneven corrosion morphology. However, H_x and H_z curves only reveal limited information about uneven corrosion.

To further explore the relationship between SMFL field variation and uneven corrosion, the simulated quantitative SMFL variation degree $N-\Delta H_{SA}$ in Figure 3(b) is defined according to the definition of index I in Equation (3):

$$N-\Delta H_{SA} = \frac{\Delta H_{SA}}{H} = \frac{[H_x]_{SG} - [H_x]_{AAV}}{\sqrt{H_x^2 + H_z^2}}, \quad i \in [0, H] \quad (4)$$

where $[H_x]_{SG}$ and $[H_x]_{AAV}$ are the SG smoothing ($n = 2$ and $m = 5$) (Savitzky, & Golay, 1964) and the AAV smoothing ($m = 50$) (Simonoff, 2012) results of the H_x component, respectively.

As shown in Figure 3(b), the $N-\Delta H_{SA}$ curves reflect the uneven corrosion-induced SMFL field variation better compared with the original SMFL field curve. In addition, the SMFL fields' total strength H and the component H_z can also be used to calculate $N-\Delta H_{SA}$. To establish a more intuitive quantitative relationship between SMFL field variation and uneven corrosion, the SMFL field variation ratio dH , the corrosion unevenness degree dS_n , and the cross-sectional area ratio K are defined as shown in Figure 3(b). Using the $N-\Delta H_{SA}$ and S curves of each specimen, several dH and the corresponding dS_n and K can be obtained, which satisfies the:

$$S_{\min} = \left[1 - \frac{dS_n}{K + 1} \right] \cdot S_{\text{ave}} \quad (5)$$

where S_{\min} is the minimum cross-sectional area of a certain segment of the corroded steel bar.

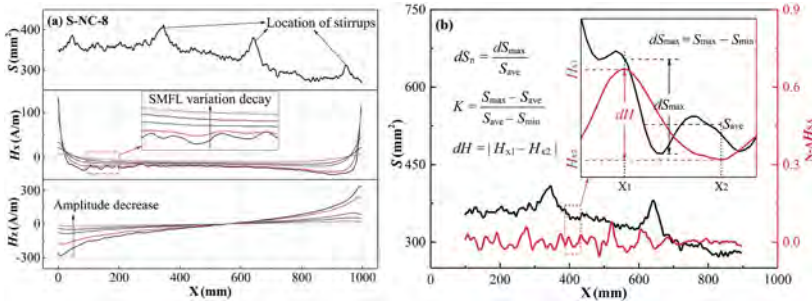


Figure 3. (a) The cross-sectional area S and experimental SMFL field components H_x and H_z of specimens S-EC-8, and (b) the geometric factors used to define indices dH , dS_n , and K .

4.2 The probability distributions of indices dS_n and K

According to Equations (4)-(5) and the data of S and total SMFL field strength H of all the specimens, dH and its corresponding dS_n and K were obtained. For brevity, only data of LFH = 30 mm are given as an example, as shown in Figure 4. The experimental result shows a clear linear correlation between dS_n and dH , which indicates the corrosion-induced cross-sectional area reduction leads to the proportional SMFL. In addition, this correlation is not affected by differences in SMFL field strength, cross-sectional area, and corrosion degree. Both the

experimental and simulated K are distributed in the interval $[0.25, 4.0]$, and most of the data points are concentrated around 1.0.

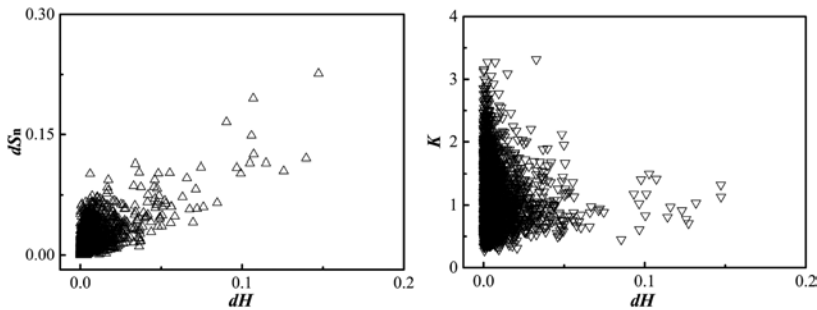


Figure 4. The experimental and simulated results of dS_n and K with LFH = 30 mm.

Probability distribution statistics and analysis of dS_n and K are further implemented based on the nonparametric kernel density estimation (KDE) method (Zhang, Yu, Liu, Dong, Li, Zang, & Xu, 2022). KDE is based on the sample points in Figure 4, and the Gaussian kernel function and the default optimal window width are used.

First, the probability density of dS_n is estimated. The range of the experimental dH is divided into 11 intervals, and then the probability density of dS_n of each dH interval is estimated using the KDE method one by one. Then, the complete probability distribution of dS_n is obtained by combing these KDE results, as shown in Figure 5(a). The Kolmogorov-Smirnov method is used to test the distribution type of dS_n in each dH interval, and the test results show that at the 95% confidence level, dS_n of all dH intervals obey the Weibull distribution:

$$f(x; \lambda, k) = \begin{cases} \frac{k}{\lambda} \left(\frac{x}{\lambda}\right)^{k-1} \exp\left(-\left(\frac{x}{\lambda}\right)^k\right), & x > 0 \\ 0, & x < 0 \end{cases} \quad (6)$$

where λ and k are two parameters of Weibull distribution.

As shown in Figure 5, the distribution parameters λ and k of dS_n of each dH are approximately linearly and inversely proportional correlated with dH , respectively, and thus λ and k are fitted. Then, the fitting results of λ and k are substituted into Equation (5) to acquire the fitted Weibull distribution of dS_n as shown in Figure 5(b). The fitted Weibull distribution is similar to the KDE result, which indicates the potential of the Weibull distribution to determine the probability density distribution of dS_n .

Second, the probability density of K is estimated. According to trial calculation, it is found that the probability distribution estimation of $(K - 0.25)$ is more feasible than that of K . The probability distribution estimation of $(K - 0.25)$ is the same as that of dS_n . As shown in Figure 6(a), the change of LFH has no significant influence on the form and magnitude of the probability distribution of $(K - 0.25)$. However, as shown in Figure 6(b), the probability distribution of $(K - 0.25)$ shows a local mutation that includes 90.1% of the data volume with the increase of dH . Therefore, the influence of dH on the probability distribution of $(K - 0.25)$ needs to be considered. The complete KDE probability distribution of $(K - 0.25)$ is shown in Figure 6(c). The Kolmogorov-Smirnov method is also used to test the distribution type of $(K - 0.25)$, and the test results show that at the 95% confidence level, $(K - 0.25)$ of all intervals obey the Gamma distribution:

$$f(x; \alpha, \beta) = \begin{cases} \frac{1}{\beta^\alpha \Gamma(\alpha)} x^{\alpha-1} \exp\left(-\frac{x}{\beta}\right), & x > 0 \\ 0, & x < 0 \end{cases} \quad (7)$$

where α and β are two parameters of Gamma distribution.

As shown in Figure 6(d), the fitted probability density distribution of $(K - 0.25)$ is similar to the KDE result, which indicates that it is appropriate to use the Gamma distribution to

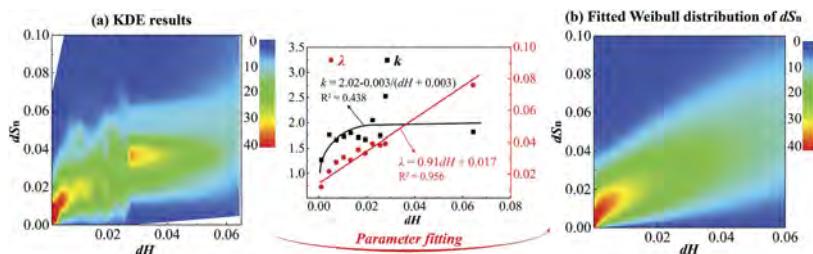


Figure 5. The (a) KDE result and (b) fitted Weibull distribution of dS_n with LFH = 30 mm.

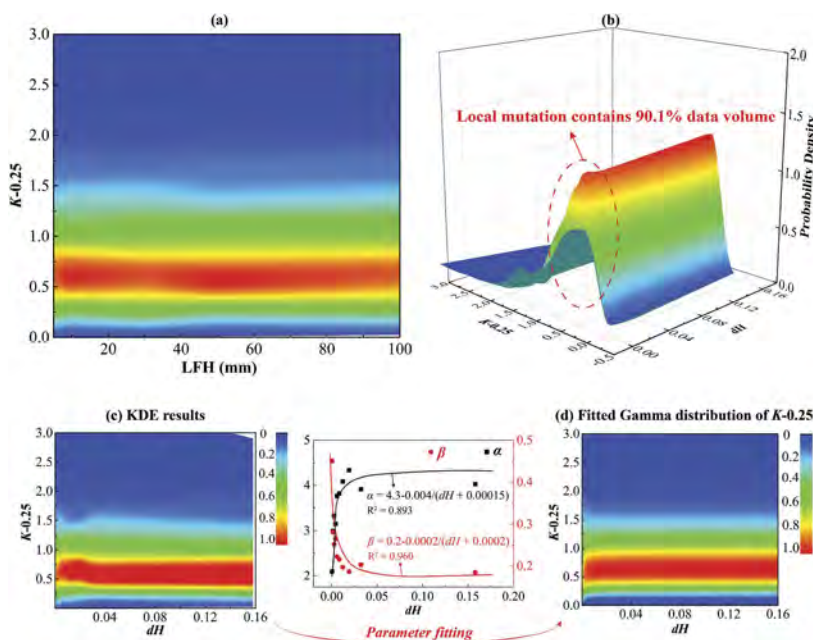


Figure 6. The effects of (a) LFH and (b) dH on $(K - 0.25)$, the (c) KDE result, and (d) fitted Weibull distribution of $(K - 0.25)$ with LFH = 30 mm.

determine the probability density distribution of $(K - 0.25)$. According to Equation (5), Figures 5 and 6, the probability density distribution of S_{min} can be determined.

5 CONCLUSIONS

The corrosion unevenness degree dS_n and cross-sectional area ratio K of the corroded rebar obey the Weibull distribution and the Gamma distribution at the 95% confidence level, respectively, based on which the probability density distribution of the minimum cross-sectional area S_{min} of the corroded steel bar can be established.

REFERENCES

- Akiyama, M., Frangopol, D. M., & Ishibashi, H. (2020). Toward life-cycle reliability-, risk-and resilience-based design and assessment of bridges and bridge networks under independent and interacting hazards: emphasis on earthquake, tsunami and corrosion. *Structure and Infrastructure Engineering*, 16(1), 26–50.
- Bojórquez, J., Ponce, S., Ruiz, S. E., Bojórquez, E., Reyes-Salazar, A., Barraza, M., ... & Baca, V. (2021). Structural reliability of reinforced concrete buildings under earthquakes and corrosion effects. *Engineering Structures*, 237, 112161.
- Dutta, S. M., Ghorbel, F. H., & Stanley, R. K. (2009). Dipole modeling of magnetic flux leakage. *IEEE Transactions on Magnetics*, 45(4), 1959–1965.
- Frangopol, D. M., Lin, K. Y., & Estes, A. C. (1997). Reliability of reinforced concrete girders under corrosion attack. *Journal of structural Engineering*, 123(3), 286.
- Guo, H. Y., Dong, Y., Gardoni, P., & Gu, X. L. (2021). Time-Dependent Reliability Analysis Based on Point-Evolution Kernel Density Estimation: Comprehensive Approach with Continuous and Shock Deterioration and Maintenance. *ASCE-ASME Journal of Risk and Uncertainty in Engineering Systems, Part A: Civil Engineering*, 7(3), 04021032.
- Gu, X., Guo, H., Zhou, B., Zhang, W., & Jiang, C. (2018). Corrosion non-uniformity of steel bars and reliability of corroded RC beams. *Engineering Structures*, 167, 188–202.
- Huang, J., Dong, Z., Fu, C., Qiu, T., Liu, C., Li, Z., & Che, X. (2022). Evaluation of Nonuniform Corrosion of Steel in Concrete Based on Two-Yoke Magnetic Sensor. *Journal of Materials in Civil Engineering*, 34(9), 04022204.
- Kaminski, M. (2013). *The stochastic perturbation method for computational mechanics*. John Wiley & Sons.
- Li, J., & Chen, J. (2009). *Stochastic dynamics of structures*. New York: John Wiley & Sons.
- Li, Q., Dong, Z., He, Q., Fu, C., & Jin, X. (2022). Effects of Reinforcement Corrosion and Sustained Load on Mechanical Behavior of Reinforced Concrete Columns. *Materials*, 15(10), 3590.
- Qiu, J., Zhang, H., Zhou, J., & Zhang, W. (2021). An SMFL-based non-destructive quantification method for the localized corrosion cross-sectional area of rebar. *Corrosion Science*, 192, 109793.
- Qiu, J., Zhou, J., Zhao, S., Zhang, H., & Liao, L. (2020). Statistical quantitative evaluation of bending strength of corroded RC beams via SMFL technique. *Engineering Structures*, 209, 110168.
- Savitzky, A., & Golay, M. J. (1964). Smoothing and differentiation of data by simplified least squares procedures. *Analytical chemistry*, 36(8), 1627–1639.
- Shi, P. P., & Zheng, X. J. (2016). Magnetic charge model for 3D MMM signals. *Nondestructive Testing and Evaluation*, 31(1), 45–60.
- Simonoff, J. S. (2012). *Smoothing methods in statistics*. Springer Science & Business Media.
- Stewart, M. G., & Al-Harthy, A. (2008). Pitting corrosion and structural reliability of corroding RC structures: Experimental data and probabilistic analysis. *Reliability engineering & system safety*, 93(3), 373–382.
- Veneziano, D., Cornell, C. A., & Grigoriu, M. (1977). Vector-process models for system reliability. *Journal of the Engineering Mechanics Division*, 103(3), 441–460.
- Zhang, H., Li, H., Zhou, J., Tong, K., & Xia, R. (2023). A multi-dimensional evaluation of wire breakage in bridge cable based on self-magnetic flux leakage signals. *Journal of Magnetism and Magnetic Materials*, 170321.
- Zhang, K., Yu, X., Liu, S., Dong, X., Li, D., Zang, H., & Xu, R. (2022). Wind power interval prediction based on hybrid semi-cloud model and nonparametric kernel density estimation. *Energy Reports*, 8, 1068–1078.
- Zhang, M., Song, H., Lim, S., Akiyama, M., & Frangopol, D. M. (2019). Reliability estimation of corroded RC structures based on spatial variability using experimental evidence, probabilistic analysis and finite element method. *Engineering Structures*, 192, 30–52.
- Zhang, W., Zhou, B., Gu, X., & Dai, H. (2014). Probability distribution model for cross-sectional area of corroded reinforcing steel bars. *Journal of Materials in Civil Engineering*, 26(5), 822–832.

Reliability analysis considering epistemic uncertainties with small initial sample and successive updating data

Yi-hua Fei, You-bao Jiang, Yu Leng & Lei Wang

School of Civil Engineering, Changsha University of Science and Technology, Changsha, China

Zheng Chen

School of Civil Engineering and Architecture, Guangxi University, Nanning, China

ABSTRACT: In structural engineering, the epistemic uncertainties of random variables, including distribution parameters and distribution type uncertainties, usually exist due to initial data scarcity. Moreover, the data will be updated over time, which causes the structural reliability updating. In this paper, for the initial data scarcity and successive data updating cases, a random variable model is developed to quantify the uncertainties of distribution parameter and distribution type based on the Bootstrap method, Akaike information criterion and Bayes update method. Considering the epistemic uncertainties, the reliability index of structure becomes a random variable and its probability density function (PDF) is presented. The numerical results show that the variability of the distribution parameters gradually decrease as the data update, and so does the variability of the reliability index. The PDF of the reliability index with the uncertainties of both distribution parameters and distribution type is largely different from that with only the uncertainty of distribution parameters.

1 INTRODUCTION

There are many uncertainties in engineering structures (Enright & Frangopol 1998, Li et al. 2015). And these uncertainties can be divided into aleatory uncertainties and epistemic uncertainties (Kiureghian & Ditlevsen 2007, Wang & Roger 2021, Jiang et al. 2020). The former is objective and its uncertainty cannot be reduced, and the latter is due to incomplete knowledge and data scarcity and so on and its uncertainty can be reduced with the deepening of cognition (Kiureghian & Ditlevsen 2007).

The aleatory uncertainty has been intensively and extensively studied in the past few decades, however the studies regarding the epistemic uncertainty are relatively less. In engineering, aleatory uncertainty is usually described by a deterministic probability distribution function. While for epistemic uncertainty, it can usually be characterized and quantified by using fuzzy models (Moens & Vandepitte 2002) and non-probabilistic methods such as interval analysis and convex set theory (Ben-Haim 1994, Elishakoff & Elisseff 1994). Many probabilistic methods have also been developed in recent years to quantify epistemic uncertainty. For example, an engineering design parameter usually has the distribution parameters and distribution type uncertainty due to data scarcity. In view of this, Most et al. (Most & KNABE 2010) employed the Bootstrap method to model the variability of the mean and standard deviation of soil shear strength parameters and their influences on the reliability of foundation bearing capacity. Sankararaman et al. (Sankararaman & Mahadevan 2013) used the likelihood method to model the distribution parameters as random variables, and pointed out that the distribution type also has uncertainty due to data scarcity. From the above, the uncertainty of distribution parameters and distribution type usually exist with small samples, but it is considered less in the data updating for the current reliability methods.

In this paper, the epistemic uncertainty is unified in the probabilistic framework with the aleatory uncertainty. For the cases of small initial sample size and subsequent data updates, a model is developed to quantify the uncertainties of distribution parameter and distribution type based on the Bootstrap method, Akaike information criterion (AIC) and Bayes update method. First, the initial

samples are sampled by the Bootstrap method to obtain the prior distribution of the distribution parameters, and then the prior distribution of the distribution type is obtained with the aid of AIC. Then the posterior distribution after the data updates is obtained by the Bayes update method. Herein the distribution parameters are considered as continuous random variables and the distribution type is considered as discrete random variables. Next, a reliability analysis was performed to investigate the effects of uncertainty in the distribution parameters and distribution types on the conditional reliability index (Based on Bayesian statistical theory, the traditional reliability index are defined as conditional reliability index (CRI) (Kiureghian 1989)). Finally, the practicality and validity of the proposed method is demonstrated by example analysis.

2 EPISTEMIC UNCERTAINTY QUANTIFICATION METHODS

2.1 Bootstrap method

The Bootstrap method (EFRON 1979) is usually applied for random sampling with put-back of the initial test data to obtain information on the epistemic uncertainty of the distribution parameters. The method can obtain a large amount of new data with the characteristics of the original test data by sampling when the actual test data are relatively sparse. So it is an effective way to quantify epistemic uncertainty under small sample conditions.

2.2 Akaike information criterion

For the distribution types, the AIC (Akaike information criterion) (AKAIKE 1974) is often used in engineering to identify the optimal distribution type by comparing the AIC values corresponding to each distribution type. The distribution type corresponding to the smallest AIC value is considered to be the optimal distribution type.

In this section we can identify the optimal distribution type by comparing the AIC values corresponding to each distribution type calculated for each Bootstrap subsample, with each subsample corresponding to an optimal distribution type. And the uncertainty of the distribution type can be characterized by this method by calculating the number of times that different distribution types are identified as the optimal distribution among 10,000 Bootstrap subsamples. And then we divide the number of times by 10,000 as a priori probability of distribution type.

2.3 Bayes update method

For the distribution parameters, let D_1 and D_2 denote the initial data and the updating data of the random variable Θ , respectively. Also, the probability density function obtained by statistical inference from D_1 is $p_{\Theta}^{(1)}(\theta|\zeta_1)$, where ζ_1 is the distribution parameter obtained from the statistical analysis of the data D_1 . If there is epistemic uncertainty in this analysis process, i.e., ζ_1 is inherently uncertain. In general, the prior distribution $p_{\zeta}(\zeta)$ of ζ_1 is artificially assumed. But in this paper, this prior distribution is given based on the Bootstrap method. The posterior distribution of the distribution parameters is obtained by the Bayes update method when the additional updating samples D_2 are introduced:

$$p_{\zeta}(\zeta|D_2) = \frac{L(D_2|\zeta)}{\int L(D_2|\zeta)p_{\zeta}(\zeta)d\zeta} \cdot p_{\zeta}(\zeta) \quad (1)$$

where $L(\cdot)$ is the maximum likelihood function, with.

$$L(D_2|\zeta) = \prod_{i=1}^{n_2} p_{\Theta}^{(1)}(\theta_i|\zeta) \quad (2)$$

where, n_2 denotes the number of new updated data.

And for the distribution type, the Bayes formula for discrete random variables should be considered, i.e:

$$P(A_i|D_2) = \frac{P(A_i) \cdot P(D_2|A_i)}{\sum_{i=1}^n P(A_i) \cdot P(D_2|A_i)} \quad (3)$$

where A_i is the distribution type, A_1 is normal distribution, A_2 is lognormal distribution and A_3 is extreme value distribution, $P(A_i)$ is the prior probability of each distribution type given by the Bootstrap method combined with AIC, $P(D_2|A_i)$ is the conditional probability its calculation formula is:

$$P(D_2|A_i) = \prod_{j=1}^n p(\theta_j|A_i, \zeta) \quad (4)$$

where $p(\theta_j|A_i, \zeta)$ is the value of the probability density function of the distribution type corresponding to A_i at the data point θ_j , and n is the number of samples. The posterior probability of each distribution type can be determined by Equation (5).

In this paper, the M-H algorithm in the Markov Chain Monte Carlo (MCMC) method (Chib & Greenberg 1995) is used to solve the posterior distribution of the distribution parameters.

Based on the above basic theory, the steps of epistemic uncertainty characterization under a small initial samples and continuous update conditions are as follows:

- 1) Based on the initial data, the prior distribution of the distribution parameters is given based on the Bootstrap method. And the prior probability of the distribution type is then given by Bootstrap combined with the AIC.
- 2) Calculate the likelihood function and conditional probability by Equation (2) and Equation (4) based on the updating data, then solve Equation (1) to obtain the posterior distribution of the distribution parameters after the updating using the MCMC method. And solve Equation (3) to obtain the posterior distribution of the distribution type.
- 3) Repeat the step 2 according to the continuous updating data, and use the previous posterior distribution as the prior distribution of this update, Then perform multiple updates to obtain the final posterior distribution of the parameter distribution type and distribution parameters.

2.4 Reliability analysis under epistemic uncertainty

The probability of structural failure under epistemic uncertainty can be expressed as:

$$P_f(\Theta) = \int_{G(\mathbf{X}, \Theta) \leq 0} f_{\mathbf{X}, \Theta}(x, \theta) dx \quad (5)$$

where $P_f(\Theta)$ is the failure probability, \mathbf{X} denotes the random uncertainty variables, Θ denotes the epistemic uncertainty variables, $G(\mathbf{X}, \Theta)$ denotes the performance function, and $f_{\mathbf{X}, \Theta}(x, \theta)$ is the joint probability density function of \mathbf{X} and Θ . Since the distribution parameters and distribution type of the variable Θ are uncertain, the failure probability $P_f(\Theta)$ is also uncertain. The corresponding reliability index is also uncertain, and defined as:

$$\beta(\Theta) = \Phi^{-1}[1 - P_f(\Theta)] \quad (6)$$

where Φ^{-1} denotes the inverse function of the standard normal cumulative distribution function.

For the calculation of the CRI, we adopted a two-loop approach and used the Monte Carlo simulation (MCS). That is, the CRI is calculated in two loops. The first loop being the determination of the distribution parameters and the distribution type by random sampling of its probability distribution. The second loop is to compute the CRI of the distribution parameter and distribution type from the first loop repeatedly. In this paper, the number of loops is 10,000, which means that we can obtain 10,000 CRI samples. And we can obtain the PDF of CRI through these samples. Then we can evaluate the mean and coefficient of variation of CRI, too.

3 NUMERICAL EXAMPLES AND INVESTIGATIONS

Consider the stability analysis model of the retaining wall in slip damage mode (Li et al. 2015), as shown in Figure 1.

In the case that the bearing capacity is satisfied, its corresponding performance function is:

$$g = \frac{c_{\text{int}}(a + b) + (W_1 + W_2) \tan \phi_{\text{int}}}{P_a} - 1 \quad (7)$$

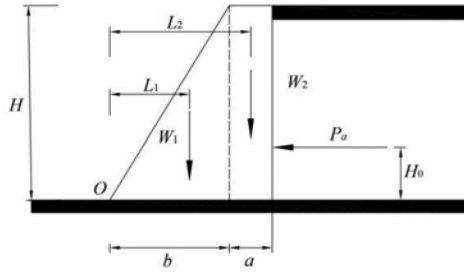


Figure 1. Stability analysis model of retaining wall.

where: $c_{int} = 1/3 \cdot c_b$ and $\varphi_{int} = 2/3 \cdot \varphi_b$ are the cohesion and friction angle of interface shear strength. Respectively, and c_b and φ_b are the cohesion and friction angle at the corresponding foundation soil, P_a is the active earth pressure, whose expressions are:

$$P_a = \frac{1}{2} \gamma_s H^2 K_a - 2cH \sqrt{K_a} + \frac{2c^2}{\gamma_s} \quad (8)$$

where K_a is the coefficient of active earth pressure, given by Rankine's theory:

$$K_a = \tan^2(\pi/4 - \phi/2) \quad (9)$$

The other parameters are defined and their values are shown in Table 1.

Table 1. Stability analysis model parameters of retaining wall.

Parameters	Value	Physical meaning
a/m	0.5	Retaining wall geometry parameters
b/m	2.5	Retaining wall geometry parameters
H/m	10	Retaining wall geometry parameters
$\gamma_s /(\text{kN/m}^3)$	18	Unit weight of backfill
$\gamma_w /(\text{kN/m}^3)$	24	Unit weight of retaining wall
$\gamma_b /(\text{kN/m}^3)$	18	Unit weight of foundation
W_1	$0.5bH\gamma_w$	Unit retaining wall gravity
W_2	$aH\gamma_w$	Unit compartment gravity
c_b /kPa	300	Cohesion of foundation soil
$\varphi_b /(^{\circ})$	30	Friction angle of foundation soil

The actual engineering test data of consolidated-drained triaxial compression shear strength parameters (c and φ) are limited, and the literature (Li et al. 2015) provides 63 sets of test data of shear strength parameters. This example examines the effect of epistemic uncertainty of parameters on the stability analysis of retaining walls using the shear strength test data.

Case 1: Consider only the distribution parameters uncertainty

We first study the uncertainty of the distribution parameters for these 63 sets of data. And we divide the 63 groups of data into two groups. Next, we use the first 30 groups of data to construct the prior distribution of the distribution parameters by the Bootstrap method. The literature (Wang & Cao 2015) shows that the mean and standard deviation samples obtained by the Bootstrap method sampling fit better with the normal distribution. So in this paper, the prior distribution is taken as normal distribution. And the posterior distribution of the distribution parameters is then obtained by the MCMC method using the latter 33 sets of data as the updated data. It is known that the posterior distribution is also normal from the theory of conjugate distribution (Bolstad 2007). It can be seen from Table 2 that the posterior distribution has less variability compared to the prior distribution, i.e., it can narrow the range of the distribution parameters and reduce the epistemic uncertainty after updating the data.

To further considered the effect of continuous updating of the samples of the distribution parameters uncertainty. It is assumed that there are 4 sets of data and each with 100 samples form random

sampling. The additional 100 samples of each updating are form random sampling of the sampling PDF (normal distribution). The mean and standard deviation of the sampling PDF is determined by the first 63 sets of data. And the scatter plot of the the additional 100 samples of each updating is shown in Figure 2. The distribution parameters are updated using these 4 sets of data, and the posterior distribution of the distribution parameters is also shown in Table 2. As can be seen from Table 2, with continuous updating of the sample, the variability of the distribution parameters keeps decreasing and the epistemic uncertainty also decreases.

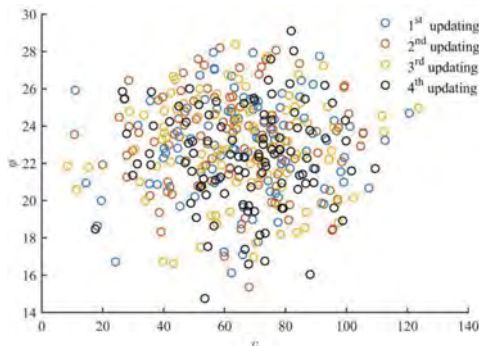


Figure 2. Scatter plot of the additional 100 samples in each updating (case 1).

Table 2. Uncertainty of distribution parameters.

Distribution parameters	Priori distribution	Posterior distribution	1 st updating	2 nd updating	3 rd updating	4 th updating
Sample size	30	63	163	263	363	463
μ_c	$N^*(66.56, 3.27)$	$N(65.97, 2.26)$	$N(66.07, 1.55)$	$N(65.73, 1.25)$	$N(65.08, 1.07)$	$N(65.47, 0.95)$
σ_c	$N(17.84, 2.44)$	$N(21.19, 1.61)$	$N(21.17, 1.08)$	$N(21.47, 0.86)$	$N(21.75, 0.74)$	$N(21.72, 0.66)$
μ_ϕ	$N(21.82, 0.41)$	$N(22.65, 0.28)$	$N(22.76, 0.19)$	$N(22.88, 0.15)$	$N(22.85, 0.13)$	$N(22.74, 0.12)$
σ_ϕ	$N(2.22, 0.28)$	$N(2.61, 0.19)$	$N(2.59, 0.13)$	$N(2.61, 0.1)$	$N(2.61, 0.09)$	$N(2.63, 0.08)$

* where $N(\mu, \sigma)$ denotes a normal distribution with mean μ and standard deviation σ .

In the following, we use the proposed method to calculate the CRI. The PDF of CRI determined by the probability distribution of some of the distribution parameters in Table 3 is shown in Figure 3, and the statistical parameters of CRI determined by each updating are shown in Table 4. It can be seen that the CRI also has a larger range of variation when the epistemic uncertainty is large. When the distribution parameters are updated to reduce the epistemic uncertainty, the range of uncertainty of the CRI becomes narrower. Also it can be seen through Figure 3 and Table 3 that the coefficient of variation of both the distribution parameter and the CRI decreases with the continuous updating of the samples.

Case 2: Considering both distribution parameters and distribution type uncertainty

In this case, we further investigate the effect of distribution type uncertainty of shear strength parameters on the reliability of retaining wall stability. Firstly, we discuss the distribution type uncertainty by 63 sets of data in the literature (Li et al. 2015), and the data are grouped as in case 1. Then the prior and posterior probability are obtained by the proposed quantification method of distribution type uncertainty, as shown in Table 4.

We next consider the uncertainty of the distribution types under the condition of continuous updating of the samples. Similar to case 1, it is assumed that there are 4 sets of data and each with 100 samples form random sampling. The additional 100 samples in 1st updating and 3rd updating are form random sampling of the sampling PDF(lognormal distribution). The additional

100 samples in 2nd updating and 4th updating are form random sampling of the sampling PDF (extreme value distribution). The mean and standard deviation of the sampling PDF is determined by the first 63 samples. The scatter plot of additional 100 samples in each updating is shown in Figure 4. And the posterior distribution of the distribution types of the shear strength parameters obtained by the Bayes update method is shown in Table 5. From Table 5, it can be seen that the posterior probabilities of the distribution type will tilt toward a certain distribution type under the condition of continuous update of the samples generated by the different distribution types.

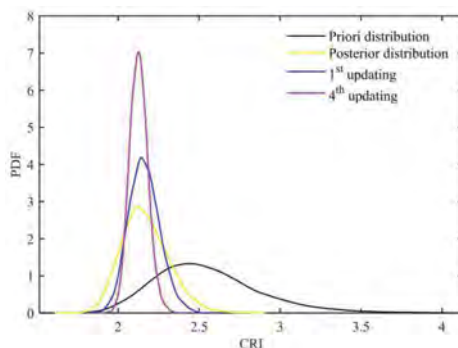


Figure 3. PDF of conditional reliability index in case 1.

Table 3. Statistical parameters of CRI in case 1.

Statistical parameters	Priori distribution	Posterior distribution	1 st updating	2 nd updating	3 rd updating	4 th updating
Sample size	30	63	163	263	363	463
Mean	2.552	2.168	2.162	2.138	2.130	2.127
Standard deviation	0.333	0.144	0.106	0.075	0.063	0.058
Coefficient of variation	0.130	0.067	0.049	0.035	0.030	0.027

Table 4. Prior and posterior probability of the distribution type.

Distribution Type	Priori probability		Posterior probability	
	c	φ	c	φ
Normal distribution	0.9844	0.9865	0.9990	0.8756
Lognormal distribution	0.0132	0.0129	0.0008	0.1095
Extreme value Distribution	0.0024	0.0006	0.0002	0.0149

Based on this, we use the proposed method to calculate the CRI. The statistical parameters of CRI (case 1 and case 2) after each update are shown in Table 6. And The PDF of the CRI corresponding to the partially updated batch is shown in Figure 5. From Table 6 and Figure 5, it can be seen that the mean value of CRI and the variability increase in some cases when both distribution parameter and distribution type uncertainties are considered, and the shape of the PDF may also change. This is because the uncertainty of distribution type is considered in the reliability analysis, while the traditional method only adopts a fixed distribution type of shear strength parameter in the reliability analysis. These results prove the importance of considering the uncertainty of the distribution type of the shear strength parameters in the reliability analysis.

Table 5. Posterior distribution of distribution types.

(a) Friction angle φ				
Distribution Type	1 st updating	2 nd updating	3 rd updating	4 th updating
Normal distribution	0.5609	0.0275	0.0056	0.0003
Lognormal distribution	0.4018	0.4434	0.9942	0.9989
Extreme value distribution	0.0373	0.5291	0.0002	0.0008
(b) Cohesion c				
Distribution Type	1 st updating	2 nd updating	3 rd updating	4 th updating
Normal distribution	0.8424	0.0008	0.0001	0.0003
Lognormal distribution	0.1275	0.7031	0.7394	0.3986
Extreme value Distribution	0.0301	0.2961	0.2605	0.6011

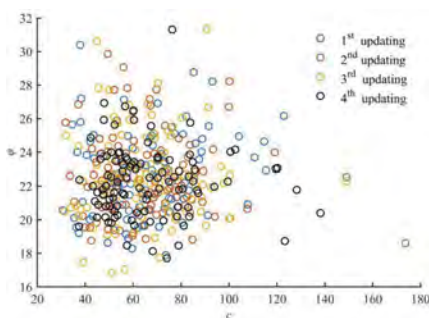


Figure 4. Scatter plot of the additional 100 samples in each updating (case 2).

Table 6. Statistical parameters of CRI in case 2.

Statistical parameters	Posterior distribution	1 st updating	2 nd updating	3 rd updating	4 th updating
Sample size	63	163	263	363	463
Mean(Case 1)	2.168	2.162	2.138	2.130	2.127
Mean(Case 2)	2.726	2.618	2.128	2.123	2.108
Coefficient of variation(Case 1)	0.067	0.049	0.035	0.030	0.027
Coefficient of variation(Case 2)	0.085	0.095	0.036	0.031	0.026

4 CONCLUSION

In this paper, a method is developed to quantify the epistemic uncertainties of random variable, including the uncertainties of distribution parameter and distribution type, which unifies the epistemic uncertainty in the probabilistic framework with the aleatory uncertainty. Then, the reliability analysis is performed to obtain the PDF of the CRI, and the influences of these uncertainties on the CRI are investigated.

The main conclusions are drawn as follows:

- (1) The uncertainties of distribution parameter and distribution type can be quantified well by the AIC combined with the Bootstrap method in case of data scarcity.
- (2) The variability of the distribution parameters gradually decreases as the data successively updates with Bayes update method, and the variability of CRI continuously decreases, too.
- (3) The PDF of CRI with the uncertainties of both distribution parameters and distribution type is largely different from that with only the uncertainty of distribution parameters.

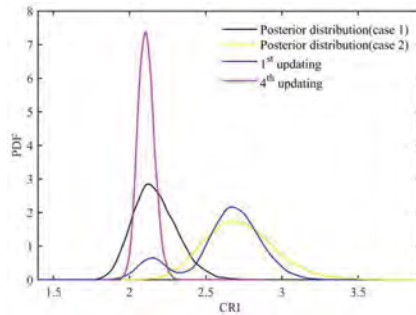


Figure 5. PDF of conditional reliability index in case 2.

ACKNOWLEDGMENTS

The research is supported by the National Key R&D Program of China (Grant No. 2021YFB2600900), Natural Science Fund for Distinguished Young Scholars of Hunan Province, China (Grant No. 2022JJ10050), Hunan Provincial Natural Science Foundation of China (Grant No. 2021JJ30716). This support is gratefully acknowledged.

REFERENCES

- AKAIKE H. 1974. A new look at the statistical model identification. *IEEE Transactions on Automatic Control*. 19(6): 716–723.
- Ben-Haim Y. 1994. A non-probabilistic concept of reliability. *Structure Safety*. 14(4): 227–245.
- Bolstad W. 2007. Introduction to Bayesian Statistics. *NJ: John Wiley and Sons*.
- Chib S & Greenberg E. 1995. Understanding the MetropolisHastings algorithm. *American Statistician*. 49(4): 327–335.
- Der Kiureghian A & Ditlevsen O. 2007. Aleatory or epistemic? Does it matter?. *Structural Safety*. 31: 105–112.
- Der Kiureghian A. 1989. Measures of structural safety under imperfect states of knowledge. *Journal of Structural Engineering*. 115 (5) 1119–1140.
- Enright M P & Frangopol D M. 1998. Probabilistic analysis of resistance degradation of reinforced concrete bridge beams under corrosion. *Engineering Structures*. 20(11): 960–971.
- EFRON B. 1979. Bootstrap methods: Another look at the jackknife. *The Annals of Statistics*. 7(1): 1–26.
- Elishakoff I. & Elisseeff P. 1994. Non-probabilistic,convex-theoretic modeling of scatter in material properties. *AIAA JOURNAL*. 32:843–849.
- Li D Q, Zhang L, Tang X S, et. al. 2015. Bivariate distribution of shear strength parameters using copulas and its impact on geotechnical system reliability. *Computers and Geotechnics*. 68: 184–195.
- Moens D & Vandepitte D. 2002. Fuzzy finite element method for frequency response function analysis of uncertain structures. *AIAA Journal*. 40(1): 126–136.
- MOST T & KNABE T. 2010. Reliability analysis of the bearing failure problem considering uncertain stochastic parameters. *Computers and Geotechnics*.37(3): 299–310.
- Sankararaman S. & Mahadevan S. 2013. Distribution type uncertainty due to sparse and imprecise data. *Mechanical System and Signal Processing*. 37: 182–198.
- Wang, X. & Cao, Z. B. 2015. Determination of the Standard Value of Geotechnical Parameters Using a Bootstrap Method. *Journal of Earthquake Engineering*. 37(S1):7–11. (in Chinese)
- X. Jiang, X. Hu, G. Liu, X. Liang, R. Wang. 2020. A generalized active subspace for dimension reduction in mixed aleatory-epistemic uncertainty quantification. *Computer Methods in Applied Mechanics and Engineering*. 370 113240.
- Z.H. Wang & G. Roger. 2021. An extended polynomial chaos expansion for PDF characterization and variation with aleatory and epistemic uncertainties. *Computer Methods in Applied Mechanics and Engineering*. 382 113854.

Numerical simulation of freeze-thaw damage deterioration of concrete in cold region

Jinyang Jiang, Yuncheng Wang & Zhiyong Liu

Jiangsu Key Laboratory for Construction Materials, Southeast University, Nanjing, China
School of Materials Science and Engineering, Southeast University, Nanjing, China

Zheng Chen

School of Civil Engineering and Architecture, Guangxi University, Nanning, China

ABSTRACT: Concrete is subject to the alternate action of positive and negative temperatures of the environment frequently in cold regions. The freeze-thaw cycle causes the spalling of concrete surface. In view of this, the investigation of the changes of fluid migration and icing in concrete during the temperature change process were carried on, the critical pore radius of frozen pore at different temperatures was determined based on the thermodynamic law. Then, considering the thermal deformation of all constituents, the deformation induced by the micro-cryosuction process and the deformation caused by the phase change of water-ice during the freeze-thaw cycle, the internal pore stress of a representative volume element is analyzed. Finally, considering the effect of the phase change of water ice, a numerical model of concrete freeze-thaw failure under the coupling of thermal-water-mechanical field is established. It is found that, influenced by the temperature, the concrete will shrink first and then expand under the freeze-thaw effect. The stress during freezing process of the concrete surface is higher than that of thawing process and the concrete will be more prone to spalling damage.

1 INTRODUCTION

The repeated freeze-thaw cycle will cause damage and destruction of concrete structures or components in cold regions, such as concrete pavement, retaining wall, bridge deck and railing, which is a major reason for the huge expenditure to repair and replace concrete structures. As one of the three main factors of concrete damage, freeze-thaw action plays an important role in the field of concrete durability research and has received extensive attentions (Mehta, 1991). With the service life of concrete structural components increasing, the safety of concrete structures is facing the challenge of freezing and thawing in many countries (Asphaug et al., 2020).

A range of achievements have been made in the study of freeze-thaw damage mechanism at present (Gong et al., 2015), among which the hydrostatic pressure theory and osmotic pressure theory (Powers and Helmuth, 1953) proposed by Powers have the highest recognition. The biggest difference between the osmotic pressure theory and the hydrostatic pressure theory lies in the migration direction of the solution in the unfrozen pores. According to the theory of hydrostatic pressure, pore solutions leave ice crystals and migrate from large pores to small ones. Furthermore, osmotic pressure theory suggests that pore solution migrates from pores to ice crystals. In general, when the water cement ratio of concrete is large, the strength is low, the age is early and the hydration degree is small, the hydrostatic pressure will lead to the freeze-thaw damage of concrete; For the concrete frozen in the environment with small water cement ratio, high strength and large salt content, the osmotic pressure will lead to the freezing and thawing damage of concrete. However, hydrostatic pressure and osmotic pressure can neither be measured by test, nor can they be accurately calculated by the formula of physical chemistry, which makes many scholars unable to reach an agreement on which of hydrostatic pressure and osmotic pressure is the main factor of

freeze-thaw damage. Although Powers himself later preferred the osmotic pressure hypothesis (Powers and Helmuth, 1953), the research results of Fagerlund (ouml and Ran, 2004), Pigeon (Pigeon and Lachance, 1981) and others supported the hydrostatic pressure hypothesis from different aspects.

The freeze-thaw damage of concrete involves complex physical changes. Although there are many researches on the freeze-thaw damage mechanism of concrete, most scholars believe that the freeze-thaw damage mechanism of concrete is closely related to its pore structural members. Since Powers put forward the theories of hydrostatic pressure and seepage pressure, there has been no more outstanding progress in the research on the mechanism of concrete freeze-thaw damage, and no unified theory has been formed. In the past twenty or thirty years, some scholars have made further quantitative research on the micro dynamic development, internal stress and strain state of concrete during icing based on the theory of Powers. However, more scholars started from the material test level to study the influence of the properties of concrete and its components and the external environment on concrete freezing and thawing, such as cooling rate, water saturation, self-healing effect, environmental humidity and minimum freezing and thawing temperature (Lee et al., 1994). Therefore, the research on the freeze-thaw damage mechanism needs to be further deepened, so as to obtain a consistent freeze-thaw damage mechanism.

Numerical simulation, as an effective research method, can obviously shorten the research cycle, save the cost and avoid the shortcomings of dispersion. Nowadays, some achievements have been made in the numerical model research on the freezing and thawing damage layer (Olsen, 1984). Among them, Olsen (Olsen, 1984) established a two-dimensional finite element calculation model that can simulate the freezing process of saturated concrete based on the differential equation of humidity and temperature, the relationship between the amount of ice and temperature, and the calculation of pore pressure; Bazant et al. (Bazant et al., 1988) proposed a mathematical model that can predict the frost resistance durability of concrete, and theoretically determined the stress and strain of freeze-thaw damaged concrete. Zuber et al. (Zuber and Marchand, 2004) proposed a two-dimensional analysis model that can predict the expansion of freeze-thaw damaged concrete. Ueda et al. (Ueda et al., 2009) established the micro constitutive model of freeze-thaw concrete based on the two-dimensional rigid body spring model, and carried out numerical analysis on the mechanical properties of freeze-thaw damaged concrete. Numerical simulation is an effect method to predict the freeze-thaw damage of concrete. Stress caused by freezing of pore liquid is the main reason of freeze-thaw damage, however, these researches paid less attention to the relationship between freeze-thaw expansion force and damage.

Based on the pore structure of concrete in cold regions, this study establishes the relationship between the saturation of pore structure and the internal expansion force of concrete during freezing and thawing. The multi-factor coupling effect is then considered to establish the multi-factor coupling numerical model of concrete under freezing and thawing. Finally, the numerical model is used to predict the stress and strain evolution of various parts of concrete under freeze-thaw cycles.

2 PORE STRUCTURE AND FREEZING

2.1 *Pore structure and pore size distribution*

As a multiphase material, concrete has complicated porosity, which depends on the material composition and the hydration of cement. Due to the change of cementitious hydration time, the total porosity of concrete can be calculated by Equation (1) (Clifton et al., 1994)

$$\phi_t = f_c \frac{w/b - 0.17\alpha}{w/b + 0.32} \quad (1)$$

where ϕ_t = total porosity of concrete, f_c = volume fraction of binder in concrete, w/b = water-to-binder ratio of concrete, α = hydration degree of cement. The hydration degree of cement is related to the w/b and hydration time.

The pore size distribution of concrete is continuous, including nano scale gel pores to millimeter scale macropores. Duan(Duan, 2009) analyzed several groups of samples in the experiment, and obtained the pore distribution function close to the actual test results through fitting:

$$\phi(r) = \frac{1 - \phi_r}{1 + \left(\frac{\log r}{2.0783}\right)^{3.8059}} \quad (2)$$

where ϕ_r = function of pore size distribution, r = pore size, nm. The pore size distribution of concrete can be obtained by combining Equations (1) and (2).

2.2 Freezing and ice saturation

The concrete is unsaturated in most cold regions, and it is difficult to achieve full saturation even if the concrete is immersed in frozen water for a long time (Liu et al., 2021a). The unsaturated concrete element in the freezing process is taken as the research object, it can be assumed that there are only three kinds of substances in its pores: ice crystal, liquid and gas. It can be considered that in the pores of a certain temperature state, these three-phase substances in concrete have the following relationships:

$$\phi = \phi_C + \phi_L + \phi_G \quad (3)$$

$$S_C + S_L + S_G = 1 \quad (4)$$

where, ϕ = porosity, ϕ_C = porosity of ice crystal, ϕ_L = porosity of liquid, ϕ_G = porosity of gas, S_C = saturation of ice crystal, S_L = saturation of liquid, S_G = saturation of gas.

The freezing of water in concrete is related to the pore size. Due to the complexity of the pore structure of cement-based materials, the process of water freezing in the pores is different from that of large volume water in nature. When ice crystals are generated, there is a certain balance in the pores, as shown in the Figure 2:

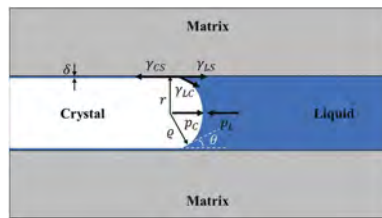


Figure 1. Ideal pore freezing at the microscopic level.

When the liquid water and ice crystals in the pores are in steady state, the ice crystal pressure p_C and liquid pressure p_L satisfies Young-Laplace equation:

$$p_C - p_L = \frac{2\gamma_{CL}}{\varrho} = \frac{2\gamma_{CL} \cos \theta}{r} \quad (5)$$

where p_C = ice crystal pressure, MPa, p_L = liquid pressure, MPa, γ_{CL} = interface energy of crystal and liquid, MPa/m, ϱ = curvature radius of ice crystal, m, r = pore radius of the cylindrical pore, m, θ = contact angle of crystal and liquid. According to the thermodynamic theory of phase transition of water in pores, the thermodynamic equilibrium of ice crystal coexisting with liquid water requires that their chemical potentials be equal (Gibbs, 1878). Restricting to the terms of higher order of magnitude, this condition implies (see for instance (Coussy, 2005))

$$p_C - p_L = \sum_m (T_m - T) \quad (6)$$

where T_m = melting temperature, K, Σ_m = melting entropy, MPa/K. As for water, $T_m \cong 273.15$ K, $\Sigma_m = 1.2$ MPa/K at 273.15 K (Petrenko and Whitworth, 2002).

Combining Equations (5) and (6), we can get the famous Gibbs-Thomson equation:

$$r = \frac{2\gamma_{CL} \cos \theta}{\Sigma_m(T_m - T)} \quad (7)$$

Generally, the ice crystal does not directly contact the hole wall, there is a layer of water film around the edge of solid matrix, with a thickness of δ . It is generally 1.0~1.2 nm. The manifestation of water ice phase transition at molecular scale is regular redistribution of water molecules. However, it is difficult to verify through experiments and simulations. It is difficult to observe the icing process in the nanoscale pores of cement-based materials even at absolute zero (Matsumoto et al., 2002). For cement-based materials, Liu et al. and Xu (Liu et al., 2021b) found through molecular dynamics that the mobility of water molecules within 0.7 nm from the wall of C-S-H gel is lower than that far away, indicating that water molecules are adsorbed by the wall of C-S-H in this range. The adsorption of water molecules on the near wall surface of C-S-H gel will affect the redistribution of water molecules. Therefore, it is assumed that the thickness of the unfrozen liquid film is consistent with the thickness of the water adsorption zone near the wall surface of the pores of cement-based materials. For cement paste, assuming that the contact angle between ice crystal and hole wall is equal to 180° , Equation (7) is:

$$r_c = \frac{2\gamma_{CL}}{\Sigma_m(T_m - T)} + \delta \quad (8)$$

where $\delta = 0.7$ nm.

According to Equation (8), the corresponding relationship between the critical pore radius and temperature can be obtained.

When the temperature drops to the freezing point, the water in the large pores freezes first. With the temperature decreasing, the ice crystals gradually grow into the small pores. For the pore size distribution curve of concrete, the corresponding frozen and unfrozen pores can be determined. The relationship between ice crystal saturation and temperature can be calculated by Equation (9):

$$S_C = \phi(r_c)/\phi_t \quad (9)$$

When the pore is completely saturated, it can be considered that the gas phase saturation is zero, then the liquid saturation can be calculated by Equation (10):

$$S_L = 1 - \phi(r_c)/\phi_t \quad (10)$$

In unsaturated concrete, the gas phase saturation of each pore is the same value, the pore phase saturation can be calculated according to Equations (4), (9) and (10).

3 VOLUME DEFORMATION AND PORE PRESSURE DURING FREEZING AND THAWING

3.1 Volume deformation

During the freezing process, the deformation and mechanical behavior of concrete are complex, including the deformation caused by temperature change, the volume deformation caused by water migration, and the volume expansion caused by water ice phase change. Poromechanics is one of the effective methods to study the mechanical behavior of cement-based materials during freezing. Select representative volume element (RVE) from porous media as Figure 2. Applying the first and second laws of thermodynamics to RVE, Clausius-Duhem equality without considering the energy dissipation of cement skeleton is obtained. When there is no external stress, the strain of RVE can be obtained as follow (Coussy and Monteiro, 2007):

$$\begin{aligned} \epsilon = & \frac{bp_L + (b_c \Sigma_m - 3\alpha_s K)\Delta T}{K} = -3 \left[\alpha_s + \frac{\phi Mb}{K + b^2 M} (S_C \alpha_C + S_L \alpha_L - \alpha_s) \Delta T \right] \\ & + \frac{M}{K + b^2 M} \left(\frac{b_c}{K_L} - \frac{b_L}{K_C} \right) \Sigma_m \Delta T + \frac{\phi Mb}{K + b^2 M} S_C \left(1 - \frac{\rho_C^0}{\rho_L^0} \right) \end{aligned} \quad (11)$$

Equation (11) contains the strain of thermal deformation of all constituents, the deformation induced by the micro-cryosuction process and the deformation caused by the phase change of water-ice during the freeze-thaw cycle.

3.2 Pore pressure

It is assumed that the cross section of pore is circular. Then the pore cross section is taken as the research object as shown in Figure 2.

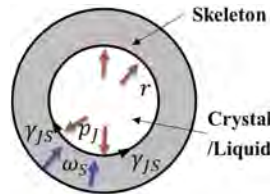


Figure 2. Stress of pore structure cross section.

For the pore structure in Figure 2, its pore diameter is r , and there may be one or two of the three substances of crystal, liquid and gas in the pore. It is assumed that the pore wall is only affected by the pressure of one substance p_j . Hydrostatic pressure and crystallization pressure of the pore can be calculated according to Equation (11):

$$\omega_S = \begin{cases} p_C = \frac{K\epsilon + b_L \Sigma_m \Delta T + 3\alpha_s K \Delta T}{b} \\ p_L = \frac{K\epsilon - b_c \Sigma_m \Delta T + 3\alpha_s K \Delta T}{b} \end{cases} \quad (12)$$

Equation (12) is the pressure on the pore wall with pore diameter r , combined with the pore diameter distribution equation (Equation (2)), and the saturation distribution of the corresponding pores (Equations (9) and (10)). The load received by the concrete during freezing and thawing can be obtained through integration:

$$p^* = \int_{r_{min}}^{r_{max}} \omega_S \frac{d\phi(r)}{dr} dr \quad (13)$$

where p^* = average pressure, r_{min} = minimum pore radius, r_{max} = maximum pore radius.

4 FREEZE-THAW DAMAGE DETERIORATION

In cold region, freeze-thaw damage of concrete is the result of the coupling of stress, thermal and humidity field.

4.1 Thermal field

A certain amount of energy is absorbed by the transformation of water ice in concrete, which is a phase change process. The Fourier quantification considering the latent heat of water ice phase change can be calculated as follows:

$$\rho C_p \frac{dT}{dt} = \nabla \cdot (\lambda \nabla T) - L \frac{dS_L}{dt} \quad (14)$$

$$\lambda = \frac{nS_L\lambda_L + nS_C\lambda_C + \lambda_s}{nS_L + nS_C + 1} \quad (15)$$

$$C_p = \frac{nS_L C_{pL} + nS_C C_{pC} + C_{ps}}{nS_L + nS_C + 1} \quad (16)$$

where C_p = specific heat capacity, λ = thermal conductivity coefficient, L = latent heat of liquid and crystal, 333.3 kJ/kg. C_p and λ can be calculated by homogenization method.

4.2 Stress field

For the volume force inside the porous medium, the equation can be written as:

$$\begin{cases} \frac{\partial \sigma'_x}{\partial x} + \frac{\partial \tau_{xy}}{\partial y} + \frac{\partial \tau_{xz}}{\partial z} - b \frac{\partial p^*}{\partial x} = 0 \\ \frac{\partial \tau_{xy}}{\partial x} + \frac{\partial \sigma'_y}{\partial y} + \frac{\partial \tau_{zy}}{\partial z} - b \frac{\partial p^*}{\partial y} = 0 \\ \frac{\partial \tau_{xz}}{\partial x} + \frac{\partial \tau_{yz}}{\partial y} + \frac{\partial \sigma'_z}{\partial z} - b \frac{\partial p^*}{\partial z} = 0 \end{cases} \quad (17)$$

4.3 Humid field

Saturation degree is one of the humidity formation in concrete, and the governing equation of saturation degree is represented by Fick's second law(Liu et al., 2021a):

$$\frac{\partial S}{\partial t} = \nabla(D_0 e^{nS} k_T \nabla S) \quad (18)$$

where $S = S_l + S_c$, D_0 = reference humid transport coefficient, m^2/s n = coefficient, and usually $n = 6$, k_T = temperature correction coefficient of humid transport coefficient which follows Arrhenius equation $k_T = \exp(U(1/T_{ref} - 1/T)/R_g)$. U = activation energy of liquid transport, kJ/mol, R_g = relative gas constant J/mol/K, T_{ref} = reference temperature, K.

4.4 Modelling

The size of concrete specimen used for simulation is 40 mm×40 mm×160 mm, one eighth of the overall structure is selected in this model. Three adjacent surfaces are set as the boundary of contact with the environment, and the other three surfaces are symmetric boundaries. Finally, the deformation and damage of the overall structure are reconstructed in a symmetrical form. The geometric model and boundary conditions of this numerical model are shown as Figure 3.

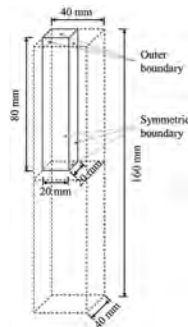


Figure 3. Geometric model and boundary conditions.

Taking a certain environment in northern China as an example, it is assumed that the daily temperature change of concrete in the cold region is -6 ~ 6 °C, which satisfies the cosine function relationship.

$$T_b(t) = \frac{T_{max} - T_{min}}{2} \cos\left(\frac{2\pi t}{t_{cycle}}\right) + \frac{T_{max} + T_{min}}{2} \quad (19)$$

where $T_b(t)$ = temperature in cold region, 267.15 K, T_{max} = maximum temperature in cold region, 299.15 K, T_{min} = minimum temperature in cold region, K, t_{cycle} = time period of a freeze-thaw cycle, 1 d.

4.5 Results of model

According to the equations in Section 3, when the ambient temperature changes, the saturation of and pore pressure of concrete change with time. Figure 4 shows the relationship between time and pore saturation at the center of the largest concrete surface and the center of concrete:

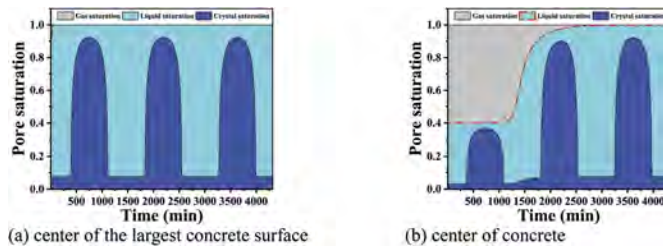


Figure 4. Pore saturation evolution.

Figure 4 shows the distribution of pore water saturation in concrete with a water-cement ratio of 0.26 in cold regions. The initial pore liquid saturation S_{l0} is 0.4, and the liquid saturation at the boundary is 1.0. Therefore, there is no gas saturation at the boundary, only the change of liquid saturation and crystal saturation occurs at the boundary. However, the obvious difference is that with the migration of moisture to the center of the concrete, the liquid saturation in the center of concrete gradually increases (as shown by the dotted line in Figure 4), and the ice crystal saturation of concrete also gradually increases under the influence of freezing and thawing. In the first cycle, the first cover of water transfer has not yet reached the center of the concrete, but in the second freeze-thaw cycle, the pore water saturation and crystal saturation in the concrete have increased. The contribution of crystallization pressure to pore pressure is greater than that of hydrostatic pressure, crystallization of the liquid in pores is the main factor of freeze-thaw damage. The same result is also reflected in the deformation of concrete as shown in Figure 6.

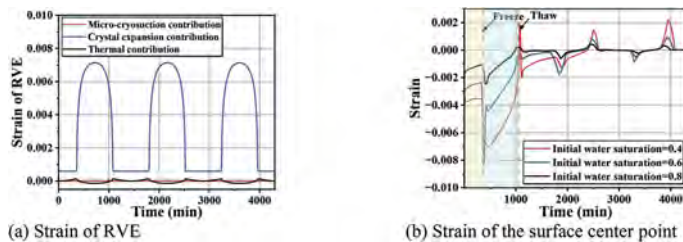


Figure 5. Evolution of strain.

Figure 5 shows that the contribution of micro-cryosuction, crystal expansion and thermal contribution to the strain of RVE is quite different. The second is the leading factor causing the volume deformation of RVE, and the thermal contribution dominates the shrinkage of concrete. Before freezing, the following interesting phenomena can be observed: the shrinkage of concrete occurs when the temperature is reduced, and the water invades the unsaturated concrete at the

same time, resulting in a certain humidity expansion of concrete. Within a short time after the temperature reaches below zero, the concrete still shrinks, which is caused by the contribution of micro-cryosuction. With the increase of the crystal saturation in the pores, the concrete gradually expands, which occurs during the whole process of the temperature below the freezing temperature. After thawing, the water in the concrete pores did not thaw at the first time due to the phase change effect of water to ice. Different concrete saturation has certain influence on the freeze-thaw strain of concrete. The freeze-thaw peak value of concrete with lower initial water saturation should greatly, due to the lower the initial water saturation, the faster the water absorption, the more obvious the frost heaving of surface concrete, and the lower the initial saturation, the later the peak value of concrete strain appears.

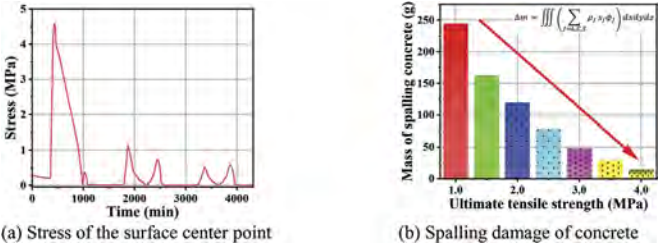


Figure 6. Stress and spalling damage.

The surface stress of the concrete is shown in Figure 6(a). There is shrinkage stress during the cooling process. With the occurrence of freezing, the stress of the concrete increases sharply, and there is another peak stress during thawing. With the continuous increase of freeze-thaw cycles, the peak stress of concrete freezing decreases and gradually equals the peak stress generated by thawing. When the concrete stress exceeds its tensile strength, it can be considered that spalling damage occurs at this part of concrete. With the increase of concrete strength, the loss of concrete freeze-thaw quality can be greatly reduced.

5 CONCLUSION

In this paper, a multi-factor coupling numerical simulation method is used to reveal how the damage of concrete occurs in cold regions. The investigation of the changes of fluid migration and icing in concrete during the temperature change process was carried on, and a numerical model of concrete freeze-thaw failure under the coupling of thermal-water-mechanical field is established. The following results can be concluded:

- (1) The ice crystal saturation of concrete is directly related to the temperature and pore size. The lower the temperature, the greater the ice content of the pores, making the pore size smaller, and the more difficult it is for the concrete to freeze.
- (2) The transport of water in unsaturated concrete will affect the frost resistance of concrete. When the initial saturation of the pore structure is low, the transport of water in the concrete will become easier. Meanwhile, the water transfer rate of concrete will be so large that a large freezing strain will form in concrete.
- (3) The stress during freezing process of the concrete surface is higher than that of thawing process and the concrete will be more prone to spalling damage. Increasing the strength of the matrix can intuitively reduce the spalling damage of the concrete.

REFERENCES

Asphaug, S. K., Kvande, T., Time, B., Peuhkuri, R. H., Kalamees, T., Johansson, P., Berardi, U. & Lohne, J. 2020. Moisture control strategies of habitable basements in cold climates. *Building and Environment*, 169.

- Bazant, Z. P., Chern, J.-C., Rosenberg, A. & Gaidis, J. 1988. Mathematical Model for Freeze-Thaw Durability of Concrete. *Journal of the American Ceramic Society*, 71, 776–783.
- Clifton, J. R., Bentz, D. P. & Ponnensheim, J. M. 1994. Sulfate Diffusion in Concrete.
- Coussy, O. 2005. Poromechanics of freezing materials. *Journal of the Mechanics & Physics of Solids*, 53, 1689–1718.
- Coussy, O. & Monteiro, P. 2007. Unsaturated poroelasticity for crystallization in pores. *Computers & Geotechnics*, 34, 279–290.
- Duan, A. 2009. *Research on Constitutive Relationship of Frozen-Thawed Concrete and Mathematical Modeling of Freeze-Thaw Process*. Doctor of Engineering, Tsinghua University.
- Gibbs, J. W. 1878. On the equilibrium of heterogeneous substances. *American Journal of Science*, S3-16, 441–458.
- Gong, F., Sicat, E., Zhang, D. & Ueda, T. 2015. Stress Analysis for Concrete Materials under Multiple Freeze-Thaw Cycles. *Journal of Advanced Concrete Technology*, 13, 124–134.
- Lee, S. K., Reddy, D. V. & Hartt, W. H. 1994. Marine Concrete Durability–Condition Survey of Certain Tensile Crack Exposure Beams at Treat Island, Maine, USA.
- Liu, Z., Wang, Y., Wang, J., Liu, C., Zhang, Y. & Jiang, J. 2021a. Experiment and simulation of chloride ion transport and binding in concrete under the coupling of diffusion and convection. *Journal of Building Engineering*, 45, 103610.
- Liu, Z., Wang, Y., Xu, D., Zang, C., Zhang, Y. & Jiang, J. 2021b. Multiple ions transport and interaction in calcium silicate hydrate gel nanopores: Effects of saturation and tortuosity. *Construction and Building Materials*, 283.
- Matsumoto, M., Saito, S. & Ohmine, I. 2002. Molecular dynamics simulation of the ice nucleation and growth process leading to water freezing. *Nature*, 416, 409.
- Mehta, P. K. 1991. Durability of concrete—fifty years of progress. *Special Publication*, 126, 1–32.
- Olsen, M. P. J. 1984. Mathematical modeling of the freezing process of concrete and aggregates. *Cement and Concrete Research*, 14, 113–122.
- Ouml & Ran, F. 2004. A service life model for internal frost damage in concrete.
- Petrenko, V. F. & Whitworth, R. W. 2002. *Physics of ice*, Physics of ice.
- Pigeon, M. & Lachance, M. 1981. Critical air void spacing factors for concretes submitted to slow freeze-thaw cycles. *Journal of the American Concrete Institute*, 78, 282–291.
- Powers, T. C. & Helmuth, R. A. 1953. Theory of Volume Changes in Hardened Portland Cement Paste During Freezing. *Highway Research Board Proceedings*.
- Ueda, T., Hasan, M., Nagai, K., Sato, Y. & Wang, L. 2009. Mesoscale Simulation of Influence of Frost Damage on Mechanical Properties of Concrete. *Journal of Materials in Civil Engineering*, 21, 244–252.
- Zuber, B. & Marchand, J. 2004. Predicting the volume instability of hydrated cement systems upon freezing using poro-mechanics and local phase equilibria. *Materials and Structures*, 37, 257–270.

Smart aggregate-based automated concrete stress monitoring via deep learning of impedance signals

J.T. Kim, Q.B. Ta, Q.Q. Pham & N.L. Pham
Pukyong National University, Busan, Korea

T.C. Huynh
Duy Tan University, Da Nang, Vietnam

ABSTRACT: A 1-D CNN regression model is designed for autonomously monitoring stress in concrete specimens utilizing the raw impedance signatures of smart aggregate (SA) sensors. The fundamental theory of the impedance measurement model of SA is presented. Next, the compression experiment on SA-embedded concrete cylinders is carried out, and the impedance signals of the cylinders are recorded under different stress levels. The 1-D CNN regression model learned the impedance signals for predicting the concrete stress is constructed. Then, the average performance of the proposed model is verified via the 10-fold cross-validation method. Consequently, the feasibility of the developed model is investigated under the effect of noises in signals and reduction of the input training data.

1 INTRODUCTION

Recently, the convolutional neural network (CNN)-based deep learning techniques have been considered as an efficient approach for assessing damage conditions of civil infrastructures (Yuan et al. 2020, Abdeljaber et al. 2018, Wang et al. 2021, Abdeljaber et al. 2017, Ta et al. 2022, Azimi & Pekcan 2019, Ta & Kim 2020, Huynh 2021, Ta et al. 2022, Huynh et al. 2019). In comparison with traditional multi-step damage detection methods (Yuan et al. 2020), CNN-based approaches can extract damage sensitivity and predict damage occurrence in one procedure (Abdeljaber et al. 2018, Wang et al. 2021); besides, the CNN has the ability to learn damage features from raw signals, which considerably decreases initial processing workload (Abdeljaber et al. 2017).

Several studies have shown the effectiveness of CNN for impedance response-based damage assessment. For example, Oliveira et al. 2018 applied a CNN based deep learning algorithm to detect damage in an aluminum plate based on changes in impedance responses. The algorithm was able to accurately detect and locate damage in the plate. Nguyen et al. 2021 proposed a 1-D CNN model learnt impedance signatures for classifying different damage conditions of a smart PZT interface. In the following year, Nguyen et al. 2022 developed a novel 1-D CNN-based autonomous feature extraction model for impedance-based PS force prediction. Their experimental verification indicates that the proposed model significantly outperforms the traditional approach using manual feature extraction. Also, the applications of CNN models learned impedance signals for damage identification have been extensively studied in various structures (Zheng et al. 2022, Li et al. 2023, Ai & Cheng 2023, Rezende et al. 2020). However, the applicability of the 1-D CNN regression model for stress monitoring inside concrete specimens using smart aggregate (SA) has not been investigated.

In this study, a 1-D CNN regression model is developed for autonomously predicting stress in concrete structures utilizing the raw impedance signatures of SA sensors. The fundamental theory of the impedance measurement model of SA is presented. The compression experiment on SA-embedded concrete cylinders is carried out, and the impedance signals of the cylinders are recorded

under different stress levels. A 1-D CNN regression model learned the impedance signals for evaluating the concrete stress is constructed. The feasibility of the developed model for predicting stress under the effect of noises in signals and reduction of the input training data is also investigated.

2 SMART AGGREGATE-BASED IMPEDANCE MEASUREMENT

Figure 1 shows a model of SA-based impedance monitoring for concrete structures. The SA is fabricated by embedding a protected PZT sensor in a small concrete block, and it is installed in an inspected structure to obtain impedance signals via the interaction between the SA and the structure (see Figure 1a). The coupling motions of the coated layer, the concrete block, and the monitored structure could be demonstrated as a 3-degrees of freedom (3-DOF) impedance model (Huynh et al. 2020, Pham et al. 2021) (see Figure 1b). The electromechanical impedance $Z(\omega)$ is computed using the SM impedance of the PZT sensor and that of the SA-host structure:

$$Z(\omega) = \left\{ j\omega A_p \left[\hat{\epsilon}_{33}^T - \frac{1}{Z_p(\omega)/Z_s(\omega) + 1} d_{31}^2 \hat{Y}_{11}^E \right] \right\}^{-1} \quad (1)$$

where A_p is the geometric constants of the PZT patch; $\hat{\epsilon}_{33}^T$ is the complex dielectric constant of at zero stress; $Z_p(\omega)$ is the structural-mechanical (SM) impedance of the PZT; $Z_s(\omega)$ is the SM impedance of the protective layer, concrete block, and host structure; d_{31} is piezoelectric constant in one-direction at zero stress; \hat{Y}_{11}^E denotes complex Young's modulus of the PZT at zero electric field.

As shown in Equation (1), the real impedance $Z(\omega)$ is the function of the SM impedance of the PZT patch, the SA, and the host structure. Once the PZT patch has no changes in its characteristics, thus, any structural changes can lead to a change in the measured impedance signatures.

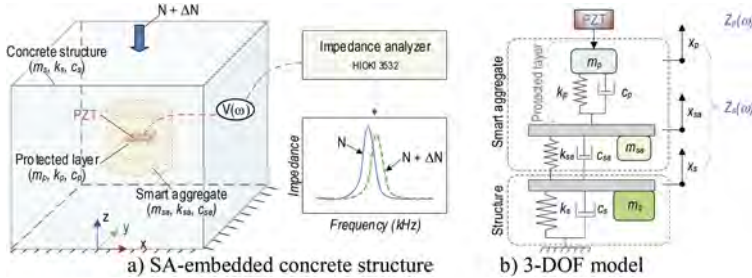


Figure 1. Model of SA-based impedance monitoring for concrete structure.

3 COMPRESSION EXPERIMENT ON SA-EMBEDDED CONCRETE CYLINDER

3.1 Fabrication of SA

Figure 2 shows the fabrication of the SA. A PZT 5A patch soldered with electric wires was protected by an epoxy layer (see Figure 2a). Then, the coated PZT was embedded in the center of a PVC mold during concrete casting to form a SA sensor (see Figure 2b). The concrete mixture used for the monitored structures (without coarse aggregates), was employed for the SA's construction (see Table 1). The SA samples are shown in Figure 2c. The compressive strength of concrete after 28 days was 25.3 MPa, which was achieved via uniaxial compressive tests.

3.2 Fabrication of SA-embedded concrete cylinder

Figure 3 shows the fabrication of a concrete cylinder embedded with the SA sensor. The SA was localized at the center of a standard cylinder mold having a size of 100×200 mm (see Figure 3a). The distance between the center of the SA and the top and bottom surfaces of the mold was

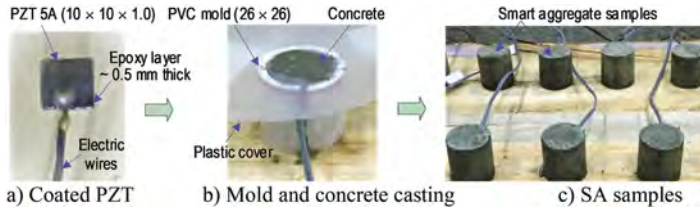


Figure 2. SA's fabrication (dimension in mm).

Table 1. Concrete mixture for SA sensor*.

Material for 1 m ³	Mass (kg)
Sand	710
Coarse aggregate (D _{max} 25)**	948
Cement	425
Water (liter)	170

* Concrete mixture was used for concrete cylinder specimens in next section.

** SA sensor was constructed without coarse aggregate.

about 100 mm. Figure 3b shows the casting process for the concrete cylinder. The concrete mixture was selected as listed in Table 1. After 28 days of the curing process, three concrete cylinders (Cylinders 1-3) embedded with three SAs (SAs 1-3), respectively, were used for the impedance test.

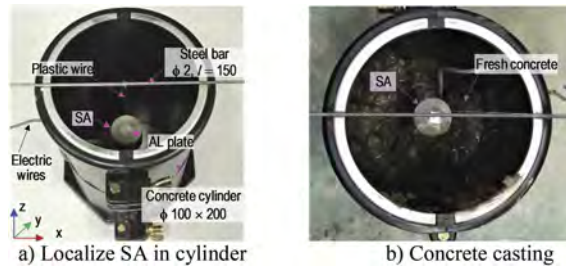


Figure 3. Fabrication of SA-embedded concrete cylinder (dimension in mm).

3.3 Experimental setup for impedance measurement under compression

Figure 4a shows an impedance testing setup of the concrete cylinders (i.e., Cylinders 1-3) embedded with SAs 1-3, respectively, under compression forces. As shown in the figure, the concrete samples were placed inside a load frame of an MTS system. A load cell with a capacity of 500 kN was used to monitor the real compression force. In the experiment, a wired impedance analyzer HIOKI 3532 was used to obtain impedance responses from the SA sensors corresponding to each loading case. The laboratory temperature was also monitored via Kyowa EDX-100A.

Figure 4b shows twelve loading cases, $S_1 = 0$ MPa to $S_{12} = 22.32$ MPa with an interval of 2.03 MPa, which were applied on the cylinders. The applied stresses were gradually increased in an automatic loading procedure with a loading speed of $0.0113 \text{ MPa.s}^{-1}$. The amplitude of a harmonic excitation was set at 1 V to obtain impedance signatures from the SAs (i.e., SAs 1-3). The impedance responses were swept in the frequency range from 100 kHz to 600 kHz with 501 points. Four ensembles of the signals were recorded in each loading. The monitored temperature varied around a variation of 1°C.

3.4 Impedance signals of SAs

Figure 5 shows impedance signals (in the range of 100 - 600 kHz) of SAs 1-3, respectively, under twelve loading cases (i.e., S_1 to S_{12}). Three resonant peaks, Peaks 1-3, were observed. Peak 1 is

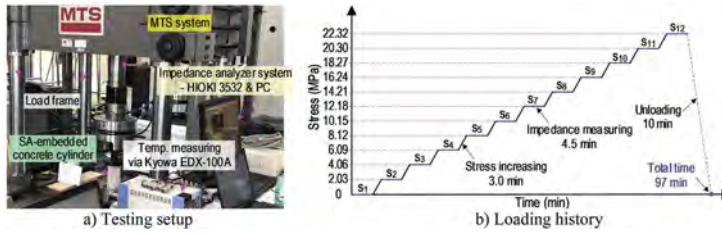


Figure 4. Testing setup for impedance measuring from SA-embedded cylinder under compression.

about 200 kHz, Peak 2 is about 270 kHz, and Peak 3 is around 500 kHz. The signals of SAs 1-3 were slightly changed with respect to each increasing applied stress, but variations were slight.

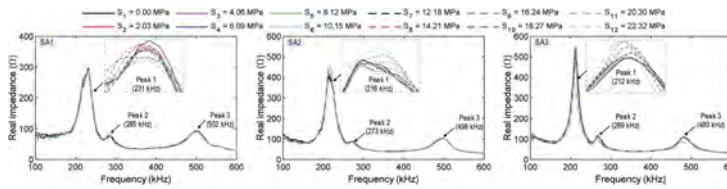


Figure 5. Impedance signals of SAs 1-3 under twelve applied stresses.

4 IMPEDANCE-BASED STRESS MONITORING USING 1-D CNN DEEP LEARNING

4.1 1-D CNN model

As shown in Figure 6, the schematic of 1-D CNN deep learning consists of two phases: 1) data acquisition and preparation and 2) 1-D CNN training and evaluation. In the first phase, a K-fold cross-validation is adopted to classify the stored datasets into training and validation datasets. In the second phase, a series of deep learning stages are performed to identify the 1-D CNN regression model. The impedance datasets and their corresponding stress levels are utilized for training the 1-D CNN model. For a stress level trained in the 1-D CNN model, the validation datasets are used to evaluate the accuracy of stress prediction.

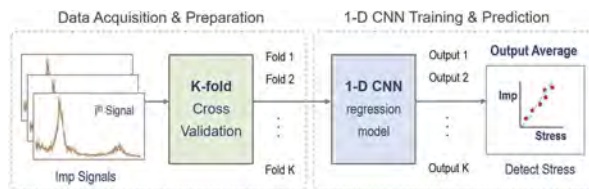


Figure 6. Schematic of 1-D CNN deep learning.

Figure 7 illustrates a typical 1-D CNN architecture with three counterparts called input, output, and hidden layers. The 1-D CNN regression model takes 1 x 501 series raw signal as input, then returns output, which can be used for evaluating and predicting stress in concrete structures.

4.2 Stress monitoring of SA-embedded concrete cylinder by 1-D CNN model

4.2.1 Data preparation for SA sensors in concrete cylinders

This study uses a specific K-Fold Cross Validation technique called stratified shuffle-split to divide data from dataset. Of the twelve impedance signals (four ensembles per SA sensor)

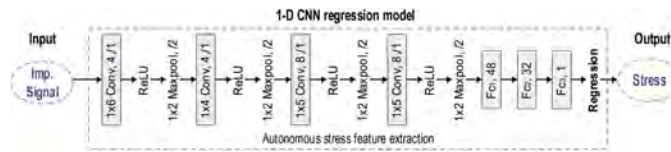


Figure 7. Designed architecture of 1-D CNN using raw impedance signals of smart aggregate.

measured at each compressive stress stage, 75 % were randomly assigned to the training fold data set, and the remaining 25 % were assigned to the evaluation fold data set. Repeat this procedure K(10) times and create K(10) fold data sets. In summary, there are 144 signals in the impedance data set, of which 108 and 36 signals are used for 1-D CNN training and validation, respectively.

4.2.2 Training and evaluation of 1-D CNN regression model

Figure 8 shows the typical training process of 1-D CNN regression model using the training fold data sets as input. The loss and root-mean-square error (RMSE) values of training and validation for fold 4 were plotted because this fold produced the best predictive model. In general, the loss and RMSE values show that the proposed 1-D CNN regression model has a good performance. Figure 9 shows the performance of the 1-D CNN regression model trained with three presentative fold datasets. The smaller the RMSE index value, the higher the prediction accuracy. Figure 10 shows the average performance of the trained 1-D CNN regression model. Figure 10a presents the RMSE values of 10 test folds ranging from 0.85 to 2.14, with an average of 1.38 MPa. Figure 10b emphasizes the relative between the average predicted stresses and actual stresses. Note that the average predicted stress results in each stress level were quite consistent with the actual ones. Compared to the stress prediction result of the 1-D CNN model trained with each single-fold dataset, the average stress prediction result of 10 folds was more accurate.

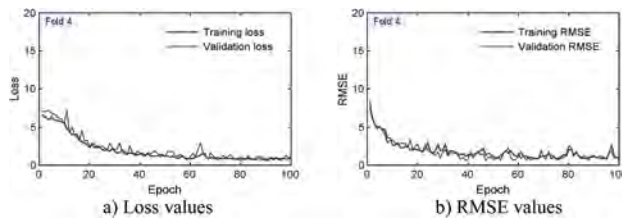


Figure 8. Loss and RMSE values of 1-D CNN regression model after 100 epochs.

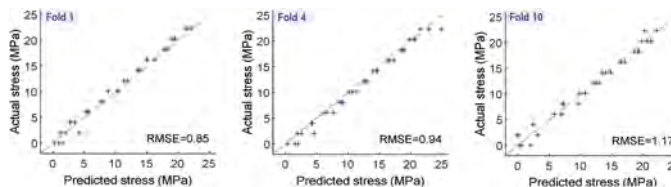


Figure 9. Evaluation results of 1-D CNN regression model.

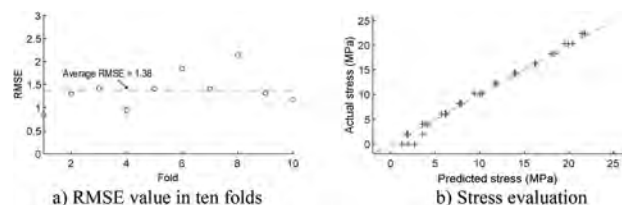


Figure 10. Average performance of trained 1-D CNN regression model.

5 CONCRETE STRESS PREDICTION USING 1D CNN REGRESSION MODEL

5.1 Databank and training 1-D CNN regression model

5.1.1 Noise-contaminated databank

The whole impedance signals of SA 2 under twelve stress levels were used to build a databank for training and testing the proposed model. These signals were injected with noises to simulate realistic circumstances. Four ensembles of signals were repeatedly measured for each stress level. First three impedance signals were randomly noised by adding a standard deviation of 0%, 1%, 2%, 3%, 4%, and 5% of the signal amplitude. A total of 216 signals were used to train the 1-D CNN model. Remaining ones were injected with different levels of noise ranging from 1% to 16% (interval of 1%). A total of 1932 signals were used for testing the model. Adding such noises to signals could help to test the reliability of 1-D CNN model on unseen test data. Examples of impedance signals with and without noise injections at the stress level S_1 are shown in Figure 11.

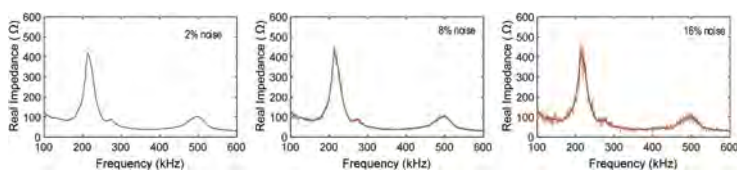


Figure 11. Adding noises to impedance signals for data argumentation (stress level S_1).

5.1.2 Training 1-D CNN model with noise-injected datasets

Figure 12 shows loss and RMSE values after 100 epochs of the 1-D CNN regression model using the training dataset. Generally, the training loss and training RMSE were reduced, while validation loss and validation RMSE fluctuated during 100 epochs.

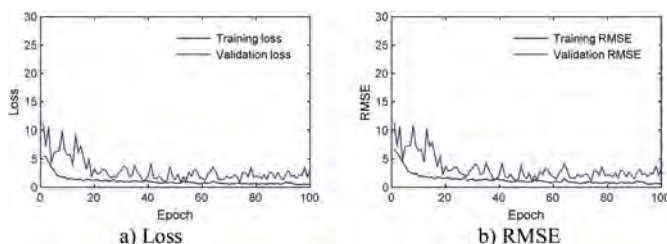


Figure 12. Loss and RMSE values of 1-D CNN regression model after 100 epochs.

5.2 Prediction for untrained levels of noises

Figure 13 shows three typical results of investigating the effects of noises on the accuracy of the model. It can be observed that the accuracy of the model in predicting stress decreased as the levels of noise increased. The relationship between the RMSE index and noise levels is illustrated in Figure 14. Note that the RMSE values increased with increased percentages of noise.

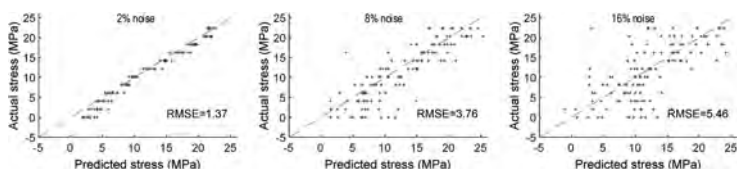


Figure 13. Effect of noise on the accuracy of 1-D CNN regression model.

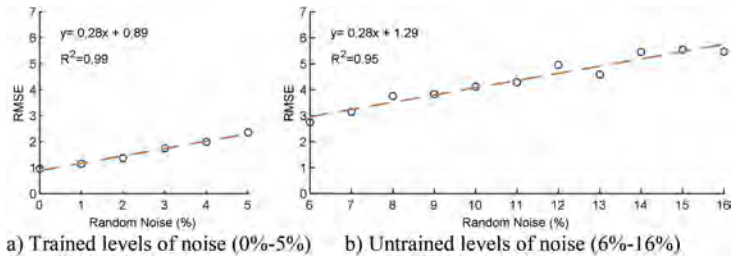


Figure 14. Relation between RMSE and noise levels.

5.3 Prediction for untrained stresses in concrete cylinder

5.3.1 Untrained-stresses databank

The robustness of the 1-D CNN regression model was investigated for stress monitoring using limited impedance data. The 1-D CNN regression model was trained by using the untrained-stress databank. The untrained-stress databank was generated by excluding impedance datasets corresponding to a few stress levels. Then the performance of the 1-D CNN model was evaluated for the untrained stress levels. The 216 impedance signals were utilized to build a training dataset. One untrained-stress dataset was designed. The untrained-stress dataset (198 signals) excluded stress level S4 from the 216 impedance signals. The testing dataset (untrained-stress datasets) was 216 impedance signals measured, completing all stress levels.

5.3.2 Train 1-D CNN regression model using untrained-stress databank

Figure 15 shows the training process of the 1-D CNN regression model using the designed dataset. It is observed that the training loss and training RMSE gradually converged, while validation and RMSE loss fluctuated during the whole training process (100th epoch).

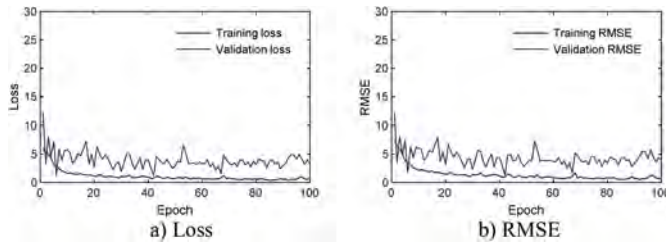


Figure 15. Training 1-D CNN regression model using training dataset 1 (excluded S4).

5.3.3 Prediction results for untrained concrete stresses

Figure 16 plots the results of predicted stresses versus actual stresses. It is observed that there was only a small variation in RMSE values between the cases of the excluded and included stress levels. The results demonstrated that the retrained model was capable of predicting stress values even when a stress level was not trained.

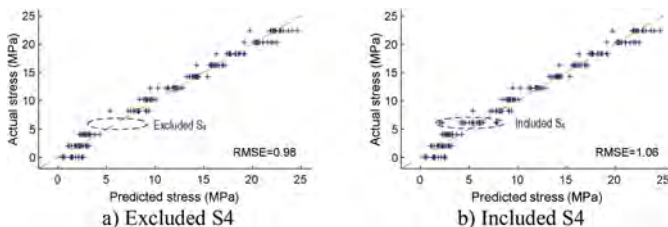


Figure 16. Stress prediction on the training dataset 1 (Std: 0-5%).

6 CONCLUSION

In this study, the 1-D CNN regression model was developed for autonomously predicting stress in concrete structures utilizing the raw impedance signals of SA sensors. The fundamental theory of the impedance measurement model of SA was presented. The compression experiment on SA-embedded concrete cylinders was carried out, and impedance signals of cylinders were recorded under different stress levels. The 1-D CNN regression model learned impedance signals for evaluating the concrete stress was constructed. The feasibility of developed model for predicting stress under the effect of noises in signals and reduction of the input training data was also investigated.

REFERENCES

- Abdeljaber, O., Avci, O., Kiranyaz, S., Gabbouj, M. & Inman, D.J. 2017. Real-time vibration-based structural damage detection using one-dimensional convolutional neural networks. *Journal of Sound and Vibration*, 388: 154–170.
- Abdeljaber, O., Avci, O., Kiranyaz, M.S., Boashash, B., Sodano, H. & Inman, D.J. 2018. 1-D CNNs for structural damage detection: Verification on a structural health monitoring benchmark data. *Neuro-computing*, 275: 1308–1317.
- Ai, D. & Cheng, J. 2023. A deep learning approach for electromechanical impedance based concrete structural damage quantification using two-dimensional convolutional neural network. *Mechanical Systems and Signal Processing*, 183.
- Azimi, M. & Pekcan, G. 2019. Structural health monitoring using extremely compressed data through deep learning. *Computer-Aided Civil and Infrastructure Engineering*, 35(6): 597–614.
- De Oliveira, M.A., Monteiro, A.V. & Vieira Filho, J. 2018. A New Structural Health Monitoring Strategy Based on PZT Sensors and Convolutional Neural Network. *Sensors (Basel)*, 18(9).
- De Rezende, S.W.F., de Moura, J.d.R.V., Neto, R.M.F., Gallo, C.A. & Steffen, V. 2020. Convolutional neural network and impedance-based SHM applied to damage detection. *Engineering Research Express*, 2(3).
- Huynh, T.-C. 2021. Vision-based autonomous bolt-looseness detection method for splice connections: Design, lab-scale evaluation, and field application. *Automation in Construction*, 124.
- Huynh, T.C., Park, J.H., Jung, H.J. & Kim, J.-T. 2019. Quasi-autonomous bolt-loosening detection method using vision-based deep learning and image processing. *Automation in Construction*, 105: 102844.
- Huynh, T.C., Nguyen, T.D., Ho, D.D., Dang, N.L. & Kim, J.T. 2020. Sensor Fault Diagnosis for Impedance Monitoring Using a Piezoelectric-Based Smart Interface Technique. *Sensors (Basel)*, 20(2).
- Li, G., Luo, M., Huang, J. & Li, W. 2023. Early-age concrete strength monitoring using smart aggregate based on electromechanical impedance and machine learning. *Mechanical Systems and Signal Processing*, 186.
- Nguyen, T.-T., Kim, J.T., Ta, Q.B., Ho, D.D., Phan, T.T.V. & Huynh, T.C. 2021. Deep learning-based functional assessment of piezoelectric-based smart interface under various degradations. *Smart Structures and Systems*, 28(1): 69–87.
- Nguyen, T.-T., Tuong Vy Phan, T., Ho, D.-D., Man Singh Pradhan, A. & Huynh, T.-C. 2022. Deep learning-based autonomous damage-sensitive feature extraction for impedance-based prestress monitoring. *Engineering Structures*, 259.
- Pham, Q.Q., Dang, N.L. & Kim, J.T. 2021. Piezoelectric Sensor-Embedded Smart Rock for Damage Monitoring in a Prestressed Anchorage Zone. *Sensors (Basel)*, 21(2).
- Ta, Q.-B., Huynh, T.-C., Pham, Q.-Q. & Kim, J.-T. 2022. Corroded Bolt Identification Using Mask Region-Based Deep Learning Trained on Synthesized Data. *Sensors*, 22(9).
- Ta, Q.-B., Dang, N.-L., Kim, Y.-C., Kam, H.-D. & Kim, J.-T. 2022. Semantic crack-image identification framework for steel structures using atrous convolution-based Deeplabv3+ Network. *Smart Struct. Syst*, 30(1): 17–34.
- Ta, Q.B. & Kim, J.T. 2020. Monitoring of corroded and loosened bolts in steel structures via deep learning and Hough transforms. *Sensors (Basel)*, 20(23).
- Wang, X., Zhang, X.a. & Shahzad, M.M. 2021. A novel structural damage identification scheme based on deep learning framework. *Structures*, 29: 1537–1549.
- Yuan, F.-G., Zargar, S.A., Chen, Q. & Wang, S. 2020. Machine learning for structural health monitoring: challenges and opportunities. *Sensors and smart structures technologies for civil, mechanical, aerospace systems*, 11379: 1137903.
- Zheng, D., Li, Z., Du, Z., Ma, Y., Zhang, L., Du, C., Li, Z., Cui, L., Zhang, L., Xuan, X. & Deng, X. 2022. Design of Capacitance and Impedance Dual-Parameters Planar Electrode Sensor for Thin Ice Detection of Aircraft Wings. *IEEE Sensors Journal*, 22(11): 11006–11015.



Taylor & Francis

Taylor & Francis Group

<http://taylorandfrancis.com>

*MS14: Coupled chemical, physical, and mechanical processes
in cementitious materials for short- and long-term behavior
of R.C. and P.C. structures*

Organizers: G. Di Luzio, R. Wan-Wendner, M. Alnaggar & J. Vorel



Taylor & Francis

Taylor & Francis Group

<http://taylorandfrancis.com>

LCA assessment related to the evolution of the earthquake performance of a strategic structure

D. di Summa

Ghent University, Ghent, Belgium
Politecnico di Milano, Milan, Italy

A. Marcucci, M. Nicolò, F. Martignoni, A. Carrassi & L. Ferrara

Politecnico di Milano, Milan, Italy

N. De Belie

Ghent University, Ghent, Belgium

ABSTRACT: Several buildings and infrastructures, located in urban areas, are identified as strategic in the case of an earthquake event. This is the case of a water treatment plant which is currently built in Genoa, Italy, and which has been assessed for the scope of this research. Since the structure has been designed following the seismic design prescriptions, this work aims to provide a preliminary assessment of how the degradation mechanisms do affect its earthquake response. To this purpose, both chloride attack and carbonation are taken into account as main degradation mechanisms. Moreover, due to the importance of the water treatment plant, to develop a realistic Life Cycle Assessment (LCA) analysis, the earthquake resistance of the structure and its evolution over time as a function of the aforesaid degradation mechanisms, have been accounted as Serviceability Limit State to estimate the frequency of the maintenance activities needed in a timeframe of 100 years.

1 INTRODUCTION

Nowadays, the large use of concrete within the construction sector outlines the need to investigate in deep the degradation phenomena that occur over the time in which a structure, an infrastructure or, simply, a structural element is designed to ensure an adequate serviceability. This, also in view of the environmental, economic and social consequences associated to the production of cement-based materials in general when not characterized by an appropriate durability. As an example, not only the production of all concrete components, including Portland Cement (PC) that is responsible for 2 billion tons/year of CO₂ (Szabo et al., 2006) (Turner & Collins, 2013)(Ouellet-Plamondon & Habert, 2015)(McLellan et al., 2011), must be taken into consideration, but also the maintenance activities that could contribute to 55% of the CO₂ emissions generated from the construction phase until the dismissal of a structure (Kumanayake & Luo, 2018). These data, when referred to the worldwide total production of concrete per year, clearly highlight the magnitude of the overall sustainability issue that, as stated by Huntzinger and Eatmon (2008) can be at local, global or regional scale. To overcome the latter, some studies focused their attention, in the recent past, on the development of advanced cement based materials such as the self-healing ones, able to restore their integrity in the case of a crack creation (Shields et al., 2021)(di Summa et al., 2022)(Van den heede et al., 2018)(Cappellesso et al., 2023). Moreover, the behaviour of concrete when exposed to aggressive environmental scenarios (e.g. carbonation or chlorides penetration) generated an increasing interest also because of the market awareness regarding the need of having long durability, reduced maintenance costs and adequate environmental performance. In this framework, the scope of this investigation is to address the effects that certain aggressive

degradation phenomena have on the structural performance of a construction in the event of an earthquake. More specifically, the largest water treatment plant within Northern Europe, identified as a strategic structure, has been assessed. Moreover, the moment when a specific damage affects the structural performance is taken into consideration as serviceability limit state in correspondence of which the maintenance activities have to be carried out to restore the normal functionality. Thus, the Life Cycle Assessment (LCA) methodology has been employed to assess the environmental performance within the defined service life (SL). In line with other researches (Kannikachalam et al., 2022)(di Summa et al., 2022)(Al-Obaidi et al., 2021)(Al-Obaidi et al.2022), the idea is to propose an approach that can help the decision process of the designers, accounting for, a priori, the overall sustainability performance due to the interaction of the material with the surrounding environment. Such approach could be then replicated, in the future, for strategic structures similar to the one here assessed.

2 DESCRIPTION OF THE CASE STUDY AND DEGRADATION MECHANISMS

2.1 Description of the case study

The water treatment structure is located in Genoa, northern Italy, within the port area and aimed at serving a population of 250,000 inhabitants. It has been identified as a strategic structure in the case of an earthquake event, reason why a SL equal to 100 years has been taken into consideration for the following analysis. A frame structure, with beams which are sometimes eccentric in relation to the corresponding pillars, characterizes the ground level. The beams have a cross section equal to 0.70m x 0.70m or 0.70m x 1.00m, the pillars of 0.70m x 0.70m while the walls of the basins at the first floor have a thickness varying between 0.30m and 0.25m. Figure 1 gives an overview of the layout of the entire structure. To have a complete knowledge of the structure, the behaviour in the event of an earthquake has been assessed prior to estimating the durability of the construction within the SL. This was possible by carrying out a modal analysis in which the vibration response has been identified for each element of the structure. Figure 1 also details a vibration example in which it is possible to highlight how the overall behaviour is not uniform. The analysis hereinafter presented is focused on the 26 pillars of the structure. The pillars are characterized by 24 Φ 24 steel reinforcement bars equally located along the 4 sides. They are subjected to a biaxial compression and bending with an average axial force of 2,300 kN and the highest value of the acting bending moment (M_{Ed}) is equal to 1200 kNm. Figure 2 details the cross section of the pillars besides the M-N interaction diagrams due to the eccentric axial force. The structure being located at the seaside and being characterized by an XS1 exposure class, both the carbonation and the chlorides penetration phenomena have been taken into consideration. With regard to the concrete, the structure has been realized by employing ordinary reinforced concrete (ORC) and ORC containing crystalline admixture (1% by mass of cement). The latter was added to enhance not only the self-healing properties but also to reduce the permeability of the concrete, avoiding the ingress of harmful substances. Even though the pillars have been realized without the addition of the crystalline admixture (CA), hereinafter two cases are assessed. The first one, corresponding to the reality, with the pillars made with ORC (referred as P_ORC) and the second one, purely hypothetical, in which they are made with the addition of the crystalline admixture (referred as P_CA).

2.2 Carbonation

To estimate the carbonation penetration, 12 cube specimens (150mm x 150mm) have been cast during the structure casting phases (March 2022). Half of the specimens were realized with the mix design of P_ORC while the remaining ones with the one of P_CA. With regard to the carbonation tests, after being exposed to open air within the worksite for 3, 6 and 9 months, as shown in Figure 3 each specimen was split into two halves and each half was then divided in two equal parts to have two perpendicular areas on which phenolphthalein was then sprayed. Table 1 indicates the average penetration depth achieved after 3 months and 6 months respectively and it is also possible to observe an overall better performance of P_CA at both ages.

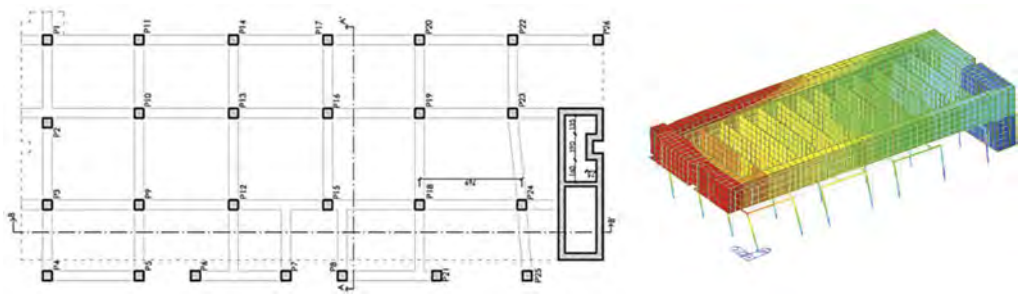


Figure 1. Layout of the structure (left) and the vibration response (right) in which the color red represents the parts more vulnerable to vibration.

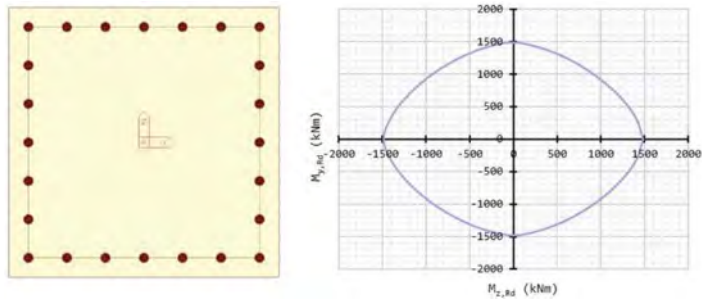


Figure 2. Cross section of the pillars (left) and biaxial interaction diagram due to an eccentric axial force.

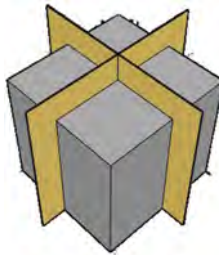


Figure 3. Example of the division of the specimen to spray the phenolphthalein.

Table 1. Carbonation depth (mm), Average and standard deviation after 3, 6 and 9 months.

	Average	SD
P_ORC (3 months)	3.8	0.60
P_CA (3 months)	1.72	0.35
P_ORC (6 months)	3.92	0.33
P_CA (6 months)	2.54	0.53
P_ORC (9 months)	4.3	0.75
P_CA (9 months)	3.03	0.25

The values presented in Table 1 have been then employed to predict the evolution of the carbonation over the SL of the structure through Equation 1 where x_c represents the depth of the carbonation, t the time expressed in years, $W(t)$ a weather function used to consider the time in which the concrete is wet and k is the carbonation coefficient measured in $\text{mm}/(\text{years})^{0.5}$. The latter depends

on several factors such as water to cement ratio, relative humidity and CO₂ concentration. While $W(t)$ has been assumed as equal to 1 due to the fact that the pillars are inside a prefabricated structure and, then, they are not wet, k has been determined by employing a non-linear regression analysis for Equation 1 and using the values reported in Table 1. The values obtained were 6.23 mm/(years)^{0.5} for P_ORC and 3.53 mm/(years)^{0.5} for P_CA. Thus, it was then possible to calculate the time needed for the carbonation process to reach the reinforcement bar surfaces located at a depth of 0.40mm according to the standards prescriptions for structures exposed to a XS1 environment. This corresponded to 41.3 years for P_ORC and 128.1 years for P_CA.

$$x_c = W(t)k\sqrt{t} \quad (1)$$

The result of P_CA being even higher than the accounted SL, the reduction of the diameter of the steel reinforcement bars have been estimated only for P_ORC by employing Equation 2 in which ϕ_0 represents the initial diameter of the reinforcement (mm), t the time (years), t_n is the time that the carbonation needs to reach the steel bars surface. Moreover, j is a constant equal to 0.0116 for the case of the steel and i_{corr} represents the power intensity in $\mu\text{A}/\text{cm}^2$ assumed as equal to 0.5 $\mu\text{A}/\text{cm}^2$ for the scope of this analysis according to (Bertolini & Pedferri, 1996).

$$\phi(t) = \phi_0 - 2i_{corr}j(t - t_n) \quad (2)$$

By employing Equation 2 it has been possible to estimate for P_ORC, a reduction of the cross section of each bar equal to 5.60% at the time of 100 years. These results are reported in Figure 3 which also contains the behaviour that the bars would have had in the case of P_CA. Then, following the model proposed by Maaddawy (El Maaddawy & Soudky, 2006) the time needed to form the first cracks because of the expansion products of the corrosion has been calculated. Such phenomenon is dictated by the thickness of the concrete cover, the diameter and the expansion volume of the steel bars, the elastic modulus of concrete and the thickness of the porous layer between concrete and steel. It was then estimated that the complete detachment of the concrete cover happens 11 years after the corrosion onset, in correspondence of the obtainment of 1 mm cracks, meaning after 52 years in total for P_ORC. Nevertheless, it must be specified that these results have to be considered as optimistic predictions since they are referring to a non-cracked state which is practically never achievable in the reality.

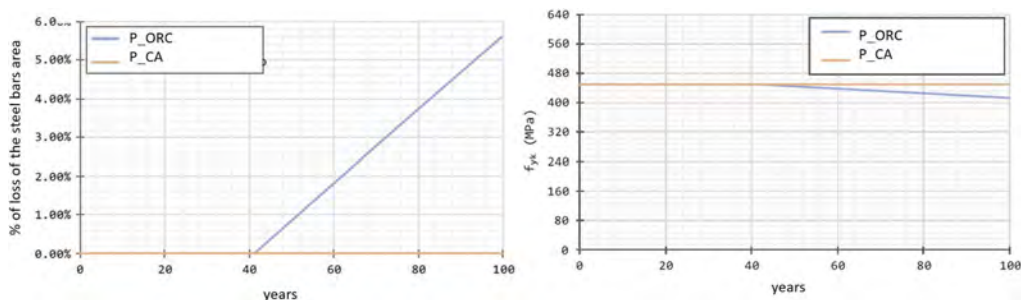


Figure 4. Loss of the cross section of the reinforcement bars in percentage (left) and decrease of steel tensile strength (F_{yk}).

2.3 Chlorides induced corrosion

As for the carbonation tests, 12 cubic specimens (150 mm x 150 mm) were realized during the casting procedures and were then split along two perpendicular areas to spray the 0.1-N AgNO₃ solution and check the chlorides penetration after 3 and 6 months of exposure to open air. Also in this case the results have shown a better performance for the case of the mix design of P_CA. Table 2 reports the value observed for the chloride penetration.

Table 2. Chlorides depth (mm), Average and standard deviation after 3, 6 and 9 months.

	Average	SD
P_ORC (3 months)	1.24	0.45
P_CA (3 months)	0.97	0.34
P_ORC (6 months)	2.10	0.81
P_CA (6 months)	1.13	0.22
P_ORC (9 months)	3.03	0.57
P_CA (9 months)	2.10	0.64

The values presented in Table 2 have then been used to calculate the apparent chloride diffusion coefficient (D_{app}) which, as already highlighted in other works (di Summa et al., 2022) (Cappellesso et al., 2023) (Kannikachalam et al., 2023) is a key parameter to predict the penetration of the chlorides within a certain time. Thus, considering a critical chloride content equal to 0.11% by weight of concrete as in (Stipanovic Oslakovic et. al, 2008), it has been possible to calculate a value of $9 \times 10^{-13} \text{ m}^2/\text{s}$ and $3.4 \times 10^{-13} \text{ m}^2/\text{s}$ for P_ORC and P_CA respectively by employing the second Fick's law. Figure 5 provides an overview of the chloride content for both P_ORC and P_CA at the age of 20, 40, 60, 100, 140 and 180 years for which both Cs and D_{app} have been assumed as constant over the time for the scope of these calculations. As it is possible to observe, the latter is reached, in correspondence of the reinforcement bars surface (namely 40 mm as the designed concrete cover) after 137 years for P_ORC and after more than 300 years for the case of P_CA. These years correspond to the corrosion initiation time. Moreover, considering that these values are based on the results obtained from the experimental campaign conducted on the uncracked state the influence of the cracks on the D_{app} value has also been checked. More specifically, considering a crack opening equal to 0.2 mm as suggested for the assumed environmental condition in the Eurocode and employing the model suggested by Wang et al., (Wang et al., 2022) an initiation time equal to 82 years for P_ORC and 135 years for P_CA was then calculated. Both periods are much higher than the ones previously estimated for the carbonation.

2.4 Structural performances of the case study subjected to the degradation phenomena

According to what has been stated in sections 2.2 and 2.3, P_ORC has a worse durability performance for both carbonation and chlorides penetration. Therefore, also its structural performance has been checked within the SL. More specifically, since carbonation is the degradation phenomenon which first leads to the reduction of the reinforcement cross section in the columns, it is the one hereinafter taken into account. Thus, the following timeframes have been assessed for the scope of the structural analysis: i) from 0 to 41 years, during when the cross section of the column doesn't show any variation; ii) from 42 to 51 years, when the corrosion starts to occur with the consequent cracks creation; iii) from 52 to 100 years, when, if no maintenance activities are going to be carried out, the concrete cross section is reduced because of the detachment of the concrete cover and the reduction of reinforcement area further continues. It has been calculated that, due to the corrosion consequences, the cross section design resistant moment M_{Rd} reduces from 1,216 kNm to 902 kNm in the M-N interaction diagrams which anyway keep their symmetry within the time. Then, the dynamic behaviour of the structure has been further assessed, hypothesizing the worst scenario in which all the pillars are subject to isotropic degradation. This represents the most dangerous scheme since in the reality there are sides of the pillars that could be more protected against the deterioration, simply because of their location and the cladding in the actual structure,. In general, it can be commented that a redistribution of the actions and a top column deflection not higher than 7.17 mm have been calculated. The latter is anyway within the limits allowed by the current codes which correspond, for a structure like the one here assessed, to a maximum value of 25.7 mm. Moreover, also a non-linear pushover analysis has

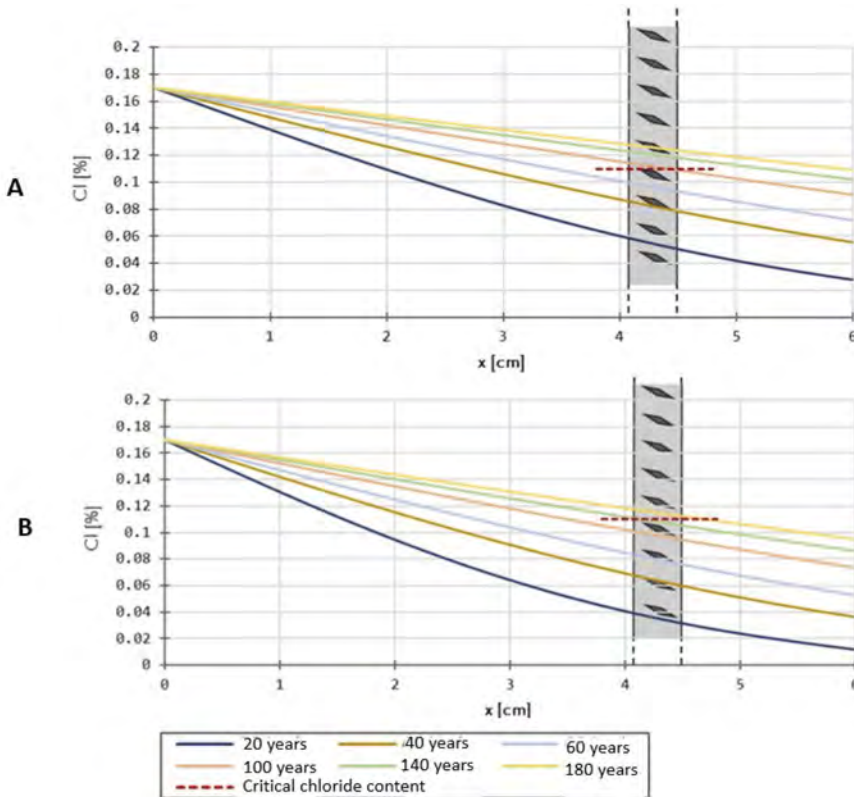


Figure 5. Calculated chlorides content at different ages for different depths for P_ORC (A) and P_CA (B).

been carried out with the consequent observation that plastic hinges form in correspondence of the edge of the pillars instead of along the beams. This is due to the design of the structure as a non-dissipative one. Nevertheless, the analysis demonstrated that the reduction of the cross section of the pillars doesn't cause any relevant changes in terms of structural resistance.

3 LIFE CYCLE ASSESSMENT AND LIFE CYCLE COST

3.1 *The system boundary of the analysis*

A cradle to grave system boundary has been employed to develop the LCA taking into consideration a SL of 100 years in total and supposing the need of one maintenance activity at 52 years only for the case of P_ORC. This is due to the carbonation that, based on the results of experiments, turned out to be the most severe degradation phenomenon for the case here assessed. The hypothesized maintenance activities consisted in the removal of the damaged concrete cover and reinforcement bars with the substitution of the latter and the casting of a new layer for the concrete cover after having applied a primer to favor its adhesion to the substrate. Ten impact indicators have been employed in total to describe the outcomes of the analysis according to the 10 CML IA impact method which aims to describe the overall consequences on a local, regional and global scale. More in detail, the following impact categories have been accounted for the scope of this analysis: global warming (GWP); acidification (AP); ozone depletion (ODP); photochemical oxidation (POCP); eutrophication (EP); abiotic depletion potential (ADP); human toxicity potential (HTP); freshwater aquatic ecotoxicity potential (FAETP); marine aquatic ecotoxicity (MAETP) and terrestrial ecotoxicity potential (TETP).

3.2 LCA and LCC outcomes

The LCA analysis highlighted a relevant reduction of the impacts of P_CA compared to P_ORC up to 40% as for HTP, FAETP and TETP. This is mainly due to the complete absence of the maintenance activities within the predefined SL for the case of P_CA. In this regard it must also be highlighted that all the steel scraps generated because of the maintenance activities of P_ORC are accounted as recycled, representing an environmental benefit, and for this reason are numerically counted with a negative value. If that were not the case, the reduction of the impacts of P_CA in comparison to P_ORC would have been even higher. In general, cement has a relevant contribution to some impact indicators as 45 % for GWP for both P_ORC and P_CA. Such percentage value is even higher in the case of MAETP impacts of reinforcement, with a value equal to 98% for P_ORC. Moreover, the effect of reinforcement on the overall impacts is smaller in the case of P_CA due to the fact that no replacement of the steel bars is supposed for the latter. Figure 6 presents some results in this regard.

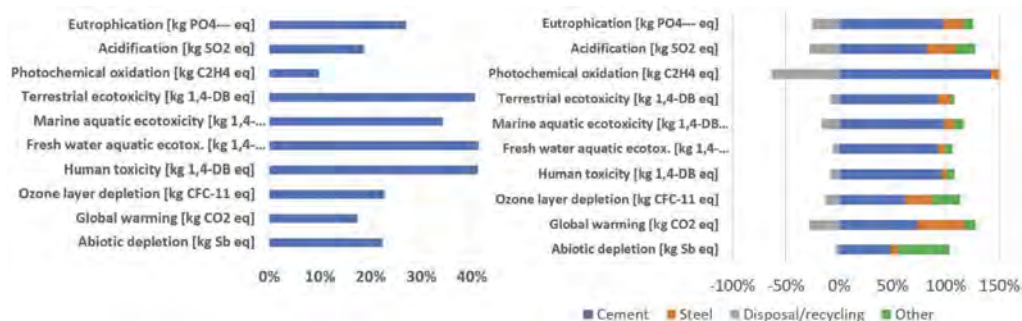


Figure 6. Impacts reduction of P_CA relative to P_ORC (left) and indication of the incidence of the main components on the overall impacts for P_ORC.

4 CONCLUSIONS

This research aimed to quantify the sustainability of a structure defined as strategic for the urban metropolitan area, comparing an ordinary technological solution to a self-healing one. To this purpose, the seismic resistance has also been checked after the appearance of a consistent degradation at the age of 52 years, because of the carbonation, for P_ORC. One of the first observations that can be made is that the use of CA for P_CA results in better durability parameters and hence longer predicted SL. In addition to this, the structural analysis demonstrated that the degradation mechanisms may affect the structural response but, for the case studied here, having been basically designed as non-dissipative, there is no significant problem though a reduction of the safety factor does actually occur. Moreover, the LCA outcomes, showing the consistent advantages of P_CA in comparison to P_ORC, highlight their importance as a decision making tool. They allow to make an “a priori” evaluation of the potential sustainability already starting from the design phase, to improve, in the future, the economic and environmental efficiency of the case study.

ACKNOWLEDGEMENTS



This project has received funding from the European Union’s Horizon 2020 research and innovation programme under the Marie Skłodowska-Curie grant agreement No 860006.

The authors thank Penetron Italia and the construction management team, responsible for the works execution of “Nuovo Impianto di Depurazione Area Centrale di Genova D.A.C”, for allowing us access to the construction site besides giving us the opportunity to cast the samples necessary for the laboratory tests.

REFERENCES

- Szabó, L.; Hidalgo, I.; Ciscar, J.C.; Soria, A. CO₂ emission trading within the European Union and Annex B countries: The cement industry case. *Energy Policy* 2006, 34, 72–87, doi:10.1016/j.enpol.2004.06.003.
- Turner, L.K.; Collins, F.G. Carbon dioxide equivalent (CO₂) emissions: A comparison between geopolymers and OPC cement concrete. *Constr. Build. Mater.* 2013, 43, 125–130, doi:10.1016/j.conbuildmat.2013.01.023.
- Ouellet-Plamondon, C.; Habert, G. Life cycle assessment (LCA) of alkali-activated cements and concretes; 2015; ISBN 9781782422884.
- McLellan, B.C.; Williams, R.P.; Lay, J.; Van Riessen, A.; Corder, G.D. Costs and carbon emissions for geopolymer pastes in comparison to ordinary portland cement. *J. Clean. Prod.* 2011, 19, 1080–1090, doi:10.1016/j.jclepro.2011.02.010.
- Kumanayake, R.; Luo, H. A tool for assessing life cycle CO₂ emissions of buildings in Sri Lanka. *Build. Environ.* 2018, 128, 272–286, doi:10.1016/j.buildenv.2017.11.042.
- Huntzinger, D.N.; Eatmon, T.D. A life-cycle assessment of Portland cement manufacturing: comparing the traditional process with alternative technologies. *J. Clean. Prod.* 2009, 17, 668–675, doi:10.1016/j.jclepro.2008.04.007.
- Shields, Y., Van Mullem, T., De Belie, N., et al. “An investigation of suitable healing agents for vascular-based self-healing in cementitious materials,” *Sustainability (Switzerland)*, V. 13, No. 23, 2021.
- di Summa, D., Tenório Filho, J. R., Snoeck, D., et al. “Environmental and economic sustainability of crack mitigation in reinforced concrete with SuperAbsorbent polymers (SAPs),” *Journal of Cleaner Production*, V. 358, 2022.
- Van den Heede, P., De Belie, N., Pittau, F., et al. “Life cycle assessment of self-healing engineered cementitious composite (SH-ECC) used for the rehabilitation of bridges.” *Life-Cycle Analysis and Assessment in Civil Engineering: Towards an Integrated Vision - Proceedings of the 6th International Symposium on Life-Cycle Civil Engineering, IALCCE 2018*. 2019. pp. 2269–75.
- Cappelleso, V., di Summa, D., Pourhaji, P., et al. “A review of the efficiency of self-healing concrete technologies for durable and sustainable concrete under realistic conditions,” *International Materials Reviews*, 2023, pp. 1–48.
- Bertolini, L., and Pedferri, P. “Tecnologia dei materiali. Leganti e calcestruzzo,” Torino, Citta studi edizioni, 1996.
- de Alcantara, N., da Silva, F., Guimarães, M., et al. “Corrosion Assessment of Steel Bars Used in Reinforced Concrete Structures by Means of Eddy Current Testing,” *Sensors*, V. 16, No. 1, 2015, p. 15.
- El Maaddawy, T., and Soudki, K. “A model for prediction of time from corrosion initiation to corrosion cracking,” *Cement and Concrete Composites*, V. 29, No. 3, 2007, pp. 168–75.
- Kannikachalam, N.P., di Summa, D., Borg, R.P., Cuenca, E., Parpanesi, M., De Belie, N., and Ferrara, L. Assessment of sustainability and self-healing performances of Recycled Ultra-High Performance Concrete (R-UHPC). *ACI Materials Journal*, 2023.
- Stipanovic Oslakovic, I., Bjegovic, D., and Mikulic, D. “Evaluation of service life design models on concrete structures exposed to marine environment,” *Materials and Structures/Materiaux et Constructions*, V. 43, No. 10, 2010, pp. 1397–412.
- Wang, X.-H., Hu, D.-G., Hong, A. K. B., et al. “Prediction of Equivalent Chloride Ion Diffusion Coefficient in Cracked Concrete of the in-Service RC Element,” *KSCE Journal of Civil Engineering*, V. 26, No. 5, 2022, pp. 2369–80.
- Al Obaidi, S., Bamonte, P., Animato, F., Lo Monte, F., Mazzantini, I., Luchini, M., Scalari, S. and Ferrara, L.: “Innovative Design Concept of Cooling Water Tanks/Basins in Geothermal Power Plants using Ultra High Performance Fiber Reinforced Concrete with Enhanced Durability”, *MDPI Sustainability*, 13(17), 2021, pp., 1–26, <http://doi.org/10.3390/su13179826>

The influence of the expansive site of delayed ettringite formation on the anisotropy of expansion evaluated by mesoscale discrete model

M. Fujishima, T. Miura & H. Nakamura

Department of Civil Engineering, Nagoya University, Nagoya, Japan

ABSTRACT: In this study, the effect of the expansive site ratio on the anisotropy of expansion due to delayed ettringite formation (DEF) was numerically evaluated considering creep. In this analysis, aggregates and mortar were separately modeled using 3D-Rigid Body Spring Model. The expansion strain was applied to the expansive site for 200 days. Each analysis was conducted under stress-free and restraint conditions. As a result of the 1 % expansive site, the expansion under restraint condition was smaller than that under stress-free condition. In the case of a higher expansive site ratio, the expansion under restraint condition was larger, and the larger compressive stress was generated in the restraint direction. The reason why the expansion under restraint condition was smaller for the 1 % expansive site case is the less accumulated compressive stress due to the localization of expansion origin. Consequently, the expansion origin may be scattered in the actual phenomenon.

1 INTRODUCTION

When concrete materials undergo the high-temperature history at 70 °C and over at the early hydration stage, delayed ettringite formation (DEF) occurs and expansion cracks are possibly induced. The DEF mechanism was suggested by Taylor et al. 2001 as follows. When concrete is applied to the high temperature at the early hydration stage, ettringite is decomposed, and sulfate ions are absorbed in calcium silicate hydrate (C-S-H). In the curing stage, sulfate ions are gradually released, and ettringite is secondary precipitated. The crystal growth pressure of secondarily produced ettringite possibly causes expansion cracks inside the concrete. The expansion due to DEF reaches up to 2 %, which is larger than the alkali-silica reaction (ASR) which is one of the internal swelling reactions.

The cracking at the concrete surface due to ASR and DEF shows a similar crack distribution. However, the cracks inside the concrete shows different trend, because the origin of the expansion is different. The origins of ASR and DEF expansion are aggregates and cement paste, respectively. The internal cracks due to DEF are formed at the interfacial transition zone (ITZ). The crack propagation process due to DEF was proposed as follows (Sanchez et al. 2018). At the first stage of expansion, the bond between aggregates and cement paste is weakened. Then, the width and length of the cracks at the aggregates interface become larger, and they propagate to the mortar phase and are connected to adjacent aggregates. On one hand, for the internal cracks due to ASR, the cracks are generated from the inside aggregates and propagate to mortar.

For ASR and DEF expansion under restraint condition, the cracks show the directionality, which is parallel to the restraint direction, and the anisotropic expansion can be observed (Liaudat et al. 2018, Hansen et al. 2021, Anca et al. 2021, Kawabata et al. 2021). In the case of ASR under uniaxial restraint condition, the transversal expansion without any restraint is larger than that under stress-free condition, which is called expansion transfer (Multon et al. 2006, Gautam et al. 2017, Liaudat et al. 2018). By contrast, in the case of DEF under uniaxial restraint condition, because the transversal expansion is smaller than that under stress-free condition, the volumetric strain decreases approximately by 20 % (Bouzabata et al. 2012, Kawabata et al. 2021).

Comparing ASR and DEF expansion, the internal cracking and the anisotropy of expansion indicate different trends, and it may be attributed to the difference in expansion origins.

Currently, the numerical analysis for DEF expansion has been developed by some researchers. Roubin et al. 2014 modeled DEF expansion using FEM, and confirmed that the crack pattern at the interface of aggregates was consistent with the experimental observations. Wang et al. 2019 directly modeled spherical aggregates and simulated ASR and DEF expansion using 3D-RBSM (rigid body spring model) to reproduce the crack patterns and the change in compressive properties. Miura et al. 2020 evaluated the effect of the expansion origins of DEF on the expansion behaviors using 3D-RBSM. The result indicated that the expansive site ratio has a large influence on the anisotropy of expansion under restraint condition. However, creep behavior was not considered in the expansion model used in the simulation.

In this study, the anisotropy of expansion under the uniaxial restraint condition was numerically evaluated to discuss the influence of the expansion origins of DEF and the time-dependent behavior. In the analysis, coarse aggregates and mortar were separately modeled using 3D-RBSM as well as the previous modeling Miura et al. 2020. The creep model was applied to the mortar phase to consider the time-dependent behavior of concrete. To reproduce DEF expansion, the expansive site was randomly selected from mortar elements with various expansive site ratio, and the expansion strain was applied to the expansive site for 200 days. DEF expansion under stress-free and restraint conditions was numerically simulated. From the results, the effect of the expansion origin on the expansion behaviors under different expansion conditions was discussed.

2 OVERVIEW OF NUMERICAL ANALYSIS

2.1 3D-RBSM

RBSM can directly evaluate discrete behavior such as cracks. The elements are the rigid body, and the mechanical springs are placed at the boundary surface between rigid body elements. To reduce the element size dependency (Thomure et al. 2001), the rigid body element is described by random voronoi particle. Figure 1 shows voronoi elements and mechanical springs. Mesoscale material constitutive law is applied to mechanical springs to reproduce the macroscopic mechanical behaviors of concrete. Mechanical springs are composed of one normal spring and two shear springs, and the three springs are placed at integral points of the boundary surface.

Figure 2 Shows the mesoscale constitutive laws. Normal spring behaves based on the tensile and compressive constitutive laws and does not indicate a yielding due to compression so material failure is attributed to only tensile and/or shear failure. Shear spring behaves based on the shear constitutive law and is related to the compressive stress of normal spring to consider the stress dependency of normal spring. The mesoscale parameters for mesoscale constitutive law are calculated based on compressive strength as shown in Table 1. The other analytical parameters were described in reference (Miura et al. 2022).

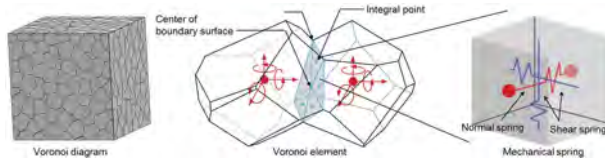


Figure 1. 3D-RBSM.

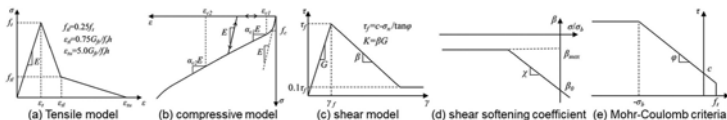


Figure 2. Mesoscale constitutive laws for normal and shear spring.

Table 1. Mesoscale parameters for mesoscale constitutive law.

NORMAL SPRING							
Elastic modulus	Tensile constitutive law		Compressive constitutive law				
E (MPa)	σ_t (MPa)	g_f (N/mm)	f'_c (MPa)	ε_{c1}	ε_{c2}	α_{c1}	α_{c2}
1.4 E^*	0.8 f_t^*	0.5 G_f^*	1.5 f'_c	$-2\sigma_c / (E(1+\alpha_{c1}))$	-0.015	0.15	0.25
SHEAR SPRING							
Shear stiffness	Mohr-Coulomb fracture criteria			Softening coefficient			
$\eta = G/E$	c (MPa)	φ	σ_b (MPa)	β_0	β_{max}	X	k
0.35	0.14 f'_c	37	f'_c	-0.05	-0.02	-0.01	-0.3

* indicates macroscopic mechanical properties.

2.2 Expansion model for DEF

The course aggregates and mortar are separately modeled as shown in Figure 3(a). The analytical concrete model is cubic shaped with 75x75x75 mm. The coarse aggregate size is uniformly 10 mm in diameter, and the number of course aggregates is 200. The aggregate diameter used in this analysis was selected as representative diameter which is the greatest number of aggregates in the grain size distribution. The average element size of the coarse aggregate phase and mortar phase is 1.3 and 3.0 mm, respectively. The mortar elements around the aggregate were smaller than 1.0 mm so at least two mortar elements exist between the adjacent aggregates to describe the cracking of the mortar phase. The material properties of mortar and aggregate are shown in Table 2.

The creep model was applied to mortar elements to consider the time-dependent behavior during expansion. The creep model of the JSCE model (JSCE 2017) was modified as shown in Equation 1 to apply to the mesoscale discrete analysis.

$$\varepsilon_{i,t} = \alpha \sum_{t_j=0}^t \Delta\sigma_{i,t_j} \cdot \frac{4W(1 - RH) + 350}{12 + f'_c} \cdot \log(t - t_j + 1) \cdot 10^{-6} \quad (1)$$

where, $\varepsilon_{i,t}$: total creep strain, α : mesoscale coefficient, $\Delta\sigma_{i,t_j}$: increment stress from t_{j-1} to t_j , W : water content per unit (kg/m^3), RH : relative humidity, f'_c : compressive strength (MPa), respectively.

When the JSCE model is directly applied to the mesoscale discrete analysis, the effect of creep is much larger. Thus, the mesoscale coefficient α was induced to reduce the creep effect. The mesoscale coefficient α was determined by sensitivity analysis to fit the deformation of concrete without expansion under restraint stress. The creep model was applied to a normal spring, and creep strain was calculated by a step-by-step method. Although in mesoscale discrete analysis, different creep models between normal and shear springs or between concrete, mortar, and cement paste should be applied, the simple creep model was used in this analysis.

To reproduce DEF expansion, the expansive site was randomly selected from all mortar elements corresponding to the expansive site ratio. The expansive site ratio was 1, 5, 10, and 100 % as a parameter to discuss the effect of expansive site on the anisotropy of DEF expansion. Figure 3 shows each expansive site as gray elements. The expansion strain of 100 μ /day had been applied to normal springs of expansive sites for 200 days.

The expansion under free and uniaxial restraint conditions was analyzed to evaluate the expansion behavior of DEF under restraint condition. In the case of expansion under restraint condition, top and bottom surfaces in y direction were restrained by steel plates. To consider only the expansion behavior of DEF, the friction between restraint plate and concrete was not taken into account.

2.3 Definition of macroscopic expansion strain

The expansion strain was defined by the points on the concrete surface of x and z directions. The points were placed on elements 10 mm inside from each side. The strains were obtained from the change in length of 55 mm. The number of obtained strains was 4 in each x and z direction and 8 in the y direction, they were averaged and the expansion in each direction was obtained. One of the

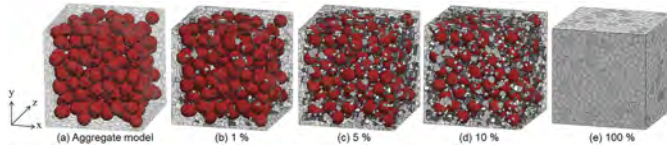


Figure 3. Expansion models.

Table 2. Material properties for mortar and aggregate.

Scale	Material	f_c (MPa)	E (GPa)	f_t (MPa)	c (MPa)	G_f (Nm)
Macro	Aggregate ^{*1}	100.0	50.0	11.00	-	-
	Mortar ^{*2}	35.0	29.5	2.46	-	0.0559
Meso	Aggregate ^{*3}	150.0	70.0	8.80	14.0	0.0005 ^{*4}
	Mortar ^{*3}	52.5	41.3	1.97	4.9	0.0280
	ITZ ^{*5}	26.25	20.65	0.98	2.45	0.0140

*1 Material properties for aggregate were based on (Roubin et al. 2014) and (JSCE 2017). f_c for the aggregate was assumed as 100 MPa.

*2 The compressive strength of the mortar was set to 35 MPa and the other material properties of the mortar were calculated based on the formulation from the JSCE (JSCE 2017).

*3 The fracture energy is unknown. In this analysis, it was applied using a small value as the aggregate cannot represent softening after cracking.

*4 The properties of the ITZ are unknown. This analysis halved the mortar properties, similar to Wang's approach in (Roubin et al. 2014, Giorla et al. 2015).

purposes of this study is to understand the anisotropy of expansion under uniaxial restraint condition. Thus, average expansion and transversal expansion were calculated as follows under stress-free and restraint conditions, respectively. The average expansion was defined as the average expansion of the x, y, and z directions in the stress-free expansion case, and the transversal expansion was defined as the average expansion of the x and z directions in the restraint case.

3 NUMERICAL RESULTS

3.1 Expansion evolution

Figure 4 shows the expansion evolutions under stress-free and restraint conditions for all expansive site ratios. In the case of stress-free expansion, the expansion increased with time, and the expansion rose with an exponential trend for the lower expansive site ratio while it linearly increased for the higher expansive site ratio. The maximum expansion is also strongly influenced by the expansive site ratio. It is approximately 2 % for a 100 % expansive site ratio and similar to the experimental trend (Bouzabata et al. 2012, Kawabata et al. 2021). In this analysis, the imposed strain was fixed for all analytical parameters, and the maximum expansion and its evolution are directly influenced by the imposed strain. Therefore, it is difficult to conclude that the analytical result of the 100 % expansive site ratio is coincident with the actual phenomena from only the stress-free expansion trend. In the cases of 1, 5, and 10 % expansive sites, the expansion in each direction indicated variation. By contrast, in the case of the 100 % expansive site, the isotropic expansion evolution was observed. The variations would be attributed to the distribution and ratio of randomly selected expansive sites as shown in Figure 3. In the case of restraint condition,

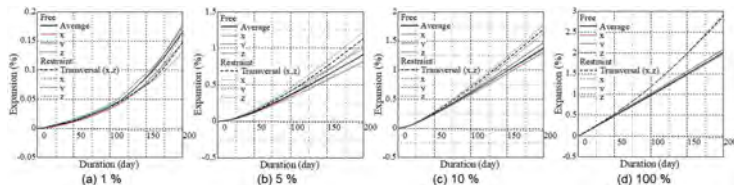


Figure 4. Expansion evolution under stress-free and restraint conditions.

the expansion in the restraint direction is almost zero. This is because the restraint plates at the top and bottom of the concrete were fixed in this analysis. The transversal expansion indicates the remarkable difference between the 1 % expansive site ratio and others. The transversal expansion under restraint condition for the 1% expansive site ratio is smaller than that under stress-free expansion while it is higher for a higher expansive site ratio. The anisotropic expansion for the 1 % expansive site ratio is similar to the experimental trend (Bouzabata et al. 2012, Kawabata et al. 2021). The expansive site ratio would be one of the dominant factors to explain the inherent phenomena of DEF expansion such as the expansion evolution and the anisotropic of expansion.

3.2 Deformation

Figure 5 shows the deformation diagrams after 200 days. For the stress-free expansion, the expansion cracks were randomly distributed, and the number of cracks increased with the increase in the expansive site ratio. In the case of the 100 % expansive site, the expansion cracks were generated on the entire surface of mortar elements without any localized cracks. As the expansive site ratio decreases, the expansion cracks were gradually localized and the width of the crack was wider than that of the 100 % expansive site ratio. This map cracking is the unique crack behavior generated by DEF expansion. Regarding the restraint condition, the expansion cracks were generated in parallel to the restraint direction. Therefore, the directionality of crack can be clearly observed. This trend is consistent with the previous experimental results (Kawabata et al. 2021).

3.3 Internal crack distribution

Figure 6 shows the internal crack distributions under stress-free and restraint conditions at the center of the cross section at 25, 50, 100 and 200 days. From this figure, the crack propagation process due to DEF was confirmed as follows. Firstly, the cracks at the interface of aggregates, which is the unique internal cracking due to DEF, are generated. Then, the width of the cracks at the interface of aggregates becomes larger and it propagates to the mortar with time. This crack propagation process is consistent with the previous experiments (Sanchez et al. 2018, Diamond 1998). For the larger expansive site ratio cases, the cracks propagated earlier and more cracks were generated in mortar independent of the restraint conditions. However, the case of the 100 % expansive site under stress-free condition showed a different trend that no-cracked mortar area existed in spots although the cracks at the interface of aggregates were generated.

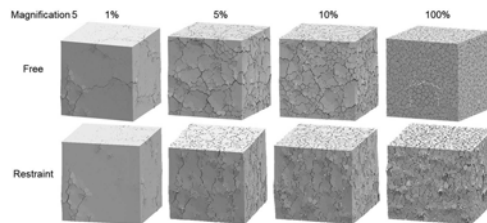


Figure 5. Deformation diagrams after 200 days under stress-free and restraint conditions.

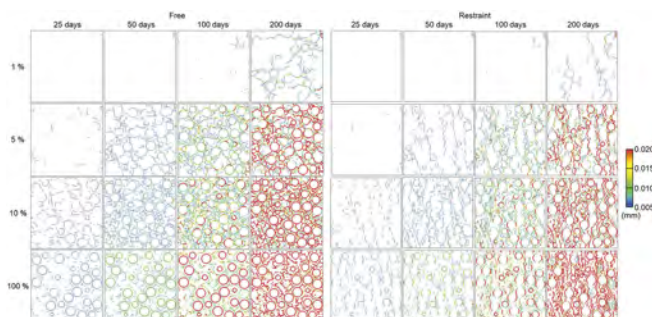


Figure 6. Crack distributions at the center of cross section under stress-free and restraint conditions.

Regarding the restraint condition, the expansion cracks were generated at only the interface of aggregates in the restraint direction, while the entire interface of aggregate was cracked in the stress-free expansion. In addition, the vertical cracks at the mortar phase can be observed. This trend is coincident with the surface crack distribution as shown in Figure 5.

4 DISCUSSION

According to the analytical results of DEF expansion under stress-free and restraint conditions, the transversal expansion under restraint condition was smaller than the average expansion under the stress-free condition in the 1 % expansive site case. This trend is similar to the experimental evidence (Bouzabata et al. 2012, Kawabata et al. 2021). Probably, the mechanisms of the expansion and crack generation process for the 1% expansive site ratio would be different from that for the higher expansive site ratio. In this chapter, the reason why the less expansive site ratio can reproduce the anisotropy of DEF expansion is discussed.

First, in order to assess the characteristic expansion behavior, the changes in the expansion rate of one expansive site for each expansive site ratio were calculated. The normalized expansion rate was defined as the increment of macroscopic expansion in a day divided by the expansive site ratio as shown in Equation 2 to compare the expansion rate between different expansive site ratio cases.

$$R_{macro,t} = \frac{\partial \varepsilon_{ave}}{\partial t} / S_{ex} \quad (2)$$

where, $R_{macro,t}$: normalized expansion rate (%/day), ε_{ave} : average expansion (%), S_{ex} : expansive site ratio, respectively. ε_{ave} under restraint condition is the averaged transversal expansion in the x and z directions. This index indicates the contribution of one expansive site to macroscopic expansion.

Figure 7 shows the change in the normalized expansion rate. In terms of stress-free expansion, the normalized expansion rate of the 100 % expansive site ratio is very low, while that of the 1 % expansive site ratio is the highest and indicates a different trend. This trend means that one expansive site largely contributes to macroscopic expansion in smaller expansive site cases. Regarding restraint condition, the trend is similar to the stress-free expansion case. The normalized expansion rate under restraint condition is higher than that of stress-free expansion, while the trend of the 1 % expansive site ratio is the opposite. In the case of the 1 % expansive site ratio, the normalized expansion rate under restraint condition is smaller than that of stress-free expansion within 100 to 175 days. Therefore, the contribution of one expansive site to macroscopic expansion under the restraint condition was smaller.

Figure 8 shows the stress distributions in the y-direction at the center of the cross-section under stress-free and restraint conditions at 25, 50, 100 and 200 days. For the stress-free condition, compressive and tensile stresses were locally generated in the cases of 1, 5 and 10 % expansive site. Tensile stress was released with the development of cracking and, subsequently, compressive stress was gradually decreased. By contrast, in the case of the 100 % expansive site under stress-free condition, compressive stress was generated at the entire cross-section while it was relatively lower than the others. Based on the stress distribution, the no-cracked mortar area in spots as shown in Figure 6 is probably attributed to that compressive stress was accumulated at entire mortar elements and, therefore, cracks cannot be generated at some parts so that internal stresses are balanced. For the restraint condition, compressive stress in the direction parallel to the restraint was increased with time. For the larger expansive site ratio cases, larger compressive stress was promptly accumulated in comparison to the stress-free condition.

Considering the expansion behavior as shown in Figures 7 and 8, the process of expansion evolution is described as follows. At the initial expansion stage, the expansion did not increase so much. This would be attributed to the internal constraint effect of the cross-section against the internal expansion pressure. After cracking, the internal constraint effect would be decreased, and then, the expansion rate increases. After that, the normalized expansion rate of 5 and 10 % expansive site ratio is in a plateau. These trends can be explained by the crack development process and internal stress accumulation. As many expansion cracks are generated in the cross-section, the internal stresses cannot be accumulated so much because the resistance force against the imposed strain is

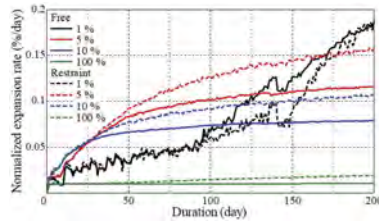


Figure 7. Expansion rate evolution.

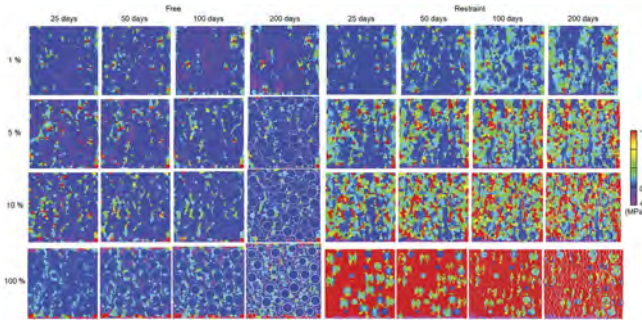


Figure 8. Stress distributions in the y-direction at the center of cross section.

decreased due to the existence of cracks. Therefore, the expansion trend of the 100 % of the expansive site ratio can be explained by a much faster cracking process and dissipation of internal stress corresponding to imposed strain. With the same concept, the expansion trend of the 1 % expansive site ratio can be also explained by the slow cracking process due to the small expansive site.

In the case of the 1 % expansive site ratio, the expansion rate increased around 100 days (Figure 7). This is because compressive stress against the internal expansion pressure was small before 100 days and, then, the accumulated compressive stress became larger. After that, expansion cracks were generated and the expansion subsequently developed. In other cases, for the stress-free condition, the locally accumulated compressive stress was not largely changed corresponding to the expansive site ratio. By contrast, for the restraint condition, larger compressive stress accumulated in the higher expansive site ratio cases. When larger compressive stress accumulates in the y-direction, larger deformation in the lateral direction occurs. This is attributed to the deformation due to the Poisson effect during compressive loading. Thus, in the higher expansive site ratio cases, the transversal expansion under restraint condition was larger than the average expansion under stress-free condition. As a result of the 1 % expansive site ratio, the less accumulated compressive stress resulted in the anisotropy of DEF expansion. Consequently, the compressive stress accumulated in the restraint direction possibly effects on the expansion behavior.

Generally, expansion cracks due to DEF with small width are distributed at the first stage of expansion and, then, the width of cracks locally becomes large. Kchakech (2015) investigated the relationship between the expansion due to DEF and the crack propagation of concrete surface. The result indicated that the crack length increased after the expansion was developed. Especially, even if the expansion plateaued, the crack length increased. Based on the analytical results, although such inherent trends were not confirmed, the expansive site may be scattered in the actual DEF expansion such as in the case of the 1 % expansive site. Furthermore, the unique crack propagation process may involve a complicated expansion process, such as the time-dependent change in the expansive site distribution or ratio.

5 CONCLUSIONS

In this study, considering creep behavior, the effect of the expansive site ratio on the anisotropy of expansion due to DEF was numerically evaluated. To reproduce DEF expansion

under stress-free and restraint conditions, coarse aggregates and mortar were separately modeled using 3D-RBSM, and the expansive site was randomly selected from mortar elements.

- 1) In the 1 % expansive site case, the expansion under restraint condition was smaller than that under stress-free condition, which is consistent with previous experiments. This may be attributed to less accumulated compressive stress due to scattered expansive sites.
- 2) In the 1 % expansive site case, the expansion rate significantly increased after the crack generation. This indicates that the crack generation and propagation involve in the increase in the expansion rate of DEF.
- 3) Based on the deformation diagrams, map cracking was observed on the concrete surface under stress-free condition, which is the characteristic cracking due to DEF expansion. For the cases under restraint condition, cracks indicated the orientation parallel to the restraint direction. This trend is consistent with the previous experimental results
- 4) Based on the crack distribution, cracks at the interface of aggregates were generated at first. Then, the width of the cracks at the interface of aggregates became larger and it propagated to mortar. This crack propagation process is consistent with the previous experiments.

REFERENCES

- Anca C.F., Frank J.V. 2021. Mechanical Properties of Alkali-Silica Reaction-Affected Concrete. *ACI Materials Journal* 119-M21: 251–262.
- Bouzabata H., Multon S., Sellier A., Houari H. 2012. Effects of restraint on expansion due to delayed ettringite formation. *Cement and Concrete Research* 42: 1024–1031.
- Gautam B.P., Panesar D.K., Sheikh S.A., Vecchio F.J. 2017. Multiaxial expansion-stress relationship for alkali silica reaction-affected concrete. *ACI Materials Journal* 114-M17: 171–184.
- Giorla A.B., Scrivener K.L., Dunant C.F. 2015. Influence of visco-elasticity on the stress development induced by alkali-silica reaction. *Cement and Concrete Research* 70: 1–8.
- Hansen S.G., Hoang L.C. 2021. Anisotropic compressive behavior of concrete from slabs damaged by alkali-silica reaction. *Construction and Building Materials* 267: 120377.
- JSCE. 2017. *Standard Specifications for Concrete Structures -Design-*.
- Kawabata Y., Ueda N., Miura T., Multon S. 2021. The influence of restraint on the expansion of concrete due to delayed ettringite formation. *Cement and Concrete Composites* 121: 104062.
- Kchakech B. 2015. Etude de l'influence de l'échauffement subi par un béton sur le risque d'expansions associées à la Réaction Sulfatique Interne, Doctoral Thesis, The University of Paris-Est.
- Liaudat J., Carol I., Lopez C.M., Saouma V.E. 2018. ASR expansion in concrete under triaxial confinement. *Cement and Concrete Composites* 86: 160–170.
- Miura T., Nakamura H., Yamamoto Y. 2020. Impact of origination of expansion on three-dimensional expansion crack propagation process due to DEF evaluated by mesoscale discrete model, *Construction and Building Materials* 260: 119911.
- Miura T., Nakamura H., Yamamoto Y. 2022. Reduction mechanism of the compressive properties of concrete with primary crack of different widths and angles evaluated by 3D-RBSM. *Engineering fracture mechanics* 276: 108877.
- Multon S., Toutlemonde F. 2006. Effect of applied stresses on alkali-silica reaction-induced expansions. *Cement and Concrete Research* 36: 912–920.
- Roubin E., Shamaa M.A.I., Colliat J.-B., Pavoine A., Divet L., Torrenti J.-M., Nahas G. 2014. A nonlinear meso-macro approach to modelling delayed ettringite formation and concrete degradation. *Materials and Structures* 47: 1911–1920.
- Sanchez L.F.M., Drimalas T., Fournier B., Mitchell D., Bastien J. 2018. Comprehensive damage assessment in concrete affected by different internal swelling reaction (ISR) mechanisms. *Cement and Concrete Research* 107: 284–303.
- Taylor H.F.W., Famy C., Scrivener K.L. 2001. Delayed ettringite formation. *Cement and Concrete Research* 31: 683–693.
- Thomure J., Bolander Jr. J., Kunieda M. 2001. Reducing mesh bias on fracture within Rigid-Body-Spring Networks, *Structural Eng./Earthquake Eng. JSCE* 18(2): 95–103.
- Wang Y., Meng Y., Jiradilok P., Matsumoto K., Nagai K., Asamoto S. 2019. Expansive cracking and compressive failure simulations of ASR and DEF damaged concrete using mesoscale discrete model. *Cement and Concrete Composites* 104: 1–17.

Chemo-physics and mechanics of RC for behavioral simulation in micro-seconds to years

K. Maekawa

Yokohama National University, Yokohama, Japan

K. Iwama

The Hong Kong Polytechnic University, Kowloon, Hong Kong

Y. Takahashi

The University of Tokyo, Tokyo, Japan

ABSTRACT: Integrated chemo-physics and mechanistic modeling is presented with regard to the multi-scale referential volume for behavioral simulation of reinforced concrete in service. The timescale of application ranges from nano-second for explosive events to years or century for life cycle of building and infrastructures. The developed simulation platform is being applied to the performance assessment of both new-designed and existing reinforced concrete on the scheme of performance-based design.

1 INSTRUCTIONS

Structural safety performances and durability of reinforced concrete (RC) are closely associated with chemo-physics and mechanistic events developing inside the microscopic spaces like pores which is thermodynamically equilibrated with surrounding environments. At the same time, the chemo-physics is mutually influenced by macroscopic structural damages and deformation like cracking, which plays a substantial role as high-speed path of substances such as water, carbon dioxide, chloride. Thus, the integration of structural kinetics and material mechanics shall be performed to meet the challenge of infrastructure design and maintenance.

This paper presents an integrated chemo-physics and mechanistic modeling with regard to the multi-scale referential volume. The timescale of simulation in cyber spaces ranges from micro-seconds for explosive events to years or century for life cycle of building and infrastructures. The developed simulation platform is being applied to the safety and durability performance examination of newly constructed RC and life-cycle assessment of existing RC on the scheme of performance-based design and maintenance.

2 INTEGRATED SCHEME OF CHEMO-PHYSICS AND MECHANICS

The microstructure modeling of concrete composite with micro-pores and the macroscopic structural concrete constitutive modeling are integrated as shown in Figure 1. The microstructure of porous media consists of capillary, gel and interlayer pores which is stochastically described by the pore size distribution function (Maekawa et al. 2008). The moisture state is identified by solving the thermodynamic equilibrium under the paths of wet and drying cycles. Here, the motion of liquid and vapor through the connected micro-pore network is idealized so that the mass balance is satisfied. The solids of hardened cement are consequently built according to the cement hydration, which is formulated by the multi-mineral hydration

model. The kinetics of substances solved in pore water is formulated together with the mutual equilibrium of multi-ions (Cl^- , Mg^{2+} , Ca^{2+} , OH^- , SO_4^{2-} , Na^+ , K^+ , Fe^{2+}) and the solved O_2 and CO_2 (Ishida et al. 2004, Maekawa et al. 2004, Elakneswaran and Ishida 2014, Wang et al. 2022). The macroscopic modeling of structural concrete with cracking was presented by integrating shear transfer along crack, transversal tension stiffening and softening and compression-tension along crack. This has been practically applied for static and dynamic behavioral simulation of RC structures (Maekawa et al. 2004).

These sub-frameworks are combined through the meso-scale modeling for crack kinetics as shown in Figure 1. Liquid water, compressive gas, frozen ice, corrosion rust and ASR gels are allowed to stay and flow in spaces surrounded by crack planes whose volume may dynamically vary. Then, the wide range of time-dependency of RC and constituent materials can be covered systematically. Figure 1 shows the governing equations of crack substances by poromechanical scheme (Biot et al. 1973). Here, the driving force of pore substance's motion denoted by " ω " is the gradient of pore pressure indicated by " p " in Figure 1. The poromechanical scheme can be multi-overlaid to handle the mixed system of several pore substances (Gong et al. 2019).

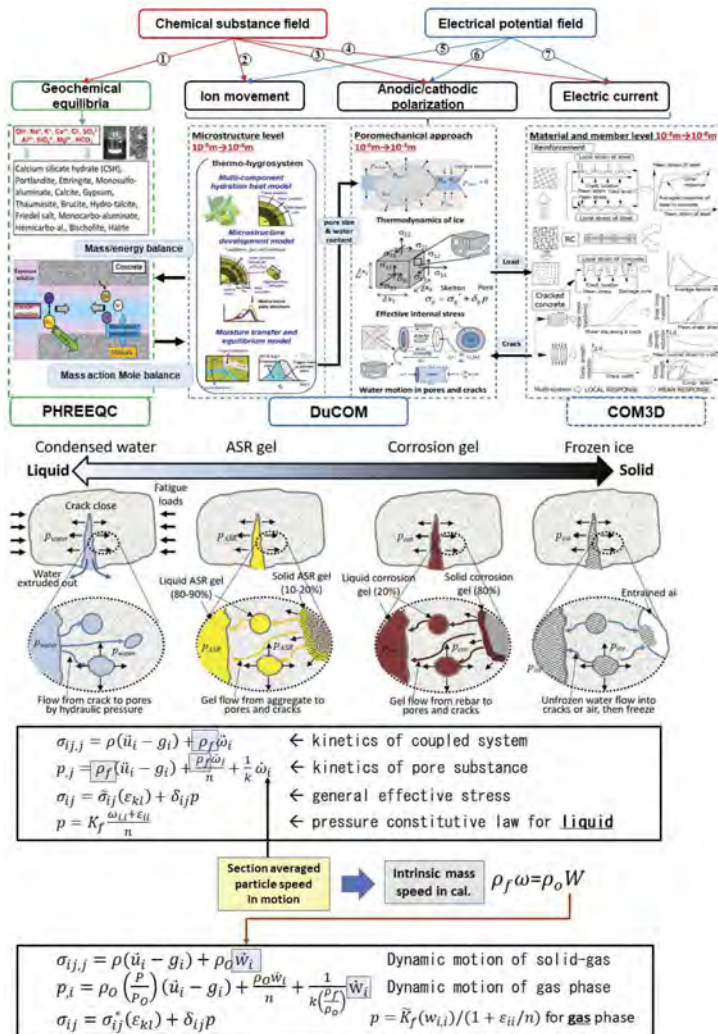


Figure 1. Integrated scheme of micro, meso and macroscopic modeling and the governing equations of kinetics of substances inside mores and crack spaces.

3 EXTENDED POROMECHANICS OF COMPRESSIVE MEDIA - MICRO-SECOND

As shown in Figure 1, the formulae of poro-mechanical kinetics can be applied to compressive gas by defining the mass rate of pore substance instead of the original particle in motion. Here, the constitutive model of gaseous pore-substance becomes highly nonlinear unlike the uncompressive liquid phase, which has been applied to consolidation and liquefaction of foundation. Figure 2 shows the numerical solution of dynamics inflation of gas (micro-second) at the gravity center of RC slab for verification of the extended gaseous poro-mechanics. The gas pressure develops inside crack spaces and spread out in a circle accompanying progressive cracking. We have a similar event of corrosion cracking which the corrosion gel introduces the cracking and at the same time it migrates into the crack spaces. Thus, the meso-scale model may build the multi-phase functionality with different timescale.

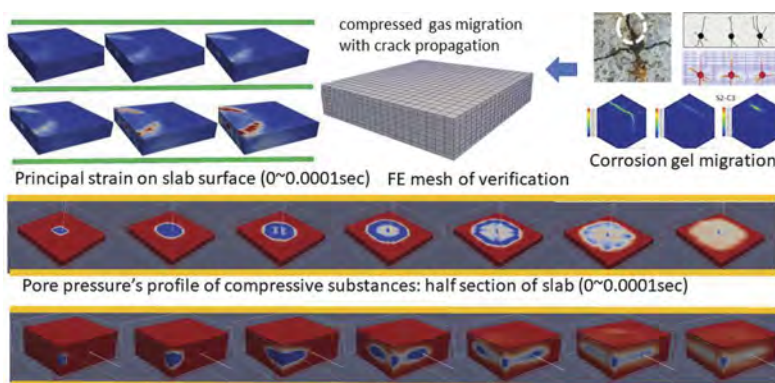


Figure 2. Verification of the computational scheme for extended poro-mechanics of compressive idealized gas substance associated with crack propagation of reinforced concrete – nano and micro-second event.

4 CHEMICAL REACTION, DECOMPOSITION AND RE-HYDRATION – HOUR SCALE

Hardened cement binder of concrete may be deteriorated owing to chemical reactions in the micro-scale volume under high temperature, which also causes the meso-scale cracking. The former chemical event results in the varying micro-pore structures and released crystal water inflates inside concrete and introduce the explosive mechanical damages of meso and macro-scales. The fire performance assessment requires the integrated modeling of chemo-physics and mechanics.

Figure 3 shows the chemical reaction formula under high temperature and consequent reform of the micro-pore structures (Iwama et al. 2022). Through the meso-scale modeling of compressive strength of concrete composites, digital data of microscopic events are linked with the macroscopic behavioral simulation of structural concrete via meso-scale modeling as shown in Figure 4. The experimental validation of the predictive platform was conducted in use of the weight change of extremely heated concrete cylinders as well as RC beams whose ductility was upgraded by the high temperature history over 1,000°C. It is computationally confirmed that the structural behaviors after exposure to fire are governed by the microscopic reform of crystals and macroscopic damage caused by thermal stress and explosion provoked by the rising vapor pressure.

5 LONG-TERM PERFORMANCE ASSESSMENT – NON-POROMECHANICS

Moisture migration and thermodynamic equilibrium may cause volumetric change related to the self-equilibrated time-dependent stresses which lead to structural performances. If no

cracking is introduced, moisture migrates through the micro-pores. Figure 5 shows the long-term excessive deflection of hollow-type long span PC viaducts over a half century (Ohno et al. 2012), and the chemo-physics and mechanics modeling can capture the long-term serviceability, and this has been included in the code specification of JSCE. Since the moisture kinetics is highly size-dependent, macroscopic mechanistic behaviors do follow the size-effect as shown in Figure 5. The impact of moisture migration arises appears slowly for structures with large-sized members like nuclear power plants compared to the normal RC building (Kurihara et al. 2017). When cracks are introduced, moisture migration is accelerated since cracks are the path of substances. The multi-scale modeling may capture the timeline of structural concrete.

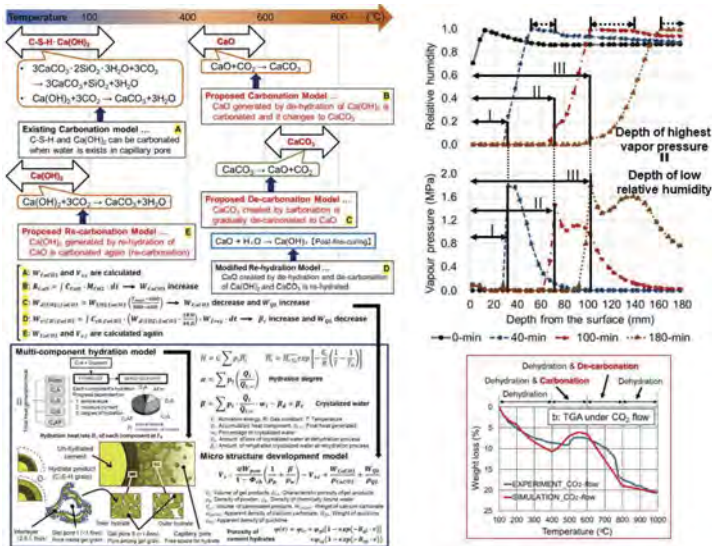


Figure 3. Chemical reaction, decomposition and re-hydration formula of cement hydrates with moisture and carbon dioxide under high temperature (left): The time-dependent vapor pressure and relative humidity profiles inside concrete (right) – minutes and hours events.

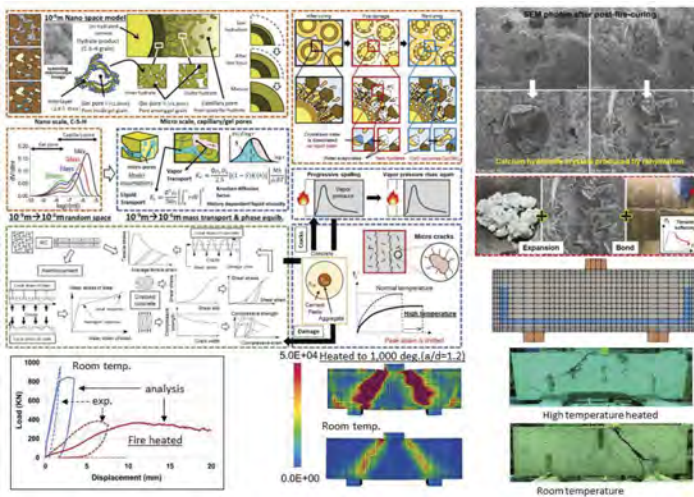


Figure 4. Varying micro-pore structures of concrete and associated structural capacity over the different scales (left); Re-hydrated Ca(OH)₂ solids with moisture after the fire heating (right).

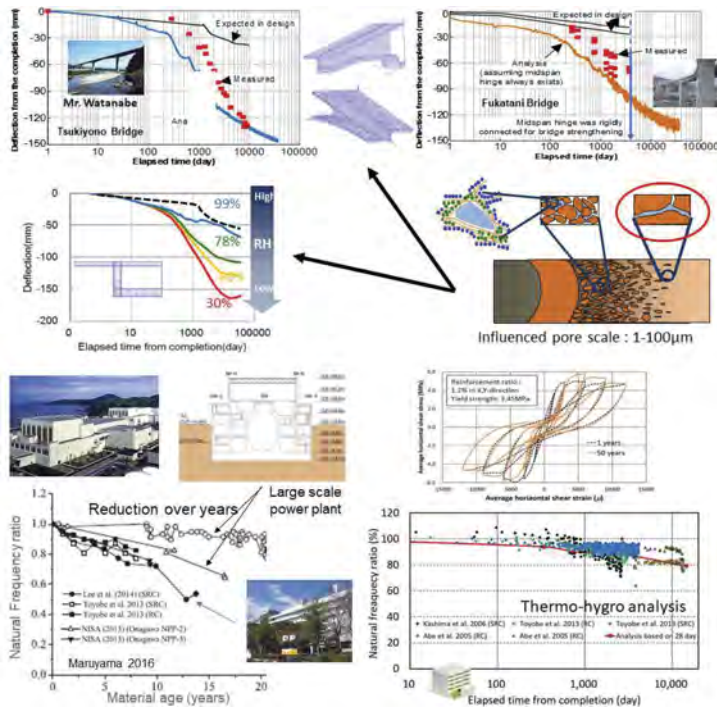


Figure 5. Varying global stiffness of RC building and nuclear power plants of different scales, which may have some impact to the earthquake resistance.

6 POROMECHANICS OF INCOMPRESSIVE MEDIA

6.1 Assessment of fatigue life of RC bridge deck – condensed water in pores

The meso-scale plays a critical role on the coupling problems of liquid water and cracked reinforced concrete under repeated actions as shown in Figure 6. The cyclic crack open & closure may create the pressure rise of pore substances owing to its viscosity and incompressibility. Thus, this impact may reach the micro-pore structures and consequent erosion. This microscopic action in seconds is similar to concrete damage by freeze-thaw cycles in days. This scheme successfully reproduces the shortened life of RC decks under wheel-type moving load with stagnant water in cyber space (Maekawa and Fujiyama 2013) and was validated by comparing the simulation with the real bridge deck lifetime over a half century (Takahashi et al. 2022) as shown in Figure 6.

Crack is one of critical factors, since it offers the pore-pressure rises caused by external loading to structures. At the same time, cracking brings about large-sized continuous paths of pore substances which may reduce the pore pressure. In some cases, ASR induced cracks may prolong the fatigue life of RC decks even under the condensed water which can escape through cracks.

6.2 Coupled chemical reaction and solid formation

Figure 7a shows the coupling of ASR gel formation driven by alkalinity of pore-solution and cracking of concrete. For computing the rate of reaction, the migration and equilibrium of sodium and potassium ions are computed (Takahashi et al. 2016) by solving the mass balance requirement. Since the ASR gel is formed inside aggregates, the micro pore structure is assumed not to be changed but it can absorb the gels inside the pore spaces including the space of aggregates. Here, it should be noted that ASR expansion of macroscopic concrete composite is apparently size dependent, because produced silica gel is hardly in motion when

the concrete composite is large and kept longer inside the composite with sustained pore pressure. It means that ASR expansion is not a material characteristics but the macroscopic structural behavior.

The ASR gels are known to be solidified in years after the creation. Thus, crack spaces are filled by the solidified gels and the mechanical properties of concrete may change (Takahashi et al. 2016, 2018). The impact of cracking is taken into account in the RC constitutive modeling in accordance with the field of strains as for the macroscopic indicator. The integrated scheme can handle these coupling of micro and macroscopic events to meet the challenge of simulating overall structural concrete subjected to forces and ambient conditions (Figure 5).

Figure 8 shows the simulation of cracking around a single reinforcing bar embedded in concrete. If the sequence of actions to cause cracking (corrosion of steel, ASR and freeze-thaw cycle: FTC) would be changed, damage profiles are predicted to be different (Gong and Maekawa 2019). The authors assume that each substance is driven by the gradient of its concentration with mutual interaction among them (see Figure 8). These attribute to the nonlinearity of each chemo-physical and mechanistic events. Here, the authors hope to be validated experimentally and by some site-inspection of real infrastructures under natural climates.

Recently, the chemo-physics and mechanical scheme for structural concrete and cementitious composites was applied to the design and construction of underground LNG storage tanks as shown in Figure 9 (Takahashi et al. 2019). The construction processes including the excavation of foundation and settlement of retaining walls were traced. The curing of fresh concrete was also re-produced inside the cyber space according to the specification of constructions. In each stage, the path-dependent parameters were taken over from the previous one. After overall 23 stages of construction, the maintenance stage begun in a long timeline till 100 years. During the period of maintenance, the safety check was conducted under statics as well as dynamics as for assessing earthquake resistance, because the seismic resistance and deformability would vary in time as shown in Figure 5.

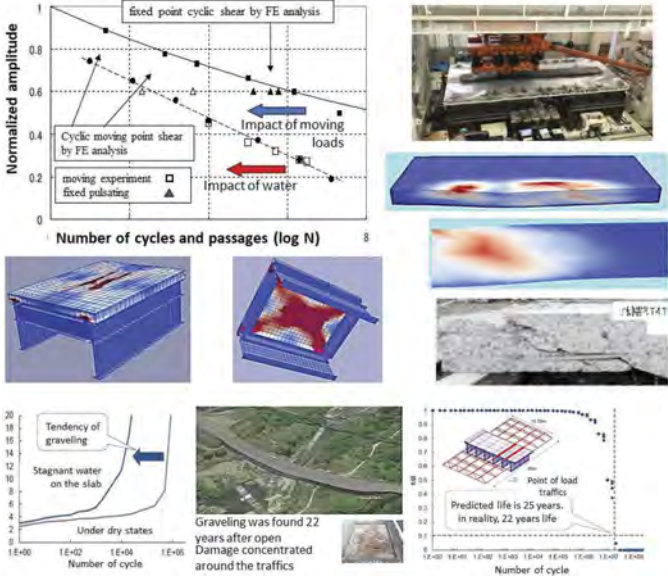


Figure 6. Deteriorated fatigue life of RC bridge deck subjected to wheel running loads and damage accelerated by condensed water trapped inside the structural cracking.

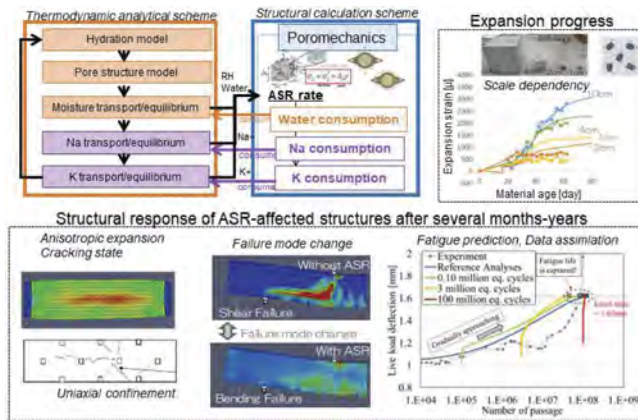


Figure 7a. ASR gel formation, cracking and its migration into the crack spaces.

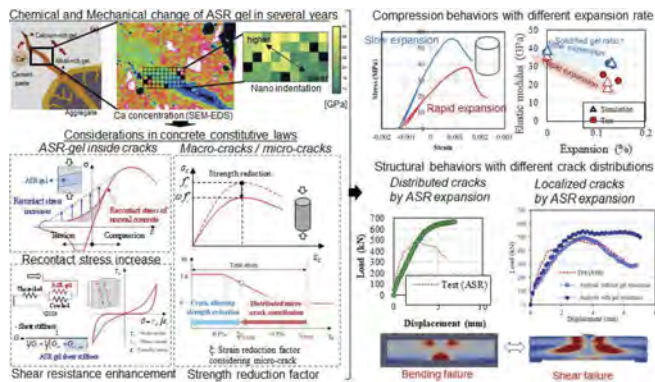


Figure 7b. ASR gel's subsequent solidification of gels for long timelines.

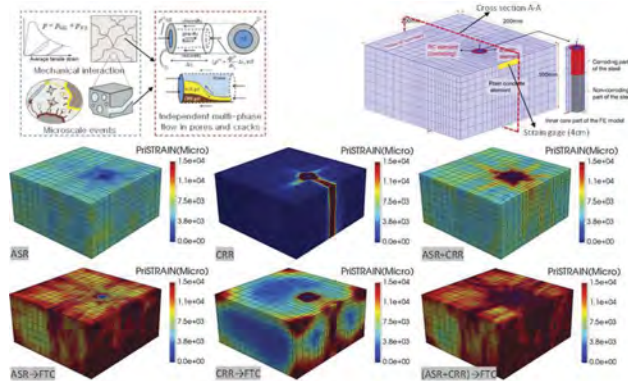


Figure 8. Chemical reaction modeling of ASR with formation of ASR gels which may cause concrete cracking where the gel itself runs away and gets solidified over the decades.

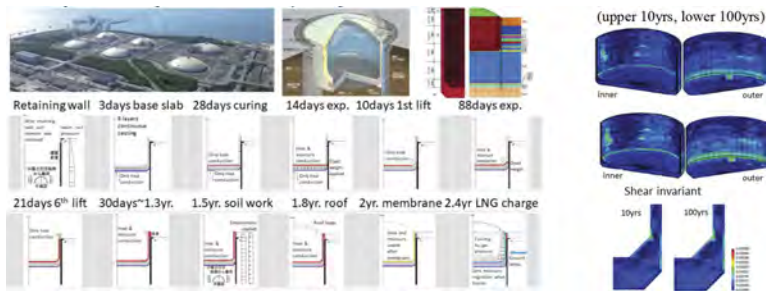


Figure 9. Practical performance-based design of a new underground LNG storage tank by means of multi-scale and chemo-physics and mechanics.

7 CONCLUSIONS

Integration of modeling for chemo-physics of cement composites and structural concrete mechanics with cracking was presented in multi-scale spaces and time domains from micro-seconds to hundred years as follows.

- (1) Kinematic modeling for substances in crack spaces may integrate the micro chemo-physics and macro mechanical modeling by poro-mechanical scheme.
- (2) The framework of poro-mechanics can be extended to compressive gaseous media which may migrate and accompany the progressive cracking similar to the corrosion and freeze-thaw actions.
- (3) The grand system is applied to the design and construction of real infrastructures on the scheme of performance-based design.

REFERENCES

- Bažant, Z.P., Hübner, M.H. & Yu, Q. 2011. *Excessive creep deflections: An awakening -Concrete international*. American Concrete Institute.
- Biot, M.A. 1973. Nonlinear and semilinear rheology of porous solids, *Journal of Geo. Research* 78(23).
- Elakneswaran, Y. & Ishida, T. 2014. Development and verification of an integrated physicochemical and geochemical modeling framework for performance assessment of cement-based materials, *Jr. of Adv. Conc. Tech.* 12: 111–126.
- Gong, F. & Maekawa, K. 2019. Proposal of poro-mechanical coupling among ASR, corrosion, and frost action for damage assessment of structural concrete with water, *Engineering Structures* 188: 418–429.
- Iwama, K. & Maekawa, K. 2022. Modeling of carbonation, de-carbonation and re-carbonation processes of structural concrete subjected to high temperature heating, *Cement and Concrete Composites* 129.
- Kurihara, R., Chijiwa, N. & Maekawa, K. 2017. Thermo-hygral analysis on long-term natural frequency of RC buildings with different dimensions, *Jr. of Adv. Conc. Tech.*, 15(8): 381–396.
- Maekawa, K., Ishida, T. and Kishi, T. 2008. *Multiscale Modeling of Structural Concrete*, Taylor & Francis.
- Maekawa, K. & Fujiyama, C. 2013. Rate-dependent model of structural concrete incorporating kinematics of ambient water subjected to high-cycle loads, *Engineering Computations* 30(6): 825–841.
- Ohno, M., Chijiwa, N., Suryanto, B. & Maekawa, K. 2012. An investigation into the long-term excessive deflection of PC viaducts by using 3D multi-scale integrated analysis, *Jr. of Adv. Conc. Tech.* 10(2): 47–58.
- Takahashi, T., Kosaka, R., Yonetsu, K., Tsuchiya, S. & Ishida, T. 2019. Thermo-hygro-dynamic analysis of LNG underground LNG tank by using multi-scale integrated simulation method, *Jr. of JSCE* 75(2).
- Takahashi, Y., Ogawa, S., Tanaka, Y. & Maekawa, K. 2016. Scale-dependent ASR expansion of concrete and its prediction coupled with silica gel generation and migration, *Jr. of Adv. Conc. Tech.* 14(8).
- Takahashi, Y., Tanaka, Y. & Maekawa, K. 2018. Computational life assessment of ASR-damaged RC decks by site-inspection data assimilation. *Jr. of Adv. Conc. Tech.* 16(1): 46–60.
- Takahashi, Y., Furukawa, T., Fang, J., Ishida, T. & Tsuchiya, S. 2022. Full-scale fatigue simulations for reinforced concrete bridge slabs with multi-scale FEM system with solid-liquid two phase model, *Challenges for Existing and Oncoming Structures; IABSE Symp. Prague, 25-27 May 2022*.
- Wang, Z., Maekawa, K., Takeda, H. & Gong, F. 2022. Multi-ion kinetics in pseudo-concrete electrolyte associated with macro-cell corrosion, *Cement and Concrete Composites* 133: 104690.

Temperature dependent modelling approach for early age behavior of printable mortars

A. Robens-Radermacher & J.F. Unger

Modelling and Simulation, Bundesanstalt für Materialforschung und -prüfung (BAM), Berlin, Germany

A. Mezhov & W. Schmidt

Technology of Construction Materials, Bundesanstalt für Materialforschung und -prüfung (BAM), Berlin, Germany

ABSTRACT: Structural build-up describes the stability and early-age strength development of fresh mortar used in 3D printing. It is influenced by several factors, i.e. the composition of the printable material, the printing regime, and the ambient conditions. The existing modelling approaches for structural build-up usually define the model parameters for a specific material composition without considering the influence of the ambient conditions. The goal of this contribution is to explicitly include the temperature dependency in the modelling approach. Temperature changes have significant impact on the structural build-up process: an increase of the temperature leads to a faster dissolution of cement phases and accelerates hydration. The proposed extended model includes temperature dependency using the Arrhenius theory. The new model parameters are successfully calibrated based on Viskomat measurement data using Bayesian inference. Furthermore, a higher impact of the temperature in the re-flocculation as in the structuration stage is observed.

1 INTRODUCTION

For extrusion-based 3D concrete printing, the early age of printable mortars is of great importance, which is affected by various time dependent phenomena like structural build-up, plasticity as well as viscosity. Structural build-up is the time dependent structuration of cementitious material at rest due to thixotropy and early hydration processes. It influences the printability, buildability, and open time of printing processes (Reiter et al., 2018, Mohan et al., 2021). For a deeper introduction it is referred to (Roussel et al., 2012). Generally, the structural build-up is influenced by several factors from the raw material constituents to external conditions such as temperature as discussed in detail in (Jiao et al., 2021).

There are several approaches to model the structural build-up of cementitious materials. Most phenomenological models are based on a time-dependent internal structural parameter describing the flocculation state, which is assumed to be zero after mixing and increases with time (Roussel, 2006). The approaches differ in the definition of the time dependency (linear, exponential, bi-linear). In the most often used model proposed by (Roussel, 2006), the static yield stress at rest increases linearly in time with the constant structuration rate A_{thix} from an initial value τ_{y0} :

$$\tau_y(t) = \tau_{y0} + A_{thix} t. \quad (1)$$

Covering the speed-up of the structural build-up after a certain time due to an onset of the acceleration period of hydration, an exponential dependency is proposed in (Perrot et al., 2015). The static yield stress following this exponential model is given as:

$$\tau_y(t) = A_{thix} t_c \left(e^{\frac{t}{t_c}} - 1 \right) + \tau_{y0}, \quad (2)$$

with an additional parameter of the characteristic time t_c . Recently, (Kruger et al., 2019) developed a bi-linear approach considering two stages of the structural build-up development with different rates: re-flocculation and structuration. By differentiating between those stages a higher precision of the first rapid re-flocculation stage dominated by physical processes is possible. The structuration stage is mainly governed by chemical reactions. The static yield stress according to the Kruger model is then given by two equations:

$$\tau_y(t) = \begin{cases} \tau_{y0} + R_{thix}t & \text{if } t < t_{rf} \\ \tau_y(t_{rf}) + A_{thix}(t - t_{rf}) & \text{if } t > t_{rf} \end{cases} \quad (3)$$

In the latter, the re-flocculation time t_{rf} defines the time period between the first stage with the re-flocculation rate R_{thix} and the second structuration stage (A_{thix}). The ratio between both rates depends on the material mixture composition (Kruger et al., 2019). In (Ivanova et al., 2022) the bilinear model is applied in the context of constant rotational velocity tests of printable mortar and concrete and for several characterization methods of 3D printable cementitious mortars in (Bos et al., 2021).

Usually, the model parameters are defined for a specific material composition without considering the influence of ambient conditions. Nevertheless, ambient conditions such as temperature and humidity will change in real life printing processes due to weather conditions, summer, winter, day, night as well as the printing process itself (pumping process changes the temperature due to pressure changes (Strangfeld, 2022)). In the discussion of eight implemented 3D concrete printing projects from around the world by (Bos et al., 2022), the challenges of the ambient temperatures' influence were also pointed out. Printings were stopped or shifted to the night by increased ambient temperature or a continuous measurement of the system temperature were applied. The temperature has a particularly significant influence on the structural build-up process because an increase of the temperature leads to a faster dissolution of cement phases and accelerates hydration. Nevertheless, there are only limited studies available to date. (Bos et al., 2019) investigated the influence of material temperature and they have shown that warm water accelerates the structural build-up rate but reduces the bonding strength between layers. (Huang et al., 2019) have shown that the increase of the temperature in a constant shear rate test of cement pastes results in an increase of the structural build-up rate. The temperature sensitivity is studied by calculating the activation energy by Arrhenius theory. They extend their studies by measuring the storage modulus by small amplitude oscillatory shear test (SAOS) in (Huang et al., 2022). It was pointed out that a rise of the temperature leads to a faster storage modulus development for cement paste samples with the same hydration degree. However, (Bogner et al., 2020) using SAOS tests at 10, 20, 25 and 30°C, found out that regardless of the ambient temperature, all investigated samples demonstrated a similar evolution of the complex shear modulus during the first 1.4 h of hydration. After that, a significant temperature influence on the modulus was observed. The discrepancy between those results could also be related to the different material compositions, methods, and time scales. The authors themselves observed a significant temperature influence on the storage moduli for cement pastes measured by SAOS with a bi-linear increase over the resting time (Mezhov et al., 2022).

The goal of this contribution is to develop a temperature dependent structural build-up model. Therefore, the bi-linear Kruger model (Equation 3) is extended by temperature dependent parameters modelled based on the Arrhenius theory. The new model parameters are estimated using Bayesian inference. Therefore, static yield stress data measured via Viskomat at four different temperature levels are used.

2 MATERIALS AND METHODS

2.1 Mixture composition and measurement set-up

Mortar samples were prepared according to the mixture composition given in Table 1. First cement CEM I 42.5 R, silica fume, sand, fly ash and superplasticizer were mixed with a spoon

around 30 sec in a 600 ml cup. The water was added within 15 sec during the second mixing at 200 rpm for 1 min by IKA STARVISC 200–2.5 mixer. After a pause and hand mixing for 30 sec, the mortar samples were mixed at 400 rpm for 2 min.

Table 1. Mixture composition.

Components	Amount [kg/m ³]
Cement (CEM I 42.5 R)	650
Sand (0.1/0.5)	980
Fly ash	190
Silica fume	90
Superplasticizer powder	4.3
Water	260
Spread by DIN EN 1015-3:1999-04	190 mm
Water cement ratio	0.4
Temperature after mixing	27°C

The structural build-up measurements were performed using a Schleibinger Viskomat NT with a double gab basket cell. The used device can measure torque from 0 to 500 Nmm. Note, the mixture composition was designed in such a way that the maximum torque does not exceed those range for all investigated temperature levels. Ten points with a rotational velocity of 0.1 rpm within 30 min were measured. The test protocol is summarized in Figure 1. Three tests for every temperature were carried out using a waterbed temperature control system with constant temperatures 17, 22, 27, 32 and 42°C. The initial temperature of the mortar after mixing was always 27°C.

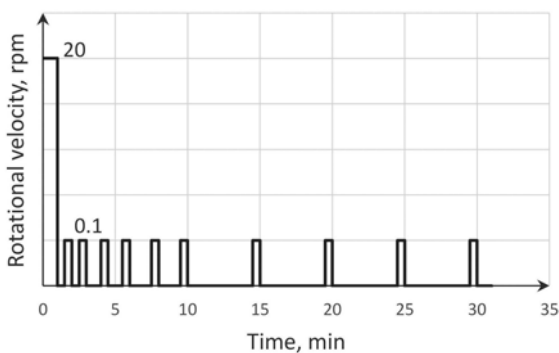


Figure 1. Test protocol for Viskomat NL measurements.

2.2 Temperature dependent structural build-up model

The bi-linear model of (Kruger et al., 2019) given in Equation 3 is extended to model the temperature influence on the early age behavior of the static yield stress τ_y . Therefore, the model parameters re-flocculation rate, structuration rate, re-flocculation time and initial static yield stress are introduced as temperature (T) dependent functions. So that the temperature dependent bi-linear model reads:

$$\tau_y(t, T) = \begin{cases} \tau_{y0}(T) + R_{thix}(T)t & \text{if } t < t_{rf}(T) \\ \tau_y(t_{rf}(T), T) + A_{thix}(T)(t - t_{rf}) & \text{if } t > t_{rf}(T) \end{cases} \quad (4)$$

Where the temperature dependent parameter functions are defined as:

$$\gamma(T) = \alpha_\gamma \exp\left(\beta_\gamma \left(\frac{1}{T} - \frac{1}{T_{ref}}\right)\right) \quad (5)$$

for $\gamma \in [\tau_{y0}, R_{thix}, A_{thix}, t_{rf}]$. This exponential functionality of a reaction rate of chemical as well as physical processes is known as Arrhenius equation. In the Arrhenius equation, the pre-factor β_γ in Equation 5 is defined by the negative ratio of a specific activation energy E_a and the gas constant R . Among other things, the Arrhenius theory is usually applied to model and characterize the temperature dependency of the cement hydration, see e.g. (Poole et al., 2007, Carette and Staquet, 2016). The unknown activation energy is thereby usually determined by calorimetry. Here, the Arrhenius equation is used to consider the temperature dependency of the structural build-up rates (re-flocculation rate and structuration rate) as well as for the re-flocculation time and the initial yield stress. The extended temperature dependent bi-linear model in Equation 4 and 5 has in total nine new unknown model parameters: the four α 's and β 's and the reference temperature T_{ref} . Those are to be defined via measurement data at different ambient temperatures for each mixture composition.

2.3 Bayesian model parameter estimation

In general, the estimation of unknown model parameters based on measured data is an inverse problem. The aim is to find appropriate values for a set of unknown model parameters θ (here the model parameters in Equation 4 and 5) minimizing the error between a given set of measurement data y and the corresponding model output values $g(\theta)$ (here Equation 4). In deterministic methods, the best parameter set is found by minimizing this difference by optimization approaches e.g. least-squares, L_p norm or weighted least square ansatz (see e.g. (Mohammad-Djafari, 1998)). The solution is a single set of the parameters' estimates and carry no information about how reliable or likely they are. In contrast, probabilistic methods provide a probabilistic description of information and beliefs, allowing the consideration of various uncertainties. In those approaches, the posterior probability distribution is computed using the Bayes' rule via

$$P(\Theta|y) = \frac{P(y|\Theta)P(\Theta)}{\int P(y|\Theta)p(\Theta)d\Theta}. \quad (6)$$

In the latter, the unknown parameter vector $\Theta = (\theta, \sigma)$ includes beside the model parameters θ additional noise parameters σ (describing e.g. the standard deviation of a Gaussian distributed additive noise $e \sim \mathcal{N}(0, \sigma^2)$). The prior probability density function $P(\Theta)$ reflects the prior knowledge on the parameters, while the likelihood $P(y|\Theta)$ defines the probability that the model has generated the data under the given model parameters. The normalization term in the denominator describes the evidence for the data considering the model. More details on the mathematical background can be found e.g. in (Watanabe, 2018).

The computation of the posteriori (Equation 6) is cumbersome, especially with increasing dimensionality of the parameter space. For that reason, sampling-based methods (Lye et al., 2020) are usually applied to evaluate Equation 6. In this paper, the well-known Markov Chain Monte Carlo (MCMC) sampling (Metropolis et al., 1953) is used. The parameter estimation is conducted via the open-source Python package *probeye* (<https://pypi.org/project/probeye/>).

3 RESULTS AND DISCUSSION

The measured temperature effect on the static yield stress evaluation in the first 30 minutes is given in Figure 2. The mean and standard deviation of the static yield stress based on three tests (stars) for all investigated temperature levels are given over the time as solid line and bars, respectively. The static yield stress is computed from the measured torque multiplied by the conversion factor for the specific cell. Two aspects are shown. First, a significant temperature effect in the yield stress evaluation is observed. With increasing ambient temperature, the rate of the static yield stress evolution increases confirming the need of a temperature dependent modelling approach. Second, the evaluation is split into two stages: a re-flocculation stage followed by

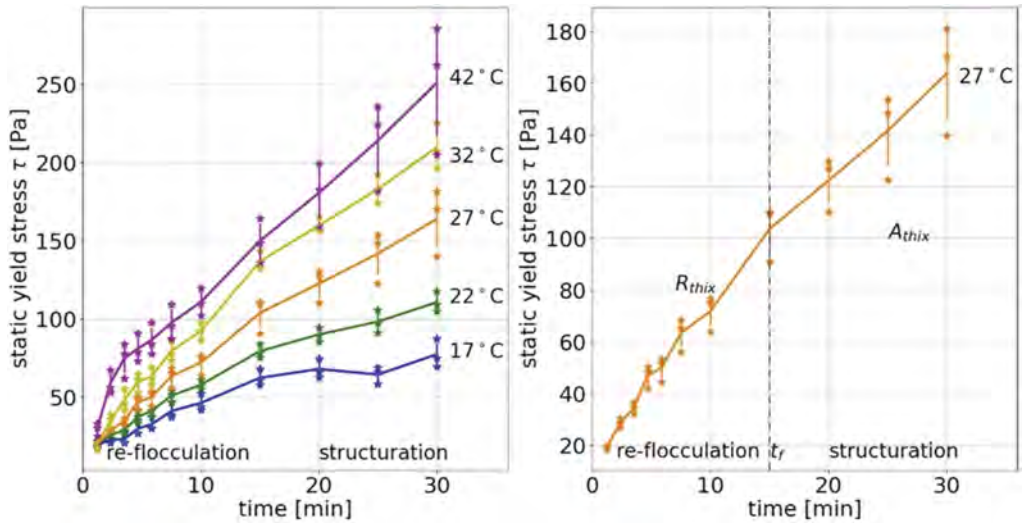


Figure 2. Mean and standard deviation of static yield stress measurements over time for five different temperatures. Separation into re-flocculation and structuration stage demonstrated for the data at 27 °C.

a structuration stage which is additionally demonstrated using the data at 27°C on the right side of Figure 2. The change between the two stages, the re-flocculation time, happens around 15 min. Independent of the ambient temperature, the first (re-flocculation) rate is usually higher than the second (structuration) rate. The rate's ratio depends on the temperature.

In a Bayesian parameter estimation, the model parameters of the proposed temperature dependent model were inferred using the measured data at temperature 17, 22, 27 and 42°C (the data at $T = 32^\circ\text{C}$ is used for the verification). Therefore, a MCMC solver with 10^6 steps in 20 chains and 5000 initial steps were running using the open-source Python module *probeye*. The prior distribution for the nine model parameters were chosen as:

$$\begin{aligned} \alpha_{\tau_{y0}} &\sim N(20, 6^2) \text{ [Pa]}, \alpha_{R_{thix}} \sim N(6, 2^2) \text{ [Pa/min]}, \alpha_{A_{thix}} \sim N(4, 1^2) \text{ [Pa/min]}, \alpha_{t_{rf}} \sim N(10, 3^2) \text{ [min]} \\ \beta_{\tau_{y0}} &\sim N(-30, 9^2) \text{ [1/K]}, \beta_{R_{thix}} \sim N(-30, 9^2) \text{ [1/K]}, \beta_{A_{thix}} \sim N(-10, 3^2) \text{ [1/K]}, \beta_{t_{rf}} \sim N(0, 3^2) \text{ [1/K]} \\ \sigma &\sim U(1, 30) \text{ [Pa]}. \end{aligned}$$

For the reference temperature, the sample's temperature after mixing was used: $T_{ref} = 27^\circ\text{C}$.

The resulting predictive posterior probability is plotted in Figure 3 as a pair plot. Here, the advantage of using a probabilistic approach can be seen. Instead of one parameter set (like the result of a deterministic approach), the deviation and correlation of the model parameters are estimated. Especially, the parameter $\alpha_{R_{thix}}$ (in the figure α_2) and $\alpha_{\tau_{y0}}$ (α_1) as well as $\beta_{\tau_{y0}}$ (β_2) and $\beta_{R_{thix}}$ (β_1) are clearly correlated, showing the ill-posedness of the inverse problem. Note, the results are also influenced by the here chosen prior distributions. Furthermore, a close to zero mean of $\beta_{t_{rf}}$ (β_4) indicates a neglectable temperature dependency of the re-flocculation time. An averaged ratio between $\beta_{R_{thix}}$ (β_2) and $\beta_{A_{thix}}$ (β_3) of around two suggests a significant higher activation energy of the re-flocculation stage compared to the structuration stage.

The inferred temperature dependency of the primary parameters: initial yield stress τ_{y0} , re-flocculation rate R_{thix} , structuration rate A_{thix} and re-flocculation time t_{rf} , modelled by the functionality given in Equation 5 is evaluated in Figure 4. The solid line represents the mean values, whereas the bars give the first standard deviation based on the MCMC samples. The plot visualizes the significant temperature dependency in the rates. But the structuration rate is less temperature dependent as the re-flocculation rate. The physical processes in the re-flocculation stage seems to have a higher temperature sensitivity, where rising temperatures increase the Brownian motion between the particles. Additionally, the shape of the temperature dependency of the two rates differs. The re-flocculation rate increases nearly linear, where

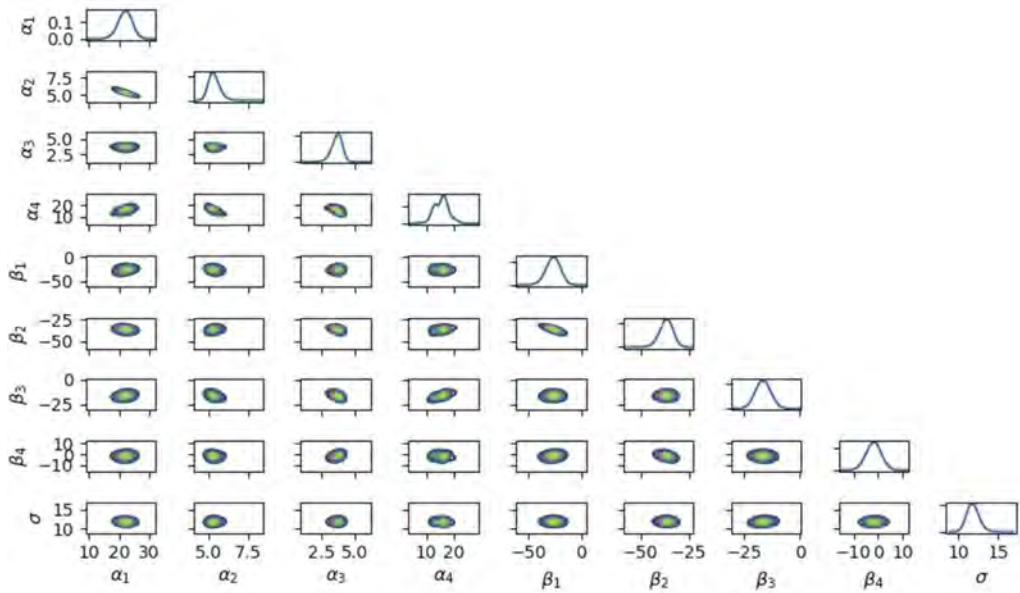


Figure 3. Pair plot of the posterior distribution with the abbreviations 1 : τ_{y0} , 2 : R_{thix} , 3 : A_{thix} , 4 : t_{rf} .

the structuration rate temperature function seems to be logarithmic. Furthermore, the initial static yield stress increases like the re-flocculation rate since both parameters describe the re-flocculation stage. In contrast, the re-flocculation time is approximately independent of the temperature with an aver-aged value of around 15 min. The measurement noise was assumed to be temperature independent, and its mean is estimated as 12 Pa.

As verification of the proposed temperature dependent structural build-up model in Equation 4 and 5 the model is reevaluated for the training temperature values 17, 22, 27 and 42°C using the estimated parameter distribution as well as newly evaluated at temperature 32°C and compared to the corresponding measured data. That comparison is shown in Figure 5 given the mean model

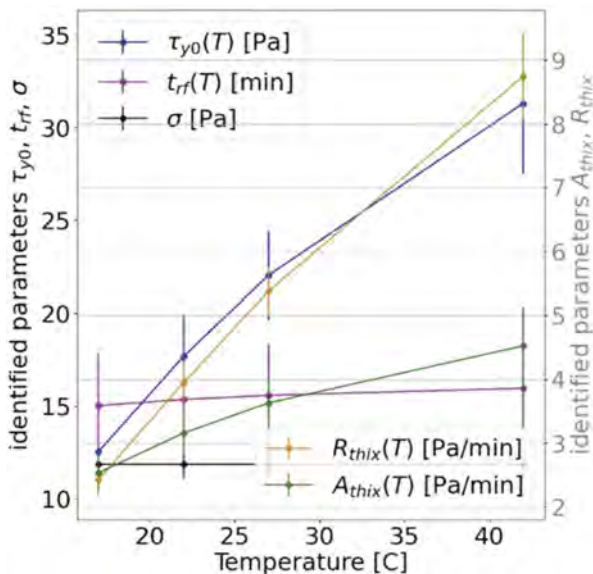


Figure 4. Inferred temperature dependency computed with Equation 6.

response as well as its first standard deviation for each temperature value and the measured data. A very good agreement for all investigated temperature values is reached even for those which were not included in the calibration part. In this way, the proposed model seems promising in predicting the temperature influence on the structural build-up of fresh mortar.

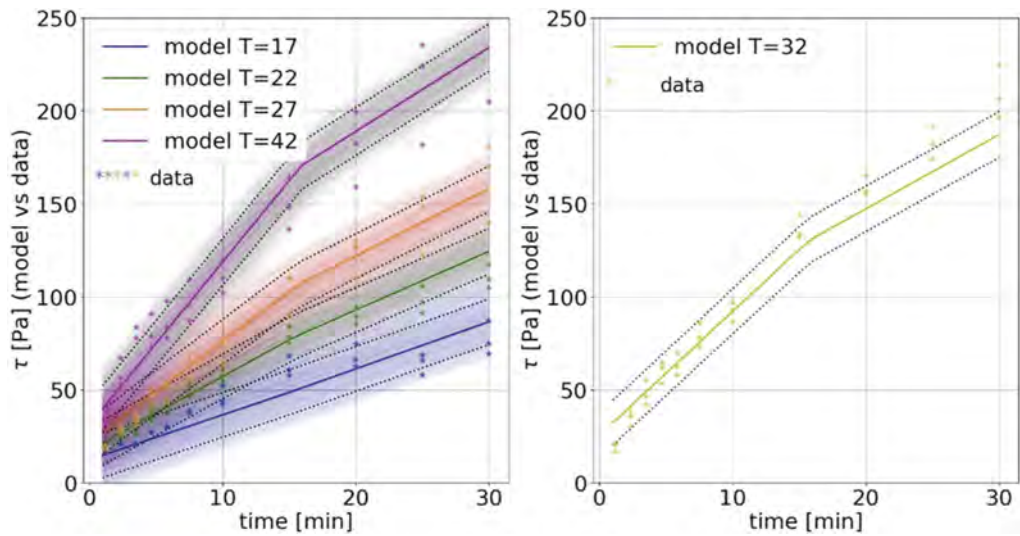


Figure 5. Inferred temperature dependency (mean as solid line and first standard deviation as dashed line of the static yield stress according to Equation 5 compared to the measured data (stars).

4 CONCLUSION

The present paper presents experimental results of the constant shear rate test indicating the influence of different ambient temperatures on the structural build-up evolution of mortar. The measured yield stress data show a presence of two stages: a re-flocculation period and a structuration stage. The temperature influence is more pronounced in the first re-flocculation stage dominated by physical processes. A new temperature dependent model approach is derived by extending the bi-linear Kruger model capturing this temperature sensitivity of the structural build-up for fresh cementitious materials. The model assumes temperature dependent functions based on the Arrhenius equation for the rates (re-flocculation and structuration rate) as well as for the initial yield stress and re-flocculation time parameters. In a Bayesian parameter estimation, the proposed model parameters are estimated for the investigated mortar composition. The analysis identifies a nearly linear temperature dependency in the re-flocculation rate, whereas the re-flocculation time is nearly temperature independent. Furthermore, a lower temperature sensitivity of the structuration rate with a logarithm shape over temperature is detected. The identified model shows very good agreement with the measured data, even for those not included in the parameter estimation process. Therefore, the proposed model could be used predicting the temperature sensitivity of structural build-up of cementitious materials. Of course, for more general conclusions further verification studies are required based on additional experimental data e.g. varying the cement type, the water content as well as using different admixtures and additions.

REFERENCES

Bogner, A., Link, J., Baum, M., Mahlbacher, M., Gil-Diaz, T., Lützenkirchen, J., Sowoidnich, T., Heberling, F., Schäfer, T., Ludwig, H.-M., Dehn, F., Müller, H.S. & Haist, M. 2020. Early hydration

- and microstructure formation of Portland cement paste studied by oscillation rheology, isothermal calorimetry, ¹H NMR relaxometry, conductance and SAXS. *Cement and Concrete Research* 130: 105977.
- Bos, F.P., Kruger, P.J., Lucas, S.S. & van Zijl, G.P.A.G. 2021. Juxtaposing fresh material characterisation methods for buildability assessment of 3D printable cementitious mortars. *Cement and Concrete Composites* 120: 104024.
- Bos, F.P., Menna, C., Pradena, M., Kreiger, E., da Silva, W.R.L., Rehman, A.U., Weger, D., Wolfs, R. J.M., Zhang, Y., Ferrara, L. & Mechtcherine, V. 2022. The realities of additively manufactured concrete structures in practice. *Cement and Concrete Research* 156: 106746.
- Bos, F.P., Wolfs, R.J.M., Ahmed, Z.Y., Hermens, L.J. & Salet, T.A.M. 2019. The influence of material temperature on the in-print strength and stability of a 3D print mortar. *Advances in Engineering Materials, Structures and Systems: Innovations, Mechanics and Applications*: 425–430.
- Carette, J. & Staquet, S. 2016. Monitoring and modelling the early age and hardening behaviour of eco-concrete through continuous non-destructive measurements: Part I. Hydration and apparent activation energy. *Cement and Concrete Composites* 73: 10–18.
- Huang, H., Huang, T., Yuan, Q., Zhou, D., Deng, D. & Zhang, L. 2019. Temperature dependence of structural build-up and its relation with hydration kinetics of cement paste. *Construction and Building Materials* 201: 553–562.
- Huang, T., Yuan, Q., Zuo, S., Yao, H., Zhang, K., Wang, Y., Xie, Y. & Shi, C. 2022. Physio-chemical effects on the temperature-dependent elasticity of cement paste during setting. *Cement and Concrete Composites* 134: 104769.
- Ivanova, I., Ivaniuk, E., Bisetti, S., Nerella, V.N. & Mechtcherine, V. 2022. Comparison between methods for indirect assessment of buildability in fresh 3D printed mortar and concrete. *Cement and Concrete Research* 156: 106764.
- Jiao, D., de Schryver, R., Shi, C. & de Schutter, G. 2021. Thixotropic structural build-up of cement-based materials: A state-of-the-art review. *Cement and Concrete Composites* 122: 104152.
- Kruger, J., Zeranka, S. & van Zijl, G. 2019. An ab initio approach for thixotropy characterisation of (nanoparticle-infused) 3D printable concrete. *Construction and Building Materials* 224: 372–386.
- Lye, A., Cicirello, A. & Patelli, E. 2020. A review of stochastic sampling methods for Bayesian inference problems. In: Zio, E & Beer, M. (eds.) *Proceedings of the 29th European Safety and Reliability Conference*. Singapore: Research Publishing.
- Metropolis, N., Rosenbluth, A. W., Rosenbluth, M.N., Teller, A.H. & Teller, E. 1953. Equation of State Calculations by Fast Computing Machines. *Journal of Chemical Physics* 21: 1087–1092.
- Mezhov, A., Robens-Radermacher, A., Zhang, K., Kühne, H-C., Unger, J.F. & Schmidt, W. 2022. Temperature Impact on the Structural Build-Up of Cementitious Materials – Experimental and Modelling Study. In: Buswell, R., Blanco, A., Cavalaro, S., Kinnell, P. (eds) *Third RILEM International Conference on Concrete and Digital Fabrication*. DC 2022. Loughborough: RILEM Bookseries,
- Mohammad-Djafari, A. 1998. From deterministic to probabilistic approaches to solve inverse problems, In: *Proceeding SPIE 3459, Bayesian Inference for Inverse Problems*. San Diego.
- Mohan, M.K., Rahul, A.V., de Schutter, G. & van Tittelboom, K. 2021. Extrusion-based concrete 3D printing from a material perspective: A state-of-the-art review. *Cement and Concrete Composites* 115: 103855.
- Perrot, A., Pierre, A., Vitaloni, S. & Picandet, V. 2015. Prediction of lateral form pressure exerted by concrete at low casting rates. *Materials and Structures* 48: 2315–2322.
- Poole, J.L., Riding, K.A., Folliard, K.J., Juenger, M. C. G. & Schindler, A. K. 2007. Methods for Calculating Activation Energy for Portland Cement. *ACI Materials Journal* 104: 303–311.
- Reiter, L., Wangler, T., Roussel, N. & Flatt, R.J. 2018. The role of early age structural build-up in digital fabrication with concrete. *Cement and Concrete Research* 112: 86–95.
- Roussel, N. 2006. A thixotropy model for fresh fluid concretes: Theory, validation and applications. *Cement and Concrete Research* 36: 1797–1806.
- Roussel, N., Ovarlez, G., Garrault, S. & Brumaud, C. 2012. The origins of thixotropy of fresh cement pastes. *Cement and Concrete Research* 42: 148–157.
- Watanabe, S. 2018. *Mathematical Theory of Bayesian Statistics* (1st ed.), Chapman and Hall/CRC.

Experimental study on effect of winter curing conditions on mechanical properties of concrete

F.L. Li, W.L. Lu, W.Q. Peng & Y.D. Tang
Beijing Jiaotong University, Beijing, China

L.F. Xu
Beijing Municipal Design Institute, Beijing, China

ABSTRACT: Compressive strength and elastic modulus are important mechanical properties of concrete, which are closely related to curing age, temperature, humidity and other conditions. The cube compressive strength, prism axial compressive strength, stress-strain relationship and elastic modulus of C50 concrete were tested under winter construction and curing condition. The effects of curing age, curing temperature and humidity on the development of mechanical properties were analyzed. The results show that with the increase of curing age, the compressive strength and elastic modulus of concrete increased rapidly in the early stage and slowly in the later stage. The compressive strength and elastic modulus of concrete cured under the natural conditions were lower than those of standard curing. The curing method had a great influence on the mechanical properties of short age specimens. Finally, according to the test results, the curing suggestions of concrete in winter construction were put forward, which provides reference for speeding up the project progress and ensuring the quality of the project.

1 INTRODUCTION

Concrete curing conditions, especially environmental temperature and environmental humidity, have a great influence on the mechanical properties of concrete. The lower environmental temperature and humidity values in the winter in northern China resulted in a large difference between the mechanical property growth of concrete and that under standard indoor curing. In recent years, to meet the development needs of transportation facilities, there are many bridges, especially assembled bridges, using winter construction methods, which brings challenges to the project schedule control (Freyermuth, 1999). Early strength and elastic modulus growth of concrete is particularly important under winter construction conditions. On the one hand, the reasonable connection between processes is a strong guarantee to speed up the project progress. If the early strength and elastic modulus values of concrete do not meet the construction requirements, it will seriously delay the project progress and reduce the project quality (Chen, & Duan, 2014). On the other hand, the early strength of concrete develops more rapidly than the elastic modulus, and concrete beams with small values of elastic modulus will lead to increased creep in the later stages of the beam after prestressing tendons are tensioned. Large-span continuous rigid frame bridge and continuous beam bridge will produce large deformation and deflection after several years of use, which will seriously affect the safety and durability of the bridges (Yan & Xie 2017; Xie & Cui 2019). Therefore, in the construction of bridge superstructures, dual parameter control of concrete strength and elastic modulus is usually required. Mechanical property parameters such as compressive strength and elastic modulus of concrete are influenced by a variety of conditions such as material composition, curing age and curing method, and have obvious regional and climatic characteristics (Xie & Li 2014). Among the existing research (Xie & Yan 2018), there are more studies on the mechanical properties of concrete at 28 days, while there is a relative lack of

research on the effects of winter construction and curing conditions on the developmental changes of concrete mechanical properties.

In this paper, cube compressive strength, prismatic axial compressive strength, stress-strain relationship during compression and elastic modulus of concrete were tested under winter construction and curing conditions, and the effects of curing age, curing temperature and curing humidity on the development of mechanical properties were analyzed, which can provide a reference to ensure the safety, suitability and durability of the project.

2 EXPERIMENTAL PROGRAM

2.1 Specimen fabrication and maintenance

2.1.1 Fabrication

Cube specimens with size of 100 mm×100 mm×100 mm were used for cubic compressive strength test, 3 pieces in each group. Prismatic specimens with size of 100 mm×100 mm×300 mm were used for axial compressive strength and elastic modulus test. 6 pieces of each group were used, 3 pieces for axial compressive strength test and the other 3 pieces for elastic modulus test. When testing the axial compressive strength of prisms, the stress-strain relationship during compression is also tested. The specimens are formed by mechanical mixing and artificial vibrating.

2.1.2 Maintenance

The maintenance methods are divided into two types of standard curing and natural curing. The environmental temperature for standard curing is 20±1 °C, and the environmental humidity is >95 %rh. The process of natural curing is as follows: the specimens were left in the natural environment with temperature 6~9 °C and humidity about 40% rh for 3 hours after the specimens were poured, and then the specimens were steam cured by steam curtain(steam curing temperature 30~35 °C, humidity>85 %rh), and the steam curtain was withdrawn after 7 hours of steam curing, and the specimens were placed in the natural environment to continue curing.

The cube compressive strength of 1 day, 6 days, 7 days, 28 days and 60 days and the axial compressive strength and elastic modulus of 7 days, 10 days and 60 days were tested. Take the specimens of different curing methods under the same age for testing, one curing method corresponds to a group of specimens.

2.2 Material properties

The cement was P·O 42.5 grade cement, and the physical and mechanical properties are shown in Table 1. The sand was natural river sand, and the indicators are shown in Table 2. The coarse aggregate was continuous graded aggregates from 5 to 25 mm, and the performance indexes are shown in Table 3. The indicators of fly ash are shown in Table 4. The external additive was high performance water reducing agent, which meets the requirements of Chinese standard GB 50119-2013 (2013) Mixing water was daily drinking water. The concrete was C50 pea gravel concrete with water-cement ratio of 0.37 and slump of 210 mm, as shown in Table 5.

Table 1. Physical and mechanical properties of cement.

Flexural strength (MPa)		Compressive strength(MPa)		Condensation time (mins)		Standard consistency water (%)
3 days	28 days	3 days	28 days	Initial	final	27.4
5.4	8.1	26.4	54.1	214	265	

Table 2. Indicators of river sand.

Fineness modulus	Mud content (%)	Mud lump content (%)	Apparent density (kg/m ³)	Bulk density (kg/m ³)
3.2	5.1	0.4	2710	1660

Table 3. Indicators of coarse aggregate.

Mud content (%)	Mud lump content (%)	Needle flake particle content (%)	Crushing value index (%)	Apparent density (kg/m ³)	Bulk density (kg/m ³)
0.9	0.3	5	8.6	2710	1660

Table 4. Indicators of fly ash.

Fineness (%)	Burning loss (%)	Water demand ratio (%)
9.4	4.1	97

Table 5. Mix ratio of C50 pea gravel concrete.

Amount of materials (kg/m ³)					
Cement	Water	Sand	Coarse aggregate	Fly ash	water reducing agent
400	147	726	1088	83	5.9

2.3 Test method

The tests of concrete cubic compressive strength, axial compressive strength and elastic modulus were carried out according to Chinese standard GB/T 50081-2019 (2019). The stress-strain relationship of the concrete during compression was tested as follows: after wiping and grinding the surface of the prismatic specimen, four strain gauges were symmetrically pasted at the center of the four sides of the specimen, as shown in Figures 1(a)-(b). The test setup was YA-3000C automatic pressure machine with accuracy level 1, as shown in Figure 1(c). The strain was collected by the static strain test and analysis system, and the stress was calculated by Equation (1).

$$\sigma = \frac{F}{A} \quad (1)$$

Where σ is the specimen stress (MPa); F is the value of the loading force (N); A is the cross-sectional area of the specimen (mm²).

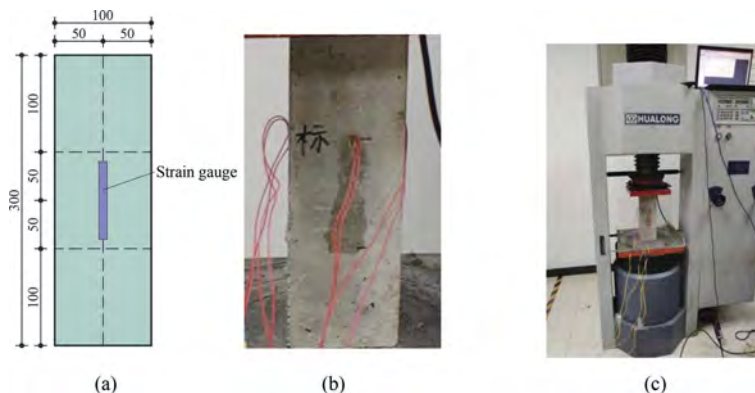


Figure 1. Strain gauge arrangement and test setup: (a) 3D view, (b) Photo, and (c) Test setup.

2.4 Test results

The cubic compressive strength, axial compressive strength and elastic modulus data of the same group of specimens were averaged and the results were summarized in Tables 6 and 7.

Table 6. Test results of the cube compressive strength.

Age (day)		1	6	7	28	60
Standard curing	Strength (MPa)	34.8	50.1	50.9	68.3	72.1

Table 7. Test results of the axial compressive strength and elastic modulus.

Age (day)	Axial compressive strength (MPa)		Elastic modulus (GPa)	
	Standard curing	Natural curing	Standard curing	Natural curing
7	43.0	39.2	31.4	28.7
10	45.7	41.4	34.7	30.2
60	59.3	53.3	46.6	43.4

3 EFFECT OF CURING AGE ON THE MECHANICAL PROPERTIES OF CONCRETE

3.1 Cube compressive strength

The variation of the cube compressive strength of concrete under standard curing with the curing age is shown in Figure 2. From Figure 2, the cube compressive strength grew monotonically with the curing age, but the growth rate slowed down and tended to converge. The cube compressive strength of the specimens with ages of 1 day, 6 days, 7 days and 60 days were 50.95 %, 73.35 %, 74.52 % and 105.56 % of the cube compressive strength of the specimens with ages of 28 days, respectively. Compared with the standard value of cube compressive strength of 50 MPa for C50 concrete, the percentage increase in cube compressive strength of the specimens with age of 1 day, 6 days, 7 days, 28 days and 60 days were -30.4 %, 0.2 %, 1.8 %, 36.6 % and 44.2 %, respectively. The data show that the cube compressive strength of this batch of specimens grew faster in the early stage and slowed down in the later stage, with early strength characteristics.

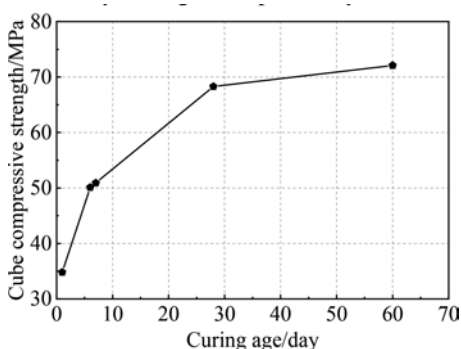


Figure 2. Variation curve of cube compressive strength with curing age.

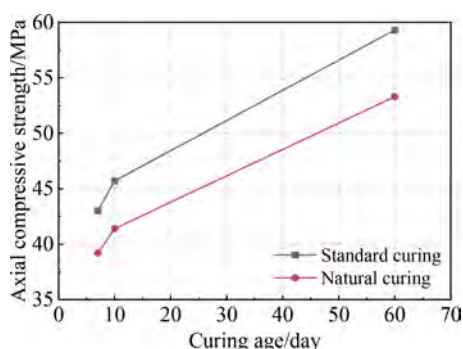


Figure 3. Variation curve of axial compressive strength with curing age.

3.2 Axial compressive strength

The variation of axial compressive strength of concrete with the curing age for different curing methods is shown in Figure 3. From Figure 3, the variation pattern of axial compressive strength with the curing age tended to be the same for different curing methods, all of which showed a fast growth of strength in the early stage and a slow growth of strength in the later stage. At the age of 7 days, the axial compressive strength of standard curing and natural curing reached 72.51% and 73.55% of the 60-day strength, respectively. At the age of 10 days, the axial compressive strength of standard curing and natural curing reached 77.07% and 77.67% of the 60-day strength, respectively.

3.3 Elastic modulus

The elastic modulus is an important mechanical parameter of concrete, which reflects the relationship between force and deformation. The factors affecting the value of the elastic modulus of concrete include external factors and internal factors. The external factors are specimen age, specimen size, load holding time, curing temperature and curing humidity, etc. The internal factors are mainly concrete raw materials and mix ratio. The variation of the elastic modulus of concrete with the curing age for different curing methods is shown in Figure 4.

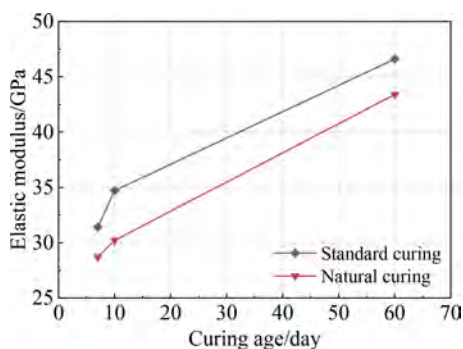


Figure 4. Variation curve of elastic modulus with curing age.

As can be seen from Figure 4, the variation of elastic modulus of concrete with the curing age was similar for different curing methods. At the age of 7 days, the elastic modulus of standard curing and natural curing were 67.38% and 66.13% of the 60-day elastic modulus, respectively. At the age of 10 days, the elastic modulus of standard curing and natural curing were 74.46% and 69.59% of the 60-day elastic modulus, respectively.

3.4 Elastic modulus

The stress-strain relationship of concrete is an important basis for studying the strength, deformation and crack development of specimens. The shape of the stress-strain curve reflects the elastic, plastic and fracture processes occurring in the material under the action of external forces, which is important for analyzing the force behavior of the specimen. The stress-strain curves of concrete under different curing methods are shown in Figure 5, where the strain is positive in compression.

Figure 5 (a) shows that: i) at the initial stage of loading, the strains of the specimens at different ages varied approximately linearly. ii) The slope of the stress-strain curve at the initial stage of loading was progressively larger for the specimens at 7, 10 and 60 days of age, indicating that the degree of concrete hardening gradually increased for the specimens at 7, 10 and 60 days of age. This also reflected the increase of the elastic modulus value with the increase of the curing age. iii) Loaded to failure, the stresses in the specimens at 7, 10 and 60 days of age were approximately 40 MPa, 50 MPa and 65 MPa, respectively, indicating that the compressive strength of concrete gradually increased with the growth of the curing age. iv) The stress-strain curves of the specimens at 7 and 10 days of age grew more stable, without obvious turning points, and with lower elastic modulus values. There was an obvious turning point (stress value approximately 20 MPa, strain value approximately $375 \mu\epsilon$) in the growth process of the stress-strain curve for the specimens aged 60 days, after which the slope of the curve decreased, indicating the rapid development of microcracks inside the specimens, resulting in a decrease in the ability of the specimens to resist deformation.

Figure 5 (b) shows that: i) the development of stress-strain curves for specimens at 10 and 60 days of age were closer at the initial stage of loading. ii) The specimens with an age of 7 days had larger strain values at the initial stage of loading and larger strain growth in the middle and late stages, indicating that the resistance to deformation of the specimens under

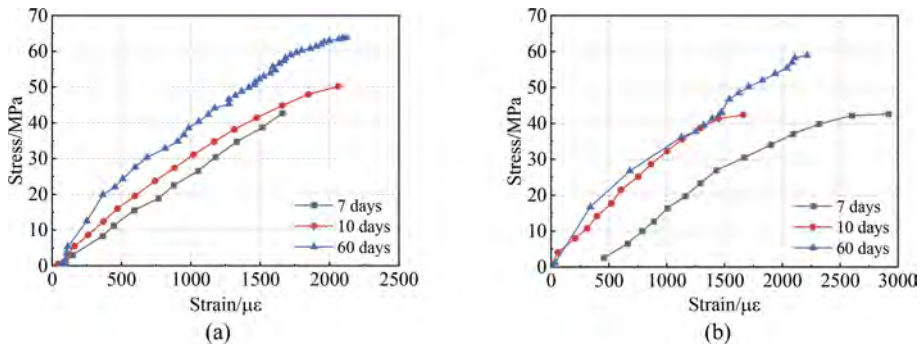


Figure 5. Stress-strain relationship of concrete under different curing methods: (a) Standard curing and (b) Natural curing.

natural curing was poor. iii) With the growth of the curing age, the compressive strength and elastic modulus of concrete also gradually increased.

4 EFFECT OF CURING METHOD ON THE MECHANICAL PROPERTIES OF CONCRETE

4.1 Axial compressive strength

According to the Chinese standard GB 50010-2010 (2010), the standard value of axial compressive strength of C50 concrete is 32.4 MPa, and the percentage increase of axial compressive strength under different curing methods was calculated using this value as the strength base value, as shown in Figure 6. From Figure 6, the percent increase of axial compressive strength under standard curing was approximately 15 % higher than that under natural curing for the specimens at 7, 10 and 60 days of age. This is because the higher environmental temperature and environmental humidity of standard curing make the cementitious material hydrate faster and therefore the axial compressive strength is higher.

4.2 Elastic modulus

According to the Chinese standard GB 50010-2010, the standard value of elastic modulus of C50 concrete is 34.5 GPa, and using this value as the base value of elastic modulus, the percentage increase of elastic modulus under different curing methods was calculated, as shown in Figure 7.

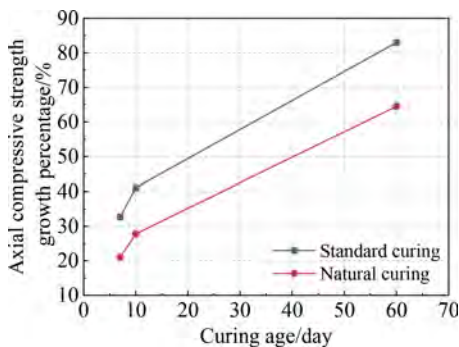


Figure 6. Variation curve of the percentage growth of axial compressive strength with the curing age.

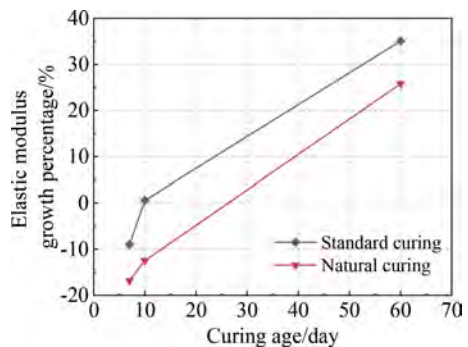


Figure 7. Variation curve of the percentage growth of elastic modulus with the curing age.

As can be seen from Figure 7, the percentage increase of the elastic modulus under standard curing was approximately 10% higher than that under natural curing for the specimens at 7, 10 and 60 days of age, which is consistent with the law of development of axial compressive strength of concrete, where the value of elastic modulus under standard curing was higher.

4.3 Stress-strain relationship

The stress-strain curves of concrete at different ages of specimens under standard curing and natural curing are shown in Figure 8. Figure 8 shows that: i) the specimens with an age of 7 days, especially under natural curing, had larger strain values at the initial stage of loading and larger strain growth at the middle and late stages, indicating that the resistance to deformation of the specimens under natural curing was poorer than under standard curing. ii) At the early stage of loading, partial overlap was observed at the initial section of the stress-strain curves for the 10-day and 60-day age specimens under different curing methods, while it did not occur for the 7-day age specimens (Figure 8 (a)). This may be because the short-age specimens under natural curing were more sensitive to environmental temperature and environmental humidity, resulting in inadequate hydration reaction of cement, which in turn caused poor resistance to deformation of the specimens, indicating that the curing method had a greater effect on the mechanical properties of the short-age specimens than the long-age specimens. iii) The slope of the concrete stress-strain curves began to differ for specimens at 7, 10 and 60 days of age under different curing methods in the middle and late stages of loading. The slope of the curve under natural curing was smaller and gradually flattened, while the slope of the curve under standard curing varied more than that of natural curing, which indicated that the compressive strength of concrete under standard curing was higher than that under natural curing.

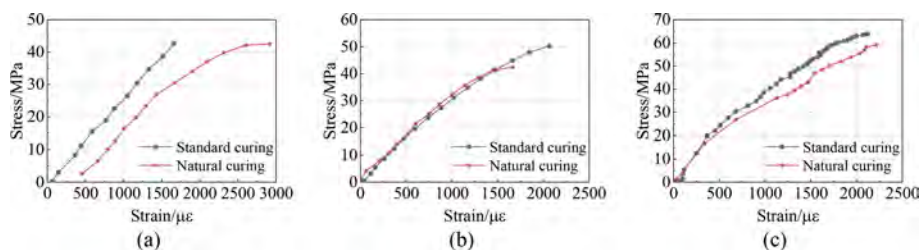


Figure 8. Stress-strain relationship of concrete at different ages: (a) 7 days of age, (b) 10 days of age, and (c) 60 days of age.

5 CONCRETE MAINTENANCE RECOMMENDATIONS UNDER WINTERCONSTRUCTION

Under winter construction conditions, the growth of early strength and elastic modulus of concrete is particularly important (Xie & Zhao 2018). For concrete beams with prestressed tendons, if the early elastic modulus value does not meet the design requirements, the later deformation and prestress loss of the beam after tensioning of prestressed tendons increases, thus reducing the safety and durability of the structure. For the project with time limit, only the early strength and elastic modulus value of concrete reach the construction requirements, so that the next process can be carried out as scheduled or ahead of schedule, thus speeding up the project progress and improving the quality of the project.

The early strength and elastic modulus values of concrete depend on the rate of hydration reaction of cement. The higher the external temperature, the faster the hydration process of the cement. The higher the external humidity and the longer the time, the slower the relative humidity inside the specimen decreases and the more complete the cement hydration reaction is (Gao & Shi 2021; Chen & Zhou 2021).

To guarantee the quality of winter concrete maintenance, the following recommendations are proposed in this paper combined with the test results: i) increase the curing temperature and curing humidity, and extend the period of steam curing, to approach or reach the standard curing conditions is better. ii) Under the premise of not affecting the progress of the project, properly extend the specimen curing age. iii) Age as a variable, increase the number of specimen groups, and increase the frequency of compressive strength and elastic modulus tests to grasp the development of mechanical properties of concrete in real time. iv) The specimens under natural curing are cured for at least 10 days before the subsequent processes are carried out.

6 CONCLUSIONS

By testing the mechanical properties of concrete under winter construction and winter curing conditions, the following main conclusions were obtained.

- (1) Under standard curing, the cube compressive strength of C50 concrete grew monotonically with the gradual increase of curing age, but the growth rate was decreasing. The cube compressive strength of concrete exhibited early strength characteristics.
- (2) With the increase of the curing age, the axial compressive strength and elastic modulus of concrete developed similarly, both showing the law of fast growth of early strength and slow growth of late strength.
- (3) The compressive strength and elastic modulus values of concrete under natural curing were lower than those of standard curing. The resistance of concrete to deformation under natural curing was worse than standard curing.
- (4) The curing method had a greater effect on the mechanical properties of the short-age specimens than the long-age specimens.
- (5) The paper proposed recommendations for winter concrete maintenance, which accumulates experience for speeding up the project progress and guaranteeing the project quality.

REFERENCES

- Chen, W. F. & Duan, L. 2014. *Bridge engineering handbook: construction and maintenance*. CRC press.
- Chen, H. B., Zhou, J.C., Wang, B. B. 2021. Experimental study on compressive strength of concrete after high temperature. *Concrete*. 10:23–26. (In Chinese)
- Cmc (China Ministry of Construction), 2013. Code for concrete admixture application, Cmc, Bei jing, GB 50119-2013. (In Chinese)
- Cmc (China Ministry of Construction), 2019. Concrete physical and mechanical properties test method standards, Cmc, Beijing, GB/T 50081-2019. (In Chinese.)
- Cmc (China Ministry of Construction), 2010. Design standards for concrete structures, Cmc, Bei jing, GB 50010-2010. (In Chinese)
- Freyermuth, C.L. 1999. Ten years of segmental achievements and projections for the next century. *PCI Journal*.
- Gao, Y., Shi, H. L., Gao, Q. Q. 2021. Influence of different curing regimes on the mechanical properties of ultra-high performance concrete. *Concrete*. 06:108–111. (In Chinese)
- Xie, J., Cui, N., Yan, J. B., Yu, J. 2019. Experimental study on prestress losses of post-tensioned concrete members at ultra-low temperatures. *Structural Concrete*. 20, 1828–1841.
- Xie, J., Li, X., Wu, H. 2014. Experimental study on the axial-compression performance of concrete at cryogenic temperatures. *Construction and Building Materials*. 72, 380–388.
- Xie, J., & Yan, J. B. 2018. Experimental studies and analysis on compressive strength of normal-weight concrete at low temperatures. *Structural Concrete*. 19, 1235–1244.
- Xie, J., Zhao, X., Yan, J. B. 2018. Experimental and numerical studies on bonded prestressed concrete beams at low temperatures. *Construction and Building Materials*. 188, 101–118.
- Yan, J. B. & Xie, J. 2017. Behaviours of reinforced concrete beams under low temperatures. *Construction and Building Materials*. 141, 410–425.

Hygro-thermo-chemo-mechanical coupled discrete model for the self-healing in Ultra High Performance Concrete

A. Cibelli, L. Ferrara & G. Di Luzio

Department of Civil and Environmental Engineering, Politecnico di Milano, Milan, Italy

ABSTRACT: Reliable durability predictions and design for advanced cement-based materials cannot disregard the modelling of their inherent self-healing capability. A discrete meso-scale model to simulate the recovery in water tightness, stiffness and strength induced by the (stimulated) autogenous healing of cracks for Ultra High Performance Concrete is presented. In this paper the model is implemented into the numerical framework of the Multiphysics-Lattice Discrete Particle Model (M-LDPM), resulting from the coupling of the Hygro-Thermo-Chemical (HTC) model and Lattice Discrete Particle Model (LDPM). Consistently with experimental evidence, the development of the self-repairing process is modelled as consisting of two independent stages: (a) the healing of matrix cracks, affecting both moisture permeability and fracture strength in the cracked state, and (b) the recovery in terms of fibre bridging action, relying on the adhesion between the healing products and the walls of the tunnel cracks which form during the fibre debonding process. This research activity is framed into the Horizon 2020 project ReSHEALience (GA 760824).

1 INTRODUCTION

Concrete cracks, even in service conditions, represent a predisposing factor for several degradation phenomena. As a consequence, in the last decades the comprehension of the processes affecting the concrete long-term performance has gathered an increasing interest among concrete professionals and researchers. Reliable durability predictions and design for either ordinary and/or advanced cementitious materials cannot disregard a proper modelling of their inherent self-healing capability. As demonstrated in a number of experimental works (e.g. Snoeck and De Belie 2015; Ferrara et al. 2018), the latter might lead to a significant recovery of physical and, in some cases, mechanical properties in the cracked state.

In structural concrete research, the term self-healing refers to the material capacity of repairing the damage in cracked state autonomously. Three major categories of concrete self-healing can be identified: (i) autogenous when the mixture composition only includes regular concrete constituents, (ii) stimulated autogenous when tailored constituents of akin chemical nature are employed to facilitate the process, and (iii) autonomic/engineered when the inclusion of specific additions, not normally employed as such, is used with the explicit purpose of favouring/activating the healing reactions.

From an accurate literature survey it stands out that, over the years, researchers have placed much more effort on the experimental investigation of the self-healing process, rather than on the modelling issues. As a matter of fact, only few models have been developed to simulate how mechanical performance of concrete are affected by the healing of cracks (Barbero et al. 2005, Voyiadjis et al. 2011, Aliko-Benítez et al. 2015, Hilloulin et al. 2016, Davies and Jefferson 2017, Oucif et al. 2018, Di Luzio et al. 2018, Jefferson et al. 2018, Yang et al. 2020, Chen et al. 2021). To the best of the authors' knowledge, none of them addresses the issue concerning the reduction of moisture permeability due to the autonomous cracks clogging. Furthermore, the majority of the published models relies on continuum-based

approaches, and consider the healing-induced effects on the mechanical properties as a smeared contribution in terms of stiffness and strength recovery in the cracked state. With this approach, they miss in simulating the local nature of the phenomena.

In this paper a discrete model to simulate the recovery in water tightness, stiffness and strength induced by the (stimulated) autogenous healing of cracks for Ultra High Performance Concrete is presented. The model is implemented into the numerical framework of the Multi-physics-Lattice Discrete Particle Model (M-LDPM) (Alnagar et al. 2017), resulting from the coupling of the Hygro-Thermo-Chemical (HTC) model (Di Luzio and Cusatis 2009, Pathirage et al. 2019) with the Lattice Discrete Particle Model (LDPM) (Cusatis et al. 2011) and its extension to fibre-reinforced concrete (LDPM-F) (Schauffert and Cusatis 2012). Consistently with experimental evidence, the development of the self-repairing process is modelled as consisting of two independent stages: (a) the healing of matrix cracks, affecting both moisture permeability and fracture strength in the cracked state, and (b) the recovery in terms of fibre bridging action, relying on the friction between the healing products and the walls of the tunnel cracks which form during the fibre debonding process.

This research activity was framed into the Horizon 2020 project ReSHEALience, which was terminated in March 2022 and delivered two valuable results: (i) the concept of Ultra High Durability Concrete, articulated into a sound approach to tailor the mix design depending on the environmental conditions to face (Lo Monte and Ferrara 2020, Lo Monte and Ferrara 2021), and (ii) a Durability Assessment-based Design strategy, validated against laboratory evidences and on-site monitoring data (Al-Obaidi et al. 2021).

2 MODELLING APPROACH

The modelling approach herein presented can be classified as a multi-scale model, in which two different scales of damage phenomena are considered: (i) matrix cracks at the mesoscale, and (ii) fibre-matrix interface cracks, which are governed by mechanisms occurring at the microscale (Figure 1). In the following, the latter are also referred to as *tunnel* cracks.

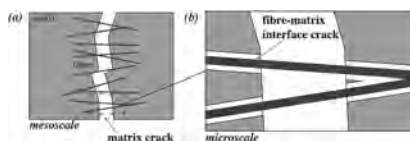


Figure 1. (a) matrix cracks at the mesoscale; (b) fibre-matrix interface cracks at the microscale.

The modelling approach relies on the idea for which the self-healing of matrix and tunnel cracks affect the material mechanical behaviour differently. For this reason, the autogenous repairing of the matrix cracks is implemented within the constitutive fracture law at the meso-scale, whereas the effect of healing on the fibres response is taken into account within the calculation of the bridging force carried by the discrete fibre reinforcement.

In the proposed model, the moisture permeability is assumed to be affected only by the matrix cracks, then only their closure contributes to the recovery in water-tightness that healed material might experience. The healing of the tunnel cracks has been considered to play a role exclusively on the mechanical behaviour.

3 NUMERICAL IMPLEMENTATION IN M-LDPM

3.1 Evolution of the healing process

The healing kinetic law formulated for plain cementitious materials (Di Luzio et al. 2018) can be employed for fibre-reinforced composites as well. Since the damage in the mechanical model evolves a two different scales (i.e. meso- and microscale), the implementation in the HTC module within the M-LDPM framework is performed by following the same conceptual

differentiation between matrix and tunnel cracks. This yields a two-fold advantage: (i) the possibility of having two separate internal variables describing the damage healing phenomena (i.e. λ_{sh}^m for matrix cracks and λ_{sh}^f for tunnel cracks) feeding the mechanical model at two different levels, and (ii) the chance of capturing the effect that the self-sealing of the matrix cracks has on the moisture permeability in the cracked state. In the following the formulation emphasising this differentiation is reported, with no theoretical differences with respect to the original one (Di Luzio et al. 2018).

Hereinafter the superscript k can be either m or f depending on which scale of damage is of interest. When $k = m$ formulas and parameters refer to the matrix cracks at the mesoscale, whereas with $k = f$ they refer to tunnel cracks at the microscale.

The kinetic laws reads

$$\dot{\lambda}_{sh}^k = \tilde{A}_{sh}^k (1 - \lambda_{sh}^k) \quad (1)$$

in which \tilde{A}_{sh}^k , inversely proportional to the reaction characteristic times, is calculated as

$$\tilde{A}_{sh}^k = \tilde{A}_{sh0}^k \cdot f_h(h) \cdot f_w^k(w_c) \cdot \exp\left[-\frac{E_{sh}^k}{R} \left(\frac{1}{T} - \frac{1}{T_{ref}}\right)\right] \quad (2)$$

where $\tilde{A}_{sh,0}^k$, namely the inverse of the reaction characteristic times in standard conditions (RH=100%, $T = T_{ref}$, $w_c = 0$), values

$$\tilde{A}_{sh0}^k = \tilde{A}_{sh1}^k (1 - \alpha_c^{sh0}) c + \tilde{A}_{sh2}^k \cdot ad \quad (3)$$

where c and ad are the cement and healing-promoting admixture content, respectively. The material parameters E_{sh}^k , \tilde{A}_{sh1}^k , and \tilde{A}_{sh2}^k are calibrated against experimental data, allowing to capture the key aspects of phenomena occurring at two different scales (Cibelli et al. 2022). In Eq. 2 the relative humidity, h , and temperature, T , fields are provided by the HTC model.

It is worth highlighting that the coefficient $f_w^k(w_c)$ provides the possibility of calibrating the effect of crack width on the process kinetic differently for matrix and tunnel cracks. Such double degree of freedom allows to trigger the healing model (i) at the mesoscale for cracks larger than the material macroporosity ($\approx 10 \div 20 \mu\text{m}$), and (ii) at the microscale for crack openings one order of magnitude smaller, as the debonding stage is typically characterised by narrower cracks.

The coefficient $f_h(h)$ accounts for relative humidity and simulates the relevant role played by the moisture supply, making the process proceed or stop whether the healing water-driven reactions are fed or not.

3.2 Moisture permeability in the healed material

The healing process has a significant effect on the moisture diffusion in presence of cracks due to the crack closure effect. This phenomenon is taken into account straightforwardly in the factor governing the crack size dependence of water permeability $f_D(w_c)$, whose formulation reads

$$f_D(w_c) = \frac{D_h^{cracked}(h, T, w_c)}{D_h^{uncracked}(h, T)} = 1 + \frac{999e^{n_c} \xi}{1 - (1 - e^{n_c}) \xi} \quad (4)$$

in which $\xi = \min[\max(w_c - w_{c0}; 0) / w_{c1} - w_{c0}; 1]$, by replacing the crack opening w_c with $w_c \cdot (1 - \lambda_{sh}^{(m)})$. It means that the actual damage affecting the moisture permeability is reduced proportionally to the evolution of the self-healing process up to completion, i.e. $w_c \cdot (1 - \lambda_{sh}^{(m)}) = 0$ for $\lambda_{sh}^{(m)} = 1$. It is worth emphasising that $\lambda_{sh}^{(m)}$ assumes the meaning of matrix crack closure degree. w_{c0} and w_{c1} express two threshold values. When $w_{c0} \leq w_c \leq w_{c1}$, D_h and moisture transport phenomena undergo a sudden and steep increment, due to a material permeability up to 1000 times larger. For $w_c \geq w_{c1}$, instead, the moisture flux stops growing even though cracks continue widening.

3.3 Self-healing of matrix cracks in LDPM

The matrix cracks (Figure 1a) are induced by the loads, either mechanical or environmental, and are responsible of the fibres mechanical activation: as long as no cracks intersect a fibre, the latter does not contribute to the structural response.

For matrix cracks, the healing effect is modelled by enforcing a homothetic expansion of the LDPM boundary limit curve $\sigma_{bt}(\varepsilon, \omega) = \sigma_0(\omega) \exp[-H_0(\omega) \langle \varepsilon_{max} - \varepsilon_0 \rangle / \sigma_0(\omega)]$, as more pronounced as more the repairing process has developed. Experimental evidences have confirmed that even plain concrete specimens, once loaded, fractured and unloaded, might show a recovery in strength and stiffness if re-loaded after a curing period in a moist environment. This is mainly due to two water-driven phenomena occurring in the cracks: delayed hydration and calcium carbonation precipitation. The healing products partially restore the material continuity, lowering, at least locally, the material bulk permeability and limiting the ingress of aggressive agents. The effect on the mechanical response, instead, depends on: (i) the chemical bounds between the filling products and the crack walls, and (ii) the nature, strength and stiffness of the healing products. Because of this, it is not granted that the crack sealing results in an actual concrete healing.

In this work, the modelling strategy adopted relies on the homothetic expansion of the boundary curve $\sigma_{bt}(\varepsilon, \omega)$ (Figure 2a) proportional to the healing degree λ_{sh}^m . Then, it allows to capture the recovery in strength, without varying the crack width within the numerical framework. Therefore, the healed material must be allowed to have a fracture strength exceeding that of the same material with the same level of damage with no healing occurred.

In LDPM, the healing implementation affects the strength limit calculation, thus, on turn, the limit curve. The updated version of the healing dependent-constitutive law relevant to the fracture behaviour reads

$$\sigma_0(\omega, \lambda_{sh}^m) = \sigma_0(\omega) (1 + c_{sh} \cdot \lambda_{sh}^m) \quad (5a)$$

$$\sigma_{bt}(\varepsilon, \omega, \lambda_{sh}^m) = \sigma_0(\omega, \lambda_{sh}^m) \exp \left[-H_0(\omega) \frac{\langle \varepsilon_{max} - \varepsilon_0 \rangle}{\sigma_0(\omega, \lambda_{sh}^m)} \right] \quad (5b)$$

In Eq. 5a, c_{sh} is an empirical coefficient steering the impact of crack closure on mechanical strength. It is defined as *healing mechanical impact coefficient*. The parameter c_{sh} depends on several aspects, e.g. curing conditions and mixture composition, therefore, it has to be calibrated experimentally. Looking at the updated equation of the boundary curve (Eq. 5b), it is important to notice that the healing, through the product $c_{sh} \cdot \lambda_{sh}^m$, governs the shape of the softening branch and sets the stress limit for the earlier stage of the constitutive law, namely when the maximum strain does not exceed the elastic limit. However, though the modelling strategy involves both linear and post-peak behavior, the former is never imposed at the mesoscale, being the limit curve expanded exclusively on those facets which experience cracking and healing.

3.4 Self-healing of tunnel cracks in LDPM-F

The fibre-matrix interface cracks (Figure 1b) develop during the interface debonding. Experimental evidences, collected through single-fibre pull-out tests, stopped after the first load drop and resumed up to rupture upon curing featuring different duration and exposure conditions (Qiu et al. 2019), confirmed that the healing of the interface cracks does affect the pull-out strength. As a matter of fact, whenever the healing process happens, delayed hydration products and CaCO_3 crystals fulfill the tunnel between the fibre and the surrounding mortar. This results in a recovery of the interface frictional bond. The phenomenon is implemented in LDPM-F by updating the value of the fibre bridging force $P(v)$ with a coefficient proportional to λ_{sh}^f . The updated constitutive law for the fibre load reads

$$P(v, \lambda_{sh}^f) = (1 + \gamma_{sh} \cdot \lambda_{sh}^f) P(v) \leq \alpha \cdot P_0 \quad (6)$$

Referring to a single-fibre pull-out test, in Figure 2b the effect of the tunnel crack self-healing on the mechanical response is qualitatively shown. After the loading and unloading stages (branches L and U), the specimen is exposed to given environmental conditions for a time span long enough to permit the self-healing process to develop. The cured specimen is then reloaded (branch R) up to rupture. Due to the recovered frictional bond, the specimen might experience a recovery in stiffness and strength, to an extent proportional to the degree of completion of the healing process. By means of the device in Eq. 6, LDPM-F is updated to be capable of capturing this experimental evidence. In Figure 2b the updated constitutive law is plotted with reference to increasing self-healing degrees, in the hypothesis of $\gamma_{sh} = 1.00$.

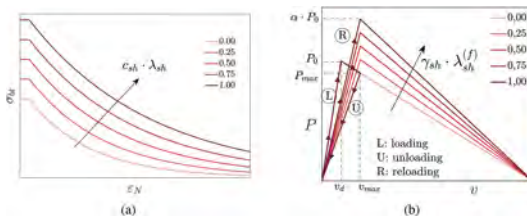


Figure 2. Healing model: (a) matrix cracks; (b) fibre-matrix interface (or tunnel) cracks.

The coefficient γ_{sh} has a physical meaning similar to c_{sh} . It governs the impact that the healing of the tunnel cracks has on the fibres contribution to the mechanical equilibrium. With $\gamma_{sh} = 0$ it is possible to capture the crack sealing, whereas if $\gamma_{sh} \geq 0$ the load carried by the fibre is enhanced thanks to the increased friction along the crack walls. The latter has an upper bound ($\alpha \cdot P_0$) in which the bridging force at full debonding P_0 is either amplified or reduced by the coefficient α . Both γ_{sh} and α are material parameters to calibrate against experimental data. Depending on the composition of the cementitious composites, the technique adopted to engineer the process, the type of the fibres (i.e. material, geometry), the curing conditions and the loading regimes, the healing might allow to recover either partially or entirely the fibre load bearing capacity. The parameter α sets the maximum achievable level of recovery. Once calibrated experimentally, γ_{sh} must comply with the condition for which, in case of full fulfilment of the tunnel crack:

$$\text{if } \lambda_{sh}^f = 1.00 \Rightarrow \gamma_{sh} \leq \frac{\alpha \cdot P_0}{P(v)} - 1 \quad (7)$$

4 VALIDATION OF THE IMPLEMENTED MODEL

4.1 Matrix cracks

The model implementation is expected to affect the mechanical response of the material in tension and shear. In order to investigate the reliability of the implemented model, the numerical simulations of how two ordinary plain concrete (OPC) specimens behave after being damaged in tension and brought to collapse, after curing, either in pure tension or shear have been executed. The material adopted has been an ordinary plain concrete whose mix composition included: (i) cement (300 kg/m³), (ii) water (190 kg/m³), and (iii) aggregates 5.5 ÷ 16 mm (1950 kg/m³).

The behaviour in tension has been investigated for a dogbone (DB) specimen, as usual for pure tensile tests, having the dimensions reported in Figure 3a and thickness of 20 mm. The dimensions have been chosen in order to localise the damage in the narrowest part of the sample, namely the mid-span cross-section. The other geometrical characteristics have been set accordingly. For the shear behaviour, instead, a double edge notched prismatic (DENP) specimen has been used (Figure 3b), having dimensions 100×70×20 mm³, and the notches 2 mm wide and 25 mm deep. It has been necessary to avoid a slender sample, as the dog-bone specimen presented above is. As a matter of fact, a stocky element presents a larger proneness

to shear failure. For both specimens it has been necessary (i) to shape the sample in order to have all the mechanical energy channelled into the growth of the fracture at the mid-span, with no dispersion due to multi-cracking scenarios, and (ii) to have the smallest dimension larger than the maximum aggregate size of the simulated material.

Once the samples geometry has been generated, both specimens have been damaged by means of an increasing tensile loading, up showing a single crack roughly $350\mu\text{m}$ wide (Figures 3c,d). Afterwards, the dog-bone sample has been brought to failure in tension, whereas the one in shear. This second stage has been repeated after having imposed an increasing value of the normalised healing degree, λ_{sh}^m , ranging from 0.00 to 1.00, and in the hypothesis of having unit healing mechanical impact coefficient, c_{sh} . Then, in Figures 3e,f, the model ability of catching the healing-induced recovery in tensile and shear strength is shown plotting the (e) tensile load vs. displacement and (f) shear load vs. slip curves.

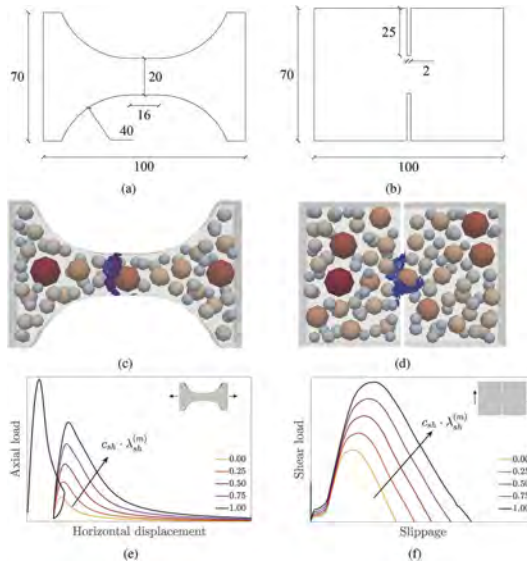


Figure 3. (a,b) DB and DENP dimensions in mm; (c,d) DB and DENP specimens: aggregate particles and cracks; (e,f) DB and DENP specimens: pure tension for pre- and re-cracking.

4.2 Tunnel cracks

The dogbone specimen in Figure 3a has been used also for testing the implementation of the tunnel cracks healing, by generating a FRC-based mesh with the same geometry. The concrete composition included: (i) cement (600 kg/m^3), (ii) water (200 kg/m^3), (iii) aggregates ranging between $3 \div 6 \text{ mm}$ (1518 kg/m^3), and (iv) steel fibres with diameter and length equals to 0.22 mm and 20 mm , respectively (0.50% by volume).

As for matrix cracks, the purpose of investigating if the healing implementation affects the fibre load-slip constitutive law as expected is achieved through a simple set of numerical simulations. The dogbone specimen has been loaded in uniaxial tension up to feature a single prominent crack ($w_c \approx 60 \mu\text{m}$). Then, it has been completely unloaded; afterwards, the sample has been reloaded up to failure. The reloading stage has been performed by assuming for λ_{sh}^f increasing fixed values: 0.00, 0.25, 0.50, 0.75, and 1.00. The numerical simulations have been carried out in two different scenarios: with no matrix cracks healing, $\lambda_{sh}^m = 0.00$, and in the hypothesis of matrix and tunnel cracks healing evolving identically, $\lambda_{sh}^m = \lambda_{sh}^f$.

Firstly, it is important to assess how the model performs at the single fibre-facet intersection. The comparison between the fibre load vs. slip curves on one of the most damaged LDPM facets obtained with λ_{sh}^f equals to 0.00 and 1.00 are shown in Figure 4b. The effect of healing acts as expected, though the re-loading in presence of healing stops before reaching

the ultimate slip (Figure 4b). As it stands out from Figure 4c, the numerical model is able to capture what has been experimentally observed in (19), where the authors detected a recovery in load-bearing capacity at macroscale with a negligible matrix crack healing. Finally, in Figure 4d, the model captures the coupled effect also on the fracturing behaviour induced by the simultaneous autogenous repairing of both matrix and tunnel cracks.

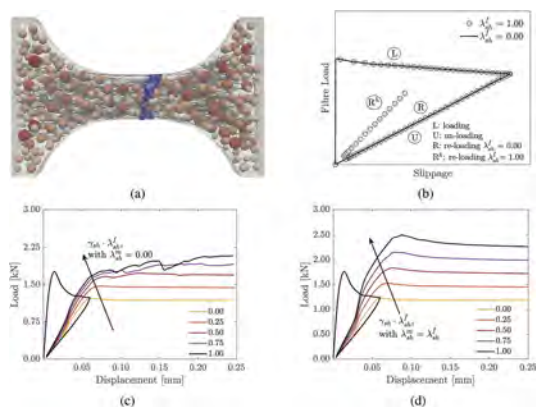


Figure 4. (a) DB FRC specimen: aggregate particles, fibres and cracks; (b) fibre load vs. slip curve experienced along one of the most damaged facets; (c) only tunnel cracks healing; (d) both matrix and tunnel cracks healing.

5 CONCLUSIONS

The model presented in this work has proved to have the potential for capturing phenomenological trends and mechanics standing out from the experimental investigations available in the literature.

The proposed numerical model presents a framework allowing to simulate the self-healing capacity of fibre reinforced cementitious composites, as affected by both the matrix crack sealing (i.e. reconstruction of material through crack continuity) and fiber-matrix interface crack healing, also called tunnel cracks, resulting into a recovery of the fibre-matrix bond capacity.

The validation against laboratory results, currently matter of study, might help in further improving the proposed approach.

ACKNOWLEDGMENTS

The work described in this paper has been performed in the framework of the Horizon 2020 project ReSHEALience (funded by European Commission, GA No 760824), whose funding the authors gratefully acknowledge. The information and views set out in this publication do not necessarily reflect the official opinion of the European Commission. Neither the European Union institutions and bodies nor any person acting on their behalf, may be held responsible for the use which may be made of the information contained therein. The numerical analyses have been performed by means of MARS, distributed by ES3 Inc. (Engineering and Software System Solutions), which is gratefully acknowledged.

REFERENCES

- Al-Obaidi, S., Bamonte, P., Animato, F., Lo Monte, F., Mazzantini, I., Luchini, M., Scalari, S. and Ferrara, L. 2021. Innovative design concept of cooling water tanks/basins in geothermal power plants using ultra-high-performance fiber-reinforced concrete with enhanced durability. *Sustainability* 13(17): 9826.

- Aliko-Benítez, A., Doblaré, M. and Sanz-Herrera, J. 2015. Chemical-diffusive modeling of the self-healing behavior in concrete. *Int. J. of Sol. and Struct.* 69–70:392–402.
- Alnaggar, M., Di Luzio, G. and Cusatis, G. 2017. Modeling time-dependent behavior of concrete affected by alkali silica reaction in variable environmental conditions. *Materials* 10(5): 471.
- Barbero, E. J., Greco, F. and Lonetti, P. 2005. Continuum damage-healing mechanics with application to self-healing composites. *Int. J. of Dam. Mech.* 14(1): 51–81.
- Chen, Q., Liu, X., Zhu, H., Ju, J. W., Yongjian, X., Jiang, Z. and Yan, Z. 2021. Continuum damage-healing framework for the hydration induced self-healing of the cementitious composite. *Int. J. of Dam. Mech.* 30(5): 681–699.
- Cibelli, A., Pathirage, M., Ferrara, L., Cusatis, G. and Di Luzio, G. 2022. A discrete numerical model for the effects of crack healing on the behaviour of ordinary plain concrete: Implementation, calibration, and validation. *Eng. Frac. Mech.* 263: 108266.
- Cusatis, G., Pelessone, D. and Mencarelli, A. 2011. Lattice discrete particle model (LDPM) for failure behavior of concrete. I: Theory. *Cem. and Con. Comp.* 33(9): 881–890.
- Davies, R. and Jefferson, A. 2017. Micromechanical modelling of self-healing cementitious materials. *Int. J. of Sol. and Struct.* 113–114:180–191.
- Di Luzio, G. and Cusatis, G. 2009a. Hygro-thermo-chemical modeling of high-performance concrete. I: Theory. *Cem. and Con. Comp.* 31(5): 301–308.
- Di Luzio, G., Ferrara, L. and Krelani, V. 2018. Numerical modeling of mechanical regain due to self-healing in cement based composites. *Cem. and Con. Comp.* 86: 190–205.
- Ferrara, L., Van Mullem, T., Alonso, M. C., Antonaci, P., Borg, R. P., Cuenca, E. A., Jefferson, A., Ng, P. L., Peled, A., Roig, M., Sanchez, M., Schroeff, C., Serna, P., Snoeck, D., Tulliani, J. M. and De Belie, N. 2018. Experimental characterization of the self-healing capacity of cement based materials and its effects on the material performance: a state of the art report by COST Action SARCOS WG2. *Constr. and Build. Mat.* 167: 115–142. Amsterdam: Elsevier.
- Hilloulin, B., Hilloulin, D., Grondin, F., Loukili, A. and De Belie, N. 2016. Mechanical regains due to self-healing in cementitious materials: Experimental measurements and micro-mechanical model. *Cem. and Con. Res.* 80: 21–32.
- Jefferson, A., Javierre, E., Freeman, B., Zaoui, A., Koenders, E. and Ferrara, L. 2018. Research Progress on Numerical Models for Self-Healing Cementitious Materials. *Adv. Mat. Interf.* 5: 1701378.
- Jefferson, A. and De Belie, N. 2016. Mechanical regains due to self-healing in cementitious materials: Experimental measurements and micro-mechanical model. *Cem. and Con. Res.* 80: 21–32.
- Lo Monte, F. and Ferrara, L. 2020. Tensile behaviour identification in ultra-high performance fibre reinforced cementitious composites: indirect tension tests and back analysis of flexural test results. *Mat. and Struct.* 53(6):145. Berlin: Springer.
- Lo Monte, F. and Ferrara, L. 2021. Self-healing characterization of UHPFRCC with crystalline admixture: Experimental assessment via multi-test/multi-parameter approach. *Constr. and Build. Mat.* 283: 122579. Amsterdam: Elsevier.
- Oucif, C., Voyiadjis, G. Z. and Rabczuk, T. 2018. Modeling of damage-healing and nonlinear self-healing concrete behavior: Application to coupled and uncoupled self-healing mechanisms. *Th. and Ap. Fract. Mech.* 96: 216–230.
- Pathirage, M., Bentz, D., Di Luzio, G., Masoero, E. and Cusatis, G. 2019. The ONIX model: a parameter-free multiscale framework for the prediction of self-desiccation in concrete. *Cem. and Con. Comp.* 103: 36–48.
- Qiu, J., He, S., Wang, Q., Su, H. and Yang, E. 2019. Autogenous healing of fiber/matrix interface and its enhancement. In G. Pijaudier-Cabot, P. Grassl and C. La Borderie (Eds.), *10th Int. Conf. on Fracture Mechanics of Concrete and Concrete Structures – FraMCoS-X, Bayonne, France*, 24–26 June 2019.
- Schauffert, E. A. and Cusatis, G. 2012. Lattice Discrete Particle Model for fiber-reinforced concrete. I: Theory. *J. of Eng. Mech.* 138(7): 826–833.
- Snoeck, D. and De Belie, N. 2015. From straw in bricks to modern use of microfibers in cementitious composites for improved autogenous healing – a review. *Constr. and Build. Mat.* 95: 774–787.
- Voyiadjis, G. Z., Shojaei, A. and Li, G. 2011. A thermodynamic consistent damage and healing model for self healing materials. *Int. J. of Plast.* 27(7): 1025–1044.
- Yang, S., Aldakheel, F., Caggiano, A., Wriggers, P. and Koenders, E. 2020. A Review on Cementitious Self-Healing and the Potential of Phase-Field Methods for Modeling Crack-Closing and Fracture Recovery. *Materials* 13(22): 5265.

Crack healing under sustained load in concrete: An experimental/numerical study

G. Di Luzio, A. Cibelli, S.M.J. Al-Obaidi, S.M.I. Radwan, M. Davolio & L. Ferrara
Politecnico di Milano, Milan, Italy

R. Wan-Wendner & Y. Wang
Ghent University, Ghent, Belgium

ABSTRACT: The need of sustainable resilient structures and infrastructures push towards the use of cementitious materials able to heal micro-cracks and defects. For real structural application under service loading the time-dependent behavior is of the utmost importance, especially in presence of cracks which can lead to a nonlinear creep behavior that might cause the structural failure. Now the new challenge is to study and quantify the effect of crack-healing on the nonlinear creep behavior. This study aims at the following goals: 1) to characterize with experimental investigations the effect of the healing in tests in which the specimens, along the exposure time and under controlled environmental conditions, are under sustained load, the expected service load, determined as a fraction of the pre-cracking load; 2) develop a comprehensive numerical framework for the interpretation and simulation of the experimentally observed results. To this purpose an experimental investigation is currently ongoing at Politecnico di Milano with reference to an Ultra High-Performance Concrete developed in the framework of the H2020 ReSHEALience project for exposure to extremely aggressive environments. The numerical framework is based on the recent developments of the multiphysics lattice particle model.

1 INTRODUCTION

Creep and shrinkage of concrete are time-dependent deformations that influence primarily the serviceability, and in some cases also the safety, of reinforced concrete structures with and without prestressing, and of composite concrete and steel structures. Shrinkage is mainly due to the changes in the moisture content/status dictated by both self desiccation and drying if exposed to lower humidity environments.

Shrinkage alone may cause damage and early age cracking of concrete with a huge impact on the durability of the structure. In addition and in combination to that, the large and widely unrecoverable creep deformations of concrete can cause significant modifications of action effects in structures in terms of internal stress distributions, excessive deflections and loss of prestressing forces, and produce large cracks.

All these effects affect the serviceability and the durability of structures, and may impact on their structural safety as well. In tall structures, absolute and differential shortening and deviations from verticality due to creep and shrinkage of concrete may be a matter of concern requiring serviceability and safety checks and proper remedial actions (Khan et al. 1997; Jirásek & Bažant 2002; Bažant & Jirásek 2018).

For long-term prediction and design the inherent self-healing capability of either ordinary and/or advanced cementitious materials cannot be disregard. The term self-healing refers to the material capacity of repairing the damage in cracked state autonomously.

However, time-dependent behavior of concrete must be contextualized in a more wide comprehensive framework since it is a result of interplay between multiple chemical, physical, and mechanical processes that are functions of the material composition and its curing as well as the surrounding environmental and loading conditions. Chemical processes include the

continued reactions of cementitious materials, aging, healing in the cracks, in addition to a variety of deleterious reactions, such as Alkali-Silica Reaction (ASR), Sulphate Attack, Physical Salt Attack, and others. Physical changes are typically related to thermal and hygral changes. As the hygro-thermal environmental conditions surrounding concrete vary, moisture and heat diffusion processes take place within the material and result in volumetric deformations, such as during thermal shocking, exposure to fire, repeated freeze and thawing, temperature rise in early-age massive structures, or moisture drying that in thick or restrained elements can be induce serious damage.

This paper reports the initial results of an ongoing activity. In the manuscript, first it is presented an experimental investigation on the effect of the crack healing in tests in which the specimens, along the exposure time and under controlled environmental conditions, are under sustained load, close to the expected service load and determined as a fraction of the pre-cracking load. The tests are performed on an Ultra High-Performance Concrete developed in the framework of the H2020 ReSHEALience project for exposure to extremely aggressive environments. Second the mesoscale approach, which is the Multiphysics-Lattice Discrete Particle Model (M-LDPM) (Alnaggar et al. 2017; Yang et al. 2021), resulting from the coupling of the Hygro-Thermo-Chemical (HTC) model (Di Luzio & Cusatis 2009a; Di Luzio & Cusatis 2009b) with the Lattice Discrete Particle Model (LDPM) (Cusatis et al. 2011b), is here for the first time adopted the numerical simulations of the creep and healing phenomena acting simultaneously. In this framework, creep and shrinkage deformations are modeled based on a discrete version (Abdellatef et al. 2015; Alnaggar et al. 2017) of the Microprestress-Solidification theory (Bažant & Prasannan 1989; Bažant et al 1997; Bažant et al. 2004; Di Luzio & Cusatis 2013). This framework has also been recently extended for the crack healing modeling in plain cementitious materials (Cibelli et al. 2022b) and fiber reinforced concrete (Cibelli et al. 2022a), but never considering the shrinkage and creep deformations during crack healing.

2 EXPERIMENTAL INVESTIGATION

Three different UHPC mixes – two with nano-additives, alumina nano-fibres (ANF) and cellulose nano-crystals (CNC), and one as reference – were characterised with both non-destructive and destructive tests; the tests were performed on $500 \times 100 \times 30 \text{ mm}^3$ thin beams obtained cutting pre-cast slabs. The main goal of the experiments was to analyse the material behaviour under real service conditions and its evolution over time; for this purpose, both mechanical loading and environmental exposure were simultaneously applied to the specimens. The experimental campaign was carried out in three different stages, defined as follows: (i) uncracked specimens, (ii) pre-cracked specimens, and (iii) cured/healed specimens (i.e., after exposure). Material properties were first evaluated on beams in virgin conditions, then the specimens were pre-cracked by means of 4-point bending, targeting a crack opening displacement (COD) of $200 \mu\text{m}$ under load, resulting in a residual COD of $75\text{-}125 \mu\text{m}$. The properties were then investigated again through non-destructive measurements, setting the reference for the effectiveness of the self-healing process. A new setup was specifically designed to apply a constant sustained load on the beams during the environmental exposure. After the pre-cracking process, beams were coupled referring to the peak load achieved during the process itself. The couple was braced and loaded with a steel frame, as shown in Figure 1; two cylinders (pink colour) act as hinges in the mid span of the beams, while four bars (black colour) are used to hold the specimens on the sides. With the system described, it was possible to emulate the 4-point bending condition during the curing and healing process, guaranteeing the presence of a constant moment in the central region of the beams. The loading process can be described in three different stages, starting from unloaded and pre-cracked specimens; (a) two load cells (blue colour) are positioned above the second layer of steel bars and braced with the top bars, (b) the targeted load, derived from the pre-cracking process, is first applied to the cells tightening the top nuts (red colour), ensuring that the exact value will be transferred to the beams, then (c) the load is finally applied to the specimens tightening the nuts in the middle (brown colour) and simultaneously releasing the load cells, allowing to remove them. The sustained loading setup was previously tested on a couple of samples to validate the effective maintenance of a constant load over time on the braced pair, keeping the load cells in position for the whole

duration of the test; the system was able to guarantee an almost constant load, with less than 10% reduction. An extensive summary of the results has been provided in Al-Obaidi et al. (2023).

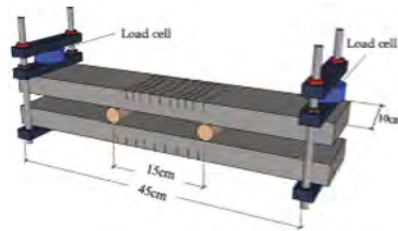


Figure 1. Sustained loading setup.

The specimens paired and braced with the sustained loading system were exposed into chloride solution (3.3% NaCl), geothermal water, and tap water as reference, to simulate the chloride and sulphate environmental attack respectively. The curing period varied between 1 and 12 months, and the specimens were tested at 1, 2, 3, 6, 9, and 12 months. The effect of healing and the crack sealing – promoted by crystalline admixture and nano-additives – were evaluated at the end of each exposure period, allowing to define the evolution of the performance that can be expected in a real structure. The material proved to be substantially resilient even under aggressive conditions such as sustained loads and different chemical attacks, maintaining constant mechanical performance over time.

3 GENERAL MULTI-PHYSICS FRAMEWORK

This section presents the numerical framework that merges the Hygro-Thermo-Chemical (HTC) model with a discrete meso-scale (LDPM) model for concrete. For time-dependent mechanical analysis, it is essential to use a multi-physics model that simulates all the relevant chemical/physical phenomena in a cement based material, such as the chemical reactions of the binder coupled with moisture transport and heat transfer in interaction with the environmental changes. Especially in the cracks chemical/physical phenomena are fundamental to characterize the healing evolution.

3.1 *Hygro-Thermo-Chemical (HTC) model*

The HTC model (Di Luzio & Cusatis 2009a; Di Luzio & Cusatis 2009b) simulates the moisture and temperature evolution in a cementitious material considering the simultaneous chemical reactions – hydration of cement and pozzolanic reactions. The reaction kinetics are formulated in terms of reaction degrees that represent the progress of a chemical reaction as the ratio between the amount of reacted material and the total initial amount of it. Similarly, if a pozzolanic material is utilized in the mixture, such as silica-fume, the rate of its reaction degree can be describe using a similar approach (Di Luzio & Cusatis 2009a).

The coupling between chemical reactions and transport processes (water and heat) is achieved by combining the water mass and enthalpy balance equations with the reaction degree kinetic equations, in which the cement hydration degree and the pozzolanic material reaction degree are assumed as an internal variables, leading to a system of partial differential equations with only two state variables, i.e. the temperature T and the pore relative humidity h . All the details of the formulation can be found in Di Luzio & Cusatis (2009a); Pathirage et al. (2019); Bousikhane et al. (2018).

3.2 *Discrete mesoscale mechanical model*

The mesoscale discrete model employed in the framework is the so-called Lattice Discrete Particle Model (LDPM) (Cusatis et al. 2011a; Cusatis et al. 2011b). It simulates the heterogeneity of concrete considering the mechanical interaction of coarse aggregates in the cementitious matrix. The

discretized concrete mesostructure creates a system of polyhedral cells interacting through triangular facets and a lattice system composed by the line segments connecting the particle centers. A rigid body kinematics is assumed to describe the deformation of the LDPM lattice/particle system. By summing up the stress contributions of all the facets and equating the total internal work with the total external work, one can obtain the discrete equilibrium equations of the LDPM formulation.

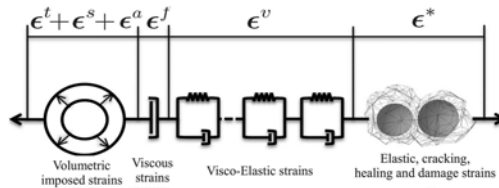


Figure 2. Equivalent rheological model based on strain additivity at the meso-scale.

The LDPM has been used successfully to simulate concrete behavior under a large variety of loading conditions (Cusatis et al. 2011a). It has been also formulated for fiber reinforced concrete (Schauffert & Cusatis 2012) and for ultra-high performance concrete (UHPC) (Smith et al. 2014). Assuming the additivity of strains at mesoscale level of each facet, one can write

$$\dot{\epsilon} = \dot{\epsilon}^* + \dot{\epsilon}^a + \dot{\epsilon}^s + \dot{\epsilon}^t + \dot{\epsilon}^v + \dot{\epsilon}^f \quad (1)$$

where $\dot{\epsilon}$ is the total strain, $\dot{\epsilon}^*$ represents the effect of instantaneous elasticity and damage, $\dot{\epsilon}^a$ represents the strain rate due to material degradation such as ASR; $\dot{\epsilon}^s$ and $\dot{\epsilon}^t$ are shrinkage and thermal strain rates, respectively; $\dot{\epsilon}^v$ is the viscoelastic strain rate and $\dot{\epsilon}^f$ is the purely viscous strain rate. The strain additivity of Eq. 1 can be represented as a rheological model of elements in series that is depicted in Figure 2.

3.2.1 Elastic, cracking, and damage behavior

In the elastic regime, the normal and shear stresses are proportional to the corresponding strains. In vectorial form, one has $\dot{\epsilon}^* = \frac{1}{E_0} \mathbf{G} \sigma$, where $\mathbf{G} = [1, 0, 0; 0, 1/\alpha, 0; 0, 0, 1/\alpha]$, E_0 = effective normal modulus, and α = shear-normal coupling parameter. It must be observed that, E_0 represents the instantaneous deformation since all creep strains, which always occurs during quasi-static loading, are included in the Kelvin chain of the rheological model. However, the Kelvin chain has a limited number of elements and, in this case, E_0 will also include the effect of very short term creep whose characteristic time is smaller than the smallest of the discrete chain. All the detail on the LDPM constitutive law can be found in Cusatis et al. (2011b).

3.2.2 Rate effect

The loading rate has a direct effect on the mechanical properties of concrete as it has been shown by many authors, among others Watstein (1953), Hughes & Gregory (1972), Reinhardt (1985). This phenomenon is explained by three main contributions: the creep of the material, the rate effect on the bond rupture in the mesoscale fracture, and the effect of inertia force on the crack propagation. For quasi-static loads, the first two mechanisms mentioned above are dominant. While increasing the strain rate loading the third contribution becomes more and more dominant. Since the fracture can be seen as the consequence of the rupture of atomic or molecular bonds dominated by a thermal activation of the bond breakages, the rate effect can be modeled by the concept of a rate dependence on the fracture process (Di Luzio & Cedolin 2005).

As proposed in Wu & Bažant (1993), the cohesive crack model can be made a time-dependent process characterized by its aforementioned activation energy. This concept has been implemented in LDPM (Smith & Cusatis 2016; Boumakis et al. 2018) by scaling the tensile stress-strain boundary by the function with the normal strain rate.

3.2.3 Solidification Theory for visco-elastic deformations

According to the Solidification Theory (Bažant & Prasanna 1989; Bažant et al 1997; Bažant et al. 2004; Di Luzio & Cusatis 2013), the visco-elastic behavior of concrete comprises the

visco-elastic strain of the aging hardened cement gel. A non-aging micro-compliance function of cement gel produces strains that reduces overtime with a function that represents the volume fraction of cement gel produced by early-age chemical reactions. This formulation is expressed in an incremental stress/strain relation using the approximation of the creep function with a Dirichlet series with the introduction of a continuous retardation spectrum based on the Post-Widder formula to calculate the parameters of the Dirichlet series (Bažant & Xi 1995; Bažant & Jirásek 2018; Di Luzio et al. 2020).

3.2.4 *Microprestress Theory for viscous deformations*

The purely viscous strain rate represents the totally unrecoverable part of the creep strain and it is associated to long-term creep, drying creep effect (also called Pickett effect), and transitional thermal creep. From the microprestress theory the purely viscous strain rate can be expressed with the dashpot in Figure 2 whose viscosity is function of the microprestress (Bažant et al 1997; Bažant et al. 2004; Di Luzio & Cusatis 2013).

Recently it has been shown that the microprestress theory arises in nanoscale numerical simulations of C-S-H in which the logarithmic creep and power-law microprestress relaxation emerge from generic deformation kinetics in such disordered systems (Masoero & Di Luzio 2020).

3.2.5 *Hygral and thermal deformation*

The variation of the relative humidity in the material pores causes free hygroscopic strain ϵ^s (swelling or shrinkage, for positive or negative relative humidity change, respectively). Similarly, temperature changes cause thermal strain rates, $\dot{\epsilon}^t$ (Abdellatef et al. 2019).

3.2.6 *Self-healing modeling*

The modelling approach consider the matrix cracks at the mesoscale, and the fibre-matrix interface cracks (*tunnel* cracks). The modelling approach relies on the idea for which the self-healing of matrix and tunnel cracks affect the material mechanical behaviour differently. For this reason, the autogenous repairing of the matrix cracks is implemented within the constitutive fracture law at the mesoscale, whereas the effect of healing on the fibres response is taken into account within the calculation of the bridging force carried by the steel reinforcement. In the proposed model, the moisture permeability is assumed to be affected only by the matrix cracks, then only their closure contributes to the recovery in water-tightness that healed material might experience.

The healing kinetic is described by an internal variable that characterized the crack close. It is formulated for plain cementitious materials can be also employed for fibre-reinforced composites as well. For all the details on the formulation an interested reader has to refer to Di Luzio et al. (2018); Cibelli et al. (2022a); Cibelli et al. (2022b).

3.2.7 *Aging*

As widely known concrete properties typically improve in course of time, especially in the early weeks after casting. This complex process is called aging and its principal source is the ongoing hydration, which depends on the mix design and the environmental boundary conditions (Cernuschka et al. 2022).

The evolution of mechanical properties are expressed as a function of an aging degree internal variable making some meso-scale parameters age-dependent that are the normal modulus, the tensile strength, the tensile characteristic length, and the shear strength ratio. For all the details on the formulation an interested reader has to refer to Di Luzio & Cusatis (2013); Wan et al. (2016).

4 MODEL APPLICATIONS

The initial results of the application of the computational framework presented in the previous Section are reported here. The proposed computational framework has been first calibrated for the aging mechanical properties of the considered material, by simulating an extensive laboratory campaign conducted at the Politecnico di Milano and looking for the best match between numerical and experimental results. As an example, in Figure 3 the comparison between numerical and experimental curves is shown for the fracture behaviour of notched specimens after three different ages from casting: 6, 28 and 180 days.

The same approach has been adopted also for the healing model, which has been calibrated and validated by using the evidences presented in Cuenca et al. (2021). In Figure 4 the model capability of capturing (i) the effect of cracks on the moisture transport phenomena and (ii) the time evolution of crack sealing due to the self-healing (Index of Crack Sealing, ICS) is shown.

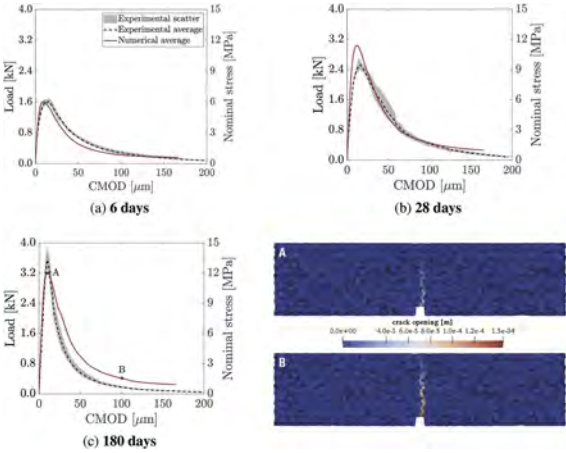


Figure 3. Ageing model – Comparison between experimental and numerical results relevant to three different ages from casting: 6, 28 and 180 days.

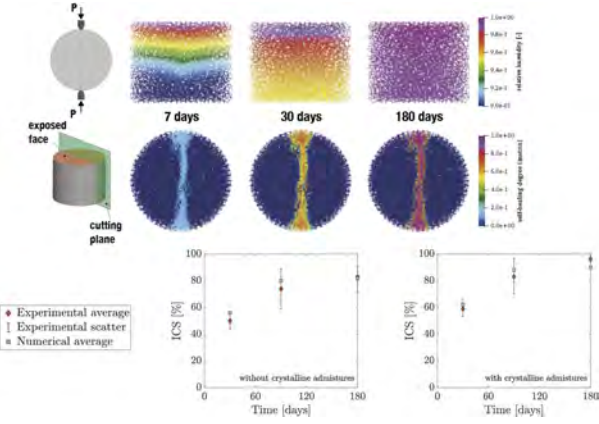


Figure 4. Healing model – Moisture gradient and healing evolution in cracked conditions over time.

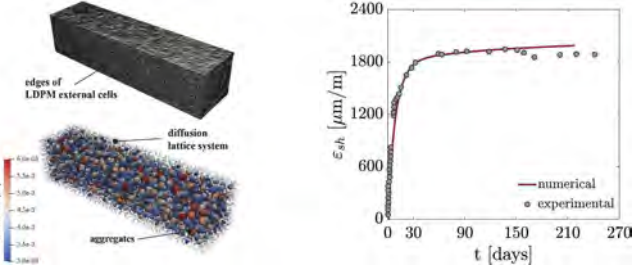


Figure 5. Shrinkage model – Comparison between experimental and numerical autogenous shrinkage in UHPC.

Finally, the proposed computational framework is being calibrated for the shrinkage and creep properties of the considered mixes. Some preliminary results are reported in Figure 5.

5 CONCLUSIONS

This study presents the initial results of an experimental/numerical research on the cross effects of the crack healing and creep in typical expected service load condition. The numerical model is based on the mesoscale Multiphysics-Lattice Discrete Particle Model (M-LDPM) for the characterization of the long- and short-term mechanical behavior with coupled thermal, shrinkage, creep deformations, and self-healing. Preliminary results are presented in this manuscript. This research allows to learn something new about the behavior of crack healing under loading condition, which is of utmost importance for practical applications.

ACKNOWLEDGMENTS

The work described in this paper has been performed in the framework of the project ReSHEALience (funded by European Commission with grant agreement No 760824), whose funding the authors gratefully acknowledge. The numerical analyses have been performed by means of MARS, distributed by ES3 Inc. (Engineering and Software System Solutions), which is gratefully acknowledged. The grant for Senior Resident research 2021/2022 to Roman Wan-Wendner from Department of Civil and Environmental Engineering is gratefully acknowledge.

REFERENCES

- Abdellatef, M., Alnaggar, M., Boumakis, G., Cusatis, G., Di Luzio, G., Wendner, R. 2015. Lattice discrete particle modeling for coupled concrete creep and shrinkage using the solidification microprestress theory. In Christian Hellmich and Bernhard Pichler and Johann Kollegger (eds.), *CONCREEP 10: Mechanics and Physics of Creep, Shrinkage, and Durability of Concrete and Concrete Structures*. ASCE, pp. 184–193.
- Abdellatef, M., Boumakis, I., Wan-Wendner, R., Alnaggar, M. 2019. Lattice Discrete Particle Modeling of concrete coupled creep and shrinkage behavior: A comprehensive calibration and validation study. *Construction and Building Materials* 211, 629–645.
- Alnaggar, M., Di Luzio, G., Cusatis, G. 2017. Modeling time-dependent behavior of concrete affected by alkali silica reaction in variable environmental conditions. *Materials* 10(5), 417.
- Al-Obaidi, S., Davolio, M., Recchia, G., Lo Monte, F. and Ferrara, L. 2023. How Does Self-Healing under Sustained Loadings in Aggressive Water Affect the Constitutive Response of a UHPFRC? In *RILEM Bookseries, Strain Hardening Cementitious Composites*, March, 2023. Springer.
- Bažant, Z. P., Cusatis, G., Cedolin, L. 2004. Temperature effect on concrete creep modeled by microprestress-solidification theory. *Journal of Engineering Mechanics* 130(Special Issue: Constitutive Modeling of Geomaterials), 691–699.
- Bažant, Z. P. & Xi, Y. 1995. Continuous retardation spectrum for solidification theory of concrete creeps. *Journal of Engineering Mechanics, ASCE* 121, 281–288.
- Bažant, Z. & Prasannan, S. 1989. Solidification theory for concrete creep. I: Formulation, II: verification and application. *Journal of Engineering Mechanics* 115 (7), 1691–1725.
- Bažant, Z. P., Hauggaard, A. B., Baweja, S., Ulm, F.-J. 1997. Microprestress-solidification theory for concrete creep. i: Aging and drying effects. *Journal of Engineering Mechanics* 123(11), 1188–1194.
- Bažant, Z. P. & Jirásek M. 2018. *Creep and Hygrothermal Effects in Concrete Structures*. Dordrecht, The Netherlands: Springer.
- Boumakis, I., Di Luzio, G., Wan-Wendner, R. 2018. Discrete element framework for modeling tertiary creep of concrete in tension and compression. *Engineering Fracture Mechanics* 200, 263–282.
- Bousikhane, F., Li, W., Di Luzio, G., Cusatis, G. 2018. Full coupling between diffusion and mechanical analysis in a discrete computational framework. In G. Meschke, B. Pichler, and J. G. Rots (Eds.), *Proceedings of the Conference on Computational Modelling of Concrete and Concrete Structures (EURO-C 2018)*, Bad Hofgastein, Austria, February 26 - March 1, 2008. CRC Press Book, 305–310.
- Cernuschka, L.M., Boumakis, I., Ninčević, K., Vorel, J., Wan-Wendner, R. 2022. Relationship of LDPM meso-scale parameters and aging for normal and high strength concretes. *RILEM Materials and Structures* 55, 219.

- Cibelli, A., Di Luzio, G., Ferrara, L. 2022. Numerical modelling via a coupled discrete approach of the autogenous healing for fibre-reinforced cementitious composites (frccs). In G. Meschke, B. Pichler, and J. Rots (Eds.), *Proceedings of the Conference on Computational Modelling of Concrete and Concrete Structures (EURO-C 2022), Vienna, Austria, February 26 - March 1, 2022* . CRC Press Book, 86–95.
- Cibelli, A., Pathirage, M., Cusatis, G., Ferrara, L., Di Luzio, G. 2022. A discrete numerical model for the effects of crack healing on the behaviour of ordinary plain concrete: Implementation, calibration, and validation. *Engineering Fracture Mechanics* 263, 108266.
- Cuenca, E., Lo Monte, F., Moro, M., Schiona, A., Ferrara, L. 2021. Effects of Autogenous and Stimulated Self-Healing on Durability and Mechanical Performance of UHPFRC: Validation of Tailored Test Method through Multi-Performance Healing-Induced Recovery Indices. *Sustainability* 13(20), 11386.
- Cusatis, G., Mencarelli, A., Pelessone, D., Baylot, J. 2011. Lattice Discrete Particle Model (LDPM) for Failure Behavior of Concrete. II: Calibration and Validation. *Cement and Concrete Composites* 33 (9), 891–905.
- Cusatis, G., Pelessone, D., Mencarelli, A. 2011. Lattice Discrete Particle Model (LDPM) for Concrete failure Behavior of Concrete. I: Theory. *Cement and Concrete Composites* 33(9), 881–890.
- Di Luzio, G. & Cedolin, L. 2005. Concrete response under dynamic loading. *Studies and Researches* 25, 155–176.
- Di Luzio, G., Cedolin, L., Beltrami, C. 2020. Tridimensional long-term finite element analysis of reinforced concrete structures with rate-type creep approach. *Applied Sciences* 10(14), 4772.
- Di Luzio, G. & Cusatis, G. 2009a. Hygro-thermo-chemical modeling of high performance concrete. I: Theory. *Cement and Concrete Composites* 31(5), 301–308.
- Di Luzio, G. & Cusatis, G. 2009b. Hygro-thermo-chemical modeling of high performance concrete. II: Numerical implementation, calibration, and validation. *Cement and Concrete Composites* 31(5), 309–324.
- Di Luzio, G. & Cusatis, G. 2013. Solidification–Microprestress–Microplane (SMM) theory for concrete at early age: Theory, validation and application. *International Journal of Solids and Structures* 50, 957–975.
- Di Luzio, G., Ferrara, L., Krelani, V. 2018. Numerical modeling of mechanical regain due to self-healing in cement based composites. *Cement and Concrete Composites* 86, 190–205.
- Hughes, B. P. & Gregory, R. 1972. Concrete subjected to high rates of loading in compression. *Magazine of Concrete Research* 24(78), 25–36.
- Jirásek, M. & Bažant, Z. P. 2002. *Inelastic Analysis of Structures*. London and New York: J. Wiley & Sons.
- Khan, A. A., Cook, W. D., Mitchell, D. 1997. Creep, shrinkage, and thermal strains in normal, medium, and high-strength concretes during hydration. *ACI Materials Journal* 94(2).
- Masoero, E. & Di Luzio, G. 2020. Nanoparticle simulations of logarithmic creep and microprestress relaxation in concrete and other disordered solids. *Cement and Concrete Research* 137, 106181.
- Pathirage, M., Bentz, D., Di Luzio, G., Masoero, E., Cusatis, G. 2019. The ONIX model: a parameter-free multiscale framework for the prediction of self-desiccation in concrete. *Cement and Concrete Composites* 103, 36–48.
- Reinhardt, H. W. 1985. Strain rate effects on the tensile strength of concrete as predicted by thermodynamic and fracture mechanics models. *MRS Proceedings* 64, 1.
- Schauffert, E. A. & Cusatis, G. 2012. Lattice discrete particle model for fiber reinforced concrete (LDPM-F): I. theory. *Journal of Engineering Mechanics* 138(7), 826–833.
- Smith, J. & Cusatis G. 2016. Numerical analysis of projectile penetration and perforation of plain and fiber reinforced concrete slabs. *International Journal for Numerical and Analytical Methods in Geomechanics* 41(3), 315–337.
- Smith, J., Cusatis, G., Pelessone, D., Landis, E., O’Daniel, J., Baylot, J. 2014. Discrete modeling of ultra-high-performance concrete with application to projectile penetration. *International Journal of Impact Engineering* 65, 13–32.
- Wan, L., Wendner, R., Liang, M., Cusatis, G. 2016. Analysis of the behavior of ultra high performance concrete at early age. *Cement and Concrete Composites* 74, 120–135.
- Watstein, D. 1953. Effect of straining rate on the compressive strength and elastic properties of concrete. *ACI Journal* 49(4), 729–744.
- Wu, Z. S. & Bažant, Z. P. 1993. Finite element modeling of rate effect in concrete fracture with influence of creep. In *Creep and Shrinkage of concrete, Proceedings of the 5th International RILEM symposium*, Barcelona, Spain, 427–432.
- Yang, L., Pathirage, M., Su, H., Alnaggar, M., Di Luzio, G., Cusatis, G. 2021. Computational modeling of temperature and relative humidity effects on concrete expansion due to alkali-silica reaction. *Cement and Concrete Composites* 124, 104237.

Homogenized mesoscale discrete model for coupled multi-physical analysis of concrete

J. Eliáš

Faculty of Civil Engineering, Brno University of Technology, Brno, Czechia

G. Cusatis

Department of Civil and Environmental Engineering, Northwestern University, Evanston, IL, USA

ABSTRACT: The contribution develops an asymptotic expansion homogenization of a mesoscale model based on rigid-body kinematics. The model is capable of solving coupled mechanics and mass transport in concrete. Two coupling phenomena are considered: the Biot's theory and an effect of cracks on the material conductivity. The homogenization technique is used to deliver a two scale model: (i) the macroscale emerges as a homogeneous Cosserat continuum coupled with mass transport. Each integration point contains (ii) a mesoscale periodic Representative Volume Element (RVE), a submodel replacing the constitutive function. The RVE is discrete, loaded by a projection of Cosserat strain tensor and macroscopic pressure gradient. The homogenized model is compared to the full model by simulating two examples: the Terzaghi's consolidation and hydraulic fracturing of a hollow cylinder.

1 INTRODUCTION

Life-cycle assessment of concrete structures demands robust numerical models capable of solving multi-physical problems. The contribution focuses on coupled mechanics and mass transport in concrete solved by a meso-scale model based on rigid body kinematics. Each rigid particle represents a larger mineral aggregate and the surrounding matrix. Cohesive contacts between particles lump both elastic and inelastic mechanical behavior. The constitutive relations are vectorial and naturally account for crack orientation (Cusatis, Pelessone and Mencarelli, 2011; Eliáš, 2020).

The mass transport is coupled with mechanics via Biot's theory where (i) the effective stress at the contacts is composed of the stress in the solid and the pressure component and (ii) the rate of volumetric deformation is linked to the pressure. (iii) Another coupling terms account for cracking which enhances the permeability coefficient of the associated conduit elements. The importance of cracking in the transport solution resulted in special coupling scheme based on a dual lattice (Grassl, 2009; Grassl and Bolander, 2016; Fahy et al., 2017; Li et al., 2018), which is employed here as well.

This high fidelity *full* model is computationally expensive because it is formulated at the meso-scale. Eliáš and Cusatis (2022) developed a homogenization technique capable of reducing computational cost of the model. It extends work of Rezakhani and Cusatis (2016) where the mechanical discrete model was homogenized. Identical homogenization technique is applied also in Rezakhani et al. (2019, 2017) and Eliáš et al. (2022). This contribution is a brief summarization of results published in the journal paper of Eliáš and Cusatis (2022).

2 DISCRETE MODEL OF COUPLED MECHANICAL AND TRANSPORT PROBLEM

The model to be homogenized is a discrete mesoscale model of concrete mechanical behavior extended by coupling with mass transport in fully saturated medium. It is similar to the well known Lattice Discrete Particle Model (LDPM) (Cusatis, Pelessone and Mencarelli, 2011; Cusatis, Mencarelli, Pelessone and Baylot, 2011). The most recent applications of LDPM are simulations of the cyclic behavior of concrete (Zhu et al., 2022) and size effect (Pathirage

et al., 2023). The model used in this contribution has different internal geometry derived from the power tessellation on spheres representing mineral aggregates (Eliáš, 2017). The constitutive functions are adopted from Cusatis and Cedolin (2007) and slightly modified, see Eliáš and Cusatis (2022) or Eliáš (2016).

The model features two types of nodes and elements. The transport nodes P and Q bear only one degree of freedom called pressure and denoted p . The mechanical nodes I and J bear displacement vector \mathbf{u} and rotation vector $\boldsymbol{\theta}$. h and S are length and area of the transport element, l and A are length and area of the mechanical element. Vectors \mathbf{c}_I and \mathbf{c}_J connect nodes I and J with the centroid of the mechanical element facet, where the constitutive equations are defined.

The kinematic equations give the pressure gradient, g , the strain vector, $\boldsymbol{\varepsilon}$, and the curvature, χ .

$$g = \frac{p^Q - p^P}{h} \quad (1)$$

$$\varepsilon_\alpha = \frac{1}{l} (\mathbf{u}^J - \mathbf{u}^I + \boldsymbol{\varepsilon} : (\boldsymbol{\theta}^J \otimes \mathbf{c}_J - \boldsymbol{\theta}^I \otimes \mathbf{c}_I)) \cdot \mathbf{e}_\alpha \quad (2)$$

$$\chi_\alpha = \frac{1}{l} (\boldsymbol{\theta}^J - \boldsymbol{\theta}^I) \cdot \mathbf{e}_\alpha \quad (3)$$

Note that displacement and rotation vectors are transformed into the local coordinate system by multiplication by directional vectors \mathbf{e}_α , $\alpha = N, M, L$ being the normal and two tangential directions.

The constitutive equations are stated in a general form and provide the flux scalar, j , the traction vector, \mathbf{t} , and the couple traction vector, \mathbf{m}

$$j = -\lambda(p, \delta)g \quad \mathbf{t} = f_s(\varepsilon) - bp_a\mathbf{e}_N \quad \mathbf{m} = f_m(\chi) \quad (4)$$

Functions λ , f_s and f_m can be defined arbitrarily. The first constitutive equation introduces the effect of crack opening, δ , on the material permeability. The second constitutive equation brings Biot's effect of fluid pressure on the normal component of the traction (Biot, 1941; Detournay and Cheng, 1995), b is a material parameter called Biot coefficient. The pressure p_a is the weighted average pressure from control volumes surrounding the mechanical element.

The final set of equations consists of the balance of fluid mass and the balance of linear and angular momentum of particles

$$\rho_{w0} \left(3b\dot{\varepsilon}_V + \frac{\dot{p}_\lambda}{M_b} \right) + q = \sum_{Q \in W} \left[\frac{Sj}{W} - \rho_{w0}\dot{v}_c \left(1 - b + \frac{p_\lambda - p_0}{K_w} \right) - \rho_{w0}v_c \frac{\dot{p}_\lambda}{K_w} \right] \quad (5)$$

$$V\rho\ddot{\mathbf{u}}^I + \mathbf{M}_{u\theta} \cdot \ddot{\boldsymbol{\theta}}^I - V\mathbf{b} = \sum_J A t_\alpha \mathbf{e}_\alpha \quad (6)$$

$$\mathbf{M}_\theta \cdot \ddot{\boldsymbol{\theta}}^I + \mathbf{M}_{u\theta}^T \cdot \ddot{\mathbf{u}}^I = \sum_J A [\mathbf{w} + m_\alpha \mathbf{e}_\alpha] \quad (7)$$

where J runs over all neighbors of particle I and Q runs over all simplices surrounding the control volume of node P , q and \mathbf{b} are external loads, M_b is Biot's modulus, K_w is the bulk modulus of fluid, ε_V is the volumetric strain reduced by the amount of cracks, v_c is volume of cracks, ρ and ρ_{w0} are densities of solid and fluid, \mathbf{M} represents various inertia tensors, $\mathbf{w} = \boldsymbol{\varepsilon} : (\mathbf{c}_I \otimes \mathbf{t}) = t_\alpha \boldsymbol{\varepsilon} : (\mathbf{c}_I \otimes \mathbf{e}_\alpha)$ is the moment of traction with respect to the mechanical node I , and $\boldsymbol{\varepsilon}$ is the Levi-Civita permutation tensor. Further details can be found in Eliáš and Cusatis (2022).

3 SEPARATION OF SCALES

The separation of scales is employed now. The macroscopic, slow variable \mathbf{x} and the microscopic, fast variable \mathbf{y} are related via separation of scales constant $\mathbf{x} = \eta\mathbf{y}$. The model appears

continuous from the viewpoint of the reference system \mathbf{x} but discrete in the reference system \mathbf{y} . Furthermore, a unique global reference system \mathbf{X} defines positions in the continuous macroscopic space.

The primary variables p , \mathbf{u} and $\boldsymbol{\theta}$ are now asymptotically expanded into components with different powers of η

$$p(\mathbf{X}, \mathbf{y}) = \eta^{-1}p^{(-1)}(\mathbf{X}, \mathbf{y}) + p^{(0)}(\mathbf{X}, \mathbf{y}) + \eta p^{(1)}(\mathbf{X}, \mathbf{y}) + \dots \quad (8)$$

$$\mathbf{u}(\mathbf{X}, \mathbf{y}) = \mathbf{u}^{(0)}(\mathbf{X}, \mathbf{y}) + \eta \mathbf{u}^{(1)}(\mathbf{X}, \mathbf{y}) + \dots \quad (9)$$

$$\boldsymbol{\theta}(\mathbf{X}, \mathbf{y}) = \eta^{-1}\boldsymbol{\omega}^{(-1)}(\mathbf{X}, \mathbf{y}) + \boldsymbol{\omega}^{(0)}(\mathbf{X}, \mathbf{y}) + \boldsymbol{\varphi}^{(0)}(\mathbf{X}, \mathbf{y}) + \eta \boldsymbol{\varphi}^{(1)}(\mathbf{X}, \mathbf{y}) + \dots \quad (10)$$

The neighboring mechanical nodes I and J are close to each other from the viewpoint of the \mathbf{X} reference system. One can use the macroscopic gradient ∇_X at node I to approximate the mechanical field variables at node J , see Fish et al. (2007). The same is valid for pressure. The Taylor expansions of the primary fields yield

$$p(\mathbf{X}_Q, \mathbf{y}_Q) = p(\mathbf{X}_P, \mathbf{y}_Q) + \frac{\partial p(\mathbf{X}_P, \mathbf{y}_Q)}{\partial X_i} x_i^{PQ} + \frac{1}{2} \frac{\partial^2 p(\mathbf{X}_P, \mathbf{y}_Q)}{\partial X_i \partial X_j} x_i^{PQ} x_j^{PQ} + \dots \quad (11)$$

$$\mathbf{u}(\mathbf{X}_J, \mathbf{y}_J) = \mathbf{u}(\mathbf{X}_I, \mathbf{y}_J) + \frac{\partial \mathbf{u}(\mathbf{X}_I, \mathbf{y}_J)}{\partial X_j} x_j^{IJ} + \frac{1}{2} \frac{\partial^2 \mathbf{u}(\mathbf{X}_I, \mathbf{y}_J)}{\partial X_j \partial X_k} x_j^{IJ} x_k^{IJ} + \dots \quad (12)$$

$$\boldsymbol{\theta}(\mathbf{X}_J, \mathbf{y}_J) = \boldsymbol{\theta}(\mathbf{X}_I, \mathbf{y}_J) + \frac{\partial \boldsymbol{\theta}(\mathbf{X}_I, \mathbf{y}_J)}{\partial X_j} x_j^{IJ} + \frac{1}{2} \frac{\partial^2 \boldsymbol{\theta}(\mathbf{X}_I, \mathbf{y}_J)}{\partial X_j \partial X_k} x_j^{IJ} x_k^{IJ} + \dots \quad (13)$$

The asymptotic expansion along with Taylor expansion is inserted into the kinematic equations to deliver scale separation of the pressure gradient, strain and curvature. The scale separation is also applied to constitutive equation. Due to assumed complex nonlinear nature of functions $\lambda(p, \delta)$, $f_s(\boldsymbol{\varepsilon})$ and $f_m(\boldsymbol{\chi})$ which are yet unknown, the separation is delivered by Taylor expansion with respect to variables p , δ , $\boldsymbol{\varepsilon}$ and $\boldsymbol{\chi}$ (see details in Eliáš and Cusatis (2022)).

Finally, all these quantities are inserted into the balance equations. The resulting expressions contain terms at different scale, distinguished by power of η . The balance needs to be satisfied at each of these scales, one therefore needs to solve several sets of balance equations. Some of them are trivial and can be solved analytically, two of them become the *macroscale* and *mesoscale* problems that are solved numerically.

4 MACROSCOPIC LEVEL

The macroscale delivers the following balance equations

$$\rho_{w0} \left[\dot{v}_{c0} \left(1 - b + \frac{p^{(0)} - p_0}{K_w} \right) + v_{c0} \frac{\dot{p}^{(0)}}{K_w} + 3b\dot{\varepsilon}_V^{(0)} + \frac{\dot{p}^{(0)}}{M_b} \right] + q = \nabla_X \cdot \mathbf{f} \quad (14)$$

$$\nabla_X \cdot \boldsymbol{\sigma}_s - \nabla_{Xp}^{(0)} \cdot \boldsymbol{\xi} = \langle \rho \rangle \ddot{\mathbf{u}}^{(0)} - \mathbf{b} \quad (15)$$

$$\nabla_X \cdot \boldsymbol{\mu}_s - \nabla_{Xp}^{(0)} \cdot \boldsymbol{\zeta} + \boldsymbol{\varepsilon} : \sigma_s - p^{(0)} \boldsymbol{\varepsilon} : \boldsymbol{\xi} = 0 \quad (16)$$

These equations describe Cosserat continuum coupled with mass transport in saturated solids. The new tensors emerging in these equations are collected from the mesoscale solution

$$\mathbf{f} = \frac{1}{V_0} \sum_{d \in V_0} h S_j^{(0)} \mathbf{e}_\lambda \quad (17)$$

$$\boldsymbol{\sigma}_s = \frac{1}{V_0} \sum_{e \in V_0} l A s_\alpha^{(0)} \mathbf{e}_N \otimes \mathbf{e}_\alpha \quad (18)$$

$$\boldsymbol{\mu}_s = \frac{1}{V_0} \sum_{e \in V_0} l A \mathbf{e}_N \otimes \left[\eta m_\alpha^{(1)} \mathbf{e}_\alpha + s_\alpha^{(0)} \boldsymbol{\varepsilon} : (\mathbf{x}_c \otimes \mathbf{e}_\alpha) \right] \quad (19)$$

$$\boldsymbol{\xi} = \frac{1}{V_0} \sum_{e \in V_0} l A b e_N \otimes \mathbf{e}_N \quad (20)$$

$$\boldsymbol{\zeta} = \frac{1}{V_0} \sum_{e \in V_0} l A b e_N \otimes [\boldsymbol{\varepsilon} : (\mathbf{x}_c \otimes \mathbf{e}_N)] \quad (21)$$

\mathbf{f} is the flux vector, $\boldsymbol{\sigma}_s$ is the solid stress tensor, $\boldsymbol{\mu}_s$ is the solid couple stress tensor and $\boldsymbol{\xi}$ and $\boldsymbol{\zeta}$ are second order tensors describing RVE internal structure producing an effect of pressure on the macroscopic stress and couple stress.

The primary fields (unknowns) at the macroscale are pressures $p^{(0)}$, displacements $\mathbf{u}^{(0)}$ and rotations $\boldsymbol{\varphi}^{(0)}$. Several emerging coupling terms are obtained describing storage of the fluid in cracks, an effect of volumetric changes on the pressure, an effect of the pressure gradient on the linear momentum balance, and effects of the pressure gradient and the pressure on the angular momentum balance. The macroscopic equations are naturally anisotropic due to the heterogeneity and cracking at the microscale.

The macroscale problem, supplemented with boundary conditions, is solved by the finite element method. Each integration point contains an embedded RVE with subscale model derived in the next section. The macroscopic pressure gradient \mathbf{a} and the Cosserat strain tensor $\boldsymbol{\gamma}$ are computed and sent to the RVE as loads. RVE serves as a macroscopic constitutive routine; after solving it, the stress like tensors (Eqs. 17–21) are received by the macroscale. According to Rezakhani and Cusatis (2016) the Cosserat effect does not contribute in a significant way and simplification to Cauchy continuum is possible.

5 MESOSCOPIC LEVEL

The RVE problem is described by the following balance equations

$$\sum_{Q \in W} S_j^{(0)} = 0 \quad (22)$$

$$\sum_{J \in V} A s_\alpha^{(0)} \mathbf{e}_\alpha = p^{(0)} \sum_{J \in V} A b e_N \quad (23)$$

$$\sum_{J \in V} A \left(s_\alpha^{(0)} \mathbf{e}_\alpha \boldsymbol{\varepsilon} : (\mathbf{c}_I \otimes \mathbf{e}_N) + \eta m_\alpha^{(1)} \mathbf{e}_\alpha \right) = p^{(0)} \boldsymbol{\varepsilon} : \sum_{J \in V} A b c_I \otimes \mathbf{e}_N \quad (24)$$

with degrees of freedom being $\eta p^{(1)}$, $\eta \mathbf{u}^{(1)}$ and $\omega^{(0)}$, the microscopic pressure, translation and rotation, respectively.

It turns out that load is provided by the eigen-pressure gradient \hat{g} and eigen-strain $\hat{\boldsymbol{\varepsilon}}_\alpha$, which are expressed as negative projections of the macroscopic pressure gradient $\mathbf{a} = \nabla_X p^{(0)}$ and the Cosserat strain tensor $\boldsymbol{\gamma} = \nabla_X \otimes \mathbf{u}^{(0)} - \boldsymbol{\varepsilon} \cdot \boldsymbol{\varphi}^{(0)}$

$$\hat{g} = - \frac{\partial p^{(0)}}{\partial X_i} e_i^\lambda = -\mathbf{a} \cdot \mathbf{e}_\lambda \quad (25)$$

$$\hat{\epsilon}_\alpha = -e_i^\alpha \left[\frac{\partial u_i^{(0)}}{\partial X_k} - \mathcal{E}_{ijk} \varphi_j^{(0)} \right] e_k^N = -\mathbf{e}_N \cdot \boldsymbol{\gamma} \cdot \mathbf{e}_\alpha \quad (26)$$

The RVE balance equations are solved numerically by the discrete mesoscale model. The constitutive equations are the original constitutive functions of the full model, λ , f_s , and f_m . Note that unlike the macroscale the RVE problem is steady state (or static).

Since the primary field $\eta p^{(1)}$ has no effect on the mechanical behavior, the mechanical RVE is partially decoupled from the transport one, which needs crack openings and it is therefore solved after the mechanical RVE.

According to the homogenization theory, the unknown fields should be periodic. Thus, the periodic boundary conditions must be enforced for pressure, displacements and rotations. Additional boundary conditions are needed for pressure and displacements as the balance equations consider only differences in these primary fields and are therefore ill-conditioned without some additional constraint. These fields are lower scale fluctuations which are supposed to be zero on average, therefore the last boundary conditions should prescribe zero volumetric average of these fields over the RVE: $\langle \eta p^{(1)} \rangle = 0$, $\langle \eta \mathbf{u}^{(1)} \rangle = 0$ where the weighted volumetric average reads $\langle \bullet \rangle = \frac{1}{V_0} \sum_{w \in V_0} V_w \bullet$.

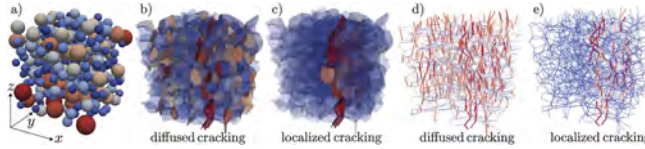


Figure 1. Single RVE loaded by straining in x direction and pressure gradient in z direction. Both diffused and localized cracking states are captured. One can see how cracks enhance conductivity of transport elements. The red (or blue) color indicates high (or low, respectively) values of depicted variables. a) RVE internal structure – aggregate diameters; b)+c) crack opening in the mechanical RVE; d)+e) fluxes in the transport RVE.

Example of fractured RVE is shown in Figure 1. The constitutive model features strain softening and therefore the mechanical problem suffers from strain localization. The localization phenomenon cannot be homogenized as the scale separation does not hold (Gitman et al., 2007), the RVE response becomes dependent on its size. Some researchers (Coenen, Kouznetsova, Bosco and Geers, 2012; Unger, 2013) suggested remedies to incorporate the strain localization into the homogenization scheme, but these techniques are not adopted here yet. The only way to simulate localized fracture is therefore to use RVE volumes corresponding to volumes associated to integration points in the macroscale model (Rezakhani and Cusatis, 2016). Unfortunately, the major benefit of the homogenization, that the large material volume can be macroscopically represented by a small RVE, would be lost.

6 IMPLEMENTATION, VERIFICATION AND APPLICATION

The constitutive models and material parameters are described in Eliáš and Cusatis (2022). The mechanical model is taken from Cusatis and Cedolin (2007) and simplified. However, any functions f_s and f_m can be easily used at the RVE level. The transport constitutive function λ can also be chosen arbitrarily. It is here considered as a simple linear dependency of the flux on the pressure gradient in the intact material with additional terms according to Grassl and Bolander (2016) when cracks are present. The macroscopic equations are rewritten into the weak form and implemented in an in-house software called OAS (Open Academic Solver). Computational domain is discretized into Cosserat trilinear isoparametric brick elements extended by additional pressure degrees of freedom.

The model is verified by simulating Terzaghi’s consolidation and applied to simulate hydraulic fracturing of hollow cylinder. These examples compare the *full* discrete model and the *homogenized* model. The comparison should ideally be repeated several times and statistically evaluated because of the intrinsic randomness of the mesoscale discrete model (Eliáš and Vořechovský, 2020), but only single realization is used. Also, only one computational thread was employed. There is a huge potential to speed-up the *homogenized* model further by distributing independent RVE problems over several processors.

6.1 Linear Terzaghi’s consolidation

The model is verified by simulating Terzaghi’s consolidation, a transient simulation of classical poromechanical problem. A partially sealed prism from a linear elastic material, initially under zero pressure and zero strain, is loaded by prescribed fluid pressure 1 MPa at the front end. Biot coefficient is $b = 0.5$.

The problem is analyzed using the *full* discrete model, and the *homogenized* continuous model composed of five trilinear 8-node isoparametric finite elements. Evolution of displacement and pressure along the central axis of the 3D prism is shown in Figure 2. There is also an analytical solution included in the comparison. Small differences are attributed to (i) heterogeneity and (ii) boundary layer effect (Eliáš, 2017), or wall effect, that is present in the *full* model and modify the mechanical properties in the vicinity of the boundary.

The *full* model features approx. 124,000 DoF and run for approx. 3 hours. The *homogenized* model has only 40 DoF and calculation took approximately 1 s. The speed-up factor is about four orders of magnitude thanks to the enforced linearity of the RVE response, which can be pre-computed at the simulation initialization.

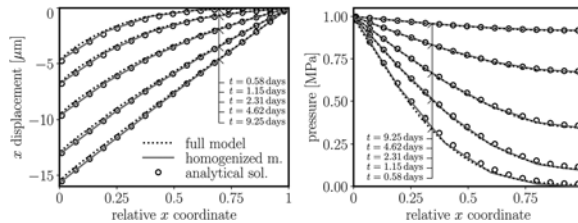


Figure 2. Comparison of results of the Terzaghi’s consolidation problem: displacement profiles and fluid pressure at various times of simulation as computed by the *homogenized* model (macroscopic component only) and the *full* model.

6.2 Hydraulic fracturing of hollow cylinder

The specimen is a hollow cylinder with transport boundary conditions prescribing zero pressure at the outer cylinder shell, pressure linearly increasing in time at the inner surface and zero normal flux at the upper and bottom surfaces. Mechanical boundary conditions restrict normal movements at the upper and bottom surface and apply inward traction on the inner surface of a magnitude equal to the prescribed pressure. Three variants of Biot’s coefficient are simulated: $b = 0, 0.05$, and 1 .

The *full* model has approximately 323,000 DoF. The *homogenized* model has only 4 elements in radial direction and 10 element along circumference. In total, it has 40 element, 320 RVEs and approx. 1.3 mil. DoF (macroscale and microscale combined). This number is, however, only virtual as most of the RVEs remain linear elastic during the calculation so their response is pre-computed and their degrees of freedom are not activated. The simulation is controlled by an increasing pressure so it eventually reaches a state when a macroscopic crack runs across the whole cylinder and solver fails due to loss of convergence. Another complication arises in *homogenized* models because the macroscopic crack may develop in any direction. Standard periodic boundary conditions cannot handle such situation (Stránský and Jirásek, 2011) and advanced approach is needed (Coenen, Kouznetsova and Geers, 2012). Instead, the RVEs are rotated in this study so they are all aligned with the radial direction under which the crack is expected.

Reasonable correspondence between the *full* and *homogenized* solution is documented in Figures 3 and 4. The larger differences occurring in the later stages of the simulations are attributed to the developed strain localization, which cannot be homogenized by the standard technique.

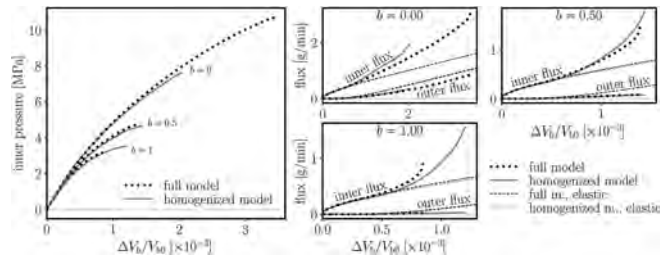


Figure 3. Left: loading pressure vs. volumetric change of the central hole; right: inner and outer fluxes.

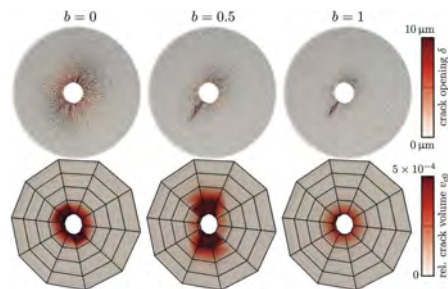


Figure 4. Cracks developed in the *full* and *homogenized* models at the last valid step of the simulation.

The *full* model simulations took 2970 min, 1220 min and 730 min for Biot coefficients 0, 0.5 and 1, respectively; the *homogenized* models run for 330 min, 150 min and 120 min (in the same order). The speed-up factors are approximately 9, 8.1 and 6.1, respectively.

7 CONCLUSIONS

Asymptotic expansion homogenization is developed for the discrete mesoscale models of coupled mechanics and mass transport in a fully saturated heterogeneous medium. Only brief description is given in this conference paper, detail are provided in Eliáš and Cusatis (2022).

- The macroscale problem corresponds to transient Cosserat continuum coupled with mass transport. It is solved with a help of the finite element method; the constitutive function is supplied by a subscale RVE problem. The homogenized macroscopic material exhibits natural anisotropy due to cracking at the microscale, both for the mass transport and mechanical behavior.
- The microscale problems are discrete and steady state. RVE loading is given by a projection of macroscopic strain and pressure gradient into eigen-strains and eigen-pressure gradients of the discrete elements. Summations of discrete stress-like quantities over the RVE then provide macroscopic stress, couple stress and flux.
- Reasonable correspondence between the *full* and *homogenized* solution and significant speed-up factors are achieved.
- The strain localization remains unsolved, the localized solution is dependent on RVE size. Possible remedies described in literature (Coenen, Kouznetsova, Bosco and Geers, 2012; Unger, 2013) shall be implemented in the future.

ACKNOWLEDGEMENTS

Jan Eliáš gratefully acknowledges financial support provided by the Faculty of Civil Engineering, Brno University of Technology under project No. FAST-J-22-8014.

REFERENCES

- Biot, M. A. 1941, General theory of three-dimensional consolidation, *Journal of Applied Physics* 12(2):155–164.
- Coenen, E., Kouznetsova, V., Bosco, E. and Geers, M. 2012, A multi-scale approach to bridge microscale damage and macroscale failure: a nested computational homogenization-localization framework, *International Journal of Fracture* 178:157–178.
- Coenen, E., Kouznetsova, V. and Geers, M. 2012, Novel boundary conditions for strain localization analyses in microstructural volume elements, *International Journal for Numerical Methods in Engineering* 90(1):1–21.
- Cusatis, G. and Cedolin, L. 2007, ‘Two-scale study of concrete fracturing behavior’, *Engineering Fracture Mechanics* 74(1):3–17. Fracture of Concrete Materials and Structures.
- Cusatis, G., Mencarelli, A., Pelessone, D. and Baylot, J. 2011, Lattice discrete particle model (LDPM) for failure behavior of concrete. II: Calibration and validation, *Cement and Concrete Composites* 33(9):891–905.
- Cusatis, G., Pelessone, D. and Mencarelli, A. 2011, Lattice discrete particle model (LDPM) for failure behavior of concrete. I: Theory, *Cement and Concrete Composites* 33(9):881–890.
- Detournay, E. and Cheng, A. H.-D. 1995, *Comprehensive Rock Engineering: Principles, Practice & Projects*, Vol. II, pp. 113–171.
- Eliáš, J. 2016, Adaptive technique for discrete models of fracture, *International Journal of Solids and Structures* 100–101:376–387.
- Eliáš, J. 2017, Boundary layer effect on behavior of discrete models, *Materials* 10:157.
- Eliáš, J. 2020, Elastic properties of isotropic discrete systems: Connections between geometric structure and poisson’s ratio, *International Journal of Solids and Structures* 191–192:254–263.
- Eliáš, J. and Cusatis, G. 2022, Homogenization of discrete mesoscale model of concrete for coupled mass transport and mechanics by asymptotic expansion, *Journal of the Mechanics and Physics of Solids* 167:105010.
- Eliáš, J. and Vořechovský, M. 2020, Fracture in random quasibrittle media: I. Discrete mesoscale simulations of load capacity and fracture process zone, *Engineering Fracture Mechanics* 235:107160.
- Eliáš, J., Yin, H. and Cusatis, G. 2022, Homogenization of discrete diffusion models by asymptotic expansion, *International Journal for Numerical and Analytical Methods in Geomechanics* 46:3052–3073.
- Fahy, C., Wheeler, S. J., Gallipoli, D. and Grassl, P. 2017, Corrosion induced cracking modelled by a coupled transport-structural approach, *Cement and Concrete Research* 94:24–35.
- Fish, J., Chen, W. and Li, R. 2007, Generalized mathematical homogenization of atomistic media at finite temperatures in three dimensions, *Computer Methods in Applied Mechanics and Engineering* 196(4):908–922.
- Gitman, I., Askes, H. and Sluys, L. 2007, Representative volume: Existence and size determination, *Engineering Fracture Mechanics* 74(16):2518–2534.
- Grassl, P. 2009, A lattice approach to model flow in cracked concrete, *Cement and Concrete Composites* 31(7):454–460.
- Grassl, P. and Bolander, J. 2016, ‘Three-dimensional network model for coupling of fracture and mass transport in quasi-brittle geomaterials’, *Materials* 9(9):782.
- Li, W., Zhou, X., Carey, J. W., Frash, L. P. and Cusatis, G. 2018, Multiphysics lattice discrete particle modeling (M-LDPM) for the simulation of shale fracture permeability, *Rock Mechanics and Rock Engineering* 51:3963–3981.
- Pathirage, M., Tong, D., Thierry, F., Cusatis, G., Grégoire, D. and Pijaudier-Cabot, G. 2023, Discrete modeling of concrete failure and size-effect, *Theoretical and Applied Fracture Mechanics* 124:103738.
- Rezakhani, R., Alnagar, M. and Cusatis, G. 2019, Multiscale homogenization analysis of alkali–silica reaction (ASR) effect in concrete, *Engineering* 5(6):1139–1154.
- Rezakhani, R. and Cusatis, G. 2016, Asymptotic expansion homogenization of discrete fine-scale models with rotational degrees of freedom for the simulation of quasi-brittle materials, *Journal of the Mechanics and Physics of Solids* 88:320–345.
- Rezakhani, R., Zhou, X. and Cusatis, G. 2017, Adaptive multiscale homogenization of the lattice discrete particle model for the analysis of damage and fracture in concrete, *International Journal of Solids and Structures* 125:50–67.
- Stránský, J. and Jirásek, M. 2011, Calibration of particle-based models using cells with periodic boundary conditions, in ‘II International Conference on Particle-based Methods - Fundamentals and Applications’, pp. 1–12.
- Unger, J. F. 2013, An FE2-X1 approach for multiscale localization phenomena, *Journal of the Mechanics and Physics of Solids* 61(4):928–948.
- Zhu, Z., Pathirage, M., Wang, W., Troemner, M. and Cusatis, G. 2022, Lattice discrete particle modeling of concrete under cyclic tension–compression with multi-axial confinement, *Construction and Building Materials* 352:128985.

Early-age cracking in concrete slabs with FRP reinforcement

J.E. Bolander

University of California, Davis, California, USA

H. Roghani & A. Nanni

University of Miami, Coral Gables, Florida, USA

ABSTRACT: This paper reports on a combined experimental and numerical modeling investigation of cracking of concrete slabs with FRP reinforcement. At this stage of the project, attention is given to early-age cracking driven by plastic shrinkage, preceding longer term considerations of cracking resistance over the service life of field applications. Small-scale slab specimens are subjected to controlled evaporation rates. Images of crack development are acquired periodically, from which crack width estimations are made. Comparisons are made between slabs reinforced with conventional steel and those reinforced with FRP, along with control specimens that lack reinforcement. During the period of plastic shrinkage, the time of crack initiation and subsequent crack openings do not appear to be influenced by the presence of the reinforcing bars.

The numerical modeling component of the research is based on a Voronoi-cell lattice model. The relative humidity, temperature, and displacement fields are discretized in three-dimensions, which allows for a comprehensive investigation of fracture development. For the reduced bond properties that are expected at early ages, the simulations confirm that cracking behavior is not significantly influenced by the presence of the reinforcing bars.

1 INTRODUCTION

Corrosion of reinforcing steel is a primary factor affecting the durability of structural concrete, especially for exposures to severe environments. The potential for corrosion-induced durability problems can be reduced by controlling crack formation in the concrete, particularly at early ages when the concrete is susceptible to cracking. Alternatively, non-corroding materials can be used as concrete reinforcement.

This research involves the use of fiber reinforced polymer (FRP) bars to reinforce concrete exposed to severe conditions, such as those presented by marine environments. Despite the fact that FRP bars have been successfully used for structural reinforcement in concrete members in building and bridge projects for the past 30 years, there has recently been interest in using FRP bars and meshes as secondary reinforcement for non-structural concrete members, such as plain concrete footings, concrete slabs-on-ground, and plain concrete walls, in place of conventional temperature and shrinkage steel reinforcement (Ekenel et al. 2022). Of interest is the effectiveness of such reinforcement in restricting plastic shrinkage cracking at early ages. It is known that conventional steel reinforcement does not restrict the opening of plastic shrinkage cracks. However, the nature of the bond mechanisms is potentially different and, in relative terms, the mismatch in stiffness between FRP and immature concrete is smaller.

FRP bar performance, relative to that of conventional steel reinforcement, is investigated through a combination of physical experimentation and numerical modeling. The bases for the experiments and modeling exercises are first described, after which preliminary results are presented. In particular, based on the assumption of poor bonding at early stages of matrix development, the type of reinforcement does not significantly influence time of cracking and crack opening driven by plastic shrinkage.

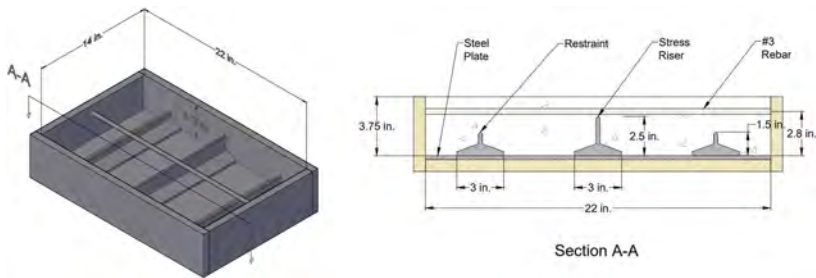


Figure 1. Device for simulating plastic shrinkage cracking.

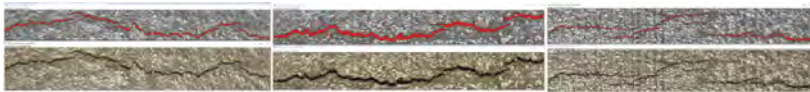


Figure 2. Post-processed (above) and original (below) images of cracking of the slab surface above the stress riser; P-SC-1, S-3S-SC-1, G-3S-SC-1 from left to right.

2 EXPERIMENTAL PROGRAM

2.1 Test set-up and procedure

Potential for plastic shrinkage cracking is assessed using a modified form of the set-up described in ASTM C1579 (ASTM 2021). The set-up involves small-scale slab specimens that incorporate metallic inserts attached to the formwork base. The insert is a 1/4 in. steel plate with 3 welded T-bars as illustrated in Figure 1. The T-bars at both ends restrain plastic shrinkage of the concrete, which fosters crack formation; the one at mid-span acts as a stress riser that influences the point of crack initiation.

Whereas ASTM C1579 pertains to the testing of fiber reinforced (or plain) concrete materials, a reinforcing bar is positioned within each of reinforced specimens, as shown in Figure 1. Along with plain concrete specimens, two types of bars were considered: glass FRP (GFRP) bars and conventional steel reinforcing bars, both having a nominal diameter of 10 mm. The main challenge is to consistently ensure the occurrence of cracking at the early stages. Therefore, an environmental chamber was designed and built to provide the critical rate of evaporation for plastic shrinkage cracking. In addition to the environmental condition considerations, several mixture designs were evaluated to maximize the plastic shrinkage. Moreover, the mixing water was heated to 50°C before addition to the mixture to increase the initial concrete temperature and rate of evaporation.

Crack initiation and development were monitored by acquiring images of the drying surface. Post-processing of the images provided data regarding time of crack initiation and the evolution of crack openings.

2.2 Experimental results

All specimens exhibited cracking within three hours after the first contact between water and cement. Images of the middle portion of the cracked specimens are presented in Figure 2. Table 1 provides crack data measured after six hours of exposure to the specified conditions of evaporation. Crack widths did not noticeably narrow in the vicinity of reinforcement, but were rather uniform over the crack lengths. The premature bond between the reinforcement and concrete during this time span results in a poor stress transfer between the concrete and reinforcement. As expected, the reinforcement is ineffective in controlling plastic shrinkage cracking.

Using the same mixture design, a companion set of pullout tests according to ASTM D7913 (ASTM 2020) was conducted to measure the bond properties of the GFRP bars at early age.

It was found that the bond strength at $t = 2\text{h}$ (the approximate time of initial cracking) is only about 0.14 MPa. For comparison, the ASTM D7957 (ASTM 2022) requires a minimum guaranteed bond strength of 7.6 MPa after 28 days of concrete hardening and the guaranteed value is the mean minus three standard deviations of the samples.

Table 1. Measured crack data at six hours after concrete casting.

Specimen ID	Reinforcement	Crack area (mm ²)	Crack length (mm)	Crack width (mm)
P-SC-1	Plain	133.5	345.4	0.39
S-3S-SC-1	Steel	246.5	353.1	0.70
S-3S-SC-2	Steel	73.5	188.0	0.39
S-3S-SC-3	Steel	129.7	342.9	0.38
G-3S-SC-1	GFRP	112.9	340.4	0.33
G-3S-SC-2	GFRP	58.1	139.7	0.42
G-3S-SC-3	GFRP	219.4	322.6	0.68

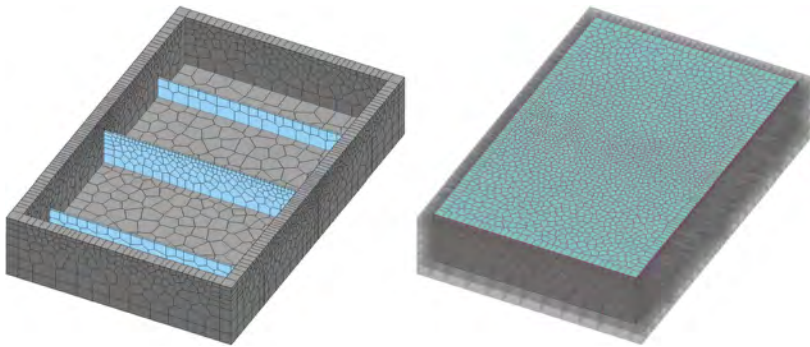


Figure 3. Discretization of test specimens: a) plywood formwork with restraining device inserts; and b) concrete specimen cast within the formwork.

3 MODELING APPROACH

Voronoi-cell lattice models (VCLM) are used to simulate the early-age thermal and hygral fields acting in the concrete, as well as the mechanical response to those actions. Such discrete modeling approaches are particularly effective in simulating cracking and other forms of displacement discontinuity (Bolander et al. 2021). A VCLM discretization of the test specimens and plywood formwork is shown in Figure 3. The study of reinforcing bars within the concrete volume requires three-dimensional simulations.

The thermal-hygral-mechanical model employed herein utilizes the analysis framework developed by Pan et al. (2017), which has the following features:

- Cementitious materials hydration is based on the model proposed by Riding et al. (2012). The degree of cementitious materials reaction can be expressed by the amount of chemically combined water or, equivalently, by

$$\alpha(t) = \frac{H(t)}{H_u} \quad (1)$$

where $H(t)$ is the cumulative amount of heat produced by the hydration reaction (J/g); and H_u is total heat available for reaction (J/g). The total available heat depends on the composition and proportioning of the cementitious materials (Riding et al. 2012);

- The temperature field within the model domain is simulated using a lattice composed of conduit elements. A convective boundary layer models heat transfer between the exposed surface of the specimen and the environment. For field exposure conditions, heat exchange with the environment is due to convection, solar radiation, thermal radiation, evaporation and condensation. For the lab specimens considered herein, convection and evaporation will be the dominant forms of heat exchange. Convective heat exchange across exposed surfaces (including the outer surfaces of the plywood formwork) depends on the difference between the solid surface temperature T_s and that of the surrounding ambient medium T_a

$$q_{conv} = A_T(T_s - T_a) \quad (2)$$

where A_T is the coefficient of convective heat transfer, which depends on material type, wind speed and other conditions (Bentz 2000). Heat of hydration is calculated at the lattice nodes and used as a source term in the thermal analyses;

- The humidity field is simulated using a parallel set of conduit elements, based on the same set of nodal points and element connectivities. After setting of the concrete, moisture transport is assumed to be governed by a diffusion process (i.e., according to Fick's 2nd law). A convective boundary layer accounts for moisture transfer between the drying surface of the concrete and the environment. The modeling of this layer is analogous to that of the temperature field, expressed by Eq. 2, although governed by different mechanisms;
- The solution process involves a time-stepping scheme in which, for each time step, the temperature and humidity fields are solved using the Crank-Nicholson method in conjunction with a fixed-point algorithm to achieve convergence;
- The simulated thermal and hygral fields produce thermal and hygral strains, respectively, within the mechanical component of the analysis framework. These strain increments produce stress that might lead to crack formation;
- Concrete property development, including strength and stiffness, depends on the degree of cementitious materials hydration. In particular, solidification theory is used to simulate creep processes and stiffness development (di Luzio & Cusatis, 2013). The development of tensile strength is represented by

$$f(\alpha) = f(\alpha_u) \left(\frac{\alpha - \alpha_0}{\alpha_u - \alpha_0} \right)^\zeta \quad (3)$$

where $f(\alpha_u)$ is the tensile strength at the ultimate degree of hydration; α_0 is the degree of hydration associated with setting; and coefficient $\zeta = 1$ when tensile strength is being modeled (de Schutter & Taewre, 1996);

- At a given stage of strength development, concrete fracture is simulated using an energy-conserving crack band model (Berton & Bolander, 2006). The geometry of neighboring Voronoi cells define the extents of the crack band;
- Each reinforcing bar is represented by series of frame elements, which connect to the concrete nodes via special link elements (Kang et al., 2014). The link elements account for the nonlinear bond actions between the concrete and reinforcement, including FRP bars as described by Focacci et al. (2000).

The model has been modified to approximate behavior of concrete in the plastic state. In particular, the modeling of plastic shrinkage is based on the simulations of Ghourchian et al. (2019), as presented in Figure 4. Plastic settlement produces volumetric strain that begins with a vertical component. A smaller horizontal strain component appears at a later time. By studying the behavior of different concrete types, Ghourchian et al. suggest that crack initiation is governed by a limiting value of horizontal strain (e.g., $\epsilon_{h-crack} \approx 0.003$), rather than a stress measure.

Herein, volumetric strain is introduced into the lattice model from the time of horizontal strain commencement; the preceding accumulation of vertical strain is neglected. This volumetric straining continues until the end of the plastic stage, after which drying shrinkage is assumed to be caused by moisture diffusion, as described above. The rate and duration of this form of volumetric straining are model parameters. The stress-based fracture criterion, as expressed by Eq. 3, is retained.

The model has also been extended to include the effects of evaporation on concrete temperature. Heat flux due to evaporative cooling is determined by

$$q_e = -E_c h_l \quad (4)$$

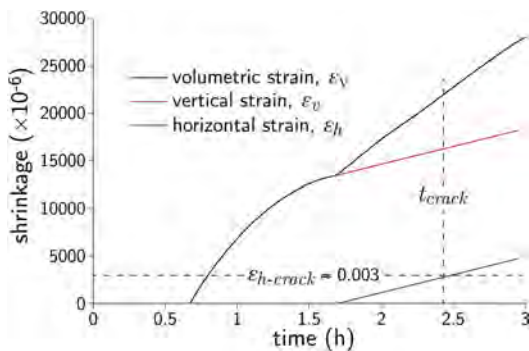


Figure 4. Volumetric instability of concrete in the plastic state (adapted from Ghourchian et al., 2019).

where E_c is evaporation rate from the concrete surface ($\text{kg/m}^2/\text{s}$) and h_l is latent heat of vaporization (J/kg). The evaporation rate from the fresh concrete surface is calculated according to Uno (1998) in the following form

$$E'_c = 5(V + 4) \left[(T_c + 18)^{2.5} - r(T_a + 18)^{2.5} \right] \times 10^{-6} \quad (5)$$

in which V is wind velocity (km/h); T_c is temperature of the concrete surface ($^\circ\text{C}$); T_a is the ambient temperature ($^\circ\text{C}$); and r is relative humidity of the environment. The evaporation rate is modified to account for maturation of the concrete according to

$$E_c = E'_c \exp \left[-(t/a)^{1.5} \right] \quad (6)$$

where t is maturation time (h) and a is a time constant set equal to 3.75h for concrete (Schindler et al., 2004).

4 SIMULATION RESULTS AND DISCUSSION

4.1 Thermal analyses

As previously noted, the thermal analyses, as well as the simulation of property development, are based on a modeling of cementitious material hydration. The recorded wind speed was used to determine transfer of heat from the upper concrete surface due to convection and evaporative cooling, as described above. Specimen temperature was measured using a thermocouple device, inserted through the plywood formwork and extending into the concrete specimen. A computational node was introduced at the location of the thermocouple tip to have one-to-one correspondence with respect to the measurement location.

Figure 5 compares the measured and simulated temperature results from the time of casting for specimen S-3S-SC-1. The initial decline in temperature was typical of the results of most of the other specimens. In the numerical simulations, the decline was found to be caused mainly by evaporative cooling, rather than other environmental factors.

4.2 Cracking behavior

In agreement with experimental observations, cracks form across the midspan width of the specimen, over the central restraint (Figure 6). Although not evident in the figure, microcracking also occurs local to the peripheral restraints, which has been observed in other experimental programs (Combrinck et al., 2018).

Prior to simulating plastic shrinkage in terms of volumetric strain, as shown in Figure 4, attempts were made to simulate plastic shrinkage as a diffusion phenomenon, as done for drying shrinkage. In addition to being conceptually invalid, these attempts failed in several respects. The resulting crack widths at $t = 6$ h were much smaller than those observed in the experiments. Furthermore, significant distributed microcracking occurred over the drying surface and the resulting macrocrack (which formed over the central device) propagated from the upper surface downward. In contrast, by introducing plastic shrinkage as a volumetric strain, the central device acts as a stress riser, such that cracking initiates at the device tip and propagates upward. Ghourchian et al. (2019) observed such upward propagation of plastic shrinkage cracking from images produced by x-ray radiography.

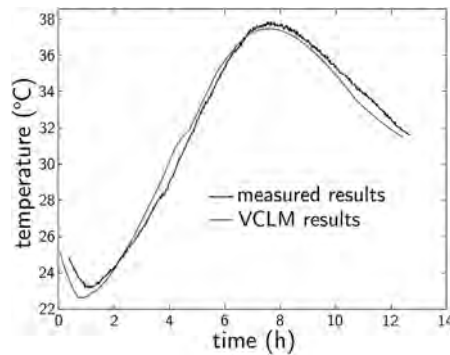


Figure 5. Measured and simulated temperatures at the thermocouple location in specimen S-3S-SC-1.

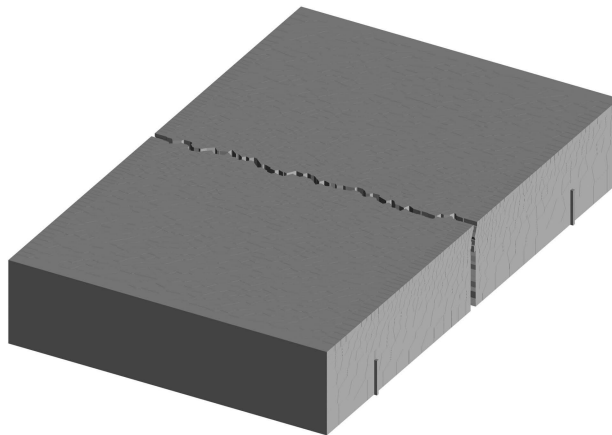


Figure 6. Crack pattern in specimen S-3S-SC-1 at $t = 4$ h.

In Pan et al. (2021), the VCLM has been extended to simulate such hygro-mechanical behavior using the effective stress concept of Biot (1941). Transport of water in the porous media is driven by gravity and described using Darcy's Law in rate format. Work toward integrating this capability with fracture modeling, and the other relevant chemo-physical processes, is ongoing.

4.3 Effects of reinforcing bars

As noted in Section 3, each reinforcing bar is represented by a series of frame elements, which connect to concrete nodes via nonlinear link elements. The frame elements are assigned the geometric and material properties of the steel or FRP bars, as the case may be. The bond strength assigned to the link elements was determined through the aforementioned pullout tests conducted at $t = 2\text{h}$, the approximate time of plastic shrinkage crack initiation.

Figure 7 presents the simulated crack opening profile for specimen S-3S-SC-1, which contains steel bar reinforcement; similar results are obtained for GFRP bar reinforcement. From these results, it is apparent that the presence of the reinforcement (of either type) does not have an appreciable effect on the crack opening profile. Given the low bond strength at this early age, this result was foreseeable. Short distributed fibers, which supply a much larger bonded surface area, are seen as a solution.

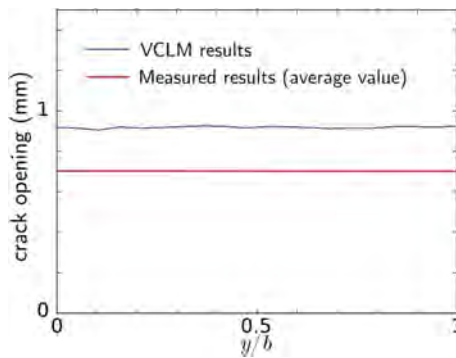


Figure 7. Simulated crack opening profile for specimen S-3S-SC-1 at $t = 6\text{h}$ (where y represents position along the crack within width b of the specimen).

5 CONCLUSIONS

The physical testing and numerical modeling of plastic shrinkage cracking is complicated by many factors. These factors include uncertainties regarding the thermo-hydro-mechanical processes and their couplings, the roles of sustained load and plastic settlement on the fracture process, frictional effects along the specimen base, and bond properties at early ages. To help address these uncertainties, more comprehensive test and analysis efforts are needed. Nonetheless, several statements can be made based on the results presented herein.

- Consistent cracking behavior of the control specimens was obtained by optimizing the concrete mixture design, controlling the environmental boundary conditions, and raising the initial temperature of the concrete which increased the evaporation rate from the drying surface. Initial temperature was raised by heating the mixing water, before its addition to the dry materials.
- For the specimens considered herein, crack opening does not appear to be restricted in the vicinity of a bar, but rather openings are fairly uniform over the specimen width. This suggests poor bond properties between the reinforcing bars and the concrete at these early ages. In other words, the presence of the reinforcing bar of either type, GFRP or steel, does not have an appreciable effect on time of plastic shrinkage crack initiation and ensuing crack opening.
- The proposed numerical analyses elucidate the roles of the various thermo-hydro-mechanical processes that affect early-age cracking of the specimens. In particular, by modeling plastic shrinkage as a bulk material phenomenon (in the form of volumetric strain), the central device acts as a stress riser. The simulated cracking initiates from the device tip and propagates upward, as seen by others using images based on x-ray radiography.

- Concrete temperatures, and thus properties of the concrete, are influenced by the thermal properties of the formwork and related boundary conditions. The modeling of evaporative cooling was found to be essential in simulating the concrete temperatures, particularly early in the testing period where temperature decreased with time.
- The numerical analyses support the notion that, due to poor bonding properties, both the steel and GFRP bars do not significantly influence crack formation and opening. To address the potential for early-age cracking, short distributed fibers are seen as an option.

REFERENCES

- ASTM C1579-21, 2021. Standard test method for evaluating plastic shrinkage cracking of restrained fiber reinforced concrete (Using a steel form insert). ASTM International, West Conshohocken, PA, USA.
- ASTM D7913-14, 2020. Standard test method for bond strength of fiber-reinforced polymer matrix composite bars to concrete by pullout testing. ASTM International, West Conshohocken, PA, USA.
- ASTM D7957-22, 2022. Standard specification for solid round glass fiber reinforced polymer bars for concrete reinforcement. ASTM International, West Conshohocken, PA, USA.
- Bentz, D.P. 2000. A computer model to predict the surface temperature and time of wetness of concrete pavements and bridge decks. Technical Report NISTIR 6551, National Institute of Standards and Technology.
- Bentz, D.P. 2007. Transient plane source measurements of the thermal properties of cement-based materials. *Materials and Structures* 40: 1073–1080.
- Biot, M.A. 1941. General theory of three-dimensional consolidation. *Journal of Applied Physics* 12: 155–164.
- Bolander, J.E., Eliáš, J., Cusatis, G. & Nagai, K. 2021. Discrete mechanical models of concrete fracture. *Engineering Fracture Mechanics* 257: 108030.
- Combrinck, R., Steyl, L. & Boshoff, W.P. 2018. Interaction between settlement and shrinkage cracking in plastic concrete. *Construction and Building Materials* 185: 1–11.
- di Luzio, G. & Cusatis, G. 2013. Solidification-microprestress-microplane (SMM) theory for concrete at early age: Theory, validation and application. *International Journal of Solids and Structures* 50(6): 957–975.
- Ekenel, M., Roghani, H., De Caso, F. & Nanni, A. 2022. Evaluation of FRP bars & meshes used as secondary reinforcement for nonstructural concrete members for building code compliance. *Special Publication* 356: 109–119.
- Focacci, F., Nanni, A. & Bakis, C.E. 2000. Local bond-slip relationship for FRP reinforcement in concrete. *Journal of Composites for Construction* 4(1): 24–31.
- Ghourchian, S., Wyrzykowski, M., Plamondon, M. & Lura, P. 2019. On the mechanism of plastic shrinkage cracking in fresh cementitious materials. *Cement and Concrete Research* 115: 251–263.
- Kang, J., Kim, K., Lim, Y.M. & Bolander, J.E. 2014. Modeling of fiber-reinforced cement composites: Discrete representation of fiber pullout. *International Journal of Solids and Structures* 51(10): 1970–1979.
- Pan, Y., Kang, J., Ichimaru, S. & Bolander, J.E. 2021. Multi-field models of fiber reinforced concrete for structural applications. *Applied Sciences* 11: 184.
- Pan, Y., Prado, A., Porras, R., Hafez, O.M. & Bolander, J.E. 2017. Lattice modeling of early-age behavior of structural concrete. *Materials* 10: 231.
- Riding, K.A., Folliard, K.J., Juenger, M.C.G. & Schindler, A.K. 2012. Modeling hydration of cementitious systems. *ACI Materials Journal* 109: 224–234.
- Schindler, A.K., Ruiz, J.M., Rasmussen, R.O., Chang, G.K. & Wathne, L.G. 2004. Concrete pavement temperature prediction and case studies with the FHWA HIPERPAV models. *Cement and Concrete Composites* 26: 463–471.
- de Schutter, G. & Taerwe, L. 1996. Degree of hydration-based description of mechanical properties of early age concrete. *Materials and Structures* 29: 335–344.
- Uno, P.J. 1998. Plastic shrinkage cracking and evaporation formulas. *ACI Materials Journal* 95(4): 365–375.

Toward distinguishing the chemical, physical, and wetting-drying sulfate attack on concrete

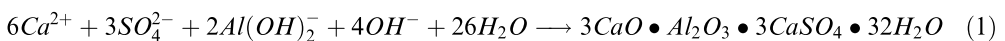
I.A.N. Omrani, M. Koniorczyk & D. Bednarska
Lodz University of Technology, Poland

ABSTRACT: Depending on the mode of exposure, concrete structures might experience various forms of sulfate attack during their service life. In the case of a concrete element which is partially subjected to a sulfate-contaminated solution, the immersed sections receive intense alterations in their mineralogical composition that affect their mechanical properties, known as “Chemical sulfate attack”. The upper sections of the element which experience no direct exposure to the solution are prone to face the crystallization and dissolution of various kinds of sulfated salts, known as “Physical sulfate attack”. The middle parts of the element that might receive a cyclic exposure to the sulfated solution via waves are vulnerable to the combination of the both noted phenomena, known as the “Wetting-drying sulfate attack”. A particular exposure condition has been designed in this paper to distinguish the three mentioned modes of sulfate attack in terms of the concrete’s mechanical response.

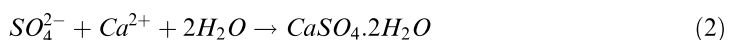
1 INTRODUCTION

Unlike the ideal laboratory regulations on the topic of “sulfate attack” under which cementitious samples face a saline solution in a constant immersed mode, concrete structures in real service environments mostly experience the external sulfate-contaminated sources through a partial exposure; i.e. foundation elements or basic columns of concrete structures in marine environments or industrial zones are partially immersed in the external saline sources.

Under such circumstances, the immersed sections of the element receive severe chemical alterations such as crystallization of secondary ettringite, gypsum, etc., and de-calcification of their portlandite and C-S-H gel (Santhanam et al. 2003). For an ordinary Portland cement paste and under the assumption that the aggressive sulfated source mainly possesses sodium and sulfate ions, ettringite crystallization as a through-solution reaction can be written as:



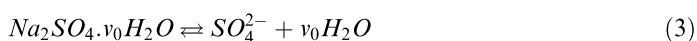
Where the Ca^{2+} cations are obtained from the decalcification of portlandite and C-S-H gel, the Al^{3+} cations come from the destabilization of the aluminate-containing hydrates (Afm, etc.) and/or clinker phases (C_3A , etc.), and the hydroxyl ions arise from the paste’s alkali elements (Marchand et al. 2002). Once the aluminate sources become exhausted in certain zones of the matrix, further intrusion of sulfate ions leads to the through solution generation of gypsum crystals as:



Which fully consumes the local portlandite and accordingly decrease the hydroxyl sources of the system, causing the destabilization of the remaining intact C-S-H gels (Marchand et al.

2002). The excessive precipitation of secondary ettringite and gypsum forces a crystallization pressure upon the solid matrix which results in the induction of expansive microcracks within the concrete's microstructure; Together with this, the decalcification of the C-S-H gel lessens the cementitious quality of the structure. Such typical aftermaths are known as "chemical sulfate attack" which makes the material vulnerable against other aggressive factors of the field and decreases its service-life (Zhang et al. 2019).

On the other hand, the cyclic precipitation/dissolution of sodium sulfate salts, namely, decahydrate and its anhydrous forms, induces expansive microcracks and surface scaling in case of sub-florescence in the dried sections of the concrete element (Scherer 2004), known as "physical sulfate attack". Such situation can be written as:



Where v_0 is the number of water molecules of the hydrated salt, 10 in case of decahydrate.

Distinguishing the above noted chemical and physical modes of sulfate attack on cementitious materials has been a topic of discussion for years (Neville 2004).

Recently, some attempts were carried out in order to regulate the physical sulfate attack in concrete (Hartell et al. 2011, Alyami et al. 2019, Najjar et al. 2017, Zhao et al. 2021); mass measurement, assessing the expansion and mechanical strength of the samples were the main approaches of such works; yet, since these analyses were conducted on the total scale of the material, the separate contribution of the chemical and physical modes of aggressions could not be clarified. Some of the cited studies also tended to evaluate the microstructural properties of the partially immersed concretes, however, their sampling locations were limited and again a clear distinction between the different forms of sulfate attack could not be recognized.

Consequently, to fill the current gap in the literature, this paper is a simple experimental approach toward distinguishing the contribution of different modes of sulfate attack; i.e. chemical degradation & physical damage. To do so, a novel exposure condition has been designed, detailed in the upcoming sections.

2 EXPERIMENTAL PROGRAM

2.1 Materials

Table 1 presents the mix proportions of the prepared concrete samples.

Table 1. Mix proportions of the concrete samples (kg/m³).

Cement	Water	W/C	Coarse agg*	Fine agg	Sand
390	195	0.5	558	648	594

* Aggregate

The utilized cement was Portland CEM I 42.5. Coarse and fine aggregates were obtained from a local river with the diameters of 8-16 and 2-8mm, respectively. Also, the diameter of the used sand was 0-2mm.

After homogeneous stirring for 5 minutes in a laboratory mixer, the fresh mixture was poured in rectangular prism moulds having the length of 200mm and cross-sectional height & width of 100mm. Subsequently, samples were de-moulded after 24h of resting in laboratory conditions. Next, they were immersed in water tanks for curing at 25°C until the age of 28th day. Finally, samples were ready for the sulfate exposure.

2.2 Exposure conditions

Anhydrous sodium sulfate salt and distilled water were utilized for preparing the aggressive sulfated environment having a concentration of 5%. Samples faced the prepared sulfate solutions as illustrated in Figure 1.

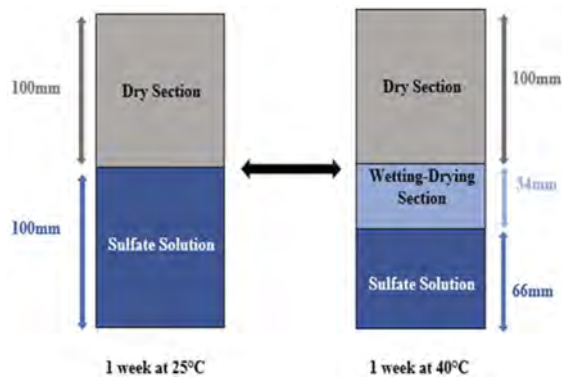


Figure 1. Schematic sulfate exposure condition.

As can be seen, samples received sulfate solution up to half of their length for 7 days at 25°C; subsequently, samples were moved to an oven drier at 40°C for 7 days where the height of the sulfate exposure was decreased to 1/3 of the sample's length. Next, samples were removed from the sulfated environment and dried at room temperature for 24h; following this, the crystallized salts of the concrete were gently removed via a brush and samples got ready for the analysis. After the analysis, samples were returned to the solutions to repeat the described cycle. Hence, sulfate solution was renewed every two weeks.

Such cyclic exposure design created three sections within the concrete; namely, the bottom 1/3 of the concrete was always immersed in the solution, denoted as the “immersed section”, the middle section which got weekly wetting-drying cycles is denoted as the “W-D section”, and the upper half of concrete that was constantly kept dry is denoted as the “dry section”.

As noted above, the employed temperature cycles are 25°C and 40°C. Such temperature ranges were chosen as realistic temperatures that might be experienced in warm zones of the planet. In addition, since the samples faced wetting-drying cycles in their middle sections, the exposure design of this study can simulate the conditions of the concrete columns which are in partial contact with a moving saline source that can produce splashing waves, i.e. marine environments.

3 RESEARCH OBJECTIVE AND METHOD

The objective of this paper is to assess and compare the mechanical properties of the immersed, W-D, and dry sections of the concrete. To do so, the conventional through transmission ultrasonic method has been employed. This method is based on the speed of the stress wave propagation through the sample which is a function of the concrete's elastic constants and density (ACI committee 228 1998). Thus, it is expected that the sulfate-induced expansive microcracks and other interruptions within the cementitious phases prolongs the stress wave's propagation speed and decreases the ultrasonic pulse velocity (UPV) of the samples.

The utilized device was Controls E48. Water was used as the coupling agent between the device's probes and concrete.

Accordingly, UPV of each section of concrete was assessed every two weeks for six months. Measurements were conducted on at least three samples to assure their reproducibility.

4 RESULTS

4.1 Visual inspection

Figure 2 illustrates the visual conditions of a typical sample at the beginning, after 3 and 6 months of the exposure.

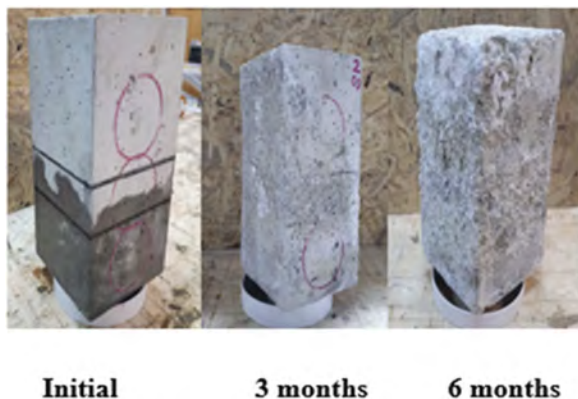


Figure 2. Typical appearances of the samples at different ages.

As can be observed, after 3 and 6 months of exposure, it is the W-D section of the sample that received the most intense damage. In this region, surface scaling was evident and coarse aggregates which lies beneath the paste surface of the concrete began to reveal themselves. Next, it is the dry section that had received a notable surface scaling, particularly after 6 month of exposure. Finally, the appearance of the immersed section remained approx. intact after 3 month, and moderately affected after 6 month of sulfate exposure.

Based on the mentioned visual inspections, one can assume that those sections of the concrete that were prone to physical sulfate attack failed more abruptly compared with the immersed section of the material.

4.2 UPV measurements

Figure 3 shows the results of the UPV measurements on different sections of the concrete.

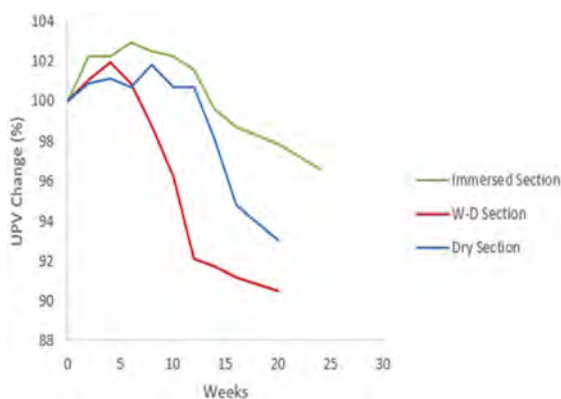


Figure 3. UPV changes of the samples.

According to Figure 3, the W-D section had the most abrupt drop of UPV. During the first four weeks of the exposure, the UPV of the W-D section was enhanced for approx. 2%. Such initial improvement is possibly due to the capillary suction of the sulfated solution which partially enhanced the material's density. After this enhancement, however, a sudden drop in the stress-wave propagation's speed was observed for approx. 10% until the 20th week which indicated the induction of the microstructural damages within the section. After the 20th week, the quality of the concrete's surface at the W-D section became so low that more contact between the device's probe and surface was not possible.

In the dry section of the material, the UPV retained approx. constant with partial enhancements during the first 12 weeks of the measurements. Such prolonged time of soundness stated that the dry section of the material had more resistance against the sulfate exposure compared with W-D section of the concrete. After this period, the UPV dropped suddenly for approx. 8% until the 20th week, after which the measurements were not possible due to the severe surface scaling of this section.

The immersed section of the concrete had the highest improvement in its UPV compared with the other two sections (approx. 3%). This section also revealed the longest soundness period, lasting for 14 weeks. After 14 weeks of exposure, the UPV of this section began to drop gradually until the final measurement point for only 4%. Such trends indicated that compared with the W-D and dry sections, the immersed section of concrete had the least sulfate-induced microstructural damages.

5 DISCUSSIONS

In this section, the possible mechanisms which led to the failure of the three sections of concrete are discussed.

At the beginning, it is important to note that concrete is a cementitious medium which is chemically active against sulfate ions, therefore, one cannot say that the W-D and dry sections of the material only received physical sulfate attack and chemical alterations were just limited to the immersed section of the samples. In other words, an interconnected network of chemical and physical phenomena is expected to occur in various sections of a concrete element which is partially subjected to sulfate solution and a rigid distinction between the various mechanisms of failure is not correct. However, it can be stated that some failure mechanisms are likely to play a more dominant role than others in precise sections of the concrete.

The notable initial improvement of the UPV in the immersed section of concrete is probably due to the precipitation of secondary ettringite and gypsum crystals as hinted in the section 1. At first, such crystals tend to precipitate through the microstructural gaps and free spaces of the matrix (Santhanam 2002); thus, their crystallization densifies the material and accordingly improves its mechanical properties. However, once the mentioned free gaps of the matrix became filled by the excessive formation of the sulfate-induced crystals, their continuous formation in time can lead to the generation of expansive crystallization pressure upon their surrounding solid skeleton, causing microcracks and failure of the material.

The dominant mechanism of failure in the W-D section of concrete was probably due to the cyclic dissolution/re-crystallization of decahydrate within the porous matrix of concrete. When exposed to 40°C, the previously wetted W-D section of concrete was dry as detailed in section 2.1; therefore, evaporation of saline pore solution occurred in this section, which eventually led to the supersaturation of its remaining saline pore solution and salt crystallization; the salt which crystallizes at 40°C is thenardite based on the phase diagram of $\text{Na}_2\text{SO}_4 \cdot n\text{H}_2\text{O}$ system (Steiger & Asmussen 2008). Now, once the concrete was returned under 25°C and its W-D section became immersed again, the previously crystallized thenardite became de-stable and dissolved. Under the assumption that such dissolving continued until pore solution became saturated with respect to thenardite, decahydrate could crystallize from a supersaturated solution for 1 week which probably generated expansive microcracks throughout the medium.

Higher up, in the dry section of the material, sub-florescence of the sodium sulfated crystals in the sections where the rate of evaporation exceeded the rate of capillary rise, could be the main mechanism of damage. Such destructive process was expected precisely when samples were placed at 40°C for 1 week.

6 CONCLUSION

In this paper, a novel sulfate exposure condition was designed under which concrete samples experienced chemical, wetting-drying and physical sulfate attack simultaneously under 25°C and 40°C temperature cycles. Such exposure conditions are common in concrete structures at marine environments. The objective was to distinguish the response of concrete when receiving the three mentioned modes of sulfate attack.

It was observed that the most intense damage was occurred in those sections of the material that were under wetting-drying sulfate attack. The dominant mechanism which causes failure in such sections are likely the dissolution and recrystallization of decahydrate. Following this, it was the dry section of concrete that got damaged. This section was mainly under physical mode of sulfate attack caused by salt sub-florescence. The immersed section of the concrete that was likely under dominant chemical alteration was the most resistant section that had a gradual damage.

The reports of this paper were solely focused on the mechanical response of the designed sections of concrete in terms of their ultrasonic pulse velocity. A more detailed analysis of the situation via different techniques at both macro- and microscopic scales are to be conducted by the authors in near future to develop an un-ambiguous and precise description of the contribution of different modes of sulfate attack on the failure of the partially subjected concrete samples.

REFERENCES

- Santhanam, M, Cohen, M.D, Olek, J. 2003. Mechanism of sulfate attack: a fresh look: Part 2 Proposed mechanisms. *Cement and Concrete Research* 33, 341–346.
- Marchand, J, Older, I, Skalny, J.P. 2002. *Sulfate Attack on Concrete (Modern Concrete Technology)*, Spon Press, London and New York.
- Zhang, Z, Jin, X, Luo, W. 2019. Long-term behaviors of concrete under low-concentration sulfate attack subjected to natural variation of environmental climate conditions, *Cement and Concrete Research* 116, 217–230.
- Scherer, G.W. 2004. Stress from crystallization of salt, *Cement and Concrete Research* 34, 1613–1624.
- Neville, A. 2004. The confused world of sulfate attack on concrete, *Cement and Concrete Research* 34, 1275–1296.
- Hartelll, J.A, Boyd, A.J, Ferraro, C.C. 2011. Sulfate Attack on Concrete: Effect of Partial Immersion, *Journal of Materials in Civil Engineering*, 23(5).
- Alyami, M.H, Alrashidi, R.S, Mosavi, H, Almarshoud, M.A, Riding, K.A. 2019. Potential accelerated test methods for physical sulfate attack on concrete, *Construction and Building Materials* 229, 116920.
- Najjar, M.F, Nehdi, M.L, Soliman, A.M, Azabi, T.M. 2017. Damage mechanisms of two-stage concrete exposed to chemical and physical sulfate attack, *Construction and Building Materials* 137, 141–152.
- Zhao, G, Guo, M, Cui, J, Li, J, Xu, L. 2021. Partially-exposed cast-in-situ concrete degradation induced by internal-external sulfate and magnesium multiple coupled attack, *Construction and Building Materials* 294, 123560.
- ACI Committee 228. *Nondestructive test methods for evaluation of concrete in structures*. Report ACI 228.2R-98. American Concrete Institute, Farmington Hills, MI. 1998.
- Santhanam, M, Cohen, M.D, Olek, J. 2002. Modeling the effects of solution temperature and concentration during sulfate attack on cement mortars, *Cement and Concrete Research* 32, 585–592.
- Steiger, M, Asmussen, S. 2008. Crystallization of sodium sulfate phases in porous materials: The phase diagram Na₂SO₄-H₂O and the generation of stress, *Geochimica et Cosmochimica Acta* 72, 4291–4306.

*MS15: Deconstruction and reuse of steel and lightweight
metal structures*
Organizers: M. Kuhnhenne & P. Kamrath



Taylor & Francis

Taylor & Francis Group

<http://taylorandfrancis.com>

Requirements for gutting and demolition cost index

H. Kesting

University of Siegen, Siegen, Germany

M. Helmus

University of Wuppertal, Wuppertal, Germany

ABSTRACT: The development of a gutting and demolition cost index is essential to determine the life cycle costs and to design recyclable buildings appropriately. Accordingly, it is important to record and analyze the dismantling phase and the existing concepts for planning recyclable buildings. In addition, the available cost indices for dismantling and demolition must be researched and analyzed with regard to their structure and information content. Taking a top-down approach into account, the essential parameters are to be worked out. Consequently, a framework was established in terms of pollutants, gutting, demolition and disposal. In addition, certain standards such as the Cradle 2 Cradle concept, the determination of the actual residual value of a building according to Madaster, the Urban Mining Index and the DGNB certificate requires a valid cost index related to the demolition. This should also meet the demand for secured dismantling costs. The integration of the cost groups according to DIN 276, the STL-Bau as well as the waste key and the statistical processing of costs on the subject of demolition is needed to be considered. By analyzing the offer documents and further discussions with experts, further factors can be worked out that influence the unit price. A database system is to be developed in a bottom-up approach, taking into account the identified requirements. Madaster and Concular and Cradle2Cradle requirements are met as digital planning and documentation are included.

1 PLANNING OF RECYCLABLE STRUCTURES

In the future, architects and planners will be asked to plan and build buildings that are capable of recycling. If one considers the entire life cycle of a building, the life cycle phase of operation must be emphasised. Between 50 % and 80 % of all costs related to the entire life cycle are incurred in the operation phase. (Litau 2015)

With the focus on the use of resources, however, the planning and execution of the building project is of particular importance. This is because the course is set during planning and execution for the later use phase, deconstruction and thus for the ecological sustainability of the building. “The EU assumes that 80% of the effects of a product can be influenced or predicted in the planning phase.” (Alt 2018, p. 28) It can also be stated that “whether a product is recyclable, what materials it is made of and what quantities of materials are to be used, is largely determined by the product design.” (Alt 2018, p. 29) However, the necessary quantitative assessment standards for dismantling are still lacking.

1.1 *Cradle 2 Cradle – A circular economy concept*

“According to the wording, circular economy means management without beginning and end. Applied to the management of materials or resources, this means that they should be managed in such a way that they do not leave the cycle, but rather remain in the cycle. At the end of

their life, they should be returned to the material cycle and thus continue to be used for other or the same product.” (Alt 2018, p. 36) A concept based on this quote for the design of circular buildings is the Cradle 2 Cradle (C2C) concept. Based on the valid regulations in the construction of buildings to comply with safety-relevant standards, we speak of C2C-inspired buildings. (C2C im Bau: Orientierung für Kommunen 2022a)

One instrument for the implementation of a C2C-inspired building is also seen in the subsequent digitisation of the building stock. (C2C im Bau: Orientierung für Kommunen 2022c)

According to the EU Commission, “85 to 95% of the buildings that exist today will probably still exist in 2050, so we should use the potential of the materials already present in them. This can be done on the basis of parameters such as year of construction, type or volume, as well as through the exchange of experience between experts.” (C2C im Bau: Orientierung für Kommunen 2022d)

The C2C project phases (C2C im Bau) are based on the life cycle of a property. In the planning project phase, reference is made to the planning of deconstruction, which addresses the main processes of the demolition life cycle phase from the life cycle of a property. (Bresser *et al.* 2020) In addition, digital planning and digital documentation of the execution and building operation of the C2C project phases is another criterion of the C2C concept. Here, attention is paid to the fact that possible material flows and material values can be mapped in the sense of urban mining. (C2C im Bau: Orientierung für Kommunen 2022d) Furthermore, the C2C concept states: “In addition, a comparison of demolition or deconstruction and the costs of a new building should be obligatory in all profitability calculations - always taking into account the ecological effects and their financial implications.” (C2C im Bau: Orientierung für Kommunen 2022b)

1.2 Urban Mining Index (UMI)

The Urban Mining Index (UMI) provides a method for assessing the circular potential of building structures. The assessment of the loop potentials of building constructions is based on the consideration of open and closed loops for materials and recyclables. For this purpose, the UMI determines a loop potential (open) and a closed loop potential (closed).

The Urban Mining Index defines “The closed-loop potential is the percentage of materials and building materials of a construction that can be kept in closed loops without loss of quality, taking into account defined criteria. Reuse and recycling are among the after-use strategies where no loss of quality occurs.” (Rosen März/2021, p. 25) Furthermore, the Urban Mining Index states that “The loop potential of a construction includes, in addition to the percentage closed-loop share, shares of materials and building materials that, taking into account defined criteria, enable material recovery with a loss of quality (reuse/downcycling). The loop potential thus represents open loops in addition to the closed loops. The closed-loop potential is thus part of the loop potential.” (Rosen März/2021, p. 25)

Furthermore, the UMI divides the life cycle of building structures into the three phases listed below:

- Pre-use phase
- Use phase
- Post-use phase.

The determination of the loop potentials is carried out separately for the pre-use and post-use phases. Thus, a closed-loop potential pre- and post-use as well as a loop potential pre- and post-use can be determined for the assessment.

Essential parameters for determining the loop and closed-loop potentials are the

- material level
- constructive level
- economic level.

Here, effects can be seen from the material via the constructive level to the economic level. These effects serve to quantify a cost value for the deconstruction or separation of materials. The UMI makes clear: “Basically, what is needed for this is a “demolition cost index”, similar to the BKI construction cost index, which provides demolition costs for both conventional and circular constructions.” (Rosen März/2021, p. 98)

1.3 DGNB certificate deconstruction

In order to close the material flows in the building industry and to establish a promotion of the building fabric in terms of value in the sense of the circular economy, the DGNB has, with a view to the planning of deconstruction measures, developed the DGNB Deconstruction Certificate (Deutsche Gesellschaft für Nachhaltiges Bauen 2022) for sustainable deconstruction. “By creating transparency with regard to the data quality underlying the calculation of the deconstruction costs as well as the remaining risks, the building owner is to be supported in the decision-making process.” (Frank, p. 49)

The certificate is issued on the basis of criteria to be evaluated. The criteria to be assessed are divided into the five subject areas of ecological quality, economic quality, socio-cultural and functional quality, technical quality and process quality. The five subject areas are equally weighted. Each weighting is included in the assessment of the DGNB certificate with a 20% share of the overall result. (Deutsche Gesellschaft für Nachhaltiges Bauen 2022)

The assessment within the DGNB certificate for building deconstruction is implemented via 12 criteria in Figure 1, which are assigned to the aforementioned five thematic fields.

This makes it clear that the topic area of “risk assessment and cost security” as well as “pure separation and recycling” and “material flow balance” were given a high priority.

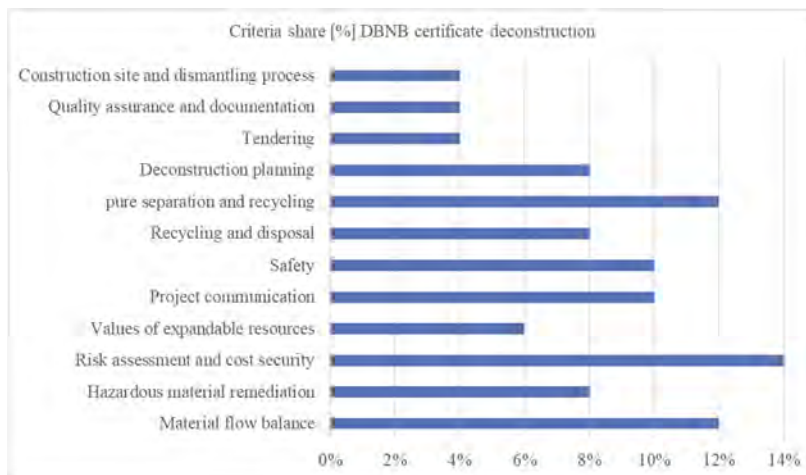


Figure 1. Criteria share DGNB certificate deconstruction.

2 COST(PLANING) IN CONSTRUCTION

If one pursues the question of transparently available demolition costs, one comes to the conclusion that there is a lack of available knowledge on this topic area. With reference to new construction, for which there is commercially available literature on object-related construction cost indices, no sources for object-related demolition costs in the sense of demolition cost indices have been identified for the area of deconstruction and demolition.

The production, repair as well as the demolition and subsequent disposal of a building are constantly affected by cost shifts. Especially the disposal costs of non-recyclable construction waste will increase in the future, also due to the shortage of landfills. (Thorsten Thörner,

Sigrid Hams, Dr.-Ing. Gabriele Becker, Dr. Bärbel Birnstengel, Arno Häusler, Nadja Schütz 2014) (AU Consult GmbH, Bayerisches Landesamt für Umwelt LfU 2015) (Iswing Dehne, Florian Knappe, Rüdiger Oetjen-Dehne, Stefanie Theis 2016)

The aim is to develop a structured planning tool that makes it possible to include the end of use of a property in the life cycle cost analysis in monetary terms. Assured costs for gutting, demolition and disposal expenses are to be compiled, which will ensure transparency in the cost calculation.

2.1 Life cycle costs

The main certification systems on the German market include the BREEAM, LEED and DGNB certificates. The DGNB has the largest market share.. (Litau 2015) For the evaluation of sustainability certificates, the determination of life cycle costs is also taken into account. Of these, the DGNB certificate for the assessment of life cycle costs has a 13 % share of the total. This is the largest share within an assessment for sustainability certificates. (Kasper Guldager, Harpa Birgisdottir, Gitte Gylling, Paul Stoller, Stefan Holst, Tiffany Broyles Yost 2018)

Life cycle costs in the narrower sense include the

- Building costs
- Operating costs
- Costs for cleaning, care and maintenance
- Costs for dismantling and disposal
- or other end-of-life scenarios. (Koschlik 2022)

The basis for calculating the life cycle costs are the production costs according to DIN 276 for the cost groups 300 and 400. Selected utilisation costs according to DIN 18960 are also used. The calculated costs are related to the gross floor area (GFA) in the area unit m². (Litau 2015)

If we look at the development of the cumulative costs along the vertical axis in relation to the horizontal life cycle phases (concept, planning, construction, use and demolition), we see that the ability to influence the resulting life cycle costs is mainly concentrated on the life cycle phases concept and planning. As time progresses, the influence on the resulting life cycle costs decreases. The cost difference between conventional planning and life-cycle-optimised planning is presented as “potential savings at the end of the life cycle” in Figure 2.

Figure 2 clearly shows that the influence on life cycle costs is decisive in the early phase of a building’s life cycle.

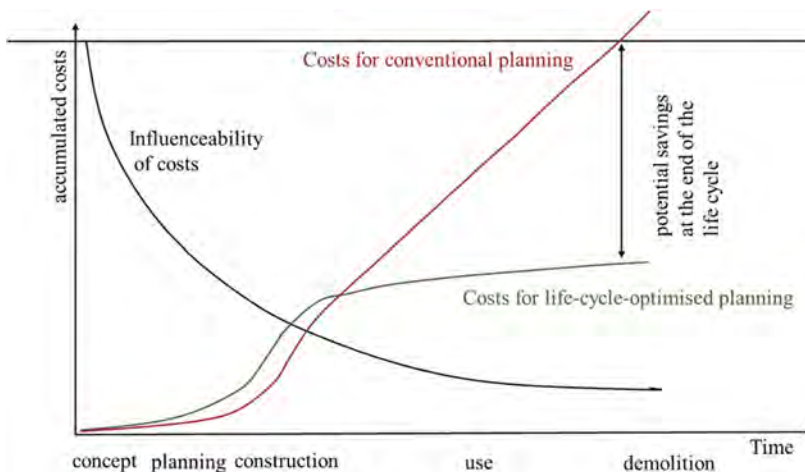


Figure 2. Influencing life cycle costs (Litau 2015, p. 24).

2.2 *Cost in construction – DIN 276*

Cost planning in construction is implemented using the standard DIN 276:2018-12 “Costs in construction” (DIN 276). DIN 276 is essentially used for cost determination and cost classification in new construction, reconstruction and modernisation of buildings and facilities. Cost planning pursues the goals of economic efficiency, cost security and cost transparency for a construction project. In addition, the cost calculations are used as a basis for financing, decision-making with regard to awarding and execution, as well as for the subsequent assessment and evaluation of construction costs incurred. The use of DIN 276 ensures that the cost calculations to be carried out are comparable. Depending on the point in time within a construction project, different cost investigations are carried out. These can be carried out once at a specific point in time or repeatedly in several steps during the course of the project. (DIN Deutsches Institut für Normung e. V. 2018)

The cost determination “cost framework” represents the beginning of the cost determination within a construction project. Based on the information available for the preparation of the “cost framework” cost calculation, the accuracy of the calculated costs is still subject to uncertainties. As the project progresses, the underlying information for the preparation of the further cost calculations becomes more detailed. At the end of each construction project, the cost determination “cost statement” is carried out. The information provided for the cost determination is based on the actual expenses incurred. (DIN Deutsches Institut für Normung e. V. 2018)

The analysis of the minimum information to be taken as a basis for the implementation of each cost calculation are the following parameters

- Service descriptions
- Quantities
- Auditable supporting documents - Evidence
- Grouping of costs to the levels of the cost groups according to DIN 276.

2.3 *Cost indices in construction*

In addition to the application of cost groups for the preparation of cost determinations, the underlying costs for the preparation of a cost determination are also required. Cost indices available on the market support this.

When conducting the market analysis according to available indices with reference to construction costs in general, the following providers could be identified:

- Building Cost Information Centre of German Chambers of Architects (BKI)
- SIRADOS construction data
- Baukosten 2020/21

The BKI construction cost database is published, among other things, in the form of reference books, which in turn are grouped into reference book series. Within the BKI reference books, statistical cost parameters for construction projects are published. The basis for the evaluation of the statistical cost parameters is formed by construction projects that have already been completed. The data is made available to the BKI by external planners or tenderers. (BKI Baukosteninformationszentrum Deutscher Architektenkammern GmbH and Baukosteninformationszentrum Deutscher Architektenkammern)

The statistical cost parameters shown in the individual reference books differ in terms of their level of detail. The level of detail is based on the cost group level of DIN 276. Here the variants

- Building
- Components
- Positions

are differentiated. The analysis of the BKI’s reference book series has shown that the reference book series “Altbau” is the only reference book series that presents cost parameters with reference to the topic of demolition and dismantling work.

The SIRADOS construction data are published, among other things, as reference books for the preparation of cost calculations according to DIN 276 and for the preparation of tenders. In addition, SIRADOS Baudaten provides several reference books as costing aids. In the reference books, construction prices are documented on the basis of price receipts of current tenders. The analysis of the SIRADOS Baudaten reference books has shown that the following reference books

- Loose-leaf work on old buildings
- SIRADOS Construction Price Manual
- SIRADOS costing atlas for shell and finishing work in old buildings

report key cost data with reference to the topic of demolition and dismantling work.

The technical book series *Baukosten 2020/21 Volume 1: Altbau - Instandsetzung, Sanierung, Modernisierung, Umnutzung* can be used to prepare cost calculations according to DIN 276. The assignment to the service areas of the STL-Bau is also given. The technical book is also dedicated to the topic of demolition and dismantling work. The content on demolition and dismantling work is very limited compared to the other products. (Schmitz *et al.* 2020)

3 REQUIREMENTS FOR A GUTTING AND DEMOLITION COST INDEX

Considering the aforementioned analyses on the planning of circular structures and cost planning in the construction industry, the first requirements for the development of a gutting and demolition cost index (EKI) can be derived from this.

3.1 *Requirements from the planning of recyclable structures*

From the analysis of the C2C concept (cf. Chap. 1.1), it can be deduced that the requirement of a disposal assignment of materials and, if applicable, the services to the waste codes and the waste designation from the “Regulation on the European Waste Catalogue - (Waste Catalogue Regulation - AVV)” must be fulfilled. At the same time, it should be possible to evaluate materials and the associated allocation to the AVV for an entire building. This would allow statements to be made about the recycling potential for buildings. Likewise, possible statements on polluted materials are possible. This in turn can lead to statements about the composition of a building in the sense of a C2C concept. Furthermore, C2C demands that digital planning and documentation are included. It can thus be deduced that a gutting and demolition cost index should serve this basis.

The Urban Mining Index (cf. Chap. 1.2) goes further in its statement and demand, and calls for a demolition cost index following the example of the BKI. Possible requirements from cost indices have been examined separately (cf. Chap. 2.3). The requirements from the Urban Mining Index can essentially be narrowed down to the parameters for determining the loop and closed-loop potentials.

The requirements from the DGNB certificate Deconstruction are based on the analysis of the catalogue of criteria to be complied with. The criterion that is highlighted most is the criterion “risk assessment and cost security”. Support for “deconstruction planning”, “separation and recycling”, “recycling and disposal”, “hazardous materials clean-up” and the “material flow balance” are further possible requirements that could be implemented with the EAKI.

3.2 *Requirements from cost planning in construction*

Possible requirements from life cycle costing (cf. Chap. 2.1) for the development and construction of an EAKI can be derived on the one hand from the provision of costs for dismantling and disposal as well as other end-of-life scenarios. Furthermore, the integration of cost groups according to DIN 276 should be considered. The preparation of the provided data of an EAKI should also meet the requirements that the data for the calculation of life cycle costs is possible in the early phases “concept” and “planning”.

The requirements from DIN 276 (cf. Chap. 2.2) refer to the fact that the data of the gutting and demolition cost index can be used for the cost determination based on DIN 276. Furthermore, the minimum information for carrying out any cost determination should be

- Service descriptions
- Quantities
- Auditable supporting documents - Evidence
- Grouping of costs to the levels of the cost groups according to DIN 276

taken into consideration. Whereas the “Verifiable Evidence - Evidence” is due to the fact that the data provided for the content of the EAKI is based on estimates of actual offers calculated by demolition companies.

The requirements from the cost indices in construction (cf. Chap. 2.3) can be summarised in connection with the aforementioned requirements on further additional points. The provision of statistical cost parameters, the integration of the STL-Bau, the allocation of the cost parameters to cost groups of DIN 276, the provision of data from external partners of already completed construction projects for the determination of statistical cost parameters, as well as the publication as a reference book and as an online version are to be mentioned here.

4 CONCLUSION

In addition to the above-mentioned requirement parameters, additional parameters for the evaluation of statistical cost parameters must be determined. Here, the documents of supporting partners are to be consulted. On the one hand, these are service specifications and additional planning and tender documents related to deconstruction and demolition. Here, the deconstruction and disposal concept as well as the deconstruction application can be named. A more in-depth analysis of the processes of the demolition life cycle phase may reveal further documents. Further expert discussions can contribute to the determination of influencing factors for the formation of the unit price of deconstruction, demolition and disposal services.

The allocation of waste code numbers to service and disposal items should also be worked out in expert discussions. In the sense of circular construction, the allocation of cost groups according to DIN 276 should not be limited to demolition and disposal. Here, an allocation should be made in the same way as for new constructions.

In order to be able to map and evaluate the complex interrelationships for a subsequent evaluation of demolition costs, coupled with the demand for digitisation, implementation in the form of a database system (DBMS) (Heuer 2018) should be preferred and developed.

REFERENCES

- Alt, M., 2018. *Ökodesign und Kreislaufwirtschaft*: Nomos Verlagsgesellschaft mbH & Co. KG.
- AU Consult GmbH, Bayerisches Landesamt für Umwelt LfU, 2015. Bedarfsprognose Deponien der Klasse 0, I und II in Bayern, 2015, 1–38.
- BKI Baukosteninformationszentrum Deutscher Architektenkammern GmbH and Baukosteninformationszentrum Deutscher Architektenkammern. *Baukosten Gebäude + Bauelemente + Positionen Neubau 2021: Statistische Kostenkennwerte Teil 1 + Teil 2 + Teil 3*. Stuttgart: BKI.
- Bresser, et al., 2020. *Building Information Modeling (BIM) als Basis für den Umgang mit digitalen Informationen zur Optimierung von Stoffkreisläufen im Bauwesen: BIM - Prozesse - Stoffkreislauf* [online]. Wuppertal, Lehr- und Forschungsgebiet Baubetrieb und Bauwirtschaft, Lehrstuhl für Werkstoffe im Bauwesen. Available from: https://www.dbu.de/projekt_33110/01_db_2848.html [Accessed 11 Apr 2022].
- C2C im Bau: C2C in den Projektphasen [online]. Available from: https://c2c-bau.org/wp-content/uploads/2022/02/3.3_Abb8_C2C-im-Bau-C2C-in-den-Projektphasen.pdf [Accessed 14 Jun 2022].
- C2C im Bau: Orientierung für Kommunen, 2022a. *3.1 C2C-inspirierte Gebäude - C2C im Bau: Orientierung für Kommunen* [online]. Available from: <https://c2c-bau.org/3-grundlagen-c2c-bau/3-1-c2c-inspirierte-gebäude/> [Accessed 14 Jun 2022].

- C2C im Bau: Orientierung für Kommunen, 2022b. 7.3 *Neubau oder Bestandssanierung - C2C im Bau: Orientierung für Kommunen* [online]. Available from: <https://c2c-bau.org/7-bedarf-und-ziele/7-3-neubau-oder-bestand/> [Accessed 13 Apr 2022].
- C2C im Bau: Orientierung für Kommunen, 2022c. 8.1 *Rückbau - C2C im Bau: Orientierung für Kommunen* [online]. Available from: <https://c2c-bau.org/8-ist-situation/8-1-rueckbau/> [Accessed 14 Jun 2022].
- C2C im Bau: Orientierung für Kommunen, 2022d. 3.2 *Instrumente für C2C Mehrwerte in Gebäuden - C2C im Bau: Orientierung für Kommunen* [online]. Available from: <https://c2c-bau.org/3-grundlagen-c2c-bau/3-2-instrumente/> [Accessed 13 Apr 2022].
- Deutsche Gesellschaft für Nachhaltiges Bauen, 2022. *Gebäude Rückbau | DGNB System* [online]. Available from: <https://www.dgnb-system.de/de/gebaeude/rueckbau/> [Accessed 14 Jun 2022].
- DIN Deutsches Institut für Normung e. V., 2018. DIN 276: 2018-12: Kosten im Bauwesen, 2018, 1–56.
- Frank, A. DGNB System – Kriterienkatalog Gebäude Rückbau: ECO1-R Risikobewertung und Kostensicherheit. Ökonomische Qualität [online], 49–57. Available from: https://static.dgnb.de/fileadmin/dgnb-system/de/gebaeude/rueckbau/kriterien/DGNB-Kriterium-Gebaeude-Rueckbau_ECO1-R_Risikobewertung_und_Kostensicherheit.pdf?m=1594385372& [Accessed 12 Apr 2022].
- Heuer, A., 2018. *Datenbanken – Konzepte und Sprachen*. 6th ed. Frechen: MITP Verlags GmbH & Co. KG.
- Iswing Dehne, Florian Knappe, Rüdiger Oetjen-Dehne, Stefanie Theis, 2016. Abschätzung des zukünftigen Bedarfs an Deponiekapazitäten in Rheinland-Pfalz: Kurzfassung der Studie im Auftrag des Landesamtes für Umwelt Rheinland-Pfalz, 2016, 1–68.
- Kasper Guldager, Harpa Birgisdottir, Gitte Gylling, Paul Stoller, Stefan Holst, Tiffany Broyles Yost, 2018. Guide to sustainable building certifications [online], 13–152. Available from: <https://build.dk/Assets/Guide-to-sustainable-building-certifications/Guide-to-sustainable-building-certifications-August-2018-e-bog.pdf> [Accessed 11 Apr 2022].
- Koschlik, M. Prof. Dr.-Ing., 2022. Vortrag BDB Bezirksgruppe Heidelberg: DGNB und nachhaltiges Bauen [online], 2022, 1–84. Available from: https://media-exp1.licdn.com/dms/document/C4D1FAQHxwo3sresadg/feedshare-document-pdf-analyzed/0/1649579998054?e=2147483647&v=beta&t=_h7H3VpZZYEx5oCAg8D9Ui0qlaj3OuCHctUWzbjc82k [Accessed 10 Apr 2022].
- Litau, O., 2015. *Nachhaltiges Facility Management im Wohnungsbau*. Wiesbaden: Springer Fachmedien Wiesbaden.
- Rosen, A., März/2021. *Urban Mining Index: Entwicklung einer Systematik zur quantitativen Bewertung der Kreislaufkonsistenz von Baukonstruktionen in der Neubauplanung*. Dissertation.
- Schmitz, H., et al., 2020. *Baukosten 2020/21: Band 1: Altbau - Instandsetzung, Sanierung, Modernisierung, Umnutzung*. 24th ed. Essen: Verlag für Wirtschaft und Verwaltung Hubert Wingen.
- Thorsten Thörner, Sigrid Hams, Dr. Ing. Gabriele Becker, Dr. Bärbel Birnstengel, Arno Häusler, Nadja Schütz, 2014. Bedarfsanalyse für DK I-Deponien in Nordrhein-Westfalen: Endbericht, 2014, 1–100.

Numerical determination of the wrinkling stress of steel polyurethane sandwich panels for reuse scenarios

K. Janczyk & M. Kuhnhenne

Institute of Steel Construction - Sustainable Metal Building Envelopes, RWTH Aachen University, Aachen, Germany

ABSTRACT: Sandwich panels are generally used as building envelopes in industrial and commercial buildings. They consist of two metallic face sheets and a core that provides the heat-insulating function of these components. The core material most commonly used is polyurethane (PUR) rigid foam. Due to the factory production of the sandwich panels, they can be quickly installed on the building and meet high building physics requirements. For those reasons, they are ideally suited for reuse. In addition, there is currently little to no possibility of recycling rigid polyurethane foam. Furthermore, recycling the steel is also energy-intensive and requires complex separation of the materials. The reuse of sandwich panels is therefore not only possible but also necessary from an ecological point of view. In this context, it is important to be able to assess the load-bearing behaviour of the panels after the first life-cycle in order to ensure a safe design. Generally, the material properties of the composite panels are determined by tests according to *EN 14509, 2013*. The modulus of elasticity and the shear modulus as well as the tensile, compression and shear strengths are determined in small specimen tests. The wrinkling stress of the panels is determined by component tests. Due to the size and number of test specimens, the effort to determine the wrinkling stress by tests is generally very high. To ensure that the reuse of sandwich panels remains attractive, the effort required to determine the material properties must be as low as possible. Avoiding the tests to determine the wrinkling stress could make an important contribution. This paper presents investigations to determine the wrinkling stress based on small-scale tests and numerical simulations, which represent an important step towards the reuse of sandwich panels.

1 INTRODUCTION

1.1 *Sandwich panels as building envelopes*

Sandwich panels are space-enclosing components that are commonly used as building envelopes in industrial and commercial construction. They consist of two metallic face sheets and a core, which takes over the heat-insulating function of these components. The core layer is usually made of mineral wool (MW), polyurethane (PUR) or polystyrene rigid foam (PIR). Due to the factory production and the low dead weight, sandwich panels allow a quick assembly while maintaining a high level of building physics quality. This leads to a great popularity and high demand of this construction method. In 2020, orders for sandwich panels amounted to over 17 million m² in Europe, *IFBS, 2021*. Sandwich panels are usually considered as self-supporting building components and are regulated by the corresponding standard *EN 14509, 2013*. Figure 1 shows a typical sandwich wall of an industrial building.

1.2 *End-of-life scenario and reuse*

Currently, end-of-life scenarios for sandwich panels do not consider reuse scenarios. The state of the art can be taken from the Environmental Product Declarations of *PPA-Europe, 2018*.



Figure 1. Typical wall made of sandwich panels.

These focus on the recovery of materials. First, the materials of the deconstructed sandwich panels are separated. Since the face sheets of the panels are usually made of steel, they can be easily recycled. The processes for the core material of the panels depend on the core material. Polyurethane core materials are usually used for energy recovery. The advantages of reuse compared to the usual end-of-life scenarios were clarified in the European research project PROGRESS as well as the difficulties and special requirements, *PROGRESS, 2020*. Furthermore, it was shown that sandwich panels in general meet the requirements for reuse. Those are in particular the possibility of standardisation, the durability, the maintenance of the physical properties of the building at a high level and sufficient material properties after the end of one life-cycle. In *Kuhnhenne et al., 2020*, it was shown that the mechanical properties of the sandwich panels after one life-cycle are basically at a sufficient level to be reused. Furthermore, rigid polyurethane foams retain their thermal properties permanently *IVPU, 2009*.

However, the high effort required to determine the mechanical properties and the associated uncertainty represent barriers to the reuse of sandwich panels. In general, the mechanical properties of sandwich panels are investigated experimentally in small-scale and component tests according to EN 14509, 2013. The small-scale tests usually refer to the properties of the core material and the component tests to the resistance of the entire panel.

1.3 Numerical investigations for the removal of uncertainties

The fact that component tests involve high effort and that it is questionable whether the results even meet the requirements represents a hurdle in the reuse of sandwich panels. Numerical simulations carried out as preliminary investigations can reduce the uncertainty about the outcome of the tests and thus represent an important barrier for future reuse. These simulations are performed on the basis of small-scale tests according to *EN 14509, 2013* and the measurement of geometric imperfections. Since both the small-scale tests and the measurement involve significantly less effort than component tests, especially with regard to the disassembly and transport of the panels, this method is suitable for making an initial statement about the reuse potential of sandwich panels.

In the following, this method is validated under laboratory conditions. First, a brief overview of the theory of wrinkling stress is given. Afterwards, experimental investigations on sandwich panels are presented. Both small-scale and component tests are carried out. In addition, the geometric imperfections of the face sheets are recorded with a high definition laser scanner before the bending tests are performed on the panel. The simulations are used to determine the wrinkling stress and are based on the small-scale tests and the measurement of the geometric imperfections. Subsequently, the numerical simulations are validated by comparing the numerical and experimentally determined wrinkling stress.

2 WRINKLING STRESS

Sandwich panels are characterised by a high load-bearing capacity with a simultaneously low dead weight. The so-called sandwich principle is created by the shear- and tension-resistant connection of the two extensional-stiff face layers with the shear-stiff core material. A bending moment is transferred by a pair of forces consisting of normal forces, which are divided between the two faces. In the case of a positive bending moment, a compressive stress occurs in the upper and a tensile stress in the lower face. Due to the high extensional stiffness and tensile strength of the metallic cover layers, the tensile stress can be absorbed without any problems. The upper face layer, which is subjected to pressure, is at risk of buckling. This face layer is elastically bedded by the core material. Exceeding the buckling stress leads to failure, the so-called wrinkling. In this case, a wrinkle forms across the width of the panel. The supporting core material allows compressive stresses in the face layer, which in turn allows for practical span lengths. From a mechanical point of view, the face layer can be seen as an elastically bedded plate under uniaxially acting normal stress, Figure 2. It can be seen that the elastic bedding is essentially dependent on the Young's modulus and shear modulus of the core material.

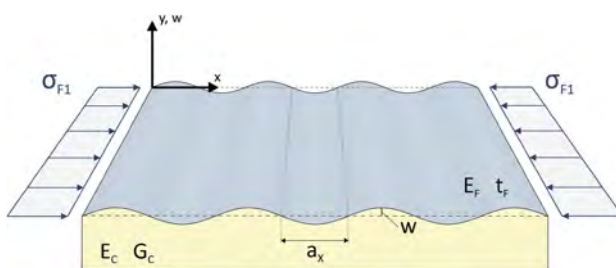


Figure 2. Wrinkling of elastic bedded steel layer.

The theoretical principles of sandwich panels have been extensively derived and presented by *Stamm & Witte 1974, Davies 2001 and Plantema 1967*, among others. The derivation takes place via the differential equation of an elastically bedded plate under uniaxial normal force loading according to Equation (1).

$$\frac{E_F \cdot t^3}{12(1 - \nu_F^2)} w(x)^{IV} + N_F w(x)'' + p(x) = 0 \quad (1)$$

where E_F = Young's modulus of the face; ν_F = Poisson's ratio of the face; w = vertical deflection of the face; $p(x)$ = function for elastic bedding.

The initial function according to Equation (2) describes the sinusoidal deformation of the cover layer.

$$w(x) = \sin\left(\frac{\pi}{a_x} x\right) \quad (2)$$

where a_x = The half wavelength.

After several transformations, the solution for the critical wrinkling stress is given by Equation (3).

$$\sigma_{w,cr} = \chi \sqrt[3]{G_C E_C E_F} \quad (3)$$

where E_F = Young's modulus of the face; G_C = Shear modulus of the core material; E_C = Young's modulus of the core material; and

$$\chi = \sqrt[3]{\frac{9(1 - \nu_C)^2}{2(1 + \nu_C)(3 - 4\nu_C)^2(1 - \nu_F^2)}} \quad (4)$$

where ν_F = Poisson’s ratio of the face; ν_C = Poisson’s ratio of the core.

Stamm & Witte 1974 also extended the approach of the critical wrinkling stress by taking imperfection into account. This should make it possible to determine the wrinkle stress under bearing load. The solution found its way into the current standard *EN 14509, 2013* and is expressed through Equation (5):

$$\sigma_w = 0.5 \sqrt[3]{G_C E_C E_F} \tag{5}$$

where E_F = Young’s modulus of the face; G_C = Shear modulus of the core material; E_C = Young’s modulus of the core material.

However, the theoretical approach underestimates the actual wrinkling stress under bearing load. In practice, this leads to manufacturers of sandwich panels resorting to the much more component tests to determine the wrinkling stress.

3 EXPERIMENTAL INVESTIGATIONS

3.1 Measurement of geometric imperfections

As described in chapter 1.3, the accuracy of the numerical analysis should be increased by taking into account the geometry of the lined surface layers on the one hand and the geometric imperfections on the other hand. To ensure the latter, a laser scanner was used to record the actual geometry of the face layer in the area of the maximum moment in the test. The accuracy of the laser is in the range of a few hundredths of a millimetre. Subsequently, the result of a scan was superimposed on the nominal geometry in the GOM-Correlate software. This makes it possible to determine the deviation of the actual geometry from the nominal geometry and thus the initial imperfections. Figure 3 shows the scanning of the surface layers on the left and the overlay of the nominal and actual geometry on the right.

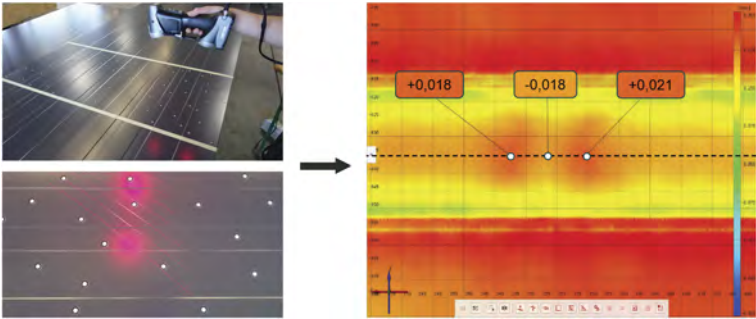


Figure 3. Determination of geometric imperfections.

The results of the measurement of the geometric imperfection are shown in Table 1. Those are the maximum deviation of the actual from the nominal geometry found in the scanned area of the respective test specimen.

Table 1. Measured geometric imperfection.

Specimen	Imperfection
-	mm
Bending test 1	0.018
Bending test 2	0.040
Bending test 3	0.029

3.2 Small-scale tests

Within the framework of the small-scale test program, tensile tests, compression tests and shear tests were carried out. Figure 4 shows the test set ups for the tensile test (left) and the compression test (centre). Both types of test were carried out in a Zwick-Roell testing machine. The test specimens had dimensions of 100 x 100 mm for both types of test. In addition, Figure 4 shows the corresponding diagram with the force-compression and force-elongation curves of individual test series.

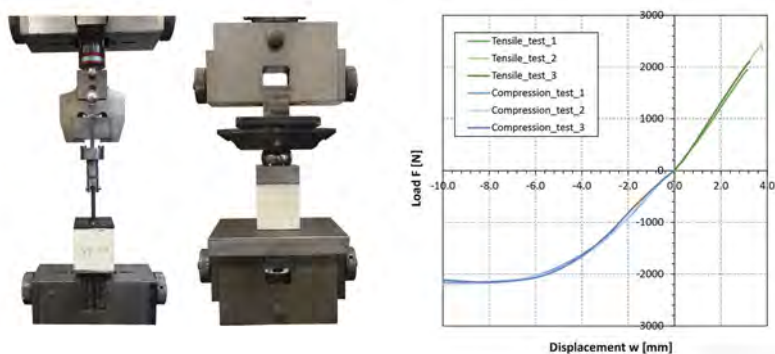


Figure 4. Test set up of tensile test (*left*); Test set up of compression test (*centre*); load-displacement diagram (*right*).

The shear tests were carried out on a 1000 mm long beam, which was then loaded to failure in a 4-point bending test. In the evaluation, the proportion of bending deformation is subtracted from the total deformation. This results in the pure shear deformation of the test specimen, so that it is possible to determine the shear modulus of the core material. The shear strength results from the maximum load related to the beam cross-section. The test set up and the load-deflection-diagram of the shear test is shown in Figure 5.

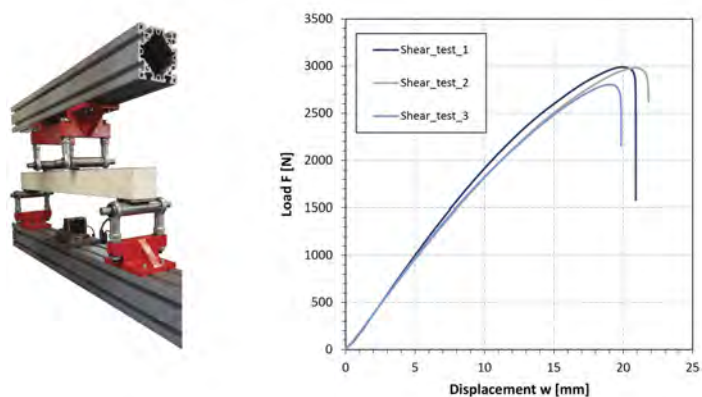


Figure 5. Test set up of shear test (*left*); load-displacement diagram (*right*).

Table 2. Experimentally determined modules of the core material.

	Young's Modulus E_{Ct}	Shear Modulus G_C
	N/mm^2	N/mm^2
Meanvalue	6.21	4.74

3.3 Component tests

Furthermore, three component tests were carried out to determine the wrinkling stress. This was done by means of a 6-point bending test. The panels had a span length of 6000 mm in accordance with *EN 14509, 2013*. The load transfer was realised over all 4 points by means of air cushions. Compared to the commonly used cross beams, air cushions have the advantage that they transfer the load over a large area and do not concentrate on one point at the top face layer of the panel. This avoids stress concentrations and the wrinkling stress is determined realistically. The test setup is shown in Figure 6 (left). The right of Figure 6 shows the load-deflection diagram of the tests.

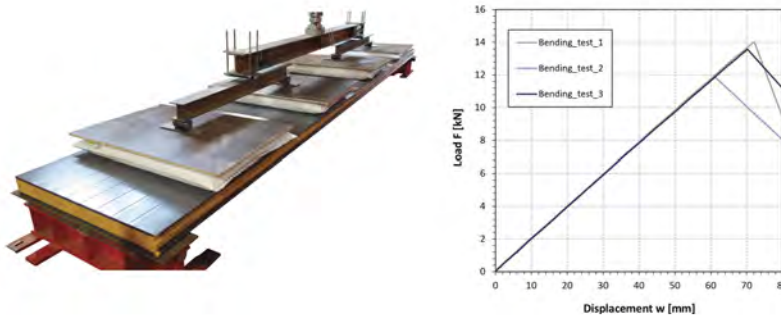


Figure 6. Test set up of bending test (*left*); load-displacement diagram (*right*).

The results of the bending tests are shown in the Table 3. It shows the maximum applied load, the resulting bending moment and the resulting wrinkling stress of the face sheet. Both the scatter of the results and the values determined are within a typical range for sandwich panels *Lange et al, 2020*.

4 NUMERICAL INVESTIGATIONS

4.1 Buckling analysis

The numerical simulations were carried out using the ABAQUS software. First, the top face layer and the core material were created separately from each other. The face layer consists of shell elements of the type S4R. The core material consists of volume elements of the type C3D8R. The top layer and core material are connected to each other with the “Tie” function. The model is supported in three places Figure 7 (*left*). First, the surface on the left is constrained in the plane of symmetry and displacements are only possible on this surface in the y-direction. Second, the surface at the bottom is supported flat against displacements in all directions. Third, the right-hand edge of the face layer is clamped and displacements are only possible in the Z-direction. This leads to the typical eigenform, the wrinkling of an elastic bedded plate under uni axial compression stress, Figure 7 (*right*).

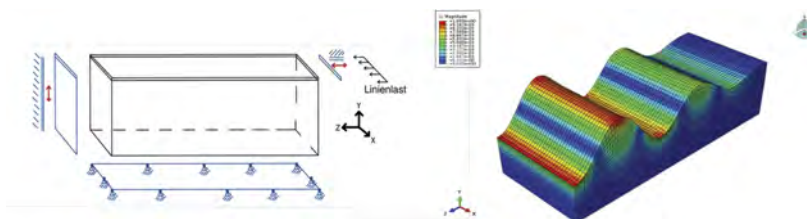


Figure 7. Numerical model: Boundary conditions and load (*left*); typical 1. eigenform (*right*).

The face layer of the core material is made of steel and the material model was made with the usual Young's modulus of 210,000 N/mm² and a Poisson's ratio of 0.3. The core material consists of rigid polyurethane foam. The modulus of elasticity is entered directly in the material model in ABAQUS. The input of the shear modulus, however, is only indirect via Poisson's ratio of the material. Since Young's modulus and shear modulus often have a similar order of magnitude in rigid polyurethane foams, the Poisson's ratio becomes negative. This is actually only the case with auxetic materials, to which polyurethane does not belong. Due to the simplification, it was necessary to validate the model in different combinations of Young's modulus and shear modulus. For this purpose, the analytical results according to equation (3) were compared with the results from the buckling analysis. The limits were defined in the range of $-0.5 < \nu_C < 0.5$. Figure 8 shows on the left all combinations of shear modulus and Young's modulus in the usual orders of magnitude of polyurethane foam. On the right, Figure 7 shows the comparison of the results of the numerical simulations and the analytical solutions.

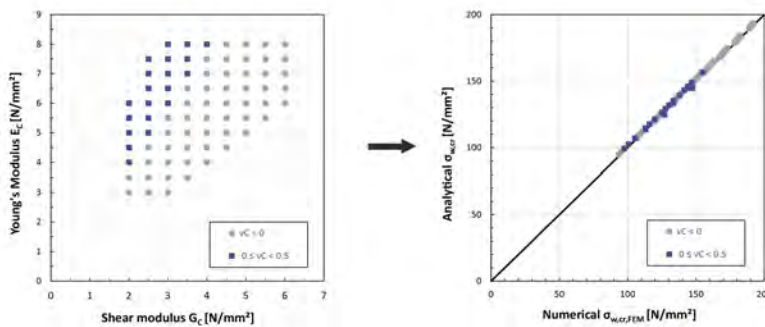


Figure 8. Results of wrinkling stresses.

It is clearly visible that the results agree very well. This applies to both the results with positive and negative Poisson's ratio. The deviation of the results is 0.94 % on average. Therefore, it can be concluded that the model is very well suited for determining the critical wrinkle stress.

4.2 Post-buckling analysis

The postbuckling analysis is done after the linear buckling analyses. Here, the eigenform from the linear buckling analysis is used to apply the imperfection. In this case, three post-buckling analyses were carried out. In each case, the maximum values of the measured imperfections from chapter 3.1 were applied. In addition, a non-linear material behaviour of the steel was assumed. Therefore, the experimental data from the manufacturer were used. Since the core material only undergoes minor deformation, the linear material behaviour from the buckling analysis was also applied here.

The evaluation of the presented method, in particular the applicability of the numerical analysis, is performed by comparing the experimentally determined wrinkle stress with the numerical. The determined wrinkling stresses are shown in Table 4. The comparison between experimental and numerical results shows a quite good agreement. In particular, the mean values of the results have only a slight deviation from 1.57%. However, it becomes clear that the dispersion of the results is much larger in the experimental investigation. This is most likely due to structural imperfections in the composite or in the core material. These could not yet be reproduced in the simulations. Nevertheless, it can be briefly summarised that the ultimate load analysis of the numerical model is capable of predicting the real ultimate load behaviour.

Table 3. Comparison between experimental and numerical wrinkling stresses.

Specimen	Experimental	Numerical	$\left(\frac{exp.}{num.} - 1\right) \cdot 100$
-	N/mm^2	N/mm^2	%
Maximum	172.11	160.03	9.91
Median	151.96	157.36	3.55
Minimum	141.32	155.34	-7.02
Meanvalue	155.13	157.57	1.57

5 CONCLUSIONS

In this paper, numerical investigations were presented that can increase the planning reliability in the reuse scenario of steel-polyurethane sandwich panels. It was shown that it is basically possible to determine the wrinkling stress of sandwich panels under bearing load with numerical simulations. The simulation was performed on the basis of small-scale tests to determine the material behaviour, as well as the measurement of the real geometric imperfections in the top face layer of the panels. The numerical simulations were able to predict the load-bearing behaviour of the component tests.

In the future, it might therefore be possible to first carry out small-scale tests on test specimens from existing panels and measure the imperfections. Here, the results of the simulations can serve as a decision-making aid. These can be considered as expected values of the results of the component tests. If the expected values meet the requirements for reuse, the component tests can be carried out with significantly less risk.

In order to show that the results are reproducible, further random tests must be carried out. Of particular interest are tests on panels that have already gone through a life cycle and could be prepared for reuse.

REFERENCES

- EN 14509, 2013. Self-supporting double skin metal faced insulating panels – Factory made products – German version EN 14509:2013 DIN Deutsches Institut für Normung e. V.
- Davies, 2001. *Lightweight Sandwich Construction*; Oxford, United Kingdom; John Wiley and Sons Ltd.
- IFBS, 2021. Internal Report, Krefeld, Germany Internationaler Verband für den Metalleichtbau.
- IVPU, 2009. *Wärmedämmstoffe aus Polyurethan-Hartschaum*, Germany, IVPU – Industrieverband Polyurethan-Hartschaum e.V.
- Kuhnhenne et. al 2020. Reuse of Sandwich Panels. *In Life-Cycle Analysis and Assessment in Civil Engineering; 2020*, Frangopol.
- Lange et. al 2020. Sandwichelemente im Hochbau. *In Stahlbau-Kalender 2020: Neue Normung im Hochbau - Leichtbau; 2020 Ernst & Sohn GmbH & Co. KG*. Kuhlmann.
- Plantema, 1967. *Sandwich Construction*; New York, London, Sydney; John Wiley & Sons, Inc.
- PROGRESS, 2020. Final Report; PROGRESS Project, European Commission, 2020.
- PPA-Europe, 2018. European Association for Panels and Profiles e. V. (PPA-Europe), Institut Bauen und Umwelt e.V. (IBU).
- EN 14509, 2013. Self-supporting double skin metal faced insulating panels – Factory made products – German version EN 14509:2013 DIN Deutsches Institut für Normung e. V.

Allowable strength estimation of vertical members used for system scaffolds considering reusability

N.G. Jang & J.H. Won

Chungbuk National University, Cheongju City, Republic of Korea

S.S. Ko

Hanwha corporation, Cheongju City, Republic of Korea

J.K. Bong

Daewoo Engineering & Construction Co., Ltd., Cheongju City, Republic of Korea

D.H. Chung

Hyundai Engineering Co., Ltd., Cheongju City, Republic of Korea

ABSTRACT: System scaffolds used in construction sites have the reused characteristic that members are used repeatedly without discarding it in terms of price, environment, and recycling. It is known that the performance of reused products could be decreased compared to the nominal allowable stress due to ‘reuse of members’ and ‘residual stress by manufacturing method’. Therefore, there is a possibility that there is a difference between the structural safety intended by the designer and that of the reused members to be installed. In this study, the performance test report of the scaffold vertical members of the reused scaffold stored and managed at the construction site in Korea was collected, and the strength reduction was analyzed considering the buckling curve specified in the design standard (Eurocode 3).

1 INTRODUCTION

Temporary structures are essential structures used in most construction sites, and many studies are being conducted on the structural safety of temporary structures. However, in research on temporary structures or temporary equipment constituting temporary structures, unused products have generally been considered (Lee et al. 2020). In general, temporary equipment at construction sites uses reusable products. At construction sites, the reused system scaffolding and system support, which are relatively inexpensive, have been used by rent avoiding high purchase costs for new products. Note that the temporary equipment such as system scaffolding are usually used for a short period of time, but they are susceptible to degradation like corrosion due to exposure to the surrounding environment and are likely to gradually lose the load-carrying capacity as usage history accumulates. The use of temporary equipment with reduced load-carrying capacity resulting from the repeated reuses can cause the collapse of the temporary structure even if design and construction are conducted by conventional practice (Jeong & Lee 2016).

In South Korea, it is legally required to check the structural safety of temporary structures before construction, and the design of a temporary structure follows the allowable stress design method. When designing temporary structures, it is difficult to verify the actual strength of temporary equipment in the site so that in practice, the structural safety of the temporary structure is checked by applying the nominal allowable stress of steel stipulated in the design standards. However, in general, the allowable stress for the design standards is mainly for the unused new steel members (Kim et al. 2008). Therefore, there might be a difference between the actual performance of reused temporary equipment at the site and that expected in the design process.

Therefore, there might be a difference between the actual performance of reused temporary equipment at the site and that expected in the design process. Thus, when designing temporary structures, some design experts often apply a reduced value 15-20% lower than the nominal allowable stress under consideration of the characteristics related to the repeated reuses. However, the background for the strength reduction rate is not clear; in fact, there are not many studies on the actual strength reduction effect of reused temporary equipment, which can be referred to in the design. Several studies on the pipe support as a typical type of temporary equipment were carried out to track the long-term changes in load-carrying capacity according to reuse history (Paik & Ro 2004; Paik 2005; Paik & Choi, 2006;). However, depending on the type of temporary equipment, the result of the decrease in resistance capacity of the reuse pipe support cannot be applied to other reused temporary equipment such as system scaffolding because of the difference in structural shape and load carrying system.

This study analyzes the decrease in the load-carrying capacity of the vertical member of system scaffold due to the reuse. In order to analyze the degradation in the load-carrying capacity of the reused temporary equipment, the quality test reports for the temporary equipment were collected from the construction sites, and then a comparative study considering the unused new temporary equipment was done to quantify the difference and characteristics. In addition, the ratio of the reused temporary equipment that did not satisfy the design standard was analyzed for the case when the allowable stress suggested by the design standard (Eurocode 3) was applied to the reused temporary structure design.

2 BUCKLING CURVE OF EUROCODE 3

The equation for the ultimate load of columns in Eurocode 3The buckling strength (P_{ut}) of the compression member subjected to concentric axial compression is calculated by the following equation based on the compressive class according to the diameter-thickness ratio (D/t).

The design equation for the ultimate load (P_{ut}) of the compression member subjected to concentric axial compression in Eurocode 3 is calculated by the following equation based on the compressive class (for class 1, 2, 3 sections) according to the diameter-thickness ratio (D/t).

$$P_{ut} = \chi A_g \sigma_y \quad (1)$$

where χ = buckling reduction factor; A_g = total cross section; σ_y = yield stress.

The reduction factor considering compression buckling is calculated by Equation 2 below:

$$\chi = \frac{1}{\phi + \sqrt{\phi^2 - \bar{\lambda}^2}} \leq 1 \quad (2)$$

where $\phi = 0.5(1 + \alpha(\bar{\lambda} - 0.2) + \bar{\lambda}^2)$; α = imperfection factor for the circular hollow section columns, 0.21 for the steel pipes with buckling shapes; $\bar{\lambda} = \sqrt{A\sigma_y/N_{cr}}$, non-dimensional slenderness; N_{cr} = critical buckling load according to the slenderness ratio and is calculated by Equation 3 below:

$$N_{cr} = \frac{\pi^2 EI}{(KL)^2} \quad (3)$$

3 ALLOWABLE STRENGTH OF REUSED VERTICAL MEMBERS BY QUALITY CERTIFICATION REPORTS

In South Korea, quality tests and inspections are required for quality assurance of temporary equipment at construction sites. The quality test report should be filed at the site according to the Enforcement Decree of the ‘‘Construction Technology Promotion Act’’ (Articles 91 and 93).

The quality test method and steel materials (STK400) for vertical members of system scaffolding are stipulated in the “Safety certification notice for protective devices” of the “Occupational Safety and Health Act.” A compression load test is performed as a quality test method for vertical members. In this study, the information for material (only ‘STK400’), diameter, thickness, length, and maximum test strength of the vertical member were collected from the certificate for quality test after confirming the authenticity of the quality test report filed at the construction site and the content appropriateness of the quality test. A total of 500 vertical member test result data were collected from the quality test reports. The specification is summarized as shown in Table 1. The experimentally determined buckling reduction factor (hereafter ‘Experimental buckling factor’) was calculated by dividing the collected maximum load of the quality test report by the product of cross-sectional area and tensile strength of each vertical member.

Table 1. Specifications of the collected reused vertical member test data.

Diameter	Thickness	Length	Count
mm	Mm	mm	
48.6	2.2	475	3
		950	4
		1900	4
		3800	4
	2.3	475	47
		900	54
		1900	63
		3800	63
	2.4	475	51
		900	54
		1900	69
		3800	84
Total			500

4 THE DIFFERENCE IN LOAD-CARRYING CAPACITY BETWEEN UNUSED AND REUSED VERTICAL MEMBERS

The load-carrying capacity of unused vertical member of system scaffolds against the compression load test was referenced by Jang (2020). The compression load test objects are the vertical member with 950 mm and 1900 mm length; both are frequently used structural members for the assembly at construction sites. The test was conducted according to the method specified in Korean national standard KS F 8021 (Components for tied post system scaffolding and shoring). Table 2 shows the detailed specifications of the unused system scaffolds. The material of the unused system scaffolds is STK400 steel.

Table 2. Specifications for the unused vertical members.

Diameter	Thickness	Length	Count
mm	mm	mm	
48.6	2.2	950	18
		1900	18

As seen in Table 3, the reused system scaffold group with a length of 950 mm ($\bar{\lambda}$: 0.67) has an average load-carrying capacity of 107.1 kN, which is about 7.4% smaller than the unused system scaffold group (115.7 kN). The reused system scaffold group with a length of 1900 mm ($\bar{\lambda}$: 1.33) has an average load-carrying capacity of 48.3 kN, which is about 8.7% smaller than the unused

system scaffold group (52.9 kN). In addition, the coefficient of variation (COV) of the reused system scaffold increased by 121.4% in the group with a length of 950 mm and 29.3% in the group with a length of 1900 mm respectively, compared to the unused system scaffold. In the case of reused products of the system scaffold, the average load-carrying capacity tends to decrease while the COV increases. Therefore, when designing a structure of a system scaffold using a reused product and determining the nominal allowable stress according to the design standard, there might be a high probability that the actual structural strength may be smaller than the designer’s calculation.

Table 3. Comparison of the load-carrying capacity between the reused and the unused system scaffolds.

Length		Reuse or not	Mean	Reduction ratio	COV	Increase rate
mm	Slenderness		kN	%	kN	%
950	0.67	Unused	115.7	-	0.089	-
		Reused	107.1	7.4	0.197	121.4
1900	1.33	Unused	52.9	-	0.174	-
		Reused	48.3	8.7	0.225	29.3

5 COMPARISON OF EXPERIMENTAL BUCKLING FACTOR AND BUCKLING CURVE OF EUROCODE 3

Figure 1 shows the buckling reduction factor according to the non-dimensional slenderness of the reused system scaffolds in the form of a box plot in the buckling reduction curve of Eurocode 3. Tables 4 show the average and standard deviation of the buckling reduction factor.

Excluding the reused vertical member group with a slenderness ratio of 0.67, about 75% of the remaining recycled vertical member groups are below the Eurocode 3 buckling curve. In the group of vertical members with a slenderness ratio of 2.67, all collected vertical member data are below the buckling curve of Eurocode 3. The higher the slenderness of the collected vertical members, the smaller the ratio of the experimental buckling factor to Eurocode 3, and in the case of the vertical member group with a slenderness of 2.67, it decreased to 70.6% compared to buckling curve of Eurocode 3. Therefore, considering the imperfection factor (α) of 0.21 in the buckling curve of Eurocode 3, the buckling curve of Eurocode 3 may not be suitable for the structural analysis of systems scaffolding for reused products. Even when using the highest value of 0.76 among the imperfection factor suggested by Eurocode 3, about 50% and 80% of vertical members with slenderness of 1.33 and 2.67, respectively, do not meet the criteria of Eurocode 3. When designing system scaffolding using reused products in consideration of Eurocode 3, a reasonable reduction method for the imperfection factor of the buckling curve is required.

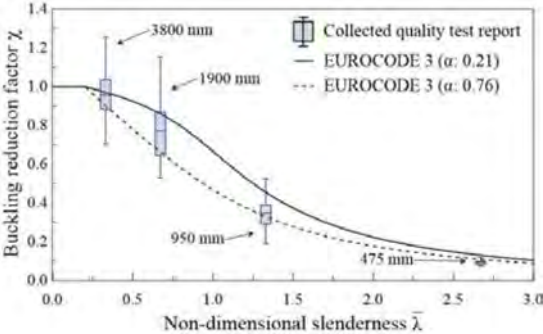


Figure 1. Comparison of buckling reduction factor between the reused system scaffolds and Eurocode 3.

Table 4. Comparison of the buckling reduction factor between the reused system scaffolds and Eurocode 3.

Non-dimensional slenderness	0.33		0.67		1.33		2.67	
	Mean	COV	Mean	COV	Mean	COV	Mean	COV
Collected quality test report	0.95	0.13	0.77	0.19	0.34	0.22	0.09	0.22
Eurocode 3 (α : 0.21)		0.97	-	0.86	-	0.45	-	0.13
Reduction ratio (%)	93.3		88.8		76.2		70.6	

6 CONCLUSIONS

In this study, based on the test reports of the system scaffold, which is filed and managed at the construction site, the difference between the buckling reduction factor of the vertical member of the reused products and the buckling curve evaluated by the Eurocode 3 was investigated.

In the case of slender reused vertical members, it decreased to about 71% of the buckling curve of Eurocode 3. In addition, the coefficient of variation in vertical member groups of some slenderness more than doubled compared to unused vertical members. The buckling curve of Eurocode 3 may not be suitable for the structural analysis of systems scaffolding for reused products. Further studies are needed on the imperfection factor of Eurocode 3 buckling curves that may be considered for the use of reused products.

REFERENCES

- Jeong, S.C., & Lee, H.K. 2016. A study on the survey and improvement of safety certifications in temporary equipment and material, *Journal of the Regional Association of Architectural Institute of Korea*, 18 (2), 171–180.
- Jang, N.G., 2020. Probabilistic characteristics of young's modulus and evaluation of buckling strength on a vertical member of system scaffold. Master's thesis, *Chungbuk National University*, Korea
- Kim, J.R., Lee, E.T., Lee, S.Y., & Baek, K.Y. 2008. A study on the structural property of structural steel tubes under axial compression. *International Journal of Steel Structures*, 20(3), 437–444.
- Lee, H.D., Won, J.H., Jang, N.G., Mha, H.S., Jeong, S.C., & Kim, S.J. 2020. Experimental study on load carrying capacity enhancement of system supports considering full installation of bracing members. *International Journal of Steel Structures*, 20(6), 2051–2067.
- Paik, S.W., & Ro, M.L. 2004. A study on the strength changes of used pipe support (1). *Journal of the Korean Society of Safety*, 19(2), 93–97.
- Paik, S.W. 2005. A study on the strength changes of used pipe support (2). *Journal of the Korean Society of Safety*, 20(3), 120–125.
- Paik, S.W., & Choi, J.S. 2006. A study on the strength changes of used pipe support (3). *Journal of the Korean Society of Safety*, 21(3), 101–106.

Limits of reuse of steel

P. Kamrath

Paul Kamrath Ingenieurrückbau GmbH, Germany

ABSTRACT: Demolition is the traditional technique, which handles the end-of-lifetime of any building, if refurbishing is not applicable anymore. Demolition is one of the biggest source of waste all over the world. The will to reduce waste leads to different recycling techniques. While waste of concrete can only go through a downcycling process and produces recycled gravel, steel and iron are used as source for new steel parts for decades. Old Steel will be generally separated and is used as a resource to produce new steel. Because steel is an expensive resource, the recycling quota of steel is above 90%. Nevertheless, the recycling of steel is energy hungry and produces a huge CO₂-footprint. Thus, the reuse of steel-elements can minimize this ecologic footprint. While for most C&D waste the focus lies on additional recycling options and the concept of urban mining is adapted, the future of steel-based buildings should be the reuse of steel-parts. The conceptual idea starts already when a building is planned by the application of a “design for deconstruction”. This paper discusses practical aspect of the reuse of steel-based parts and defines limits of reuse. Those limits are given by the steel quality as well as by aspects of contamination (tar, asbestos). Examples of succeeded recovering of steel parts are introduced.

1 INTRODUCTION

Demolition work in the modern building environment produces about 60% of the total waste occurring in Germany. One important key issue of demolition are strategies to prevent waste and therefore to reach high recycling quotes. For most objects to demolish, techniques are based only on a material-view as a waste. In other words: The building will become waste, which is first sorted and then it will be decided depending on the different materials of waste whether certain recycling techniques are useful. Thus, steel is sorted and is being put back into the cycle. Concrete may be downcycled to gravel. With these techniques and decisions the waste is going to be minimized. Such techniques are calls “urban mining”, which describes the view of something to demolish as a store of more or less usable materials.

A new view to the building to be demolishes does not focus on materials and their use as a recycled product but on parts of buildings as they are. Wouldn't it be good to keep columns and beams in-tact and to reuse them as already premanufactured used parts for a new building and to give them a new life? To precisely differentiate demolition with the intend of reusing parts from demolition intending the use of raw materials from now on deconstruction is used to describe the intend to keep parts or whole building intact and demolition is used only in the meaning of a total teardown with focusing on materials (see Figure 1).

2 DECONSTRUCTION VS. DEMOLITION

2.1 *Reuse, deconstruction and demolition*

Handling the end-of-lifetime of any building leads to three scenarios of renewing a building (Kamrath & Hechler, 2011b):

Deconstruction: A clearance could extend the lifetime and could be an alternative to demolition. During a building clearance, any non-load bearing parts of the building will be deconstructed. The rebuild process starts with the old skeleton.

Reuse of Structure: Deconstruction and reuse of the structure itself could be an alternative for some structures, especially those made of steel. This method helps to generate a second life for the load bearing structure e.g. for bridges or halls at another place.

Demolition: Complete demolition is the typical end-of-life scenario. To avoid waste and landfilling, reuse and recycling of materials should be considered.

The lowest impact on natural resources is achieved by reuse of whole structures or even a whole building. If a whole building can be deconstructed and rebuilt elsewhere, no waste is produced at all. If this possibility is considered prior to build, this is called “design for deconstruction”.

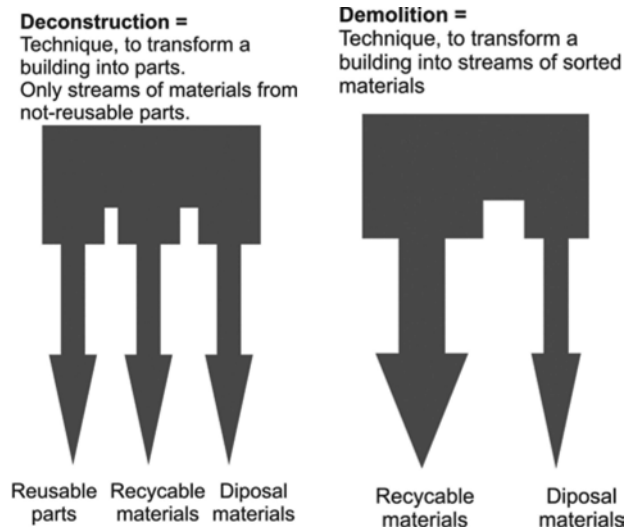


Figure 1. Waste streams occurring for general demolition work which is dividing the stream into recyclable materials and disposal materials only (e.g. hazardous). Comparison to a deconstruction waste streams, which handles reusable parts as a third stream.

2.2 Recycling

If whole structural elements cannot be reused or deconstruction is not applicable (e.g. structure failure), demolition and recycling of materials is the best choice. Recycling is divided into three stages, which are:

1st order recycling is the complete recycling of material with the focus of creating a new product with the resources of used materials. This is possible with all kinds of metals, plastics and glass. Steel is the world’s most recycled material. After melting the sorted materials, a new product of the same quality can be made.

2nd order recycling or downcycling can be done with all not-polluted mineral materials such as concrete, brick-stone and general masonry. Recycling of concrete is the process of producing gravel which can be used instead of natural gravel. Concrete however, unlike a 1st order material, while made from cement cannot be recreated into more or new cement. Once concrete has been made, there is no practical way to decompose it into the basic elements of sand, water, aggregate and cement that went into its formation. Nevertheless, processing waste concrete to produce recycled concrete aggregate (RCA) or recycled crushed concrete (RCC) has the potential to greatly reduce the quantity sent to landfill each year and complements the government’s sustainable development and waste minimization policies. The potential of RCC/RCA differs according to the local market. If natural gravel is cheap, the demand

for recycled concrete is low. If no natural resources exist (e.g. the Netherlands) the potential is high and the possibilities for recycling are high as well.

3rd order recycling concerns thermal use. Wooden materials and plastics with no possibility of 1st order recycling are possible sources of energy for power plants. If no thermal use is possible (e.g. due to pollution or contamination) landfilling is the only possibility.

2.3 *End-of-Life data for common parts*

Deconstruction is a special way of demolition with the goal, to keep as much from structures intact for a latter use as possible. The conceptual idea for matching deconstructing techniques is the “reverse building” technique (Hechler et al. 2011).

Demolition is focused on safety and materials while reverse building keeps elements intact. This technique is not applicable to any building. The lighter weighting the structures are, the better a reverse building concept is possible. Most of today buildings to deconstruct or demolish were not planned for a later use. Thus, the boundary conditions do not fit to perform a full reverse building deconstruction. There are a few examples of buildings, which apply to a “design for deconstruction”. That means, those buildings were already planned to deconstruct and reuse the whole on another site later (Dorsthorst & Kowalczyk 2002).

The life cycle of as structure consist of the production, fabrication, transport and erection of the construction materials, the use of the construction and finally the end-of-life of the construction.

Steel is here from the world’s most recycled material. The main conclusion from the diagram is, that it is mainly of interest to recycle materials which can be recycled cost-effectively and indefinitely, e.g. aluminum cans and glass bottles, can be reclaimed and recycled into more of the original product: new cans and bottles. The energy and material savings are substantial, and there are high consumer recycling rates in many countries.

The recycling of C&D Waste only partially addresses the problem, because it can lead to considerable consumption of resources in re-processing and transportation. Only a fraction of construction elements can be reclaimed and reused for their original purpose, and this is normally the best environmentally sustainable option at a local level. The average end-of-life scenario for construction materials is shown in Table 1 (SCI).

Recycling is hereby defined as the end-of-life recovery and reprocessing of a product (e.g. by re-melting of steel construction products to form new steel products) and Reuse is defined as the end-of-life recovery and reuse (e.g. of steel construction products as a product filling the same function with or without some reprocessing). The recycling rate (within a defined system) is defined as:

The tonnage of a product recycled/Tonnage of the product arising on demolition sites

The reuse rate is similar defined by replacing the word recycled with reuse (Hechler et al. 2011).

Confusion in existing in peoples’ minds about the nature of concrete recycling. Concrete, however, while made from cement, cannot be recycled into more cement. Once concrete has been made, there is no practical way to decompose it into the basic elements of sand, water, aggregate and cement that went into its formation. However, there are opportunities to crush and reuse concrete recovered from construction demolition. The recycled material can be substituted for fresh aggregate in some applications (World Business Council for Sustainable Development, 2008).

3 EXAMPLE: DECONSTRUCTION AND REUSE OF ROOFTOP MADE OF STEEL

3.1 *Overview*

The single storey hall was part of an old fabrication plant and located in Wuppertal, Germany. The production company has two fabrication sites. Due to growth over the years, this site was planned to be demolished and to be replaced by modern fabrication buildings afterwards.

Table 1. Average end-of-life scenario data.

Material	Recycling (%)	Reuse (%)	Landfill (%)
girder	88	11	1
Lintel	88	10	2
Road barrier	65	34	1
Post coated inner wall components	59	7	34
Doorframes	90	9	1
Insulated inner wall box	87	11	2
Metalstud wall	92	7	1
Services	87	11	2
Light gauge steel (housing)	87	11	2
Purlins and rails	87	1	2
Composite floor decking	81	15	4
Composite sandwich cladding panels	53	37	10
Roof plate (coated)	81	15	4
Profiled cladding and roofing panels	81	15	4
Heavy structural sections	87	11	2
Reinforcement [Steel Recycling Institute]	65	0	35

Total there existed 2 halls as well as an office building. While the office building and the greater part of the fabrication halls from the 1950s were planned to be demolished, the oldest hall was planned to keep for historical reasons. Unfortunately, modifications in the 1950s combined the bearing constructions of the office building with the historical hall. Because the fabrication started once in this hall, there was a deep interest, to keep as least the roof-structure and to integrate this as a remembrance to the beginning of the company.

3.2 Deconstruction

Demolition techniques are quite different from deconstruction. While demolition is fast because nothing needs to be kept intact, deconstruction or reverse building needs other machines as well as more care to the parts which should be deconstructed. It is evident to plan, when the technique has to be switched from demolition by excavators to techniques which keep parts intact (Figure 4 top).

The construction of the roof structure consists of steel-timbering. Up-on the bearing structure, the roof was build of wood with a regular sealing of old tar-based cardboard. Due to the filigree steal-structure preliminary cardboard and wood were deconstructed by man-power. Afterwards, all jointing's of the girders to columns were dismantled.

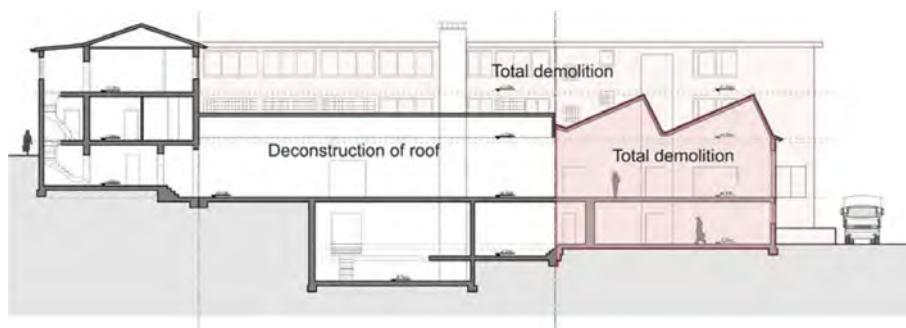


Figure 2. Overview of demolition and deconstruction. An office-building was demolished while the roof of an earlier fabrication hall was deconstructed and reused for the new building.



Figure 3. Deconstruction process: All not-bearing parts are removed. The steel-structure will be removed by crane.



Figure 4. Single storey hall after demolition of inner parts with intact roof. Steel-based roof structure after deconstruction.

Only the horizontal links retained for stability reasons. The links were dismantled just in time when the girders were removed.

To keep the steel timbering intact after the deconstruction, it was evident, to build a construction to store the elements. This construction was fabricated of steel (Figure 4 bottom).

In general, deconstruction is applicable. A general application needs to analyze costs and time for such techniques.

3.3 *Limitation of deconstruction for reuse*

Dismantling of structures for reuse issues is quite different from the regular demolition process. For regular demolition there is no need to keep anything intact. For demolition the boundary condition are safety of neighboring buildings and a focus on raw materials, while

the deconstruction focuses on the construction itself to be kept intact. Thus, there is an increase of hand-made work instead of the use of excavators.

In fact, both methods lead to the same rates of steel-reuse from the material view. If the costs are considered, the costs of deconstruction for reuse are much higher. Probably there are savings for the new building using the dismantled parts.

Nevertheless, deconstruction for reuse is possible even for single-storey-halls originally built the early 20th century. For this case, it was helpful, that the new use for the girder-structure is at the same site. Especially if only parts of structures are identified for reuse, it is evident to find a suitable building to integrate the used parts later. This building needs to fit the geometrical dimensions.

As long as the used structures are integrated on the same site, an additional benefit is the omission of any transports. Thus, there is a high saving of energy.

3.4 Deconstruction of modern SSH

The example was dealing with the architectural idea to keep the roof structure for later use as a remembrance of older times.

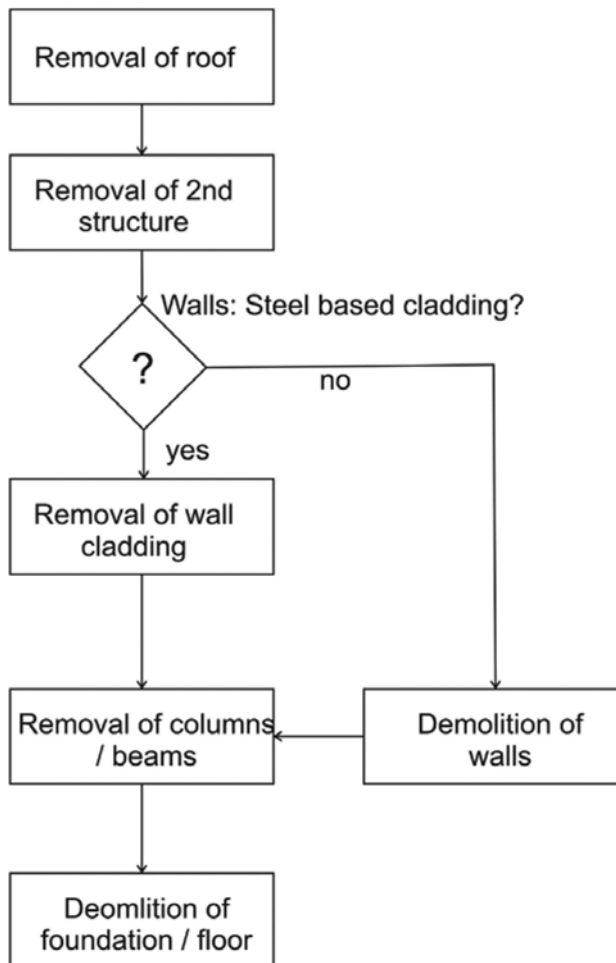


Figure 5. Demolition/deconstruction plan of a single storey hall. In general, there exist parts with a low interest to keep intact (roof cladding), the primary steel construction and the founding made of concrete, which can be downcycled in the end.

Mostly, deconstruction is interesting for SSH which were build in the last 20 years. It is assumed, that those halls meet nearly the same standards as we have today.

At first, all parts are sorted into parts to keep and parts not to keep. Thus, the waste streams as given in Figure 1 are identified. For demolition a precise division into parts is not necessary. As soon as parts are identified for deconstruction, the whole technique has to follow the needs of keeping the identified parts intact. Instead of a combined demolition of the roof including the primary structure, the cladding must be handled carefully for example (Figure 5).

For a general SSH the deconstruction plan should be as presented in Figure 5: Deconstruction becomes a mixture from reverse building (Roof, cladding removal), deconstruction of structure and demolition of concrete-based parts as funding and possibly walls.

The time consumption for reverse building is about 3 times higher than the time consumption for general, not parts-based demolition. Thus, costs and time for deconstruction are higher than for demolition. This may be worth the extra costs if the SSH can be sold to begin a new life on another place.

4 CONCLUSIONS

Reuse is limited by technical and economic issues. Technically mostly structures which are screwed are favored for deconstruction and reusing. The secondary structure may be welded and be renewed. The less parts are made of concrete such as walls, the better the reuse potential will be. For deconstruction the technique needs to be switched from excavator-work to crane based work. In fact, during a deconstruction, excavators are only needed for demolition of the foundation/ground-floor. If walls are made of concrete or masonry, an excavator needs to work parallel to cranes and lifts, which extends costs. Thus, the perfect reusing case are SSH (Single Storey Halls) with cladding on a screwed steel-based structure.

Besides technical issues, deconstruction possibilities are limited by economic issues. Deconstruction will take much more time than demolition on site. Today, the removal of buildings is mostly done as the begin of a new building. So, the removal goes ahead and is mainly performed as a preliminary clearance. The costs of removing steel-based structures are very low, because even regular recycling of the steel-based parts creates a high income and is described with urban mining. Thus, for the customer there is no need to put extra-effort or time into performing a deconstruction. His interest is mainly to have the new building/hall as fast as possible being built. Costs of regular demolition are about 5% of the building costs due to the high recycling potential of steel.

In western parts of Europe, the willing to use or reuse something is little as well. The intention to sale a complete SSH which is deconstructed cannot be a decision of the demolition contractor. Such an effort will not fit the time-planning of a building project. Thus, during the planning already a possible deconstruction needs to be taken into account. This must include a plan for storing the parts, the search for a new reconstruction place, planning for the reconstructed foundation and material tests. While demolition would be cheap, deconstruction will increase costs first.

Unfortunately, even the environmental effect is little. Especially steel is known as an up to 100% recyclable material. While construction made of concrete for example have small recycling potential and the former concrete can only be downcycled to gravel of concrete, steel-based parts can be remelted for unlimited times. Reusing may further lower the CO₂-footprint, but steel construction are already performing well.

Deconstruction for reusing today is a niche. Such projects are done for the great fairs such as the Bauma in Munich or the IAA in Frankfurt. Additional halls were planned as steel-based, light-weight constructions which are build such for the one-week lasting event and are deconstructed afterwards. The BAUMA for example is being held only every 4 years. Thus, the temporary hall is being rebuild on the same place for each fair again. The key for these temporary buildings is the possibility to rebuild them as additional place on exact the same place. Regular deconstruction with intended rebuilding needs the finding of a total new place.

The construction parts are intended to be sold. Selling complete halls as used parts need a market which does not exist today.

ACKNOWLEDGEMENTS

The research presented in this paper received funding from European Commission's Research Fund for Coal and Steel project under grant agreement No 747847.

REFERENCES

- Dorsthorst, B.J.H & Kowalczyk, T. 2002: Design for recycling. CIB Publication 272, Paper n.8. In: Proc. of the CIB TG39 Deconstruction Meeting, Design for Deconstruction and Materials Reuse, Karlsruhe, Germany. Rotterdam: CIB.
- Hechler, O. & Larsen, O.P. & Nielsen, S. 2011: Design for deconstruction. In: COST Action C25 "Sustainability of Constructions - Integrated Approach to Life-time Structural Engineering", Volume 2: Summary Report of the Cooperative Activities. Malta. 2011. ISBN 978-99957-816-2-0
- SCI: LCA for steel construction
- Kamrath, P. & Hechler, O. 2011b: Eine Einführung in den Stand der Technik bei Abbruch- und Rückbauarbeiten: Konzepte, Möglichkeiten, Potential. In: Der Bauingenieur, Band 86, June 2011, pp. 269–280, Springer Verlag, ISSN 0005–6650
- World Business Council for Sustainable Development, 2008

The deconstruction of a steel based single story hall

P. Kamrath

Paul Kamrath Ingenieurrückbau GmbH, Germany

ABSTRACT: As part of the PROGRESS research project a steel-based single-story hall was deconstructed and the primary and secondary structure of the building was recovered. The structure was explored by UAV devices. The SSH is built of 7 different parts. From up to down the hall consists of the roof insulation build out of Styrofoam with a foil, the roof itself made of trapezoidal sheets, a secondary steel structure connected to the primary arcs. The steel-based construction is founded on a reinforced concrete plate. The plate and fundaments are located ca. 1,0m above the ground. The space in between is filled with sand or any other material suitable at the original building time. Exploring materials and even chemical tests of mineral waste is common and important due to the risk to contaminate the environment or risk health of people. To create drawings of buildings to demolish or dismantle is not worth the effort. Nevertheless, exact geometry knowledge is very helpful for the planning of a demolition project and was rebuild by the use of UAV devices. A technique was developed to perform the deconstruction for reuse of steel parts mainly by excavators. Thus, the recovering of usable parts and the demolition of the concrete based ground plate was performed by the same machines. This paper presents the results and discusses the possibilities of excavator-based deconstruction.

1 INTRODUCTION

Typically, single story halls are not built as temporary objects. Although costs for building are little compared to structures based on concrete, today's buildings are not intended for reuse. Nevertheless, a perfect SSH to test the reuse capabilities was found in Cologne, Germany. The owner had to remove a single-story hall from the area of the great market in Cologne. His intention was just the clearing of the area as he was committed by contracts with the operator of the market area. The building itself was about 25 years old, thus the structure had not reached the end of lifetime, which is at least 50 years.

For the practical work a compromise needed to be found between traditional demolition with the advantages such as little costs and high performance and new technologies which intend the reuse of the whole building.

So the goal was to explore a technology based on machines which are typical for demolition work and to perform a deconstruction with them. The use of the standard demolition machines is helpful because it opens the possibility to switch from deconstruction to demolition extremely fast. Even for projects not intended for deconstruction during planning this might open the possibility to optimize the project for reuse on a later stage. (see Figure 1).

2 OVERVIEW OF THE PROJECT

2.1 *General*

The great market of Cologne is an area, where different sellers of food and fruits store imported goods for reselling to companies, restaurants, and general food stores (Figure 1). The areal consists of many buildings and halls from all decades. The great market itself is not operating as seller itself. It generates the framework for other companies, which are selling the

goods. The idea is to have all the big players of imported fruits on one place. Most bigger cities in Germany have such markets for almost a century. Nevertheless, today there is little need for the idea of a centralized market. Thus, the market area in Cologne is closing during the next years and first companies are leaving the area today.

Especially the bigger companies were running out of space somewhere in the past and built additional storage halls. To extend their capabilities. Unfortunately, when leaving the area, they are contracted to remove “own” buildings.

The result is the need to remove even newer buildings which are perfectly reusable (Figure 2).



Figure 1. Area of the great market of Cologne with the object to deconstruct for reuse (left).



Figure 2. View through the market area with the single story hall to be deconstructed on the right (right).

2.2 Exploring the structure

In most cases for objects to remove there exists a lack of information. The original planning of a building does not exist anymore after some decades and the change of owners. In most cases there is no information about materials used, possible hazardous waste which in general was unknown to be hazardous in older times and no drawings of the formerly planned building.

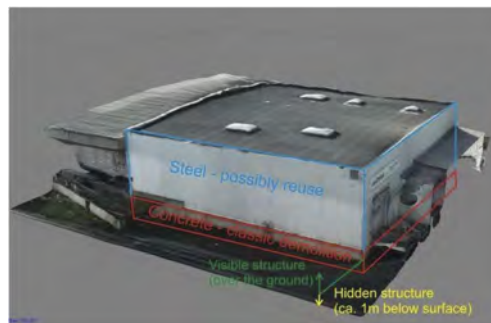


Figure 3. Overview of the SSH on a UAV model: The hall consists of a visible over the ground structure which is made of steel with attached cladding (blue), a concrete structure which ends ca. 1m below the surface (red).

Exploring materials and even chemical tests of mineral waste is common and important due to the risk to contaminate the environment or risk health of people. To create drawings of buildings to demolish is not worth the effort. Nevertheless, exact geometry knowledge is very helpful for the planning of a demolition project.

During the planning, the steel-based part was identified as a possible reuse item while the concrete founding are to be demolished. For the crushed concrete there is a general possibility to downcycling and reuse the material as recycling-gravel. This is obviously the lowest form of recycling.

The concrete structure is mainly unknown. From general experience it can be assumed, that floor plate and walls were made of 20cm reinforced concrete. The space below the floor plate is assumed to be filled with sand or a similar filling. For calculation, a box with no holes and no empty spaces is assumed.

The steel-work is easier to explore. While the roof is made of trapezoidal sheets with insulation, the primary structure consists of 4 arcs made of 2 parts which are connected in the middle axis. The arcs are made of non-standard steel beams. The secondary structure is made of small beams. It was planned to deconstruct the primary and secondary structure. The trapezoidal sheets and the cladding are not recommended for reuse possibilities since a deconstruction of the light-weight parts is very time intensive (Figures 3 and 4).

Table 1 lists the main parts of the objects from the roof down to the fundamentals. In General, the concrete and filling are about 700m³/1.500to. The steel-base hall with cladding is approximately 50to only. Even if the structure is going to be reused, this causes that most materials of the building are still becoming waste.

The height of the hall is below 10m. That means, that the machines used for demolition may be used for deconstruction as well. This is important to switch during the work process between parts to deconstruct for reuse and concrete demolition work without changing the machines used. As a test case this opens up the possibility as well for projects not initially intended for reuse to deconstruct parts if it suits.

Table 1. Calculated masses and parts.

No.	Part	Size	Waste management
1	Roof	531 m ²	Recycling, disposal
2	Wall (steel)	414 m ²	Recycling, disposal
3	Ground plate	106,2 m ³	Recycling off-site
4	Fundaments (concrete)	55,2 m ³	Recycling off-site
5	Filling	630 m ³	Recycling
6	Reusable structure	20 to	Deconstruction reuse

2.3 Additional object information

Besides the exploration of a structure all known historical information were collected. Especially on industrial sites it is urgently important to collect data about bombings due to World War II. Close to the building a probably not-exploded bomb was detected. Also, exactly at the position of today's hall, a German gun emplacement was located. The bomb itself is not affecting the demolition of the hall – the distance will not become closer as 30m. Since the hall was built around the year 2000 the former gun emplacement was already known at times of building the hall. During earthwork at that time possible remains were already removed.

The result of the analysis of leftovers is, that there is no danger due to the found unexploded bomb as well as there is no need for further local investigations. Nevertheless, work below the ground-level should be done with care.

While the finding of a World War II leftover doesn't affect the deconstruction/demolition project itself, the possible bomb will be investigated by authorities soon.

Any building is connected to the sewage system in the ground as well as to electricity and other medias. It is evident that a building to remove needs to be cut from all the media systems before the demolition. The connection to the sewer system needs to be sealed to prevent pollution of the sewer system with ground material causing blockage of the sewage pipe.

The owner of the sewage system postulates a partly removal of the sewer system as well as sealing of the connections with concrete. The sewer system of the area is well documented.

3 DECONSTRUCTION OF SSH BY EXCAVATORS

3.1 Idea of excavator-based deconstruction

Generally, demolition is excavator based while deconstruction is based on lifting parts up. In easier words: Demolition is a technique to destroy a building or hall controlled and sort the masses into classes of materials. Deconstruction needs to survey the former elements. While



Figure 4. Steel structure: The primary structure is made of 4 arcs of steel. There is no visible connection plate on the ground. Obviously, the columns are poured into the concrete. (left).

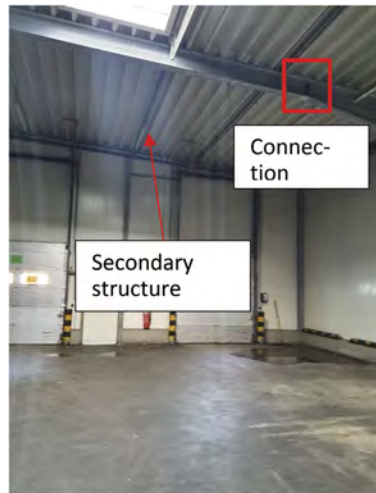


Figure 5. Between each of the arcs smaller steel beams as a secondary structure are visible. The connections are screwed. (right).

during demolition connections of steel beams can be cutted with the help of the excavator (e.g. steel shear devices), a deconstruction project needs the connections to be unscrewed. Thus, an excavator seems not to be the right instrument for deconstruction.

On the other hand, after deconstruction of the steel parts an excavator is needed to remove the concrete basement parts. That means, that even a deconstruction of all reusable parts ends in traditional demolition of concrete-based parts. Today, the removal of halls or other buildings is mostly entitled as a demolition. Thus, the contract of the client only describes the total removal of a specific object but does not describe the technique. The contractor owes the removal of the object in a given time span. Mostly, the contract will not specify that the former object has to be destroyed and become waste. Thus, it is up to the contractor how he plans to remove the object. Deconstruction is only an alternative, if the deconstruction can be performed fast enough to follow the given time span for the demolition project. To minimize costs of the extra work for deconstruction it would be a good to use the same machines as for the demolition. Then, a deconstruction could be performed as an alternative with the later chance to sell the reusable parts.

The less additional machines are used, the better the deconstruction can perform against the demolition.

For the Cologne SSH the deconstruction by excavators was tested. As a first step, the different parts of the SSH were analyzed if deconstruction would be an alternative to demolition.

The SSH is built of 7 different parts. From up to down the hall consists of the roof insulation build out of styrofoam with a foil, the roof itself made of trapezoidal sheets, a secondary steel structure connected to the primary arcs. The steel-based construction is founded on a reinforced concrete plate. The plate and fundaments are located ca. 1,0m above the ground. The space in between is filled with sand or any other material suitable.

The deconstruction causes higher costs. Thus, it is important that parts are suitable for reuse after deconstruction. If they fail to be reused, those parts would be handled as waste/recycling materials only with the same effect as generally demolished parts. That means, that only those parts shall be deconstructed, which are not predisposed for deformation during the deconstruction process. Trapezoidal sheets are not deconstructable without deformation as well as sandwich elements could easily be damaged. Thus, it was chosen to deconstruct the primary and secondary structure while demolish the light-weight parts such as the cladding and the trapezoidal sheets.

Deconstruction of a SSH

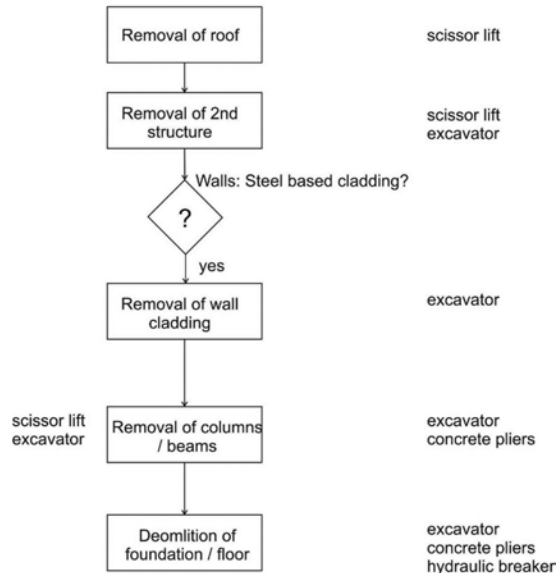


Figure 6. Deconstruction of the Cologne SSH by excavators. The primary and secondary structure is deconstructed for reuse. Cladding and light-weight materials are chosen for recycling only. Foundation is handled as regular demolition.

Table 2 lists the parts and the decision about the handling for the testcase. Figure 6 shows the deconstruction plan.

3.2 Dismantling of structure by excavator

For general demolition of an SSH the safe technique for demolition of the structure is given in Figure 7. The technique is based on flame cutting the adjacent girders and pulling the structure down. If the primary structure is poured in concrete, there exist cutting techniques to create a hinge that allows the needed movement.

Further in the project, it will be checked, if the connection can be uncovered so that flame cutting will become evident.

In fact, the technique is the same for deconstruction, except that no flame cutting is used. Instead the joints need to be unscrewed. The poured parts have to be dismantled by small excavators. It is evident not to release joints of the secondary structure before the anchoring in the ground. As well, deformation may become an issue. Thus, it is recommended to use two excavators for pulling the arcs to the ground.

Modern roof structures are insulated by a 30cm or more tick insulation of styrofoam. Removal by machines causes parts of the styrofoam to be destroyed and being blown away. To avoid the waste to be blown away it is recommended to remove the insulation by manual work. After the insulation removal, above the trapezoidal sheets all non-steel materials are deconstructed.

After the insulation of the roof the side walls were dismantled. During the dismantling by excavators with an attached gripper it was tested, whether the sandwich elements can be dismantled without damage. Thus, it was tested, if those elements were usable for reuse.

In fact, the gluing between the metal sheet and the insulation was weathered so much, that the connection was not stable anymore.

For separation the following technique was invented:

- 1) A Single element is laid down the ground.
- 2) The excavator grips one corner and pulls the metal sheet up. While pulling the sheet up the weight of the element is used to separate the metal sheet.

Table 2. List of parts of the SSH and decision of deconstruction vs. demolition.

Part	Description	Demolition	Deconstruction	Comment
Roof insulation	Foil with insulation of styrofoam		(x)	Recycling, disposal
Roof	Trapezoidal sheets	x		Recycling, disposal
Secondary structure	Steel beams, scerwed		x	Recycling off-site
Primary structure	Steel arcs, screwed but spilled into concrete		x	Recycling off-site
Side walls	Sandwich elements	x		Recycling
ground plate	reinforced concrete	x		Deconstruction reuse
Filling	Sand, earth or equal	(x)		

- 3) Two workers remove parts of insulation which adhere on the sheet.
- 4) The separated materials are sorted into metals and general waste.

Figure 8 shows the dismantling by excavator without deforming the sandwich elements. It was determined that separation of the different materials is best function, if the elements are not badly brought up but mostly in shape.

Thus, although in this example the sheets could not be reused, in general a dismantling technique open for reuse is recommended for the sheets. Even if reuse seems not practicable separating the materials will be easier if the elements are not deformed yet.

The main advantage of excavators in opposite to dismantling structures by hand is the better efficiency. Trapezoidal sheets are very light weight compared to the secondary or primary structure. If the sheets are not needed anymore the use of an excavator avoids unnecessary unscrewing of the sheets. In fact, screws will burst if the excavator grabs a sheet. Because the sheets are much thinner than any structure, no parts of the secondary or primary structure are affected. In fact, it seems that the excavator just pulls off the sheets without any resistance.

At this stage, most materials from the object became waste. All metals became part of the recycling process and are put back into the cycle for remelting. All insulation was used for energy recovery – in other words the styrofoam was burned and only used as energy source.

But, at this stage no parts were put back on the market as reusable parts. The reasons, why no parts were suiting the idea of reusing were:

- 1) Thickness of flat parts. Parts to be reused should be able to be handled without to much care. If parts tend to deform the chance is high that a certain percentage does not fit the claim of later reusing. If the parts are sold later for reusing but are not reusable due to deformation, they might be returned. The effort to deconstruct parts with zero deformation would be higher than the costs for generally new parts.
- 2) Especially the cladding on walls and roof are used during the first life for connecting certain building equipment parts to it. That causes changes in original colour, holes from connections and scratches to the sheets. While the bearing structure is mostly as on the first day of usage, the metal sheets look used. Reusing means that the whole SSH never will fit the definition of a new building.
- 3) It remains an open question, who will be responsible for deformations. If the former SSH was sold as one piece of reusable hall, each deformed part can cause claims by the buyer for a additional part which is free of deformation. Unfortunately, the risk is high to be responsible for the costs of those additional parts.
- 4) Even if just dismantled parts are sold, which may fit or not fit the needs for reusing, a price above the price of general scrap metal is only possible, if the percentage of not-deformed parts is at least 90%. To reach such a high percentage of intact parts, the efforts is becoming very high which may result in prices not inline with the market.

Generally, the deconstruction of parts is mainly done by cranes. For the test case it was chosen to use excavators. On the one hand, excavators are the typical machines for demolition and are multifunctional. Excavators can be used not only to lift things up but also with attached tools to remove concrete, to load materials and to separate waste.

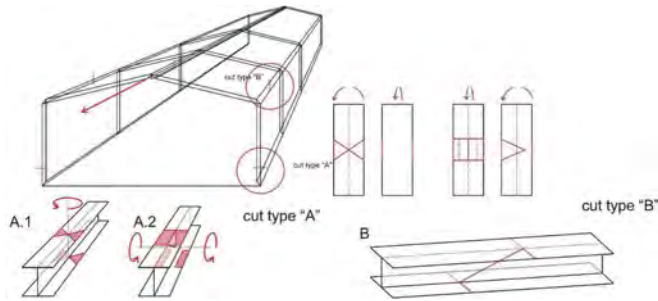


Figure 7. Combined technique to dismantle the primary/secondary structure for demolition.



Figure 8. Removal of roof insulation and sealing; Left picture before removal.

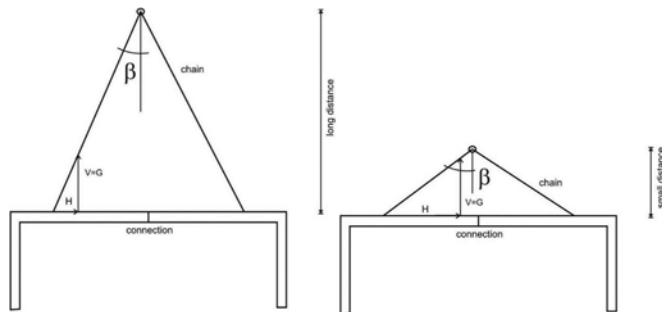


Figure 9. Forces in dependence to the vertical distance of the crane. The smaller the distance becomes, the more horizontal forces arise. It may affect the connections so that other techniques are needed instead of classical up lifting by excavators.

If excavators are planned to be used, they are limited by height. If the object is larger than the height of the excavator, a deconstruction by excavator work will fail. The possible height of excavators already reaches 50m and more. Beside those special machines standard excavators reach ca. 15m in height. That matched most SSH.

Nevertheless, the higher the distance between the structure and the excavator, the little horizontal forces are (see. Figure 9). Especially if the arc is made of connected parts additional forces should be avoided. It was chosen to pull the arcs down by two parallel working excavators.

Figure 10 shows the solution: Lifting the whole arc up by one excavator would affect the connection point in the middle of the arc and is not recommended. Instead, two excavators

were used with grabbers to slightly pull down the arc. On the ground, all connections were released without the danger of collapse of parts of structure.

Before pulling the arc down, it was important to explore the connection of the steel-based arc to the concrete floor. From first explorations it was known that the steel arcs were not having plates on the concrete plate but were shed into the concrete.

Figure 10 shows the solution: Lifting the whole arc up by one excavator would affect the connection point in the middle of the arc and is not recommended. Instead, two excavators were used with grabbers to slightly pull down the arc. On the ground, all connections were released without the danger of collapse of parts of structure.

Before pulling the arc down, it was important to explore the connection of the steel-based arc to the concrete floor. From first explorations it was known that the steel arcs were not having plates on the concrete plate but were shed into the concrete.

Before pulling the arc down, it was important to explore the connection of the steel-based arc to the concrete floor. From first explorations it was known that the steel arcs were not having plates on the concrete plate but were shed into the concrete.



Figure 10. To avoid instabilities, two excavators carefully pull down the structure to the ground.



Figure 11. Removing concrete at jointing of steel arcs.

3.3 Reusable parts

All parts identified for reuse needed to be checked afterwards. In general, all parts suited the quality needed. No parts were deformed. Some screw holes were damaged during flame cutting. Flame cutting was used, if unscrewing was not possible due to rust, mechanical errors, or impaired supply of the threaded rods.



Figure 12. Deconstructed parts of primary structure ready to be reused.

4 CONCLUSIONS

A SSH suitable to become a test case was found in Cologne. The hall was created in the beginning of the year 2000. It was important to test the possibilities to perform deconstruction with the same machines as the regular demolition is done.

The identification of parts which were deconstructed for reuse tried to estimate the risk of damage due to deformation. Thus, the primary and secondary structure was deconstructed while all light-weight parts were recycled only. During the deconstruction and demolition, it was realized, that the sandwich elements were aged so much over 20 years, that the glue failed at the connection of metal sheets and insulation was too bad for reuse. On the other hand, it was experimented, how separation of sheets could be possible on site.

Nevertheless, most waste masses are created by the demolition of concrete parts. The total masses only change little if reuse is applied.

On the other hand, if reuse is prepared with deconstruction techniques performed by excavators, the total costs are only little higher compared to general demolition. The additional time for deconstruction was only 20% higher than for a demolition without deconstructing parts. Thus, to increase the decision to deconstruct parts of modern SSH for later reuse, the later reuse has to be seen as an additional chance with low extra costs. This might help to start deconstruction as an idea performed even without having a special client or buyer. The risk of high costs is little. The chance to increase income of demolition of SSH due to selling reusable parts may justify more experiments.

From the practical view the deconstruction of light-weight parts seems the challenging thing in the future. Besides technical issues it is important to find a solution for the following question:

Who is responsible for parts which are not reusable after deconstruction due to deformation? What percentage of loss is acceptable? At the moment it seems difficult to put a hall on the market with only 75% of cladding. Additionally, sandwich profiles undergo an evolutionary process and may not be the same some years in future as today. That could result in a higher percentage of parts which are needed to be renewed. On the other hand: Deconstruction of light-weight parts is even competing against new parts if about 20% loss is included. Besides the technical problems the reuse of light-weight parts is a legal question of acceptable contract conditions.

The main result is the possibility to perform deconstruction by excavators instead of cranes. Deconstruction for reuse becomes so something, any demolition contractor could do or at least try.

Nevertheless, planning becomes important. A view to temporary situations as well as a higher risk of collapse follows the deconstruction idea.

ACKNOWLEDGEMENTS

The research presented in this paper received funding from European Commission's Research Fund for Coal and Steel project under grant agreement No 747847.

REFERENCES

- Dorsthorst, B.J.H & Kowalczyk, T. 2002: Design for recycling. CIB Publication 272, Paper n.8. In: Proc. of the CIB TG39 Deconstruction Meeting, Design for Deconstruction and Materials Reuse, Karlsruhe, Germany. Rotterdam: CIB.
- Hechler, O. & Larsen, O.P. & Nielsen, S. 2011: Design for deconstruction. In: COST Action C25 "Sustainability of Constructions - Integrated Approach to Life-time Structural Engineering", Volume 2: Summary Report of the Cooperative Activities. Malta. 2011. ISBN 978-99957-816-2-0.
- Kamrath, P. & Hechler, O. 2011b: Eine Einführung in den Stand der Technik bei Abbruch- und Rückbauarbeiten: Konzepte, Möglichkeiten, Potential. In: Der Bauingenieur, Band 86, June 2011, pp. 269–280, Springer Verlag, ISSN 0005-6650.
- SCI: LCA for steel construction.
- World Business Council for Sustainable Development, 2008.

On the development of regulations for the increased reuse of steel structures

H. Bartsch, F. Eyben, J. Voelkel & M. Feldmann

Institute of Steel Construction, RWTH Aachen University, Germany

ABSTRACT: When designing steel components, the industrial cycle is important to consider. At present, iron production in blast furnaces and the recycling of steel scrap predominate. However, there is great potential in the reuse of components instead of recycling. To date, only a small amount of structural steel is reused. Many steel constructions are, e.g. due to serviceability requirements, requirements without making use of the plastic material reserves and the usual over-strengths with large safety margins. Currently, components are recycled despite high quality and good condition, instead of being directly reused. So far, concrete regulations are missing.

This paper presents first approaches for the development of regulations for the increased reuse of steel structures. There are already initial drafts for design standards that address the reuse of structural steel. Research approaches are concerned with defining the suitability of different components for reuse. It needs the development of evaluation criteria, evaluation categories as well as conformity testing of existing components. Possible is the definition of different component quality groups or a designation according to the traffic light system. A special focus should be placed on the safety of reused components. Furthermore, approaches to determine the environmental and economic benefits of reuse help to show the great potential of reusing steel components.

Additionally, components subjected to fatigue loading can be designed efficiently by constructing connections obtaining high fatigue classes, e.g. the machined butt joint. Alternatively, post-treatments methods like mechanical treatments or heat-treatment methods provide important tools to create extremely fatigue strength structural elements.

In the future, structured and consistent recommendations should be made for safe reuse of steel, for which the paper presents proposals.

1 INTRODUCTION

With the “Green Deal”, the European Commission is pursuing the goal of counteracting the existential threats posed by climate change and environmental destruction. Future buildings must be designed and built to be as material-efficient, dismantling-friendly and recycling-friendly as possible, so that the reuse of components and the recycling of building materials can reduce waste, CO₂ emissions and energy requirements. The present paper presents approaches to design guidelines for an efficient reuse of steel structures and components, also including optimised fatigue loaded parts in the future. Therefore, the state of art focussing on the reuse of steel structures or components, as it is addressed in different historical and current standards and product declarations, is presented to give an overview on the existing regulations. A concept for designing a guideline for an economical reuse-procedure is then derived and extended to parts optimised for fatigue loading.

2 STATE OF THE ART REGARDING REUSE OF STEEL COMPONENTS

The reuse of steel structures or at least steel components is addressed in many outdated as well as present standards or guidelines. Nowadays, due to the need for sustainable solutions in the

construction-sector, reusing steel structures is becoming more increasingly important, which is also reflected in the fact that a lot of research is being carried out. Some approaches of outdated and current standards will be presented in the following. A historical approach for using “Old Steel” in Germany is given in the DIN 1050 Blatt 2 (DIN 1050 Blatt 2, 1947) of 1947. Old Steel is defined as steel which is extracted from destroyed components or buildings. It can be steel bars, shaped steel or plates. Due to the standard, old steel can be reused in new components or buildings under predominantly static load, but it has to be marked with a certain label. The marking, as exemplarily shown in Figure 1, contains information on the company, the supervising specialist engineer, who has to ensure the correct extraction and processing of the old steel, as well as the label for the old steel as defined in (DIN 1050 Blatt 2, 1947).

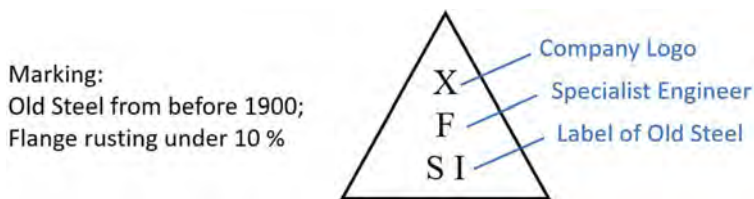


Figure 1. Example Marking for an Old Steel as defined in (DIN 1050 Blatt 2, 1947).

The label is defined referring to the production year of the steel as well as flange rusting. Steels with flange rusting, so reduced thickness due to rusting, smaller than 10 % are category I steels, while steels with a flange rusting between 10 and 25 % are category II. Steels, which were produced before 1900 gets an additional label “S”. Steels with more than 25 % thickness reduction due to flange rusting, are forbidden to be reused. For steels of category I, the allowed stresses according to DIN 1050 can be applied. For steels of category II, the cross-section resistances must be reduced to 80 %.

In current standards, Reuse of steel is for example addressed in the American standard ANSI/AISC 360-16 (ANSI/AISC 360-16, 2016), but more focused on applications outside the structural building. Especially for pipe supports and scaffolding, the usage of old steel is allowed. Annex 5 presents some testing procedures to check the material properties of steel to be reused. Here, mainly destructive testing methods, e.g. tensile tests with defined specimens at the defined spots of an old component, has to be done (ANSI/AISC 360-16, 2016) .

In the current development or revision of standards, the reuse-aspect is often discussed. In the current version of the revision of the prEN 1090-x (prEN 1090-x:2022, 2022) the reuse of steel structures or components is included. Rules for the deconstruction of steel structures as well as testing procedures for the materials are given. It is mainly valid for warm and cold-formed profiles. For connections and welded parts are no regulations defined. The standard is a supplement for the execution of steel structures in EXC1, EXC2 and probably EXC3 (with limits regarding fatigue) acc. to EN 1090-2 (EN 1090-2, 2015) with reused steel. An evaluation scheme, see Figure 2, to check the suitability of a steel/component to be reused is presented in (prEN 1090-x:2022, 2022). In a first step, all accessible information on the construction must be collected. In an early stage of the deconstruction, a visual inspection should be done to identify unsuitable components for reuse due to huge plastic deformations, cross-sectional weakening or corrosion. After that, components which are similar can be divided into groups (prEN 1090-x:2022, 2022). These groups or components are then assorted to one of the four defined evaluation procedures (A, B, C and D) based on the scheme in Figure 2.

The procedures contain regulations on material testing and checking the documentations. For procedure A for example, only non-destructive testing methods are required to validate the original documentations. Then the material properties can be assumed as listed in the documents. For procedure D, additional destructive tests have to be carried out, to determine the material properties, e.g. yield strength, tensile strength or chemical composition (prEN 1090-x:2022, 2022).

In addition to the standards, there are many guideline-documents focussing on reuse. The Steel Construction Centre Switzerland published a guideline-document (Technische

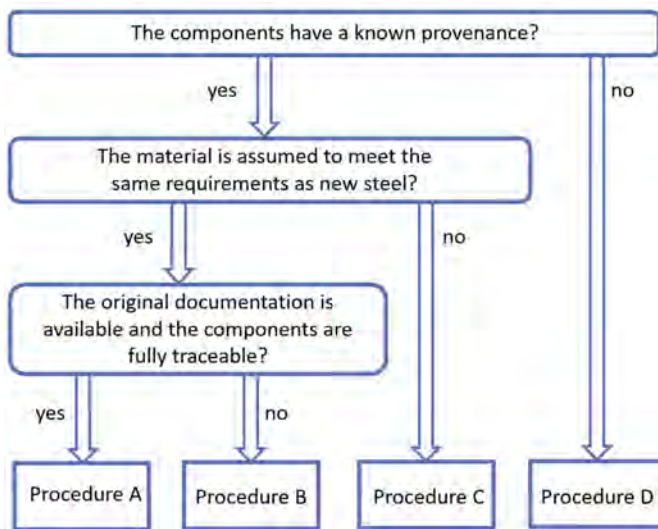


Figure 2. Evaluation scheme to check the suitability of components for reuse acc. to prEN 1090-x (prEN 1090-x:2022, 2022).

Kommission Stahlbau Zentrum Schweiz, 2022) on the reuse of steel components regarding structural analysis, surface protection and quality management. Here, recommendations regarding fatigue-loaded components are given to ensure the suitability for reuse (Technische Kommission Stahlbau Zentrum Schweiz, 2022) .

Product declarations for buying reused steel profiles are developed by the British Constructional Steelwork Association (The British Constructional Steelwork Association Ltd, 2022). Guidelines for the seller and buyer of reused steel, e.g. how to deal with tolerances in geometry or material properties, are given. In detail, also testing procedures, destructive and non-destructive, to determine material properties are listed (The British Constructional Steelwork Association Ltd, 2022).

Additional rules are implemented in (The British Constructional Steelwork Association Ltd, 2022), where sustainable requirements for steel structures are defined. In the field of steel products, there are constant changes, which influences different standards e.g. prEN 17662 prEN 17662, 2021(). In (prEN 17662, 2021), product declarations are increasingly supplemented with sustainable and reusable options. With this development, steel structures or components are seen within the whole live cycle and different scenarios of reuse in different stages of the live cycle are defined (prEN 17662, 2021).

Nowadays, reuse of steel, steel structures or components is also increasingly being investigated and promoted in the field of research. For example, as part of the railway project “i2030 – More rail for Berlin and Brandenburg”, a method was developed, to ensure the quality and steel grade of old steels from a disused existing bridge using non-destructive tests, see Figure 3 (IWT-AG, 2022).

The bridge is part of the Siemensbahn, was finished 1929 and closed down in the 80s. The bridge is under monument protection and should now be reused. In the project, the chemical composition was determined with an optical emission spectrometer (OES), which enables one to analyse many measuring points. The chemical composition was used to infer the steel grade of the different components (IWT-AG, 2022).

In the process of the revision of ONR 24008 (ONR 24008, 2014), an Austrian standard for assessing the load-bearing capacity of existing railway and road bridges, static and cyclic tests were carried out on riveted components from old bridges as part of a research project (Taras & Greiner, 2008). The static tests made it possible to determine the resilience of the riveted joint and the existing clamping forces. This allowed to compare the crack propagation in the fatigue tests with fracture mechanics models (Taras & Greiner, 2008).



Figure 3. Preparation and measurement of optical emission spectrometer to determine the steel grade (IWT-AG, 2022), © IWT-Solutions AG 2022, www.iwt-ag.de.

Furthermore, the reuse and further use of building components was investigated within the framework of a research project at the University of Applied Sciences in Constance; a building material lexicon with the evaluation of the reusability of various building materials was developed on the basis of a pilot project (John & Stark, 2021)

These partly very old regulations as well as the present approaches to reuse steel components must be bundled in a targeted manner to define innovative and practicable rules. Furthermore, the reuse of whole structures (e.g. entire hall frames or crane runway girders) including connection areas or cross-section changes are not addressed in detail in the current state of art. Also, the reuse of fatigue loaded components or to reuse the component for a fatigue loaded reuse-case, is not considered well.

3 PROPOSAL FOR A DEVELOPMENT OF GUIDELINES ON THE REUSE OF STEEL COMPONENTS

Against the background of the problematic situation described above with regard to the high CO₂ emissions in the steel construction industry and the major economic and ecological advantages of the reuse of steel components, the preparation of a recommendation for guideline on reuse, also consolidating the different approaches as shown in chapter 2, represents the first important step.

Since broad-based reuse in Germany is a new concept, the current possibilities for reusing steel products must first be analysed in detail. It must be clarified which products are already reused in which processes and how the potential for future reuse can be derived from this. Also, the current market of steel products and the adaptability of it has to be considered, whereby also the supply chain, with a view to the demolition sector and the current treatment of steel scrap in Germany, should be taken into account. The ecological benefits and economic potential should be displayed. In addition, the legal framework must be investigated to identify the possibilities and current limits of reuse. The determination whether and, if so, which legal obstacles must be overcome in the future is also related to this.

To determine the suitability of components for potential reuse, a subdivision of steel structures into typical component groups, e.g. according to the traffic light scale, can represent a simple designation system. In order to evaluate steel products already in use and to categorize them for reuse, a standardized concept must be developed. For this purpose, it is necessary to know the essential aspects that have a decisive influence on the reusability of components and that must be given special consideration. The history of the component and its documentation (production, coating, loading, etc.) as well as the results of possible material tests

(strength, ductility, toughness, chemistry) and the condition of the component are relevant. Based on this, it is possible to work out how the components can be classified on the basis of evaluation criteria for reuse.

The components should be assigned to different classes according to their suitability. The classes are graded from components that can be used adequately for new products to components that are no longer suitable as a construction product. The evaluation criteria can be divided into:

- A. Criteria on initially available information about a component (e.g. function) and
- B. Criteria for the evaluation of results from additionally required tests (e.g. characteristic yield strength).

Especially if no or little initial information is available, additional testing procedures are indispensable. For this purpose, test methods as well as specifications for sampling must be developed to determine the actual properties of the dismantled components. In addition to destructive testing, non-destructive testing methods are also particularly useful.

Optical laser measurement methods, such as handheld 3D scanners, cf. Figure 4, can be considered for recording the real geometry including imperfections. Further, e.g. hardness tests could be used to estimate the actual yield strength of the material. Such a testing concept requires detailed validation by means of a detailed test program.



Figure 4. Measurement of steel components using laser technology.

Provided that components can be classified; however, no statement can be made about the corresponding safety levels. To overcome this, a statistical evaluation must be developed in accordance with the semi-probabilistic safety concept according to DIN EN 1990 (EN 1990, 2020) and safety analysis in determining the actual prevailing properties of a component. Here, statistical distributions of the measured values from the previously defined test methods must be critically analysed and transferred to the safety concept of the Eurocode. The component resistances of reused components are subject to greater uncertainty with respect to geometry and material, so that the derivation of a partial safety factor, especially for reused components, must be realized.

After that, safe classifications for the reuse of steel components can be worked out. The classification should be based on the known information and additional test results. Here, components can also be classified individually area by area (i.e. areas with constant cross-sections or areas between discontinuities/defects). The overall class could, for example, be made analogous to the cross-section classification according to EN 1993-1-1 (EN 1993-1-1, 2005), considering the subclasses of the individual areas. Furthermore, the quality (also of areas) could be increased, e.g. on the basis of specifications for the post-treatment of individual areas or entire components, and thus an overall better class for reuse could be achieved. In order to verify the entire evaluation procedure, verification on the basis of different exemplary old building components is essential.

Finally, a guideline for the safe and efficient dismantling, testing and reinstallation of previously installed steel components and entire steel structures would be desirable. This guideline should represent a uniform procedure for the practical implementation of reuse on the basis of the normative specifications and further regulations to be developed. In this context, care should be taken to ensure that the instructions are as simple, clear and efficient as possible, e.g. in the form of tables or flow charts. In order to make reuse future-proof, design recommendations for the new construction of structures that are to be suitable for dismantling and reuse are also advisable.

These regulations should relate in particular to the steel materials to be used, the special design requirements and the structural design of the connections and connection details.

4 PROPOSAL FOR DESIGN OF FATIGUE-OPTIMISED STRUCTURAL DETAILS

When it comes to the reuse of steel components, fatigue-stressed structures are usually excluded from the outset. This is because for fatigue strength, the previous stress ranges on the component play a major role in its future service life – which in most cases are not precisely known. However, if we want to focus our approach to component design in the future more on long-term benefits, the reuse of fatigue-stressed structures is an option.

Since fatigue cracks initiate at notches the detailing of a steel connection is crucial for a long lifetime. The following three-level approach is suggested to design fatigue optimised details:

1. In order to be able to provide multi-variant recommendations for different structural details of a structure, a critical survey of the known fatigue standards is a necessary prerequisite to be carried out. Fatigue detail catalogues found in European and international standards (e.g. (EN 1993-1-9, 2010; Hobbacher, 2016) as well as regulations, e.g. in crane construction (EN 13001-3-1, 2019) list structural details in fatigue classes (FATs) depending on their execution. Here, design and execution options with particularly high FATs can be considered for various constructions. For the future, an adaptation of valid guidelines in the area of steel construction should be considered in this context as a first step.
2. At the Institute of Steel Construction, a detailed fatigue database has been developed together with the Karlsruhe Institute of Technology and the University of Stuttgart, in which more than 20.000 individual test results for various details of EN 1993-1-9 are documented (Bartsch, et al., 2020). This database (in 2024 to be published by the Deutscher Ausschuss für Stahlbau DASt e.V. online) has already proven to be a very valuable tool for deriving better detail categories and calculating more accurate fatigue strengths based on well-documented test results, see (Bartsch, et al., 2020; Bartsch, et al., 2021; Bartsch & Feldmann, 2021). Using the information of the data base, particularly favourable fatigue designs and executions that have achieved good results in the documented tests could be identified. This includes also post-treatment methods which lead to higher fatigue resistances and longer lifetimes for a possibly reused component, e.g. by grinding or remelting of the weld toe by TIG, peening, high frequency mechanical impact (HFMI), stress relieving, cf. (Drebenstedt, et al., 2021)
3. Finally, for very specific problems, finite element-based (FEM) numerical simulation techniques are also a useful tool, that allow assessment of stress concentrations resulting from different designs of typical details. Based on local fatigue concepts, the most favourable detailing of a structural part can be worked out.
4. For fatigue stressed-components to be reused, a specific prescription of the documentation of any information on applied stress ranges in terms of an accurate stress history and number of cycles is the basic requirement. Especially for components that are constantly exposed to the same repetitive stress ranges, e.g. certain crane runway girders, an exact documentation of the loads can be easily achieved.

5 CONCLUSIONS

To conclude, this paper presents first approaches for the development of guidelines to reuse steel structures and components. It was shown that the reuse of steel components was already used after the Second World War to counteract the shortage of materials, but due to economic growth did not become common afterwards. Nevertheless, several standards and guidelines have been developed since then to regulate or facilitate the reuse of steel components. Those different regulations in historical and present standards as well as ongoing and completed research projects were summarised and transferred to design recommendations for an approach to develop a guideline. The aim was to make the reuse of steel components as efficient, workable and user-friendly as possible. In a first step the suitability of a component for reuse must be checked by analysing the available information and the condition of the component itself. Depending on the results predefined additional tests must be carried out before a component can be classified. The extent to which a steel component can be reused depends on the class in which it is classified. To develop the classes for reuse, safety investigations acc. to the semi-probabilistic safety concept according to DIN EN 1990 (EN 1990, 2020) has to be made for all classification tools (e.g. 3D-scan, tensile tests etc.). The classification then can be done area by area for individual components resulting in an overall classification for the component with regards to the lowest classified area. The quality can be increased, e.g. on the basis of specifications for the post-treatment of individual areas or entire components. In addition to that, an approach to implement fatigue-loaded components in the reuse concept was presented. Fatigue detail catalogues and data bases should be used to seek out details with high FATs or favourable fatigue design and execution. Thus, numerical methods could be used to optimize typical details. Nevertheless, reuse of steel components with a history of fatigue loading is only possible if the stress ranges and load-cycles during service life are well documented.

In this paper it is shown that there already are standards, guidelines and research dealing with the reuse of steel. However, there is still a lack of guidance regards proper reuse on a daily basis. To exploit the economic and ecological potential of steel reuse a key factor will be a handy guideline making reuse easy to apply for those companies operating in the steel industry. Developing such a guideline still some research is needed specially to make the future investigation and classification of components as simple, clear and efficient as possible.

REFERENCES

- ANSI/AISC 360-16, 2016. *Specification for Structural Steel Buildings*. s.l.: s.n.
- Bartsch, H., Citarelli, S. & Feldmann, M., 2021. Investigations on the fatigue behaviour of welded-in stiffeners with gaps. *Journal of Constructional Steel Research*, p. 107075.
- Bartsch, H. et al., 2020. Analysis of fatigue test data to reassess detail categories of EN 1993-1-9. *Steel Construction*, 13(4), pp. 280–293.
- Bartsch, H. & Feldmann, M., 2021. Numerical and data-based investigations on the fatigue resistance of load-carrying cruciform joints with gaps. *Journal of Constructional Steel Research*, Volume 185, p. 106843.
- Bartsch, H., Hoffmeister, B. & Feldmann, M., 2020. Fatigue analysis of welds and bolts in end plate connections of I-girders. *International Journal of Fatigue*, Volume 138, p. 105674.
- DIN 1050 Blatt 2, 1947. "Alistahl im Hochbau - Richtlinien für Aufarbeitung und Verwendung". s.l.:s.n.
- Drebenstedt, K. et al., 2021. Neubewertung des Kerbfallkatalogs nach DIN EN 1993-1-9. In: *Stahlbau Kalender 2021*. Ernst & Sohn: s.n., p. Kapitel 6.
- EN 1090-2, 2015. "Execution of steel structures and aluminium structures - Part 2: Technical requirements for steel structures". s.l.:s.n.
- EN 13001-3-1, 2019. *Cranes – General design – Part 3-1: Limit states and proof competence of steel structure*, s.l.: s.n.
- EN 1990, 2020. *Basis of structural design*. s.l.:s.n.
- EN 1993-1-1, 2005. *Design of steel structures – Part 1-1: General rules and rules for buildings; EN 1993-1-1*. s.l.:s.n.
- EN 1993-1-9, 2010. *Design of steel structures – Part 1-9: Fatigue*. s.l.:s.n.

- Hobbacher, A. F., 2016. *Recommendations for Fatigue Design of Welded Joints and Components - Second Edition - IIW document IIW-2259-15 ex XIII-2460-13/XV-1440-13*, s.l.: International Institute of Welding.
- IWT-AG, 2022. *Projekthomepage i2030*. [Online] Available at: <https://www.i2030.de/> [Accessed 15 08 2022].
- John, V. & Stark, T., 2021. *Wieder- und Weiterverwendung von Baukomponenten (RE-USE)*, s.l.: BBSR-Online-Publikation.
- ONR 24008, 2014. *Evaluation of load capacity of existing railway and highway bridges*, s.l.: s.n.
- prEN 1090-x:2022, 2022. "Execution of steel structures and aluminium structures - Steel structures - Part X: Reuse of structural steel". s.l.: s.n.
- prEN 17662, 2021. *Execution of steel structures and aluminium structures - Environmental Product Declarations - Product category rules complementary to EN 15804 for steel, iron and aluminium products for use in construction works*, s.l.: s.n.
- Taras, A. & Greiner, R., 2008. *Versuche an genieteten Brückenlängsträgern - Statisches Verhalten, Ermüdungsfestigkeit und Rissausbreitung. Stahlbau 77*.
- Technische Kommission Stahlbau Zentrum Schweiz, 2022. *Re-Use: Wiederverwendung von Stahlbauteilen*, s.l.: s.n.
- The British Constructional Steelwork Association Ltd, n.d. *Model specification for the purchase of reclaimed steel sections*, s.l.: s.n.
- The British Constructional Steelwork Association Ltd, n.d. *National Structural Steelwork Specification for Building Construction - Annex J - Sustainability Specification*, s.l.: s.n.

RFID-based traceability system for constructional steel reuse

P. Hradil & K. Jaakkola

VTT Technical Research Centre of Finland Ltd., Espoo, Finland

K. Tuominen

Purkupiha Group Oy, Lahti, Finland

ABSTRACT: This paper introduces a traceability system based on radio-frequency identification tags attached to the steel building components to provide a link to the cloud-based electronic material passport and 3D information model obtained by aerial scanning of the building before deconstruction. With such traceability system, the complete and accurate information about the building components, their quality and history can be readily available before the deconstruction of the building. This will allow more efficient reuse and better decision-making in deconstruction planning phase. For instance, it would be also possible to check actual demand for the particular component or the whole assembly. The technology was demonstrated on a real deconstruction and reuse of industrial steel hall in Tampere, Finland.

1 INTRODUCTION

Deconstruction of assembled steelwork is generally a straightforward task. However, facility owners and contractors are facing many challenges when trying to streamline the process into the successful reuse project when the recovered components are assembled again in a different place or configuration. It is important to understand the whole deconstruction process and its difference from the ordinary demolition already in the preliminary planning, allocation of time and resources, tendering and local approval procedures.

One of the barriers for successful reuse is lack of reliable and accurate information about the steel components, their age, material quality, coating or modifications made during their previous life. This paper introduces a traceability system based on radio-frequency identification (RFID) tags attached to the steel components to provide a link to the cloud-based electronic material passport and 3D information model obtained by aerial scanning of the building before deconstruction. VTT and Purkupiha are partners in Horizon 2020 project ICEBERG coordinated by Tecnalia, in which such technology has been demonstrated on a real deconstruction and reuse of industrial steel hall in Tampere, Finland.

Building information modelling is rather new in demolition and deconstruction business, but a lot of experience already exists in building design, construction and renovation works. The challenge related to the RFID technology is the selection of proper transponders that are cost-efficient but readable when attached to the steel surface, and can survive harsh treatment during deconstruction, storage, transport and repeated assembly. Contractors or facility owners can nowadays offer deconstructed building components for sale on various trading portals, but the information about their material and dimensions is typically produced after deconstruction. With our new traceability system, the information can be ready before deconstruction allowing more efficient reuse and better decision-making in deconstruction planning phase.

1.1 *Constructional steel reuse*

The reuse of building components is one of the international strategic spearheads in developing the circular economy in the construction sector. The need for more efficient building materials recovery is becoming more important for the contractors in building industry who will have to change their operations from the traditional demolition process to more difficult deconstruction in order to retain the value of the building elements. It is clear that among the existing buildings, only those connected by reversible connections (e.g. bolted) are ready to be disassembled and reused without large effort and damaging of the fabricated elements. Therefore, most of the constructional steel frames can be disassembled and we can see many good examples of their successful reuse, relocation, in-situ adaptive reuse, or further separation into reusable constituent products (Ungureanu et al. 2020). Constructional steel reuse is in many cases economically feasible solution (Kuhnhenne et al. 2018, Vares et al. 2019) and has very low environmental footprint (Ungureanu et al. 2019). We believe that the innovations in the reuse of constructional steel components can be directly projected into the reuse of other materials such as prefabricated concrete construction and engineered wood assemblies.

2 CONSTRUCTION PRODUCTS TRACEABILITY

2.1 *Digital Product Passport and Digital Building Logbook*

The proposal for new European Ecodesign for Sustainable Products Regulation (EU 2022b) strongly emphasizes digitalization of the products information and introduces ‘Digital Product Passport’ to electronically register, process and share product-related information amongst supply chain actors, authorities and end-users. Digital Product Passport means a set of data specific to a product and that is accessible via electronic means through a linear bar code symbol, a two-dimensional symbol or other automatic identification data capture medium (data carrier) that can be read by a device. Examples of the requirements for product-specific data defined in the regulation and its annexes are presented in Table 1.

Table 1. Digital Product Passport (EU 2022b), the most relevant data fields.

Data category	Examples of data fields
Administrative information	unique product identifier, data carrier, passport level, accessibility
Substances of concern	names, locations, concentrations, instructions for safe removal
Product performance	durability and reliability of the product or its components, ease of repair, maintenance, upgrading, re-use, remanufacturing, refurbishment and recycling, weight and volume, environmental or carbon footprint of the product, microplastic release, generated waste
Instructions and guidance	installation, maintenance, repair, disassembly, return and disposal Information for consumers, end-users and treatment facilities
Other relevant information	information under other Union law and so on

The proposal for new European Construction Products Regulation (EU 2022a) empowers the European Commission to establish Union construction products database or system that builds on the Digital Product Passport introduced by the proposed Regulation on ecodesign for sustainable products (EU 2022b). It also establishes the need for ‘Digital Building Logbook’. The logbook is specifically required in Article 12 of the Construction Products Regulation about used, remanufactured and surplus products, and therefore relevant for the reuse of construction products. The Construction Products Regulation refers for more details about the information requirements for the Digital Building Logbook to the EASME report (Volt & Toth 2020). Table 2 shows the outcome of the research conducted in their study in the form of the most relevant data categories and fields. Some of the information under ‘Product performance’ category can be readily available by the relevant certificates, such as Declaration of

Performance or Environmental Product Declaration. Therefore, it is important to standardize open data format for such declarations compatible with the other linked data such as various 3D information models.

Table 2. Digital Building Logbook (Volt & Toth 2020), the most relevant data fields.

Data category	Examples of data fields
Administrative information	unique building identifier, ownership, tenancy, maintenance, utilities, insurance and licenses
General information	year built, district heating access, solar potential, soil/terrain, climate, accessibility, safety manual
Building description/ characteristics	BIM, design documentation, technical systems and utilities, expected lifetime, fire evacuation plan, surroundings, historical context
Building operation and use	number of occupants, functions, energy/water consumption and production, behavioral insights
Building performance	EPC rating, envelope, total calculated energy consumption, renovation recommendations, climate resilience potential
Building material inventory	types, locations, volumes/weights, embodied carbon, life span, fire resistance classes, waste categories, chemical declarations, certificates, Global Trade Item Numbers
Smart readiness	SRI result, smart district potential, demand/response potential, charging infrastructure for e-mobility
Finance	Property value, tax, rent, maintenance cost, yield, valuation, other costs

It can be seen that most of the Digital Product Passport data fields from Table 1 may be allocated to the relevant category in the Digital Building Logbook in Table 2. Ideally, the former should be a subset of the latter.

2.2 ICEBERG solution

The goal of materials and products traceability system developed in the EU project ICEBERG is to collect and communicate all the relevant information to ensure better recovery, recycling and reuse of end-of-life building materials. The development, testing and implementation of the digital cloud platform and its relevant databases is still on-going, but the preliminary data fields relevant to reusable building components have been identified in its deliverable D1.4 “Functional Identification and Authentication Toolkit” (see Table 3).

Table 3. Data fields recommended for implementation in EU ICEBERG project.

Data category	Examples of data fields
Administrative information	unique product identifier, product type, etc.
Product operation and use	dates and geolocations of demolition, sorting, storage, transport, use within the current building
Product description/ characteristics	real properties observed or measured during inspections/testing such as range of sizes, lengths and thicknesses, total volume or mass, surface coating, impregnation or another treatment, classification (quality, decay rating, strength grading . . .), observed damage
Nominal properties and certification	Declaration of Performance, Environmental Product Declaration and other characteristics declared by the manufacturer/dealer
Other relevant information	photos

The information recommended for product reuse in Table 3 is partly overlapping with the requirements of Digital Product Passport (Table 1) and partly with the recommended information in the Digital Building Logbook (Table 2), but contains some additional data fields and categories. Therefore, more effort will be done in the development of the final version of the traceability platform to harmonize its data fields with the new European regulations.

3 RFID TECHNOLOGY FOR CONSTRUCTION PRODUCTS

3.1 Selection of RFID technology

Over the past years, NFC (Near Field Communication) reader has become a standard component of a modern smart phone, which has increased the popularity of the technology in general. However, the very limited read range of NFC, just a few centimeters at its practical maximum, is not enough considering the special requirements of the construction application (NFC Forum 2022). Fast readability of the tags in construction components while in place as well as when stored or transported requires a longer read range. Therefore, UHF RFID operating at 868 MHz, nowadays also commonly referred to as RAIN RFID, was selected as the RFID technology for this application (RAIN RFID alliance 2022). The maximum read range of several meters enables automated and fast reading of tagged items as well as reading of several, often also hidden tags at a time from one spot. In many cases, the exact position of the tag is not even known. Thanks to the passive, batteryless technology, the tags are practically ageless and due to their simplicity, still low-cost (Finkenzeller 2004). This enables individual tagging of even small construction parts and their life-cycle long traceability. The data structure and wireless interface of the selected system is based on EPC Gen2 and ISO 18 000 - 6C standards (EPCglobal 2013).

3.2 RFID components

The practical performance of a passive UHF RFID system depends a lot on the selection of the tag. There is a lot of misconception regarding the performance of UHF RFID systems, which is often based on using wrong types of tags that are not suitable for the intended use environment. The main categories of UHF RFID tags used here are label-type single-layer tags for dielectric objects and hard on-metal tags. Even within these main categories, it is important to find the right types according to the aimed read range, the physical limitations of the object, cost and e.g. durability aspects. As the tags are selected from the range of commercially available products, they are always somewhat of a compromise, but by proper selection, good performance can be achieved (Finkenzeller 2004, Nikitin & Rao 2006, Mercer et al. 2011).



Figure 1. UHF RFID Tags used for construction elements. SmarTrac Belt label tag (left) for wooden elements and Confidex Ironside (right) for large metallic parts.

For tagging the construction parts to be reused, three tag types were selected: SmarTrac Belt as a label for dielectric parts such as wooden beams (Avery Dennison 2021), Confidex Ironside for large metal objects (Confidex 2015) and Confidex Ironside Micro (Confidex 2021) for smaller or thinner metal parts. Figure 1 (left) shows Belt tag on a wooden beam, secured with two staples. Figure 1 (right) presents Ironside secured on a roof panel with

a cable tie. Figure 2 shows the assembly of Ironside Micro tag with a self-drilling screw and two tags assembled on door rails. Before assembly, the read range of the selected tags was verified by Tagformance Pro RFID measurement system (Voyantic 2022). Based on the measurements, Belt provides read range of 6 meters on wood, Ironside 6 meters on metal and Ironside Micro 4 meters on metal. Read range of Belt depends on the moisture of the tagged wood and that of the on-metal tags depends on the size of the metallic object, so the results are indicative. However, they confirm that the read ranges are adequate for remote and automatic reading of tags in the construction environment. The unit cost of the used transponders in large quantities is 0.08 € for Belt, 3 € for Ironside and 2 € for Ironside Micro.



Figure 2. Confidex Ironside Micro UHF RFID tag for small and thin metal objects and its assembly with a self-drilling screw (left and middle) and Nordic ID HH85 handheld UHF RFID reader (right).

The main RFID reader of the demonstrations is a handheld device, namely Nordic ID HH85 shown in Figure 2 right (Nordic ID 2022). The reader provides the maximum allowed power of 2 ERP for the both orthogonal polarizations, which enables the maximum read range of the tags also in the construction environment.

Of the coding schemes available within EPC Gen2 standard, SGTIN-96 was selected as a simple and efficient data format (EPCglobal 2013). In the demonstrator, the tags were preprogrammed using a data structure shown in Figure 3. The individual running number of the tag and its respective item was then associated with BIM. Another method of associating the data is to program the tags during the tagging process. However, operation range of programming is shorter than that of reading and the challenge of differentiating tags is greater due to the risk of unwanted programming, so preprogramming tags before installation is the preferable concept.

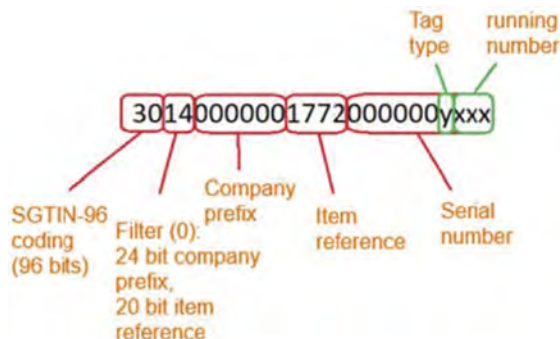


Figure 3. Data format used in the tags attached to the construction elements.

4 DECONSTRUCTION AND REUSE OF STEEL HALL IN TAMPERE, FINLAND

Purkupiha demolished 15 industrial properties on one jobsite during the year 2022 in Lamminpää Tampere. The demolition job was part of the area development actions. Buildings were demolished due to the area being transformed to accommodate residential blocks, commercial buildings and office buildings. Four buildings in the area were deconstructed, and the rest were demolished by using traditional methods. One of the deconstruction projects was an example of a case where the demolition contractor incorporates circular economy into the demolition job without the client's separate request. Purkupiha disassembled the steel hall and transported the reusable components to a new user (see Figure 4).



Figure 4. Manual deconstruction of the roof cladding (left) and the aerial view of the deconstruction site (right).

A 3D model of this building was generated for the purposes of deconstruction and reuse (see Figure 5). Tools and processes for creating an electronic material pass for buildings and building components were developed in the project ICEBERG. The goal of this study was the development of working methods for reuse, removal of suitable products from the structure in high quality, evaluation and traceability of building parts and development of documentation using digital information modeling to support planning of deconstruction and new installation of those parts. In the tests carried out in the project, the validity of the products and solutions was demonstrated in practice.



Figure 5. 3D scanning (left) and creating of building information model (right) of the steel hall.

Data collection and documentation of demolished buildings with the help of data modeling is completely new in Finland. It was shown in practice how digitization may promote reuse of construction parts and 3D data modeling is fully scalable in terms of technology. In this project its applicability and the added value was tested at the real demolition site. Purkupiha collaborated in this study with VTT Technical Research Centre of Finland Ltd. and Spanish Tecnalia, Research and technological development center. Additional information was produced for the design of new buildings and to the traceability of the original construction parts: RFID tags are linked to the cloud database and scanned to the data model directly from the site using a cloud service.

5 SUMMARY AND CONCLUSIONS

One of the largest barriers to reuse of building products is the lack of reliable information at its end of life and the complicated chain of contractors, material dealers and owners in the process. This results in expensive, and often repeated, testing and measurements of the material and product performance. Development of the digital traceability system will greatly improve this situation and has a potential to reduce costs and time needed for successful reuse project. Moreover, it may also improve the confidence of the potential buyers in the quality and performance of the second hand products. Many architects are afraid to use used parts because they don't know what condition they are in and where they have been used. In the future, they will have this data available in the cloud service. With the help of the database, designers can use a lot of accurate information they didn't have before. This will take reuse to a whole new level. RFID technology is promising solution because it is cheap, durable and reliable and the tags do not need dedicated power supply.

ACKNOWLEDGEMENTS

The research presented in this paper was supported by the EU project ICEBERG. This project has received funding from the European Union's Horizon 2020 research and innovation programme under grant agreement No 869336.

REFERENCES

- Avery Dennison 2021. *Smartrac Product Datasheet, Belt-UCODE-G2iL/03/21/DS*, Miamisburg: Avery Dennison. <<https://rfid.averydennison.com/content/dam/rfid/en/products/rfid-products/data-sheets/datasheet-Belt-UCODE-G2iL.pdf>>
- Confidex 2015. *Confidex Ironside™ Product Datasheet*, Confidex Ltd. <https://www.confidex.com/wp-content/uploads/Ironside_Datasheet.pdf>
- Confidex 2021. *Confidex Ironside Micro™ Product Datasheet*, Confidex Ltd. <https://www.shenghero.co.jp/product/confidex/Ironside_Micro_Datasheet.pdf>
- EU 2022a. *Proposal for a Regulation laying down harmonised conditions for the marketing of construction products, amending Regulation (EU) 2019/1020 and repealing Regulation (EU) 305/2011*, Brussels: European Union.
- EU 2022b. *Proposal for a Regulation of the European Parliament and of the Council establishing a framework for setting ecodesign requirements for sustainable products and repealing Directive 2009/125/EC*, Brussels: European Union.
- EPCglobal 2013. *EPC™ Radio-Frequency Identity Protocols, Generation-2 UHF RFID: Specification for RFID Air Interface Protocol for Communications at 860 MHz – 960 MHz, Version 2.0.0 Ratified*, EPCglobal Inc. <https://www.gs1.org/sites/default/files/docs/epc/uhf1g2_2_0_0_standard_20131101.pdf>
- Finkenzeller, K. 2004. *RFID Handbook: Fundamentals and Applications in Contactless Smart Cards and Identification*, 2nd ed., New York, NY, USA: Wiley.
- Kuhnhenne, M., Pyschny, D., Hradil, P., Sansom, M., Kesti, J., Dubina, D. & Ungureanu, V. 2018. *Report on the reuse potential of single-storey steel buildings*, Deliverable D1.2 of PROGRESS project, Aachen: RWTH.

- Mercer, A.J., James, R.K., Bennett, G., Patel, P., Johnston, C. & Cai, J. 2011. Performance testing of RFID systems with RF-harsh materials, In *Proc. 2011 IEEE International Conference on RFID-Technologies and Applications*, pp. 537–543.
- NFC Forum 2022. *NFC Forum website*, accessed 8.12.2022. <<https://nfc-forum.org/>>
- Nordic ID 2022. *Nordic ID HH85 datasheet v1.1*, Salo: Nordic ID Group. <https://www.nordicid.com/wp-content/uploads/Nordic_ID_HH85-_datasheet_1v1.pdf>
- Nikitin, P.V. & Rao, K.V.S. 2006. Performance limitations of passive UHF RFID systems, In *Proc. 2006 IEEE Antennas and Propagation Society International Symposium*, pp. 1011–1014.
- RAIN RFID alliance 2022. *RAIN RFID alliance website*, accessed 8.12.2022. <<https://rainrfid.org/>>
- Ungureanu, V., Greca, D., Hradil, P., Vares, S., Sansom, M., Pyschny, D. 2019. *Report on the methodology to declare environmental benefits of reused elements*, Deliverable D5.1 of PROGRESS project, Timișoara: Universitatea Politehnica Timișoara.
- Ungureanu, V., Fechete, H. & Dubina, D. 2020. *Factsheets on review of existing deconstruction cases*, Deliverable D1.1 of PROGRESS project, Timișoara: Universitatea Politehnica Timișoara.
- Vares, S., Hradil, P., Sansom, M., Ungureanu, V., Kamrath, P. 2019. *Economic assessment of reusing steel-based elements*, Deliverable D5.2 of PROGRESS project, Espoo: VTT Technical Research Centre of Finland, 2019.
- Volt, J., Toth, Z. 2020. *Definition of the Digital Building Logbook: Report 1 of the Study on the Development of a European Union Framework for Buildings' Digital Logbook*, Brussels: Executive Agency for Small and Medium-sized Enterprises.
- Voyantic 2022. *Tagformance Pro catalogue*, accessed 8.12.2022. <<https://voyantic.com/lab/tagformance-pro/>>.

Environmental and economic impact of steel industrial buildings made of reclaimed elements

R. Buzatu

Politehnica University of Timisoara, Timisoara, Romania

V. Ungureanu

Politehnica University of Timisoara, Timisoara, Romania

Romanian Academy, Timisoara Branch, Timisoara, Romania

P. Hradil

VTT Technical Research Centre of Finland, Espoo, Finland

ABSTRACT: The paper presents a comparative environmental and economic analysis of several steel structures, starting from an optimal design case considering a new steel structure made with new materials, along with further design possibilities of the same steel building made using reclaimed elements. The analysis is based on a single-storey industrial hall, quantifying the savings achievable by reusing construction materials in a comparative life cycle assessment and life cycle cost assessment. The paper shows the environmental benefits together with the structural feasibility of a strategy based on the reuse approach in construction. The results show that the greatest gain is achieved in the production stage when the reuse approach is adopted rather than recycling. A 29-35% reduction in emissions is observed when the structure is built with reused steel, while the potential financial benefits are greater.

1 INTRODUCTION

Waste management policies in the EU aim to reduce waste generation and increase resource efficiency by using the potential of resources derived from waste to the utmost, reducing in this way the environmental impact of waste. The Waste Framework Directive 98/2008/EC (Directive 2008/98/EC of The European Parliament) promotes a waste conduct where prevention is first preferred, followed by reuse and recycling, having disposal as the last alternative. As construction and demolition waste (CDW) generates more than a third of all waste produced in the EU (Eurostat 2022), it has become a priority waste stream, challenging the sector for a higher amount of recycling, reusing, or other types of material recovery from CDW. A greater amount of CDW-recovered materials will not only promise a resource-efficient and competitive economy, but will also reduce high greenhouse gas (GHGs) emissions from the building sector.

There were several successful reuse projects in Europe (Coelho et al. 2020) demonstrating that structural steel reuse is possible and represents a viable solution in the construction sector, producing considerable benefits in terms of carbon emissions savings, time savings, or cost savings. Building with reclaimed elements requires additional engaging in deconstruction, reconditioning (e.g. sandblasting, coating steel elements) and transport, which may bring burdens in environmental impact but, at the same time, avoids the loads of the impact caused by the production of new structural elements which demand material sourcing and energy-intensive fabrication processes (Brütting et al. 2020).

The purpose of the analysis carried out in this work is to compare the environmental and economic impact of industrial steel structures (using indicators such as climate change in terms of GHG emissions, resource use, eutrophication and cost indicators). The assessment includes single-storey steel structures made of completely new materials, as well as structures made of reused elements for the entire structure, for components (elements of the primary structure), or just for some individual members of the structure. The study is based on a life cycle assessment (LCA) and a life cycle cost (LCC) of a single-storey industrial hall erected in Romania and for the cases where reclaimed steel elements were considered, it involved relocation from Germany to Romania.

2 ASSESSMENT SCENARIOS

Five scenarios were selected for the assessment.

Case 0: the study is built on a single-storey industrial hall located in Romania that has a total length of 30 m, with six identical frames at a spacing of 5 m. The span is 17.5 m and the height at the eaves is 6 m. The load bearing structure is made of hot-rolled steel sections (columns - HEA320, beams - IPE300, S355) and the envelope involves steel sandwich panels with mineral wool insulation (120 mm sandwich panels for the roof and 80 mm sandwich panels for the walls). All elements of the structure were designed as elements made from new materials. The total weight of steel consumption was 23682.8 kg + 2550.4 kg (hot-rolled steel profiles + cold-formed purlins).

Case 1: The structure originated in Germany and had (initial dimensions) a span of 17.5 m, a length of 35 m (7 bays of 5 m each), and a height of 6 m at the eaves. The columns were HEA300 and the beams were IPE 360 steel profiles with variable cross-sections at the beam-to-column connection. The steel grade is S355. To relocate to Romania, the structure had to withstand higher loadings than in Germany. To achieve this condition, it was concluded that only the portal frames of the structure can be reused either with a smaller bay than the initial one or by reinforcing the frames to be able to carry the new loads. Due to the high price of the second option, it was decided to build the structure with a bay of 0.5 m smaller than the original one. In the end, the structure to be rebuilt in Romania has a length of 31.5 m, seven bays of 4.5 m, and a width of 17.5 m. The existing roof, the wall bracing systems and the longitudinal beams were not strong enough to conform to the seismic requirements, which constrained their manufacture of new steel. In the end, the total weight of the steel structure is 24812.7 kg + 2695.1 kg (hot-rolled steel profiles + cold-formed purlins), from which 17907.1 kg represents reused steel. The existing envelope consisting of 80 mm steel sandwich panels with mineral wool insulation was reused for the structure erected in Romania, but to comply with the U-values existing in Case 0, an additional layer of 60 mm sandwich panels (new elements) was added to the entire envelope.

Case 2: Existing profiles (as individual members) for beams and columns have been identified in a stockyard in Germany derived from deconstructed buildings. The beams are IPE360 steel profiles and the columns are HEA400. The steel grade is S275. All other components represent new steel. As in Case 0, the structure has a total length of 30 m, with six frames at a 5 m spacing, a span of 17.5 m, and a height at the eaves of 6 m. The weight of the steel structure is 27716.3 kg + 2550.4 kg (hot-rolled steel profiles + cold-formed purlins), from which 16795.4 kg represents reused steel. The envelope has the same composition as in Case 1.

Case 3: Individual members of the steel profiles for beams and columns have been identified in a stockyard in Germany along with end plates for beams and columns. The beams are IPE360 steel profile, the columns are HEA400 and the end plates are 30 mm thick. The steel grade is S275. All other components of the steel structure represent new steel. The dimensions of the steel structure are the same as in Case 0 and Case 2. The total weight of the steel structure is 29112.1 kg + 2550.4 kg (hot-rolled steel profiles + cold-formed purlins), from which 19919.7 kg represents reused steel. The envelope has the same composition as in Case 1.

Case 4: The structure originated in Germany and has a total length of 30 m, with six identical frames at 5 m, a span of 17.5 m, and a height at the eaves of 6 m. The total weight of the steel structure is 27716.3 kg + 2550.4 kg (hot-rolled steel profiles + cold-formed purlins), from which all 27716.3 kg represent reused steel. Practically, the entire superstructure was relocated and reused in this scenario. The dimensions of the steel structure are the same as in Case 0 and Case 2. Only the purlins of the steel structure represent new steel in the superstructure. The same solution as in Case 1, was considered for the envelope.

The amount of steel consumption and the percentage of reused steel, for each case scenario, is presented in Table 1.

Table 1. Steel consumption (for the superstructure) - total steel vs. reused steel.

Case no.	Total weight [t]	Reused steel [t]	%	Purlins [t]
Case 0	23.7	-	-	2.55
Case 1	24.8	17.9	72.2	2.69
Case 2	27.7	16.8	60.6	2.55
Case 3	29.1	19.9	68.3	2.55
Case 4	27.7	27.7	100	2.55

3 SYSTEM BOUNDARIES

The case studies in the assessment considered the following system boundaries: (1) the main building components are the foundations and the ground floor slab (concrete and steel rebars), the steel load-bearing structure (hot-rolled and cold-formed steel elements), sandwich panels (steel sandwich panels with mineral wool insulation), triple glazed windows and sectional sliding gates; (2) other materials and components considered in addition to steel: (a) concrete foundations and concrete floor: 185 m³; (b) triple glazed windows: 22.5 m²; (c) sectional sliding gates: 48 m²; (3) the steel rebars were counted as new material, with an input of 73% steel scrap in the manufacturing process and an end-of-life scenario with 95% recycling potential and 5% landfilling or loss of material after sorting (Celsa Steel 2020); (4) for all scenarios, the same U-values/components were considered in the assessment, i.e. for the external walls, roof elements, ground floor slab, windows and entrance door; (5) the heated floor area of the industrial hall is 525 m²; (6) the operational lifetime of the building is 25 years.

4 ENVIRONMENTAL ASSESSMENT

Using the LCA, the environmental impact of secondary products can be evaluated when recycling or reuse is involved. It demands the allocation of environmental impact over different uses, and there are various approaches to reporting this in LCA, which may characterise the process as upstream (Allacker et al. 2017). The approach to accounting for recycling and reuse in LCA, in this paper, was evaluated using the modular approach, based on the principles of European standards (EN 15643:2021, EN 15804:2012).

Production stage: Modules A₁-A₃. This assessment considers the manufacture of the load-bearing structure, foundations, floor slab, envelope, windows, and industrial sectional doors. The LCA results are calculated for each case scenario considering a “new structure with new materials” and “reused elements” in which different amounts of reused steel were evaluated from the deconstructed industrial building halls. The product stage for the reused elements includes blasting and coating (where required) (JSC Litana ir Ko 2021).

Construction stage: Modules A₄-A₅. In these modules, the assessment includes the transportation of all construction materials from the manufacturer to the building site, the transportation of equipment, and the construction of the structure. As the location of the building site was considered close to the site, all the distances from the manufacturers to the building site are between 10 and 70 km.

For the reused steel structure (Case 1) and elements (Cases 2, 3 and 4) the distance considered for the transport of reused steel and sandwich panels was 1200 km. Euro 5 articulated

truck transport (27 t payload capacity) and Euro 4 concrete mixer transport (12-14 t) were assigned to the transport of construction materials from the GaBi database (Sphera Solutions 2021) and 65-80% of the payload was considered in the evaluation; also a return journey of empty trucks was taken into account in the evaluation.

Building construction included excavation of soil for the foundation and floor slab, concreting and assembly of steel structure and envelope using a 10 t auto-crane, forklifts, man-lifts, wheel loader, bulldozer, excavator, concrete pump and packaging waste processing (Sphera Solutions 2021), (European Association for Panels and Profiles 2018), (JSC Ameko Konstrukcijos 2018).

Use stage: Modules B₁-B₇. The use stage refers to the lifetime of the building, which starts from the completion of building construction, and ends when the building is deconstructed or demolished. As the industrial hall life expectancy in each case study in this evaluation is 25 years, maintenance, repair, replacement of elements, or refurbishment was not considered during this lifetime. The evaluation of operational energy consumption was based on the energy demand for a distribution warehouse (Konrad et al. 2021) and includes energy consumption for space heating, cooling, lighting, IT, security, computers, and other systems. In the assessment, neither heat recovery nor mechanical cooling were considered. The use stage was identical for each case scenario. Therefore, both new and reused buildings have the same environmental impact during the use stage.

End-of-life: Modules C₁-C₄. In this assessment, the end-of-life scenario for each one of the five cases studies involved an instance for “demolition and recycling” and another one for “deconstruction and reuse” (Module C1). The deconstruction included the dismantling of steel structure and envelope using a 10 t auto-crane, forklifts, man-lifts, hydraulic breaker excavator, and wheel loader (Vares et al. 2019), while demolition included working with a 10 t auto-crane, bulldozer, hydraulic breaker excavator, hydraulic scrap shear and wheel loader. The energy demand for the demolition of the steel load-bearing structure was assumed to be 0.239 MJ/kg of steel product if the product is recycled and 0.432 MJ/kg of steel product if the product is to be reused (Gordon Engineering 1997). For cold-formed steel elements, the impacts of deconstruction were modelled based on data from the literature on energy use in demolition, accounting for 0.085 kWh of diesel-powered machinery work per kg of deconstructed steel (Europrofil AB 2020). For concrete, the environmental impact included the use of diesel in the demolition process (Interbeton 2021), while for reinforcement, it included the consumption of diesel for the recovery of reinforcement from crushed concrete (Celsa Steel 2020). The deconstruction process of the steel structure follows the reverse assembling process, to which additional effort is added to preserve the integrity of the deconstructed components for reuse (EN 15804:2012). Where no other data were available, the supplementary effort was generated in the study as a 1.5 workload multiplier for the amount of reused elements at the end-of-life (Coelho et al. 2020).

Benefits and loads beyond the system boundary: Module D. Recovered materials, recovered structures or elements of the structure, steel scrap recycling can result in benefits in the form of CO₂ (or other impacts) savings. In this paper, the data for Module D are based on scenarios that consider current practises and current rates of materials recycling. The calculation model used for the assessment of Module D - Climate Change-total [kg CO₂eq] is based on an innovative calculation model (Hradil et al. 2019), compatible with the methodology of the standard EN 15804:2012. The calculated impact involving potential environmental credits or burdens generated by future lifecycles is based on the impacts of reuse and recycling of the materials jointly operated. The calculation is based on the inputs and outputs of recycled and reused materials, the impact of virgin material production, and the impact of theoretical pure recycling. The yield of the recycling process was considered 0.916 t of recycled steel per 1 t of steel scrap (as specified by the World Steel Association 2017) and the information about Modules A1-3 was based on Environmental Product Declarations (EPDs) by Ruukki Construction (2020).

4.1 Assessed scenarios for the environmental impact

Each of the five cases studied covered a scenario for “demolition and recycling” and one for “deconstruction and reuse” in the end-of-life module. It was assumed in the assessment that

when it comes to the reuse of construction materials, both steel and envelopes are reused materials, as described in the following scenarios.

- *New steel - demolition and recycling (Case 0)*: in the assessment it was considered that the external input of steel scrap includes 20% from manufacturing processing (both the blast furnace and the electric arc furnace are used in the fabrication processing) (Sphera Solutions 2021) and that 90% of the steel is recycled at the structure's end-of-life;
- *New steel - deconstruction and reuse (Case 0)*: in the assessment it was considered that the external steel scrap input includes 20% from manufacturing processing, 90% of the steel is reused at the end-of-life of the structure and 90% of the remaining steel is recovered for recycling. Furthermore, 90% of the envelope was considered reused and from the remaining sandwich panels 90% of the steel sheets were recovered for recycling (3.45% of the total mass of the sandwich panels);
- *Reused steel structure - demolition and recycling (Case 1)*: 65.1% of the total steel weight in the superstructure (incl. purlins) represented reused steel and the remaining new steel has an external scrap input of 20%. At the end-of-life of the structure, 90% of the steel is recycled (including 90% of the steel sheets from the sandwich panels);
- *Reused steel structure - deconstruction and reuse (Case 1)*: 65.1% of the total steel weight of the structure (incl. purlins) represented reused steel and the remaining new steel has an external scrap input of 20% from manufacturing processing. At the end-of-life of the structure, 72% of the steel load-bearing structure (representing steel frames only) is reused and 90% of the remaining steel is recovered for recycling (25% of the total steel mass). Also, it was considered that 90% of the envelope is reused and 90% of the steel sheets are recovered from the remaining sandwich panels for recycling (3.45% of the total mass of the sandwich panels);
- *Reused steel elements - demolition and recycling (Case 2)*: 55.49% of the total steel weight in the superstructure (incl. purlins) represented reused steel and the remaining new steel has an external scrap input of 20%. At the end-of-life of the structure, 90% of the steel is recycled (including 90% of the steel sheets in the sandwich panels);
- *Reused steel elements - deconstruction and reuse (Case 2)*: 55.49% of the total steel weight of the structure (incl. purlins) represented reused steel and the remaining new steel has an external scrap input of 20%. At the end-of-life of the structure, 55.49% of the steel load-bearing structure (representing only columns and beams only) is reused and 90% of the remaining steel is recovered for recycling (40.06% of the total steel mass of the superstructure). Also, it was considered that 90% of the envelope is reused and 90% of the remaining sandwich panels are recovered for recycling;
- *Reused steel elements - demolition and recycling (Case 3)*: 62.91% of the total steel weight of the structure (incl. purlins) represented reused steel and the remaining new steel has an external scrap input of 20%. At the end-of-life of the structure, it is assumed that 90% of the steel is recycled (including 90% of the steel sheets in sandwich panels);
- *Reused steel elements - deconstruction and reuse (Case 3)*: 62.91% of the total steel weight of the structure represents reused steel and the remaining new steel has an external scrap input of 20%. At the end-of-life of the structure, 62.91% of the steel load-bearing structure (representing columns and beams only) is reused and 90% of the remaining steel is recovered for recycling. Also, 90% of the envelope was considered reused and from the remaining sandwich panels 90% of the steel sheets were recovered for recycling;
- *Reused structure - demolition and recycling (Case 4)*: 100% of the total steel weight in the superstructure (incl. purlins) represented reused steel, only the rebars in the foundations were considered new steel, with an input scrap of 20%. At the end-of-life of the structure, 100% of the steel is recycled (including 100% of the steel sheets in the sandwich panels);
- *Reused structure - deconstruction and reuse (Case 4)*: 100% of the total steel weight in the superstructure (incl. purlins) represented reused steel. At the end-of-life of the structure, all the steel in the load-bearing structure is reused.

The percentage of steel used in the description below refers to the steel used in the superstructure (main and secondary structure) only (see Table 2).

Table 2. Assessed scenarios for steel in the superstructure - Input and output flow of the material.

End-of-life scenario for steel: Recycle scenario	In			Out		
	New material	Reused material	Recycled material (scrap)	Waste	Material for reuse	Material for recycling
Case 0	80%	0%	20%	10%	0%	90%
Case 1	27.92%	65.10%	6.98%	10%	0%	90%
Case 2	35.61%	55.49%	8.90%	10%	0%	90%
Case 3	29.67%	62.91%	7.42%	10%	0%	90%
Case 4	0%	100%	0%	0%	0%	100%

End-of-life scenario for steel: Recycle scenario	In			Out		
	New material	Reused material	Recycled material (scrap)	Waste	Material for reuse	Material for recycling
Case 0	80%	0%	20%	1%	90%	9%
Case 1	27.92%	65.10%	6.98%	3%	72%	25%
Case 2	35.61%	55.49%	8.90%	4.45%	55.49%	40.06%
Case 3	29.67%	62.91%	7.42%	3.71%	62.91%	33.40%
Case 4	0%	100%	0%	0%	100%	100%

5 LIFE CYCLE ASSESSMENT RESULTS

The assessment of the environmental impact was expressed using Total Climate Change as a pointer following the rules described in EN 15804 (2012). Table 3 presents the greenhouse gas (GHG) emissions for each case study. As the results show, in the production stage (A1-A3), the savings are between 25-26% when reclaimed steel is used in construction compared with the case using new materials only. Relocating the entire superstructure of the industrial hall and reusing it as it involves a decrease in the emissions in the production stage of up to 33%. In the end-of-life stage (C1-C4), when the deconstruction process requires additional effort to preserve the integrity of the deconstructed components for reuse, the savings are acquired by the recycling scenarios.

Table 3. LCA results of the assumed scenarios.

Scenario	Demolition and recycle [tCO ₂ e]				
	Case 0	Case 1	Case 2	Case 3	Case 4
Environmental impacts (A-C)	1230.14	1193.99	1195.22	1195.81	1185.32
Production stage (A1-3)	143.97	104.94	106.43	106.76	96.45
Construction stage (A4-5)	22.46	25.00	24.79	24.97	24.93
Use stage (B)	1048.83	1048.83	1048.83	1048.83	1048.83
Dem./Dec. stage (C1-4)	14.88	15.23	15.16	15.22	15.22
Loads and benefits (D)	-58.39	43.12	31.37	42.63	58.10

Scenario	Demolition and recycle [tCO ₂ e]				
	Case 0	Case 1	Case 2	Case 3	Case 4
Environmental impacts (A-C)	1242.93	1207.42	1207.42	1209.00	1209.99
Production stage (A1-3)	143.97	143.97	104.94	106.43	106.76
Construction stage (A4-5)	22.46	25.00	24.79	24.79	24.97
Use stage (B)	1048.83	1048.83	1048.83	1048.83	1048.83
Dem./Dec. stage (C1-4)	27.68	27.68	28.95	28.95	29.40
Loads and benefits (D)	-128.44	-45.75	-46.18	-43.72	26.88

According to the results, the highest environmental impact is shown in the case where structures erected with new elements are deconstructed for the next reuse case ($2.35 \text{ t CO}_2 \text{ e/m}^2$ – Case 0), while the lowest emission rate is registered when structures are built with reused portal frames and at the end-of-life of the structure, steel is recovered for recycling ($2.25 \text{ t CO}_2 \text{ e/m}^2$ – Case 4).

LCA savings are reflected as negative values, while positive values define the burdens of material utilisation. Benefits and loads beyond the system boundary are not aggregated with the life cycle impacts (Modules A to C). In scenarios where the structures are built with reused elements and the end-of-life steel is recovered for recycling, a burden is recorded in the assessment. The highest potential savings ($0.244\text{-}0.269 \text{ t CO}_2 \text{ e/m}^2$) appear in the scenario in which the industrial hall was erected with new elements, which are deconstructed for the next reuse case at the end-of-life. Figure 1 presents the total LCA results of the scenarios assessed in the industrial hall.

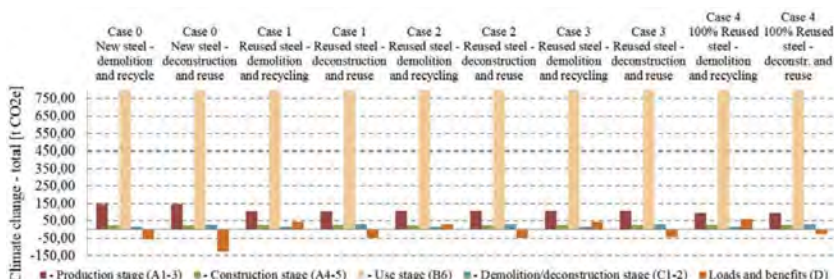


Figure 1. Total LCA results of the scenarios including loads and benefits beyond the system boundary.

6 ECONOMIC ASSESSMENT

The calculation of economic indicators is based on the same scenarios and modules as in the LCA analysis, referring to new steel and reused steel structures, which were associated with time and financial costs. The assessment of the economic performance of the cases studied follows the rules described in EN 16627 (2015). Potential cost savings include revenues for recycled steel (earnings from sold steel scrap), revenues from the sold steel elements or sold structure, and revenues from the sold sandwich panels. The returns considered in the case of recycling were 193 euro/ton of sold steel scrap (the value represents the price of auctioned steel scrap in Romania at the time of the assessment) while the gains from the sold recovered structure (without refurbishment) were calculated at a value of 639 euro/ton of steel. Additional costs for expertise, redesign, testing, sandblasting, and repainting were counted in cases where reused steel was involved.

The results of the life cycle cost assessment show that the economic impact in the production stage (Modules A1-A3) is represented by a 1-8% decrease in the cost when construction materials are reused. When the entire superstructure is relocated and reused, the economic impact in the production stage is less than the economic impact of structures built with new materials with more than 13%. The higher economic impact of the scenarios that involve reused materials is maintained also in the assessment of the total life cycle when the costs increase by 6 to 45 euro/m² compared to the scenarios that relate only to new materials. Total life cycle cost also considers the costs of demolition, deconstruction, and transportation of dismantled materials, which is why the savings gained in the production stage related to the reuse of the construction materials are counterbalanced by the costs of the deconstruction of the structure in the end-of-life stage. The life cycle cost results of the assessment for all stages of the life cycle, including potential savings, are given in Table 4 (potential savings are reflected as negative values). According to the results, the highest LCC (modules A-C) is shown in the cases where the structures erected with reclaimed elements are deconstructed for the next reuse case (911 €/m^2) and the lowest LCC in the case where the construction uses new steel structures and after demolition recovered steel is sold for recycling (858 €/m^2).

Table 4. LCC results of the assumed scenarios.

Scenario	Demolition and recycle [k€]				
	Case 0	Case 1	Case 2	Case 3	Case 4
Environmental impacts (A-C)	454.60	456.53	459.73	459.36	450.53
Production stage (A1-3)	112.66	104.71	108.19	107.28	97.70
Construction stage (A4-5)	36.13	44.61	44.25	44.67	45.55
Use stage (B)	294.90	294.90	294.90	294.90	294.90
Dem./Dec. stage (C1-4)	10.91	12.31	12.39	12.51	12.39
Loads and benefits (D)	-6.55	-7.37	-7.82	-8.05	-7.82

Scenario	Demolition and recycle [k€]				
	Case 0	Case 1	Case 2	Case 3	Case 4
Environmental impacts (A-C)	469.65	474.27	478.17	478.31	468.98
Production stage (A1-3)	112.66	104.71	108.19	107.28	97.70
Construction stage (A4-5)	36.13	44.61	44.25	44.67	45.55
Use stage (B)	294.90	294.90	294.90	294.90	294.90
Dem./Dec. stage (C1-4)	25.96	30.05	30.83	31.46	30.83
Loads and benefits (D)	18.71	-16.83	-18.22	-18.93	-18.22

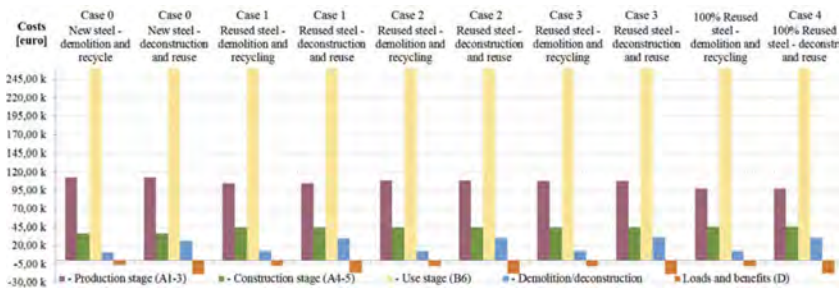


Figure 2. LCC results of the scenarios, including loads and benefits beyond the system boundary.

Figure 2 presents the total LCC results of the assessed scenarios, where the savings are reflected as negative values. When considering the loads and benefits from Module D only, the highest savings (32.50 euro/m² – 36.66 euro/m²) come when the structure is deconstructed for future reuse at the end-of-life, but when the total life cycle is considered, the costs of the structure built with reused construction materials (Cases 1, 2, 3 and 4) exceed the costs of the structure designed with elements from new materials (Case 0).

7 CONCLUSIONS

The end-of-life quality of construction products plays an important role in considering the circular economy, as buildings have a long-intended life span and require a significant amount of material resources. To maintain circularity, these resources have to be kept in service through reuse, reclaim or recycling. The present assessment considered five different case studies, where the building is constructed from new or reused components, and in which the components will be reused or recycled in the future. The results of the environmental assessment showed that reuse is a strategy that offers superior environmental benefits to recycling (modules A-C), the greatest gain being visible in the production stage (A1-3), where the GHG emissions are between 25-33% lower when the structure is built with reused steel (183.71 kg CO₂ e/m² for structures built with reused steel compared to 274.22 kg CO₂ e/m² for structures built

with new steel). According to the results, when it comes to the economic potential of the reuse stages in various reuse and recycle scenarios, the scenario with reused steel elements resulted in higher potential savings (between 32.50 €/m² and 36.66 €/m²) compared to the recycling scenario (between 12.47 €/m² and 15.33€/m²). However, due to the large variety of materials and building practises, it is recommended to perform LCA and LCC calculations on a case-by-case basis, as the results could differ significantly from the present study.

ACKNOWLEDGMENT

This paper was financially supported by the Project “Network of excellence in applied research and innovation for doctoral and postdoctoral programs/InoHubDoc”, project co-funded by the European Social Fund financing agreement no. POCU/993/6/13/153437.

REFERENCES

- Allacker, K., Mathieux, F., Pennington, D. & Pant, R. 2017. The search for an appropriate end-of-life formula for the purpose of the European Commission Environmental Footprint initiative. *The International Journal of Life Cycle Assessment*, 22(9), 1441–1458.
- Brütting, J., Vandervaeren, C., Senatore, G., De Temmerman, N. & Fivet, C. 2020. Environmental impact minimization of reticular structures made of reused and new elements through Life Cycle Assessment and Mixed-Integer Linear Programming. *Energy and Buildings*, 215, 109827.
- Celsa Steel, S.A. (2020). *EPD - Steel reinforcement products for concrete*. The International EPD® System.
- Coelho, A.M.G., Pimentel, R., Ungureanu, V., Hradil, P. & Kesti, J. 2020. *European Recommendations for Reuse of Steel Products in Single-Storey Buildings*. ECCS.
- EN 15643:2021. *Sustainability of construction works - Framework for assessment of buildings and civil engineering works*. CEN, Brussels, Belgium.
- EN 16627:2015. *Sustainability of construction works. Assessment of economic performance of buildings. Calculation methods*. CEN, Brussels, Belgium.
- EN 15804:2012+A2:2019. *Sustainability of construction works - Environmental product declarations - Core rules for the product category of construction products*. CEN, Brussels, Belgium.
- European Association for Panels and & Profiles. (2018). *EPD - Double skin steel faced sandwich panels*.
- Europrofil AB. (2020). *EPD - Light gauge steel profiles and components*.
- Eurostat 2022. Generation of waste-by-waste category, hazardousness and NACE Rev. 2 activity. https://ec.europa.eu/eurostat/databrowser/view/env_wasgen/default/table?lang=en.
- Hradil, P., Fülöp, L., & Ungureanu, V. 2019. Reusability of components from single-storey steel-framed buildings. *Steel Construction: Design and Research*, 12(2), 91–97.
- Interbeton 2021. *EPD - Environmental Product Declaration for Ready Mixed Concrete C25/30 XC3, S2*.
- JSC Ameko Konstrukcijos 2018. *EPD - Steel Structures*.
- JSC Litana ir Ko. 2021. *EPD - Primed and painted steel structures*.
- Konrad, L., Kłodawski, M. & Gepner, P. 2021. Energy Consumption in a Distributional Warehouse: A Practical Case Study for Different Warehouse Technologies. *Energies* 14(9), 2709.
- Gordon Engineering 1997. *Demolition Energy Analysis of Office Building Structural Systems*. The Athena Sustainable Materials Institute.
- Ruukki Construction Oy 2020. *EPD - Hot-dip galvanised building products*.
- Sphera Solutions 2021. *GaBi: Product Sustainability Software*. (10.6).
- Vares, S., Hradil, P., Sansom, M., & Ungureanu, V. 2019. Economic potential and environmental impacts of reused steel structures. *Structure and Infrastructure Engineering* 16:1–12.



Taylor & Francis

Taylor & Francis Group

<http://taylorandfrancis.com>

MS16: Assessment of existing masonry arch bridge infrastructure
Organizers: M. Gilbert, G. Cardani, T. Boothby & D. Coronelli



Taylor & Francis

Taylor & Francis Group

<http://taylorandfrancis.com>

Optimal strengthening of masonry arch bridges with externally bonded reinforcing layers

M. Bruggi & A. Taliercio

Department of Civil and Environmental Engineering, Politecnico di Milano, Milan, Italy

ABSTRACT: Strengthening is a natural step following a failed bridge assessment. Referring to masonry bridges, a numerical tool is presented to find the optimal distribution of reinforcement to be externally bonded to two-dimensional elastic no-tension structural elements, with the aim of maximizing their overall stiffness. Notwithstanding the non-linearity of the adopted material model, no incremental procedure is needed to prescribe equilibrium of the strengthened element. Indeed, the same minimization procedure handles both the energy-based solution of the no-tension elastic body and the topology optimization problem that distributes the optimal reinforcement. A few numerical simulations are presented to assess the capabilities of the proposed procedure in defining the optimal reinforcement layouts for masonry arches and arch bridges, subjected to gravity loads and resting on fixed or elastic foundations. Designers can exploit the tool to sketch a preliminary layout of the FRP strengthening, which should be subsequently detailed according to technical codes.

1 INTRODUCTION

Externally bonded Fiber Reinforced Polymers (FRPs) are nowadays widely used to strengthen, upgrade, or retrofit deteriorated masonry structural elements (Foraboschi 2001, Grande et al. 2008). FRPs have several positive properties, including resistance to wear and corrosion, flexibility, high strength-to-weight ratio, etc. Unlike other materials (e.g., reinforced concrete and steel) that were widely used in the past to strengthen existing buildings, FRPs do not significantly increase the weight of the of the building and, as such, are extremely appropriate in seismic regions (Shrive 2006). FRPs compensate the limited tensile strength of masonry, and increase the load-carrying capacity and ductility of the repaired structural element, as experimentally and numerically shown by several authors (see e.g. Caporale & Luciano 2012).

Drawbacks related to the use of FRPs as retrofitting materials for masonry structures are the possibility of debonding, which can nullify the effectiveness of the reinforcement (see e.g. Capozucca 2010, 2011), or worsening in crack diffusion in the unreinforced regions (Angelillo et al. 2014). Debonding can be avoided by appropriate surface treatments, using fasteners, or applying carbon FRP plates at the intrados of masonry arches, rather than strips or sheets, as suggested by Borri et al. (2011).

According to these remarks, the interest in obtaining methodologies suitable to identify effective reinforcing layouts for masonry constructions under given load conditions is apparent. Some authors basically propose to arrange the reinforcement according to a strut-and-tie scheme, either in such a way as to heal the cracks formed in the unreinforced element (Li et al. 2013), or using optimization procedures (Krevaikas & Triantafillou 2005). A simple strut-and-tie scheme, however, might not be the most appropriate one to retrofit elements of complex geometry, or subjected to nontrivial load conditions. Accordingly, Bruggi & Taliercio (2013) and Bruggi et al. (2013) proposed a general approach based on Topology Optimization (TO - see e.g. Bendsoe & Kikuchi 1988) for 2D, in-plane loaded structural elements, to obtain reinforcing layouts that

minimize a suitable maximum equivalent stress for a prescribed amount of reinforcement. A similar approach was later proposed by Cunha & Chaves (2014) and Bruggi & Taliercio (2015a) for transversely loaded 2D structural elements. In these papers, the optimal reinforcing layout maximizes the elastic stiffness of the reinforced element for a given amount of fiber reinforcement; in the latter paper, the anisotropic and unsymmetric behavior in tension and compression of the reinforcing layers is also taken into account.

Recently, Bruggi & Taliercio (2017) proposed an approach to define the optimal fiber-reinforcement of 2D structural elements made of no-tension materials (e.g. plain concrete or masonry). Here, this approach is specialized to masonry arches and arch bridges that have to be retrofitted by externally bonded FRP strips. The reinforcement is supposed to be unable to carry compressive stresses. A TO formulation is presented to distribute a prescribed amount of fiber-reinforcement at either the intrados or the extrados of the arch, or at both sides, to maximize the overall elastic stiffness of the strengthened element. Unlike the papers quoted above, where the structural elements to be reinforced are linearly elastic, a no-tension model is used to account for the negligible tensile strength of the material. The stress analysis of the no-tension element is itself reduced to a TO problem, according to the approach recently proposed by Bruggi (2014). Indeed, following Del Piero (1989), masonry is supposed to be a hyperelastic, no-tension material. The possible anisotropy associated with the brickwork bond is neglected, and masonry behaves isotropically if all the principal stresses are strictly negative (compressive). The occurrence of positive (tensile) principal stresses is prevented by replacing the isotropic material by an equivalent, orthotropic material whose elastic constants depend on the principal stresses and on the orientation of the principal stress directions. Hyperelasticity allows the equilibrium of the body to be enforced by solving a topology optimization problem, i.e. finding the distribution of the equivalent orthotropic material that minimizes the overall strain energy of the no-tension body.

The main advantage of the approach proposed here is that both the analysis of the no-tension solid and the definition of the layout of the optimal no-compression reinforcement are embedded within the same minimization procedure.

Following Amir & Sigmund (2013) and Gaynor et al. (2013), a combined truss-continuum approach is adopted to model the strengthened element.

2 EQUILIBRIUM OF NO-TENSION BODIES AS A TOPOLOGY OPTIMIZATION PROBLEM

Consider a 2D no-tension isotropic solid, occupying a volume Ω . Typically, the solid can be made of plain concrete or masonry: in the latter case, the macroscopic anisotropy of the material is neglected, as the tensile strength of masonry is actually negligible only perpendicularly to the joints. Mathematical formulations aimed at analyzing no-tension materials were proposed by several authors since the '80s of last century (see e.g. Giaquinta & Giusti 1985, Del Piero 1989, Cuomo & Ventura 2000). More recently, Angelillo et al. (2010) proposed to analyze no-tension solids by replacing the real material by an 'equivalent' orthotropic material that exhibits negligible stiffness in any direction along which the principal stresses in the real medium are non-negative. This idea was later exploited by Bruggi (2014) to re-formulate the analysis of 2D no-tension solids as a TO problem: the distribution of the equivalent material is obtained by minimizing the strain energy of the solid. This non-incremental approach provides the solution under given loads through a one-shot energy-based optimization procedure, provided that the applied loads are compatible with the no-tension constraint. The collapse load of no-tension 2D solids can also be determined by an algorithm based on the approach outlined above (Bruggi & Taliercio 2015b).

The problem formulation is only briefly recalled hereafter; further details can be found in the papers referred above. Let \mathbf{t}_0 denote tractions prescribed over the free boundary of the solid, Γ_t , whereas \mathbf{u}_0 denote displacements prescribed over the constrained boundary, Γ_u . Also, let (z_1, z_2) be the symmetry axes of the equivalent orthotropic material. These axes are assumed to be locally aligned with the directions (z_I, z_{II}) of the principal stresses (σ_I, σ_{II}) at any point of the real

solid, to maximize the material stiffness (Pedersen 1989). Let θ denote the angle between (z_I, z_{II}) and the axes of a given Cartesian reference system. In weak form, the problem solution can be sought as follows:

$$\left\{ \begin{array}{l} \min_{\rho_1, \rho_2} \quad \frac{1}{2} \int_{\Omega} \mathbf{D}(\rho_1, \rho_2, \theta) : \varepsilon(\mathbf{u}) : \varepsilon(\mathbf{u}) d\Omega \\ \text{s.t.} \quad \int_{\Omega} \mathbf{D}(\rho_1, \rho_2, \theta) : \varepsilon(\mathbf{u}) : \varepsilon(\mathbf{v}) d\Omega = \int_{\Gamma_t} \mathbf{t}_0 \cdot \mathbf{v} d\Gamma \quad \forall \mathbf{v}, \\ \mathbf{u}|_{\Gamma_u} = \mathbf{u}_0, \\ \theta \text{ s.t. } z_1 = z_I \text{ and } z_2 = z_{II}, \\ \rho_1, \rho_2 \text{ such that } \sigma_I \leq 0 \text{ and } \sigma_{II} \leq 0, \\ 0 < \rho_{min} \leq \rho_1, \rho_2 \leq 1, \end{array} \right. \quad (1)$$

where \mathbf{u} denotes the (infinitesimal) displacement field, $\varepsilon(\mathbf{u})$ is the (infinitesimal) strain tensor, \mathbf{D} is the fourth-order elasticity tensor of the equivalent orthotropic material, and ρ_1, ρ_2 are nondimensional parameters defined hereafter. In plane stress conditions, and using Voigt's notation, the matrix of the elastic stiffness constants in the material reference frame (z_1, z_2) can be expressed as

$$[D] = \frac{1}{1 - \nu_m^2} \begin{bmatrix} \tilde{E}_1 & \tilde{\nu}_{12} \tilde{E}_2 & 0 \\ \tilde{\nu}_{21} \tilde{E}_1 & \tilde{E}_2 & 0 \\ 0 & 0 & \tilde{G}_{12} (1 - \nu_m^2) \end{bmatrix}, \quad (2)$$

where \tilde{E}_i ($i = 1, 2$) are the Young's moduli of the orthotropic equivalent material, \tilde{G}_{12} its shear modulus, $\tilde{\nu}_{12}, \tilde{\nu}_{21}$ its Poisson's ratios (with $\tilde{\nu}_{12}/\tilde{E}_2 = \tilde{\nu}_{21}/\tilde{E}_1$). To prevent the principal stresses from being positive in the equivalent solid, the stiffness of the orthotropic material is prescribed to vanish along the direction(s) of the tensile principal stress(es) in the real solid. To avoid numerical instabilities, the elastic constants of the equivalent material are related to those (E_m, ν_m) of the real isotropic material according to a generalization of the so-called SIMP model (Bendsøe & Sigmund, 1999), which reads

$$\tilde{E}_i = \rho_i^p E_m, \quad \tilde{\nu}_{ij} = \sqrt{\frac{\rho_i^p}{\rho_j^p}} \nu_m, \quad \tilde{G}_{12} = \sqrt{\rho_1^p \rho_2^p} \frac{E_m}{2(1 + \nu_m)} \quad (3)$$

for $i, j = 1, 2$. The parameters ρ_i ($i = 1, 2$) range from a strictly positive value ρ_{min} to 1 (see Eq. (1)), the extreme values corresponding to a negligible stiffness or a non-penalized stiffness along z_i , respectively, depending on the sign of the relevant principal stress; these parameters can be interpreted as 'nondimensional material densities' along the symmetry axes of the orthotropic solid. A strictly positive lower bound is prescribed, to avoid singularity of the stiffness matrix in a finite-element formulation. p is a penalization parameter, usually taken equal to 3 (Bendsøe & Sigmund, 1999).

The expressions of the equivalent constants in Eq. (3) are similar to those proposed by Cordebois & Sidoroff (1982) for anisotropic damaged materials, thus considering the penalization of the elastic constants as a form of tensile damage.

3 OPTIMAL FIBER-REINFORCEMENT OF 2D NO-TENSION BODIES

Assume now that the no-tension solid has to be retrofitted by unidirectional FRP layers. These layers are assumed to withstand only tensile stresses along the fibers. A given amount of reinforcement, V_f , normalized to the maximum amount that can be bonded over the entire free boundary of the body, is prescribed. A minimization problem is formulated to find the optimal distribution of reinforcement that maximizes the stiffness of the strengthened body. The no-compression constraint is enforced using a SIMP-type approach similarly to Eq. (3).

The solution of the nonlinear equilibrium problem for the reinforced body is sought by embedding the minimization procedure within the energy-based approach presented in the previous Section: the discretized FE form of the procedure is presented hereafter. A mesh made of N truss elements for the reinforcement layers, and M four-node plane elements for the underlying no-tension solid, is used. The non-dimensional densities used to enforce the no-tension constraint in the original solid and the no-compression constraint in the reinforcement are assumed to be element-wise constant. In the j -th truss-like element the density of the reinforcement is denoted by x_j , whereas in the i -th plane element the densities that govern the stiffness of the ‘equivalent material’ along its symmetry axes are denoted by x_{1i}, x_{2i} . The orientation of the material symmetry axes of the i -th FE with respect to the global Cartesian reference frame is denoted by θ_i .

The stiffness matrix of the j -th truss element can be expressed as $x_j^p \mathbf{K}_{0j}$, where \mathbf{K}_{0j} is the stiffness matrix if the element undergoes tensile stresses (so that $x_j = 1$). The stiffness matrix of the i -th plane element will be denoted by $\mathbf{K}_i(x_{1i}, x_{2i}, \theta_i)$. The implemented discrete form of the problem formulated above reads:

$$\left\{ \begin{array}{l} \min_{x_j, x_{1i}, x_{2i}} C = \\ \text{s.t.} \quad \sum_{i=1}^M \mathbf{U}_i^T \mathbf{K}_i(x_{1i}, x_{2i}, \theta_i) \mathbf{U}_i + \sum_{j=1}^N \mathbf{U}_j^T x_j^p \mathbf{K}_{0j} \mathbf{U}_j \\ \sum_{i=1}^M \mathbf{K}_i(x_{1i}, x_{2i}, \theta_i) \mathbf{U}_i + \sum_{j=1}^N x_j^p \mathbf{K}_{0j} \mathbf{U}_j = \mathbf{F}, \\ \theta_i \text{ such that } z_1 = z_I \text{ and } z_2 = z_{II}, \\ x_{1i}, x_{2i} \text{ such that } \sigma_{i,I} \leq 0 \text{ and } \sigma_{i,II} \leq 0, \\ 0 < \rho_{min} \leq x_{1i}, x_{2i} \leq 1, i = 1 \dots M \\ x_j \text{ such that } \sigma_j \geq 0, \\ 0 \leq x_j \leq 1, j = 1 \dots N \\ \frac{\sum_{j=1}^N x_j A_j}{\sum_{j=1}^N A_j} \leq V_f, \end{array} \right. \quad (4)$$

where $\mathbf{U}_i, \mathbf{U}_j$ are the arrays of the d.o.f.s of the 2D and the truss-like finite elements, respectively; \mathbf{F} is the array of the equivalent nodal loads.

In Eq. (4), the objective function is the structural compliance C , i.e. the work of the external loads at equilibrium. The overall strain energy (half of the structural compliance C) is the sum of that stored in the underlying no-tension material and in the fiber-reinforcement to be optimized. Note that the adopted objective function is the same suggested by building codes (EN 1992-1-1, 2004) to derive optimal reinforcement layouts for r.c. members.

In Eq. (4), the constraints in Eq. (1) are reported in discretized form. Additionally, the third last constraint avoids the presence of any strengthening material carrying compressive stresses. The second-last constraint concerns the reinforcement density in any truss element, which is allowed to vanish if the element undergoes compressive stresses. Finally, the last constraint enforces an upper bound on the volume of reinforcement, depending on the area of each truss element, A_j , and the relevant density.

The constrained minimum compliance problem stated in Eq. (4) can be numerically solved by the so-called Method of Moving Asymptotes (MMA – see e.g. Svanberg, 1987). This gradient-based method uses sequential convex programming and the analytical computation of the sensitivities of the objective function. At each iteration, the MMA solves a sequence of simpler approximate sub-problems, which are separable, convex and constructed according to the sensitivity information at the current step, as well as to the iteration history. This approach has been found to be effective in solving large-scale TO problems, giving results in agreement with those achieved through optimality criteria, see e.g. Bendsøe & Sigmund (2003).

The stress constraints in Eq. (4) are enforced by implementing the penalization approach proposed by Ananiev (2005), with the main aim of reducing the computational effort related to the implementation of clusters of local stress constraints. Whenever a principal stress is found to be positive in any element i of the no-tension material, or the stress is found to be

negative in any element j of the reinforcing layer, the corresponding design variables are penalized, and a modified compliance \widehat{C} is computed. The penalized densities are defined as

$$\begin{aligned}\widehat{x}_{1i} &= kx_{1i}, \widehat{x}_{2i} = kx_{2i}, i = 1 \dots M, \\ \widehat{x}_j &= kx_j, j = 1 \dots N,\end{aligned}\tag{5}$$

where $k < 1$ is a penalization factor (herein $k = 0.5$). This heuristic approach was shown to be effective in the treatment of stress constraints (Ananiev, 2005).



Figure 1. Optimal fiber-reinforcement of a single arch made of linear elastic NT material: the principal compressive stresses in the strengthened element are also shown.

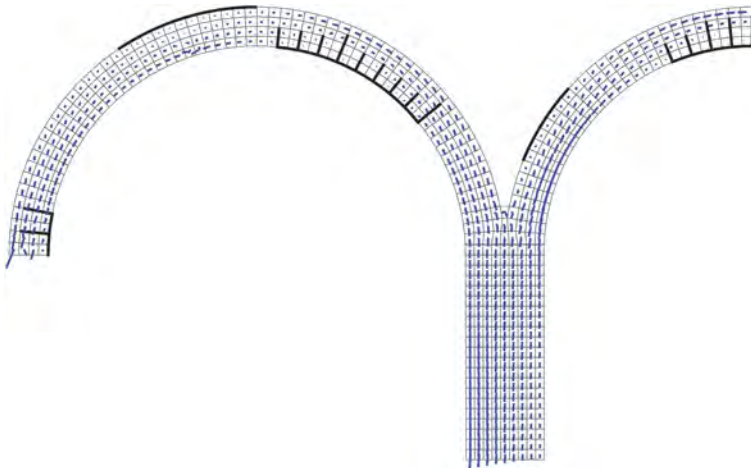


Figure 2. Optimal fiber-reinforcement of a three-span arch bridge made of linear elastic NT material resting on rigid supports: the principal compressive stresses in the strengthened element are also shown.

Providing the MMA with the reduced objective function \widehat{C} and the relevant sensitivities, the gradient-based minimizer updates the design variables x_{1i} , x_{2i} ($i = 1 \dots M$) and x_j ($j = 1 \dots N$), and prevents any stiff material to exist along the weak direction(s) of the no-tension body, as well as any compressed reinforcement element. Computing the sensitivities of the reduced objective function \widehat{C} with respect to the minimization unknowns is straightforward (see Bruggi & Taliercio, 2017).

4 NUMERICAL APPLICATIONS

In the numerical applications shown hereafter, attention is focused on the reinforcement of arch-like structural elements. The elastic properties of the no-tension isotropic material are $E_m = 4,500$ MPa

and $\nu_m = 0.2$. The thickness of the FRP layer is $t_{fr} = 1.40$ mm, whereas the elastic modulus of the reinforcement is $E_r = 205,000$ MPa.

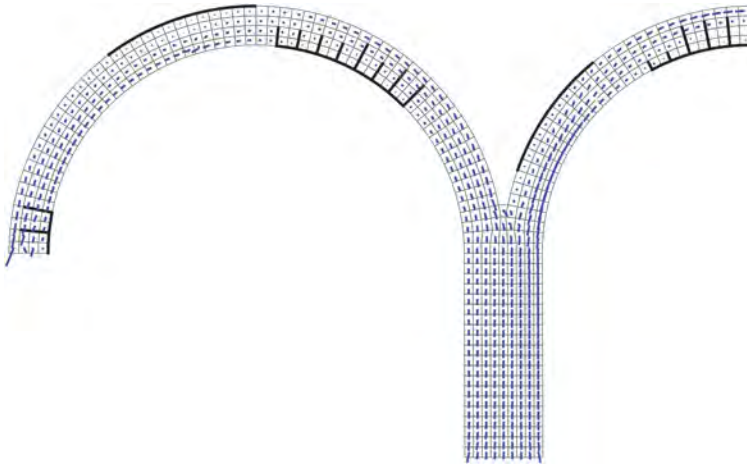


Figure 3. Optimal fiber-reinforcement of a three-span arch bridge made of linear elastic NT material assuming the pier to rest on an elastic support: the principal compressive stresses in the strengthened element are also shown.

First of all, a single semi-circular arch, with an external radius of $R_{em} = 4.75$ m, an internal radius of $R_{im} = 4.00$ m, and an out-of-plane thickness of $t_{hm} = 1$ m, is considered. The arch undergoes its self-weight, being $\gamma_m = 18$ kN/m³ the unit weight, and the weight of an infill up to the top of the extrados of the arch, being $\gamma_i = \gamma_m$ the unit weight of the added material.

The optimal layout of two tension-only reinforcing layers, which can be located along the intrados and/or the extrados of the arch, is sought. To make the fiber-reinforcement at the intrados effective, tension-resistant fasteners must be provided to connect the reinforcement to the inner (compressed) part of the body. Otherwise, radial tensile stresses would occur and nullify adhesion. A maximum volume fraction of reinforcement $V_f = 0.5$ is prescribed.

Figure 1 shows the optimal reinforcement, along with the principal compressive stresses in the strengthened specimen. The FRP layers are located at the crown, where a cracked area is found, at the intrados of the abutments, and at the extrados of the haunches. Note the presence of fasteners around the crown, to fulfil equilibrium of the reinforcing curved layer. Fasteners also help the flow of the compressive stresses deviate towards the bulk of the no-tension body, as shown by the orientation of the principal stresses at the abutments. It must be noticed that the overall amount of distributed reinforcement is less than V_f . The need to consider a volume fraction stems from the use of a topology optimization formulation, having the aim of limiting the amount of reinforcement to be used. In this example and those that follow, the no-compression requirement for the FRP layers prevents the optimizer from exploiting any compressive reinforcement to improve the overall stiffness. Hence, the upper bound becomes active depending on the values of V_f .

Then, a three-span arch bridge is considered, assuming that each span has the same geometry as the arch investigated above and that the same loads (gravity and fill) are applied. Symmetry is exploited, and only the left part of the bridge (including an arch, half of the central span, and the supporting pier) is analyzed. In Figure 2 the layout of the optimal fiber-reinforcement and the principal compressive stresses in the strengthened element are shown, assuming the supports to be fixed. The optimal reinforcement of the central arch is quite similar to that of the single arch, see Figure 1. However, both the location and the extension of the reinforcing layers of the outer arch are remarkably different. Thus, modeling the entire bridge is an essential task to achieve an effective strengthening.

As a peculiar feature of the adopted linear elastic no-tension model, elastic supports may be straightforwardly introduced in the numerical simulations. In Figure 3, the optimal layout of the fiber-reinforcement in the same three-span arch is presented, along with the principal compressive stresses in the strengthened element, assuming now the base of the pier to rest on an elastic foundation, with a modulus of subgrade reaction $k_p = 0.1 \text{ N/mm}^3$. This accounts for the deformability of the supporting foundation and the underlying soil. Compared to the case of fixed support shown in Figure 2, a more homogeneous stress distribution is found at the base of the pier. Concerning the optimal layout of the reinforcing layers, minor modifications are found in the outer arch, whereas a larger amount of reinforcement is used in the central one.

5 CONCLUSIONS

A theoretical formulation based on Topology Optimization has been proposed to define the optimal layout of a given amount of reinforcement to be applied on 2D masonry arch-like structural elements to maximize their stiffness. Assuming masonry to be an elastic, isotropic, no-tension material and FRPs to resist only tensile stresses, the formulation simultaneously avoids principal tensile stresses in the arch and compressive stresses in the reinforcement.

The main advantage of the proposed approach is that no incremental procedure is needed to compute the objective function, notwithstanding the inherent non-linearity of the adopted material model. The same minimization procedure deals with both the energy-based analysis of the no-tension elastic body, and the topology optimization problem that distributes the optimal reinforcement.

The examples presented in Section 4 show that when FRP strips are used to retrofit no-tension arches, fasteners are required at the intrados: otherwise, any reinforcement would be simply blown out, owing to the inability of the material to withstand radial tensile stresses. In all the applications, smooth convergence of the objective function was found in a reasonable number of iterations. Also, soil deformability was found to affect the optimal reinforcing layout (compare Figures 2 and 3).

The implementation described in this contribution considers a single load case, meaning that it is directly applicable to long span masonry arch bridges, where live loads are small in comparison to dead loads. When small and medium-span bridges are addressed, multiple load cases must be considered. This may be done by optimizing separately for each one of the relevant load cases and, then, looking at the envelope of the achieved solutions as the effective reinforcement to be used. However, this procedure does not guarantee that the amount of reinforcement is less than the prescribed volume fraction. To overcome this issue, a single optimization procedure may be implemented adopting as objective function a weighted sum of the strain energy for each one of the load cases, while taking into full account the volume constraint.

In the continuation of the research, an extension of the formulation to 3D no-tension solids is planned. The aim is to propose optimal reinforcing layouts for masonry vaults of any geometry, typically groin, rib, and domical vaults, possibly including lunettes. Refined finite element meshes, or higher-order finite elements, are expected to be required to obtain meaningful solutions, with a dramatic increase in computational cost compared to 2D problems. On the other hand, the possibility of avoiding incremental solutions is expected to make the proposed numerical approach more robust and less expensive than ‘classical’ optimization procedures for nonlinear bodies.

REFERENCES

- Amir, O. & Sigmund, O. 2013. Reinforcement layout design for concrete structures based on continuum damage and truss topology optimization. *Struct. Multidisc. Optim.* 47(2): 157–174.
- Ananiev, S. 2005. On equivalence between optimality criteria and projected gradient methods with application to topology optimization problem. *Multibody System Dynamics* 13(1):25–38.
- Angelillo, M., Cardamone, L. & Fortunato, A. 2010. A numerical model for masonry-like structures. *J. Mech. Mater. Struct.* 5(4):583–615.

- Angelillo, M., Babilio, E., Cardamone, L., Fortunato, A. & Lippiello, M. 2014. Some remarks on the retrofitting of masonry structures with composite materials. *Compos. Part B: Eng.* 61:11–16.
- Bendsoe, M.P. & Kikuchi, N. 1988. Generating optimal topologies in structural design using a homogenization method. *Comp. Meth. Appl. Mech. Eng.* 71:197–224.
- Bendsoe, M.P. & Sigmund, O. 1999. Material interpolation schemes in topology optimization. *Arch. Appl. Mech.* 69(9-10):635–654.
- Bendsoe, M.P. & Sigmund, O. 2003. *Topology Optimization - Theory, Methods and Applications*. Springer, Berlin.
- Borri, A., Castori, G. & Corradi M. 2011. Intrados strengthening of brick masonry arches with composite materials. *Compos. Part B: Eng.* 42(5):1164–1172.
- Bruggi, M. 2014. Finite element analysis of no-tension structures as a topology optimization problem. *Struct. Multidisc. Optim.* 50(6):957–973.
- Bruggi, M., Milani, G. & Taliercio, A. 2013. Design of the optimal fiber-reinforcement for masonry structures via topology optimization. *Int. J. Solids Struct.* 50(13):2087–2106.
- Bruggi, M. & Taliercio, A. 2013. Topology optimization of the fiber-reinforcement retrofitting existing structures. *Int. J. Solids Struct.* 50(1):121–136.
- Bruggi, M. & Taliercio, A. 2015a. Optimal strengthening of concrete plates with unidirectional fiber-reinforcing layers. *Int. J. Solids Struct.* 67-68:311–325.
- Bruggi, M. & Taliercio, A. 2015b. Analysis of no-tension structures under monotonic loading through an energy-based method. *Comput. Struct.* 159:14–25.
- Bruggi, M. & Taliercio, A. 2017. Optimal strengthening of no-tension structures with externally bonded reinforcing layers or ties. *Struct. Multidisc. Optim.* 55(5):1831–1846.
- Caporale, A. & Luciano, R. 2012. Limit analysis of masonry arches with finite compressive strength and externally bonded reinforcement. *Compos. Part B: Eng.* 43(8):3131–3145.
- Capozucca, R. 2010. Experimental FRP/SRP-historic masonry delamination. *Compos. Struct.* 92(4):891–903.
- Capozucca, R. 2011. Experimental analysis of historic masonry walls reinforced by CFRP under in-plane cyclic loading. *Compos. Struct.* 94(1):277–289.
- Cordebois, J.P. & Sidoroff, F. 1982. Anisotropic damage in elasticity and plasticity (in French). *J. Méc. Th. Appl.* special issue:45-60.
- Cunha, J. & Chaves, L.P. 2014. The use of topology optimization in disposing carbon fiber reinforcement for concrete structures. *Struct. Multidisc. Optim.* 49(6):1009–1023
- Cuomo, M. & Ventura, G. 2000. Complementary energy formulation of no tension masonry-like solids. *Comput. Methods Appl. Mech. Eng.* 189(1):313–339.
- Del Piero, G. 1989. Constitutive equation and compatibility of the external loads for linear elastic masonry-like materials. *Meccanica* 24(3):150–162.
- EN 1992- 1-1 2004. *Eurocode 2: Design of concrete structures - Part 1-1: General rules and rules for buildings*.
- Foraboschi, P. 2001. Strength assessment of masonry arch retrofitted using composite reinforcements. *Masonry Int.* 15(1):17–25.
- Gaynor, A.L., Guest, J.K. & Moen, C.D. 2013. Reinforced concrete force visualization and design using bilinear truss-continuum topology optimization. *J. Struct. Eng.* 139(4):607–618.
- Giaquinta, M. & Giusti, E. 1985. Researches on the equilibrium of masonry structures. *Arch. Rat. Mech. An.* 88:359–392.
- Grande, E., Milani, G. & Sacco, E. 2008. Modelling and analysis of FRP-strengthened masonry panels. *Eng. Struct.* 30(7):1842–1860.
- Krevaikas, T.D. & Triantafyllou, T.C. 2005. Computer-aided strengthening of masonry walls using fibre-reinforced polymer strips. *Mater. Struct.* 38(275):93–98.
- Li, B., Qian, K. & Tran, C.T.N. 2013. Retrofitting earthquake-damaged RC structural walls with openings by externally bonded FRP strips and sheets. *J. Compos. Constr.* 17(2):259–270.
- Pedersen, P. 1989. On optimal orientation of orthotropic materials. *Struct. Optim.* 1:101–106.
- Shrive, N.G. 2006. The use of fibre reinforced polymers to improve seismic resistance of masonry. *Constr. Build. Mater.* 20(4):269–277.
- Svanberg, K. 1987. Method of moving asymptotes - A new method for structural optimization. *Int. J. Numer. Methods Eng.* 24:359–373.

Static and seismic assessment of Ponte delle Capre, a masonry arch bridge

F. Casarin, S. Bellin & M. Mocellini

R-Struct Engineering srl, Padova, Italy

R. Fabris

Public Works Office Director, Municipality of Torrebelticino, Torrebelticino (VI), Italy

ABSTRACT: Ponte delle Capre (Goats Bridge) is a masonry arch bridge located in Torrebelticino (Vicenza, Italy) above the Leogra creek. Its origins are not documented, but it is supposed to date back to XIV century. The bridge is 25 m long and 4.30 m wide; it has one arch: its span is 21 m and the rise 8.50m. The structure is composed of stone masonry and lime mortar. The structure is currently subject to the transit of heavy vehicles, as it is the only access route to a nearby steel carpentry factory. The present study describes the assessment of the structural behavior of the existing bridge, considering static (traffic) and seismic actions, in order to evaluate the safety level and define retrofitting interventions.

The bridge has been analysed through Finite Element Model: a 3D model of the bridge has been built with solid elements (bricks), using MIDAS FEA NX software, starting from the 3D physical layout acquired with laser-scanner methodology and managed using Autodesk Recap Pro software. A deep on-site investigation campaign has been performed to calibrate morphological features and mechanical characteristics of structural materials.

Linear analysis has been initially used for static assessment and dynamic frequencies evaluation; static and seismic nonlinear analysis (pushover) has been then performed, considering the total strain crack model for structural materials.

In conclusion, a proposal for the structural retrofitting of the existing bridge is presented, with the aim of combining structural performance and cultural heritage preservation, by using compatible materials and maintaining the original function of the existing arch.

1 INTRODUCTION

In the framework of the Italian Recovery and Resilience Plan (Next generation EU), the European Union financed interventions for the protection of land and water resources, including the restoration and structural retrofitting of Ponte delle Capre (Goat Bridge), an existing arch bridge located in Torrebelticino, a small town near Vicenza, on the Vicentine Prealps.

Ponte delle Capre is an ancient masonry bridge dated back to XIV century, built above the Leogra creek, a water course that flow from mount Pasubio to Vicenza.

This paper describes structural analysis carried out for the static and seismic assessment of the existing bridge and then for the design of the retrofitting intervention. The engineering challenge was constituted by the heavy loads to which the bridge is exposed: it is the only access route to a nearby steel carpentry factory, which entails a daily crossing of the bridge with heavy vehicles. The intervention had to combine the cultural heritage preservation and the static and seismic retrofitting to the current national standards.

The combination of traffic loads, safety factor and actions has been defined following the new Italian guidelines for risk classification and management, safety assessment and monitoring of existing bridges, published by Italian Ministry of Transportation in July 2022, considering

the Operativity Condition, that means 30 years reference time and reduced safety factors, but traffic loads as prescribed by the current national standard.



Figure 1. View of the bridge.

2 DESCRIPTION OF THE BRIDGE

2.1 *Historical context*

Ponte delle Capre is a masonry arch bridge with a humpback shape. Its origins are not documented, but it is supposed to date back at least to the XIV century, since it is mentioned in a document dated 1332 A.D. The shape of the arch recalls the type of masonry arch bridge often defined in Europe with the name “devil’s bridge”, originally considering the structure so complex and daring that its construction could only be considered possible by means of an artifice of the devil: a similar legend occurs also for this bridge.

An important historical document, dated 1590, attests the reconstruction of the bridge, damaged by the flood of the Leogra creek in 1572. The extent of the works carried out is not known, but probably the different masonry composition between basal and central part is connected to these interventions, as well as the insertion of the tie-rods visible on the arch (Snichelotto & Pretto 2022).

Other restoration interventions date back to 1791 and 1891.

The original pavement was raised around 1960, reducing the original shape, substituting the stone finishing with asphalt. The raising of the filling caused the out-of-plane overturning of the spandrel walls, which was restored in 2010, with the realization of a reinforced concrete slab 40cm thick on the lateral quarters of the arch, anchored to the walls by steel ties and rounded anchor plates, still visible on the spandrel walls.

Currently the structures of the bridge show signs of degradation and deterioration: on the arch intrados widespread efflorescence and biological patina are visible, together with severe mortar degradation on joints, mostly caused by the infiltration of water, due to the absence of extrados waterproofing. Moreover, some cracks are visible, especially located at the base of the arch and at the middle span, as shown on the crack pattern survey of the bridge’s intrados, shown in Figure 2; this mechanical distress can be related to the material deterioration (i.e. mortar washout due to water leakage) but also to the high traffic loads passing on the bridge today, surely not previewed in the original design of the bridge; indeed the structural assessment analysis highlighted as most stressed areas the abutments and the middle span, where main cracks have been detected.

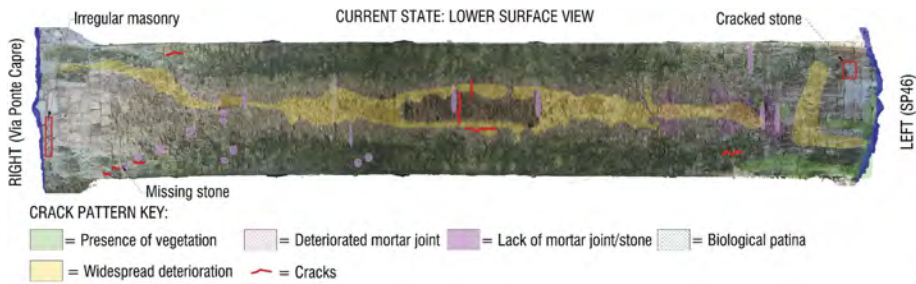


Figure 2. Intrados plan view of the bridge, current state and crack pattern survey.

2.2 Geometrical and structural description

The bridge has a length of about 25m, a height of approximately 21m and a width of 4.30m. It is composed by a single arch: its span is 21 m and the rise 8.50m. The thickness of the arch is 65 cm in the central part, while increase to 120cm near the supports. The stone arch is laid directly on the rocky bank of the river, with a reduction of the thickness, as seen during investigations.

The road path is composed of a single lane carriageway (3.70m wide) limited by the masonry parapets that act also as road barrier; parapets have a variable height from 65cm to 100cm, due to the rise of the slope of the pavement. On Figures 3-4 the survey of the bridge is shown.

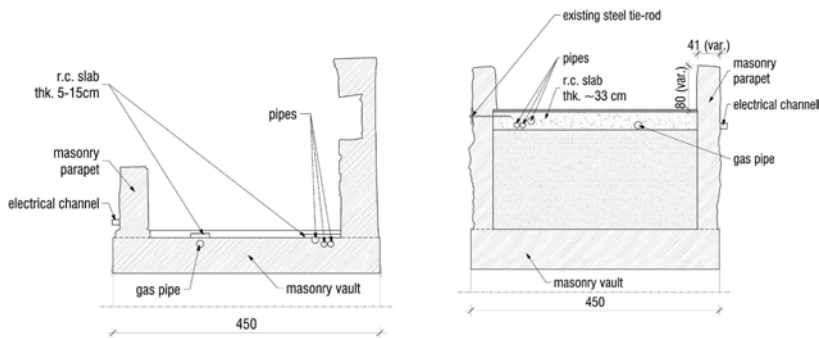


Figure 3. Transversal sections, at keystone on left, at quarter on right, current state.

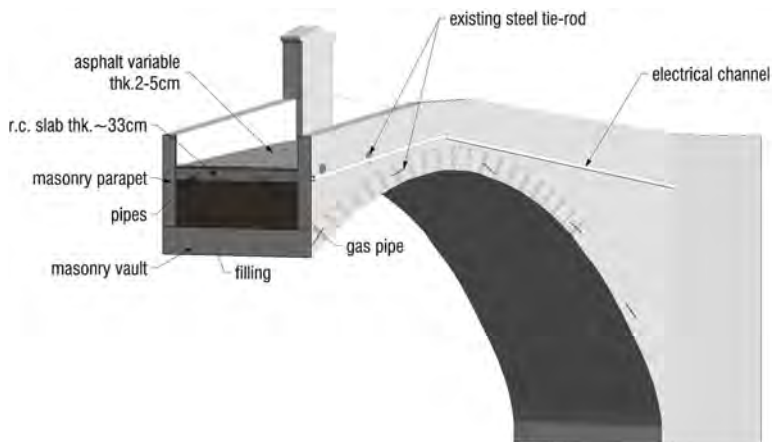


Figure 4. Axonometric view of the bridge, current state.

From the structural point of view, the bridge is composed of stone masonry, but different typologies are present. The basement of the arch is of regular squared stones, while the rest of

the vault is built with rounded local stone (named “lardaro”, a quartz phyllade), such as spandrel walls and parapets. Lateral arches present a more regular texture, made with squared stones interspersed with bricks as regularization elements. Masonry joints are made with lime mortar, even if there is a widespread surface with cement mortar repointing.

The filling of the arch consists of a mixture of soil, gravel and stones; a reinforced concrete slab 40cm thick is present above the filling on the lateral quarters, while in central part the asphalt pavement (6-10cm thick) is directly laid above the structural arch. R.c. slab is anchored to the spandrel walls by means of steel bars and external rounded plates, visible on the two spandrel walls. Steel tie-rods (6 elements) have been inserted through the arch during previous consolidation interventions, probably in the XVI century (Snichelotto & Pretto 2022).

3 STRUCTURAL INVESTIGATIONS

3.1 *On site investigation campaign*

A thorough structural investigation campaign was conceived and executed to achieve an adequate knowledge level for the design of the interventions. Considering the needs of preservation of the existing structures, as requested by the Cultural Heritage Authority, non-destructive and slightly destructive tests have been used: single and double flat jack tests to obtain information on the local state of stress and the mechanical characteristics of masonry, carried out in the regular stone masonry and in the irregular one; micro-core drillings with video-endoscopic inspection, for the evaluation of the internal composition of the arch and of the filling; collection of mortar samples for characterization and mineralogical-petrographic study, performed on samples extracted from the flat jack tests or core drillings; georadar on the pavement surface in order to identify the extension of the reinforced concrete slab. Soil investigations (DPSH, Dynamic Probing Super Heavy) and geophysics tests (MASW) completed the on-site campaign.

3.2 *Obtained results*

The endoscope investigations allowed to obtain the morphology of the bridge, identifying the thickness of the arch (65cm in the central part, 120cm at the springers), of the filling layer and of the r.c. slab below the asphalt. The abutments area was also inspected, noting that the arch thrust is directly transferred to a stone substrate.

Single flat jack tests highlighted a high compression stress on the arch near the support, 2.80 MPa on the West side, 3.59 MPa on the East side; this difference between the two sides of the arch may be due to local stress concentration, considering that the East flat jack was made on the regular stone masonry with very thin mortar layer.

Despite the high compression stress, the double flat jack registered a very good masonry mechanical properties, both in terms of stiffness and of resistance; the comparison between the obtained results and the Italian Standards recommended values for the considered masonry typologies shows much higher values for the masonry of the arch. In Table 1 flat jack test results are reported, together with the comparison to the National Standard recommended values (NTC18).

Table 1. On site tests on masonry (flat jack).

Test ID	Location	Local stress N/mm ²	Max stress N/mm ²	Elastic mod. N/mm ²	fc (NTC18) N/mm ²	E (NTC18) N/mm ²
MD.01	West support Irregular stones	2.80	5.56	7435	1.80	1260
MD.02	East support Squared stones	3.59	7.08	23788	7.00	2850

Flat jack tests usually do not allow a suitable determination of the compression resistance, however in this case curves of the flat jack tests were almost straight and registered an almost complete recovery in the unloading phase, sign that the inelastic phase was not reached. Maximum compression stress reached in the tests can safely be considered as compression resistance of the masonry. Additional tests would have been useful to confirm these results, but for preservation reasons were not authorised.

Mortar samples tests shown two main mortar types: recent cementitious mortar and original/ancient lime mortar, which registered an average compression resistance of 7,25 MPa (punch test), highlighting a very good composition.

3.3 Material properties

Considering the structural survey and the on-site investigation tests results, two main masonry typologies have been considered: regular squared stone masonry (for basement and lateral arches) and irregular stone masonry (for the central part of the vault); corresponding mechanical properties are shown in Table 2. For the filling a density of 24 kN/m³ and deformability modulus E=50 MPa have been considered.

Table 2. Mechanical properties of the two masonry typologies.

Type ID	Masonry typology	f_c N/mm ²	$\tau_0 - f_v0$ N/mm ²	E N/mm ²	G N/mm ²	γ kN/m ³
01	Irregular stone masonry	5.00	0.074	7435	2974	24
02	Squared regular stones masonry	7.00	0.230	23788	9515	24

For non-linear analysis a Total Strain Crack model has been used (Rots, 1988, Lourenço, 1996), that allows to consider an equivalent homogeneous material with elastic-plastic behavior (with softening curve) in compression, and elastic-fragile (with behavior controlled by the fracture energy) in traction.

Non-linear properties of materials have been defined based on results of flat jack tests (for compression resistance and elastic modulus) and on National Standards parameters (for tensile resistance); fracture energy values have been initially defined based on literature parameters: a sensitivity analysis has been performed for the final value definition, comparing the nonlinear behavior with cinematic and linear analysis results (i.e. hinge positions, maximum stressed zones, etc.). In Table 3 considered non-linear material properties are shown.

Table 3. Non-linear properties of the two considered materials.

Type ID	Masonry typology	f_t N/mm ²	G _{f,t} N/mm	h mm	f_c N/mm ²	G _{f,c} N/mm	h mm
01	Irregular stone masonry	0.11	0.07	400	5.00	5.00	400
02	Squared regular stones masonry	0.23	0.15	400	7.00	10.00	400

4 NUMERICAL MODEL

A three-dimensional model of the bridge is constituted using MIDAS FEA NX finite element software. The finite element model of the bridge is generated using brick elements with 6 or 8 nodes and 3 degrees of freedom for each node. The mesh is generated automatically by the software and counts 20007 nodes and 19472 brick elements.

The model creation started from the 3D laser-scanner survey, which provided the physical model of the bridge. Point cloud has been managed and simplified using Autodesk Recap Pro and Revit software; geometry has hence been imported in Midas FEA NX software, by which the mesh has been automatically generated. Considering the bridge directly laid on the rock, fixed external constraints have been applied.

Self-weight analysis has been performed for the model calibration, comparing the compression stress with single flat jack tests result: a good match is noted with the MD01 test (West support), while a slight discrepancy is present on the MD02 (east support), probably due to local stress concentration.

Dynamic modal analysis has also been done to evaluate the natural frequencies of the bridge, briefly reported in Figure 5.

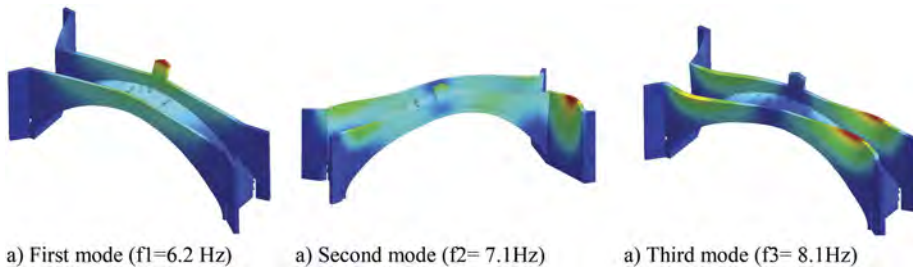


Figure 5. Natural frequencies and mode shapes of the bridge.

5 PRESENT STATE STRUCTURAL ANALYSIS

The assessment of the structural capacity of the existing bridge has initially been done using simplified kinematic analysis (Heyman, 1982), considering the traffic loads in different positions and combinations (Figure 6b).

Linear static analysis has been performed using the described FE model, considering permanent and live loads (wind, snow, and traffic) as prescribed by National Standards. Principal stresses have been compared with resistance values, properly reduced considering safety factor and knowledge factor. In order to consider a no-tension masonry capacity even in the context of the linear analysis, a redistribution of the tensile stresses in the verification section was considered, partializing its thickness (Figure 6a).

Kinematic and linear static analysis highlighted that the existing bridge does not meet the requirements of National Standards for static loads. Considering the peculiarity of the bridge case-study, dated back to 1300, Italian guidelines for risk classification and management, safety assessment and monitoring of existing bridges (D.M. 01/07/2022) has been used to define the traffic loads: “Operating” and the “Transitability” conditions have been considered. The first one provides for the transit of all vehicular traffic categories, but considering lower load combination factors, calculated considering 30 years as reference time. Such verifications are not satisfied in the current state analysis, both in case of tandem traffic load 300 kN (in two axis) considered in the center position of the arch or in the asymmetric position (at the thirds of the arch). In particular, in the first case the most stressed section is the key of the arch, while in the latter the most stressed sections are the thirds of the arch and the abutments. This behaviour is consistent with the influence line of the arch structures. In the current state, the minimum static safety coefficient calculated is 0,67 in the middle section.

Therefore, the analysis has been performed considering the “Transitability” condition, that means a 5 years reference time, and two different load cases: 75 kN distributed in two axis and 180 kN distributed in three axes. These traffic categories, together with only light vehicles case, have been selected considering the real traffic conditions, connected to the nearby steel carpentry factory. In both cases the most stressed section is in the abutment when the tandem load is in the asymmetric position at the thirds of the arch. The safety coefficient in the “Transitability” condition is equal to 1,02, giving the positive verification results in every section.

Comparing the performed analysis, the unsatisfactory static situation of the structure has been proven, identifying the most stressed sections in every loading scheme; most stressed area in the elastic FEM model match with the crack pattern survey, confirmed also by the kinematic analysis and by the position of the plastic-hinges highlighted in the non-linear analysis.

Considering the presented results, a traffic limitation to the bridge has been imposed, allowing the transit only to intermediate heavy vehicles (180kN, three axes), until the design interventions execution.

Nonlinear analysis has also been performed for seismic assessment, highlighting a seismic safety level around 40% of the design action.

Intervention design has been thus developed to guarantee the “Operating” condition, in order to remove the traffic limitation, but also considering the Culture Heritage Authority prescriptions.

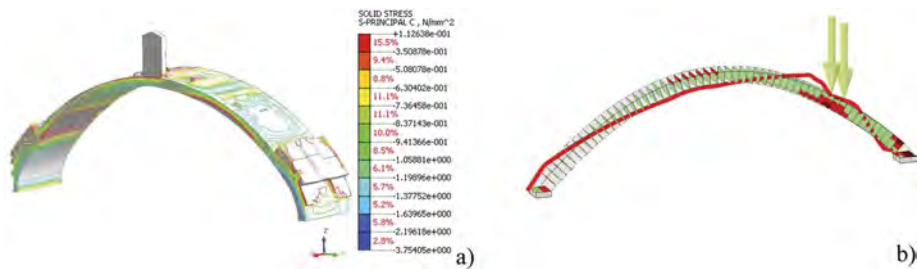


Figure 6. Linear static analysis result from F.E. Model (a) and kinematic analysis results (b) with the thrust line in the most unfavorable tandem load condition.

6 RETROFITTING INTERVENTIONS AND DESIGN ANALYSIS

The challenge of the design activity consisted of combining the cultural heritage preservation and the retrofitting of the structure to the design traffic loads, considering that the transit to heavy vehicles had to be maintained, at least until the realization of a new bridge for the access to the steel carpentry factory. Present state analysis highlighted the main vulnerabilities of the bridge, connected to excessive tensile stresses on the arch section in case of eccentric traffic load.

The design planned to increase the resistance section of the arch and insert tensile resistance elements, by means of a new r.c. slab above the existing masonry arch. To maximize the material compatibility, the new slab - 10cm thick - will be realized using lime concrete (C12/15) and stainless steel rebars. Confining of the arch for containment of pressure curve is granted by masonry walls at arch extrados (masonry stiffeners), made with clay bricks and lime mortar, reinforced by stainless steel rebars inserted on joints. The filling of the vault is designed with lightweight material, with an upper lime concrete slab for point loads distribution. The retention of the spandrel walls is provided by slab connection and by the insertion of stainless-steel tie-rods with external anchors, to avoid out-of-plane overturning. The intervention is completed by the restoration of the masonry walls and arch, by the means of traditional technique such as grouting and repointing.

The structural function of the arch has been maintained, improving its behavior and capacity by inserting confining devices and tensile resistance elements, applying the structural honesty concept (than means maintain original function, reinforcing only critical aspects). To do this, verification procedure has been deepened considering values of material strength linked directly to the on-site tests and less conservative than those one required by the Technical Standard.

Seismic design level has been checked considering non-linear pushover analysis, which was performed applying a monotonically increasing pattern of transversal forces, calculated from the linear dynamic spectral analysis, so proportional to the vibration modes of the structure. Both directions have been considered.

Pushover analysis was performed in two main steps: first static vertical loads have been applied, then the incremental horizontal forces were added. The seismic capacity of the structure is defined by the curve of the base shear force versus the horizontal displacement (considered in the middle of the arch) which has been converted in the response of an equivalent nonlinear

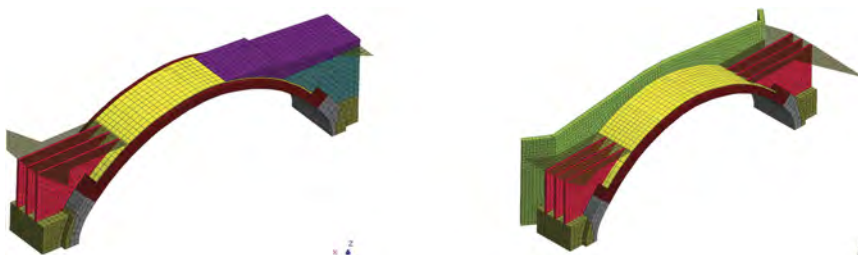


Figure 7. Design FEM numerical model - 3D views.

single degree of freedom system, for its comparison with the design spectrum (Fajfar 2000, 2002). In the design state the displacement capacity results higher than the seismic demand.

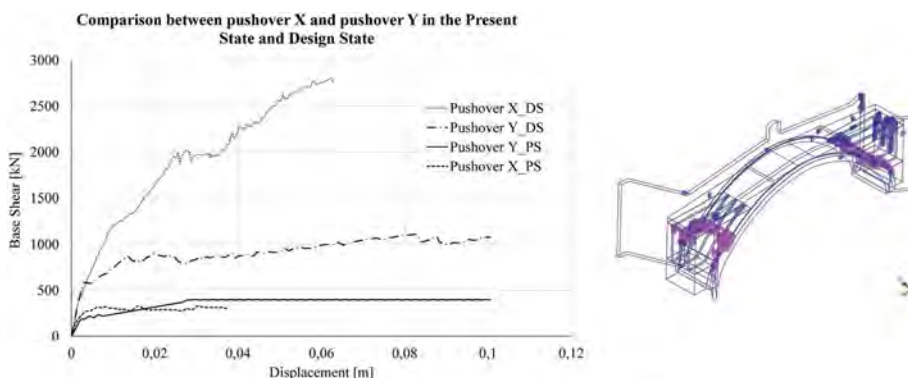


Figure 8. Pushover curves (on left) and pushover analysis results in terms of plasticized elements in the design state (on right): pink= partially open -loading; blue= partially open -unloading.

7 CONCLUSIONS

In this paper an intervention proposal for the structural retrofitting of Ponte delle Capre is presented. The design approach sought the structural consolidation with improvement of the static and seismic behavior adhering to the concept of *structural honesty*, this implying the respect of the structural function of the original resistant elements of the bridge. At the same time, the use of new structural reinforcement systems is based on the selection of new materials that respect as much as possible the principles of conservation also imposed by the Cultural Heritage Authority, aiming however to return to the community an infrastructure that is called to resist project actions required for newly built structures, considering the particular need to maintain transit for heavy vehicles. Designers called to intervene on Cultural Heritage need a greater project sensitivity than for new buildings design. Considering that the risk linked to the design choices is higher, the use of more refined calculation as nonlinear analysis is required, to minimize over-design that can cause the loss of historical values. The professional risk is also linked to the interpretation of the Technical Standards which are appropriate for newly built structures but often have technical limits if dogmatically applied to cultural heritage. The Guidelines for existing bridges, as well as the ISO 13822 Standards and the ISCARSAH Directives help in the appropriate assumption of more suitable calculation hypotheses.

REFERENCES

- Fajfar, P. 2000. A nonlinear analysis method for performance-based seismic design. *Earthq Spectra*. 16: 573–92.
- Fajfar, P. 2002. Structural analysis in earthquake engineering - a breakthrough of simplified nonlinear methods. *Proceeding of 12th European conference on earthquake engineering*.
- Heyman, J. 1982. *The masonry arch*. Chichester: Ellis Horwood.
- ICOMOS, Iscarsah. Guidelines: recommendations for the analysis, conservation, and structural restoration of architectural heritage.
- Lourenço, P.B. 1996. Computational strategies for masonry structures. PhD. Thesis, Delft: Delft Technical University of Technology.
- Ministry of Infrastructure and Transportations 2022. Guidelines for classification and risk management, safety evaluation and monitoring of existing bridges (DM 01/07/2022). Rome: Official Gazette.
- Milani, G. & Lourenço, P.B. 2012. 3D non-linear behavior of masonry arch bridges. *Computers & Structures*. 110(111): 133–150.
- Pelà, L. Aprile, A. & Benedetti, A. 2009. Seismic assessment of masonry arch bridges. *Engineering structures*. 31: 1777–1788.
- Ozmen, A. & Sayin, E. 2018. Seismic assessment of a historical masonry arch bridge. *Journal of Structural Engineering & Applied Mechanics*. 1(2): 95–104.
- Snichelotto, P. & Pretto P. 2022. Il ponte delle capre. Torrebelvicino.

Damage accumulation in the structural life and assessment of masonry bridges

T.E. Boothby

The Pennsylvania State University, University Park, PA, USA

D. Coronelli

Politecnico di Milano, Milan, Italy

ABSTRACT: Structural conditions along the life of masonry bridges show changes in geometry caused by load effects, settlements, environmental actions and material deterioration, with accumulation of damage in time. Particular attention should be paid to transverse load effects on spandrel walls, together with the consequences of water ingress in the structure. The paper first analyses the approaches in the Italian CNR DT213 and the British CIRIA C800 to consider damage accumulation in the assessment. The effects of water ingress are then shown through a review of case studies. Example of limit analysis accounting for damage due to cracking and water seepage is proposed. The conclusions address the needed research developments

1 INTRODUCTION

Failure mechanisms that actually occur in masonry arch bridges are characterized by the progressive development of cracks in various positions (Harvey, 2012). The design and maintenance codes for masonry bridges and for masonry-earthwork structures in general pay scant attention to the transverse load effects that can be observed in masonry bridges. This is contrary to the authors' experience that the effects of lateral loads on the spandrel walls precipitate the majority of the failures of such bridges. These effects include the following: bulging of spandrel walls; sliding of spandrel walls with respect to the arch barrel; overturning of spandrel walls; longitudinal cracking in the arch barrel.

Whether one of these effects appears, or which one of these effects appear, is a function of the relative strength of the spandrel wall and the arch barrel. Each of the failure modes listed above is a function of some weakness in the load path for lateral loads. Overturning of the spandrel wall generally indicates a slender wall, while sliding indicates a more stocky wall. Bulging seems to indicate some lateral restraint, as provided by a bond beam or a concrete parapet. Cracking of the arch barrel indicates that the wall is sufficiently proportioned to resist failure of the wall itself, or that the bonding within the arch barrel is insufficient to resist the lateral forces in direct tension. A further effect, which will be modelled later in this article, is that transverse bending in the arch barrel due to heavy concentrated wheel loads induces longitudinal cracking adjacent to the inside of the spandrel wall, as the spandrel wall stiffens the arch barrel in both directions: longitudinally and transversely. Similar cracks can form in ribbed bridges.

These effects have been described by a few authors, most often in a qualitative manner. Harvey (2012) describes qualitatively the evolution of damage in the arch barrel that may result from the stiffening influence of the spandrel wall. Sokolovich et al. (2021) attribute the longitudinal cracking to the shear stresses induced in the arch barrel by the passage of trucks relatively close to the spandrel wall. Polatsu et al. (2019) simulate the separation of a spandrel wall by discrete elements, which incorporates three different effects described above: the failure initiated by a separation of the spandrel wall from the arch ring, then sliding of the spandrel wall, and finally an overturning failure of the spandrel wall. They identify this failure as

occurring at a lower load than the global failure of the arch ring—it is probable that the former would be considered as a failure of a real bridge.

A careful study of the causes of these phenomena includes lateral loads on the spandrel walls, vehicle impact, transverse bending of the arch barrel and water entry into the fill. The last item is a significant cause of the appearance of transverse damage, or may exacerbate transverse damage due to another cause.

This article will focus primarily on the changes in material properties and assemblies induced by entry of water into the bridge structure and possible means of assessing the damage that results from this factor.

2 ASSESSMENT GUIDELINES

The assessment approaches in the Italian CNR DT213 (2015) and the British CIRIA C800 (Gilbert et al., 2022) are considered. Two ways of accounting for damage accumulation are highlighted. The Italian guidelines define a factor of confidence related to knowledge of geometry, cracking, texture and material properties. CIRIA C800 defines the permissible limit state analysis, i.e. the point beyond which progressive load-induced degradation occurs in the bridge life, using a model including actual geometry and damage.

2.1 *Italian CNR DT 213*

2.1.1 *Damage in limit state verifications*

The “Instructions for the evaluation of structural safety of masonry road bridges” (CNR, 2015) define a factor of confidence on the basis of the knowledge of material properties and the structural damage. The factor is used to multiply the partial safety factor, dividing in turn resistance in limit state verification.

The knowledge is built by the survey of the geometry, the crack pattern and interpretation of their causes, analysis of the deterioration; exam of the masonry texture and structural details; determination of the material strength and physical properties, through testing or based on the literature. The factor of confidence is quantified in the range 1.0-1.35 as a function of the knowledge level, with the highest value corresponding to limited knowledge.

An additional factor of non-conformity measures the difference between the bridge proportions and the state of the art proportion rule. The range is 0.85-1.15, corresponding to the best and worse level respectively. Also this factor multiplies the partial safety factor.

A coefficient for material deterioration (section 6.5.4) is defined in the range 1.0-1.20 based on the type of deterioration observed and its extension. This is multiplied by the partial safety factor to divide the material strength in verifications.

The document indicates that knowledge on cracking is essential for structural analysis and repair and strengthening interventions. Cracking is defined physiological if it does not alter the use of the carriageway and displacements do not alter in a significant way the geometry.

The document defines serviceability limit states, with the structure bearing stresses limited within allowable stresses and physiological cracking. Formulations for crack width calculation are proposed. The ultimate limit states are defined for the activation of collapse scenarios.

The values of partial safety factors in the Italian code are in a range 2.0-30.0 according to masonry units and mortar quality.

2.1.2 *Transverse load effects*

Section 3.10.1 and 3.10.2 prescribe the verification of the load bearing capacity of the fill and the spandrel walls, under lateral pressure given by the fill material, with the most critical position of the live loads. For the former the document reports the methods of the Italian national code. This in turn considers the possibility to use an observational method (NTC2018 6.2.5), by monitoring relevant displacements or crack widths with respect to limits determined for safety reasons.

2.2 CIRIA C800

2.2.1 Damage

The CIRIA C800 Guidelines (Gilbert et al., 2022) define a Permissible Limit State (PLS), to determine the point beyond which progressive load-induced degradation occurs in the bridge life. This is analysed using a model including actual geometry and damage in the material strength properties.

The document underlines the need to model defects directly rather than applying global condition factors. Mortar loss should be modelled by a loss of cross-section. In a similar way, fine transverse cracks in a PLS assessment (because of the deterioration effect of opening and closing of joints over time) and large transverse cracks (>1mm) in an ULS assessment should be modelled as cross-section loss.

Alternatively it is possible to assess the PLS via monitoring, checking the stability of cracks and displacements.

2.2.2 Transverse load effects and spandrel walls

The Guidelines highlight the effect of stiff elements attracting high stresses such as those generated at the interface of a barrel bearing on a stiff spandrel, with flexible soil fill, showing that this may result in a common defect of longitudinal cracks detaching the wall (Section 3.6 “Common defects”). The document underlines that the principal load bearing action depends on the masonry thickness and the weight of the masonry and superimposed fill, considering horizontal mobilized pressures and attached spandrel walls as secondary, as they may become detached. Nevertheless the guidelines indicate the need to assess the principal as well as the secondary elements, and concerns over their safety may lead to an “assessment failure”.

Amongst the preliminary assessment operations a survey of the voids in the internal areas adjacent to spandrels is indicated (section 5.2.3).

Building the model of the bridge, spandrel walls should be considered in 3D models, defined as level 3. Spandrel walls should not be considered in more simple 2D models, because of their possible detachment. This last event leads to an increase of flexibility and can be captured by monitoring displacements, and modelled considering a reduced effective width.

The verification of bridges in flood conditions should consider modelling of water pressure and effective stresses if seepage conditions are anticipated. Stability of spandrels under flooding with rapid drawdown should consider the effect of saturated fill with no supporting hydrostatic pressure (section 7.2.4).

3 WATER INGRESS AND BRIDGE FAILURE

The entry of large amounts of rainwater into the fill of the bridge has been documented as a cause of failure or incipient failure in several arch bridges. Many of these collapses were initiated or exacerbated by the entry of water into the fill adjacent to the spandrel wall. This was the clear cause of the simultaneous loss of both spandrel walls of the Blaine viaduct in Eastern Ohio (Figure 1). The bridge was in poor condition generally and endured a collapse of both spandrel walls due to the combined effect of heavy rains and floodwater (USGS, 1999).

The Wyebrook Bridge, Chester County, PA also underwent a spandrel wall collapse as a result of poor drainage facilities and heavy rains (Boothby and Craig, 1996). A spandrel wall collapse of Rockville Bridge, PA, (Froio, 2012) precipitated a train derailment. Although this failure does not appear to be described in refereed literature, newspaper and other popular articles (Guida, 2010; Stonearchbridges.com, 2019; Explore Pennsylvania History, 2022), attribute this failure variously to water intrusion, freeze-thaw and settlement.

A similar issue is present on a large population of bridges of the former Pennsylvania Railroad (built between 1899 and 1910) especially the bridges that consist of ‘ribbed arches’ (Figure 2). This is a system for overcoming a skew crossing by approximately one meter wide arches offset from each other. The joint between the arches is susceptible to opening, water intrusion, and ballast leakage. The bridges noted had pre-existing issues with the spandrel



Figure 1. Collapse of Blaine, OH viaduct 1999 (viewed from above).

walls including longitudinal cracking of the arch barrel and leaning of the spandrel walls. It is not entirely clear that these collapses were due to the entry of rainwater, but the accumulating damage was most probably due in part to the entry of water, weakening of the fill and erosion of the fill.

These effects are primarily due to earth pressures on the spandrel walls, although they are usually exacerbated by the flow of water through the fill. Often, as a result of the structural effects described here, a path is opened for this flow of water that potentially causes an acceleration of the adverse effects.

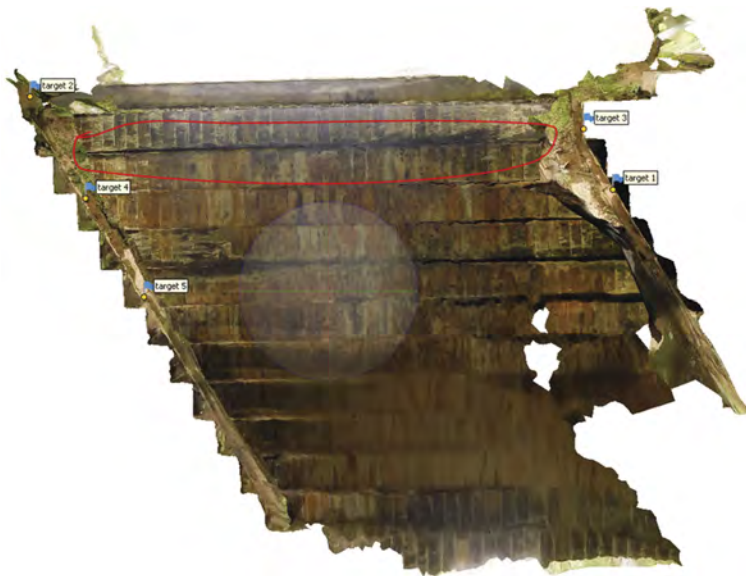


Figure 2. Photogrammetric reconstruction of crack in a ribbed skew railway arch bridge 2022 (viewed from below).

4 MODELLING OF DAMAGE RELATED TO WATER INGRESS

A limit analysis model (Coronelli and Giangregorio, 2023) for vaults is here extended to simulate the effects of water ingress. The kinematic model divides the system with discontinuities joining nodes on a regular square mesh. The kinematics include three relative rotations and three displacements, and compatibility is enforced at each node. The flow rule considers no-tension, infinite compression strength for axial force and bending, friction and cohesion for shear and torsion.

As a first example of analysis, the bridge geometry considers a span of 3m, the barrel with a 0.2m thickness and spandrel walls with a 1m depth, 0.6m thick, flush with the barrel at the intrados. A live load is applied at 3/4 of the span, along a line parallel to the support, with a length of 1.8m.

Two analyses are carried out (Figure 3). The first considering the same strength properties for the interfaces in all discontinuities: friction angle 35 degrees and cohesion 0.2 N/mm². The second analysis considers the damage caused by water flowing at a crack formed at the interface of one spandrel wall and the barrel, reducing to zero friction and cohesion.

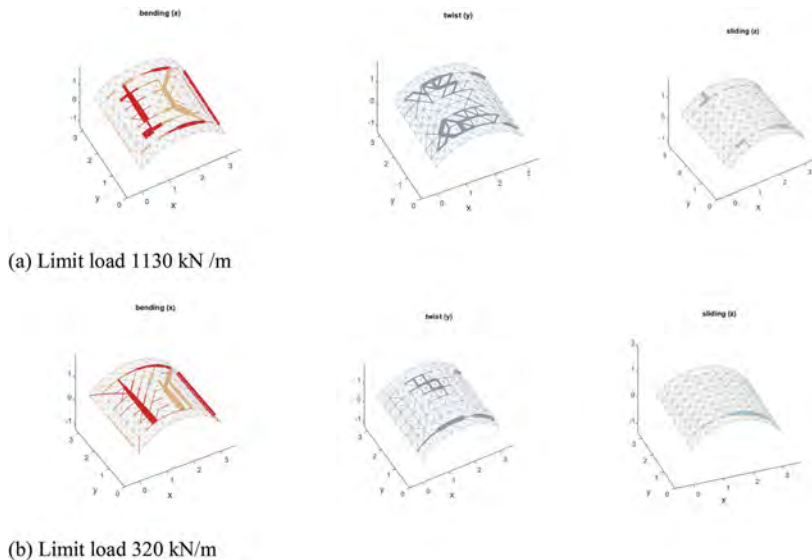


Figure 3. Failure mechanism change and limit load reduction related to water flow damage: (a) sound bridge; (b) cracking along spandrel-vault interface.

The effect of the material degradation is a significant reduction in the limit load with a change in the failure mechanism. The first analysis shows a symmetric mechanism in the barrel between the spandrels, with four line hinges as well as torsion and sliding. In the latter case the mechanism is non-symmetric, with the barrel sliding relative to the spandrel and twist occurring without torsion damage on one side.

As a second example, a bridge barrel is considered, with a span of 3m and a 45° skew in plan (Figure 4a). A construction with unskewed masonry is considered, with a bonding pattern parallel to the abutments. Damage is considered to occur in correspondence of transverse cracks opening at 1/4 of the span; here the friction and cohesion for shear stresses are reduced to 10%.

The mechanism without damage (Figure 4b) shows four line hinges. The mechanism with damage (Figure 4c) shows twist and sliding under the load, and a more complicated flexural hinge pattern. The failure load is reduced by 14%.

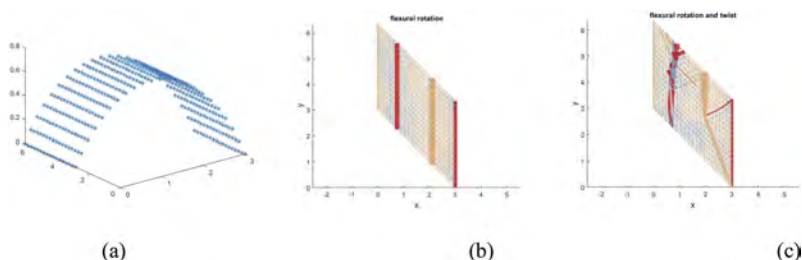


Figure 4. Effects of water ingress at transverse crack location: (a) geometry. Yield lines at failure load: (b) no damage from water ingress; (c) damage at transverse sagging crack at $\frac{1}{4}$ span, corresponding to live load location. Legend: red=sagging; yellow= hogging; grey=twist.

5 CONCLUSIONS

Two relevant National guidelines have been analysed, for the consideration of existing damage in assessment of masonry arch bridges. The Italian CNR DT213 defines a factor of confidence including evaluation of the damage conditions of the structure. The factor is used in ultimate limit state verifications, reducing the factored resistance for higher damage levels; hence the value can be adjusted to consider local conditions of sections considered in verifications. CIRIA C800 indicates methods for direct modelling of damage, and defines a performance limit state (PLS) to verify that stress levels do not overcome a reference level. Both documents suggest the use of monitoring for safety verification as an alternative to analytical methods and limit state verifications.

Amongst the causes of damage, the paper highlights the importance of considering transverse effects of loads on masonry arch bridges. These cause different types of cracking, that can be connected to water ingress causing further damage. Spandrel wall collapse has been shown to be related to water ingress in many cases of real bridge failure.

The effects of water ingress have been shown to affect the failure mechanisms and resistance of masonry arch bridges, using a 3D limit analysis model to study the failure of bridge barrel vaults.

The research developments will address the study of existing bridges with the development of models for the structure including fill, spandrel and abutment walls.

ACKNOWLEDGEMENTS

The Authors are grateful to Mohammed Rakeh and Joe Kallas for completing the photogrammetric study and providing the image in Figure 2.

REFERENCES

- Boothby, T. and Craig R. 1996. Stone arch bridge behavior: a case study. *Proceedings of the North American Masonry Conference. The Masonry Society*. pp. 400–407.
- Boothby, T.; Yurianto, Y. and Erdogmus, E. 2005. Experimental Replication of Masonry Arch Bridge Spandrel Wall Collapse. *TMS Journal* 23 (1) December.
- Coronelli D., Giangregorio, M.C. 2023. Three-dimensional Limit Analysis of Barrel Arch Bridges. *IALCCE 2023 Proceedings, Eighth International Symposium on Life-Cycle Civil Engineering*, Milan, July 2nd-6th.
- CNR .2015. “Istruzioni per la Valutazione della Sicurezza Strutturale di Ponti Stradali in Muratura” CNR-DT 213/2015, Rome, Italy, pp. 108 (in Italian).
- Erdogmus and Boothby 2004. Strength of spandrel walls in masonry arch bridges. *Journal of the Transportation Research Board* 1892, No. 1. pp.47–55
- Explore Pennsylvania History. 2022. <https://explorepahistory.com/hmarker.php?markerId=1-A-1B3>
- Froio, M. 2012. Philadelphia Division: Shocks Mills Bridge. Michaelfroio.com <http://michaelfroio.com/blog/2012/10/04/philadelphia-division-shocks-mills-bridge>, Michael Froio, 2022.

- Gilbert, M., Smith, C., Cole, G., Melbourne, C. 2022. Guidance on the assessment of masonry arch bridges. *CIRIA C800*, London, 143 pp.
- Guida, M. 2010. Rockville: the bridge built to last forever. Pennsylvania Center for the Book (2022) <https://pabook.libraries.psu.edu/literary-cultural-heritage-map-pa/feature-articles/rockville-bridge-built-last-forever>, accessed 10 December 2022.
- Hendry, A. and Royles, R. 1991. Model tests on masonry arches. *Proceedings of the Institution of Civil Engineers Part 2*. 91:299–321.
- Pennsylvania Railroad. 1997. Rockville Bridge Collapse of 1997, WHTM TV-27, Harrisburg.
- Polatsu, B; Erdogmus, E. and Lourenco, P. 2019. Comparison of in-plane and out-of-plane failure modes of masonry arch bridges using discontinuum analysis. *Engineering Structures*. 178:24–36.
- Sokolovic, N.; Petrovic, M.; Kontic, A.; Koprivica, S. and Sekularac, N. 2021. Inspection and assessment of masonry arch bridges, Ivanjica case study. *Sustainability* 13,13363. doi: 10.3390/su132313363.
- Stonearchbridges.com. 2019. <https://stonearchbridges.com/2019/11/15/on-spandrel-walls/>. accessed 10 December 2022.
- United States Geological Survey. 1999. *USGS report*, U.S. Government Printing Office: 2000-573-047/20201 Region No. 8.

Three-dimensional limit analysis of barrel arch bridges

D. Coronelli

Politecnico di Milano, Milan, Italy

M.C. Giangregorio

Milan Order of Architects, Milan, Italy

ABSTRACT: A model based on the kinematic approach of limit analysis is here described and applied to analyze barrel arch bridges up to collapse. The approach extends concepts of the Discontinuity Layout Optimization (DLO), formulated by Smith and Gilbert (2007), applied for two-dimensional geotechnical, slabs and arch bridges to the three dimensional geometry and structural response of a cylindrical shell. This is done by describing the barrel structure with nodes connected to each other by the possible fracture lines and imposing compatibility and associated flow rules for rotation, sliding and twist. The simplified model of a bridge is formulated according to the component structural analysis proposed by the Italian CNR DT213/215. Experiments on masonry barrels up to collapse are considered as benchmark for the application of the model, including straight and skew barrels.

1 INTRODUCTION

The response to failure of masonry arch bridges is understood as a three-dimensional structure (Royles and Hendry, 1991). Limit analysis is one of the most commonly used tools to study the failure mechanism and predict the limit load. An upper bound approach is formulated here, allowing the calculation of the collapse multiplier and relative mechanism for the barrel vault of a bridge. Such simplified model of the bridge is formulated according to the component structural analysis, one of the approaches proposed by the Italian CNR DT213/215, as a first step to a more comprehensive three dimensional analysis including the fill, spandrel walls and abutments.

The discontinuity layout optimization (DLO) was proposed by Smith and Gilbert (2007) for plane plasticity geotechnical problems, then extended to slabs with arbitrary geometry (He, 2014) and to masonry arch bridges (Gilbert et al., 2010). Given a set of nodes in the structure geometry, the procedure allows the determination of the collapse mechanism and associated upper bound limit load, through the identification of the subset of inter-node discontinuities which are present in the critical failure mechanism.

A step to extend the general formulation of DLO to three-dimensional shell problems is proposed here. The structure geometry is described with nodes connected to each other by the possible segmental fracture lines and imposing compatibility and associated flow rules for rotation, sliding and twist.

Experiments on masonry barrel vaults tested up to collapse (Vermeltfoort, 2001) are considered as benchmarks for the application of the kinematic algorithm.

2 MODEL

2.1 *Geometry and kinematics*

It is possible to describe the geometry of the vault as an arch with a translation in the orthogonal direction to the plane where it is drawn. In Figure 1 the arch is positioned in the plane

x-z and the direction of the translation is the y axis. The origin of the global axis (x-y-z) is at one corner of the vault. The thickness of the shell is considered directed in an orthogonal direction respect to the middle surface.

On the middle surface a grid of nodes is defined. The nodes are connected to each other by fracture lines. Smith and Gilbert (2007) study 2D problems with segmental fracture lines connecting each node with all other nodes. In the formulation proposed here for barrel vaults each fracture line connects one node to the adjacent.

Compared to a rigid block analysis, obtained dividing the shell along circumferential and longitudinal planes, a more general set of possible fracture lines is considered. The two-dimensional Discontinuity Layout Optimization method in the literature consider all fracture lines obtained connecting each node to all others in the mesh. As a first step for the extension to three-dimensional geometry in shells, the formulation proposed here considers fracture lines connecting each node to the adjacent nodes in the mesh, thus limiting the length of fracture lines i.e. only a subset of fracture lines are considered.

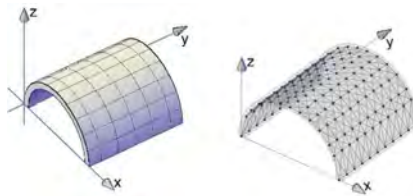


Figure 1. Division of the surface in a grid with nodes.

The formulation is three-dimensional. Two different reference systems are considered: global (x, y, z), and local (x', y', z'); the latter is different for every fracture line (YL). The local reference system chosen has the direction of the axis x' from the first node to the second node of the fracture line; axis z' is the normal to the shell surface; y' is obtained by the right-hand rule.

2.2 Formulation

The general discretized “Discontinuity Layout Optimization” (DLO) problem stated as kinematic formulation is (Smith and Gilbert, 2007):

$$\min \lambda f_L^T d = -f_D^T d + g^T p \quad (1a)$$

$$Bd = 0 \quad (1b)$$

$$N_{flow} p - d = 0 \quad (1c)$$

$$f_L^T d = 1 \quad (1d)$$

where λ is a dimensionless load factor that is found by the solution of the problem; f_D is the vector of dead load and f_L is the vector of live load; p and g are vectors of plastic multipliers and their corresponding work equation coefficients, and d contains the relative displacements and rotations along the discontinuities in the local reference system. The equation of the principle of virtual work is imposed; minimizing the collapse multiplier for the live loads, leads to Equation (1a). Considering the kinematic problem formulation for shells, a given fracture-line i contributes to the global compatibility constraint Equation (1b). B is the compatibility matrix that resolves all discontinuity displacement in global (x,y,z) components at each node; d is the vector of relative displacements and rotations in the local reference system (x', y', z'). Equation (1b) imposes that the sum of the displacements and rotations at all nodes must be zero, in the global reference system. N_{flow} is a flow matrix where the yield functions are considered (see the

following section), with positive plastic multipliers p . In this kinematic formulation the discontinuity displacements d and the plastic multipliers p are the variables solved by a linear programming algorithm, to obtain the minimum value of the multiplier of the live loads representing the collapse load, λ . The constraint in Equation (1d) allows to obtain the value of the load multiplier with the minimization on the right hand side of Equation (1a).

The vectors f_D and f_L (Figure 2) represent the forces to calculate the work of the dead load with the self-weight and the live load (Equation 1a) on the part of the structure above the fracture line.

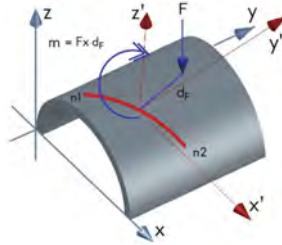


Figure 2. Load on a generic fracture line.

2.3 Plastic flow and dissipation.

Given the resistance criteria, the plastic flow components are given by the product of the N_{flow} matrix by the plastic multipliers, expressed with positive and negative parts.

The flexural rotation ϑ_x , the twist ϑ_y , the in plane rotation ϑ_z , and the three displacements sliding δ_x δ_z and the positive only δ_y for tension are allowed. Rotations and sliding displacements are coupled with normal displacements (Figures 3 and 4). If the line represents a free boundary, all the rotations and displacements are allowed, and there is no coupling between the different displacements.

$$Np - d = \begin{bmatrix} 1 & -1 & 0 & 0 & 0 & 0 & 0 & 0 & 0 & 0 & 0 \\ 0 & 0 & 1 & -1 & 0 & 0 & 0 & 0 & 0 & 0 & 0 \\ 0 & 0 & 0 & 0 & 1 & -1 & 0 & 0 & 0 & 0 & 0 \\ 0 & 0 & 0 & 0 & 0 & 0 & 1 & -1 & 0 & 0 & 0 \\ t/2 & t/2 & \tan \phi \cdot cT & \tan \phi \cdot cT & l/2 & l/2 & \tan \phi & \tan \phi & 1 & 0 & \tan \phi & \tan \phi \\ 0 & 0 & 0 & 0 & 0 & 0 & 0 & 0 & 0 & 0 & 1 & -1 \end{bmatrix} \begin{bmatrix} p_{1i}^+ \\ p_{1i}^- \\ p_{2i}^+ \\ p_{2i}^- \\ p_{3i}^+ \\ p_{3i}^- \\ p_{4i}^+ \\ p_{4i}^- \\ p_{5i}^+ \\ p_{5i}^- \\ p_{6i}^+ \\ p_{6i}^- \end{bmatrix} - \begin{bmatrix} \vartheta_{ni} \\ \vartheta_{zi} \\ \delta_{x'i} \\ \delta_{y'i} \\ \delta_{z'i} \end{bmatrix} = \mathbf{0}$$

Linear relations are used to define the yield functions, and normality is assumed for the fracture line representing a constrained boundary or an internal discontinuity. The length of the segment connecting two adjacent nodes is indicated as l . The flexural yield function is based on infinite compression and no tension, with the section rotating around the intrados or extrados edge for ϑ_{ni} and around the discontinuity ends for ϑ_{zi} . The flow is formulated with friction angle ϕ and non-zero cohesion for shear and torsion. The torsion moment cT on the cross section is calculated following Portioli et al. (2014).

The analysis of skew bridge vaults requires considering the shear and torsion stresses acting together with normal stress, in relation to the masonry texture used (CNR, 2015; Sarhosis et al., 2014). Lourenço (2000) studied the out-of-plane response of masonry panels and shells,

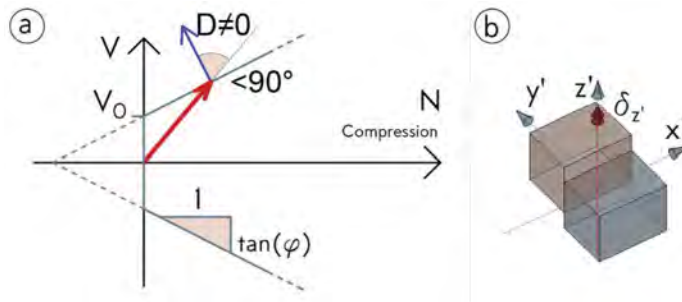


Figure 3. a) Yield function with shear and normal force and b) sliding.

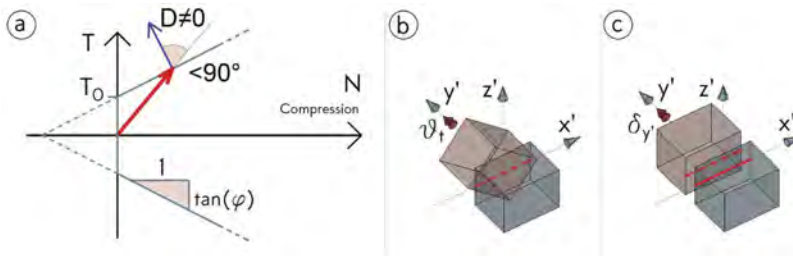


Figure 4. a) Yield function with torsion and axial forces and b) twist c) displacement.

showing that the flexural resistance in the plane orthogonal to the courses can be the double of that parallel to the masonry bed joints. Tassios and Avramidou (1988) discussed the variability of friction angle, considering failures in directions equal to or different from the bed joints plane.

To consider the effect of the masonry texture, in the formulation used here values of the friction coefficient and cohesion based on tests are considered for the discontinuities parallel to the joint planes, and the one for the other directions which was 50% greater.

3 RESULTS

The case of a square barrel vault tested by Vermeltoort (2001) is shown (Figure 4). The span is 3m, and the width 1.25m, with a vault thickness of 0.1m. The masonry texture has courses parallel to the support lines. Load lines were spaced 0.6m in plan. Three constant loads of 5KN were applied at the first, third and fourth transverse lines, while the live load was in the second position from the left support (see Figure 5).

A coefficient of friction $\tan(30^\circ)$ and cohesion 0.1MPa are considered for the discontinuities parallel to the joint planes, and 50% greater for the other directions.



Figure 5. Test results (Specimen R1, Vermeltoort, 2001): cracking close to failure.

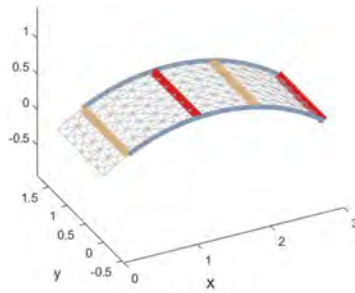


Figure 6. Analysis results, flexural fracture lines (red sagging, yellow hogging).

Figure 6 shows the collapse mechanism analysis results, with four flexural hinge lines, sagging under the load and right support, hogging on the left near to support and at the right of the live load. The limit load prediction was 37.5kN, while the test result was 40.7kN.

The case of a skew bridge vault tested by Vermeltoort (2001) is shown (Figure 7). The span of the bridge is 3m, and the width 1.25m, with a vault thickness of 0.1m. The skew is obtained by translating in plan one support over a distance equal to the bridge width. The masonry texture has courses parallel to the support lines. Three constant loads of 5kN were applied at the first, third and fourth transverse lines (see Figure 5), in the direction perpendicular to the inclined edge. A variable load at the second line was increased to failure, reaching a limit load of 26kN, with the mechanism showing the hinging described in Figure 7.



Figure 7. Test results (specimen S2, Vermeltoort 2001): cracking at failure.

The results (Figure 8) show flexural hinging at location corresponding to those observed experimentally, together with twist, in particular along the hinging directions. The limit load predicted is 36.75 kN.

The model was developed focusing on obtaining a mechanism comparable to the test results. The overestimation of the experimental result can be explained by the absence of the interaction of shear and torsion in the formulation, and the associated flow used. In addition, the fixed position of discontinuities can contribute to this result of an upper bound discrete approach.

4 CONCLUSIONS AND DEVELOPMENTS

A kinematic limit analysis model is proposed to consider the 3D collapse mechanism and failure load of arch bridge vaults. Three relative displacements and three rotations are considered at the interface between portions of the structure. Infinite compression strength and no-tension are considered for normal stresses; constant friction with non-zero cohesion are considered for shear stresses. The masonry orthotropy is modelled assuming higher friction and cohesion along the directions different from the masonry bed-joints.

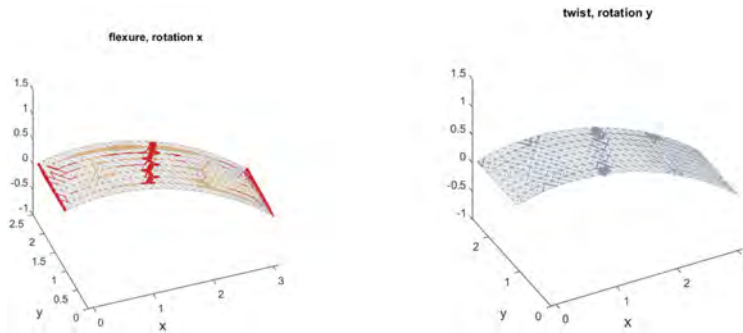


Figure 8. Analysis results: (a) flexural rotations (red sagging, yellow hogging); (b) twist.

As a first step for the extension of Discontinuity Layout Optimization to three-dimensional geometry in shells, the formulation proposed here considers fracture lines connecting each node to the adjacent nodes in the mesh. The developments should consider all possible fracture lines, extending the formulation proposed.

Results for square and skew arch bridge vaults show fair agreement with test results. The model setup considers only the barrel vault; further research will include other parts of the bridge structure.

The collapse mechanism prediction provides indications for the assessment, with the possibility to compare the crack pattern in a survey to the analytical results, and supports the choice of the position of monitoring locations.

ACKNOWLEDGEMENTS

The authors acknowledge the collaboration with prof. Matthew Gilbert, during a visiting PhD period at the University of Sheffield in 2019. The authors are grateful to Prof. A.T. Vermeltoort for the personal communications and the photographic material on the test results.

REFERENCES

- CNR. 2015. Istruzioni per la Valutazione della Sicurezza Strutturale di Ponti Stradali in Muratura. CNR-DT 213/2015, Rome, Italy, pp. 108 (in Italian).
- Gilbert M., He L., Smith C.C., Le C.V. 2014. Automatic yield-line analysis of slabs using discontinuity layout optimization. *Proc. R. Soc. A* 470: 20140071.
- Gilbert M., Smith C.C., Pritchard T.J. 2010. Application of discontinuity layout optimization to geotechnical limit analysis problems. *Proceedings of the Institution of Civil Engineers, Engineering and Computational Mechanics*, 163 September 2010 Issue EM3, Pages 155–166, doi: 10.1680/eacm.2010.163.3.155.
- Royles, R., Hendry, W.A. 1991. Model tests on masonry arches. *Proceedings of the Institution of Civil Engineers*, Part 2, 91, June, 299–321.
- Lourenço, P.,B. 2000. Anisotropic softening model for masonry plates and shells. *J. Struct. Eng., ASCE*, 2000, 126(9): 1008–1016.
- Portioli F., Casapulla C., Cascini L., D’Aniello M., Landolfo R. 2013. Limit analysis by linear programming of 3D Masonry structures with associative friction laws and torsion interaction effects. *Arch Appl Mech*, 83, pp 1415–1438.
- Sarhosis V., Oliveira D.V., Lemos J.V., Lourenco P. B. 2014. The effect of skew angle on the mechanical behaviour of masonry arches. *Mechanics research communications*. 61, pp. 53–59.
- Smith C.C., Gilbert M. 2007. Application of discontinuity layout optimization to plane plasticity problems. *Proc. R. Soc. A* 463, pp. 2461–2484.
- Tassios, T.P., Avramidou, N. 1988. *Meccanica delle murature*. Liguori Ed. ISBN-13: 9788820716387, 240 pp. (in Italian).
- Vermeltoort A.T. 2001. Analysis and experiments of masonry arches. In: P.B. Lourenço & P. Roca (Eds.), *Proc. Historical Constructions*, Guimarães, PT.

The Reinforced Arch Method for the life of the ancient bridge of Omegna

L. Jurina & E.O. Radaelli

JURINA e RADAELLI Studio Associato, Milan, Italy

D. Coronelli

Politecnico di Milano, Milan, Italy

ABSTRACT: Extending the life of historic masonry bridges frequently requires strengthening of arches showing damage or limited load bearing capacity. The “Reinforced Arch Method” (RAM) uses a cable on the extrados and/or the intrados, prestressing the blocks. A recent application is the xv century bridge (Ponte Antico) in Omegna (Verbania, IT) along a route of an historic quarrying district. Originally formed of two stone arches, today a damaged structure with one arch remains after a 20th century collapse. The structure is modelled numerically and assessed in the present condition and with the strengthening by four extrados cables, comparing the results of a linear elastic finite element model and limit state verifications, and static limit analyses with optimization of the thrust line and limit load. The strengthening and the intervention proposed for the collapsed arch are discussed, in relation to their new life as a footbridge on a touristic route.

1 INTRODUCTION

The necessity of interventions on arch structures is frequent in the field of the strengthening of historic masonry bridges showing damage conditions or limited load bearing capacity for live loads. The damage is generally related to the limited tensile and flexural strength of masonry, particularly in the presence of non-symmetrical gravity loading, horizontal seismic actions or, as in the case considered in this paper the effects of water pressure during a flood.

Historic bridges suffer from the environmental actions along centuries of life, and the lack of maintenance. Climate change causes flooding and extreme flow conditions causing increasing threats for these systems (Drdacky and Slizkova, 2012).

A strengthening technique denominated “Reinforced Arch Method” (RAM) has been proposed by the first author (Jurina, 2012). The method consists in the laying of a tension cable on the extrados and/or the intrados of the arch, in order to prestress the blocks thus providing flexural strengthening. The cable tension brings the system in action by applying a set of radial forces on the arch, leading to a reduction of the thrust-line eccentricity, thus avoiding or anyway delaying the formation of flexural hinges. The over 500 experimental tests carried out on scale models have demonstrated the validity of this method, using arches with different geometries: roman, pointed and segmental arches.

A recent application of the RAM method, with ongoing worksite activities, has been the historic bridge on the Strona torrent in Omegna (Verbania, IT). This construction which dates back to the xv century was originally formed of two stone arches, each measuring 13.30 metres, along a route of an historic quarrying district. Today a damaged system with only one arch remains after a collapse at the start of the 20th century. Restoration and strengthening activities have been undertaken. Within the structural assessment and design, the structure has been

modelled numerically both in the present condition and with the strengthening by way of four extrados cables, pre-tensioned by 30KN each. The paper shows the assessment results obtained by a linear elastic finite element method, and limit analyses with a static approach to calculate the collapse load multiplier, using a recently developed calculation model.

The intervention proposed for the masonry arch of the bridge that collapsed is discussed, in relation to its compatibility with the surviving structure and its new life as a footbridge on a touristic route.

2 BRIDGE DESCRIPTION AND CONDITIONS

The bridge over the Strona torrent is located in the municipality of Omegna (VB). The construction dates back to the 15th century, by the will of Duke Gian Galeazzo Sforza, and consisted of two stone arches. The eastern bank humped back arch collapsed at the beginning of the 20th century.



Figure 1. Life of the bridge (a) in the early 20th century (left); (b) in 1952 after the collapse (right) of the eastern span; (c) conditions prior to the restoration works; (d) rendering of the restoration project.

The arch span is 13.6m, the cross section thickness 0.4m and width 2.1m. The standing Western wing walls extend 6m on the bank. The central support is on rock elevating above the water flow. The collapsed span to the East corresponded to a lower elevation above water flow; the collapse was related to erosion of the foundation on this bank side with the torrent in full spate. Figure 1a shows the conditions prior to the collapse. Figure 1 b-c show the conditions in recent times, after the collapse and prior to the start of restoration works. Further damage of the walls and parapet above the standing arch is visible. Figure 1d shows a rendering of the restoration project described in the next section.

3 INTERVENTION AND RECONSTRUCTION

The intervention (Figure 2) includes foundation strengthening by piles reaching rock at 4.5m depth, strengthening of the stone arch (RAM), spandrel and wing walls ties, reinforced concrete arch construction and a reinforced concrete slab for the whole length of the bridge roadway. The missing span is replaced with a reinforced concrete arch structure faced with stone. This choice, approved by the Ministry of Cultural Heritage, was the fruit of the comparison of different alternative solutions (see Section 6).

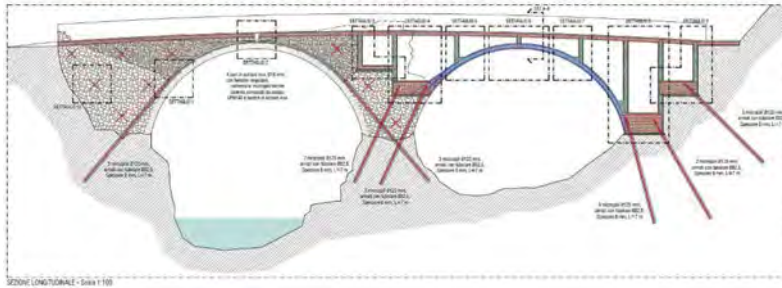


Figure 2. Structural restoration with cable layout and anchoring, and new bridge span.

4 THE REINFORCED ARCH METHOD (RAM)

The main purpose of the “RAM – Reinforced Arch Method” is to modify the distribution of loads, acting on the arch, vault or dome so that the combination of the old loads plus the new loads can be the “right one” for the given and known geometry of the masonry structure. It’s worth to mention that cables can be applied with similar effects either on the extrados or the intrados of the arch, obtaining the same consolidation results. In the first case (i.e. at the extrados) cables can be simply laid down on the masonry or, if needed, a thin layer of fiber reinforced mortar can be interposed to regularize the surface. In the second case (i.e. at the intrados) some connection devices are needed to transfer the loads between cables and masonry.

Experimental and numerical results showed a linear relationship between the load multiplier factor μ and the tension force N applied to the cables.

The Reinforced Arch Method, in its several variations, is an innovative solution that adjusts many different geometries, with acceptable aesthetic results and other important advantages, such as: necessity, lightweight, minimally invasive, removability.

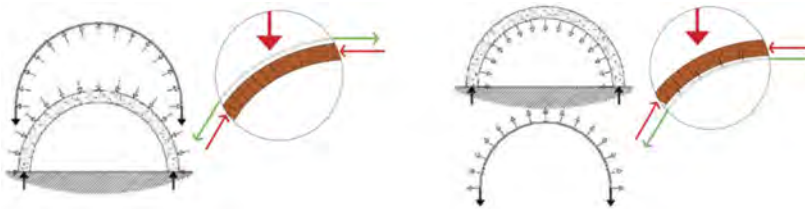


Figure 3. Radial forces applied on the arch by means of RAM (extrados and intrados).

The extrados solution was chosen for the Omega bridge because the conditions of the structure easily allowed the removal of the remaining part of the construction on top of the arch, to install the system.

5 MODELS FOR ASSESSMENT AND DESIGN

5.1 Materials

The arches, spandrels and abutments are made of roughly cut stone masonry. The fill is made of rubble with an estimated unit weight of 10 KN/m^3 . Material properties were determined with the Italian Code NTC2018. The characteristic compression strength is 3.2 MPa and the factored strength for ultimate limit state verifications is 0.95 MPa . For shear the friction coefficient is equal to 0.4 and the characteristic cohesive bond strength 0.065 MPa (factored 0.02 MPa). The strengthening ties are made of stainless steel INOX AISI 316, diameter $\Phi 16 \text{ mm}$ with 222 wires, grade 1470 MPa .

5.2 Finite element analysis and verifications

The design and verifications were carried out based on the Italian code NTC 2018. Four linear elastic FEM models were set up using SAP2000 (CSI, 2019) – see Figure 4:

- 1) 3D model with plane shell elements for the existing arch and spandrel and wing walls, for static loading; this corresponds to the as built configuration prior to the intervention.
- 2) 3D model with the addition of brick elements for the fill; this corresponds to the strengthened existing stone masonry structure;
- 3) 2D model with one-dimensional frame elements for the new RC arch span, for static loading;
- 4) 3D model of the whole bridge for seismic verifications.

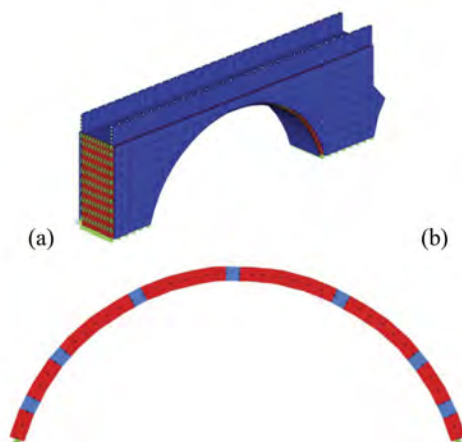


Figure 4. Finite element model: (a) the western span (model n.2); (b) the barrel and reference sections.

Flexural resistance verifications were based on the eccentricity e calculation, from the calculated axial force and moment in the arch cross-section; cracking occurs for $e > t/6$ and loss of resistance for $e > t/2$ (t = cross-section depth).

The strengthening effect is considered by an increase of the axial force in each cross section, equal to the tension in the cables.

The load conditions were the gravity loading ultimate limit state and the seismic actions; the latter are low in relation to the seismicity of the site and are not discussed in the following.

5.3 Limit analysis

A 2D limit analysis model has been developed. The arch is divided into rigid blocks separated by interfaces where flexural and sliding verifications are carried out. No-tension interfaces are used. Finite compression strength is considered, limiting the thrust line position within a band interior to the block depth. For the shear interface a constant friction coefficient equal to 0.4 is used. A linear program is solved obtaining the maximum static multiplier, corresponding to the limit load and the optimized thrust line position.

The effect of the RAM strengthening is modelled as resultant radial forces on each block, calculated as components of the tie tension forces along the extrados with a circular shape.

The model is set up with 20 blocks for the arch; the remaining parts are modelled as loads:

- Case 1: arch weight (20 KN/m³), fill weight (10 KN/m³), spandrel walls (18 KN/m³) and live load.
- Case 2: the same as Case 1, with the addition of radial forces transferred by RAM ties.

Table 1. FEM analyses, internal forces and normal stress.

A) Non-reinforced bridge.								
Section	Comb.	N (KN)	M (KNm)	e=M/N (m)	condition	Stress σ_{N+M} * (MPa)	Strength f_d (MPa)	σ_{N+M} / f_d
1	A	182	27	15	Cracked	1.39	0.95	1.46
	B	260	29	11	Cracked	1.09	0.95	1.15
2	A	163	39	24	e > h/2		0.95	
	B	221	41	19	Cracked	5.37	0.95	5.65
3	A	147	1	1	e < h/6	0.21	0.95	0.22
	B	156	1	1	e < h/6	0.21	0.95	0.22
4	A	111	30	27	e > h/2		0.95	
	B	157	31	20	Cracked	20.10	0.95	21.16
5	A	144	2	1	e < h/6	0.21	0.95	0.22
	B	203	5	1	e < h/6	0.33	0.95	0.35
6	A	158	34	10	e > h/2		0.95	
	B	231	35	10	Cracked	1.61	0.95	1.69
7	A	242	29	12	Cracked	1.09	0.95	1.15
	B	176	28	16	Cracked	1.63	0.95	1.72
B) RAM reinforced bridge.								
Section	Comb.	N (KN)	M (KNm)	e=M/N (m)	condition	Stress σ_{N+M} * (MPa)	Strength f_d (MPa)	σ_{N+M} / f_d
1	A	272	27	10	Cracked	0.99	0.95	1.46
	B	350	29	8	Cracked	1.06	0.95	1.15
2	A	253	39	15	Cracked	1.92	0.95	
	B	311	41	13	Cracked	1.56	0.95	5.65
3	A	237	1	0	No cracking	0.31	0.95	0.22
	B	246	1	0	No cracking	0.32	0.95	0.22
4	A	201	30	15	Cracked	1.28	0.95	
	B	247	31	13	Cracked	1.07	0.95	21.16
5	A	234	2	1	No cracking	0.32	0.95	0.22
	B	293	5	2	No cracking	0.44	0.95	0.35
6	A	248	34	14	Cracked	1.33	0.95	
	B	321	35	11	Cracked	1.17	0.95	1.69
7	A	332	29	9	Cracked	1.03	0.95	1.15
	B	266	28	11	Cracked	1.00	0.95	1.72

A = combination for maximum flexural stress; B = combination for maximum axial force effect.

(*) calculated with no tension assumption, linear stress distribution

Figure 5 shows the comparison of design moments in combination 2 and cross-section resistance for the non-reinforced and reinforced configurations; in addition the moment distribution for the limit load is shown. Figure 6 shows the increase of the limit load relative to the design load, for increasing tension of the reinforcement. The masonry strength increase given by bed-joint repointing and injections is considered as well, in the passage from non strengthened (tension = 0) to strengthened cases.

5.4 Comparison of results

The project allows the comparison of different analysis and verification methods. Elastic finite element analysis sets up a model with geometrical features closely related to the survey results for

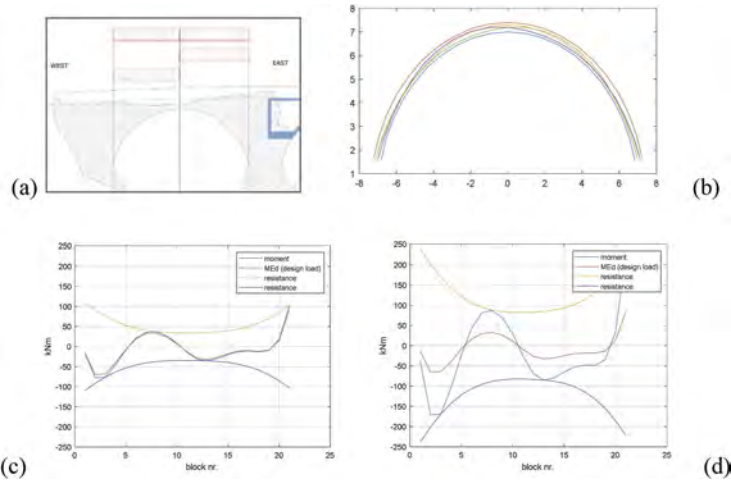


Figure 5. (a) Variable load distributions and (b) strengthened arch lines of thrust for limit loads. Comparison of moment load effects for arch (c) without strengthening (combination 1, limit multiplier = 1.1) and (d) with RAM strengthening (combination 1, limit multiplier = 2.64).

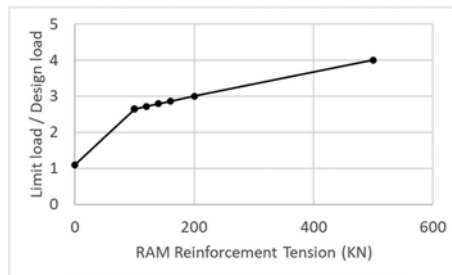


Figure 6. Increase of the limit load relative to design load as a function of RAM reinforcement tension.

arch vault, spandrel walls and fill. With a choice of elastic material properties the model furnishes an equilibrium solution for selected load distributions. This can be used for the structural verifications prescribed by codes, such as the Italian national specifications, under the assumptions of no-tension and limited compression and shear strength. The assumed elastic behavior highlights critical structural conditions by elevated eccentricity of the normal force in the arch sections, resulting in very high compression stress or even eccentricity beyond the section limits.

Limit analysis model considers only the arch as load bearing element. The cross section limit moments are calculated with finite compression and no tension strength, without the possibility of exceeding the cross-section resistance with a model closer to the masonry arch mechanical response.

Figure 7 shows the comparison of the ratio of maximum compression stresses and strength in the FEM based design (Section 5.2) with the ratio of the design moments to the resistance for the limit analysis (Section 5.3). The design moments are obtained dividing the limit moments by the maximum load multiplier obtained. The two models are based on different assumptions. The limit state verifications are carried out for the maximum compression and shear stresses compared to the corresponding strength. The stress distribution is linear in the compression zone. This leads to determine more critical conditions, particularly for the non-reinforced arch (see Table 1) and for the reinforced arch as well.

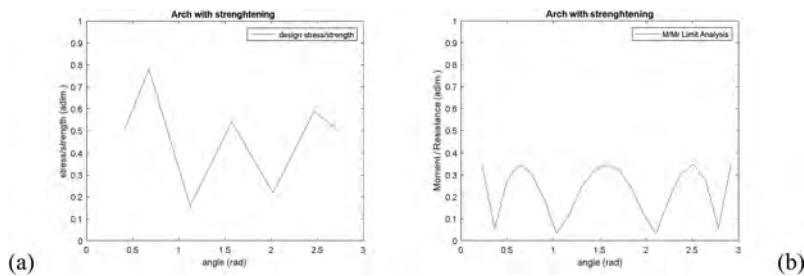


Figure 7. Comparison of assessment results for the resistance of the RAM reinforced arch, full load combination 1 (a) ratio of design stress and strength (from elastic analysis); (b) ratio of design load moments to moment resistance (limit analysis).

6 DISCUSSION

The life of the bridge started in the XV century in relation to mining and quarrying activities of the Strona valley. The intervention was urgent because of the risk of collapse of the remaining span, damaged by the flow of the Strona torrent. A new phase will start with the restoration and strengthening of the bridge, aiming at providing a path for pedestrians within a cultural and touristic project.



Figure 8. Study of alternative solutions: examples of projects: a) medieval bridge in Su Ponti Ecciu - Allai (Oristano) b) Pont Trencat (Catalunya); c) Roman bridge in Sogliano al Rubicone (www.jurina.it).

The solution chosen for the span that collapsed was the result of a multidisciplinary work in collaboration with the Ministry of Cultural Heritage. The structural and the architectural designers, evaluated multiple solutions relating to the method of reconstruction of the collapsed span; examples of projects in the practice were taken into consideration (Figure 8). In fact, different structural materials were considered, including masonry, steel and concrete, analyzing their advantages and disadvantages in terms of ease of execution, durability, maintenance and, last but not least, costs. The final choice was the use of reinforced concrete, finished with roughly cut stones.

7 CONCLUSIONS

The following conclusions can be drawn, based on the case study shown, concerning the RAM strengthening system, analytical methods for verification and design solutions to extend the life of the historic bridge in Omega.

The strengthening system provides an increase in resistance proved by two different verification methods, maintaining the features of the original construction where this was still standing. The project allows the comparison of different analysis and verification methods. Finite element analysis provides a good geometric model with relative ease, using available commercial packages. The elastic solution with equilibrium, though different from the real behavior

of a masonry structure, gives indications for design based on a lower bound approach. These can be integrated with a limit analysis lower bound model, with a more simple geometry but assumptions closer to masonry response. Thrust line analysis with limits for eccentricity can be easily set up e.g. using a spread sheet, predicting the limit load. Developments considering limited compression strength and shear sliding within an optimization solution have been shown in the paper.

The solution chosen to reconstruct the part that collapsed was the result of a comparative study considering different configuration and materials. The elements in favor of a reinforced concrete system with a stone facing were the structural stability and cost of this solution.

ACKNOWLEDGEMENTS

The authors acknowledge the role of the project committee coordinated by Don Gianfranco Lanfranchini, the financial support provided by CARIPLO, 2019 “Interventi emblematici”, the construction works carried out by Panizza 1914 srl (Trenzano, BS), and architects A. Baldioli and G. Ciuffo

REFERENCES

- CSI. 2019 CSI Analysis Reference Manual – SAP 2000 Advanced Research, Computers and Structures Inc.
- Drdácký M., Slížková Z. 2012. Structural strategies and measures reducing flood action on architectural heritage. www.witpress.com, ISSN 1743-3517 (on-line) *WIT Transactions on Information and Communication Technologies*, Vol 44, © 2012 WIT Press. doi:10.2495/RISK120221.
- Jurina, L. 2012. Strengthening of masonry arch bridges with RAM - Reinforced Arch Method. *Bridge Maintenance, Safety, Management, Resilience and Sustainability*. Proceedings of the Sixth International Conference on Bridge Maintenance, Safety and Management, p.1063–1070.
- Ministero degli Interni. 2018. NTC2018 - Norme Tecniche per le Costruzioni. D.M.17 Gennaio 2018 (in Italian).

Numerical investigation of 3D response characteristics of masonry bridges by detailed mesoscale masonry models

M.S. El Ashri, S. Grosman, L. Macorini & B.A. Izzuddin
Imperial College London, London, UK

ABSTRACT: This paper adopts a detailed 3D mesoscale modelling strategy to tackle the pressing challenge of assessment for masonry arch bridges. Most of these structures have undergone severe deterioration during their service-life under both increasing traffic loads and environmental actions. However, they still represent a major portion of existing infrastructure for roadway and railway traffic in Europe. The development of reliable assessment methods for such structures is urgently required. However, this is clearly hindered by their complex behaviour. In the adopted modelling strategy, the heterogeneous nature of masonry arch bridges is addressed by adopting a discrete mesoscale modelling for masonry components in conjunction with a continuous modelling for backfill. In addition, the interaction between the different bridge parts is accounted for using nonlinear interface elements at the physical interfaces, where a mesh tying approach is employed to connect non-conforming meshes. The computational effort associated with such detailed models is efficiently optimised using a domain partitioning technique, where the bridge is subdivided into smaller partitions allowing for an efficient parallel computation. This modelling strategy aims at capturing the overall behaviour of masonry arch bridges, which is dominantly three-dimensional mainly due to the asymmetry of typical traffic loads and the complex geometry in the case of skew bridges. In the paper, the response of realistic 3D bridge samples with various loading and geometric configurations is investigated leading to an improved understanding of their typical 3D behaviour to collapse.

1 INTRODUCTION

To identify the main behavioural characteristics of masonry arch bridges, both experimental and analytical investigations have been carried out over the past few decades. The experimental tests carried out by Transport Research Laboratory (TRL) (Page, 1995), as well as Melbourne and his collaborators (Melbourne & Gilbert, 1995, Hodgson, 1996) have demonstrated a 3D behaviour associated with masonry arch bridges. Such 3D behaviour can be fully captured only by using 3D assessment methods, a need which has been recently addressed by several researchers. Milani & Lourenco (2012) developed a macro-scale FE homogenised strategy to investigate the 3D behaviour of masonry arch bridges. Thereafter, Papa et al. (2021) put forward a 3D adaptive limit analysis procedure, which can be used to predict the ultimate behaviour of skew arches interacting with backfill. Discrete Element Method (DEM) has been lately used by Forgács et al. (2018) and Pulatsu et al. (2019) to develop 3D models for masonry arch bridges taking into account the contribution of both backfill and spandrel walls.

The 3D mesoscale modelling approach adopted in this paper has been previously utilised to analyse both single span (Zhang et al., 2018) and multi-span masonry arch bridges (Tubaldi et al., 2018). In these previous studies, a simplified continuum approach was adopted for modelling spandrel walls, where they were considered as a lateral extension for the backfill but with different material parameters. Recently, a mesoscale description for spandrel walls that allows for the actual masonry bond has been developed, and it has been adopted for the

analysis of single span square arch bridges (Grosman et al., 2021). In this paper, this full mesoscale description is further extended to analyse single span skew arch bridges, as outlined in the following sections.

2 METHODOLOGY

To develop an improved understanding for the complex 3D behaviour of masonry arch bridges, a 3D modelling strategy that can capture cracks and plastic deformations within the structure up to collapse is adopted in this paper. This strategy accounts for the nonlinear behaviour of different bridge components, as well as their mutual interaction. This is achieved by using the discrete 3D mesoscale modelling approach developed by Macorini & Izzuddin (2011) to model the masonry components in the bridge, allowing for the actual masonry bond within the arch barrel and spandrel walls. This approach utilises 3D elastic solid elements to model masonry units and 2D zero-thickness nonlinear interface elements to model both mortar joints and potential fracture planes within bricks. Each brick unit is modelled using two solid elements with an interface element in the middle of the brick to allow for cracking within the brick itself due to tension or shear. The material nonlinearity in masonry is lumped within the interfaces using the cohesive-frictional material model developed by Minga et al. (2018a), whereas geometric nonlinearity is considered using a co-rotational approach for interface elements and using Green's strains for solid elements. This is complemented with a continuous elastoplastic modelling approach for backfill, where the backfill domain is discretised using 3D solid elements. The plastic response for backfill is defined by a modified Drucker-Prager yield criterion as described by Zhang et al. (2018).

In addition, the interaction between the different parts of the bridge is considered using nonlinear interface elements at the physical interfaces between the different domains, where the same material model used for the interface elements within the mesoscale representation of masonry is adopted. Having matching interfaces between the different components could be impractical. Therefore, a mesh tying method, which has been developed by Minga et al. (2018b) based on the mortar method, is adopted to allow for the connectivity between non-conforming meshes between the arch barrel, backfill, and spandrel walls.

Such detailed models are associated with a significant computational cost which is efficiently reduced using a domain partitioning technique (Jokhio & Izzuddin, 2015), where the bridge is subdivided into smaller partitions. These partitions are linked together using a parent structure allowing for an efficient parallel computation, where each partition is analysed using an independent processor. This whole proposed methodology is implemented in the nonlinear finite element program ADAPTIC (Izzuddin, 1991).

3 NUMERICAL SIMULATIONS

3.1 *Validation*

To demonstrate the capability of the adopted mesoscale modelling strategy to simulate the response of masonry arch bridges, two experimental tests are used for validating the proposed numerical models. The first test is on the square arch bridge "Square Bridge 3-3" tested at Bolton Institute (Melbourne & Gilbert, 1995), while the second test is on the skew arch bridge "Skew Bridge 3-3" tested by Hodgson (1996). The two bridges have similar dimensions with a span of 3m, a rise of 0.75m and a width along the abutments of about 3.5m. Also, the arch barrel for both bridges is composed of 2 rings following the stretcher bond with a total thickness of 0.215m. The spandrel walls are built according to the English bond on top of the arch barrel at each face to confine a crushed limestone backfill. The two bridges are tested up to failure under a line load applied at quarter-span parallel to the abutments. It should be noted that the skew bridge is constructed according to the helicoidal method with a 45° skew angle.

Since the two bridges have been tested within the same experimental programme, the properties for the construction materials of the two bridges are comparable as indicated in (Melbourne & Gilbert, 1995) and (Hodgson, 1996). The material parameters for the mesoscale models are calibrated based on the material tests performed within the experimental programme. These properties include the compressive strength, Young’s modulus and Poisson’s ratio for brickwork. Also, the properties for the backfill are provided based on the material tests performed within the experimental programme, where the friction angle is 60° and the cohesion is almost negligible. However, the provided properties do not cover all the parameters required for the numerical models. Therefore, the remaining parameters are calibrated based on previous research by Zhang et al. (2018) and Grosman et al. (2021) to validate the square arch bridges “Bridge 3-1” and “Bridge 3-3” tested at Bolton Institute (Melbourne & Gilbert, 1995). The main material parameters used for the validation of the numerical model are provided in Table 1.

Table 1. Material parameters for interface elements.

		Mortar joints	Backfill-Arch	Spandrel wall-Arch
Normal stiffness (k_n)	N/mm ³	100	40	100
Tangential stiffness (k_t)	N/mm ³	50	20	50
Tensile strength (f_{ti})	MPa	0.20	0.002	0.10
Compressive strength (f_{ci})	MPa	26	26	26
Cohesion (c)	MPa	0.25	0.003	0.15
Fracture energy in tension (G_{ti})	N/mm	0.01	1E5	0.01
Fracture energy in shear (G_{si})	N/mm	0.05	1E5	0.05
Internal friction angle (ϕ_i)	Rad	0.464	0.54	0.464
Dilatancy angle (ψ_i)	Rad	0.00	0.00	0.00

The numerical load-displacement curves for both square and skew bridges provide a good approximation to the experimental response as shown in Figures 1(a) and (b). The numerical response in both cases slightly overestimates the peak load by about 10%, and slightly underestimates the experimental initial stiffness. The deformed shapes at failure for both square and skew bridges, as outlined in Figures 2-4, agree in having a four-hinge failure mechanism for the arch barrel, where the hinges form below the load, around three-quarter span, and at the two springings. However, the failure mode in the case of square bridge is purely two-dimensional under the effect of the line load. This is not the case for the skew bridge which fails under a three-dimensional four-hinge mechanism, where the formed hinges are not parallel to the abutments. Moreover, the hinges take a saw-toothed pattern due to the helicoidal construction method for skew arches. In addition to the four-hinge mechanism, a notable sliding between the two rings of the arch barrel is predicted for both bridges, which agrees with the experimental observations (Melbourne & Gilbert, 1995, Hodgson, 1996). The numerical

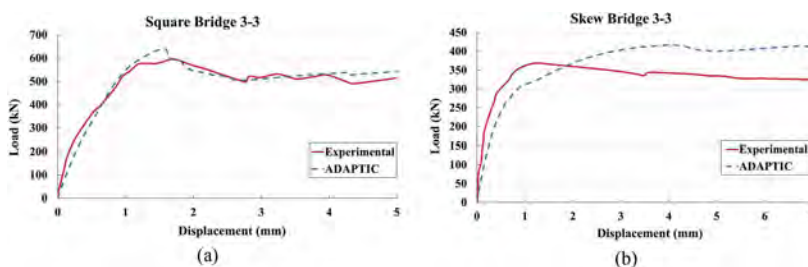


Figure 1. Numerical and experimental load-displacement curves for the vertical displacement below line load on the intrados of (a) square bridge 3-3 (Melbourne & Gilbert, 1995); (b) skew bridge 3-3 (Hodgson, 1996).

deformed shapes clearly exhibit out-of-plane deformations for the two spandrel walls close to the loading beam. The crack pattern for spandrel walls at failure includes two main vertical cracks close to the loading beam and at three-quarter span due to the deformations of the arch barrel. These two cracks are accompanied by a horizontal crack at the base of the spandrel/wing wall away from the load. Although this crack pattern applies to the two spandrel walls in the square bridge, it only applies to the Eastern spandrel wall in the skew bridge due to the three-dimensional response associated with asymmetric skew geometry.



Figure 2. Square Bridge 3-3 (Melbourne & Gilbert, 1995) (a) experimental crack pattern; (b) deformed shape at failure.

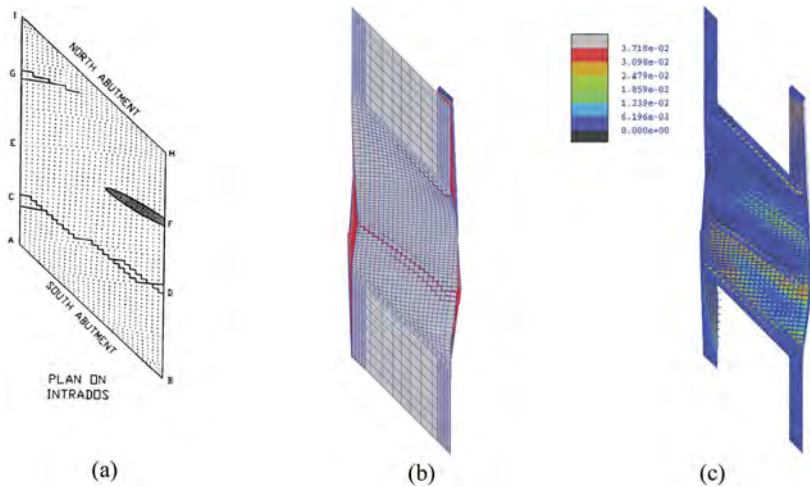


Figure 3. Skew Bridge 3-3 intrados (Hodgson, 1996) (a) experimental crack pattern; (b) deformed shape at failure; (c) contours of plastic work developed in the interfaces due to tension W_{cr1} .

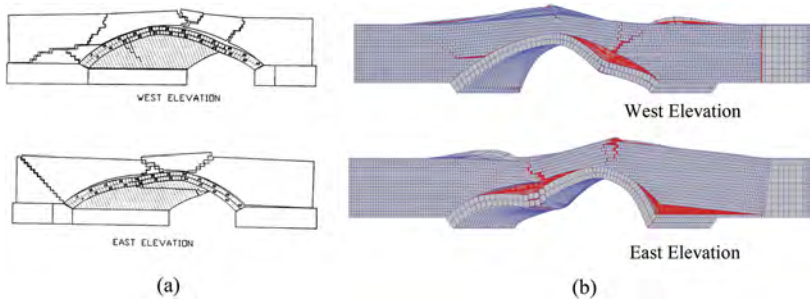


Figure 4. Skew Bridge 3-3 (Hodgson, 1996); West Elevation (top) and East Elevation (bottom); (a) experimental failure mechanism; (b) deformed shape at failure.

3.2 Parametric study on masonry arch bridges

The validated numerical models for both the square and skew arch bridges are considered as control specimens for the development of a parametric study on masonry arch bridges. This parametric study aims at developing a more profound understanding for the complex behaviour of masonry arch bridges under various loading conditions.

3.2.1 Line load parallel to abutments

First, a line load parallel to the abutments is applied at mid, third, quarter, and eighth span. For the case of square bridges, the load capacities under line loads at third, quarter and eighth of the span are almost identical, where the load at the third span is the most critical. Conversely, the line load at the mid-span exhibits the highest load capacity compared to the other locations, as depicted in Figure 5(a). The load-displacement response for the case of skew bridges, as shown in Figure 5(b), indicates that line load at quarter span is the most critical, followed by the loads at third, eighth, and mid span respectively. For both the square and skew bridges, the initial stiffness for the bridge under line loads declines as the load is applied further from the abutments as indicated in both Figures 5(a) and (b).

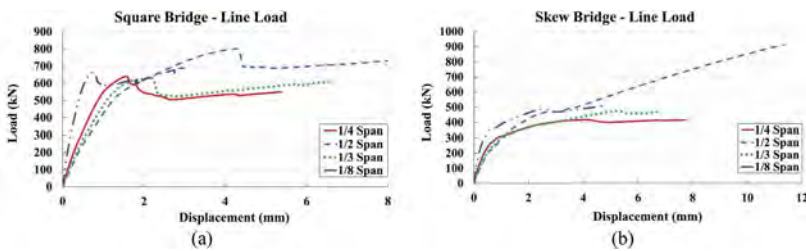


Figure 5. Numerical load-displacement curves for the vertical displacement below line load on the intrados of (a) square bridge; (b) skew bridge, showing the influence of line load at different locations.

For square bridges, the line loads at third and eighth span produce the same two-dimensional four-hinge mechanism as in the case of load at quarter span. The only difference is the location of the hinge below the load, which shifts in each case. In contrast, the line load at mid span results in a two-dimensional five-hinge mechanism, where the hinges form below load, around quarter and three-quarter span and at the two springings, as displayed in Figure 6. This is reflected in Figure 5(a) with the high load capacity associated with the mid span case in the load-displacement curve. These observations for square bridges also apply for the skew bridges. However, the mechanisms convert from being two-dimensional into three-dimensional, where the hinges take a saw-toothed shape, as well as being not parallel to the abutments. Regarding spandrel walls, the same crack pattern of the quarter-span case is observed in all the other cases for the square bridge. Again, this pattern is only applicable to

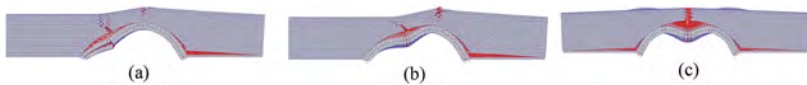


Figure 6. Numerical deformed shape at failure for square bridge under line load at (a) eighth span (b) third span (c) mid span.

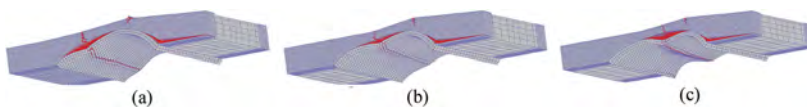


Figure 7. Numerical deformed shape at failure for skew bridge (showing the Eastern spandrel wall) under line load at (a) eighth span (b) third span (c) mid span.

the Eastern spandrel wall in the case of skew bridges, whereas the Western wall undergoes a more complex cracking pattern which varies based on the load location.

3.2.2 Patch load

In this section, both concentric and eccentric patch loads of size (500mm×600mm) are applied at quarter and mid span. The load-displacement curves for square bridges, shown in Figure 8 (a), indicate that patch loads at mid span exhibit a higher load capacity compared to those at quarter span. This observation is consistent with that in the case of line loads. In terms of load eccentricity, concentric patch loads applied at mid-width generally tends to provide a higher capacity compared to eccentric loads applied at quarter width. However, the effect of eccentricity on load capacity is more significant at quarter span than at mid span. In reference to the initial stiffness, square bridges provide a higher stiffness under patch loads at quarter span than at mid span, which is compatible with the behaviour under line loads. In case of skew bridges, patch loads at three-quarter width are also considered due to their asymmetric geometry. Most of the observations for square bridges also apply to skew bridges except for the effect of eccentricity on load capacity, which is less significant in the skew bridges.

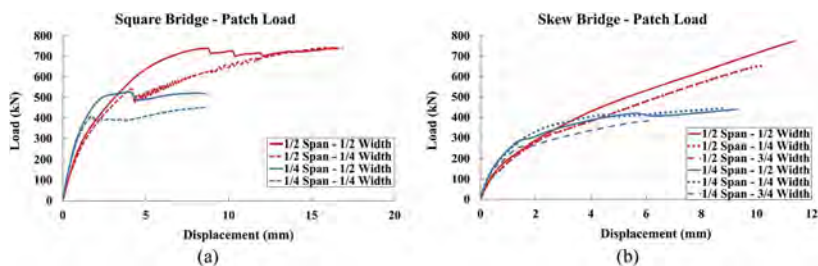


Figure 8. Numerical load-displacement curves for the vertical displacement below patch load on the intrados of (a) square bridge; (b) skew bridge, showing the influence of patch load at different locations.

The deformed shapes at failure for square bridges under patch load at various locations outline the complex cracking behaviour within the arch barrel, as outlined in Figure 9. This complex behaviour is expressed in the form of diagonal cracks extending from below the patch load to the faces of the arch barrel. It is also obvious that the previous hinge mechanisms associated with line loads are no longer observed, where more complex three-dimensional failure mechanisms develop within the arch barrels. For spandrel walls, the crack pattern is almost identical to that observed for the case of line loads. However, the severity of the cracks is dependent on the proximity level for the patch load with respect to the spandrel wall.

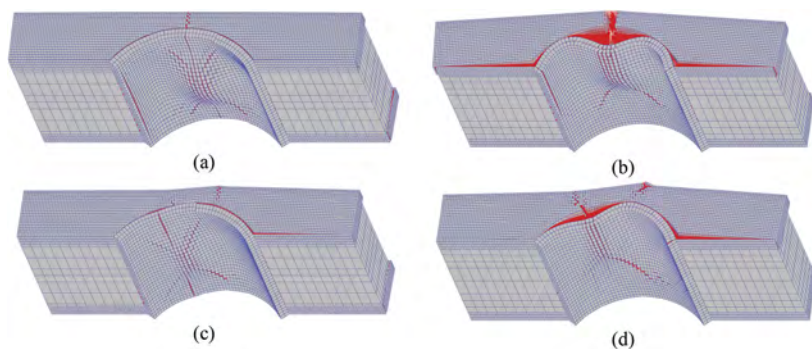


Figure 9. Numerical deformed shape at failure for square bridge under patch load at (a) mid-span mid-width; (b) mid-span quarter-width; (c) quarter-span mid-width; (d) quarter-span quarter-width.

Unlike square bridges, hinges along the whole width of the arch barrel form below the patch load in the case of skew bridges. The formed hinges are saw-toothed due to the helicoidal construction method, but in this case, they are diffused over a larger area below the applied load. This can be due to the characteristics of the patch loads which tend to trigger 3D effects compared to the line loads. These observations are supported by the failure mechanisms predicted for the different cases, as shown in Figure 10. It can be noted that patch loads at quarter span result in a four-hinge mechanism, whereas loads at mid span lead to a five-hinge mechanism, which is compatible with the failure modes under line loads. These observations agree with the load-displacement curves in Figure 8 which shows that load eccentricity is less significant in the case of skew bridges. This is further indicated here by the fact that patch loads do not significantly alter the failure mode for skew bridges compared to the case of line loads. Regarding spandrel walls, the Eastern spandrel wall maintains the same crack pattern composed of two vertical cracks and one horizontal crack in most of the cases. On the other hand, the Western spandrel wall undergoes more complex cracking based on the load location along both the span and width of the bridge.

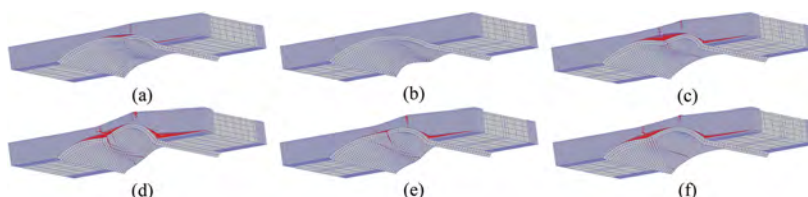


Figure 10. Numerical deformed shape at failure for skew bridge (showing the Eastern spandrel wall) under patch load at (a) mid-span mid-width; (b) mid-span quarter-width; (c) mid-span three quarter-width (d) quarter-span mid-width; (e) quarter-span quarter-width; (f) quarter-span three quarter-width.

4 CONCLUSIONS

This paper explores the main characteristics of the 3D response for masonry arch bridges using detailed 3D mesoscale models, considering the actual masonry bond in all the masonry components. Both square and skew single-span multi-ring masonry arch bridges are investigated in this paper to develop an improved understanding of the complex behaviour of these structures. The validated numerical models have demonstrated the capability of 3D mesoscale models to simulate the behaviour of masonry arch bridges, representing the experimental behaviour in terms of both the load-displacement response and the failure mechanisms. These validated models are used afterwards in a parametric study on both square and skew masonry arch bridges. This study led to the development of a better understanding for the 3D behaviour of these structures, summarised in the following main findings:

- The most common failure mechanism for both square and skew masonry arch bridges is a four-hinge mechanism. The four hinges form normally at the load location, away from the load (three-quarter span), and at the two springings.
- The previous observation takes place mainly when line load is applied at quarter, third, or eighth of the bridge span. When the load is applied at mid-span, this failure mechanism converts into a five-hinge mechanism, where the hinges form below the load, at quarter and three-quarter span, and at the two springings.
- In the case of square bridge, the failure mechanism under line loads is mostly two-dimensional. However, it is different in the case of skew bridges, where the hinge mechanism becomes three-dimensional with the hinges non-parallel to the abutments, also exhibiting a saw-tooth shape due to the nature of the helicoidal construction method.
- Under the effect of patch loads, the behaviour of both square and skew bridges becomes dominantly three-dimensional. For square bridges, failure mechanisms with diagonal cracks take place regardless of the location for patch load, whereas mechanisms with diffused hinges form in the case of skew bridges.

- It was found that the least critical load position for both square and skew bridges is at mid-span, whereas the most critical position is at third span for square bridges and at quarter span for skew bridges.
- The initial stiffness for both square and skew bridges tends to decrease as the load is applied further away from the abutments.
- The effect of eccentricity for patch loads on the load capacity is more significant at quarter-span than at mid-span in the case of square bridges. For skew bridges, the effect of eccentricity is less significant.

ACKNOWLEDGEMENTS

The authors gratefully acknowledge support from EPSRC grant EP/T001607/1 (Project title: Exploiting the resilience of masonry arch bridge infrastructure: a 3D multi-level modelling framework). Additionally, the authors would like to thank Prof. Matthew Gilbert for the data he has provided on the experimental tests performed at Bolton Institute.

REFERENCES

- Forgács, T., Sarhosis, V. & Ádány, S. (2018) Discrete element modelling of skew masonry arch bridges taking into account arch ring-backfill interaction. In: *Proceedings of the International Masonry Society Conferences. 10th International Masonry Conference, 2-4 July 2018, Milan, Italy*. International Masonry Society, 337–346.
- Grosman, S., Bilbao, A. B., Macorini, L. & Izzuddin, B. A. (2021) Numerical modelling of three-dimensional masonry arch bridge structures. *Proceedings of the Institution of Civil Engineers - Engineering and Computational Mechanics*, 174, 96–113.
- Hodgson, J. A. (1996) *The behaviour of skewed masonry arch bridges*. PhD thesis. University of Salford.
- Izzuddin, B. A. (1991) *Nonlinear dynamic analysis of framed structures*. PhD thesis. Imperial College London (University of London).
- Jokhio, G. A. & Izzuddin, B. A. (2015) A Dual Super-Element Domain Decomposition Approach for Parallel Nonlinear Finite Element Analysis. *International Journal for Computational Methods in Engineering Science & Mechanics*, 16, 188–212.
- Macorini, L. & Izzuddin, B. A. (2011) A non-linear interface element for 3D mesoscale analysis of brick-masonry structures. *International Journal for Numerical Methods in Engineering*, 85, 1584–1608.
- Melbourne, C. & Gilbert, M. (1995) The behaviour of multi-ring brickwork arch bridges. *Structural Engineer*, 73, 39–47.
- Milani, G. & Lourenco, P. B. (2012) 3D non-linear behavior of masonry arch bridges. *Computers & Structures*, 110, 133–150.
- Minga, E., Macorini, L. & Izzuddin, B. A. (2018a) A 3D mesoscale damage-plasticity approach for masonry structures under cyclic loading. *Meccanica*, 53, 1591–1611.
- Minga, E., Macorini, L. & Izzuddin, B. A. (2018b) Enhanced mesoscale partitioned modelling of heterogeneous masonry structures. *International Journal for Numerical Methods in Engineering*, 113, 1950–1971.
- Page, J. (1995) Load tests to collapse on masonry arch bridges. In: *Arch Bridges. Proceedings of the first international Conference on arch bridges, 3-6 September 1995, Bolton, UK*. Thomas Telford, 289–298.
- Papa, T., Grillanda, N. & Milani, G. (2021) Three-dimensional adaptive limit analysis of masonry arch bridges interacting with the backfill. *Engineering Structures*, 248, 113189.
- Pulatsu, B., Erdogmus, E. & Lourenço, P. B. (2019) Simulation of Masonry Arch Bridges Using 3D Discrete Element Modeling. In: *Structural Analysis of Historical Constructions*. Springer International Publishing, 871–880.
- Tubaldi, E., Macorini, L. & Izzuddin, B. A. (2018) Three-dimensional mesoscale modelling of multi-span masonry arch bridges subjected to scour. *Engineering Structures*, 165, 486–500.
- Zhang, Y., Tubaldi, E., Macorini, L. & Izzuddin, B. A. (2018) Mesoscale partitioned modelling of masonry bridges allowing for arch-backfill interaction. *Construction and Building Materials*, 173, 820–842.

Experimental investigation of the effect of masonry infill on the performance of masonry arch bridges

S. Amodio, M. Gilbert & C.C. Smith
The University of Sheffield, UK

ABSTRACT: Numerical modelling forms a fundamental part of most masonry arch bridge assessments. However, the numerical models employed need to be validated against full-scale bridge tests, or, alternatively, against tests on scale models. This contribution describes a programme of tests carried out on medium-scale masonry arch bridges to explore the effects of internal spandrel walls and masonry backing on structural performance, since the effects of these elements appear to have been little investigated previously. The tests have provided high quality benchmark results that have been used to validate numerical models developed using the discontinuity layout optimization (DLO) limit analysis method. It has been found, both experimentally and numerically, that internal spandrels and backing can contribute significantly to bridge load-carrying capacity.

1 INTRODUCTION

Masonry arch bridges continue to form an essential part of the transport systems of many countries around the world. However, many aspects of their behaviour remain quite poorly understood. For example, although the behaviour of masonry arch bridges containing soil backfill has been extensively investigated over the last few decades (Page 1993, Melbourne & Gilbert 1995, Boothby et al. 2004, Augustus-Nelson & Swift 2020), significantly fewer studies have examined the effects of other infill materials, such as backing and internal spandrel walls, which are common in long span bridges and viaducts. Harvey & Harvey (2017) and Gilbert et al. (2022) have observed that the presence of backing can potentially trigger different modes of response, by moving the effective arch springing locations. Also, experimental evidence has suggested that external spandrel walls may have a significant stiffening effect on the arch barrel (Royles & Hendry 1991, Melbourne et al. 1997). However, due to a lack of research, internal spandrel walls are in practice often modelled using a fictitious soil fill material, with the unit weight adjusted to take account of internal voids (Network Rail 2006); this approach appears likely to lead to inaccurate predictions of load carrying capacity.

In order to improve our understanding of the modes of response of bridges containing masonry backing and internal spandrel walls, a programme of quasi-static load tests to failure on laboratory bridges has recently been conducted at the University of Sheffield, with the aim of quantifying their contributions to bridge load-carrying capacity. Medium-scale models have been employed as these have the advantage of allowing rapid test turnaround and also reducing costs. The main aim of the research was to provide high quality test data that could be used to validate numerical models. In the present study, test results are compared with predictions from numerical limit analyses conducted via discontinuity layout optimization method (DLO). Preliminary outcomes from the study are presented herein.

2 EXPERIMENTAL INVESTIGATION

2.1 General test arrangement and design

An experimental test campaign was developed that included single and multi-span bridges incorporating either masonry backing, internal spandrels or sand backfill, with the principal aim of comparing their respective contributions to load carrying capacity and influence on failure modes. The multi-span models only included two spans as this was considered sufficient to investigate the primary failure modes likely to be encountered in full-scale multi-span bridges, which typically involve two adjacent spans (Melbourne et al. 1997).

The models had segmental arch barrels composed of voussoir blocks extending across the full width of the bridge (198mm) and were built without external spandrel walls to represent approximately plane strain conditions. This aided interpretation of the test data and also allowed direct comparison with 2D numerical models.

The bridges were constructed with sandstone blocks, cut using precise CNC manufacturing process to obtain high geometrical accuracy, with thin joints used to achieve closely fitting arch barrels; this was designed to increase repeatability of the tests. For convenience, masonry joints were filled with fast setting 'liquid magnesium' (or 'liquid chalk'), a commercially available product, composed of isopropyl alcohol, magnesium carbonate hydroxide and resin.

Both backing and internal spandrels were built with a typical stretcher bonding pattern. However, a number of bridges with spandrels were constructed with an alternative bonding pattern to emulate the presence of cracks in correspondence of the load and to allow investigation of the effect of different load distributions on load carrying capacity. The main bridge dimensions are shown in Figure 1.

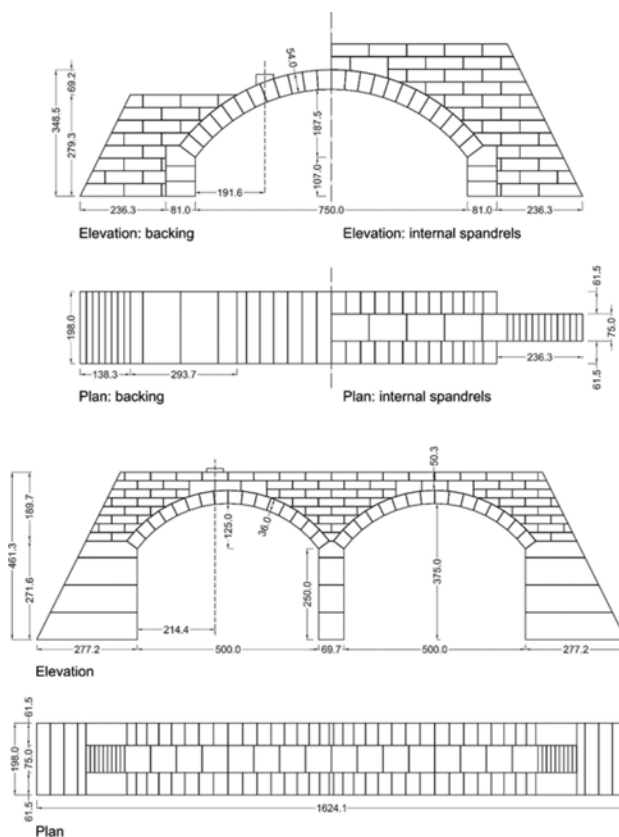


Figure 1. Main dimensions of single and multi-span bridge models tested, with backing and internal spandrel masonry shown (all dimensions in mm).

The tests were performed in a purpose-made test rig apparatus (described in Pytlos 2015) that features a stiff and transparent test chamber and an automated sand filling process via pluviation to ensure uniform and consistent backfill density, in the case of the soil filled bridges. The loading system included an electric actuator operated in displacement control mode while bridge displacements were measured using five LVDT transducers positioned perpendicular to the arch intrados.

2.2 *Single span bridge tests*

All the single span models were tested to failure by alternately applying the load at the $\frac{1}{4}$ span and $\frac{3}{4}$ span points, except in the case of the sand backfilled models, which were tested only at the $\frac{1}{4}$ span point.

A first series of tests on bare arch models indicated that the chalk material used in the joints provided a small bond strength that was lost once cracks in the joints were formed. Also, when a given arch was first tested, it exhibited a slightly stiffer response and higher load-carrying capacity compared to subsequent repeat tests. However, the chalk material appeared to foster good test repeatability; for the three benchmark bare arches tested, each loaded four times, the average failure load was 191.1N and the coefficient of variation was 3.8%.

Tests on models with backing included three nominally identical bridges (named B1, B2, B3), though in B1 and B2 the abutments were left free to move (albeit movement of these was observed only in the case of B2), while B3 had fixed abutments. The backing had the same width as the arch barrel and covered $\frac{2}{3}$ of the arch height on each side; it provided an increase in load-carrying capacity of approximately 40% in the case of the bridge with free abutments and 77% (on average) in the case of the bridges where abutments were fixed (or were not observed to move). However, the failure load was observed to be particularly sensitive to the form of the crack pattern that developed in the masonry infill far from the load, following deformation of the arch. Here sliding and/or rocking failure were observed to occur, though the extent of these mechanisms appeared to be influenced by the variable nature of the masonry bond strength and/or by slight differences in the construction. As a consequence, variability in the results was observed to be higher (approximately 8%). These differences in load-carrying capacity can be observed by comparing the load-displacement responses of bridges B1 and B3 when tested at $\frac{1}{4}$ and $\frac{3}{4}$ span (see Figure 2). Finally, in the case of bridge B2 the abutment far from the load rotated outwards, pushing into the backing, which also rotated rigidly. This failure mechanism led to a reduced capacity and less smooth load-displacement response, as also shown in Figure 2.

Similar considerations and differences in failure loads were observed for the models with internal spandrels. These bridges contained a single longitudinal wall of 75mm width, over-arching the barrel along its centreline. Failure was via formation of hinged mechanisms, dividing the spandrel walls into three main sections, with major cracks forming close to the $\frac{1}{4}$ and $\frac{3}{4}$ span hinges. Additionally, more diffused, cracks were observed in the wall section far from the load, where combined hinging and sliding failure occurred. Also in this case, the wall failure modes were likely influenced by the variable masonry bond strength and possible small differences in wall construction. The substantial strengthening effect of the spandrels provided an increase in load-carrying capacity of approximately 4.3 times compared to that of a bare arch, with an average failure load of 828N.

Furthermore, some of the models incorporated non-interlocking wall blocks in the region close to the load to emulate the presence of cracks, effectively directing the applied load onto the arch. This reduced bridge load carrying capacity to an average load of 472.2N, that is 57% of the failure load obtained from other models with a regular masonry bond.

Tests on two bridges with sand backfill exhibited very similar failure loads (average = 862.1N) and mechanisms to those observed in bridges with internal spandrels. However, the main difference is that the spandrel walls occupied only 38% of the bridge width; therefore, these provided a greater stiffening effect per unit width, i.e. 11N/mm versus 4.4N/mm of the sand.

Finally, tests were carried out on bridges containing both backing and internal spandrels. These bridges performed similarly to models that included spandrels only, though the presence of backing provided an increase in load-carrying capacity of approximately 12%. Results from all single span bridge tests are summarized in Table 1.

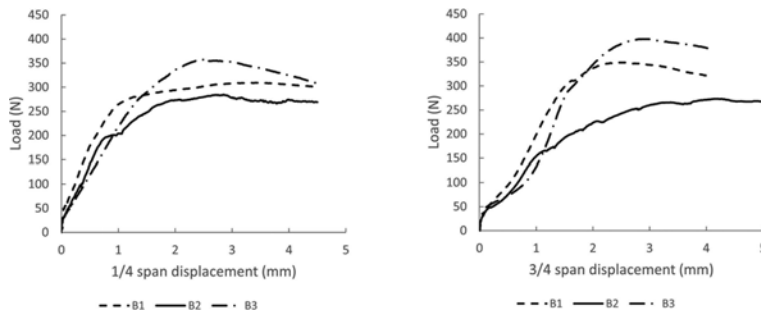


Figure 2. Load displacement responses of single span bridges with backing when loaded at $\frac{1}{4}$ span (left) and $\frac{3}{4}$ span (right). Note that in bridges B1 and B2 the abutments were left free to slide (though abutment movement were only observed in the latter model), while in B3 these were fixed.

Table 1. Experimental and numerical results of single and multi-span bridge models.

Bridge series	Backfill type	No. of models	No. of tests	Average experimental load (N)	Numerical load (N)	Numerical/Experimental
Single span	Bare arch	7	28	191.1	200.2	1.05
	Backing (free abutments)	1	4	268.1	238.4	0.89
	Backing	2*	8	338.1	317	0.94
	Spandrels ('cracked' wall)	3	5	472.4	508.9	1.08
	Spandrels	2	8	828	827.6	1
	Backing + Spandrels (free abutments)		8	474	439.9	0.93
	Backing + Spandrels	2**	8	926.8	928.5	1
Multi-span	Sand backfill	2	2	862.1	763.6	0.86
	Bare arches	2	8	66	70.6	1.07
	Spandrels	2	8	234.6	261.2	1.11
	Sand backfill	2	2	306.7	316.5	1.03

*One of the models (B1) had free abutments, though these were not observed to move during the tests.

**The same two models were first tested with fixed abutments and then with free abutments.

2.3 Multi-span bridge tests

The multi-span bridges tested comprised bare arch models and models with either internal spandrels or sand backfill. Preliminary numerical investigations were conducted to find the critical load position for these bridges, and it was found to be near the arch crown (as also found by Melbourne et al. 1997). Thus, the bridges were loaded near the crown of each of the two arches in turn. All the models failed via formation of a typical 7 hinge mechanism involving both spans and rotation of the intermediate pier. Results from the bare arch tests had a variability of just 3%.

The internal spandrel walls provided an increase in bridge load-carrying capacity of approximately 3.5 times compared to the bare arches. At failure, major cracks developed close to the hinges that formed at the crown of each arch, dividing the wall into three main sections, that rotated rigidly as the arches pushed sideways. Also, further cracks developed in the wall section furthest from the load. After the first test, the deformed geometry and the loss of masonry bonding strength affected the load-displacement response observed in subsequent repeat tests, with the peak load also reducing by approximately 13%.

Bridges with sand backfill failed in similar hinged mechanisms, though these exhibited a significantly increased load-carrying capacity (+31%). Nonetheless, the spandrels still provided higher strength per unit width than the sand fill (3N/mm vs. 1.55N/mm respectively). Results from all multi-span bridge tests are summarized in Table 1.

3 NUMERICAL MODELLING

3.1 Model details

Numerical analyses were carried out employing the discontinuity layout optimization (DLO) limit analysis method (Smith & Gilbert 2007). This has been developed for both 3D and 2D problems, though the latter has been adopted here since the bridge models exhibited 2-dimensional failure modes. The analyses were conducted using the LimitState:GEO software (2021), which implements the DLO technique.

A key advantage of this method is that both masonry and soil elements can be modelled directly. However, the mathematical formulation assumes that the friction behaves in an associative manner, which can potentially lead to overestimations of load-carrying capacity.

The masonry is represented as an assemblage of discrete rigid blocks, with sliding and crushing failure permitted at the interfaces between blocks. The soil is modelled as a Mohr-Coulomb material, with a mobilized strength assumed in the region of soil remote from the load to take account of the fact that deformations at peak load are not sufficient to mobilize the full strength of the soil in the passive region (Smith et al. 2004). However, defining appropriate mobilization factors is not straightforward (Gilbert et al. 2010, Callaway et al. 2012).

Here it has been assumed that full soil strength is mobilized on the active side of the bridge, while a factor of 0.5 has been applied to the soil internal angle of friction and cohesion on the passive side. Also, a strength multiplier of 0.5 has been applied to the soil-arch interface. These values enabled reasonable correlation to be obtained between the numerical model and experimental results.

The material properties adopted in the models are provided in Table 2. The sand internal angle of friction was measured via shear box tests and found to be 37 degrees. Pilot wrench tests were also carried out on masonry samples to determine the joint bending resistance, with regression analyses performed to characterize the masonry in compression. These regression analyses appeared to suggest that the very edges of the joints were very weak but very much stronger elsewhere. Although this two-crushing strength model was adopted in the DLO models involving sand fill material, more experiments are required to investigate this further; in all the other models a low compressive strength (of 0.25N/mm²), applied to the whole joint, was adopted. The masonry joint friction angle was measured via tilt table tests and was found to be 37 degrees; however, to take account of the non-conservatism arising from the assumption of associative friction, a reduced angle of friction of 33 degrees was used in the models. Finally, a reduced unit weight was assigned to the spandrel walls to take account of the reduced width relative to the barrel.

Table 2. Material properties adopted in the numerical models. A mobilization factor of 0.5 was applied to the soil strength parameters in the passive region of the bridge.

Material properties					
Masonry			Sand		
Arch/Backing unit weight (kN/m ³)	Spandrels unit weight (kN/m ³)	Compressive strength (kN/m ²)	Joints' friction angle (deg)	Unit weight (kN/m ³)	ϕ (c') [deg (kN/m ²)]
23.618	8.946	250*	33	17.554	37 (0)

*Assumed value, adopted in all models except the ones with sand backfill.

3.2 DLO validation

Using the aforementioned assumptions led to reasonable computed DLO failure loads being obtained (all within 15% of the experimental values, see Table 1), together with failure mechanisms that are representative of those observed during the experiments in most cases (e.g. see Figure 3 and 4).

As discussed in Section 2.2, the load-carrying capacity of the single span bridges appeared quite sensitive to the failure modes that occurred in the infill masonry remote from the load.

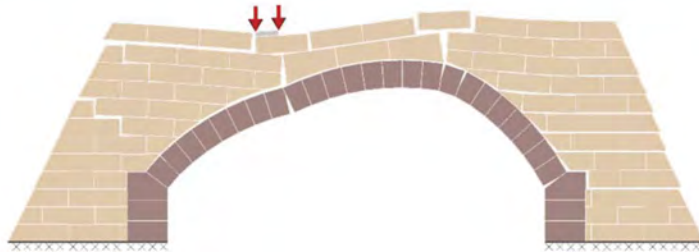
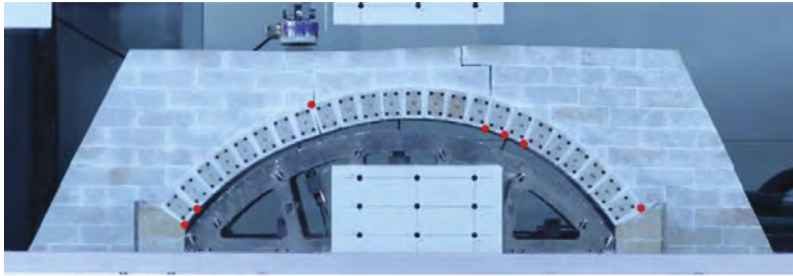


Figure 3. Failure mechanism of single span bridge with internal spandrels and superimposed hinges (top image) and failure mechanism predicted by DLO (bottom image).

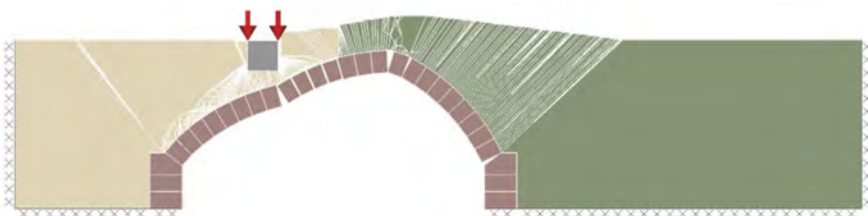
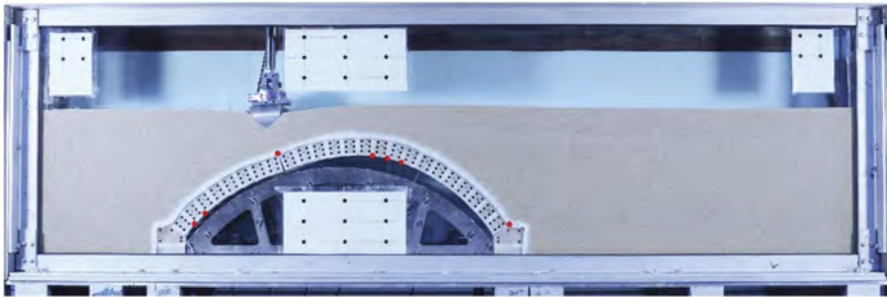

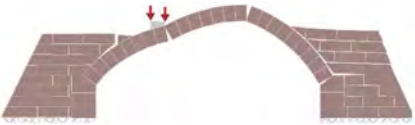


Figure 4. Failure mechanism of single span bridge with sand backfill and superimposed hinges (top image) and failure mechanism predicted by DLO (bottom image).

These involved a combination of sliding and hinging modes, which led to various crack patterns and thus differences in failure loads of over 10% in some cases.

Although in the DLO models primarily sliding modes in the backing and spandrels were predicted, in some of the experiments, rotation of a large portion of masonry was observed. This can be modelled by preventing sliding in relevant joints to ensure that rotation becomes the critical failure mode. An example is shown in Table 3, in which similar differences in peak loads are also predicted by DLO if the same failure modes observed in the experiments are induced.

Table 3. Predicted mechanisms of a bridge with backing, modified to replicate the failure modes observed in specific tests.

Bridge test	Failure mechanism	Experimental load (N)	Numerical load (N)	Numerical/Experimental
B 1-1		309.3	336.8	1.09
B 1-2		349	366.3	1.05

3.3 Commentary

In addition to the results presented in the previous sections a series of parametric studies have been performed. These indicate that the numerical models are relatively sensitive to the soil properties and to the chosen masonry crushing strength and angle of friction. In relation to the latter, it is also known (e.g. see Valentino et al. 2023) that the assumption of associative friction can lead to quite significant over-predictions of capacity when relatively few masonry blocks are involved, as is the case here.

Furthermore, in the DLO analyses of bridges containing soil backfill, as this is modelled directly, a mobilization factor needs to be applied to the passive side soil strength. However, determining an appropriate mobilization factor and identifying the extent of passive region is not always straightforward.

Nevertheless, a major benefit of DLO is that results can be obtained rapidly and directly, with relatively few input parameters and without the need to perform a time-consuming and often unreliable incremental analysis.

4 CONCLUSIONS

A programme of quasi-static load tests to failure on laboratory bridges has been carried out to investigate the effect of masonry backing and internal spandrels on bridge load carrying capacity. The tests have confirmed the significant strengthening effect of these two infill materials. It was found that bridge models containing internal spandrels and sand backfill performed similarly, with failure via hinged mechanisms in both cases, though the internal spandrels provided a greater stiffening effect per unit width. Masonry backing also measurably increased load carrying capacity.

The discontinuity layout optimization (DLO) numerical procedure has been found to provide results that are in reasonably close agreement with experimental failure loads (within 15% in most cases), using input parameters common across bridge models. Experimentally observed failure modes could be reliably modelled in most cases. However, additional masonry joint characterization tests are required to improve confidence in the results obtained.

ACKNOWLEDGEMENTS

The authors wish to acknowledge the financial support provided by Network Rail and EPSRC.

REFERENCES

Augusthus-Nelson, L. & Swift, G. 2020. Experimental investigation of the residual behaviour of damaged masonry arch structures. *Structures*, 27:2500–2512.

- Boothby, T., Erdogmus, E., & Yurianto, Y. 2004. Transverse strength of a model masonry arch bridges. In *Proceedings of the 4th International Arch Bridges Conference*, Barcelona.
- Callaway, P., Gilbert, M., & Smith, C. 2012. Influence of backfill on the capacity of masonry arch bridges. *Proceedings of the Institution of Civil Engineers: Bridge Engineering*, 165(3):147–158.
- Gilbert, M., Cole, G., Smith, C., & Melbourne, C. 2022. *CIRIA C800: Guidance on the assessment of masonry arch bridges*. CIRIA, London, UK.
- Gilbert, M., Smith, C., and Pritchard, T. (2010). Masonry arch analysis using discontinuity layout optimization. *Proceedings of the Institution of Civil Engineers: Engineering and Computational Mechanics*, 163:155–166.
- Harvey, B. & Harvey, H. 2017. On the service behaviour of masonry viaducts. *Proceedings of the Institution of Civil Engineers: Bridge Engineering*, 170(4):248–254.
- LimitState 2021. *LimitState:GEOManual, version 3.6.1*. LimitState Ltd, Sheffield. See <https://www.limitstate.com/geo-documentation>.
- Melbourne, C. & Gilbert, M. 1995. The behaviour of multi-ring brickwork arch bridges. *The Structural Engineer*, 73(3):39–47.
- Melbourne, C., Gilbert, M., & Wagstaff, M. 1997. The collapse behaviour of multi-span brickwork arch bridges. *The Structural Engineer*, 75(17):297–305.
- Network Rail 2006. *The structural assessment of underbridges*, NR/GN/CIV/025. Network Rail, UK.
- Page, J. 1993. *Masonry arch bridges – state-of-the-art review*. HM Stationery Office, London.
- Pytlos, M. 2015. *New Tools for Modelling Soil-filled Masonry Arch Bridges*. PhD thesis, The University of Sheffield, Sheffield, UK.
- Royles, R. & Hendry, A. 1991. Model tests on masonry arches. *Proceedings of the Institution of Civil Engineers*, 91(2):299–321.
- Smith, C. & Gilbert, M. 2007. Application of discontinuity layout optimization to plane plasticity problems. *Proceedings of the Royal Society A: Mathematical, Physical and Engineering Sciences*, 463 (2086):2461–2484.
- Smith, C., Gilbert, M., & Callaway, P. 2004. Geotechnical issues in the analysis of masonry arch bridges. In *Proceedings of the 4th International Conference on Arch Bridges*, pages 343–352, Barcelona.
- Valentino, J., Gilbert, M., Gueguin, M., & Smith, C.C. 2023. Limit analysis of masonry walls using discontinuity layout optimization and homogenization. *International Journal for Numerical Methods in Engineering*, 124(2): 358–381.

Multi-fidelity modelling of masonry arch bridges under traffic loading

S. Grosman, Q. Fang, L. Macorini & B.A. Izzuddin

Imperial College London, London, UK

ABSTRACT: Masonry arch bridges are part of the historical heritage from the Industrial Age in the UK and Europe. To preserve this infrastructure, robust assessment methodologies are required to adequately account for the effects of evolving loading and material degradation. This work presents 3D multi-fidelity modelling strategies for masonry viaducts which can be used for accurate assessment. The masonry components of the bridge structure are modelled using high-fidelity mesoscale models or efficient macroscale models. Filling materials are represented using elasto-plastic models considering their cohesive and frictional nature. The interaction between the different parts is taken into account by adopting non-linear interface elements allowing for sliding and separation. The results of numerical investigations on a realistic viaduct under traffic loading, which were conducted by performing nonlinear simulations under transient loading, showcase the potential of accurate 3D modelling comparing the results from mesoscale and macroscale models.

1 INTRODUCTION

The pressing need to predict the structural performance of a massive amount of masonry arch bridges in the UK and around the world has prompted the development of assessment methods for these complex structural systems. Various numerical modelling strategies have been developed over the past few decades, and they generally entail nonlinear analysis capabilities and numerical solution procedures of various degrees of sophistication. The paradigm of numerical simulation of masonry bridges at different loading levels up to collapse is mainly based on the Finite Element (FE) or Discrete Element methods. Accurate predictions under different loading conditions require the use of 3D models providing a complete geometric description of masonry bridges and viaducts. In particular, the 3D representation is the only way to accurately represent such complex phenomena as complex arch cracking patterns observed in real masonry bridges or the frequently reported outward movement (walking) of spandrel walls (Ozaeta García-Catalán & Martín-Caro Alamo, 2020).

Conventionally, 3D continuum-based methods rely on a macroscale description of the different masonry constituents (Fanning & Boothby, 2001, Caddemi et al., 2019). That is, masonry is considered a single homogeneous and isotropic continuum where nonlinear effects are captured in a ‘smeared’ fashion. Although this offers computational efficiency, it simplifies the real heterogeneity arising from the combination of brick/stone units and mortar. The main limitation of such a macroscale strategy is associated with substantial difficulty when determining reliable material parameters.

The mesoscale description, in contrast, comprises separate representations of the two distinct constituents of masonry: the brick/stone unit as solid elements and the mortar layers as zero-thickness interface elements (Macorini & Izzuddin, 2011). This strategy has been recently applied to investigate the response of masonry arches (Zhang et al., 2016) and bridges (Zhang et al., 2018, Tubaldi et al., 2020, Grosman et al., 2021). The mesoscale description facilitates the explicit consideration of masonry bonds as well as the modelling of complex arch

geometries such as a skew arch. It also enables the capturing of radial cracking, ring separation and more complex 3D cracks in masonry bridges.

While the 3D mesoscale models generally provide more realistic predictions, they are also associated with substantial difficulties in mesh generation and significant computational costs, which can hinder their use for the practical assessment of large structures. In the following section, multi-fidelity modelling strategies, based on meso- and macroscale masonry models, with a parametric mesh generator tool developed at Imperial College London for accurate 3D simulations of masonry viaducts are presented and used to investigate the response of a realistic brick-masonry railway viaduct under traffic loading.

2 MULTI-FIDELITY MODELLING STRATEGY

This section introduces the detailed modelling strategy developed to investigate masonry viaducts which has been implemented in ADAPTIC (Izzuddin, 1991), a finite element code for advanced nonlinear analysis of structures. Macroscale and mesoscale masonry models are used to simulate material nonlinearity in the masonry components of the analysed structure. The two strategies can be also combined leading to mixed meso- macroscale models (Grosman et al., 2023). As specified before, in the macroscale modelling strategy, the masonry components are modelled using 3D continuum elements, sized independently from the dimensions of bricks and mortar joints (Figure 1a). The material described in this case is based on a constitutive model combining the concepts of plasticity and damage (Lee & Fenves, 1998, Chisari et al., 2020). It is worth noting that appropriate interpretation is needed to relate the results obtained with such models to real material behaviour. On the other hand, in the mesoscale description (Figure 1b), the masonry material is modelled based on separate representations for units and joints. More specifically, as elaborated in Macorini and Izzuddin (2011), elastic solid elements are used to describe units and nonlinear interface elements to represent mortar joints and potential failure surfaces within bricks. The material description for nonlinear interfaces employs a cohesive-frictional constitutive model (Minga et al., 2018), providing computationally robust solutions to the local nonlinear problem. The latter approach can capture the propagation of local damage, but it is associated with significant computational costs. Mixed meso- macroscale models employ detailed mesoscale descriptions only for critical spans or segments and more efficient macroscale representations for the remaining parts of the analysed viaduct (Figure 1c). This combination improves computational efficiency while allowing for capturing the local damage phenomena.

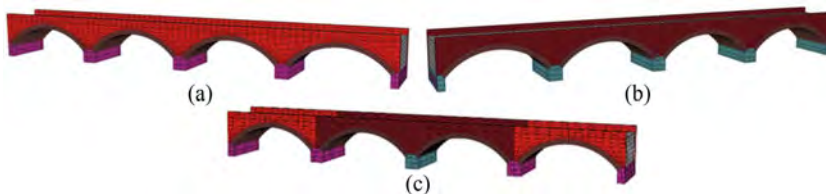


Figure 1. Modelling strategies for masonry viaducts: (a) macroscale, (b) mesoscale and (c) mixed meso-macroscale models.

To facilitate extensive numerical analysis of masonry viaducts featuring diverse geometries, materials, and loading characteristics, a novel parametric design tool has been recently developed by the authors (Grosman et al., 2023) as an add-on component within the Rhino & Grasshopper environment (McNeel & Associates, 2010). The developed tool provides a comprehensive parametric description for each distinct structural component of the bridge (arch barrel, backing/backfill, spandrel wall, pier etc.) and allows for a robust way of joining these components together to form the masonry bridge as depicted in Figure 2. Each component can support both meso- and macroscale definition and is fully parametric. Connectivity

between distinct adjacent components is established via a set of nonlinear interfaces. 3D modelling of large and complex structural systems, such as realistic masonry viaducts, bears a high computational cost, even when using the more computationally efficient macroscale models. Thus, to improve computational efficiency further, the advantage is taken of the domain decomposition approach earlier developed at Imperial to parallelise the solution procedure between multiple processor cores (Jokhio & Izzuddin, 2015, Izzuddin & Jokhio, 2017). To accurately represent transient railway loading for nonlinear dynamic simulations, the developed tool integrates capabilities for the automatic generation of traffic loading according to the vehicle axle profile and speed. In comparison to static analysis with incremental application of train loading, dynamic analysis with transient loading is capable of capturing more realistic propagation of the damage in the brickwork.

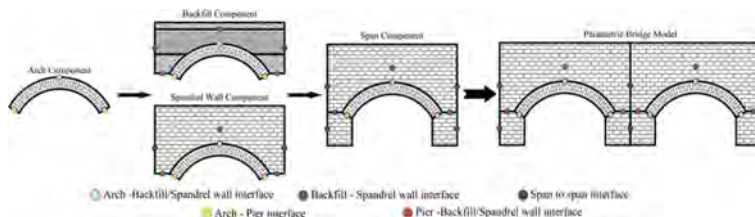


Figure 2. The modular approach to bridge assembly.

According to the developed modelling strategy for accurate simulations of masonry viaducts under train loading, model material parameters for masonry, backfill and backing should be obtained from material tests on masonry specimens taken out from the analysed structure. More specifically, physical tests on masonry cores can provide stiffness and strength properties of units and mortar joints, which can be used directly in mesoscale masonry models. Subsequently, calibrated mesoscale models can be employed within a multi-level computational strategy (Chisari et al., 2020) to determine suitable material properties for more efficient macroscale models. Of course, where results from material tests are not available, a range of material properties for masonry can be assumed from the literature. In this case, the results of the numerical simulations with assumed material properties provide performance limits for the analysed structure.

3 NUMERICAL EXAMPLES

In this work a realistic multi-span multi-ring masonry viaduct with a backing layer above the masonry piers, which contain concrete infill, is analysed under traffic loading. Figure 3 depicts the main geometrical characteristics of the bridge structure. In the numerical simulations, only four spans are represented, where the investigation is focused on the response of the two internal spans. Two alternative strategies are compared by modelling the two internal spans using a detailed mesoscale model, Model 1 in Figure 4a, or an efficient macroscale model, Model 2 in Figure 4b, to represent material nonlinearity in the masonry components of the viaduct segment. On the other hand, the external spans, which are modelled with the same macroscale mesh for the internal spans of Model 2 but assuming elastic behaviour for the masonry parts, are included in the viaduct model mainly to provide appropriate boundary conditions for the investigated internal spans. The two alternative models for the analysed 4-span viaduct segment, Model 1 with a mixed meso- macroscale mesh and Model 2 with a macroscale mesh, are shown in Figure 1c, a. Table 1 and Table 2 provide the material parameters used in Model 1 and Model 2 for solid elements and interface elements, respectively. The material parameters include Young's modulus (E), Poisson ratio (ν), compressive strength (f_c), tensile strength (f_t), tensile fracture energy (G_t), shear fracture energy (G_s), compressive fracture energy (G_c), cohesion (c), friction angle (ϕ), dilatancy angle (ψ), normal stiffness (k_n) and tangential stiffness (k_t). In the macroscale model, masonry compressive strength,

tensile strength, and tensile fracture energy are set to the same values as those used for the mortar interface in the mesoscale model. The masonry Young's modulus used in the macroscale model is calculated via simple homogenisation along the circumferential direction of the masonry arches, which represent the main masonry components of the analysed bridge structure, based on the brick unit Young's modulus and the normal stiffness of the mesoscale mortar interface adopted in the mesoscale model.

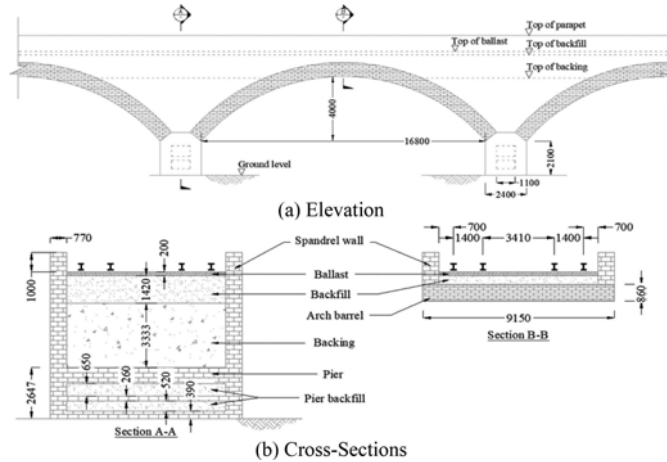


Figure 3. Geometrical characteristics of the analysed viaduct.



Figure 4. Mesoscale and macroscale descriptions for one span of the analysed viaduct.

Table 1. Material properties of solid elements adopted in numerical models.

	E [MPa]	ν [MPa]	f_t [N/mm]	f_c [MPa]	G_t [N/mm]	Ψ [deg]
Mesosopic elastic brick unit*	16259	0.15	-	-	-	-
Macroscopic masonry (middle spans)**	10388	0.15	0.15	26.0	0.10	35
Macroscopic masonry (side spans)***	10388	0.15	10.10	53.5	10.10	35
Macroscopic elastic ballast***	150	0.15	-	-	-	-
Macroscopic backing and backfill***	6000	0.15	1.50	15.0	0.15	35

* Adopted in the two middle spans of Model 1

** Adopted in the two middle spans of Model 2

*** Adopted in all the spans in both Model 1 and Model 2

The response of the structure under traffic loading has been investigated by performing nonlinear dynamic analyses representing a ballast-laying train travelling over the viaduct. More specifically, the ballast-laying train is composed of one locomotive and five coaches with standard axle configurations, as indicated in Figure 5. The viaduct has 2 separate tracks,

Table 2. Material properties of interface elements adopted in the numerical models.

	k_n [MPa]	k_t [MPa]	f_t [MPa]	f_c [MPa]	G_t [N/mm]	G_s [N/mm]	G_c [N/mm]	c [MPa]	ϕ [deg]
M	100	50	0.15	26	0.1	0.25	20	5	26.6
B	100	50	5	26	10^5	10^5	10^5	5	0.0
I	90	40	0.002	24	10^5	10^5	10^5	0.0003	31.0

M - Mortar interfaces between brick units*

B - Brick-bisecting interfaces to allow for the potential cross-sectional crack in bricks*

I - Interfaces between superstructure infill (backfill and backing) and spandrel wall or arch barrel***

as shown in Figure 3b. Track 1 is the track on which the train is travelling, whereas Track 2 is the opposite unoccupied track. The train is travelling at speed of 80 km/h.

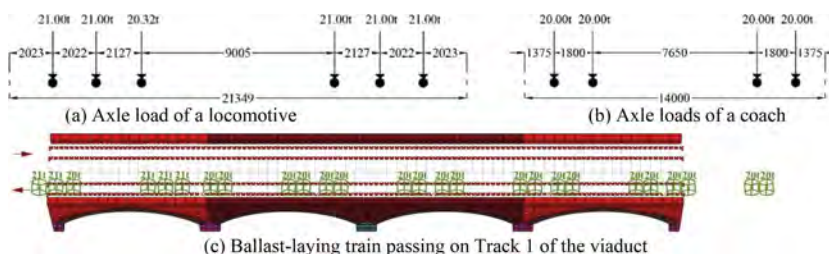


Figure 5. Configuration of the ballast-laying train.

4 RESULTS

4.1 Viaduct behaviour under standard axle loading

The predictions provided by Model 1 and Model 2 are compared focusing on the 3D displacement components at locations T1 and T2 under Track 1 and Track 2 at the arch crown intrados in the right middle span (Figure 6). The time-history displacement curves are compared in Figure 7, where a very good agreement is found between detailed mesoscale and simplified macroscale models. This confirms the accuracy and potential of the macroscale model, even with unsophisticated calibration of model parameters for the masonry material, to predict the serviceability response of a complex masonry viaduct.

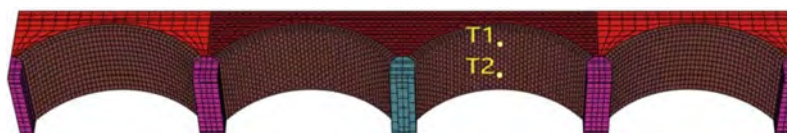


Figure 6. Locations where the displacement components are analysed under train loading.

It is also of interest to examine the damage pattern in the brickwork of the masonry component of the viaduct. The damage pattern is obtained when the train travelling through the viaduct, at the position shown in Figure 8, where the first bogie of the locomotive just passes through the middle pier. Figure 9 depicts the damage patterns in the middle span resulting from the mixed-meso- macroscale model (Model 1) and the macroscale model (Model 2). In order to visualise the deformed shape of the viaduct under traffic loading, the traffic-induced displacements are scaled up by 1000 in Figure 9a.

Figure 9a shows bed joint separations at the top of the spandrel wall above each pier. It is worth noting that the predicted damage in this location is due mainly to the application of the

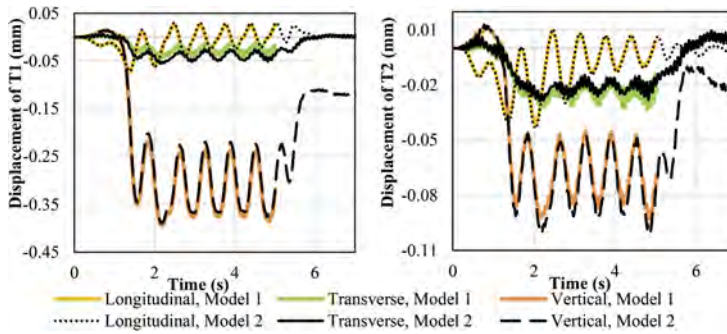


Figure 7. Displacement of the nodes under Track 1 (left) and Track 2 (right) in both mixed-scale and macroscale models.

bridge self-weight prior to the passage of the train. A medium level damage is observed also at the bed joint at the soffit of the arch barrel at the right intermediate span, where 5 train axles pass through. Longitudinal and transverse cracks have not yet appeared in the arch barrel under the assumed train loading, as suggested by the undamaged transverse mortar interfaces and longitudinal brick-brick interfaces.

Figure 9b confirms that the macroscale model (Model 2) can provide a realistic prediction of damaged regions in the spandrel walls and arch barrel, based on comparison against the reference Model 1. Although the progression of the crack in the brickwork cannot be accurately captured by the macroscale model, considering its much-improved computational efficiency, it can be utilised to study displacement time-histories and damage patterns of realistic viaducts under serviceability train loading.



Figure 8. Position of the train when damage patterns are studied.

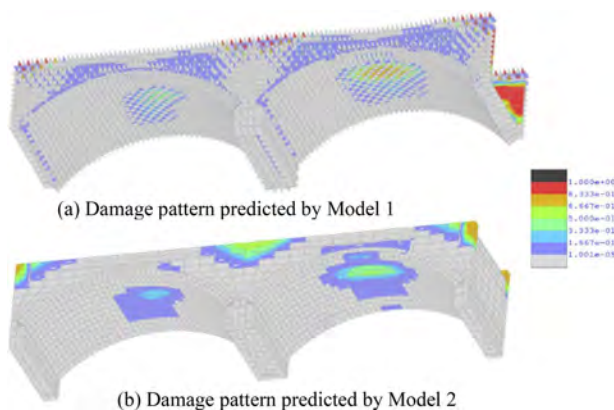


Figure 9. Damage pattern of the middle spans when the ballast-laying with typical axle load passing.

4.2 Viaduct behaviour under increased axle loading

To further investigate the nonlinear behaviour of the masonry viaduct under increased loading scenarios, a three times heavier train is applied to the viaduct. More specifically, a ballast-

laying train with the same speed and axle arrangement, but with triple axel loading, is applied on Track 1 of the viaduct. Both models with different levels of fidelity are generated. The damage patterns of the viaduct when the train passes through the viaduct at the position shown in Figure 8 are studied.

Figure 10a shows the damage pattern in the middle spans predicted by the mesoscale model. As indicated by Figure 9b, the separation of the brick head joints at the top of the spandrel wall above the pier - initially induced by self-weight - propagates radially, culminating in a step-crack damage pattern at this location. Figure 10c depicts the damage pattern in the arch barrel, where a substantial portion of the mortar joints is entirely open in the transverse direction resulting in transverse fractures at the intrados of the arch.

In addition to the progression of cracks that appear under standard service loading, triple service loading causes damage in further locations. Figure 10d shows shear sliding between the spandrel wall and the arch and the onset of ring separation, and Figure 10e shows some evolving head joint separation at the spandrel wall and bed joint separation at the soffit of the arch barrel.

Figure 11 shows the damage pattern predicted by the macroscale models, which provides a satisfactory indication of the location and degree of damage in the spandrel walls and arch barrels.

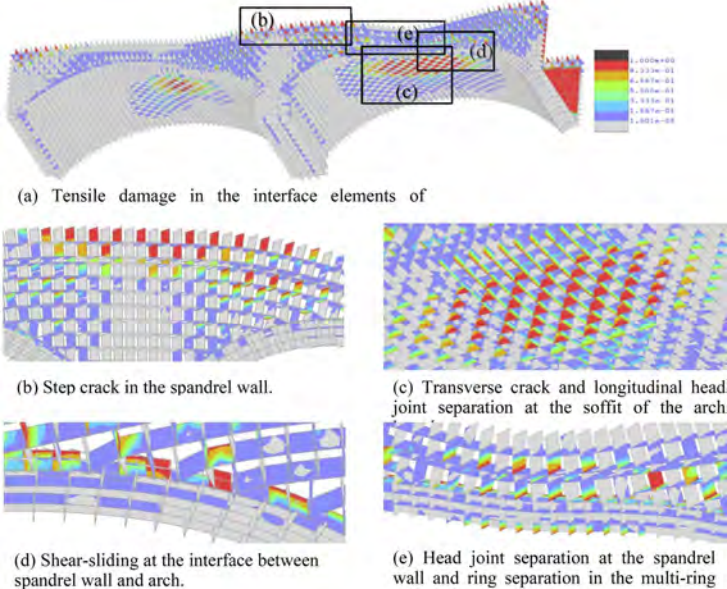


Figure 10. Damage pattern in the middle spans predicted by the mixed meso- macroscale model (Model 1) when a train under the passage of a train with triple axle load.

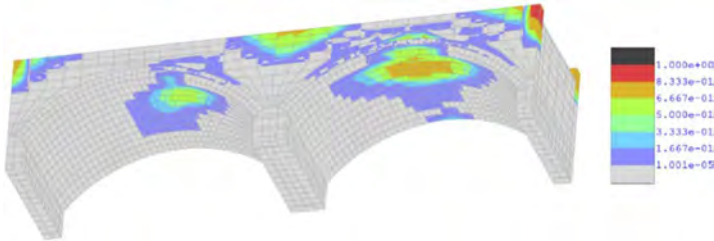


Figure 11. Damage pattern of middle spans predicted by macroscale model when a train with triple axle load passing.

5 CONCLUSION

This work showcases the potential of using 3D models with different degrees of complexity for predicting the response of a realistic multi-span viaduct segment under train loading. A mixed meso- macroscale model, representing specific viaduct segments with detailed numerical descriptions explicitly modelling masonry bond, was developed and used as a baseline model to assess the ability of a more efficient macroscale model to predict the response under serviceability and increased traffic loading. The results obtained indicate that the simpler macroscale model, including a straightforward calibration of the model material parameters for the masonry components, enables an accurate prediction of the viaduct displacements and the location of damage. On the other hand, the detailed mesoscale model offers an improved description of cracking in the brickwork of the analysed structure and enables a practical incorporation of a wide range of defects as found in real masonry viaducts, but at the expense of an increased computational cost. In future research, the developed multi-fidelity modelling strategies will be validated against monitoring data and used to investigate the response of realistic masonry viaducts under different loading conditions.

REFERENCES

- Caddemi, S., Calì, I., Cannizzaro, F., D'urso, D., Pantò, B., Rapicavoli, D. & Occhipinti, G. (2019) 3D Discrete Macro-Modelling Approach for Masonry Arch Bridges. Zurich, Switzerland, International Association for Bridge and Structural Engineering (IABSE).
- Chisari, C., Macorini, L. & Izzuddin, B. A. (2020) Multiscale model calibration by inverse analysis for nonlinear simulation of masonry structures under earthquake loading. *International Journal for Multi-scale Computational Engineering*, 18, 241–263.
- Fanning, P. J. & Boothby, T. E. (2001) Three-dimensional modelling and full-scale testing of stone arch bridges. *Computers & Structures*, 79, 2645–2662.
- Grosman, S., Bilbao, A. B., Macorini, L. & Izzuddin, B. A. (2021) Numerical modelling of three-dimensional masonry arch bridge structures. *Proceedings of the Institution of Civil Engineers - Engineering and Computational Mechanics*, 174, 96–113.
- Grosman, S., Macorini, L. & Izzuddin, B. A. (2023) Parametric Nonlinear Modelling of 3D Masonry Arch Bridges. *Advances in Engineering Software*, (under review).
- Izzuddin, B. A. (1991) Nonlinear Dynamic Analysis of Framed Structures.
- Izzuddin, B. A. & Jokhio, G. A. (2017) Mixed-Dimensional Coupling for Parallel Partitioned Nonlinear Finite-Element Analysis. *Journal of Computing in Civil Engineering*, 31, 04016062–04016062.
- Jokhio, G. A. & Izzuddin, B. A. (2015) A Dual Super-Element Domain Decomposition Approach for Parallel Nonlinear Finite Element Analysis. *International Journal for Computational Methods in Engineering Science and Mechanics*, 16, 188–212.
- Lee, J. & Fenves, G. L. (1998) Plastic-Damage Model for Cyclic Loading of Concrete Structures. *Journal of Engineering Mechanics*, 124, 892–900.
- Macorini, L. & Izzuddin, B. A. (2011) A non-linear interface element for 3D mesoscale analysis of brick-masonry structures. *International Journal for Numerical Methods in Engineering*, 85, 1584–1608.
- Mcneel, R. & Associates (2010) Rhinoceros 3D, Version 6.0. *Robert McNeel & Associates, Seattle, WA*.
- Minga, E., Macorini, L. & Izzuddin, B. A. (2018) A 3D mesoscale damage-plasticity approach for masonry structures under cyclic loading. *Meccanica*, 53, 1591–1611.
- Ozaeta García-Catalán, R. & Martín-Caro Alamo, J. A. (2020) *Catalogue of Damages in masonry arch bridges*, Paris, UIC.
- Tubaldi, E., Minga, E., Macorini, L. & Izzuddin, B. A. (2020) Mesoscale analysis of multi-span masonry arch bridges. *Engineering Structures*, 225, 111137–111137.
- Zhang, Y., Macorini, L. & Izzuddin, B. A. (2016) Mesoscale partitioned analysis of brick-masonry arches. *Engineering Structures*, 124, 142–166.
- Zhang, Y., Macorini, L. & Izzuddin, B. A. (2018) Numerical investigation of arches in brick-masonry bridges. *Structure and Infrastructure Engineering*, 14, 14–32.

Analysis of masonry arch bridges using multi-scale discontinuity layout optimization

Linwei He, Nicola Grillanda, John Valentino, Matthew Gilbert & Colin C. Smith
Department of Civil and Structural Engineering, University of Sheffield, Sheffield, UK

ABSTRACT: Masonry arch bridges are still in active usage in many countries across the globe. However, the analysis tools that generally underpin the assessment process for these structures have traditionally been 2D, which means that 3D modes of response cannot be captured. This contribution introduces a multi-scale limit analysis method for 3D masonry arch bridges using discontinuity layout optimization (DLO), which is a highly efficient limit analysis technique that automatically identifies the collapse load and associated failure mechanism of a solid or structure. Using this approach, a macroscopic shell continuum is assumed, using a homogenized material that is obtained by analysing the microscopic behaviour of a representative pattern of masonry units in the structure. Therefore, potential 3D failure modes for masonry arch bridges can be revealed. The basic model assumes rigid masonry units, and takes into account key engineering features such as aspect ratio of masonry units. Simple examples are used to validate the proposed method; then simple square and skew masonry arch bridges are analysed to demonstrate the efficacy of the proposed method.

1 INTRODUCTION

Masonry arch bridges are long-lived structures that are still in widespread usage across western Europe and other parts of the world. Modern techniques for the structural analysis of masonry arch bridges can be traced back to works by Kooharian (1953) and Heyman (1966), where masonry was assumed to possess infinite stiffness, infinite crushing strength and sliding resistance and to have joints with zero tensile strength. Under these assumptions, an arch will collapse via the opening of a sufficient number of hinges, with the stability of the structure depending only on its geometry (Heyman 1969).

Many numerical tools have been developed to analyse the 2D behaviour of masonry arch bridges. For example, Livesley (1978) introduced a computational limit analysis tool to model the collapse behaviour of assemblies of rigid blocks, using linear programming (LP) to obtain solutions. Other computational methods based on the static or kinematic theorems of plastic analysis, have also been proposed since. Practical software tools have also been developed to analyse masonry arch bridges for industrial users, e.g., LimitState:RING (Gilbert 2001) and ArchNURBS (Chiozzi et al. 2016). Furthermore, strategies have been proposed to allow masonry crushing and sliding phenomena to be modelled (the latter with both associated and non-associated flow behaviour); see Gilbert (2007).

However, the main focus of previous work has been on the development of 2D modelling tools, which are clearly not capable of modelling the 3D behaviour of masonry arch bridges, which can be important in some cases (e.g. when skew bridges are involved). Whilst it is in principle straightforward to extend 2D methods to 3D if all constituent masonry units are explicitly modelled, and potential hinge locations coincide with the locations of mortar joints (e.g. see Portioli et al. (2014) and Grillanda et al. (2022)), this requires detailed geometrical information about the locations of all voussoirs in the bridge. Such information may not be readily available, and collecting it may involve laborious processes. Alternatively, a multi-scale (or homogenized) approach can be utilized, where the model is represented by a continuous material characterized by a suitable (homogenized) yield domain. de Buhan and

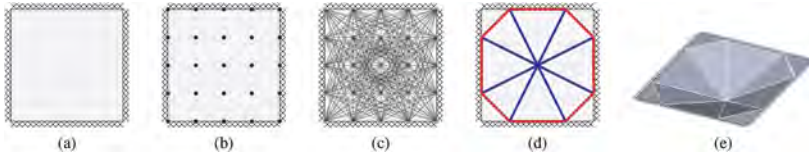


Figure 1. Steps in general DLO procedure (a) problem specification (square slab under out-of-plane UDL); (b) node discretization; (c) interconnection of nodes with all potential discontinuities; (d) identification of critical subset of potential discontinuities using optimization; (e) corresponding collapse kinematics.

de Felice (1997) and Sab (2003) respectively introduced homogenization methods for in-plane and out-of-plane masonry structures. Their work has attracted significant interest, and several strategies have been presented to deduce the homogenized properties depending on the initial assumptions, and various numerical approaches have been developed; see Milani et al. (2006a,b, 2008).

Discontinuity layout optimization (DLO) is a highly efficient numerical method that can be used to automatically identify the collapse load and the associated failure mechanism of a solid or structure. DLO directly models the potential discontinuities that can occur at failure, and utilizes efficient mathematical programming solution methods to obtain solutions. DLO has been applied to a broad range of applications, including geotechnical engineering problems (e.g., Smith and Gilbert 2007) and slab yield-line analysis problems (e.g., Gilbert et al. 2014). Although DLO can be used to directly analyse masonry structures by modelling joints as discontinuities, following a ‘heterogeneous’ approach (e.g., Gilbert et al. 2010), the full potential of DLO becomes apparent when used in conjunction with a multi-scale representation of the constituent masonry, since it obviates the need to model all constituent masonry units explicitly. Initial work in this area was recently carried out by Valentino et al. (2023), who introduced a multi-scale DLO method for in-plane masonry problems. In the present work the approach is extended to model 3D shell problems such as masonry arch bridges, where a macroscopic shell continuum is assumed and where a homogenized material obtained by analysing the microscopic in- and out-of-plane behaviour of a representative pattern of masonry units in the structure is employed. The paper is organized as follows: firstly, the standard DLO method is introduced; secondly, the proposed multi-scale approach is developed and relevant mathematical expressions are given; thirdly, several numerical examples are used to demonstrate the efficacy of the method; finally, conclusions are drawn.

2 GENERAL DLO FORMULATION

The main steps in DLO are illustrated in Figure 1. Firstly, the geometry of the problem, together with boundary and load conditions are specified (Figure 1a). Secondly, the problem domain is discretized using nodes (Figure 1b). Thirdly, potential discontinuities are created by interconnecting nodes (Figure 1c). For a shell structure, each discontinuity involves 6 kinematic variables, as shown in Figure 2, including in-plane shear displacement d_t , in-plane normal displacement d_n , out-of-plane shear displacement d_z , bending rotation r_t , twisting rotation r_n and in-plane rotation r_z . Finally, the most critical failure mechanism is identified (Figure 1d) by solving the following optimization problem (after Smith and Gilbert 2007):

$$\text{minimize } -\mathbf{f}_D^T \mathbf{d} + \mathbf{g}^T \mathbf{p} \quad (1a)$$

$$\text{subject to } \mathbf{Bd} = 0 \quad (1b)$$

$$\mathbf{f}_L^T \mathbf{d} = 1 \quad (1c)$$

$$\mathbf{Np} - \mathbf{d} = 0 \quad (1d)$$

$$\mathbf{p} \geq 0, \quad (1e)$$

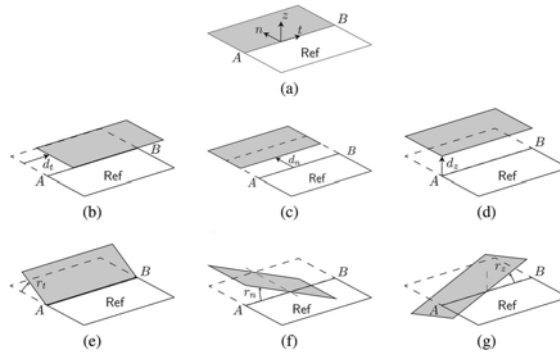


Figure 2. Kinematic variables in a discontinuity AB : (a) coordinate system; (b-g): in-plane shear displacement d_t , in-plane normal displacement d_n , out-of-plane shear displacement d_z , bending rotation r_t , twisting rotation r_n and in-plane rotation r_z .

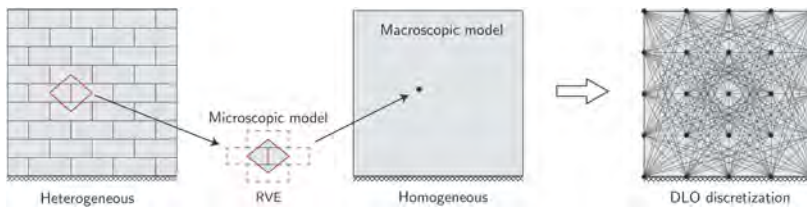


Figure 3. Multi-scale approach: modelling a periodic masonry structure using a microscopic model defined via a RVE and a macroscopic model solvable via DLO.

where \mathbf{f}_D and \mathbf{f}_L are vectors containing respectively specified dead and live loads, \mathbf{d} and \mathbf{p} are, respectively, vectors containing all kinematic variables shown in Figure 2 and their associated non-negative plastic multipliers. Also \mathbf{g} is a work coefficient vector, so that $\mathbf{g}^T \mathbf{p}$ describes the internal energy dissipation along discontinuities. \mathbf{B} is a compatibility matrix, used to ensure all kinematic variables are compatible at nodes. Finally, \mathbf{N} is a flow rule matrix describing the failure criteria with respect to kinematic variables. With respect to variables \mathbf{d} and \mathbf{p} , optimization problem (1) is a LP problem, so that a globally optimal solution can be identified. In addition, a post-processing step can be carried out to visualize the failure mechanism; see Figure 1e. Note that the steps in Figure 1 will create a large number of potential discontinuities (e.g., see Figure 1c), so a vast number of potential failure modes can be replicated. This means that DLO is capable of obtaining highly accurate solutions.

3 MULTI-SCALE APPROACH

As mentioned previously, DLO can readily be applied to masonry structures simply by only modelling joints as potential discontinuities (e.g., the heterogeneous model in Figure 3). However, this approach does not take full advantage of DLO, since the numbers of potential discontinuities involved is limited, such that a full ‘layout optimization’ is not required.

However, DLO becomes more valuable when a multi-scale approach is adopted, and the locations of discontinuities are not known *a priori*. As shown in Figure 3, the multi-scale approach first defines a representative volume element (RVE), which captures the microscopic behaviour of a periodic masonry structure, including interlocking effects and the failure criteria at joints. Then a macroscopic model is created, assuming a continuum problem solvable via well-developed limit analysis methods, though which now involves the use of a homogeneous material model derived by analysing the heterogeneous behaviour of the RVE. To develop a multi-scale DLO method, the RVE, microscopic and macroscopic models are now examined.

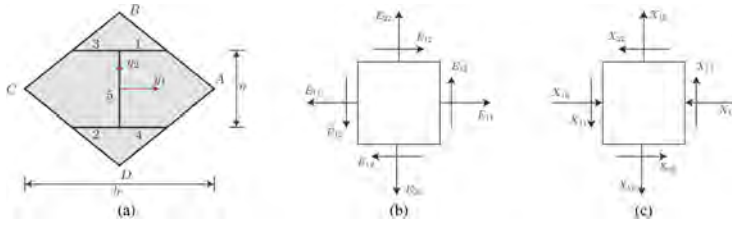


Figure 4. RVE and the corresponding macroscopic strain rate tensor: (a) geometry of the RVE, comprising four rigid bodies (*A*, *B*, *C* and *D*) and five joints (1,2,...,5); (b) in-plane macroscopic strain rate tensor; (c) macroscopic curvature tensor.

3.1 RVE

For sake of simplicity, the RVE in de Buhan and de Felice (1997) is used here (Figure 4a). The kinematic properties of the RVE are defined by a macroscopic strain rate tensor \mathbf{E} , following the Love-Kirchhoff plate model (after Cecchi and Sab 2002):

$$\mathbf{E} = \begin{bmatrix} E_{11} & E_{12} & X_{11}y_1 + X_{12}y_2 \\ E_{21} & E_{22} & X_{12}y_1 + X_{22}y_2 \\ -\frac{X_{11}y_1 + X_{12}y_2}{2} & -\frac{X_{12}y_1 + X_{22}y_2}{2} & 0 \end{bmatrix}, \quad (2)$$

where E_{11} , E_{22} and E_{12} are components of the in-plane strain rate tensor; also X_{11} , X_{22} and X_{12} are components of the curvature tensor and y_1 and y_2 are the position coordinates in the RVE, as shown in Figure 4. Taking into account the periodicity conditions (see e.g. Cecchi and Sab 2002 for detailed derivations), the displacements and rotations of the four vertices $ABCD$ can be written with respect to variables in \mathbf{E} :

$$\mathbf{u}_A = \begin{bmatrix} E_{11}b/2 \\ E_{12}b/2 \\ a^2X_{22}/4 - b^2X_{11}/16 \end{bmatrix} + \mathbf{u}_c, \quad \mathbf{\Omega}_A = \begin{bmatrix} -0.5bX_{12} \\ 0.5bX_{11} \\ 0 \end{bmatrix} + \mathbf{\Omega}_c \quad (3a)$$

$$\mathbf{u}_B = \begin{bmatrix} E_{12}a \\ E_{22}a \\ -a^2X_{22}/4 + b^2X_{11}/16 \end{bmatrix} + \mathbf{u}_c, \quad \mathbf{\Omega}_B = \begin{bmatrix} -aX_{22} \\ aX_{12} \\ 0 \end{bmatrix} + \mathbf{\Omega}_c \quad (3b)$$

$$\mathbf{u}_C = \begin{bmatrix} -E_{11}b/2 \\ -E_{12}b/2 \\ a^2X_{22}/4 - b^2X_{11}/16 \end{bmatrix} + \mathbf{u}_c, \quad \mathbf{\Omega}_C = \begin{bmatrix} 0.5bX_{12} \\ -0.5bX_{11} \\ 0 \end{bmatrix} + \mathbf{\Omega}_c \quad (3c)$$

$$\mathbf{u}_D = \begin{bmatrix} -E_{12}a \\ -E_{22}a \\ -a^2X_{22}/4 + b^2X_{11}/16 \end{bmatrix} + \mathbf{u}_c, \quad \mathbf{\Omega}_D = \begin{bmatrix} aX_{22} \\ -aX_{12} \\ 0 \end{bmatrix} + \mathbf{\Omega}_c. \quad (3d)$$

where \mathbf{u}_A , \mathbf{u}_B , \mathbf{u}_C and \mathbf{u}_D are the displacement vectors of the four vertices respectively; also $\mathbf{\Omega}_A$, $\mathbf{\Omega}_B$, $\mathbf{\Omega}_C$ and $\mathbf{\Omega}_D$ are the rotation vectors and \mathbf{u}_c and $\mathbf{\Omega}_c$ are constant displacement and rotation vectors of the RVE, respectively. Figure 5 shows the relative displacements and rotations of the RVE with respect to the variables in \mathbf{E} .

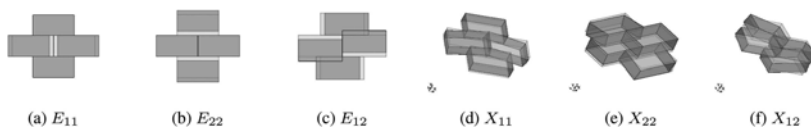


Figure 5. Associated displacements and rotations of the RVE (showing kinematics without reference to applicable flow rules).

3.2 Microscopic model

Since the displacement and rotation vectors at the four vertices of the RVE are given in (3), the relative displacements at the five joints in Figure 4a can be calculated using:

$$[\mathbf{u}]_{\alpha\beta} = \mathbf{u}_\alpha + \boldsymbol{\Omega}_\alpha \times (\mathbf{y}_d - \mathbf{y}_\alpha) - \mathbf{u}_\beta - \boldsymbol{\Omega}_\beta \times (\mathbf{y}_d - \mathbf{y}_\beta), \quad \text{for } \alpha, \beta \in \{A, B, C, D\} \quad (4)$$

where $[\mathbf{u}]_{\alpha\beta}$ is the relative displacement vector (or ‘displacement jump’) between masonry blocks α and β . Also \mathbf{y}_d is a vector containing coordinates of a point at the joint. Note that for each joint, $[\mathbf{u}]_{\alpha\beta}$ comprises the normal displacement $[u_n]$, in-plane shear displacement $[u_i]$ and out-of-plane shear displacement $[u_z]$.

Given the relative displacements at joints, flow rules can now be written. Here Mohr-Coulomb failure criteria is assumed:

$$[u_n]_j \geq \mu \sqrt{[u_i]_j^2 + [u_z]_j^2}, \quad \text{for } j \in \{1, 2, 3, 4, 5\}, \quad (5)$$

where μ is the coefficient of friction, $[u_n]_j$, $[u_i]_j$ and $[u_z]_j$ are the relative displacements of joint j shown in Figure 4, calculated by substituting (3) in (4). The average energy dissipation within the RVE can be derived as:

$$\Pi = \frac{1}{ab} \sum_{j=1}^5 \int_0^{l_j} \int_{-\frac{t}{2}}^{\frac{t}{2}} \frac{[u_n]_j c}{\mu} dt dl = \frac{ct(E_{11} + E_{22})}{\mu}, \quad (6)$$

where Π is the average energy dissipation within the RVE, c is the cohesion, l_j is the length of joint j in Figure 4a, and t is the thickness of masonry blocks. The inequality constraints in (5) and the equation in (6) define the microscopic behaviour of the RVE.

3.3 Macroscopic model

The macroscopic model assumes a continuum problem solvable via the standard DLO approach shown in Figure 1. Variables of the macroscopic strain rate tensor \mathbf{E} can be derived as:

$$\mathbf{E} = \mathbf{T}\mathbf{d} \quad (7)$$

where \mathbf{T} is a transformation matrix, readers interested in its derivations are referred to Valentino et al. (2023). Also $\mathbf{E} = [E_{11}, E_{22}, E_{12}, X_{11}, X_{22}, X_{12}]^T$ is a vector containing components of macroscopic strain rate tensor in Equation (2) and $\mathbf{d} = [d_t, d_n, dz, r_t, r_n, r_z]^T$ is a vector of kinematic variables in DLO.

3.4 Multi-scale DLO formulation

Given both microscopic and macroscopic models, the full DLO formulation can be written as:

$$\text{minimize } -\mathbf{f}_D^T \mathbf{d} + \sum_{i=1}^m l_i \Pi_i \quad (8a)$$

$$\text{subject to } \mathbf{B}\mathbf{d} = 0 \quad (8b)$$

$$\mathbf{f}_L^T \mathbf{d} = 1 \quad (8c)$$

$$\left. \begin{array}{l} \mathbf{E}_i = \mathbf{T}\mathbf{d}_i \\ \mathbf{N}(\mathbf{E}_i) \leq 0 \end{array} \right\} \text{ for } i = 1, 2, \dots, m \quad (8d)$$

where \mathbf{d}_i and \mathbf{E}_i are, respectively, vectors containing DLO kinematic variables and macroscopic strain rate tensors for discontinuity i and m is the number of discontinuities. Also Π_i is the averaged energy dissipation in the RVE, obtained in Equation (6), such that $\sum_{i=1}^m l_i \Pi_i$ is the

total internal energy dissipation within the structure. \mathbf{B} is a compatibility matrix, \mathbf{f}_L and \mathbf{f}_D are load effect vectors, as shown in Problem (1). Finally, $\mathbf{N}(\cdot)$ is the microscopic flow rule defined in Constraint (5). Since in (5) the constraints are quadratic cones, Problem (8) is a conic programming problem, which can be solved efficiently via modern convex optimization solvers such as MOSEK (MOSEK ApS 2022).

4 NUMERICAL EXAMPLES

4.1 Simple validation example: L-shaped wall

This example is a L-shaped wall previously studied by Portioli et al. (2014). The geometry of the wall is shown in Figure 6a. The masonry blocks have a dimension of $0.8 \text{ m} \times 0.03 \text{ m}$ and a thickness of 0.04 m . Cohesion c and the coefficient of friction μ are set to 0 and 0.7, respectively. The wall is subject to a horizontal body force $w = \lambda G$, where G is the self-weight of the structure, and λ is the load factor. Solutions obtained using rigid block and DLO methods are shown in Figure 6b-d, with the resulting failure mechanisms being quite similar. The load factor obtained using rigid block analysis was 0.195 (identical to that found by Portioli et al. 2014), while the result obtained by multi-scale DLO is 0.155, which is lower than the former. This is because that the multi-scale approach effectively assumes that the constituent masonry blocks are infinitely small, and block interlocking effects in this case become less significant than when blocks are larger; see Valentino et al. (2023) for more details.

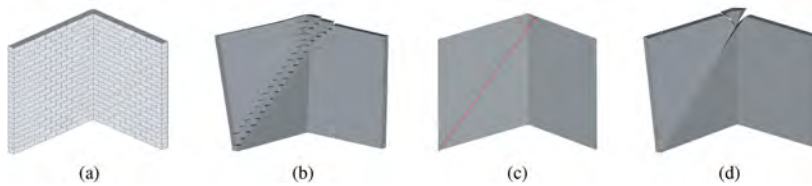


Figure 6. L-shaped wall: (a) geometry; (b) rigid-block analysis using a heterogeneous approach via standard DLO, $\lambda = 0.195$; (c) multi-scale DLO, $\lambda = 0.155$; (d) failure mechanism of (c).

4.2 Square masonry arch bridge

The second example involves a square masonry arch bridge subject to a centreline point load $F = 1 \text{ kN}$ applied at quarter span. The geometry of the bridge is shown in Figure 7a, where the bridge span is $L = 0.75 \text{ m}$, width is $L/2$, and thickness is $t = 0.054 \text{ m}$, and the unit weight is set to 23.6 kN/m^3 . Cohesion c and the coefficient of friction μ are set to 0 and 0.75, respectively. In the rigid block model, a total of 24 voussoirs with an aspect ratio of 2.318 (full block measured at the mid-surface) are used, and the resulting failure mechanism is shown in Figure 7(b). On the other hand, using multi-scale DLO, the curved geometry is approximated via piecewise-linear surfaces; see solution obtained using a coarse (150 node) numerical discretization in Figure 7(c). Note that discontinuities (e.g., hinges) can now occur within a given arch segment, so the computed load factor is lower than that obtained via rigid block methods, where hinges can only occur at joints. Also, two intersecting discontinuities are observed to form under the point load applied on the arch centreline.

4.3 Skew bridge

In the third example two skew bridges are considered, using the same base configuration as in the previous example. In this case the arch geometries are obtained by ‘shearing’ the arch by 15 and 45 degrees (i.e., the skew angle). In addition, voussoirs are configured using the helicoidal method (see Forgács et al. 2017), which can be taken into account in DLO by rotating the local coordinate system in each piecewise-linear surface. Figure 8a and b show the results obtained using a skew angle of 15°; the load factor is 0.488, which is 57% higher than that obtained for the square bridge. This is due to interlocking effects arising from the helicoidal voussoir configuration, leading to rotated hinge lines. If the skew angle is increased to 45°, the

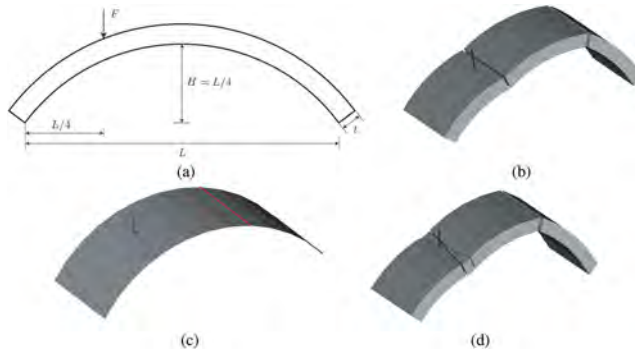


Figure 7. Square bridge: (a) geometry; (b) rigid-block analysis (with 24 voussoirs), $\lambda = 0.327$; (c) multi-scale DLO, $\lambda = 0.311$; (d) failure mechanism of (c).

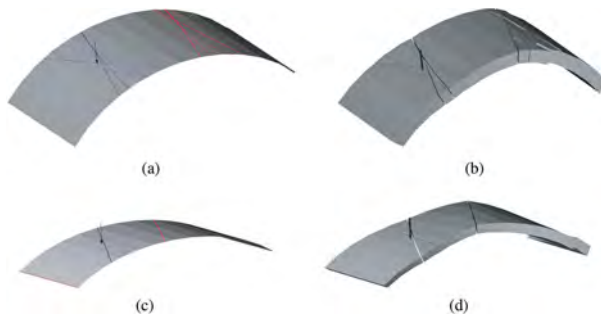


Figure 8. Skew bridge: (a) and (b), skew angle 15° , $\lambda = 0.488$; (c) and (d), skew angle 45° , $\lambda = 0.774$.

load factor increases further, with the failure mode clearly showing rotated hinge lines and twisting failure near the right abutment.

5 CONCLUSIONS

In this paper the powerful and highly efficient discontinuity layout optimization (DLO) procedure is applied to the analysis of masonry arch bridge structures. Here DLO is used in conjunction with a multi-scale representation of the constituent masonry, obviating the need to model individual masonry units explicitly. In the multi-scale approach, a macroscopic shell continuum is assumed, using a homogenized material model that is obtained by analysing the microscopic behaviour of the representative volume element (RVE) of masonry units in the structure. Several numerical examples, including those involving square and skew arch bridges, are used to demonstrate that 3D responses of masonry arch structures can be captured via the proposed approach. Bridges with complex geometries and spandrel walls can directly be modelled using the homogenized shell DLO method, though further developments are required to ensure soil-structure interaction in soil-filled masonry bridges.

ACKNOWLEDGEMENTS

The financial support of EPSRC under grant reference EP/T001305/1 is gratefully acknowledged.

REFERENCES

- Cecchi, A. and K. Sab (2002, January). Out of plane model for heterogeneous periodic materials: the case of masonry. *European Journal of Mechanics - A/Solids* 21(5), 715–746.
- Chiozzi, A., M. Malagù, A. Tralli, and A. Cazzani (2016). Archnurbs: Nurbs-based tool for the structural safety assessment of masonry arches in MATLAB. *Journal of Computing in Civil Engineering* 30(2), 04015010.
- de Buhan, P. and G. de Felice (1997, July). A homogenization approach to the ultimate strength of brick masonry. *Journal of the Mechanics and Physics of Solids* 45(7), 1085–1104.
- Forgács, T., V. Sarhosis, and K. Bagi (2017, June). Minimum thickness of semi-circular skewed masonry arches. *Engineering Structures* 140, 317–336.
- Gilbert, M. (2001). RING: a 2D rigid-block analysis program for masonry arch bridges. In *ARCH'01: 3rd International Arch Bridges Conference (Paris, 19-21 September 2001)*, pp. 459–464.
- Gilbert, M. (2007). Limit analysis applied to masonry arch bridges: state-of-the-art and recent developments. In *5th International Arch Bridges Conference*, pp. 13–28.
- Gilbert, M., L. He, C. C. Smith, and C. V. Le (2014). Automatic yield-line analysis of slabs using discontinuity layout optimization. *Proceedings of the Royal Society A: Mathematical, Physical and Engineering Sciences* 470(2168), 20140071.
- Gilbert, M., C. Smith, and T. Pritchard (2010, September). Masonry arch analysis using discontinuity layout optimisation. *Proceedings of the Institution of Civil Engineers - Engineering and Computational Mechanics* 163(3), 155–166.
- Grillanda, N., A. Chiozzi, G. Milani, and A. Tralli (2022). Nurbs solid modeling for the three-dimensional limit analysis of curved rigid block structures. *Computer Methods in Applied Mechanics and Engineering* 399, 115304.
- Heyman, J. (1966). The stone skeleton. *International Journal of Solids and Structures* 2(2), 249–279.
- Heyman, J. (1969). The safety of masonry arches. *International Journal of Mechanical Sciences* 11(4), 363–385.
- Kooharian, A. (1953). Limit analysis of voussoir (segmental) and concrete arches. *Proc. American Concrete Institute* 89, 317–328.
- Livesley, R. K. (1978). Limit analysis of structures formed from rigid blocks. *International journal for numerical methods in engineering* 12(12), 1853–1871.
- Milani, E., G. Milani, and A. Tralli (2008). Limit analysis of masonry vaults by means of curved shell finite elements and homogenization. *International Journal of Solids and Structures* 45(20), 5258–5288.
- Milani, G., P. Lourenço, and A. Tralli (2006a). Homogenization approach for the limit analysis of out-of-plane loaded masonry walls. *Journal of Structural Engineering* 132(10), 1650–1663.
- Milani, G., P. B. Lourenço, and A. Tralli (2006b). Homogenised limit analysis of masonry walls, part i: Failure surfaces. *Computers & Structures* 84(3-4), 166–180.
- MOSEK ApS (2022). *MOSEK Optimizer API for Python*. MOSEK.
- Portioli, F., C. Casapulla, M. Gilbert, and L. Cascini (2014, September). Limit analysis of 3D masonry block structures with non-associative frictional joints using cone programming. *Computers & Structures* 143, 108–121.
- Sab, K. (2003). Yield design of thin periodic plates by a homogenization technique and an application to masonry walls. *Comptes Rendus Mécanique* 331(9), 641–646.
- Smith, C. and M. Gilbert (2007). Application of discontinuity layout optimization to plane plasticity problems. *Proceedings of the Royal Society A: Mathematical, Physical and Engineering Sciences* 463, 2461–2484. doi:10.1098/rspa.2006.1788.
- Valentino, J., M. Gilbert, M. Gueguin, and C. C. Smith (2023). Limit analysis of masonry walls using discontinuity layout optimization and homogenization. *International Journal for Numerical Methods in Engineering* 124(2), 358–381.

The role of history in the structural assessment of a multi-span masonry arch bridge

G. Zani, P. Martinelli, G. Cardani & M. di Prisco

Department of Civil and Environmental Engineering, Politecnico di Milano, Milan, Italy

ABSTRACT: The long history of an important multi-span masonry arch bridge built in 1336 in Lecco, Italy, across the Adda River and still in use today is presented here. The study was one of the preliminary stages of an extensive structural investigation project that led to prescriptions on the current use and management of this bridge. The objective is to describe the historical-constructive evolution of the Azzone Visconti Bridge, named after its creator and Lord of Milan; because of its complex and long history, the bridge appears today as the structural assemblage of several substructures. The intent is to present a comparison of different structural modeling approaches, already adopted in the safety assessment of the bridge. Finally, the possibility of implementing the valuable information recovered from the historical study (e.g., existing material heterogeneities, cracking patterns, and past interventions) into alternative analytical models is discussed.

1 INTRODUCTION

Historical bridges are an important part of a country's cultural heritage because their evolution has accompanied the history of a civilization, ready to overcome natural obstacles and facilitate exchanges with neighboring populations. However, in times of battle they were often subject to attack, demolition and reconstruction. For this reason, many of them are registered as protected architectural heritage. Some of them have survived many centuries of use through constant maintenance but have undergone numerous transformations to better adapt to the new demands of the 20th century. Not only external agents, but also increased vehicular traffic, as well as increased maximum allowable accidental loads, represent possible damage factors for the structure. To ensure safe working conditions, the load-bearing capacity of these bridges must be evaluated and demand levels carefully assigned.

The long history of an important multi-span masonry arch bridge built in 1336 in Lecco, Italy, across the Adda River and still in use today is presented here. The study was one of the preliminary stages of an extensive structural investigation project that led to prescriptions on the current use and management of this bridge. As part of an institutional collaboration between the Politecnico di Milano (Lecco Campus) and the Municipality of Lecco, extensive research activity involving different disciplines and research groups was initiated in 2014, with the aim of investigating the load-bearing capacity of the bridge, under the scientific coordination of the last author.

This paper focuses attention on the Azzone Visconti Bridge, a masonry arch bridge that was for centuries (until 1955) the only road connection between the two banks of the Adda River, the only outlet of Lake Como, and is still an important access route to the city of Lecco (northern Italy). The bridge had several abutments and drawbridges and, after later enlargement, now has 11 spans of different sizes. The bridge is considered to be the most important medieval evidence in the city, and is one of the most impressive masonry works in the entire region.

The bridge has been profoundly modified in the 20th century. Because of its complex and long history, it now evidences the structural assemblage of several substructures and has thus lost its homogeneity, becoming more vulnerable.

The intent is to present here a comparison of different structural modeling approaches, of varying degrees of sophistication, that have already been adopted in bridge safety assessment. Finally discussing the possibility of implementing the valuable information recovered from the historical study (e.g., existing material heterogeneities, cracking patterns, and past interventions) into alternative analytical models.

2 THE HISTORIC-CONSTRUCTIVE EVOLUTION OF THE BRIDGE

The Azzone Visconti Bridge (also known as *Ponte Vecchio*) is a historic masonry arch bridge built in the 14th century, consisting of ten piers, eleven arches and two abutments, one on the east side of Lecco and one on the west side of Malgrate of the Adda River. It has an overall length of about 133 m and an average deck width of about 6.2 m. Although the bridge appears today to be very different from the original construction, it remains one of the most important examples of military engineering from the Middle Ages.

2.1 From the origin in the 14th century to the 17th century

The bridge was built at the behest of the Lord of Milan, Azzone Visconti, between 1336 and 1338, connecting for the first time in the territory the two banks of the Adda River, which until then had belonged to the Duchy of Milan and the Republic of Venice. The bridge was equipped with a stronghold, a central tower and a larger one towards Lecco, while the two heads were equipped with a ravelin (Figure 1a,b). The bridge was also defended by three drawbridges, placed at the fortifications, and was armed with bombs and thrusters. In the 17th century, those who wanted to cross had to pay a toll managed by a consortium composed of several co-owners, nobles from Lecco and Milan, as well as of a monastery.

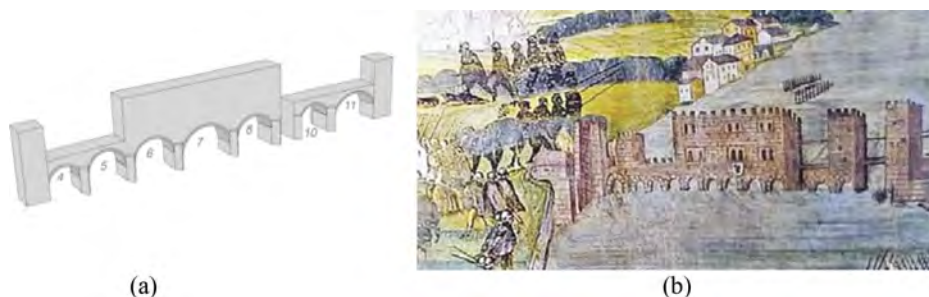


Figure 1. Azzone Visconti Bridge: a) model of the 1st phase, mid 14th century (bridge as a fortress with only 8 spans, adapted from di Prisco et al. 2019) and b) detail of the fresco depicting the Battle of Lecco and the bridge with the fortress, in the Medici castle in Melegnano (MI); dating of the painting estimated between 1544 and 1555 (adapted from Comandù et al. 2005).



Figure 2. The bridge after 1533, when the great tower was destroyed and already with 11 spans (courtesy of Ambrosiana Library of Milan).

The Azzone Visconti Bridge was originally built with eight arches. The bridge was later expanded in two phases (1350 and 1434) to 11 arches to widen the cross section of the river, favoring faster water flow and reducing flooding in the Como area. The bridge has undergone continual modifications over time due to wars and the water level of Lake Como. In fact, the Adda River is the only emissary of the lake, and the bridge piers constitute an obstacle to the water flow. For this reason, due to repeated flooding of Como at the far end of the other closed branch of the lake, the riverbed was lowered even in the last century and the piers were consequently consolidated.

After the wars fought by Gian Giacomo Medici, known as the Medeghino in 1531, the bridge was severely damaged (Figure 2) (Belloni et al. 1992) and, in the early 17th century (1600-1608), it was renovated on behalf of the Spanish Governor.

2.2 The 18th and 19th century

Its strategic and economic importance would last for centuries (Figure 3a,b), until the last battle won by the Austrian-Russians of the Holy Alliance against the French and Cisalpine troops between April 25 and 27, 1799. On that occasion, the French blew up an archway to slow down the enemy's passage and flight, and this damage would not be repaired until after the end of Napoleonic rule (Figure 4). As a sign of gratitude for the victory, a small chapel was erected in the center of the bridge (Figure 4b), but which is no longer present. In the 19th century, the abolition of the military stronghold of Lecco gave the start to many changes made with the intention of facilitating transit. The lateral towers were demolished to facilitate the passage of carriages (Figure 4).

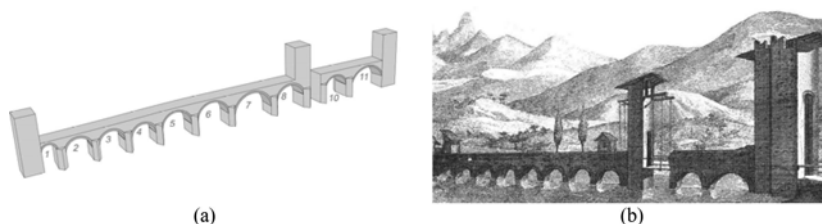


Figure 3. Azzone Visconti bridge: a) 2nd phase model, end of 18th century (11-span bridge with towers and drawbridge, adapted from di Prisco et al. 2019); b) view of the bridge, 1760-1771, etching of G.C. Bianchi (Giulini 1760).

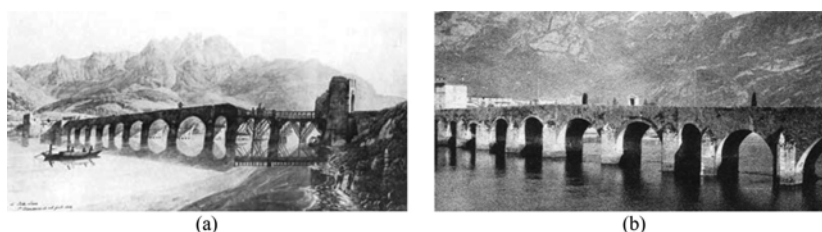


Figure 4. Azzone Visconti bridge: a) in 1806 (water-colour by P. Birmann) with two demolished towers and two arches destroyed after the Napoleonic damages and b) with reconstructed arches and a small chapel visible in the center of the bridge in the early 20th century (extracted from Resegoneonline.it 2014).

2.3 The 20th century

In 1909-1910 the existing bridge deck was enlarged by means of cantilever steel beams to host a tramway and to cope with the increasing traffic. Additional engaged piers were added on both sides to support the cantilevers (visible in Figure 5b). In 1949-1950, a radical intervention was carried out by Prof. Eng. A. Danusso: a) to facilitate the outflow of the river, the riverbed was lowered by about 2 m; b) to protect the bridge piers, the foundations of 7 piers were strengthened; c) the foundation of each pier was reinforced by introducing a large diameter

steel encasing ring, about 5 m deep, filled with concrete and constrained at the top by an additional reinforced concrete (RC) outer ring (Figure 6); d) to widen the roadway, the deck was completely removed (Figure 5) and a continuous RC caisson was inserted between the two masonry spandrel walls and filled with coarse granular material (mix of pebbles and mortar). The caisson was made square or U-shaped, depending on the varying height between the extrados of the arches and the deck. e) In addition, the engaged piers (or pilasters) added around 40 years earlier above the cutwaters, were removed.

Three arches damaged by the out-of-plumb of the piers were strengthened. External pedestrian footbridges were also added using cantilever steel beams and RC slabs resting on the aforementioned beams. Over the next 70 years, after this invasive intervention, no further work was carried out other than routine maintenance. Figure 7 shows a view of the bridge as it appears today.



Figure 5. Azzone Visconti bridge: a) model of the bridge with the most significant strengthening intervention depicted in blue: removal of the original deck and infill, insertion of a continuous concrete caisson and enlargement of the foundations. b) photo before the strengthening when the deck was removed in 1949-1950 and grafted piers were still present. The zoom shows the inner side of the deck after the removal of the infill (courtesy of Lecco Municipality, “Consorzio Fiume Adda” and Ministry of Culture).

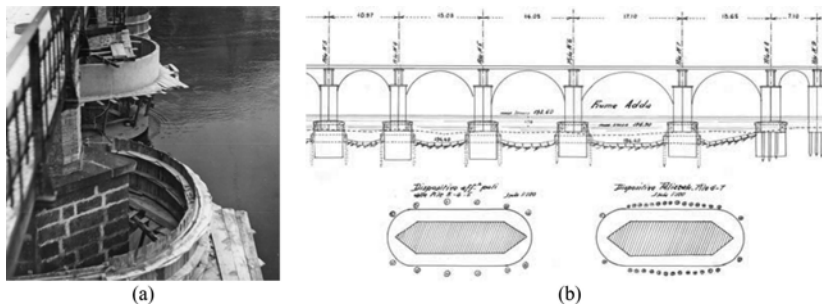


Figure 6. Azzone Visconti bridge: a) strengthening of the piers foundations; b) original drawings of the 1949-1950 project (courtesy of Lecco Municipality, ‘Consorzio Fiume Adda’ and Ministry of Culture).



Figure 7. Azzone Visconti bridge: a) model representing the current shape (adapted from di Prisco et al. 2019) and b) current view.

3 REMARKS ON THE HISTORICAL ANALYSIS FOR STRUCTURAL EVALUATION

The bridge has a very irregular geometry, as evidenced by an accurate laser scanner survey (Barazzetti et al. 2016), and has piers with different rotations and very different arch spans, as confirmed by the historical-constructive evolution described above.

Different masonry textures are observed in the spandrels (Figure 8b), from river pebbles arranged in a herringbone pattern in the original arches to roughly cut stones in the modified and/or repaired parts, to more rectangular stones and slabs for the added parts; discontinuities are clearly visible.

Masonry repairs can be observed at the ends of the fortress demolished during the 16th century war (occupying three spans: n. 6, 7 and 8 as in Figure 1). Metallic anchorages placed approximately at the haunches of the arches and arranged in such a way as to have the iron tie-rods in a transverse rather than longitudinal direction are visible (Figure 8b); there is no date of insertion.

The crack pattern, after the last intervention, shows small vertical cracks in the 3 oldest buttresses to the east of the former fortress, where the out-of-plumb of the 5th bay (from the east) already repaired in the 1950s is evident and of about 50 cm (Figure 8a).

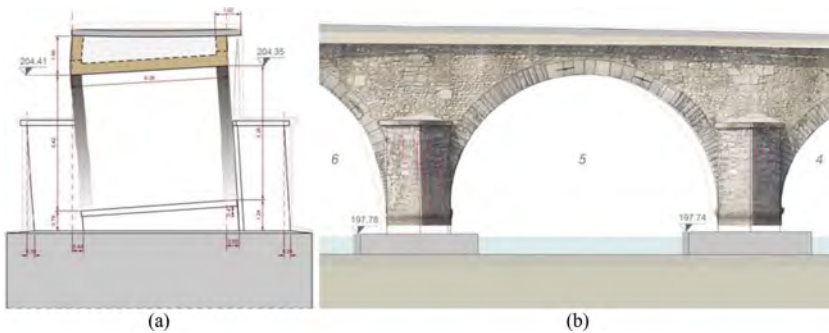


Figure 8. a) Out-of-plumb of the 5th bay southwards and b) photogrammetric view of two piers (south side) at the barrels of arch 5 with the crack pattern survey highlighted in red.

The historical research provided crucial information for future investigations, such as the strong heterogeneity of the bridge structure, modified over the centuries with different constructive techniques. The classification of masonry textures and the crack pattern survey also confirmed the sequence of construction phases showing the discontinuities in the structure highlighted by the historical research (Figure 9), resulting in a refined identification of structural heterogeneities (di Prisco et al. 2019) and helping to better understand the current state of conservation of the bridge. The historical occurrence of damage and cracking, in fact, identifies critical areas that have suffered over time from exceeding the elastic limits of the materials or from the interaction with the river.

At least six different substructures highlighted in different colors were recognized in Figure 9: i) the central portion highlighted in gray, which corresponds to the original construction; ii) the first extension (green) toward the Lecco shore, built about ten years later; iii) the last pier

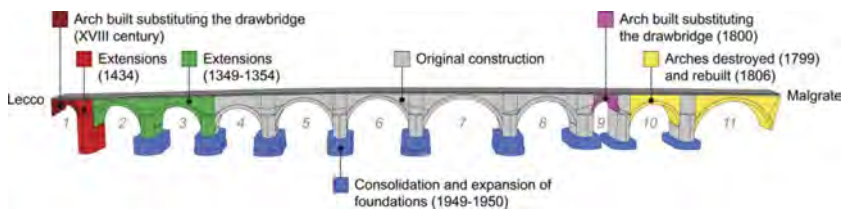


Figure 9. Azzone Visconti bridge: configuration of the historical construction evolution (view of the North side of the bridge, adapted from di Prisco et al. 2019).

finished around one century later (red); iv) the arch built to replace a drawbridge (magenta) at the end of the 18th century; v) the last two arches toward Malgrate (yellow) destroyed in 1799, and rebuilt 7 years later and, finally, vi) the consolidation of the pier foundations in the middle of the last century.

Although in similar cases greater accuracy must be used in modelling the discontinuities and different properties of the masonry must be taken into account, in this precise case, the massive intervention carried out in the 1950s achieved such a stiffening of the deck that it dominated over the underlying inhomogeneities and discontinuities, at least with respect to gravitational forces. Therefore, it can be assumed that the homogeneous models adopted up to now and presented in Martinelli et al. 2018, Zani et al. 2019, 2020 succeed in representing well the actual behavior of the structure.

4 MODELLING APPROACHES FOR HISTORICAL MASONRY BRIDGES

To analyze the response of the Azzone Visconti bridge subjected to a specific load configuration imposed during an acceptance load test, several interpretation models were set up during the investigation (Figure 10). Specifically, limit analysis models using the RING software (RING 2021) and two-dimensional (2D) finite element (FE) analyses implemented in Abaqus (Dassault Systèmes 2016) were developed for the central arches 6-8; additional three-dimensional (3D) FE models, also implemented in Abaqus, were employed to simulate the response of the entire bridge.

RING (Figure 10a) is a simplified and user-friendly analysis tool based on the rigid block limit analysis technique and designed to quickly check the adequacy of masonry arch bridges against the most recurrent failure modes. The 2D FE model depicted in Figure 10b is made with beam-type and plane stress elements combined with translational springs simulating the soil and the infill materials. The full 3D FE model (Figure 10c) is made of solid elements combined with rotational and translational non-linear springs representing the soil. In the 2D FE model the nonlinearity was partially accounted for assuming the tensile strength of the arches equal to zero and assuming a rigid-plastic generalized constitutive relationship with strain hardening and non-associated flow rule for the soil (Nova & Montrasio 1991). The 3D FE model accounted for the material nonlinearity in most of the bridge components by means of the concrete damaged plasticity model (Lubliner et al. 1989; Lee & Fenves 1998). A detailed description of the 2D and 3D FE models is herein omitted but can be found in Martinelli et al. (2018) and Zani et al. (2020), respectively.

Table 1 reports the potentials and limitations of each modelling approach observed in their practical application. The following factors/effects have been considered: (1) role of spandrel walls (if present), (2) role of infill material, (3) transverse behavior, (4) reproduction of existing cracking patterns and local damage, (5) reproduction of material heterogeneities, (6) reproduction of strengthening intervention(s), (7) soil-structure-interaction beneath the foundations, (8) rapid prediction of the ultimate bearing capacity and (9) ease in creating the model and extracting the results.

Table 1. Potential of the modelling approaches described in Section 4 (Y: yes; P: partly; N: no).

Factors/effects	RING model			2D FE model			3D FE model		
	Y	P	N	Y	P	N	Y	P	N
Spandrel walls			•		•			•	
Infill material	•				•			•	
Transverse behavior			•			•		•	
Cracking patterns and local damages		•			•				•
Material heterogeneities	•			•				•	
Strengthening intervention(s)		•			•			•	
Soil-structure-interaction beneath the foundations			•		•			•	
Rapid prediction of the ultimate bearing capacity	•				•				•
Ease in creating the model and extracting the results	•			•					•

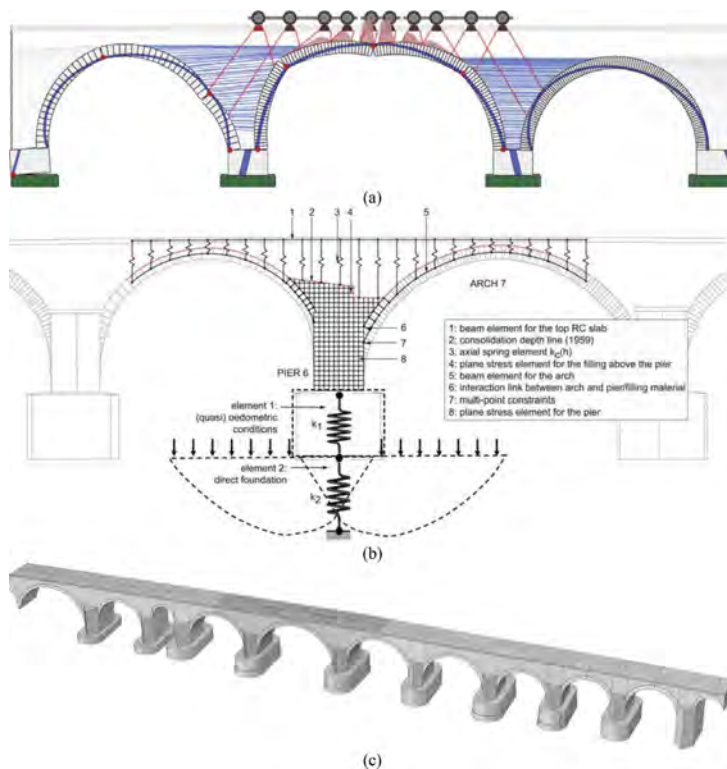


Figure 10. Representation of (a) limit analysis model (arches 6-8), (b) 2D FE model (arches 6-8) and (c) full three-dimensional FE model (adapted from Zani et al. 2020).

Regarding the RING model, the main limitations are due to the difficulty in correctly reproducing reinforcement interventions (such as the presence of a complex RC caisson) and simulating the nonlinear soil-structure interaction beneath the foundations. On the other hand, one of the main advantages – aside from the ease of model creation and results extraction – is the rapid assessment of the ultimate capacity of the bridge with regard to masonry components.

As for the 2D FE model, the main limitations include the difficulty in reproducing the transverse behavior and the partial reproduction of the infill and spandrel walls. The ease in creating the model and extracting the results is one of the main merits.

Concerning the 3D FE model, the main limitation is the computational burden combined with significant effort in model creation and result extraction. Strengthening interventions and transverse behavior can be captured correctly. The 3D FE model also allows reliable reproduction of the nonlinear soil-structure interaction. According to the authors, both the 2D and 3D nonlinear FE models risk providing a less reliable estimate of ultimate capacity than that provided by limit analysis, as the increased sophistication of the simulations could lead to a reduced control over unpredicted numerical phenomena.

5 CONCLUSIONS

The paper presents the historical-constructive evolution of an important multi-span masonry arch bridge (named Azzone Visconti Bridge) built in 1336 in Lecco. The bridge has undergone several transformations over the centuries, growing from the original eight arches to the current eleven. The bridge was also profoundly modified in the 20th century with strengthening works aimed at adapting it to the new requirements of vehicular traffic, but distorting its homogeneity.

A comparison of three different structural modeling approaches with varying degrees of sophistication, namely limit analysis, 2D nonlinear FE analysis, and 3D nonlinear FE analysis, is presented. The potentials and limitations of each approach are highlighted using the Azzone Visconti Bridge as a case study. The strengthening interventions, which played a key role in correctly reproducing the structural behavior of the Azzone Visconti bridge, are difficult to reproduce with limit analysis models and require the use of advanced 3D FE analysis. Correct reproduction of the bridge transverse behavior and soil-structure interaction also requires the use of 3D FE analysis. Limit analysis provides a rapid assessment of the ultimate bearing capacity of ordinary multi-span masonry arch bridges, whereas 2D and 3D FE analyses, given their increasing level of sophistication, require more effort to provide reliable predictions.

Finally, the work also highlights the importance of uncovering and interpreting historical information related to the bridge. For example, the past presence of towers later destroyed may play a decisive role in the over-consolidation of the soil beneath the foundations and can provide useful information about the significant loads sustained by the structure over time.

REFERENCES

- Barazzetti, L., Banfi, F., Brumana, R., Previtali, M., Roncoroni, F. 2016: Bim from Laser Scans... not just for buildings: Nurbs-based parametric modelling of a medieval bridge. *ISPRS Ann. Photogramm. Remote Sens. Spatial Inf. Sci.*, III-5, 51–56. doi: 10.5194/isprs-annals-III-5-51-2016
- Belloni, L.M., Besana, R., Zastrow, O. 1991. *Castelli basiliche e ville - Tesori architettonici lariani nel tempo*. Alberto Longatti (ed.), Como – Lecco: La Provincia S.p.A. Editore-riale
- Comandù, A., Mariani, E., Mazzi, C., Rossi, R., Santoro, A., Vaiani Rossi, E. 2005. *Il castello Mediceo di Melegnano. Luoghi di storia, arte, cultura*. Melegnano: Galli Thierry ed.
- Dassault Systèmes. 2016. Analysis user's manual, version 6.14. Providence, RI: Dassault Systèmes.
- di Prisco, M., Scola, M., Zani, G. 2019. On site assessment of Azzone Visconti bridge in Lecco: limits and reliability of current techniques. *Construction and Building Materials* 209: 269–282. doi: 10.1016/j.conbuildmat.2019.02.080
- Giulini, G. 1857. *Memorie spettanti alla storia, al governo ed alla descrizione della città e campagna di Milano ne' secoli bassi*. vol. X, Milano: Francesco Colombo Librajo editore
- Lee, J., Fenves, G.L. 1998. Plastic-Damage Model for Cyclic Loading of Concrete Structures. *J Eng Mech* 124: 892–900. doi: 10.1061/(ASCE)0733-9399(1998)124:8(892)
- Lubliner, J., Oliver, J., Oller, S., Oñate, E. 1989. A plastic-damage model for concrete. *Int J Solids Struct* 25: 299–326. doi:10.1016/0020-7683(89)90050-4.
- Martinelli, P., Galli, A., Barazzetti, L., Colombo, M., Felicetti, R., Previtali, M., Roncoroni, F., Scola, M., di Prisco, M. 2018. Bearing capacity assessment of a 14th century arch bridge in Lecco (Italy). *International Journal of Architectural Heritage* 12(2): 237–256. doi: 10.1080/15583058.2017.1399482
- Nova, R., Montrasio, L. 1991. Settlements of Shallow Foundations on Sand. *Geotechnique* 41 (2):243–56.
- Resegoneonline.it, Lecco editorial Board. 31-5-2014. Il ponte Azzone Visconti: perché non trasformarlo in museo a cielo aperto? Varese: Resegone 3000 s.r.l. <http://www.resegoneonline.it/articoli/II-ponte-Azzone-Visconti-perch-non-trasformarlo-in-museo-a-cielo-aperto-20140530/#prettyPhoto> (accessed: 9.1.2023)
- RING. 2021. 'LimitState:RING- Powerful masonry arch analysis software.' <https://www.limitstate.com/ring> (accessed: 15. 11.2022)
- Rovelli, G., Vidus Rosin, L. 2016. Indagini diagnostiche e analisi statica del ponte Azzone Visconti (Msc. Thesis), Politecnico di Milano (in Italian).
- Zani, G., Martinelli, P., Galli, A., Gentile, C., di Prisco, M. 2019. Seismic Assessment of a 14th-Century Stone Arch Bridge: Role of Soil-Structure Interaction. *Journal of Bridge Engineering* 24 (7)n.05019008: 1–20. doi: 10.1061/(ASCE)BE.1943-5592.0001441
- Zani, G., Martinelli, P., Galli, A., di Prisco, M. 2020. Three-dimensional modelling of a multi-span masonry arch bridge: influence of soil compressibility on the structural response under vertical static loads. *Engineering Structures* 221 n.110998: 1–16. doi: 10.1016/j.engstruct.2020.11099

Stochastic load-carrying capacity assessment of brick masonry arch bridges

B. Liu

School of Civil Engineering, University of Leeds, Leeds, UK

I.B. Muhit

School of Civil Engineering, University of Leeds, Leeds, UK

School of Computing, Engineering & Digital Technologies, Teesside University, Middlesbrough, UK

V. Sarhosis

School of Civil Engineering, University of Leeds, Leeds, UK

ABSTRACT: Masonry arch bridges form an integral part of our infrastructure network, and their safety is important for the functioning of our society. Now, assessing the structural performance of ageing masonry infrastructure is a complex task. Existing ageing masonry arch bridges are characterized by inherent variability and may have stochastic material properties even in the same bridge. Hence, a realistic methodology for structural assessment of masonry arch bridges is crucial to protect the ageing masonry bridges and utilize these resources efficiently. In this study, stochastic-based assessment on the load-carrying capacity of masonry arch bridges has been performed, which introduces material variabilities into a two-dimensional structural analysis model based on the Discrete Element Method (DEM). Over 100 probabilistic analyses have been developed to assess the ultimate load that a bridge can carry when subjected to monotonic loading at a quarter span. The bond properties of mortar joints, including cohesion, tensile strength, and friction angle, were considered as stochastic variables following a normal distribution. The computational results were compared against the experimental results obtained from the literature. From the results analysis, it was shown that the computational model considering the random variability of bond strength properties can better predict the load-carrying capacity of the masonry arch bridge than the deterministic one. The bond strength at the unit-to-mortar interface significantly affected the ultimate strength of the masonry arch bridge.

1 INTRODUCTION

Masonry arch bridges form a significant part of the UK and European infrastructure network. It is estimated that there are approximately 200,000 masonry arch bridges and culverts in Europe and 40,000 masonry arch bridges in the UK. Most of these bridges were constructed between the 17th and 19th centuries and are still in service today (Forgács et al. 2021). After being used for over a hundred years, the significant structural deterioration caused by several environmental impacts may result in a reduction in the durability and load-bearing capacity of the bridges. On the other hand, most of these old masonry arch bridges support traffic loads much higher than those originally designed to carry, which can pose a serious threat to the safety of the bridges. Thus, there is an urgent need to assess the in-service behavior and predict the load-bearing capacity of masonry arch bridges to inform their repair, maintenance, and rehabilitation strategies.

Assessing the structural performance of ageing masonry arch bridges is challenging due to the inherent variability in their material properties. So far, several computational approaches, ranging from simple to high-fidelity, have been developed to predict the ultimate load-carrying capacity of

masonry arch bridges (D’Altri et al. 2019). Within these numerical methods, a large number of input parameters are required to describe the mechanical behavior of materials and define the interactions between different elements. These parameters need to be carefully selected so that the model can accurately reproduce the behavior of real structures (Sarhosis & Sheng 2014).

Now, in order to assess the influence of material variability on the ultimate load-carrying capacity of masonry structures, high fidelity numerical modelling approaches coupling with Monte-Carlo simulations have been used (Li et al. 2014, Muhit et al. 2022). For example, Sarhosis et al. (2019) proposed a methodology which considers the spatial variability of masonry materials. The proposed method was integrated into a two-dimensional (2D) discrete element modelling approach to predict the stochastic strength of masonry walls containing openings. The study also carried out a series of sensitivity analyses to determine the factors affecting the load-carrying capacity of masonry walls. Later, the approach was adopted and incorporated within the three-dimensional (3D) Discrete Element Method (DEM) software for assessing the mechanical behavior of other masonry structures (Pulatsu et al. 2022, Gonen et al. 2022).

Following the research carried out by Sarhosis et al. (2019), this paper presents a stochastic-based assessment of the load-carrying capacity of masonry arch bridges subjected to static load. More than 100 realizations were carried out on a masonry arch bridge model developed based on the 2D DEM. Computational results were compared against the experimental findings obtained from the literature. The stochastic parameters considered in the current study included the friction angle, tensile strength, and cohesion at the unit-to-mortar interface, representing the bond properties of mortar joints. Moreover, sensitivity analysis was carried out to investigate the influence of these mortar bond properties on the load-carrying capacity of the masonry arch bridge.

2 METHODOLOGY

The heterogeneity and inherent variability in material properties are the most remarkable characteristics of ageing masonry arch bridges, which considerably affect the structural behavior and load-carrying capacity of the bridge. However, most of the computational models in previous research have failed to consider material variabilities. In other words, the same (uniform) material parameters were usually assigned throughout the masonry domain by engineers/researchers (Sarhosis et al. 2019). This study has adopted a probabilistic approach to investigate the influence of random material properties on the mechanical behavior of masonry arch bridges. The framework of the methodology adopted in this study is summarized in Figure 1.

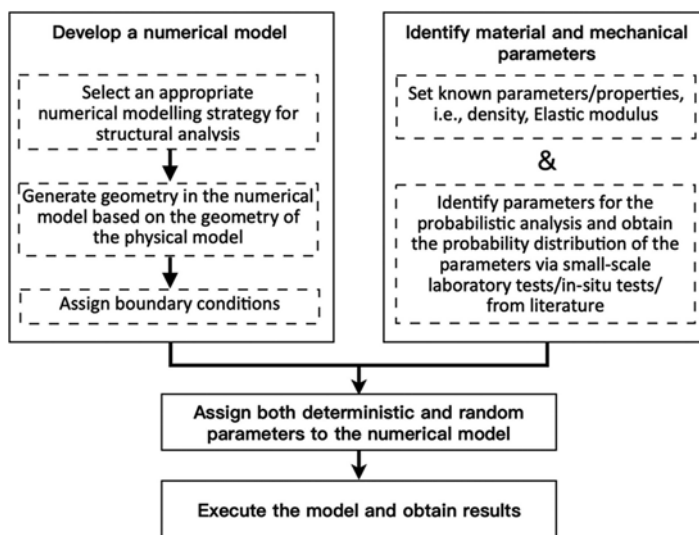


Figure 1. Framework for introducing material variabilities in computational models.

Overall, the methodology involved introducing material variabilities into the computational model. As the first step, the critical parameters for the probabilistic analysis need to be identified, and the mean values and probability distributions of these parameters can be obtained from either small-scale laboratory/in-situ tests or the literature. Having assigned deterministic and stochastic parameters to the computational model, simulations and sensitivity analyses can then be executed. It is worth noting that the parameters used for the probabilistic analysis should be selected based on the characteristics of the structure. For example, as the low bond strength of mortar joints has been found to be one of the dominant factors affecting the mechanical behavior of historical masonry arch bridges (Sarhosis et al. 2019), the bond properties of the unit-to-mortar interface, including friction angle, tensile strength, and cohesion, have been selected as random variables for probabilistic analysis in the study.

3 EXPERIMENTAL TESTING OF A MASONRY ARCH WITH BACKFILL

Full-scale static tests on brickwork masonry arch bridges were carried out by Augustus-Nelson et al. (2018, 2020) at the University of Salford. Figure 2 shows the experimental setup and dimensions for the test chamber and the bridge model. The test was carried out under plain-strain conditions with two stiff walled chambers to restrict any out-of-plane movement of the fill and arch barrel. Class A Engineering bricks and a lime mortar with a mix ratio of 1:2:9 (cement:lime:sand) were used to construct the bridge model to produce the low bond strength characteristic found in real masonry arch bridges.

The experimental model mainly contained an arch barrel constructed with a header bond configuration. The span and thickness of the arch barrel were equal to 3 m and 0.215 m, respectively, and the span-to-rise ratio of the arch was 4:1. The cohesionless MOT type I limestone was selected as the backfill material, which was placed into the test chamber and compacted layer by layer until it reached the 0.3 m over the crown of the arch. During the test, a monotonic load was applied by a hydraulic actuator via a load-spreading beam to the level surface of the backfill above the quarter of the arch barrel.

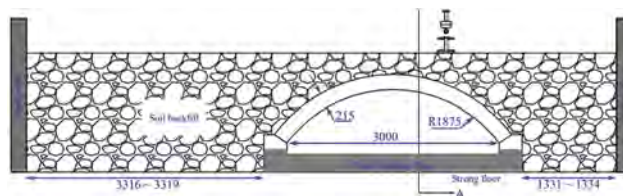


Figure 2. Masonry arch bridge model tested in the laboratory (Augustus-Nelson et al. 2018).

4 DISCRETE ELEMENT MODELLING AND THE COMPUTATIONAL MODEL

Past experience has demonstrated that cracking in masonry arch bridges occurs at the unit-to-mortar interfaces due to the low tensile and shear resistance of the mortar joints. This characteristic makes the discontinuum modelling approach more appropriate compared with other approaches (e.g., homogeneous ones) in simulating the cracking behavior and failure mechanism of masonry arch bridges. In this study, the 2D commercial software, Universal Distinct Element Code (UDEC), based on the DEM, was used to develop the numerical model (Itasca 2011).

Developing a model in UDEC starts with creating a single block covering the domain to be analyzed. Then, the original block generated is discretized into several small blocks in accordance with the geometry feature of the target structures. In the numerical model shown in Figure 3, the arch barrel was assembled by several individual bricks, which were represented by independent deformable blocks with a linear elastic behavior. Mortar joints were

represented by zero-thickness interface elements between blocks as shown in Figure 4a. The mechanical behavior of joints in the normal and shear directions (see Figure 4b and c) are subjected to the following equations:

$$\Delta\sigma_n = -K_n\Delta u_n \quad (1)$$

$$\Delta\tau_s = -K_s\Delta u_s \quad (2)$$

where $\Delta\sigma_n$ and $\Delta\tau_s$ are the change in normal and shear stress, respectively; K_n and K_s stand for the stiffness in the normal and shear directions, respectively; and Δu_n and Δu_s are the change of displacement in the normal and shear directions, respectively.

The numerical model developed in the present work had the same geometry and dimensions as the large-scale bridge tested in the laboratory. Table 1 lists the material and mechanical properties of masonry units, backfill, and backfill-to-arch ring interfaces in the numerical model. These parameters were kept constant (deterministic) throughout the stochastic analysis. On the other hand, material properties of mortar joints, including the tensile strength (J_{ten}), cohesion (J_{coh}), and friction angle (J_{fric}) were considered stochastic to isolate the influence of remaining parameters (i.e., backfill properties and backfill-to-arch ring interface properties) on the load-carrying capacity of the masonry arch bridge and highlight the effect of bond properties with inherent variability found in most real masonry arch bridges. The mean and coefficient of variations (COV) of the stochastic parameters are listed in Table 2 which were obtained from material characterization tests in the laboratory. J_{coh} and J_{fric} were assumed to be normally distributed (Gaussian distribution) while J_{ten} was assumed fully correlated to J_{coh} according to the following equation (Milani & Lourenco 2013):

$$J_{ten} = J_{coh} / 1.4 \quad (3)$$

In terms of loading and boundary conditions of the computational model, the blocks representing the tank walls, basement, and abutments were considered fixed. A monotonic load was applied by controlling a block with the same width as the load-spreading beam to move downwards at a constant velocity. It is worth noting that adaptive damping was assigned to the model to obtain a convergent static solution. In this way, the large displacement of blocks was allowed with the sequential contact detection and update.

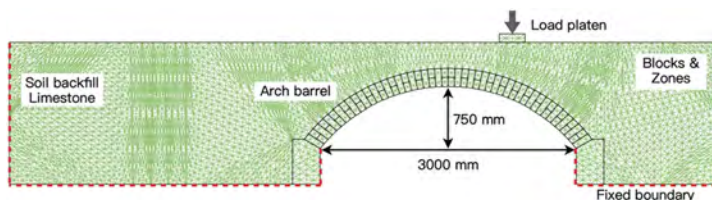


Figure 3. 2D numerical model of the masonry arch bridge based on the DEM showing meshing at the backfill and arch barrel.

5 RESULTS AND DISCUSSION

Figure 5a shows a typical failure mechanism of the masonry arch bridge obtained from the computational model. From all simulations, the same four-hinge failure mechanism was observed, with high compressive stresses concentrated at the hinge locations, which was consistent with the experimental observation (see Figure 5b). In particular, with the downward movement of the load platen, a tensile crack initiated at the intrados of the arch underneath the load platen, forming one hinge at the quarter of the arch. The other three hinges occurred

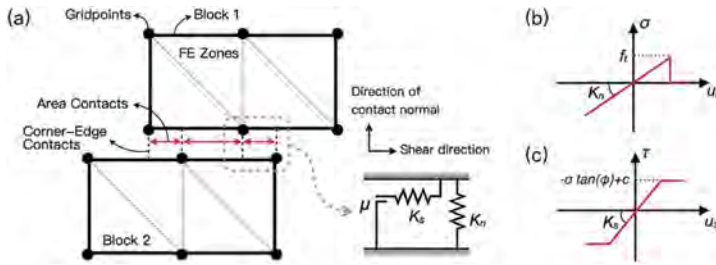


Figure 4. (a) Contacts between blocks; Mechanical behavior of the zero-thickness interface at the (b) normal and (c) shear direction.

Table 1. Material and mechanical properties of masonry units, backfill and backfill-to-arch interfaces adopted in the numerical model (assumed).

Material	Unit weight	Young's modulus	Poisson's ratio	Friction angle	Tensile strength	Cohesion
Units	kN/m ³	MPa	-	degree	MPa	MPa
Backfill	20	300	0.3	45	0	0.0005
Bricks	22	9	0.2	-	-	-
Backfill-to-arch interface	-	-	-	35	0	0

Table 2. Statistics of the bond properties of unit-to-mortar interfaces.

Property	Symbol	Mean value	COV	Distribution
Unit-to-mortar interface friction angle	J_{fric}	35 degrees	0.06	Normal
Cohesion at the unit-to-mortar interface	J_{coh}	0.02 MPa	0.2	Normal
Tensile strength at the unit-to-mortar interface	J_{ten}	$J_{ten} = J_{coh}/1.4$	-	-

at approximately the two edges and three-quarters of the arch barrel. Furthermore, the independence of the failure mechanism from the unit-to-mortar bond characteristics suggested that the failure mechanism of the masonry arch bridge was governed by the boundary conditions and bond configurations of the arch barrel, rather than by the material properties of mortar joints.

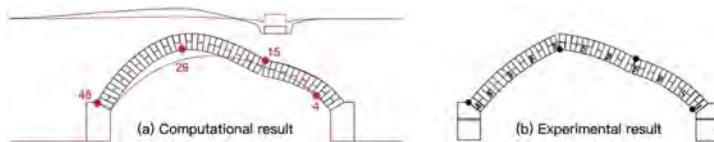


Figure 5. Failure mechanism and deformation of the masonry arch bridge obtained from the (a) computational (magnitude factor is 5) and (b) experimental model.

Figure 6 compares the numerical results against the experimental load-displacement relationships of the masonry arch bridge. The mean values for J_{fric} and J_{coh} were equal to 35 degrees and 0.02 MPa, respectively, and the respective COV of these two parameters were equal to 6% and 20%. As the load platen moved downwards, the load carried by the bridge increased until it reached a peak. The fluctuations and reductions observed in the load-displacement curves were related to the crack initiation and propagation process, as well as

the stiffness degradation of the bridge under loading. The results also illustrated the influence of the stochastic bond strength properties on the load-carrying capacity of the masonry arch bridge. In principle, a relatively large range of ultimate loads, from 124.33 kN to 273.65 kN, was obtained from the computational model with stochastic bond strength properties. The experimental model had an ultimate load of 142.7 kN, which fell within the range obtained from the computational model and was closer to the lower limit of the range.

Figure 7 shows the sensitivity analysis results of the ultimate load on the bond strength of the mortar joint. In numerical simulations, the mean values of J_{coh} varied from 0.015 MPa to 0.04 MPa with a COV of 20%. The values of tensile strength and cohesion were fully correlated according to Equation 3. For all the simulations, the mean value and COV for J_{fric} remained at 35 degrees and 6%, respectively. In Figure 7, the red lines are trend curves for the maximum, average, and minimum loads obtained from the simulations. It was calculated that the standard deviations for the results of four groups with different mean values of bond strength were all equal to approximately 40%, which highlighted the influence of stochastic bond properties of the unit-to-mortar interface on the ultimate load of the masonry arch bridge. With the stochastic properties of mortar joints, a range of peak loads was obtained from the computational model with different mean values of cohesion and tensile strength. Nevertheless, a significant positive correlation between the bond strength and ultimate loads was observed. With the increase in the mean bond strength, the average load-carrying capacity of the bridge increased, suggesting that the bonding strength of the mortar joints is one of the dominant factors affecting the overall strength of the masonry arch bridge.

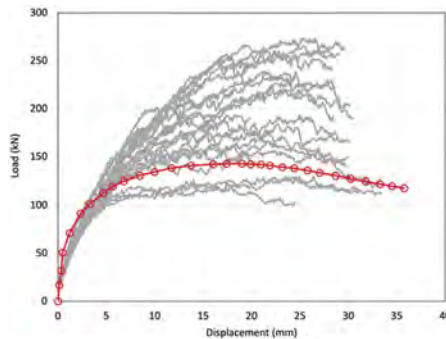


Figure 6. Experimental (red line) against numerical (grey lines) load-displacement curves.

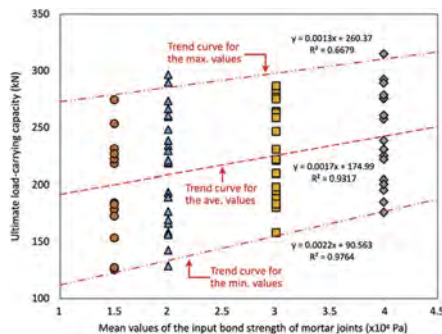


Figure 7. Sensitivity of the ultimate load on the bond strength of mortar joints (the mean value of J_{coh} at the unit-to-mortar interface varied from 0.015 MPa to 0.04 MPa, with COV remaining at 20%).

6 CONCLUSION

Ageing masonry arch bridges are characterized by inherent variability and may have stochastic material properties even in the same bridge. Such random properties could result in a considerable variation in the strength and stiffness of the masonry arch bridge. However, most of the previous studies have ignored this variation in material properties and instead assigned the same (uniform) parameters through the masonry structure for simplicity, which can lead to an inaccurate evaluation of the ultimate strength of a real masonry arch bridge.

This paper presents a stochastic-based assessment of the ultimate strength and mechanical behavior of masonry arch bridges to address this issue. Stochastic bond properties of unit-to-mortar interfaces were assigned to a 2D computational model developed based on the DEM, and over 100 simulations were executed to predict the load-carrying capacity of the masonry arch bridge. From the analyses of the results, it is shown that the computational model with stochastic material properties can better predict the load-carrying capacity of a real masonry arch bridge with inherent material variabilities. Moreover, the random bond properties did not affect the failure mechanism of the masonry arch bridge investigated and all computational models had a four-hinged behavior. However, with the stochastic bond strength of unit-to-mortar interfaces, the predicted ultimate loads of the bridge had a variation with a COV of approximately 40%, which is expected as the mean value of bond strength increased, the load-carrying capacity of the bridge increased significantly.

The study reported herein is the preliminary findings of the more sophisticated computational model being developed. Hence, such finding assumes and considers the simplest case, while more complicated scenarios like spatially variable bond strength properties of masonry, the correlation between unit-to-mortar interfaces in the same course and different courses, complicated statistical relationships between strength properties, more sophisticated considerations of the backfill materials, etc. can be considered in future studies.

ACKNOWLEDGEMENT

This work was funded by the EPSRC project “Exploiting the resilience of masonry arch bridge infrastructure: a 3D multi-level modelling framework” (ref. EP/T001348/1). The financial contribution is very much appreciated.

REFERENCES

- Augusthus-Nelson L. & Swift G. 2020. Experimental investigation of the residual behavior of damaged masonry arch structures. *Structures* 27: 2500–12.
- Augusthus-Nelson L., Swift G., Melbourne C., Smith C. & Gilbert M. 2018. Large-scale physical modelling of soil-filled masonry arch bridges. *International Journal of Physical Modelling in Geotechnics* 18: 81–94.
- D’Altri A.M., Sarhosis V., Milani G., Rots J., Cattari S., Lagomarsino S., Sacco E., Tralli A., Castellazzi G. & de Miranda S. 2019. A review of numerical models for masonry structures. In B. Ghiassi & G. Milani (eds), *Numerical Modeling of Masonry and Historical Structures*: 3–53. Woodhead Publishing.
- Forgács T., Sarhosis V. & Ádány S. 2021. Shakedown and dynamic behavior of masonry arch railway bridges. *Engineering Structures* 228: 111474.
- Gonen, S., Pulatsu, B., Erdogmus, E., Lourenço, P.B. & Soyoz, S. 2022. Effects of spatial variability and correlation in stochastic discontinuum analysis of unreinforced masonry walls. *Construction and Building Materials* 337: 127511.
- ITASCA 2011. *UDEC-universal distinct element code manual: theory and background*. Itasca Consulting Group, Minneapolis.
- Li J., Masia, M.J., Stewart, M.G. & Lawrence, S.J. 2014. Spatial variability and stochastic strength prediction of unreinforced masonry walls in vertical bending. *Engineering Structures* 59: 787–797.
- Milani, G. & Lourenco, P.B. 2013. Simple Homogenized Model for the Nonlinear Analysis of FRP Strengthened Masonry Structures. II: Structural Applications. *Journal of Engineering Mechanics* 139(1): 77–93.

- Muhit, I.B., Masia, M.J., Stewart, M.G. & Isfeld, A.C. 2022. Spatial Variability and Stochastic Finite Element Model of Unreinforced Masonry Veneer Wall System Under Out-of-plane Loading. *Engineering Structures* 267: 114674.
- Pulatsu, B., Gonen, S., Parisi, F., Erdogmus, E., Tuncay, K., Funari, M.F. & Lourenço, P.B. 2022. Probabilistic approach to assess URM walls with openings using discrete rigid block analysis (D-RBA). *Journal of Building Engineering* 61: 105269.
- Sarhosis V., Forgács T. & Lemos J.V. 2019. Stochastic strength prediction of masonry structure: a methodological approach or a way forward? *RILEM Technical Letters* 4: 122–129.
- Sarhosis V. & Sheng Y. 2013. Identification of material parameters for low bond strength masonry. *Engineering Structure* 60:100–10.

New UK guidance for the assessment of masonry arch bridges

Matthew Gilbert, Colin C. Smith & Serena Amodio

Department of Civil and Structural Engineering, University of Sheffield, Sheffield, UK

ABSTRACT: Masonry arch bridges are long-lived structures that continue to form a vital part of our transport infrastructure. However, they are facing a number of challenges associated with their extended period in service and the changing requirements of modern transport systems. CIRIA C800 provides new, freely available, guidance for the assessment of masonry arch bridges, building on recent research findings and advice already available in existing CIRIA guidance and in UK highway and railway assessment codes. Most significantly, the new guidance promotes the use of the Permissible Limit State (PLS), the point beyond which progressive load-induced degradation occurs under service loads during the intended life of a bridge. This is designed to allow engineers to more reliably identify the bridges that are likely to be most susceptible to the damaging effects of repeated cyclic loading. Background information on the new guidance is presented in the paper, including details of a simplified PLS calculation method and an example that demonstrates how it can be applied in practice.

1 INTRODUCTION

Approximately one million masonry arch bridges are currently in use worldwide, the majority of which are over 100 years old, and which are handling traffic that is very different to that which their builders originally intended. These bridges include one or more masonry arches serving as the primary means of supporting the applied loads, though incorporate a wide range of construction details. Given the large numbers of such bridges currently in service, it is important that bridge owners have access to information that can inform their efficient management, ensuring that limited maintenance budgets are focused appropriately. Central to this is having access to useful information garnered from periodic bridge assessments.

In the middle of the last century the well-known MEXE method of assessment was developed for masonry arch bridges (National Highways, 2022). This sought to determine the level of service load that could be carried and includes both ‘analysis’ and ‘observational’ elements. However, since the ‘analysis’ element of the method has known flaws (Wang & Melbourne, 2010), the observational element of the method is arguably more useful, albeit this does not provide a predictive capability. These flaws have led to reduced usage of the MEXE method in recent years, with the current UK assessment code for highway bridges (National Highways, 2022) indicating that the MEXE method cannot be applied to bridges with spans of less than 5m or greater than 18m. Instead limit analysis methods (after Heyman, 1982) have increasingly been used in recent years. These are used to determine the Ultimate Limit State (ULS) load, with a fixed factor of safety then applied to determine the Serviceability Limit State (SLS) load. This is because no widely accepted SLS criteria for masonry arch bridges have been developed to date.

Of course, bridge assessment requires the availability of competent assessment engineers, who also need to have access to effective tools. Unfortunately, two issues have been found to adversely affect the quality of these assessments:

- many assessment engineers are unfamiliar with masonry arch bridges, and how they carry applied loading, in part because they are typically not treated on university syllabi;

- current generation assessment approaches are often unable to discriminate between bridges that have the capacity to carry additional loading, and those that do not.

A new guidance document, CIRIA C800 (Gilbert et al., 2022), has therefore been prepared to address both the above issues, addressing the first by providing educational material and the second by presenting a new, more discriminating, assessment approach. In the latter case the approach presented involves supplementing existing ULS calculations with independent Permissible Limit State (PLS) calculations, where the PLS is defined as the point beyond which progressive load induced degradation occurs under service loads during the intended life of the bridge. Significantly, the simplified PLS calculations presented involve the use of the same limit analysis methods used for ULS analysis, though use different inputs.

The paper is structured as follows: section 2 presents an overview of the new CIRIA C800 guidance; section 3 describes key aspects of the new limit state assessment approach presented in CIRIA C800; in section 4 these calculations are applied to a railway masonry arch bridge; finally, in section 5 conclusions are drawn.

2 NEW UK GUIDANCE: CIRIA C800

CIRIA C800, ‘Guidance on the assessment of masonry arch bridges’ (Gilbert et al, 2022), is a new document designed to provide practical guidance to practitioners involved in the assessment of bridge constructions that include masonry arch elements. It is free to download from the CIRIA website (<https://www.ciria.org>) and was designed to expand and bring up to date the sections on assessment in an existing CIRIA guidance document, CIRIA C656 (McKibbins et al, 2006), taking advantage of recent research findings as appropriate. CIRIA C800 comprises eight chapters and nine appendices, with the majority of these comprising useful background information for assessment engineers with a range of backgrounds, from those who are new to the assessment of masonry arch bridges, to experienced engineers who wish to refresh or update their knowledge in the area. Since masonry arch bridges are not covered on most university syllabi, little prior knowledge is assumed.

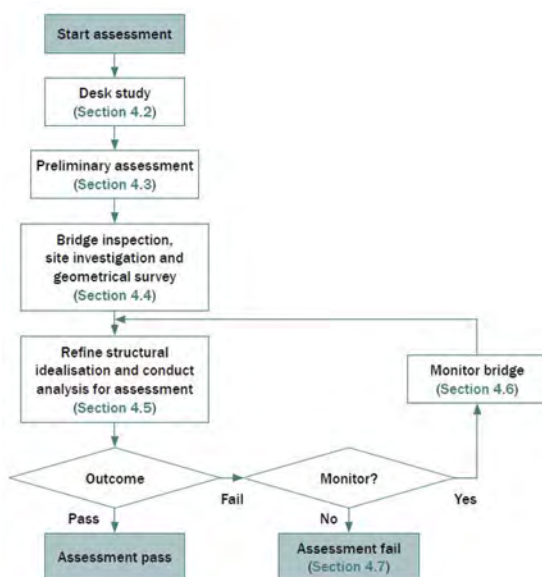


Figure 1. Steps in the bridge assessment process (from CIRIA C800, Gilbert et. al. 2022).

Steps in a typical bridge assessment process are outlined in Figure 1; this assumes that the assessment will require calculations to be performed, with monitoring of a bridge carried out only if the bridge cannot be demonstrated to have the required capacity.

It is evident from the process depicted in Figure 1 that it involves many steps that can only be carried out effectively by a competent assessment engineer, who is familiar both with masonry arch bridge constructions, and with the calculation methods that are used to analyse them. In this respect, clearly a good level of understanding is important; without it, appropriate data will likely not be gathered, or inappropriate models and/or model inputs may be used, leading to inaccurate assessment. Thus, CIRIA C800 contains numerous figures and tables designed to ensure readers are familiar with key principles; an excerpt is reproduced in Figure 2.

Observation	Notes	Illustrative examples
1. The pattern of loading in relation to the shape of a masonry gravity structure governs overall stability.	This means that it is important to accurately measure the shape of the arch barrel, piers etc when undertaking an assessment, and to use patterns of loadings that are representative of those that will be applied in practice in assessment calculations.	<p>Shallow arch: low profile where a low mid-span point load W is required to cause failure via formation of hinges (a), and pointed arch profile where a high load is required to cause failure via formation of hinges (b).</p>
2. Masonry gravity structures resist applied actions through their inherent self-weight and thickness.	Self-weight is often beneficial, so scenarios where it is not factored up should be included in assessment calculations. Also, the thickness of all masonry elements (arch barrels and piers) should be carefully measured before assessment.	<p>Force P required to cause overturning failure of a stack of blocks (a), required force reduces if blocks have lower unit weight (b), and required force reduces if blocks are thicker (c).</p>

Figure 2. Sample observations to explain fundamental behaviour (from CIRIA C800, Gilbert et. al. 2022).

In the excerpt shown in Figure 2 the aim is to emphasize the importance of arch shape, and the fact that masonry gravity structures derive their resistance from the thickness and self-weight of the masonry. It is also noted that as self-weight is often beneficial, an assessment should include calculations where this is not increased via application of partial factors – something that may be unfamiliar to engineers who are used to assessing steel or concrete structures.

In addition to providing general background information, a key element of CIRIA C800 is a chapter describing a new assessment approach that involves use of both ULS and Permissible Limit State (PLS) calculations, where the PLS is defined as the point beyond which progressive load induced degradation occurs under service loads during the intended life of the bridge; how this fits in a limit state assessment of a bridge is outlined in the next section.

3 LIMIT STATE ASSESSMENT

3.1 Ultimate Limit State (ULS) assessment calculations

A ULS assessment of a masonry arch bridge typically makes use of analysis calculations that draw upon the theorems of plastic limit analysis, firmly established in the middle of the last century, and shortly afterwards interpreted in the context of masonry arch bridges by workers such as Kooharian (1953), Heyman (1982) and Harvey (1988). Considering the lower bound (or ‘safe’) theorem of plastic analysis, this states that the structure can be deemed to be safe providing an equilibrium state can be identified and applicable ‘yield’ criteria are not violated. In the case of a masonry arch bridge, it is usual to neglect the tensile strength of the masonry, such that bending resistance is provided by the normal force, much of it arising from gravity loads, and the thickness of the masonry cross-section (Figure 2). It can be shown that the main applicable equilibrium and ‘yield’ criteria are satisfied if the thrust line (or, when masonry compressive strength is included, ‘thrust zone’) lies entirely within the thickness of the masonry. Other yield criteria can be accounted for in a similar way; for example, the line/zone of thrust should cross voussoirs at a sufficiently steep an angle to ensure that applicable shear (sliding) failure criteria are not violated. In a normal ULS analysis masonry materials are not generally considered in detail – though in reality their properties will generally degrade

over time, either due to environmental effects, long term loading (creep) or due to repeated application of loads (fatigue).

Most masonry arch bridges also contain soil backfill, which significantly increases load carrying capacity, by: (i) applying significant vertical dead weight (to effectively ‘pre-stress’ the masonry); (ii) dispersing the loads from vehicle axles (so as to be less concentrated); and (iii) providing horizontal ‘passive’ restraint to sway of the arch into the surrounding fill material; see Figure 3. In his proposed analysis method for masonry arch bridges Heyman (1982) took account of (i) and (ii), but ignored (iii). This apparent shortcoming was addressed by others in the years that followed (e.g. Harvey 1988). However, horizontal soil pressures generally require large displacements of the constituent masonry elements to be mobilized. Thus, whilst it is justifiable to include these pressures in a ULS model, it is much less so when normal vehicle load levels are involved, since the resulting deformations are likely to allow opening and closing of joints, that in turn are likely to lead to progressive degradation of the structure over time.

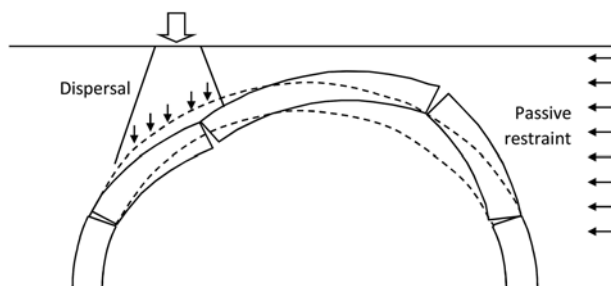


Figure 3. Soil-arch interaction (after Smith et al. 2004).

3.2 Permissible Limit State (PLS) assessment calculations

3.2.1 Background

When a masonry arch bridge is overloaded for a prolonged period, warning signs will normally become clearly evident (e.g. flexibility under live load, cracks that grow with time, increasing distortion, etc). However, once the bridge reaches this stage, the damage can be extensive and costly to repair, or in some cases, may be beyond repair. Therefore, it is important to have a way to forewarn engineers that a particular loading condition is likely to lead to distress.

Instead of trying to predict when individual cracks might form (which would require sophisticated analysis tools and extensive knowledge of the structure), it is much more practical to examine the underlying cause of why deflections under load begin to increase. In a typical bridge with soil backfill, increased deflection under load is associated with mobilization of passive soil pressures. Though these can contribute greatly to ultimate load carrying capacity, large structural movements are needed to mobilize these. (N.B. If spandrel walls are attached then, prior to large passive soil pressures being mobilized, the spandrel walls will be engaged. In this case the stiffness mismatch between the walls and surrounding backfill will be large at this point, hence often leading to cracks/detachment; the likelihood of this can be reduced if the level of load is kept below the PLS load level.) Similarly, comparatively large deformations (strains) are required in order to fully mobilize masonry strength in compression, due to the inherently inelastic, non-linear, behaviour of masonry. These observations open up the possibility of developing a first order analysis method to establish approximately when damage is likely to occur, coinciding with the point at which deflections start to grow.

3.2.2 Simple PLS assessment method

Given the background described above, CIRIA C800 describes a simple PLS assessment method for masonry arch bridges that is undertaken by performing a conventional limit analysis, though with:

- unfactored service loads;
- limited lateral soil pressures (lateral soil pressure coefficient, $K = 1$);
- reduced compressive strength (e.g., taking partial factor on the material strength, $\gamma_m = 2.0$ corresponds to a cyclic loading endurance limit for compressive loading of 0.5, after Casas (2009));
- transverse cracks modelled, if present;
- due account taken of the flexibility of other elements (e.g. near surface elements, which may increase load distribution much more at the ULS than at the PLS).

3.2.3 Commentary

A potentially useful way of conceptualizing the PLS is to consider that bridges manifesting load-induced deterioration have exhausted their primary modes of resistance, and have started to engage less reliable secondary modes of resistance, such as soil passive pressures and/or spandrel wall resistance. The resulting simple PLS assessment method described above can thus be undertaken using the same limit analysis tools traditionally used to determine ULS capacity, though now neglecting passive resistance. Also, a reduced value of masonry compressive strength is used. Since primary modes of resistance are being relied upon, the degree of modelling uncertainty is lower than when ULS calculations are being performed, which can be reflected in the partial factors used.

3.2.4 Underpinning research

A number of bridges were cyclically load tested in the laboratory to explore to provide supporting data (Augustus Nelson et al, 2018a, 2018b, Augustus-Nelson & Swift 2020); e.g. Figure 4 shows views of sections of the arch barrels of two bridges cyclically load tested to failure.



Figure 4. Observed cyclic loading induced damage in two laboratory bridges: (a) clay filled bridge; (b) crushed limestone filled bridge (from CIRIA C800, Gilbert et. al. 2022).

Due to time and cost constraints only a relatively small number of bridges could be subjected to cyclic loading regimes. Therefore quasi-static load tests undertaken on bridges from the literature were also studied to estimate the level of load required to mobilize increasing displacements, likely to correspond to the point at which passive pressures start to be mobilized and hence also to the PLS load. This is indicated by a break in the load-displacement response; best-fit bilinear and trilinear representations of load-displacement plots were extracted and used to identify experimental PLS load envelopes - a sample is shown in Figure 5.

Figure 5 also shows predicted ULS and PLS analysis results obtained using the LimitState: RING software (LimitState Ltd 2020), in the latter case using simple PLS assessment method assumptions. In this case although the predicted PLS load lies slightly below the experimental PLS load envelope derived from a load-displacement plot, it falls within the PLS load envelope obtained when a nominally identical bridge was cyclically loaded to failure (the damage shown in Figure 4b occurred when the cyclic load level was increased from 70kN to 80kN).

3.3 Assessment process

The approach presented in CIRIA C800 is, as far as possible, consistent with that used in the Eurocodes and with CS 454 (National Highways, 2022), which adopts a similar approach to the Eurocodes. Figure 6 shows an extract from CIRIA C800 that summarises the applicable inputs, including partial factors, to be applied in ULS and PLS assessments.

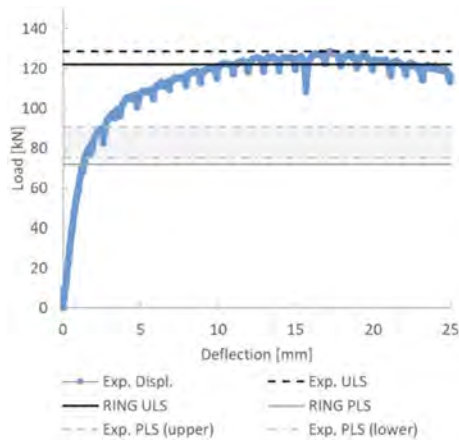


Figure 5. Sample load-deflection plot derived from test on crushed limestone filled laboratory bridge, also showing experimentally derived and predicted ULS and PLS loads (from CIRIA C800, Gilbert et. al. 2022).

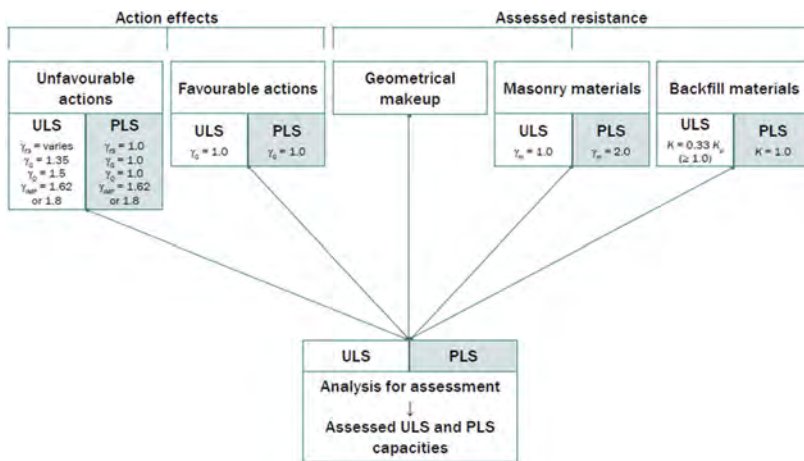


Figure 6. Key ULS and PLS analysis for assessment inputs (from CIRIA C800, Gilbert et. al. 2022).

Since primary modes of resistance are being relied upon in the PLS, the degree of modelling uncertainty is lower than when ULS calculations are being performed; this is taken account of by adopting a loads effect factor γ_{f3} of 1.0 in the former case, and above 1.0 in the latter case (except when a detailed ‘Level 3’ assessment is being carried out).

4 EXAMPLE ASSESSMENT: SINGLE-SPAN RAILWAY BRIDGE

For comparative purposes a single-span railway bridge, Whiley Hill Bridge, is here assessed using both NR GN/CE/C/025 (Network Rail, 2006) and CIRIA C800.

The bridge is a single-span masonry arch bridge located in County Durham on George Stephenson’s original Stockton to Darlington railway. The bridge comprises an approx. 3.3m span semicircular stone voussoir arch span resting on abutment walls; see Figure 7 (see CIRIA C800 for geometrical details). According to archive documents the structure was constructed in

1824 and as such is one of the oldest railway bridges still in service in the world. The bridge supports a single track carrying both freight and passenger traffic. Long term monitoring of crown deflections found these to be beyond acceptable limits, with the overall trend showing slowly increasing deflections with time, suggesting progressive load induced deterioration. Freight trains consisting of wagons laden with coal hauled by a class 66 locomotive were the most onerous traffic routinely using the bridge at the time of the original assessment. The wagons were consequently down-rated, with loading reduced to 23 tonnes per axle. Also, the track was realigned to place it nearer the centre of the structure, and crown displacements of the bridge were monitored periodically to allow deterioration of the bridge to be tracked.



Figure 7. Whiley Hill bridge: (a) elevation, (b) traffic surface (from CIRIA C800, Gilbert et. al. 2022).

A survey indicated that the abutments have a thickness similar to that of the arch and no evidence of backing was found. Monitoring of arch crown deflections revealed that live loading was causing progressive damage. A survey carried out in 2011 reported that a longitudinal crack had formed in the arch barrel and through both abutments, together with other more recent longitudinal cracks. Also, localised fractures and dropped stones were observed in the arch.

The bridge was reported to have black gravelly sand backfill with coal fragments. Tests on soil samples indicated an internal angle of friction of 40 degrees and a relatively high cohesion of 33 kN/m². However, the latter may be due to suction pressures since the soil was partially saturated and cannot be relied upon. Therefore, it was taken as zero in the analysis. The masonry unit weight and coefficient of friction were not made available, while values for the crushing strength and ballast unit weight were tNR/GN/CIV/025. The load model adopted in this study is a type RA1 (short lengths) with 23 tonnes axle loads, which correspond to the maximum live loading on the bridge. The bridge effective width is generally taken as the distance between longitudinal cracks; considering the numerous cracks present in the barrel, a conservative effective width of 1.8m has been adopted. Also, given that the bridge incorporates slender abutments, it was deemed appropriate to model two scenarios in which the abutments were either assumed to be rigid or modelled explicitly to allow these to also fail.

Results from the resulting CIRIA C800 and NR/GN/CIV/025 assessments are presented in Table 1. Note that an 'adequacy factor' above 1.0 indicates that the factored applied loading can be safely carried; below 1.0 means that this is not the case. The LimitState:RING software (LimitState 2020) was used to perform all assessment calculations.

It can be seen from Table 1 that, according to NR/GN/CIV/025, irrespective of the scenario considered, the bridge has sufficient load carrying-capacity. In contrast, the PLS capacity calculated according to the method described in CIRIA C800 results in a PLS adequacy factor of less than 1.0 in both scenarios. Given that the bridge has been showing signs of progressive load-induced deterioration, the CIRIA C800 assessment clearly appears to be much more realistic.

Table 1. Whiley Hill Bridge: summary of assessment results (from CIRIA C800, Gilbert et. al. 2022).

Scenario	Document	Limit state	γ_e (γ_{fe} for vehicle loads)	Impact factor	γ_{fs}	Analysis adequacy factor
A Model arch barrel only	NR/GN/CIV/025	Hybrid	1.9	1.8	1.0	1.23
	CIRIA C800 (this guidance)	ULS	1.5		1.1	1.41
		PLS	1.0		1.0	0.78
B Model arch barrel and abutments	NR/GN/CIV/025	Hybrid	1.9	1.8	1.0	1.04
	CIRIA C800 (this guidance)	ULS	1.5		1.1	1.19
		PLS	1.0		1.0	0.65

5 CONCLUSIONS

A new guidance document, CIRIA C800, has been produced that provides guidance on the assessment of masonry arch bridges, building on recent research findings and advice already available in existing CIRIA guidance and in UK highway and railway assessment codes. Most significantly, the new guidance promotes the use of the Permissible Limit State (PLS), the point beyond which progressive load-induced degradation occurs under service loads during the intended life of a bridge. This is designed to allow engineers to more reliably identify which bridges are most susceptible to the damaging effects of repeated cyclic loading.

REFERENCES

- Augustus-Nelson, L., Swift, G., Melbourne, C., Smith, C. & Gilbert, M. 2018a. Large-scale physical modelling of soil-filled masonry arch bridges. *International Journal of Physical Modelling in Geotechnics* 18(2):81–94.
- Augustus-Nelson, L., Swift, G.M., Smith, C.C., Gilbert, M. & Melbourne, C. 2018b Influence of railway loading on the performance of soil-filled masonry arch bridges. *Proceedings of the Institution of Civil Engineers-Bridge Engineering* 171(4):276–289.
- Augustus-Nelson, L. & Swift, G. 2020. Experimental investigation of the residual behaviour of damaged masonry arch structures, *Structures* 27:2500–2512.
- Casas J, 2009. A probabilistic fatigue strength model for brick masonry under compression, *Construction and Building Materials* 23(8):2964–2972.
- Gilbert, M., Cole, G., Smith, C. & Melbourne, C. 2022, *CIRIA C800: Guidance on the assessment of masonry arch bridges*. CIRIA, London, UK.
- Harvey W.J. 1988. Application of the mechanism analysis to masonry arches, *Struct. Eng. A*, 66 (5):77–84.
- Heyman J. 1982. *The masonry arch*, Ellis Horwood, Chichester.
- Kooharian A. 1952. Limit Analysis of Voussoir (Segmental) and Concrete Arches, *Proc. American Concrete Institute*. 49(12):317–328.
- LimitState Ltd. 2020. *LimitState:RING Manual*, Version 3.2c. LimitState Ltd, Sheffield, UK.
- McKibbins, L., Melbourne, C., Sarwar, N. & Sicillia Gallard, C. 2006. *CIRIA C656: Masonry arch bridges: Condition appraisal and remedial treatment*, CIRIA, London, UK.
- National Highways. 2022. *DMRB CS454: Assessment of highway bridges and structures*, The Stationery Office, London UK.
- Network Rail, 2006. *NR/GN/CIV/025: The structural assessment of underbridges*, Network Rail, UK.
- Smith C.C., Gilbert, M. & Callaway, P.A. 2004. Geotechnical issues in the analysis of masonry arch bridges, *Proc. 4th Int. Arch Bridges Conf.*, Barcelona, pp. 343–352.
- Wang, J. & Melbourne, C. 2010. Mechanics of MEXE method for masonry arch bridge assessment. *Proc. ICE - Engineering and Computational Mechanics*, 163(3):187–202.



Taylor & Francis

Taylor & Francis Group

<http://taylorandfrancis.com>

*MS17: Recent advance in seismic protection systems: Design, modeling
and testing strategies of traditional and innovative solutions
Organizers: A. Pavese & M. Furinghetti*



Taylor & Francis

Taylor & Francis Group

<http://taylorandfrancis.com>

Prestressed Lead Damper for seismic protection of structures

V. Quaglini, C. Pettoruso & E. Bruschi

Department of Architecture, Built environment and Construction engineering, Politecnico di Milano, Milan, Italy

M. Sartori

Freyssinet Products Italy SpA, Milan, Italy

ABSTRACT: The study presents the design and experimental characterization of a lead friction damper with improved resistance to repeated seismic loads. The damper provides energy dissipation by the friction force triggered between a moving shaft and a lead core prestressed within a steel chamber. Thanks to the ability of lead to restore its properties by strain relief due to static recrystallization immediately after deformation, the damper is not affected by low-cycle fatigue. Prototypes of the damper were subjected to the test procedure recommended by the European standard EN 15129 for Displacement Dependent Devices, fulfilling the relevant requirements. The damper provides a stable response over repeated cycles, characterized by an essentially rectangular hysteresis loop with an equivalent viscous damping ratio $\xi_{\text{eff}} > 55\%$, a low sensitivity on the loading rate, and the ability to withstand multiple cycles of deformation without deterioration of performance, ensuring maintenance-free operation in presence of repeated ground shakes.

1 INTRODUCTION

Supplemental energy dissipation has proved, through research and practical applications, to be a viable solution to mitigate the effects of earthquakes and reduce the seismic vulnerability of ordinary constructions, such as residential, school and industrial buildings (Aliakbari et al. 2020, Gandelli et al. 2019, Garivani et al. 2020, Martinez-Rueda 2002). This strategy is generally implemented by inserting dissipative devices, or dampers, in the bays of the building frame or at column-to-beam connections, with the aim of (i) increasing the structural stiffness, with reduction of inter-story displacements, and (ii) dissipating much of the seismic energy, with limitation of floor accelerations (Bruschi et al. 2022, Bruschi & Quaglini 2022).

Among supplementary energy dissipation devices, the lead extrusion damper developed by Rodgers et al. (2007a), known as HF2V (High Friction to Volume) damper, has been revealed to provide large energy dissipation capability combined with compact dimensions (Rodgers et al. 2019, Quaglini et al. 2021, Quaglini & Bruschi 2022), which make this system suitable for the seismic upgrade of existing structures, since it has a limited impact on the architectural aesthetics or function of the building (Rodgers 2009). The HF2V consists of a steel shaft with a protruding bulge encased in a lead core which is in turn confined within a steel chamber. The deflection of the shaft causes the lead to extrude through the orifice created between the bulge and the internal wall of the chamber as it moves from one side of the bulge to the other; this mechanism ensures a constant force upon yielding, similar to the behavior of conventional steel hysteretic dampers (Rodgers et al. 2008), but avoiding at the same time the typical drawbacks that affect such devices. In fact, because of low-cycle fatigue issue and permanent deformation at unloading, steel hysteretic dampers need to be replaced after a major earthquake. The HF2V damper has been developed starting from the earlier studies of Robinson and Greenbank (1976). The dimensions of these prior devices were very large to provide

sufficient reaction forces, and for this reason their use was mainly limited as part of base isolation systems (Bruschi 2021). In this damper, as the shaft moved, the material was compressed into a smaller volume leading to the formation of a trailing void; as the bulge passes through this void, the damper experiences less resistance and dissipates less energy (Rodgers et al. 2007a). On the other hand, Rodgers et al. (2007a, 2008, 2009, 2019) disclosed to increase the force and the dissipation capability of the damper by preloading the lead core during the assembly of the device. Compressing the lead reduced the formation of trailing voids and boosted the force-to-volume ratio, allowing a more compact design, able to fit into tight volumetrically constrained applications, such as directly into beam–column joints (Mander et al. 2009, Rodgers et al. 2007b, 2008). Further research on this technology was carried out by Yang et al. (2015), Soydan et al. (2015, 2018), Patel (2017), Bruschi et al. (2020), Pettorruso et al. (2021), Quaglini et al. (2021).

Recently, a novel lead damper, called the PreStressed Lead Damper (PS-LED), has been introduced (Pettorruso et al. 2021, Bruschi & Quaglini 2022, Quaglini et al. 2022). The paper illustrates the conceptual design of the PS-LED, presents the tests performed on two prototypes of PS-LED for the characterization of the device.

2 DESIGN OF THE PS-LED

The PS-LED consists of four main components: a straight shaft, a rigid tube, a cap and a lead core (Figure 1). Tube, shaft and cap are made of high strength steel, and the shaft is plated with hard chromium. A bushing provided in the cap drives the linear motion of the shaft.

The PS-LED is intended to be inserted in conventional damped brace systems, and connected at one end of the shaft and at the opposite end of the tube. When the structure oscillates under the effects of the ground motion, the shaft moves relative to the tube, activating a friction force at the interface with the lead core, through which energy is dissipated. Since the coefficient of friction between lead and chromium plated steel is noted to remain almost steady once sliding is triggered (Pettorruso et al. 2021), the damper provides a constant force over its entire stroke with an ensuing essentially rectangular hysteretic curve, which maximizes the amount of energy dissipation. The theoretical amount of energy dissipated in a full cycle is $EDC = 4 N_0 d_b$, where N_0 is the resisting force developed by friction during deflection of the shaft and d_b is the amplitude of displacement. The axial force is controlled by prestressing the lead core during the assembling process; in this way, voids in the working material are removed, resulting in a perfect fit to the tube and the shaft and avoiding clearances at motion reversals (Quaglini et al. 2022).

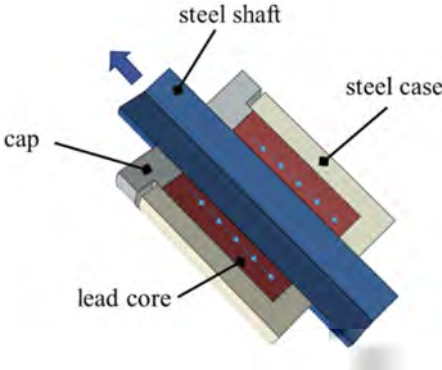


Figure 1. Longitudinal section of the PS-LED (Quaglini et al. 2022).

Over the HF2V device which exploits the plastic deformation of lead, the PS-LED relies on friction only for energy dissipation. This is expected to reduce the influence of heating (which has indeed a major effect on the extrusion resistance of lead) on the output force, and increase

the stability of the damping characteristic during repeated cycles. Another feature of the PS-LED is that the straight shaft does not require complex and expensive machining operation as its bulged counterpart does, permitting the use of commercial chromed shafts and reducing manufacturing costs.

3 MATERIALS & METHODS

3.1 Description of the prototype

In the study two prototypes of PS-LED were tested. The main geometrical and performance properties of the devices are reported in Table 1, where D_s is the diameter of the shaft, D_{cyl} is the inner diameter of the tube wall, L_s is the length of the lead core – shaft interface and L_d is the axial length of the device, N_d is the design axial force and d_{bd} the design seismic displacement in either direction (i.e. one half of the total stroke).

Raw materials are the same for both prototypes. Tube, shaft and cap are made of structural steel S355, while the working material is 99.99% pure lead. The shafts are plated with 70 μm thick hard chromium in order to minimize friction and wear during sliding through the bushing provided in the cap. In order to avoid off-axis loads, self-lubricating spherical hinges with a minimum rotation capacity of $\pm 2^\circ$ are provided at both ends of the dampers, namely at one end of the shaft and on the bottom of the tube (Figure 2). A picture of the devices is shown in Figure 3(a).

Table 1. Properties of tested PS-LED prototypes.

	D_s	D_{cyl}	L_s	L_d	N_d	d_{bd}
Test	mm	mm	mm	mm	kN	mm
Prototype 1	32.5	60	80	410	220	10
Prototype 2	20	70	70	385	50	15

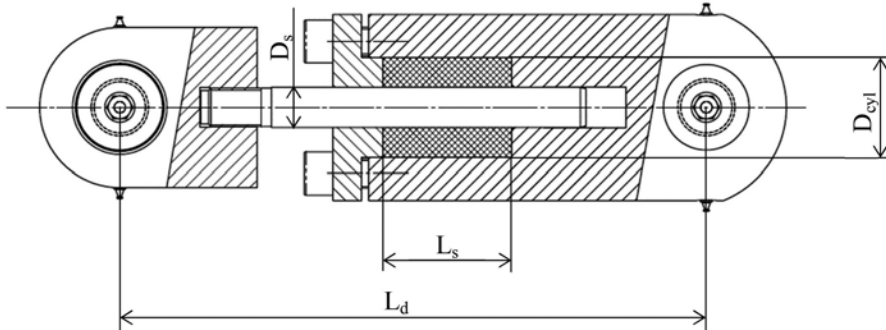


Figure 2. Characteristic dimensions of PS-LED prototypes.

3.2 Testing protocol

The tests were performed at the Materials Testing Laboratory of Politecnico di Milano, using a 500 kN servohydraulic testing machine (MTS Systems, Eden Prairie, MN) (Figure 3(b)), and following the testing protocol prescribed by the European Standard EN 15129 (CEN 2009) for Displacement Dependent Devices (DDD). Harmonic cycles of increasing amplitude at 25%, 50% and 100% of the design deflection d_{bd} were imposed to the specimens, performing five cycles for each intermediate amplitude and ten cycles for the maximum amplitude. The loading frequency was $f_0 = 0.5$ Hz for prototype 1, and 0.25 Hz for prototype 2. Then, a ramp test at 0.1 mm/s speed was performed to two times the amplified design displacement $\gamma_x \gamma_b d_{bd}$

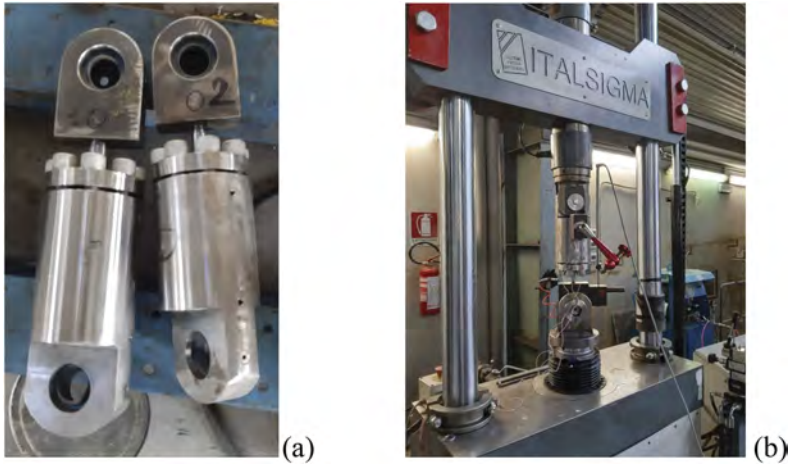


Figure 3. Picture of the tested PS-LED prototypes (a); test configuration showing one prototype on the testing machina (b).

recommended in the standard (where $\gamma_b = 1.1$ and $\gamma_x = 1.2$ are the amplification factor and the reliability factor), to assess the non-failure condition under quasi-static condition.

At the end of the protocol according to EN 15129, in order to investigate the dependence of the response on the speed, three additional tests were performed at the design deflection d_{bd} for different frequencies, with 4 cycles at each frequency. The test plan is reported in Table 2.

Table 2. Test plan.

Test	amplitude	frequency	rate	Cycles
Cyclic	$0.25 d_{bd}$	f_0	0.1 mm/s	5
	$0.5 d_{bd}$	f_0		5
	$1.0 d_{bd}$	f_0		10
Ramp	$2 \gamma_x \gamma_b d_{bd}$	=	0.1 mm/s	1
	$1.0 d_{bd}$	$0.5 f_0$		4
Rate	$1.0 d_{bd}$	$1.0 f_0$		4
	$1.0 d_{bd}$	$1.5 f_0$		4

4 RESULTS

The experimental force – displacement hysteresis loop of the PS-LED is shown in Figure 4. At the beginning of loading the PS-LED shows a linear behavior, corresponding to the elastic deflection of the shaft. After the friction resistance at the lead – shaft interface is overcome and sliding of the shaft relative to the lead core is engaged, the force – deflection diagram displays a plastic branch characterized by a constant force independent of the accommodated deflection, and the same behaviour occurs after motion reversal. The axial force of the plastic branch is almost symmetric in extension ($N > 0$, shaft moving outwards) and in compression ($N < 0$, shaft moving inwards), according to Coloumb friction. It is worth noting that owing to the high elastic stiffness of the steel members, the hysteresis loop exhibits the rectangular shape assumed in design. The small changes in the output force close to motion reversals suggest that the friction between the shaft and the working material has a shallow dependence on the velocity, though this dependency does not affect too much the overall response.

The response of the PS-LED is evaluated on the basis of two quantities, namely the effective stiffness K_{eff} and the equivalent viscous damping ratio ζ_{eff} , which are determined through Equations (1) and (2):

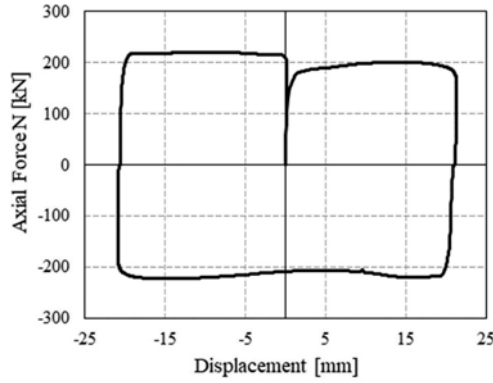


Figure 4. Hysteresis loop of a tested prototype of PS-LED observed in a reversed cycle.

$$K_{eff} = \frac{N}{d_0} \quad (1)$$

$$\zeta_{eff} = \frac{2 EDC}{\pi d_0 N} \quad (2)$$

where N is the force at d_0 deflection, d_0 is the maximum deflection in the cycle and EDC is the energy dissipated per cycle.

The standard (CEN 2009) requires that both K_{eff} and ζ_{eff} remain almost constant during a sequence of cycles of same amplitude, and fulfilling the conditions of Equations (3) and (4):

$$\frac{|K_{eff,i} - K_{eff,3}|}{K_{eff,3}} \leq 0.10 \quad (3)$$

$$\frac{|\zeta_{eff,i} - \zeta_{eff,3}|}{\zeta_{eff,3}} \leq 0.10 \quad (4)$$

where i is the cycle number ($i \geq 2$), and $K_{eff,3}$ and $\zeta_{eff,3}$ are the effective stiffness and the viscous equivalent damping ratio evaluated at the third cycle of a test sequence at the same displacement amplitude, respectively.

Figure 5 and Figure 6 show the variation of K_{eff} and ζ_{eff} during the Cyclic test of Table 2. Disregarding the first cycle, in the most challenging test sequence at the design deflection d_{bd} , K_{eff} and ζ_{eff} respect the stability requirements, showing maximum variations (with respect to $K_{eff,3}$ and $\zeta_{eff,3}$) of 9.9% and 2.4% for prototype 1, and of 7.6% and 0.9% for prototype 2, respectively. The average value of the equivalent damping ratio over 10 cycles performed at the design seismic displacement d_{bd} is $\zeta_{eff} = 0.55$ for prototype 1 and $\zeta_{eff} = 0.60$ for prototype 2, close to the maximum theoretical value of 0.63, confirming the excellent dissipation capacity of the PS-LED. On the other hand, for standard buckling-restrained steel hysteretic dampers made of mild steel, the equivalent viscous damping ratio generally lies in the range of 20% to 40%, depending on the geometry and the design deflection (Sina et al. 2021, Sitler et al. 2020, Tonon et al. 2013).

In the Ramp test, both prototypes were able to sustain the amplified design deflection $\gamma_x \gamma_b d_{bd}$ without any cracking, demonstrating the ability of the PS-LED to accommodate the prescribed displacement without any mechanical damage or deterioration of its stiffness (Figure 7).

Figures 8 and 9 show the cyclic variation of the effective stiffness and the effective damping ratio of the two prototypes at different frequencies. The influence of the rate of deflection is quite low: for both devices the variation of $K_{eff,3}$ and $\zeta_{eff,3}$ with respect to the values evaluated

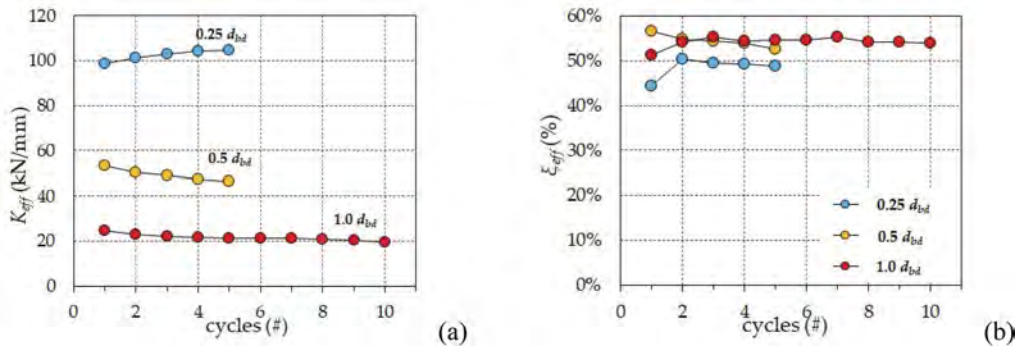


Figure 5. Prototype 1: effective stiffness K_{eff} (a) and equivalent viscous damping ζ_{eff} (b) of the PS-LED vs. number of cycles at different deflection amplitudes d_{bd} .

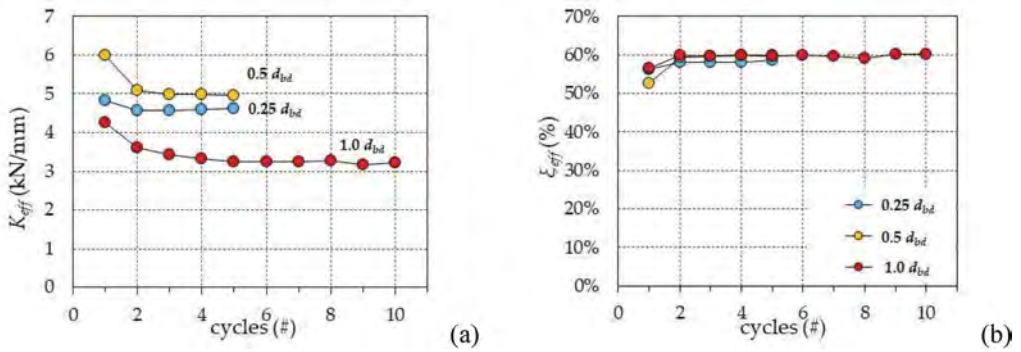


Figure 6. Prototype 2: effective stiffness K_{eff} (a) and equivalent viscous damping ζ_{eff} (b) of the PS-LED vs. number of cycles at different deflection amplitudes d_{bd} .

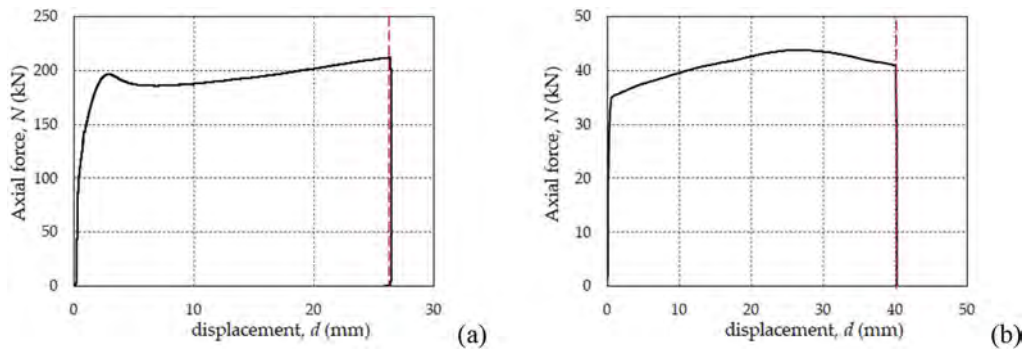


Figure 7. Ramp test to the amplified design deflection $2 \gamma_x \gamma_b d_{bd}$: (a) Prototype 1; (b) Prototype 2.

at the central frequency f_0 is less than 10% as required for Displacement Dependent Devices, and can be neglected in practical applications according to the standard (CEN 2009).

5 CONCLUSIONS

In this paper the design of a novel energy dissipation device, the PS-LED, has been experimentally evaluated following the provisions for Displacement Dependent Devices of the European

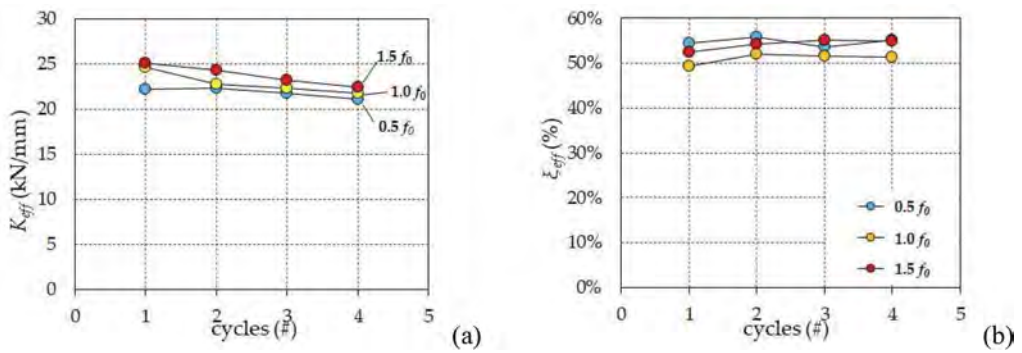


Figure 8. Prototype 1: effective stiffness K_{eff} (a) and equivalent viscous damping ζ_{eff} (b) of the PS-LED vs. number of cycles at different frequencies.

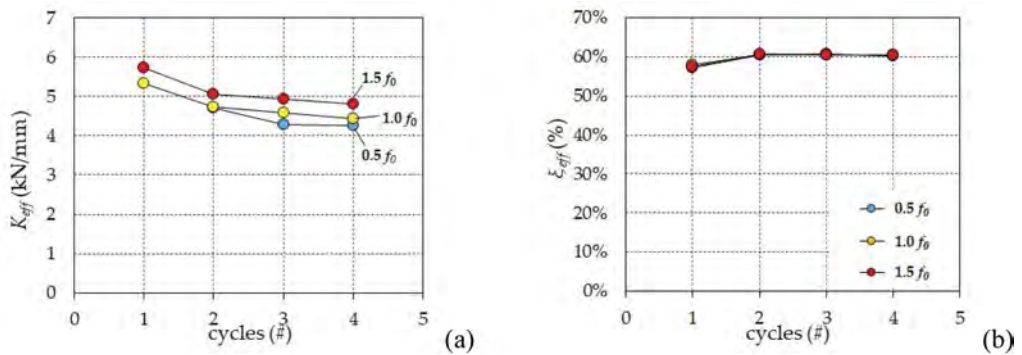


Figure 9. Prototype 2: effective stiffness K_{eff} (a) and equivalent viscous damping ζ_{eff} (b) of the PS-LED vs. number of cycles at different frequencies.

standard EN 15129 (CEN 2009). The PS-LED is characterized by an essentially rigid–plastic behaviour, with a constant axial force and an equivalent viscous damping ratio ζ_{eff} close to 60%, independent of the maximum cyclic displacement and of the rate of deformation. The two tested prototypes have shown a stable and predictable mechanical response over a series of cycles with an amplitude equal to the design seismic displacement, respecting the limits of variation prescribed in the European standard.

FUNDING

This research was partially funded by the Department of the Italian Civil Protection (DPC) in the Frame of the National Research Project DPC – ReLUIS (National Network of Laboratories of Seismic Engineering) 2019–2021, Work Package 15 “Regulatory Contributions for Isolation and Dissipation”.

REFERENCES

- Aliakbari, F., Garivani, S., Aghakouchak, A.A. 2020. An energy based method for seismic design of frame structures equipped with metallic yielding dampers considering uniform inter-story drift concept. *Engineering Structures* 205: 110114, doi: 10.1016/j.engstruct.2019.110114.
- Bruschi, E., Macobatti, F., Pettorosso, C., Quaglino, V. 2020. Characterization and numerical assessment of Lead Extrusion Damper with adaptive behavior. *17th World Conference on Earthquake Engineering*, Sendai.

- Bruschi, E. 2021. *Seismic retrofit of RC framed buildings with supplementary energy dissipation: modelling and application of a novel lead damper*. PhD Thesis, Milan: Politecnico di Milano.
- Bruschi, E., Quaglini, V., Calvi, P.M. 2022. A simplified design procedure for seismic upgrade of frame structures equipped with hysteretic dampers. *Engineering Structures* 251: 113504, doi: 10.1016/j.engstruct.2021.113504.
- Bruschi, E., & Quaglini, V. 2022. Assessment of a novel hysteretic friction damper for the seismic retrofit of reinforced concrete frame structures. *Structures* 46: 793–811, doi: 10.1016/j.istruc.2022.10.113.
- Gandelli, E., Taras, A., Distl, J., Quaglini, V. 2019. Seismic retrofit of hospitals by means of hysteretic braces: influence on acceleration-sensitive non-structural components. *Frontiers in Built Environment* 5: 100. doi: 10.3389/fbuil.2019.00100.
- Garivani, S., Askariani, S.S., Aghakouchak, A.A. 2020. Seismic design of structures with yielding dampers based on drift demands. *Structures* 28: 1885–1899, doi: 10.1016/j.istruc.2020.10.019.
- Mander, T.J., Rodgers, G.W., Chase, J.G., Mander, J.B., MacRae, G.A. 2009. A damage avoidance design steel beam-column moment connection using High-Force-To-Volume dissipators. *Journal of Structural Engineering* 135(11): 1390–1397.
- Martínez-Rueda, J.E. 2002. On the evolution of energy dissipation devices for seismic design. *Earthquake Spectra*. 18(2): 309–346, doi: 10.1193/1.1494434.
- Patel, C.C. 2017. Seismic analysis of parallel structures coupled by lead extrusion dampers. *International Journal of Advanced Structural Engineering* 9: 177–190.
- Pettoruso, C., Quaglini, V., Bruschi, E. 2021. Supplemental energy dissipation with prestressed Lead Extrusion Dampers (P-LED): Experiments and modeling. *COMPdyn 2021, The 8th ECCOMAS Thematic Conference on Computational Methods in Structural Dynamics and Earthquake Engineering*.
- Quaglini, V., Pettoruso, C., Bruschi, E. 2021. Experimental and numerical assessment of prestressed lead extrusion dampers. *International Journal of Earthquake Engineering* 38(2), 46–69.
- Quaglini, V., Pettoruso, C., Bruschi, E. 2022. Design and Experimental Assessment of a Prestressed Lead Damper with Straight Shaft for Seismic Protection of Structures. *Geosciences* 12(5): 182. doi: 10.3390/geosciences12050182.
- Robinson, W.H., Greenbank, L.R. 1976. Extrusion energy absorber suitable for the protection of structures during an earthquake. *Earthquake Engineering & Structural Dynamics* 4(3): 251–259.
- Rodgers, G.W., Chase, J.G., Mander, J.B., Leach, N.C., Denmead, C.S., 2007a. Experimental development, tradeoff analysis and design implementation of high force-to-volume damping technology. *Bulletin of the New Zealand National Society for Earthquake Engineering* 40(2): 35–48.
- Rodgers, G.W., Mander, J.B., Chase, J.G., Dhakal, R.P., Solberg, K.M. 2007b. DAD post-tensioned concrete connections with lead dampers: analytical models and experimental validation. *8th Pacific Conference on Earthquake Engineering*, Singapore.
- Rodgers, G.W., Solberg, K.M., Chase, J.G., Mander, J.B., Bradley, B.A., Dhakal, R.P., Li, L. 2008. Performance of a damage-protected beam-column subassembly utilizing external HF2V energy dissipation devices. *Earthquake Engineering and Structural Dynamics* 37(13): 1549–156. doi: 10.1002/eqe.830.
- Rodgers, G.W. 2009. Next generation structural technologies: implementing high force-to-volume energy absorbers. Christchurch: Ph.D. Thesis, University of Canterbury.
- Rodgers, G.W., Chase, J.G., Mander, J.B. 2019. Repeatability and high-speed validation of supplemental lead-extrusion energy dissipation devices. *Advances in Civil Engineering* 2019: 7935026.
- Sina, F., Amir, H.A., Lars, D. 2021. Equivalent viscous damping for buckling-restrained braced RC frame structures. *Structures* 34: 1229–1252.
- Sitler, B., Takeuchi, T., Matsui, R., Terashima, M., Terazawa, Y. 2020. Experimental investigation of a multistage buckling-restrained brace. *Engineering Structures* 213: 110482. doi: 10.1016/j.engstruct.2020.110482.
- Soydan, C., Yüksel, E., İrtem, E. 2015. The Behavior of a steel connection equipped with the Lead Extrusion Damper. *Advances in Structural Engineering* 17(1): 25–39. doi: 10.1260/1369-4332.17.1.25.
- Soydan, C., Yüksel, E., İrtem, E. 2018. Retrofitting of pinned beam-column connections in RC precast frames using lead extrusion dampers. *Bulletin of Earthquake Engineering* 16: 1273–1292. doi: 10.1007/s10518-017-0246-z.
- Tonon, E., Forte, M., Mammino, A., Moro, S. 2013. Protezione sismica degli edifici mediante dissipatori d'energia: Applicazione pratica della nuova sede della prefettura de L'Aquila. *XV Conference of the Italian Association of Seismic Engineering ANIDIS*, Padua.
- Yang, M.F., Xu, Z.D., Zhang, X.C. 2015. Experimental study on lead extrusion damper and its earthquake mitigation effects for large-span reticulated shell. *Steel and Composite Structures* 18(2): 481–496.

Nonlinear analysis of base isolated buildings with curved surface sliders including over-stroke displacements

Felice Carlo Ponzo, Antonio Di Cesare & Nicla Lamarucciola
University of Basilicata, Potenza, Italy

ABSTRACT: Seismic isolation represents one of the most suitable strategies for mitigating the seismic risk of structures and infrastructures. Acceptable probabilities of collapse for seismically isolated buildings could be achieved by an appropriate isolator displacement capacity. This paper investigates the effects of the over-stroke capacity of double concave curved surface sliding isolators, in addition to the nominal displacement capacity, on the seismic response of base isolated structures. The case study building is a reinforced concrete frame structure designed for high hazard seismic site. The level of performance of global collapse prevention has been investigated considering the earthquake intensity levels at the Collapse Limit State (with a return period of 1000 years). The results of the nonlinear static and dynamic analysis highlights that the seismic isolation without the over-stroke capability show a limited margin against collapse for seismic intensities beyond the design limit state level.

1 INTRODUCTION

The minimization of potential seismic damaging of a building can be achieved introducing flexibility at the base of the structure in the horizontal direction and damping element to reduce the amplitude of displacements. In recent years, one of the most widespread technologies is the seismic isolation, as a practical and economical alternative to traditional seismic reinforcement.

Nowadays there are many isolation devices that differ in construction technology, materials, geometry and operation. The most common seismic devices are elastomeric isolators and sliding isolation systems. The latter are composed of a certain number of moving parts (at least two) made of steel and composite materials which slide over each other expressing a specific friction force. One of the mainly used seismic isolation system is the Curved Surface Slider (CSS), also known as Friction Pendulum Slider® (FPS), firstly developed by Zayas (Zayas et al. 1987), which includes both re-centering and good dissipation capabilities being based on the pendulum mechanic principle.

The double CSS bearing (or Double Concave Curved Surface Slider - DCCSS) consists of two facing concave stainless-steel surfaces separated by a slider which can be either articulated or rigid. The DCCSS can be modelled as two CSS in series associated with same coefficient of friction μ and effective radius of curvature R_{eff} (Fenz & Constantinou 2006, Ponzo et al. 2017).

The CSS devices can be further divided in two main groups: devices with or without a displacement restrainer, which prevent the inner slider to slid past a certain point which usually is the perimeter of the housing pad. These elements can be for example displacement restraining rings, which are made of the same material of the housing plate and can be welded, bolted to it or even form a single block with the pad itself (Bao et al. 2018). Retaining elements such as restraining ring (Figure 1a) are widely used in America (Kitayama & Constantinou 2019) in order to control displacements and to avoid the isolator disassembly when displacements higher than the design ones occur. Anyways, the impact against such retaining elements may induce significantly high acceleration onto the superstructure. On the contrary, the European Standards (UNI EN 15129:2018) do not allow the presence of restraining end-stroke element that can be damaged in case of a seismic event higher than the Maximum Credible Earthquake (MCE) and only approves

the use of structural joints separating the superstructure from the surrounding constructions, in order to safely accommodate the seismic movement. In particular, the European Standard allows the use of ground retaining walls, (Figure 1b), or specific devices such as rubber bumpers attached to the walls, to be used as end-over-stroke. Usually in Europe, the gap separating the superstructure from the retaining wall is much larger than the displacement capacity of the isolators, and consequently, the inner slider can run on the edge of the sliding surfaces for earthquakes producing displacement larger than the isolators capacity. When displacement restraining elements are not employed, and concave plates feature a flat rim (Bao et al. 2018b), the inner slider movement beyond the geometric capacity displacement d_c of the isolator is allowed entering in the so-called over-stroke displacement regime. The slider running in the over-stroke displacement regime it is capable of providing the DCCSS device with an increased displacement capacity d_{lim} and sliding force (Di Cesare et al. 2019, Ponzo et al. 2020, Di Cesare et al. 2021, Ponzo et al. 2021, Furinghetti et al. 2021a). Figure 1 shows the DCCSS in two deformed conditions: with a restraining ring and with overstroke capacity and moat wall.

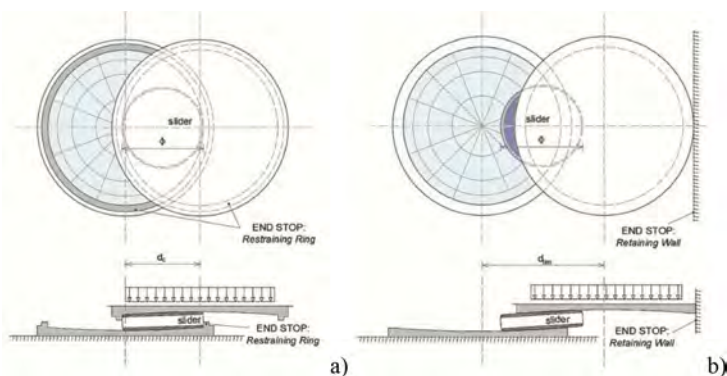


Figure 1. DCCSS bearing in deformed condition a) with a restraining ring d_c ; b) with overstroke capacity and retaining wall $d_{lim} \geq d_c$; in plan and cross section view (Di Cesare et al. 2021).

The equations of motion and the limit displacements for the over-stroke sliding regime have been characterized by (Di Cesare et al. 2022, Furinghetti et al. 2021b) but a proper argumentation is needed in order to provide designers with the accurate displacement capacities and forces of DCCSS isolators.

This paper focuses on a case study of isolated building by means of DCCSS isolators with and without over-stroke displacement and moat wall, designed following the Italian seismic code (NTC 2018, Ragni et al. 2018). The building is a six-storey concrete frame structure assumed located in the city of L'Aquila (Italy) on soil class C. Nonlinear static and dynamic analyses were performed considering earthquake intensity levels at Collapse Limit State. Analyses results in terms of global drift and base shear are presented.

2 DESCRIPTION OF THE CASE STUDY BUILDING

The prototype structure considered in this study represents a typical residential RC-frame buildings located in L'Aquila, characterized by a regular plan of approximately 240 square meters and 6 stories above ground (Figure 2). The ground level height is 3.4 m while the other stories heights are 3.05 m. The building includes a staircase, designed with knee beams, and all stories have the same 25 cm-thick slab.

Infill panels have been considered as regularly distributed in plan and elevation, with different opening percentages. Infills dead loads have been considered in the design process. More details about RC structural members and masonry infills can be found in (Ricci et al., 2019).

In the base-isolated configuration, a supplementary RC base slab has been implemented below the ground floor columns (Figure 2). Elastic beams have been added at the base floor

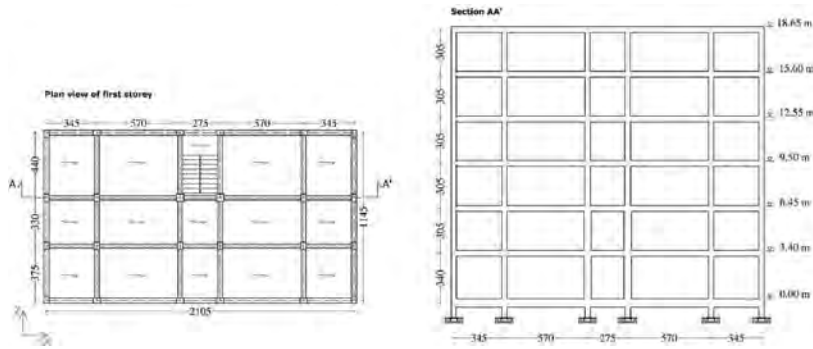


Figure 2. Case study building: plan view and longitudinal sections.

to realize the grid above the isolation system, consisting of 24 DCCSS isolators placed below the columns. Both concave plates of the DCCSS are characterized by the same radii of curvature and the same coefficients of friction ($R_1 = R_2$ and $\mu_1 = \mu_2$), and the assumed hypothesis is that sliding occurs simultaneously on both surfaces, considering a rigid cursor. The maximum displacement d_{max} has been assumed by catalogue, taking into account torsional effects, and the geometric capacity displacement d_c has been assumed as $d_c = 1.10 \cdot d_{max}$.

The total seismic weight W of the isolated frame is about 22380 kN and the vertical loads on the internal isolators N_{Sd} is about 1000 kN. The isolation system is designed considering the MCE spectrum shown in Figure 3a (UNI EN 1998-1:2004)

The seismic inputs considered in this study are reported in Figure 3b and consisted of a set of 20 ground motion for the intensity level corresponding to the Collapse Limit State (return period of 1000 years). The 5%-damped elastic spectra of the seismic records selected to represent the earthquake intensity level at MCE of the isolated structures is shown in Figure 3b. A reference period (conditioning period) closes to the design value of the fundamental period of vibration of $T = 3$ s has been considered. More details about the seismic hazard evaluation and the record selection for nonlinear dynamic analysis can be found in previous studies (Iervolino et al. 2018).

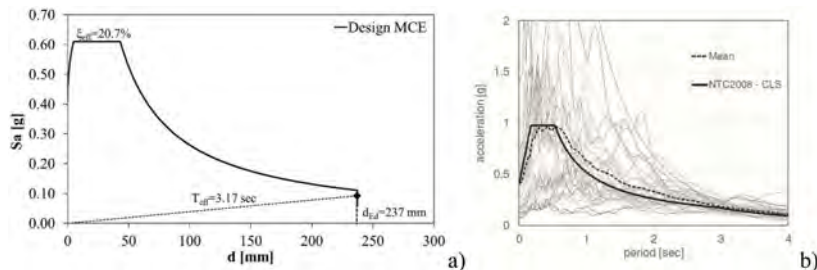


Figure 3. Acceleration response spectra of ground motion for Collapse Limit State (CLS) and Isolation systems design procedure on ADRS Spectra for LLS and CLS for L'Aquila site (Di Cesare, A., & Ponzio, F. C., 2023).

The geometric characteristics and main design parameters of the designed isolation system are reported in Table 1, in terms of: equivalent radius R_{eff} , friction coefficient μ , equivalent stiffness K_{eff} , effective period T_{eff} , effective damping ξ_{eff} , slider dimension, the maximum displacement d_{max} , the design displacement d_{Ed} of the isolation system at the MCE. For the over-stroke stage of motion the mechanical parameters are the increase of stiffness k_2 and friction coefficient $\Delta\mu$.

The oversizing due to the industrial discretization of the devices has been taken into account considering the ratio between the actual isolator displacement capacity d_c and the design displacement d_{Ed} equal to 1.4 in this study. The overstroke limit has been defined as the ratio between the ultimate displacement d_{lim} and d_c , equal to 1.25.

Table 1. Geometric characteristics and main design parameters of the isolation system at the CLS.

	R_{eff}	μ	K_{eff}	T_{eff}	ζ_{eff}	d_{Ed}	Φ	d_{max}	d_c	d_{lim}
Case Study	[mm]	[%]	[kN/mm]	[sec]	[%]	[mm]	[mm]	[mm]	[mm]	[mm]
AQ_New	3700	2.5	0.357	3.17	21	237	200	± 300	± 330	± 414

3 NUMERICAL MODELLING

The numerical model of the superstructure has been implemented in (OpenSEES 2006). A lumped plasticity approach has been considered for the structural elements of the superstructure, whereas elastic beams have been used for the base floor grid above the isolation system. The structural model also includes the staircase featuring inclined beams and cantilever steps. The cyclic degrading behaviour of plastic hinges (*modIMKmodel*) in the OpenSEES framework has been described implementing the model proposed by (Ibarra et al. 2005). In this study, 5% Rayleigh damping is used to model the viscous damping of the superstructure. Second order effects have not been considered. The masonry infills In-Plane (IP) behaviour has been modelled with an equivalent compression-only strut. The backbone curve of the diagonal strut has been defined on the basis of a modified version of the (Decanini et al. 2014) model, while the effect of openings has been taken into account through suitable strength/stiffness reduction factors. Both the Out-Of-Plane (OOP) and the IP/OOP interaction effects have been taken into account in the modelling strategy. Finally, local shear interactions, between masonry infills and adjacent RC columns, have been represented implementing shear springs at the ends of the columns to reproduce their nonlinear shear response triggered and amplified by the action of the adjacent equivalent compression-only diagonal. More information about superstructure modelling can be found in (Ricci et al. 2018).

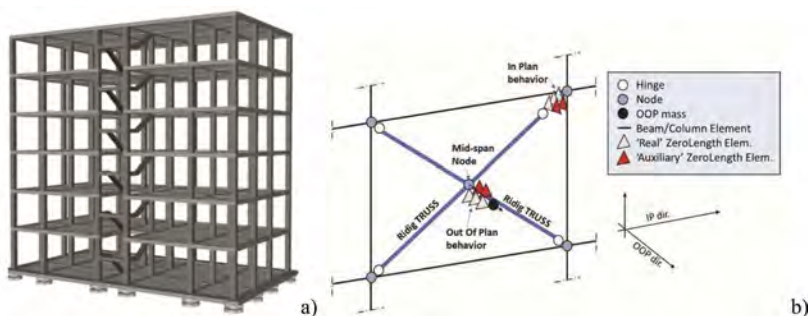


Figure 4. Schematic representation of the base-isolated prototype building and b) IP/OOP infill panels model.

The basic *SingleFPBearing* element (Figure 5) in OpenSees (OpenSees 2006) has been implemented to describe the DCCSS cyclic behaviour composed of a zero-length sliding hinge. The basic model has been modified in order to simulate the DCCSS behaviour during the over-stroke displacement, by adding three zero length parallel elements from the top j -node to a new fixed k -node (Figure 5). Two of these three zero length parallel elements have been modelled as elastic-perfectly plastic gap elements (*elasticPPGap*) defined by a gap displacement d_c , an elastic stiffness k_2 , increased friction coefficient and a yielding force F_y , no hardening ratio or damage accumulation are considered so the gap material can recenter on load reversal. The last zero length element has been implemented considering a multi-linear elastic material (*elasticMultiLinear*), characterized by a nonlinear elastic behaviour without energy dissipation, defined by a set of stress-strain points.

The Rigid Gap has been modelled with a zero-length hinge, from j -node to s -node of Figure 5, consisting of an elastic-perfectly plastic gap element (*elasticPPGap*) with infinite stiffness ($k=\infty$) and at a gap displacement of d_c for models of rings or d_{lim} for models of rigid moat walls.

The ultimate displacement d_{lim} threshold value considered in the over-stroke regime is linked to the attainment of the first of the following conditions (Di Cesare et al. 2022): (i) vertical load instability; (ii) the displacement exceeds a limit value related to the maximum contact pressure between sliding interfaces (60 MPa) (iii) the device undergoes more than two over-stroke cycles. Plastic deformations of the end-stroke models, as example due to moat wall nonlinearity, were not taken into account. More details about numerical modelling of DCCSS in overstroke regime can be found in (Di Cesare et al. 2020, Ponzo et al. 2020, Di Cesare & Ponzo 2023).

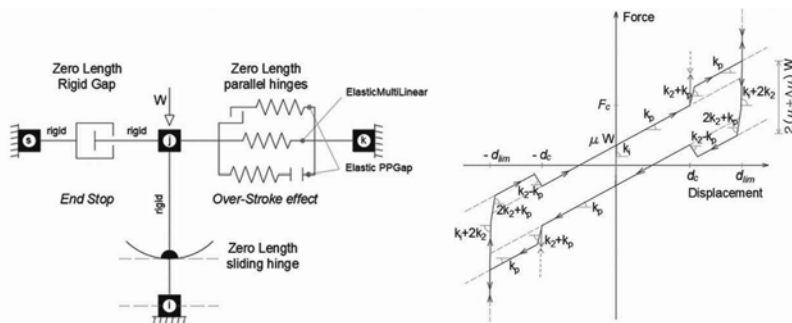


Figure 5. Spring model representation of the Modified SingleFPBearing with End-Stop and force vs displacement relationships for the retaining wall model.

4 NON-LINEAR STATIC AND DYNAMIC ANALYSES RESULTS

Nonlinear analyses have been performed considering different conditions of the isolation system. The seismic performance of the isolated structure and isolation system was evaluated by comparing the results of nonlinear static analysis (Pushover) in both horizontal directions with those of nonlinear dynamic analysis. A distribution of lateral forces proportional to the floor masses was used in the pushover analyses. In Figure 6 the pushover curves of not-isolated, base-isolated building, without and with overstroke and without and with rigid end-stop are compared. Pushover curves of base-isolated building model without displacement restraints (black dashed lines) show the basic behaviour of the isolation system, with a first quasi-rigid branch (pre-sliding stage), followed by a second branch accounting for isolators restoring stiffness. The isolated model with displacement restraints highlights a pushover behaviour of the not-isolated superstructure for displacement greater than the base displacement capacity d_c . In particular, as can be observed in Figure 6, for the configuration with isolation system and stop, after the pre-sliding stage and the second branch accounting for isolators restoring stiffness, the isolation system stops when the base displacement reaches d_c and superstructure pushover curve is shown again. The system with isolation system, over-stroke and stop perfectly overlaps the previous one for the first two branches, then, when the geometric capacity displacement is reached, the isolation system enters in the over-stroke regime with a third branch with increased stiffness friction force, and finally, when the end-over-stroke is reached (end of sliding), the superstructure pushover curve is shown again. It is possible to observe that the shape of the first part of the pushover curve of isolated structures can be approximated by an elastoplastic hardening behavior.

In order to evaluate the behaviour of the isolation system with and without rigid end-stop, the seismic response of base-isolated model has been investigated by means of multi-stripe nonlinear time-history analyses considering 20 real ground motions at intensity level corresponding to the collapse limit state and compared with pushover curves. The seismic input consisted of bi-directional horizontal ground motions time histories. In Figure 7 nonlinear dynamic results are expressed in terms of the acceleration displacement response spectrum, considering the maximum superstructure top displacement vs ratio between maximum base shear and total seismic weight. The dynamic results are in good agreement with the pushover curves both in sliding stage and in over-stroke stage. It is worth noting that the over-stroke regime has been reached

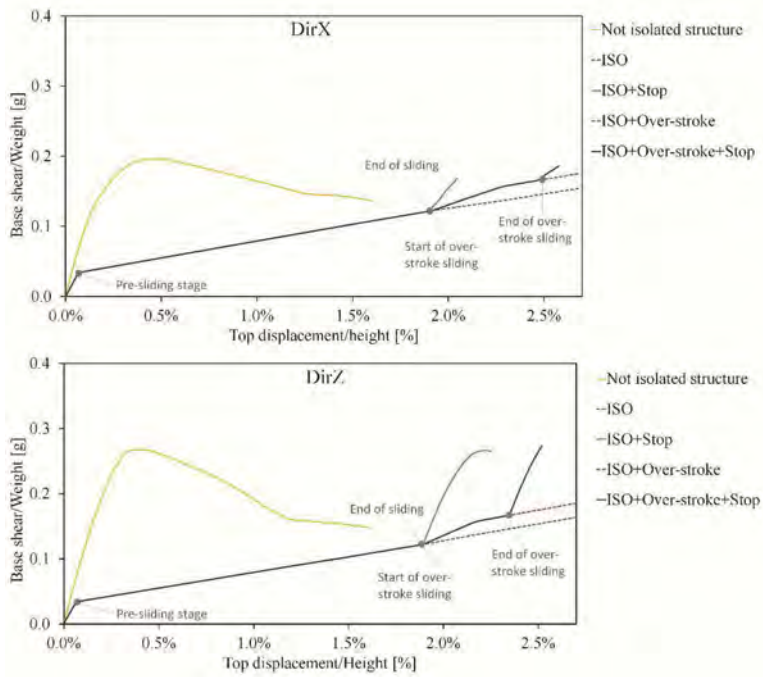


Figure 6. Pushover curves of not-isolated building and isolated with and without overstroke and with and without end-stop for horizontal directions.

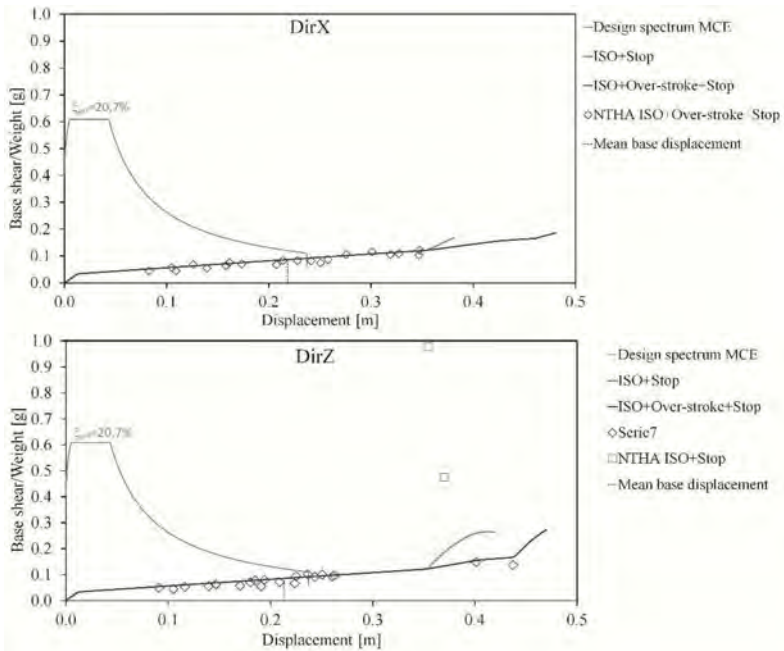


Figure 7. Nonlinear static versus nonlinear dynamic results in terms of maximum top displacement and acceleration at the base level for horizontal directions.

for two earthquakes of the spectra-compatible inputs, mainly due to the variability of the selected ground motion. For the same seismic inputs in the configuration with isolation system and rigid end-stop in the case of impact between the superstructure and the end stop dynamic analyses provide values of the base shear significantly higher than those obtained from the push-over curves, due to the dynamic effects. Figure 7 also reports the mean values of maximum base displacements and the design MCE spectrum (see Figure 3b). The mean base displacement is slightly lower than the design displacement d_{Ed} .

5 CONCLUSIONS

In this paper a case study of a seismically isolated RC frame structure with DCCSS in high seismic zone was numerically investigated based on non-linear static and dynamic analyses. Coherently with commercially available DCCSS devices, the oversizing due to industrial discretization and the over-stroke displacement capacity of the bearings before reaching the end-stroke were considered. For the case of base isolation with overstroke, characterized by a ratio between the overstroke displacement d_{lim} and actual isolator displacement capacity d_c (d_{lim}/d_c) equal to 1.25, and by a ratio between d_c and the design displacement d_{Ed} (d_c/d_{Ed}) equal to = 1.4, non-linear dynamic analyses showed that the impacts against the end-stop are avoided in all seismic inputs spectra-compatible with the MCE. In all cases, the design displacement evaluated by equivalent static analysis and the mean value of maximum base displacement evaluated by nonlinear dynamic analysis are in good agreement.

Results from nonlinear static analysis and nonlinear time history analysis pointed out that over-stroke displacement of the isolators may significantly increase the safety factor in case of earthquakes bigger than the design ones, without drawing on the plastic resources of the superstructure and changing the construction costs. Further analyses are currently underway considering different case studies of retrofitted RC frame.

ACKNOWLEDGEMENTS

Authors would like to acknowledge the financial support of RELUIS 2022–2024 project (Work Package no. 15: Contributions to the Italian seismic code for base isolation and energy dissipation systems) funded by the Italian Civil Protection Department.

REFERENCES

- Zayas, V.A., Low, S.S. & Mahin, S.A. 1987. The FPS earthquake protection system, *Earthquake Engineering Research Center*, Report, No. 87–01, Berkeley, California.
- Fenz, D.M. & Constantinou, M.C. 2006. Behavior of the Double Concave Friction Pendulum Bearing. *Earthq. Eng. Struct. Dyn.*, 35, 1403–1424.
- Ponzo, F.C., Di Cesare, A., Leccese, G. & Nigro, D. 2015. Shaking table tests of a base isolated structure with double concave friction pendulum bearings. *Bulletin of the New Zealand Society for Earthquake Engineering*, 48(2), pp. 136–144
- Bao, Y., Becker, T. C., Sone, T. & Hamaguchi, H. 2018. Experimental study of the effect of restraining rim design on the extreme behavior of pendulum sliding bearings. *EESD*, 47(4), 906–924.
- Kitayama, S. & Constantinou, M.C. 2019. Effect of displacement restraint on the collapse performance of seismically isolated buildings. *BEE*, 1–20.
- UNI EN. 15129:2018 2009. Anti-seismic devices. *European committee for standardization (CEN)*, Bruxelles, Belgium.
- Bao Y, Becker TC, Sone T & Hamaguchi H. 2018b. To limit forces or displacements: collapse study of steel frames isolated by sliding bearings with and without restraining rims. *SDEE* 2018;112:203–14.
- Di Cesare, A., Ponzo, F. C., Telesca, A., Nigro, D., Castellano, G., Infanti, S., et al. 2019. Modelling of the over stroke displacement of curved surface sliders using OpenSEES, *OpenSEES Days Eurasia*. Hong Kong.

- Ponzo, F. C., Di Cesare, A., Telesca, A., Nigro, D., Castellano, M. G., & Infanti, S. 2020. Influence of DCCSS Bearings Over-Stroke and breakaway on the seismic response of isolated buildings. *Proceedings of the 17th World Conference on Earthquake Engineering*, September 2020, Sendai, Japan.
- Di Cesare, A., Ponzo, F.C., & Telesca, A. 2021. Improving the earthquake resilience of isolated buildings with double concave curved surface sliders. *Eng. Struct.* 2280, 111498.
- Ponzo, F.C., Di Cesare, A., Telesca, A., Pavese, A. & Furinghetti, M. 2021. Advanced modelling and risk analysis of RC buildings with sliding isolation systems designed by the Italian Seismic Code. *Appl. Sci.* 11, 1938.
- Furinghetti, M., Yang, T., Calvi, P.M., & Pavese, A. 2021a. Experimental evaluation of extra-stroke displacement capacity for curved surface slider devices. *Soil Dyn. Earthq. Eng.* 146.
- Di Cesare A, Ponzo FC & Telesca A 2022. Mechanical model of the overstroke displacement behaviour for double concave surface slider antiseismic devices. *Front. Built Environ.* 8:1083266. doi: 10.3389/fbuil.2022.1083266
- Furinghetti, M. & Pavese, A. 2021b. Modeling strategies for the lateral response of curved surface slider devices under extreme displacement demands. *Proceedings of the COMPDYN 2021, 8th ECCOMAS Thematic Conference on Computational Methods in Structural Dynamics and Earthquake Engineering*, June 2021, Streamed from Athens, Greece.
- NTC 2018. Italian technical code for constructions (in Italian). Ministry of Infrastructures, Italy 2018.
- Ragni, L., Cardone, D., Conte, N., Dall'Asta, A., Di Cesare, A., Flora, A., Leccese, G., Micozzi, F. & Ponzo, F.C. 2018. Modelling and Seismic Response Analysis of Italian Code-Conforming Base-Isolated Buildings. *Journal of Earthquake Engineering*, Vol 22(2), doi: 10.1080/13632469.2018.1527263
- Ricci, P., Manfredi, V., Noto, F., Terrenzi, M., Petrone, C., Celano, F., et al. 2018. Modeling and seismic response analysis of Italian code-conforming reinforced concrete buildings. *Journal of Earthquake Engineering*, Vol 22, doi: 10.1080/13632469.2018.1527733
- EN1998-1. Eurocode 8 2004. Design of structures for earthquake resistance—Part 1: general rules, seismic actions and rules for buildings. *European committee for standardization (CEN)*, Bruxelles, Belgium.
- Iervolino, I., Spillatura, A., & Bazzurro, P. 2018. Seismic reliability of code-conforming Italian buildings. *Journal of Earthquake Engineering* 22, 5–27. doi:10.1080/13632469.2018.1540372
- OpenSEES 2006. Open system for earthquake engineering simulation. *PEER Center, University of California*, Berkeley. Available at <http://opensees.berkeley.edu/>.
- Di Cesare, A., & Ponzo, F. C. 2023. Effect of Over-Stroke Capacity of Curved Surface Sliders on the Collapse Safety of Seismically Isolated Buildings. In *Seismic Isolation, Energy Dissipation and Active Vibration Control of Structures: 17th World Conference on Seismic Isolation (17WCSI)* (pp. 254–263). Cham: Springer International Publishing.
- Ibarra, L.F., Medina, R.A., & Krawinkler, H. 2005. Hysteretic models that incorporate strength and stiffness deterioration. *Earthquake Engng Struct. Dyn.* 34, 1489–1511. <https://doi.org/10.1002/eqe.495>.
- Decanini, L., Liberatore, L. & Mollaioli, F. 2014. Strength and stiffness reduction factors for infilled frames with openings. *Earthquake Engineering and Engineering Vibration* 13(3). doi: 10.1007/s11803-014-0254-9
- Ponzo, F.C., Di Cesare, A., Telesca, A. & Nigro, D. 2021. Base isolated buildings with curved surface sliders including displacement restraints. In: *Proceeding of 14th World Congress in Computational Mechanics (WCCM) ECCOMAS 2020*, Virtual Congress, 11–15 Jan 2021.

Effects of wear on the friction coefficient of a curved surface slider

V. Quaglini & E. Bruschi

Department of Architecture, Built environment and Construction engineering, Politecnico di Milano, Milan, Italy

Esengül Çavdar, Gökhan Özdemir & Volkan Karuk

ESQUAKE Seismic Isolator Test Laboratory, Eskişehir Technical University, Eskişehir, Turkey

Uğurcan Özçamur

TIS Technological Isolation Systems, Ankara, Turkey

ABSTRACT: The study investigates the modification in the friction coefficient of a Curved Surface Slider (CSS) due to service movements through complementary tests performed on a small-scale specimen of the sliding material and a full-scale prototype, both of them subjected to a sliding distance of 1000 m. The changes in the coefficient of friction vs. the sliding distance are compared, demonstrating that small-scale tests provide fair estimates of the friction properties of the full-scale CSS. Moreover, the seismic response of the CSS remains almost the same regardless of the sliding distance.

1 INTRODUCTION

Sliding isolation system with curved surfaces, also known as Friction Pendulum System®, or FPS® (Zayas et al. 1987, 1990, Mokha et al. 1991) in North America, and Curved Surface Sliders (CSS) in Europe, are among the most popular antiseismic hardware nowadays (Calvi & Calvi 2018). Such system accommodates the horizontal displacements of the superstructure by means of one or more pair(s) of curved sliding surfaces, which also provide a restoring force due to the effect of gravity, and dissipate the seismic energy through friction forces that are activated during sliding (Quaglini et al. 2017a, 2017b). In bridges and viaducts, the CSS behaves throughout its service life as a conventional sliding bearing, accommodating the low velocity movements induced from temperature changes and traffic loads. On the other hand, in the event of an earthquake, the CSS provides the seismic displacement, which generally occur at high speeds, on the order of some hundred mm/s.

The sliding surfaces of the isolators usually consist of a pad made of a self-lubricating polymeric material and a mating concave surface made of stainless steel or plated with hard chromium. Since the introduction of the Pendulum system in the '80s of the last century (Zayas et al. 1987), a number of self-lubricating polymeric materials have been proposed, including filled polytetrafluoroethylene (PTFE) (Zayas et al. 1990, Quaglini 2012), polyethylene (PE) and polyamide (PA) (Barone et al. 2019). A viable sliding material for CSSs must fit different requirements regarding the expected performance in both service and seismic situations, providing high load bearing capacity combined with wear endurance, low coefficient of friction at low speeds in order not to constrain service movements, and stable coefficient of friction at high speeds.

Current standards (CEN 2009, AASHTO 2020, ASCE/SEI 2017) recommend to perform displacement controlled dynamic tests on full scale prototypes of the isolators to assess the friction coefficient under seismic loading. The number of cycles in these tests is generally three for most of the loading conditions. However, since prototype tests are generally performed on

new devices, the influence of the wear of the sliding surfaces on the high-speed coefficient of friction is disregarded. Nevertheless, such wear may be not negligible in the event that the earthquake hits the isolated structure after several years of service of the isolators. On the other hand, the friction coefficient for slow and small amplitude service motions is assessed by performing cyclic tests on small-scale samples of the sliding material, considering in this case large accumulated sliding distances, up to 1000 m for buildings, and 10000 m for bridges (CEN 2009), and including also changes in the environmental temperature.

The reliability of small-scale tests for the characterization of sliding materials has been extensively debated among tribologists. In conventional tribotesting, small-scale tests performed on unidirectional rotating pin-on-disc, block-on-ring or reciprocating cylinder-on-plate test rigs are mainly used because of their cost- and time-effectiveness and ease of handling small samples (Samyn et al. 2006). However, test conditions can strongly differ from real application, and scale effects are neglected, therefore making extrapolations towards the actual working conditions hard to make, and possibly leading to substantial errors.

This study investigates the modification of the friction coefficient of a sliding isolator due to service movements through complementary investigations performed on both small-scale specimens of the sliding material and a full-scale double concave friction pendulum (DCFP). Both small- and large-scale specimens are subjected to a total sliding distance of 1000 m, and the change in the coefficient of friction vs. the sliding distance obtained in the two tests are compared. Moreover, the coefficient of friction of the DCFP at different sliding distances is evaluated experimentally under the effect of ground motion excitations.

2 MATERIALS & METHODS

2.1 *Small-scale tests*

The small-scale tests were performed at the Material Testing Laboratory of Politecnico di Milano following the method provided in the European standard on antiseismic devices EN 15129 (CEN 2009).

The specimen consists of a circular pad made of a proprietary slider material consisting of filled PTFE, combined with a mating surface made of stainless-steel mirror finished to roughness $R_z \leq 1 \mu\text{m}$, to replivate the same sliding interface used in the DCFP. The pad has a diameter of 75 mm and a thickness of 7 mm, and is recessed by 4.5 mm into a steel plate, leaving a sliding gap of 2.5 mm.

The specimen is placed in a custom testing machine at Politecnico di Milano (Quaglini et al. 2012). The machine consists of a four-column steel frame equipped with two servo-hydraulic jacks aligned at 90 degrees to each other (Figure 1). The vertical jack, rated 300 kN, applies a compression force to the specimen producing the target contact pressure on the sliding interface. The horizontal jack, rated 50 kN, drives a sledge that carries the sliding material pad. The stainless-steel mating plate is screwed to a backing plate fixed to the rod of the vertical jack. Load cells and inductive displacement transducers are used to measure the loads and the movements applied to the sliding material pad. The whole specimen is enclosed in a thermal chamber operating between $-70 \text{ }^\circ\text{C}$ and $90 \text{ }^\circ\text{C}$. A digital controller coupled with a thermal sensor allows to control the temperature within the chamber within a tolerance of $\pm 1 \text{ }^\circ\text{C}$.

The tests are performed in accordance with the long term friction test method prescribed in the standard (CEN 2009), modified to extend the maximum temperature to $+70 \text{ }^\circ\text{C}$. The sliding material pad is subjected to the application of axial load and concurrent back-and-forth sliding motion in horizontal direction. The test program consists of 3 phases as shown in Table 1 and Figure 2. In phase 1 the temperature is varied between $-35 \text{ }^\circ\text{C}$ and $+70 \text{ }^\circ\text{C}$ and the static and dynamic coefficients of friction are assessed at the velocity of 0.4 mm/s. Phase 2 is performed at $21 \text{ }^\circ\text{C}$ and at the velocity of 2 mm/s over a total sliding distance of 1000 m. The aim of this phase is to wear the sliding surfaces of the pad and the stainless steel sheet. Then, in phase 3 the coefficient of friction is assessed again at the various temperatures.

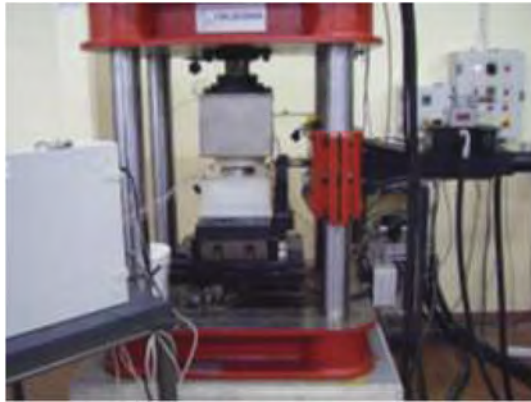


Figure 1. Testing machine for small-scale friction tests.

Table 1. Long term friction test program.

Phase Number	1	2	3
pressure on sliding material pad	45 MPa	45 MPa	45 MPa
temperature	-35 ... +70 °C	+21 °C	-35 ... +70 °C
velocity	$0.4_0^{+0.5}$ mm/s	2 ($\pm 0,1$)	$0.4_0^{+0.5}$ mm/s
distance (per phase)	30 m	1000 m	30 m

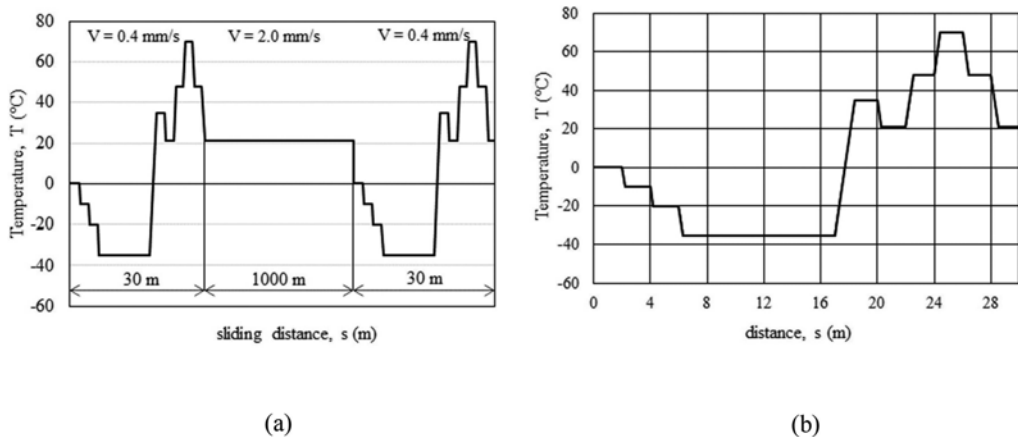


Figure 2. (a) Temperature profile vs. accumulated sliding distance in the long term friction test; (b) detail of temperature profile in phases 1 and 3.

2.2 Full-scale tests

Full-scale tests were performed at the ESQUAKE Seismic Isolator Test Laboratory of Eskişehir Technical University on a double concave friction pendulum (DCFP).

The specimen consists of a convex slider between two concave plates as shown in Figure 3(a), having two curved sliding surfaces with radius of curvature of 1800 mm each. Figure 3(b) shows the tested DCFP and its main dimensions. The equivalent radius of curvature is 2500 mm and the displacement capacity is 300 mm in any direction.

The test set-up is represented in Figure 4. The system is capable of applying force and displacement controlled dynamic motions in both horizontal and vertical directions. The maximum loading capacities are 2000 kN and 20000 kN in horizontal and vertical

directions, respectively. In the horizontal direction, the maximum stroke is ± 600 mm and the maximum loading velocity is 1000 mm/s.

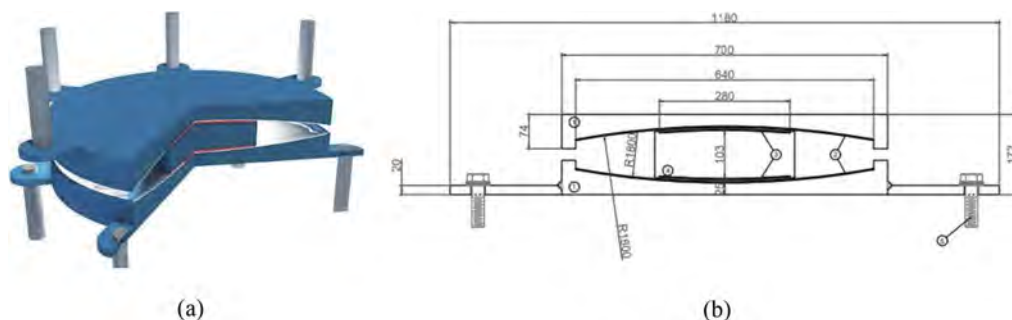


Figure 3. (a) Picture of the tested DCFP, (b) geometrical properties (dimensions in mm).

The DCFP is subjected to cyclic displacements with amplitude of 70 mm. The imposed velocity is 5 mm/s and the accumulated sliding distance was 1000 m. The vertical force applied to the DCFP is 3500 kN corresponding to an average normal stress on the sliding pads of 57 MPa. The test program is composed of 20 phases of 50 m each, with a dwell period of at least 40 minutes between two consecutive phases. After accumulated distances of 250, 500, 750 and 1000 m the DCFP is subjected to scaled down displacement histories of the strong motion component of Kocaeli Yarimca record (Figure 5), scaled by factors of 0.2, 0.3, 0.4 and 0.5 which correspond to maximum displacements of 100, 150, 200 and 250 mm, respectively. The displacement histories are applied to the DCFP in order of increasing amplitude with a 15 minutes of dwell time between two consecutive tests.

The ambient temperature at the laboratory was 21.3 °C at the beginning of the cyclic motion and varied between 21.1 °C and 27.1 °C throughout the whole test.

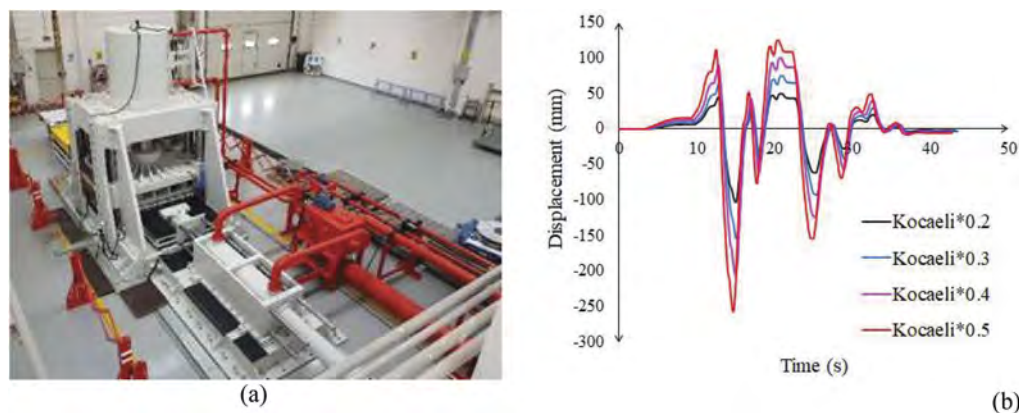


Figure 4. (a) Seismic isolator test set-up at ESQUAKE Seismic Isolator Test Laboratory; (b) displacement histories applied to simulate the seismic loading on the DCFP.

3 RESULTS

3.1 Small-scale tests

Figure 5 reports the maximum values of the static and dynamic low-velocity coefficient of friction at the relevant test temperatures, labelled as $\mu_{st}(T)$ and $\mu_{dyn}(T)$ respectively, measured in small-scale tests at the beginning of the test and after an accumulated sliding distance of 1000 m.

The coefficient of friction of the virgin material is about 7% at $T = +21^{\circ}\text{C}$, and undergoes significant variations with temperature changes: $\mu_{st}(T)$ and $\mu_{dyn}(T)$ vary from 2.1% at $T = +70^{\circ}\text{C}$ to about 16% at $T = -35^{\circ}\text{C}$. The rate of the friction coefficient vs. temperature has a steep increase below 0°C , switching from $0.073\% \text{ }^{\circ}\text{C}^{-1}$ in the range between 0°C and $+70^{\circ}\text{C}$, to $0.287\% \text{ }^{\circ}\text{C}^{-1}$ in the range between 0°C and -35°C . On the other hand, the sliding distance has a weak effect on the low-velocity coefficient of friction, which exhibits just a small growth at the end of the 1000 m path in comparison to the values assessed at the beginning of the test: the increase is less than 0.5% at every temperature but for 0°C where the variation is about +1.2%.

It is also worth noting that at each temperature the values of $\mu_{st}(T)$ and $\mu_{dyn}(T)$ are very close to each other. This behavior, which is possibly due to the fillers embedded in the sliding material, prevents the occurrence of the sticking phenomenon that affects the performance of CSS isolators characterized by a high ratio of static to dynamic friction coefficient in case of weak or moderate ground motions (Gandelli et al 2020; Gandelli & Quaglini 2020; Gandelli et al. 2019).

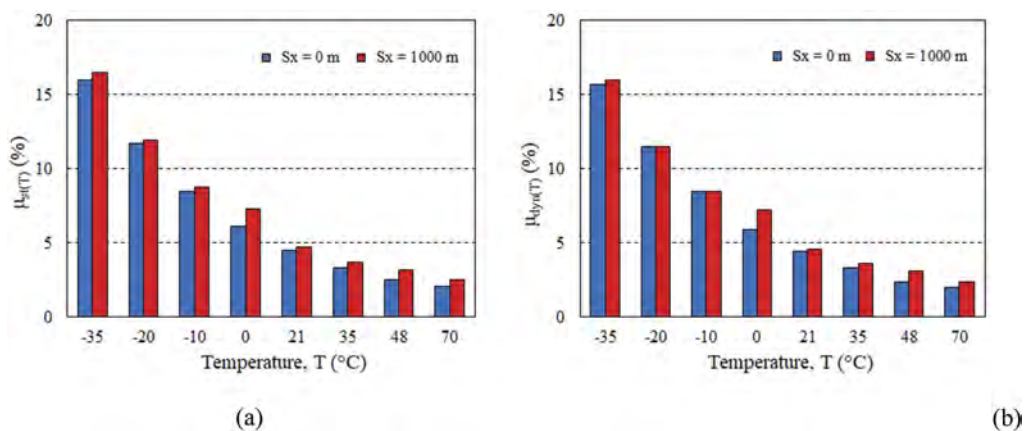


Figure 5. Coefficients of friction assessed in small-scale tests on the virgin specimen ($S_x = 0\text{ m}$) and after the accumulated sliding distance of 1000 m ($S_x = 1000\text{ m}$) at various temperatures: (a) static coefficient of friction, (b) dynamic coefficient of friction.

3.2 Full-scale tests

Figure 6 shows the coefficient of friction μ of the DCFP against the accumulated sliding distance observed in the full-scale test at 5 mm/s. In each test phase (of 50 m sliding distance), the coefficient of friction gradually decreases as the travelled distance increases, tending to a steady value at the end of the phase. On the other hand, at the very beginning of each phase, the friction coefficient shows a larger value than the one recorded at the end of the previous phase. The behavior is ascribed to two mechanisms: the heating of the sliding surfaces during sustained motion promotes a decrease in μ , while the cooling down of the sliding surfaces during the dwell time between two consecutive phases promotes the contrary effect (Quaglini et al. 2014, Cavdar & Ozdemir 2021, Cavdar et al. 2022). Considering the maximum value of μ (which must be considered for calculating the design force for the sizing of the anchorages of the isolator and of the adjacent elements), the low-velocity coefficient of friction of the DCFP decreases from 5.4% at 0 m to 4.8% after 1000 m, and achieves a peak of 5.6% at a distance of 600 m.

Eventually Figure 8 reports the increase in the maximum isolator force measured during the earthquake simulations performed at various sliding distances, normalized to the maximum isolator force at the beginning of the test. As a general trend, the isolator force

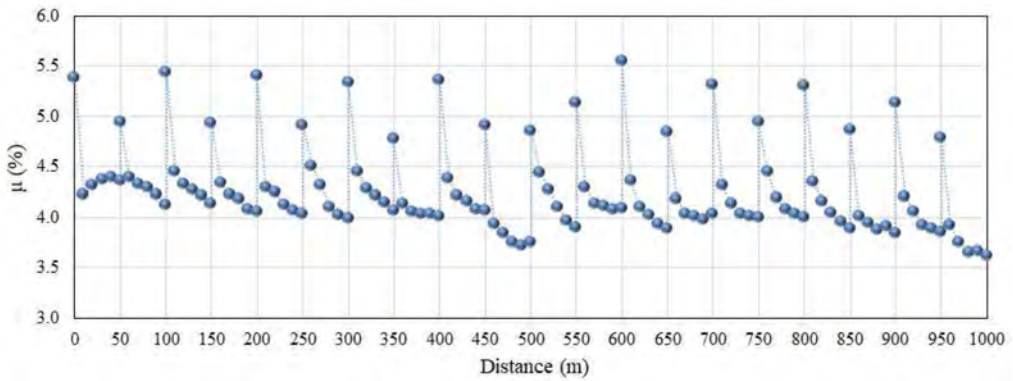


Figure 6. Coefficient of friction of DCFP at $v = 5 \text{ mm/s}$.

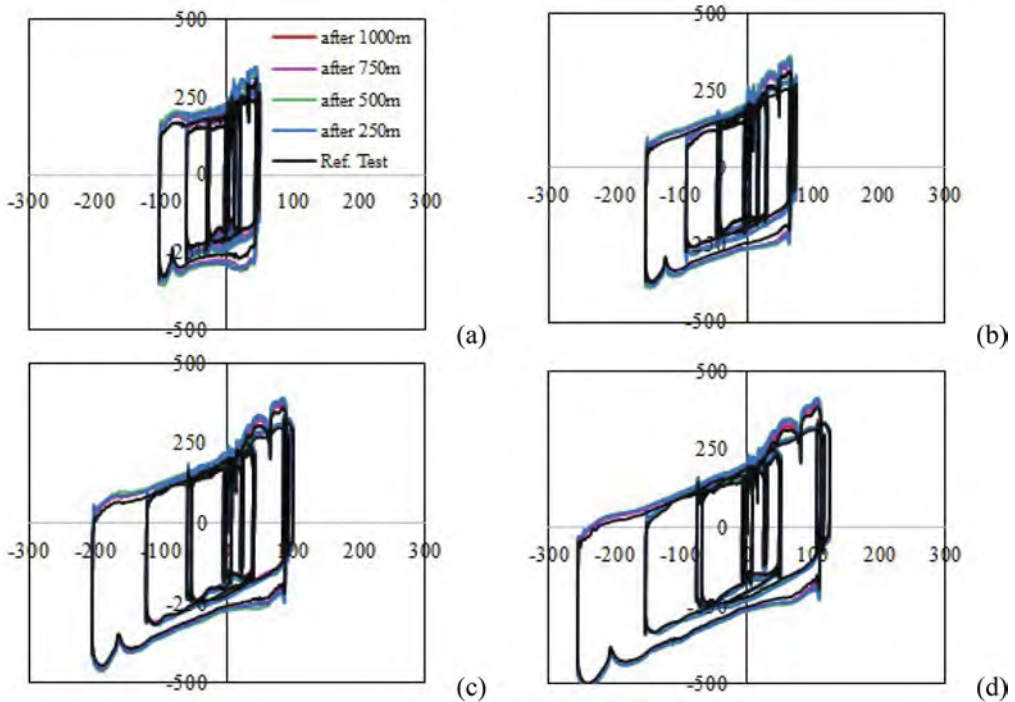


Figure 7. Force-displacement curves of DCFP obtained from ground motion excitations using modified displacement histories of Kocaeli Yarımca record by scale factors of: (a) 0.2, (b) 0.3, (c) 0.4 and (d) 0.5.

increases up to a distance of 500 m, and then it decreases as the travelled distance has a further increase. Only under the maximum amplification of the displacement history (by a 0.5 scale factor) the maximum increase is observed at 250 m, followed by a steady decrease at longer paths. In general, the stronger the seismic excitation, the lower is the effect of the sliding distance. However, it must be underlined that considering a different displacement history (i.e. with large number of cycles having large amplitude or with large number of small-amplitude cycles prior to large amplitude motion) in the tests of DCFP may lead to different results, as such a variation in the loading may affect the heating of the sliding interface and the corresponding hysteresis loops will be different from those presented in Figure 7.

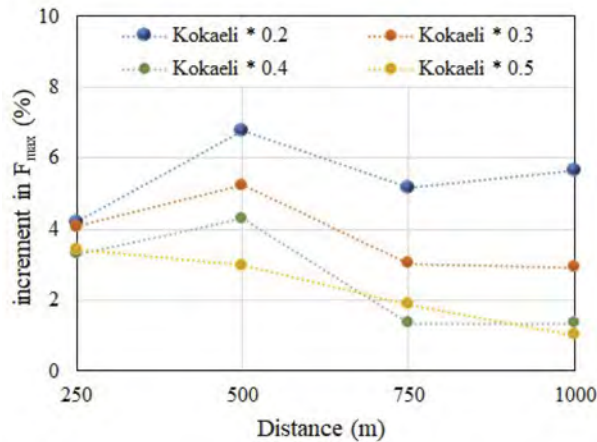


Figure 8. Increase of maximum force of DCFP under ground motion excitations.

4 CONCLUSIONS

According to current practice, small-scale tests on sliding material samples are aimed at estimating the coefficient of friction activated during service movements that generally occur at low velocity, in order to derive design values for non-seismic conditions. On the other hand, full scale tests are performed to assess the coefficient of friction at high speeds during seismic movements, relevant to earthquake conditions. In the present study, full-scale tests are performed to investigate the effect of the sliding distance both the low-velocity and high-velocity coefficients of friction of a real isolator, considering a sliding distance of 1000 m. Additionally, a sample of the sliding material is subjected to a long term friction test over the same distance in order to evaluate the consistency with large-scale results.

Both small- and large-scale tests show that, for the examined slider material, the effect of the accumulated sliding distance, and the associated wearing of the sliding surface, on the coefficient of friction at low velocity is small. Small-scale tests highlight an increase of both μ_{st} and μ_{dyn} less than 0.5% after 1000 m, and in particular at +21 °C μ_{st} increases from 4.5% to 4.7%. Large-scale tests show a slight decrease of the coefficient of friction μ of the DCFP; however the value $\mu = 4.8\%$ measured at 1000 m matches the equivalent coefficient of friction of the DCFP $\mu_{st} = 4.7\%$.

Force-displacement curves of the tested DCFP obtained for dynamic loadings, simulating different seismicity levels, provide the confirmation that accumulated sliding distance has a negligible effect also on the hysteresis loop and the friction behavior of DCFP under seismic loading.

To the knowledge of the Authors, this is the first experimental study investigating the effect of wear on the coefficient of friction of full scale sliding isolators. However, it must be emphasized that the results presented in the paper concern the particular sliding material examined in the study, and other sliding materials may undergo a different effect of wear. A proper investigation is therefore required before extrapolating the conclusions of this work to other materials.

ACKNOWLEDGEMENTS

The Authors gratefully acknowledge the support of TIS Technological Isolation Systems SA for providing the DCFP for the experimental campaign.

REFERENCES

- AASHTO. 2020. LRFD Bridge Design Specifications, 9th Edition. Washington: American Association of State Highway and Transportation Officials.
- ASCE/SEI 7. 2016. Minimum design loads for buildings and other structures. Reston: American Society of Civil 1801 Alexander Bell Drive, VA 20191.
- Barone, S., Calvi, G.M., Pavese A. 2019. Experimental dynamic response of spherical friction-based isolation devices. *Journal of Earthquake Engineering* 23(9):1465–1484, doi: 10.1080/13632469.2017.1387201
- Calvi P.M. & Calvi. G.M. 2018. Historical development of friction-based seismic isolation systems. *Soil Dynamics and Earthquake Engineering* 106: 14–30, doi: 10.1016/j.soildyn.2017.12.003
- Cavdar E., & Ozdemir. G., 2021. Investigation on both experimental and analytical response of a double friction pendulum. In: *Proc. 6th International Conference on Earthquake Engineering and Seismology (6ICEES), Gebze, 13-15 October*.
- Cavdar E., Ozdemir. G., Ozcamur U., 2022. Experimental investigation on hysteretic behavior of a Double Friction Pendulum and frictional heating. In: *Proc. 17th World Conference on Seismic Isolation, Energy Dissipation and Active Vibration Control of Structures (17WCSI), Turin, 11-16 September*. CEN EN 15129. 2009. Anti-Seismic Devices. Brussels: European Committee for Standardization.
- Gandelli E., De Domenico, D., Dubini, P., Bruschi, E., Quaglini, V. 2020. Influence of the breakaway friction on the seismic response of buildings isolated with curved surface sliders: Parametric study and design recommendations. *Structures* 27: 788–812, doi: 10.1016/j.istruc.2020.06.035.
- Gandelli, E., & Quaglini, V. 2020. Effect of the static coefficient of friction of curved surface sliders on the response of an isolated building. *Journal of Earthquake Engineering* 24(9): 1361–1389, doi: 10.1080/13632469.2018.1467353.
- Gandelli E., Penati, M., Quaglini, V., Lomiento, G., Miglio, E., Benzoni, G.M. 2019. A novel OpenSees element for single curved surface sliding isolators. *Soil Dynamics and Earthquake Engineering* 119: 433–453, doi: 10.1016/j.soildyn.2018.01.044.
- Quaglini V. 2012. High damping curved surface sliding isolators for bridges. In: *Bridge Maintenance, Safety, Management, Resilience and Sustainability; Proc. 6th International Conference on Bridge Maintenance, Safety and Management (IABMAS 2012), Stresa, 8-12 July*: 3685–3692. Rotterdam: Balkema.
- Quaglini V., Dubini, P., Poggi, C. 2012. Experimental assessment of sliding materials for seismic isolation systems. *Bulletin of Earthquake Engineering* 10(2): 717–740, doi: 10.1007/s10518-011-9308-9.
- Quaglini V., Bocciarelli, M., Gandelli, E., Dubini, P. 2014. Numerical assessment of frictional heating in sliding bearings for seismic isolation. *Journal of Earthquake Engineering* 18(8): 1198–1216, <http://10.1080/13632469.2014.924890>.
- Quaglini V., Gandelli, E., Dubini, P. 2017a. Experimental investigation of the re-centring capability of curved surface sliders. *Structural Control and Health Monitoring* 24 (2):e1870, <http://10.1002/stc.1870>.
- Quaglini V., Gandelli, E., Dubini, P. 2017b. Effect of friction on the re-centring capability of sliding bearings with curved surfaces. In: *Proc. 7th International Conference on Advances in Experimental Structural Engineering (AESE 2017), Pavia, 6-8 September*.
- Samyn, P., De Baets, P., Schoukens, G., Van Peteghem, A. P. 2006. Large-scale tests on friction and wear of engineering polymers for material selection in highly loaded sliding systems. *Materials & Design* 27: 535–555, doi: 10.1016/j.matdes.2004.12.021.
- Zayas, V. A., Low, S.S., Mahin, S. A. 1987. The FPS earthquake protection system: experimental report. Berkeley: Report No. UCB/EERC-87/01, Earthquake Engineering Research Center, University of California.
- Zayas, V. A., Low, S.S., Mahin, S. A. 1990. A simple pendulum technique for achieving seismic isolation. *Earthquake Spectra* 6: 317–333, doi: 10.1193/1.1585573.

Effects of rubber shear modulus variability on the seismic response of isolated bridges

M. Marra & S. Silvestri

University of Bologna, Bologna, Italy

ABSTRACT: The mechanical behavior of bridge decks equipped with High Damping Rubber Bearings is strongly affected by the rubber shear modulus that governs their lateral stiffness. It is a random variable, which can be described by a normal distribution.

In this paper, the effects of the variability of the shear modulus are investigated in terms of displacements for both the isolators and the piers, with reference to a case-study RC bridge with continuous caisson deck over four spans. The bridge is modelled with minimal systems with a reduced number of degrees of freedom along the longitudinal and transversal directions. Linear time-history analyses have been carried out using 7 natural seismic records, by considering 10,000 samples for the shear modulus fitting the chosen distribution. A statistical analysis has been then developed on the numerical results in order to obtain percentile values. Finally, Upper and Lower Bounds are identified for design purposes.

1 INTRODUCTION

The dynamic and seismic behaviour of bridges is governed by the connection system (“bearings layout”) between the superstructure (deck) and the substructures (piers and abutments). Among all possible traditional and innovative solutions (Tubaldi et al. 2015, Silvestri et al. 2019), nowadays the seismic isolation (Naeim & Kelly 1999, Franchin et al. 2001) of the bridge deck with respect to the substructures is widely used for both the seismic design of new bridges and the seismic retrofit of existing ones. Even though in the last years the adoption of Curved Surface Sliders is fast increasing (Furinghetti 2022), High Damping Rubber Bearings (HDRBs) still represent a viable choice (De Luca & Guidi 2019). Design of HDRB isolation system is typically conducted by practitioners assuming a deterministic value of the shear modulus of the rubber material of the HDRB devices (Furinghetti 2022). However, it is a random variable with a non-negligible coefficient of variation, that can be reasonably described by a Gaussian distribution, as highlighted by the analysis of the results of several experimental campaigns carried out for commercial orders at various laboratories (Furinghetti & Pavese 2019). The objective of this paper is to investigate the effects, in terms of displacements, of the variability of the shear modulus of the rubber material of HDRBs and to eventually provide coefficients, to be applied to the displacement response parameter values obtained using the mean value of the shear modulus, for the estimation of Upper and Lower Bound coefficients, for design purposes.

2 THE CASE-STUDY BRIDGE

The considered bridge is characterised by a continuous deck over four equal spans, for a total length $L = 180$ m. The three piers are characterised by different heights, equal to 8 m, 20 m and 10 m (Figure 1). The configuration is thus symmetric with reference to the longitudinal direction, while it is slightly eccentric with reference to the transversal direction. The RC caisson deck is 11.50 m wide and 0.50 m thick (Figure 2a), whilst the RC piers have a squared cellular cross-section with side length equal to 1.75 m and thickness equal to 0.30 m (Figure 2b). On the

top of the piers there are RC prismatic transversal elements with a rectangular cross-section of 2.00 m x 1.90 m and a length of 6.40 m, which provide the support base for the isolators. There are two isolators for each pier and for the two abutments, for a total number of ten isolators. Concrete class is C40/50. The bridge is supposed to be located in L'Aquila, Italy. The weight of the RC structural elements is 37723 kN, whilst the weight of the non structural elements (slope screed and bituminous layers, such as waterproofing, binder and wear layer) is 10624 kN. Consequently, the total dead load of the bridge is 48347 kN.

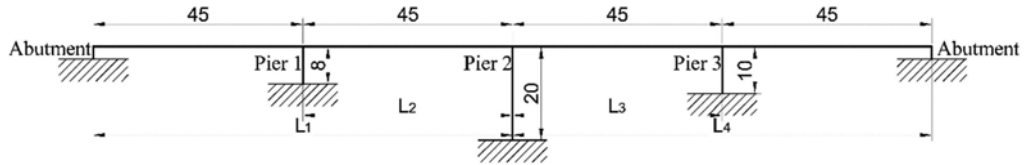


Figure 1. Schematised longitudinal view of the case-study bridge.

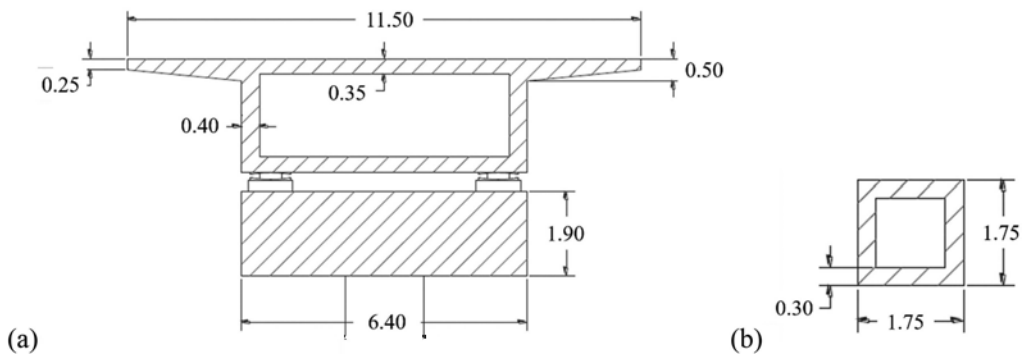


Figure 2. (a) Cross-section of the RC cassoin deck and pier top. (b) Cross-section of the three RC piers.

3 MODELLING OF THE ISOLATED BRIDGE

Different models are possible for the isolated bridge depending on the objective of the analysis: (i) a Single-Degree-Of-Freedom (SDOF) idealisation, representing the deck mass connected through the lateral stiffness of the isolation system to the substructures (assumed as fixed); (ii) minimal systems, that describe the behaviour of the deck and the piers by means of a reduced number of degrees of freedom (Silvestri et al. 2019); (iii) Finite Element models, that describe the bridge behaviour by means of several nodes and beam and/or shell elements.

The first one is usually sufficient for the dimensioning of the isolation system. The second one allows to perform time-history analyses with lower computational effort than the third one.

In the minimal systems, the masses that define the degrees of freedom in the equations of motion are the mass of the deck and the masses of each half pier (the remaining parts are assumed to be directly transferred to the ground base). Figure 3 shows the minimal systems used for the evaluation of the seismic response of the bridge along the two directions (u referring to longitudinal displacements; v referring to transversal displacements):

- along the (symmetric) longitudinal direction, the minimal system is composed of four degrees of freedom: the displacement of the deck (u_{deck}) and the three displacements of the top of the piers (u_{pier1} , u_{pier2} , u_{pier3});
- along the (slightly eccentric) transversal direction, the minimal system is composed of five degrees of freedom: the displacement of the deck (v_{deck}), the three displacements of the top of the piers (v_{pier1} , v_{pier2} , v_{pier3}), and the in-plane rotation of the deck (φ_{deck}).

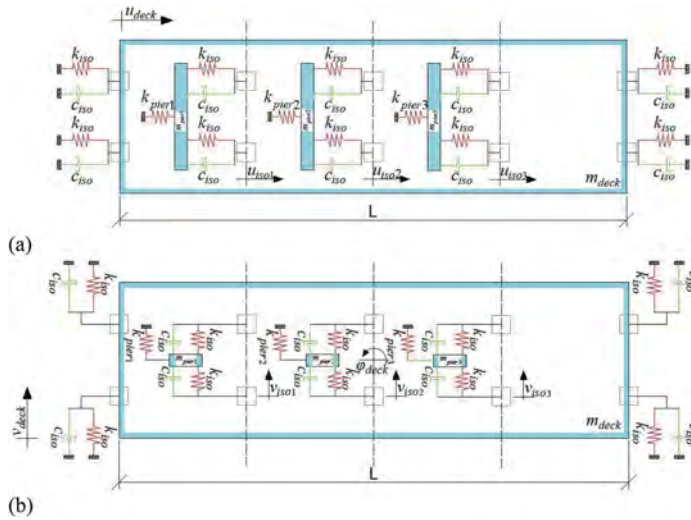


Figure 3. Minimal systems: (a) along the longitudinal direction and (b) along the transversal direction.

4 SEISMIC INPUT

The pseudo-acceleration elastic response spectrum of the horizontal component of the earthquake input is reported in Figure 4. Peak ground acceleration is equal to 0.459g. The maximum (plateau) spectral acceleration is equal to 1.103g. To perform time-history analyses seven natural earthquakes have been chosen in such a way as to result compatible with the 5% damped elastic spectrum.

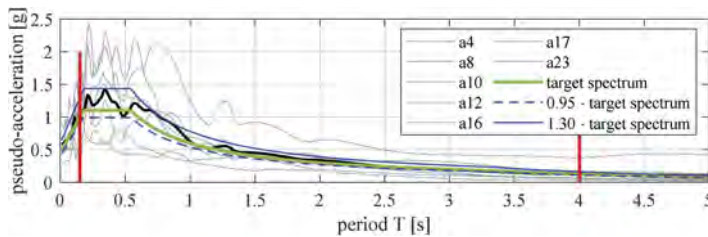


Figure 4. Horizontal elastic spectrum and spectra of the seven natural seismic records.

5 PROCEDURE ADOPTED FOR THE IDENTIFICATION OF THE HDRB ISOLATORS

The isolation system (to be placed between the deck and the substructures) has been pre-identified according to a simplified procedure based on the SDOF idealization, in which the degree of freedom is represented by the horizontal displacement of the deck. The SDOF model consists of the mass of the deck (m_{deck}) concentrated at the deck level. The stiffness ($k_{iso,tot}$) and the damping coefficient ($c_{iso,tot}$) are provided by the isolation system, which is made of ten devices. Since they work in a parallel system, the values of the stiffness and the damping coefficient of the equivalent SDOF model are given by the sum of the stiffness values and the damping coefficient values of the ten isolators, respectively.

The simplified procedure is based on the following hypotheses: (i) the deck is rigid in both horizontal (longitudinal and transversal) directions, (ii) the piers are rigid in the vertical (axial) direction, (iii) the target lateral deformation γ_{iso} of the isolator is imposed to be equal to the height h_{iso} of the isolator itself (i.e. shear deformation $\gamma_{iso} = d_{iso}/h_{iso}$ equal to 100%, where d_{iso} is the displacement of the isolator), (iv) the shear modulus of the rubber material that governs the lateral stiffness of the isolator is assumed in the range 0.7-1.0 MPa (this corresponds to a normal rubber and

to a damping ratio ζ_{iso} of the isolation system around 10%), (v) the total damping coefficient provided by the isolation system is evaluated as: $c_{iso,tot} = 2 \cdot m_{deck} \cdot \omega_{iso} \cdot \zeta_{iso}$ (where ω_{iso} is the fundamental circular frequency of the isolated bridge and ζ_{iso} is the damping ratio), (vi) the isolators have radial symmetry (i.e. the procedure keeps its validity along the two horizontal directions). The procedure is summarized in the following steps:

1. Choice of the target period T_{iso} for the isolated bridge, typically in the range 2.5-3.5 s.
2. Evaluation of the spectral acceleration corresponding to the target period: $S_a(T_{iso})$. Note that it has to be evaluated on the 10%-damped elastic spectrum since an isolation system usually provides a damping ratio ζ_{iso} of around 10%.
3. Evaluation of the spectral displacement:

$$S_d(T_{iso}) = S_a(T_{iso}) / \omega_{iso}^2 = S_a(T_{iso}) \cdot (T_{iso} / 2\pi)^2 \quad (1)$$

Then, assuming that $\gamma_{iso} = d_{iso} / h_{iso} = 100\%$ leads to:

$$h_{iso} = d_{iso} = S_d(T_{iso}) \quad (2)$$

4. Choice of the diameter of the isolators in order to avoid instability phenomena. The ratio between diameter D_{iso} and height h_{iso} should be larger than 2.0 (Furinghetti & Pavese 2019, Furinghetti 2022). Therefore a typical relationship is:

$$D_{iso} = 2.5 \cdot h_{iso} \quad (3)$$

5. Calculation of the lateral stiffness of each single isolator k_{iso} , assuming that all isolators are equal to each other:

$$k_{iso} = \frac{m_{deck} \cdot \omega_{iso}^2}{n_{iso}} \quad (4)$$

where n_{iso} is the total number of isolators.

6. Check that the shear modulus G falls within the assumed range (0.7-1.0 MPa):

$$G = \frac{4 \cdot k_{iso} \cdot \chi_V \cdot h_{iso}}{\pi \cdot D_{iso}^2} \quad (5)$$

where χ_V represents the shear shape factor.

If the hypothesis is not satisfied, then G is taken equal to 1.0 MPa and the diameter of the isolator is calculated as:

$$D_{iso} = 2 \cdot \sqrt{\frac{k_{iso} \cdot \chi_V \cdot h_{iso}}{\pi \cdot G(=1\text{MPa})}} \quad (6)$$

7. Check that the isolator shear displacement roughly respects the assumption $\gamma_{iso} = d_{iso} / h_{iso} = 100\%$ (made in Step 3).
8. Evaluation of the maximum vertical axial force on the isolators. They have to carry out the function of support during the entire life of the bridge both in static conditions, with reference to the Ultimate Limit State (ULS), and in seismic conditions, with reference to the Collapse Limit State (CLS). The axial force can be evaluated either according to tributary areas afferent to each isolator or by means of a numerical model.
9. Check that the isolators satisfy the two conditions: in terms of target lateral stiffness k_{iso} (Steps 1-7) and in terms of axial force capacity (Step 8). If this latter is not satisfied, then the geometric characteristics of the isolators should be updated.

The procedure has been applied to the case-study bridge. The following data have been adopted: the elastic spectrum represented in Figure 4 reduced to account for a damping ratio of 10%, $m_{deck} = 4717$ t, $T_{iso} = 3.25$ s, $n_{iso} = 10$. The following outcomes have been obtained: $h_{iso} = 420$ mm, $D_{iso} = 1040$ mm, $k_{iso} = 1.756$ kN/mm, $G = 0.94$ MPa, $c_{iso} = 167$ kN m/s. However, the isolator obtained following Steps 1-7 does not satisfy the axial force capacity condition (Step 8). Therefore, the geometric characteristics have been slightly changed to meet this condition (the height has been reduced). The following final properties for each single isolator have been thus identified: $h_{iso} = 326$ mm, $D_{iso} =$

1000 mm, $k_{iso} = 2.99$ kN/mm, $G = 0.8$ MPa, $c_{iso} = 202$ kN m/s, leading to $T_{iso} = 2.50$ s for the SDOF idealisation, to $T_{iso} = 2.78$ s for the minimal system along the longitudinal direction (roughly including the flexibility of the three piers), and to $T_{iso} = 2.92$ s for the more refined FE model (also including the flexibility of the deck and a better representation of the piers behaviour).

6 ANALYSES PERFORMED

The effects of the aleatory variability in the shear modulus G of the rubber material of the HDRB isolators have been investigated by means of time-history dynamic analyses carried out using the minimal systems detailed in Section 3 and the seven seismic records described in Section 4. The isolators identified in Section 5 are constituted by rubber layers with mean shear modulus G equal to 0.8 MPa and equivalent viscous damping ratio of around 10%. Consequently, G is assumed as a random variable characterized by a normal distribution with mean value equal to 0.8 MPa and coefficient of variation equal to 14.5% (as per the results of experimental campaigns carried out for commercial orders at various laboratories, see Furinghetti & Pavese 2019). The following assumptions have been made:

- The shear modulus is the parameter that mainly governs the mechanical behaviour of the isolator device.
- A linear relationship is assumed between the rubber shear modulus G and the horizontal stiffness k_{iso} of the isolator device:

$$G = \left(\frac{4 \cdot \chi_V \cdot h_{iso}}{\pi \cdot D_{iso}^2} \right) \cdot k_{iso} \quad (7)$$

where the geometric parameters of the isolator have been considered as deterministic.

- The variability of the shear modulus has been taken into account by acting directly on the mean horizontal stiffness of the isolator device ($k_{iso,mean} = 2.99$ kN/mm corresponding to a mean shear modulus equal to 0.8 MPa) by means of an adimensional factor g , for which a normal distribution has been assumed:

$$k_{iso} = g \cdot k_{iso,mean} \quad (8)$$

$$g = N(\mu = 1, \sigma = \text{cov} = 0.145) \quad (9)$$

- A number of 10,000 realizations of the normal random variable corresponding to multiplication factor g have been randomly generated and seven time-history simulations have been carried out (with the seven seismic records) for each realisation.
- The damping coefficient of the isolator devices has been updated for each realisation adopting the equivalent SDOF model and assuming a damping ratio equal to $\xi_{iso} = 10\%$:

$$c_{iso} = \frac{2 \cdot \xi_{iso} \cdot \omega_{iso} \cdot m_{deck}}{n_{iso}} \quad (10)$$

- The same damping coefficient c_{iso} has been assumed in both longitudinal and transversal directions.

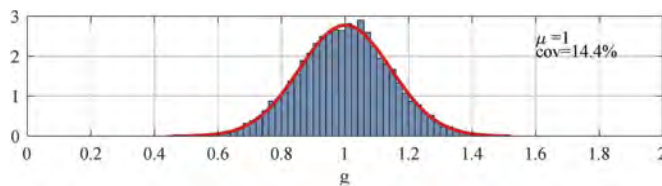


Figure 5. Histogram of the relative frequencies of the sample of the 10,000 realizations of factor g .

Figure 5 shows the histogram of the relative frequencies of the sample of the randomly generated 10,000 realizations, which have mean value equal to 1 and coefficient of variation equal to 14.4% (compared to the 14.5% target).

To sum up, a total number of 140,000 numerical simulations have been performed:

- 70,000 analyses along the longitudinal direction, conducted on 10,000 minimal models with 4 DOFs assuming the 7 natural accelerograms as input.
- 70,000 analyses along the transversal direction, conducted on 10,000 minimal models with 5 DOFs assuming the 7 natural accelerograms as input.

7 RESULTS OBTAINED

The results are expressed in terms of *mean displacement* of each degree of freedom of the two minimal systems along the two directions. For each direction, it is evaluated as the mean of the seven maximum values of the displacement obtained during the seven accelerograms. With reference to the nomenclature introduced in Figure 3, the attention has been paid on the following displacements:

- $u_{isoAB} = u_{deck}$ and $v_{isoAB} = v_{deck}$ are the displacements sustained by the isolators on the abutments that coincide with the displacements of the deck with respect to the abutment;
- $u_{iso1} = u_{deck} - u_{pier1}$ and $v_{iso1} = v_{deck} - v_{pier1}$ are the longitudinal and transversal displacements sustained by the isolators on pier 1 that coincide with the relative displacements of the deck with respect to the top of pier 1;
- $u_{iso2} = u_{deck} - u_{pier2}$ and $v_{iso2} = v_{deck} - v_{pier2}$ are the displacements sustained by the isolators on pier 2;
- $u_{iso3} = u_{deck} - u_{pier3}$ and $v_{iso3} = v_{deck} - v_{pier3}$ are the displacements sustained by the isolators on pier 3.

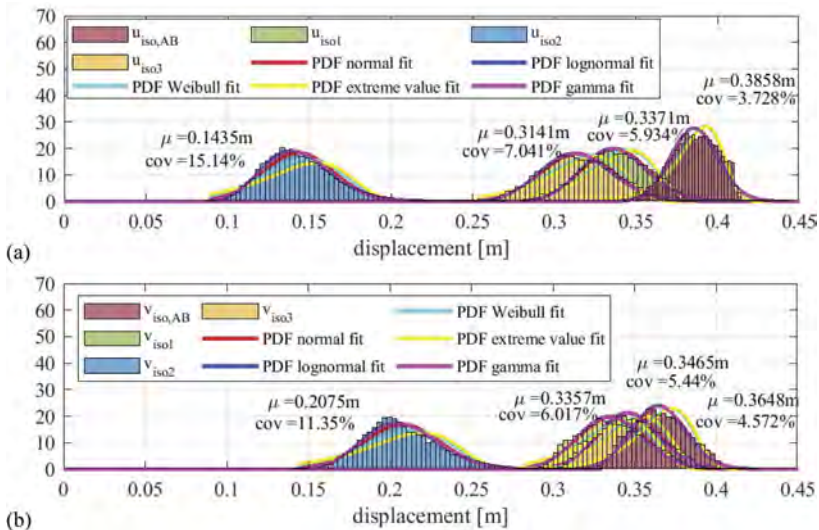


Figure 6. Results in terms of isolators displacements: (a) longitudinal direction, (b) transversal direction.

For each one of the above-mentioned displacements, a set of 10,000 *mean displacement* values (mean of the seven maximum values obtained for the seven accelerograms) are obtained. Each set is considered as a sample of a random variable whose distribution is unknown and has to be identified. A fitting has been then performed of the relative frequency histogram of each set of 10,000 values of the above-mentioned displacements with the Probability Density Function that better represents the set itself. The best fitting has been conducted by considering four well-known Probability Density Functions (PDFs): (i) Normal, (ii) LogNormal, (iii) Weibull, (iv) Extreme Values and (v) Gamma (Ang & Tang 2007). Figures 6a and b show an example of the results obtained in terms of isolators displacements, for the longitudinal and transversal directions, respectively. The

best fit has been evaluated by means of two statistical tests: (i) the Chi-Square test and (ii) the Kolmogorov-Smirnov test (Ang & Tang 2007).

On the basis of the results of the numerical simulations (or through their best fits), also the percentile values associated with selected percentages can be obtained. Then, from the values of the percentiles, it is possible to calculate the coefficients that allow considering the variability of the rubber shear modulus on the structural response of the bridge. These coefficients can be applied to the displacements of the isolators obtained considering the mean value of the rubber shear modulus. In fact, as it can be seen from Figure 6, the coefficient of variation that characterizes the variability of the shear modulus does not keep unaltered in the variability of the response parameters, i.e. of the displacements of the deck, of the top of the piers, and of the isolator devices. Therefore, starting from the theoretical probability functions for each response parameter these coefficients can be calculated according to: $c_{x\%} = \delta_{x\%} / \delta_{G_{mean}}$, where $\delta_{x\%}$ indicates the percentile of the displacement response parameter characterized by a probability of non-exceedance equal to $x\%$, and therefore by a probability of being exceeded equal to $1-x\%$, and $\delta_{G_{mean}}$ is the corresponding response parameter obtained considering the design mean value of the shear modulus G_{mean} . In this respect, Table 1 reports those coefficients for all the displacements, both in the longitudinal and transversal directions.

Table 1. Coefficients for taking into account the variability of the rubber.

DOF		C _{1%} (Lower Bound)	C _{5%}	C _{16%}	C _{50%}	C _{84%}	C _{95%}	C _{99%} (Upper Bound)
Longitudinal direction	u_{deck}	0.9132	0.9386	0.9629	1	1.0371	1.0612	1.0866
	u_{pier1}	0.7674	0.8535	0.9231	1.011	1.0769	1.1117	1.1447
	u_{pier2}	0.9413	0.9652	0.983	1.0032	1.0174	1.0247	1.0312
	u_{pier3}	0.8061	0.8793	0.9378	1.0098	1.0634	1.0915	1.1171
	u_{isoAB}	0.9132	0.9386	0.9629	1	1.0371	1.0612	1.0866
	u_{iso1}	0.8621	0.9024	0.941	1	1.059	1.0976	1.1379
	u_{iso2}	0.699	0.7735	0.853	0.9889	1.147	1.2641	1.3993
	u_{iso3}	0.8364	0.8841	0.93	1	1.07	1.1159	1.164
Transversal direction	v_{deck}	0.8936	0.9268	0.9556	1	1.0463	1.0776	1.1064
	v_{pier1}	0.758	0.8493	0.9224	1.0137	1.0822	1.1233	1.1553
	v_{pier2}	0.9098	0.9358	0.9612	1	1.0388	1.0642	1.0909
	v_{pier3}	0.7633	0.8521	0.9231	1.0118	1.0799	1.1154	1.1479
	$\Delta v_{deck,max}$	0.717	0.8113	0.8868	1	1.1321	1.2264	1.3019
	v_{isoAB}	0.8936	0.9268	0.9556	1	1.0463	1.0776	1.1064
	v_{iso1}	0.8733	0.9105	0.9457	1	1.054	1.0837	1.1264
	v_{iso2}	0.7658	0.8265	0.8892	0.9937	1.1108	1.1947	1.2896
	v_{iso3}	0.868	0.9044	0.9404	0.9982	1.0599	1.1019	1.148

Starting from the values of these percentiles, for each structural element and for each isolator, the multiplicative coefficients have been calculated which, once applied to the result ($\delta_{G_{mean}}$) obtained assuming the mean design value of the rubber shear modulus, allow to immediately obtain the Upper Bound (here selected as the 99% percentile) and Lower Bound (1% percentile) values which take into account the variability of the rubber shear modulus: $\delta_{UpperBound} = c_{UB} \cdot \delta_{G_{mean}} = c_{99\%} \cdot \delta_{G_{mean}}$ and $\delta_{LowerBound} = c_{LB} \cdot \delta_{G_{mean}} = c_{1\%} \cdot \delta_{G_{mean}}$. Regarding the isolators displacements: (i) the Upper Bound coefficient increases as the flexibility of the underlying structural element (pile/abutment) increases; (ii) the Lower Bound coefficient decreases (and therefore deviates more and more from 1) as the flexibility of the structural element (pile/abutment) increases. Regarding the top piers displacements: (i) the Upper Bound coefficient decreases as the flexibility of the pile increases, with a trend qualitatively opposite to the coefficient for the displacement of the corresponding isolator; (ii) the Lower Bound coefficient increases (and therefore gets closer and closer to 1) as the flexibility of the pile increases, with a trend qualitatively opposite to the coefficient for the displacement of the corresponding isolator. It has been verified that, by applying a typical variability (cov = 14.5%) to the mechanical properties of the elastomeric

isolators (specifically: to the shear modulus of the rubber material), with linear dynamic analyses, a variability is obtained in the main displacement response parameters (underestimates/overestimations with respect to the results obtainable assuming the design mean values) no higher than 20% with reference to the 84th-percentile and no higher than 30% with reference to the 99th-percentile. This result is substantially in line with what is reported in the last sentence of paragraph 7.10.5.1 of the Italian code (NTC 2018).

8 CONCLUSIONS

A simplified procedure for the identification of HDRB isolators has been presented and applied to a RC bridge. The effects of the variability in the mechanical properties of the isolators (rubber shear modulus) on the structural behaviour of the isolated bridge emerged from several time-history analyses carried out on minimal models. They are characterized by few degrees of freedom, four in the longitudinal direction and five in the transversal one. The rubber shear modulus G is assumed as a random variable characterized by a normal distribution with mean value equal to 0.8 MPa and coefficient of variation equal to 14.5%. From 10,000 sets of numerical simulations (each one carried out with seven natural accelerograms) which are representative of the realizations of the random variable G , the best fitting of the probability functions of the mean values of the displacements (for both isolators and piers) have been performed. The analyses of the associated percentiles allow the definition of coefficients for taking into account the variability of the rubber, i.e. Upper and Lower bounds values.

ACKNOWLEDGEMENTS

Financial supports of Department of Civil Protection (DPC-RELUIS 2019–2021 and 2022-2024 Grants - Research line WP15: “Contributi normativi relativi a Isolamento e Dissipazione”) is gratefully acknowledged.

REFERENCES

- Ang, A.H-S. & Tang, W.H. 2007. *Probability Concepts in Engineering: Emphasis on Applications to Civil and Environmental Engineering*. 2nd Edition. New York, NY, U.S.A.: John Wiley & Sons, Inc.
- De Luca, A. & Guidi, L.G. 2019. State of art in the worldwide evolution of base isolation design. *Soil Dynamics and Earthquake Engineering* 125: 105722. <https://doi.org/10.1016/j.soildyn.2019.105722>.
- Franchin, P., Monti, G. & Pinto, P.E. 2001. On the accuracy of simplified methods for the analysis of isolated bridges. *Earthquake Engineering and Structural Dynamics* 30: 362–382. <https://doi.org/10.1002/eqe.12>
- Furinghetti M. & Pavese A. 2019. Numerical Parametric Study on Property Modification Factors of Isolation Devices. *Atti del XVIII Convegno ANIDIS 2019 - L'Ingegneria sismica in Italia*, Ascoli Piceno (Italy), 15-19 September 2019.
- Furinghetti, M. 2022. Definition and Validation of Fast Design Procedures for Seismic Isolation Systems. *Vibration* 5(2): 290–305. <https://doi.org/10.3390/vibration5020017>
- Naeim, F. & Kelly, J.M. 1999. *Design of seismic isolated structures: from theory to practice*. New York, NY, U.S.A.: John Wiley and Sons, Inc.
- NTC 2018. *Decreto Ministeriale del 17/ 01/2018: Norme Tecniche per le Costruzioni*. Roma, Italy: Ministero delle Infrastrutture.
- Silvestri, S, Palermo, M., Palma, P.M., Tangocci, F., Zampini, N., Tomaselli, F. 2019. Sistemi minimi per la progettazione sismica di ponti con diverse soluzioni per lo schema di vincolo. *Atti del XVIII Convegno ANIDIS 2019 - L'Ingegneria sismica in Italia*, Ascoli Piceno (Italy), 15-19 September 2019: 18–28.
- Tubaldi, E., Dall'Asta, A., Dezi, L. 2015. Seismic Response Analysis of Continuous Multispan Bridges with Partial Isolation. *Shock and Vibration*. Vol. 2015, Article ID 183756, 15 pages, 2015. <https://doi.org/10.1155/2015/183756>

Prediction of the response of a lead-core rubber bearing using machine learning

T. Zhelyazov

Technical University of Sofia, Sofia, Bulgaria

S. Ólafsson & R. Rupakhety

Earthquake Engineering Research Centre, University of Iceland, Selfoss, Iceland

ABSTRACT: Lead-core rubber bearing is a widely used device for seismic isolation. It remains a preferred option for important structures such as bridges, nuclear power plants, hospitals, etc., mainly due to its considerable energy dissipation capability. Accurate predictive models are a prerequisite for a safe and efficient design and thus prolong the life cycle of buildings and structures. A detailed finite element model generally provides insight into the complex behavior of the lead-core rubber bearing. However, being demanding computational resources, its implementation in the base-isolated structure analysis might not be appropriate. The contribution focuses on a more efficient model from a computational point of view – a neural network. Although the neural network doesn't use the physical model, the latter is employed to produce the target data. Some technological aspects of the multilayer perceptron are discussed, such as architecture, choice of the activation function, and training strategies.

1 INTRODUCTION

The contribution considers a machine learning algorithm designed to predict the response of Lead-Core Rubber Bearings (LCRB). Specifically, a multilayer perceptron model is implemented. Such a model generally comprises an input layer, several hidden layers, and an output layer. It operates on statistical data or a set of parameters considered crucial for the complex behavior of LCRB without explicitly formulating an underlying predictive model. The output obtained for each set of input features is compared with corresponding target values providing a basis to improve the model parameters (or to train the model) in order to minimize the divergence to the desired or targeted output. Typically, such a multilayer perceptron, in contrast to, for example, a finite element model, is less demanding in computational resources. The intensive computational process related to the final element simulation might hinder its application in the investigation of the LCRB response within a base-isolated structure.

For some time, LCRB devices have been a subject of research and have been successfully implemented as a base isolation of bridges and buildings. Some early examples are the Scamperdown Bridge (Park & Blakeley 1978) and the base isolation of the William Clayton Building (Megget 1978). Because of their considerable energy-dissipation capacity, they are a preferred option for base isolation of buildings and structures of primary societal importance, such as hospitals or nuclear power plants. Generally, the lead-core rubber bearing consists of (i) elastomeric layers separated by (ii) steel shims; (iii) a central plug (or plugs); (iv) top and bottom steel plates (Figure 1).

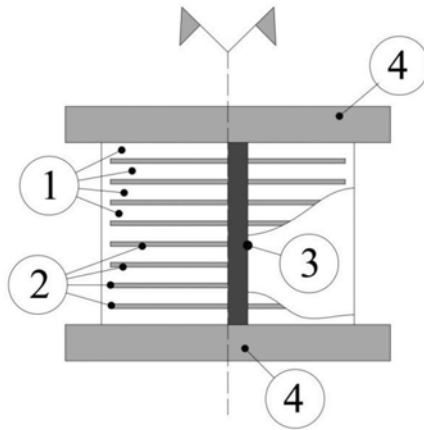


Figure 1. Lead-core bearing device: rubber layers (1); steel shims (2); central plug (3); steel plates (4).

The steel shims provide the isolator with the vertical stiffness needed to resist loads transferred from the superstructure. Under horizontal loads, for example, during an earthquake, lateral deformation of the elastomeric layers assures the decoupling of the superstructure from the ground. Also, the yielding of the central plug material due to the horizontal forces' action leads to more-pronounced hysteresis loops in the isolator's response, thus enhancing the energy dissipation capacity. Reportedly, the lead (in the lead plug) recovers its mechanical properties quickly when subjected to deformation, and due to the confinement provided by steel and rubber plates, the lead core deforms in pure shear (Skinner et al. 1980); among the LCRB features is also the re-centering capability (Robinson & Tucker 1977). Figure 2 schematizes the response of a lead-core bearing device.

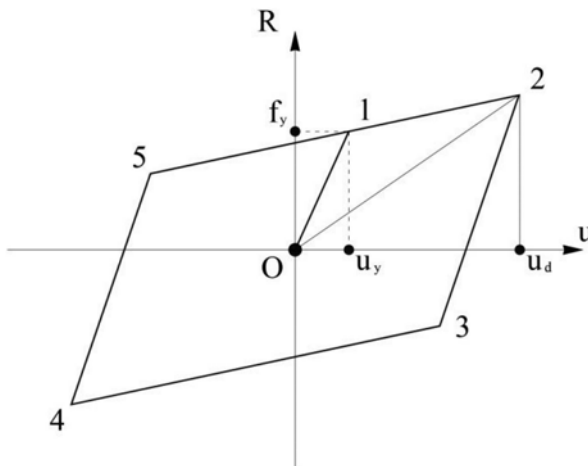


Figure 2. Idealized hysteresis response of a lead-core bearing device.

2 THE ARCHITECTURE OF THE MULTILAYER PERCEPTRON

A recurrent neural network has been instantiated. The network contains a few hidden layers of neurons equipped with the rectified linear unit activation function,

$$\eta(x) = \begin{cases} 0 & \text{if } x < 0 \\ x & \text{if } x \geq 0 \end{cases} \quad (1)$$

which provides for some argument x the nonlinear overall behavior of the machine. Figure 3 schematizes the feed-forward propagation in the multilayer perceptron (which is, in fact, recurrent).

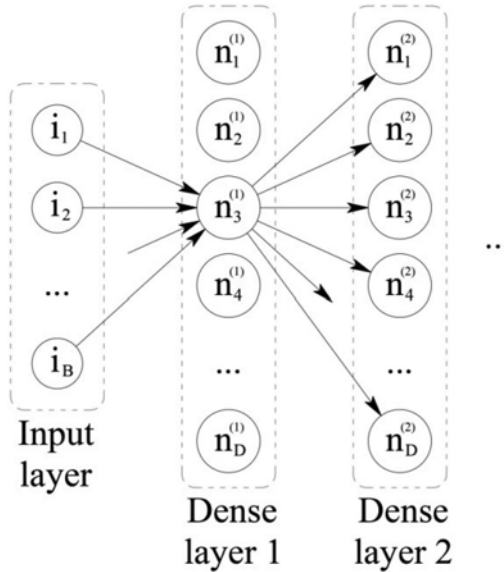


Figure 3. Schematized architecture of the neural network.

The figure visualizes the inputs that take a given neuron of the multilayer perceptron, as well as the connections of this neuron to the neurons of the next layer. The connections between the other neurons are not shown. It depicts the first or the input layer and the following two layers. The considered neuron is $n_3^{(1)}$; the subscript denotes the neuron's position in the layer, and the superscript is the layer number. This neuron takes inputs from all the neurons in the previous layer (the input) layer. The data that this neuron sends to all of the neurons in the subsequent layer (in the dense layer network, all of the neurons in a given layer are initially connected to all of the neurons in the following layer) is provided by the following relation

$$z_3^{(1)} = \eta \left(\left(W^{(1)} \right)^T I + b_3^{(1)} \right) \quad (2)$$

where $W^{(1)}$ denotes an array containing the weights of the connections providing data from the previous layer to that neuron, $W^{(1)} = (w_1^{(1)}, w_2^{(1)}, \dots, w_B^{(1)})$, B is the dimension of the input layer, T in the superscript denotes the transpose of this array considered as a matrix, and I stands for an array containing the data provided by the previous layer (the input layer), $I = (i_1, i_2, \dots, i_B)$; $b_3^{(1)}$ is the bias of the neuron; η is a function defined in Equation (1). In Figure 3, D denotes the length of the dense layers, as all layers are designed to be equal in size.

The loss function is identified with the mean squared error.

$$\psi = \frac{1}{N} \sum_{i=1}^N (y_i - \tilde{y}_i)^2 \quad (3)$$

where y_i and \tilde{y}_i are the target and output values, respectively, and N is the number of output values.

To generate the target sets, the Bouc-Wen model is employed, named after the authors of the first contributions to the topic (Bouc 1967, Wen 1976). As pointed out by Sivaselvan & Reinhorn (2000), for various combinations of the model parameters, it can be reduced to a rate-independent model (Ozdemir 1976) or a nonlinear elastic model (Menegotto & Pinto 1973). This approach has also been used by Constantinou and Tadjbakhsh (1985); its generalized version has been implemented by Song and Der Kiureghian (2006) with introduced shape parameters capable of simulating highly asymmetric hysteresis, and it is still employed in some recent studies (Shoaei et al. 2018).

$$R = \alpha \frac{f_y}{u_y} u(t) + (1 - \alpha) f_y z(t) \tag{4}$$

$$\frac{dz}{dt} = \frac{1}{u_y} \left[A \frac{du}{dt} - \gamma \left| \frac{du}{dt} \right| z(t) |z(t)|^{n-1} - \beta \frac{du}{dt} |z(t)|^n \right] \tag{5}$$

In Equation (4), R stands for the restoring force generated in the isolator, u – for the current displacement, α is the post-yielding to initial stiffness ratio, u_y and f_y are the yield displacement, and the yield shear force, respectively; $z(t)$ is the hysteresis variable defined in Equation (5). In Equation (5), the parameters γ and β control the size and the shape of the hysteresis loops, and n is responsible for the smoothness of the transition from elastic to post-elastic behavior. The material parameters needed for the constitutive relation, an elastic-perfectly plastic model, are taken from (Doudoumis et al. 2005), and, more precisely, the elasticity modulus of the lead core is set to $E=18e^6$ kN/m², the Poisson’s ratio - $\nu=0.43$, and the unidirectional yield stress - $f_y=19.5e^3$ kN/m².

The database is split into a training and a validation set. Figure 4 displays a typical sample of target data points obtained for a current combination of input parameters.

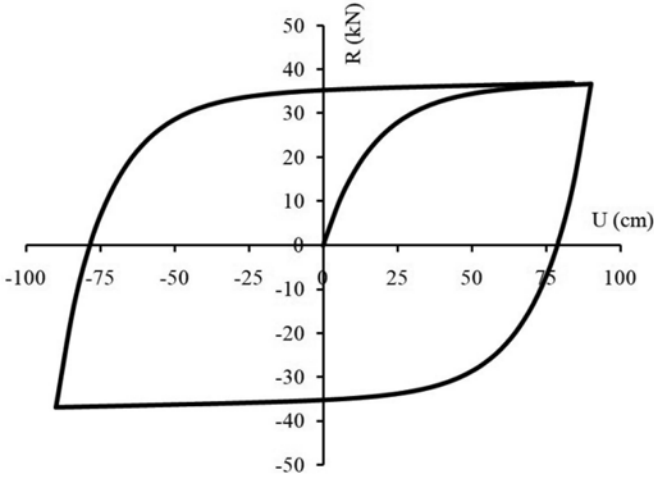


Figure 4. A typical displacement-restoring force relationship providing a target set of data points for a given set of input parameters.

To obtain the restoring force-displacement relationship (Figure 4), the Bouc-Wen model described by Equations (4)–(5) is used. By assumption, the bottom face of the bearing is fixed, while uniaxial displacements are applied to the top surface. Figure 5 provides a simplified image of the synthetic design space of the perceptron.

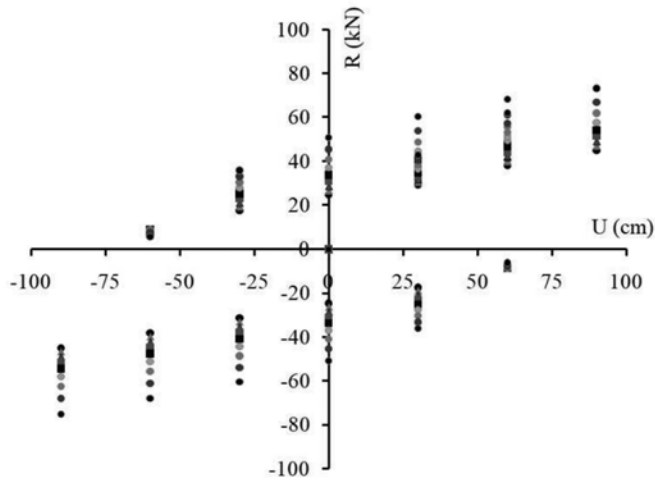


Figure 5. A portion of the database.

The hyperparameters, such as the learning rate or the loss function type, are tuned to enhance the overall behavior of the network (Figure 6).

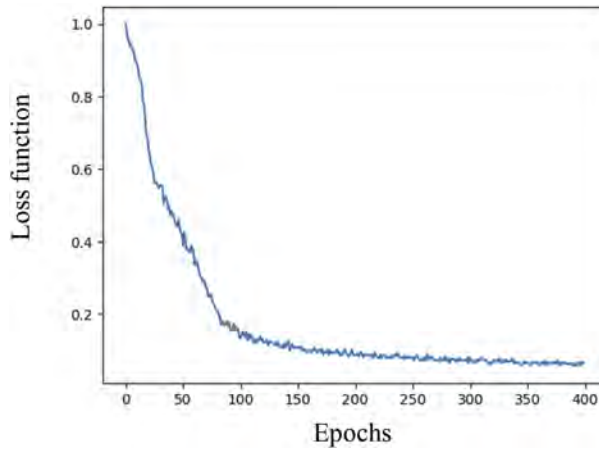


Figure 6. The loss function evolution.

3 DISCUSSION

The LCRB response is typically defined through the relationship between the generated restoring force and the applied displacement. Based on this relationship, some conventional characteristics of the bearing device (energy dissipation capacity, secant stiffness, etc.) can be assessed. A possible way to evaluate the energy dissipation capacity is the hysteresis viscous damping ratio (see for example Ahmadipour & Alam 2017).

$$\zeta_H = \frac{E_H}{4\pi E_S}, \quad (6)$$

where E_S and E_H are the elastic and dissipated hysteresis energies, respectively. These two quantities are assessed using the hysteresis loops in the bearing device's response.

The model defined by Equations (4)–(5) neglects some characteristics of the bearing device, such as the geometrical dimensions of the lead core and the rubber layers and the material properties of the rubber layers. Furthermore, it doesn't take into account the magnitude of the applied vertical force, e.g. the loads transferred from the superstructure. In this context, a more detailed model, for example, a finite element model (Figure 7a–b), could provide a more accurate output.

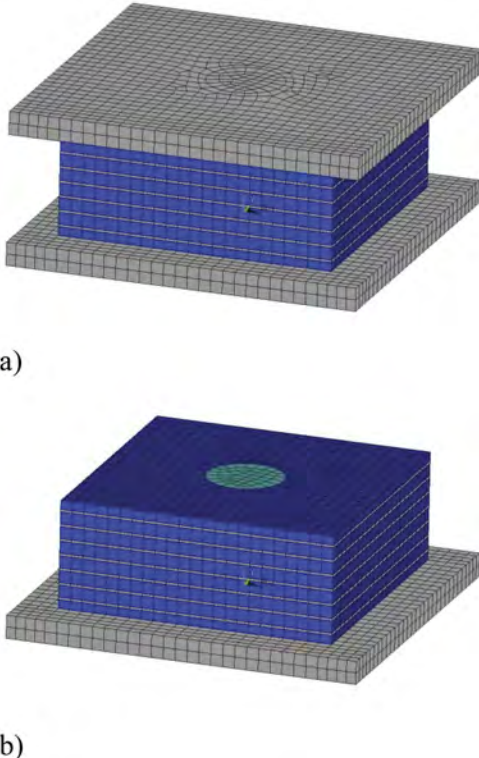


Figure 7. Detailed finite element model of the lead-core bearing device: steel shims and steel plates are displayed in grey, rubber layers are shown in dark blue, and the lead core is in light blue.

Besides the precise geometrical representation, constitutive relations are formulated for the lead (in the lead plug), the rubber layers, and steel (in the top and bottom steel plates and the steel shims). An elastic-plastic model with hardening after yielding is employed for the lead core, and a Neo-Hookean model is used for the rubber layer. Steel is assumed to have a linear elastic response.

It is well-known that such a detailed model might be highly computationally intensive. This might hinder their implementation in the dynamic analysis of a base-isolated structure. On the other hand, finite element models could provide data for artificial neural network training or validation.

4 CONCLUSIONS

A multilayer perceptron has been developed to predict the ‘restoring force-applied displacement’ relationship for a lead-core rubber bearing device. The model architecture, instantiation, and back-propagation rules have been discussed in the contribution.

The multilayer perceptron employs synthetic data for training and validation, which implies a restriction on the input parameters due to the choice of the model used to create the

corresponding target datasets needed for the learning procedure. Compared to models of detailed and comprehensive output, which are at the same time computationally intensive, the light Bouc-Wen type models are relatively easily implemented in the simulation of the bearing device response when considered as parts of a base-isolated structure. Collecting datasets based on detailed finite element simulation results and data found in the available literature is in progress. In this context, the number of parameters taken into account by the neural network (or the number of input parameters) will be increased.

ACKNOWLEDGEMENTS

The financial support of the Research and Development Sector at the Technical University of Sofia for funding the registration fee is acknowledged with gratitude.

REFERENCES

- Ahmadipour, M. & Alam, M.S. 2017. Sensitivity analysis on mechanical characteristics of lead-core steel-reinforced elastomeric bearings under cyclic loading. *Engineering Structures* 140: 39–50.
- Bouc, R. 1967. Forced vibration of mechanical systems with hysteresis. *Proc. of the 4th Conf. on Non-linear Oscillations*.
- Constantinou M.C. & Tadjbakhsh M. 1985. Hysteretic Dampers in base isolation: random approach. *Journal of Structural Engineering* 111(4): 705–721.
- Doudoumis, I.N., Gravalas, F. & Doudoumis, N.I. 2005. Analytical Modeling of Elastomeric Lead-Rubber Bearings with the use of Finite Element Micromodels. In *Proc. 5th GRACM Int. Congr. Comput. Mech.* Limassol.
- Megget, L.M. 1978. Analysis and design of a base-isolated reinforced concrete frame building. *Bulletin of the New Zealand Society for Earthquake Engineering* 11(4): 245–254.
- Menegotto, M. & Pinto, P. 1973. Method of analysis for cyclically loaded RC plane frames including changes in geometry and non-elastic behavior of elements under combined normal force and bending. In *Proc., Symp. Resistance and Ultimate Deformability of Struct. Acted on by Well-Defined Repeated Loads, IABSE Reports, Vol. 13*.
- Ozdemir, H. 1976. Nonlinear transient dynamic analysis of yielding structures. PhD dissertation, University of California, Berkeley, California.
- Park R. & Blakeley R.W.G. 1978. Seismic Design of Bridges. Structures Committee Summary 3, *Road Research Unit*, National Roads Board, New Zealand.
- Robinson, W.H. & Tucker, A.G. 1977. A Lead-Rubber Shear Damper. *Bulletin of the New Zealand National Society for Earthquake Engineering* 10(3): 151–153.
- Shoaei, P., Orimi, H.T. & Zahrai, S.M. 2018. Seismic reliability-based design of inelastic base-isolated structures with lead-rubber bearing systems. *Soil Dynamics and Earthquake Engineering* 115: 589–605.
- Sivaselvan, M.V. & Reinhorn, A.M. 2000. Hysteretic models for deteriorating inelastic structures. *Journal of Engineering Mechanics* 126(6): 633–640.
- Skinner, R.I., Tyler, R.G., Heine, A.J. & Robinson, W.H. 1980. Hysteretic dampers for the protection of structures from earthquakes. *Bulletin of the New Zealand Society for Earthquake Engineering* 13(1): 22–36.
- Song J, & Der Kiureghian A. 2006. Generalized Bouc–Wen model for highly asymmetric hysteresis. *Journal of Engineering Mechanics ASCE* 132(6): 610–618.
- Wen, Y.-K. 1976. Method for random vibration of hysteretic systems. *J. Engrg. Mech. ASCE* 102(2): 249–263.

Experimental assessment of anti-seismic devices performance

Alberto Pavese, Simone Reale & Matthew J. Fox

Civil Engineering and Architecture Department – DICAr, University of Pavia, Pavia, Italy

ABSTRACT: In the last years, anti-seismic devices have benefitted from numerous advances in the materials and technological fields, which have increased global performance in terms of durability and capacity to sustain dynamic loading and thus allowing improved design of structures. Anti-seismic devices are required, by the design codes, to sustain an experimental protocol to characterise their main response parameters and allow for a global evaluation. The tests intend to replicate the worst operative conditions the devices could face during their design life. In this paper, two residential buildings equipped with curved surface slider isolators are analysed through Non-Linear Time History Analyses using a large number of accelerograms to assess the realistic combinations of external actions applied during their life. Based on the analysis outcomes, tentative general rules to define an optimised testing protocol for devices will be derived and compared to the testing requirements given in the codes.

1 INTRODUCTION

1.1 *Principles of seismic isolation*

The principle of seismic isolation has been developed because of the need to protect human lives and reduce damage to structures during earthquakes, with seismic isolation typically being employed in high seismicity regions. The main difference between traditional seismic design philosophy and seismic isolation is that in the former the energy dissipation is achieved through the inelastic response of the building (the dissipated energy corresponds directly to structural damage) while in the latter the structure is essentially protected. It has to be pointed out that other structural systems, such as viscous dampers, allow for energy dissipation without sustaining damage. Furthermore, most isolated buildings will be designed to still sustain some damage due to inelastic behaviour in very large earthquakes. A seismic isolation system is designed employing devices with low lateral stiffness to obtain a longer fundamental period with respect to the structure without seismic isolation devices. The basic principle of seismic isolation is to decouple the building from the ground motion. Several types of devices are nowadays available to obtain this effect. The devices must be able to accommodate high levels of displacement. Out of the available devices, Curved Surface Slider (CSS) isolators have been largely employed because of their simplicity and ease of manufacturing. (Avinash et al. 2022, Calvi & Calvi 2018) In the last years anti-seismic devices have benefitted from numerous advances in the materials and technological fields, which have increased global performance in terms of durability and capacity to sustain dynamic loading and thus allowing improved design of structures. (Furinghetti 2022) To briefly introduce the devices studied in this work, CSS isolators present a sliding surface and a puck, which moves to generate the relative displacement between upper and lower parts of the device. The horizontal surfaces of the device must remain parallel through the motion. Careful consideration is given to the choice of materials for the sliding surfaces, with PTFE being a popular choice. The careful selection of materials allows a good degree of control

over the frictional behaviour during sliding, which not only dissipates energy but also prevents movement under small, frequent loading.

1.2 Experimental protocol for anti-seismic devices

As in the case of construction materials or structural components, anti-seismic devices are required, by the design codes, to sustain an experimental protocol to characterise their main response parameters and allowing a global evaluation. Examining the testing protocols given in the main design and assessment codes of practice, it can be seen that devices must be subjected to several combinations of external actions: displacement, velocity, pressure etc. These tests intend to replicate the worst operative conditions the devices could face during their design life. Testing protocols are defined by codes, like EN 15129:2009 (CEN 2009). EN 15129:2009 introduces the various types of anti-seismic devices and prescribes the properties the devices must have to be considered safe and adequate to be employed. The code is currently being reviewed. The paragraph 8.3, dedicated to CSS isolators, defines the specific testing protocol for this type of device. The factory production control tests consist in the verification of the load bearing capacity, in the calculation of the friction force in service conditions and in three symmetrical test cycles at the design displacement d_{bd} . This last production test verifies if the slider is able to slide on the curved surface with velocity v_{ed} corresponding to the Collapse Prevention Limit State (SLC) spectral velocity in presence of an acting axial force N_{ed} . The code specifies that at least the 5% of the produced CSS isolators must be tested.

The present study aims to investigate what are the most severe conditions a CSS isolator may have to face during a seismic event. Non-Linear Time History Analyses (NLTHA) will be performed on two numerical models of base isolated buildings and the analysis outcomes will be compared with the actions specified by the code for the testing protocol of CSS isolators. Based on the analysis outcomes, tentative general rules to define an optimised testing protocol for devices will be derived and later compared to the testing requirements given in the EN 15129:2009.

2 CASE STUDIES

2.1 Characteristics of the case studies

Two case study structures have been considered in this work. Each case study has been modeled and NLTHAs have been performed. The main characteristics of the case studies are briefly reported in Table 1. The first case study is a residential building with a reinforced concrete (RC) frame structure including a central core of RC walls. The interface slab with the isolation system is 0.5 m thick. 28 seismic isolation devices have been employed. It has been assumed that the structure was located in L'Aquila, Abruzzo. The second case study is a residential building with an RC frame structure, without a central core since the stairs have been modeled using frame elements. 24 seismic isolation devices have been employed. It has been assumed that the structure was located in Cosenza, Calabria.

Table 1. Characteristics of the case studies.

Characteristics	Case study 1	Case study 2
Plan dimensions [m]	26.05 x 13.08	21.05 x 11.45
Total height [m]	15.25	18.65
Fundamental period [s]	0.743	0.959
Total mass [ton]	2266	2080
Number of devices [#]	28	24

2.2 Characteristics of the seismic isolation system

The characteristics of the seismic isolation systems employed in the case studies are reported in Table 2. Only CSS isolators have been used. The motivation is that these devices are subjected to vertical and horizontal displacements during the earthquake and the vertical displacement can be accommodated only if all the devices oscillate in the same way. The main characteristics of CSS isolators are equivalent radius R_{eq} and friction coefficient μ .

Table 2. Characteristics of the seismic isolation systems.

Characteristics	Case study 1	Case study 2
Number of devices [#]	28	24
Equivalent radius R_{eq} [m]	4.23	4.23
Friction coefficient μ [#]	0.036	0.036
Diameter of the slider Φ [m]	0.184	0.190
Friction force F_{μ} [kN]	28	37
Maximum force F_{max} [kN]	60	78
Maximum displacement d_{max} [m]	0.170	0.206

2.3 Definition of the seismic input

The analyses performed in this study considered both natural and artificial accelerograms for the SLC, with analyses being performed in two orthogonal horizontal directions. For each structure:

- 7 artificial accelerograms have been generated to match the SLC response spectrum;
- 7 natural accelerograms have been selected to match the SLC response spectrum.

For the generation of artificial accelerograms, the methodology proposed by Vanmarcke and Gasparini (1977) was followed. The selection of natural records has been performed using REXEL (Iervolino, Galasso & Cosenza 2009). Spectrum compatibility has been taken into account, following the prescriptions given by the NTC2018 (D.M. 17/01/2018). Figure 1 shows the result of the spectrum compatibility check of artificial records for Case Study 1. Figure 2 shows the same results for natural records. The results for Case Study 2 are similar and so are not reported.

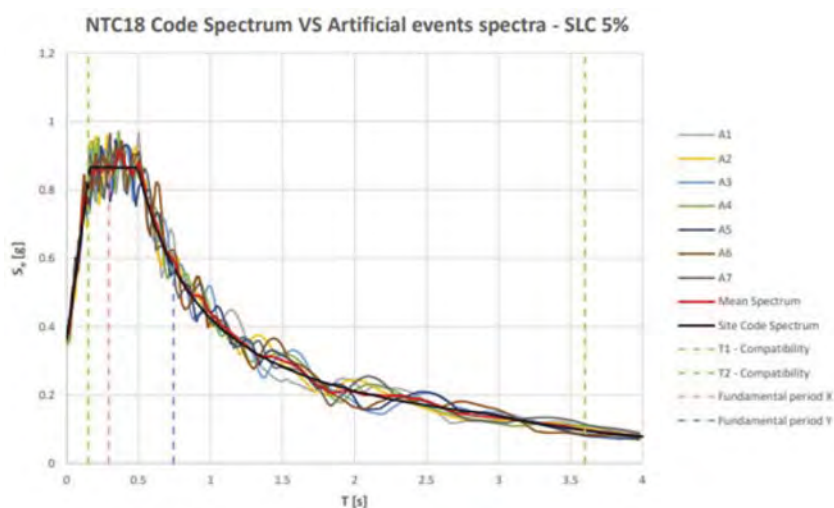


Figure 1. Spectral compatibility check for artificial records, Case Study 1.

3 COMPARISON BETWEEN ANALYSES OUTCOMES AND TEST PROTOCOLS

3.1 Sliding isolation tests-dynamic

In the sliding isolation tests, EN 15129:2009 requires consideration of three displacement levels (d_{bd} , $0.5d_{bd}$ and $0.25d_{bd}$) with the same velocity v_{ed} . To discuss if maintaining the same velocity for all the tests is correct, it is useful to consider separately artificial records and natural records. Considering the artificial records, the resulting displacements are never greater than d_{bd} and the velocity has values comparable with the design velocity. For Case study 1, the mean velocity in the X direction is equal to $1.05v_{ed}$, while the mean velocity in Y is equal to $1.15v_{ed}$. For Case study 2, the mean velocity in X direction is equal to $1.12v_{ed}$, while the mean velocity in Y is equal to $1.15v_{ed}$. Artificial records seem to confirm the code prescription about the velocity that has to be maintained during the tests. Considering natural records, in 6 and 8 analyses extra stroke displacements are present for Case study 1 and Case study 2 respectively. Considering only the events without extra stroke displacement in the devices, the mean velocity is around $1.08v_{ed}$, confirming the code prescriptions. Considering the events with extra stroke displacements in the devices, it has been noted that the velocity tends to scale coherently with the deformation level. The maximum value of velocity that has been reached is equal to $2.13v_{ed}$, for an extra stroke displacement of $1.18d_{bd}$. The results seem to confirm the code prescriptions for displacement levels below d_{bd} , but the code does not present tests for displacement levels higher than d_{bd} where the velocity is different.

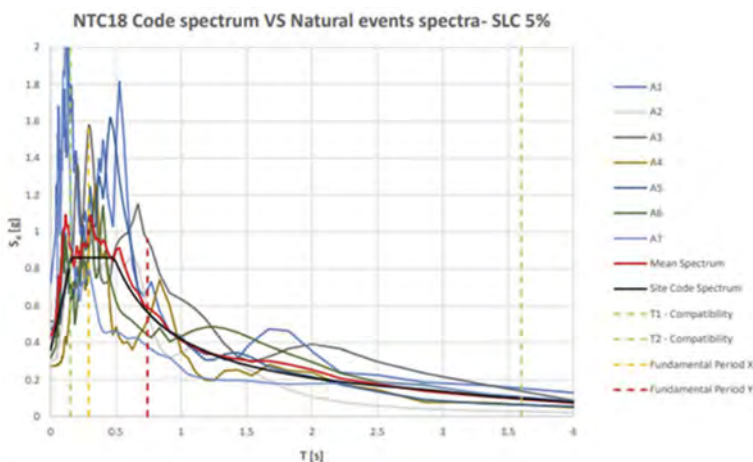


Figure 2. Spectral compatibility check for natural records, Case Study 1.

3.2 Sliding isolation tests-seismic

In the seismic test, the device is subjected to 3 displacement cycles. The maximum displacement is d_{bd} , the test is performed with velocity v_{ed} and maximum and minimum levels of axial force, called $N_{ed, max}$ and $N_{ed, min}$ respectively, are alternatively present. Some considerations concerning the relationship between axial action and design displacement are due. Given the design axial force N_{sd} , Figure 3 shows the comparison between normalised displacement and normalised axial force of a device for the Case study 2. The analysis outcomes in Figure 3 are about an artificial record. The peak displacement is around $0.7d_{bd}$, but the contemporary axial force is $1.8N_{sd}$. Figure 4 shows the comparison between normalised displacement and normalised axial force of a device for the Case study 1. The analysis outcomes in Figure 4 are about a natural record. The peak displacement is around $0.85d_{bd}$, but the contemporary axial force is $1.3N_{sd}$. In both the examples, the maximum axial force

takes place in correspondence of the maximum displacement. However, it has to be pointed out that the oscillation frequency seems to be much higher for the axial force than for the displacement. For this reason, the correspondence between extreme axial forces and extreme displacements is not particularly frequent in the set of analyses. A significative variation of N_{sd} (at least 10%) happens in correspondence of the maximum displacement only in few analyses. A relationship between displacement and axial action oscillations was not observed.

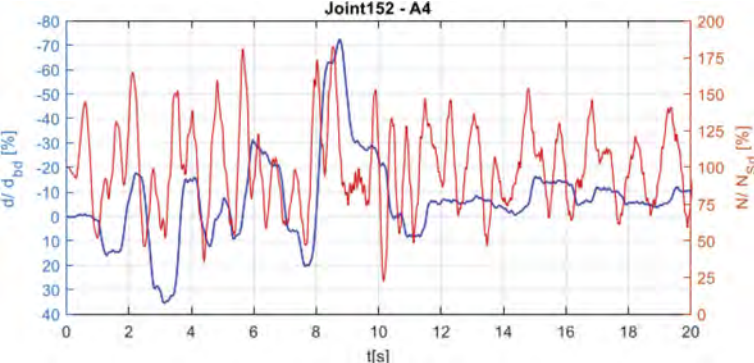


Figure 3. Time histories of normalised displacement and axial force - Case Study 2, artificial record.

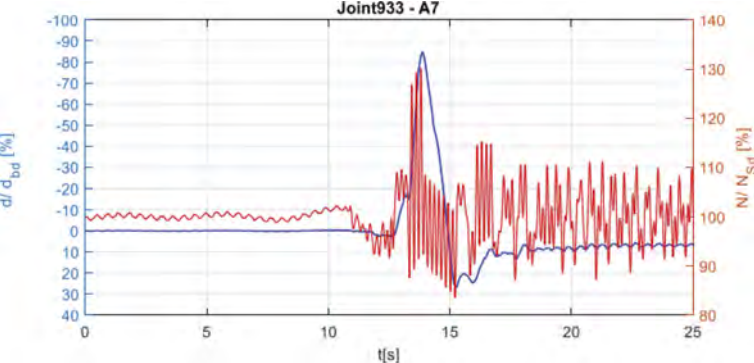


Figure 4. Time histories of normalised displacement and axial force - Case Study 1, natural record.

3.3 Load bearing capacity

EN 15129:2009 prescribes that a seismic isolation device must be able to carry a vertical load equal to $2N_{sd}$ when in its zero-displacement position, maintaining the load for 1 minute. The purpose of the test is to verify the device in an overload condition. The range $0-2N_{sd}$ contains the possible variations of axial forces in the devices during a seismic event, but some exceptions have been noted in the analysis outcomes. Joint 152 of the Case study 2 is in the corner of the isolation interface. Joint 933 of Case study 1 and Joint 156 of the Case study 2 are near the stairs. In correspondence of these points, values of axial force up to $3.1N_{sd}$ have been observed. These values are beyond the limits prescribed by the codes and happen for high displacements (extra stroke displacements, in most cases). Table 3, Table 4 and Table 5 show the axial force variation in the previously introduced points.

Table 3. Axial force variation through the set of analyses for Joint 152 - Case study 2, natural records.

Joint 152 – Case study 2 – Natural events – SLC – X				
Events	d_{\max}^+/d_{bd}	d_{\max}^-/d_{bd}	N_{\max}/N_{sd}	N_{\min}/N_{sd}
A1	1.11	-0.62	1.81	0.07
A2	0.23	-0.53	1.62	0.02
A3	0.53	-0.41	1.67	0.30
A4	0.48	-0.63	1.75	0.26
A5	1.27	-1.06	1.87	0.00
A6	1.32	-0.29	1.76	0.00
A7	1.14	-0.96	2.69	0.00

Table 4. Axial force variation through the set of analyses for Joint 933 - Case study 1, natural records.

Joint 933 – Case study 1 – Natural events – SLC – Y				
Events	d_{\max}^+/d_{bd}	d_{\max}^-/d_{bd}	N_{\max}/N_{sd}	N_{\min}/N_{sd}
A1	1.59	-1.18	2.16	0.00
A2	0.51	-0.28	1.79	0.09
A3	1.73	-1.33	2.23	0.00
A4	0.47	-0.51	1.94	0.32
A5	0.24	-0.76	2.16	0.06
A6	1.45	-0.69	2.00	0.33
A7	0.27	-0.89	1.52	0.44

Table 5. Axial force variation through the set of analyses for Joint 156 - Case study 2, natural records.

Joint 156 – Case study 2 – Natural events – SLC – Y				
Events	d_{\max}^+/d_{bd}	d_{\max}^-/d_{bd}	N_{\max}/N_{sd}	N_{\min}/N_{sd}
A1	1.15	-0.51	2.51	0.10
A2	0.17	-0.62	2.48	0.12
A3	0.41	-0.42	2.26	0.00
A4	0.41	-0.76	1.92	0.00
A5	1.21	-1.03	2.86	0.00
A6	1.21	-0.28	2.49	0.00
A7	1.18	-1.12	3.10	0.00

3.4 Number of cycles

CSS isolators are characterised by high non-linearities and analysing the outcomes of the simulations only few relevant cycles have been observed. EN 15129:2009 prescribes three symmetrical cycles for the sliding isolation tests. Three cycles are justifiable for $0.5d_{bd}$ or $0.25d_{bd}$ displacement levels but considering the analysis outcomes seem to be excessive for the d_{bd} displacement level. To properly address this issue, it is possible to compare the numerical results with an experimental test, computing the work on the device in both cases. The work can be calculated integrating over time the product of shear, S , and displacement, d , time histories. Figure 5 shows the time histories of S and d for an experimental test and a numerical simulation. For CSS isolators positive work W^+ and negative work W^- on the device must be distinguished since S and d are not always with the same

sign. For the reported example, considering the numerical results, W^+ and W^- are equal to 35 kJ and 12 kJ respectively and a total work of 47 kJ is obtained. The work of the experimental test W_T is equal to 73 kJ. It has been observed that the work on the isolator in presence of the most intense natural event of the set is around the 64% of the work in the dynamic tests.

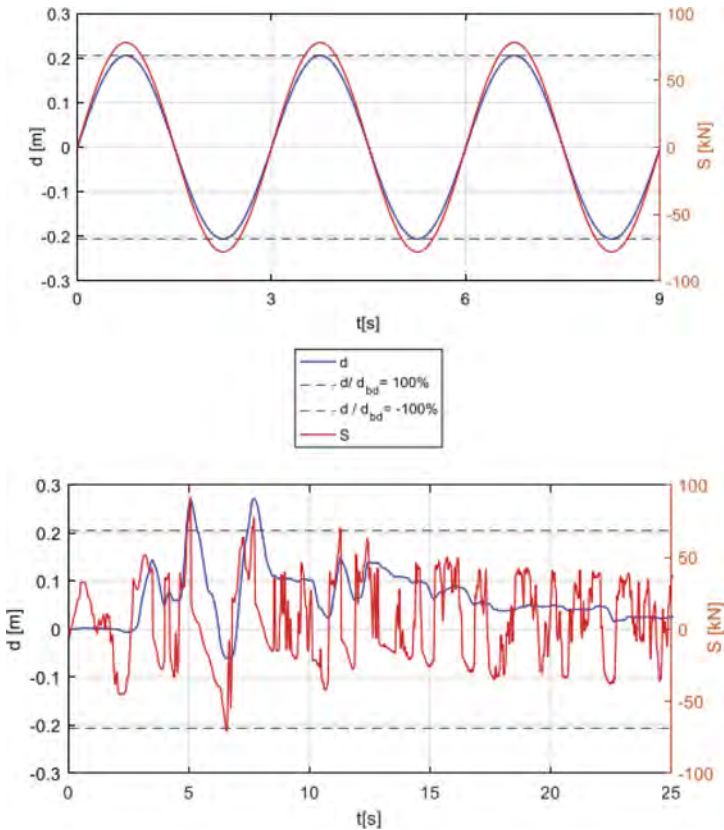


Figure 5. Time histories of shear and displacement for an experimental test (top) and a numerical simulation (bottom).

4 CONCLUSIONS

Two base isolated structures have been selected and modeled. NLTHAs have been performed using both artificial and natural records. The analysis outcomes have been compared with the testing protocols contained in the EN 15129:2009 to provide a critical evaluation of the performances required for a CSS isolator. Considering the Dynamic tests, the results seem to confirm the code prescriptions for displacement levels below d_{bd} , but the code does not present tests for displacement levels higher than d_{bd} . Considering Seismic tests, a relationship between displacement and axial action oscillations was not observed. In terms of load bearing capacity, the range $0-2N_{sd}$ contains the possible variations of axial forces in the devices during a seismic event, but some exceptions have been noted in the analysis outcomes. Regarding the number of cycles in the tests, the code prescribes three symmetrical cycles for the sliding isolation tests. Three cycles are justifiable for $0.5d_{bd}$ or $0.25d_{bd}$ displacement levels but considering the analysis outcomes seem to be excessive for the d_{bd} displacement level. It has to be pointed out that

the present study has considered only two base isolated structures, a higher number of case studies would enhance the confidence on the results.

ACKNOWLEDGMENTS

Part of the current work has been carried out under the financial support of the Italian Civil Protection, within the frameworks of the national Research Project DPC – ReLUIS (National Network of Laboratories of Seismic Engineering) 2022–2024, WP15.

REFERENCES

- Avinash, A. R., Krishnamoorthy, A., Kamath, K., & Chaithra, M. 2022. Sliding Isolation Systems: Historical Review, Modeling Techniques, and the Contemporary Trends. *Buildings*, 12(11), 1997.
- Calvi, P. M., & Calvi, G. M. 2018. Historical development of friction-based seismic isolation systems. *Soil Dynamics and Earthquake Engineering*, 106, 14–30.
- CEN 2009 Comité Européen de Normalisation TC 340, European Code UNI EN 15129:2009 Anti-seismic devices, European Committee for Standardization, Brussels, Belgium
- D.M. 17/01/2018. Norme Tecniche per le Costruzioni, D.M. 17/ 01/2018. Italia: Gazzetta Ufficiale
- Furinghetti, M. 2022. Definition and Validation of Fast Design Procedures for Seismic Isolation Systems. *Vibration*, 5(2), 290–305.
- Iervolino, I., Galasso, C., & Cosenza, E. 2010. REXEL: computer aided record selection for code-based seismic structural analysis. *Bulletin of Earthquake Engineering*, 8(2), 339–362.
- Vanmarcke, E. H., & Gasparini, D. A. 1977. Simulated earthquake ground motions.

Vulnerability assessment of bridges within the Italian highway network

Simone Reale & Alberto Pavese

Department of Civil Engineering and Architecture – DICAr, University of Pavia, Pavia, Italy

Marco Furinghetti

Department of Civil Engineering and Architecture – DICAr, University of Pavia, Pavia, Italy

EUCENTRE Foundation, Pavia, Italy

ABSTRACT: Bridges are fundamental for the transportation system of a nation and they can be subject to significant deterioration phenomena linked to the fact that the construction period typically dates back to the 1960s. This study involves the analysis of four case study bridges belonging to the Italian highway network. Analytical fragility curves have been constructed for each of the bridges. The case studies have also been analysed to determine the Structural and Foundational and Seismic Classes of Attention, following the approach proposed by the 2020 Italian Guidelines. It was possible to compare two different assessment approaches. In regions with higher seismicity the main problems in bridges are related to bearings and connecting elements located in the piers. These problems may be linked to the fact that at the time of the design of the structures there was less understanding of need for seismically resilient bridge design.

1 INTRODUCTION

The safety of existing bridges represents a serious problem since these structures are fundamental for the transportation system of a nation and, at the same time, they can be subject to significant deterioration phenomena linked to the fact that the construction period typically dates back to the 1960s (Fox et al. 2022). Considering that at the time durability was not one of the goals in projects and that the service life of the structures has been in most cases already reached or exceeded, proper maintenance and retrofit interventions are needed. The rise in frequency of bridge collapses is an indicator of the effects of aging and lack of maintenance (Cosenza & Losanno 2022). Proper maintenance is fundamental because the most important element in the durability of bridges is the correct evolution of the structure through the years. The main causes of collapse in existing bridges are flooding, impacts and foundational problems, while the design loads are responsible only for a small number of collapses (Deng et al. 2016). The analysis of the Italian infrastructure stock reveals that the railway system is smaller, more uniform and more organised in terms of maintenance with respect to the roadway system. Shortage of resources for the maintenance of structures and the increasing traffic are also relevant factors (Di Prisco 2019).

This study involves the analysis of four case studies belonging to the Italian highway network. The case studies have been built around the same period (early-60s to mid-70s) and all of them belong to the Italian highway network. At the time, there was a less developed understanding of the seismic behaviour of structures and crucial facets of the design process, like bearing design and anti-seismic details, were addressed with simplified approaches. Table 1 reports the main characteristics of the case studies. The available documentation provided information about the structural elements, both in terms of sections and reinforcement. The documents reported also information about the original materials. When available, results of

experimental tests performed on the structures have been taken as a reference for material properties. In the cases where there were not test results available, assumptions about the deterioration of materials have been made.

For each of the case studies, fragility curves have been computed referring to the overall response of the bridge and to the response of bearings and individual structural elements. The results have been used to evaluate the efficiency of the procedure set out by the new “Guidelines for the classification and management of risk, safety evaluation, and monitoring of existing bridges” (2020), which have been introduced in 2020 and will be herein referred to as “the Guidelines”. In particular, the Level 2 assessment has been applied to the case studies, defining Structural and Foundational and Seismic Classes of Attention, allowing for evaluation of the proposed approach.

Table 1. Main characteristics of the case studies.

Case study	Year	Structural scheme	Bearings	Number of spans	Total length [m]	Soil category (NTC2018)
Bridge 1	1960	Continuous beams with Gerber saddles	Neoprene	13	421	A
Bridge 2	1969	Simply supported beams	Neoprene and steel plates	4	124	A
Bridge 3	1973	Simply supported beams with Gerber saddles	PTFE-Steel	5	157	B
Bridge 4	1969	Simply supported beams	Neoprene and steel plates	3	87.8	A

2 THE GUIDELINES

2.1 *Bridge assessment guidelines*

The Guidelines have been introduced in 2020. The proposed multilevel and multi-risk approach is organised into six progressively more detailed levels. Level 0 involves a stocktake of bridges, gathering information about, for instance, location, structural system, period of construction and, eventually, retrofit interventions. Level 1 requires visual inspection to detect damage on the structure. At the end of the inspection, a report is produced using a standardised format provided with the Guidelines. In Level 2, Classes of Attention are defined by combining in a simplified way data related to hazard, vulnerability and exposure. There are 5 Classes of Attention (Low, Medium-low, Medium, Medium-high, High). Level 3 consists in a preliminary assessment of structural safety and is performed by comparing the design actions provided by the codes at the time of construction with the design actions provided by NTC2018 (D.M. 17/01/2018). Level 4 is a detailed safety assessment of the bridge considering current code requirements. Level 5, not directly covered by the Guidelines, is related to the resilience of the bridge network.

From level 0 to level 5 the analyses become more demanding in terms of engineering effort, but it is expected that the number of structures that have to be assessed progressively decreases. The Guidelines also introduce the structural monitoring of bridges. Considerations on structural monitoring are beyond the scope of this work, given the extremely broad nature of the topic.

2.2 *Structural and foundational class of attention*

The definition of Structural and Foundational Class of Attention for the case studies is based on the determination of hazard, vulnerability and exposure classes. In terms of hazard class, the main parameters are the load level of the bridge and frequency of commercial vehicles. To estimate the vulnerability class, level of defectiveness, structural scheme, span length, number of spans, materials, design code and speed of degradation are considered. The exposure class is defined on the basis of mean daily traffic (MDT), average length of spans, presence of road

alternatives, type of entity under the bridge and transit of dangerous goods. These three classes, defined using decisional trees that combine the parameters introduced above, are then employed to derive the Structural and Foundational Class of Attention using tables in the Guidelines.

In the definition of the Class of Attention, vulnerability is the most important factor because if it is high the Class of Attention will be High independently from the classes related to the other two factors. In fact, the vulnerability class is directly connected with the level of defectiveness of the structure. Table 2 reports the Structural and Foundational Class of Attention for each of the case studies. For all the four case studies, the Structural and Foundational Class of Attention is High.

Table 2. Assessment of structural and foundational class of attention.

Structural and Foundational Class of Attention				
Case studies	Hazard class	Vulnerability class	Exposure class	Class of Attention
Bridge 1	High	High	High	High
Bridge 2	High	Medium-high	High	High
Bridge 3	High	High	High	High
Bridge 4	High	Medium-high	High	High

2.3 Seismic class of attention

The definition of the Seismic Class of Attention follows the same approach presented for the Structural and Foundation Class of Attention. In terms of hazard class, the main parameters are PGA, topographic category and subsoil type. Structural scheme, span length, materials, level of defectiveness and design criteria are considered to derive the vulnerability class. The exposure class is derived from the level of MDT, medium length of the spans, presence of road alternatives, type of entity under the bridge, transit of dangerous goods and strategic importance of the infrastructure. Table 3 reports the Seismic Class of Attention for each of the case studies. For Bridge 1, Bridge 2 and Bridge 3 the Seismic Class of Attention is High, while for Bridge 4 is Medium-high.

Table 3. Assessment of seismic class of attention.

Seismic Class of Attention				
Case studies	Hazard class	Vulnerability class	Exposure class	Class of Attention
Bridge 1	Medium-high	Medium-high	High	High
Bridge 2	Medium-high	Medium-high	High	High
Bridge 3	Medium	High	High	High
Bridge 4	Medium-low	Medium-high	High	Medium-high

3 FRAGILITY CURVES

3.1 Methodology

Fragility curves represent the link between the seismic hazard at a site and the effects on the exposed elements. The fragility curves associated with each case study have been derived using the so-called Multiple Stripes Analysis (MSA). This approach requires structural analyses to be performed at a discrete set of Intensity Measure (IM) levels, using different ground motions at each level. Target properties of the ground motions vary at different IM levels and the selection of different accelerograms allows the variation of the seismic hazard parameters to be taken into consideration (Baker 2015). The fundamental aspects of the methodology used to derive the fragility curves are reported below.

10 code-based elastic spectra have been defined according to the NTC2018. The spectra are characterised by an increasing value of return period T_r , from 30 to 2475 years, as reported in

Table 4. The definition of these spectra is fundamental to ensure that the selected ground motions represent a broad enough range of IM levels (Manfredi et al. 2022).

The number of ground motions that have to be selected to provide reliable results in the analyses is still an open issue, but 7 ground motions appear to be the minimum requirement (Manfredi et al. 2022). 7 pairs of natural records for each IM level have been selected using the ground motion selection software REXEL (Iervolino et al. 2009). The selection of the ground motions required that seismic hazard disaggregation be undertaken first (Bazzurro & Cornell 1999, Fox et al. 2016). In the matching of the ground motions to the spectra, NTC2018 has been taken as reference for the issue of spectral compatibility. In particular, given the first period T , the highest value between $2T$ and 2 s has been selected as maximum value of the range of periods in which spectral compatibility must be ensured.

The definition of the criteria used to compute capacity and demand for each structural element is fundamental. In terms of shear actions, considering the indications of the 2019 Commentary of NTC2018, the capacity of an existing structure has to be computed taking into account the ductility demand on the elements. The main contributors to shear capacity, in this formulation, are normal actions N , concrete and steel contributions and interaction between flexural rotation of the element and plastic component of ductility demand. Considering the chord rotation capacity, in the 2019 Commentary of NTC2018, three different formulations are proposed in relation to Collapse Prevention Limit State (SLC), Life-safety Limit State (SLV) and Damage-limitation Limit State (SLD). The first two formulations refer to an ultimate capacity, while the last formulation gives a capacity correlated with yielding tension.

For bearing displacement, the chosen approach consisted in monitoring the horizontal deformations of each bearing through the analyses, defining four Limit States associated with different conditions of the devices. The definition of Limit States correlated to the seismic response of the bearings is crucial to properly describe the structural behaviour of the case studies. The Limit States specified for bearings are slightly different for elastomeric and PTFE-steel bearings. For elastomeric bearings, the shear deformation γ has been computed as the ratio between horizontal displacement d and total height of the elastomer, while for PTFE-steel devices the ratio between d and the total height of the device h has been considered.

Two Global Limit States, Damage and Collapse, have also been defined to describe the global response of the bridge. The former is associated with an operating condition of the structure while the latter defines a condition where critical failures in piers or bearings are present. It has been assumed that to reach Collapse Limit State it was necessary to exceed Damage Limit State. The criteria listed in Table 5 are alternative possibilities and reaching just one of them is enough to consider the corresponding Limit State as being exceeded.

Table 4. Values of T_r for each IM level.

IM level	1	2	3	4	5	6	7	8	9	10
T_r	30	50	101	201	475	712	975	1462	1950	2475

Table 5. Global Limit States.

Limit States	Criteria
Damage	$\gamma=0.5$; Reaching of chord rotation capacity (SLD) in at least one pier; Failures in secondary elements.
Collapse	$\gamma=2$; Reaching of shear capacity in at least one pier; Reaching of chord rotation capacity (SLV) in at least one pier; Reaching or exceeding $\gamma=1$ and failures in secondary elements.

Non-Linear Time History Analyses (NLTHA) have been performed to obtain the data required to derive the fragility curves. For each of the considered Limit States, the fraction of analyses that for a given IM level reached or exceeded the associated threshold was computed. The fitting procedure, which allowed to finally obtain the fragility curves, was performed applying the maximum likelihood method, which is the most appropriate with this type of data (Baker 2015).

3.2 Fragility curves for the case studies

Figure 1 reports the fragility curves for bearings, structural elements and global response of Bridge 1. The response of the bearings is not particularly detrimental. The pier behaviour is acceptable both in terms of shear and chord rotation.

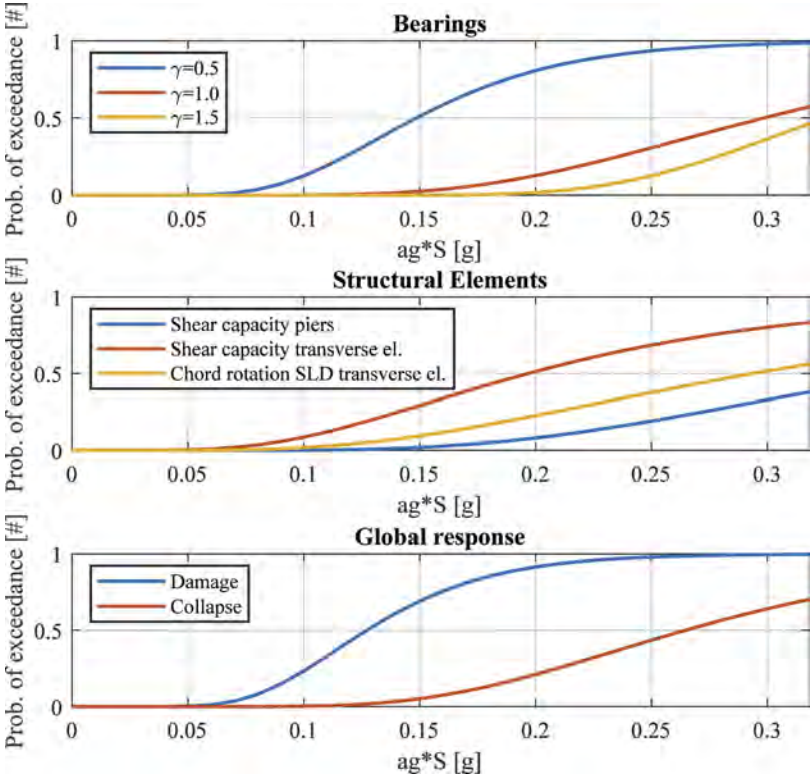


Figure 1. Fragility curves related to bearings, structural elements and global response of Bridge 1.

Local problems, mainly in terms of shear failures, are present in the transverse connecting elements of the piers. Local failures must not be underestimated because they can have an influence on the global dynamic behaviour of the structure. The global behaviour of Bridge 1 is acceptable, but the presence of local problems is relevant in the assessment of the structure.

Figure 2 reports the fragility curves for bearings, structural elements and global response of Bridge 2. The response of the bearings is critical for this case study. This result may be due to factors such as the high seismicity of the region and the structural scheme of the bridge. Also, analysing the documentation it has been noted that the design, which dates back to 1969, did not take into account seismic actions. The pier behaviour is acceptable both in terms of shear and chord rotation. Local problems, mainly in terms of shear failures, are present in the connecting element between the two parts of each pier. The global behaviour of Bridge 2 is acceptable, but the presence of local problems is relevant in the assessment of the structure.

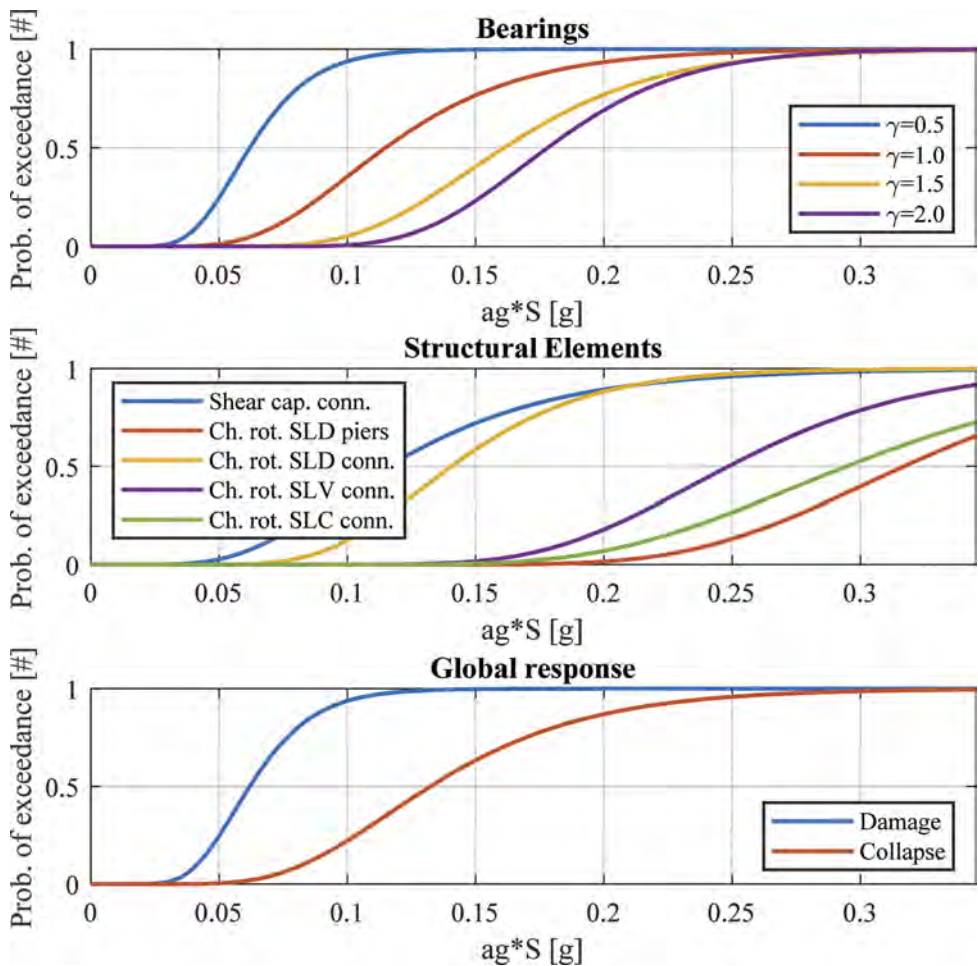


Figure 2. Fragility curves related to bearings, structural elements and global response of Bridge 2.

Figure 3 reports the fragility curves for bearings, structural elements and global response of Bridge 3. The bearings of Bridge 3 are made of polytetrafluoroethylene (PTFE) and steel. This type of devices is characterised by high displacement capacity. The seismicity of the region (the ground acceleration on rock, a_g , corresponding to $T_r = 2475$ years is equal to 0.191 g) leads to significant displacements of the bearings. In terms of structural elements, the shear response generates some problems, while the response in terms of chord rotation does not highlight particular problems. This type of behaviour can be explained considering the large spacing between the stirrups and that concrete properties have been obtained using experimental tests as reference (which showed a state of deterioration with respect to design properties).

Figure 4 contains the fragility curve related to reaching $\gamma=0.5$ in the bearings of Bridge 4. This was the only relevant curve for this case study since the other curves were not characterised by enough discrete points to perform the fitting procedure. No significant issues related to the seismic response of structural elements have been detected. The only relevant curve, $\gamma=0.5$, corresponds to a normal condition for the bearings. These results can be explained considering the low seismicity of the zone, with a_g corresponding to $T_r = 2475$ years equal to 0.081 g.

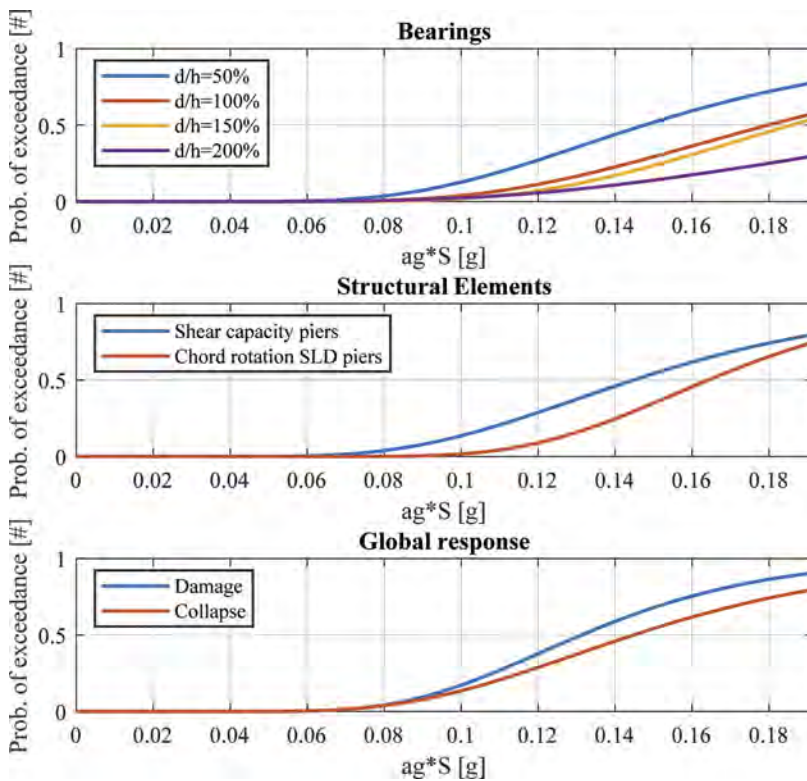


Figure 3. Fragility curves related to bearings, structural elements and global response of Bridge 3.

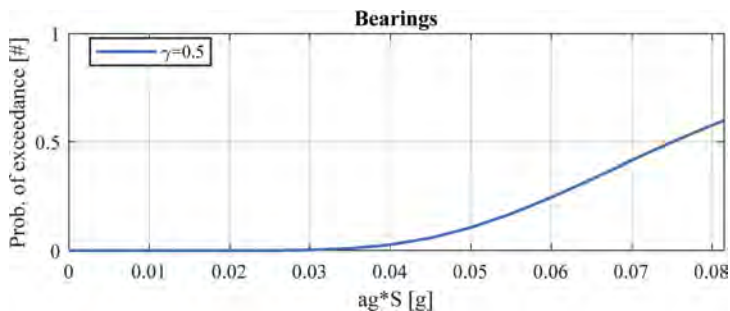


Figure 4. Fragility curve related to $\gamma=0.5$ for Bridge 4.

4 CONCLUSIONS

On the basis of what has been discussed in previous sections, the conclusions reported below can be drawn. In regions with higher seismicity the response of the bearings is critical, while in areas with lower seismicity there are not particular problems in the bearings. A good behaviour of the piers has been noted regarding ductile failures. Except for Bridge 3, a good response in terms of brittle failures has been found. Considering the connecting elements in frame piers, local problems (mainly in terms of brittle mechanisms) have been found. This is an aspect that must not be underestimated as failures in these elements can modify the flexural behaviour of the piers and so the overall response of the structure. The results obtained

interpreting the analytical fragility curves are in agreement with the fact that the seismic behaviour of existing bridges can be problematic, and that a higher seismicity can be associated with a more detrimental behaviour.

Considering the Guidelines, each case study is associated to the High Structural and Foundational Class of Attention. The three bridges in higher seismicity zones have been associated to the High Seismic Class of Attention, while Bridge 4 has been associated to the Medium-high Seismic Class of Attention. For bridges in areas with higher seismicity there is therefore a result in agreement with that of the fragility curves, while for Bridge 4 there is a discrepancy that could be due to the different level of conservatism of the analyses, the procedure of the Guidelines could lead to a poor reflection of the true seismic behaviour of bridges when the seismicity of the area is lower. Since the assessment of Classes of Attention is based on decisional trees and visual inspections it is expected that it will be more conservative than an analytic approach based on NLTHA.

Note that the results obtained cannot be considered as general since the number of considered case studies is relatively small and considering that this study could be developed and extended in the future, this consideration has to be intended only as a qualitative evaluation.

ACKNOWLEDGMENTS

This work was funded by the agreement between the Italian Consiglio Superiore dei Lavori Pubblici and the ReLUI Consortium on “Sperimentazione delle linee guida per la classificazione e gestione del rischio, la valutazione della sicurezza ed il monitoraggio dei ponti esistenti”, Decreto del Ministero delle Infrastrutture n. 578 del 17.12.2020.

REFERENCES

- Baker, J. W. 2015. Efficient analytical fragility function fitting using dynamic structural analysis. *Earthquake Spectra*, 31(1), 579–599.
- Bazzurro, P., & Allin Cornell, C. 1999. Disaggregation of seismic hazard. *Bulletin of the Seismological Society of America*, 89(2), 501–520.
- Cosenza, E., & Losanno, D. 2021. Assessment of existing reinforced-concrete bridges under road-traffic loads according to the new Italian guidelines. *Structural Concrete*, 22(5), 2868–2881.
- Deng, L., Wang, W., & Yu, Y. 2016. State-of-the-art review on the causes and mechanisms of bridge collapse. *Journal of Performance of Constructed Facilities*, 30(2), 04015005.
- Di Prisco, M. 2019. Critical infrastructures in Italy: State of the art, case studies, rational approaches to select the intervention priorities. In *fib Symposium 2019: Concrete-Innovations in Materials, Design and Structures* (pp. 49–58). International Federation for Structural Concrete.
- D.M. 17/01/2018. Norme Tecniche per le Costruzioni, D.M. 17/ 01/2018. Italia: Gazzetta Ufficiale
- Fox, M. J., Stafford, P. J., & Sullivan, T. J. 2016. Seismic hazard disaggregation in performance-based earthquake engineering: occurrence or exceedance?. *Earthquake Engineering & Structural Dynamics*, 45(5), 835–842.
- Fox MJ, Furinghetti M, Pavese A. Application of the new Italian assessment guidelines to a 1960s prestressed concrete road bridge. *Structural Concrete*. 2022. <https://doi.org/10.1002/suco.202200884>
- Manfredi, V., Masi, A., Özcebe, A. G., Paolucci, R., & Smerzini, C. 2022. Selection and spectral matching of recorded ground motions for seismic fragility analyses. *Bulletin of Earthquake Engineering*, 1–27.
- High Council of Public Works. Linee Guida per la classificazione e gestione del rischio, la valutazione della sicurezza ed il monitoraggio dei ponti esistenti (in Italian). 2020.
- Iervolino, I., Galasso, C., & Cosenza, E. 2010. REXEL: computer aided record selection for code-based seismic structural analysis. *Bulletin of Earthquake Engineering*, 8(2), 339–362.

Life-Cycle Assessment (LCA) of fiber-reinforced reclaimed-rubber seismic isolators

F. Cilento

Institute of Polymers, Composite and Biomaterials, CNR (National Research Council of Italy), Portici, Italy

D. Losanno, C. Menna, C. Ciriello & F. Parisi

Department of Structures for Engineering and Architecture, University of Naples Federico II, Naples, Italy

ABSTRACT: During the last few years, a growing interest has been observed in the development of low-cost seismic isolation systems with the aim of reducing seismic risk in developing countries. Fibre-reinforced elastomeric isolators (FREIs) in unbonded configuration demonstrated to be an effective alternative solution to conventional steel-reinforced elastomeric isolators (SREIs). The use of reclaimed rubber compounds in FREIs has the potential to further reduce the environmental impact associated with this technology. Reclaimed rubber FREIs reinforced with polyester fabrics have shown adequate deformation capacity, stable hysteretic behaviour, and satisfactory damping properties. In this study, the environmental burden associated with the FREI technology when using reclaimed rubber compound and flexible reinforcement is computed by performing a life cycle environmental assessment. The sustainability outcome in terms of resource use/savings, energy and emissions to the environment is preliminary quantified and compared to that of classical SREIs.

1 INTRODUCTION

Base isolation is one of the most effective technologies for the seismic protection of structures. Despite all, the system is still rarely used in emerging countries and common housing projects because classical Steel-Reinforced Elastomeric Isolators (SREIs) are large, heavy, and expensive, requiring a highly labor-intensive manufacturing process. In recent years, the development of new low-cost seismic isolators made it possible to extend this technology to common building projects (Calabrese et al. 2019; Losanno et al. 2021). During the last decade, Fiber Reinforced Elastomeric Isolators (FREIs) were introduced as a lower-cost option to SREI (Konstantinidis & Kelly 2014). The use of flexible reinforcement in extension and bending, such as carbon, glass, nylon, and polyester fiber sheets, significantly reduces the weight of the device and the installation costs also increasing the ability of the device to dissipate elastic strain energy providing higher damping capacity due to friction between different layers.

FREIs could be installed in an unbonded configuration by mounting the devices between the sub-structure and superstructure without any mechanical restraint, just relying on friction at the contact surfaces (Toopchi-Nezhad et al. 2011). In terms of isolation effectiveness, FREIs take benefit of the roll-over phenomenon that reduces the bearing contact area resulting in lower secant stiffness than SREI. The lack of both flexural rigidity of internal reinforcement and external fastening significantly reduces tensile and peeling stress in the rubber compound in comparison to classical SREIs (Losanno et al. 2019; Losanno et al. 2021). Hence, virgin rubber can also be replaced by lower-performance reclaimed rubber compounds when manufacturing unbounded FREIs. This not only turns into a further cost reduction but also a positive environmental impact when comparing FREIs to traditional SREIs. Habieb et al. (Habieb et al. 2021) conducted a preliminary investigation on recycled rubber for building isolation systems in the form of reactivated (i.e. devulcanized) Ethylene-Propylene Diene Monomer (EPDM) from industrial waste. Along the same line, these

authors recently developed with the company ITALGUM and experimentally tested a prototype polyester-fabric reclaimed-rubber FREI (P-RU-FREI) showing promising performance in terms of both displacement and damping capacity (Cilento et al. 2022; Italgum S.r.l et al. 2022). Very recent experimental works on full-scale prototypes and numerical analyses on both RC frame and unreinforced masonry buildings confirmed the suitability of FREIs for protecting low-rise buildings (Calabrese et al. 2019; Madera Sierra et al. 2019; Losanno et al. 2022a; Losanno et al. 2022b).

To further address the development of sustainable solutions for the design of new buildings and retrofit existing ones both in developed and developing countries, a life cycle environmental assessment of the different isolator solutions has become necessary. Life cycle assessment (LCA) is considered an efficient and comprehensive tool to evaluate the environmental impacts of a product throughout its life cycle, starting with the extraction and processing of raw materials, manufacturing and production, product transportation, use and maintenance, until its waste disposal. The method was successfully applied in the construction sector (Ortiz et al. 2009) to evaluate the environmental performance of construction products (Napolano et al. 2015) or to support the decision-making process oriented towards environmental sustainability (Caruso et al. 2017).

To the best of the authors' knowledge, no literature has been published on the process LCA of FREI compared to SREI systems. Hence, this study aims to provide an LCA-based environmental assessment of FREIs and SREIs, with a specific focus on the product stage of the life cycle.

2 P-RU-FREI VERSUS SREI: MATERIALS AND PROCESS

Previous studies (Strauss et al. 2014; Madera Sierra et al. 2019) demonstrated the convenience of using FREIs in unbounded configuration rather than SREI due to the following features: (i) simplification of the installation process, (ii) reduction of energy consumption and cost, and (iii) reduction of internal stresses with the possibility to adopt lower performance elastomeric materials (Losanno et al. 2020).

The reference FREI prototype was assumed according to (Cilento et al. 2022) where P-RU-FREIs were dimensioned for a low-rise RC frame in a length scale of 2. In this study, the corresponding full-scale P-RU-FREI is considered as the reference geometry for the LCA study. In detail, the environmental assessment is conducted on both P-RU-FREI and its SREI counterpart sharing the same rubber geometry (i.e. equal diameter and total rubber height) and compound (i.e. equal soft compound with $G = 0.4$ MPa). However, a different source of rubber is considered in the comparative study (reclaimed rubber for P-RU-FREI against virgin rubber for SREI) to better highlight the potential environmental benefits of the different isolation systems.

The main properties of both the isolators are given in Figure 1 and listed in Table 1 where the diameter of the isolator D and the corresponding rubber height H_r , the total height of the device H , the thickness of the rubber layer t_r , and the thickness of reinforcement t_f are given. For the sake of comparison, the same value of the second shape factor $S_2 = D/H_r = 4.4$ is obtained for both P-RU-FREI and SREI, which is capable of ensuring lateral stability up to 200% shear strain-imposed deformation. The primary shape factor S_1 (defined as the ratio of the loaded area over the rubber layer free-to-bulge area) is approximately equal to 20 for both isolators in the same way.

Table 1. Properties of P-RU-FREI and SREI.

	P-RU-FREI	SREI
Reinforcement type	2D polyester fabric	Steel shim
Rubber compound	Reclaimed	Virgin
D [mm]	400	400
t_r [mm]	5	5
t_f [mm]	0.53	3
n [-]	18	18
H_r [mm]	90	90
H [mm]	99	141

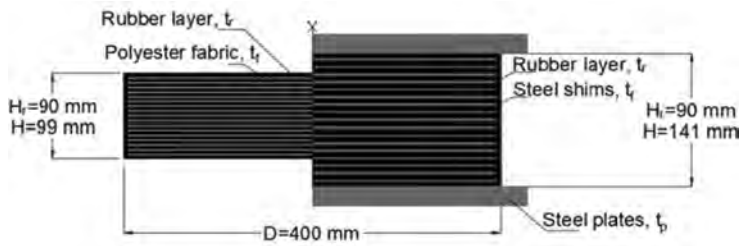


Figure 1. Stratigraphy of P-RU-FREI (left) and SREI (right).

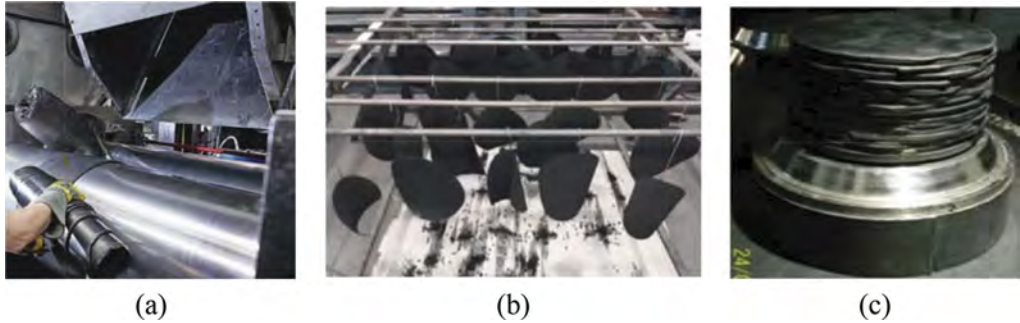


Figure 2. Manufacturing process of elastomeric isolators: (a) rubber compound preparation; (b) flexible reinforcement preparation; (c) isolator assembly.

2.1 Manufacturing process

The manufacturing process for both isolators can be divided into three main phases: (1) rubber compound preparation (Figure 2a); (2) reinforcement preparation (Figure 2b); (3) isolator assembly and vulcanization (Figure 2c).

Phase (1) consists of a mixing and milling process of the rubber compound. It follows the same steps for both types of isolators and differs only for the process duration, which is 40 min for the virgin compound and 60 min for the reclaimed compound. The latter compound was obtained as a hybrid mix of virgin rubber and tyre rubber crumb (mixture of butadiene rubber SBR, and natural rubber NR) in a weight ratio equal to 1:1.

A longer process is required in the case of steel reinforcement with respect to fibre reinforcement for phase (2), which includes sandblasting of metals, primer and adhesive application in the former case, while it reduces to fibre sheets impregnation with proper adhesive only in the latter case.

Phase (3) consists in stacking in a preheated mould alternated layers of rubber and reinforcement. This multilayer structure is vulcanized by applying heat and pressure to the mould for a sufficient time (180 min for SREI and 120 min for P-RU-FREI) to ensure that an optimal linkage activation is achieved.

3 LCA MODEL AND RESULTS

To assess the environmental performances of both seismic isolation systems in the product stage, a comparative life cycle assessment (LCA) was carried out. According to (ISO14040 2006) and (ISO14044 2006), the LCA method includes four steps: (1) goal and scope definition; (2) life cycle inventory (LCI) analysis; (3) life cycle impact assessment (LCA); and (4) interpretation (Klöppfer 2012; Curran 2013). The goal of this study is to analyze the environmental impacts of P-RU-FREI and SREI isolators with the geometry described above and assumed as a functional unit in order to compare the results for the different impact categories and determine which is the least impacting device from the production point of view. Production of the isolators is a complex process that can be divided into three steps: rubber compound preparation, reinforcement preparation, and isolator

assembly. The main processes involved in the production of P-RU-FREI and SREI isolators were included in the system boundary shown in Figure 3(a) and (b), respectively. The grey boxes refer to end-product, i.e. the isolator; the blue boxes refer to the main steps involved during the isolators production. The green boxes refer to material or energy inputs to system (raw material supply, transport to the plant, energy needed to process raw materials); the orange boxes refer to waste flows in which the dashed arrows refer to recycled material reintroduced into the process.

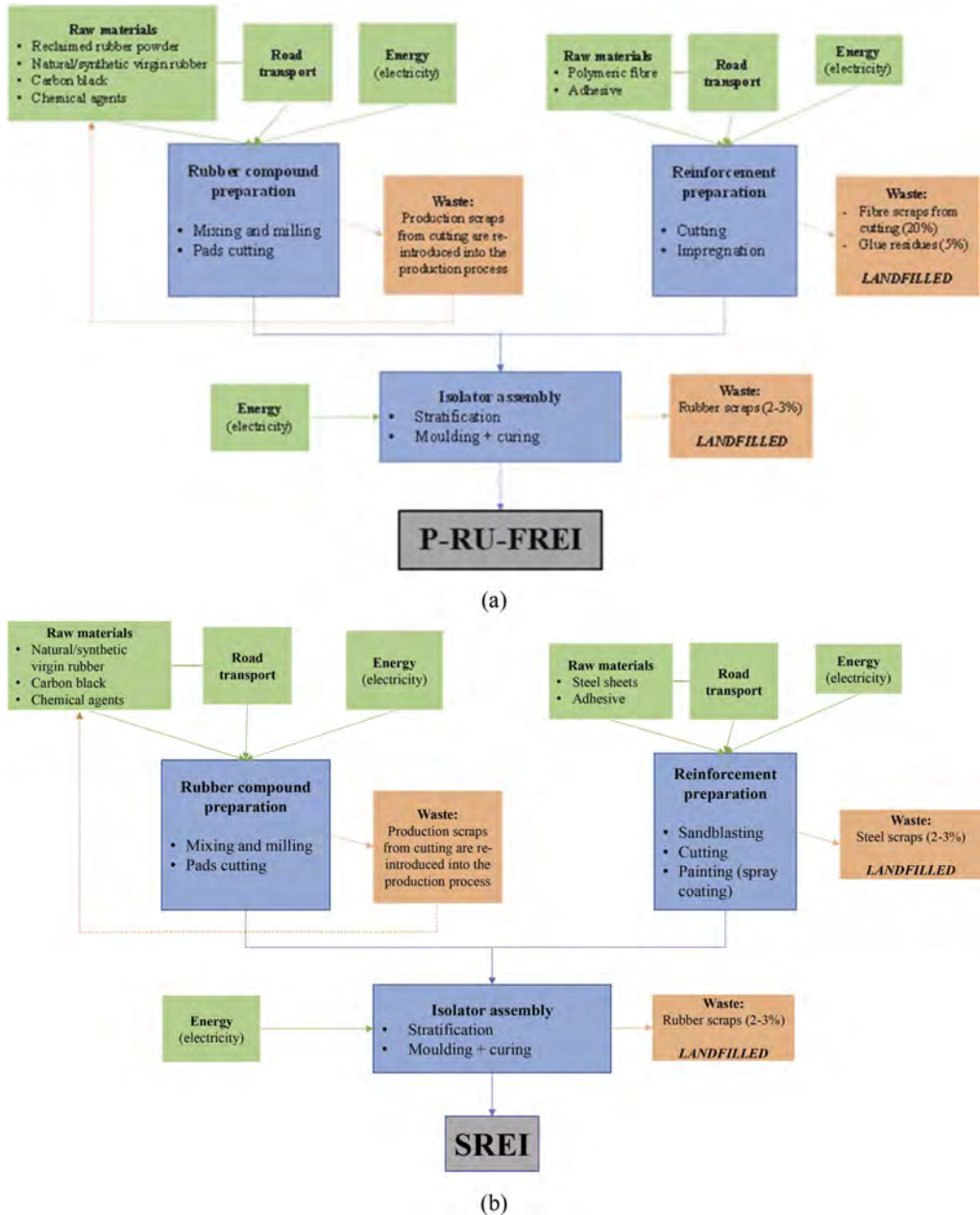


Figure 3. The system boundary of P-RU-FREI (a) and SREI (b) production stage.

Table 2. The inventory of the LCA of processing P-RU-FREI and SREI.

Step	Materials and energy	
	P-RU-FREI	SREI
Rubber compound preparation		
Input	NR/SBR tyre reclaimed rubber Natural rubber Styrene - butadiene rubber Polybutadiene Zinc oxide Paraffins Hydrocarbon resin Carbon black Naphthenic oil Transport Electricity	Natural rubber Styrene - butadiene rubber Polybutadiene Zinc oxide Paraffins Hydrocarbon resin Carbon black Naphthenic oil Transport Electricity
Reinforcement preparation		
Input	Polyester fibre/resin Chemosil 231 G Transport Electricity	Steel reinforcement Plates Adhesive Connecting plates Transport Electricity
Output	Fibre scraps Glue residues	Steel scraps
FREIs Isolator assembly		
Input	Rubber compound Reinforcement Electricity	Rubber compound Reinforcement Electricity
Output	Rubber scraps	Rubber scraps

IMPACT2002+ methodology (Joliet et al. 2003) was selected for the impact assessment phase of the study. It proposes a feasible implementation of a combined midpoint/damage approach, linking all types of life cycle inventory results via several midpoint categories to several damage categories. IMPACT2002+ considers 15 midpoint categories which are expressed in reference units of a given substance and are quantified starting from preexisting impact assessment methods. Midpoint categories are then combined to define four damage categories: human health, ecosystem quality, climate change, and resources. These four damage categories are expressed in DALY, PDF m² y, kg CO_{2-eq} and MJ, respectively. For the sake of brevity, only the results in terms of mid-point categories are considered in this study.

Environmental Impacts are first characterized; then, they are normalized with reference to mean European values representative of a certain period of time, either at the midpoint or at the damage level. Normalization allows the different categories to be plotted on the same graph, making the interpretation of results easier and contextualizing the results.

3.1 Life Cycle Inventory (LCI) analysis

LCI is a phase to list all the data collected and identify inputs/outputs (Li et al. 2010). The detailed foreground data of this study are summarized in the Table 2. Moreover, the ecoinvent database (<https://ecoinvent.org/the-ecoinvent-database/>) was applied in this study to provide detailed background data on generic materials, energy, transportation, and waste.

Data for the raw materials were further elaborated by taking into account cut-off criteria. Cut-off rules enable LCA practitioners to conduct LCA without having to model 100% of the product system. According to the ILCD Handbook (Curran 2012), the cut-off criteria refer to the omission of non-relevant life cycle stages, activity types, specific processes and products and elementary flows from the system model. In this specific case all materials with a percentage in weight less than 1% have been neglected. The use of NR/SBR tyre reclaimed rubber in the P-RU-FREI production

process was modelled as avoided impact in terms of virgin natural rubber. Data for the electricity input was selected in ecoinvent as “Electricity mix, AC, consumption mix, at the consumer, 1kV - 60kV IT S”. It represents the Italian specific electricity supply for final consumers, including electricity own consumption, transmission/distribution losses and electricity imports from neighboring countries. The transportation of raw materials (expressed in ton*Km) for both isolators was selected as “transport, freight, lorry 3.5-7.5 metric ton, EURO4”.

3.2 Life cycle impact assessment and interpretation

LCA results are summarized in Figures 4 and 5 by reporting the 15 environmental impact categories for both types of isolators after the execution of the characterization and normalization steps. For each impact category, the environmental impacts are shown by dividing the different stages of the isolator production (rubber compound preparation, reinforcement and assembly). In terms of product stage contribution, Figure 4 (a) and (b) highlight that there is a different environmental burden (in the percentage of the whole impact) associated with the rubber and reinforcement components for P-RU-FREI and SREI isolators. In particular, the rubber compound preparation in the P-RU-FREI production is responsible for the highest environmental impact in all the categories (with an average value of greater than 60%). The reinforcement production accounts for approximately 25% of the total impacts whereas the assembly phase (mostly associated with energy consumption) is responsible for 10% of production impacts. On the contrary, the highest contribution to the environmental burden of the SREI isolator is given by the reinforcement preparation with an average value of 74.7%; while the step of rubber compound preparation and assembly have an average contribution of 22 and 3%, respectively.

Figure 5 shows the results of the mid-point impact categories by comparing the P-RU-FREI and SREI systems. It can be observed that the P-RU-FREI has a lower environmental impact (i.e. 20% on average) in all the categories compared to SREI (reported as 100% in the histogram solid bars) mainly due to the dominant contribution of steel reinforcement production and transformation (orange bars). The beneficial effects of reclaimed rubber in the P-RU-FREI raw material production can be clearly identified only in a few impact categories (e.g., carcinogens, respiratory organics, global warming potential); in the remaining ones, the impacts are comparable to SREI.

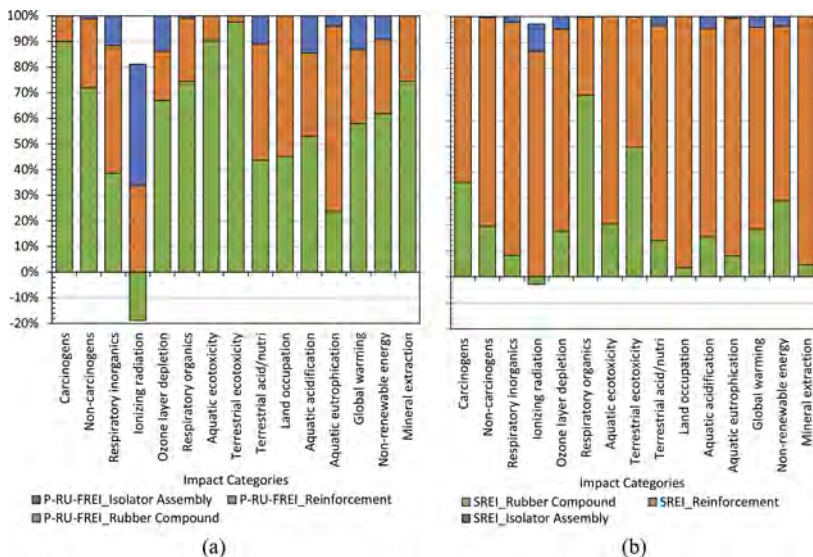


Figure 4. Characterization of environmental impacts for P-RU-FREIs (a) and SREIs (b).

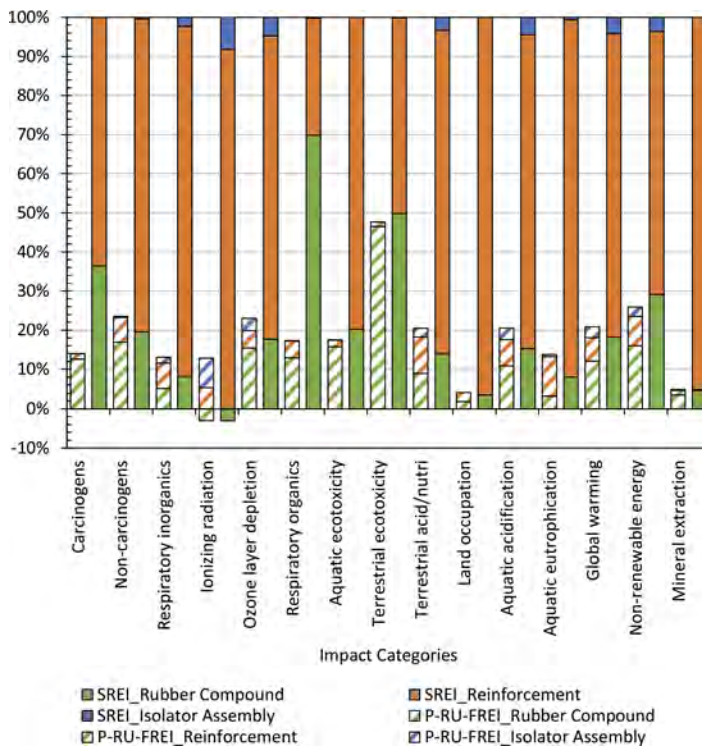


Figure 5. Comparison of P-RU-FREIs and SREIs for the 15 mid-point categories (IMPACT 2002+).

4 CONCLUSIONS

In this study, the environmental performances of two isolation systems have been assessed by means of LCA. Preliminary results – focusing on the isolator production stage – demonstrate the interesting potential of reducing environmental impacts in the case of P-RU-FREI devices; lighter reinforcements compared to steel ones might be an effective solution to reduce the burden of steel-related transformation processing in SREI. The use of reclaimed rubber in the P-RU-FREI raw material production can provide additional benefits. However, further investigations should be considered to achieve a comprehensive evaluation of both systems, such as the extension of LCA to the building scale, durability and maintenance, and end-of-life scenarios.

ACKNOWLEDGMENTS

The company ITALGUM (<https://www.italgum.com/>) and Dr. Luigi Piga are gratefully acknowledged for providing relevant information about the manufacturing process for LCA.

REFERENCES

Calabrese A., Losanno D., Spizzuoco M., Strano S. & Terzo M. 2019. Recycled Rubber Fiber Reinforced Bearings (RR-FRBs) as base isolators for residential buildings in developing countries: The demonstration building of Pasir Badak, Indonesia. *Engineering Structures*. 192:126–144.

Caruso M.C., Menna C., Asprone D., Prota A. & Manfredi G. 2017. Methodology for life-cycle sustainability assessment of building structures. *ACI Structural Journal* 114(2):323.

Cilento F., Losanno D. & Piga L. 2022. An experimental study on a novel reclaimed rubber compound for fiber-reinforced seismic isolators. *Structures*. 45:9–22.

Curran M.A. 2012. Life cycle assessment handbook: a guide for environmentally sustainable products. New Jersey.

- Curran M.A. 2013. Life cycle assessment: a review of the methodology and its application to sustainability. *Current Opinion in Chemical Engineering* 2(3):273–277.
- Habieb A.B., Milani G., Cerchiaro R., Quaglini V. & Milani F. 2021. Numerical study on rubber compounds made of reactivated ethylene propylene diene monomer for fiber reinforced elastomeric isolators. *Polymer Engineering and Science*. 61(1):258–277.
- ISO14040. 2006. Environmental management—Life cycle assessment: Principles and framework.
- ISO14044 2006. Environmental management—Life cycle assessment: Requirements and Guidelines.
- Italgum S.r.l, Piga L, Losanno D & Cilento F. 2022. “Dispositivo isolatore, quale un isolatore sismico o un elemento di appoggio, metodo per il suo ottenimento e materiale comprendente almeno un elastomero recuperato n.ro 102022000013360.”:1–32 (patent application).
- Jolliet O., Margni M., Charles R., Humbert S., Payet J., Rebitzer G. & Rosenbaum R. 2003. IMPACT 2002+: a new life cycle impact assessment methodology. *The international journal of life cycle assessment* 8(6):324–330.
- Klöppfer W. 2012. The critical review of life cycle assessment studies according to ISO 14040 and 14044. *The international journal of life cycle assessment* 17(9):1087–1093.
- Konstantinidis D. & Kelly J.M. 2014. Advances in low-cost seismic isolation with rubber. *NCEE 2014-10th U.S. National Conference on Earthquake Engineering: Frontiers of Earthquake Engineering*
- Li X., Xu H., Gao Y. & Tao Y. 2010. Comparison of end-of-life tire treatment technologies: A Chinese case study. *Waste management* 30(11):2235–2246.
- Losanno D., Madera Sierra I.E., Spizzuoco M., Marulanda J. & Thomson P. 2019. Experimental assessment and analytical modeling of novel fiber-reinforced isolators in unbounded configuration. *Composite Structures*. 212(December 2018):66–82.
- Losanno D., Calabrese A., Madera-Sierra I.E., Spizzuoco M., Marulanda J., Thomson P. & Serino G. 2020. Recycled versus Natural-Rubber Fiber-Reinforced Bearings for Base Isolation: Review of the Experimental Findings. *Journal of Earthquake Engineering*. 00(00):1–20.
- Losanno D., Ravichandran N., Parisi F., Calabrese A. & Serino G. 2021. Seismic performance of a Low-Cost base isolation system for unreinforced brick Masonry buildings in developing countries. *Soil Dynamics and Earthquake Engineering*. 141:106501.
- Losanno D., De Domenico D. & Madera-Sierra I.E. 2022a. Experimental testing of full-scale fiber reinforced elastomeric isolators (FREIs) in unbounded configuration. *Engineering Structures*. 260:114234.
- Losanno D., Ravichandran N. & Parisi F. 2022b. Seismic fragility models for base-isolated unreinforced masonry buildings with fibre-reinforced elastomeric isolators. *Earthquake Engineering & Structural Dynamics*
- Madera Sierra I.E., Losanno D., Strano S., Marulanda J. & Thomson P. 2019. Development and experimental behavior of HDR seismic isolators for low-rise residential buildings. *Engineering Structures*. 183:894–906.
- Napolano L., Menna C., Asprone D., Prota A. & Manfredi G. 2015. Life cycle environmental impact of different replacement options for a typical old flat roof. *The international journal of life cycle assessment* 20(5):694–708.
- Ortiz O., Castells F. & Sonnemann G. 2009. Sustainability in the construction industry: A review of recent developments based on LCA. *Construction and building materials* 23(1):28–39.
- Strauss A., Apostolidi E., Zimmermann T., Gerhaher U. & Dritsos S. 2014. Experimental investigations of fiber and steel reinforced elastomeric bearings: Shear modulus and damping coefficient. *Engineering Structures*. 75:402–413.
- Toopchi-Nezhad H., Tait M.J. & Drysdale R.G. 2011. Bonded versus unbonded strip fiber reinforced elastomeric isolators: Finite element analysis. *Composite Structures*. 93(2):850–859.

Definition of a design procedure of seismic isolation systems based on rubber bearings

Marco Furinghetti

Civil Engineering and Architecture Department – DICAr, University of Pavia, Pavia, Italy
EUCENTRE Foundation, Pavia, Italy

ABSTRACT: Among the many protective strategies against earthquake excitations, Rubber Bearings represent the easiest solution for seismic isolation systems, even though a number of issues have to be considered, especially related to vertical buckling and limitations on the maximum vertical load which can be applied to the single isolator. In this work a fast design procedure is defined specifically for Rubber Bearing isolators, by considering initial assumptions, which can be easily managed by practitioners. With hand computations in few steps, devices can be determined in terms of both geometrical and mechanical properties, able to provide the proper period shift and energy dissipation, in agreement with the assumed performance point, avoiding buckling behavior with respect to the vertical direction. The presented procedure has been applied to a case study structure, which has been numerically analyzed, in order to assess the efficiency of the designed isolation system.

1 INTRODUCTION

Passive isolation represents one of the most effective techniques for the reduction of the seismic vulnerability of both newly designed and existing poorly designed structural systems. (Brunesi et al. 2016, Calvi and Calvi 2018). In the recent past, both numerical and experimental campaigns have led to the development of a number of devices, able to provide specific energy dissipation, associated to low values of lateral stiffness, which directly implies a period shift (Constantinou et al. 1990, Constantinou et al. 1999, De Domenico et al. 2018, Dolce et al. 2005, Fenz and Constantinou 2006, Kumar et al. 2013). Consequently, low internal forces are induced into the superstructure, and the high displacement demand expected at the isolation system can be limited. Thanks to the outcomes of experimental tests, a number of numerical models have been developed with high levels of sophistication, which are able to reproduce the force response of the implemented devices. This allows realistic numerical seismic simulations, which can return precious results for both vulnerability and risk assessments (Dall’Asta et al. 2020, Cardone et al. 2019, Mazza and Mazza 2017). On the other hand, even though come general guidelines for the design of an isolation system are provided by commonly adopted standard codes worldwide, the definition of specific design rules would help practitioners to obtain the geometrical and mechanical parameters for isolation devices, in order to guarantee a certain performance point.

In this work fast design rules for seismic isolation systems based on elastomeric devices are defined and validated, through Non-Linear Time-History Analyses. Special attention will be focused on the definition of geometrical and mechanical properties of the isolators, in order to consider eventual buckling effects since the design phase.

2 FAST DESIGN RULE

In this work, fast design rules are defined, specifically for elastomeric isolators (Figure 1). The aim is to provide a few-step procedure to come up with an initial configuration of the isolation system of a building, by accounting for buckling and local failures.

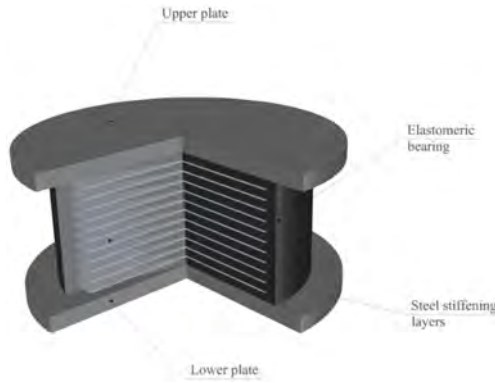


Figure 1. Internal components of a Rubber Bearing isolation device.

The adopted fast design procedure has been developed in a recent research work (Furinghetti, 2022). The presented procedure starts with the assumption of a performance point, in terms of design period and equivalent viscous damping (Figure 2). Consequently, the displacement demand of the isolation system can be computed, in terms of displacement spectral coordinate, at the design period, as a function of the assumed equivalent viscous damping.



Figure 2. Definition of the performance point.

Once the displacement demand is computed, the total height of the device can be obtained, by assuming a design shear strain, generally equal to 100% (Step (1)). Then, the horizontal diameter of the single elastomeric isolator can be computed as a function of the displacement demand, through the application of a scale factor: this is to ensure that the isolator is able to transfer the applied vertical load from the superstructure to the substructure even when the maximum displacement is achieved, with no buckling phenomena; this implies scale factors β higher or equal to 2,0. Hence, all the geometrical parameters of the single device are defined, and the lateral stiffness of the single device can be computed, as a function of the shear modulus of the adopted compound. Finally, the number of elastomeric isolators can be determined, by considering the ratio between the global stiffness of the system (as a function of the design period and the global isolated mass) and the stiffness of the single isolator; it can be noted that the overall procedure does not consider any additional force response related to the eventual Flat Sliders, needed to cover all the bearing points of the structure.



Figure 3. Steps of the fast design procedure.

Step 2) is strongly related to possible buckling phenomena of the designed isolators, especially when the device is subjected to the maximum shear deformation (De Luca et al. 2019).

To this aim, elastomeric isolation bearing can be characterized by a Critical Vertical Load, depending on two shape factors S_1 and S_2 , and accounting for the effective reduced plan area which is addressed to transfer the vertical load from the superstructure to the substructure, as shown in eq.(1) (De Luca et al. 2019).

$$\left\{ \begin{array}{l} N_{crit} = G_r \cdot A_r \cdot S_1 \cdot S_2 \\ S_1 = \frac{\phi}{4t_r} \\ S_2 = \frac{\phi}{t_e} \\ A_r = A_{iso} \cdot \left(1 - \frac{D_d}{\phi}\right) \end{array} \right. \quad (1)$$

Thus, in order to obtain a better definition of the plan diameter of the elastomeric isolator, all these parameters have been combined, by assuming a design target value of vertical pressure, defined as the ratio between the critical vertical load and the gross plan area of the device.

$$\left\{ \begin{array}{l} N_{crit} = G_r \cdot A_{iso} \cdot \left(1 - \frac{D_d}{\phi}\right) \cdot \frac{\phi}{4t_r} \cdot \frac{\phi}{t_e} \\ t_e = n_r \cdot t_r \\ \sigma_d = \frac{N_{crit}}{A_{iso}} \end{array} \right. \quad (2)$$

In agreement with such assumptions, the following expression of the design vertical pressure σ_d can be obtained, as a function of the maximum displacement D_d , the shear modulus of the elastomeric compound G_r , the diameter of the device Φ , the number and the thickness of the rubber layers (n_r and t_r respectively).

$$\sigma_d = G_r \cdot \left(1 - \frac{D_d}{\phi}\right) \cdot \frac{\phi^2}{4 \cdot n_r \cdot t_r^2} \quad (3)$$

If the thickness of the single elastomeric layer is assumed, then a second order equation with respect to the diameter of the isolator is obtained.

$$\phi^2 + (-D_d) \cdot \phi + \left(-\frac{4 \cdot n_r \cdot t_r^2 \cdot \sigma_d}{G_r}\right) = 0 \quad (4)$$

Finally, the diameter of the device can be obtained, and thanks to the proposed formulation, the returned value is directly associated to a critical vertical load, which is related to a specific design vertical pressure.

3 APPLICATION TO A CASE STUDY STRUCTURE

In order to validate the efficacy of the proposed fast design rule, a case study structure has been considered, consisting of a 6-storey reinforced concrete frame building, with all members designed according to Italian code-conforming provisions (Cardone et al. 2019). The horizontal sizes are approximately 21m and 12m for x and y directions respectively, with an interstorey height of 3.05m for all the floors, and 3.4m for the first, resulting in a total height of 19m.

The seismic mass for all the levels of the building is approximately equal to 300tons, with a total weight of the structure of 2080tons. If the modal analysis is performed, by modeling linear elastic frame elements for both beams and columns, a first mode period of vibration around 1.0 seconds is obtained. For the proper evaluation of the protection level provided by the designed isolation system, a non-linear static analysis (push-over) has been computed, through an OpenSees model of the fixed-base configuration.

In Figure 4 results are shown in terms of capacity curve of the structure.

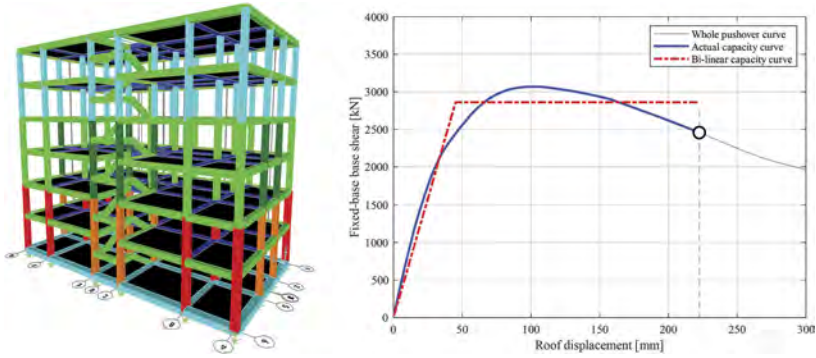


Figure 4. Case study structure.

In order to determine the ultimate point of the building, a reduction of 20% of the maximum strength has been considered. Then, the non-linear capacity curve has been approximated through a bi-linear behavior, by implementing a special least-square procedure, which minimizes the sum of square errors of the base shear values, by ensuring the same area below each curve, corresponding to an energy balance.

Non-Linear Time History Analyses (NLTHA), performed on a linear elastic model of the building, implemented within SAP2000 (CSI 2021), by applying a selection of seven unidirectional natural seismic events (Iervolino et al. 2009). The spectrum-compatibility of the adopted suite of ground motions has been studied, in agreement with the Italian Building Code (NTC 2018), as a function of the seismic hazard level defined for the construction site: namely, L'Aquila city, with Soil class C and topography category T1. The Collapse Limit State has been assumed, corresponding to a return period of 975 years. The spectrum-compatibility has been checked, by considering 90% and 130% respectively of the code target spectrum as lower and upper bounds, in comparison to the mean spectrum of the selected events, within a period range between 0,15s and 3,0s.

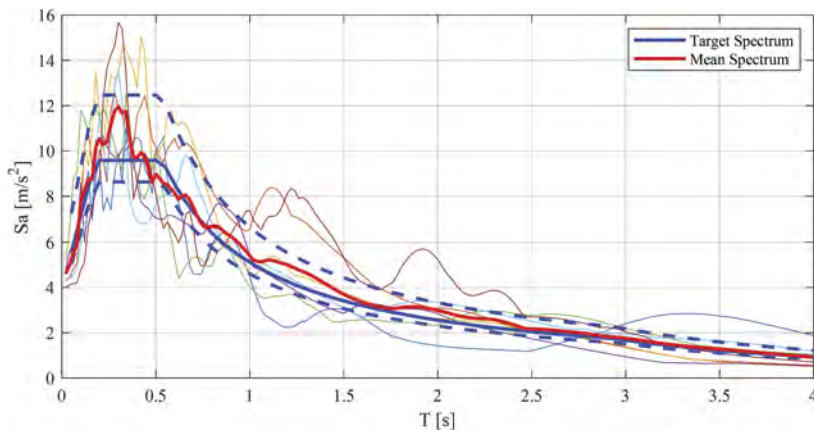


Figure 5. Selection of code-based spectrum compatible seismic events.

Single-events ground acceleration time series have been scaled, in order to better achieve spectrum-compatibility prescriptions; moreover, scale factors have been bounded between 0.5 and 2.0, aiming at preserving the correct frequency content for the considered Peak Ground Acceleration (PGA) values.

For the application of the aforementioned fast design procedure, a number of mechanical and geometrical quantities have been initially assumed. Firstly, a performance point has been

detected, at a design period value of 2.8sec, together with an equivalent viscous damping of 15%, corresponding to High Damping Rubber Bearings. Then, 100% of design lateral shear strain has been considered, and the adopted compound has been characterized by a shear modulus value equal to 0.8MPa. For the proper definition of the plan diameter of the device, as a design value of the vertical pressure, 9.0MPa has been considered, as the reference value for the testing protocol for elastomeric bearings in agreement with the European Standard Code UNI:EN15129:2018 (CEN 2018 - namely 6.0MPa), increased by 50%. Finally, 12mm and 2mm have been considered as thickness values for rubber and steel layers respectively.

In Table 1 all the design parameters returned by the adopted procedure are summarized.

Table 1. Design parameters for the case study structure.

T_d [sec]	ξ_d [%]	h_{is} [mm]	γ_d [%]	G_r [MPa]	σ_d [MPa]	Φ_r [mm]	n_{is} [#]
2.8	15	252	100	0.8	9.0	516	16

As can be noted, the design procedure has led to an isolation system of 16 elastomeric devices. Since the considered case study structure has 24 bearing points, Flat Sliders have to be implemented, in order to correctly support the structural weight of the building. In addition, seismic elastomeric isolators have been placed in the most external regions of the plan view of the building, in order to increase as much as possible the resulting torsional stiffness of the isolation system, by providing a symmetric layout. In Figure 6 the final configuration of the designed isolation system is shown.

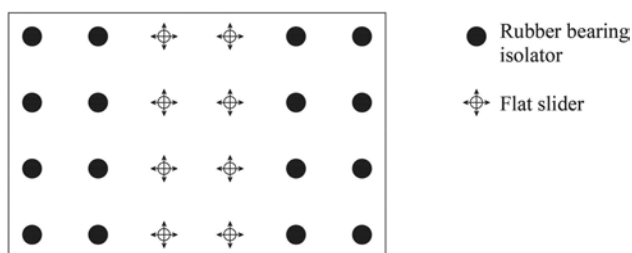


Figure 6. Distribution of devices for the designed isolation system.

4 RESULTS OF N.L.T.H.A.

In this section global results are presented, in terms of single-event and mean values of peak isolation displacement (Figure 7) and peak building base shear (Figure 8).

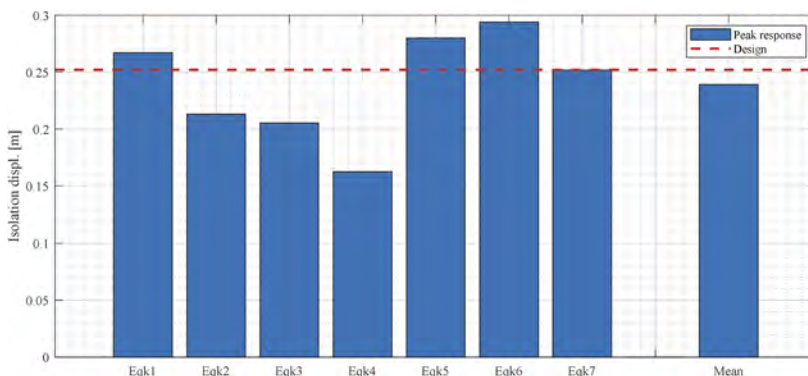


Figure 7. Results: peak isolation displacement.

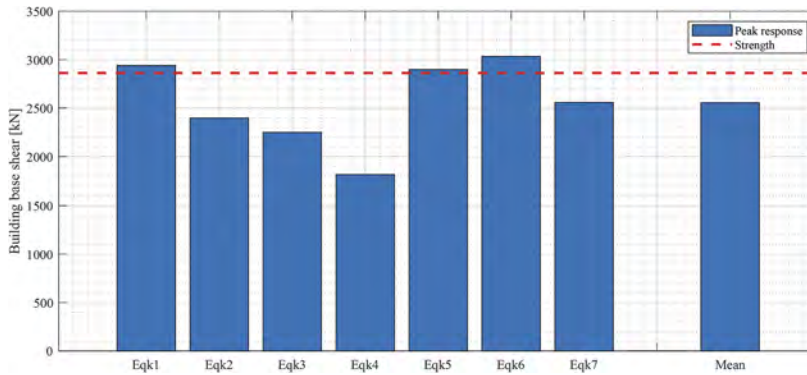


Figure 8. Results: peak building base shear.

As can be noted, the mean isolation displacement, which represents the reference value, in agreement with the Italian building Code, is close to (but lower than) the target design displacement of the devices; in addition, also the single-event values are fairly close to the target design displacement, thanks to both the proper adopted design procedure and the high level of spectrum-compatibility of the applied suite of ground motions.

Furthermore, if the efficacy and the protection capabilities of the designed isolation system are considered, through the analysis of the single-event and the mean peak base shear of the building, it can be assessed that the building force response falls within the elastic range in almost all cases; in some seismic events larger values can be detected, with limited variation percentages (below 10%), which can still be considered as included in the elastic linear elastic response.

5 CONCLUSIONS

In this work a fast design procedure for elastomeric bearings has been presented. More specifically, special attention has been focused on the protection against the buckling critical load at maximum displacement, so that the isolator is able to provide the proper support for the whole range of applied vertical loads. The procedure has been applied to a case study structure, by performing Non-Linear Time History Analyses, and results have led to the following remarks:

- The adopted procedure has led to the proper geometrical characteristics of the implemented isolators, and the plan diameter has been computed, in order to guarantee that a specific value of average vertical pressure, as correspondent to the critical load;
- For safety reasons, the reference value of average vertical pressure has been defined as the vertical load generally applied in testing protocols, in agreement with the European Standard Code UNI:EN15129:2018 (namely 6.0MPa), increased of 50%, resulting into 9.0MPa.
- The proposed procedure leads to a sufficiently safe definition of the displacement demand for the isolation system, and low variations can be detected also for the single-event response;
- Concerning the base-shear response of the building, it can be assessed that all values are approximately lower than or equal to the maximum strength of the bi-linear capacity curve of the building, ensuring a linear-elastic response for both the single-event and the mean cases, even though slightly higher values can be detected for some earthquake simulations.

ACKNOWLEDGEMENTS

Part of the current work has been carried out under the financial support of the Italian Civil Protection, within the frameworks of the Executive Project 2017–2019 (Project 3 – Assessment

of the seismic isolation of building structures through hybrid tests with numerical substructuring) and the national Research Project DPC – ReLUIIS (National Network of Laboratories of Seismic Engineering) 2022–2024, WP15.

REFERENCES

- Brunesi E., Nascimbene R., Pavese A. (2016) Mechanical model for seismic response assessment of lightly reinforced concrete walls. *Earthquake and Structures*, Volume 11, Issue 3, Pages 461–481.
- Calvi P.M., Calvi G.M. (2018) Historical development of friction-based seismic isolation systems. *Soil Dynamics and Earthquake Engineering* 106(2018):14–30.
- Cardone D., Conte N., Dall’Asta A., Di Cesare A., Flora A., Lamarucciola F., Micozzi F., Ponzo F.C., Ragni L. (2019), “RINTC_E Project: the Seismic Risk of Existing Italian RC Buildings Retrofitted with Seismic Isolation”, *COMPdyn 2019, 7th ECCOMAS Thematic Conference on Computational Methods in Structural Dynamics and Earthquake Engineering*, Crete, Greece, 24–26 June 2019.
- CEN – Comité Européen de Normalisation TC 340 (2018) “European Code UNI EN 15129:2018 Anti-seismic devices”, Brussels.
- Constantinou M., Mokha A., Reinhorn A. (1990). Teflon bearings in base isolation II: modeling. *Journal of Structural Engineering*, 116:455–474.
- Constantinou, M. C., Tsopelas, P., Kasalanati, A., and Wolff, E. (1999). “Property modification factors for seismic isolation bearings.” Report No. 99-0012, MCEER.
- CSI, “SAP2000 v.21.2.0, Integrated Software for Structural Analysis and Design,” Computers and Structures Inc., Berkeley, California.
- Dall’Asta A, Leoni G, Micozzi F, Gioiella L and Ragni L (2020) A Resilience and Robustness Oriented Design of Base-Isolated Structures: The New Camerino University Research Center. *Front. Built Environ.* 6:50. doi: 10.3389/fbuil.2020.00050
- De Domenico D., Ricciardi G., Benzoni G. (2018). Analytical and finite element investigation on the thermo-mechanical coupled response of friction isolators under bidirectional excitation. *Soil Dynamics and Earthquake Engineering*, 106, 131–147.
- De Luca, A.; Guidi, L.G., 2019, “State of art in the worldwide evolution of base isolation design” *Soil Dynamics and Earthquake Engineering*, 125, 105722, <https://doi.org/10.1016/j.soildyn.2019.105722>.
- Dolce M., Cardone D., Croatto F. (2005) Frictional behavior of steel-PTFE interfaces for seismic isolation. *Bulletin of Earthquake Engineering*, 3, 75–99.
- Fenz D., Constantinou M.C. (2006). Behaviour of the double concave friction pendulum bearing. *Earthquake Engineering And Structural Dynamics*, 35,1403–1424.
- Furinghetti, Marco. 2022. “Definition and Validation of Fast Design Procedures for Seismic Isolation Systems” *Vibration*, 5, no. 2: 290–305. <https://doi.org/10.3390/vibration5020017>.
- Iervolino I., Galasso C., Cosenza E. (2009). REXEL: computer aided record selection for code-based seismic structural analysis. *Bulletin of Earthquake Engineering*, DOI: 10.1007/s10518-009-9146-1.
- Kumar M., Whittaker A.S., Constantinou M.C. (2015). Characterizing friction in sliding isolation bearings. *Earthquake Engineering and Structural Dynamics*, 44,1409–1425.
- Mazza F., Mazza M. (2017) Sensitivity to modelling and design of curved surface sliding bearings in the nonlinear seismic analysis of base-isolated r.c. framed buildings. *Soil Dynamics and Earthquake Engineering*, 79, 951–970.
- NTC 2018, Norme Tecniche per le Costruzioni, Decreto ministeriale del 17 gennaio 2018, in Italian (Italian Building Code, 2018).

Inverse design of isolated structures using predicted FEMA P-58 decision variables

H.G. Pham & T.C. Becker

University of California, Berkeley, California, USA

ABSTRACT: Base isolation systems are often chosen in structural engineering to outperform conventional designs, allowing designers to achieve high performance goals. However, achieving specific performance targets requires numerous high-fidelity analyses and often involves iterative design. To address this, a database of diverse structural designs under earthquake inputs is constructed, and probabilistic loss and downtime estimation is carried out. Several machine learning models are utilized to fit the design parameters to their performance, allowing for prediction over a wide space of new design combinations. The prediction models find that accurate cost estimation relies on classification of impact against the moat wall, which is strongly predicted by the moat capacity of the isolators. The developed model is used to for an inverse design procedure in which acceptable design regions are attained by defining acceptable limits for repair cost, downtime, etc, and the resulting design is verified to outperform a typical code compliant design.

1 INTRODUCTION

Recent research into performance based engineering has significantly improved engineers' and stakeholders' capabilities in quantifying losses and risks associated with seismic threats. Past studies involving such assessments for conventional steel special moment frames found that significant losses are retained in replacement costs (Hwang & Lignos 2017) as well as lengthy disruption in the building's functionality and occupancy status (Molina Hutt et al. 2016). With regards to these societal consequences, however, the incorporation of economic performance metrics into a targeted design process remains a large challenge, even for fixed based structures. Although ASCE 7-22 (2022) code provisions provide safety measures aimed at meeting collapse risk targets, they do not ensure the functionality of buildings after an event. Under these contexts compounded with the extensive time and computational cost associated with iterative design and performance assessment, the development of a design process to optimize building performance subjected to targets in decision variables and economic metrics warrants additional research.

The FEMA P-58 (2018) methodology is the state-of-the-art loss estimation approach in structural design, but fully carrying out the performance assessment for design is a time-consuming task. Full design considering these economic metrics have been studied for conventional fixed-base moment frames (Ghasemof et al. 2022), and while the effect of base isolation on building resiliency have been analyzed in case studies (Moretti et al. 2014), the inverse design that directly targets the economic consequences as estimated by FEMA P-58 remains an unexplored topic. The continued development of data learning and prediction models offers a solution to bypass the lengthy assessment process of early estimations in structural design. This combination of machine learning aided estimations and the FEMA loss assessment has been previously utilized to evaluate the effect of design parameters and modeling uncertainty on lifetime costs for fixed based structures (Hwang et al. 2022), but has not been

used to carry out an inverse design problem, especially for isolated structures. Thus, this research seeks to provide a data learning assisted inverse design procedure that can aid in preliminary design of a broad range of isolated building given clear design goals such as desired downtime and/or costs.

2 DATABASE CONSTRUCTION

To create the database, a set of inputs is generated from which the building design is automated and a ground motion is scaled. A set of 400 points is generated to train the prediction models. The structure is a three-story steel moment frame, isolated with triple friction pendulum (TFP) bearings. The superstructure is 3 bays and 3 stories. Figure 1 shows an elevation of the structure with dimensions along with several important design parameters used in the problem.

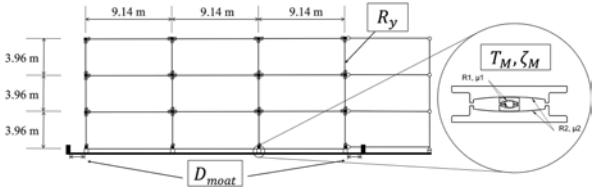


Figure 1. Elevation view: isolated moment frame and TFP bearing.

The design of the structure is based on typically used design parameters. The descriptions and ranges for each parameter are presented in Table 1. Parameter ranges are chosen to reflect typical values that might be seen in the design of an isolated structure in coastal California. The range for the amplification of the moat gap, A_δ , is chosen to investigate potential overdesign of the displacement capacity that might be needed. The strength reduction factor, R_y , is defined as the reduction applied onto the elastic base shear for the structure and is treated as a random variable to explore the effects of increasing the superstructure strength. Its upper bound (2.0) is the ASCE 7-22 recommended value for isolated steel moment frames. For the purpose of creating a space of input variables, Latin hypercube sampling with uniform distribution is utilized to generate design input combinations to ensure that an evenly distributed input set is achieved and to provide a well-supported basis for the prediction models.

Table 1. Design inputs for Latin hypercube sampling.

Input	Description	Lower bound	Upper bound
S_1	Target spectral acceleration at $T = 1$ sec	0.8	1.3
T_M	Target effective period for bearing design	2.5 sec	4.0 sec
ζ_M	Target effective damping for bearing	0.10	0.20
μ_1	Inner slider friction coefficient	0.01	0.05
R_1	Inner slider radius of curvature	380 mm (15 in)	1140 mm (45 in)
A_δ	Amplitude for moat gap	1.0	2.0
R_y	Strength reduction factor	0.5	2.0

2.1 Design of the bearings and superstructure

The TFP bearing design is derived from the unidirectional multi-stage behavior of TFP bearings. Figure 1 shows a cross section of the bearing used in the study. For simplicity, this study examines bearings with the outer sliding surfaces sharing the same friction coefficient and radius of curvature. The expected displacement D_M under a given spectrum serves as the nominal recommended moat gap capacity by ASCE 7-22 without amplification for torsion as the analysis is

conducted with a unidirectional ground motion. For this study, to explore the effect of the moat gap on the cost and downtime, the displacement capacity is modified by multiplying by A_δ .

Given the target T_M and ζ_M and two randomly generated design parameters, the remainder of the bearing parameters can be solved. This study randomly selects inner friction coefficients (μ_1) and inner radii of curvature (R_1) to solve for the other bearing parameters as shown in Fenz & Constantinou (2008) or Becker & Mahin (2013). The superstructure is then designed following ASCE 7-22 Chapter 12 procedures, with maximum story drift at $\theta = 0.015$. The lightest compact W-shapes are selected for the beams, and then the columns are selected to ensure a strong column weak beam mechanism. The beams are selected from suitable W-shapes through the process determining sufficient second moment of area (I_x) and section modulus (Z_x) to meet the drift and strength requirements, respectively. The beams are then selected from the lightest compact shape, while the columns are selected to ensure a strong column weak beam mechanism. From the design procedure, the friction coefficients (μ), slider radii of curvature (R), moat gap (D_{moat}), column sections, and beam sections are attained.

2.2 Modeling and analysis in OpenSees

The 2-D model is constructed in OpenSees (McKenna et al. 2010). Beam and column elements are modeled as elastic elements with a rotational spring at each end using the modified Ibarra-Krawinkler material model to account for strength deterioration. Parameters for the material model are adapted to reduce the elastic beam length to 80%, placing each plastic hinge at 10% of the member length away from each joint (Lignos & Krawinkler 2011). To simulate P Δ effects, a leaning column is used to carry the loads from the unmodeled gravity frames. A rigid diaphragm using elastic elements spans the layer above the isolators. The superstructure has Rayleigh damping of 5% and 2% at the first and third superstructure modes.

The bearings are modeled with triple friction pendulum elements using simple Coulomb friction (Dao et al. 2013) without accounting for uplift failure of the bearings. The moat wall is implemented using zero-length impact elements. The impact model uses a damped Hertz contact model (Muthukumar & DesRoches 2006), and the parameters are calibrated assuming that the isolation layer diaphragm is 152 mm (6 in) thick and collides against a 304 mm (12 in) thick moat wall that is 2.74 m (9 ft) tall.

A library of 68 ground motion records from the PEER NGA-West database (Ancheta et al. 2014) from events of magnitudes ranging from 6.0 to 8.0 and distances from 0.0 km to 80.0 km is used. $V_{s,30}$ velocities were limited from 200 m/s to 600 m/s to select for site with dense soil or soft rock. Given a S_1 , the random ground motion is selected and scaled over a range of interest defined as $T = [0.2T_{\text{isol}}, 1.5T_{\text{isol}}]$, where T_{isol} is a typical average period for isolated structures, estimated as 3.0 seconds. The isolated structural model is then subjected to a nonlinear dynamic analysis for a randomly selected ground motion, scaled based on the S1 parameter. The peak interstory drift ratios, floor accelerations, and floor velocities are collected. For this study, analyses are stopped when any story drift ratio exceeds $\theta = 0.20$, and their last committed state and response are recorded.

2.3 Loss and downtime estimation

To perform repair cost and time estimation, a Monte Carlo approach is carried out as called for by the FEMA P-58 guidelines and implemented by the Pelicun (Zsarnóczy & Deierlein 2020) tool for assessment of structural performance. For each design in the database, the engineering demand parameters (EDP) consisting of the peak interstory drift ratios, peak floor accelerations, and peak floor velocities are treated as deterministic samples, and the residual story drift ratios are estimated using the methodology provided in FEMA P-58 using an assumed yield story drift ratio of $\theta_y = 0.0075$. For all structures, non-structural building content is specified assuming that all floors contain 100% office occupancy, except for the first floor which contains 80%-20% retail-office mixed occupancy. All fragility data uses FEMA P-58's database.

For the study, two replacement conditions that trigger the maximum replacement cost for the building are specified: building collapse and irreparable damage. The building collapse damage

state is determined using a collapse fragility curve dependent on story drift. The parameters for the curve is defined by assuming a dispersion of 0.25 (Yun & Hamburger 2002) and that a moment frame with 10% peak drift ratio has a 84% (mean + one standard deviation) collapse frequency. The irreparable damage state is based on values found in FEMA P-58 and has a fragility curve that assumes the risk is distributed lognormal given residual story drift with a mean of $\theta = 0.01$ and a dispersion of 0.3. For both of these cases, the replacement cost is set as 250 USD per 0.092 m² (\$250 per ft²) of floor area, which amounts to 8,100,000 USD for the example structure. Likewise, a replacement downtime is calculated using an assumption that 40% of the replacement cost is labor at the rate of 680 USD per worker-day which is typical for the San Francisco Bay Area. The assessments are then carried out using 10,000 realizations per experiment, and the statistics of the repair cost, repair time, collapse frequency, and irreparable damage frequency are recorded. In this study, the repair time is specified as the time required for a team of 25 workers to repair damaged components sequentially.

3 PREDICTION MODEL

To facilitate the inverse design of structures, several prediction models are built to estimate the expected value of the repair cost, sequential repair time, and collapse risk of a design. From the results of the time history analyses and loss estimations, response parameters and decision variables are greatly increased when the structure experiences impact with the moat wall, and their relationships with the design variables also differ when impact occurs. Additionally, regression performed without considering the effect of impact leads to predictions that underfit the true data, often underestimating loss in scenarios where impact is likely and overestimating loss in the other extreme. Thus, the expected value of a decision variable DV given design variables X is conditioned against I , impact of the moat wall, and the total expected value can be expressed as

$$E[DV | X] = E[DV | X, I = 1]\Pr(I = 1) + E[DV | X, I = 0]\Pr(I = 0) \quad (1)$$

For a single decision variable, three prediction models are then trained: a classification model to perform probabilistic estimation of impact given the design parameters and two regression models to fit decision variables under impact and no impact conditions. To form the covariate vector X that is used to predict outcomes, several important design variables are identified as variables that can characterized structures of different isolated systems and are selected as covariates for the prediction models. The first variable, $\frac{D_{\text{moat}}}{(S_{aT_M}/B_M)T_M^2}$, the moat gap ratio relates the moat gap to the elastic displacement demand and is effectively a multiplier of the displacement capacity required by ASCE 7-22. To account for the stiffness of the structural system in the design process, the variable T_M is retained as the period of the isolation system. Lastly, the variables ζ_M and R_y represent the structural damping and strength reduction factor, respectively. The list of covariates for the surrogate model is then finalized as $\frac{D_{\text{moat}}}{(S_{aT_M}/B_M)T_M^2}$, ζ_M , R_y , and T_M .

3.1 Classification model for impact

For classification of isolation impact, Gaussian process classification (GPC) is used for several reasons. Like the regression methods discussed, Gaussian process classifiers (Williams & Rasmussen 2006) allow for the usage of a kernel in order to expand its feature space to account for nonlinear interaction between variables. However, GPC is a non-parametric method that does not rely on a small weight vector to make prediction, thus allow for prediction to be directly influenced by the size of the training set. Moreover, GPC is a probabilistic model that allows for predictions of outcome's likelihood directly, which is not a well-calibrated option when support vector classifiers.

The database is split into 320 training points and 80 testing points, and the model achieved a prediction score of 90% in the testing set. Figure 2 shows the Gaussian process classification model for impact against the moat wall as predicted using the design variables.

As expected, the likelihood that the isolation layer will impact against its wall is primarily dependent on the gap ratio. The GPC model shows that higher T_M results in a lower predicted probability of impacting the moat wall, visible in the contours moving towards lower gap ratios as T_M increases. R_y and ζ_M show less effect on predicting impact, resulting in relatively stagnant contours as those variables change. The results are reasonably expected, since the gap ratio and T_M most directly affect the flexibility of the bearings as well as the capacity provided to the isolation layer. It should be noted that at higher gap ratios where fewer points lie, the model regresses to a more moderate prediction in absence of data support which results in the slight increase in impact probability seen.

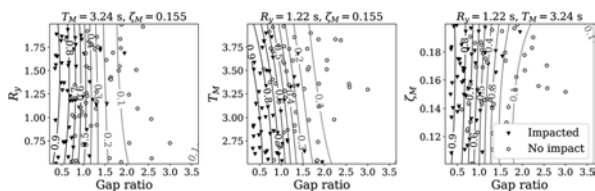


Figure 2. GPC impact probabilities by variables.

3.2 Regression models for decision variables

Two machine learning methods are considered to fit the decision variables (cost and downtime) given an impact condition: support vector regression (SVR) and kernel ridge regression (KR), with the radial basis function (RBF) kernel utilized for both models. Although more complex methods like Gaussian process regression could be considered to carry out the fit, the two methods chosen achieve a similar fit at a much reduced computational cost. The models are fit against the mean decision variable value of the estimation. To fit the model, the 400 points in the database are grouped by their impact status with 188 trials experiencing impact. Each subset is then fit with a separate model, and the regression results are used as conditioned expected values in Equation 1. Ultimately, different models are chosen for different decision variables due to their fit qualities. SVR is used for cost and KR is used for downtime.

Figure 3 details the predictions of the models for repair cost and downtime, weighted by the likelihood of impact as predicted by the GPC model. When predicting cost, the SVR model shows that an increase in T_M reduces the expected mean repair cost across all gap ratios shown. In contrast, a decrease in ζ_M reduces the repair cost, with the decrease more notable at higher damping levels at larger gap ratios where impact is not expected. With respect to R_y , low gap ratios seem to suggest that either extrema of the superstructure strength bounds leads to a lower predicted repair cost, though this may be possible due to the high variance in EDPs that are experienced when impact happens. The SVR model shows that an increase in R_y at larger gap ratios leads to a very moderate decrease in repair cost. Similar trends are noted in the prediction of downtime using the GPC-KR model with the noted exception that the model perceives that lower R_y leads to lower downtime across all gap ratios.

4 EXAMPLE DESIGN

4.1 Inverse design

Upon creating the prediction models based on generalized parameters, acceptable design regions can be identified based on desired performance limits. The prediction models are applied to a design space that spans the bounds of the input space (Table 1). For this example, the final design

is selected as that with the cheapest upfront cost that satisfies a repair cost limit of \$1,620,000 (20% of the replacement cost) and a repair time of one month for a team of 25 workers.

The upfront cost for this study considers the construction and development costs of the steel in the superstructure and the land given the moat distance. The land cost is taken as \$2837 per m² (\$263 per sq ft) for a special moment frame isolated system located in San Francisco, CA, with a moat wall (Kitayama & Cilsalar 2022). To estimate the cost of the superstructure strength, a unit cost of \$4.40 per kg (\$2.00 per lb.) is taken for steel and the cost of each structure in the initial database is calculated. A linear regression is then performed for the steel cost on the design base shear for the superstructure (V_s), and the coefficients are used to estimate costs of new designs. Table 2 shows the design selected by the prediction models in conjunction with the upfront cost minimization.

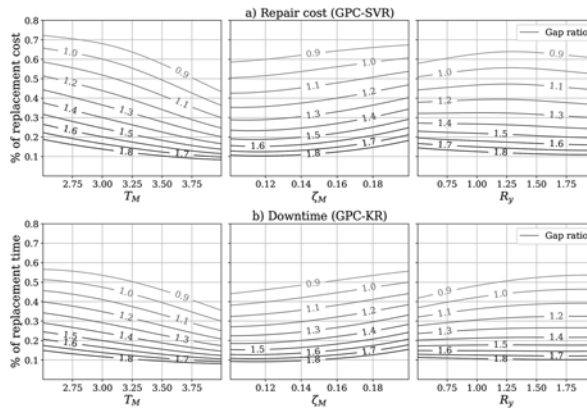


Figure 3. GPC-SVR prediction of mean repair cost and downtime at different gap ratios.

Table 2. Inverse design chosen by grid search.

Variable	Source	Value
Gap ratio	Prediction models & grid search	1.383
T_M	Prediction models & grid search	3.93 s
ζ_M	Prediction models & grid search	0.20
R_y	Prediction models & grid search	2.0
S_1	Arbitrarily chosen by location	1.017 g
D_{moat}	Calculated from gap ratio	91.6 cm (36.1 in)
μ_1	Selected by designer	0.036
μ_2	Calculated from design	0.067
R_1	Selected by designer	1015 mm (40 in)
R_2	Calculated from design	2844 mm (112 in)

4.2 Validation

To validate the design, a series of nonlinear time history analyses is performed using a suite of 60 ground motions. For each ground motion ran, the set of EDPs are collected for the purpose of performance estimation with Pelicun. However, since a distribution of EDPs are now available for a single designed structure, they are processed in the FEMA P-58 framework as a single set of EDPs distributed lognormal rather than as 60 deterministic samples. Additionally, a baseline run that represents a typical code-compliant design is conducted in order to compare the inverse design against a representative one that is very likely seen in practice. The baseline has a specified gap ratio of 1.0, $R_y = 1.0$, $T_M = 3.5$ seconds, and $\zeta_M = 0.15$. Figure 4 reports the distribution of the cost estimates for both structures generated from 10,000

realizations of component damage, loss, and repair time as calculated by the Pelicun module as well as the selection limit for those criteria.

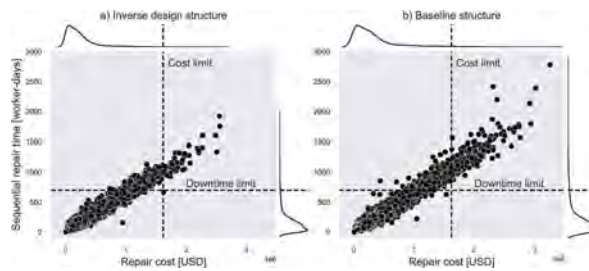


Figure 4. Distribution of estimated decision variable for designed structures.

From the distributions shown in Figure 4, the inverse design has results that are generally distributed at lesser costs and repair times than the baseline design. From the predicted values shown in Table 3, downtime (sequential repair time) is the variable that controlled the selection of the inverse design, since the predicted value lies just short of the limit compared to the repair cost. For the limits chosen, the inverse design achieved the targets more often than the baseline design. Of the 10,000 realizations shown, 91.7% of the inverse design realizations fell within the repair cost limit, and 90.1% met the repair time limit, compared to the baseline design’s 80.5% and 77.2% for cost and time, respectively.

Table 3. Performance evaluation of inverse design structure at MCE_R .

Variable	Targeted Limit	Prediction	Design performance (Δ baseline)
Mean repair cost	\$1,620,000	\$1,233,381	\$854,430 (-49.8%)
Mean downtime (days)	28.0	27.8	20.8 (-48.9%)
Upfront cost	—	—	\$348,602 (-12.0%)

Table 3 presents the performance of the inverse design compared against the baseline structure. The inverse design meets all of the required targets. Overall, the inverse design outperforms the baseline in all metrics presented, including upfront cost. The inverse design’s lower upfront cost is a result of lowering the steel cost in superstructure strength in exchange for a higher land cost to accommodate the moat gap capacity.

5 CONCLUSION

To better identify acceptable isolation designs for targeted building performance, several data learning models are developed to identify admissible design parameter ranges given performance targets without relying on high-fidelity dynamic analysis. From the support database, it is found that prediction models rely on conditioning the data on the impact against the moat wall to provide more accurate loss predictions. The inverse design is then selected by narrowing down the design space on the repair cost model predicted by a GPC-SVR model and repair downtime predicted by a GPC-KR model. The selected design is shown to achieve the targeted performance objectives with the following observations:

- The inverse design selected to achieve a repair cost amounting to 15.2% of the replacement cost and 4 weeks of downtime, achieved 10.5% of replacement cost and 3 weeks of downtime, while a typical baseline structure following code recommendation achieved 21.0% of replacement cost and 5.8 weeks of downtime.
- Depending on feasibility in increasing land plot size, an 38% increase in moat gap and displacement capacity could result in up to a 50% reduction in expected repair cost, even when

compounding with a lowered superstructure strength ($R_y = 2.0$), as shown by comparing the inverse design to the baseline design in the validation study.

The design process as assisted by prediction models is shown to be capable of meeting performance objective, with possible expansion to additional objectives to be considered, such as collapse risk, red-tag risk, or component group-specific level losses. Future work would greatly benefit from the combination of the loss prediction model with more sophisticated upfront cost considerations.

REFERENCES

- Ancheta, T.D., Darragh, R.B., Stewart, J.P., Seyhan, E., Silva, W.J., Chiou, B.S.J., Wooddell, K.E., Graves, R.W., Kottke, A.R., Boore, D.M. and Kishida, T. 2014. NGA-West2 database. *Earthquake Spectra* 30(3): 989–1005. London: SAGE Publications Sage UK.
- ASCE/SEI 7-22 2022. *Minimum Design Loads and Associated Criteria for Buildings and Other Structures*. Reston, VA: American Society of Civil Engineers.
- Becker, T.C. and Mahin, S.A. 2013. Approximating peak responses in seismically isolated buildings using generalized modal analysis. *Earthquake engineering & structural dynamics* 42(12): 1807–1825. Wiley Online Library.
- Dao, N.D., Ryan, K.L., Sato, E. and Sasaki, T. 2013. Predicting the displacement of triple pendulum bearings in a full-scale shaking experiment using a three-dimensional element. *Earthquake engineering & structural dynamics* 42(11): 1677–1695. Wiley Online Library.
- FEMA P-58 2018. *Seismic Performance Assessment of Buildings*. Washington D.C.: Federal Emergency Management Agency.
- Fenz, D.M. and Constantinou, M.C. 2008. Modeling triple friction pendulum bearings for response-history analysis. *Earthquake Spectra* 24(4): 1011–1028. London: SAGE Publications Sage UK.
- Ghasemof, A., Mirtaheri, M. and Mohammadi, R.K., 2022. Multi-objective optimization for probabilistic performance-based design of buildings using FEMA P-58 methodology. *Engineering Structures* 254: 113856. Elsevier.
- Hwang, S.H. and Lignos, D.G. 2017. Earthquake-induced loss assessment of steel frame buildings with special moment frames designed in highly seismic regions. *Earthquake Engineering & Structural Dynamics* 46(13): 2141–2162. Wiley Online Library.
- Hwang, S.H., Mangalathu, S., Shin, J. and Jeon, J.S. 2022. Estimation of economic seismic loss of steel moment-frame buildings using a machine learning algorithm. *Engineering Structures* 254: 113877. Elsevier.
- Lignos, D.G. and Krawinkler, H. 2011. Deterioration modeling of steel components in support of collapse prediction of steel moment frames under earthquake loading. *Journal of Structural Engineering* 137(11): 1291. Reston, VA: American Society of Civil Engineers.
- Kitayama, S. and Cilsalar, H. 2022. Seismic loss assessment of seismically isolated buildings designed by the procedures of ASCE/SEI 7-16. *Bulletin of Earthquake Engineering* 20(2): 1143–1168. Springer.
- McKenna, F., Scott, M.H. and Fenves, G.L. 2010. Nonlinear finite-element analysis software architecture using object composition. *Journal of Computing in Civil Engineering* 24(1): 95–107. Citeseer.
- Molina Hutt, C., Almufti, I., Willford, M. and Deierlein, G. 2016. Seismic loss and downtime assessment of existing tall steel-framed buildings and strategies for increased resilience. *Journal of Structural Engineering* 142(8): C4015005. Reston, VA: American Society of Civil Engineers.
- Moretti, S., Trozzo, A., Terzic, V., Cimellaro, G.P. and Mahin, S. 2014. Utilizing base-isolation systems to increase earthquake resiliency of healthcare and school buildings. *Procedia Economics and Finance* 18: 969–976. Elsevier.
- Muthukumar, S. and DesRoches, R. 2006. A Hertz contact model with non-linear damping for pounding simulation. *Earthquake engineering & structural dynamics* 35(7): 811–828. Wiley Online Library.
- Williams, C.K. and Rasmussen, C.E. 2006. *Gaussian processes for machine learning* (Vol. 2, No. 3, p. 4). Cambridge, MA: MIT press.
- Yun, S.Y., Hamburger, R.O., Cornell, C.A. and Foutch, D.A. 2002. Seismic performance evaluation for steel moment frames. *Journal of Structural Engineering* 128(4): 534–545. Reston, VA: American Society of Civil Engineers.
- Zsarnóczay, A. and Deierlein, G.G. 2020. PELICUN—A Computational Framework for Estimating Damage, Loss and Community Resilience. In *Proceedings, 17th World Conference on Earthquake Engineering*. Sendai: WCEE.

Seismic behaviour of building using damage-avoidance shearwall hold-downs

L. Budi

PT. Pertamina (Persero), Dumai, Indonesia

ABSTRACT: Concrete coupled wall is the outstanding seismic resisting system for mid to high-rise building structures. In this system, the link beam provides coupling action between the beam and the adjacent wall panel, which increases the lateral stiffness and reduces the footprint of the seismic resisting system. However, once the link beam is damaged due to a severe earthquake, it is difficult, costly, and time-consuming to repair. To deal with this issue, the Resilient Slip Friction Joint (RSFJ) is used to couple the wall limb in this study. RSFJ is a novel seismic technology which can satisfy the “life safety” and “immediate occupancy” criteria post-earthquake. An eight-storey reinforced concrete building is designed using the forced-based design method, and its seismic performance is evaluated by non-linear static pushover and nonlinear dynamic time-history simulations. The results showed that this system can provide a high level of structural ductility while providing fully self-centring behaviour.

1 INTRODUCTION

Studies showed that the concrete coupled wall is one of the most effective seismic resisting systems for mid to high-rise building structures, particularly for those located in an active seismic region. In this system, the link beam provides coupling action between the beam and the adjacent wall panel, which significantly increases the wall system’s lateral stiffness and eventually reduces the footprint for the seismic resisting system. However, once the link beam is damaged due to a severe earthquake, it is difficult, costly, and time-consuming to repair, which results in business disruption and increased building life cycle costs.

To comply with the “life-safety” and “immediate occupancy” criteria, the researchers conducted many studies to develop the low damage concept for concrete structures, where they still have the benefits of concrete shear walls. The general principle of the low-damage design concept is to control damage by using rocking connections, which are typically combined with supplemental damping devices, to dissipate energy. These damping devices act as sacrificial fuses which can be easily repairable or replaceable after moderate to severe earthquakes. Housner (1963) initially introduced the rocking concept by undertaking an experimental study on a rigid rocking block. He reported that the rocking motion had a considerable contribution in enhancing the structural stability against the overturning moment. Aslam et al. (1978) studied the rocking response of rigid structures and stated rocking resistance of the structure can be improved by anchoring it to the ground. Priestley et al. (1999) developed a hybrid post-tensioned connection on a concrete shear wall and reported that the prototype has an extremely satisfactory performance when subjected to severe seismic force. Yielding, friction, and viscous damping are proposed, tested, and used in rocking shear walls (Sritharan et al. 2015).

The above studies have advanced the concept of low-damage design for concrete structures, but there remains a significant literature gap. The poor repairability of the sacrificial elements requires the element replacement after a severe earthquake which is costly and causes business disruption for the building. In addition, as the residual capacity of these sacrificial elements will not be sufficient to resist severe aftershocks, the structure will still be vulnerable until

getting fully repaired by replacing the damaged fuses. Furthermore, regular inspection is required to deal with the creep issue in post-tensioning steel strand cables and their supporting members. Therefore, there is still a remaining step to achieve an ideal maintenance-free rocking wall system which provides an efficient and high-performance lateral load-resisting system and excellent self-centring mechanism during earthquakes and aftershocks.

To respond to the above challenges, Zarnani and Quenneville (2015) introduced a new technology, known as the Resilient Slip Friction Joint (RSFJ). It provides essential energy absorption and self-centring capability, and other excellent features, including secondary fuse activation, easy reparability, and free maintenance, to ensure life “safety” and “immediate occupancy” criteria post-earthquake. This research project proposed a concrete coupled wall structure using the RSFJ to produce an efficient and high-performance lateral load-resisting system.

The objective of this research is to analyze and assess the implementation of the RSFJ device in concrete coupled wall systems. The basic equations and the hysteresis curve of the RSFJ are introduced. The specific configuration of the RSFJ will be proposed, and the procedure to design RSFJ specifications will be developed. The effect of the RSFJ damping device in increasing the seismic performance of the building structure will be further investigated. Finally, the numerical modelling is developed, and its structural analysis result is verified.

2 RESILIENT SLIP FRICTION JOINT (RSFJ)

2.1 Analytical model

The RSFJ technology is a novel friction joint that provides energy absorption and self-centring behaviour in one compact package. The main component of the RSFJ comprises an elongated holes steel plate, metal cap plate, high strength bolts, and disc springs, as shown in Figure 1. In RSFJ, the restoring force comes from specific steel grooved plates which are tied through high-strength bolts and disc springs. By slipping of grooved plates, the input energy is dissipated through frictional resistance. Based on the free body diagrams presented in Figure 1, the design procedure is developed for the prediction of the performance of the RSFJ (Zarnani et al. 2016). The slip force (F_{slip}) and residual force (F_{res}) can be determined by Equations (1) and (2), respectively:

$$F_{RSFJ,slip} = 2 * n_b * F_{b,pr} \left(\frac{\sin\theta + \mu_s * \cos\theta}{\cos\theta - \mu_s * \sin\theta} \right) \quad (1)$$

$$F_{RSFJ,res} = 2 * n_b * F_{b,pr} \left(\frac{\sin\theta - \mu_k * \cos\theta}{\cos\theta + \mu_k * \sin\theta} \right) \quad (2)$$

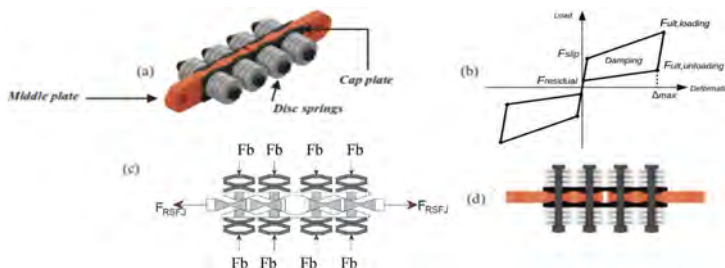


Figure 1. RSFJ device: a) assembly; b) hysteresis; c) free body diagram; d) the joint at rest.

Where n_b = number of bolts on each splice, θ = groove angle, $F_{b,pr}$ is the clamping force of prestressing and the μ_s and μ_k are the static and kinetic coefficient of friction respectively, while considered $\mu_k = 0.85\mu_s$ (Hashemi et al. 2017). The general hysteresis behaviour of RSFJ

is illustrated in Figure 1(b). $F_{ult,loading}$ and $F_{ult,unloading}$ are the system forces at the maximum disc springs displacement and bolts force.

$$F_{b,u} = F_{b,pr} + K_s * \Delta_s \quad (3)$$

$F_{ult,loading}$ and $F_{ult,unloading}$ is derived by replacing the bolt forces in Equation 1 and Equation 2 by Equation 3, and μ_s, μ_k with μ_k, μ_s .

2.2 RSFJ as the hold-downs

Figure 2(a) shows the proposed rocking wall system. The free-body diagram of a rocking shear wall with RSFJ and the hysteretic behaviour of the system is shown in Figure 2(b). The deflection of the joints is related to their lever arm, which is the horizontal distance between the RSFJ centre to the rotating edge of the shear wall. Therefore, $\Delta_{RSFJ,1}/\Delta_{RSFJ,2} = L_1/L_2$, where Δ_{RSFJ} and L are, the expansion of the RSFJ and the associated lever arms, respectively.

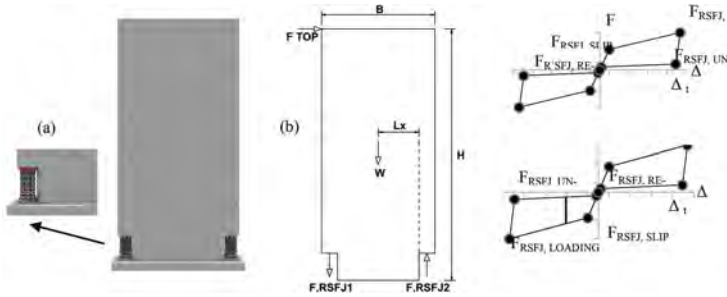


Figure 2. The concrete rocking shear wall: (a) RSFJ as hold-downs; (b) free body diagram of the wall.

Hashemi et al. (2017) explained that the horizontal force acting at the top of the wall (F_{top}) can be calculated from the moments of the centre of rotation (the base of the wall). In this way, F_{top} can be further obtained using the following formula:

$$F_{top,slip} = \frac{1}{H} * [(W * L_w + F_{RSFJ,slip}(L_1 + L_2))] \quad (4)$$

In this equation, H is the height of the wall, W is the vertical loads, L_w is the horizontal distance from the vertical load to the centre of rotation, and $F_{RSFJ,slip}$ is the slip force of the RSFJ. After the slip stage, the force within the RSFJ corresponds to the deflection within them. Therefore, Equation (1) can be used to determine the lateral strength of the wall, $F_{RSFJ,1}$ and $F_{RSFJ,2}$ are the forces within the tensioned and compressed RSFJ, respectively. During the loading of the wall, Equation (2) can be employed to develop a correlation between $F_{RSFJ,1}$ and $F_{RSFJ,2}$. Then, Equations (1) and (2) can be combined to determine the overall load-deformation behaviour of the wall.

2.3 RSFJ as the shear links

In the coupled walls system, the coupling beam could be replaced by RSFJ (as the shear links). Similar to the single shear wall, the horizontal displacement on all columns and walls is equal because all columns and walls is connected to the floor. Sahami et al. (2019) proposed a formula to calculate the rocking base moment (M_{rock}) and rocking stiffness (k_{rock}) on the coupled wall system.

$$M_{rock} = M_{weight} + M_{damper} = W * B + n_d \quad (5)$$

$$k_{rock} = n_d * k_{d,ini} * [n_w * (L + d)^2 + (d)^2] \quad (6)$$

where n_w is the number of coupled walls and n_d is the number of dampers on each side of the walls, respectively. Meanwhile, W is the seismic weight of the wall, B is the width of the wall and d is the length of the shear link. The numerical analysis results showed that the coupled wall system using RSFJ as the shear link could achieve the capacity of two identical single walls.

3 THE DESIGN OF THE CASE STUDY BUILDING

An eight-storey reinforced concrete building structure with a concrete coupled wall as its seismic resisting system is proposed in this research project to evaluate the seismic performance of the system and the adopted design philosophy. The concrete coupled walls are used in the middle of the building to minimise the torsional effects. Meanwhile, the RSFJs are used as the hold-down at the bottom corner of the wall and as the shear link in the middle of the coupling beam. To satisfy the requirement of NZS1170.5: 2004, the following criterion is set for the design philosophy: (a) the Ultimate Limit State (ULS) lateral drifts are kept under 1.4 % to minimize the damage to structural and non-structural components (b) the structure remains elastic, the dampers are not activated and the lateral drift ratios are kept 1.5 % and 0.33 % for Ultimate Limit State (ULS) and Serviceability Limit State (SLS) cases, respectively (c) the structure has zero or negligible residual displacement at the end of the seismic event.

The building plan is 35 m by 35 m and is symmetrical about the two main axes. Along each axis, a concrete coupled wall equipped with RSFJ is used as the Lateral Load Resisting System (LLRS). A novel type of shear key is installed at the wall's base to provide displacement compatibility and transfer the shear forces from the wall to the foundation (Hashemi and Quenneville, 2017). The total building height is 28 m and has an identical storey height of 3.5 m. The building is designed for office application (i.e. importance level 3), is located in Christchurch, and is built on the soft soil layer (i.e. soil class type D). Figure 3. illustrates the developed model used in this research project.

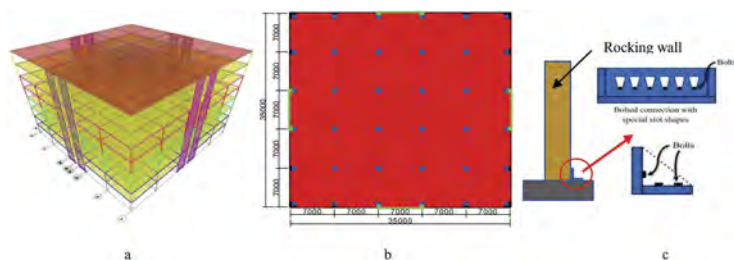


Figure 3. The proposed model: (a) 3D Model; (b) plan view; (c) novel shear key.

The loads applied during the preliminary design are a self-weight (for the frame) of $0,006 \text{ kg/cm}^2$, a super-imposed dead load of $5 \times 10^{-3} \text{ kg/cm}^2$, a floor weight of $3 \times 10^{-2} \text{ kg/cm}^2$, a cladding weight of 10^{-2} kg/cm^2 , a floor live load of $3 \times 10^{-2} \text{ kg/cm}^2$ and a roof live load of $2.5 \times 10^{-3} \text{ kg/cm}^2$. The calculated seismic weights for the structure are $1.3 \times 10^6 \text{ kg}$ for floor one and floor two, $11 \times 10^6 \text{ kg}$ for floor three and floor four, $9.44 \times 10^5 \text{ kg}$ for floor five and floor six, $8.34 \times 10^5 \text{ kg}$ for floor seven, and $6.75 \times 10^5 \text{ kg}$ for roof.

A ductility factor of $\mu = 4.0$ and a structural performance factor of $S_p = 0.7$ are adopted for the design. The value of S_p is linked to the design ductility/level of detailing used and the value of 0.7 is appropriate for structures designed under NZS3101:2006. However, for other structural systems that use damage avoidance technologies, this value might be unconservative and may need to be re-evaluated. The period of the structure is determined as $T_1 = 0.43$ seconds using the empirical equation provided in NZS1170.5: 2004. Note that for periods equal to or more than 0.7 seconds, $k_\mu = \mu$. The base shear of the structure is specified as $V_b = 9.11 \times 10^5 \text{ kg}$ and $V_b = 1.584 \times 10^6 \text{ kg}$ for SLS and ULS cases, respectively. This base shear is distributed in the structure respecting the storey weights and heights as per the recommendations in NZS1170.5: 2004.

4 NUMERICAL ANALYSIS

In this section, a structural analysis using the SAP2000 program is performed to investigate the performance of the structure and to check the seismic lateral drift. A 3D model of an eight-storey building with concrete coupled walls and RSFJs is considered for the numerical modelling. The

beam-column connections and base connections are designed as pinned joints while the column sections are continuous as required by NZS3101.1:2006. A rigid diaphragm is assigned to each floor to constrain the horizontal displacement of the beams. The gravity loads have been applied to the beam and the seismic weights have been assigned to the nodes in each elevation.

The “Damper-Friction Spring” element in SAP2000 is adopted to represent the load-displacement behaviour of the RSFJs as the shear link and hold-down. The accuracy of using this link element for the RSFJs has previously been verified by comparing the experimental data with numerical results (Hashemi, 2017). The shear force demand and axial force demand on the wall’s toe from the elastic numerical model are used to determine the shear link and hold-down stiffness value, respectively. To achieve the rocking behaviour of the wall, the rocking foundation model which is represented by the “Gap” element in SAP 2000 is used.

Table 1. Summary of the key parameter of the RSFJ system.

Level	Parameter							
	F_{ult} (kg)	F_{slip} (kg)	$F_{restore}$ (kg)	$F_{residual}$ (kg)	$K_{initial}$ (kg/cm)	$K_{slip\ loading}$ (kg/cm)	$K_{slip\ unloading}$ (kg/cm)	Δ_{max} (cm)
1	6.8200	37130	27280	10230	682	52.7	289	5.9
2	103200	55800	41280	15480	1032	80.3	437	5.9
3	124700	67200	49880	18705	1247	97.5	528	5.9
4	142000	76400	56800	21300	1420	111.2	602	5.9
5	123100	66400	49200	18465	1231	96	522	5.9
6	122200	66000	48800	18330	1222	95.3	518	5.9
7	103200	56000	41200	15480	1032	80	437	5.9
8	91700	49300	36680	13750	917	71.8	389	5.9
HD-1	1858700	912000	743480	278805	18587	1604.6	7876	5.9
HD-2	1277600	740200	511040	191640	12776	910.8	5414	5.9
HD-2	1021000	473000	408400	153150	10210	928.8	4326	5.9
HD-2	2133500	1198600	853400	320025	21335	15846	9040	5.9

The Nonlinear Push-over Analyses (NPA) are carried out to estimate the shear force for a specified lateral drift and calculate hysteresis damping values. The numerical model and analysis procedure are considered valid if the base shear and maximum roof displacement obtained from nonlinear pushover analysis is less than 5 % than that calculated using Equivalent Static Method (ESM) formula. Besides, the cyclic pushover analysis curve should represent the flag-shape hysteresis curve, which is the main characteristic of the self-centring structure. Furthermore, the nonlinear time history analysis is carried out to validate the initial ductility factor used in the design process and investigate the structure’s behaviour. Seven seismic events are selected and scaled for ULS based on method described in NZS 1170.5 for the given location and soil type. The ‘peak of three’ or the ‘average of seven’ records may be considered when designing using time-history analysis (Bradley, 2014). The numerical model and the design process are considered valid if the discrepancy between ESM estimation and NLTHA outcomes (i.e. base shear and roof displacement) are less than 5 %.

5 RESULTS AND DISCUSSION

The base shear generated from pushover analysis is 9.99×10^5 kg, which is slightly lower than that of the ESM calculation (1.0235×10^6 kg). Meanwhile, the lateral drift from pushover analysis is 1.5 % (i.e. 420 mm), which satisfies the target displacement. Moreover, the flag-shaped hysteresis curve, which is the main characteristic of the self-centring system can be reasonably achieved. It is observed from the hysteresis curve that the structure remains elastic up to 0.2 %. After this point, the RSFJs start to activate, resulting in the observed bi-linear pushover curve. It should be noted that since not all RSFJs are activated at the same time, a transition zone from the linear elastic zone to the geometrically nonlinear zone is observable in the pushover curve. Nevertheless, the entire structure remains elastic, and no material nonlinearity is expected within the transition zone. Figure 4. depicts the final hysteresis curve obtained from pushover analysis for the proposed structural system.

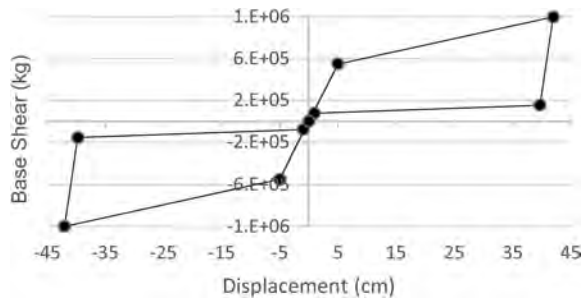


Figure 4. The final hysteresis curve obtained from non-linear pushover analysis.

5.1 Nonlinear dynamic time-history simulations

The NLTHA results are about 4 % lower than that calculated with the ESM. In this study, the average of seven ground motions is considered for analysis and an equivalent ductility factor of $\mu = 2.9$ is used for the developed model. Figure 5. illustrates the base shear and roof displacement obtained from NLTHA. NLTHA H1 and NLTHA H2 refers to analysis for x-axis and y-axis, respectively.

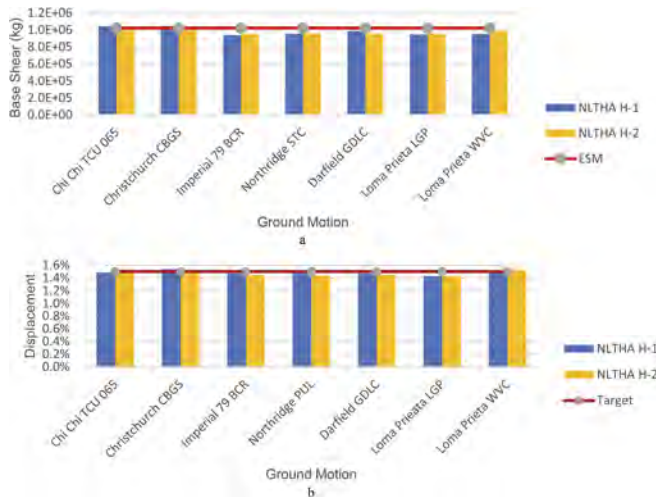


Figure 5. NLTHA Result: (a) base shear comparison; (b) roof displacement comparison.

The chart shows that the highest base shear is obtained from the Christchurch CBGS and Chi-Chi TCU event which are accounted at 1.048×10^6 kg and 1.045×10^6 kg, respectively. Similarly, the highest roof displacement is generated from the Christchurch and Chi-Chi TCU event, which are recorded at 43.1 cm and 42.6 cm. The average base shear is accounted for at 9.824×10^5 kg, which is slightly lower than that of the ESM estimation (10.235×10^5 kg). Meanwhile, the average roof displacement is calculated at 1.46 %, which is 0.04 % lower than the target drift (i.e. 1.5 %). If the mean of the recorded drifts is taken, it reasonably satisfies the target drift and confirms the predicted seismic performance of the developed structural model.

5.2 Inter-storey drifts

It can be seen in form Figure 6. that the maximum inter-storey drift of the proposed model is about 1.5 %, which is significantly lower than the requirement in the NZS 1170.5. It means that the configuration of the RSFJ and the lateral resisting system can prevent the “soft storey” formed at any building level. The highest and the lowest inter-storey drift is recorded for the Loma Prieta

LGP (1.61 %) and the Imperial 79 BCR (1.37 %), respectively. These values are well close to the target lateral drift, which shows the accuracy of the proposed design and analysis method.

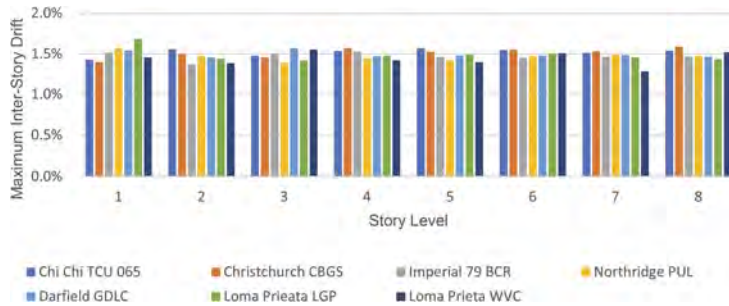


Figure 6. NLTHA Result: Inter-storey drift.

5.3 The residual drift

To achieve the full self-centring behaviour, the maximum residual drift at the end of NLTHA shall be limited at 0.2% and 0.25% for the design level intensity earthquake and for the maximum considered earthquake (MCE) intensity, respectively (Henry et al., 2011). Figure 7 shows the residual drift from Chi-Chi and Christchurch event which is less than 8mm (i.e., less than 0.2%). The residual drift from other events is less than 6mm. Therefore, these residual drifts will result in the negligible structural damage and minor cosmetic repairs after earthquake. It confirms the fully self-centring behaviour (i.e., with-out relying on any supplementary devices such as the post-tensioned strands), which can be attributed to the RSFJs used in the LLRS.

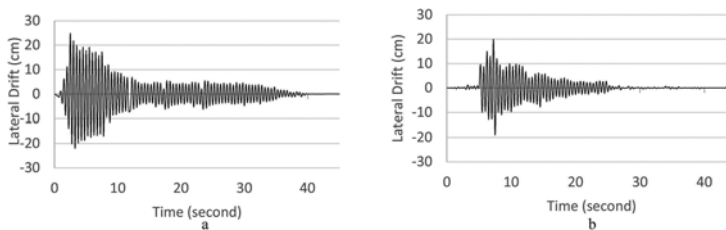


Figure 7. Residual drift: (a) Chi-Chi event; (b) Christchurch event.

5.4 Response of the individual RSFJ

Overall, each RSFJ performs within its capacity and achieve its desired lateral displacement. According to the analysis results, the internal forces (i.e. shear force for the shear links and axial force for the hold-downs) are lower than their ultimate force ($F_{ult,loading}$). Similarly, their lateral displacements are slightly lower than the specified displacement. In other words, the secondary fuse activation is not needed for the proposed structural model. Furthermore, these individual responses of the RSFJs show the efficiency of the proposed structural wall system and design procedure in controlling lateral drift. It means that the self-centring behaviour does not rely on any external mechanism (i.e. gravity resisting system), which is particularly advantageous for the structural systems in which the lateral load resisting system is separated from the gravity load resisting system.

6 CONCLUSIONS

This paper discusses the seismic behaviour of building using damage-avoidance shear wall hold-downs. In this system, the application of self-centring friction damping on the building

structure is proposed and its performance is analytically and numerically observed. This innovative RSFJ system is incorporated in a coupled concrete wall system with the aim of achieving damage avoidance.

To investigate the performance of the novel concept on the system level, an eight-storey concrete building structure with concrete coupled wall as Lateral Resisting System is proposed in this study. The design philosophy used was to limit the inter-storey drift ratios to 0.33 % and 1.4 % for SLS and ULS, respectively. The results of the NLTHA showed that the structure is well designed and was able to meet the target performance criteria. Moreover, a fully self-centring behaviour was observed for all analysed cases. Therefore, the proposed model can be considered as an efficient alternative to traditionally high-damage lateral resisting systems to minimise and localise damages.

ACKNOWLEDGEMENT

The authors would like to thank Ministry of Foreign Affairs and Trade of New Zealand (MFAT) for the financial support of this research.

REFERENCES

- Aslam, M., Godde, W. G., & Scalise, D. T. (1978). Earthquake rocking response of rigid bodies. University of California, Berkeley. <https://escholarship.org/uc/item/07b7w0rv>
- Darani, F. M., Zarnani, P., Hashemi, A., Bagheri, H., Quenneville, P., & Hammerle, E. (2019). Self-centring pre-cast concrete shear walls with resilient slip-friction joints: a new seismic damage avoidance structural system. Fifth Conference on Smart Monitoring, Assessment and Rehabilitation of Civil Structures.
- Hashemi, A. (2017). Seismic resilient multi-story timber structures with passive damping. University of Auckland, New Zealand
- Henry, R. S., Sritharan, S., & Ingham, J. M. (2011). Recentring requirements for the seismic design of self-centring systems. the Ninth Pacific Conference on Earthquake Engineering Building an Earthquake-Resilient Society, Auckland, New Zealand.
- Housner, G. W. (1963). The behaviour of inverted pendulum structures during earthquakes. *Bulletin of the Seismological Society of America*, 53(2), 403–417.
- NZS 1170.5:2004 (2004). Structural design action part 5: Earthquake actions. New Zealand Standard Executives. <https://www.standards.govt.nz/>
- NZS 3101.1:2006 (2006). Concrete Structure Standard part 1: The design of concrete structures. New Zealand Standard Executives. <https://www.standards.govt.nz/>
- Priestley, M.J.N., Sritharan, S., Conley, J.R. & Pampanin, S. (1999). Preliminary results and conclusions from the PRESSS five-story precast concrete test building. *PCI Journal*, 44(6), 42–67.
- Sahami, K., Veismoradi, S., Zarnani, P., & Quenneville, P. (2019, April 4-6). Seismic performance of rocking concrete shear walls with Innovative Rotational Resilient Slip Friction Joints. 2019 Pacific Conference on Earthquake Engineering and Annual NZSEE Conference.

*MS18: Safety and maintenance of masonry arch bridges:
Diagnostic, monitoring, modelling, risk analysis
and retrofit interventions*
*Organizers: F. Cannizzaro, N. Cavalagli, C. Chisari,
B. Pantò, F. Scozzese, P. Zampieri & M. Zizi*



Taylor & Francis

Taylor & Francis Group

<http://taylorandfrancis.com>

Preliminary investigation on the response sensitivity of masonry arch bridges subjected to scour

F. Scozzese & A. Dall'Asta

School of Architecture and Design, University of Camerino, Ascoli Piceno, Italy

E. Tubaldi

University of Strathclyde, Glasgow, UK

ABSTRACT: Flood-induced scour represents an insidious phenomenon affecting bridges. In the last 20 years, several bridge collapses have been registered all over the world. Considering that masonry bridges characterize most of the existing infrastructure heritage worldwide, it is essential to quickly and effectively deal with this problem, through inspection campaigns, continuous monitoring activities and interventions aimed at mitigating the risk. This paper analyses numerically the response of a masonry arch bridge under local scour actions. A real case study is considered and an accurate 3D finite element model of the bridge is developed in Abaqus, accounting for both mechanical and geometrical nonlinearities. This study represents a preliminary investigation aimed at quantifying the sensitivity of different response parameters to the scour evolution, information that can be used at a later stage for damage identification and quantification.

1 INTRODUCTION

Scour represents one of the main causes of bridge collapse all over the world (Pizarro et al., 2020; Tubaldi et al., 2022a; Eidsvig et al., 2021; Malena et al., 2021; Tubaldi et al., 2020).

Masonry arch bridges are a widespread typology characterizing a large part of the existing infrastructural networks (Borlenghi et al., 2021a; Leoni et al., 2021; Zampieri et al., 2021; De Matteis et al., 2021; Zizi et al. 2023) and they have proved to be very vulnerable to flood-induced scour actions, due to their high stiffness and the usually shallow foundations (Zampieri et al., 2017; Ragni et al., 2019; Solan et al., 2020).

The relevance of the problem is substantiated by the large number of scour-induced collapses registered in the last decades, as well as by the always increasing number of scientific studies on the topic. Indeed, according to the most recent scientific literature in the field, several works have been dedicated to the development of numerical modelling strategies able to describe the evolution of damage (Tubaldi et al., 2020; Pantò et al., 2022; Cannizzaro et al., 2018; Pepi et al., 2021) and numerical analysis on masonry arch bridges subjected to scour (Cabanzo 2022; Tecchio et al., 2022; Scozzese et al., 2021).

Structural monitoring represents a key strategy to identify and prevent damages on bridges (Nicoletti et al. 2023; Innocenzi et al. 2022; Gara et al. 2020). Several studies have been oriented towards the assessment and development of techniques for scour detection, based for instance on dynamic identification via operational modal analysis or similar continuous monitoring strategies (Civera et al. 2022; Borlenghi et al 2021b; Scozzese et al., 2021; Rainieri et al 2020; Malekjafarian et al., 2020; Scozzese et al., 2019); some authors (Zhang et al., 2022) have investigated scour detection methods exploiting the input provided by passing vehicles; experimental and full-scale studies have also been conducted on scoured bridge piers (Hamidifar et al., 2022; Tubaldi et al., 2022b).

In this paper, a multi-span masonry arch bridge is considered as case study and a preliminary numerical investigation is performed to quantify to which extent different response parameters, including some main global kinematic parameters (e.g., transversal displacements on piers, spandrels and arches, vertical settlements, etc.) are influenced by scour. The study results allow providing some preliminary but useful insights about the parameters that are most sensitive to scour and that can be used, at a later stage, for damage identification and quantification. They also provide useful information for the development of optimal monitoring strategies for masonry arch bridges subjected to scour.

2 METHOD

A masonry arch bridge is considered as case study and an accurate 3D finite element model is developed in Abaqus [28], accounting for both mechanical and geometrical nonlinearities.

A set of kinematic response parameters is defined, consisting in vertical and transversal displacements of several characteristic structural nodes of the bridge.

The bridge response evolution is assessed at different stages of the scour process acting underneath one of the piers, under the assumption of a meandering river configuration which only involves one single pier of the bridge.

The scour process evolution is numerically modelled according to the procedure proposed in (Ragni 2010), i.e., by gradually deactivating the boundary conditions at the pier base depending on the current level of scour excavation. In particular, a pre-fixed, simplified inverted pyramid shape is considered to represent the scour hole, which is defined entirely by the friction angle of the bed material φ , and by the maximum depth of scour y_s . The pyramid height coincides with the depth y_s , the upstream scour hole slope is assumed equal to φ , whereas the downstream slope is $\varphi/2$.

The progression of scour is simulated by considering increasing values of y_s and by removing the springs that are located into the scour hole. This approach allows to describe the two joint effects of scour, namely the loss of support and the settlements that consist in a translation and rotation at the pier base.

A schematic representation of the gradual sediments removal numerically simulated is provided in Figure 1, where the different stages of the process are characterized by increasing values of the normalized scour parameter y_s/h , i.e., the ratio between the scour depth, y_s , and the foundation height, h (assumed as fully embedded at starting conditions).

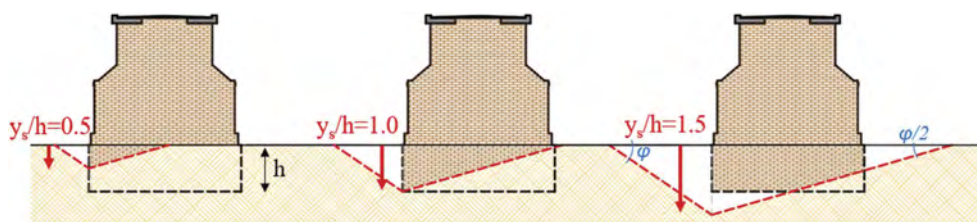


Figure 1. Geometry of the scour hole and scour excavation evolution.

3 APPLICATION

3.1 Case study

The case study is taken from a previous work (Ragni et al., 2019) and consists of a masonry arch bridge of six piers and seven spans (16.00 m long) with segmental brick vaults. Piers have shallow foundations of height $h = 4.0\text{m}$.

The bridge total length is about 130 m and its longitudinal representation is provided in Figure 2.

The river crossed by the bridge has the features of a meandering river, as testified by the photographs of Figure 3, showing the various paths assumed by the main channel of the river within its riverbed. Due to this particular feature of the river, the bridge experienced several localized scour actions over the year, where single piers were involved depending on the specific path of the water in a given year or period of the year.

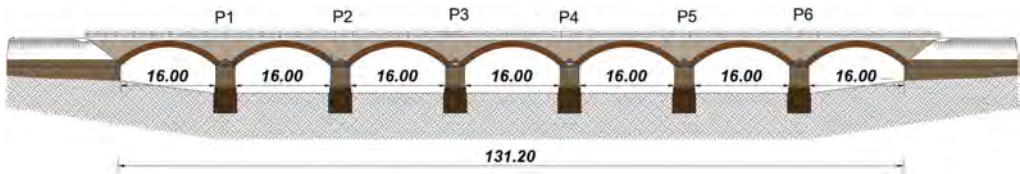


Figure 2. Longitudinal scheme of the bridge.



Figure 3. Meandering path of the Aso river and modification over the years: 2012, 2013, 2016 (half bridge collapsed), 2021 (rebuilt). Source: Google Maps/Google Earth.

3.2 Solid elements model

A 3D model is developed in ABAQUS 2017, by accounting for both geometrical and mechanical nonlinearities. The bridge model is built by using continuum solid linear hexahedral 8-nodes elements of type C3D8R, with 6 degrees of freedom per node.

The non-linear response of the masonry parts is accounted for by using the Concrete Damage Plasticity (CDP) model with the parameters reported in (Scozzese et al., 2019).

For the fill material (granular mixture), the Mohr-Coulomb failure criterion is used, with friction angle of 55° and cohesion $c = 10 \text{ kN/m}^2$. The interaction between the different bridge components is simulated by means of the nonlinear frictional and cohesive interfaces (Scozzese et al., 2019): a frictional interface is used to describe the interaction between the fill and the other bridge components along the tangential direction; a “hard-contact” behaviour is assumed along the normal direction, allowing separation but preventing penetration between the parts in contact; cohesive interactions are used for the other interfaces and simulate the behaviour of mortar joints between the parts.

The main material properties are summarized in Table 1, namely: density ρ , Young’s modulus E , yield stress in compression $f_{y,c}$, peak tensile stress $f_{y,t}$, backfill cohesion c .

For what concerns the riverbed properties, the following parameters are considered: friction angle $\phi=38^\circ$, Young’s modulus $E=1065000 \text{ kN/m}^2$, Poisson’s ratio $\nu = 0.45$, shear modulus $G=370000 \text{ kN/m}^2$, soil density $\rho = 2.0 \text{ t/m}^3$, and average shear waves velocity $V_s= 430 \text{ m/s}$.

The soil-foundation interaction is modelled through three sets of springs (X, Y and Z) with equivalent soil stiffness constants taken from a previous work by the authors (Scozzese et al., 2019). However, it is worth to note that more refined impedances formulations might also be used (Carbonari et al. 2018; Morici et al., 2019; González et al. 2020; Minnucci et al., 2022).

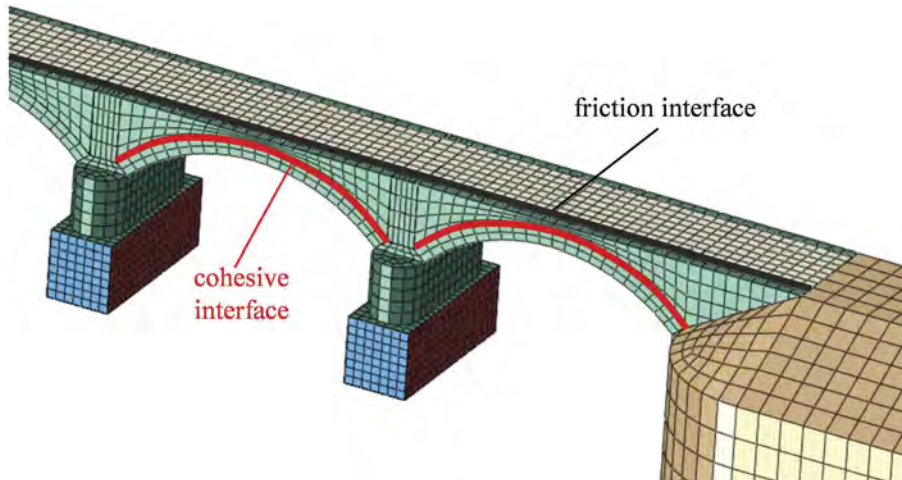


Figure 4. Numerical model of the bridge with parts highlighted with different colors.

Table 1. Main structural material properties.

	Masonry	Masonry (Piers)	Backfill	Abutment
ρ [t/m^3]	1.80	1.75	1.70	1.90
E [t/m^2]	3100000	2900000	250000	300000
c or $f_{y,c}$ [kN/m^2]	2000	2000	10	\
$f_{y,c}$ [kN/m^2]	150	150	0	\

3.3 Scour simulation and monitored response parameters

Because of the specific (meandering) features of the river, a localized scour scenario is considered in which a single pier is involved. The selected pier is the number 6, i.e., the last pier close to the abutment 2.

A scour process characterized by values of the ratio y_s/h from 0.0 to almost 1.5 is analyzed. For value of y_s/h close to 1.5, indeed, convergence issues are encountered within the numerical simulation, testifying the attainment of a unstable structural condition (collapse).

The following nodes placed on the up-stream face of the bridge (see Figure 5) are considered to evaluate the structural displacements during the scour process evolution:

- Top spandrel nodes, namely $S5_{top}$ (on the Pier 5 adjacent to the scoured one), $S6_{top}$ (on the scoured Pier 6), and Ab2 (on the abutment 2);
- Arch nodes, namely A6 (arch on the left of the scoured pier), A7 (arch on the right of the scoured pier);
- Foundation nodes of the scoured pier, namely $P6_{top}$ (upper upstream corner of the foundation), and $P6_{bottom}$ (lower upstream corner of the foundation).

Both vertical (Z) and transversal (Y) displacements are monitored at nodes $S5_{top}$, $S6_{top}$, Ab2, A6, A7. Vertical displacements are monitored at nodes $P6_{top}$ and $P6_{bottom}$.

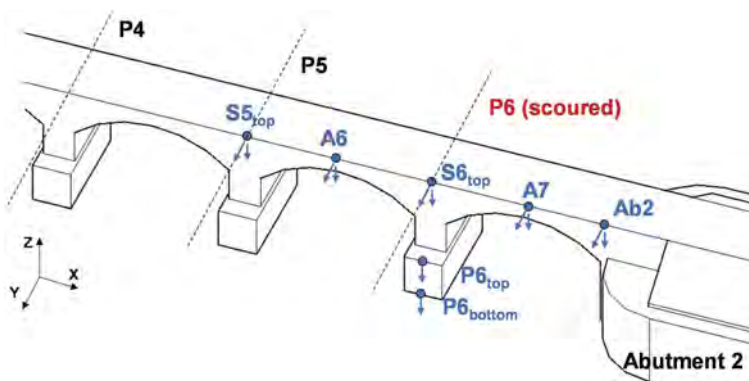


Figure 5. Scheme of the nodes monitored during the numerical analysis to asses the response variation induced by the scour process.

4 RESULTS

The response of the bridge is shown in Figure 6 (vertical displacements) and Figure 7 (transversal displacements). A near-collapse limit state (named failure in legend plot) is also added to the charts, highlighted by a vertical grey dotted line. This condition correspond to the development of critical diagonal cracks on the arches close to the scoured pier, as shown in Figure 8.

According to the results, the following comments can be made:

- Displacements at the nodes located on the Pier 5 ($S5_{top}$) and the Abutment 2 (Ab2) are very small (negligible);
- For what concerns the vertical displacements, the nodes most sensitive to scour are represented by those aligned along the vertical face of the Pier 6 (scoured), with magnitude rising from the bottom ($P6_{bottom}$) to the top of the bridge ($S6_{top}$);
- For what concerns the transversal displacements, the nodes most sensitive to scour are again those aligned along the vertical face of the Pier 6 (scoured) but the magnitude follows a reverse order, i.e., from the top ($S6_{top}$) to the bottom ($P6_{bottom}$);
- Nodes on the arches (A7 and A6) also show a quite important sensitivity to scour;
- The most sensitive nodes identified in this study develop displacements up to 20 mm before of the attainment of a severe irreversible damage state on the bridge (failure), thus they can be used within a continuous monitoring campaign to predict dangerous situations.

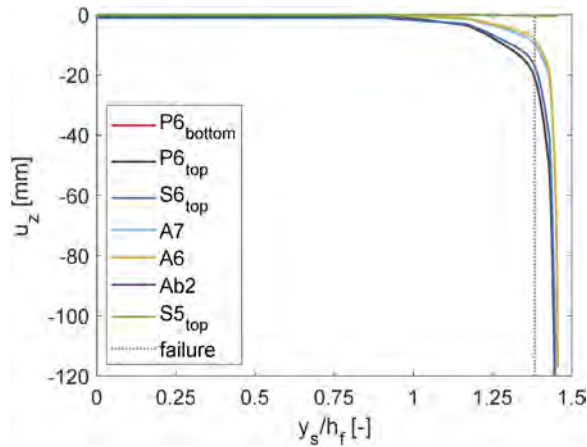


Figure 6. Vertical displacements at the monitored nodes on the up-stream face of the bridge.

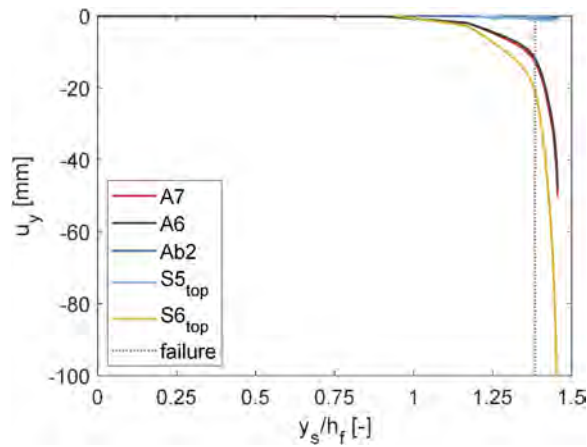


Figure 7. Transversal displacements at the monitored nodes on the up-stream face of the bridge.

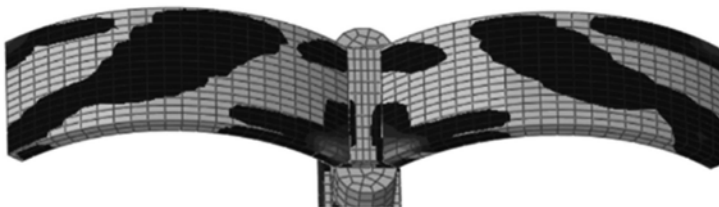


Figure 8. Plastic strains highlighting typical diagonal cracks on the arches (failure condition).

5 CONCLUSIONS

This paper analyses numerically the response of a masonry arch bridge under local scour actions and aims at analyzing the sensitivity of different response parameters (transversal and vertical displacements at different structural nodes of the bridge) to the scour evolution.

A real case study is considered and an accurate 3D finite element model of the bridge is developed. Numerical simulations are carried out to describe the scour hole progression around the foundation of a single pier until the attainment of an incipient bridge collapse condition.

As a major result, it is observed that the most sensitive nodes (e.g., at the top of the spandrel on the up-stream face of the piers) identified in this study develop non-negligible displacements (up to 20 mm) before the attainment of a severe irreversible damage state on the bridge. A continuous monitoring campaign based on the observation of such response parameters might thus be suitable to predict and anticipate dangerous conditions.

The study is preliminary and calls for a deeper investigation in which the effectiveness of a wider set of response parameters shall be assessed to derive information that can be used at a later stage for damage identification and quantification.

Different scour scenario should also be investigated in future papers.

REFERENCES

- Borlenghi, P., D'Angelo, M., Ballio, F., & Gentile, C. (2021b). Continuous monitoring of masonry arch bridges to evaluate the scour action. In *International Conference of the European Association on Quality Control of Bridges and Structures* (pp. 400–408). Springer, Cham.
- Borlenghi, P., Saisi, A., & Gentile, C. (2021a). Determining and Tuning Models of a Masonry Bridge for Structural Assessment. In *International Conference of the European Association on Quality Control of Bridges and Structures* (pp. 409–417). Springer, Cham.
- Cannizzaro, F., Pantò, B., Caddemi, S., & Calì, I. (2018). A Discrete Macro-Element Method (DMEM) for the nonlinear structural assessment of masonry arches. *Engineering Structures*, *168*, 243–256.
- Carbonari, S., Morici, M., Dezi, F., Leoni, G., 2018. A lumped parameter model for time-domain inertial soil-structure interaction analysis of structures on pile foundations. *Earthquake Engng Struct Dyn* *47*, 2147–2171. <https://doi.org/10.1002/eqe.3060>
- Civera, M., Mugnaini, V., & Zanotti Fragonara, L. (2022). Machine learning-based automatic operational modal analysis: A structural health monitoring application to masonry arch bridges. *Structural Control and Health Monitoring*, *29*(10), e3028.
- De Matteis, G., Bencivenga, P., Zizi, M., & Prete, A. D. (2021). Critical Issues of Typical Existing Masonry Road Bridges Handled by the Province of Caserta. In *International Conference on Protection of Historical Constructions* (pp. 1081–1092). Springer, Cham.
- Eidsvig, U., Santamaría, M., Galvão, N., Tanasic, N., Piciullo, L., Hajdin, R., ... & Matos, J. (2021). Risk assessment of terrestrial transportation infrastructures exposed to extreme events. *Infrastructures*, *6*(11), 163.
- Gara F., Nicoletti V., Carbonari S., Ragni L., Dall'Asta A. Dynamic monitoring of bridges during static load tests: influence of the dynamics of trucks on the modal parameters of the bridge. *J Civil Struct. Health Monit.*, *10*(2),197–217, 2020. DOI: 10.1007/s13349-019-00376-1.
- González, F., Carbonari, S., Padrón, L.A., Morici, M., Aznárez, J.J., Dezi, F., Maeso, O., Leoni, G., 2020. Benefits of inclined pile foundations in earthquake resistant design of bridges. *Engineering Structures* *203*, 109873. <https://doi.org/10.1016/j.engstruct.2019.109873>
- Hamidifar, H., Mohammad Ali Nezhadian, D., & Carnacina, I. (2022). Experimental study of debris-induced scour around a slotted bridge pier. *Acta Geophysica*, 1–15.
- Innocenzi R.D., Nicoletti V., Arezzo D., Carbonari S., Gara F., Dezi L. A Good Practice for the Proof Testing of Cable-Stayed Bridges. *Applied Sciences (Switzerland)*, *12* (7), 3547, 2022. DOI: 10.3390/appl2073547.
- Leoni, G., Gara, F., & Morici, M. (2021). Evaluation of Seismic Vulnerability of the Historical SS Filippo e Giacomo Masonry Arch Bridge in Ascoli Piceno (Italy). In *International Conference of the European Association on Quality Control of Bridges and Structures* (pp. 613–622). Springer, Cham.
- Li, Z., Tang, F., Chen, Y., Hu, X., Chen, G., & Tang, Y. (2021). Field experiment and numerical verification of the local scour depth of bridge pier with two smart rocks. *Engineering Structures*, *249*, 113345.
- Malekjafarian, A., Kim, C. W., O'Brien, E. J., Prendergast, L. J., Fitzgerald, P. C., & Nakajima, S. (2020). Experimental demonstration of a mode shape-based scour-monitoring method for multispan bridges with shallow foundations. *Journal of Bridge Engineering*, *25* (8), 04020050.
- Malena, M., Angelillo, M., Fortunato, A., de Felice, G., & Mascolo, I. (2021). Arch bridges subject to pier settlements: Continuous vs. piecewise rigid displacement methods. *Meccanica*, *56*(10), 2487–2505.

- Maroni, A., Tubaldi, E., Ferguson, N., Tarantino, A., McDonald, H., & Zonta, D. (2020). Electromagnetic sensors for underwater scour monitoring. *Sensors*, 20(15), 4096.
- Mendoza Cabanzo, C., Santamaría, M., Sousa, H. S., & Matos, J. C. (2022). In-Plane Fragility and Parametric Analyses of Masonry Arch Bridges Exposed to Flood Hazard Using Surrogate Modeling Techniques. *Applied Sciences*, 12(4), 1886.
- Minnucci, L., Morici, M., Carbonari, S., Dezi, F., Gara, F., & Leoni, G. (2022). A probabilistic investigation on the dynamic behaviour of pile foundations in homogeneous soils. *Bulletin of Earthquake Engineering*, 20(7), 3329–3357.
- Morici, M., Minnucci, L., Carbonari, S., Dezi, F., & Leoni, G. (2019). Simple formulas for estimating a lumped parameter model to reproduce impedances of end-bearing pile foundations. *Soil Dynamics and Earthquake Engineering*, 121, 341–355. <https://doi.org/10.1016/j.soildyn.2019.02.021>
- Nicoletti V., Martini R., Carbonari S., Gara F. Operational Modal Analysis as a Support for the Development of Digital Twin Models of Bridges. *Infrastructures*, 8 (2), 24, 2023. DOI: 10.3390/infrastructures8020024.
- Pantò, B., Chisari, C., Macorini, L., & Izzuddin, B. A. (2022). A hybrid macro-modelling strategy with multi-objective calibration for accurate simulation of multi-ring masonry arches and bridges. *Computers & Structures*, 265, 106769.
- Pepi, C., Cavalagli, N., Gusella, V., & Giofrè, M. (2021). An integrated approach for the numerical modeling of severely damaged historic structures: Application to a masonry bridge. *Advances in Engineering Software*, 151, 102935.
- Pizarro, A., Manfreda, S., & Tubaldi, E. (2020). The science behind scour at bridge foundations: A review. *Water*, 12(2), 374.
- Ragni, L., Scozzese, F., Gara, F., & Tubaldi, E. (2019, March). Dynamic identification and collapse assessment of Rubbianello Bridge. In *Towards a Resilient Built Environment Risk and Asset Management: IABSE Symposium Guimarães 2019* (pp. 619–626).
- Rainieri, C., Notarangelo, M. A., & Fabbrocino, G. (2020). Experiences of dynamic identification and monitoring of bridges in serviceability conditions and after hazardous events. *Infrastructures*, 5(10), 86.
- Scozzese, F., Ragni, L., Tubaldi, E., & Gara, F. (2019). Modal properties variation and collapse assessment of masonry arch bridges under scour action. *Engineering Structures*, 199, 109665.
- Scozzese, F., Ragni, L., Tubaldi, E., Gara, F. 2021. Scour-induced dynamic properties modification of masonry arch bridges with different geometry. *COMPdyn Proceedings*.
- Solan, B., Ettema, R., Ryan, D., & Hamill, G. A. (2020). Scour concerns for short-span masonry arch bridges. *Journal of Hydraulic Engineering*, 146(2), 06019019.
- Tecchio, G., Donà, M., Saler, E., & da Porto, F. (2022). Fragility of single-span masonry arch bridges accounting for deterioration and damage effects. *European Journal of Environmental and Civil Engineering*, 1–22.
- Tubaldi, E., Antonopoulos, C., Mitoulis, S. A., Argyroudis, S., Gara, F., Ragni, L., ... & Anastasiadis, A. (2022b). Field tests and numerical analysis of the effects of scour on a full-scale soil–foundation–structural system. *Journal of Civil Structural Health Monitoring*, 1–21.
- Tubaldi, E., Minga, E., Macorini, L., & Izzuddin, B. A. (2020). Mesoscale analysis of multi-span masonry arch bridges. *Engineering Structures*, 225, 111137.
- Tubaldi, E., White, C. J., Patelli, E., Mitoulis, S. A., De Almeida, G., Brown, J., ... & Zonta, D. (2022a). Invited perspectives: Challenges and future directions in improving bridge flood resilience. *Natural hazards and earth system sciences*, 22(3), 795–812.
- Zampieri, P., Tetougueni, C. D., & Pellegrino, C. (2021). Nonlinear seismic analysis of masonry bridges under multiple geometric and material considerations: Application to an existing seven-span arch bridge. In *Structures* (Vol. 34, pp. 78–94). Elsevier.
- Zampieri, P., Zanini, M. A., Faleschini, F., Hofer, L., & Pellegrino, C. (2017). Failure analysis of masonry arch bridges subject to local pier scour. *Engineering Failure Analysis*, 79, 371–384.
- Zhang, B., Zhao, H., Tan, C., O'Brien, E. J., Fitzgerald, P. C., & Kim, C. W. (2022). Laboratory Investigation on Detecting Bridge Scour Using the Indirect Measurement from a Passing Vehicle. *Remote Sensing*, 14 (13), 3106.
- Zizi, M., Bencivenga, P., & De Matteis, G. (2023, February). Handling policies for Italian existing bridges with a territorial approach: the case study of Caserta, Italy. In *Structures* (Vol. 48, pp. 1306–1321). Elsevier.

A methodology to derive scour fragility functions for masonry arch bridges

G. Degan Di Dieco & M. Pregnolato

Department of Civil Engineering, University of Bristol, Bristol, UK

A.R. Barbosa

School of Civil and Construction Engineering, Oregon State University, Corvallis, USA

ABSTRACT: Frequency and intensity of hydrological hazards have increased. Consequently, riverine bridges are suffering damage due to flooding. Fragility functions are used to estimate such damage conditioned on hazard intensity. However, flood fragility functions are limited for riverine bridges, and generally lack for masonry bridges. This paper presents a methodology to derive flood fragility functions for masonry arch bridges accounting for component failure modes. Demand and capacity of bridge components are derived from existing analytical expressions, and account for aleatory uncertainties via Monte Carlo simulations. The methodology is illustrated using a UK masonry bridge, which collapsed due to winter flood-induced scour. The investigated bridge is divided into its components (e.g., arches, pier) and a scour fragility function is derived for the arch, based on a lognormal cumulative distribution fitting to the derived failure probability data. Future research will develop scour fragility functions for other bridge components.

1 INTRODUCTION

In recent years various bridges have collapsed because of increasing precipitations, floods, and lack of maintenance (Schaap and Caner, 2021). In the United Kingdom (UK), recent collapses have highlighted the vulnerability of masonry arch bridges to flooding (Solan et al., 2020). For instance, eight masonry bridges collapsed in the Cumbria region alone (Northwest of England) during the 2009 and 2015 floods, resulting in £10.49 million of reconstruction costs (Li et al., 2021). Flood-induced bridge damage can result from scour, hydrostatic or hydrodynamic actions (HE, 2020a). The literature indicates that scour is the leading cause of bridge damage (Sasidharan et al., 2021), including natural, general, contraction, and local scour (HE, 2020a).

Quantifying the flood risk of bridge portfolios is becoming crucial to reduce economical and human losses (Swiss Re, 2021). Risk is typically obtained as the product of hazard, exposure, and vulnerability (Ang and Tang, 1975). Vulnerability represents the likelihood of losses as a function of hazard intensity measure(s) (Galasso et al., 2021), where expected losses are given as the product of the expected level of damage and bridge restoration costs for the various levels of damage (Gidaris et al., 2017). The expected level of damage conditioned on hazard intensity measure(s) is referred as “fragility” and estimated via fragility functions (Wen and Ellingwood, 2005). For applying fragility functions in vulnerability assessments, structures within a portfolio are grouped in vulnerability classes (Burns et al., 2021; Mangalathu et al., 2017), i.e. groups of structures which do not have statistically significant different responses (e.g. reinforced concrete multi-column bent bridges).

Bridge flood vulnerability classes that explicitly account for bridge structural performance and their possible failure modes are currently scarce in the literature (Gidaris et al., 2017; Degan Di Dieco et al., 2022). When considering masonry arch bridges, Lamb et al. (2019) derived scour fragility functions by fitting lognormal fragility functions to probability data of historical failures, and flood return period as intensity measure. Eidsvig et al. (2021) and Mendoza Cabanzo et al. (2022) derived scour fragility functions via limit state analyses of load carrying capacity and flow discharge as intensity measure. George and Menon (2021) proposed scour fragility functions derived via

kinematic chain limit analyses with scour-induced pier rotation as intensity measure. Maroni et al. (2020) developed a Bayesian scour fragility function using a qualitative risk classification, scour depth data from monitoring, and relative scour depth as intensity measure. The reviewed studies show that their fragility functions do not consider failure modes of components. Subdividing a bridge into key structural components affects damage estimates of bridge portfolios (Minnucci et al., 2022; Nielson and DesRoches, 2007) and consequently their risk. As a result, the first step to build robust estimates for flood-induced damage and risk is the investigation of significant failure modes of bridge components and their interdependencies (Argyroudis and Mitoulis, 2021; Ren et al., 2019).

This paper proposes a methodology of fragility functions for masonry arch bridges which accounts for failure modes of key structural components. Figure 1 illustrates the rationale of the proposed methodology for pier local scour inducing compressive rotational failure of a masonry arch; however, the methodology is derived to accommodate further components and their failure modes. In this methodology, existing analytical expressions are used to estimate bridge component capacities, while structural analysis schemes are used to estimate demands on bridge components. As a proof-of-concept, the proposed methodology is applied to a two-span masonry arch bridge which was spanning over River Calder in Halifax (West Yorkshire, North of England) and that collapsed in winter 2015 because of flood-induced scour (Tubaldi et al., 2018). This paper is divided into five sections. Section 2 details the methodology for developing fragility functions, the approach to account for scour effects on estimates of masonry arch capacity and demand, and the case study bridge. Section 3 shows the derived fragility function. Section 4 discusses underpinning assumptions and suggests future work. Section 5 summarizes the key findings.

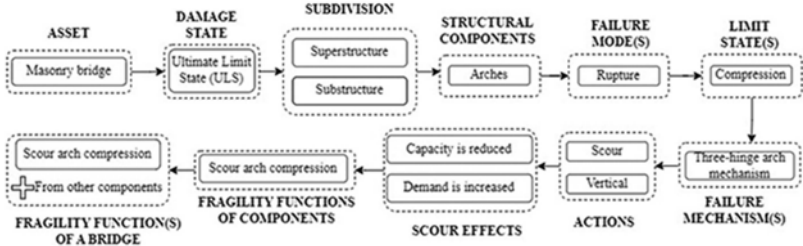


Figure 1. The proposed methodology for deriving flood fragility functions for masonry arch bridges.

2 METHODS

2.1 Fragility function derivation

Fragility functions can be derived empirically or analytically (Shinozuka et al., 2000). While empirical fragility functions are derived from observed damage data, analytical fragility functions are defined upon failure probability data, i.e. the ratio of the number of cases that exceed the failure state to the total number of simulations, for each investigated intensity measure (Mendoza Cabanzo et al., 2022). Based on structural reliability theory, the limit state function $M(x)$ (Mendoza Cabanzo et al., 2022) is given by:

$$M(x) = R(x) - E(x) \tag{1}$$

where $M(x)$ measures the difference between resistance effects $R(x)$ (i.e. capacity) and load effects $E(x)$ (i.e. demand), and x is a vector of a particular sample point. From Equation 1, it follows that failure is defined when $M(x) \leq 0$. Failure data can be generated via simple Monte Carlo (MC) simulations (Schmidt et al., 2019) and fitted with a cumulative distribution function, such as the lognormal fragility function (Baker, 2015). This study focuses on the limit state function for ultimate compressive strength only.

The compressive resistance of masonry elements R (i.e. capacity) is given by Equation 4.7.1 of CD 376 (HE, 2020b):

$$R(R_c) = 0.6 \cdot F_c \cdot [R_c \cdot b \cdot (t - 2e)] \quad (2)$$

where b (mm) is the element width, R_c (N/mm^2) is the basic random variable defining the masonry compressive strength, t (mm) is the overall element thickness, e (mm) is the eccentricity of the centre of compression in the element, 0.6 is a deterministic coefficient, and F_c is the condition factor and function of cracking in the arch (see Equation 6). Note that the 0.6 coefficient derives from Equation 4.7.1 in CD 376 (HE, 2020b), where $0.6 = 0.4 \gamma_M$, and $\gamma_M = 1.5$ is a partial safety factor. The masonry compressive strength R_c is assumed normally distributed with mean value \bar{r}_c and coefficient of variation CoV_c . For the normal random variable R_c , the mean value \bar{r}_c is obtained from the characteristic value f_k as follow (Melchers and Beck, 2018):

$$\bar{r}_c = f_k / (1 - k_{0.05} \cdot CoV_c) \quad (3)$$

where $k_{0.05}$ is the value of the standard normal variable for a probability of 0.05, f_k is given by Equation 3.1 of BS EN 1996-1-1:2005 (BSI, 2013):

$$f_k = K f_b^\alpha f_m^\beta \quad (4)$$

where α , β , and K are constants, function of mortar and unit type, and listed at paragraph 3.6.1.2 of BS EN 1996-1-1:2005 (BSI, 2013), f_m is the mean compressive mortar strength, and f_b is the normalised mean compressive unit strength (i.e. brick), in the direction of the applied action effect, and all these variables have been considered deterministic. Annex 2 of Morton (2012) provides the equation for f_b :

$$f_b = CF \cdot \delta \cdot f_{bm} \quad (5)$$

with both CF conditioning factor and δ shape factor related to brick tests given by Annex A of BS EN 772-1:2011 (BSI, 2015), f_{bm} is the mean compressive strength of the unit, and all these variables have been considered deterministic. The condition factor F_c , given by Equations 7.5.1a,b of CS 454 (HE, 2020c), is used to consider the material degradation defects in arch conditions:

$$F_c = F_{cM} F_j = F_{cM} (F_w F_d F_{m0}) \quad (6)$$

where F_{cM} is the arch barrel condition factor, F_j is the joint factor for arch diagonal cracks, F_w is the joint width factor, F_d is the joint depth factor, and F_{m0} is the mortar factor. The value of F_{cM} and F_j shall be determined according to Tables 7.5.1a,b,c,d of CS 454 (HE, 2020c) after a bridge inspection; however, their values have been assumed in this study, and considered deterministic.

The compressive load effect E (i.e. demand) is determined according to the assessment level 1 of CS 454 (HE, 2020c), where simple structural analyses are carried out and the masonry tensile strength is neglected:

$$E(\Gamma_m) = S_a(\Gamma_m) / \Phi_i \quad (7)$$

where $S_a(\Gamma_m)$ is the compressive force in the component, linear function of the unit weight of masonry Γ_m [see Equation 45 in Chapter 3 of Como (2013)], and Φ_i is the slenderness and eccentricity factor given by Equation 6.4 of BS EN 1996-1-1:2005 (BSI, 2013). Note that the compressive force in the component $S_a(\Gamma_m)$ is derived from the structural analysis, Γ_m is the basic random variable, Φ_i is considered deterministic and constant with scour depth, and load partial factors have been assumed equal to 1.0. The unit weight of masonry Γ_m is assumed normally distributed with mean value $\bar{\gamma}_m$ and coefficient of variation CoV_γ . The eccentricity of loads has been considered in the verification via the slenderness and eccentricity factor Φ_i (BSI, 2013)

$$\Phi_i = 1 - 2(e_i/t) \quad (8)$$

where $e_i = 0.05t$ is the minimum eccentricity at the element top and t is the element thickness.

In this study, dead loads, superimposed dead loads and pier local scour are the considered actions (HE, 2020c). To determine the thrust maximum value, Méry's method (Méry, 1840) is applied in the main plane (X-Y) of the case study bridge (Figure 2a). Méry (1840) supposed a three-hinge mechanism for the arch, with hinges located at the springing lines and crown, and the masonry material assumed linear elastic. The resulting scheme is structurally determined, the maximum thrust occurs at the springing level and e is equal to 1/6 of the arch's thickness. Therefore, the expressions for $S_a(\Gamma_m)$ was derived using equilibrium equations, and then implemented in Jupiter notebooks with Python (PSF, 2022).

Subsequently, R_c in Equation 2 and Γ_m in Equation 7 have been sampled with simple MC simulations (Schmidt et al., 2019) to estimate $R(R_c)$ and $E(\Gamma_m)$. Then, the arch probability of failure P_f has been calculated as:

$$P_f \approx n(M(x) \leq 0)/N \quad (9)$$

where N is the number of conducted simulations and $n(M(x) \leq 0)$ is the number of simulations n for which $M(x) \leq 0$ according to Equation 1. A convergence assessment of the MC estimator for both R_c and Γ_m was performed in terms of CoV following procedures in Ballio and Guadagnini (2004), i.e. root mean square of sample mean/variance divided by sample mean/variance, to identify the needed number of simulations for stabilisation of CoV values. Finally, failure probability data was fitted with a lognormal fragility function by following procedures in Baker (2015):

$$P_f = \Phi \left[\ln \left(d_{s,loc} / \hat{\theta} \right) / \hat{\beta} \right] \quad (10)$$

where $d_{s,loc}$ is the pier local scour depth, $\hat{\theta}$ and $\hat{\beta}$ are the estimates of median and log standard deviation, respectively, obtained using the maximum likelihood estimation method.

2.2 Case study

The fragility assessment was carried out on a two-span masonry arch bridge in Halifax (West Yorkshire, England), which was spanning over River Calder and that collapsed in December 2015 due to flood-induced scour (Tubaldi et al., 2018). The geometry of the bridge is typical in terms of span of various UK riverine bridge portfolios (Mathews and Hardman, 2017; Stevens et al., 2020). Figure 2a depicts the geometry of the investigated bridge, including: length of 20.30m between abutment faces; out-to-out width along the transverse direction of 3.80m; the two arches are segmental in shape, assumed of one ring, with span length of 9.26m, intrados rise of 3.45m, arch thickness of 0.50m ($r_i/L = 0.37$, $t_a/L = 0.05$); the pier has a rectangular transverse section of width 1.8m and depth 3.40m; bridge total length of 33.40m.

The masonry of arches, pier, spandrel walls, and parapet has unit weight γ_m 22 kN/m³ (Tubaldi et al., 2018), assumed as mean value $\bar{\gamma}_m = \gamma_m$, and $CoV_v = 10\%$ (Su et al., 2020), while backfill soil has unit weight of 19 kN/m³ (Tubaldi et al., 2018) and considered deterministic.

Regarding mechanical properties: (i) for general purpose mortar M4: $\alpha = 0.7$, $\beta = 0.3$, $f_m = 4$ MPa; (ii) for group 1 calcium silicate units: $K = 0.55$; (iii) for red sandstone wide blocks (Wiggins et al., 2019): $CF = 1$, $\delta = 1.18$ for air-dry brick testing, $f_b = 10$ MPa; (iv) resulting masonry: $f_k = 4.69$ MPa, $COV_c = 15\%$ (Conde et al., 2020), $k_{0.05} = 1.6449$, $\bar{r}_c = 6.23$ MPa.

Regarding the structural scheme (Figure 2b), parapet, spandrel walls, and backfill are considered as dead loads; the three-hinged arch lies on beam-like pier and abutments; the pier lies on beam-like shallow foundation, while abutments do not have any foundation; the foundation lies on Winkler-like spring soil; the soil-foundation modelling is outside of the scope of this study, as well as considering lateral earth pressures. Given the structure's vertical symmetry, the structural analysis is limited to half of a span; a one-meter arch barrel depth (i.e. $t = 1.00m$) is examined.

Before performing the probabilistic assessment, the deterministic assessment identified the arch as the component at the highest risk of failure among other components. Therefore, the

arch is the main focus of the reliability analysis performed in this study and for which the fragility function is derived.

Failure probability data was derived for six different discrete levels of local scour depth, $d_{s,loc} = [1.20, 1.50, 2.00, 2.30, 2.49, 2.54]m$, previously investigated by Tubaldi et al. (2018), and related to a not-symmetric scour hole. Scour effects on capacity and demand were considered via the empirical coefficients of Equation 6 and Equation 8, respectively, to reflect that pier local scour induces (Tubaldi et al., 2018): cracks in the arch barrel, central pier, pier-foundation interface, and eccentricity of vertical loads. Considering that the diagonal crack F_{cM} values reduce capacity the most (HE, 2020c), this case study investigates arch diagonal cracks only. Input values for F_c are: $F_{cM} = 0.3$ to 0.9 for diagonal cracks, while the variation of F_{cM} with scour depth is assumed linear between $F_{cM} = 0.3$ for $d_{s,loc} = 2.54m$ and $F_{cM} = 0.9$ for $d_{s,loc} = 120m$; $F_w = 1.0$ for width of joint = $6mm$; $F_d = 0.8$ for joints with 10% of thickness of barrel insufficiently filled; $F_{mo} = 0.9$ for loose joint condition; the multiplication of F_w , F_{mo} , and F_d leads to $F_j = 0.576$; while $F_c = 10$. For $d_{s,loc} = 1.00 m$. The assumption of F_{cM} values is based on the interpretation of arch cracking patterns and damages in tension due to pier vertical displacement and rotation determined by Tubaldi et al. (2018) via three dimensional finite element analyses. For an arch barrel depth $L/2 = 3.1m$, $e_i = 0.05 \cdot 3.1m = 0.16m$, Equation 8 gives $\Phi_i = 0.90$ and assumed constant with scour depth.

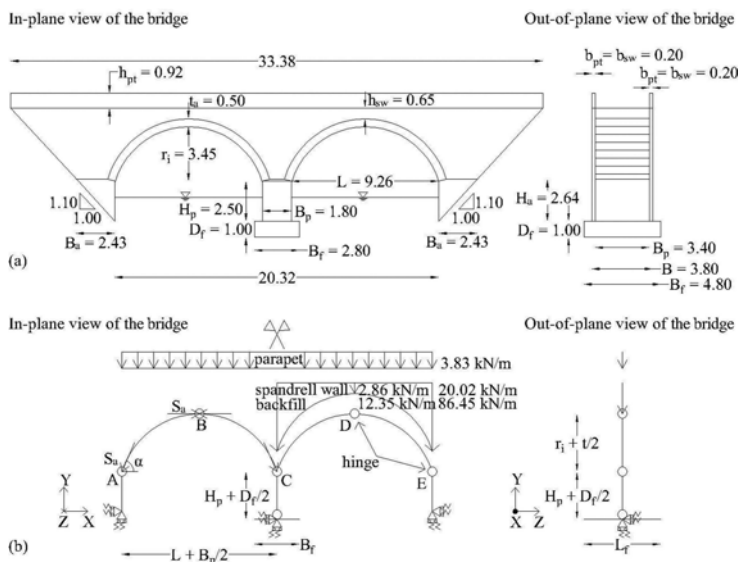


Figure 2. (a) Illustration of the case study bridge (dimensions in m); (b) model of the system bridge-river in scoured conditions.

3 RESULTS

The proposed methodology is demonstrated for the compressive failure mechanism of arches due to pier local scour for the UK case study described previously. 100.000 MC simulations were needed to obtain convergence for R_c and Γ_m in terms of CoV ; the results of MC simulations are here forth referred to as “realisations”. The 100.000 realisations of R_c and Γ_m were used to estimate capacity and demand according to Equation 2 and 7, respectively. Then, the obtained capacity and demand were used to estimate the limit state function (Equation 1) for the six investigated scour depths and the number of simulations for which $M(x) \leq 0$ was recorded. For instance, for $d_{s,loc} = 1.50m$, $F_c = 0.900$ and $\Phi_i = 0.90$, lead to 39.879 failures ($M(x) \leq 0$). Therefore, the first-not-null failure probability point is $(1.50m, 0.3988)$; further points were determined by changing F_c at each investigated scour depth, while Φ_i was considered constant, followed by performing MC simulations.

The derived scour fragility function for the arch is shown in Figure 3 for a scour depth range of 1.00m to 2.6m, where 1.0m is the foundation's depth and 2.6m is just above the 2.54m collapse scour depth estimated by Tubaldi et al. (2018). Note that the minimum value considered for scour depth is 1.20m because pier displacements develop only after scour depth exceeds the foundation depth (i.e. 1.0m). From fitting the failure probability data, a median $\hat{\theta} = 1.52m$ and log standard deviation of $\hat{\beta} = 0.05$ were estimated.

The proposed approach for deriving arch scour fragility functions could be repeated for a different bridge geometry and the resulting fragility function could be used to predict the failure probability of a masonry arch, if measurements of pier scour depth is available at the bridge site. Provided the made assumptions (see Section 4), the derived fragility function shown in Figure 3 represents one of the inputs needed to determine the bridge fragility function(s) in a failure mode analysis when multiple components are considered (e.g. piers, foundation). To the authors' knowledge, the derived arch scour fragility function represents the first attempt in the literature to determine flood fragility functions of masonry arch bridges from component fragilities.

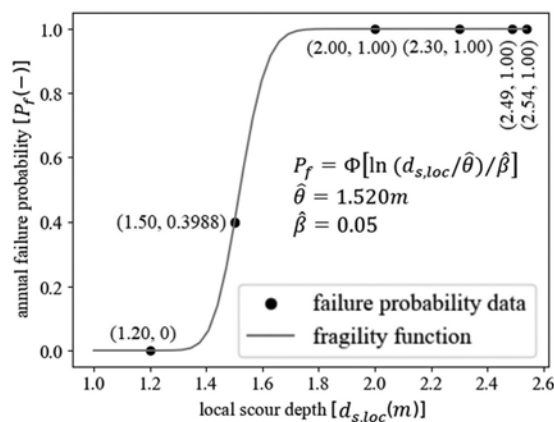


Figure 3. Derived scour fragility function for the investigated masonry arch.

4 DISCUSSION AND FUTURE RESEARCH

The proposed deriving methodology for flood fragility functions for masonry arch bridges advances the existing literature. Towards defining reliable fragility estimates, this study investigated the fragility of a masonry arch for the compressive resistance assessment, considering effects of pier local scour on arch demand and capacity; a UK case study was used to demonstrate the methodology. Results (Figure 3) showed that the investigated arch presents a median value of pier local scour depth of approximately 1.50m.

In the calculations, assumptions were made for dimensions and quality of bricks and mortar because no information was available. The effects of scour on the arch were considered via empirical coefficients (i.e. F_c , Φ_i), subjectively linked to scour depth because no relations were found. Furthermore, this study investigated a reduction of arch capacity due to diagonal cracks only, but other cracks (e.g. longitudinal) are possible (HE, 2020c). In addition, the interaction between backfill-arch-spandrel walls shall be investigated since it may affect the bridge flood response (Sarhosis et al., 2016). Failure probability data was fitted with a lognormal fragility function, which was shown to provide equal failure probabilities of other possible functions (Lallemant et al., 2015); however, more failure data shall be generated from the discretization of the expressions of condition factor F_c and eccentricity factor Φ_i as function of scour depth.

Although this work presents a fragility function for one component only (arch), it recommends to extend the methodology to the other components, to avoid underestimating the risk failure of a bridge (Nielson and DesRoches, 2007). Future work will develop scour fragility functions for compression limit state of other bridge components, such as pier, to obtain the global failure fragility

function(s). Further studies could consider additional random variables, e.g. shear strength of the mortar, to understand if there is more than one fragility function for a considered damage state; epistemic uncertainties, e.g. variability in the parameters of the used probability distribution function, shall be addressed and validated to enable implementation of fragility functions.

5 CONCLUSIONS

This study proposes a deriving methodology for scour fragility functions of masonry arch bridges able to account for failure modes of significant bridge components, which represents a novelty in the existing literature. Using a UK case study, a fragility function for the arch of a masonry bridge subjected to pier local scour was derived via simple MC simulations and analytical design expressions as an example. Future research opportunities include: (a) applying the proposed methodology to other bridge components; (b) investigating the relations scour depth-masonry capacity and demand; (c) investigating effects of various epistemic uncertainties; (d) validating the developed fragility functions.

DATA STATEMENT

Data and codes underpinning this paper are available upon request to the main author.

ACKNOWLEDGMENTS

Giuseppe Degan Di Dieco and Maria Pregolato acknowledge the Engineering and Physical Sciences Research Council (EPSRC) (Scholarship 2444849; Fellowship EP/R00742X/2), The Alan Turing Institute (ATI) (2021/22 Enrichment Scheme), Dr Mark Hobbs from The ATI for his supervision, and Sophia Nunn for proofreading.

REFERENCES

- Ang, A. H. S. & Tang, W. H. 1975. *Probability Concepts in Engineering Planning and Design, Vol. 1 - Basic Principles*. New York: John Wiley & Sons.
- Argyroudis, S. A. & Mitoulis, S. A. 2021. Vulnerability of bridges to individual and multiple hazards-floods and earthquakes. *Reliability Engineering & System Safety* 210.
- Baker, J. W. 2015. Efficient analytical fragility function fitting using dynamic structural analysis. *Earthquake Spectra* 31(1): 579–599.
- Ballio, F. & Guadagnini, A. 2004. Convergence assessment of numerical Monte Carlo simulations in groundwater hydrology. *Water Resources Research* 40(4).
- BSI. 2013. *BS EN 1996-1-1:2005+A1:2012. General rules for reinforced and unreinforced masonry structures*. London: British Standards Institute.
- BSI. 2015. *BS EN 772-1:2011+A1:2015. Methods of test for masonry units - Part 1: Determination of compressive strength*. London: British Standards Institute.
- Burns, P. O., Barbosa, A. R., Olsen, M. J. & Wang, H. 2021. Multihazard Damage and Loss Assessment of Bridges in a Highway Network Subjected to Earthquake and Tsunami Hazards. *Natural Hazards Review* 22(2).
- Como, M. 2013. *Statics of Historic Masonry Constructions*. New York: Springer.
- Conde, B., Matos, J. C., Oliveira, D. V. & Riveiro, B. 2020. Probabilistic-based structural assessment of a historic stone arch bridge. *Structure and Infrastructure Engineering*: 1–13.
- Degan Di Dieco, G., Barbosa, A. R. & Pregolato, M. 2022. A taxonomy of riverine roadway bridges at risk of flooding: towards bridge classes and damage models. *Proceedings of the Institution of Civil Engineers - Bridge Engineering*: 1–15.
- Eidsvåg, U., Santamaría, M., Galvão, N., Tanasic, N., Piciullo, L., Hajdin, R., Nadim, F., Sousa, H. S. & Matos, J. 2021. Risk Assessment of Terrestrial Transportation Infrastructures Exposed to Extreme Events. *Infrastructures* 6(11).
- Fang, D. L., Napolitano, R. K., Michiels, T. L. & Adriaenssens, S. M. 2019. Assessing the stability of unreinforced masonry arches and vaults: a comparison of analytical and numerical strategies. *International Journal of Architectural Heritage* 13(5): 648–662.
- Galasso, C., Pregolato, M. & Parisi, F. 2021. A model taxonomy for flood fragility and vulnerability assessment of buildings. *International Journal of Disaster Risk Reduction* 53.

- George, J. & Menon, A. 2021. A mechanism-based assessment framework for masonry arch bridges under scour-induced support rotation. *Advances in Structural Engineering* 24(12): 2622–2636.
- Gidaris, I., Padgett, J. E., Barbosa, A. R., Chen, S., Cox, D., Webb, B. & Cerato, A. 2017. Multiple-Hazard Fragility and Restoration Models of Highway Bridges for Regional Risk and Resilience Assessment in the United States: State-of-the-Art Review. *Journal of Structural Engineering* 143(3): 04016188.
- HE. 2020a. *CD 356: Design of highway structures for hydraulic action - Revision 1*. London: Highways England.
- HE. 2020b. *CD 376: Unreinforced masonry arch bridges - Revision 0*. London: Highways England.
- HE. 2020c. *CS 454: Assessment of highway bridges and structures - Revision 1*. London: Highways England.
- Lallemant, D., Kiremidjian, A. & Burton, H. 2015. Statistical procedures for developing earthquake damage fragility curves. *Earthquake Engineering & Structural Dynamics* 44(9): 1373–1389.
- Lamb, R., Garside, P., Pant, R. & Hall, J. W. 2019. A Probabilistic Model of the Economic Risk to Britain's Railway Network from Bridge Scour During Floods. *Risk Analysis* 39(11): 2457–2478.
- Li, X., Cooper, J. R. & Plater, A. J. 2021. Quantifying erosion hazards and economic damage to critical infrastructure in river catchments: Impact of a warming climate. *Climate Risk Management* 32: 100287.
- Mangalathu, S., Soleimani, F. & Jeon, J.-S. 2017. Bridge classes for regional seismic risk assessment: Improving HAZUS models. *Engineering Structures* 148: 755–766.
- Maroni, A., Tubaldi, E., Val, D., McDonald, H., Lothian, S., Riches, O., Zonta, D. & Huang, H. 2020. A Bayesian network-based decision framework for managing bridge scour risk. *Sensors and Smart Structures Technologies for Civil, Mechanical, and Aerospace Systems* 2020.
- Mathews, R. & Hardman, M. 2017. Lessons learnt from the December 2015 flood event in Cumbria, UK. *Proceedings of the Institution of Civil Engineers - Forensic Engineering* 170(4): 165–178.
- Melchers, R. E. & Beck, A. T. 2018. *Structural Reliability Analysis and Prediction*. Hoboken: Wiley.
- Mendoza Cabanzo, C., Santamaría, M., Sousa, H. S. & Matos, J. C. 2022. In-Plane Fragility and Parametric Analyses of Masonry Arch Bridges Exposed to Flood Hazard Using Surrogate Modeling Techniques. *Applied Sciences* 12(4).
- Méry, E. 1840. Sur l'équilibre des voûtes en berceau. *Annales des Ponts et Chaussées* 1er Série(1er Semestre).
- Minnucci, L., Scozzese, F., Carbonari, S., Gara, F. & Dall'Asta, A. 2022. Innovative Fragility-Based Method for Failure Mechanisms and Damage Extension Analysis of Bridges. *Infrastructures* 7(9).
- Morton, J. 2012. *Designers' Guide to Eurocode 6: Design of Masonry Structures*. London: ICE Publishing.
- Nielson, B. G. & DesRoches, R. 2007. Seismic fragility methodology for highway bridges using a component level approach. *Earthquake Engineering & Structural Dynamics* 36(6): 823–839.
- PSF. 2022. *Python 3.11.1 documentation*. The Internet: Python Software Foundation.
- Ren, L., He, S., Yuan, H. & Zhu, Z. 2019. Seismic Fragility Analysis of Bridge System Based on Fuzzy Failure Criteria. *Advances in Civil Engineering*: 1–13.
- Sarhosis, V., De Santis, S. & de Felice, G. 2016. A review of experimental investigations and assessment methods for masonry arch bridges. *Structure and Infrastructure Engineering* 12(11): 1439–1464.
- Sasidharan, M., Parlikad, A. K. & Schooling, J. 2021. Risk-informed asset management to tackle scouring on bridges across transport networks. *Structure and Infrastructure Engineering*: 1–17.
- Schaap, H. S. & Caner, A. 2021. Bridge collapses in Turkey: causes and remedies. *Structure and Infrastructure Engineering*: 1–16.
- Schmidt, R., Voigt, M., Pisaroni, M., Nobile, F., Leyland, P., Pons-Prats, J. & Bugeđa, G. 2019. *General Introduction to Monte Carlo and Multi-level Monte Carlo Methods. Uncertainty Management for Robust Industrial Design in Aeronautics*. Springer International Publishing.
- Shinozuka, M., Feng, M. Q., Lee, J. & Naganuma, T. 2000. Statistical Analysis of Fragility Curves. *Journal of Engineering Mechanics* 126(12).
- Solan, B., Ettema, R., Ryan, D. & Hamill, G. A. 2020. Scour Concerns for Short-Span Masonry Arch Bridges. *Journal of Hydraulic Engineering* 146(2).
- Stevens, N. A., Lydon, M., Marshall, A. H. & Taylor, S. 2020. Identification of Bridge Key Performance Indicators Using Survival Analysis for Future Network-Wide Structural Health Monitoring. *Sensors (Basel)* 20(23).
- Su, L., Li, X.-l. & Jiang, Y.-p. 2020. Comparison of methodologies for seismic fragility analysis of unreinforced masonry buildings considering epistemic uncertainty. *Engineering Structures* 205.
- Swiss Re 2021. Global insured catastrophe losses rise to USD 112 billion in 2021, the fourth highest on record. *Swiss Re Press Releases*.
- Tubaldi, E., Macorini, L. & Izzuddin, B. A. 2018. Three-dimensional mesoscale modelling of multi-span masonry arch bridges subjected to scour. *Engineering Structures* 165: 486–500.
- Wen, Y. K. & Ellingwood, B. R. 2005. The Role of Fragility Assessment in Consequence-Based Engineering. *Earthquake Spectra* 21(3): 861–877.
- Wiggins, D., Mudd, K. & Healey, M. 2019. Rehabilitation of Brougham Castle Bridge, UK. *Proceedings of the Institution of Civil Engineers - Engineering History and Heritage* 172(1): 7–18.

Experimental modal analysis and finite element model updating of a historical masonry arch bridge

M. Morici

School of Architecture and Design, University of Camerino, Ascoli Piceno, Italy

V. Nicoletti

Department ICEA, Engineering Faculty, Università Politecnica delle Marche, Ancona, Italy

G. Leoni

School of Architecture and Design, University of Camerino, Ascoli Piceno, Italy

F. Gara

Department ICEA, Engineering Faculty, Università Politecnica delle Marche, Ancona, Italy

ABSTRACT: This paper presents the experimental test campaign to calibrate a finite element model intended to evaluate the seismic vulnerability of the SS Filippo e Giacomo historical masonry arch bridge in Ascoli Piceno (Italy). The bridge has undergone very complex vicissitudes related mainly to exceptional river floods; it was partially rebuilt twice and other strengthening works were carried out over the time. The bridge, which is almost completely built with travertine blocks, has a total length of 146 m and follows a slightly curved path. Six arches, the main of which is semi-circular with span of 25 m and the others are lancet arches with span of about 8 m, support the carriageway that is about 8 m wide. The piers and abutments are founded on the bed-rock and consequently some piers are deeply embedded in the sandy gravel deposit. A campaign of experimental tests was executed encompassing onsite measurements of stresses and modulus of elasticity, as well as laboratory measurements on specimens taken from the structures. Vibration tests were also carried out to evaluate the modal properties of the bridge. The acquired experimental data were used to calibrate a 3D Finite Element Model that has been developed considering the complex geometry of the bridge also including the deformable soil deposit. A very good consistency was achieved between experimental and theoretical behaviours.

1 INTRODUCTION

Evaluation of a historical masonry structure is a challenging task due to the numerous unknown factors surrounding the structure's actual conditions (Minnucci et al. 2022) (original structure, structural changes brought on by repair, enlargement, retrofit works, various construction systems, various materials, degradation and damages to the structure and materials, changes to the soil and foundation, etc.), as well as the complexity of modelling techniques and analysis methods (Pavia et al. 2021). In this regard, advanced measuring techniques are required to capture the true behaviour of the structure, particularly the mechanical properties of the structural materials and the overall dynamic behaviour, following a thorough study and geometrical and structural survey (Ragni et al. 2019).

Regarding the material survey, both conventional and cutting-edge techniques are accessible, however non-destructive procedures are typically favored when working with historically significant and priceless structures. A thorough material testing campaign may make it possible to fix a significant number of the key parameters used to define the structural finite element model. By employing modal identification methods and a variety of test types, such as forced, impulse, release, or ambient vibration testing, it is possible to empirically assess the structure's overall

dynamic behaviour (Aras et al. 2011, Beolchini and Vestroni 1997, Benedetti and Gentile 1994, Nicoletti et al. 2023, Dall'Asta et al. 2022, Tubaldi et al. 2021). Since no artificial excitation is needed and the test can be conducted in operational conditions with minimal disruption to the structure's use, ambient vibration tests with the appropriate output-only modal identification methods have recently emerged as the preferred test typology for evaluating the modal parameters of full-scale structures, particularly historic ones. (Gentile and Saisi 2007, Nicoletti et al. 2022a) The updated improved finite element models, which are needed for structural verifications, as well as for the design of repair and retrofit works, may then be created based on the experimental modal parameters (De Sortis et al. 2005, Ahmadian et al. 1994, Mottershead et al. 1993, Nicoletti et al. 2022b, Gara et al. 2021, Cipriani et al. 2022).

The paper presents the experimental test campaign and the updating of the finite element model of the SS. Filippo and Giacomo Bridge over the Tronto River, in Ascoli Piceno, Central Italy. The bridge was constructed in the 14th century, after which it underwent several modifications for renovation, strengthening, modernization, and enlargement work. As a result of interactions between parts with varied mechanical properties and ages, the structural organism becomes very complicated. Given these uncertainties and the significance of the bridge, a precise examination of its current state was deemed necessary in order to create a reliable predictive finite element model that would be utilized to develop the seismic retrofit design. First, a geometric survey and historical analysis of the bridge were developed. In order to assess the quality of the travertine block masonry, both destructive and non-destructive in-situ testing for material characteristics were performed. In particular, the young modulus of some materials, which was initially defined according to standard values suggested by codes, was calibrated to fit the dynamic behaviour obtained experimentally. A refined 3D finite element model was developed using these data and tuned based on the experimental modal parameters.

2 CASE STUDY: THE SS. FILIPPO AND GIACOMO BRIDGE

2.1 *General description*

In Ascoli Piceno town, the SS. Filippo and Giacomo bridge rises in a less urbanized area and spans the Tronto River in a modest straight valley located between two loops. The bridge highest height is almost 20 m, and its overall length is 146 m. The bridge is constructed between two rock escarpments, one of which has a significant slope (Figure 1). The left escarpment has a rather high slope (52°) whereas the right one is less sloping (31°). The gorge is characterized by a sandy gravel deposit on the right riverbank, with variable thickness up to 10 m, whereas the sandstone bedrock is outcropping at the left riverbank.



Figure 1. Aerial view of the SS Filippo and Giacomo bridge.

The bridge consists of six arches. The main one, which is semicircular in shape and has a span of around 25 meters, crosses the river during its normal flow. The remaining five arches have a span of roughly 8 meters and are lancet-shaped. During unusual floods, the river occupies the right bank where all of the piers are located. With a curve close to the left abutment, the plan

route is mainly rectilinear. The bridge was widened in the first part of the 20th century using a double series of pensile semicircular tiny arches, with spans of approximately 4 m, supported by stone corbels. The two-lane road is about 6 m wide and is bordered by two sidewalks of about 1 m width. With the exception of the 20th-century pensile arches and the interior lighting chambers, the bridge is entirely constructed of travertine stones.

2.2 Bridge damages during the centuries

The current SS. Filippo and Giacomo bridge's appearance is the result of a complicated series of incidents that transpired during its almost 600-year history (Figure 2).

The previous bridge, which was built in the second part of the XIV century, was most likely made up of four semicircular arches. A flood that occurred in 1453 severely damaged it, resulting in the collapse of three arches on the right side, likely as a result of the river flowing down the canyon on that side at the time, as may be inferred from geological studies.

The reconstruction of the bridge began about 1464; the portion that had survived was left intact, while the piece that had fallen was reconstructed using lancet arches with shorter spans than the original ones. The requirement to shift the pier spacing without changing the height or the original top level led undoubtedly to the selection of lancet arches. It is believed that the five new arches have not undergone any significant changes as of right now. The major arch that had survived the first flood collapsed as a result of a second exceptional flood that took place in 1528. This was rebuilt beginning in 1545 and using two parallel barrel-vaults. The downstream vault, which is about 3 m wide, has remained largely unchanged, while the upstream vault, which has a variable width, underwent a significant vertical settlement (of about 0.4 m). The vault was finally rebuilt in 1667 by installing wooden and iron ties intended to tighten together the two parts. A poorly designed wall collapsed in 1721 due to a fresh flood (probably a wing wall or a part of the abutment at the left riverbank). In 1794, a cutwater was constructed to safeguard the main pier. Between 1835 and 1836, the two arches supported by the main pier were repaired. In order to make maintenance of the structure easier, two barrel-vaults were constructed at the conclusion of these works rather than reinstalling the earth fill at the extrados of the main arch. The spandrel walls of the bridge support the two vaults. Between 1849 and 1850, work was done to lessen the slope of the upper road. The spandrel walls were lifted and filled with dirt after transverse ties were put two meters from the previous top level to support the structure. In order to enlarge the roadway, the final curve was changed by adding side travertine corbels with various spans up to 1 m. These corbels were subsequently joined by 0.30 m thick brick arches. During this phase, a new arrangement of interior lighting rooms was constructed over the main arch; the rooms are spaced equally between the external pensile arches to allow for the installation of stone corbels in the walls dividing the rooms. Each chamber has an orthogonal vault to the previously realized lower level. The bridge's current configuration was determined by the last significant intervention, which took place in 1932. By using a series of pensile arches similar to those previously mentioned, the remaining portion of the bridge is widened.

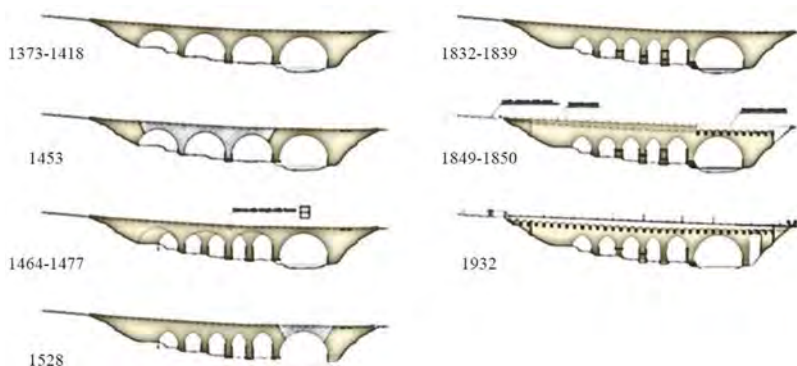


Figure 2. Bridge damages and reconstructions over centuries.

3 EXPERIMENTAL CAMPAIGN

3.1 Tests on construction materials

On-site experiments, including two tests using single flat jacks and one test using double flat jacks, were used to characterize the construction materials. Additionally, three compression experiments on travertine specimens obtained via masonry coring, were carried out. Locations for sampling and testing are reported in Figure 3.

Masonry coring allowed for the observation that the pier structure is made up of a significant internal rubble stone infill that is characterized by the presence of water in the lower parts, as well as an external curtain that is made of Ascoli Piceno travertine square blocks and has a variable thickness. Compressive tests carried out on the three specimens gave scattered results with minimum strength 16.9 N/mm^2 . The double flat jack test carried out at the base of pier P2 provided a linear behavior in the stress range investigated (up to about 4 N/mm^2), characterized by Young modulus of about 6600 N/mm^2 . At the bases of piers P1 and P2, single flat jack tests were conducted to estimate the stress status in the exterior brickwork curtains. As anticipated, the stress state for pier P1 is greater than that for pier P2. In particular, the normal vertical stress in pier P1 is approximately 1.3 N/mm^2 , whereas that for pier P2 is around 0.5 N/mm^2 . Testing was not done for the inner vaulted rooms masonry since it was clear through examination and laser scanner survey that it is a solid brick masonry. Nonetheless, it is important to note that, with the exception of the mass, these elements are not anticipated to have a substantial impact on the structure's overall behaviour. The two kinds of masonry constituting the bridge structure can be classified according to catalogs reported in design guidelines and standards (Decree 17/01/2018, Circular 21/01/2019), and the main characteristics are reported in Figure 3.

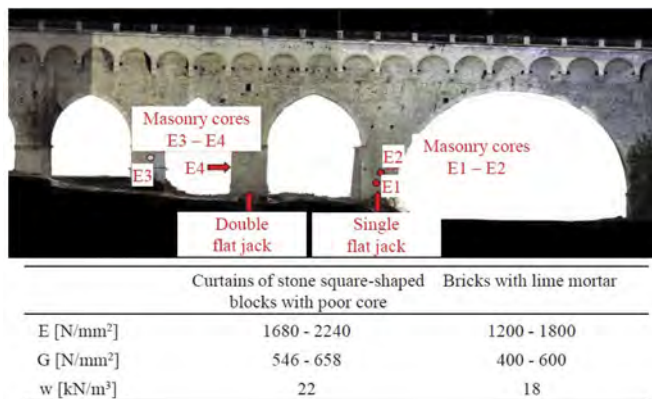


Figure 3. Experimental campaign and estimated properties of the construction materials.

3.2 Ambient vibration tests and operational modal analysis

The accelerations of the deck recorded during ambient vibration measurements, which are mostly caused by traffic, wind, and microtremors, are used to experimentally determine the modal characteristics of the bridge, including natural frequencies, damping ratios, and mode shapes. Eight low noise piezoelectric uniaxial accelerometers, a 24-bit data collecting device, and coaxial cables are used to conduct the testing.

Many tests were used to determine the bridge overall dynamic behaviour, but only those helpful to explore the transversal behaviour are described and analyzed in this work. The chosen measurement setup is seen in Figure 4a and consists of 8 accelerometers that are positioned in the middle of each span and measure in a transversal direction. The minimum sampling rate for the utilized data collecting equipment was 2048 Hz, and time histories measuring 1000 seconds in length were obtained. According to Cantieni (2005), this length of time gives adequate data to accurately determine the modal parameters, and a collection duration greater than about 1000–2000 times the

fundamental period is advised (in this case a value of about 2.5 Hz was obtained by preliminary measurements, which leads to 400-800 s). Before performing the operational modal analysis all the recorded data were processed by means of suitable signal processing techniques: trend removal, low pass filtering (to eliminate the contribution of high frequencies and to avoid aliasing phenomena) and down-sampling at 51.2 Hz, in order to decrease the amount of data and make faster the successive analyses.

Based on the accelerations collected during the ambient vibration test, the modal parameters are estimated using the Covariance-Driven Stochastic Subspace Identification (SSI-Cov). This approach converts the second-order system of differential equations that describes the dynamic issue into a first-order system using a stochastic state-space model (Juang 1994, Van Overschee & De Moor 1996). Depending on the model order employed in the state-space model, the SSI-Cov enables the estimate of a variety of modes. The stabilisation diagram (Figure 4b) allows the separation of the physical modes from the spurious ones, allowing the identification of the stable modes, i.e., natural frequencies, damping ratios, and mode shapes that remain consistent as the model order increases. In this work models with up to 40 order are used and the modes are considered to be consistent if, when increasing the model order one by one: natural frequency variation is less than 1%, damping ratio variation is less than 2%, and MAC between the modes is greater than 98%.

In the frequency range of 2–6 Hz, Table 1 lists the natural frequencies with the pertinent damping ratios, and Figure 5 displays the normalised modal shapes derived using the SSI-Cov approach. These modes are the transversal modes typical of a masonry bridge of this type.

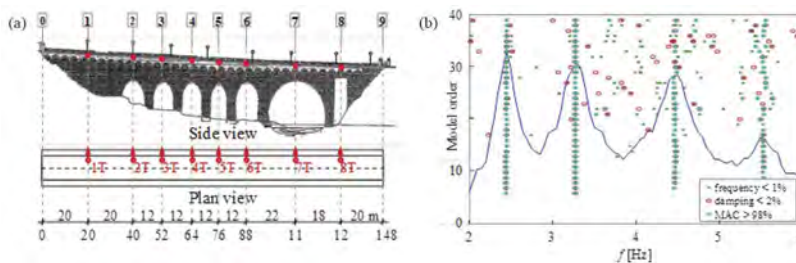


Figure 4. Ambient vibration tests: (a) sensor configuration, (b) stabilization diagram from SSI-Cov.

Table 1. Experimental modal parameters.

Mode	f [Hz]	ξ [%]	Mode shape
1	2.46	2.11	1 st transverse
2	3.30	2.97	2 nd transverse
3	4.54	2.54	3 rd transverse
4	5.61	2.50	4 rd transverse

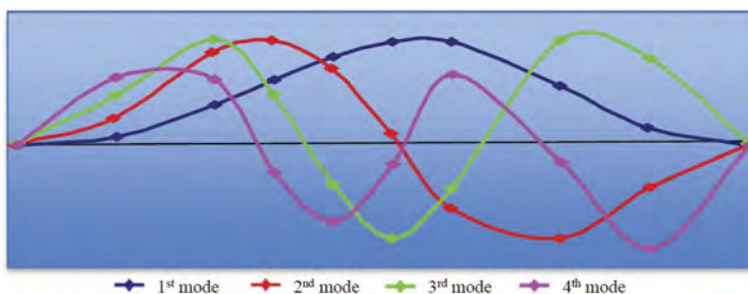


Figure 5. Experimental mode shapes.

4 NUMERICAL MODELLING

4.1 Finite element model of the bridge

Utilizing data from the laser scanner survey, a model for the overall structural analysis has been developed in Straus7. To account for the specific geological arrangement and capture the impacts of soil-pier interaction, the 3D model contains an appropriate area of the soil deposit with varying depth (Figure 6). A mesh of 4-node tetrahedral elements with linear interpolation shape functions is used to create the finite element model (Tetra4). By importing a closed poly-surface that approximates the geometry discovered by the laser scanner survey, the mesh is automatically generated. All internal chambers and the earth fill are modelled in order to accurately reflect the true stiffness and mass distribution of the structure. This avoids over-refinement of the mesh owing to features that do not directly affect the general behaviour of the bridge. The maximum length imposed to the element edge is 1.0 m, while it is extended to 4.5 m for the elements of the soil deposit. The deposit foundation and the structural portions engaging with the sand stone formation are both fixed with restraints. The model has a total of 75,204 degrees of freedom and is made up of 120,545 elements. All of the materials, including soil deposits and earth fills, are regarded as being linear elastic and isotropic.

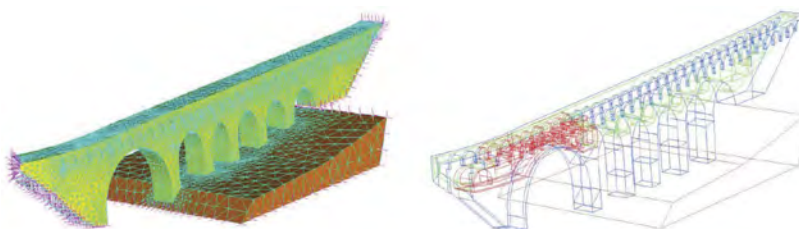


Figure 6. Finite element model of the bridge (Straus7).

4.2 Finite element model updating

By matching the experimental modal parameters with numerical ones pertinent to the finite element model previously stated, the mechanical parameters of the finite element model are calibrated adopting the manual tuning technique. Figure 7 displays the first four mode shapes that were achieved by calibrating the model by merely altering the elastic modulus of the travertine masonry that makes up the structure. Moreover, the comparison among the first four experimental and numerical mode shapes is reported as well, while Table 2 reports the percentage errors relevant to the frequencies and the approximation of the mode shapes by means of the Modal Assurance Criterion (MAC) (Allemang and Brown 1982). The parameters achieved at the end of the updating procedure are reported in Table 3. The soil parameters are supposed based on available geotechnical tests, while infill materials are hypothesized.

Table 2. Comparison between experimental and numerical modal parameters after the model updating.

Mode	Frequency [Hz]		Error [%]	MAC [%]
	Experimental	Numerical		
1	2.46	2.42	1.55	98
2	3.30	3.45	-4.67	95
3	4.54	4.87	-7.34	93
4	5.61	6.23	-10.99	86

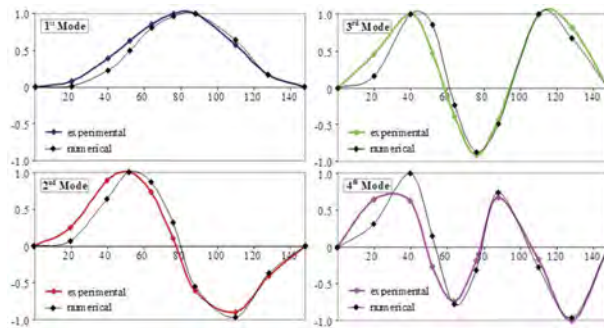


Figure 7. Comparison between experimental and numerical mode shapes.

Table 3. Comparison between experimental and numerical modal parameters after the model updating.

Material	E [N/mm ²]	G [N/mm ²]	W [kN/m ³]
Travertine masonry	7000	2414	22
Brick masonry	1282	427	18
Earth fill	666	238	18
Soil deposit	666	243	19

5 CONCLUSIONS

A finite element model of a mediaeval masonry bridge with distinctive geometry resulting from extremely complicated historical vicissitudes, has been calibrated through an experimental test campaign that has been presented. The bridge is built on a sand-stone deposit that is outcropping at the abutments and rises in a canyon. The bridge is made up of six separate arches, each supported by piers that extend up to 10 meters into the river deposit of sandy-gravel soil. The piers are built on a sand-stone formation. In order to create a model that included all significant aspects of the original building, including the interior lighting rooms highly asymmetrical geometry and the pensile arches built to widen the highway, a laser scanner survey was essential.

The onsite tests permitted to evaluate the main mechanical characteristics of the materials and to estimate the stress state in critical sections of the piers. The operational modal analysis, used to detect the dynamic behavior of the bridge, was decisive for tuning a finite element model capable of predicting the overall behavior of the bridge.

The calibrated model very well reflect the dynamic behaviour of the real bridge and it could be a fundamental support in the numerical analyses required for the bridge safety verifications.

REFERENCES

- Allemang R. J., Brown D. L. 1982. A correlation coefficient for modal vector analysis. Proc. of 1st Int. Modal Analysis Conf., Bethel, CT, USA, 110–15.
- Aras F., Krstevska L., Tashkov L. 2011. Experimental and numerical modal analyses of a historical masonry palace. *Constr Build Mat*, 25(1), 81–91.
- Benedetti D., Gentile C. 1994. Identification of modal quantities from two earthquake responses. *Earthq Eng Struct Dyn*, 23(4), 447–462.
- Beolchini G.C., Vestroni F. 1997. Experimental and analytical study of dynamic behaviour of a bridge. *J Struct Eng ASCE*, 123(11), 1506–1511.

- Cantieni R. 2005. Experimental methods used in system identification of civil engineering structures. Proc. 1st Int. Operational Modal Analysis Conf., Copenhagen, Denmark, pp. 249–260.
- Cipriani L., Dall’Asta A., Leoni G., Morici M., Zona A. 2022. First results of long-term monitoring of Portico Varano in the Camerino Ducal Palace (Italy). *COMP-DYN Proceedings*, 8th International Conference on Computational Methods in Structural Dynamics and Earthquake Engineering (COMP-DYN 2021) Athens, 28-30 June 2021.
- Circular 21/01/2019, n.7, Instructions for the application of «Adjournment of “Technical code for constructions”», (D.M. 17/ 01/2018). Superior Council of Public Works, G.U. - n.5, 11/ 02/2019. In Italian language.
- Dall’Asta A., Leoni G., Gioiella L., Micozzi F., Ragni L., Morici M., Scozzese F., Zona A. 2022. Push-and-release tests of a steel building with hybrid base isolation. *Eng Struct* 272, 114971. <https://doi.org/10.1016/j.engstruct.2022.114971>.
- Decree 17/01/2018, n. 42, Adjournment of «Technical code for constructions», Italian Ministry of Infrastructures and Transports. In Italian language
- Gara F., Arezzo D., Nicoletti V., Carbonari S. 2021. Monitoring the Modal Properties of an RC School Building during the 2016 Central Italy Seismic Swarm. *J Struct Eng ASCE*, 147(7), 05021002.
- Gentile G., Saisi A. 2007. Ambient vibration testing of historic masonry towers for structural identification and damage assessment. *Constr Build Mat*, 21(6), 1311–1321.
- Juang J.N. 1994. Applied System Identification. Prentice-Hall Englewood Cliffs, New Jersey, USA.
- Minnucci, L., Scozzese, F., Carbonari, S., Gara, F., & Dall’Asta, A. (2022). Innovative Fragility-Based Method for Failure Mechanisms and Damage Extension Analysis of Bridges. *Infrastructures*, 7(9), 122.
- Nicoletti V., Arezzo D., Carbonari S., Gara F. 2023. Detection of infill wall damage due to earthquakes from vibration data. *Earthq Eng Struct Dyn*, 52(2), 460–481.
- Nicoletti V., Arezzo D., Carbonari S., Gara F. 2022a. Vibration-Based Tests and Results for the Evaluation of Infill Masonry Walls Influence on the Dynamic Behaviour of Buildings: A Review. *Arch Comp Methods Eng*, 29(6), 3773–3787.
- Nicoletti V., Arezzo D., Carbonari S., Gara F. 2022b. Dynamic monitoring of buildings as a diagnostic tool during construction phases. *J Build Eng*, 46, 103764.
- Pavia A, Scozzese F, Petrucci E, Zona A. Seismic Upgrading of a Historical Masonry Bell Tower through an Internal Dissipative Steel Structure. *Buildings*. 2021; 11(1):24.
- Ragni L., Scozzese F., Gara F., Tubaldi E. (2019). Dynamic identification and collapse assessment of Rubbianello Bridge. In *Towards a Resilient Built Environment Risk and Asset Management: IABSE Symposium Guimarães 2019* (pp. 619–626).
- Tubaldi, E., Scozzese, F., De Domenico, D., Dall’Asta, A. (2021). Effects of axial loads and higher order modes on the seismic response of tall bridge piers. *Engineering Structures*. 247, 113134.
- Van Overschee P., De Moor B. 1996. Subspace identification for linear systems: theory–implementation–applications. Dordrecht, The Netherlands: Kluwer Academic Publishers.

Influence of site effects on the seismic vulnerability of masonry arch bridges

Ö. Saygılı

Department of Civil Engineering, Yeditepe University, Istanbul, Turkey

J.V. Lemos

National Laboratory for Civil Engineering (LNEC), Lisbon, Portugal

ABSTRACT: Historical masonry structures are vulnerable to seismic loadings due to their architectural characteristics, unsuitable strengthening or retrofit techniques, according to post-earthquake scenarios observed in Turkey during the previous 50 years. Masonry arch bridges are among the most important architectural heritage buildings vulnerable to earthquake motion. Historic masonry bridges that have suffered severe damage highlight the need for preventive and focused risk reduction strategies. This study aims to analyze the seismic vulnerability of two historical masonry arch bridges located in the Northeast and Northwest of Turkey, considering the seismotectonic parameters of the region. Nonlinear behavior of the masonry arch bridges under the seismic excitations that can be expected at the site was simulated in order to predict the potential damage levels. Discrete element method based on the numerical integration in time of the equations of motion of the system by means of an explicit finite difference method was used. The explicit solution procedure uses small time steps for numerical stability and this methodology allowed a general analysis to assess the joint separation and sliding of stone blocks. The seismic responses of these two masonry bridges showed that the geometry of the bridge has a significant effect on the structural performance, especially the arch span, which increases the seismic vulnerability of the bridges. More research is still needed on the approaches available to improve the seismic safety of damaged masonry arch bridges while preserving their historical value.

1 INTRODUCTION

Many old stone and brick bridges from the past still stand in Turkey, serving as important transportation infrastructures that were built long ago to help people get around. Most of these bridges have a round or pointed arch shape and rise high on both sides of the river. These bridges are specifically designed to withstand floods, and their lengths and heights depend on the width and depth of the valley where they are located. The investigation of the structural behavior of masonry structures is an active research subject, as evidenced by several studies (Çaktı et al., 2016; Karaton et al., 2017; Özmen & Sayın, 2018; Pulatsu et al., 2019; Saygılı, 2019, 2020; Saygılı & Lemos, 2020, 2021). To understand the structural behavior of these bridges, it is essential to know about the structural elements that contribute to their weight. The arch is the primary load-bearing element in a masonry bridge, transferring the compressive forces to the piers or foundation. Other structural elements, such as spandrels, abutments, and piers, also play an important role in resisting the loads. Stone arch bridges of various sizes and shapes are among the most common masonry bridges, belonging to different historical periods. Generally, the arch is made of cut stone, and the spandrels are made of gravel or rubble stone. The stone material resists gravity forces with its high compressive

strength, while the mortar between the stones acts as binding. Steel/metal elements are sometimes used to resist tensile forces. Parapets of these bridges are formed with a single row of cut stones on both sides of the bridge road.

This study focused on the seismic behavior of two historical masonry bridges located in Turkey. The Historical Kazan Bridge is a historic bridge that originally belonged to the Ottoman city's water systems. It has a rectangular plan with projected spandrel walls that are pierced by a pointed arch. The arch is made of cut stones, and other parts are made of rubble stone. The pointed arch span is 7.18 meters, composed of 37 stones, with a width of 6 meters. The keystone at the top of the arch is larger than the other stones. Along the roadway, the bridge has parapet stones above its spandrel wall, and the inclination on both sides of the roadway is around 6%. The outer shells of the spandrel walls are cut limestone, and two abutments support each end of the bridge. The thickness of the spandrel wall is 0.7 meters, and filling materials are placed between the stone walls. The second case study is about Şenyuva Bridge, which is made of stone and is an arch bridge. The arch is made of regular stone, and the side walls are made of regular rubble stone. The bridge has a pointed arch with a span of 24 meters and a width of 3.5 meters. The thickness of the spandrel walls is 0.5 meters, and filling materials are present between the cut stones. The bridges were found to be vulnerable to earthquakes, and it is crucial to assess their structural response to ensure their safety for the future. This was done by using 3-D non-linear numerical analyses to see how the bridges responded under simulated and real ground motions. The material properties of Kazan Bridge were established by relying on experimental data obtained from masonry structures constructed during the same period. In contrast, Bayraktar et al. (2009) conducted ambient vibration tests on Şenyuva Bridge to determine its dynamic characteristics through experimental means. These tests enabled the calibration of the existing data on the material properties of Şenyuva Bridge.

2 SEISMICITY

2.1 Kazan Bridge

This article explores the history of the first masonry bridge, known as the Historical Kazan Bridge, currently located in Edirne, a city with a rich cultural and historical background. The city boasts a variety of ancient buildings and monuments that reflect the religious and cultural life of different periods. The tectonic setting of the region is controlled by the Anatolian and

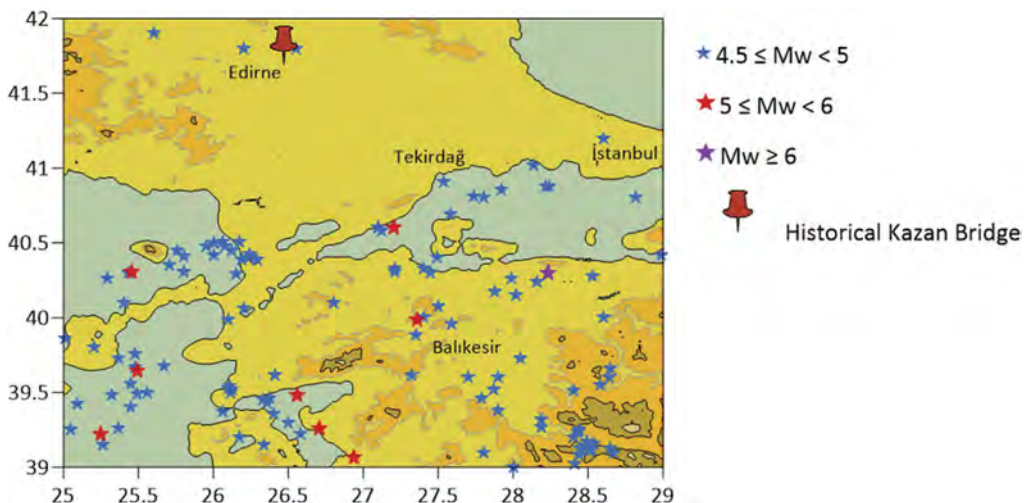


Figure 1. Seismic activity of the Thrace region.

Eurasian Plates, which rotate in opposite directions (Ambraseys & Finkel 1991, Gök et al. 2016). Additionally, there are several active and inactive faults in the area. Seismic activity is concentrated on the southern side of the Edirne provincial border, with less activity to the north of the city center (see Figure 1). The most significant earthquake in the region occurred in 1912, resulting in casualties and the destruction of many masonry buildings.

2.2 Şenyuva Bridge

The Şenyuva Bridge, a historical landmark, can be found in the city of Rize, located in the eastern Black Sea region. The area surrounding the Black Sea basin is characterized by geological fault lines such as the Southeast Black Sea Fault in the south, the North Anatolian Fault (NAF), and the North-East Anatolian Fault (NDAF) in the north, and the Eastern Pontide active deformation zone in the east. This region is known for experiencing earthquakes caused by thrust mechanisms, particularly on the northeast coast of the Black Sea where compressional tectonics are prominent. Research has revealed that the compressional zone of the region has caused an increase in crust thickness, ranging from 42-46 km, due to the convergence of the Arabian Plate and the Eurasian Plate. The Eastern Pontide active deformation zone is responsible for creating three distinct seismic belts from south to north: The South seismic zone (NAF and EAF Erzincan-Erzurum), the Middle seismic zone (Eastern Black Sea Region and coastal zone), and the Northern seismic zone (Black Sea). Seismic activity increases in magnitude from north to south, as observed in the 1939 Erzincan earthquake with a magnitude of $M_w=7.9$ occurring in the south seismic zone. Furthermore, earthquake focus depths also increase from north to south, which could be attributed to the nature and thickness of the earthquake-generating crust, transitioning from oceanic crust to continental crust (Figure 2).

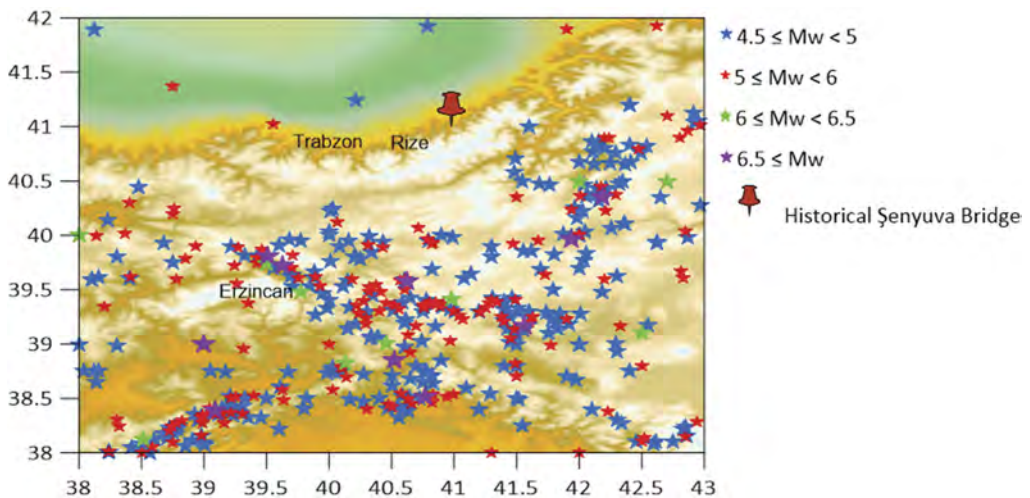


Figure 2. Seismic activity of the Rize region.

3 SELECTION OF SEISMIC MOTION RECORDS

3.1 Synthetic strong ground motions

Artificial ground motions are commonly used in dynamic analyses of seismic structures to simulate the effect of an earthquake on a structure. These simulations are crucial in determining the likely response of a structure to a specific earthquake, or in comparing the responses of different structures to each other. In this study, artificial ground motions were generated to

match the target spectrum of a specific earthquake and produce a realistic ground motion. To generate these artificial ground motions, the method of matching the target spectra was employed, which involved adjusting the acceleration, velocity, and displacement of the ground motion to fit a specific target spectrum. Figures 4 and 5 provide visual representations of the target spectra and the resulting artificial ground motions.

In addition to the artificial ground motions, real ground motions were also used as inputs in response history analysis. Three real ground motions were selected from the Pacific Earthquake Engineering Research Center (PEER) ground motion database for shallow crustal earthquakes in active tectonic regimes. These ground motions were chosen based on their compatibility with the target spectrum. Furthermore, eight records were scaled to the target spectrum ordinate using the method of minimizing the Mean Squared Error (MSE). This technique was applied in the frequency domain over a specified period range according to the requirements given in the Turkish Building Seismic Code 2018 (TBSC 2018).

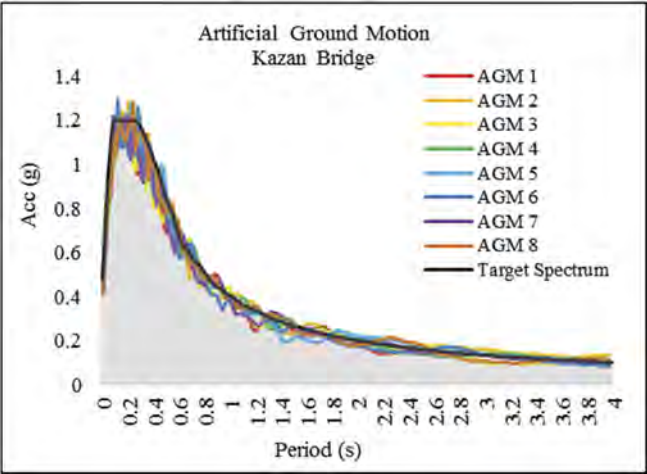


Figure 3. Artificial ground motion data set for historical Kazan Bridge.

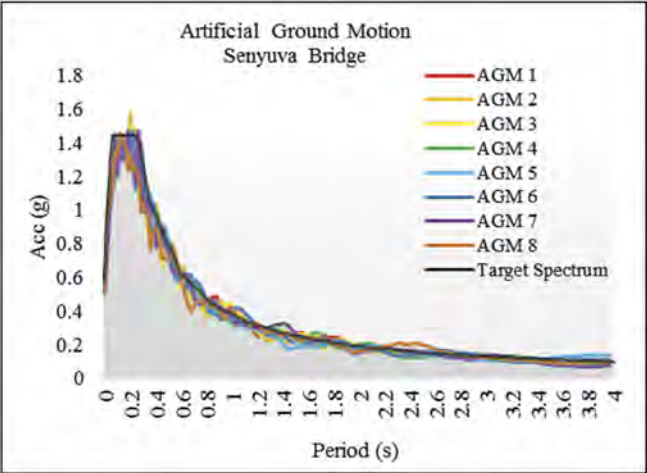


Figure 4. Artificial ground motion data set for historical Senyuva Bridge.

4 DAMAGE STATES OF THE BRIDGES

4.1 Continuum and discrete models

This study employed two different modeling approaches to create models of historical stone-masonry bridges. One model was based on a continuum approach, while the other was based on a discontinuum approach. To create these models, the finite element method was used with a macro modeling strategy, using the SAP2000 (CSI 2004) computer program. The models consisted of four components: a spandrel wall, a barrel, fill material, and a roadway (slab). The mechanical behavior of these components was assumed to be linearly elastic, and Hooke's law was used to model the elasticity of the system. The continuum models were only used for elastic analysis, while more elaborate macro-models were used for nonlinear analysis.

For the discontinuum models, the code 3DEC computer program was used (Itasca 2016). This approach allowed for the modeling of the discontinuities and fractures that are inherent in stone-masonry bridges, providing a more accurate representation of their behavior under load. Bending mode shapes of the numerical models are given in Figure 5, providing a visual representation of the deformation patterns that occur when the bridges are subjected to loading. These mode shapes can help to identify potential failure modes and guide the design of interventions to improve the safety and resilience of these historic structures.

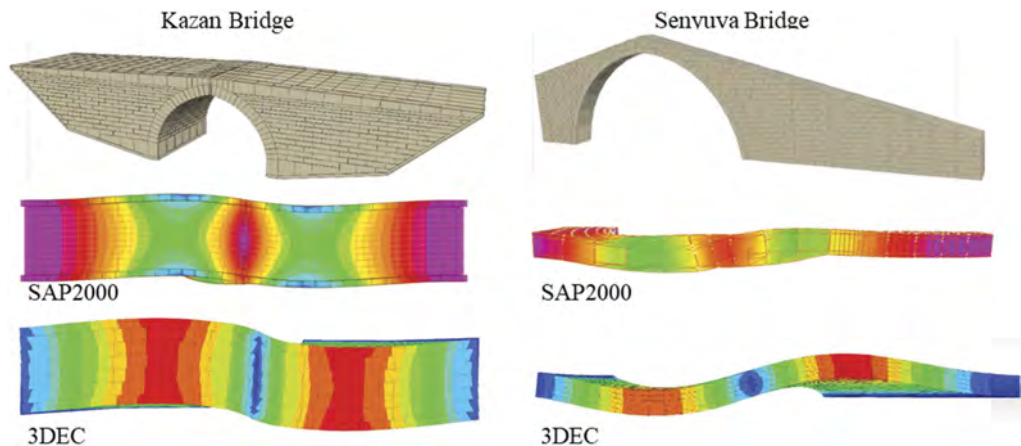


Figure 5. Bending mode of the Kazan Bridge and Şenyuva Bridge.

4.2 Kazan Bridge

To model the seismic response of different ground motions, nonlinear dynamic analyses were performed using the 3DEC program (Itasca 2016). The input was defined in terms of velocity time series, which were applied at the base of the model. This approach allowed for a detailed evaluation of the behavior of the bridge under seismic loading, taking into account the complex nonlinearities and material behavior that are present in such structures. The results of the analysis showed that the maximum displacement occurred in the middle of the transverse span during seismic excitation. Furthermore, the maximum vertical stress and tensile stress were observed at the same location. These findings are consistent with the expected behavior of stone-masonry bridges under seismic loading, where the mid-span region is subjected to the greatest stresses and deformations. Interestingly, the results also indicated that the brick bridge under artificial seismic data experienced higher velocities than scaled or unscaled seismic data (Figure 6). This may be due to the fact that the artificial record was specifically designed to match the design spectrum, which represents the envelope of multiple earthquakes. In contrast, the scaled or unscaled seismic data may not fully capture the range of

possible seismic events that the structure could be subjected to. However, it should be noted that the use of artificial records could potentially lead to further deformation of the structure under artificial recording.

4.3 Senyuva Bridge

Şenyuva Bridge was found to be vulnerable to severe damage or collapse under artificial earthquakes, with a return period of 2475 years. The damage process typically involved a series of shear cracks and openings around the eastern part of the downstream side of the bridge, starting from the crown of the arch and extending towards the support region. This type of failure is consistent with the expected behavior of stone-masonry arch bridges under seismic loading, where shear and tensile stresses can cause cracking and separation in the masonry blocks. The analysis also revealed that areas of significant stress concentration developed in the upper part of the arch curve during the seismic excitation. This finding highlights the importance of accurately modeling the complex geometry and material behavior of stone-masonry bridges when assessing their seismic performance. The variation of permanent displacement magnitudes in the Şenyuva Bridge at the end of the dynamic analysis using artificial ground motion data sets is

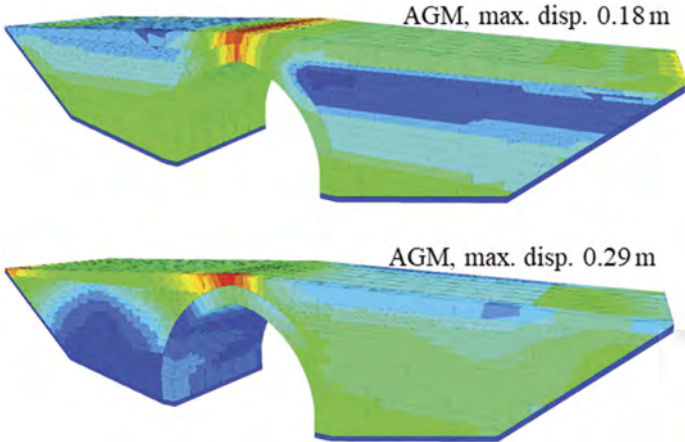


Figure 6. Permanent displacement magnitudes in Kazan Bridge.

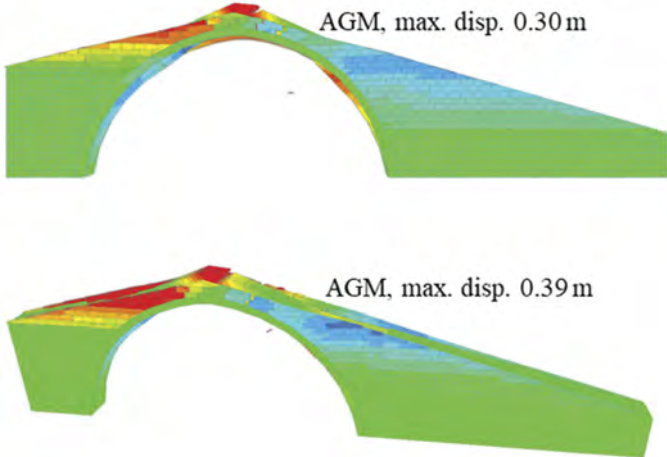


Figure 7. Permanent displacement magnitudes in Senyuva Bridge.

shown in Figure 7. These results provide important insights into the long-term behavior of the bridge under seismic loading, and can help guide efforts to improve its safety and resilience in the face of future seismic events.

5 CONCLUSION

This study investigated the seismic behavior of two historical stone masonry bridges located in Turkey. The bridges were subjected to both artificial and real ground motions to assess their vulnerability to seismic excitation. The results showed that Kazan Bridge would experience some damage from the stresses produced by dynamic effects. However, based on the results of all cases presented, it was found that the bridge can withstand the applied seismic excitations. Moderate damage, especially from AGM records, occurred at the mid-span of the arch, mostly as slight openings. The bridge demonstrated a stiff behavior, confirming its durability, strength, and ability to sustain the seismic loading prescribed by present regulations.

The author indicates that the Şenyuva Bridge is significantly vulnerable to earthquakes and that its structural behavior is influenced by the bridge's geometry. The bridge has a 2475-year return period, and its performance under artificial ground motion is worse than that of the Kazan Bridge. This study concluded that dynamic analysis is a useful tool for assessing the seismic safety of masonry bridges. Under strong ground motions, DEM models provide insight into the levels of damage and the collapse patterns that may be expected. Further research is necessary to understand the impact of structural design features on the seismic safety of deficient masonry bridges.

REFERENCES

- Ambraseys, N.N, Finkel, C. 1991. Long-term seismicity of Istanbul and of the Marmara Sea region. *Terra Nova* 3:527–539.
- Bayraktar, A., Birinci, F., Altunışık, A.C, Türker, T., Sevim, B. 2019. Finite element model updating of Şenyuva historical arch bridge using ambient vibration tests. *The Baltic Journal of Road and Bridge Engineering* 4(4):177–185.
- Caktı, E., Saygılı, Ö., Lemos, J.V., Oliveira, C.S. 2016. Discrete element modeling of a scaled masonry structure and its validation. *Engineering Structures* 126, 224–236.
- CSI (Computers and Structures Inc.). 2004. SAP2000 Integrated finite element analysis and design of structures. CSI, Berkeley.
- Gök, R., Mellors, R.J., Sandvol, E., Pasyanos, M., Hauk, T., Takedatsu, R., Yetirmişli, G., Teoman, U., Turkelli, N., Godoladze, T., Javakishviri, Z. 2016. Lithospheric velocity structure of the Anatolian plateau-Caucasus-Caspian region. *Journal of Geophysical Research: Solid Earth* 116 (B5):2156–2202.
- Itasca. 3DEC (3-Dimensional distinct element code) Version 5.2 2013 Minneapolis (MN).
- Karaton, M., Aksoy, H.S., Sayın, E., Calayır, Y. 2017. Nonlinear seismic performance of a 12th century historical masonry bridge under different earthquake levels. *Eng Fail An* 79:408–421.
- Özmen, A., Sayın, E. 2018. Seismic assessment of a historical masonry arch bridge. 2018. *J Struct Eng* 1 (2):95–104.
- Pulatsu, B., Erdogmus, E., Lourenço, P.B. 2019. Comparison of in-plane and out-of-plane failure modes of masonry arch bridges using discontinuum analysis. *Eng Struct* 178:24–36.
- Saygılı, O. 2019. Estimation of structural dynamic characteristics of the Egyptian Obelisk of Theodosius. *Earthquakes and Structures* 16(3): 311–320.
- Saygılı, Ö. 2020. Seismic Performance Evaluation of a Masonry Building Subjected to Near and Far Field Ground Motions. *Civil Engineering Journal* (3).
- Saygılı, Ö., Lemos, J.V. 2020. Investigation of the structural dynamic behavior of the Frontinus Gate. *Applied Sciences* 10(17): 5821.
- Saygılı, Ö., Lemos, J.V. 2021. Seismic vulnerability assessment of masonry arch bridges. *Structures* 33: 3311–3323.
- Turkish Building Seismic Code 2018. Prime Ministry, Disaster and Emergency Management Presidency (AFAD), Ankara.

Computational strategy for the design of monitoring for masonry arch bridges using DIC procedures

S. Grosman, Q. Fang, L. Macorini & B.A. Izzuddin
Imperial College London, London, UK

ABSTRACT: Masonry arch bridges are old structures characterised by a complex behaviour. Detailed monitoring is essential to improve the understanding of the response under different loading conditions, to identify damaged structures, and to validate numerical models for accurate structural assessment. Generally, standard monitoring techniques necessitate direct access and contact to the analysed structure, which can be problematic in many cases. The use of Digital Image Correlation (DIC) overcomes these critical limitations offering an improved potential for detailed and streamlined monitoring. This work focuses on the development of advanced computational tools to support the practical application of DIC monitoring in field conditions. The proposed procedure utilises results from 3D numerical models to generate synthetic video files representing the bridge response under traffic loading, which can be subsequently employed to calibrate camera setups for DIC monitoring.

1 INTRODUCTION

A substantial part of European bridge infrastructure consists of masonry bridges and viaducts. Maintaining good condition of such structures is paramount to their continued use and to ensuring effective and safe transportation links. To this end, it is necessary to establish robust approaches for bridge monitoring. While there are multiple techniques to accurately measure deflections, they usually necessitate direct access to the bridge structure, which might be difficult to achieve especially for structures featuring tall piers and long spans. This access problem can be tackled by utilising non-contact monitoring methods (Feng et al., 2015, Xu et al., 2018). Among these monitoring strategies, vision-based methods utilising pattern matching between temporal sets of images of the considered structure (Koltsida et al., 2013, Busca et al., 2014) are of particular interest, as they guarantee an effective approach for monitoring the response at multiple points at once while maintain reasonable levels of accuracy (Kim & Kim, 2011, Wang & Li, 2020). However, the utilisation of vision-based systems poses new challenges for monitoring. In particular, stable camera mounting becomes critical to achieve accurate measurement (Lava et al., 2009, Brownjohn et al., 2017). Sudden lighting changes present another source of vulnerability as they might cause over- or under-exposure of some images in the analysed sequence (Acikgoz et al., 2018b). Another source of uncertainty comes from the environmental condition that affects the light refraction, which becomes especially pronounced in long range measurements (Lages Martins et al., 2015).

Considering all of these issues, it is important to plan monitoring work very carefully to maximise the amount of useful output that can be collected. This paper focuses on ways to provide information on the design of monitoring setups to achieve this goal. To this end a “Numerical Camera” technique is proposed. In this procedure, prior to monitoring, the structure under investigation is analysed using a 3D finite element (FE) model considering realistic traffic loading scenarios. The numerical results from the FE simulations are then used

to construct a “digital twin” of the bridge to be monitored, that is used to create a series of synthetic videos capable of simulating different camera positions and properties. The obtained videos are then processed with Digital Image Correlation (DIC) tools to obtain 3D displacements at some key points on the structure. These results are then compared against numerical results for the structure, to validate the accuracy of the proposed strategy. This approach can be used to determine DIC setup requirements for each point of interest. The following section will provide a brief overview of DIC techniques as well as a more detailed description of the “Digital twin” generation and the “Numerical camera” capabilities. Finally, an application of the developed approach is presented for the determination of key camera parameters (frame rate, resolution) for the monitoring of a realistic masonry viaduct.

2 METHODOLOGY

DIC is a vision-based technique used to measure displacements and strains of the monitored object by comparing temporal sets (captured over a continuous time frame) of images of the object surface. In DIC, the process of matching or “correlating” corresponding points is typically done using algorithms that compare the intensity of pixels values in different images, as well as their spatial relationship to each other (Feng et al., 2015). Once the corresponding points have been identified, the displacement and strain between them can be calculated based on the difference in their positions in subsequent images.

Masonry bridges are complex structures that exhibit pronounced 3D behaviour under loading. This behaviour should be reflected in the dataset obtained via monitoring. A substantial obstacle to practical DIC application is the fact that 2D DIC was originally developed under the premise that the camera viewing angle would remain normal to the object plane. One way to address this is by installing targets on the monitored bridge (Lages Martins et al., 2015) that would be normal to the camera orientation. The other relies on a complex calibration to correct for the perspective distortion that occurs due to non-orthogonality of the viewing angle. A typical approach to achieve such a correction is to use vanishing points (points where projections of parallel lines intersect) to construct transformation matrix (Santana-Cedr es et al., 2017). In practice this is usually realised by defining a series of geometric features on the image that will be used for perspective correction in conjunction with camera intrinsic parameters (Acikgoz et al., 2018b).

Prior research (Lava et al., 2009, Feng et al., 2015, Acikgoz et al., 2018a) indicates a clear need for pre-monitoring calibration of DIC techniques to achieve the best result. When it comes to field monitoring, it becomes exceedingly difficult to achieve consistent calibration, as environmental factors are unique and uncontrollable. To address this Lava et al., (2009, 2020) suggests the utilisation of finite element models as substrates for the DIC analysis, where FE model deformations are used to morph the image of the patterned structure, that are then utilised in the DIC analysis. This work extends such a technique to larger structures with naturally occurring patterns (masonry bond), generating an effective digital twin of an actual bridge. A “digital twin” is a virtual representation of a physical object or system that can be used for monitoring and analysis. In the context of masonry arch bridge monitoring, such model can be created from two sources of information: 1) displacement data obtained from the FE simulation of the considered structure, and 2) general bridge geometric data combined with brick size and bond pattern.

According to the proposed approach, a FE macroscale model of the masonry structure is generated using a recently developed parametric modelling tool for masonry arch bridges and viaducts (Grosman et al., 2023). For large-scale masonry bridge structures, the use of the macroscale approach (Tubaldi et al., 2020, Grosman et al., 2021) is shown to yield good results, especially in the serviceability loading range. According to the macroscale modelling strategy, masonry is modelled using continuum solid elements, sized independently from the actual dimensions of masonry units and mortar joints, resulting in computationally efficient models. Material models combining plasticity and damage are employed in this approach (Lee & Fenves, 1998, Chisari et al., 2020) to represent material nonlinearity in the masonry assumed as

a uniform material. The developed model (Figure 1) is then analysed using the advanced non-linear FE software ADAPTIC (Izzuddin, 1991) considering realistic traffic loading scenarios.

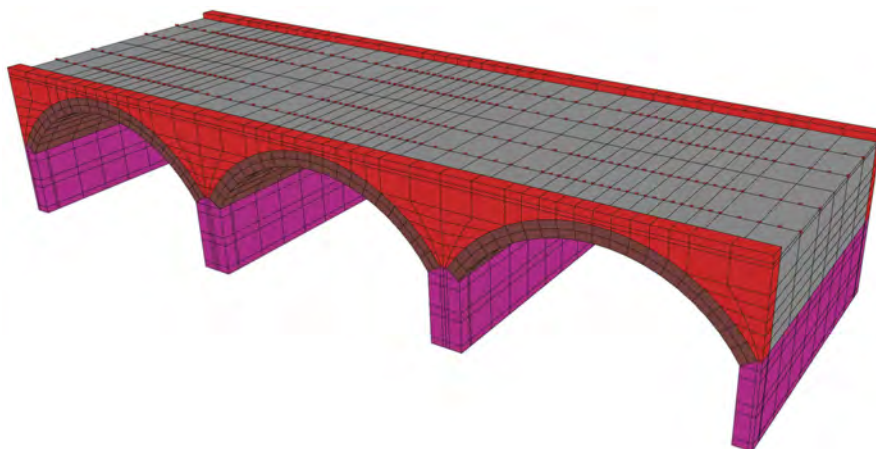


Figure 1. Numerical model of the Mill Road Viaduct.

Bridge geometric data is utilized for generation of the façade mesh on top of the bridge external surfaces. This process can be subdivided into the following two steps: 1) the geometric features and bounding surfaces of the bridge are identified, including the arches, which may have a different bond pattern; 2) a new façade mesh is then created to cover the entire structure, with each brick being subdivided into four triangular segments with a point in the center. To accurately represent the appearance of the brick surface, a small variation of color is added to each mesh segment to account for the natural patterning on the brick faces. The resulting mesh provides a detailed virtual representation of the bridge that can then be used for monitoring.

All of this data is utilised inside a MATLAB software environment (The MathWorks, 2012) to generate a virtual model of a bridge that can be interacted with via a newly developed tool – “Numerical Camera” – that connects MATLAB in-built visualisation properties with camera hardware specifications. This tool allows users to capture synthetic videos of the bridge as if it were being viewed through a real camera. The “Numerical Camera” has a number of features that can be controlled by the user (Figure 2). These include control over the field of view, via the size of the camera sensor and the focal distance. The camera can also be repositioned and rotated around the bridge to change the perspective from which the bridge is being viewed. The frame rate and resolution of the camera can also be adjusted to control the desired video output.

3 NUMERICAL EXAMPLE

The potential of the developed computational strategy for the design of DIC monitoring tests is illustrated in a numerical example investigating the response of a realistic masonry viaduct under traffic loading.

3.1 *Mill Road Viaduct*

Mill Road Viaduct (Figure 3) is a multi-span masonry bridge located in Lewisham, South London. A portion of the viaduct serves as a platform for the Lewisham train station. This is a busy junction that experiences a high volume of relatively slow-moving traffic, in both directions. The viaduct consists of four straight masonry arches and two skew masonry arches with the last one crossing the Ravensbourne River.

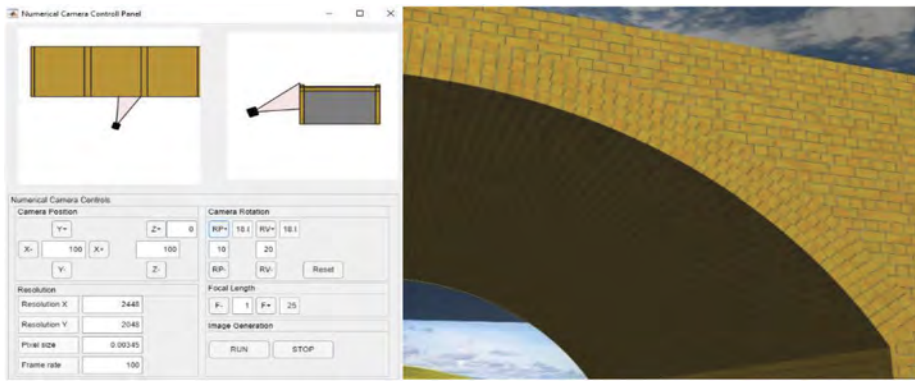


Figure 2. Numerical camera rotation control panel.



Figure 3. Mill Road Viaduct.

Out of the six spans, only three internal spans are considered in the numerical simulation, with edge spans serving as boundary conditions for the mid span (Span 3 in Figure 4). On average, the span of the considered arches is 7400 mm long with a rise of 2000 mm. The arch bridge is 8510 mm wide, with piers of 1930 mm high and 920 mm length.

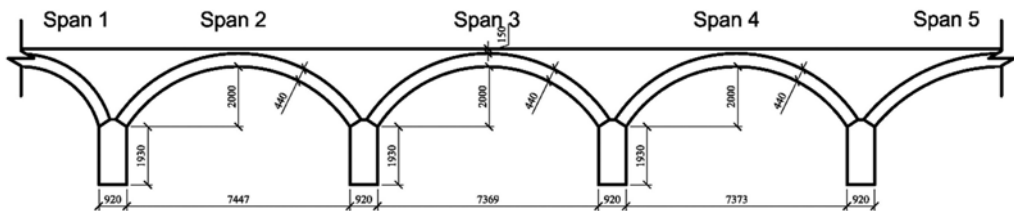


Figure 4. Mill Road Viaduct sizing information.

The analysed bridge structure is modelled in ADAPTIC (Izzuddin, 1991) and analysed under the effects of traffic loading due to the passage of a ballast train (65 km/h) consisting of 10 coaches. The specific axel loading for each coach, as well as the order and number of coaches in considered train are presented in Figure 5. The material properties utilised in the numerical simulations are presented in Table 1.

Table 1. Material properties used in the numerical analysis.

Material Properties	Masonry	Backing	Backfill
Young's modulus [N/mm ²]	7000.00	2500.00	2500.00
Poisson ratio	0.15	0.15	0.15
Tensile strength [N/mm ²]	0.20	0.15	0.05
Fracture energy in uniaxial tension [N/mm]	0.05	0.05	0.05
Maximum uniaxial compressive strength [N/mm ²]	25.00	10.00	5.00

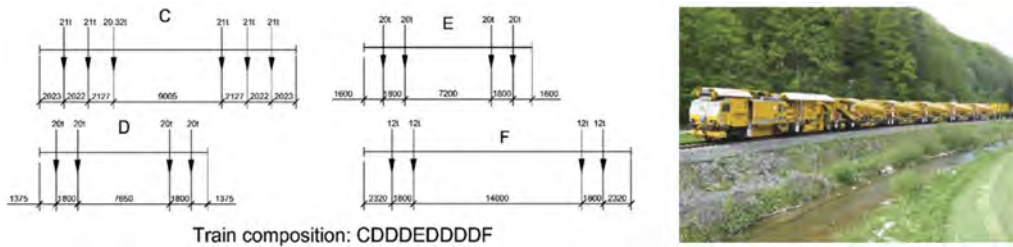


Figure 5. Traffic loading considered in the analysis.

3.2 Numerical camera verification

3.2.1 DIC setup

To verify the proposed approach for the design of DIC monitoring tests on the analysed bridge, the numerical model (Figure 1) described in the previous section is processed, and its visually accurate counterpart (Figure 6) is generated in MATLAB. Utilising nodal displacements obtained during the time-history FE analysis, a series of synthetic images corresponding to specific time frames are generated and combined into a video file to be analysed using DIC. To remove uncertainty associated with the generated videos, image compression is not utilised when generating images.



Figure 6. Tiled model of the Mill Road Viaduct spans 2 – 4.

The generated video are then processed with “Imetrum: Video Gauge” software (Imetrum, 2016). To address perspective correction, rectangular regions are specified in 3D space for each target to determine vanishing points and to provide calibration for transformation from the image scale to the real scale. Displacements are calculated based on an 80×80 pixels target defining the region of interest where the correlation procedure takes place. Each target is defined in such a way as to include bond features, specifically orthogonal bond intersections or mortar loops, to improve correlation accuracy.

The conducted simulation pursues the following goals: 1) verification of the proposed procedure via direct comparison of DIC and numerical displacements at the monitored points; 2) establishment of minimal camera parameters (frame rate and resolution) ensuring a good match; 3) preliminary investigation of the influence of the camera standoff distance (from the bridge face) on the quality of DIC result.

3.2.2 Comparison between DIC and numerical results

An initial trial is conducted considering a camera resolution of 2448×2048 pixels and a frame rate of 100 frames per second (fps). The camera is positioned at the middle of span 3, at a 5 m distance from the bridge face, resulting in a camera elevation of 20 degrees (Figure 7a). Good agreement is generally observed for the monitored points (Figure 7b).

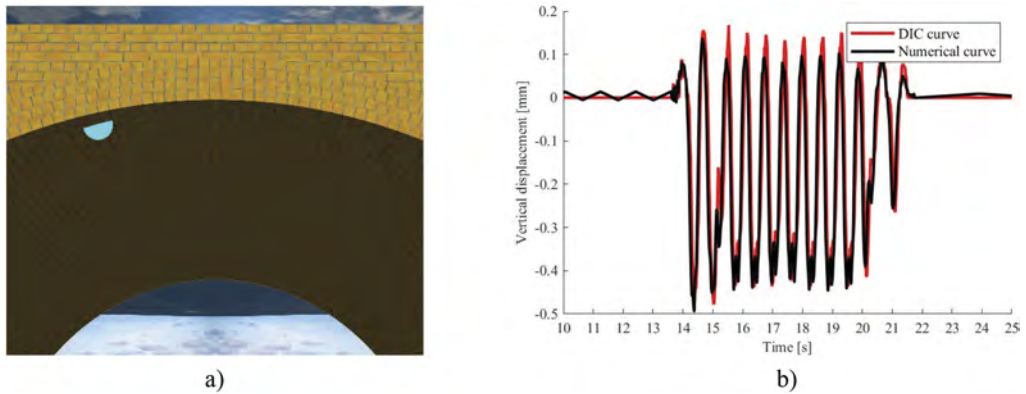


Figure 7. Camera view for verification test a) and verification results b).

The next investigation considers the effects of the assumed camera frame rate on the DIC result. To this end 5 different frame rates are considered: 100, 50, 25, and 12 fps. It is important to note that the frame rate should always be selected based on train speed, as faster trains generally require higher frame rates. Comparisons of different DIC curves and associated numerical results are presented in Figure 8a. In general, all the results indicate reasonable agreement, with only the 12 fps option showing reduced accuracy.

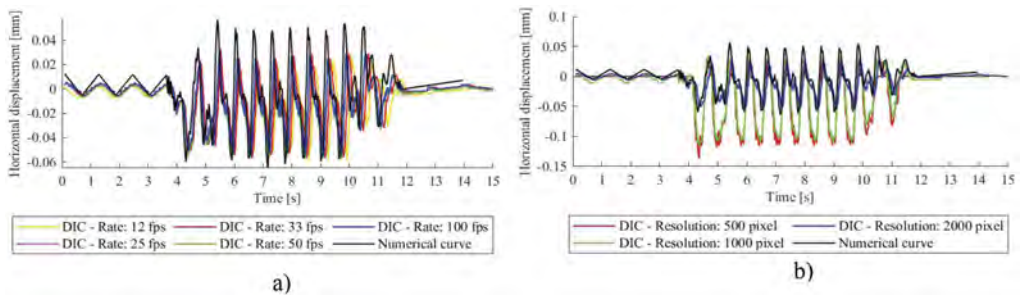


Figure 8. Influence of camera parameters on DIC results: a) frame rate; b) resolution.

The camera resolution is also investigated to establish its influence on the observed DIC response. Three options are considered: 1) 2448×2048 pixels denoted as 2000 for brevity from now on; 2) 1224×1024 pixels denoted as 1000; and 3) 612×512 pixels denoted as 500. Comparison results are presented in Figure 8b. In this case emphasis is put on horizontal deformations on the arch due to their small magnitude, as this can be more readily affected by camera resolution. Obtained results support this conclusion, as only the 2000 pixel camera led to good agreement with numerical inputs, for displacement range of 0.1 mm. It should be noted that although results obtained with 1000 and 500 pixel cameras do not conform with numerical results magnitude, they do depict all of the response features.

In a final investigation, the effects of different stand-off distances between the camera and monitored bridge are considered. This numerical test was conducted considering a camera

resolution of 2448×2048 pixels and a rate of 100 fps and standoff distances of: 1) 3.5 m (Figure 9a); 2) 5 m (Figures 7a); and 3) 10 m (Figure 9b).

The results obtained for 10 m standoff highlight that an increased distance can result in a drastic drop in accuracy of the DIC prediction, as shown in Figure 9c. It is also worth noting that the standoff distance is connected to the camera elevation, with a small standoff corresponding to larger elevation, where an increase in camera elevation can cause some discrepancy in the response prediction as well (Figure 9c). The performed study confirms that the developed approach can be effectively used to maximize the effectiveness of on-site DIC monitoring establishing acceptable levels for standoff and elevation and camera characteristics.

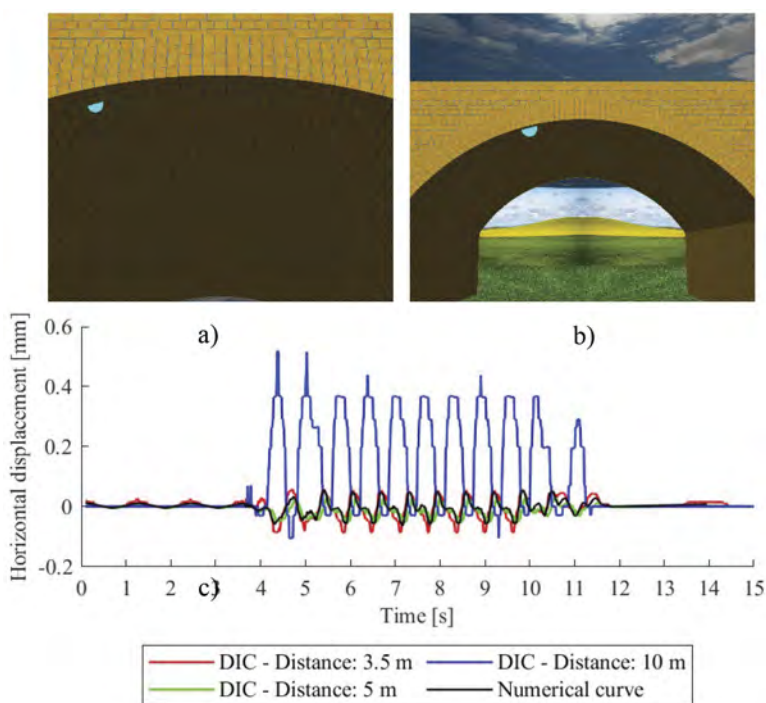


Figure 9. Influence of standoff distance on DIC result: a) camera view 3.5 m; b) camera view 10 m; c) results comparison.

4 CONCLUSIONS

Masonry arch bridges constitute a substantial portion of bridge infrastructure. A considerable proportion of these bridges is older than 100 years, resulting in an increasing need for monitoring due to regular deterioration due to environmental factors as well as increasing loading due to the evolution of rolling stock and locomotive design. This study investigated the applicability of DIC to displacement tracking of bridges under typical traffic loading in field conditions, where small displacements and environmental noise can substantially affect the accuracy of DIC algorithms. To this end, a numerical strategy was developed to verify the applicability of DIC in ideal conditions. The proposed approach utilises results from 3D FE simulation of the analysed structures to construct a realistic representation of the bridge under traffic loading, which can then be captured via a Numerical Camera as a synthetic video to be processed with DIC algorithm. This approach can be used to assist the design of the monitoring work, taking into account topographic constraints, possible configurations for the camera lenses, camera position and camera orientation.

The proposed strategy is verified by comparing numerical input against DIC output, where good agreement is found for the monitored data point, for some of the considered monitoring strategies. Ability of camera to accurately capture structural response is shown to be heavily dependent on camera resolution with 2448×2048 pixel resolution proving to be sufficient for the considered testing options. Further simulations highlight applicability of the developed approach to maximising the effectiveness of on-site DIC monitoring establishing acceptable levels for standoff and elevation and camera characteristics. It is worth noting though that obtained results characterise ideal recording conditions, and may be adversely affected when conducting monitoring in adverse weather situations (e.g. wind, rain, dust pollution).

REFERENCES

- Acikgoz, S., Dejong, M. J., Kechavarzi, C. & Soga, K. (2018a) Dynamic response of a damaged masonry rail viaduct: Measurement and interpretation. *Engineering Structures*, 168, 544–558.
- Acikgoz, S., Dejong, M. J. & Soga, K. (2018b) Sensing dynamic displacements in masonry rail bridges using 2D digital image correlation. *Structural Control and Health Monitoring*, 25, 1–24.
- Brownjohn, J. M. W., Xu, Y. & Hester, D. (2017) Vision-based bridge deformation monitoring. *Frontiers in Built Environment*, 3, 1–16.
- Busca, G., Cigada, A., Mazzoleni, P. & Zappa, E. (2014) Vibration Monitoring of Multiple Bridge Points by Means of a Unique Vision-Based Measuring System. *Experimental Mechanics*, 54, 255–271.
- Chisari, C., Macorini, L. & Izzuddin, B. A. (2020) Multiscale model calibration by inverse analysis for nonlinear simulation of masonry structures under earthquake loading. *International Journal for Multi-scale Computational Engineering*, 18, 241–263.
- Feng, D., Feng, M. Q., Ozer, E. & Fukuda, Y. (2015) A vision-based sensor for noncontact structural displacement measurement. *Sensors (Switzerland)*, 15, 16557–16575.
- Grosman, S., Bilbao, A. B., Macorini, L. & Izzuddin, B. A. (2021) Numerical modelling of three-dimensional masonry arch bridge structures. *Proceedings of the Institution of Civil Engineers - Engineering and Computational Mechanics*, 174, 96–113.
- Grosman, S., Macorini, L. & Izzuddin, B. A. (2023) Parametric Nonlinear Modelling of 3D Masonry Arch Bridges. *Advances in Engineering Software*, (under review).
- Imetrum, L. (2016) Video Gauge User Manual - Version 5.0.1.
- Izzuddin, B. A. (1991) Nonlinear Dynamic Analysis of Framed Structures.
- Kim, S. W. & Kim, N. S. (2011) Multi-point displacement response measurement of civil infrastructures using digital image processing. *Procedia Engineering*, 14, 195–203.
- Koltsida, I. S., Tomor, A. K. & Booth, C. A. (2013) the Use of Digital Image Correlation Technique for Monitoring Masonry Arch. *7th International Conference on Arch Bridges*, 681–690.
- Lages Martins, L. L., Rebordão, J. M. & Silva Ribeiro, A. S. (2015) Structural observation of long-span suspension bridges for safety assessment: Implementation of an optical displacement measurement system. *Journal of Physics: Conference Series*, 588.
- Lava, P., Cooreman, S., Coppieters, S., De Strycker, M. & Debruyne, D. (2009) Assessment of measuring errors in DIC using deformation fields generated by plastic FEA. *Optics and Lasers in Engineering*, 47, 747–753.
- Lava, P., Jones, E. M. C., Wittevrongel, L. & Pierron, F. (2020) Validation of finite-element models using full-field experimental data: Levelling finite-element analysis data through a digital image correlation engine. *Strain*, 56, 1–17.
- Lee, J. & Fenves, G. L. (1998) Plastic-Damage Model for Cyclic Loading of Concrete Structures. *Journal of Engineering Mechanics*, 124, 892–900.
- Santana-Cedr s, D., Gomez, L., Alem n-Flores, M., Salgado, A., Esclar n, J., Mazorra, L. & Alvarez, L. (2017) Automatic correction of perspective and optical distortions. *Computer Vision and Image Understanding*, 161, 1–10.
- The Mathworks, I. (2012) *MATLAB and Statistics Toolbox Release 2012b*, Natick, Massachusetts, United States.
- Tubaldi, E., M nga, E., Macorini, L. & Izzuddin, B. A. (2020) Mesoscale analysis of multi-span masonry arch bridges. *Engineering Structures*, 225, 111137–111137.
- Wang, J. & Li, G. (2020) Study on bridge displacement monitoring algorithms based on multi-targets tracking. *Future Internet*, 12, 11–22.
- Xu, Y., Brownjohn, J. & Kong, D. (2018) A non-contact vision-based system for multipoint displacement monitoring in a cable-stayed footbridge. *Structural Control and Health Monitoring*, 25, 1–23.

Influence of uncertain mechanical parameters on the load-bearing capacity of multi-span masonry arch bridges

M. Zizi, C. Chisari & G. De Matteis

Department of Architecture and Industrial Design, University of Campania “Luigi Vanvitelli”, Aversa (CE), Italy

ABSTRACT: The present paper deals with the assessment of the load-bearing capacity of existing masonry arch bridges by means of numerical models. The problem related to the selection of uncertain parameters is addressed by reproducing a past experimental test performed on a reduced-scale bridge prototype vertically loaded until its collapse. The test is reproduced in Abaqus software by representing masonry elements through the Finite Element macro-modelling approach, in which masonry is considered as a homogeneous material having a plastic-damage constitutive behaviour in the nonlinear field. The fill material is introduced by means of a nonlinear continuum behaving under similar Mohr-Coulomb hypotheses. An appropriate interaction law that entails a frictional response in the tangential direction, avoids interpenetration, and allows for the separation between the two materials, is also considered. A wide parametric investigation is performed to obtain a good fitting with the experimental evidence by varying the uncertain mechanical parameters (i.e. Elastic Modulus of backfill, tensile strength of masonry and contact law between the two materials). Thus, a reliable numerical model exhibiting a response consistent with the experimental outcome in terms of both failure mode and force-displacement curve is proposed. The influence of each investigated parameter on the overall response of the bridge is then deeply analysed and discussed, also with the aim to identify possible retrofitting strategies.

1 INTRODUCTION

The structural safety of the worldwide existing infrastructural heritage is a complex challenge that, in recent times, has involved an ever-increasing number of researchers and practitioners (Zizi et al. 2023). In this field, reliable numerical models to interpret the response under external loads of in-service infrastructures, on the one hand, are considered one of the most valuable tools, while, on the other, their calibration still represent a serious issue to be addressed. Whilst, nowadays, the suitability of the available assessment methodologies for existing reinforced concrete and steel structures and infrastructures are widely corroborated, the study of masonry structures is generally recognized as an open issue, mainly related to the mechanical complexity of the base materials, as well as their interaction (Melbourne 1990, Sokolovic et al. 2021, Zampieri et al. 2021, Zhang et al. 2018, Pantò et al. 2022).

Several assessment methodologies, including for instance limit analysis and various space- and time-discretisation numerical approaches, may be adopted for the study of masonry structures. In this context, numerical methods as finite element or discrete element modelling are considered very effective tools to interpret the response under vertical and horizontal loads of these structures, despite characterized by a certain difficulty in the selection of the mechanical parameters adopted for describing the material behaviour. Within such methods, the behaviour of masonry structures is simulated by discretizing the structural elements according to different detail levels (i.e. mono-dimensional, bi-dimensional or three-dimensional elements in combination with detailed or simplified micromodelling and macromodelling discretization), and post-elastic material descriptions (e.g. plastic, damage, damage-plastic, etc.) (Lourenço 2009).

Focusing on finite element methods based on a macro-modelling discretization, masonry infra-structures, and in particular masonry arch bridges, may represent a very interesting benchmark case study, being their response dependent on (i) the material description adopted for the masonry material, generally constituting arch rings, piers, abutments and spandrel walls, (ii) the material description adopted for the backfill material, generally characterized by a soil-like behaviour, and (iii) the laws adopted for describing the interaction between the two materials. In this sense, a rational selection of the mechanical parameters adopted for the assumed material descriptions and interaction laws is required since they can significantly affect the overall response of the numerical model.

Based on this premise, in the present study, the calibration of a reliable finite element model in Abaqus software for reproducing the evidence of a past experimental test retrieved from the literature is proposed (Melbourne et al. 1997). Given the uncertainties related to the definition of some mechanical parameters, an iterative calibration procedure has been performed, entailing the execution of 27 numerical analyses. Such a calibration allowed for identifying the most influencing parameters on the response of the investigated case study.

2 THE REFERENCE EXPERIMENTAL TEST

2.1 Test description: Set-up and characteristics of the material

The reference experimental test consisted of a three-span arch bridge prototype vertically loaded until collapse at one-fourth of the central span. Hereinafter, some general notions about the adopted test set-up and materials are provided, but further information can be found in Melbourne et al. (1997), referring to “*Bridge no. 2*”.

The specimen counts three 3 m-long spans. The two piers are characterized by a height of 1.5 m and a length of 0.44 m, while the abutments have a height and a length equal to 0.92 m and 1.8 m, respectively. The segmental arch rings present a thickness of 0.215 m and a height (from the impost to the keystone at the intrados) of 0.75 m. A backfill material is also present over the arch rings and abutments, with a height of 1.095 m and 0.13 m at the abutments and arch keystones, respectively. No spandrel walls are present in the specimen, but detached walls guaranteed the confinement in the transversal direction of the backfill material. Arch rings, piers and abutments are in brickwork masonry while a cohesionless soil is adopted as fill material. The width of the specimen is equal to 3.54 m and 2.88 m for masonry elements and fill material, respectively.

As regards the characteristics of the material, the following parameters were provided by the authors of the test:

- Compressive strength of the masonry $f_c = 26.8$ MPa;
- Elastic modulus of the masonry $E_m = 16,200$ MPa;
- Specific weight of the masonry $\gamma_m = 22.4$ MPa;
- Cohesion of the backfill $c = 0$ MPa;
- Internal friction angle of the backfill $\phi_b = 60^\circ$;
- Specific weight of the backfill $\gamma_b = 22.2$ MPa.

Thus, no information was provided about the elastic modulus of backfill, tensile strength of masonry, backfill-arch interface behaviour and the post-peak response of any of the materials. This is rather usual in experimental characterisation of masonry arch bridges, and thus it is of great interest to understand how the uncertain/missing parameters should be selected and how they affect the final prediction of the numerical simulation.

2.2 Experimental test results

The tested specimen exhibited a capacity of about 320 kN. The test was interrupted at a radial displacement of the intrados point in correspondence with the load application of about -45 mm due to the damage occurred. In particular, the damage interested the central and the north (opposite side with respect to the load application point) arches, as well as the in-between pier at the base. The results in terms of force-displacement curve and crack pattern are shown in Figure 1.

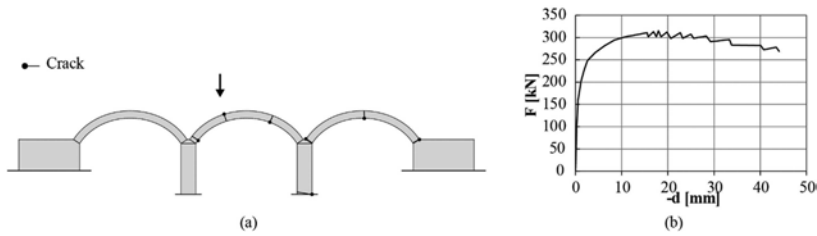


Figure 1. Main results of reference experimental test: (a) damage pattern and (b) force-radial displacement curve (adapted from Melbourne et al. 1997).

3 FINITE ELEMENT MODELLING

3.1 Description of the model

The bridge at hand was modelled in Abaqus software by means of 8-node solid elements. In particular, elements with reduced (C3D8R) and full (C3D8) integration were adopted for backfill and masonry elements, respectively. Reduced integration for the backfill was adopted to decrease computational efforts. Such a choice has been preliminary validated by checking that it did not substantially influence the analysis results. An average mesh size of 0.1 m was adopted for both materials, after a preliminary sensitivity analysis.

Given the symmetry with respect to the longitudinal axis and in order to reduce the computational efforts, half bridge has been modelled and appropriate boundary conditions have been assigned to the nodes lying on the longitudinal cutting plane. Also, the transversal displacements of the backfill were restrained to simulate the presence of the additional walls. The base node at piers and abutments were considered fully fixed. A three-dimensional view of the model is provided in Figure 2.

Perfect node continuity was considered between masonry elements, while their contact with the backfill material was modelled by an interaction law. The adopted law avoids the interpretation but allows the node separation in case of tensile stresses once the contact is occurred. Moreover, a frictional behaviour with $\mu = \tan(30^\circ)$ in the tangential direction has been also considered.

The masonry material was represented as a homogeneous material. The Concrete Damage Plasticity (CDP) material model (Lubliner et al. 1989, Lee & Fenves 1998), available in the software's library, was assumed to describe the masonry behaviour in the non-linear field. A parabolic law was assumed in compression (Sawko 1982), while in tension a linear softening was considered as function of the fracture energy.

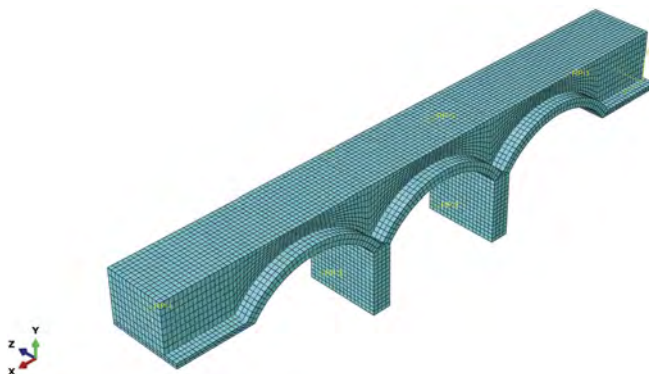


Figure 2. The adopted finite element model.

The mechanical parameters assumed for the masonry, i.e. elastic modulus and compressive strength, were the ones reported in Melbourne et al. (1997). As for the behaviour in tension, a strength $f_t=0.2$ MPa was assumed, while the fracture energy $G_{f_t}=13.2$ N/m was defined according to Lourenço (2009), as per Equation 1.

$$G_{f_t} = 0.025(2 \cdot f_t)^{0.7} \quad (1)$$

Also, linear damage laws in both compression (d_c) and tension (d_t) were introduced: the onsets of damage were defined at maximum compression or tension stresses, while at the maximum inelastic strain (compression) and displacement (tension) the maximum damage values (100%) were considered attained. The remaining parameters for defining the CDP behavior were set by considering conventional values: i. uniaxial-to-biaxial compressive strength ratio $f_{c0}/f_{b0}=1.16$; ii. dilation angle $\psi_{CDP}=10^\circ$; iii. $K_c=0.667$; iv. eccentricity $\varepsilon=0.1$.

The backfill material was simulated by means of a Mohr-Coulomb-like formulation with an elastic modulus $E_b=50$ MPa and a perfectly plastic post-elastic behaviour. At this purpose, and to avoid convergence issues when the stress state approaches the corner of the failure surface, the linear Drucker-Prager material model implemented in Abaqus software was adopted. To approximate the outer cone of the Mohr-Coulomb failure surface with the Drucker-Prager constitutive relationship, a friction angle $\beta=50.5^\circ$ was assumed. Moreover, a small cohesion was also introduced ($c=0.001$ MPa) to ensure robustness to the analysis.

3.2 Numerical calibration

The numerical analysis was phased in two steps: in the first step the gravitational load was applied, while in the second one the increasing vertical load until collapse was introduced at one-fourth span of the central bay. Given the complexity of the model, as well as the significant displacements attained in the real experimental test, a dynamic/implicit analysis method was adopted in the second step with a velocity of the load application such that guaranteeing the quasi-static load transmission (i.e. 0.01 mm/s). A fictitious damping coefficient equal to 20% was also introduced for both materials to avoid abrupt losses of strength and consequent convergence issues. The validity of this approach was verified against the static approach, showing that in such a way convergence issues were avoided and computational effort reduced without affecting the accuracy of the analysis.

Whilst some mechanical parameters were known and reported in the reference literature work (i.e. elastic modulus and compressive strength of the masonry, cohesion and friction angle of the backfill soil and specific weights of the material), no information were available with reference to tensile strength of the masonry f_t and elastic modulus of backfill material E_b . Moreover, in the considered case, it must be mentioned also the uncertainty affecting the friction coefficient μ defining the tangential law adopted for describing the interaction between the different materials.

Based on this, the proposed model has been defined by performing a parametric study where the unknown parameters were varied according to the following values:

- Tensile strength of the masonry: $f_t = 0.2$ MPa, 0.4 MPa, 0.8 MPa;
- Elastic modulus of the backfill material: $E_b = 25$ MPa, 50 MPa, 100 MPa;
- Friction coefficient for the interaction law: $\mu = \tan(15^\circ)$, $\tan(30^\circ)$, $\tan(60^\circ)$.

Moreover, the fracture energy in tension was obtained from the selected value of tensile strength. These preliminary analyses were pushed until a vertical displacement of the point of load application of -20 mm. This was sufficient to operate a comparison between reference and numerical curves, which was performed by evaluating, for each displacement level u , the absolute total relative percentual error $E_{r\%}$ of the force values. In particular, the percentual error $E_{r\%}$ was estimated according to Equation 2:

$$E_{r\%} = \int_0^{u_{\max, \text{num}}} \frac{|F_{\text{num}}(u) - F_{\text{exp}}(u)|}{F_{\text{exp}}(u)} du \quad (2)$$

where: the vertical displacement u ranges from 0 to the maximum displacement of the numerical curve $u_{max,num}$ and $F_{num|exp}(u)$ indicates the force value in the numerical or experimental curve obtained at each displacement value.

3.3 Validation of the implemented numerical model

Based on the described calibration procedure, the unknown parameters were defined by selecting the case that returned the lowest value of the relative percentage error. In particular, when $E_b=50$ MPa, $f_i=0.2$ MPa and $\mu=\tan(30^\circ)$ were adopted, the minimum value of the relative error ($E_{r\%}=3.1\%$) was obtained.

The calibrated model returned, at the end of the analysis, results strongly consistent with the experimental evidence. This is confirmed by the comparison in terms of both failure modes and force-displacement curves shown in Figure 3. In particular, in Figure 3a the tensile damage at the last displacement value is plotted together with the experimental crack position overlapped, while in Figure 3b the comparison between the numerical and experimental curves is shown.

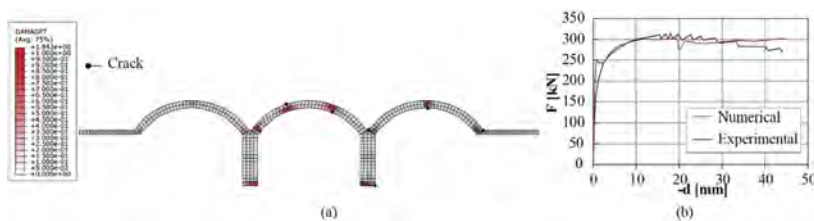


Figure 3. Results of numerical analysis in comparison with experimental evidence: (a) damage pattern and (b) force-radial displacement curves.

4 EFFECTS OF UNCERTAIN PARAMETER ON BRIDGE RESPONSE

4.1 Influence of the uncertain parameters

The wide set of analyses performed for calibrating the numerical model has led to make some considerations about the effects of the investigated parameters on the bridge response. A first consideration about the effects of uncertainty relate to the unknown parameters has been performed by quantifying their influence on the response of the bridge in comparison with the reference case.

Firstly, the percentage variation $\Delta F_{max,i}$ between the i -th numerical ($F_{max,num,i}$) and experimental ($F_{max,exp,i}$) capacities (maximum force) has been determined for each analysed case, as per Equation 3.

$$\Delta F_{max,i} = \frac{F_{max,num,i} - F_{max,exp,i}}{F_{max,exp,i}} \quad (3)$$

Considering the design of experiments described above, triplets of these values have been defined by considering the cases where two of the unknown parameters were constant and one sole parameter was varied. This leads to 9 triplets for each investigated parameter.

For each of these triplets, the influence has been assessed by calculating the range R_i , according to Equation 4.

$$R_i = \max(\Delta F_{max,i}) - \min(\Delta F_{max,i}) \quad (4)$$

R represents the variation in accuracy due to the variation of the single parameter, since all the other parameters are fixed.

Clearly, R changes depending on the basic point, i.e., the fixed value assumed by the other parameters. Thus, a quantitative measure of the influence of the parameters under

investigation (i.e. E_b , f_t and μ) is represented by the distribution of R , and in particular by the average and standard deviation over the 9 triplets. The results are shown in Figure 4 where the obtained R_i values are plotted together with their average R_m and standard deviation σ_R .

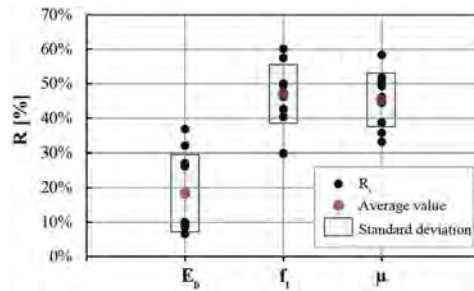


Figure 4. Influence of uncertain parameters.

As it can be observed, according to this elaboration, the most influencing parameters resulted the tensile strength of the masonry f_t ($R_m=47\%$) and the tangential friction μ ($R_m=45.3\%$). Conversely, the elastic modulus of the backfill material resulted the less influencing parameter on the bearing capacity, being $R_m=18.4\%$.

4.2 Effects of the uncertain parameters on the capacity

Once the most influential parameters have been identified, their effects on the capacity of the bridge have been estimated. In particular, in Figure 5, the influence of the f_t and μ parameters is shown for each value of E_b by means of 3d bar charts where the ΔF_{max} values are plotted on the vertical axis.

According to Figure 5, a dependency of the overall vertical loading capacity of the bridge on all parameters can be clearly recognised. Such a dependency is even more evident in the graphs of Figure 6, which represent the F_{max} dependency on f_t and μ given a value of the E_b parameter. In particular, in Figure 6, the filled indicators refer to the primary horizontal axis (f_t) and show the F_{max} for constant values of the tangential friction, while the empty indicators refer to the secondary horizontal axis (μ).

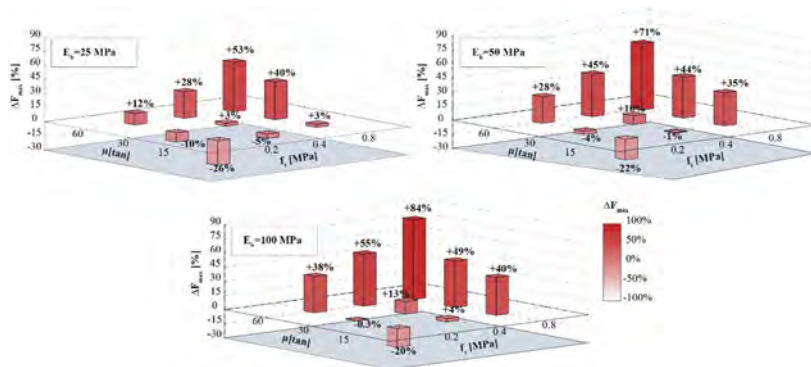


Figure 5. Influence of unknown parameters on strength capacity by means of 3d bar charts.

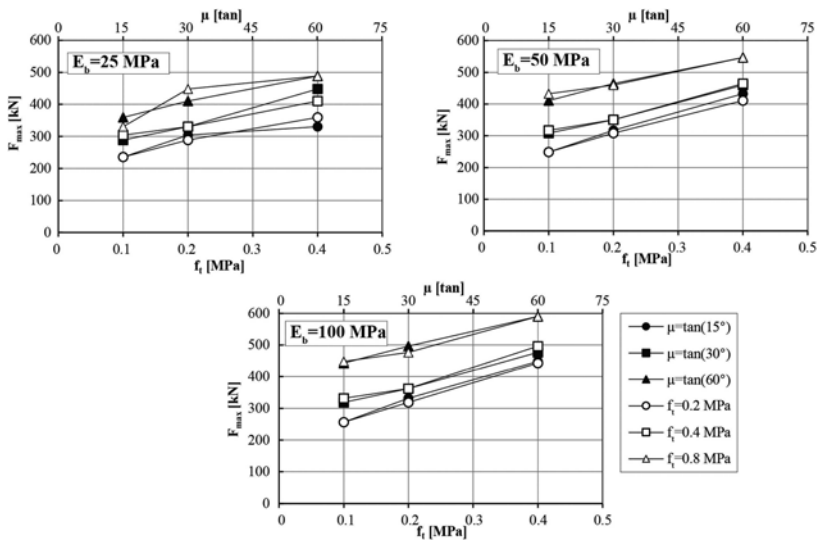


Figure 6. Influence of unknown parameters of strength capacity by means of dispersion graphs.

The graphs of Figure 6 show that generally a linear dependency can be identified between the variations of the investigated parameters and the maximum strength capacity exhibited by the numerical model with respect to the reference experimental case.

5 CONCLUSIONS

In the present study, the calibration of a reliable numerical model for reproducing the evidence retrieved from a literature experimental test has been addressed. The calibration entailed a parametric study including a number of numerical analyses aimed at fixing the mechanical unknown parameters. Such a calibration procedure allowed for some considerations about the influence of some parameters on the response of the bridge, as well as identifying possible retrofitting solutions for existing masonry arch bridge.

In general, it has been observed that the response of masonry arch bridges is mostly influenced by the tensile strength of masonry elements and the law describing the interaction between masonry and backfill material. Whilst the strong influence of the former parameter (i.e. f_t) on the capacity of the bridge was expectable, on the other hand, the parametric study highlighted that selection of the μ value, for which closed-form methodologies are actually missing, can considerably affect the bridge response. Nonetheless, in other similar literature applications, an approach consistent with the one proposed in this study was adopted, confirming the reliability of the calibrated finite element model, as well as of the determined μ value (e.g. Scozzese et al. 2019).

It has been also observed that the stiffness of the soil material used as backfill can modify the capacity of the bridge, even though in a less influential manner: the stiffer the backfill material, the higher the capacity of the bridge in facing external vertical loads.

Therefore, it can be concluded that conferring tensile strength (i.e. by means of steel-, FRP or FRCM-based techniques) to masonry arch elements in existing bridges may represent one of the most effective and convenient retrofitting solutions for structural enhancement. This holds true also if a better connection between masonry and backfill is guaranteed despite, further studies need to be performed aimed at identifying compatible, sustainable and convenient retrofitting solutions based on this concept. Finally, a beneficial effect can be also obtained by stiffening the backfill material for instance by means of injections by means of mortar or materials of other nature. Nonetheless, given that when such a solution is also

expected to modify the dynamical characteristics of the entire structure, hence having effect on its seismic response, and considered the smaller influence of backfill stiffness on the capacity assessed by this study, in many cases this may not represent the most convenient solution.

ACKNOWLEDGMENTS

Part of the present study has been developed within the activities of project “SAFE_MAB - Advanced procedures for SAFETY assessment of existing Masonry Arch Bridges”, funded by the University of Campania “Luigi Vanvitelli”. The first author is funded by MUR (Ministry of University and Research) through PON FSE 2014-2020 program (contract: 49-I-32603-3).

REFERENCES

- Lee, J. & Fenves, G.L. 1998. Plastic-Damage Model for Cyclic Loading of Concrete Structures. *Journal of Engineering Mechanics* 124(8): 892–900.
- Lourenço, P.B. 2009. Recent Advances in Masonry Modelling: Micromodelling and Homogenisation. In U. Galvanetto & M. H. Ferri Aliabadi (eds), *Multiscale Modeling In Solid Mechanics: Computational Approaches*. London: Imperial College Press.
- Lublliner, J., Oliver, J., Oller, S. & Oñate, E. 1989. A Plastic-Damage Model for Concrete. *International Journal of Solids and Structures* 25(3): 299–326.
- Melbourne, C., Gilbert, M., & Wagstaff, M. 1997. The Collapse Behaviour of Multispan Brick-work Arch Bridges. *Structural Engineer* 75(17): 297–305.
- Melbourne, C. 1990. The Assessment of Masonry Arch Bridges—The Effects of Defects. In J. E. Harding, G. A. R. Parke & M. J. Ryall (eds), *Bridge Management*. New York: Springer.
- Pantò, B., Chisari, C., Macorini, L. & Izzuddin, B.A. 2022. A Hybrid Macro-Modelling Strategy with Multi-Objective Calibration for Accurate Simulation of Multi-Ring Masonry Arches and Bridges. *Computers & Structures* 265: 106769.
- Sawko, F. 1982. Numerical Analysis of Brick Walls under Compressive Loading. In Proceedings of British Ceramic Society, Load-Bearing Brickwork, edited by West HWH, 213–22.
- Scozzese, F., Ragni, L., Tubaldi, E. & Gara, F. 2019. Modal Properties Variation and Collapse Assessment of Masonry Arch Bridges under Scour Action. *Engineering Structures* 199: 109665.
- Sokolovic, N.M., Petrovic, M., Kontic, A., Koprivica, S. & Šekularac, N. 2021. Inspection and Assessment of Masonry Arch Bridges: Ivanjica Case Study. *Sustainability* 13(23): 13363.
- Zampieri, P., Tetougueni, C.D. & Pellegrino, C. 2021. Nonlinear Seismic Analysis of Masonry Bridges under Multiple Geometric and Material Considerations: Application to an Existing Seven-Span Arch Bridge. *Structures* 34: 78–94.
- Zhang, Y., Tubaldi, E., Macorini, L. & Izzuddin, B.A. 2018. Mesoscale Partitioned Modelling of Masonry Bridges Allowing for Arch-Backfill Interaction. *Construction and Building Materials* 173: 820–42.
- Zizi, M., Bencivenga, P. & De Matteis, G. 2023. Handling Policies for Italian Existing Bridges with a Territorial Approach: The Case Study of Caserta, Italy. *Structures* 48: 1306–1321.

Simplified analysis on multiring masonry arch bridges

R. Piazzon, P. Zampieri & C. Pellegrino

Department of Civil, Environmental and Architectural Engineering, University of Padua, Padua, Italy

ABSTRACT: Multi-ring brickwork masonry arch bridges in service in the European railway and roadway network represents a typology of masonry bridges that generally have lower load carrying capacity with respect to masonry arch bridges with different arch texture. These bridges differ from the single-ring arches for their peculiar mechanical behaviors and collapse modality. This paper presents the evaluation of the load carrying capacity of multi-ring masonry arches by means of a simplified numerical strategy, that permits to investigate the in-plane failure mechanism of the element. In the simplified approach the arch geometry is subdivided in rigid elements, interacting along their rigid edges through non-linear bidimensional links in which the stiffness and the material nonlinearities are concentrated. The numerical results obtained with the proposed approach are compared with experimental outcomes.

1 INTRODUCTION

The multi-ring brickwork masonry arch bridge is a bridge category diffuse all around the world. The majority of them were built over a century ago and the increasing of the traffic loads demand and the deterioration of the materials bring the necessity of the static and seismic assessment of these structures. The peculiarity of this category is the presence of the rings joints that can be potential surfaces of weakness for the arch (Melbourne & Gilbert 1995). For this reasons, several different numerical approaches have been developed to perform the structural safety assessment of this type of bridge. Among them, the Finite Element Method (FEM), the Rigid Block analysis Method and the Discrete element method are most diffuse.

The FEM models, despite the high computational cost and the problems with the convergence of the solution, can reaches accurate prediction of the response of the bridge (Zampieri & Tetougueni & Pellegrino 2021). One among the FEM models, is the mesoscale approach (Zhang & Macorini & Izzuddin 2018) that reproduces the geometry subdividing the bricks into 3D solid elastic elements and the mortar joints into 2D non linear interface elements in which the nonlinearities are concentrated obtaining good prediction of the results.

The Rigid block analysis considers the geometry of the arch as a mesh of rigid block, investigate the structural equilibrium and collapse model through limit analysis obtaining with less computational cost good results (Melbourne & Gilbert 1995).

The discrete element method has the possibility of using deformable or rigid element and non-linear interfaces recreating the arch geometry (Kassotakis & Sarhosis & Forgács & Bagi 2017).

The aim of this paper is to present a simplify numerical method for the evaluation of the capacity of multi-ring masonry arches, capable of simulate the failure modes typical of this category, for example the detachment between rings, using less computational cost than another sophisticated methods.

2 DESCRIPTION OF THE NUMERICAL STRATEGY

The approach considered in this paper simulates the geometry of the original arch by means of rigid panels connected through a distribution of 2D nonlinear links capable of simulating

the flexural and shear-sliding masonry behaviors and coupling between them (Zampieri & Piazzon & Pantò & Pellegrino 2022, Caddemi & Calì & Cannizzaro & D'Urso & Pantò & Rapicavoli & Occhipinti 2019, Cannizzaro & Pantò & Caddemi & Calì 2018) (Figure 1).

The interface link is composed by two in series mono-dimensional springs, the normal spring is disposed perpendicularly to the edge meanwhile the tangential spring is parallel to it (Figure 2). The mechanical coupling is obtained according to the Mohr-Coulomb yield criterion, based on the friction coefficient (μ) and the cohesion (c). The links are capable of simulate the material cracking that leads to the formation of the hinges, typical mechanism of the masonry arches.

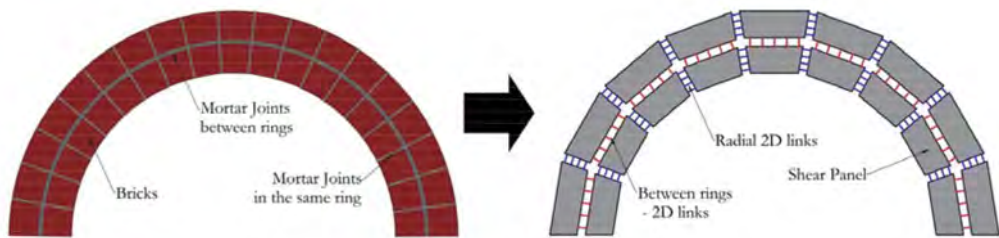


Figure 1. Real masonry arch (left); numerical representation of the geometry with discrete elements (right).

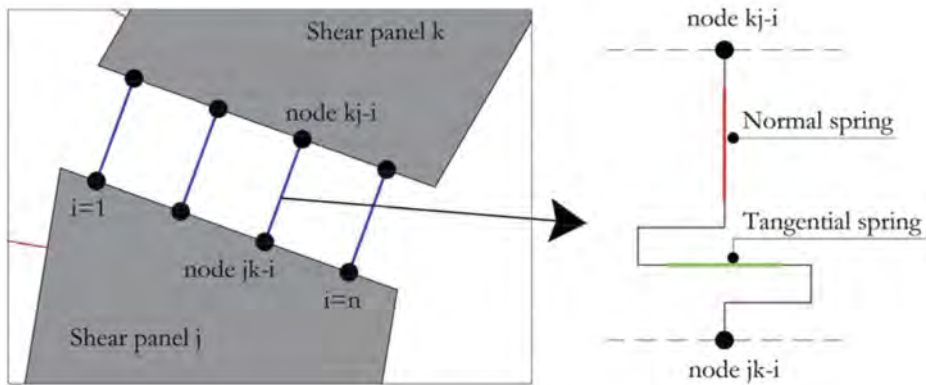


Figure 2. Discrete element interface with nodes connected with links (left) and numerical representation of the 2D link (right).

3 MODEL CALIBRATION

The normal springs reproduces the joint and brick compressive behaviour by means of a parabolic relationship reaching the peak-strength, followed by a linear softening and a residual strength. The tensile behavior is simulated with a linear elastic law with linear softening after the peak-value. The linear softening ends with a zero force residual, that corresponds to the cracking of the material. The link that simulates cracked masonry maintains the original behavior in compression but, if tensile displacement occur, it is considered detached and it doesn't contribute in the normal and tangential directions. The initial normal stiffness $K_{N,0}$, the peak force in tension and the peak force in compression are modelled considering

the potential mortar joint and unit failure modes. The tangential spring describes the sliding behavior with an linear elasto-plastic constitutive law with linear softening, controlled by a damage function that reduces cohesion, friction coefficient and tangential stiffness. Considering the Mohr-Coulomb yielding surface, the peak force value $F_{T,lim}$ is calculated as:

$$F_{T,lim} = \mu \cdot F_N + F_0 \tag{1}$$

Where the μ is the friction coefficient, F_N the normal force acting in the link, $F_0=c \cdot \lambda \cdot s$, c the cohesion, λ is the influence length in the direction parallel to the edge, and s is the thickness of the arch represented.

The shear stiffness is calibrated in function of the shear moduli of the brick and the mortar, and the actual thickness of the joint.

4 NUMERICAL SIMULATIONS OF TESTS ON MASONRY ARCHES

To evaluate the effectiveness of the proposed method, two experimental tests, one executed on a two-rings masonry arch with 3m span and one on a three-rings arch with 5m span, are numerically simulated (Melbourne & Wang & Tomor 2007). Both arches has the span-rise ratio of 4:1. The arches, built using high quality bricks and cement mortar, were pre-loaded using hydraulic jacks at $\frac{1}{4}$ and $\frac{3}{4}$ of the arch, each of which applies 10 kN for the 3m-span arch and 22.5 kN for the 5m-span arch. In the experimental tests the live vertical load is applied monotonically with load control at $\frac{1}{4}$ of the span and the vertical and horizontal displacement at the previously reported points are recorded. In the numerical simulation, permanent non-structural loads(G2) are implemented as concentrated forces meanwhile the live load (Q) is applied as imposed displacement to a single control point positioned at $\frac{1}{4}$ of the span considering displacement control, condition that permits to analyzing the post-peak behavior as resumed in the Figure 3. The meshes reproduce the actual number of rings and number of bricks utilized in the experimental tests. The numerical mechanical properties are calibrated on the materials properties obtained from previously cited work.

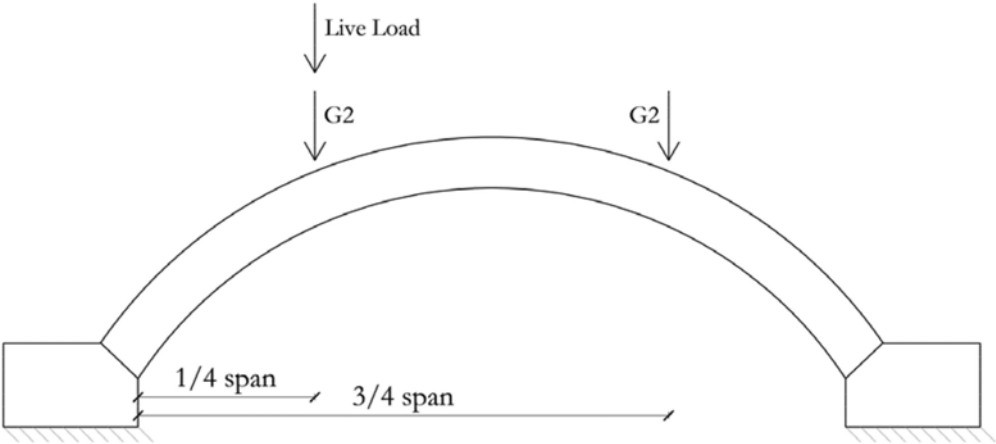


Figure 3. Test set-up.

The results are reported in Figure 4 and Figure 5, compared to the experimental findings, in terms of load-displacement curves, considering the vertical displacement of a point in the intrados in correspondence of $\frac{3}{4}$ of the span for the 2-rings arch and $\frac{1}{4}$ of the span for the 3-rings span.

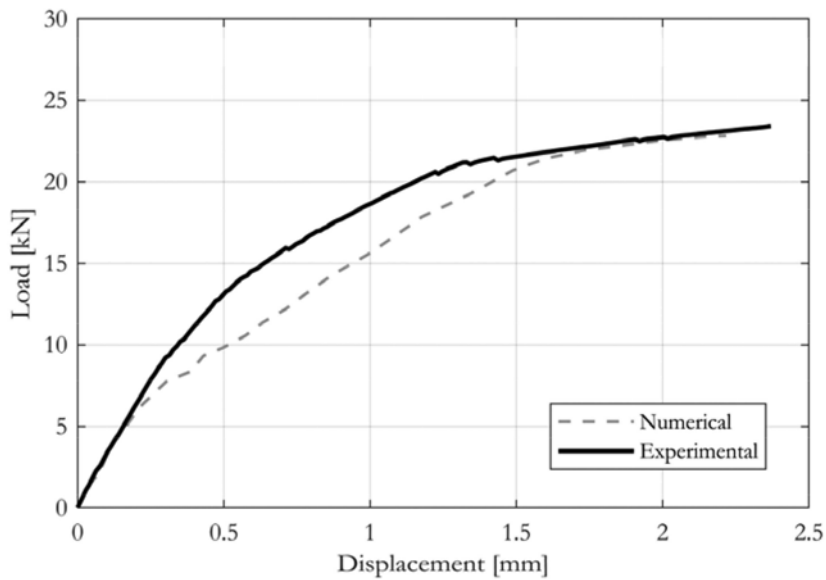


Figure 4. Comparison between the experimental and numerical results for the 2-rings arch.

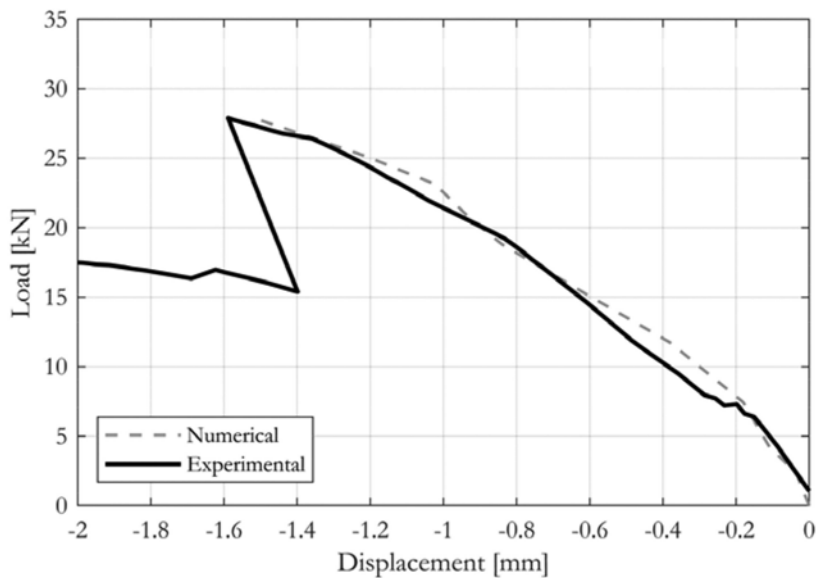


Figure 5. Comparison between the experimental and numerical results for the 3-rings arch.

5 DISCUSSION OF THE RESULTS

In the Figure 6 and Figure 7, the numerical deformed shapes are reported, in comparison with the experimental deformed shape for the 2-ring arch and a representation of the position of the 4 hinges for the 3-rings arch. The results highlight good correspondence between the numerical and the experimental tests in terms of peak load, initial stiffness and failure mode. In particular the first arch, with two brick rings, exhibit the typical 4-hinges mechanism, even

in the highest hinge is diffuse and it is not assimilable to a unique crack. Neither the experimental and the numerical model present between-rings separation. The numerical capacity curve (Figure 4) approximates the experimental one especially in the initial and final part, reproducing the effective initial stiffness of the arch. The numerical test ends because of convergence limits. The 3-rings arch's exhibits a first phase in which it manifests the 4-hinges mechanism meanwhile the failure mode is governed by the shear/sliding mechanism between rings and between elements of the same ring. As presented in the deformed shape, the sliding between rings is the primary failure mode, at which result the sliding in the opposite direction. In the Figure 5 can be observed the well prediction of the model in terms of initial stiffness and degradation of the stiffness before the failure point. The peak load corresponds to the rings separation/sliding and the activation of the mechanism presented in the Figure 7, after which the load registered decreases in value.

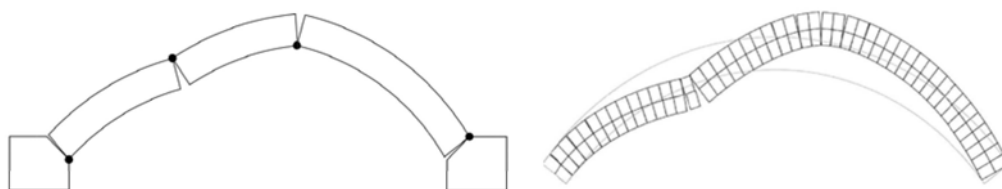


Figure 6. Failure mechanism of the experimental test for the 2-rings arch (left) and deformed shape obtained from the numerical model, considering an amplification factor of 50 (right).

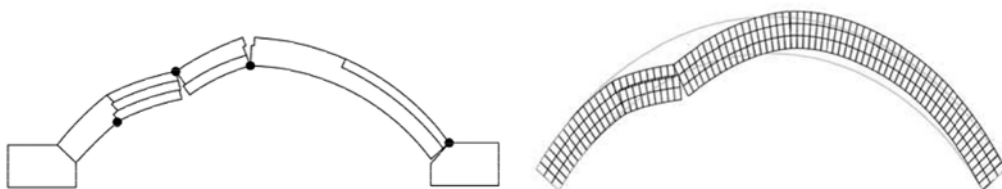


Figure 7. Failure mechanism of the experimental test for the 3-rings arch (left) and deformed shape obtained from the numerical model, considering an amplification factor of 50 (right).

6 CONCLUSIONS

This paper introduces a simplified numerical strategy for the simulation of the nonlinear in-plane response of masonry multi-rings arches. The geometry of the masonry is represented by a mesh of discrete elements, connected with links able to simulate the flexural and shear-sliding collapse modes typical of masonry material. The case studies present two typical failure mode of masonry arches, well reproduced in the numerical tests. In particular, the proposed model is able to reproduce the sliding between rings, failure mode not visible in the single-ring arches.

REFERENCES

- Caddemi, S. & Calì, I. & Cannizzaro, F. & D'Urso, D. & Pantò, B. & Rapicavoli, D. & Occhipinti, G. 2019. 3D discrete macro-modelling approach for masonry arch bridges. *IABSE Symposium, Guimarães 2019: Towards a Resilient Built Environment Risk and Asset Management*: 1825–1835.

- Cannizzaro, F. & Pantò, B. & Caddemi, S. & Calì, I. 2018. A Discrete Macro-Element Method (DMEM) for the nonlinear structural assessment of masonry arches, *Engineering Structures* 168: 243–256.
- Kassotakis, N. & Sarhosis, V. & Forgács, T. & Bagi, K. 2017. Discrete element modelling of multi-ring brickwork masonry arches. In *13th Canadian Masonry Symposium*. Newcastle University.
- Melbourne, C. & Gilbert, M. 1995. The behaviour of multi-ring brickwork arch bridges, *The Structural Engineer* 73(3): 39–47.
- Melbourne, C. & Wang, J. & Tomor, A. 2007. *Masonry Arch Bridges*, Sustainable Bridges.
- Zampieri, Paolo & Tetougueni, Cyrille Denis & Pellegrino, Carlo 2021. Nonlinear seismic analysis of masonry bridges under multiple geometric and material considerations: Application to an existing seven-span arch bridge, *Structures*, 34: 78–94.
- Zampieri, P. & Piazzon, R. & Pantò, B. & Pellegrino, C. 2022. A Simplified Modelling Approach for the In-Plane Analysis of Masonry Structures Strengthened by FRCCs. In *Key Engineering Materials* 916: 201–206.
- Zhang, Yanyang & Macorini, Lorenzo & Izzuddin, Bassam A. 2018. Numerical investigation of arches in brick-masonry bridges, *Structure and Infrastructure Engineering*, 14:1: 14–32.

Effects of changing temperature in the vibration-based model updating of a masonry bridge

P. Borlenghi, A. Saisi & C. Gentile
DABC, Politecnico di Milano, Milan, Italy

ABSTRACT: FE model updating of structures is commonly based on the modal parameters evaluated in a single vibration test. Nevertheless, the influence of changing temperatures on modal parameters – especially on natural frequency – is well known. The paper presents an investigation on the effects of (temperature-induced) frequency variations on the estimate of the elastic properties of a historical masonry bridge. Firstly, documentary research, geometric survey, minor destructive tests and ambient vibration tests were performed. Subsequently, the numerical model of the masonry bridge is developed based on the collected data, and the updating procedure is performed by using the two sets of modal parameters identified in July 2018 (average temperature 30.4°C) and April 2021 (average temperature 13.2°C). The results show that the (temperature-induced) frequency decrease seems to affect more significantly the estimate of the Young's modulus of spandrels and backing.

1 INTRODUCTION

The calibration of FE models is fundamental to obtaining reliable results in the structural assessment of existing bridges and infrastructures. In the engineering practice, the modal parameters identified from vibration data are often used as targets for the model parameters adjustment (see e.g. Costa et al 2015, Pepi et al. 2021, Aytulun et al. 2022 for recent applications on masonry bridges); however, the influence of environmental factors (e.g. outdoor temperature) on modal parameters, and especially on natural frequencies, is well known and extensively documented in the scientific literature (Ramos et al. 2010, Saisi et al. 2015, Ubertini et al. 2017, Roselli et al. 2018). Consequently, when a FE model is calibrated for structural assessment purposes, it would be appropriate to consider that the identified structural parameters also result from specific environmental conditions and the related variability might propagate along the structural identification process.



Figure 1. The *Olla* bridge: (a) picture from the Stura River; (b) existing damages on the second arch.

In the present paper, the effects of temperature-induced frequency variations on FE model updating of a historical masonry arch bridge are investigated. The selected structure is the *Olla* bridge, a masonry viaduct built in the second half of the 19th century in the northwest of Italy. High piers characterise the bridge; therefore, operational modal testing and analysis are well suited for evaluating its dynamic behaviour. Firstly, the numerical model is developed by integrating topographic survey, historical research, visual inspections and limited tests on materials. Subsequently, two ambient vibration tests are performed in different environmental conditions and the two different sets of identified modal parameters are used to estimate the optimal structural parameters. The presented results highlight that major variations of the optimal estimates are observed in the structural elements with lower compressive forces.

2 THE *OLLA* BRIDGE: DESCRIPTION AND PRELIMINARY ANALYSIS

The investigated structure (Figure 1a) – called *Olla* bridge (Borlenghi et al. 2023) – is a multi-span masonry arch bridge that crosses the Stura River between the small municipalities of Gaiola and Borgo San Dalmazzo. The structure is approximately 120 m long and comprises 5 arches, with a maximum span of 25 m, 4 piers and end abutments, with the tallest pier being 26 m high. Piers and abutments are in a good quality ashlar stone masonry, whereas arches and spandrel walls are in brick masonry.

The documentary research revealed the collapse of the central arch in 1944 (Figure 2) and the subsequent reconstruction in 1945.

The complete representation of the structure was obtained with the Terrestrial Laser Scan and topographic survey. The processing of the point clouds allowed the extraction of an accurate 3D model and a series of conventional 2D drawings from which the FE model was developed. In addition, the visual inspections highlighted the presence of local damages on the arches (Figure 1b) and diffused surface decay.



Figure 2. The collapse of the central arch occurred in 1944.

3 EXPERIMENTAL SURVEYS

The experimental survey on the *Olla* bridge included some Minor Destructive Tests (MDTs) to retrieve information on internal morphology and material distribution and two series of Ambient Vibration Tests (AVTs) to characterise the dynamic behaviour of the structure under different environmental conditions.

The MDTs – consisting of limited coring tests – were performed to obtain information on arches, spandrels and fill. Due to the limited extension of the core drill machine, no information on the backing was obtained. The coring tests were performed in the Autumn of 2018. Six coring samples were taken from the following elements: 2 on the arches, 2 on the spandrels and 2 on the deck (Figure 3a). The tests revealed that the arches are constituted only by brick masonry while the spandrels are a mixture of stone and brick masonry. The fill consists of compacted soil and pebbles. The thickness of the asphalt over the fill is equal to 20 cm.

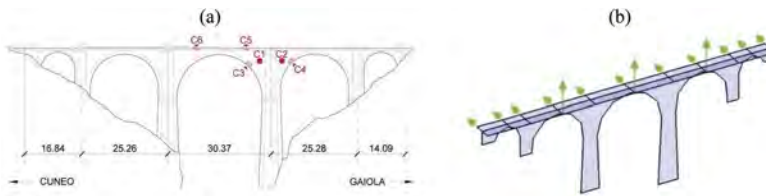


Figure 3. (a) Layout of the samples coring; (b) Sensor layout adopted for the AVTs.

Overall, the adopted measuring devices for the AVTs included 14 high-sensitivity piezoelectric accelerometers (WR model 731A, 10 V/g sensitivity and ± 0.50 g peak) and a multi-channel acquisition system with 4 DAQ modules (NI 9234, 24-bit resolution, 102 dB dynamic range and anti-aliasing filters). In addition, each accelerometer was connected with a 1-meter cable to a power unit/amplifier (WR P31) to improve the performance of the acquisition chain: the power unit/amplifier was aimed at providing a constant current to power the accelerometer's internal amplifier, signal amplification and selective filtering.

Regarding the dynamic testing, a preliminary prompt test was performed with a single triaxial geophone (SARA GEOBOX SS45), revealing that the fundamental vibration mode of the structure involved the transversal motion of the deck. Therefore, the sensor layout for both tests was arranged to guarantee a complete representation of the lateral mode shapes and a partial reconstruction of the vertical ones (Figure 3b): the transversal response was recorded in 11 measuring points, while the vertical response was measured in 3 points (i.e. the centre of the three major arches). The tests were performed with one lane open to vehicular traffic.

The sampling frequency adopted in both AVTs was equal to 200 Hz, which is more than enough for the considered structure whose dominant frequencies are below 10 Hz. Therefore, low pass filtering and decimation were applied to down-sample the data to 40 Hz, obtaining a Nyquist frequency of 20 Hz. The modal identification was performed with time windows of 2400 s using the covariance-driven Stochastic Subspace Identification technique (SSI-Cov, Peeters & De Roeck 1999). The reader can refer to (Cabboi et al. 2017) for full details on the applied SSI-Cov procedure.

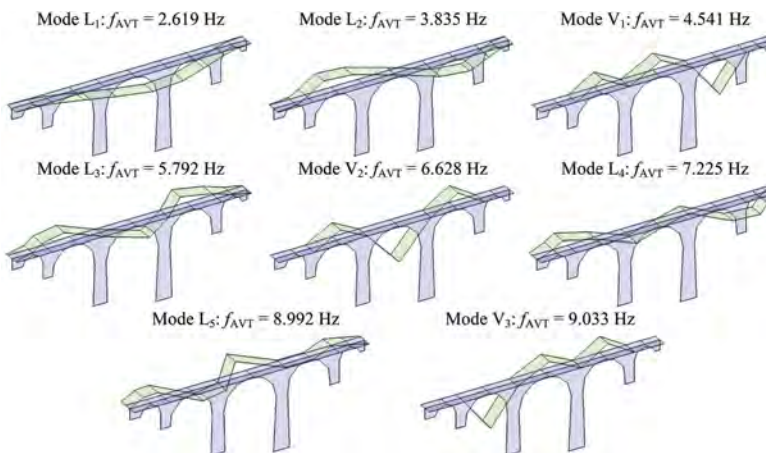


Figure 4. Modal identification from Dataset 1, July 2018: L denotes the dominant lateral vibration modes, and V denotes the dominant vertical vibration modes.

The first dynamic test was performed on July 31st, 2018, with an average temperature of 30.4°C, while the second dynamic test was performed on April 22nd, 2021, with an average temperature of 13.1°C. Overall, 5 transverse and 3 vertical vibration modes are identified in

both tests for the frequency range of 0-10 Hz. The identified mode shapes are shown in Figure 4. It should be noticed that: (a) the transverse modes exhibit an increasing number of half-sine waves and inflexion points; (b) each identified vertical mode is characterised by the dominant deformation of one of the three longer spans, respectively.

The comparison of identified natural frequencies is shown in Table 1. The decrease in the outdoor temperature among the two tests is equal to 17.3°C, and the corresponding average reduction of natural frequencies is equal to 4%.

4 FE MODELLING AND UPDATING CONSIDERING ENVIRONMENTAL EFFECTS

In a previous study (Borlenghi et al. 2020), a simplified model of the *Olla* bridge was developed to investigate the contribution of backing and spandrels in the dynamic response of the structure in operational conditions. The simplified model emphasised the importance of the stiffening effects given by the structural elements above the arches. Nevertheless – due to the simplified nature of the model – a good experimental-numerical correlation was obtained for the lateral modes while an imperfect correlation was obtained for the vertical modes. Consequently, the 3D FE model herein presented reproduces as closely as possible the external geometry of the bridge with reasonable assumptions on its internal morphology. Therefore, spandrels, backing and fill material have been modelled along with arches, abutments and piers, considering a perfect connection among each structural element.

4.1 Development of the FE model

The 3D FE model of the bridge was developed in the ABAQUS software using ten-node tetrahedral elements (C3D10). The regular distribution of masses, the accurate description of geometrical details and the negligible mesh sensitivity on natural frequencies were obtained using a relatively large number of elements. Overall, the FE model consists of 45604 tetrahedral elements with 211818 degrees of freedom and an average mesh size of 1.15m.

Regarding the adopted geometry, the geomatic survey allowed the definition of all external dimensions with high accuracy; in contrast, the thickness of arches, the thickness of spandrels, and the height of backing were identified with a multi-step procedure. The characteristics of the internal morphology were initially assumed from historical research and then verified with local tests. For the spandrels, it was possible to assume a constant thickness equal to 1.0 m, while for the arches, the thickness visible from outside corresponds with the internal one. Due to the limited length of the drilling machine, no information on the backing was retrieved from the local tests. Consequently, the height of the backing was directly assumed from the construction handbook of Curioni (1873) and then validated with the FEMU procedure.

Furthermore, the main assumptions regarding the definition of the numerical model are herein listed: (i) the effect of soil-structure interaction was neglected, and the boundary conditions of piers and abutments were assumed fixed; (ii) all the materials were considered isotropic; (iii) the Poisson's ratio of masonry materials was held constant and equal to 0.15; (vi) the weight per unit volume of each structural component was held constant and equal to 20 kN/m³ for the piers and abutments, 17 kN/m³ for the arches, 19 kN/m³ for the spandrels, 21 kN/m³ for the base of the central piers, 18 kN/m³ for the backing, and 16 kN/m³ for fill. In view of the clear presence of superficial rocks at the river level (Figure 1a), the base nodes of piers and abutments were assumed as pinned. Similarly, the longitudinal translation of the abutments was restrained.

Different materials were considered for each structural element: (a) piers and abutments are built in ashlar stone masonry, (b) arches are in solid brick masonry, (c) spandrels are characterised by a first layer of bricks, and then rough-cut stones, (d) the bases of two central piers are in regular ashlar stone masonry, (e) the backing – as shown in the historical pictures of Figure 2 – is in masonry, (f) the fill is made up of loose soil and pebbles. In addition, the information coming from the historical research was considered: the central arch was rebuilt after the second world war, and so it was for the backing above the nearby piers. Consequently, different material properties were considered for the central arch (rebuilt in 1945) and the backing over the central piers. Figure 5 summarises the adopted elements with constant material properties.

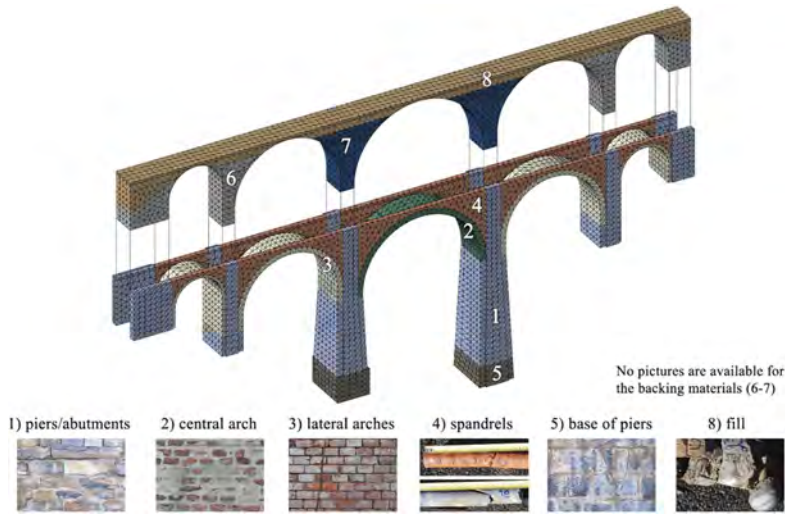


Figure 5. FE model of the Olla bridge with the indication of different materials.

4.2 FE Model Updating (FEMU)

Firstly, the (frequency) sensitivity of the selected Young's modulus was checked: all the parameters have a certain influence on the natural frequencies, with the only exception of the fill material. Due to its low sensitivity, the Young's modulus of fill was set equal to 0.30 GPa like a gravels/sand well-graded.

Subsequently, the selected structural parameters were manually updated until an acceptable solution was reached. The adopted values of the Young's modulus are the following: 16.5 GPa for the piers and abutments, 4.50 GPa for the arches, 15.0 GPa for the spandrels, 22.0 GPa for the base of the central piers, and 2.0 GPa for the backing. A one-to-one correspondence of the experimental-numerical modes was obtained, providing a preliminary verification of the main modelling assumptions. However, a maximum frequency discrepancy ($DF = 100 \cdot (1 - f_i^{FEM}/f_i^{AVT})$) equal to 7.4% showed the need for model updating.

The adopted FEMU procedure was implemented in MATLAB environment and it is based on the Douglas-Reid method (Douglas & Reid 1982) with the Particle Swarm Optimisation (PSO) algorithm: the updating parameters are iteratively corrected in a constrained range until a stable minimum solution for an objective function is found. Particularly, the following objective function was adopted:

$$J(\mathbf{x}) = \frac{100}{n} \sum_{i=1}^n \left| 1 - \frac{f_i^*(\mathbf{x})}{f_i^{AVT}} \right| \quad (1)$$

where f_i^{AVT} are the i -th experimentally identified natural frequency and $f_i^*(\mathbf{x})$ are the i -th polynomial approximations (Douglas & Reid 1982) of the numerical natural frequencies, expressed as functions of the \mathbf{x} updating parameters. The interested reader can refer to Borlenghi et al. 2023 for full details on updating procedure.

4.3 Discussion of the effects of environmental parameters on optimal models

Table 1 shows the comparison between the experimentally identified and numerically estimated natural frequencies in the two considered ambient conditions: July 2018 with a $T_{mean}=30.4^\circ\text{C}$ and April 2021 with a $T_{mean}=13.1^\circ\text{C}$. In both cases, an excellent

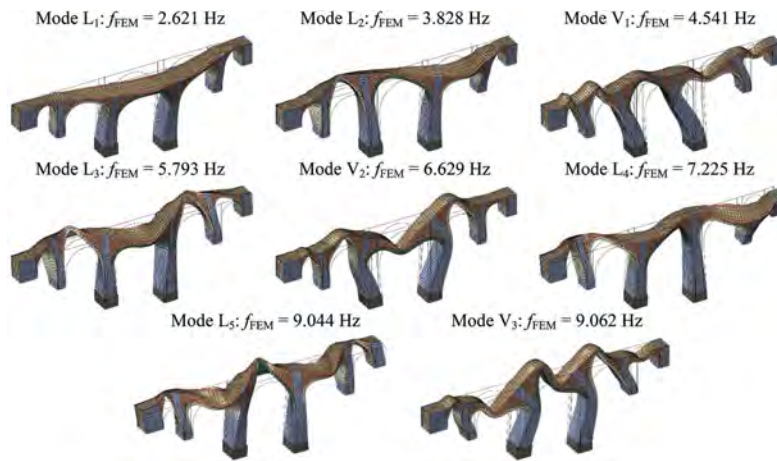


Figure 6. Vibration modes of the updated FE model (modal data from July 2018).

experimental-numerical correlation is obtained with an average frequency discrepancy DF of 0.15% and 0.57%, respectively, and an average mode shape correlation MAC of 0.95 in both cases. As expected, the numerical natural frequencies follow the variations of the experimental ones, with an average decrease equal to 4%, while the mode shapes exhibit negligible changes.

Table 2 lists the optimal estimates of the updated structural parameters of the two models. The differences between the Young's modulus of the central and lateral arches, as well as the one of the backing, are motivated by the reconstruction of 1945. As demonstrated by the coring tests, the spandrels are made of bricks externally and stone internally, justifying the high values elastic modulus obtained. Finally, the base of the central piers is built in a better-quality stone masonry with respect to the rest of the piers and, moreover, the optimal elastic modulus conceivably accounts for the stiffening effect provided by the compacted soils surrounding the piers.

The decrease in temperature between July 2018 and April 2021 implies a decrease in natural frequencies, which, in turn, determines an average reduction in Young's modulus equal to 8%. In detail, Table 2 shows the percentage of decrease for each parameter. The Young's modulus of piers, abutments, central arch, the base of central piers, and the backing of central piers exhibits a variation of less than 2%, while the Young's modulus of lateral arches shows a decrease of about 4%. However, major variations of the Young's modulus estimate are observed for spandrels and lateral backing.

The interpretation of structural parameter variations due to temperature-induced frequency changes is not straightforward. The natural frequencies of the *Olla* bridge tends to increase with increased temperature. Similar behaviour has been observed in long-term monitoring of masonry towers (Ramos et al. 2010, Saisi et al. 2015, Ubertini et al. 2017), as well as, from the repeated dynamic testing of a masonry viaduct (Roselli et al. 2018). The most accepted explanation is that the thermal expansion of materials induces the closure of micro-cracks, minor discontinuities or mortar gaps (defects typically present in masonry elements). Hence, the temporary compacting of the masonry induces a temporary increase of stiffness and natural frequencies, as well. In addition, small gaps and micro-cracks are expected to be more frequent in structural element with a low level of compressive stresses. It is worth noting that spandrels and backing are bearing less compressive forces than piers and arches. Consequently, it might be expected that the relatively high temperature measured during the first test of July 2018 generated a significant stiffening effect on backing and spandrels due to the expansion of masonry material and the consequent closure of micro-cracks, resulting in an apparent higher elastic modulus.

Table 1. Comparison between experimental and numerical natural frequencies considering different environmental conditions: July 2018 with $T_{\text{mean}}=30.4^{\circ}\text{C}$ and April 2021 with $T_{\text{mean}}=13.1^{\circ}\text{C}$.

Mode Id.	July 2018				April 2021			
	OMA		Optimal model		OMA		Optimal model	
	f_{AVT} (Hz)	f_{FEM} (Hz)	DF (%)	MAC (-)	f_{AVT} (Hz)	f_{FEM} (Hz)	DF (%)	MAC (-)
L ₁	2.619	2.621	-0.07	0.998	2.555	2.570	-0.61	0.997
L ₂	3.835	3.828	0.18	0.994	3.700	3.687	0.35	0.995
V ₁	4.541	4.541	-0.01	0.976	4.235	4.246	-0.28	0.972
L ₃	5.792	5.793	-0.02	0.989	5.554	5.553	0.02	0.991
V ₂	6.628	6.629	-0.02	0.995	6.477	6.441	0.56	0.995
L ₄	7.225	7.225	-0.01	0.902	6.789	6.908	-1.75	0.909
L ₅	8.992	9.044	-0.57	0.794	8.605	8.631	-0.31	0.784
V ₃	9.033	9.062	-0.32	0.951	8.671	8.697	-0.30	0.938

$$\text{DF} = 100 \cdot (1 - f_i^{\text{FEM}}/f_i^{\text{AVT}})$$

Table 2. Summary of the structural parameters identified from model updating considering different environmental conditions: July 2018 with $T_{\text{mean}}=30.4^{\circ}\text{C}$ and April 2021 with $T_{\text{mean}}=13.1^{\circ}\text{C}$.

No.	Structural elements	Optimal model	Optimal model	$\Delta E/E$ (%)
		A (July 2018)	B (April 2021)	
		E_A (GPa)	E_B (GPa)	
1	Piers/abutments	16.10	15.81	1.8%
2	Central arch	7.73	7.63	1.2%
3	Lateral arches	3.23	3.10	4.3%
4	Spandrels	16.85	12.00	28.8%
5	Base of central piers	27.49	27.34	0.5%
6	Backing lateral piers/abut.	1.38	1.13	17.6%
7	Backing central piers	4.56	4.49	1.7%

$$\Delta E/E = 100 \cdot (E_A - E_B)/E_A$$

5 CONCLUSIONS

The paper illustrates the effects of different environmental conditions on the model updating procedure of a historical masonry viaduct called *Olla* bridge.

The investigations in the *Olla* bridge included documentary research, geometric survey, minor destructive tests and ambient vibration tests. Particularly, the AVTs were performed in different environmental conditions: the first test was performed in July 2018 with an average temperature of 30.4°C , and the second test was performed in April 2021 with an average temperature of 13.2°C . Based on the information collected onsite, a 3D FE model was developed, and the uncertain structural parameters were estimated using the modal parameter identified in the two dynamic tests.

In summary, the following conclusions can be drawn:

- The onsite visual inspections highlighted the presence of local damages on the arches and diffused surface decay;
- During both dynamic tests, 5 lateral and 3 vertical vibration modes were identified in the frequency range of 0-10 Hz;
- The outdoor temperature variation between the two tests (July 2018 and April 2021) is equal to 17°C ;
- The percentage of variation in natural frequencies between the two tests has an average of 4%, a maximum of 6.7% for mode V₁ and a minimum of 2.3% for mode V₂;

- The Young's modulus of selected structural elements is estimated for both environmental conditions, showing an average variation of 8%;
- The Young's modulus of spandrels and lateral backing is the most affected by the changes in environmental conditions, with a decrease of 29% and 18%, respectively;
- The more pronounced variation in the elastic modulus of spandrels and backing is most likely related to the expansion of masonry material and the consequent closure of micro-cracks and small gaps during the hot season.

The reported results have demonstrated the importance of accurately evaluating the temperature effects for model updating purposes in masonry structures: the apparent stiffening effect given by the high temperatures of the hot season can lead to an over-estimation of the elastic properties of structural elements characterised by low loading levels. However, the apparent increase of stiffness is negligible for the main load-bearing elements, i.e. arches and piers. Consequently, the influence of testing conditions (and consequently of temperature-induced frequency variations) is conceivable negligible in the structural safety assessment of the investigated bridge.

ACKNOWLEDGEMENTS

The support of ANAS (Struttura territoriale Piemonte e Valle d'Aosta) is gratefully acknowledged. Sincere thanks are due to M. Cucchi and M. Iscandri (LPMSC, Politecnico di Milano) who assisted the authors in conducting the field tests.

REFERENCES

- Aytulun, E., Soyoz, S. & Karcioğlu, E. 2022. System identification and seismic performance assessment of a stone arch bridge. *Journal of Earthquake Engineering* 26(2):723–743.
- Borlenghi, P., Saisi, A. & Gentile, C. 2020. Preliminary structural assessment of a multi-span masonry arch bridge. In Arède, A. & Costa, C. (eds) *Proceedings of ARCH 2019; Porto, 2-4 October 2019*. Structural Integrity 11:56–463.
- Borlenghi, P., Saisi, A. & Gentile, C. 2023. ND testing and establishing models of a multi-span masonry arch bridge. *Journal of Civil Structural Health Monitoring* in press.
- Cabboi, A., Magalhães, F., Gentile, C. & Cunha, A. 2017. Automated modal identification and tracking: Application to an iron arch bridge. *Structural Control and Health Monitoring* 24(1):e1854.
- Costa, C., Arède, A., Costa, A., Caetano, E., Cunha, A. & Magalhaes, F. 2015. Updating numerical models of masonry arch bridges by Operational Modal Analysis. *International Journal of Architectural Heritage* 9(7):760–774.
- Curioni, G. 1873. *L'arte del costruire: costruzioni civili, stradali ed idrauliche* (in Italian). Augusto Federico Negro Editore, Turin.
- Douglas, B.M. & Reid, W.H. 1982. Dynamic tests and system identification of bridges. *Journal of the Structural Division* 108(ST10): 2295–2312.
- Peeters, B. & De Roeck, G. 1999. Reference-based stochastic subspace identification for output-only modal analysis. *Mechanical Systems and Signal Processing* 13(6):855–878.
- Pepi, C., Cavalagli, N., Gusella, V. & Giofrè, M. 2021. An integrated approach for the numerical modelling of severely damaged historic structures: Application to a masonry bridge. *Advances in Engineering Software* 151:102935.
- Ramos, L.F., Marques, L., Lourenço, P.B., De Roeck, G., Campos-Costa, A. & Roque, J. 2010. Monitoring historical masonry structures with Operational Modal Analysis: Two case studies. *Mechanical Systems and Signal Processing* 24(5):1291–1305.
- Roselli, I., Malena, M., Mongelli, M., Cavalagli, N., Giofrè, M., De Canio, G. & de Felice, G. 2018. Health assessment and ambient vibration testing of the “Ponte delle Torri” of Spoleto during the 2016–2017 Central Italy seismic sequence. *Journal of Civil Structural Health Monitoring* 8(2):199–216.
- Saisi, A., Gentile, C. & Guidobaldi, M. 2015. Post-earthquake continuous dynamic monitoring of the Gabbia Tower in Mantua, Italy. *Construction and Building Materials* 81:101–112.
- Ubertini, F., Comanducci, G., Cavalagli, N., Pisello, A.L., Materazzi, A.L. & Cotana, F. 2017. Environmental effects on natural frequencies of the San Pietro bell tower in Perugia, Italy, and their removal for structural performance assessment. *Mechanical Systems and Signal Processing* 82:307–322.

Numerical approaches to assess the load capacity of FRCM strengthened masonry bridges

D. Santinon, P. Zampieri & C. Pellegrino
University of Padova, Padova, Italy

D. Ricci, F. Iodice, A. Vecchi & F. Iacobini
Rete Ferroviaria Italiana RFI, Roma, Italy

ABSTRACT: Numerous railway masonry arch bridges located in regions with high seismic hazard, are still part of the Italian railway networks. In order to increase the safety level of masonry bridges with respect to the seismic action, as it is required by the Italian technical Standards (NTC2018), strengthening interventions are necessary. The use of FRCM (Fiber Reinforced Cementitious Matrix) system applied onto the masonry arch intrados represents an alternative to the traditional retrofit techniques common used in the past. This strengthening method allows to increase the masonry bridge capacity without changing: the weight, the geometry and the stiffness of the structure. Moreover, the railway line can still in service during the realization of the strengthening intervention. In this work, based on the results obtained from experimental tests, a simplified numerical approach is calibrated for the evaluation of the load carrying capacity of masonry arch bridges strengthened with FRCM system applied onto arch intrados. The calibration process provides simple and practical guidelines for modelling masonry bridges strengthened with FRCM.

1 INTRODUCTION

Nowadays, more and more masonry buildings with several decades of life are in need of restoration, improvement or retrofitting (Zizi, et al., 2023). In Italy, the masonry construction heritage, both buildings and bridges, represents the majority of all present constructions and, therefore, their study and preservation require special attention. Masonry is known to be an anisotropic material with multiple failure modes, which contributes to making masonry constructions difficult to study and evaluate. In current practice, simplified but functional approaches are preferred in order both to limit errors due to excessively complex and unmanageable modelling and to limit computational time. The aim of this paper is to present a simplified methodology for evaluating the load-bearing capacity of masonry semicircular arch bridges, both reinforced and not (Chisari, et al., 2021). Nowadays, there are several studies proving the ability of natural and sustainable materials to reinforce arch bridges (Gioffrè, et al., 2023; Gioffrè, et al., 2021), however, these materials may have durability problems. Both to avoid this problem and due to the presence of established studies, the choice has turned to the use of carbon fibre (CFRCM). The numerical methodology applied to the results of two masonry arch specimens, realised with the contribution of the Italian railway network (RFI, Rete Ferroviaria Italiana), will be illustrated in this paper.

2 DESCRIPTION OF EXPERIMENTAL SPECIMENS

Two masonry arches were constructed with lime mortar-based conglomerate backfill (Zizi, et al., 2023), with a net length of 3.00 m and a rise of 1.32 m. In particular, the arches were built using pressed fired clay bricks measuring 250x120x55 mm, using the four-headed laying technique shown in Figure 1, with a lime mortar thickness of 10 mm at the intrados. The resulting section of the arch is 250 mm in thickness and 510 mm in width. The backfill is made of a lime mortar-based conglomerate with 450 mm in width and 650 mm in length.

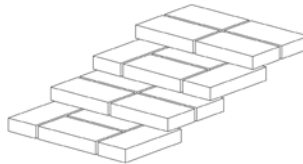


Figure 1. Example of a four-headed laying technique.

Finally, an FRCM reinforcement with both fabric and spike anchors made of a dry carbon fiber were applied to the intrados, of one of them, for a total thickness of 10 mm.

The arches are supported on rigid substructures that were fixed to the laboratory slab, by means of special tie rods, when the tests were carried out by applying an eccentric load.

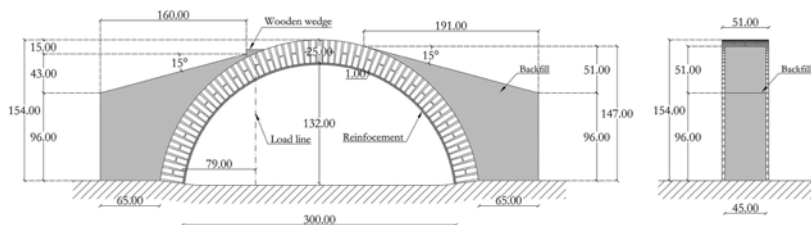


Figure 2. Front view and side view of the semicircular arches, here represented also with the reinforcement; measure are in cm.

3 DESCRIPTION OF THE FEM MODELS

3.1 Modelling

The numerical study of reinforced and unreinforced arch specimen was carried out through the use of the MidasFEA software. Two-dimensional elements were used for the masonry and the backfill, since the failure mechanism is symmetrical with respect to the longitudinal axis x , and one-dimensional “truss” type elements were used for the intrados reinforcement. The restraints used are interlocking, with the exception of the vertical direction y , for which infinitely rigid springs reacting only to compression were used. The interaction between the arch and backfill was taken into account by using a “discrete cracking” interface, while a special interface between the arch and the reinforcement was not used. This either because the spike anchors severely limit the sliding and also because the maximum tension attributed at the fabric is equal to the debonding tension, which implicitly allows for the detachment of the net.

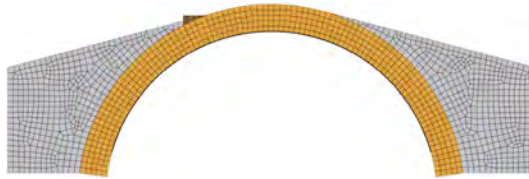


Figure 3. Model for the semicircular arches, here represented also with the reinforcement (blackline at the intrados).

3.2 Materials

Masonry is a tensile low-reactive material with mechanical behavior that can be represented by a stress-strain constitutive bond with a non-linear law. Since masonry consists of blocks and joints, it is generally characterized by anisotropy. However, there are numerous mathematical models in the literature that are able to approximate the real behavior of masonry by modelling a continuous homogeneous and isotropic material. One of the most used and adopted models for the modelling of masonry is the “Total Strain Crack Model”, it allows to treat the elements that discretize the masonry in an isotropic way until a stress-strain point is reached, which leads to the formation of a crack, beyond this point the behavior becomes anisotropic.

This model, in addition to the definition of the classical mechanical parameters (elastic modulus, Poisson’s coefficient, density, etc.) is uniquely defined by assigning the following parameters: compressive and tensile stress-strain law, compressive strength f_c , tensile strength f_t , tensile fracture energy G_t , compressive fracture energy G_c and type of crack modelling. In particular, the constitutive law for masonry and backfill in tension adopted is a non-linear relation with exponential softening (Figure 5) while in compression a parabolic law was used (Figure 4).

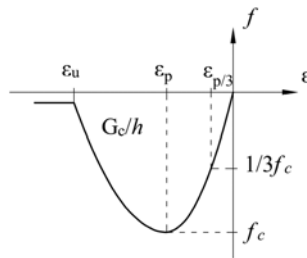


Figure 4. Compression law for masonry and for the backfill.

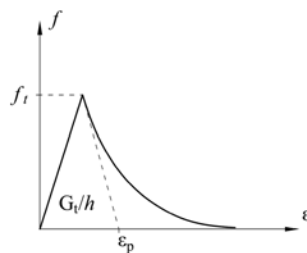


Figure 5. Tensile law for masonry and for the backfill.

The mechanical and deformation parameters used for masonry and the backfill are summarized in Table 1:

Table 1. Parameters used for the finite element modelling of masonry and backfill.

Parameter	Masonry	Backfill
Tensile strength f_t [MPa]	0.08	0.173
Compressive strength f_c [MPa]	3.45	1.725
Tensile fracture energy G_t [N/mm]	0.004	0.005
Compressive fracture energy G_c [N/mm]	1	1
Average FEM element size h [mm]	50	50
Elastic modulus E_m [MPa]	1500	750
Poisson's coefficient ν	0.25	0.2
Volume weight W [kN/m ³]	18	17

These values were determined from the Italian code “Norme Tecniche per le Costruzioni” considering a confidence level LC2 and the material safety coefficient $\gamma_m = 1$, as the analyses were non-linear. The tensile fracture energy was determined using the empirical formulations (1) and (2) (Ghiassi & Milani, 2019), in order to define the range of possible values:

$$G_{t1} = 0.025(f_c/10)^{0.7} \quad (1)$$

$$G_{t2} = 0.029f_t \quad (2)$$

Finally, the compression fracture energy was set at 1 N/mm².

The parameters used for the discrete cracking interface are: normal stiffness $k_n = 50\text{N}/\text{mm}^3$; tangential stiffness $k_t = 20\text{N}/\text{mm}^3$ and tensile strength $f_{ct} = 0.04\text{N}/\text{mm}^2$. The value of the normal stiffness (following a parametric analysis) was set at $50\text{N}/\text{mm}^3$, a value for which successive increases in stiffness do not lead to significant changes in the solution, while the value of f_{ct} was defined again from a sensitivity analysis in order to capture the detachment mechanism between the backfill and the arch as shown by the experimental tests. The tangential stiffness value was determined by imposing $k_t/k_n = 0.4$ (Gaetani, et al., 2017).

Finally, for the strengthened arch specimen, a brittle-type tensile law with residual strength was imposed on the fabric (Figure 6), while an elasto-plastic relation was adopted in compression.

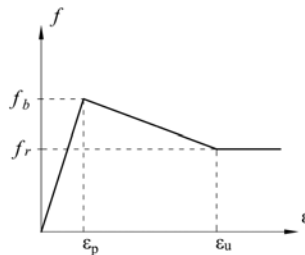


Figure 6. Tensile law for the fabric.

The fabric area was determined as the product of the width of the arch by the equivalent thickness, determined with the Equation (3), following the indications of the Italian code “Linea Guida per la identificazione, la qualificazione ed il controllo di accettazione di compiti fibrorinforzati a matrice inorganica (FRCM) da utilizzarsi per il consolidamento strutturale di costruzioni esistenti”:

$$t_{eq} = 1000 \cdot \frac{G}{g} = 0.0648mm^2 \quad (3)$$

Where $G = 0.11kg/m^2$ weight of the wires only in the resistant direction, $g = 1700kg/m^3$ density of the carbon fiber.

The mechanical parameters of the fabric are summarized in the Table 2:

Table 2. Parameters used for the finite element modelling of the fabric.

Parameter	
Area A [mm ²]	33.04
Poisson's coefficient ν	0.2
Volume weight W [kN/m ³]	24
Compressive strength f_c [MPa]	3.45
Debonding tensile strength f_b [MPa].	470

The debonding tensile strength value is the average debonding value obtained from appropriate shear-lap tests with a radius of curvature equal to the arches here presented. These experiments produced an average tensile strengths of 470 MPa for the semicircular arch specimen.

3.3 Applied loads

In addition to the elements' own weight, a yielding constraint is applied to reproduce the load in displacement control relative to the experimental test. Loads are applied in two phases:

- Phase 1: gravitational loads only;
- Phase 2: displacement-controlled load with a maximum value of 10 mm, applied using 100 incremental steps.

4 RESULTS COMPARISON

Comparisons between numerical and experimental test results in terms of load-displacement are given below.

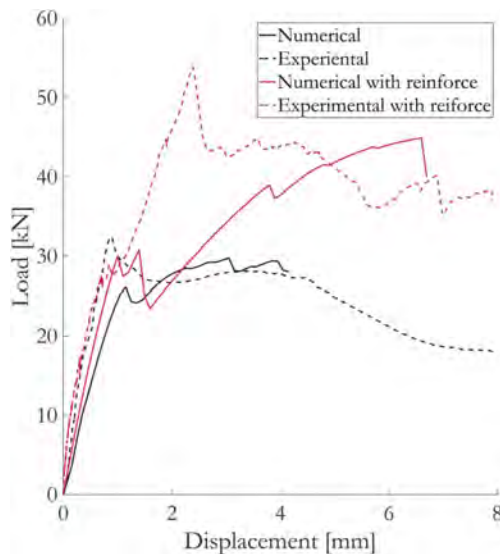


Figure 7. Comparison graph between experimental and numerical test results.

As regards the failure modes, a representation of the real failure mode with that obtained numerically for the unreinforced arch is shown in Figure 8 and for the reinforced one in Figure 9.

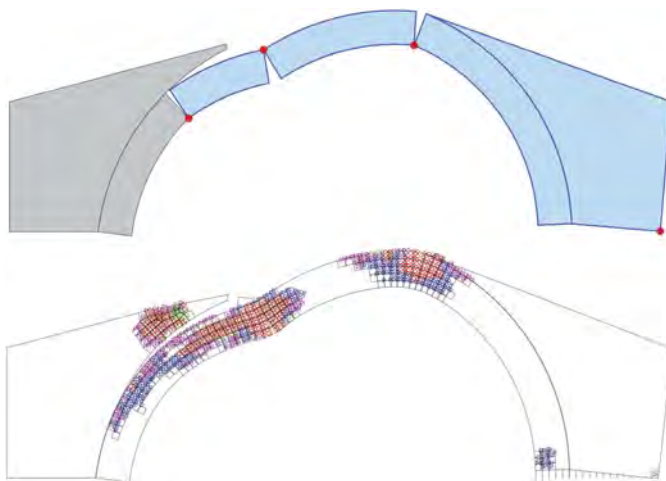


Figure 8. Comparison of the actual rupture pattern, upper image, with the numerically determined pattern, lower image. Unreinforced case.

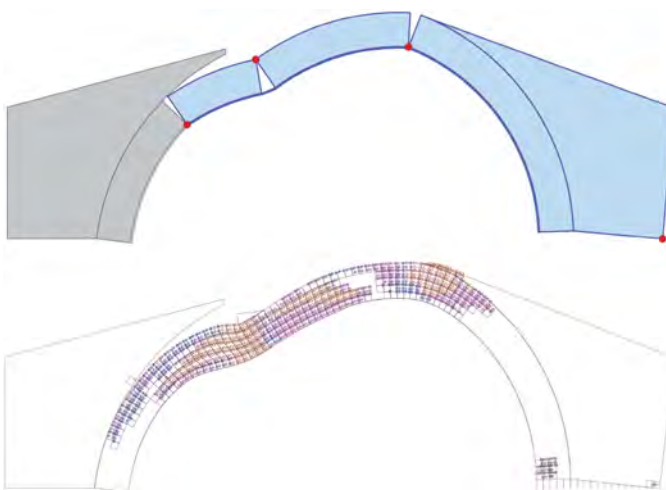


Figure 9. Comparison of the actual rupture pattern, upper image, with the numerically determined pattern, lower image. Reinforced case.

5 CONCLUSIONS

From the analysis introduced above, it can be seen that, despite the approximation derived from the continuous modelling of the masonry, it is possible to obtain good results in terms of both load-displacement and failure modes. Indeed, for the semicircular arch, the results show a good correspondence in the elastic phase between the numerical case and the experimental one. In particular, the numerical method shows a slightly lower elastic peak load and stiffness, which is positive as it provides a margin of safety. In the post-peak, some more marked differences can be seen, but only for the cases with reinforcement.

As far as failure modes are concerned, the numerical models show a good correspondence with the hinges formed in the experimental specimens. In particular, the numerical models cannot show a perfect hinge, due to the continuous modelling approximations, however, the higher damage zone of the finite elements (red region) for unreinforced arches approximates the experimental evidence correctly.

REFERENCES

- Chisari, C., Cacace, D. & De Matteis, G., 2021. Parametric Investigation on the Effectiveness of FRM-Retrofitting in Masonry Buttressed Arches. *Buildings*, Volume 11 (9), 406.
- Consiglio Superiore dei Lavori Pubblici, December 2018. *Linea Guida per la identificazione, la qualificazione ed il controllo di accettazione di compositi fibrorinforzati a matrice inorganica (FRCM) da utilizzarsi per il consolidamento strutturale di costruzioni esistenti*.
- Gaetani, A., Lourenco, P., Monti, G. & Moroni, M., 2017. Shaking table tests and numerical analyses on a scaled dry-joint arch undergoing windowed sine pulses. *Bulletin of Earthquake Engineering*, November.p. 15: 493961.
- Ghiassi, B. & Milani, G., 2019. *Numerical Modeling of Masonry and Historical Historical. From Theory to Application*. Duxford: Woodhead Publishing Series in Civil and Structural Engineering.
- Gioffrè, M. et al., 2023. Effect of hemp bio composite strengthening on masonry barrel vaults damage. *Construction and Building Materials*, 27 February .367(130100).
- Gioffrè, M. et al., 2021. A novel hemp-fiber bio-composite material for strengthening of arched structures: Experimental investigation. *Construction and Building Materials*, 15 November 308(124969).
- Ministero delle infrastrutture e dei trasporti, 17 January 2018. *Norme tecniche per le costruzioni*. Roma. Gazzetta ufficiale.
- Zizi, M., Bencivenga, P. & De Matteis, G., 2023. Handling policies for Italian existing bridges with a territorial approach: the case study of Caserta, Italy. *Structures*, February, Volume 48, pp. 1306–1321.
- Zizi, M., Chisari, C. & De Matteis, G., 2023. Effect of the backfill material in the seismic response of multi-span masonry arch bridges under seismic loading. *Procedia Structural Integrity*, Volume 44, pp. 673–680.

3D collapse mechanisms of masonry bridges subjected to horizontal actions

L. Niero, P. Zampieri & C. Pellegrino

Department of Civil, Environmental and Architectural Engineering, University of Padova, Padova, Italy

ABSTRACT: A large number of existing masonry arch bridges are still in use in the Italian roadway and railway networks. Most of them were built more than one hundred years ago, designed considering only gravitational loads without any seismic analysis. To keep these works in service, it is necessary to have tools that can describe and predict the structural behavior of the bridge when subjected to extreme actions. For this reason, a three-dimensional rigid-block analysis for masonry arch bridges has been developed. In the model, the main structural masonry elements (vault, pier, abutments, spandrel wall) are discretized as an assemblage of rigid blocks, which interact via no-tension contact surface with Coulomb friction. This approach allows reproducing with good accuracy the tri-dimensional collapses mechanisms of some real masonry arch bridges recently collapsed due to extreme events.

1 INTRODUCTION

Masonry is one of the most widely used materials in ordinary structures and monumental buildings in Italy and, for this reason, there are several masonry arch bridges in the Italian road and rail network which are still in service today. Most of them were built more than a hundred years ago and were designed considering only gravity loads, without taking into account any seismic or extreme actions. For this reason, several existing bridges are characterized by structural and functional deficiencies: first, they were designed for less severe service conditions than those required today and, in addition, besides suffering progressive damage and natural deterioration, they can also be subjected to extreme actions such as earthquake, flooding and foundation settlements. In addition, flood-induced scour problems can occur on masonry piers because of the erosive effect and removal of bank material from bridge foundations located within the riverbed (Ragni, et al., 2019; Scozzese, et al., 2019).

To keep existing masonry arch bridges in service, it is necessary to have tools that can describe and predict their behavior. Currently, in the literature there are several structural models that enable the analysis of these structures up to the collapse condition (Zizi, et al., 2022; Galassi, 2023; Galassi & Zampieri, 2023) but, one of the most popular is rigid blocks analysis, which quickly provides an estimation of the carrying capacity of the structure and the associated failure mechanism. Koocharian (1952) and Heyman (1969) were among the first to apply plastic limit analysis theorems to masonry structures, assuming constituent blocks have infinite compressive strength, joints have zero tensile strength and sliding failures are not allowed. In the 1970s Livesley (1978) developed a formal linear programming (LP) procedure to compute the load factor of structures and plot their collapse mechanisms, considering also sliding failures. A similar approach was used by Melbourne & Gilbert (1995) to successfully model two-dimensional masonry arch bridges, assuming an associative friction model governed by Mohr-Coulomb law. Subsequently, to achieve more realistic behavior of structures, several authors such as Gilbert (2006), Ferris & Tin-Loi (2001), Orduña & Lourenço (2003) extended the formulation of the problem considering also a finite compressive strength of the material and a non-associated flow law. Some authors

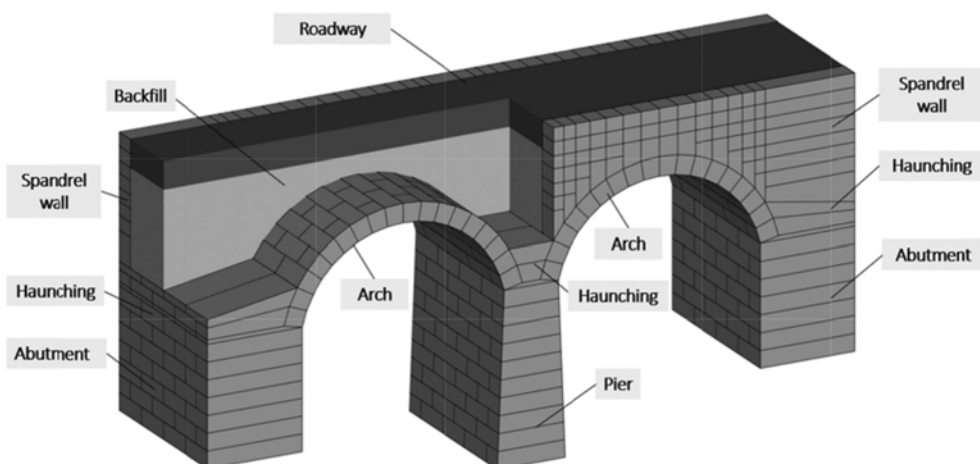


Figure 1. Three-dimensional rigid block model of a masonry arch bridge.

like Orduña & Lourenço (2005) and more recently Portioli et al. (2014) and Cascini et al. (2020) have proposed a three-dimensional formulation of the problem by applying it to out-of-plane loaded walls and arches.

This paper aims to develop a three-dimensional rigid block analysis for masonry arch bridges, capable of capturing the out-of-plane behavior of the structures subjected to extreme actions. The main structural masonry elements, such as vaults, pier, abutments and spandrel wall are discretized as an assembly of rigid blocks, interacting through contact surfaces with no-tensile strength and Mohr-Coulomb friction. The developed code, based on rigid-block analysis, defines the collapse multiplier and the associated failure mechanism without taking load history into account, using a linear optimization procedure and an associated flow law.

2 THE RIGID BLOCK MODEL

To analyze the three-dimensional behavior of the masonry arch bridge in Figure 1, its structural elements (arches, central pier, side abutments and spandrel wall) are modeled using a set of rigid blocks to study the interaction between the different elements. Instead, the backfill and road pavement are considered as external forces acting on the structural masonry elements, proportional to their load area.

Rigid blocks typically have larger geometric dimensions than physical blocks to also account the mortar joint, which is not modeled explicitly. This approach is particularly appropriate for analyzing existing masonry structures characterized by poor quality mortar (Baggio & Trovalusci, 1993). In fact, some experimental tests (Trovalusci, 1992) have validated the use of discrete, rather than homogeneous and isotropic, models and have shown how the global behavior of the structure is strongly influenced by the size, arrangement and orientation of the different elements rather than by their mechanical properties. For this reason, in the rigid-block analysis the collapse multiplier is obtained from local equilibrium conditions, assuming the hypothesis of: i) absence of tensile stresses at the interface and ii) the impossibility of crushing failure. In fact, masonry bridges are old structures subjected to cyclic loading, fatigue phenomena and freeze-thaw cycles for a long time so it is realistic to assume zero tensile strength in mortar joints. Finally, the attritive resistance at the interface is considered using the Mohr-Coulomb law and an associated flow law. The presented model is therefore capable of predicting the three-dimensional behavior of a masonry arch bridge subject to both vertical loads and hazard events such as earthquakes. In this paper, the constraint and loading conditions shown in Figure 2 are applied to the discrete model of a masonry arch bridge.

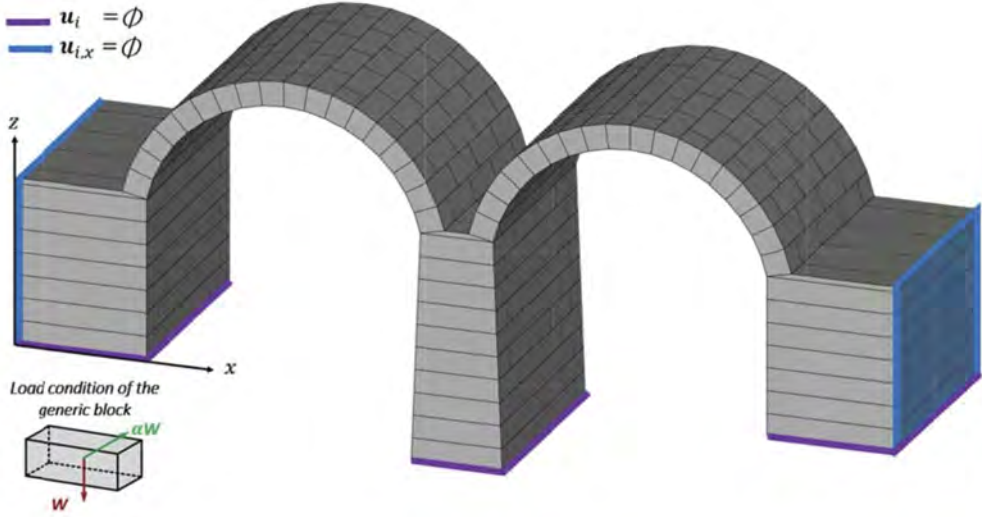


Figure 2. Loading and constraint condition of the masonry arch bridge.

3 LINEAR PROGRAMMING FOR RIGID-BLOCK ANALYSIS

The numerical model of a masonry arch bridge is composed of n rigid blocks and m contact points, located at the vertexes of interfaces (Figure 3). External loads and the displacement rates applied to the centroid of each 3D rigid block are respectively collected in vector $\mathbf{f} \in \mathbb{R}^{6n}$ and $\mathbf{u} \in \mathbb{R}^{6n}$:

$$\mathbf{f} = [f_{x1}, f_{y1}, f_{z1}, m_{x1}, m_{y1}, m_{z1}, \dots, f_{xn}, f_{yn}, f_{zn}, m_{xn}, m_{yn}, m_{zn}]^T \quad (1)$$

$$\mathbf{u} = [u_{x1}, u_{y1}, u_{z1}, u_{\theta x1}, u_{\theta y1}, u_{\theta z1}, \dots, u_{xn}, u_{yn}, u_{zn}, u_{\theta xn}, u_{\theta yn}, u_{\theta zn}]^T \quad (2)$$

The loads in \mathbf{f} can be expressed as the sum of the known dead loads \mathbf{f}_D and live loads \mathbf{f}_L , multiplied by an unknown scalar factor α :

$$\mathbf{f} = \mathbf{f}_D + \alpha \mathbf{f}_L \quad (3)$$

The three internal resultant forces (i.e., axial force n_k , shear force t_{1k} and t_{2k}) acting at each k -th point of contact can be arranged in vector $\mathbf{x} \in \mathbb{R}^{3m}$:

$$\mathbf{x} = [n_1, t_{11}, t_{21}, \dots, n_k, t_{1k}, t_{2k}, \dots, n_m, t_{1m}, t_{2m}]^T \quad (4)$$

The kinematic variables $\mathbf{q} \in \mathbb{R}^{3m}$, that correspond to the static variables \mathbf{x} in a virtual work sense, are the relative displacement rates at the contact points (i.e., normal displacement rates ε_{1k} , tangential displacement rates γ_{1k} and γ_{2k}) defined as:

$$\mathbf{q} = [\varepsilon_1, \gamma_{11}, \gamma_{21}, \dots, \varepsilon_k, \gamma_{1k}, \gamma_{2k}, \dots, \varepsilon_m, \gamma_{1m}, \gamma_{2m}]^T \quad (5)$$

The compact equilibrium equation can be written as follows

$$\mathbf{B}\mathbf{x} = \mathbf{f}_D + \alpha \mathbf{f}_L \quad (6)$$

where $B \in \mathbb{R}^{6n \times 3m}$ is the equilibrium matrix.

The following constraint conditions are then specified for each contact point:

$$\begin{aligned} y_{rk} &= n_k \geq 0 \\ y_{sk} &= -\sqrt{t_{1k}^2 + t_{2k}^2} + \mu n_k \geq 0 \end{aligned} \quad (7)$$

where μ is the friction coefficient and the compressive force n_k is positive according to the convention shown in Figure 3. Equation (7) represent the failure modes by opening and sliding but the interaction of contact points considers other failure modes that may occur such as rocking and twisting.

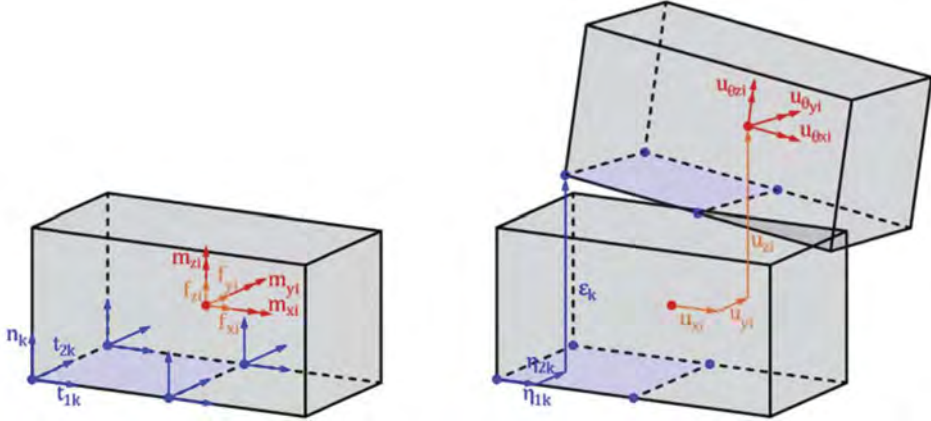


Figure 3. (a) Static and (b) kinematic variables at the block centroid i and contact point k (rearranged from Portioli et al., 2014).

In order to use linear programming techniques, the Lorentz cone, which describes the sliding failure condition, is linearized using 8 hyperplanes. The constraint conditions can be written as follows:

$$\begin{aligned} y_{rk} &= n_k \geq 0 \\ y_{s1,k} &= -t_{1k} \cos \frac{k\pi}{4} - t_{2k} \sin \frac{k\pi}{4} + \mu n_k \geq 0 \quad k = 1, \dots, 8 \end{aligned} \quad (8)$$

In general, constraint conditions are defined as:

$$\mathbf{y} = \mathbf{N}^T \mathbf{x} \leq \mathbf{0} \quad (9)$$

where \mathbf{y} is the vector of failure conditions and \mathbf{N}^T is the matrix that collects the constraints conditions.

Both the static and kinematic approaches of limit analysis (Ferris & Tin-Loi, 2001; Portioli, et al., 2014; Zampieri, 2020; Hua & Milani, 2023) are used to identify the collapse condition of the masonry arch bridge, then solving the problem through linear programming techniques. In particular, the LP related to the static theorem is given by

$$\begin{aligned} &\text{maximize} && \alpha \\ &\text{subject to} && \mathbf{B}\mathbf{x} - \alpha \mathbf{f}_L = \mathbf{f}_D \\ &&& \mathbf{N}^T \mathbf{x} \leq \mathbf{0} \end{aligned} \quad (10)$$

whereas the LP arising from the kinematic theorem is

$$\begin{aligned}
& \text{minimize} && -f_D^T u \\
& \text{subject to} && f_L^T u = 1 \\
& && -B^T u + N z = 0 \\
& && z \geq 0
\end{aligned} \tag{11}$$

where z is the vector of resultant strain rates (analogous to plastic multipliers in classical plasticity).

4 RESULTS AND DISCUSSION

In this section, the results of a rigid block analysis performed on a masonry arch bridge, expressed in terms of load multiplier and associated mechanism, are presented.

The structure under consideration is composed by two arches with a thickness of 0.55 m, a span $L = 6.0$ m and rise $f = 2.4$ m. They are connected to a central pier of height 5.0 m and two side abutments of height 3.5 m. A coefficient of friction at the interface of 0.75 is assumed.

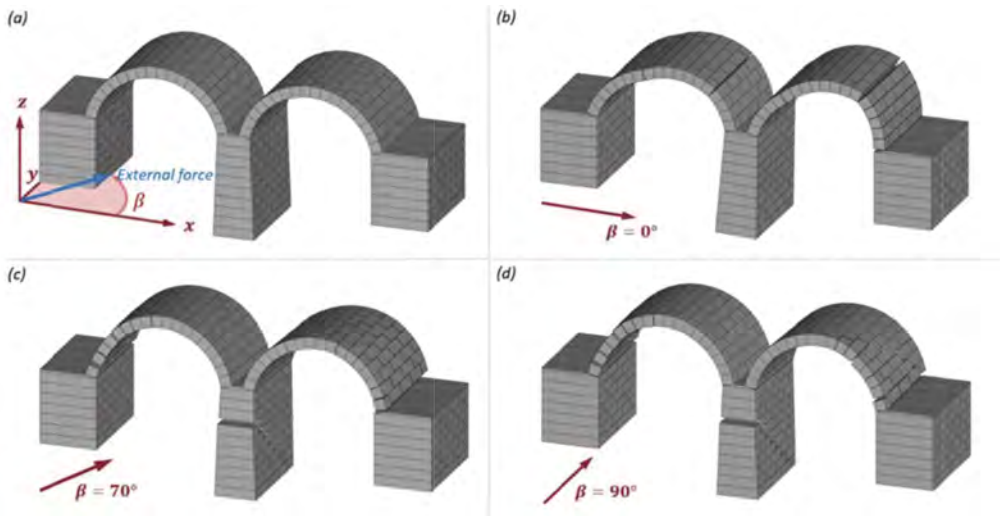


Figure 4. (a) Representation of the external horizontal force applied with variable angle β ; (b) Failure mode for $\beta = 0^\circ$ (c) Failure mode for $\beta = 70^\circ$ (d) Failure mode for $\beta = 90^\circ$.

In addition to considering the self-weights of each element, calculated proportionally to the geometry of the block assuming a unit weight of 22 kN/m^3 , variable horizontal loads are applied on each element, proportional to their weight force (Figure 4).

A parametric analysis is then performed, calculating the collapse multiplier and the associated failure mechanism when the angle of inclination $\beta \in [0; 90]$ of the horizontal force f_L is varied (Figure 4). For $\beta = 0^\circ$ the variable load acts in the longitudinal direction while for $\beta = 90^\circ$ the horizontal action is parallel to the transverse direction.

Analyzing Figure 5, an increment in collapse multipliers is observed as the angle β increases, representative of a greater resistance of the structure to transverse actions than to longitudinal ones.

The collapse mechanisms shown in Figure 4 highlight that, for values of $\beta \geq 60^\circ$, there are transverse failures affecting the central pier and the two masonry arches. In fact, the discretization employed is functional to the failure mechanisms: the pile is a slender element in the plane, subject to failure by rocking and sliding. In contrast, transversely it has a considerable size and a discretization with more elements is made in order to capture the classical mechanisms of rocking and sliding but also diagonal shear failure, evident in Figure 4(c,d).

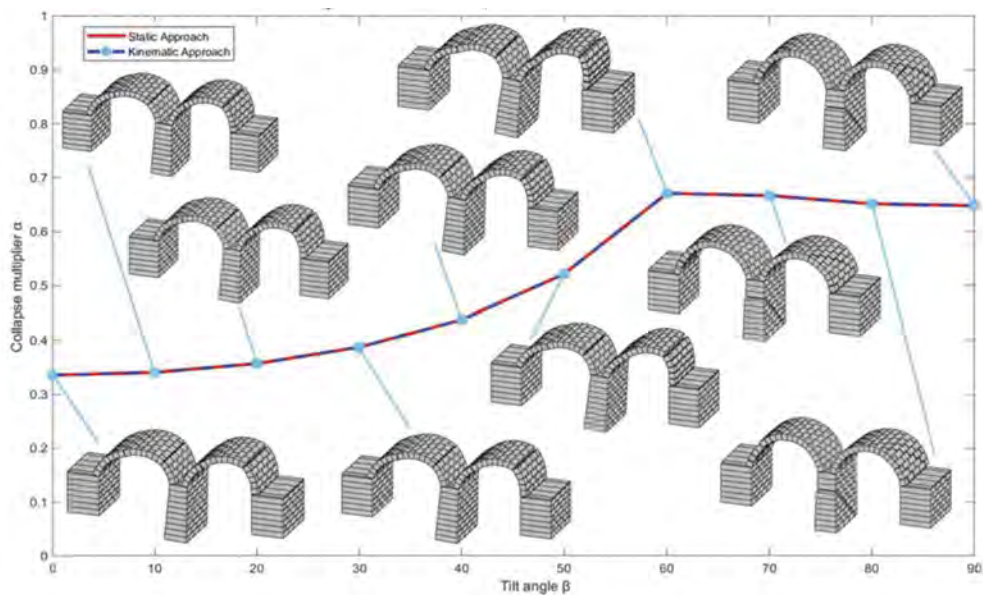


Figure 5. Collapse multiplier vs. tilt angle β of the external horizontal action.

Like most bridges in Italy, the arches are discretized with a single element on the thickness, allowing for rocking and sliding mechanisms. In contrast, multiple elements are used at depth to also capture diagonal cracking mechanisms and localized sliding.

5 CONCLUSIONS

In this paper, results on the collapse condition of masonry arch bridge subject to inclined horizontal inertial action have been presented.

To identify the collapse condition, expressed in terms of load multiplier and associated failure mechanism, rigid-block analysis has been performed, assuming the absence of tensile stresses at the interfaces and the impossibility of crushing failure. An attritive resistance at the interface has been considered, using the Mohr-Coulomb principle and an associated flow law.

A parametric analysis has been performed on the structure, varying the angle of application of the horizontal external actions, expressed as a function of the self-weight of each block. The results obtained showed that the use of a three-dimensional analysis of the structure is also capable of capturing transverse failure mechanisms, which occur on the structural elements of the masonry arch bridge for out-of-plane actions, in addition to longitudinal in-plane actions.

REFERENCES

- Baggio, C. & Trovalusci, P. 1993. *Discrete models for jointed block masonry walls*. Philadelphia, Pennsylvania, pp. 939–49, Vol. 2.
- Cascini, L., Gagliardo, R. & Portioli, F. 2020. LiABlock_3D: A Software tool for collapse mechanism analysis of historic masonry structures. *International Journal of Architectural Heritage*, 14(1): pp. 75–94.
- Ferris, M. & Tin-Loi, F. 2001. Limit analysis of frictional block assemblies as a mathematical program with complementarity constraints. *Mechanical sciences*, 43(1): pp. 209–224.
- Galassi, S. 2023. An alternative approach for limit analysis of masonry arches on moving supports in finite small displacements. *Engineering Failure Analysis*, 145.

- Galassi, S. & Zampieri, P. 2023. A new automatic procedure for nonlinear analysis of masonry arches subjected to large support movements. *Engineering Structures*, 276.
- Gilbert, M., Casapulla, C. & Ahmed, H. 2006. Limit analysis of masonry block structures with non-associative frictional joints using linear programming. *Computers & Structures*, 84(13-14): pp. 873–887.
- Heyman, J. 1969. The safety of masonry arches. *International Journal of Mechanical Sciences*, 11(4): pp. 363–385.
- Hua, Y. & Milani, G. 2023. Simple modeling of reinforced masonry arches for associated and non-associated heterogeneous limit analysis. *Computer and Structures*, 280.
- Kooharian, A. 1952. Limit analysis of voussoir (segmental) and concrete arches. *ACI Journal*, 49(12): pp. 317–28.
- Livesley, R. 1978. Limit analysis of structures formed from rigid blocks. *International Journal for Numerical Methods in Engineering*, 12(12): pp. 1853–1871.
- Melbourne, C. & Gilbert, M. 1995. The behaviour of multiring brickwork arch bridges. *The Structural Engineer*, 73(3): pp. 39–47.
- Orduña, A. & Lourenço, P. 2003. Cap Model for Limit Analysis and Strengthening of Masonry Structures. *Journal of Structural Engineering*, 129: pp. 1367–1375.
- Orduña, A. & Lourenço, P. 2005. Three-dimensional limit analysis of rigid blocks assemblages. Part II: Load-path following solution procedure and validation. *International Journal of Solids and Structures*, 45(18-19): pp. 5161–5180.
- Portioli, F., Casapulla, C., Gilbert, M. & Cascini, L. 2014. Limit analysis of 3D masonry block structures with non-associative frictional joints using cone programming. *Computers & Structures*, 143: pp. 108–121.
- Ragni, L., Scozzese, F., Gara, F. & Tubaldi, E. 2019. *Dynamic identification and collapse assessment of Rubbianello Bridge*. Guimarães.
- Scozzese, F., Ragni, L., Tubaldi, E. & Gara, F. 2019. Modal properties variation and collapse assessment of masonry arch bridges under scour action. *Engineering Structures*, 99.
- Trovalusci, P. 1992. *No-tension discrete model with friction for jointed block masonry walls using interface elements*. Pittsburgh, pp. 11.73–82, Vol. 2.
- Zampieri, P. 2020. Horizontal capacity of single-span masonry bridges with intrados FRCM strengthening. *Composite Structures*, 244.
- Zizi, M., Cacace, D., Rouhi, J., Lourenço, P. & De Matteis, G. 2022. Automatic procedures for the safety assessment of stand-alone masonry arches. *International Journal of Architectural Heritage*, 16 (9): pp. 1306–1324.

Near-collapse deformed configuration of masonry arch bridges

G. Stagnitto

University of Pavia, Pavia, Italy

P. Zampieri

University of Padova, Padova, Italy

ABSTRACT: The near collapse-deformed configuration of a structure can be evaluated directly through mathematical programming, without the classical nonlinear incremental analysis. In this work, with the assumption of no elastic returns of the material, the theoretical deformed shaped at collapse of masonry bridges is directly defined using a variational principle, in the simplifying assumption of perfect elastoplastic behavior. The proposed approach is an extension of the well-known paper of Heyman. In the Heyman work, the final configuration of the structure that respect the restrain conditions is due to two contributions: the contribution of the elastic deformations of the structure portions between plastic-hinges and the contribution of the rotations concentrated in the plastic-hinge sections. In this work, the final configuration of the masonry bridges is evaluated considering the elastoplastic deformation of the structure obtained by the integration of the curvature that tends to infinity in the plastic-hinges sections and the rotations concentrate in the plastic-hinge sections

1 THE ELASTIC-PLASTIC DEFLECTION OF BEAMS AT THE POINT OF COLLAPSE (THE PROCEDURE PROPOSED BY HEYMAN)

Heyman proposed a procedure to assess the deformed configuration (rotation and displacement functions) at the incipient collapse condition of fixed-ended beam of Figure 1a (Heyman 1961).

The simplification adopted by Heyman is the absence of elastic-plastic behavior: the maximum elastic moment M_e coincides with the plastic moment M_p .

When the limiting moment is reached, concentrated plastic rotation θ_i is formed in the section i (Figure 1b). The concentrated rotations θ_2 and θ_3 at the point of collapse are given by the conditions that the θ_1 rotation is zero because in 1 the last plastic hinge forms. The rotations θ_i have limited value and are not the rotations concentrated in the plastic hinges ϕ_i (with unlimited value and limited ratio) when the structure is reformed in a kinematic mechanism (Figure 1b).

Heyman uses the Principle of Virtual Work (PVW) for the determination of the beam deflection at the point of collapse. Considering Figure 1a, M is the bending moment distribution that is equal to the elastic curvature distribution if the beam flexural stiffness (EJ) is equal to 1; m is a most general bending moment distribution specified in terms of end moments m_1 e m_2 ; m^* is one moment distribution that is in equilibrium with the unit load P (Figure 1a).

Considering the moment distribution m , the unknown plastic rotation and the elastic curvature distribution ϕ_i , by the equation of the PVW:

$$\sum m \theta_i + \int m \frac{M}{EJ} ds = 0 \quad (1)$$

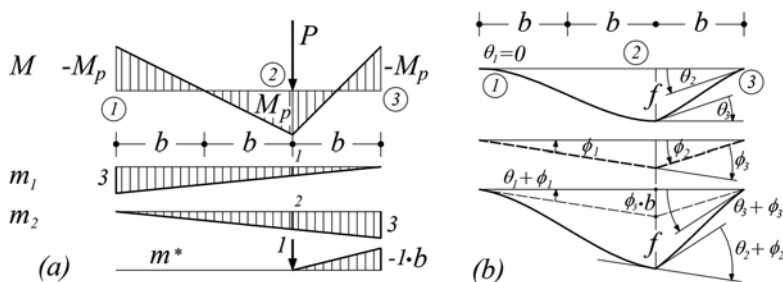


Figure 1. Elastic-plastic deflection and collapse kinematic.

The second term is equal to zero because the virtual work of the external forces considering an auto-equilibrated moment distribution m is zero.

Considering the independent distribution of moment m_1 and m_2 (Figure 1a) the plastic rotations different to zero are defined as follow:

$$\theta_2 = \frac{M_p \cdot b}{2EJ} \theta_3 = -\theta_2 = -\frac{M_p \cdot b}{2EJ} \quad (2)$$

The sign of rotations agrees with that of moment distribution: then the last plastic hinge is in the section 1. Considering the bending moment distribution m^* in equilibrium with the load $P=l$ (Figure 1a) and the rotations θ_2 and θ_3 then, by the equation of virtual work is possible to define the deflection f :

$$f = \sum m^* \theta_i + \int m^* \frac{M}{EJ} ds = \frac{2}{3} \frac{M_p b^2}{EJ} \quad (3)$$

2 THE ELASTIC-PLASTIC BEAMS DEFLECTION AT THE COLLAPSE POINT: THE PROPOSED PROCEDURE

The procedure proposed by Heyman is general and is applicable to beams and frames. In this paper an alternative simplified procedure is proposed. The procedure, valid for beams or and (open) frames, allows to evaluated the structure deflection at the collapse considering the plastic bending moment distribution without the application of the PVW for writing the compatibility equations. The procedure is still valid if an elastoplastic bending moment distribution is considered.

From the “moment area theorems” (Ghali et al 2003) in the fixed-ends beam, the area of the curvature distribution and the static moment respect to the beam ends are zero. Fixed the origin of referring system in the left end and considering a generic beam section: the curvature integral from the right end to the generic section is the beam rotation in the considered section and the static moment of the same curvature area respect to the vertical axis is the beam deflection. The theorems are applicable also in the case of concentrate rotations (R^+ , R^-).

The deflection of section 1 is equal to:

$$u_1 = \left(M_p \frac{b}{2} \right) \cdot \left(\frac{4}{3} b \right) - \left(M_p \frac{b}{4} \right) \cdot \left(\frac{2}{3} b \right) = \frac{M_p \cdot b^2}{2} = \left(M_p \frac{b}{2} \right) \cdot b \quad (4)$$

In the hypothesis that the last plastic hinge is in 1: the concentrate rotations in sections 2 and 3 must equal with opposite sing: $|R^+| = |R^-| = M_p \frac{b}{2}$.

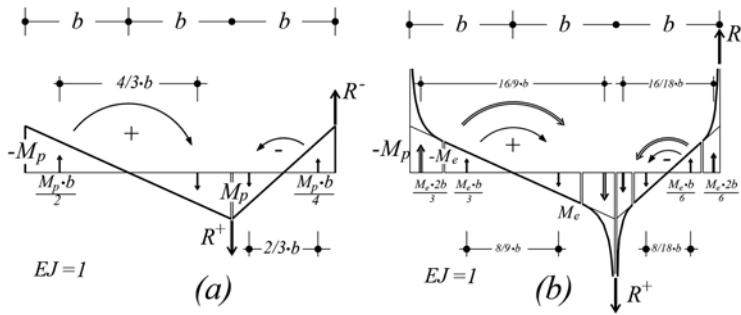


Figure 2. Curvature distribution: (a) elastic and plastic concentrated, (b) elastic, elastoplastic and plastic concentrated.

The deflection of section 2, considering also the contribution of the concentrate rotation, is equal to:

$$u_2 = -\left(M_p \frac{b}{4}\right) \cdot \left(\frac{2}{3}b\right) - \left(M_p \frac{b}{2}\right) \cdot b = -\frac{2}{3}M_p b^2 \quad (5)$$

3 THE ELASTOPLASTIC BEAMS DEFLECTION AT THE COLLAPSE POINT: THE PROPOSED PROCEDURE

Considering a beam portion Δ between section a and section b . Suppose that in section a the bending moment is equal to M_e and in section b is equal to M_p .

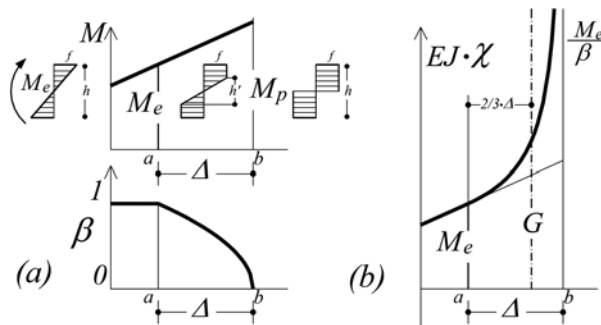


Figure 3. Bending moment a) and curvature b) distribution.

The curvature is equal to M/EJ for bending moment values lower and equal to M_e , otherwise:

$$\chi = \frac{1}{EJ} \cdot \frac{M_e}{\beta}, \quad \beta = \frac{h'}{h} = \sqrt{3 - 2 \frac{M(x)}{M_e}} \quad (6)$$

The curvature integral ($EJ = 1$), in the interval $(a-b)$, is evaluated in the hypothesis of linear distribution of the bending moment as follows:

$$\begin{aligned}
y = \frac{x}{\Delta}, M_p = \frac{3}{2} \cdot M_e \rightarrow M(y) = M_e + y(M_p - M_e) \rightarrow \frac{M_e}{\beta} &= M_e \cdot \left[3 - 2\left(1 + \frac{y}{2}\right) \right]^{-\frac{1}{2}} \\
&= M_e(1 - y)^{-\frac{1}{2}} \\
\theta_{ab} = \int_0^{\Delta} \frac{M_e}{\beta} dx = \Delta M_e \int_0^1 \frac{1}{\sqrt{1-y}} dy = \Delta M_e \left[-2\sqrt{1-y} \right]_0^1 &= \Delta M_e \cdot 2
\end{aligned} \tag{7}$$

The interesting result is that the relative rotation θ_{ab} between section a and section b is 2 time the maximum elastic moment time Δ (if $EJ=1$)

Then, the center of the curvature in the considered beam segment (Δ) is equal to:

$$\begin{aligned}
\eta\Delta &= \frac{\int_0^{\Delta} x \frac{M_e}{\beta} dx}{\int_0^{\Delta} \frac{M_e}{\beta} dx} = \frac{M_e\Delta^2 \int_0^1 y \frac{1}{\beta} dy}{M_e\Delta \int_0^1 \frac{1}{\beta} dy} = \frac{M_e\Delta^2 \int_0^1 y \frac{1}{\sqrt{1-y}} dy}{2\Delta M_e} = \frac{M_e\Delta^2 \left[-\frac{2}{3}(2+y)\sqrt{1-y} \right]_0^1}{2\Delta M_e} \\
&= \frac{M_e\Delta^2 \frac{4}{3}}{2\Delta M_e} = \frac{2}{3}\Delta
\end{aligned} \tag{8}$$

The second interesting result is that the center of the curvature diagram between section a and section b is $2/3 \Delta$.

For the symmetry of the positive and negative areas, the elastoplastic curvature diagram (Figure 2b) has global area equal to zero: then the rotation of the section 1 is equal to zero. Therefore, the deflection in section 1 is equal to:

$$u_1 = \frac{10}{9} M_e \cdot b^2 = \frac{20}{27} M_p \cdot b^2 \tag{9}$$

Because the arm of the concentrate rotations is equal to b , and because $M_e = \frac{2}{3} M_p$, the rotation $|R^+| = |R^-| = R$ are defined as follows:

$$R = \frac{u_1}{b} = \frac{10}{9} M_e \cdot b = \frac{20}{27} M_p \cdot b \tag{10}$$

Therefore, the deflection in section 2 is equal to:

$$u_2 = -\left(M_e \frac{1}{6} b\right) \frac{8}{18} b - \left(M_e \frac{2}{6} b\right) \frac{16}{18} b + R \cdot b = -\frac{40}{27} M_e \cdot b^2 = -\frac{80}{81} M_p \cdot b^2 \tag{11}$$

These results were compared with a numerical procedure: the Figure 4a shows the elastoplastic deformation of the fixed-ends beam. The Figure 4b, instead, shows the elastoplastic deformation of the beam and the additional term due to the concentrate rotations (R^+ , R^-). It is important to observe: The beam deformation (Figure 4b) respect the boundary condition in the left end, in the section 2 and in section 3 there is a beam axis discontinuity and in section 1 the beam deformed axis tangent is zero.

Assuming $M_e = 12 \rightarrow M_p = 18 : u_1 = 13.3333, R = 13.3333 u_2 = -17.7777$

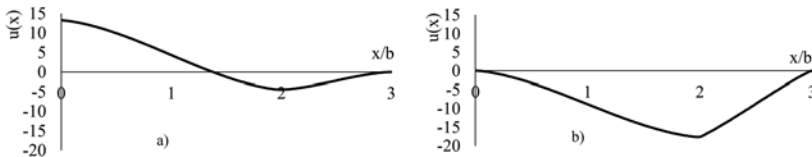


Figure 4. Beam deflection at the collapse point, the elastoplastic contribution (a) and the elastoplastic contribution plus the plastic concentrated rotations (b).

4 THE ELASTOPLASTIC ROTATIONS AROUND THE NEUTRAL AXIS METHOD

A method that extends the validity of the *moment area theorems and related corollaries* (Ghali et al 2003) to the elastoplastic no-tension arched structures is presented here. The idea of the method is to consider the relative rotations applied to the neutral axis (instead of the beam axis) to automatically take into account the axial force contribution (Stagnitto 2022).

Figure 5 shows the collapse thrust line of the masonry arch railway bridge for the critical position of the moving load. The elastoplastic analysis, conducted using a variational procedure (Stagnitto et al 2022), considering the collapse load multiplier, finds the same solution of the limit analysis (Zampieri 2020, Zampieri et al 2019, Stagnitto et al 2019).

The relative rotation $\Delta\theta_k$, concentrated in the arch interface k and obtained by integrating the curvatures of each arch block considered, is represented as a vector applied on the neutral axis position of each section (Figure 5). Moreover, the plastic hinges are located in sections 1, 11, 19, 27.

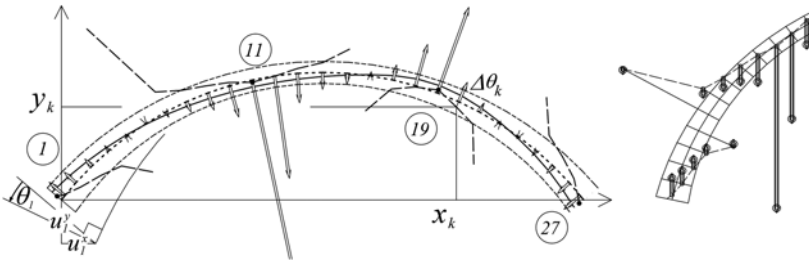


Figure 5. Arch thrust line at the point of collapse, neutral axis diagram, relative rotations vectors.

For example, the calculation of the rotation and the displacement components of point 1 on the axis of the section 1, if (x_k, y_k) are the coordinates of the intersection between the neutral axis and the trace of section k with respect to a reference system with origin in point 1, is given by:

$$\theta_1 = \sum_{k=1}^n \Delta\theta_k \quad u_x^1 = \sum_{k=1}^n y_k \cdot \Delta\theta_k \quad u_y^1 = \sum_{k=1}^n x_k \cdot \Delta\theta_k \quad (12)$$

5 THE CURVATURE INTEGRAL OF ELASTOPLASTIC NO-TENSION STRUCTURES

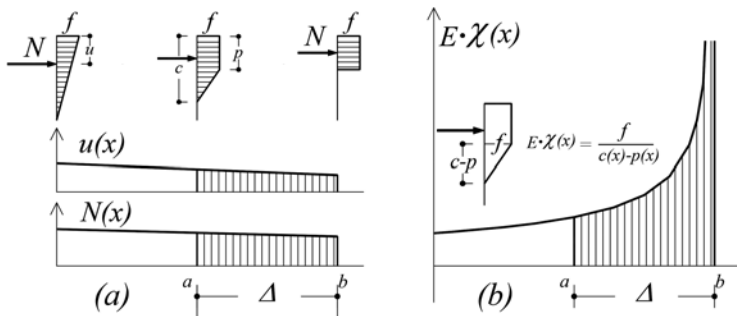


Figure 6. The curvature integral of elastoplastic no-tension structures.

If Δ is the integration interval of the elastic-plastic curvatures $\chi(x)$, the relative rotation between sections a and b (unit width beam) is equal to:

$$E \cdot \Delta \vartheta = \int_0^\Delta \chi(x) dx \quad (\text{where } E = 1) \quad (13)$$

$$\chi(x) = \frac{f}{c(x)-p(x)} = \frac{f^2/2\sqrt{3}}{\sqrt{2 \cdot f \cdot N(x) \cdot u(x) - 3 \cdot N^2(x)}}$$

c is the section compressed area and p is the plasticized section zone. If we assume a linear trend of the functions $N(x)$ and $u(x)$ between section a and b , we obtain (Abramowitz and Stegun 1972):

$$y = \frac{x}{\Delta} \rightarrow \int \chi(x) dx = \Delta \int \chi(y) dy = \Delta \int \frac{f^2/2\sqrt{3}}{\sqrt{2fNu-N^2}} = \Delta \frac{f^2}{2\sqrt{3}} \int \frac{1}{\sqrt{Ay^2+By+C}} \quad (14)$$

$$\int \frac{1}{\sqrt{Ay^2+By+C}} = \frac{1}{\sqrt{A}} \ln \left| 2\sqrt{A} \cdot \sqrt{Ay^2+By+C} + 2Ay+B \right|$$

Since at b the curvature is infinite, $\chi(y)$ diverges for $y = 1$; therefore, the denominator of the integrand function is zero for $y = 1$ and therefore $\chi(y)$ can be expressed in the form: $\chi(y) = F(y) \cdot \frac{1}{\sqrt{1-y}}$.

Inverting the transformation function $t = \sqrt{1-y}$ we obtain: $y = 1 - t^2 \rightarrow dy = -2t \cdot dt$

Changing the sign of the integrand (and consequently inverting the extremes of integration) we obtain a different integral equation:

$$\Delta \cdot \int_0^1 \chi(y) dy = \Delta \cdot \int_{\sqrt{1-1}}^{\sqrt{1-0}} \chi(1-t^2) \cdot 2t \cdot dt \quad (15)$$

The integral obtained, free of singular points, is calculated numerically using Gauss's formulae.

6 LINEAR SYSTEM OF EQUATIONS IN UNKNOWN PLASTIC ROTATIONS

The direct method proposed to derive plastic rotations in elastoplastic beams can be extended to masonry arches.

If we suppose that the hinge in 1 is the last: $R_1 = 0$.

Let us denote by (x_2, y_2) , (x_3, y_3) , (x_4, y_4) , the coordinates of the first three plastic hinges with respect to a reference system in point 1.

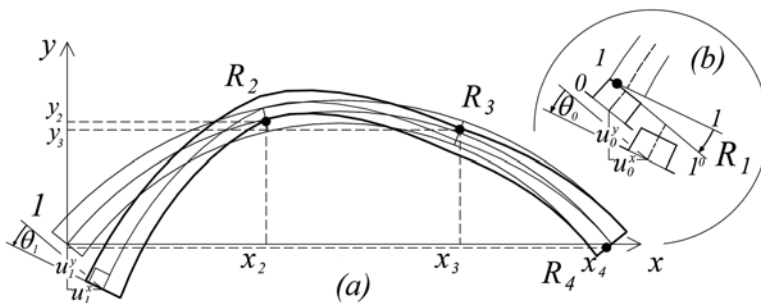


Figure 7. The elastoplastic deflection of the no-tension arch.

Figure 7 shows the elastoplastic deformation, i.e. the deformation produced by relative rotations obtained by integrating the elastoplastic curvatures corresponding to the solution of the limit analysis, including curvatures tending to infinity.

The relative rotations were applied at the neutral axis points of the limit analysis solution. At point 1 (center of section 1) we have the two displacement components u_1^x , u_1^y e and the rotation θ_1 .

The three concentrated plastic rotations R_2, R_3, R_4 , applied consecutively from the fixed right-end, must return point 1 to its original position, also cancelling the rotation θ_1 .

The solving system is therefore as follows:

$$\begin{aligned} R_2 + R_3 + R_4 &= -\theta_1 \\ R_2 \cdot x_2 + R_3 \cdot x_3 + R_4 \cdot x_4 &= -u_1^y \\ R_2 \cdot y_2 + R_3 \cdot y_3 + R_4 \cdot y_4 &= -u_1^x \end{aligned} \tag{16}$$

A linear system of three equations in three unknowns was obtained; the coefficient matrix is defined by the coordinates of the first three plastic hinges:

$$\begin{bmatrix} 1 & 1 & 1 \\ x_2 & x_3 & x_4 \\ y_2 & y_3 & y_4 \end{bmatrix} \cdot \begin{bmatrix} R_2 \\ R_3 \\ R_4 \end{bmatrix} = \begin{bmatrix} -\theta_1 \\ -u_1^y \\ -u_1^x \end{bmatrix} \tag{17}$$

The calculation should be performed assuming the hinge develops last and is correct when the three rotations are in agreement with those corresponding to the limit thrust line (obtained from the limit analysis).

A case study in which the proposed procedure is applied is illustrated in Figure 8, which shows the elastoplastic arch deformation before the application of concentrated plastic rotations (Figure 8a) and the elastoplastic-plastic collapse arch deformation (Figure 8b), drawing with amplification of displacements.

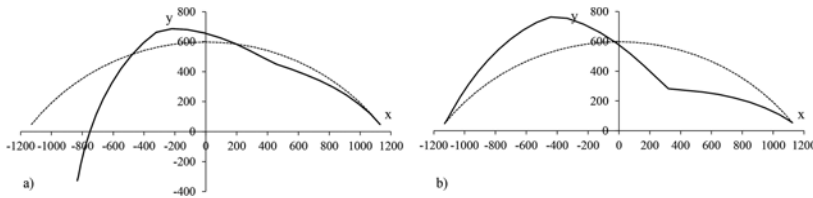


Figure 8. The elastoplastic arch deformation before the application of concentrated plastic rotations (a) and the elastoplastic-plastic collapse arch deformation (8b).

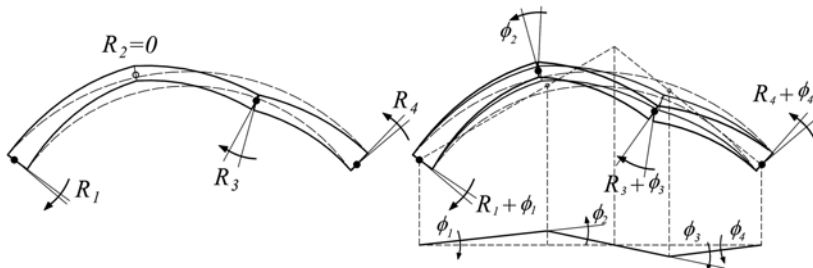


Figure 9. Arch deformation at the point of collapse and arch deformation during the collapse.

For the sake of clarity, this deformation corresponds to the incipient arch collapse condition (Figure 9). From this configuration, the effects of the four plastic rotations of the collapse kinematism are summed when the structure is transformed into a mechanism.

7 THE CENTER OF ELASTOPLASTIC ROTATIONS

Based on the elastoplastic arch deflection (obtained by integrating the elastoplastic curvatures), one can derive the center of instantaneous rotation G of the initial section of the arch,

which we will call *the center of elastoplastic rotations* of the initial section or the *center of gravity of the elastoplastic weights* (by analogy to the center of gravity of the elastic weights in the theory of the ellipse of elasticity).

With respect to point 1, the center G is positioned at a horizontal distance of $\frac{u_c}{\vartheta_1}$ and a vertical distance of $\frac{u_c}{\vartheta_1}$.

As seen, concentrated plastic rotations must cancel the displacement and rotation of the center point of the initial section, i.e. they must cancel the rotation ϑ_1 around the elastoplastic center.

It is useful to verify that the vector composition of the concentrated plastic rotations is a rotation applied at the same point G and of equal and opposite value to the elastoplastic rotation.

The graphical method to derive the center G of the resultant of the three rotations R_1 , R_3 , R_4 is as follows.

The vector R_3 is plotted in 1 and 4. The two vectors are plotted in 3:

- R_4 on the same side as R_3 (with respect to the conjunction 4-3) since they are discordant;
- R_1 on the opposite side of R_3 (with respect to conjunction 1-3) since they are concordant.

The points of the vectors are joined, obtaining intersections 1-3 and 4-3 on sides 1-3 and 4-3 (or on their prolongation). We join 1 with 1-3 and 4 with 4-3: the center G , intersection of these two conjunctions, must correspond to the center of the elastoplastic rotations.

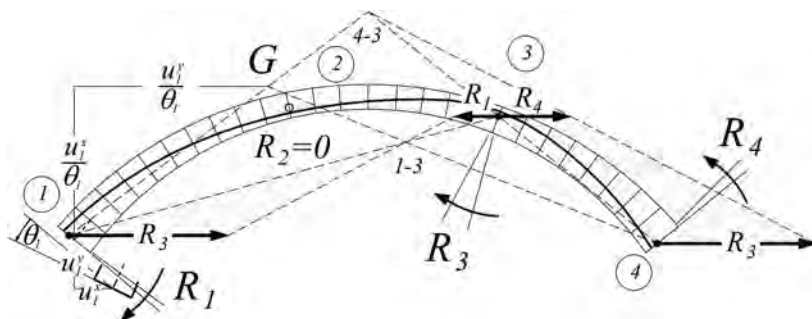


Figure 10. The center of elastoplastic rotations.

REFERENCES

- Ghali, A.M. Neville, T.G. Brown, Structural Analysis, 5th ed., London, 2003 Abramowitz and Stegun, Handbook of Mathematical Functions, New York, 1972
- Heyman J.: On the estimation of deflexions in elastic-plastic framed structures, Proceedings of the Institution of Civil Engineers, 19 (1), (1961)
- Maier G., Grierson D.E., Best M.J.: Mathematical programming methods for deformation analysis at plastic collapse, Computers & Structures, 7(5), (1977)
- Stagnitto G., Pederzani A.: An innovative approach for the assessment of masonry bridges based on two new limit analysis theorems, IABSE Conf. Guimarães, pp.176–183, (2019).
- Stagnitto G., Siccardi R. Ghioni M.: The Somigliana’s Double Dislocation method for the calculation of the live loads collapse multiplier of masonry arch bridges, Proceedings of the 1st Conference of the European Association on Quality Control of Bridges and Structures, EUROSTRUCT 2021, Padova, pp. 304–312 (2022)
- Stagnitto G.: The Consecutive Rotations Around Neutral Axis (C.R.A.N.A.) method for the calculation of deformations of masonry arches in the elastoplastic state, University of Pavia, Pavia (2022)
- Page J., Masonry Arch Bridges – State of the art review, Transport Research Laboratory, HMSO, London, (1993)
- Zampieri P.: Horizontal capacity of single-span masonry bridges with intrados FRCM strengthening Composite Structures, 244, DOI: 10.1016/j.compstruct.2020.112238, (2020)
- Zampieri, P., Amoroso M., Pellegrino C.: The masonry buttressed arch on spreading support Structures, 20, pp. 226–236. DOI: 10.1016/j.istruc.2019.03.008 (2019)

Safety checking at point and section level of masonry arch bridges

G. Stagnitto

University of Pavia, Pavia, Italy

R. Siccardi

EPFL employed by Ferrovie Federali Svizzere, SA Bellinzona, Switzerland

M. Ghioni

Anastasi & Partners S.A., Locarno, Switzerland

P. Zampieri

University of Padova, Padova, Italy

ABSTRACT: Through the variational method based on the Somigliana's Double Dislocation, the theoretical elastoplastic solution of a masonry arch bridge is evaluated under a generic load condition, obtaining the live loads multiplier, which corresponds to the achievement of a predetermined ductility limit. The well-known experimental campaign performed by Schwartz e Thürlimann showed that the ultimate limit state of a masonry wall subjected to high eccentric compressive axial force is reached when there are high rotational capacity of the critical sections. From these results, the Swiss national standard proposed a ductility check at sectional level. In this work, the final configuration of the masonry bridges is evaluated considering the elastoplastic deformation of the structure obtained by the integration of the curvature that tends to infinity in the plastic-hinges sections and the rotations concentrate in the plastic-hinge sections necessary for the respect of the restrain conditions of the structure. Using this approach, a double ductility check is possible: at point and section level.

1 CONSIDERATION ABOUT THE PUNCTUAL AND SECTIONAL DUCTILITY IN A MASONRY CROSS-SECTION

The solution of the limit analysis is theoretically valid if the ductility of the material is assumed infinite. In fact, the final equilibrated solution - which corresponds to the theoretical collapse of the structure - must effectively be reached without local collapses of the structure that would prevent the development of the plastic deformations necessary to reach the tensional state associated with the final equilibrated solution.

However, in a masonry arch, the no-tension solution that respects the prefixed material ductility $\mu_e \leq \bar{\mu}_e$ at every point in some cases does not justify the collapse loads observed in real bridges (Page, 1993). In fact, it has been found experimentally (Schwart and Thürlimann 1988) that collapse of masonry sections subjected to eccentric compressive axial force occurs for high local values of rotation (up to 0.1 rad) as shown in Figure 1 where the results of experimental tests performed by Thurlimann and Schwartz (Schwart and Thürlimann 1988) are reported.

The conclusion of the authors (Schwart and Thürlimann 1988) (which is taken from the Swiss standard SIA 266/2) is as follows: if the dimensionless limit axial force $v=N/(s f_c)$ (in an arch of unit width, section of thickness s and made of masonry with compressive strength equal to f_c) is less than 0.25, no limits should be considered on the rotation capacity of the section.

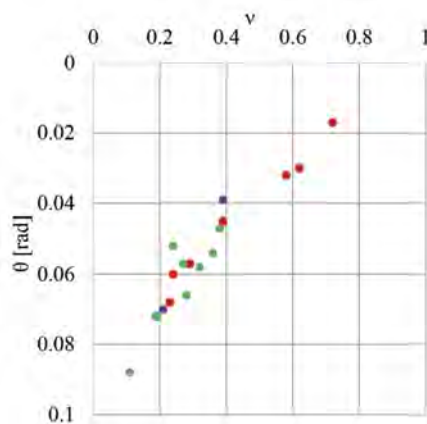


Figure 1. Experimental results obtained by Schwartz and Thurlimann, 1988.

2 SIMPLIFIED VERIFICATION WITH TWO PARALLEL ANALYSES AND PROPOSED SINGLE VERIFICATION

The considerations of the previous points suggest a simplified load capacity of a masonry bridge that determines the minimum strength required to reach the limit situation (for each load combination and for each position of the moving load). This can be done by means of two structural analyses conducted in parallel: the classical limit analysis using the static method (Stagnitto and Pederzani 2019, Zampieri 2020 and Zampieri et al. 2019) (and kinematic admissibility check) and the nonlinear elastoplastic analysis (Stagnitto et al. 2022).

In the first case, the required strength is derived in a way that the rotational capacity of the sections is not limited; in the second case, the required strength is derived in a way that the predetermined ductility is respected at each point.

If a single verification is to be defined, the most reasonable procedure would seem to be that of checking the concentrated rotations actually required to reach the ultimate theoretical collapse situation; as we will see, the concentrated rotations must also include the integrals of the curvatures in the areas near the plastic hinge where the punctual ductility limit value has been exceeded.

The purpose of this paper is to define a method for checking total concentrated rotations, verifying that they are internal to the domain of allowable rotations as a function of axial action.

3 COLLAPSE DEFORMATION DUE TO ELASTOPLASTIC DEFORMATIONS ONLY

For the understanding of the method, we focus on an example of a masonry arch railway bridge of about 20 meters net span (Stagnitto et al. 2022).

The load combination that maximizes the dissymmetric effects of vertical loads is considered: vertical and horizontal forces for permanent [G] and variable [Q] loads are considered in the analysis, multiplied by the corresponding safety coefficients: $1.0[G] + \lambda[Q]$.

Theoretical collapse corresponds to $\lambda=1$.

From the limit analysis, the critical position of the railway load is the one identified in Figure 2, corresponding to the highest value of the required resistance f_c equal to 3.50 MPa: this stress value is located in the four sections 1, 11, 19, 27 where the plastic hinges are formed. Therefore, the set of equilibrated solutions subjected to $0 \leq \sigma \leq f_c$ is theoretically reduced to the equilibrated solution obtained by limit analysis.

Internal actions in plastic hinges correspond to points that pertain to the limit domain:

- Figure 3a, in the space of dimensionless internal actions v , μ : $\mu = \frac{1}{2} \cdot (v - v^2)$;

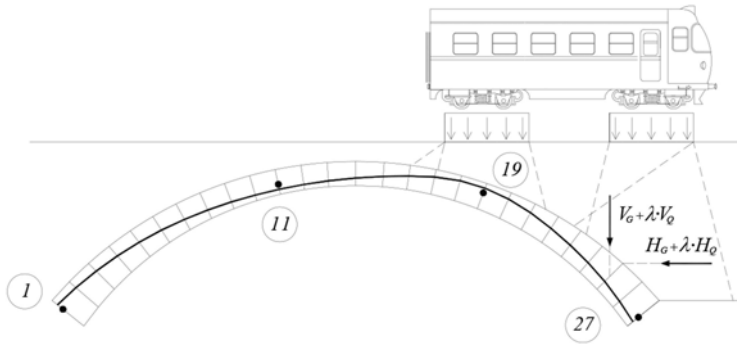


Figure 2. Critical load condition in a railway masonry bridges.

-Figure 3b, in the space of axial action and dimensionless eccentricity: $\frac{\varepsilon}{s} = \frac{t}{v} = \frac{1}{2} \cdot (1 - \nu)$ (since we have considered the absolute values of eccentricities, we graphically overlap the values of sections 1 and 27).

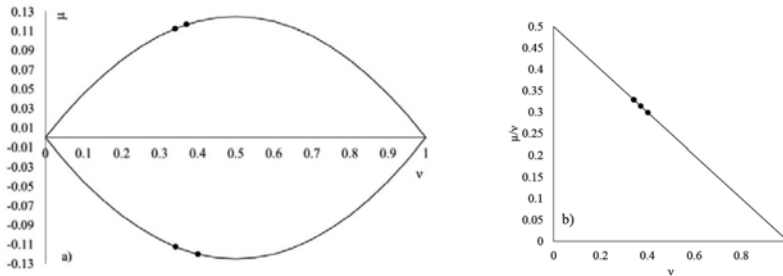


Figure 3. Limit domains (v, μ) and $(v, \mu/v)$.

Since the equilibrated collapse solution is the only one that, under ultimate load, respects the strength conditions, the elastoplastic calculation conducted by variational procedure (Stagnitto et al 2022) can only find the same solution.

We observe that the final equilibrium solution (theoretically valid under the assumption of non-limited ductility) does not depend on the elastic parameters of the arch and is valid even in the presence of elastic returns. A rigorous, only in the absence of elastic returns can the diagrams of unit strains be derived directly from those of stresses.

Any local unloading would still have a negligible influence on the deformation profile of the arch at collapse (Maier et al. 1977).

On the basis of the equilibrated collapse solution, we calculate, at each node, the relative rotations $\Delta\theta$ by integrating the curvatures χ over the arc length of the corresponding segment.

In the four plastic hinges, appropriate integration techniques are used because the curvature theoretically tends to infinity (Stagnitto and Zampieri 2023). Although this theoretical assumption is unrealistic, finite values of the concentrated rotations are obtained that have the same order of magnitude as the experimentally enslaved ones.

As we shall verify the elastoplastic deformation thus obtained does not verify compatibility with the hyperstatic constraint, and therefore concentrated plastic rotations will form in the first three plastic hinges.

In the presence of such concentrated rotations there is a discontinuity of absolute rotation; concentrated rotation is the result of a process of abstracting on a phenomenon that always actually concerns a finite length of an arch.

Thus, at each node, the relative rotation is equal to:

- (i) to Simpson’s integral if the section is not a plastic hinge: $\Delta\vartheta_i = \frac{L_i}{6} \cdot (\chi_1 + 4\chi_2 + \chi_3)$
- (j) to the improper integral over the relevant ashlar + the concentrated rotation, if any, if the plastic hinge is not the initial or final section of the arch: $\Delta\vartheta_j = \int_0^{L_j} \chi ds + (R_j)$
- (k) to any concentrated plastic rotation if the plastic hinge is the initial or final section of the arch:

$$\Delta\vartheta_k = (R_k) \quad k = 1, n$$

In fact, the elastoplastic rotations of the extreme segments are located at the additional nodes (in the middle of the initial and final elements, of shorter length) 1^* and n^* :

$$\Delta\vartheta_{1^*} = \int_0^{L_1} \chi ds \quad \Delta\vartheta_{n^*} = \int_0^{L_n} \chi ds$$

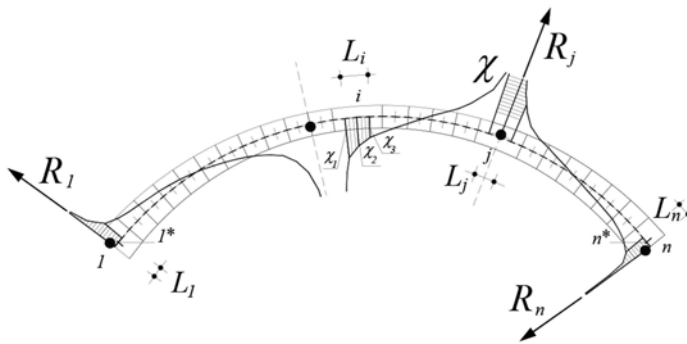


Figure 4. Curvature diagram and concentrated rotations.

Deformation is obtained by the method of elastoplastic rotations around the neutral axis: the “key” of the method is to place the relative rotations on the neutral axis instead of the geometric axis, so as to automatically account for section partialization and the influence of axial force (Stagnitto and Zampieri 2023).

Positioning on the neutral axis the relative rotations in the nodes preceding each section, their sum gives the rotation in section θ , the sums of their static moments, with respect to the vertical and horizontal axes passing through the center of gravity of the section, give the vertical displacements u_y and horizontal displacements u_x of the center point of the section. The resulting elastoplastic deformation (drawing with amplification of displacements) is plotted in Figure 5.

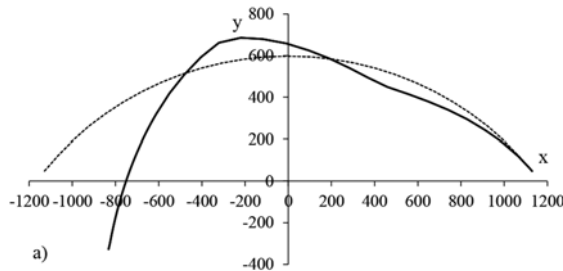


Figure 5. Elastoplastic deformation of the arch (x10).

4 CONCENTRATED PLASTIC ROTATIONS IN THE FIRST THREE PLASTIC HINGES

As can be seen from Figure 5, the elastoplastic deformation does not verify compatibility with the constraint: at point 1 (geometric center of the initial section) there are nonzero values of the absolute rotation $\theta_1 \cong 0,05 \text{ rad}$ and vertical displacements $u_1^y \cong 37,5 \text{ cm}$ and horizontal displacements $u_1^x \cong 37,5 \text{ cm}$.

A nominal value of $E=1000 \text{ MPa}$ was assumed, which is suitable for catching the deformation at full-scale collapse (Figure 6).

These three components of the displacement of node 1 are canceled by the plastic rotations in the first three plastic hinges (Stagnitto and Zampieri 2023), since the equilibrium solution obtained corresponds to the last possible equilibrium, i.e., to the act of formation of the fourth plastic hinge. From this point on, plastic rotations of unlimited value appear, affecting all four hinges.

By sequential elastic-plastic analysis (Stagnitto et al. 2022), it is found that the last plastic hinge is formed in section 11. If only the limit analysis is carried out, the last plastic hinge can still be identified: the calculation should be performed assuming one of the four hinges as the last and is correct when the three rotations agree with those that would cause the limit analysis thrust line.

We report, in Figure 6, the deformation configuration at incipient collapse. This deformation takes into account the partialization of the sections, the elastic rotations in the sections that remained elastic (compressive), the elastoplastic rotations in the sections where the maximum compression f_c was reached, and the concentrated plastic rotations in the sections that reached the ultimate limit state.

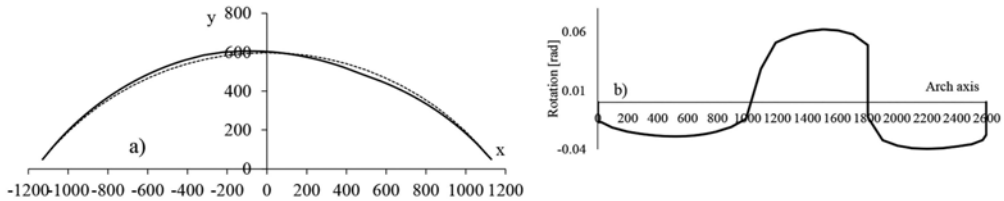


Figure 6. Final deformation of the arch and rotations diagram at bridge collapse (with plastic rotations).

We observe how, in the absolute rotations diagram, the three plastic rotations concentrated in sections 1, 19, 27 appear as discontinuities (and there is no discontinuity in section 11, however, because that is the last hinge to be formed). However, the total concentrated rotations actually needed to reach the collapse situation (before the mechanism is triggered) must still include a contribution.

5 CONCENTRATED TOTAL ROTATIONS IN THE FIRST THREE PLASTIC HINGES

It has been found experimentally (Page 1933) that in a plasticized arch section the rotations are concentrated in a single section at the plastic hinge. To reproduce this situation with a mathematical model, the relative rotations of the ashlar near the plastic hinge are calculated and considered as an increase in the rotations in the plastic section.

The assumption at the basis of the verification is as follows: the fiber-level ductility check in each section is replaced by an internal action-level check in a single section, in which the plastic rotation of the section itself, the elastoplastic rotation of the relevant ashlar and the elastoplastic rotations of adjacent segments with greater ductility than allowed are added together. When the concentrated rotations are internal to the domain of admissibility, it is justified to calculate them in a one-dimensional model that, for the advantage of safety, maximizes them by admitting infinite curvature at the plastic hinges. For simplicity, let us consider the limit case, i.e., suppose we accept a maximum ductility of 1: then all elastoplastic rotations (derived

from compressive strength) are concentrated in plastic hinges. The total concentrated rotations (see Figure 7) include the concentrated plastic rotations (R) of the fully plasticized sections, the elastoplastic rotations of the related segments ($|\chi| \rightarrow \infty$), and the elastoplastic rotations of the neighboring segments with ductility greater than the allowable ductility ($\mu_\epsilon > \bar{\mu}_\epsilon$).

Therefore, the ductility verification:

- or is positive in segments where the distribution of elastoplastic curvatures ($\mu_\epsilon \leq \bar{\mu}_\epsilon$) and the resulting regularity of absolute rotation are accepted;
- or is replaced, for the other segments (regarded as infinitely stiff) by the verification of the total rotations that are concentrated in the critical sections.

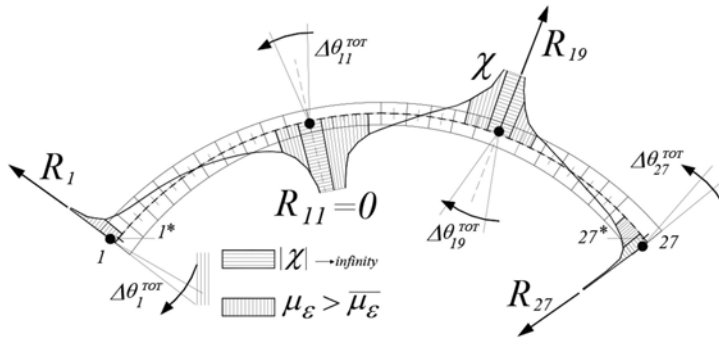


Figure 7. Curvature diagram (elastic and elastoplastic range).

Even assuming, for simplicity $\bar{\mu}_\epsilon = 1$, the solution does not correspond to the classical elastic-plastic solution, which, instead, considers the entire arch elastic with the exception of the sections where plastic hinges are formed.

In the proposed method, however, the solution must be called elastoplastic-plastic because the transition zones between the elastic state and the plastic final state, and concentrated plastic rotations are considered.

The deformation obtained after concentration of the elastoplastic rotations (Figure 8) is a more “angular” than that in Figure 5.

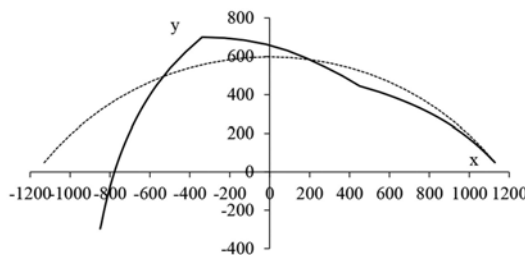


Figure 8. Elastoplastic deformation of the arch (x10), after concentration of elastoplastic rotations.

When plastic R rotations are applied, the deformation and absolute rotations diagram (Figure 9) show that the displacements and rotation of the initial node are all canceled.

Keeping the total rotation of the last hinge (sec. 11), the diagram of absolute rotations according to the collapse kinematism (in dashed line) was plotted for comparison.

If all relative rotations, including elastic ones, were concentrated according to their sign (regarding all ashlar as infinitely rigid), the two diagrams would be coincident: this suggests

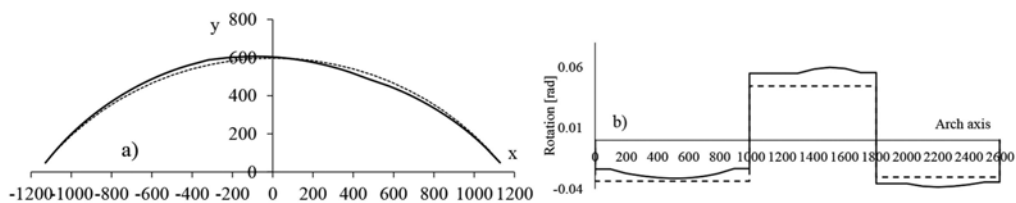


Figure 9. Final deformation of the arch and rotations diagram at bridge collapse (with total rotations).

simplified methods that assume for collapse deformation estimation the rigid kinematism calibrated according to the total rotation of the last hinge.

For a nominal value of $E=1000$ MPa, the maximum (vertical) displacement is about 22 cm, in section 19; for comparison, under the forces $1.0[G] + 0.8[Q]$ the maximum displacement—also at the same point 19—was about 7 cm (Stagnitto et al. 2022), compared to a bridge of about 20 meters of span.

6 ASSESSMENT OF ADMISSIBILITY OF TOTAL ROTATIONS

In the following figure, based on the experimental evidence cited by Schartz and Thurliman (1988), the domain of permissible rotations as a function of the dimensionless axial force v was plotted as an example.

The limit domain, drawn for conceptual purposes only to illustrate the proposed assessment method, contains all the points in Figure 1.

Instead, the actual domain for design purposes will have to take into account other experimental evidence and other considerations, including statistical ones, in order to define a design domain as a function of a given fractile, in probabilistic terms. On the domain we reported the four total concentrated rotations, placing them according to the value of the axial force. The maximum concentrated rotation is in section 19, where, for $E=1000$ MPa, it is equal to 0.09 radians (Figure 10a).

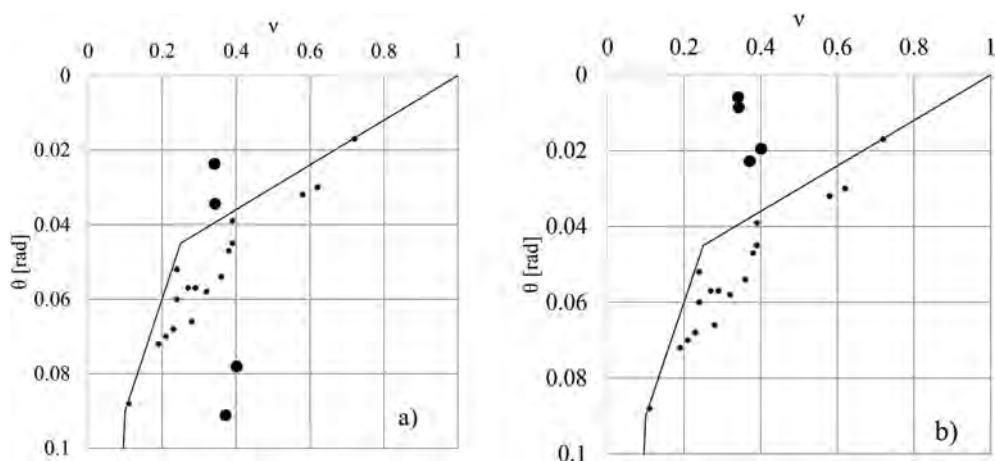


Figure 10. Assessment of admissibility of total rotations ($E = 1000$ $E = 4000$).

Assuming $E = 4,000$ MPa (realistic value for bridges: Cappini et al. 2010), the rotations are 4 times smaller and the maximum rotation (in 19) becomes: $0.09 \text{ rad}/4 = 0.0225 \text{ rad} = 1^\circ, 30$.

Therefore, the verification of the total rotations is positive (Figure 10b) and the equilibrated collapse solution can actually be achieved.

7 CONCLUSIONS

For the purpose of realistic estimation of the collapse multiplier, a calculation of the rotations actually required to reach the theoretical collapse solution has real practical utility.

The method presented in this contribution derives the elastoplastic deformation associated with the equilibrated solution of the limit analysis, taking into account the concentrated rotations in the plastic hinges that precede the formation of the final hinge.

Analytical developments of the method are explained in (Stagnitto and Zampieri 2023). The concentrated rotations thus estimated must be less than those allowed—based on experimental evidence—as a function of the dimensionless axial force in the section.

Since it has been experimentally observed that, in a plasticized arch section, rotations are concentrated around a single section, the estimation of the total rotation must also include the integral of the curvatures in the adjacent zones where the point ductility limit value is exceeded. In this way, the verification considers both failure conditions, at the point level and at the sectional level.

Assuming elastoplastic idealizations, in the presence of progressive plasticizations, the proposed method does not know the disadvantage of convergence problems when the load multiplier increases.

REFERENCES

- Brenchich A., de Felice G.: Brickwork under eccentric compression: Experimental results and macroscopic models, *Construction and Building Materials*, Volume 23, Issue 5, Pages 1935–1946, (2009)
- Cappini A., Stagnitto G., Pederzani A., Rossi C., Rossi P.P., Structural analysis and strengthening intervention of the multispan stone masonry bridge of Ribellasca between Italy and Switzerland, 6th International Conference on Arch Bridges, Fuzhou, China 11-13 October 2010
- Maier G., Grierson D.E., Best M.J.: Mathematical programming methods for deformation analysis at plastic collapse, *Computers & Structures*, 7(5), (1977)
- Page J.: *Masonry Arch Bridges – State of the art review*, Transport Research Laboratory, HMSO, London, 1993
- Stagnitto G., Siccardi R., Ghioni M.: The Somigliana’s Double Dislocation method for the calculation of the live loads collapse multiplier of masonry arch bridges, *Proceedings of the 1st Conference of the European Association on Quality Control of Bridges and Structures, EUROSTRUCT 2021, Padova*, pp. 304–312, (2022)
- Stagnitto G., Pederzani A.: An innovative approach for the assessment of masonry bridges based on two new limit analysis theorems, *IABSE Conf. Guimarães*, pp.176–183, (2019).
- Stagnitto G., Zampieri, P.: Near-collapse deformed configuration of masonry arch bridges, 8th IALCEE-MS19, Milano, (2023)
- Schwartz J., Thürlimann B.: *Masonry Walls under Centric or Eccentric Normal Force*, *Proceedings 8th International Brick Masonry Conference, Dublin, Ireland*, (1988)
- Zampieri P.: Horizontal capacity of single-span masonry bridges with intrados FRCM strengthening *Composite Structures*, 244, DOI: 10.1016/j.compstruct.2020.112238 (2020).
- Zampieri P., Amoroso M., Pellegrino C.: The masonry buttressed arch on spreading support *Structures*, 20, pp. 226–236. DOI: 10.1016/j.istruc.2019.03.008 (2019).

Discrete Macro-Element structural assessment of a railway masonry arch bridge subjected to pier settlements

D. Rapicavoli, F. Cannizzaro, S. Caddemi & I. Calìò

Department of Civil Engineering and Architecture, University of Catania, Catania, Italy

ABSTRACT: Settlements in bridges can induce structural damage that can be limited and affect only the serviceability of the infrastructure or, in the worst scenario, can cause local or global failure. To assess the structural behaviour of masonry arch bridge and identify the occurrence of damage, also in presence of structural health monitoring, reliable numerical models to perform sufficiently accurate nonlinear simulations are needed. The innovative strategy known as discrete macro-element model (DMEM) is here employed to assess the performance of a masonry arch bridge in presence of piers settlements. The adopted numerical strategy assures an easy and geometrically consistent model characterized by a low computational burden with very accurate results. The numerical investigation here reported is also devoted to detect the main structural parameters that have to be controlled in health monitoring bridge survey and to identify threshold levels to be considered for automatic early warning alerts. A masonry arch bridge located in Maletto (Italy), belonging to the rail network of Ferrovia Circumetnea (FCE), which was subjected to a retrofitting intervention due to the presence of extensive damage at the haunches of the arches, is here studied in its original configuration. A sensitivity analysis with respect to the settlement magnitude of a pier foundation is performed considering the operational loads by conducting nonlinear static analyses. The role of the settlements in masonry arch bridges and the relevant effects on the structural performance are shown and discussed also with the aim to associate the severity of damage to the structural performance of the bridge.

1 INTRODUCTION

Masonry arch bridges can be subjected to structural damage that can be induced by different causes, such as degradation of the materials (Tecchio et al. 2022), scours (Ragni et al. 2019, Scozzese et al. 2019, Solan et al. 2020, Zampieri et al. 2017), settlements (DeJong 2016, Malena et al. 2021, Grillanda et al. 2022). Damage in masonry arch bridges can be also due to settlements of the pier foundations induced by scour, under-sizing of the foundations, soft soil (Bayraktar and Hökelekli, 2021).

The interpretation and the prediction of the reduction of structural performance due to damage related to different causes require advanced numerical models capable to perform nonlinear static and/or dynamic analyses. Refined Finite Element (Tubaldi et al. 2020, Pepi et al. 2021) or Discrete Element (Saygılı and Lemos, 2021) simulations have been proposed in the scientific literature. An alternative modelling strategy, specifically introduced for the numerical modelling of masonry structures (Caddemi et al. 2017), known as discrete macro-element model (DMEM) was recently extended and applied for the simulation of the complex nonlinear static and dynamic behaviour of masonry arch bridges (Caddemi et al. 2018, Caddemi et al. 2019, Caddemi et al. 2020). The DMEM is based on the adoption of shear deformable three-dimensional macro-elements interacting with each other by means of nonlinear zero-thickness interfaces, and its main advantages rely on the limited amount of degrees of freedom required by each element, on the adoption of simple but effective constitutive laws based on a fiber

discretization, which make the numerical approach reliable, robust and characterized by a simple interpretation of the results. In addition, the low computational cost allows to perform static and dynamic nonlinear analyses in reasonable computer time even for large models.

The DMEM strategy is here applied for modelling a four span railway masonry arch bridge located in Maletto (Italy), and belonging to the Ferrovia CircumEtna (FCE) company. The bridge is a curved one with a constant slope, and was characterised by a diffused crack pattern at the intrados of the arches evidenced during an inspection made in 1984, caused by settlements at the base of a central pier. The precarious safety condition of the bridge required a retrofitting intervention. Here the bridge is studied in the original structural layout for different severity of the settlement of the central pier with the aim to evaluate the structural performance of the bridge due to central pier settlements and assessing the bridge capacity as a function of the settlement magnitude. The study is also motivated by the need to define thresholds levels of foundation displacements to be assigned to health monitoring system that could be installed in the masonry bridge.

2 THE CASE STUDY: A MASONRY ARCH BRIDGE IN MALETTTO

2.1 Description

The case study is a masonry arch bridge (Figure 1) built in the 19th century and located in the south of Italy, in the municipality of Maletto (Sicily) at km 62 on the FCE rail network. It is a four-span bridge with 0.60 m thick circular arches separated by three piers with an average span length of 7.30 m, rises ranging from 3.37 m to 4.05 m. The arches are composed by regular volcanic ashlar; the spandrels, whose thickness is equal to 0.40 m, and the piers are made by rectangular shaped volcanic stones.

The railway has a 1.1% slope and a constant radius of curvature equal to 97.3 m and belongs to a single-track non-electrified non-standard railway line where the distance between the inner edges of the rails is 0.95 m allowing a maximum velocity of 35 km/h. In November 1984 an inspection of the structure revealed a severe crack pattern at the arch haunches due to settlements at the central pier, whose cause was attributed to the characteristics of the soil (sandy clay), and to an insufficient size of the foundations, Figure 2. Due to the findings of the inspection, the maximum velocity over the bridge was limited to 10 km/h, and a structural reinforcement was applied. The retrofitting solution included the introduction of a concrete layer at the intrados of the vaults confined by an external steel corrugated thick plate used as formworks. The new structure was founded on a new reinforced concrete enlargement of the existing masonry foundation.



Figure 1. Railway Maletto masonry arch bridge: pictures (a) of 1926 (Sergi 2019) and (b) 2014.

The bridge was further investigated in 2022 within a research project involving the University of Catania, as a consultant, the FCE and the private company Systemia. The main focus of the project is on the health monitoring of bridge by means of innovative sensor boxes (Ferritta et al. 2020). The campaign of research activities also included a detailed survey of the bridge with a Terrestrial Laser Scanning (TLS) and Unmanned Aerial Vehicle (UAV) techniques, and a geological risk assessment. The outcome of the mentioned activities included the



Figure 2. Crack pattern at the haunches of the arch evidenced during the inspection of 1984.

definition of a geometrical digital twin of the bridge by capturing digital images and applying photogrammetric processing technique (Garozzo et al. 2022), Figure 3, results here employed as a base to implement the numerical structural model of the bridge.



Figure 3. 3D point cloud of the Maletto Bridge.

3 DAMAGE SCENARIO AND NUMERICAL MODELING

Based on the geometrical survey of the bridge, a numerical model of the structure was implemented in a DMEM software environment HiStrA Bridge (Caliò et al. 2015). The adopted model, whose theoretical approach is described in references (Caddemi et al. 2017), is based on shear deformable spatial macro-element interacting with other elements through nonlinear zero-thickness interfaces embedding the membrane element deformability. In the model here adopted each element is governed by seven degrees of freedom only, associated to the six rigid body motion and a single additional degree of freedom associated to a shear deformability of the element with respect to a significant plane.

The computational model here implemented is characterized by 4844 shear deformable spatial elements and 238 rigid elements, Figure 4, with a total amount of 35336 degrees of freedom. Four different materials have been identified in the bridge, depicted with different colors in Figure 4, corresponding to the fill, the zero-thickness friction interfaces connecting the fill to the other components of the bridge, the stone volcanic arches and spandrel walls. The overall views of the different parts of the bridge and a legend associated to the different material are reported in Figure 4. The adopted mechanical properties, estimated according to realistic values for the adopted material typologies, are summarised in Table 1. The constitutive laws adopted for each structural element are specialized for the flexural, shear and sliding behavior. The arches and spandrel walls are characterized for the flexural behavior by a parabolic constitutive law in compression and exponential softening in traction; the shear-diagonal behavior is assumed elastic while the shear-sliding is ruled by a Mohr-Coulomb criteria. The fill is considered as elasto-plastic with almost zero tensile strength and membrane behavior lumped in the interfaces; an elasto-plastic constitutive law, associated with a Turnsek-Cacovic yielding

criteria, is adopted for the generalized shear diagonal behavior, at the macro-scale. The interaction of the fill with the arches and the spandrel walls are ruled by ad hoc interfaces with zero cohesion. All the adopted parameters are reported Table 1.

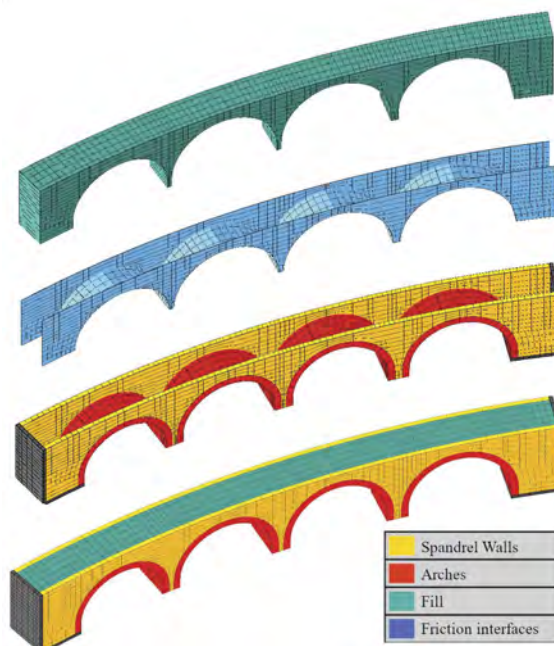


Figure 4. The implemented numerical model: exploded and overall views of the bridge.

Table 1. Mechanical parameters.

Material	E	G	f_c	f_{ct}	G_{fc}	G_{ft}	c	μ_c	τ_0	μ_τ	w
	MPa	MPa	MPa	MPa	N/mm	N/mm	MPa	-	MPa	-	kN/m ³
Arches	1800	600	3.0	0.02	4.0	0.001	0.01	0.6	-	-	22
Spandrel walls	1800	600	2.0	0.05	1.5	0.001	0.01	0.6	0.3	0.4	22
Fill	300	115	0.5	0.01	∞	∞	-	-	0.0005	-	18
Friction interfaces	300	115	1.0	0.01	∞	∞	0.0	0.6	-	-	-

where E = normal elastic modulus; G = shear elastic modulus; f_c = compressive strength; f_{ct} = tensile strength; G_{fc} = compressive fracture energy; G_{ft} = tensile fracture energy; c = sliding cohesion; μ_c = sliding friction ratio; τ_0 = diagonal shear strength; μ_τ = diagonal shear friction ratio; w = self-weight.

The piers are founded on elastic soil foundation whose normal flexibility k_n has been assumed equal to 12.75 kg/cm³ corresponding to a sandy clay soil.

To investigate the effect of the settlement of the soil on the nonlinear response of the superstructure, some numerical analyses have been conducted applying different levels of vertical settlement enforced on the central pier. Precisely, three-stage nonlinear static analyses are performed, including the following steps: i) application of the self-weight of the structure, ii) application of the settlement in the central pier, iii) incremental analyses till collapse associated with the operational load. For stage ii) four configurations have been considered corresponding to no settlement ($u=0.0$ m) and five magnitudes of the vertical settlements ($u=0.01$ m, $u=0.025$ m, $u=0.04$ m, $u=0.08$ m, $u=0.12$ m).

The operational load is evaluated according to the actual locomotive model currently in service in the FCE rail network, that is called ADe 21-25, Figure 5. The total weight of the vehicle

is 310 kN and the vertical load on each wheel axle is $Q_{vi}=38.75$ kN. Push-down analyses have been performed considering 5 different abscissae $x_i = \{2.00, 12.39, 22.25, 32.32, 43.26 \text{ m}\}$ of the loading scheme, corresponding to locating the centre of gravity of the locomotive in correspondence of the axes of the abutments and of the piers. The reference gravity and the operational loads have been magnified by coefficient equal to 1.35 and 1.45, respectively, according to the Italian regulation for ultimate limit state combinations (see tab. 5.2.V in D.M. 17.01.2018).

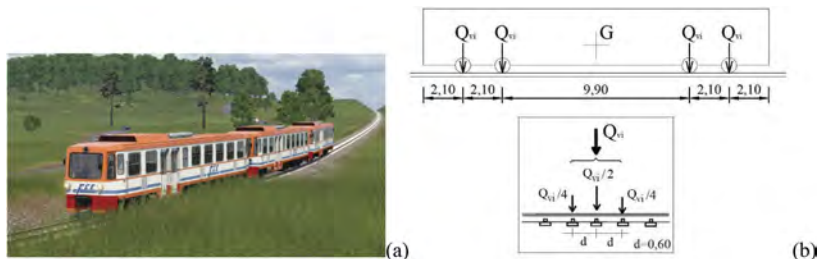


Figure 5. (a) Adopted locomotive ADe 21-25 for the evaluation of the operational loads and (b) corresponding scheme (measures expressed in m).

4 INFLUENCE OF SETTLEMENTS ON THE STRUCTURAL PERFORMANCE

The considered positions of the operational load and the adopted loading scheme are summarised in Figure 6, together with two positions of monitored displacement considered in the following.

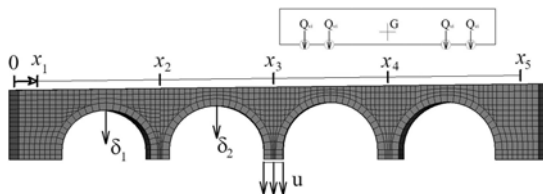


Figure 6. Applied loads and positions of the operational load, base settlement u , monitored vertical displacements.

The results of the performed analyses are reported in terms of deformed shape and crack patterns at the end of the stages ii) and iii) of the analyses for a specific position of the operational load (x_2) in Figure 7. The reported configurations correspond to the configuration in absence of settlements (top), $u=0.04$ (middle) and $u=0.12$ m (bottom).

The results, expressed in terms of distribution of damage, show that the settlement of the central pier leads to a crack pattern consistent with that observed during the bridge inspection in 1984 and reported in Figure 2. In terms of collapse mechanism associated to the magnification of the operational load, all the models, with and without settlement, show the involvement of the second arch and the rotation of the central pier. A more pronounced rotation of the pier, partially involving the third arch, is shown for the configurations with settlement of the central pier with different extension associated to the settlement magnitude.

In Figure 8, the load-displacement curves are reported for the first two positions of the operational load associated with the different magnitude of settlements. As expected, for the second position, higher values of the vertical settlements lead to a loss of the capacity of the bridge. In the worst scenario, the bearing capacity is about 75% of that associated to the configuration in absence of settlements.

Unexpectedly, for the first position of the operational load higher values of the settlements lead to slightly higher load multipliers than in the absence of settlements. The latter circumstance could be due to the state of compression induced by the settlement in the first arch (the

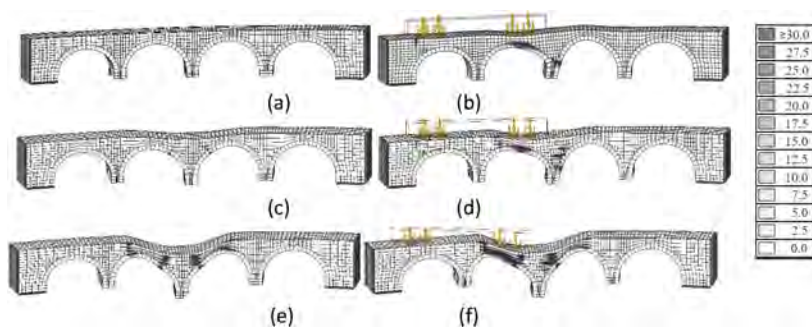


Figure 7. Deformed shapes and damage patterns (a-b) in absence of settlements and with settlements $u=0.04\text{m}$ (c-d) and $u=0.12\text{m}$ (e-f): before (a, c, e) and after (b, d, f) the application of the operational load magnified until collapse.

part of the bridge mainly involved in the collapse mechanism), which slightly delays the development of damage.

It is also worth to mention that the considerable load multipliers are due to the low weight of the adopted locomotive (310 kN), currently operating on the line, if compared with the weight corresponding to the standard D4 operational load indicated in the UIC Code-700 (900 kN).

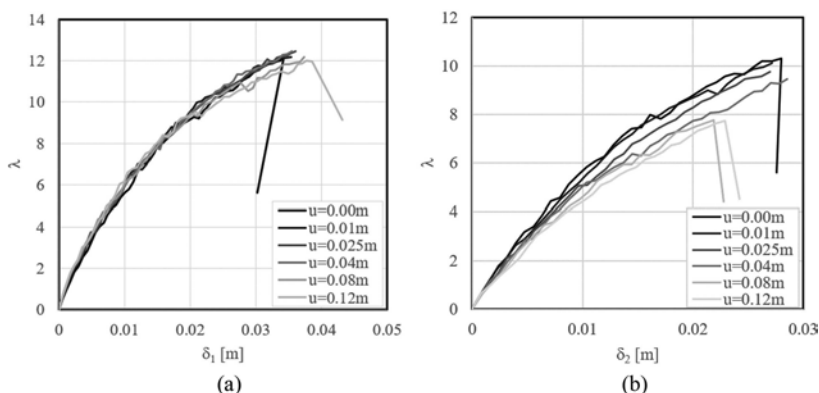


Figure 8. Load-displacement curves for all the analysed settlement configurations at positions (a) x_1 and (b) x_2 of the operational load: vertical displacement δ_1 and δ_2 at the crown of the vault respectively of the first and second arch (see Figure 7).

Finally, in Figure 9, the influence line reporting the abscissa x_1 of the centre G of the operational load versus the vertical bearing capacity of the bridge is reported for all the analysed configurations. Except for the first position of the operational load (which has been already discussed), in all the other cases the collapse load multiplier reduces as the magnitude of the vertical settlements increases (with a maximum reduction of 56% for the third position). Positions x_2 and x_4 of the operational load are associated to the lowest and highest load multipliers respectively (for settlements lower than 0.08 m), whereas for large settlements the weakest performance of the bridge occurs for position x_3 of the operational load. In absence of settlements the load multiplier ranges between 10.29 and 13.30, whereas for $u=0.12\text{m}$ it ranges between 5.56 and 12.44. The results highlight how the slope of the bridge, affecting the rise of the arches (ranging from 3.38 m of the first arch to 4.03 m), has a direct effect on the load capacity of the bridge, and the importance of an accurate geometry modelling of the bridge.

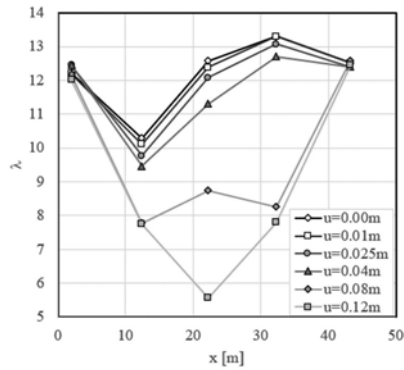


Figure 9. Bearing capacity of the bridge versus the abscissa x of the centre of gravity of the operational load.

5 CONCLUSIONS

In this study, a nonlinear numerical strategy based on a DMEM approach has been applied for the assessment, under operational loads, of a four span railway masonry arch bridge. The study required to upgrade the modelling strategy with respect to two aspects: i) allowing a more complex geometry accounting for a curved track with slope and ii) upgrading the non-linear static procedure analysis introducing the pier settlements after the application of gravitational loads and before the incremental operational load phase till collapse.

The Maletto railway bridge was numerically investigated considering different magnitudes of settlements of the central pier, which induce a loss of the bearing capacity of the bridge compromising the operational conditions of the line. The performed sensitivity analyses allowed to evaluate, for each position of the operational load, the influence of the settlement magnitude in the collapse mechanism and the load bearing capacity of the bridge. The role of the settlements in masonry arch bridges and the relevant effects on the structural performance have been also evaluated with the aim to associate the severity of the settlement to the structural performance of the bridge in view of the design of health monitoring system of masonry bridges and the definition of typical early warning thresholds to be considered in advanced monitoring systems taking into account also the possible occurrence of piers settlement.

ACKNOWLEDGEMENTS

This study was partially funded by: FCE (CircumEtnea Railway); The MonVia project “Sviluppo e ottimizzazione di un sistema general purpose modulare per il monitoraggio strutturale” within the ‘Programma Operativo Nazionale – Imprese e Competitività – 2014/2020 FESR (leader of the research group SYSTEMIA S.r.l. Catania).

REFERENCES

- Bayraktar, A. & Hökelekli, E. 2021. Nonlinear soil deformability effects on the seismic damage mechanisms of brick and stone masonry arch bridges. *International Journal of Damage Mechanics*. 30(3): 431–452.
- Caddemi, S., Calìò, I., Cannizzaro, F., & Pantò, B. 2017. New frontiers on seismic modeling of masonry structures. *Frontiers in Built Environment*. 3, 39.
- Caddemi, S., Calìò, I., Cannizzaro, F., D’Urso, D., Occhipinti, G., Pantò, B., Pisanelli, G., Rapicavoli, D., Spirolazzi, G., & Zurlo, R. 2018. A ‘parsimonious’ 3D discrete macro-element method for masonry arch bridges. In: *Proceedings of the International Masonry Society Conferences*. 222279: 541–551.
- Caddemi, S., Calìò, I., Cannizzaro, F., D’Urso, D., Pantò, B., Rapicavoli, D., & Occhipinti, G. 2019. 3D discrete macro-modelling approach for masonry arch bridges. In: *Towards a Resilient Built Environment Risk and Asset Management*. IABSE Symposium, Guimaraes 2019. 1825–1835.

- Caddemi, S., Calìo, I., Cannizzaro, F., Rapicavoli, D., Pantò, B., Occhipinti, G., D'Urso, D., Corti, L., Spirolazzi, G., & Zurlo, R. 2020. An automatic discrete macro-element method based procedure for the structural assessment of railway masonry arch bridges. *REHABEND*. 1004–1012.
- Calìo, I., Cannizzaro, F., Pantò, B., & Rapicavoli, D. 2015. “HiStrA (Historical Structure Analysis),” in HISTRA s.r.l (Catania, Italy). Available at: <http://www.grupposismica.it>
- DeJong M.J. 2016. Settlement effects on masonry structures. In Koen Van Balen, Els Verstrynghe (eds.), *Structural Analysis of Historical Constructions: Anamnesis, diagnosis, therapy, controls - Proceedings of the 10th International Conference on Structural Analysis of Historical Constructions, SAHC 2016, Leuven (Belgium), 13-15 September 2016*: 449–456.
- Fertitta, G., Costanza, A., D'Anna, G. & Patanè, D. 2020. The Earth Lab 5s (ETL3D/5s) seismic sensor. Design and test. *Annals of Geophysics*.
- Garozzo, R., Calìo, D., Galizia, M., Pappalardo, G., & Santagati, C. 2022. Integration of remote surveying methodologies for geological risk assessment of masonry arch bridges. *D-SITE 2022 Drones - Systems of Information on cultural hEritage International Seminar meeting 16th-18th June 2022* Museum of Electrical Technology, Pavia Italy
- Grillanda, N., Scacco, J., & Milani, G. 2022. Fast Adaptive Limit Analysis of Masonry Arch Bridges in Presence of Differential Settlements of Bridge Piles. *Lecture Notes in Civil Engineering*, 200 LNCE. 437–443.
- Malena, M., Angelillo, M., Fortunato, A., de Felice, G. & Mascolo, I. 2021. Arch bridges subject to pier settlements: continuous vs. piecewise rigid displacement methods. *Meccanica* 56: 2487–2505.
- Ministerial Decree 17 January 2018. Aggiornamento delle «Norme tecniche per le costruzioni». *Gazzetta Ufficiale Serie Generale*, n. 42, 20-02-2018, *Suppl. Ordinario* n. 8
- Pepi, C., Cavalagli, N., Gusella, V., & Giofrè, M. 2021. An integrated approach for the numerical modeling of severely damaged historic structures: Application to a masonry bridge. *Advances in Engineering Software*, 151, 102935.
- Ragni, L., Scozzese, F., Gara, F., & Tubaldi, E. 2019. Dynamic identification and collapse assessment of Rubbianello Bridge. In *Towards a Resilient Built Environment Risk and Asset Management: IABSE Symposium Guimarães 2019* (pp. 619–626).
- Saygili, Ö., & Lemos, J.V. 2021. Seismic vulnerability assessment of masonry arch bridges. *Structures*, 33: 3311–3323.
- Scozzese, F., Ragni, L., Tubaldi, E., & Gara, F. 2019. Modal properties variation and collapse assessment of masonry arch bridges under scour action. *Engineering Structures*, 199, 109665.
- Sergi, G. 2019. La ferrovia circumetnea: cento anni intorno al vulcano. *Arti grafiche Etna Molino*, Catania.
- Solan, B., Ettema, R., Ryan, D., & Hamill, G. A. 2020. Scour concerns for short-span masonry arch bridges. *Journal of Hydraulic Engineering*, 146(2), 06019019.
- Tecchio, G., Donà, M., Saler, E. & da Porto, F. 2022. Fragility of single-span masonry arch bridges accounting for deterioration and damage effects. *European Journal of Environmental and Civil Engineering* 1–22.
- Tubaldi, E., Minga, E., Macorini, L., & Izzuddin, B. A. 2020. Mesoscale analysis of multi-span masonry arch bridges. *Engineering Structures*, 225, 111137.
- UIC CODE-700 2004. Classification of lines – Resulting load limits for wagons. *International Union of Railways, November 2004, 10th Edition*
- Zampieri, P., Zanini, M. A., Faleschini, F., Hofer, L., & Pellegrino, C. 2017. Failure analysis of masonry arch bridges subject to local pier scour. *Engineering Failure Analysis*, 79, 371–384.



Taylor & Francis

Taylor & Francis Group

<http://taylorandfrancis.com>

SPECIAL SESSIONS

*SSI: Climate change effects on life-cycle safety, reliability,
and risk of structures and infrastructure systems*

Organizers: F. Biondini, Z. Lounis & M. Ghosn



Taylor & Francis

Taylor & Francis Group

<http://taylorandfrancis.com>

Framework for life-cycle tsunami risk assessment considering sea-level rise effects due to climate change

A.K. Alhamid, M. Akiyama & K. Aoki

Waseda University, Tokyo, Japan

S. Koshimura

Tohoku University, Sendai, Japan

D.M. Frangopol

Lehigh University, Bethlehem, USA

ABSTRACT: The colossal impact of tsunamis has been responsible for a significant loss to coastal infrastructure world-wide. However, due to the sea-level rise effects, the life-cycle risk assessment associated with the cumulative loss becomes intractable since hazards due to tsunami are time-dependent. A more accurate life-cycle tsunami risk assessment is needed to enhance the disaster preparedness of coastal communities. This paper presents a framework for life-cycle risk assessment of coastal residential buildings subjected to tsunami under sea-level rise effects. Earthquake occurrences are predicted probabilistically using a Poisson process based on historical data. Time-variant sea-level rise hazard assessment is carried out based on various climate models considering the uncertainties of emission scenarios. Monte Carlo simulation-based tsunami hazard assessment is performed to estimate the tsunami hazard curves considering sea-level rise effects. With the fragility curve of building structures developed from historical tsunami damage data, the tsunami risk of coastal building is estimated based on tsunami hazard considering sea-level rise effects, fragility curve, and the unit loss of individual buildings. An illustrative example is presented by applying the proposed framework to several municipalities in Kochi Prefecture of Japan. The effects of sea-level rise and earthquake occurrence on the life-cycle risk are discussed.

1 INTRODUCTION

In the last two decades, tsunami disasters have severely affected the coastal infrastructure, including massive disaster waste and road network disruption (Akiyama et al., 2020). One notable instance was the 2011 Great East Japan earthquake that generated a massive tsunami and eradicated the coastal infrastructure of the Tohoku region. The loss was estimated at around 16.9 trillion yen, constituting one of the most expensive natural disasters in history (Kajitani et al., 2013). However, progressive sea-level rise due to climate change has become an uprising issue and is projected to cause not only coastal inundation but also the extension of future natural disasters such as tsunamis (Alhamid et al., 2022a). Therefore, the existing tsunami risk assessment should be improved by considering the effects of sea-level rise to enhance the disaster preparedness of coastal communities.

Life-cycle risk assessments have been widely implemented as a basis for evaluating the socio-economic impact of natural disasters over the lifetime of an infrastructure (Mechler, 2016). For instance, De Risi et al. (2018) performed a life-cycle cost assessment of urban areas under flood risk in developing countries. Furthermore, since the number of earthquake arrival times is the governing variable in determining the cumulative monetary loss, Pandey & van der Weide (2018) presented a life-cycle cost assessment of seismic damage based on a compound Poisson process. Nevertheless, these studies have not integrated the nonstationary sea-level rise effects on the life-cycle tsunami risk assessment.

Due to the nonstationary sea-level rise effects, the tsunami hazard and risk become time dependent. In addition, the number of earthquake arrivals and their corresponding arrival times are of great importance in the life-cycle tsunami risk assessment (Sepúlveda et al., 2021, Alhamid et al., 2022b). Therefore, a more comprehensive life-cycle tsunami risk assessment that considers the abovementioned aspects should be established to promote a more accurate assessment of potential infrastructure loss due to tsunamis.

This paper presents a framework for life-cycle risk assessment of coastal residential buildings subjected to tsunamis under sea-level rise effects. Probabilistic earthquake occurrences are developed based on historical data under a Poisson process. On the other hand, time-variant sea-level rise hazard assessment is carried out based on various climate models considering the uncertainties of emission scenarios. Monte Carlo simulation-based tsunami hazard assessment is employed to estimate the tsunami hazard curves considering sea-level rise effects. With the fragility curve of building structures developed from historical tsunami damage data, the tsunami risk of a coastal building is estimated based on tsunami hazard considering sea-level rise effects, fragility curve, and the unit loss of individual buildings. An illustrative example is presented by applying the proposed framework to several municipalities in Kochi Prefecture of Japan. The effects of sea-level rise and earthquake occurrence on the life-cycle risk are discussed.

2 BASIC PROCEDURE FOR LIFE-CYCLE TSUNAMI RISK UNDER SEA-LEVEL RISE

The procedure for life-cycle tsunami risk assessment considering nonstationary sea-level rise effects mainly comprises probabilistic earthquake occurrence modeling, tsunami hazard assessment considering sea-level rise effects, fragility assessment, and risk assessment. In addition, the structural types, location, and failure probability of the corresponding structures are integrated with the aid of the Geographic Information System (GIS). A compound renewal theory (Alhamid et al. 2022b) is developed to consider the effects of nonstationary sea-level rise in the life-cycle tsunami risk assessment. The flowchart for estimating the life-cycle tsunami risk of a building portfolio, including the overview of the MCS-based numerical solution associated with the compound renewal process, is presented in Figure 1.

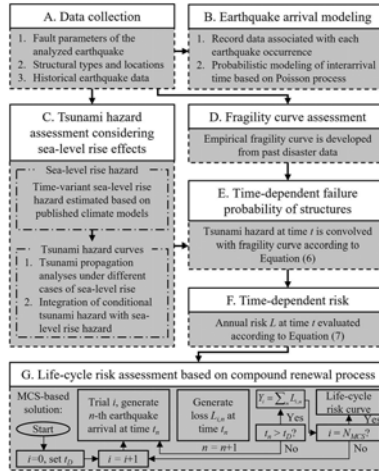


Figure 1. Procedure for life-cycle tsunami risk assessment of building portfolio under nonstationary sea-level rise effects.

2.1 Probabilistic earthquake arrival modeling

The probabilistic earthquake occurrence can be developed by inferring the statistics associated with the interarrival times from the historical record data of the corresponding analyzed

earthquake. A key parameter from the statistical inference is the mean annual rate of occurrence of tsunamigenic earthquakes (hereafter denoted as λ). Various probabilistic models of natural disasters can be developed based on the mean recurrence rate. Specifically, the Poisson process has been widely adopted, where each event is assumed to occur randomly in time and independently of each other. Under the Poisson point process, the interarrival time of the earthquake event is described as an exponential distribution with a generic form:

$$f_W(t) = \lambda e^{-\lambda t} \quad (1)$$

where W is the random variable associated with the interarrival time of the earthquake event.

2.2 Time-variant sea-level rise hazard assessment

The nonstationary sea-level rise hazard assessment has been reported in Alhamid et al. (2022a) and is briefly presented herein. The regional sea-level rise hazard at time t is estimated by multiplying each global mean sea-level rise component with its corresponding spatial variability and can be expressed as (Alhamid et al. 2022a):

$$\begin{aligned} \psi(\mathbf{x}_r, t) &= FG_{STR}(\mathbf{x}_r) \cdot S(\mathbf{x}_r, t) + FG_{GLA}(\mathbf{x}_r) \cdot G(\mathbf{x}_r, t) + FG_{ICS}(\mathbf{x}_r) \cdot I(\mathbf{x}_r, t) \\ &= \omega(\mathbf{x}_r, t) + \zeta(\mathbf{x}_r, t) + \eta(\mathbf{x}_r, t) \end{aligned} \quad (2)$$

where $\psi(\mathbf{x}_r, t)$ is the total regional sea-level rise value at time t and coordinate vector \mathbf{x}_r of the corresponding analyzed fault, $FG_{STR}(\mathbf{x}_r)$, $FG_{GLA}(\mathbf{x}_r)$, and $FG_{ICS}(\mathbf{x}_r)$ are the sea-level spatial variability associated with sterodynamic, glacier, and ice-sheet sea-level rise, respectively, $G(t)$ and $I(t)$ are the global mean glacier and ice sheet sea-level rises at time t , respectively, $S(\mathbf{x}_r, t)$ is the sterodynamic sea-level rise, $\omega(\mathbf{x}_r, t)$, $\zeta(\mathbf{x}_r, t)$, and $\eta(\mathbf{x}_r, t)$ are the total, sterodynamic, glacier, and ice sheet regional sea-level rise values, respectively.

The cumulative distribution function (CDF) of each regional sea-level rise component described in Equation (2) can be developed from statistical analysis of the published climate models, as described in Alhamid et al. (2022a). Considering the emission scenarios (i.e., Representative Concentration Pathways (RCPs)), the CDF of total regional sea-level rise hazard can be expressed as (Alhamid et al. 2022b):

$$F_\psi(\psi(\mathbf{x}_r, t)) = 1 - \int_0^\psi \sum_{RCP=1}^4 \left[\iint_{\Omega_{G,I}} f_{SGI}(\omega(\mathbf{x}_r, t), \zeta(\mathbf{x}_r, t), \eta(\mathbf{x}_r, t) | \Pi_{RCP}) d\zeta d\eta \right] \cdot P(\Pi_{RCP}) d\psi \quad (3)$$

where $F_\psi(\psi(\mathbf{x}_r, t))$ is the CDF of the regional total sea-level rise, $f_{SGI}(\omega(\mathbf{x}_r, t), \zeta(\mathbf{x}_r, t), \eta(\mathbf{x}_r, t) | \Pi_{RCP})$ is the multivariate probability distribution based on sterodynamic, glacier, and ice sheet sea-level rises given climate change scenario Π_{RCP} , where Π_1 , Π_2 , Π_3 , and Π_4 correspond to RCP 2.6, RCP 4.5, RCP 6.0, and RCP 8.5, respectively, $\Omega_{G,I}$ is the joint domain of integration for regional glacier sea-level rise ζ and ice sheet sea-level rise η , and $P(\Pi_{RCP})$ is the occurrence probability of climate change emission scenario Π_n , where $P(\Pi_{RCP}) = 1/4$ is assumed.

2.3 Tsunami hazard assessment considering nonstationary sea-level rise effects

The tsunami hazard curve considering sea-level rise effects is evaluated by performing tsunami propagation analyses under several sea-level rise cases. The fault movement models and their associated parameters (i.e., average stress drop and rake angle) adopted from the Cabinet Office Government of Japan (2012) and Ishibashi et al. (2021) are employed in the surface deformation formula developed by Okada (1986) to generate initial tsunami heights. Sea-level rise effects are taken into account by modifying the bathymetry and roughness coefficient data prior to the propagation analyses. Based on the tsunami's initial height and sea-level rise model, 2D tsunami propagation simulations are performed according to the nonlinear long-wave theory for each case of sea-level rise.

To reduce computational time, Radial Basis Function (RBF) network surrogate model is constructed to develop the relationship between tsunami inundation depth and its corresponding fault parameters. The conditional tsunami hazard curve given a specific sea-level rise is evaluated based on the constructed surrogate model and fault movement uncertainties via MCS. The details of the RBF network model and its validation of the conventional MCS-based tsunami hazard assessment can be found in Alhamid et al. (2022a). Finally, the tsunami hazard curve considering sea-level rise effects is estimated according to the total probability theorem as (Alhamid et al. 2022a):

$$F_{H(\mathbf{x}_r, t)}(h) = \int_0^\infty \left\{ F_{H|\Psi}(h|\psi(\mathbf{x}_r, t)) \cdot \left| -\frac{dF_\Psi(\psi(\mathbf{x}_r, t))}{d\psi} \right| \right\} d\psi \quad (4)$$

where $F_{H(\mathbf{x}_r, t)}(h)$ is the tsunami CDF considering sea-level rise effects over the analyzed target earthquake fault \mathbf{x}_r at time t , and $F_{H|\Psi}(h|\psi(\mathbf{x}_r, t))$ is the conditional tsunami CDF given sea-level rise intensity over the analyzed target earthquake fault \mathbf{x}_r at time t equals ψ . The tsunami hazard described in Equation (4) is utilized to evaluate the time-dependent reliability and risk of structures.

2.4 Fragility assessment of individual structures subjected to tsunami

The fragility of an individual structure subjected to tsunamis can be evaluated from an analytical or empirical approach. This study adopts the empirical fragility curve from De Risi et al. (2017) to reflect realistic post-earthquake conditions. In addition, the fragility curve has considered the prior damage due to seismic and has been used for risk assessment in Japan (Goda, 2020).

By approximating the fragility curve as a lognormal distribution, the probability of a structure jb with structural type st having damage state ds_q given a tsunami inundation depth h (i.e., $P_{jb(st)}(DS = ds_q | H = h)$) can be expressed as:

$$P_{jb(st)}(DS = ds_q | H = h) = \Phi \left[\frac{\ln h - \ln(\nu_{t,q}(st))}{\sigma_{t,q}(st)} \right] \quad (5)$$

where ds_q with $q = 1, 2,$ and 3 correspond to none, moderate, and complete damage state, respectively, $\Phi(\cdot)$ denotes the CDF of the standard normal distribution and $\nu_{t,q}(st)$ and $\sigma_{t,q}(st)$ are the mean and standard deviation of the tsunami fragility curve associated with damage state q and structural type st , respectively. For illustrative purposes, two structural types, wooden and nonwooden structures, are considered and denoted as $st = 1$ and $st = 2$, respectively. The fragility curves for each structural type are presented in Figure 2. It should be noted that the nonwooden structures' fragility adopted herein is equivalent to the concrete fragility in De Risi et al. (2017).

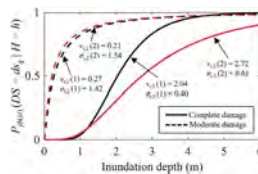


Figure 2. Tsunami fragility curves for building structures (adapted from De Risi et al. 2017).

2.5 Time-dependent failure probability of structures

The failure probability of an individual structure is calculated by convolving the tsunami hazard with the fragility curve. However, due to the nonstationary sea-level rise effects, the failure probability of an individual structure is no longer constant and becomes time-dependent. The time-dependent failure probability of structure jb with structural type st can be evaluated as:

$$P_{jb(st)}(DS = ds_q, T = t) = \int_0^\infty \left\{ P_{jb(st)}(DS = ds_q | H = h) \cdot \left| -\frac{dF_{H(x_r, t)}(h)}{dh} \right| \right\} dh \quad (6)$$

Based on the time-dependent failure probability described in Equation (6), the life-cycle risk of building portfolios under nonstationary sea-level rise effects is developed according to a compound renewal process.

2.6 Life-cycle risk assessment based on a compound renewal process

Due to the effects of sea-level rise, the distribution associated with annual risk becomes conditionally dependent on the earthquake arrival time. The procedure for life-cycle risk assessment under such nonstationary conditions is developed herein.

The direct economic loss L incurred by a building portfolio due to a single earthquake at a particular time t can be expressed as:

$$L(t) = \sum_{st=1}^{nst} \sum_{jb=1}^{njb(st)} \sum_{q=1}^3 P_{jb(st)}(DS = ds_q, T = t) \cdot R_{Ljb(st)}(ds_q) \cdot C_{Rjb(st)} \cdot A_{jb(st)} \cdot g_{DR}(r, t) \quad (7)$$

where $njb(st)$ is the total number of buildings of structural type st , nst is the total number of structural types considered ($nst = 2$), $R_{Ljb(st)}(ds_q)$ is the loss ratio of the damage state q for building structure $jb(st)$, $C_{Rjb(st)}$ is the unit replacement cost of building structure $jb(st)$ per unit area depending on the structural type st , $A_{jb(st)}$ is the floor area associated with structure $jb(st)$, $g_{DR}(r, t)$ is the discounting function to convert loss at time t into net present worth with discount rate r . The building loss ratios $R_{Ljb(st)}(ds_q)$ is assigned as 0.0, 0.3, and 1.0 for none, moderate, and complete damage, respectively, following Goda (2020).

In this study, the structures are assumed to be restored to those in the pre-hazard stage after each earthquake. Furthermore, let T_n describe the earthquake's n -th arrival time, such that $T_n = W_1 + W_2 + \dots + W_n$. The interarrival time W_i is assumed to be an independent and identically distributed random variable with PDF described in Equation (1). Furthermore, let $Y(t_D)$ represents the cumulative economic loss resulting from all possible earthquake occurrences from the last earthquake occurrence until an analyzed time t_D . Therefore, the probability of cumulative economic loss $Y(t_D)$ exceeding a value y can be expressed as:

$$P(Y(t_D) > y) = P(L(t_1) + \dots + L(t_n) > y | \mathbf{T} = \mathbf{t}) \cdot P(\mathbf{T} = \mathbf{t}) \quad (8)$$

$$P(L(t_1) + \dots + L(t_n) > y | \mathbf{T} = \mathbf{t}) = 1 - \int_0^\infty \dots \int_0^\infty \left\{ f_{L_1 | T_1} \left(\left[y - \sum_{a=2}^n l_a \right] | t_1 \right) \cdot \prod_{b=2}^n f_{L_b | T_b}(l_b | t_b) \right\} dl_1 \dots dl_n \quad (9)$$

where $\mathbf{T} = \{T_1, T_2, \dots, T_n\}^T$ represents the combination of random variables associated with arrival time with a value of $\mathbf{t} = \{t_1, t_2, \dots, t_n\}^T$, and $f_{L | T}(l | t)$ is the conditional PDF of economic loss L with a value l given $T = t$.

The term $P(\mathbf{T} = \mathbf{t})$ in Equation (8) represents the joint probability distribution of arrival time, which can be defined according to Jung (1963) as:

$$P(\mathbf{T} = \mathbf{t}) = \lambda^n e^{-\lambda t_D} dt_1 dt_2 \dots dt_n \quad (10)$$

As shown in Equations (8) to (10), the cumulative economic loss $Y(t_D)$ depends on the number of earthquake occurrences n and arrival time T , where both variables are substantially uncertain. To circumvent this difficulty, an MCS procedure is proposed and employed to carry out the life-cycle risk assessment, as presented in Figure 3. A case study is provided in the following subsection to illustrate the effectiveness of the proposed framework.

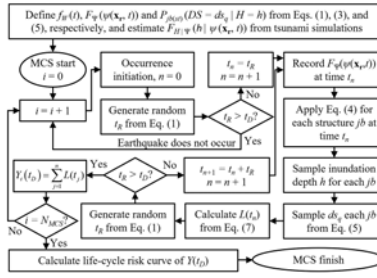


Figure 3. MCS procedure to estimate life-cycle tsunami risk of building portfolio under nonstationary sea-level rise effects based on the compound renewal process.

3 ILLUSTRATIVE EXAMPLE

As an illustrative example, the framework is implemented for building portfolios in Kochi Prefecture of Japan subjected to the anticipated Nankai Trough earthquake, namely Kochi and Kounan cities. The analyzed municipalities and their corresponding building population are shown in Figure 4.

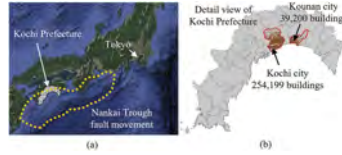


Figure 4. (a) Location of Kochi Prefecture and the Nankai Trough fault movement, and (b) location of the analyzed municipalities and the corresponding building population.

3.1 Tsunami hazard assessment considering nonstationary sea-level rise effects

To estimate the inclusive tsunami hazard curve considering sea-level rise effects, sea-level rise hazard information over the analyzed earthquake is necessary. The time-variant sea-level rise hazard curve evaluated over the Nankai Trough earthquake is adopted from Alhamid et al. (2022b) and shown in Figure 5.

Tsunami propagation analyses are carried out using 15 tsunami fault movements from Ishibashi et al. (2021) considering the uncertainties associated with average stress drop and rake angle. The average stress drop is modeled as a lognormal distribution with a mean and standard deviation of 1.2 and 1.0 MPa, respectively, truncated at 3.0 MPa. As for the rake angle, a normal distribution is assumed with a mean and standard deviation of 0° and 10°, respectively. To convert the fault parameters into slip dislocation for initial tsunami height, the following formula is used (Alhamid et al. 2020a):

$$D_f = \frac{16(\Delta\sigma)S_f^{0.5}}{f_R \cdot 7\pi^{1.5}} \quad (11)$$

where D_f is the slip dislocation, $\Delta\sigma$ is the average stress drop, S_f is the fault area, and f_R is the fault rigidity.

The tsunami propagation analyses are performed based on the RBF network surrogate model described in Alhamid et al. (2022b). Based on the RBF network, the conditional tsunami hazard curve is evaluated and convolved with sea-level rise hazard according to Equation (4) to obtain the tsunami hazard curve considering sea-level rise effects.

Figure 5(a) and (b) show the tsunami propagation analysis results in Kochi and Kounan cities for average stress drop and rake angle of 2 MPa and 10°, respectively, under 0.6 meters

of sea-level rise. The tsunami intensity is greater in Kounan city, while Kochi city shows a higher inundation area due to lower topography. Therefore, the tsunami impacts considerably depend on the geographical characteristics of the analyzed municipalities. To develop the tsunami hazard considering sea-level rise effects, the sea-level rise hazard over the Nankai Trough fault movement is evaluated following the procedure in Alhamid et al. (2022a) and is shown in Figure 5(c).

Figure 5(d) shows the tsunami hazard curve for the analyzed cities assuming that the anticipated Nankai Trough earthquake will occur in 2022 and 2100. Due to the effects of sea-level rise, the tsunami hazard curves for both analyzed cities are exacerbated.

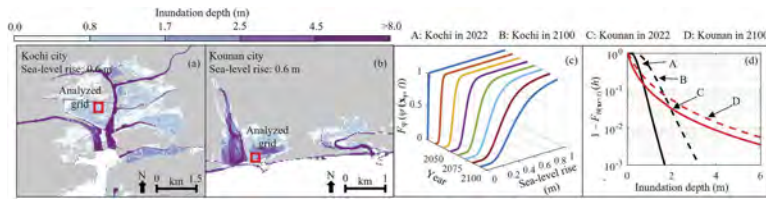


Figure 5. (a) Tsunami inundation map in Kochi city, (b) Tsunami inundation map in Kounan city, (c) Sea-level rise hazard evaluated over the Nankai Trough fault movement (Alhamid et al., 2020b), and (d) Tsunami hazard evaluated in the analyzed grid.

3.2 Life-cycle tsunami risk of building portfolio under nonstationary sea-level rise effects

The life-cycle tsunami risk is assessed according to the procedure described in Figure 3. In this study, the replacement cost $C_{R/b(st)}$ is assumed as 160,000 JPY/m² and 150,000 JPY/m² for wooden and nonwooden structures, respectively (Goda, 2020). For illustrative purposes, a discount rate of 0.3% is assumed. In addition, building structures in the same tsunami grid cell depicted in Figure 5 are assumed to be under the same tsunami hazard and share the same failure probability.

Figure 6 shows the life-cycle tsunami risk of building portfolios in the analyzed municipalities, assuming a Poisson process of earthquake occurrence with a mean recurrence interval of 117 years/event. With an exceedance probability of more than 0.2, the risk associated with cumulative loss in Kounan city is higher than that in Kochi. However, the risk in Kochi city increases and exceeds that of Kounan when the exceedance probability is lower than 0.2. Comparing this result to previous tsunami disasters such as the 2011 Great East Japan earthquake, Nankai Trough earthquake is expected to cause a more significant loss when other affected cities are accounted.

According to the results presented in Figure 6, when the effects of sea-level rise are considered, the tsunami risk in Kochi city is consistently higher than in Kounan city for all exceedance probabilities. Therefore, considering sea-level rise is imperative to enhance the accuracy of life-cycle tsunami risk assessment and improve disaster preparedness for coastal communities.

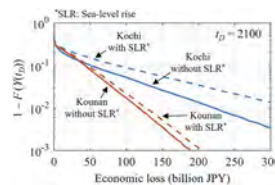


Figure 6. Life-cycle tsunami risk of building portfolios in the analyzed cities under the Poisson process.

4 CONCLUSIONS

The following conclusions are drawn:

1. A framework for estimating the life-cycle tsunami risk of building portfolios under nonstationary sea-level rise effects is established. The framework systematically considers the uncertainties associated with the number of earthquake occurrences and their arrival time.
2. An MCS-based compound renewal process is proposed to integrate the nonstationary sea-level rise effects with cumulative economic loss assessment. Based on the MCS numerical solution, the proposed framework promotes a better risk information decision by enabling the estimation of the risk curve of cumulative loss.
3. Sea-level rise affects the life-cycle tsunami risk of the analyzed municipalities differently depending on the associated geographical characteristics. Nevertheless, the life-cycle tsunami risks substantially increase when considering sea-level rise effects.

To enhance the life-cycle tsunami risk assessment, future studies should try to develop a more realistic model of earthquake occurrence such as the non-Poisson model and consider various mean recurrence intervals of earthquake occurrence.

REFERENCES

- Akiyama, M., Frangopol, D.M. & Ishibashi, H. 2020. Toward life-cycle reliability-, risk- and resilience-based design and assessment of bridges and bridge networks under independent and interacting hazards: emphasis on earthquake, tsunami and corrosion. *Structure and Infrastructure Engineering*. 16(1):26–50.
- Alhamid, A.K., Akiyama, M., Ishibashi, H., Aoki, K., Koshimura, S. & Frangopol, D.M. 2022. Framework for probabilistic tsunami hazard assessment considering the effects of sea-level rise due to climate change. *Structural Safety*. 94.
- Alhamid, A.K., Akiyama, M., Aoki, K., Koshimura, S. & Frangopol, D.M. 2022. Stochastic renewal process model of time-variant tsunami hazard assessment under nonstationary effects of sea-level rise due to climate change. *Structural Safety*. 99.
- Cabinet Office Government of Japan. 2012. *Investigative commission on the modeling of giant earthquake caused by Nankai Trough earthquake: Modeling of tsunami fault*.
- Goda, K. 2020. Multi-Hazard Portfolio Loss Estimation for Time-Dependent Shaking and Tsunami Hazards. *Frontiers in Earth Science*. 8.
- Ishibashi, H., Akiyama, M., Frangopol, D.M., Koshimura, S., Kojima, T. & Nanami, K. 2021. Framework for estimating the risk and resilience of road networks with bridges and embankments under both seismic and tsunami hazards. *Structure and Infrastructure Engineering*. 17(4):494–514.
- Jung, J. 1963. A theorem on compound poisson processes with time-dependent change variables. *Scandinavian Actuarial Journal*. 1963(1–2):95–98.
- Kajitani, Y., Chang, S.E. & Tatano, H. 2013. Economic Impacts of the 2011 Tohoku-oki earthquake and tsunami. *Earthquake Spectra*. 29.
- Mechler, R. 2016. Reviewing estimates of the economic efficiency of disaster risk management: opportunities and limitations of using risk-based cost–benefit analysis. *Natural Hazards*. 81(3):2121–2147.
- Okada, Y. 1986. Surface deformation due to shear and tensile faults in a half-space. *International Journal of Rock Mechanics and Mining Sciences & Geomechanics Abstracts*. 23(4):128.
- Pandey, M.D. & van der Weide, J.A.M. 2018. Probability distribution of the seismic damage cost over the life cycle of structures. *Structural Safety*. 72:74–83.
- De Risi, R., Goda, K., Yasuda, T. & Mori, N. 2017. Is flow velocity important in tsunami empirical fragility modeling? *Earth-Science Reviews*. 166:64–82.
- De Risi, R., De Paola, F., Turpie, J. & Kroeger, T. 2018. Life Cycle Cost and Return on Investment as complementary decision variables for urban flood risk management in developing countries. *International Journal of Disaster Risk Reduction*. 28:88–106.
- Sepúlveda, I., Haase, J.S., Liu, P.L.F., Grigoriu, M. & Winckler, P. 2021. Non-Stationary Probabilistic Tsunami Hazard Assessments Incorporating Climate-Change-Driven Sea Level Rise. *Earth's Future*. 9(6).

Life-cycle design of concrete highway bridge decks under climate change

H. Shirkhani, Z. Lounis & J. Zhang

National Research Council of Canada, Ottawa, ON, Canada

ABSTRACT: Chloride-induced corrosion is the main deterioration mechanism that governs the service life design of many concrete structures such as concrete bridge decks in Canada. The annual average surface air temperature over Canada has warmed historically and is projected to rise approximately twice the global average due to climate change. The temperature increase will lead to an increase in the probability of corrosion initiation of reinforcing steel and a shortening of service life of concrete structures. Current approaches for life cycle design of concrete bridge decks do not consider the impact of climate change. A probabilistic and mechanistic approach is proposed and demonstrated through an illustrative test case to assess the impact of climate change on life cycle design of concrete bridge decks exposed to corrosive environments. The time-dependent probability of corrosion was found to increase with temperature. In corrosive environments, corrosion-resistant steel reinforcement and high performance concrete can be used to reduce the corrosion probability significantly in the changing climate.

1 INTRODUCTION

Infrastructure systems, such as bridges, are critical to the social welfare, growth of the economy and protection of the environment. Bridge systems in North America are aging and deteriorating which can be exacerbated by climate change. Corrosion is one of the most costly deteriorating mechanisms and causes the most widespread damage in reinforced concrete (RC) and steel bridges, particularly in regions with harsh winters that require the use of road de-icing salts. The Federal Highway Administration (FHWA, 2002) estimated the annual direct cost of corrosion of highway bridges in the U.S. at \$8.3 billion and consisting of \$3.8 billion to replace structurally deficient bridges over ten years. In particular, climate change can also exacerbate the RC infrastructure corrosion-induced deterioration. Corrosion processes are known to be temperature dependent. For instance, RC samples can experience higher rates of corrosion at increasing temperatures (Guest et al., 2020). Moreover, the increasing ambient temperature will reduce the chloride threshold of reinforced concrete (Zhang et al., 2018; Shirkhani et al., 2020). Therefore, it is essential to consider the climate change impacts in the design of RC structures against corrosion.

Development of methodologies for the prediction of service life of RC bridge decks built in corrosive environments and subjected to changing climate is therefore of great importance. These methodologies can help with the effective design and management of bridge infrastructure through reducing the risk of failure and extending the service life. A comprehensive model for the estimation of the service life of RC bridge decks may include various stages of corrosion. However, many important RC infrastructures consider the corrosion initiation time as the design service life, which conservatively assumes the initiation of corrosion as the limit state (Zhang and Lounis 2006 and 2009; Sudret et al., 2008). In addition, there are different approaches for the assessment of the probability of failure of infrastructure systems and components. Some of these approaches, such as Markovian-based models require limited amount of data on the condition of the infrastructure. These approaches rely on statistical deterioration modelling methods that use historical data to predict the future deterioration of bridges (e.g. see Roelfstra et al. 2004; Agrawal, et al. 2010). The main drawbacks of these

models include dependency on the availability, quality, and applicability of historical data as well as lack of consideration of ambient climatic conditions and de-icing agent applications.

On the other hand, mechanistic and probabilistic approaches require more data on loads, material properties, and ambient climatic conditions as well as the uncertainties in the governing parameters and models (Lounis and Daigle, 2008; and Lounis and McAllister, 2016). Considering the physical corrosion processes, mechanistic models allow for the simulation of bridge deck deterioration over time, which makes these models an appropriate choice for considering the effects of climate change.

Most of the current approaches for service life design are based on prescriptive requirements regarding the minimum concrete cover depth, maximum water/cement ratio, etc. Current prescriptive requirements and inadequate design and maintenance have led to a large number of structurally and /or functionally deficient concrete infrastructures in North America, including highway bridges. In addition, between 1948 and 2016, the best estimate of mean annual temperature increase is 1.7°C for Canada, and depending on the level of greenhouse gas (GHG) emissions, the average temperatures in Canada are expected to rise by an additional 1.5 to 6.3°C by 2100, which is approximately twice the global average (Bush and Lemmon, 2019). It is expected that increases in temperatures will lead to increases in the diffusion coefficients and reductions in the chloride threshold levels, which in turn will lead to reduced service life of concrete infrastructures built in corrosive environments (Zhang et al. 2018). On the other hand, the increase in temperature may lead to a reduction of the surface chloride concentration due to a reduction in the use of de-icing salts during winter in some regions in North America, which is not considered in this study.

Previous research studied the service life design of RC bridge decks. Zhang and Lounis (2009) presented a performance-based approach for the service life design of RC structures by analyzing the relationships and sensitivity of four design parameters that govern the time to corrosion initiation of reinforced concrete structures built in chloride-laden environments. However, the literature lacks studies on climate change impacts on the corrosion of RC structures. Wang et al. (2010a,b) studied the impacts of climate change on the corrosion of concrete structures by taking into account the change of CO₂ concentration in the atmosphere and the temperature effect on the diffusion of chlorides into concrete. Shirkhani et al. (2020) studied the impact of temperature rise on the design service life of concrete bridge decks under different climate change conditions in different regions of Canada. Guest et al. (2020) developed a bridge deck design model by simulating three deterioration stages of concrete bridge decks, including the initiation of steel corrosion, the generation of concrete cracks, and the propagation of cracks.

In this paper, a probabilistic-mechanistic approach is used to assess the impact of climate change on life cycle performance of RC bridge decks in corrosive environments. Chloride-induced corrosion is the main deterioration mechanism that is assumed to govern the service life of RC bridge decks. The Monte Carlo approach together with a chloride diffusion-based model are used to determine the probability of corrosion initiation of steel reinforcement, which is assumed as the design service life of RC bridge decks. This assumption is adequate for critical concrete infrastructures such as RC bridge decks, while for other structures the service life can be assumed the sum of the corrosion initiation time and a corrosion propagation time such as time to cracking, spalling, or delamination. The proposed methodology can help achieve a long service life and minimize the risk of failure of RC bridge decks, including the minimization of the risk of capacity and/or functionality loss due to excessive deterioration. In this paper, the focus is on the probabilistic modeling of the service life and durability design of concrete infrastructures subjected to corrosion from de-icing salts and climate change-induced temperature rise.

2 METHODOLOGY

2.1 Corrosion model

The corrosion of concrete structures is a two-stage process that includes a corrosion initiation stage and a corrosion propagation stage (Tuutti 1982). In this study, the service life is defined as the time to the onset of corrosion of bridge decks exposed to chlorides. Equation 1 shows a simplified diffusion-based model that is implemented to estimate the time variation of chloride ingress into concrete using Crank's (1975) solution of Fick's second law of diffusion:

$$C(x, t) = C_s \left[1 - \operatorname{erf} \left(\frac{x}{2\sqrt{Dt}} \right) \right] \quad (1)$$

where $C(x, t)$ is the chloride concentration at depth x (cm) after time t (year), D is the chloride diffusivity (cm^2/year) corresponding to the type of the concrete, C_s is the surface chloride concentration (kg/m^3), which is a measure of the environmental corrosion load applied on the RC structure, and erf is the error function. The time to the onset of corrosion (t_i) is defined as when the chloride concentration C at the rebar level (i.e. $x=d_c$ the concrete cover depth) exceeds the rebar chloride threshold (C_{th}), which depends on the type of the reinforcing steel and its resistance to chloride ions.

It should be noted that uncertainties are associated with the parameters in the model. For instance, the concrete chloride diffusivity (D) is not a constant but rather depends on time, temperature, and depth. Moreover, the chloride threshold value of the rebar (C_{th}) is reported with a considerable scatter in the literature, and the level of uncertainty of the concrete cover depth (d_c) depends on the quality of construction. In addition, the surface chloride concentration (C_s) is subjected to a continually changing chloride exposure. Given the level of uncertainties and the stochastic nature of the problem, we will consider these uncertainties through the application of a probabilistic approach, which will be explained in the following section.

2.2 Impact of temperature on time to corrosion initiation

Temperature can directly affect the oxidation and reduction rates in corrosion as an electrochemical process, and it also affects the diffusion of chlorides in the concrete. The dependence of the chloride diffusion coefficient on temperature is given by the following Arrhenius relationship (Saetta et al. 1993):

$$D_T = D_{T_0} e^{\frac{E_a - D}{R} \left(\frac{1}{T_0 + 273.16} - \frac{1}{T + 273.16} \right)} \quad (2)$$

where D_T is a function of temperature T ($^{\circ}\text{C}$) and D_{T_0} is the reference chloride diffusion coefficient at the reference temperature T_0 , with R being the gas constant ($R=8.314 \times 10^{-3}$ kJ/mol). There is considerable uncertainty associated with the estimation of the chloride diffusion coefficient. It was shown by Zhang et al. (2018) that the mean value of D can be considered to be $0.32 \text{ cm}^2/\text{year}$ for high performance concrete (HPC) and $2.52 \text{ cm}^2/\text{year}$ for normal performance concrete (NPC), with corresponding activation energy values of $E_a - D = 47$ and 30 KJ/mol, respectively.

As Equation 2 shows, the chloride diffusion coefficient varies with temperature. We consider the temperature rise of ΔT , which indicates the difference between the temperature in the future (T_{fut}) and baseline (T_{base}) time periods due to climate change. The relative change in the chloride diffusion coefficient due to the temperature rise can be then estimated from Equation 3:

$$\frac{D_{fut}}{D_{base}} = \exp \left[\frac{E_a - D}{R} \left(\frac{1}{T_{base}} - \frac{1}{T_{fut}} \right) \right] \quad (3)$$

With the temperature-dependence assumption of the corrosion rate and following the Arrhenius law, the chloride threshold value can be assumed inversely proportional to the corrosion reaction rates and follows thus inversely the Arrhenius law with temperature. Temperature can also affect the rebar chloride threshold value in a different way through concrete chemistry. With a rising temperature, the chloride threshold value is reduced due to the release of more chloride ions from concrete with higher temperatures, and at the same time by accelerated corrosion reactions. These two mechanisms can be assumed independent of each other, and the chloride threshold values with temperature is thus expressed as follows (Zhang et al., 2018; Shirkhani et al., 2020):

$$C_{th-T} = C_{th-T_0} \exp \left[\frac{(E_{Cl-concr} + E_{Cl-steel})}{R} \left(\frac{1}{T} - \frac{1}{T_0} \right) \right] \quad (4)$$

where (C_{th-T_0}) is the chloride threshold value at the reference temperature T_0 , and $E_{Cl-concr}$ and $E_{Cl-steel}$ are the activation energy for release of free chlorides and the rebar activation energy, respectively. The above analysis is based on the assumption that the chloride threshold value of rebar decreases with temperature following the inverse of the Arrhenius law based on very limited available studies. The activation energy value can range from 22 to 48 KJ/mol depending on the mechanisms.

Similar to the chloride diffusion coefficient, Equation 4 can be used to estimate the relative change in the chloride threshold value due to temperature rise as follows:

$$\frac{C_{thfut}}{C_{thbase}} = \exp\left[\frac{(E_{Cl-concr} + E_{Cl-steel})}{R}\left(\frac{1}{T_{fut}} - \frac{1}{T_{base}}\right)\right] \quad (5)$$

As Equations 2 to 5 show, the time to corrosion initiation is a function of temperature. Therefore, the temperature variation within the future periods under climate change will lead to deviations of the design service life from the indented design service life obtained under historical climatic conditions.

2.3 Life cycle performance prediction model

In this paper, the time to corrosion initiation is assumed as the service life of RC bridge decks. As discussed above, the values of chloride concentration at the rebar level and the rebar chloride threshold are not deterministic parameters but are associated with high levels of uncertainty. The chloride concentration at the rebar level is a random variable which depends on several uncertain parameters including the chloride diffusion coefficient, and concrete cover depth. The uncertainty in these parameters can be reflected through assuming a specific type of statistical distribution (e.g. normal, lognormal, gamma, Weibull, uniform, etc.), which can be obtained from field measurements, experience or literature.

Given the uncertainty in the performance model parameters, we formulate the model to estimate the probability that the chloride concentration at the reinforcing steel level is higher than the chloride threshold level i.e. $P[C(d_c, t) > C_{th}]$ as a probabilistic problem. This probability represents a realistic measure of the probability of corrosion of RC bridge decks, which can be expressed as:

$$P_{cor}(t) = P[C(d_c, t) > C_{th}] \quad (6)$$

Assume that both $C(d_c, t)$ and C_{th} are independent random variables with probability density functions (pdf) $f_C(d_c, t)$ and $f_{C_{th}}(c_{th})$ and cumulative distributive functions (cdf) $F_C(d_c, t)$ and $F_{C_{th}}(c_{th})$, respectively. Then, the probability of corrosion at time t , can be determined as follows:

$$P_{cor} = \int_0^{\infty} F_{C_{th}}(x) f_{C(d_c, t)} dx \quad (7)$$

We employ the Monte Carlo method in order to compute the probability of corrosion over the corrosion domain. In this method, we identify first the parameters and variables in Equation 7 that are considered as random variables. Then, a distribution will be assigned to each parameter. We then generate inputs randomly from a probability distribution over the domain and perform a deterministic computation and aggregate the results to determine to the probability of corrosion.

3 TEMPERATURE RISE UNDER CLIMATE CHANGE

Since 1950, the annual average surface air temperature over Canada's landmass has warmed by 1.7°C, and average temperatures in Canada are expected to rise by an additional 1.5°C to 4.5°C by 2070, which is approximately twice the global average (Bush and Lemmen, 2019). The rate of warming is even higher in Northern Canada.

The projected annual mean temperature change across Canada is presented in the Canadian Climate Change Report (Bush and Lemmen, 2019). Both low (RCP 2.6) and high (RCP8.5) emission scenarios are considered with two time periods of: (i) near term (2031–2050) – when differences in emission scenarios are modest; and (ii) the late century (2081–2100) – when climatic

responses to the low and high emission scenarios will have diverged considerably – are selected and the changes are estimated relative to the baseline period of 1986–2005 (see Figure 1).

As it can be seen, all regions across Canada are warming under both low and high emission scenarios with enhanced warming at higher latitudes. In the near term (2031–2050), the differences between the low and the high emission scenarios are in the order of 0.5°C to 1°C and not significant. However, for the late century (2081–2100), the differences become very large. For instance, for Canada as a whole the projected temperature increases are roughly 4°C higher under the high emission scenario while regional temperature increase can be as high as 11 °C.

4 ILLUSTRATIVE TEST CASE

We consider a bridge deck located in Ottawa, Ontario with a deck thickness of 225 mm and reinforced with isotropic reinforcement with a percentage of 0.3% for both top and bottom layers in both longitudinal and transverse directions.

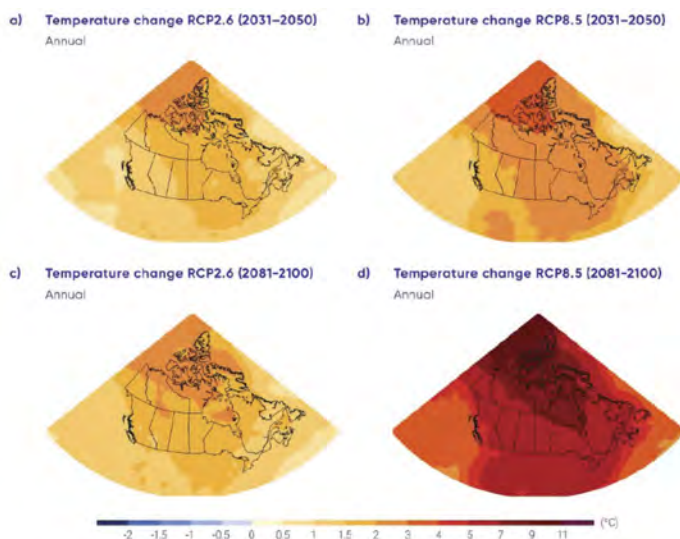


Figure 1. Projected annual mean temperature change (°C) relative to 1986–2005 for the 2031–2050 (top) and 2081–2100 (bottom) periods under RCP2.6 (left) and RCP8.5 (right) [Bush and Lemmen, 2019].

We assume a baseline scenario together with three future scenarios considering temperature increase of $\Delta T = 2, 4$ and 6°C , which can be achieved under low and high emission scenarios in southern Canada. The average annual temperature for the baseline scenario is estimated using the Environment and Climate Change Canada historical climatic data for the period of 1986–2005 for Ottawa, Canada ($T_{\text{base}}=6.3^\circ\text{C}$). Then, for each parameter in Equation 1, we assume the distribution type and its corresponding mean and coefficient of variation. For instance, for the high performance concrete in the baseline scenario, we set the mean value of the diffusion coefficient as $0.20\text{ cm}^2/\text{year}$ with a coefficient of variation of 25% (Lounis and Daigle 2008). Moreover, we assume log-normal distributions for all parameters.

For the investigated bridge deck, the corrosive environment is defined by the surface chloride concentration with a mean value of 6 kg/m^3 and a coefficient of variation of 25%, while the concrete cover depth has a mean value of 70 mm and a coefficient of variation of 25% (Lounis and Daigle 2008). Two types of reinforcing steel are investigated: (i) Conventional black steel with a mean chloride threshold value of 0.70 kg/m^3 and a coefficient of variation of 20% (Lounis and Daigle 2008); and (ii) Corrosion-resistant steel with a mean chloride threshold value of 1.4 kg/m^3 and a coefficient of variation of 20% (Lounis and Daigle 2008). The selected corrosion-resistant steel has a chloride threshold value that is double that of black steel, which could correspond to the case of galvanized steel reinforcement.

Table 1. Mean value and coefficient of variation (COV) for parameters in baseline and future scenarios.

Parameter	Baseline		$\Delta T = 2^\circ\text{C}$		$\Delta T = 4^\circ\text{C}$		$\Delta T = 6^\circ\text{C}$	
	Mean	COV	Mean	COV	Mean	COV	Mean	COV
Surface chloride content (kg/m^3)	6	25	6	25	6	25	6	25
Concrete cover depth (mm)	70	25	70	25	70	25	70	25
Threshold chloride content (kg/m^3) for black steel	0.70	20	0.63	22	0.56	24	0.51	26
Threshold chloride content (kg/m^3) for corrosion-resistant steel	1.40	20	1.25	22	1.13	24	1.01	26
HPC diffusion coefficient (cm^2/year)	0.20	25	0.23	27	0.27	29	0.31	31
NPC diffusion coefficient (cm^2/year)	0.30	25	0.33	27	0.36	29	0.39	31

To design long life concrete bridge decks, one may consider using high performance concrete or ultra-high performance concrete, which have lower apparent chloride diffusion coefficients compared to normal concrete (Table 1). In this test case, we consider two concrete types: (i) High performance concrete (HPC) with a mean value of the diffusion coefficient of $0.20 \text{ cm}^2/\text{year}$ and a coefficient of variation of 25%, and (ii) Normal performance concrete (NPC) with a mean value of the diffusion coefficient of $0.30 \text{ cm}^2/\text{year}$ and a coefficient of variation of 25%.

Using the Arrhenius relationship (Equations 3 and 5), the mean values of the chloride diffusion coefficient and chloride threshold value for the temperature rise scenarios are estimated. It is assumed that the increase of diffusion coefficient and decrease of chloride threshold value with temperature are time-invariant; i.e. we assume that the temperature rise occurs on the average of the annual temperature over the design life of the RC bridge deck. Since the future projected changes in temperature rise is uncertain, we assume that the uncertainties in the diffusion coefficient and chloride threshold value with temperature rise are higher than the base case. Hence, for these two parameters, the coefficient of variation is assumed to increase with temperature rise in future scenarios.

5 RESULTS AND DISCUSSION

We consider different scenarios of the test case to evaluate the impact of climate change and the role of using HPC and corrosion-resistant steel in achieving better performance. In all simulations, we use 100,000 random samples for the model variables in the Monte-Carlo simulations, and consider a 50-year planning horizon.

In the first test case, we assess the impact of climate change on a bridge deck with NPC and black steel rebar. Figure 2a shows the variations in the probability of corrosion with time. It can be seen that the climate change induced temperature increase can significantly affect the performance of bridge decks. The probability of corrosion under climate change induced warming becomes larger with time. The probability of corrosion at almost half of the planning horizon (26 years) is about 20% in the baseline scenario (i.e. with no warming) while it increases to 30%, 40% and 50% for warming levels of $\Delta T = +2^\circ\text{C}$, $+4^\circ\text{C}$ and $+6^\circ\text{C}$, respectively.

The second test case examines the performance in terms of time-variations of probability of corrosion of RC bridge decks made with corrosion-resistant steel in a changing climate. We compare the performance of two NPC bridge decks, one reinforced using black steel and the other one using corrosion-resistant steel. Figure 2b illustrates the time-variations of the probability of corrosion for these two RC bridge decks subject to various warming levels under climate change. As expected, the time-varying probability of corrosion of concrete bridge decks reinforced with corrosion-resistant steel is much lower than the one corresponding to black or carbon steel. For example, under the warming level of $\Delta T = +2^\circ\text{C}$ after 30 years, the probability of corrosion of a bridge deck with corrosion-resistant steel is 28%, which is 40% lower than the corrosion probability of the deck with black steel (68%). The results show the benefit of using corrosion-resistant steels for designing long life concrete infrastructures.

In the third test case, we examine the use of HPC as an alternative for designing long life RC bridge decks as HPC benefits from having lower chloride diffusion coefficients. In this example,

the probability of corrosion of bridge decks made with HPC is compared to that of NPC under $\Delta T=+2^{\circ}\text{C}$ and $\Delta T=+6^{\circ}\text{C}$. Figure 2c illustrates that after 50 years, the probability of corrosion of the bridge deck made with HPC is about 48% and 72% while the probability of corrosion for NPC deck is about 68% and 83% under $\Delta T=+2^{\circ}\text{C}$ and $\Delta T=+6^{\circ}\text{C}$ warming levels, respectively.

These examples illustrate the importance of the consideration of climate change in service life prediction and service life design of RC bridge decks, and the essential role of using high performance concrete and corrosion-resistant rebar materials in reducing the probability of corrosion. It should be noted that the final choice of the optimal design should include a comparison of the life cycle costs of the different design alternatives (Lounis and Daigle 2008).

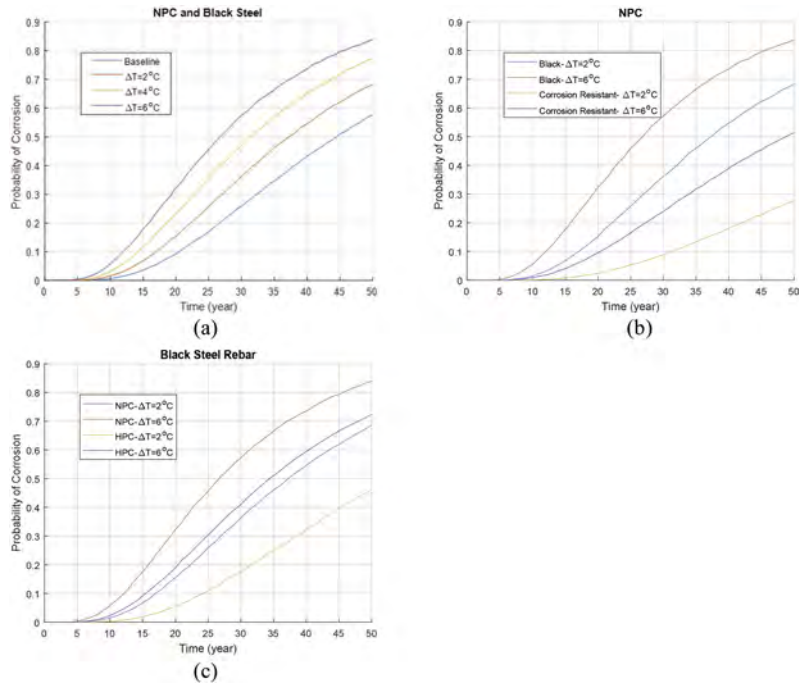


Figure 2. Probability of corrosion under various warming levels for RC bridge decks with (a) NPC and black steel reinforcement (b) black steel and corrosion-resistant steel reinforcement and (c) NPC and HPC.

6 CONCLUSIONS

Temperature increase due to climate change can lead to an increase in chloride diffusivity of concrete while decreasing the threshold chloride values of rebars, which yields an increase in the probability of corrosion and a shortening of service life of RC bridge decks. Using a probabilistic-mechanistic approach, the impact of temperature rise due to climate change on the probability of the time of corrosion onset of RC bridge decks is modelled. We employed a simplified diffusion-based model to estimate the time variation of chloride ingress into concrete and used the Arrhenius relationship to quantify the impact of temperature increase on the chloride diffusivity of concrete and the threshold chloride values of rebars. Based on the projected changes in annual average temperatures in near term and late century time periods under low and high emission scenarios, we defined warming levels of $\Delta T = +2^{\circ}\text{C}$, $+4^{\circ}\text{C}$ and $+6^{\circ}\text{C}$ and compared the performance of RC bridge decks to a baseline scenario with no warming. Uncertainties in the parameters governing the service life, such as concrete cover depth, chloride threshold, chloride diffusion, and surface chloride concentration are considered by modeling them as random variables using the Monte Carlo method. The service life of concrete structures can be defined as the time at which the probability of corrosion reaches an acceptable value for the different types of concrete, reinforcing steel and concrete cover depths. Different test cases were illustrated to assess the impact of temperature increase on RC bridge decks and investigate the effects of using HPC and corrosion-

resistant steel for designing long life RC bridge decks. The results illustrated that the time-dependent probability of corrosion increases with temperature. For the RC bridge decks made with NPC and black steel, the results indicated that at the end of a 50-year planning horizon, the probability of corrosion increases approximately by 10% per 2°C temperature increase. To reduce the high probability of corrosion due to temperature increase, corrosion-resistant steel reinforcement and HPC can be used. For instance, the use of corrosion-resistant steel reduced the corrosion probability by 40% and 30% after 50 years for the warming levels of $\Delta T = +2^{\circ}\text{C}$ and $+6^{\circ}\text{C}$, respectively compared to black steel reinforcement. The final selection of service life design should take into account the life cycle costs incurred within a given life cycle of RC bridge decks.

REFERENCES

- Agrawal, A.K., Kawaguchi, A. and Chen, Z., 2010. Deterioration rates of typical bridge elements in New York. *Journal of Bridge Engineering*, 15(4), pp.419–429.
- Bush, E., and D. S. Lemmen. 2019. Canada's changing climate report, 444. Ottawa: Government of Canada.
- Crank, J., 1979. *The mathematics of diffusion*. Oxford university press.
- G. Koch, M. Brongers, N. Thompson, Y. Virmani, and J. Payer, *Corrosion cost and preventive strategies in the United States*. Report No. FHWA-RD-01-156, R315-01. Washington, DC: Federal Highway Administration, 2002.
- Grove, A.T. 1980. Geomorphic evolution of the Sahara and the Nile. In M.A.J. Williams & H. Faure (eds), *The Sahara and the Nile*: 21–35. Rotterdam: Balkema.
- Guest, G., Zhang, J., Atadero, R. and Shirkhani, H., 2020. Incorporating the effects of climate change into bridge deterioration modeling: The case of slab-on-girder highway bridge deck designs across Canada. *Journal of Materials in Civil Engineering*, 32(7), p.04020175.
- Jappelli, R. & Marconi, N. 1997. Recommendations and prejudices in the realm of foundation engineering in Italy: A historical review. In Carlo Viggiani (ed.), *Geotechnical engineering for the preservation of monuments and historical sites; Proc. intern. symp., Napoli*, 3-4 October 1996. Rotterdam: Balkema.
- Johnson, H.L. 1965. Artistic development in autistic children. *Child Development* 65(1): 13–16.
- Lounis, Z. and Daigle, L., 2008, September. Reliability-based decision support tool for life cycle design and management of highway bridge decks. In *Annual Conference of the Transportation Association of Canada* (pp. 1–19).
- Lounis, Z. and McAllister, T.P., 2016. Risk-based decision making for sustainable and resilient infrastructure systems. *Journal of Structural Engineering*, 142(9), p.F4016005.
- Polhill, R.M. 1982. *Crotalaria in Africa and Madagascar*. Rotterdam: Balkema.
- Roelfstra, G., Hajdin, R., Adey, B. and Brühwiler, E., 2004. Condition evolution in bridge management systems and corrosion-induced deterioration. *Journal of Bridge Engineering*, 9(3), pp.268–277.
- Shirkhani, H., Seidou, O., Mohammadian, A. and Qiblawey, H., 2016. Projection of significant wave height in a coastal area under RCPs climate change scenarios. *Natural Hazards Review*, 17(1), p.04015016.
- Shirkhani, H., Zhang, J. and Lounis, Z., 2020. Ensemble analysis of climate-change impacts on design-service life of reinforced concrete bridge decks across Canada. *Natural Hazards Review*, 21(3), p.04020030.
- Sudret, B., 2008. Probabilistic models for the extent of damage in degrading reinforced concrete structures. *Reliability Engineering & System Safety*, 93(3), pp.410–422.
- Tuutti, K., 1982. *Corrosion of steel in concrete*. Cement-och betonginst.
- Vetter, T., Reinhardt, J., Flörke, M., Van Griensven, A., Hattermann, F., Huang, S., Koch, H., Pechlivanidis, I. G., Plötner, S., Seidou, O. and Su, B., 2017. Evaluation of sources of uncertainty in projected hydrological changes under climate change in 12 large-scale river basins. *Climatic Change*, 141(3), pp.419–433.
- Wang, X., Nguyen, M., Stewart, M.G., Syme, M. and Leitch, A., 2010. Analysis of climate change impacts on the deterioration of concrete infrastructure—part 1: mechanisms, practices, modelling and simulations—a review. *Published by CSIRO, Canberra. ISBN, 9780(4310365)*, p.8.
- Wang, X., Nguyen, M., Stewart, M.G., Syme, M. and Leitch, A., 2010. Analysis of climate change impacts on the deterioration of concrete infrastructure—Part 3: Case Studies of Concrete Deterioration and Adaptation. *Canberra, Australia: Commonwealth Scientific and Industrial Research Organisation*.
- Zhang, J. and Lounis, Z., 2006. Sensitivity analysis of simplified diffusion-based corrosion initiation model of concrete structures exposed to chlorides. *Cement and concrete research*, 36(7), pp.1312–1323.
- Zhang, J. and Lounis, Z., 2009. Nonlinear relationships between parameters of simplified diffusion-based model for service life design of concrete structures exposed to chlorides. *Cement and Concrete Composites*, 31(8), pp.591–600.
- Zhang, J., Shirkhani, H. and Lounis, Z., 2018. Climate change impact on design service life of concrete bridge decks exposed to chlorides. In *Proc., 10th Int. Conf. on Short and Medium Span Bridges. Quebec, Canada: Canadian Society for Civil Engineering*.

Climatic design data for buildings and infrastructure under changing climate in Canada

H. Shirkhani & Z. Lounis

National Research Council Canada, Ottawa, Canada

ABSTRACT: This paper investigates the future climate data required for the design and evaluation of buildings and infrastructure systems considering climate change. Currently, the climatic design data of buildings and infrastructure are based on historical observations, which due to climate change, can result in higher risks of failure. The future climatic conditions largely depend on human-induced greenhouse gas emissions described by emission scenarios. The responses of different climate models to the future emissions result in uncertainty in climatic data projections. Moreover, the projected climatic data are expected to vary with time, which is known as climate non-stationarity, which depends on the type of the climatic parameter and the design life. The building or infrastructure with longer design life are more prone to uncertainty and non-stationarity. A number of climatic design values for locations across Canada are analyzed to illustrate the implications of climate change for climatic design parameters.

1 INTRODUCTION

Buildings and infrastructure systems such as bridges, roads, transit, water supply and wastewater systems provide basic and core services, which are critical to the stability of the economy, wellness of the environment and people's quality of life. According to the Canadian Infrastructure Report Card (CIRC, 2019), one third of Canada's municipal infrastructure is in fair, poor or very poor condition, which can be exacerbated by climate change impacts.

It is certain that Canada's climate has warmed and that it will warm further in the future. Between 1948 and 2016, the best estimate of mean annual temperature increase is 1.7°C for Canada as a whole and 2.3°C for northern Canada. Both the observed and projected increases in mean temperature in Canada are about twice the corresponding increases in the global mean temperature, regardless of future emission scenario.

Current approaches for design, evaluation and rehabilitation of buildings and infrastructure are based on historical climatic data that: (i) do not consider the projected changes in the magnitude of the climatic loads; and (ii) assume stationary loads and resistance. However, climate change may increase climatic loads while decreasing the resistance of buildings and infrastructure systems. As a result of the combined effects of climate change and aging, the probability of failure of buildings and infrastructure could exceed the prescribed target values assumed in current codes, standards and guides, which in turn may lead to early failure (shortened service life) as well as higher probability of failure with serious social, economic and environmental consequences (Figure 1).

Nearly 35% of infrastructure assets are in need of maintenance, repair and rehabilitation, which means that Canada's infrastructure deficit estimates ranging from \$50 billion to \$570 billion (INFC 2018). Therefore, there is a need to develop design codes, standards and guidelines based on future climatic loads to build climate-resilient buildings and infrastructure. There are existing climate resiliency studies in the literature including climate change resiliency adaptation (Lounis and Daigle 2008; Lounis and McAllister, 2016; Knott et al., 2019). However, the selection and use of the projected climatic design data is a challenging task due to the high level of uncertainty associated with climate projections as well as the time variation of climatic

design values and their statistics – known as non-stationarity. Previous studies observed a high level of non-stationarity in climatic data (Rootzen and Katz 2013; Lee and Ellingwood 2017).

In order to predict the GHGs concentration trajectory, the Intergovernmental Panel on Climate Change (IPCC) developed emission scenarios including four Representative Concentration Pathway (RCP) scenarios, RCP2.6, RCP4.5, RCP6.0 and RCP8.5, as well as a core set of five scenarios based on the Shared Socioeconomic Pathways (SSPs): SSP1-1.9, SSP1-2.6, SSP2-4.5, SSP3-7.0, and SSP5-8.5. Previous studies investigated these uncertainties for various engineering applications (Shirkhani et al., 2020; Shirkhani et al., 2015; Stott et al., 2002). Selection of an appropriate emission scenario to obtain future climatic data is a non-trivial and delicate task.

In this study, the challenges for selection and use of the future climatic data required for the design and management of climate-resilient buildings and infrastructure systems are presented. In order to illustrate these challenges, we use the future-looking climatic design data, which was generated as an outcome of the Climate Resilient Buildings and Core Public Infrastructure (CRBCPI, 2020) initiative led by the National Research Council Canada (Cannon et al., 2020). In this paper, the projected changes of selected climatic design data are presented for various locations across Canada in order to illustrate the impact of climate change across various climatic regions over Canada. In addition, to shed some lights on the challenges for selection of an appropriate emission scenario, the future climatic design parameters are presented under various emission scenarios. The concept of global warming levels (GWLs) and timing of these waring levels are also presented. The role of the infrastructure design life in the time horizon of climatic projections and selection of emission scenarios are discussed for short and long life assets. The non-stationarity issue of projected climatic design data is discussed through assessing the time variation of selected climatic design parameters under various emission scenarios.

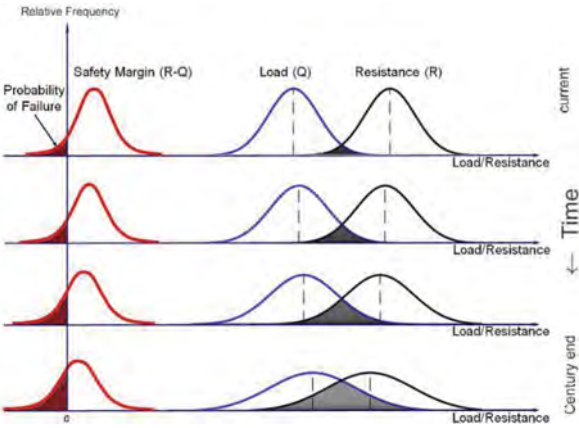


Figure 1. Impact of climate change on climatic load and probability of failure of infrastructure: increasing probability of failure with time (from top to bottom) due to the non-stationary climatic loads and accelerated deterioration.

2 CLIMATE CHANGE DRIVER AND EMISSION SCENARIOS

2.1 Climate change driver

Future global climate change is driven primarily by emissions, and hence increasing atmospheric concentrations of GHGs and changing concentrations of aerosols. Human influence on the climate system is now an established fact (IPCC, 2014; IPCC, 2022; USGCRP, 2018; Bush and Lemmen, 2019) and that human influence is the principal driver of many changes observed across the atmosphere, ocean, cryosphere and biosphere. The Sixth Assessment Report by IPCC (AR6; IPCC, 2022) concludes that it is now an established fact that human-induced GHG emissions have led to an increased frequency and/or intensity of some weather and climate extremes, in particular for temperature extremes. In addition, evidence of observed changes and attribution to human influence

has strengthened for several types of extremes, in particular for extreme precipitation, droughts, tropical cyclones and compound extremes.

2.2 Emission scenarios: RCP and SSP

The future emissions of GHGs and aerosols are highly uncertain and depend on several socio-economic factors. Therefore, different emission scenarios or “pathways” of future GHG concentrations, aerosols, and land-use change were specified by Intergovernmental Panel on Climate Change (IPCC, 2014). The emission scenarios that were used in AR5 (IPCC, 2014) and were widely used in the literature before AR6 report (IPCC, 2022) were called “Representative Concentration Pathways” (RCPs). RCPs were identified by approximating the radiative forcing at the end of the 21st century: RCP2.6, RCP4.5, RCP6.0 and RCP8.5.

IPCC (2022) used a core set of five scenarios based on the Shared Socioeconomic Pathways (SSPs) in AR6: SSP1-1.9, SSP1-2.6, SSP2-4.5, SSP3-7.0, and SSP5-8.5. Figure 2 shows the global warming under RCP and SSP emission scenarios.

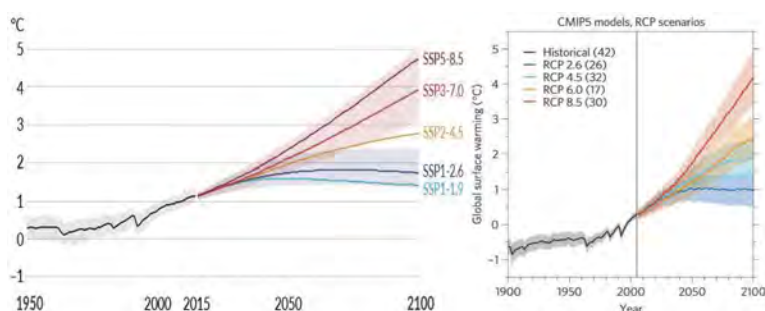


Figure 2. Increase in surface temperature under SSP (left) and RCP (right) emission scenarios relative to 1850-1900 [IPCC, 2022; IPCC 2014].

Although, like RCPs, SSPs are also labelled by the level of radiative forcing they reach in 2100 and can in principle be related to the core set of SSP scenarios, the RCPs and SSP-based scenarios are not directly comparable since: (i) the gas-to-gas compositions differ; (ii) the projected 21st-century trajectories may differ; and (iii) the overall effective radiative forcing tends to be higher for the SSPs.

3 GLOBAL WARMING LEVELS AND TIMING

Traditionally, projections of climate variables are summarized and communicated as a function of time and emission scenarios. However, for many indicators of climate change, such as seasonal and annual mean and extreme surface air temperatures and precipitation, the geographical patterns of changes are well estimated by the level of global surface warming, independently of the details of the emission pathways that caused the warming, or the time at which the level of warming is attained. Therefore, recently, quantifying global and regional climate at specific global warming levels (GWLs) has become widespread. In this approach, scenario-based climate projections are translated into GWLs by aggregating the climate model response at specific GWL across scenarios.

This approach is also implemented in the CRBCPI initiative (Cannon et al., 2020). However, in the CRBCPI initiative, the regional climate projections are translated into GWLs by aggregating single-model initial-conditions large ensembles under one emission scenario (RCP8.5). The timing of when a certain GWL is reached under a particular scenario needs to be estimated. In AR6, results of 20-year averaged change in global surface temperature were estimated relative to the 1850–1900 reference period using the CMIP6 output through a combined assessment taking into

account the observed warming. The timing of GWLs in CRBCPI are estimated using 31-year averaged changes relative to 1986-2016 baseline period based on the CMIP5 ensemble under RCP emission scenarios. Canadian Regional Climate Model (CanRCM4) simulations driven by Canadian Earth System Model (CanESM2), for which the warming levels relative to the 1986-2016 baseline are approximately 1°C lower than levels relative to the preindustrial period (Cannon et al., 2020). Using this approximation, and for the level of global warming that are available in both Cannon et al. (2020), and the AR6, Table 1 presents the timing of the global warming under both RCP and SSP emission scenarios.

4 FUTURE CLIMATIC DESIGN DATA

4.1 Methodology and data

As part of the CRBCPI initiative, future-looking climate data were developed to be implemented in future editions of building and infrastructure codes and standards. In this section, we will provide an overview and summary of the methodology and findings of Cannon et al., (2020) for the projected changes in climatic data across Canada.

The output of a 50-member initial-conditions large ensemble of the Canadian Regional Climate Model (CanRCM4-LE) forced by RCP 8.5 emission scenario was used to estimate the projected changes in the selected climatic design data at specified GWLs. CanRCM4 dynamically downscales Canadian Earth System Model (CanESM2) to a grid with 0.44° (~50km) resolution over North America (Scinocca et al., 2016). In order to associate the projected climatic data under RCP8.5 with other emission scenarios, the timing of GWLs under each RCP emission scenario is estimated using the CIMP5 ensemble relative to the baseline period of 1986-2016 (See Table 2). Years that are presented in Table 1, indeed, indicate the centre year of the 31-year period for which the average change in global mean temperature is reached by the corresponding RCP emission scenario. For example, the future time horizon of 2070 corresponds to the time period of 2055-2085. For the end of the century time horizons, however, the time period might be shorter due to the data availability up to the end of century (year 2100). For instance, the warming level of $\Delta T = 3.5^\circ C$ is projected to be reached under RCP8.5 scenario by 2090 time horizon, which corresponds to the 2080-2100 period. It should be noted some ΔT warming levels do not occur before 2100 under specific emission scenarios (shown as dash in Table 2).

4.2 Projected changes in climatic data

The climatic loads that are required for design of new and evaluation and management of existing buildings and bridge infrastructure include wind, snow, rain, temperature, ice and flood. Figure 3 provides examples of projected changes in climatic design data used in the National Building Code (NBCC, 2015) and Canadian Highway Bridge Design Code (CHBDC, 2014).

The projected changes in the wind load are relatively small for most of locations across Canada. The wind load decreases at some stations and increases at other locations. Due to the increasing temperature, both hot and cold extremes are projected to become warmer in future for all locations across Canada. The minimum mean daily temperature is projected to increase significantly with larger changes in the North. The scientific confidence in climate change projections varies depending on the climate variable and, in some cases, region. Confidence in temperature change is higher than confidence in precipitation change, in large part because temperature change is a direct consequence of the radiative imbalance associated with changing GHG and aerosol emissions while precipitation change is affected by a number of complex processes that cannot be resolved or simulated by climate models. Moreover, confidence about changes in compound events, involving multiple variables, e.g., snow loads, driving rain wind pressures, etc., is lower.

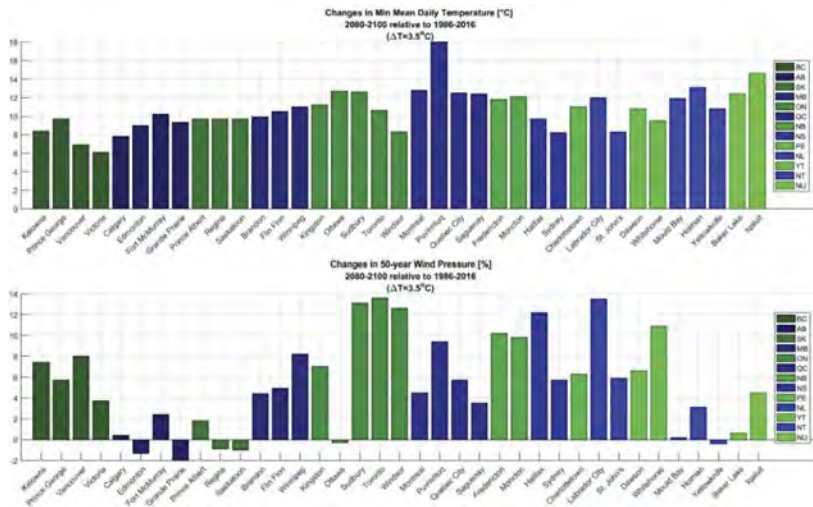


Figure 3. Projected changes corresponding to GWL of $\Delta T = 3.5^{\circ}\text{C}$ (see Table 2) for: Minimum Mean Daily Temperature (top) and 50-year Wind Pressure (bottom).

Table 1. Timing of global warming levels under RCP and SSP emission scenarios (relative to 1850–1900 reference period) as the period during which the average global surface temperature change exceeds the specified level. For RCP and SSP emission scenarios 31-year and 20-year periods are used, respectively.

$\Delta T^{\circ}\text{C}$ (GWL)	Timing of Global Warming							
	RCP 8.5	SSP5-8.5	RCP 6.0	SSP3-7.0	RCP 4.5	SSP2-4.5	RCP 2.6	SSP1-2.6
+1.5	2008-2038	2018-2037	2008-2038	2021-2040	2008-2038	2021-2040	2008-2038	2023-2042
+2.0	2020-2050	2032-2051	2031-2061	2037-2056	2031-2061	2043-2062	-	-
+3.0	2044-2074	2055-2074	2074-2100	2066-2085	-	-	-	-
+4.0	2065-2095	2075-2094	-	-	-	-	-	-

Table 2. – Year at which indicated GWL is exceeded under different emission scenarios (Cannon et al., 2020).

$\Delta T^{\circ}\text{C}$ (GWL)	RCP 8.5	RCP 6.0	RCP 4.5	RCP 2.6
+0.5			2023	
+1	2035		2046	-
+1.5	2047		2070	-
+2	2059	2087	-	-
+2.5	2069	-	-	-
+3	2080	-	-	-
+3.5	2090	-	-	-

5 CLIMATE CHANGE UNCERTAINTIES AND NON-STATIONARITY

Climate models are computer models that simulate the global climate system driven by future GHG emission scenarios, and provide projections of future climatic variables. Since climate change is driven by GHG emissions, the future projections of climatic variables highly depend on the assumption of the future emission scenario. The spread of climatic projections under various emission scenarios represents a measure of uncertainty due to future GHG emissions. In addition, climate models respond differently to the same GHG emission forcing, which represents the model uncertainty associated with future climate change projections. The future

GHG emissions and the climate model are two major sources of uncertainty associated with future climate projections that can be captured by performing a multi-model multi-scenario approach (Vetter et al., 2017; Shirkhani et al., 2015, Shirkhani et al., 2020). The third source of uncertainty in climate projections is the internal climate variability, which stems from the natural chaotic variability of the climate system. This uncertainty is irreducible as it is intrinsic to the climate system’s behaviour. The spread from output of simulations from a single-model initial-conditions large ensembles can represent uncertainty due to internal climate variability. The relative influence of internal variability, forcing uncertainty, and model uncertainty on future climate projections depends on the variable, spatial scale, and time horizon of interest.

The current codes and guidelines for the design of infrastructure are based on the assumption of the stationarity of the climate. However, in the presence of non-stationarity the conventional methods and models for load estimation as well as reliability and risk assessment are not valid. The nonstationary of climatic data is illustrated in Figure 4, which shows the time variation of projected changes in 50-year wind pressure and minimum mean daily temperature under various emission scenarios. As can be seen, the projected changes in wind pressure show a trend with time and emission scenarios. The level of non-stationarity of climatic design values clearly depends on the length of the design life and the climate non-stationarity may become more critical for infrastructure with longer design life.

6 SELECTION OF EMISSION SCENARIO

The design life of the buildings and infrastructure determines the planning horizon and the future time frame required for projections of climatic design data. Appropriate selection of a future emission scenario is a complex task, which presents a challenge to engineering communities. Cannon et al., (2020) provided preliminary recommendations. For the 50-year horizon (i.e. infrastructure with design life of up to 50 years, such as buildings), it is recommended that RCP8.5 scenario in the period with the center year of 2069 be used since the incremental change in design values relative to those for RCP4.5 or RCP6.0 is not large for this time frame. This means that for the infrastructure with design life of 50 years or shorter, the RCP8.5 can be used.

For the 75-year time horizon (such as bridges), the selection of an appropriate scenario is more complicated because the difference between different scenarios near the end of the century can be quite large (as can be also seen in Figure 2 for the global average temperature). In this case, a judgment must be made on which scenario to adopt. Consultation with experts to assess the probability of different forcing scenarios may be needed to arrive at a final decision. For most design values, a conservative choice would be the RCP8.5 scenario in the time period with the center year of 2090, acknowledging that this could lead to more expensive designs or greater risk associated with the underestimation of some types of loads, such as snow loads.

The projected changes in 10-year and 50-year wind loads as structural climatic design parameters for buildings with a 50-year planning horizon are compared under various emission scenarios in Figure 5 for different locations across Canada. As Table 2 shows, the GWLs of $\Delta T = +2.5^{\circ}\text{C}$ and $\Delta T = +1.5^{\circ}\text{C}$ correspond to the 50-year planning horizon under RCP8.5 and RCP 6.0/RCP 4.5 respectively. Figure 5 shows that the projections of wind pressures are relatively close under various scenarios for most locations. It should be noted that the projected changes in wind pressure remain relatively small, therefore, even high differences in projected changes under various RCPs may not be significant.

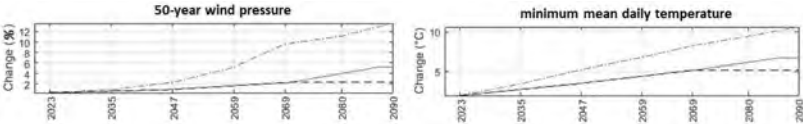


Figure 4. Time variation of projected changes in 50-year wind pressure and minimum mean daily temperature for Toronto under RCP8.5 (blue), RCP6.0 (red) and RCP4.5 (black) emission scenarios. Changes are relative to 1986-2016 baseline period.

For bridge infrastructure with a design life of 75-year, in Figure 6 we compare the projected changes in ice thickness and minimum mean daily temperature under RCP6.0 and RCP8.5 for the 75-year time horizon. As Table 1 shows, we may approximate the 75-year horizon by GWLs of $\Delta T = + 2^{\circ}\text{C}$ and $\Delta T = + 3.5^{\circ}\text{C}$ under RCP6.0 and RCP8.5, respectively. As for the extreme temperatures, the results of RCP8.5 are consistently higher than those of RCP6.0, at least by 2°C . The difference is higher for 75-year planning horizon and in the northern region, particularly for the cold extreme temperatures. The differences between the projected changes of extreme temperatures under RCP8.5 and RCP6.0/4.5 are higher for the extreme cold temperatures (up to 4°C in most of locations) while it is lower for the extreme hot temperatures (up to 2°C for most of the locations).

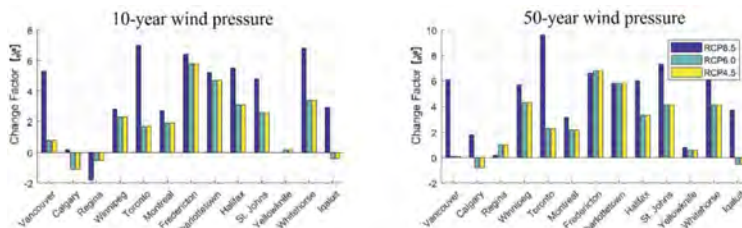


Figure 5. Comparison of projected changes in 10-year (left) and 50-year (right) wind loads under RCP8.5 and RCP6.0/4.5 for 50-year time horizon.

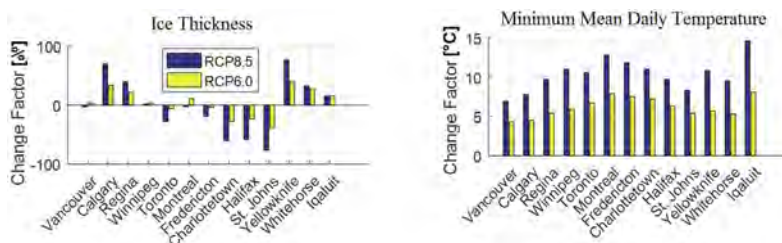


Figure 6. Comparison of projected changes in ice thickness (left) and minimum mean daily temperature (right) under RCP8.5 and RCP6.0 for 75-year time horizon.

The role of the infrastructure design life in the time horizon of climatic projections and selection of emission scenarios were discussed for short and long life assets. It was shown that selection of an appropriate emission scenario is a complex task and is more challenging for long-life assets.

7 CONCLUSIONS

In this study, the future climatic data for design and evaluation of buildings and infrastructure systems are discussed. The challenges for the selection and use of the future climatic data are presented. For selected climatic design data that are used in NBCC (2015) and CHBDC (2014), future-looking climatic data from the NRC-led CRBCPI initiative were presented. The average warming across Canada is twice the global average, with even greater warming occurring in the North. For temperature-related elements, every region of Canada is projected to experience warming. The extreme cold temperature is projected to increase even more than extreme hot temperatures. The shift in phase of precipitation from snow to rain with warming leads to larger relative increases in rain across Canada. The future ice accretion loads are projected to increase in several locations, particularly for latitudes higher than 50°N . While the future projections of wind loads are lacking in confidence due to the gap in climate science, the future changes in wind load over Canada will be relatively small.

The concept of GWLs and timing of these waring levels are also presented. It was shown that the GWLs under RCP and SSP emission scenarios can be linked through the timing when GWLs are attained. It was discussed that there is relatively high uncertainty associated with the

climate change projections. There are different sources of uncertainties including future emission scenarios, climate model uncertainty and natural internal variability of the climate system. It was noted that scientific confidence in climate change projections varies by region and by climate variable. The confidence in temperature change is higher than confidence in precipitation change and wind speed. Furthermore, confidence about changes in climatic loads involving multiple variables, e.g., snow loads, driving rain wind pressures, and ice accretion is lower than individual parameters. The extreme values are also more uncertain compared to cumulative and averaged ones. These uncertainties are significant obstacles for the design and management of infrastructure systems under climate change. The non-stationarity issue of projected climatic design data is discussed through assessing the time variation of selected climatic parameters. The stationarity assumption may not be valid anymore given the changing climate. In a non-stationary climate, the climatic design value can change over the design life of the infrastructure. The projected climatic design data at the end of the design life will then be different, and depends on the infrastructure design life and the choice of the emission scenario.

REFERENCES

- Bush, E., and Lemmen, D.S. (Eds.) 2019. Canada's Changing Climate Report-CCCR. Government of Canada, Ottawa, ON, 444p. <https://changingclimate.ca/CCCR2019/>
- Cannon AJ, Jeong DI, Zhang X, Zwiers FW Climate-resilient buildings and core public infrastructure, An assessment of the impact of climate change on climatic design data in Canada; 2020. Ottawa, ON: Government of Canada. p. 106. <https://publications.gc.ca/pub?id=9.893021&sl=0>.
- CIRC. (2019). Canadian Infrastructure Report Card. <http://canadianinfrastructure.ca/downloads/canadian-infrastructure-report-card-2019.pdf>
- CRBCPI: Climate Resilient Buildings and Core Public Infrastructure, 2020, <https://www.infrastructure.gc.ca/plan/crbcp-irccipb-eng.html>
- Infrastructure Canada (2018). About Infrastructure Canada. <https://www.infrastructure.gc.ca/about-apropos/index-eng.html#1> (accessed Nov. 7, 2018)
- IPCC (2014). Climate Change 2014: Synthesis Report. Contribution of Working Groups I, II and III to the Fifth Assessment Report of the Intergovernmental Panel on Climate Change [Core Writing Team, R.K. Pachauri and L.A. Meyer (eds.)]. IPCC, Geneva, Switzerland, 151 pp.
- IPCC, 2022: Climate Change 2022: Impacts, Adaptation, and Vulnerability. Contribution of Working Group II to the Sixth Assessment Report of the Intergovernmental Panel on Climate Change [H.-O. Pörtner, et al., (eds.)]. Cambridge University Press. Cambridge University Press, Cambridge, UK and New York, NY, USA, 3056 pp., doi:10.1017/9781009325844.Knott,
- Jayne F., et al. "A framework for introducing climate-change adaptation in pavement management." *Sustainability* 11.16 (2019): 4382.
- Lee, Ji Yun, and Bruce R. Ellingwood. "A decision model for intergenerational life-cycle risk assessment of civil infrastructure exposed to hurricanes under climate change." *Reliability Engineering & System Safety* 159 (2017): 100–107.
- Lounis, Z., and McAllister, T. (2016). Risk-based Decision Making for Sustainable and Resilient Infrastructure Systems. *ASCE J. Struct. Engng.*, 142(9),pp.1–14.
- Lounis, Z., Daigle, L., (2008). Reliability-based Decision Support Tool for Life Cycle Design and Management of Highway Bridge Decks. Annual Conf. of the Transportation Association of Canada, Toronto, 19 p.
- Rootzén, Holger, and Richard W. Katz. "Design life level: quantifying risk in a changing climate." *Water Resources Research* 49.9 (2013): 5964–5972.
- Scinocca, J. F., Kharin, V. V., Jiao, Y., Qian, M. W., Lazare, M., Solheim, L. & Dugas, B. (2016). Coordinated global and regional climate modeling. *Journal of Climate*, 29(1),17–35.
- Shirkhani, H., et al. (2015). Projection of Significant Wave Height in a Coastal Area under RCPs Climate Change Scenarios. *J. Natural Hazards Review* 17.1: 04015016.
- Shirkhani, H., Zhang, J., and Lounis, Z. (2020). Ensemble Analysis of Climate Change Impacts on Design Service Life of Reinforced Concrete Bridge Decks across Canada. *ASCE J. Natural Hazards Review*, 21(3).
- Stott, P., Kettleborough, J. Origins and estimates of uncertainty in predictions of twenty-first century temperature rise. *J. Nature* 416, 723–726 (2002). <https://doi.org/10.1038/416723a>
- USGCRP, 2018: Impacts, Risks, and Adaptation in the United States: Fourth National Climate Assessment, Volume II [Reidmiller, D.R., C.W. Avery, D.R. Easterling, K.E. Kunkel, K.L.M. Lewis, T.K. Maycock, and B.C. Stewart (eds.)]. U.S. Global Change Research Program, Washington, DC, USA, 1515 pp. doi: 10.7930/NCA4.2018.

Life-cycle structural reliability of RC bridge piers under corrosion in a changing climate

G.V. Nava, L. Capacci & F. Biondini

Politecnico di Milano, Milan, Italy

L. Casti

Université Gustave Eiffel, Champs-sur-Marne, France

ABSTRACT: Aging and deterioration processes of structures and infrastructure systems can be severely affected by the long-term evolution of environmental conditions expected in a changing climate. This paper aims at investigating the interaction between climate change and environmental aggressiveness on the probabilistic life-cycle performance of concrete structures under corrosion. A simulation-based framework is proposed for life-cycle structural reliability analysis under climate change scenarios. The framework is applied to a bridge pier with hollow core cross-section exposed to chloride-induced corrosion. The results allow to quantify the impact of climate change on long-term probabilistic structural response and highlight the need for proper modeling of the environmental parameters and climate evolution over the entire lifespan of aging structures for optimal life-cycle maintenance and management of structural and infrastructural facilities.

1 INTRODUCTION

Civil engineering structures are designed to guarantee the functionality and resilience of the served communities and the safety of its users over a service life spanning several decades. Multiple deterioration processes may affect the original performance of materials and structures and severely impair the level of structural safety and reliability over time (Ellingwood 2005). Design practice and management strategies of structural and infrastructural facilities should therefore account for the detrimental impact of deterioration processes, taking into account multiple factors such as durability of construction materials, quality of structural detailing, type of structural systems, and environmental exposure (Biondini & Frangopol 2016, 2019).

Daily weather fluctuations and long-term change in climate conditions can influence structural deterioration as well as the intensity and frequency of natural hazards. As highlighted by the Intergovernmental Panel on Climate Change (IPCC), climate change is unequivocal and the non-stationarity of climate and weather conditions is substantially connected to greenhouse emissions (IPCC 2021). It is hence important to investigate the impact of climate change effects on structural systems exposed to aging and deterioration, including bridges and infrastructure facilities (Nasr et al. 2020). To support the decision making process of new and existing assets, incorporating climate factors in structural performance indicators is critical to inform design, assessment, maintenance, retrofit, and repair in a life-cycle perspective (Capacci & Biondini 2019).

This paper presents a probabilistic framework for life-cycle assessment of aging structural systems exposed to environmental aggressiveness, with emphasis on Reinforced Concrete (RC) structures under corrosion processes (Biondini et al. 2004, Biondini & Vergani 2015). Climate change effects are incorporated in the proposed framework considering the long-term evolution of climate parameters affecting the deterioration rate, such as temperature and relative humidity.

The methodology is applied to a RC bridge pier subjected to chloride-induced corrosion. The results allow quantifying the detrimental impact of climate change on corrosion damage and related effects on lifetime structural safety and reliability of aging RC bridge structures.

2 LIFE-CYCLE STRUCTURAL ASSESSMENT IN A CHANGING CLIMATE

2.1 Climate change scenarios

The future climate is predicted through the definition of emission scenarios in relation to the evolution of population, economy, technology, energy, land use and agriculture, and described by different reference scenarios, such as the four Representative Concentration Pathways (RCPs) (Van Vuuren et al. 2011). RCP 2.6 is a mitigation scenario, RCP 4.5 and RCP 6.0 are medium stabilization scenarios and RCP 8.5 is a very high baseline emission scenario. These RCPs are representative of a larger set of scenarios reported in the literature and their denomination is associated to the value of Radiative Forcing predicted in 2100. The choice of an even number of scenarios is linked to the decision of avoiding a middle RCP, providing a manageable set of scenarios able to describe also extreme projections. RCPs have been recently integrated with the Shared Socioeconomic Pathways (SSPs) in order to characterize a range of uncertainties in the mitigation efforts required to achieve particular climate outcomes and in the adaptation efforts that could be taken to cope with the climate change effects (O'Neill et al. 2016).

Predicting spatially and temporally dependent environmental parameters considering different scenarios is a complex task. Indeed, the future climate projection depends on the selected Global Circulation Model (GCM), which is subjected to several sources of uncertainty classified in internal, model and scenario uncertainty (Madsen 2013). The inner variability of the climate systems is referred as internal uncertainty, while model uncertainty is related to the assumption and simplification considered for the definition of the GCM. Lastly, scenario uncertainty is associated with the assumptions implemented in the definition of the different climate scenarios. These uncertainties evolve in time depending on the selected environmental parameter projection and the spatial scale considered. Different analyses should be applied in order to deal with these uncertainties for the assessment of climate change impact on civil engineering structures, e.g. using different trajectories from the same GCM and considering different scenarios.

The spatial resolution of GCMs is usually ranging from tens to hundreds of kilometers while civil engineering problems often require the evaluation at the local scale. For this purpose, downscaling techniques are used in order to retrieve environmental projections for specific location. Advantages and disadvantages of the most common techniques, i.e. statistical and dynamics downscaling, are discussed in Trzaska & Schnarr (2014).

2.2 Conceptual framework for life-cycle structural assessment

The proposed methodology for life-cycle assessment of aging structures under climate change is illustrated in Figure 1. The structure of the flowchart comprises three constitutive dimensions: climate scenario modeling, mechanical damage assessment, and structural performance analysis.

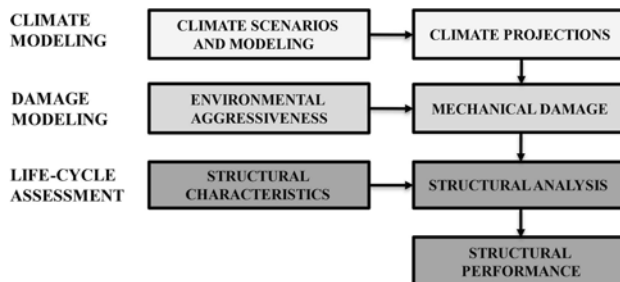


Figure 1. Methodology flowchart for performance assessment of aging structures in a changing climate.

Climate modeling provides the projections of relevant environmental parameters affecting the deterioration process based on the investigated climate scenario (e.g., RCP selection) and the input data required by the selected predictive model for climate change (e.g., site, timeframe). The projections retrieved in this phase concern the climate parameters that affect capacity deterioration and hazard rate of the investigated structural problem (e.g., temperature, relative humidity, wind speed). Then, mechanical damage is governed by environmental aggressiveness exacerbated by detrimental projections of climate parameters. Based on analytical or empirical formulations, this phase allows to describe onset and propagation of aging and deterioration processes (e.g., corrosion, freeze-thaw cycles, sulphate attacks). The characterization of mechanical damage informed by non-stationary climate conditions allows to establish the numerical models for structural analysis over time (e.g., sectional analysis, static and dynamic analysis). The problem can be formulated in probabilistic terms and integrated for practical implementation within a Monte Carlo simulation framework to account for uncertainties of basic modeling parameters encompassing all dimensions of the life-cycle structural assessment.

3 CORROSION MODELLING UNDER TIME-VARIANT ENVIRONMENTAL FACTORS

For RC structures exposed to chloride ingress, damage induced by the diffusive attack follows corrosion initiation and propagation and may involve corrosion of steel reinforcement and deterioration of concrete (Bertolini et al. 2013).

3.1 Corrosion initiation

The initiation time can be defined as the time necessary to achieve a critical chloride concentration at the reinforcing steel surface. Chloride ingress in concrete is generally modelled using the Fick's diffusion equation in the one-dimensional formulation:

$$D \frac{\partial^2 C}{\partial x^2} = \frac{\partial C}{\partial t} \quad (1)$$

where D is the concrete diffusivity and C is the chloride concentration at the depth x and time t . This simplified approach is considered in this paper. However, it is worth noting that for structural members with complex geometry and non-uniform chloride concentration exposure the diffusion process should be more accurately described by two- or three-dimensional patterns of concentration gradients (Biondini et al. 2004, Titi & Biondini 2016).

Over time, the aging process and the evolution of the environmental parameters, such as temperature and relative humidity, may affect the concrete diffusivity. Experimental studies show that the diffusion coefficient increases with temperature (Stewart et al. 2011). Moreover, chloride penetration occurs in the presence of water in the capillary pores. Indeed, a small relative humidity hinders chloride penetrations (Saetta et al. 1993). In order to account for non-stationary climatic conditions, the diffusion coefficient at time t is evaluated as follows:

$$D(t) = D_{ref} f_T(t) f_{RH}(t) f_a(t) \quad (2)$$

where D_{ref} is the reference diffusion coefficient for $T=20$ °C and $RH=75\%$, f_T accounts for the variation of temperature, f_{RH} accounts for the variation of relative humidity, and f_a is an aging function.

The function f_T is evaluated as follows based on the Arrhenius law (Peng & Stewart 2016):

$$f_T(t) = e^{\frac{E}{R} \left(\frac{1}{293.15} - \frac{1}{273.15+T(t)} \right)} \quad (3)$$

where E is the activation energy of the chlorides diffusion process, R is the gas constant (8.314×10^{-3} kJ/mol), and T is the temperature in Celsius degrees. The function f_{RH} is defined based on following empirical model (Saetta et al. 1993):

$$f_{RH}(t) = \left[1 + \frac{(1 - RH(t))^4}{(1 - 0.75)^4} \right]^{-1} \quad (4)$$

where RH is the concrete pore relative humidity. Finally, the function f_a is evaluated as follows:

$$f_a(t) = \left(\frac{0.0767}{t} \right)^a \quad (5)$$

where a is an aging coefficient.

3.2 Corrosion propagation

Corrosion initiates with the attainment of a critical concentration threshold C_{cr} . The propagation phase is described based on the Faraday's law in terms of corrosion penetration rate (mm/year):

$$\frac{\partial p_s}{\partial t} = 0.0116 R_f i_{corr} \quad (6)$$

with p_s = corrosion penetration depth (mm), i_{corr} = corrosion electric current density ($\mu\text{A}/\text{cm}^2$) and R_f = pitting factor, i.e. the ratio between the maximum depth measured at pit and the average penetration calculated indirectly from the weight loss of the steel bar (Stewart & Al-Harthy 2008).

Corrosion propagation may be significantly affected by the variation of environmental parameters. Indeed, a gradual reduction in the concrete resistivity along with an increase in temperature leads to increase the corrosion rate (Stewart et al. 2011). In addition, the corrosion rate is low for relative humidity values lower than 50%, it increases exponentially for relative humidity ranging from 50% to 65%, it remains nearly constant for relative humidity from 65% to 85%, and then tends to decrease (Guo et al. 2015). Moreover, the corrosion rate increases over time due to the increase of chloride concentration (Liu & Weyers 1998) and decreases due to the formation of corrosion products (Vu & Stewart 2000). Based on these results, the influence of environmental parameters on the time-variant corrosion penetration rate is investigated in this paper based on the following relationship (Casti 2021, Nava 2022):

$$i_{corr}(t) = i_{corr,ref} \varphi_{RP}(t) \varphi_T(t) \varphi_{RH}(t) \varphi_C(t) \quad (7)$$

where $i_{corr,ref}$ is the reference corrosion rate for $T=20$ °C and $RH=75\%$, and the time-variant functions $\varphi_{RP}(t)$, $\varphi_T(t)$, $\varphi_{RH}(t)$, and $\varphi_C(t)$ account for the effects associated with formation of rust products and variation of temperature, relative humidity, and chloride concentration, respectively. The function φ_{RP} is described as follows (Vu & Stewart 2000):

$$\varphi_{RP}(t) = 0.85 t_p^{-0.29} \quad (8)$$

where t_p is the corrosion initiation time. The function φ_T is based on the following stepwise linear relationship (Stewart et al. 2011):

$$\varphi_T(t) = [1 + K_T(T(t) - 20)] \quad (9)$$

where $K_T=0.025$ or $K_T=0.073$ for temperature $T \leq 20^\circ\text{C}$ and $T > 20^\circ\text{C}$, respectively. Finally, the functions φ_{RH} and φ_C are based on the following formulations (Guo et al. 2015):

$$\varphi_{RH}(t) = e^{-6000(RH(t)-0.75)^6} \quad (10)$$

$$\varphi_C(t) = \frac{C(t) + C_{cr}}{2 C_{cr}} \quad (11)$$

Sensitivity analyses on the proposed corrosion model are reported in Nava (2022).

3.3 Mechanical damage modeling

Corrosion damage is modeled considering the reduction in the mass of steel reinforcement, concrete strength, and steel ductility as proposed in Biondini & Vergani (2015). The reduction of cross-sectional area A_s of steel bars is the most relevant damage induced by corrosion:

$$A_s(t) = [1 - \delta_s(t)]A_{s0} \quad (12)$$

where A_{s0} is the area of the undamaged bar and δ_s is a damage function of the corrosion penetration depth related to the type of corrosion, i.e. uniform or localized (pitting) corrosion. Delamination and spalling are related to the propagation of longitudinal cracks along the concrete cover due to the formation of oxidation products on the steel bars. The effects of such degradation process can be modelled by reducing the effective concrete compression strength f_c in terms of the damage indices evolution of the steel longitudinal reinforcement. Furthermore, reduction of steel ductility is experimentally reported to be related to percentage of steel mass loss induced by corrosion to brittle failure. This effect can be modelled reducing the ultimate strain capacity ε_{su} of the steel bars.

4 APPLICATION

4.1 RC bridge pier

The proposed methodology is applied to life-cycle reliability assessment of the RC two-column bridge pier shown in Figure 2. Each column has hollow-core rectangular cross-section with overall dimensions $3.8 \text{ m} \times 3.4 \text{ m}$ (Figure 2a). The steel reinforcement varies over the length of the pier with a concrete cover of 75 mm. The bending capacity of the RC cross-sections A-A' (Figure 2b) and B-B' (Figure 2c), with overall reinforcement $A_s=1491 \text{ cm}^2$ and $A'_s=745 \text{ cm}^2$ for cross-section A-A' and $A_s=718 \text{ cm}^2$ and $A'_s=583 \text{ cm}^2$ for cross-section B-B', is investigated. An axial force $N=67.09 \text{ MN}$ associated with dead loads is considered. The cross-sections are modelled based on a fiber approach in OpenSees (Mazzoni et al. 2006). The constitutive model for concrete (Concrete04) accounts for confinement (Figure 2d). The stress-strain law for steel bars is elastic-plastic with strain hardening (Steel01). The bridge pier is assumed to be exposed to chloride attack over internal and external surfaces with uniform concentration C_s .

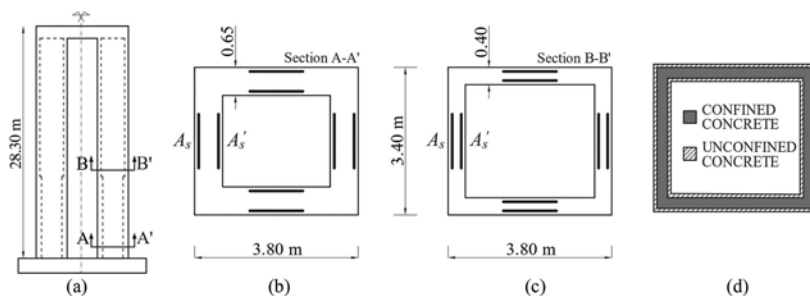


Figure 2. (a) RC bridge pier; (b) cross-section A-A'; (c) cross-section B-B'; (d) concrete confinement.

The analysis timeframe ranges from the year 2000 to the year 2100. The three climate scenarios shown in Figure 3 are considered: (1) very high baseline emission scenario (RCP 8.5); (2) mitigation scenario (RCP 2.6); and (3) No Climate Change (NCC). Temperature projections in Figure 3a are based on the fourth version of the Community Climate System Model (Gent et al. 2011). Projections are downscaled with respect to the station located in Viale Marche, Milan, Italy (Casti 2021) and the analyses are performed considering annual time scale for scenario NCC and monthly time scale for scenarios RCP 2.6 and RCP 8.5, by taking into account also cyclic temperature variations. Linear projections of relative humidity as shown in Figure 3b are considered based on Bastidas-Arteaga et al. (2013).

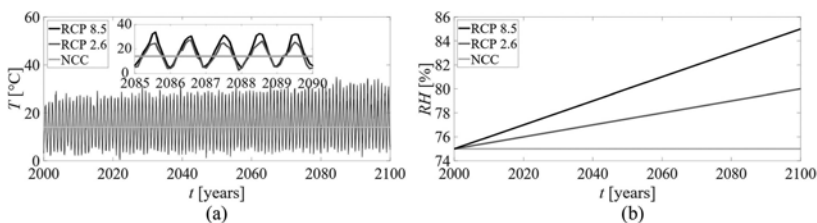


Figure 3. Temperature and relative humidity projections under different climate scenarios.

The probabilistic analysis accounts for uncertainties in mechanical and environmental damage stressors, including surface chloride concentration C_s , critical chloride concentration C_{cr} , reference diffusivity coefficient D_{ref} , aging coefficient a , reference current density $i_{corr,ref}$, pitting factor R_f , concrete strength f_c , and steel strength f_y . Probability distribution types, probabilistic descriptors and bounds of the random variables are listed in Table 1.

Table 1. Random variables, distribution types, and descriptors. Adapted from multiple sources (Nava 2022).

Random Variable	Distribution Type	Mean μ	C.o.V	Bounds
Surface chloride concentration C_s [%wt./c]	Truncated Normal	3.0	0.30	$C_s \geq 0$
Critical chloride concentrations C_{cr} [%wt./c]	Beta	0.60	$0.15/\mu$	$0.2 \leq C_{cr} \leq 2$
Reference diffusivity D_{ref} [10^{-12} m ² /s]	Truncated Normal	15.8	0.20	$D_c \geq 0$
Aging coefficient a [-]	Beta	0.30	$0.12/\mu$	$0 \leq a \leq 1$
Reference current density $i_{corr,ref}$ [μ A/cm ²]	Lognormal	2.586	0.67	$i_{corr} \geq 0$
Pitting factor R_f [-]	Gumbel	7.1	$0.17/\mu$	$R_f \geq 0$
Unconfined concrete strength f_c [MPa]	Lognormal	40.02	$5/\mu$	$f_c \geq 0$
Steel yielding strength f_y [MPa]	Lognormal	487.58	$30/\mu$	$f_y \geq 0$

4.2 Nominal structural analysis

Deterministic structural analyses are carried out for the two investigated cross-sections by assuming the mean values of the random variables as nominal values.

The bending moment M vs curvature χ diagrams in the vertical plane normal to the bridge axis (strong axis of the cross-sections) are shown in Figure 4a at the years 2000 (light gray line) and 2100 considering scenarios NCC (dark gray line) and RCP 8.5 (black line). Limit states are also reported over the capacity curves for concrete first cracking (star marker), concrete cover spalling (circle marker), and ultimate curvature (square marker). At the time 2100, cover spalling is not reported since it occurs earlier for corrosion products expansion. The results highlight that the effect of climate change significantly reduces the lifetime structural capacity of the bridge pier.

Figure 4b and Figure 4c show the axial force N vs bending moment M capacity curves associated with cracking and peak bending capacity limit states, respectively for cross-section A-A' (Figure 4b) and cross-section B-B' (Figure 4c). These results show that the detrimental impact

of climate change on the cracking limit state is exacerbated by the axial force level, while the effects on the peak bending capacity are almost independent on the axial force. Additional results related to multiple limit states of the cross-sections are available in Nava (2022).

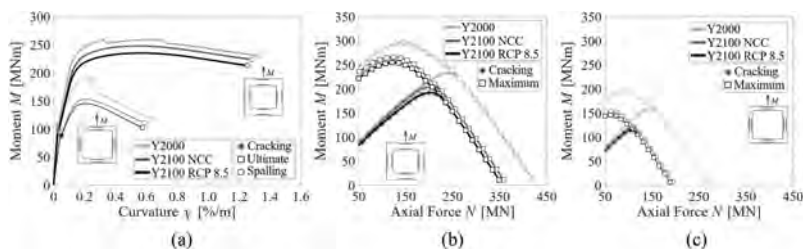


Figure 4. (a) M - χ diagrams; M - N capacity curves of (b) cross-section A-A' and (c) cross-section B-B'.

4.3 Life-cycle structural reliability analysis

The results of a Monte Carlo simulation from a sample of 10^5 realizations are shown in Figure 5 in terms of bending moment M vs curvature χ diagrams of cross-section A-A'. Figure 5a compares median, 16% and 84% fractiles at years 2000 and 2100 under no climate change (NCC) and RCP 8.5. The results for the entire samples are also shown by strong transparency in Figure 5b (Year 2000) and Figure 5c (Year 2100 under RCP 8.5) to better highlight relevant statistical features of the M - χ diagrams, such as centrality, variability, and skewness.

Life-cycle structural reliability is assessed with a 10-year time step considering as limit state the attainment of a target peak bending strength $M_t=166$ MN. The sample size is adaptively selected to mitigate the computational effort and guarantee a sufficient level of estimate accuracy. The results in terms of time-variant reliability index $\beta(t)$ are reported in Figure 6a. The detrimental impact of climate change can be appreciated at the year 2100 by a larger reliability index decay, approximately of 20% for RCP 2.6 and 30% for RCP 8.5, with respect to NCC scenario. These results confirm the relevant effects of climate change on life-cycle structural reliability.

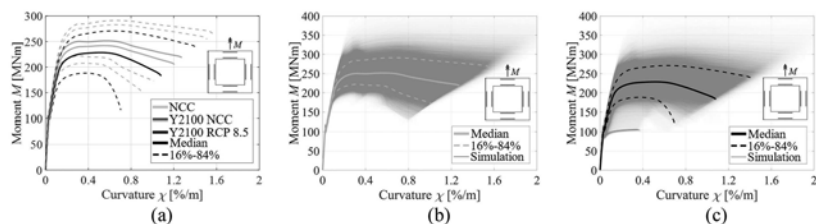


Figure 5. M - χ diagrams of cross-section A-A': (a) Median, 16% and 84% fractiles at years 2000 and 2100 under no climate change (NCC) and RCP 8.5; Results for the entire samples of 10^5 Monte Carlo realizations at years (b) 2000 and (c) 2100 under RCP 8.5.

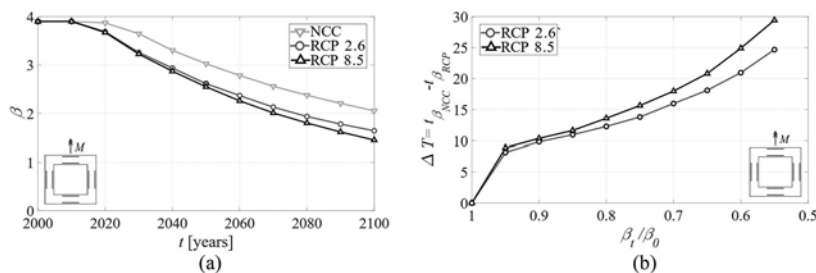


Figure 6. Life-cycle reliability analysis of cross-section A-A' under no climate change (NCC) and two climate change scenarios (RCP 2.6 and RCP 8.5): (a) Time-variant reliability index $\beta(t)$; (b) Time lag ΔT between NCC and RCP scenarios vs target reliability index β_t .

An effective quantitative measure of the impact of a changing climate can also be achieved by computing the time lag associated with the attainment of a target reliability index β_t between two scenarios with and without climate change effects. Figure 6b shows the time lag ΔT vs the target reliability index β_t , normalized with respect to the initial reliability index β_0 (i.e., β_t/β_0). As an example, for $\beta_t=0.55\beta_0$ the time lag is approximately 30 years for the RCP 8.5 scenario and 25 years for the RCP 2.6 scenario. It is worth noting that the relevant time lag associated to the mitigation scenario RCP 2.6 is mainly due to the effects of the cyclic variation of temperature. Indeed, neglecting it, as highlighted in additional analyses reported in Nava (2022), the detrimental effects of climate change are reduced.

5 CONCLUSIONS

The effects of non-stationary climate conditions on life-cycle performance and reliability of RC structures under corrosion has been investigated. The deterioration model incorporates future projections of climate parameters leading to increase damage caused by corrosion. The results obtained for a RC bridge pier cross-section allowed to quantify the impact of climate change on long-term structural reliability and highlighted the importance of modeling degradation taking environmental exposure and climate evolution into account. Neglecting seasonal fluctuations and climate trends may lead to an underestimation of the reliability index over time and, in turn, an overestimation of times for inspections, maintenance, retrofit, and repair.

This paper focused on the impact of climate change on the life-cycle reliability of individual concrete structures under corrosion. Life-cycle maintenance and management of resilient infrastructure systems should also be investigated accounting for climate change effects on the interaction of an increasingly aggressive environment with multiple hazards and considering the harmful impact of loss of functionality in critical system components. Further research is hence necessary to incorporate the proposed framework into risk-based procedures for optimal mitigation and adaptation strategies with a systemic perspective.

REFERENCES

- Bastidas-Arteaga, E., Schoefs, F., Stewart, M. G., & Wang, X. 2013. Influence of global warming on durability of corroding RC structures: A probabilistic approach. *Engineering Structures*, 51: 259–266.
- Bertolini, L., Elsener, B., Pedeferri, P., Redaelli, E., & Polder, R. 2013. *Corrosion of Steel in Concrete: Prevention, Diagnosis, Repair*. Weinheim: Wiley-VCH.
- Biondini, F., Bontempi, F., Frangopol, D. M., & Malerba, P. G. 2004. Cellular Automata Approach to Durability Analysis of Concrete Structures in Aggressive Environments. *Journal of Structural Engineering*, 130(11): 1724–1737.
- Biondini, F., & Frangopol, D. M. 2016. Life-Cycle Performance of Deteriorating Structural Systems under Uncertainty: Review. *Journal of Structural Engineering*, 142(9): F4016001.
- Biondini, F., & Frangopol, D. M. 2019. *Life-Cycle Design, Assessment, and Maintenance of Structures and Infrastructure Systems*. American Society of Civil Engineers.
- Biondini, F., & Vergani, M. 2015. Deteriorating beam finite element for nonlinear analysis of concrete structures under corrosion. *Structure and Infrastructure Engineering*, 11(4): 519–532.
- Capacci, L., & Biondini, F. 2019. Seismic Resilience of Deteriorating RC Bridges and Road Networks under Climate Change. *20th Congress of IABSE*, New York, NY, USA, September 4-6, 2019.
- Casti, L. 2021. *Life-Cycle Reliability of Aging Structures Under Climate Change*, MSc Dissertation. Politecnico di Milano.
- Ellingwood, B. R. 2005. Risk-informed condition assessment of civil infrastructure: state of practice and research issues. *Structure and Infrastructure Engineering*, 1(1),7–18.
- Gent, P. R., Danabasoglu, G., Donner, L. J., Holland, M. M., Hunke, E. C., Jayne, S. R., Lawrence, D. M., Neale, R. B., Rasch, P. J., Vertenstein, M., Worley, P. H., Yang, Z. L., & Zhang, M. 2011. The community climate system model version 4. *Journal of Climate*, 24(19): 4973–4991.

- Guo, Y., Trejo, D., & Yim, S. 2015. New Model for Estimating the Time-Variant Seismic Performance of Corroding RC Bridge Columns. *Journal of Structural Engineering*, 141(6): 04014158.
- IPCC 2021. *Climate Change 2021: The Physical Science Basis, the Working Group I contribution to the Sixth Assessment Report*. Cambridge: Cambridge University Press.
- Liu, T., & Weyers, R. W. 1998. Modeling the Dynamic Corrosion Process in Chloride Contaminated Concrete Structures. *Cement and Concrete Research*, 28(3): 365–379.
- Madsen, H. O. 2013. Managing structural safety and reliability in adaptation to climate change. *11th International Conference on Structural Safety and Reliability (ICOSSAR 2013)*, New York, NY, USA, June 16-20, 2013.
- Mazzoni, S., McKenna, F., & Fenves, G. L. 2006. *Open system for earthquake engineering simulation user manual*. Pacific Earthquake Engineering Research Center: University of California, Berkeley (<http://opensees.berkeley.edu/>).
- Nasr, A., Kjellström, E., Björnsson, I., Honfi, D., Ivanov, O. L., & Johansson, J. 2020. Bridges in a changing climate: a study of the potential impacts of climate change on bridges and their possible adaptations. *Structure and Infrastructure Engineering*, 16(4),738–749.
- Nava, G. V. 2022. *Effect of Climate Change on Life-Cycle Reliability of Concrete Structures under Corrosion*, MSc Dissertation, Politecnico di Milano.
- O’Neill, B. C., Tebaldi, C., van Vuuren, D. P., Eyring, V., Friedlingstein, P., Hurtt, G., Knutti, R., Kriegler, E., Lamarque, J.-F., Lowe, J., Meehl, G. A., Moss, R., Riahi, K., & Sanderson, B. M. 2016. The Scenario Model Intercomparison Project (ScenarioMIP) for CMIP6. *Geoscientific Model Development*, 9(9): 3461–3482.
- Peng, L., & Stewart, M. G. (2016). Climate change and corrosion damage risks for reinforced concrete infrastructure in China. *Structure and Infrastructure Engineering*, 12(4),499–516.
- Saetta, A., Scotta, R., & Vitaliani, R. 1993. Analysis of chloride diffusion into partially saturated concrete. *Materials Journal*, 90(5): 441–451.
- Stewart, M. G., Wang, X., & Nguyen, M. N. 2011. Climate change impact and risks of concrete infrastructure deterioration. *Engineering Structures*, 33(4): 1326–1337.
- Stewart, M. G., & Al-Harthy, A. 2008. Pitting corrosion and structural reliability of corroding RC structures: Experimental data and probabilistic analysis. *Reliability Engineering and System Safety*, 93(3): 373–382.
- Titi, A., & Biondini, F. 2016. On the accuracy of diffusion models for life-cycle assessment of concrete structures. *Structure and Infrastructure Engineering*, 12(9): 1202–1215.
- Trzaska, S., & Schnarr, E. 2014. *A Review of downscaling methods for climate change projection*. Washington: United States Agency for International Development.
- Van Vuuren, D. P., Edmonds, J., Kainuma, M. et al K. 2011. The representative concentration pathways: An overview. *Climatic Change*, 109: 5–31.
- Vu, K. A. T., & Stewart, M. G. 2000. Structural reliability of concrete bridges including improved chloride-induced corrosion models. *Structural Safety*, 22(4): 313–333.

Risk based life-cycle planning for flood-resilient critical infrastructure

S. Skaric Palic

Infra Plan Consulting, Zagreb, Croatia

I. Stipanovic

University of Twente Faculty of Engineering Technology, Enschede, The Netherlands

E. Ganic

University of Belgrade Faculty of Transport and Traffic Engineering, Belgrade, Serbia

M. Kosic & A. Anzlin

Slovenian National Building and Civil Engineering Institute, Ljubljana, Croatia

M. Bacic & M.S. Kovacevic

Faculty of Civil Engineering, University of Zagreb, Zagreb, Croatia

K. Gavin

InGEO Consulting, & TU Delft Faculty of Civil Engineering and Geosciences, Delft, The Netherlands

ABSTRACT: The paper presents a risk assessment model, developed in the project oVER-FLOW and further implemented in the project CROSScade, for determining the direct and indirect impacts of flooding hazards. As a consequence of flooding, transport infrastructure and flood protection systems can be significantly damaged and cause cascading effects on other infrastructure. To achieve flood resilient infrastructure, it is necessary to assess the vulnerability of critical assets in the affected area. The model uses novel vulnerability assessment methods for embankments and bridges exposed to different flood hazard scenarios allowing the asset owners to understand risk and performance of their infrastructure. Scarce financial resources are allocated on the critical assets allowing significant cost savings and avoiding the waste of non-renewable resources in strengthening large sections which have sufficient resilience. The consequence analysis is based on an improved quantification model for direct and indirect impacts of different flood hazard scenarios used for risk mapping of the affected area.

1 INTRODUCTION

Climate change is leading to more extreme weather events in most parts of the world (EEA, 2016; World Economic Forum, 2019). High water levels caused by increased frequency of heavy rainfall are causing flooding hazards and higher impacts such as increased financial consequences and human losses. The complete life-cycle management for critical infrastructure needs to consider these new extreme loads by applying different climate change scenarios to prepare for future hazardous events. Infrastructure managers require tools to support decision-making and prioritize intervention measures, either during the response or during the prevention stage. A risk-based safety approach regarding flood events provides information by combining data about the chance of a flood event, vulnerability and exposure of community, property and infrastructure.

The overall objective of the oVERFLOW project (<https://projectoverflow.eu/>) is strengthening resilience to climate change impacts, with the specific objective being the development of climate-resilient infrastructure. The key step to achieving the project objective focuses around the refinement of the risk-based approach for vulnerability assessment of levees (Rijkswaterstaat VNK Project Office, 2012, 2014) and using physical (sensor-based) real-time condition data rather than periodic visual condition assessment. Data-driven enhanced knowledge about the vulnerability of the weakest links in the flood protection systems and bridges led to the reduction of uncertainties and improved numerical models. This serves as the basis for decision-making processes regarding the prioritization of strategic investments and to further develop civil protection protocols for flooding events as prevention and response measures. The methodology developed in the oVERFLOW project was validated in a flood-prone case study areas of South Holland Region in the Netherlands and the city of Karlovac in Croatia. This paper presents the methodology validation on Croatian case study area, shown in Figure 1.



Figure 1. Karlovac city center next to the Kupa river: a) <https://aktivirajkarlovac.net/>; 2014 flood in Karlovac, b) <https://www.jutarnji.hr/vijesti/hrvatska/>).

2 FLOOD RISK ASSESSMENT

The intersection of a flood scenario for a specific return period and the area impacted by the hazard, for which vulnerability or damage functions are developed, forms the basis of flood risk assessment methodology. Using the framework presented in Figure 2, the vulnerability analysis results are combined with potential flood effects to create the risk forecasting tool. The tool provides information on the possible financial cost of flood consequences, as well as the population at risk, critical infrastructure, and evacuation routes in the flood-affected area.

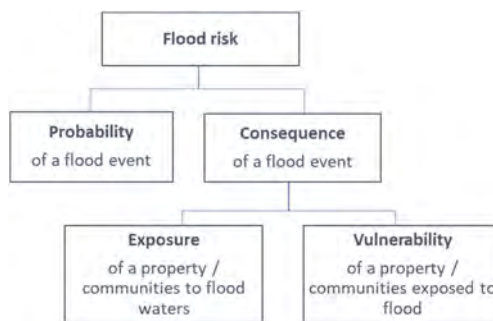


Figure 2. Risk assessment framework.

2.1 Flood hazard scenarios

Climate change is affecting the global mean temperature and the total amount of precipitation. However, the precipitation quantities are regionally significantly varying and have no clear trend compared to the temperature. Observations show that precipitation changes are occurring in the amount, intensity, frequency and type. Basic theory, climate model

simulations and empirical evidence all confirm that warmer climates, owing to increased water vapour, lead to more intense precipitation events even when the total annual precipitation is reduced slightly, with prospects for even stronger events when the overall precipitation amounts increase. The warmer climate, therefore, increases the risks of both drought and floods (IPCC, 2014). The effect of climate change on precipitation is similar to that of the river flows. Future changes in the mean and extreme river flow will show regional variety.

In the development of flood scenarios, historical and predicted climatological and hydrological parameters were analyzed for a period of one hundred years from 1970 to 2070 for the case study in Croatia. A machine learning technique was applied to predict changes in water flow and water level using an ensemble of temperature and precipitation data from the regional climate change model RegCM4 (MZOE, 2017). The model was used to calculate change (projections) for the future climate in two periods: 2011 - 2040 and 2041 - 2070, assuming the IPCC scenarios RCP4.5 and RCP8.5. The RCP4.5 scenario (moderate scenario) predicts the medium level of greenhouse gas concentrations while for the RCP8.5 scenario (extreme scenario) there is continuous increase of greenhouse gas concentrations. Simulations of water flow and water level show that climate change is likely to impact the Kupa river's future flows and water levels. Although the changes in annual average flows and water levels are expected to be small and not significant, models predict a significant increase in flow and water level in winter months and its decrease in summer months for both moderate and extreme scenarios, with bigger changes in the extreme scenario, shown in Figure 3. The climate change data and flood maps obtained with this analysis were further used for vulnerability analysis of critical infrastructure (Burić&Grgurić, 2020).

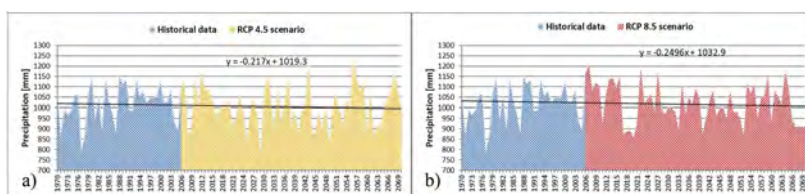


Figure 3. Modelled ensemble mean annual precipitation with RegCM4 for model point nearest to Karlovac 1970 – 2070; a) scenario RCP 4.5, b) scenario RCP 8.5. Data source: DHMZ (Burić&Grgurić, 2020).

2.2 Vulnerability analysis of embankments and bridges

Within the oVERFLOW project, the vulnerability analysis of critical assets focuses on the embankments and bridges, which are the most important components of the flood protection system and the transportation infrastructure as potential evacuation/emergency routes. The methodology is based on in-situ data collection and numerical models for bridges and embankments. The major outcomes of the proposed methodology are fragility curves for assessing the integrity of embankments and fragility surfaces for the serviceability and ultimate limit state for bridges. These data explicitly account for both material and loading uncertainty and can be used to interpret how likely a failure is, given a certain flood event.

The input data for the analysis of two bridges from the Karlovac case study area is obtained from archived projects, which were complemented with results of a drone and bathymetric survey and ambient vibration measurements (Kosić et al., 2021). The results of the drone and bathymetric surveys were used to define the geometry, whereas measurements of ambient vibration allowed the estimation of the bridge's modal properties. Due to specific hydraulic conditions, i.e. non-stationary flow (Burić&Grgurić, 2020), both velocity and water height are found to be necessary for precise estimation of the bridge performance, so the result of the vulnerability analysis is presented with fragility surfaces, which represents an extension of the classical fragility curve concept.

An advanced modelling approach for simulation of the bridge response considering soil-structure interaction is applied (Kosić et al. 2023a). The study examines different flood-loading scenarios, including hydrodynamic loads, debris and scour. Special attention is devoted to the

explicit simulation of the effect of scouring on the distribution of forces in the structure. Several failure mechanisms are considered, and the most unfavorable mechanism for the given flooding scenario is identified. The vulnerability analysis is performed separately for the serviceability (SLS) and ultimate limit state (ULS). The results of the analyses indicate that the SLS of the bridges is affected significantly by the accumulation of debris, which constricts the flow of the water and leads to an amplification of scour due to the local increase of the flow velocity (Kosič et al., 2023b). The fragility surfaces provide crucial input for developing the risk forecasting tool with the so-called traffic light indicators, representing a safe/unsafe evacuation route during the response.

The implementation of the methodology to the Karlovac case study area includes calculating the probability of failure of 3 km of riverbanks on the left and right side of river Kupa. Riverbank stability is assessed for both rapid drawdown and seismic loading scenarios, for which fragility curves were developed (Bačić et al, 2022). Characteristic riverbank sections are identified from a remote photogrammetric survey, geometry for different sections and probabilistic calculations are performed on each of them. Calculated values of probability of failure for different scenarios provide the basis for classifying the embankments and riverbanks based on their vulnerability and developing an inventory of critical flood protection infrastructure in the case study area.

To evaluate the vulnerability of the riverbank slopes, global stability is identified as the relevant failure mechanism. For each riverbank section, analysis is performed so that the water level external to the riverbank slope experienced a rapid reduction in level while residual water levels (RWL) in the riverbank remained at higher levels. For the seismic stability during the increase of the pseudo-static loads (acceleration), the probability of stability failure also increases. The maximum considered value of peak horizontal acceleration is selected as 0.3g, which is double the value of the 475-year return period in the city of Karlovac (<http://seizkarta.gfz.hr>). These analyses are performed by using drained parameters in the first step analyses and undrained parameters in the second step analyses, in which upper clay was modelled with undrained parameters. In further project developments, these results are incorporated into the risk forecasting tool for the purpose of classification of the embankments and riverbanks based on their vulnerability and development of an inventory of critical flood protection infrastructure (Gavin&Reale, 2021).

2.3 *Direct and indirect consequences*

Flood effects may be both direct, through the immediate interaction of flood water with built, natural and human environments, and indirect, through damage or disruption of transportation and economic activities that impact people's livelihoods. Damage to buildings, economic assets, loss in agriculture, loss of human life, immediate health impacts and loss of ecological goods are generally applied quantifiable parameters. Indirect flood damages are damages caused by disruption of physical and economic linkages and the extra costs of emergency and other actions taken to prevent flood damage and other losses. This includes, for example, the loss of production of companies affected by the flooding, induced production losses of their suppliers and customers, the costs of traffic disruption or the costs of emergency services. Indirect damage is often measured as a loss of flow values (WMO, 2015).

oVERFLOW methodology for quantification of different flood impact categories includes two approaches developed for different types of users:

- i. The quantification of impacts in monetary value to show direct flood damage to different assets can be used by infrastructure managers, owners or local authorities. This information can support decisions such as the prioritization of assets which need to be upgraded, identification of possible needed interventions and investments for flood protection systems, transport infrastructure or any other endangered asset. The model is used in the final risk assessment and can also be used for cost-benefit analysis (Bruijn et al., 2015).
- ii. Mapping of the vulnerability of critical infrastructure and population density gives the insights of direct impacts on humans, especially important for Civil Protection Agencies (CPAs) and first responders about the endangered population, areas with low rise buildings or buildings with people without self-sufficiency (preschools, schools, retirement homes etc.) where their immediate attention is needed in case of floods. It also provides information about safety evacuation routes so they can reach certain areas without delay or endangerment.

The main parameters for the risk evaluation and calculation of direct economic damage are the value of elements at risk and water depth-damage curves (Moel&Aerts, 2011; Klijn et al., 2007). In the oVERFLOW methodology, damages of industrial and residential buildings, businesses, infrastructure and land per different usage types are quantified in monetary terms, using literature and historical values from the case study area (Huizinga et al. JRC, 2017; Kok et al., 2005, Wagenaar et. al, 2016;). For the oVERFLOW project, mainly for the case study area of the city of Karlovac, different categories for residence and industrial buildings are taken into account with damage curves developed for the analyzed area, see Figure 4.

Special assets and areas, including vulnerable assets (critical infrastructure such as transport, healthcare, electricity, and water supply), cultural heritage, installations, and vulnerable nature areas, are identified and mapped. The flooding of these assets is of relevance for flood risk managers, infrastructure managers and evacuation services. Also, mapping buildings per number of stories, provides with the information needed to prioritize evacuation in certain areas. Higher buildings mean more space for people to evacuate themselves on higher floors which is why buildings are mapped according to the number of stories and number of residents.

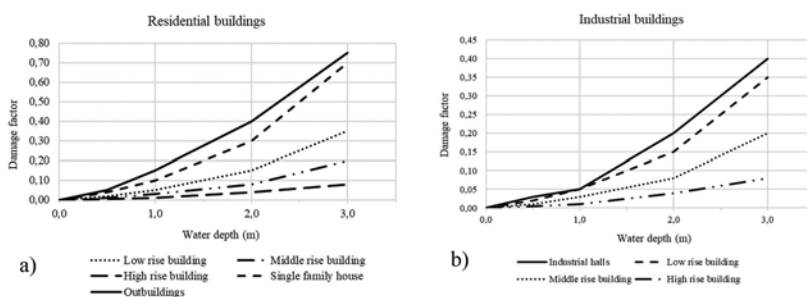


Figure 4. Proposed damage values for Croatian case study for a) Residential and b) Industrial buildings (Skaric&Stipanovic, 2022).

Safe evacuation routes and accessibility for first responders are determined by highlighting critical transport infrastructure. The safe evacuation routes are established based on reaching the nearest safe place within buildings, building blocks and city districts. Areas with higher buildings safer in case of a flood hazard can be highlighted. The main constraints associated with the emergency are structural vulnerabilities along escape routes (failure of bridges or flood protection structures), uncertain road conditions due to landslides, and parts of roads under the water, including traffic congestion, road blockage, etc. Optimal evacuation alternatives in the form of the safest and most efficient routes for evacuation of the population from the affected region are determined based on the results of the vulnerability assessment of bridges and embankments.

Losses to any business in the area affected by flood include loss of business value that would have been produced if a flood event had not occurred. Production is stopped due to the Material Damage (MD) of installations or disrupted supply chains. It could be that other businesses or productions, processes before or after, have also been stopped or delayed due to a hazardous flood event. These are indirect losses, defined as Loss due to Business Interruption (LBI), which do not include direct economic losses to a company caused directly by contact with water. Loss of business category implies the long-term economic effect of a flood due to business interruption. Indirect losses to a business are often expressed as a share of the material damage in flood (Vilier et.al, 2014). In the 1993 Netherlands flood, 75% of the damage to the industry was related to property, and 25% was related to productivity loss (Kok, 2001, Genovese, 2006).

Following the economic scenario that there is no income while the business is interrupted, but the expenditures remain, if the business is to be restored after the flood event, the economic loss due to business interruption (LBI) is calculated based on the following:

$$LBI = (I_{tot} + E_{tot}) \times Nr_{emp} \times T \quad (1)$$

where LBI = loss due to business interruption (€); I_{tot} = total income per employee per day; E_{tot} = total expenditure per employee per day; Nr_{emp} = a number of employees in the flood-affected area; T = time for the return of business to pre-flood conditions.

3 RISK MAPPING

Calculation of risk implies the combination of flood hazard scenarios with the exposed area, and the verification of direct and indirect consequences. The overall product is the spatial distribution of flood risks for selected areas. Direct impacts are quantified in monetary values, while indirect qualitative analysis with pre-designed risk classification and highlighting of different risk levels is proposed. The results are integrated into the existing GIS platforms as two different operational layers: for Infrastructure Managers (IMs) for future planning of investment measures and for CPAs in order to enhance the emergency response and ensure safe and efficient evacuation. Flood hazard maps, which show flood depths for different probabilities of occurrence of a flood, are overlapped with spatial data of area's exposure and vulnerability of critical assets.

3.1 Hazard maps

For the case study area in Croatia, the city of Karlovac, three different flood scenarios have been analyzed and compared. Flood scenarios are based on Croatian Waters flood hazard maps with three different return periods: high (HP), medium (MP) and low probability (LP) of occurrence, with return periods 25, 100 and 1000 years, respectively. Water depths are grouped into four categories: < 0.5 m, 0.5 – 1.5 m, 1.5 – 2.5 m and > 2.5 m (Croatian Waters, 2019).

3.2 Risk tool layers for Civil Protection Agencies

Based on the performed analysis, the following information is provided in the form of a GIS-based risk forecasting tool to be used by CPAs in a case of a flood event:

- Number of people to be evacuated, and their location in the affected area, see Figure 5;
- Crucial institutions affected by flood (hospitals, schools, retirement homes...);
- Available shelters for evacuation (flooded/not flooded);
- Safe and available evacuation routes (flooded roads; operating infrastructure – embankments and bridges that are safe or not safe for usage during flooding), see Figure 6.

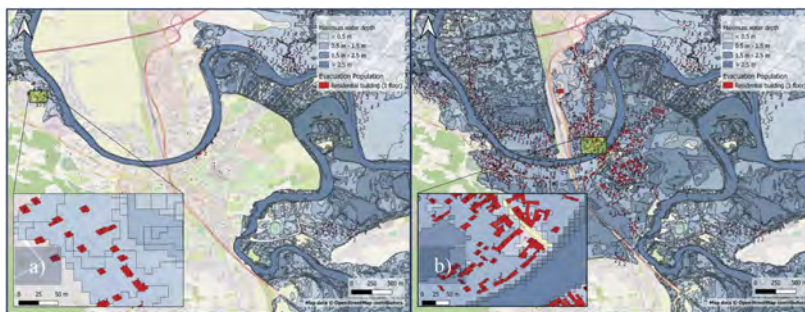


Figure 5. Population flood risk map – Map of low rise buildings (red) and number of residents overlapped with a) Flood map HP and b) Flood map LP.

3.3 Risk tool layers for infrastructure managers

Based on the performed analysis, information about possible direct and indirect impacts is provided through a risk forecasting tool to be used by IMs for prioritization and strategic planning. Direct impacts to transport infrastructure and to industrial and residential buildings, businesses, infrastructure and land per type, all quantified in monetary terms. Indirect impacts regarding loss of business disrupted due to the flood event.

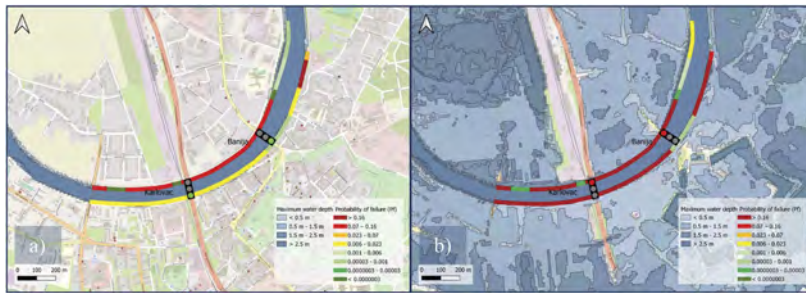


Figure 6. Results of the vulnerability analysis for embankments and bridges for a) HP of flood occurrence and b) LP of flood occurrence.

Figure 7 presents total estimated damage values (including direct and indirect damages) for different flood events for the City of Karlovac area. It can be seen from this graph that the total damage costs are increasing with the increase of the return period, or the extent of the flood event.

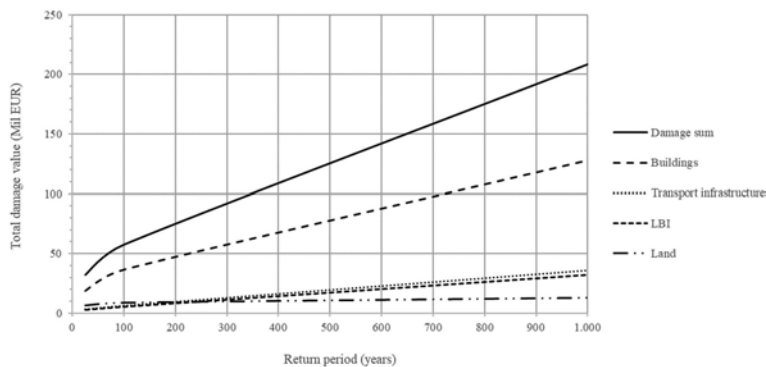


Figure 7. Graphical representation of economic damage (€) per category for three different flood probabilities for the city of Karlovac area.

4 CONCLUSIONS

Much effort is directed towards improving prevention and response measures for flood events to protect the population, their belongings, assets, businesses, and society at large. Experience has shown that, for the most part, consequences of flood hazard cannot be completely mitigated. As a result, the focus should be placed on reducing or avoiding adverse consequences on people, the environment, and property. Targeted data, which is frequently already available, can be used to extract relevant information from a range of users, including CPAs and IMs. This paper presents an overview of the risk assessment methodology developed within the oVERFLOW project and further implemented in the CROSScade project, which uses the improved vulnerability assessment of the critical infrastructure based on the actual monitoring data and consequence analysis of direct and indirect impacts using local exposure data. The main contribution of the methodology is a better prediction of the areas with the highest risk, which can be used to support decision-making during the response stage and to plan investments to strengthen most vulnerable parts of the critical infrastructure.

ACKNOWLEDGEMENT

This research was co-funded by UCPM program, GA 874421: oVERFLOW (Vulnerability assessment of embankments and bridges exposed to flooding hazard), GA 101048395: CROSScade (Cross-border cascading risk management for critical infrastructure in Sava river Basin). We would also like to acknowledge great collaboration with City of Karlovac.

REFERENCES

- Bačić, M., Kovačević, M.S., Jurić Kačunić, D., Librić, L., Car, M., Gavin, K., Stipanović, I., Reale, C., Classification of a flood protection infrastructure based on its vulnerability to various loads, CETRA 2022, Proceedings of the international conference, May 2022.
- Burić M., Grgurić S. (2020). oVERFLOW Deliverable 2.2 Climate downscaling and flooding scenarios for selected area.
- Bruijn de K., Wagenaar D., Slager K., Bel de M., Burzel A., Deltares for Rijkswaterstaat Water, Updated and improved method for flood damage assessment: SSM2015 (version 2), 2015
- Croatian Waters, 'Water area management plan 2022 – 2027', Flood risk management, Preliminary Flood Risk Assessment 2018.', published July 2019
- EEA. (2016). Flood risks and environmental vulnerability - Exploring the synergies between floodplain restoration, water policies and thematic policies. In EEA Report No 1/2016. (Issue 1).
- Gavin K., Reale C. (2021). oVERFLOW Deliverable 4.1 D4.1 Report on Vulnerability Assessment Methodology - Fragility curves for embankments subjected to flooding.
- Genovese E., 2006, 'A methodological approach to land use-based flood damage assessment in urban areas: Prague case study', EUR 22497 EN ISSN 1018-5593, Luxembourg: Office for Official Publications of the European Communities.
- Huizinga J., Moel de H., Szewczyk W., Global flood depth-damage functions - Methodology and the database with guidelines, JRC Technical Reports, 2017, Pdf ISBN 978-92-79-67781-6, ISSN 1831-9424, doi: 10.2760/16510
- Klijn F, Baan PJA, De Bruijn KM, Kwadijk J (2007) Overstromingsrisico's in Nederland in een veranderend klimaat, vol Q4290. Delft, Netherlands, WL, Delft hydraulics, pp 1–166
- Kok M. (2001), "Damage functions for the Meuse River floodplain", Internal report, JRC (Ispra).
- Kok M., et al., 2004, Standaardmethode 2004 Schade en Slachtoffers als gevolg van overstromingen, DWW-2005-005, HKV LIJN IN WATER, November 2004.
- Kosić, M., Anžlin, A. (2022). oVERFLOW Deliverable 4.2 Report on Vulnerability Assessment Methodology - Fragility curves for bridges subjected to flooding.
- Kosić, M.; Prendergarst, L.; Anžlin, A. Analysis of the response of a roadway bridge under extreme flooding-related events: scour and debris loads. *Engineering Structures* (accepted, in the process of publication).
- Kosić, M.; Anžlin, A.; Bau, V. Flood Vulnerability Study of a Roadway Bridge Subjected to Hydrodynamic Actions, Local Scour and Wood Debris Accumulation. *Water* 2023, 15, 129. <https://doi.org/10.3390/w15010129>.
- Kosić M., Hekić D., Kalin J., Oostwegel L., Anžlin A. (2021). oVERFLOW Deliverable 3.2: Report on investigation works and monitoring of bridges.
- Moel de H., Aerts J. C. J. H., 'Effect of uncertainty in land use, damage models and inundation depth on flood damage estimates', *Nat Hazards* (2011) 58:407–425. DOI 10.1007/s11069-010-9675-6.
- MZOE, 2017. Rezultati klimatskog modeliranja na sustavu HPC Velebit za potrebe izrade nacrtu Strategije prilagodbe klimatskim promjenama Republike Hrvatske do 2040. s pogledom na 2070. i Akcijskog plana (Podaktivnost 2.2.1.).
- World Economic Forum. (2019). *Global Risks Report 2019*, 14th Edition. World Economic Forum
- Rijkswaterstaat VNK Project Office (2012) *Flood Risk in the Netherlands, VNK2: The Method in brief – Technical background*, <https://www.helpdeskwater.nl/onderwerpen/waterveiligheid/programma-projecten/veiligheid-nederland/publicaties/>
- Rijkswaterstaat VNK Project Office (2014) *The National Flood Risk Analysis for the Netherlands*, <https://www.helpdeskwater.nl/onderwerpen/waterveiligheid/programma-projecten/veiligheid-nederland/>
- Skaric Palic S., Stipanovic I. (2022). oVERFLOW Deliverable 5.1 D5.1 Quantification framework for direct and indirect impacts of flooding hazards.
- Vilier J., Kok M. Nicolai R.P., 'Assessment of the losses due to business interruption caused by large-scale floods', *Safety, Reliability and Risk Analysis: Beyond the Horizon – Steenbergen et al. (Eds), 2014 Taylor & Francis Group, London, ISBN 978-1-138-00123-7, p.2415–2423*
- Wagenaar D.J., Bruijn de K.M., Bouwer L.M., Moel de H., 'Uncertainty in flood damage estimates and its potential effect on investment decisions', *Nat. Hazards Earth Syst. Sci.*, 16, 1–14, 2016 www.nat-hazards-earth-syst-sci.net/16/1/2016/, doi:10.5194/nhess-16-1-2016.
- World Meteorological Organization (WMO), 2015 'Integrated flood management tools series: Effectiveness of flood management measures', Issue 21 https://www.floodmanagement.info/publications/tools/Tool_21_Effectiveness_of_Flood_Management_Measures.pdf
- <http://aktivirajkarlovac.net/2018/09/plan-za-plan-razvoja-zvijezde/>
- <http://Jutarnji.hr/vijesti>
- <http://projectoverflow.eu/>

Equitable climate adaptation framework for levees

A. Mohammed & F. Vahedifard

Richard A. Rula School of Civil and Environmental Engineering, Mississippi State University, Starkville, Mississippi, USA

ABSTRACT: The evolving risk of floods significantly threatens the economy, safety, and well-being of several regions globally. In 2020, the average annual loss due to floods in the United States was over \$32 billion, projected to increase by over 26% by 2050 due to climate change. This calls for a critical need to proactively develop and implement climate adaptation strategies to ensure the integrity of earthen levees, which play a fundamental role in the nation's flood protection systems. The levees in the United States have an average age of 57 years, most of which are under marginal conditions. Approximately two-thirds of the American population lives in counties protected by levees where floods disproportionately affect disadvantaged communities. We present a risk-based equitable adaptation strategy for levees in a changing climate that concurrently considers changes in hazard levels, vulnerability, and exposure. Identifying new patterns of climatic extremes and natural hazards (i.e., hazard levels) that impact the performance of current and future levee systems is the first step in achieving a climate-ready levee system. The next step involves characterizing the vulnerability of levee systems while considering the influence of climate-adjusted hazard levels. Finally, the proposed adaptation framework suggests considering changes in the exposure of assets and communities in levee-protected areas due to various factors (e.g., climate change, urbanization, land use, and land cover changes). The proposed adaptation framework intertwines engineering factors and socio-demographic attributes toward achieving resilient, sustainable, and equitable levee systems in a warming climate.

1 INTRODUCTION

The evolving risk of floods significantly threatens the economy, safety, and well-being of several regions globally. In 2020, the average annual loss due to floods in the United States was over \$32 billion, projected to increase by over 26% by 2050 due to climate change (Wing et al. 2022). This calls for a critical need to proactively develop and implement climate adaptation strategies to ensure the integrity of earthen levees, which play a fundamental role in the nation's flood protection systems. The levees in the United States have an average age of 57 years, most of which are under marginal conditions. Approximately two-thirds of the American population lives in counties protected by levees where floods disproportionately affect disadvantaged communities (ASCE 2021).

We present a risk-based equitable adaptation strategy for levees in a changing climate that concurrently considers changes in hazard levels, vulnerability, and exposure. Identifying new patterns of climatic extremes and natural hazards (i.e., hazard levels) that impact the performance of current and future levee systems is the first step in achieving a climate-ready levee system. The next step involves characterizing the vulnerability of levee systems while considering the influence of climate-adjusted hazard levels. Finally, the proposed adaptation framework suggests considering changes in the exposure of assets and communities in levee-protected areas due to various factors (e.g., climate change, urbanization, land use, and land cover changes).

The proposed adaptation framework intertwines engineering factors and socio-demographic attributes toward achieving resilient, sustainable, and equitable levee systems in a warming climate.

2 LEVEE RISK

Risk is defined in this study as the likelihood of adverse effects on people and assets. (IPCC 2021). In climate change-related studies, the risk is identified as the result of the interaction of hazard, vulnerability, and exposure. Thus, levee risk in this study is defined as the product of evolving hazards, vulnerabilities, and rising exposure. This implies that there is no risk in areas where the hazard does not cause harm to communities or assets. Risk is found when there is an overlap of extreme events, people and assets, and vulnerability in the levee system. Here consider three scenarios i) Extreme event causing levee failure in a remote area with no people or assets. ii) Extreme events lowered levee performance in an urban area with adaptation measures in place. iii) Extreme event lowered levee performance in an urban area with no adaptation measures in place. The first option indicates the most significant hazard, while the third option indicates the highest risk. Delineating the evolving levee risk with climate change is critical to achieving a climate-ready levee system. Hence, the study considers these three components (hazard, vulnerability, and exposure) to constitute the key elements of a comprehensive risk assessment for levees (Figure 1).

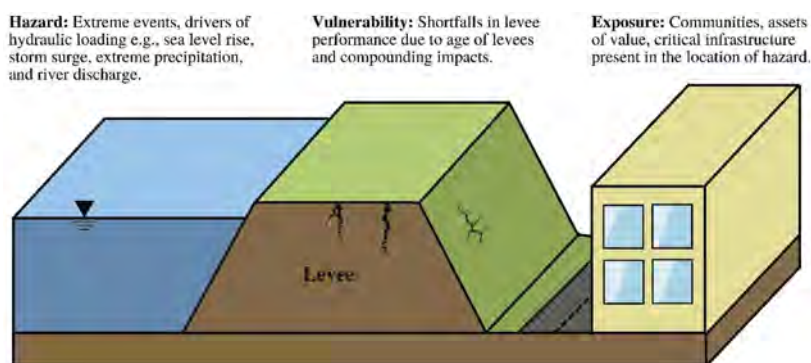


Figure 1. Interaction between hazard, vulnerability, and exposure.

2.1 Hazard

The consequences of anthropogenic climate change are felt through the exacerbating intensity and frequency of extreme events in the form of rising water levels, particularly on levees (Milly et al. 2002; Buchanon et al. 2017; Vitousek et al. 2017; Taherkhani et al. 2020). The increase in the water level can be a result of storm surges, extreme precipitation, river discharge, increased surface runoff, and land subsidence. Changes in land use and urban developments in floodplains directly lead to a reduction in the storage capacity of natural storage systems. River channels are often confined within dikes or levees to accommodate new settlements. This can lead to higher river velocities increasing flood risk downstream. Measures to curtail flooding in one location may increase flood risk in different locations (Wang et al. 2018). Urban development also results in larger areas of impervious surfaces such as roads, pavements, and parking yielding increased surface water runoff. The failure of drainage systems can have severe impacts on the land side of the levee. Thus, it is critical to identify new patterns of climatic extremes and natural hazards (i.e., hazard levels) that affect the performance of existing and future levee systems.

Climate change can have an impact on individual extreme events as well as compounding and cascading hazards (e.g., co-occurrence of extreme precipitation and storm surge) (Moftakhari et al. 2017). Variations in the probabilities of storm surge, sea level rise, and even droughts can, either individually or combined can have a significant impact on levee performance in the short and long term. Levees are designed for rainfall through extreme precipitation estimates, which are derived from the assumption that the probability of extreme events does not change drastically over time. This assumption can lead to underestimation in the levee design (Vahedifard et al. 2017). Levees are also typically designed to withstand single or multiple extreme events. However, most design criteria, operating procedures, and levee maintenance and management practices do not consider the impact of compounding extremes, i.e., the simultaneous occurrence of multiple extreme events, or cascading impacts, i.e., successive extreme events contributing to the reduction in levee performance. Most often, the interdependencies of two or more hazards which may or may not be extreme events in and of themselves, are overlooked. This phenomenon is known as a compound event. The following scenarios provide examples of circumstances leading to compounding events i) two or more co-occurrences of extreme events (extreme rain and storm surge), ii) co-occurrence of extreme events with underlying conditions that amplify impact (earthquake and extreme rain) or iii) combination of events that are not themselves extreme but collectively lead to severe impacts (moderate rain and drainage failure).

2.2 *Vulnerability*

Vulnerability is defined as susceptibility in levee performance due to factors such as age and gaps in understanding the impacts of compounding events. Addressing vulnerability requires the development of frameworks that associate climate change data with physical performance measures (e.g., probability of failure) of levees. Levees were used to protect farmlands and livestock primarily. However, due to rapid urbanization, levee-protected areas now accommodate critical infrastructure. There is a growing number of studies into developing resilient levees; however, despite the advances in climate adaptation, there are several critical gaps in the current state-of-the-art, including i) uncertainties in changing hazard levels, particularly future extremes are often ignored. Typical levee performance studies consider one or a few sources of uncertainty, such as soil property. However, there are several sources of uncertainty including hydraulic loading scenarios, response thresholds, material properties, and uncertainties related to future representative concentration pathways (RCPs). ii) land vegetation atmosphere interactions, their impacts on the performance of levee systems, and their underlying uncertainties are typically overlooked. iii) interactions between different modes of failures, e.g., slope stability failure, under seepage, and over-topping failure under single and compound loading scenarios, need to be better understood and addressed in the design. iv) The changes in levee resilience over their service life are not well understood or modeled. Levees are subject to various hazards that may occur with non-stationary intervals and uncertain magnitudes throughout their service life. In addition, the residual effects of a hazard will affect levee performance in the subsequent hazard. Prolonged drought, for example, can cause desiccation cracks in earthen levees, leading to increased infiltration during extreme precipitation and eventual depreciation in levee performance. Awareness programs, monitoring, and mitigation efforts can all help to reduce vulnerability. A classic example is the \$500 million flood damage caused by levee failure in the Secchia river in northern Italy in January 2014 (Orlandini et al. 2015). In this incident, the failure of the levee raised awareness, which led to government agencies identifying a potential second breach. A quick mitigation response prevented a second levee failure and subsequent damage (Orlandini et al. 2015).

2.3 *Exposure*

The rising global population and encroachment in areas particularly close to natural water bodies constitute one of the main reasons that damages from extreme events have significantly increased in the past decade. Over half of the world's population lives within 3 kilometers of

a natural water body (Kummu et al. 2011). Despite covering less than 15% of the earth's total area, coastal regions susceptible to flooding accommodate a substantial proportion of the world's population. In the U.S., seventeen million people live behind a levee (ASCE 2021). The rising exposure to flood risk directly results from the growing population, assets, more frequent and severe extreme events due to anthropogenic climate change, and land-use/ land-cover changes. Most often, flood plains are attractive locations for new settlements due to the ease of access to water and the natural flat terrain for development. An example of increasing exposure is observed when the local public and decision-makers believe that the levee has controlled river flow and continues to develop flood-prone areas. Developed areas eventually become urban centers, where a levee breach can have serious consequences for people and assets. Therefore, a levee adaptation framework should account for the changes in the exposure of assets and communities.

Rising exposure increases the dependency and importance of other critical infrastructure systems, such as power grids, for a community's resilience. The uneven spread of post-flooding resilience can lead to pockets of areas with higher exposure. This is especially noticeable in areas with high concentrations of underserved and socially vulnerable communities. For example, people living below the poverty line have a lower capacity to recover from hazards than those who are affluent. This variability can be curbed by incorporating environmental justice into the adaptation strategy.

3 5-STEP FRAMEWORK FOR EQUITABLE LEVEE ADAPTATION

Broadly climate adaptation of infrastructure is viewed as a changing of the existing status quo and adopting new practices to enable the development of climate-resilient infrastructure. Here, we present a five-step framework for the equitable adaptation of levees. A comprehensive levee adaptation strategy requires concurrent consideration of both geotechnical and socioeconomic factors to achieve equitable risk. Despite rising interest in climate-resilient infrastructure, the state-of-the-art practice currently lacks in terms of ensuring equity in investments and adaptation. Historically underserved and vulnerable communities (HUSVCs) are considerably more vulnerable to flooding due to pre-existing conditions stemming from socioeconomic characteristics such as poverty, lack of education and awareness, health, and no vehicle access. Furthermore, these communities are ill-equipped to prepare for and respond to floods due to a limited understanding of forecast terminologies and the severity of floods. HUSVCs are found to disproportionately occupy levee-protected areas due to various factors such as segregation by race and ethnicity, low property value, language, employment status, and immigration status. Hence, any attempts to create a climate adaptation strategy should explicitly include considerations for environmental justice to ensure equitable adaptation outcomes. Such a framework should seamlessly integrate physical performance measures and socioeconomic characteristics.

This study proposes a five-step framework for equitable levee adaptation that considers rising flood risk and prioritizes HUSVCs (Figure 2). The framework is built to achieve equal flood risk for all communities, regardless of socioeconomic status. Moreover, the framework is designed to be iterative, meaning past shortfalls are identified and corrected for the next cycle. The five steps that constitute the adaptation framework is as follows.

- i) **Community assessment:** The main objective of the first step is to identify communities most in need of levee adaptation. This step entails geospatial analysis of levee-protected areas in conjunction with population characteristics. Two datasets used here include Levee-protected areas: regions protected from flooding by levees obtained from the national levee database (NLD 2022), and Census data: For levee-protected areas, the census bureau provides socioeconomic and demographic data such as African Americans, Asians, Native Americans, Hispanic or Latino, persons below poverty, persons with low education, households without access to a vehicle, and persons with disabilities at the tract level. The findings of the first step inform decision-makers about which areas require priority for adaptation and identify areas of higher exposure.

- ii) **Community engagement:** The second step is to broaden public participation to better understand their needs and priorities, knowledge gaps, and perceived risk. This step aims to identify stakeholders (public, political, environmental, and commercial) in the adaptation. Moreover, by engaging the community, knowledge disconnects between stakeholders can be evaluated and addressed through informal education (Collins and Ison, 2009). An effective strategy for improving hazard awareness in the general public is to provide a platform for discussions between the people, government, and researchers. A truly integrative approach can be reached when the local public, decision-makers, and researchers work together towards a common goal. Open discourse on preparedness, lack of awareness, response to the event, existing evacuation strategies, and funding available should take priority. The primary objective of this step is to establish a two-way dialogue with impacted communities and ensure their concerns are addressed during the adaptation process.
- iii) **Flood risk assessment:** Following community identification and engagement, this step entails the assessment of levee performance for different modes of failure under current and projected future climate conditions. Extensive research methods have been used to perform a risk assessment of levees (Zhang et al. 2013; Zimmaro et al. 2019; Lanzafame & Sitar, 2019; Vahedifard et al. 2020). These methods use fragility curves, which provide the relationship between the probability of failure and hydraulic loading. This step quantifies the impact of climate change by considering changes in hazard levels. Assessment should quantify the impact of worsening hydraulic loading on levees, individually or combined, which can severely impact levee performance. (Vahedifard et al. 2020). Furthermore, the assessment also provides guidelines and risk thresholds to initiate adaptation measures.
- iv) **Adaptation assessment:** The fourth step entails weighing feasible and practical adaptation options based on the outcomes of the previous three steps. The type of vulnerable communities, their needs, perceived risk, concerns, and the current state of the levee should all be used to determine the preferred adaptation option. Both soft and hard adaptation options can be proposed to determine the most practical approach in terms of funding availability, federal government support, and the viability of adapting the current levee system. Furthermore, it is necessary to estimate the financial resources required to implement adaptation measures and compare the potential cost savings from adaptation. It is also critical to

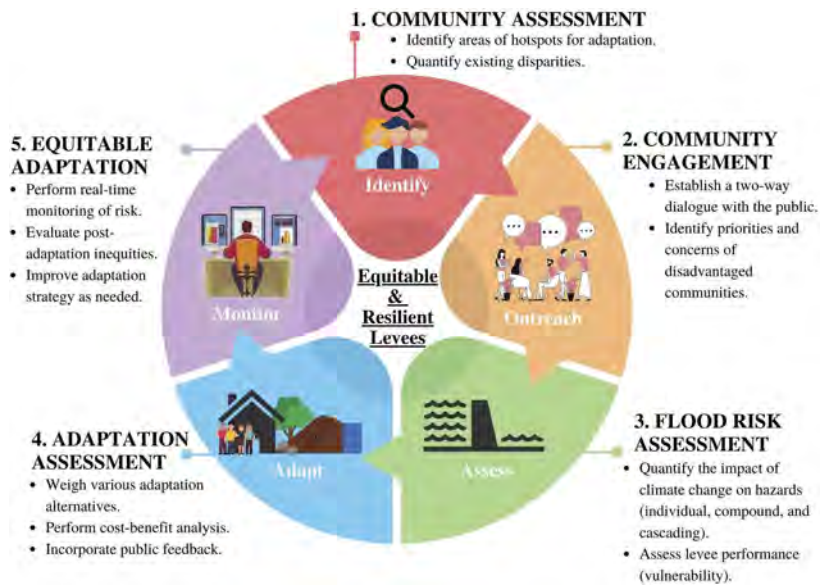


Figure 2. Five-step framework for equitable climate adaptation of levees that incorporates evolving flood risk and prioritizes disadvantaged communities.

debate the benefits and drawbacks of the proposed adaptation strategy at various stages of the framework and incorporate local public feedback into the design.

- v) Equitable adaptation: The final step is the implementation of a selected adaptation strategy. However, adaptation alone is not adequate; this step aims to establish long-term monitoring protocols to evaluate evolving risk. This step sets up protocols for long-term monitoring of evolving hazards, developing vulnerabilities, and rising exposure. This step also takes a look back at the adaptation process to identify room for improvement. For instance, an evaluation of how public participation influenced adaptation planning or tradeoffs between parties for reaching a consensus on adaptation strategy needs to be recorded. The proposed five-step framework is an iterative process that improves with each cycle by addressing shortcomings in the strategy for future adaptation efforts.

4 ADAPTATION STRATEGIES

Feasible levee design based on short and long-term hydraulic loading scenarios is required for levee adaptation. The uncertainties and intermodal variability in future climate extremes will elevate the probability of levee failure. As a result, developing resilient current and future levees requires accounting for the variability and uncertainty associated with a changing climate future. A viable approach is to have a risk-based adaptation strategy, which allows for the design to adapt to changes in hazard levels, vulnerability, and exposure. Levees can be built with a capacity for adaptation, allowing for adaptation measures to be implemented when water levels reach a particular threshold. This approach has a lower upfront cost but with the option of additional investment to respond to future extreme events (Hinkel et al. 2014). A risk-based adaptive strategy considers and identifies potential hazards and their likelihood of occurrence and prepares for the future decline in levee performance. However, rebuilding the nation's levee systems is prohibitively expensive. As a result, soft measures such as elevating levees, fail-safe options, land acquisition, flood warning systems, and land use regulations are frequently used in levee adaptation strategies.

To mitigate the effects of flooding, several adaptation options can be used. The list of possible soft measures is lengthy and frequently region/climate dependent. Some soft measures that can be implemented include i) complete mapping of levees across the U.S. as outlined in the national flood insurance reform bill. ii) Designate levees based on current conditions iii) Inspecting and bringing up to code current levee systems using updated loading scenarios. iv) Designate high-exposure zones to identify areas that require priority. v) Develop policies for maintenance and upgrading deteriorating levees. vi) Develop systems that reduce reliance on levees for flood protection, such as having safe-to-fail options. vii) Ensure adequate funding for the operation and routine maintenance of levees. viii) develop alternative water storage infrastructure or systems to route excess water. Finally, establish several funding streams to develop and maintain resilient levee systems that can withstand future climate change.

5 CONCLUSION

Despite the rising severity and magnitude of extreme events as a result of climate change, there are few studies that present a comprehensive framework that incorporates environmental justice into climate adaptation for levees. Here, we present a framework for climate-resilient levees that incorporates possible metrics to quantify progress and approaches that are grounded on environmental justice. In the proposed framework, First, we identify disparities in leveed protected areas, which serve to identify hotspots for equitable adaptation. Second, we approach at-risk communities to determine their needs, goals, and perceived risk. For an equitable outcome, it is critical that community feedback be incorporated into the adaptation process. The third step involves flood risk assessment, which entails detecting vulnerabilities in levee systems using physical performance measurements (probability of failure). The fourth

step is then used to evaluate adaption alternatives based on cost-benefit analysis and community feedback. The final step involves implementing adaptation and long-term monitoring of levee performance and social impacts. It is crucial that environmental justice is incorporated into each step of the framework. Finally, a robust five-step adaptation framework is proposed that incorporates both engineering and socioeconomic factors. Comprehensive studies are required to explore each step of the framework to develop a set of objectives, outcomes, and prerequisites for moving forward.

Maintaining levee resilience in a changing world while addressing existing inequities is a complicated and multidisciplinary problem. To address this issue, close collaborations between experts from various fields, including geotechnical engineering, climate science, social science, and hydrology, as well as decision-makers and authorities responsible for maintaining and operating levees, are required. Finally, climate adaptation of levees will fail to reach an equitable outcome unless the public is actively involved throughout the adaptation process to identify and recognize resilience and equity concerns.

ACKNOWLEDGMENT

The work is supported by the National Oceanic and Atmospheric Administration (NOAA) (Grant # NA22NWS4680007).

REFERENCES

- ASCE. 2021. America's Infrastructure Report Card 2021. American Society of Civil Engineers.
- Buchanan, M. K., Oppenheimer, M., & Kopp, R. E. (2017). Amplification of flood frequencies with local sea level rise and emerging flood regimes. *Environmental Research Letters*, 12(6), 064009.
- Collins, K., & Ison, R. 2009. Jumping off Arnstein's ladder: social learning as a new policy paradigm for climate change adaptation. *Environmental policy and governance*, 19(6), 358–373.
- Hinkel, J., Lincke, D., Vafeidis, A. T., Perrette, M., Nicholls, R. J., Tol, R. S., ... & Levermann, A. 2014. Coastal flood damage and adaptation costs under 21st century sea-level rise. *Proceedings of the National Academy of Sciences*, 111(9), 3292–3297.
- IPCC, C. C. 2021. The physical science basis. Contribution of working group I to the sixth assessment report of the Intergovernmental Panel on Climate Change. *Cambridge University Press*, Cambridge, United Kingdom and New York, NY, USA
- Kummu, M., De Moel, H., Ward, P. J., & Varis, O. (2011). How close do we live to water? A global analysis of population distance to freshwater bodies. *PloS one*, 6(6), e20578.
- Lanzafame, R., & Sitar, N. (2019). Reliability analysis of the influence of seepage on levee stability. *Environmental Geotechnics*, 6(5), 284–293.
- Milly, P. C. D., Wetherald, R. T., Dunne, K. A., & Delworth, T. L. 2002. Increasing risk of great floods in a changing climate. *Nature*, 415(6871), 514–517.
- Moftakhari, H. R., Salvadori, G., AghaKouchak, A., Sanders, B. F., & Matthew, R. A. 2017. Compounding effects of sea level rise and fluvial flooding. *Proceedings of the National Academy of Sciences*, 114(37), 9785–9790.
- National Levee Database. 2022. U.S. Army Corps of Engineers (USACE)
- Orlandini, S., Moretti, G., & Albertson, J. D. 2015. Evidence of an emerging levee failure mechanism causing disastrous floods in Italy. *Water Resources Research*, 51(10), 7995–8011.
- Taherkhani, M., Vitousek, S., Barnard, P. L., Frazer, N., Anderson, T. R., & Fletcher, C. H. 2020. Sea-level rise exponentially increases coastal flood frequency. *Scientific reports*, 10(1), 1–17.
- Vahedifard, F., Sehat, S., & Aanstoos, J. V. 2017. Effects of rainfall, geomorphological and geometrical variables on vulnerability of the lower Mississippi River levee system to slump slides. *Georisk: Assessment and Management of Risk for Engineered Systems and Geohazards*, 11(3), 257–271.
- Vahedifard, F., Jasim, F. H., Tracy, F. T., Abdollahi, M., Alborzi, A., & AghaKouchak, A. 2020. Levee fragility behavior under projected future flooding in a warming climate. *Journal of Geotechnical and Geoenvironmental Engineering*, 146(12), 04020139.
- Vitousek, S., Barnard, P. L., Fletcher, C. H., Frazer, N., Erikson, L., & Storlazzi, C. D. 2017. Doubling of coastal flooding frequency within decades due to sea-level rise. *Scientific reports*, 7(1), 1–9.
- Wang, R. Q., Stacey, M. T., Herdman, L. M. M., Barnard, P. L., & Erikson, L. 2018. The influence of sea level rise on the regional interdependence of coastal infrastructure. *Earth's Future*, 6(5), 677–688.

- Wing, O. E., Lehman, W., Bates, P. D., Sampson, C. C., Quinn, N., Smith, A. M., . . . & Kousky, C. 2022. Inequitable patterns of US flood risk in the Anthropocene. *Nature Climate Change*, 12(2), 156–162.
- Zhang, L. M., Xu, Y., Liu, Y., & Peng, M. 2013. Assessment of flood risks in Pearl River Delta due to levee breaching. *Georisk: Assessment and Management of Risk for Engineered Systems and Geohazards*, 7(2), 122–133.
- Zimmaro, P., Stewart, J. P., Brandenburg, S. J., Kwak, D. Y., & Jongejan, R. 2019. Multi-hazard system reliability of flood control levees. *Soil Dynamics and Earthquake Engineering*, 124, 345–353.



Taylor & Francis

Taylor & Francis Group

<http://taylorandfrancis.com>

*SS2: SHM for life-cycle informed management
of degrading structures*

Organizers: M.P. Limongelli, P. Gardoni, S. Thöns & D. Lu



Taylor & Francis

Taylor & Francis Group

<http://taylorandfrancis.com>

Integration of information quality assessment in bridge resilience management

N. Makhoul & M.P. Limongelli
Politecnico di Milano, Milan, Italy

ABSTRACT: Bridge conditions assessment is increasingly relying on Structural Health Monitoring (SHM) which allows the continuous acquisition of information on the structural state and overcomes problems that affect visual inspection such as subjectivity of the assessment, and difficulty to access hidden damages. However, the quality of SHM data is scarcely considered when information extracted from data is used to support management decisions, even though it plays an important role in the optimization of the management strategy and relevant decision-making process. In this article, a proposal to integrate the assessment of SHM information quality into bridge condition assessment management is presented. Mainly are discussed a general bridge management assessment procedure, and a decision-making scheme based on the Value of Information analysis to quantify the Value of Information Quality Assessment (IQA), and the impact of SHM IQA on bridge performance indicators.

1 INTRODUCTION

Modern bridges, constructed primarily in the past century, are aging worldwide and require maintenance. It is a challenge to extend their lifetime due to population growth, and increased natural risks from climate change.

Transportation is a necessity for the economy, the appropriate operation of modern society, and its continuous welfare (Schroten et al. 2019). However, due to the scarcity of resources required for adequate maintenance, preserving the required functionality level of aging critical infrastructures such as bridges is problematic. The average annual loss on transport infrastructure due to floods during the years 2010 to 2015 (European Environment Agency 2019) represents an average annual loss of 13.3 billion euros, with a constant upward trend in the coming years. Therefore, one main objective of the European Union (EU) is to preserve transport infrastructures appropriately functional. This led the EU, for example, to invest solely €38 billion in maintenance (Schroten et al 2019). These figures call for the development of a strategy to optimize bridge integrity management accounting for our scarce capacity to precisely predict the occurrence, long-term evolution, and spatial distribution of disruptive events.

In the last 30 years, research efforts have been devoted to a change of perspective from a condition-based to a risk-based approach in pursuit of efficient bridge integrity management subject to limited budgets. This is demonstrated by the extensive literature on this theme resumed in (Makhoul & Argyroudis 2018) and by the several research projects funded by the EU, such as COST TU1406 (Casas & Matos 2021). However, risk-based approaches to bridge integrity management do not account for the need to improve the recovery phase after the disruption thereby reducing the indirect consequences related to its loss of functionality ((Bruneau et al 2003), (Faber 2007), (Cimellaro et al. 2009), (Linkov et al. 2014), (Sharma et al. 2018), (Faber 2018)). Furthermore, interconnections between networks and domains are neglected most of the time. This does not replicate the real world which is shaped by increasingly

interconnected technological, economical, sociological, and ecological networks (Havlin et al. 2012, Linkov et al. 2014). Thus, a systemic approach is needed to account for these interconnections allowing us to describe the resilience across and within these domains.

In (Faber 2018) a systemic approach was suggested for sustainable and resilient engineered systems. It allows for building decision support and management tools using an indicator-based approach, which was suggested for interconnected subsystems (i.e., physical, social, and economical). In (Turksezer et al 2020) the concept of resilience indicators was used to define the characteristics of the managed system in terms of physical, information, and organizational subsystems. In this framework, the management of the system operated by the organizational subsystem is supported by the information flow managed by the information subsystem. However, in this, as in many other approaches, information quality is not considered, implicitly assuming that the available information possesses the required quality to support decisions. Studies addressing information quality and discussing the role of information quality in resilience management are still absent (Makhoul & Argyroudis 2018, Makhoul & Argyroudis 2019, Faber 2018, NAP 2012s). The scope of this article is to propose a step toward this direction through the integration of information quality into a framework for managing the resilience of bridge infrastructure.

This article recalls in Section 2 indicators for data quality (DQ) assessment previously published (Makhoul 2022, Makhoul & Limongelli 2022) and in Section 3 their deterministic and probabilistic metrics (Makhoul 2022). In Section 4, which constitutes the core of the paper, a possible framework based on Value of Information (VoI) analysis is proposed to account for SHM information quality in the management of bridge condition assessment. Finally, the integration of SHM information quality assessment into VoI analysis and the impact of SHM information quality on bridge performance indicators are briefly discussed.

Table 1. Data quality indicators and sub-indicators.

Data management phase	Indicator	Definition
<i>Acquisition</i>	Correctness	data is accurate, precise, and consistent
	Accuracy	the measured value of data is close to the real-world
	Precision	the measured data values are close to each other
	Consistency	the measured data is free of internal contradictions with respect to a rule.
	Redundancy	the measured data is not unique (multiple sets of data exist).
<i>Processing and sharing</i>	Accessibility	the measured data is available and can be shared reliably
	Interoperability	the measured data is concise and interpretable by machines
	Security	the access to data can be restricted to other parties and kept secure.
	Traceability	the sources of data are known
<i>Supporting decisions</i>	Timeliness	the data is up-to-date when needed
	Completeness	all required data are available in the dataset
	Relevance	the data is useful for the task at hand

2 SELECTION OF INDICATORS FOR QUALITY ASSESSMENT OF SHM DATA

Data quality indicators for structural health monitoring were suggested in (Makhoul 2022) and (Makhoul & Limongelli 2022). Those indicators were clustered and assigned sub-indicators to describe their different aspects. Overall, six indicators, and five sub-indicators were designated as presented in Table 1 with their allocated definitions. The indicators were grouped into three phases of data management (i.e., acquisition, processing and sharing, and Supporting decisions). The classification aims to highlight proper data quality aspects for each one of the SHM data management phases.

3 METRIC FOR THE GLOBAL QUALITY INDICATOR INDICATORS

The data quality metrics were reviewed (Makhoul 2022), and two methods were suggested for assessing DQ metrics in SHM Context. Those methods are 1) A deterministic method, and a probabilistic method accounting for uncertainties.

3.1 Deterministic metrics

The deterministic method assigns data quality metrics using scales. Those scales range from 0 (i.e., the lowest quality) to 1 (i.e., the highest quality). Metrics are defined as discrete or continuous scales as follows.

The discrete scale, where the metric has at least two or more discrete values:

$$\text{metric} = \begin{cases} 1 & \text{yes} \\ 0 & \text{no} \end{cases} \quad (1)$$

$$\text{metric} = \begin{cases} 1 & \text{yes} \\ 0.5 & \text{partially} \\ 0 & \text{no} \end{cases} \quad (2)$$

where ‘yes’ and ‘no’ means that the data is accurate (for accuracy), or not, etc., and ‘partially’ means that the data partially possess the quality under consideration (e.g., 0.5).

The continuous scale, where the metric is defined as a percentage of the data having this quality (i.e., 50% of the data is accurate, etc.).

Then, (Makhoul 2022) introduced a global metric accounting for all quality attributes. This DQ is computed using the equation:

$$DQ = \sum_u \omega_u * DQ_u \quad (3)$$

where DQ_u is the metric for the u^{th} quality attribute and ω_u the relative normalized weight.

The normalized weights are calculated by:

$$\omega_u = \frac{S_u}{\sum_u S_u} \quad (4)$$

where S_u are the weights of the quality attributes which, for example, might be based on expert opinion. They enable us to distinguish between the importance levels of selected attributes. The decision-maker is required to allocate scales (S_u) to each quality indicator based on its assigned importance for the decision-making case at hand. The definition of the weights in equation (4) guarantees that the sum of all the weights equals 1:

$$\sum_u \omega_u = 1 \quad (5)$$

This global metric is used to assess the level of data quality by suggesting adequate thresholds.

3.2 Probabilistic metrics

Probabilistic metrics were proposed in (Makhoul 2022) in the form of probability distribution functions. They were offered for the cases of permanent and occasional monitoring to account for different data flows (Table 2). The probabilistic approach assigns an adequate probability distribution function to the indicator metrics. As discussed in (Makhoul 2022) probabilistic metrics varies based on the type of data and associated uncertainties. In SHM, the probability distribution function assigned is highly dependent on the flow of the SHM data. The flow is scarce in the case

Table 2. The probabilistic metrics for DQ for permanent and occasional SHM.

Indicators				
Measurement	Accuracy	Precision	Consistency	Completeness
Permanent	$A = R - M \sim N(\mu, \sigma)$	σ_d	$Co \sim N(\mu_{co}, \sigma_{co})$	$C \sim N(\mu_c, \sigma_c)$
Occasional	$A = R - M \sim B(n, p)$	σ_d	$Co \sim B(n_{co}, p_{co})$	$C \sim B(n_c, p_c)$
Indicators				
Measurement	Timeliness	Accessibility	Redundancy	Relevancy
Permanent	$Q_{Time} = 1$	$Ac \sim N(\mu_c, \sigma_c)$	$R \sim N(\mu_r, \sigma_r)$	$Re \sim N(\mu_{re}, \sigma_{re})$
Occasional	$Q_{Time}(T) = e^{-\lambda T}$	$Ac \sim B(n_c, p_c)$	$R \sim B(n_r, p_r)$	$Re \sim B(n_{re}, p_{re})$

of occasional SHM measurements, thus the data is discrete and the binomial distribution can be used (Faber 2012). The flow is abundant in the case of permanent SHM measurements, thus the data is continuous and the normal distribution can be used (Faber 2012).

4 ACCOUNTING FOR DATA QUALITY OF SHM IN THE LIFE CYCLE ASSESSMENT MANAGEMENT

In this section, the integration of SHM information quality assessment into bridge condition assessment is proposed. In Section 4.1, a general bridge management assessment procedure considering the SHM information quality is presented. Then in Section 4.2, the integration of SHM information assessment into the Value of Information analysis is presented. Finally, in Section 4.3, the impact of SHM information quality assessment on the estimation of bridge performance indicators is briefly discussed.

4.1 General bridge management assessment procedure considering the SHM data quality

A General Assessment Procedure (GAP) for the existing structure was presented in (ISO 13822 2010). Herein an Updated General Assessment Procedure (UGAP) that includes the assessment of SHM information quality in the process is introduced (Makhoul 2023). It is presented in Figure 1. This step was included after the inspection tests such as surveillance, visual, etc. The outcome of the VoI analysis may lead – or not – to perform an Information Quality Assessment (IQA). Two outcomes are possible i.e., whether the value of information equals zero, then the IQA is skipped, and GAP is followed straightforwardly. If the IQA leads to a value of information greater than zero, then IQA is performed on the collected information. The word ‘inspections’ is generically used herein to address the process of collecting information about the bridge condition. This process can be carried out through visual surveys, destructive and nondestructive testing, SHM, etc. The selection of the specific type of inspection can be carried out through a Value of Information analysis. However, herein the focus is on the integration of information quality assessment (IQA) into condition assessment thereby the selection of the inspection type will not be addressed. Without loss of generality, it will be assumed that the inspection process is carried out through SHM. The management actions considered in the flowchart in (Figure 1) can be operation actions (i.e., monitoring, and change in use) or construction actions (i.e., rehabilitation such as repair or upgrading, and demolition). In the following, they will be generically addressed as ‘interventions’.

4.2 Value of information analysis accounting for the SHM information quality assessment

The suggested decision-making framework to assess the benefit of performing SHM IQA is based on VoI analysis. The approach is based on pre-posterior Bayesian analysis and expected

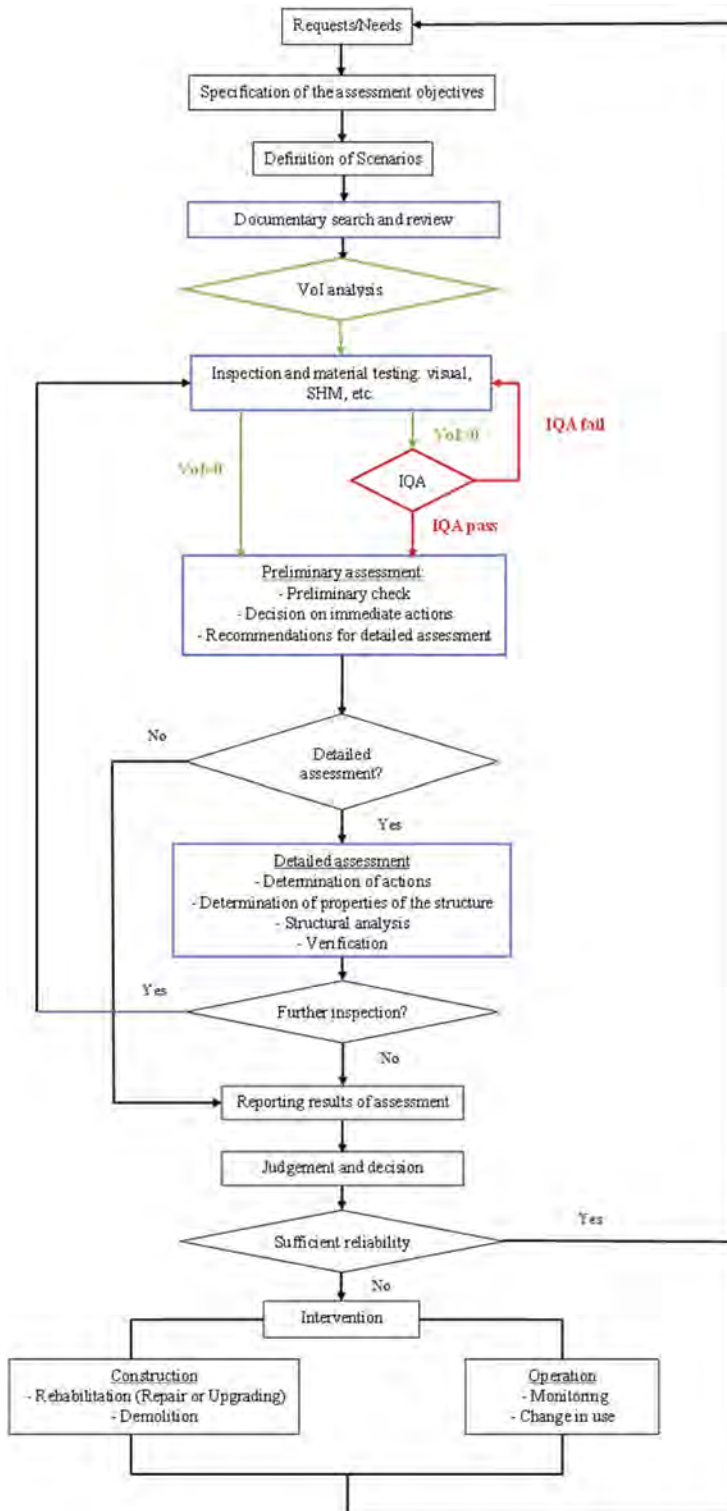


Figure 1. Flowchart for the updated general assessment procedure of existing structure considering the SHM IQA.

value theory (Schlaifer & Howard 1961, Benjamin & Cornell 1970, von Neumann & Morgenstern 2007).

In Figure 2 the process to quantify the VoI of IQA for information collected through inspections is represented through a decision tree. In reference (Giordano et al. 2023) the complete framework is described and applied using a machine-learning-based tool for the assessment of the information quality. Herein the decision tree that describes the VoI quantification is illustrated.

Decision nodes are depicted by a square, and chance nodes by a circle. Branches stemming from squares represent decision alternatives, and branches stemming from circles represent states of nature. Herein the decisions are about the implementation of the information quality assessment (IQA), and of the intervention action (a). The upper branch of the tree represents the prior decision analysis where the selection of the optimal intervention is carried out without performing IQA. The bottom branch is the pre-posterior decision analysis where the decision about the intervention is performed with the support of IQA. The difference between the expected consequences of the optimal actions (schematically reported in equation 6) selected with the two types of decision analyses (prior and pre-posterior) quantifies the values of IQA. The full processed equations are detailed further in (Makhoul 2023), and for utility counterpart and computations (Makhoul, 2019).

$$VoI = C_{preposterior} - C_{prior} \tag{6}$$

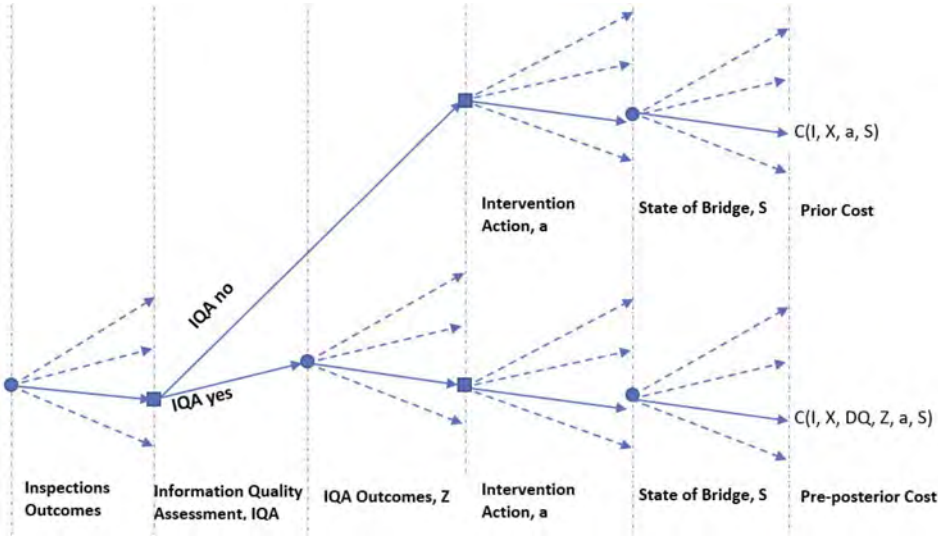


Figure 2. Decision tree for the quantification of the Value of Information Quality assessment (IQA).

4.3 System performance indicators accounting for SHM information quality

Bridge performance can be analyzed using several available performance indicators, such as for instance risk and resilience. Herein reference is made to a generic performance indicator.

The structural performance – and thereby its indicators – will generally decrease in time due, for instance, to deterioration associated with insufficient maintenance. The estimation of performance indicators can benefit from SHM information that provides an improved knowledge of the bridge condition (Bocchini et al. 2012) and (Capacci & Biondini 2020). If also SHM IQA is carried out, a further update of the performance indicator can be carried out, leading to a different estimation of the service life as shown in (Figures 3-4).

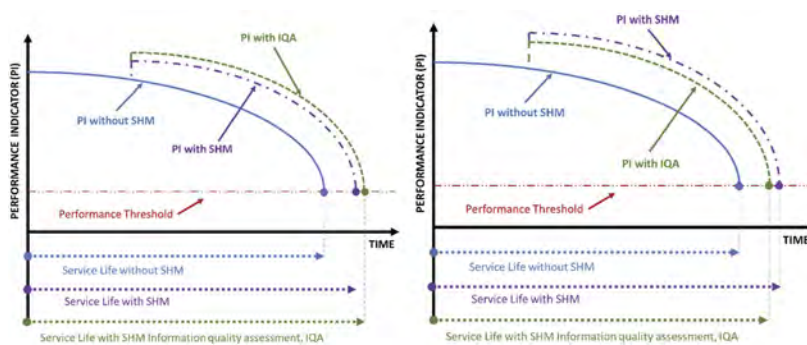


Figure 3. Performance indicator profile with and without SHM IQA: a) case of Service life longer with SHM and with SHM IQA, b) case of Service life greater with SHM but shorter without SHM IQA.

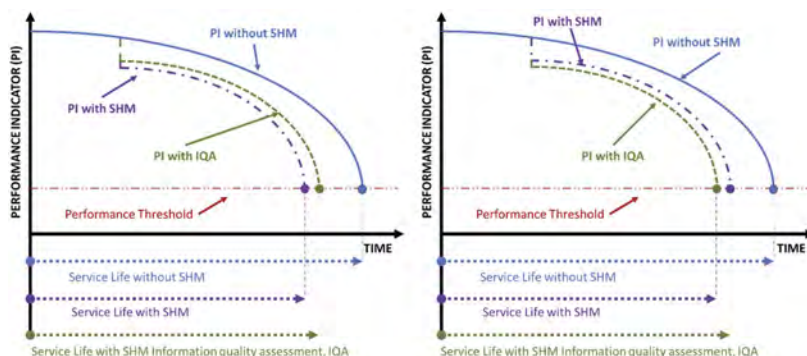


Figure 4. Resilience indicator profile with and without SHM IQA: a) case of Service life longer without SHM and longer with IQA than without IQA, b) case of Service life longer without SHM but shorter without IQA than with IQA.

5 CONCLUSIONS

Bridge conditions assessment is increasingly relying on Structural Health Monitoring (SHM). However, the quality of SHM information is rarely considered although it plays a vital role in management strategy optimization and relevant decision-making. To address this issue, this article suggests the integration of SHM information quality assessment on a Value of Information analysis base. The integration of SHM information quality assessment into VoI analysis and the quantification of resilience indicators and bridge service life are briefly discussed.

ACKNOWLEDGEMENT

I thank Politecnico di Milano for funding this research through the Seal of Excellence project.

REFERENCES

- Benjamin, J.R. & Cornell, A.C. 1970. *Probability, Statistics, and Decision for Civil Engineers*. Courier Corporation.
- Bocchini, P., Decò, A & Frangopol, D. 2012. Probabilistic functionality recovery model for resilience analysis. In F. Biondini & D. M. Frangopol (Eds.), *Bridge maintenance, safety, management, resilience and sustainability. Proceedings of the Sixth International IABMAS Conference* (pp. 1920–1927).

- Bruneau, M., Chang, S.E., Eguchi, R.T., Lee, G.C., O'Rourke, T.D., Reinhorn, A.M., Shinozuka, M., Tierney, K., Wallace, W.A. & von Winterfeldt, D. 2003. A Framework to Quantitatively Assess and Enhance the Seismic Resilience of Communities. *Earthquake Spectra*, 19(4), 733–752. <https://doi.org/10.1193/1.1623497>
- Capacci, L. & Biondini, F. 2020. Probabilistic life-cycle seismic resilience assessment of aging bridge networks considering infrastructure upgrading. *Structure and Infrastructure Engineering*, 16(4), 659–675. <https://doi.org/10.1080/15732479.2020.1716258>
- Casas, J. R. & Matos, J.C. 2021. Quality specifications for roadway bridges in Europe: Overview of COST Action TU1406. In *Bridge Maintenance, Safety, Management, Life-Cycle Sustainability and Innovations* (pp. 1985–1992). CRC Press.
- Cimellaro, G.P., Fumo, C., Reinhorn, A.M. & Bruneau, M. 2009. *Quantification of Disaster Resilience of Health Care Facilities. Technical Report MCEER-09-0009*. <https://nehrlsearch.nist.gov/static/files/NSF/PB2010103200.pdf>
- European Environment Agency. 2019. <https://www.eea.europa.eu/>
- Faber, M.H. 2007. Assessing and Managing Risks due to Natural Hazards. *ISGSR2007 1st International Symposium on Geotechnical Safety & Risk*.
- Faber, M.H. 2012. *Statistics and Probability Theory* (Vol. 18). Springer Netherlands. <https://doi.org/10.1007/978-94-007-4056-3>
- Faber, M.H. 2018. On sustainability and resilience of engineered systems. In *Routledge Handbook of Sustainable and Resilient Infrastructure* (pp. 28–49). Routledge. <https://doi.org/10.4324/9781315142074-3>
- Giordano, P.F., Quqa, S. & Limongelli, M.P. 2023. The value of monitoring a structural health monitoring system. *Structural Safety*, 100, 102280. <https://doi.org/10.1016/j.strusafe.2022.102280>
- Havlin, S., Kenett, D.Y., Ben-Jacob, E., Bunde, A., Cohen, R., Hermann, H., Kantelhardt, J.W., Kertész, J., Kirkpatrick, S., Kurths, J., Portugali, J. & Solomon, S. 2012. Challenges in network science: Applications to infrastructures, climate, social systems and economics. *The European Physical Journal Special Topics*, 214(1), 273–293.
- ISO 13822. 2010. *ISO 13822:2010, Bases for design of structures – Assessment of existing structures*. <https://www.iso.org/standard/46556.html>
- Linkov, I., Bridges, T., Creutzig, F., Decker, J., Fox-Lent, C., Kröger, W., Lambert, J.H., Levermann, A., Montreuil, B., Nathwani, J., Nyer, R., Renn, O., Scharte, B., Scheffler, A., Schreurs, M. & Thiel-Clemen, T. 2014. Changing the resilience paradigm. *Nature Climate Change*, 4(6), 407–409. <https://doi.org/10.1038/nclimate2227>
- Makhoul, N. 2019. Seismic risk mitigation in buildings using a new method to encode a joint weighting function in multi-attribute utility theory. *SN Applied Sciences*, 1(9). <https://doi.org/10.1007/s42452-019-1136-6>
- Makhoul, N. 2022. Review of data quality indicators and metrics, and suggestions for indicators and metrics for structural health monitoring. *Advances in Bridge Engineering*, 3(1), 17. <https://doi.org/10.1186/s43251-022-00068-9>
- Makhoul, N. 2023. Bayesian Decision-Making Process Including Structural Health Monitoring Data Quality for Bridge Management. *KSCCE Journal of Civil Engineering, Fortcoming*.
- Makhoul, N. & Argyroudis, S. 2018. Loss estimation software: developments, limitations and future needs. *16ECEE - 16th European Conference on Earthquake Engineering*.
- Makhoul, N. & Argyroudis, S. 2019. Tools for Resilience Assessment: Developments, Limitations and Future Needs. *ICONHIC2019 – 2nd International Conference on Natural Hazards & Infrastructure*.
- Makhoul, N. & Limongelli, M.P. 2022. Quality indicators for Structural Health Monitoring data: A tool for enhanced resiliency assessment and decision-making. *ICONHIC2022 – 3rd International Conference on Natural Hazards & Infrastructure*.
- NAP. 2012. *Disaster Resilience*. National Academies Press. <https://doi.org/10.17226/13457>
- Schlaifer, R. & Howard, R. 1961. *Applied statistical decision theory*. Harvard University.
- Schroten, A., van Wijngaarden, L., Brambilla, M., Gatto, M., Maffii, S., Trosky, F., Kramer, H., Monden, R., Bertschmann, D., Killer, M., Lambla, V., El Beyrouty, K. & Amaral, S. 2019. *Overview of transport infrastructure expenditures and costs*. https://cedelft.eu/wp-content/uploads/sites/2/2021/03/CE_Delft_4K83_Overview_transport_infrastructure_expenditures_costs_Final.pdf
- Sharma, N., Tabandeh, A. & Gardoni, P. 2018. Resilience analysis: a mathematical formulation to model resilience of engineering systems. *Sustainable and Resilient Infrastructure*, 3(2), 49–67. <https://doi.org/10.1080/23789689.2017.1345257>
- Turksezzer, Z.I., Pina Limongelli, M. & Havbro Faber, M. 2020. On a generic framework for systems resilience modelling of bridges - accounting for historic and cultural values. *Sustainable and Resilient Infrastructure*, 1–14.
- von Neumann, J. & Morgenstern, O. 2007. *Theory of Games and Economic Behavior (60th Anniversary Commemorative Edition)*. Princeton University Press. <https://doi.org/10.1515/9781400829460>

Optimum inspection scheduling of steel storage tanks based on past ultrasonic thickness measurements

S.A. Faroz

Infrastructure Risk Management (IRM), Mumbai, India

M.S. Khan

Department of Civil Engineering, Monash University, Clayton, Australia

S. Ghosh

Structural Safety, Risk & Reliability (SSRR) Lab, Department of Civil Engineering, Indian Institute of Technology Bombay, Mumbai, India

ABSTRACT: In the oil and gas industry, storage tanks play an important role, ensuring a continuous flow of the petroleum based products. Interruption in their performance due to unforeseen failure and subsequent repairs can result in losses running into millions of dollars. Even the prescribed inspection and maintenance regimes cause interruptions in their service resulting in monetary losses. Although such inspections are routine in the industry, information collected from non-destructive evaluations are rarely used in planning the life-cycle management of these structures. This work proposes a framework for planning the life-cycle management of steel oil and gas storage tanks by optimizing the inspection interval (or, minimizing the inspection cost and business losses). In this, a minimum reliability-based performance criterion is selected as the constraint. The time-varying probabilistic performance of the structure (considering uncertainty in loading, material and geometric parameters) is assessed through Bayesian updating of the deterioration model based on ultrasonic thickness measurements from past inspections. This framework is demonstrated on a “Horton sphere” liquefied petroleum gas storage tank subjected to corrosion deterioration.

1 INTRODUCTION

The oil and gas industry have a large number of metallic structures in their infrastructure asset portfolio. Steel storage tanks play a significant role in the storage of flammable and hazardous crude oil and its derivatives. A review of accidents of 242 storage tanks show that 74% of accidents occurred in petroleum refineries, oil terminals or storage (Chang & Lin 2006). A small accident may lead to property loss of million dollars and few days of production interruption. A large accident results in lawsuits, stock devaluation, or company bankruptcy. For example, a recent chemical spill in Charleston, West Virginia, USA resulted in more than 40,000 litres of toxic liquid from storage tank into a nearby river contaminating the drinking water of approximately 300,000 people for 12 days and resulting in the responsible company filing for bankruptcy shortly after (Larson 2014). An investigation into the disaster made by the US Chemical Safety and Hazard Investigation Board found that pitting corrosion on the tank degraded the thickness of the tank and was the direct cause of the incident (CSB 2014). Corrosion is one of the top factors responsible for such accidents (Esouilem, Bouzid, & Nadeau 2020).

Above-ground steel storage tanks are prone to atmospheric corrosion or interior corrosion or both, which causes reduction of shell thickness. The interior of a tank, that is in contact with the petroleum products, should not corrode since the hydrocarbons are not corrosive to metals and alloys. However, dissolved water and oxygen, hydrogen sulphide, certain organic sulphur and oxygen-containing compounds in petroleum products can cause corrosion (Groysman 2014b).

Annual report of economic losses from corrosion at a oil refinery near Haifa, Israel, with a capacity of 12 million ton crude per year had direct losses from corrosion of US\$ 4-8.5 million per year. The cost loss of production downtime (indirect losses) can sometimes be even more: US\$ 7.5-30.4 million per year. Thus, the total loss from corrosion amounts to US\$ 13.8-34.5 million per year (Groysman 2014a). It is no wonder that this cost of corrosion to our society is included in the price of many products that we buy, be it a car or everyday commodities like bread.

Conventionally, to keep the tank structural performance from deteriorating due to corrosion over the intended service-life, a corrosion allowance (CA) in terms of additional shell thickness is provided over the required thickness to bear the loads. CA is usually based on the expected deterministic corrosion rate for the service-life. However this deterministic method may be inadequate considering the uncertainties of the corrosion process over a long service life.

To track the life-cycle performance, an inspection interval of 5 years is usually prescribed, from 10 years after its commissioning. In this inspection the residual shell thickness of the tank is measured using ultrasonic thickness gauge. This prescriptive inspection interval approach may be either short or elongated with respect to the condition of the tank. When the interval is shortened, the cost of cleaning tanks (for inspection) and the temporary loss of storage volume or plant operating issues can be extremely costly. For elongated inspection intervals, there is the risk of environmental damage caused by leaking tanks and the high cost of environmental cleanup due to missed detection of corrosion. Therefore, tank owners have a keen interest in lengthening the service interval of their tanks to the extent that the safety of the tank is still maintained prior to the next scheduled inspection.

This work proposes a novel framework for planning the life-cycle management of Horton tanks (Figure 1) by optimizing the inspection interval. In this, a minimum reliability-based performance criterion is selected as the constraint. The time-varying probabilistic performance of the structure (considering uncertainty in loading, material and geometric parameters) is assessed through Bayesian updating of the deterioration model based on ultrasonic thickness measurements from past inspections. The next inspection is scheduled at the half remaining life computed (BIS 1969).

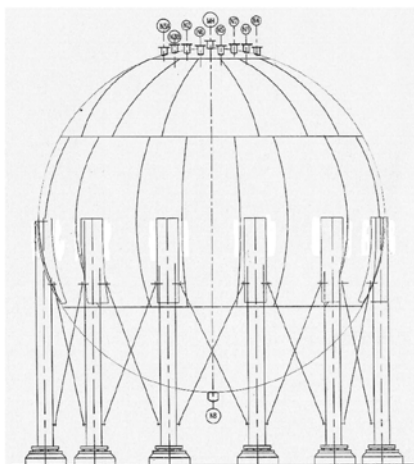


Figure 1. LPG Horton sphere tank.

2 TANK INFORMATION

In this paper a LPG/propane storage steel Horton sphere located in India is investigated (Figure 1). The sphere was designed following BS 5500 (BSI 1997) and SMPV rules (PESO 1981) with internal diameter $D_i = 18.0$ m for a design pressure $p = 21.2$ kg/cm² at top and design shell thickness of 50 mm. The grade of steel is A-537 CL-1. This tank was commissioned in 1999. The first set of measurements of shell thickness was taken in the year 2009 with a total of 734 measurements. The minimum shell thickness found in this survey was 49.4 mm. The second set of

thickness measurements was performed in 2014, with 684 measurements in total, with a minimum shell thickness of 49.7 mm. For these two sets, different agencies were involved in the measurements. It is inferred that in these measurements the locations of measurement were not identical, which is realistic considering that such locations are not marked for future usages.

The data along with a deterministic linear regression line is shown in Figure 2. As seen in this figure, there is a considerable scatter in the thickness data for every year of measurement. The most significant drawback in adopting a deterministic regression is that it ignores this scatter and results in (erroneous) point estimates of the model parameter and the estimation itself (actual corrosion level is above and below the regression curve as in Figure 2). Since failure of these tanks can be based on a local corrosion pit, any best-fit approach ignoring the scatter is not a suitable choice. Furthermore the absolute minimum thickness may not be captured during measurement. As a result, such deductions may also result in a misinformed decision making (Zheng & Ellingwood 1998).

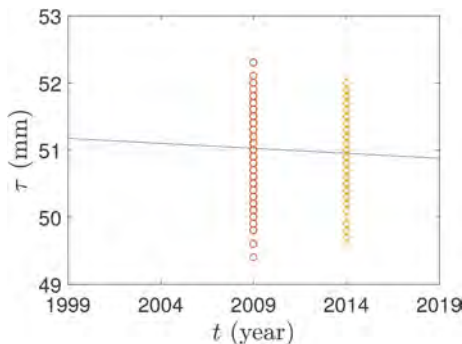


Figure 2. Thickness data and deterministic regression corrosion model.

The A-537 CL-1 steel has a characteristic yield strength of $f_{yk} = 345$ MPa and tensile strength of $f_{uk} = 485$ MPa. As per BS 5500 (BSI 1997), the nominal design stress is $f = \min\left(\frac{f_{yk}}{1.5}, \frac{f_{uk}}{2.35}\right) = 206$ MPa = 2100kg/cm². Thus, the required thickness for design pressure is

$$\tau = \frac{pD_i}{4f - 1.2p} = \frac{21.2 \times 18000}{4 \times 2100 - 1.2 \times 21.2} = 45.56 \text{ mm} \quad (1)$$

The thickness provided was 50 mm.

3 BAYESIAN UPDATING OF SHELL THICKNESS

In oil and gas industry, a deterministic linear corrosion model is most widely used (API 2008). A probabilistic linear corrosion model is considered for this paper

$$\tau(t) = \tau_0 - Ct + \varepsilon \quad (2)$$

where τ_0 is the initial thickness of the shell i.e. at year 1999, $\tau(t)$ is the time-varying thickness of the shell, C is the corrosion rate and $\varepsilon \sim \mathcal{N}(0, \sigma)$ is the randomness.

It is assumed that the tank is effectively coated externally and the atmospheric corrosion is negligible. All corrosion occurs at the internal surface where there is no coating.

3.1 Prior distribution

The tolerance on thickness of plate for the present design is 50 ± 1.2 mm (BIS 2009), (BIS 2002). The corresponding lower thickness is adopted as the 2.5 percentile value and the upper thickness as the 97.5 percentile value of a normal distribution to form the prior distribution of τ_0 , given by

$$f(\tau_0) \sim \mathcal{N}(50, 0.61)(\text{mm}) \quad (3)$$

The minimum required thickness without corrosion allowance was 45.56 mm, and the provided thickness was 50 mm. Thus the effective corrosion allowance provided is 4.44 mm for a life of 50 years. Considering this information, an average corrosion rate of 0.09 mm/year is adopted a-priori as mean. Assuming a large coefficient of variation (CoV) of 50%, the lognormal distribution of C is

$$f(C) \sim \mathcal{LN}(-2.52, 0.47)(\text{mm/year}) \quad (4)$$

The lognormal distribution here is specified with the parameters of the lognormal distributions, i.e. the mean and the standard deviation of the logarithm of the lognormally distributed random variable.

In the absence of any specific data on σ , we assume it to be lognormally distributed with a mean of 1 and very large standard deviation of 5 (i.e., a CoV of 500%). Therefore, the prior distribution of σ is given by

$$f(\sigma) \sim \mathcal{LN}(-1.63, 1.81)(\text{mm}) \quad (5)$$

The joint prior distribution for the parameters $\theta = [\tau_0 \ C \ \sigma]$ is taken as the product of the densities of individual parameters, by considering each parameter to be independent of other:

$$f'(\theta) = f(\tau_0) \times f(C) \times f(\sigma) \quad (6)$$

3.2 Likelihood function

The parameter θ conditioned predictive distribution of remaining thickness based on Eq. 2 is

$$f(\tau|t, \theta) = \frac{1}{\sqrt{2\pi\sigma^2}} \exp\left\{-\frac{[\tau - \tau(t)]^2}{2\sigma^2}\right\} \quad (7)$$

Eq. 7 is used to form the likelihood function for a thickness measurement τ_i at time t_j as $f(\tau_i|t_j, \theta)$. For m_j number of measurements at time t_j , $\mathcal{D} = \{\tau_{i=1:m_j}, t_j\}$, assuming each to be statistically independent of the other the overall likelihood function can be formed as

$$L(\theta, \mathcal{D}) = \prod_{i=1}^{m_j} f(\tau_i|t_j, \theta) \quad (8)$$

3.3 Parameter updating

The model parameters are updated to the posterior $f''(\theta)$ using Bayesian inference:

$$f''(\theta) \propto L(\theta, \mathcal{D})f'(\theta) \quad (9)$$

using the Markov chain Monte Carlo (MCMC) approach. For this Bayesian updating, we use a MATLAB toolbox for uncertainty quantification, UQLab (Marelli & Sudret 2014). We use the adaptive Metropolis algorithm for MCMC with 100 chains and 1×10^5 steps. The Markov chains indicate convergence and a 50% of the samples are discarded as burn-in. Three updating scenarios are considered:

1. data from year 2009 only
2. data from year 2014 only
3. data from year 2009 and 2014 combined

3.4 Results

Figures 3a, 3b, and 3c provide the posterior distributions of τ_0 , C , and ε , respectively. As the measurements indicated less corrosion, the impact of the data on corrosion model parameters

is found to be likewise. The posterior distribution of τ_0 indicates a higher value while the posterior distribution of C suggests a much lower rate of corrosion.

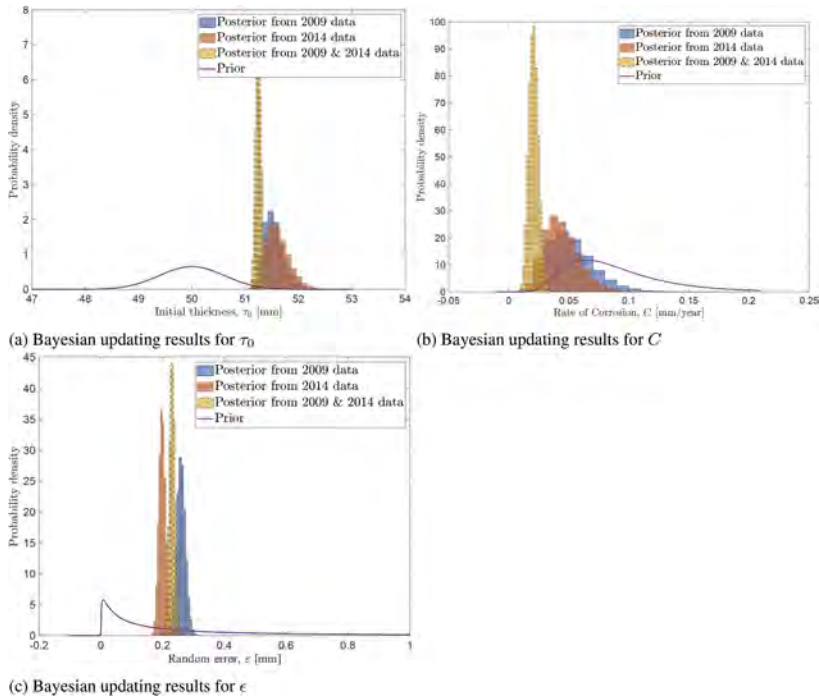


Figure 3. Bayesian updating results for different parameters.

3.5 Robust prediction of corrosion

θ -conditioned predictive distribution of the residual thickness (τ) for any time t is as per Eq. 7. Once the corrosion model is updated, the parameters θ are available in the form of sample values. In most of Bayesian inferences applied to model updating in engineering problems, either the sample mean or the sample median value is used for prediction (Faroz 2017). This ignores the parameter uncertainty. In the present work, a single parameter-unconditioned distribution of τ , which includes the variability due to the random samples of θ , is obtained using the total probability theorem for a robust predictive distribution for any time t (Faroz & Ghosh 2021)

$$f(\tau|t) = \int_{\Theta} f(\tau|t, \theta) f''(\theta) d\theta \quad (10)$$

4 REMAINING LIFE ANALYSIS

4.1 Uncertainty quantification

The remaining life analysis (RLA) is performed based on a minimum reliability-based performance criterion. The limit state for the reliability analysis is formulated as

$$G(t) = \tau(t) - \tau_{req} \quad (11)$$

where $\tau(t)$ is given by Equation 10, and τ_{req} is the thickness required as specified in the design standard (BSI 1997). τ_{req} is calculated by removing all safety factors from the equation specified in BSI 1997:

$$\tau_{req} = \frac{pD_i}{4f_y - p} \quad (12)$$

In Equation 12, it is assumed that fatigue strength for the steel is not critical. In this study, only the internal pressure is assumed as the governing load.

As per BIS (1969) the difference between the minimum and maximum values of D_i shall not exceed 1% of the nominal internal diameter (18000 mm) with a maximum of $\frac{D_i+1250}{200}$ (96.25 mm). Based on this, we assume D_i to be a uniformly distributed random variable:

$$f(D_i) \sim \mathcal{U}(17952, 18048) \text{ (mm)} \quad (13)$$

ASME CRTD-86 (2007) quantified statistical uncertainties in the yield strength of steels (f_y). For high strength carbon steel, a lognormally distributed yield strength with a bias of 1.2 and a COV of 0.09 are recommended. Therefore, for a nominal value of 345 MPa, the distribution of the yield strength is

$$f(f_y) \sim \mathcal{LN}(6.02, 0.09) \text{ (MPa)} \quad (14)$$

In the absence of statistical data on hydraulic pressures in spherical tanks, a normally distributed pressure with a bias of 0.91 and a COV of 0.25 are assumed. Therefore, for a design pressure of 21.2 kg/cm² we have

$$f(p) \sim \mathcal{N}(1.9, 0.47) \text{ (MPa)} \quad (15)$$

The samples obtained from MCMC simulations are used for reliability estimation using Monte Carlo simulation (MCS) with 5×10^6 samples.

4.2 Optimal next inspection

API (2008) provides ‘generic failure frequency’ (gff), a value representative of the refining and petrochemical industry’s failure data. In other words, gff is the average probability of failure in a large population of components. The gff is intended to be the failure frequency prior to any specific damage occurring from the operating exposure conditions. The accepted gff for tank shell course as per API (2008) is 1×10^{-4} . Helle (2012) demonstrated how this value of gff specified by API (2008) is too high. Therefore, in the present work we have adopted a lower value of gff , i.e. 1×10^{-5} , for a demonstration of the proposed methodology.

BIS (1969) specifies that the maximum period between inspections should not exceed one-half of the estimated remaining safe operating life of the vessel. Therefore, the maximum period between the inspections will be half of the time predicted by the model for the tank to reach a probability of failure equal to gff i.e. 1×10^{-5} .

4.3 Results and discussion

Figure 4 presents the resulting probability of failure (P_f) calculated from a MCS of the posterior distributions. The posterior distributions indicate very low corrosion of the tank consistent with the measurements, and consequently Figure 4 indicates a very slow progression of corrosion with the time elapsed in service. For the case with measurements only from year 2009, the gff is exceeded in the 74th year of service. Therefore, the resulting optimal next inspection is 32 years after 2009 or 42nd year of the service life. For the case with data only from 2014, the resulting optimal next inspection is $(95-15)/2 = 40$ years after 2015 or 55th year of the service life. For the case when data from both years are taken for updating (with corrosion measured very low), the estimated probability of failure crosses gff in the year 175 of the service life. Therefore, next optimal inspection as per this updating scenario should be on the 95th year of the service life.

Figure 5 presents a comparison of the thickness required as per the code with the thickness predicted by the updated model at a year far later in the service life of the tank, i.e. the

120th year of service. The relative lack of overlap between the histograms of model predicted thickness (with the required thickness), particularly for the case when both years data is used for updating, explains the highly safe condition of the structure estimated in Figure 4.

Taking a deterministic approach with the nominal thickness of 50 mm at year zero, the linear regression yields into thickness increasing with years, which cannot be realistic. If only the data from years 2009 and 2014 are used in linear regression (Figure 2), we find, $\tau(t) = 51.176 - 0.0149t$ (mm). Based on the minimum required thickness of 45.56 mm (Equation 1), the age to reach failure is 376.91 years. Thus, the next inspection will be on year $(376.91 - 15)/2 \approx 181$, which is almost double of the estimation based on the framework proposed here.

We note that the estimated tank performance and the consequent maximum interval between inspections is subject to the assumptions made in the study. Hierarchical probabilistic models and incorporation of correlation between the measurements can check for any potential Bayesian model over-fitting and lead to more accurate and practical results. This study has adopted a single linear corrosion model for Bayesian fitting. Other models such as an exponential model can also be adopted and a Bayesian model selection strategy can be used to choose the best model (Faroz & Ghosh 2021). A spatial model for nonlinear progression of corrosion could potentially lead to much different results. Similarly, this study adopted a non-hierarchical model while assuming statistically independent measurements.

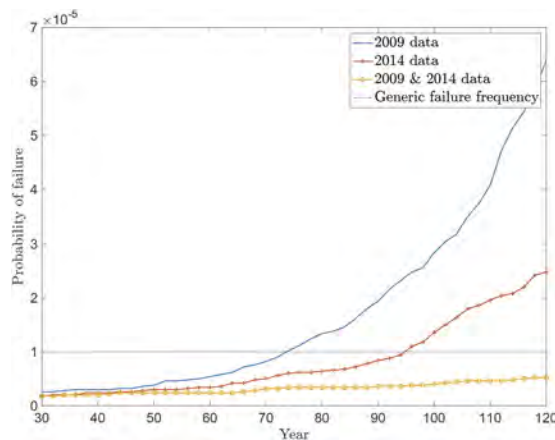


Figure 4. Predicted probability of failure for various Bayesian updating scenarios.

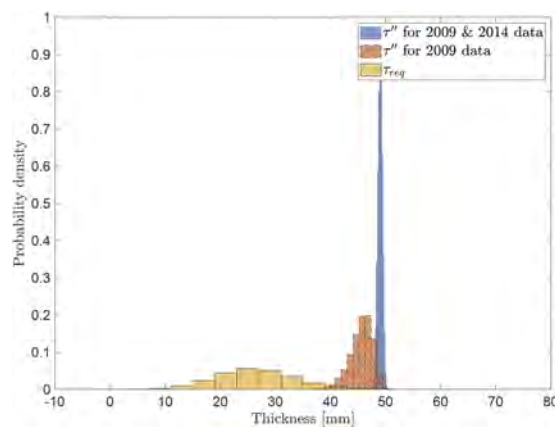


Figure 5. Comparison of posterior model predicted thickness and required thickness as per code at year 120.

5 CONCLUSION

Conventional methods for performance based inspection planning of petroleum storage steel tanks rely on deterministic methods. Structural reliability methods can be used to incorporate the uncertainties that govern the performance of a steel storage tank. Bayesian statistics provides a conceptual framework to incorporate corrosion pit depth measurements into the existing models for corrosion progression. In this study, the authors propose a novel framework to determine the optimal next corrosion inspection of petroleum storage steel tanks. This framework is based on Bayesian statistics and structural reliability methods. It is expected to assist practicing engineers in conducting a reasonably thorough uncertainty quantification for the performance estimation of LPG storage steel tanks.

Tank shell thickness measurements are taken at two different time instances during the service life of the tank. Based on three different scenarios of data assimilation, a Markov chain Monte Carlo approach based on an adaptive Metropolis-Hastings algorithm is adopted for Bayesian updating. The study assumes a linear model for corrosion progression. The Bayesian updating results indicate a very slow progression of corrosion. The consequent probability of failure of the tank is very low and the performance indicates a highly safe structure. The optimal next inspection is found to be on the 42nd, 55th, and 95th year of the service life, for three different data considerations.

Future work along this line should incorporate combined load effects on the shell, nonlinear corrosion progression models, and spatial data analysis.

REFERENCES

- API (2008). *API RP 581. Risk-Based Inspection Technology*. Washington, D.C., USA: American Petroleum Institute.
- ASME CRTD-86 (2007). *Development of reliability-based load and resistance factor design (LRFDF) methods for piping: research and development report*. Number 86 in CRTD. New York, NY: ASME.
- BIS (1969). *IS 2825. Code for Unfired Pressure Vessel*. New Delhi, India: Bureau of Indian Standards.
- BIS (2002). *IS/ISO 7452. Hot-Rolled Structural Steel Plates - Tolerances on Dimensions and Shape*. New Delhi, India: Bureau of Indian Standards.
- BIS (2009). *IS 2002. Steel Plate for Pressure Vessel for Intermediate and High Temperature Service Including Boilers*. New Delhi, India: Bureau of Indian Standards.
- BSI (1997). *BS 5500. Specifications for Unfired Fusion Welded Pressure Vessel*. London, UK: British Standards Institution.
- Chang, J. I. & C.-C. Lin (2006). A study of storage tank accidents. *Journal of Loss Prevention in the Process Industries* 19.
- CSB (2014). Freedom Industries Chemical Release. <http://www.csb.gov>.
- Esouilem, M., A.-H. Bouzid, & S. Nadeau (2020). Frequency Failure Causes Analysis of Pressure Vessel and Piping Equipment: Case Study of the Alberta Petrochemical Industry. *ASCE-ASME J Risk and Uncert in Engrg Sys Part B Mech Engrg* 6(4).
- Faroz, S. A. (2017). *Assessment and Prognosis of Corroding Reinforced Concrete Structures through Bayesian Inference*. Ph. D. thesis, Indian Institute of Technology Bombay, Mumbai, India.
- Faroz, S. A. & S. Ghosh (2021). Comprehensive framework for the hyper-robust bayesian calibration of a nondestructive testing instrument. *Structural Safety* 92, 102105.
- Groysman, A. (2014a). Corrosion education: present and future. In *The 19th International Corrosion Congress*, Jeju, Korea.
- Groysman, A. (2014b). *Corrosion in Systems for Storage and Transportation of Petroleum Products and Biofuels: Identification, Monitoring and Solutions*. Springer.
- Helle, H. P. E. (2012). Five fatal flaws in API RP 581. In *Proceedings of the 14th Middle East Corrosion Conference and Exhibition, Manama, Bahrain*.
- Larson, E. (2014). Freedom Industries Files Bankruptcy After Elk River Spill. <http://www.bloomberg.com>.
- Marelli, S. & B. Sudret (2014, June). UQLab: A framework for uncertainty quantification in Matlab. In *Vulnerability, Uncertainty, and Risk*, pp. 2554–2563. American Society of Civil Engineers.
- PESO (1981). *The Static and Mobile Pressure Vessels (Unfired) Rules*.
- Zheng, R. & B. R. Ellingwood (1998). Role of non-destructive evaluation in time-dependent reliability analysis. *Structural Safety* 20(4), 325–339.

The role of life-cycle civil engineering practices in smart and sustainable cities

M.D. Lepech, A.S. Kiremidjian & K.H. Law

Department of Civil and Environmental Engineering, Stanford University, USA

ABSTRACT: Globally, civil infrastructure and our built environment is being embedded with dense sensing networks. These networks form the technological foundation of “smart cities” and enable a new, data-driven era of infrastructure engineering for increased lifecycle performance. But smart cities require more than simply embedding IT hardware into existing urban infrastructure, or the application of artificial intelligence to analyze municipal data streams. This paper discusses the set of physical infrastructures, digital technologies, regulations and policies, financing mechanisms, community outreach, businesses and business models, partnerships, institutions, and other engagement mechanisms that must be established in concert with each other to provide a high quality of life in smart and sustainable cities. Specifically, the role of infrastructure life-cycle evaluation is studied in the context of smart city traffic management systems. Results show that smart city traffic management can result in significant reductions in life cycle impacts associated with urban mobility and transportation.

1 INTRODUCTION

1.1 *The smart city paradigm and smart city models*

Around the world, civil engineering infrastructure and our built environment is being embedded with dense sensing networks. These networks form the technological and IT underpinnings of “smart cities” and are increasingly enabling a new, data-driven era of infrastructure engineering for increased lifecycle performance. This “smart city paradigm” was introduced out of a global need to respond to the challenges of increasing populations in megacities and significant growth in the demand for limited resources (Bačić et al. 2018). Today, smart city projects in many countries are being planned or implemented as a pathway toward greater urban sustainability in the face of global challenges such as climate change, as summarized by Kiremidjian & Lepech (2023).

To facilitate more successful implementation of the smart city paradigm, several models have been proposed to structure smart city services. These models include a theoretical foundation for the smart city concept by Harrison and Donnelly (2011), along with more detailed implementation models by Sánchez et al. (2013) and Li et al. (2015). A comprehensive summary of these models has been presented by Bačić et al. (2018). Some of the approaches to smart city development emphasize technological aspects (e.g., Park et al. 2018), while other approaches consider social and economic aspects that must also be addressed (e.g., Baraniewicz-Kotasińska 2022).

1.2 *Urban metastructure*

While dense sensing networks may form the technological foundation of smart cities, implementation requires much more than simply embedding information technology hardware into existing urban infrastructure systems or the application of artificial intelligence to analyze municipal data streams. Recognizing that large cities are complex systems of physical, environmental, social, economic, and financial systems, among others, smart city implementation requires a set of physical infrastructures, digital technologies, regulations and policies, financing mechanisms, community

outreach, businesses and business models, partnerships, institutions, and other engagement mechanisms that need to be established and operated in concert with each other to provide a high quality of life in smart and sustainable cities. This set of interconnected technologies, policies, and organizations, first applied to urban transportation systems (Rogers 2016), is referred to herein as urban metastructure (Lepech 2017, Lepech 2021, Kiremidjian & Lepech 2023)

This metastructure can be parsed into three critical elements. The foundational element is (I) a dense sensing and data collection network. This sensing and data collection network comprises the “set of physical infrastructures” within the urban metastructure. Such sensing networks can be constructed specifically for smart city purposes (i.e., CCTV cameras, traffic sensors) or leverage the increasing numbers and capabilities of smartphones. Built upon this sensing network is (II) a computational layer that translates the ever-growing stream of smart city data into information that can be used by residents, businesses, and visitors. This computational layer, which leverages advanced computational algorithms (i.e., machine learning, artificial intelligence) to efficiently and rapidly process incoming data streams, can provide the public with information via smartphone applications or direct alerts. These two basic layers of smart city metastructure, (I) sensing and (II) computation, are commonly associated with smart city research.

The final component of metastructure is (III) an engagement mechanism. This is a less commonly studied, yet critically important component. Effective engagement mechanisms comprise the “regulations and policies, financing mechanisms, community outreach, businesses and business models, partnerships, and other institutions” of urban metastructure and are necessary to substantially increase the quality of life for residents in smart and sustainable cities.

2 ELEMENTS OF URBAN METASTRUCTURE

2.1 *Physical infrastructure for smart and sustainable cities*

Sensors are a crucial component of any intelligent control system and a foundational component of smart city metastructure. The performance of an urban system can be improved via control systems that enhance awareness of its environment and its operational status, and therefore is equipped with an array of sensors (Bačić et al. 2018). Different types of sensors are typically deployed to collect a variety of data that are then synchronized and analyzed to extract information that enables robust decision making and control. In situ sensors, embedded on a structure, road, or other infrastructure system components, collect information locally (e.g., at traffic loops). Beyond local sensor networks, remote sensors (e.g., CCTV cameras, satellites) collect data from a distance. Data streams from smartphones are an increasingly critical component of smart city sensor networks. Today, an important part of this smartphone dataset are data from human-generated measurements which “include subjective observations on the environment, social media posts, mobile phone calls and text messages, and physiological measurements by wearable body sensors” (Bačić et al. 2018). Data and information transmission and storage are achieved through wired or wireless communications networks.

For illustration, the smart city of Songdo in South Korea has deployed a dense network of traffic loops and CCTV cameras. These systems are now generating terabytes of smart city vehicle traffic data for a complete network of intersections in Songdo and throughout the Incheon Free Economic Zone (IFEZ) in South Korea. In addition to traffic data, smart city physical infrastructure systems include air quality sensors that are dispersed in street lighting for pollution metering (Szarata et al. 2017, Vasiutina et al. 2022) and environmental monitoring systems that track air and water quality in buildings to identify airborne pathogens (e.g., Chew et al. 2022). Systems for tracking footsteps in buildings are being developed to optimize foot traffic flow and, in healthcare and assisted living facilities, monitor elderly occupants to prevent falls (e.g., Pan et al. 2017). Surely, these examples represent only a subset of the myriad types of physical infrastructure which comprises the first layer of metastructure; a dense sensing and data collection network.

2.2 *Smart city computational infrastructure*

A robust computational layer is necessary to support good decision making and infrastructure management. Data collected from the complex combination of sensors are meaningless until

information is extracted and used in the management and control of various urban systems. Computational and data science tools such as advanced statistical analysis, machine learning, and artificial intelligence have been under development for some time for these purposes and have greatly advanced over the past decade.

For example, a novel, adaptive traffic signal control algorithm has been developed for Songdo, South Korea that utilizes a new traffic signal control design relying on deep reinforcement learning (Gu et al. 2022). Unlike current approaches used in traffic signal design, the Songdo system is based on a multi-discrete soft-Q-networks (MD-SQN) algorithm and uses real-time traffic conditions (i.e., queue lengths, approaching traffic counts, presence of non-vehicle actors) to set traffic light durations. The MD-SQN algorithm results in traffic signal actions that are more practical than those devised by current traffic signal algorithms.

Embedding new forms of computational layers, like MD-SQN, into rapidly evolving digital twins is also key to the development of smart cities. These technologies can be used in many ways for managing critical systems in smart cities (Farsi et al. 2020). It is also important to link digital twins to the physical and functional properties of systems (Lepech et al. 2016) to map and study interdependencies and conflicts, thereby enhancing the ability to tackle difficult interactions.

2.3 *Smart city engagement mechanisms*

Engagement mechanisms are an important component of the metastructure, essential to the effective implementation of smart city systems. Engagement includes regulations and policies, financing mechanisms, community outreach, businesses and business models, partnerships, and other institutions. Without integration of these elements in smart city implementation, the value proposition of technologies remains ambiguous to residents and fails to achieve long-term goals.

There exist examples of successful engagement mechanisms around the world. For example, Virtual Singapore provides residents with “a geo-visualization, analytical tools and 3D semantics-embedded information platform to connect and create awareness and services that enrich their community.” Digital Dubai now has over 90 government services that are digitalized and accessible to citizens through its DubaiNow App.

Building upon the MD-SQN computational layer that is being implemented in Songdo, South Korea for integrated urban mobility management, Songdo city operations are controlled at a centralized command center that can enact smart mobility solutions in near real time. But it is important to recognize that smart city technologies must be implemented with people in mind to engage with citizens and create value for residents. Therefore, unlike other traffic optimization algorithms, the new MD-SQN traffic signal algorithm maintains the “cycle concept” (i.e., a recognizable repeating pattern of protected turns and free traffic flow) to account for human drivers’ preferences and habits (Gu et al. 2022). Using MD-SQN traffic signal timing, each agent (the traffic light) decides on the duration of its own phase, and multiple agents jointly control the duration of all phases in one cycle of intersection light timing and execute it in the next cycle. Additionally, MD-SQN explicitly considers non-vehicle travelers (e.g., pedestrians and bicyclists) and can deal with potential data transmission delays and interruptions, which are common in real-world traffic sensing conditions. Such engagement approaches that maintain the citizen-centered or user-centered focus of smart cities will be essential for their ultimate success.

3 SMART AND SUSTAINABLE CITIES

3.1 *Songdo, South Korea case study*

Songdo Smart City, located within Incheon Municipal City and near Seoul, South Korea is a purpose-built “ubiquitous city” constructed with sensors to track traffic conditions, feeding that information into traffic light timing routines to minimize traffic and local air pollution. Construction started with over US\$40 billion in investment from Gale International, POSCO E&C, Morgan-Stanley Real Estate, Asia Development Institute, Arup & Partners, and CISCO Services Korea.

The Stanford Center at the Incheon Global Campus (SCIGC) is currently conducting research in collaboration with Songdo Smart City on dynamic traffic management systems to

solve urban mobility issues along with urban sustainability challenges. SCIGC is an interdisciplinary research center located in Songdo and focusing on smart city technology implementation, sustainable urban systems and wellness, innovative smart city entrepreneurship and business models, and sustainable development and financing.

In this case study, the focus is a major traffic intersection in Songdo, South Korea. The intersection connects the major thoroughfares of Convensia Road and Incheon Tower Road in Songdo. The purpose of this study is to assess the impact of implementing the new MD-SQN traffic signal algorithm as compared to existing signal timing algorithms on the basis of social, environmental, and economic lifecycle impacts. The functional unit of measurement in this study is 1000 passenger vehicles traversing the intersection at Convensia Road and Incheon Tower Road.

To determine traffic conditions at the intersection, CCTV footage of traffic flow at the intersection was obtained in 5-minute-long videos taken at the start of each hour during a 24-hour period. Traffic counts for these intervals throughout the day are provided in Table 1. This results in a traffic mix of 95% automobiles, 2% busses, and 3% trucks. The collection of this type of data represents the sensing layer of the Songdo smart city metastructure.

Table 1. Extrapolated hourly traffic counts from 5-minute CCTV data for the convensia road and incheon tower road intersection.

Time	Auto	Bus	Truck	Time	Auto	Bus	Truck
00:00 – 03:00	276	12	0	13:00 – 17:00	2544	132	144
03:00 – 06:00	132	12	0	17:00 – 21:00	5220	78	30
06:00 – 09:00	3606	108	90	21:00 – 24:00	2058	42	6
09:00 – 13:00	2820	48	192				

3.2 Traffic signal control optimization using MD-SQN

A novel multi-discrete soft-Q-network (MD-SQN) approach is proposed for optimization of traffic signal actions at the Convensia Road and Incheon Tower Road intersection. In this case, MD-SQN is implemented to solve for the optimal traffic signal policy under a multi-discrete action space scenario. A complete description of the MD-SQN formulation, and a comparison of MD-SQN with other traffic signal control algorithms, can be found in Gu et al. (2022).

The traffic signal control problem is one with multiple agents jointly deciding an action plan. Such action design introduces a multi-discrete action space reinforcement learning (RL) problem, which is difficult for many existing RL methods to solve. One approach to this multi-discrete action space problem is multi-agent reinforcement learning (e.g., Foerster et al (2018), Sunehag et al. (2017)). Assuming that all agents are a part of the environment and do not interfere with each other, multi-agent reinforcement learning approaches can devise a rational policy, π , for traffic signal timing (i.e., red, yellow, and green light sequencing and timing in all directions). However, if interference between agents is ignored the result is that all agents compete for the limited resource (i.e., green duration). This creates more congestion and causes chaotic actions.

To solve this problem, instead of solving for π we can solve for a q-value, which is strongly correlated with π in value-function-based RL. The q-value can be determined by changing the policy from a base case and observing differences in performance. The optimization problem can then be solved with appropriate objective and constraint functions. Once again, a complete mathematical description of the MD-SQN algorithm can be found in Gu et al. (2022). The implementation of an optimal traffic signal timing algorithm represents the computational layer of the Songdo smart city metastructure.

Based on vehicle traffic counts, arrival times, and departure times determined from CCTV data, the time spent by vehicles currently traversing the Convensia Road and Incheon Tower Road intersection is determined. This is the base case traffic management scenario. Based on vehicle traffic counts and arrival times, and implementing MD-SQN as the signal timing algorithm, an alternative traffic management scenario is devised. The frequency of time spent (seconds) by 1000 vehicles waiting at the Convensia Road and Incheon Tower Road

intersection for the base case and MD-SQN traffic management scenarios are shown in Figure 1(left) and Figure 1(right), respectively. For each scenario, the idling time spent at the intersection was computed in two simulations, one during daytime (Simulation 1) conditions, and one during nighttime (Simulation 2) conditions.

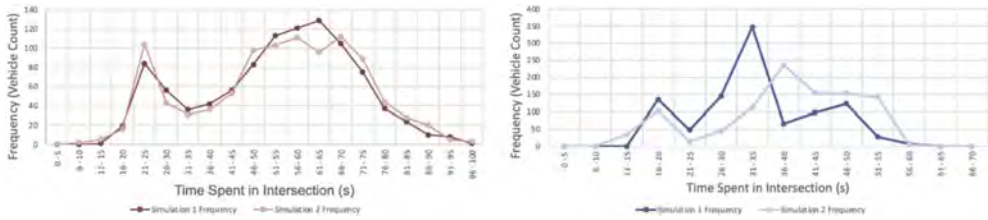


Figure 1. The frequency of idling time spent (seconds) by 1000 vehicles in the Convensia Road and Incheon Tower Road intersection for the base traffic management scenario (left) and MD-SQN traffic management scenarios (right).

As seen in Figure 1, the number of vehicles experiencing shorter times idling at the intersection is much larger for the MD-SQN traffic management scenario. For those vehicles that do have to stop at the intersection, the MD-SQN traffic control scenario reduces the average total time a vehicle spends idling at the intersection from approximately 53 seconds to approximately 36 seconds. The reduction seen in average idling time spent at the intersection represents the engagement layer of the Songdo smart city metastructure.

3.3 Electrification of South Korean automobile fleet

South Korea has national goals for electrification of the national automobile vehicle fleet by 2030. In 2030, the South Korean automobile fleet is expected to be 33% electric vehicles (EV) and 67% internal combustion engine (ICE). For this study, three EV market penetration scenarios are assumed when comparing the potential sustainability impact of the new MD-SQN traffic signal algorithm with the base case for traffic management. Combining the 3 EV scenarios with the 2 traffic management scenarios, a total of 6 life cycle analysis scenarios are shown in Table 2.

Table 2. Vehicle fleet composition and traffic signal control algorithm for six life cycle analysis scenarios.

Scenario	ICE %	EV %	Signal Algorithm	Scenario	ICE %	EV %	Signal Algorithm
S1	100	0	Base Case	S2-MDSQN	90	10	MD-SQN
S1-MDSQN	100	0	MD-SQN	S3	67	33	Base Case
S2	90	10	Base Case	S3-MDSQN	67	33	MS-SQN

4 LIFE CYCLE ANALYSIS

4.1 Goal and scope of analysis

The goal of this analysis is to assess the impact of implementing an MD-SQN traffic signal management algorithm as compared to the base case (current) traffic signal management algorithm at the Convensia Road and Incheon Tower Road intersection in Songdo, South Korea. The functional unit of analysis is 1000 vehicles traversing the intersection. The boundaries of analysis include raw material acquisition, production, processing, transportation, use, and disposal for fossil fuels used in ICE vehicles and raw material acquisition, production, processing, transportation, use, and disposal for batteries used in EVs. The analysis excludes fuels and energy expended in vehicle acceleration or crossing the intersection, since these impacts are identical in both management scenarios. The analysis also excludes impacts associated with the manufacturing of ICE vehicles or EVs, along with exclusion of the impacts of tires, repair parts, and other maintenance.

4.2 Life cycle inventory and economic costs

The ICE vehicle fuel life cycle inventory analysis was split into two components. One component is raw material extraction, with the other being fuel processing, distribution, and combustion. The unit processes used in SimaPro databases were “crude oil inventory” and “light oil inventory”, respectively. For EV battery production, the unit process used in the SimaPro database was “rechargeable lithium-ion battery.” The impacts associated with this unit process were scaled to match the amount of wasted battery lifetime associated with waiting at the intersection. The assumed average EV battery lifetime is 10 years.

Idle time spent at the intersection was converted to cost per second based on ICE idling fuel costs and EV lost battery life. For ICE vehicles, average idling fuel consumption is 1.9 L/hr (South Carolina Dept. of Health 2022). The average price for gasoline in South Korea as of November 2022 was US\$1.16/L. Thus, the ICE vehicle idling cost is US\$6.1e-6/sec. The cost of an EV battery in South Korea is US\$15,300 with no cost for end-of-life disposal (Da-sol 2022). Based on the initial cost and expected lifetime of the battery, the EV idling cost is US\$4.9e-7/sec.

4.3 Life cycle impact assessment

Social, environmental, and economic indicators are reported for this analysis. These indicators, and their respective metrics, are summarized in Table 3.

Table 3. List of reported life cycle assessment indicators for the Songdo case study.

Indicator	Unit	Type
Idling Time	sec	Social
Global Warming Potential	kg CO ₂ -eq	Environmental
Ozone Depletion Potential	kg CFC11-eq	Environmental
Acidification Potential	kg SO ₂ -eq	Environmental
Eutrophication Potential	PO ₄ -eq	Environmental
Economic Cost	US\$	Economic

4.4 Interpretation and results

The impacts measured for each of the scenarios and indicators shown in Tables 2 and 3, respectively, are shown in Table 4. The results indicate that the reduction in idle time associated with implementation of the MD-SQN traffic signal control algorithm broadly reduces social, environmental, and economics indicators in each of the categories reported. Across the three EV penetration scenarios, implementation of MD-SQN traffic signal control algorithm generally results in consistent reductions in impacts, aside from eutrophication potential, which sees the benefits of MD-SQN implementation decrease with higher EV market penetration (Scenario S3). This is due to relatively high eutrophication potential emissions associated with battery production as compared to fossil fuel production.

Sensitivity analyses were carried to account for uncertainty in the assumptions that drive life cycle impact and cost calculations. Specifically, the idling fuel consumption of ICE vehicles and the battery lifetime of EVs batteries were varied. Uncertainties of $\pm 20\%$ on idling fuel consumption, battery lifetime, and fuel price were considered. This extent of sensitivity was selected as a likely magnitude of variation depending on vehicle age, manufacturer, and model. The analysis was performed for each scenario and impact category. A sample result of the sensitivity analysis for CO₂-eq emissions is shown in Figure 2. Results of all sensitivity analyses show that all impact categories, except eutrophication, are more sensitive to changes in the idling fuel consumption than to changes in the EV battery life. For each scenario, sensitivity is higher in the base case than in the MD-SQN case due to the larger absolute impacts associated with the base case. Across all scenarios and all variations, the conclusion that implementation of MD-SQN traffic signal control algorithm generally results in consistent reductions in impacts did not change.

Table 4. Life cycle indicators for Scenarios S1, S2 and S3 for each of the six indicators quantified.

Indicator	Scenario								
	S1	S1-MDSQN	Δ (%)	S2	S2-MDSQN	Δ (%)	S3	S3-MDSQN	Δ (%)
Idling Time (sec)	53.1	35.6	-33.0	53.1	35.6	-33.0	53.1	35.6	-33.0
Global Warming Potential (kg CO ₂ -eq)									
ICE	2.21E+01	1.48E+01		1.99E+01	1.34E+01		1.48E+01	9.95E+00	
EV	0	0		9.20E-02	6.20E-01		3.04E-01	2.04E-01	
Total	2.21E+01	1.48E+01	-32.9	2.00E+01	1.40E+01	-30.1	1.51E+01	1.01E+01	-33.0
Ozone Depletion Potential (kg CFC11-eq)									
ICE	6.75E-06	4.52E-06		6.07E-06	4.07E-06		4.52E-06	3.03E-06	
EV	0	0		3.89E-09	2.61E-09		1.28E-08	8.61E-09	
Total	6.75E-06	4.52E-06	-33.0	6.07E-06	4.07E-06	-32.9	4.53E-06	3.04E-06	-33.0
Acidification Potential (kg SO ₂ -eq)									
ICE	3.36E-02	2.26E-02		3.03E-02	2.03E-02		2.25E-02	1.51E-02	
EV	0	0		6.36E-04	4.27E-04		2.10E-03	1.41E-03	
Total	3.36E-02	2.26E-02	-32.7	3.09E-02	2.07E-02	-33.0	2.46E-02	1.65E-02	-32.9
Eutrophication Potential (kg PO ₄ -eq)									
ICE	7.74E-03	5.01E-03		6.73E-03	4.51E-03		5.01E-03	3.36E-03	
EV	0	0		1.99E-03	1.33E-03		6.56E-03	4.40E-03	
Total	7.74E-03	5.01E-03	-35.3	8.72E-03	5.84E-03	-33.0	1.16E-02	7.76E-03	-32.9
Economic Cost (US\$)									
ICE	32.39	21.72		29.16	19.55		21.70	14.56	
EV	0.00	0.00		0.26	0.17		0.85	0.57	
Total	32.39	21.72	-32.9	29.42	19.72	-33.0	22.55	15.13	-32.9

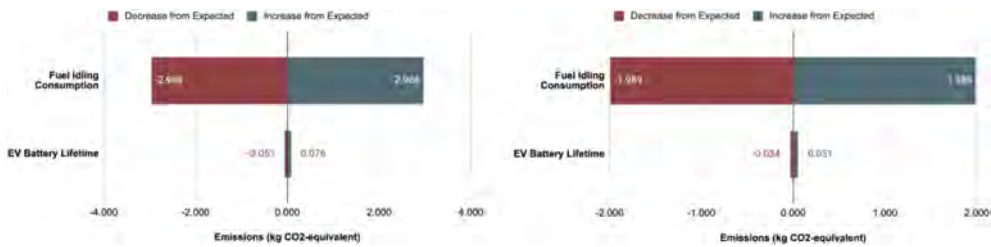


Figure 2. Sensitivity in greenhouse gas potential emissions (kg CO₂-eq) by varying idling fuel consumption and EV battery lifetime by $\pm 20\%$ for Scenario S3 (left) and Scenario S3-MDSQN (right).

The results presented in Table 4 are calculated for a functional unit of 1000 vehicles traversing the intersection of Convensia Road and Incheon Tower Road. Summing the traffic counts provided in Table 1 for an entire day, over 60000 automobiles cross the intersection on a typical workday. Assuming 250 workdays annually, implementation of the MD-SQN traffic signal control algorithm can reduce greenhouse gas emissions by over 100 metric tons of CO₂-eq annually. Applied more broadly to traffic intersections throughout Songdo and other South Korean cities, the potential impact reductions associated with smart city implementations at scale can become a substantial part of meeting current sustainability challenges at a global scale.

5 CONCLUSION

This paper introduces the concept of urban metastructure as a transcendent set of physical, technological, and social infrastructure systems that must be built in concert with one another to increase the likelihood of smart and sustainable city success. Specifically, the three layers of urban metastructure - sensing, computation, and engagement – were discussed and examples from numerous smart city efforts around the world were presented. A specific case study, advanced traffic signal control management in the smart city of Songdo, South Korea, was used to illustrate all three of the layers and connect their results to life cycle assessment and life cycle engineering of smart city transportation systems. Results from this case study show that implementation of a newly developed MD-SQN traffic signal control algorithm at one intersection in Songdo smart city generally results in consistent reductions in social, environmental, and economic impacts over time.

The promise of future smart and sustainable cities is exciting. But there remain numerous challenges and obstacles to their successful implementation over the coming decades. These challenges include privacy concerns, data security, financial shortfalls, and instrumentation of legacy infrastructure with advanced sensors, among others (Kiremidjian & Lepech 2023). Therefore, as urban designers, municipal officials, IT specialists, civil engineers, and other disciplines we must

come together to deliver on this promise, and the concept of metastructure can increase the likelihood of smart and sustainable city success. Such success will ultimately result in smarter, more sustainable urban environments that offer high quality of life to city residents around the globe.

ACKNOWLEDGEMENTS

Work at the Stanford Center at the Incheon Global Campus (SCIGC) is supported in part under the National Program to Subsidize Attracting Foreign Educational Institution and Research Institutes published by the Ministry of Trade, Industry, and Energy of the Republic of Korea and managed by the Incheon Free Economic Zone Authority. The authors would also like to thank contributions by Stanford Master of Science students Sheena Dichoso Echano, James Keo-Kosal, Celine Phua, Laura Vanderweyen, Katie Wheeler, Karissa Collins, Pascal Flury, Santiago Ossa, Gabriel Reygrobelle, and Derek Salas, along Stanford PhD Candidate Yirong Chen.

REFERENCES

- Bačić Ž, Jogun T, Majić I. 2018. Integrated sensor systems for smart cities. *Tehnički Vjesnik* 25(1):277–84.
- Baraniewicz-Kotasińska S. 2022. Smart city: Four approaches to the concept of understanding. *Urban Research & Practice* 15(3):397–420.
- Chew LW, Chen C, Gorlé C. 2022. Improving thermal model predictions for naturally ventilated buildings using large eddy simulations. *Building & Environment* 220:109241.
- Da-sol K. 2022. Will battery subscriptions lower EV prices? *The Korea Herald*. 16 Aug 2022.
- Dept. of Health & Env. Control. 2022. Idling: Why It's a Problem and What You Can Do. S. Carolina Dept. of Health & Env. Control Bureau of Air Quality, Air Programs and Implementation. Columbia, S. Carolina. <https://scdhec.gov/sites/default/files/Library/CR-010109.pdf>.
- Farsi M, Daneshkhal A, Hosseinian-Far A, Jahankhani H, eds. 2020. *Digital Twin Technologies and Smart Cities*. Cham, Switzerland: Springer
- Foerster J, Farquhar G, Afouras T, Nardelli N, Whiteson S. 2018. Counterfactual multi-agent policy gradients. In *Proceedings of the AAAI Conference on Artificial Intelligence*, volume 32.
- Gu X, Chen Y, Kan Y, Xu C, Wang M, Lepech M. 2022. A Real-World Signal Control Framework with Novel Action Design and MD-SQN Approach. *Proceedings of the 25th IEEE International Conference on Intelligent Trans. Systems*. Sept 18 – Oct 18, 2022. Macau, China.
- Harrison C, Donnelly IA. 2011. *A Theory of Smart Cities*. Proceedings, 55th Annual Mtg of the ISSS, Hull, UK.
- Kiremidjian A.S. & Lepech, M. 2023. An Infrastructure Systems Approach to Smart and Sustainable Cities. *US National Academy of Engineering The Bridge*. 53 (1). In Press.
- Li Y, Lin Y, Geertman S. 2015. The development of smart cities in China. *Proceedings, 14th Internatl Conf on Computers in Urban Planning & Urban Management*, Cambridge MA.
- Lepech M, Geiker M, Michel A, Stang H. 2016. Probabilistic design and management of sustainable concrete infrastructure using multi-physics service life models. *1st Internatl Conf on Grand Challenges in Construction Materials*. Los Angeles, California, USA.
- Lepech, M 2017. Where city intelligence leads: a strategy for global smart city development. *Keynote Address. Smart Cities Innovation Summit (SCIS) Asia 2017*. Seoul, South Korea. September 6, 2017.
- Lepech, M 2021. A Vision for Smart and Sustainable Cities. *Keynote Address. SCIGC First International Symposium: Envisioning Smart Cities and Beyond*. Incheon, South Korea. June 4, 2021.
- Pan S, Yu T, Mirshekari M, Fagert J, Bonde A, Mengshoel OJ, Noh HY, Zhang P. 2017. FootprintID: Indoor pedestrian identification through ambient structural vibration sensing. *Proceedings, ACM on Interactive, Mobile, Wearable and Ubiquitous Technologies* 1(3):89.
- Park E, Del Pobil AP, Kwon SJ. 2018. The role of Internet of Things (IoT) in smart cities: Technology roadmap-oriented approaches. *Sustainability* 10(5):1388.
- Rogers A. 2016. Welcome to the metastructure: The new internet of transportation. *Wired*, Jan 4.
- Sánchez L, Elicegui I, Cuesta J, Muñoz L, Lanza J. 2013. Integration of utilities infrastructures in a future internet enabled smart city framework. *Sensors* 11(13):14438–65.
- Sunehag P, Lever G, Gruslys A, Marian Czarnecki W, Zambaldi V, Jaderberg M, Lanctot M, Sonnerat N, Leibo J Z, Tuyls K, et al. 2017. Value-decomposition networks for cooperative multi-agent learning. *arXiv preprint arXiv:1706.05296*.
- Szarata A, Nosal K, Duda-Wiertel U, Franek L. 2017. The impact of the car restrictions implemented in the city centre on the public space quality. *Transportation Research Procedia* 27:752–59.
- Vasiutina H, Naumov V, Szarata A, Rybicki S. 2022. Estimating the emissions reduction due to the use of cargo bikes: Case studies for the selected European cities. *Energies* 15(14):5264.

Value of information under random decision, model, and measurement errors

Z.Y. Mir Rangrez

IITB-Monash Research Academy, Mumbai, Maharashtra, India

J. Ghosh & S. Ghosh

Indian Institute of Technology Bombay, Mumbai, Maharashtra, India

C. Caprani

Monash University, Melbourne, Victoria, Australia

ABSTRACT: Value of Information (VoI) analysis provides a quantitative measure to justify the adoption of a structural health monitoring (SHM) strategy for civil infrastructure maintenance. The VoI analysis adopts predictive and measurement-based models to characterise the infrastructure state and monitoring quality. The uncertainties in such models have been explicitly considered in the current VoI framework and the decision maker is expected to choose the action maximizing the expected utility defined by a deterministic utility function. However, under the influence of some tangible or intangible factors like budget availability, bias, etc., the decision maker may end up choosing a sub-optimal action. The present study characterizes such decisions by introducing a concept of cost of decision and models such decisions by a random error, in addition to the predictive model and measurement errors, to assess their influence on the VoI. The results indicate the negative influence of such decisions on VoI.

1 INTRODUCTION

Civil infrastructure is crucial to the social and economic development of all communities worldwide (Calderón and Servén, 2004; Frangopol, 2011). This infrastructure, however, ages with time due to the effect of environmental stressors like corrosion, fatigue, etc. and therefore requires maintenance during its service life. The maintenance or repair needs to be carried out optimally both in terms of when (i.e., the point(s) in time) during the service life as well as the extent required. A decision maker, responsible for the maintenance, usually decides based on pre-defined degradation models or expert judgment (Konakli et al., 2016). However, the resulting maintenance may not be optimal for the specific structure as the actual degradation of the structure may deviate from the predicted one. Therefore, a decision maker faces the uncertainty regarding the actual state of the structure, wherein the decision may result in a conservative maintenance or a riskier one. A conservative maintenance leads to unnecessary costs resulting in the over-utilization of maintenance budget and in the presence of budget constraints, it would be highly undesirable. On the other hand, inadequate maintenance poses high risk of infrastructure failure leading to adverse consequences both in terms of direct costs including the loss of human life and an indirect effect on the country's economy.

Structural health monitoring (SHM) has the potential to aid a decision maker by providing additional information about the state of the system which may be a structure or a component, thus reducing the uncertainty and leading to relatively optimal maintenance decisions (Faber and Thons, 2014; Biondini and Frangopol, 2016). However, the cost saving obtained from a monitoring information must exceed the cost of monitoring strategy for its rational adoption. The value of information (VoI) analysis provides a metric to estimate the expected benefit from an information acquirement strategy (Schlaifer and Raiffa, 1961; Howard, 1962). For civil infrastructure

maintenance, VoI has the potential to assist the optimal utilization of additional information from monitoring (Pozzi and Der Kiureghian, 2011; Thöns, 2018; Khan et al., 2022). In this context, VoI is defined as the expected cost savings obtained by adopting a monitoring strategy for a given maintenance decision scenario consisting of (i) an action model, (ii) a cost model, and (iii) a probabilistic state degradation model (Pozzi and Der Kiureghian, 2011; Faber and Thöns, 2014; Thöns, 2018; Khan et al., 2022). VoI is obtained as the difference between the costs of prior optimal action and the optimal action after using the monitoring information. The conditional value of information (*CVoI*) is defined corresponding to a particular monitoring outcome and is estimated by posterior analysis of VoI framework (Thöns, 2019). Moreover, the expected value of information (*EVoI*) is obtained by pre-posterior analysis which involves taking the expectation over all the possible monitoring outcomes, thus giving the value metrics before implementation of the monitoring strategy (Thöns, 2019).

The VoI estimate is affected by the quality of information (Pozzi and Der Kiureghian, 2011; Srinivasan and Parlikad, 2013). Some studies (Khan et al., 2020; Zhang et al., 2023) have evaluated the effects of model and measurement errors on the value of information estimate. Consequently, these errors are being explicitly incorporated in a VoI based decision analysis. However, a common assumption in such an analysis is that the decision maker will always act rational and this behaviour is modelled as per the expected utility theory (EUT) (Cappello et al., 2016). Although the decision maker is expected to act rationally most of the time, chances are that the behaviour may deviate in some cases and a sub-optimal decision is preferred relative to the EUT frame of reference, for example, some studies have discussed the scenarios where a decision maker is affected by bias (Verzobio et al., 2021) or their preference may not align with the regulations (Li and Pozzi, 2021). Moreover, at times, social and political pressure may also play a role in such deviations from a rational or optimal decision making. Therefore, a number of factors, tangible as well as intangible, may influence the final decision and the actual benefit obtained from a monitoring strategy would be different from the predicted one. This may lead, in some cases, to an incorrect verdict on the monitoring adoption. The existing VoI framework lacks the robustness towards the realization of such random sub-optimal decisions and therefore, the resulting estimates are relatively ideal than the ones actually realized in the field.

The present study aims to incorporate the instances of sub-optimal decisions in a VoI framework by modelling them as generic random decision errors. The concept of the cost of decision is introduced to characterise a sub-optimal decision for a given knowledge about the state of the structure. Moreover, a parametric analysis is carried out to analyse the extent of effects on the VoI estimate by adopting a maintenance case study of a component and treating random model, measurement and decision errors as the parameters of interest.

2 SUB-OPTIMAL DECISIONS

In a maintenance decision problem, for a given level of knowledge regarding the actual state of the structure, the optimal action is the one incurring minimum expected cost. All other actions are sub-optimal relative to this action, that is, the expected costs of such actions is high. The posterior VoI analysis gives the optimal action for a given information and it is expected that a rational decision maker will choose the same action for maintenance. However, in reality, the decision maker may choose a sub-optimal action instead. The potential cause for this behaviour may include a random risk averse or risk seeking attitude of the decision maker. The word “random” is important here, as it is usually assumed that a properly elicited utility function would suffice for describing the decision maker’s risk attitude. However, an accurate calibration of the risk attitude is very difficult (Hey and Orme, 1994), if not impossible, and the risk attitude at any time may depend on various intangible factors if the decision maker’s judgment is influenced by some heuristics or bias (Tversky and Kahneman, 1987; Verzobio et al., 2021). Additionally, it has been observed that the decisions under risk vary with the choices available, and the way these choices are framed at the moment of decision-making (Stewart et al., 2019). The possibility of sub-optimal actions may be relatively high around the threshold outcomes, where the difference between the expected costs of two

actions is relatively less and the decision maker may decide to incur some extra cost and ends up with a sub-optimal decision to satisfy the intangible influencing factors like budget availability, social and political pressures, etc.

2.1 Cost of decision

For a given level of knowledge about the state of structure, a decision, whether optimal or sub-optimal, can be characterized by a quantity by which it offsets the potential cost saving corresponding to that level of knowledge. This quantity is defined here as the ‘cost of decision’. This cost is different from the actual expected cost incurred from doing an action and in fact forms an element of the incurred expected cost.

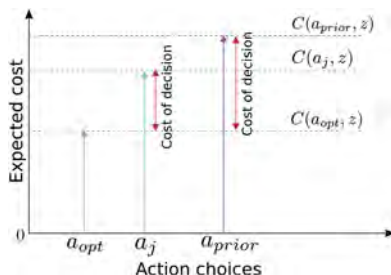


Figure 1. Cost of decision corresponding to different action choices for a given information z .

Let $C(a_j, z)$ denote the expected cost corresponding to an action a_j , for a given information z . Figure 1 depicts the concept of cost of decision. In a posterior analysis, the conditional value corresponding to a given information z is obtained as

$$CVoI(z) = C_{prior} - C(a_{opt}, z) \quad (1)$$

where, C_{prior} = expected cost for optimal maintenance action a_{prior} without information, and $C(a_j, z)$ = expected cost incurred by choosing the optimal action a_{opt} corresponding to the knowledge refinement due to an information z .

Therefore, a rational decision maker is expected to receive the benefit equal to $CVoI$. However, if the decision maker chooses a sub-optimal decision, it would decrease the benefit obtained from the information and may even bring the benefit to zero, if he ends up choosing the same decision as that without information, i.e., a_{prior} . The cost of decision is given as

$$\text{Cost of decision} = C(a_j, z) - C(a_{opt}, z) \quad (2)$$

where, $C(a_j, z)$ = the expected cost incurred from some chosen action a_j for a given information z .

The cost of a particular decision can be zero if it is an optimal decision or can have a positive value if it is a sub-optimal decision. This cost reduces the potential $CVoI$ that could be obtained from a given information.

2.2 Modelling sub-optimal decisions

The present study considers random occurrences of sub-optimal decisions; i.e., a cost utility function for a decision maker is available, however, the decision maker under some tangible or intangible scenario may deviate from the elicited behaviour. If $C(a_i, a_j)$ denotes the difference between the expected costs of action a_i and a_j , then

$$C(a_i, a_j) = C(a_i, z) - C(a_j, z) \quad (3a)$$

and as per EUT,

$$C(a_i, a_j) > 0 \Rightarrow a_j \text{ is chosen} \quad (3b)$$

In order to incorporate the possibility of a sub-optimal decision, a normally distributed error term is incorporated in the decision criteria as in Hey and Orme (1994) and Equation 3b becomes:

$$C(a_i, a_j) + \epsilon_d C_{ref} > 0 \Rightarrow a_j \text{ is chosen} \quad (4)$$

where, $\epsilon_d C_{ref}$ constitutes the decision error, $\epsilon_d \sim N(0, \sigma_d^2)$, and C_{ref} is a reference cost. If $\sigma_d^2 = 0$, the decision maker does not deviate from the expected rational behaviour and increase in the value of σ_d^2 results in higher chances of sub-optimal decisions.

3 CASE STUDY

A component case study, adopted originally from Konakli et al. (2016) which was further developed by Khan et al. (2020), is considered for the demonstration of sub-optimal decision making and its treatment. Khan et al. (2020) developed the VoI framework incorporating additive bias, multiplicative bias, and random errors in both the predictive model and measurements. However, the present study considers only the random model and measurement errors. The structural component is assumed to have a service life of $L = 30$ years. The component resistance at time t (years) is given as:

$$R(t) = R_0 G(t) \quad (5)$$

where R_0 = resistance at the start of service life at $t_0 = 0$ years, t = time discretized in years, and $G(t)$ is a degradation function:

$$G(t) = 1 - at^b \quad (6)$$

where, a and b are the degradation parameters characterizing the degradation mechanism (Mori and Ellingwood, 1993). a and b are assumed deterministic with values 0.01 and 1.0, respectively. R_0 is assumed as a lognormal random variable with mean = 2.5 units and coefficient of variation = 0.1. Load on the component S is also assumed to be a lognormal random variable with mean = 1.0 units and coefficient of variation = 0.3. It is assumed that the prediction model for the component performance estimates the lognormal resistance with the random error (ϵ_{M_o}). The predicted resistance $X(t)$ is therefore given as:

$$\ln X(t) = \ln R(t) + \epsilon_{M_o} \quad (7)$$

where, ϵ_{M_o} is a zero-mean normal random variable with variance $\sigma_{M_o}^2$. The limit state function at any year t is:

$$g(t) = X(t) - S \quad (8)$$

In terms of normal random variables, the limit state function can also be written as:

$$z(t) = \ln X(t) - \ln S \quad (9)$$

where, $z(t)$ is a normally distributed random variable

$$z(t) \sim \mathcal{N}(\mu_z, \sigma_z^2) \quad (10a)$$

where,

$$\mu_z = \mu_{\ln R_0} + \ln(1 - at^b) - \mu_{\ln S} \quad (10b)$$

$$\sigma_z^2 = \sigma_{R_0}^2 + \sigma_{M_o}^2 + \sigma_{\ln S}^2 \quad (10c)$$

and the annual probability of failure during year t is obtained as:

$$P_f(t) = \Phi_{z(t)}(0) \quad (11)$$

where, $\Phi_{z(t)}(\cdot)$ = cumulative distribution function of $z(t)$.

Two action choices are available to the decision maker; viz. (i) do nothing (a_0) and (ii) replacing the component (a_1) by a new component of similar type. The present cost of component replacement $c_r = 10$ cost units, and on the other hand, component failure cost $c_f = 1000$ cost units. The high cost of component failure is due to the resulting failure of the structure of which the component forms a critical part. For the present study, the utility function of the decision maker is assumed to be linear and the utility of a consequence is equal its negative costs. Therefore, the present analysis would express the utilities directly in terms of the costs. Moreover, the action decision is assumed to be taken at the start of any particular year. The discounted costs for the action decisions at any decision year t_a are obtained as:

$$c_{a_0} = c_f \sum_{t=t_a}^{L-1} \frac{P_f(t)}{(1+\lambda)^t} \quad (12)$$

$$c_{a_1} = \frac{c_r}{(1+\lambda)^{t_a}} + c_f \sum_{t=t_a}^{L-1} \frac{P_f(t-t_a)}{(1+\lambda)^t} \quad (13)$$

where, c_{a_0} and c_{a_1} = discounted cost corresponding to decisions a_0 and a_1 respectively, $L=30$ years, $t_a \in [0,30)$, λ = discount rate with due consideration to the inflation, and $\lambda = 0.02$ is assumed. Moreover, for the present study $t_a = 5$ years.

In addition, the decision maker has a choice to adopt monitoring strategy that measures the predicted lognormal resistance ($\ln X$). The measurements are not perfect and exhibit a zero-mean normally distributed random error ϵ_{M_x} with variance equal to σ_{Me}^2 . Therefore, a particular measurement at time t can be expressed as:

$$Y(t) = \ln X(t) + \epsilon_{Me} \quad (14)$$

The decision maker can use the information from these measurements to update the predicted lognormal resistance using Bayes theorem (Gelman et al., 2013). Consequently, an updated component failure probability could be obtained, which may change the cost of action decisions, resulting in different posterior costs of these actions. These costs are obtained using Equations 12 and 13, by replacing the prior probability of failure with the updated posterior probability of component failure.

3.1 Sub-optimal decision scenario

The adopted scenario considers a decision maker who behaves rationally during the prior decision making and the possibility of sub-optimal decision is present only after taking the measurements. For example, based on the established degradation models or maintenance guidelines, a decision maker is keen to adopt a particular action before taking the measurements, however, the measurements on a particular component in the field may suggest a different level of intervention compared to the prior one, but the decision maker may still follow prior regulations and may not modify his decision based on the measurement results. In such a scenario the prior and posterior decisions are obtained as:

$$\text{Prior decision} = \begin{cases} a_1 & \text{if } C_{prior}(a_0, a_1) > 0 \\ a_0 & \text{if } C_{prior}(a_0, a_1) < 0 \end{cases} \quad (15)$$

$$\text{Posterior decision} = \begin{cases} a_1 & \text{if } C_{post}(a_0, a_1) + \epsilon_d C_{ref} > 0 \\ a_0 & \text{if } C_{post}(a_0, a_1) + \epsilon_d C_{ref} < 0 \end{cases} \quad (16)$$

where, $\epsilon_d C_{ref} =$ decision error, $\epsilon_d \sim \mathcal{N}(0, \sigma_d^2)$, and $C_{ref} =$ reference cost. In the present study, the failure cost of component c_f is taken as the reference cost.

4 PARAMETRIC STUDY

A parametric study of the expected value of information, at the end of 5th year, is carried out considering the variation in random decision, model and measurement error parameters. The effect of each parameter on $EVoI$ is analysed individually. In addition, effects of different combinations of these error parameters is studied. The error combinations considered are shown in Table 1. The range of values considered for model error parameter is within the recommended bounds (Joint Committee on Structural Safety, 2001). However, due to a lack of such recommendations for decision errors in civil infrastructure literature, the range of values for decision error parameter have to be assumed. The sole aim of assuming these values is to analyse the magnitude of effect on $EVoI$. The actual expected values can be established by a survey of sub-optimal decisions encountered in civil infrastructure maintenance.

Table 1. Error combinations for parametric study.

Combination	σ_d	$\frac{\sigma_{Me}}{\mu_{in} R_0}$	$\frac{\sigma_{Mo}}{\mu_{in} R_0}$
EC1	0.0	0.0	0.0
EC2	0.05	0.1	0.0
EC3	0.05	0.0	0.15
EC4	0.0	0.1	0.15
EC5	0.05	0.1	0.15

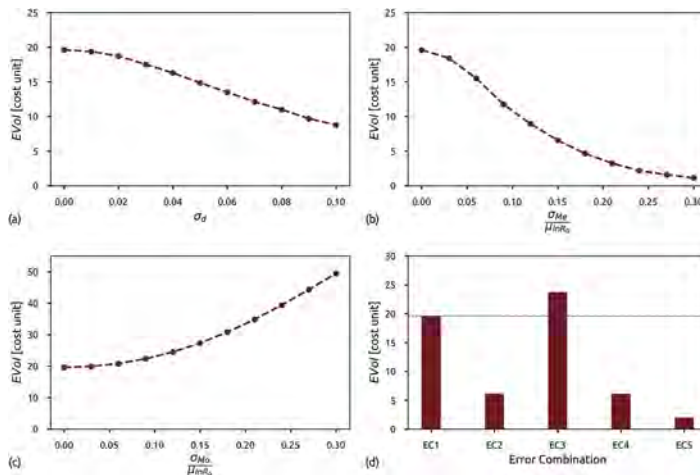


Figure 2. Variation of $EVoI$ at the end of 5th year with change in (a) standard deviation of decision error, (b) normalized standard deviation of random measurement error, (c) normalized standard deviation of random model error, and (d) different error combinations (Table 1).

4.1 Results and discussion

Figure 2 shows the results from the parametric study. Figure 2a shows the variation of $EVoI$ with changes in the decision error parameter. $EVoI$ generally decreases with increase in the possibility of high cost decision errors. The effect is marginal for small decision errors with only 4.5% decrease in $EVoI$ at $\sigma_d = 0.02$. This is due to the fact that small magnitude errors lead to sub-optimal decisions having marginally higher costs compared to the optimal decisions. Consequently, the influence of small additional expected costs of sub-optimal decisions on resulting $EVoI$ is negligible. However, for large decision errors, the resulting sub-optimal

decisions have high expected costs, thereby decreasing the *EV_{oI}*. This can be observed through the rapid decrease in *EV_{oI}* value beyond $\sigma_d = 0.02$.

Figure 2b depicts the negative effect of measurement error on *EV_{oI}*, with 94% decrease in *EV_{oI}* at $\sigma_{Me} = 0.3\mu_{ln R_0}$. The more imperfect the information, the less is its value. This is in conformity with previous parametric studies conducted on *EV_{oI}* (Pozzi and Der Kiureghian, 2011; Konakli et al., 2016; Li and Pozzi, 2019). In fact, the concept of cost of decision is applicable in the case of imperfect information as well, and due to inaccuracy the decision maker in some cases may end up choosing sub-optimal decisions (Ali et al., 2022). Thus leading to expected costs that decrease the value of information relative to the perfect information case, i.e., at $\sigma_{Me} = 0$.

Figure 2c shows the effect of the model error on *EV_{oI}*. With increase in the model error, *EV_{oI}* increases – having a 152% increase at $\sigma_{Mo} = 0.3\mu_{ln R_0}$ with respect to the perfect scenario at $\sigma_{Mo} = 0$. The positive influence of model error is due to the increase in uncertainty at the prior analysis stage. Consequently, the information acquirement would be more beneficial under such scenario.

Figure 2d shows the effect of different error combinations on *EV_{oI}*. EC1 corresponds to a perfect model, perfect measurement and a perfectly rational decision maker. The presence of measurement and decision errors in EC2 results in a 68% decrease in *EV_{oI}* relative to EC1. For EC3 (i.e., with a model and decision error combination), the resulting *EV_{oI}* depends on the severity of each error, since the model error has a positive effect unlike the decision error, which negatively effects *EV_{oI}*. Consequently, for the error values adopted in EC3, the resulting *EV_{oI}* is 21% more than that corresponding to EC1. The negative effect of the measurement error is observed to be relatively large in the presence of the model error for EC4 resulting in *EV_{oI}* = 6.11 cost units, i.e., a 69% decrease compared to *EV_{oI}* = 10.82 cost units without any model error. In the presence of all these errors, the negative effect of decision and measurement errors overshadows the positive effect of model error as observed for EC5, where the resulting *EV_{oI}* is only 10% of that for the EC1 combination.

5 CONCLUSIONS

The existing VoI framework neglects the possibility of sub-optimal decisions and therefore gives relatively ideal VoI estimates that may lead to incorrect monitoring adoption. The present study considers random occurrences of sub-optimal decisions where the decision maker deviates from the elicited utility function. A quantity defined as the cost of decision is introduced to characterize a sub-optimal decision. Moreover, the occurrence of such decisions is modelled by incorporating a normally distributed random error in the conventional VoI framework. An attempt is made to evaluate the effect of incorporating such decision errors on the resulting *EV_{oI}* for civil infrastructure maintenance by considering the case study of a structural component.

It is observed that low magnitude decision errors result in marginal decrease in the information value. For the selected case, the decrease in *EV_{oI}* is found to be 4.5% at $\sigma_d = 0.02$. However, the effect is appreciable if the decision maker deviates significantly from the rational behaviour and chooses an action decision having large cost differences with the optimal decision for the given level of knowledge about the state of the structure. Therefore, it is recommended to include a reasonable level of uncertainty, specific to a particular decision maker, in the decision criteria for the purpose of carrying out a practical VoI analysis. The presence of measurement error, which is always present in different amounts in a practical measurement process, further brings down the value obtained from the information. The model error contributes to the uncertainty at prior stage and leads to more value in adopting the new information. However, in combination with measurement error, the overall effect is to decrease the *EV_{oI}*.

Finally, the VoI analysis is sensitive to the decision problem characterization and therefore the effect of different errors may vary, in quantitative terms, for different VoI decision problems. However, the general trend for the error influence on *EV_{oI}* is expected to remain the

same. Moreover, in this study, a range of decision errors is assumed, however, the incorporation of such decision errors in a practical VoI application requires the proper quantification of such errors in order to obtain a reasonable VoI estimate.

REFERENCES

- Ali, K., J. Qin, & M. H. Faber (2022). On information modeling in structural integrity management. *Structural Health Monitoring* 21(1), 59–71.
- Biondini, F. & D. M. Frangopol (2016). Life-Cycle Performance of Deteriorating Structural Systems under Uncertainty: Review. *Journal of Structural Engineering* 142(9), 1–17.
- Calderón, C. & L. Servén (2004). The Effects of Infrastructure on Growth and Income Distribution. *Central Bank of Chile Working Papers*, 1–43.
- Cappello, C., D. Zonta, & B. Glisic (2016). Expected utility theory for monitoring-based decision-making. *Proceedings of the IEEE* 104(8), 1647–1661.
- Faber, M. H. & S. Thons (2014). On the value of structural health information. *Safety, Reliability and Risk Analysis: Beyond the Horizon - Steenbergen et al. (Eds)*, 2535–2544.
- Frangopol, D. M. (2011). Structure and Infrastructure Engineering Life-cycle performance, management, and optimisation of structural systems under uncertainty: accomplishments and challenges Life-cycle performance, management, and optimisation of structural systems under uncertainty.
- Gelman, A., J. B. Carlin, H. S. Stern, D. B. Dunson, A. Vehtari, & D. B. Rubin (2013). Bayesian Data Analysis Third edition (with errors fixed as of 13 February 2020). (February), 677.
- Hey, J. D. & C. Orme (1994). Investigating Generalizations of Expected Utility Theory Using Experimental Data. *Econometrica* 62(6), 1291–1326.
- Howard, R. A. (1962). Information Value Theory. *Systems Science* (1).
- Joint Committee on Structural Safety (2001). Part 3: Resistance Models. Technical report.
- Khan, M. S., C. Caprani, S. Ghosh, & J. Ghosh (2022, apr). Value of strain-based structural health monitoring as decision support for heavy load access to bridges. *Structure and Infrastructure Engineering* 18(4), 521–536.
- Khan, M. S., S. Ghosh, C. Caprani, & J. Ghosh (2020). Sensitivity of Value of Information to Model and Measurement Errors. *ASCE-ASME Journal of Risk and Uncertainty in Engineering Systems, Part A: Civil Engineering* 6(4), 04020038.
- Konakli, K., B. Sudret, & M. H. Faber (2016). Numerical Investigations into the Value of Information in Lifecycle Analysis of Structural Systems. *ASCE-ASME Journal of Risk and Uncertainty in Engineering Systems, Part A: Civil Engineering* 2(3), 1–13.
- Li, S. & M. Pozzi (2019). What makes long-term monitoring convenient? A parametric analysis of value of information in infrastructure maintenance. *Structural Control and Health Monitoring* 26(5), 1–18.
- Li, S. & M. Pozzi (2021). Information Avoidance and Overvaluation in Sequential Decision Making under Epistemic Constraints.
- Mori, Y. & B. R. Ellingwood (1993). Reliability-based service-life assessment of. *Journal of Structural Engineering* 119(5), 1600–1621.
- Pozzi, M. & A. Der Kiureghian (2011). Assessing the value of information for long-term structural health monitoring. *Health Monitoring of Structural and Biological Systems 2011 7984* (510), 79842W.
- Schlaifer, R. & H. Raiffa (1961). *Applied statistical decision theory*. New York: John Wiley & Sons, Inc.
- Srinivasan, R. & A. K. Parlikad (2013, oct). Value of condition monitoring in infrastructure maintenance. *Computers & Industrial Engineering* 66(2), 233–241.
- Stewart, N., E. Canic, & T. Mullett (2019). On the futility of estimating utility functions: Why the parameters we measure are wrong, and why they do not generalize. *PsyArXiv preprint*, 1–23.
- Thöns, S. (2018). On the Value of Monitoring Information for the Structural Integrity and Risk Management. *Computer-Aided Civil and Infrastructure Engineering* 33(1), 79–94.
- Thöns, S. (2019). Quantifying the Value of Structural Health Information for Decision Support: Guide for Scientists. *COST Action TU 1402: Quantifying the Value of Structural Health Monitoring* (May), 1–61.
- Tversky, A. & D. Kahneman (1987). Judgment under Uncertainty: Heuristics and Biases. *185*(4157), 1124–1131.
- Verzobio, A., D. Bolognani, J. Quigley, & D. Zonta (2021). Consequences of representativeness bias on SHM-based decision-making. *Structure and Infrastructure Engineering* 0(0), 1–13.
- Zhang, W.-H., J. Qin, D.-G. Lu, M. Liu, & M. Havbro (2023). Quantifying the value of structural health monitoring information with measurement bias impacts in the framework of dynamic Bayesian Network. *Mechanical Systems and Signal Processing* 187(November 2022), 109916.

A review on low-cost sensors compatible with open-source platforms used for life-cycle monitoring of civil structures

M. Komary, S. Komarizadehasl & J. Turmo

Department of Civil and Environment Engineering, Universitat Politècnica de Catalunya, BarcelonaTech, Barcelona, Spain

F. Lozano & J.A. Lozano-Galant

Department of Civil Engineering, Universidad de Castilla-La Mancha, Ciudad Real, Spain

X. Ye

Department of Bridge Engineering, Tongji University, Shanghai, China

ABSTRACT: Lately, the need for adopting sensors in buildings and infrastructures for monitoring and inspection of the health state of those structures is increasing. This demand is due to the increasing age of the structural stock worldwide. Consequently, more economical ways of Structural Health Monitoring applications are getting huge attention. This paper presents and evaluates several low-cost electronics compatible with open-source digital technologies for static and dynamic Structural System Identification applications. Firstly, an open-source microcontroller (Arduino), the main programable logic controller, and a Raspberry pi, a small single-board computer, are introduced. Secondly, various economic sensors with diverse measurement applications, such as ultrasonic and laser ranging, acceleration, temperature, and humidity, are discussed. Thirdly, multiple experiments in different controlled ambients are applied to assess and compare their tolerances as well as advantages and disadvantages of their use, among their price. Some problems with the Arduino codes and sensor positions emerged during the installation of the sensors and the data collection process. Finally, to attain an effective manner of using these low-cost electronics, this article offers answers to the issues faced.

1 INTRODUCTION

Lately, the demand for adopting sensors in infrastructures and buildings is increasing. This need is due to the monitoring and inspection of the health state of those structures. Consequently, more economic ways of SHM applications are getting huge attention (Komarizadehasl et al. 2022). In this article, several models of low-cost sensors have been introduced. Furthermore, the features of each one of them have been explained. Each sensor could be applied in a particular circumstance. Every sensor has benefits as well as weaknesses in various conditions. To be able to work with them, firstly Arduino Uno (which is the main programable logic controller (PLC) in this project), and a Raspberry pi, a small single-board computer, are introduced. Secondly, diverse types of sensors along with their specifications have been introduced. Each type of sensor may use a different way to send its data. Thirdly, different ways of communicating with this PLC will be presented. Finally, the results of these sensors have been illustrated.

2 STATE OF THE ART

In this section the sensors and a microcontroller that has been used in the project will be reviewed along with their technical descriptions.

2.1 *Arduino Uno*

Arduino is an open-source electronics platform based on easy-to-use hardware and software. Aduino Uno is a microcontroller board based on the ATmega328P. It has 14 digital input/output pins, 6 analog inputs to measure and convert the voltage to a digital value. It facilitates numerous interfaces to communicate with other microcontrollers and computers such as Inter-Integrated Circuit (I2C), Serial Peripheral Interface (SPI) and Universal asynchronous receiver/transmitter (UARTA) (Pathak et al. 2019) (Komarizadehasl et al. 2022) (Mahyad Komary et al. 2023). Figure 1 is the schematic of the Arduino Uno circuit.



Figure 1. Schematic of the Arduino Uno (Pathak et al. 2019).

2.2 *Raspberry Pi*

Raspberry Pi is a low cost, small and portable size of computer board. It can be used to plug-in to computer monitor or television, keyboard, mouse, pen-drive etc. Raspberry Pi has built in software such as Scratch which enables users to program and design animation, game or interesting video. In addition, programmers can also develop script or program using Python language; it is main core language in Raspbian operating system (Komarizadehasl, Lozano Galant, et al. 2022b).



Figure 2. Schematic of the Raspberry pi.

2.3 *Ultrasonic sensor*

Ultrasonic ranging module HC - SR04 provides 2cm - 400cm non-contact measurement function which on Figure 3 its schematic has been presented. For this sensor, the ranging accuracy can reach to 3mm. The modules have transmitters, receiver and processing circuit. The basic concept of work is: firstly, using I/O trigger for at least 10uS (microsecond) high level signal. Secondly, The Module automatically sends frequency of 40 kHz and detect whether there is

a pulse signal back. Finally, the range can be calculated through the time interval between sending trigger signal and receiving echo signal. Test distance = (time × velocity of sound (340M/S)) (Kamal and Hemel 2019).



Figure 3. Schematic of an Ultrasonic ranging module HC-SR04 (Kamal and Hemel 2019).

2.3.1 Humidity sensor

As it has been written on section 2.3, for measuring the distance using that sensor the speed of sound is needed. The sound travels in different speeds in different temperatures and humidity (M. Komary et al. 2022). The schematic of this sensor has been shown on Figure 4. DHT22 has already been calibrated during production process and provides accurate information (Patil, Khedkar, and Jadhav 2019) (Liu 2013).



Figure 4. Schematic of a DHT22, digital temperature/humidity sensor.

2.4 The VL53L1X

The VL53L1X, which has been shown on Figure 5 is a state-of-the-art, Time-of-Flight (ToF), laser-ranging sensor, enhancing the ST FlightSense™ product family.



Figure 5. Schematic of a VL53L0X (Adafruit 2018).

It is the fastest miniature ToF sensor on the market with accurate ranging up to 4 m and fast ranging frequency up to 50 Hz. Housed in a miniature and reflowable package, it integrates a SPAD receiving array, a 940 nm invisible Class1 laser emitter, physical infrared filters, and optics to achieve the best ranging performance in various ambient lighting conditions with a range of cover window options. Unlike conventional IR sensors, the VL53L1X uses

ST's latest generation ToF technology which allows absolute distance measurement whatever the target color and reflectance. It is also possible to program the size of the ROI on the receiving array, allowing the sensor FoV to be reduced (Adafruit, 2018).

2.5 MPU 9250

The MPU-9250, delivered in a 3x3x1mm QFN package, is the world's smallest 9-axis Motion-Tracking device and incorporates the latest InvenSense design innovations, enabling dramatically reduced chip size and power consumption, while at the same time improving performance and cost. The MPU-9250 Motion-Tracking device sets a new benchmark for 9-axis performance with power consumption only 9.3μA and a size that is 44% smaller than the company's first-generation device. Gyro noise performance is 3 times better, and compass full-scale range is over 4 times better than competitive offerings(Mahyad Komary et al. 2022).

The MPU-9250 is a System in Package (SiP) that combines two chips: the MPU-6500, which contains a 3-axis gyroscope, a 3-axis accelerometer, and an onboard Digital Motion Processor™ (DMP™) capable of processing complex Motion-Fusion algorithms; and the AK8963, the market leading 3-axis digital compass (Komarizadehasl et al. 2022). Improvements include supporting the accelerometer low power mode with as little as 6.4μA of and it provides improved compass data resolution of 16-bits (0.15 μT per LSB) (InvenSense 2014). On Figure 6 schematic of this sensor can be seen.



Figure 6. Schematic of accelerometer sensor(InvenSense 2014).

3 COMMUNICATION WAYS

While many sensors use digital and analog ports for uploading the measured data to the microcontroller, some sensors use the inter-integrated circuit (i2c) protocol. This is a protocol that allows multiple “slave” digital integrated circuits (sensors) to communicate with one or more “master” chips (arduino). Like the serial peripheral interface (spi) which is only intended for short-distance communications within a single device. The ultrasonic sensor and dht22 have been connected to the arduino's digital ports. The laser and the accelerometer had to be connected to i2c port (scl, sda) on the board.

All the different types of ranging circuits have been connected and glued together, so data from all 3 of them would be measured almost simultaneously on the static experiment. A different circuit had to be made for the accelerometer, in order to perform the dynamic experiment. Finally, 2 different codes were written on the Arduino platform and uploaded to the board via a usb cable. In addition, a Raspberry Pi which is a small size Linux-based computer that can be connected to Arduino microcontrollers, was used as the wireless file server in this study (Komarizadehasl, Lozano Galant, et al. 2022b). This way, the operator can access the Arduino codes for modifying or upgrading purposes (Komarizadehasl, Lozano Galant, et al. 2022a). To save and acquire provided data of the accelerometers, a python code was written to save the acquisition data on the Raspberry Pi memory card. For getting the main characteristics of these sensors, a few dynamic and static tests have been carried on.

4 STATIC EXPERIMENT

The device was tested against for the purpose of same measurement against different materials. In the static experiment, tests with and without extreme ambient light has been done for getting the distance from the big book. For the one with the light bulb, the temperature sensor has been moved a bit far from the source of the light and heat. The reason was that the excruciating heat coming from the light bulb would not harm the sensor. standard deviations driven from the performed tests has been illustrated. On Table 1 ranging result of same experiment under different circumstances has been shown.

Table 1. Results of ranging experiments.

Sensors	Thick book	White paper	Black paper	Tissue	Transparent plastic cover	Extreme ambient light
Ultra	0.61	1.87	1	352	0.7	3.23
Laser	2.5	2.67	7.18	4.66	5.46	3607

It should be mentioned that the ultrasonic sensor which was the chipset sensor and the easiest one to install, had shown better performances compare to the laser ones. On down side, this sensor needs 5v interaction digital ports and needs at least 4 volts for its full functionality. The only problem with this sensor could be its data providing speed. Although the laser has a faster rate (50Hz data production), this sensor has a frequency of only 20Hz. In other words, this sensor can provide up to 20 data each second. The biggest problem with the ultrasonic sensors would be their dependence on the ambient temperature and humidity. Since the speed of sound changes from an environment to another. This sensor needs the accurate speed of sound for its calculations. The proposition of this paper would be using the ultrasonic sensor with a laser sensor if there was the probability of a changing temperature or of an extreme ambient light. Using the first laser sensor or the second one is due to what range and circumstances the experiment may experience.

5 DYNAMIC EXPERIMENT

For testing the accelerometer sensor and its reliability, an experiment has been implemented. With a dynamic jack, a sinus signal has been programed and the vibrations had been saved by the accelerometer. This jack can shake its bottom plate as was programmed. The instructions to the hydraulic jack was to make a wave with a fixed frequency 5 hertz (5 complete waves in one second). The movement of the jack was to go up to 0.1 millimeter up and -0.1 millimeter down from its null axis to make a sinus wave. With a very simple two time differential, the acceleration equation could be calculated.

$$y = d * \sin(\omega * t + \varphi) \quad (1)$$

$$\omega = 2 * \pi * f \quad (2)$$

In the above equation y is the displacement in time t, d is the maximum allowed movement of the jack in each cycle, ω is the angular frequency and f is the set frequency which equal to 5Hz and φ is the phase constant. On the equ.3, acceleration has been calculated from the equ.1 and equ.2. this was done by getting the second order derivative of the equ.1. By putting all the data in the equ.3 the maximum acceleration was calculated as $10.4352 \text{ g} * 10^{-3} \text{ m/s}^2$.

$$a = \frac{d^2 * y}{dt^2} = \ddot{y} = -d * \omega^2 * \sin(\omega * t + \varphi) \quad (3)$$

The very first faced problem in this experiment was that the sensor could not record data or if recorded, the data were messy. It was deduced that the sensor had to be glued to the bottom plate of the jack for getting accurate information. The second problem was that the written python code could save only 120 data per second while the sensor was reporting more than 300 data per second. Although by using a serial port commercial software on the computer it could have been possible to save data with the same speed of their production. Since here getting the accurate time of capture was vital, it was obligatory to use python to attach the provided data with their corresponding time. To tackle this problem, the speed of data capture had to be dialed down, so the python could get and save them. To be on the safe side the speed of capture had been set on 84Hz.

The other unexpected issue that this project faced was that, though this sensor had been calibrated in the company, it had a constant number added to all provided data which from now here it would be named as the white noise. As on the Figure 7a it has been illustrated, the averaged data is around -50milig while they had to fluctuate around zero. This -50milig was considered as the white noise of this sensor. In order to measure this correctly, the average of 10000 set of data in a vibration free test has been calculated. For this sensor the white noise had been calculated as -49.8535 milig. By removing this amount from the provided accelerations, the values had been pulled up where they needed to be. The data were clearer and more understandable when this white noise had been removed. This improvement can be seen on Figure 7b.

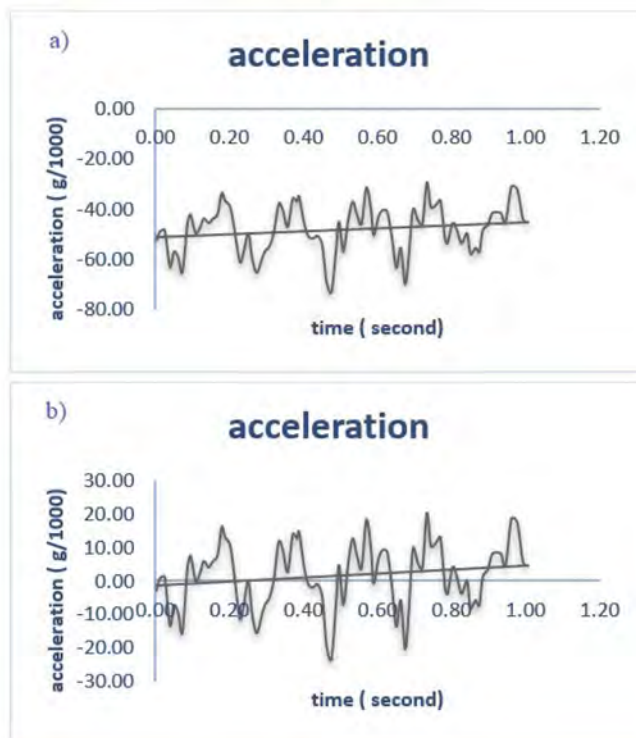


Figure 7. 7a shows Acceleration, Time diagram with white noise & 7b shows Acceleration, Time diagram without the white noise.

6 CONCLUSIONS

Notwithstanding that the laser sensors did not have as good results as the ultrasonic one, they can be useful as well. They are smaller, they are lighter and faster and have noise-free technology (no noise can enter from the wires). Moreover, they work independent of the temperature of their testing situation. Best results would only appear if an ultrasonic sensor (attached to its temperature and humidity sensor) be used alongside of a Laser sensor. They can cover the downsides of each other and provide accurate, useful set of data.

As on the Figure 7b it is visible the sinus wave conducted from the accelerometer is quite close with the expected behavior. As it is observable the sinus wave is fluctuating about 10.5 milig from its average. As it was calculated on the last section the graph should have had a 10.453 milig fluctuation. It is quite notable to see that they have worked out almost the same.

On the Figure 7b the filtered data from the 5Hz experiment has been shown. As it can be seen, the result is not so accurate, for the fluctuation has other unexpected data or noises as well. In the future works, filters must be applied to delete the unwanted data and ambient noises which may have entered in to this experiment unwantedly.

ACKNOWLEDGEMENTS

The authors are indebted to the Spanish Ministry of Economy and Competitiveness for the funding provided through the research project BIA2017-86811-C2-1-R directed by José Turmo. This project was funded with FEDER funds. Authors are also indebted to the Secretaria d' Universitats i Recerca de la Generalitat de Catalunya for the funding provided through Agaur (2017 SGR 1481). It is also to be noted that funding for this research has been provided for MR. Seyedmilad Komarizadehasl by Agencia Estatal de Investigación del Ministerio de Ciencia Innovación y Universidades grant and the Fondo Social Europeo grant (PRE2018-083238).

REFERENCES

- Adafruit. 2018. "STMicroelectronics, VL53L1X - A New Generation, Long Distance Ranging Time-of-Flight Sensor Based on ST's FlightSense™ Technology." <https://www.st.com/resource/en/datasheet/vl53l1x.pdf>.
- InvenSense, TDK. 2014. "MPU-9250, Nine-Axis (Gyro+ Accelerometer+ Compass) MEMS MotionTracking™ Device."
- Kamal, AM, and SH Hemel. 2019. "Comparison of Linear Displacement Measurements Between A Mems Accelerometer and Hc-Sr04 Low-Cost Ultrasonic Sensor." *ieeexplore.ieee.org*. <https://ieeexplore.ieee.org/abstract/document/8934569/>.
- Komarizadehasl, Seyedmilad et al. 2022. "A Novel Wireless Low-Cost Inclinometer Made from Combining the Measurements of Multiple MEMS Gyroscopes and Accelerometers." *Sensors 2022, Vol. 22, Page 5605* 22(15):5605. <https://www.mdpi.com/1424-8220/22/15/5605/htm> (February 24, 2023).
- Komarizadehasl, Seyedmilad, Fidel Lozano Galant, et al. 2022a. "Development of an Accurate Low-Cost Device for Structural Vibration Acquisition." *IABSE Symposium Prague 2022 Report: Challenges for Existing and Oncoming Structures*: 1–6.
- Komarizadehasl, Seyedmilad et al. 2022. "Low-Cost Accurate Acceleration Acquisition Sensor." *Bridge Safety, Maintenance, Management, Life-Cycle, Resilience and Sustainability: Proceedings of the Eleventh International Conference on Bridge Maintenance, Safety and Management (IABMAS 2022), Barcelona, Spain, July 11-15, 2022*: 803–10.
- Komarizadehasl, Seyedmilad, Fidel Lozano Galant, et al. 2022b. "Resolution Improvement of Low-Cost MEMS Accelerometer by Aligning Simulations Sensors." *IABSE Symposium Prague 2022 Report: Challenges for Existing and Oncoming Structures*: 1–6.
- Komarizadehasl, Seyedmilad et al. 2022. "Using Few Accelerometer for Improving the Resolution and Accuracy of Low-Cost Accelerometers." *Bridge Safety, Maintenance, Management, Life-Cycle, Resilience and Sustainability: Proceedings of the Eleventh International Conference on Bridge Maintenance,*

- Safety and Management (IABMAS 2022)*, Barcelona, Spain, July 11- 15, 2022: 1575–79. <https://upcommons.upc.edu/handle/2117/371037> (September 29, 2022).
- Komary, M., S. Komarizadehasl, G. Ramos, and V. Torralba. 2022. “Full Review of Low-Cost Electronics Implemented in Structural Health Monitoring Applications for Bridges.” In *Bridge Safety, Maintenance, Management, Life-Cycle, Resilience and Sustainability*, London: CRC Press, 980–85. <https://www.taylorfrancis.com/chapters/edit/10.1201/9781003322641-117/full-review-low-cost-electronics-implemented-structural-health-monitoring-applications-bridges-komary-komarizadehasl-ramos-torralba> (February 24, 2023).
- Komary, Mahyad et al. 2023. “Low-Cost Technologies Used in Corrosion Monitoring.” *Sensors* 2023, Vol. 23, Page 1309 23(3):1309. <https://www.mdpi.com/1424-8220/23/3/1309/htm> (February 24, 2023).
- Komary, Mahyad, Seyedmilad Komarizadehasl, Gonzalo Ramos Schneider, and Victor Torralba Mendiola. 2022. “Developing and Validation of an Inclinometer Sensor Based on Fusion of a Magnetometer, an Accelerometer and a Gyroscope Sensor for SHM Applications.” *Bridge Safety, Maintenance, Management, Life-Cycle, Resilience and Sustainability: Proceedings of the Eleventh International Conference on Bridge Maintenance, Safety and Management (IABMAS 2022)*, Barcelona, Spain, July 11- 15, 2022: 1607–11. <https://upcommons.upc.edu/handle/2117/371039> (September 14, 2022).
- Liu, Thomas. 2013. *arduino.ru Digital-Output Relative Humidity & Temperature Sensor/Module DHT22 (DHT22 Also Named as AM2302) Capacitive-Type Humidity and Temperature Module/Sensor*. <http://www.datasheet4u.com>.
- Pathak, B, P Kumar, A Sharma, and R Kumar. 2019. “Earthquake Detector Using Arduino Uno.” <http://122.252.232.85:8080/jspui/handle/123456789/22911>.
- Patil, TS, SR Khedkar, and MS Jadhav. 2019. “Internet of Things (IoT) Based Warehouse Monitoring and Control Interface Implementation.” <https://www.academia.edu/download/60437773/IRJET-V6I678520190830-121843-gk14fp.pdf>.

On the utilization of multiple information for the integrity management of deteriorating systems

G. Costa

Politecnico di Milano, Milan, Italy

BAM Federal Institute for Materials Research and Testing, Berlin, Germany

M.P. Limongelli

Politecnico di Milano, Milan, Italy

Faculty of Engineering, Lund University, Lund, Sweden (Lisa Meitner guest professor)

S. Thöns

Faculty of Engineering, Lund University, Lund, Sweden

BAM Federal Institute for Materials Research and Testing, Berlin, Germany

ABSTRACT: Recent years' publications have shown how valuable information can be in the integrity management of civil structures. Monitoring systems increase the knowledge about the structural state, improving the prioritization of the interventions, and the selection of optimal maintenance strategy and thereby allowing for budget optimization and risk minimization. This paper investigates the effect of multiple information on integrity management throughout a deteriorating structure's life cycle. Pre-posterior analysis and the concept of the Value of Information (VoI) are used to quantify the benefit multiple information provide in structural integrity management. Multiple information (e.g., local information about the condition state of the several components of a system) and actions are associated with an expected utility. Optimization is performed by determining the lowest total expected cost of the maintenance strategy for a given set of information.

1 INTRODUCTION

Decision-making is a crucial aspect of civil and infrastructure engineering due to the large social, economic, and structural consequences decisions can result in. Several factors may undermine the performance of civil structures as the deterioration effects, the intervention quality, the extreme load conditions, and environmental phenomena. Furthermore, these factors are affected by significant uncertainties and cannot be quantified effectively. Monitoring systems and techniques may reduce such uncertainties and increase the knowledge about the structural performance of a system. Collecting and analyzing information entails a cost that should be compensated by the benefit achieved by their use in integrity management. In this context, an optimization process may be performed by determining if, when, and which type of information is optimal to collect. This optimization process requires the utilization of the concept of Value of Information (VoI) from the Bayesian decision theory. Schlaifer and Raiffa (1961) formulated the VoI in the Bayesian context providing the base for the theoretical framework and many applications, see e.g., (Zhang *et al.*, 2021) for a review. The VoI provides a quantification of the expected benefit, e.g., in terms of saved expected budget, which information may provide in decision-making. Information may be obtained by destructive and non-destructive tests, inspections, and by deploying sensors on a structure. Multi-component deteriorating systems, multi-sensor information integration, and sensor arrangement optimization are investigated e.g., in (Long, Döhler and Thöns, 2020) and (Malings and Pozzi, 2016). However, in both papers, the

case studies only account for serial systems neglecting the system redundancy, the capacity to redistribute the loads, and the component behavior characteristics.

This paper extends the available VoI framework for engineering structures to account for multi-component measurements in the evaluation of the optimal maintenance strategy of a deteriorating structural system, accounting for its redundancy and the correlation among the components. A novel deterioration model is adapted from the literature and a new description for the information model is formulated and implemented. Furthermore, VoI is evaluated at several times during the service life of a deteriorating structure and accounting for different numbers of monitored components. The value of obtaining multi-component measurements rather than a single-component measurement is evaluated in terms of how it affects the selection of the optimal maintenance strategy. In Section 2, a generalized system state model is reported and discussed. The initial resistance, deterioration, load, and structural model are defined. Section 3 encompasses a novel description of the information model when multiple information on the structural state is obtained. Section 4 reports the decision scenario and utility model. Section 5 describes the analytical formulation which is later implemented in the case study in Section 6. Finally, the conclusions are drawn in Section 7.

2 SYSTEM STATE MODEL

A structural system is typically characterized by its capacity, i.e., initial resistance that decreases over time due to deterioration effects, and demand, i.e., effect of the load that will be herein addressed as load. Following the semi-probabilistic approach, the design resistance of a structure may be described as:

$$R_0 = \gamma_S \cdot \gamma_R \cdot A \cdot R_{mat} = \gamma \cdot A \cdot R_{mat} \quad (1)$$

where γ_S is the load safety factor for one dominating action, γ_R is the safety factor for the material, A represents the geometrical properties of the system (cross-section area, inertia etc.), and R_{mat} corresponds to the material strength (Thöns, 2022). The deterioration description accounts for degradation and damage. Degradation evolves gradually over time (e.g. due to corrosion, fatigue, crack growth, etc.) and damage corresponds to a shock deterioration process (e.g. due to earthquakes, floods, etc.). In reference (Mori and Ellingwood, 1993), the authors introduce a general modeling of deterioration proposing different parameters for the deterioration type and rate. Long, Döhler and Thöns (2020) apply this model in the analyses of an articulated structure and simulate different types of deterioration encompassing diffusion-controlled deterioration, corrosion, and fatigue as well as sulfate attack induced concrete deterioration. Furthermore, Kamariotis, Chatzi and Straub (2023) implement an empirical deterioration model to consider shock deterioration processes. In this study, the overtime resistance of a structure is defined as:

$$R(t) = R_0 \cdot (1 - \alpha(t - T_0)^\beta - \sum_{i=1}^{N(t)} D_i) \quad (2)$$

where the first term $\alpha(t - T_0)^\beta$ represents the gradual damage (Mori and Ellingwood, 1993), and the second term $\sum_{i=1}^{N(t)} D_i$ represents the shock deterioration processes modelled as a homogeneous Poisson process (Kamariotis, Chatzi and Straub, 2023). In the equation α is the annual deterioration rate, t is the time, T_0 is the deterioration initiating time, β indicates the deterioration type, $N(t)$ is the number of shock events in a year, and D_i is the amount of a shock deterioration. Herein two system states are considered: state X_1 indicating the failure and state X_2 indicating a safe state (Thöns, 2018). The limit state equation can be written as:

$$X_1: g_X = M_R \cdot R(t) - M_S \cdot S \leq 0 \quad (3)$$

$$X_2: g_X = M_R \cdot R(t) - M_S \cdot S > 0 \quad (4)$$

where M_R and M_S represent the resistance and load model uncertainties, $R(t)$ is the resistance defined by eq. (2) and S is the load considered constant in time. The load description, the resistance and the load model uncertainties are provided by the JCSS (JCSS, 2001). The probability of a failure event $P(X_1)$, and the probability of a safe state $P(X_2)$, i.e., the reliability, may be calculated with Eq. (3) and Eq. (4). When dealing with multi-components and multi-information systems, the structural system performance can be described through Daniels systems (DS) models. The DS enables the modeling of a structural system taking into consideration the system's redundancy, the capacity to redistribute loads, and the component behavior (ductile or brittle). The DS model is a parallel system representative of a wide range of redundant structures with an initial resistance R_0 , a current resistance $R(t)$ that depends on the deterioration level, and load S (Thöns, 2018). The initial resistance $R_0 = R(t=0)$ is fixed through a design iteration process, i.e., setting a target reliability $P_t = 10^{-5}$ and adjusting R_0 such that $P(X_2(R_0)) = P_t$. For a ductile DS with n components, the system reliability may be written as:

$$P(X_2): P\left(g_X = \sum_i^n M_{R_i} \cdot R_i(t) - \sum_i^n M_{S_i} \cdot S_i > 0\right) \quad (5)$$

where the resistance $R_i(t)$, the load S_i , and the model uncertainties M_R and M_S refer to the i -th structural component. For a brittle DS, system reliability can be written as:

$$P(X_2) = P\left(g_X = \max((n - i + 1) \cdot m_{R_i} \cdot r_i(t)) - \sum_i^n M_{S_i} \cdot S_i > 0\right) \quad (6)$$

with $m_{R_1} \cdot r_1(t) \leq \dots \leq m_{R_n} \cdot r_n(t)$

where m_{R_i} and $r_i(t)$ are individual realizations of the resistance model and resistance distributions and $R_i(t)$ and they are used for the maximization process, equivalent to an intersection set operator (Gollwitzer and Rackwitz, 1990). The structural properties, the deterioration, and the load on the single components of a multi-component system may be dependent, i.e., correlated. Indeed, the components' material resistance $R_{i,mat}$ is usually correlated since it depends on the material production and fabrication. Load on each component is fully correlated and depends on its structural properties, e.g., component stiffness. The annual degradation rate may not be correlated for localized degradation (e.g., degradation induced by fatigue) or may be fully correlated for system degradation (e.g., corrosion due to an aggressive environment). The damage due to shock events, e.g. earthquakes, floods, and fire, may be correlated if the event affects the whole structure or may not if it affects only some components (e.g. plastic hinges in seismically designed structures). Furthermore, model uncertainties' correlation is high in the case the same model for all the components is used.

3 INFORMATION MODEL

Information about the structural performance usually enhances the knowledge of the structural state thereby supporting integrity management and budget optimization. Information on the system or component resistance and load may be obtained directly or indirectly by measuring quantities that are related to them. For example, the load may be estimated indirectly from the measurement of the deflection it causes, when their relationship is known.

Taking basis in the definition and the determination process of model uncertainties (JCSS, 2001), measurements may be modeled as realizations of model uncertainties, i.e. normalized model-predictions, affected by measurement uncertainty. Furthermore, this modeling accounts for the fact that the structural probabilistic model cannot be usually completely determined with available measurement strategies (Thöns, 2018). For each component of a multi-component system, measurements can be modeled on the component model resistance and load uncertainty, i.e., with the realizations m_{R_i} and m_{S_i} , affected by the measurement uncertainty. When a measurement of the structural state has been obtained, the posterior probability of failure can be recalculated. The updated posterior probability of failure for a single component system is:

$$X_1|m_R: g_{X|m_R} = M_U \cdot m_R \cdot R(t) - M_S \cdot S \leq 0 \quad (7)$$

where m_R is the measurement obtained by the monitoring system and M_U is the measurement uncertainty. As indicated in the introduction, a contribution of this paper lies in the expansion of Eq. (7) to multi-component systems and multiple measurements. Measurements may be obtained on one or more components and the probability of failure of the system can be updated. For a redundant multi-component system, the posterior probability of failure can be written as in Eq. (8) for ductile component behavior, and as in Eq. (9) for brittle component behavior.

$$X_1|\mathbf{O}_R: g_{X|\mathbf{O}_R} = \sum_i^n O_{R_i} \cdot R_i(t) - \sum_i^n M_{S_i} \cdot S_i \leq 0 \quad (8)$$

$$X_1|\mathbf{O}_R: g_{X|\mathbf{O}_R} = \max((n - i + 1) \cdot o_{R_i} \cdot r_i(t)) - \sum_i^n M_{S_i} \cdot S_i \leq 0 \quad (9)$$

where \mathbf{O}_R includes the resistance model uncertainties M_{R_i} and measurements m_{R_i} (realizations of M_R) affected by a measurement uncertainty M_U . o_{R_i} is the individual realization of the i^{th} distribution in \mathbf{O}_R that are ordered as in Eq. (6), i.e. $o_{R_1} \cdot r_1(t) \leq \dots \leq o_{R_i} \cdot r_i(t) \leq \dots \leq o_{R_n} \cdot r_n(t)$. In the case a measurement is obtained only on the first component, the terms in Eq. (8) and (9) can be written as vectors as follows:

$$\mathbf{O}_R = \begin{Bmatrix} M_U \cdot m_R \\ M_{R_2} \\ M_{R_3} \\ \vdots \end{Bmatrix}, \quad \mathbf{R}(t) = \begin{Bmatrix} R_1(t) \\ R_2(t) \\ R_3(t) \\ \vdots \end{Bmatrix}, \quad \mathbf{M}_S = \begin{Bmatrix} M_{S_1} \\ M_{S_2} \\ M_{S_3} \\ \vdots \end{Bmatrix}, \quad \mathbf{S} = \begin{Bmatrix} S_1 \\ S_2 \\ S_3 \\ \vdots \end{Bmatrix}$$

4 DECISION SCENARIO AND UTILITY MODEL

The decision scenario adopted in the analysis accounts for five distinct actions, namely a_0 the do-nothing action, a_1 the strengthening action, a_2 the repair action, a_3 the load reduction action and a_4 the consequence reduction utility. Along with (Thöns, 2022), a_1 , a_2 and a_3 are system state actions, i.e. enhancing the structural state and reliability, whereas a_4 is a utility action, i.e. affecting consequences and functionality of the structural system. Each action is associated with an implementation uncertainty, which reflects the quality of the implemented intervention. Therefore, an implementation state, i.e., posterior to the action $X_1(t)|a_k, Y_k$, can be defined accounting for the full, partial or failed action implementation. Implementation uncertainty is exemplarily formulated in (Thöns, 2022). Table 1 illustrates the action types, effects, cost, and implementation uncertainty. The updated limit state equations are reported for the simple case of a single-component system. Information can be considered in these equations by substituting the model distribution M_R by its realization m_R and related measurement uncertainty M_U as in Eq. (7).

The strengthening action a_1 is representative of the case in which an action aiming to enhance the structural resistance is performed. The action effect is quantified to an increase of 50% of the resistance (e.g., Fiber Reinforced Polymers (FRP) strengthening on the resisting moment of a beam). The repair action a_2 results in the restoration of the initial resistance at the time of the action implementation (t_a). The load reduction action a_3 is assumed to result in a constraint of 50% of the acting load, e.g., by limitation of the traffic. The consequence reduction action a_4 is assumed to reduce the cost of failure by 15%. For simplicity reasons, the cost of failure c_F is set equal to 1. Action costs, information costs, and therefore, the utilities are calculated as a percentage of c_F . The cost of a single measurement, i.e., information, is set equal to 0.1 % c_F .

5 DECISION ANALYTICAL FORMULATION

The pre-posterior decision analysis is performed at different times to investigate how the VoI varies within the structure's service life. The posterior and pre-posterior utilities have been

Table 1. Action types, descriptions, effects, costs, and implementation uncertainties.

Action type	Description	Action effect	Cost (% C_F)	Implementation uncertainty
a_0	Do nothing	-	-	-
$g_{X_1(t) a_0} = M_R \cdot R(t) - M_S \cdot S \leq 0$				
a_1	Strengthening	$1.5 R$	2%	$Y_1 = Tr(0.95,1.05,1.10)$
$g_{X_1(t) a_1, Y_1} = M_R \cdot 1.5 \cdot R(t) \cdot Y_1 - M_S \cdot S \leq 0$				
a_2	Repair	$R(t = t_{a2}) = R_0$	10%	$Y_2 = Tr(0.90,0.95,1.00)$
$g_{X_1 a_2, Y_2} = M_R \cdot R_0 \cdot Y_2 - M_S \cdot S \leq 0$				
a_3	Load reduction	$S/2$	1.0%	$Y_3 = N(1,0.1)$
$g_{X_1(t) a_3, Y_3} = M_R \cdot R(t) - M_S \cdot S/2 \cdot Y_3 \leq 0$				
a_4	Consequence reduction	$c_{F,red} = 0,85$	1.0%	$Y_4 = Tr(0.85,0.95,1.05)$
$g_{X_1(t) a_4, Y_4} = M_R \cdot R(t) - M_S \cdot S \leq 0 c_{F,red} = 0,85 \cdot c_F \cdot Y_4$				

formulated to include the cost of the information as proportional to the number of measurements. Thereby, posterior and preposterior utilities can be compared in the evaluation. The extensive analytical formulation from (Schlaifer and Raiffa, 1961) is adopted in the analysis as allowing for the calculation of the posterior utilities and total expected costs which are later used in the exemplary case study. The consideration of system state actions and implementation uncertainties in the analysis led to an equivalence issue between the two decision analytical formulations from the literature, namely the normal and the extensive formulations. The analysis highlighted that the preposterior utility equivalence holds for utility actions but not for system-state actions. Therefore, an adjustment factor $r_E(X_l, Y_k, a_k)$ has been derived equal to $\frac{P(X_l|a_k, Y_k)}{P(X_l)}$. Eq. (12) includes such adjustment factor for the calculation of the preposterior utility. Table 2 reports the analytical formulation which is adopted in the analysis.

Table 2. Analytical formulation.

	Objective function
Prior	$U_{prior} = \max_{a_k} E_{X_l a_k, Y_k} [u(X_l, a_k, Y_k)] =$ $= \max_{a_k} \sum_{X_l} P(X_l a_k, Y_k) \cdot u(X_l, a_k, Y_k) - c_{a_k}$ (10)
Posterior	$U_{post}(O_{i,j}) = \max_{a_k} E_{X_l O_{i,j}, a_k, Y_k} [u(X_l, a_k, Y_k)] =$ $= \max_{a_k} \sum_{X_l} P(X_l O_{i,j}, a_k, Y_k) \cdot u(X_l, a_k, Y_k) - c_{a_k} - n_i \cdot c_i$ (11)
Pre-posterior	$U_{pre-post} = \max_{a_k, i_i} E_{oi,j} \left[\max_{a_k} E_{X_l O_{i,j}, a_k, Y_k} [u(X_l, a_k, Y_k)] \right] \cdot r_{E(X_l, Y_k, a_k)} =$ $\max_{i_i} \sum_{O_{i,j}} P(O_{i,j}) \cdot \max_{a_k} \sum_{X_l} \left(\frac{P(X_l a_k, Y_k)}{P(X_l)} \cdot P(X_l O_{i,j}, a_k, Y_k) \cdot u(X_l, a_k, Y_k) \right) - c_{a_k} - n_i \cdot c_i$ (12)

Where X_l indicates the structural states, a_k indicates the action k , Y_k is the implementation uncertainty, c_{a_k} indicate the action cost, i_i is the information strategy characterized by n_i , number of monitored components and c_i , cost of the measurement on a single component, $O_{i,j}$

corresponds to the information set (including the measurements) relative to an information strategy i_s , and u is utility associated to a state and, in the case of an utility action, to the action effect and its implementation uncertainty. According to (JCSS, 2001), durability needs to be taken into account by imposing the survival condition (X_2) of the structure at the time of analysis. Therefore, when calculating the $P(X_1(t))$ at the time t of analysis, the condition of survival in the previous time steps ($t-t_{step}$) is considered as:

$$P(X_1(t)|X_1(t-t_{step})) = \frac{P(X_1(t))}{1 - P(X_2(t-t_{step}))} \quad (13)$$

VoI is a quantification of the benefit that information provides in integrity management. The evaluation of such benefit over the structural service life is performed by calculating a pre-posterior and a prior utility at the different steps of analysis. VoI can be calculated as the difference between the pre-posterior and prior utilities at the time t .

$$VoI(t) = U_{prepost}(t) - U_{prior}(t) \quad (14)$$

6 EXEMPLARY STUDY

The calculation of the VoI is performed for an existing structure deteriorating over time due to degradation and damage effects. The structural system is modeled as a DS with five parallel components, e.g., a bridge with five piers, and the number of monitored components is made to vary from one to five. In the first case, information is obtained on a single component, in the second case, information is obtained on two components, etc. In the analysis, the current resistance of the components is monitored. Each measurement is local and provides information on the component state. Therefore, the system current resistance is estimated accounting for the components' brittle and ductile behaviors. Moreover, actions are assumed to be implemented simultaneously to the five elements of the structure. These hypotheses are made as herein the parallel components of the DS are modeled with the same initial resistance and being affected by the same deterioration phenomena. Further studies may concentrate on the study of component actions of more complex structures. The several decision options are compared by their total expected cost being the cheapest selected as the optimal. The probabilistic models assumed in the analysis are based on (Thöns, 2022) and here presented in Table 3.

Table 3. Probabilistic models.

Variable	Mean	Variance	Distribution	Reference
Load S	1.0	0.2	Gumbel	E.g., (JCSS, 2001)
Load model uncertainty M_S	1.0	0.1	Lognormal	JCSS Probabilistic Model Code Part 3.9 (2001) (JCSS, 2001)
Resistance R_{mat}	1.0	0.05	Lognormal	Generic, (JCSS, 2001)
Resistance model uncertainty M_R	1.0	0.05	Lognormal	(JCSS, 2001) Part 3.9
Measurement uncertainty M_U	1.0	0.3	Normal	(Thöns, 2022)
Annual degradation rate α	Medium $7.6 \cdot 10^{-5}$	0.001	Lognormal	(Kamariotis, Chatzi and Straub, 2023)
Jumps number $N(t)$	$0.04 t$	-	Poisson	(Kamariotis, Chatzi and Straub, 2023)
Shock deterioration D_i	$E(R_0)/50$	0.25	Lognormal	Generic
Deterioration type β	$\beta = 1$ corresponds to the most applied corrosion models			(Mori and Ellingwood, 1993)
Safety factor γ_S	1.5 for one dominating action			(EN 1990: Eurocode - Basis of structural design, 2002)
Safety factor γ_R	1.0 for steel			(EN 1990: Eurocode - Basis of structural design, 2002)

Several considerations on the components' properties, load conditions, and deterioration phenomena are made in the analysis. The components, the load S is fully correlated and distributes evenly to the parallel components.

The components' material resistance R_{mat} is assumed to be fully correlated as the parallel components are equal, degradation (α) and damage ($N(t)$, D_i) are assumed as fully correlated since in the analyzed parallel structure corrosion and shock events are assumed to affect equally. The correlation of the model uncertainties is modeled with 0 and 1 as hardly any such considerations can be found in the scientific literature. In this analysis measurement uncertainty is assumed not to be correlated for simplicity reasons. In the first part of the analysis, three times during the service life of a five non-correlated component structure are investigated, namely the construction year ($t = 0$), half of the service life ($t = 25$ years), and the end of the service life ($t = 50$ years). Figure 1(a), (b), and (c) present the total expected costs at the three times in the case a single sensor is installed whereas Figure 1(d) presents the case in which two measurements are obtained on the structure at $t = 25$ years. The optimal action given one or two resistance measurements is identified as the one with the lowest total expected cost and consequences. At time 0, for any measurement of one component resistance, the optimal action is a_0 (do nothing). This is because at the beginning of the service life and in the case component resistance measurements are not correlated, the other components can fully compensate the load demand maintaining a low system probability of failure. The other actions involve implementation costs, which are not compensated by their effect on risk reduction. When the service life approaches 25 years, the optimal action depends on the obtained resistance measurement varying from the load reduction action to the consequence reduction and do-nothing action when a high resistance value is measured. At $t = 50$ years, the repair action, and the consequence reduction action are found to be the optimal actions, respectively, for low and high resistance measurements. In Figure 1(d), the case of two monitored structural components (over five) is considered. The combination of two or more measurements may induce the selection of a different action with respect to the case when a single measurement is available.

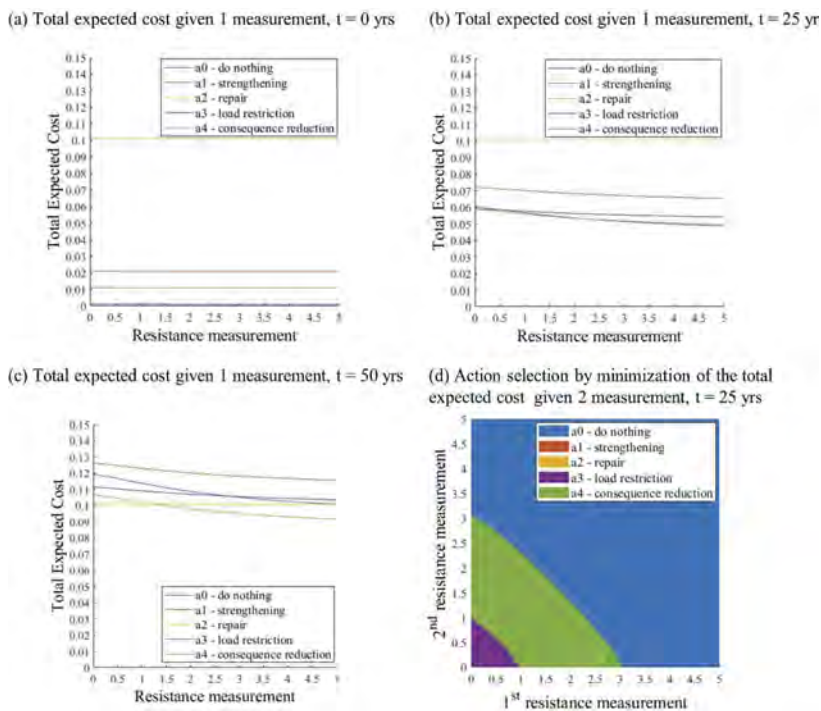


Figure 1. Total Expected cost given one measurement (a),(b),(c) and two measurements(d) at $t = 0$, 25, and 50 years.

This is the case where a low resistance measurement is obtained on the first component and a high one is obtained on the second component. The second measurement leads to the selection of a different action and thereby results in a higher VoI. The second part of this analysis aims to analyze VoI throughout the service life of a structure when different assumptions on the measurement's correlation, i.e., model uncertainty realization correlation, and DS component behaviors are made. This analysis aims to analyze how valuable information is throughout the structure's service life.

In Figure 2(a), a fully correlated ductile system is analyzed, i.e., resistance, deterioration, load, and the collected measurements are assumed to be fully correlated. In Figure 2(b), the same resistance, load, and damage characteristics are assumed for the DS whereas a non-correlated resistance model uncertainty is considered. Along with the deterioration processes and the decrease of the resistance in time, the VoI increases. It is found that at the very beginning of the structural service life (in this case before five years) measurements do not provide any support in the management. Later, in this case, after five years but before ten years, measurements do support the selection of the action, but their costs are not compensated by the risk reduction. Indeed, only after the first ten years, VoI has a positive value. Moreover, in the case of fully ductile and brittle correlated systems, it is found that monitoring a single component results more advantageous than monitoring several components accordingly to (Giordano *et al.*, 2020) . This is since the obtained measurements on the different components would reveal correlated measurements and therefore, the same action would be selected. On the contrary, when non-correlated components are assumed, a single component measurement provides optimal integrity management support in only a specific time interval. With the decrease of the structural capacity to due deterioration, a higher number of monitored components would provide optimal integrity management, e.g. in the case of the non-correlated brittle components the optimal management would be provided by no measurement in the first 10 years, 1 measurement in the range 10-13 years, 2 measurements in the range 13-17 years, 3 measurements in 17-20 years, 4 measurements in 20-25 years and successively by 5 measurements (one on each component).

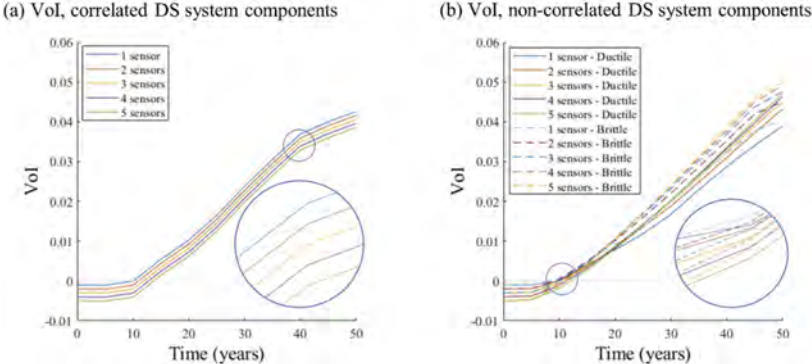


Figure 2. VoI for a full correlated DS (a), non-correlated DS with ductile or brittle components (b).

7 CONCLUSIONS

This paper presents the analysis of VoI throughout the service life of an idealized structural system. DSs are used to schematize a redundant structure with five components, e.g., a bridge with 5 piers, and a newly adapted deterioration model has been adopted in the analysis. Local information on one or more components of the structure is assumed to be obtained. The optimal action is selected by performing a minimization of the total expected cost. The decision scenario has been formulated for a wide range of actions including interventions enhancing the structural performance and interventions reducing the consequences of collapse. Information value analysis utilizing multiple measurements and system state actions in conjunction with a DS contributes to the novelty of the paper. Furthermore, the equivalence of the normal and extensive formulation has been stated. The results from the analysis show that the VoI increases throughout the service

life of the structure and that obtaining multiple information may not always be preferable. Indeed, in the case of fully correlated systems, a single measurement provides optimal management. On the contrary, in the case of non-correlated systems, it is found that a different number of measurements provide optimal management throughout the service life.

REFERENCES

- EN 1990: *Eurocode - Basis of structural design* (2002).
- Giordano, P. F. *et al.* (2020) 'Value of Information analysis for degrading engineering systems', *Proceedings of the 7th International Symposium on Life-Cycle Civil Engineering, IALCCE 2020*, (i), pp. 671–678. doi: 10.1201/9780429343292-87.
- Gollwitzer, S. and Rackwitz, R. (1990) 'On the reliability of Daniels systems', *Structural Safety*, 7(2–4), pp. 229–243. doi: 10.1016/0167-4730(90)90072-W.
- JCSS (2001) *Part 3.09 of the Probabilistic Model Code*. JCSS Joint Committee on Structural Safety.
- Kamariotis, A., Chatzi, E. and Straub, D. (2023) 'A framework for quantifying the value of vibration-based structural health monitoring', *Mechanical Systems and Signal Processing*, 184(September 2022), p.109708. doi: 10.1016/j.ymsp.2022.109708.
- Long, L., Döhler, M. and Thöns, S. (2020) 'Determination of structural and damage detection system influencing parameters on the value of information', *Structural Health Monitoring*. doi: 10.1177/1475921719900918.
- Malings, C. and Pozzi, M. (2016) 'Value of information for spatially distributed systems: application to sensor placement', *Reliab Eng Syst Saf*, 154. doi: 10.1016/j.res.2016.05.010.
- Mori, Y. and Ellingwood, B. R. (1993) 'Reliability-based service-life assessment of', 119(5), pp. 1600–1621.
- Schlaifer, R. and Raiffa, H. (1961) *Applied Statistical Decision Theory*. Boston: Harvard University Press.
- Thöns, S. (2018) 'On the Value of Monitoring Information for the Structural Integrity and Risk Management', *Computer-Aided Civil and Infrastructure Engineering*, 33(1), pp. 79–94. doi: 10.1111/mice.12332.
- Thöns, S. (2022) 'Structural assessment and expected utility gain', in *IPW22*, pp. 1–13.
- Zhang, W.-H. *et al.* (2021) 'Value of information analysis in civil and infrastructure engineering: a review', *Journal of Infrastructure Preservation and Resilience*, 2(1). doi: 10.1186/s43065-021-00027-0.



Taylor & Francis

Taylor & Francis Group

<http://taylorandfrancis.com>

SS3: Monitoring of structures for informed decision making
Organizers: A. Strauss & D.M. Frangopol



Taylor & Francis

Taylor & Francis Group

<http://taylorandfrancis.com>

Recent progress developing a rating framework for evaluating SHM for bridge scour

P.J. Vardanega, G. Gavriel & M. Pregolato

University of Bristol, Bristol, UK

ABSTRACT: Scour is a complex phenomenon and one of the most frequent causes of riverine bridge failures. Detecting scouring effects is a complex geotechnical/structural/hydraulic engineering challenge. Incorporating more risk-based approaches into scour assessment frameworks may allow for enhancements over current processes which remain reliant on visual inspection to detect bridge scour. Scour detection and monitoring is inherently a ‘damage detection’ task. A wide range of technologies for scour monitoring are available which may partially replace or supplement visual inspection activities. Recently, a new rating framework has been presented to assist engineers to assess the relative merits of different sensor technology options on scour-prone bridges. In this paper, the development of this framework is reviewed and compared with other scour rating frameworks; suggestions for future development and calibration are proposed.

1 INTRODUCTION

1.1 *Bridge scour*

Scour is a complex phenomenon and a frequent reason for bridge failures across the world (e.g. Briaud *et al.* 2011, Maddison 2012, Prendergast & Gavin 2014, Dikanski *et al.* 2017, Ettema *et al.* 2017, Kerényi & Flora 2019). Scour effects on individual bridges may change with time due to changes in flows and flooding levels (cf. Dikanski *et al.* 2017). Detecting scouring effects is a complex forensic engineering challenge (see Vardanega *et al.* 2021 for a recent review). Incorporating more risk-based approaches into scour assessment frameworks may allow for enhancements over current processes which remain largely reliant on visual inspection to detect bridge scour (cf. Pregolato *et al.* 2021). Maroni *et al.* (2022) highlighted the need for probabilistic assessments of scour risk along with integration of ‘quasi-real-time’ monitoring data into scour risk management frameworks.

The categorization system for bridge Structural Health Monitoring (SHM) proposed by Webb *et al.* (2015) (summarized in Figure 1) includes the following five categories: (i) ‘Anomaly Detection’; (ii) ‘Sensor Deployment Studies’; (iii) ‘Model Validation’; (iv) ‘Threshold Check’ and (v) ‘Damage Detection’. These categories are presented in order of increasing complexity but arguably also of increasing value to the asset owner (Webb *et al.* 2015). Scour detection and monitoring is inherently a ‘damage detection’ task. Damage detection is a difficult challenge for many SHM systems, but it is necessary to prevent collapses of bridges over waterways in the case of scour.

1.2 *Rating systems*

Figure 2 shows some of the key considerations when specifying new SHM systems (Vardanega *et al.* 2016). Ahlborn *et al.* (2010a) and Vaghefi *et al.* (2012) offer a methodology to determine the efficiency of different remote sensing options for assessing bridge condition indicators (see also Ahlborn *et al.* (2010b) for a review of various remote sensing options for bridge condition detection). Vardanega *et al.* (2016) proposed a rating system to determine if a planned SHM system

would deliver value to a bridge asset owner. The framework from Vardanega *et al.* (2016) was in part inspired by the framework proposed to assign geotechnical reduction factors presented in Poulos (2004) and the system to assess the value of remote sensing technologies from Vaghefi *et al.* (2012) (see also Ahlborn *et al.* 2010a). The framework from Vardanega *et al.* (2016) was tested using information from five previous monitoring deployments (see Table 1, see also Nepomuceno *et al.* (2019, 2022) who used the framework for further case studies).

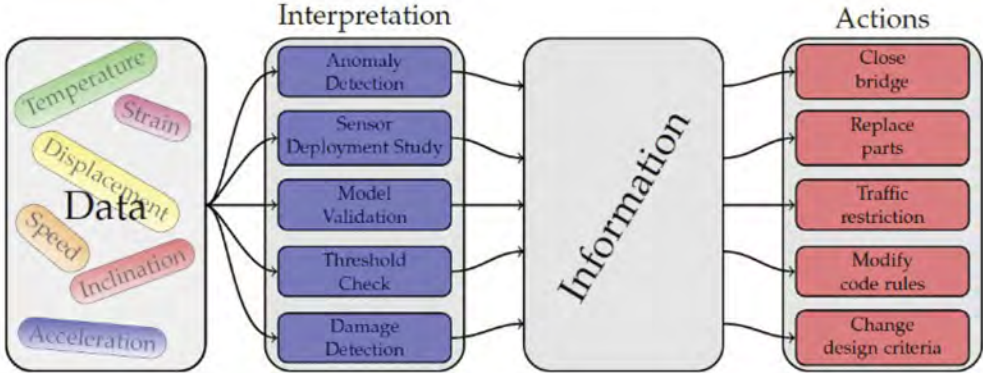


Figure 1. Categories of SHM systems (taken from Webb *et al.* (2015) and used under the terms of the cc by 4.0 license).

Table 1. Summary of Bridge Projects evaluated in Vardanega *et al.* (2016) using the framework (see also Nepomuceno *et al.* 2022).

Bridge Structure	References	Outcome from Vardanega <i>et al.</i> (2016) rating
Walton Bridge	Middleton <i>et al.</i> (2014) Webb (2014)	Project unlikely to yield value to asset owner/ manager
Nine Wells Bridge	Hoult <i>et al.</i> (2009) Schwamb (2010) Webb (2014) Webb <i>et al.</i> (2017)*	Project may yield value to the asset owner/manager
Humber Bridge (Hessle Anchorage)	Hoult <i>et al.</i> (2008) Fidler <i>et al.</i> (2021)*	Project likely to yield value to the asset owner/ manager
Ferriby Road Bridge	Hoult <i>et al.</i> (2010)	Project may yield value to the asset owner/manager
Hammersmith Flyover	Webb <i>et al.</i> (2014)	Project likely to yield value to the asset owner/ manager

* paper not published when Vardanega *et al.* (2016) framework first published

The framework from Vardanega *et al.* (2016) was further tested for a planned monitoring effort on a proposed footbridge (Nepomuceno *et al.* 2019) and has recently been examined in the context of prior monitoring efforts (Nepomuceno *et al.* 2022). Vardanega *et al.* (2021) have recently presented a new rating framework to assist engineers with answering the ‘Which sensor?’ question from Figure 2 in the context of bridge scour detection (see Gavriel (2019) for an early version of the rating framework for scour).

1.3 Paper aims

This paper briefly outlines some of the key monitoring devices used for scour monitoring and then discusses the new rating framework presented in Vardanega *et al.* (2021); it makes comparison of this framework with that discussed in Pregnotato *et al.* (2022) and the Scour Monitoring Decision Framework (SMDF) in Lueker *et al.* (2010). This comparison may allow the development of a new, comprehensive framework for planning and assessing scour monitoring efforts.

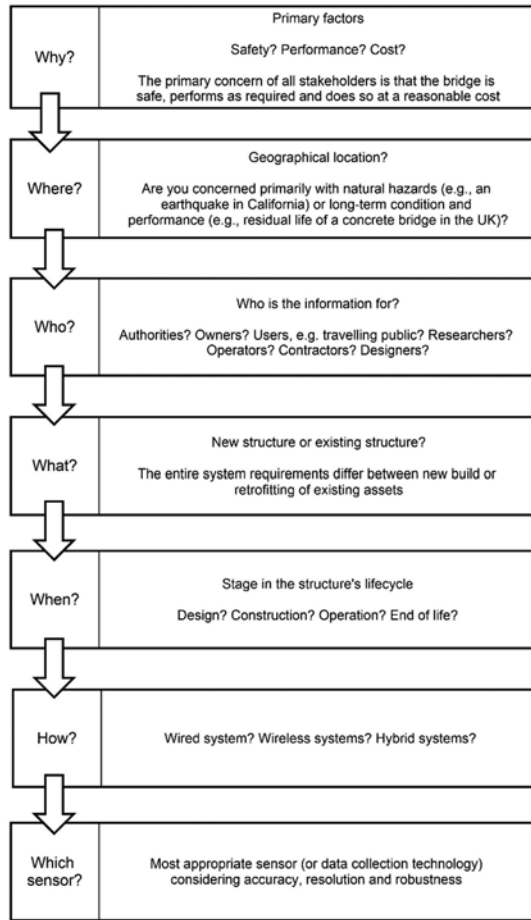


Figure 2. Key considerations when deciding whether to employ SHM (taken from Vardanega *et al.* 2016 and used under the terms of the cc by 4.0 license).

2 BRIDGE SCOUR MONITORING DEVICES

2.1 Scour monitoring technologies

A range of technologies for scour monitoring are available which may partially replace or supplement visual inspection activities (see Briaud *et al.* 2011, Prendergast & Gavin 2014, Wang *et al.* 2017 and Prendergast *et al.* 2018 for detailed reviews of scour monitoring devices). Sections 2.2 to 2.4 briefly outline the use of Accelerometers, Fiber-Bragg grating sensors and Sonar in some scour monitoring case studies. Further reviews on general bridge monitoring technologies can be found in Webb *et al.* (2015) and Middleton *et al.* (2016).

2.2 Accelerometers

Accelerometers are used to measure dynamic response of bridges subject to scour damage by detecting changes in the natural frequency (e.g. Prendergast & Gavin 2014, Bao & Liu 2016, Kariyawasam *et al.* 2019a, 2019b, 2020). The collected data can then be analysed using spectral analysis methods (e.g. Brincker *et al.* 2001, Briaud *et al.* 2011). Briaud *et al.* (2011) reported that based on studies of two bridges in Texas (USA) that draw-backs from accelerometers were 'lack of efficient excitation' from loading and high-power consumption (the latter may be mitigated with solar panels).

2.3 Fiber-Bragg grating sensors

Fiber-Bragg grating sensors can be installed on bridge piers to detect changes in soil levels during (and post) flood events (e.g. Lin *et al.* 2006, Prendergast & Gavin 2014 and Kong *et al.* 2017). According to the review of Prendergast & Gavin (2014, p.140) embedded rods that are “partially exposed due to scour will be subjected to hydrodynamic forces from the flow of water that induce bending in the exposed rod” and progression of scouring can be detected with an array of strain gauges installed along the rod (see the field studies of Lin *et al.* 2006 and Kong *et al.* 2017).

2.4 Sonar

Sonar devices can be mounted to vessels or on bridge piers to detect changes in riverbed conditions by sending out sound waves and measuring the time taken for the sound wave to return (e.g. De Falco & Mele 2002, Briaud *et al.* 2011, Prendergast & Gavin 2014 and Clubley *et al.* 2015). Briaud *et al.* (2011, p.15) explain that for sonar sensors: “The time taken for the signal to propagate from the emitter to the receiver in combination with the material properties gives an estimate of the distance from the emitter to the interface of the two mediums.” Briaud *et al.* (2011) also explain that fixed sonar devices can be damaged or destroyed due to the effects of debris.

3 SCOUR RATING FRAMEWORK

A preliminary version of a rating framework to compare various scour monitoring technologies was proposed by Gavriel (2019). Vardanega *et al.* (2021) further developed the framework and used it to evaluate seven monitoring deployments reported in the literature (see Table 2 for a summary of this recent work).

Table 2. Summary of the application of the scour monitoring rating framework to seven installed monitoring systems from Vardanega *et al.* (2021).

Bridge Structure(s)/Location	References	Score (/25)
Mezzana Corti & Borgoforte Bridges (River Po, Italy)	De Falco & Mele (2002)	16
Dadu Bridge (Wu River, Taiwan)	Lin <i>et al.</i> (2006)	17
Railway viaduct (River Hamble, England, UK)	Clubley <i>et al.</i> (2015)	14
Concrete bridge (Redwood Creek, Louisiana, USA)	Kong <i>et al.</i> (2017)	11
Tadcaster bridge (River Wharfe, England, UK)	Selvakumaran <i>et al.</i> (2018)	17
Baildon bridge (River Aire, England, UK)	Kariyawasam (2019a, 2019b)	17
A76 200 bridge (River Nith, Scotland UK)	Maroni <i>et al.</i> (2020)	19

When using the framework, it is important to understand how monitoring systems may be used to capture different aspects of scouring. For example, Highways England (BD 97/12: HA (2012): clause 7.14) considers three categories of scour monitoring techniques: “(i) those that seek to measure the maximum scour levels that have occurred at the bridge site; (ii) those that seek to measure the development of scour adjacent to the structure as it develops during a flood; (iii) systems based on monitoring analogues (conditions that may correlate with the development of scour) such as flow velocities, water level, or weather warnings.”

Monitoring devices may be used to capture data relevant to one or more of the aforementioned categories from HA (2012). The rating framework (Vardanega *et al.* 2021) includes five criteria (Q1 to 5) each of which are rated from 1 to 5, with a higher score given to a device with improved capability:

- “Q1 – Ease of installation”
- “Q2 – Ease of operation”
- “Q3 – Ease of data-logging/capture”
- “Q4 – Ease of data interpretation”
- “Q5 – Measurement frequency”.

Figure 3 shows a diagrammatic description of the scoring system (for a complete description of the rating system see Vardanega *et al.* 2021). The following classification is used to describe the level of applicability of devices scored using the rating framework (Vardanega *et al.* 2021):

- “Very high applicability” (score 23-25)
- “High applicability” (score of 18-22)
- “Moderate applicability” (score of 13-17)
- “Low applicability” (score of 8-12)
- “Very low applicability” (score of 5-7).

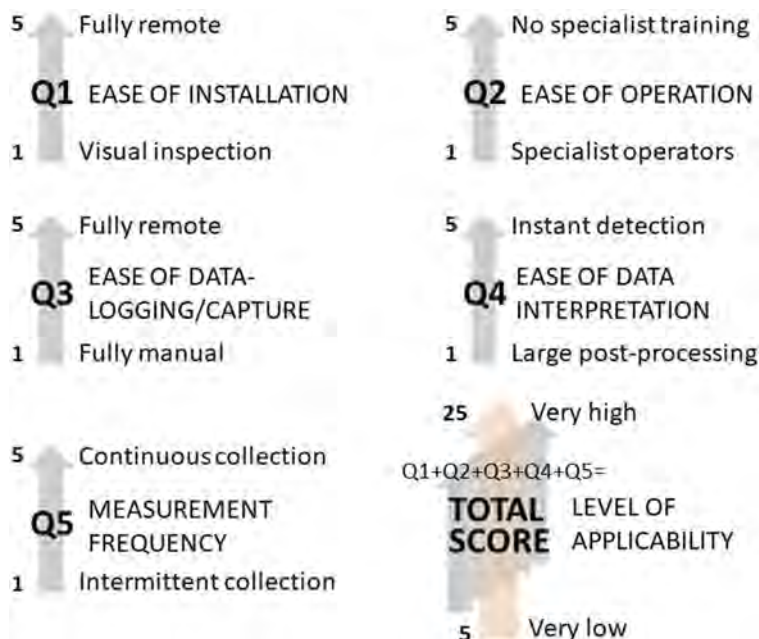


Figure 3. Schematic of the scour device rating system proposed in Vardanega *et al.* (2021).

4 COMPARISON WITH OTHER FRAMEWORKS

Pregolato *et al.* (2022) built on the framework presented in Vardanega *et al.* (2021) by introducing nine criteria versus the five criteria suggested by Vardanega *et al.* (2021). The updated framework by Pregolato *et al.* (2022) introduced two cost related criteria one related to the initial cost of the measuring apparatus and one related to the whole-life cost of the measuring apparatus. Pregolato *et al.* (2022) also considered the environmental limitations which are associated with the use of the examined apparatus as suggested by the original framework (Gavriel 2019). The updated framework from Pregolato *et al.* (2022) accounts for the robustness of the measuring apparatus. Pregolato *et al.* (2022) incorporated weighting factors for the criteria (albeit assigned by engineering judgement), such as those shown in Figure 3.

Lueker *et al.* (2010) applied the Minnesota ‘Scour Monitoring Decision Framework’ (SMDF) to five sites and demonstrated that a range of scour devices may be selected with sonar being the generally preferred option. The SMDF has many more criteria than Vardanega *et al.* (2021) with more details on the nature of the riverine conditions being considered, as well as e.g. the traffic levels on the bridge.

5 CONCLUSIONS

5.1 Summary

A rating framework (Vardanega *et al.* 2021) has been proposed to assist engineers to answer the ‘which sensor?’ question when considering SHM systems for scour monitoring and assessment. The framework has five key criteria which are rated from 1 to 5 depending on the capability of the technology in terms of “Ease of installation”, “Ease of operation”, “Ease of data logging/capture”, “Ease of data interpretation” and “Measurement frequency”. The framework can also be used to assess a full scour SHM deployment, which may involve multiple technologies which form a more complex SHM system. Finally, the comparison with other frameworks (Pregolato *et al.* 2022 and Lueker *et al.* 2010) highlighted the possibility to include other criteria, such as sensor cost or traffic levels.

5.2 Further work

The framework should also be tested for proposed monitoring efforts on new projects to see its use in both selecting and comparing different sensing device options and to evaluate the designed monitoring specification on such projects. As previously stated, the possibility of adding further criteria or weightings for different criteria depending on the situation should also be explored. In addition, the rating-frameworks of Vardanega *et al.* (2021) (with the additions proposed by Pregolato *et al.* 2022) along with other methods such as the ‘Scour Monitoring Decision Framework’ (Lueker *et al.* 2010) should be applied to a wider range of past case-studies to improve calibration and determine the minimum number of criteria needed for successful specification of scour monitoring systems. While the cost of the initial deployment and operation of the monitoring system should be added to the framework a consideration of the cost of data-interpretation and processing should also be considered to supplement the ‘Ease of data interpretation’ criterion. This would allow for better consideration of the life-cycle costs of the specified monitoring system.

ACKNOWLEDGMENTS

The third author was supported by the Engineering and Physical Sciences Research Council (EPSRC) Living with Environmental Change (LWEC) Fellowship (EP/R00742X/2).

DATA AVAILABILITY

This study has not generated new experimental data.

REFERENCES

- Ahlborn, T.M., Shuchman, R., Sutter, L.L., Brooks, C.N., Harris, D.K., Burns, J.W., Endsley, K.A., Evans, D.C., Vaghefi, K. & Oats, R.C. 2010a. An evaluation of commercially available remote sensors for assessing highway bridge condition. Available from: <https://mtri.org/bridgecondition/doc/RITA_BCRS_Commercial_Sensor_Evaluation.pdf> [28/02/2023].
- Ahlborn, T.M., Harris, D.K., Brooks, C.N., Endsley, K.A., Evans, D.C. & Oats, R.C. 2010b. Remote sensing technologies for detecting bridge deterioration and condition assessment. *NDE/NDT for highways and bridges: Structural materials technology (SMT) 2010*. New York: American Society for Non-destructive Testing (ASNT).
- Bao, T. & Liu, Z. 2016. Vibration-based bridge scour detection: A review. *Journal of the International Association for Structural Control Monitoring* 24(7):[e1937].
- Briaud, J-L., Hurlebaus, S., Chang, K-A., Yao, C., Sharma, H., Yu, O-Y., Darby, C., Hunt, B.E. & Price, G.R. 2011. Realtime monitoring of bridge scour using remote monitoring technology. *Report 0-6060-1*. Texas, USA: Texas Transportation Institute. <<http://tti.tamu.edu/documents/0-6060-1.pdf>> [28/02/2023].

- Brincker, R., Zhang, L. & Andersen, P. 2001. Modal identification of output-only systems using frequency domain decomposition. *Smart Materials and Structures* 10(3): 441–445.
- Clubley, S., Manes, C. & Richards, D. 2015. High-resolution sonars set to revolutionise bridge scour inspections. *Proceedings of the Institution of Civil Engineers – Civil Engineering* 168(1): 35–42.
- De Falco, F. & Mele, F. 2002. The monitoring of bridges for scour by sonar and sediment. *NDT&E International* 35(2): 117–123.
- Dikanski, H., Hagen-Zanker, A., Iman, B. & Avery, K. 2017. Climate change impacts on railway structures: bridge scour. *Proceedings of the Institution of Civil Engineers – Engineering Sustainability* 170(5): 237–248.
- Ettema, R., Constantinescu, G. & Melville, B. 2017. Flow-field complexity and design estimation of pier-scour depth: Sixty years since Laursen and Toch. *Journal of Hydraulic Engineering* 143 (9):[03117006].
- Fidler, P.R.A., Middleton, C.R., Vardanega, P.J. & Hoult, N.A. 2021. Long-term monitoring of the Humber Bridge Hesse anchorage chamber. In Yokota, H. & Frangopol, D.M. (eds.), *Bridge Maintenance, Safety, Management, Life-Cycle Sustainability and Innovations: Proceedings of the Tenth International Conference on Bridge Maintenance, Safety and Management (IABMAS 2020)*, Sapporo, Japan, 11-15 April 2021: 1779–1786, The Netherlands, CRC Press/Balkema Taylor & Francis Group.
- Gavriel, G. 2019. An Innovating Rating System for Assessing Scour Monitoring Devices. *Undergraduate Research Report No. 1819RP009*, Department of Civil Engineering, University of Bristol, Bristol, UK.
- Highways Agency (HA) 2012. The Assessment of Scour and Other Hydraulic Actions at Highway Structures. BD97/12. Design Manual for Roads & Bridges. The Stationery Office. London, UK. Available from: <<https://www.standardsforhighways.co.uk/dmrb/search/8ff7a31b-1ce0-4e34-9e94-b2372f125f34>> [28/02/2023].
- Hoult, N.A., Fidler, P.R.A., Wassell, I.J., Hill, P.G. & Middleton, C.R. 2008. Wireless structural health monitoring at the Humber Bridge UK. *Proceedings of the Institution of Civil Engineers – Bridge Engineering* 161(4): 189–195.
- Hoult, N.A., Bennett, P.J., Fidler, P.R.A., Middleton, C.R. & Soga, K. 2009. Distributed fibre optic strain measurements for pervasive monitoring of civil infrastructure. *Proceedings 4th International Conference on Structural Health Monitoring of Intelligent Infrastructure (SHMII-4)*, Zurich, Switzerland, Winnipeg, MB, Canada, International Society for Structural Health Monitoring of Intelligent Infrastructure.
- Hoult, N.A., Fidler, P.R.A., Hill, P.G. & Middleton, C.R. 2010. Long-term wireless structural health monitoring of the Ferriby Road Bridge. *Journal of Bridge Engineering* 15(2): 153–159.
- Kariyawasam, K.K.G.K.K., Fidler, P.R.A., Talbot, J.A. & Middleton, C.R. 2019a. Field deployment of an ambient vibration-based scour monitoring system at Baildon-Bridge, UK. In Dejong, M.J. et al. (eds.), *International Conference on Smart Infrastructure and Construction 2019 (ICSIC): Driving Data-Informed Decision Making*: 711–719, London, ICE Publishing.
- Kariyawasam, K., Fidler, P., Talbot, J. & Middleton, C. 2019b. Field assessment of ambient vibration-based bridge scour detection. In: Chang et al. (eds.), *Structural Health Monitoring 2019: Enabling Intelligent Life-cycle Health Management for Industry Internet of Things (IIOT): Proceedings of the Twelfth International Workshop on Structural Health Monitoring, September 10-12, 2019, Stanford, CA, USA*: 374–381.
- Kariyawasam, K.D., Middleton, C.R., Madabhushi, G., Haigh, S.K. & Talbot, J.P. 2020. Assessment of bridge natural frequency as an indicator of scour using centrifuge modelling. *Journal of Civil Structural Health Monitoring* 10(5): 861–881.
- Kerenyi, K. & Flora, K. 2019. A hybrid approach to forensic study of bridge scour. *Proceedings of the Institution of Civil Engineers – Forensic Engineering* 172(1): 27–38.
- Kong, X., Cai, C.S., Hu, J.X., Xiong, W. & Peng, H. 2017. Field application of an innovative bridge scour monitoring system with fiber Bragg grating sensors. *Journal of Aerospace Engineering* 30 (2):[B4016008].
- Lin, Y.B., Lai, J.S., Chang, K.C. & Lin, L.S. 2006. Flood scour monitoring system using fiber Bragg grating sensors. *Smart Materials and Structures* 15(6): 1950–1959.
- Lueker, M., Marr, J., Ellis, C., Winsted, V. & Akula, S.R. 2010. Bridge Scour Monitoring Technologies: Development of Evaluation and Selection Protocols for Application on River Bridges in Minnesota. *Report MN/RC 2010-14*. St. Paul, MN: Minnesota Department of Transportation.
- Maddison, B. 2012. Scour failure of bridges. *Proceedings of the Institution of Civil Engineers – Forensic Engineering* 165(1): 39–52.
- Maroni, A., Tubaldi, E., Ferguson N., Tarantino, A., McDonald, H. & Zonta, D. 2020. Electromagnetic Sensors for Underwater Scour Monitoring. *Sensors* 20(15):[4096].
- Maroni, A., Tubaldi, E., McDonald, H. & Zonta D. (2022). A monitoring-based classification system for risk management of bridge scour. *Proceedings of the Institution of Civil Engineers – Smart Infrastructure and Construction* 175(2): 92–102.
- Middleton, C., Vardanega, P., Webb, G. & Fidler, P. 2014. Smart infrastructure – are we delivering on the promise? Keynote Paper: 6th Australian Small Bridges Conference, Sydney, Australia, 27–28 May 2014, <https://doi.org/10.13140/RG.2.1.1463.5288>

- Middleton, C.R., Fidler, P.R.A. & Vardanega, P.J. 2016. *Bridge Monitoring: A practical guide*. London, UK: ICE Publishing.
- Nepomuceno, D.D.T., Bennetts, J., Webb, G.T., Langhorne, M., Johnson, M., Macdonald, J.H.G., Tryfonas, T. & Vardanega, P.J. 2019. Assessing the Potential Value of a SHM Deployment on a Proposed Footbridge. In Rodrigues, H. & Elnashai, A. (eds.), *Advances and Challenges in Structural Engineering: Proceedings of the 2nd GeoMEast International Congress and Exhibition on Sustainable Civil Infrastructures, Egypt 2018, Sustainable Civil Infrastructures*: 151–166. Cham, Springer.
- Nepomuceno, D.T., Vardanega, P.J., Tryfonas, T., Pregnotato, M., Bennetts, J., Webb, G., Foster, A., Augustine, L. & Holland, M. 2022. SHM deployments for two bridge structures: assessing potential value. In: J.R. Casas, D.M. Frangopol & J. Turmo (eds.) *Bridge Safety, Maintenance, Management, Life-Cycle, Resilience and Sustainability: Proceedings of the Eleventh International Conference on Bridge Maintenance, Safety and Management (IABMAS 2022), Barcelona, Spain, July 11-15, 2022*: 1078–1086, CRC Press/Balkema Taylor & Francis Group, London, UK.
- Poulos, H.G. 2004. An approach for assessing geotechnical reduction factors for pile design. In: *Proceedings of the 9th Australia New Zealand Conference on Geomechanics*: vol. 1, 109–115. Auckland, New Zealand: New Zealand Geotechnical Society and the Australian Geomechanics Society.
- Pregnotato, M., Vardanega, P.J., Limongelli, M.P., Giordano, P.F. & Prendergast, L.J. 2021. Risk-based scour management: A survey. In: Yokota, H. & Frangopol, D.M. (eds.), *Bridge Maintenance, Safety, Management, Life-Cycle Sustainability and Innovations: Proceedings of the Tenth International Conference on Bridge Maintenance, Safety and Management (IABMAS 2020), Sapporo, Japan, 11-15 April 2021*: 693–701, The Netherlands, CRC Press/Balkema Taylor & Francis Group.
- Pregnotato, M., Gavriel, G., Thompson, D., Anderson, M., Fox, I. & Giles, K. 2022. Scour monitoring for railway assets (UK). In: J.R. Casas, D.M. Frangopol & J. Turmo (eds.) *Bridge Safety, Maintenance, Management, Life-Cycle, Resilience and Sustainability: Proceedings of the Eleventh International Conference on Bridge Maintenance, Safety and Management (IABMAS 2022), Barcelona, Spain, July 11-15, 2022*: 879–884, CRC Press/Balkema Taylor & Francis Group, London, UK.
- Prendergast, L.J. & Gavin, K. 2014. A review of bridge scour monitoring techniques. *Journal of Rock Mechanics and Geotechnical Engineering* 6(2): 138–149.
- Prendergast, L.J., Limongelli, M.P., Ademovic, N., Anžlin, A., Gavin, K. & Zanini, M. 2018. Structural health monitoring for performance assessment of bridges under flooding and seismic actions. *Structural Engineering International* 28(3): 296–307.
- Schwamb, T. 2010. Optical Strain Sensing for Piled Foundations at Ninewell's Bridge. *M.Res. thesis*, University College London–University of Cambridge, London–Cambridge, UK.
- Selvakumaran, S., Plank, S., Geiß, C., Rossi, C. & Middleton, C. 2018. Remote monitoring to predict bridge scour failure using Interferometric Synthetic Aperture Radar (InSAR) stacking techniques. *International Journal of Applied Earth Observation and Geoinformation* 73: 463–470.
- Vaghefi, K., Oats, R.C., Harris, D.K., Ahlborn, T.M., Brooks, C.N., Endsley, K.A., Roussi, C., Shuchman, R., Burns, J.W. & Dobson, R. 2012. Evaluation of commercially available remote sensors for highway bridge condition assessment. *Journal of Bridge Engineering* 17(6): 886–895.
- Vardanega, P.J., Webb, G.T., Fidler, P.R.A. & Middleton, C.R. 2016. Assessing the potential value of bridge monitoring systems. *Proceedings of the Institution of Civil Engineers – Bridge Engineering* 169(2): 126–138.
- Vardanega, P.J., Gavriel, G. & Pregnotato, M. 2021. Assessing the suitability of bridge-scour-monitoring devices. *Proceedings of the Institution of Civil Engineers – Forensic Engineering* 174(4): 105–117.
- Wang, C., Yo, X. & Liang, F. 2017. A review of bridge scour: mechanism, estimation, monitoring and countermeasures. *Natural Hazards* 87(3): 1881–1906.
- Webb, G.T. 2014. Structural Health Monitoring of Bridges. *Ph.D. thesis*, University of Cambridge, Cambridge, UK.
- Webb, G.T., Vardanega, P.J., Fidler, P.R.A. & Middleton, C.R. 2014. Analysis of Structural Health Monitoring Data from Hammersmith Flyover. *Journal of Bridge Engineering* 19(6):[05014003].
- Webb, G.T., Vardanega, P.J. & Middleton, C.R. 2015. Categories of SHM Deployments: Technologies and Capabilities. *Journal of Bridge Engineering* 20(11):[04014118].
- Webb, G.T., Vardanega, P.J., Hoult, N.A., Fidler, P.R.A. Bennett, P.J. & Middleton, C.R. 2017. Analysis of Fiber-Optic Strain-Monitoring Data from a Prestressed Concrete Bridge. *Journal of Bridge Engineering* 22(5):[05017002].

Predicting the usefulness of monitoring information for structural evaluations of bridges

N. Bertola & E. Brühwiler

Ecole Polytechnique Fédérale de Lausanne (EPFL), Lausanne, Switzerland

ABSTRACT: With economic, environmental, and material resources becoming increasingly scarce, more sustainable solutions for the management of civil infrastructure are required. Accurately evaluating the structural capacity is primordial to avoid unnecessary replacement of existing bridges. The assessment of existing structures is currently made based on construction drawings, recorded information on the materials used, and visual inspection. The remaining uncertainties on the structural behavior are compensated by conservatism assumptions. Monitoring data collected through bridge load testing, structural performance monitoring, and non-destructive tests provide additional information on the structural behavior leading to decision regarding bridge safety and reducing considerably the costs and environmental impacts of management. Nonetheless, collecting this information is often costly as the sensor deployment and the data management are expensive. The monitoring costs may not always be justified by the benefits in terms of information gain. This paper proposes a methodology to evaluate the potential impact of monitoring activities on the evaluation of structural performance. A full-scale bridge in Switzerland is used to assess the usefulness of several monitoring techniques. Results show that the monitoring leads to more accurate evaluations of structural verifications, and each method provides complementary information.

1 INTRODUCTION

Civil structures are designed using conservative assumptions and simple design models. Existing structures have thus untapped reserve capacity, and monitoring the structural behavior can unlock this potential (Smith, 2016). A better knowledge of the behavior and properties of a complex structure through monitoring may be then leveraged to optimize structural rehabilitation, focus inspection, and extend service durations (Frangopol et al., 2008).

Monitoring of structural behavior can be separated into two activity subsets depending on the monitoring goal: the evaluation of the structural capacity at a given time, called structural performance monitoring (SPM) (Feng et al., 2004), and the evolution of the structural behavior over time, called structural health monitoring (SHM) (Farrar & Worden, 2010). These two uses of monitoring data have different implications for infrastructure management. SPM provides information for structural-capacity evaluations (Proverbio et al., 2018) and the structural behavior in its environment (i.e., traffic loading and environmental actions) (Sawicki & Brühwiler, 2022). SHM aims to detect current and future damage in structures (J. M. Brownjohn, 2007), improving their maintenance and safety assessments in the future (Orcesi & Frangopol, 2011). Despite the undeniable potential of structural monitoring, both SHM and SPM are still rarely put into practice by asset managers (Ye et al., 2022). Several reasons explain this reluctance: the lack of time, the lack of resources, and missing related courses in curricula (Große et al., 2019).

The assessment of existing structures is made based on construction drawings (if they are recorded), and visual inspection. The remaining missing information is compensated by conservative assumptions following new-design principles (Brühwiler et al., 2012). Several

methods have been proposed to assess existing-structure performance (Ghosn et al., 2016a; Ghosn et al., 2016b). In Switzerland, structural safety is evaluated based on the indicator of the degree of compliance n calculated using Equation (1). A value of n exceeding 1.0 means that structural safety is ensured and that there is reserve capacity (Swiss Society of Engineers and Architects, 2011). This generic metric has the advantage that it can be applied to any structural verification for ultimate limit states (ULS), fatigue limit states (FLS), and service limit states (SLS). Analytical or numerical models are required to compute structural capacity and load effects. Typically, several structural verifications are made for each limit state.

$$n = \text{Capacity} / \text{Demand} \quad (1)$$

SPM aims to update the evaluations of the degrees of compliance using field measurements. Several monitoring techniques are possible for this task, such as non-destructive tests (NDT) (Helal et al., 2015), bridge load testing using static and/or dynamic excitations (Brownjohn et al., 2011), and continuous monitoring to measure the real bridge condition (i.e., through a bridge weight in motion process) (Lydon et al., 2016). Evaluation of structural behavior based on monitoring data may require an inverse analysis (Pasquier & Smith, 2016). Sensor data do not directly support the structural-property evaluation, meaning that the data interpretation is complex (Catbas et al., 2013). Conventional residual-minimization approaches have provided unsafe parameter estimates and population-based methodologies (i.e., Bayesian model updating, error-domain model-falsification) are recommended (Pai & Smith, 2022).

The choice of the monitoring system significantly influences the success of SPM (Ercan & Papadimitriou, 2021). Studies have developed strategies to predict the information gain of monitoring systems, for instance, based on information entropy (Bertola et al., 2017; Papadimitriou, 2004). Recently, efforts have been made to quantify the value of information by comparing maintenance intervention with and without including expected information gain (Bertola et al., 2020; Kamariotis et al., 2022). Nonetheless, the first choice of engineers is to select the appropriate monitoring techniques rather than sensor configuration. This paper proposes a methodology to evaluate the usefulness of several monitoring systems in terms of their potential influence on the degrees-of-compliance evaluations.

2 METHODOLOGY

In this section, the methodology to predict the benefit of monitoring data on the evaluation of bridge structural capacity. This methodology is shown in Figure 1 and involves four main phases.

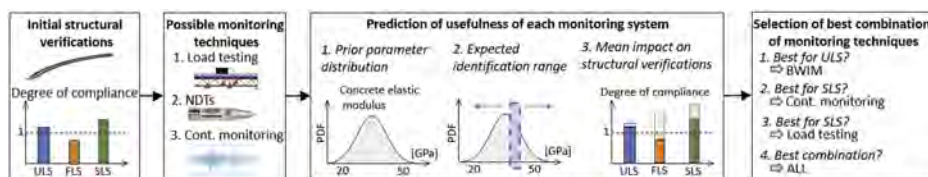


Figure 1. Methodology predicting the usefulness of monitoring techniques for structural-performance evaluation.

The first phase involves evaluating structural performance without monitoring information. After a visual inspection, the main structural characteristics (i.e., material properties) and load levels are estimated. These estimations are based on recorded information (such as structural drawings) and conservative bridge-parameter values on missing information.

Several structural verifications are made for serviceability, fatigue, and ultimate limit states. The results are expressed in terms of degrees of compliance (Equation 1). Typically, a finite-element model is built to improve the accuracy of structural verifications. At this stage, the first evaluation of bridge potential deficiencies is made, and potential uncertainties on the structural behavior are assessed.

The second stage involves defining the potential monitoring techniques that could be applied. Estimations of sensor types, the number of devices, and the duration of monitoring are made. Additionally, it must be evaluated which bridge parameters can be more precisely estimated using monitoring data from each technique.

The third stage involves assessing the usefulness of each monitoring technique independently and is performed using three steps. First, the prior distribution of each bridge parameter (i.e., material properties, boundary conditions, load levels) is estimated. Then, based on monitoring-technique accuracy, the expected identification range is defined. The identification range may sometimes be complex to estimate, especially when monitoring involves updating multiple parameters using inverse analysis. Nonetheless, studies on sensor placement have shown that it is possible to predict expected parameter ranges after monitoring (Bertola et al., 2017, 2020). As measurements are unpredictable, this step only involves defining possible ranges of parameter identification rather than a predicted value. For instance, bridge load testing will enable the identification of the bridge girder stiffness from which concrete elastic modulus with a precision range of 5 GPa, called the identification range. Let's assumed that the elastic modulus has an expected value defined between 20 and 50 GPa with a mean value of 35 GPa. Expected parameter values after monitoring are evaluated based on the most conservative value when centering the identification range on the mean value of the prior distribution. In the previous, the expected identification value is equal to $35 - 5/2 = 32.5 \text{ GPa}$. The third step is to reevaluate the degrees of compliance based on expected identification values for each monitoring technique. It may happen that the re-evaluations of the degrees of compliance may not vary if the parameter is not influencing the structural verification. In this example, the elastic modulus will have influence on the SLS verifications but no impacts on the ULS verifications. Each method may provide information on a subset of bridge parameters, and the expected influence on structural verification can vary significantly.

The last step is selecting the appropriate combination of monitoring techniques that maximize the information gain for all limit states. As each monitoring technique provides different information, the best technique will often differ between structural verifications of limit states. A combination of monitoring techniques is thus often recommended to maximize the information gain. Another strategy would be to pick only monitoring techniques that may significantly influence structural verifications with a degree of compliance smaller than 1.0.

3 CASE STUDY

3.1 *Bridge presentation*

In this section, the methodology proposed in Section 2 is implemented on a full-scale case study in Switzerland. This eight-span viaduct was built in 1959 is an eight-span viaduct (Figure 2) and is one of the first steel-concrete composite bridges built in Switzerland. The superstructure involves a reinforced concrete (RC) slab fixed to two steel box girders. The spans vary between 12 and 25.6 m, and the bridge width is 12.7 m. The RC slab has a varying thickness between 0.17 and 0.24 m, while the two steel girders have a constant height of 1.30 m. The structure was subject to an intervention in 2002, where longitudinal stiffeners on the steel girders and bolts at the Gerber joints between the spans were added.

3.2 *Monitoring systems*

This bridge was monitored between 2016 and 2019. Strain gauges and thermocouples were installed to monitor traffic effects and temperature variations directly on rebars in both longitudinal and transverse directions with potential fatigue issues (see Section 3.3). These sensors were also used for bridge weight-in-motion and calibrated using load tests. Several static load tests were performed on the fourth span in 2016. The sensor network during these tests involved five LVDTs at mid-span, and five strain gauges both in the transverse and longitudinal directions near midspan were mounted (Bayane et al., 2021). Two non-destructive tests were performed: rebound hammer and sound-velocity measurements on the RC slab on the same span.



Figure 2. Composite steel-concrete bridge case study in Switzerland and the finite-element model.

3.3 Prior evaluation of bridge capacity

The bridge performance before monitoring was assessed following the rules given in Swiss standards for existing structures (Brühwiler et al., 2012), using construction and intervention drawings, and visual inspections. A numerical model was built using SCIA software, and the model involves 1D and 2D elements. The entire bridge is modeled (including bridge piers) to improve the accuracy of the predictions at the monitored span (Figure 2). The bridge deck geometry has been modeled accurately, especially the complex shape of the RC slab. The size of the finite elements is set to 400 mm, except for the monitored span, where it is reduced to 100 mm to improve the quality of the predictions.

Several structural verifications have been made: 13 for ULS, 10 for FLS, and 2 for SLS. Of these 25 structural verifications, only two have degrees of compliance smaller than 1.0, and both involve FLS on longitudinal and transverse rebars in the RC deck (Figure 4).

3.4 Expected information gain

3.4.1 Step 1 – Prior distribution and potential information gain

In this section, the usefulness of information gain is made. First, the main bridge parameters that can be identified using the three monitoring techniques (bridge load testing, B-WIM, and continuous monitoring) are defined. These parameters involved: the deck stiffness (approximated as the elastic modulus of concrete), the rotational stiffness at the Gerber joints, the daily maximum stress differences in rebars due to traffic loading, the ULS load level (in terms of maximum axle force), and the concrete compressive strength. The prior distribution of each distribution is shown in Figure 3. Value ranges and distributions of these parameters are selected based on engineering judgment.

Figure 2 also qualitatively presents the potential information gain of each monitoring technique on these parameters. Rebound hammer and sound-velocity measurements provide information on the uncracked elastic modulus and compressive strength of concrete. Static load testing helps update concrete elastic moduli and the rotational stiffness at boundary conditions, but these estimates may not be precise enough to provide reliable safety verifications. The continuous monitoring provides accurate estimations of maximum stress differences necessary for fatigue safety verification, while B-WIM helps to define more accurate load models for ULS. These monitoring techniques thus provide complementary information.

3.4.2 Step 2 – precision of monitoring output

The second step involves estimating the precision of monitoring outputs. For each parameter that can be updated by a monitoring technique, an identification range is estimated (Table 1). For NDTs, these identification ranges mostly depend on the sensor precision and the number of tests performed. The continuous monitoring and B-WIM have precisely measured the traffic on the bridge for three years. Nonetheless, these techniques require estimating tails of distributions to

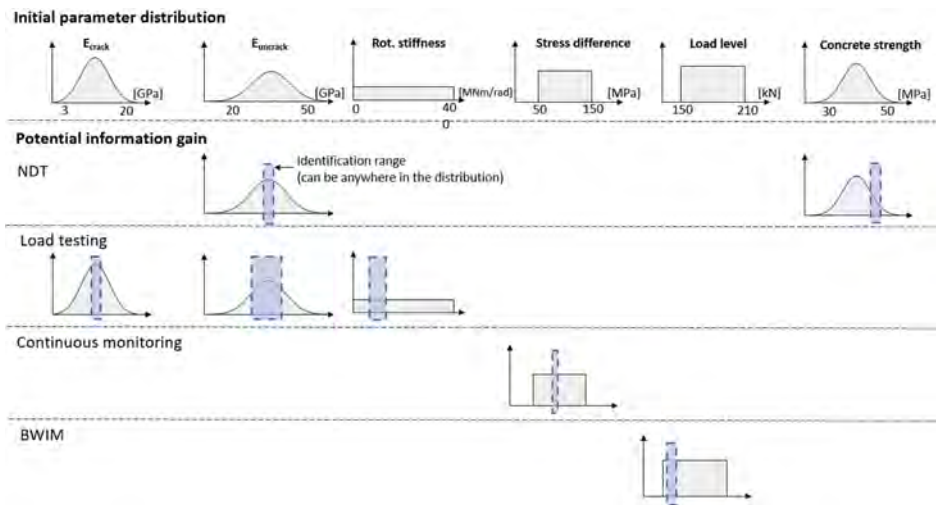


Figure 3. Prior bridge-parameter distributions and potential information gain of each monitoring technique on these parameter distributions.

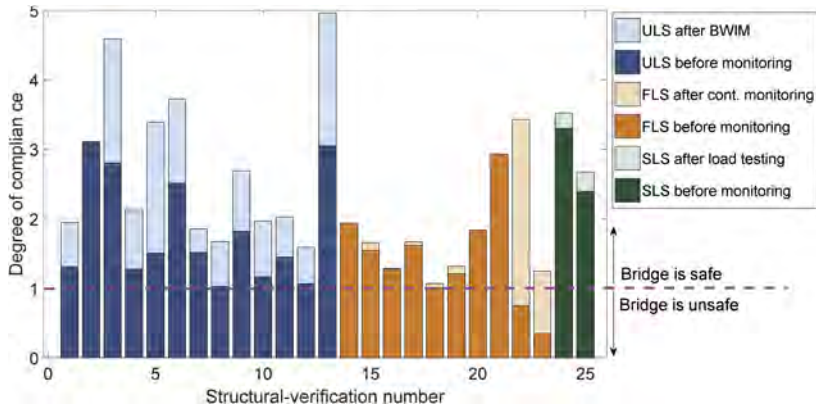


Figure 4. Degrees of compliance prior to and after monitoring for each structural verification.

define accurate evaluations of maximal stress differences and axle load levels which may have some extrapolation errors. Bridge load testing provides simultaneous information on three bridge parameters based on an inverse analysis. The precision of identification ranges is determined using the hierarchical algorithm based on the sensor configuration and performed load test. More information on this information gain can be found in (Bertola et al., 2022).

3.4.3 Step 3 – Influence on degrees of compliance

Based on the results in Steps 2 and 3, the expected values used for structural verification after monitoring are obtained. These values are calculated as the mean value in the prior distribution (Figure 1) minus half of the precision range (Table 1), and the results are shown in Table 2. Each monitoring technique helps increase a subset of bridge parameter values.

For each monitoring technique, the influence of expected monitoring outputs on the degrees of compliance is evaluated (Table 3). Except for the NDT (only updating and E_{ncr}), all monitoring techniques provide useful information for the bridge structural verifications. Nonetheless, only load testing provides useful information for SLS verifications, while FLS verifications are mostly influenced by continuous monitoring and ULS verifications by the BWIM data. When all techniques are combined, an average increase of degrees of compliance of 19 % over the 25 structural verifications is obtained, showing that monitoring can provide

Table 1. Estimates of value-range identification for each parameter and each monitoring technique.

Bridge parameter	Precision of identification range of monitoring technique			
	NDT	Load testing	Cont. Monitoring	B-WIM
Cracked RC section E_{cr} [GPa]	-	6	-	-
Uncracked RC section E_{ncr} [GPa]	5	15	-	-
Rot. Stiffness [MNm/rad]	-	100	-	-
Stress difference [MPa]	-	-	2	-
Load level [kN]	-	-	-	5
Concrete strength [MPa]	2	-	-	-

Table 2. Expected parameter values obtained after monitoring.

Bridge parameter	Mean expected values after monitoring			
	NDT	Load testing	Cont. Monitoring	BWIM
Cracked RC section E_{crack} [GPa]	6	10	6	6
Uncracked RC section E_{ncr} [GPa]	30	28	20	20
Rot. Stiffness [MNm/rad]	0	100	0	0
Stress difference in steel rebar [MPa]	150	150	73	150
Maximum axle load [kN]	210	210	180	210
Concrete compressive strength [MPa]	38	30	30	30

significant information for bridge performance evaluation. Nonetheless, in a value of information perspective (only measuring when it can change the safety assessment of the bridge), only the continuous monitoring is justified.

Table 3. Expected influence of monitoring information on structural-verification degrees of compliance.

Structural verification	Mean degrees of compliance before monitoring	Expected mean degrees of compliance after monitoring				
		NDT	Load testing	Cont. Monitoring	BWIM	Combined
SLS	2.84	2.91 (+3%)	3.23 (+14%)	2.84 (+0%)	2.84 (+0%)	3.23 (+14%)
FLS	1.45	1.45 (+0%)	1.45 (+0%)	1.76 (+21%)	1.45 (+0%)	1.76 (+21%)
ULS	1.82	1.88 (+2%)	1.82 (+0%)	1.82 (+0%)	2.12 (17%)	2.1 (+18%)
Combined	1.75	1.79 (+2%)	1.79 (+2%)	1.88 (+7%)	1.91 (+9%)	2.08 (+19%)

3.5 Result validation

In this Section, predictions in terms of monitoring usefulness are compared to observed information gain based on field measurements. Details of the data interpretation and evaluations of degrees of compliance after monitoring can be found in (Bertola et al., 2022).

In the previous section, it was concluded that each monitoring technique (except NDT) provides useful information, and their combination should improve degrees of compliance by a mean average of 19 %. The results of the information gain after monitoring are shown in Figure 4. On average, the monitoring data increases degrees of compliance by 36 %. As predictions were evaluated as mean values, both prediction and observed results can be evaluated as similar.

It is also worth looking at information-gain predictions in terms of the performance of each monitoring technique individually. For SLS verifications, it was predicted that the most useful technique is static load testing, and this result is validated by field measurement. The prediction for ULS verifications showed that only the B-WIM could provide significant information, and this result is also validated by field measurements. Continuous monitoring is the

most useful monitoring technique for FLS verifications, and this prediction is verified using monitoring data. These results confirm that the proposed methodology can provide accurate estimations of the usefulness of monitoring techniques.

Thanks to monitoring data, the bridge safety is now verified as FLS verifications that had a degree of compliance smaller than one has updated values larger than 1.0. This result confirms that structural performance monitoring can lead to untap reserve capacity of bridges.

4 CONCLUSIONS

In this study, a methodology is provided to estimate the usefulness of serval monitoring techniques for bridge performance evaluations. This methodology supports engineers and bridge owners by selecting the optimal combination of monitoring techniques to maximize the information gain in terms of increasing the metric for structural-safety assessments. A bridge case study in Switzerland, where four monitoring techniques were performed, showed that most monitoring techniques provide useful and unique information. Additionally, the predictions in terms of expected information gain for each technique and their combinations are in agreement with results based on monitoring data. In the next step, this methodology will be extended for a comprehensive value-of-information framework to select the optimal combination of monitoring techniques.

REFERENCES

- Bayane, I., Pai, S. G. S., Smith, I. F. C., & Brühwiler, E. 2021. Model-Based Interpretation of Measurements for Fatigue Evaluation of Existing Reinforced Concrete Bridges. *Journal of Bridge Engineering*, 26(8), 04021054.
- Bertola, N. J., Bayane, I., & Brühwiler, E. 2022. Cost-benefit evaluation of a monitoring system for structural identification of existing bridges. In *Bridge Safety, Maintenance, Management, Life-Cycle, Resilience and Sustainability*. CRC Press
- Bertola, N. J., Henriques, G., & Brühwiler, E. 2022. Assessment of the information gain of several monitoring techniques for bridge structural examination, *Journal of Civil Structural Health Monitoring*, Under review.
- Bertola, N. J., Papadopoulou, M., Vernay, D., & Smith, I. F. C. 2017. Optimal multi-type sensor placement for structural identification by static-load testing. *Sensors*, 17(12), 2904.
- Bertola, N. J., Proverbio, M., & Smith, I. F. C. 2020. Framework to Approximate the Value of Information of Bridge Load Testing for Reserve Capacity Assessment. *Frontiers in Built Environment*, 6.
- Brownjohn, J. M. 2007. Structural health monitoring of civil infrastructure. *Philosophical Transactions of the Royal Society of London A: Mathematical, Physical and Engineering Sciences*, 365 (1851),589–622.
- Brownjohn, J. M. W., De Stefano, A., Xu, Y.-L., Wenzel, H., & Aktan, A. E. 2011. Vibration-based monitoring of civil infrastructure: Challenges and successes. *Journal of Civil Structural Health Monitoring*, 1(3–4), 79–95.
- Brühwiler, E., Vogel, T., Lang, T., & Lüchinger, P. 2012. Swiss standards for existing structures. *Structural Engineering International*, 22(2),275–280.
- Catbas, F., Kijewski-Correa, T., Lynn, T., & Aktan, A. 2013. *Structural identification of constructed systems*. Reston: American Society of Civil Engineers.
- Ercan, T., & Papadimitriou, C. 2021. Optimal Sensor Placement for Reliable Virtual Sensing Using Modal Expansion and Information Theory. *Sensors*, 21(10).
- Farrar, C. R., & Worden, K. 2010. An introduction to structural health monitoring. *New Trends in Vibration Based Structural Health Monitoring* (pp. 1–17). Springer.
- Feng, M. Q., Kim, D. K., Yi, J.-H., & Chen, Y. (2004). *Baseline Models for Bridge Performance Monitoring*. 130(5), 562–569. Reston: American Society of Civil Engineers.
- Frangopol, D. M., Strauss, A., & Kim, S. 2008. Use of monitoring extreme data for the performance prediction of structures: General approach. *Engineering Structures*, 30(12),3644–3653.
- Ghosn, M., Dueñas-Osorio, L., Frangopol, D., McAllister, T., Bocchini, P., Manuel, L., Ellingwood, B., Arangio, S., Bontempi, F., Shah, M., Akiyama, M., Biondini, F., Hernandez, S., & Tsiatas, G. 2016a.

- Performance indicators for structural systems and infrastructure networks. *Journal of Structural Engineering*, 142(9), F4016003.
- Ghosn, M., Frangopol, D. M., McAllister, T. P., Shah, M., Diniz, S. M. C., Ellingwood, B. R., Manuel, L., Biondini, F., Catbas, N., Strauss, A., & others. 2016b. Reliability-based performance indicators for structural members. *Journal of Structural Engineering*, 142(9), F4016002.
- Große, C. U., Arndt, R. W., Mähner, D., Niederleithinger, E., & Taffe, A. 2019. Zerstörungsfreie Prüfung im Bauwesen: Memorandum zur Lehre an deutschsprachigen Hochschulen. *Bautechnik*, 96(4), 360–368.
- Helal, J., Sofi, M., & Mendis, P. 2015. Non-Destructive Testing of Concrete: A Review of Methods. *Electronic Journal of Structural Engineering*, 14(1), Article 1.
- Kamariotis, A., Chatzi, E., & Straub, D. 2022. Value of information from vibration-based structural health monitoring extracted via Bayesian model updating. *Mechanical Systems and Signal Processing*, 166, 108465.
- Lydon, M., Taylor, S. E., Robinson, D., Mufti, A., & Brien, E. J. O. 2016. Recent developments in bridge weigh in motion (B-WIM). *Journal of Civil Structural Health Monitoring*, 6(1), 69–81.
- Orcesi, A. D., & Frangopol, D. M. 2011. Optimization of bridge maintenance strategies based on structural health monitoring information. *Structural Safety*, 33(1), 26–41.
- Pai, S. G. S., & Smith, I. F. C. 2022. Methodology Maps for Model-Based Sensor-Data Interpretation to Support Civil-Infrastructure Management. *Frontiers in Built Environment*, 8.
- Papadimitriou, C. 2004. Optimal sensor placement methodology for parametric identification of structural systems. *Journal of Sound and Vibration*, 278(4), 923–947.
- Pasquier, R., & Smith, I. F. C. 2016. Iterative structural identification framework for evaluation of existing structures. *Engineering Structures*, 106, 179–194.
- Proverbio, M., Vernay, D. G., & Smith, I. F. C. 2018. Population-based structural identification for reserve-capacity assessment of existing bridges. *Journal of Civil Structural Health Monitoring*, 1–20.
- Sawicki, B., & Brühwiler, E. 2022. Quantification of influence of monitoring duration on measured traffic action effects on fatigue of RC deck slabs of road bridges. *Structure and Infrastructure Engineering*, 0(0), 1–15.
- Smith, I. F. C. 2016. Studies of Sensor Data interpretation for Asset Management of the Built environment. *Frontiers in Built Environment*, 2, 2–8.
- Swiss Society of Engineers and Architects. 2011. Existing structures, SIA 269, 269/1-269/7. Swiss Society of Engineers and Architects, Zurich, Switzerland.
- Ye, C., Kuok, S.-C., Butler, L. J., & Middleton, C. R. 2022. Implementing bridge model updating for operation and maintenance purposes: Examination based on UK practitioners' views. *Structure and Infrastructure Engineering*, 18(12), 1638–1657.

Monitoring and data informed approaches for the condition assessment of existing structures

E. Apostolidi

Institute of solid structures, Technical University of Darmstadt, Darmstadt, Germany

M.F. Granzner & A. Strauss

Institute of Structural Engineering, University of natural resources and life sciences, Vienna, Austria

R. Geier

Schimetta consult zt gmbh, Vienna, Austria

ABSTRACT: For the appropriate decision-making on maintenance and safety of existing infrastructure, obtaining accurate monitoring information is of crucial importance. Both at a European and national level, current standards and monitoring practice lack standardized approaches to monitoring and this could be partially attributed to the high diversity of the transport infrastructure assets and their environments that increases the complexity of this matter. The new *fib* Model Code 2020 (MC2020) paves the way to new European standards for monitoring and maintenance of structures. Furthermore, MC2020 aims to improve the rules in the structural design codes by bridging the gaps in the current knowledge in theory and practice regarding the monitoring of structures. The main objectives of MC2020 should facilitate and support the various standardization bodies to prepare new standards in monitoring, maintenance, and safety of transport infrastructure. In addition to MC2020, the EU Horizon 2020 IM-SAFE project suggests a respective methodology that tries to be in line with classical engineering procedures, presented in the form of a flow chart. Based on these multi-level condition assessment processes, which are briefly presented in the current paper, an Austrian bridge is used as a case study. The Seitenhafenbridge in Vienna has been monitored over the past 10 years and the acquired data with respect to the condition assessment of the bridge are used for the implementation of the IM-SAFE flow chart aiming to increase the service life for the structure.

1 INTRODUCTION

In the last decades, codes and standards focused mainly on the documentation of guidelines and recommendations for the design of new structures, aiming to ensure the safety and serviceability. At the same time, another goal was to provide the designers with a set of recommendations that are simple, transparent and that avoid potential critical errors. The relative simplicity of those rules includes some conservatism. For new structures this has hardly any influence on the cost, whereas, conversely, this conservatism may turn out to be favourable in the future, if new unforeseen conditions develop, different to the initial design assumptions and criteria adopted.

More recently, as the existing road and railway infrastructure in Europe and worldwide has aged significantly, many existing structures, after having functioned satisfactorily for decades, no longer meet the demands placed upon them for structural safety. Partially, this can be due to a change in the loads which may be larger than envisaged in the stage of design, like the traffic loads on many bridges. Another reason can be that the structures have experienced deterioration, leading to a reduction of the bearing capacity as a result of diminished mechanical properties, and loss of cross-sectional area of concrete and steel. Furthermore, it is possible that it turns out that structures have been designed on basis of design rules from the past, which are actually not accepted anymore.

Therefore, there is an urgent need to provide the engineering community with standards on monitoring and maintenance of existing structures, in an effort to address the question of how the condition of an existing structure can be assessed and how potential deteriorations affect its remaining service.

At this moment *fib* TG 10.1 works to develop a new *fib* Model Code for Concrete Structures (*fib* MC2020, 2023), which should integrate rules for both the design of new and the assessment of existing structures. The behaviour of existing structures is, therefore, an important new component to be considered. This contribution is developed as a part of a collaboration between *fib* TG 10.1 and *fib* Commission 3 “Existing Structures” that consists of several Task Groups. Particularly TG 3.3: Existing Concrete Structures: Life Management, Testing and Structural Health Monitoring has produced a state-of-the-art Bulletin (under publication) that serves an accompanying document to the MC2020 and summarises available scientific information on the subject (*fib* TG 3.3 Bulletin, 2023).

Furthermore, the ongoing European Horizon 2020 project IM-SAFE (<https://im-safe-project.eu/>) also deals with the same thematic and has managed to gather valuable number of case studies and monitoring data information that will serve a new and harmonized European standard for monitoring, maintenance and safety of transport infrastructure in a standardized digitalization approach. The aim of this contribution is to briefly mention the performance condition assessment methods proposed by *fib* (and are also in line with IM-SAFE), including monitoring and data informed approaches and to present a case study of an existing bridge in Vienna, Austria, which was equipped with a certain monitoring setup right after its erecting, where this specific multi-level performance assessment finds application up to date, helping the continuous assessment of the present and future behaviour of this structure.

2 PERFORMANCE ASSESSMENT OF EXISTING STRUCTURES

2.1 *Data informed approaches for the assessment*

Based on practical experience, the performance assessment of a structure is reasonable to break down into a minimum of three levels to support the decision-making process with regards to performance assessment and maintenance optimization. These levels are: Level I - Visual Inspections, Level II - Detailed Inspections, Testing and Monitoring and Level III – Structural Health Monitoring (SHM) & Modelling.

This multi-level performance assessment approach has been reflected in the decision-making flow developed as part of the IM-SAFE Project objectives, a framework of the data-informed safety assessment (H2020 CSA IM-SAFE, 2022a and 2022b) highly interrelated with the life-cycle management of the transport infrastructure. The proposed flow describes the different stages of the assessment of new and existing structures, focusing on various levels (network, system and component) and taking into account the available data during the lifespan and maintenance process of the structure. The same proposed flow is also adopted and can be found in the (*fib* MC2020, 2023) and (*fib* TG 3.3 Bulletin, 2023).

Very briefly, the purpose of Level I is to remove existing doubts about the performance using simple methods, which must, however, be adequate. The preliminary evaluation consists of an approximate assessment based on inspection, an accompanying study of the available documents, and a simplified check on structural safety. An added value can be achieved by using drone-based inspections with AI controlled cameras (Bergmeister et al., 2022). In this first level, it makes sense to distinguish between key performance indicators, which allow an initial assessment, and performance indicators for detailed inspection and to define performance targets and performance thresholds. The performance evaluation based on detection of visible anomalies can either lead to Key Performance Requirements (KPR) level or, in case of an insufficient condition, to a Level II evaluation.

Structural investigations and updating of information are typical of Level II – it comprises detailed inspection, testing and monitoring, among other activities. The additional information gained e.g., from the performance indicators of these investigations can be introduced into confirmatory calculations with the aim of finally dispelling or confirming any doubts as to whether the structure is safe. A detailed inspection of the structure or structural part in question is

extremely important, especially the recognition of typical hazard scenarios that could endanger the structure's residual service life. Further any defects and damage process due to excessive loading or some fragility of important structural members must be detected e.g., by using the visual inspection associated observations and/or performance indicators. As in the first level, it is recommended to distinguish between key performance indicators, which allow an assessment based on a minimum of detailed inspection, testing or monitoring related observations, and performance indicators associated with detailed testing and monitoring. The results of Level II must be summarised in a report. In particular, the report must give information on the structural safety based on the performance indicator findings of Levels I and II and must contain the information about the Performance Requirement Indexes (PRIs) for e.g., network assessment purposes as in Level I.

For important structural members or important structures and for problems with substantial consequences, an advanced analysis (including material and geometry nonlinearity) for performance assessment and performance prediction should be planned to check carefully the proposal for the pending decision that results from Level I and II evaluations. This advanced analysis that includes SHM and FE Modelling with the data acquired by the first ideally updating the second, constitute Level III of the performance assessment methodology.

2.2 *Data informed associated performance indicators*

A particular challenge is the utilisation of measurement data and its use in the performance assessment processes. This topic is already partly addressed in MC2020 (*fib* MC2020, 2023), also to a greater extent in the associated background Bulletin documents (*fib* TG 3.3 Bulletin, 2023) and in further literature sources (Strauss et al. 2017; Strauss et al. 2021). However, some differentiation is also required, associated with informed performance indicators, as will be shown below. A performance indicator can be considered as a measurable/testable parameter that quantitatively describes a property of a structure. The multi-level methodology presented above mainly involves the concept of gathering information through observations/inspection/monitoring that leads to the potential identification of e.g., a degradation mechanism affecting structure. These observations or damage indicators (DIs) can be further defined as performance indicators (PIs), that can interact with one or all levels of bridge management, which are: a) the network, b) the system and the component.

2.2.1 *Performance indicators at the network level*

At the network level, based on bridge condition assessment gained through standard inspection and evaluation procedures with additional evaluation of bridge importance in the network, the primary goal to be reached is supporting the maintenance management and asset management decision process. Priority repair ranking is an example of the essential indicator for the final goal: optimal management plan of road-/railway bridges, which is to be evaluated through decision ranking by power and weakness of decisions. While the bridge structural performance assessment is based on four criteria: structural safety, serviceability, durability and robustness related to the (general) condition of the structure, the bridge importance in the network is based on five criteria: road or corridor category, annual average daily traffic, detour distance, largest span and total length. Such criteria are usually reduced to comparable values with the help of preference functions and with the help of an adequate thresholds of indifference and preference for each criterion. Indicators for the key performance requirements are determined at this level.

2.2.2 *Performance indicators at the system level*

A qualitative assessment can show how the collapse of a particular element would affect the individual Structural Performance Requirements. Structural performance assessment at the system level will require an adequate knowledge level on particular PIs and DIs with related properties, such as stiffness changes and traffic load characteristics, which may require investment in additional inspection, testing or monitoring methods, advanced modelling techniques and updating data on resistance and loads. Besides technical indicators, at this level sustainability and socio-economic indicators will be an essential component of the set of the performance requirements. Additionally, indicators related to scientific achievements in, for example, testing and monitoring, dynamic behaviour and reliability of structures, should be elaborated at this level, as well.

2.2.3 Performance indicators at the component level

Inspections of structures are generally carried out at the level of components. For bridges, three main subsystems can be distinguished: substructure, superstructure and road-/railway, with specific bridge components associated with these systems, including constitutive materials. For tunnel systems, a similar decomposition is possible, distinguishing e.g., ridge, callous, abutment and base area, or inner shell, outer shell and sealing level. At the component level, one of the important goals to be reached (or task to be performed) is the damage assessment. This implies the detection of damages but also the identification and evaluation of damage within the set thresholds. The categorization of damage as a primary performance indicator at the component level, requires considering related detection methods, performance thresholds and evaluation methods. PIs, DIs, damage processes, surveying technologies and performance assessment levels can be correlated.

3 THE CASE STUDY OF THE SEITENHAFENBRIDGE IN VIENNA, AUSTRIA

In the framework of the performance condition assessment presented in section 2, the Seitenhafen-bridge is used as a case study to partially apply this methodology, highlighting the three levels of assessment for a newly constructed structure. The bridge, shown in Figure 1(a), is part of a new road connection in the city of Vienna, crossing the Danube Channel. It is a concrete/steel composite bridge, constructed in 2011, and it was designed for road, pedestrian and bicycle traffic. The total length of the bridge is 128,69 m, divided in 5 fields, and a width of 15 m. The road deck is a solid reinforced concrete structure, and its support was realized through steel columns, arranged in pairs

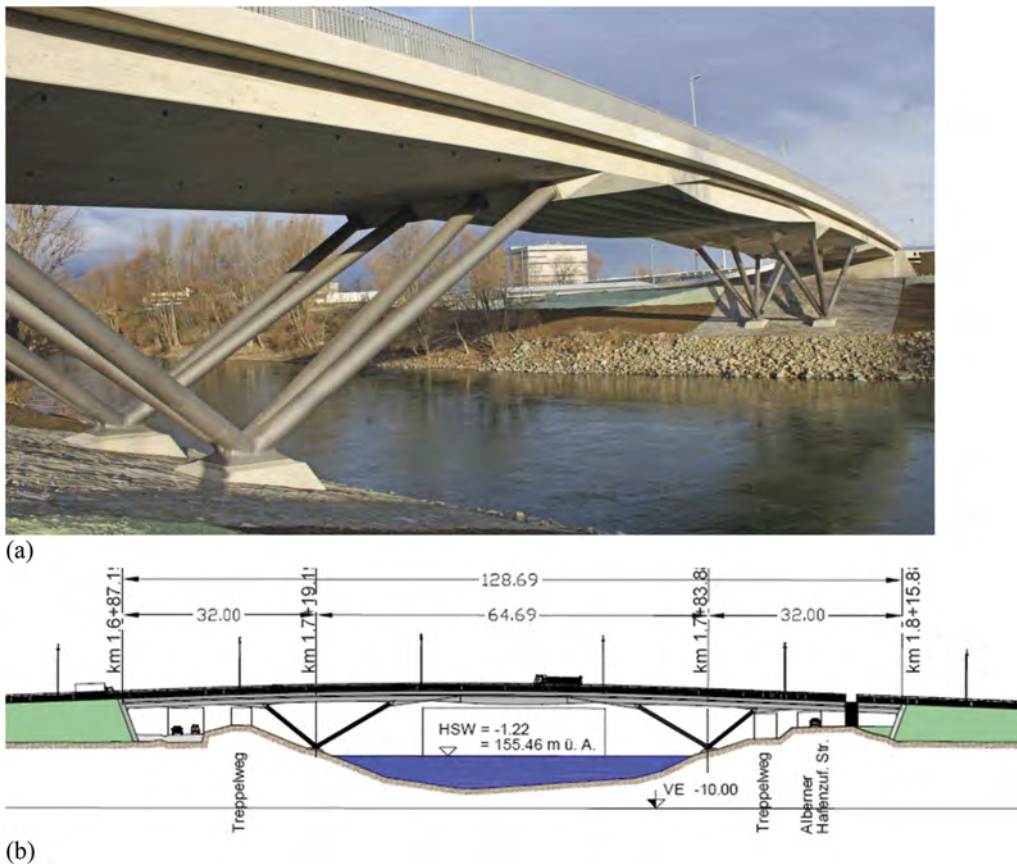


Figure 1. The Seitenhafenbridge crossing the Danube Channel in Vienna, Austria. (a) General overview and (b) Longitudinal section (Geier et al., 2009).

next to the bearings. The abutments are not aligned at right angles with the road axis, as it can be seen in the longitudinal section of Figure 1(b) (Geier et al., 2009).

The Seitenhafenbridge in Vienna is currently the longest integral bridge in Austria and due to its significance, the infrastructure manager requested and installed a complex system for the monitoring of the movements of the construction. This step leads to a more detailed inspection level (Level II) and the infrastructure manager along with the consulting company defined performance and key indicators and their thresholds that go hand in hand with the monitoring setup.

The monitoring set up is shown in Figure 2 and it was designed to serve the particularities of this integral bridge, constantly measuring temperature and the movements of the construction, like for example deflection, inclination, length variation and ground pressure at the abutment. The data are continuously assessed and summed up in intermediary reports showing the actual behaviour of the structure.

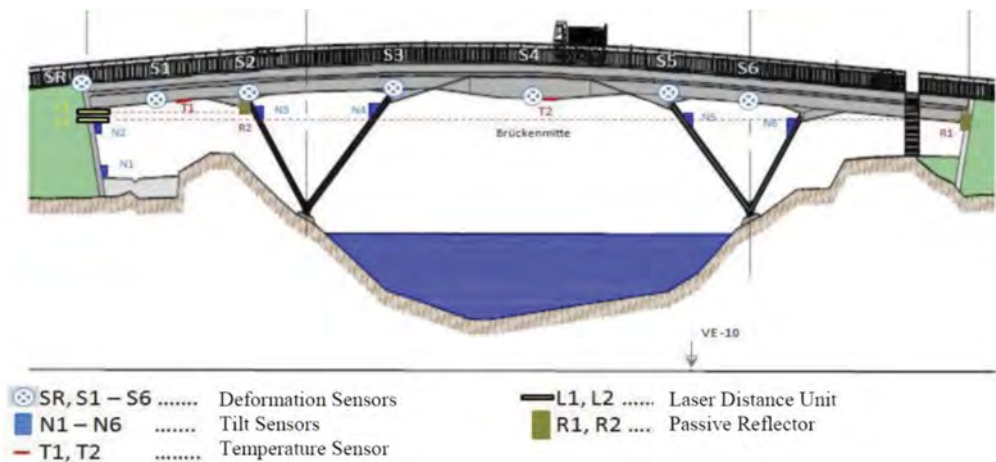


Figure 2. Monitoring setup at the Seitenhafenbridge crossing the Danube Chanel in Vienna, Austria (Geier et al., 2009).

In parallel to the application of the monitoring system, a detailed finite element (FE) model of the structure was created, going into level II of the performance assessment process. After monitoring the structure for a significant period of time, important information on its behaviour in terms of temperature, deformations and overall movement of the structure could be extracted. The monitoring data was used to update the FE model and verify the performance of the critical details of the structure. In Figure 3, within a period of 3 years (12.2011 to 12.2014), the variation of the measured vertical deformations (Figure 3(a)) and temperature (Figure 3(b)) is documented. It can be noticed that at the middle of the structure a maximal vertical deformation of $\sim +30\text{mm}$ was measured during the summertime, while during the winter months a vertical deformation of $\sim -10\text{mm}$ was documented.

In the following Figure 4, the generic framework and process flow for risk management proposed by the IM-SAFE project is applied step by step for the Seitenhafenbridge, highlighting the 8 most important points for this particular structure. In this flowchart, one can also see on the left side of each step which levels in terms of bridge management (e.g., component, system, network) should be considered for the PI definition. The exact elaboration of the process steps is described in detail in the (H2020 CSA IM-SAFE. 2022a) and (H2020 CSA IM-SAFE. 2022a).

In more detail, for the Seitenhafenbridge the following main points of the risk management flow are listed below, showing the flow indicated by the blue arrows in Figure 4:

1. Classification and Prioritization: This new bridge is currently the longest integral bridge in Austria. Due to the total length of approx. 130 meters, an in-depth performance analysis and risk assessment was requested, classifying this structure as medium to high priority structure.

2. Detailed investigation (Yes/No): In this context, the monitoring of the movements of the structure was required.
3. Condition survey at level II: Performance and key indicators and their thresholds were defined in order to reach condition survey level II.
4. Level II Performance monitoring: The monitoring system continuously measures temperatures and movements of the structure, such as deflection, inclination, length change, and soil pressure at the abutment.
5. Detailed structural assessment: A detailed digital twin model was developed using the monitoring data to verify the performance of the critical details, reaching condition survey level III.
6. Condition survey at level II: The digital twin models were updated, and the functionality of the critical details was verified.
7. Level III Performance monitoring: Thresholds were set for the monitored performance indicators using the digital twin models.
8. Alert level assessment: An alarm system was set up in combination with the monitoring system and the client.
9. Continuous monitoring and diagnostics are active since 2011, on all the 5 spans of the bridge, with a real-time alerting system active to support proactive maintenance intervention figure.

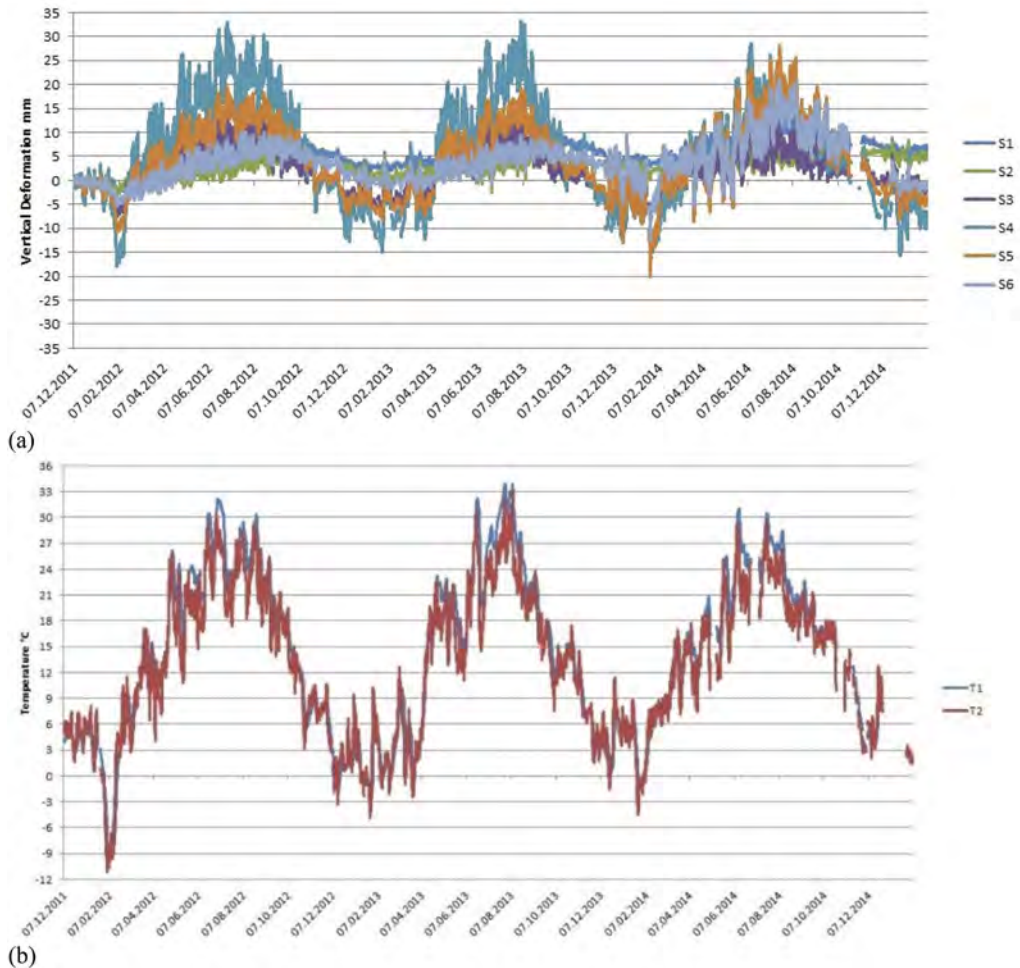


Figure 3. Measured data within a period of 3 years for (a) vertical deformations at the location of sensors S1 to S6 and (b) temperatures at the location of sensors T1 and T2 (Geier et al., 2009).

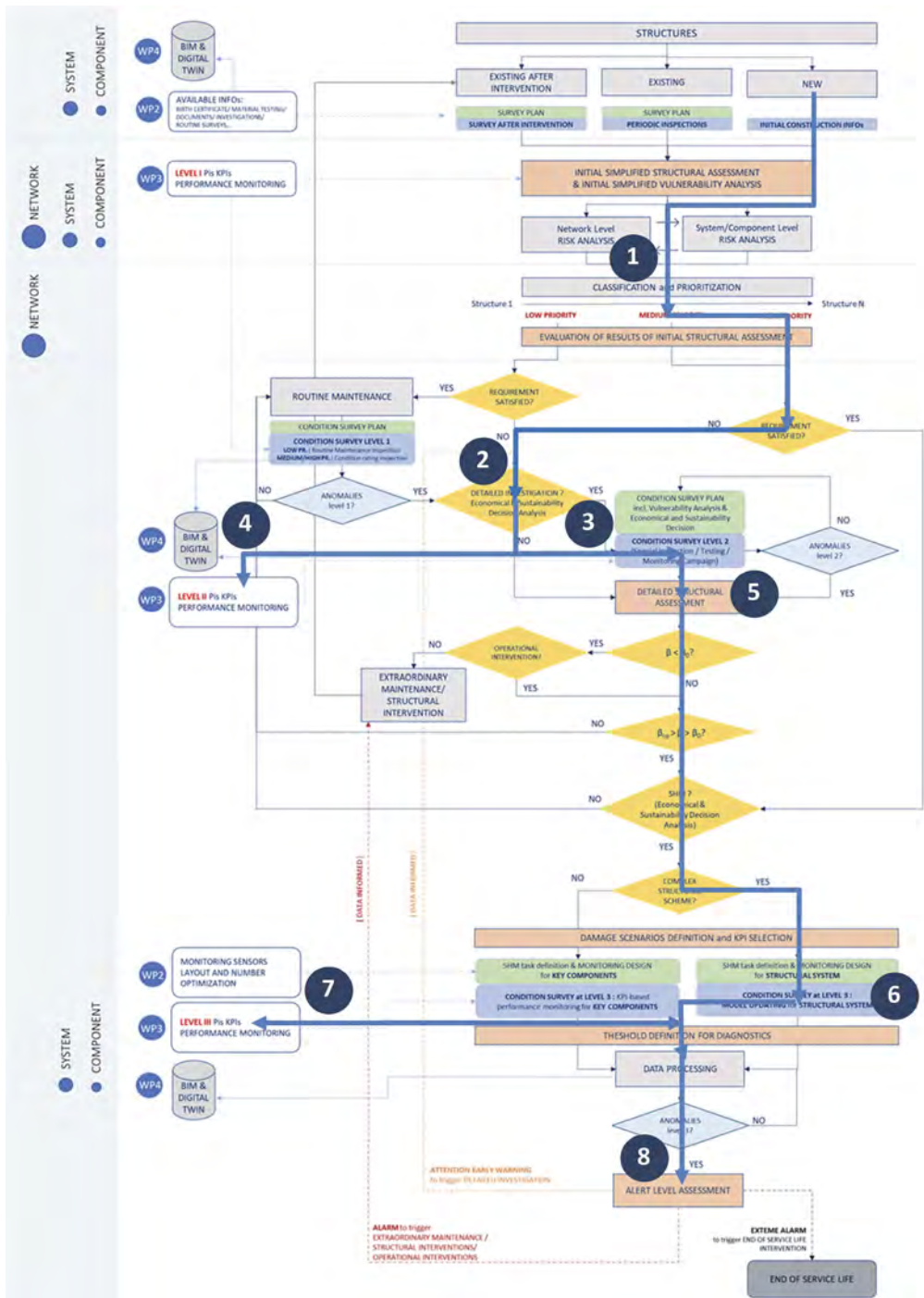


Figure 4. Generic framework and process flow for risk management, from IM-SAFE project report D3.1, particularly adjusted for the Seitenhafenbrücke in Vienna, Austria (H2020 CSA IM-SAFE. 2022a).

4 CONCLUSIONS

In the current paper, a brief overview of the framework for the data-informed safety assessment and its high interrelation with the through-life management of the transport infrastructure is presented. The relevant performance assessment methodologies developed by the *fib* MC 2020 and the IM-SAFE project are briefly presented. Through the application in a specific bridge structure, the Seitenhafenbridge in Vienna, of the generic framework and process flow for risk management adopted by the IM-SAFE project, an assessment process more in line with the classical engineering procedure is verified. This framework assists the more organized and systematic assessment of the structure throughout its lifetime, enabling a better understanding and communication of its condition not only to the owners and the involved engineers, but also to other related disciplines. Furthermore, it assists the systematic definition of PIs based on the different levels of assessment targeting a longer service life of infrastructure.

ACKNOWLEDGEMENTS

The authors would like to acknowledge the support of the research project IM-SAFE and its working team (<https://im-safe-project.eu/>).

REFERENCES

- Bergmeister, K., Strauss, A., Hoffmann, M. 2022. Digitale Zustandserfassung von Gebäuden, Infrastrukturbauwerken und Naturgefahren. In: *Betonkalender 2022*, Ernst & Sohn. P. 533–606 (in German).
- fib* Model Code. 2023 Model Code for Concrete Structures Fédération internationale du béton (*fib*) (under review).
- fib* TG 3.3. 2023. Existing concrete structures: Life management, testing and structural health monitoring. State-of-the-art Report. Fédération internationale du béton (*fib*) (under publication).
- Geier, R., Mack, T., Strauss, A. 2009. Monitoring Experiences on Integral Bridges, IABSE Symposium Report.
- Hajdin, R., Kušar, M., Mašović, S., Linneberg, P., Amado, J. & Tanasić, N. 2018. TU1406 COST Action: Quality Specifications for Roadway Bridges, Standardization at a European Level: *WG3-Technical Report: Establishment of a Quality Control Plan*. Braga: Boutik.
- H2020 CSA IM-SAFE. 2022a. Progress Report D3.1: Appraisal of methods for safety evaluation and risk management. <https://im-safe-project.eu/> (OER Format).
- H2020 CSA IM-SAFE. 2022b. Progress Report D3.2: Background materials for implementation of decision-making regarding maintenance strategies. <https://im-safe-project.eu/> (OER Format).
- Strauss, A., Ivanković, A. M., Campos e Matos, J. & Casas, J. 2017. Performance indicators for road bridges – overview of findings and future progress. Joint COST TU1402 – COST TU1406 – IABSE WC1 Workshop: The Value of Structural Health Monitoring for the reliable Bridge Management, Zagreb, Croatia.
- Strauss, A., Sattler, F., Hoffmann, M., Apostolidi, E. Fernandez, S. & Campos e Matos, J. 2021. Performance indicators for European bridge management. Bridge Maintenance, Safety, Management, Life-Cycle Sustainability and Innovations: 1993-2005, CPR Press.
- Strauss A., Bigaj-van Vliet A., Daró P., Sanchez, A., Granzner, M., Bergmeister, K. 2022. Performance indicators for an objective assessment and through-life management of bridges and tunnels, *fib Congress Oslo*.

A novel low-cost inclinometer sensor based on fusion technology for structural health monitoring applications

M. Komary, A. Alahmad, S. Komarizadehasl & J. Turmo

Department of Civil and Environment Engineering, Universitat Politècnica de Catalunya, BarcelonaTech, Barcelona, Spain

J.A. Lozano-Galant

Department of Civil Engineering, Universidad de Castilla-La Mancha, Ciudad Real, Spain

Y. Sun

School of Civil and Hydraulic Engineering, Huazhong University of Science and Technology, Wuhan, China

ABSTRACT: The fundamental purpose of structural health monitoring (SHM) is to examine the accuracy of the structural health state and predict its future strength. Lately, researchers have been paying close attention to the structural damage detection process employing inclinometers. However, this technique can only be used with unique structures with a sizable Structural Health Monitoring (SHM) budget due to the high cost of inclinometers. Therefore, the use of low-cost sensors by implementing various techniques to improve their accuracy compared to high-cost precision sensors has attracted much attention for structural assessment. This paper introduces a novel, low-cost inclinometer that measures inclination by fusion technology combining gyroscopes and accelerometers. The microcontroller technology used in this gadget is an open-source Internet of Things (IoT) based platform, allowing for wireless data streaming and free commercial software for data collecting. Not only are the coding and placement issues of these sensors thoroughly explained, but detailed answers to the problems mentioned above are also provided, as well as an efficient way to assemble and prepare the sensors.

1 INTRODUCTION

Structural Health Monitoring (SHM) has attracted the attention of engineers over the past decades as a control system to measure the structural response of structural elements to prevent future potential failures in civil infrastructures. A number of factors and situations such as construction defects, fatigue and environmental factors might decrease the structure's serviceability and safety over time (Kaloop et al., 2022), (Mahyad Komary et al., 2022), (Seyedmilad Komarizadehasl et al., 2022). Therefore, monitoring and assessing structures' health state throughout their life cycle are essential to minimize the future reparation costs and to confirm the Structural safety and serviceability (Proske, 2020), (Farré-Checa et al., 2022). SHM applications provide vital information about the actual structural response of infrastructures, the condition of the structures and their performance (Mahyad Komary et al., 2023).

For measuring static and dynamic responses, sensors are widely used in SHM systems (S. Komarizadehasl et al., 2022). Accelerometers are commonly used for monitoring the dynamic response of the structures, while the most common sensors for static measurements include strain gauges, inclinometers and thermometers (Lei et al., 2021), (M. Komary et al., 2022).

Even though accelerometers can detect global structural damages to a structure, they traditionally fail to detect the damage location and its severity (Hester et al., 2019). Displacement

sensors such as Laser Displacement Sensors (LDS) can be used in load tests to help to locate the damage and its extension as long as a particular reference point exists (Raghuwanshi & Parey, 2018), (Yao et al., 2022). Unfortunately, a number of limitations on-site can make the proper definition of the required reference points difficult (Park et al., 2013). Alternative strain-type sensors can be used to evaluate the extent of the damage and its location. In fact, this type of sensor has shown remarkable accuracy and applicability in the literature (Li et al., 2020), (Iriarte et al., 2021), (Copertaro, 2022). However, a large number of this type of sensor might be needed to monitor the structure's structural properties entirely.

In order to overcome the drawback of the aforementioned sensors, inclinometers can be used. Angular sensors (inclinometers, tilt sensors) are manufactured to estimate the angular rotation of a target object respected to an artificial horizon (Hester et al., 2019), (Seyedmilad Komarizadehasl et al., 2022). Most inclinometers follow the principle of measuring responses induced by pendulum behaviour due to gravity (Huseynov et al., 2020). Furthermore, this slope can be used to calculate the drift of vertical members and vertical deflection of the horizontal elements (Ha et al., 2013).

Table 1 illustrates the characteristics of some of the commercially available inclinometers and is sorted by the price of the sensors. It should be noted that prices are based on the recent producer declaration and are VAT excluded.

Table 1. Characteristics of some of the commercially available inclinometers.

Model	Sampling Rate (Hz)	Resolution (Degrees)	Measurement Range (Degrees)	Price (€)
ZEROTR ONIC	10	$100 \times 10^{-5} \text{ }^\circ$	$\pm 0.5^\circ$	3950
ACA2200	20	$10 \times 10^{-5} \text{ }^\circ$	$\pm 0.5^\circ$	710
HI-INC	100	$100 \times 10^{-5} \text{ }^\circ$	$\pm 15.0^\circ$	650
ZCT-CX09	8	$100 \times 10^{-5} \text{ }^\circ$	$\pm 15.0^\circ$	350
DNS	100	$300 \times 10^{-5} \text{ }^\circ$	$\pm 85.0^\circ$	348

Analysis of Table 1 shows a wide range of prices (varying between 350€ up to 3950 €) and measurement ranges (varying between 0.5 and 85.0 degrees). It can be seen that inclinometers with a lower range have a higher resolution and price. Furthermore, inclinometers with higher resolution typically have higher costs and lower sampling frequencies.

On the contrary to the benefits of using inclinometers (Hester et al., 2019), this monitoring system presents limited precedents in the literature of SHM of bridges (Erdenebat et al., 2018), (Alten et al., 2017). Among the reasons given by Huseynov (Huseynov et al., 2020) to explain the lack of the use of the inclinometers is to highlight the lack of sensor technology, low-frequency sampling, and the cost of the current inclinometers.

To solve the aforementioned drawback of inclinometers, low-cost sensors can be used. In fact, Micro-Electro-Mechanical Systems (MEMS) accelerometers have revolutionized the measuring applications with reduced size and price (Seyedmilad Komarizadehasl, Lozano Galant, et al., 2022a). It should be noted that other low-cost MEMS accelerometers were already published for SHM applications in the literature.

MEMS sensors are typically coupled with gyroscopes. MEMS Gyroscopes measure the angular rate by Coriolis acceleration, enabling the rotational speed measurement. The main drawback of the gyroscopes is bias instability or Flicker noise (Hiller et al., 2019).

Almost all current MEMS inclinometers use sensor fusion capability to improve the individual drawbacks of the accelerometer and the gyroscope. In addition, the negative impacts of a sudden movement of the accelerometer estimations are controlled with the gyroscope measurements (Ghasemi-Moghadam & Homaeinezhad, 2018).

The literature review shows no accurate, low-cost inclinometers based on the Arduino or NodeMCU technology that could be used in SHM of bridges due to the special peculiarities of this type of monitoring (Huseynov et al., 2020). To fill these gaps, this paper presents, for the first time in the literature, a Low-cost Adaptable Reliable Angle-meter (LARA) system for SHM of bridges. LARA is a low-cost wireless inclinometer based on an IoT-based microcontroller (NodeMCU) technology with an accuracy of 0.003 degrees based on the performed experiments of this paper.

LARA is based on MEMS technology and uses the complementary filter to couple the outputs of its accelerometer and gyroscope calculated angles.

In addition, to build an inclinometer with higher accuracy, better resolution and lower noise density, this paper develops a custom-designed Printed Circuit Board (PCB) containing five low-cost aligned MEMS MPU9250 chipsets, each of one incorporating a gyroscope, an accelerometer and a magnetometer (Seyedmilad Komarizadehasl, Lozano Galant, et al., 2022b).

2 THE PROPOSED INCLINOMETER

2.1 Low-cost Adaptable Reliable Angle-meter (LARA) system

2.1.1 Hardware architecture of LARA

This paper proposes multiple combinations of gyroscopes and accelerometers for producing a more accurate inclinometer. To this end, five chipsets of MPU9250 are engineered together on a single PCB and synchronized using a multiplexor (TCA9548A). To avoid the problems of a manual fabrication (such as nonalignment of the circuits, time-consuming process of aligning, soldering and sensor quality control and size), the PCB of LARA was designed and produced to satisfy the delicacy of current project measurements. In addition, the required components of LARA are soldered to the PCB using machine assembly. The cost of a LARA made by connecting five MPU9250 and TCA9548A and a bulk company-produced PCB with assembled components is around 37 and 51 €, respectively.

As shown in Figure 1.a, LARA has four output ports. These wires should be connected to a microcontroller to power up the sensors, acquire the sampled data, and convert the gyroscope and the accelerometer to tilt and pitch inclination. The used microcontroller of this paper is NodeMCU and shown in Figure 1.b. This low-cost open-source Internet of Things (IoT) platform runs on the ESP8266 chipset. ESP8266 is a low-cost WiFi microchip with the Internet protocol suite (also known as TCP/IP) capability (Chiesa et al. 2020).

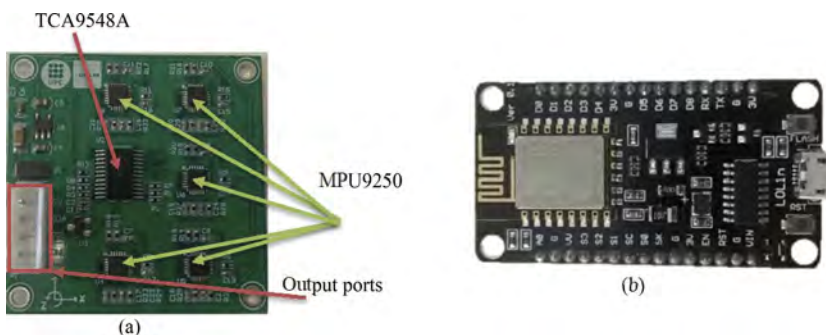


Figure 1. Illustration of LARA: (a) The produced product, and (b) NODE MCU microcontroller.

2.1.2 Software architecture of LARA

In this section, the used software for this project is presented in the following:

Arduino platform: NodeMCU is first programmed using the Arduino platform. This program first estimates the angle in real-time from each of the individual MPU9250 chipsets. Then, the formulas for calculating the rotation using a triaxial accelerometer for X and Y axes are presented in Eq.1 and Eq.2, respectively.

$$\text{angle}_{accX} = \tan^{-1} \left(\frac{\text{acc}Y}{\sqrt{\text{acc}Z^2 + \text{acc}X^2}} \right) \times \left(\frac{360}{2\pi} \right) \quad (1)$$

$$\text{angle}accY = \tan^{-1}\left(\frac{accX}{\sqrt{accZ^2 + accY^2}}\right) \times \left(\frac{360}{2\pi}\right) \quad (2)$$

In Eq.1 and Eq.2, where, $\text{angle}accX$ and $\text{angle}accY$ are the calculated angles from the acquired data of a MPU9250 accelerometer around the X-axis and Y-axis, respectively. The $accX$, $accY$ and $accZ$ represent the obtained acceleration data of X, Y and Z axes. Eq.3 and Eq.4 present the used complementary equation for the fusion of the gyroscope and the accelerometer results for measuring the rotation around X and Y axes, respectively.

$$\text{angle}X = (0.96 \times (\text{angle}X_0 + \text{gyro}X \times \text{time})) + 0.04 \times \text{angle}accX \quad (3)$$

$$\text{angle}Y = (0.96 \times (\text{angle}Y_0 + \text{gyro}Y \times \text{time})) + 0.04 \times \text{angle}accY \quad (4)$$

In Eq.3 and Eq.4, where, $\text{angle}X$ and $\text{angle}Y$ are the final calculated rotations around X and Y-axes, respectively. The $\text{angle}X_0$ and $\text{angle}Y_0$ are the estimated angle of the system from the previous measurement. The $GyroX$ and $GyroY$ represent the measured angular speed of the gyroscope for X and Y axes, respectively. The time presents the interval time between two measurements. Further analysis of these equations shows that the angle calculated from the accelerometer is multiplied by a smaller coefficient than that of the gyroscope (Yi et al., 2018). This low coefficient factor of $\text{angle}acc$ is for mitigating the impact of environmental vibrations (also known as cross-talk of vibration) and can vary between 0.02 and 0.05 (Shen et al., 2012).

Data acquisition: Unlike the Arduino platform, free commercial software like SerialPlot can represent the sampled data in real-time in a graphical interface and save the data with the date and timestamp of data acquisition.

3 STATISTICAL REPRESENTATION OF COMBINING DYNAMIC-SENSOR THEORY

3.1 Noise reduction of Inclinometers

It was noticed that the average value of outputs of several aligned synchronized inclinometers has lower noise density than the those of a single one. The standard deviation of up to five combined inclinometers is presented in Figure 2.

The analysis of Figure 2 shows that the higher the number of sensors considered the lower the noise density of their averaged measurements that the more combined inclinometers have a lower noise density. The reason behind the beneficial behaviour of combined inclinometers is within the inherent dynamic noises of the produced accelerometers and gyroscopes chipsets.

These results led to investigating the beneficial impact of dynamic sensor combinations. Analysing the individual outputs, the five used MPU9250 sensors showed that every single sensor has unique dynamic noises.

By improving the noise density, the inclinations that in the first place were smaller than the noise density of the sensor can now be detected due to the improved noise level.

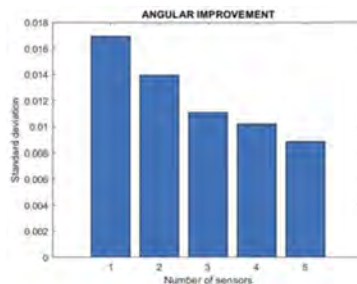


Figure 2. Representation of the noise ratio of a single and up to five combined inclinometers using standard deviation.

4 LABORATORY EXPERIMENTS

4.1 LARA resolution and accuracy verification using a beam model

In order to present the resolution and accuracy of LARA more clearly, a load test is performed on a small-scale beam with a length of 1.24m. This section compares the slope estimation of two sensors (LARA and HI-INC) located on the support of a simply supported aluminium beam model under a point load of 467 gr (4.58 kN) with hand calculation of slope at the beam edges.

This test is carried out using a U-shaped aluminium profile with section dimensions of 25×25×3×3 mm. The effective length of the beam model, which is the distance between the null axis of its support, is fixed as 1080 mm.

The test aim was to read the maximum slope of the beam model deck under a known applied load on the mid-span. The maximum slope at the supports can be calculated by Equation 5. Therefore, LARA and HI-INC were attached to achieve this objective on top of the beam model support. First, LARA and HI-INC worked for a while without any loads and their estimations were acquired. Next, the point load was set on the mid-span of the beam model (Figure 3) and then another data acquisition process was carried out to measure the slope of the beam by LARA and HI-INC. It is essential to mention that this test was repeated three times.



Figure 3. Load test of a beam model.

The used formula for calculating the slope of a simply supported beam with a load located on its midspan by hand is presented in Eq.5 (Hibbeler, 2017).

$$\Delta\theta_1 = \frac{P \times L^2}{16 \times E \times I} \quad (5)$$

In Eq.5, where, $\Delta\theta_1$ (Radians) is the maximum slope at the supports, P is the value of the applied load at the mid-span, L is the effective beam length, E (69637.05 MPa) is the beam elasticity module, and I (12853.08 mm⁴) is the beam moment of inertia.

Table 2. Comparing the inclination estimation of LARA and HI-INC.

Number of the experiments	Hand calculation slope (degrees)	LARA Difference (degrees)	LARA (degrees)	HI-INC difference (degrees)	HI-INC (degrees)
1	0.021372	0.001613	0.022985	0.002447	0.018925
2	0.021372	0.002316	0.023688	0.000853	0.020519
3	0.021372	0.001362	0.022734	0.005196	0.016176

The analysis of Table 2 shows that the accuracy of LARA based on these experiments is less than 0.002 degrees. Further study of Table 2 illustrates that the accuracy of HI-INC is around 0.005 degrees. In fact, this is very close to accuracy value detailed in its datasheet ($\pm 0.003^\circ$ for $\pm 15^\circ$ version).

Another experimental test was carried out on this beam model using a heavier weight (21.942 N). In this experiment, instead of putting the weight only on the midspan, the weight was set on various beam locations.

Figure 4 presents the slope measurement comparison of HI-INC and LARA with the hand calculation values. It is vital to mention that this experiment is carried out on the same beam model presented in Figure 3. As showed in this figure, the inclinometer is mounted on a pinned support.

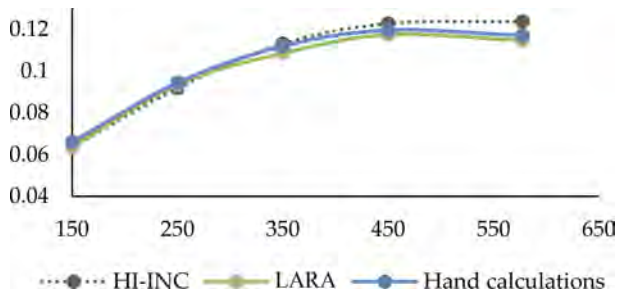


Figure 4. Support slope of a simply supported beam under a point load located on various spots.

Analysis of Figure 4 shows that LARA has a maximum measured difference of 0.003 degrees from the hand calculation slope. In addition, it can be seen that LARA has a closer trend to the hand calculation values compared to those of HI-INC.

It can be seen from Table 1 that HI-INC, ZCT-CX09 and DNS have a resolution of 0.003 degrees. Therefore, LARA can be compared with them. Figure 5 presents the price comparison of these inclinometers.

Analysis of Figure 5 shows a significant difference between the price of LARA and inclinometers with the same resolution. LARA is 12, 6 and 6 times cheaper than HI-INC, ZTC-CX09 and DNS inclinometers, respectively. Also, it does not need extra paid commercial software for data acquisition, and it is based on open-source software and hardware.

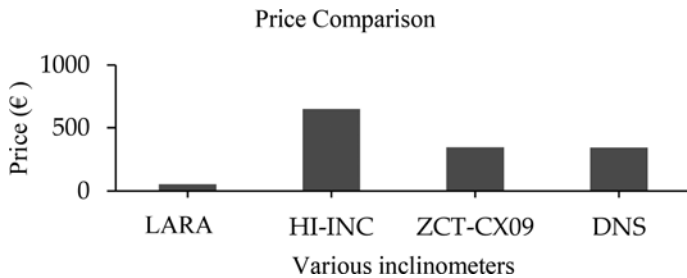


Figure 5. Price comparison of LARA with traditional commercial inclinometers with a resolution of 0.003 degrees.

5 CONCLUSION

Lately, the implantation of inclinometers for SHM of bridges is receiving a lot of attention from engineers and researchers. In fact, unlike accelerometers, inclinometers can enable easily the evaluation of both the location and severity of the structural damage. This characteristic makes them suitable for long-term Structural Health Monitoring (SHM) of bridges. However, the current inclinometers' high price has limited their use. There is gap in the literature with the development of a low-cost inclinometer for long term SHM of bridges with a low budget for their health assessments.

To fill these gaps, in this paper, a Low-cost Adaptable Reliable Angle-meter (LARA) system is presented. LARA is a low-cost wireless IoT-based inclinometer with a sampling frequency of 250 Hz. The main novelty of LARA is combining the results of five aligned inclinometers for reducing the inherent noise density of individual accelerometers and gyroscopes of LARA.

In order to validate the assumption of noise reduction and signal improvement of inclination measurements using the averaged results of several aligned inclinometers, four laboratory experiments were carried out. The results of tests show that averaging the values of

a number of aligned accelerometers reduces the noise density of the frequency domain representation of a vibration acquisition experiment.

In addition, in order to compare the accuracy of the used commercial inclinometer and LARA a load test is performed on a beam. In this test, the reported values of the commercial inclinometer are compared with LARA's. It is shown that LARA estimated the theoretical slope with less than 0.003 degrees of difference from the hand calculated values. However, HI-INC showed an accuracy higher than its datasheet data with a magnitude of $\pm 0.005^\circ$.

REFERENCES

- Alten, K., Ralbovsky, M., Vorwagner, A., Topplitzer, H., & Wittmann, S. (2017). Evaluation of Different Monitoring Techniques during Damage Inflection on Structures. *Procedia Engineering*, *199*, 1840–1845. <https://doi.org/10.1016/J.PROENG.2017.09.106>
- Copertaro, E. (2022). Assessment of resistive strain gauges measurement performances in experimental modal analysis and their application to the diagnostics of abrasive waterjet cutting machinery. *Measurement*, *188*, 110626. <https://doi.org/10.1016/J.MEASUREMENT.2021.110626>
- Erdenebat, D., Waldmann, D., Scherbaum, F., & Teferle, N. (2018). The Deformation Area Difference (DAD) method for condition assessment of reinforced structures. *Engineering Structures*, *155*, 315–329. <https://doi.org/10.1016/J.ENGSTRUCT.2017.11.034>
- Farré-Checa, J., Komarizadehasl, S., Ma, H., Lozano-Galant, J. A., & Turmo, J. (2022). Direct simulation of the tensioning process of cable-stayed bridge cantilever construction. *Automation in Construction*, *137*, 104197. <https://doi.org/10.1016/J.AUTCON.2022.104197>
- Ghasemi-Moghadam, S., & Homaeinezhad, M. R. (2018). Attitude determination by combining arrays of MEMS accelerometers, gyros, and magnetometers via quaternion-based complementary filter. *International Journal of Numerical Modelling: Electronic Networks, Devices and Fields*, *31*(3), e2282. <https://doi.org/10.1002/JNM.2282>
- Ha, D. W., Park, H. S., Choi, S. W., & Kim, Y. (2013). A Wireless MEMS-Based Inclinometer Sensor Node for Structural Health Monitoring. *Sensors 2013, Vol. 13, Pages 16090-16104*, *13*(12), 16090–16104. <https://doi.org/10.3390/S131216090>
- Hester, D., Brownjohn, J., Huseynov, F., O'Brien, E., Gonzalez, A., & Casero, M. (2019). Identifying damage in a bridge by analysing rotation response to a moving load. *Structure and Infrastructure Engineering*, *16*(7), 1050–1065. <https://doi.org/10.1080/15732479.2019.1680710>
- Hibbeler, R. C. (2017). *Structural Analysis*. Pearson; 10th edition (July 28, 2017), ISBN: 0134610679.
- Hiller, T., Pentek, Z., Liewald, J. T., Buhmann, A., & Roth, H. (2019). Origins and Mechanisms of Bias Instability Noise in a Three-Axis Mode-Matched MEMS Gyroscope. *Journal of Microelectromechanical Systems*, *28*(4), 586–596. <https://doi.org/10.1109/JMEMS.2019.2921607>
- Huseynov, F., Kim, C., O'Brien, E. J., Brownjohn, J. M. W., Hester, D., & Chang, K. C. (2020). Bridge damage detection using rotation measurements – Experimental validation. *Mechanical Systems and Signal Processing*, *135*, 106380. <https://doi.org/10.1016/J.YMSSP.2019.106380>
- Iriarte, X., Aginaga, J., Gainza, G., Ros, J., & Bacaicoa, J. (2021). Optimal strain-gauge placement for mechanical load estimation in circular cross-section shafts. *Measurement*, *174*, 108938. <http://dx.doi.org/10.1016/J.MEASUREMENT.2020.108938>
- Kaloo, M. R., Eldiasty, M., & Hu, J. W. (2022). Safety and reliability evaluations of bridge behaviors under ambient truck loads through structural health monitoring and identification model approaches. *Measurement*, *187*, 110234. <https://doi.org/10.1016/J.MEASUREMENT.2021.110234>
- Komarizadehasl, S., Komary, M., Turmo, J., Torralba, V., Lozano, F., & Lozano-Galant, J. A. (2022). Using few accelerometer for improving the resolution and accuracy of low-cost accelerometers. In *Bridge Safety, Maintenance, Management, Life-Cycle, Resilience and Sustainability* (1st Edition, Vol. 5, pp. 1575–1579). CRC Press. <https://doi.org/10.1201/9781003322641-193>
- Komarizadehasl, Seyedmilad, Komary, M., Alahmad, A., Lozano-Galant, J. A., Ramos, G., & Turmo, J. (2022). A Novel Wireless Low-Cost Inclinometer Made from Combining the Measurements of Multiple MEMS Gyroscopes and Accelerometers. *Sensors 2022, Vol. 22, Page 5605*, *22*(15), 5605. <https://doi.org/10.3390/S22155605>
- Komarizadehasl, Seyedmilad, Komary, M., Turmo Coderque, J., Torralba Mendiola, V., Lozano Galant, F., & Lozano Galant, J. A. (2022). Low-cost accurate acceleration acquisition sensor. *Bridge Safety, Maintenance, Management, Life-Cycle, Resilience and Sustainability: Proceedings of the Eleventh International Conference on Bridge Maintenance, Safety and Management (IABMAS 2022), Barcelona, Spain, July 11- 15, 2022*, 803–810. <https://doi.org/10.1201/9781003322641-96>

- Komarizadehasl, Seyedmilad, Lozano Galant, F., Komary, M., Lozano Galant, J. A., & Turmo Coderque, J. (2022a). Development of an accurate low-cost device for structural vibration acquisition. *IABSE Symposium Prague 2022 Report: Challenges for Existing and Oncoming Structures*, 1–6.
- Komarizadehasl, Seyedmilad, Lozano Galant, F., Komary, M., Lozano Galant, J. A., & Turmo Coderque, J. (2022b). Resolution improvement of low-cost MEMS accelerometer by aligning simulations sensors. *IABSE Symposium Prague 2022 Report: Challenges for Existing and Oncoming Structures*, 1–6.
- Komary, M., Komarizadehasl, S., Ramos, G., & Torralba, V. (2022). Developing and validation of an inclinometer sensor based on fusion of a magnetometer, an accelerometer and a gyroscope sensor for SHM applications. In *Bridge Safety, Maintenance, Management, Life-Cycle, Resilience and Sustainability* (1st Edition, Vol. 5, pp. 1607–1611). CRC Press. <https://doi.org/10.1201/9781003322641-198>
- Komary, Mahyad, Komarizadehasl, S., Ramos Schneider, G., Tošić, N., Turmo Coderque, J., & Torralba Mendiola, V. (2022). Full review of low-cost electronics implemented in structural health monitoring applications for bridges. *Bridge Safety, Maintenance, Management, Life-Cycle, Resilience and Sustainability: Proceedings of the Eleventh International Conference on Bridge Maintenance, Safety and Management (IABMAS 2022), Barcelona, Spain, July 11-15, 2022*, 980–985. <https://doi.org/10.1201/9781003322641-117>
- Komary, Mahyad, Komarizadehasl, S., Tošić, N., Segura, I., Lozano-Galant, J. A., & Turmo, J. (2023). Low-Cost Technologies Used in Corrosion Monitoring. *Sensors*, 23(3), 1309. <https://doi.org/10.3390/s23031309>
- Lei, L., Song, D., Liu, Z., Xu, X., & Zheng, Z. (2021). Displacement Identification by Computer Vision for Condition Monitoring of Rail Vehicle Bearings. *Sensors*, 21(6), 2100–2119. <https://doi.org/10.3390/s21062100>
- Li, Y., Wang, H., Cai, W., Li, S., & Zhang, Q. (2020). Stability monitoring of surrounding rock mass on a forked tunnel using both strain gauges and FBG sensors. *Measurement*, 153, 107449. <https://doi.org/10.1016/J.MEASUREMENT.2019.107449>
- Park, H., Son, S., Choi, S., & Kim, Y. (2013). Wireless laser range finder system for vertical displacement monitoring of mega-trusses during construction. *Sensors*, 13, 5796–5813. <https://doi.org/10.3390/s130505796>
- Proske, D. (2020). Fatalities due to bridge collapse. *Proceedings of the Institution of Civil Engineers - Bridge Engineering*, 173(4), 1–24. <https://doi.org/10.1680/jbren.20.00001>
- Raghuwanshi, N. K., & Parey, A. (2018). Experimental measurement of mesh stiffness by laser displacement sensor technique. *Measurement*, 128, 63–70. <https://doi.org/10.1016/J.MEASUREMENT.2018.06.035>
- Shen, X., Yao, M., Jia, W., & Yuan, D. (2012). Adaptive complementary filter using fuzzy logic and simultaneous perturbation stochastic approximation algorithm. *Measurement*, 45(5), 1257–1265. <https://doi.org/10.1016/J.MEASUREMENT.2012.01.011>
- Yao, X., Xing, Z., Zhang, Z., & Sheng, A. (2022). The online monitoring system of pantograph slider based on 2D laser displacement sensors. *Measurement*, 194, 111083. <https://doi.org/10.1016/J.MEASUREMENT.2022.111083>
- Yi, C., Ma, J., Guo, H., Han, J., Gao, H., Jiang, F., & Yang, C. (2018). Estimating Three-Dimensional Body Orientation Based on an Improved Complementary Filter for Human Motion Tracking. *Sensors* 2018, Vol. 18, Page 3765, 18(11), 3765. <https://doi.org/10.3390/S18113765>

Sensor monitoring for engineering structures: Applications to tunnels

A. Strauss, F. Sattler & B. Täubling-Frueleux

Vienna Department of Civil Engineering and Natural Hazards, University of Natural Resources and Life Sciences, Vienna, Austria

C. Seywald

ÖBB-Infrastruktur AG, Streckenmanagement und Anlagenentwicklung, Fachbereich Bautechnik Tunnelbau, Vienna, Austria

H. Neuner & V. Kostjak

Department for Geodesy and Geoinformation, TU Wien, Vienna, Austria

D.M. Frangopol

Lehigh University, ATLSS Research Center, Bethlehem, PA, USA

ABSTRACT: The validation of behaviour of existing structures and its materials characteristics requires the application of tests and monitoring to gather information about the actual response. The comparison of the actual performance and the designed performance enables the validation of the design assumptions in terms of implied loads and materials resistance. In case of non-compliance of the design with the current performance, the design assumptions need to be updated. The application of prescribed loads to a structure to check its load carrying capacity is a powerful tool for evaluating existing structures. In particular, in this research, different types of load tests are employed on a tunnel profile. The system responses to validate the structural performance is recorded with innovative monitoring in tunnel systems, such as accelerometer arrays, fibre optic sensors, and laser distance sensors. Special attention is paid to the capabilities of digital image correlation and nonlinear finite element analysis.

1 INTRODUCTION

Austrian railway infrastructure operator maintains and operates about 150 tunnels with an age of more than 100 years. Most of these are masonry tunnels whose lining can be made of different materials, e.g. rubble masonry, brick masonry, bricks. Damages in such tunnels, e.g. due to ageing and operational influences as well as requirements for current clearance profiles, sometimes require extensive repair or renewal measures on the existing masonry. These measures, which are partly carried out during ongoing railway operations, are usually accompanied by a temporary weakening of the existing tunnel. Measurement systems that have become established in conventional tunnel construction, such as 3D displacement measurements, are not always suitable for carrying out construction measures in masonry tunnels, or are only suitable as an additional aid. In order to select an appropriate monitoring system, the prevailing boundary conditions in the tunnel are crucial. These include operational boundary conditions, e.g. during installation, and on the boundary conditions during continuous monitoring. Typical parameters/conditions to be considered for tunnel monitoring are: (a) condition of the masonry (e.g. geometry, roughness), (b) overhead power supply line (e.g. electromagnetic field), (c) temperature or temperature fluctuations, (d) humidity, (e) aerodynamic effects due to passing trains, (f) dust (e.g. due to passing

trains, construction work), (g) impacts/vibrations (e.g. due to train travel or construction work), and (f) lightning conditions. Beyond that, experience shows that when monitoring the load-bearing capacity of masonry tunnels, the displacements resulting from the construction measures have very low levels and these can be detected in form of local spalling, brittle fracture of masonry or detachment (Zimmermann et al., 2010, 2011). Locally, these can occur even at extremely low displacement values and cannot be detected with conventional monitoring methods (Spyridis and Strauss, 2020). Therefore, when selecting the monitoring instruments, it is important to consider which phenomena are to be recorded during the monitoring (e.g. displacements, spalling, strains, skewing) associated with short and longer reaction times. The aim of this research project was therefore to analyse classic and innovative monitoring systems that can be used reliably and economically in the reconstruction of old masonry tunnels under tunnel conditions.

2 FIELD TEST

2.1 Preliminary studies

The preliminary studies were carried out together with the Austrian Federal Railways, the Vienna University of Technology and the University of Natural Resources and Life Sciences to analyse modern measuring systems for recording deformations in tunnel structures. Tachymeters and laser trackers were used as reference systems, which have been in use for many years and can be compared with newer innovations in terms of accuracy and manageability. With these systems, horizontal and vertical angles as well as the oblique distance from the measuring device to the measuring point are recorded, usually by means of a standardised mirror prism. The recorded measuring points can also be easily integrated into higher-level coordinate systems. The systems to be analysed were profile laser scanners, which use a reflectorless distance measurement principle, an inclinometer chain system mounted along the ring in the inner wall of the tunnel, a fibre optic system and a Digital Image Correlation system. Special attention is given in this paper to the analysis of the Digital Image Correlation System and its suitability for the monitoring of masonry tunnels in the process of retrofitting (Neuner et al., 2022).

2.2 Demonstrator and monitoring systems

As a demonstrator for the experimental investigations, the HABA reinforced concrete mouth profile 3600/2250, manufactured according to ÖNORM EN 1916 and ÖNORM B5074, was used (see Figure 1). As can also be seen in Figure 2, the profile was designed with 30 cm deep and 20 cm wide slots in the crown area, in the upper and lower strut area in order to reduce the bending stiffness of the mouth profile and thus to generate significant 3D deformations which can occur in real tunnel shells. The loading processes has been applied via tie rods, shown in the illustrations.

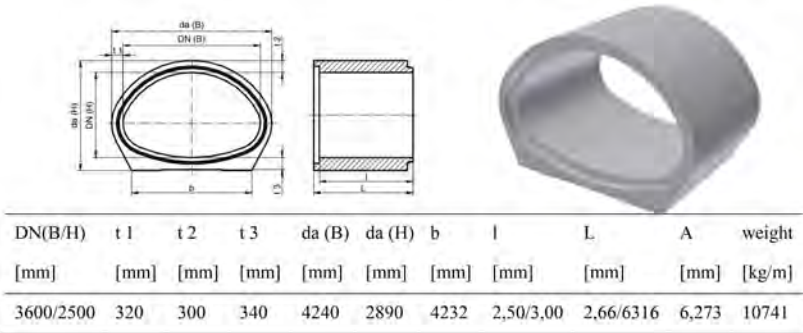


Figure 1. Data sheet of the HABA mouth profile (Strauss et al., 2022c) and 3D NLFEA drawing of the mouth profile.

The HABA mouth profile is a reinforced concrete profile C25/30 with a 4 cm concrete cover and 36 pieces of $d = 8$ mm longitudinal reinforcement on the inner and outer circumference of the profile as well as $d = 9$ mm ring reinforcement every 8 cm on the outside and 6 cm on the inside, see Figure 2(b) and 2(c) (top view) and Figure 2(d) (front view) show the arrangement of the operated monitoring systems. In particular, the following systems were operated in the profile shown in these figures: (1) Longitudinal inclinometer from HBK, (2) Fibre optic sensor system from HBK, (3) Profile laser scanners from TripleIn, (4) Digital Image Correlations System DIC from DANTEC, and (5) SAA inclinometer system from Measurand. In addition, a laser tracker and a tachymeter – both from Leica - were operated from outside the profile.

The *Digital image correlation* captures the surface of the object being measured and correlates the images from different cameras or viewing angles to create a 3D model. By comparing the model at different load levels, pixel displacements and subsequently strains, in-plane and out-of-plane displacements can be determined. Since not only individual measuring points but the entire surface is recorded, the subsequent evaluation with the help of modern software is very versatile. For example, a line element can be defined and the strain calculated over time. In this project, the focus was on the evaluation of the local strain determination and the evaluation of the out-of-plane displacements - profile deformation.

The *SAA inclinometer* is a chain of 41 accelerometer triads connected sequentially by rigid rods with a length of 125 mm. It enables the measurement of inclination angles in 3D-space by sensing the components of the gravity vector. By means of an initial zero measurement followed by repeated measurement cycles, the SAA inclinometer can be used to derive displacements and deformations along the chain and thus of the deformations of the mouth profile due to the applied loads. The measurement interval was 10 minutes and the starting point of the system was monitored by laser tracker or a tachymeter respectively.

The *fibre-optic inclinometer* system HBK records the strains, i.e. the changes in length between the fixation points on the tunnel profile. The geometric deformations of the tunnel profile can only be determined indirectly via the strain changes along the FOS inclinometer band.

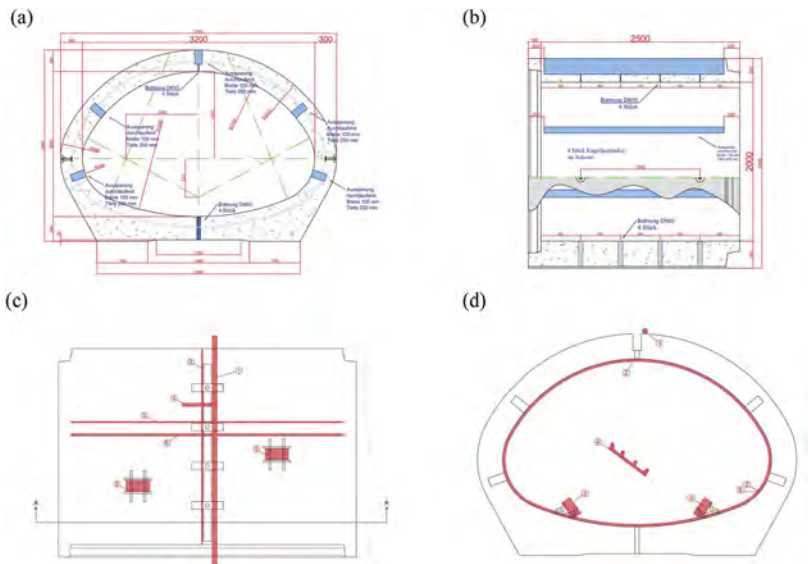


Figure 2. Modified HABA mouth profile and the location of the monitoring systems (a) mouth profile cross-section, (b) reinforcement plan, (c) profile floor plan with measuring system arrangement and (d) mouth profile cross-section with measuring system arrangement. Monitoring systems: (1) Longitudinal inclinometer by HBK, (2) Fibre optic sensor system by HBK, (3) Profile laser scanners, (4) Digital Image Correlations System DIC by DANTEC (5) SAA – inclinometer by Measurand. In addition, a laser tracker and a total station were operated, which were located outside the profile.

Profile laser scanner and laser tracker are polar measurement devices and basically deliver coordinates of measured points related to an instrument specific coordinate system. While the laser tracker measures the distances on corner cube reflectors using the interferometric principle, the laser scanner uses reflectorless distance measurements based on Time-of-Flight principle. The distance, the alignment angle and thus the position of the measured point are recorded. Occurring displacements result from coordinate difference of points.

Table 1 gives an overview of the measured variables that have been recorded (+) or derived (~) on the mouth profile (Beigel, 2023).

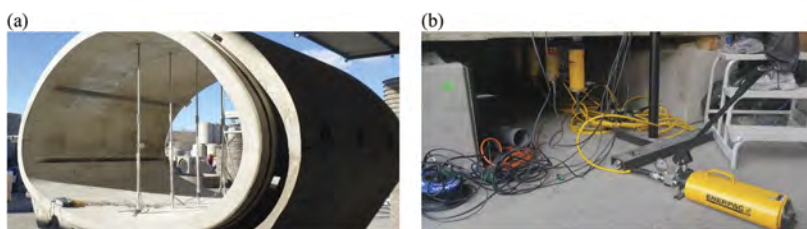


Figure 3. Load transmission by means of strain-controlled bars: (a) bar arrangement in the symmetry plane of the mouth profile, (b) load transmission by means of hydraulic cylinders beneath the profile (Neuner et al., 2022).

Table 1. Measured parameters of the monitoring systems applied to the tunnel/mouth profile (Beigel, 2023).

System	DIC	SAA	FOS	L-Tracker	Laserscanner
Strains	+	-	+	-	-
Displacements	+	+	~	+	+
Inclinations	+	+	~	~	~
Ranking*	1	2	3	ref.	4

*) with respect to the measurement accuracy in tunnel environment

2.3 Loading procedures and processes

The HABA Mouthprofil on the factory grounds of HABA GmbH was subjected to a temporally rapid load regime in predefined load steps. The load was applied in static, uniform load steps in the vertical symmetry plane of the profile. The uniform load application by means of hydraulic cylinders was achieved by four rods (diameter M24), which were guided through holes in the apex and in the base plate to the outside of the profile and anchored accordingly on the outer sides, see Figure 3. The tests on the demonstrator were carried out on 7th, 9th and 23rd February 2022. During the entire loading procedures, see Figure 4, the deformations were continuously recorded with SAA. The increase or decrease of the load was always done gradually with a step size of 40 kN. On 7th February 2022, a load of 0 to 80 kN (4 x 20 kN thread force) had been applied. The test was used to record the elastic system response and profile stiffness information for the creation of the digital twin. The digital twin was then used to obtain a numerical prediction of the maximum load, which was set at 400 kN (4 x 100 kN). Visible cracks on the inner surface of the mouth profile and also on the outside of the profile first appeared at about 120 kN.

The tests on February 9th, 2022, were used to obtain a non-elastic system response and to initiate cracks in order to verify the suitability of the monitoring system for crack detection and plastic deformations. As shown in Figure 4, the load level of 80kN (from February 7th, 2022), at which the digital imaging correlation (DIC) system was set up, was gradually reduced to 0 kN. Thereafter, the load was twice gradually increased up to a maximum load of 200kN.

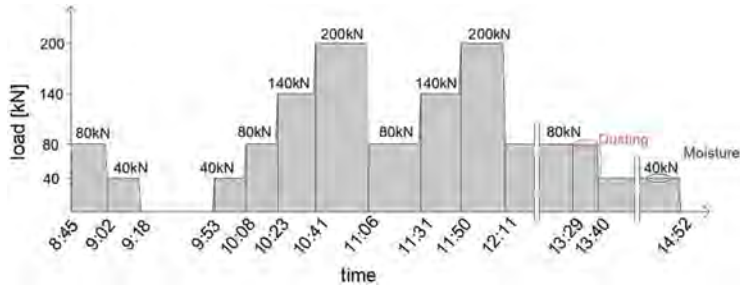


Figure 4. Loading process on 9th February 2022.

3 DIGITAL IMAGE CORRELATION AS MONITORING SYSTEM IN TUNNELS

Dantec's Q-400 system was used as a digital monitoring system for the mouth profile. Details of the system setup and system can be found in Beigel, 2023. Of particular interest in these analyses was the monitoring of the entire displacement and strain field of the inner surface of a defined profile section near the ridge, see Figure 2(d). As shown in Figure 5, the z-deformations in the ridge area (blue) and the flank area (red) were analysed at different load levels (stages 1 to 6), see Figures 4 and 6, as well as the crack development. The complete deformation curves of the individual stages are shown in the upper right graph. As can be seen from these images, the vertical deformations in the range $\leq 1/10$ mm can be clearly detected and followed. Up to a load of 200kN, a ridge deformation of 3mm was detected.

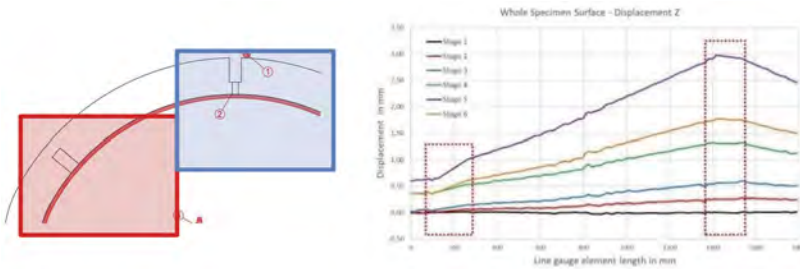


Figure 5. Z displacement | loading process 0 → 200 kN → 80 kN (9th February 2022) Stage 1 to 6.

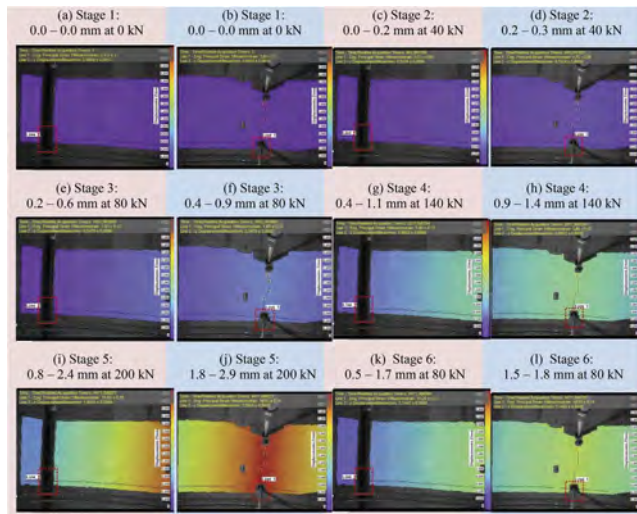


Figure 6. DIC z displacement | loading process 0 → 200 kN → 80 kN (9th February 2022) Stage 1 to 6.

As shown in Figure 7, in addition to the vertical displacements z of the profile, the horizontal movements of the entire profile as well as the local horizontal movements of e.g. cracks and crack surfaces as well as localizations were of particular interest. As can be seen in Figure 8(b), (d), (j) and (l), a crack has developed in the ridge area and the two crack surfaces move in opposite directions according to the applied load level. These deformations and crack pattern development can also be seen in the graphs in the upper right area of the figure, especially the non-linear and partly opposite movements are of high interest. These observations show the high potential of this monitoring technique. The general strain and principal strain developments are also analysed with a non-linear analysis method in Beigel (2023). Details on the monitoring procedures are provided in Polt (2023).

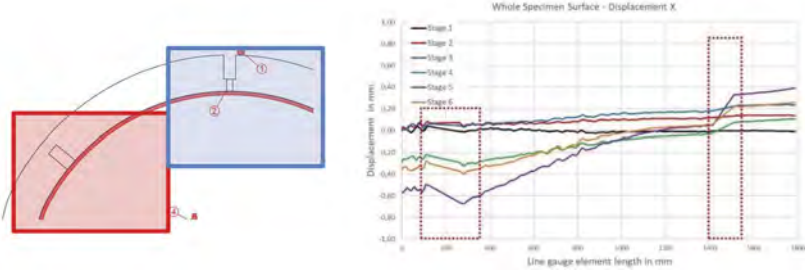


Figure 7. X displacement | loading process 0 → 200 kN → 80 kN (9th February 2022) Stage 1 to 6.

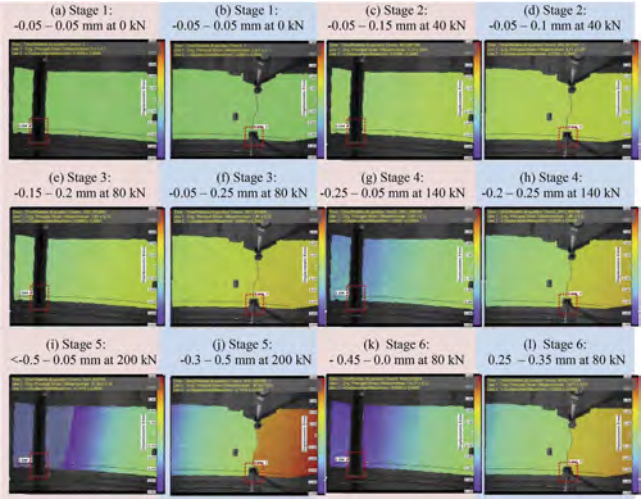


Figure 8. DIC x displacement | loading process 0 → 200 kN → 80 kN (9th February 2022) Stage 1 to 6.

4 DIC VS. OTHER INVESTIGATED MONITORING SYSTEMS

The aim of this research was not only to analyse the capabilities and strengths of innovative monitoring systems in tunnel systems that are renewed, such as the digital image correlation, the SAA inclinometer, the fibre-optic system, the laser distance measurement and laser tracker measurement (see also Neuner et al., 2022, Beigel, 2023) but also to assess the accuracy and measurement reliability as well as the stability of the monitoring systems and their installation possibilities in tunnels under renovation. Figure 9 shows one of these analyses from these

investigations, in which the measurement accuracies of the vertical and horizontal displacements of the DIC were compared with the results of the SAA measurements and the laser tracker reference measurements. As can be seen from this diagram, the differences between the observed monitoring systems are in the range of 1/100 for the displacements both vertically and horizontally.

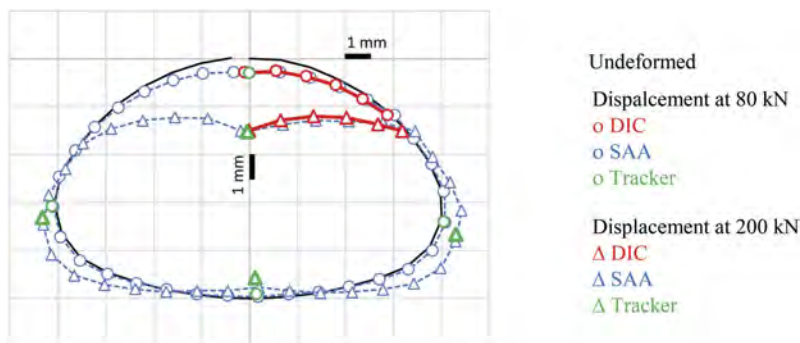


Figure 9. Measurement accuracies of the vertical and horizontal displacements of the DIC vs. SAA and Tracker measurements.

The digital image correlations system can be classified as an innovative system based on these analyses, which can provide exact results for local monitoring of e.g. strains as well as very precise solutions for the global monitoring of the profile geometry. However, the investigations also showed that site conditions such as dust, humidity and vibrations can limit the applicability of the system. Nevertheless, it should also be noted that systems, like the DIC, provide an excellent basis for the development of digital twins which subsequently allow evaluation and prediction models for degradation, deterioration processes and the detection of service life changes as well as for in-depth probabilistic simulations, as shown for example in (Canestro et al., 2021, Slowik et al., 2021, Spyridis and Strauss et al. 2020, Strauss et. al. 2004, 2006, 2010, 2018, 2020, 2022).

5 CONCLUSIONS

In this research project, several innovative monitoring systems were investigated for their suitability for use in tunnel retrofitting processes in controlled field experiments. The studies have shown that modern innovative systems such as the Digital Image Correlation (DIC) system provide very comprehensive detailed results at the different levels of monitoring (micro-strain analysis and global profile deformation). However, the use of the DIC systems is still sometimes limited by site conditions.

ACKNOWLEDGEMENTS

The authors thank the ÖBB-Infrastruktur AG for commission the MONTUN Research Project. The authors also thank the fib COM3 “Existing Concrete Structures” for discussions and support and the IABSE TG1.4.

REFERENCES

- Beigel, A. 2023. Verifizierung innovativer Monitoringsysteme für Tunnelinstandsetzungen mittels digitaler Zwillingsanalysen. Vienna, Universität für Bodenkultur.
- Canestro, E., Strauss, A. & Helder, S. 2021. Multiscale modelling of the long-term performance of pre-stressed concrete structures – Case studies on T-Girder beams. *Engineering Structures*, 231, 111761.

- Neuner, H., Kostjak, V., Linzer, F., Loderer, W., Seywald, C., Strauss, A., Rigler, M. & Polt, M. 2022. Assessing Deformation Monitoring Systems For Supporting Structural Rehabilitation under Harsh Conditions. *EGU General Assembly 2022*. Vienna.
- Polt, M. 2023. Verifizierung innovativer Sensortechnologien für Tunnelinstandsetzung. Vienna, Universität für Bodenkultur.
- Slowik, O., Novák, D., Novák, L. & Strauss, A. 2021. Stochastic modelling and assessment of long-span precast prestressed concrete elements failing in shear. *Engineering Structures*, 228, 111500.
- Spyridis, P. & Strauss, A. 2020. Robustness Assessment of Redundant Structural Systems Based on Design Provisions and Probabilistic Damage Analyses. *Buildings*, 10, 213.
- Strauss, A., Andrea, M. & Konrad, B. 2006. Nonlinear Finite Element Analysis of Reinforced Concrete Corbels at Both Deterministic and Probabilistic Level. *Computers and Concrete*, 3, 123–144.
- Strauss, A., Bergmeister, K., Novák, D. & Lehký, D. 2004. Stochastische Parameteridentifikation bei Konstruktionsbeton für die Betonerhaltung. *Beton- und Stahlbetonbau*, 99, 967–974.
- Strauss, A., Bien, J., Neuner, H., Harmening, C., Seywald, C., Österreicher, M., Voit, K., Pistone, E., Spyridis, P. & Bergmeister, K. 2020. Sensing and monitoring in tunnels testing and monitoring methods for the assessment of tunnels. *Structural Concrete*, 21, 1356–1376.
- Strauss, A., Castillo, P., Bergmeister, K., Krug, B., Wan-Wendner, R., Marcon, M., Matos, J. & Casas, J. R. 2018. Shear Performance Mechanism Description Using Digital Image Correlation. *Structural Engineering International*, 28, 338–346.
- Strauss, A., Frangopol, D. M. & Bergmeister, K. 2010. Assessment of Existing Structures Based on Identification. *Journal of Structural Engineering*, 136, 86–97.
- Strauss, A., Neuner, H., Rigler, M., Polt, M., Seywald, C., Kostjak, V., Linzer, F. & Loderer, W. 2022. Verification of the performance of reinforced concrete profiles of alpine infrastructure systems assisted by innovative monitoring. *EGU General Assembly 2022*. Vienna.
- Zimmermann, T., Strauss, A. & Bergmeister, K. 2010. Numerical investigation of historic masonry walls under normal and shear load. *Construction and Building Materials*, 24, 1385–1391.
- Zimmermann, T., Strauss, A. & Bergmeister, K. 2011. Structural behavior of low- and normal-strength interface mortar of masonry. *Materials and Structures*, 45, 829–839.

Digital twins for bridges – concept of a modular digital twin based on the linked data approach

T. Zinke & S. Reymer

HochTief ViCon GmbH, Essen, Germany

S. Kosse, P. Hagedorn & M. König

Lehrstuhl für Informatik – Ruhr-Universität Bochum, Bochum, Germany

F. Wedel, S. Schneider & S. Marx

Gesellschaft für Wissens- und Technologietransfer – TU Dresden – Institut für Massivbau, Dresden, Germany

S. Nieborowski & S. Windmann

Bundesanstalt für Straßenwesen (BASt), Bergisch Gladbach, Germany

ABSTRACT: Bridges are essential transport infrastructure components that are subjected to degradation due to dynamic loads and environmental impacts. Continuous condition monitoring is essential to ensure the safe and economical use of the structures until the end of their life cycle. Predictive maintenance can be implemented using modern information and communication technologies such as the digital twin (DT) combined with structural health monitoring methods. DTs are virtual real-time representations of structures that collect, evaluate, and provide data for informed decision-making. However, a unified approach still needs to be developed for application in the civil engineering domain. This paper proposes a concept to implement modular DT for bridge structures based on the linked data approach. Modularity is realized by use cases that integrate existing heterogeneous data sources providing a closed view of an aspect. An exemplary implementation of one use case is realized using a container-based approach.

1 INTRODUCTION

Bridges are an integral part of an efficient transport infrastructure. Therefore, ensuring their safety, reliability, and availability is a very high priority for authorities and operators. Due to the aging of structures, increasing traffic loads, and climate change influences, considerable measures must be taken to maintain and modernize structures. Meeting these challenges is one of the most urgent future tasks in transport infrastructure. For this reason, new innovative approaches for information delivery and assessment will be integrated and further developed to provide the basis for an optimized predictive life cycle management. This includes, among other things, the minimization of life cycle costs, optimized structure inspection, and improved availability, safety, and reliability of engineering structures.

The digital twin (DT), as a virtual representation of a real asset or structures, is an essential component for the collecting, evaluating, and providing data and information along all life cycle phases. It provides the basis for smart services and other artificial intelligence based methods for condition prediction, maintenance planning, or traffic control. The Federal Highway Research Institute in Germany has initiated the research project “concept study for the

unification of digital twin bridge components”, which focuses on developing a modular concept for DTs of bridges.

This paper provides a basis for the future realization of modular DTs of bridge structures on a conceptual and technical level. The modular concept ensures the expandability and future viability. The concept is validated in a case study in which the technical implementation of the use case of interval-based condition inspection (structure inspection) is demonstrated.

2 STATE OF THE ART

A DT is commonly understood as a formal virtual representation of a physical object, process, or system that captures the properties and behaviors of the respective entity and enables context-specific communication, data storage, interpretation, and evaluation (Industrial Internet Consortium 2020). Since its introduction as the conceptual ideal of product life cycle management (PLM), many industries have recognized the potential the DTs. As a result, the DT is becoming a key concept for digital transformation in many industries, each with its definition that considers individual industry-specific requirements so that no uniform understanding of the concept exists (Kritzinger et al. 2018).

The term DT is often used synonymously with other concepts. Kritzinger et al. (Kritzinger et al. 2018) distinguish the DT based on the degree of integration, making it differentiable from concepts like the digital shadow and digital model. They define the DT as a digital representation with an automatic bidirectional data flow. In contrast, they define the digital shadow as a digital representation with unidirectional and a digital model as a representation without any form of automatic data exchange. In construction, the adoption of the DT is still in its infancy. It is seen as an extension, complementary to, or completely independent of existing Building Information Modeling (BIM) approaches (Shahzad et al. 2022). For Delgado et al. (Delgado et al. 2021), BIM and the DT serve different industry needs. According to Boje et al. (Boje et al. 2020) the DT is a virtual representation of components or structures that goes beyond a BIM model by exploiting the bidirectional data connection enabling an ever-updated representation of a building.

The DT for bridges is mostly discussed in the context of structural health monitoring for continuous condition monitoring. The DT captures the data measured by the structural sensors and can predict about the structural behavior of the structures in conjunction with structural reliability techniques to deal with uncertainties (Bittencourt et al. 2021). The main features and capabilities of a DT for structural health monitoring of bridge structures are essentially a digital representation consisting of geometry and other relevant metadata, a connection to the structure, for example, through sensors, and a common data environment for data access as well as for the integration of visualization and simulation tools (Ye et al. 2019).

In their work, Shim et al. (Shim et al. 2019) present a DT framework for bridge structure maintenance. Their solution consists of a maintenance information management system based on a 3D information model combined with a digital inspection system with image processing. A major challenge in modeling DTs of bridge structures is the creation of basic geometrical models, especially for existing structures. Lu et al. (Lu et al. 2019) propose an object-matching method for existing reinforced concrete bridges in IFC format using four types of point clusters to create geometric twins based on point clouds. Their method generates a geometric twin with LOD 250 to LOD 300.

AR & VR methods can be used to make the results of structural inspection accessible. Omer et al. (Omer et al. 2019) propose a novel bridge inspection method in which bridges are digitized using LIDAR (light detection and ranging) so that they can later be inspected in a virtual reality (VR) environment. Their approach enables access to critical areas and increases the safety of inspectors. Furthermore, Wenner et al. (Wenner et al. 2022) present the realization of a DT of the Köhlbrand Bridge, which can detect damage and changes in condition by collecting data in real-time. The real-time data, as well as the collected data history, are used as the basis for predictive maintenance. Lazoglu et al. (Lazoglu et al. 2023) present

a concept of a DT, which is realized for the Filstal bridges. This includes integrating, processing, and aggregating of data from bridge inspections and calculated structural safety verifications, as well as monitoring and diagnostic data to display the bridge condition continuously.

3 CONCEPT

The prerequisite for the transition from reactive to predictive life cycle management of bridges is the DT for the acquisition, evaluation, and provision of data enabling informed decision-making using, among others, current engineering models and methods from the field of artificial intelligence. The high fragmentation and complexity of the construction industry require the development of a flexible DT concept that facilitates the integration of heterogeneous data sources. As life cycle phases change, so do the requirements for bridges and new functionality consisting of data and processes must be continuously integrated into DT. A modular approach to implementing the DT is one way to ensure the necessary flexibility.

The following sections present a modular DT concept for bridges, which considers modularity separately regarding the business processes and software-technical implementation. Modularization generally means dividing a whole into largely independent, exchangeable, and modifiable modules, forming a closed functional unit. Interaction between the individual modules takes place via standardized interfaces (Balzert, 2010).

The present concept is based on a top-down approach in which the objectives of DT have been defined first. Based on these objectives, the associated business processes and use cases required for implementation were identified. The business processes and use cases form the process modularity and are based on existing regulations. Each use case consists of any number of process steps. For example, the use case of continuous condition monitoring is divided into data acquisition, evaluation, and information generation and uses context-specific methods, software tools, and data. A deep understanding of the corresponding processes and their input and output data is essential for a modular implementation. In order to develop suitable data structures and identify data exchange and interaction needs, it is recommended to develop a detailed use case description.

The software-technical implementation must integrate the modules described at the process level into modules that contain all relevant data, methods, tools, and models. In addition, the technical requirements placed on the digital twin regarding information modeling, compilation, synchronization, interfaces, connectivity, and interoperability must be met by the software-technical implementation (cp. Industrial Internet Consortium 2020).

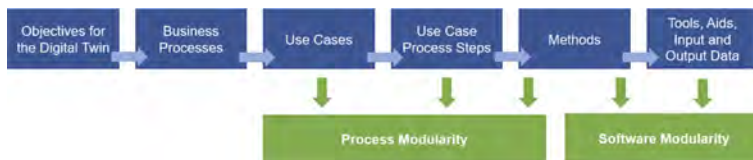


Figure 1. Top-down approach for the development of the complete modular concept.

3.1 Process modularity

Process modules are use cases that provide specific services or specific data as a self-contained functional unit with clearly defined input and output data. A distinction is made between mandatory and optional use cases. Mandatory use cases create a data baseline, while optional use cases provide additional services that can be individually integrated into the DT. For example, a mandatory use case is of interval-based condition inspection (bridge inspection), while visualization of traffic restrictions is optional.

Process modularity is divided into different levels. The use case level and subordinate process levels of the individual use cases are modular. The various use cases describe the

superordinate level of process modularity. The subordinate level of process modularity represents the detailing of the individual use cases into different process steps. Depending on the requirements profile and the level of detail of the use case within DT, the individual process steps are exchanged, transformed, or extended. In particular, the implementation of the use case and the associated process steps can change significantly as the level of digitization progresses. Despite the variable methodical implementation of the use case, the required input data and the defined output data remain unchanged.

3.2 Description of the use cases

Some general conditions have to be defined to identify and describe the individual use cases. An essential aspect is the structure of the bridge. It has to be ensured that each bridge can be implemented by the modular concept of the DT regardless of its design. Furthermore, the superordinate structure of a use case within the virtual representation has to be described.

A bridge structure is composed of several components, so the DT is also formed by several DTs on the component level. This structure corresponds to the classification systems used in civil engineering, such as ASB-ING (BMVBS 2013). This decomposition of the DT also makes it possible to understand components or hotspots as subsystems and, thus, to compose the overall bridge system from individual components.

The general structure of a virtual use case representation can also be divided into four levels, see Figure 2. At the lowest level, various data can be used, e.g., a BIM model enriched with data from the building database, measurement data, or user data. Depending on the data type, these data can be collected once, cyclically, or continuously. Different evaluation methods can generate information for different business processes on the second level from the various data sources. Business processes representing the third level can be divided into methods for monitoring, analyzing, or predicting the state of the physical object. Finally, the information can thus be obtained and converted into knowledge at the top level by making it available to the user in a suitable manner. In this way, the use cases serve as decision support for the user.

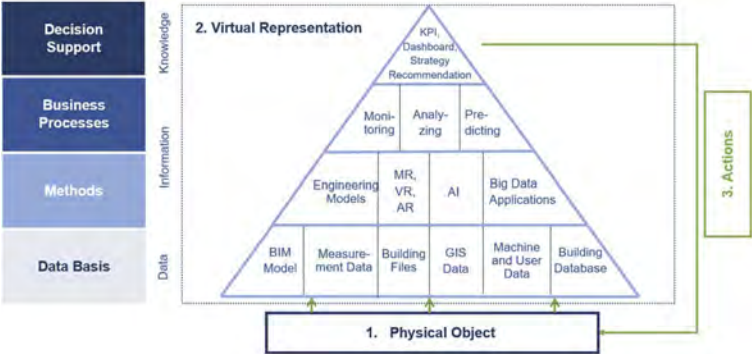


Figure 2. Layer concept of the virtual representation.

Within the underlying project, 21 use cases were identified which can be divided into three areas of operational processes, maintenance planning and execution, and strategic life cycle management. Each area serves different business processes in the use phase. The goal of the operational processes area is the optimal execution of structural maintenance and ensuring operational processes. The use cases of this area focus on a short-term time horizon of 1 to 3 months and relate to the entire roadway, such as winter maintenance or car accident management. The maintenance planning and implementation area aims to maintain the required condition of the structure, including, for example, the use cases of interval-based condition

inspection (structure inspection), continuous condition monitoring, or traffic data acquisition. These use cases cover a time horizon of 1 to 5 years and only consider components at the structure and component level. The third area of use cases covers strategic life cycle management with a time horizon of 3 to 50 years. Examples mentioned here are degradation analyses, the formulation of maintenance strategies, and EU-taxonomy analyses. In the future, this area will ensure the application of predictive management for the operation and maintenance of bridges at the structure, component, and portfolio levels.

3.3 Software modularity

A modular implementation of a DT must allow access to existing and established heterogeneous data sources, such as digital building databases, for running the business processes embedded in the use cases. Access is granted utilizing queries and web interfaces that differ from database to database. The different data sources, therefore, form data islands that must be software-technically integrated into the modular DT concept. Additionally, the data must be provided in a uniquely identifiable and machine-readable way. Linked data enables the linking of building-related databases to relevant data sources so that information can be related in a partially automated way. An update of interconnected data sets enables processes to adapt by automatically processing specialized inquiries, enabling reactions to new and changed contents. With linked data, access to data is provided via standardized interfaces.

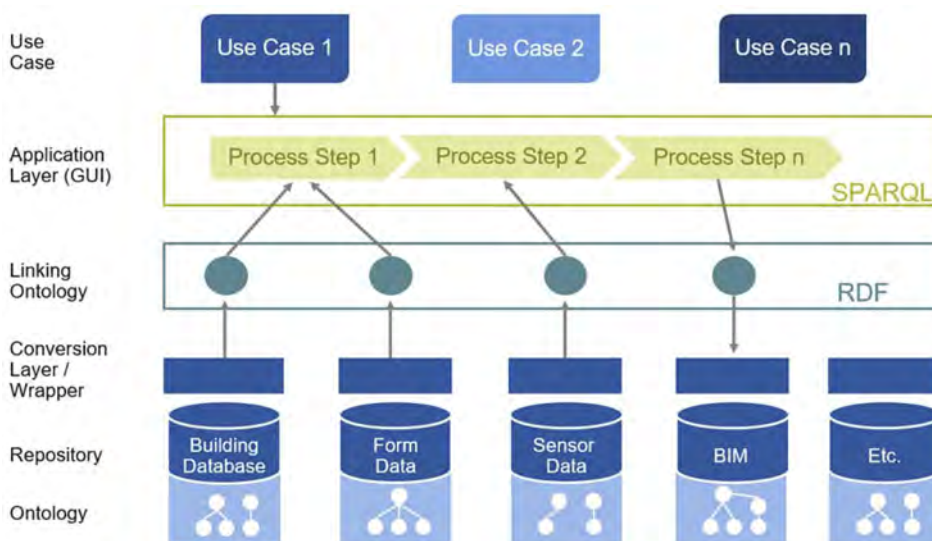


Figure 3. Framework of software modularity.

Figure 3 shows a layer-based framework for implementing a linked data-based modular DT. The framework is based on an ontology-based description of linked resources to uniquely associate data. For this purpose, data are formalized in a graph-based manner using the resource description framework (RDF). RDF defines data in subject-predicate-object triples emerging as a directed graph representation. Ontologies are used to model RDF-based data sources on a schema level and connect them to business processes invoked by use cases. For this purpose, existing ontologies must be reused, or new ontologies must be developed for each data source providing corresponding class and properties definitions.

Uniform resource identifiers (URI) enable unique identification and mapping of RDF entities. Various conversion tools and wrappers convert existing databases into RDF format, thus ensuring data access via uniform interfaces. Semantic searches and queries can be

performed using the SPARQL protocol and RDF query language (SPARQL) in conjunction with the used ontologies. Semantic information from data sources of other use cases can be systematically defined and linked to existing data sets using appropriate ontologies. Data sources can be automatically converted to RDF format using conversion tools and wrappers as mentioned above in conjunction with ontology definitions and added to the module with an ontology for a formal schematic description of the data.

4 CASE STUDY

Information containers for linked document delivery (ICDD) are suitable for implementing modular DTs based on linked data. ICDD containers integrate heterogeneous data sources to enable context-specific simplified information delivery. All data relevant to an aspect or use case can be stored in the container or linked externally. In addition, it is possible to express links and relationships between the various data, making them an ideal foundation for implementing the presented concept. Besides the usage as an exchange format, due to the employment of semantic web technologies, the ICDD schema is suited to be implemented in web applications, such as common data environments (CDE) or asset management applications (Hagedorn et al. 2023).

The structure of ICDD containers is specified by ISO 21597-1:2020 (ISO 2020). The file format with the extension `.icdd` complies with the ZIP64 standard defined by ISO/IEC 21320. Essentially, the data structure of an ICDD container consists of an index file and the three folders ontology resources, payload documents, and payload triplets. The index file describes the data content and identifies the container. The folder ontology resources contains the container ontology and linkset ontologies. The container ontology specifies classes and properties to describe the container contents associated with the index dataset. Linkset ontologies specify classes and properties for describing links and relationships between the data contents of the container. All ontologies are available as RDF(s)/OWL files. The payload documents folder contains all data and documents relevant to the use case. Through the link datasets in the payload triples folder, relationships and links between the data contents can be specified in conjunction with the corresponding linkset ontologies.

In this paper, ICDD containers are created per use case to implement a modular DT. The federation of all container modules forms the DT. As part of a proof of concept, an ICDD container has been equipped for the interval-based condition inspection use case. The container has been created using the web platform developed in the work of Hagedorn et al. (Hagedorn et al. 2023). The use case of interval-based condition inspection is utilized for data collection and damage assessment as part of structural inspections based on existing regulations and codes such as DIN 1076 or ASB ING. The data collected during the structural inspection must be structured to create a basis for other use cases based on interval-based condition monitoring. Therefore, the ICDD container for representing the interval-based condition recording must contain, among other things, a digital building model and digital images, plans, and structural documents. Furthermore, an interface for building databases, such as digital ones, must be ensured.

Figure 4 shows the ICDD container for the interval-based condition recording comprised of the ICDD ontologies, a folder with located damage images, a bridge IFC 2x3 model, and an “ExternalBridgeDatabase” entry in the payload documents folder, and a linkset file “DamageLocalization.rdf” interconnecting the damage images and the results from the interval-based condition inspection to their matching elements in the IFC model in the payload triples folder. The “ExternalBridgeDatabase” is an instance of the ICDD extension class “ExternalDatabase” provided in an extension ontology. It acts as a connector between the container and the relational database storing the condition data. The connector applies the RDB to RDF Mapping Language (R2RML) for generating RDF triples from the condition database, which can be linked and queried in the container context. In addition, the used software implementation supports direct mapping and custom R2RML mapping files stored within the container. In this use case, the R2RML direct mapping is employed to retrieve all

unfiltered database entries and in their relational structure. RDF triples are generated to the “ExternalBridgeDatabase.instances.ttl” file in the payload triples folder whenever the procedure is triggered manually or via a webhook request.

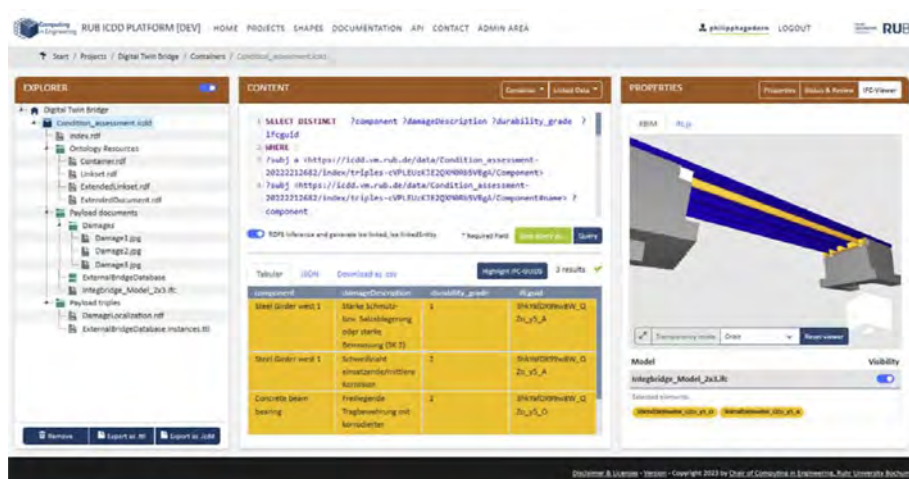


Figure 4. Querying and visualizing recorded conditions from database registered in the ICDD container.

In the context of the ICDD container, the retrieved condition data can be queried using SPARQL, resulting in textual damage descriptions, damaged components and their interconnections to IFC elements, and the assessment of durability, stability, and safety. The interconnection between the damaged IFC elements and the respective on-site damage images is shown in Figure 4.

Further use cases of this dynamic integration of bridge condition and maintenance data can be found in Hagedorn et al. (Hagedorn et al. 2023). The present case study shows the feasibility to deploy a modular DT using ICDD and Linked Data.

5 CONCLUSIONS

In this paper, a concept of a modular DT based on linked data has been developed. Modules are use cases consisting of data, methods, business processes, and decision support, each providing a closed view of a single aspect. A container-based implementation demonstrates the functionality of the presented concept. The following findings and can be summarized:

- The division into the process and software modularity enables the overall design of a modular concept for DT of bridges.
- Use cases are suitable as modules of process modularity because they each form a self-contained functional unit that provides specific services or data for business processes.
- The implementation of the individual process steps of the corresponding use cases is realized within the software modularity using various methods tools, utilities, and input and output data.
- Linked data enables a modular software-technical implementation through which all data sources belonging to a use case are linked, uniquely identifiable, and accessible via standardized interfaces.
- ICDD containers are ideal for implementing modular linked data-based DTs. For each use case, an ICDD container can be created that contains all relevant data sources and provides methods for the semantic description of the data and standardized access to the data. The individual containers together form the DT.

In future research, the developed concept will be validated by implementing a pilot project. On this basis, further digital services enable optimization and expansion of DT processes.

ACKNOWLEDGMENT

This paper is based on parts of the research project carried out at the request of the Federal Ministry for Digital and Transport, represented by the Federal Highway Research Institute, under research project No. 15.0677/2020/IRB. The authors are solely responsible for the content. We would like to thank the members of our project's advisory board for their useful advices and feedback.

REFERENCES

- Balzert, H. (2010). Textbook of software engineering: basic concepts and requirements engineering. Spektrum: Heidelberg.
- Bittencourt, T. N. & Futai, M. M. & Da Conceição Neto, A. P. & Ribeiro, D. M. (2021). Digital transformation of bridges inspection, monitoring and maintenance processes. In: Hiroshi Yokota/Dan M. Frangopol (Eds.). *Bridge Maintenance, Safety, Management, Life-Cycle Sustainability and Innovations*. CRC Press, 11–30.
- BMVBS (2013). *Instruction Road Information Bank for Engineering Structures, Building Data Subsystem (ASB-ING), Bridge and Civil Engineering Collection*, as of 10/2013.
- Boje, C. & Guerriero, A. & Kubicki, S. & Rezgui, Y. (2020). Towards a semantic Construction Digital Twin: Directions for future research. *Automation in Construction* 114, 103179. <https://doi.org/10.1016/j.autcon.2020.103179>.
- Davila Delgado, J. M. & Oyedele, L. (2021). Digital Twins for the built environment: learning from conceptual and process models in manufacturing. *Advanced Engineering Informatics* 49, 101332. <https://doi.org/10.1016/j.aei.2021.101332>.
- DIN 1076: 1999-11, *Engineering structures in connection with roads – inspection and test*.
- Hagedorn, P. & Liu L. & König M. & Hajdin R. & Blumenfeld T. & Stöckner, M. & Billmaier M. & Grossauer, K. & Gavin, K. (2023). BIM-enabled Infrastructure Asset Management using Information Containers and Semantic Web. *ASCE Journal of Computing in Civil Engineering*, 37 (1), DOI: 10.1061/(ASCE)CP.1943-5487.0001051.
- Industrial Internet Consortium (2020). *Digital Twins for Industrial Applications. Definition, Business Values, Design Aspects, Standards and Use Cases*.
- ISO (2020). *Information container for linked document delivery—Exchange specification—Part 1: Container*. ISO 21597-1. Geneva: International Organization for Standardization.
- Kritzinger, W. & Karner, M. & Traar, G. & Henjes, J. & Sihn, W. (2018). Digital Twin in manufacturing: A categorical literature review and classification. *IFAC-PapersOnLine* 51 (11), 1016–1022. <https://doi.org/10.1016/j.ifacol.2018.08.474>.
- Lazoglu, A. & Naraniecki, H. & Zaidman, I. & Marx, S. (2023). A monitoring based digital twin for the Filstal bridges. *Proceedings of the 8th International Symposium on Life-Cycle Civil Engineering (IALCCE 2023), Milan, 2-6 July 2023, Italy*.
- Lu, R. & Brilakis, I. (2019). Digital twinning of existing reinforced concrete bridges from labelled point clusters. *Automation in Construction* 105, 102837. <https://doi.org/10.1016/j.autcon.2019.102837>.
- Omer, M. & Margetts, L. & Hadi Mosleh, M. & Hewitt, S. & Parwaiz, M. (2019). Use of gaming technology to bring bridge inspection to the office. *Structure and Infrastructure Engineering* 15 (10), 1292–1307. <https://doi.org/10.1080/15732479.2019.1615962>.
- Shahzad, M. & Shafiq, M. T. & Douglas, D. & Kassem, M. (2022). Digital Twins in Built Environments: An Investigation of the Characteristics, Applications, and Challenges. *Buildings* 12 (2), 120. <https://doi.org/10.3390/buildings12020120>.
- Shim, C.-S. & Dang, N.-S. & Lon, S. & Jeon, C.-H. (2019). Development of a bridge maintenance system for prestressed concrete bridges using 3D digital twin model. *Structure and Infrastructure Engineering* 15 (10), 1319–1332. <https://doi.org/10.1080/15732479.2019.1620789>.
- Wenner, M. & Meyer-Westphal, M. & Herbrand, M. & Ullerich, C. (2022). smartBRIDGE Hamburg: a digital twin to optimise infrastructure maintenance. *Proceedings of the 11th International Conference on Bridge Maintenance, Safety and Management (IABMAS 2022), Barcelona, 11-15 July 2022, Spain*.
- Ye, C. & Butler, L. & Calka, B. & Iangurazov, M. & Lu, Q. & Gregory, A. & Girolami, M. & Middleton, C. (2019). A Digital Twin of Bridges for Structural Health Monitoring. <https://doi.org/10.12783/shm2019/32287>.

*SS4: Artificial intelligence-based life-cycle management
of infrastructure systems
Organizers: Y. Dong, D.M. Frangopol & X. Lei*



Taylor & Francis

Taylor & Francis Group

<http://taylorandfrancis.com>

Sustainability-informed intelligent management of aging civil infrastructure systems with emphasis on bridge networks

Xiaoming Lei & You Dong

Department of Civil and Environmental Engineering, The Hong Kong Polytechnic University, Hong Kong, China

Dan M. Frangopol

Department of Civil and Environmental Engineering, ATLSS Engineering Research Center, Lehigh University, PA, USA

ABSTRACT: Infrastructure systems are subjected to deterioration throughout the duration of their life-cycle from exposure to the environment. The bridge network systems play a crucial role in urban, and their safety are highly related to the carbon emissions within the construction field. This study suggests a deep reinforcement learning (DRL) approach for the sustainability-informed life-cycle management of aging infrastructure systems to meet the goal of dropping the global carbon emissions. The management of aging structures completely considers the environmental, economic, and safety impacts. The management optimization with Markov decision process is achieved with the DRL approach. The effectiveness and efficiency of the approach are validated with a bridge network. The proposed DRL-based management approach maximizes structural conditions while minimizing overall carbon emissions and economic expenses. The proposed approach could also assist stakeholders in efficiently allocating funds to maintain aging structures and understanding the performance, risk, sustainability, and life-cycle of infrastructure assets.

1 INTRODUCTION

With the expansion of human civilization, the number of infrastructure systems has unavoidably increased, causing a significant daily CO₂ footprint on the environment (Bianchi and Biondini 2022, Biondini and Frangopol 2015). Recently, the idea of carbon neutrality has been promoted with the aim of achieving zero net worldwide CO₂ emissions. Therefore, it is urgent to improve civil infrastructure management and operation processes in order to reduce carbon emissions over the course of a civil infrastructure's life and encourage the creation of a low-carbon smart world.

The sustainable policy-making process typically includes a number of factors, such as the effects on the environment, economy, society, and safety (Capacci and Biondini 2020, Capacci et al. 2020). In previous research projects, risk assessments for network-level bridges under service loads or multi-hazard scenarios were completed empirically, qualitatively, and quantitatively (Lei et al. 2022a). Dong et al. (2014) calculated the sustainable metrics for a transportation network in the USA under a seismic scenario. Abdelkader et al. (Abdelkader et al. 2022) developed a multi-stage policy-making approach to involve a neural network model and an optimization model for predicting sustainable resource allocation. These studies mainly used the Markov decision processes (MDPs) to simulate the deterioration and maintenance progress. Genetic algorithms are often employed to give good policies for optimizing infrastructure system management.

Deep reinforcement learning (DRL) is an effective deep learning method to optimize complicated infrastructure systems. Cheng and Frangopol (2021) proposed a DRL-based approach for load rating projects of network-level bridges. Andriotis and Papakonstantinou (2021) presented a management optimization method with a decentralized multi-agent DRL model. This study efficiently formulated the plans, considering the life-cycle risks and budget constraints. Zhang and Si (2020) advanced the conventional condition-based management plans for infrastructure systems based on DRL. Lei et al. (2022b) proposed the DRL life-cycle maintenance framework for network-level bridges, and the proposed method effectively improved the regional safety of bridge structures and reduced the management cost simultaneously. Very few studies have been performed on aging infrastructure systems with life-cycle management optimization using DRL methods and taking sustainable metrics and risk attitudes into account.

This study develops a DRL-based sustainable life-cycle maintenance policy-making system for aging infrastructure systems. The environmental, economic, and safety metrics are transformed into multi-utility models to construct the reward function for DRL. The time-variant structural failure probability is developed based on the measured data. Within the employed structural features, system topology, and sustainable metrics in the DRL environment, the CNN-based policy-making agent could suggest optimal life-cycle management policies. An existing highway bridge network in China is used to validate the suggested approach.

2 DRL-BASED MANAGEMENT POLICY OPTIMIZATION FRAMEWORK

2.1 Sustainable life-cycle management framework

Figure 1 shows the DRL-based management policy-making framework, which consists of a CNN-based management policy-making agent, service environment, state and sustainable reward, and management outputs. The CNN-based agent gives the management actions for the infrastructure. The service environment contains structural deterioration and management effects, which could be obtained from theory, inspection, and monitoring. The state and reward represent the service condition of infrastructure, and the sustainable reward feeds back to the agent to evaluate the policies. The DRL method enables the policy-making agent to learn better management actions in an interactive environment to maximize cumulative rewards.

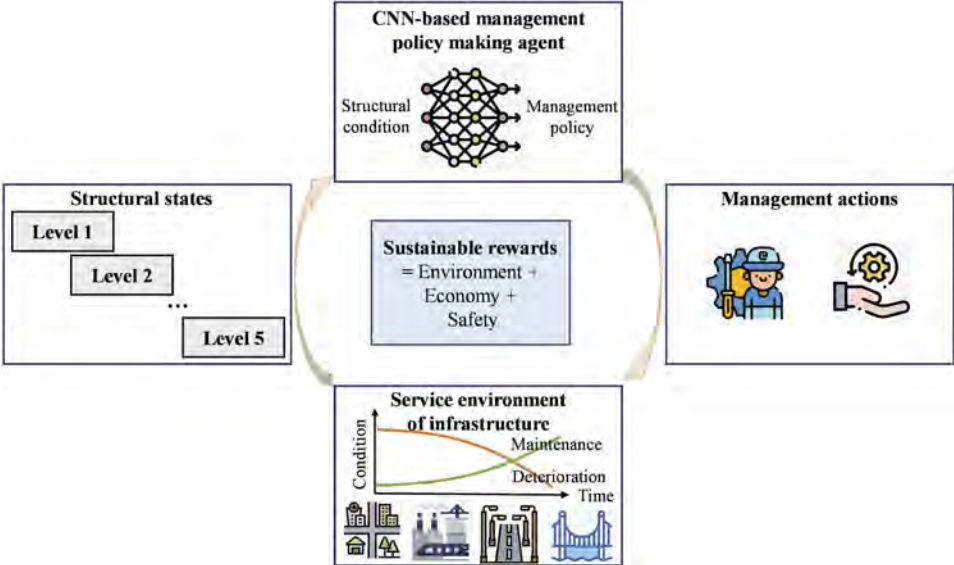


Figure 1. DRL framework considering multi-attribute utilities.

2.2 Convolutional neural network-based policy-making agent

Normally, the MDPs method assumes offline information of detailed stochastic models for the whole environment and provides optimum management policies. DRL uses domain information and learns to perform efficiently by engaging directly with environments. Figure 2 illustrates the Convolutional neural network (CNN) -based policy-making agent with Q learning. It is a model-free technique that uses a CNN model to output the value function. In Q learning of Figure 2, grey blocks are the main parts of the algorithm. The hollow blocks are the outputs of estimated states, actions, and rewards. Some primary operations are illustrated beside the arrow lines, and the blue arrows are the updating of the model parameters.

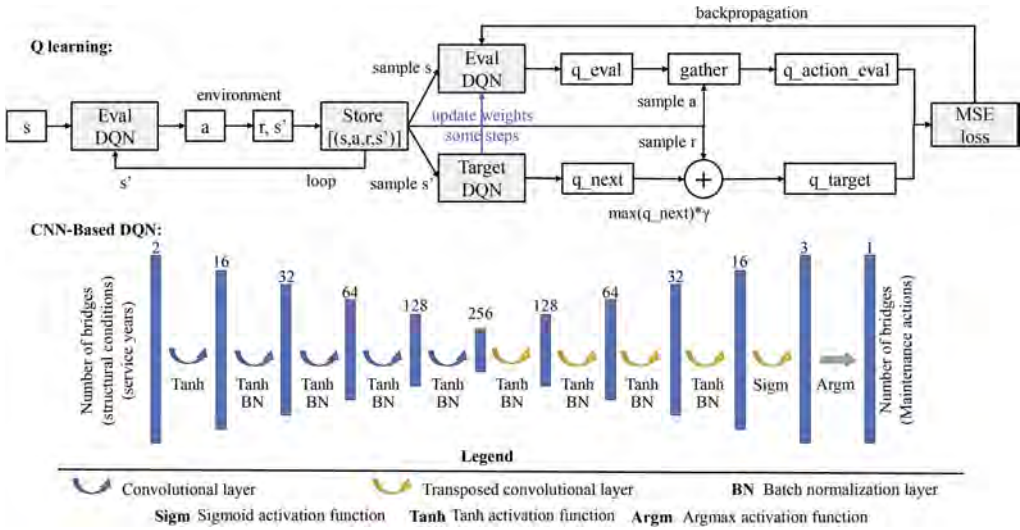


Figure 2. The CNN-based policy-making agent with Q learning.

The DRL agent observes the structural state s_t , recommends a management action a_t , and outputs a reward r_t at each step. The output management policy $\pi(a|s)$ links structural states with management procedures (Lei and Dong 2022). The agent receives feedback to evaluate the action. The purpose of the DRL agent is to maximize its predicted total reward, which is weighted by $\gamma \in [0, 1]$ at each step to express their value to the current state. At the same time, the return is $R_t = \sum_{t'=t}^T \gamma^{t'-t} r_{t'}$ where T is the step taken after the episode ends. The predicted return after monitoring the structural state and conducting a management action under a management policy is the action-value function $Q^\pi(s, a) = E[R_t | s_t = s, a_t = a, \pi]$. With the help of the greedy algorithm, the Q value is determined by

$$Y_t^{DQN} = R_{t+1} + \gamma \max_a Q(S_{t+1}, a; \theta_t) \quad (1)$$

The Q-learning has two critical advantages (Busoniu et al. 2008): 1) Experience replay could take random samples from the replay memory and break the data correlation. 2) Two separate Q-networks contain the current parameters θ and the old parameters θ^- , respectively. At every update iteration i the current parameters θ are updated to minimize the mean-squared error concerning old parameters θ^- by optimizing the following DQN loss function:

$$L_i(\theta_i) = E \left[\left(r + \gamma \max_{a'} Q(s', a'; \theta_i^-) - Q(s, a; \theta_i) \right)^2 \right] \quad (2)$$

The CNN-based agent is used as the policy-making agent, as shown in Figure 2. The CNN-based agent receives the measured data of civil infrastructure and extracts their hidden features. The inputs contain the spatial-temporal structural condition data of civil infrastructure. The CNN model gives the management actions of infrastructures with compressed features. The obtained high-level abstracts are unsampled and decompressed into valuable information using the transposed convolutional layers. Up until the targets are reached, the feature extracted by the convolutional layers is sampled nonlinearly with weights. The recommended management action for civil infrastructure is the output of the CNN-based agent.

2.3 Multi-attribute utility model with sustainability metrics

The utility model defines management costs taking the policy maker’s perspective into account. To reduce the impact of different ranges, utility models normalize cost values from 0 to 1. The risk attitude of the policy maker also can be taken into account in the model. The single-attribute utility model is

$$u(t) = \frac{1}{1 - \exp(-\gamma)} \left[1 - \exp\left(-\gamma \frac{C_{max} - C(t)}{C_{max}}\right) \right] \quad (3)$$

where, C_{max} denotes the maximum single-attribute sustainable metric; γ denotes the risk attitude, where $\gamma > 0$ and $\gamma < 0$ represent risk aversion and acceptance attitudes, respectively; and $C(t)$ denotes the time-variant single-attribute sustainable metric.

Along with the aforementioned single-attribute utility model, the sustainable multi-attribute utility model also incorporates the contribution of economic, environmental, and safety metrics. The sum of all the weights equals 1. The sustainable multi-attribute utility model is shown in Figure 3, and is formed as

$$u_f = w_c u_c + w_m u_m + w_s u_s \quad (4)$$

where, u_f is the sustainable multi-attribute utility model; w_c , w_m , and w_s are the weights for the environmental, economy, and safety single-attribute utility in the sustainability perspective.

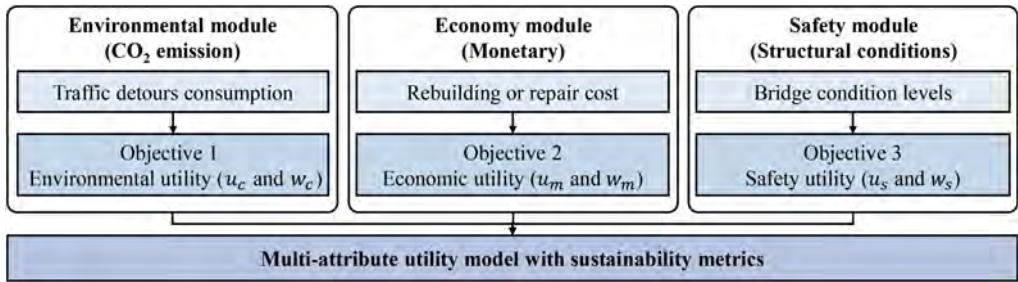


Figure 3. Sustainable multi-attribute utility model for infrastructure system.

3 CASE STUDY FOR LOCAL BRIDGE NETWORK

3.1 Bridge network descriptions

The proposed sustainable intelligent management of aging civil infrastructure systems is implemented on an existing highway bridge network in China. Eight roads link the six cities together, which is depicted in Figure 4. The network contains a total of 308 middle- and small-span RC bridges. This study aims to optimize the 100-year maintenance policy.

In this case, the failure of network elements other than bridges is regarded as insignificant in comparison to those of bridges.

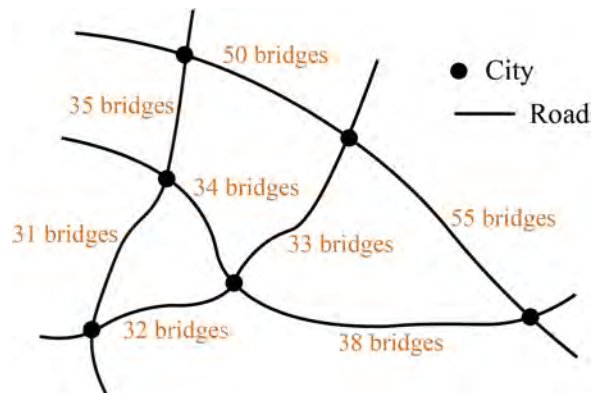


Figure 4. Bridge network layout.

These bridges range in width from 5 to 20 meters. The largest proportion is found in bridges with a width of roughly 20 meters and 5 to 10 meters. Although the span length of these bridges ranges from 5 to 96 meters, most of them have a length of less than 50 meters. The sustainable maintenance policy takes traffic volume into account when calculating CO₂ emissions from traffic detours. The CO₂ emission per kilometer for each type of vehicle is defined by a survey in 2016.

3.2 Structural deteriorations

The actual structural deterioration features can be extracted from the measured data, such as inspection reports and structural health monitoring systems. The failure probabilities of constructed bridges and the network links are essential for managing the bridge. Generally, the bridge condition and safety levels comprehensively determine the structural failure probability.

The structural condition level, which ranges from 1 to 5, describes the general structural condition of the bridge structure. Level 1 denotes the best structural conditions for the bridge, while Level 5 denotes the worst conditions. Considering the impacts of material and load uncertainties, the life-cycle time-variant structure failure probability distribution of this network is shown in Figure 5. It can be shown that the probability of failure in later phases of operation is vast, indicating a significant need for optimal management to improve structural performance. The maintenance effects also could be determined in similar approaches.

The deterioration model for each bridge in the network is sampled from this distribution. Without maintenance, the average value of environmental, economic, and safety metrics are 9174.07, 2537.93, and 981.0, respectively, in the 100th year. They could also be used as the maximum value of each metric to form the multi-attribute utility model.

3.3 Model setting and training

To fully retrieve the high-dimensional features and generate optimal policies in practice, the training epoch is set at 1000. In order to allow agents to remember and reuse previous experiences, the memory capacity is set to 50. The weights are updated during training at a rate of 0.001, which is the learning rate. The value of the discount factor is set to 0.05. It could be used to gauge how motivated the agents are by rewards and provide evidence of the convergence of some techniques.

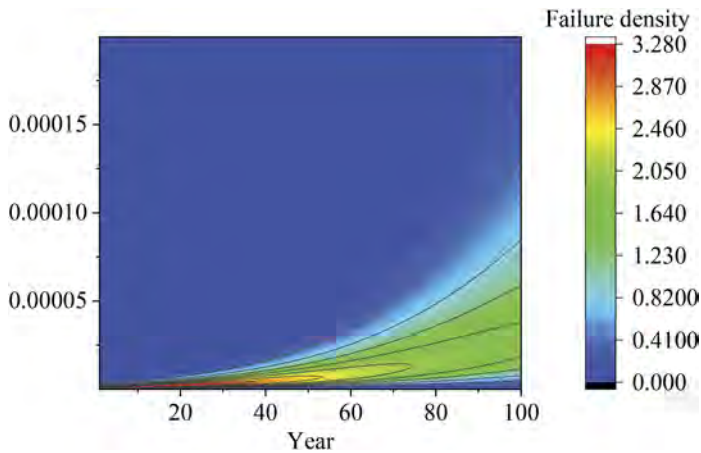


Figure 5. Probability density distributions of life-cycle failure probability under no maintenance.

The coordinate value of each point in Figure 6 denotes the life-cycle accumulated values of the economic, environmental, and safety of network-level bridges. Figure 6 also contains the optimized policy for each training epoch. The smaller the metric (coordinate) value, the better the management policy. The output management policies become more efficient at maximizing sustainable metrics as the number of epochs rises. The optimal management policies in terms of environmental, economic, and safety metrics are 3443.8, 5248405.3, and 2612.0, respectively, as shown by the green point with projection lines. The trained optimal policy outperforms the most successful conventional policy in terms of environmental, economic, and safety metrics by 32.12%, 47.52%, and 41.96%, respectively.

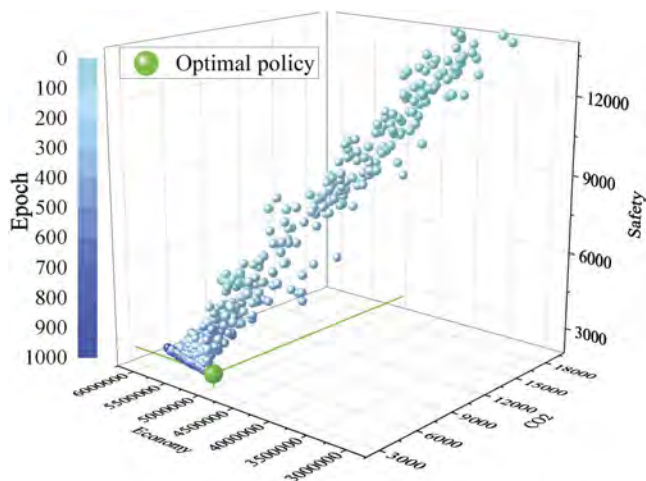


Figure 6. Optimized management policies during model training.

3.4 Optimal life-cycle management policies

The annual changes in network-level bridge conditions and management actions are displayed in Figure 7 from the regional view. Figure 7 (a) displays that most bridges are in condition Level 1 during the life-cycle. Bridges with condition Level 2 are around 7%, and bridges with condition Level 3 are less than 1%. The optimal management policy keeps the network-level

bridges in better service performance. Figure 7 (b) shows that the optimal management policy employs a small number of efficient management actions to ensure the good condition of network-level bridges. Among all the management actions, the repair action is mostly selected as preventative.

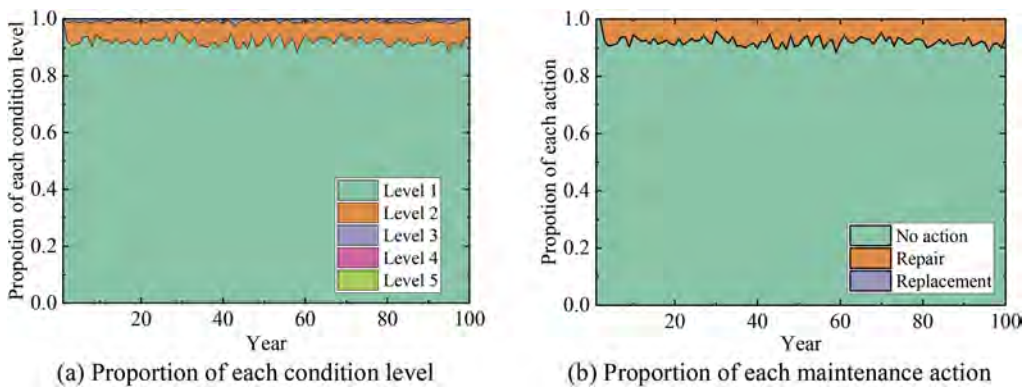


Figure 7. Annual changes in structural conditions and maintenance actions of the optimal policy.

From the individual view, Figure 8 displays the condition level of each bridge in four typical years. Each bridge holds a distinct structural condition variation and maintenance scheme. In the four subfigures, only seven bridges (one in the 20th, 40th, and 60th year and four in the 80th year) deteriorated to condition Level 3. The additional CO₂ emissions are 37.42, 31.52, 34.35, and 37.53 tons in these four years. The available budgetary resources maintain a balance between regional structural safety and environmental impact.

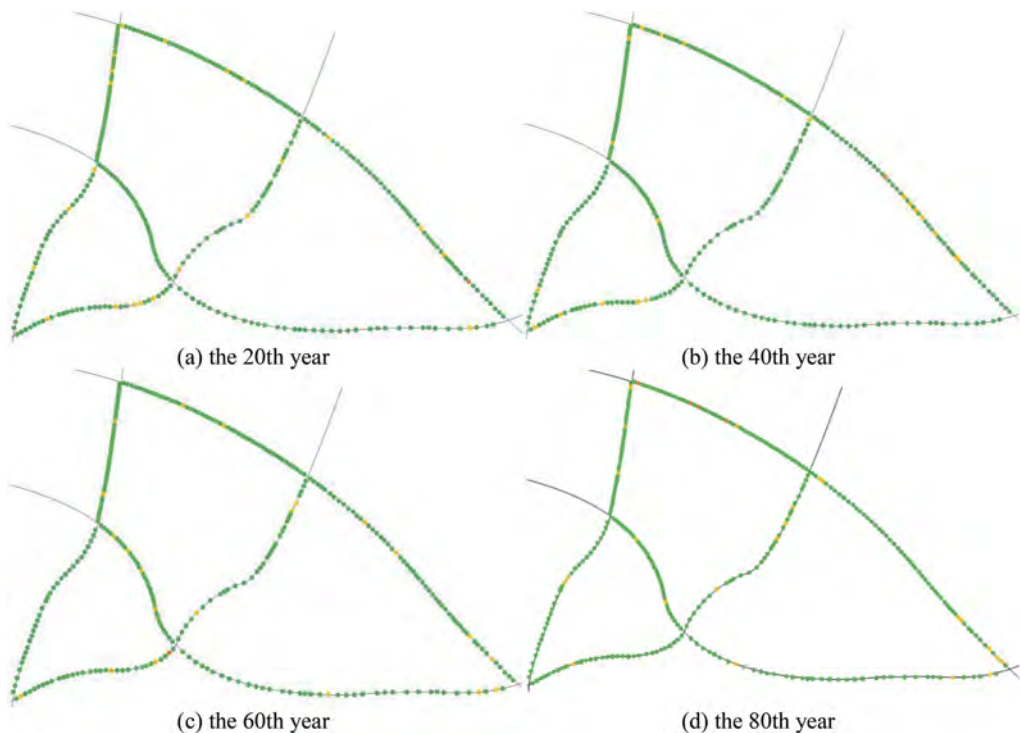


Figure 8. Individual bridge conditions in four typical years.

4 CONCLUSIONS

This study provides a DRL-based framework to determine life-cycle sustainable management policies for aging infrastructure systems. The following are the main conclusions:

- 1) The sustainability metrics are transformed into utility models to construct the reward function for DRL. DRL could output more efficient and sustainable life-cycle management policies than traditional condition-based methods. It also proved to have a better trade-off between the three main objectives of the infrastructure system.
- 2) The optimal management policy keeps the network-level bridges in better service performance. It employs a small number of efficient management actions to ensure the good condition of network-level bridges. Among all the management actions, the repair is mostly selected as preventative.
- 3) From an individual perspective, each bridge holds a distinct structural condition variation and management scheme. Very few bridges that deteriorated to condition Level 3. The available budgetary resources maintain a balance between sustainable regional impact.

FUNDINGS

The study has been supported by the Research Grant Council of Hong Kong (project no. PolyU 15219819 and 15221521) and the Centrally Funded Postdoctoral Fellowship Scheme (P0043893). The support is gratefully acknowledged. The opinions and conclusions presented in this study are those of the authors and do not necessarily reflect the views of the sponsoring organizations.

REFERENCES

- Abdelkader, E. M., Moselhi, O., Marzouk, M. & Zayed, T. 2022. An exponential chaotic differential evolution algorithm for optimizing bridge maintenance plans. *Automation in Construction*, 134.
- Andriotis, C. P. & Papakonstantinou, K. G. 2021. Deep reinforcement learning driven inspection and maintenance planning under incomplete information and constraints. *Reliability Engineering & System Safety*, 212.
- Bianchi, S. & Biondini, F. 2022. Life-Cycle Assessment of Deteriorating RC Bridges Using Artificial Neural Networks. *Journal of Infrastructure Systems*, 28.
- Biondini, F. & Frangopol, D. M. 2015. Design, assessment, monitoring and maintenance of bridges and infrastructure networks. *Structure and Infrastructure Engineering*, 11, 413–414.
- Busoniu, L., Babuska, R. & de Schutter, B. 2008. A comprehensive survey of multiagent reinforcement learning. *Ieee Transactions on Systems Man and Cybernetics Part C-Applications and Reviews*, 38, 156–172.
- Capacci, L. & Biondini, F. 2020. Probabilistic life-cycle seismic resilience assessment of aging bridge networks considering infrastructure upgrading. *Structure and Infrastructure Engineering*, 16, 659–675.
- Capacci, L., Biondini, F. & Titi, A. 2020. Lifetime seismic resilience of aging bridges and road networks. *Structure and Infrastructure Engineering*, 16, 266–286.
- Cheng, M. H. & Frangopol, D. M. 2021. A Decision-Making Framework for Load Rating Planning of Aging Bridges Using Deep Reinforcement Learning. *Journal of Computing in Civil Engineering*, 35.
- Dong, Y., Frangopol, D. M. & Saydam, D. 2014. Sustainability of Highway Bridge Networks Under Seismic Hazard. *Journal of Earthquake Engineering*, 18, 41–66.
- Lei, X. & Dong, Y. 2022. Deep reinforcement learning for optimal life-cycle management of deteriorating regional bridges using double-deep Q-networks. *Smart Structures and Systems*, 30, 571–582.
- Lei, X., Xia, Y., Dong, Y. & Sun, L. 2022a. Multi-level time-variant vulnerability assessment of deteriorating bridge networks with structural condition records. *Engineering Structures*, 266, 114581.
- Lei, X. M., Xia, Y., Deng, L. & Sun, L. M. 2022b. A deep reinforcement learning framework for life-cycle maintenance planning of regional deteriorating bridges using inspection data. *Structural and Multidisciplinary Optimization*, 65.
- Zhang, N. L. & SI, W. J. 2020. Deep reinforcement learning for condition-based maintenance planning of multi-component systems under dependent competing risks. *Reliability Engineering & System Safety*, 203.

Meta-learning method for efficient time-variant reliability analysis of deteriorating structures

T. Gao, J. Cheng & Y. Liu

Huazhong University of Science and Technology, Wuhan, China

M. Cheng

Cornell University, Ithaca, USA

D.M. Frangopol

Lehigh University, Bethlehem, USA

ABSTRACT: Time-variant reliability analysis is an essential computational procedure to quantify the failure probability and risk throughout the life-cycle of structures. A major challenge of time-variant reliability analysis is the computational effort and expense, especially when sampling-based methods are involved. Artificial Intelligence inspires a new perspective for developing advanced life-cycle computational tools in this field. This paper presents a meta-learning method to provide an alternative computational scheme that can achieve higher efficiency in terms of utilizing the evaluations from earlier point-in-time reliability analysis. The proposed meta-learning method uses the deep neural network (DNN) as the surrogate for reliability analysis. The model-agnostic meta-learning (MAML) method is adopted as the meta-learning algorithm to learn a set of adaptable parameters for subsequent DNN training. A corrosion problem is used to illustrate the applicability and efficiency of the proposed method.

1 INTRODUCTION

Civil and marine structures are often exposed to severe environment that can cause deterioration of structural performance. A rational assessment of deteriorating structural performance during life-cycle is critical for effective intervention strategies. In this regard, time-variant reliability analysis (Liu & Frangopol 2018; Gong & Frangopol 2019) became an essential computational tool for life-cycle management of aging structures (Frangopol 2011). Reliability analysis usually adopts sampling techniques to quantify the failure probability accurately. As a result, the required number of simulations is considerably high, especially when dealing with low failure probability events. The computational efficiency problem remains a key challenge for reliability tools as decision-makers demand rapid solutions for life-cycle management.

Machine learning methods can be used to address the computational expensive problem associated with reliability analysis (Saraygord Afshari et al. 2022). The trained DNN model can approximate the limit state function, therefore, helping to accelerate the computation process. A series of machine learning methods are successful in the structural reliability analysis domain such as Kriging (Yi et al. 2021) and Artificial Neural Network (Chojaczyk et al. 2015). DNN modeling research also concerns with the refinement of models for computational accuracy. An extensive review of adaptive DNN model methods for reliability analysis can be referred to Teixeira et al.(2021). The application of deep neural networks (Bao et al. 2021) in this field has shown an enlarged capability to deal with more complex reliability problems. However, the training of deep neural

networks is non-trivial as a large number of episodes are required for convergence. In addition, refinement samples are often needed to ensure the quality of DNN predictions (Xiang et al. 2020; Zhang et al. 2022).

Despite the improvement of structural reliability analysis with machine learning methods, time-variant reliability analysis still lack an appropriate surrogate method. The DNN modeling process has to repeat from scratch in each point-in-time reliability assessment. The traditional way of training and tuning a large number of DNNs is not considered an ideal solution for time-variant analysis. A key aspect of artificial intelligence is the capability to utilize experience and knowledge. Meta-learning is the concept of learning a model that can generalize and adapt to new tasks with prior knowledge from learned tasks (Finn et al. 2017). Cheng et al. (2022) proposed a meta-learning framework for DNN modeling with reduced sampling data. A similar idea of utilizing prior data for Gaussian process modeling is presented in the work of Pfingstl and Zimmermann (2022). The concept of meta-learning is appealing to address the computational problem with time-variant reliability analysis.

This paper proposed a meta-learning framework for time-variant reliability analysis in a way to significantly reduce the computational effort for surrogate training. Time-variant surrogate-assisted reliability problem is treated as a series of similar training tasks. The goal of the proposed meta-learning is to learn the prior knowledge that can generalize across the various training tasks, thereby accelerate the subsequent training process. This computational scheme can achieve higher efficiency in terms of utilizing the deep neural network training from earlier point-in-time reliability analysis. In other words, the computational scheme “learned” to improve the efficiency of reliability analysis as time evolves. The proposed method is illustrated with a simple corrosive beam problem.

2 META-LEARNING FRAMEWORK FOR TIME-VARIANT RELIABILITY ANALYSIS

2.1 Time-variant reliability analysis

It is considered that a time-variant reliability problem can be defined with a limit state function, $G(t) = g(X(t))$, where $X(t) = [X_1(t); X_2(t), \dots, X_n(t)]$ is an n-dimensional time-variant random variable vector. If $G(t) \leq 0$, the structure is considered to be in the failure domain, otherwise it is safe. The probability failure over time is expressed as:

$$P_f(T) = P(G(t) \leq 0), \exists t \in [0, T] \quad (1)$$

where T is the point in time during the life cycle; $P_f(\cdot)$ denotes the probability of failure.

2.2 Deep neural network for limit state function approximation

A reliability analysis framework based on the DNN model can be used to approximate the limit state function in order to improve efficiency. The DNN model transforms the feature representation of the sample from the original space to a new feature space to make classification or prediction easier. The typical structure of the DNN is shown in Figure 1. It consists of the input layer, several hidden layers, and the output layer. In this work, the input is the time-variant random variable $X(t)$ of specific problems, and the output is the predicted value of the limit state equation $G(t)$.

2.3 Model-agnostic meta-learning algorithm

This work proposes a meta-learning method for time-variant reliability analysis. The reliability analysis framework has a meta-training phase and a learning phase as shown in Figure 2. For the meta-training phase, Model-agnostic meta-learning algorithm (MAML) (Finn et al.

2017) is used to obtain the meta-trained model, which represents the knowledge learned from the earlier time DNN training tasks. For the learning phase, DNN models are adapted from the meta-trained model to accelerate training for subsequent tasks.

The meta-trained model parameterized by θ'_{mt} and the DNN model for new task T_w parameterized by θ'_w are denoted as f'_{mt} and f'_w . The goals of the meta-training phase and the learning phase are to find the optimal neural networks parameters θ'_{mt} and θ'_w .

To obtain the optimal θ'_{mt} , each epoch of MAML consists of the following steps.

- (a) Sample N_s tasks $(T_{s1}, T_{s2}, \dots, T_{sn})$ from the earlier time tasks.
- (b) For $T_{si} \in (T_{s1}, T_{s2}, \dots, T_{sn})$, the DNN model f'_{mt} is adapted from θ'_{mt} by using data points from T_{si} . The specific process is as follows, θ'_{si} is updating using one gradient descent

$$\theta'_{si} = \theta'_{mt} - \alpha \nabla_{\theta'_{mt}} \mathcal{L}_{T_{si}}(f'_{\theta'_{mt}}) \quad (2)$$

where α is the learning rate of the inner loop, and $\mathcal{L}_{T_{si}}$ is the loss function associated with T_{si} .

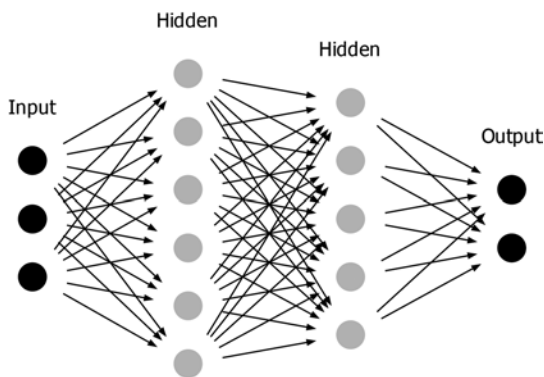


Figure 1. The construction of the DNN model.

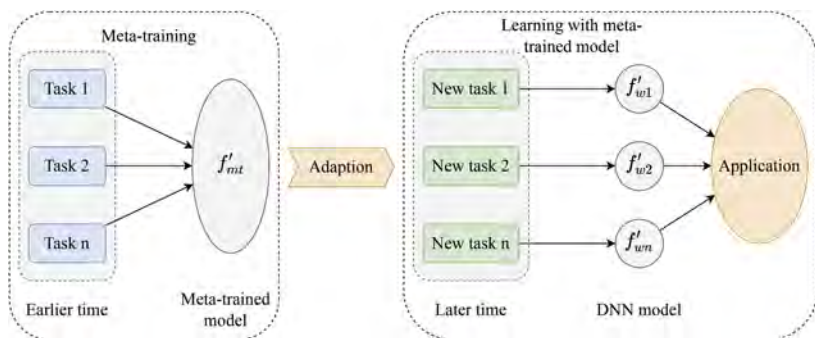


Figure 2. Meta-learning-based DNN modelling framework(Adapted from (Cheng et al. 2022)).

- (c) The DNN model θ'_w is adapted from θ'_{mt} by using new data points from all tasks. θ'_w is updated using gradient descent

$$\theta'_{mt} \leftarrow \theta'_{mt} - \beta \nabla_{\theta'_{mt}} \sum_{T_{si}} \mathcal{L}_{T_{si}}(f'_{\theta'_{si}}) \quad (3)$$

where β is the learning rate of the main loop. The purpose of meta-training is to find θ'_{mt} that minimizes \mathcal{L}_{T_m} . The procedure is shown in Algorithm 1.

Once the meta-trained model is available, the next step is to update the DNN model from the meta-trained model on specific tasks. When optimizing θ'_w , the first update is an update from θ'_{mt} , which represents the adaptation from the meta-trained model:

$$\theta'_w = \theta'_{mt} - \alpha \nabla_{\theta'_{mt}} \mathcal{L}_{T_w}(f'_{\theta'_{mt}}) \quad (4)$$

while later updates using the same data points are

$$\theta'_w = \theta'_w - \alpha \nabla_{\theta'_w} \mathcal{L}_{T_w}(f'_{\theta'_w}) \quad (5)$$

In this paper, stochastic gradient descent is used for Eq.(2), while the Adam optimizer (Kingma & Ba 2014) is used for other updates.

Algorithm 1 MAML for the meta-training phase (adopted from (Finn et al. 2017))

Require: α, β : step size hyperparameters
1: Randomly initialize θ'_{mt}
2: **while** not done **do**
3: Sample N_s tasks $(T_{s1}, T_{s2}, \dots, T_{sn})$;
4: **for** all T_i **do**
5: Sampling data points from existing data points;
6: Evaluate $\nabla_{\theta'_{mt}} \mathcal{L}_{T_{si}}(f'_{\theta'_{mt}})$;
7: Compute adapted parameters with gradient descent: $\theta'_{si} = \theta'_{mt} - \alpha \nabla_{\theta'_{mt}} \mathcal{L}_{T_{si}}(f'_{\theta'_{mt}})$;
8: **end**
9: Update $\theta'_{mt} \leftarrow \theta'_{mt} - \beta \nabla_{\theta'_{mt}} \sum_{T_{si}} \mathcal{L}_{T_{si}}(f'_{\theta'_{si}})$;
10: **end**

2.4 Meta learning for time-variant reliability analysis

For time-variant reliability analysis, the meta-training set is obtained by selecting the time interval. As shown in Figure 3, tasks in the earlier time interval are sampled as the meta-training set, and DNN models are adapted from the meta-trained model by training on data points from the later time interval.

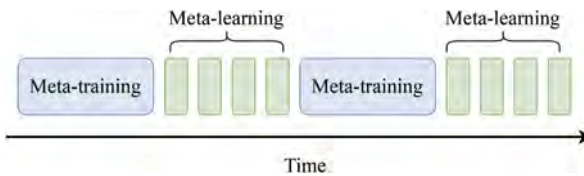


Figure 3. Division for meta-training and meta-learning tasks.

To implement the framework for specific problems, it is important to know what can be categorized as meta-training tasks. In this work, tasks within a time interval have a certain degree of similarity. In the meta-training phase, when using tasks in an appropriate time interval as the meta-trained model training set, the meta-trained model will show better performance in predicting tasks at later time, and it can reduce the number of epochs required for the learning phase. In contrast, if an inappropriate meta-training set is selected, the trained meta-trained model may not be effective. In the learning phase, the converged meta-trained model is used to predict tasks at later time points. As the time point moves away from the time interval which is used to construct the meta-trained model training set, the performance of the meta-trained model gradually degrades. In this case, it is possible that the meta-trained model is less effective than a randomly initialized DNN.

3 ILLUSTRATIVE EXAMPLE

3.1 Corrosion beam problem

For illustrative purposes, a simple-supported beam corrosion problem is used here. The cross-section shape of the beam is shown in Figure 4. The size of the cross-section decreases with time due to the corrosion.

Considering the material properties and manufacturing errors, the yield strength of the material σ (MPa) and the length of corroded beam L (m) are treated as random variables that follow normal distributions, where $\sigma \sim N(200, 20^2)$ and $L \sim N(8.5, 0.2^2)$. The material mass density, ρ (kN/m³), the height $h(t)$ and the beam breadth $b(t)$ (m) are assumed to be uniform distributed variables listed in Table 1. An stochastic load F (kN) is applied on the middle point of the beam, which follows normal distribution, where $F \sim N(5000, 700^2)$.

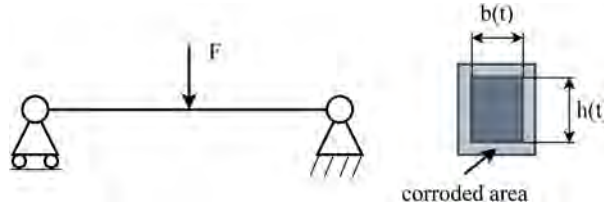


Figure 4. Corroded beam under midspan load.

Table 1. Uniform random variables in the corroded beam problem.

Variable	Distribution	Mean	Radius
ρ (kN/m ³)	uniform	78	0.5
$b(t)$ (m)	uniform	$0.3-5 \times 10^{-4}t$	0.015
$h(t)$ (m)	uniform	$0.05-4 \times 10^{-4}t$	0.004

According to the mechanical analysis, the failure event occurs when the maximum stress exceeds the yielding limit of the beam, and the limit state function associated with the failure is expressed as:

$$G(\sigma, L, \rho, F, b(t), h(t)) = \frac{b(t)h(t)^2}{4} \sigma - \left(\frac{FL}{4} + \frac{\rho b(t)h(t)L^2}{8} \right) \quad (6)$$

3.2 Results

The considered time period is given as [20, 30] month in this problem. For the DNN architecture, the hidden layer number is set to two. The first hidden layer has 128 neurons and the second has 64 neurons. For meta-training, t varies from time t_1 to time t_2 , where t_1 and t_2 belong to [1, 30] and t_1 is less than t_2 . For task after time t_2 , the surrogate $\hat{G}(\sigma, L, \rho, F, b(t), h(t))$ is adapted from the meta-trained model. As a comparison, a randomly initialized DNN is used to solve the same task. The following concrete example can illustrate the performance of MAML.

In this illustrative example, t_1 and t_2 are set to 20, and 25 in meta-training, respectively. The number of Monte Carlo simulations is 10^6 . For new tasks, the DNN training is adapted from a meta-trained model or randomly initialized DNN. As shown in Figure 5, the time-variant failure probability in the time interval [20, 30] is illustrated. For the randomly initialized neural network and meta-trained model, when updating the model, the number of data points and convergence epochs are the same. The specific improvement of efficiency is shown in Table 2 and Figure 6. The difference between the predicted failure probabilities and those obtained by Monte Carlo sampling is less than 3%, which represents the model has converged. In this example, it is found that randomly initialized DNN models cannot converge to the

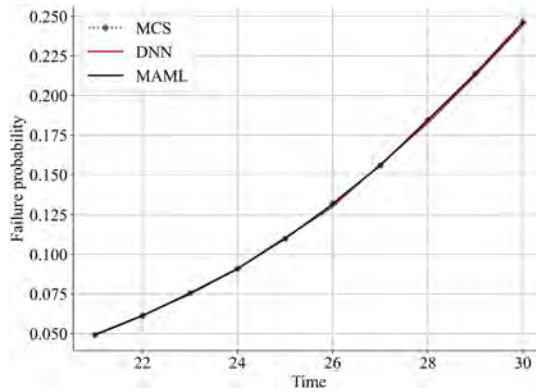


Figure 5. Time-variant probability failure of the corroded beam.

target value when using a small number of data points. Therefore, the number of sampling data points is selected to be 5000 to ensure that both MAML and DNN can meet the requirements. The DNN model based on the meta-trained model converges with fewer epochs, and the failure probability curve varies smoothly. As the time point of a new task becomes farther away from the time interval set in the meta-training phase, the efficiency of the meta-trained model will decrease, and it may be worse than a randomly initialized DNN. This problem can be solved by changing the time interval set in the meta-training phase.

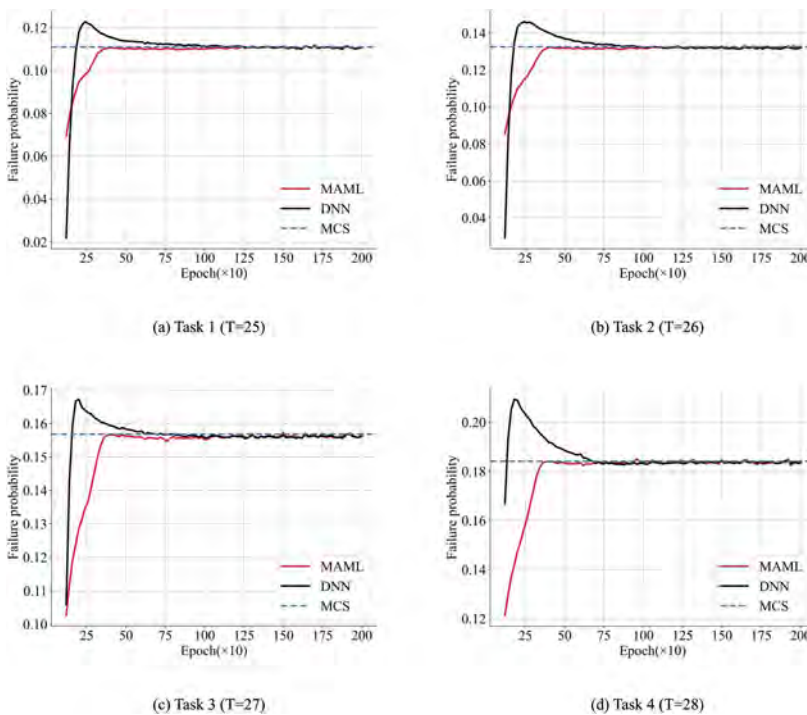


Figure 6. Task 1, 2, 3 and 4, comparison of results on the same data points.

4 CONCLUSIONS

This paper presents an initial study of applying the meta-learning method for time-variant reliability analysis. Time-variant reliability analysis is an essential computational procedure to

Table 2. Comparison results of the proposed method with randomly initialized DNN on the same data points.

Task	Time	Failure Probability	Epoch ($\times 10$)		
			DNN	MAML	Reduction of epoch
1	25	0.111	78.8	32.6	0.586
2	26	0.132	61.4	32.2	0.476
3	27	0.157	63.8	32.0	0.498
4	28	0.184	54.6	31.6	0.421
5	29	0.214	42.4	31.2	0.264
6	30	0.247	39.0	31.8	0.185

* Each value in Epoch column is the average of 5 runs.

quantify the failure probability and risk over the life-cycle of deteriorating structures. Based on the model-agnostic meta-learning algorithm, the meta-trained model is obtained by using data points from an earlier time as the meta-training set. The DNN model is adopted from a DNN initialized with meta-trained model parameters. This method can speed up the training process and achieve higher efficiency for life-cycle analysis.

ACKNOWLEDGMENTS

This research is supported by State Key Laboratory of Ocean Engineering (Shanghai Jiao Tong University) (Grant No. GKZD010084) and the Fundamental Research Funds for the Central Universities (HUST:No. 2020kfyXJJS047).

REFERENCES

- Bao, Y., Z. Xiang, & H. Li 2021. Adaptive subset searching-based deep neural network method for structural reliability analysis. *Reliability Engineering & System Safety*, 213, 107778.
- Cheng, M., C. Dang, D. M. Frangopol, M. Beer, & X.-X. Yuan 2022. Transfer prior knowledge from surrogate modelling: *A meta-learning approach*. *Computers & Structures*, 260, 106719.
- Chojaczyk, A., A. Teixeira, L. Neves, J. Cardoso, & C. Guedes Soares 2015. Review and application of artificial neural networks models in reliability analysis of steel structures. *Structural Safety*, 52, 78–89.
- Finn, C., P. Abbeel, & S. Levine 2017. Model-agnostic meta-learning for fast adaptation of deep networks. *In International Conference on Machine Learning* (pp.1126–1135). PMLR.
- Frangopol, D. M. 2011. Life-cycle performance, management, and optimisation of structural systems under uncertainty: accomplishments and challenges. *Structure and Infrastructure Engineering*, 7(6), 389–413.
- Gong, C. & D. M. Frangopol 2019. An efficient time-dependent reliability method. *Structural Safety*, 81, 101864.
- Kingma, D. P. & J. Ba 2014. Adam: A method for stochastic optimization. *arXiv preprint*, arXiv:1412.6980.
- Liu, Y. & D. M. Frangopol 2018. Time-dependent reliability assessment of ship structures under progressive and shock deteriorations. *Reliability Engineering & System Safety*, 173, 116–128.
- Pfingstl, S. & M. Zimmermann 2022. On integrating prior knowledge into gaussian processes for prognostic health monitoring. *Mechanical Systems and Signal Processing*, 171, 108917.
- Saraygord Afshari, S., F. Enayatollahi, X. Xu, & X. Liang 2022. Machine learning-based methods in structural reliability analysis: *A review*. *Reliability Engineering & System Safety*, 219, 108223.
- Teixeira, R., M. Nogal, & A. O'Connor 2021. Adaptive approaches in metamodel-based reliability analysis: *A review*. *Structural Safety*, 89, 102019.
- Xiang, Z., J. Chen, Y. Bao, & H. Li 2020. An active learning method combining deep neural network and weighted sampling for structural reliability analysis. *Mechanical Systems and Signal Processing*, 140, 106684.
- Yi, J., F. Wu, Q. Zhou, Y. Cheng, H. Ling, & J. Liu 2021. An active-learning method based on multi-fidelity kriging model for structural reliability analysis. *Structural and Multidisciplinary Optimization*, 63(1), 173–195.
- Zhang, K., N. Chen, P. Zeng, J. Liu, & M. Beer 2022. An efficient reliability analysis method for structures with hybrid time-dependent uncertainty. *Reliability Engineering & System Safety*, 228, 108794.

Optimization of sewer flushing programs: A deep reinforcement learning approach

A. Keshvari Fard & X.-X. Yuan

Department of Civil Engineering, Toronto Metropolitan University, Toronto, ON, Canada

ABSTRACT: Flushing programs are critical for managing municipal sewer assets and require efficient planning and funding. The multi-year flushing program planning decision is a complex and challenging problem involving a vast number of decision alternatives and dependencies among asset components. This paper presents a deep reinforcement learning (DRL) approach to solve this problem. The sewer network is divided into catchments and flushing decisions are made at the catchment level. The problem is formulated as a Markov decision process with the goal of maximizing the expected cumulative flushing effectiveness reward. The annual budget has a lower and upper bound, and unused budget can be saved for future years. The results show that the DRL approach performs better than a conventional genetic algorithm and is close to the Pareto frontier, particularly for longer planning horizons.

1 OVERVIEW

Sanitary sewer systems are an important class of municipal infrastructure assets. As the service age of these infrastructure assets accumulates, they deteriorate in both functional capacity and structural integrity (Yuan, 2016). Obstructions in the sewer network, such as tree roots, solidified grease, and illegally dumped waste, can impede the flow of water and decrease the system's overall capacity, which is considered an operational failure. If this capacity falls below the amount of water being discharged into the system, it can lead to overflowing, which poses risks to properties, the environment, and public health (Phillips et al., 2012). Municipalities are therefore responsible for developing proactive maintenance interventions, such as flushing, for maintaining the networks at the desired level of service and reducing the risk of blockages and overflows (Weatherly et al., 2017; Halfawy et al., 2009).

Municipalities need optimization tools to prioritize sewer segments for flushing at the network level due to their limited workforce and budgets allocated for maintenance activities. In most flushing programs, the flushing cycle is designed for a finite horizon, thus ensuring that every pipe segment is flushed at least once during the cycle. This requires determining which sewer segments need to be flushed each year so as to achieve maximum network performance while remaining within budget constraints. To reach an optimal solution, this problem requires integrated planning for the entire period since each sewer segment may degrade at different rates, and its condition at a specific time depends on the flushing decisions taken in previous years. For multi-year planning, the problem is traditionally formulated as integer programming. However, due to the nonlinear relationship between the network performance and the decision variables, this is a challenging optimization problem to solve. Moreover, when the annual budget is allowed to be transferred between years, this budget variation allowance adds another layer of complexity to the problem. All of these call for more effective solution strategies.

Recently, researchers have explored various approaches for optimizing sewer system maintenance. Abraham et al. (1998) proposed an optimization model for sewer management using a Markovian approach and dynamic programming. Elmasry et al. (2019) used mixed integer linear programming for multi-objective optimization of sewer inspection scheduling. Fontecha et al. (2020) employed linear programming for short-term maintenance scheduling. Many studies have also used evolutionary optimization methods, such as genetic algorithms, but

they have limitations in reaching the optimal solution (Tack and J. Chou, 2002; Altarabsheh et al., 2018; Chan et al., 1994; Fwa et al., 1994; Liu et al., 1997).

Markov Decision Processes (MDP) is a mathematical framework for making decisions in systems where the future state of the system depends only on the current state and the action taken rather than the entire history of states and actions. MDPs are often used to model and optimize the long-term behaviour of engineering systems, such as infrastructures (Golabi et al., 1982; Madanat, 1993), through the use of dynamic programming (Bellman, 1966). Machine learning techniques, particularly deep reinforcement learning, have been applied to optimize maintenance and renewal plans modelled by MDP. Mohammadi and He (2022) used deep reinforcement learning to optimize rail maintenance, with a reward function based on cost-effectiveness and hazard improvement. Cheng et al. (2022) compared two reinforcement learning methods for optimizing dynamic inspection policies in condition-based maintenance. Du and Ghavidel (2022) developed a deep reinforcement learning framework for maintenance decision-making in a highway bridge portfolio, and Cheng and Frangopol (2021) used deep reinforcement learning for load rating planning of bridges.

Overall, it is clear that there are a variety of approaches that have been proposed for optimizing the maintenance of sewer systems. While traditional optimization methods have been widely used for maintenance planning, there is also a growing interest in the use of machine learning techniques, such as deep reinforcement learning to improve the decision-making process. However, more research is needed to evaluate the effectiveness of these approaches in real-world scenarios and to identify the best practices for implementing them in practice. The objectives of the paper are twofold: First, develop a deep reinforcement learning approach for sewer network maintenance planning problem, and second, evaluate the performance of the proposed algorithm by comparing its optimality with genetic algorithm results.

2 PROBLEM STATEMENT

The optimization of sewer flushing programs is a complex problem for municipalities to enhance network performance while utilizing limited resources efficiently. The flushing program is usually optimized for a defined horizon to determine which sewer segments should be flushed every year to achieve maximum network performance while maintaining budget constraints. The flushing program usually starts in the summer and covers a certain percentage of the network each year. The annual budget can be flexible and may include a predefined level of variation tolerance. A sewer network is typically divided into catchment areas to account for the operational and spatial dependencies between sewer segments. All segments within a catchment must be flushed together to maximize the flushing effectiveness. This means that all segments within a catchment are considered as a single unit in the decision-making process, and asset managers must determine which catchments to flush in each year of the planning horizon.

2.1 Deterioration model

Markov chain models are frequently used to represent the deterioration of sewer conditions (Baik et al., 2006; Altarabsheh, Kandil, and Ventresca, Altarabsheh et al.). Protocols like WRC-MSCC and NASSCO-PACP categorize sewer condition data into five levels, where 1 represents excellent condition, and 5 represents the worst. The deterioration transition probability matrix for each sewer segment, represented by \mathbf{P} , is a 5×5 matrix, where each element, p_{ij} , is the probability of transitioning from state i to state j in one year. The maintenance effectiveness matrix, \mathbf{M} , models the improvement in sewer condition after flushing.

Considering all the segments in a catchment as a single unit simplifies the problem. This allows the overall condition of catchments to be considered instead of the condition of each segment. The catchment state vector represents the percent of the total length at each state. The initial state vector is determined by averaging the initial states of all sewer segments within the catchment. The equivalent transition probability matrix of the catchment is a weighted average of its sewer segments' matrices. The equivalent maintenance effectiveness matrix is also derived with the same method. The expected catchment condition is predicted following the Kologmorov-Chapman equation once the initial state vector and the catchment deterioration transition matrix are determined.

2.2 Problem formulation

The objective of this optimization problem is to minimize the overall average condition of a sewer network, which is made up of n catchments, over a h -year planning period. This objective function can be represented mathematically as:

$$\text{Minimize } \frac{1}{Lh} \sum_{j=1}^h \sum_{i=1}^n l_i \mu_{ij} \quad (1)$$

where l_i is the length of catchment i ; L is the total length of the network ($L = \sum_{i=1}^n l_i$); and μ_{ij} is the average condition of catchment i at the end of year j , which can be calculated by $\mu_{ij} = s_{i,j}v'$, where v is the state space vector (1,2,3,4,5) and $s_{i,j}$ is the state probability vector represents the probabilities that the catchment i is being in each state, at the end of year j .

The change in the condition of each catchment over time is affected by both the natural deterioration process and the flushing decisions made. This is modelled using Equation 2, where x_{ij} is a binary variable representing the decision to flush catchment i in year j . If flushing is done, the variable is set to 1, and 0 otherwise. The equation states that without flushing, the condition follows the natural deterioration process described by the matrix P_i , but with flushing at the end of the decision year, the condition is updated by the maintenance effectiveness matrix M_i .

$$s_{ij} = (1 - x_{ij})s_{i,j-1}P_i + x_{ij}s_{i,j-1}P_iM_i \quad (2)$$

The flushing program is subject to the following constraints:

$$\sum_{j=1}^h \sum_{i=1}^n c_F l_i x_{ij} \leq B \quad (3)$$

$$\left| \sum_{i=1}^n c_F l_i x_{ij} - \frac{B}{h} \right| \leq \frac{B}{h} \tau, \forall j \in (1, 2, \dots, h) \quad (4)$$

$$\sum_{j=1}^h x_{ij} \geq 1, \forall i \in (1, 2, \dots, n) \quad (5)$$

Constraint (3) limits the total program cost with respect to the total available budget (B). In this constraint, c_F is the cost of flushing per unit length of the sewer. According to constraint (4), annual budget variations, with regards to the average annual budget (B/h), must not exceed the allowable tolerance (τ). Also, constraint (5) guarantees that every catchment will be flushed at least once within the planning horizon.

The condition of each catchment at a specific year is determined by all the decisions made in previous years. Therefore, the overall condition of each catchment, represented by μ_{ij} , is a function (Equation 6) of the initial condition vector of the catchment, $s_{i,0}$, the transition probability matrix, P_i , the flushing effectiveness matrix, M_i , and decision variables (x_{ij}), from year one (x_{i1}) up year j (x_{ij}). Therefore, the objective function is not a linear function of the decision variables for planning horizons greater than one year ($h > 1$).

$$\mu_{ij} = f(s_{i,0}, P_i, M_i, x_{i1}, x_{i2}, \dots, x_{ij}) \quad (6)$$

3 PROPOSED RL METHODOLOGY

An MDP environment is defined by a set of discrete states, S , a finite set of actions, A , a stochastic transition model, P , and a reward function, r . At each decision step, the agent observes the current state, s_t , takes action a_t , and receives a reward r_t based on the reward function. The agent then proceeds to the next state, s_{t+1} , according to a known stochastic model with transition probability $p(s_{t+1}|s_t, a_t)$.

In this framework, a policy, π , is defined as a state-dependent sequence of actions. It is a mapping from states to actions. The decision-maker's goal is to maximize the total return, R_t , it receives in the long run from any time step, t , to the end of the planning horizon, and this criterion is the primary basis of altering a policy. The total return, from time t to the end of the planning horizon, is calculated as follows:

$$G_t = r(s_t, a_t) + \gamma r(s_{t+1}, a_{t+1}) + \dots + \gamma^{T-t} r(s_t, a_t) = \sum_{i=t}^T \gamma^{i-t} r(s_i, a_i) \quad (7)$$

where γ is a discount factor, $0 \leq \gamma \leq 1$, that determines the present value of future rewards. The total return can be conditioned on the current state and action pair, called *action-value function* $Q^\pi(s_t, a_t)$, and denoted the value of taking action a_t in state s_t under a policy π . In other words, $Q^\pi(s_t, a_t)$ is the expected return starting from s_t , taking action a_t , and thereafter following policy π :

$$Q_\pi(s_t, a_t) = \mathbb{E}_{s_t > r, a_t > r} [G_t | s_t, a_t] \quad (8)$$

and using Equation 7, the action-value function can be formulated recursively as follows:

$$Q_\pi(s_t, a_t) = r(s_t, a_t) + \gamma \mathbb{E}_{s_{t+1}, a_{t+1}} [Q_\pi(s_{t+1}, a_{t+1})] \quad (9)$$

The best action at each given state s is determined by selecting the action that maximizes the expected return starting from s . By having optimal action-value function, Q^* , we can directly find the optimal action by $a^*(s) = \arg \max_a Q^*(s, a)$. It can be proven that for an MDP with a discount factor less than 1, there exists at least one optimal deterministic policy (Sutton and Barto, 2018). The optimal action-value function $q^*(s_t, a_t)$, follows the Bellman equation and can be recursively formulated by Equation 10:

$$Q^*(s_t, a_t) = r(s_t, a_t) + \gamma \sum_{s_{t+1} \in S} p(s_{t+1} | s_t, a_t) \left[\max_{a_{t+1} \in A} Q^*(s_{t+1}, a_{t+1}) \right] \quad (10)$$

3.1 Deep reinforcement learning

Reinforcement learning can be viewed as a broad class of learning problems in which an agent interacts with a dynamic, stochastic, and incompletely known environment to find a decision-making strategy (policy) for taking actions in order to optimize a measure of its long-term performance (Sutton and Barto, 2018). The Q-learning algorithm (Watkins and Dayan, 1992) is a popular method for solving RL problems using a value-based approach. It aims to find the optimal action-value function, $Q^*(s, a)$. The Q-learning algorithm uses a Q-table to store the estimated action-value function and updates the Q-values iteratively using the temporal difference (TD) error, which measures the difference between the current estimate and the expected future return. The Q-table is updated according to the following update rule:

$$Q(s_t, a_t) \leftarrow Q(s_t, a_t) + \alpha (r + \gamma \max_{a_{t+1} \in A} Q(s_{t+1}, a_{t+1}) - Q(s_t, a_t)) \quad (11)$$

where α is the learning rate. The Q-learning algorithm converges to the optimal action-value function as the number of iterations increases.

The conventional Q-learning method uses a tabular form to represent the action-value function. However, this method becomes intractable for systems with a large number of states and actions. To overcome this problem, deep reinforcement learning (DRL) utilizes deep neural networks as a function approximator to provide an accurate representation of the value function in large state-action spaces. This allows for the problem of determining the action-value function for every point in the state-action space to be reduced to determining the optimal value of the parameters of the neural network function approximator. One popular DRL method is using deep Q-learning (DQL), which was first introduced by Mnih et al. (2013) and allows for the estimation of the value of an action using a function approximator, $Q(s, a; \theta) \approx Q^*(s, a)$, instead of using a Q-table. As a function approximator for Q-values, a simple deep neural network called deep Q-network (DQN) is used under the principle of

Q-learning. This deep neural network gets the states as input and estimates the Q-values for all possible actions in the output layer. Therefore, the number of nodes in the input layer and output layer equals the size of the state space and action space, respectively. At time step t , the approximate target value of an action is calculated as follows:

$$y_t = r(s_t, a_t) + \gamma \max_{a_{t+1} \in A} Q(s_{t+1}, a_{t+1}, \theta) \quad (12)$$

where θ represents the parameters of DQN, which are updated by minimizing the mean squared error (MSE) between the approximated and the target Q-value. The parameters of DQN are updated using stochastic gradient descent through the back-propagation process according to Equation 13:

$$\theta_{i+1} = \theta_i + \alpha [y_t - Q(s_t, a_t; \theta_i)] \nabla_{\theta} Q(s_t, a_t; \theta_i) \quad (13)$$

3.2 DQN configuration for sewer flushing program

Figure 1 presents the DQN designed to optimize the flushing program for a sewer network. The state space includes the overall condition of the network, current decision year, remaining budget, and each catchment's condition. The action space consists of all possible binary decisions for all catchments, making it a combinatorial space of 2^n possible actions. The DQN architecture includes two hidden layers with 64 neurons each, with input and output layers. The reward function is the effectiveness of the annual flushing plan and is calculated as $1 - s_{t+1}$, where s_{t+1} is the normalized overall condition of the network at the beginning of the next year. The annual budget and one-flush constraints are also considered in the reward function, with penalties applied if violated.

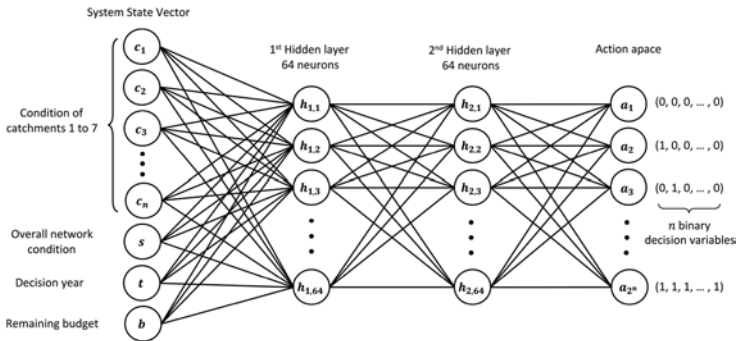


Figure 1. Neural network architecture of the proposed methodology.

4 RESULTS

The case study is based on a real-world example of a town's sewer network in Ontario. The studied network is composed of 531 sewer segments, which are grouped into seven catchments. The planning horizon for this study is seven years, with a time interval of one year. The transition probability matrix for each sewer segment is calculated using a regression equation that takes into account the pipe attributes of length, diameter, and slope (Lin et al., 2019). It is assumed that the flushing procedure is perfect maintenance, meaning that after flushing a segment, its condition is immediately changed to excellent. The cost of flushing per unit length of sewer is \$1.38, and the available budget for the whole period is \$70,000. Therefore, the average available budget for each year is \$10,000. The allowable tolerance for annual budget variation with regard to the average budget is 15 percent, meaning that the allowable range for the annual budget is [\$8,500, \$11,500].

In this study, a DQL agent was trained¹ to optimize the flushing program for a 7-year period in the case study. The training involved 20,000 simulations (episodes), each representing a simulation

1. <https://github.com/amirkfard/Deep-Q-Learning-Infrastructure-network-planning>

of seven years using Markov decision processes. The agent’s goal is to select the optimal catchments to flush each year in order to achieve the highest possible flushing effectiveness over the 7-year horizon. All the results are obtained on a desktop computer operating 64-bit Microsoft Windows with a Xeon(R) W-2155 processor at 3.3 GHz and 32GB RAM. During the learning process, the DQN learning rate (α) is 0.0005, the discount factor (γ) is 0.99, and the epsilon decay rate is 0.9995.

The result of the training process is shown in Figure 2. Each point represents one simulation and the associated total reward. Through repeated training episodes, the DQL agent was able to learn and improve its decision-making strategies, ultimately leading to the selection of a flushing plan that achieved high flushing effectiveness (minimizing overall network condition). The outcome of the optimized policy is presented in Table 1. The objective value (seven-year average network condition) of this plan is 2.412. Each column in the table provides the annual flushing plan and specifies the catchments which must be flushed that year. The last row of the table presents the cost of the plan for each year, and the total program cost is \$69,494.9.

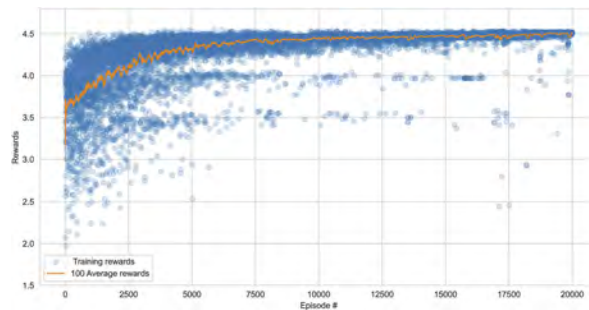


Figure 2. The performance of DQL during training for 7-year plan.

Table 1. Optimized flushing program.

Catchment	Year 1	Year 2	Year 3	Year 4	Year 5	Year 6	Year 7
1		✓				✓	
2		✓			✓		✓
3	✓		✓		✓		✓
4		✓				✓	
5				✓			
6			✓		✓		
7	✓					✓	
Annual cost	9,471.9	9,564.0	9,836.5	10,155.7	11,430.9	9,552.2	9,483.7

The OR-Tools library (Perron and Furnon, 2019) was used to find feasible solutions using a constraint programming method based on considering all possible decision sequences for each catchment. The total number of feasible solutions found was 10,571,631. The results are presented in Figure 3, which shows the distribution of feasible solutions in terms of the flushing program cost and the performance of the program. The best solution found is highlighted in green, with an objective value of 2.400 and a total cost of \$69,814.0.

The performance of a proposed methodology is also compared with Genetic Algorithm, which is a commonly used method in the literature. The python library Deep (Fortin et al., 2012) was used to implement GA. The initial population consisted of 300 random individuals, each having 49 binary genes representing a seven-year flushing plan for seven catchments. The two-point crossover and mutation probabilities were set at 0.9 and 0.1, respectively. The Hall of Fame method was also used to improve performance. For each optimization round, the number of generations was set at 1000, which took about 508.7 seconds on average to complete. This computation time is roughly the same as the 20,000 episodes in the DQL algorithm (which took 507.8 seconds to complete), making the comparison fair in terms of optimization time.

The solutions obtained from two different methods, GA and DQL (100 results each), are highlighted in blue and red, respectively. The graph shows that the solutions found by DQL are more consistent and lie on the Pareto frontier, while the solutions found by GA are more scattered with lower flushing program performance.

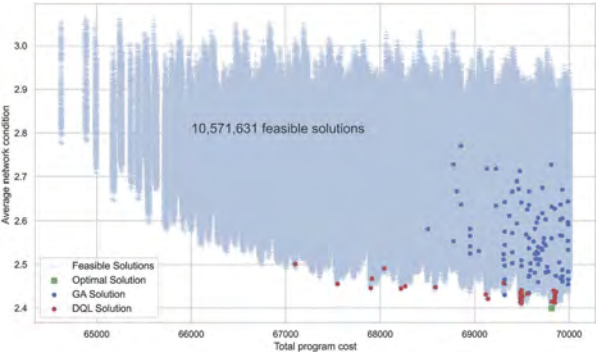


Figure 3. Feasible solution region and distribution of DQL and GA results.

The results presented in Table 2 provide insight into how the length of the planning horizon affects the performance of two different approaches for solving the problem of sewer network flushing optimization. The average performance of plans generated by DQL and GA are compared for different planning horizon lengths of 7, 14, 21, and 28 years. The results show that as the planning horizon increases, the performance of GA decreases, while the performance of the DQL approach remains relatively consistent. The numbers in the parenthesis show the portion of infeasible outcomes of each method at different planning horizons, which demonstrates, e.g., for 28-year planning horizon, the GA method cannot reach a feasible plan in 57% of the solution outcomes. This suggests that the GA may not be an effective algorithm for longer planning horizons. On the other hand, the DQL approach appears to be less affected by the length of the planning horizon, and it is a more suitable approach for longer planning horizons.

Table 2. The effect of planning horizon on the performance of DQL and GA.

Horizon	7 years	14 years	21 years	28 years
GA	2.564 (0.02)	2.732 (0.09)	2.791 (0.38)	2.823 (0.57)
DQL	2.423 (0.00)	2.491 (0.00)	2.496 (0.00)	2.493 (0.00)

5 CONCLUSION

In this paper, we proposed a DQL approach to solve the flushing program optimization problem for sewer networks. Results showed that the DQL approach produces plans with a higher overall performance than the GA approach, particularly for longer planning horizons. DQL’s solution landscape is also closer to the Pareto frontier, which represents the set of optimal solutions. However, the limitations of DQL in dealing with combinatorial action spaces need further research. To address this, solutions such as multi-agent RL, hierarchical RL, or changing the decision variables to continuous ones have been proposed. Overall, the DQL approach is a promising solution for infrastructure network maintenance planning and a valuable addition to existing methods for solving sewer network flushing program planning.

REFERENCES

Abraham, D. M., R. Wirahadikusumah, T. J. Short, and S. Shahbahrami (1998). Optimization modeling for sewer network management. *Journal of Construction Engineering and Management* 124(5), 402–410.

- Altarabsheh, A., A. Kandil, and M. Ventresca. Multi-objective optimization algorithm for sewer network rehabilitation using life cycle cost analysis and semi-markov deterioration models. In *Construction Research Congress* 2016, pp. 2089–2099.
- Altarabsheh, A., A. Kandil, and M. Ventresca (2018). New multiobjective optimization approach to rehabilitate and maintain sewer networks based on whole lifecycle behavior. *Journal of Computing in Civil Engineering* 32(1), 04017069.
- Baik, H.-S., H. S. Jeong, and D. M. Abraham (2006). Estimating transition probabilities in markov chain-based deterioration models for management of wastewater systems. *Journal of water resources planning and management* 132(1), 15–24.
- Bellman, R. (1966). Dynamic programming. *Science* 153(3731).
- Chan, W., T. F. Fwa, and C. Tan (1994). Road-maintenance planning using genetic algorithms. i: Formulation. *Journal of transportation engineering* 120(5), 693–709.
- Cheng, J. D., Y. Liu, M. H. Cheng, W. Li, and T. Y. Li (2022). Optimum condition-based maintenance policy with dynamic inspections based on reinforcement learning. *Ocean Engineering* 261.
- Cheng, M. and D. M. Frangopol (2021). A decision-making framework for load rating planning of aging bridges using deep reinforcement learning. *Journal of Computing in Civil Engineering* 35(6), 04021024.
- Du, A. and A. Ghavidel (2022). Parameterized deep reinforcement learning-enabled maintenance decision-support and life-cycle risk assessment for highway bridge portfolios. *Structural Safety* 97.
- Elmasry, M., T. Zayed, and A. Hawari (2019). Multi-objective optimization model for inspection scheduling of sewer pipelines. *Journal of Construction Engineering and Management* 145(2), 04018129.
- Fontecha, J. E., O. O. Guaje, D. Duque, R. Akhavan-Tabatabaei, J. P. Rodríguez, and A. L. Medaglia (2020). Combined maintenance and routing optimization for large-scale sewage cleaning. *Annals of Operations Research* 286(1), 441–474.
- Fortin, F.-A., F.-M. De Rainville, M.-A. G. Gardner, M. Parizeau, and C. Gagné (2012). Deap: Evolutionary algorithms made easy. *The Journal of Machine Learning Research* 13(1), 2171–2175.
- Fwa, T., C. Tan, and W. Chan (1994). Road-maintenance planning using genetic algorithms. ii: Analysis. *Journal of transportation engineering* 120 (5), 710–722.
- Golabi, K., R. B. Kulkarni, and G. B. Way (1982). A statewide pavement management-system. *Interfaces* 12(6), 5–21.
- Halfawy, M., L. Dridi, and S. Baker (2009). A multi-objective optimization decision support model for renewal planning of sewer networks. *Journal of Water Management Modeling*.
- Hordijk, A. and L. Kallenberg (1979). Linear programming and markov decision chains. *Management Science* 25(4), 352–362.
- Lin, P., X. Yuan, and E. Tovilla (2019). Integrative modeling of performance deterioration and maintenance effectiveness for infrastructure assets with missing condition data. *Computer-Aided Civil and Infrastructure Engineering* 34(8), 677–695.
- Liu, C., A. Hammad, and Y. Itoh (1997). Maintenance strategy optimization of bridge decks using genetic algorithm. *Journal of transportation engineering* 123(2), 91–100.
- Madanat, S. (1993). Optimal infrastructure management decisions under uncertainty. *Transportation Research Part C: Emerging Technologies* 1(1), 77–88.
- Mnih, V., K. Kavukcuoglu, D. Silver, A. Graves, I. Antonoglou, D. Wierstra, and M. Riedmiller (2013). Playing atari with deep reinforcement learning. *arXiv preprint arXiv:1312.5602*.
- Mohammadi, R. and Q. He (2022). A deep reinforcement learning approach for rail renewal and maintenance planning. *Reliability Engineering & System Safety* 225.
- Perron, L. and V. Furnon (2019). Or-tools, version 7.2 (<https://developers.google.com/optimization/>).
- Phillips, P., A. Chalmers, J. Gray, D. Kolpin, W. Foreman, and G. Wall (2012). Combined sewer overflows: an environmental source of hormones and wastewater micropollutants. *Environmental science & technology* 46(10), 5336–5343.
- Sutton, R. S. and A. G. Barto (2018). *Reinforcement learning: An introduction*. MIT press.
- Tack, J. N. and E. Y. J. Chou (2002). Multiyear pavement repair scheduling optimization by pre-constrained genetic algorithm. *Transportation Research Record* 1816(1), 3–8.
- Watkins, C. and P. Dayan (1992). Q-learning. *Machine Learning* 8(3-4), 279–292.
- Weatherly, R., K. Ryan, and C. Reed (2017). How to prevent your wastewater cip from being flushed—the intersection of master planning and business planning. *Proceedings of the Water Environment Federation* 2017(2), 470–486.
- Yuan, X.-X. (2016). Principles and guidelines of deterioration modelling for water and waste water assets. *Infrastructure asset management* 4(1), 19–35.

Carbon emission reduction in railway maintenance using reinforcement learning

J. Sresakoolchai & S. Kaewunruen

School of Civil Engineering, University of Birmingham, Birmingham, UK

ABSTRACT: At present, the effect of global warming becomes more severe due to carbon emissions. This negative effect attracts the interest of the international community to minimize it. The railway industry is an industry in which carbon emission cannot be neglected due to the sizes of projects, long operation and maintenance stages in the service life, including sources of energy that might not be clean in some areas. This study aims to minimize the negative effect of the railway industry on the maintenance aspect by using reinforcement learning to optimize maintenance activities. The maintenance in the railway industry is a complicated task and might not be optimized in terms of cost efficiency, serviceability, and environmental impact. The use of reinforcement learning can improve the overall efficiency of railway maintenance as it has been proven in many tasks in the railway industry and other industries. Data used to develop the machine learning model are based on field data collected during 2016-019. The length of the studies section is 30 km. Sources of data are from track geometry cars, maintenance reports, defect reports, and maintenance manuals of the sampled railway operator. The methodology used in the study is Proximal Policy Optimization (PPO). The results show that the use of reinforcement learning can reduce the carbon emission from railway maintenance activities by 48% which causes a significant amount of carbon emission while the railway defects are reduced by 68% which improved maintenance efficiency.

1 INTRODUCTION

Carbon emission is one of the causes of severe global warming and climate change nowadays. Therefore, carbon emission attracts more attention. The international community then tries to reduce it to minimize the negative effect on the environment. Although someones claim that railway transportation is one of the transportation modes that are environmentally friendly. However, it cannot be denied that many activities in the railway industry also create carbon emissions. For example, the construction of a railway project needs a lot of construction materials their production processes emit carbon or the sources of energy that are used to operate the railway may not totally clean. In addition, railway projects have long service life so the operation and maintenance phase also cause carbon. Therefore, minimizing carbon emissions in railway activities will be able to significantly minimize the negative effect on the environment.

This study aims to reduce carbon emissions from railway maintenance activities using reinforcement learning (RL). A technique used to develop a deep RL model is Proximal Policy Optimization (PPO). Data used to develop the RL model is collected from field data. The samples section is 30 km long. The duration of data collection is 2016-2019. Sources of data are from track geometry parameters collected using track geometry cars, track inspection reports showing track component defects, and maintenance reports showing performed maintenance activities during the interesting duration. Data from different sources are processed and combined together to feed into the RL model. Then, a maintenance manual of the sampled authority will be used to compare and define thresholds to create the customized RL

environment which will be used to define rewards for the RL's agent in the RL model training process. The expected contributions of the study are the developed RL model can be used by railway operators to plan railway maintenance activities more efficiently when carbon emission from maintenance activities is reduced as well as the number of railway defects. These will result in the improvement of an environmentally friendly railway system, and better serviceability, reliability, and safety in the railway system due to few defects occurring in railway networks. In addition, the developed RL model can be used to support decision-making for railway maintenance if railway operators are not ready to use a data-driven scheme in which decision-making completely relies on data and the RL model.

2 LITERATURE REVIEW

RL was first introduced in the early 1980s. It was developed to solve problems about how to react or what to do when we are in different situations (Sutton and Barto, 2018). The purposes of different reactions are to maximize rewards or outcomes from actions. As a representative, an agent is used and trained to know how to respond to different situations. The agent is not told how to do but it has to explore by itself how to maximize rewards at the latest stage. A challenge is each action not only affects the immediate rewards but also what happens next (stage). All of these are the important characteristic of RL that other types of machine learning techniques do not have and cannot resolve.

Examples of popular RL applications are chess and other game players, robots in industries, or pilot assistance in passenger cars (Sutton and Barto, 2018). Many methods are used to solve RL problems. One of the first methods is Tabular Solution Method which is the simplest. Then, other techniques were developed to be used with RL such as Markov Decision Processes, Dynamic Programming, or Monte Carlo Methods. During the last decade, many techniques have been developed to extend the potential of RL and other recent RL models have been developed and proven that the performance is better.

RL is one of the main categories of machine learning among supervised and unsupervised learning. RL becomes more popular because it has a capability that supervised and unsupervised have not. RL can react to specific environments and be trained to respond to environments that optimize rewards. Therefore, RL can be used to solve problems by finding the best responses or actions under specific situations. The interaction of the RL model is done through an agent over time or stage. The agent will use the process of trial and error to find the optimum policy under different situations.

In each timestep or stage, two components continuously interact which are the agent and the environment. The environment will provide information to the agent through stages and rewards. Then, the agent will react to the environment by taking action. After that, new stages and rewards will be provided by the environment to the agent again. This process will repeat until the end of the training. A simple flowchart of this process is shown in Figure 1. In every stage, a reward is provided to the agent based on how well the agent reacts to the environment. This will be used to find the best policy for the agent.

Reinforcement learning (RL) has been more popular in the last few years. It has been applied in many fields (Li, 2019) such as communication and networking (Luong et al., 2019), biology (Mahmud et al., 2018), electrical systems (Zhang et al., 2019), robotics (Kormushev et al., 2013), transportation (Abdulhai and Kattan, 2003), medical (Zhou et al., 2021), finance (Kolm and Ritter, 2020), or engineering (Andriotis and Papakonstantinou, 2019). Shaker et al. (2010) proposed a technique applying RL to assist in the landing of unmanned aerial vehicles. In that study, it was found that the RL agent could learn very fast and achieve the goal. Sun et al. (2017) applied RL to control and improve water use or agricultural irrigation. They found that RL could increase productivity while decreasing water use.

RL has been applied in the railway industry in different aspects. Šemrov et al. (2016) applied Q-Learning for rescheduling single-track trains. The action spaces of the agent consisted of two actions which were stop and go. Rewards were calculated based on delay. The model was tried with a three-station scenario. It was found that using RL could reduce delays

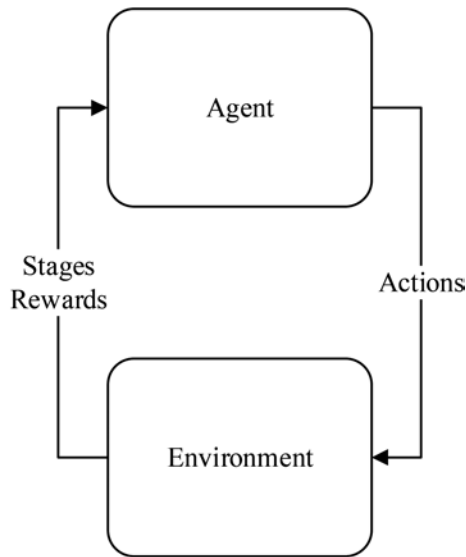


Figure 1. Simple flowchart of RL model.

in train schedules. This finding was also confirmed by Khadilkar (2018), Cui et al. (2016), Zhu et al. (2020b), and Cui et al. (2020). Other applications of RL in the railway industry were alignment optimization (Gao et al., 2022), power management (Xu and Ai, 2021, Zhu et al., 2020a, Deng et al., 2022), inspection (Zhong et al., 2021), and control (Wang et al., 2022).

For the environmental aspect, RL was used to manage the building energy (Yu et al., 2020) which showed that efficiency was improved by up to 30%. Cao and Wang (2022) applied RL to schedule the carbon emission of electric vehicles. They found that the use of RL could reduce carbon emissions by up to 20%.

From the literature review, there has never been a study applying RL for railway maintenance and carbon emission reduction. This research gap is interesting and is possible to be fulfilled using RL. Therefore, this study aims to apply RL to reduce carbon emissions generated from railway maintenance activities.

3 METHODOLOGY

3.1 *RL model*

This study applied PPO to develop the RL model. Referring to OpenAI (2017), PPO provides a better result than the state-of-the-art approaches while it is simple and easy to use and tune. PPO includes the supervised learning technique to implement a cost function. A concept is the RL model will try to minimize the cost function in each stage while keeping the deviation from the previous policy small. This creates less variance during the training process. As a result, the training will be smoother and prevent the agent from unreasonably reacting to the environment.

PPO applies the Actor-Critic scheme for the RL agent. The RL model comprises two parts which are the Deep Neural Nets of the Actor and the Critic. For the actor part, the model learns what action to take in specific situations. In other words, the agent will receive information from the environment. Information can be images or numerical data in the form of features like supervised learning. For the critic part, the model will receive information about actions and observe the next stage to evaluate how well those actions are. The positive and negative outcomes will be evaluated and updated by the critic part. In conclusion, the actor part has the function to select actions and the critic part has the function to tell whether those actions are good or bad. From this process, the agent will have the ability to learn which actions are good. If the new policy is better than the current one, the agent will update its policy. If not, the agent will keep the current policy.

3.2 Data characteristics and preparation

Data are obtained from a selected section of the 30-km track during 2016-2019. Sources of data are track geometry measurements, defect inspection reports, and maintenance records.

Track geometry measurement contained data of superelevation, longitudinal level (10m chord), longitudinal level (20m chord), alignment (10m chord), alignment (20m chord), gauge, and twist (20m chord).

Defect inspection reports contain data on different track component defects. To simplify the defects, defects are categorized using types of track components consisting of ballast, fastener, rail, sleeper, and switch and crossing. Track geometry parameters and component defects will be used as states of the RL model. Therefore, there are 12 features used as states to determine whether track sections have defects. For component defects, it is straightforward. However, for track geometry parameters, defective sections will be considered using thresholds defined by the railway authority. If track geometry parameters exceed the thresholds, they will be considered defective. The thresholds are shown in Figure 2.

Maintenance records collect data on performed maintenance activities on each track section. There are seven maintenance activities which are tamping, rail grinding, ballast cleaning, sleeper replacement, rail replacement, fastening components replacement, and ballast unloading.

Every source of data is combined to process and analyze the characteristic of data. These data will be used to develop the custom RL environment. Maintenance activities can be considered seven binary action spaces. In each stage, different maintenance activities can be combined and it will create a lot of diversity in performed maintenance activities. However, the data sources are rich enough to be numerically processed to support this diverse action space. In other words, the size of the data is big enough to tell how much track geometry parameters will improve or deteriorate when any maintenance activities are performed. At the same time, how much the probability of each track component defect will increase or decrease when different maintenance activities are performed. More detail will be described in the following section.

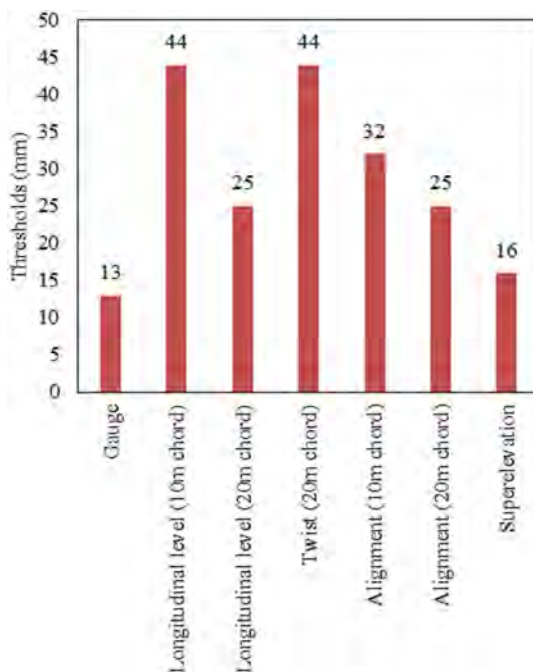


Figure 2. Track geometry thresholds.

3.3 Problem description

In the RL model, there are five components consisting of agent, environment, states, actions, and rewards.

In this study, the agent will learn how to perform maintenance activities according to 12 states which are seven track geometry parameters and five track component defects. There are five maintenance activities which are tamping, rail grinding, ballast cleaning, sleeper replacement, rail replacement, fastening components replacement, and ballast unloading that can be independently combined. Therefore, there are possible 128 combinations of maintenance activities. Different combinations of maintenance activities result in different improved and deteriorated track geometry parameters and the probability of track component defect occurrence that is obtained from the analysis of collected field data. The RL agent aims to minimize the maintenance activities to minimize the carbon emission while keeping tracks free from defects. Non-defective track means every track geometry parameter does not exceed defined thresholds and there is no track component defect.

The first stage of the RL model will have states or features as the field data. Then, the agent will randomly take actions that generate a new stage. This process will repeat 100 times which is the defined number for the agent to learn. Then, the reward will evaluate based on the actions. Rewards are defined by setting negative values of maintenance activities creating carbon emissions and penalties when tracks are defective. The penalties are set relatively high because maintenance aims to keep track in good conditions or defect-free. In a study done by Kaewunruen et al. (2021), they found that the maintenance activities of a 2.45 km track caused carbon emissions of 3,017 tCO₂e. In this study, the length of a section is 1 foot or 0.3 m. Form the calculation, the average carbon emissions per maintenance activity in a section is 0.37 tCO₂e. The agent is trained until the loss converges which demonstrates that the policy is optimized.

Then, results from field data and the RL model will be compared to evaluate the carbon emissions and the number of defects.

4 RESULTS AND DISCUSSION

The RL model is set to train for 100,000 epochs or training times. The RL model is developed using Python language. The technique used to develop the RL model is PPO as mentioned. The loss of the training is shown in Figure 3. It can be seen that after the model is trained for 30,000 epochs, the loss is equal or close to 0 which means the RL model is optimized and the training is done.

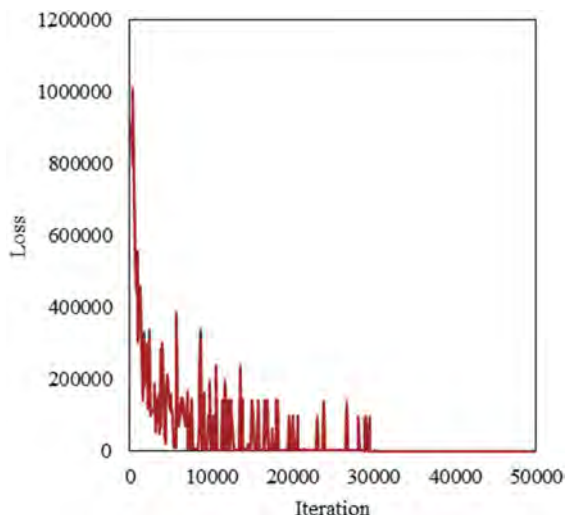


Figure 3. Training loss.

Figure 4 presents the differences between the number of performed maintenance activities and defects from field data and the RL model. From the field data, the number of performed maintenance activities and defects are about 963k and 520k respectively. However, the results from the RL model are 503k and 164k respectively. Therefore, the use of the RL model can reduce the number of performed maintenance activities by 48% and the number of defects by 68% which significantly improves the overall maintenance efficiency.

In terms of carbon emissions, assume that one maintenance activity causes a carbon emission of 0.37 tCO₂e. Therefore, the maintenance activities from the field data will create a carbon emission of 356,404 tCO₂e while the carbon emission from the maintenance when the RL model is applied is only 186,154 tCO₂e which is only 52% of the current carbon emission. Therefore, it can be concluded that the developed RL model can significantly reduce carbon emissions from the maintenance activities in the railway industry which conforms to the aim of the study.

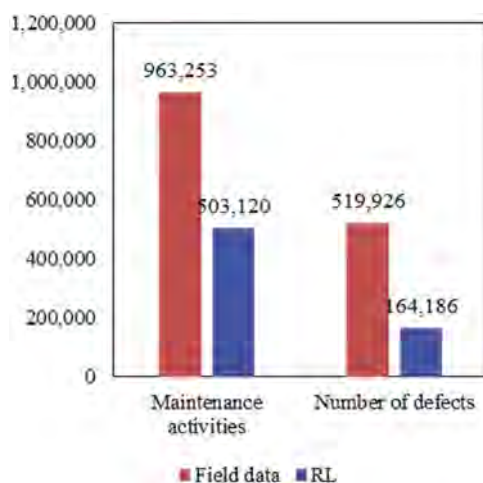


Figure 4. Differences in the number of performed maintenance activities and defects from field data and the RL model.

5 CONCLUSION

This study aims to apply the RL model to reduce carbon emissions from railway maintenance. The technique used to develop the RL model is PPO. States used to train the agent consist of 12 parameters from track geometry parameters and track component defects. Combinations of seven maintenance activities are used to create the action spaces for the RL agent. Rewards are based on the number of performed maintenance activities and defects found in track sections. Therefore, the RL agent is trained to minimize the maintenance activities to reduce carbon emissions while keeping railway tracks defect-free. Data used to develop the RL model are from field data collected from the 30km track in 2016-2019.

The developed RL model can fulfill the aim of the study. It demonstrates the potential in reducing carbon emissions from railway maintenance by minimizing maintenance activities while limiting occurred defects. Compared to field data, the results from the RL model shows that it can reduce carbon emission by 48% and the number of defects by 68%.

Contributions of the study are the railway operators can use the concept from this study to develop their own RL model to support decision-making and plan the maintenance using their data. More states can be added to meet different requirements such as setting a limited budget for maintenance or time constraints to perform maintenance activities.

ACKNOWLEDGMENT

The authors also wish to thank the European Commission for the financial sponsorship of the H2020-RISE Project no.691135 “RISEN: Rail Infrastructure Systems Engineering Network”, which enables a global research network that addresses the grand challenge of railway infrastructure resilience and advanced sensing in extreme environments (www.risen2rail.eu).

REFERENCES

- Abdulhai, B. & Kattan, L. (2003) Reinforcement learning: Introduction to theory and potential for transport applications. *Canadian Journal of Civil Engineering*, 30, 981–991.
- Andriotis, C. P. & Papakonstantinou, K. G. (2019) Managing engineering systems with large state and action spaces through deep reinforcement learning. *Reliability Engineering & System Safety*, 191, 106483.
- Cao, Y. & Wang, Y. (2022) Smart Carbon Emission Scheduling for Electric Vehicles via Reinforcement Learning under Carbon Peak Target. *Sustainability*, 14, 12608.
- Cui, L., Yuan, Z., Ming, Z. & Yang, S. (2020) Improving the congestion control performance for mobile networks in high-speed railway via deep reinforcement learning. *IEEE Transactions on Vehicular Technology*, 69, 5864–5875.
- Cui, Y., Martin, U. & Zhao, W. (2016) Calibration of disturbance parameters in railway operational simulation based on reinforcement learning. *Journal of Rail Transport Planning & Management*, 6, 1–12.
- Deng, K., Liu, Y., Hai, D., Peng, H., Löwenstein, L., Pischinger, S. & Hameyer, K. (2022) Deep reinforcement learning based energy management strategy of fuel cell hybrid railway vehicles considering fuel cell aging. *Energy Conversion and Management*, 251, 115030.
- Gao, T., Li, Z., Gao, Y., Schonfeld, P., Feng, X., Wang, Q. & He, Q. (2022) A deep reinforcement learning approach to mountain railway alignment optimization. *Computer-Aided Civil and Infrastructure Engineering*, 37, 73–92.
- Kaewunruen, S., Sresakoolchai, J. & Lin, Y.-H. (2021) Digital twins for managing railway maintenance and resilience. *Open Research Europe*, 1, 91.
- Khadilkar, H. (2018) A scalable reinforcement learning algorithm for scheduling railway lines. *IEEE Transactions on Intelligent Transportation Systems*, 20, 727–736.
- Kolm, P. N. & Ritter, G. (2020) Modern perspectives on reinforcement learning in finance. *Modern Perspectives on Reinforcement Learning in Finance (September 6, 2019)*. *The Journal of Machine Learning in Finance*, 1.
- Kormushev, P., Calinon, S. & Caldwell, D. G. (2013) Reinforcement learning in robotics: Applications and real-world challenges. *Robotics*, 2, 122–148.
- Li, Y. (2019) Reinforcement learning applications. *arXiv preprint arXiv:1908.06973*.
- Luong, N. C., Hoang, D. T., Gong, S., Niyato, D., Wang, P., Liang, Y.-C. & Kim, D. I. (2019) Applications of deep reinforcement learning in communications and networking: A survey. *IEEE Communications Surveys & Tutorials*, 21, 3133–3174.
- Mahmud, M., Kaiser, M. S., Hussain, A. & Vassanelli, S. (2018) Applications of deep learning and reinforcement learning to biological data. *IEEE transactions on neural networks and learning systems*, 29, 2063–2079.
- Openai (2017) Proximal Policy Optimization.
- Šemrov, D., Marsetič, R., Žura, M., Todorovski, L. & Srdic, A. (2016) Reinforcement learning approach for train rescheduling on a single-track railway. *Transportation Research Part B: Methodological*, 86, 250–267.
- Shaker, M., Smith, M. N. R., Yue, S. & Duckett, T. (2010) Vision-based landing of a simulated unmanned aerial vehicle with fast reinforcement learning. *IEEE*.
- Sun, L., Yang, Y., Hu, J., Porter, D., Marek, T. & Hillyer, C. (2017) Reinforcement learning control for water-efficient agricultural irrigation. *IEEE*.
- Sutton, R. S. & Barto, A. G. (2018) *Reinforcement learning: An introduction*, MIT press.
- Wang, H., Han, Z., Liu, Z. & Wu, Y. (2022) Deep Reinforcement Learning Based Active Pantograph Control Strategy in High-Speed Railway. *IEEE Transactions on Vehicular Technology*.
- Xu, J. & Ai, B. (2021) Experience-driven power allocation using multi-agent deep reinforcement learning for millimeter-wave high-speed railway systems. *IEEE Transactions on Intelligent Transportation Systems*.
- Yu, L., Qin, S., Zhang, M., Shen, C., Jiang, T. & Guan, X. (2020) Deep reinforcement learning for smart building energy management: A survey. *arXiv preprint arXiv:2008.05074*.
- Zhang, Z., Zhang, D. & Qiu, R. C. (2019) Deep reinforcement learning for power system applications: An overview. *CSEE Journal of Power and Energy Systems*, 6, 213–225.

- Zhong, J., Liu, Z., Wang, H., Liu, W., Yang, C., Han, Z. & Núñez, A. (2021) A looseness detection method for railway catenary fasteners based on reinforcement learning refined localization. *IEEE Transactions on Instrumentation and Measurement*, 70, 1–13.
- Zhou, S. K., Le, H. N., Luu, K., Nguyen, H. V. & Ayache, N. (2021) Deep reinforcement learning in medical imaging: A literature review. *Medical image analysis*, 73, 102193.
- Zhu, F., Yang, Z., Lin, F. & Xin, Y. (2020a) Decentralized cooperative control of multiple energy storage systems in urban railway based on multiagent deep reinforcement learning. *IEEE Transactions on Power Electronics*, 35, 9368–9379.
- Zhu, Y., Wang, H. & Goverde, R. M. P. (2020b) Reinforcement learning in railway timetable rescheduling. *IEEE*.

Intelligent monitoring and control method of the life-cycle cable-stayed bridge with steel-concrete composite beam

G.W. Yao, G.F. Zhang & S.Y. Li

State Key Laboratory of Mountain Bridge and Tunnel Engineering, School of Civil Engineering, Chongqing Jiaotong University, Chongqing, China

Y.F. Wu, E.G. Jiang & Y.D. Zhu

Chongqing Fengjian Expressway Co., Ltd, Chongqing, China

ABSTRACT: Relying on the Science and Technology Demonstration Project of the Ministry of Transport for the safe and intelligent construction of the Fengjian Expressway in the Three Gorges Reservoir Area, this paper focuses on the long-term performance evolution and construction and operation safety of Daxihe Bridge, a steel-concrete composite beam cable-stayed bridge with a main span of 650m, and carries out the research and application of intelligent monitoring and fine construction control technology throughout the entire bridge construction and operation life cycle. Based on BIM and GIS, an intelligent monitoring and early warning system is constructed that incorporates monitoring of bridge construction, completed bridge load test, and operation-related health monitoring. This system realizes intelligent bridge construction monitoring and measurement, online monitoring of incremental and full data of completed bridge load test and health monitoring during operation, and guarantees the data continuity of construction monitoring and health monitoring, seamlessly connects the whole process of bridge construction, management, maintenance, and operation, and realize online perception, monitoring, identification, evaluation, and real-time warning of the effects of the environment and load on the bridge as well as the structural response, performance, state, and safety level.

1 INSTRUCTIONS

Bridge projects have high complexity, long periodicity, and numerous construction phases (Shang 2007), bridge workers suggest an intelligent whole-life design to address the flaws in bridge engineering, and the approach improves the basic framework and design methodologies in the design phase (Zhang et al. 2019), requiring that the comprehensive costs of operation, maintenance, management, and demolition after completion should be fully considered in bridge design to achieve long-term service levels with minimal input (Gu 2008), utilizing BIM technology in tandem with the most recent computer, information, and management technology to fundamentally address deficiencies in intelligent bridge construction (Chen et al. 2009 & Zou 2014).

The intelligent bridge structure consists of three parts: monitoring subsystem, diagnostic subsystem, and assessment subsystem (Zhou et al. 2019). Sensors are used in bridge health monitoring research to monitor key bridge parameters and thus predict structural degradation and damage mechanisms (Shan 2010, Hawk et al.1998, Söderqvist et al. 1998 & Thompsonet 1998). Cable-stayed bridges, as a cable-stayed load-bearing system, have greater spanning capacity than girder bridges, as well as good mechanical properties and economic indicators, are widely used in the construction of various types of bridges (Wu 2015, Wu 2015 & Jiang 2013). The bridge health monitoring team has conducted health monitoring studies on structures such as marine platforms and proposed a system design for construction monitoring, bridge

completion testing, operational health monitoring, and maintenance management of cable-stayed bridges (Zhang 2010, Li 2006 & Li 2006). The application of intelligent construction and control technology for cable-stayed bridges is gradually gaining attention (Tan 2006, Jiang et al. 2021, China J. Highw. Transp. 2021 & Lai et al. 2021).

In view of the long-term performance evolution of cable-stayed bridges and construction and operation safety issues, the intelligent construction and refined monitoring and control technology demonstration application is carried out during the construction-operation period based on the Daxihe Bridge, and an intelligent monitoring system considering bridge construction monitoring, bridge load test and operation health monitoring is built. The bridge construction monitoring and measurement is intelligent, and the online monitoring of the incremental and full data of the bridge load test and operation health monitoring ensures the continuity of the data of the construction monitoring and measurement and operation health monitoring, and the real-time monitoring and warning of the bridge structural status and safety level.

2 WHOLE LIFE-CYCLE INTELLIGENT MONITORING AND CONTROL SYSTEM SCHEME

2.1 *Project overview*

The Fengjian Expressway is located in Fengjie and Wushan counties in the hinterland of the Three Gorges Reservoir Area, with a total length of 48.752km. It has 20 bridges totaling 10533 m, including 5 extra-large bridges that are 6898m long and 13 great bridges that are 3483m long, for an 88.2% bridge to tunnel ratio. The project has a high ratio of bridges and tunnels, complex terrain, and difficult construction. Construction and operation safety is the focus of this project, and the durability and reliability of the bridges and their appurtenances need to be enhanced, as well as the use of advanced monitoring and control technologies to ensure construction safety and improve the quality of construction.

The Daxihe Bridge, a representative mega-span cable-stayed bridge in the project, adopts a double-tower, double-cable deck fan-shaped arrangement of cable-stayed wires, and the main bridge is a 650m steel-hybrid combination girder with a full-width of 27.6m. The main tower is a reinforced concrete structure with a diamond-shaped shape, and the tower pier is a single-box, three-compartment section. The diagonal cables are anchored by external steel anchor tubes at the ends of the girders, 208 diagonal cables with 1860MPa epoxy-coated steel strands are used throughout the bridge. The diagonal cables use a double corrosion protection system to ensure that they are corrosion-free throughout their design life (Yu et al. 2021). Because of the long cable and low self-vibration frequency, vibrations are extremely easy to happen under the excitation of wind load or vehicle load (Zhou et al. 2014, Zhang et al. 2016 & Sun 2020), which needs to be monitored and controlled to keep the amplitude of cable vibrations within an acceptable range. The effect of the whole bridge after the completion of the construction is shown in Figure 1.



Figure 1. Rendering of Daxihe Bridge, a mega-span cable-stayed bridge.

2.2 Program design

With 5G communication, cloud computing, big data, the Internet of Things, and intelligent control as the basic core technologies, the demonstration application of intelligent monitoring and refined construction control technology during the construction and operation of large cable bridges is carried out for the long-term performance evolution, construction and operation safety of bridges with large cable structure systems such as cable-stayed bridges and suspension bridges, and a comprehensive bridge construction monitoring, bridge load test, and operation health monitoring system is built on the Daxihe Bridge. The intelligent monitoring and early warning system (Figure 2), which integrates bridge construction, management, maintenance, and transportation, can sense, monitor, identify, evaluate, and warn about the effects of the environment and the load on the bridge as well as the structural response, performance, status, and safety level in real-time.

During the construction of the bridge, long-life maintenance-free intelligent sensors are buried to avoid damage to the bridge structure at a later stage of deployment and to provide instantaneous and cumulative monitoring of environmental parameters such as temperature, humidity, wind field, load effects such as automobile, ship impact, earthquake, structural mechanical responses including steel structure and concrete stress and cracks, main girder deformation, main cable and deck alignment, cable force, tower deflection, foundation settlement and dynamic characteristic parameters such as vibration and damping. It provides flawless structural response data to understand the long-term performance evolution of the bridge, uses 5G communication to wirelessly transmit stored data, images, and videos, and combines with IOT technology to realize bridge safety assessment and real-time warning on the BIM integrated management platform, records and responds to disasters promptly, and generates analysis reports quickly. It can effectively enhance the quality of bridge projects and guarantee the safety of construction and operation while also enhancing the scientific nature of bridge-bearing capacity assessment and safety warning. It can also significantly improve the quality of large cable-stayed bridge construction and operation management.

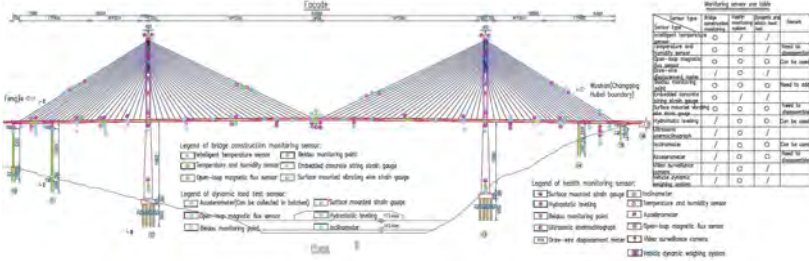


Figure 2. Design of the whole life-cycle intelligent monitoring and control system of Daxihe Bridge.

3 INTELLIGENT MONITORING AND CONTROL OF BRIDGE PROJECTS DURING THE CONSTRUCTION PERIOD

3.1 Monitoring and control of bridge structure

Intelligent monitoring and control of bridge structure during the construction period is an important part of the construction quality control system, which is a macro regulation of bridge construction quality and a supplement and prerequisite for bridge construction quality control. The stress of the main stress sections, the deformation of the main measurement points, and the stress of the main components are measured during the bridge construction process to apply the structural testing technology and field analysis technology to the construction and combined with the actual construction process to form a complete system of structural calculation and analysis, monitoring and feedback control, its importance is self-

evident. The general arrangement of monitoring during the construction period of the bridge is shown in Figure 3.

The cable-stayed bridge is a high-order statically indeterminate structure, and the construction method and installation sequence used are closely related to the alignment and internal force state of the main girders after the bridge is finished, and the structural system and loading conditions change continuously during the construction phase (Li 2020), monitoring the stress state of the key parts of the piers and towers during the construction period can control the stress state and geometric deflection of the piers and towers. Considering the need for later monitoring or bridge load tests, buried steels and concrete strain gauges are used on both sides of the tower column, and the test section is chosen to be the control section against the bottom of the tower and the section near the anchorage area of the cable tower, with a total of 32 sensors arranged. During construction, the major girders will experience the combined effect of axial pressure and shifting bending moment, therefore, 98 sets of external affixed stress transducers are installed in the key control sections of the main girders for stress monitoring, and the concrete girders use embedded steel string strain gauges and the steel girders use external affixed steel string strain gauges. The main girder elevation measurement is carried out by precision level, and the main tower deformation measurement is carried out by distance measurement method and high precision total station.

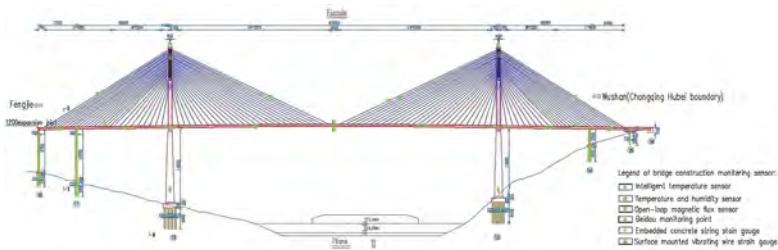


Figure 3. General arrangement of monitoring during the construction period of Daxihe Bridge.

During the construction of cable-stayed bridges, the cables not only bear the self-weight and construction load of the girders, but also control the alignment of the girders by adjusting the cable force, which is critical to the smooth progress of the main span closure. Usually, after the tensioning of each construction stage, the cable force of 2-3 pairs of cables in the vicinity needs to be checked, and the control of the cable force includes the adjustment of the tensioning force of the cable at the current stage after the completion of each construction stage of the main girder and the adjustment of the multi-cable force at the stage. The bridge primarily employs the frequency method to monitor the cable force, using the highly sensitive sensor attached to the cable to pick up the vibration signal of the cable under the environmental excitation vibration, after filtering and analysis, amplification and spectrum analysis, determine the cable's self-oscillation frequency according to the spectrum graph, and then determine the cable force according to the relationship between the self-oscillation frequency and the cable force.

The main structure of the cable-stayed bridge, diagonal cable and tower girder are spatially non-linear structures, and the temperature difference will have an important impact on the internal force and alignment of the structure, so the temperature field of the cable-stayed girder and tower need to be measured for a long time during the construction period, and the temperature impact will be adjusted at every step of construction to avoid the alignment and internal force of the bridge deviating from the design target value. Temperature sensors are arranged in designated sections of the tower, span, tower pillar, and cable, and the temperature sensor system adopts an analog and digital hybrid semiconductor temperature sensor system, with a total of 168 temperature sensors required to be deployed during the bridge's construction period.

3.2 Monitoring and control of large construction equipment

The intelligent hydraulic climbing formwork monitoring system of Daxihe Bridge adopts the technical route of *intelligent control* and *safety monitoring*, deploying strain sensors on the key stress parts of the climbing formwork system such as formwork, frame, track, etc. The main implementation contents include:

- (1) Hydraulic climbing formwork Programmable logic controller (PLC) closed-loop intelligent control system. PLC closed-loop control system is adopted to realize intelligent control of climbing, real-time monitoring, and automatic control of the load at each position of the climbing device by microcomputer, real-time display of the load value at each position, with the functions of over and loss of load warning and automatic shutdown.
- (2) Hydraulic climbing formwork safety monitoring system. Stress sensors are positioned in critical areas of the formwork to automatically, wirelessly and in real-time monitor the formwork's stress, compare the measured and theoretical values of the formwork's stress and deformation in real-time, assess the safety level of the hydraulic climbing formwork's stress, and implement early warning.
- (3) Real-time monitoring data display and analysis system. The system mainly displays the monitoring data in real-time, and the site staff can clarify the real-time height, plane position information, and force deformation of the hydraulic climbing device.

The monitoring system of intelligent cable hoisting system is similar to the intelligent hydraulic climbing formwork monitoring system, which also adopts the technical route of *intelligent control* and *safety monitoring*. It adopts sensor integration technology and video monitoring technology and establishes an intelligent control platform to realize digital control and management of the hoisting system, which greatly reduces manual operation in the process of hoisting and abnormal risk. Strain sensors and cable force sensors are deployed on key stress parts of the hoisting system, such as the main truss, flat beam, and cable, and the data is connected to the bridge construction intelligent monitoring and control system to perform online intelligent monitoring and safety warnings on the stress and deformation of key parts of the hoisting system.

4 BRIDGE STRUCTURE LOAD TEST INSPECTION AFTER BRIDGE COMPLETION

After bridge completion, the bridge structure load test inspection mainly includes the tower and pier displacement, the stress and strain of the bridge body, and the cable force of the cable-stayed bridge under load (Shi et al. 2022). The stability of the cable-stayed bridge body, pier tower, and cable-stayed bridge state is the prerequisite for ensuring its safe operation throughout its life. Bridge load test detection points are laid out as shown in Figure 4.

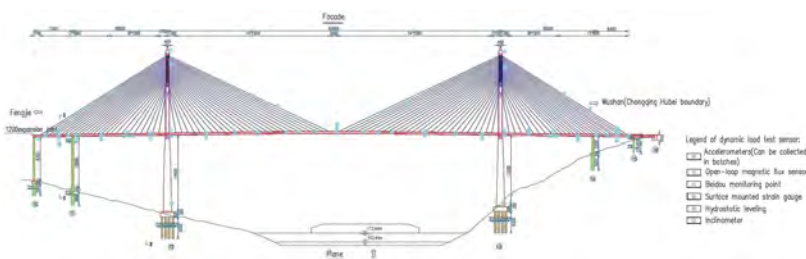


Figure 4. Daxihe Bridge load test measurement point arrangement.

Under the static load test, the pier tower displacement monitoring points are laid at the top of the bridge tower or the pier position at the junction of the bridge deck and the pier, the bridge body stress-strain detection points are laid in the key section of the main beam at the middle

and both sides of the top and bottom, the section is laid out in the main span's 1/2 and 1/4 position, through the stress-strain monitoring of the key sections of the main beam, the stress of the bridge in the load test can be understood and the disease can be diagnosed in time. The frequency, vibration type, damping, vibration intensity, and amplitude of the cable-stayed bridge are the signs of the bridge's overall safety, and the change of the material strength on the dynamic characteristics of the bridge should be given special attention in the early stages of bridge formation. The change in the self-vibration frequency or local mode shape of the bridge may indicate local structural damage, and the vibration monitoring measurement point is arranged at the bottom of the span beam with more obvious vibration, attempting to be in the same position as the strain monitoring section, and cooperating with the accelerometer to detect the dynamic characteristics and vibration level of the tower beam structure under the dynamic load test, the dynamic monitoring state of the bridge strain and the measurement results of the accelerometer can effectively evaluate the safety of the bridge function.

After completion of the bridge, each pair of cables is measured once to provide a basis for subsequent cable force control, and the cable force data under constant load is used to further fine-tune the bridge alignment and adjust the cable force to the optimum cable force to achieve or approach the design value. The cable force under dynamic and static load is measured and compared to the design value during the load test to ensure that the dynamic and static characteristics of the cable meet the specifications and design requirements. The measurement points are usually placed at the longest and shortest diagonal cables, and a flux sensor is placed every few cables according to the density of the cables in the bridge design, with the flux acquisition system used for data collection.

5 INTELLIGENT MONITORING AND SAFETY WARNING OF BRIDGE STRUCTURE DURING OPERATION

According to the idea of whole-life monitoring and safety warning for cable-stayed bridges, intelligent monitoring and safety warning are required for the traffic volume, wind load, ambient temperature and humidity, and micro-cracks under different service states and service environments during the operation period, in addition to the conventional stress-strain monitoring for each structure of the bridge. A video monitoring system is used to monitor bridge traffic and structural status, while a dynamic weighing system provides load data support for assessing bridge safety status, and an inspection and maintenance system conducts electronic inspections to collect, process, and analyze bridge management and maintenance data. The health monitoring system monitors the bridge's overall, local, environmental, and load response, whereas the electromechanical monitoring system is mainly responsible for monitoring and maintaining electromechanical equipment such as dehumidifiers.

To evaluate the traffic flow during bridge operation, the load cell and other equipment are set up near the approach bridge. According to the structural characteristics of the Daxihe Bridge, the wind speed and direction meter (Figure 5a) is positioned at the top of the bridge tower or the open area of the bridge deck, by monitoring wind speed and direction. The ambient temperature and humidity monitoring use temperature sensors and moisture-sensitive

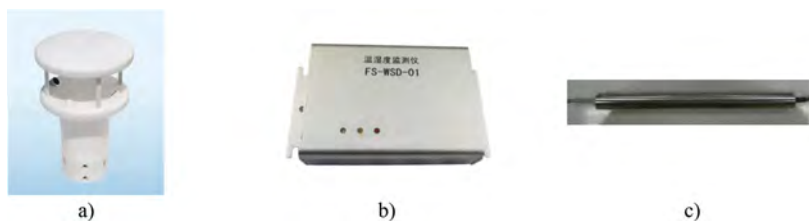


Figure 5. Monitoring instruments during operation: a). ambient temperature and humidity sensor; b). ultrasonic wind speed and direction meter; c). crack meter.

elements (Figure 5b), and the measurement points are placed at the bottom of the span at the same location of the section as vibration or strain. Microcracks are monitored by a high-precision crack meter (Figure 5c), and the measurement points are placed at the expansion joints and the bottom of the bridge, the location of easy cracks is determined by calculation analysis and engineering experience.

In terms of safety warning, it is mainly divided into stress warning and displacement warning. The stresses in the main beam, main tower, diagonal cable, and subsidiary members are monitored in areas where model calculations indicate that stresses may be exceeded. At the beginning of the service phase, the frequency of stress monitoring of key sections is increased to keep abreast of the stress state of the main beam. In addition, it is also necessary to analyze and deal with the tower top offset and bridge deck elevation monitoring results in time, when the load and environmental effects of the bridge alignment deviation trend, or displacement abnormalities exceed the warning value, the early warning system provides timely warnings through intelligent control platforms and all units to consult and find countermeasures to solve the problem.

6 CONCLUSIONS

The Fengjian high-speed bridge project uses information technology synergy, sensor integration technology, and video monitoring technology to establish a digital intelligent control platform, achieve online intelligent monitoring and safety warning of large construction equipment, protect the bridge structure and construction equipment safety, and improve engineering quality. Long-life maintenance-free intelligent sensors are buried during bridge construction to prevent later deployment from causing damage to the structure. These sensors monitor in real-time the instantaneous incremental and cumulative full amount of structural mechanical response and dynamic characteristic parameters, such as pier and tower displacement, bridge stress and strain, and cable force, to provide perfect structural response raw data for mastering the long-term performance evolution of the bridge. It will significantly raise the standard of large cable-stayed bridge girder construction and operation management, as well as the scientific nature of bridge capacity assessment and safety warning, all of which have important promotion and application value and industry-leading significance for the building of mountain bridges.

ACKNOWLEDGEMENTS

This paper was supported by the National Natural Science Foundation of China (Grant No. 52178273), the Natural Science Foundation of Chongqing (Grant No. cstc2021jcyj-msxmX1159), the Chongqing Talent Plan Project (Grant No. cstc2022ycjh-bgzxm0124), the Open Fund Project of State Key Laboratory of Mountain Bridge and Tunnel Engineering (Grant No. SKLBT-YF2105) and the Chongqing Project of Joint Training Base Construction for Postgraduates (Grant No. JDLHPYJD2020004).

REFERENCES

- Chen, A.R. 2009. Design processes of bridges based on given structural life [M]. *Beijing: China Communications Press.*
- Editorial Department of China Journal of Highway and Transport. 2021. Review on China's bridge engineering research: 2021 [J]. *China Journal of Highway and Transport*, 34(02): 1–97.
- Gu, F.H. 2008. Research of the information classification coding oriented the enterprise information sharing and management system [D]. *Jiangxi University of Science and Technology.*
- Hawk, H. & Small E.P. 1998. The BRIDGIT bridge management system [J]. *Structural Engineering International*, 8(4): 309–314.
- Jiang, D.X. 2013. Experimental study of cable environmental corrosion damage under alternating stress [D]. *Chongqing Jiaotong University.*
- Jiang, Z.L. & Zang, G.G. 2021. Research on full-process management of bridge engineering assembly intelligent construction [J]. *Highway Engineering*, 46(04): 39–45.

- Lai, M.G., Yang, M., Zhai, M.G. & Yao, X.F. 2021. Industrialized intelligent construction of bridge [J]. *Highway*, 66(07): 195–202.
- Li, C.C. 2020. Research on the key technology of tower deformation control in the synchronous construction of cable stayed bridge [D]. *Chang'an University*.
- Li, H. & Ou, J.P. 2006. Design and implementation of health monitoring systems for cable-stayed bridges (I): design methods [J]. *China Civil Engineering Journal*, 36(4): 39–44.
- Li, H. & Ou, J.P. 2006. Design and implementation of health monitoring systems for cable-stayed bridges (II): implementations [J]. *China Civil Engineering Journal*, 39(4): 45–54.
- Shan, D.S. 2010. Smart bridge health monitoring and damage diagnosis [M]. *Beijing: China Communications Press*.
- Shang, C.J. 2007. Research on Construction industry management informatization based on construction life-cycle [D]. *Beijing Jiaotong University*.
- Shi, Z., Yu, W.Q., Yang, S.L., Yan, A.G. & Li, D.P. 2022. Experimental study on mechanical and deformation performance of steel-concrete composite box girder of high-speed railway cable-stayed bridge [J]. *Journal of The China Railway Society*, 44(01): 111–118.
- Sun, H.B. 2020. Analysis of vehicle-bridge coupling vibration of long-span cable-stayed bridge considering initial deformation of bridge deck [J]. *Railway Engineering*, 60(10): 25–30.
- Söderqvist, M.K. & Veijola, M. 1998. The finnish bridge management system [J]. *Structural Engineering International*, 8(4): 315–319.
- Tan, X.H. 2006. A Study and application of monitoring and measurement technology for cable tensions on cable-stayed bridge [J]. *Highway*, 03: 146–154.
- Thompson, P.D. 1998. The PONTIS bridge management system [J]. *Structural Engineering International*, 8(4): 303–308.
- Wu, G.Q. 2015. Experimental study on stress corrosion and corrosion fatigue of stay cables under acid rain condition [D]. *Chongqing Jiaotong University*.
- Wu, W.J. 2015. Experimental study of stay cable electrochemical corrosion fatigue under alternating stress state [D]. *Chongqing Jiaotong University*.
- Yu, X.R., Yao, G.W., Zhong, H. & Jiang, Y.X. 2021. Corrosion characteristics and mechanical properties of steel strands under coupling effect of alternating load and chloride salt environment [J]. *Journal of Building Materials*, 24(06): 1315–1321.
- Zhang, X.J. & Yao, M. 2016. Parametric study of wind stability of long span partially ground-anchored cable stayed bridges [J]. *Bridge Construction*, 46(03): 23–28.
- Zhang, Y.F., Gao, Z.Y. & Mei, X.Y. 2010. Study of options for multi-pylon long span railway cable-stayed bridge [J]. *Bridge Construction*, 03: 55–58+82.
- Zhang, Y.C., Zeng, S.W., Du, W.Z., Li, X.J. & Zhao, Q. 2019. Research based on Bentley about BIM system solution for rapid and intelligent construction of bridge [J]. *Highway Engineering*, 44(04): 140–148.
- Zhou, Q., Hong, Y.W. & Ren, P.J. 2014. Experimental investigation on wind-resistant performance improvement of cable-stayed bridge at the bottom of canyon [J]. *Highway Engineering*, 39(02): 49–53.
- Zhou, X.H. & Zhang, X.G. 2019. Thoughts on the development of bridge technology in China [J]. *Engineering*, 5(6): 1120–1130.
- Zou, Y. 2014. Study on bridge information modelling (BrIM) implemented framework in design and construction stages [D]. *Chongqing Jiaotong University*.

Integrating unstructured data analytics and BIM to support predictive maintenance

S. Sobhkhiz & T. El-Diraby

Centre for Information Systems in Infrastructure and Construction, Department of Civil & Mineral Engineering, University of Toronto, Toronto, Canada

ABSTRACT: Maintenance resource prediction is difficult because it is influenced by a multitude of factors such as the rate of system deterioration, operational effectiveness, and the efficiency of the asset management program. Work orders (WO) can provide useful insights to account for such factors, but they come in unstructured non-standardized forms that is difficult to analyze. This paper proposes an approach that leverages semantic networks for WO text analytics to support predictive maintenance. The proposed system pulls the basic facility attributes from BIM and historical work orders. This is primarily done by transferring the text of WOs into semantic networks. Using network-based machine learning, clusters of WO typical concepts are extracted. The clusters are categorized to act as prototypes for future WOs. Along with BIM features, these clusters help match the scope of work to previous similar WOs, which are used to estimate the required resources for a new WO.

1 INTRODUCTION

While predicting future maintenance budgets is essential to any life cycle analysis (LCA), enhancing the quality of asset management (AM) is the key to reducing LCA. If assets are well-managed, the speed of deterioration can be reduced; and we can decide more accurately on timely proactive maintenance, which optimizes the life cycle performance of buildings. One key aspect in optimizing maintenance strategies is resource allocation. Facility managers need to have accurate estimates of how much resources each maintenance task requires. Otherwise, they may end up spending a significant amount of their limited resources on tasks that have less priority. Depending on the size and number of the buildings, a facility manager needs to make such estimates for a large number of work orders on a daily basis. For instance, in the institutional building sector, a significant number of work orders are issued every year. As an example, the University of Toronto has around 40,000 work orders per year for its 150 buildings.

However, facility managers do not usually have access to the right information to make such estimates. For instance, consider a problem/failure that has occurred with a mechanical part of an HVAC system. Such issues are usually submitted to building managers using work orders by building engineers or inspectors. A building manager has to use her domain knowledge to estimate how much this problem is going to cost, how long it's going to take to resolve, and how many people are going to be engaged in resolving it. Furthermore, it is very likely that a maintenance task will trigger a few other tasks as well. For instance, if the asset is located in a sensitive and secure area, then for an engineer to access it, a number of security access requests are needed as well. Or if the asset is part of a larger more complex system, then maybe more than one expertise is needed for resolving the issue. A facility manager has to consider all such issues in her decision-making processes. With the existing practices, most of the decisions are made without the needed data and solely based on the manager's experience and expertise.

Most of the required information for FM decisions can be found in the text of the current and previous work orders. However, work orders come in unstructured non-standardized

forms, which makes it very challenging to extract knowledge from. Work orders can be submitted by a wide range of users (e.g., occupants, engineers, managers) which use different terms and ways to describe a wide range of issues. With the recent advances in natural language processing (NLP), there has been a number of ongoing lines of research which focus on resolving the challenges of work order analytics. For instance, some studies used text mining to extract performance metrics from work order data (Gunay et al. 2019; Dutta et al. 2020; Yang et al. 2018). More complex studies used text mining to extract keywords and topics which can help profile/classify issues (McArthur et al. 2018; Yang et al. 2022; Hong et al. 2022). Finally, some researchers have focused on linking work orders (and other FM documents) to BIM.

One common trend in these studies is the use of standardization and structured analytics. In other words, studies often tend to transform the unstructured work order data into structured forms to make them easier for training predictive models, or extracting key performance indicators (KPIs). For instance, using ontological approaches or developing static templates is very common. The purpose of this study is to investigate a different approach which considers the unstructured and non-parametric nature of work orders (and unstructured data in general). Mainly, we will investigate the use of network theory for work order analytics and linking work orders text data to IFC concepts.

2 BACKGROUND

Work orders contain valuable knowledge which is directly relevant to a building's performance. Gunay et al. (2019) recognize this potential as an untapped opportunity, and propose a method where fault frequencies of different building systems are calculated based on work order text analytics. Similarly, Dutta et al. (2020) proposed a method which used text mining on four different classes of work orders (Lighting, thermal & air quality, janitorial, and maintenance) to develop performance metrics. In another study, Yang et al. (2018) developed a method for analyzing the failure modes of HVAC equipment using work order data.

One key area of focus has been work order profile classification. The purpose in these studies is to automatically classify a record into a set of predefined classes such as mechanical or electrical. It can be argued that if work orders are automatically classified into such topics, it facilitates processes such as resource allocation (Mukhopadhyay et al. 2020). For instance, the work order would be sent to its pertinent division much faster, if its topic is known. To this end, Naqvi et al. (2022) developed a work order classifier for a manufacturing company that classified work orders into four groups of mechanical, electrical, electronic, and miscellaneous, and achieved an accuracy of 82%. Such studies are recently being conducted in the domain of building maintenance as well. The work of Yang et al. (2022) is a good example. In their study, Yang et al. developed a classifier that considers several aspects of work orders such as location, associated element, and defect type. Their classifier used 11 defect classes and achieved an f-1 score of 0.93. In another study, Hong et al. (2022) used work orders submitted regarding HVAC issues and developed a SVM classifier that achieved an accuracy of 85% over 25 classes.

Linking work orders to BIM has also been investigated in several studies. For instance, Lee et al. (2016) proposed an ontological approach where a defect ontology was developed that included concepts from BIM and defective issues. The ontology was used to model a given work order by including the relevant BIM concepts as well as the relevant defect concepts. Given that the concepts are linked before-hand (when developing the ontology) a link between the defect and corresponding BIM concepts is established. In another similar study, Kim et al. (2018) proposed a method using semantic web technologies. Their proposed ontology was more comprehensive in the sense that in addition to BIM and work order concepts, they included COBie concepts. As a result, their proposed method covered asset information as well as BIM and defect information. Designing ontologies with the purpose of adding BIM to the AM process is an ongoing line of research.

Farghaly et al. (2019) also proposed the use of semantic web technologies to support BIM-based asset management. The study develops an ontology that integrates concepts from three domains of IFC, maintenance scheduling, and procurement documents. The approach employed a participatory action research in which focus groups and interviews were

conducted to determine key concepts and their relationships for building the ontology. Next, a framework is presented where asset maintenance data as well as data extracted from BIM is converted to RDF according to the proposed ontology. The ontology uses encoding systems from standards such as Uniclass2 and requires maintenance data to be generated according to the same standards as well.

These methods mostly rely on using standardized processes to add some sort of a structure to the unstructured work order data. For instance, all the studies on linking work orders to BIM either require the user to use a coding mechanism (such as using object IDs when submitting work orders) or static mapping mechanisms where the links are predefined in an ontology or a relational schema. Even when developing work order classifiers, the common practice is to define a set of generic classes (such as mechanical, electrical, and so on), then label work orders according to these classes and train a classifier. This approach implies that work orders will always be submitted within the scope of the predefined classes, which is not necessarily true. Given that the work orders are unstructured text, they may very likely include concepts and classes that do not fit with the predefined set of classes the classifier is trained on. In such cases, the classifier will push the work order into one of its classes, nonetheless.

3 SEMANTIC NETWORKS AS AN ALTERNATIVE

It can be argued that one of the key challenges in working with an unstructured data source such as work orders is the data modeling approach that is chosen. Currently, studies tend to restructure the data into relational or ontological forms (Sobhkhiz et al. 2021). This process usually requires defining the structure, either in the form of an ontology or a relational schema, in advance. Here, we aim to investigate an alternative approach where instead of pre-modeling the data, we use techniques for extracting patterns from the unstructured data in an unsupervised process. Semantic networks can be a potential candidate. Semantic networks allow us to formally represent the concepts in a graph structure without parametrizing it. It extracts the knowledge inductively as opposed to the traditional top-down methods where knowledge is deducted (Yun and Park 2018; Shi et al. 2018).

The purpose of this study is to investigate the potentials of network analytics and concept networks in resolving the challenges discussed in the previous sections. The motivation behind using concept networks is that they are obtained in an unsupervised manner without the need of using top-down modeling. In other words, we do not need to define the concepts and relationships in the data, rather they are extracted in a bottom-up manner from the data. This can be viewed as a way of formalized representation of the data which can be used for a variety of purposes such as work order classification or linking work orders to structured schemas such as that of IFC (Sobhkhiz and El-Diraby 2022). Another advantage of network modeling is that it can easily adapt to the changes in the data. If a new concept or relationship appears or an existing relationship changes, the network can adapt itself to represent those changes. In the following we will examine the usability of these features in two contexts of 1) work order modeling, and 2) linking work orders to BIM.

To generate a semantic network, we need to identify the concepts and their relationships in the data. This can be done through data mining techniques such as association rule mining. Figure 1 shows the overall step-by-step process for extracting a semantic network. After text preprocessing, the method employs association rule mining in order to identify association relationships between different concepts. Namely, we will be using the 'lift' measure to define how strongly connected two different concepts are. In association rule mining, the lift value determines how the probability of appearance of one concept changes when another is present. If the lift value is 1, then it indicates that there is no dependency between the two. Values greater than 1 indicate that the presence of one concept increases the presence probability of the other. Once the lift measures are calculated, the rules can be represented in a graph structure where the concepts are the nodes, and lift measures the weight of the edges between them.

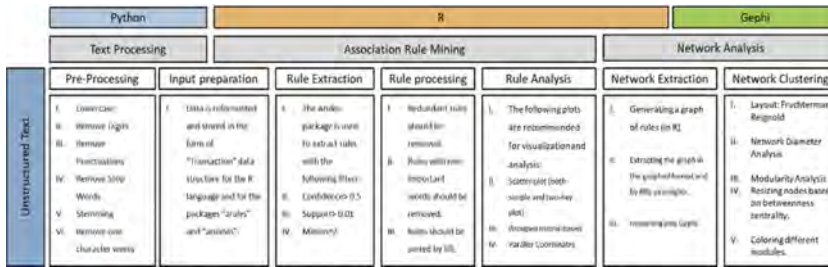


Figure 1. Extracting semantic networks from text sources.

3.1 Use case 1 - Extracting AM-related concepts using network analytics

As discussed in the literature review, one of the challenges in the studies related to work order analytics is to develop classification systems. The common trend so far has been to use expert defined top-down classes for modeling AM concepts. But the problem is that these classes do not necessarily represent the specific AM trends that are occurring within an organization. An alternative approach would be to use data-driven solutions that extract the key topics and classes from the data. Here, we propose using a semantic network that is extracted from the work orders and algorithms such as network modularization and topic modeling for extracting the work order classes. Figure 2 shows a proposed algorithm for this purpose. More details will be published in a subsequent paper.

The proposed method works by extracting the classes level by level from high-level generic classes in the highest layer to more detailed classes in the lowest ones. The high-level classes would be the by-the-book classes that are common across all organizations. Mechanical or electrical classes are examples of such high-level classes. As the layers increase, the classes become more AM relevant. For instance, mechanical systems in a hospital are not the same as the ones in an institutional building. These differences start to emerge when the classes become more detailed in lower levels.

3.2 Use Case 2- Linking work orders to BIM using semantic networks

The use of non-standardized language makes it difficult to link a given work order to its corresponding element/s in a BIM model. Consider a work order that is discussing an issue regarding a door located on the second floor of a building. Linking the work order to the 'door' object of the building's BIM model would not be a very straightforward process. This cannot be done using simple keyword matching. An issue with a door could include its different systems such as lock, fob, key, cylinder (for controlling its closing and opening), shafts, handle, or different functions such as closing, opening, being noisy, and so on. And all of these are just for a simple door. How would we match other systems and issues? Back to using structured approaches, some studies suggest using standardized mechanisms such as adding a BIM object code to the work order which is not really feasible in practice. Not everyone knows these codes and IDs. Also, many times the user does not know which element the issue is originating from (for instance, a burning smell with unknown source).

Semantic networks can also help here. When we extract a semantic network from work order data, we are essentially providing a semantic representation for different concepts based on their co-occurrence with other concepts. As such, when the term 'door' appears with concepts such as 'entrance' and 'access' it will be indirectly connected to concepts such as 'fob' which itself will be connected to the same concepts ('entrance' and 'access'). If we use the same network representation for the BIM concepts, we will be able to link the two networks using logical relationships. For instance, linking 'IfcDoor' to 'Door' is a logical link. But since 'Door' is itself connected to other concepts such as 'fob' we are essentially linking 'IfcDoor' to 'fob' as well. We can use these connections and train a classifier that will determine whether the concepts in a work order text are close enough to a given IFC concept. If so, the work

order will be linked to its associated IFC concept. We can extract a semantic network for BIM concepts from the text sources such as buildingSmart Data Dictionary (bSDD). Figure 3 shows the general idea behind the approach. More details will be published in another subsequent paper.

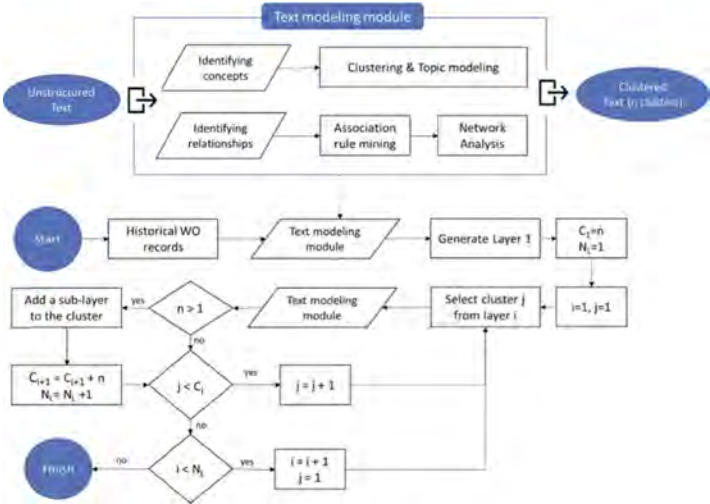


Figure 2. An algorithm for extracting a hierarchical class from work order texts.

4 CASE STUDY

In this study, we used the database of a facilities and services department responsible for the operation and maintenance of institutional buildings in the city of Toronto. The department uses its in-house developed CMMS solution for managing service orders where a digital form is used for work order submission. The dataset contains 36 columns including the information of the people involved with the work order (e.g., who requested the work order, who is supervising it, and who is directly solving it), the date and time of when the work order was submitted and closed, status code, building, location, description, and so on. We used a dataset of 1055 work orders that was collected for an institutional building over a period of 8 months.

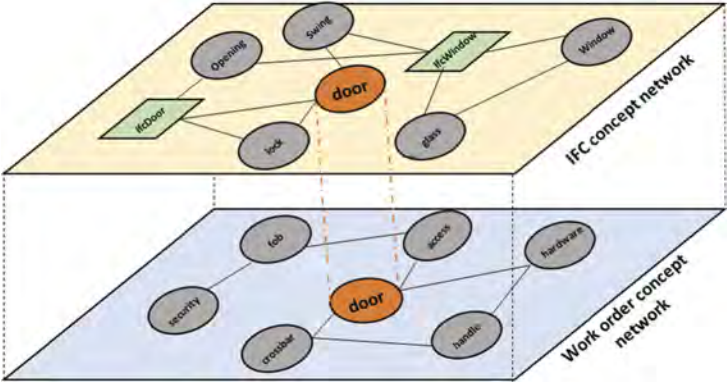


Figure 3. Linking work order semantic network to IFC semantic network.

4.1 Work order modeling

In this section, we employ the algorithm proposed in the first use case to develop a classification model for the work orders that can be used for a variety of purposes such as KPI development or automated work order classification. In the first step, a semantic network needs to be extracted. Figure 4 shows the modularized semantic network that was extracted from the work order sample database. Next, we perform topic modeling to extract the probabilistic features of similar documents. By employing the proposed algorithm, the hierarchical classification system can be extracted from the work order data. In the first step, the high-level classes are determined according to the results of network modularization. Figure 5 shows the 9 classes that were identified as follows: mechanical, electrical, plumbing, janitorial, event management, access & security, space comfort, carpentry, and elevator.

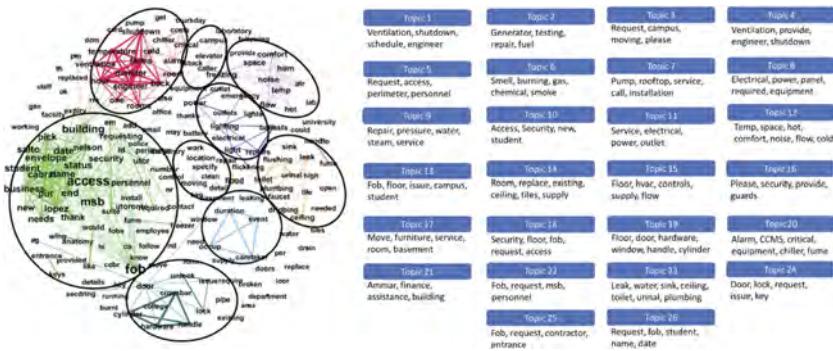


Figure 4. Extracting work order semantic network and topic models.

As can be seen, these classes are generic (or by-the-book) classes that are common across all organizations. Next, we start adding details to the model and extract low-level classes. These classes represent the specific AM practices of an organization. Given the limited size of the database, this can be done for a few classes that have large enough samples. For instance, the class mechanical is broken down into four more sub-classes of failure alarm, HVAC services, generic repair, planned maintenance, and contractor administrative. The access and security class also included a large number of samples and could be further broken down into two sub-classes of fob/key request and door/window hardware services. In a future study, we will use these classes to develop a dynamic hierarchical classifier for work order data.

4.2 Linking work orders to BIM

In this section, we use semantic networks to link work order documents to IFC concepts. This would be the essential first step to link a document to its associated BIM object/s. To this end, we first need to extract a similar concept network for the IFC concepts from the records in the bSDD database. Figure 6 shows a snapshot of such a network for the two classes of IfcDoor and IfcWindow. Once the IFC network is constructed, we can link the two networks through their common nodes. For instance, the node 'door' is common between the two networks, and will be one of the nodes that connects the two networks. Now, we can calculate the distance between a given concept, say 'fob', to a given IfcClass such as 'IfcDoor'.

In the next step, we label 80% of the documents with their associated IFC classes. For instance, a work order requesting a service to fix a door would have a label of Ifcdoor. Work orders may include more than one class. The dataset in this study included 28 IFC classes. Next, for each pair of work order and IfcClass, we extract the distance features from the networks. For instance, consider the work order 'please fix the closing cylinder in room gb229'. For each concept in the work order, we calculate the distance of the concept to a given IFC

class (28 classes in this study). Next, if the instance is related to the IFC class, it will have a label of 1, if not, a label of 0. Now we can train a classifier that can learn whether the distances of the concepts in a work order represent relatedness to a given IFC class based on the semantic networks. Our initial analysis on the remaining 20% of the work orders achieved an average f-score of 0.97 over all classes which is very promising. More detailed analyses will be published in a subsequent paper.

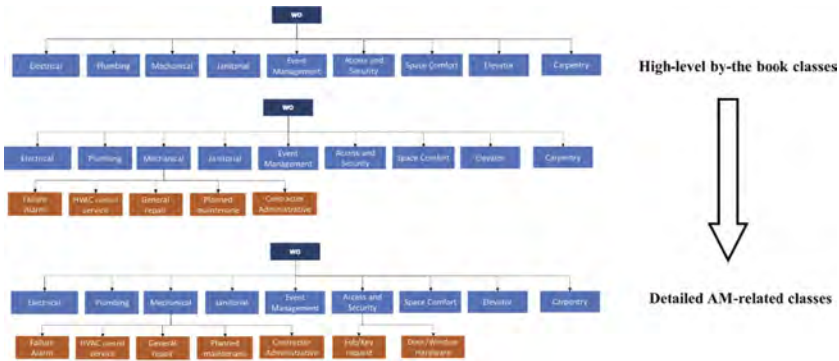


Figure 5. Developing a hierarchical work order model.

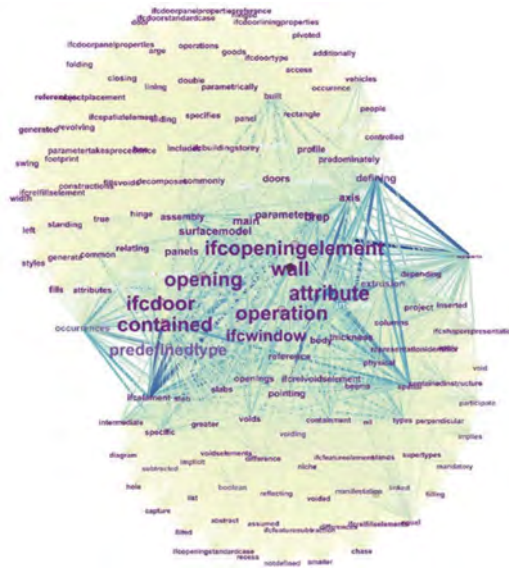


Figure 6. IFC semantic network.

5 CONCLUSIONS

The majority of building data is unstructured in the form of inspection forms, specifications, communications (e.g., emails), complaints, feedback and so on. Unstructured data is the most valuable source for capturing business and operational knowledge and is central to developing business intelligence applications. Considerably, studies focus on the structured side with applications that aim to develop real-time digitized models of physical entities for services such as monitoring and prediction. For instance, a well-studied subject on this matter is using

building asset data (e.g., HVAC systems) for predicting asset failure and developing maintenance strategies. These types of studies require using predefined data models to make data machine-readable and usable for applications such as predictive analysis. Although top-down model-based analysis is reasonable for data coming from sensors, this is not the case for unstructured data such as texts. Unstructured data, inherently, does not follow a specific form or standard, and pushing it into any predefined standard will limit the analysis to the extent of that standard. Nevertheless, many studies use top-down modeling approaches for analyzing unstructured data. Pre-defined data models that are developed heuristically and by experts can cause critical limitations for unstructured data analytics.

As such in this study, we investigate an alternative approach where a structure is not imposed on the data, rather, it is extracted in a bottom-up unsupervised process. We narrowed down the scope to using semantic networks and the domain of work order data analytics. Obviously, other techniques and domains are yet to be explored. Hypothetically, such approaches should broaden the opportunities for analytics. For instance, semantic networks can be easily updated according to the changes in the data. If more classes and relationships emerge (which is likely in the case of unstructured sources) semantic networks have the capacity to accommodate those changes. This allows for developing dynamic and self-updating solutions for cases such as classification. This particular issue will be investigated in a follow-up study.

REFERENCES

- Dutta, S., Burak Gunay, H. and Bucking, S., 2020. A method for extracting performance metrics using work-order data. *Science and Technology for the Built Environment*, 26(3), pp.414–425.
- Farghaly, K., Abanda, F.H., Vidalakis, C. and Wood, G., 2019. BIM-linked data integration for asset management. *Built Environment Project and Asset Management*.
- Gunay, H.B., Shen, W. and Yang, C., 2019. Text-mining building maintenance work orders for component fault frequency. *Building Research & Information*, 47(5), pp.518–533.
- Hong, S., Kim, J. and Yang, E., 2022. Automated Text Classification of Maintenance Data of Higher Education Buildings Using Text Mining and Machine Learning Techniques. *Journal of Architectural Engineering*, 28(1), p.04021045.
- Kim, K., Kim, H., Kim, W., Kim, C., Kim, J. and Yu, J., 2018. Integration of ifc objects and facility management work information using Semantic Web. *Automation in Construction*, 87, pp.173–187.
- Lee, D.Y., Chi, H.L., Wang, J., Wang, X. and Park, C.S., 2016. A linked data system framework for sharing construction defect information using ontologies and BIM environments. *Automation in Construction*, 68, pp.102–113.
- McArthur, J.J., Shahbazi, N., Fok, R., Raghubar, C., Bortoluzzi, B. and An, A., 2018. Machine learning and BIM visualization for maintenance issue classification and enhanced data collection. *Advanced Engineering Informatics*, 38, pp.101–112.
- Mukhopadhyay, A., Pettet, G., Vazirizade, S., Vorobeychik, Y., Kochenderfer, M. and Dubey, A., 2020. A review of emergency incident prediction, resource allocation and dispatch models. arXiv preprint arXiv:2006.04200.
- Naqvi, S.M.R., Varnier, C., Nicod, J.M., Zerhouni, N. and Ghufran, M., 2022. Leveraging Free-Form Text in Maintenance Logs Through BERT Transfer Learning. In *International Conference on Deep Learning, Artificial Intelligence and Robotics* (pp. 63–75). Springer, Cham.
- Shi, F., Chen, L., Han, J. and Childs, P., 2017. A data-driven text mining and semantic network analysis for design information retrieval. *Journal of Mechanical Design*, 139(11).
- Sobhkhiz, S. and El-Diraby, T., 2022. A network-based framework for dynamic linkage of unstructured data to BIM: supporting predictive analysis in work order management.
- Sobhkhiz, S., Taghaddos, H., Rezvani, M. and Ramezani-pour, A.M., 2021. Utilization of semantic web technologies to improve BIM-LCA applications. *Automation in Construction*, 130, p.103842.
- Yang, C., Shen, W., Chen, Q. and Gunay, B., 2018. A practical solution for HVAC prognostics: Failure mode and effects analysis in building maintenance. *Journal of Building Engineering*, 15, pp.26–32.
- Yang, D.U., Kim, B., Lee, S.H., Ahn, Y.H. and Kim, H.Y., 2022. AutoDefect: Defect text classification in residential buildings using a multi-task channel attention network. *Sustainable Cities and Society*, p.103803.
- Yun, E. and Park, Y., 2018. Extraction of scientific semantic networks from science textbooks and comparison with science teachers' spoken language by text network analysis. *International Journal of Science Education*, 40(17), pp.2118–2136.



Taylor & Francis

Taylor & Francis Group

<http://taylorandfrancis.com>

SS5: Concrete damage assessment using coda waves
Organizers: C. Gehlen, E. Niederleithinger, J. Timothy & T. Kränkel



Taylor & Francis

Taylor & Francis Group

<http://taylorandfrancis.com>

Ultrasonic monitoring of large-scale structures - input to engineering assessment

N. Eppe, C.A. Sanchez-Trujillo & E. Niederleithinger
Bundesanstalt für Materialforschung und -prüfung, Berlin, Germany

ABSTRACT: Ultrasonic coda wave interferometry can detect small changes in scattering materials like concrete. We embedded ultrasonic transducers in the Gänstorbrücke Ulm, a monitored road bridge in Germany, to test the methodology. Since fall 2020, we've been monitoring parts of the bridge and comparing the results to commercial monitoring systems. We calculate signal and volumetric velocity changes using coda waves, and long-term measurements show that the influence of temperature on strains and ultrasound velocity changes can be monitored. Velocity change maps indicate that different parts of the bridge react differently to environmental temperature changes, revealing local material property differences. A load experiment with trucks allows calibration to improve detectability of possibly damaging events. Our work focuses on measurement reliability, potential use of and distinction from temperature effects, combination with complementary sensing systems, and converting measured values to information for damage and life cycle assessment.

1 INTRODUCTION

Monitoring concrete bridges is necessary to ensure a safe and reliable transport infrastructure. Bridges require monitoring, maintenance, and, if needed, restoration of damage, especially when they were built some decades ago and started suffering from aging effects. Damage can include discontinuities, like the formation of new fractures, deformation, or deterioration, like corrosion of the rebar and pre-stressing systems. Some of this damage is visible on the exterior. But what happens when it isn't? Then, the need for a reliable Structure Health Monitoring (SHM) system arises.

Ultrasonic (US) monitoring with coda waves is an SHM technique that has been highlighted as particularly sensitive to the effects of stress, temperature, moisture, and cracking of scattering materials like concrete (Snieder et al. 2002). These effects are encrypted in the velocity variation of ultrasonic waves. Coda Wave Interferometry, CWI, is a technique to measure velocity variations. This method has been widely applied by seismologists to measure and localize wave velocity changes in the interior of the earth (Sens-Schönfelder & Wegler 2006). With the right adjustments, it can be used for civil engineering structures (Zhang et al. 2016). This method has been tested in small concrete samples but it must be adapted to larger structures. This is part of the goal of the DFG research unit CoDA. This unit aims for an integral development of the application of CWI on concrete specimens and real structures. It's supported by simulations and experiments designed by experts in diverse domains from signal processing, structural engineering, material science, and numerical modeling. The Gänstorbrücke is the first large-scale structure to be equipped with a measuring system monitored with this technique by the research unit. In this paper, we will show results from permanent monitoring as well as a load experiment after a brief introduction to CWI. It is followed by an outlook on the possible integration into existing bridge monitoring frameworks and the benefits towards engineering assessment.

2 METHODOLOGY

Concrete is a peculiar material for ultrasonic testing, as it is composed of aggregates of varying sizes and a fine matrix around them. Elastic waves propagating through the structure will encounter these aggregates and get scattered if the wavelength is about the size of the aggregate. For classical non-destructive testing, looking at reflections from backwalls and delaminations this is reducing the resolution power. In Ultrasonic Monitoring with coda waves, on the other hand, we take advantage of this property. Let's suppose two sensors are installed and active on a bridge. When one of the transducers sends a pulse, a certain part of the energy might go through a straight path, without scattering, from the transmitter to the receiver. Nevertheless, some waves will be inevitably scattered by the aggregates of the medium. The path these scattered waves take is longer than the direct one and makes them "sensitive" to a larger area than the direct ones. The scattered waves are recorded later in time by the receiver. If a small change in the medium occurs, the direct waves might not show any change but the scattered waves will, as shown in Figure 1. This late part of the recorded waveform corresponds to the so-called coda. The ultrasonic methods have been proven effective to monitor concrete structures (Zhang et al. 2016, Clauß et al. 2020, Epple et al. 2022). Ultrasonic sensors can be embedded directly into the structure either during construction or later on when the necessity to monitor the structure arises (Wang et al. 2022). The transducers used in the study act as transmitters but also as receivers. This property allows switching sources and receivers to create different sensor arrangements with different spatial sensitivities and therefore to acquire more information without having to replace the sensors. Additionally, the measurements can be stored in the cloud almost in real time making the data accessible from remote places and monitoring a much easier task for engineers.

2.1 Ultrasonic monitoring

2.1.1 Correlation coefficient

The objective of this parameter is to provide a value for the similarity of the waveforms of a pair of signals. The first signal recorded $u_o(t)$ is taken as the reference. If the medium is subjected to a small change, the second signal $u_c(t)$, recorded after the perturbation, is supposed to have the small change encoded in its coda. With a similarity measure, one can estimate the magnitude of the medium change. The similarity between these pairs of signals is measured by a simple correlation coefficient, CC , ranging from -1 to 1:

$$CC = \frac{\int_{t_1}^{t_2} u_o(t)u_c(t)dt}{\sqrt{\int_{t_1}^{t_2} u_o^2(t)dt \int_{t_1}^{t_2} u_c^2(t)dt}} \quad (1)$$

The two signals are compared on a finite time interval between t_1 and t_2 . A correlation coefficient approaching zero means that the waveforms are dissimilar and when it approaches 1 it means that there's no change at all between the reference, $u_o(t)$, and the later waveform, $u_c(t)$. In the rare case of a complete phase shift, the correlation coefficient would approach -1.

To monitor, many signals must be acquired through time and all of them are then directly compared with the reference. Therefore, is very important to choose the reference carefully. In case of small changes in the material, it is sufficient to choose the first measurement as a baseline corresponding to the potential undamaged state. When the damage level continuously increases with time, if there's not enough recovery of the structure, the waveforms acquired later can change so much that the reference becomes obsolete in the long run. Therefore, using a step-wise reference is advised to asses relative changes over time (Zotz-Wilson et al. 2019). The correlation coefficient method does not provide a direct quantitative measure of the change induced by strain or environmental factors like temperature. It is not suitable for distinguishing between global velocity changes and changes in local scattering behavior, nor the kind of damage that the medium suffered. Therefore, to extract information valuable for structural engineers, we need to apply a more advanced method.

2.1.2 Stretching method

When the properties or condition of the medium changes, the waves are expected to propagate either a little bit faster or slower than before. The longer their travel path, the more head start or delay they'll have compared to the reference measurement. If one can measure how much a signal apparently dilates or compresses by this effect, it would be possible to determine the average velocity change in the medium. The stretching method (Lobkis & Weaver 2003, Sens-Schönfelder & Wegler 2006, Hadzioannou et al. 2009) is used to detect subtle dilation or compression of the waveform with respect to a reference initial state and link- it to a relative velocity change $\Delta v/v$. To do this, the reference trace, $u_o(t)$, is stretched and compressed by a series of epsilon factors, ϵ , creating a series of stretched references $u_o(t + \epsilon t)$. The measured waveform, $u_c(t)$, is then correlated to all the traces in the series:

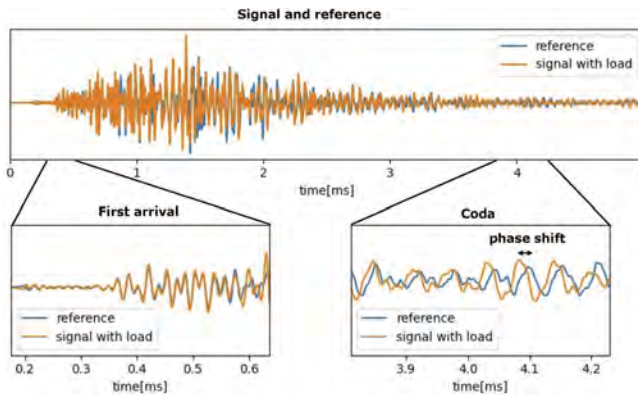


Figure 1. Two signals recorded with the same source and receiver. Emphasis is on the first arrival of the signal and the coda. The waveforms of both recordings are similar in the first arrival but on the coda, it's possible to appreciate a phase shift between the two signals. Figure adapted from Epple et al. (2022).

$$CC(\epsilon) = \frac{\int_{t_1}^{t_2} u_o(t + \epsilon t)u_c(t)dt}{\sqrt{\int_{t_1}^{t_2} u_o^2(t + \epsilon t)dt \int_{t_1}^{t_2} u_c^2(t)dt}} \quad (2)$$

The epsilon corresponding to the highest correlation value, $CC(\epsilon)$, corresponds to the representative velocity change due to the disturbance in the medium. When this method is applied to waveforms acquired at different times, it provides information on the temporal evolution of the medium. The method can be applied to different parts of the coda. It is possible to select the whole coda, the early part, or even the later part, resulting in a slightly different spatial sensitivity. Both, the stretching method and the correlation coefficient provide a temporal evolution of the medium but both lack the ability to locate the area of the changes and the type of damage encountered by the structure. In this case, advanced inversion algorithms are needed.

2.2 Experiment

The Gänstorbrücke (Figure 2) is one of the many bridges that traverse the river Danube and connects the cities of Ulm and Neu-Ulm in Germany. The 96m reinforced concrete bridge was constructed in 1950. Since damage has been detected in the form of corrosion and subsequent fractures of prestressing wires, the bridge is currently monitored with acoustic emission and strain sensors until its dismantled and rebuilt. This base monitoring makes it the perfect structure to test ultrasonic monitoring. Therefore, in 2020 the bridge was equipped with 24 embedded ultrasonic sensors as well as several external transducers. These transducers have a center frequency of 60 kHz (ACS and 25 kHz (ACS S0205), respectively. Thus, we have unscattered energy as well as

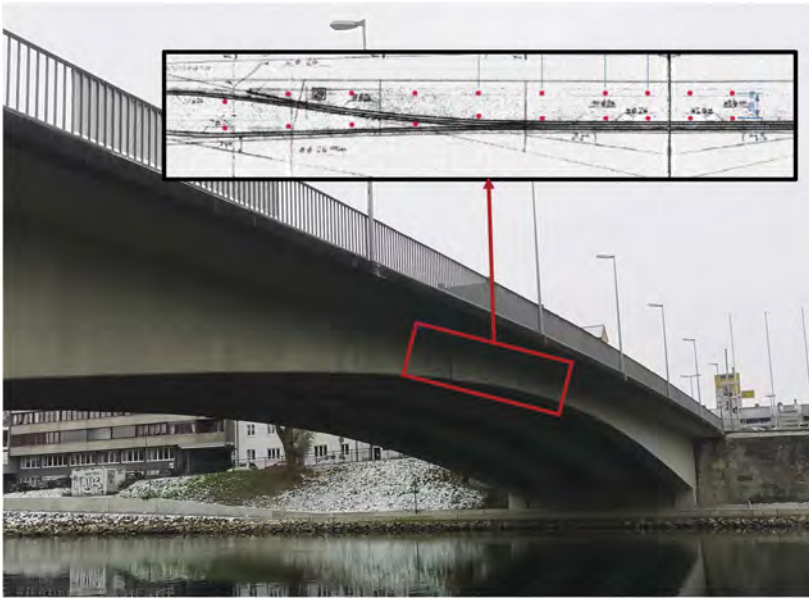


Figure 2. Photo of the Gänstorbrücke bridge with the location of the sensors indicated by red dots on the schematics of the bridge.

scattered coda in the recordings. 20 of these embedded transducers are located in the center of the bridge (Figure 2, schematics) to perform active ultrasonic measurements with an array for monitoring and imaging applications. The measurement device is a raspberry-pi based instrument for permanent ultrasonic monitoring developed at BAM (Barroso et al. 2021), especially for this kind of data acquisition. In December 2021, a load test was carried out during the night. This decision was made to calibrate the system and compare the changes induced by load and the effects of temperature to determine if the detection of cracks is in fact possible. In the experiment, two trucks of 15 and 32 tons were placed in 5 different positions over the bridge while ultrasonic consecutive measurements were taken. To reduce the acquisition time, a commercial device similar to the raspberry-pi-based was used for the acquisition (Wang et al. 2022).

3 RESULTS

All data were bandpass filtered to remove low and high-frequency noise. In Section 3.1 the relative velocity change is multiplied by negative one to indicate the correlation of velocity change and temperature change.

3.1 Long term analysis

The monitoring system at Gänstorbrücke has been running since installation in late 2020 with some downtime due to device maintenance. For most transducers, the signal quality has remained comparable. Comparisons of signals re We have identified in previous experiments (Epple et al. 2021) that the environmental temperature change has a significant influence on the signal, and can lead to strong decorrelations during a single day. While this is a reversible structural change, it is important to quantify it to determine thresholds and possible overshadowing of damage events. Figure 3 shows the CWI results from December 2021, the same month the load experiment was conducted. It is important to note that in this graph we have the sign for the velocity change reversed. Positive numbers refer to a decrease, to emphasize the correlation with temperature. A comparison of strain (gray), temperature (black), and three exemplary source-receiver combinations evaluated with the stretching technique using a fixed reference show that temperature

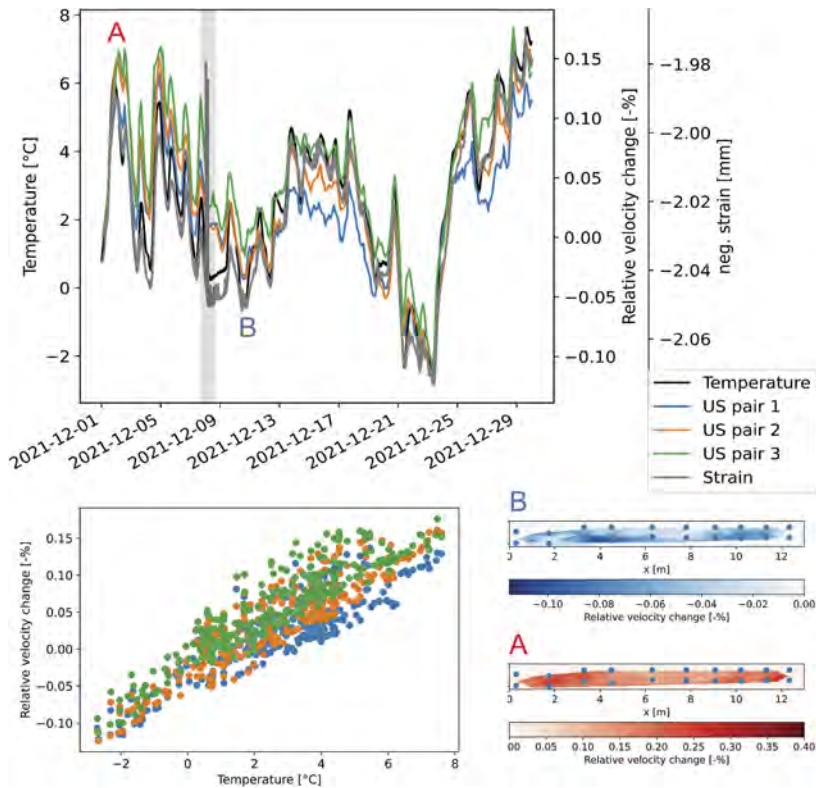


Figure 3. The results of a fixed reference analysis in Dec. 2021 show a strong correlation between temperature, strain, and negative velocity change (top). The time of the load experiment is marked in gray. The relationship between relative velocity change and temperature is linear (bottom left). An analysis of the sensor array at a warm (A) and cold (B) time shows an increased reaction to temperature change in two distinct areas of the array.

influences both strain and ultrasound velocity in a similar manner, while the strain measurements have a better temporal resolution. An increase in temperature reduces the stiffness of the material (and leads to material expansion) and therefore increases strain and decreases the velocity. Here, the relationship between temperature and velocity change is almost linear with $\approx 0.025 \frac{\%}{\text{C}}$ which is about the same magnitude as found in the aforementioned studies. With the focus on damage detection, we have plotted an areal map of velocity change from measurement during the day (A, warm) and during the night (B, cold) to evaluate if there are areas significantly reacting to temperature changes. The areal plots are created in accordance to Niederleithinger et al. (2018) where we attribute the calculated value for every transducer pair to their respective midpoint and interpolate between the results. In both cases, we see that the velocity decrease/increase is larger at the edges of the array compared to the center of the array. The anomalies on the left side of the array we mainly attribute to the separation of tendon ducts (see Figure 2). For the increased velocity change in the very center of the bridge, we are lacking an obvious interpretation and need to consult numerical simulations of the bridge strain fields under changing environmental conditions.

3.2 Load test

Figure 4 shows the result and setup of the load test. After data evaluation, we detected bad data quality in two combinations (8-9 and 17-18). The long-term analysis has shown that these two combinations are having some consistency issues from time to time, which might be caused by issues with transducer coupling. The experiment was conducted at night and temperature data shows a constant temperature during the entire experiment. Therefore, we do not

need to correct or account for any influence of temperature. As the influence of trucks on positions 1 and 5 was minimal, we focus on analyzing the influence of both trucks on measurements recorded with horizontal source-receiver combinations and both trucks at positions 2,3, and 4. The results are attributed to the midpoint between the source and receiver and shown over the distance in the sensor array. We separated the analysis for both trucks and plotted the results of the transducer combinations at the bottom of the array separately from the results from the top combinations. With these results, we see how our measurements are reacting to the load, which on the one hand induces compression and bending in the beam in the upper part and on the other hand opens existing cracks in the bottom, altering our ultrasonic signal.

The maximum changes in the load experiment exceed the influences of temperature variations below 10°C. Unsurprisingly, the 32 T truck induces a larger velocity change, the biggest change occurs in both cases when the truck is at position 3 directly above the array. When comparing the bottom and top zone with the truck at position 3, we see that velocity changes in the lower area are exceeding the changes on the top. These results are in accordance with bending experiments (Clauß et al. 2020) where the tensile forces are larger on the bottom, which decreases the ultrasonic velocity. In general, the velocity decreases even on the top zones, where numerical models suggest compression and therefore a velocity increase. We assume that the strong tensile forces, combined with the areal analysis of CWI will always lead to velocity reduction below a strong load on a bridge.

At positions 2 and 4 mainly sensors 1-3 and 11-13 are influenced. While this position 2 is close to these sensor positions (5 m), we would expect almost no influence from the load at position 4 due to the large distance to sensors 10 and 20 (15 m). Furthermore, in these cases, the velocity increases, indicating compression instead of tension. Also, this is the only scenario where the velocity change in the top part exceeds the change in the bottom part. We attribute this to the tendon duct layout. As shown in Figure 2, the tendon ducts are split in this region re-distributing strain. While this effect is most prominent with load at position 4, it can also be observed for sensor combinations 11-12 and 1-2 with load at position 3.

4 CONCLUSIONS

We have instrumented the Gänstorbrücke with a reliable ultrasonic monitoring system that can be used for permanent monitoring and short-time experiments. During monitoring operations, daily temperature changes can change the velocity by about 0.25% with a mostly linear relation between

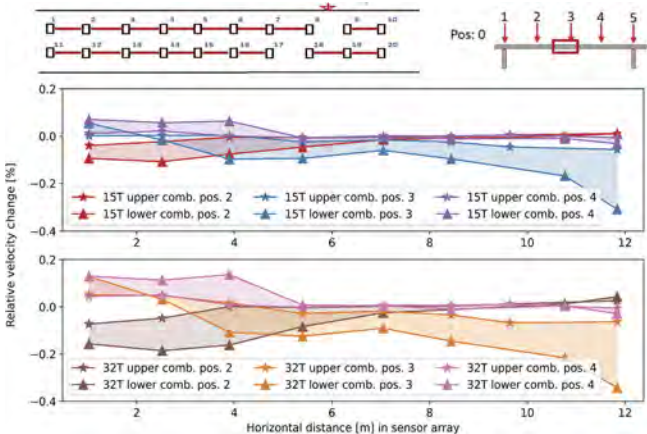


Figure 4. The results of the load test: For both trucks (15T and 32T) we analyze the relative velocity change throughout the array for horizontal combinations with load at positions 2,3 and 4 (schematics top). In the areas directly affected by load, the tensile forces induced by the bridge bending cause a strong velocity change predominantly in the bottom part of the array. The influence of load at positions further away is more complex and can lead to velocity increase caused by compression.

temperature and velocity change. Correction of these influences is complicated because it is not fully linear. Therefore, for the evaluation of material changes, we suggest choosing the reference measurement at the same ambient temperature and time of day instead of attempting a correction. The temperature changes can also be seen in the localized strain measurements installed for commercial bridge monitoring. Strain data has a better temporal resolution but no spatial resolution. The benefit of active ultrasonic monitoring lies in the areal analysis where we can identify parts of the bridge more influenced by temperature change than others. This can for example indicate cracks or other material damages reacting to temperature change. Furthermore, there is a nonlinear portion in the temperature-velocity relation. This non-linear part might be more sensitive to damages (Sun & Zhu 2019), so we hope to analyze and use this effect in future works.

The observations made in the load experiment show that load influences are stronger than influences of temperature change but of similar dimensions. This might cause problems in damage detection if no additional devices are available, e.g. acoustic emission. For damage detection, we advise using data collected at similar temperatures, preferably during the night time to minimize temperature gradients in the material. The array monitoring system helps localize the origin of changes, which opens possibilities for advanced damage localization algorithms based on inverse calculations. This has already been applied on several occasions (e.g. Zhang et al. (2016)) but not in an operational bridge with embedded 60 kHz transducers. Research on this topic will show the added value of a coda-based active ultrasonic monitoring system. It is not meant to replace but complement other monitoring technologies. A combination with AE is straightforward. It can be implemented at a relatively low cost and help to improve maintenance and repair strategies as well as general LCA/LCC analysis.

ACKNOWLEDGMENTS

The authors would like to thank the DFG for funding DFG FOR 2825 CoDA, the German Road Research Institute BAST for funding the instrumentation of the Gänstorbrücke (Project 89.0345/2022), the cities of Ulm and Neu-Ulm for access to the bridge and continued support, and Ingenieurbüro Schiessel Gehlen Sodeikat for providing access to measurement data and infrastructure during instrumentation and data evaluation.

REFERENCES

- Barroso, D. F., Epple, N., & Niederleithinger, E. (2021). A portable low-cost ultrasound measurement device for concrete monitoring. *Inventions* 2021, Vol. 6, Page 36 6(2):36.
- Clauß, F., Epple, N., Ahrens, M. A., Niederleithinger, E., & Mark, P. (2020, 7). Comparison of experimentally determined two-dimensional strain fields and mapped ultrasonic data processed by coda wave interferometry. *Sensors* 2020, Vol. 20, Page 4023 20: 4023.
- Epple, N., Barroso, D. F., Hau, J., & Niederleithinger, E. (2021). Accounting for long term environmental influences on ultrasonic monitoring measurements of reinforced concrete constructions with embedded transducers. *Proceedings of the 10th International Conference on Structural Health Monitoring of Intelligent Infrastructure, SHMII 10*: 1–7.
- Epple, N., Niederleithinger, E., & Fontoura Barroso, D. (2022). Coda wave interferometry for monitoring bridges with embedded ultrasonic transducers—lessons learned at the gänstorbrücke bridge ulm, germany. In *NDT. net Issue-2022-09-*, pp. 1–8.
- Hadziioannou, C., Larose, E., Coutant, O., Roux, P., & Campillo, M. (2009). Stability of monitoring weak changes in multiply scattering media with ambient noise correlation: Laboratory experiments. *The Journal of the Acoustical Society of America* 125(6): 3688–3695.
- Lobkis, O. I. & Weaver, R. L. (2003). Coda-wave interferometry in finite solids: Recovery of p-to-s conversion rates in an elastodynamic billiard. *Physical Review Letters* 90: 4.
- Niederleithinger, E., Wang, X., Herbrand, M., & Müller, M. (2018). Processing ultrasonic data by coda wave interferometry to monitor load tests of concrete beams. *Sensors* 18(6): 1971.
- Sens-Schönfelder, C. & Wegler, U. (2006, 11). Passive image interferometry and sea-seasonal variations of seismic velocities at merapi volcano, indonesia. *Geophysical Research Letters* 33.
- Nieder, R., Grêt, A., Douma, H., & Scales, J. (2002, mar). Coda wave interferometry for estimating non-linear behavior in seismic velocity. *Science* 295(5563): 2253–2255.

- Sun, H. & Zhu, J. (2019). Thermal modulation of nonlinear ultrasonic wave for concrete damage evaluation. *The Journal of the Acoustical Society of America* 145(5): EL405–EL409.
- Wang, X., Niederleithinger, E., & Hindersmann, I. (2022). The installation of embedded ultrasonic transducers inside a bridge to monitor temperature and load influence using coda wave interferometry technique. *Structural Health Monitoring* 21(3): 913–927.
- Zhang, Y., Planès, T., Larose, E., Obermann, A., Rospars, C., & Moreau, G. (2016). Diffuse ultrasound monitoring of stress and damage development on a 15-ton concrete beam. *The Journal of the Acoustical Society of America* 139(4): 1691–1701.
- Zotz-Wilson, R., Boerrigter, T., & Barnhoorn, A. (2019). Coda-wave monitoring of continuously evolving material properties and the precursory detection of yielding. *The Journal of the Acoustical Society of America* 145(2): 1060–1068.

A new technique to detect altered stresses in tendons early

N. Sträter, F. Clauß, M.A. Ahrens & P. Mark

Institute of Concrete Structures, Ruhr University Bochum, Bochum, Germany

ABSTRACT: Prestressing is the decisive component for achieving large spans with concrete bridges. For the long-term preservation of prestressed concrete bridges, the early detection of damage to tendons is particularly important. As tendons are often located within the concrete, the assessment of their condition is difficult with conventional methods. Ultrasonic measurements with sensors embedded in the concrete and evaluated with coda wave interferometry offer a promising new approach for assessing the internal health of concrete structures. To demonstrate the detection of tendon failures, two experiments—one with pre-tensioning and one with post-tensioning—were carried out at Ruhr University Bochum, Germany. By simulating a tendon failure, the prestressing force drops abruptly. The experimental results prove that the coda technique detects such tendon failures unambiguously, although no external changes seem to have appeared.

1 INTRODUCTION

Prestressing is the key technique to economically bridge large spans with concrete structures (Fischer et al. 2014, Sanio et al. 2014). In contrast to ordinary reinforced concrete (RC), the prestressing enables to reduce deformations, closes cracks and utilizes the high compressive strength of concrete. Typically, tendons used to apply prestress to the concrete are embedded in it, which renders visual inspection impossible. If failures of individual tendons occur, for example due to fatigue (Sanio et al. 2018) or stress-corrosion cracking (Nürnberger 2002), the concrete remains under compression. Only progressive damage and further tendon failures lead to visible cracks on the surface, resulting in the risk that the entire structure may collapse.

Nowadays, techniques such as strain gauges, fiber optics (Konertz et al. 2019, Clauß et al. 2021) or acoustic emission (Tonelli et al. 2020) exist for assessing the health of reinforced and prestressed concrete structures. It is the nature of the beast that many of them have disadvantages, as they either only provide local information, are not suitable for permanent monitoring or are of uneconomical use.

A promising approach for the condition assessment of concrete structures lies in coda waves. Coda is the late part of an ultrasonic (US) signal sent from a transmitter to a receiver. The corresponding coda waves are scattered many times in the concrete and pass through a large volume. The waves react sensitively to influences from strain (Clauß et al. 2020, 2022, Diewald et al. 2022), temperature (Epple et al. 2021), moisture (Ju et al. 2015, Legland et al. 2018) and structural changes like cracks (Finger et al. 2021, Grabke et al. 2021, Grabke et al. 2022). The ultrasonic signals are evaluated using coda wave interferometry (CWI) originating from the field of seismology. In the past, the method was transferred to the health assessment of concrete structures (Larose & Hall 2009, Planès & Larose 2013).

This contribution aims at how tendon failures can be detected with coda waves. As a method for their evaluation, the CWI is first introduced briefly. Afterwards, the experiment of an unbonded post-tensioned beam is presented, where the prestressing can be adjusted and

changed in a controlled manner. Here, a tendon failure is simulated by a gradual release of the prestressing. Furthermore, a more complex test of a pre-tensioned beam was carried out, in which tendons are in bond with the concrete. In this test, a tendon rupture was initiated by drilling from the outside. The results collected in both tests for the artificial generation of tendon failures are discussed and compared with each other.

2 METHODS

2.1 Principles of coda wave interferometry

Conventional US methods from the field of non-destructive testing mainly avail the arrival of a ballistic wave for evaluation. In contrast, CWI is based on the coda part, i.e., the rear part of an US signal (Snieder 2006). The associated waves spend a longer time in the medium, are scattered several times and thus repeatedly record information in a large volume. When using CWI, knowledge is not gained from individual US measurements, but rather two signals before and after an event are compared with each other to obtain measure of changes happened.

Coda waves are known to be very sensitive to changes in strain (Clauß et al. 2020, 2022, Diewald et al. 2022), temperature (Epple et al. 2021), moisture (Ju et al. 2015, Legland et al. 2018) and structural changes such as cracks (Finger et al. 2021, Grabke et al. 2021, Grabke et al. 2022). Figure 1 depicts an example of two US signals measured before and after a small event. In the direct part (at the beginning of the signals), hardly any differences are notable, whereas in the later coda part, which is enlarged here, a clear change is apparent.

In mathematical terms, the CWI compares two signals u_1 and u_2 within a time window t_1 to t_2 . The correlation coefficient CC is determined as a measure of similarity of the two signals in the given time window. If the signals are identical, CC reaches the value 1. If the signals are completely different, it approaches 0.

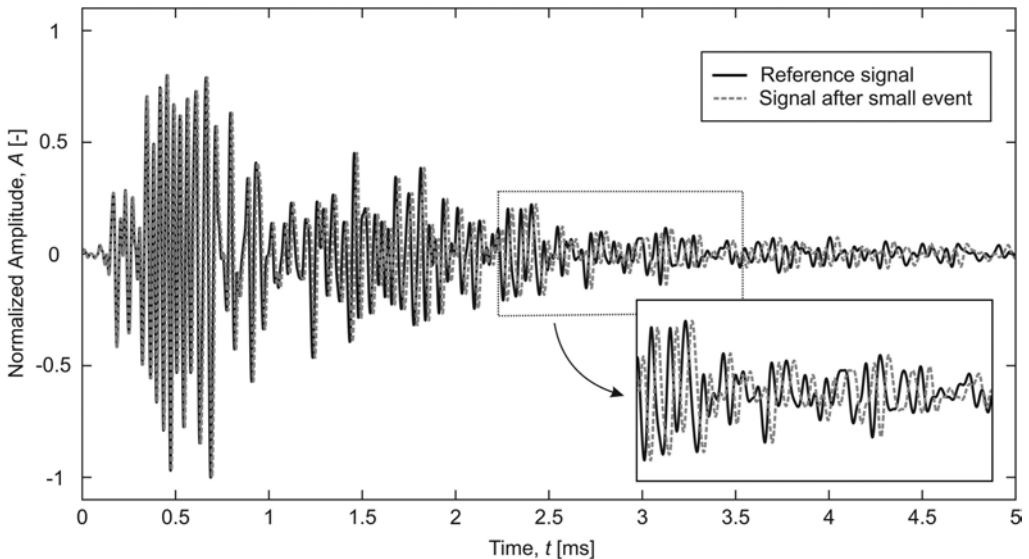


Figure 1. Ultrasonic measurement for the same source-receiver combination before and after a small event on a test specimen.

From the wave shift of both coda signals, another quantity the relative velocity change dv/v can be derived. To this end, the stretching technique (Niederleithinger et al. 2018) is used here, which compares the signal u_2 to a stretched version of u_1 being the reference signal. The

stretching factor ε maximizing the correlation coefficient CC corresponds to the negative relative velocity change dv/v . An increase in the velocity of the signal u_2 compared to u_1 causes a positive value of the relative velocity change and vice versa.

$$-\frac{dv}{v} = \arg \max_{\varepsilon \in \mathbb{R}} CC(t, \varepsilon) = \arg \max_{\varepsilon \in \mathbb{R}} \frac{\int_{t_1}^{t_2} u_1(t(1-\varepsilon)) u_2(t) dt}{\sqrt{\int_{t_1}^{t_2} u_1^2(t(1-\varepsilon)) dt \int_{t_1}^{t_2} u_2^2(t) dt}} \quad (1)$$

2.2 Experiments

To investigate the detection of tendon failure by the application of coda waves, a stepped series of experiments was conducted in the labs of Ruhr University Bochum, Germany. Therefore, two externally identical test specimens ($w/d/l = 200/200/1500$ [mm]) were manufactured. In the first step, an internal bondless prestressing (test 1: post-tensioned beam) is explored. Possible influences from the bond between tendons (in this case threaded rods) and the concrete are completely excluded. In this way, the focus lays on the pure effect of the prestressing force within the concrete and its effect on the coda waves. In the ensuing step (test 2: pre-tensioned beam), the tendons (still threaded rods) are completely embedded in the concrete, i.e., as an additional effect, only the bond between concrete and tendons is added. The results reveal the detection of externally invisible tendon failure.

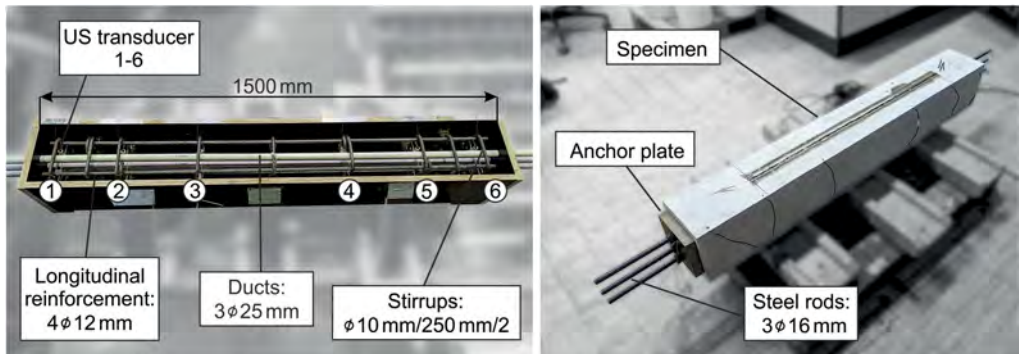


Figure 2. Test specimen of an unbonded post-tensioned beam before (left) and after (right) concreting.

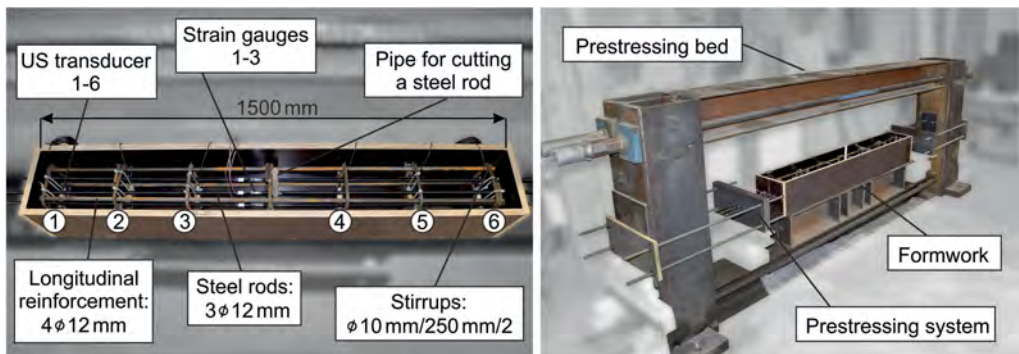


Figure 3. Test specimen of a pre-tensioned beam before concreting: formwork (left) and prestressing bed (right).

Three threaded rods ($\varnothing 16 \text{ mm}$) pass through the first test specimen. The threaded rods run in ducts, which were concreted in beforehand. The rods are prestressed by tightening nuts against anchor plates on both sides of the hardened specimen (cf. Figure 2, right). Via the anchor plates, the intended total force of 100 kN is transferred directly to the concrete. Guiding the tendons bondless in the ducts renders it possible to apply and release prestress in a controlled manner in order to set altered tendon stresses. As there is no bond to the concrete, tendon failure—in other words, a drop in force—can be simulated by loosening the nuts. In the experiment, the application of the prestress is monitored via the strain of the threaded rods measured with strain gauges. The post-tensioned beam was reinforced with longitudinal bars ($4 \varnothing 12 \text{ mm}$) and stirrups ($\varnothing 10 \text{ mm}/250 \text{ mm}/2$). An additional stirrup was inserted at load application.

Also the second specimen is passed through by three threaded rods (now $\varnothing 12 \text{ mm}$, cf. Figure 3, left). Before concreting, the rods are prestressed in the casting bed. They protrude from the formwork and can be prestressed by tightening nuts, which is again monitored by measuring the steel strains (Figure 3, right). To compensate for possible losses due to slip, prestressing was slightly above the target level of 100 kN (cf. Figure 6). After concreting and during hardening, the force is carried by the prestressing bed for another 12 days until it is transferred to the concrete. The nuts are loosened gradually to apply the stress evenly. Due to the bond between the concrete and the threaded rods, the test specimen is set under compression.

To create an artificial tendon failure on the pre-tensioned beam, a rod had to be drilled from the outside. Drilling into the concrete would lead to its damage, to which the coda waves react sensitively. To obtain comparable results before and after tendon rupture, the concrete is not allowed to be damaged by the drilling. For this purpose, a plastic tube was inserted during concreting to provide free access from the outside to the tendon later.

3 RESULTS AND DISCUSSION

3.1 Post-tensioning

The post-tensioned beam was prestressed in 10 uniform steps up to 100 kN. Figure 4 ($t = 0$ to 3000 s) reveals the successive increase of the measured strains in the threaded rods in increments of $125 \mu\text{m}/\text{m}$. Afterwards, to simulate tendon failure, the middle bar is gradually released. For this reason, the strain profile of the central rod decreases in steps of $125 \mu\text{m}/\text{m}$ (3000 to 4600 s), whereas the steel strains of the other two tendons rise negligibly from 1250 to 1280 $\mu\text{m}/\text{m}$.

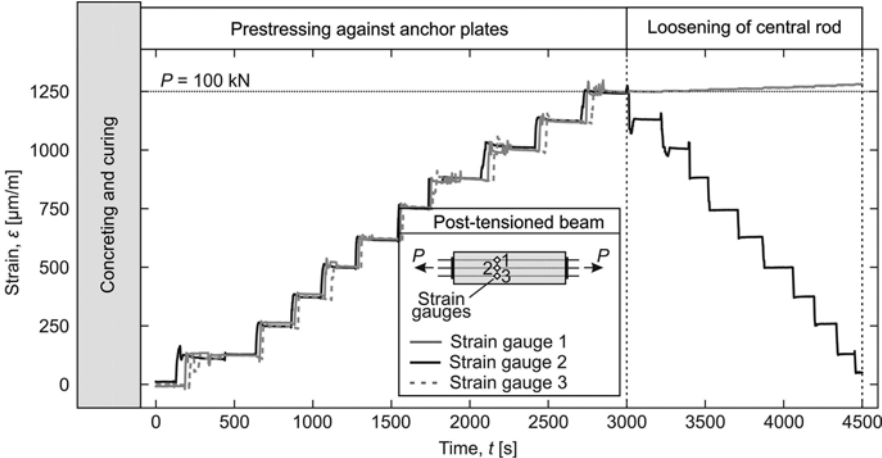


Figure 4. Measurement results of the strain gauges for the post-tensioned beam during prestressing and loosening.

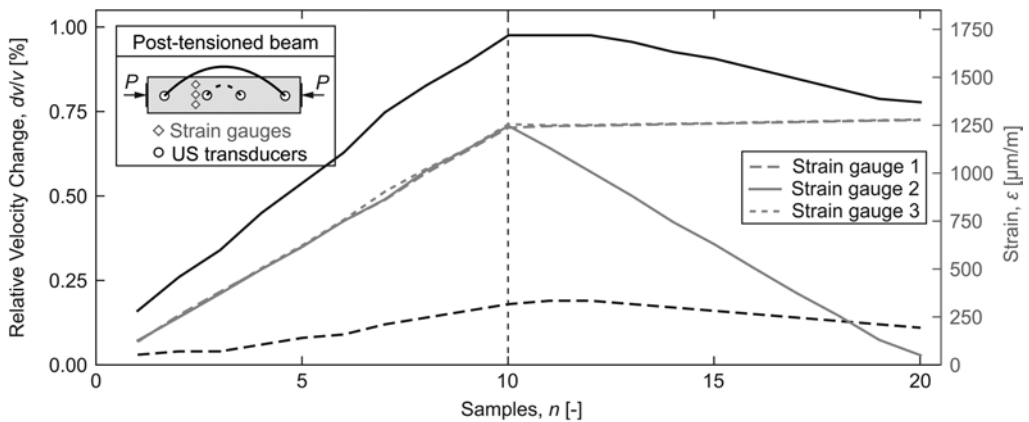


Figure 5. Comparison of the ultrasonic measurements and the strains in the rods for the post-tensioned beam.

Accompanying these strain measurements, US measurements were performed on each prestressing level. Figure 5 compares both the relative velocity changes for an inner and outer transducer pair (in black) and the measured strains of the threaded rods (in grey) for each prestress level (cf. Samples). The elevation in prestress is evident from the nearly linear increase in strain in all three threaded rods ($n = 0$ to 10). With the increasing prestress of the threaded rods comes—the actual goal of prestressing—the increase of concrete’s compressive stress. In accordance to the acoustoelastic effect (Lillamand et al. 2010), the relative velocity change becomes positive, thus indicates a speeding up of the coda waves. For both transducer pairs, there is an almost linear increase in the velocity change, which is in line with the uniformly applied prestress. The larger spacing of the outer US transducers leads to a greater rise in the relative velocity change (max. 0.98%) with increasing load than it is the case for the inner pair (max. 0.18%).

After reaching the maximum force, the prestressing of the central threaded rod is released by loosening the nut in 10 even steps ($n = 10$ to 20) to simulate the failure of a tendon. The measured strain in the middle bar therefore drops linearly, whereas again a slight increase in strain can be observed in the other two tendons. With the gradual failure of a tendon and the resulting decrease in the total prestressing force in the concrete, the relative velocity changes also fall approximately linearly. After the total failure of the middle rod ($n = 20$), the relative velocity changes decrease by 26% (outer pair) and 39% (inner pair). Therefore, the failure of the tendon becomes visible in an evident reduction of the relative velocity change.

3.2 Pre-tensioning

In the case of the pre-tensioned beam, the threaded rods were prestressed in the casting bed before concreting. Figure 6 left illustrates the gradual increase in steel strains in all three tendons and elucidates the exceeding prestressing beyond the target of 100 kN to compensate for effects from slip (relative displacement between the concrete and the threaded rods). After concreting and curing, the load is transferred to the concrete by releasing the prestressing bed (Figure 5, right). Between 0 and 4000 s, the steel strains decrease slightly, which can be attributed to the slip mentioned.

From 4000 s on, the cutting of the central tendon begins. Since the drill bit tends to slip of the threaded rod during drilling, several attempts had to be made and the cutting succeeds only gradually. This results in the stepwise decrease of strain in the middle bar. Due to the bond to the concrete, the tendon is anchored again with increasing distance from the cutting location. Thus, even at the location of the strain gauges, a residual strain of about 500 $\mu\text{m/m}$ remains in the central threaded rod. During tendon failure, the strains in the undamaged bars stay constant.

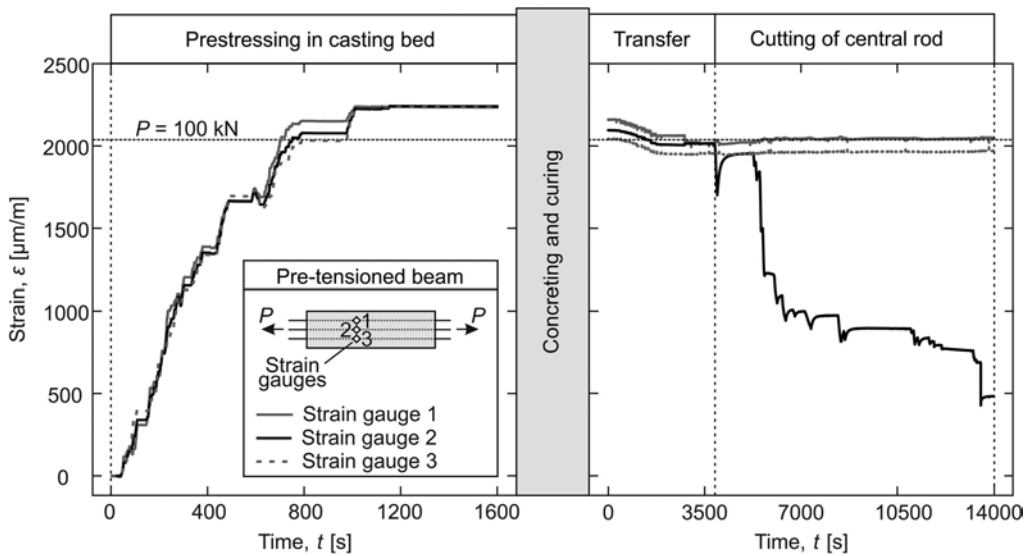


Figure 6. Measurement results of the strain gauges for the pre-tensioned beam during prestressing, load transfer and cutting.

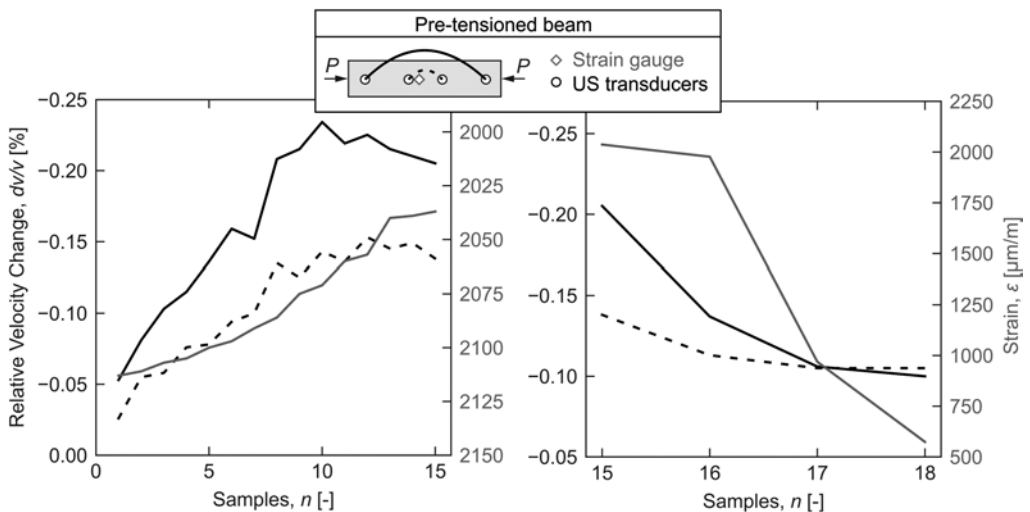


Figure 7. Comparison of the ultrasonic measurements and the strain in the central rod for the pre-tensioned beam.

Again, accompanying US measurements were carried out several times during the load transfer to the concrete (loosening of the prestressing bed) and the cutting of the tendon. Figure 7 highlights the measured relative velocity changes dv/v again for an inner and outer transducer pair as well as the strains of the middle tendon (left: load transfer, right: cutting). The force transfer to the concrete was not measured directly, but the slight decrease in strain in the tension rods due to slip ($n = 1$ to 15) allows it to be traced. As the load transfer progresses, the measured relative velocity changes for both pairs of transducers are also altered.

Cutting the threaded rod at center triggers a significant drop in the relative velocity change of 50% for the outer and 25% for the inner transducer pair. The damage to the tendon can be clearly recognized by the change in the ultrasonic signals.

3.3 Comparison

In contrast to the post-tensioned beam, all measured relative velocity changes in the pre-tensioned beam have a negative sign. According to the acoustoelastic effect, positive relative velocity changes dv/v would have been expected here since both beams are prestressed. It is assumed that local tensile stresses and cracks occur due to the bond between concrete and threaded bars, which cause a reduction of the ultrasonic velocity. These side effects seem to dominate the measurements, so that the results do not indicate any compressive stresses as a result of the prestressing. Since there is no bond in the post-tensioned beam, these side effects do not appear, making it possible to measure positive values for dv/v there.

4 CONCLUSIONS

A post-tensioned and a pre-tensioned beam were experimentally investigated to detect tendon failures using coda wave interferometry. On both beams, the transmission of the prestressing force as well as the artificial generation of a tendon failure were monitored with ultrasonic and strain measurements.

Provided there is no bond between the concrete and the tendon, as is the case with the post-tensioned beam, the ultrasonic results indicate compressive stresses in the beam. For the pre-tensioned beam, the results are overlaid by local effects—in the form of cracks and tensile stresses—of the bond, so that negative relative velocity changes are measured despite the applied compressive force. Nevertheless, for both types of prestressing, tendon failures could be clearly identified by distinct changes in the ultrasonic signal. The results underline the potential of using the coda wave technique as a permanent measuring instrument to monitor tendons.

In the future, the investigations will be extended to a post-tensioned beam, whose tendons are grouted so that there will be bonding to the concrete. Subsequently, larger prestressed structures will be investigated that are additionally subjected to bending.

ACKNOWLEDGMENTS

This research was funded by the Deutsche Forschungsgemeinschaft (DFG, German Research Foundation) —Project number 398216472.

REFERENCES

- Clauß, F., Ahrens, M.A. & Mark, P. 2021. A comparative evaluation of strain measurement techniques in reinforced concrete structures—A discussion of assembly, application, and accuracy. *Structural Concrete*, 22 (5): 2992–3007.
- Clauß, F., Epple, N., Ahrens, M.A., Niederleithinger, E. & Mark, P. 2020. Comparison of Experimentally Determined Two-Dimensional Strain Fields and Mapped Ultrasonic Data Processed by Coda Wave Interferometry. *Sensors (Basel, Switzerland)*, 20 (14).
- Clauß, F., Epple, N., Ahrens, M.A., Niederleithinger, E. & Mark, P. 2022. Correlation of Load-Bearing Behavior of Reinforced Concrete Members and Velocity Changes of Coda Waves. *Materials (Basel, Switzerland)*, 15 (3).
- Diewald, F., Epple, N., Kraenkel, T., Gehlen, C. & Niederleithinger, E. 2022. Impact of External Mechanical Loads on Coda Waves in Concrete. *Materials (Basel, Switzerland)*, 15 (16).
- Epple, N., Barroso, D.F. & Niederleithinger, E. 2021. Towards Monitoring of Concrete Structures with Embedded Ultrasound Sensors and Coda Waves – First Results of DFG for CoDA. In: P. Rizzo and A. Milazzo (eds.), *European Workshop on Structural Health Monitoring*. Cham: Springer International Publishing: 266–275.
- Finger, C., Saydak, L., Vu, G., Timothy, J.J., Meschke, G. & Saenger, E.H. 2021. Sensitivity of Ultrasonic Coda Wave Interferometry to Material Damage-Observations from a Virtual Concrete Lab. *Materials (Basel, Switzerland)*, 14 (14).

- Fischer, O., Müller, A., Lechner, T., Wild, M. & Kessner, K. 2014. Ergebnisse und Erkenntnisse zu durchgeführten Nachrechnungen von Betonbrücken in Deutschland. *Beton- und Stahlbetonbau*, 109 (2): 107–127.
- Grabke, S., Bletzinger, K.-U. & Wüchner, R. 2022. Development of a finite element-based damage localization technique for concrete by applying coda wave interferometry. *Engineering Structures*, 269: 114585.
- Grabke, S., Clauß, F., Bletzinger, K.-U., Ahrens, M.A., Mark, P. & Wüchner, R. 2021. Damage Detection at a Reinforced Concrete Specimen with Coda Wave Interferometry. *Materials (Basel, Switzerland)*, 14 (17).
- Ju, T., Li, S., Achenbach, J. & Qu, J. 2015. Effects of moisture on ultrasound propagation in cement mortar. In: AIP Publishing LLC: 1409–1414.
- Konertz, D., Löschmann, J., Clauß, F. & Mark, P. 2019. Faseroptische Messung von Dehnungs- und Temperaturfeldern/Fiber optic sensing of strain and temperature fields. *Bauingenieur*, 94 (07-08): 292–300.
- Larose, E. & Hall, S. 2009. Monitoring stress related velocity variation in concrete with a 2×10^{-5} relative resolution using diffuse ultrasound. *The Journal of the Acoustical Society of America*, 125 (4): 1853–1856.
- Legland, J., Thery, R., Abraham, O., Villain, G., Durand, O., Larose, E. & Tournat, V. 2018. Influence of moisture on the estimation of nonlinear parameters in concrete with Nonlinear ultrasonic Coda Wave Interferometry. *e-Journal of Nondestructive Testing, Vol.23, No.08*.
- Lillamand, I., Chaix, J.-F., Ploix, M.-A. & Garnier, V. 2010. Acoustoelastic effect in concrete material under uni-axial compressive loading. *NDT & E International*, 43 (8): 655–660.
- Niederleithinger, E., Wang, X., Herbrand, M. & Müller, M. 2018. Processing Ultrasonic Data by Coda Wave Interferometry to Monitor Load Tests of Concrete Beams. *Sensors (Basel, Switzerland)*, 18 (6).
- Nürnberg, U. 2002. Corrosion induced failure mechanisms of prestressing steel. *Materials and Corrosion*, 53 (8): 591–601.
- Planès, T. & Larose, E. 2013. A review of ultrasonic Coda Wave Interferometry in concrete. *Cement and Concrete Research*, 53: 248–255.
- Sanio, D., Ahrens, M.A., Mark, P. & Rode, S. 2014. Untersuchung einer 50 Jahre alten Spannbetonbrücke zur Genauigkeitssteigerung von Lebensdauerprognosen. *Beton- und Stahlbetonbau*, 109 (2): 128–137.
- Sanio, D., Löschmann, J., Mark, P. & Ahrens, M.A. 2018. Bauwerksmessungen versus Rechenkonzepte zur Beurteilung von Spannstahlermüdung in Betonbrücken. *Bautechnik*, 95 (2): 99–110.
- Snieder, R. 2006. The Theory of Coda Wave Interferometry. *Pure and applied geophysics*, 163 (2-3): 455–473.
- Tonelli, D., Luchetta, M., Rossi, F., Migliorino, P. & Zonta, D. 2020. Structural Health Monitoring Based on Acoustic Emissions: Validation on a Prestressed Concrete Bridge Tested to Failure. *Sensors (Basel, Switzerland)*, 20 (24).

Comparison of structural analysis results with coda wave interferometry measurements

S. Grabke & K.-U. Bletzinger

Chair of Structural Analysis, Technical University Munich, Germany

ABSTRACT: Coda wave interferometry is an ultrasound-based technology for structural health monitoring of concrete structures that is based on a correlation evaluation of two ultrasonic signals. To detect damage locations, sensitivities of the coda waves are used. These sensitivities are derived from wave propagation approximations that are computed with the finite element method applied on a diffusion problem. So far, the actual value of localized damage has little meaning in real experiments. This study compares results from structural analysis to the actual measurements. The analysis results should be used as the basis of a measurement classification that in the end should identify damage with a threshold. The comparison is performed at a real four-point bending test of a reinforced concrete specimen.

1 INTRODUCTION

Coda wave interferometry (CWI) is an ultrasound-based structural health monitoring technology for concrete structures. With increasing age of build infrastructure combined with heavier traffic loads, monitoring structures is essential for an evaluation and lifetime extension. The non-destructive CWI is an ideal candidate for a permanent monitoring. Due to a high sensitivity to changes in the medium it can detect cracks at very early stages. Several studies (Niederleithinger et al. (2018); Wang & Niederleithinger (2018); Wang et al. (2019, 2020); Zhan et al. (2020)) have shown the immense potential of damage detection with CWI in large scale field experiments. With a measurement network even a damage localization is possible. In general, the authors refer to damage as an irreversible change of the structure caused by exceeding the elastic load bearing capacity of the material which leads to cracking. So far a classification of detected damage in terms of e.g. crack size is difficult. For a reliable permanent monitoring, a good calibration of the equipment is essential. This is complicated by varying stresses in different regions of a structure. This study compares CWI measurements to stress computations on a structural analysis model to evaluate the possibility of a computation based measurement calibration.

2 METHODOLOGY

The CWI is a relative measurement technology that always needs a reference measurement. This means that the technology can only detect additional damage compared to the reference. Existing damage is only detectable if e.g. a crack is increasing. Also it is of major importance that the ultrasonic signal is scattered multiple times on the way from a source to a receiver. Thus, concrete with its heterogeneous mix of cement, aggregates, pores and reinforcement is an ideal material for the technology. The scattering not only extends the sensing area but also increases the sensitivity to small changes in the medium. A good review on the basics of CWI in concrete can be found in Planès & Larose (2013). The present study is based on an experiment that is further described in Grabke et al. (2021, 2022).

The central element in CWI is a cross-correlation (CC) evaluation of the measurements. Changes in the medium e.g. by cracks but also temperature (Wunderlich & Niederleithinger (2011)), moisture (Ju et al. (2015)) and stresses (Larose & Hall (2009); Lillamand et al. (2010))

affect the coda signal. The CC in the signal φ at time t is measured in a time frame of length T with the following formula:

$$CC(t) = \frac{\int_{t-T/2}^{t+T/2} \varphi_{ref}(t)\varphi(t) dt}{\sqrt{\int_{t-T/2}^{t+T/2} \varphi_{ref}^2(t) dt \int_{t-T/2}^{t+T/2} \varphi^2(t) dt}} \quad (1)$$

Depending on the type of monitoring the CC is either evaluated for a time frame with length of the whole signal or several shorter consecutive time frames that measure a development within the signal. The CC can be used directly as a measurement or with a network of several measurements a damage localization can be performed. For the localization, the sensitivities of a coda wave K are computed as follows (Pacheco & Snieder (2005)):

$$K(S, R, x, t) = \frac{\int_0^t I(S, x, u)I(x, R, t - u) du}{I(S, R, t)} \quad (2)$$

In Equation 2, I (*position 1, position 2, t*) stands for the wave intensity at *position 2* after time t of a wave starting from *position 1*. Looking at the numerator of Equation 2 one can see that the integral sums up all the time combinations of a wave going from the source position S to position x to the receiver position R in time t . Since the waves going through position x are just a fraction of all wave paths arriving at the receiver R , the numerator term is normalized by the general possibility of a wave travelling from source S to receiver R in time t .

In order to reduce computational complexity and the possibility to apply a damage localization at large structures, the diffuse coda wave intensities are approximated. Ryzhik et al. (1996) have shown that the spread of a waves energy in a random media as concrete can be approximated with a diffusive spread in a homogeneous medium. This study uses the finite element method (FEM) to solve the diffusion problem. With the coda wave sensitivities an inverse problem can be formulated whose solution is the damage localization. Grabke et al. (2022) gives further insights on the FEM based computation and damage localization that is based on Planès et al. (2015).

The inversion based damage localization has the advantage that it is mapping a localized damage on the structure but without calibration contains no reliable information about the damage size. A calibration is rather tricky because measurements are strongly depending on the given setup and ideally would require a test damage which is impractical. Also the damage localization requires a steady-state for the time it takes to perform all measurements. Depending on the amount of measurement pairs and used equipment this takes several seconds up to minutes. In conclusion, this means that for a practical application with traffic load only a few measurements are active during a critical loading. Thus this study investigates the possibility to calibrate each measurement pair individually based on computed stresses for critical load cases and derive a damage threshold for each measurement pair. In typical applications the stress state is multiaxial and the principal stress directions indicate crack formations. The von Mises stresses $\sigma_{v,M}$ are fictitious equivalent stresses computed for each element from the Cauchy stress tensor and describe the overall material utilization. Important to note here is that von Mises stresses are actually not a good stress measure for concrete because compressive and tensile load bearing capacity differ by a factor of approximately 10. Later the von Mises stresses are thus modified. Further improvements can be achieved by applying a non-linear material model that contains the actual yield criteria of concrete (e.g. Kupfer & Gerstle (1973)) on the simulation. In this study the Cauchy stresses are first transferred to principal stresses $\sigma_{1,2}$:

$$\sigma_{1,2} = \frac{\sigma_x + \sigma_y}{2} \pm \sqrt{\left(\frac{\sigma_x - \sigma_y}{2}\right)^2 + \tau_{xy}^2} \quad (3)$$

The von Mises stresses are then computed as follows:

$$\sigma_{v,M} = \sqrt{\frac{1}{2}[(\sigma_1 - \sigma_2)^2 + \sigma_1^2 + \sigma_2^2]} \quad (4)$$

This study uses a simple first order linear structural analysis on the same mesh as the FEM computations for the diffusion problem. In order to classify CC measurements the coda wave sensitivities are superposed with stresses in the medium. With stresses being an element related quantity and coda wave sensitivities being an node related quantity they need to be transferred to a common basis. This study thus interpolates the coda wave sensitivities on the elements. In order to compare measurements among each other a weighting factor w for each pair is introduced. For comparison this weighting factor is later normed with the maximum norm.

$$w(S, R) = \int_{\Omega} \int_T K(S, R, x, t) dt \sigma_{v,M}(x) dx \quad (5)$$

3 EXPERIMENTAL SETUP

The comparison of structural analysis and coda measurements is made at the experiment described in Grabke et al. (2021). The experiment performed by the Institute of Concrete Structures at the Ruhr University Bochum is a four point bending test. Figure 1 gives an overview on the experimental setup. Figure 2 shows the CC development of selected measurement pairs for increasing loading. In the given experimental setup the concretes tensile strength f_{ctm} is

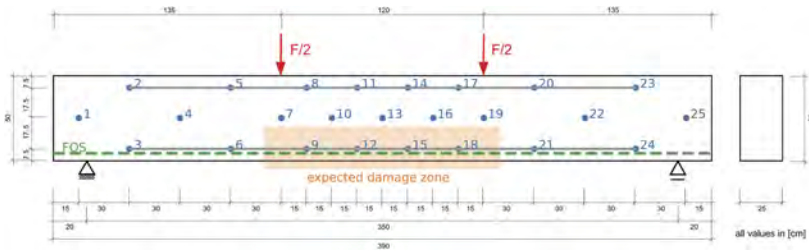


Figure 1. Overview of the four-point bending test conducted at a real reinforced concrete specimen by the Institute of Concrete Structures at the Ruhr University Bochum. Blue dots show the 25 embedded ultrasound transducers used and green marks the reference measurement with Fiber Optic Sensor. Grey lines indicate the evaluated measurement pairs.

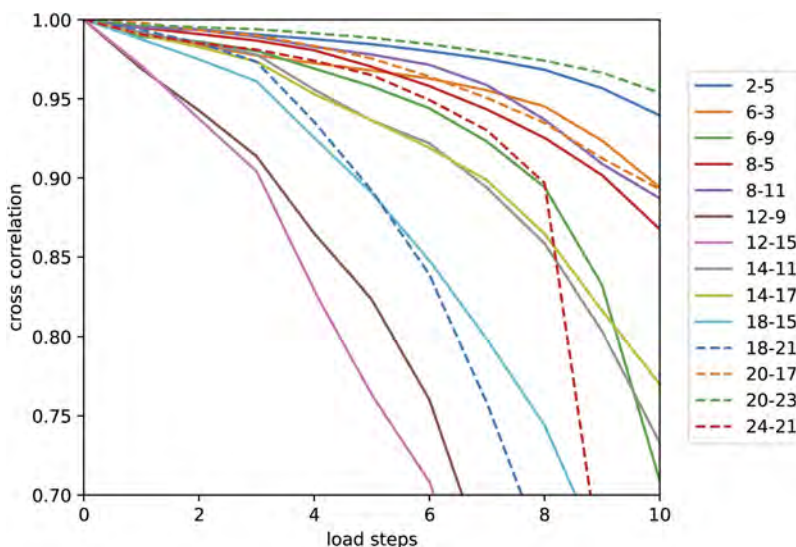


Figure 2. Cross-correlation development of selected pairs over the first load steps.

reached around load step 10. This is the load steps where computationally cracks occur. In the CC development one can see that even before cracking, correlation drops can be measured. One can see that depending on the position of measurement pairs within the structure, the CC values are of different magnitude. In general, measurements near the damage zone show the lowest correlation whereas measurements in zones further away from cracks are comparable little. For the investigated four point bending test Figure 3 gives the von Mises stresses $\sigma_{v,M}$.

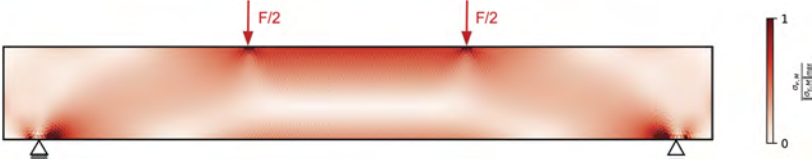


Figure 3. Normed von Mises stresses $\sigma_{v,M}$ for the investigated four-point bending test.

4 RESULTS

For evaluation load step 8 is closer investigated. This load step is computationally uncracked and thus the used computations are applicable. On the other hand the measured CC for some measurements are already comparably large. Figure 4 shows the CC measurements at load step 8 mapped onto the structure. One can see that the CC values for each measurement are of very

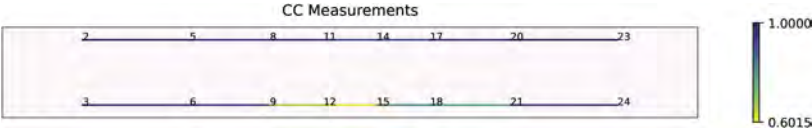


Figure 4. CC measurements at load step 8 mapped onto the structure.

different magnitudes. The weights from Equation 5 that superpose coda wave sensitivities and stresses in the specimen should help explain these differences. They are shown in Figure 5. One can see that due to the formation of an arch under pressure for the four point bending test,

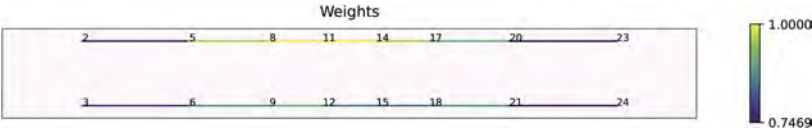


Figure 5. Weights computed with Equation 5.

especially the measurement pairs in the middle on the top have larger weights, whereas the CC on the bottom in the tensile zone are that lowest. The CC values are most probably due to the fact that concrete works well under pressure but cracks comparably early under tension. Concluding the comparison one can say that a comparison of the measurements in Figure 4 and the weights in Figure 5 is not satisfying. With the CWI as a technology that especially measures cracks with a high sensitivity, the focus is now put on the principle tensile stresses in the specimen. Therefore the compressive principle stresses from Equation 3 are neglected for the von Mises stress computation of Equation 4. The resulting von Mises stresses are shown in

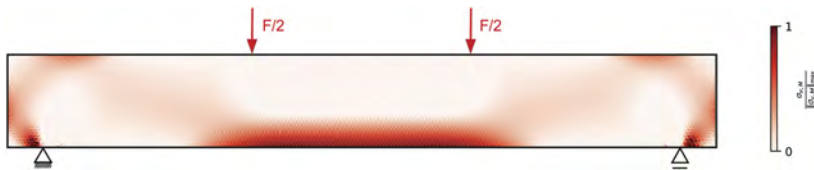


Figure 6. Normed von Mises stresses $\sigma_{v,M}$ with compressive principal stresses neglected.

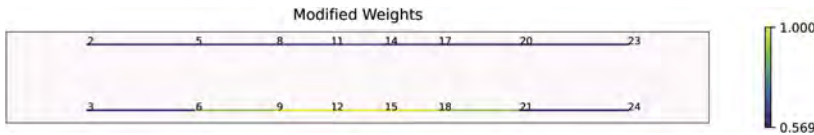


Figure 7. Weights computed with Equation 5 with neglected compressive principle stresses for the von Mises stress computation of Figure 6.

Figure 6 and the resulting computation of weights is shown in Figure 7. One can see that overall there is a correlation of the value distribution between Figures 4 and 7. Further investigations will deal with the question of how to use the weights to calibrate the CC measurements in order to have an overall damage threshold. Out of the box the results were not satisfying. A big role play selected measurements with over-proportionally little CC. These unusual measurements can come from cracks very close to transducer positions. The weights of Figure 7 however, are an ideal tool to find malfunctioning of measurement equipment.

5 CONCLUSIONS

Concluding one can say that structural analysis can help explain and understand CWI measurements. The study has shown that especially changes in the specimen due to tensile stresses are measured. As mentioned earlier the used modified von Mises stresses are a simple technique and further improvements can be achieved by applying a non-linear material model that contains the actual yield criteria of concrete on the simulation. With a model that can approximate expected measurement values there is immense potential for the future. Future research will try to classify CC measurements based on the structural analysis results.

REFERENCES

- Grabke, S., Clauß, F., Bletzinger, K.-U., Ahrens, M. A., Mark, P. and Wüchner, R. 2021. Damage detection at a reinforced concrete specimen with coda wave interferometry. *Materials*, 14(17): 5013, sep 2021. doi: 10.3390/ma14175013.
- Grabke, S., Bletzinger, K.-U., and Wüchner, R. 2022. Development of a finite element-based damage localization technique for concrete by applying coda wave interferometry. *Engineering Structures*, 269:114585, oct 2022. doi: 10.1016/j.engstruct.2022.114585.
- Ju, T., Li, S., Achenbach, J., and Qu, J. 2015. Effects of moisture on ultrasound propagation in cement mortar. *AIP Conference Proceedings*, 1650(1):1409–1414, 2015. doi: 10.1063/1.4914756.
- Kupfer, Helmut B., and Kurt H. Gerstle. 1973. Behavior of concrete under biaxial stresses. *Journal of the engineering mechanics division*, 99.4: 853–866, aug 1973.
- Larose, E. and Hall, S. 2009. Monitoring stress related velocity variation in concrete with a relative resolution using diffuse ultrasound. *The Journal of the Acoustical Society of America*, 125: 1853–1856, January 2009.
- Lillamand, I., Chaix, J.-F., Ploix, M.-A., and Garnier, V. 2010. Acoustoelastic effect in concrete material under uni-axial compressive loading. *NDT & E International*, 43(8):655–660, nov 2010. doi: 10.1016/j.ndteint.2010.07.001.

- Niederleithinger, E., Wang, X., Herbrand, M., and Müller, M. 2018. Processing ultrasonic data by coda wave interferometry to monitor load tests of concrete beams. *Sensors*, 18(6):1971, jun 2018. doi: 10.3390/s18061971.
- Pacheco, C. and Snieder, R. 2005. Time-lapse travel time change of multiply scattered acoustic waves. *The Journal of the Acoustical Society of America*, 118(3):1300–1310, sep 2005. doi: 10.1121/1.2000827.
- Planès, T. and Larose, E. 2013. A review of ultrasonic coda wave interferometry in concrete. *Cement and Concrete Research*, 53: 248–255, nov 2013. doi: 10.1016/j.cemconres.2013.07.009.
- Planès, T., Larose, E., Rossetto, V., and Margerin, L. 2015. Imaging multiple local changes in heterogeneous media with diffuse waves. *The Journal of the Acoustical Society of America*, 137(2):660–667, feb 2015. doi: 10.1121/1.4906824.
- Ryzhik, L., Papanicolaou, G., and Keller, J. B. 1996. Transport equations for elastic and other waves in random media. *Wave Motion*, 24(4):327–370, dec 1996. doi:10.1016/s0165-2125(96)00021-2.
- Wang, X. and Niederleithinger, E. 2018. Coda wave interferometry used to detect loads and cracks in a concrete structure under field conditions. 2018. doi: 10.5281/ZENODO.1402380.
- Wang, X., Niederleithinger, E., Chakraborty, J., and Klikowicz, P. 2019. Monitoring a concrete bridge girder with the coda wave interferometry method. 2019. doi: 10.5281/ZENODO.3520603.
- Wang, X., Chakraborty, J., Bassil, A., and Niederleithinger, E. 2020. Detection of multiple cracks in four-point bending tests using the coda wave interferometry method. *Sensors*, 20(7):1986, apr 2020. doi: 10.3390/s20071986.
- Wunderlich, C. and Niederleithinger, E. 2011. Evaluation of temperature influence on ultrasound velocity in concrete by coda wave interferometry. In *Nondestructive Testing of Materials and Structures*, pages 227–232. Springer Netherlands, sep 2011. doi: 10.1007/978-94-007-0723-8_33.
- Zhan, H., Jiang, H., Zhang, J., and Jiang, R. 2020. Condition evaluation of an existing t-beam bridge based on neutral axis variation monitored with ultrasonic coda waves in a network of sensors. *Sensors*, 20(14):3895, jul 2020. doi: 10.3390/s20143895.

About the separation of impacts on coda waves in concrete

F. Diewald

Centre for Building Materials, Technical University of Munich, Munich, Germany

ABSTRACT: Our built environment during the last 100 years has expanded more than ever referring to material consumption of the construction industry. Especially for engineering structures, the most common building material is reinforced concrete due to its performance, cost-efficiency and availability. However, this material poses special challenges regarding non-destructive monitoring of both the condition and integrity of civil engineering structures, which is an increasingly important part within life cycle analysis. Ultrasound-based Coda Wave Interferometry (CWI) is one of the most promising monitoring techniques as it can detect and localize even weak changes in the microstructure of heterogeneous materials. Recent research has shown that this technique is also applicable for identifying precursors of deterioration processes.

One of the challenges for concrete monitoring using CWI is the separation of reversible changes due to temperature and moisture as well as mechanical stresses from irreversible changes such as damage in the structure. Previous studies investigated these impacts in the framework of ‘one-dimensional’ experiments at the specimen scale under laboratory conditions. From each experiment, we derived calibration curves for the relation between the individual external impact and the Coda Waves’ velocity variations, which are consistent for one concrete mix. In this contribution, we summarize these relations and propose equations, allowing us to distinguish between the causes of velocity variations of Coda Waves propagating in concrete. With this research, we aim at generating a model that will enable the separation of reversible and irreversible changes in concrete using Coda Wave Interferometry. Our results will contribute to establishing CWI as an early-warning-system for engineering structures made from reinforced concrete and therefore increasing the safety of large parts of our infrastructure.

1 INTRODUCTION

Using Germany as an example, the largest proportion of our infrastructural buildings is raised from structural concrete and the majority of the over 52,000 bridges have been constructed between 1960 and 1990 (BASt 2021). Amongst novel reliability models (Gehlen 2000; Breit et al. 2011; von Greve-Dierfeld & Gehlen 2016a; von Greve-Dierfeld & Gehlen 2016b; von Greve-Dierfeld & Gehlen 2016c) and updated building codes, the scientific community addresses the safety needs of the ageing infrastructure, which has to deal with a steadily increasing traffic volume at the same time, by developing new monitoring methods for damage detection. Structural concrete poses a special challenge to monitoring techniques, mainly because of its distinctive heterogeneity and complex microstructure. One of the most promising techniques to detect even weak changes in the microstructure of concrete is ultrasound-based coda wave interferometry.

A most discussed process of damage development is corrosion-induced deterioration. Figure 1 (Gehlen 2000) illustrates that microstructural changes, or in other words micro-scale damage formation, starts after depassivation of the reinforcement. The damage level becomes critical after exceeding a limit state for the crack width (Gehlen et al. 2010) as

self-reinforcing effects occur due to facilitated gas and liquid transport mechanisms until the structure reaches the Ultimate Limit State, which is equal to its failure. Within this process, detection of mechanical damage is desired as early as possible for safety and economical reasons. It is realized by either inspection at discrete points in time or by a continuous monitoring system. Due to its extraordinary sensitivity in heterogeneous media like concrete, CWI is suitable for damage detection at an unprecedented early stage in comparison with conventional NDT techniques.

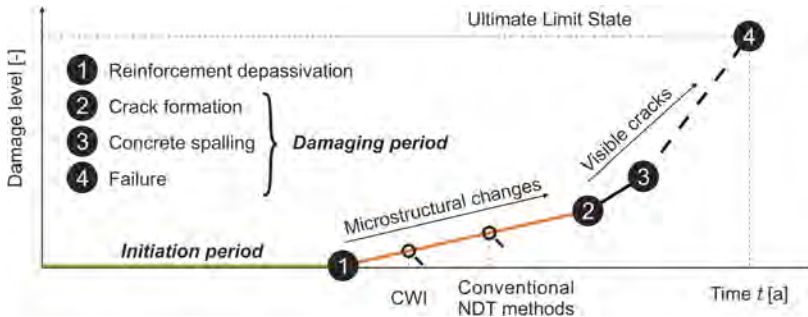


Figure 1. Time-depending progress of corrosion-induced deterioration and damaging of reinforced concrete structures and their limit state, adapted from (Gehlen 2000), characterized by the initiation period and the damaging period, during which mechanical damage occurs. In comparison with many conventional non-destructive testing methods in heterogeneous media, coda wave interferometry is more sensitive and has the potential to detect damage before other techniques.

The research presented in this study summarizes the main findings of a doctoral thesis (Diewald 2023), where the content in this article is taken nearly verbatim from the thesis. The results will contribute to establishing CWI for its application as an early-warning monitoring system for integrity assessment of structures made from reinforced concrete. The research is motivated by the need for a general safety increase of our built environment.

2 METHODS

The potential sensitivity of coda waves to weak changes in heterogeneous media has been recognized much before its application to concrete structures. Early studies from the geophysical community investigated the seismic source, attenuation and scattering effects of coda waves from small local earthquakes already in 1969 (Aki 1969; Aki & Chouet 1975). Finite difference and finite element methods have already been suggested for the case of known model parameters to interpret the seismograms regarding the geometrical localization of any change. The model parameters were typically unknown for the earth's crust, however, they may be well-known in static models for engineering structures today. Later in 2002, CWI was introduced by revealing the relationship between the seismic velocity in granite and temperature changes together with the associated acoustic emissions (Snieder et al. 2002). Furthermore, the at first sight chaotically and noisily appearing coda waves were found to be highly repeatable as no change in the medium appears (Snieder 2006).

Multiple methods for CWI analysis are based on the calculation of a stretching factor $\varepsilon = dt/t = -dv/v$ (Snieder et al. 2002; Sens-Schönfelder & Wegler 2006; Hadziioannou et al. 2009), using a maximum signal correlation coefficient CC between a reference signal $u(t)$ and a perturbed signal $\tilde{u}(t)$, where t_1 and t_2 mark the time window in which the velocity change is derived. Equation (1) states the basic equation of the stretching technique (Sens-Schönfelder & Wegler 2006) to determine relative velocity changes dv/v .

$$CC(\varepsilon) = \frac{\int_{t_1}^{t_2} u(t)\tilde{u}(t(1-\varepsilon))dt}{\sqrt{\int_{t_1}^{t_2} u^2(t)dt \int_{t_1}^{t_2} \tilde{u}^2(t(1-\varepsilon))dt}} \quad (1)$$

The exceptional sensitivity, together with the signal repeatability, led to a large number of studies about detecting and locating weak changes in concrete using CWI dealing with the ultrasonic wave speed, affected by thermal, mechanical and chemical damage (Planès & Larose 2013). However, these impacts may affect a structure at the same time and add various terms to the total velocity change. This superimposition is a big challenge regarding the interpretation of the velocity variation as their exact separation into the single effects is unknown. Irreversible changes are of particular interest because they are generally synonymous to occurring damage in the structure. Therefore, another aspect of interpreting the velocity variation is the separation between changes that are reversible and the irreversible ones that indicate damage. Figure 2 shows different impacts on engineering structures that affect the properties of coda waves.

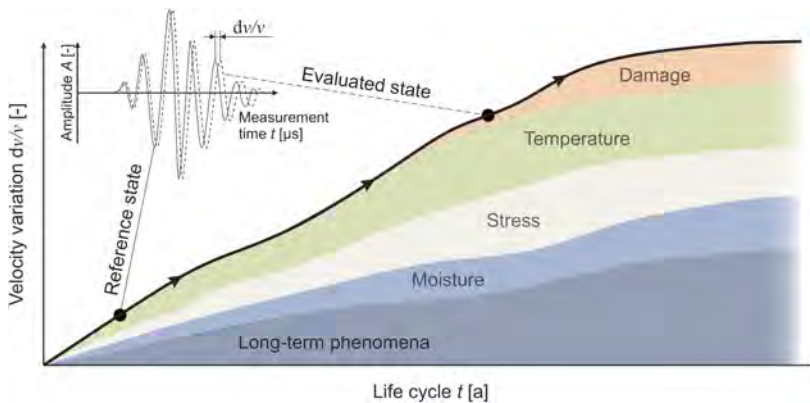


Figure 2. Summarized effects on the velocity variation dv/v between two ultrasonic signals propagating in a structure at a reference state and at the evaluated state. The term long-term phenomena aggregates further concrete-specific phenomena, e.g., shrinkage, creep, carbonation, and corrosion, whereas the remaining effects act on a short-term scale.

3 RESULTS

For each sender-receiver pair in a structure, we can collect one ultrasonic signal at a time and determine the total velocity change between the measurements at a reference state and the evaluated state. The measured velocity variation can be expressed as a sum of three terms that change at different rates over time as in Equation (2). The transient term covers the impacts from state changes due to temperature, stress, or moisture, where the changes in dv/v are expected immediately, e.g., for stress, or over a few hours up to days, e.g., for temperature and moisture in large structures. A second stationary term includes velocity variations that steadily develop over longer periods, in the range of over months or years. This term is affected by long-term strain or chemical changes of the phase composition. In this formulation, the first two terms are considered reversible, whereas a third term includes changes that are induced by any irreversible material change. Therefore, any value greater than zero is an indicator for damage in the structure.

$$\left(\frac{dv}{v}\right)_{measured} = \left(\frac{dv}{v}\right)_{transient} + \left(\frac{dv}{v}\right)_{stationary} + \left(\frac{dv}{v}\right)_{irreversible} \quad (2)$$

The individual effects on Equation (2), coming from the structural system, are presented in greater detail in Figure 3.

The left side of Equation (2) is the result of ultrasonic measurements followed by the calculation of dv/v , while the irreversible term on the right side is usually the critical one that should be determined to identify any damage in the structure. To solve the equation, both the remaining terms must be evaluated in detail. Equation (3) further breaks down the transient term of dv/v , where individual effects of temperature T , saturation degree S of the material, i.e., the pore space, and stress σ are included. In this notation, x_0 refers to the value of each variable at the reference state, while Δx refers to its change.

$$\left(\frac{dv}{v}\right)_{transient} = \frac{dv}{v}(T_0, \Delta T) + \frac{dv}{v}(S_0, \Delta S) + \frac{dv}{v}(\sigma_0, \Delta\sigma) \tag{3}$$

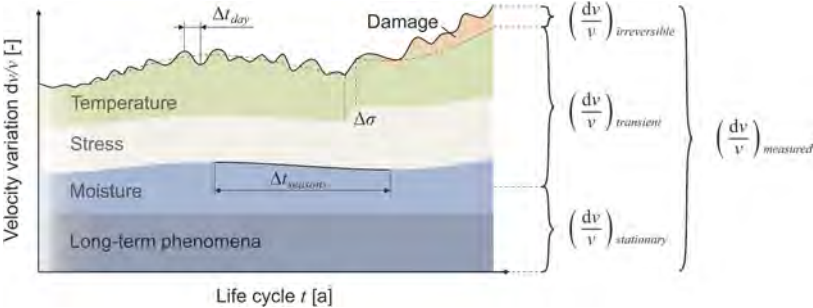


Figure 3. Summarized effects on the velocity variation dv/v refined from Figure 2. Originating from the measured total velocity variation, dv/v splits into three terms according to Equation (2). Transient changes occur on a short time scale, whereas stationary changes are only visible over a long period. Assuming that these two terms can be predicted, any remainder can be considered an irreversible change that indicates damage in the structure.

Both temperature ($T_0, \Delta T$) and saturation degree ($S_0, \Delta S$) are variables that must be considered together, as they affect each other due to the temperature-affected moisture content of the structure’s environment and the moisture gradient that arises in the material. It is important to note that the saturation degree of the pore space affects the anelastic seismic properties of concrete. However, S is usually not directly measurable and must be expressed by external variables, e.g., relative humidity RH or electric resistance of the electrolyte Ω . Equation (3) emphasizes the impact on dv/v as a result of the state change of the material due to the saturation degree rather than using an external variable, for which a delayed system response should be considered.

The relationship between temperature and dv/v is quasi-linear for the same water-to-cement ratio (Larose et al. 2006; Wunderlich & Niederleithinger 2012). For relative humidity variation, a steady decrease of dv/v develops for an increase of water in the pore system between 35%RH up to 80%RH at a reference temperature of 20°C (Diewald 2023). Furthermore, a saturation degree above this value can disrupt the trend, where dv/v increases compared to the lower values of RH . Combining all observations and the additional consideration of the water-to-cement ratio, which influences the pore space, leads to a third order polynomial model that covers the variation of the three variables and their effect on the velocity variation dv/v at a high degree of confidence.

The saturation degree exposes particularly well the fact that any relationship stated for the individual arguments depends on the material composition as the amount of water in the pore space is also affected by the volume of the pore space which again depends on the water-to-cement ratio w/c . We showed this in the polynomial model that had dominant terms depending on w/c . Furthermore, also elastic, anelastic and scattering properties may change for different material mixes. This implies that any experimentally determined relationship for both the transient and the stationary terms is only valid for the particular material. The relationships between the transient and stationary impacts on the velocity variation can either be

experimentally determined for the particular case, for which Equation (2) should be solved, or predicted by material models in combination with wave propagation simulations (Vu et al. 2021a; Vu et al. 2021b; Saenger et al. 2021; Holla et al. 2021). Such models can be calibrated by means of the physical relationships and the data from experimental studies with the objective to be transferable for arbitrary material mixes. Nevertheless to compensate for velocity changes due to temperature and the saturation degree, the T and S of the structure must be known and measured on a continuous basis, e.g., in the same grid as ultrasonic transducers are embedded.

The relationship between stress ($\sigma_0, \Delta\sigma$) and the velocity variation is also affected by the material mix as the crack formation process changes for different material mixes. A stress increase can be approximated by a linear relationship in the elastic range up to 30% of the material strength for both compression and tension, while an irreversible velocity decrease occurs above this load level (Diewald, Epple, Kraenkel, Gehlen, & Niederleithinger 2022).

The influence of the cross correlation value CC on the calculation of dv/v must also be considered and its computation should be standardized during the entire evaluation cycle (Diewald et al. 2022). This becomes especially important for major changes in the structural system, i.e., irreversible ones or long-term changes with a great effect on the ultrasonic waveforms. Equation (4) provides the arguments of the long-term stationary term, where the effects of strain ε and chemical phase changes Ψ are included.

$$\left(\frac{dv}{v}\right)_{stationary} = \frac{dv}{v}(\varepsilon_0, \Delta\varepsilon) + \frac{dv}{v}(\Psi_0, \Delta\Psi) \quad (4)$$

Typical phenomena that induce long-term strain ($\varepsilon_0, \Delta\varepsilon$) in concrete are shrinkage and creep, where the resulting strains have an impact on the velocity variation in addition to immediate change of dv/v due to stress. It was shown that the characteristic shrinkage and creep behavior of concrete can be measured for several load levels using CWI (Diewald et al. 2022). Consequently, these changes must be considered especially for long-term state comparisons using CWI and, thus, appear in in the stationary term.

Furthermore, the velocity variation is affected by chemical phase changes ($\Psi_0, \Delta\Psi$). Phase changes are a continuous process in cementitious materials, whereas two types of phase changes should be distinguished here. First, early hydration is the most extreme case, during which cement and water react, develop strength, and develop to the solid form cement paste. It was shown that the velocity variation development using stepwisely compared ultrasonic signals correlates with the dissolution of the main clinker phases over time (Diewald et al. 2022). CWI shows similarly high accuracy in detecting characteristic hydration periods compared to conventional techniques, e.g., heat flow calorimetry and Vicat test, but also to a thermodynamic model of early-age phase formation using CemGEMS. Although the study showed that ultrasonic velocity changes can detect the early-age strength development of concrete during the early hydration, CWI is usually designed to detect weak changes in a structural concrete system as expressed by Equation (2). Hence, phase changes addressed in Equation 4 are rather long-term and must be considered as a source for velocity changes.

4 CONCLUSIONS

In order to make Equation (2) fully interpretable, we will need material models that can cover all the summarized effects for individual material mixes with arbitrary scattering properties. In turn, the scattering properties should be defined by material parameters, e.g., elasticity, pore and aggregate size, which can be easily determined for each concrete. As soon as the individual arguments for the transient and the stationary terms can be predicted by concrete models, the total measured velocity variation may be evaluated regarding any remaining value that can be assigned to the irreversible term as an indicator for damage.

However, this requirement only exists, when a full interpretation becomes necessary. This is mostly the case regarding the identification of long-term damage development together with the separation from other long-term phenomena that are non-destructive. For the identification of spontaneous or short-term damage development in general, CWI is a suitable technology due to its sensitivity to changes in the microstructure, even if the transient and the stationary terms or the scattering properties are not fully known. In this case, even without an exact interpretation of the causes for velocity changes, CWI is applicable as an early-warning system.

ACKNOWLEDGEMENTS

Funded by the Deutsche Forschungsgemeinschaft (DFG, German Research Foundation) - 398216472. This research was conducted in the framework of the research unit *Concrete Damage Assessment by Coda Waves (CoDA)*.

REFERENCES

- Aki, K. (1969, 1). Analysis of the seismic coda of local earthquakes as scattered waves. *Journal of Geophysical Research* 74: 615–631.
- Aki, K. & Chouet, B. (1975, 8). Origin of coda waves: Source, attenuation, and scattering effects. *Journal of Geophysical Research* 80: 3322–3342.
- BASt (2021). BASt - Brückenstatistik. <https://www.bast.de/DE/Statistik/Bruecken/Brueckenstatistik.html>. Accessed: 2023-01-06.
- Breit, W., Dauberschmidt, C., Gehlen, C., Sodeikat, C., Taffe, A., & Wiens, U. (2011, 5). Zum ansatz eines kritischen chloridgehaltes bei stahlbetonbauwerken. *Beton- und Stahlbetonbau* 106: 290–298.
- Diewald, F. (2023). Unpublished: Impact of microstructural changes in concrete on coda waves. *Doctoral Dissertation, Technical University of Munich*.
- Diewald, F., Epple, N., Kraenkel, T., Gehlen, C., & Niederleithinger, E. (2022, 8). Impact of external mechanical loads on coda waves in concrete. *Materials* 2022, Vol. 15, Page 5482 15: 5482.
- Diewald, F., Irbe, L., Kraenkel, T., Machner, A., & Gehlen, C. (2022). Monitoring early cement hydration with coda wave interferometry. *Proceedings of the 13th International Workshop on Structural Health Monitoring*: 5482.
- Gehlen, C. (2000). Probabilistische lebensdauerbemessung von stahlbetonbauwerken – zuverlässigkeitsbetrachtungen zur wirksamen vermeidung von bewehrungskorrosion. *Doctoral Dissertation, RWTH Aachen*.
- Gehlen, C., Greve-Dierfeld, S. V., & Ostermink, K. (2010, 1). Modelling of ageing and corrosion processes in reinforced concrete structures. *Non-Destructive Evaluation of Reinforced Concrete Structures: Deterioration Processes and Standard Test Methods*: 57–81.
- Hadziioannou, C., Larose, E., Coutant, O., Roux, P., & Campillo, M. (2009). Stability of monitoring weak changes in multiply scattering media with ambient noise correlation: laboratory experiments. *The Journal of the Acoustical Society of America* 125(6): 3688–3695.
- Holla, V., Vu, G., Timothy, J. J., Diewald, F., Gehlen, C., & Meschke, G. (2021). Computational generation of virtual concrete mesostructures. *Materials* 14(14).
- Larose, E., Rosny, J. D., Margerin, L., Anache, D., Gouedard, P., Campillo, M., & Tiggelen, B. V. (2006, 1). Observation of multiple scattering of khz vibrations in a concrete structure and application to monitoring weak changes. *Physical Review E - Statistical, Nonlinear, and Soft Matter Physics* 73: 016609.
- Planès, T. & Larose, E. (2013, 11). A review of ultrasonic coda wave interferometry in concrete. *Cement and Concrete Research* 53: 248–255.
- Saenger, E. H., Finger, C., Karimpouli, S., & Tahmasebi, P. (2021). Single-station coda wave interferometry: A feasibility study using machine learning. *Materials* 14(13).
- Sens-Schönfelder, C. & Wegler, U. (2006, nov). Passive image interferometry and seasonal variations of seismic velocities at Merapi Volcano, Indonesia. *Geophysical Research Letters* 33(21).
- Snieder, R. (2006). The theory of coda wave interferometry. *Pure and Applied Geophysics* 163(2-3): 455–473
- Snieder, R., Grêt, A., Douma, H., & Scales, J. (2002). Coda wave interferometry for estimating nonlinear behavior in seismic velocity. *Science (New York, N. Y.)* 295(5563): 2253–2255.

- Snieder, R., Grêt, A., Douma, H., & Scales, J. (2002, mar). Coda wave interferometry for estimating non-linear behavior in seismic velocity. *Science* 295(5563): 2253–2255.
- von Greve-Dierfeld, S. & Gehlen, C. (2016a, 9). Performance based durability design, carbonation part 1 – benchmarking of european present design rules. *Structural Concrete* 17: 309–328.
- von Greve-Dierfeld, S. & Gehlen, C. (2016b, 12). Performance-based durability design, carbonation part 2 – classification of concrete. *Structural Concrete* 17: 523–532.
- von Greve-Dierfeld, S. & Gehlen, C. (2016c, 12). Performance-based durability design, carbonation, part 3: Psf approach and a proposal for the revision of deemed-to-satisfy rules. *Structural Concrete* 17: 718–728.
- Vu, G., Diewald, F., Timothy, J. J., Gehlen, C., & Meschke, G. (2021a). Reduced order multiscale simulation of diffuse damage in concrete. *Materials* 14(14).
- Vu, G., Diewald, F., Timothy, J. J., Gehlen, C., & Meschke, G. (2021b, 7). Reduced order multiscale simulation of diffuse damage in concrete. *Materials* 2021, Vol. 14, Page 3830 14: 3830.
- Wunderlich, C. & Niederleithinger, E. (2012). Evaluation of temperature influence on ultrasound velocity in concrete by coda wave interferometry. *RILEM Bookseries* 6: 227–232.

A virtual lab for damage identification in concrete using coda waves

G. Vu & G. Meschke

Institute for Structural Mechanics, Ruhr University Bochum, Germany

J.J. Timothy

Centre for Building Materials (cbm), Technical University of Munich, Germany

E.H. Saenger

Bochum University of Applied Sciences, Germany; Fraunhofer IEG, Germany; Ruhr University Bochum, Germany

ABSTRACT: Identifying and preventing damage in concrete structures at an early stage of material degradation can significantly reduce costs associated with the maintenance and repair of concrete infrastructure. Weak material degradation, such as load-induced initiation and propagation of microcracks, is a precursor of localized damage (macrocracking) in concrete structures and can be detected by means of multiple-scattered late arriving ultrasonic signals, also called coda waves. In order to reliably identify and quantify damage initiation and propagation using coda waves, a systematic tool that translates ultrasonic coda signals into the state of damage is required. To this end, we systematically investigate the effect of material degradation on the coda variations at the specimen level using a combination of multiscale computational modeling, forward wave propagation simulations and feature extraction. At the specimen scale, damage initiation and propagation in realistic mesoscale concrete models is simulated using a virtual lab and a novel reduced order multiscale method. The concrete specimens subjected to specific level of damage in the virtual lab are subsequently analyzed by wave propagation simulations. Finally, a strategy for using specimen scale information for predicting the state of damage at the structural scale will be presented.

1 INTRODUCTION

Throughout their service life, concrete structures undergo a gradual degradation process as they are constantly exposed to a wide spectrum of environmental and mechanical loads. These influences promote the growth of pre-existing defects in concrete. Without appropriate maintenance of the structure, microcrack growth might lead to microcrack coalescence and crack localization and ultimately to complete loss of load bearing capacity of a concrete structure. In this regard, detection of early stage degradation of concrete structures can help reduce costs associated with maintenance and repair of concrete structures (Gharehbaghi et al., 2021, Inaudi 2009). This can be potentially achieved by the use of coda wave based monitoring system as it is highly sensitive to weak changes.

Coda Wave Interferometry (CWI) (Snieder et al. 2002) is a technique used in seismology that utilizes the late arrival part of an recorded ultrasonic signal (typically called coda waves). On one hand, this part of the signal contains rich information of concrete microstructure thanks to the multiple sampling process within the concrete medium. By analyzing the evolution of coda features, information of subtle material changes can be extracted. On the other hand, the high sensitivity of the coda wave constitutes a challenge in reliably translating the variation of coda waves into the corresponding level of damage in concrete structures. Various experimental

investigations have been conducted to explore the potential of CWI to quantify load induced damage in concrete. Yet, under laboratory environment, two underlying issues arise: damage quantification and effect discrimination.

Therefore, numerical simulations can provide insights regarding the physical phenomena and consequently help establish the relationship of damage and coda variations quantitatively. In this contribution, we present a computational framework that simulates 1) load induced distributed damage in concrete, and 2) wave propagation process in an affected concrete specimen. The usefulness of the proposed framework is demonstrated through data generation for ultrasonic waves based investigation of damage.

2 CONCEPT OF CODA BASED VIRTUAL LAB FOR DAMAGE IDENTIFICATION IN CONCRETE

The design of a coda based virtual lab is analogous to a standard setup for non-destructive evaluation of concrete specimens in laboratory condition (see, e.g., Diewald et al. 2022, Stähler et al. 2011). We designed our simulation workflow as follows: the first step is called Data Generation, in which simulated coda signals are generated for various damage conditions of a concrete specimen by means of mechanical and wave propagation simulations. Here, the uniaxial compression load case is considered. In the second step–Feature Extraction, the feature of simulated signals at increasing damage levels obtained from the CWI operation is further validated with the experimental data. See Figure 1 for a schematic illustration of the workflow.

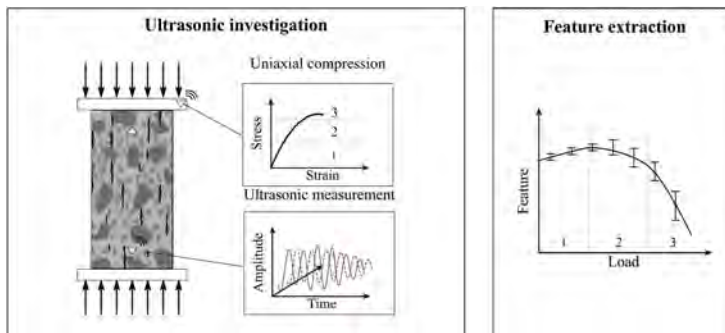


Figure 1. Schematic illustration of the virtual concrete laboratory.

3 UNIAXIAL COMPRESSION SIMULATION OF LOAD INDUCED DISTRIBUTED DAMAGE IN CONCRETE

Under uniaxial compression, damage process in concrete involves various complex mechanisms taking place simultaneously across scales (Van Mier 1998). The complex behavior originates from the heterogeneous nature of concrete ranging from nanometer scale to decimeter scale. Particularly, at microscopic scale (approx. 10^{-3} m), mortar consists of hardened cement matrix hosting sand particles, pores, as well as defects known as microcracks. At the meso-level, concrete consists of irregular coarse aggregates randomly distributed in a mortar matrix. As a result, concrete under loading exhibits a highly perturbed stress field. Such stress fluctuation causes microcracks to first deform and subsequently propagate, playing a governing role in the pre-peak behavior of concrete.

In this regard, from the modeling viewpoint, it is important to consider these microstructure details and its evolution induced by the external load. Therefore, to simulate distributed damage in concrete, we adopted the reduced order multiscale modeling strategy proposed in Vu et al. 2021a. The schematic illustration of the multiscale model is presented in Figure 2.

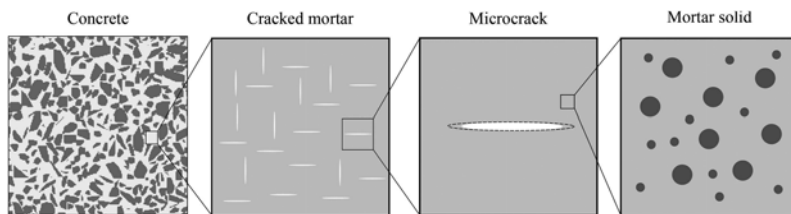


Figure 2. Schematic illustration of the multiscale model showing distributed penny-shaped microcracks and coarse aggregates embedded in the mortar matrix made of hardened cement paste and sand.

3.1 Methodology

In general, a multiscale modeling framework requires two primary operations to efficiently transfer information across scales: *Localization* and *Homogenization*. This approach mitigates the need of relying on conventional empirical constitutive models and enables the generation of microstructure-property relationships (Matouš et al. 2016). If the microstructure is explicitly resolved, such a multiscale modeling scheme is generally computationally demanding as one has to solve a large number of sub-problems at each material point. Thus, it is often appropriate to employ a model order reduction technique. In the proposed multiscale approach for modeling concrete, we use a K-means clustering based model reduction (Liu et al. 2016) to group material points (voxels) that have a similar mechanical behavior into a finite number of groups denoted as clusters. Subsequently, a microscopic continuum micromechanics based sub-problem is incorporated to each cluster during numerical simulation. In the *Localization* step, given the applied macroscopic strain, the mesoscopic strain field is computed by means of the Fast Fourier Transform (FFT) based computational homogenization method (Moulinec & Suquet 1994). This information (mesoscopic strain tensor) is transferred to the microscopic scale, where the evolution of microcrack topology is modeled using a damage law based on the framework of Linear Elastic Fracture Mechanics (LEFM) (Pichler et al. 2007, Iskhakov et al. 2021). In the *Homogenization* step, the effect of evolving microcracks results in the change of the effective secant stiffness tensor, computed using the modified Interaction Direct Derivative (IDD).

3.2 Mesomodel of concrete

One of the important simulation inputs is the mesoscopic description of concrete. To generate a highly realistic virtual specimen, we used the computational tool developed by co-authors. Input of the mentioned tool includes the measured size distribution of coarse aggregates and geometrical description of each aggregate family (e.g., size, aspect ratio, smoothness, concave surface parameters). The generated mesomodel is also periodic, which shows clear advantage in computational homogenization and in the forward wave simulations. Further details regarding the algorithmic implementations can be found at (Holla et al. 2021).

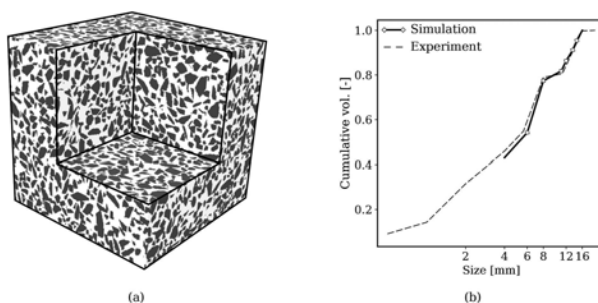


Figure 3. Visualization of the simulated concrete specimen of standard AB16 (a) and its corresponding grain size distribution.

Concrete specimens of size 10 cm, standard AB16 were considered for the analysis. The high-fidelity concrete specimen is discretized using 201^3 voxels of size 0.5 mm (Figures 3 a, b). Moreover, via k-means based model reduction procedure, the information of the meso-model is compressed into 72 clusters: 64 clusters of mortar matrix, and 8 clusters of quartzitic aggregates. Also, the material parameters for each constituent at this scale are listed in Table 1.

Table 1. Material parameters of quartzitic aggregate, mortar matrix ($\varphi_{quartz}=43.95\%$), and concrete standard AB16.

Material parameter	Quartzitic aggregate	Mortar matrix	Concrete
Young's Modulus E [GPa]	84.6	30.1	48.03
Poisson's ratio ν [-]	0.12	0.19	0.15
Density ρ [kg/m^3]	2650	2104	2364

3.3 Micro-parameters of mortar cementitious material

Regarding the material and numerical parameters, we used parameters provided in (Vu et al. 2021a). It is to be noted that, the model has been validated with the experimental data. The microcrack parameters and the corresponding mechanical properties of mortar matrix used in the numerical simulations are summarized in Table 2.

Table 2. Microcrack geometrical parameters.

Microcrack radius	a	0.023	mm
Microcrack half thickness	c	0.001	mm
Total microcrack volume fraction	φ_{crack}	8.3	%
Solid mortar's fracture energy	g_f	0.661	N/mm

3.4 Uniaxial compression

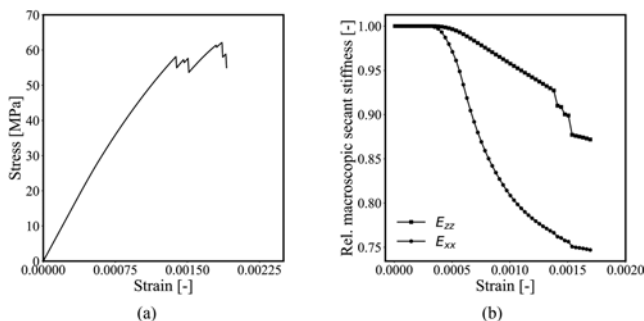


Figure 4. Stress-strain response obtained from the numerical simulation (a), and the evolution of secant stiffnesses (b).

The clustered virtual sample is then subjected to the uniaxial compression test with the strain increment of 10^{-5} . The stress-strain curve obtained from the simulation is presented in Figure 4 a. From the simulation, one can specify 3 pre-peak regimes: elastic deformation, microcrack growth, and microcrack coalescence. The elastic regime is characterized by the elastic relation between global stress and strain. The microcracking regime starts at 15.89 MPa (20.4% f_c). At this stage, microcracks whose plane parallel to major stress axis grows, resulting in a steady reduction of the axial secant stiffness. At the near peak regime (45-55 MPa), concrete undergoes a rapid reduction in stiffness. This can be attributed to the coalescence of microcracks and crack localization. Also from Figure 4b, it can be seen that, the lateral secant stiffnesses reduce at much faster rate than the longitudinal one due to the selective direction of propagation of the microcracks.

At a given load step, local information of the degraded secant stiffness tensor is exported and serves as input for the forward wave propagation simulations.

4 SIMULATION OF ULTRASONIC WAVES IN CONCRETE MEDIUM

In this section, we demonstrate the use of the wave propagation simulation for generating simulated coda signals. These simulated signals, once validated with measured ones, can be utilized for coda wave based investigations and help the development of a data-driven damage classifier, especially when measured data are not often available for training. Moreover, another advantage of numerical modeling is that damage information is known at each simulation step and therefore reliable damage labeling is possible.

4.1 Simulation setup

The simulation setup is analogous to the setup for ultrasonic investigation of concrete under uniaxial compression described in Diewald et al. 2022. The test subjects are prism concrete samples of $10 \times 10 \times 40$ cm. Two transducers are embedded at the center axis, located at 30 cm away from each others and at 5 cm distance to the nearest boundary. The high slenderness ratio is desired to keep the distance between the transducers longer than the wave length of the excitation source (60 kHz).

This setup can be realized by stacking 4 periodic cubic concrete samples from previous simulation in the vertical direction. It is important to note that, the frictionless boundary condition can be applied to impose the true uniaxial compression stress state. As such, the pre peak behavior of concrete is then independent of the specimen slenderness (Van Vliet & Van Mier 1996, Van Mier et al. 1997).

Ultrasonic 3D wave simulations are performed using a rotated staggered-grid finite-difference scheme (Saenger et al. 2000) over 40,000 time steps (2 ms duration), with the gridsize of 0.5 mm and the time step size of 5×10^{-8} s. The mentioned scheme is ideal for simulating the wave field in heterogeneous medium and has been successfully applied to concrete as demonstrated in Kocur et al. (2010). To simulate the attenuation phenomenon observed in ultrasonic measurement, a specific viscoelastic model is used and thus 4 additional parameters are introduced. Frequency-dependent attenuation is simulated with 2 Maxwell bodies with $\gamma_1 = 0.04$, $\gamma_2 = 0.1$ (defining $\bar{Y}_m^{ijkl} = c_{ijkl} \gamma_m$) at frequencies $\omega_1 = 2\pi 20$ kHz, $\omega_2 = 2\pi 1$ MHz, respectively. See Equation (4) of Saenger et al. (2005) for further details regarding the parameters. In addition, to simulate reflective boundary, additional vacuum layers have been added to all sides of the concrete model. For the simulation of concrete at the initial condition, the material parameters for each phase are taken from Table 1. In the remaining 12 damaged cases, the stiffness is computed by taking the average of lateral and longitudinal stiffnesses. Whereas, the stiffness and Poisson's ratio of vacuum are set to zero and its density is set to 10^{-5} kg/m^3 .

Following the approach outlined in (Finger et al. 2021), the excitation source is a moment tensor source with 2 non-zero components (xx and zz). The wavelet form was also taken from (Finger et al. 2021) with a central frequency of 60 kHz. This is within the recommended frequency range for ultrasonic testing in concrete (Fröjd & Ulriksen 2017).

Multiple receivers are considered in the analysis. Here, a total of 27 receivers positioned at 3 zz-planes of 27.5, 30.0, 32.5 cm distance to the source, respectively. The spacing between receivers on the same planes is 2.5 cm. The simulated signals are the average of temporal displacement in x, y, and z directions. An exemplary numerical setup is illustrated in Figure 5.

5 CODA WAVE INTERFEROMETRY (CWI) ANALYSIS

5.1 The CWI-method

Given 2 ultrasonic signals recorded from a fixed source and a fixed receiver, CWI can be applied on their coda parts to evaluate the similarity of two signals. In this process, changes in

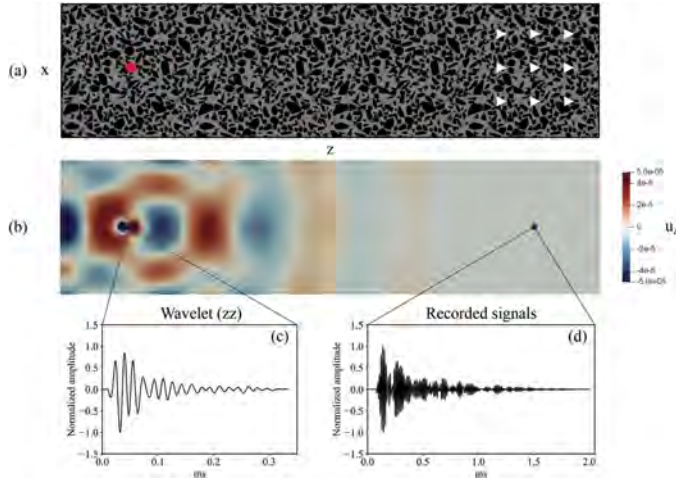


Figure 5. Summary of a 3D simulation setup. a) Visualization of the model at mid-plane ($y = 5$ cm), aggregate phase and mortar phase are marked in black and grey, respectively, red circle denotes source location ($z = 5$ cm), white triangles denote receiver locations. b) Displacement (z) snapshot at 0.04 ms. c, d) Visualization of the pulse signal used to induce a seismic wavefield in concrete medium, and the recorded signal at location $x = y = 5$ cm, $z = 35$ cm.

the examined medium can be detected. Various CWI methods have been proposed in recent decades. In most methods, velocity variation and cross correlation features are calculated. In our analysis, the stretching technique (Niederleithinger et al. 2018) is adopted as the method is stable regardless of the choice of the time-window. Given two signals $u_u(t)$, $u_p(t)$, evaluated within the time window $[t_1, t_2]$, the relative velocity change $\frac{dv}{v}$ is the value of the stretch factor ε that maximizes the cross correlation of two signals and is calculated as:

$$\frac{dv}{v} = \operatorname{argmax}_{\varepsilon \in \mathbb{R}} CC(\varepsilon) = \operatorname{argmax}_{\varepsilon \in \mathbb{R}} \frac{\int_{t_1}^{t_2} u_u(t) u_p(t(1 + \varepsilon)) dt}{\sqrt{\int_{t_1}^{t_2} u_u^2(t) dt \int_{t_1}^{t_2} u_p^2(t(1 + \varepsilon)) dt}}, \quad (1)$$

Here u_u and u_p denotes signals travelling through unperturbed and perturbed medium, respectively.

5.2 Numerical results

The stretching method has been applied for all 27 sender-receiver pairs over 13 load steps (1 intact, and 12 affected conditions). The time window $[0, 1]$ ms was selected for the evaluation, this includes both direct and coda parts of the ultrasonic signal.

Figure 6 shows the correlation of $\frac{dv}{v}$ and the applied stress. Three stages can be identified, marked in Figure 6. In the elastic stage, the simulation could not reproduce the typical increase in wave velocity typically seen in the experiment, this is because the current model is not yet accounting for microcrack closure. In stage 2 (18–32 MPa), we see a reduction of $\frac{dv}{v}$ at the rate of 0.0041 MPa^{-1} due to diffuse microcracking. At stage 3, measurement at different receiver locations shows a higher deviation as compared to stage 2. This could imply an uncertainty and robustness of CWI technique at higher load level, which should no longer be considered a weak change. Overall, the trend reproduced from the simulation is similar to the experimental range reported in He et al. 2022. Moreover, an almost linear correlation between $\frac{dv}{v}$ and the global stiffness reduction can be seen in Figure 6 b. The rate of change is 0.799 with maximum standard deviation of 0.988.

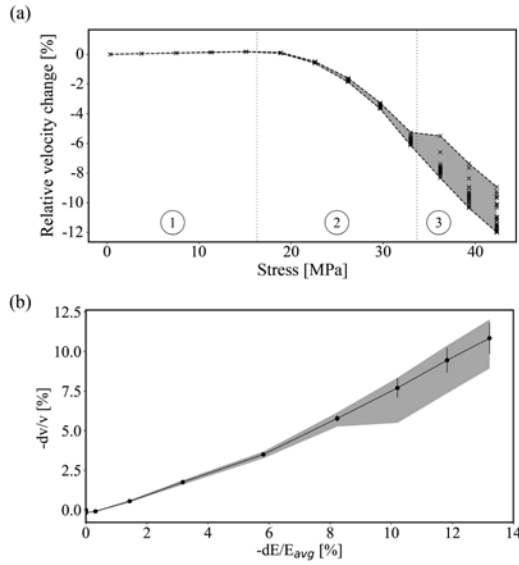


Figure 6. a) The relative velocity change $\frac{dv}{v}$ in relation with the applied stress. Each mark ‘x’ represents measurement from one transducer-receiver pair. In total, 351 $\frac{dv}{v}$ measurements were calculated. b) Correlation of reduction in velocity and the reduction in average stiffness.

6 CONCLUSIONS

In this contribution, we demonstrated the use of a computational framework for damage evaluation of concrete using ultrasonic waves. First, mechanical simulations were performed using a multiscale reduced order modeling methodology. It was followed by performing wave propagation simulation in the concrete specimen at different damage levels. The recorded signals were analyzed by means of the CWI method and a relation between the relative velocity change and global stiffness change was derived. Based on the numerical results, the following remarks can be drawn:

- A virtual environment for ultrasonic testing has been established. The proposed methodology is able to reproduce experimentally observed phenomena and can be used to generate a large synthetic dataset for data-driven damage classification.
- From the structural health monitoring viewpoint, one can evaluate the level of global material degradation in concrete using CWI method, provided that the type of damage is known a-priori. In general, concrete is highly resistant to compression loads and can sustain a prolonged microcracking stage. While under uniaxial tension, concrete fails at much lower threshold of microcracking (see Diewald et al. 2022).

To realize a robust tool for structural health monitoring at the structural level, the following aspects should be taken into account:

- Material uncertainty has to be introduced into the numerical model, for instance, by simulating more concrete samples with varied grain size distribution, strength, and stiffness.
- Damage in tension should also be considered, and a strategy to distinguish critical damage threshold in tension and compression has to be formulated.
- It is important to analyze the effect of the geometrical condition on the signals features. This can be achieved by using absorbing boundary condition in the wave simulations.

ACKNOWLEDGEMENT

The authors would like to thank the German Research Foundation (DFG) for their financial support in the framework of Subprojects RUB1 and BU of the Research Unit FOR 2825.

REFERENCES

- Diewald, F., Epple, N., Kraenkel, T., Gehlen, C. and Niederleithinger, E., 2022. Impact of External Mechanical Loads on Coda Waves in Concrete. *Materials*, 15(16), p.5482.
- Finger, C., Saydak, L., Vu, G., Timothy, J.J., Meschke, G. and Saenger, E.H., 2021. Sensitivity of Ultrasonic Coda Wave Interferometry to Material Damage—Observations from a Virtual Concrete Lab. *Materials*, 14(14), p.4033.
- Gharehbaghi, V.R., Noroozinejad Farsangi, E., Noori, M., Yang, T.Y., Li, S., Nguyen, A., Málaga-Chuquitaype, C., Gardoni, P. and Mirjalili, S., 2021. A critical review on structural health monitoring: definitions, methods, and perspectives. *Archives of Computational Methods in Engineering*, pp.1–27.
- Fröjd, P. and Ulriksen, P., 2017. Frequency selection for coda wave interferometry in concrete structures. *Ultrasonics*, 80, pp.1–8.
- He, Y., Song, L., Xue, K., Liu, S., Li, H., Yang, W. and Huang, J., 2022. Ultrasonic Coda Wave Experiment and Simulation of Concrete Damage Process under Uniaxial Compression. *Buildings*, 12(5), p.514.
- Holla, V., Vu, G., Timothy, J.J., Diewald, F., Gehlen, C. and Meschke, G., 2021. Computational generation of virtual concrete mesostructures. *Materials*, 14(14), p.3782.
- Inaudi, D., 2009. Structural Health Monitoring of bridges: general issues and applications. In *Structural health monitoring of civil infrastructure systems* (pp. 339–370). Woodhead Publishing.
- Iskhakov, T., Giebson, C., Timothy, J.J., Ludwig, H.M. and Meschke, G., 2021. Deterioration of concrete due to ASR: Experiments and multiscale modeling. *Cement and Concrete Research*, 149, p.106575.
- Kocur, G.K., Saenger, E.H. and Vogel, T., 2010. Elastic wave propagation in a segmented X-ray computed tomography model of a concrete specimen. *Construction and Building Materials*, 24(12), pp.2393–2400.
- Liu, Z., Bessa, M.A. and Liu, W.K., 2016. Self-consistent clustering analysis: an efficient multi-scale scheme for inelastic heterogeneous materials. *Computer Methods in Applied Mechanics and Engineering*, 306, pp.319–341.
- Matouš, K., Geers, M.G., Kouznetsova, V.G. and Gillman, A., 2017. A review of predictive nonlinear theories for multiscale modeling of heterogeneous materials. *Journal of Computational Physics*, 330, pp.192–220.
- Moulinec, H. and Suquet, P., 1994. A fast numerical method for computing the linear and nonlinear mechanical properties of composites. *Comptes Rendus de l'Académie des sciences. Série II. Mécanique, physique, chimie, astronomie*.
- Niederleithinger, E., Wang, X., Herbrand, M. and Müller, M., 2018. Processing ultrasonic data by coda wave interferometry to monitor load tests of concrete beams. *Sensors*, 18(6), p.1971.
- Pichler, B., Hellmich, C. and A. Mang, H., 2007. A combined fracture-micromechanics model for tensile strain-softening in brittle materials, based on propagation of interacting microcracks. *International Journal for Numerical and Analytical Methods in Geomechanics*, 31(2), pp.111–132.
- Saenger, E.H., Gold, N. and Shapiro, S.A., 2000. Modeling the propagation of elastic waves using a modified finite-difference grid. *Wave motion*, 31(1), pp.77–92.
- Saenger E.H., Shapiro S.A. and Keehm Y., 2005: Seismic effects of viscous Biot-coupling: Finite difference simulations on micro-scale, *Geophysical Research Letters* 32, L14310.
- Snieder, R., Grêt, A., Douma, H. and Scales, J., 2002. Coda wave interferometry for estimating nonlinear behavior in seismic velocity. *Science*, 295(5563)
- Stähler, S.C., Sens-Schönfelder, C. and Niederleithinger, E., 2011. Monitoring stress changes in a concrete bridge with coda wave interferometry. *The Journal of the Acoustical Society of America*, 129(4), pp.1945–1952.
- Van Mier, J.G.M., Shah, S.P., Arnaud, M., Balaýssac, J.P., Bascoul, A., Choi, S., Dasenbrock, D., Ferrara, G., French, C., Gobbi, M.E. and Karihaloo, B.L., 1997. Strain-softening of concrete in uniaxial compression. *Materials and Structures*, 30(4), pp.195–209.
- Van Mier, J.G.M., 1998. Failure of concrete under uniaxial compression: An overview. *Fracture mechanics of concrete structures*, 2, pp.1169–1182.
- Van Vliet, M.A. and Van Mier, J.M., 1996. Experimental investigation of concrete fracture under uniaxial compression. *Mechanics of Cohesive-frictional Materials: An International Journal on Experiments, Modelling and Computation of Materials and Structures*, 1(1), pp.115–127.
- Vu, G., Diewald, F., Timothy, J.J., Gehlen, C. and Meschke, G., 2021a. Reduced order multiscale simulation of diffuse damage in concrete. *Materials*, 14(14), p.3830.
- Vu, G., Timothy, J.J., Singh, D.S., Saydak, L.A., Saenger, E.H. and Meschke, G., 2021b. Numerical simulation-based damage identification in concrete. *Modelling*, 2(3), p.19.

The hydration of cement paste: Thermodynamics driven multi-scale modeling of elastic properties and coda wave interferometry based monitoring

E. Jäggle, J.J. Timothy, F. Diewald, T. Kränkel & C. Gehlen

Chair of Materials Science and Testing, Department of Materials Engineering, TUM School of Engineering and Design, Centre for Building Materials, Technical University of Munich, Munich, Bavaria, Germany

A. Machner

Professorship for Mineral Construction Materials, Department of Materials Engineering, TUM School of Engineering and Design, Centre for Building Materials, Technical University of Munich, Munich, Bavaria, Germany

ABSTRACT: Concrete is produced by mixing hydraulic cement and aggregates with water. In contact with water, the cement particles first dissolve and subsequently hydrates form through various chemical reactions determining the overall mechanical material properties. Modeling, simulation, and monitoring of the cement hydration provide insights into the processes involved and allow prediction of overall material properties. Thereby, linking the underlying chemical processes to macroscopic material properties remains a key challenge. In this contribution, thermodynamic simulation and a multi-scale modeling approach were employed for Young's modulus development prediction for an ordinary Portland cement paste during the first 24^h of hydration. Further, ultrasound based Coda Wave Interferometry (CWI) methods were applied for monitoring of corresponding cement paste specimens. Coinciding trends were found for model and monitoring based results: Initial small alterations are followed by a period of strong material changes with an accelerated stiffness development and a strong increase in wave velocity.

1 INTRODUCTION

Reinforced concrete is used extensively for the construction of infrastructure around the globe. To produce concrete, cement, and aggregates are mixed with water. Through various reactions of the cement with the water, a cement paste matrix is formed, binding the aggregates together and leading to the overall solidification and strength development of the material. This process is referred to as hydration. The hydration determines the short- and long-term strength of concrete and is therefore an essential part of holistic durability assessment. Previous researchers have focused on understanding and predicting the chemical processes (e.g., Ouzia & Scrivener 2019; Lothenbach & Zajac 2019), strength and stiffness development (e.g., Pichler et al. 2009), as well as the development of new monitoring methods (e.g., Diewald et al. 2022b). Nevertheless, it remains challenging to link the complex microstructural changes to macroscopic material properties. Advances have been made in thermodynamic simulation of the chemical reactions, including the development of a web application (CemGEMS) for thermodynamic simulations by Kulik et al. (2021). Using existing concepts of multi-scale modeling for macroscopic material properties there is potential to predict stiffness development during hydration based on thermodynamic simulation results. Such predictions need to be validated by experimental information. Therefore, in-situ monitoring of material changes is required. Recently, ultrasound (US) based Coda Wave Interferometry (CWI) is extensively

investigated for low-cost, in-situ monitoring of concrete structures (Diewald et al. 2022a). Diewald et al. (2022b) applied CWI methods for investigating early hydration and compared the respective results to conventional hydration monitoring techniques.

2 THEORETICAL BACKGROUND

2.1 *Microstructure development during cement hydration*

Cement is a multi-phase material, which is comprised of the cement clinker, calcium sulfates such as gypsum and anhydrite, and optional mineral additives. In ordinary Portland cement (OPC), the cement clinker is the main component (Taylor 1997). Within the clinker, grains of alite (C_3S) and belite (C_2S) are bound together by aluminates (C_3A) and ferrite (C_4AF) (Stutzman 2004). When the cement is mixed with water, it dissolves and hydrates form out of the aqueous solution, which build the solid cement paste matrix. The main hydrates during early hydration up to 24 h are needle shaped calcium silicate hydrates (C-S-H), plate-like portlandite (CH), and ettringite needles (AFt) (Scrivener 1984). Other phases might occur in smaller quantities (Scrivener 1984; Li et al. 2022), including plates of monocarbonate, flake-like hydrotalcite, or spherical hydrogarnet. The hydrates precipitate mainly on or near the cement grain surface and grow, leading to the connection of individual cement grains, when a certain hydration degree (percolation threshold) is reached (Garboczi & Bentz 1998; Torrenti & Benboudjema 2005). The development of the microstructure through hydrate formation and percolation causes the transition of the initial workable, liquid mixture to a solid material. The related development of elastic properties, such as the Young's modulus is therefore intrinsically linked to the underlying chemical reactions.

2.2 *Thermodynamic simulation*

Thermodynamic modeling and simulation provide information on the thermodynamically stable phase assemblage at a certain degree of reaction of the cement and therefore indicate microstructural changes. It predicts hydrate formation based on cement consumption and thermodynamic information. Appropriate thermodynamic data for cement based systems is available through databases (Lothenbach et al. 2019). For predictions, the hydration process is typically depicted in two steps (Lothenbach & Zajac 2019): (I) Modeling of cement dissolution. (II) Thermodynamic simulation of hydrate formation. Forecasts on cement dissolution are usually based on empirically derived models, e.g., by Parrott & Killoh (1984). As their model was developed using long-term data, it has been reported by Kulik et al. (2021) to insufficiently describe cement dissolution during early hydration. Alternatively, they propose to use the five-parameter logistic (5PL) function fitted to experimentally obtained dissolution data. Given the dissolution information, thermodynamic calculations predict the phase assemblage as the most stable composition at the temperature and pressure stated, while simultaneously considering all aqueous, solid, and gaseous phases. Therefore, thermodynamic equilibrium is assumed, i.e., that the system has reached its most stable state under the given external conditions. However, during hydration, the system changes extensively, especially within the first hours. Thus, the equilibrium condition is not met during early hydration and calculations need to be restrained to mirror experimental observations. Therefore, the formation of certain phases is suppressed, as their formation is kinetically hindered.

Common software solutions for thermodynamic calculation, such as GEMS (Kulik et al. 2012), use the Gibbs free energy minimization approach to predict hydrate formation. Methods and software are under continuous improvement. Recently Kulik et al. (2021) developed the web application CemGEMS based on the GEMS-Selektor code and thermodynamic information from established databases for facilitated thermodynamic simulations. Customizable templates enable individual adjustments for the cement paste mixture and hydration conditions. They further provide simulation options including dissolution modeling according to the 5PL function.

2.3 Microstructure modeling

As discussed above, the microstructure of hydrating cement is heterogeneous. The properties of such a heterogeneous material can be described using the concept of a representative elementary volume (REV). An REV describes a volume (length scale L) containing heterogeneities (length scale l). The size of the REV is chosen such that $l \ll L$. The REV represents the effective behavior of a heterogeneous structure. If the properties of the individual constituents in the REV are given, the corresponding overall property can be obtained by homogenization using analytical or computational methods. If multiple geometries over a wide range of scales are involved, REV's are specified at each scale and homogenization is performed sequentially. In general, the stiffness (henceforth, the fourth order tensor of elasticity will be called the stiffness) of an REV with n different components with n different stiffness can be estimated using the following expression (Timothy & Meschke 2016):

$$\mathbb{C}_{REV} = \sum_{i=1}^n \phi_i \mathbb{C}_i : \mathbb{A}_i \quad (1)$$

In the above equation, \mathbb{C}_{REV} is the homogenized and effective stiffness of the REV; \mathbb{C}_i is the stiffness and ϕ_i the volume fraction of the i^{th} component. The fourth order tensor \mathbb{A}_i is the localization tensor that downscales an applied strain at the REV level to the phase level. It also specifies geometrical information corresponding to the i^{th} material component. The localization tensor can be approximated by several methods depending on the material morphology (i.e. spatial distribution of the phases in an REV). For a material with a clear matrix-inclusion morphology, the Mori-Tanaka (MT) method can be used (Timothy & Meschke 2016):

$$\mathbb{C}_{REV}^{MT} = \mathbb{C}_h + \sum_{i=1}^n \phi_i (\mathbb{C}_i - \mathbb{C}_h) : \mathbb{A}_i : \left[\phi_h \mathbb{I} + \sum_{i=1}^n \phi_i \mathbb{A}_i \right]^{-1} \quad (2)$$

$$\mathbb{A}_i = \left[\mathbb{I} + \mathbb{S} : \mathbb{C}_h^{-1} : (\mathbb{C}_i - \mathbb{C}_h) \right]^{-1} \quad (3)$$

In the above expression, \mathbb{S} is the Eshelby tensor and \mathbb{C}_h is the elastic tensor of the matrix (host) phase. In case there is no clear matrix-inclusion morphology, but the phases are mixed together, the cascade micromechanics model (CCM) can be applied.

$$\mathbb{C}_{REV}^{CCM}(n+1) = \sum_{i=1}^n \phi_i \mathbb{C}_i : \mathbb{A}_i(n) : \left[\sum_{i=1}^n \phi_i \mathbb{A}_i(n) \right]^{-1} \quad (4)$$

$$\mathbb{A}_i(n) = \left[\mathbb{I} + \mathbb{S} : \mathbb{C}_{REV}^{-1}(n) : (\mathbb{C}_i - \mathbb{C}_{REV}^{-1}(n)) \right]^{-1} \quad (5)$$

At $n \rightarrow \infty$ the self-consistent scheme is recovered. In this paper the Mori-Tanaka scheme and the CCM model (Timothy & Meschke 2016) at the regularized self-consistent limit is used.

2.4 Ultrasound based monitoring with CWI methods

State-of-the-art transmission techniques for US based hydration monitoring assess the development of wave velocity. A concise overview of these methods is given by Gabrijel et al. (2020). Currently, a new US approach is under investigation for monitoring reinforced concrete structures: Coda Wave Interferometry (CWI) uses multiply scattered waves for the detection of even marginal material changes. The term coda thereby refers to the tail of the US signal (Aki 1985), which contains information from these waves. Multiply scattered waves sample the material extensively, and therefore the coda is more sensitive to material changes than the direct wave.

Numerically, two waves recorded at different times $u(t')$ and $\tilde{u}(t')$ can be compared by a time-shifted correlation coefficient with a center-time t , and a window length from t_1 to t_2 (Snieder 2006). The stretching technique (Lobkis & Weaver 2003) describes the change in the waveform via stretching or compression such that the correlation coefficient $CC(\varepsilon)$ is maximized:

$$CC(\varepsilon) = \frac{\int_{t_1}^{t_2} u(t')\tilde{u}(t'(1-\varepsilon)) dt'}{\sqrt{\int_{t_1}^{t_2} u^2(t') dt \int_{t_1}^{t_2} \tilde{u}^2(t'(1-\varepsilon)) dt'}} \quad (6)$$

The stretching factor ε thereby corresponds to the velocity variation dv/v :

$$\varepsilon = \frac{dv}{v} \quad (7)$$

Signals can be compared stepwise, or relative to a fixed reference signal. When using a stepwise reference, the cumulated velocity variation ε_c for the n^{th} signal can be calculated as well:

$$\varepsilon_c = \begin{cases} \varepsilon_n, & n = 1 \\ (\varepsilon_{n-1} + 1)(\varepsilon_n + 1) - 1, & n > 1 \end{cases} \quad (8)$$

CWI is usually applied for the detection of subtle material alterations. Cement hydration, however, is associated with major changes in the material structure and properties. Nevertheless, the application of CWI methods with stepwise comparison enables tracing of time-dependent modifications. The ability of stepwise CWI to capture trends during early hydration was shown by Diebold et al. (2022b) by comparing CWI results for repeated US measurements for OPC concrete to corresponding information from conventional monitoring and thermodynamic simulation.

3 METHODS

3.1 Thermodynamic simulation

CemGEMS (Kulik et al. 2021) was used for the thermodynamic simulation of the cement phase assemblage during the first 24 h of hydration. Therefore, the phase assemblage of the anhydrous cement used for the US experiments as determined by quantitative X-ray diffraction, the water-to-cement ratio of 0.45, and conditions of 20 °C and 1 bar were implemented. For hydration simulation, the 5PL dissolution modeling approach was selected, setting the process parameters as proposed by CemGEMS. The calculation was performed for 24 h with 101 linear steps. To prohibit the formation of corresponding, kinetically hindered phases, the formation of specified phases, e.g., gibbsite and dolomite, were disabled as proposed by CemGEMS, and phosphorus, titanium, and manganese containing oxides were removed from the cement composition.

3.2 Multi-scale modeling

In order to model the evolution of the elastic properties of hydrating cement paste, a multi-level micromechanics homogenization model that uses the Mori-Tanaka and the CCM model was employed. The temporal evolution of the volume content of the material phases was obtained from the CemGEMS thermodynamic simulation. The corresponding elastic properties were obtained from literature (Haecker et al. 2005). To use Equation 1 and 2 also the geometry of the phases had to be specified. The hydrate phases C-S-H and ettringite are assumed to be needle-shaped (prolate spheroidal) while portlandite and monocarbonate are assumed to be disc shaped (oblate spheroidal). All other phases are assumed to be spherical in shape. All phases are assumed to be isotropically distributed. In total 6 REV's are used to upscale the elastic properties of hydrating cement paste. The REV's used in the homogenization procedure are shown in Figure 1.

REV-1 is modeled as a mixture of aluminat and ferrite without a clear matrix-inclusion morphology. Here the CCM model is applied. REV-2 corresponds to alite and belite embedded in a material mixture whose properties are obtained by homogenization of REV-1. The Mori-Tanaka scheme is applied for the homogenization of REV-2. REV-3 represents a heterogeneous

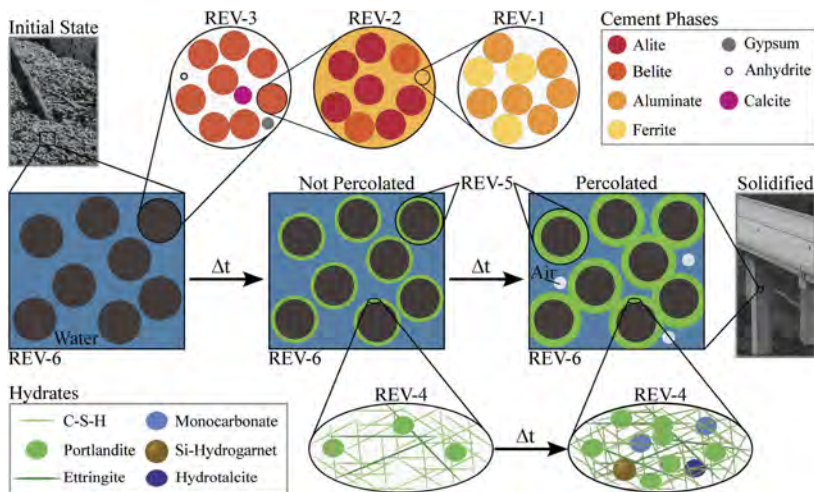


Figure 1. Schematic representation of the multi-scale model for stiffness development based on thermodynamically predicted phase assemblage by volume. All geometries represent 3-dimensional objects. For the representative elementary volumes REV-1 to REV-5 the material properties are homogenized and used as input for the larger scale REV. Through homogenization of REV-6 the overall material stiffness is obtained.

mixture of particles such as gypsum, anhydrite, calcite and the material phase whose properties have been obtained from homogenization of REV-2. As no clear matrix-inclusion morphology can be specified, the CCM model is used for homogenization of REV-3. The cement phase, i.e., REV-3 surrounded by REV-4 that represents the hydrates, is homogenized using the Mori-Tanaka scheme. This morphology refers to REV-5. REV-5 is finally embedded in the aqueous solution. REV-5 together with the aqueous solution is homogenized using the CCM model to obtain the effective elastic properties of REV-6. The evolution of the elastic properties using multi-scale homogenization was simulated using PyMatSim a Python based research software for materials simulation currently developed by the authors.

3.3 Ultrasound based monitoring with CWI methods

Cement paste with a water-to-cement ratio of 0.45 was produced using a CEM I 42.5 R with a density of 3.12 g/cm^3 and a Blaine specific surface of $3,400 \text{ cm}^2/\text{g}$. The raw materials were equilibrated at $20 \text{ }^\circ\text{C}$ and 37.619 kg of CEM I 42.5 R and 16.928 kg of tap water were mixed using a compulsory mixer with a capacity of 75 L for a total of 150 s . Each specimen was prepared with two piezoelectrical US transducers symmetrically embedded at a distance of 300 mm . Figure 2 shows (A) one US transducer (ACSYS S0807) with a center frequency of 60 kHz , (B) the transducer positioning within the specimen, and (C) one specimen with embedded transducers after solidification and demolding. After casting, the specimens were covered with a moist jute cloth and stored in a climate chamber at $20 \text{ }^\circ\text{C}$ and 65% relative humidity.

The US transducers were connected to the measuring system, which transmits pulses with a frequency of 60 kHz to the selected transducer and records the signal at the corresponding

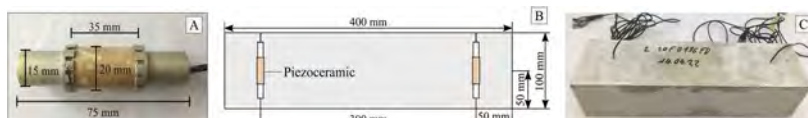


Figure 2. (A) New piezoelectrical US transducer. (B) Symmetrical transducer positioning within $400 \times 100 \times 100 \text{ mm}^3$ specimen for US monitoring. (C) Solidified CEM I 42.5 R pure cement paste specimen after demolding with two embedded US transducers as illustrated in (B). The mean temperature of the sample during the first 24 h of hydration was determined as approximately $30 \text{ }^\circ\text{C}$.

receiver with a sampling rate of 2 MHz and 10,000 samples. Signals were collected every 5 min for the first 22 h with both embedded transducers acting as a sender and receiver once.

The recorded signals were processed by performing offset compensation, pretrigger, and crosstalk removal as well as frequency filtering as described by Niederleithinger et al. (2018). Further, the signals were clipped to the length of 4,500 μs and faulty signals were removed for which the maximum amplitude was less than 0.1 times the amplitude of the previous signal or with a maximum tail amplitude exceeding half the maximum amplitude of the early signal and maximum amplitudes greater than the noise.

4 RESULTS AND DISCUSSION

The simulated cement phase assemblage for the first 24 h of cement hydration in terms of volume fractions is shown in Figure 3(A). The thermodynamic simulation predicts a continuous decline in clinker content and an increase in hydrate volumes with increasing hydration time. Thereby, the total volume loss of solid and liquid phases was compensated artificially by the addition of air. The volume loss appears as a linear trend over time. However, the alterations of phase assemblage of cement phases and hydrates follow a non-linear behavior with striking events occurring between 6 h and 9 h: After about 7 h of hydration, gypsum disappears and at about 8 h the slope of volume increase in solid phases decreases. Moreover, from 8 h onwards, less ettringite is formed. The associated evolution of the material structure, expressed using the Young's modulus predicted by the multi-scale model is shown in Figure 3(B). Within the first hours, the Young's modulus increases only marginally below 0.1 GPa until the increase becomes visible at approximately 5 h of hydration and further accelerates after about 6 h. From this point on, the Young's modulus increases monotonously. After 24 h a maximum value of 8.65 GPa is reached.

The results of the CWI-based monitoring are shown in Figure 3(C)-(E). The entire processed signals were used to calculate the velocity variation dv/v , the correlation coefficient CC and the cumulated velocity variation ε_c by stepwise comparison according to Equations 6-8. The general trends are consistent with those reported by Diewald et al. (2022b). Initially, a 4 h long period of stagnating values is observed for all CWI parameter. Subsequently, strong changes occur between 4 h and 12 h, and a transition to minor parameter changes takes place from 12 h onwards. Within the first hours, the velocity variation fluctuates around zero due to noise dominating signal alterations. A switching process in the early signal leads to stabilization of the corresponding correlation coefficient within this period. During the second period, the velocity variation drops to negative values, indicating a velocity increase. Meanwhile, the correlation coefficient first deviates from and subsequently converges again to 1 as the US signals initially develop and later stabilize. Corresponding to the velocity variation, the cumulative velocity variation decreases to negative values within the second period and merges into a trend of smaller slope in the last hours.

The development of the cumulated velocity variation and the Young's modulus correlate, as both exhibit an initial period of no alteration, followed by a monotonous trend of declining or increasing values. This compliance can be explained by the underlying microstructure development: At first, the fluid suspension of solid particles in water does not yield significant stiffness. This remains unchanged until a certain hydration degree is reached, at which point the hydrates have grown so that the individual particles are bonded together. Progressing connectivity leads to the development of a continuous solid matrix and its densification. Consequently, the stiffness and the wave velocity increase, whereby the increase in velocity is reflected in an increasingly negative cumulated velocity variation. However, the transition time from the initial to the second phase differs between the model based prediction and experimental observations by about 2 h. This discrepancy is assumed to be mainly attributed to the difference in temperature, which is 20 °C for the model based results and 30 °C for the experimental data. The temperature has a major influence on the hydration progress and can enhance the hydration in the range of hours.

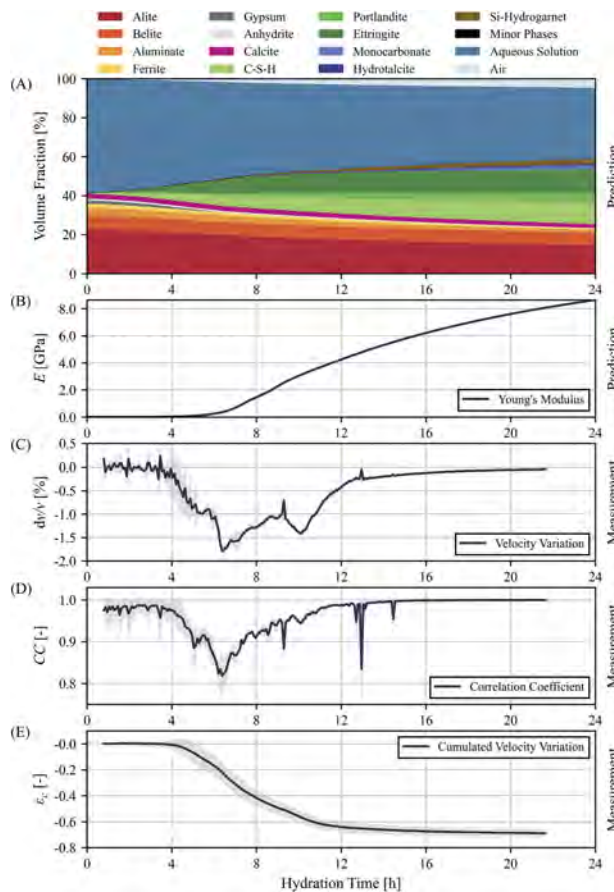


Figure 3. Thermodynamically predicted cement paste phase assemblage over hydration time at 20 °C (A). Composition as volume fractions relative to initial cement paste volume. Volume loss due to chemical shrinkage is compensated by air. (B) Young's modulus E , predicted by multi-scale modeling based on the thermodynamic prediction at 20 °C. Velocity variation dv/v (C), correlation coefficient CC (D), and cumulative velocity variation ϵ_c (E) retrieved by CWI with a stepwise comparison. Average values (solid blue lines) and standard deviation (grey shadowed areas) from two specimens and two measurement directions each. Specimens for US monitoring exhibited an average temperature of approximately 30 °C during the observed period.

5 CONCLUSIONS

In this study, thermodynamic simulation of cement paste phase assemblage was combined with a multi-scale model for stiffness prediction. The development of the Young's modulus retrieved was compared to experimental results of US monitoring using CWI methods. The validity of the model was indicated by correlation of the Young's modulus and the cumulated velocity variation. A period of major microstructural change was observed within the predicted phase assemblage, Young's modulus development, and the CWI parameter at about 4 to 8 hours of hydration. Agreement of results is limited by the thermodynamic equilibrium assumption and a hydration temperature of 20 °C, which underlie the thermodynamic simulation and the idealized stiffness model.

The feasibility and potential of an integrated approach, combining thermodynamic simulation, multi-scale modeling, and CWI monitoring was demonstrated. Further refinement of the models and simulations, as well as the evaluation by means of corresponding experimental data, is required for improved predictions. A deepened understanding of CWI parameter

development during hydration seems further promising for the linkage of microstructural developments to macroscopic material properties.

ACKNOWLEDGEMENTS

We thank the German Research Foundation (DFG) for the funding of the Research Unit FOR 2825 (project number 398216472). This research was enabled in the framework of Subprojects TUM1 and RUB1 with the provided measurement devices of BAM. We thank Sara Niedenzu, Felix Bachl, Manuel Gebhart and Karin Hartlieb-Pfüller for their valuable contribution.

REFERENCES

- Aki, K. 1985. Theory of Earthquake Prediction with Special Reference to Monitoring of the Quality Factor of Lithosphere by the Coda Method. In C. Kisslinger & T. Rikitake (eds), *Practical Approaches to Earthquake Prediction and Warning*: 219–230. Dordrecht: Springer Netherlands.
- Diewald, F. et al. 2022a. Impact of External Mechanical Loads on Coda Waves in Concrete. *Materials* 15 (16): 5482.
- Diewald, F. et al. 2022b. Monitoring Early Cement Hydration with Coda Wave Interferometry. In S. Farhangdoust et al. (eds), *Proceedings of the 13th International Workshop on Structural Health Monitoring*: 141–148. Stanford.
- Gabrijel, I. et al. 2020. Ultrasonic Techniques for Determination and Monitoring Various Properties of Cementitious Materials at Early Ages. In M. Serdar et al. (eds), *Advanced Techniques for Testing of Cement-Based Materials*: 23–68. Cham: Springer International Publishing.
- Garboczi, E.J. & Bentz, D.P. 1998. The microstructure of portland cement-based materials: computer simulation and percolation theory. In *Proceedings of the Spring 1998 Materials Research Society on Computational Materials Science*: 89–100. San Francisco.
- Haecker, C.-J. et al. 2005. Modeling the linear elastic properties of Portland cement paste. *Cement and Concrete Research* 35(10): 1948–1960.
- Kulik, D.A. et al. 2012. GEM-Selektor geochemical modeling package: revised algorithm and GEMS3K numerical kernel for coupled simulation codes. *Computational Geosciences* 17: 1–24.
- Kulik, D.A. et al. 2021. CemGEMS – an easy-to-use web application for thermodynamic modeling of cementitious materials. *RILEM Technical Letters* 6: 36–52.
- Li, B. et al. 2022. The Early Age Hydration Products and Mechanical Properties of Cement Paste Containing GBFS under Steam Curing Condition. *Buildings* 12(10): 1746.
- Lobkis, O.I. & Weaver, R.L. 2003. Coda-wave interferometry in finite solids: recovery of P-to-S conversion rates in an elastodynamic billiard. *Physical review letters* 90(25): 254302.
- Lothenbach, B. et al. 2019. Cemdata18: A chemical thermodynamic database for hydrated Portland cements and alkali-activated materials. *Cement and Concrete Research* 115: 472–506.
- Lothenbach, B. & Zajac, M. 2019. Application of thermodynamic modelling to hydrated cements. *Cement and Concrete Research* 123: 105779.
- Niederleithinger, E. et al. 2018. Processing Ultrasonic Data by Coda Wave Interferometry to Monitor Load Tests of Concrete Beams. *Sensors* 18(6): 1971.
- Ouzia, A. & Scrivener, K. 2019. The needle model: A new model for the main hydration peak of alite. *Cement and Concrete Research* 115: 339–360.
- Parrott, L.J. & Killoh, D.C. 1984. Prediction of Cement Hydration. *British Ceramic Procedures* 35: 41–53.
- Pichler, B. et al. 2009. Spherical and acicular representation of hydrates in a micromechanical model for cement paste: prediction of early-age elasticity and strength. *Acta Mechanica* 203(3): 137–162.
- Scrivener, K. 1984. *The development of microstructure during the hydration of cement*. PhD Thesis: Imperial College.
- Snieder, R. 2006. The Theory of Coda Wave Interferometry. *Pure and applied geophysics* 163: 455–473.
- Stutzman, P. 2004. Scanning electron microscopy imaging of hydraulic cement microstructure. *Cement and Concrete Composites* 26(8): 957–966.
- Taylor, H.F.W. 1997. *Cement Chemistry*. London: Thomas Telford Publishing.
- Timothy, J.J. & Meschke, G. 2016. A cascade continuum micromechanics model for the effective elastic properties of porous materials. *International Journal of Solids and Structures*, 83: 1–12.
- Torrenti, J.M. & Benboudjema, F. 2005. Mechanical threshold of cementitious materials at early age. *Materials and Structures* 38(3): 299–304.



Taylor & Francis

Taylor & Francis Group

<http://taylorandfrancis.com>

*SS6: Life-cycle redundancy, robustness, and resilience indicators
for aging structures and infrastructure systems under multiple hazards
Organizers: F. Biondini & D.M. Frangopol*



Taylor & Francis

Taylor & Francis Group

<http://taylorandfrancis.com>

Financial risk assessment of flexible infrastructure systems

N. Acuña-Coll & M. Sánchez-Silva

Department of Civil and Environmental Engineering, Universidad de Los Andes, Bogotá, Colombia

ABSTRACT: Extreme natural hazards impact infrastructure systems, causing economic losses and environmental problems, affecting well-being and quality of life. During the last decades, the public and private sectors have focused on developing approaches to manage infrastructure capable of accommodating changes in demand and responding efficiently to uncertain damaging events. This paper presents a new strategy to assess the financial value of incorporating flexibility. First, the paper describes infrastructure systems as processes and briefly describes how to incorporate flexibility in design and management. Afterward, the paper reviews traditional approaches for the financial evaluation of infrastructure throughout its lifetime and offers a proposal based on the Decoupled Net Present Value (DNPV). Finally, the proposed method is illustrated by three different infrastructure management approaches. The results indicate that the DNPV is a better indicator of the system's financial performance. Besides, financial validation strengthens the value of flexible systems over standard design and construction strategies.

1 INTRODUCTION

It is estimated that urbanization in developing countries will reach values above 90% between 2012 and 2032 (Baker, 2012). Rapid urbanization is a challenge to all sectors of society since it demands the adaptation and rapid growth of new sustainable infrastructure. In addition, in most developing countries, the growth of urban areas leads low-income people to relocate to areas with high exposure to risk (e.g. landslides and flooding). Furthermore, the increasing number of high-intensity hazard events due to climate change will significantly impact communities, especially in the most vulnerable sectors. The World Bank calculates that natural hazards cost the global economy about \$ 520 billion annually. Within this context, governments and worldwide institutions seek to develop approaches to manage complex infrastructure systems capable of adapting to events in an uncertain future.

The main task behind hazard management is managing large uncertainties. Currently, it is possible to create models that support managing under deep uncertainty, such as decision trees, roadmaps, and stochastic programming, among other planning approaches. More recently, the idea of flexible design and management of infrastructure systems has emerged as an alternative in this direction. Flexible systems can easily respond to or change operational parameters, or their design, to keep or add value to the system when subjected to external or internal demands. Furthermore, flexible systems change their state by modifying their internal structure, thus moving to a new state defined by a continuous or discrete set of options (e.g. Adaptation Pathways). Overall, introducing flexibility in the development of infrastructure contributes to better management of planned/unplanned events, taking advantage of investment/business opportunities, reducing possible cost overruns, and handling the perceptions and interests of stakeholders. The most common method for evaluating infrastructure performance over time is a Life Cycle Cost Analysis (LCCA). Most studies support this evaluation by a financial assessment that includes the Net Present Value (NPV). Several authors have shown that, financially, incorporating flexibility in infrastructure management is much better than the implementation of traditional designs. (Cardin et al., 2015; De Neufville & Scholtes, 2011; Sánchez-Silva & Calderón-Guevara, 2022). The objective of this paper is to compare the traditional LCCA that uses the NPV as the fundamental financial strategy with

a new financial tool called Decoupled NPV (DNPV) proposed by Espinoza and Morris (Espinoza & Morris, 2013). This comparison is carried out within the context of systems that evolve and change with time. In addition, this comparison provides new insights into project performance in relation to risk management.

2 MODELING INFRASTRUCTURE SYSTEMS

2.1 *System thinking approach*

Large infrastructures could be modeled as *systems* based on the ideas of systems theory (Checkland, 1999). Systems are an organized assembly of elements with a purpose (Meadows & Wright, 2008). Mainly, the three pillars for system thinking are (Blockley & Godfrey, 2017): i) structuring information hierarchically, ii) identifying and recognizing the importance of loops, and iii) understanding the system as a set of processes. Similarly, Ackoff (2010) considers that system thinking focuses on connectivity, relationship, process, patterns, and context. Many researchers have identified the importance of analyzing systems as processes over the life cycle, especially in the area known as project management. For example, Lean construction, which is currently widely used, is a broad practice and philosophy that is key to controlling and improving the processes in the construction industry (Babalola, Ibem & Ezema, 2019). Overall, systems are a set of interacting processes that are organized hierarchically and exhibit emergent properties. This last element is the key to the so-called holistic view of projects. Understanding systems from this perspective requires recognizing the continuously changing nature of infrastructure and the importance of focusing on the interactions of components (subsystems) and emerging properties at different levels.

2.2 *Flexible and adaptable infrastructure systems*

Flexibility is “the ability of a system to respond or change some of its design or operational parameters easily to keep or add value to the system when subjected to either internal or external demands.” (Sánchez-Silva, 2021; Torres-Rincón, Sánchez-Silva & Bastidas-Arteaga, 2021). Flexible systems are designed with specific features that facilitate future changes in system parameters, such as the implementation of new technology or the expansion or contraction of the system according to demand (Cardin et al., 2015). Likewise, adaptability describes the system’s ability to change its functionality or structure when required (Chester & Allenby, 2019). Flexibility and adaptability are sometimes used as synonyms; however, in most cases, flexible systems are also adaptable, but the contrary is not always true.

There is a distinction between fully flexible systems and systems whose flexibility is defined by the so-called Adaptation Pathways (AP). In form, the system can change its state at any time to any value; this is, actions that modify system parameters can take values in a continuous space. However, in the case of Adaptation Pathways, possible actions (system interventions) are limited by a finite set of actions that can only initiate after a particular point in time and that limit the system to take specific state values. In a way, Adaptation Pathways are a specific case of fully flexible systems. Note that incorporating flexibility in infrastructure is linked with the design and management strategies, which define the type and nature of changes (interventions) that are executed over time. In this context, we do not consider systems that can change their internal structure autonomously. Note also that at the heart of Infrastructure management, there is the need for sequential decision-making to guarantee that the systems operate as planned.

3 FINANCIAL PERFORMANCE

3.1 *Life cycle cost analysis*

Life cycle cost analysis (LCCA) is a technique to evaluate the financial performance of projects. Many institutions, such as the FIB or the Federal Highway Administration (FHWA) in the U.S., have established a guide to carry out LCCA. This paper uses the basic LCCA approach to evaluate the performance of three design and management system types:

standard, fully flexible, and Adaptation Pathways. The paper focuses mainly on their financial performance when carrying out a discounted cash flow analysis.

3.2 Net present value and the role of risk in discounting

There are different economic indicators for the economic assessment of infrastructure projects, such as Net Present Value (NPV), Benefit/Cost Ratio (B/C), and Internal Rate of Return (IRR). NPV is the most widely used method to analyze the profitability of projects. Not only infrastructure projects but any investment projects. Net Present Value is calculated as the total discounted difference between the expected cash inflows or benefits (\bar{B}) and the expected cash outflows or investments (\bar{I}). The benefits result from the fulfillment of the purpose of the system. They are usually calculated from the demand met or payments agreed upon by contract. In contrast, the investments are an outcome of the operation, maintenance, or modification of the design or operation parameters of the infrastructure. Then NPV is computed as:

$$NPV = \sum_{t=0}^N \left[\frac{\bar{B}_t - \bar{I}_t}{(1 + \delta)^t} \right] \quad (1)$$

where t is a specific time, N is the finite time window and δ is the discount rate. Projects are profitable if the NPV value exceeds zero ($NPV > 0$). Large NPV values imply better financial performance. The NPV is extensively used, mainly due to its simplicity. However, the main implementation problem is the choice of the discount rate, δ . This parameter is not standard; it depends on the type of project, the economic, social, and environmental conditions and perceptions, the risk of the investment, and the funds' origin, among others. In a nutshell, this rate should reflect the time value of money (time preference) and the uncertainty of the project.

Selecting a particular discount rate, δ , have important implications on the feasibility of the project and the decisions that follow. Note that if all the benefits and costs of an infrastructure project were certain, the project should be evaluated with a *risk-free rate*. The risk-free rate is the theoretical rate of return of an investment with zero risk. In practice, cash flows include some degree of uncertainty; therefore, the risk-free rate of return does not truly exist. For example, there is uncertainty coming from the randomness in the operation's income or the size of interventions throughout the project's lifetime. This variability imposes some risks on investors and stakeholders. In infrastructure, the risk is often quantified as the expected value of the losses. However, quantifying the cash flow's risk is challenging when defining the project's financial structure. Loss metrics are generally based on property conservation, public safety, economic losses, or business continuity (Lounis & McAllister, 2016).

In traditional financial assessments, risks are frequently considered within the discount rate. Then, in this setting, the discount rate is called *risk-adjusted discount rate*. This rate is increased according to the project's risk profile, i.e. larger uncertainty means larger discounting. Experts often select the rate for the specific conditions of a project based on the project location and the origin of funds.

Espinoza and Morris (2013) identified several problems with selecting risk-adjusted discount rates when making traditional NPV evaluations. These are: 1) the use of a single discount rate throughout the project's entire life cycle is not consistent with the fact that risks may increase or decrease over time; 2) discounting benefits and costs at the same rate fail to recognize that they have different risk profiles; and 3) the NPV method substantially minimizes future cash flows in high-risk projects. Based on these observations, Espinoza and Morris (2013) proposed an alternative approach to performing the financial assessment of projects in which the risks are explicitly considered, called Decoupled Net Present Value (DNPV).

3.3 Decoupled net present value

Espinoza and Morris (2013) proposed an alternative method to the NPV based on separating the risky part from both benefits and costs in the cash flow. This solution allows discounting the "known" cash flow part at a risk-free rate while risks are transferred to a third party via some premium. As a result, the DNPV formula can be written as follows:

$$DNPV = \sum_{t=0}^N \left[\frac{\bar{B}_t - \bar{I}_t - \bar{R}_t}{(1+r)^t} \right] \quad (2)$$

where N is the number of cash flows occurring during the project's lifetime (known and finite). The term \bar{R}_t is the expected risk premium paid at time t , and r is the risk-free rate.

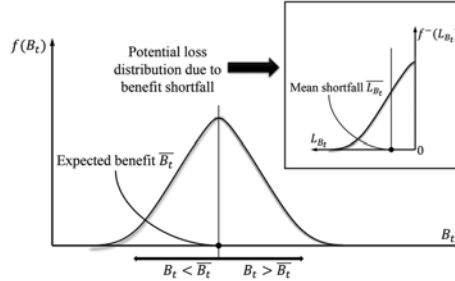


Figure 1. Distribution of benefits at a specific time and potential loss distribution at that time due to benefit shortfall (adapted from Espinoza & Morris, 2013).

The expected risk premium is obtained by identifying all the sources of risk in the specific period or stage. Since the DNPV differentiates between risks associated with the outflow or the inflow, $\bar{R}_t = \bar{R}_{B_t} + \bar{R}_{I_t}$. The premiums are calculated as a percentage of profits ($\eta_B B_t$) or investments ($\eta_I I_t$). The specific values of η_B or η_I can be obtained using various methods, including a probabilistic approach and option pricing (Espinoza & Morris, 2013). In the probabilistic approach, it is necessary estimating the probability distribution of benefits and investments at each time. Consider, for example, the distribution of the project's benefits at time t , as shown in Figure 1. In this case, the premium of the cash inflows at time t is related to the mean shortfall (\bar{L}_{B_t}), i.e. the mean value of the distribution of potential losses (Espinoza & Morris, 2013). The premium of the cash inputs at time t is computed as follows:

$$\bar{R}_{B_t} = \bar{L}_{B_t} \times P(\bar{B}_t > B_t) \quad (3)$$

Similarly, for the case of costs, it is possible to calculate the investment mean excess cost (\bar{L}_{I_t}). In this case, the premium of the cash outflows at time t is calculated as:

$$\bar{R}_{I_t} = \bar{L}_{I_t} \times P(\bar{I}_t < I_t) \quad (4)$$

Equations 3 and 4 associate the risk premium with the possibility of obtaining lower benefits or higher costs than expected. The larger the average drop in benefits or cost overruns, the larger the risk premium.

3.4 Value of the DNPV in dynamic adaptable management

The project's risk profile often changes with time; therefore, the DNPV methodology requires computing the premium at every time. However, this way of calculating the discounted values has two drawbacks when modelling dynamic adaptable systems. First, the distributions of costs could be skewed because the costs in adaptive problems do not occur at fixed times; they will depend on a prediction of future demands, in particular of extreme events, which add large uncertainties to cost estimations. Second, the distribution of costs or benefits is not easy to obtain, given the lack of data and demand variability.

Based on the previous discussion, a proposal to approximate the solution is as follows. First, the time mission of the project can be divided into a set of time intervals with similar lengths. Then, the percentage of profits or investment, i.e. η_B or η_I , could be computed and kept constant for every interval. For example, for a time horizon of 60 years, it might be

reasonable to have intervals of 15 years. Finally, the mean shortfall or mean excess cost is calculated by simulation. Equations 2 y 3 could be rewritten as:

$$\bar{R}_{B_t} = \frac{1}{K} \left[\sum_{k=0}^k \mathbf{1}_{B_t,k} (\bar{B}_t - B_{t,k}) \right] \quad (5)$$

$$\bar{R}_{I_t} = \frac{1}{K} \left[\sum_{k=0}^k \mathbf{1}_{I_t,k} (I_{t,k} - \bar{I}_t) \right] \quad (6)$$

where K is the number of simulations, $B_{t,k}$ represents the benefits at time t in simulation k , $\mathbf{1}_{B_t,k}$ is an indicator function that is 1 if $\bar{B}_t > B_{t,k}$ and 0 otherwise. Similarly, $I_{t,k}$ is the investment at time t in simulation k , $\mathbf{1}_{I_t,k}$ is an indicator function that is 1 if $\bar{I}_t < I_{t,k}$ and 0 otherwise.

Equation 5 illustrates the mean shortfall (\bar{L}_{B_t}). Each shortfall value is subtracted from the benefit \bar{B}_t to build the cash flow in the DNPV. The probability distribution of the benefits is calculated from simulations; and the number of simulations where we find a shortfall over the number of simulations. With this simplification, we find that the number of times we observe shortfalls is trivial. Similarly, Equation 6 shows the \bar{L}_{I_t} as the average of overruns. In this case, the expected investment is subtracted from each excess value to make the potential overruns distribution. The probability of the cost overruns is computed as the number of simulations where we find overruns over the number of simulations. Then, the number of times we find overruns results irrelevant to the estimation.

4 ILLUSTRATIVE EXAMPLE

4.1 Case description

Let us consider a system with a vector of parameters that depends on time, $X(t)$. The system state $X(t)$ moves to a new state $X(t + \Delta t)$ by choosing an action a from a set of possible actions \mathbf{A} . This system has some emergent properties, such as capacity, resistance, or safety, which conform to a vector of system performance indicators $V(t)$. For simplicity, in this paper, we will consider $V(t)$ as the system's capacity (single parameter). Furthermore, let us consider that the system is subjected to a time-variant demand $D(t)$. The system is designed to withstand the demand for some specific time τ , $0 \leq \tau \leq t_m$, with t_m the expected service life (i.e. time mission). Then, the system initial state $V(0)$ satisfies $P(V(0) \leq D(\tau)) = \zeta$. The acceptable failure probability is $\zeta = 10^{-3}$. Finally, it was assumed that the project's lifetime is 60 years.

In this example, three design and management system types were considered: a fully flexible system, a flexible system subjected to changes constrained by adaptation pathways, and the standard (traditional) design. The illustrative case also considers that if the system fails (sudden drop in capacity), it will recover its initial capacity almost instantly. In the first two cases in which flexibility plays an important role, the system is equipped with some flexibility features that are part of the management and operation. In other words, the system's capacity can be modified when required to accommodate changes in demand. These changes respond to specific intervention strategies (policies) that follow certain rules, such as when to make changes and the size of those changes. In addition, a strategy also considers aspects such as the critical capacity v , the time window t_q used for recurrent predictions, the restriction between capacity expansions t_k ; and the flexibility range h . The basic parameters that define the performance of the three systems: fully flexible, Adaptation Pathways and standard are, respectively: $V(0) = \{93.17, 93.17, 197.28\}$, $v = \{52.20, 52.20, 112.42\}$, $t_p = 8$, $t_q = 5$, $t_k = 5$ and $h = 3 \times V(0)$.

Figure 2a shows a sample path of the standard and flexible strategies subjected to extreme events and specific demand. Likewise, Figure 2b presents the standard case and Adaptation Pathway strategies under the same conditions. In Figure 2b we can observe the discretized set of actions or paths $\mathbf{A} = \{a_1, a_2, a_3, a_4\}$ adopted in this illustrative example. In these realizations, it was assumed that extreme events occur with a return period of 40 years, which causes most failures to occur towards the end of the project's lifetime.

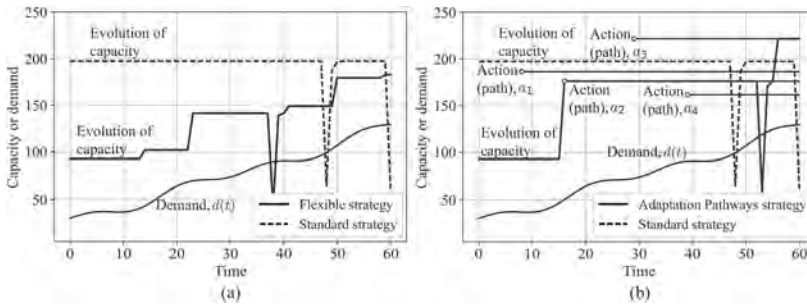


Figure 2. Realization of flexible, Adaptation Pathways and standard strategies under a random demand.

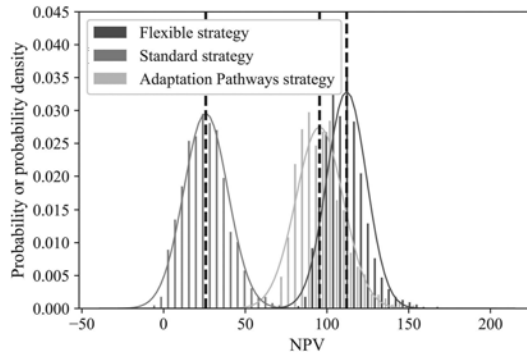


Figure 3. Distribution of the Net Present Value for the three strategies with a discount rate of 6%.

4.2 Financial risk assessment

Selecting the best design and management strategy depends on many factors. This paper focuses on a financial assessment based on evaluating discounted cash flows. Because the system response depends on the demand, which is unknown, the financial response of the three system types was evaluated statistically using simulation. Then, for every policy, every system was subjected to 2000 different demand paths. Initially, the NPV for every simulation was computed with a risk-adjusted discount rate of 6%. The histograms of the NPV for the three system types are shown in Figure 3. It can be observed that the best performance, i.e. the largest expected NPV, corresponds to the fully flexible strategy with $\mathbb{E}[\text{NPV}] = 113.04$, followed by the Adaptation Pathways and the standard cases with expected NPV 15.28% and 76.27% smaller than the flexible strategy respectively. The probability that the project is not feasible tends to zero in the flexible and Adaptation Pathways strategies, while this value is 0.7% for the standard case. To assess the sensitivity of the risk-adjusted discount rate, we calculated the expected value of the NPV for various discount rates. The results are reported in Table 1. It can be observed that the standard strategy is the most sensitive to the risk-adjusted discount rate. This result is consistent with the systems dynamic because the main cost in the standard case occurs in the initial year or early stages, which means that only the total benefits

Table 1. Expected NPV for different discount rates.

Strategy	Discount rate [%]			
	2	4	6	8
Flexible	311.34	177.66	113.04	77.70
Adaptation pathways	258.60	148.11	95.77	67.51
Standard	154.47	66.00	26.82	7.78

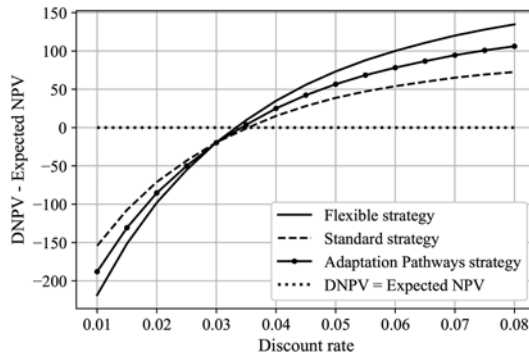


Figure 4. Difference between DNPV and Expected NPV vs discount rate with a risk-free rate of 3%.

vary significantly with the discount rate. In contrast, the discount rate influences adaptable systems in both total benefits and costs, achieving a less variable difference in the NPV method.

The NPV financial evaluations were compared with DNPV. In the latter, the risk-free rate was chosen as $r = 3\%$. Repeating the analysis performed to assess the NPV, the DNPV was also evaluated for the three system types. As in the NPV analysis, the best option for DNPV is the flexible strategy with a DNPV of 212.2, followed by the Adaptation Pathways and the standard case. Note that by using the DNPV strategy, the expected discounted value almost doubles for the flexible case, which has implications when defining the project's feasibility. The value of the discounted risk premiums (\bar{R}) for the fully flexible, Adaptation Pathways and standard cases were 21.04, 19.36, and 20.79, respectively. However, if the risk is expressed as a percentage of the expected profitability, the riskiest strategy is the standard, then the Adaptation Pathways, and finally, the fully flexible strategy. The standard case has a larger risk since the expected profitability is highly uncertain; it depends significantly on the evolution of the demand. On the contrary, for adaptable systems, there is less uncertainty in profitability, and the risks of cost overruns are transferred to future years. Furthermore, the fully flexible case manages risks better than the Adaptation Pathways approach because the adaptations are made in a continuous space; that is, better adaptability and greater certainty of profits.

To compare the DNPV and the NPV, the indicator $W = \text{DNPV} - \mathbb{E}[\text{NPV}]$ for each system type was calculated for various discount rates δ (see Figure 4). A value of W closer to 0 indicates that the discount rate used in the NPV analysis approaches the most accurate risk-adjusted discount rate based on the understanding of the system dynamic. The risk-adjusted discount rate, δ_m for which $\text{DNPV}(r) - \text{NPV}(\delta_m) = 0$. The value of δ_m for flexible and Adaptation Pathways strategies is 3.32% and 3.40%, respectively, while this rate reaches 3.50% for the standard approach. Note that for the three system types, the value of $\delta_m - r$ is the inherent risk derived from the system performance and management.

This analysis might be an important tool for a financial institution considering funding an infrastructure project. In this case, the minimum discount rate on loans may be conditioned on the management strategy (policy) used to operate the system. Any value above δ_m depends on other factors such as credit history, the country's risk, the exchange rate, and political stability, among others. In most cases, these factors dominate the ultimate selection of the final rate. Funding institutions using discounting rates above δ_m have the possibility of larger profitability margins. Note that it does not make much sense to use values of $\delta < \delta_m$; this clearly underestimates risk.

In Figure 4, different discount rates can be selected to keep the index W constant. For example, to establish a margin of $W = \text{DNPV} - \mathbb{E}[\text{NPV}] = 50$ units, the standard management strategy will require a risk-adjusted discount rate of $\delta = 5.8\%$, while this value will be $\delta = 4.75\%$ and $\delta = 4.45\%$ for the Adaptation Pathways and the fully flexible cases, respectively. These results are consistent, given that the flexible strategy is the least risky, followed by the Adaptation Pathways. Finally, note that if the three project types are evaluated with the same discount rate (larger than any δ_m), the flexible case will always render the largest W due to its risk profile.

5 CONCLUSION

Infrastructure systems are subjected to a large variety of external and internal demands, which include social, environmental, and economic pressures, as well as operational and extreme natural events. The traditional approach to managing the uncertainties derived from these demands consists of designing for solicitations expected to occur at the end of the project's lifetime. This approach yields over designs for most of the project's lifetime. In this context, flexible strategies emerge as a new paradigm. This paper aims to compare the LCCA of three systems types, i.e. fully flexible systems, systems whose evolution is defined by a set of adaptation pathways, and the standard design. Specifically, the comparison is based on two different strategies to assess the financial value of incorporating flexibility: Net Present Value (NPV) and Decoupled Net Present Value (DNPV). Despite being widely used, the NPV has important drawbacks, among which is the difficulty of estimating the risk-adjusted discount rate. Then, the DNPV is presented as an alternative indicator that addresses the problems of the NPV. The results indicated that the NPV does not account properly for the project risk, especially in the fully flexible design strategy. The results also showed that when the LCCA is based on the NPV only, the flexible system is the most efficient, with a high Net Present Value and a low variance. Furthermore, the flexible management strategy has the lowest financial risk, while the standard strategy has the highest risk due to the large uncertainties that it involves.

REFERENCES

- Ackoff, R.L., Addison, H.J. & Carey, A. Jappelli. 2010. Systems Thinking for Curious Managers: With 40 New Management F-laws. In Triachy Press (ed.).
- Babalola, Ibem, E. O., & Ezema, I. C. 2019 Implementation of lean practices in the construction industry: A systematic review. *Building and environment*, 148, 34–43.
- Baker, J. L. 2012. Climate change, disaster risk, and the urban poor: cities building resilience for a changing world. Washington, D.C.: World Bank.
- Blockley, D., & Godfrey, P. (2nd edition) 2017. Doing it differently. In ICE Publishing (ed.).
- Cardin, M.A., Ranjbar-Bourani, M., & De Neufville, R. 2015. Improving the Lifecycle Performance of Engineering Projects with Flexible Strategies: Example of On-Shore LNG Production Design. *Systems Engineering*, 18 (3), 253–268.
- Checkland, P. 1999. Systems Thinking, Systems Practice: Includes a 30-Year Retrospective. In Wiley (eds).
- Chester, M., & Allenby, B. 2019. Toward adaptive infrastructure: flexibility and agility in a non-stationarity age. *Sustainable and Resilient Infrastructure*, 4 (4), 173–191.
- De Neufville, R. & Scholtes, S. 2011. Flexibility in engineering design. Cambridge, Mass: MIT Press.
- Espinoza, & Morris, J. W. F. 2013. Decoupled NPV: a simple, improved method to value infrastructure investments. *Construction Management and Economics*, 31(5),471–496.
- Haasnoot, M., Middelkoop, H., Offermans, A., Van Beek, E., & van Deursen, W. 2012. Exploring pathways for sustainable water management in river deltas in a changing environment. *Climatic Change*, 115, 795–819
- Lounis, Z. & McAllister, T.P. 2016. Risk-based decision making for sustainable and resilient infrastructure systems. *Journal of Structural Engineering*, 142(9).
- Meadows, D., & Wright, D. E. 2008. Thinking in systems. Chelsea Green Publishing.
- Sánchez-Silva, M. 2021. Design of flexible and adaptable infrastructure systems. *ICE Infrastructure Asset Management*, 8 (8), 36–48
- Sánchez-Silva, M., & Calderón-Guevara, W. 2022. Flexibility and adaptability within the context of decision-making in infrastructure management. *Structure and Infrastructure Engineering*, 18 (7), 950–966.
- Torres-Rincón, S., Sánchez-Silva, M., & Bastidas-Arteaga, E. 2021. A multistage stochastic program for the design and management of flexible infrastructure networks. *Reliability Engineering & System Safety*, 210, 107549.

Time-dependent assessment of corrosion impact on R/C members

M. Calò & G. Gabbianelli

Department of Civil Engineering and Architecture, University of Pavia, Pavia, Italy

ABSTRACT: The assessment of structures subject to deterioration is a non-negligible aspect that engineers must deal with to correctly estimate the structural response, retrofit strategies as well as maintenance plans. In fact, inaccurate estimation could result in an inappropriate design or require premature and additional interventions that were not initially planned, thus increasing the maintenance costs of the structure. Consider in this regard that in the United States alone, investment in the replacement and rehabilitation of reinforced concrete structures and infrastructures can be estimated at around \$20 billion annually. Thus, accurate estimation of structural response can result in resource savings. To this end, a simplified approach to consider the impact of corrosion on reinforced concrete structural elements is proposed here. Material deterioration, in terms of reduced area and spatial and temporal concrete degradation with a reduction in strength and deformation capacity, is numerically incorporated through a fibre approach with the advantage of not increasing the computational cost of analysis. The technique is validated by comparing numerical results with experimental tests available in the literature considering nonlinear static and dynamic analyses due to corrosive attack. The results demonstrate the ease and efficiency of the proposed technique to capture the impact of deterioration in the response of structural elements during the nominal life period.

1 INTRODUCTION

1.1 *Rationale, literature review and research objectives*

Ageing of structures is a problem that our society must be able to deal with both for new construction as well as for those buildings that have reached the end of their nominal design life. The influence of environmental exposure (i.e. variation in atmospheric temperatures and humidity), carbon dioxide concentration levels and the infiltration of harmful substances such as chloride ingress have an effect on the entire lifecycle of a construction, in addition to the materials used and the construction processes. Recent studies, in fact, focused on understanding the impact of climate change and the implications of rising CO₂ levels and temperatures on corrosion (Rianna et al. 2020). On the other hand, in developed countries, chloride attack appears to be the major environmental stressor capable of affecting the structural capacity of elements and producing a significant economic impact. Indeed, considering only the United Kingdom and Scotland, the corrosion damage to infrastructure can be estimated at around £1 billion (Wall-bank 1989). In the U.S., on the other hand, the Federal Highway Administration (FHWA) estimates a direct annual cost of corrosion on infrastructure (i.e. highway bridges, gas and liquid transmission pipelines, waterways and ports, hazardous materials storage, airports and railroads) at \$22.6 billion, of which \$8.3 billion is due to highway bridges (Koch et al. 2002).

To this end, in the previous decades, several efforts have been made both to assess the impact of corrosion on the behavior of structural components through accelerated degradation procedures in the laboratory (Val and Melchers 1997, Stewart 2004) as well as individual reinforcing steel rebars (Du et al. 2005a, Kashani et al. 2013), or, in a more comprehensive

approach, de-tecting the overall dynamic characteristics of the building or structural and non-structural elements (Gara et al. 2021, Nicoletti et al. 2022a, 2022b).

From a phenomenological point of view, degradation is induced by a kinetic process of diffusion of chemical components, such as sulphates and chlorides, caused by concentration gradients within the volume of the material (Mehrer 2007). Chlorides, which are critical in the marine environment but also result from the application of de-icing salts, penetrate through the concrete cover, locally breaking the passive film of the reinforcement and producing oxidation. Corrosion of reinforcement steel induces concrete cracking and produces rusting at the inter-face, delamination and potential cover expulsion (Vidal et al. 2004). Furthermore, at a local material level, with regard to individual reinforcing bars, experimental studies show premature buckling, low-cycle fatigue, and loss of ductility and strength. Consequently, the foremost effects of deterioration on the response of structural elements are loss of adherence and cross-sectional area of the reinforcement, change of mechanical properties of the degraded materials, as well as of the overall ductility of the members due to the variation in flexural stiffness and shear capacity (Vu et al. 2016). Localised embrittlement can seriously compromise the capacity of an element and cause abrupt failure with nefarious consequences.

The evaluation of the influence of corrosion has not only been observed experimentally, but several researchers have adopted analytical and numerical criteria. From what emerges in the literature, efforts placed to capture the degradation by structural analysis are diverse (Kashani et al. 2019). For example, through 3D finite element analysis (di Carlo et al. 2017) but given the high computational burden, it is not yet extendable for large-scale analysis. Alternatively, through sophisticated methods such as implementing nonlinear mechanical bonds to simulate the effects of deterioration on the reinforcing bars (Kashani et al. 2015, Dizaj et al. 2018) or, globally, by means of damage indices (Ghosh and Padgett 2010, Berto et al. 2020) while, in other cases, this is taken into account through the reduction of reinforcing bars alone (Rao et al. 2017). In the case of structural elements subject to corrosive attack, the mechanical properties of materials and the effects of confinement of transverse stirrups should be updated, thereby capturing both the spatial extent and the accumulation of damage during the propagation of the phenomenon. Therefore, the present study aims to provide a numerical approach considering spatial and temporal deterioration. Thus, in this study, the effect of deterioration is explicitly considered at the local material level without increasing the computational onus. The intent is to propose a model that is easy to implement in commercial finite element software so that practitioners may address structural assessments while also considering the actual durability of structures.

2 STRUCTURAL MODELING OF DEGRADATION DUE TO CORROSION IMPACT

As reported in the previous section, the intent of the framework presented in this study is to develop a refined procedure for encompassing the corrosion degradation in finite element software - that employ beam-column elements - without increasing the computational burden; in this way, it would be possible to perform vulnerability analyses with the traditional tools currently adopted by practitioners. Although fibre beam-column elements are particularly efficient from a computational viewpoint and in terms of accuracy (Spacone *et al.* 1996a, 1996b), simulation of reinforced concrete elements is primarily appropriate when the response is flexural-dominant. Where the response is brittle-type, thus marked by shear failure, these models are not so accurate because they do not capture the coupling of the complete stress state, i.e. the axial-shear-flexural interaction. Some researchers (Jeon *et al.* 2015), in order to overcome this obstacle, have set up shear springs to account for shear strain, but in any case, this strategy does not account for the complete interaction, as previously recalled. To overcome this issue, future work could improve the proposed methodology by evaluating, for each individual member, the minimal value of shear capacity corresponding to the stirrup yielding, bonding failure and flexural-bonding failure (Belletti *et al.* 2013, Walraven *et al.* 2013) and so the possible violation of the member shear capacity in order to be removed from the analysis.

The modelling approach proposed here can account for the actual state and extent of damage across the distributed integration point sections (IPs) by pointwise variation of the

fibres at the sectional level. The idea stems from the usual in situ inspections, aiming to recreate the structure's actual condition, as depicted in Figure 1. In this way, following the inspection of an artefact, it is possible to tackle the future structural behaviour hypothesising extensions and the progressive deterioration thus performing temporal analysis.

In the following, the methodology employed will be presented and validated by experimental case studies.

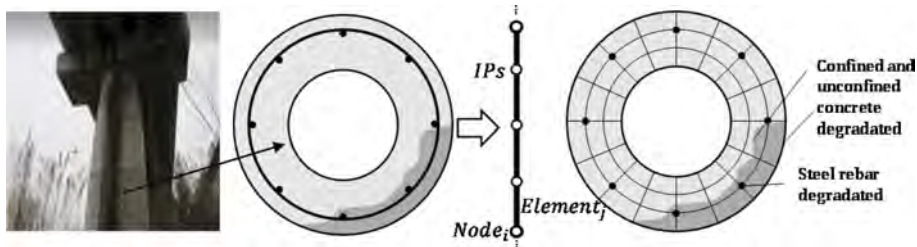


Figure 1. Conceptual depiction of the proposed approach: material-level degradation is accounted for by means pointwise variation of the fibres at the sectional level.

2.1 Description of corrosion modelling

Corrosion is a phenomenon that alters the mechanical properties of materials over the nominal life of a structure. All of this, as is well-known, can have effects on the reduction of steel in reinforcing bars, or strands in the case of prestressed concrete structures, affecting the strength and ductility of the concrete due to cracking and altering the adherence. In the case of chloride attack, pitting is the typical corrosion mechanism that occurs in reinforcement embedded in concrete. Unlike uniform corrosion that spreads uniformly over metal surfaces, pitting corrosion is a highly localised type of corrosion where a break in the protective film of the reinforcement results in a crater or pit. To explain the model, in the literature, a representation of the phenomenon has been proposed through geometric considerations (Stewart 2004). For what concerns the modelling of degradation as a spatial and temporal phenomenon, the evaluation procedure begins with the notion of the chloride profile in structural elements so that appropriate time-decay relationships of physical properties of materials can be considered. Therefore, given the environmental conditions, the following steps can be performed to assess the capacity of a concrete member (Imperatore et al. 2016):

1. Evaluation of the chloride distribution and content in time.
2. Definition of the critical corrosion content related to the corrosion initiation period.
3. Evaluation of the corrosion rate.
4. Evaluation of the rebar mass loss in time.
5. Definition of the strength decay laws of the corroded rebars versus the mass loss (or the time).
6. Structural analysis and check of corroded elements.

Regarding steps 1-2, we can refer to the diffusive models known in the literature (Chatterji 1994, 1995). Typically, unlike experimental tests with accelerated corrosion, the chloride content on the surface is about 0.4 % (by concrete weight), with a critical content of 0.05 % (by concrete weight). The evaluation of the pit depth over time can be expressed as (Stewart 2004):

$$P_x \left(\frac{\text{mm}}{\text{yr}} \right) = 0.0116 \cdot i_{\text{corr}} \cdot R \cdot t \quad (1)$$

Where the corrosion rate i_{corr} is measured as a current density $\mu\text{A}/\text{cm}^2$ (Otieno et al. 2011), R is the ratio between the maximum localised attack on steel and the average attack along the rebar surface, and it can be estimated between 4 and 8, finally, t is the time since initiation of corrosion. Focusing then on step 3, the corrosion rate, i_{corr} , should not be assumed constant

since it reduces over time due to rust which decreases the irons of steel surface. An expression of corrosion rate is:

$$i_{\text{corr}}(t) = 0.85 \cdot i_{\text{corr}}(1) \cdot t^{-0.29} \quad (2)$$

where $i_{\text{corr}}(1)$ is the corrosion rate at the beginning of propagation:

$$i_{\text{corr}}(1) = \frac{3.78 \cdot \left(1 - \frac{w}{c}\right)^{-1.64}}{c} \quad (3)$$

with c the concrete cover expressed in centimetres.

Starting from relations Equations 1-3, it is possible to evaluate the corrosion loss of the cross-sectional area of individual reinforcing steel rebars relative to the uncorroded configuration (step 4). In what follows, $X(t)$ will denote this relative reduction. In this study, the model used to predict the loss of cross-sectional area of reinforcing bar due to pitting is that proposed by Val & Melchers (1997). Then, in conjunction with the adoption of empirical factors, the constitutive laws of materials account for the spread of the spatial and temporal decay of the phenomenon (step 5) and so the structural analysis (step 6).

2.2 Impact of corrosion on mechanical behavior

A model for reducing the strength of reinforcing steel rebars was investigated by Du et al., conducting accelerated corrosion tests on reinforcing rebars embedded in concrete (Du et al. 2005b). The relationship that the authors proposed to determine the time loss of yield strength, $f_{y,\text{corr}}$ relative to the initial condition, $f_{y,\text{uncorr}}$, is:

$$f_{y,\text{corr}}(t) = (1 - 0.005 \cdot X(t)) \cdot f_{y,\text{uncorr}} \quad (4)$$

In addition, the change in strengths is interrelated with strain; therefore, the material's ductility reduction appears evident for the same modulus of elasticity. This type of corrosive process changes the expected failure from ductile to brittle.

The corrosive process of steel produces rust that expands, causing splitting stresses in the concrete and affecting the concrete's mechanical properties around the deteriorated reinforcing bar. Shayanfar *et al.* investigated the reduction of concrete strength as a function of the degree of corrosion through an experimental accelerated corrosion test (Shayanfar et al. 2016), proposing the relation:

$$f_{c,\text{corr}}(t) = (1 - \lambda(t)) \cdot f_{c,\text{uncorr}} \quad (5)$$

The percentage of loss strength compared to the initial configuration, $f_{c,\text{uncorr}}$, is related by empirical factors that consider the water/cement ratio (w/c). For instance, the reduced compressive strength due to reinforcement corrosion, Equation 5, for a specimen with a w/c equal to 0.5, can be assumed as: $\lambda(t) = 2.576 \cdot X(t) - 1.876$. The relationships Equations 4-5 make it possible to differentiate not only the individual reinforcing rebars of a section subject to degradation but also the stirrups, reflecting the loss of confinement in the mechanical property of the concrete.

3 CASE STUDIES

3.1 Experimental test of a simply supported beam subjected to a monotonic load

A laboratory test conducted by Rodriguez *et al.* in 1997 was carried out to investigate the effect of reinforcing bar corrosion on the service limit state and ultimate capacity of reinforced concrete beams (Rodriguez *et al.* 1997). The study also sought to investigate the influence of different variables, such as the level of degradation, reinforcement detailing, and interaction

versus load. The beams had a length of 2.3 m, with a cross-section of 200 x 150 mm². The diameter of the rebar used was distinguished between lower ($\Phi 10$, $\Phi 12$) and upper ($\Phi 8$) rebars, while the brackets had a diameter of 6 mm, spaced every 170 mm. Regarding the mechanical properties of the concrete, the compressive strength value is assessed around 34-37 MPa, with a water/cement ratio of 0.5. The concrete used to induct corrosion, is featured by 3% calcium chloride. The steel had a yield strength of 585 and 628 MPa, with an ultimate strength equal to 655 MPa. The accelerated corrosion process occurred for about 200 days, and the steel was subjected to a current intensity of about 0.1 mA/cm². When the corrosion process was completed, the simply supported beam was subjected to a four-point bending test loading scheme.

In Table 1, the specific values of test named 114 are reported and considered for the analysis performed. Values of numerical steel and concrete corroded reported in the mentioned table refer to the rebars $\Phi 10$. The structural analysis conducted in this study was performed using the OpenSees software framework (McKenna et al. 2010), while the deteriorated mechanical properties over time were computed by means of a set of specific subroutines written in MATLAB (The MathWorks Inc. n.d.). The user can specify the duration of corrosion, the environmental conditions, the structural configuration of a specific member and the selected rebars subjected to a deterioration process. The output files are constituted by the pointwise fibres of the section and the materials. In this way, the accurate extension of the damage around the reinforcing steel rebars is captured. The depth of crack propagation and the concrete cracked around the rebars are taken as twice the concrete cover of the section. The constitutive relations of concrete and steel material were adequately scaled. In Figure 1, a depiction of the deteriorated section after 130 days of accelerated corrosion and the comparison of the numerical-experimental test considered is represented.

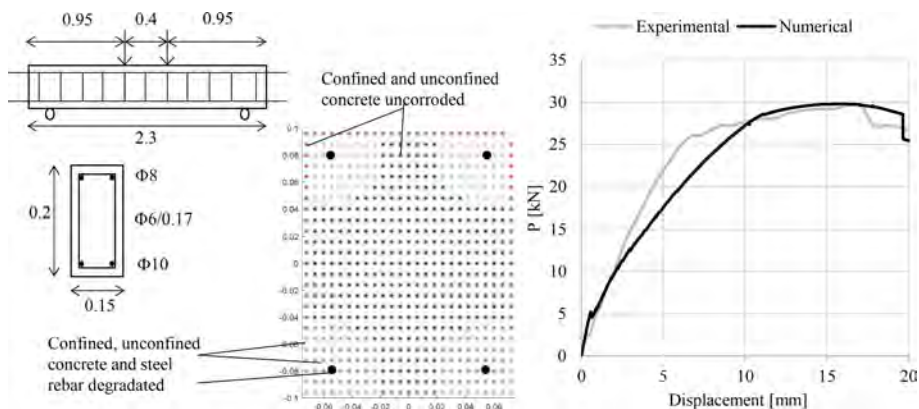


Figure 2. A) Experimental test readapted from literature (Rodriguez et al. 1997); b) section deteriorated and c) numerical response.

In the present study, five uniform nonlinear beam-column elements, with a force-based formulation and five Gauss-Lobatto integration sections, are adopted. Moreover, to capture geometric nonlinearities, the co-rotational formulation is adopted. A displacement control with an adaptive solution of the algorithm is implemented through scripts in the usual tcl programming language. In fact, the analysis is carried out through the Newton-Raphson iterative solution, and if convergence is not achieved, the displacement increment is reduced. The convergence criterion adopted is the norm of displacements, with a tolerance of 1×10^{-6} obtained through, at most, 50 iterations.

3.2 Experimental test of a pier in dynamic conditions

To the authors' knowledge, the unique available experimental test in the literature on corroded RC columns under dynamic earthquake loading is the one performed by Yuan et al.

Table 1. Properties of the test specimen 114. Unit of measure: MPa unless otherwise specified.

Uncorroded	f_c	f_{ct}	E_c	$f_{sy-su}(\Phi 10)$			
Experimental	34	3.1	27405	575-655			
Corroded	$f_{c,corr.}$	$f_{ct,corr.}$	$E_{c,corr.}$	$f_{sy,corr}(\Phi 10)$	R [-]	$p_{130 \text{ days}}(\text{mm/year})$	$X_{130 \text{ days}}(\text{mm}^2/\text{mm}^2)$
Numerical*	17.24	1.7	19515	518	7.75	4.2	0.3

* Symbols here of last three columns, refer to Equations (1-5).

(Yuan et al. 2018). In this study, the results of shaking table tests conducted for coastal bridge piers by considering the effect of a non-uniform corrosion are described. Four structural specimens with different degrees of corrosion at the designed splash and tidal zone are first fabricated by the electrochemical accelerated corrosion method and then subjected to incrementally increasing ground motions. For the complete experimental campaign, the reader may refer to the literature (Yuan et al. 2018); here, for the sake of simplicity, only a few pieces of information are reported. The diameter of the column is 200 mm with a 15 mm concrete cover and an effective height of 1.66 m. Figure 3a shows a scheme of the test as well as the time-relative displacement relationship of the specimen.

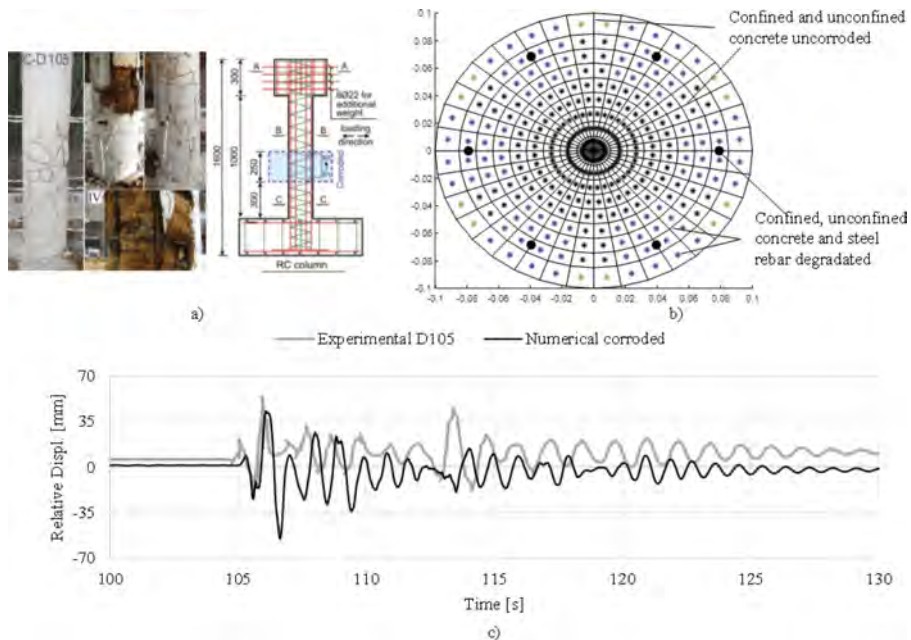


Figure 3. A) Schematic of test specimen readapted from literature (Yuan et al. 2018); b) section deteriorated and c) numerical response of the four time history.

The section consisted of 6Φ10 reinforcing steel rebars with a yield and ultimate strength of 662 MPa and 422 MPa, respectively, while the stirrups had a diameter Φ6 mm. The water-cement ratio of the concrete was equal to 0.38. The 28-day average compressive strength and modulus of elasticity were tested to be 36.27 MPa and 19.5 GPa, respectively. A mass of about 7.86 tons was placed at the head, while the extent of the zone subjected to accelerated corrosion with a current density of 300 $\mu\text{A}/\text{cm}^2$ for 105 days was 250 mm and 300 mm above the footing as represented in Figure 3. The corrosion region was immersed in a 4.0 % NaCl solution before the current was applied with the purpose to allow enough chloride ions to penetrate. The Imperial Valley “El-Centro” 1940 recording set was chosen by scaling the motion to investigate the damage process (eight-time histories were applied to the specimen with a peak-table acceleration of: 0.112 g, 0.32 g, 0.64 g, 0.85 g, 1.10 g, 1.35 g, 1.6 g and 1.85 g). The numerical degraded

section considered in the analysis is shown in Figure 3b, where the explicit representation of the deterioration can be appreciated around the rebars through the integration points, here taken as twice the concrete cover of the section. As mentioned before, even in this case the model used to predict the loss of cross-sectional area of reinforcing bars is that proposed by Val & Melchers (1997). In this study, four force-based beam-column elements are used to reproduce the specimen with five Gauss-Lobatto integration point sections. For the top node, a lumped transverse mass and an axial load were applied. In addition, the “Bond_SP01” model was used to capture the bond-slip phenomenon of the fully anchored bars at the column-to-footing in conjunction with the adoption of a single zero-length section to consider the strain penetration effects.

OpenSees model was created to perform the transient analysis of the corroded specimen using an implicit response integration scheme, namely the HHT method. Figure 3c shows the test and simulation results of the time histories of the relative displacement (between the mass block and shaking table) under the excitation of earthquake number four according to the test campaign (E4). From the figure, it can be observed that the simulated responses of the displacement match reasonably well, even though the model does not fully capture the accumulated residual displacement.

4 CONCLUSIONS

In the present study, the spreading of material’s degradation subjected to corrosion by means of the pointwise modification of fibres at the sectional level of beam-column elements was validated through the results of experimental tests. A specific subroutine developed in MATLAB has been developed to conceive this aim. Firstly, a simply supported beam subjected to a monotonic load was considered, while subsequently, the only test currently available in the literature of a column subjected to accelerated corrosion and subjected to a series of dynamic incremental loads was examined. In both cases, nonlinear beam-column type elements with diffuse plasticity were used, subjected to spatial and temporal updating of the fibres around the reinforcing bars. Specifically, the reduction of steel area and change of mechanical properties of concrete due to cracking were considered in the volume of material affected by the degradation.

One of the main advantages of the presented approach is its accuracy and feasibility; as a matter of fact, practitioners can accurately reproduce the geometry of the degradation by means of in-situ inspection and then assess the elements’ capacity without adopting more sophisticated tools. Further studies will allow the model to include brittle failure modes and additional local detailing exploring the use for large-scale analyses.

REFERENCES

- Belletti, B., Damoni, C., den Uijl, J. A., Hendriks, M. A. N., & Walraven, J. C. 2013. Shear resistance evaluation of prestressed concrete bridge beams: fib Model Code 2010 guidelines for level IV approximations. *Structural Concrete*, 14(3),242–249.
- Berto, L., Caprili, S., Saetta, A., Salvatore, W., & Talledo, D. 2020. Corrosion effects on the seismic response of existing rc frames designed according to different building codes. *Engineering Structures*, 216, 110397.
- Chatterji, S. 1994. Transportation of ions through cement based materials. Part 3 experimental evidence for the basic equations and some important deductions. *Cement and Concrete Research*, 24 (7),1229–1236.
- Chatterji, S. (1995). On the applicability of Fick’s second law to chloride ion migration through portland cement concrete. *Cement and Concrete Research*, 25(2),299–303.
- di Carlo, F., Meda, A., & Rinaldi, Z. 2017. Numerical cyclic behaviour of un-corroded and corroded RC columns reinforced with HPRC jacket. *Composite Structures*, 163, 432–443.
- Dizaj, E. A., Madandoust, R., & Kashani, M. M. 2018. Exploring the impact of chloride-induced corrosion on seismic damage limit states and residual capacity of reinforced concrete structures. *Structure and Infrastructure Engineering*, 14(6),714–729.
- Du, Y. G., Clark, L. A., & Chan, A. H. C. 2005a. Effect of corrosion on ductility of reinforcing bars. *Magazine of Concrete Research*, 57(7),407–419.

- Du, Y. G., Clark, L. A., & Chan, A. H. C. 2005b. Residual capacity of corroded reinforcing bars. *Magazine of Concrete Research*, 57(3), 135–147.
- Gara, F., Arezzo, D., Nicoletti, V., & Carbonari, S. 2021. Monitoring the Modal Properties of an RC School Building during the 2016 Central Italy Seismic Swarm. *Journal of Structural Engineering (United States)*, 147(7).
- Ghosh, J., & Padgett, J. E. 2010. Aging considerations in the development of time-dependent seismic fragility curves. *Journal of Structural Engineering*, 136(12), 1497–1511.
- Imperatore, S., Leonardi, A., & Rinaldi, Z. 2016. Strength decay of RC sections for chloride attack. *International Journal of Structural Integrity*, 7(2), 194–212.
- Jeon, J.-S., DesRoches, R., Lowes, L. N., & Brilakis, I. 2015. Framework of aftershock fragility assessment–case studies: older California reinforced concrete building frames. *Earthquake Engineering & Structural Dynamics*, 44(15), 2617–2636.
- Kashani, M. M., Alagheband, P., Khan, R., & Davis, S. 2015. Impact of corrosion on low-cycle fatigue degradation of reinforcing bars with the effect of inelastic buckling. *International Journal of Fatigue*, 77, 174–185.
- Kashani, M. M., Crewe, A. J., & Alexander, N. A. 2013. Nonlinear stress–strain behaviour of corrosion-damaged reinforcing bars including inelastic buckling. *Engineering Structures*, 48, 417–429.
- Kashani, M. M., Maddocks, J., & Dizaj, E. A. 2019. Residual Capacity of Corroded Reinforced Concrete Bridge Components: State-of-the-Art Review. *Journal of Bridge Engineering*, 24(7), 3119001.
- Koch, G. H., Brongers, P. H., Thompson, N. G., Virmani, Y. P., & Payer, J. H. (2002). Corrosion costs and preventive strategies in the United States, FHWA-RD-01-156.
- McKenna, F., Scott, M. H., & Fennes, G. L. 2010. Nonlinear Finite-Element Analysis Software Architecture Using Object Composition. *Journal of Computing in Civil Engineering*, 24(1), 95–107.
- Mehrer, H. (2007). *Diffusion in Solids (Vol. 155)*. Springer Berlin Heidelberg.
- Nicoletti, V., Arezzo, D., Carbonari, S., & Gara, F. 2022a. Detection of infill wall damage due to earthquakes from vibration data. *Earthquake Engineering and Structural Dynamics*.
- Nicoletti, V., Arezzo, D., Carbonari, S., & Gara, F. 2022b. Dynamic monitoring of buildings as a diagnostic tool during construction phases. *Journal of Building Engineering*, 46.
- Otieno, M., Beushausen, H., & Alexander, M. 2011. Prediction of Corrosion Rate in RC Structures - A Critical Review. In C. Andrade & G. Mancini (Eds.), *Modelling of Corroding Concrete Structures* (pp. 15–37). Springer Netherlands.
- Rao, A. S., Lepech, M. D., Kiremidjian, A. S., & Sun, X.-Y. 2017. Simplified structural deterioration model for reinforced concrete bridge piers under cyclic loading. *Structure and Infrastructure Engineering*, 13(1), 55–66.
- Rianna, G., Mercogliano, P., Villani, V., Nogal, M., Gervasio, H., Neves, L., Bastidas-Arteaga, E., & Tsionis, G. 2020. Expected implications of climate change on the corrosion of structures.
- Rodriguez, J., Ortega, L. M., & Casal, J. 1997. Load carrying capacity of concrete structures with corroded reinforcement. *Construction and Building Materials*, 11(4), 239–248.
- Shayanfar, M. A., Barkhordari, M. A., & Ghanooni-Bagha, M. 2016. Effect of longitudinal rebar corrosion on the compressive strength reduction of concrete in reinforced concrete structure. *Advances in Structural Engineering*, 19(6), 897–907.
- Spacone, E., Filippou, F. C., & Taucer, F. F. 1996a. Fibre beam-column model for non-linear analysis of r/c frames: part II. Applications. *Earthquake Engineering & Structural Dynamics*, 25(7), 727–742.
- Spacone, E., Filippou, F. C., & Taucer, F. F. 1996b. Fibre beam–column model for non-linear analysis of r/c frames: part I Formulation. *Earthquake Engineering & Structural Dynamics*, 25(7), 711–725.
- Stewart, M. G. 2004. Spatial variability of pitting corrosion and its influence on structural fragility and reliability of RC beams in flexure. *Structural Safety*, 26(4), 453–470.
- The MathWorks Inc. (n.d.). MATLAB 2022b.
- Val, V. D., & Melchers, R. 1997. Reliability of deteriorating RC slab bridges. 1993, 1638–1644.
- Vidal, T., Castel, A., & François, R. 2004. Analyzing crack width to predict corrosion in reinforced concrete. *Cement and Concrete Research*, 34(1), 165–174.
- Vu, N. S., Yu, B., & Li, B. 2016. Prediction of strength and drift capacity of corroded reinforced concrete columns. *Construction and Building Materials*, 115, 304–318.
- Wallbank, E. J. 1989. The performance of concrete in bridges: A survey of 200 highway bridges.
- Walraven, J., Belletti, B., & Esposito, R. 2013. Shear Capacity of Normal, Lightweight, and High-Strength Concrete Beams according to Model Code 2010. I: Experimental Results versus Analytical Model Results. *Journal of Structural Engineering*, 139(9), 1593–1599.
- Yuan, W., Guo, A., Yuan, W., & Li, H. 2018. Shaking table tests of coastal bridge piers with different levels of corrosion damage caused by chloride penetration. *Construction and Building Materials*, 173, 160–171.

Resilience-based optimal management of aging bridge networks under mainshock-aftershock sequences

L. Jafari, L. Capacci & F. Biondini
Politecnico di Milano, Milan, Italy

M. Khanmohammadi
University of Tehran, Tehran, Iran

ABSTRACT: This paper presents a mathematical framework for optimal management of aging bridge networks subjected to mainshock-aftershock sequences. The pre- and post-earthquake management of the highway systems is addressed considering performance objectives based on seismic resilience and life-cycle costs. Structural capacity of vulnerable bridges and traffic performance of the transportation network are investigated accounting for the effects of aftershocks by state-dependent fragility curves informing cumulative damage scenarios, and the effects of aging and deterioration process by time-dependent fragility curves. Optimal intervention sequences are identified under uncertainties involved related to bridge damage levels and mainshock-aftershock sequences based on a bi-objective optimization problem aiming at maximizing network resilience and minimizing costs associated with pre-event maintenance and retrofit interventions as well as post-repair restoration activities.

1 INTRODUCTION

Community seismic resilience has been defined as the ability of social units (e.g. organizations and communities) to mitigate hazards, contain the effects of disasters when they occur, and carry out recovery activities in ways that minimize social disruption and mitigate the effects of future earthquakes (Bruneau et al. 2003). An outstanding example of seismic event is the 1989 Loma Prieta earthquake on California's Central Coast, hitting the Bay Area in San Francisco, which caused numerous fatalities and injuries besides serious damage to physical facilities. The 1994 Northridge earthquake in Los Angeles was another major event that led to severe social and economic losses, especially concerning electric power outage and disruptions in the water system. In 1995, the Hyogo-ken Nanbu earthquake in Japan induced thousands of deaths and injuries along with prolonged downtime of integral lifelines such as electric, gas, water, telecommunication and transportation system. In addition to the disruptive effects of mainshocks, major seismic events such as 1994 Northridge, 2008 Wenchuan, and 2012 Emilia were followed by noticeable aftershocks, which may exacerbate the damage scenarios on mainshock-damaged structures and bridges leading to functional issues up to collapse.

Transportation networks play a significant role in the resilience of communities after extreme events such as earthquakes, by providing communication service to critical units (e.g. hospitals, fire stations, among others) and transition to damaged areas. Bridges are among the most vulnerable components of transportation networks and their damage can disrupt the emergency response (Bocchini & Frangopol 2011a, 2012a, Capacci et al. 2022). The vulnerability of bridges depends on its resistance to earthquakes which is also affected by its damage state due to aging and deterioration process (Capacci & Biondini 2020, Capacci et al. 2020a, 2020b). Retrofitting and maintenance activities as well as restoration interventions would

enhance the seismic capacity of bridges, but existing limitations for available manpower, equipment or financial resources requires an optimal management. Nonetheless, priorities are largely influenced by uncertainties in seismic hazard (e.g. ground motion variability) and structural vulnerability as well as, subsequently, bridge damage conditions and their consequence at the network scale. Optimization can aid the decision-making process defining prioritization patterns for these activities aimed at enhancing the resilience of networks accounting for the related uncertainties and constraints.

Based on this background, this paper is devoted to plan management strategies for resilient bridge networks by jointly considering pre-event management to enhance emergency response and post-event management to promote the recovery procedure by considering mainshock-aftershock sequences affecting aging bridges. A multi-objective optimization process is proposed to find Pareto-Front of optimal solutions representing optimal retrofit methods and prioritized start time of restoration activities to maximize the network resilience exposed to mainshock-aftershock sequences and minimize costs related to these strategies. The vulnerability of bridges is estimated based on fragility curves taking into account the effect of retrofitting, aging and deterioration processes and damage accumulation caused by previous shocks. A congestion-based functionality metric is used to evaluate travel time delay and distance increase due to using detours when bridges traffic capacities decrease due to damage. The proposed methodology is applied to a small-scale six-bridge transportation network exposed to a seismic scenario considering the effect of mainshock and aftershocks. The results show that one can enhance seismic resilience of transportation network with the lowest cost by selection of critical bridges to be properly retrofitted before extreme events and prioritization of bridges to start restoration activities after extreme events based on their effectiveness in functionality, their proximity to epicenters and aging or deterioration condition.

2 SEISMIC VULNERABILITY

Seismic vulnerability of bridges can be evaluated by fragility analysis. Fragility curves represent the cumulative probability of being in or exceeding each damage state for a given seismic intensity. Seismic demands i_b at bridge sites exposed to given mainshock-aftershocks sequences are evaluated by seismic hazard analysis for spatially distributed networks (Jayaram & Baker, 2009). If a bridge gets damaged with a mainshock and not recovered at the occurrence time of aftershock, its seismic capacity decreases and a state-dependent fragility curve considering damage accumulation is needed to assess seismic vulnerability. The detrimental effects of deterioration processes, such as chloride-induced corrosion, may be exacerbated by climate change and lead to increase over time the seismic vulnerability of bridges. Therefore time-dependent fragility curves are required to evaluate damage states. Retrofitting is a solution to improve seismic resistance of bridges and decrease vulnerability. Proper retrofit methods can be based on bridge type and structural damage condition.

Vulnerable elements of bridges include piers, bearings, cap beams, and joints, among others. Different retrofit methods can be applied to decrease the vulnerabilities of these components. Seismic isolator bearings and seismic restrainers are retrofit methods to decrease vulnerability related to bearings. Seat extender and reinforced concrete jacketing are effective to reduce the damage in cap beams and concrete joints. Shear keys or traverse bumpers are used to restrain traversal movement of bridges. Different kinds of jacketing such as concrete, steel, fiber reinforced polymer (FRP), engineered cementitious composite (ECC), and fabric reinforced cementitious matrix (FRCM) jacketing are used to increase the ductility and shear capacity of bridge piers. In addition, FRCM confinement may decrease the vulnerability related to environmental deterioration caused by dioxide emission or chloride diffusion, and preserve its functionality under high temperatures (Padgett & DesRoches 2009, Billah et al. 2013, Zanini et al. 2020, Skokandić et al. 2022). According to literature, retrofit, pre-existing damage condition, and deterioration may lead to considerable changes in median values, but slight changes in dispersion of fragility curves (Padgett & DesRoches 2009, Iervolino et al. 2020, Capacci et al. 2020, Ghosh & Padgett 2010).

A general formulation for fragility curves considering possible conditions leading to as-built, retrofitted, state-dependent, and time-dependent fragility curves, can be formulated as follows:

$$P[S_b \geq s_b | \hat{s}_b, r_b, i_b, t_b] = \Phi \left[\frac{\ln(i_b) - \ln(MF_a(s_b, t_b) \cdot MF(s_b, \hat{s}_b, r_b) \cdot i_{b,m}(s_b))}{\zeta_{s,b}(s_b)} \right], \quad s_b > \hat{s}_b \quad (1)$$

where S_b = variable representing the damage state of the b -th bridge in the network with values $s_b = 0, 1, 2, 3, 4$ associated with no damage, slight, moderate, extensive, and complete damage state, respectively; \hat{s}_b = pre-existing damage state; r_b = retrofit method and takes the value 1 for a non-retrofitted bridge, and values 2, 3, ... for different types of retrofit interventions; i_b = seismic intensity at b -th bridge site; $i_{b,m}(s_b)$ = median intensity measure leading to the exceedance of a given damage state s_b ; $\zeta_{s,b}(s_b)$ = standard deviation of the natural logarithm of the intensity measure leading to the exceedance of a given damage state s_b ; t_b = bridge age; $MF(s_b, \hat{s}_b, r_b)$ = modification factor for median values of fragility curves for damage state s_b considering retrofit measure r_b and pre-existing damage state \hat{s}_b ; $MF_a(s_b, t_b)$ = modification factor for median values of fragility curves for damage state s_b considering the bridge age t_b at occurrence time of shocks, with $MF_a(s_b, t_b) \leq 1$. Figure 1 shows typical trends of modification factors.

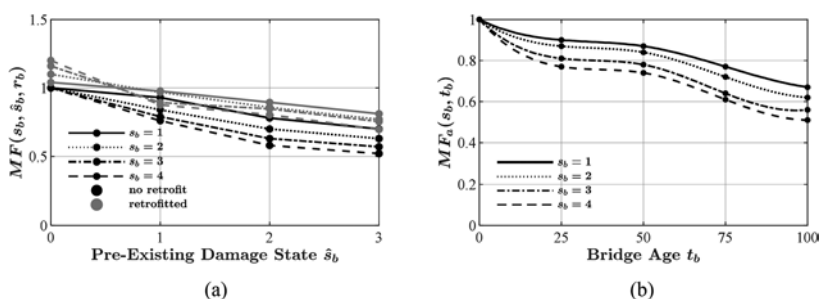


Figure 1. Typical trends for modification factors: (a) $MF(s_b, \hat{s}_b, r_b)$; (b) $MF_a(s_b, t_b)$.

For $s_b = \hat{s}_b$, $P[S_b \geq s_b | \hat{s}_b, r_b, i_b, t_b] = 1$, and for $s_b = 5$, $P[S_b \geq s_b | \hat{s}_b, r_b, i_b, t_b] = 0$. The occurrence probability of damage state s_b on bridge b is hence evaluated based on fragility curves as follow:

$$P[S_b = s_b | \hat{s}_b, r_b, i_b, t_b] = P[S_b \geq s_b | \hat{s}_b, r_b, i_b, t_b] - P[S_b \geq s_b + 1 | \hat{s}_b, r_b, i_b, t_b], \quad s_b \geq \hat{s}_b \quad (2)$$

It is worth noting that for $s_b < \hat{s}_b$, the probability of being in damage state s_b is equal to zero ($P[S_b = s_b | \hat{s}_b, r_b, i_b, t_b] = 0$). An average of occurrence probabilities of different damage states can be used to quantify damage level l_b of each bridge affected by an earthquake (Bocchini & Frangopol 2011a):

$$l_b = E(S_b) = \sum_{s_b \geq \hat{s}_b}^4 s_b \cdot P[S_b = s_b | \hat{s}_b, r_b, i_b, t_b] \quad (3)$$

The damage level l_b is bounded within the interval $[0, 5) \subset \mathbb{R}$.

3 RESILIENCE FRAMEWORK

Spatially distributed bridges in a transportation network exposed to earthquakes might experience different damage levels. These damage levels combination is representative of bridge network damage state. Since damage level l_b takes values in the interval $[0, 5)$, the total number of possible network damage level combinations are discretized by rounding the damage level

l_b to the nearest smaller integer to define the expected damage state for each bridge (i.e. 0, 1, 2, 3, 4). The expected damage state combinations can be collected in a vector s representing the bridge network damage state, with N_b columns denoting the number of bridges and N_s rows denoting the total number of possible network damage combinations. The damage levels l_b can be evaluated by using fragility curves, explained in seismic vulnerability section.

To quantify resilience, a proper performance metric representing the network functionality for each damage state combination s caused by shocks is required. In this paper, a performance metric based on total travel time $TTT(s)$ and total travel distance $TTD(s)$ is used (Bocchini & Frangopol 2012a, b). These functionality indicators are computed by combined traffic assignment and distribution problem (Bocchini & Frangopol 2011b) for each damage state combination s . Damage states of bridges are taken into account by considering the time delay and distance increase caused by using detours when bridges are partially or completely closed. In this case, it is considered that for expected damage states 0, 1, 2, 3, and 4, the bridge traffic capacity is respectively 100, 75, 50, 25, and 0 percentage of the undamaged bridge. Considering different factors such as bridge type, available resources affect the restoration process of damaged bridges. It is assumed that each bridge will restore from a damage level to the next one over a definite time interval.

Therefore, by selecting proper retrofit method and start time of restoration activities for each bridge, network functionality can be evaluated at each time step based on the current damage state. In this way, the network resilience can be computed as follow (Capacci & Biondini 2020):

$$R = \frac{1}{\Delta t_h} \sum_{i=0}^{N_t} Q_i(s) \cdot \Delta T_i \quad (4)$$

where Δt_h = time horizon; ΔT_i = time step; N_t = total number of time steps in the network recovery process; and $Q_i(s)$ = network functionality at i -th time step with respect to the damage state combination s .

Resilience R to be maximized and cost C to be minimized are considered as targets in a bi-objective optimization problem to inform the decision-making process addressing the retrofitting and restoring interventions. Decision variables are retrofit methods and start time of restoration activities selected from a time horizon, for each bridge. Constraints on the maximum number of simultaneous restoration activities and maximum time duration for simultaneous restoration activities that can be done on different bridges, are applied due to limited resources. This multi-objective constrained problem is solved by NSGA-II (Deb et al. 2002) meta-heuristic algorithm using penalty functions. Decision makers can select optimal solutions from Pareto-Front obtained by solving the optimization problem, based on their required resilience, budgets and available resources. Further details can be found in Jafari et al. (2023).

4 APPLICATION

The proposed methodology is applied to the small-scale six-bridge network shown in Figure 2a, exposed to a mainshock- aftershocks scenario at times 0, 3, and 7 months with magnitudes m equal to 7.0, 6.8, and 7.5, respectively. The ages of bridges are 50, 20, 40, 100, 70, and 80 years at the occurrence time of mainshock. Modification Factors $MF_a(s_b, t_b)$ are based on Figure 1. The seismic demands i_b obtained by attenuation law (Bindi et al. 2011) are shown in Figure 2b. The bridge network functionality for each damage state combination $Q(s)$ is computed by the combined traffic assignment and distribution problem.

It is assumed that B1 is a multi-span continuous (MSC) steel girder bridge, B2 and B5 are multi-span simply supported (MSSS) concrete girder bridges, B3 is MSSS steel girder bridge, and B4 and B6 are MSC concrete girder bridges. The details of these four types of bridges and their as-built fragility curves parameters can be found in Padgett (2007) and Padgett & DesRoches (2009). The optimal retrofit methods are selected from those listed in Table 1 and 2. Modification factors $MF(s_b, \hat{s}_b=0, r_b)$ and costs of these retrofit methods are supported by engineering judgments and based on literature (Padgett 2007, Raza et al. 2019, Zanini et al. 2020). It is assumed

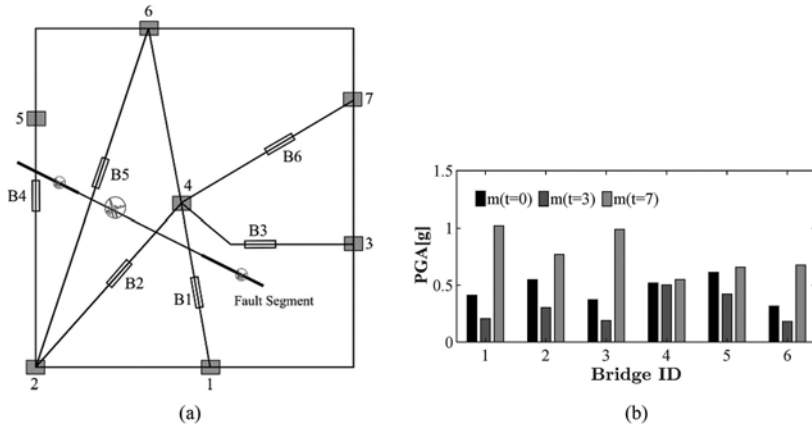


Figure 2. (a) Bridge network layout and fault segment. (b) Seismic demands at bridge sites associated with mainshock and aftershocks.

that the modification factor $MF(s_b, \hat{s}_b, r_b)$ for each s_b and $\hat{s}_b = 1, 2,$ and 3 is $0.9, 0.8,$ and 0.7 times the corresponding modification factor $MF(s_b, \hat{s}_b=0, r_b)$ for each s_b , respectively. A detour of 30 km is assumed for each bridge. Restoration cost for one month time unit is considered 250 k\$. More details about bridge network traffic characteristics, as well as the required recovery time for each damage state of each bridge type, can be found in Jafari et al. (2023).

Table 1. Modification factors $MF(s_b, \hat{s}_b=0, r_b)$ for bridges with steel girders.

r_b	Retrofit methods	MSSS Steel girder				MSC Steel girder				Cost [k\$]
		$s_b=1$	$s_b=2$	$s_b=3$	$s_b=4$	$s_b=1$	$s_b=2$	$s_b=3$	$s_b=4$	
1	No retrofit	1.00	1.00	1.00	1.00	1.00	1.00	1.00	1.00	0.0
2	Steel Jackets	1.06	1.06	1.07	1.13	1.04	1.14	1.14	1.18	36.0
3	Elastomeric Isolation Bearings	1.57	1.00	1.37	1.39	1.37	1.00	1.27	1.61	70.4
4	Restrainer Cables	1.03	1.03	1.04	1.11	1.03	1.05	1.11	1.17	16.5
5	Seat Extenders	1.00	1.00	1.00	1.26	0.99	1.01	1.00	1.21	12.0
6	Shear Keys	0.99	0.98	0.98	0.97	1.08	1.14	1.13	1.09	12.0
7	Restrainer Cables & Shear Keys	1.02	1.02	1.04	1.09	1.09	1.17	1.21	1.21	28.5
8	Seat Extenders & Shear Keys	0.99	0.98	0.99	1.23	1.09	1.15	1.15	1.41	24.0
9	Concrete Jacketing	1.05	1.03	1.04	1.11	1.03	1.07	1.09	1.15	100.0
10	ECC Jacketing	1.08	1.12	1.12	1.16	1.05	1.29	1.23	1.22	120.0
11	CFRP Jacketing	1.07	1.10	1.11	1.17	1.05	1.23	1.22	1.23	32.0
12	FRCM Jacketing	1.07	1.20	1.30	1.50	1.05	1.26	1.37	1.58	70.0

The solution of the bi-objective optimization problem involves several computational steps. The damage level of bridges is firstly evaluated at each time step (0.2 month), based on recovery process and fragility curves, for restoration and retrofit strategies selected by NSGA-II algorithm, to obtain the bridge network damage state s at each time step of selected time horizon $\Delta t_h = 2$ years. Therefore, the bridge network functionality at each time step $Q_\lambda(s)$ is determined. Then the bridge network resilience R and cost C of selected retrofit and restoration strategies are quantified. Start times of restoration intervention are selected from a time horizon $\Delta t_h = 2$ years and it is assumed that maximum three simultaneous restoration activities with maximum time interface of 12 months can be done on different bridges. The optimal Pareto-Front solutions obtained by solving the optimization process are shown in Figure 3. Several optimal solutions are selected from the Pareto-Front and reported in Table 3. The outputs extracted from these solutions include network functionality (Figure 4) and bridge damage profile with the corresponding recovery schedule charts (Figure 5) that provide essential information for decision makers.

Table 2. Modification factors $MF(s_b, \hat{s}_b=0, r_b)$ for bridges with concrete girders.

r_b	Retrofit methods	MSSS Concrete girder				MSC Concrete girder				Cost [k\$]
		$s_b=1$	$s_b=2$	$s_b=3$	$s_b=4$	$s_b=1$	$s_b=2$	$s_b=3$	$s_b=4$	
1	No retrofit	1.00	1.00	1.00	1.00	1.00	1.00	1.00	1.00	0.0
2	Steel Jackets	1.05	1.30	1.33	1.41	1.03	1.16	1.17	1.20	36.0
3	Elastomeric Isolation Bearings	1.62	1.00	1.05	1.17	2.94	1.31	1.21	1.17	70.4
4	Restrainer Cables	1.01	1.07	1.10	1.13	1.04	0.96	1.01	1.05	16.5
5	Seat Extenders	0.99	1.03	1.02	1.32	1.01	1.00	1.00	1.31	12.0
6	Shear Keys	1.04	0.97	0.92	0.87	1.01	0.98	0.99	1.01	12.0
7	Restrainer Cables & Shear Keys	1.06	1.03	1.06	1.07	1.04	0.96	1.04	1.12	28.5
8	Seat Extenders & Shear Keys	1.04	1.01	0.95	1.22	1.01	0.97	0.99	1.37	24.0
9	Concrete Jacketing	1.04	1.14	1.20	1.33	1.03	1.08	1.10	1.16	100.0
10	ECC Jacketing	1.07	1.62	1.54	1.51	1.04	1.33	1.28	1.25	120.0
11	CFRP Jacketing	1.06	1.49	1.52	1.53	1.03	1.26	1.27	1.26	32.0
12	FRCM Jacketing	1.06	1.50	1.63	1.88	1.04	1.27	1.38	1.59	70.0

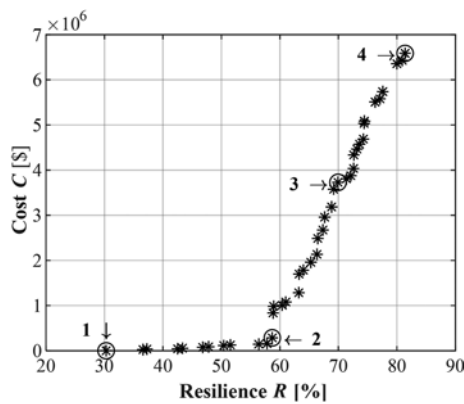


Figure 3. Pareto- Front of optimal solutions.

Table 3. Details of selected Pareto-Front solutions.

#	Retrofit strategy						Start time of restoration intervention						Resilience [%]	Cost [M\$]
	B1	B2	B3	B4	B5	B6	B1	B2	B3	B4	B5	B6		
1	1	1	1	1	1	1	24.0	24.0	24.0	24.0	24.0	24.0	30.3	0.0
2	6	11	12	12	12	11	24.0	24.0	24.0	24.0	24.0	24.0	58.7	0.3
3	6	11	12	5	12	11	7.0	24.0	24.0	24.0	24.0	7.2	69.9	3.7
4	6	11	12	12	12	11	7.0	11.0	6.8	24.0	24.0	6.8	81.4	6.6

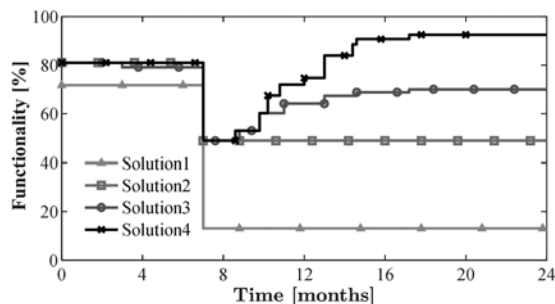


Figure 4. Network functionality profile for selected optimal solutions.

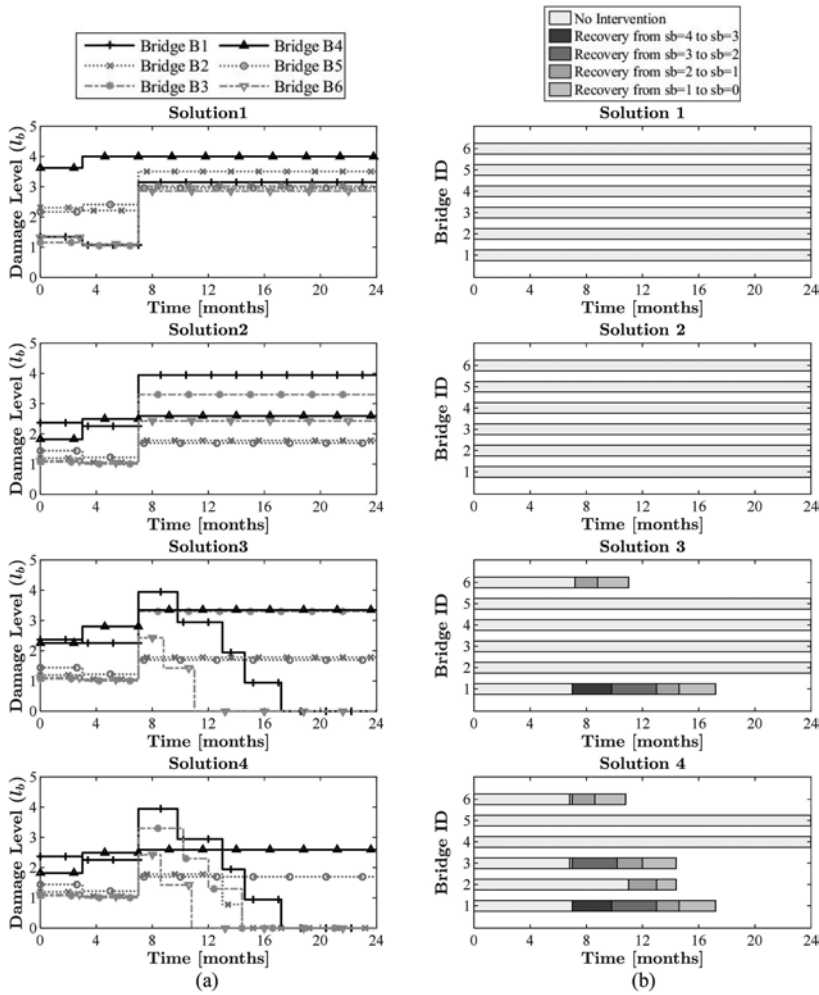


Figure 5. (a) Damage levels profiles and (b) corresponding recovery schedule charts for selected optimal solutions.

5 CONCLUSIONS

A resilient transportation network is an integral part of a resilient community, and bridges as the most susceptible components to extreme events such as earthquakes, should be the center of attention. The seismic performance of existing aged bridges might decrease due to deterioration process such as chloride induced corrosion or climate changes. Also, most of these bridges were not designed based on seismic design codes. As pre-event interventions, different retrofit methods based on bridge type and structural condition can be applied. Also, effective post-event activities are needed to recover rapidly the bridge network functionality after an extreme earthquake. After a mainshock, corresponding aftershocks might also strictly affect the bridge network resilience. Optimal resource allocation is the priority of managers and decision makers to improve the resilience of infrastructures. This paper presented an optimization methodology to find optimal interventions for applying to bridges taking into account all possible factors affecting resilience. The vulnerability of bridges has been calculated based on time-dependent, state-dependent, retrofitted and pristine bridge fragility curves. The objectives are maximizing resilience and minimizing cost of rehabilitation interventions, considering retrofit methods and start time of restoration activities as decision variables. The optimization

problem has been applied to a small-scale bridge network. Decision makers could select optimal solutions of Pareto-Front obtained from optimization process based on their budget and available resources. Further research is needed to extend the proposed approach to large scale networks and to account for a wider spectrum of retrofitting interventions and maintenance strategies.

REFERENCES

- Billah, A. M., Alam, M. S. & Bhuiyan, M. R. 2013. Fragility analysis of retrofitted multicolumn bridge bent subjected to near-fault and far-field ground motion. *Journal of Bridge Engineering* 18(10): 992–1004.
- Bindi, D., Pacor, F., Luzi, L., Puglia, R., Massa, M., Ameri, G. & Paolucci, R. 2011. Ground motion prediction equations derived from the Italian strong motion database. *Bulletin of Earthquake Engineering* 9(6): 1899–1920.
- Bocchini, P. & Frangopol, D. 2011a. Resilience-driven disaster management of civil infrastructure. *Computational methods in structural dynamics and earthquake engineering*: 25–28.
- Bocchini, P. & Frangopol, D. M. 2011b. A stochastic computational framework for the joint transportation network fragility analysis and traffic flow distribution under extreme events. *Probabilistic Engineering Mechanics* 26(2): 182–193.
- Bocchini, P. & Frangopol, D. M. 2012a. Optimal resilience-and cost-based post disaster intervention prioritization for bridges along a highway segment. *Journal of Bridge Engineering* 17(1): 117–129.
- Bocchini, P. & Frangopol, D. M. 2012b. Restoration of bridge networks after an earthquake: Multicriteria intervention optimization. *Earthquake Spectra* 28(2): 427–455.
- Bruneau, M., Chang, S. E., Eguchi, R. T., Lee, G. C., O'Rourke, T. D., Reinhorn, A. M., Shinozuka, M., Tierney, K., Wallace, W. A. & Von Winterfeldt, D. 2003. A framework to quantitatively assess and enhance the seismic resilience of communities. *Earthquake spectra* 19(4): 733–752.
- Capacci, L. & Biondini, F. 2020. Probabilistic life-cycle seismic resilience assessment of aging bridge networks considering infrastructure upgrading. *Structure and Infrastructure Engineering* 16(4): 659–675.
- Capacci, L., Biondini F. & Frangopol D. M. 2022. Resilience of aging structures and infrastructure systems with emphasis on seismic resilience of bridges and road networks. *Resilient Cities and Structures* 1(2): 23–41.
- Capacci, L., Biondini F. & Kiremidjian, A. 2020a. Damage disaggregation for seismic resilience assessment of aging bridge networks. *17th World Conference on Earthquake Engineering (17WCEE)*: 1–12.
- Capacci, L., Biondini, F. & Titi, A. 2020b. Lifetime seismic resilience of aging bridges and road networks. *Structure and Infrastructure Engineering* 16(2): 266–286.
- Deb, K., Pratap, A., Agarwal, S. & Meyarivan, T. 2002. A fast and elitist multi objective genetic algorithm: Nsga-ii. *IEEE transactions on evolutionary computation* 6(2): 182–197.
- Ghosh, J. & Padgett, J. E. 2010. Aging considerations in the development of time-dependent seismic fragility curves. *Journal of Structural Engineering* 136(12):1497–1511.
- Iervolino, I., Chioccarelli, E., & Suzuki, A. 2020. Seismic damage accumulation in multiple mainshock–aftershock sequences. *Earthquake Engineering & Structural Dynamics* 49(10): 1007–1027.
- Jayaram, N. & Baker, J. W. 2009. Correlation model for spatially distributed ground-motion intensities. *Earthquake Engineering & Structural Dynamics* 38(15): 1687–1708.
- Jafari, L., Khanmohammadi, M., Capacci, L. & Biondini, F. 2023. Resilience-based optimal seismic retrofit and recovery strategies of bridge networks under mainshock-aftershocks sequences. *Journal of Infrastructure Systems*, ASCE (submitted).
- Padgett, J. E. 2007. *Seismic vulnerability assessment of retrofitted bridges using probabilistic methods*. Ph.D. thesis, Georgia Institute of Technology, USA.
- Padgett, J. E. & DesRoches, R. 2009. Retrofitted bridge fragility analysis for typical classes of multispan bridges. *Earthquake Spectra* 25(1): 117–141.
- Raza, S., Khan, M. K., Menegon, S. J., Tsang, H.-H. & Wilson, J. L. 2019. Strengthening and repair of reinforced concrete columns by jacketing: State-of-the-art review. *Sustainability* 11(11): 3208.
- Skokandić, D., Vlašić, A., Kušter Marić, M., Srbić, M. & Mandić Ivanković, A. 2022. Seismic assessment and retrofitting of existing road bridges: state of the art review. *Materials* 15(7): 2523.
- Zanini, M. A., Toska, K., Faleschini, F. & Pellegrino, C. 2020. Seismic reliability of reinforced concrete bridges subject to environmental deterioration and strengthened with FRCC composites. *Soil Dynamics and Earthquake Engineering* 136: 106224.

Risk-based optimal life-cycle maintenance of post-tensioned concrete bridges considering accuracy of inspection methods in structural model updating

M. Taeb, A.B. Mehrabi & K. Lau
Florida International University, Miami, USA

ABSTRACT: This paper recommends a procedure for risk-based lifetime cost optimization of maintenance for PT bridges. To demonstrate the procedure, an actual segmental post-tensioned bridge is used for which the inspection results are available. Hands-on and nondestructive tests were performed on several external PT tendons to verify the accuracy. The results showed that non-destructive evaluation (NDE) and hands-on inspection results are correlated, as such, the level of accuracy for the selected methods to be used for the inspection was determined to be acceptable for the inspection to continue in large scale. External tendons of the bridge were then inspected using the selected NDE method. The inspection results were used to calculate the reduction in the cross section of post tensioning elements. Investigation is underway to optimize the lifetime risk of the bridge, simplified reliability analysis associated with updated finite element model subjected to deterioration of the external post tensioning elements.

1 INTRODUCTION

Considerable number of Post-Tensioned (PT) bridges have been constructed because PT systems enable them to carry significant traffic loads and have an aesthetical structure at the same time. However, corrosion has been a long-standing issue for PT tendon that leads to the weakening and failure of tendons and deterioration of the structural performance. In the case of external PT tendons, the limited interaction points between the post-tensioning elements and the main structure increases the redundancy and reliability concerns for the PT elements in terms of deterioration. Because of this, the inspection of post-tensioning system, updating structural model, and reliability analysis of deteriorating PT bridges are of great importance. To address this need, a risk-based decision support system for maintenance of post tensioned concrete bridges (Taeb & Mehrabi 2019) can be adopted. Figure 1 shows the modules of the corresponding decision support system, research modules completed, and ongoing research modules. This paper aims to demonstrate the application of such decision support system on a bridge, called here the bridge of case study. The first module of the decision support system is the selection of inspection method which is developed in the independent paper (Taeb & Mehrabi 2022). Normally, the inspection results are used deterministically to estimate the existing condition of the bridge ignoring the probability of false results. To address this shortcoming, the second module is the stochastic condition assessment covers the applicable condition ratings and probability of true and false condition diagnostic during the inspection, and proposes a new approach in considering inspection results. The third Module is the inspection of external post tensioning elements of the bridge of case study and discussion on the inspection results. The fourth Module focuses on the available maintenance scenario for the post tensioning elements which include “No action”, “Repair”, and “Replacement” of the external tendons. The fifth module proposes a deterioration model for the post tensioning elements which will be used in the structural simulation of maintenance scenarios in time and the

lifetime risk analysis of the bridge of case study. Ongoing research modules include finite element modeling, updating structural model based on the inspection results, structural simulation of the maintenance scenarios, reliability analysis, and scenario-based lifetime risk analysis that are under investigation and will be presented in future works.



Figure 1. Risk-based decision support system for maintenance of post-tensioned concrete bridges.

2 STOCHASTIC CONDITION ASSESSMENT

Structural condition assessment is based on condition rating, and the post-tensioning system is not an exception. A variety of condition rating methods are available in the literature (AASHTO 2018). The purpose of this module is determination of stochastic parameters of the rating diagnosis in NDE test, which will be used in modules to follow. An arrangement of condition rating for post tensioning elements is used in this study which was developed by Taebay and Mehrabi (Taebay & Mehrabi 2022) based on comparable SNBI rating.

To determine the actual accuracy and the analysis of rating diagnostic, twenty tendons among more than one thousand were randomly selected. Figure 2 is the sketch showing the cross-section of the bridge of the case study in the bridge span.

True rating diagnosis are the cases where the result of the NDE and destructive test are the same. False diagnosis refers to cases where the result of the impact testing is not the same as the dissection inspection method, however, the result of the NDE method in this case could have indicate a condition worse or better than the result of the dissection test which assumed to be as the inspection method with zero false diagnostic. Overrated false diagnosis is the case that NDE reports the condition rating better than the condition assessed by the dissection test, which can be considered as non-conservative. Underrated false diagnosis is the case that NDE reflects the condition rating more than the condition assessed by the dissection test, which can be considered as conservative.

Based on the results of investigation among the twenty cases investigated, fourteen true diagnosis (70%), three (15%) underrated false diagnosis, and three (15%) Overrated false diagnosis were reported. Figure 3 shows the results of the investigation on stochastic parameters of condition assessment in the bridge of case study.

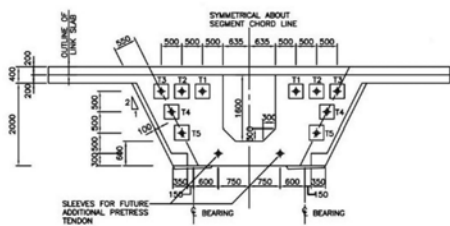


Figure 2. Typical cross section of the approach viaduct.

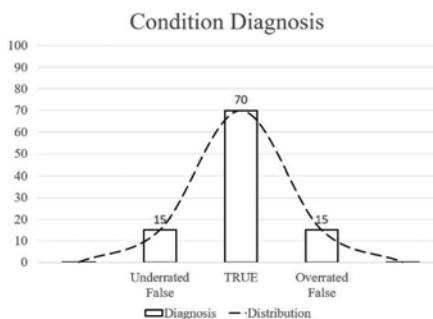


Figure 3. Stochastic parameters of condition assessment in the bridge of case.

3 INSPECTION OF EXTERNAL POST TENSIONING ELEMENTS AND THE RESULTS

The bridge of case study is one span of the approaches which is constructed as a post-tensioned segmental bridge. The bridge is simply supported and is spanned 35 meter with 10 external post-tensioned tendons along the entire span. There are three deviators inside the box and the external tendons were passed through pipes embedded in these deviators. There are two holes in the deviators and diaphragms anticipated by the designer to accommodate additional PT tendons if necessary. There are 5 tendons at the left side of the section (from L1 to L5) and there are 5 tendons at the right side of the section (from R1 to R5). The inspection results based on SNBI rating for corresponding tendons are concluded in Table 1. Figure 4 shows one of the anchorage caps in the bridge of case study which strands are exposed to the environment. Figure 5 shows one of the tendons in the critical condition (Condition Rating 2).

Table 1. Inspection results for the ramp bridge of the case study.

Tendon	L1	L2	L3	L4	L5	R1	R2	R3	R4	R5
Condition	7	6	0	6	8	3	7	5	5	4



Figure 4. One of the anchorages without proper cap.



Figure 5. Critical condition of a tendon.

4 MAINTENANCE SCENARIO IDENTIFICATION

Three scenarios considered for maintenance of external post tensioning elements are, “no action”, “repair”, and “replacement”. “No action” means that there is no need to change the current condition of the tendon and the tendon will be kept in the same condition as it is.

In the case of “repair,” there are actions that needed for the free length of the tendons as well as the anchorages. These actions cannot change the structural condition of the tendons, however nonstructural parts of the tendons which are the corrosion protection barriers will be repaired.

To address the issues in anchorage zones activities such as cleaning and brushing the anchor plate/wedge plate, and installation of new galvanized steel caps on the anchorage zone will also be needed.

In the case of “Replacement”, that is removing the existing tendon and installing a new tendon, both structural and nonstructural conditions will be changed to “excellent” condition. The replacement procedure includes the steps of structural safety determination, submittal of theoretical elongations and jacking forces, cutting the old tendon, new strands and HDPE pipe installation, stressing of the new strands, grouting, and quality control check.

5 DETERIORATION MODEL FOR POST-TENSIONING ELEMENTS

In this research, the authors considered the localized corrosion in addition to uniform corrosion. Localized corrosion is normally one of the serious side effects of excess bleed water and

usually appears within ten years from construction (Permeh, Samanbar & Lau 2022; Carsana & Bertolini 2015). The slope and height of the tendons in post tensioning system influences the chance of grout segregation and probability of the localized corrosion. Uniform corrosion is characterized by corrosive attack progressing evenly over the entire surface area. Corrosion protection barriers prevent the uniform corrosion to occur on strands. Proposed deterioration model includes parameters involved in both local and uniform corrosion.

To follow the risk-based decision support system for maintenance of post tensioned concrete bridges, the probability of failure in a deteriorating PT tendon is needed. Equation (1) is introduced to represent the probability of failure of a tendon due to local and uniform corrosion.

$$P_f(t) = \omega P_f^L(t) + (1 - \omega) P_f^U(t) \quad (1)$$

P_f is the probability of failure of a tendon, ω is the percentage of the tendons impacted by localized corrosion, P_f^L is the probability of failure of the tendon due to localized corrosion and P_f^U is the probability of failure of the tendon due to uniform corrosion. It is assumed that the chance of occurrence of severe local and uniform corrosion at the same time is zero. This assumption supports the thinking that the bleeding is within the corrosion protection system while uniform corrosion occurs when the protection system fails. Since the research on the corrosion speed due to bleed water is still ongoing, the probability of the failure caused by localized corrosion should be considered stochastic. Suitable distribution to demonstrate the failure of the tendon due to localized corrosion is an exponential distribution. The exponential distribution is frequently used for reliability calculations as a first cut based on its simplicity to generate the first estimate of reliability when more details failure modes are not described (Ott/Longnecker 2015). If the expected service life of a tendon attacked by bleed water is assumed t_L , the corresponding coefficient of the exponential distribution and the probability then will be determined using Equation (2).

$$P_f^L(t) = 1 - e^{-\lambda t}; \lambda_L = \frac{1}{t_L} \quad (2)$$

The probability of failure due to uniform corrosion, however, needs further assumptions. It can be assumed that the rate of corrosion in protected tendon by corrosion protection barriers is diminished. Nonetheless there is a chance for the protection system to fail. Therefore, the probability of failure of a tendon due to uniform corrosion includes the failure of the corrosion protection system and probability of structural failure of the tendon considering the time for tendon to be corroded. Penetration time for external ions and moisture content needed for the corrosion to occur is considered at the time to failure of the corrosion protection system (t_1).

$$P_f^U(t) = P_f^P(t = t_1) \times P_f^S(t = t) \quad (3)$$

In Equation (3) P_f^P is the probability of failure of the corrosion-protection system, P_f^S is the probability of structural failure of the tendon due to uniform corrosion, t_1 is the time which the protection system fails, and t is the time. The probability of failure of the corrosion protection barriers can be estimated by exponential distribution based on expected remaining lifetime of the protection system (t_0). It is based on the condition of the corrosion protection system. The probability of failure of the corrosion protection system is determined by Equation (4).

$$P_f^P(t) = 1 - e^{-\lambda_P t}; \lambda_P = \frac{1}{t_0} \quad (4)$$

Equations (5) to (8) are to determine the probability of structural failure of a tendon.

$$P_f^S(t) = P(Y < 1) \quad (5)$$

$$Y = \frac{\text{Capacity}}{\text{Demand}} = \frac{R}{Q} \quad (6)$$

$$R = \varphi_c f_y A_0 (1 - \omega) g_U \quad (7)$$

$$Q = \frac{f_y A_0}{S} \quad (8)$$

In Equations (5) to (8), Y is the capacity to demand ratio, R is the capacity of the tendon based on the corresponding condition and Q is the demanding design load which the tendon should carry. It is assumed that the distribution for both R and Q are lognormal (Nowak & Collins 2000), hence the distribution for Y is also lognormal. It is also assumed that the tensile stress is uniformly distributed across the cross section.

φ_c is the condition factor, f_y is the yielding stress of high stress steel, A_0 is the intact cross section of the strand, ω is the percentage of the tendons attacked by the localized corrosion, g_U is the deterioration function, and S is the design safety factor.

Equation (9) represents the parameters involved in the deterioration function.

$$g_U(t) = \begin{cases} 1, & t < t_1 \\ (1 - R_U(t - t_1))^2, & t \geq t_1 \end{cases} \quad (9)$$

R_U is the corrosion rate which is selected based on the environmental condition of the bridge location. Table 2 summarizes the recommended corrosion rates for variety of environments based on literature (Sivakumar et al. 2011; Ghosn et al. 2013). Corrosion rates are dependent on variety of parameters as discussed in the last section of this paper, therefore, the rates in the Table 2 should be considered as rough estimates for the decision support system and are subject to change on case-by-case basis. The time which corrosion protection system fails is t_1 . In Equation (9) it is assumed that the corrosion reduces the radius of the strand. It is also assumed that the residual materials caused by the corrosion does not influence the corrosion rate. It is also assumed that the corrosion is uniformly distributed along the free length of the tendon.

Table 2. Uniform corrosion rates based on the environmental condition of the bridge.

Climate type	$I_{\text{corr}} \left(\frac{\mu\text{A}}{\text{mm}^2} \right)$	Metal Loss (mmpy)
Dry	$<1.2 \times 10^{-4}$	5.817×10^{-3}
Temperate/Continental	$1.2 \times 10^{-4} - 2.4 \times 10^{-4}$	$5.817 \times 10^{-3} - 11.61 \times 10^{-3}$
Tropical	$2.4 \times 10^{-4} - 24 \times 10^{-4}$	$11.61 \times 10^{-3} - 116 \times 10^{-3}$

For determination of the structural failure of the tendon, since Y is lognormally distributed, coefficient of variance and mean value of the parameters involved in corrosion are needed. In the proposed deterioration model, it is recommended to estimate t_0 based on the condition of the corrosion protection system, therefore, Table 3 includes the recommended coefficient of variance for the deterioration function (g_U) with respect to t_0 .

5.1 Case study

The bridge of case study (Figure 2) is one of the spans in a 6-km long bridge for which damages to the external tendons was found during a routine inspection. Inspection results for all 10 external tendons for this span were available. In this paper, the deterioration of one tendon with poor condition of corrosion protection barrier is investigated ($t_0=25$ year). Design safety factor is considered $S=1.45$. The structural condition of the tendon is satisfactory $\varphi_c = 1$. Coefficient of variance for the condition factor φ_c is 15% and for safety factor, S, is diminished. Inspection

Table 3. Estimated t_0 and coefficient of variance for g_U based on condition of corrosion protection system.

Condition	Explanation	Recommended t_0 (year)	COV g_U
Good	No defect is observed in the corrosion protection system. Few defects such as small voids are observed through the free length of the tendon. Anchorage cap has some minor defects. Defects are not correlated together. There is no clue for sever environmental interaction for the strand.	75	0.2
Fair	Significant voids in the grout are observable. Initial clues of fatigue in the HDPE layer are observable. The chance of environmental interaction for the strand is not significant. The anchorage zone is not properly sealed. No evidence for the environmental interaction.	50	0.3
Poor		25	0.4

results 8 years after the operation of the bridge shows that 10% of the external tendons are impacted by local corrosion and almost in the failed condition ($\omega=10\%$, $t_L=8$ year). It is worth noting that the true and false probability of diagnosis for the inspection is 0.7 and 0.3, respectively. The bridge of case study is located in the region with tropical climate, therefore, the inspection team decided to consider uniform corrosion rate of $R_U=0.075$ mmpy.

Effective percentage of the tendons impacted by local corrosion based on the stochastic parameters of condition assessment will be determined using Bayesian updating.

$$\omega' = P(\text{local}|\text{true}) + P(\text{uniform}|\text{false}) = 0.1 \times 0.7 + 0.9 \times 0.3$$

$$\omega' = 0.34, 1 - \omega' = 0.66$$

By substitution of corresponding values in the Equations (1) to (9) for different values of t_1 (time to failure of corrosion protection barrier), Figures 6a and 6b show the probability of failure (P_f) of the tendon which was described in the bridge of case study associated with probability of failure due to local corrosion (P^L) and probability of failure due to uniform corrosion (P^U).

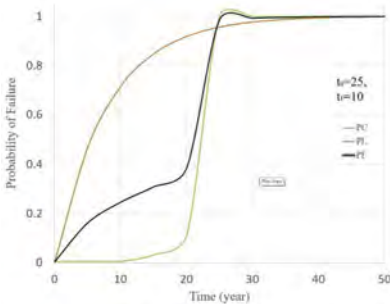


Figure 6a. Probability of failure of a tendon in the bridge of case study in poor condition $t_0=25$, $t_1=10$.

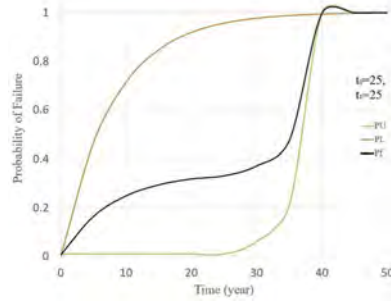


Figure 6b. Probability of failure of a tendon in the bridge of case study in poor condition $t_0=25$, $t_1=25$.

Proposed probabilistic deterioration model is a simplified probabilistic model to estimate the time dependent reliability of the post tensioning elements. Proposed deterioration model will be used in the ongoing research modules to determine the time dependent reliability of the bridge of case study.

6 ONGOING RESEARCH MODULES

The overall goal of this research is to obtain the optimum total risk among available maintenance scenarios while the probability of failure of the bridge meets the minimum threshold

during remaining service life. The previous sections described the tasks and modules completed to date. In the following, the approach for conducting the remaining tasks as described.

Equation (10) demonstrates the optimization goal, while Equation (11) defines the parameters involved. In Equations (10) and (11), R_T is the total risk, C_M is the maintenance cost, C_B is the value of the bridge, and P_f is the probability of the failure of the bridge. There are three identified scenarios ($i=3$) in this study including “no action”, “repair”, and “replace” which each has two different scenarios of deterioration ($j=2$).

$$\text{Min}(R_T); P_f(t) \leq P_{\text{threshold}} \quad (10)$$

$$R_{Ti}(t) = C_{Mi}(t) + P_{ij}(t)C_B \quad (11)$$

The limit state of study which is illustrated in Equation (12) is based on Strength I of AASHTO LRFD bridge design specification (AASHTO 2021) and AASHTO manual for bridge evaluation (AASHTO 2018).

$$R_n \geq 1.25DC + 1.5DW + 1.75LL \quad (12)$$

In Equation (12), R_n is nominal resistance capacity, DC is dead load, DW is the load associated with wearing surface, and LL is the live load.

To investigate the limit state for the flexural capacity of the bridge due to compression crushing of concrete, finite element modelling of the bridge of case study is developed and verified for intact structure. The finite element modelling simulates 11 segments, 3 deviators, and 2 diaphragms at both ends. Ten (10) external PT tendons are connected to the segments via deviators and diaphragms properly to model the behavior of the segmental post tensioned (PT) bridge. Figures 7 shows the corresponding finite element model.

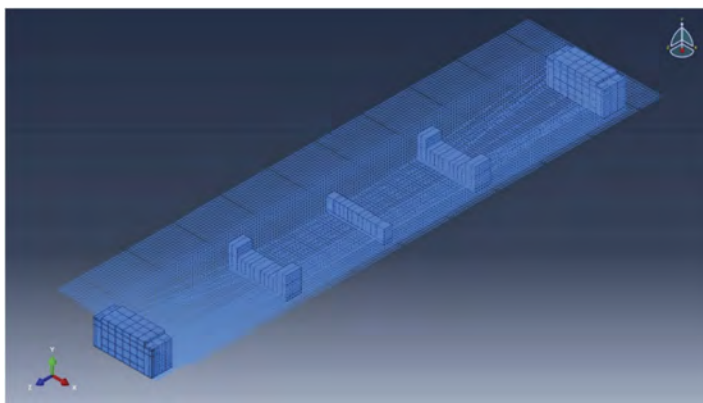


Figure 7. Finite element model for the bridge of case study (3D).

The live load data for the bridge of case study is gathered from Florida department of transportation reports and converted to HS-20 truck. HS-20 is the truck that used by NCHRP 368 during the calibration of the AASHTO LRFD as design truck and associated calibration parameters and factors then used in literatures to simplify the reliability evaluation of the bridges. One of the realistic representations of live load effects on bridges would take the form of Equation (13) (Sivakumar et al. 2011).

$$LL_T = L_{\text{max}} \times L_{\text{HS20}} \times IM_{\text{fact}} \times \lambda_T \quad (13)$$

Where LL_T = total live load effect on the bridge member or on the bridge system, L_{max} = maximum projected load due to the random trucks on the bridge presented in the function of the number of HS-20 equivalent trucks, $L_{\text{HS-20}}$ is the load effect of the HS-20 truck used as the base line for analysis, IM_{fact} = dynamic amplification factor of the total load effect, and λ_T

is the adjacent data parameter. Hence, in this study, HS-20 truck represents the live load of the bridge and the capacity of the bridge will be presented as the number of HS-20 trucks.

Updating of the finite element modeling is based on inspection results for the external post tensioned tendons. Based on condition factor (ϕ_c) reported by the inspection, the cross sections of the strands will be updated and adjusted. Future deteriorating updated models associated with corresponding maintenance and deterioration scenarios then will be used to determine the capacity of the structure for each scenario.

Simplified reliability analysis then will be used to calculate the reliability of the structure using nominal capacity achieved by finite element modeling and the equivalent HS-20 trucks. The method is called simplified since it assumes that both the demand and capacity, have the lognormal distribution (like Equation (5)). The results then will be used in equation (11) with associated costs to determine the cost of the scenarios to give the owner the options to choose.

7 CONCLUSION

Post-tensioning elements play a critical role in the structural integrity of post-tensioned bridges and their maintenance is important for the asset managers and bridge owners. A risk-based decision support system (DSS) for maintenance of post tensioned concrete bridges was introduced in this study and implemented to investigate the safety of a bridge of case study. Some of the research modules are complete and some are ongoing. Among subjects covered in this paper is a unified and reliable risk-based methodology for selecting the inspection method with minimum risk as the subsystem of DSS. Normally, the inspection results are used deterministically to estimate the existing condition of the bridge ignoring the probability of false results. In the proposed method, the true and false diagnostics probability of condition assessment using a variety of available inspection methods was investigated in the module of stochastic condition assessment. Accordingly, the optimum inspection method was selected for the bridge of case study and inspection on the external post tensioning system of the bridge was carried out. Maintenance scenarios were presented and elaborated in detailed steps. The parameters which influence the deterioration of post tensioning elements were discussed and a deterioration model was introduced. Finite element modeling is ongoing to investigate the capacity, safety, and reliability of the structure. The FE model will be used to determine the capacity of the structure in each maintenance scenario and to calculate the reliability index and probability of failure accordingly. Determined probabilities of failure then will be used with associated costs to have the optimal scenario.

REFERENCES

- American Association of State Highway and Transportation Officials, (AASHTO). (2018). *Manual for bridge evaluation*. Washington, DC:
- American Association of State Highway and Transportation Officials, (AASHTO). (2021). *AASHTO LRFD bridge design specifications*. Washington, DC: American Association of State Highway and Transportation Officials.
- Carsana, M., & Bertolini, L. (2015). Corrosion failure of post-tensioning tendons in alkaline and chloride-free segregated grout: A case study. *Structure and Infrastructure Engineering*, 11(3), 402–411.
- Ghosn, M., Sivakumar, B., & Miao, F. (2013). Development of state-specific load and resistance factor rating method. *Journal of Bridge Engineering*, 18(5), 351–361. doi:10.1061/(ASCE)BE.1943-5592.0000382
- Nowak, A. S., & Collins, K. R. (2000). *Reliability of structures*. New York, NY: McGraw-Hill.
- Permeh, S., & Lau, K. (2022). Localized corrosion of steel in alkaline solution with low-level chloride and elevated sulfate concentrations. *Cement*, 10, 100051.
- Sivakumar, B., Ghosn, M., & Moses, F. (2011). *Protocols for collecting and using traffic data in bridge design*. Transportation Research Board.
- Taeb, M., & Mehrabi, A. B. (2019). Decision support framework for inspection and maintenance: A focus on bridges using post-tensioning tendons. *Curr. Trends Civil Struct. Eng.*, 3
- Taeb, M., & Mehrabi, A. B. (2022). Risk-based selection of inspection method for external post-tensioning system of bridges. *Applied Sciences*, 12(14), 7103.
- Terzioglu, T., Karthik, M. M., Hurlebaus, S., & Hueste, M. B. D. (2019). Nondestructive evaluation of external post-tensioning systems to detect grout defects. *Journal of Structural Engineering (New York, N. Y.)*, 145(1), 5018002. doi:10.1061/(ASCE)ST.1943-541X.0002229

Seismic safety assessment of “Palácio do Itamaraty” at Brasília reliability-based

P.Q. Rodrigues & J.C. Pantoja

University of Brasilia, Brasilia, Federal District, Brazil

P.S.T. Miranda

Federal Institute of Education, Science and Technology of Ceará - IFCE, Ceará, Brazil

ABSTRACT: In Brasilia (Brazil) heritage buildings have been designed without considering seismic loads. The aim of the paper is to assess seismic behavior of reinforced concrete structure of “Palácio do Itamaraty”. In this study, Monte Carlo simulation technique is implemented in Hirosawa method to examine structural level of safety. Reliability indexes for each floor are estimated and comparisons to target reliability indexes are made. The sensitivity of different input variables is also studied. Seismic indexes of structure for each floor remained greater than seismic demand indexes in all Brazilian seismic zones through Hirosawa method. Despite of, inadequate reliability indexes is noticed in all floor, which implies that structure is not enough to guarantee an adequate performance. Sensitivity analysis shows the influence of irregularity of structure in seismic response. The results highlight the importance of a probabilistic approach by Hirosawa Method to assertive decisions of conservation and rehabilitation of architectural heritage subject to seismic hazards.

1 INTRODUCTION

The “Palácio do Itamaraty” in Brasilia is a symbol of modern architecture designed by the architect Oscar Niemeyer. The headquarter of Ministry of Foreign Affairs of Brazil was opened in 1970 and from a structural point of view the building is carried by a sequence of reinforced concrete frames with floors and the span of the slab is quite large. Once this historic heritage owns architectural and historic relevance it must be preserved and conserved (ICCOMOS, 2013).

Due to low seismicity in Brazil, “Palácio do Itamaraty” was not designed to withstand seismic loads and few researchers have evaluated seismic vulnerability of Brazilian buildings. Nevertheless, increasing of seismic hazard in localized areas have been recorded (Petersen et al. 2018). Miranda (2021) developed an exhausted study of structures from Brazilian city with high seismicity. In this context, the purpose of the present work is to evaluate the seismic performance of “Palácio do Itamaraty” in a probabilistic approach. Assessment is carried out by Hirosawa method adopted by Japan Building Disaster Prevention Association (JBDPA) and adapted to Brazilian reality (Miranda, 2013). The uncertainties involved in the problem are taken into account by Monte Carlo simulation implemented in Hirosawa Method.

Japanese Seismic Index Method or Hirosawa Method has been used to evaluate seismic performance of existing reinforced concrete buildings with less than six stories (Calvi et al, 2009). Pan American Health Organization adjusted this methodology and have implemented in Latin America, mainly in Chile, Peru, Mexico and Ecuador (PAHO, 2000). Ozdemir et al (2005) proposed an adaptation and calibration to Turkish buildings using nonlinear static analyses of 12 buildings. Letelier & Parodi (2021) analyzed a sample of 116 buildings in Chile comparing their real behavior during the 2010 earthquake with seismic performance specified by Hirosawa method.

2 SEISMIC ASSESSMENT

In first level of procedure, Hirosawa method seeks to evaluate the strength of a story on the basis of average stresses and the cross-sectional area of columns without demanding for ductility (Hiroyuki, 1981). The seismic index I_S for the total earthquake resisting capacity of a story is defined by the product of three indices (1): basic seismic index E_0 , irregularity index S_D and time index T_D .

$$I_S = E_0 \cdot S_D \cdot T_D \quad (1)$$

and E_0 :

$$E_0 = \left(\frac{n+1}{n+i} \right) \cdot a_1 \left[\frac{f_c}{20} \cdot \frac{\tau_c \cdot A_c}{W} \right] \cdot F_c \quad (2)$$

where n = number of stories of a building, i = number of the story for evaluation, W = total weight, A_c = total cross-sectional area of columns in the story studied, τ_c = average shear stress at the ultimate state of columns, which may be taken as 7 kgf/cm² and F_c = ductility index of columns which may be taken as 1.0, a_1 = effective strength factor of the columns and should be taken as 1.0. The influence of the deterioration is taken into account in the index T_D varying from 0.7 to 0.8 according to inspection of the building (Hirosawa, 1992). For more advanced model see Biondini & Bianchi (2019). The methodology also estimates another index: seismic demand index of structure I_{S0} and should be calculated by eq. 3 regardless of the story building.

$$I_{S0} = E_S \cdot Z \cdot G \cdot U \quad (3)$$

where E_S = basic seismic demand index of structure, Z = zone index namely factor accounting for the seismic activities in the region of the site, G = ground index and considers the effects of the amplification of the surface soil and geological conditions and usage index (U) contemplates the use of the building. Seismic safety of structure shall be judged by $I_S > I_{S0}$. If this inequation is satisfied the building possess the seismic capacity required against the considered earthquake motions (JBDPA, 2001).

3 RELIABILITY ANALYSIS

3.1 Probability of failure and reliability index

According to Holicý & Vruouwenvelder (2005) one of the most important term in the theory of structural reliability is the probability of failure p_f . Structural behavior may be defined as the set of basic variables $\mathbf{X} = [X_1, X_2, \dots, X_n]$ and limit state is given by the limit state function and It is defined as $g(\mathbf{X}) = \mathbf{0}$. In general, probability of failure p_f (4) remains below a given target probability. The failure is defined when a limit state is reached i.e. solicitation S exceeds resistance R . Probability of violation of limit state may be expressed as:

$$p_f = P\{g(X) \leq 0\} = \int \dots \int_{g(X) \leq 0} f_X(x) dx < p_{target} \quad (4)$$

where $f_X(x)$ is the probability density function for the randomic variable X . Commonly reliability is quantified in terms of index of reliability:

$$\beta = -\Phi^{(-1)}(p_f) \quad (5)$$

where $\Phi^{-1}(\cdot)$ = inverse normal distribution. For system in series involving multiples mode of failure, Equation 6 demonstrates failure probability of system composed of m members and then probability of survivor in Equation 7:

$$p_f = P(F_1 \cup F_2 \cup F_3 \cup \dots \cup F_m) \tag{6}$$

$$p_s = P\left(\bigcap_{i=1}^m G_i(X) \geq 0\right) = \int_{\bar{D}} \dots \int f_X(x) dx \tag{7}$$

where $\bar{D} : \bar{F}_1 \cap \bar{F}_2 \cap \bar{F}_3 \cap \dots \cap \bar{F}_m$ is the region or mode of survivor. A numerical approach is required and reliability analysis can be performed by Monte Carlo simulation (Melchers, 2001) where repeated analyses are carried out with random outcomes of the basic variables X generated in accordance to their marginal density function $f_{X_i}(x_i)$, $i = 1, \dots, n$.

3.2 Target reliability level

The Probabilistic Model Code (2001) suggests target reliabilities for the ultimate limit state considering several consequence classes and cost of safety measures (Table 1).

Table 1. Target reliabilities considering one year reference period according to JCSS (2001).

Relative cost of safety measure	Consequences of failure		
	Minor	Moderate	Large
Large	$\beta = 3.1$	$\beta = 3.3$	$\beta = 3.7$
Normal	$\beta = 3.7$	$\beta = 4.2$	$\beta = 4.4$
Small	$\beta = 4.2$	$\beta = 4.4$	$B = 4.7$

4 SENSITIVITY ANALYSIS

In order to determine the most contributing input variable to an output behavior in Hiroswawa Method or even ascertain some interactions effects within the model Sensitivity Analysis are need (Ioss & Lemaitre, 2015). SA allows to verify how the model responses varies when the input parameters of the model vary (Marelli et al, 2017). Also, how the uncertainty in the input of a model can be apportioned to different sources of uncertainty in the model input (Saltelli et al. 2000). There are several methods to evaluate sensitivity, the most complete and most costly is Morris Method that consists in discretizing input space for each variable and then performing a giving number of one at a time design allowing to classifying inputs in groups of having negligible effects, inputs having large linear effects without interactions and. Morris method offers two sensitivity measures for each factor (8, 9): μ estimates the overall effect of the factor on the output and σ that measures nonlinearity and interaction effects of the input factor.

$$\mu_j = \frac{1}{r} \sum_{i=1}^r |E_j^{(i)}| \tag{8}$$

$$\sigma_j = \sqrt{\frac{1}{r} \sum_{i=1}^r \left(E_j^{(i)} - \frac{1}{r} \sum_{i=1}^r E_j^{(i)} \right)^2} \tag{9}$$

5 APPLICATION

5.1 Structural model

The building is characterized by a squared plan with sides measuring about 84 m (Figure 1). The overall building height is about 14 meters. The three-story RC structure is composed of

beam span of 6.0 m, 18.0 m and 36.0 m. The nominal material strength is $f_c = 40\text{MPa}$ for concrete in compression. Beams depth varies depending on the floor between 40 cm to 120 cm and width also varies between 8 cm to 400 cm. The free interstory height differs in each story. For first floor height is 2.88 m, the second one is 3.50 m and the last one is 4.82 m. The geometry of cross-section varies in both shapes: trapezoid and rectangular. The structural modelling of “Palácio do Itamaraty” is exhibited in Figure 2.



Figure 1. The external view of the “Palácio do Itamaraty”.



Figure 2. Structural model of the “Palácio do Itamaraty”.

5.2 Deterministic assessment

Analysis of the seismic behavior of the structure were developed first in a deterministic approach of Hirosawa Method. The period of the structure is about 0.4765 second. Seismic index of each floor was estimated and a summary of information are presented in Table 2 and Table 3.

Table 2. Summary of input variables related to the floor 1 and 2 of “Palácio do Itamaraty”.

	Floor 1	Floor 2
Level of floor	+0.00	+3.60
Weight of the building upper the story (W) in kgf	18298435.02	14646983.91
Floor area in m ²	5774.30	4424.28
Sum of cross-sectional area of column (Ac) in cm ²	380800.00	418200.00
Fundamental Period (Ta) in seconds	0.4765	0.4765
Basic seismic index of structure E_0	0.6474	0.7448
Irregularity Index S_D	1.2	1.14
Time Index T_D	0.7	0.7
Seismic index of Structure I_S	0.6215	0.6792

Note that seismic indices of first, second and fourth are increasing owing to basic seismic index E_0 . This index takes in account cross sectional area of column and as the weight of the building upper the story decreases, the index E_0 increases. As presented in Table 3 cross sectional area reduces in third floor and impacts in index E_0 . The lower value of seismic index $I_S = 0.6215$ is applied to all structure. Even though detailed inspection indicated the time index $T = 0.8$ due to the fact the age of building is upper to 30 years, it was considered the minimum

Table 3. Summary of input variables related to the floor 3 and 4 of “Palácio do Itamaraty”.

	Floor 1	Floor 2
Level of floor	+7.82	+13.24
Weight of the building upper the story (W) in kgf	11002432.15	773435.97
Floor area in m ²	5342.28	6649
Sum of cross-sectional area of column (Ac) in cm ²	401200.00	326200.00
Fundamental Period (Ta) in seconds	0.4765	0.4765
Basic seismic index of structure E_0	0.8154	0.8254
Irregularity Index S_D	1.14	1.14
Time Index T_D	0.7	0.7
Seismic index of Structure I_S	0.7436	0.7527

value in method T = 0.7. A class E soil is considered in this study. The seismic demand index of “Palácio do Itamaraty” concerning seismic activities in the Brasilia is estimated about $I_{S0} = 0.08$. Regarding the region with moderate seismic activity in Brazil (State of Ceará) the seismic demand index $I_{S0} = 0.3922$ still satisfies inequation $I_S > I_{S0}$. To describe the seismic index I_S for every floor, surfaces of seismic response are developed. Figure 3 presents seismic index I_S versus Irregularity Index S_D and Time Index T_D related to first floor.

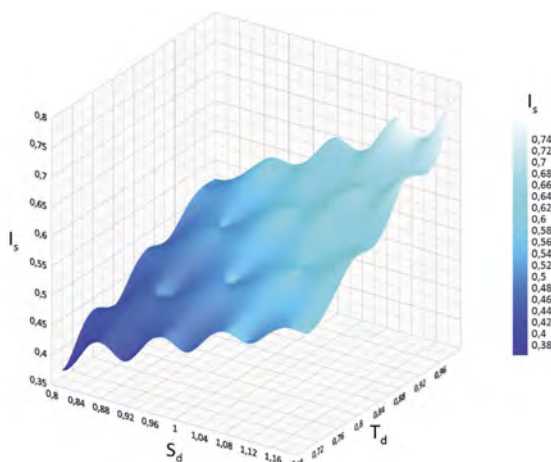


Figure 3. Surface of seismic index I_S .

5.3 Numerical simulation and reliability assessment

The assessment of seismic performance is based on probabilistic model assuming W, dead load, as normally distributed random variable (Ellingwood et al. 1982) and concrete compressive strength f_c is considered lognormal distributed random variable (Table 4). The time index (T_D) and irregularity index (S_D) is taken as random variable uniformly distributed between the values $\lambda_{min} = 0.7$ and $\lambda_{max} = 1.0$ and values $\lambda_{min} = 0.4$ and $\lambda_{max} = 1.2$, respectively.

Figure 4 exhibits reliability indices $\beta = -\Phi^{-1}(p_f)$ for each floor (SC 00 – Scenario 00). It is worth noting that lower probability of failure is detected in fourth floor $P_F \approx 0.0133$ and the elevated failure probability is found in first floor. The relation between dead load of structure and cross-sectional area of floor influences in reliability index. The number of simulation (n = 300.000) has been properly chosen in order to detect probability of failure. Comparing every single floor reliability index these values are lower than the recommended limits provided by JCSS (Table 5). Even regarding three different scenarios (SC 01, SC 02 and SC 03) where time index T_D was set constant for each floor (Table 6) structure of “Palacio do Itamaraty” depicts

inadequate probability of failure. For the scenario 01, β decreased when T_D was reduced to the minimum.

Table 4. Probability distribution and their parameters (mean value μ and standard deviation σ).

Random variables	Distribution type	μ	σ
Concrete Strength f_c	Lognormal	6.0998	0.0998
Dead Load W	Normal	1.05W	0.10 μ
Cross-Sectional Area A_c	Normal	381600	39972.99

Table 5. Reliability indices for each floor.

β	Floor	Probability of Failure
1.6955	1 st	0.0450
1.9885	2 nd	0.0234
2.1596	3 rd	0.0154
2.2179	4 th	0.0133

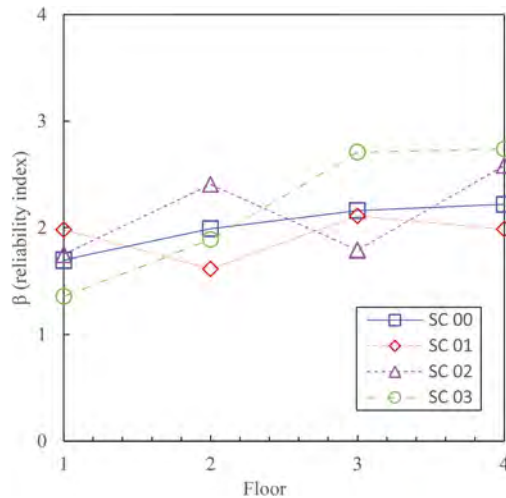


Figure 4. β versus floor of building.

Table 6. Reliability indices with T_D for each floor set constant.

Floor	Scenario 01		Scenario 02		Scenario 03	
	Time index T_D	β	Time index T_D	β	Time index T_D	β
1 st	0.95	1.9784	0.85	1.7474	0.7	1.3590
2 nd	0.7	1.6167	1.0	2.4035	0.8	1.8874
3 rd	0.8	2.1072	0.7	1.7886	1.0	2.7075
4 th	0.75	1.9834	0.95	2.5814	1.0	2.7370

The sensitivity of seismic behavior obtained from the model with respect to the uncertain input variables are presented in Figure 5. It can be seen that the most influential basic variable in this analysis is the irregularity index (S_D) that quantifies the effect of the shape, complexity and the stiffness unbalance distribution and also followed by the concrete strength (f_c),

cross-sectional area (A_c), weight (dead load W), Time Index (T_D). It is also observed that model linearly depends on the inputs and there is no input interaction once $\sigma_j \ll \mu_j^* \forall j$.

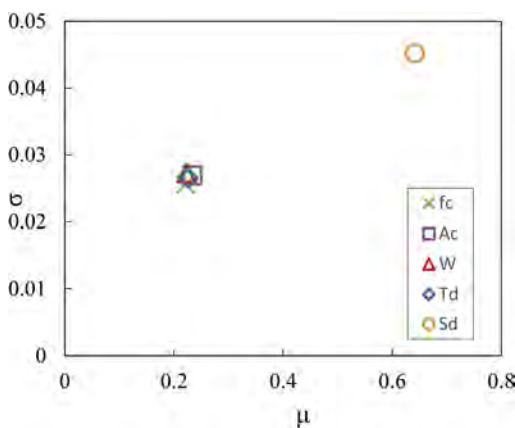


Figure 5. Sensitivity of seismic index.

6 CONCLUSIONS

A probability-based approach to qualitative assessment of seismic behavior of existing building has been presented. This approach considering uncertainties related to the materials and load was implemented in Hirosawa Method. Furthermore, the sensitivity of seismic behavior of structure regarding the basic variables was studied. It has been showed that “Palácio do Itamaraty” do not possess the seismic capacity required against the considered earthquake motions once seismic index of structure is lower to seismic demand index.

The unacceptable failure probability is noticed in all floor, which implies that the structure is not enough to guarantee an adequate performance. Moreover, Sensitivity analysis showed the influence of irregularity of building in the seismic response of structure by Hirosawa Method followed by cross-sectional area, deterioration, total weight of structure and concrete strength.

The results showed that small contraction in total cross section area columns of third floor did not affect reliability index. In contrast constant time index modified directly probability of failure and since the level of deterioration was low, the reliability expanded but still remained below JCSS target reliabilities. Though Hirosawa Method structure of “Palácio do Itamaraty” has acceptable performance against seismic load because was established the lower importance factor and risk category of building (category I) referring to buildings that represent a low risk to human life in the event of failure. Thereby if it alters category of risk the seismic demand index will be upper than seismic index of structure and meet the reliability indices.

REFERENCES

- A. Hiroyuki., 1981. A method for the evaluation of the seismic capacity of existing reinforced concrete buildings in Japan,” Bulletin of the New Zealand National Society for Earthquake Engineering, vol. 14, no. 3, pp. 105–130.
- Biondini, F., & Bianchi, S. 2019. Life-cycle seismic performance prediction of deteriorating RC structures using artificial neural networks. Life-Cycle Analysis and Assessment in Civil Engineering: Towards an Integrated Vision. London: Taylor & Francis Group.
- Calvi, G., Pinho, R., Magenes, G. 2009. Traditional and Innovative Methods for Seismic Vulnerability Assessment at Large Geographical Scales. In: The 1755 Lisbon Earthquake: Revisited. Geotechnical, Geological, and Earthquake Engineering, vol 7. Springer, Dordrecht. https://doi.org/10.1007/978-1-4020-8609-0_12

- Ellingwood, B., Galambos, T.V., MacGregor, J.G. & Cornell, C.A. 1980. Development of a ProbabilityBased Load Criterion for American National Standard A58. Washington, DC, USA: National Bureau of Standards.
- Hirosawa, M. 1992. Retrofitting and Restoration of Buildings in Japan. International Institute of Seismology and Earthquake Engineering, Lecture Note of Seminar Course.
- Holicý, M. & Vruouwenvelder, T. 2005. Chapter I – Basic concepts of structural reliability. *Implementation of Eurocodes Handbook 2 Reliability Backgrounds*. Available at: <http://eurocodes.jrc.ec.europa.eu/>.
- ICOMOS. International Council on Monuments and Sites. 2013. The Burra Charter: The Australia ICOMOS Charter for Places of Cultural Significance. Australia. Available at: <https://australia.icomos.org/publications/burra-charter-practice-notes/#bc>.
- Iooss, B., & Lemaître, P. 2015. A review on global sensitivity analysis methods. In C. Meloni and G. Dellino (Eds.), *Uncertainty management in Simulation-Optimization of Complex Systems: Algorithms and Applications*. Springer.
- JCSS. 2001. Joint Committee on Structural Safety. Probabilistic Model Code. *Internet Publication*. Available at: www.jcss-lc.org.
- Marelli, S. *et al.* 2017. UQLabuser manual – Structural Reliability, Report UQLab-V1.0-107, Safety & Uncertainty Quantification, ETH Zurich.
- Miranda, P. S. T. 2021. A influência das ações sísmicas nas edificações brasileiras em concreto armado. Tese (Doutorado em Engenharia Civil) - Faculdade de Engenharia da Universidade do Porto. Universidade do Porto, Porto.
- Miranda, P. S. T. 2013. Avaliação da Vulnerabilidade Sísmica na realidade predial brasileira. Fortaleza: Expressão Gráfica e Editora
- PAHO. Pan American Health Organization. 2000. Principles of disaster mitigation in health facilities. Washington, D.C.
- Parodi, C. Letelier, V. 2020. Application of Hirosawa Method to Compare Seismic Performance of Reinforced Concrete Buildings during the Earthquake of 2010 in Chile. *International Journal of Structural and Civil Engineering Research*.
- Petersen M.D., Harmsen S.C., Jaiswal K.S., Rusktales K.S., Luco N., Haller K.M., Mueller C.S., Shumway A.M. 2018. Seismic Hazard, Risk, and Design for South America. *Bulletin of the Seismological Society of America*, Vol. 108, pp. 781–800.
- Melchers, R.E. 2001. *Structural reliability analysis and prediction*. JohnWiley & Sons.
- Saltelli, A., Chan, K., Scott, E.M. 2000. (eds.): *Sensitivity Analysis*. Wiley Series in Probability and Statistics. Wiley, New York.
- JBDPA. Japan Building Disaster Prevention Association. 2001. *Technical Manual for Seismic Evaluation and Seismic Retrofit of Existing Reinforced Concrete Buildings*. Building Research Institute.

*SS7: Bridge weight-in-motion systems and applications
to structural health monitoring
Organizers: S. Mustafa & D. Cantero*



Taylor & Francis

Taylor & Francis Group

<http://taylorandfrancis.com>

Bridge weigh-in-motion to support SHM

D. Cantero

NTNU Norwegian University of Science and Technology, Trondheim, Norway

ABSTRACT: Bridge Weigh-in-motion (BWIM) is an established technology that allows estimating the wheel weights, axle spacing and velocity of travelling vehicles moving at full speed. It relies on the structural response of a bridge to infer the desired vehicle properties. These systems provide an enormous amount of information on the traffic's characteristics that can be used to develop accurate site-specific road traffic models. However, BWIM technology has matured sufficiently and there is a trend to find additional uses, not only for the traffic data obtained, but also for existing instrumentation on the bridge. In particular, various recent publications suggest that the information extracted from such systems can also be used for the purpose of SHM. The integration of the vehicle loading characteristics should further extend the capabilities and reduce the cost of SHM systems.

1 INTRODUCTION

Weight-in-Motion (WIM) is a group of technologies and methods that allow the weighing of passing road traffic at full speed, without having to stop or divert the vehicles. Originally, the aim of WIM technology was to enforce axle weight limits on freight vehicles. However, the information gathered by WIM systems can be used to elaborate more precise site-specific traffic models for improved infrastructure design, assessment and management (van Loo and Žnidarič, 2019). Yet a more recent application has been found as possible Structural Health Monitoring (SHM) technique. More precisely, the recorded signals and estimated information about individual vehicles can be used to evaluate the structural integrity of bridges.

This paper gives an overview of WIM technology, a description of some recent results and an exploratory discussion on the potential usage for SHM. First, the paper provides a brief introduction of the technology in order to introduce WIM to a broader audience. Secondly, a summarized description of some of the latest published ideas by the author is presented. Amongst others, a level I damage detection method (i.e. capable of detecting the existence of damage) for short- to medium-span bridges is outlined, that combines information from pavement-based and bridge-based WIM systems. In addition, the Virtual Axle concept is introduced. This theoretical finding shows that it is possible to assess damages in certain types of bridges by introducing a fictitious weightless axle in the WIM algorithm. Finally, this paper wants to put forward a discussion on the potential and applicability of WIM technology (hardware, methods, measurements and inferred data) for SHM, based on published experiences and the author's own view.

2 WIM TECHNOLOGY

WIM systems consist of a wide range of technologies that weight road vehicles moving at full speed and are able to estimate their wheel weights and axle spacing. Two main categories of WIM systems exist, namely pavement-based and bridge-based.

In Pavement-based WIM systems, sensors are located on the road surface or embedded in the pavement, which can be pressure cells, bending plates and inductive loops, among others. Adequate processing of the recorded signals will provide the sought information about the passing vehicles (axle weights, spacing and speed). The accuracy of the weight estimates is affected by the road unevenness that increases the variability of the axle forces due to the vehicle's dynamic response. Because the sensor in a pavement-based WIM system is only able to weigh the axle for a very short period of time, the estimated axle weight might be corrupted by the vehicle dynamics. However, its accuracy has been enhanced, since its appearance in the 1950's and is nowadays a technology used worldwide (van Loo and Žnidarič, 2019).

On the other hand, Bridge-based WIM systems (BWIM) utilize measured bridge responses (generally strain) during a vehicle passage to infer the axle weights by means of the approach introduced by Moses in 1979 (Moses, 1979) and can be summarized as follows. To estimate each individual axle weight $\{P_i\}$ for a vehicle with N axles it is necessary to calibrate the system and obtain the corresponding influence line $\{I_i\}$ for every sensor location. For every vehicle-crossing event, the system measures the strain $\{\epsilon_i^{me}\}$ and extracts information about the vehicle's speed, number of axles and distance between them. This is in practice achieved in modern BWIM systems utilizing various strain gauges along the bridge with the so-called Nothing-on-Road strategy (Kalin et al., 2006). With this information it is possible to describe the theoretical strain $\{\epsilon_i^{th}\}$ and compare it to the measured strain. The minimization of the squared difference between measured and theoretical responses can be expressed in matrix form reducing the problem to a system of linear equations (OBrien et al., 2009).

$$\{P_i\} = \frac{[I_{t,i}]^T \{\epsilon_i^{me}\}}{[I_{t,i}]^T [I_{t,i}]} \quad (1)$$

The solution of this linear system provides the weight estimates for each individual axle of a passing vehicle. In Equation (1), the term $[I_{t,i}]$ is the matrix of influence line's ordinates of dimension $(T \times N)$ where T is the total number of sampling points. The matrix $[I_{t,i}]$ is composed of multiple copies of the influence $\{I_i\}$ line for the particular sensor location considered and shifted accordingly to the axle spacings of the vehicle. The accuracy of the BWIM system depends on the bridge span and the vehicle's axle spacing, where stiff short straight spans are best suited for BWIM purposes (Gonzalez, 2010). However, over the past decades (Yu et al., 2016) many improvements have been incorporated to this technology. This has increased the applicability of BWIM and allowed to successfully implement it in other bridge sites.

During the installation of a BWIM system, the structure's influence line $\{I_i\}$ must be obtained and calibrated on-site using a vehicle of known speed, axle spacing and weights. However, over time, the structural behaviour of the bridge might change due to damage. As a result, the influence line $\{\tilde{I}_i\}$ at a sensor of the BWIM system has changed with respect to the influence line obtained during calibration. The axle weight estimates provided by the system have an inherent error for any subsequent event since the influence line has not been recalibrated. This is, the predicted axle weights are computed using the original influence line $\{I_i\}$ whereas the actual measured strain is related to the new influence line $\{\tilde{I}_i\}$. Therefore, the estimated axle weights $\{\tilde{P}_i\}$ are different from the actual axle weights of the traversing vehicle $\{P_i\}$. In the remaining of the document the influence line obtained during calibration is termed healthy influence line, whereas the modified one is termed damaged influence line.

3 COMBINATION OF WIM AND BWIM

In (Cantero and González, 2015) a level I damage detection technique is proposed for short to medium span road bridges using the input provided by two different WIM systems: a pavement-based WIM station located in the same route as the bridge and a bridge-based WIM system. If the bridge suffers some local or global damage, the structure's response will change and as a result, the BWIM system will provide incorrect GVW estimations.

This idea can be further elaborated following the notation in Section 2. Consider that the actual axle loads of a passing vehicle $\{P_i\}$ are correctly obtained from a nearby pavement-based WIM station, while the BWIM provides the estimates $\{\tilde{P}_i\}$ based on the current bridge responses. If both weight estimates are available their relationship can potentially be used for SHM of the bridge. More specifically, it is proposed to study the error in total vehicle weight estimation of the BWIM system (E_{BWIM}) defined as:

$$E_{BWIM} = \frac{\sum_{i=1}^N \tilde{P}_i - \sum_{i=1}^N P_i}{\sum_{i=1}^N P_i} \times 100 \quad (2)$$

When the bridge is undamaged, the error is close to zero, but not exactly zero because of the influence of the inherent system inaccuracies (dynamics, noise, inaccurate truck location). However, significant changes of E_{BWIM} over time indicates that the structural response to traffic has changed. Incorrect axle weight predictions by the BWIM system indicate changes in the structure's influence line and that probably damage has occurred.

This indicator E_{BWIM} can be used as an indicator of structural integrity and it can be periodically updated with additional frequent vehicle crossing events. Furthermore, it can be shown that this indicator is more sensitive to damage than a frequency-based indicator. Figure 1 shows the relative variation of the beam's natural frequencies compared to the variation of E_{BWIM} for a range of degrees of global damage. For the same amount of global damage, the BWIM error-based indicator approximately doubles the sensitivity to damage of a frequency-based approach.

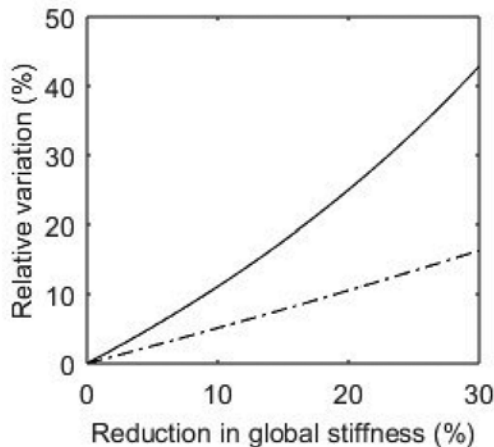


Figure 1. Theoretical relative changes (in absolute value) in E_{BWIM} (solid) and natural frequency (dashed) due to global damage.

The identification of local damage on the bridge is more complex than for global damage. The results and sensitivities depend on the damage location, severity and bridge boundary conditions and sensor locations. However, the proposed indicator E_{BWIM} provides some indication of damage. To evaluate this, in (Cantero and González, 2015) a numerical investigation is performed by simulating one month of traffic within a Monte Carlo scheme to vary the passing vehicle properties. Different damage locations are explored for a local stiffness reduction of 50% using the signals from strain sensors located at three different positions along the damaged beam. The results are summarized in Figure 2. Even though the average E_{BWIM} due to local damage are smaller than for global damage, the stiffness loss is still identifiable. For a given damage, the average E_{BWIM} is different for each sensor location. This information could be used to roughly estimate the location of the damage.

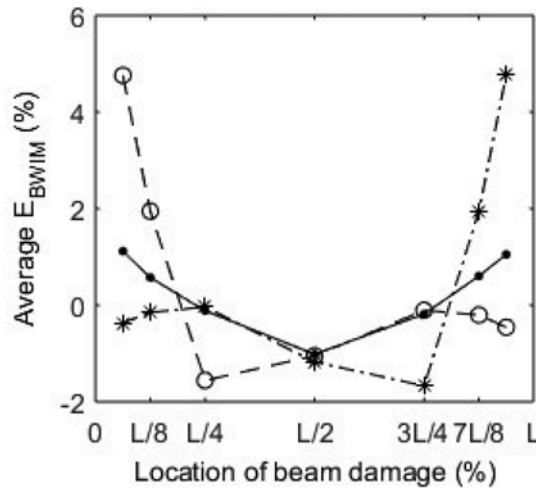


Figure 2. One-month average EBWIM for sensor located at $\frac{1}{4}L$ (dashed); $\frac{1}{2}L$ (solid); $\frac{3}{4}L$ (dash-dot) and a 50% local damage at seven different locations (dots).

This idea could be applied to a road network with multiple critical bridges, as schematically represented in Figure 3. Each bridge should have a monitoring system capable of performing BWIM that calculate axle weight estimates. A pavement-based WIM station along the network would provide the reference weight estimates. The information can be correlated to identify the corresponding reference values to the estimated values considering the expected arrival time of the vehicle to each bridge. Traffic congestions, vehicle delays or even vehicles abandoning the road network at some exit, would difficult or reduce the number of correlated vehicles. However, because this idea is not based on the results of one single vehicle crossing but rather on the aggregate results of multiple events, with time sufficient correlated events can be found.

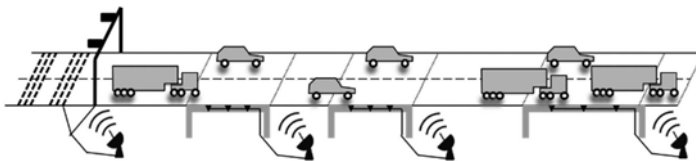


Figure 3. Weigh-In-Motion based damage identification concept for structural health monitoring of bridges.

4 THE VIRTUAL AXLE CONCEPT

In (Cantero et al., 2015), the authors introduce a level I damage identification method for statically indeterminate bridges using the information provided by a BWIM system. It is theoretically shown that for damage detection it is useful to assume the presence of an additional weightless axle, which has been termed ‘Virtual Axle’ (VA). A change in structural behavior will lead to weight estimates different from zero for this fictitious VA load by the BWIM system. It is possible to identify even small changes in influence lines by applying the VA concept. The proposed idea can be used to define a new robust output-only model-free level 1 SHM technique.

To illustrate this idea, the linear system in Equation (1) is solved for the particular case of a vehicle with only two axles. The linear system can be solved, resulting in expressions for the estimated axle weights as seen in Equation (3).

$$\begin{Bmatrix} \tilde{P}_1 \\ \tilde{P}_2 \end{Bmatrix} = \begin{bmatrix} \frac{(P_1 D_{1,1} + P_2 D_{1,2}) H_{2,2} - (P_1 D_{2,1} + P_2 D_{2,2}) H_{2,1}}{H_{1,1} H_{2,2} - H_{1,2}^2} \\ \frac{(P_1 D_{2,1} + P_2 D_{2,2}) H_{1,1} - (P_1 D_{1,1} + P_2 D_{1,2}) H_{1,2}}{H_{1,1} H_{2,2} - H_{1,2}^2} \end{bmatrix} \quad (3)$$

where matrix $[H]$ derives from the matrix product of healthy influence lines, and matrix $[D]$ is the result of the matrix product of healthy $\{I_i\}$ and damaged $\{\tilde{I}_i\}$ influence lines. (It is acknowledged that this text does not provide a full description of the terms in Equation (3). Refer to (Cantero et al., 2015) for a complete description of the formulation.) Furthermore, if we assume that one of the traversing axles is weightless ($P_2 = 0$) it reduces to Equation (4).

$$\begin{Bmatrix} \tilde{P}_1 \\ \tilde{P}_2 \end{Bmatrix} = \begin{bmatrix} \frac{P_1 D_{1,1} H_{2,2} - P_1 D_{2,1} H_{2,1}}{H_{1,1} H_{2,2} - H_{1,2}^2} \\ \frac{P_1 D_{2,1} H_{1,1} - P_1 D_{1,1} H_{1,2}}{H_{1,1} H_{2,2} - H_{1,2}^2} \end{bmatrix} \quad (4)$$

Equation (4) shows that the installed BWIM system provides an estimate for both axles, even though one of the axles traversing the system is known to have no weight. This weightless axle has been termed Virtual Axle (VA) and its properties are listed below:

- The VA is zero if there is no damage, i.e. when $\{\tilde{I}_i\} = \{I_i\}$.
- The VA is zero if the axle distance d is greater than the length of the influence line L . This result sets the limits of possible axle distances to consider in any VA calculation to the interval $[-L, +L]$.
- The VA is zero if the damaged influence line is a linear transformation of the healthy one, i.e. when $\{\tilde{I}_i\} = \lambda\{I_i\}$ for λ a constant.
- A value of VA different to zero indicates that the influence line obtained during calibration is different in shape to the current influence line of the structure.

Figure 4 shows a schematic representation of the concept of Virtual Axle. An existing BWIM system would render an actual weight estimate for a fictitious weightless axle if the current influence line has changed in shape with respect to the one obtained during calibration. The derivation of VA was presented for the case of a hypothetical 2-axle vehicle (one real and one virtual). However, it is possible to extend the expressions to vehicles with more axles obtaining the same properties listed above.

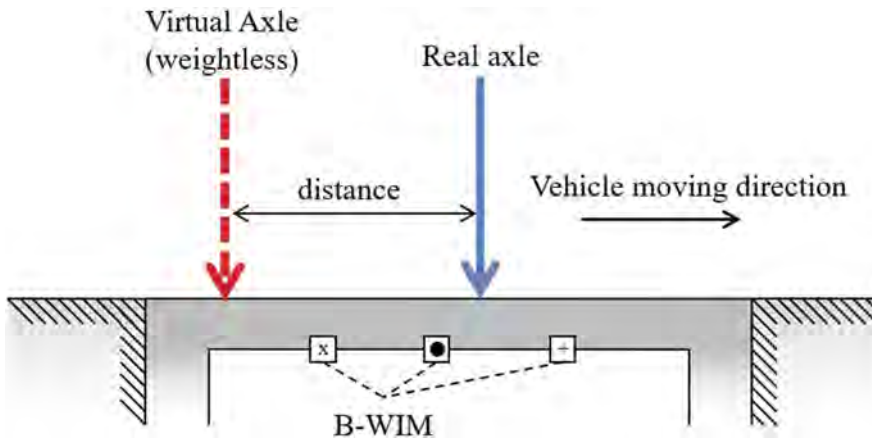


Figure 4. Schematic Description of Virtual Axle Concept.

The location of this additional weightless axle with respect to the other two is a key parameter. In fact, it can be located either in front or to the back of the vehicle. The maximum distance between the virtual axle and the vehicle is limited by the length of the influence line L . Therefore, it is possible to obtain weight estimates for virtual axles located between $-L$ (back of vehicle) and $+L$ (front of vehicle).

This idea is checked numerically in (Cantero et al., 2015) using the results from a Vehicle-Bridge interaction model for a 2-axle vehicle traversing a fixed beam. The generated strain signals are corrupted with additional noise and an example reproduced in Figure 5. This signal is used to calculate weight estimates including the additional weightless axle at different distances from the vehicle. Figure 6 shows the VA estimates within the valid distance range and compares the results between healthy and damaged bridges. The VA values are given as a percentage of the Gross Vehicle Weight (GVW). Because this example also includes the dynamic behavior of the bridge the VA results are not exactly zero even for the healthy bridge case. However, Figure 6 shows some clear differences in VA estimates between healthy and damaged cases.

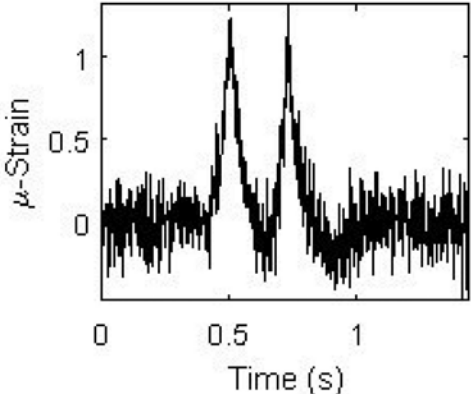


Figure 5. Strain signal with noise for a sensor located at $\frac{1}{4}$ span.

An inherent limitation of the BWIM algorithm is related to closely spaced axles, which renders an ill-conditioned linear system to solve. Small perturbations in the signal (e.g. noise), produce unreliable and unrealistic results. Therefore, in order to avoid ill-conditioning of the system, the location of the virtual axle is placed at a minimum distance L_0 (equal to $\pm 10\%$ of L) away from the vehicle. The assumed range of ill-conditioned virtual axle distances correspond to the shaded area shown in Figure 6.

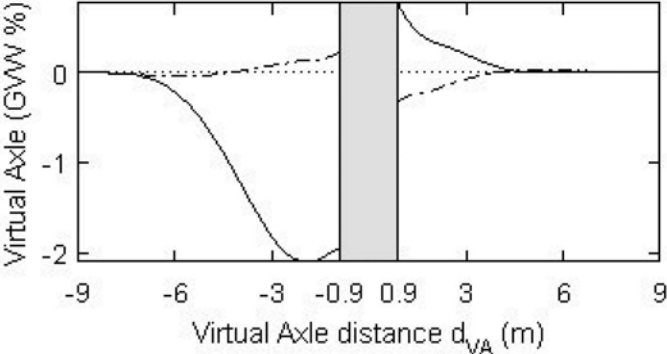


Figure 6. Virtual axle results for healthy (dashed) and damaged (solid) bridge with a 30% stiffness reduction at mid-span. Sensor location $\frac{1}{4}L$.

As shown in (Cantero et al., 2015) it is possible to derive a damage index from the results of VA analysis. The repeated calculation of this index for several vehicle crossing events can be used to detect small local damages in statically indeterminate structures. The method is applicable to a wide range of road conditions, while it shows very little sensitivity to noise. The numerical results show that the sensitivity of the proposed method is good enough to compensate for the variability in results due to: difference in vehicle properties, bridge dynamics and signal noise. Therefore, the method could be classified as a level I SHM technique. The VA methodology could also provide some indication on damage location.

The VA concept is applicable to standard BWIM systems that are already installed since no changes in hardware are required. It is only necessary to update the software to include the calculations of a fictitious load. However, its scope is limited to identification of local damages in statically indeterminate structures. It is important to note that in general BWIM systems provide more reliable results the shorter the length of the influence line. This is why most of currently operational installations are on short span bridges. However, BWIM systems can also be used in longer multiple-span continuous bridges locating the sensors in members that feature local responses. In those cases, the effective length of the influence line can be small and good accuracies can be achieved too.

Nevertheless, the proposed idea has inherent limitations. The sensitivity to local damages greatly depends on the actual location of the damage. In addition, the idea relies on the use of extracted influence lines, which are known to be dependent on environmental conditions. These factors will affect the damage detection effectiveness. The proposed idea can be considered as one possible strategy for damage detection, that should be supplemented with other methods. Further investigations are necessary to confirm the practical potential of the proposed idea.

5 DISCUSSION

SHM of bridges and its ultimate goal of correct assessment of existing structures is not an easy task. In recent decades multiple approaches and ideas have been proposed. Many research groups continue exploring this topic because of its scientific interest and potential cost reduction capabilities on infrastructure management. However, the reality of the bridge assessment problem is very broad because of the heterogeneity in structural solutions, construction materials, loading and environmental conditions. It is unlikely that there will ever be a single method or technology for the correct structural integrity evaluation. Most likely, any relevant progress in this field will emerge from the combination of multiple methods and sources of information.

In this regard, BWIM technology should be considered as one important technology that can contribute positively to SHM. Standard BWIM installations provide information about the passing traffic and the recorded structural responses can be further processed to infer additional information on the structural integrity. On the other hand, existing long-term monitoring systems can be adapted or improved to estimate traffic loading based on the BWIM algorithm. However, future long-term monitoring systems should ideally include sensors and algorithms that maximize the information that can be extracted. The author believes those systems should also include BWIM capabilities.

As shown in this article, the direct analysis of the predicted vehicle weights and their change in time gives an indication of the structural integrity. Also, the processing of the signals gathered for the BWIM problem can be analysed with the novel Virtual Axle concept to infer additional indications of possible structural changes. Furthermore, the information gathered by such BWIM systems can be used to elaborate more precise site-specific traffic models for improved infrastructure design, assessment and management. Together with other sources of information, this data constitutes a valuable source of information to be used as input in data-driven bridge model updating procedures. Furthermore, there is a large potential when combining the supplementary information provided by ITS (Intelligent Transport Systems). The real-time data flow should allow to move forward from BIM (Building information modelling) models towards the desirable goal of having digital twins of existing bridges, which in turn would facilitate the predictive maintenance of the infrastructure.

It is worth mentioning that this article has only discussed two recent developments on BWIM for SHM that the author has been part of. However, there are more developments in BWIM technology led by other research groups internationally. A non-exhaustive list of recent advances includes: sensing technology (fibre sensors, wireless, energy harvesting, . . .), measured response (acceleration, shear strain, displacements, . . .), processing techniques (machine learning, signal processing, . . .), system calibration methods (influence line extraction . . .), information management (data compression, . . .) and extension to other bridge types (railway). Therefore, the potential applications of BWIM have not been exhausted yet and many more might arise in the coming future to support SHM.

6 CONCLUSIONS

This paper has provided a short overview of WIM technology with more emphasis on bridge-based solution. Then it presented the idea of combining the information from different WIM systems (one pavement-based and one bridge-based). The error in weight estimates has been reported to be a reliable and robust indicator of structural integrity, more sensitive to damage than the traditional method based on variation in natural frequencies. Secondly, a qualitative description of the Virtual Axle concept was provided. The addition of a weightless axle in the BWIM algorithm can be used to derive a damage index in certain structures. This novel idea can readily be tested on existing BWIM installations since it does not require any physical modification. To apply the VA concept, only modifications on the calculation algorithm are required. In summary two different level I SHM methods based on WIM technology that can be integrated into a broader SHM strategy in road network.

REFERENCES

- Cantero, D. & González, A. 2015. Bridge Damage Detection Using Weigh-in-Motion Technology. *Journal of Bridge Engineering*, 20, 04014078.
- Cantero, D., Karoumi, R. & González, A. 2015. The Virtual Axle concept for detection of localised damage using Bridge Weigh-in-Motion data. *Engineering Structures*, 89, 26–36.
- Gonzalez, A. 2010. *Development of a Bridge Weigh-In-Motion System*, Germany, LAP Lambert Academic Publishing AG & Co.
- Kalin, J., Žnidarič, A. & Lavrič, I. 2006. Practical implementation of nothing-on-the-road bridge weigh-in-motion system. *Slovenian National Building and Civil Engineering Institute*, 207, 3–10.
- Moses, F. 1979. Weigh-In-Motion system using instrumented bridges. *ASCE Transportation Engineering Journal*, 105, 233–249.
- Obrien, E. J., Rowley, C. W., Gonzalez, A. & Green, M. F. 2009. A regularised solution to the bridge weigh-in-motion equations. *International Journal of Heavy Vehicle Systems*, 16, 310–327.
- Van Loo, H. & Žnidarič, A. 2019. *Guide for Users of Weigh-In-Motion - An introduction to Weigh-in-Motion*, ISWIM, International Society for Weigh-in-Motion.
- Yu, Y., Cai, C. & Deng, L. 2016. State-of-the-art review on bridge weigh-in-motion technology. *Advances in Structural Engineering*, 19, 1514–1530.

Bayesian-based bridge influence line identification and uncertainty estimation

S. Mustafa

Department of Civil Engineering, Indian Institute of Technology (BHU), Varanasi, India

I. Yoshida & H. Sekiya

Department of Urban and Civil Engineering, Tokyo City University, Tokyo, Japan

ABSTRACT: Being a unique characteristic of a structure, the identification of an accurate bridge influence line from real measurement of bridge response under moving loads is on high demand for new structural design, model calibration, structural condition assessment and bridge weigh-in-motion. Despite its uniqueness, the identified influence lines from different measured signals tend to differ due to perturbations owing to the dynamic effect, road surface roughness, difference in calibration trucks and so on. This paper proposes a robust method using Bayesian framework for the identification of a single influence line by considering multiple measured signals. The effectiveness of the proposed method is demonstrated through a field experiment on a simply-supported steel girder bridge using three calibration trucks with different axle numbers and axle configurations. Using Bayesian framework, the uncertainties associated with the identified influence lines are also estimated which are useful for knowing the accuracy of predicted signals and estimated axle weights using a particular influence line.

1 INTRODUCTION

Over the last few decades, a large number of civil infrastructures, such as bridges, have emerged worldwide as a part of social-economic development. They are considered as important asset of every society. However, many of the existing bridges have already crossed a significant amount of their service life. On the other hand, there is a rapid increase of demands on these infrastructures because of the ever-increasing nature of traffic loads and operational speeds. Consequently, various types of damage, such as corrosion and fatigue, have been discovered. The combined effects of aging and increasing load conditions has prompted the needs to intensify maintenance and implementation monitoring of these assets. Therefore, it is becoming increasingly important to know the actual in-service condition of bridges for the evaluation of their remaining service life and performances so that appropriate countermeasures be taken to ensure their safety and operation.

The above goals can be achieved by analyzing the load-deformation characteristics of a bridge and obtaining an accurate information about the past, present and future traffic conditions. Among these two, the former can be achieved by simply looking into the bridge influence line which represents a unique characteristic of a bridge that shows the variation of response at a certain location when a unit concentrated load traverses the bridge (Timoshenko & Goodier 1934). The later can be achieved by implementing a bridge weigh-in-motion (BWIM) system that gives information about traffic loads by utilizing the measured response and bridge influence line (O'Brien et al. 1999, Cardini & DeWolf 2009, Mustafa et al. 2021). Therefore, bridge influence line plays a crucial role in achieving both the goals. Moreover, because it gives a direct relationship between the load and the response, it is also used for other applications such as improving structural design (Fiorillo & Ghosn 2015), finite-element model updating (Lin et al. 2022, Xiao et al. 2015), structural condition assessment and damage detection (Chen et al. 2015, He et al. 2017).

Due to the practical significance of bridge influence line in many important applications, the accurate identification of it from real measurements on the bridge is becoming an important research topic.

For instance, the backbone of BWIM algorithms is bridge influence line and their accuracy is highly governed by the accuracy of identified influence line. Accordingly, many methods have been developed to extract the bridge influence line from measured responses induced by a calibration truck. The measured responses can be either measured displacements, strains or bending moments, depending on the measurement system and their intended purpose. Depending on the analysis domain, the influence line identification methods can be categorized into two: time-domain method and frequency-domain method, although both uses the same mathematical framework (Mustafa et al. 2021). McNulty & O'Brien (2003) first developed a crude way of estimating bridge influence line using a point-by-point graphical method. An improved method was developed later by O'Brien et al. (2006) in time-domain using a linear least-squares method. It is basically an inverse approach where the influence line is identified by minimizing the residual norm between the measured and theoretical bridge responses. However, this method is often ill-posed due to the fact that a slight change in the measured response leads to a considerable change in the identified influence line. To overcome this issue, regularization methods (Chen et al. 2015, Zheng et al. 2019) and base function method (Wang et al. 2017), that are commonly used to solve an ill-posed problem, have been introduced recently. In case of frequency-domain analysis, the response equation is first converted to frequency-domain by using the Fourier transformation and then, the influence line is obtained by dividing the response function by a quantity that is a product of axle weights and complex exponential (Mustafa et al. 2021). Finally, the influence line in original domain can be obtained by applying the inverse Fourier transform. Alternatively, the convolution theorem can be applied to extract the influence line in frequency-domain as done by Frøseth et al. (2017). The main issue with frequency-domain analysis is that it makes the solution unstable for shorter length of measured data due to the inherent assumptions involved in discrete Fourier transform (Mustafa et al. 2021). A comprehensive review and comparison among different influence line identification methods can be found in Zheng et al. (2019).

In all the methods described above, the bridge influence line was extracted from a single measured signal induced by a single calibration truck. Clearly, such methods are not robust to perturbations, and they may produce different influence lines for different measured signals. The measured signals induced by the same calibration truck in different test runs could also be different due to many factors such as bridge vibration, road roughness, measurement noise, disturbances from other loadings and so on (O'Brien et al. 2009). Thus, the variations in the measured signals are inevitable. Hence, the influence line identification method should be robust against such perturbations. For this reason, it would be worthy to know the underlying uncertainty associated with the identified influence line. One of the ways to address this issue is by simultaneously considering multiple signals, either induced by the same or several different calibration trucks. The goal is to determine a single influence line that is capable to predict all bridge responses induced by different calibration trucks. Only one example of addressing this issue is found in Ieng (2015) where the author used the maximum likelihood estimation and considered many signals for the estimation of influence line numerically. The limitation of this method is that the uncertainty associated with the identified influence line was not calculated.

This paper presents a new method for the identification of bridge influence line using Bayesian framework that addresses the aforementioned issues. The advantages of using a Bayesian method are that it allows to take into account all types of available information along with their associated uncertainties by modelling them probabilistically. At first, the mathematical model for influence line identification using conventional time-domain formulation is provided. Then, a Bayesian framework with consideration of multiple measured signals is introduced. The proposed method is then validated through field tests on a simply-supported steel girder bridge and measuring the bridge displacement responses. Three calibration trucks with different axle numbers and axle configurations are used for investigating the variability in the measured bridge response and their effect on the influence line identification process.

2 CONVENTIONAL FORMULATION OF INFLUENCE LINE

In conventional formulation, the bridge influence line is identified from measured response induced by a single passage of a calibration truck. It assumes that the measured response due

to a traversing vehicle is a summation of contributions from individual axles plus an additive noise term that represents a combined effect of bridge and vehicle dynamics, road roughness, measurement noise and so on (Obrien et al. 2006, Yoshida et al. 2021). This is a valid assumption when the response is linear and axle-load effects are independent. Subsequently, for a calibration truck with known axle weights w_i , and axle distance d_i with respect to the first axle, the observation equation for bridge response $z_t(t_k)$, at k th scan of time, is given by

$$z_t(t_k) = \sum_{i=1}^N w_i x_s(s_i(t_k)) + \varepsilon \cdots \cdots; s_i(t_k) = k\Delta t v - d_i \quad (1)$$

where N is the total number of axles of a calibration truck, $x_s(s)$ is the influence line coefficients corresponding to the i th axle, ε is the observation error, Δt is the sampling time of measurement, and v is the speed of calibration truck. The above expression in Eq. (1) can be conveniently written in matrix form as

$$\mathbf{z} = \mathbf{H}\mathbf{x} + \varepsilon \quad (2)$$

where $\mathbf{z} \in \mathbb{R}^{N_m \times 1}$ is the measured bridge response vector with N_m sampling points, $\mathbf{x} \in \mathbb{R}^{N_m \times 1}$ is the influence line vector to be determined with N_l number of coefficients, and $\mathbf{H} \in \mathbb{R}^{N_m \times N_l}$ is the vehicle information matrix. The \mathbf{H} matrix is constructed based on the information of a calibration truck such as its axle weights and axle spacings, as given below.

$$\mathbf{H} = \begin{bmatrix} w_1 & 0 & \dots & \dots & 0 \\ 0 & w_1 & 0 & \dots & \vdots \\ \vdots & \vdots & \ddots & \dots & \vdots \\ w_2 & 0 & \dots & \ddots & \vdots \\ 0 & w_2 & 0 & \dots & w_1 \\ \vdots & \vdots & \ddots & \dots & \vdots \\ w_N & 0 & \dots & \ddots & \vdots \\ 0 & w_N & 0 & \dots & w_2 \\ \vdots & 0 & \ddots & \dots & \vdots \\ \vdots & \vdots & \dots & \ddots & 0 \\ 0 & 0 & \dots & \dots & w_N \end{bmatrix} \quad (3)$$

The \mathbf{H} matrix defined above is a constant matrix with known axle weights that are separated according to their sampling point difference. It should also be noted that the \mathbf{H} matrix is a non-square matrix due to the consideration of presence of only the first (last) axle at the time entry (exist) on the bridge. For this reason, the identified influence line has a shorter length than the measured response vector by a number C_N , where C_N represents the sampling point difference between the first and the last axles. The significance of \mathbf{H} matrix is that each row of this matrix represents a relationship between one bridge response and N_l influence coefficients. For a non-square \mathbf{H} matrix, Eq. (2) is solved by ordinary least-square method using the following objective function J of sum of squared residuals

$$J = (\mathbf{z} - \mathbf{H}\mathbf{x})^T (\mathbf{z} - \mathbf{H}\mathbf{x}) \quad (4)$$

The solution for unknown influence line \mathbf{x} is obtained by minimizing J

$$\mathbf{x} = (\mathbf{H}^T \mathbf{H})^{-1} \mathbf{H}^T \mathbf{z} \quad (5)$$

Clearly, the conventional method of influence line identification using ordinary least-squares does not consider the measurement noise and associated uncertainty explicitly. Moreover, as the influence line is identified from a single measured signal, it can't include the variability of measured

responses due to different calibration trucks and different test conditions, such as road roughness, driving lane of calibration trucks and travelling speeds.

3 BAYESIAN FRAMEWORK CONSIDERING MULTIPLE SIGNALS

3.1 Basic Bayesian framework

A probabilistic framework incorporating multiple signals and various uncertainties is introduced in this section. In Bayesian method, the posterior probability of uncertain model parameters \mathbf{x} given some measured data \mathbf{D} can be obtained using Bayes' theorem (Beck & Katafygiotis 1998)

$$p(\mathbf{x}|\mathbf{D}) = \frac{p(\mathbf{D}|\mathbf{x})p(\mathbf{x})}{p(\mathbf{D})} \quad (6)$$

where $p(\mathbf{D}|\mathbf{x})$ is the probability density function (PDF) of observed data based on a model specified by the model parameters \mathbf{x} . It reflects a probability model for the prediction error between the actual measured response \mathbf{D} and model prediction specified by \mathbf{x} . The term $p(\mathbf{x})$ represents the prior PDF of \mathbf{x} which is based on previous knowledge or user's judgement, and $p(\mathbf{D})$ is the normalizing constant.

3.2 Posterior PDF considering multiple signals

A probability model is first developed for $p(\mathbf{D}|\mathbf{x})$. If there are N_s number of measured signals available resulting from N_s test runs of one or several different calibration trucks on the bridge, then the observed data set will be $\mathbf{D}_{N_s} = \{z_1, \dots, z_{N_s}\}$. Using the axioms of probability, we can write

$$p(\mathbf{D}_{N_s}|\mathbf{x}) = \prod_{n=1}^{N_s} p(z_n|\mathbf{D}_{n-1}, \mathbf{x}) = \prod_{n=1}^{N_s} p(z_n|\mathbf{x}) \quad (7)$$

where $p(z_n|\mathbf{D}_{n-1}, \mathbf{x})$ can be written as $p(z_n|\mathbf{x})$ when the user's uncertainty in the n th measured signal specified by model parameter \mathbf{x} is not influenced by the previous measured signals. Moreover, in the problem of influence line identification, only the measured response is used to identify it. Therefore, in the absence of any prior knowledge, $p(\mathbf{x})$ can be treated as a constant i.e., non-informative prior (Yuen et al. 2002). Hence, the expression for posterior PDF in Eq. (6) can be simplified as

$$p(\mathbf{x}|\mathbf{D}_{N_s}) = c \prod_{n=1}^{N_s} p(z_n|\mathbf{x}) \quad (8)$$

where c is a constant term incorporating normalizing constant and non-informative prior that do not include \mathbf{x} . Therefore, by simply extending the product by one term, new measured data can be incorporated in a systematic and consistent fashion for the estimation of posterior PDF of model parameters \mathbf{x} . This is an important feature of Bayesian framework.

3.3 Identification of influence line using Bayesian framework

For a linear response, the probabilistic forward model for predicting the observation $z_n \in \mathbb{R}^{N_n \times 1}$ from \mathbf{x} is expressed by

$$\mathbf{z}_n = \mathbf{H}_n \mathbf{x} + \varepsilon_n \quad (9)$$

where $\varepsilon_n \in \mathbb{R}^{N_n \times 1}$, is the prediction or observation error between the measured and predicted response for the n th test. If the PDF model for ε_n is a zero-mean Gaussian with covariance matrix $\mathbf{R}_n \in \mathbb{R}^{N_n \times N_n}$, then the posterior PDF in Eq. (8) can be written as

$$p(\mathbf{x}|\mathbf{D}_{N_s}) = c \prod_{n=1}^{N_s} \frac{1}{(2\pi)^{N_n/2} |\mathbf{R}_n|^{1/2}} \exp \left[-\frac{1}{2} (\mathbf{z}_n - \mathbf{H}_n \mathbf{x})^T \mathbf{R}_n^{-1} (\mathbf{z}_n - \mathbf{H}_n \mathbf{x}) \right] \quad (10)$$

The most probable value of \mathbf{x} is obtained by maximizing the above posterior PDF. Using asymptotic approximation for Gaussian distribution, a maximum-a-posteriori (MAP) is estimated for optimal value of \mathbf{x} by minimizing the negative of logarithm of posterior PDF i.e., $\hat{\mathbf{x}} = \arg \min[-\ln p(\mathbf{x}|\mathbf{D}_{N_s})]$. Therefore, the MAP estimate is obtained by minimizing the following objective function and ignoring the constant terms

$$J = \frac{1}{2} \sum_{n=1}^{N_s} (\mathbf{z}_n - \mathbf{H}_n \mathbf{x})^T \mathbf{R}_n^{-1} (\mathbf{z}_n - \mathbf{H}_n \mathbf{x}) \quad (11)$$

The MAP estimate can be obtained analytically by performing $\partial J / \partial \mathbf{x} = 0$

$$\hat{\mathbf{x}} = \mathbf{P} \sum_{n=1}^{N_s} \mathbf{H}_n^T \mathbf{R}_n^{-1} \mathbf{z}_n \quad (12)$$

$$\mathbf{P} = \left(\sum_{n=1}^{N_s} \mathbf{H}_n^T \mathbf{R}_n^{-1} \mathbf{H}_n \right)^{-1} \quad (13)$$

where $\hat{\mathbf{x}}$, \mathbf{P} represents the mean and covariance matrix of posterior PDF, respectively. The influence line calculated using Eq. (12) takes into account multiple measured signals. If the observation error is independent, then the covariance matrix for observation noise can be simplified as $\mathbf{R}_n = \sigma_n^2 \mathbf{I}$ where σ_n is the standard deviation of observation error in n th test and \mathbf{I} is the unit matrix.

4 VALIDATION OF PROPOSED METHOD

4.1 Description of test bridge and field experiment

The test bridge is a single-span slab-on-girder steel girder bridge consisting of three main girders with two traffic lanes (Yoshida et al. 2021). It has a span length of 33.65 m and a width of 6.25 m. As a part of the BWIM system for the target bridge, a displacement gauge was installed at the longitudinal center of girder no. 2 (G2) for measuring the bridge displacement responses induced by the travelling vehicles. The schematic views of the test bridge along with sensor layout is shown in Figure 1.

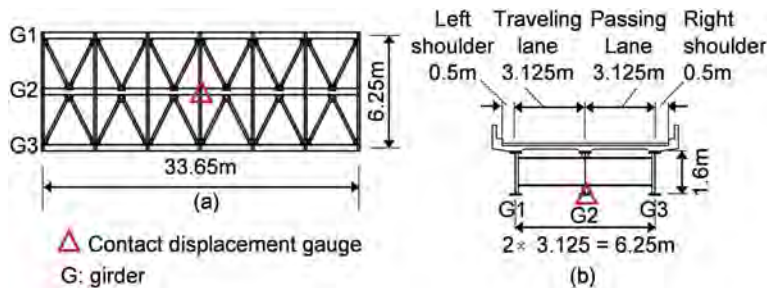


Figure 1. Schematic diagrams of the test bridge with sensor layout: (a) Plan view; (b) Sectional view.

Table 1 shows the specifications of the contact displacement gauge used in this study. Multiple test runs were conducted using three different calibration trucks to consider the variability in the measured bridge responses. The specifications of three calibration trucks are listed in Table 2. A total of ten calibration runs involving different test conditions, listed in Table 3, were considered in this study. The measured bridge responses corresponding to these calibration runs are shown in Figure 2. As can be seen, a lot of variability exists in the measured bridge responses owing to the perturbation in the dynamic component. Due to this variability in the measured responses, the calculated bridge influence lines will also vary from one to another. Therefore, it would be difficult to judge the actual influence line of the bridge calculated using the single measured signal corresponding to anyone of the calibration trucks. Hence, incorporating multiple measured signals corresponding to different calibration trucks

and test conditions (mainly driving lanes and travelling speeds) would make the influence line identification process a lot more robust. This can be done easily using Bayesian framework as discussed in the preceding section, namely by using Eq. (12).

Table 1. Specifications of contact displacement gauge.

Model	Sampling Frequency (Hz)	Capacity (mm)	Nonlinearity (mm)	Sensitivity ($\times 10^{-6}$ strain/mm)
CDP-25 (Tokyo Sokki Kenkyujo Co., Ltd.)	100	0–25	0.1% of rated output	500

Table 2. Specifications of three calibration trucks.

Axle type	Axle weights and GVW (kN)					Axle spacing (m)		
	1st axle	2nd axle	3rd axle	4th axle	GVW	1st-2nd	2nd-3rd	3rd-4th
4-axle	44.7	44.2	53.8	52.5	195.2	1.85	4.18	1.2
3-axle	53.6	34.9	35.0	-	123.5	3.23	1.31	-
2-axle	22.8	24.1	-	-	46.9	2.87	-	-

Table 3. Description about calibration runs on the test bridge.

Run No.	Driving lane	Types of calibration truck used	Travelling speed (m/s)
1	Travelling	4-axle	10.87
2	Passing	4-axle	12.94
3	Travelling	4-axle	12.74
4	Passing	4-axle	13.71
5	Passing	3-axle	14.29
6	Travelling	3-axle	13.92
7	Passing	3-axle	14.04
8	Passing	2-axle	13.88
9	Travelling	2-axle	13.52
10	Travelling	2-axle	12.23

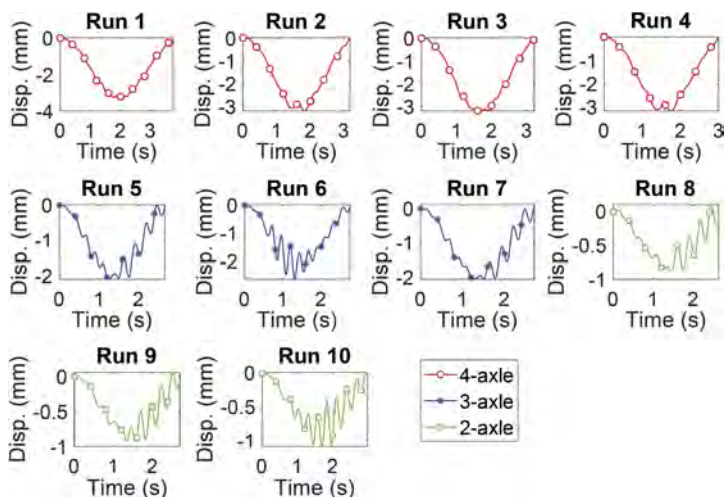


Figure 2. Measured displacement responses under three different calibration trucks.

4.2 Bayesian-based influence line identification considering multiple signals

At first the influence lines were identified by the conventional method (using Eq. (5)) which considers only one signal at a time and treat the observation error as the white noise (uncorrelated). Figure 3 shows the identified influence line from each measured signal using conventional method. Clearly, the conventional method could not identify a unique influence line since it is very sensitive to perturbations. Hence, the influence line identified using the measured signal of one type of calibration truck cannot predict well the measured response due to another type of calibration truck.

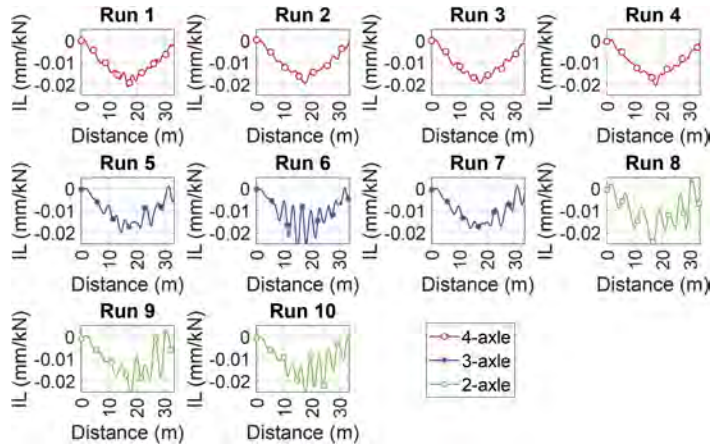


Figure 3. Identified influence line for each measured signal using conventional method.

To address these issues, the influence line was identified using the proposed Bayesian method considering multiple measured signals simultaneously, namely by using Eq. (12). Figure 4(a) shows the identified influence lines using the proposed method. A single influence line was identified accounting all measurement signals collected during the ten passages of calibration runs. The uncertainties associated with the identified influence lines were estimated using the proposed method. Figure 4(b) shows the standard deviations of identified influence lines. Since the standard deviation of identified influence line is very small, it could be considered as accurate. Hence, the identified influence line considering multiple signals could be used for the accurate prediction of the theoretical bridge responses due to any vehicle types or the estimation of axle weights of unknown vehicles traversing the test bridge.

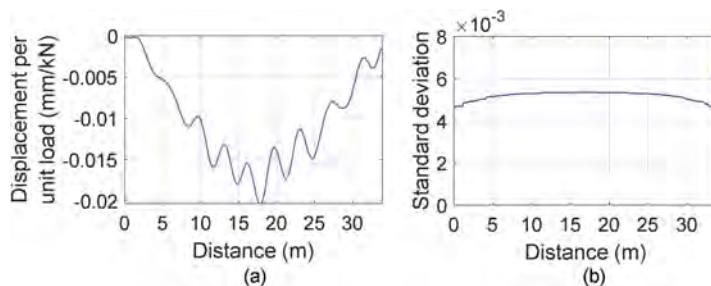


Figure 4. (a) Identified influence lines using the proposed method considering multiple signals; (b) Standard deviation of identified influence lines using Bayesian method.

5 CONCLUSIONS

It is important to calculate an accurate and robust influence line due to its wide range of applications. The conventional methods of influence line identification are limited to the use a single

measured signal which is why it is not so robust against the various perturbations in the measured signals. In this work, an accurate and robust influence line was identified using the Bayesian method and considering multiple measured signals of different types of calibration trucks. The proposed method makes it possible to estimate a single influence line using as many measured signals as desired. Moreover, using proposed Bayesian framework, the uncertainty in the identified influence line could be quantified which provides a valuable information for predicting the theoretical responses due to any vehicles and axle weights estimation of unknown vehicles.

REFERENCES

- Beck, J. & Katafygiotis, L. 1998. Updating models and their uncertainties. I: Bayesian statistical framework. *Journal of Engineering Mechanics*, 124(4): 455–461.
- Cardini, A.J. & DeWolf, J.T. 2009. Implementation of a long-term bridge weigh-in-motion system for a steel girder bridge in the interstate highway system. *Journal of Bridge Engineering* 14(6): 418–423.
- Chen, Z.W., Zhu, S.Y., Xu, Y.L., Li, Q. & Cai, Q.L. 2015. Damage detection in long suspension bridges using stress influence lines. *Journal of Bridge Engineering*, 20(3): 05014013.
- Fiorillo, G. & Ghosn, M. 2015. Application of ILs for the ultimate capacity of beams under moving loads. *Engineering Structure*, 103: 125–133.
- Frøseth, G.T., Rønnquist, A., Cantero, D. & Øiseth, O. 2017. Influence line extraction by deconvolution in the frequency domain. *Computers and Structures*, 189: 21–30.
- He, W.Y., Ren, W.X. & Zhu, S.Y. 2017. Damage detection of beam structures using quasi-static moving load induced displacement response. *Engineering Structures*, 145: 70–82.
- Ieng, S. 2015. Bridge influence line estimation for bridge weigh-in-motion system. *Journal of Computing in Civil Engineering*, 29(1): 0000384.
- Lin, S.W., Du, Y.L., Yi, T.H. & Yang, D.H. 2022. Model Updating Using Bridge Influence Lines Based on an Adaptive Metamodel Global Optimization Method. *Journal of Bridge Engineering*, 27(3): 04022003.
- McNulty, P. & O'Brien, E.J. 2003. Testing of bridge weigh-in-motion system in a sub-Arctic climate. *Journal of Testing and Evaluation*, 31(6): 1–10.
- Mustafa, S. & Sekiya, H. & Hirano, S. & Miki, C. 2021. Iterative linear optimization method for bridge weigh-in-motion systems using accelerometers. *Structure and Infrastructure Engineering*, 17(9): 1245–1256.
- Mustafa, S., Yoshida, I. & Sekiya, H. 2021. An investigation of bridge influence line identification using time-domain and frequency-domain methods. *Structures*, 33: 2061–2065.
- O'Brien, E.J., Znidaric, A. & Dempsey, A.T. 1999. Comparison of two independently developed bridge weigh-in-motion systems. *International Journal of Heavy Vehicle Systems* 6(1–4): 147–161.
- Obrien, E.J. & Quilligan, M.J. & Karoumi, R. 2006. Calculating an influence line from direct measurements. *Bridge Engineering*, 159(1), 31–4.
- Obrien, E.J., Rowley, C.W. & Gonzalez, A. & Green, M.F. 2009. A regularised solution to the bridge weigh-in-motion equations. *International Journal of Heavy Vehicle Systems*, 16(3), 310–327.
- Timoshenko, S. & Goodier, J.N. 1934. *Theory of elasticity*. New York: McGraw-Hill.
- Wang, N.B., He, L.X., Ren, W.X. & Huang, T.L. 2017. Extraction of influence line through a fitting method from bridge dynamic response induced by a passing vehicle. *Engineering Structures*, 151: 648–664.
- Xiao, X., Xu, Y.L. & Zhu, Q. 2015. Multiscale modeling and model updating of a cable-stayed bridge. II: model updating using modal frequencies and influence lines. *Journal of Bridge Engineering*, 20(10): 04014113.
- Yoshida, I., Sekiya, H. & Mustafa, S. 2021. Bayesian bridge-weigh-in-motion and uncertainty estimation. *ASCE-ASME Journal of Risk and Uncertainty in Engineering Systems, Part A: Civil Engineering*, 7(1): 04021001.
- Yuen, K.V. & Katafygiotis, L.S. 2002. Bayesian Modal Updating using Complete Input and Incomplete Response Noisy Measurements. *Journal of Engineering Mechanics*, 128: 340–350.
- Zheng, X., Yang, D.H., Yi, T.H. & Li, H.N. 2019. Development of bridge influence line identification methods based on direct measurement data: a comprehensive review and comparison. *Engineering Structures*, 198: 109539.

Bridge weigh-in-motion: Feedback on various types of bridges

F.B. Cartiaux, V. Le Corvec & J. Semiao
OSMOS Group SA, Paris, France

A. Brouste
Laboratoire Manceau de Mathématiques, Le Mans Université, Le Mans, France

ABSTRACT: Bridge Weigh-in-Motion (B-WIM) systems use the bridge deck itself as a scale for the estimation of the vehicle gross weight and axle loads. This implies that the performance of a B-WIM is strongly dependent on the bridge structure, even more than on the quality of the sensors used for collecting the raw data necessary to derive the WIM results. This paper describes the feedback of the use of B-WIM systems by OSMOS Group since 2018, focusing on the incidence of the bridge deck material and geometry on the WIM results. The feedback relies on a sample of fifteen different bridges of various types, including reinforced concrete slab or beam girder decks, steel truss bridges, composite decks with steel beam girders, and prestressed concrete beam or box girders. The incidence of geometrical parameters is discussed, with span length from 10 m to 50 m, a number of main beam girders from two to ten, and also some bridges with a significant skew angle. The examples are located mainly in France and Italy, but also in Asia and the Middle East. Based on this feedback, some general guidelines are given for the applicability of B-WIM on different types of bridges, and cases for which the expected performance is the best are pointed out. Further improvements of the B-WIM system are finally discussed, to deal with the conditions which still induce some difficulties for an efficient B-WIM.

1 INTRODUCTION

Road infrastructure owners and managers can get significant benefit from an accurate knowledge of the real traffic level, in terms of asset management (Dolcemascolo et al., 2015), road and truck safety including overweight detection (Jacob et al., 2010), and assessment of the impact of the traffic in terms of damages to optimize the maintenance operations (Schmidt et al., 2013). To get this knowledge, Weigh-in-Motion (WIM) solutions allow to estimate the gross vehicle weight (GVW) of each individual vehicle, sometimes along with its silhouette and load by axle, without interrupting the traffic flow.

Usual WIM solutions use devices that must be installed inside the pavement, which implies works with road closures, sensitivity to the pavement condition, and inconvenience when the road must undergo pavement maintenance works. Bridge-WIM (B-WIM) solutions offer a way to remedy to the above-mentioned issues, by using a bridge located anywhere along the road as a scale. Sensors are installed on the bridge deck, on well-chosen locations, usually under the main girders, thus avoiding works on the road itself and allowing a high robustness of the WIM system, insensitive to pavement condition.

As a counterpart, the performance of a B-WIM system in terms of accuracy for GVW and axle load estimation is strongly dependent on the bridge deck itself and may highly vary from one bridge to another. This issue is discussed in this paper by analyzing the feedback of OSMOS Group, which developed and used a specific B-WIM system called “WIM+D” in the last years. Fifteen different bridges have been instrumented with this system since 2018, covering a large variety of typologies and materials.

2 DESCRIPTION OF THE BRIDGE-WIM SYSTEM

2.1 General principle for the Bridge-WIM

B-WIM systems use strain sensors on critical parts of the bridge deck, where the variations of the strain are the most significant under the effect of the traffic loads: for example, on the lowest member of main girders at the middle of one span, where the bending of the deck is maximal.

The WIM+D system specifically uses Optical Strand (OS) strain sensors, which measure the average longitudinal strain over a length of one meter, to smooth the potential effects of the heterogeneity of the material, especially for reinforced concrete bridges which may present microcracks.

The set of sensors is divided into three categories, according to the purpose of each measurement:

- “Gross Weight Sensors” are set on main girders of one span, if possible, on all girders, or a selection of them equally distributed along the deck width, if there are more than six girders,
- “Speed Sensors” are similarly set on the next span if the bridge has more than one span. The speed of the vehicle is computed and then used to calculate the GVW. For single span bridges, the speed may be deduced from the gross weight sensors, but with a lower accuracy.
- “Axle Load Sensors” are optional. They are set on locations subject to a local strain while axles are crossing the bridge. One axle load sensor per traffic lane is enough. Not all types of bridge structures are suitable for axle weighting: some bridges do not have sensitive enough local strain.

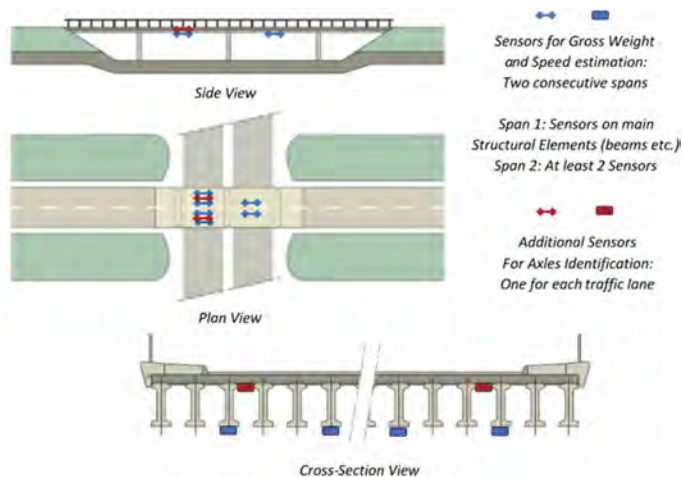


Figure 1. A typical WIM+D sensors layout.

The usual set-up of the WIM+D system comprises six to twelve sensors, depending on the bridge deck structure (Figure 1), incl. two to six gross weight sensors, two speed sensors and two to four axle load sensors, if applicable. All sensors are connected to an Expert Data Acquisition System (EDAS), allowing a continuous recording at a sampling rate of 100 Hz. The records are automatically triggered by thresholds applied to the strain variations, to associate each record to one – or a few successive – passages of vehicles on the bridge.

2.2 The Optical Strand technology

The strain sensors used by the WIM+D system are Optical Strands (OS). They are using the principle of the modulation of the intensity of light in fiber optics through micro-bending: three fiber optics are braided together inside a common one-meter-long coating duct which

ensures their protection, and the intensity of the light returned by the device to its interrogator directly depends on the elongation (or shortening) of the braided part.

Thus, it is possible to measure an average strain over the one-meter length of the sensor, at a high sampling rate (here, 100 Hz), and without the need of complex optoelectronics and specific light sources, unlike other fiber optic sensing technologies. Due to their easy and robust installation (Figure 2), OS have been widely used for Structural Health Monitoring (SHM) purpose, but they are also convenient for B-WIM (Cartiaux et al., 2019).

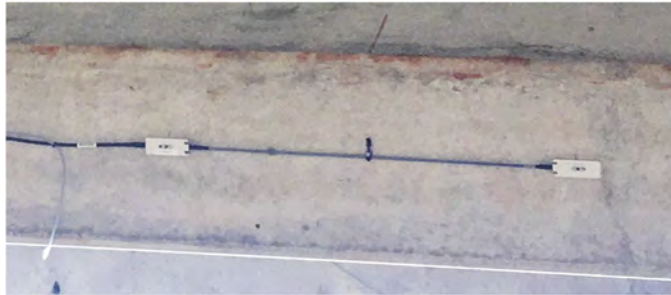


Figure 2. Optical Strand set under one of the main beam girders of a prestressed concrete viaduct.

2.3 Data flow, processing, and release of the results

The raw strain measurements are acquired by the system at the sampling rate of 100 points every second. The EDAS ensures the synchronicity of the data on all the different sensors set on the bridge deck and carries out a first data selection: only the data which correspond to significant strain variations on any of the OS are kept for further analysis, with a few seconds (usually, five) of pre- and post-trigger buffer. After this first step of recording and preprocessing, the data is organized as a succession of dynamic records of a few seconds, each one of them gathering the effects of one heavy vehicle on the bridge as they are recorded by all the synchronized OS.

After this first step, the strain data are sent through the 4G network to a cloud, which will keep them for further analysis, including the WIM but also SHM-dedicated ones like spectral decomposition or rainfall counting. For the WIM feature, a dedicated algorithm identifies the results related to the truck, like GVW and axle loads, from the response of the bridge deck as recorded by the OS. Indeed, heavier vehicles induce a stronger mechanical response with higher strain. The algorithm is also able to distinguish vehicles driving on the bridge at the same time in opposite directions, or vehicles which follow each other at short distance and triggered the same dynamic record.

The final WIM results are released after one to two minutes delay on a web interface, on which they are available for any user interested in the traffic data on the monitored bridge. The results available are time of passage, gross vehicle weight, direction, and speed. On specific types of bridges, it is also possible to release the vehicle length, number of axles, silhouette, and load of each axle. In addition, the system can be coupled with a video camera to get images and even plate numbers of the vehicles.

3 BRIDGE-WIM IMPLEMENTATION AND ACCURACY ASSESSMENT

3.1 Description of the bridges

The WIM+D system has been in use on fifteen different bridges since its first release in Italy in 2018. Some of these individual experiments have been documented more in detail already (Cartiaux et al., 2021 and 2023). In this paper, we present a general overview of all the fifteen cases: it is interesting that the bridges have a high variety of typologies, span length, and number of girders. This allows a discussion on the incidence of these characteristics on the performance of B-WIM.

Table 1 gives the brief description of each bridge with the main characteristics: number of spans and span length, number of main girders, type of material and typology, along with a geographical indication and the year of installation of the WIM+D system. The span length ranges from 10 m to 59 m, and the typologies from historical iron truss beams to prestressed concrete or composite decks. It is also indicated whether the spans are isostatic (6 cases among 15).

Table 1. Brief description of the bridges, sorted by chronological order of WIM+D installation.

Bridge	Country	Date	Typology	Nb of spans	Span length (m)	Nb of girders	Nb of sensors
1	Italy	2018	Composite deck	3	32	4 steel beams	8
2	Italy	2018	Concrete slab	2	19	None (slab)	8
3	Italy	2018	Composite deck	2	28	2 steel beams	6
4	France	2018	Reinforced concrete (RC)	15	17	3 RC beams	4
5*	France	2019	Prestressed precast concrete beams (PPCB)	4	15	10 PPCB	12
6	Italy	2019	Prestressed concrete (PC) box girder (isostatic)	1	16	1 box girder	6
7	Kuwait	2020	Concrete slab	2	18	None (slab)	12
8	France	2021	PC beams (isostatic)	1	26	4 PC beams	6
9	Taiwan	2021	PC beams (isostatic)	1	35	5 PC beams	8
10	France	2021	Composite deck (isostatic)	1	10	3 iron beams	3
11	France	2021	PC beams	5	59	2 PC beams	6
12*	Italy	2021	PC beams (isostatic)	9	32	4 PC beams	8
13	Ukraine	2021	RC beams (isostatic)	4	33	8 RC beams	10
14	France	2021	Iron truss, historical	5	45	2 truss beams	4
15	France	2022	Iron truss, historical	11	45	2 truss beams	6

* Bridges 5 and 12 have been documented more in detail, see resp. Cartiaux et al., 2021, and 2023.

3.2 Methods for the accuracy assessment

Assessing the accuracy of an on-site WIM system requires a dedicated verification procedure, which implies to use a sample of vehicles as reference loads and let them drive on the bridge at various speeds, in all available traffic lanes (and even out of lane). The GVW of each one of the test vehicles is measured on a homologated weighbridge just before and after each test day. If the silhouette and axle load results are assessed as well, their reference value are measured at the same occasion.

The accuracy assessment is carried out by comparing the results given by the B-WIM as the vehicles are driven on the bridge to these reference values. It implies a statistical analysis of the difference between reference values of GVW or axle load and values given by the B-WIM. Thus, a significant number of test passages is required. A usual accuracy assessment of the WIM+D system implies two or three different vehicles, each one of them running at least 10 to 20 times back-and-forth on the bridge.

Once all the measured weights of the B-WIM are recorded for the whole test, the relative error with respect to the reference values of GVW and – if required – axle load is analyzed to eventually accept the system into an accuracy class. A few different standards define such classes. For this study, we have chosen to give the estimation of the 95% quantile of the absolute value of the relative errors, which means that 5% (or less) of the measured absolute value of relative errors are above this quantile (percentage of accuracy).

In a second step, for some of the bridges only, a more robust statistical analysis of the percentage of accuracy has been carried out, according to the COST 323 methodology, which considers the uncertainty related to the number of runs and the environmental conditions of the test through categories of reproducibility and repeatability (Jacob et al., 2002, Brouste, 2021). The COST 323 defines accuracy classes ranking from A to E: the class A (best one) means that the percentage of accuracy (for GVW) is less than 5%, and the class E (worst one) that it is above 25%.

In the case of the bridge 12, an additional accuracy assessment according to the OIML standard has been carried out, for information only, as the OIML requirements are technically not applicable to such a B-WIM system, not used for legal metrology (OIML, 2006). This methodology simply considers the maximal measured relative errors.

3.3 Test plans

The fifteen bridges have been tested for accuracy assessment of the WIM+D system according to the plans summarized in Table 2 (in which “-” means “not tested”). In some cases, two of the test vehicles happen to have the same GVW (rounded at tons) but they had different silhouettes and number of axles.

Table 2. Test plans.

Bridge	Nb of vehicles	GVW (t)	Nb of runs (total)	Axle load test	COST 323	OIML
1	2	36 and 56	22	-	-	-
2	2	35 and 57	27	-	-	-
3*/Test 1:	2	35 and 57	31	-	-	-
3*/Test 2:	3	19, 39, and 50	30	Yes	-	-
4	3	12, 16, and 19	18	-	-	-
5*/Test 1:	3	19, 32, and 44	33	Inconclusive	Yes	-
5*/Test 2:	3	19, 40, and 40	194	Inconclusive	Yes	-
6	3	20, 35, and 50	9	Yes	-	-
7	3	20, 25, and 30	26	-	-	-
8	3	19, 32, and 40	36	Yes	-	-
9	2	21 and 36	27	Yes	-	-
10	3	19, 32, and 40	36	-	-	-
11	3	19, 32, and 38	36	-	-	-
12*/Test 1:	3	24, 42, and 42	75	Inconclusive	Yes	Yes
12*/Test 2:	3	17, 29, and 34	42	Inconclusive	Yes	Yes
13	6	13, 21, 29, 32, 44, 45	67	Inconclusive	Yes	-
14	1	10	20	-	Yes	-
15	2	10 and 12	36	Yes	Yes	-

* Bridges 3, 5 and 12 have been tested twice at different dates, with different vehicles.

The design of the WIM+D system allows an accurate estimation for the GVW in any case, but the axle identification is strongly dependent on the possibility of measuring some local bending effect, typically the local bending of a thin slab between two main girders. Not all bridge deck types allow this possibility. Concrete slabs (bridges 2 and 7) are not suited to this feature, for example. Thus, one third only of the fifteen cases were tested for the axle identification and axle load estimation. Moreover, in some cases there was no demand for axle load estimation from the asset manager, so the system was optimized for GVW only, which enabled to use less sensors.

In the case of bridges 3, 6, 8, 9, and 15, the accuracy assessment of the system for the axle load estimation was successful. In the case of bridges 5, 12, and 13, some axle load sensors were set up to investigate whether these bridge types would fit the requirements for axle detection by the WIM+D system, but without acceptable accuracy. This gives valuable feedback for further improvement of the system.

In any case, the estimation of the GVW is totally independent of the one of the axle loads, unlike classical WIM devices installed inside the pavement.

4 MAIN RESULTS OF THE FEEDBACK

4.1 Accuracy assessment for the Gross Vehicle Weight (GVW)

The results of the accuracy assessment for GVW are released in Table 3. The bridge typology is reminded, and the tolerance is given as the percentage of accuracy, which corresponds to

the 95% quantile of absolute values of all measured relative errors during each test. That means that (less than) 5% of the measured relative errors are above this percentage of accuracy. The equivalent absolute error is also given, in tons.

Whenever it is applicable, the COST 323 and OIML classes in which the WIM+D system is accepted are released as well.

Table 3. Accuracy assessment for the Gross Vehicle Weight.

Bridge	Typology	Tolerance (%)	Tolerance (t)	COST 323	OIML
1	Composite deck	8	4.5		
2	Concrete slab	12	5.2		
3*/Test 1:	Composite deck	7	3.1		
3*/Test 2:	Composite deck	10	5.1		
4	RC beams	7	1.3		
5*/Test 1:	PPCB	9	3.6	C(15)	
5*/Test 2:	PPCB	14	4.7	C(15)	
6	PC box girder (isostatic)	15	5.7		
7	Concrete slab	15	3.8		
8	PC beams (isostatic)	12	3.9		
9	PC beams (isostatic)	14	3.3		
10	Composite deck (isostatic)	12	3.7		
11	PC beams	15	3.4		
12*/Test 1:	PC beams (isostatic)	4	1.0	A(5)	5
12*/Test 2:	PC beams (isostatic)	5	1.0	B+(7)	10
13	RC beams (isostatic)	6	2.1	B+(7)	
14	Iron truss, historical	9	0.9	C(15)	
15	Iron truss, historical	7	0.9	B(10)	

* Bridges 3, 5 and 12 have been tested twice at different dates, with different vehicles.

The WIM+D system shows good performances for a WIM device, with no tolerance above 15% whatever the bridge and test conditions. When the assessment according to COST 323 is released, the accepted class is always C(15) or better for the GVW. In one case (bridge 12) the class A(5), which is the best possible one, is even reached.

The bridges 3, 5, and 12 have been tested twice, and the difference in the assessment results depending on the test deserves some explanation:

In the case of bridge 3, the second test was carried out three months after the first one, after adding two additional sensors for the axle detection. For bridge 5, it was even twenty months between the two tests. In both cases, the environment conditions were very different, and the second test was carried out without re-adjusting the system, so we have an insight on the evolution of the performance without maintenance actions. In the case of bridge 5, it is shown that even after almost two years, the accuracy class C(15) assessed initially remains valid.

In the case of bridge 12, the second test was carried out the day after the first one, with the same vehicles, but they were half-loaded. So, the results of the first test, with accuracy class A(5) and even OIML class 5, are valid for full-loaded vehicles – the most interesting ones in regard to overweight detection, and the results of the second test are valid for half-loaded vehicles only.

The best performance is reached by PC or RC beams isostatic bridges, at the condition that they have more than one span (bridges 4, 12, and 13). Indeed, bridges 6, 8, 9 and 10 have only one span, which induces some uncertainty for the estimation of the speed, a result not only useful for the asset manager but also mandatory to compute the GVW. Iron truss and composite decks, even hyperstatic, give also good results (bridges 1, 3, 14, and 15). The concrete slabs (bridges 2 and 7) are the least performant, however both bridges have a significant skew angle, which also induces some difficulties.

The case of bridge 11 is specific: it is a long hyperstatic PC beams bridge of 200 m, with a central span of 59 m, on which the length of the influence lines and the density of the traffic poorly allows to separate properly the strain measurements due to successive vehicles, thus inducing a poor performance compared to other PC beams bridges.

4.2 Accuracy assessment for the silhouette and axle loads

The silhouette and axle loads are detected on five among the fifteen bridges, with results released in Table 4:

Table 4. Accuracy assessment for the axle load.

Bridge	Typology	Tolerance (%)		COST 323
		Single axles	Groups of axles	
3 (Test 2)	Composite deck	30	28	
6	PC box girder (isostatic)	19	22	
8	PC beams (isostatic)	24	15	
9	PC beams (isostatic)	39	22	
15	Iron truss, historical	10	not tested*	B(10)

* Due to weight limitation, the test vehicles for bridge 15 were 2-axles vehicles without groups of axles.

On the few cases on which the test for axle load is available, the results reflect the difficulty of analyzing a relevant local bending effect, which strongly depends on the bridge type. Moreover, in the case of bridges 6, 8, and 9, the single-span configuration already mentioned has an incidence on the axle load results, which are speed-dependent as well.

In the case of bridge 15 however, the axle load estimation gives good results, consistent with the results for the GVW. This is due to a favorable configuration of the bridge deck, with a thin ultra-high-performance fiber reinforced concrete (UHPFRC) slab located between the two lateral historical iron truss girders, used as “axle detector” with a very clear local bending effect under traffic loads.

5 GUIDELINES FOR THE APPLICATION OF BRIDGE-WIM

5.1 Best suitable types of bridge deck structures

The feedback on various types of bridges and the results in terms of tolerance for the GVW estimation allow to formulate guidelines as follows for the expected performance of the WIM +D system, depending on the characteristics of the bridges. We classify the performance in three main categories, each one gathering one third of the fifteen tested bridges:

Table 5. Performance categories.

Category	Tolerance (%)	Bridges	Number of girders	Span length
Very good	8% or less	1, 4, 12, 13, 15	4, 3, 4, 8, 2	32, 17, 32, 33, 45
Good	8% to 12%	2, 3, 8, 10, 14	0 (slab), 2, 4, 3, 2	19, 28, 26, 10, 45
Acceptable	12% to 15%	5, 6, 7, 9, 11	10, 1 (box), 0 (slab), 5, 2	15, 16, 18, 35, 59

To expect a very good performance, the bridge for the application of the WIM+D system should be chosen as follows:

- Number of main girders ideally between 2 and 4, and up to 8,
- Span length ideally between 30 m and 45 m,
- Isostatic decks with more than one span give the best results (bridges 12 and 13).

The type of material, whether reinforced or prestressed concrete, composite deck with steel main girders or even historical iron truss, has no significant incidence on the performance.

5.2 Additional conditions for axle detection

The previous considerations apply for the GVW estimation only. The axle detection and axle load estimation come as an option and are not possible for every bridge. The technical

condition to ensure an efficient axle detection is to be able to measure, on some locations on the bridge deck, a significant local bending effect, the influence line of which is shorter than the usual spacing between successive axles (around 2 m, for example).

This is achieved on thin slab structures which carry the pavement between girders. However, the slab must be thin enough to present sufficient bending under the effect of a single wheel, and the usual transverse location of the wheels needs to be somewhere on the slab, ideally just above the dedicated axle load sensors, and not right on the main girders.

These constraints leave only few possibilities among the fifteen tested bridges. The only one with good performance for the axle detection is bridge 15, with a very thin UHPFRC slab spanning the two lateral girders, and thus ensuring that we have both always the wheels on the slab, and the slab itself flexible enough.

6 CONCLUSIONS

With fifteen very different bridges monitored since 2018, the WIM+D system by OSMOS Group has significant feedback to get conclusions about its applicability depending on the type of bridge.

For the gross vehicle weight (GVW) estimation, the ideal bridge would be a reinforced or pre-stressed concrete beams, or composite bridge deck, with few main girders (2 to 4) and a span length between 30 m and 45 m, with more than one span, and, for the best performance, isostatic. This case allows to expect a percentage of accuracy of 5% or less, and one of the tested bridges was accepted in class A(5) of COST 323. At the opposite, thick concrete slabs with significant skew angle, and very long highly hyperstatic bridge decks, give less accurate results. Interestingly, very good performance has been achieved on historical iron truss bridges, despite of hyperstaticity.

Axle load detection through the WIM+D process still deserves some improvements. One of the tested bridges was accepted in class B(10) of COST 323 for the axle load estimation, with a very favorable configuration comprising an UHPFRC thin slab for measuring local bending effects. Research is currently going on for that specific point, to allow axle detection through a better identification of superimposed influence lines inside the measured signal, involving advanced regression and regularization methods.

REFERENCES

- Brouste, A. 2021. Testing the accuracy of WIM systems: application to a B-WIM case. *Measurement*, 185.
- Cartiaux, F.-B., Koutsonika, S., Andrikopoulos, G., Pelletier, P. 2019. Bridge Monitoring & Assessment via OSMOS Optical Strands. *Proceedings of the Fourth Joint International Symposium on Deformation Monitoring JISDM 2019*.
- Cartiaux, F.-B., Le Corvec, V., Semiao, J., Jacob, B., Schmidt, F., Brouste, A., Ehrlacher, A. 2021. Real Condition Experiment on a new Bridge Weigh-in-Motion Solution for the Traffic Assessment on Road Bridges. *Proceedings of the IABSE Congress Ghent 2021 – Structural Engineering for Future Societal Needs*, pp. 1242–1248. IABSE.
- Cartiaux, F.-B., Fort, V., Pelletier, P.M., Jacob, B., Brouste, A. 2023. Combined Bridge Weigh-In-Motion and Structural Health Monitoring on Road Bridges: Case Study on the Salso Viaduct (Italy). In: Rizzo P., Milazzo A. (eds) *European Workshop on Structural Health Monitoring. EWSHM 2022. Lecture Notes in Civil Engineering*, vol 254. Springer, Cham. https://doi.org/10.1007/978-3-031-07258-1_8
- Dolcemascosto V., Hornych P., Jacob B., Schmidt F., Klein E. 2015. Heavy Vehicle Traffic and Overload Monitoring in France and Applications. *Proceedings of the XXVth World Road Congress, Road and Mobility creating new Value from Transport, Seoul, Nov. 2-6, 2015*.
- Jacob, B., O'Brien, E., Jehaes, S. 2002. COST 323, European Specification on Weigh-in-Motion of Road Vehicles. EUCOCOST/323/8/99.
- Jacob B., Feypell de la Beaumelle V. 2010. Improving truck safety: Potential of weigh-in-motion technology. *IATSS Research*, 34, 2010, 9–15.
- OIML. 2006. Automatic Instruments for weighing Road Vehicles in Motion and Axle Load measuring. Part 1: Metrological and technical requirements – Tests. R 134-1.
- Schmidt F., Glaeser K.-P., Hornych P., Piau J.-M., Jacob B. 2013. Impacts from Truck Traffic on Road Infrastructure. *PIARC, Routes/Roads 358, 2013, 74–83*.

Estimation of remaining fatigue life of railway bridges using measurements from the WIM system

M. Zakharenko, G.T. Frøseth & A. Rönquist

Norwegian University of Science and Technology (NTNU), Trondheim, Norway

ABSTRACT: This study presents an approach to estimate the remaining fatigue life of railway bridges using the fatigue load model and its calibration with the data from a Weigh-in-Motion (WIM) System. The basement of the model is an assumption that damage caused to the infrastructure by each train passage equals the damage of the most damaging train of the traffic at the site. The calibration of the model is performed using the measurements of strains on rails of the Sokna bridge (Dovreline), Norway. The idea of calibration is to guarantee that the load model induces the same fatigue damage as actual traffic. To simplify and unify the analysis influence lines (IL) approach, the standard method for predicting the stress histories of railway bridges, is used in the load model. Correction factors for calibration the model estimations are obtained for the fifteen most common IL for five main groups of trains.

1 INTRODUCTION

Railway infrastructure is an essential part of every country, and its degradation is an important question. Railway infrastructure, especially in Norway, includes a lot of bridges. For example, Norwegian railway system includes more than 2300 bridges. About 40% of all bridges are steel bridges, and they have material fatigue as a primary damage mechanism (Sustainable Bridges, 2007). Collapses of bridges lead to catastrophic consequences such as loss of human lives and high expenses to renovation. The above facts make fatigue of railway bridges a significant topic to study.

There are two approaches to estimate remaining fatigue life. In the case of a crack that has already been detected, the fracture mechanics approach is applicable for the estimation of the remaining fatigue life (Lovejoy, 2003). When the initial crack size is not available, the combination of a fatigue endurance model (Taras & Greiner, 2010) and a damage accumulation model is used (Fatemi, & Yang, 1998). The description of loading cycles experienced by the material is necessary for both approaches, and a fatigue load model is required. Fatigue load model represents traffic conditions at the bridge and usually it consists of a reference load and a set of calibrating the damage from reference load to the actual damage in the bridge (Hirt, 1982). Based on rolling stock data, statistics, and operational rules the Norwegian load model was established (Frøseth & Rönquist, 2019a). The measurement station collecting loads and geometries of trains was presented (Zakharenko et al., 2022a). The calibration coefficients for the Norwegian fatigue load model were calculated (Zakharenko et al., 2022b).

This paper is organized as follows. First, the theoretical background behind the fatigue load model is presented at Section 2.1. Next, the measurement station that was used to obtain traffic conditions is described at Section 2.2. Methodology to calculate correction factors for the calibration of the fatigue load model is described at Section 2.3. Section 3.1 presents measured traffic conditions and defines five main groups of trains. Section 3.2 demonstrates the level of conservatism of the load model and represents obtained correction factors. Finally, conclusions regarding the estimation of fatigue life using weigh-in-motion system are drawn.

2 METHODS

2.1 Fatigue damage and load model

Fatigue is a damage mechanism characterized by the initiation and propagation of the crack under cyclic loading of the material. Fatigue endurance curve (Wagener & Melz, 2018), S-N curve, is a dependency defining the number of loading cycles N with a stress range S that material can resist before failure. The classical and simple fatigue endurance curve is defined by Basquin's relation (Taras & Greiner, 2010):

$$N(S) = CS^{-m} \quad (1)$$

where C and m are experimentally obtained fatigue resistance parameters.

Miner's damage accumulation rule is used to consider different stress ranges induced by varying loads. It states that the cumulative fatigue damage D is equal to the sum of damages induced by each stress range individually (Fatemi & Yang, 1998):

$$D = \sum_i \frac{1}{N(S_i)} = \frac{1}{C} \sum_i S_i^m \quad (2)$$

where stress ranges S_i can be obtained from stress history by rainflow cycle counting (Amzlag et al., 1994).

The stress histories are usually described with static load function $f(x)$. The function can be defined through sum of influences of train axles:

$$f(x) = \sum_{i=1}^{n_p} p_i \delta(x - x_i) \quad (3)$$

where n_p is the number of the axles in train, p_i is axle load of the axle i , $\delta(x)$ is the Dirac delta function, x_i is coordinate of axle i .

Influence lines (IL) approach to static analysis is a common approach to predict stress histories in studying of railway bridges (Imam & Righiniotis, 2010). Influence line is a representation of a fatigue component in the form of the response of a structure to a unit load located at horizontal line. Table 1 shows IL representing the majority of critical components of railway bridges. IL can be obtained from measurements (OBrien et al., 2006) on real structures as well as from numerical modeling (Jepsen & Damkilde, 2018).

The response of a structure consists of two parts: static and dynamic. The static response $z_0(s)$ is a convolution of the load function and the IL (4), where $*$ is a convolution operator, s is a distance that the train has passed along the load path of the IL.

$$z_0(s) = (f * l)(s) \quad (4)$$

The dynamic part is defined through dynamic amplification factor (Liu et al., 2013):

$$\Phi = \Phi(v, L_\Phi) \quad (5)$$

where v is a train speed, L_Φ is length of IL.

The total response of a structure $z(s)$ than:

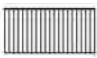



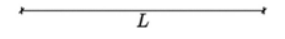

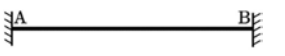
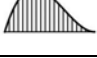
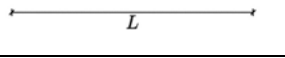

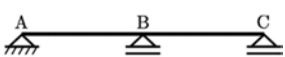

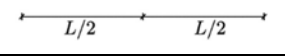



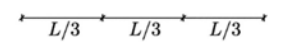
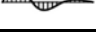
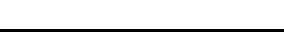
$$z(s) = \Phi(v, L) \cdot \sum_{i=1}^{n_p} p_i l(s - x_i) \quad (6)$$

The damage caused to the infrastructure by the train passage can be calculated using formulas above. To estimate the remaining fatigue life the first step is to establish a load model of past traffic at the site. Taking the assumption that each train passing a bridge causes to the infrastructure damage that is equal to the damage from the most damaging train at the site the fatigue load model was established for Norway. The traffic conditions of Norwegian railway system were collected (Frøseth & Rönquist, 2019a). Most damaging trains were identified with the help of the late acceptance hill climbing method for four time periods (1900–1930,

1930–1960, 1960–1985 and 1985–present) and two train types (Frøseth & Rönnquist, 2019b). The load functions of identified passenger and freight trains for the last period are presented in Figure 1. Then the load model was established on the rolling stock data, operational rules, and statistics (Frøseth & Rönnquist, 2019c).

However, fatigue load model includes load model as well as its calibration. To calibrate the model to actual traffic real loads were measured, see details in next section.

Table 1. Influence lines representing the majority of critical components of railway bridges. The table is adopted from Zakharenko et al. (2022b).

IL	Shape	Base system	Description
1		-	Total load effect
2			M_{AB}
3			V_{AB}
4			M_{AB}
5, 5r			M_A, M_B
6, 6r			M_{AB}, M_{BC}
7			M_B
8			M_{BC}
9, 9r			M_B, M_C
10, 10r			M_{AB}, M_{CD}

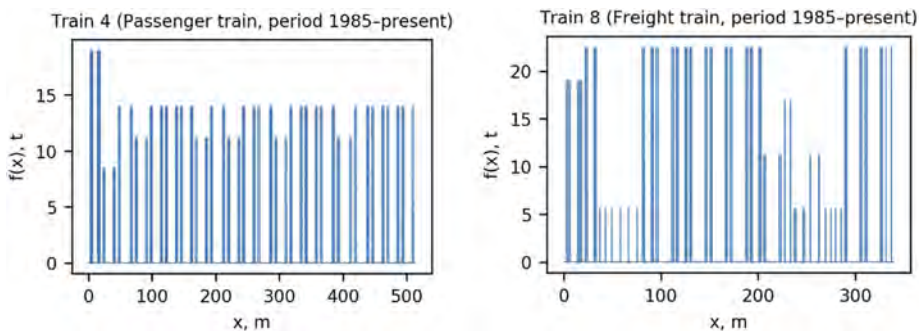


Figure 1. Load functions of the most damaging trains (last time period) from Norwegian fatigue load model. Figures are adopted from Zakharenko et al. (2022b).

2.2 Measurements

The measurement station is placed at one of the Norwegian railway lines, Dovreline, that connects Oslo and Trondheim. The Sokna bridge (Lundamo station) has low permissible speed (50 km/h) which helps the measurements to represent static part of the loading mostly (the dynamic part is negligible). The station uses for measurements six strain gauges placed at rails (three channels are at right rail, three are at left rail) and one temperature sensor. A photo of strain gauges of one channel is depicted in Figure 2. Every strain gauge forms one of the six strain channels.

The signal from one channel is filtered with the help of the moving average filter that removes random noise and smooths the signal. Next, the bias is removed from the smooth signal (Figure 3). Figure 4 shows the example of the final result (output of the strain channel) of measurement of the passage of one passenger train (one locomotive, six wagons).

The wheel loads are obtained from the output of the strain channels with Equation (7):

$$F(t) = V \cdot \frac{G}{4} \cdot C \cdot \varepsilon \tag{7}$$

where $F(t)$ is a vertical force from the wheel that the rail is subjected to in the middle between gauge pair, V is the input excitation voltage, G is a gauge factor, C is a calibration factor converting the voltage output of the system to tonnes, ε is an output signal of one channel.

To obtain the axle load p_{axle} of the train passing the measurement station the Equation (8) is used:

$$p_{axle} = median(w_{L1}, w_{L2}, w_{L3}) + median(w_{R1}, w_{R2}, w_{R3}) \tag{8}$$

where w_i is the final load obtained from channel i (the wheel load since gauges placed on the rails). The examples of load functions that are the goal of measurements can be found in Table 2.

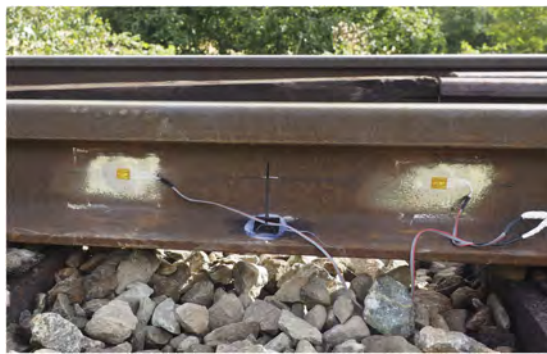


Figure 2. Placement of strain gauges of one channel on the rail.

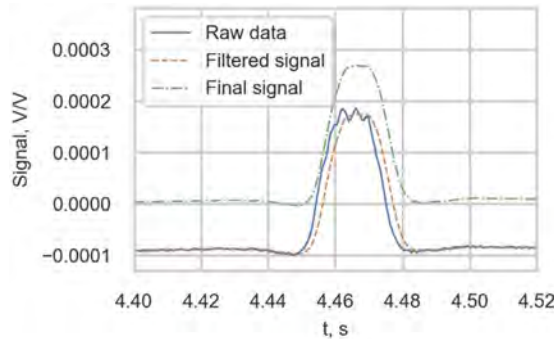


Figure 3. Processing of the signal from the strain gauge.

The details regarding the measurement station, the thorough description of an approach to proceed raw measured data and question of the measurement errors can be found at Zakharenko et al. (2022a).

2.3 Model calibration

The fundamental idea of the calibration is to adjust damage induced by the load model to the damage of the actual traffic. To achieve this goal the damage D_{model} caused by the model train (the most damaging train) and damage D_i caused by the real measured train are compared. The relationship γ_i between these damages (9) shows the level of conservatism of the model.

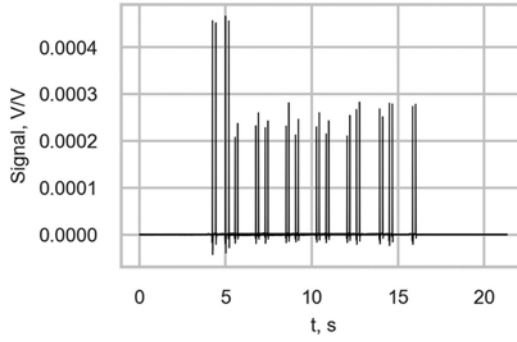


Figure 4. Example of output of one channel after passage of the passenger train consisting of one locomotive and six wagons.

$$\gamma_i = \frac{D_{model}}{D_i} \quad (9)$$

The total damage of n trains passed measurement station should cause to the infrastructure the same damage that induced by the model (n passages of the model train corrected by the correction factor γ_m).

$$\sum_{i=1}^n D_i = n \frac{D_{model}}{\gamma_m} \quad (10)$$

Finally, plugging D_{model} from (9) we obtain a formula for the calculation of the correction factor γ_m that calibrates the model to the actual traffic:

$$\gamma_m = \frac{n}{\sum_{i=1}^n 1/\gamma_i} \quad (11)$$

3 RESULTS AND DISCUSSION

3.1 Main train groups

The measurement station has registered more than 10,500 passages of trains. The main groups of trains are presented in Table 2, the algorithm to filter trains by types is published in Zakharenko et al. (2022a). There are two train types in Norway, passenger and freight. Passenger trains can be categorized in a sense of moving force, passenger trains moving by the locomotive and passenger Multiple Units (one of the wagons is motorized, locomotive is absent).

The distribution of percentage of measured trains by types is next: the passenger trains with locomotives consists about 6% of measured traffic, freight trains is 24%, MU Class 93 is 5%, MU Class 92 is the greatest part, and it composes about 49% of traffic, MU Class 73 is 10%. The remaining trains are service trains, single or double locomotives that do not have great damage potential and consequently can be excluded from the analysis. There are also MU compositions consisting of two or three MU of one type attached together, they are extremely limited in number and included in the main MU groups.

3.2 Calibration factors

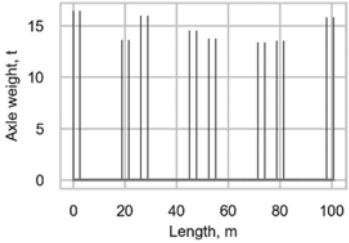

To study the level of conservatism and to obtain calibration coefficients for the model all announced trains were compared with the model trains (the most damaging trains) in a sense of damage that a train causes to the infrastructure. In different words, γ_i were calculated individually for every single train (passenger trains were compared with the most damaging passenger train, freight trains with the most damaging freight train), γ_m were calculated for each train group. γ_m are presented in Figure 5.

Table 2. Main groups of trains. Illustrations are adopted from Zakharenko et al. (2022a), Zakharenko et al. (2022b).

Train type	Load function	Photo
Passenger (with locomotive) 6%		
Freight (with locomotive) 24%		
MU Class 935%		
MU Class 9249%		

(Continued)

Table 2. (Continued)

Train type	Load function	Photo
MU Class 7310%	 <p>A bar chart showing axle weight in tonnes (t) on the y-axis (0 to 15) and length in meters (m) on the x-axis (0 to 100). The chart displays several vertical bars representing axle weights at various positions along the train length.</p>	 <p>A photograph of a high-speed train, likely a Shinkansen, stopped at a station platform. The train is white with red and blue accents.</p>

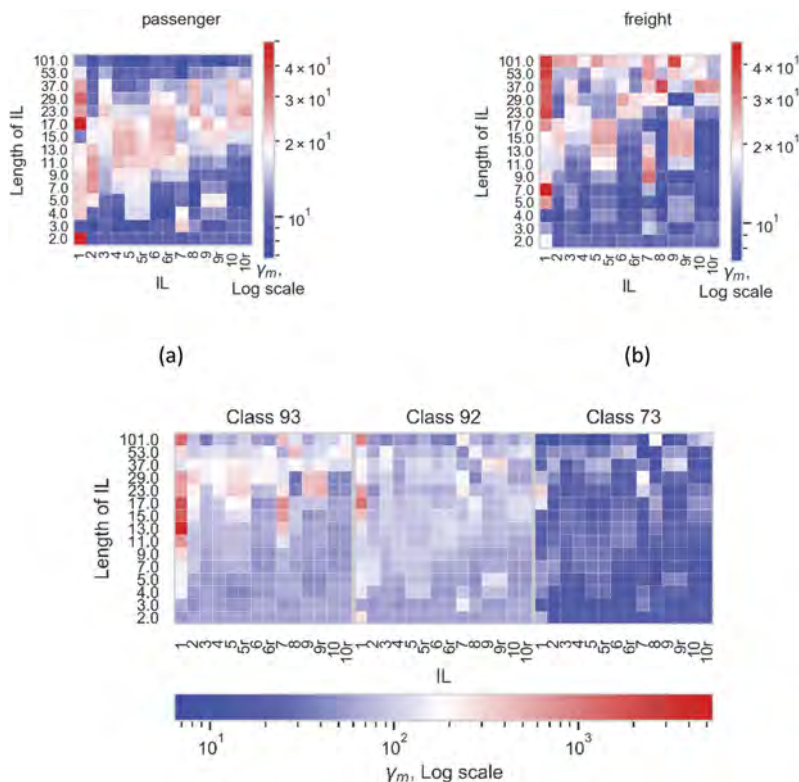


Figure 5. Correction coefficient γ_m for a) passenger trains, b) freight trains with locomotive and MU c) Class 93, Class 92, Class 73. The red lines are γ_m for studied cases.

The most conservative estimations the model gives for MU Class 92 since the train is much lighter than the model train and has a smaller number of axles. The closest to reality estimations the model gives for passenger trains. However, estimations are too conservative.

As the result, the calibration must be done since the level of conservatism of the model is excessive. The tables with exact numbers for the model calibration are presented in Zakharenko et al. (2022b). For quick estimations the minimum correction coefficients among all damage cases (IL length with the type of IL) can be used. According to Zakharenko et al. (2022b) the calibration can be performed with $\gamma_m=6.4$ for freight, passenger with locomotive and Class 73 trains, and $\gamma_m=32.7$ for Class 92 and Class 93.

4 CONCLUSIONS

The question of accurate estimation of the remaining fatigue life, and consequently maintenance, of railway bridges is essential for countries around the world because of a high importance of railways and catastrophic consequences of bridge collapses. The fatigue load model for estimation of residual life of railway bridge consists of artificial load and calibration coefficients.

At current work the Norwegian load model plays the role of the artificial load. The basic assumption of the model is that each train that passes the bridge is equal to the most damaging train at the site in a sense of damage causing to the infrastructure. The load model incorporated the influence lines (IL) approach to represent most critical details in the structure of the railway bridge. The model distinguishes two types of trains, passenger trains, and freight trains.

The calibration of the model is suggested to be made with the help of the weigh-in-motion (WIM) system having the six strain gauges. The method to proceed raw data from the measurement system is described. The main train groups are defined: freight train with locomotive, passenger train with locomotive, Multiple Units of three classes (Class 93, Class 92, Class 73).

The calibration coefficients (correction factors) for the fatigue load model are defined and discussed. The correction factors for the individual trains were calculated, the correction factors for each of the main group of trains were obtained. The load model is acknowledged to be too conservative. The suggestion is to use correction coefficients. The quick estimations can be performed with calibration of model with the coefficient 6.4 for freight, passenger with locomotive and Class 73 trains, and $\gamma_m = 32.7$ for Class 92 and Class 93.

REFERENCES

- Amzallag, C., Gerey, J. P., Robert, J. L., & Bahaud, J. 1994. Standardization of the rainflow counting method for fatigue analysis. *International journal of fatigue* 16(4): 287–293.
- Fatemi, A., & Yang, L. 1998. Cumulative fatigue damage and life prediction theories: A survey of the state of the art for homogeneous materials. *International Journal of Fatigue* 20(1): 9–34.
- Frøseth, G. T., & Rønnquist, A. 2019a. Evolution of load conditions in the Norwegian railway network and imprecision of historic railway load data. *Structure and Infrastructure Engineering* 15(2): 152–169.
- Frøseth, G. T., & Rønnquist, A. 2019b. Finding the train composition causing greatest fatigue damage in railway bridges by Late Acceptance Hill Climbing. *Engineering Structures* 196: 109342.
- Frøseth, G. T., & Rønnquist, A. 2019c. Load model of historic traffic for fatigue life estimation of Norwegian railway bridges. *Engineering Structure*, 200: 109626.
- Hirt, M. A. 1982. Remaining fatigue life of bridges. In *IABSE Symposium (Washington DC): Maintenance, Repair and Rehabilitation of Bridges* 113–129. Zürich, Switzerland: International Association for Bridge and Structural Engineering.
- Jepsen, M. S., & Damkilde, L. 2018. A direct and fully general implementation of influence lines/surfaces in finite element software. *Advances in Engineering Software* 120: 55–61.
- Liu, K., Zhou, H., Shi, G., Wang, Y. Q., Shi, Y. J., & De Roeck, G. 2013. Fatigue assessment of a composite railway bridge for high speed trains. Part II: Conditions for which a dynamic analysis is needed. *Journal of Constructional Steel Research* 82: 246–254.
- Lovejoy, S. C. 2003. Determining appropriate fatigue inspection intervals for steel bridge members. *Journal of Bridge Engineering* 8(2): 66–72.
- O'Brien, E. J., Quilligan, M. J., & Karoumi, R. 2006. Calculating an influence line from direct measurements. *Proceedings of the Institution of Civil Engineers-Bridge Engineering* 159(1): 31–34.
- Sustainable Bridges. 2007. *Sustainable bridges – Assessment for future traffic demands and longer lives* (Technical Report). Retrieved from www.sustainablebridges.net
- Taras, A., & Greiner, R. 2010. Development and application of a fatigue class catalogue for riveted bridge components. *Structural Engineering International* 20(1): 91–103.
- Wagner, R., & Melz, T. 2018. Fatigue life curve—A continuous Wöhler curve from LCF to VHCF. *Materials Testing* 60(10): 924–930.
- Zakharenko, M., Frøseth, G. T., & Rønnquist, A. 2022a. Train classification using a weigh-in-motion system and associated algorithms to determine fatigue loads. *Sensors* 22(5): 1772.
- Zakharenko, M., Frøseth, G. T., & Rønnquist, A. 2022b. How conservative is the Norwegian fatigue load model for service life estimation of railway bridges? *Structure and Infrastructure Engineering* 1–14.

Bridge-weigh-in-motion by strain of transverse stiffener and heavy-truck traffic characteristics in Fukuoka area, Japan

E. Yamaguchi, Y. Furusato, R. Nakamura & K. Horiuchi
Kyushu Institute of Technology, Kitakyushu, Japan

ABSTRACT: Information on actual traffic loads travelling along highways is valuable to determine maintenance scheme of bridges. The techniques that weigh trucks in motion, known as weigh-in-motion have attracted many highway engineers and researchers. One of such techniques is based on the deformation of a bridge and is called bridge-weigh-in-motion (BWIM). Although relatively inexpensive, the conventional BWIM requires the strains of transverse stiffeners for supplemental information in addition to the strains of main girders. Effort has been made to conduct BWIM only by the strains of transverse stiffeners. It was successful for truck-load estimation and then extended to estimate axle loads. By this economical axle-load estimation method, the axle loads are evaluated and analyzed. The susceptibility of the lane to fatigue is then discussed.

1 INTRODUCTION

Needless to say, the road infrastructure is of vital importance for the society. However, in many countries their deterioration due to age is now a big concern, and a good maintenance scheme is urgently needed to balance maintenance cost and the serviceability of road infrastructure. A factor that deteriorates the road infrastructure is traffic load. The information on actual traffic loads travelling along highways is therefore valuable to determine maintenance scheme of bridges. Because of that, the techniques that weigh trucks in motion without disturbing traffic flow have attracted many highway engineers and researchers. Those techniques are called collectively weigh-in-motion.

One of the weigh-in-motion techniques is based on the deformation of a bridge and is called bridge-weigh-in-motion (BWIM). The technique was first explored by Moses (1979). Because of its lower cost than pavement scales, much attention has been drawn to BWIM in Japanese bridge engineering community (Matsui & El-Hkim 1989, Ojio et al. 2001, 2018, 2019, Miki et al. 1987, 2001, Ishio et al 2002), as maintenance work is getting very important in recent years in Japan.

A group of the authors has applied BWIM to a regional project in 2002 (Yamaguchi et al. 2004, 2009). It was to find out actual truck loads on National Route 201. A problem encountered in this project was that a two-span continuous bridge with skew was the only bridge available to the project while a short, simply-supported steel bridge with no skew is ideal for BWIM. Therefore, a careful preliminary field test with known truck loads was conducted, having shown that even this type of bridge could be used for BWIM. The method for this BWIM is based on that employed by Miki et al. (1987, 2001). The estimates of truck loads are obtained by the strains of main girders. Those strains are however insufficient to conduct BWIM. The supplemental information such as truck velocity is required, for which the strains of transverse stiffeners are also needed.

After the project, the possibility of estimating truck loads solely by the strains of transverse stiffeners was explored (Yamaguchi et al. 2010). It was successful, showing that the proposed approach can give a good estimate of the truck load, provided that the transverse stiffeners

are chosen carefully. The method is economical, reducing the BWIM cost, since the required strain measurements are much less.

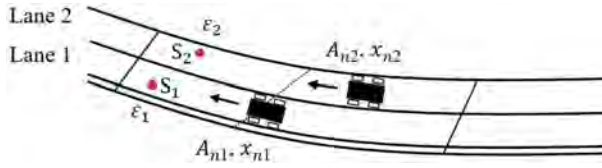


Figure 1. Illustration of variables in Equations (2) and (3).

The renewal project of intercity expressway is now underway in Japan. This is a big project, the cost of which is estimated at JPY 3 trillion (about USD 231 billion). Much of the cost would be spent for the replacement/repair of the bridge deck. For the damage of the bridge deck, axle load is known to be more responsible than truck load. Against this background, the method of estimating axle load by using the strains of transverse stiffeners only has been explored successful (Yamaguchi et al. 2021, 2022) which is economical and of much help for the maintenance of the bridge deck and thus the bridge itself. In Japan, a large number of bridges, 71% of them, belong to municipal governments that suffer budget deficit constantly. The proposed method should be able to help those bridge owners assess the influence of traffic loads and construct efficient maintenance scheme with affordable cost.

The axle-load estimation method is given first in this paper. Solving a set of simultaneous equations each of which is associated with a different lane, the approach is mathematically more consistent than that in the past approach. The axle loads are evaluated and analyzed by this approach, based on which the susceptibility of the lane to fatigue is discussed.

2 AXLE-LOAD ESTIMATION

The axle load of a truck is estimated from the strain in the transverse stiffener induced by the truck running on the bridge.

Suppose that at time t , an n -th axle of a truck in Lane l is located at a position x_{nl} . The strain ε_i induced in the transverse stiffener S_i in Lane i is expressed as

$$\varepsilon_i(t) = \sum_{l=1}^{N_l} \sum_{n=1}^{N_k} I_{il}(x_{nl}(t)) A_{nl} \quad (1)$$

where N_l = the total number of lanes of the highway; N_k = the total number of axles of the truck; A_{nl} = the axle load of the n -th axle of a truck in Lane l ; and I_{il} = the influence line function, giving the normal strain in the vertical direction in S_i induced by the unit load of 1 kN at the position x_{nl} . I_{il} is therefore a function of x_{nl} . The influence line function is obtained by the 3-D finite element analysis.

In the case of a two-lane bridge, $N_l = 2$, as illustrated in Figure 1, Equation (1) is written explicitly as

$$\varepsilon_1(t) = \sum_{n=1}^{N_1} I_{11}(x_{n1}(t)) A_{n1} + \sum_{n=1}^{N_2} I_{12}(x_{n2}(t)) A_{n2} \quad (2)$$

$$\varepsilon_2(t) = \sum_{n=1}^{N_1} I_{21}(x_{n1}(t)) A_{n1} + \sum_{n=1}^{N_2} I_{22}(x_{n2}(t)) A_{n2} \quad (3)$$

If the estimated axle loads are good, $\varepsilon_f(t)$ should be close to the measured strain ε_f^* . Therefore, the axle loads should be estimated by minimizing D defined by the following equation:

$$D = \sum_{m=1}^M \{\varepsilon_1^*(t_m) - \varepsilon_1(t_m)\}^2 + \sum_{m=1}^M \{\varepsilon_2^*(t_m) - \varepsilon_2(t_m)\}^2 \quad (4)$$

where M = the number of strain measurements; and t_m = the time at the strain measurement. The axle load A_{nl} is to be obtained by solving the following set of simultaneous equations:

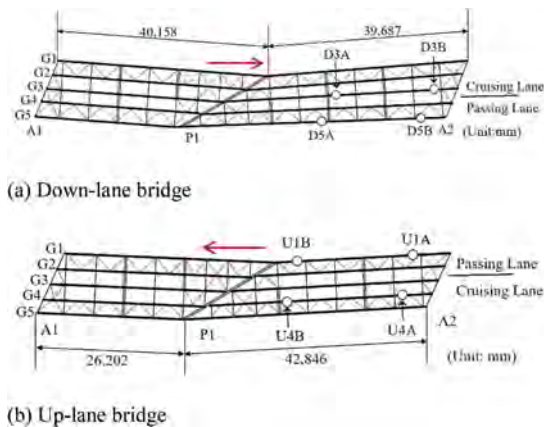


Figure 2. Plans of Sasaguri Bridge.

$$\frac{\partial}{\partial A_{n1}} \left[\sum_{m=1}^M \{\varepsilon_1^*(t_m) - \varepsilon_1(t_m)\}^2 \right] + \frac{\partial}{\partial A_{n1}} \left[\sum_{m=1}^M \{\varepsilon_2^*(t_m) - \varepsilon_2(t_m)\}^2 \right] = 0 \quad (5)$$

$$\frac{\partial}{\partial A_{n2}} \left[\sum_{m=1}^M \{\varepsilon_1^*(t_m) - \varepsilon_1(t_m)\}^2 \right] + \frac{\partial}{\partial A_{n2}} \left[\sum_{m=1}^M \{\varepsilon_2^*(t_m) - \varepsilon_2(t_m)\}^2 \right] = 0 \quad (6)$$

As discussed in Yamaguchi et al. (2010, 2021), depending on the layout of the lateral members of the bridge such as a cross girder between main girders, the influence of axle loads of the truck traveling on an adjacent lane would be negligible. In that case,

$$I_{il} = 0 \text{ for } i \neq l \quad (7)$$

The equations would be simpler and easier to solve.

The truck velocity is obtained by measuring the strains of two transverse stiffeners under each traffic lane. To that end, the identification of the strain responses due to the same truck is required. This has been done by using the auto-correlation function. (Yamaguchi et al. 2004). Once the axle loads are obtained, the truck load can be computed by simply taking the sum of the axle loads.

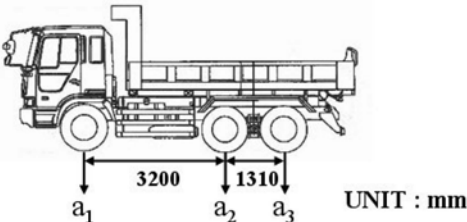
3 VALIDITY

3.1 Field test

The validity of the proposed method is studied by using the field test data with Sasaguri Bridge. The field test was conducted in 2003. Sasaguri Bridge is located on National Route

201 and consists of two parallel bridges, the up-lane bridge and the down-lane bridge. Each bridge has two lanes, and each bridge is for traffic in one specific direction, up or down. The up-lane bridge is about 70 m long while the down-lane bridge is about 80 m long. Otherwise, they are very similar to each other. Both are a two-span continuous plate-girder steel bridge with five main girders. The plans are presented in Figures 2.

The circles in Figure 2 show the locations of the transverse stiffeners whose strains were measured in the field test. The strain measurement was carried out using two transverse stiffeners in each lane to evaluate the truck velocity. The strains measured at U1A, U4B, D3A and D5A are made use of also for the axle-load estimation. Therefore, the strain influence line at each of these four transverse stiffeners is obtained by the three-dimensional finite element analysis of Sasaguri Bridge with the single axle load travelling on the lane. The magnitude of the axle load for the analysis is 1 kN. Nastran (MSC 2014) is used for the analysis.



	AXLE WEIGHT			GROSS WEIGHT
	a ₁	a ₂	a ₃	
TRUCK A	48.1	77.1	74.2	199.4
TRUCK B	58.7	71.1	66.2	196.0
TRUCK C	52.6	58.4	49.6	160.6

UNIT : kN

Figure 3. Calibration trucks.

The field test was conducted with three calibration trucks shown in Figure 3. The following four patterns of traffic situation were considered in the field test:

- Pattern 1: Only one truck runs
- Pattern 2: Two trucks run in the same lane
- Pattern 3: Two trucks run side by side
- Pattern 4: Two trucks run in the same lane while the other runs in the other lane

Figure 4 illustrates the four traffic patterns. For each pattern, various combinations of the three trucks were considered and the same truck-running test was repeated three times since variation in the measurement is expected. The number of the truck-running tests amounted to 60. It is noted that to enhance the reliability of the field test data, traffic was controlled so that no public vehicles would run on the bridge during each truck-running test. The same test data were used previously and more details of the test are available in there (Yamaguchi et al. 2004, 2009).

3.2 Estimation result

First, the axle loads are estimated, assuming that the influence of axle loads of the truck traveling on the adjacent lane is negligible. In short, Equation (7) is applied, which then requires much less computational cost.

For all the patterns in the up-lane bridge and Patterns 1 and 2 in the down-lane bridge, the average errors are smaller than 10%. Some of the maximum errors are a slightly larger than 20%, which are still considered acceptable for practical purpose. This result ensures that the influence line function obtained by the 3-D finite element analysis is good. On the other hand, much larger

error is observed for Patterns 3 and 4 in the down-lane bridge, the patterns where trucks run on both the cruising and passing lanes. Which suggests that the influence of the truck on the adjacent lane cannot be ignored in the down-lane bridge.

The axle loads for Patterns 3 and 4 in the down-lane bridge are re-estimated without applying Equation (7). The estimations are improved considerably with the average error of up to 7.2%, and the estimate accuracy is now considered acceptable for practical purpose. Besides, these traffic patterns are seldom observed, little influencing the overall result of axle loads on this highway anyway. The improvement is more discussed by Yamaguchi et al. (2022).

It is therefore concluded that the estimation of axle loads solely by the strains of transverse stiffeners is possible.

4 AXLE LOADS OF HEAVY TRUCKS

Strain measurement was carried out from March 3, 2004 to November 30, 2004. Because of the trouble of the measurement device, no data were taken for 44 days and hence the total number of the measurement days is 229.

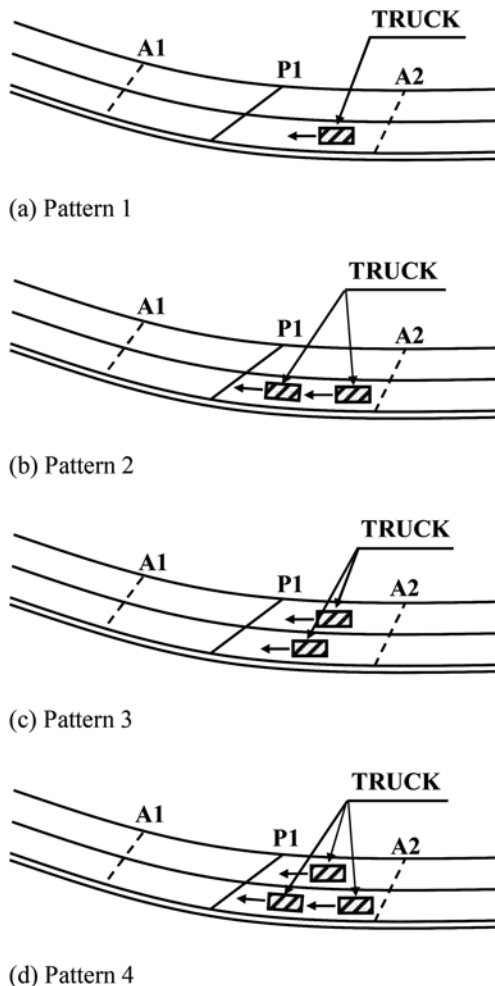


Figure 4. Traffic situations in field test.

The legal limit on the truck load is 245 kN in Japan. For a truck heavier than the limit to run, permission must be obtained. Yet it is generally believed that quite a few heavy trucks run on highways. In the present research, the characteristics of the traffic flow of those heavy trucks is focused on, because the information on the traffic flow of those heavy trucks is very scarce if available. The strain measurement was 18 years ago, yet the traffic volume on this highway hasn't changed much: the traffic volume per day is 35363 in 2005, 35235 in 2010 and 36289 in 2015 (because of the COVID-19, the survey hasn't been conducted in recent years). Hence, the data to be used can be considered still good. In what follows, a truck heavier than 245 kN is simply referred to as a heavy truck or merely a truck for the sake of simplicity. Photos of heavy trucks were also taken. The heaviest truck found in the project is shown below. The truck didn't run in the way that a heavy truck is supposed to run: it should be accompanied by two cars, one in front and the other behind, but no such cars were observed. The truck weight was estimated as 97 metric tons (951 kN), which is about 3.9 times larger than the legal limit.

The damage due to traffic load is greatly influenced by the magnitude of the load and the number of loads. The influence on the fatigue damage is not simply proportional to the magnitude of the load. The welding is one of the most susceptible parts to fatigue damage in a steel bridge, and it is known that the damage would be in proportion to the cube of the applied load. In short, the axle load of 200 kN gives the damage 8 times larger than 100 kN-axle-load, for example. Based on that, Figure 6 shows how many axle loads effectively equivalent to 98 kN-axle-load, the legal limit, passed on each lane during the period of the measurements for the project UL and DL



Figure 5. The heaviest truck observed in the project.

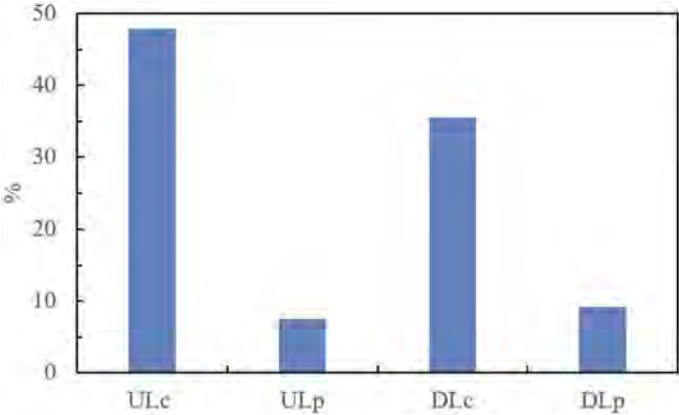


Figure 6. 98 kN-axle-loads travelling on each lane.

stand for the up-lane bridge and the down-lane bridge, respectively, and the subscripts of c and p stand for the cruising lane and the passing lane, respectively.

As observed, since 45% of the 98 kN-equivalent axle loads traveled on UL_C , the members that support UL_C are most susceptible to fatigue damage. The members that support DL_C are also susceptible to fatigue damage since 35% are passing on DL_C . On the other hand, fatigue damage is much less expected in in the members that support UL_P or those that support DL_P . The possibility of fatigue crack development in the members that support UL_C is 7 times larger than that in the members supporting UL_P . The possibility of fatigue crack development in the members that support DL_C is 4 times larger than that in the members supporting DL_P . Members related to the cruising lane should be inspected very carefully.

Figure 7 presents the rate of heavy trucks in terms of the number passing on each lane. Obviously much more heavy trucks run on the cruising lanes than on the passing lanes. To be interesting, the proportions in Figures 5 and 6 are not much different. They are indeed very similar to each other, as can be seen in Figure 8, although the truck weight varies widely. The similarity of the two figures implies that a heavy truck tends to have more axles so as to reduce the axle load. Which is indeed confirmed by the result of Yamaguchi et al. (2022).

By estimating axle loads travelling on various bridges in a region, it can be figured out which lane of a bridge is the most susceptible to damage, which lane follows it and so forth. Such data on axle loads should then be able to help construct an effective scheme for the maintenance of the bridges in the region.

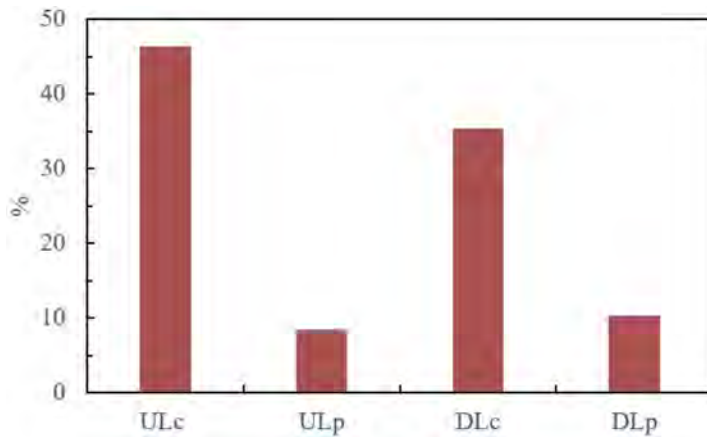


Figure 7. Number of heavy trucks travelling on each lane.

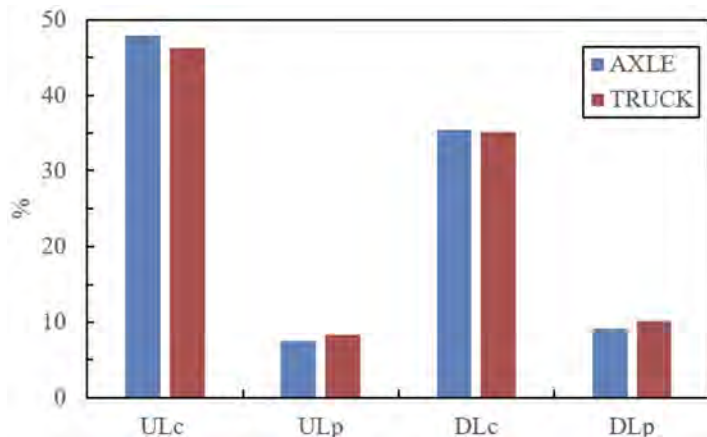


Figure 8. Combination of Figures 6 and 7.

5 CONCLUDING REMARKS

An economical BWIM to estimate axle loads was briefly reviewed. Only strains in two transverse stiffeners per lane are needed for the method. It is therefore much inexpensive to evaluate the influence of traffic loads. In this paper, an application of the method to bridge maintenance was demonstrated: in Sasaguri Bridge the cruising lanes are 4 to 7 times more susceptible to fatigue crack development than the passing lanes, suggesting that cruising lanes and the members that support cruising lanes should be taken care of much more in maintenance work. The estimation and analysis of traffic loads should thus help construct a good maintenance scheme.

REFERENCES

- Ishio, M., Nakamura, S., Tamakoshi, T. & Nakasu, K. 2002. About the WIM system using the influence line. *Proc. of 57th Annual Conference of The Japan Society of Civil Engineers, JSCE*, 1447–1448.
- Ojio, T., Yamada, K. & Kobayashi, N. 2001. Development of bridge weigh-in-motion system using stringers of steel plate girder bridge. *Journal of Structural Engineering* 47(A): 1083–1092.
- Ojio, T., Yamada, K. & Kozuka, M. 2018. Bridge Weigh-in-Motion by reaction force method using PC-girder bridges. *Journal of Structural Engineering* 64(A): 709–714.
- Ojio, T., O'Brien, E. & Taylor, S. 2019. Contactless bridge weigh-in-motion using PC-girder bridges. *Journal of Structural Engineering* 65(A): 600–606.
- Matsui, S. & El-Hkim, A. 1989. Estimation of axle loads of vehicles by crack opening of RC slab. *Journal of Structural Engineering* 35(A):407–418.
- Miki, C., Murakoshi, J., Yoneda, T. & Yosimura, H. 1987. Weighing trucks in motion. *Bridge and Foundation* 87(4): 41–45.
- Miki, C., Mizunoue, T. & Kobayashi, Y. 2001. Monitoring system of bridge performance with fiber-optic communications. *Journal of Construction Management and Engineering* 686/VI-52: 31–40.
- Moses, F. 1979. Weigh-in-motion system using instrumented bridges. *Transportation Engineering, Journal of ASCE* 105(TE3): 233–249.
- MSC. Nastran 2014.
- Yamaguchi, E., Matsuo, K., Kawamura, S., Kobayashi, Y., Mori, M., Momota, K. & Nishinohara, T. 2004. Accuracy of BWIM using two-span continuous steel girder bridge. *Journal of Applied Mechanics* 7: 1135–1140.
- Yamaguchi, E., Kawamura, S., Matsuo, K., Matsuki, Y. & Naito., Y. 2009. Bridge-weigh-in-motion by two-span continuous bridge with skew and heavy-truck flow in Fukuoka area, Japan. *Advances in Structural Engineering* 12(1): 115–125.
- Yamaguchi, E., Naitou, Y., Matsuo, K., Matsui, Y., Takaki, Y. & Kawamura, S. 2010. BWIM by transverse stiffeners of steel I-girder bridge. *Journal of Civil Engineering, Division F* 66(2), JSCE: 251–260.
- Yamaguchi, E., Tsuzuki, K. & Oda, K. 2021. Estimation of axle loads by bridge-weigh-in-motion using strain measurement of transverse stiffeners. *Bridge Maintenance, Safety, Management, Life-Cycle Sustainability and Innovations*, CRC Press: 4089–4094.
- Yamaguchi, E. & Furusato, Y. 2022. Axle-load-estimation based on strain of transverse stiffener and characteristics of traffic loads due to heavy trucks. *Bridge Safety, Maintenance, Management, Life-Cycle, Resilience and Sustainability*, CRC Press: 1280–1286.

Deep sensor-fusion approach to vehicle detection on bridges using multiple strain sensors

H.T. Vuong & A. Takasu

National Institute of Informatics, Tokyo, Japan
Graduate University for Advanced Studies, Kanagawa, Japan

T.P. Doan

Hanoi University of Science and Technology, Hanoi, Vietnam

ABSTRACT: Bridge weighing in motion (BWIM) detects heavy vehicles passing a sensor or multiple sensors. Sensor technology with rapid development enables us to monitor bridges with multiple types of sensors and cameras. These sensors are installed at different positions and require synchronization. In this paper, we propose a novel vehicle detection framework for the multiple strain sensors BWIM systems based on a novel deep sensor-fusion approach. The proposed framework is composed of three components. The first component collects and denoises the strain sensor signal. Then, the cleaning signals are processed by the Wavelet transform in the second component to obtain the corresponding coefficient matrices. Finally, the third component feeds the coefficient results into an improved deep neural network. It extracts complex features through multiple neural layers and can detect vehicle properties from multi-view signals. The performance of the proposed framework is evaluated on real-world bridge health monitoring datasets. The results of the experiments show that the proposed framework is reliable and effective for vehicle detection in the BWIM system.

1 INTRODUCTION

Advanced technology in the fields of sensors, data collection and communication, signal analysis, and data processing have brought great benefits to structural health monitoring. Bridge Health Monitoring System (BHMS) usually deploys surveillance cameras to visually identify passing vehicles. BHMS also set up multiple types of sensors at different positions to measure its changes over time. The sensor signal data provide meaningful information on passing vehicles. There are two main types of sensors, such as accelerometers and strain meters, for using vehicle detection task (Alegre-Sanahuja et al. 2016, Doan and Takasu 2017, Doan and Takasu 2020). The accelerometer sensor senses the vibration, while the strain meters measure the strain of the bridge induced by passing vehicles. However, the authors in (Alegre-Sanahuja et al. 2016) only use one strain signal view to detect spikes for vehicle passing, whereas (Doan and Takasu 2017, Doan and Takasu 2020) only use accelerometers signal data to detect oscillations for vehicle crossing in a bridge. According to (Alegre-Sanahuja et al. 2016), the Wavelet method transforms each signal into scale-time space before searching for spikes in the originals signals. In (Doan and Takasu 2017), the acceleration signal is denoised using morphological component analysis with the tunable Q-factor wavelet transform to reveal oscillations that indicate events of passing vehicles in the signal. These researchers only focus on spike-by-spike sequences after applying wavelet transform to identify passing vehicles for a strain sensor or an accelerometer. There are two main vehicle-weighing aims. The first proposal is that the BWIM system detects overloaded vehicles to enforce laws. Then, the BMHS system can estimate the damage progression of bridges. Many researchers have been interested in the heavy vehicles detection task, which is an important component of the BWIM system. For BWIM, we consider the problem of vehicle detection in terms of multiple strain sensing.

(Kawakatsu et al. 2017, Kawakatsu et al. 2018, Kawakatsu et al. 2020) proposed the deep neural networks (DNNs)-based techniques for detecting overloaded vehicles crossing a bridge. These systems can help us to alert the serious damage caused by vehicle overloading to the bridge. The authors built a Traffic Surveillance System (TSS) that interacts with a surveillance camera. The system identifies a vehicle from the collected video by combining a moving-object detector. More specifically, the authors exploited a deep Convolutional Neural Network (CNN) (Ren et al. 2015) to recognize the individual passing vehicles. Their main aim is to extract free oscillations from the observed vibration data following vehicle-passing events. They observed that the extracted oscillations from sensor signals data caused by a large, heavy vehicle are preferred. However, the research projects only consider detecting vehicle passing based on CNN from image data. On the other hand, multiple strain meters provide the speed of the vehicles as well as their weight. Combining the multiple strain sensors from different views enables us to obtain the same information like vehicle speed and vehicle weight, which can be improved the performance of the system. Therefore, we consider how to use the rich information from sensor signals to support image-based TSS for the vehicle detection task. Deep multi-view representation learning methods aim to exploit consistency and complementary information between these views to learn new representations for the data. Therefore, these methods often have better generalization ability. Specifically, in our previous work (Vuong et al. 2022), we proposed an improved sensor signal alignment framework that combined dynamic time warping and the objective function of DNNs to align multiple sensor signals. It employs the generalized sequentially correlated autoencoders (GSCAE) model (Doan & Takasu 2020) for multiple sensor signal alignment. In this paper, we propose an improved vehicle detection framework based on a deep sensor-fusion approach. Firstly, the difference with the previous research, we process the original sensor signals by Wavelet transform methods to get the coefficients matrix. The signal processing can make rich information for the system instead of only using raw sensor signals. Based on exploiting DCCA method (Andrew et al. 2013), we propose deep sensor-fusion learning by using two autoencoders instead of feed-forward neural networks as in DCCA. It extracts complex features through multiple neural layers and can detect vehicle properties from the multi-view sensor signals.

The paper is organized as follows. Section 2 describes the problem settings for BWIM system. In section 3, we briefly present some background for the methods proposed in this article. The proposed framework and its main components are described in section 4. Section 5 empirically evaluates the performance of the proposed framework, and section 6 concludes the paper.

2 PROBLEM SETTINGS

Many researchers have been interested in the heavy vehicles detection task which is an important component of the BWIM system. A simple approach is to install an axle load meter on the road surface. It is difficult to retrofit existing bridges because paving requirements and meters can be fragile and require frequent repair. To solve the problems, BWIM systems address them by treating the bridge structure itself as a large weighing scale. The system uses data from strain sensors. These sensors are installed at different positions of the bridge, such as deck, girder, beam, and flange. Figure 1 (a) shows a typical BWIM, which installed multiple strain sensors at different positions on the bridge. Note that signal sensor datasets are synchronous and require alignment. Figure 1 (b) describes a strain signal sequence example with two spikes corresponding to the events that the wheels of vehicles pass over the sensor. Based on strain sensors analysis, we use multiple strain signals for vehicle detection to improve the performance of BWIM systems.

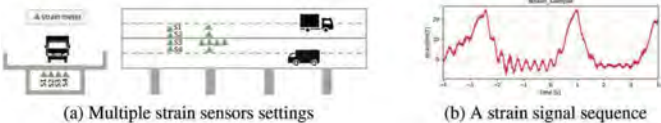


Figure 1. A BWIM with multiple strain sensors.

3 BACKGROUND

3.1 Continuous Wavelet Transform (CWT)

With the capability to provide both time and frequency domain information, wavelet analysis is mainly a technique for time-frequency analysis of signals, signal compression, signal denoising, and feature extraction. Wavelet transform decomposes a signal into a linear combination of basic functions, which are derived from one mother wavelet by means of dilation and translation. More specifically, given a 1D signal $f(t)$ that is a function w.r.t time t , CWT (Rhif et al. 2019) computes a 2D scale-time representation as follows:

$$C(a, b) = |a|^{-\frac{1}{2}} \int_{-\infty}^{\infty} f(t) \psi^* \left(\frac{t-b}{a} \right) dt, \quad (1)$$

where $C(a, b)$ represents the coefficients of CWT, (*) denotes the complex conjugate, ψ is the wavelet mother, a denotes the scaling parameter, and b is the time shifting parameter or translation.

For effectively representing patterns in the signal, the selection of the wavelet mother is crucial. According to (Ngui et al. 2013), the main challenge of using Wavelet transform is to select the most optimal mother for the different problems. Because the different mother Wavelets applied on the same signal may produce different results. The different Wavelets in scales and time are shifted along the entire movement and multiplied by its sampling interval to obtain significant physical, resulting in coefficients. This enables better characterizing oscillated behavior in signals.

3.2 Deep sensor-fusion learning

An event can be presented from multiple different views. We denote the data matrices for each view by $\mathbf{A} = [a_1, a_2, \dots, a_N]$, $\mathbf{B} = [b_1, b_2, \dots, b_N]$ with N samples. We consider paired observations from two views, denoted $(a_1, b_1), (a_2, b_2), \dots, (a_N, b_N)$ for $i = [1, N]$. We also denote \mathbf{f} function to map inputs by kernel machines or DNNs with a corresponding set of learning parameters \mathbf{W}_f . For example, the projection of view 1, and view 2 are as follows $\mathbf{f}(\mathbf{A}) = [\mathbf{f}(a_1), \dots, \mathbf{f}(a_N)]$, $\mathbf{f}(\mathbf{B}) = [\mathbf{f}(b_1), \dots, \mathbf{f}(b_N)]$, respectively. The dimensionality of the projection is denoted L . The deep canonical correlation analysis (DCCA) (Andrew et al. 2013) is a DNN extension of canonical correlation analysis (CCA) (Hardoon et al. 2004). Inspired by DCCA, we propose the deep sensor-fusion learning approach based on DCCA. Instead of feed-forward neural networks in DCCA, we use two autoencoders (AE) combined with CCA. The schematic diagram of the deep sensor-fusion learning is described in Figure 2. Both two feature extraction networks \mathbf{f} , \mathbf{g} , and the two reconstruction networks \mathbf{q} and \mathbf{p} are separate for each view to get reconstruction errors $\mathbf{R}_A, \mathbf{R}_B$. The objective of this model is optimized as follows:

$$\min_{\mathbf{w}_f, \mathbf{w}_g, \mathbf{w}_q, \mathbf{w}_p, \mathbf{U}, \mathbf{V}} \frac{-1}{N} \text{tr}(\mathbf{U}^\top \mathbf{f}(\mathbf{A}) \mathbf{g}(\mathbf{B})^\top \mathbf{V}) + L_{AE} \quad (2)$$

$$L_{AE} = \frac{\lambda}{N} \sum_{i=1}^N (\|\mathbf{a}_i - \mathbf{q}(\mathbf{f}(\mathbf{a}_i))\|^2 + \|\mathbf{b}_i - \mathbf{p}(\mathbf{g}(\mathbf{b}_i))\|^2), \quad (3)$$

where $\lambda > 0$ is a trade-off parameter, two CCA directions \mathbf{U}, \mathbf{V} with L dimensions. L_{AE} is the sum of reconstruction errors. Similar to the optimization of DCCA, we also use stochastic optimization for the deep sensor-fusion objective.

4 PROPOSED FRAMEWORK

We present a novel vehicle detection framework based on the deep sensor-fusion approach using multiple sensor signal data for BWIM. In particular, we utilize two strain signal sensors

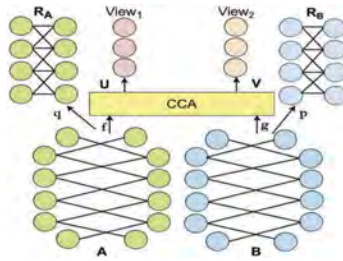


Figure 2. Schematic diagram of deep sensor-fusion approach.

at different positions on the bridge. We observe that two views corresponding to the two strain sensors can identify a passing vehicle event. The flowchart of the proposed framework is depicted in Figure 3. Our framework includes three phases. The first phase (in a gray area), *data pre-processing*, collects sensor signal datasets from the BWIM database. Then, we apply the Wavelet denoising methods (El-Dahshan 2011, Wink and Roerdink 2004) to get two denoising signals S_1 and S_2 . The second phase (in a blue area), *signal transformation*, uses Wavelet transform methods (Vuong et al. 2022) to decompose a denoised signal sequence from 1D frequency space into 2D scale-time space to obtain coefficient results in C_1 , and C_2 . In the final phase (in a yellow area), *vehicle detector*, the coefficient matrix is fed into the deep sensor-fusion learning as Figure 2 to find the sharing representations for each view. Then, the output results of deep sensor-fusion learning are used to train with a simple classifier (Quinlan 1996) to detect vehicles.

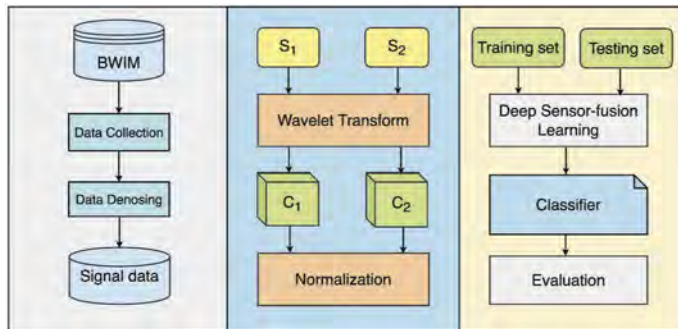


Figure 3. The general flowchart of the proposed framework.

We further depict a strain signal sequence as Figure 4(a) and its coefficients of CWT using Morlet Wavelet and Mexican Hat Wavelet (Vuong et al. 2022) in Figure 4(b) and Figure 4(c), respectively. It can be easily seen that the coefficients at time scales, where the oscillations appear in the original signal, are larger than those at the other time scales. Thus, the coefficients matrix is an informative representation of the signal. In addition, it also owns sequential nature as its columns are sequentially related.

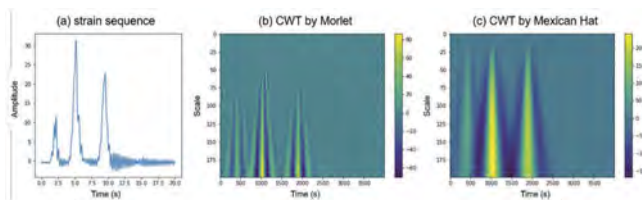


Figure 4. (a) strain signal sequence, (b) CWT by Morlet, (c) CWT by Mexican Hat.

5 EXPERIMENTS

5.1 Data pre-processing and transform

We evaluate the performance of the proposed framework on two real-world strain signal datasets. These data are collected from BHMS on two bridges in Japan. One is a prestressed concrete bridge (Bridge A) and the other is a metal bridge (Bridge B). Note that the two selected sensors on the same bridge are installed at different positions. These sensors require synchronization. The sampling frequency of the strain meters is 100Hz and 200Hz, respectively. We use 50K samples for signals in these experiments. The length of each sample is 128 time steps. The ground-truth data are collected from the surveillance cameras installed on the bridge. We use the TSS proposed in (Kawakatsu et al. 2017) to retrieve the number of vehicles along with the time epochs that they pass over the sensors. Then, the raw signals are reduced noise. For example, the denoising sensor signal is illustrated in Figure 5 (a), 5 (b), respectively, for the first and second sensor positions in Bridge A.

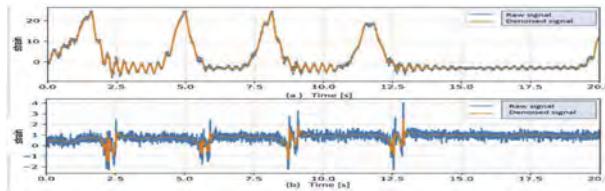


Figure 5. Example of raw signals and denoised signals at different positions in Bridge A.

After denoising signal data, we use CWT to transform the inputs into scale-time space to obtain coefficients. For strain signals, we use the Mexican Hat Wavelet or the Morlet Wavelet. In many experiments, we set up scale parameters from 10 to 200. With a scale equal to 200, we obtain the meaning coefficients with an accuracy of the classifier is more than 92 %. Therefore, we use a scale parameter equal to 200 for each sensor signal data. The coefficient results are used as inputs to feed the deep sensor-fusion learning for vehicle detectors.

5.2 The compared methods

To evaluate the performance of the deep sensor-fusion learning in our proposed framework, we employ many experiments with the compared methods, which are based on the multi-view representation approach as follows:

- *Traditional CCA-based methods:* CCA, Kernel CCA (Hardoon et al. 2004, Kawano et al. 2019) are foundation techniques for finding a common space between two views without DNNs.
- *AE-based methods:* SplitAE (Ngiam et al. 2011), CorrAE, DistAE (Wang et al. 2015) find a sharing representation by reconstructing errors for each view. These methods use two autoencoders without CCA to find a common subspace for multiple views.
- *Hybrid CCA and DNN methods:* Both DCCA and deep sensor-fusion learning use hybrid DNNs and CCA. However, we propose two autoencoders for deep sensor-fusion learning instead of using two feed-forward neural networks as in DCCA.

Deep sensor-fusion learning has hyperparameters that are selected by using the tuning set. The final dimensionality L is selected from $\{5, 10, 15, 20, 25, 30, 35, 40, 45, 50\}$. The feature mappings (\mathbf{f}, \mathbf{g}) are implemented by networks of 4 hidden layers and a linear output layer of L units; reconstruction mappings (\mathbf{q}, \mathbf{p}) are implemented by networks of 4 hidden layers and an output layer of L units. We use SGD for optimization with minibatch size, learning rate, and momentum tuned on the tuning set. Then, we use a very simple decision tree classifier (Quinlan 1996) for embeddings of views to train efficiently on low-dimensional projections and achieve high accuracy for vehicle detection.

5.3 Evaluation metric

The ground truth consists of the number of vehicles and sequence samples. The i -th sample is described as triplet $\{\mathbf{s}_{1i}, \mathbf{s}_{2i}, \mathbf{g}_i\}$. Here, \mathbf{s}_{1i} is a sequence of the first sensor signal input, \mathbf{s}_{2i} is a sequence of the second sensor signal input. \mathbf{g}_i indicates the presence of a vehicle at the bridge entrance at the observation time. We estimate the length of a sequence input based on the average speeds and bridge length. Each dataset in our experiments is divided into training, tuning, and test sets according to the ratio of 80%, 10%, and 10%, respectively. The trained model is used to classify the label of test data. To evaluate the performance of the deep multi-view models, we use metrics such as accuracy (Acc), precision (P), recall (R), and F_1 scores for the classification problem. The main standard parameters include True Positive (TP), False Positive (FP), True Negative (TN), and False Negative (FN) are defined in the confusion matrix (Susmaga 2004). Based on the confusion matrix, Acc, P, R, and F1 are defined as follows:

$$Acc = \frac{TP + TN}{TP + FP + TN + FN}, \quad (4)$$

$$P = \frac{TP}{TP + FP}, R = \frac{TP}{TP + FN}, F1 = \frac{2 \times P \times R}{P + R}. \quad (5)$$

We use five folds cross-validation with ten experiment times for each fold to evaluate the proposed method and the compared methods, particularly the averaged Acc, P, R, and F1 scores.

5.4 Results

The averaged accuracy results of the proposed framework and the compared methods on two bridges are given in Table 1. The mean accuracy along with standard deviation on the training data and testing data by our proposed framework are $97.87 \pm 1.41\%$ and $93.62 \pm 1.73\%$ on Bridge A, respectively, $96.76 \pm 1.53\%$ and $94.24 \pm 1.85\%$ on Bridge B. It can be clearly observed that the deep sensor-fusion learning in our proposed framework surpasses the compared methods. More specifically, our framework achieved better accuracy on both two bridges than those of the traditional CCA-based methods (CCA, Kernel CCA) from 10% to 20%. In comparison with the AE-based methods, they could not beat our proposed framework. In particular, the performance of our framework is higher than SplitAE, Corre AE, and DistAE from 10% to 22% for Bridge A and from 5% to 15% for Bridge B. Results also show that our framework is more effective than the DCCA method about 5%. The results also validate the importance of the deep sensor-fusion model in our framework. The reason may be that the peak detection procedure in our framework is more effective than the compared methods. In addition, reconstruction errors computed by the AEs model integrating with the CCA objective can account for different types of anomalies. As we can observe, substituting it with the two separate autoencoders significantly degenerates the performance of the proposed framework by the SplitAE method. The deep sensor-fusion learning can leverage complementary information between the two signals to compute more discriminative reconstruction errors. The outputs of deep sensor-fusion learning make classification much easier on vehicle detector. So, we only use a simple classifier that can be trained efficiently on low dimensional projections that already achieve high accuracy instead of using a heavily nonlinear classifier on the original inputs. Deep sensor-fusion learning plays an important role in improving the framework's performance.

The mean P, R, and F1 results, along with standard deviation for five folds cross-validation of the proposed framework, are described in Figure 6 (a), and Figure (b), for Bridge A, and Bridge B, respectively. Performance of our proposed framework obtains from 90% to 95% with F1 score on two datasets. Both P and R results are high over five folds. In Bridge A, the mean P results obtained more than 95%, and the mean R results are about 90% on five folds. For Bridge B, we also observe that the similarity results of P and R are from 90% to 95%. The results show that the deep sensor-fusion approach is the effective method for finding a sharing projection between two views for both strain signals datasets. Therefore, the proposed framework can be generalized for multiple strain signal datasets on bridges. Furthermore, it can be integrated and improve the accuracy of vehicle detection task for BWIM systems.

Table 1. Comparison of the proposed method with the compared methods.

Method	Mean Acc (%)			
	Bridge A		Bridge B	
	Training data	Testing data	Training data	Testing data
CCA	78.72 ± 2.24	74.47 ± 2.83	82.01 ± 2.45	80.94 ± 2.64
Kernel CCA	85.11 ± 2.24	80.85 ± 2.45	85.49 ± 2.64	80.16 ± 2.82
SplitAE	89.36 ± 1.41	85.36 ± 2.24	91.37 ± 1.95	89.93 ± 2.24
CorrAE	82.56 ± 1.73	75.36 ± 2.24	87.46 ± 2.24	81.35 ± 2.45
DistAE	75.62 ± 2.24	72.36 ± 2.45	84.96 ± 1.85	80.81 ± 2.24
DCCA	93.62 ± 1.73	89.36 ± 2.23	94.96 ± 1.73	92.81 ± 1.75
Proposed framework	97.87 ± 1.41	93.62 ± 1.73	96.76 ± 1.53	94.24 ± 1.85

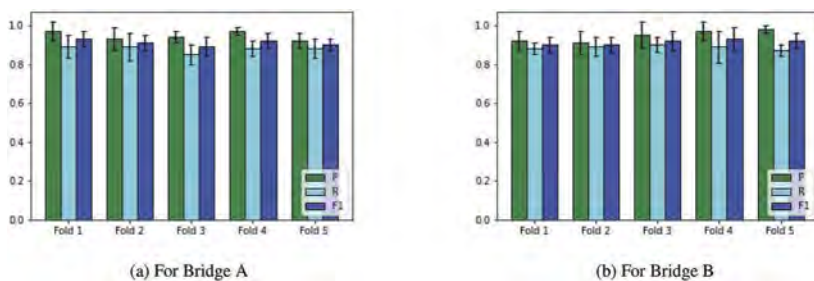


Figure 6. Averaged P, R, and F1 score of 5 folds cross-validation both bridges.

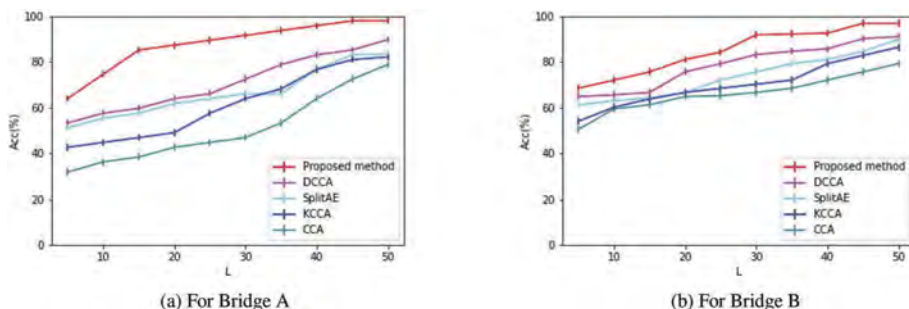


Figure 7. Comparison the proposed method and the compared methods at the different L.

Each algorithm has hyper-parameters that are selected using the tuning set. We evaluate the mean accuracy of the proposed method and the compared methods with the different L parameters from $\{5, 10, 15, 20, 25, 30, 35, 40, 45, 50\}$ on two strain sensor datasets. The averaged accuracy results at different L are described in Figure 7. In Figure 7 (a) for Bridge A, the results show that the performance of our proposed method is better than the compared methods at the different values L. Similarly, our proposed method surpasses the compared methods in Figure 7 (b) for Bridge B. Both the traditional CCA methods without DNNs and AE-based methods without CCA can not find an effective subspace to share between views when lower L from 5 to 40. The proposed framework based on deep sensor-fusion learning can improve the performance of vehicle detection by integrating CCA and AEs. The performance of the proposed framework significantly increases along with increasing L values from 5 to 40. When L is from 45 to 50, the implementation of the proposed framework has almost no increase and is stable. The experiment results show the effectiveness of the proposed framework when we choose L equal to 50.

6 CONCLUSIONS

In this paper, we propose a novel vehicle detection framework for multiple strain sensors of BWIM systems based on deep sensor-fusion learning. The proposed framework transforms the signal into a scale-time space by CWT. Then, we propose a deep sensor-fusion learning approach based on AEs and CCA for multiple sensors. It extracts complex features through multiple neural layers and can detect vehicle properties from the multi-view sensor signals. The performance of the proposed framework is evaluated on two real-world datasets collected from bridge health monitoring systems. The results of the experiments show that the proposed framework is reliable and effective for vehicle detection in the BWIM system.

After detecting vehicles on bridges, we consider how to estimate the heavy vehicles and detect overload vehicles by multiple strain sensor signals in future work. The overload vehicle detection task may reduce the costs of both installation and system maintenance for BHMS.

REFERENCES

- Alegre-Sanahuja, J., W. Lu, & A. Takasu (2016). Wavelet transform based vehicle detection from sensors for bridge weigh-in-motion. In *Proceedings of the 31st Annual ACM Symposium on Applied Computing*, pp. 935–940.
- Andrew, G., R. Arora, J. Bilmes, & K. Livescu (2013). Deep canonical correlation analysis. In *International conference on machine learning*, pp. 1247–1255. PMLR.
- Doan, T. & A. Takasu (2017). Robust vehicle detection from noisy acceleration signal for bridge monitoring systems. In *Proceedings of the 19th International Conference on Information Integration and Web-based Applications & Services*, pp. 136–140.
- Doan, T. & A. Takasu (2020). Deep multiview learning from sequentially unaligned data. *IEEE Access* 8, 217928–217946.
- El-Dahshan, E.-S. A. (2011). Genetic algorithm and wavelet hybrid scheme for ecg signal denoising. *Telecommunication Systems* 46 (3), 209–215.
- Hardoon, D. R., S. Szedmak, & J. Shawe-Taylor (2004). Canonical correlation analysis: An overview with application to learning methods. *Neural computation* 16 (12), 2639–2664.
- Kawakatsu, T., K. Aihara, A. Takasu, & J. Adachi (2018). Deep sensing approach to single-sensor vehicle weighing system on bridges. *IEEE Sensors Journal* 19 (1), 243–256.
- Kawakatsu, T., K. Aihara, A. Takasu, & J. Adachi (2020). Fully-neural approach to heavy vehicle detection on bridges using a single strain sensor. In *ICASSP 2020-2020 IEEE International Conference on Acoustics, Speech and Signal Processing (ICASSP)*, pp. 3047–3051. IEEE.
- Kawakatsu, T., A. Kakitani, K. Aihara, A. Takasu, & J. Adachi (2017). Traffic surveillance system for bridge vibration analysis. In *2017 IEEE International Conference on Information Reuse and Integration (IRI)*, pp. 69–74. IEEE.
- Kawano, K., S. Koide, & T. Kutsuna (2019). Canonical soft time warping. In *Asian Conference on Machine Learning*, pp. 551–566. PMLR.
- Ngiam, J., A. Khosla, M. Kim, J. Nam, H. Lee, & A. Y. Ng (2011). Multimodal deep learning. In *ICML*.
- Ngui, W. K., M. S. Leong, L. M. Hee, & A. M. Abdelrhman (2013). Wavelet analysis: mother wavelet selection methods. *Applied mechanics and materials* 393, 953–958.
- Quinlan, J. R. (1996). Learning decision tree classifiers. *ACM Computing Surveys (CSUR)* 28 (1), 71–72.
- Ren, S., K. He, R. Girshick, & J. Sun (2015). Faster r-cnn: Towards real-time object detection with region proposal networks. *Advances in neural information processing systems* 28.
- Rhif, M., A. Ben Abbes, I. R. Farah, B. Martinez, & Y. Sang (2019). Wavelet transform application for/ in non-stationary time-series analysis: a review. *Applied Sciences* 9 (7), 1345.
- Susmaga, R. (2004). Confusion matrix visualization. In *Intelligent information processing and web mining*, pp. 107–116. Springer.
- Vuong, T. H., T. Doan, & A. Takasu (2022). Sensor data alignment for multi-view bridge monitoring. In *Bridge Safety, Maintenance, Management, Life-Cycle, Resilience and Sustainability*, pp. 1598–1606. CRC Press.
- Wang, W., R. Arora, K. Livescu, & J. Bilmes (2015). On deep multi-view representation learning. In *International conference on machine learning*, pp. 1083–1092. PMLR.
- Wink, A. M. & J. B. Roerdink (2004). Denoising functional mr images: a comparison of wavelet denoising and gaussian smoothing. *IEEE transactions on medical imaging* 23 (3), 374–387.

*SS8: Performance, safety, and cost of civil infrastructure
in a life-cycle context*
Organizers: Y. Li, P. Yuan, Y. Dong & D.M. Frangopol



Taylor & Francis

Taylor & Francis Group

<http://taylorandfrancis.com>

Masonry design for extended life-time usage by implementing joint behaviour

T. Molken, J. Smits & S. Van Hout

Department of Civil Engineering, Materials and Constructions division, KU Leuven, De Nayer Campus, Sint-Katelijne-Waver, Belgium

R. Meuleman

Product developer, Wienerberger Belgium nv, Kortrijk, Belgium

ABSTRACT: New structures are designed for a specified design working life according to (EN 1990, 2015). Facing sustainability requirements, designers need to account for extended lifetime usage beyond the original purpose of the building. Increasing the spans of the floors is one way to do so. Though, it significantly limits the use of masonry structures. (EN 1996-1-1, 2012) states that the designer should account for out-of-plane eccentricities of the masonry wall. Annex C of this document allows for a simplification with a fully restrained connection between floor and wall elements. Therefore, the eccentricity is directly related to the span of the neighbouring elements. Though, in the same annex, it is acknowledged that this is too conservative so a reduction is allowed. Nevertheless, they are not able to implement the stiffness of mortar joints or bearing paths. To take these interface materials into account, an easy-at-hand analytical approach is developed and tested.

1 INTRODUCTION

For centuries, masonry structures have shown a proven adaptability to new occupations and even resilience. Up till now, old masonry structures are still a valid research subject throughout all of Europe as they can still be found in existing structures (Bertolesi, et al., 2019; Vitti, 2021). Figure 1 shows some examples of repurposed masonry buildings in Europe. From that point of view, masonry structures can be seen as sustainable structures.



Leopoldskazerne, Ghent



La Piscine, Roubaix



LX factory, Lisbon

Figure 1. Repurposed masonry buildings in Europe.

Currently, the design of masonry bearing wall structures is carried out uniformly throughout Europe and certain other countries in accordance with the Eurocodes (EN 1996-1-1, 2012) or the American code (ACI 530-13, 2013) in Northern America. However the simplified rules of annex

C out of (EN 1996-1-1, 2012) will lead to conservative results in the case of unreinforced masonry. In combination with rather limited normal forces, the negative influence of eccentricities on the bearing capacity is a handicap for the application of big spans. However, in the future, the demand is rising for masonry in combination with big spans to apply adaptable design (Malabi-Eberhardt, et al., 2021) where a building during his lifetime could facilitate different occupations.

One common way of limiting eccentricities and obtaining equally distributed load transfers is by the application of bearing paths made out of elastic material. Loads are not anymore concentrated near the borders of the brick but distributed over the width which should lead to smaller eccentricities. This paper presents the results of some theoretical approaches and the results of experiments on a two-storey high scaled model of a masonry structure. Further, it can be noted that the bearing path also has the advantage to limit the transfer of vibrations through the building.

2 HANDLING ECCENTRICITIES

2.1 Code provisions out of EN 1996-1-1 together with annex C

The verification of unreinforced masonry walls in the ultimate limit state uses a reduction factor Φ applied on the product of the thickness of the wall t and the design compressive strength of the masonry f_{db} see Eq. (1). The reduction factor accounts for the effects of slenderness and the eccentricity caused by the loading. While for the thickness of the wall, the bearing length t_b may be taken at the top and bottom of the wall in the case of a partial support of the floor. On the other hand, it is known that with small values of t_b stresses will increase rapidly, and plasticisation will occur. Reason why a rectangular stress block in the code is proposed (EN 1996-1-1, 2012) with an upper limitation of $0.33 \cdot t$ (or level arm $\geq 0.33 \cdot t$ to the gravity centre, Figure 2).

$$N_{Ed} \leq N_{Rd} = \Phi_i \cdot t \cdot f_d = \left(1 - \frac{2e_i}{t}\right) \cdot t \cdot f_d \leq 0.9 \cdot t \cdot f_d \quad (1)$$

The eccentricity e_i is the sum of the eccentricities due to: the floor load M_{id}/N_{id} , horizontal loads mostly coming from the wind e_{he} , and imperfections e_{init} . A minimum value of $0.05t$ should be respected, see Eq. (2). Note that in the American code (ACI 530-13, 2013) the reduction factor is depending on the square of the slenderness ratio defined by the height of the masonry and the radius of gyration without the impact of out-of-plane loads (for unreinforced masonry).

$$e_i = \frac{M_{id}}{N_{id}} + e_{he} + e_{init} \geq 0,05t \quad (2)$$

Where M_{id} : Design value of the bending moment caused by the eccentricity of the floor load at the support (at the top as M_1 and at the bottom as M_2).

N_{id} : Design value of the vertical load at the top middle or bottom of the wall.

e_{he} : Eccentricity resulting from horizontal loads.

e_{init} : Initial eccentricity due to construction imperfections $\geq h_{ef}/450$

The information needed to calculate the out-of-plane eccentricity M_{id}/N_{id} from Eq. (2) can be found in Annex C of (EN 1996-1-1, 2012). It is a simplified method applicable to masonry walls supporting concrete floors. The end moment is given by Eq. (3) for M_1 (and likewise for M_2) and can be used for local analysis of the wall-floor joint and starts from an uncracked wall-section assuming elastic behaviour of materials. This implies that normal forces should be sufficiently high to guarantee full contact without cracking. For non-timber joist floors the moment distribution can be found in Figure 2. On the other hand, it is also stated that when the bearing length is limited to $t_b < t$, the relevant moments of inertia need to be used. As it is known that true fixity will not occur, the moments obtained may be reduced by a semi-empirical factor η varying between 0.5 and 1, depending on the bending stiffness ratio k_m of the adjacent floor to the upper and lower walls, see Eq. (4) valid for slabs loaded with uniform distributed loads.

$$M_1 = \frac{n_1 \frac{E_1 I_1}{h_1}}{n_1 \frac{E_1 I_1}{h_1} + n_2 \frac{E_2 I_2}{h_2} + n_3 \frac{E_3 I_3}{l_3} + n_4 \frac{E_4 I_4}{l_4}} \cdot \left[\frac{w_3 l_3^2}{4(n_3 - 1)} - \frac{w_4 l_4^2}{4(n_4 - 1)} \right] \quad (3)$$

$$\eta = 1 - \frac{k_m}{4} = 1 - \frac{1}{4} \cdot \left[\frac{n_3 \frac{E_3 I_3}{h_3} + n_4 \frac{E_4 I_4}{h_4}}{n_1 \frac{E_1 I_1}{h_1} + n_2 \frac{E_2 I_2}{h_2}} \right] \geq 0.5 \quad (4)$$

Where:

w_i = distributed load on element i

n_i = stiffness factor equal to 4 with both ends fixed, 3 for members simply supported at the end, 0 for the stiffness term for the cantilever and 1.5 for the loading

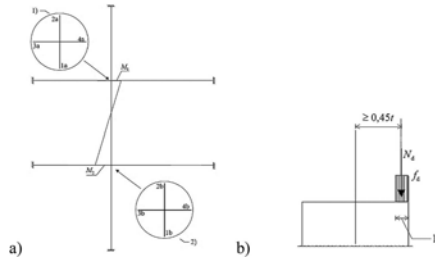


Figure 2. Simplified presentation for moment distribution (a) and maximum values (b) out of (EN 1996-1-1, 2012).

2.2 Önorm B 3350.

The old Austrian masonry code (Pauser, 1993) presents another interesting structural model, based on a strut mechanism, which makes horizontal stiff bracings needed. Nevertheless, the final outcomes in the meaning of stress fields at the contact surface are not meaningfully different.

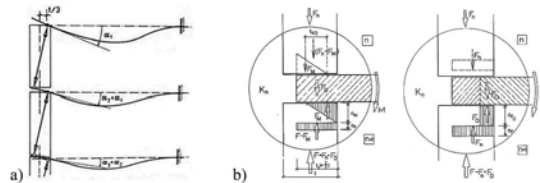


Figure 3. Structural model out of the old Austrian code (a) and proposed stress distributions at the contact surface (b), following (Pauser, 1993).

It can be highlighted that in the presented structural model an indication is made of the effects of higher loads and therefore higher bending moment capacities of the joints. Decreasing rotations (and linked to this also deflections) are marked: $\alpha_1 > \alpha_2 > \alpha_3$.

2.3 Literature

Most, if not all, of the experimental research has been devoted to refining the reduction factor η from Eq. (4) to obtain a more consistent relation between the results following from Eq. (3) with observations based on experiments. Sahlin (Sahlin, 1959) was one of the first to carry out a study of wall-floor connections in which the influence of crack formations at connection sites was investigated using tests on frameworks. This study laid the foundation for further research into the behaviour of floor-wall connections. Decades later, Hendry A.W (Hendry, 1998) conducted real-size tests to derive the same joint fixity factor η (= moment reduction

factor). Lewicki (Lewicki, et al., 2004) published similar research at different loads. This was done for both hollow clay bricks and aerated concrete walls.

2.4 Proposed theoretical model

Despite the considerable efforts made by the cited researchers so far a methodology based on fundamental mechanics is missing which allows for including the beneficial effect of elastic bearing paths. In practice, neoprene is often inserted between the hollow core slab and the masonry wall to distribute the load (avoiding local failure of the wall), limit acoustic emissions and avoid the transition of vibrations. This neoprene also inhibits the transition of a bending moment between the slab and the wall. In a first step, the rotational stiffness of a wall against an externally applied constant moment M is written as a function of the rotation angle φ , see Eq. (5). With σ a constant bending stress in the masonry and b , t and h respectively the length, the thickness and the height of the masonry wall.

$$C_{constant} = \frac{M}{\varphi} = \frac{\sigma \frac{bt^2}{6}}{\frac{\Delta h}{t/2}} = \frac{\sigma \frac{bt^3}{12}}{\varepsilon \cdot h} = \frac{\sigma \frac{bt^3}{12}}{\frac{\sigma}{E} \cdot h} = \frac{E * I}{h} \quad (5)$$

As already shown in Figure 2 (a), the bending moment is varying over the height in such a way that $M_1 = -M_2$ in the case of equal loads, heights and spans. The shortening Δh is now due to the averaged strain or half value of the maximum strain (corresponding with the maximum stress or moment at the top and bottom) which develops only over half of the height. In a next step, a reasonable assumption is made that the bending moment is not varying over the limited thickness of the bearing path h_n , width t_n and Young modulus E_n . As before, but accounting for the varying moment, Eq. (6) can be found where the stress in the bearing path is related to the one in the masonry wall by the square of the width.

$$\begin{aligned} C_{wall+bp} &= \frac{M}{\varphi} = \frac{\sigma \frac{bt^2}{6}}{\frac{\Delta h_n + \Delta h}{t/2}} = \frac{\sigma \frac{bt^3}{12}}{\varepsilon_n \cdot h_n + \varepsilon/2 \cdot h/2} = \frac{\sigma \frac{bt^3}{12}}{\sigma \left(\frac{t}{t_n}\right)^2 / E_n \cdot h_n + \sigma/E \cdot h/4} \\ &= \frac{EI}{\left(\frac{E}{E_n} \left(\frac{t}{t_n}\right)^2 \frac{h_n}{h} + \frac{1}{4}\right) h} = \frac{1}{n_i \frac{E}{E_n} \left(\frac{t}{t_n}\right)^2 \frac{h_n}{h} + 1} n_i \frac{EI}{h} = \alpha_i n_i \frac{EI}{h} \end{aligned} \quad (6)$$

To account for the presence of a bearing path in the equation of Annex C (EN 1996-1-1, 2012) a new reduction factor α_i is introduced depending on the geometrical, material parameters of the bearing path and the boundary condition by the stiffness factor n_i , without the need for η -factor. Previous Eq. (3) can be rewritten as Eq. (7) by introducing the corresponding α_i -factors. To adjust this formula for concentrated loads (P) instead of distributed loads (w), the calculation of the load effect changes from factor $1/4 \cdot w l^2$ to $3/8 \cdot P l$.

$$M_1 = \frac{\alpha_1 n_1 \frac{E_1 I_1}{h_1}}{\alpha_1 n_1 \frac{E_1 I_1}{h_1} + \alpha_2 n_2 \frac{E_2 I_2}{h_2} + \alpha_3 n_3 \frac{E_3 I_3}{h_3} + \alpha_4 n_4 \frac{E_4 I_4}{h_4}} \cdot \left[\frac{w_3 l_3^2}{4(n_3 - 1)} - \frac{w_4 l_4^2}{4(n_4 - 1)} \right] \quad (7)$$

3 EXPERIMENTAL PROGRAM

3.1 Development of a scaled model.

Typical multi-purpose buildings are characterized by spans of 8.1 m and free heights of at least 3.0 m. The masonry wall thickness is in such cases about 0.30 m to obtain a sufficient acoustic performance. In the case of multi-span applications, the slab thickness will be about 0.25 m for an in-situ casted concrete floor slab.

Out of practical reasons, a test set-up was developed at a scale of 1/3 respecting the same slenderness ratio (h/t) or a storey height of 1 m with a brick width of only 0.10 m. A single-span standard reinforced hollow core precast floor element with a free span of 2.8 m and thickness of 0.13 m was used. A two-storey building was realized to capture differences in deformation at both levels as mentioned in section 2.2, see Figure 3. Two types of execution have been tested. In the first one, no bearing path or even mortar joint was used. A practice which is frequently seen on smaller single-house sites in Belgium. Secondly, bearing paths (width limited to 80 mm instead of 100 mm of the brick) are inserted at the top and bottom to facilitate the best possible distribution of forces. The depth of the test set-up was fixed to 0.60 m, the width of the hollow core element used. Horizontal stability was guaranteed by wooden beams attached to the hollow cores in the middle of the span, supported by the stiff testing frame (allowing vertical deformations). Dimensions of the test set-up and measuring devices can be found in Figure 4, together with a picture of both test set-ups in the laboratory.



Figure 4. Test set-up of the scaled model (Meylemans, 2023).

3.2 Geometrical and material properties.

Material properties have been derived based on material tests, with stress levels equal to the one applied under the real testing conditions, see Table 1. Adhesives have been used by a professional (from the Wienerberger factory) for the bricklaying of the glued bricks.

Table 1. Mechanical material properties.

Component	Producer	Type	ρ	f_{ck}	f_{cm}	E
			[kg/m ³]	[N/mm ²]	[N/mm ²]	[N/mm ²]
Bricks	Wienerberger	PLS500-15N	850*	5.94	15*	15000°
Adhesive	Wienerberger	Dry-fix	1*	-	-	-
Mortar	Handmade	C300	1800	-	12°	27000°
Hollow core	Vets	V13-60GL	1653	40*	48°	35000°
Bearing path	Hakron	Neoprene 60	-	-	5*	18

* Out of datasheet of the producer, °based on information out of (EN 1992-1-1, 2005) or (EN 1996-1-1, 2012) and - = not relevant. Characteristic values based on tests on wall elements EN1025-1.

3.3 Measuring devices

Up-to-date measuring techniques have been used with a differentiation between the ones related to the slab, loadcells and Linear Variable Differential Transformers LVDT's, and the ones related to the vertical wall elements. For these latter elements, Digital Image Correlation (DIC) techniques have been used with front and side views in combination with classic DEMEC strain measurements as validation of the DIC (gauge length of 150 mm and an accuracy of 0.02 mm).

Three-dimensional digital image correlation (3D-DIC), an optical-numerical contactless technique, is used for measuring the strain distribution and full-field displacement at the surface of a specimen. Two synchronized stereovision cameras (Manta G-895B cameras with Kowa LM12XC lenses) take images of a speckled object in the undeformed and deformed state (20 images at each load step). The images are post-processed in DuoDIC, an open source MATLAB toolbox (Solav & Silverstein, 2022). In the undeformed state of the specimen, some images are taken of a flat checkerboard pattern. DuoDIC uses these images for calibrating both cameras.

The DIC measurement, see *Figure 5*, consists of a two-step approach. The first step includes the full view of the specimen. The field of view in step two is concentrated on the region just above and just below the hollow core slab. In such a way, displacements over the thickness of the wall are obtained by DIC measurements on the headers of the masonry.



Figure 5. DIC test-setup (a) full view of the specimen and, (b) detailed concentrated view.

3.4 Numerical simulation

With the aid of the Finite Element Method (FEM), shell elements, and contact elements (avoiding the transition of tensile stresses) first insight can be obtained. Figure 6 shows, by the aid of the principal stresses, and a concentrated load of 14.4 kN applied at each floor level, a huge influence of the bearing path. Compression stresses are divided by a factor of about 10, parasitic stresses are disappearing and stresses are introduced more centrally with an elastomer bearing path. Additionally, the inclined strut (almost disappearing with the elastomer) of Figure 3 can be visualized by the principal stresses of Figure 6.

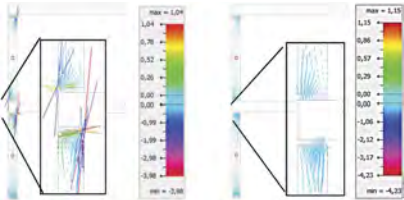


Figure 6. FEM simulation - hard contact left (minimum -3,98 N/mm²), elastomer right (-0,41 N/mm²).

4 RESULTS AND VALIDATION

A concentrated load was applied to achieve the ultimate bearing capacity of the hollow core slab based on the mean values of the material properties (JCSS, 2001) and a rectangular stress distribution in the concrete. Three characteristic moments can be derived (EN 1992-1-1, 2005) the cracking moment $M_{cr} = 4.54$ kNm; the design moment for the ultimate limit state (ULS) $M_{Rd} = 7.78$ kNm; and the expected failure moment $M_u = 11.69$ kNm. For a simply supported element, the corresponding concentrated loads are respectively: $P_{cr} = 4.5$ kN, $P_{Rd} = 9.0$ kN, and $P_u = 14.4$ kN or 30, 63 and 100% of the estimated failure load. During the tests, no failure was observed which made it possible to repeat the tests several times.

4.1 Deformations of the wall elements

The DIC measurements on the headers of the wall show the displacements at the location of the connection at the lower floor level, Figure 7. Due to a recording error, only the displacements at a load level of 7.2 kN/ each level can be shown, in the figure also some noise can be seen due to the tongue-and-groove shape of the blocks. Unfortunately, the measurements during the experimental testing are not accurate enough to compare them with the results of the finite element model in the linear-elastic FE software. Though, when looking more generally at displacements, similar trends and magnitudes can be observed between test results and numerical modelling.

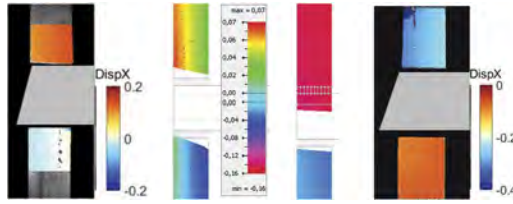


Figure 7. Results out of the FEM model (central) and DIC measurements (outer sides) at 7.2 kN of the header parts on top and bottom of the lower floor, respectively without and with elastic bearing path. Different scales have been used.

The results of the LE-FE model can then be compared to the analytical approaches as shown in Table 2. The first three columns show the outcome of applying the formula (Eq. (3)) and the reduction (Eq. (4)) proposed in Eurocode 6. As stated before, these formulas do not account for interface materials such as neoprene. The two following columns, ‘New-Neoprene’, apply the newly proposed factor α (Eq. (6)). It is seen that the obtained compression stresses are relatively close to each other for the lower wall. However, the tensile stresses are more deviating which is also the case for all stresses at the level of the upper wall with limited normal forces.

Table 2. Comparison analytical and numerical results.

	EC6 – non incl. interface material			New - Neoprene		LE-FEM*	
	$M_{1,EC6}$ [kNm]	$M_{1,EC6,red \eta}$ [kNm]	$\sigma_{zz, ana, red \eta}$ [N/mm ²]	$M_{1,red \alpha}$ [kNm]	$\sigma_{zz, ana, red \alpha}$ [N/mm ²]	$\sigma_{zz, num, neoprene}$ [N/mm ²]	$\sigma_{zz, num, cold}$ [N/mm ²]
Upper wall	-0,323	-0,162	-0,27/0,13	-0,134	-0,23/0,10	-0,14/0,02	-0,22/0,09
Lower wall	-0,287	-0,143	-0,31/0,04	-0,127	-0,29/0,02	-0,23/0,00	-0,42/0,16

* Values not obtained in the joint, but slightly lower since the boundary conditions of the joint were adjusted to avoid the floor slab pulling on the wall.

4.2 Deformations of the hollow cores

In the end, also a comparison is made between the deformations (compensated for the settlements of the supports) of the hollow cores, see Figure 8. On the left hand side, the data out of the first loading cycle is shown, some scatter is seen due to the cracking and a loading and unloading cycle. This scatter is completely disappeared in the second loading cycle (only the A and E series are shown), at the right hand side, except for the lower one with an elastic bearing path (N).

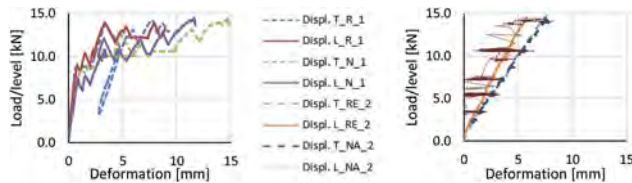


Figure 8. Measured deformations of the hollow core slab at the top (T), lower (L), with rigid (R), neoprene (N) bearing paths, after a first (1) and second test cycle (2). Measurements of L_N_2 are presented dotted, due to the high scatter.

It is noted that the deformation of the upper hollow cores is always more important than the ones of the lower floor, indicating that the double clamping moment of the lower floors plays a role, see also section 2.2. A reset was done of the deformations between the first and subsequent loading cycles, reason why no residual deformations (after the first loading cycle) in the

right graph of Figure 8 can be found. Residual deformations of 5.9 (rigid)/- (neoprene) mm of the lower and about 7.9 (rigid)/7.5 (neoprene) mm of the top slabs have been measured. In the reloading phase, it is remarkable that no difference can be found between the system with rigid supports and with elastomer, which is clearly the case during the first loading cycle.

5 CONCLUSIONS

A new approach was presented to handle the influence of elastic bearing paths in the formulation of Annex C out of (EN 1996-1-1, 2012). Based on more advanced FEM approaches it seems that the proposal works well and there is no need more for a semi-experimental joint fixity factor. For the experimental setup, a reduction factor of more than 10 can be achieved.

Experimental results clearly indicated that there is still a certain ‘fixity’ in the connections even with the application of an elastic bearing path. However, no important bending strains could be observed which is an indication that the actual code is far too negative. This is the reason why other researchers cited launched the semi-empirical so-called joint fixity reduction factor η . The α -factor proposed in this contribution is based on mechanical sound engineering principles and allows to take into account the beneficial effects of bearing paths. Results shows an even better performance than the actual fixity-factor out of the code provisions. Nevertheless, further improvements should be made to obtain full correspondence with FEM- and test-results.

ACKNOWLEDGEMENTS

This research would never have been possible without the question raised by the company Wienerberger, who also delivered the needed material together with Vets (Belgium) for the hollow cores. Our master thesis student Miro performed all the described experiments together with Luc our lab technician. This work will be continued in the near future.

This work was supported by FWO – Research Foundation of Flanders [grant number 1SG3523N].

REFERENCES

- ACI 530-13, 2013. Building code requirements for masonry structures. *American Concrete Institute*.
- Bertolesi, E., Adam, J. M., Rinaudo, P. & Calderón, P. A., 2019. Research and practice on masonry cross vaults - A review. *Engineering Structures*, pp. 67–88.
- EN 1990, 2015. *Eurocode 0 Basis of structural design (consolidated version including AI:2005 and AC:2010)*. Brussels, Belgium: CEN250.
- EN 1992-1-1, 2005. *Design of concrete structures - Part 1-1: General rules and rules for buildings (+AC 2008)*. Brussels: CEN250.
- EN 1996-1-1, 2022. *Design of masonry structures - Part 1-1: General rules for reinforced and unreinforced masonry structures (consolidated version including AC:2009 and AI:2012)*. Brussels: CEN250.
- Hendry, A., 1998. *Structural masonry*. 2nd ed. London: Red Globe Press.
- JCSS, 2001. *Probabilistic Model Code*, Denmark: <https://www.jcss-lc.org/jcss-probabilistic-modelcode/>.
- Lewicki, B., Lechman, M. & Szczygielski, A., 2004. *A method of testing of floor-wall joints*, Warsaw: Building Research Institute.
- Malabi-Eberhardt, L. C. et al., 2021. Environmental design guidelines for circular building components: The case of circular building structure. *Sustainability*, 18 May, pp. 13, 5621.
- Meylemans, M., 2023. *Invoed van oplegrubber op de krachtwerking in metselwerk, bij meervoudige verdiepingstoepassingen*. Sint-Katelijne-Waver: KU Leuven, FIIW.
- Pauser, A., 1993. Önorm B 3350 Tragende Wände - Kurzfassung miet Kommentar. In: P. Funk, ed. *Mauerwerk-Kalender 1993*. Berlin: Ernst & Sohn, pp. 539–554.
- Sahlin, S., 1959. *Structural interaction of walls and floor slabs*, Stockholm: Inst. for byggnadsstatik KTH.
- Solav, D. & Silverstein, A., 2022. DuoDIC: 3D Digital Image Correlation in MATLAB. *JOSS*, 26 June.
- Vitti, P., 2021. Mortars and masonry-structural lime and gypsum mortars in antiquity and middle ages. *Archaeological and anthropological sciences*, p. 10.

Data-driven life-cycle risk assessment of bridge networks using Bayesian network

M. Cheng & H.O. Gao

Cornell University, Ithaca, NY, USA

ABSTRACT: Bridge failures within the transportation network can lead to significant losses. Such failures are attributable to many factors from design to usage, internal to external, historic to present. It is therefore important to monitor and assess these risks in a holistic life-cycle approach. Generally, life-cycle risk assessment involves the evaluation of bridge failure probability over time and the associated consequences/losses. With increasing capabilities to harvest big data from various sources, the risk profile can be updated by integrating the power of data into the assessment. This paper presents a framework based on Bayesian network to perform data-driven life-cycle risk assessment for bridge networks. The life-cycle risk is updated with data from count stations and the bridge monitoring data. 13 bridges in a bridge network in New Jersey is used to demonstrate how the framework fuses the data and complex model of the system for risk assessment of the bridge network.

1 INTRODUCTION

Bridges are vulnerable assets in a transportation network and infrastructure systems. Failures of bridges can lead to significant losses such as injuries, casualties, traffic delays, and lost productivity. Such failures are attributable to many factors such as natural hazards, deterioration, and overloads (Frangopol et al. 2017). The failure analysis is further complicated by confounding factors changing over time such as the increasing traffic loads and failure consequences due to stressors such as population growth in urban areas and the increasing magnitudes and frequencies of natural hazards exacerbated by climate change (Yang and Frangopol 2019). Hence, it is important to monitor and assess these risks in a holistic life-cycle approach across the bridge network. In general, life-cycle risk assessment (LCRA) of a bridge network involves evaluating the failure probability profiles of bridges and the corresponding failure consequences within the transportation network. In existing studies, LCRA has been performed for bridge networks under different hazards such as earthquakes (Bocchini and Frangopol 2011) and riverine floods (Zhang and Alipour 2022). The outputs of risk assessment can then be used for decision-making such as life-cycle management (Liu et al. 2020) and recovery optimization (Bocchini and Frangopol 2012).

Recently, the ability to harvest big data to support the risk assessment of the transportation network has been advanced significantly. The newly available data can better reflect the capacity of and demand for the transportation network. For example, data from sensors embedded in the bridges and pavements can indicate bridge performance and diagnose road conditions, respectively (Frangopol et al. 2017; Guerrero-Ibáñez et al. 2018), which provides key information for up-to-date network capacity evaluation, while radar sensors and cameras can capture traffic flows (Guerrero-Ibáñez et al. 2018) that reflect demands over the network. The power of big data offers LCRA of bridge networks new improvement opportunities as the data/information on the network capacity and demand can be continuously acquired to update the failure probability profiles and the associated consequences. Structural health monitoring (Sun et al. 2020), intelligent transportation systems (Zhu et al. 2018), and smart manufacturing systems (Qu et al. 2019) are some examples of efforts in related fields that started incorporating the

power of data in their respective practices (i.e., structural engineering, transportation, and manufacturing). However, these existing endeavors tend to work in silos without taking a comprehensive systems approach. It is therefore important to develop a general methodology that accounts for different analyses and integrates disparate sources of data as a leverage for complex system level analysis and decision making.

This paper presents a framework based on Bayesian network (BN) to incorporate data from various sources into LCRA of bridge networks. BN presents an intuitive graphical framework that can model the relationships among random variables (i.e., nodes) using conditional probabilities. With recent advances, it's made its way into risk assessment (Marcot and Penman 2019). More specifically, the proposed framework uses BN to (1) model the interdependencies across and correlations within sub-systems analyses and (2) update the probability distributions of variables of interest when data is available for any nodes and subsystems. The framework also classifies the nodes into either data nodes or analysis nodes to guide Bayesian inference. In this paper, reliability analysis of the bridges and traffic prediction are joined together to perform data-driven LCRA of the bridge network. Using the framework, the life-cycle risk of the bridge network is updated when data from count stations and/or bridge monitoring devices is available. A bridge network located in Camden County, New Jersey, is used as an illustrative example to demonstrate how this framework can unify different analyses and disparate sources of data into LCRA for better informed and educated decision.

2 DATA-DRIVEN LIFE-CYCLE RISK ASSESSMENT (LCRA) OF A BRIDGE NETWORK

The risk of a bridge network is the joint risk of bridges in the network, usually summation of the individual bridge risks under reasonable independency assumption across bridge failures. For each evaluation time interval, typically a year, it involves the evaluation of the bridge failure probabilities and the corresponding consequences, which is expressed as

$$R_{netw}(t) = \sum_{i=1}^{N_b} P_{f,i}(t)C_{f,i}(t) \quad (1)$$

where N_b is the number of bridges considered in the bridge network, $P_{f,i}(t)$ is the failure probability of the i th bridge in year t , and $C_{f,i}(t)$ is the failure consequence associated with bridge i .

The performance function of a bridge to determine $P_{f,i}(t)$ is (Cheng et al. 2020)

$$g(t) = \alpha_m \alpha_a R_n(t) - a_{dl} L_{dl} - \alpha_{ll} L_{ll}(t) \quad (2)$$

where α_m and α_a are the uncertainty factors associated with material strength and the analysis, respectively, $R_n(t)$ is the nominal resistance in year t , a_{dl} and α_{ll} are the uncertainty factors associated with the dead load and live load, respectively, L_{dl} is the nominal dead load, and $L_{ll}(t)$ is the nominal live load for year t . Due to deterioration from different stressors, $R_n(t)$ decreases over years, while the live load effects can increase due to the increase in the truck weight and volume (Yu et al. 2019). The specific formulation of Equation 1 depends on various factors, such as the configurations of the bridge and the axle spacing of the trucks. Since the focus of this paper is not on the reliability analysis of bridges, we let L_{dl} and L_{ll} be normalized by $R_n(0)$ and only focus on the time-varying factors. A general form of the performance function is

$$g(t) = \alpha_m \alpha_a F_d(t) - a_{dl} A_{dl} - \alpha_{ll} A_{ll} F_{trk,W}(t) F_{trk,V}(t) \quad (3)$$

where $F_d(t)$ (<1) is the deterioration factor in year t , A_{dl} and A_{ll} are normalized factors associated with the dead load and live load, respectively, and $F_{trk,W}(t)$ and $F_{trk,V}(t)$ are the time-varying factors associated with the truck weight and truck volume, respectively. The effect of the truck volume on the failure probability is minimal, so $F_{trk,V}(t)$ is set to 1. $F_d(t)$ is modeled using a linear function

$$F_d(t) = 1 - B_d t \quad (4)$$

where B_d is the linear factor for deterioration. $W_{trk}(t)$ is modeled using an exponential decay function (Yu et al. 2019)

$$F_{trk,W}(t) = 2 \cdot \exp(-0.15t) \quad (5)$$

In this paper, $C_{f,i}(t)$ is estimated as the indirect loss due to detour cost after the closure of the bridge. The indirect loss is the summation of the running costs and the time loss associated with the vehicles supposed to pass the bridge (Dong et al. 2013). The running cost is

$$C_{run}(t) = L_d V_{ADT}(t) T_d [c_{r,car}(1 - r_{trk}) + c_{r,trk} r_{trk}] \quad (6)$$

where L_d is the detour length of the bridge, $V_{ADT}(t)$ is the annual average daily traffic (AADT) volume at year t , T_d is the time duration of the detour, $c_{r,car}$ and $c_{r,trk}$ are running costs for car and trucks, respectively, and r_{trk} is the ratio of truck traffic. The time loss is

$$C_{time}(t) = \frac{L_d V_{ADT}(t) T_d}{S_d} [c_{w,car} O_{car}(1 - r_{trk}) + c_{w,trk} O_{trk} r_{trk}] \quad (7)$$

where S_d is the speed of detour, $c_{w,car}$ and $c_{w,trk}$ are wages for car and truck drivers, respectively, and O_{car} and O_{trk} are average occupancies per car and truck, respectively.

In traditional risk assessment, some model parameters (e.g., V_{ADT} and W_{trk}) are treated as constants across years. Their values can be either taken from some existing sources (e.g., national bridge inventory database) or pre-determined using established models (e.g., linear extrapolation). However, such values are not necessarily best representations of the real conditions. Data-driven LCRA can address this caveat by utilizing data from monitoring devices. Newly available data can help reduce the discrepancy between the values adopted in risk assessment modeling and the true conditions. This in turn reduces the uncertainty when evaluating the risk.

In this paper, the deterioration factor F_d is estimated through data from bridge monitoring devices. Since the devices are usually embedded in the bridges, it is assumed that $F_d(t)$ can be obtained each year. V_{ADT} and $F_{trk,W}$ are estimated using the data from count stations in the traffic monitoring program operated by Department of Transportation (DOT). The traffic data mainly comes from continuous count stations (CCSs) and the short term count stations (STCS). The goal of the CCS is to understand the temporal pattern of traffic flow by installing permanent sensors to collect data all year round, while the goal of the STCS is to understand the spatial pattern of the investigated area by using portable sensors to measure traffic flow on road segments for one to three days. Specifically, the truck weight is monitored by CCSs and it is assumed that $F_{trk,W}(t)$ is perfectly observed. The estimation of V_{ADT} of a bridge is more complicated. Though the number of STCSs are large, it is still not enough to cover all the roads and bridges. Therefore, $V_{ADT}(t)$ of a bridge is approximated by the nearby STCSs (Wang and Kockelman 2009)

$$V_{ADT}(t) = \frac{1}{2} [V_{STCS,1}(t) \alpha_{iv,s1} + V_{STCS,2}(t) \alpha_{iv,s2}] \quad (8)$$

where $\alpha_{iv,s1}$ and $\alpha_{iv,s2}$ are uncertainty factors for traffic volume due to the spatial interpolation for the first and second STCSs, respectively, and $V_{STCS,1}(t)$ and $V_{STCS,2}(t)$ are AADT measured at the two nearby STCSs. It should be noted that if there is only one nearby STCS, then $V_{ADT}(t) = \alpha_{iv,s} V_{STCS,1}$. Besides, if the nearby count site is a CCS, then the acquired data $V_{CCS}(t)$ can be used to calculate $V_{ADT}(t)$. When data is provided for all nearby STCSs, $V_{ADT}(t)$ can be immediately determined. However, missing data complicates the problem as the STCSs do not have measurements every year. In that case, $V_{STCS}(t)$ is estimated using temporal extrapolation (Huynh et al. 2021)

$$V_{STCS,1}(t) = \alpha_{iv,t} \cdot V_{STCS,1}(t-1) F_{C,V}(t) \quad (9)$$

where $\alpha_{tv,t}$ is the uncertainty factor for traffic volume due to the temporal extrapolation, $V_{STCS,1}(t-1)$ is the AADT measured in the previous year, and $F_{C,V}(t)$ is the annual growth factor for the traffic volume measured at CCSs in year t . $V_{STCS,2}(t)$ is calculated in the same way. The underlying assumption is that growth rates are the same for all locations in the investigated area. Overall, F_d , $F_{trk,W}$, $F_{C,V}$, and V_{CCS} are observed every year, while V_{STCS} are obtained every few years. The data from these sources are used to update the failure probability profiles and the associated failure consequences of the bridge network.

3 FRAMEWORK FOR DATA-DRIVEN LCRA USING BAYESIAN NETWORK (BN)

BN is a directed acyclic graph (DAG) consisting of nodes that represent random variables and links that connect the nodes showing the dependencies and statistical correlations. BN models a joint probability distribution as the product of marginal distributions and conditional probability distributions. Consider a BN with four nodes in Figure 1. X_1 and X_2 , both random variables, represent root nodes and are described by marginal distribution $P(X_1)$ and $P(X_2)$, respectively. X_3 is a child node of X_1 and X_2 and is described by conditional probability $P(X_3|X_1, X_2)$, while X_4 is the child node of X_2 and is described by conditional probability $P(X_4|X_2)$. The joint distribution is then

$$P(X_1, X_2, X_3, X_4) = P(X_1)P(X_2)P(X_3|X_1, X_2)P(X_4|X_2) \quad (10)$$

More information regarding BN can be found in Straub and Der Kiureghian (2012).

Constructing a BN involves (1) building the graphical model (i.e., DAG) and (2) eliciting and storing the conditional probability tables (CPT) that define the relationships among nodes (Bensi 2010). The first step is related to the system one wants to analyze, while for the second step, conditional probability tables can be established based on expert knowledge tables (Marcot and Penman 2019), or determined using the simulation data (Bensi 2010). After constructing the BN, inference can be efficiently performed via query from the distributions of a set of random variables given the evidence of another set of random variables. Classical algorithms for inference include the variable elimination algorithm and junction tree algorithm (Bensi 2010).

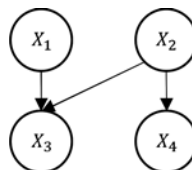


Figure 1. Example BN with four nodes.

Here we propose a framework for data-driven LCRA using BN. Based on the function of the nodes in system analysis, we define three types of nodes: performance nodes (PN), data nodes (DN), and analysis nodes (AN). Performance nodes are represented by random variables that are considered as the performance indicators that can be monitored and/or quantified for a system or a subsystem. The PNs depend on the system and the analysis objectives. For LCRA of the bridge network, the PN represents risk in each year. Data nodes are the random variables with data coming in reflecting conditions of a system. In the model discussed in Section 2, F_d , $F_{trk,W}$, $F_{C,V}$, and V_{STCS} are DNs that can be further categorized as continuous or intermittent DNs. If the updating frequency of a DN is higher than that of the monitoring frequency of the system PN, then it is a continuous DN (CDN); otherwise, it's an intermittent DN (IDN). Analysis nodes (AN) are the random variables representing the outputs from certain analyses or models. The analysis can be as simple as estimating V_{ADT} using nearby STCSs (i.e., Equation 9), or as complicated as the reliability analysis of a bridge (i.e., Equations 2 and 3).

Based on the temporal property, the framework also classifies the nodes as time-dependent or not. Suppose a non-time-dependent node is the child node of a list of parent nodes in the

graph, then a time-dependent node depends not only on this list of nodes, but also on itself in the previous time step. In this paper, for a time-dependent node, a virtual root node representing itself in the previous step is added. When PN, IDN, and AN are time-dependent, they are denoted as PN-T, IDN-T, and AN-T, respectively. An example of IDN-T is traffic volume from short term count stations (STCS) V_{STCS} . When they are not time-dependent, they are denoted as PN-NT, IDN-NT, and AN-NT, respectively.

Once the classification of nodes in a BN is done, Bayesian inference can be made. An inference consists of query variables and evidence variables. Query variables include PN-T, PN-NT, IDN-T when receiving no data, and AN-T, while evidence variables include IDN-T and IDN-NT when receiving data, and CDN.

4 ILLUSTRATIVE EXAMPLE

Thirteen bridges in a transportation network in Camden county, New Jersey, are used as an illustrative example. The bridges, STCSs, and the CCS are shown in Figure 2. There are 3 STCSs and 1 CCS on the road link. Based on the entrances and exits on the highways, these count stations are used to estimate the AADT of the 13 bridges (i.e., V_{ADT}). Gadda et al. (2007) investigated the errors in estimating AADT using count stations. Based on their results, the temporal uncertainty $\alpha_{t,v,t}$, is assumed to follow a triangular distribution with a mode of 1.0, a lower limit of 0.6, and an upper limit of 1.4, indicating an estimation error around 20%. For spatial uncertainty $\alpha_{t,v,s}$, it is also assumed to follow a triangular distribution with a mode of 1.0. The estimation error depends on the distance between the count sites and the bridge. It is 20% when the distance is smaller than 0.5 mile, otherwise, it is 40%. Please note that when there is no entrance or exit between the bridge and the count station, the error is 10% to reflect the error due to the adjustment from a two-day measurement to a one-year estimate. As mentioned previously, V_{ADT} is used for the calculation of failure consequence. The additional parameters for failure consequence evaluation are as follows (Cheng and Frangopol 2023). $c_{r,car} = 0.11$, $c_{r,trk} = 0.30$, $t_d = 180$, $r_{trk} = 0.04$, $c_{w,car} = 22.82$, $c_{w,trk} = 26.97$, $O_{car} = 1.5$, $O_{trk} = 1.05$, and $V = 50$. L_d of bridges are obtained from national bridge inventory database. The parameters to evaluate failure probabilities are based on the computation results in Cheng and Frangopol (2022). A_{dl} and A_{ll} are estimated to be 0.10 and 0.35, respectively, and are used for all bridges, while B_d varies from 0 to 0.002.

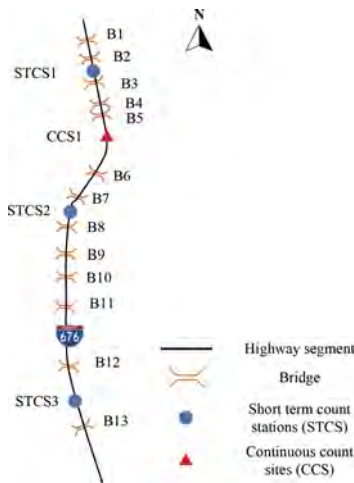


Figure 2. Bridges and traffic count sites in the transportation network in Camden County, New Jersey.

The graphical model of the BN is shown in Figure 3. On the right, the figure shows brief explanations of the nodes. On the left, the figure shows the relationships among the nodes. The graph mainly depicts the estimation of (1) AADT and (2) the reliability indices of the

bridges before the final bridge network risk assessment. For estimation of the AADT, the links between V_{Bi} and the measurements at count stations depend on the topography of the highway segments shown in Figure 2. For estimation of the reliability indices, the node $F_{Trk,W}$ affects the reliability indices of all bridges since the truck weight is only measured at the CCS. Deterioration of each bridge is measured to update its reliability index. As a result, a node $F_{d,Bi}$ is connected to β_{Bi} for each bridge. After the AADT and reliability index are estimated, the risk of each bridge can be determined. Finally, the risk of the network is the summation of the risk across all the individual bridges studied.

With the BN graphical model, next step is to construct marginal distributions and conditional probability tables. Monte Carlo simulation is used to generate the data for all the nodes (Bensi 2010). It should be noted that such simulation is different from those in reliability analysis where random data is generated according to the prescribed usually normal distribution. Instead, here the ranges of certain random variables are determined first; samples are then drawn uniformly from these while calculations are performed for other random variables. Before the learning of conditional probability tables of BN, discretization is carried out for all the nodes. The binning intervals for all traffic volume nodes are the same except that the ranges are different based on the current value. Specifically, the upper and lower limits are 1.8 and 0.8 times of the current AADT, respectively. The ranges of $F_{d,Bi}$, $F_{Trk,W}$, and β_{Bi} are from 0.93 to 1.0 with an interval of 0.01, from 1.0 to 1.8 with an interval of 0.01, and from 2.8 to 4.2 with an interval of 0.1, respectively. Since the risk of bridges can vary drastically, the ranges of the risk for all bridges are first determined using the simulated data for parameter learning. The interval is then set by calculating the 20th, 40th, 50th, 60th, 70th, 80th, 90th, 92th, 94th, 96th, 98th, 99th, 99.5th, and 99.9th percentiles. The reason for the irregular intervals is that higher risk should be paid more attention to.

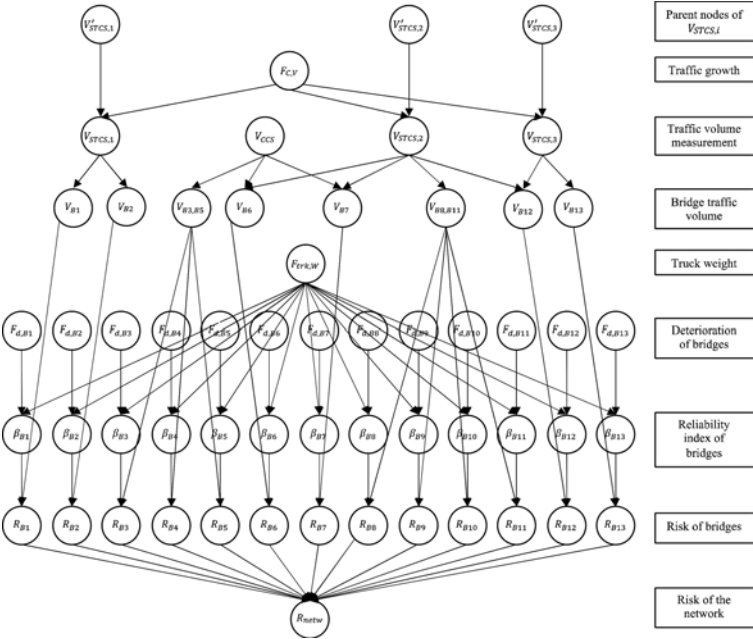


Figure 3. BN for the data-driven LCRA of the bridge network.

A future scenario is hypothesized to illustrate how BN can perform the risk assessment. As mentioned previously, LCRA is complemented by the available data from F_d , $F_{Trk,W}$, $F_{C,V}$, V_{CCS} , and V_{STCS} . Monte Carlo simulation is used to generate the profiles of data for these random variables. The deterioration profile of each bridge $F_d(t)$ is simulated by first randomly sampling B_d using a normal distribution with a mean of 0.001 and a COV of 0.2 and then calculate F_d in each year. $F_{Trk,W}(t)$ is calculated by Equation (5). Annual growth rate in each year $F_{C,V}(t)$ is

simulated using a normal distribution with a mean of 1% and a standard deviation of 1%. With a starting AADT of 62456 (i.e., $V_{CCS}(0) = 62456$), $V_{CCS}(t)$ is calculated by multiplying $V_{CCS}(t-1)$ and $F_{C,V}(t-1)$. $V_{STCS}(t)$ of the three STCSs are generated in the same way as $V_{CCS}(t)$. Specifically, $V_{STCS,1}(0) = 65436$, $V_{STCS,2}(0) = 67874$, and $V_{STCS,3}(0) = 85124$. $F_d(t)$, $F_{trk,W}(t)$, $F_{C,V}(t)$, and $V_{CCS}(t)$ can be observed at each year, while according to NJDOT, STCS measurements are generally conducted in a three-year cycle. Hence, it is assumed that data of $V_{STCS,1}(t)$, $V_{STCS,2}(t)$, and $V_{STCS,3}(t)$ are observed every three years with $V_{STCS,1}(0)$, $V_{STCS,2}(1)$, and $V_{STCS,3}(2)$ being first obtained at the three corresponding STCSs.

BN is implemented using the python package pgmpy (Ankan and Panda 2015). Figure 4 shows the total risk of the whole bridge network. As time elapses, the risk generally increases due to the deterioration of bridges and increases in the traffic volumes. However, we see decreases in total risk in years 15, 16, and 28, when $V_{STCS,3}$ are observed. This indicates that observed data helps adjust downward the overestimation of V_{B12} and V_{B13} . Figure 5 shows the risk of a selected bridge B2. Based on Figure 3, V_{B2} has only one parent node, $V_{STCS,1}$. Since the CDN $F_{c,v}$ and the failure probability are always increasing, the risk estimation can only be reduced when data from $V_{STCS,1}$ indicates a decrease in V_{B2} . In year 21, the risk significantly drops. This matches with the availability of observed $V_{STCS,1}$ in that year. Together, Figures 4 and 5 demonstrate the ability of the BN framework in using available observations to update the risk estimation of the bridge network.

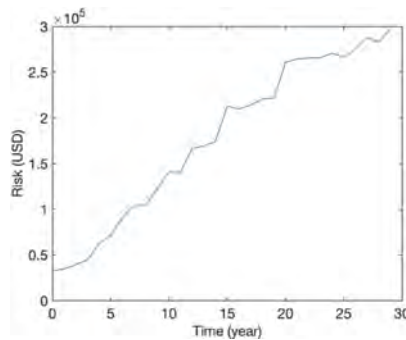


Figure 4. Risk of the bridge network.

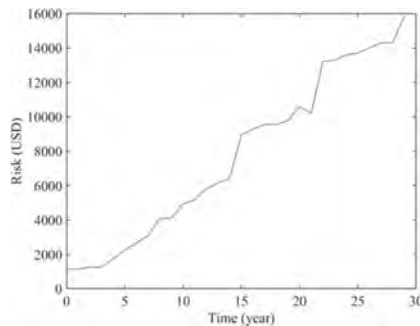


Figure 5. Risk of a representative bridge B2.

5 CONCLUSIONS

In this paper, a framework based on Bayesian network (BN) is proposed for data-driven life-cycle risk assessment (LCRA). Based on the function of the nodes in a BN, three types of nodes including performance nodes, data nodes, and analysis nodes are defined. The data nodes are further classified to be intermittent or continuous given the frequency of receiving data. Based on the temporal properties, these nodes can also be grouped as time-dependent or not. With the classification of nodes, the framework specifies the procedure to perform Bayesian inferences.

The framework is then applied to LCRA of bridge networks with the inclusion of data from three sources. Particularly, the traffics on the bridges are updated by data from traffic count stations and used to update the failure losses of bridges, while reliability of the bridges is updated by truck weight data fused with bridge monitoring data. A bridge network in Camden County, New Jersey, is used to demonstrate the ability of the framework in supporting life-cycle risk assessment and management of infrastructure systems.

REFERENCES

- Ankan, A. & Panda, A. 2015. pgmpy: Probabilistic graphical models using python. In Kathryn Huff & James Bergstra (eds), *Proceedings of the 14th python in science conference, Austin, Texas, 6-12 July 2015*.
- Bensi, M.T. 2010. *A Bayesian Network Methodology for Infrastructure Seismic Risk Assessment And Decision Support*. University of California, Berkeley.
- Bocchini, P. & Frangopol, D.M. 2011. A stochastic computational framework for the joint transportation network fragility analysis and traffic flow distribution under extreme events. *Probabilistic Engineering Mechanics* 26(2): 182–193.
- Bocchini, P. & Frangopol, D.M. 2012. Restoration of bridge networks after an earthquake: Multicriteria intervention optimization. *Earthquake Spectra* 28(2): 426–455.
- Cheng, M. & Frangopol, D.M. 2022. Life-cycle optimization of structural systems based on cumulative prospect theory: Effects of the reference point and risk attitudes. *Reliability Engineering & System Safety* 218: 108100.
- Cheng, M. & Frangopol, D.M. 2023. Efficient scenario analysis for optimal adaptation of bridge networks under deep uncertainties through knowledge transfer. *Structural Safety* 100: 102278.
- Cheng, M. Frangopol, D.M. & Gong, C. 2020. Acceptance of corrosion-resistant steel in design of steel girder bridges based on expected utility theory. *Journal of Bridge Engineering* 25 (11):04020098.
- Dong, Y. Frangopol, D.M. & Saydam, D. 2013. Time-variant sustainability assessment of seismically vulnerable bridges subjected to multiple hazards. *Earthquake Engineering & Structural Dynamics* 42 (10): 1451–1467.
- Frangopol, D.M. Dong, Y. & Sabatino, S. 2017. Bridge life-cycle performance and cost: analysis, prediction, optimisation and decision-making. *Structure and Infrastructure Engineering* 13(10): 1239–1257.
- Gadda, S. Kockelman, K.M. & Magoon, A. 2007. Estimates of AADT: Quantifying the uncertainty. Presented in *World Conference on Transportation Research, Berkeley, California, 2017*.
- Guerrero-Ibáñez, J. Zeadally, S. & Contreras-Castillo, J. 2018. Sensor technologies for intelligent transportation systems. *Sensors* 18(4): 1212.
- Huynh, N., Wang, J. DeVine, R. Chowdhury, M.R. Jin, W. Biswas, P. & Comert, G. 2021. *Estimating AADT On Non-coverage Roads*. Columbia, SC: South Carolina Department of Transportation.
- Liu, L. Yang, D.Y. & Frangopol, D.M. 2020. Network-level risk-based framework for optimal bridge adaptation management considering scour and climate change. *Journal of Infrastructure Systems* 26 (1):04019037.
- Marcot, B.G. & Penman, T.D. 2019. Advances in Bayesian network modelling: Integration of modelling technologies. *Environmental Modelling & Software*, 111: 386–393.
- Padgett, J.E. DesRoches, R. & Nilsson, E. 2010. Regional seismic risk assessment of bridge network in Charleston, South Carolina. *Journal of Earthquake Engineering* 14(6): 918–933.
- Qu, Y.J. Ming, X.G. Liu, Z.W. Zhang, X.Y. & Hou, Z.T. 2019. Smart manufacturing systems: state of the art and future trends. *International Journal of Advanced Manufacturing Technology*, 103(9), pp. 3751–3768.
- Straub, D. & Der Kiureghian, A. 2012. Bayesian network enhanced with structural reliability methods: methodology. *Journal of Engineering Mechanics* 136(10): 1248–1258.
- Sun, L. Shang, Z. Xia, Y. Bhowmick, S. & Nagarajaiah, S. (2020). Review of bridge structural health monitoring aided by big data and artificial intelligence: From condition assessment to damage detection. *Journal of Structural Engineering* 146(5): 04020073.
- Wang, X. & Kockelman, K.M. 2009. Forecasting network data: Spatial interpolation of traffic counts from texas data. *Transportation Research Record* 2105(1): 100–108.
- Yang, D.Y. & Frangopol, D.M. 2019. Societal risk assessment of transportation networks under uncertainties due to climate change and population growth. *Structural Safety* 78: 33–47.
- Yu, Y. Cai, C. S. He, W. & Peng, H. 2019. Prediction of bridge maximum load effects under growing traffic using non-stationary Bayesian method. *Engineering Structures* 185: 171–183.
- Zhang, N. & Alipour, A. 2022. Flood risk assessment and application of risk curves for design of mitigation strategies. *International Journal of Critical Infrastructure Protection* 36: 100490.
- Zhu, L. Yu, F. R. Wang, Y. Ning, B. & Tang, T. 2018. Big data analytics in intelligent transportation systems: A survey. *IEEE Transactions on Intelligent Transportation Systems* 20(1): 383–398.

Risk-based life-cycle loss assessment using statistical moments

Y. Zhang

Department of Civil and Environmental Engineering, The Hong Kong Polytechnic University, Hong Kong, China

Y. Li

Department of Construction and Quality Management, Hong Kong Metropolitan University, Hong Kong, China

ABSTRACT: Evaluating the economic loss of civil infrastructure subjected to hazards can be significant for life-cycle risk assessment. In the past, the expected value of loss has been widely investigated during risk assessment and employed as a standard decision-making criterion. However, the inherent uncertainties may be neglected when focusing on the mean value. Hence, other statistical moments, especially the higher-order moments, and the probability density function of the long-term loss should be considered. In this paper, a probabilistic analysis framework is proposed for risk quantification to compute the probability density function of the long-term loss using statistical moments. By using the first-four statistical moments of the long-term loss, the maximum entropy method can construct the probability density function of the long-term loss effectively and accurately. The proposed method can enhance the computation efficiency during risk assessment and benefit the decision-making process.

1 INTRODUCTION

Over the past few decades, there were significant financial and social losses caused by various natural hazards, which have gained increasing awareness of the public to risk management of civil infrastructures. Risk assessment and life cycle performance of infrastructures are becoming key concerns of researchers to conduct risk management. Recently, the long-term loss of civil infrastructures subjected to hazards such as earthquakes, hurricanes and flooding have received special attention (Cheng & Frangopol, 2022, Giouvanidis & Dong, 2020, Zhu et al., 2021). The long-term loss is also known as risk during life-cycle risk assessment, and it refers to the cumulative financial loss of the civil infrastructures resulting from the damage under hazards over the service life. Previously, the expected long-term loss has been regarded as a standard decision criterion. However, more recent studies have stated that the expectation of long-term loss is not informative and other statistical indicators should be involved (Cheng & Frangopol, 2022, Goda & Hong, 2006, Goda & Hong, 2008). Then several studies started to investigate the statistical parameters of the long-term loss such as the standard deviation and higher-order moments. For instance, an analytical renewal model was proposed to assess the mean and standard deviation of the life-cycle cost (Pandey & Van Der Weide, 2017). Li et al. (2020) stated that the importance of evaluating the higher-order moments of the long-term loss under stationary and non-stationary hazard models. The higher-order moments of long-term loss under non-stationary hazards such as the skewness and kurtosis are of interest. Uncertainties arising from the stochastic occurrence and the intensity of hazards are taken into account.

In addition to statistical parameters, the probability distribution of the long-term loss could also be significant information for decision-making process (Pandey & van der Weide, 2018, Wang & Zhang, 2018). Although Monte Carlo simulation (MCS) is the most direct way to assess the probability distribution of the long-term loss, it could be time-consuming when considering different hazard conditions and scenarios. To address this research gap, a probabilistic approach incorporating the maximum entropy method and the statistical moments of the long-term loss is developed for capturing the probability density function (PDF) of long-term loss.

Maximum entropy method (MEM) refers to the moment method for deriving the unknown PDF of a random variable with its statistical moments (Rahman & Xu, 2004, Xu & Rahman, 2004, Zhao & Ono, 2001). Various distribution models were developed to fit the unknown PDF such as the Pearson system and Johnson system (Johnson et al., 1995, Xu et al., 2020). However, the MEM could be seen as the most unbiased one among different distribution models. The MEM originates from the maximum entropy principle (Jaynes, 1957), which can select the most possible distribution towards the underlying PDF of interest. In the field of structural reliability analysis, MEM has been widely utilized to derive the unknown PDF of structural responses (Li & Zhang, 2011, Xu & Kong, 2019). Overall, MEM could be a versatile tool for the derivation of the unknown PDF of a random variable. The computational effort of using MEM can be remarkably reduced compared with that of MCS. In this study, MEM with the first-four analytical statistical moments, i.e., mean, standard deviation, skewness and kurtosis, are employed for the derivation of the PDF and CDF of long-term loss. The following section introduces a stochastic hazard model to provide the stochastic model for risk assessment. Section 3 summarizes the theory of MEM and the analytical first-four statistical moments of long-term loss is also included. Section 4 presents a case study to validate the efficiency and accuracy of the proposed method. Finally, conclusions are stated in Section 5.

2 LIFE-CYCLE RISK MODEL

2.1 Stochastic hazard model

The risk assessment within the life-cycle is dependent on the stochastic hazard model. The homogeneous Poisson process has been widely utilized to model probabilistic uncertainties of hazards (e.g., earthquakes and typhoons) in previous studies. In this paper, the typhoon hazard and the homogeneous Poisson model is taken as an example for illustrative purposes. According to the Poisson process, the arriving time of a typhoon event is a random variable. If the life-cycle of the civil infrastructure is $(0, t_{\max}]$, the arriving times within the period can be denoted as a series of $\{T_1, T_2, \dots, T_k\}$, i.e., T_k is the arriving time of the k th typhoon event during the life cycle. The inter-arriving time between the two adjacent events is also a random variable and can be noted as S_k . The relationship between the arriving time and the inter-arriving time can be described as $T_k = S_1 + S_2 + \dots + S_k$. The homogeneous Poisson process specifies that the inter-arriving time follows exponential distribution

$$f_s(s) = \lambda \exp(-\lambda s) \quad (1)$$

where λ is the occurrence rate associated with the hazard.

The total number of occurrences can be given as $N(t_{\max})$ and let $N(t_{\max}) = n$. It follows a Poisson distribution

$$P[N(t_{\max}) = n] = \frac{(\lambda t_{\max})^n \exp(-\lambda t_{\max})}{n!}, \quad n = 0, 1, 2, \dots \quad (2)$$

2.2 Risk assessment within the life cycle

Given the stochastic hazard model, the risk-based economic loss of each typhoon event can be noted as L , which is a series of random variables $\{L_1, L_2, \dots, L_k\}$. For instance, the loss associated with the first typhoon event is L_1 . Herein, the investigated loss is restricted to the economic cost of civil infrastructure system due to repair or restoration. Other costs such as social impact are not investigated in this context. By quantifying the losses of all the typhoon events, the accumulated loss within the life cycle can be given as

$$AL(t_{\max}) = \sum_{k=1}^{N(t_{\max})} L_k e^{-rT_k} \quad (3)$$

where $AL(t_{\max})$ is the accumulated loss within the life cycle, r is the monetary discount rate, L_k and T_k are the loss and the arriving time associated with the k th typhoon event.

3 PROBABILISTIC LOSS USING STATISTICAL MOMENTS

3.1 Statistical moments

To compute the probabilistic distribution of the accumulated loss, the four statistical moments should be determined firstly. The statistical moments of the accumulated loss are the key inputs for the proposed probabilistic loss assessment framework. Herein, the first-four moments (i.e., mean, standard deviation, skewness and kurtosis) are calculated based on the moment generating function (MGF). The MGF of X about ϖ can be defined as

$$M_X(\varpi) = E[e^{\varpi X}] \quad (4)$$

The theory of the MGF gives that the m th order moment of X can be calculated by taking the m th order derivatives of the MGF. Based on this theorem, the MGF of the accumulated loss within the life cycle should be calculated and can be given as

$$M_{AL(t_{\max})}(\varpi) = \exp\left[\lambda \int_0^{t_{\max}} [M_L(\varpi e^{-rx}) - 1] dx\right] \quad (5)$$

Subsequently, the first four statistical moments of the accumulated loss within life cycle can be computed analytically by taking the derivatives at zero. Accordingly, the first four analytical statistical moments can be calculated (Li et al. 2020).

3.2 Maximum entropy method

Once the first-four analytical statistical moments of long-term loss are obtained, the maximum entropy method can be employed to derive the probabilistic distribution of the long-term loss. The general idea of the MEM is presented as follows.

Given a random variable Y , the information entropy of Y can be expressed as

$$H(f_Y(y)) = - \int_y f_Y(y) \log(f_Y(y)) dy \quad (6)$$

On the basis of the maximum entropy principle, the underlying PDF of Y can be found by the following constrained optimization problem

$$\begin{cases} \text{Find:} & f_Y(y) \\ \text{Maximize:} & H(f_Y(y)) = - \int_Y f_Y(y) \log[f_Y(y)] dy \\ \text{s.t.:} & E[Y^i] = \int_Y Y^i f_Y(y) dy, \quad i = 1, 2, \dots, k \end{cases} \quad (7)$$

where $E[Y^i]$ is the i -th raw moment of Y . Hence, the MEM uses a series of statistical moments of Y as constrains to find an underlying PDF with the maximum information entropy, which can be seen as an unbiased estimation of the unknown PDF. Conventionally, the number of the commonly used statistical moments is adopted as four, which refers to the first-four statistical moments.

To solve the optimization problem in Equation (7), the Lagrangian function is introduced first

$$\begin{aligned} L[\varphi, f_Y(y)] = & - \int_Y f_Y(y) \log[f_Y(y)] dy - (\varphi_0 - 1) \left[\int_Y f_Y(y) dy - 1 \right] - \\ & \sum_{i=1}^k \varphi_i \left[\int_Y y^i f_Y(y) dy - \mathbb{E}[Y^i] \right] \end{aligned} \quad (8)$$

where $\varphi = [\varphi_0, \varphi_1, \dots, \varphi_k]^T$ is the vector of the Lagrangian multipliers. Given the following condition

$$\frac{\partial L(\varphi, f_Y(y))}{\partial f_Y(y)} = 0 \quad (9)$$

The underlying PDF of random variable Y is expressed as

$$\hat{f}_Y(y) = \exp\left(-\varphi_0 - \sum_{i=1}^k \varphi_i y^i\right) \quad (10)$$

where φ_0 is calculated as follows by using the normalization axiom in probability theory

$$\varphi_0 = \log \left[\int_Y \exp\left(-\sum_{i=1}^k \varphi_i y^i\right) dy \right] \quad (11)$$

However, the constrained optimization problem shown in Equation (7) is difficult to solve. To address this issue, K-L divergence can measure the discrepancy between the true PDF and the estimated one

$$K[f_Y(y), \hat{f}_Y(y)] = \int_Y f_Y(y) \log \left[\frac{f_Y(y)}{\hat{f}_Y(y)} \right] dy = \int_Y f_Y(y) \log[f_Y(y)] dy - \int_Y f_Y(y) \log[\hat{f}_Y(y)] dy \quad (12)$$

By substituting Equation (10) into Equation (12), we can obtain

$$K[f_Y(y), \hat{f}_Y(y)] = -H(f_Y(y)) + \varphi_0 + \sum_{i=1}^k \varphi_i \mathbb{E}[Y^i] \quad (13)$$

Minimizing the K-L divergence can be an alternative way to find the underlying true PDF. Likewise, the objective function can be revised as

$$\Gamma(\varphi) = \varphi_0 + \sum_{i=1}^k \varphi_i E[Y^i] = \log \left[\int_Y \exp\left(-\sum_{i=1}^k \varphi_i y^i\right) dy \right] + \sum_{i=1}^k \varphi_i E[Y^i] \quad (14)$$

Then, the hyper parameters φ can be determined by the following un-constrained optimization problem

$$\begin{cases} \text{Find:} & \varphi = [\varphi_0, \varphi_1, \dots, \varphi_k]^T \\ \text{Minimize:} & \Gamma(\varphi) = \log \left[\int_Y \exp\left(-\sum_{i=1}^k \varphi_i y^i\right) dy \right] + \sum_{i=1}^k \varphi_i E[Y^i] \end{cases} \quad (15)$$

3.3 Probabilistic distribution of life-cycle loss

Before using the maximum entropy method for deriving the probabilistic distribution of the long-term loss, a standardized transformation is employed to transform the long-term loss (i.e., AL) into a standard random variable Y

$$Y = \frac{AL - u_1}{u_2} \quad (16)$$

By solving the un-constrained optimization problem shown in Equation (15), the underlying probabilistic distribution of the long-term loss can be estimated as

$$\hat{f}_{AL}(l_t) = \frac{1}{u_2} \hat{f}_Y(y) = \frac{1}{u_2} \exp\left(-\varphi_0 - \sum_{i=1}^k \varphi_i \left(\frac{l_t - u_1}{u_2}\right)^i\right) \quad (17)$$

where l_t is the long-term loss of interest.

4 ILLUSTRATIVE EXAMPLE

To validate the accuracy and efficiency of the proposed method. A coastal bridge subjected to the hurricane hazard is investigated. The bridge is a multi-span simply girder bridge, which is vulnerable to deck unseating failure encountering hurricanes. The occurrence of hurricanes is modelled by the homogeneous Poisson process over the service life of the bridge. The relevant parameters that dominate the long-term loss of the bridge are the occurrence rate λ , the parameter of the loss severity L , the monetary discount rate r and the service life of the bridge t_{\max} .

Note that the occurrence rate λ is determined as 0.245 by the annual number of hurricanes in a specific region (Li et al., 2020). The loss severity L is calculated by the product of the failure probability and the corresponding repair loss caused by the failure events (i.e., unseating failure of the bridge). In this paper, the loss severity is assumed as exponential distribution and the expected loss severity is 1.283 million USD (Li et al., 2020). The service life is 75 years of this bridge.

The first-four statistical moments can be calculated as 12.2099×10^6 USD, 4.3773×10^6 USD, 0.61 and 3.54 on the moment generating function given in Equation (5). Then, the maximum entropy method can be employed to derive the long-term loss of the coastal bridge under hurricanes by using these statistical moments as constraints. The Lagrangian multipliers of the MEM are determined as (0.3459, 0.5015, -0.1287, 0.0164). Figures 1 and 2 show the PDF and CDF in logarithm scale of the long-term loss by 10^6 MCS and the proposed method, respectively. It can be seen that the PDF and CDF by the proposed method are in good accordance with those by MCS, which reveals that the proposed method can be an alternative way to fit the unknown probabilistic distribution of loss of civil infrastructures instead of MCS. Thereby, the proposed method can significantly improve the efficiency of deriving the probabilistic distribution of the long-term loss under different scenarios.

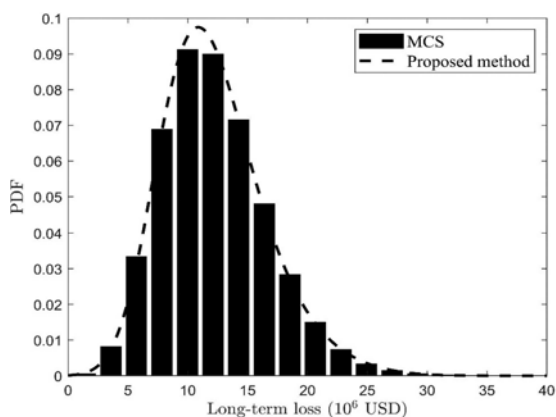


Figure 1. PDF of the long-term loss (75 years, $r = 2\%$).

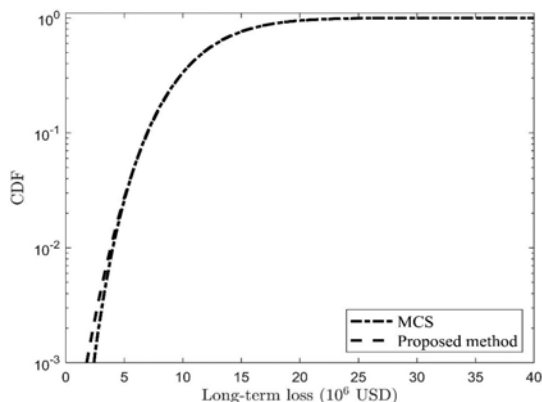


Figure 2. CDF of the long-term loss (75 years, $r = 2\%$).

5 CONCLUSIONS

In this paper, a probabilistic analysis method is developed for deriving the probability density distribution of the long-term loss of civil infrastructures. First, the analytical statistical moments,

including mean, standard deviation, skewness and kurtosis of long-term loss are calculated by using the moment generating function based on the stochastic Poisson process. Then, the maximum entropy method is employed to find an estimation of the unknown distribution of the long-term loss by fitting its first-four statistical moments. The proposed method can be an alternative way to derive the distribution of the long-term loss and achieve comparable accuracy compared with the conventional sampling technique, i.e., MCS. The proposed method will benefit the process of deriving distributions of long-term loss given different scenarios as well as the process of decision making.

ACKNOWLEDGEMENTS

The work described in this paper was substantially supported by Hong Kong Metropolitan University Research Grant (No. RD/2022/1.3).

REFERENCES

- Cheng, M. & Frangopol, D. M. 2022. Life-cycle optimization of structural systems based on cumulative prospect theory: Effects of the reference point and risk attitudes. *Reliability Engineering & System Safety*, 218, 108100.
- Giouvanidis, A. I. & Dong, Y. 2020. Seismic loss and resilience assessment of single-column rocking bridges. *Bulletin of earthquake engineering*, 18, 4481–4513.
- Goda, K. & Hong, H. 2006. Optimal seismic design considering risk attitude, societal tolerable risk level, and life quality criterion. *Journal of Structural engineering*, 132, 2027–2035.
- Goda, K. & Hong, H. 2008. Application of cumulative prospect theory: Implied seismic design preference. *Structural Safety*, 30, 506–516.
- Jaynes, E. T. 1957. Information theory and statistical mechanics. *Physical review*, 106, 620.
- Johnson, N. L., Kotz, S. & Balakrishnan, N. 1995. *Continuous univariate distributions, volume 2*, John Wiley & sons.
- Li, G. & Zhang, K. 2011. A combined reliability analysis approach with dimension reduction method and maximum entropy method. *Structural and Multidisciplinary Optimization*, 43, 121–134.
- Li, Y., Dong, Y. & Qian, J. 2020. Higher-order analysis of probabilistic long-term loss under nonstationary hazards. *Reliability Engineering & System Safety*, 203, 107092.
- Pandey, M. D. & Van Der Weide, J. 2017. Stochastic renewal process models for estimation of damage cost over the life-cycle of a structure. *Structural Safety*, 67, 27–38.
- Pandey, M. D. & Van Der Weide, J. 2018. Probability distribution of the seismic damage cost over the life cycle of structures. *Structural Safety*, 72, 74–83.
- Rahman, S. & Xu, H. 2004. A univariate dimension-reduction method for multi-dimensional integration in stochastic mechanics. *Probabilistic Engineering Mechanics*, 19, 393–408.
- Wang, C. & Zhang, H. 2018. Probability-based estimate of tropical cyclone damage: An explicit approach and application to Hong Kong, China. *Engineering Structures*, 167, 471–480.
- Xu, H. & Rahman, S. 2004. A generalized dimension-reduction method for multidimensional integration in stochastic mechanics. *International Journal for Numerical Methods in Engineering*, 61, 1992–2019.
- Xu, J. & Kong, F. 2019. Adaptive scaled unscented transformation for highly efficient structural reliability analysis by maximum entropy method. *Structural Safety*, 76, 123–134.
- Xu, J., Zhang, Y. & Dang, C. 2020. A novel hybrid cubature formula with Pearson system for efficient moment-based uncertainty propagation analysis. *Mechanical Systems and Signal Processing*, 140, 106661.
- Zhao, Y. G. & Ono, T. 2001. Moment methods for structural reliability. *Structural safety*, 23, 47–75.
- Zhu, D., Li, Y., Dong, Y. & Yuan, P. 2021. Long-term loss assessment of coastal bridges from hurricanes incorporating overturning failure mode. *Advances in Bridge Engineering*, 2, 1–15.

Effects of high temperature on web crippling strength of lean duplex stainless steel tubular sections

Yancheng Cai, Chi-Chung Lee & Shu-Lun Mak

Department of Construction and Quality Management, Hong Kong Metropolitan University, Hong Kong

Liping Wang

School of Civil Engineering, Central South University, Changsha, China

Feng Zhou

Department of Structural Engineering, Tongji University, Shanghai, China

ABSTRACT: In this paper, non-linear finite element models were developed for the web crippling of cold-formed lean duplex stainless steel (CFLDSS) square and rectangular hollow sections under the concentrated interior bearing loads at elevated temperatures (up to 950 °C). The interior bearing loads cover the loading conditions of Interior-One-Flange (IOF) and Interior-Two-Flange (ITF). The web crippling design rules in the current international specifications were examined. It was found that the predictions by the North American Specification were generally unconservative and not reliable, while the European Code provided reliable but very conservative predictions. New design method, the Direct Strength Method, was proposed for the web crippling strength of CFLDSS tubular sections at elevated temperatures under the loading conditions of IOF and ITF. The assessments indicate that the new method provides better strength predictions than the codified design rules. The new predictions are overall conservative and reliable.

1 GENERAL INSTRUCTIONS

The excellent properties of stainless steel, such as corrosion resistance with low life cycle costs, and fire resistance, make it suitable for a wide range of applications in engineering structures. The alloying elements of stainless steel have been continually developed for the goal of better mechanical properties, and higher corrosion resistance in high temperature application (Ronald et al. 2007). The relatively new stainless steel, lean duplex stainless steel is a high strength material with nominal 0.2% proof stress of 450 MPa. It offers higher strength than the traditional stainless steel, but has superior economic advantages due to its lower nickel content (around 1.5%), as the cost mainly depends on the nickel price. Therefore, it is becoming an attractive choice as a construction material in civil and structural engineering industry. In the last decade, great progress has been made in understanding the structural performance and design criteria of lean duplex stainless steel, including fundamental material properties (Saliba & Gardner, 2013), and structural members, such as beams (Huang & Young, 2014), columns (Zhao et al. 2015), and the bolted connections (Cai & Young 2014a).

However, it should be noted that these investigations were conducted at room (ambient) temperature condition instead of at elevated temperatures. It has been recognized that stainless steel has better strength and stiffness retention than carbon steel at elevated temperatures. This superior performance has been utilized in the high temperature industry for many years (Gardner et al. 2010). In the last few years, attention has been received to investigate the structural performance of stainless steel structures at elevated temperatures, for examples of tubular joints (Feng & Young, 2012), and bolted connections (Cai & Young, 2014b, 2018).

However, limited investigations have been conducted on stainless steel undergoing web crippling at elevated temperatures.

It is proposed herein to investigate the behavior of cold-formed lean duplex stainless steel (CFLDSS) tubular sections undergoing web crippling under interior loading conditions at elevated temperatures. The sections are under the interior loading conditions of Interior-One-Flange (IOF) and Interior-Two-Flange (ITF) at the nominal elevated temperatures ranged from 22 to 950 °C. The web crippling strength design rules at room temperature in the current codified design rules (EC 3-1.3, 2006, NAS, 2016) are examined for the possibility of application at elevated temperatures. The reduced material properties due to elevated temperatures were used in calculating the strength predictions. Finally, a new design method, the Direct Design Method (DSM), is proposed, which provide better strength predictions than the current codified design rules.

2 SUMMARY OF EXPERIMENTAL INVESTIGATION

The tests carried out by Cai and Young (2019b) for cold-formed lean duplex stainless steel (CFLDSS) tubular sections subjected to web crippling failure under concentrated interior bearing loads (IOF and ITF) were under room (ambient) temperature condition. The CFLDSS had square and rectangular hollow sections ($H \times B \times t$) with grades of EN 1.4162 (AISI S32101) and EN 1.4062 (AISI S32202), where H is the over height of the section web; B overall cross-sectional width, and t thickness of the section. The tensile coupon tests were carried out to obtain the material properties of the CFLDSS at room temperature condition, including the Young's modulus (E_r), 0.2% proof stress ($f_{0.2,r}$) and ultimate strength ($f_{u,r}$). Detailed descriptions of the coupon tests and web crippling tests are given in Cai and Young (2019a, b).

3 FINITE ELEMENT ANALYSIS

3.1 *Development of Finite element models*

The finite element (FE) models developed by the ABAQUS program of version 6.20 (2019) were used to simulate the web crippling tests of CFLDSS specimens. Four main components in the tests were modelled, namely, the section of CFLDSS, the steel bearing plates, the interactions between the steel bearing plates and specimen, and the boundary conditions.

The shell element type S4R, which is a four-node doubly curved element with reduced integration and hourglass control was selected to simulate the CFLDSS tubular sections. The CFLDSS members were modelled according to the centerline dimensions of the cross-sections. The solid element type C3D8R was chosen to simulate the steel bearing plates. The steel bearing plates were defined as rigid body as the steel bearing plates in the test program (Cai & Young 2019b) were fabricated by high strength steel with thickness of 50 mm, which are much thicker than the CFLDSS specimens. Contact pairs were used to model the interfaces between the CFLDSS sections and the bearing plates, with the bearing plates defined as master surface while the CFLDSS sections as slave surface. A coefficient of 0.4 was adopted to account for the friction penalty contact in the tangential direction. The geometrical nonlinearity of the FE models is considered by the NLGEOM command in ABAQUS (2019). Due to the symmetry of the geometries and failure modes of the test specimens, as well as the test setup under the IOF and ITF loading conditions (Cai & Young 2019b), half of the CFLDSS specimens and steel bearing plates were modelled by assigning appropriate symmetric boundary conditions.

The engineering stress-strain curves obtained from the tensile coupon tests were converted to true stress and logarithmic plastic strain curves. The true stress and logarithmic plastic strain curve was then imitated by means of a piecewise linear stress-strain model, especially, over the strain-hardening region. The material properties were assigned to the webs and flanges of the sections. Displacement control loading method and the general static analysis method were used in FE analysis. Detail of the development of FE models are described in Cai et al. (2021).

3.2 Validation of FE models

A total of 34 CFLDSS tubular sections tested by Cai and Young (2019b) at room temperature condition were analyzed. The comparisons of the web crippling strengths (P_t) per web obtained from the test program with those obtained from the finite element results ($P_{FE,r}$) are shown in Table 1. It is shown that a good agreement was generally achieved between test and FE strengths. The mean values of the $P_t/P_{FE,r}$ for the IOF and ITF specimens are 1.10 and 1.08, respectively; with the same corresponding coefficient of variation (COV) of 0.063. The test strengths are generally slightly higher than the predictions from the FE analysis. This could be due to the flat tensile material properties instead of the compressive material properties were used in the webs. The observed failure modes from the tests are well predicted by the FE analysis for the two different loading conditions are illustrated in Figure 1. In summary, the comparisons indicate that both the failure modes and the ultimate web crippling strengths from the test program could be replicated by the results of the FE analysis. Detail of the strength comparison between tests and FE analysis are presented in Cai et al. (2021).

Table 1. Overall comparison of test strengths with finite element predictions (Cai et al. 2021).

Loading condition	Number of tests		$P_t/P_{FE,r}$
IOF	16	Mean	1.10
		COV	0.063
ITF	18	Mean	1.08
		COV	0.063

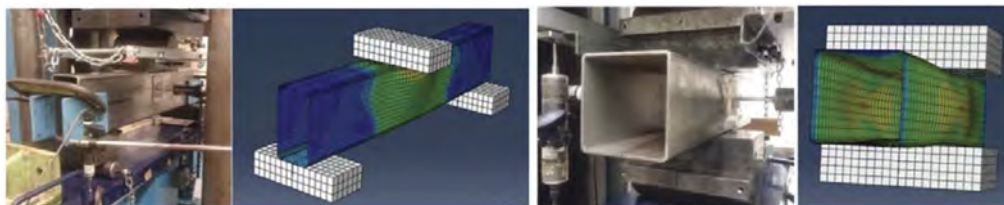


Figure 1. Comparison of tests and FE models for IOF (*upleft*) and ITF (*upright*) (Cai, et al. 2021).

Table 2. Material properties at elevated temperatures (Cai & Young, 2014b).

Material properties	Nominal Temperature (°C)						
	22 [#]	200	350	500	650	800	950
E_T (GPa)	200	190	183	169	160	60.4	13.5
$f_{0.2,T}$ (MPa)	724	564	508	448	304	119	18.0
$f_{u,T}$ (MPa)	862	710	696	627	358	138	25.0

Note: “#” represents room (ambient) temperature.

4 PARAMETRIC STUDIES AND ANALYSIS

The validated FE models were used to generate numerical data for the CFLDSS tubular sections under the IOF and ITF loading conditions at elevated temperatures. The numerical investigation in this study generally simulates the test procedure of steady state tests, where the specimens is heated to a pre-determined temperature level without any preloading, the specimen will then be loaded until failure while the specimen temperature is maintained. The material properties of CFLDSS at elevated temperature conditions were used. The stress-strain curves of the tensile flat coupons in the longitudinal direction of CFLDSS (grade EN 1.4162) rectangular section at elevated temperatures were used. These stress-strain curves were measured at elevated temperature

using steady state test method by Cai and Young (2014b), including Young's modulus (E_T), 0.2% proof stress ($f_{0.2\%,T}$) and ultimate strength ($f_{u,T}$) at elevated temperatures are presented in Table 2.

A total of 140 specimens at elevated temperatures, i.e. 22 (room temperature), 200, 350, 500, 600, 800 and 950 °C were analysed in the parametric study. The design of the CFLDSS tubular sections was done by considering the key parameters in the web crippling design rules (EC 3-1.3, 2006, NAS, 2016) for steel tubular sections. These tubular sections include five rectangular and five square hollow sections ($H \times B \times t$). The variation of the key parameters in these sections cover a wide range, including $h/t = 21.0 \sim 145.0$ and $N/h = 0.36 \sim 1.24$, where h is the flat web height. The specimens were generally identified by three segments in the labelling, as shown in Table 3. For example of specimen IOF250×250×2.0N250, where the first segment "IOF" indicates the loading condition of "Interior-One-Flange"; the following segment of "250×250×3.0" means the section dimension of " $H \times B \times t$ " in the unit of mm; and the last segment "N250" indicates that the loading plate with bearing length (N) of $N = 60$ mm was used in the test specimen.

Table 3. Web crippling strength (kN) of specimens per web in parametric study (Cai et al. 2021).

Specimen labelling	22 [#] °C	200 °C	350 °C	500 °C	650 °C	800 °C	950 °C
IOF250×250×2.0N125	44.7	37.2	34.6	30.8	22.6	8.8	1.6
IOF250×250×2.0N250	51.0	43.0	40.0	35.8	26.2	10.2	1.9
IOF250×250×5.0N125	240.1	199.6	186.9	164.7	119.1	46.3	8.4
IOF250×250×5.0N250	289.0	242.1	225.4	200.7	144.8	56.4	10.3
IOF250×250×12.0N250	1143.0	923.5	871.5	754.0	514.6	200.0	35.0
IOF300×200×2.0N200	48.7	41.1	38.2	34.2	25.0	9.7	1.8
IOF300×200×5.0N100	223.2	185.2	173.6	152.6	109.9	42.7	7.8
IOF300×200×5.0N200	272.8	227.3	211.3	187.5	135.6	52.7	9.6
IOF300×200×12.0N100	885.7	727.5	694.7	610.3	404.2	155.4	28.0
IOF300×200×12.0N200	1090.8	885.5	837.1	726.7	494.9	192.7	33.9
ITF250×250×2.0N125	33.2	30.0	28.3	26.0	20.9	8.3	1.7
ITF250×250×2.0N250	37.7	34.0	32.1	29.5	23.7	9.3	1.8
ITF250×250×5.0N125	250.1	210.7	196.7	174.8	126.6	49.4	9.1
ITF250×250×5.0N250	284.6	241.6	225.9	201.8	149.8	59.1	11.0
ITF250×250×12.0N250	1320.7	1079.0	1024.4	890.6	610.6	237.3	42.6
ITF300×200×2.0N200	33.1	30.5	29.0	26.7	22.1	8.7	1.8
ITF300×200×5.0N100	243.2	202.9	190.7	167.9	119.2	46.3	8.4
ITF300×200×5.0N200	275.9	234.5	218.5	195.6	144.0	56.0	10.4
ITF300×200×12.0N100	978.1	802.7	767.5	672.9	445.9	170.0	30.7
ITF300×200×12.0N200	1254.1	1025.6	969.7	845.1	581.3	225.3	40.4

Note: "#" represents room (ambient) temperature.

The ultimate strengths ($P_{FE,T}$) of the CFLDSS specimens per web at elevated temperatures are shown in Table 3. The reduction factors of web crippling strengths for CFLDSS specimens were obtained by normalizing the strengths at elevated temperatures ($P_{FE,T}$) with that at room temperature ($P_{FE,r}$) for the same specimen at elevated temperatures. As shown in Figure 2, these reduction factors were compared with those of material properties of CFLDSS at elevated temperatures, i.e. the reduction factors of E_T/E_r and $f_{0.2,T}/f_{0.2,r}$. The reduction factors of E_T/E_r overestimated the residual strengths of the specimens, while those of $f_{0.2,T}/f_{0.2,r}$ underestimated the residual strengths of the specimens in the temperatures ranged from 200 to 950 °C. Nevertheless, both reduction factors of E_T/E_r and $f_{0.2,T}/f_{0.2,r}$ show similar reduction trends to those of $P_{FE,T}/P_{FE,r}$.

5 CURRENT DESIGN RULES AND ASSESSMENT

5.1 General

The current codified web crippling design rules of stainless steel members are mainly based on those of carbon steel members. The differences of the design rules in current design specifications are discussed in Cai and Young (2019a). In this study, the design rules in North

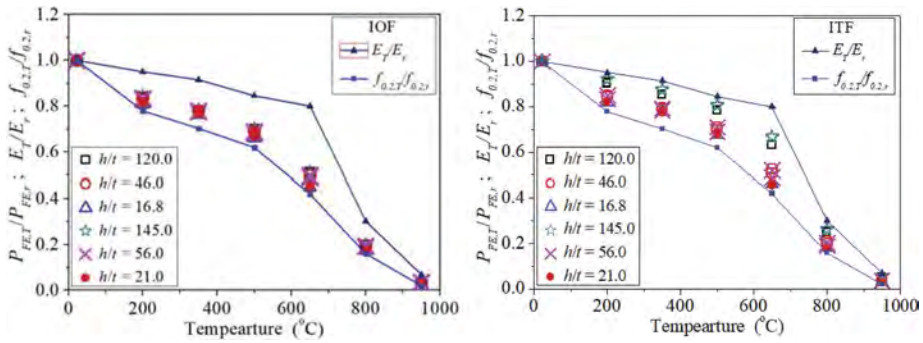


Figure 2. Comparison of reduction factors for IOF (*upleft*) and ITF (*upright*) loading conditions (Cai, et al. 2021).

American Specification (NAS, 2016) and European code (EC 3-1.3, 2006) were used. It should be noted that these design rules are only applicable for room temperature condition, but not for elevated temperature conditions. When calculating the nominal strengths, the reduced material properties (Table 2) of CFLDSS due to elevated temperatures were used. Reliability analysis was used to assess the web crippling design rules. The analysis was performed following the Commentary in the ASCE Specification (2002). The reliability index (β) of 2.5 was set in this study. The β was calculated by using the corresponding resistance factor (ϕ) specified in the design codes. Details of the analysis procedure are presented in Cai et al. (2021).

5.2 Assessment of current predictions

The ultimate strengths ($P_{FE,T}$) per web at elevated temperatures were compared with those predicted by the aforementioned design specifications. Table 4 summarizes the comparisons, where the comparisons were also presented at each temperature level.

Table 4. Comparison of test strengths with predicted strengths (Cai et al. 2021).

Temperature		IOF			ITF		
		P_{FE}/P_{NAS}	P_{FE}/P_{EC}	$P_{FE}/P_{DSM,T}$	P_{FE}/P_{NAS}	P_{FE}/P_{EC}	$P_{FE}/P_{DSM,T}$
22 °C [#]	Mean	0.80	3.27	0.95	0.63	6.30	0.90
	COV	0.109	0.152	0.163	0.095	0.165	0.116
200 °C	Mean	0.85	3.15	1.13	0.69	6.24	1.10
	COV	0.120	0.162	0.155	0.076	0.147	0.096
350 °C	Mean	0.88	3.17	1.21	0.73	6.31	1.19
	COV	0.112	0.155	0.139	0.069	0.140	0.088
500 °C	Mean	0.88	3.10	1.22	0.73	6.24	1.21
	COV	0.121	0.164	0.137	0.068	0.135	0.079
650 °C	Mean	0.93	2.77	1.58	0.80	5.74	1.63
	COV	0.153	0.191	0.129	0.108	0.144	0.064
800 °C	Mean	0.92	2.80	1.18	0.80	5.84	1.24
	COV	0.155	0.193	0.041	0.117	0.150	0.099
950 °C	Mean	1.11	2.77	1.60	0.99	5.97	1.75
	COV	0.169	0.207	0.200	0.153	0.165	0.266
Overall	Mean	0.91	3.00	1.27	0.77	6.09	1.29
	COV	0.169	0.179	0.228	0.176	0.148	0.263
	ϕ	0.90	0.91	0.80	0.80	0.91	0.80
	β	1.79	5.56	2.92	1.59	8.43	2.75

Note: “[#]” represents room (ambient) temperature.

For the IOF loading condition at each temperature, the predictions by the NAS (2016) are unconservative except for the temperature level of 950 °C due to the mean values smaller than

1.0; while the predictions by EC 3-1.3 (2006) are conservative. The conservative predictions are mainly due to the web slenderness ratio (h/t) and the actual bearing lengths (N) are not considered in the design provisions of EC 3-1.3 (2006), as discussed by Cai and Young (2019a). Note that the CFLDSS specimen sections have different web slenderness (h/t) and were loaded by steel plates with different bearing lengths (N). Similarly, for the CFLDSS specimens subjected to ITF loading condition, the predictions by the NAS (2016) are unconservative while those by EC 3-1.3 (2006) are conservative at each temperature levels.

The overall mean value of FE strength-to-predicted strength with the corresponding COV are also illustrated in Table 4. For IOF loading condition, the overall mean value for the predictions by NAS (2016) is 0.91, with the corresponding COV of 0.169. The predictions by NAS (2016) are not reliable due to the values of $\beta = 1.79$ that is smaller than 2.5. The predictions by EC3-1.3 (2006) are very conservative but reliable. Similarly, for ITF loading condition, the mean value for the predictions by NAS (2016) is 0.77 and the predictions are not reliable due to the $\beta < 2.5$. However, the overall predictions by EC3-1.3 (2006) are reliable but very conservative.

6 PROPOSED DIRECT STRENGTH METHOD AND ASSESSMENT

6.1 General

The predictions by the NAS (2016) were generally unconservative and not reliable while those by EC3-1.3 (2006) were very conservative and reliable. Hence, improvements were made for the web crippling design of CFLDSS tubular sections at elevated temperatures. The Direct Strength Method (DSM) (2008) is an alternative way to determine the strength of cold-formed steel members. The DSM has been developed and documented in the design specifications, such as the NAS (2016) for the design of steel beams and columns. It should be noted that the current DSM in design specifications does not provide design rules for web crippling design of cold-formed steel members. In this study, efforts on the DSM modifications are made for its application to web crippling design of CFLDSS tubular sections at elevated temperatures,

6.2 Modified DSM

The presented format of DSM in Cai and Young (2021) for web crippling design of CFLDSS stainless steel sections at room temperature is illustrated in Equation (1), where different sets of coefficient for a , b , n , γ and λ_k in Equation (1) were proposed depending on the loading conditions. The two different types of web crippling failure for cold-formed stainless steel square and rectangular hollow sections are, web buckling, where the web crippling capacity mainly depends on the stiffness of the material, and yielding in the web, where the web crippling capacity mainly depends on the yield strength of the material (Zhou & Young 2013). As presented in Figure 2, the reduction factors of web crippling strength, $f_{0.2,T}/f_{0.2,r}$ and E_T/E_r of CFLDSS sections depicted similar reduction trends at elevated temperature. The factor χ as shown in Equation (2) was proposed to account for the effects of reduction factors of $f_{0.2,T}/f_{0.2,r}$ and E_T/E_r at elevated temperatures. To be consistent with the design at room temperature condition, the $f_{0.2,T}$ and E_T at elevated temperatures were considered in this study. The CFLDSS tubular sections subjected to web crippling ($P_{DSM,T}$) at elevated temperatures could then be calculated by χP_{DSM} , as shown in Equation (3).

$$P_{DSM} = \begin{cases} \gamma P_{y,T} & \lambda \leq \lambda_k \\ a \left[1 - b \left(\frac{P_{cr,T}}{P_{y,T}} \right)^n \right] \left(\frac{P_{cr,T}}{P_{y,T}} \right)^n P_{y,T} & \lambda > \lambda_k \end{cases} \quad (1)$$

$$\chi = \frac{1}{0.0036} \frac{f_{0.2,T}}{E_T} \quad (2)$$

$$P_{DSM,T} = \chi P_{DSM} \quad (3)$$

where $\lambda = (P_{y,T}/P_{cr,T})^{0.5}$ is the web crippling slenderness ratio. The $P_{cr,T}$ and $P_{y,T}$ are respectively the nominal bearing strengths per web for buckling and yielding at elevated temperatures. The

calculations of $P_{cr,T}$ and $P_{y,T}$ could be done manually by referring Clause 5.13 of the AS 4100 (1998), as shown in Equations (4)-(7). It should be noted that these equations are provided for the design at room temperature condition (AS 4100, 1998), but not for elevated temperatures. Therefore, the $f_{0.2,r}$ was replaced by $f_{0.2,T}$ at elevated temperatures in calculations.

$$P_{cr} = \alpha_c t N_m f_{0.2,T} \quad (4)$$

where α_c is the slenderness reduction factor as specified in Clause 6.3.3 of the AS 4100 (1998), N_m is the mechanism length for the loading conditions of IOF an ITF, which could be determined by the following Equation (5):

$$N_m = N + 5R + h \quad (5)$$

where R is the outer corner radius.

$$P_y = \alpha_p t N_m f_{0.2,T} \quad (6)$$

$$\alpha_p = \frac{0.5}{k_s} \left[1 + \left(1 - \alpha_{pm}^2 \right) \left(1 + \frac{k_s}{k_v} - \left(1 - \alpha_{pm}^2 \right) \frac{0.25}{k_v^2} \right) \right] \quad (7)$$

where $k_s = 2R/t - 1$, $\alpha_{pm} = 1/k_s + 0.5/k_v$ and $k_v = h/t$.

Table 5. Coefficients for the design by DSM (Cai et al. 2021).

Loading condition	a	b	n	λ_k	γ	ϕ
IOF & ITF	1.00	0.18	0.45	0.60	1.13	0.80

In this study, different values of a , b , n , λ_k , γ and ϕ were proposed, as shown in Table 5. These are applicable for CFLDSS square and rectangular hollow sections having stiffened or partially stiffened flanges with the limits for $10 \leq h/t \leq 145$, $r/t \leq 2.0$, $N/t \leq 150$ and $N/h \leq 1.5$.

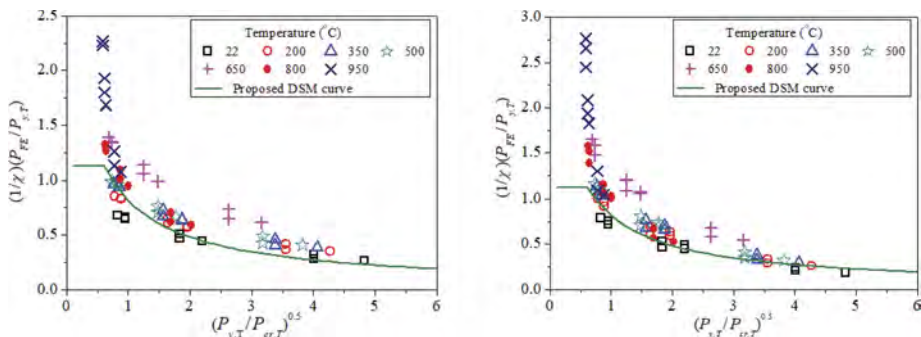


Figure 3. Comparison of FE results with proposed DSM curve for IOF (upleft) and ITF (upright) (Cai, et al. 2021).

6.3 Assessment of proposed DSM predictions

The strength predictions by the proposed DSM ($P_{DSM,T}$) were compared with those FE results, as shown in Table 4. The proposed DSM ($P_{DSM,T}$) for the web crippling strengths of CFLDSS tubular sections at elevated temperature generally provided conservative predictions at each temperature level, except at 22 °C. For each loading condition, the overall conservative predictions are mainly due to the very conservative predictions for the strengths at the temperature levels of 650 and 950 °C as reflected in the mean values of $P_{FE}/P_{DSM,T}$. The predictions by using the proposed DSM are reliable for the two loading conditions at elevated temperatures as the values of $\beta > 2.5$. The comparisons of the $P_{FE}/P_{DSM,T}$ at elevated temperatures together with the DSM curves (using Equations (1-3)) for the two loading conditions are shown in Figure 3. In each figure, the ratio of $(1/\chi)(P_{FE}/P_{y,T})$ were plotted against the web crippling slenderness ratio of $(P_{y,T}/P_{cr,T})^{0.5}$.

7 CONCLUSIONS

Non-linear finite element models were developed for the web crippling of cold-formed lean duplex stainless steel (CFLDSS) square and rectangular hollow sections under the loading conditions of Interior-One-Flange (IOF) and Interior-Two-Flange (ITF). After successful verification, an extensive parametric study of 140 CFLDSS tubular sections at elevated temperatures up to 950 °C was performed. The assessments showed the predictions by the NAS (2006) were generally unconservative and not reliable while those by EC3-1.3 (2006) were very conservative and reliable. The Direct Strength Method (DSM) was proposed. It is shown that the predictions by using the DSM are generally conservative and reliable. Therefore, the DSM is applicable for web crippling (loading conditions of IOF and ITF) design of CFLDSS tubular hollow sections at elevated temperatures with limits of $21 \leq h/t \leq 145$, $r_f/t \leq 2.0$, $N/t \leq 125$ and $N/h \leq 1.25$. The flanges of the CFLDSS tubular sections are stiffened or partially stiffened that unfastened to the supports.

ACKNOWLEDGEMENT

The work described in this paper was substantially supported by Hong Kong Metropolitan University Research Grant (No. RD/2022/2.1).

REFERENCES

- ABAQUS. 2019. Analysis User's Manual, ABAQUS, Inc., Version 6.20.
- ASCE. 2002. *Specification for the design of cold-formed stainless steel structural members*. American Society of Civil Engineers (ASCE), ASCE Standard, SEI/ASCE-8-02, Reston, Virginia.
- Australian Standard (AS). 1998. *Steel structures*. AS 4100, Sydney, Australia: Standards Australia; 1998.
- Cai, Y. & Young, B. 2014a Structural behavior of cold-formed stainless steel bolted connections. *Thin-Walled Structures*, 83: 147–156.
- Cai, Y. & Young, B. 2014b. Behavior of cold-formed stainless steel single shear bolted connections at elevated temperatures. *Thin-Walled Structures*, 75: 63–75.
- Cai, Y. & Young, B. 2018. Bearing resistance design of stainless steel bolted connections at ambient and elevated temperatures. *Steel and Composite Structures, An International Journal*, 29(2): 273–286.
- Cai, Y. & Young, B. 2019a. Web crippling of lean duplex stainless steel tubular sections under concentrated end bearing loads. *Thin-Walled Structures*, 134: 29–39.
- Cai, Y. & Young, B. 2019b. Cold-formed lean duplex stainless steel tubular members under concentrated interior bearing loads. *Journal of Structural Engineering*, 145(7): 04019056.
- Cai, Y., Wang, L. & Zhou, F. 2021. Lean duplex stainless steel tubular sections undergoing web crippling at elevated temperatures. *Journal of Constructional Steel Research*, 182: 106681.
- Cai, Y. & Young, B. 2021. Web crippling design of lean duplex stainless steel tubular members under interior loading conditions. *Engineering Structures*, 238: 112192.
- EC 3-1.3. 2006. *Eurocode 3: Design of steel structures - Part 1-3: General rules - Supplementary rules for cold-formed members and sheeting*. EN 1993-1-3, Brussels: European committee for standardization.
- Feng, R. & Young, B. 2012. Design of cold-formed stainless steel tubular joints at elevated temperatures. *Engineering Structures*, 35: 188–202
- Gardner, L., Insaustia, A., Ng, K.T. & Ashraf, M. 2010. Elevated temperature material properties of stainless steel alloys. *Journal of Constructional Steel Research*, 66 (5): 634–647.
- Huang, Y. & Young, B. 2014. Experimental and numerical investigation of cold-formed lean duplex stainless steel flexural members. *Thin-Walled Structures*, 73: 216–228.
- North American Specification (NAS). 2016. *North American Specification for the design of cold-formed steel structural members*. AISI S100–16, Washington D. C.: American Iron and Steel Institute (AISI).
- Ronald, L.P., Clara, H., Doris, M.E., Paulo, R.R. & Angelo, F.P. 2007. A Short Review on Wrought Austenitic Stainless Steels at High Temperatures: Processing, Microstructure, Properties and Performance. *Materials Research*, 10 (4): 453–460.
- Saliba, N. & Gardner, L. 2013. Cross-section stability of lean duplex stainless steel welded I-sections. *Journal of Constructional Steel Research*, 18: 1–14.
- Zhao, O., Rossi, B., Gardner, L. & Young, B. 2015. Behaviour of structural stainless steel cross-sections under combined loading-Part II: Numerical modelling and design. *Engineering Structures*, 89: 247–259.
- Zhou, F. & Young, B. 2013. Web crippling behaviour of cold-formed duplex stainless steel tubular sections at elevated temperatures. *Engineering Structures*, 57: 51–62.

Risk-based fatigue assessment of orthotropic steel decks

J. Heng

Shenzhen University, Shenzhen, China
University of Birmingham, Birmingham, UK

Y. Dong

The Hong Kong Polytechnic University, Hong Kong, China

C. Baniotopoulos & S. Kaewunruen

University of Birmingham, Birmingham, UK

ABSTRACT: The orthotropic steel deck (OSD) shows notable superiorities in bridge applications but is highly prone to fatigue cracking due to the use of massive welded connections, especially in the rib-to-deck (RD) connection. This study presents a risk-based approach to planning different management strategies for OSDs under fatigue, which is supported by the integrated fatigue assessment coupling test data, in-situ measurements and probabilistic simulations. RD connections are focused on since they account for the longest welding length, i.e., about 50 times the total bridge length. The probability-stress-life (P-S-N) curve is first derived for RD connections from fatigue test data. Meanwhile, a condition-based probabilistic model of vehicle loads is constructed using the site-measured data. The load model is then implemented with numerical simulations in a sampling-based manner to derive fatigue stress spectra of different fatigue-critical RD connections. Based on the derived P-S-N curve and stress spectra, the fatigue deterioration of RD connections is assessed in a probabilistic form. Moreover, the failure assessment diagram (FAD) is derived for OSDs considering the serviceability, in accordance with the estimation of associated consequences. Based on the probabilistic estimation, the risk assessment is carried out for the OSD by combining the probability of failure and associated consequences.

1 INTRODUCTION

The orthotropic steel deck (OSD) is a highly redundant and integrated deck system that is extensively employed in large-span bridges, in which the light self-weight is of the first priority (Zou et al., 2022). The OSD consists of massive components connected via a copious number of welded connections (Heng et al., 2022). Especially, the rib-to-deck (RD) welded joint can even account for 50 times the total bridge length. Under this situation, fatigue cracking is frequently observed in OSDs after several decades of exploitations (Connor et al., 2012). As a result, the normal operation of the bridge will be greatly affected in the presence of excessive cracks within the same lane.

The fatigue issue of RD joints in OSDs has already been investigated with great efforts in the past 20 years due to its prominence and notable influence, including both fatigue resistance (Cheng et al., 2016), life prediction (Ye et al. 2017), and repair methods (Wang et al., 2021). However, some further efforts are still lacking from the aspect of risk assessments, which helps to offer different insights into the recurring fatigue cracking issue of OSDs.

This work aims to offer novel insights into the fatigue-induced risk of lane closures in the OSD bridge, which can provide constructive supports for the further management of OSDs with massive welded joints. In section 2, stress spectra of RD joints in different lateral locations are derived by combing the finite element simulation and condition-based random vehicle model. In section 3, fatigue prognosis is carried out using a multi-level failure assessment diagram, followed by the associated risk assessment of lane closures. In section 4, the major result and findings are discussed. Finally, key conclusions are drawn in Section 5.

2 DERIVATION OF FATIGUE STRESS

2.1 Illustration of the investigated bridge

In this study, a typical OSD bridge in the urban network of Chengdu, China is selected as the prototype, as shown in Figure 1. The selected bridge consists of three spans of 45 m (side), 68 m (main) and 45 m (side). In the length, the bridge is divided into a total of 112 segments, each of which has a similar configuration except for the varying sectional height. The width of bridge (in a single direction) is 12.5 m, carrying one fast lane, one middle lane and one slow lane. Beneath the three lanes, a total of 15 longitudinal ribs (also called as U-ribs) are distributed. Each U-rib is connected to the deck by two RD joints on its left and right sides. For better illustration, the U-ribs are named as 1 to 15 from left (fast lane) to right (slow lane), e.g., U1. Accordingly, the associated RD joint is coded with L (left) or R (right), e.g., U1L or U1R.



Figure 1. The typical OSD bridge selected for investigation (courtesy of Dr Junlin HENG).

2.2 Site-specific random traffic modelling

Based on the site-specific traffic data, the random vehicle load (RVL) model (Heng et al., 2019) can be established to simulate the fatigue action on RD joints by vehicles, as shown in Figure 2. In the RVL model, vehicles are classified into a total of six categories, mainly depending on the configuration of axles and functions. It can be found that, the light-weight car accounts for the highest proportion in both the three lanes, i.e., 76.67% in total traffic. Meanwhile, it is worth noting that the heavy trucks V5 and V6 show a highly similar occupancy rate in the middle and slow lanes. As a result, equal concerns should be paid to the fatigue cracking in RD joints of both the middle and slow lanes.

Instead of the gross vehicle weight, the load of each vehicle type is modelled in detail from axle-to-axle. Due to the presence of multi-peaks in the distribution of axle weights, the Gaussian mixed model (GMM) model is leveraged. Meanwhile, the lateral distribution of vehicle within the lane is also considered by fitting the discrete distribution by Eurocode 1 (CEN, 2003) to a Gaussian distribution. Further details about the RVL model could be found in (Guo et al., 2015).

Based on the RVL model, random sampling of vehicles can be carried out in a conditional sampling manner, as illustrated by Equation 1,

$$p(W_i) = p(VC) \cdot p(W_i|VC) \quad (1)$$

where VC standards for the vehicle category; W_i is the weight of the i th axle.

Meanwhile, in terms of the average daily traffic (ADT), the mean value of 10,605 and standard deviation of 2,121 can be derived from the observation data.







Category	Illustration	Occupancy rate (%)		
		Fast	Middle	Slow
V1		41.23	25.74	9.70
V2		0.03	0.26	0.36
V3		0.1	0.87	0.6
V4		0.04	0.67	0.92
V5		0.06	1.17	1.31
V6		0.57	7.94	8.43

Figure 2. Configuration of different vehicle types and lane occupancy rate.

2.3 FE-based derivation of fatigue stress

Multi-scale finite element (FE) model of the bridge is constructed, as shown in Figure 3. The model includes the global model of the bridge structure, the sub-model of the interested segment, and the local refined model of the RD joint. The 3-dimensional shell element SHELL63 is employed in the FE modelling. Since the global modelling aims to simulate the boundary condition at the structural level, a relatively coarse meshing size is employed (i.e., 50 mm in width and 100 mm in length). Then, the segment at the mid-span is selected for the sub-model, which employs a fine mesh size of 20×20 mm at the outer edge. Further, the RD joint is highly refined with a very fine element size of 4 mm.

The global model and sub-model are connected using the interpolation of nodal displacement at the interface, which is realised by multi-point constriction (MPC). Meanwhile, the local refine model is embedded in the sub-model by sharing nodes directly.

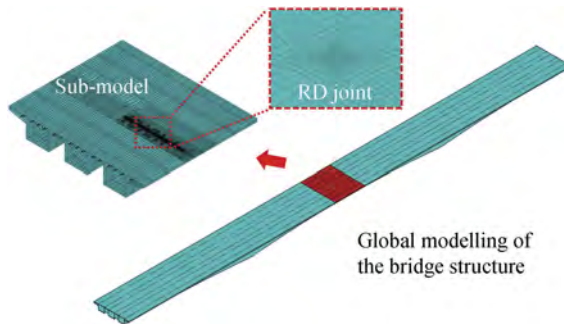


Figure 3. Finite element model of the selected bridge.

Based on the constructed FE model, the sampled vehicle can be transformed into the stress spectra of RD joints in different lateral positions, as shown in Figure 4. In the derivation, a total of 5,000,000 samples of vehicles are generated based on the RVL model discussed in Section 2.2. The influence surface technology (Heng et al., 2019) is employed to improve the solution efficiency, via which the loading of vehicles can be achieved by vector calculus. As indicated by the result, the RD joints in the fast lane (e.g., U4r) shows a low level of stress spectra due to the rare presence of heavy trucks in the lane. On the contrary, the similar RD joint in the middle lane (i.e.,

U9R) suggest a high-level stress distribution. Moreover, a very notable feature of multi-peaks can be found in the stress spectra. Moreover, the stress spectra also vary significantly within the same lane due to the lateral distribution of the car footprint. For instance, the RD joint U14L shows a very limited stress level since it is very close to the centre of the lane.

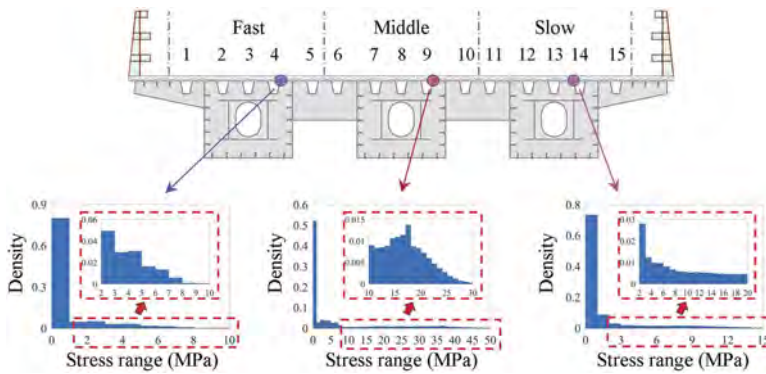


Figure 4. Stress spectra of different RD joints.

3 PROBABILISTIC PROGNOSIS AND RISK ASSEMENT

3.1 Fatigue damage model

The fatigue strength of RD joint is described using the probability-stress-life (P-S-N) curve, as illustrated by Equation 2,

$$\log(C) = m \cdot \log(\Delta\sigma_{ref}) + \log(N_{ref}) + \varepsilon \quad (2)$$

where C is a material constant marking the fatigue strength of RD joints; m is the power index, fixed as 3.0 in this work; $\Delta\sigma_i$ and N_i are respectively reference stress range and associated allowance number of loading cycle; ε stands for the uncertainty factor, which follows the lognormal distribution.

Based on the fatigue test data in (Zheng et al., 2019), the mean value of parameter C is determined as 2.27×10^{12} , while its coefficient of variance (COV) is solved as 0.59. For each RD joint, the fatigue limit state function (LSF) can be expressed by Equation 3,

$$g(D, t) = \Delta - D(t) \quad (3)$$

where $D(t)$ is the damage accumulation factor at time t ; Δ is the tolerance factor, assumed as 1.0 in this study.

Since the RD joint experience variant-amplitude fatigue action, the linear damage accumulation rule is employed in calculating the fatigue damage, as illustrated by Equation 4,

$$D(t) = \sum_i \frac{N_i \cdot \Delta\sigma_i^m}{N_{ref} \cdot \Delta\sigma_{ref}^m} \quad (4)$$

where $\Delta\sigma_i$ and N_i denote the i th applied stress range and number of loading cycle, respectively.

3.2 Failure assessment diagram and limit state functions

As aforementioned, the bridge is divided into 112 segments in the length direction. Accordingly, each lane can be also divided into 112 lane segments (LSs). Moreover, as depicted in Figure 4, each lane segment has five U-ribs and ten RD joints associated. To this end, the OSD system is idealized into a link-parallel mixed system, as indicated by the failure

assessment diagram (FAD) in Figure 5. In general, the OSD system consists of three parallel components, i.e., fast, middle and slow lanes. Then, each lane is further discretized into 112 LSs, which are also in the parallel relation. Finally, each LS is modelled by a linking system covering all the ten RD joints with the lane.

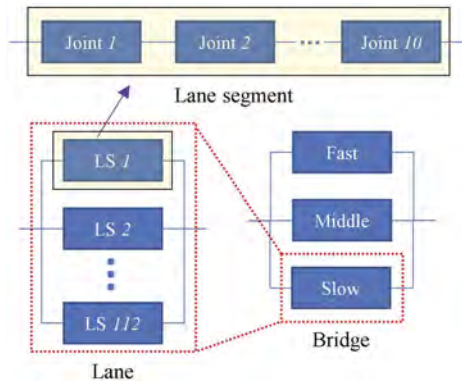


Figure 5. Failure assessment diagram of the OSD bridge.

As discussed earlier, excessive fatigue cracking within the same lane will result in mandatory lane closure due to its influence on the running safety of vehicles. To this end, after consulted with industrial colleague, the failure of the lane is assumed when the fatigue crack occurs in more than 10% of the 112 LSs, i.e., above 11 LSs. To this end, the possibility of occurrence can be further expressed for the closure in each lane, as illustrated by Equation 5,

$$p_{lc} = p(N_{f,LS} \geq 11) \quad (5a)$$

$$p_{f,LS} = \prod_{i=1}^{10} p_{f,joint}(i) \quad (5b)$$

where P_{lc} denotes the possibility of lane closure; $N_{f,LS}$ is the number of cracked lane segment; $P_{f,LS}$ is the failure probability of each lane segment; $P_{f,joint}(i)$ stands for the failure probability of i th RD joint in the lane.

3.3 Risk assessment model

Based on the above FAD, three scenarios are identified for potential risk of lane closures, i.e., one lane closure, two lanes closure and all the three lanes closure (i.e., the shutdown of the bridge). Accordingly, the associated costs can be estimated, as illustrated by Equation 6,

$$C_{LC} = (C_r + C_f + C_t) \cdot (1 + r_m)^t \quad (6)$$

where C_{LC} is the total cost for lane closure; C_r denotes the estimated repair cost; C_f is the fuel and abrasion cost of vehicles due to detour; C_t stands for the time value consumed by detour of vehicles; r_m is the annual discount rate of money, assumed as 1.5% in this study.

Detailed computation of the cost can be referred to a previous study (Zhu et al., 2016), while Table 1 lists the value considered in this study.

4 RESULT AND DISCUSSION

4.1 Fatigue reliability

Based on the proposed method, the fatigue reliability of each joint can be at first predicted, as shown in Figures 6a and b. Overall, the RD joints in the fast lane demonstrate the highest

Table 1. Key parameters for the consequence analysis.

Type	Symbol	Scenario of lane closure (in €)		
		One lane	Two lanes	Shutdown
Repair cost	C_r	93,000	166,183	230,247
Fuel cost	C_f	107,376	214,751	322,127
Time value	C_t	158,459	316,918	475,378

reliability due to the rare presence of heavy trucks. Meanwhile, very similar reliability can be found in the RD joints within the middle and slow lane, which is consistent with the distribution of heavy trucks V5 and V6. Figure 6b further plot a list of representative RD joints in the different lane. It is worth noting that the fatigue reliability of the RD joint is highly sensitive to its lateral position in the lane. For instance, the joint U14L shows the highest reliability while the nearby U14R suggests the third lowest reliability. Meanwhile, it is also revealed that the joint U12L in the slow lane is the most fatigue-critical detail. Based on the reliability prediction made using site-specific data, a tailored managing plan can be stipulated for the OSD bridge.

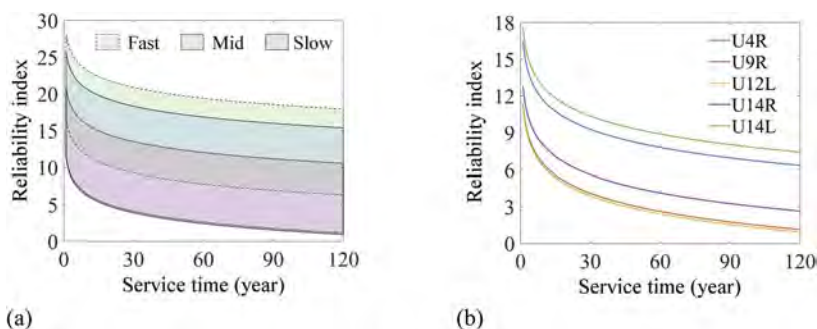


Figure 6. Reliability of welded joints: (a) distribution over lanes; (b) selected joints in different lanes.

Similarly, incorporating the FAD proposed in Figure 5, the fatigue reliability can be also assessed at the level of lane segments, as shown in Figure 7. Similar to the previous result, the middle and slow lanes show a very consistent evolution of reliability during the service life of the bridge. Meanwhile, a very prominent reliability is predicted for the fast lane due to the rare passing of heavy trucks.

In addition, the possibility of occurrence can also be estimated for the closure in different lanes, as shown in Figure 8a. Also, the fast lane is highly unlikely to closure due to the limited fatigue damage by light-weight cars. At the same time, the possibility of closure becomes very prominent in both the slow lane and middle lane as the bridge is approaching the end of its design life (i.e., 120 years in this study). Moreover, the three assumed scenarios are also investigated, as shown in Figure 8b. After about 80 years of service, the closure of a single lane becomes very notable. With the time further increase, the closure of two lanes is even apparent, while the closure of a single lane becomes unlikely. At the same time, the shutdown (i.e., the closure of all the three lane) seems to be a rare event during the entire service life.

4.2 Time-variant risk

The time-variant risk associated with the above different scenarios is also estimated, as shown in Figures 9a and b. Overall, the risk is relatively moderated before 80 years, indicating the guaranteed performance of OSDs as a highly integrated and redundant deck system. Meanwhile, it can be found that the largest risk originates from the scenario that two lanes are forced to closure. Figure 9b further investigates the contribution of the three scenarios.

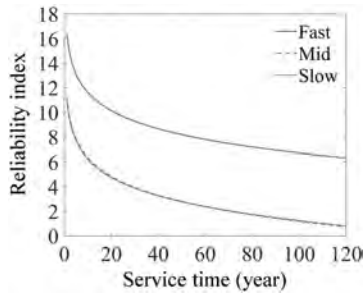


Figure 7. Reliability of lane segment.

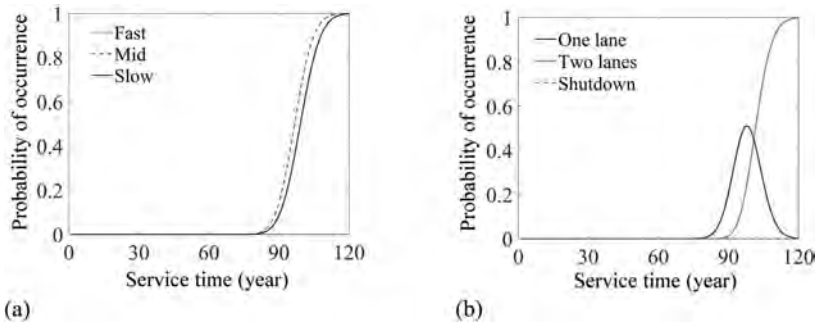


Figure 8. Probability of occurrence of lane closures: (a) different lane; (b) different scenarios.

Obviously, the “two lanes” event increase at a rapid rate and surpass the “one lane” event after roughly 100 years.

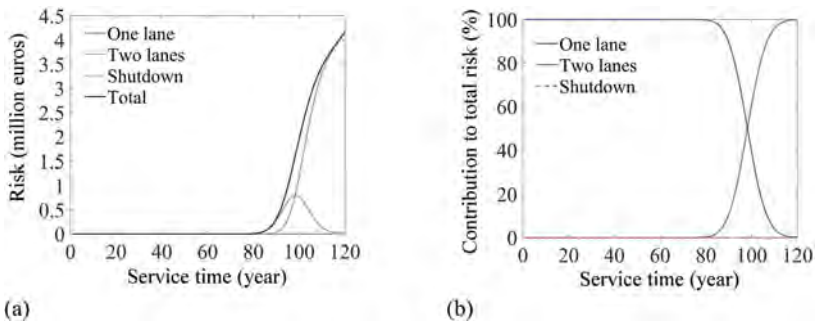


Figure 9. Time-variant risk due to fatigue: (a) different scenarios; (b) contribution of scenarios.

5 CONCLUSIONS

Based on the above investigation, the following key conclusions can be drawn.

- (1) The fatigue stress spectra in the rib-to-deck (RD) joints of orthotropic steel deck (OSD) bridges are controlled by both the lane type and lateral position within the lane. Due to the rare presence of heavy trucks in the fast lane, the stress level in all the RD joints is relatively low within the lane. Meanwhile, high fatigue stress is likely to occur in the RD joint close to the frequent foot print of vehicles. Accordingly, the fatigue damage of RD joints shows a very high sensitivity to the lane type lateral position within in the lane.

- (2) Both the middle lane and slow lane shows a similar possibility of closure, while it is a rare event for the closure of the fast lane. Different from the middle lane and slow lane, heavy trucks rarely select the fast lane. As a result, the mandatory closure of the slow lane is very unlikely to occur under the investigated traffic. To this end, more efforts are suggested to the slow lane and middle lane.
- (3) The one-lane and two lanes closure contribute remarkably to the risk of lane closure, while the shutdown scenario has little contribution. After about 80 years of service, the risk associated with the closure of a single lane becomes very notable, which is then surpassed by the closure of two lanes soon. Meanwhile, the risk of a shutdown is maintained at a very limited level during the entire service life.

ACKNOWLEDGEMENT

The support by National Natural Science Foundation of China (52208182), Natural Science Foundation of Shenzhen (JCYJ20220531101010020) and Marie Skłodowska-Curie Actions (MSCA) Fellowship via URKI (EP/X022765/1) is acknowledged with thanks by the authors.

REFERENCES

- Connor, R. J. (2012). Manual for design, construction, and maintenance of orthotropic steel deck bridges (No. FHWA-IF-12-027). United States. Federal Highway Administration.
- Cheng, B., Ye, X., Cao, X., Mbako, D., & Cao, Y. (2017). Experimental study on fatigue failure of rib-to-deck welded connections in orthotropic steel bridge decks. *International Journal of Fatigue*, 103, 157–167.
- CEN (European committee for standardization), EN 1991-2:2003 Eurocode 1: Actions on structures—part 2: traffic loads on bridges, CEN, Brussels, 2003.
- Guo, T., Liu, Z., Pan, S., & Pan, Z. (2015). Cracking of longitudinal diaphragms in long-span cable-stayed bridges. *Journal of Bridge Engineering*, 20(11), 04015011.
- Heng, J., Zheng, K., Kaewunruen, S., Zhu, J., & Baniotopoulos, C. (2019). Dynamic Bayesian network-based system-level evaluation on fatigue reliability of orthotropic steel decks. *Engineering Failure Analysis*, 105, 1212–1228.
- Heng, J., Zhou, Z., Zou, Y., & Kaewunruen, S. (2022). GPR-assisted evaluation of probabilistic fatigue crack growth in rib-to-deck joints in orthotropic steel decks considering mixed failure models. *Engineering Structures*, 252, 113688.
- Wang, Y., Shao, X., Chen, J., Cao, J., & Deng, S. (2021). UHPC-based strengthening technique for orthotropic steel decks with significant fatigue cracking issues. *Journal of Constructional Steel Research*, 176, 106393.
- Ye, X. W., Liu, T., & Ni, Y. Q. (2017). Probabilistic corrosion fatigue life assessment of a suspension bridge instrumented with long-term structural health monitoring system. *Advances in Structural Engineering*, 20(5), 674–681.
- Zheng, K., Feng, X., Heng, J., Zhu, J., & Zhang, Y. (2019). Fatigue reliability analysis of rib-to-deck joints using test data and in-situ measurements. *Applied Sciences*, 9(22), 4820.
- Zhu, B., & Frangopol, D. M. (2016). Time-variant risk assessment of bridges with partially and fully closed lanes due to traffic loading and scour. *Journal of Bridge Engineering*, 21(6), 04016021.
- Zou, Y., Yu, K., Heng, J., Zhang, Z., Peng, H., Wu, C., & Wang, X. (2022). Feasibility study of new GFRP grid web-concrete composite beam. *Composite Structures*, 116527.

Life-cycle management of offshore wind deteriorating structures under ship collision accidental events

P. Salazar L., J. Morán A. & P. Rigo

Department of Naval and Structural Engineering (ANAST), Liege, Belgium

P.G. Morato

Department of Wind and Energy Systems, Technical University of Denmark, Roskilde, Denmark

ABSTRACT: In conventional industrial practices, the structural performance is evaluated against deterioration mechanisms as well as extreme and/or accidental events. However, most existing approaches treat the aforementioned structural assessments separately. In this work, we identify system inspection and maintenance strategies by jointly modeling deterioration processes and accidental/extreme events within the overall life-cycle management optimization. In particular, the decision-making objective is formulated considering a system failure risk metric that depends on the damage caused by deterioration processes and accidental/extreme hazards. In order to enable efficient inference and uncertainty propagation, we propose an underlying probabilistic approach relying on dynamic Bayesian networks. The efficacy of the proposed approach is tested in a life-cycle management setting where the risk of an offshore wind frame substructure is controlled by timely allocating inspection and maintenance actions. Within the investigation, we also observe the influence of ship collision events frequency on the resulting asset management strategies.

1 INTRODUCTION

Civil and maritime infrastructures support societal development and are essential for economic growth. Among them, offshore wind turbines offer a sustainable solution towards the pursuit of achieving renewable energy generation. Engineering systems are, however, exposed to deterioration mechanisms throughout their service life along with occasional extreme and/or accidental events, thus inducing a risk of structural failure. There is a need, therefore, for life-cycle management capable of controlling structural failure risks while minimizing inspection and maintenance costs. Driven by modern data collection techniques, the development of decision-making methods has been intensified in the last decade (Frangopol & Soliman 2016). From a computational standpoint, the identification of life-cycle management strategies involves the solution of a challenging decision-making problem under uncertainty and imperfect information, in which the uncertainties associated with the estimation of deterioration processes and data collection systems should also be adequately quantified.

Early risk-based approaches frame the decision-making problem in a simplified decision tree, where inspections and maintenance decisions are selected based on static pre-defined heuristic rules, e.g. equidistant inspection intervals, and repairs undertaken following damage indications. Later on, heuristic-based methods are integrated with dynamic Bayesian networks (DBNs) via policy search simulations, thus providing more flexibility to the definition of the heuristic decision rules (Luque & Straub 2019). Heuristic-based policies are, however, limited by the fact that only a subset of the vast policy space is explored. Addressing this limitation, decision-making methods relying on Markov Decision Processes (MDPs) and Partially Observable MDPs (POMDPs) have been proven to provide optimal policies in high-dimensional space settings (Papakonstantinou & Shinozuka 2014, Morato et al. 2022a). In very high dimensional state, action, and observation spaces, normally characteristic of engineering systems planning problems, schemes integrating POMDP with deep reinforcement learning can efficiently identify optimal policies, resulting in substantial cost savings compared

to other heuristic-based and conventional management strategies (Andriotis & Papakonstantinou 2019, Morato et al. 2022b). The previously mentioned decision-making methods are usually applied so as to identify management strategies for deteriorating engineering components or systems. Yet, along with deterioration processes, engineering infrastructures are also occasionally exposed to extreme and/or accidental hazards. With respect to the latter, methods able to identify management strategies for engineering systems under extreme events have also been explored in the literature (Kumar et al. 2009). The severity and occurrence of extreme hazards are normally characterized as low-probability high-consequence events, (Stewart & Rosowsky 2022). In that case, the goal of adequate strategies generally involves controlling the vulnerability of affected structural systems, as well as mitigating human, social, environmental, and economic losses. However, high-probability low-consequence accidental events can also occur, and while they may be associated with less critical consequences, the structural reliability of the concerned engineering systems can be severely compromised. For example, offshore wind structures are exposed to multiple hazards throughout their lifetime, including extreme environmental loads and accidents, e.g. ship collisions. In conjunction with deterioration processes, damage due to high-probability low-consequence ship collisions detrimentally affects the capacity of offshore wind structural systems, rendering them potentially unable to withstand future hazards.

Most reported planning methods and conventional industrial practices deal with engineering systems exposed to either deterioration mechanisms or extreme events. In this work, we propose a probabilistic modeling framework based on dynamic Bayesian networks jointly treating deterioration processes and accidental/extreme events. Particularly, the system's structural reliability is formulated conditional on its components' reliability, whose evolution is modeled considering both probabilistic deterioration processes and accidental/extreme events. The proposed scheme constitutes the underlying probabilistic foundation, which integrated with heuristic- or POMDP- based decision-making methods, is able to provide management strategies for deteriorating engineering systems under accidental and/or extreme events. To test our approach, life-cycle management heuristic-based policies are identified for a structural system subject to fatigue deterioration and accidental ship collision events, also investigating the effect of accidental events occurrence and their intensity on the resulting strategies.

2 LIFE-CYCLE MANAGEMENT OF DETERIORATING STRUCTURES UNDER ACCIDENTAL AND/OR EXTREME EVENTS

In this section, we propose a probabilistic modeling approach based on dynamic Bayesian networks for the estimation and inference of the reliability of a structural system subject to both time-varying deterioration processes and accidental/extreme loads. Relying on computed system reliability metrics, along with inspection and maintenance costs, life-cycle management policies can then be identified via policy search simulations or Markov decision processes.

2.1 *Probabilistic modeling via dynamic Bayesian networks*

Encoding the conditional relationships among random variables, Bayesian networks are acyclic graphical models that enable robust inference based on observed information. Bayesian networks that track dependencies over time are commonly denoted temporal template models, or more generally, dynamic Bayesian networks (DBNs). By leveraging the inference capabilities featured by DBNs, the reliability of a structural system can be efficiently estimated. The overarching scheme for probabilistically modeling the reliability of a deteriorating structural system under accidental/extreme events over time is graphically shown in Figure 1. Chance nodes represent random variables and are bounded by circular edges in the graph, additionally filled with grey color if they are partially observable. Also, network template models are enclosed by a blue or green box, indicating whether they are repeated over components or intensity measures, respectively.

2.2 *Stochastic deterioration processes*

The damage condition state caused by a non-stationary deterioration process, e.g. fatigue or corrosion, can be updated over time based on collected information through a two-step

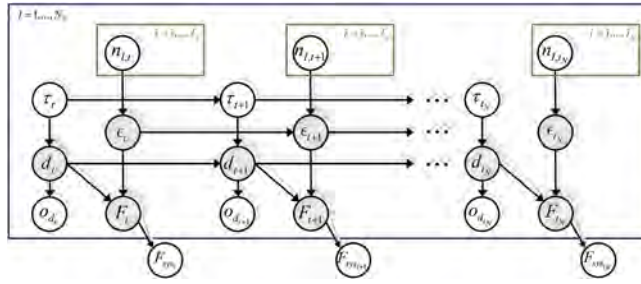


Figure 1. Overarching graphical representation of the proposed probabilistic approach. Damage evolution caused by both deterioration processes and accidental/extreme events is modeled over time through dynamic Bayesian networks. Each component's reliability is conditional on deterioration and accidental/extreme damage, whereas the system's reliability depends on the components' reliability.

process. Firstly, the joint state comprised of the damage condition, d_t , and the deterioration rate, τ_t while conditional on past observations, $\mathbf{o}_0, \dots, \mathbf{o}_t$, advances over time according to the transition model $p(d_{t+1}, \tau_{t+1} | d_t, \tau_t)$, as:

$$p(d_{t+1}, \tau_{t+1} | \mathbf{o}_0, \dots, \mathbf{o}_t) = \sum_{d_t} \sum_{\tau_t} p(d_{t+1}, \tau_{t+1} | d_t, \tau_t) p(d_t, \tau_t | \mathbf{o}_0, \dots, \mathbf{o}_t) \quad (1)$$

Based on the information collected from inspections or monitoring, the damage is then updated by applying Bayes' rule. The likelihood $p(\mathbf{o}_{t+1} | d_{t+1})$ can be directly defined from probability of detection curves or other observation uncertainty measures:

$$p(d_{t+1}, \tau_{t+1} | \mathbf{o}_0, \dots, \mathbf{o}_{t+1}) \propto p(\mathbf{o}_{t+1} | d_{t+1}) p(d_{t+1}, \tau_{t+1} | \mathbf{o}_0, \dots, \mathbf{o}_t) \quad (2)$$

2.3 Accidental and/or extreme events

Occasional accidental or extreme events can be categorized according to their severity and can be probabilistically modeled based on their occurrence rate. The frequency associated with an accidental event depends on the operational conditions, location, and specific characteristics of the structural system. Based on the specific frequency, annual event occurrences can be estimated, for example, through a Poisson random process. In Figure 1, the annual occurrence is depicted with the node n_I for each considered intensity measure, I , and graphically represented as a template model. The damage sustained due to accidental or extreme events, ϵ , can be then modeled conditional on annual event occurrence. In terms of reliability, a component or system limit state can be defined based on the structural damage, ϵ , and a case-dependent safety measure.

2.4 System structural reliability

At the system level, the failure event can be defined conditional on the component's failure probability, represented in Figure 1 with nodes F_{sys} and F , respectively (Morato et al. 2022b). And, as mentioned previously, the failure probability associated with each component depends, in turn, on the deterioration, d , and accidental, ϵ , damage condition.

2.5 Reliability-based robustness index

Along with reliability measures, quantifying the resistance of a structural system against accidental or extreme loads can also be informative for life-cycle management considerations. As explained by Biondini (2009), structural robustness can be measured by comparing the structural performance (e.g. reliability) of the system in a damaged state with respect to the system in an intact condition. A reliability-based robustness index, I_R , can be therefore formulated as (Frangopol & Curley 1987):

$$I_R = \frac{\beta_{sys,0}}{\beta_{sys,0} - \beta_{sys,d}} \quad (3)$$

where $\beta_{sys,0}$ and $\beta_{sys,d}$ correspond to the reliability index (i.e. $\beta_{sys} = -\Phi^{-1}[p_{F_{sys}}]$) estimated for the intact and damaged system, respectively.

2.6 Life-cycle management planning

As mentioned in Section 1, life-cycle strategies can be identified through heuristic-based policy search or via POMDP-based deep reinforcement learning, potentially including additional maintenance actions undertaken in response to damage caused by accidental or extreme events. In any case, the objective of the life-cycle management decision problem is stated as the minimization of the total expected cost, $\mathbf{E}[c_T]$:

$$\mathbf{E}[c_T] = \mathbf{E} \left[\sum_{t=0}^{t_N} [\gamma^t (c_{I,t} + c_{R,t} + r_{F,t})] \right] \quad (4)$$

where c_I and c_R , stand for inspection and repair costs, respectively; while the system risk, r_F , is defined as the system failure probability, $p_{F_{sys}}$, multiplied by the failure cost, c_F . Note that the total cost is discounted by the factor γ . By identifying policies on the basis of the aforementioned optimization objective, life-cycle management policies are able to jointly consider the risk induced by deterioration processes and occasional accidental/extreme events, both of them encapsulated in the system risk metric, r_F .

3 LIFE-CYCLE MANAGEMENT PLANNING FOR A DETERIORATING OFFSHORE WIND SUBSTRUCTURE SUBJECT TO SHIP COLLISIONS

The main goal of this study is to determine the influence of occasional accidental events on life-cycle management strategies. Specifically, life-cycle management policies are identified for a structural system subject to both fatigue deterioration and accidental ship collision events. A heuristic-based policy search is conducted in order to identify life-cycle strategies, evaluating each considered heuristic combination over 2,000 policy realizations on a 30-year decision horizon. In particular, a specified number of braces (and their corresponding fatigue hotspots) are inspected at equidistant inspection intervals, prioritized according to their brace failure probability. Besides, a brace is subsequently repaired if a crack is observed or once the brace failure probability exceeds 10^{-3} . The heuristic-based policy becomes the optimized heuristic combination that results in the minimum total life-cycle cost, among all evaluated heuristic rules. The inspection and repair costs are specified for each element as $c_I = 0.4$ and $c_R = 30$ monetary units, whereas the system failure cost is defined as $c_F = 50,000$ monetary units. Also, a discount factor is specified as $\gamma = 0.95$. Note that more optimal policies can be found via POMDP-based deep reinforcement learning approaches. As mentioned earlier, the primary aim of the study is not reaching policy optimality but observing the effect of considering both deterioration processes and extreme/accidental events on the retrieved life-cycle strategies.

3.1 Case study description

3.1.1 System structural reliability

The methodology proposed in Section 2 is tested for a typical engineering system in the structural reliability community, the Zayas frame, considered in this work as a 2-dimensional representation of an offshore wind substructure. The frame features 2 legs and 13 braces, with the characteristics shown in Figure 2. The failure of the system corresponds to the event in which the frame is not able to withstand a concentrated horizontal load applied at the upper-left corner, i.e. the probability of the external horizontal load exceeding the structural system

resistance $p_r[L_H > L_{push}]$. The horizontal load is characterized as a lognormal random variable with mean $\mu_{L_H} = 70$ kN and 25% coefficient of variation, while the system resistance is assumed deterministic. The system failure depends on the event of a potential brace failure, caused by fatigue deterioration and/or accidental collision damage. Particularly, a brace failure event is defined as a series system including one/two fatigue hotspots and a collision failure event, each of them estimated based on the limit states explained hereafter. To define the failure probability of the frame, pF_{sys} , conditional on all brace failure/survival state combinations, 8,192 ($= 2^{13}$) non-linear static push-over simulations have been run with the assistance of the computer code 'USFOS'. For a complete description of the frame structural reliability computation, the reader is referred to Morato et al. (2022b).

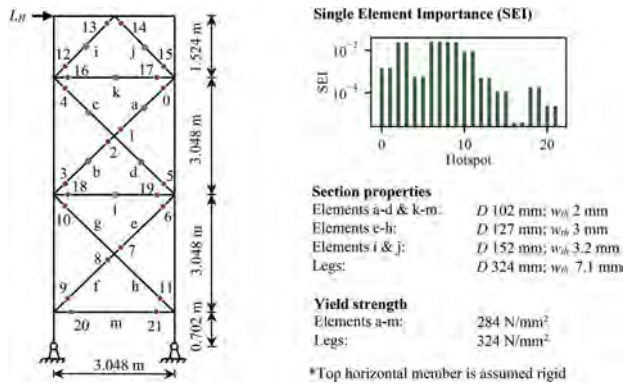


Figure 2. Zayas frame geometry and material properties, adapted from Morato et al. (2022b).

3.1.2 Fatigue deterioration

The deterioration condition of each fatigue hotspot is here described according to the Markovian model, originally proposed in Ditlevsen & Madsen (2007):

$$d_{t+1} = \left[\left(1 - \frac{m}{2} \right) C_{FM} S_R^m n^{m/2} + d_t^{1-m/2} \right]^{2/2-m} \quad (5)$$

where the evolution over time, t , of the crack depth, d , is formulated through a fracture mechanics law with material parameters $\ln(C_{FM}) \sim \mathcal{N}(\mu = -35.2, \sigma = 0.5)$ and $m = 3.5$, stress range $S_R \sim \mathcal{N}(\mu = 70, \sigma = 10)$ N/mm², $n = 10^6$ annual stress cycles, and initial crack depth $d_0 \sim \text{Exp}(\mu = 1)$ mm. At the hotspot level, fatigue failure p_{F_i} occurs once the crack depth, d , exceeds a critical size, $d_c = 20$ mm, formally defined as $p_{F_i} = \Pr[g_t \leq 0]$ and computed via a through-thickness failure criterion (Hlaing et al. 2022), i.e. $g_t = d_c - d_t$. Adopting the probabilistic methodology proposed in Section 2, the fatigue deterioration is encoded in a deterioration rate DBN model. The continuous crack depth, d , is adequately discretized into states conditional on $|\mathcal{S}_t| = 31$ fully observable deterioration rate states. In terms of the observational model, the inspection quality is quantified with a Probability of Detection curve $PoD(d) \sim \text{Exp}(\mu = 8)$. More details can be found in Morato et al. (2022a).

3.1.3 Ship collisions

The accidental event is defined as a ship bow impact on the midpoint of a brace and its damage is estimated by means of the absorbed energy. For the purpose of this study, only elements on the 'splash zone' are potentially subject to ship collisions, i.e. brace elements a-d and i-l. The mechanisms for energy absorption are assumed as plastic bending and plastic tensile strain. Local denting and global deflection of the installation, as well as local deformation of the vessel, are not accounted for. To determine the energy absorbed by the collided structure, a ship bow collision on a brace member is considered as a three-point centrally loaded beam bending problem, (Zhang

et al. 2019). The maximum capacity of energy absorbed by bending and tension, ϵ_{max} , corresponds then to the hinge rotation limit of the element, formulated as:

$$\epsilon_{max} = 4\sigma_y w_{th} (D - w_{th})^2 \alpha \left(\frac{w_{th}}{D}\right)^\beta + \pi\sigma_y w_{th} (D - w_{th}) \frac{L}{2} \left[\alpha \left(\frac{w_{th}}{D}\right)^\beta\right]^2 \quad (6)$$

where w_{th} , D , and L represent the wall thickness, outer diameter, and length of each tubular member, respectively, while σ_y corresponds to the yield strength. According to Marshall et al. (1977), a lower and upper bound solution can be specified for the plastic hinge rotation at failure for a tubular element, where the range for the multiplicative constant α may be defined between 122 and 12,800 and the exponent β may take values between 2.5 and 3. To account for the uncertainty associated with the previously mentioned parameters and defined for each considered element thickness and diameter, α is described as a uniform random variable, $\alpha \sim \mathcal{U}(122, 12800)$, and β is assumed as a Gaussian random variable, $\beta \sim \mathcal{N}(\mu = 2.75, \sigma = 0.25)$. Geometrical and material properties are treated here as deterministic variables.

Table 1. Occurrence frequency statistical description of all examined accident ship collision events, categorized according to their intensity measure (collision energy).

Occurrence frequency/intensity	0.625 kJ	3.125 kJ	6.250 kJ	9.375 kJ	12.5 kJ
Low (λ_{low})	10^{-2}	10^{-3}	$5 \cdot 10^{-4}$	10^{-5}	10^{-6}
Medium (λ_{medium})	$5 \cdot 10^{-2}$	$5 \cdot 10^{-3}$	10^{-3}	$5 \cdot 10^{-5}$	$5 \cdot 10^{-6}$
High (λ_{high})	10^{-1}	10^{-2}	$5 \cdot 10^{-3}$	10^{-4}	10^{-5}

During the computation of policy evaluations, the failure probability of an accidental event is estimated, at each time step, according to the limit state, $g_{col} = \epsilon_{max} - \epsilon_{col}$, with ϵ_{max} calculated following Equation 6. In terms of the collision energy, ϵ_{col} , which can be linked to the intensity measure of an accidental event, a set of collision intensities are here investigated ranging between 0.625 and 12.5 kJ. The intensities can be regarded as reasonable collision scenarios for the Zayas frame, corresponding specifically to a ship mass between 5 and 100 tonnes colliding at 0.5 m/s. In the numerical experiments, three collision occurrence event settings are tested, representative of low, medium, and high frequencies, all of them described as Poisson processes. Table 1 lists the mean annual frequency, λ , considered for each analyzed setting. While evaluating life-cycle policies, the number of ship collision events, $n_{I,col}$, is sampled at each time step, thereby enabling the computation of the collision energy ϵ_{col} and the accidental event failure probability.

3.2 Results and discussion

3.2.1 Robustness analysis

To better understand the ability of the analyzed frame to withstand potential ship collisions, the robustness of each brace is quantified according to Equation 3 and displayed in Figure 3. The intact reliability index, β_0 , corresponds to the case in which only deterioration damage is considered, whereas the damaged reliability index, β_{db} , also accounts for accidental events associated with a certain collision intensity, along with fatigue deterioration. As expected, more severe ship collisions lead to an overall robustness reduction, also accentuated by longer fatigue deterioration exposure. Interestingly, the observed robustness indices are clearly influenced by each brace's structural importance, defined according to Morato et al. (2022b).

3.2.2 Life-cycle costs and policies

The total expected cost, $\mathbf{E}[c_T]$, resulting from all examined accidental event frequency settings is reported in Table 2, also listing the corresponding expected inspection and repair costs along with the system failure risk, i.e. $\mathbf{E}[c_I]$, $\mathbf{E}[c_R]$, and $\mathbf{E}[r_F]$. Whereas more intense ship collision events naturally lead to higher life-cycle total expected costs, expected inspection and repair costs are also clearly influenced by the intensity of accidental events. Considering only

Table 2. Expected total cost resulting from the conducted numerical experiments for settings with varying frequency of collision event occurrence.

Occurrence frequency	$E[c_f](\% E[c_T])$	$E[c_R](\% E[c_T])$	$E[r_F](\% E[c_T])$	$E[c_T](95\% \text{ C.I.})$
Zero (λ_{zero})	15.31 (7.3 %)	55.99 (26.8 %)	137.35 (65.9 %)	208.65 (± 0.01)
Low (λ_{low})	15.29 (7.0 %)	59.75 (27.2 %)	144.41 (65.8 %)	219.45 (± 0.02)
Medium (λ_{medium})	11.99 (4.5 %)	66.01 (25.1 %)	185.08 (70.4 %)	263.08 (± 0.04)
High (λ_{high})	11.01 (3.4 %)	86.02 (26.5 %)	227.59 (70.1 %)	324.63 (± 0.05)

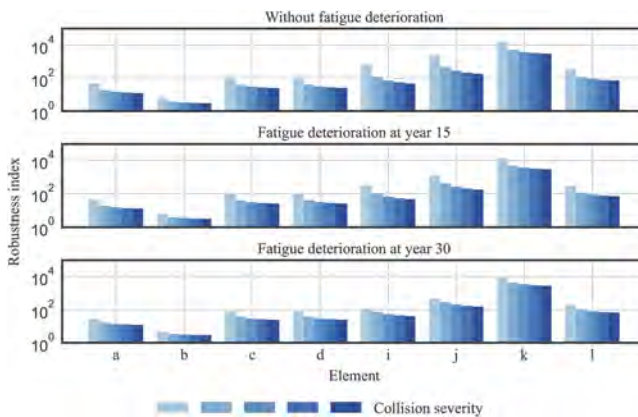


Figure 3. Reliability-based robustness index estimated for all Zayas' brace elements potentially subject to ship collision accidental events (darker colors represent major severity).

fatigue deterioration during the planning stage would have resulted in a higher failure risk for more severe collision scenarios, with negligible influence on inspection and repairs. To further investigate the effect of collision occurrence on the retrieved policies, an additional analysis is conducted comparing the heuristic decision rules evaluated for each occurrence setting against the baseline case, in which only fatigue deterioration is considered. The normalized difference between the $E[c_T]$ resulting from each evaluated heuristic rule combination h_i and the optimized heuristic-based policy h_{opt} is defined as the comparative proxy, formulated as:

$$\bar{h}_i = \frac{\mathbf{E}[c_T(h_i)] - \mathbf{E}[c_T(h_{opt})]}{\mathbf{E}[c_T(h_{opt})]} \quad (7)$$

The above-mentioned metric, \bar{h}_i , is compared in Figure 4 for three ship collision frequency settings (i.e. λ_{low} , λ_{medium} , λ_{high}) against the case where only fatigue deterioration is modeled, λ_{zero} . Additionally, optimized heuristic-based policies are marked with a plus marker for each considered collision event occurrence case and a circular marker for λ_{zero} . As seen in the figure, the optimized heuristic-based policy remains the same for λ_{low} setting, yet it is clearly different for the other two cases λ_{middle} and λ_{high} . As one could expect, the life-cycle policy is mainly driven by fatigue deterioration when the frequency of accidental events is very low. Nevertheless, life-cycle management strategies are influenced by both fatigue deterioration and ship collision for the other two examined ship collision frequency scenarios. Additionally, it can also be observed that the optimized heuristic-based policy for λ_{zero} setting is farther from the optimized life-cycle policy when considering higher frequency of ship collisions, thus demonstrating the importance of jointly modeling both fatigue deterioration and accidental events.

4 CONCLUSIONS

This study reveals the importance of accounting for the increased risk caused by accidental events in life-cycle management planning for deteriorating structural systems. In the numerical

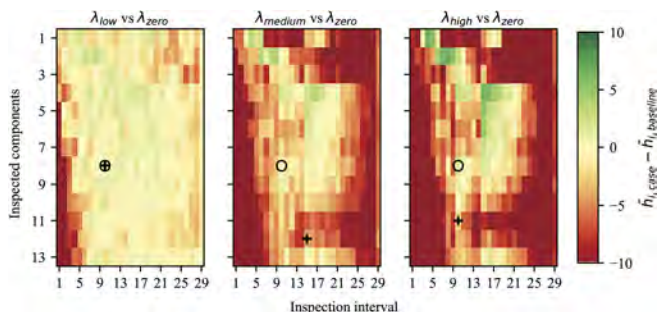


Figure 4. Heatmap representation of the difference between the normalized expected total costs resulting from settings with varying frequency of ship accidental collision events and the baseline case, in which only fatigue deterioration is accounted for.

experiments, heuristic-based life-cycle management policies are identified for an offshore wind substructure subject to fatigue deterioration and ship collisions, and the results indicate that the retrieved strategies are highly sensitive to the intensity and occurrence frequency of the examined ship collision events. In terms of decision-making, further research efforts might explore the integration of the proposed probabilistic approach with deep reinforcement learning methods.

REFERENCES

- Andriotis, C.P. & Papakonstantinou, K.G. 2019. Managing engineering systems with large state and action spaces through deep reinforcement learning. *Reliability Engineering and System Safety* 191:106483.
- Biondini, F. 2009. A measure of lifetime structural robustness. In *Proceedings of the 2009 Structures Congress - Don't Mess with Structural Engineers: Expanding Our Role*, Austin, pp. 1–9.
- Ditlevsen, O. & Madsen, H.O. 2007. *Structural reliability methods*. Department of Mechanical Engineering, Technical University of Denmark.
- Frangopol, D.M. & Curley, J.P. 1987. Effects of damage and redundancy on structural reliability. *Journal of Structural Engineering* 113(7): 1533–1549.
- Frangopol, D.M. & Soliman, M. 2016. Life-cycle of structural systems: recent achievements and future directions. *Structure and Infrastructure Engineering* 12(1): 1–20.
- Hlaing, N., Morato, P.G., Nielsen, J.S., Amirafshari, P., Kolios, A. & Rigo, P. 2022. Inspection and maintenance planning for offshore wind structural components: integrating fatigue failure criteria with Bayesian networks and Markov decision processes. *Structure and Infrastructure Engineering* 18(7): 983–1001.
- Kumar, R., Gardoni, P. & Sanchez-Silva, M. 2009. Effect of cumulative seismic damage and corrosion on the life-cycle cost of reinforced concrete bridges. *Earthquake Engineering and Structural Dynamics* 38:887–905.
- Luque, J. & Straub, D. 2019. Risk-based optimal inspection strategies for structural systems using dynamic Bayesian networks. *Structural Safety* 76: 68–80.
- Marshall, P.W., Gates, W. E. & Anagnostopoulos, S.W. 1977. Inelastic dynamic analysis of tubular offshore structures. In *9th Annual Offshore Technology Conference OTC 2908, Houston*, pp. 110–119.
- Morato, P.G., Papakonstantinou, K.G., Andriotis, C.P., Nielsen, J.S. & Rigo, P. 2022. Optimal inspection and maintenance planning for deteriorating structural components through dynamic Bayesian networks and Markov decision processes. *Structural Safety* 94:102140.
- Morato, P.G., Andriotis, C.P., Papakonstantinou, K.G. & Rigo, P. 2022. Inference and dynamic decision-making for deteriorating systems with probabilistic dependencies through Bayesian networks and deep reinforcement learning. *arXiv* 2209.01092.
- Papakonstantinou, K.G. & Shinozuka, M. 2014. Planning structural inspection and maintenance policies via dynamic programming and Markov processes. Part II: POMDP implementation. *Reliability Engineering and System Safety* 130:214–224.
- Stewart, M.G. & Rosowsky, D.V. 2022. *Extreme events for infrastructure: uncertainty and risk*, pp. 3–27. Springer International Publishing.
- Zhang, S., Pedersen, P.T. & Villavicencio, R. 2019. *Internal mechanics of ship collision and grounding*. Butterworth-Heinemann.

*SS9: Risk-based prioritization and monitoring of bridges
for road infrastructure management in Lombardy region, Italy
Organizers: F. Biondini, M.P. Limongelli, C. Gentile & M. Belloli*



Taylor & Francis

Taylor & Francis Group

<http://taylorandfrancis.com>

Static monitoring of a masonry arch bridge: Evaluating the effects of changing environment

P. Borlenghi & C. Gentile

DABC, Politecnico di Milano, Milan, Italy

M. D'Angelo

DICA, Politecnico di Milano, Milan, Italy

Tecnoindagini Srl, Cusano Milanino, Italy

F. Ballio

DICA, Politecnico di Milano, Milan, Italy

ABSTRACT: The paper presents selected results obtained in the continuous monitoring of the *Candia* bridge – a historical masonry arch bridge crossing the Sesia River in the north of Italy – to detect scour-induced effects. Generally speaking, hydraulic processes are the main cause of bridge failure, and masonry arch bridges are particularly vulnerable to scour-induced settlements. Consequently, the early detection of anomalies associated to scour is of outmost importance to ensure the safe operation of river bridges. In the present study, measurements of the piers rotation are performed using tiltmeters; in addition, environmental parameters, such as temperature, water level and riverbed changes, are measured to check possible correlation with the monitored rotations. The results from the first two years of monitoring highlight anomalous changes in the rotation-temperature correlation of various piers.

1 INTRODUCTION

Masonry bridges with shallow foundations on the riverbed are highly vulnerable to scour-induced settlements. Nevertheless, the number of studies addressing this issue is still limited. Some scholars have tackled the problem with refined numerical models (Zampieri et al. 2017, Tubaldi et al. 2018, Scozzese et al. 2019), limit analysis (George & Menon 2022) or laboratory testing of scaled-down models (Invernizzi et al. 2011). However, extensive studies on the long-term monitoring of scour effects in masonry arch bridges are still missing. The present paper summarizes the results collected in two years of continuous monitoring of the historical multi-span masonry bridge, called *Candia* bridge.

On-site inspections revealed that all pier footings resting on the riverbed underwent strengthening interventions, highlighting the vulnerability to scour actions. In addition, the bridge experienced an intense flood event in October 2020.

The quasi-static monitoring system of the *Candia* bridge was designed to measure the rotations at the top of the piers resting on the riverbed to eventually detect the onset of scour-induced settlement. In more detail, the system includes: (a) 15 MEMS tilt-meters; (b) 1 hydrometer and 1 echo-sounder; (c) 1 weather station; (d) 2 cameras. The tiltmeters measure the traverse rotation of piers at the arches skewback and 2 tilt-meters are installed on the piers that were most affected by the scour events since 2003. In addition, temperature, water level and riverbed variations are monitored by means of thermocouples, hydrometer and echosounder respectively. The system is active since November 2020.

The structure, along with other bridges has been investigated as part of a joint research between Politecnico di Milano and Regione Lombardia aimed at defining guidelines for monitoring key infrastructures (Limongelli et al. 2022) and the subsequent implementation in pilot sensing systems (see, e.g. Bianchi et al. 2022, Borlenghi et al. 2022b, D'Angelo et al. 2022).

After a concise description of the bridge and the Sesia River, the paper focuses on the data collected in the first two years of monitoring.



Figure 1. The *Candia* bridge: view from the upstream of Sesia River.

2 THE *CANDIA* BRIDGE: DESCRIPTION AND PRELIMINARY ANALYSIS

The investigated structure (Figure 1) – called *Candia* bridge (Borlenghi et al. 2022a) – is a multi-span masonry arch bridge that crosses the Sesia River between the small municipalities of Candia Lomellina and Casale Monferrato. The structure is 325 m long and it is composed of 16 segmental arches, 15 piers and end abutments. All structural components are built in brick masonry. The arches have a span – measured from the arch skewback – of 17.5 m. As shown in Figure 1, all the piers were subjected to the strengthening of the foundation. The deck width is equal to 10 m and includes a roadway and a railway track, with the latter being inactive since 2010.

2.1 *The interaction with the Sesia river*

The structure is located 5 km upstream of the confluence between Sesia River and Po River. The Sesia River has a meandering channel pattern, which appears planimetrically stable from aerial images observation since 1954. In addition, the flow regime of the Sesia River is rather torrential with flow discharges ranging between 70 m³/s and 5000 m³/s. In case of a 200-year flood event, water can reach an elevation of about 105 m above sea level (asl) and 1 m above the skewback of the bridge arches.

According to Pizarro et al. (2019), scour can be classified as (1) natural scour, (2) contraction scour, and (3) local scour. In case of *Candia* bridge, the natural scour is occurring due to a general degradation of the altimetric profile of the Sesia River: along the period 1960-2000, the river generally eroded for 2-3 m. In addition, local scour at the foundation piers may occur due to local flow turbulences induced by the obstructions in the riverbed: the large concrete plinths reduced the free flow cross-section to 13.5 m. The presence of wood debris can further intensify the local scour process and in the case of *Candia* bridge the presence of important accumulation of debris during floods is well-documented.

Armoring intervention of the riverbed were carried out on several occasions to stabilize the sediments around the foundations. To the authors' knowledge, the last intervention of riverbed stabilization - before the installation of the monitoring system - was performed after 2003 around the most eroded piers at the left side of the channel, where flow concentrates in normal condition. This operation, however, simply modified the local morphology of the riverbed, deviating the main flux - and therefore the scour process - from the left to the central-channel piers. Figure 2 shows a representation of this mechanism.

In October 2020 a serious flood of the Sesia River occurred. The maximum water level reached during the event can be estimated from available photos and it is almost equal to

105 m asl (the quota of the 200-year flood event). The flood caused severe damage to the streets, railway tracks and buildings in areas nearby the bridge. However, no evidence of damage was detected on the bridge. After the flood event, field measurements of water depth were performed with a stadia rod. The local measures on pier P05 – taken from the extrados of the foundation plinth – resulted in 5.5 m at the upstream side and 2.7 m at the downstream side.



Figure 2. Satellite images of the Sesia River before and after the armoring intervention.

2.2 Historical and documentary research

Due to the lack of available documentations, an intense historical research was performed to identify the construction period and the main structural interventions.

The bridge was conceivably built between 1868 and 1870. According to the original design drawings – found in a Thesis of the Royal Technical School for Engineers of Turin (Martinengo 1869) – the foundations of the piers were of two types: the piers most subject to the river flow, i.e. those on the river right (P01-P04), were founded at a depth of 2 m below the riverbed (96 m asl), while the remaining ones (P05-P15) were founded 1 m below the riverbed (97 m asl). Surprisingly, at the age of the construction, the main river channel was on the river right.

Between 1954 and 1955 the 9th arch – included among P08 and P09 – was reconstructed and the foundations of piers from P09 to P11 were strengthened a deepening of the foundation level (Figure 3a) up to 12 m below the riverbed. The reason of the heavy damage of the arch is still unknown but most likely it was connected to soil settlements. Subsequently, during the 1980s, a similar intervention on the foundations of piers P04-P08 was performed (Figure 3b), together with the strengthening of arches from 1 to 5.

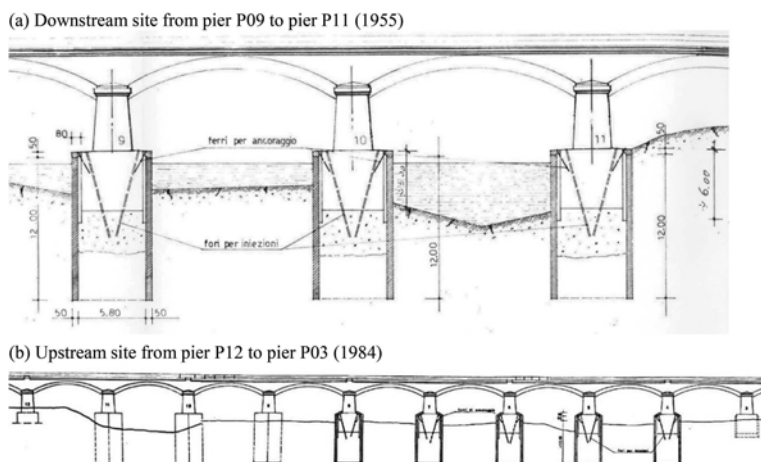


Figure 3. Historical drawings of different strengthening interventions on the piers: (a) 1955 intervention on piers P09, P10 and P11; (b) 1984 intervention on piers from P04 to P08.

To the authors' knowledge and based on the results of the documentary research, the foundation level for piers from P04 to P11 is equal to 12 m (measured from the extrados of the foundation plinth) while the foundation level of piers P01-P03 and P12-P15 is equal to 6 m.

3 THE CONTINUOUS MONITORING SYSTEM

The monitoring system installed in the *Candia* bridge (Figure 4a) is composed by: (a) 15 uniaxial MEMS analog tiltmeters (SISGEO model 0S541MA0202, accuracy $\pm 0.008^\circ$); (b) 1 weather station (measuring temperature, humidity, rainfall intensity, wind speed and direction); (c) 1 hydrometer; (d) 1 echo-sounder and (e) 2 cameras.

Figure 4b shows typical installation of one tiltmeter (before the cable connection). The tiltmeters were installed at the skewback of the arches on the upstream side of the bridge, measuring positive transverse rotations along the direction of the river flow. It is worth noting that the pier rotation due to a scour-induced settlement is expected to occur in the opposite direction of the river flow (Tubaldi et al. 2018) and therefore with negative measured rotations. As shown in Figure 4a, the tiltmeters were installed only on the piers located in the riverbed and the piers from P04 to P08 – the ones most affected by the deviation of the main river flux from the left- to the central-channel (Figure 2) – are monitored with two tiltmeters: one for each skewback.

The environmental parameters are measured with the weather station, the hydrometer and the echo-sounder. In addition, the outdoor temperatures are also recorded by the internal thermistor of the tiltmeters. The water level is measured with a hydrometer positioned at the deck level while the evolution of scouring holes is performed with an echo-sounder. As shown in Figure 4c, the echo-sounder is installed on piers 5 at the downstream side: the ideal position of the sensor should be on the upstream side, where the scour hole might develop, however, the intense debris accumulation on the upstream side suggested the installation on the downstream side. The debris accumulation on the piers is detected with 2 cameras taking pictures of the river from the upstream side (Figure 5).

The continuous monitoring system has been active since November 22nd, 2020. The sensor network has a sampling frequency of 1 Hz with the only exception of the cameras that acquire pictures every 10 minutes. The recorded data are collected every hour in 1 binary file that is transmitted to Politecnico di Milano for the analysis. In the post-processing phase the recorded data are averaged to obtain a single observation every hour.



Figure 4. The quasi-static monitoring system: (a) sensors layout; (b) mounting of tiltmeter T12; (c) position of the echosounder.

4 DATA ANALYSIS

This section summarises the main results of the quasi-static monitoring system for a period of 2 years, from 31/12/2020 to 01/01/2023. During this time period 16,510 1-h dataset were collected and analysed together with the upstream side pictures taken with the permanent cameras in the daylight (e.g. Figure 5).

Firstly, the main environmental parameters, i.e. outdoor temperature and water level, are processed. Figure 6a illustrates the evolution of the outdoor temperature measured from the internal thermistor of one tiltmeter. The maximum and minimum recorded temperatures in the selected period are equal to 45.7°C and -7.3°C, respectively. However, the temperatures below -1.2°C were ignored in the present paper due to an occasional sensor malfunctioning.

Figure 6b presents the time evolution of the river water level measured with the hydrometer in terms of elevation above sea level (m asl). The average recorded value in the selected period is 97.0 m asl while the maximum value is equal to 100.6 m asl (12 May 2021). It is worth considering that during the expected 200-year event, the river water level can reach an elevation of about 105 m asl, namely, rising about 8 m from the average water level. In the selected period the maximum detected rising is about 3.6 m from the average water level.

Regarding the analysis of debris accumulation Figure 5a shows the important wood debris accumulated over the concrete foundation basement of pier P05 after the flooding of October 2020 (estimated water level reach during the event equal to 105 m asl). After six months an event with a water level of 100 m asl occurred in May 2021 and a substantial variation in the debris accumulation is visible from Figure 5b.



Figure 5. Pictures from the permanently installed cameras: (a) debris accumulation on P05 in November 2020 resulting from the important event of October 2020; (b) debris accumulation on P05 and P04 after the event of May 2021.

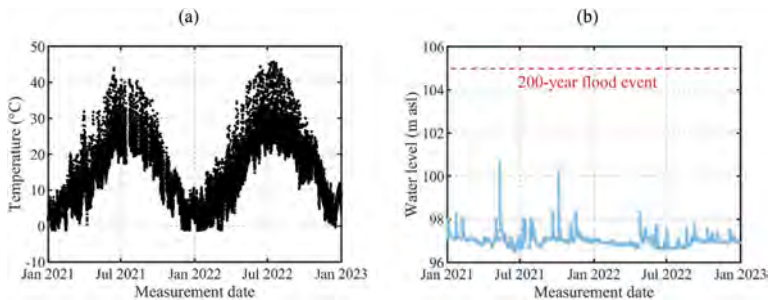


Figure 6. Time evolution of environmental parameters: (a) measured temperature and (b) water level.

Due to the limited length of the present paper only the results of the four most representative tiltmeters are reported: T3, T4, T7 and T8. The selected sensors belong to piers P04 and P06, namely two of the piers most affected by the deviation of the main river flux from the left-

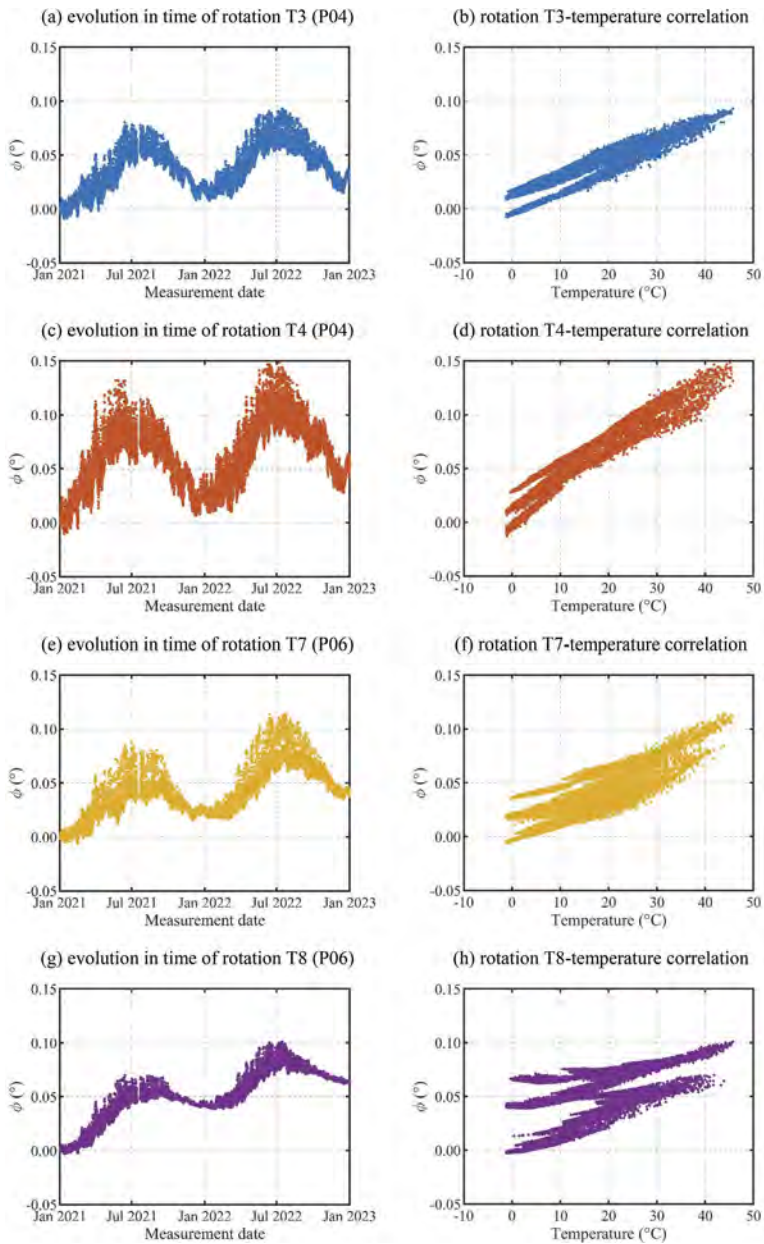


Figure 7. Time variation of rotations and rotation-temperature correlation of sensors T3 (P04), T4 (P04), T7 (P06) and T8 (P06).

Table 1. Statistics of the measured rotations from January 1st 2021 to January 1st 2023.

Tiltmeter	φ_{ave} (°)	φ_{min} (°)	φ_{max} (°)	σ_x (°)	CV (%)
T3	0.036	-0.008	0.093	0.020	56.0
T4	0.060	-0.013	0.148	0.030	50.5
T7	0.039	-0.006	0.114	0.022	57.0
T8	0.050	-0.003	0.101	0.023	46.6

the central-channel after 2003 (Figure 2). Table 1 reports the statistical analysis of the measured rotations. φ_{ave} , φ_{min} and φ_{max} denotes the average, minimum and maximum values of recorded respectively; σ_x represents the standard deviation and CV the coefficient of variation. The maximum daily variation – experienced during the summer – ranges between $\pm 0.028^\circ$ for T8 and $\pm 0.075^\circ$ for T4, while the seasonal variations are about two times larger, ranging from $\pm 0.06^\circ$ for T8 and $\pm 0.14^\circ$ for T4.

Firstly, the qualitative comparison of Figures 7a, c, e, g and Figure 6a suggest that the fluctuations of the measured pier rotations approximately follow the temperature variations with a direct correlation: the rotations increase with the increase of temperature. However, the inspection of the time evolution of measured rotations (Figure 7a, c, e, g) reveals that between January 2021 and January 2023 – periods in which temperatures are similar – there is a clear accumulation of rotation, ranging from $+0.02^\circ$ for T3 to $+0.06^\circ$ for T8. In addition, as shown in Figures 7b, d, f, h, the rotation-temperature correlation exhibits various changes during the monitoring period, highlighting the presence of different anomalies.

Tubaldi et al. 2018 analyzed scour effects on a two-span masonry bridge with a novel modelling procedure. The research highlight that: (a) the effects of scouring-induced settlements are related with pier-foundation rotations in the opposite direction of the river flow; (b) the pier displacements start to increase beyond the values induced by vertical loads only after the maximum scour depth exceeds the foundation depth. The previous considerations can be related to the present work as follow:

- The tiltmeters of *Candia* bridge experienced an accumulation of rotation in the direction of the river flow; therefore, the phenomenon that caused the residual rotations should be related to a soil settlement of the downstream side. It is worth considering that the distribution of vertical loads is not symmetric: the railway track – decommissioned in 2010 – is on the upstream side while the roadway is on the downstream side, causing an asymmetric distribution of service loads.
- According to the blueprints of the different interventions (Figure 3) the foundations depth for all the piers should be equal to approximately 12 m (measured from the extrados of the foundation plinth). During an onsite survey a local measure of the scour hole depth on the upstream side of pier P05 was equal to 5.5 m. Consequently, the system should record the negative rotation residuals only if new important hydraulic events will occur.

5 CONCLUSIONS

The paper illustrates the first two years of results from the continuous monitoring system recently designed and installed on the historical masonry arch bridge of *Candia* over the Sesia River.

The main aim of the monitoring system is to detect scour-induced pier settlements. Variations in the structural behavior of the bridge are measured with a series of MEMS tiltmeters installed on top of the bridge piers. To account for the hydraulic actions, and for the scour in particular, a hydrometer, an echo-sounder, and two cameras were installed. It is worth noting that relevant flood events – which would induce scour – did not occur during the first two years of recording. Due to the limited length of the paper, only four tiltmeters are analyzed in the presented research (i.e. T3, T4, T7 and T8).

From the analysis of the recorded data, the following conclusions can be drawn:

- The tilt variations in the considered monitoring period range from -0.013° to $+0.148^\circ$.
- The outdoor temperature is confirmed as the dominant driver for the tilt variations; however, the rotation-temperature correlation changes different times during the monitoring period.
- Between January 2021 and January 2023 there is a clear accumulation of rotation, ranging from $+0.02^\circ$ for T3 to $+0.06^\circ$ for T8.
- The water elevation does not show any correlation with the pier rotations. However, the recorded water level variations are negligible in respect to the flood events experienced by the structure in October 2020, before the monitoring system installation.

The physical phenomenon that caused the identified permanent shifts in the rotation- temperature correlation is still not clear. To this purpose onsite visual inspections are periodically performed to detect the onset of possible cracks in the arches. However, it is worth considering that the detected anomalies are not directly correlated with scour-induced settlements: the scour action induces a rotational mechanism at the base of the piers on the upstream side, while the identified permanent rotations occurred (most likely) due to settlements in the downstream side.

Within the following months, new investigations are planned using drones, laser-scanner surveys and local measures of scour hole depth at central pier foundations.

ACKNOWLEDGEMENTS

The support of Regione Lombardia is gratefully acknowledged. Sincere thanks are due to G. Cazzulani, PhD (MECC, Politecnico di Milano), G. Zonno, PhD (DABC, Politecnico di Milano), M. Cucchi and M. Iscandri (LPMSC, Politecnico di Milano) who assisted the authors during the installation of the monitoring system.

REFERENCES

- Bianchi, S., Biondini, F., Rosati, G., Anghileri, M., Capacci, M., Cazzulani, G. & Benedetti, L. 2022. Structural Health Monitoring of Two Road Bridges in Como, Italy. In Pellegrino, C., *et al.* (eds) *Proceedings of the 1st Conference of the European Association on Quality Control of Bridges and Structures, EUROSTRUCT 2021; Padua*, 29 August - 1 September 2021. Lecture Notes in Civil Engineering, vol 200. Springer, Cham.
- Borlenghi, P., D'Angelo, M., Ballio, F. & Gentile, C. 2022. Continuous Monitoring of Masonry Arch Bridges to Evaluate the Scour Action. In Pellegrino, C., *et al.* (eds) *Proceedings of the 1st Conference of the European Association on Quality Control of Bridges and Structures, EUROSTRUCT 2021; Padua*, 29 August - 1 September 2021. Lecture Notes in Civil Engineering, vol 200. Springer, Cham.
- Borlenghi, P., Gentile, C. & Zonno, G. 2022. Monitoring Reinforced Concrete Arch Bridges with Operational Modal Analysis. In Pellegrino, C., *et al.* (eds) *Proceedings of the 1st Conference of the European Association on Quality Control of Bridges and Structures, EUROSTRUCT 2021; Padua*, 29 August - 1 September 2021. Lecture Notes in Civil Engineering, vol 200. Springer, Cham.
- D'angelo, M., Menghini, A., Borlenghi, P., Bernardini, L., Benedetti, L., Ballio, F., Belloli, M. & Gentile, C. 2022. Hydraulic Safety Evaluation and Dynamic Investigations of Baghetto Bridge in Italy. *Infrastructures* 7(4): 53.
- George, J. & Menon, A. 2022. Kinematic approach for scour analysis of masonry arch bridges. *Engineering Failure Analysis* 141:106703.
- Invernizzi, S., Lacidogna, G., Manuello, A. & Carpinteri, A. 2011. AE monitoring and numerical simulation of a two-span model masonry arch bridge subjected to pier scour. *Strain* 47(SUPPL. 2):158–169
- Limongelli, M.P., Gentile, C., Biondini, F., di Prisco, M., Ballio, F., Zonno, G., Borlenghi, P., Bianchi, S., Capacci, L., Anghileri, M., Zani, G., Scalbi, A., Ferreira, K.F., D'Angelo, M., Cazzulani, G., Benedetti, L., Somaschini, C., Bernardini, L., Belloli, M., Resta, F., Vigo, P. & Colombo, A. 2022. Bridge structural monitoring: the Lombardia regional guidelines. *Structure and Infrastructure Engineering*: article in press.
- Martinengo, L. 1869. *Ponte in muratura sul fiume Sesia nella ferrovia in costruzione di Asti-Casale-Mortara*. Regia Scuola d'Applicazione per gli Ingegneri di Torino.
- Pizarro, A., Manfreda, S. & Tubaldi, E. 2020. The science behind scour at bridge foundations: A review. *Water* 12(2):374.
- Scozzese, F., Ragni, L., Tubaldi, E. & Gara, F. 2019 Modal properties variation and collapse assessment of masonry arch bridges under scour action. *Engineering Structures* 199:109665.
- Tubaldi, E., Macorini, L. & Izzuddin, B.A. 2018. Three-dimensional mesoscale modelling of multi-span masonry arch bridges subjected to scour. *Engineering Structures* 165: 486–500.
- Zampieri, P., Zanini, M.A., Faleschini, F., Hofer, L. & Pellegrino, C. 2017. Failure analysis of masonry arch bridges subject to local pier scour. *Engineering Failure Analysis* 79:371–384.

Structural health monitoring of bridges based on GNSS

S. Bianchi, L. Capacci, M. Anghileri, F. Biondini & G. Rosati

Department of Civil and Environmental Engineering, Politecnico di Milano, Milan, Italy

G. Cazzulani

Department of Mechanical Engineering, Politecnico di Milano, Milan, Italy

S. Barindelli & S. Caldera

GReD Geomatics Research & Development, Lomazzo (CO), Italy

ABSTRACT: This paper presents an overview of Global Navigation Satellite System (GNSS) technology for Structural Health Monitoring (SHM) of bridges. Peculiarities and requirements related to GNSS technology, installation features, data management, signal processing and significance of the results to ultimately support life-cycle frameworks for optimal management of critical bridge assets are discussed. A case study of GNSS-based SHM of an existing bridge is also presented. The investigated bridge is part of a group of pilot bridges equipped with different SHM systems within a project for risk-based bridge management and monitoring at regional scale. Results of the GNSS-based SHM of the bridge, with emphasis on data processing and correlation analysis, are presented for a monitoring time interval of about two years.

1 INTRODUCTION

Bridges are critical assets within infrastructure systems and their operability is fundamental to guarantee efficient mobility within transportation networks and suitable levels of system functionality and resilience (Biondini & Frangopol 2019). However, bridges are exposed to aging and deterioration processes and many countries are facing with the need of significant repair and maintenance activities on large stocks of existing bridges that are approaching the end of the service life, with huge social and economic impacts (ASCE 2021). It is therefore essential for bridge managers and owners to establish efficient management procedures to prioritize maintenance and rehabilitation interventions for a rational allocation of the available economic resources at infrastructure scale. To this purpose, Structural Health Monitoring (SHM) is an important support to bridge condition assessment procedures.

Among other SHM techniques, Global Navigation Satellite System (GNSS) technology allows to monitor three-dimensional displacements of structures and infrastructural facilities for long-term observations of the structural behavior and damage detection to inform the optimal maintenance and management planning. This paper provides a short overview of the GNSS-based monitoring systems of critical infrastructure systems, including peculiarities and requirements related to GNSS technology, installation features, data management, signal processing and results significance to ultimately support life-cycle frameworks for optimal management of bridge assets at infrastructure scale. An application to GNSS-based SHM of an existing bridge is also presented (Bianchi et al., 2021, 2022a).

The investigated bridge is part of a group of nine bridges selected as pilot case studies for the design and installation of different SHM systems (Borlenghi et al. 2021, Zani et al. 2021, Bianchi et al. 2022b, Capacci et al. 2022, D'Angelo et al. 2022) within a joint project established in Italy between Regione Lombardia and Politecnico di Milano for risk-based

management and monitoring of the regional roadway infrastructure (Biondini et. al. 2022, Limongelli et. al. 2022). The bridge is a seven-span structure with grillage deck made by pre-cast Prestressed Concrete (PC) I-beams and simply supported on each span and Reinforced Concrete (RC) piers. The bridge is crossing a river and two of the central spans have been instrumented with a GNSS-based SHM system aimed at assessing the long-term structural behavior. The system is complemented by a weather station to monitor the environmental conditions. As the bridge is exposed to hydraulic actions, a camera and a hydrometer have been integrated into the monitoring system for detecting floating debris in front of the piers and monitoring of water elevation, respectively (Bianchi et al. 2021). This paper focuses on the GNSS-based SHM system and presents some selected results over a monitoring time interval of about two years, with emphasis on data processing and correlation analysis.

2 GNSS-BASED MONITORING SYSTEMS

Permanent GNSS-based system is a well-known and reliable solution to monitor three-dimensional displacements of selected points located on structures, infrastructural facilities, and ground surface (DeLoach et al. 1989, Bock et al. 1990, Lovse et al. 1995). This system is based on the processing of GNSS satellite signals, received by ground antennas located permanently on the points of interest (Teunissen et al. 2017). There are various GNSS strategies available for signal analysis, broadly categorized into two groups: Absolute Positioning (AP) and Relative Positioning (RP). Precise Point Positioning (PPP) is an example of an AP strategy, where the position of a monitored point is calculated using only the data collected by its GNSS antenna (Zumberge et al. 1997). In contrast, RP is performed by computing the positions of a monitored point using its data together with those collected by one or more reference antennas. This approach is the most suited for SHM purposes, because it allows to compute displacements of points with the highest accuracy. In fact, accuracies in the estimation of displacements up to the millimeter level can be achieved over short baselines of a few kilometers or less (Caldera et al. 2022). Moreover, the advent of new generation and cost-effective GNSS hardware, along with improvements in data processing software, and the introduction of new satellite constellations and features, have made GNSS technology more accessible for permanent monitoring purposes. This development is significant since the use of traditional geodetic hardware was previously limited mainly by budgetary constraints (Caldera et al. 2016).

In using the RP approach for SHM purposes, it is essential to install one antenna on an unaffected point to serve as the reference monitoring point, also referred to as the Local Master (LM). The displacements of all other points are calculated with respect to this reference point. For instance, when monitoring the movements caused by a landslide on the piers of a bridge, LM should be positioned nearby, in a stable position outside the landslide area. The monitored points are then located on the piers. Notably, one advantageous feature of GNSS is that the LM position can be monitored with respect to a third-part Continuously Operating Reference Station (CORS) or a regional and/or national GNSS positioning services, if available. Although with slightly worse accuracy, this approach helps avoid a misinterpretation of the monitoring project resulting from apparent movements of the monitored points caused by LM movements. This is a unique characteristic of GNSS technology, that usually is not applicable when using other permanently installed instruments like robotic total station or Ground-Based Synthetic Aperture Radar (GBSAR).

Another characteristic of GNSS is that the displacements are provided in all weather conditions, including snowfall, fog, and heavy rain. In this way, the continuity of the monitoring is not compromised especially during weather events that can trigger anomalous structural responses. In contrast, optical instruments such as total stations or collimators may not be as well-suited for such bad weather monitoring periods.

A GNSS-based monitoring network provides straightforward and easy-to-interpret results, consisting of three-dimensional displacements of monitored points in a customized local reference system. For example, when dealing with a bridge, it is generally useful to define it with

an axis in the direction of the bridge, an axis perpendicular to this direction and the third one accordingly for the height component.

In addition, the antennas in a GNSS network do not require line-of-sight visibility, making it a flexible approach suitable for scenarios with artificial or natural obstructions, such as mountainous areas or urban environments, where the use of other monitoring techniques is difficult. It is also worth highlighting that GNSS processing is session-independent, which prevents errors from accumulating over time and avoids the slow drifts that may affect other instruments, such as MEMS-based sensors.

Although GNSS antennas collect raw GNSS data at a 1-5 second rate, computing GNSS displacements requires processing a larger temporal window to achieve higher accuracy (the rule is: the wider the window, the better the accuracy). For instance, hourly displacements are computed by processing data collected over a 1-hour window to achieve 2-3 mm accuracy, while daily displacements require processing data collected over a 24-hour window to achieve 1 mm accuracy or better. Due to latency, the technology may not be suitable for extreme real-time applications, such as collapses.

Moreover, accuracy depends on the distance of the monitoring point from the LM, with shorter baselines achieving millimeter-level accuracy, particularly within 1 km of distance (the rule is: the shorter the baseline, the better the accuracy).

Finally, the main GNSS requirement is that the antenna should have a good sky visibility, to be able to collect the signals coming from GNSS satellites. This is why GNSS is not applicable in scenarios with absent sky visibility (i.e., inside tunnels) and can suffer in urban canyons or in points with a lot of vegetation covering the sky.

3 CASE STUDY: ISOLA DOVARESE BRIDGE

The bridge considered as a case study in this paper is located in Isola Dovarese, a small town in Cremona province, Italy. This structure has a prominent role in the regional transportation systems since it overpasses the Oglio River, an affluent of the Po River, and guarantees the link with Mantova province. The two-lane SP11 road runs on the bridge, and it carries an average daily traffic of 4292 vehicles characterized by 24% of heavy trucks, up to 20 tons.

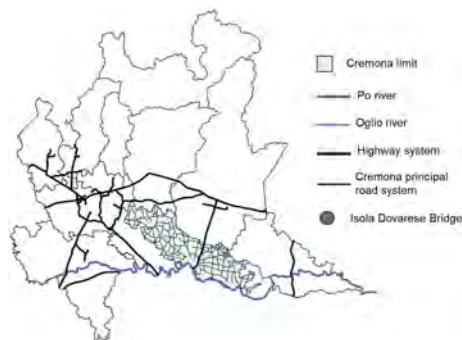


Figure 1. Map of Lombardy region with location of Isola Dovarese bridge.

Figure 2 shows a view of the bridge. Built in 1969, the Isola Dovarese bridge is a seven-span structure with total length of 107,00 m, including end spans of 8,40 m long and five central spans of 18,00 m. The bridge deck is simply supported on each span and is made by a grillage of precast PC I-beams with top RC slab and transversal stiffening RC beams. Geometry of the deck cross-section for one of the central spans is shown in Figure 3. Cast-in-situ RC piers are supported by pile foundations, each consisting of 35 circular piles 8 m deep, as shown in Figure 4.



Figure 2. View of the Isola Dovarese bridge.

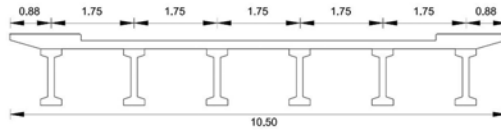


Figure 3. Bridge deck cross-section.

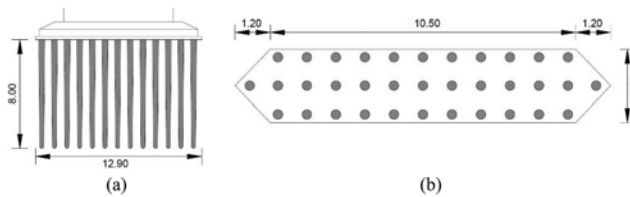


Figure 4. Bridge foundation [m]: (a) vertical and (b) plan views.

4 DESIGN AND IMPLEMENTATION OF THE GNSS-BASED SHM SYSTEM

To support the design of the monitoring system, an in-depth study of the bridge condition state was developed. Historical technical drawings and reports were provided by Cremona Province. In 2018 an experimental campaign aimed at the mechanical characterization of material was performed by means of destructive and non-destructive tests. In 2019 a detailed visual inspection activity was carried to check information gathered from available design documents and verify the current bridge condition. Visual inspection highlighted a fair condition state of the bridge characterized by extensive portions of exposed corroded reinforcement of the piers. Over the same year, a rehabilitation intervention aimed at the steel bar passivation and restring of the concrete cover was performed. Finally, in order to optimally design the monitoring network, any operational constraints related to the installation, deployment and maintenance of the GNSS monitoring system were identified (e.g., power supply availability, sky visibility of the GNSS antennas for the selected monitoring points, on-field sensors configuration to optimize deployment costs, cable routing, among other features and requirements).

The preliminary studies and observations suggested to implement a GNSS-based SHM system for the observation of the long-term structural response of the bridge. The primary objective was to evaluate the behavior of the decks and piers by monitoring the absolute displacements of selected points. GeoGuard solution (<https://www.g-red.eu/geoguard>) was selected for the implementation of the GNSS monitoring of the bridge. It is a state-of-the-art end-to-end solution that provides IoT GNSS sensors, the Brevia GNSS processing software and a web interface to access the monitoring results. A network of ten GNSS antennas was strategically positioned at representative points on two of the five central spans of the bridge that spanned the river, as shown in Figure 5a. Additionally, the LM was installed on one of the abutments, which is not affected by the movements under investigation (Figure 5b). To ensure adequate coverage and minimize the number of GeoGuard Monitoring Units (GMU) required, 6 GMUs were employed. One of them was used in a single GNSS antenna configuration (LM) and the remaining five were used with a GNSS dual-antenna configuration. This approach allowed for optimal hardware costs since fewer GMUs, that connect two GNSS

antennas instead of only one, were deployed. Each GMU was powered by a photovoltaic panel. The data gathered are displayed on a system user interface with options for setting filtering parameters, a localization map, and highlighted displacements (Figure 5c). System notifications alert users when displacement thresholds are exceeded.

The GNSS-monitoring system was installed in July 2020. In order to reach the locations of interest on the piers, the installation was carried out by a team of rock climbers who rappelled beneath the bridge deck using a rope (Figure 6a). Steel supports were specifically designed to anchor the GNSS antennas to the bridge, ensuring optimum sky visibility. The supports were carefully sized to ensure their displacements are at least an order of magnitude lower than those that can be measured with GNSS signals from the satellite constellation (Figure 6b).



Figure 5. GNSS-based SHM system. (a) Location of ten GNSS antennas on both bridge deck and piers. (b) Plan view with location of antennas, LM, and reference system. (c) System user interface.



Figure 6. (a) Installation phase (b) GeoGuard Monitoring Units and steel supports.

The GNSS system steadily recorded from October 2020. The GNSS antennas collected raw satellite data at a rate of 0.2 Hz, which were subsequently sent to a dedicated processing cloud for elaboration over various time intervals ranging from 1 to 24 hours. The resulting solutions were displayed on the system user interface (Figure 5c). The monitoring system has been dismissed in July 2022, at the end of the planned period of investigation of this specific pilot study within the project for risk-based management and monitoring of the regional roadway infrastructure.

5 RESULTS OF DATA PROCESSING AND CORRELATION ANALYSIS

Time histories for longitudinal, transversal, and vertical displacement can be accessed in the system user interface for each point over different time intervals. Figure 7a shows the longitudinal, transversal, and vertical displacements with respect to the LM for one monitored pier point (ID11) over the entire monitoring period of almost two-year, using 24-hour time interval, along with a spline interpolation of the results. Figure 7b represents the hourly movements of the same point (ID11) for a representative period of two weeks. In general, recorded bridge movements were below 5 mm and primarily resulted from seasonal variations during the observation period, especially in the transversal direction.

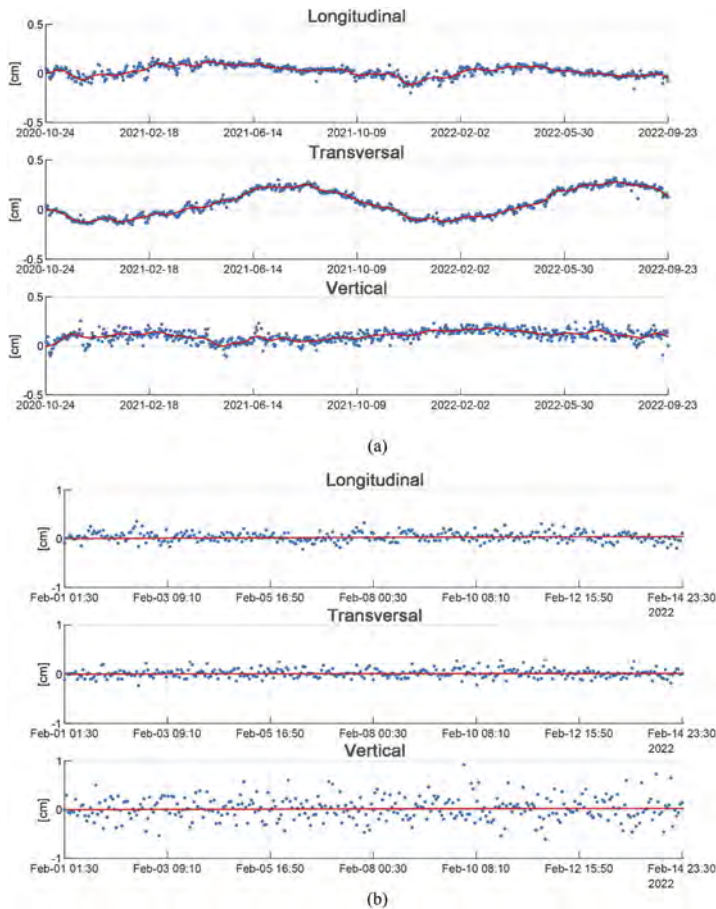


Figure 7. Longitudinal, transversal, vertical displacement components of antenna ID11 with respect to the LM (blue dots), compared with a spline interpolation of the dataset (red line): (a) Daily displacements for a monitoring period of about two years; (b) Hourly displacements for a monitoring period of two weeks.

A multiple linear regression model has been implemented to filter the effects of temperature variations on the computed displacements. Environmental temperature data has been collected by the GNSS receivers that recorded also their internal temperature at 20 minutes interval. The decorrelation of GNSS signals has been performed based on the daily average internal temperature of the reference receiver ID01. The residual displacement time-series have been then computed after decorrelation for longitudinal, transversal, and vertical displacement components of the ID11 receiver using a 24-hour time interval, as shown in

Figure 8. The decorrelated time series exhibit a stable trend over time, confirming that the detected periodic movements are mainly due to the thermal effects affecting the structure.

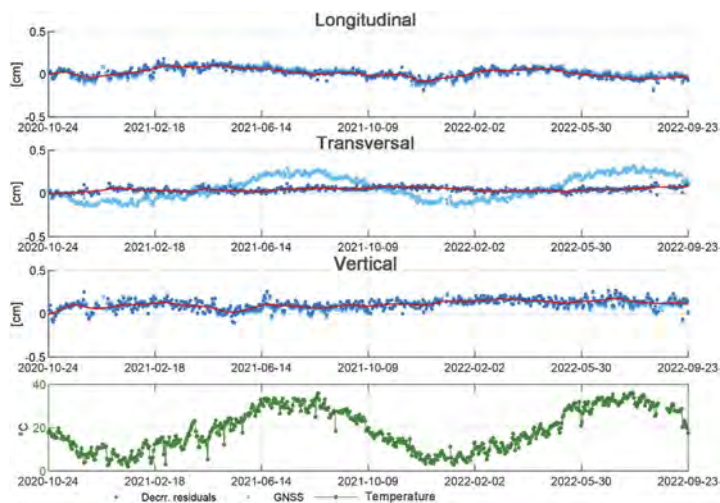


Figure 8. Temperature-decorrelated daily longitudinal, transversal, vertical displacement components of antenna ID11 with respect to the LM (blue dots) compared with a spline interpolation of the dataset (red line) and temperature time-history (green dots) for a monitoring period of about two years.

6 CONCLUSIONS

An overview of GNSS technology for permanent displacement monitoring, including its benefits and limitations, as well as some recommendations for optimal use, has been provided. An innovative GNSS-based SHM system utilizing new generation, cost-effective receivers, with application to an existing bridge, has been also presented. The SHM system designed and implemented on the investigated bridge has been active for two years as a pilot case study of a project for risk-based management and monitoring of a roadway infrastructure system at regional scale. The SHM system was intended to monitor the short-term and long-term structural behavior of the bridge, providing support for early detection of anomalous movements and maintenance planning.

The results show that the monitored points displacement accuracy is less than a millimeter for daily solutions and approximately one millimeter for hourly solutions. Analysis revealed limited bridge movements, with periodical displacements less than 5 mm primarily caused by thermal effects. Decorrelation of the measures from temperature confirms that the movements result from thermal effects on the structure and that the bridge exhibits stable behavior over time. Based on these results, it can be concluded that the good performance of the GNSS SHM system is suitable to facilitate a timely identification of damage initiation and propagation and support the bridge condition assessment to inform a proper planning of maintenance and rehabilitation interventions.

ACKNOWLEDGEMENTS

The research activities presented in this paper, including the design, installation, implementation, and management of the GNSS-based SHM system of the Isola Dovarese bridge, have been funded by a research agreement between Regione Lombardia and Politecnico di Milano for the development of criteria and guidelines for maintenance and management of the regional road infrastructure network.

REFERENCES

- ASCE 2021. *Report Card for America's Infrastructure*, American Society of Civil Engineers, Reston, USA.
- Bianchi, S., Biondini, F., D'Angelo, M., Ballio, F., Anghileri, M., Rosati, G. Cazzulani, G. 2021. Satellite-based structural and hydraulic monitoring of a 50-year-old bridge over the Oglio River in Italy. *1st Conference of the European Association on Quality Control of Bridges and Structures (EUROSTRUCT 2021)*, Padua, Italy, August 29 - September 1, 2021.
- Bianchi, S., Biondini, F., Anghileri, M., Capacci, L., Rosati, G., Cazzulani, G., Caldera, S. 2022a. GNSS-based structural monitoring of the Isola Dovarese bridge, Italy. *11th International Conference on Bridge Maintenance, Safety and Management (IABMAS 2022)*, Barcelona, Spain, July 11-15, 2022.
- Bianchi, S., Capacci, L., Anghileri, M., Biondini, F., Rosati, G., Somaschini, C., Cazzulani, G., Benedetti, L. 2022b. Structural health monitoring of a RC bridge in como, Italy. *11th International Conference on Bridge Maintenance, Safety and Management (IABMAS 2022)*, Barcelona, Spain, July 11-15, 2022.
- Biondini, F., Ballio, F., di Prisco, M., Bianchi, S., D'Angelo, M., Zani, G., Capacci, L., Anghileri, M., Scalbi, A., Flores Ferreira, K. 2022. Bridge vulnerability and hazard assessment for risk-based infrastructure Management. *11th International Conference on Bridge Maintenance, Safety and Management (IABMAS 2022)*, Barcelona, Spain, July 11-15, 2022.
- Biondini, F., Frangopol, D.M., (Eds.) 2019. *Life-cycle design, assessment and maintenance of structures and infrastructure*. American Society of Civil Engineers (ASCE), Reston, USA.
- Bock, Y., Shimada, S. 1990. Continuously monitoring GPS networks for deformation measurements. Symposium. Edinburgh, Scotland, August 7–8, 1989. In: Bock, Y., Leppard, N. (Eds.), *Global Positioning System: An Overview*. International Association of Geodesy Symposia, 102, 40–56, Springer.
- Borlenghi, P., Gentile, C. Zonno, G. 2021. Monitoring reinforced concrete arch bridges with operational modal analysis. *1st Conference of the European Association on Quality Control of Bridges and Structures (EUROSTRUCT 2021)*, Padua, Italy, August 29 - September 1, 2021.
- Caldera, S., Barindelli, S., Sansò, F., Pardi, L. 2022. Monitoring of structures and infrastructures by low-cost GNSS receivers. *Applied Sciences*, 12(23), 12468.
- Caldera, S., Realini, E., Barzaghi, R., Reguzzoni, M., Sansò, F. 2016. Experimental study on low-cost satellite-based geodetic monitoring over short baselines. *Journal of Surveying Engineering*, 142(3), 04015016.
- Capacci, L., Bianchi, S., Anghileri, M., Biondini, F., Rosati, G. Pinto, L., Ioli, F., Somaschini, C. C., Cazzulani, G., Benedetti, L. 2022. Structural health monitoring and geometric survey informed by laser scanner and UAV mapping of an existing tall RC viaduct. *11th International Conference on Bridge Maintenance, Safety and Management (IABMAS 2022)*, Barcelona, Spain, July 11-15, 2022.
- D'Angelo, M., Menghini, A., Borlenghi, P., Bernardini, L., Benedetti, L., Ballio, F., Gentile, C. 2022. Hydraulic safety evaluation and dynamic investigations of Baghetto bridge in Italy. *Infrastructures*, 7 (4), 53.
- DeLoach, S. R. 1989. Continuous deformation monitoring with GPS. *Journal of Surveying Engineering*, 115(1),93–110.
- Limongelli, M.P., Gentile, C., Biondini, F., di Prisco, M., Ballio, F., Zonno, G., Borlenghi, P., Bianchi, S., Capacci, L., Anghileri, M., Zani, G., Scalbi, A., Flores Ferreira, K., D'Angelo, M., Cazzulani, G., Benedetti, L., Somaschini, C. Bernardini, L. Belloli, M. Resta, F. Vigo, P. Colombo, A. 2022. Bridge structural monitoring: The Lombardia regional guidelines. *Structure and Infrastructure Engineering*.
- Lovse, J. W., Teskey, W. F., Lachapelle, G., Cannon, M. E. 1995. Dynamic deformation monitoring of tall structure using GPS technology. *Journal of Surveying Engineering*, 121(1),35–40.
- Teunissen, P. J., Montenbruck, O., (Eds.) 2017. *Springer handbook of global navigation satellite systems*, Vol. 10, 978–3, Springer, Cham, Switzerland.
- Zani, G., Scalbi, A., Flores Ferreira, K., Somaschini, C., di Prisco, M. 2021. Load Testing and Structural Monitoring of a Reinforced Concrete Mid-century Bridge. *1st Conference of the European Association on Quality Control of Bridges and Structures (EUROSTRUCT 2021)*, Padua, Italy, August 29 - September 1, 2021.
- Zumberge, J.F., Heflin, M.B., Jefferson, D.C., Watkins, M.M., Webb, F.H. 1997. Precise point positioning for the efficient and robust analysis of GPS data from large networks. *Journal of Geophysical Research: Solid Earth*, 102(B3), 5005–5017.

Remote monitoring of a concrete bridge through InSAR and GNSS measurements

O. Lasri, P.F. Giordano & M. Previtali

Politecnico di Milano, Milan, Italy

M.P. Limongelli

Lund Technical University, Lund, Sweden

ABSTRACT: Structural Health Monitoring (SHM) can support decision makers in structural integrity management by providing information about occurrence of damage and its evolution in time. Nevertheless, the adoption of traditional SHM systems, e.g., vibration-based SHM systems employing accelerometers, involves laborious installations and maintenance of the instrumentation (e.g., sensors, cables, acquisition systems), which is typically directly installed on the monitored structure. Recently, thanks to new Synthetic Aperture Radar missions, remote sensing provides promising methodology capable of monitoring infrastructure assets. This paper investigates the use of Multi-Temporal Interferometric Synthetic Aperture Radar (MT-InSAR) processing as a suitable tool for monitoring the structural health of bridges. The full interferometry processing chain is based on Sentinel-1 radar data and a combination of open-source routines. The feasibility of the remote monitoring strategy is assessed on a concrete bridge on which GNSS receivers are installed. To validate the methodology, MT-InSAR-derived time histories are verified against the GNSS-derived ones.

1 INTRODUCTION

Bridges and viaducts play a key role in transportation networks. An anomaly or a collapse of these structures could compromise the economy of entire communities (Clemente 2020). Due to the ageing of these infrastructures and the evolution of traffic demand, structural degradation is becoming a serious matter of concern. Furthermore, climate change is exacerbating the frequency and intensity of extreme flood events as flood-induced scour is among the main causes of the riverine bridge collapse (Wardhana 2003). According to this, a proper plan of management and security becomes crucial to avoid wasting resources. Structural Health Monitoring (SHM) systems provide a valid resource to decision-makers and nowadays there is a wide choice of instrumentations and methods (Karbhari 2009). In several geoscience fields, Synthetic Aperture Radar Interferometry (InSAR) is already a well-established monitoring technology and enables the study of geophysical processes (Milillo 2019a, Davalillo 2014). Recently, due to the development of Multi-Temporal InSAR (MT-InSAR) techniques and the increase in the temporal and spatial resolution of SAR products, InSAR technology can provide measurements of deformations of human artefacts like bridges (Giordano 2022, Milillo 2019b, Selvakumaran 2020). Selvakumaran et al. (2018), by processing 48 TerraSAR-X scenes over the Tadcaster Bridge (England), highlight the reliability of MT-InSAR to detect movements in the region of the bridge where the collapse occurred due to the scouring action. As aforementioned, several works in the literature highlight the potential for this technology to provide measurements of assets that are difficult to access for conventional SHM systems. Nevertheless, while traditional monitoring methods provide only limited and point-like

displacement data, MT-InSAR strategies facilitate coverage of wide areas with a high frequency, saving time and money (Milillo 2019b, Huang 2017, Qin 2019). Furthermore, due to the availability of SAR images relevant to past periods, MT-InSAR strategies allow for studying the past behaviour of the infrastructure. Nowadays, establishing the link between MT-InSAR outcomes in terms of displacement time histories and the structural health of bridges remains a key topic of investigation. Besides, one of the main barriers to the wide use of MT-InSAR is the scarce accessibility of relevant software and hardware tools. Most MT-InSAR software packages are patented, only available through expensive licenses, and they perform a black box processing preventing a clear understanding of all steps.

In this paper, a workflow based on SNAP-StaMPS open-source tools (Mancini 2021) is adopted to perform a PSInSAR analysis using Sentinel 1 data. Sentinel Application Platform (SNAP) is a software distributed by ESA which incorporates utilities for interferogram generation. The interferograms are the input for the free Stanford Method for Persistent Scatterers (StaMPS) package which generates the displacement time series and the displacement velocity estimated over the analysed PSs. The MT-InSAR workflow is run on ordinary hardware (a 16 GB RAM laptop) and tested on a real case study. A bridge monitored by a GNSS system is selected to carry out a comparison between MT-InSAR and GNSS results.

In the following sections, the GNSS (Section 2.1) and InSAR (Section 2.2) techniques are presented highlighting the basic concepts of each technique. The case study, a concrete bridge crossing the Oglio river, Northern Italy, is described in Section 3.1. A description of the application of the MT-InSAR and the GNSS techniques to the case of the study is presented in Sections 3.2 and 3.3, respectively. Section 3.4 reports the discussion and comparison of the results of the two techniques.

2 REMOTE MONITORING THROUGH GPS AND INSAR

2.1 GNSS

In the 1970s, the U.S. Department of Defense began developing satellite navigation systems, commissioning the design and construction of the first satellite, NAVSTAR GPS (Navigation Satellite Timing and Ranging Global Positioning System), which was launched in 1978. A Global Navigation Satellite System (GNSS) is composed of three segments: the control segment, the space segment, and the user segment. The control segment is composed of a network of monitoring stations and ground antennas that assure the proper operation of other segments. The GNSS satellites represent the space segment: satellites orbiting the Earth at a height of more than 20,000 kilometres and broadcasting an electromagnetic signal that contains ranging codes and navigation data. This data allows users (user segment) to compute both the travel time from the satellite to the receiver and the satellite coordinates at any epoch. A GNSS receiver is required to properly use the information contained in a GNSS satellite signal. The main elements of a generic GNSS receiver are an antenna and a microprocessor which allow for analyzing the information contained in the GNSS signal and obtaining the position of the antenna phase centre in a geocentric reference system (i.e., for GPS, in the WGS84 reference system). GNSS signals can be processed and analyzed in several ways with different levels of accuracy (Roberts 2015). In the civil engineering context, numerous applications replicate to some extent the traditional nature of static engineering surveying, such as coordinating control points and monitoring deformation. In the last decade, also dynamic applications and deflection monitoring of large structures have been proposed (Roberts 2015, Xinpeng 2021). Nowadays, the static methods based on Differential-GNSS strategies allow for a high-precision positioning providing coordinates of ground locations with millimetric precision, both in the horizontal and in the vertical components (Correa-Muños 2018).

2.2 InSAR

In addition to the GNSS constellations that provide navigation and geo-referencing services, there are other constellations of satellites for Earth observation purposes. These satellites orbit nearly 800 kilometres from Earth and fall into two broad categories: optical satellites and radar

(Radio Detection And Ranging) satellites. Radar satellites are active devices that irradiate electromagnetic waves at different bands of the microwave domain towards a certain area of interest or target. A fraction of the signal is backscattered and returned to the sensor, where amplitude and phase are recorded. The amplitude of the backscattered signal depends on the amount of electromagnetic field backscattered towards the satellite which depends on acquisition geometry, radar carrier frequency, radar resolution, wavelength and polarization, size of the scatterers, surface roughness and orientation. Typically, signals backscattered from exposed rocks and urban areas show strong amplitudes, whereas smooth flat surfaces (like water basins) show low amplitude. Instead, the phase of the signal is affected by the target-sensor distance, thereby it is proportional to surface topography, ground displacement along Line Of Sight (LOS), atmospheric pressure, water vapour and soil moisture (Cusson 2018). In the ideal case where the phase alteration is correlated only to the target-sensor distance, analyzing phase variations among two radar images of the same area of interest can inform about the area movement. Based on this concept, Differential Interferometric Synthetic Aperture Radar (DInSAR) techniques allow for obtaining the deformation rate of the target by analyzing radar images acquired over the same area at different times. A simple phase difference between two images cannot properly assess the target displacement, mainly because the phase change is perturbed by some decorrelations due to variations in atmospheric properties and by errors in satellite orbit and surface elevation determination (Ferretti 2001, Hooper 2012). The phase change among two images which generate the i -th interferogram can be described as follows (Ferretti 2001):

$$\Delta\varphi_i = \frac{4\pi}{\lambda} \Delta r_{Ti} + \Delta\alpha_i + \Delta n_i + \varepsilon_{topo,i} \quad (1)$$

where Δr_{Ti} is the phase change due to the movement in the LOS direction, $\Delta\alpha_i$ is the atmospheric phase contribution, Δn_i is the decorrelation noise and $\varepsilon_{topo,i}$ is the phase contribution due to possible errors in the Digital Elevation Model (DEM). According to Equation (1), the main challenge of any DInSAR technique is to assess the phase change Δr_{Ti} . An essential condition to accomplish this separation is to analyze pixels characterized by small Δn_i typically related to two types of reflectors: those where the response to the radar is dominated by a strong reflecting object and is constant over time (Permanent Scatterer, PS) and those where the response also remains constant but due to different small scattering objects (Distributed Scatterers, DSs). The first pioneer work based on Permanent Scatterer Interferometry (PSInSAR) was proposed by Ferretti et al. (2001). This strategy uses an algorithm patented and developed by a spin-off company founded by Politecnico di Milano and called Tele-Rilevamento Europa, TRE (Ferretti 2001). In the last few years, other strategies have been developed, such as the Small Baseline Subset (SBAS) technique (Crosetto, 2016) and the SqueeSAR algorithm (an extension of the PSInSAR) that allows for using both PSs and DSs (Ferretti 2011). Some validations of PSInSAR highlighted that, in ideal conditions and by exploiting high-resolution data, sub-millimeter accuracy can be obtained (Ferretti 2007). However, these performances cannot be generalized to all possible scenarios since the accuracy strictly depends on the quality of images and processing strategy. Another important PSInSAR contribution was given by Hooper et al. who proposed a novel PS selection method based on the use of phase characteristics and suitable to find low-amplitude natural targets with phase stability that cannot be identified by amplitude-based algorithms (Hooper 2004). This work originated one of the most widely used PSInSAR software packages, StaMPS (Hooper & Zebker 2007, Hooper 2008). Nowadays, due to data availability and some freely available SAR services, such as European Space Agency (ESA) services and Sentinel 1 images, PSInSAR processing becomes more accessible, and it can be run also by open-source processing chain (Mancini 2021).

3 CASE OF STUDY

3.1 *The Isola Dovarese bridge*

The case study is a concrete bridge situated in Isola Dovarese, a municipality of the Cremona province, Italy (Bianchi et al. 2022a, Bianchi et al. 2022b, Limongelli et al. 2022). The Isola

Dovarese bridge, shown in Figure 1, was built in 1969 and has a total length of 107 m including two lateral spans of 8.40 m and five central spans of 18 m. By overpassing the Oglio River, an affluent of the Po River, this bridge provides a key asset for local and regional traffic. The bridge deck is made of precast prestressed concrete I-beams with top concrete slab and transversal stiffening beams. The deck is simply supported on cast-in-situ reinforced concrete piers with a hexagonal profile. In 1979, to tackle a general scour of the riverbed, the foundations were strengthened. Recently, an extensive visual inspection activity of the river-bridge system highlighted the good condition state of the bridge but a massive woody debris accumulation in front of a couple of piers.



Figure 1. The Isola Dovarese bridge.

3.2 Processing of GNSS data

The GNSS-based SHM system designed for the Isola Dovarese Bridge consists of ten receivers mounted on the deck and the piers of two central spans (Bianchi et al. 2022a, Bianchi et al. 2022b). Each slave receiver is anchored through a special steel support guaranteeing the continuous visibility of the satellite constellation. Satellite observations are made by the receiver every 5 seconds and sent in almost real-time to the cloud where they are processed with two different rates: hourly and daily position solutions. The software used by the survey company is the BREVA GNSS Software, developed by GRd, which allows higher estimation accuracy because it is specifically made to process low-receiver data. With an accuracy of up to 1 mm for 24-hour time intervals, the GNSS monitoring system provides the relative vertical displacement with respect to the master receiver ID01, at ten key points of the bridge (Figure 2).

In previous works, findings indicate limited movements of the bridge with small upward vertical displacements likely related to water level variations (Bianchi et al. 2022b). It was also observed that the bridge's displacements are primarily caused by thermal effects and water level variations (Bianchi et al. 2022a). In this study, data relevant to the receivers mounted on deck are considered, namely ID04 and ID08 mounted on the eastern side of the bridge, and ID05 and ID09 mounted on the western side (Figure 2). Figure 3b shows the GNSS time histories of the vertical displacement in the observation period (October 2020 – August 2022). All GNSS receivers anchored on the deck show similar vertical displacement and present a clear seasonal trend. Figure 3b displays the mean value of the four vertical displacement time series.

3.3 Processing of InSAR data

In this analysis, 18 scenes covering the period from October 2020 to December 2021 and freely provided by the European Space Agency (ESA) (through Sentinel-1 satellite mission), were processed. The 18 Single Look Complex (SLC) images, acquired through the Interferometric Wide (IW) swath mode with a geometric resolution of approximately 5 m x 20 m, were processed through an open-source workflow (based on SNAP and STAMPS software) run in

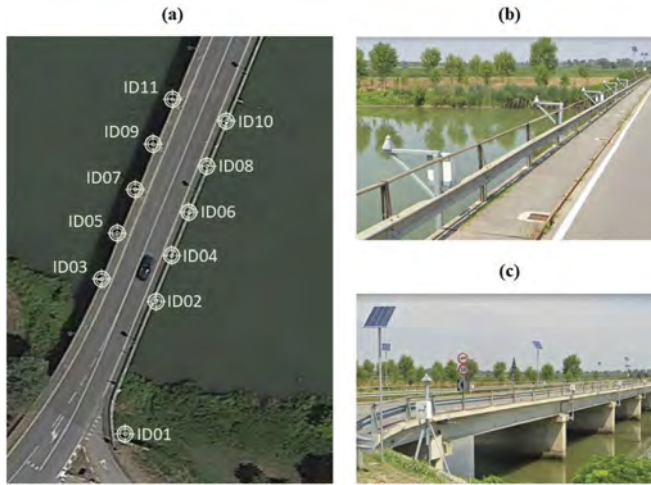


Figure 2. GNSS monitoring: (a) planimetric location of GNSS receivers; receivers mounted on the (b) West and (c) East sides of the bridge.

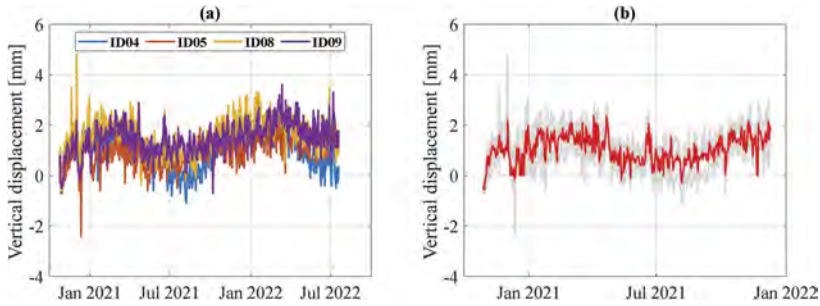


Figure 3. (a) GNSS vertical displacement of the deck receivers; (b) GNSS average vertical displacement of the deck receivers.

a consumer-grade laptop with 16 GB of RAM. To compare the outcomes of the PSInSAR and the GNSS analyses (Figure 3), an estimation of the vertical component of the InSAR LOS displacement is required. By assuming negligible planimetric displacements of the deck, an estimation of the vertical displacement is obtained as follows:

$$d_{UP} \sim \cos \tilde{\theta} d_{LOS} \quad (2)$$

where θ is the incidence angle between the LOS displacement d_{LOS} and the vertical direction, $\tilde{\theta}$ is its average value, and d_{UP} is the vertical component of the LOS displacement. In Figure 4, the available PSs in the area of interest are shown Figure 4a. The InSAR time series, in terms of LOS displacement and vertical displacement, are reported in Figures 4b and c, respectively.

3.4 Comparison of results

To compare InSAR and GNSS results, a zone idealization is carried out (Figure 5). The planar displacement of the PSs observable in Figures 4 and 5 may be due to the low accuracy of the Digital Terrain Model (DTM) used for topographic phase removal (Equation 1).

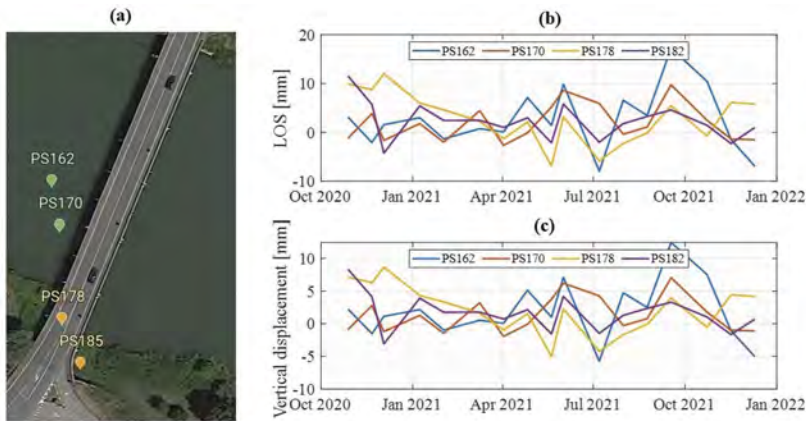


Figure 4. The PSs in the area of interest: (a) location of PSs; (b) LOS displacement of the PSs; (c) vertical components of the LOS displacements of the PSs.

According to PSs location, it is reasonable to assume that PS162 and PS170 belong to the deck portion already monitored through the GNSS system (Z1 in Figure 5b). Similarly, PS178 and PS185 are assumed to belong to the zone of GNSS master receiver ID01 (Z2 in Figure 5b). The InSAR displacement of the two zones (Z1 and Z2) are estimated each as the average displacement of the PSs in the zone.

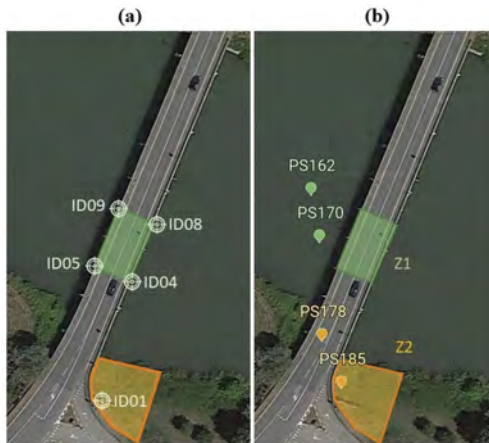


Figure 5. (a) The GNSS receivers; (b) Zone idealizations.

The GNSS system provides the relative vertical displacement of the deck (Z1) with respect to the master receiver ID01 (Z2). To make results comparable, the InSAR relative displacement of the deck is obtained by subtracting the Z1 displacement from the Z2 displacement. As shown in Figure 6a, the time histories of the vertical component of the displacements computed with the two sets of data are consistent. A downward movement of the bridge in the warmest period (July 2021) is highlighted by both time histories. Even if the entity of InSAR displacement is quite different (Figure 6a), the trend of the deck movement is consistent with the GNSS evidence. The correlation analysis between the GNSS and the InSAR displacement shows a high consistency corresponding to a Pearson Correlation Coefficient (R in Figure 6b) of $\sim 71\%$ (Figure 6b).

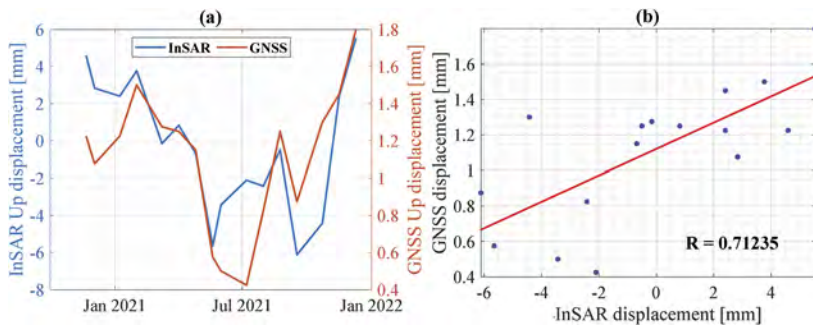


Figure 6. (a) Relative displacement of zone Z1 with respect to zone Z2: InSAR vs GNSS; (b) Correlation study among InSAR and GNSS output.

4 CONCLUSION

One of the main barriers to the use of InSAR processing is the scarce accessibility of relevant software and hardware tools as well as satellite images. In this study, a consumer-grade laptop (16 GB RAM), open-source software and low-resolution radar images (freely available) are used. The results are then validated against the GNSS-derived time histories. Despite the limited number (18) of low-resolution images and the short bridge length, some PSs have been identified in the study area. The GNSS and InSAR vertical components of the bridge displacements present different values; however, the two-displacement series shows a trend correlation. This study presents preliminary evidence suggesting a possible correlation between GNSS and InSAR vertical components. However, due to the limited number of images and potential confounding variables, it is not possible to draw definitive conclusions. Further studies utilizing a larger number of radar images and higher resolution images are necessary to thoroughly assess the PSInSAR workflow based on open-source software. Future works will aim to boost the PSInSAR processing by using high-resolution images to increase the number of PSs, as well as utilizing both ascending and descending images to improve the accuracy of vertical displacement measurements.

ACKNOWLEDGEMENTS

The installation and the management of the GNSS system on the Dovarese bridge were funded by Regione Lombardia–Politecnico di Milano agreement, 2018–2020. This study was partially funded by the Lombardy Region and by the Italian Civil Protection Department within the project RELUIS 2022–2024 WP6 “Structural Health Monitoring and Satellite Data”.

REFERENCES

- Bianchi, S., Biondini, F., Anghileri, M., Capacci, L., Rosati, G., Cazzulani, G., & Caldera, S. 2022a. GNSS-based structural monitoring of the Isola Dovarese Bridge, Italy. *11th International Conference on Bridge Maintenance, Safety and Management*: Barcelona, Spain.
- Bianchi, S., Biondini, F., D’Angelo, M., Ballio, F., Anghileri, M., Rosati, G., & Cazzulani, G. 2022b. Satellite-Based Structural and Hydraulic Monitoring of a 50-Year-Old Bridge over the Oglio River in Italy, EUROSTRUCT 2021: Proceedings of the 1st Conference of the European Association on Quality Control of Bridges and Structures: 380–389.
- Clemente, P. 2020. Monitoring and evaluation of bridges: lessons from the Polcevera Viaduct collapse in Italy, *J Civil Struct Health Monit* 10:177–182.
- Correa-Muñoz, N.A. & Cerón-Calderón, L.A. 2018. Precision and accuracy of the static GNSS method for surveying networks used in Civil Engineering. *Ingeniería e Investigación* 38: 52–59.

- Crosetto, M., Monserrat, O., Cuevas-González, M., De-vanthéry, N., & Crippa, B. 2016. Persistent Scatterer Interferometry: A review. *ISPRS Journal of Photogrammetry and Remote Sensing* 115: 78–79.
- Cusson, D., & Ozkan, I. F. 2018. Satellite-Based InSAR Monitoring of Highway Bridges: Validation Case Study on the North Channel Bridge in Ontario, Canada. *Transportation Research Record* 2672: 76–86.
- Davalillo, J.C.G. et al. 2014. DInSAR analysis of ALOS PALSAR images for the assessment of very slow landslides: the Tena Valley case study. *Landslides* 11(2): 225–246.
- Ferretti, A., Prati, C., & Rocca, F. 2001. Permanent Scatterers in SAR Interferometry. *IEEE transactions on geoscience and remote sensing* 39(1): 8–10.
- Ferretti, A., Savio, G., Barzaghi, R., Borghi, A., Musazzi, S., Novali, F., Prati, C., & Rocca, F. 2007. Submillimeter accuracy of InSAR time series: experimental validation. *IEEE TRANSACTIONS ON GEOSCIENCE AND REMOTE SENSING* 45(5).
- Ferretti, A., Fumagalli, A., Novali, F., Prati, C., Rocca, F., & Rucci, A. 2011. A new algorithm for processing interferometric data-stacks: SqueeSAR. *IEEE TGRS* 49: 3460–3470.
- Giordano, P. F., Turksezer, Z. I., Previtali, M., & Limongelli, M. P. 2022. Damage detection on a historic iron bridge using satellite DInSAR data. *Structural Health Monitoring* 21(5): 2291–2311.
- Hooper, A., Zebker, H., Segall, P., & Kampes, B. 2004. A new method for measuring deformation on volcanoes and other natural terrains using In-SAR persistent scatterers. *Geophysical Research Letters* 31(23).
- Hooper, A & Zebker, H.A. 2007. Phase unwrapping in three dimensions with application to InSAR time series. *J. Opt. Soc. Am. A* 35(16).
- Hooper, A. 2008. A multi-temporal InSAR method incorporating both persistent scatterer and small baseline approaches. *Geophysical Research Letters* 35(16).
- Hooper, A., Bekaert, D., Spaans, K., & Arkan, M. 2012. Recent advances in SAR interferometry time series analysis for measuring crustal deformation. *Tectonophysics* 13: 514–517.
- Huang, Q., Crosetto, M., Monserrat, O., & Crippa, B. 2017. Displacement monitoring and modelling of a high-speed railway bridge using c-band sentinel-1 data. *ISPRS J. Photogram. Remote Sens.* 128(4): 204–211.
- Karbhari, V. & Ansari, F. 2009. *Structural Health Monitoring of Civil Infrastructure Systems*. Cambridge: Woodhead Publishing
- Limongelli, M. P., Gentile, C., Biondini, F., Di Prisco, M., Ballio, F., & Belloli, M. 2022. The monitoring guidelines of the Lombardia region in Italy. *The 1st International Online Conference on Infrastructures*: Basel, Switzerland.
- Mancini, F., Grassi, F., & Cenni, N. 2021. A Workflow Based on SNAP–StaMPS Open-Source Tools and GNSS Data for PSI-Based Ground Deformation Using Dual-Orbit Sentinel-1 Data: Accuracy Assessment with Error Propagation Analysis. *Remote Sensing* 13: 753.
- Milillo, P., Rignot, E., Rizzoli, P., Scheuchl, B., Mougino, J., Bueso-Bello, J., & Prats-Iraola, P. 2019a. Heterogeneous retreat and ice melt of Thwaites Glacier. *West Antarctica. Science advances* 5(1).
- Milillo, P., Giardino, G., Perissin, D., Milillo, G., Coletta, A., & Terranova, C. 2019b. Pre-Collapse Space Geodetic Observations of Critical Infrastructure: The Morandi Bridge, Genoa, Italy. *Remote Sensing* 11(12).
- Qin, X., Ding, X., Liao, M., Zhang, L., & Wang, C. 2019. A bridge-tailored multi-temporal DInSAR approach for remote exploration of de-formation characteristics and mechanisms of complexly structured bridges. *ISPRS J. Photogram. Remote Sens* 156: 27–50.
- Roberts, G. W., Tang, X., & Brown, C. 2015. A review of satellite positioning systems for civil engineering. *Proceedings of the Institution of Civil Engineering - Civil Engineering* 168.
- Selvakumaran, S., Plank, S., Geiß, C., Rossi, C., & Middleton, C. 2018. Remote monitoring to predict bridge scour failure using Interferometric Synthetic Aperture Radar (InSAR) stacking techniques. *Int J Appl Earth Obs Geoinformation* 72: 463–470.
- Selvakumaran, S., Rossi, C., Marinoni, A., Webb, G., Bennetts, J., Barton, E., Plank, S., & Middleton, C. 2020. Combined InSAR and Terrestrial Structural Monitoring of Bridges. *IEEE Transactions on Geoscience and Remote Sensing* 216:71–90.
- Wardhana, K. & Hadipriono, F.C. 2003. Analysis of Recent Bridge Failures in the United States. *J. Perform. Constr. Facil.* 17(3): 144–150
- Wang, X., Zhao, Q., Xi, R., Li, C., Li, G., & Li, L. 2021. Review of Bridge Structural Health Monitoring Based on GNSS: From Displacement Monitoring to Dynamic Characteristic Identification. *in IEEE Access* 9: 43–65.

How to prioritize bridge maintenance using a functional priority index

M. Arena, G. Azzone & V.M. Urbano

Department of Management, Economics and Industrial Engineering, Politecnico di Milano Milano, Lombardy, Italy

P. Secchi, A. Torti & S. Vantini

MOX - Department of Mathematics, Politecnico di Milano, Milano, Lombardy, Italy

ABSTRACT: The progressive aging of civil infrastructures makes it essential to develop managerial tools and instrument for planning maintenance activities. As public entities, typically in charge of the management of infrastructures, have limited resources, it is crucial to define clear prioritization criteria. Addressing this need, this work introduces the usage of a functional priority index for ranking infrastructures on the basis of the impact of their closure. The impact is expressed in terms of induced travel delay for people due to path detour. To estimate this delay an analytical strategy is introduced and applied to assess the priority index on a sample of 290 bridges in Lombardy. Relevant information are gathered integrating two data sources providing information on the transportation network and on the travel demand, i.e. road network data and Origin Destination matrices. The results of this application show that the method enables the identification of the most critical infrastructures and the detection, for each bridge closure, of the most impacted areas of the region and the most impacted hours of the day.

1 INTRODUCTION

Maintaining civil infrastructures and ensuring their functioning is a crucial problem for those entities that are responsible for their management as these structures are naturally subject to both obsolescence and deterioration caused by the effects of natural hazards, operational and environmental conditions (Wang, Zhang, & Li 2017). Among civil infrastructures, bridges are crucial elements characterized by high vulnerability in terms of both natural and man-made risk. The impact of aging and natural deterioration processes could be detrimental to the infrastructure system performances under service loadings or extreme events, such as earthquakes. Moreover, considering their relevance for the transportation network system, they often represent bottlenecks as they are designed to cross obstacles as water flows or highways. Hence, the detour of these infrastructures could result in substantial extra travelling time (Biondini & Frangopol 2016). Given the importance of infrastructures for transport network users, the reliability of nodes of the network represents a key element for evaluating the quality of transport. In order to allow infrastructure reliability and safety for transportation network management purpose, maintenance activities are necessary. In the current economic context, resources available to public entities, that are typically in charge of the management of these infrastructures, are limited, making crucial the identification of some criteria for planning maintenance activities based on clear priorities (Frangopol & Liu 2007).

The evaluation of the priority of intervention and the development of an adequate maintenance planning is a complex task, because it requires to take into considerations many different variables characterizing the level of risk, that range from the age of the infrastructure, its technical characteristics, the operating conditions, and also the consequences of the unavailability

of the infrastructure (Arena, Bianchi, Biondini, Torti, & Vantini 2020). It is worth to highlight that concepts of vulnerability, risks and reliability are still not uniquely defined (see Jenelius et al., 2006 and Pan et al., 2021 for discussions on the definitions of these concepts). In this study, we adopted the definitions provided by Simmons et al., in 2017. The authors identified three different components influencing the level of risk: i) hazard, ii) vulnerability and iii) exposure (Simmons, Corbane, Menoni, Schneiderbauer & Zschau 2017). The first component refers to detrimental events that may cause losses or damage, such as long-term gradual stress events and shock events (Hughes & Healy 2014). Vulnerability refers to the likelihood of occurrence of disruptive events. Exposure is related to the consequences of the hazard on the social community; hence it requires the assessment of the impact on the societal needs. Loss of functionality or temporary closure of an infrastructure is an example of the exposure of the system.

In this paper, we will focus on the system functionality and, more specifically, on the consequence of the unavailability of the infrastructure in terms of impact on users. More in details, we will propose a methodology to evaluate the impact of a bridge closure in connection to its function of maintaining a proper connectivity between all areas of a region, allowing users to move from one point to another and reach their destinations. Despite concepts of vulnerability, reliability and risks do not have widely accepted definitions, authors agree on the usage of the increased cost of travel (measured through time, distance or money) for the users as a reasonable measure of the reduced function of the network (Jenelius et al., 2006). Therefore, this work will assess the impact of the closure of a bridge on the users in terms of delays induced on traveling people. First, a global index, measuring total travel cost in terms of travel time will be presented; second, the variability of the additional travel time along time and space will be evaluated, in order to understand within day variability and identify areas that are most affected by the closure of an infrastructure.

The rest of the manuscript is organized as follows. In Section 2 we introduce a brief review of related literature. The sample and the data sources follow in Section 3. In Section 4, we present the methodology used to evaluate the impact of a bridge closure. In Section 5 we report the results of the analysis on the selected sample. In section 7 we illustrate our conclusions and some of the potential future research paths.

2 RELATED RESEARCH

The assessment of transport failure has recently drawn the attention of both scholars and practitioners. The increasing vulnerability of infrastructures due to climate change (Schneider, Semenov, Patwardhan, Burton, Magadza & Oppenheimer 2007) and the recent collapses of transportation infrastructures, contributed to the enhancement of the relevance of the topic. Several measures of impact assessment have been introduced in the literature, looking at different indicators, such as generalized costs, user costs, efficiency measures, network topological features and congestion effects (Jenelius, Petersen, & Mattsson 2006, Taylor, Sekhar, & D'Este 2006, Stein, Young, Trent, & Pearson 1999). Jafino, Kwakkel and Verbraeck in 2020 reviewed the different measures that have been introduced in prior studies for ranking transport infrastructures on the basis of the consequences deriving from the closure of the infrastructure. Referred to as criticality analysis measures, seventeen measures have been described and compared. A first set of metrics are built on the concept of generalized travel costs derived from an infrastructure disruption. Total travel cost can be assessed only in terms of additional travel time or can be weighted according to the travel demand. A second set of measures is based on the concept of accessibility of the geographical area. In these cases, the impact is assessed in terms of reduced accessibility characterizing the area. Authors often used the Hansen's index for measuring accessibility index (Taylor et al., 2006; Hernández & Gómez, 2011; Taylor & D'Este, 2007). The third set of criticality measures are built for measuring connectivity among different places. A decrease in connectivity implies that some places of the network become unreachable from other places of the network, due to disruption of

single or multiple infrastructures. However, it is worth to highlight that these measures are highly sensitive to inaccuracies in the network data (Jeulieus et al., 2006).

These approaches allow to estimate, in different ways, the consequences of the closure of an infrastructure, generally evaluating the impact of a disruption, in terms of travel costs for the users, accessibility or connectivity of the area. However, all these approaches do not address one element crucial to the understanding of the consequence of a damaged network: the temporal variability of the effects. Since daily traffic profiles are characterized by a large within-day variability, analyzing mobility flows between an origin and a destination during the 24 hours is fundamental to investigate the consequences of closing a transportation infrastructure over the day. In this paper, the object of the analysis is the additional travel cost considering both the induced delay and the travel demand on the network. Regarding the former we represented the induced delay by means of a point belonging to a space of continuous functions defined on the time domain $(0,24)$. As for the latter, the spatial aggregation is the network wide aggregation. This approach allows to estimate the impact of the closure of one infrastructure on the overall transportation network. The impact will be assessed considering the additional delay for the trips of the whole set of origin destination pairs, hence capturing inter-dependencies among elements of the transportation infrastructure (Scott, Novak, Aultman-Hall, & Guo, 2006).

3 DATA

3.1 *The sample*

In this manuscript, for supporting the development of the methodology, we will focus on a reduced sample of road infrastructures, made of 290 bridges, selected in accordance with regional authorities from Lombardy Region. This area is characterized by a large and heterogeneous territory with an area of 23,844 square kilometers and a resident population of about 10 million inhabitants. The road network of Lombardy counts 70,000 km of roads. On this transport network there are almost 10,000 infrastructures, including bridges, tunnels and overpasses. The sample will allow us to test the methodology, understand potential criticisms and limitations before extending the approach to all the 10,000 infrastructures of the road network. The sample includes the most relevant bridges located in the twelve provinces which the region is divided into: Bergamo (BG), Brescia (BS), Milano (CMM), Como (CO), Cremona (CR), Lecco (LC), Lodi (LO), Monza Brianza (MB), Mantova (MN), Pavia (PV), Sondrio (SO) and Varese (VA). Each bridge is identified by an identification code of the road network section, the province it belongs to, and its GPS position.

3.2 *The datasets*

As follows we describe the datasets available for developing the project: the regional road network model and the regional OD matrices, both provided by the regional government of Lombardy. The road network model is a spatial network made of about 37,000 nodes and 82,000 directional edges, which model all types of roads of the real network. Nodes represent the intersections between two or more roads, whereas edges are segments of road between two intersections. For each directed edge of the network, an identification code of the road section, the type of the road (e.g. highway, regional, provincial, local) the length (km), the typical travel time (hour) and the velocity without traffic (km/h) are known.

Regione Lombardia, the administrative body of Lombardy, publishes every few years an OD matrix, containing the number of trips across different mobility areas during a typical working day. OD matrix has been estimated starting from survey data on travel behavior and merging this information with data related to the socioeconomics features of the different areas of the region. The OD matrices of Lombardy contain the number of hourly trips between 1,450 internal mobility areas. Trips are classified according to eight modalities (car driver, car passenger, motorbike, bus, train, bike, foot and others) and five purposes (work,

study, business, occasional and return home). For the scope of our analyses, we aggregated all trips with respect to their purpose and we considered only those of people moving with a motor vehicle on the road, hence aggregating the modalities car driver, car passenger, motorbike and bus, while disregarding the trips related to the other modalities. In this way, we obtain a total of almost 12.4 million of trips distributed over the day, accounting for almost 75% of the total trips contained in the matrix. For the scope of our analyses, we integrated our two sources of information, the road network data model and the OD matrices.

4 METHODOLOGY

In this section, we illustrate the main methodological choices made in this work in connection to the selection of the indicator used to measure the impact and the methodology for the assessment of the impact for the selected bridges. Specifically, we propose an approach that relies on prior literature focusing on the evaluation of consequences of the closure of the infrastructure in terms of additional travel cost, but enriches prior research, considering how this delay changes over time and space, i.e. time and space variability.

4.1 *The calculation of the global index*

The first step of analysis is the so-called traffic assignment step and consists in the estimation, for each trip, of the route on the road network. First, for each mobility area, its centroid is associated to the closest node of the road network data model. The assignment of the centroid is computed by minimizing the Euclidean distance in kilometers between the two. Next, for every OD couple the shortest time path $O \rightarrow D$ on the road network data model is found by means of the Dijkstra's algorithm (Newman 2018). Through this algorithm, the number of trips passing through it is computed. This latter is obtained by summing over all OD pairs whose shortest connecting path goes through e . The relevant indicator could either be the flow function describing the number of trips passing from e at any time t of the day:

$$f_e(t) = \sum_{(O,D):e \in O \rightarrow D} f_{(O,D)}(t - t_{(O,e)}) \quad (1)$$

where $f_{(O,D)}(t)$ is a standard function indicating the number of travelers departing from O at time t and heading at D , $t_{(O,e)}$ indicates the travel time necessary for reaching the midpoint of edge e starting from O , and $f_{(O,D)}(t - t_{(O,e)})$ the number of travelers at time t on edge e departed from O and heading at D . Coherently with previous studies we define an index on the basis of the importance of bridges in maintaining a proper connectivity between all origin and destination couples of the OD matrices in order to measure the impact of the bridge closure (Berdica & Mattsson 2007, Sullivan, Aultman-Hall, & Novak 2009, Rupi, Bernardi, Rossi, & Danesi 2015). We evaluate the effects of a bridge closure on the movement of people, by estimating an index expressed in terms of extra person-hours traveled. To measure the consequences of the closure of a bridge belonging to the edge e of the road network data model, we virtually remove the edge e from the network. Then, for every OD pair we measure the increase in travel time of the shortest time path connecting O and D after the removal of the edge e . Hence, to obtain the extra traveled person-hours we simply multiply this extra travel time by the number of trips associated to edge e :

$$I_e = \sum_{(O,D):e \in O \rightarrow D} \left[t_{(O,D)}^- - t_{(O,D)} \right] \int f_{(O,D)}(t - t_{(O,e)}) dt. \quad (2)$$

I_e is measured in person-hours and indicates the cumulative extra-time, spent on road in the typical working day by people traveling within the area, due to the closure of a bridge belonging to the edge e .

4.2 Spatial-temporal indexes

The global index I_e has the benefit of providing an estimate of the total impact of a bridge closure but does not consider the spatio-temporal variability, i.e. how this impact spreads during the hours of the day and across geographical areas of the region. To this purpose, we provide a novel two-way approach exploring both the temporal and the spatial dimensions. From a temporal perspective, we estimate how the impact of a bridge closure changes along time. To this end, we follow the same argument used above to build the global impact index I_e , but separately for each time $t \rightarrow [0, 24]$. Hence, to measure along time the impact of the closure of a bridge belonging to the edge e , we measure the temporal impact function

$$i_e(t) = \sum_{(O,D):e \in O \rightarrow D} \left[t_{(O,D)}^{-e} - t_{(O,D)} \right] f_{(O,D)}(t - t_{(O,e)}) \quad (3)$$

From a spatial perspective, we want to estimate how the impact of a bridge closure is distributed across the region, namely the most impacted areas of Lombardy. Hence, we apply again the same argument used above for the construction of I_e (2) but now we fix the origins or the destinations:

$$I_e^O = \sum_{D:e \in O \rightarrow D} \left[t_{(O,D)}^{-e} - t_{(O,D)} \right] \int f_{(O,D)}(t - t_{(O,e)}) dt \quad (4)$$

And

$$I_e^D = \sum_{O:e \in O \rightarrow D} \left[t_{(O,D)}^{-e} - t_{(O,D)} \right] \int f_{(O,D)}(t - t_{(O,e)}) dt. \quad (5)$$

5 RESULTS

5.1 Analysis of the global index

Figure 1 shows the value of I_e for each bridge. In this, each bridge is colored according to its global impact in terms of person-hours per day using a log-scale. Looking at the Figure 1, it

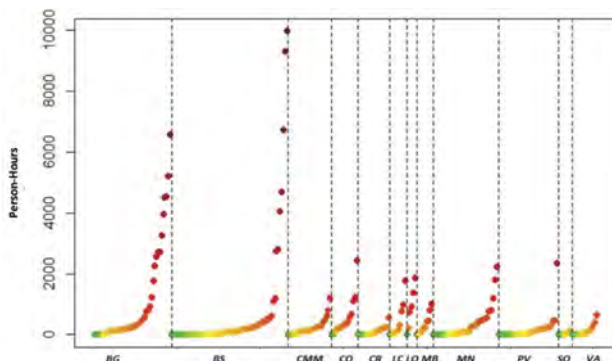


Figure 1. Distribution of the global impact (person-hours) of the 290 bridges for each province.

appears that the most critical bridges are located in the north side of the region in the provinces of Bergamo and Brescia, which are mainly in a mountain area with a sparse road network made of few main roads mostly located at the valley bottom with very time-consuming alternative paths. Moreover, the values of I_e in the different provinces follow a strongly right-skewed distribution characterized by few bridges with high values and many bridges with low values.

5.2 Analysis of the spatio-temporal effects

We now investigate the impact of each bridge closure by its temporal and spatial effect during the day using the functions $i_e(t)$. An illustrative example related to a one-way bridge is reported in Figure 2 which shows the spatio-temporal effects due to the closure of the most critical afternoon-peak bridge: on top left, the geographical position of the selected bridge is highlighted; in the top right we show the temporal impact function of its closure; at the bottom, the spatial impacts on both origins (left) and destinations (right) are reported. Results reveal a clear difference between the impacted origins, all of them located west of the bridge, and the impacted destinations, all of them located east of the bridge. This is due to the fact that the selected bridge is on a one-way road going from west to east. Looking at the temporal impact function, the afternoon peak appears to be higher than the morning peak, due to the fact that people moving on this road are likely to be mostly commuters coming back home after going west to work in the morning.

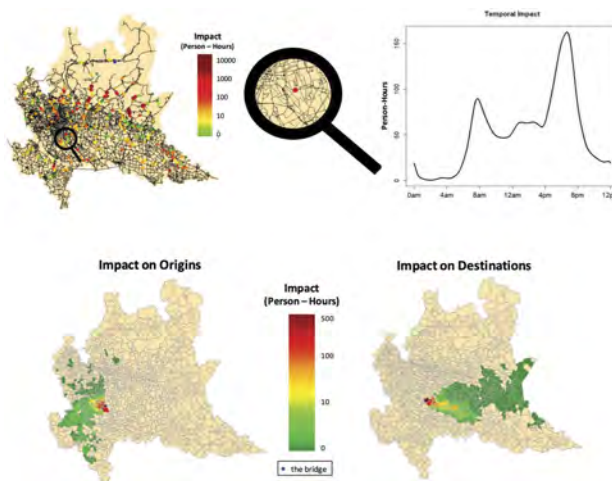


Figure 2. Top: the selected bridge on the road network of Lombardy and its temporal impact function. Bottom: the spatial impacts of the bridge closure, highlighted with a blue point, on both origins and destinations.

6 MONETARY QUANTIFICATION

Delays caused by the unavailability of an infrastructure can be expressed in monetary terms through the Value of Time (VOT), also called the value of travel time savings. The Value of Time is defined as “*the monetary value attached to the possibility of save a determined amount of travel time*” (Zamparini & Reggiani 2007). In other words, the VOT can be seen as willingness-to-pay indicator (Hess 2005), that links time to the cost that individuals have to face in order to accomplish their mobility activities (Zamparini & Reggiani 2007). The VOT is of central interest in transportation research, because it is one of the most relevant components in

the evaluation of mobility and infrastructural investments and it is a very important parameter for explaining travel behavior and modal choices.

Obviously, the VOT is not unique as it depends significantly on the characteristics of the individual, the means of transport and, more generally, the conditions in which a trip is made. In the literature, very different VOTs, estimated on the basis of the various studies are available. One relevant example is the meta-analysis provided by (Wardman, Chintakayala, & de Jong 2016), that covers more than 3100 monetary valuations deriving from 389 studies conducted in Europe between 1963 and 2011. The valuation of VOT also refer to the Italian transportation context, in line with the geographical scope of this analysis. Moreover, the study introduces different segmentation factors including travelling mode and travelling purpose, hence enabling the estimation of the VOT for people using the car as transportation mean.

7 CONCLUSIONS

This work proposes a methodology aimed to assess the functional priority of one critical infrastructure in a transport network, bridges. Specifically, we focused on the exposure risk addressing the impact of the closure of the infrastructure in connection to its function of ensuring the accessibility of an area, connecting different geographical areas. From a methodological point of view, we provided different levels of impact assessments. First and foremost, we introduced the global index for estimating the impact of a bridge closure, hence providing a means for ranking infrastructures.

Secondly, we explored both temporal and spatial variability. From a temporal point of view, we evaluated how the impact of a bridge closure varies according to the hour of the day. From a spatial point of view, we evaluated how the impact of a bridge closure is distributed over origins and destinations of trips. The analysis of the temporal results allows to identify the most critical bridges of the region and to highlight for each bridge the most impacting hours of the day. These results can be used by decision makers for communication or planning purpose. Regarding the former, decision makers can anticipate the damage on the users caused by maintenance interventions on road infrastructures. Moreover, the information on the temporal variability of the consequences of bridge closure can be instrumental in optimizing the road maintenance schedule. The impact of bridge closure is also assessed in economic terms. Using the concept of the value of time (VOT), the hours of delay for the users have been translated into monetary value, hence highlighting the socio-economic cost for one hour of infrastructure disruption for people using the examined infrastructure.

The developed methodology has proved to be scalable and repeatable, thus providing possibility for application on a larger set of bridges or to other contexts. Specifically, the proposed methodology can be applied to other geographical areas and extended to any other transportation infrastructure that can be modeled as a directional edge, such as tunnels and overpasses. In conclusion, we want to highlight some of the potential paths for future research. First, the proposed methodology focuses on one specific impact dimension, that is the impact on users. This dimension has to be complemented in order to consider the broader socio-economic impact, including the impact on the economic activities operating in the area related to supply chain management (Bell, 2000; Smith et al., 2003). The proposed approach could also be enhanced by considering elastic demand function. Further research could also be directed towards the consideration of other maintenance strategies, such as the reduced capacity due to closure of one of the two road directions.

REFERENCES

- Arena, M., S. Bianchi, F. Biondini, A. Torti, & S. Vantini (2020). Individuare le priorit  manutentive dei ponti stradali lombardi. In G. Azzone, S. Balducci, and P. Secchi (Eds.), *Infrastrutture e Citta`. Innovazione, coesione sociale e digitalizzazione*, pp. 185–223. Milan: Francesco Brioschi Editore

- Bell, M.G.H., 2000. A game theory approach to measuring the performance reliability of transportation networks. *Transportation Research Part B: Methodological* 34, 533–545.
- Berdica, K. & L.-G. Mattsson (2007). Vulnerability: a modelbased case study of the road network in stockholm. In *Critical infrastructure*, pp. 81–106. Springer.
- Biondini F, Frangopol DM (2016). Life-cycle performance of deteriorating structural systems under uncertainty: review. *J Struct Eng*;142(9): F40160011-17.
- D’Este G., M Taylor (2003). Network Vulnerability: An Approach to Reliability Analysis at the Level of National Strategic Transport Networks. In: Bell MGH, Iida Y, eds. *The Network Reliability of Transport*. Vol 1. Emerald Group Publishing Limited; 23–44. doi:10.1108/9781786359544-002
- Frangopol, D. M. & M. Liu (2007). Maintenance and management of civil infrastructure based on condition, safety, optimization, and life-cycle cost. *Structure and infrastructure engineering* 3(1), 29–41.
- Gradilla Hernández L, González Gómez O. (2011) Identification of critical segments by vulnerability for freight transport on the paved road network of Mexico. *Investig geográficas*: (74):48–57.
- Jafino BA, Kwakkel J, Verbraeck A. (2020) Transport network criticality metrics: a comparative analysis and a guideline for selection. *Transp Rev*.40(2):241–264. doi:10.1080/01441647.2019.1703843
- Jenelius, E., T. Petersen, & L.-G. Mattsson (2006). Importance and exposure in road network vulnerability analysis. *Transportation Research Part A: Policy and Practice* 40(7), 537–560.
- Hess, S. (2005). Advanced discrete choice models with applications to transport demand.1–303.
- Hughes, J.F. and Healy, K. 2014. Measuring the resilience of transportation networks. Technical Report, NZ Transport Agency Research Report 546.
- Newman, M. (2018). *Networks*. Oxford university press.
- Rupi, F., S. Bernardi, G. Rossi, & A. Danesi (2015). The evaluation of road network vulnerability in mountainous areas: a case study. *Networks and Spatial Economics* 15(2), 397–411.
- Schneider, S. H., S. Semenov, A. Patwardhan, I. Burton, C. Magadza, M. Oppenheimer, A. B. Pittock, J. B. Smith, A. Suarez, and F. Yamin. (2007) Assessing Key Vulnerabilities and the Risk from Climate Change. In *Fourth Assessment Report of the Intergovernmental Panel on Climate Change* (M. L. Parry, O. F. Canziani, J. P. Palutikof, P. J. van der Linden, and C. E. Hanson, eds.), Cambridge University Press, Cambridge, Mass, pp. 779–810.
- Scott, D. M., Novak, D. C., Aultman-Hall, L., & Guo, F. (2006). Network robustness index: A new method for identifying critical links and evaluating the performance of transportation networks. *Journal of Transport Geography*, 14(3),215–227. doi:10.1016/j.jtrangeo.2005.10.003
- Simmons, D.C., Corbane, C., Menoni, S., Schneiderbauer, S., Zschau, L. (2017). Understanding disaster risk: risk assessment methodologies and examples. In: *Science for disaster risk management: knowing better and losing less*. Chapter 2, Poljanšek, K., Marín Ferrer, M., De Groeve, T., Clark, I. eds., 38–130.
- Smith, B.L., Qin, L., Venkatanarayana, R., (2003). Characterization of freeway capacity reduction resulting from traffic accidents. *Journal of Transportation Engineering* 129, 362–368.
- Stein, S. M., G. K. Young, R. E. Trent, & D. R. Pearson (1999). Prioritizing scour vulnerable bridges using risk. *Journal of Infrastructure Systems* 5(3),95–101.
- Sullivan, J., L. Aultman-Hall, & D. Novak (2009). A review of current practice in network disruption analysis and an assessment of the ability to account for isolating links in transportation networks. *Transportation Letters* 1(4), 271–280.
- Taylor, M. A., S. V. Sekhar, & G. M. D’Este (2006). Application of accessibility-based methods for vulnerability analysis of strategic road networks. *Networks and Spatial Economics* 6(3), 267–291.
- Wang, C., H. Zhang, & Q. Li (2017). Reliability assessment of aging structures subjected to gradual and shock deteriorations. *Reliability Engineering and System Safety* 161, 78–86.
- Wardman, M., V. P. K. Chintakayala, & G. de Jong (2016). Values of travel time in europe: Review and meta-analysis. *Transportation Research Part A: Policy and Practice* 94, 93–111.
- Zamparini, L., & Reggiani, A. (2007). Meta-analysis and the value of travel time savings: A transatlantic perspective in passenger transport. *Networks and Spatial Economics*, 7(4),377–396. <https://doi.org/10.1007/s11067-007-9028-5>.

*SS10: Deterioration modeling of concrete, rebar, steel
and bond performance*
Organizers: X. Gao, X. Ren & J. Li



Taylor & Francis

Taylor & Francis Group

<http://taylorandfrancis.com>

Analysis of mechanical behavior of bond between plain rebar and concrete

X. Gao & Y. Yu

Department of Structural Engineering, Tongji University, Shanghai, China

C. Su

Department of Structural Engineering, Tongji University, Shanghai, China
Shandong Provincial Architecture Design & Research Institute

J. Li

Department of Structural Engineering, Tongji University, Shanghai, China

ABSTRACT: The analysis of the bond properties of plain rebars to concrete is of great significance for the identification and strengthening of historic buildings. This study investigates the bonding mechanism of plain rebars to concrete through theoretical analysis of pull-out tests. The normal stress at the contact interface due to the difference in Poisson's ratio between reinforcement and concrete and the resulting bond stress are quantified through the combination of elastic mechanics and fracture mechanics. The energy release rate is introduced in the analysis to elucidate that when the crack extension force is greater than the frictional resistance at the debonding interface, the bond-slip curve will drop precipitously after reaching the peak point (cliff type), and conversely the curve decreases slowly under abrasive wear (slope type). According to the theory, the bond-slip curve of plain rebar and concrete can be predicted.

1 INTRODUCTION

Plain rebars are used as reinforcement in historic buildings; therefore, the analysis of the bond properties of plain rebars to concrete has positive implications for the identification and strengthening of historic buildings (Cairns 2021, Mo & Chan 1996, Robuschi et al. 2021, Xu et al. 2019). The study of the bond performance of reinforcement and concrete has been accompanied by the application of reinforced concrete structures, however, due to the complexity of the factors and the change of the impact with different stress states, the research on the bond properties is still limited. The current research methods for bond behavior mainly include experimental studies, numerical analysis and analytical solutions. Among the experimental studies, axial pull-out tests (Darwin et al. 1996, Gao et al. 2018) and beam tests (Gao et al. 2022, Mo & Chan 1996) are the main test types where the concrete strength and component including the addition of various fibers such as CF, SF, PF, etc., the confining pressure effect such as stirrups and concrete cover depth, the longitudinal reinforcement such as the surface shape, diameter and anchorage length are the key factors; and the magnitude of the load, the strain and slip of the reinforcement are the main physical quantities measured in the tests owing to limitations of measurements.

Compared to the large number of experimental studies on the bond properties, the research on the bonding mechanism at the interface of reinforcement and concrete need to be further studied. The consensus on the bond mechanism is chemical adhesion at the interface at the

initial stage, and with the emergence of relative slip at the interface of reinforcement and concrete, mechanical interlock force and frictional force come into play. In terms of numerical analysis, the bond behavior is simulated by adding zero-thickness tangential and normal spring elements (Ngo & Scordelis 1967, Erfanian & Elwi 2019, fib 2022), or indirectly by adjusting the constitutive relations of reinforcement and concrete (Liu et al. 2020, Feng et al. 2018, Jendele & Cervenka 2006). For the study of the mechanical behavior of the bond mechanism, some researchers considered it as an axisymmetric plane strain problem based on elastic mechanics, and solved the bond stress in the limit state by using the elastic mechanical characteristics of thick-walled cylinders (Tepfers & De Lorenzis 2003, Gao et al. 2019). Ouyang & Shah (1994) analyzed the bond-slip properties of reinforcement and concrete based on fracture mechanics, and the damage caused by concrete cracking was considered to correct the bond-slip model (Phan et al. 2015).

The interfacial interaction between plain rebar and concrete is a dynamic process of bonding, damage and frictional state with the change of loadings. In this paper, considering the bond mechanism of reinforcement and concrete, the normal stress at the interface due to the difference in Poisson’s ratio between reinforcement and concrete and the resulting bond stress are quantified through the combination of elastic mechanics and fracture mechanics. By comparing the crack extension force and the frictional resistance at the debonding interface, the bond-slip curve can be judged as a cliff type with a precipitous drop after reaching the peak point and a slope type with a slow decrease under abrasive wear.

2 BASIC ASSUMPTIONS OF PULL-OUT SPECIMENS

The pull-out test of plain rebars in concrete matrix is the main test method to study the bond properties between plain rebars and concrete. A detailed theoretical analysis of the pull-out process of the rebar helps to correctly understand the bonding behavior. In most of the pull-out tests of plain rebars, the fixed end of the matrix (i.e. concrete) is at the loading end (Figure 1a). Since the bond properties of plain rebars and concrete is mechanically identical to that of fiber and concrete, Gao et al (1988) analyzed the debonding process of fiber and matrix based on elasticity and fracture mechanics, as shown in Figure 1b where the loading end is free and the other end of the matrix is fixed. In addition, there are some assumptions were used: the stress distribution of interface between fiber and matrix are uniform; the stress at the fiber-matrix bonding interface away from the crack tip is ignored; and the stress distribution length at the crack tip is ignored. Comparing Figure 1a and 1b, it found that the boundary conditions of the two are not consistent. Therefore, based on the study by Gao et al (1988), the theoretical equations are derived in this paper using the boundary conditions shown in Figure 1a, which conform to the boundary conditions of pull-out test of plain rebars.

The initial bond length of the plain rebar is s . Assuming a debonding zone of length l already exists between the fiber and matrix, the length of the bonded region is $s-l$. The radius of the plain rebar is r , its elastic modulus and Poisson’s ratio are E_f and ν_f , respectively; and the radius of the matrix is R , its elastic modulus and Poisson’s ratio are E_m and ν_m , respectively.

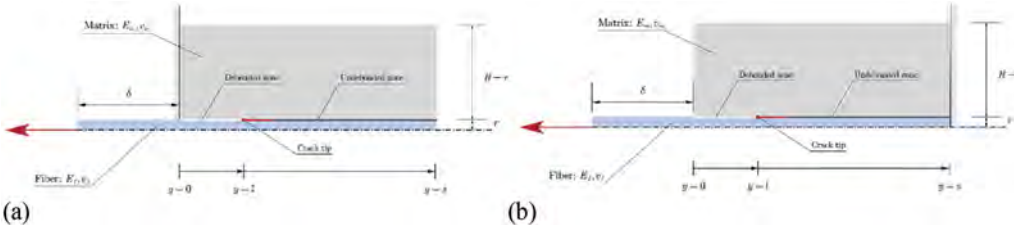


Figure 1. Specimen of pull-out test: (a) plain rebar; (b) fiber.

3 INTERFACIAL NORMAL STRESS

3.1 Basic equations

For a cylindrical pull-out specimen with the plain rebar embedded on the center line, the stress state of the plain rebar in the axial plane with its surrounding concrete can be simplified to an axisymmetric plane strain problem. Polar coordinates are used for computational simplicity in which the distance from the origin is ρ and the angle is φ , and the expressions for each stress component when the body force is ignored are:

$$\begin{cases} \sigma_\rho = \frac{A}{\rho^2} + B(1 + 2 \ln \rho) + 2C \\ \sigma_\varphi = -\frac{A}{\rho^2} + B(3 + 2 \ln \rho) + 2C \\ \tau_{\rho\varphi} = 0 \end{cases} \quad (1)$$

where σ_ρ = radial stress; σ_φ = hoop stress; and $\tau_{\rho\varphi}$ = tangential stress.

The expressions for each displacement component are:

$$\begin{cases} u_\rho = -\frac{1+\nu}{E} \left[\frac{A}{\rho} - 2B\rho(\ln \rho - 1) - (1 - 4\nu)B\rho - 2(1 - 2\nu)C\rho \right] \\ u_\varphi = \frac{4B\rho\varphi(1-\nu^2)}{E} \end{cases} \quad (2)$$

where u_ρ = radial displacement and u_φ = hoop displacement.

Based on the assumption of complete contact between the plain rebar and concrete at the initial stage, which means the plain rebar should not detach from its surrounding concrete at the normal direction, and there is no relative sliding at the tangential direction, the normal stresses of the plain rebar and the concrete at the interface ($\rho = r$) are equal, and the tangential stresses are also equal. In addition, the normal and tangential displacements of the plain rebar and the concrete at the contact interface are also equal, respectively.

3.2 Stress and displacement of the plain rebar and concrete

According to the boundary conditions, the stress and displacement components of the plain rebar can be expressed respectively as:

$$\sigma_{\rho,f} = \sigma_{\varphi,f} = q^* \quad (3)$$

$$u_{\rho,f} = \frac{1 + \nu_f}{E_f} (1 - 2\nu_f)q^*\rho \quad (4)$$

Similarly, the stress and displacement components of concrete can be expressed respectively as:

$$\sigma_{\rho,m} = \frac{\frac{R^2}{\rho^2} - 1}{\frac{R^2}{r^2} - 1} q^* \quad (5)$$

$$\sigma_{\varphi,m} = -\frac{\frac{R^2}{\rho^2} + 1}{\frac{R^2}{r^2} - 1} q^* \quad (6)$$

$$u_{\rho,m} = -\frac{1}{E_m} \left[\frac{1 + \nu_m}{\rho} \frac{r^2 R^2 q^*}{R^2 - r^2} + (1 + 2\nu_m)(1 - 2\nu_m) \frac{r^2 q^* \rho}{R^2 - r^2} \right] \quad (7)$$

3.3 Interfacial normal stress

Based on Equation 4 for the radial displacement of the plain rebar and Equation 7 for the radial displacement of the concrete, combined with the assumption of complete contact, an equation is obtained:

$$\alpha(1 - \nu_f)q^* - 2\alpha\nu_f^2q^* = -(1 + 2\gamma + \nu_m)q^* + 2\gamma\nu_m^2q^* \quad (8)$$

where $\alpha = E_m/E_f$ and $\gamma = r^2/(R^2-r^2)$.

In the plane strain problem, the out-of-plane strain can be ignored, so the axial strain of the plain rebar and concrete can be considered equal to zero, and the relationship between the out-of-plane axial stress and the in-plane stress of the plain rebar and concrete are:

$$\begin{cases} \sigma_f = \nu_f(\sigma_{\rho,f} + \sigma_{\varphi,f}) \\ \sigma_m = \nu_f(\sigma_{\rho,m} + \sigma_{\varphi,m}) \end{cases} \quad (9)$$

By substituting Equations 3, 5 and 6 into Equation 9, the relationship between the axial stress of the plain rebar and concrete and the normal stress q^* at the interface can be obtained:

$$\begin{cases} \sigma_f = 2\nu_fq^* \\ \sigma_m = -2\gamma\nu_mq^* \end{cases} \quad (10)$$

The expression of normal stress at the interface can be obtained by substituting the above Equation 10 into Equation 8:

$$q^* = \frac{\alpha\nu_f\sigma_f - \nu_m\sigma_m}{\alpha(1 - \nu_f) + 1 + \nu_m + 2\gamma} \quad (11)$$

According to the assumption that the stress distribution of both plain rebar and concrete is uniform in the cross section, the axial stress of plain rebar and concrete can be obtained directly by dividing their axial cross-sectional resultant forces (T_m , T_f) by the cross-sectional area.

The relationship between the normal stress q^* at the interface and the axial cross-sectional resultant forces (T_m , T_f) can be obtained:

$$q^* = \frac{1}{\pi r^2} \left[\frac{\alpha\nu_f T_f - \gamma\nu_m T_m}{\alpha(1 - \nu_f) + 1 + \nu_m + 2\gamma} \right] \quad (12)$$

4 SOLUTION OF THE TENSILE FORCE AND DISPLACEMENT

Take a micro-element dy in the debonding zone for analysis, the rebar is under tension, one end of the tension is T_f and the other end is $T_f + dT_f$; the concrete is under compression, one end of the resultant force is T_m and the other end is $T_m + dT_m$, the interface between concrete and rebar has a tangential stress τ_s . The equilibrium equation of the micro-element can be established:

$$\frac{dT_m}{dy} = -\frac{dT_f}{dy} = 2\pi r\tau_s \quad (13)$$

The interfacial tangential stress τ_s is generated by friction, so it can be obtained from the following equation:

$$\tau_s = \mu(q_0 - q^*) \quad (14)$$

where μ = friction factor at debonding interface.

Considering the tension force of the rebar is P at the loading end, and the compression force of the concrete is $-P$, the resultant forces of the rebar and the concrete can be obtained by substituting Equations 12 and 14 into Equation 13:

$$T_m = (\tilde{P} - P)e^{\lambda y} - \tilde{P} \quad (15)$$

$$T_f = -T_m \quad (16)$$

where

$$\tilde{P} = \frac{\pi r^2 q_0}{\alpha \nu_f + \gamma \nu_m} [\alpha(1 - \nu_f) + 1 + \nu_m + 2\gamma] \quad (17)$$

$$\lambda = \frac{2\mu}{r} \left[\frac{\alpha \nu_f + \gamma \nu_m}{\alpha(1 - \nu_f) + 1 + \nu_m + 2\gamma} \right] \quad (18)$$

According to Equation 17, when $P = \tilde{P}$, the resultant force of concrete section is equal to $-\tilde{P}$ ($T_m \equiv -\tilde{P}$), the resultant force of rebar section is equal to \tilde{P} ($T_f \equiv \tilde{P}$), the resultant force in the debonding zone does not vary with the change of cross-sectional position, which indicates that there is no tangential stress at the debonding interface, and the Poisson effect at this moment has completely offset the initial normal stress q_0 . therefore, \tilde{P} is considered as the characteristic tension force value that can completely offset the initial pressure at the interface caused by the Poisson effect.

The strains of the rebar and concrete in the debonding zone can be calculated by the following equations:

$$\frac{du_f}{dy} = \frac{T_f}{\pi r^2 E_f} - \frac{2\nu_f}{E_f} q^* \quad (19)$$

$$\frac{du_m}{dy} = \frac{\gamma T_m}{\pi r^2 E_m} + \frac{2\nu_m}{E_m} \gamma q^* \quad (20)$$

where u_f = the axial displacement of the rebar and u_m = the axial displacement of the concrete.

The axial displacement of the rebar and concrete can be obtained by substituting Equation 18 into Equation 19 and Equation 15 into Equation 20 and integrating. The displacement difference between the rebar and concrete can be obtained thereby:

$$\begin{aligned} \nu(y) &= |u_f(y) - u_m(y)| \\ &= \left[\frac{1 - 2k\nu_f}{\pi r^2 E_f} + \frac{\gamma(1 - 2k\nu_m)}{\pi r^2 E_m} \right] \cdot \left[\tilde{P}(l - y) - (\tilde{P} - P) \frac{1}{\lambda} (e^{\lambda l} - e^{\lambda y}) \right] \end{aligned} \quad (21)$$

where

$$k = \frac{\alpha \nu_f + \gamma \nu_m}{\alpha(1 - \nu_f) + 1 + \nu_m + 2\gamma} \quad (22)$$

5 LOAD-DISPLACEMENT CURVE OF PULL-OUT SPECIMENS

5.1 Threshold value of initial normal stress

Assuming the cracked body is always in the elastic state, the equilibrium equation can be established according to the energy conservation:

$$\int_{S_T} \mathbf{T} d\mathbf{u} ds = \zeta dA + \int_{S_T} \tau_s d\mathbf{v} ds + dU \quad (23)$$

where ζ = the energy release rate and U = the elastic strain energy.

The left side of Equation 23 is the mechanical work done by external forces during crack extension, the first term on the right side of Equation 23 is the energy consumed by crack extension, the second term is the energy consumed by interface friction, and the third term is the change in the elastic strain energy of the system. The elastic strain energy U of the cracked body can be directly expressed as:

$$dU = \frac{1}{2} \int_{S_T} \mathbf{T} d\mathbf{u} ds - \frac{1}{2} \int_{S_T} \tau_s d\mathbf{v} ds \quad (24)$$

The energy release rate can be obtained by substituting Equation 24 into Equation 23:

$$\zeta = \frac{1}{2} \frac{\partial}{\partial A} \int_{S_T} \mathbf{T} d\mathbf{u} ds - \frac{1}{2} \frac{\partial}{\partial A} \int_{S_T} \tau_s d\mathbf{v} ds \quad (25)$$

The pull-out specimen can be regarded as a special case of the cracked body, the external force \mathbf{T} is the loading end tension force P , and its displacement $-u_f(0)$ is the displacement of rebar at the loading end, and the minus sign here means the displacement direction of rebar at the loading end is opposite to the positive direction of the coordinate system. The relative slip between the crack surfaces is the displacement difference $v(y)$ between the rebar and concrete, the crack area A is the area of the debonding zone ($2\pi rl$), and the micro surface area ds is $2\pi r dy$. When the above-mentioned parameter is substituted into Equation 25, the energy release rate can be obtained.

$$\zeta = \frac{-P \partial u_f(0)}{4\pi r \partial l} - \frac{1}{2} \int_0^l \tau_s \frac{\partial v(y)}{\partial l} dy \quad (26)$$

The following equation can be obtained by substituting Equation 21 into Equation 26:

$$4\pi^2 r^3 E_f \zeta = (1 + \beta)(1 - 2k\nu_f)(P - Q)^2 \quad (27)$$

where

$$Q = T_m(l) + P = (\tilde{P} - P)(e^{\lambda l} - 1) \quad (28)$$

According to Equation 27, the expression of the tension force P at the loading end can be obtained:

$$P = 2\pi r^{3/2} \left[\frac{E_f \zeta}{(1 + \beta)(1 - 2k\nu_f)} \right]^{1/2} + Q \quad (29)$$

When there is no friction force at the interface of the debonding zone, i.e. $\mu = 0$, then the coefficient $\lambda = 0$ according to Equation 18, and followed by $Q = 0$ according to Equation 28. Therefore, only the first term remains on the right side of Equation 29, and P is defined as P_0 at this moment:

$$P_0 = 2\pi r^{3/2} \left[\frac{E_f \zeta}{(1 + \beta)(1 - 2k\nu_f)} \right]^{1/2} \quad (30)$$

P_0 indicates the tensile force without friction at the debonding interface, which is the force required for crack expansion. The tension force P can be simplified by substituting Equations 28 and 30 into Equation 29:

$$P = \tilde{P} - (\tilde{P} - P_0)/e^{\lambda l} \quad (31)$$

Threshold value of initial normal stress can be obtained according to Equation 31 if $P_0 = \tilde{P}$.

5.2 Typical load-displacement curves

There are two typical load-displacement curves during the pull-out process of plain rebar (Figure 2). When the initial normal stress q_0 is greater than the threshold value of initial normal stress q_{th} , the peak of the load-displacement curve of the pull-out test occurs when the rebar is about to be completely debonding from concrete ($y = s$), and before that, the force $P(s)$ at the loading end can be expressed as:

$$P(s) = \tilde{P}(1 - e^{-\lambda s}) + P_0 e^{-\lambda s} \quad (32)$$

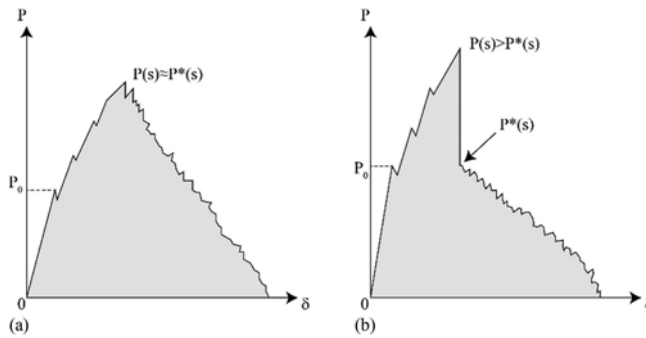


Figure 2. Two typical load-displacement curves: (a) slope type; (b) cliff type.

After complete debonding, there is only friction force at the interface between plain rebar and concrete, defining the tension force at this moment as:

$$P^*(s) = \tilde{P}(1 - e^{-\lambda s}) \quad (33)$$

When the difference between $P(s)$ and $P^*(s)$ is small, which is reflected in the load-displacement curve as a slow decline after reaching the peak (Figure 2a), and this curve is named as slope type curve. When $P(s) > P^*(s)$, the load-displacement curve will drop precipitously to $P^*(s)$ after reaching the peak (Figure 2b), this curve is named as cliff type curve.

6 CONCLUSIONS

This study analysis the reasons for two typical types load-displacement curves during the pull-out tests of plain rebar. The following conclusions were determined:

- The normal stress at the interface due to the difference in Poisson's ratio between plain rebar and concrete is quantified, and the expression of the characteristic tension force that can completely offset the initial pressure at the interface caused by the Poisson effect is derived.

- The energy release rate is introduced to elaborate the load-displacement curve. The reaction force at the loading end is divided into two parts, the friction force at the debonding interface and the crack extension force at the crack tip. When the crack extension force is greater than the frictional force, the curve, named as cliff type curve, shows a steep drop after reaching the peak point; on the contrary, the curve belongs to slope type and decreases slowly after reaching the peak under abrasive wear.
- The verification of the theory is not presented due to the page limit, and the service-life of the bond due to the corrosion of plain rebar needs further study.

ACKNOWLEDGEMENT

This work was supported by the Tongji University (No.0200219296).

REFERENCES

- Cairns, J. 2021. Local bond-slip model for plain surface reinforcement. *Structural Concrete* 22(2): 666–675.
- Darwin, D., Zuo, J., Tholen, M. L., *et al.* 1996. Development length criteria for conventional and high relative rib area reinforcing bars. *ACI Structural Journal* 93(3): 347–359.
- Erfanian, A. & Elwi, A. E. 2019. Bond plastic model for steel-concrete damaged interface element. *Journal of Structural Engineering* 145(5): 04019018.
- Feng, D. C., Wu, G. & Lu, Y. 2018. Finite element modelling approach for precast reinforced concrete beam-to-column connections under cyclic loading. *Engineering Structures* 174(10): 49–66.
- fib Bulletin No.106. Advances on bond in concrete. State-of-the-Art report, ISBN 978-2-88394-164-9, 2022.
- Gao, X. L., Ren, X. D., Li, J., *et al.* 2018. Bond behavior between steel reinforcing bars and concrete under dynamic loads. *Structural Concrete* 19(6): 1806–1817.
- Gao, X. L., LI, N. K. & Ren, X. D. 2019. Analytic solution for the bond stress-slip relationship between rebar and concrete. *Construction and Building Materials* 197: 385–397.
- Gao, Y. C., Mai, Y. W. & Cotterell, B. 1988. Fracture of fiber-reinforced materials. *Journal of Applied Mathematics and Physics (ZAMP)* 39(4): 550–572.
- Jendele, L. & Cervenka, J. 2006. Finite element modelling of reinforcement with bond. *Computers and Structures* 84(28): 1780–1791.
- Liu, Y. B., Dai, J. W., Yang, Y. Q., *et al.* 2020. Novel uniaxial concrete constitutive model considering bond-slip effect. *Earthquake Engineering and Engineering Vibration* 19(3): 649–668.
- Mo, Y. L. & Chan, J. 1996. Bond and slip of plain rebars in concrete. *Journal of Materials in Civil Engineering* 8(4): 208–211.
- Ngo, D. & Scordelis, A. C. 1967. Finite element analysis of reinforced concrete beams. *ACI J.* 64 (3): 152–163.
- Ouyang, C. S. & Shah, S. P. 1994. Fracture energy approach for predicting cracking of reinforced concrete tensile members. *ACI Structural Journal* 91(1): 69–78.
- Phan, T. S., Rossi, P. & Tailhan, J. L. 2015. Numerical modelling of the concrete/rebar bond. *Cement & Concrete Composites* 59: 1–9.
- Robuschi, S. Sumearll, J., Fernandez, I., *et al.* 2021. Bond of naturally corroded, plain reinforcing bars in concrete. *Structure and Infrastructure Engineering* 17(6): 792–808.
- Tepfers, R. & De Lorenzis, L. 2003. Bond of FRP reinforcement in concrete - A challenge. *Mechanics of Composite Materials* 39(4): 315–328.

Residual bearing capacity of corrosion-damaged reinforced concrete columns with annular cross sections

Y. Jiang, Hua-Peng Chen & W.B. Li

School of Transportation Engineering, East China Jiaotong University, Nanchang, Jiangxi, China

ABSTRACT: This paper aims to analyze the residual bearing capacity of the corroded reinforced concrete (RC) columns with annular cross sections to provide useful information for maintenance and repair. The materials and structural strength degradation models are constructed by investigating the deterioration mechanism of the corroded structures. Based on these deterioration models, the analytical models are presented to evaluate the residual bearing capacity of the corrosion-damaged annular columns. Then, the moment-axial force (M-N) interaction diagram is plotted to analyze the influences of various corrosion levels and different loading conditions on the residual bearing capacity of the corroded columns. Finally, a numerical example is applied to verify the effectiveness of the presented method. The obtained results conclude that the proposed approach can be used to quantitatively analyze the bearing capacity of the corroded annular RC columns, which grows as the compression zone area develops but decreases as the rebar corrosion level increases.

1 INTRODUCTION

The annular RC columns are often employed in bridges and port engineering structures as load-bearing components (Wang et al. 2019), prone to be attacked by aggressive environments. Research (Huang et al. 2020) shows that chloride-induced steel corrosion is one of the most critical factors leading to the degradation of RC structures. Recently, many analytical methods have been established to predict the residual strength of the corroded RC structures (Wang & Liu 2009, Jnaid & Aboutaha 2016, Chen 2018, Chen & Nepal 2018, Chen et al. 2022). Jnaid & Aboutaha (2016) developed the finite element modelling and analytical models to estimate the residual flexural strength of the corroded RC beams by accounting for the deterioration of rebar bond strength and the reduction of the rebar capacity. Moreover, the residual bearing capacity models of the corroded RC columns were constructed by analyzing the degradation of materials and structural strength by Chen et al. (2022). However, the existing studies mainly focus on analyzing the effects of rebar corrosion on RC beams and columns with rectangle cross-sections, and there are very limited investigations for the corroded annular columns.

This paper presents an analytical method to assess the performance deterioration of the corroded annular RC columns. By investigating the degradation of materials and structural strength, the residual bearing capacity models are constructed to evaluate the effects of corrosion levels and loading conditions on the residual capacity of the corroded annular columns.

2 DEGRADATION MODELS OF MATERIALS AND STRUCTURAL STRENGTH

2.1 Rebar corrosion

Chloride-induced steel reinforcement corrosion changes the yield strength and the cross-sectional area of rebar (Du et al. 2005). Generally, the corrosion level can be defined as the mass ratio between the corroded rebar and the original rebar, then expressed as the residual area ratio of the rebar cross-section. Therefore, the residual bearing capacity of the corroded rebar F_{sx} can be written as

$$F_{sx} = f_{yc} A_{sc} \quad (1)$$

where f_{yc} is the residual yield strength of the corrosion-damaged rebar, calculated from $f_{yc} = (1-\gamma X)f_{y0}$, in which f_{y0} is the yield strength of the uncorroded rebar, and γ is the influence coefficient of nonuniform corrosion obtained from experimental results (Du et al. 2005), taken as 0.5; A_{sc} is the residual area of the corroded rebar, estimated from $A_{sc} = (1-X)A_{s0}$, in which A_{s0} is the cross-sectional area of the original rebar.

2.2 Concrete cracking and spalling

The rust expansion exerts the hoop stress on the surrounding concrete. When the tensile stress of the concrete cannot bear the hoop stress from the rust expansion, the cracks generate at the rebar bond interface and then propagate to the concrete cover surface with rebar corrosion growth. Based on the thick-walled cylinder model, the crack width at the concrete surface w_c can be expressed as a function of the radial displacement at the bond interface \bar{u}_b (Chen 2018), namely

$$w_c(X) = \frac{W_u G_f}{\eta_1 f_t} \left(\frac{E_c}{f_t} \bar{u}_b(X) - \eta_2 \right) \quad (2)$$

where the radial displacement \bar{u}_b depends on the rebar volume expansion factor ζ_r , calculated from $\bar{u}_b = (\zeta_r - 1)D_b X/4$; D_b is the original diameter of rebar; G_f , f_t , and E_c are the fracture energy, tensile stress and elastic modulus of the intact concrete, respectively; W_u is the normalized value of the ultimate cohesive crack width; and coefficients η_1 and η_2 can be defined as

$$\eta_1 = (l_0 - R_b)(1 - R_{sc}(l_0 - R_{sc})\delta(R_{sc}, R_b)); \quad \eta_2 = R_b + R_{sc}(l_0 - R_b)(l_0 - R_{sc})\delta(R_{sc}, R_b) \quad (3)$$

where l_0 is the material constant estimated from $l_0 = n_c W_u l_{ch}/(2\pi)$, in which l_{ch} is characteristic length given by $l_{ch} = E_c G_f / f_t^2$; n_c is the total number of concrete cracks, $n_c \approx 2\pi R_{sc} / L_c$; L_c is the spacing of crack bands; R_{sc} is the distance from the centroid of the rebar to the concrete cover surface. Moreover, $\delta(R_{sc}, R_b)$ is the crack width coefficient associated with the radial distance between rebar surface R_b and concrete cover surface R_{sc} , expressed as

$$\delta(R_{sc}, R_b) = \frac{R_{sc} - R_b}{l_0(l_0 - R_b)(l_0 - R_{sc})} + \frac{1}{l_0^2} \ln \frac{R_{sc}|l_0 - R_b|}{R_b|l_0 - R_{sc}|} \quad (4)$$

After the cracks connect each other, the concrete cover peels off. This paper simplifies the irregular spalling of the concrete cover as uniformly damaged. Then, the residual outer radius r_c of the annular columns can be evaluated from the crack width at the concrete surface (Chen et al. 2022), as

$$r_c = r - y_c = r - \min(cw/T, c) \quad (5)$$

where r is the outer radius of the intact concrete cross-section; y_c is the average loss of the concrete cover thickness due to corrosion; w is the cumulated crack width, given by $w = w_c n_c$; c is the thickness of the concrete cover; T is the coefficient estimated from the load capacity tests of the corroded RC columns (Hui et al. 1997), taken here as $T = 0.003\text{m}$.

2.3 Rebar bond strength deterioration

Corrosion-induced rebar deformation and concrete cracking seriously weaken the rebar bond strength and affect the load transmission, leading to reduction of the bearing capacity of RC structures. Research indicated that the residual bond strength ratio ζ is strongly related to the crack width propagation at the concrete cover surface (Chen 2018), namely

$$\zeta(X) = \tau_{ux}(X)/\tau_{i0} = 1/(1 + \lambda_\eta w(X)/D_b) \quad (6)$$

where τ_{i0} and τ_{ux} are the bond strength of the rebar before and after corrosion, respectively; the coefficient λ_η is determined by the fitting of experimental results (Cairns et al. 2006), taken as $\lambda_\eta = 15\text{-}20$. When the rebar anchorage failure occurs before yielding failure, the bearing capacity of the corroded rebar F_{ux} is determined by the residual bond strength τ_{ux} (Fib 2010), expressed as

$$F_{ux} = \pi D_{bc} l_a \tau_{ux}(X) \quad (7)$$

where the residual diameter of the corroded rebar D_{bc} is given by $D_{bc} = (1-X)^{0.5}D_b$, and l_a is the rebar anchorage length. Then, the residual strength f_{ux} of the corroded rebar after bond failure can be calculated from $f_{ux} = 4\tau_{ux}l_a/D_{bc}$. Moreover, the deterioration of the rebar bond strength can also lead to the deformation incompatibility between the rebar and the concrete. Here, by introducing the bond strength interpolation factor G_d (Wang & Liu 2009), the stress-strain relationship between the rebar and the concrete under severe corrosion can be compatible, defined as

$$G_d = \frac{\varepsilon_{sx}}{\varepsilon_{sc}} = \frac{2(\varepsilon_{end} - \varepsilon_{start})Y_{xc}}{\tan(17.5^\circ)\varepsilon_{end}L_{ub}} \quad (8)$$

where ε_{sx} and ε_{sc} are the strain of the rebar and the surrounding concrete, respectively; the initial and final strains ε_{end} and ε_{start} are taken as 0.006 and 0.002, respectively; Y_{xc} is the residual height of the concrete compression zone; and L_{ub} is the unbonded length of the tensile rebar.

2.4 Buckling of corroded compressive rebar

For the corroded columns bearing the vertical loads, the longitudinal rebar has the potential failure of buckling due to the stirrup corrosion and the spalling of the concrete cover. The critical buckling stress f_{cr} of the longitude rebar can be estimated from the improved Euler's formula, as

$$f_{cr} = \pi^2 E_s I_{sc} / (L_p^2 A_{sc}) \quad (9)$$

where E_s is the elastic modulus of the steel bars; I_{sc} is the inertia moment of the corroded rebar calculated from $I_{sc} = \pi D_{bc}^4 / 64$; and the laterally unbraced length L_p of the longitude rebar is given as $L_p = n_r s$, in which s is the stirrup spacing; and $(n_r + 1)$ is the number of the failure stirrups.

3 MODELS FOR RESIDUAL BEARING CAPACITY

3.1 Basic assumption of reinforcement

The bearing capacity of the corrosion-damaged RC columns consists of the strength contributions of both concrete and steel reinforcement. For an annular concrete column with steel bars exceeding six ($n_s \geq 6$) and uniformly distributed arrangement, the stress state of the rebar can be analyzed by converting the independent steel bars into an equivalent steel ring (Wang et al. 2019) with an area of A_{nsc} and a thickness of t_{sc} , as shown in Figure 1, given as

$$A_{nsc} = \sum_{i=1}^{n_s} A_{sc}(i); \quad t_{sc} = A_{nsc} / (2\pi r_s) \quad (10)$$

where A_{sc} is the residual area of one of the corroded steel bars in the concrete section, given by Equation 1; and r_s is the distance from the centroid of the rebar to the center of the ring section.

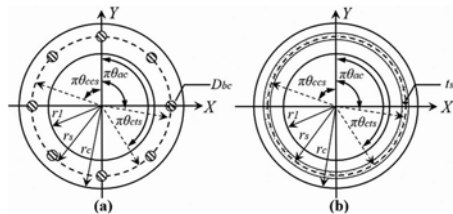


Figure 1. Basic assumption of reinforcement: (a) independent steel bars; (b) the equivalent steel ring.

3.2 Parameter definition

The typical annular cross-section of RC columns is plotted in Figure 2(a), where r_1 and r are the inner and outer radii of the ring section, respectively; r_c is the residual external radius of the ring section after corrosion damage. When $r_1/r \geq 0.5$, the area A_Y of the concrete compression zone can be approximately taken as the area of the ring section formed by a central angle of $2\pi\theta_{ac}$, where θ_{ac} is defined as $\theta_{ac} = A_Y/A_{cc}$, in which A_{cc} is the residual area of the corrosion-damaged

concrete cross-section $A_{cc} = \pi(r_c^2 - r_l^2)$, and A_{c0} is the intact concrete section area $A_{c0} = \pi(r^2 - r_l^2)$. Moreover, the area ratio θ_c is calculated from $\theta_c = A_y/A_{cc}$, in which A_y represents the equivalent compressive zone area of the concrete; the area ratio θ_{ccs} is taken as $\theta_{ccs} = A_{cs}/A_{nsc}$; A_{cs} is the area of the rebar failure under compression; θ_{cts} is equal to $1 - \theta'_{cts}$ in which the area ratio θ'_{cts} is defined as $\theta'_{cts} = A_{ts}/A_{nsc}$; and A_{ts} is the area of the rebar failure in tension.

In Figure 2(b), h_{0c} is the effective height of the damaged concrete cross-section, given by $h_{0c} = r_c + r_s$; the ratio ζ_c is defined as $\zeta_c = Y_{xc}/h_{0c}$, in which Y_{xc} is the residual compression zone height of the concrete column calculated from $Y_{xc} = y_{xc}/\beta_1$; y_{xc} is the equivalent compression zone height of the concrete; β_1 is the reduction factor of the concrete compression zone height; y_c is the average loss of the height in the concrete compression zone, estimated from Equation 5; ε_{cu} is the ultimate compressive strain of the concrete; ε_c is the concrete compressive strain corresponding to y_{xc} ; ε_{acs} is the failure strain of the corroded compressive rebar; ε_{ats} is the failure strain of the corroded tensile rebar; y_{acs} and Y_{acs} are the distances from the position of the strain ε_{acs} to the X -axis and the neutral axis, respectively; y_{ats} and Y_{ats} are the distances from the position of the strain ε_{ats} to the X -axis and the neutral axis, respectively.

The relationship between ζ_c and parameters θ_c , θ_{ac} , θ_{ccs} , and θ_{cts} associated with the cross-sectional strain distribution can be established from the plane-section assumption, as listed in Table 1. In addition, r_{tc} is equal to $(r_c + r_l)/2$; the coefficient β_c is expressed as $\beta_c = (f_{sc}/E_s)/\varepsilon_c$; the coefficient β_c is estimated from $\beta_c = (f_{szc}/E_s)/\varepsilon_c$; f_{sc} and f_{szc} represent the failure stresses of the tensile and compressive rebar, respectively, where the tensile stress f_{sc} is a negative value.

Table 1. Model parameters definition.

Coordinate position*	θ ($0 \leq \theta \leq 1$)
$r_c - Y_{xc}$	$\theta_c = \arccos(r_c/r_{tc} - \beta_1 \zeta_c (r_c + r_s)/r_{tc})/\pi$
$r_c - Y_{xc}$	$\theta_{ac} = \arccos(r_c/r_s - \zeta_c (1 + r_c/r_s))/\pi$
$y_{acs} = Y_{acs} - Y_{xc} + r_c$	$\theta_{ccs} = \arccos(r_c/r_s + (\beta_c - 1)\zeta_c (1 + r_c/r_s))/\pi$
$y_{ats} = Y_{ats} - Y_{xc} + r_c$	$\theta_{cts} = \arccos(r_c/r_s + (\beta_c - 1)\zeta_c (1 + r_c/r_s))/\pi$

* Below the X -axis gives the negative values, while above the X -axis gives positive values.

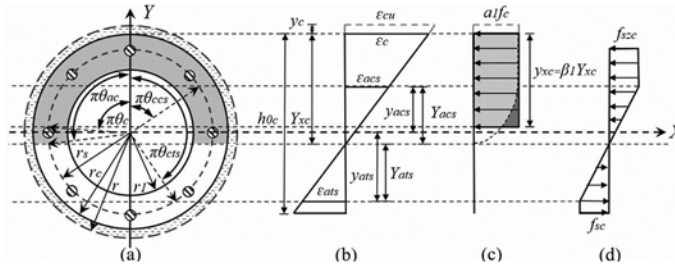


Figure 2. Stress block and parameters definition of corroded annular RC columns: (a) typical cross-section; (b) strain distribution; (c) equivalent stress distribution of concrete; (d) stress distribution of rebar based on the equivalent steel ring assumption.

3.3 Residual bearing capacity of concrete

From Figure 2(c), the axial force of the concrete F_c can be calculated from the residual area of the concrete cross-section and the compressive strength of the concrete f_c , and the concrete bending moment M_c can then be calculated by assuming the X -axis as the moment axis, namely

$$F_c = a_1 f_c A_{cc} A ; M_c = a_1 f_c A_{cc} r_s B / \pi \quad (11)$$

where a_1 is the reduction factor of the concrete compressive strength, parameters A and B are defined, respectively, as

$$A = \theta_c ; B = \sin \pi \theta_c r_{tc} / r_s \quad (12)$$

3.4 Residual bearing capacity of rebar

From the stress distribution of the rebar, as shown in Figure 2(d), the stress states of the equivalent steel ring can be divided into four parts. Based on the materials and structural strength degradation models, the axial force of the corroded rebar for different stress states can be calculated from the residual stress and area. Moreover, the bending moment of rebar for various states can be obtained by taking the moment of the X -axis.

3.4.1 Case 1: Rebar reaching the compressive failure stress ($0 \leq \theta \leq \theta_{ccs}$)

In Case 1, the failure stress of the compressive rebar f_{szc} is governed by the smaller value of the yield strength f_{yc} and the critical buckling strength f_{cr} , expressed as $f_{szc} = \min(f_{yc}, f_{cr})$. Meanwhile, the residual cross-section area can be calculated from the area ratio θ_{ccs} . Then, the force F_{cs} and moment M_{cs} of rebar can be expressed, respectively, as

$$F_{cs} = f_{szc} A_{nsc} k_{cef} ; M_{cs} = f_{szc} A_{nsc} r_s k_{cem} / \pi \quad (13)$$

where parameters k_{cef} and k_{cem} can be calculated from

$$k_{cef} = \theta_{ccs} ; k_{cem} = \sin \pi \theta_{ccs} \quad (14)$$

3.4.2 Case 2: Rebar under compression but not reaching the failure stress ($\theta_{ccs} \leq \theta \leq \theta_{ac}$)

In the case of the rebar not reaching the compressive failure stress ($\theta_{ccs} \leq \theta \leq \theta_{ac}$), the strength of the rebar can be estimated from the stress-strain relationship. In addition, the residual cross-section area can be calculated from the difference between the area ratios θ_{ac} and θ_{ccs} . The axial force F'_{cs} and bending moment M'_{cs} of rebar in Case 2 can then be expressed as

$$F'_{cs} = f_{szc} A_{nsc} k'_{cef} ; M'_{cs} = f_{szc} A_{nsc} r_s k'_{cem} / \pi \quad (15)$$

where parameters k'_{cef} and k'_{cem} are defined as

$$k'_{cef} = \frac{\mu_{acs} + \eta_{cs} \nu_{acs}}{\pi (\cos \pi \theta_{ccs} + \eta_{cs})} ; k'_{cem} = \frac{\nu_{acs} / 2 + \mu_{2acs} / 4 + \eta_{cs} \mu_{acs}}{\cos \pi \theta_{ccs} + \eta_{cs}} \quad (16)$$

in which μ_{acs} is taken as $\mu_{acs} = \sin \pi \theta_{ac} - \sin \pi \theta_{ccs}$; μ_{2acs} is calculated from $\mu_{2acs} = \sin 2\pi \theta_{ac} - \sin 2\pi \theta_{ccs}$; ν_{acs} is equal to $\pi(\theta_{ac} - \theta_{ccs})$; and the factor η_{cs} associated with the cross-section properties is given by

$$\eta_{cs} = \zeta_c (1 + r_c / r_s) - r_c / r_s \quad (17)$$

3.4.3 Case 3: Rebar in tension but not reaching the failure stress ($\theta_{ac} \leq \theta \leq \theta_{ctis}$)

The residual cross-section area of rebar in Case 3 can be calculated from the difference between the area ratios θ_{ctis} and θ_{ac} . Then, the force F'_{ts} and moment M'_{ts} of the corroded rebar can be determined by the stress-strain relationship, namely

$$F'_{ts} = f_{szc} A_{nsc} k'_{ctf} ; M'_{ts} = f_{szc} A_{nsc} r_s k'_{ctm} / \pi \quad (18)$$

When the bond effect between the rebar and the surrounding concrete is adequate, the parameters k'_{ctf} and k'_{ctm} can be defined, respectively, as

$$k'_{ctf} = \frac{\mu_{tsa} + \eta_{cs} \nu_{tsa}}{\pi (\cos \pi \theta_{ccs} + \eta_{cs})} ; k'_{ctm} = \frac{\nu_{tsa} / 2 + \mu_{2tsa} / 4 + \eta_{cs} \mu_{tsa}}{\cos \pi \theta_{ccs} + \eta_{cs}} \quad (19)$$

where μ_{tsa} is taken as $\mu_{tsa} = \sin \pi \theta_{ctis} - \sin \pi \theta_{ac}$; μ_{2tsa} is calculated from $\mu_{2tsa} = \sin 2\pi \theta_{ctis} - \sin 2\pi \theta_{ac}$; and ν_{tsa} is given by $\nu_{tsa} = \pi(\theta_{ctis} - \theta_{ac})$. However, the deformation of the tensile rebar and the surrounding concrete is incompatible after rebar bond failure. Here, the bond strength interpolation factor G_d is introduced to construct a new stress-strain relationship between the corroded rebar and the cracked concrete. Then, the parameters k'_{ctf} and k'_{ctm} can be rewritten as

$$k'_{ctf} = G_d \frac{\mu_{tsa} + \eta_{cs} \nu_{tsa}}{\pi (\cos \pi \theta_{ccs} + \eta_{cs})} ; k'_{ctm} = G_d \frac{\nu_{tsa} / 2 + \mu_{2tsa} / 4 + \eta_{cs} \mu_{tsa}}{\cos \pi \theta_{ccs} + \eta_{cs}} \quad (20)$$

3.4.4 Case 4: Rebar reaching the tensile failure stress ($\theta_{cts} \leq \theta \leq 1$)

For the case with part of the steel ring failure in tension, the stress of the corroded rebar f_{sc} depends on the smaller value of the yield strength f_{yc} and the residual bond strength f_{ux} , expressed as $f_{sc} = \min(f_{yc}, f_{ux})$, and the residual cross-section area is equal to $\theta'_{cts} A_{nsc}$. Then, the axial force F_{ts} and bending moment M_{ts} can be expressed, respectively, as

$$F_{ts} = f_{sc} A_{nsc} k_{ctf}; \quad M_{ts} = f_{sc} A_{nsc} r_s k_{ctm} / \pi \quad (21)$$

where parameters k_{ctf} and k_{ctm} are estimated from

$$k_{ctf} = \theta'_{cts}; \quad k_{ctm} = -\sin \pi \theta_{cts} \quad (22)$$

3.5 Residual bearing capacity of the corroded columns

Based on the stress state analysis, consequently the residual axial force N_{res} and bending moment M_{res} of the corroded annular RC columns can be calculated by summing the concrete load capacity and the rebar load capacity, namely

$$N_{res} = F_c + F_{cs} + F'_{cs} + F'_{ts} + F_{ts}; \quad M_{res} = M_c + M_{cs} + M'_{cs} + M'_{ts} + M_{ts} \quad (23)$$

4 NUMERICAL EXAMPLE

In this section, a short RC column of annular cross-sections is employed to illustrate the applicability of the residual bearing capacity models described above. The cross-section of this column has an inner radius of $r_I = 125\text{mm}$, an outer radius of $r = 175\text{mm}$, and a radius of $r_s = 150\text{mm}$. Nine rebars of a diameter of 10mm are uniformly distributed in the concrete section, with a tensile strength $f_{y0} = 340\text{MPa}$ and an elasticity modulus $E_s = 200\text{GPa}$. The concrete compressive strength f_c is 40MP, with the cover thickness c of 20mm. Moreover, other material properties of the concrete can be estimated from the concrete compressive strength (Fib 2010). In addition, the stirrups have a spacing of 100mm, and the total crack number n_c is taken as 4.

In Figure 3, the equivalent crack width at the concrete surface as a function of corrosion level is analytically predicted, matching well the experimental results (Vidal et al. 2004, Coronelli et al. 2013, Banba et al. 2014, Khan et al. 2014). The predicted results demonstrate a well-defined trend in which the cracks widen as the corrosion level increases.

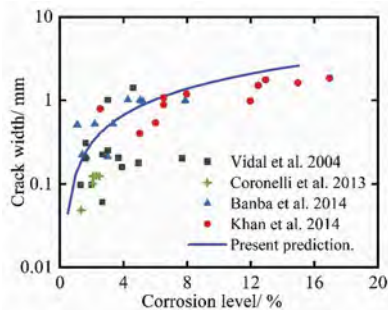


Figure 3. Predicted equivalent concrete crack width versus corrosion level, compared with experimental results from various sources.

Based on the results of crack width evolution, the normalized residual bond strength can be estimated from Equation 6. In Figure 4, the normalized residual rebar bond strength declines as the crack width increases, matching well the experimental data (Rodriguez et al. 1994, Fischer 2010, Law et al. 2011, Banba et al. 2014). Compared with the later crack propagation stage, the normalized residual bond strength has a more rapid drop in the earlier stage.

Figure 5 shows the influences of rebar corrosion and the relative compression zone area ratio θ_c on the residual bearing capacity of the corroded annular concrete columns, where the normalized

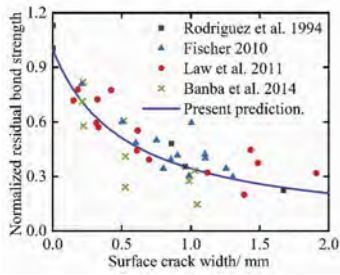


Figure 4. Predicted normalized residual bond strength versus surface crack width, compared with experimental data from various sources.

axial force n is calculated from $n = N_{res}/a_1f_cA_{c0}$. As expected, the residual bearing capacity of the corroded columns largely depends on the loading conditions and the corrosion levels, which grows as the compression zone area increases but decreases with the corrosion level increases.

To further investigate the effects of the corrosion level on the mechanical performance of the annular RC columns, various values of the corrosion level ranging from 0 to 50% are adopted to predict the residual bearing capacity of the corroded columns, as shown in Figure 6, where the normalized bending moment m is calculated from $m = \pi M_{res}/a_1f_cA_{c0}r_s$. From the results, the bearing capacity of the corroded RC column reduces obviously at the corrosion level between 4 and 15%. For corroded columns with smaller eccentricities, the loss of the concrete cross-section is the main reason causing the significant decline of the residual capacity. However, for the corroded columns with larger eccentricities, the degradation of rebar bond strength is the critical factor, leading to the rapid drop of the residual capacity.

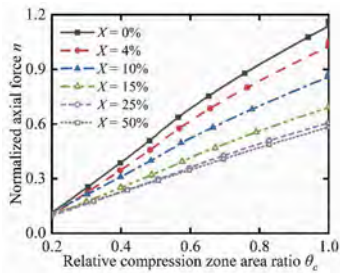


Figure 5. Normalized bearing capacity n of the corroded annular columns with various rebar corrosion levels and different relative compression zone area ratios θ_c .

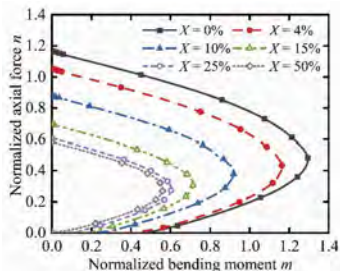


Figure 6. The M-N interaction diagram of the annular RC column with various corrosion levels.

5 CONCLUSION

This paper presents an analytical method for assessing the residual bearing capacity of the corroded RC columns with annular cross-sections. The materials and structural strength degradation models are constructed by investigating the deterioration mechanism of the corroded

columns, which consider the decrease of rebar bearing capacity, the cracking and spalling of concrete cover, rebar bond strength reduction, and the buckling of the compressive rebar. The residual bearing capacity models are then constructed to quantitatively analyze the coupling effects between corrosion levels and loading conditions on the bearing capacity of the corrosion-damaged annular columns. According to the results obtained from the numerical example, the following conclusions are drawn: (1) the developed models can effectively predict the concrete crack width growth, rebar bond strength degradation and residual bearing capacity of the corroded annular columns; (2) the effects of rebar corrosion on the residual bearing capacity of the annular concrete columns increase significantly as the compression zone area develops; (3) at the corrosion level of 4-15%, the residual bearing capacity of the corroded annular columns reduces more obviously due to concrete cover loss and rebar bond strength deterioration.

ACKNOWLEDGMENTS

The authors are very grateful for the financial supports received from the National Key Research and Development Program of China (Grant No. 2021YFE0105600), the National Natural Science Foundation of China (Grant Nos. 51978263) and the Key Project for Scientific and Technological Cooperation Scheme of Jiangxi Province (Grant No. 20212BDH80022 and 20223BBH80002).

REFERENCES

- Banba, S., Abe, T., Nagaoka, K., et al. 2014. Evaluation method for bond-splitting behavior of reinforced concrete with corrosion based on confinement stress of concrete against corrosion expansion. *J. Adv. Concr. Technol.* 12(1): 7–23.
- Cairns, J., Du, Y. & Law, D. 2006. Residual bond strength of corroded plain round bars. *Mag. Concr. Res.* 58(4): 221–231.
- Chen, H. P. 2018. Residual flexural capacity and performance assessment of corroded reinforced concrete beams. *J. Struct. Eng.* 144(12): 04018213.
- Chen, H. P., Jiang, Y. & George, M. 2022. Structural performance deterioration of corroding reinforced concrete columns in marine environments. *Ocean Eng.* 262: 112155.
- Chen, H. P. & Nepal, J. 2018. Modeling residual flexural strength of corroded reinforced concrete beams. *ACI Struct. J.* 115(6): 1625–1635.
- Coronelli, D., Hanjari, K. Z. & Lundgren, K. 2013. Severely corroded RC with cover cracking. *J. Struct. Eng.* 139(2): 221–232.
- Du, Y. G., Clark, L. A. & Chan, A. H. C. 2005. Residual capacity of corroded reinforcing bars. *Mag. Concr. Res.* 57(3): 135–147.
- Fib 2010. *Fédération internationale du Béton/international federation for structural Concrete Model code 2010*. Lausanne, Switzerland. Federation internationale du beton.
- Fischer, C. 2010. Experimental Investigations on the Effect of Corrosion on Bond of Deformed Bars. *Proceedings of the 8th fib PhD Symposium*, Kgs, Lyngby, Denmark.
- Huang, L., Ye, H. L., Jin, X. Y., et al. 2020. Corrosion-induced shear performance degradation of reinforced concrete beams. *Construct. Build. Mater.* 248: 118668.
- Hui, Y. L., Li, R. & Lin, Z. S. 1997. Experimental studies on the property before and after corrosion of rebars in basic concrete members. *Ind. Constr.* 27(6): 14–18. (in Chinese).
- Jnaid, F. & Aboutaha, R. S. 2016. Residual flexural strength of corroded reinforced concrete beams. *Eng. Struct.* 119: 198–216.
- Khan, I., Francois, R. & Castel, A. 2014. Prediction of reinforcement corrosion using corrosion induced cracks width in corroded reinforced concrete beams. *Cement Concr. Res.* 56: 84–96.
- Law, D. W., Tang, D., Molyneaux, T., et al. 2011. Impact of crack width on bond: confined and unconfined rebar. *Mater. Struct.* 44(7): 1287–1296.
- Rodriguez, J., Ortega, L. M. & Casal, J. 1994. Corrosion of reinforcing bars and service life of reinforced concrete structures: corrosion and bond deterioration. *International Conference on Concrete Across Borders 2*: 315–326.
- Vidal, T., Castel, A. & Francois, R. 2004. Analyzing crack width to predict corrosion in reinforced concrete. *Cement Concr. Res.* 34(1): 165–174.
- Wang, P., Zhou, D. & Huang, Z. 2019. Ultimate Strength of Annular Reinforced Concrete Members Under Combined Actions. *J. Shanghai Jiaotong Univ. (Sci.)* 24: 430–438.
- Wang, X. H. & Liu, X. L. 2009. Predicting the flexural capacity of RC beam with partially unbonded steel reinforcement. *Nucl. Eng. Des.* 6(3): 235–252.

Steel liner corrosion and its effects on the leak-tightness of the nuclear containment structure

X.B. Li, X.Y. Wu & J.X. Gong

State Key Laboratory of Coastal and Offshore Engineering, Dalian University of Technology, Dalian, China

ABSTRACT: To evaluate the aging effect of the steel liner on the nuclear containment structure, uniaxial tensile tests are conducted on 36 steel liner specimens with 0% to 50% corrosion rate. The corrosion effect on the degradation of the mechanical properties of the steel liner is investigated. Based on the experimental results, the stress-strain model of the corroded steel liner is established, and a corrosion simulation method for the steel liner is proposed. Combined with the finite element method, the effect of steel liner corrosion on the leak-tightness of the containment is evaluated. Finally, the proposed corrosion simulation method is compared to the Nuclear Regulatory Commission (NRC) method, and recommendations for the corrosion factor in the NRC method are made.

1 INTRODUCTION

The nuclear containment structure (containment, hereafter) serves as the ultimate physical barrier in the defense-in-depth system of the nuclear power plant. The steel liner anchored on the inner wall of the containment plays a pivotal role in ensuring the leak-tightness of the containment. As the service time increases, the containment will suffer from aging-related degradation, and steel liner corrosion is one of the major forms of degradation (Dunn et al., 2011, Petti et al., 2011). A series of large-scale experiments on the containment demonstrated that concrete cracking occurred prior to the tearing of the steel liner, and thus the leak-tightness of the containment under severe accidents is directly determined by the steel liner (Hanson et al., 1987a, Hanson et al., 1987b, Hessheimer and Dameron, 2006). Given the critical role of the steel liner as a leak-barrier, it is of great importance to investigate the mechanical properties of the corroded steel liner and the corrosion effect on the leak-tightness of the containment.

Due to the particularity of the containment, the effect of steel liner corrosion on the containment was generally carried out by testing the mechanical properties of corroded steel liner specimens and then conducting a numerical simulation of the containment based on the test results. Cherry et al. (Cherry, 1999) conducted a series of corrosion tests on A516 GR70 steel liners, and found that the ultimate strength and ultimate tensile strain of the steel liners were significantly reduced by corrosion. Based on the experimental results, the NRC proposed a simulation method and a tearing criterion for the corroded steel liner (Cherry and Smith, 2001, Spencer et al., 2006). According to research conducted by the NRC, the leak-tightness of different types of containment under steel liner corrosion conditions has been extensively studied (Spencer et al., 2006, Petti et al., 2008, Li and Gong, 2023). In general, there are few studies on the steel liner corrosion. The corrosion test carried out by Cherry et al. (Cherry, 1999) only considered the steel liner with a maximum corrosion level of 20%, and the test data were not sufficient to obtain the degradation law of the mechanical properties of the steel liner under different corrosion levels. The corrosion simulation method proposed by the NRC considered the weakening of the bearing capacity of the steel liner by reducing its thickness but ignored the degradation of the material properties of the corroded steel liner. Additionally, the tearing criterion for the

corroded steel liner proposed by the NRC is to introduce a corrosion factor that can characterize the corrosion effect on the ductility of the steel liners. However, the suggested value for the corrosion factor given by the NRC fails to reflect the corrosion level.

In the present work, the mechanical properties of the corroded steel liner are investigated by corrosion and uniaxial tensile tests, and the mechanical properties of the corroded steel liner under different corrosion rates are analyzed. Based on the experimental results, the constitutive model for the corroded steel liner is established, and a corrosion simulation method for the steel liner is proposed. Combined with the nonlinear finite element analysis method and sub-model analysis techniques, the effect of different levels of steel liner corrosion on the leak-tightness of the containment is evaluated. Finally, the proposed corrosion simulation method is compared to the NRC method, and recommendations for the corrosion factor in the NRC method are made.

2 UNIAXIAL TENSILE TESTS

2.1 Specimen preparation

In this study, P265GH steel with a thickness of 6 mm, which is widely used for containment steel liners, is selected as the test material. The tensile specimens used in this study were designed in accordance with Chinese standard GB/T228.1–2010. Six groups of corrosion rates (from 0% to 50%) are considered by using the electrochemical accelerated corrosion method, and each group includes six specimens. It should be mentioned that the corrosion level of steel liners in nuclear power plants is usually assessed by the corrosion depth and area. Therefore, the reduction in average cross-sectional area is used in this study to calculate the corrosion rate.

2.2 Test results

The tensile stress-strain curves of representative specimens are shown in Figure 1, and the detailed test results are shown in Table 1.

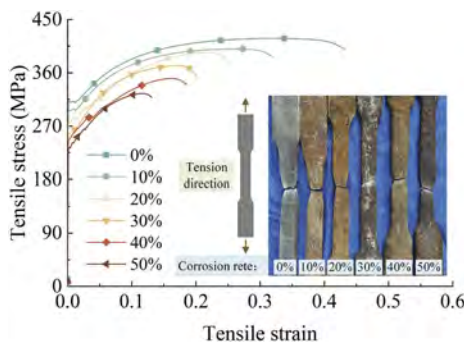


Figure 1. Tensile stress-strain curves of steel liner specimens.

Table 1. Uniaxial tensile test results of steel liner specimens.

Specimen group	η (%)	E_s (MPa)	f_y (MPa)	ϵ_{sh}	f_p (MPa)	ϵ_p	ϵ_u
L-0%	0	203958	310.57	0.02079	431.14	0.2657	0.4363
L-10%	10	201631	290.42	0.01976	394.12	0.2105	0.3009
L-20%	20	202142	264.10	0.01460	379.22	0.1792	0.2414
L-30%	30	200109	267.21	0.01108	364.65	0.1425	0.1935
L-40%	40	201966	248.34	0.00712	361.25	0.1413	0.1899
L-50%	50	199694	231.02	0.00469	335.07	0.1095	0.1464

Note: η is the corrosion rate; E_s is the elastic modulus; f_y is the yield strength; ϵ_{sh} is the strain of the steel liner for hardening initiation; f_p is the peak strength; ϵ_p is the peak strain; ϵ_u is the fracture strain.

Combined the contents in Figure 1 and Table 1, the following points can be concluded:

- (1) The elastic modulus of the steel liner is not affected by corrosion, but the yield strength, peak strength, peak strain, and fracture strain are degraded as the corrosion rate increases.
- (2) At a corrosion rate of 50%, the mean fracture strain of the steel liner is reduced by 66.45%, indicating that the ductility of the corroded steel liner is significantly degraded.
- (3) When the corrosion rate is low, the steel liner exhibits an obvious yield point and yield platform. However, when the corrosion rate reaches 30%, the yield point is no longer obvious and the yield platform gradually becomes shorter or even disappears.

To reflect the corrosion effect on each mechanical property parameter of the steel liner, statistical analysis is performed for f_y , f_p , ϵ_p , and ϵ_u , as shown in Figure 2. Moreover, regression analysis of the test results revealed that the remaining mechanical parameters of the steel liner approximately satisfy the following linear degradation law as the corrosion rate increases:

$$M(i) = 1 - k(i)\eta \quad (0 \leq \eta \leq 50\%) \quad (1)$$

where $M(i)$ represents the non-dimensional quantity for the mechanical parameter of the steel liner, i.e., $M(f_y) = f_y/f_{y0}$, $M(f_p) = f_p/f_{p0}$, $M(\epsilon_p) = \epsilon_p/\epsilon_{p0}$, $M(\epsilon_u) = \epsilon_u/\epsilon_{u0}$; f_{y0} , f_{p0} , ϵ_{p0} , and ϵ_{u0} represent the mean values of the corresponding mechanical parameters of the uncorroded steel liner, respectively; $k(i)$ represents the degradation coefficient (see Figure 2).

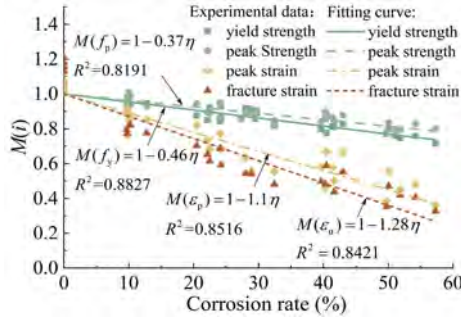


Figure 2. Degradation law of mechanical properties of steel liner specimens.

3 CONSTITUTIVE MODEL OF CORRODED STEEL LINERS

As shown in Figure 1, the tensile constitutive relationship of the steel liner generally includes four stages, a linear elastic stage, a yielding platform, a strain hardening stage, and a necking stage. Through statistical analysis of the test curves, the constitutive model of the corroded steel liner is established in this study, which has the following form:

$$\sigma_s = \begin{cases} E_s \epsilon_s & 0 \leq \epsilon_s < \epsilon_y \\ f_y & \epsilon_y < \epsilon_s \leq \epsilon_{sh} \\ f_y \left[1 + \frac{\epsilon_s - \epsilon_{sh}}{\epsilon_p - \epsilon_{sh}} \left(\frac{f_p}{f_y} - 1 \right) \exp \left(1 - \frac{\epsilon_s - \epsilon_{sh}}{\epsilon_p - \epsilon_{sh}} \right) \right] & \epsilon_{sh} < \epsilon_s \leq \epsilon_u \end{cases} \quad (2)$$

The present constitutive model considers that the modulus of elasticity of the steel liner remains constant under different corrosion rates, and thus the yield strain can be calculated from the yield strength. The f_y , f_p , ϵ_p , and ϵ_u at different corrosion rates can be calculated by Equation (1). Additionally, the mechanical property parameter ϵ_{sh} has a large dispersion due to the impact of uneven corrosion. To develop a uniform mathematical model, a linear relationship is fitted to ϵ_{sh} , and it has the following form:

$$M(\epsilon_{sh}) = \frac{\epsilon_{sh}}{\epsilon_{sh0}} = 1 - 1.48\eta \quad (3)$$

Figure 3 shows the comparison between the model curves and the test curves under different corrosion rates, which are in good agreement.

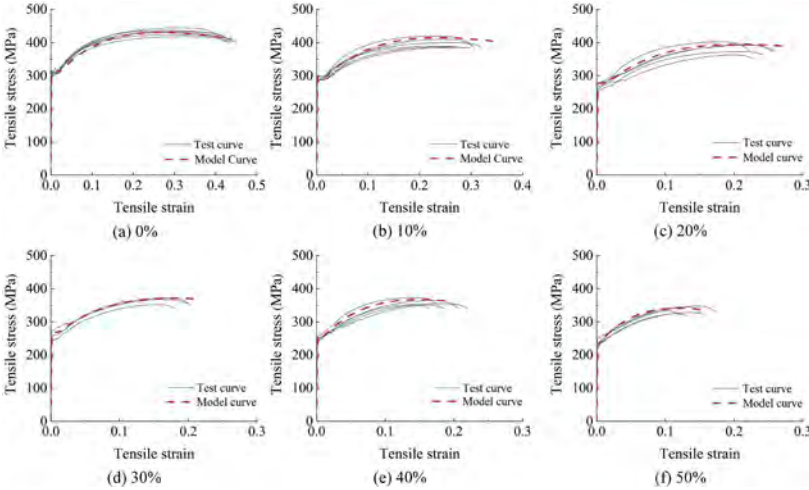


Figure 3. Comparison between the model curve and the test curve.

4 FE ANALYSIS OF THE CONTAINMENT

4.1 Global model of the containment

The containment studied in reference (Zhou et al., 2018) is adopted in this study, as shown in Figure 4. The total height of the containment is 61.7 m, and the height of the base slab is 5.5 m. The inner radius of the dome is 24 m with a wall thickness of 0.8 m, and the inner radius of the cylinder wall is 18.5 m with a wall thickness of 0.9 m. The entire inner surface of the containment is lined with a 6 mm steel liner to provide the required leak-tightness at the pressure boundary. To meet functional requirements, many penetrations are provided in the containment, such as equipment hatches and personnel airlocks. Furthermore, a complete pre-stressing tendon system is arranged in the containment.

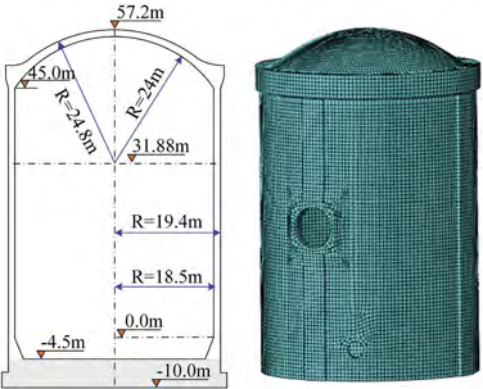


Figure 4. Schematic diagram and FE model of the containment.

In this study, a global FE model of the containment is established by ABAQUS. The modeling details of the global model are referenced in the literature (Jin and Gong, 2021). The mechanical behavior of the concrete is simulated using the plastic damage model in

ABAQUS, and the uniaxial compressive and tensile constitutions of concrete are modeled using stress-strain relationships suggested in the literature (Li and Gong, 2023). The isotropic elastic-plastic model is applied to simulate the mechanical behavior of the rebar and the prestressed tendons. For this study, we focused on the steel liner corrosion, and the mechanical behavior of the steel liner is modeled by the constitutive model proposed in Equation (2) to simulate the real corrosion situation. In addition, the nonlinear FE analysis of the global model of the containment is divided into two analysis steps. In the first step, the gravity load and the prestressing load of the tendons are applied simultaneously. In the second step, the pressure is applied uniformly to the inner surface of the containment.

4.2 Sub-model for corroded steel liners

A series of aging investigations into the containment revealed that the steel liner corrosion is strongly localized, and the corroded area is usually small (Dunn et al., 2011, Petti et al., 2011). Therefore, the FE model requires a refined mesh to reflect the strain concentration in the corroded area of the steel liner. However, due to the large size and complex structural form of the containment, the use of a refined mesh for the global model will make convergence difficult. To overcome this limitation, we performed the local corrosion analysis of the steel liner using the sub-model technique of ABAQUS, and the specific implementation process can be found in a previous work (Li and Gong, 2023). To reduce the influence of the singular zones of the containment on the calculation, the current zone of the containment, which is away from the buttress and the penetration, is selected for the sub-model. To consider the most unfavorable scenario, the sub-model for the corroded steel liner is selected at the location where the maximum strain of the steel liner is generated in the current zone of the global model, as shown in Figure 5. The corrosion region is set at the center of the sub-model, and its dimensions and shape are described in the NRC report (Spencer et al., 2006). Through mesh convergence analysis, the global mesh size of the sub-model is taken as 200 mm. Additionally, the mesh size of the corrosion area is taken as 8 mm, and a transition zone is provided around it to reduce the effect of variation in mesh size.

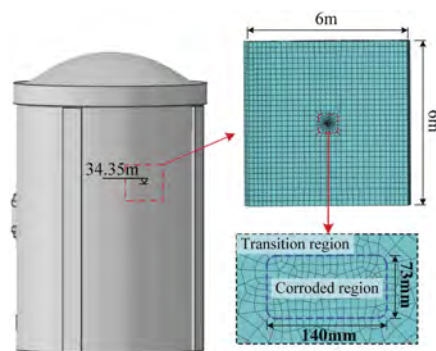


Figure 5. FE model of the sub-model.

4.3 Failure criterion

In the nuclear engineering community, it is widely acknowledged that the tearing of the steel liner means that the containment loses its leak-tightness function. The tearing of the steel liner is determined by its fracture strain, and the NRC has proposed a failure criterion for steel liners with consideration of corrosion effects in the FE analysis (Spencer et al., 2006):

$$\varepsilon_{pe} = f_m f_{cor} f_g \varepsilon_{p,eff} \quad (4)$$

where ε_{pe} is the uniaxial equivalent strain of the steel liner; f_m is the multiaxial stress factor; f_g is gauge length factor; $\varepsilon_{p,eff}$ is the effective plastic strain of the steel liner from the FE analysis.

The corrosion factor in Equation (4) reflects the corrosion effect on the ductility of the steel liner, and three suggested values of the f_{cor} are recommended by NRC (Cherry and Smith, 2001). However, these recommended values cannot directly reflect the effect of different corrosion levels on the ductility of the steel liner. Based on the test results, we propose a calculation method for the corrosion factor that takes the corrosion rate into account:

$$f_{\text{cor}}^* = \frac{1}{1 - 1.28\eta} \quad (0 \leq \eta \leq 50\%) \quad (5)$$

Therefore, an improved failure criterion for the corroded steel liner can be expressed as:

$$\varepsilon_{\text{pe}} = f_{\text{m}} f_{\text{cor}}^* f_{\text{g}} \varepsilon_{\text{p,eff}} \quad (6)$$

According to the failure criteria, when ε_{pe} exceeds the ε_{u0} of the steel liner, tearing occurs, and thus the containment is considered to lose its leak-tightness function (or functional failure).

5 SIMULATION METHOD AND ANALYSIS RESULTS

5.1 Simulation methods for corroded steel liners

The previous studies for the numerical simulation of the corroded steel liner mainly used the simulation method proposed by the NRC, which was to reduce the thickness of the steel liner in the corroded zone, and the uncorroded material properties were still adopted in the corroded zone (Cherry and Smith, 2001, Spencer et al., 2006, Petti et al., 2008, Alhanaee et al., 2018). This simulation method assumes that the substrate material properties of the steel liner after removing the corroded layer are consistent with those of the uncorroded material. However, the corrosion morphology of the steel liner shown in Figure 1 indicates that the corroded steel liner has many corrosion pits on its surface caused by the non-uniformity of corrosion. Due to the stress concentration effect, the mechanical parameters of the substrate material of the corroded steel liner are also significantly degraded. Therefore, the corrosion simulation method proposed in this study is to reduce the thickness of the corroded steel liner according to the corrosion rate and then impart the corresponding stress-strain relationship of the corroded steel liner in the corroded zone according to the proposed constitutive model. The proposed method can consider both the cross-sectional loss and the degradation of the mechanical properties of the corroded steel liner. Therefore, it is closer to the actual performance of the corroded steel liner.

To investigate the leak-tightness performance of the containment under different corrosion degrees of the steel liner, six groups of corrosion conditions with corrosion rates ranging from 0% to 50% are considered in this study. Meanwhile, the same corrosion conditions are simulated according to the NRC method to compare the differences between the proposed corrosion simulation method and the NRC method. In addition, Equations (4) and (6) are used to determine the tearing of the steel liner under the NRC method and the proposed method, respectively.

5.2 FE analysis results and discussion

A plot of the ratio of ε_{pe} to ε_{u0} as a function of pressure is shown in Figure 6, and a horizontal line is drawn at a ratio of 1.0 to indicate the failure occurs. The functional failure pressure corresponding to the tearing of the steel liner gradually decreases as the corrosion rate increases. Compared with the uncorroded condition, the functional failure pressure of the containment is reduced by 29.06% at a corrosion rate of 50%, indicating that the steel liner corrosion can easily lead to leakage of the containment at low pressures under accident conditions.

Taking the simulated condition with corrosion rate of 50% as an example, Figure 7 shows the comparison of the relationship curves between steel liner strain and pressure under the proposed corrosion simulation method and the NRC method. It should be mentioned that the corrosion factor in the failure criterion is taken as $f_{\text{cor}} = 2$ for the corrosion rate of 50% according to relevant literature (Spencer et al., 2006, Petti et al., 2008). At low pressure, the steel liner strains calculated by the proposed method and the NRC method are essentially the same. However, at

high levels of pressure, the steel liner strain calculated by the NRC method is lower than our proposed method. What's more, the NRC method overestimates the functional failure pressure corresponding to the tearing of the steel liner. Additionally, it is not conservative enough to use $f_{cor} = 2$ to determine the tearing of the steel liner in the case of a 50% corrosion rate.

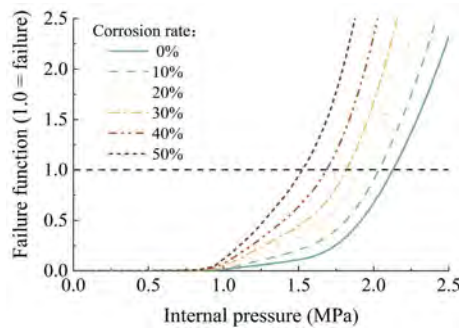


Figure 6. Failure functions under different corrosion rates.

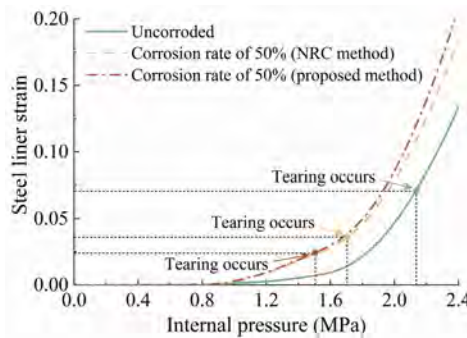


Figure 7. Comparison of corrosion simulation methods.

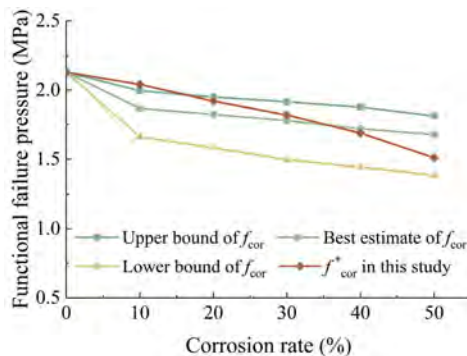


Figure 8. Comparison of functional failure pressure.

Following the three suggested values of the corrosion factor recommended by the NRC, the functional failure pressure under different corrosion rates is calculated, as shown in Figure 8. Comparing the NRC method with the proposed method, it is obvious that the proposed method can directly reflect the variation of the corrosion factor with the corrosion rate. Meanwhile, the corrosion factor obtained by our proposed method basically conforms to the value interval of the corrosion factor recommended by the NRC. Moreover, the corrosion factor

recommended by the NRC can be specified as follows: when the corrosion rate is less than 20%, the upper bound value can be selected; when the corrosion rate is 20% to 40%, the best estimate value is recommended; and when the corrosion rate exceeds 40%, the lower bound value should be adopted.

6 CONCLUSIONS

Combined with corrosion test and numerical simulation, the mechanical properties of the corroded steel liner and the corrosion effect on the leak-tightness of the containment are systematically analyzed. The following conclusions can be drawn:

- (1) The corrosion effect on the elastic modulus of the steel liner is not significant, but as the corrosion rate increases, the yield strength, peak strength, peak strain, and fracture strain show linear degradation.
- (2) The constitutive model of the corroded steel liner established in this study agrees well with the experimental results.
- (3) Functional failure pressure of the containment decreases with the increase in the corrosion degree of the steel liner, and when the corrosion rate is 50%, the functional failure pressure decreases by 29.06%.
- (4) The proposed simulation method can directly reflect the impact of corrosion on the steel liner and is closer to the actual corrosion situation. Additionally, the corrosion factor recommended by the NRC is clarified. When the corrosion rate is less than 20%, the upper bound can be chosen; when the corrosion rate is 20% to 40%, the best estimate is recommended; and when the corrosion rate exceeds 40%, the lower bound should be used.

REFERENCES

- Cherry, J. L. (1999) Analyses of containment structures with corrosion damage. *SAND96-0004C*. Albuquerque, NM.
- Cherry, J. L. & Smith, J. A. (2001) Capacity of steel and concrete containment vessels with corrosion damage. *NUREG/CR-6706*. Albuquerque, NM, Nuclear Regulatory Commission.
- Dunn, D. S., Pulvirenti, A. L. & Hiser, M. A. (2011) Containment liner corrosion operating experience summary technical letter report – Revision 1 *Technical Letter Report – Revision 1*. Washington, U.S. Nuclear Regulatory Commission Office of Nuclear Regulatory Research.
- Hanson, N. W., Schultz, D. M., Roller, J. J., Azizinamini, A. & Tang, H. T. (1987a) Testing of large-scale concrete containment structural elements. *Nuclear Engineering and Design*, 100, 129–149.
- Hanson, N. W., Schultz, D. M., Roller, J. J. & Tang, H. T. (1987b) Results of large-scale test of discontinuity region in a prestressed concrete containment. *Nuclear Engineering and Design*, 104, 321–328.
- Hessheimer, M. F. & Dameron, R. A. (2006) Containment integrity research at sandia national laboratories. *NUREG/CR-6906*. Albuquerque, NM, Nuclear Regulatory Commission.
- Jin, S. & Gong, J. X. (2021) Fragility analysis and probabilistic performance evaluation of nuclear containment structure subjected to internal pressure. *Reliability Engineering & System Safety*, 208.
- Li, X. & Gong, J. (2023) Effects of steel liner corrosion on the leak-tightness of prestressed concrete containment structure under severe accident loads. *Annals of Nuclear Energy*, 180.
- Petti, J. P., Naus, D., Sagüés, A., Weyers, R. E., Erler, B. A. & Berke, N. S. (2011) Nuclear containment steel liner corrosion workshop: final summary and recommendation report. *SAND2010-8718* Albuquerque, NM.
- Petti, J. P., Spencer, B. W. & Graves, H. L., III (2008) Risk-informed assessment of degraded containment vessels. *Nuclear Engineering and Design*, 238, 2038–2047.
- Spencer, B. W., Petti, J. P. & Kunsman, D. M. (2006) Risk-informed assessment of degraded containment vessels. *NUREG/CR-6920*. Albuquerque, NM, Nuclear Regulatory Commission.
- Zhou, L., Li, J. B., Zhong, H., Lin, G. & Li, Z. C. (2018) Fragility comparison analysis of CPR1000 PWR containment subjected to internal pressure. *Nuclear Engineering and Design*, 330, 250–264.

Influence of combined corrosion of carbonation and cyclic loading on reinforced concrete beams

L.X. Zhu, Z.J. Zhou & Y.Q. Tian
Chang'an University, Xi'an, Shaanxi, China

C.R. Chen
Gansu Province Transportation Planning, survey & design Institute Co., Ltd., Lanzhou, Gansu, China

ABSTRACT: Carbonation resistance has received prevalent attention from academia as well as industry during the last few decades. The single influence of carbonation on reinforced concrete structures has been widely considered. However, the combined effect of cyclic loading and carbonation still need to be investigated. Therefore, an optimized test procedure was proposed to simulate the damage mechanism of reinforced concrete beams with combined corrosion. The results showed different carbonation process of tensile concrete corresponding to two different test procedures, which indicated that combined corrosion was more serious than separated effects. And a carbonation model of tensile concrete under combined corrosion was proposed. Subsequently, the model was validated by comparing the prediction results with data from past literature. The research findings are significant for improving the accuracy of evaluation of residual carbonation life of reinforced concrete bridges and early warning of durability protection.

1 INTRODUCTION

Carbonation is of major concern to researchers and engineers, as the reaction of CO₂ with calcium-bearing phases in concrete infrastructure components is known to decrease alkalinity of pore water, introducing steel reinforcements corrosion in concrete (Morandea, et al. 2014, Tang, J.Z., et al. 2018). Thus, carbonation is typically considered to be a major cause of performance deterioration of reinforcement concrete (RC) structures in the atmospheric environment.

Numerous researchers have investigated the influence of material components and ambient conditions on concrete carbonation, including various mineral additions (Sisomphon, et al. 2007), mix proportions (Leemann, et al. 2015), recycled aggregates (Zhang, et al. 2021), relative humidity and temperature (Bary & Sellier, 2004, Chen & Ho, 2013), and CO₂ concentration (Visser, 2014). Considering that concrete in structures is constantly subjected to both carbonation and loads, the influences of static loads and visible cracks on concrete carbonation have also been investigated (Castel, et al. 1999, Song, et al. 2006, Talukdar, et al. 2015) and corresponding carbonation models were established (Wang, et al. 2018, Tang, et al. 2020). It is generally believed that the tensile stress had a positive association on the carbonation depth; conversely, there were thresholds existing for the influence of the compressive stress level. In large-scale concrete bridges, prestressed reinforcements are used to avoid cracking of concrete during their service life, but traffic loading cycles will promote the expansion of microcracks and pores (Jiang, et al. 2017). Compared with uncracked concrete, the diffusion of CO₂ is more likely to start in damaged concrete (Chen, et al. 2008). For example, Wang et al. (2018) observed that flexural cracks clearly affected the upward propagation of the carbonation front. Therefore, the combination of the mechanical load and environmental actions was more severe than the sum of those individual factors (Yao, et al. 2017).

However, few studies in carbonation model that accounted for the effects of fatigue damage were reported. Song, et al. (2020) proposed a numerical model for prefatigued concrete and further revealed the effects of environmental factors on the carbonation process of concrete.

Jiang, et al. (2018) established a general carbonation equation for three common damage patterns occurred in pier, the top and bottom of girders at mid-span, respectively. Nevertheless, those experimental specimens were subjected to fatigue damage before carbonation, which was inconsistent with the actual service condition of bridges. Therefore, an improvement in test process is necessary for accurate corrosion initiation prediction of steel reinforcements in reinforced concrete structures.

In this study, the environmental chamber with a loading equipment was used to realistically simulate the coupling effects of cyclic loading and carbonation on RC beams. The distribution of cracks and carbonation process of the flexural tensile concrete under combined corrosion was revealed. Furthermore, the influence of test procedure on concrete carbonation was also studied. Finally, on the basis of experimental data and theoretical analysis, the corresponding carbonation model was established and verified. The outcome of this study can provide important references for evaluation of residual carbonation life and durability protection of RC structures in atmospheric environment.

2 EXPERIMENTAL METHODS

2.1 Materials and specimens

The Chinese standard ordinary Portland cement (P.O 42.5) was used in this study with a specific surface of 363 m²/kg. And natural river sand obtained from Weihe river was chosen as the fine aggregate with a fineness modulus of 3.40 and an apparent density of 2700 kg/m³. As for the coarse aggregate, continuous graded crushed gravel was used with a size of 5-15 mm and an apparent density of 3100 kg/m³.

A total of 5 RC beams was designed and cast. One beam was loaded monotonically to failure to determine the static capacity of the beam. Two beams were carbonated after loaded cyclically and the other two beams were exposed to combined corrosion. In addition, several cubic concrete specimens were cast for carbonation. The concrete mix proportion is shown in Table 1, and the dimension of RC beams as well as the details of reinforcements are given in Figure 1. All specimens were cured for 28 days in a standard curing room, in which the temperature and relative humidity were kept at 23 ± 2°C and 95%, respectively.

Table 1. Mix proportion of Concrete.

Water	Cement	Fine Aggregate	Coarse Aggregate	
kg/m ³	kg/m ³	kg/m ³	kg/m ³	w/c
161	460	684	1116	0.35

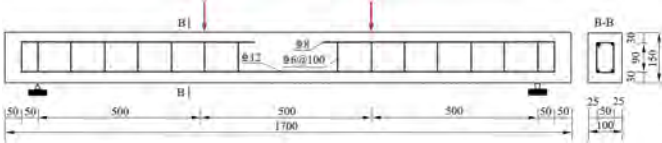


Figure 1. Dimension and reinforcement detailing of RC beams.

2.2 Load application

2.2.1 Equipment for loading test

The equipment can simulate the mechanical properties of specimens corresponding to various working conditions, either for static load or cyclic load. There were three parts to the load equipment: the loading system, the control system and the data collection system. As shown in Figure 2, the loading system was composed of a reaction frame, hydraulic jack, load distributing girder, fixture, and load sensor, etc. The base of the hydraulic jack was fixedly connected with the reaction

frame, and the lifting part was connected with the load distribution girder through the fixture. The length of the distribution girder was 500 mm and the RC beams were tested under four-point flexural loading. Furthermore, the control system can adjust the load through controlling the hydraulic jack with the automatic pressure circulation device and the maximum load that can be applied by the equipment is 300 kN. Real-time data during the test, such as displacement, strain could also be collected by the stress and strain testing and analysis system (DH3818Y).

The loading system was placed in the environmental chamber while the other two systems were placed outdoors, connecting through oil-pressure pipes and sensor lines. This was convenient for operation and could prevent it from being interfered by the high temperature and humidity in the chamber as well.

2.2.2 Calculation of loading in test

Considering that actual vehicle loads are usually variable-amplitude fatigue loads which is difficult to simulate, constant amplitude sinusoid was selected in this paper. The details of the groups and loads are given in Table 2. The maximum load F_{max} and minimum load F_{min} applied to the RC beams in the fatigue tests are presented in this table. The maximum loads were determined based on S_{max} : a percentage of the yield strength of the reference beam, which was determined from the static tests. At the beginning, the beams were first subject to the mean load between F_{max} and F_{min} , and then, the fatigue damage was accumulated under constant amplitude sinusoidal cyclic loading at a frequency of 4 Hz.

Table 2. Summary of the specimens and corrosion condition.

Spec.	Procedure	Cyclic Load	
		F_{min}/F_{max} (kN)	S_{max}
A	Carbonation	-	-
B1	Static failure	-	-
B2	SC*	4.6/13.8	0.3
B3	SC	4.6/23	0.5
B4	CC**	4.6/13.8	0.3
B5	CC	4.6/23	0.5

* SC stands for separated corrosion; **CC stands for combined corrosion.

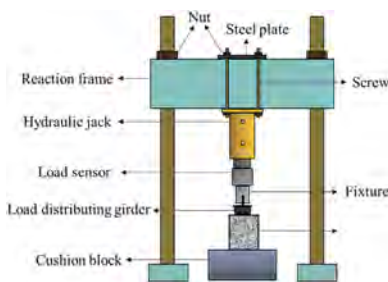


Figure 2. Equipment for loading test.



Figure 3. Carbonation chamber.

2.3 Accelerated carbonation test

After curing for 28 days, R2 and R3 were first applied to specified cyclic loads. Then the undamaged specimens R4 and R5 were successively placed on loading devices in the carbonation chamber (Figure 3) for 28 days combined corrosion. The cubic concrete specimens and damaged beams R2 and R3 were also put into the chamber for carbonation at the same time. According to the China National Standard (GB/T 50082-2009), the concentration of CO_2 was kept at $(20 \pm 3) \%$, and the values of the relative humidity and temperature were kept at $(70 \pm 5) \%$ and $(20 \pm 2) ^\circ C$, respectively.

In this study, a phenolphthalein indicator was used to measure the carbonation depth, which was an important index to evaluate the carbonation resistance of concrete. The sampling locations on the tension surface of RC beams are presented in Figure 4 and the carbonation depth was measured by a concrete carbonation depth ruler. At each location, two sample holes were dry drilled using an 8 mm diameter rotary impact drill. And the mean value of the measured carbonation depths of sample holes corresponding to different carbonation durations was chosen as the final carbonation depth of concrete.

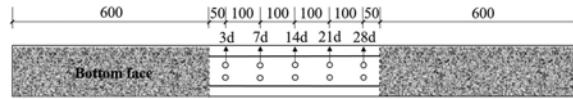


Figure 4. Measurement of carbonation depth.

3 TEST RESULTS AND ANALYSIS

3.1 Crack width of RC Beams

The maximum flexural crack width of tensile zone of RC beams is shown in Figure 5, where the crack widths of B2 and B3 were measured under individual action of cyclic loading. The graph presents that the crack width increased rapidly in the first 14 days. This increase is due to the tensile stress being greater than the tensile strength of concrete, which accelerated the appearance of new microcracks and the propagation of the existing cracks. Thereafter, the crack width only exhibited a slight increase due to the further rising load cycles. The first reason for the downward trend of cracks width development lies in that the tensile stress was mainly borne by the steel bars rather than the concrete with the increase in the number of loading cycles. Secondly, the carbonization products may also result in the partial blocking of internal pores and cracks of concrete after 14 days.

Figure 5 also illustrates that the bending cracks were mainly concentrated in the pure flexural zone of RC beams, and they expanded from the bottom of the beams to the center after thousands of loading cycles. Besides, the number and space of cracks distributed in the bottom of B4 was obviously less than that of B5, and the maximum crack width of B5 (0.12mm) was about 3 times that of B4 (0.05mm) after 28 days. The same applied to B2 and B3, which indicated that both the number and width of flexural cracks increase with the increase of the load level.

In addition, it can be found that the crack width curve of B2 lay above that of B4 for equal carbonation ages, and the same happened with B3 and B5. Further, the crack width differences between combined corrosion specimens and separated corrosion specimens increased with the increase of carbonation durations, which gave a further verification on the point that carbonation slowed down the expansion of crack.

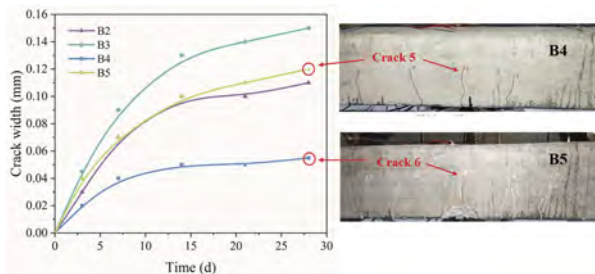


Figure 5. The maximum flexural crack width and distribution of specimens.

3.2 Carbonation depth of concrete

For the RC beams subjected to flexural loads, their lateral section could be divided into flexural tension zone and flexural compression zone by a neutral plane. The compressive load borne by

the flexural compression concrete was very low in this paper, which inhibited the carbonation. Considering that the tensile strength of concrete was much lower than the compressive strength, there existed difference in carbonation rate, which further affected the corrosion of steel in concrete. Therefore, the carbonation depth of tensile concrete should be investigated separately.

Figure 6 shows the carbonation depth of flexural tensile concrete under the combined effects of carbonation and cyclic loading, as well as that of zero-load cubic specimens. Generally, the carbonation depth of all specimens showed an increased trend, but that of fatigue-damaged specimens were all greater than that of non-damaged concrete. After 28 days of coupled corrosion, the carbonation depth of B2, B3, B4, B5 were 7.45, 12.75, 8.68, 14.36 mm, respectively, which were 22.5%, 109.7%, 42.8%, and 136.2% higher than that of A (6.08 mm). And the carbonation rate for unstressed specimens was 1.16 at 28 days, and that of B4 and B5 were 41.26% and 133.76% higher, respectively. This was consistent with previous reports (Jiang, et al. 2017, Song, et al. 2020) that fatigue damage decreased the carbonation resistance of concrete.

Under the same load level, the difference in carbonation depth of B2 and B4 increased with carbonation durations. However, that of B3 and B5 could be divided into two phases, i.e. the carbonation depth of B5 developed from less than that of B4 initially to a final exceedance. The reasons for this phenomenon are as follows. Firstly, when the load level was low, some cracks in separated corrosion specimens closed due to creep of concrete, which hindered the transportation of CO₂. In the meantime, carbonation-introduced autogenous healing also had the same effect. Secondly, compared with the combined corrosion, the separated corrosion specimen under high load level produced large unrecoverable plastic deformation earlier, so its carbonation depth was higher at the beginning. However, the carbonation rate of specimen with initial fatigue damage decreased with the decrease of hydration products. Thirdly, both length and width of flexural cracks in the combined corrosion specimens were gradually expanded, resulting in the faster growth of carbonation depth. Therefore, the difference of carbonation depth between the separated corrosion specimens and the combined corrosion specimens continued to increase.

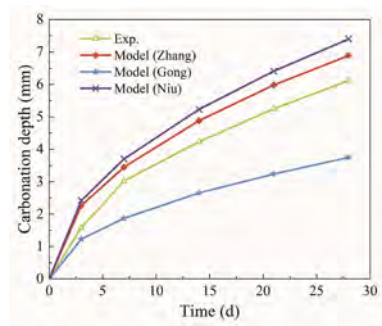
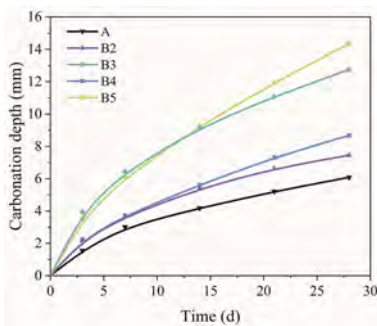


Figure 6. The carbonation depths of specimens.

Figure 7. Comparison of mathematical models.

4 CARBONATION MODEL OF FATIGUR DAMAGED CONCRETE

According to the previous researches, fatigue damage did not change the proportional relationships between carbonation depths of concrete and square roots of carbonation ages (Jiang, et al. 2018). On this basis, an influence coefficient of cyclic load K_D was introduced in order to analyze qualitatively the effect of cyclic load on the carbonation depth of concrete, as shown in Eq. (1).

$$x_D = k\sqrt{t} = K_D \cdot K_0 \cdot \sqrt{t} = K_D \cdot x_0 \quad (1)$$

Where x_D is the carbonation depth of fatigue-damaged concrete (mm); x_0 is the carbonation depth of non-damaged concrete; k is the carbonation rate coefficient; t is the carbonation age (d); K_0 is the carbonation coefficient of non-damaged concrete; K_D is the influence coefficient of cyclic loading.

4.1 The carbonation depth of non-damaged concrete x_0

To date, various prediction models for the carbonation depths of non-damaged concrete have been proposed, such as semi-theoretical model (Zhang & Jiang, 1998), multi-coefficient model (Gong, et al. 1985) and stochastic model (Niu, 2003), as shown in as shown in Eq.(2), (3), and (4), respectively.

$$x_0 = 839(1 - RH)^{1.1} \sqrt{\frac{C_0 \cdot (w/c \cdot \gamma_c - 0.34)}{c \cdot \gamma_{HD} \cdot \gamma_c}} \sqrt{t} \quad (2)$$

where RH is the relative humidity (%); C_0 is the volume concentration of CO_2 (%); w is the water mass per volume (kg/m^3); c is the cement mass per volume (kg/m^3); γ_c is the coefficient of cement type, γ_{HD} is the coefficient of cement hydration.

$$x_0 = K_1 K_2 K_3 K_4 K_5 K_6 a \sqrt{t} \quad (3)$$

in which, K_1 is the coefficient of cement content; K_2 is the coefficient of water-cement ratio; K_3 is the coefficient of fly-ash content; K_4 is the coefficient of cement type; K_5 is the coefficient of aggregate type; K_6 is the coefficient of curing method; a is the carbonation rate.

$$x_0 = 2.56 K_{mc} K_j K_{CO_2} K_p K_s \sqrt[4]{T} (1 - RH)^4 RH (57.94 m_c / f_{cu} - 0.76) \sqrt{t} \quad (4)$$

where K_{mc} is the random variable for calculation pattern indeterminacy, K_j is the coefficient of carbonation location, K_{CO_2} is the coefficient of CO_2 concentration, K_p is the coefficient of casting surface, K_s is the coefficient of stress, T is the average annual ambient temperature, f_{cu} is the cube compressive strength of concrete, m_c is the ratio between the mean and standard values of the concrete cube compressive strength.

The predicted carbonation depth of those models and experimental results is compared in Figure 7. By comparison, it can be found that the model proposed by Zhang had advantages on calculated precision and the average value of the relative error was 0.75. Hence, Zhang's model was selected as the base carbonation model of non-damaged concrete and the relative error was introduced as the adjustment coefficient, as Eq. (5) described.

$$x_0 = 0.75 \times 839 \cdot (1 - RH)^{1.1} \cdot \sqrt{C_0 \cdot (w/c \cdot \gamma_c - 0.34) / (c \cdot \gamma_{HD} \cdot \gamma_c)} \cdot \sqrt{t} \quad (5)$$

4.2 The influence coefficient of cyclic loading K_D

In order to accurately describe the accumulation and development process of fatigue damage in concrete under cyclic flexural loading, it is necessary to define an appropriate fatigue damage variable and establish the relationship between the variable and load history. Tanaka, k. et al. (1999) defined a parameter to quantitative described the damage degree of specimens which was related to the stress amplitude and loading cycles, as shown in Eq. (6).

$$D_F = \sigma / f + 0.0431 (\lg N)^{1.24} \quad (6)$$

where D_F is the degree of fatigue damage, σ is the tensile stress (MPa), f is the flexural strength (MPa), N is the number of cyclic loading.

Fitting process is conducted on test data of carbonation depth of non-damaged concrete, indicating that K_0 was 1.1056. Hence, Eq. (1) can be described as follows:

$$K_D = x_D / (1.1056 \cdot \sqrt{t}) \quad (7)$$

According to Eqs. (6) and (7), the corresponding least-square regression line of the coefficient K_D versus the variable D_F can be obtained, thus, K_D can be rewritten as Eq. (8).

$$K_D = 0.6243 + 0.0350 e^{4.67 D_F} \quad (8)$$

By introducing Eqs. (5) and (8) into Eq. (1), the carbonation depth of concrete under cyclic loading can be obtained:

$$x_D = (390.14 + 22.02e^{4.67Df}) \cdot (1 - RH)^{1.1} \cdot \sqrt{C_0 \cdot (w/c \cdot \gamma_c - 0.34) / (c \cdot \gamma_{HD} \cdot \gamma_c)} \cdot \sqrt{t} \quad (9)$$

4.3 Model validation

Experimental data that collected from literature (Zhou, 2016) in which the accelerated carbonation tests on fatigue-damaged concrete beams were carried out were used to validate the proposed carbonation model in this paper. After curing for 90 days, all specimens were subjected to repeated loads to reach the specified fatigue damage degree (D) through controlling the number of load cycles. Finally, these damaged concrete specimens were moved into the environmental chamber for 7, 14, 28, and 56 days, and the reported exposure conditions for those specimens were the same as those in this study.

Figure 8 shows the carbonation depths of fatigue-damaged concrete beams calculated by the proposed model and it is obvious that the carbonation depths obtained by different methods were almost identical when $D \leq 0.6$. When the fatigue damage degree was 0.2, 0.4, and 0.6, the average relative errors between the predicted carbonation depth and the experimental results reported by Zhou were 7.52%, 9.68%, 7.80%, respectively. In the initial stage of the test, the test results were generally greater than the prediction values, but with the increase of exposure time, the carbonation depth of the proposed model came from behind to exceed test one at 56 days when $D = 0.6$. This phenomenon was more obvious as for the specimen with fatigue damage of 0.8, and the test procedure was responsible for the increase of relative error between the measured depths and model results, as illustrated in Section 3.2.

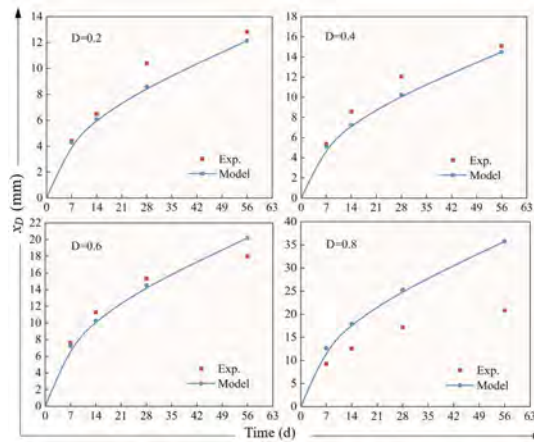


Figure 8. Comparison between predicted results and those reported by Zhou.

5 CONCLUSION

An innovative accelerated carbonation test of RC beams under the action of cyclic flexural loading was conducted in this study. Within the scope of our experiments, the following conclusions are drawn:

- (1) The decrease of carbonation resistance of concrete was related to the increase of cracks introduced by cyclic loading. The flexural crack width was positively correlated with load level and cycles, and carbonation depth was easily affected by load. However, the growth rate of the two was decreased. The carbonation process of concrete under the combined corrosion and separated corrosion was different. Hence, in the carbonation analysis of fatigue-damaged reinforced structures, the influence of test procedure should be considered.
- (2) By introducing the coefficient of fatigue damage and establishing the relationship between the coefficient and the degree of fatigue damage, a carbonation model of tensile concrete

- considering the effect of cyclic flexural loading is proposed based on Zhang 's model. It is found that the carbonation depths predicted by the theoretical carbonation model were in good agreement with the results reported by Zhou, and thereby demonstrated its validity.
- (3) Although 28 days of combined corrosion can reveal the carbonation mechanism of fatigue-damaged concrete to some extent, the degradation mechanism of mechanical properties of RC beams can be better investigated if the corrosion durations are longer. Furthermore, there are some differences between natural condition and accelerated tests, further experimental research is required.

REFERENCES

- Bary, B. & Sellier, A. 2004. Coupled moisture—carbon dioxide—calcium transfer model for carbonation of concrete. *Cement and Concrete Research* 34: 1859–1872.
- Castel, A. et al. 1999. Effect of loading on carbonation penetration in reinforced concrete elements. *Cement and Concrete Research* 29: 561–565.
- Chen, C.T. & Ho, C.W. 2013. Influence of cyclic humidity on carbonation of concrete. *Journal of Materials in Civil Engineering* 25: 1929–1935.
- Chen, D. & Mahadevan, S. 2008. Chloride-induced reinforcement corrosion and concrete cracking simulation. *Cement and Concrete Composites* 30: 227–238.
- Gong, L.S. et al. 1985. Multi coefficient carbonation equation of concrete and its application. *Concrete and Reinforced Concrete* 06: 10–16.
- Jiang, C. et al. 2017. Experimental investigation on carbonation in fatigue-damaged concrete. *Cement and Concrete Research* 99: 38–52.
- Jiang, C. et al. 2018. Modeling the effects of fatigue damage on concrete carbonation. *Construction and Building Materials* 191: 942–962.
- Leemann, A. et al. 2015. Relation between carbonation resistance, mix design and exposure of mortar and concrete. *Cement and Concrete Composites* 62: 33–43.
- Morandeau, A. et al. 2014. Investigation of the carbonation mechanism of CH and CSH in terms of kinetics, microstructure changes and moisture properties. *Cement and Concrete Research* 56: 153–170.
- Niu, D.T. 2003. *Durability and life prediction of concrete structures*. Beijing: Science Press.
- Sisomphon, K. & Franke, L. 2007. Carbonation rates of concretes containing high volume of pozzolanic materials. *Cement and Concrete Research* 37: 1647–1653.
- Song, H.W. et al. 2006. Predicting carbonation in early-aged cracked concrete. *Cement and Concrete Research* 36: 979–989.
- Song, L. et al. 2020. Carbonation Process of Reinforced Concrete Beams under the Combined Effects of Fatigue Damage and Environmental Factors. *Applied Sciences* 10: 3981.
- Talukdar, S. et al. 2015. Modelling the effects of structural cracking on carbonation front advance into concrete. *International Journal of Structural Engineering* 6: 73.
- Tanaka, K. et al. 1999. Effect of repeated load on micro structure and carbonation of concrete and mortar. *Durability of Building Materials and Components* 8: 256–265.
- Tang, G.B. et al. 2020. Prediction model of concrete carbonation depth under the combined actions of stress. *Journal of Building Materials* 23: 304–308.
- Tang, J.Z. et al. 2007. Influence of axial loading and carbonation age on the carbonation resistance of recycled aggregate concrete. *Construction and Building Materials* 137: 707–717.
- Visser, J.H.M. 2014. Influence of the carbon dioxide concentration on the resistance to carbonation of concrete. *Construction and Building Materials* 67: 8–13.
- Wang, J. et al. 2018. Influence of concrete stress state on carbonation depth. *Journal of Building Structures* 39: 397–404.
- Wang, X.H. et al. 2018. Influence of loading and cracks on carbonation of RC elements made of different concrete types. *Construction and Building Materials* 164: 12–28.
- Yao, Y. et al. 2017. Recommendation of RILEM TC 246-TDC: test methods to determine durability of concrete under combined environmental actions and mechanical load. *Materials and Structures* 50: 155.
- Zhang, K. et al. 2021. Experimental study on carbonation behavior of seawater sea sand recycled aggregate concrete. *Advances in Structural Engineering*.
- Zhang, Y. & Jiang, L.X. et al. 1998. A practical mathematical model of concrete carbonation depth based on the mechanism. *Industrial Buildings* 01: 16-19+47.
- Zhou, Y.X. 2016. An experimental study on carbonation of concrete under flexural fatigue, Xi'an University of Architecture and Technology.

*SS11: BRIDGE|50: Experimental testing and model validation
for life-cycle design and assessment of RC/PC bridges
Organizers: F. Biondini, F. Tondolo, S. Manto & C. Beltrami*



Taylor & Francis

Taylor & Francis Group

<http://taylorandfrancis.com>

Large-scale experimental testing of 50-year-old prestressed concrete bridge girder

P. Savino, A. Quattrone, D. Sabia, B. Chiaia & F. Tondolo
Politecnico di Torino, Turin, Italy

M. Anghileri, F. Biondini & G. Rosati
Politecnico di Milano, Milan, Italy

ABSTRACT: This paper reports on large-scale loading tests survey carried out on 50-year-old prestressed concrete girders as part of the BRIDGE|50 research project (www.bridge50.org). The girders were retrieved from an existing viaduct in Turin, Italy. The prestressed concrete elements were 19.2 m long and had an I-shaped cross-section with a cast-in-situ slab. Variable damages were found, due to in-service deterioration and/or subsequent lifting operations during the demolition phase. Each specimen was subjected to static tests using monotonic or cyclic loading up to the ultimate load. This paper reports the results of tests on the second group of four girders, comparing their load-deflection responses and strains with those of the first group subjected to a different static scheme. The experimental findings highlight the global structural response from bending to bending/shear failure; the outcomes will define a valuable reference database for assessing the residual structural performance of existing girder bridges.

1 INTRODUCTION

Civil infrastructures operate under adverse service conditions, which may cause durability problems at different levels and, in the worst cases, the decrease or total loss of load-carrying capacity. Meanwhile, traffic demand is continuously growing, both in terms of number and weight of vehicles. However, as civil infrastructures age, uncertainties on the prediction of structural response increase due to the deterioration mechanisms. As a result, structural assessment has received much attention in recent decades from different perspectives. Structural health monitoring technologies have been developed to report the structural health status and early warning in presence of structural damage. Indeed, full-scale load tests are conducted to better understand the structural behavior of existing structures and to calibrate structural models. However, large-scale tests on civil infrastructures, are not always straightforward. In order to learn more about non-linear behavior and the ultimate capacity of bridges, the load test involves irreversible damages which led to the dismissing of the structure. Furthermore, huge human, financial, and material efforts are required, and as reported in Recupero & Spinella (2019), only few studies have been carried out on full-scale prestressed concrete (PC) girders from decommissioned bridges around the world (Wang et al. 2020). Assessment of existing bridges requires a thorough understanding of their structural behavior. However, the investigation usually concerns few structural members, equipped to study mainly the flexural behavior. Full-scale experiments should include more variables to be controlled. A systematic assessment of several specimens should be conducted under different loading test setups for a better understanding of the failure mechanism and thus develop more reliable estimates of the residual capacity.

In this scenario, the BRIDGE|50 research project was established to study the residual structural performance of a 50-year-old viaduct and provide a framework for safety assessment and residual lifetime evaluation of existing bridges (Biondini et al. 2020, 2021). A wide experimental campaign was planned to investigate 25 prestressed concrete (PC) I-girders, 4 PC box girders, and 2 pier caps recovered from the C.so Grosseto viaduct, a viaduct built in Turin in 1970 and

decommissioned in 2018. After demolition, the structural members were stored in a testing site properly equipped to conduct a detailed structural assessment including visual inspection, deterioration mapping, and non-destructive tests (Anghileri et al. 2020). Furthermore, a large reaction steel frame of the Interdepartmental Center for the Safety of Infrastructures and Constructions (SISCON) of Politecnico di Torino was used to perform full-scale load tests up to failure. Several load test setups were considered to study the failure mechanisms under flexural, mixed flexural/shear, and shear loading modes. The first group of four PC beams was tested under three-point bending configuration and detailed in Tondolo et al. (2021, 2022) and Savino et al. (2023). This paper reports the experimental results of the second group of four beams tested under four-point bending configuration up to failure. The reported parameters not only extend the database aimed at providing further knowledge on the structural response of 50-year-old PC beams but could be used to evaluate developed theories on resisting mechanism. The observed response is also compared with the structural behavior recorded for the first group of beams.

2 DESCRIPTION OF THE C.SO GROSSETO VIADUCT

The C.so Grosseto viaduct was a multilevel road bridge located in Turin, Italy. It was built in 1970 and decommissioned in 2019 for a new urban redevelopment plan (Savino et al. 2020). Its structural topology represents a typical solution widespread in the Italian motorway heritage and consists of two structurally independent decks, one for each traffic way, with simply supported span. Each span comprised ten PC I-shaped girders and two PC box girders at the edges, with a length averaging from 16.0 to 24.0 m. Two diaphragms connected the longitudinal girders at the third points. The superstructure was completed by a cast-in-situ slab of 140 mm. The infrastructure was 1.4 km long and achieved a maximum vertical clearance of 12.4 m.

During the decommissioning works in 2018, a total of 31 structural elements were removed and stored in a testing site of about 6000 m², located in Turin. A detailed layout of the preserved structural member in the original deck configuration is shown in Figure 1. The coloured elements represent the girders recovered for BRIDGE|50 research project; the elements depicted in blue belong to the first group of tests whereas the elements highlighted in red refer to the girders investigated and reported in this work. All the elements were properly identified with a code, according to the original configuration. The PC beams studied in the present work were identified as B7-P47/46, B6-Ab/P47, B6-P48/49, and B10-Ab/P47 according to classification reported in Savino et al. 2023.

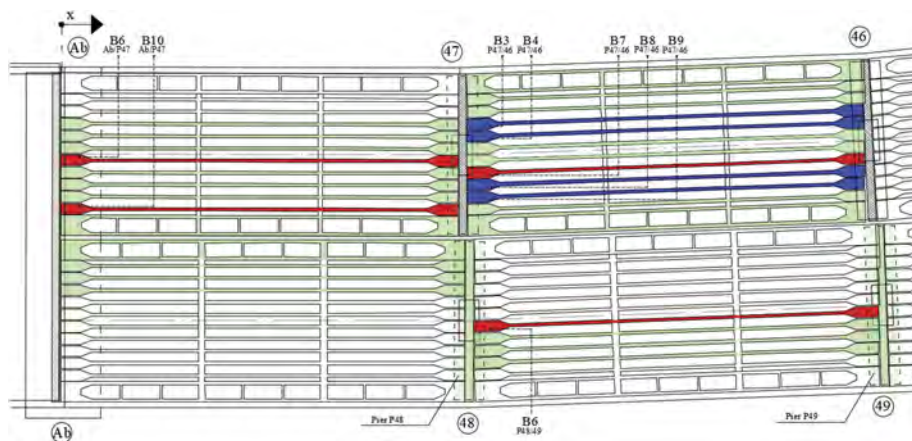


Figure 1. In-service layout of the investigated structural members (first group of tested girders in blue, second group of tested girders in red).

2.1 Details of the tested girders

All the girders were 19.5 m long, with an I-shaped cross-section of 580 x 900 mm. Cover depths were 45 mm for prestressed strands and were variable up to a minimum of 10 mm for

ordinary reinforcement. According to the design documentation, prestressing reinforcement was composed of seven-wire strands with a nominal diameter of 12.7 mm and tensile strength of 1638 MPa. The prestressed reinforcement consisted of 17 strands concentrated in the lower part of the beam and 3 strands located in the top flange as pictured in Figure 2. The stirrups are made by 8 mm ribbed steel spaced of 250 mm. The 14 cm cast-in-situ slab was reinforced with a square mesh of rebars. The maximum allowable stress for the strands at the tensioning stage was 1400 MPa. The concrete compressive strength at 28 days was designed to be 30 MPa. No specific requirements were reported for the cast-in-situ slab. The arrangement of the reinforcement as well as the cross-section geometry is given in Figure 2.

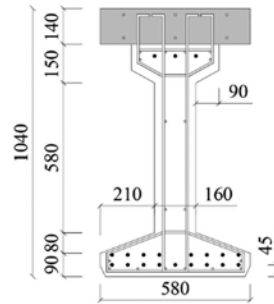


Figure 2. I-beam cross-section (units in mm).

According to the diagnostic campaign performed before the load tests session, the beams investigated in the present work were considered in good condition except for B6-P48/49 and B10-Ab/P47 girder which presented controlled damages induced by dismantling operations (Savino et al. 2023). The B6-P49/48 beam had two strands cut on both sides of the lower flange, at distances 3.7, 9.6, and 15.5 m from the end section. The B10-Ab/P47 girder had two strands cut on one side at distances of 3.8 and 15.5 m. Relying on the results provided by the preliminary diagnostic campaign, the load test program was properly planned, starting from the undamaged beams, considered as a benchmark for the subsequent beams with different degrees of damage.

3 FULL-SCALE LOAD TESTS SETUP

For the purpose of testing the PC girders with variable load configurations, a proper reaction steel frame was used (SISCON). Each beam was simply supported and loaded under a four-point bending configuration adopting shear spans of 650 cm. The loading system consisted of two couple of hydraulic jacks which transfer the load to the specimens through transverse steel beams. The loading process was conducted in two loading cycles. In the first phase, the load was increased until the opening of cracks, followed by the complete unloading of the girder. In the second loading phase, the specimens were loaded up to failure. The load tests were performed with a fixed loading rate by controlling the force and were stopped when the concrete in the compression zone crushed. The double loading cycles allowed also to perform the dynamic characterization of the specimens at different level of damages (Quattrone et al. 2020, Sabia et al. 2021, 2022).

As it is unusual to have full-scale elements of existing bridges loaded to collapse, the data gathered during such tests are of extreme interest to understand their structural response. For this reason, a proper measurement plan has been designed for each beam to measure several parameters involving displacements, strains, loads, vibrations, and acoustic emissions. This section summarizes only the equipment used to measure the parameters reported in this work and detailed below. Arrangement of the monitoring system is shown in Figure 3.

The layout of the monitoring system has been defined according to the load test setup, considering two main zones: the shear span and the bending span. Along the shear span, linear variable displacement transducers (LVDTs) were installed on aluminum frames oriented at 45° with a measurement base of 707 mm. Such sensors were denoted by the code “SHxxA/B”,

where “xx” indicates the progressive number, “A” refers to the frames with a negative slope, and “B” refers to the frames with positive slopes. In the bending zone, the LVDTs were installed on horizontal frames with a measurement base of 400 mm. Those were denoted by “BxxT/C” where “xx” indicates the progressive number, “T” refers to the LVDTs installed on the bottom flange, and “C” refers to the remaining positions. Furthermore, two electrical strain gauges were mounted on the bottom and upper flanges of the precast beam along the left vertical alignment of the B01T and B01C LVDTs.

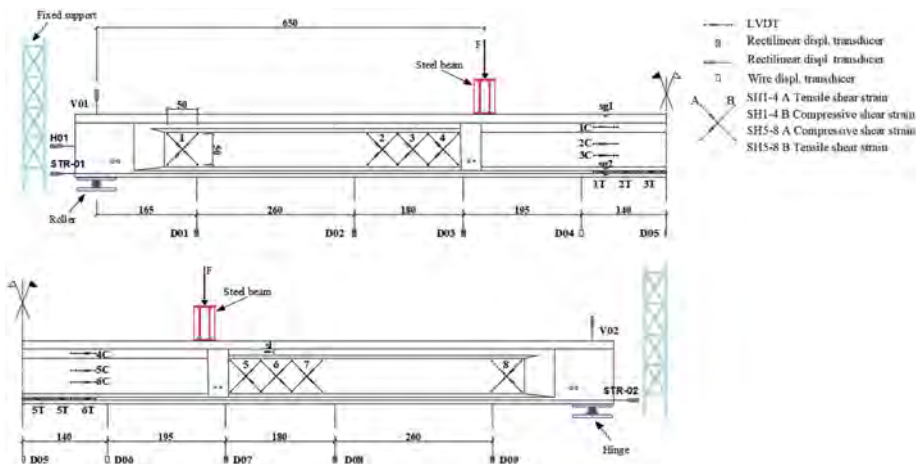


Figure 3. Layout of the monitoring system (units in cm).

Three displacement transducers were installed at each end of the girder to measure vertical and horizontal displacements at the supports, and the potential slipping of one strand. A displacement transducer was installed along the shear span to measure potential sliding of the cast-in-situ slab. The vertical deflections along the shear span were measured by nine potentiometer transducers connected to the bottom of the girders (“D01-09” in Figure 3). For the B7-P47/46 girder, the LVDTs along the shear span, in positions 2-4 and 5-7, were moved 50 cm from the transverse diaphragms. The LVDTs in positions B02/03C and B05/06C were used along the shear span, close to positions 1 and 8. The two strain gauges were moved to the same alignment as the B03T. For B10-Ab/P47 girder, the two strain gauges have been moved to the midspan.

4 TEST RESULTS

Some of the most representative results of the full-scale load tests have been reported in the present paper. These diagrams were chosen to show the overall structural response of the girder as a consequence of simultaneous shear and bending actions during the mechanical tests. All the diagrams have been obtained by referring to the load applied by a single jack. Therefore, to consider the total load applied to the specimen, the load should be multiplied by 4. Furthermore, the self-weight and the weight of the loading system (estimated as 11.82 kN per actuator) need to be considered.

The Figure 4 presents the midspan deflection versus the applied load. The diagrams highlight a similar behaviour for all the specimens, which can be described by three phases: a linear elastic relationship, a cracking-induced reduction of the stiffness and the failure after reaching the maximum load due to the crushing of the upper slab.

The failure mode was similar with that registered in the first group of specimens (Savino et al. 2023). However, a different resistance mechanism was involved, as it will be shown in the following based on the crack pattern.

The B7-P47/46 reached its maximum capacity with a load of 120.1 kN, inherent to an applied bending moment of 1561.3 kNm. The B6-Ab/P47 showed a failure load of 126.5 kN; this load

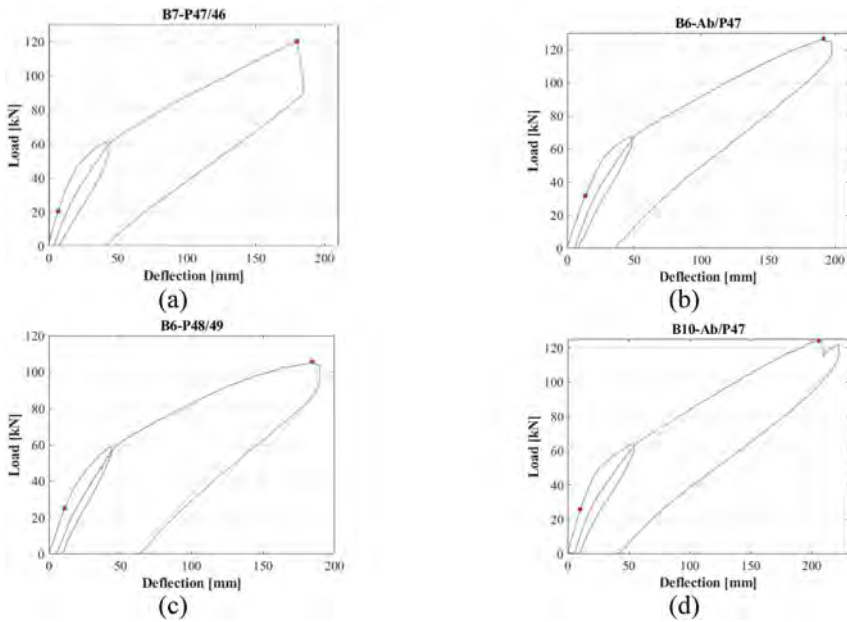


Figure 4. Load vs deflection: (a) B7-P47/46, (b) B6-Ab/P47, (c) B6-P48/49, and (d) B10-Ab/P47 girder.

corresponds to a maximum applied bending moment of 1644.5 kNm. The B6-P48/49 was loaded up to a failure load of 105.6 kN, corresponding to a bending moment of 1372.8 kNm. The B10-Ab/P47 was loaded up to a failure load of 124.0 kN, corresponding to a bending moment of 1612.0 kNm. At these load levels, the B7-P47/46, B6-Ab/P47, B6-P48/49, and B10-Ab/P47 specimen exhibited maximum midspan deflections of 179.9, 191.3, 184.3 and 205.5 mm, respectively. Referring to the load-midspan deflection diagram of the specimens tested under three-point loading configuration, the maximum bending moment and midspan deflection were 1492.2 kNm (B8-P47/46) and 167 mm (B3-P47/46) respectively (Savino et al. 2023).

Since the load-deflection curves are function of the global behavior of the specimens, the first cracking load was detected from the load-tensile strain curves recorded by local transducers installed at the bottom flange of the PC girders near the midspan. The cracking load was determined in the sections that firstly began to deviate from the linear trend. As an example, Figure 5a shows a comparison between the LVDT readings and the strain gauge sg2, which shows the lowest cracking load. The estimated cracking loads for B7-P47/46, B6-Ab/P47, B6-P48/49, and B10-Ab/P47 beam were 20.7 kN, 25.5 kN, 17.2 kN, and 22.1 kN, respectively.

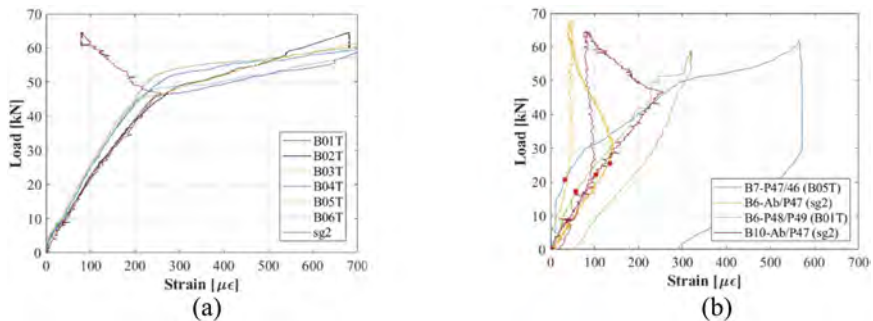


Figure 5. Load versus tensile strains: (a) signals comparison for B10-Ab/P47, (b) cracking load for B7-P47/46, B6-Ab/P47, B6-P48/49, and B10-Ab/P47 girder.

All curves start with a linear branch followed by a change in strain distribution when the applied load determines the first cracking. For B6-Ab/P47 and B10-Ab/P47 specimen, as the tensile strains were recorded by the strain gauges, a reduction in strain is observed: this can be associated to a crack opening in the nearby of the strain gauge location.

The compressive strains recorded in the top region have been reported in Figure 6. The green curves refer to the strain of the cast in situ slab recorded by strain gauges, and the other two curves refer to the top flanges of the I-beams, according to the layout in Figure 3. Furthermore, the images of the failure zones are also reported. The maximum compressive strain recorded on the top slab of the B7-P47/46 beam was -2.2‰. From Figure 6b, the failure occurred close to the strain gauge position in the midspan. For the other specimens, the compressive strains on the top slab resulted -1.4‰, -1.1‰, and -1.7‰, respectively.

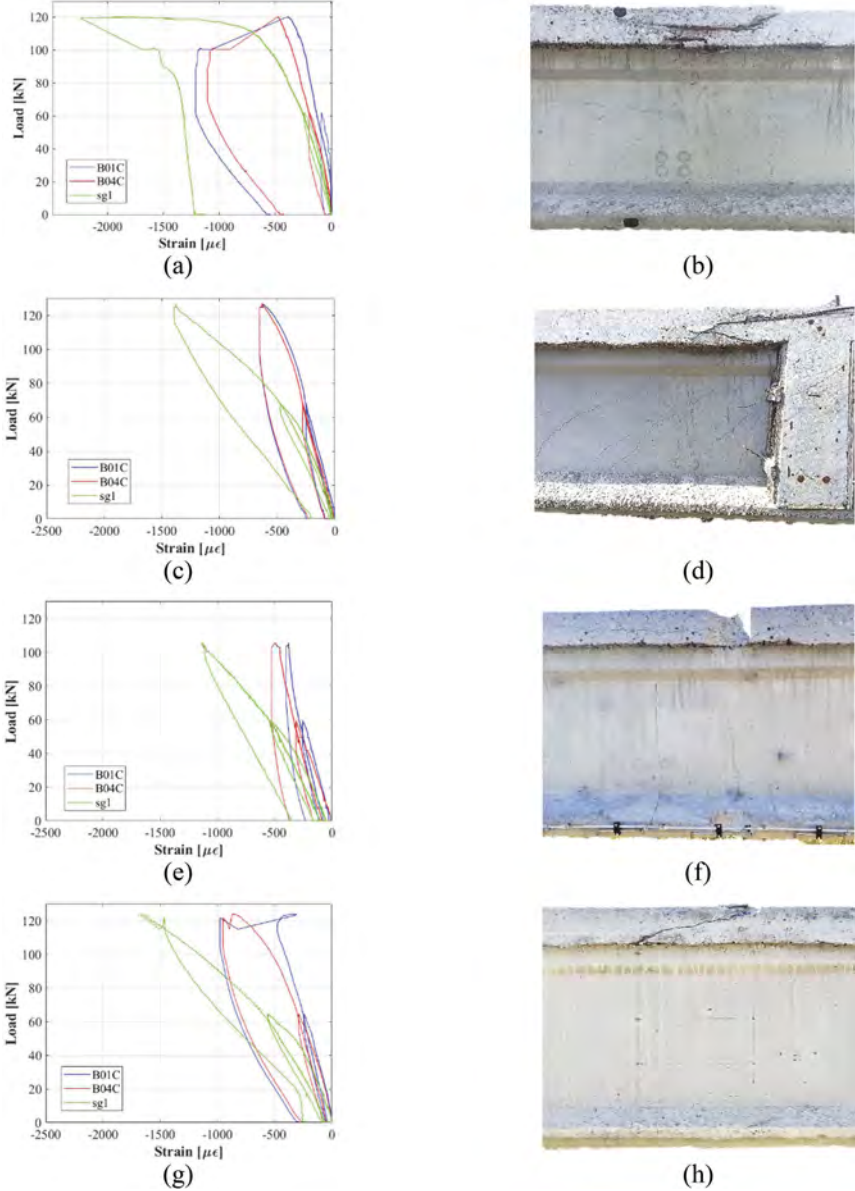


Figure 6. Load versus top compressive strain and failure zones: (a)-(b) B7-P47/46, (c)-(d) B6-Ab/P47, (e)-(f) B6-P48/49, and (g)-(h) B10-Ab/P47 girder.

During the loading process, the average strains recorded by the LVDTs installed on the diagonal frames along the shear span were considered representative of the shear strains. As an example, the shear strain curves recorded on the left side (Figure 3) of the B7-P47/46 beam are shown in Figure 7. According to these curves after the load reaches approximately 50 kN, diagonal cracks formed with an inclined angle from the longitudinal axis, and basically orthogonal to the principal tension direction.

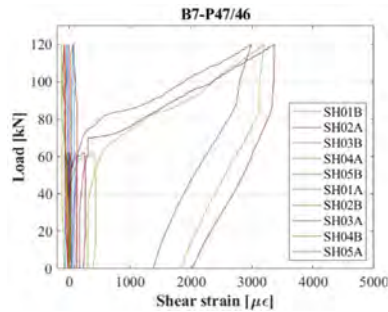


Figure 7. Load versus shear strain for B7-P47/46 beam.

The development of flexure-shear cracking for beam B7-P47/46 as representative of the four tests is reported in Figure 8a. The cracking pattern registered for girder B8-P47/46, as a representative of the previous three-point bending configurations, is reported in Figure 8b which reveals shear cracking along the whole length of the beam. Figure 8a reveals no shear strains in the constant moment region and a higher number of diagonal cracks in the shear span.

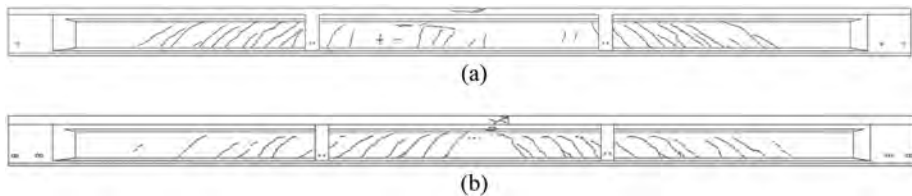


Figure 8. Crack pattern after the load tests: (a) B7-P47/46 (4-P bending test), and (b) B8-P47/46 (3-P bending test) girder.

5 CONCLUSIONS

An extensive experimental investigation has been conducted to study the structural behavior of 50-year-old PC girders at both service and ultimate load levels. The present paper summarizes the experimental part of the investigation concerning the tests involving both flexural and shear mechanisms. Specimens with different level of damage were tested, undamaged and damaged by dismantling operations, resulting in strands cut. The test results were analyzed considering deflections, strains, and cracks evolution, as well as ultimate capacities. Furthermore, the structural responses were compared with the results of specimens previously tested in three-point bending configuration. All the tests have shown a flexural compression failure with brittle crushing of the cast in situ slab.

ACKNOWLEDGMENTS

BRIDGE|50 is a research project based on a research agreement among universities, public authorities, and private companies. Members of the Management Committee: S.C.R. Piemonte

(President); Politecnico di Milano (Scientific Coordinator); Politecnico di Torino (Scientific Responsible of the Experimental Activities); Lombardi Engineering (Secretary); Piedmont Region; City of Turin; Metropolitan City of Turin; TNE Torino Nuova Economia; ATI Itinera & C.M.B.; ATI Despe & Perino Piero; Quaranta Group. BRIDGE|50 website: <http://www.bridge50.org>

REFERENCES

- Anghileri, M., Biondini, F., Rosati, G., Savino, P., Tondolo, F., Sabia, D., Manto, S., Nivriera, M., Trincianti, C., Ventura, D., Monti, G., Legramandi, C., and Caruso, C. 2020. Deconstruction of the Corso Grosseto viaduct and setup of a testing site for full scale load tests. *10th International Conference on Bridge Maintenance, Safety and Management (IABMAS 2020)*, 28 June–2 July 2020 (postponed to April 11-15, 2021), Sapporo, Japan.
- Biondini, F., Manto, S., Beltrami, C., Tondolo, F., Chiara, M., Salza, B., Tizzani, M., Chiaia, B., Lencioni, A., Panseri, L., and Quaranta, L. 2020. BRIDGE|50 research project: Residual structural performance of a 50-year-old bridge. *10th International Conference on Bridge Maintenance, Safety and Management (IABMAS 2020)*, 28 June–2 July 2020 (postponed to April 11-15, 2021), Sapporo, Japan.
- Biondini, F., Tondolo, F., Manto, S., Beltrami, C., Chiara, M., Salza, B., Tizzani, M., Chiaia, B., Lencioni, A., Panseri, L., and Quaranta, L. 2021. Residual Structural Performance of Existing PC Bridges: Recent Advances of the BRIDGE|50 Research Project. *1st Conference of the European Association on Quality Control of Bridges and Structures (EUROSTRUCT 2021)*, Padua, Italy, August 29 - September 1, 2021. In: Pellegrino, C., Faleschini, F., Zanini, M.A., Matos, J.C., Casas, J.R., Strauss, A. (Eds.) *Lecture Notes in Civil Engineering*, 200, 2022, Springer.
- Quattrone, A., Tondolo, F., Sabia, D., Capacci, L., Lencioni, A., Legramandi, C. 2020. Dynamic tests and modal identification of Corso Grosseto viaduct decks before the dismantling. *10th International Conference on Bridge Maintenance, Safety and Management (IABMAS 2020)*, 28 June–2 July 2020 (postponed to April 11-15, 2021), Sapporo, Japan.
- Recupero, A. and Spinella, N. 2019. Experimental tests on corroded prestressed concrete beams subjected to transverse load. *Structural Concrete* 20: 2220–2229.
- Sabia, D., Quattrone, A., Tondolo, F., Savino, P. 2021. Dynamic identification of damaged PC bridge beams. *1st Conference of the European Association on Quality Control of Bridges and Structures (EUROSTRUCT 2021)*, Padua, Italy, August 29 - September 1, 2021. In: Pellegrino, C., Faleschini, F., Zanini, M.A., Matos, J.C., Casas, J.R., Strauss, A. (Eds.) *Lecture Notes in Civil Engineering*, 200, 2022, Springer.
- Sabia, D., Quattrone, A., Tondolo, F., Savino, P. 2022. Experimental evaluation of the effect of controlled damages on the dynamic response of PC bridge beams. *11th International Conference on Bridge Maintenance, Safety and Management (IABMAS 2022)*, Barcelona, Spain, July 11-15, 2022. In: Casas, J.R., Frangopol, D.M., Turmo, J. (Eds.), *Bridge Safety, Maintenance, Management, Life-Cycle, Resilience and Sustainability*. CRC Press/ Balkema, Taylor & Francis Group, London, UK.
- Savino, P., Anghileri, M., Chiara, M., Salza, B., Quaranta, L. 2020. Corso Grosseto viaduct: Historical and technical overview. *10th International Conference on Bridge Maintenance, Safety and Management (IABMAS 2020)*, 28 June–2 July 2020 (postponed to April 11-15, 2021), Sapporo, Japan.
- Savino, P., Tondolo, F., Sabia, D., Quattrone, A., Biondini, F., Rosati, G., Anghileri, M., Chiaia, B. 2023. Large-Scale Experimental Static Testing on 50-Year-Old Prestressed Concrete Bridge Girders. *Applied Sciences* 13(834): 1–22.
- Tondolo, F., Biondini, F., Sabia, D., Rosati, G., Chiaia, B., Quattrone, A., Savino, P., Anghileri, M. 2021. Experimental program and full-scale load tests on PC deck beams. *1st Conference of the European Association on Quality Control of Bridges and Structures (EUROSTRUCT 2021)*, Padua, Italy, August 29 - September 1, 2021. In: Pellegrino, C., Faleschini, F., Zanini, M.A., Matos, J.C., Casas, J.R., Strauss, A. (Eds.) *Lecture Notes in Civil Engineering*, 200, 2022, Springer.
- Tondolo, F., Sabia, D., Chiaia, B., Quattrone, A., Savino, P., Biondini, F., Rosati, G., Anghileri, M. 2022. Full-scale testing and analysis of 50-year-old prestressed concrete bridge girders. *11th International Conference on Bridge Maintenance, Safety and Management (IABMAS 2022)*, Barcelona, Spain, July 11-15, 2022. In: Casas, J.R., Frangopol, D.M., Turmo, J. (Eds.), *Bridge Safety, Maintenance, Management, Life-Cycle, Resilience and Sustainability*. CRC Press/Balkema, Taylor & Francis Group, London, UK.
- Wang, J., Tang, S., Zheng, H., Zhou, C., Zhu, M. 2020. Flexural Behavior of a 30-Meter Full-Scale Simply Supported Prestressed Concrete Box Girder. *Applied Sciences* 10(3076): 1–19.

Experimental tests for mechanical characterization of prestressed concrete bridge deck beams

M. Anghileri, G. Rosati & F. Biondini
Politecnico di Milano, Milan, Italy

P. Savino & F. Tondolo
Politecnico di Torino, Turin, Italy

ABSTRACT: This paper presents the preliminary results of extensive experimental activities for mechanical characterization of 50-year-old prestressed concrete bridge deck beams within the BRIDGE|50 research project (<http://www.bridge50.org>). The experimental campaign includes non-destructive diagnostic tests (e.g. sclerometer and ultrasonic tests) carried out on several prestressed concrete deck beams and laboratory mechanical tests on concrete cores extracted from both precast beam and cast-in-situ slab. The results of these activities have been used for calibration and validation of structural analysis models and to support a proper planning of full-scale load tests up to collapse to be performed on the deck beams.

1 INTRODUCTION

Aging and deterioration processes, combined with poor durability and lack of maintenance and repair activities, may drastically affect in time the load bearing capacity reducing the structural lifetime of bridges. This is nowadays an urgent problem in many countries, including Italy, since there is a large number of bridges built over the past 50 years that are approaching the end of the service life and a significant percentage of them are in a state of moderate to severe deterioration (Malerba 2014, ASCE 2021). The amount of maintenance and repair activities necessary to restore or increase the structural capacity and functionality of deteriorated bridges is huge and represents a relevant obstacle to infrastructure facilities management for owners and public authorities. This critical situation is made more evident by recent bridge and viaduct collapse events that have occurred with alarming frequency. It is therefore of paramount importance to establish effective life-cycle criteria, methods, and tools for bridge assessment, maintenance and management under uncertainty (Biondini and Frangopol 2016, 2019).

Despite significant developments accomplished in the last decades, life-cycle approaches still need to be consolidated by robust validation and accurate calibration and gathering new information and data from existing bridges and experimental tests is key to this purpose. BRIDGE|50 is a research project established jointly by Politecnico di Milano and Politecnico di Torino as part of a research agreement with public authorities and private companies to collect data from inspection activities and experimental tests on deteriorated bridge components and investigate the residual structural performance of existing bridges. This project includes a wide experimental campaign on a set of 29 Prestressed Concrete (PC) deck beams (25 PC I-beams and 4 PC box beams) with top Reinforced Concrete (RC) slab and 2 PC pier caps stored in a testing site after the dismantling of a viaduct in service for about 50 years (Biondini et al. 2021a, 2021b, 2022, Savino et al. 2022). The on-site activities include non-destructive diagnostic tests, full-scale load tests up to collapse, and concrete samples collected for laboratory tests. This paper presents the preliminary results of the non-destructive tests and laboratory tests for mechanical characterization of the PC bridge deck beams. The results of these activities have been used for calibration and validation of structural analysis models

(Anghileri and Biondini 2022) and to support a proper planning of full-scale load tests up to collapse to be performed on the PC deck beams (Tondolo et al. 2022).

2 PRELIMINARY ON-SITE INVESTIGATION

The experimental campaign of the research project started with a series of preliminary activities conducted on-site before the dismantling of the viaduct. These activities included visual inspections of the bridge components. Visual inspections have been conducted according to national and international standards with the participation of public authorities and private managing bodies. The large and diversified amount of data gathered through these activities has been elaborated according to inspection models typically used in practice (Beltrami et al. 2021).

Concrete coring from a bridge pier and carbonation tests have been conducted to investigate the aging and deterioration effects. Concrete split cores have been extracted from a bridge pier and carbonation depth has been assessed using a phenolphthalein solution as an indicator of the location of the depassivation front. A dynamic tests campaign has been also carried out on the bridge decks to characterize the dynamic behavior of the decks under service condition. Dynamic measurements have been acquired by using instrumented hammer and free-falling mass devices. The collected data have been analyzed in order to extract the principal modal components. The comparison of these results with those provided by full-scale experimental tests conducted in the testing site have been used to investigate the effectiveness of dynamic identification procedures in the assessment of damaged bridges. A detailed description of this activity and a critical appraisal of the results are reported in Quattrone et al. (2021) and Sabia et al. (2021, 2022).

3 PC BRIDGE DECK BEAMS

The dismantling of the viaduct at the end of its service life allowed the opportunity to investigate the residual capacity of several PC elements. In particular, 29 PC deck beams and 2 PC pier caps of the viaduct have been moved and stored in a testing site. The preliminary activities of the experimental campaign started with the study of the I-shaped PC bridge deck shown in Figure 1. The beams are characterized by a total length of about 19.40 m and made of a precast PC beam with top cast-in-place RC slab.



Figure 1. PC bridge deck beams stored at the testing site.

The I-shaped bridge deck beams are reinforced with twenty 7-wire prestressing strands with straight longitudinal profile. The nominal diameter of the steel strands is 12.7 mm (effective area 99 mm²). The initial prestressing stress, net of instantaneous and estimated long-term losses reported in the technical design documentation is $\sigma_{pd}=836$ MPa. However, based on the results of full-scale load tests and diagnostic activities aimed at evaluating the residual prestressing, the actual prestressing level after a lifetime of 50 years resulted significantly lower with respect to the design value, with a prestressing stress level $\sigma_p=614$ MPa estimated to best fit the experimental results of full-scale load tests (Anghileri 2022).

4 NON-DESTRUCTIVE TESTING

Rebound hammer tests and ultrasonic tests have been conducted on several PC bridge deck beams to characterize the concrete mechanical characteristics. The tests have been carried out

by subdividing the beams in five sample portions representative of the longitudinal beam profile. Longitudinal steel bars and stirrups are detected by means of pacometer and marked on the beam surface. This allowed to define a grid of 3×3 points on both the rear and front side used for sclerometer and ultrasound emission and reception points.

Ultrasonic tests have been conducted to measure the propagation velocity of compressive mechanical waves along the beam. This method can allow to detect internal cracking and other defects as well as damage in concrete such as environmental deterioration due to aggressive chemicals and inadequate concrete cast. It is worth noting that the outcomes at beam lateral regions might be characterized by a lower accuracy with respect to the measurements over the beam web in the inner regions due to both larger irregularities in the material volume when larger distances are covered by the ultrasound waves and interaction with denser reinforcement pattern.

The ultrasonic test measures the time required by the ultrasonic waves to cross the beam depth which is converted to concrete elastic modulus assuming concrete density $\rho=25 \text{ kN/m}^3$ and Poisson ratio $\nu =0.2$, as reported in the design technical documentation. Figure 2 shows mean and standard deviation values of concrete elastic modulus E measured in correspondence of the support lateral regions and over the beam web regions for 11 PC I-shaped beams.

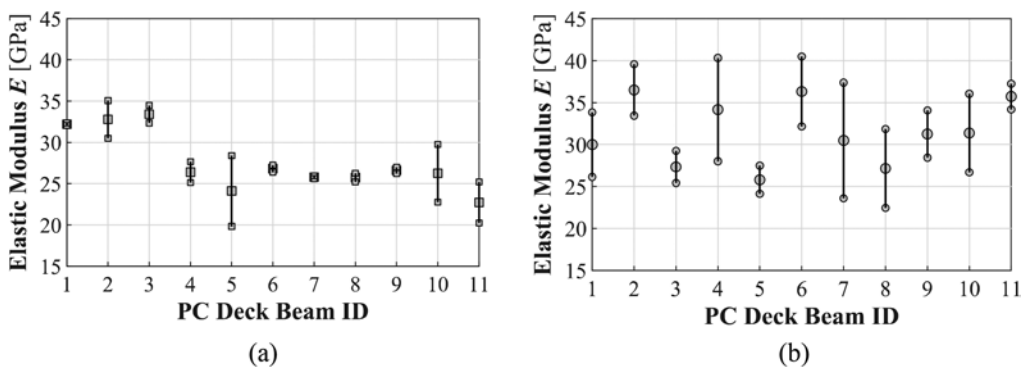


Figure 2. Mean and standard deviation values of elastic modulus E for 11 beams: (a) support regions, and (b) beam web regions.

The results show a quite large variability at the same sample zones, particularly for the elastic modulus over the beam web. This effect might be attributed to differences in local concrete composition and/or deterioration state. The overall sample mean \bar{x} and sample coefficient of variation (CoV) of the concrete elastic modulus E are 29.89 GPa and 0.17, respectively. Moreover, assuming a Student's t-distribution for the standard variate associated to concrete elastic modulus sample mean \bar{x} , the two-sided 95% and 99% confidence interval are $(\bar{x} \pm 1.54 \text{ GPa})$ and $(\bar{x} \pm 1.95 \text{ GPa})$, respectively. These statistical confidence intervals can provide a quantitative measure of accuracy of point estimates of the sample mean (Ang and Tang 2007). Also, considering the total set of samples $n=55$, Figure 3 shows the results of the χ^2 and Kolmogorov-Smirnov (K-S) statistical tests conducted to estimate the validity of probability distribution models associated to the considered random variable and discriminate the relative goodness-of-fit among assumed distribution models. The χ^2 test compares the empirical probability mass function and the theoretical probability density functions by assuming normal and lognormal distributions. The K-S test compares the experimental cumulative frequency with a lognormal cumulative distribution function. Both statistical tests are passed with a significance level of 5%.

The rebound hammer test is used to estimate the compressive concrete strength based on the correlation between material surface hardness and residual strength. In fact, the sclerometer includes a sliding mass coupled with a spring. The mass is in contact with a swinging rod used to strike the material surface. The rebound distance of the mass is converted by a graduated scale into the rebound number S , which is then converted into the estimated concrete strength through a correlation curve calibrated by the device manufacturer using standard specimens.

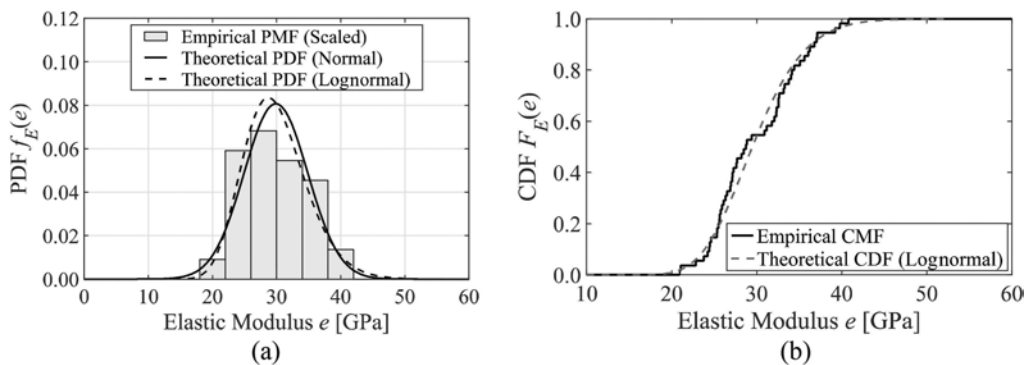


Figure 3. Concrete elastic modulus E distributions: (a) χ^2 and (b) Kolmogorov-Smirnov statistical tests.

The rebound test is carried out after the ultrasonic test because the hammer blows may leave small marks on the beam that may affect the concrete surface roughness. The sclerometer test has been applied to three PC bridge deck beams collected in the testing site for a total of 15 sampling points. The rebound number S is converted into concrete compression strength. The overall sample mean and CoV of compressive concrete strength f_{cm} are 48.25 MPa and 0.20, respectively. The rebound hammer method generally provides a good estimate only of concrete cover strength. Even though concrete carbonation may lead to steel reinforcement corrosion, it generally increases the concrete strength. Therefore, the results of rebound tests may overestimate concrete strength. A more accurate estimate of the concrete strength has been evaluated based on SonReb method, with mean value $f_{cm}=31.88$ MPa and $CoV=0.25$. A detailed description of this activity is reported in Anghileri et al. (2021).

5 LABORATORY MECHANICAL TESTS

Laboratory mechanical tests have been performed on several concrete cores extracted from the PC bridge deck beams (Figure 4) after full-scale load tests have been performed. The concrete strength has been evaluated with uni-axial compressive tests on cylindrical samples characterized by aspect ratio 1:1 or 1:2 (Figure 5) and different diameter values (i.e., $\varnothing 75$, $\varnothing 100$, and $\varnothing 150$ mm). The results showed a small variability between the samples extracted from three PC deck beams. Considering a set of $n=17$ samples, the overall sample mean and CoV of the concrete compressive strength f_c are 29.94 MPa and 0.15, respectively, showing a good agreement with the results of non-destructive tests processed through the SonReb method.



Figure 4. Coring of samples from PC bridge deck beams.

The tensile concrete strength has been evaluated through splitting tensile strength test (Figure 6). The experimental results showed a small variability between samples extracted from three PC deck



Figure 5. Uni-axial compressive strength tests on concrete samples.

beams also for the tensile concrete strength. Considering a set of $n=9$ samples, the overall sample mean and CoV of the concrete tensile strength f_{ct} are 3.33 MPa and 0.13, respectively.



Figure 6. Splitting concrete tensile strength test.

The concrete elastic modulus has been also evaluated with uni-axial compressive strength test (Figure 7). Considering a set of $n=8$ samples, the overall sample mean and CoV of the concrete elastic modulus E_c are 27.22 GPa and 0.07, respectively. Moreover, the same eight samples have been used for uni-axial compressive tests to evaluate the complete stress-strain curves (Figure 8).

The level of concrete carbonation depth has been measured on the samples spraying a solution of phenolphthalein on concrete surfaces. Figure 9 shows the concrete carbonation depth assessment through a bar graph for concrete cores extracted from the support regions (rectangular cross-section) and beam web regions (I-shaped cross-section) of three PC deck beams.

Two tensile concrete strength tests have been also performed on concrete cores extracted from the top RC slab of the deck beams. Moreover, tensile tests have been conducted on samples of both prestressing strands and reinforcing bars. Table 1 and Table 2 summarize the mechanical properties of materials for both precast PC bridge deck beams and cast-in-situ RC slab, respectively, as evaluated from the complete set of information collected from available technical documentation, results of laboratory tests on samples, and results of on-site non-destructive testing.

The deck beams, particularly in the end regions, exhibit local damage due to corrosion with steel mass loss and concrete spalling. These effects can be attributed to the inadequacy of the bridge water conveyance system and use of road salts during the service life of the bridge.



Figure 7. Uni-axial concrete compressive test for elastic modulus assessment.

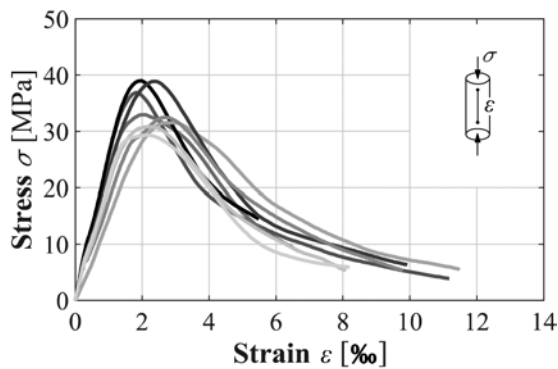


Figure 8. Uni-axial stress-strain curves of concrete in compression.

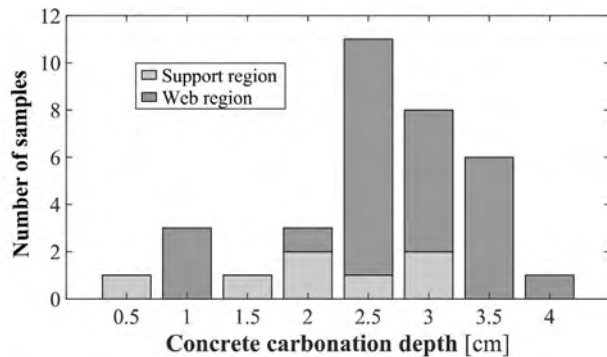


Figure 9. Concrete carbonation depth assessment.

However, based on visual inspections of the tested beams in the failure regions after the full-scale load tests, no significant corrosion of the prestressing strands has been observed. This indicates a relatively good attention during the construction phase of the precast PC beams.

The results of visual inspection activities, non-destructive and destructive tests, and laboratory tests have been also used for validation and calibration of structural modeling for non-linear analysis (Anghileri and Biondini 2021, 2022, Anghileri 2022) and a proper plan of the full-scale load tests (Tondolo et. al 2022, Savino et. al 2023).

Table 1. Nominal material characteristics of precast PC bridge deck beam.

Material characteristic	Value
Compressive concrete strength, f_c	-29.94 MPa
Tensile concrete strength, f_{ct}	3.33 MPa
Concrete elastic modulus, E_c	27.22 GPa
Steel bar yielding strength, f_{sy}	450 MPa
Steel bar ultimate strength, f_{su}	540 MPa
Steel bar elastic modulus, E_s	200 GPa
Steel strand yielding strength, f_{py}	1486 MPa
Steel strand ultimate strength, f_{pu}	1722 MPa
Steel strand elastic modulus, E_p	195 GPa

Table 2. Nominal material characteristics of cast-in-situ RC slab.

Material characteristic	Value
Compressive concrete strength, f_c	-26.00 MPa
Tensile concrete strength, f_{ct}	2.35 MPa
Concrete elastic modulus, E_c	27.00 GPa
Steel bar yielding strength, f_{sy}	450 MPa
Steel bar ultimate strength, f_{su}	540 MPa
Steel bar elastic modulus, E_s	200 GPa

6 CONCLUSIONS

Experimental activities based on non-destructive and laboratory tests carried out on concrete samples extracted from several 50-year-old PC bridge decks beams with cast-in-situ RC slab have been presented. Non destructive diagnostics included rebound hammer tests, ultrasonic tests, pacometer tests, sclerometric tests, and ultrasonic tests. The results of the non-destructive tests have been elaborated based on confidence intervals and statistical tests. The mechanical properties of materials have been estimated based on laboratory tests on concrete cores and samples of prestressing strands and reinforcing bars. For concrete, the results of laboratory tests show good agreement with the results of non-destructive tests processed through the SonReb method. Furthermore, concrete carbonation has been measured with higher carbonation depths in the web regions of the PC deck beams. For prestressing strands, no significance corrosion has been found based on visual inspections of the tested beams in the failure regions after the full-scale load tests.

The results of these experimental tests will be continuously updated based on the ongoing activities of the BRIDGE|50 research project and will be used for calibration and validation of structural analysis models and corrosion deterioration models to support a proper planning and interpretation of full-scale load tests to be performed on the deck beams.

ACKNOWLEDGMENTS

BRIDGE|50 is a research project based on a research agreement among universities, public authorities, and private companies. Members of the Management Committee: S.C.R. Piemonte (President); Politecnico di Milano (Scientific Coordinator); Politecnico di Torino (Scientific Responsible of the Experimental Activities); Lombardi Engineering (Secretary); Piedmont Region; City of Turin; Metropolitan City of Turin; TNE Torino Nuova Economia; ATI Itinera & C.M.B.; ATI Despe & Perino Piero; Quaranta Group. BRIDGE|50 website: <http://www.bridge50.org>.

REFERENCES

- Ang, A. H.-S., Tang, W. H. 2007. *Probability concepts in engineering: Emphasis on applications to civil and environmental engineering*. Vol. 1, Wiley.
- Anghileri, M. 2022. *Life-cycle structural performance of RC/PC bridges: computational modeling and experimental validation*. PhD thesis. Politecnico di Milano.
- Anghileri, M., Biondini, F. 2021. Nonlinear structural analysis of PC bridge deck beams. *1st Conference of the European Association on Quality Control of Bridges and Structures (EUROSTRUCT 2021)*, August 29 – September 1, 2021, Padua, Italy.
- Anghileri, M., Biondini, F. 2022. Formulation and experimental validation of nonlinear finite element analysis of PC bridge deck beams. *11th International Conference on Bridge Maintenance, Safety and Management (IABMAS 2022)*, July 11 –15, 2022, Barcelona, Spain.
- Anghileri, M., Savino, P., Capacci, L., Bianchi, S., Rosati, G., Tondolo, F., and Biondini, F. 2021. Non-destructive testing and model validation of corroded PC bridge deck beams. *First Conference of the European Association on Quality Control of Bridges and Structures (EUROSTRUCT 2021)*, August 29 – September 1, 2021, Padua, Italy.
- ASCE 2021. *Report card for America's infrastructure*. American Society of Civil Engineers, Reston, USA.
- Beltrami, C., Bianchi, S., Cervio, M., Anghileri, M., Felicetti, R., Quattrone, A., Chiara, M., Salza, B., and Masala, D. 2021. Bridge visual inspections: Experience of local authorities and the case study of the Corso Grosseto viaduct. *Tenth International Conference on Bridge Maintenance, Safety and Management (IABMAS 2020)*, June 28-July 2, 2020 (postponed to April 11-15, 2021), Sapporo, Japan.
- Biondini, F., Frangopol, D. M. 2016. Life-cycle performance of deteriorating structural systems under uncertainty: Review. *Journal of Structural Engineering*, American Society of Civil Engineers, 142 (9), F4016001.
- Biondini, F., Frangopol, D. M., (Eds.) 2019. *Life-cycle design, assessment, and maintenance of structures and infrastructure systems*. American Society of Civil Engineers, Reston, USA.
- Biondini, F., Manto, S., Beltrami, C., Tondolo, F., Chiara, M., Salza, B., Tizzani, M., Chiaia, B., Lencioni, A., Panseri, L., and Quaranta, L. 2021a. BRIDGE| 50 research project: Residual structural performance of a 50-year-old bridge. *Tenth International Conference on Bridge Maintenance, Safety and Management (IABMAS 2020)*, June 28-July 2, 2020 (postponed to April 11-15, 2021), Sapporo, Japan.
- Biondini, F., Tondolo, F., Manto, S., Beltrami, C., Chiara, M., Salza, B., Tizzani, M., Chiaia, B., Lencioni, A., Panseri, L., and Quaranta, L. 2021b. Residual Structural Performance of Existing PC Bridges: Recent Advances of the BRIDGE|50 Research Project. *First Conference of the European Association on Quality Control of Bridges and Structures (EUROSTRUCT 2021)*, August 29 – September 1, 2021, Padua, Italy.
- Malerba, P. G. 2014. Inspecting and repairing old bridges: Experiences and lessons. *Structure and Infrastructure Engineering*, Taylor & Francis, 10 (4), 443–470.
- Quattrone, A., Sabia, D., Tondolo, F., Capacci, L., Lencioni, A., and Legramandi, C. 2021. Dynamic tests and modal identification of Corso Grosseto viaduct decks before the dismounting. *Tenth International Conference on Bridge Maintenance, Safety and Management (IABMAS 2020)*, June 28-July 2, 2020 (postponed to April 11-15, 2021), Sapporo, Japan.
- Sabia, D., Quattrone, A., Tondolo, F., and Savino, P. 2021. Dynamic identification of damaged PC bridge beams. *First Conference of the European Association on Quality Control of Bridges and Structures (EUROSTRUCT 2021)*, August 29 – September 1, 2021, Padua, Italy.
- Sabia, D., Quattrone, A., Tondolo, F., and Savino, P. 2022. Experimental evaluation of the effect of controlled damages on the dynamic response of PC bridge beams. *11th International Conference on Bridge Maintenance, Safety and Management (IABMAS 2022)*, July 11 –15, 2022, Barcelona, Spain.
- Savino, P., Tondolo, F., Sabia, D., Quattrone, A., Biondini, F., Rosati, G., Anghileri, M., Chiaia, B. 2023. Large-scale experimental static testing on 50-year-old prestressed concrete bridge girders, *Applied Sciences*, MDPI, 13(2), 2023, 1–22.
- Tondolo, F., Sabia, D., Chiaia, B., Quattrone, A., Savino, P., Biondini, F., Rosati, G., and Anghileri, M. 2022. Full-scale testing and analysis of 50-year old prestressed concrete bridge girders. *11th International Conference on Bridge Maintenance, Safety and Management (IABMAS 2022)*, July 11 –15, 2022, Barcelona, Spain.

Experimental campaign for corrosion assessment of 50-year-old PC deck beams

M. Carsana, E. Redaelli, D.O. Valoti & F. Biondini
Politecnico di Milano, Milan, Italy

ABSTRACT: Several prestressed concrete (PC) deck beams, stored in a testing site after dismantling a 50-year-old viaduct, have been subjected to inspection and diagnostics activities within the BRIDGE|50 research project. This paper discusses the results of field and laboratory tests carried out on these structural elements. Based on visual observations and magnetic and electrochemical tests, concrete samples have been collected from different PC deck beams in order to understand the cause of their degradation conditions. Chemical, physical, and microstructural properties of samples from selected beams are investigated based on laboratory tests focusing on the measurement of the actual carbonation penetration, chloride penetration profiles, and other durability-related parameters that are fundamental for corrosion assessment of PC deck beams.

1 INTRODUCTION

Reinforced concrete (RC) and prestressed concrete (PC) structures are exposed to multiple aging and deterioration processes, especially due to corrosion of steel reinforcement (Bertolini 2008, Biondini & Frangopol 2016). The impact of these damage processes is high, particularly for the large stock of existing RC/PC structures and infrastructural facilities, such as bridges and viaducts, built around the middle of last century. A proper and effective maintenance of RC/PC structures under corrosion needs to be supported by suitable criteria, methods and procedures for the characterization of the state of materials degradation (Bertolini et al. 2013) and condition structural assessment (Biondini & Frangopol 2019). A strong impulse for advances along these lines is given by the ongoing BRIDGE|50 research project - Residual structural performance of a 50-year-old bridge (Biondini et al. 2020), conducted within a research agreement established among Politecnico di Milano, Politecnico di Torino, and several public authorities and private companies (www.bridge50.org). This project provides a wide experimental campaign to be carried out on a group of PC deck beams obtained from a viaduct demolished in Turin in 2019 after a lifetime of about 50 years. Two adjacent spans of the viaduct have been preserved and deconstructed, including 29 precast PC beams (25 I-beams and four box beams) and two PC pier caps. These structural members are currently stored in a testing area dedicated to full scale load tests up to collapse, field investigations, and collection of samples for laboratory tests.

This paper reports an overview of the ongoing research activities devoted to field diagnostics and laboratory tests for corrosion characterization. More in detail, based on results from visual observations and non-destructive testing (NDT) made through magnetic and electrochemical methods (such as those for measuring corrosion potential of steel bars and electrical resistivity of concrete), concrete samples have been collected from selected structural elements (Figure 1) in order to better understand the cause of their degradation conditions. Chemical, physical, and microstructural properties of samples collected from different PC deck beams have been investigated. Laboratory tests have been focused on the measurement of the actual carbonation depth, chloride penetration profiles, sulphates content and microstructural features of concrete for a proper degradation assessment of PC beams.



Figure 1. View of different types and condition degradation state of PC structural elements preserved in the testing area. (a) Northern and eastern fronts of I-beam 46-T9-47; (b) Southern and eastern fronts of box-beam 47-C2-SP; (c) Eastern front of pier cap 48; (d) Southern and eastern fronts of I-beam 46-T1-47.

2 FIELD TESTS

The analysis of the PC deck beams started with an accurate visual survey which has been carried out in order to assess visible signs of deterioration and to locate areas for field measurements consisting of NDT described in §2.1. The preliminary inspection of the beams has highlighted their different conditions depending on the structural type. Cracking and spalling of concrete took place on wide zones of the structural elements, especially for pier caps and box beams. The pier caps exhibit evident signs of deterioration from corrosion of the reinforcing bars with wide detachments of the concrete, often even for layers of thickness larger than the concrete cover. Moreover, parts of the reinforcement are no longer embedded in concrete and they are heavily corroded (Figure 1c). Box-beams show signs of degradation especially in the bottom parts (Figure 1b). Moreover, some zones of concrete surface are interested by phenomena of efflorescence that could be due to the use of deicing salts. Overall, most of I-beams seem to be under fair conditions as documented in Figure 1a (except for damages caused by the demolition operations). Some of I-beams present signs of concrete segregation, limited to the end zones; only two I-beams show in such end parts wide detachments of concrete cover and steel bars heavily corroded (Figure 1d). A detailed inspection has been documented in Carsana et al. (2021) in order to assess the presence of visible signs of degradation. Based on visual inspection activities, NDT have been carried out in field on selected elements (Carsana et al. 2022), one for each type of PC beams.

2.1 Methodology

In order to verify the degradation state of steel bars on different types of PC beams, the cover depth of the outermost reinforcing bars has been detected with a magnetic-type covermeter. The concrete surface has been investigated by using re-bound hammer test. The corrosion behaviour of the steel reinforcement has been investigated by means of electrochemical measurements. The corrosion potential of steel has been mapped on the concrete surface using a CSE (Cu/CuSO₄) reference electrode. The electrical resistivity has been measured by placing a resistivity probe connected to a conductivitymeter on the outside surface. Preliminary measurements of corrosion rate have been also made in some localized zones of inspected PC elements.

2.2 Preliminary results

Inspection of selected PC beams has been made along several fronts (E=East; N=North; W=West, and S=South) by means of measurements of concrete cover thickness, surface strength (R_{scler}), corrosion potential (E_{corr}) and corrosion rate (i_{corr}) of steel bars and electrical resistivity of concrete (ρ). Results of inspection are summarized in Table 1, where the minimum (m), maximum (M) and average values (ave) obtained from each measurement are shown; the number of measurements (#) is also reported.

In order to assess the quality of the concrete, Schmidt hammer tests have been carried out. It should be observed that this test can be characterised by a great scatter of results, due to not only the variability of the compressive strength of concrete but the influence of several parameters related to the surface hardness of concrete (which is the parameter actually measured by the Schmidt hammer). Overall, the mechanical performance of the concrete of different PC beams seems comparable; the average values of the estimated strength of concrete ranged from 43 MPa (pier cap 48) to 57 MPa (I-beam 46-T9-47). Major variability has only been found for pier caps due to presence of zones where the concrete is weak, such as those close to cracking and spalling of surface. In fact, Schmidt hammer tests, being a NDT measurement, can extensively be carried out throughout the elements and can be used as an index of the homogeneity of the concrete. Electrochemical measurements have been carried out to investigate the corrosion conditions of the reinforcement at the moment of inspection (Table 1). On average, the corrosion potential measured on east front of pier cap 48 is -282 mV vs CSE. In several parts of east front corrosion potential reached also minimum values of -423 mV vs CSE, lower than -350 mV vs CSE (i.e., the threshold according to American Standard ASTM C876 below which the probability of corrosion is higher than 90%). Thus, such values highlight that, at the time of the measurements, the corrosion state of steel bars was not negligible. It should however be observed that electrochemical measurements refer to the active conditions of the steel at the moment in which the measurement is carried out and they could change based on electrical resistivity of concrete. Since the survey has been carried out after a rather dry period, the concrete was dry and had high values of electrical resistivity ($>1000 \Omega m$), as reported in Table 1. Comparable conditions have been also observed on the north front of pier cap 48 that has showed average values of electrical resistivity and corrosion potential respectively equal to 614 Ωm and -334 mV vs CSE. Overall, corrosion rate values of 301 and 5.35 mA/m² have been measured on pier cap 48. Certainly, the corrosion propagation of steel bars in this structural element could increase further during wet periods and more negative corrosion potentials could be reached.

Corrosion evaluation has been carried out in the same period also both on south and west fronts of the box beam 47-C2-SP. The reinforcement potential of the box beam 47-C2-SP showed average values of -136 and -220 mV/CSE and minimum values of -351 mV and -371 mV vs CSE (Table 1), while the electrical resistivity of concrete ranged between 700 and 1080 Ωm . The corrosion risk seems comparable to that of pier cap 48 as confirmed by a value of corrosion rate of 5.31 mA/m². For comparison, electrochemical measures have been carried out also on I-beam 46-T9-47 which showed corrosion potentials (between -59 mV and -119 mV vs CSE), significantly higher than those measured on box beam and pier cap. A negligible corrosion probability is also confirmed by a corrosion rate of 0.14 – 1.19 mA/m². In order to better investigate the causes of corrosion of inspected structural elements, different samples have been collected and subjected to laboratory tests.

3 LABORATORY TESTS

Table 2 summarizes structural elements that have been considered for more detailed inspection through by collecting several samples and doing laboratory tests. Such samples have been derived from different zones selected by taking into account their representativeness and exposure conditions with respect to the original location in the dismantled viaduct.

3.1 Sampling and analysis

Initially, several small fragments of concrete (indicated as *Fi*) have been collected during inspection phases. In few cases cores of diameter 45.5 mm and length of at least 160 mm have been also taken from the longitudinal or transversal front of structural elements (*Ci*). Moreover, several samples of concrete powders (*Pi*) have been collected directly by drilling at several depth with a tip of 10 mm diameter being this method considered much less invasive than taking a concrete core. The depth of carbonation has been measured by spraying a phenolphthalein indicator on concrete powders collected at increasing depth. Same test has been repeated also in lab on concrete cores derived from PC beams.

Chloride analyses have been carried out both on concrete powder samples as well as on 10 mm concrete slices in which each core has been divided in order to determine total chlorides profile as a function of depth. Both powder samples and concrete slices, the latter once ground, have been digested in hot nitric acid. The chloride content has been measured by means of potentiometric titration and expressed as percentage of the dry concrete. Chloride content has been measured also on single concrete fragments collected from outside surface of several PC beams. The content of sulphates has been measured with traditional chemical analysis of the samples dissolved in hydrochloric acid. Moreover, the microstructure of some samples has been observed under scanning electron microscope with an EDS X-ray spectrometer.

3.2 Analysis of results

The SEM image of concrete sample collected from I beam 46-T9-47 (Figure 2a) highlights the typical features of hardened cement paste. The compact morphology of cement paste is not much different from those of concrete fragments collected from other PC beams (F28 and F27) and may justify the high strength values measured by Schmidt hammer tests (Table 1). Moreover, the presence of certain chemical elements, such as calcium (Ca), oxygen (O) and silicon (Si) in major amounts, in addition to magnesium (Mg), aluminum (Al) and sodium (Na), is associated to typical compounds of calcium silicate and aluminate hydrates (Figure 2b). Traces of chlorine (Cl) and sulfur (S) have been found in this cement matrix as well as in those of samples F27 and F28 (Table 2). These traces suggest possible contaminations in concrete which could be responsible of chemical attacks (Neville 2011). Therefore, additional chemical tests have been carried out to verify degradation state of concrete of different PC beams.

Sulphate attack of concrete has been excluded for each type of PC beams. Samples C2, C3, F35, F36 and P28 show a content of SO_3 negligible, ranging between 0.12-0.81% (Colleparidi 2006). Further analyses have been carried out in order to value carbonation and chlorides penetration in concrete elements. Figure 3 compares the results of phenolphthalein test. Concrete core named C2-SN, which crossed the entire thickness of I-beam 46-T9-47, shows a depth of carbonation of 29-30 mm on the northern and the southern fronts.

On the southern front powder concrete samples (*P1-S*) have been also collected near concrete core C2-SN by obtaining comparable values, even if less accurate. For a depth of 20 mm concrete powder turned out to be carbonated, while for an increasing depth, ranging between 20 and 40 mm, not all powders turned out to be carbonated and showed grey-pink color. Phenolphthalein test made on this second layer of the *P1-S* sample indicates that the depth of carbonation shall be considered between 20 and 40 mm. From the comparison of the average value of the carbonation depth with the average value of the concrete cover thickness (Table 1), it follows that steel reinforcement of southern front of I beam 46-T9-47 should be in contact with an alkaline concrete.

On the east front of the same structural element the carbonation depth shows a major variability, likely related with different local properties of concrete. In fact, concrete core C3-E shows a depth of carbonation of 23 mm while powder concrete samples *P2-E*, collected in a zone near segregation (Figure 3b), turned out to be carbonated up to a depth of 40 mm. Therefore, the reinforcement, for which the concrete cover is minimum (as for reinforcing bars present in the bottom part, Figure 3b) and carbonation front has reached them, are no longer in passive conditions and the risk of concrete cracking due to corrosion is present.

On other inspected structural elements (48 and 47-C2-SP) carbonation depth has been measured only by means of drilling of powder concrete. Box beam 47-C2-SP has been tested

Table 1. Main findings of the inspection of PC beams related to corrosion potential, corrosion rate, electrical resistivity, Schmidt hammer test, and concrete cover thickness (# = number of measurements; *m* = minimum value; *M* = maximum value; *ave* = average value), with indication of section (L = Longitudinal, T = Transversal), and orientation front (S = Southern, N = Northern, W = Western, and E = Eastern).

Element		<i>I-beam</i>		<i>Box beam</i>		<i>Pier cap</i>	
Front		<i>S</i>	<i>E</i>	<i>S</i>	<i>E</i>	<i>E</i>	<i>N</i>
Section		<i>L</i>	<i>T</i>	<i>L</i>	<i>T</i>	<i>L</i>	<i>T</i>
Name		46-T9-47		47-C2-SP		48	
Tests:	Time inspection	<i>summer</i>		<i>winter</i>		<i>winter</i>	
E_{corr}	<i>m</i>	-295	-227	-371	-351	-423	-424
(<i>mV vs</i>	<i>M</i>	+161	-46	+143	+2	-102	-248
CSE)	<i>Ave</i>	-59	-119	-136	-220	-282	-334
	#	328	14	325	16	58	13
ρ	<i>m</i>	70	48	51	63	188	127
(Ωm)	<i>M</i>	3000	1800	5625	3913	7500	1139
	<i>Ave</i>	482	434	1080	701	1514	614
	#	326	12	294	15	58	13
i_{corr}	<i>m</i>	0.14	1.19	1.31	-	1.87	3.30
(mA/m^2)	<i>M</i>	0.14	1.19	9.33	-	4.14	7.40
	<i>Ave</i>	0.14	1.19	5.32	-	3.01	5.35
	#	1	1	2	-	2	2
Concrete	<i>m</i>	10	-	5	-	4	-
Cover	<i>M</i>	65	-	61	-	38	-
(<i>mm</i>)	<i>Ave</i>	40	-	22	-	23	-
	#	57	-	83	-	42	-
R_{scler}	<i>m</i>	36	49	35	-	10	-
(<i>MPa</i>)	<i>M</i>	69	69	60	-	69	-
	<i>Ave</i>	56	57	46	-	43	-
	#	72	12	72	-	45	-

Table 2. Samples collected during inspection activities from PC beams and type of analysis carried out: *carb* = phenolphthalein test, *Cl* = chlorides content, *SO₃* = sulphates content, SEM = microstructure observations. Type of samples: *F* = concrete fragment; *C* = concrete core and *P* = concrete powder. ^ multiple samples collected at increasing depth.

<i>Element</i>	<i>Name</i>	<i>Samples</i>	<i>carb</i>	<i>Cl</i>	<i>SO₂</i>	<i>SEM</i>
Pier cap	48	<i>P3</i> ^, <i>P4</i> ^, <i>F28</i>	✓	✓	✓	✓
Box-beam	47-C2-SP	<i>P7</i> ^, <i>P6</i> ^, <i>F27</i> , <i>F35</i> , <i>F36</i>	✓	✓	✓	✓
I-beams	46-T9-47	<i>P1</i> ^, <i>P2</i> ^, <i>C2</i> ^, <i>C3</i> ^, <i>F12</i>	✓	✓	✓	✓
	46-T8-47	<i>P8</i> ^, <i>P9</i> ^, <i>P10</i> ^, <i>C4</i> , <i>C5</i>	✓	✓	-	-
	47-T5-SP	<i>P11</i> ^	✓	✓	-	-
	46-T1-47	<i>F16</i>	✓	✓	-	-

in terms of carbonation thickness in two zones of southern front (*P5* and *P6*), showing values of the order of 7-17 mm, and in a zone of western front (*P7*) which results to be in alkaline condition. For pier cap 48 the carbonation depth was less than 20 mm on eastern front (sample *P3*). Conversely, sample *P4* of the northern front of pier cap 48 was alkaline although it was collected near the zone with evident signs of deterioration from corrosion (Figure 1c). Concrete of pier cap 48 and box beam 47-C2-SP showed to be less carbonated than that of I beam 46-T9-47. Since their carbonation front is lower than the average depth of the reinforcement (22-23 mm), it appears that rebars were corroding at the time of inspection for other causes. Thus, several samples have been subjected to the measurement of chlorides content (Table 2). Figure 4 shows, separately for type of inspected beams, the chloride profiles measured on concrete samples. Each graph reports the chloride profiles measured on both

longitudinal and transversal fronts of inspected beams (distinguished respectively by means of filled and empty symbols) and the critical threshold of chlorides (dotted line) for carbon steel (0.05-0.125% in mass of concrete).

Chloride profiles have been interpolated based on the “erf function” obtained from the analytical solution of the one-dimensional Fick’s second law of diffusion. Often the first analysis, i.e. the outermost point (red border), has been not considered in the fitting procedure. Figure 4a shows chloride profiles obtained both from concrete cores (C2, C3) and powder concretes (P1, P2) collected from I beam 46-T9-47. In particular, comparable chloride contents have been obtained for specimens from southern front (P1) and from top part of eastern front (C3), where no segregation phenomena are visible, with negligible values (around 0.01% in mass of concrete).

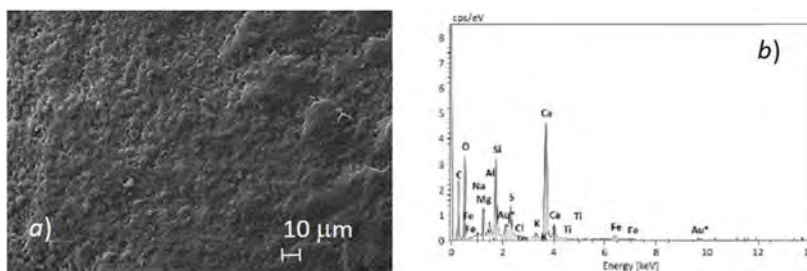


Figure 2. (a) SEM image, and (b) EDS analysis of the cement matrix of concrete sample F12 collected from I beam 46-T9-47.

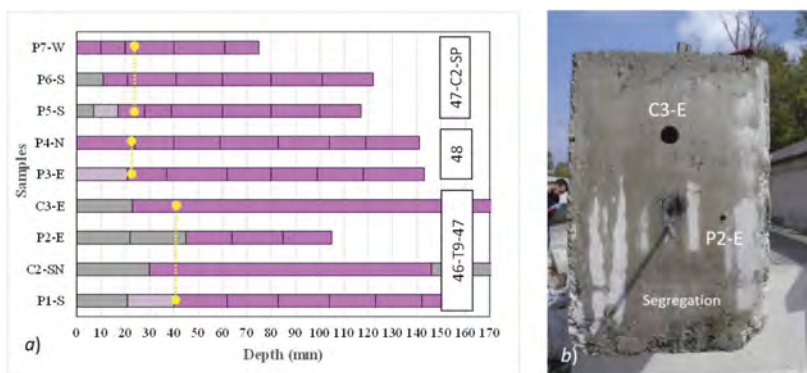


Figure 3. (a) Results of phenolphthalein test carried out both on concrete powder (P_1) and core (C_i) samples (grey = carbonated concrete; pink = alkaline concrete; mix color grey/pink = alkaline/carbonated concrete). Average concrete cover for each structural element is indicated with a yellow line. (b) View of east front of 46-T9-47 and collection positions of the samples C3-E and P2-E.

Chloride content appears only slightly higher in the first 20 mm of the eastern front of I-beam 46-T9-47 (P2, Figure 3b), although it is lower than the critical threshold of chlorides. Chloride profiles have been calculated also on powder samples derived from other I-beams (Figure 4d). Overall, it can be deduced that chlorides content is always negligible on longitudinal front (south or north) of I-beams. Only in sample P11, chlorides content has reached the critical threshold at the average concrete cover thickness (Figure 4d). Moreover, in the concrete fragment F16, collected at a depth of 25-30 mm from I-beam 46-T1-47, a high chlorides content (0.09% vs concrete mass) has been found. Thus, it can be deduced that the risk of chloride-induced corrosion should be considered for I-beams only on transversal fronts, as confirmed for I-beams 47-T5-SP and 46-T1-47 and by preliminary observations (Figure 1d).

Same analyses have been repeated on pier cap 48 and box beam 47-C2-SP. Chloride profiles measured on pier cap 48 (Figure 4c) overcome the critical chlorides threshold also far beyond

average concrete cover thickness, both on eastern and northern fronts, with maximum values of 0.14% vs concrete mass. Chloride penetration in box-beam 47-C2-SP is comparable on western and southern fronts, with values intermediate between the maximum obtained on pier cap 48 and the minimum of I-beam elements; chlorides content is higher than the critical threshold beyond steel depth.

4 CORROSION ASSESSMENT

Pier caps and box-beams present evident signs of deterioration from corrosion of reinforcement (Figure 1). Conversely, no clear signs of corrosion-induced damage have been observed on I-beams, except in their end parts where evidences of concrete segregation are visible (Figure 3b). The presence of macro-voids, observed on the concrete surface especially of eastern and western fronts of I-beams, suggests that concrete was not properly vibrated during casting phases. This phenomenon might have caused in some cases premature corrosion initiation with consequent detachments (Figure 1d) towards the ends of the I-beams or in their lower parts. However, based on chemical analyses carried out on several concrete samples collected from all inspected PC beams, both chlorides and carbonation penetration seem to be the main causes of corrosion.

As far as pier cap 48 is concerned, the depth of carbonation, measured on eastern and northern fronts, ranges between 0 and less of 20 mm. From the comparison with the values of the concrete cover thickness (Table 1), it follows that a part of steel reinforcement of the pier cap 48 could be in contact with alkaline concrete. However, where the concrete cover is low (Table 1) and carbonation has reached the steel rebars, these are no longer in passive conditions. In addition, a chloride content higher than the critical threshold has been found in pier cap 48 at average steel depth (0.14% vs concrete mass). Certainly, high corrosion probability to which steel reinforcement of pier cap 48 might be subjected is confirmed by the electrochemical measurements obtained in terms of corrosion potential (until -424 mV vs CSE) and of corrosion rate (with a value of 5.35 mA/m²) at the moment of inspection. Overall, better conditions for steel reinforcement have been observed in the I-beams. For example, I-beam

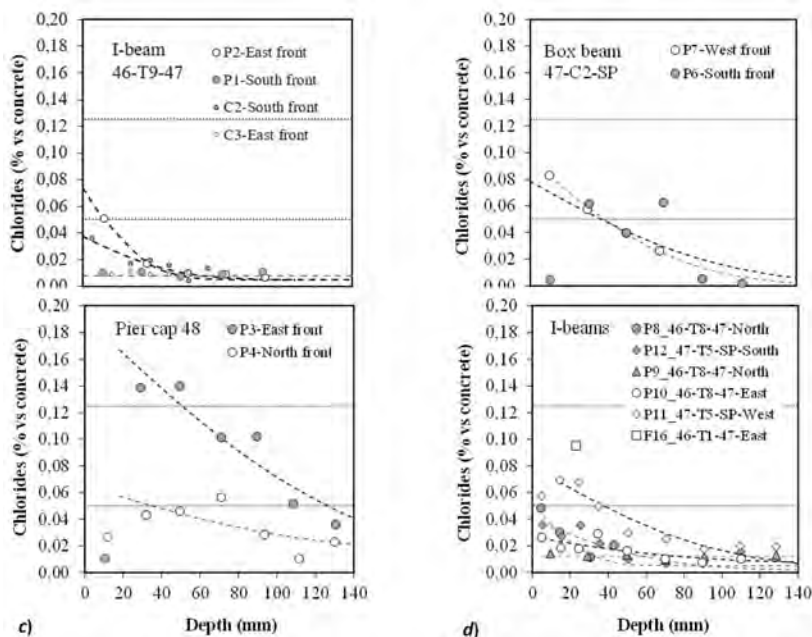


Figure 4. Chloride profiles measured on the different fronts of structural beams: (a) I-beam 46-T9-47; (b) box beam 47-C2-SP; (c) pier cap 48; (d) I-beams 46-T8-47, 46-T1-47 and 47-T5-SP. The dotted horizontal line indicates the critical chloride threshold.

46-T9-47 shows average corrosion potentials of -59 and -119 mV vs CSE respectively on southern and eastern fronts (Table 1). A negligible corrosion probability is also confirmed by an average corrosion rate ranging between 0.74 and 1.19 mA/m².

For these I-beams the risk of corrosion shall be considered high only towards their ends or in the lower parts, where the presence of macro-voids in case of segregation or an inadequate concrete cover could have favored the penetration of carbonation and chlorides (Figure 4d).

The conditions of box beams appear intermediate between those of pier caps and I-beams. Box-beam 47-C2-SP shows corrosion potentials ranging between -371 and +2 mV vs CSE with an average value of corrosion rate around 5.34 mA/m². The risk of chloride-induced corrosion from de-icing salts for box-beam 47-C2-SP is confirmed by chloride profiles.

5 CONCLUSIONS

In the framework of the multipartner project BRIDGE|50, a wide campaign of field and laboratory tests concerning real scale PC elements, such as those deriving from the viaduct demolished in Turin in 2019 after 50 years of service life, is ongoing. The results of the experimental study already carried out are allowing to evaluate statistically various electrochemical, chemical, physical and microstructural parameters of the inspected structural elements with the aim of defining an adequate procedural approach for corrosion assessment of RC/PC structures and infrastructure facilities. In particular, the results presented in this paper has highlighted that the main causes of deterioration of RC/PC elements are associated to concrete carbonation and chloride penetration due to de-icing salt especially for pier caps and box beams. Further experimental research along these lines is in progress to investigate the main factors affecting carbonation and chloride-induced corrosion of structural elements by considering different exposure conditions.

ACKNOWLEDGEMENTS

BRIDGE|50 is based on a research agreement established by universities, public authorities, and private companies. Management Committee: S.C.R. Piemonte (President); Politecnico di Milano (Scientific Coordinator); Politecnico di Torino (Scientific Responsible of the Experimental Activities); Lombardi Engineering (Secretary); Piedmont Region; City of Turin; Metropolitan City of Turin; Torino Nuova Economia; ATI Itinera & C.M.B.; ATI Despe & Perino Piero; Quaranta Group. Project website: www.bridge50.org

REFERENCES

- Bertolini, L., Elsener, B., Pedferri, Redaelli, E., Polder, R. 2013. *Corrosion of Steel in Concrete: prevention, diagnosis, repair*, Weinheim, Germany, Wiley.
- Bertolini, L. 2008. Steel corrosion and service life of reinforced concrete structures. *Structure and Infrastructure Engineering*, 4(2): 123–137.
- Biondini, F., Frangopol, D.M. 2016. Life-cycle performance of deteriorating structural systems under uncertainty: Review, *Journal of Structural Engineering*, ASCE, 142(9): 1–17.
- Biondini, F., Frangopol, D.M., (Eds.) 2019. *Life-cycle design, assessment and maintenance of structures and infrastructure systems*, American Society of Civil Engineers (ASCE), Reston, VA, USA.
- Biondini, F., Manto, S., Beltrami, C., Tondolo, F., Chiara, M., Salza, B., Tizzani, M., Chiaia, B., Lencioni, A., Panseri, L., Quaranta, L. 2020. BRIDGE|50 research project: Residual structural performance of a 50-year-old bridge, 10th *International Conference on Bridge Maintenance, Safety, and Management (IABMAS 2020)*, Barcelona, Sapporo, Japan, June 28-July 2, 2020 - postponed to April 11-15, 2021 (online).
- Carsana, M., Biondini, F., Redaelli, E., Valoti, D.O. 2021. On site-corrosion characterization of 50-year-old PC deck beams, *1st Conference of European Association on Quality Control of Bridges and Structures (EUROSTRUCT 2021)*, August 29–September 1, 2021. Padua, Italy.
- Carsana, M., Biondini, F., Redaelli, E., Valoti, D.O. 2022. Corrosion assessment of 50-year-old PC deck beams, *11th International Conference on Bridge Maintenance, Safety, and Management (IABMAS 2022)*, 11-15 July 2022. Barcelona, Spain.
- Colleparidi, M. 2006. *The new concrete*, Villorba (TV), Italy, Tintoretto.
- Neville, A.M. 2011. *Properties of concrete*, 5th ed., England, Longman.

Experimental validation of nonlinear finite element analysis of PC bridge deck beams based on the results of full-scale load tests

M. Anghileri & F. Biondini
Politecnico di Milano, Milan, Italy

ABSTRACT: Full-scale load tests on prestressed concrete (PC) deck beams extracted from a dismantled bridge have been performed within the ongoing BRIDGE|50 research project. The results of this experimental activity, along with the outcomes of non-destructive tests and laboratory tests for mechanical characterization of materials, are considered in this paper for the validation of computational structural analysis models based on PC beam finite elements with distributed nonlinearity and plane-stress finite elements formulated in accordance with the Modified Compression Field Theory. The accuracy of numerical versus experimental results is evaluated under four-point bending for different shear span ratios and by taking into account the contribution of the top concrete slab on the structural response of the tested beams.

1 INTRODUCTION

Life-cycle-oriented design, assessment, maintenance, and management of deteriorating structures and infrastructural facilities should rely on structural analysis frameworks capable to account for time-variant structural performance, loading scenarios, environmental exposures, deterioration processes, and effects of maintenance and repair interventions (Biondini and Frangopol 2016). Availability of efficient and accurate life-cycle models is particularly important for bridge structures to properly address the significant amount of maintenance and repair activities necessary to restore or increase the structural capacity and functionality of huge stocks of existing bridges and viaducts worldwide that are currently rated as structurally deficient (ASCE 2021). However, although life-cycle models are well established for some of the most detrimental damage processes, such as corrosion and fatigue, robust validation and accurate calibration are still needed (Ellingwood 2005, Biondini and Frangopol 2018). In fact, deterioration models are sensitive to change of the probabilistic parameters of the input random variables and their validation is a difficult task because of the limited availability of information about long-term performance of in-service structures. Gathering new data from both inspection of existing structures and experimental tests is therefore of essence for a successful implementation in practice of life-cycle methods.

Based on these needs, the BRIDGE|50 research project has been established by Politecnico di Milano and Politecnico di Torino as part of an agreement with public authorities and private companies for a wide experimental campaign on a prestressed concrete (PC) viaduct dismantled after a lifetime of about 50 years (Biondini et al. 2021a, 2021b). A set of 29 PC deck beams, including 25 I-beams and four box-beams with top reinforced concrete (RC) slab, and two PC pier caps have been moved and stored in a testing site. The experimental activities include non-destructive diagnostic tests, full-scale load tests, and laboratory tests. These activities are complemented by extensive numerical analyses to further investigate the structural behavior of the tested beams and support a proper planning of the ongoing load tests (Anghileri and Biondini 2021, 2022). This paper presents recent project advances aimed at validating computational structural analysis models based on RC/PC beam finite elements with distributed nonlinearity and plane-stress finite elements formulated in accordance with the Modified Compression Field Theory (MCFT).

2 EXPERIMENTAL CAMPAIGN

2.1 PC bridge deck I-beams

The PC bridge deck beams investigated in this paper have a total length of about 19.40 m and consist of precast PC I-beams with twenty 7-wire prestressing strands and top cast-in-place RC slab, as shown in Figure 1. The nominal diameter of the steel strands is 12.7 mm (effective area 99 mm²). The initial prestressing stress, net of instantaneous and estimated long-term losses reported in the technical design documentation is $\sigma_{pd}=836$ MPa. However, based on the results of full-scale load tests and diagnostic activities, the actual prestressing level after a lifetime of 50 years resulted lower of about 25-30% with respect to the design value. This reduced value can be associated to larger instantaneous and/or long-term prestressing losses and steel corrosion effects. The I-beams, particularly in the end regions, exhibit local damage due to corrosion with steel mass loss and concrete spalling. These effects can be attributed to inadequacy of the bridge water conveyance system and use of road salts during the bridge service life. However, no significance corrosion of the prestressing strands has been observed based on visual inspections of the tested beams in the failure regions after the full-scale load tests. The effects of steel corrosion are therefore not considered in the structural analysis of the beams investigated in this paper.

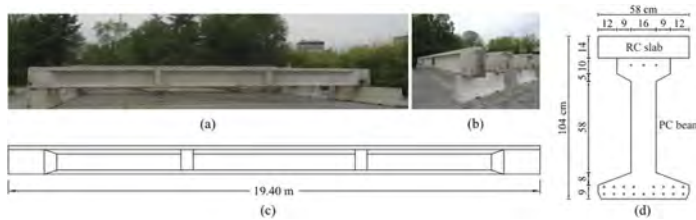


Figure 1. PC deck beams: (a-b) views, (c) longitudinal profile, and (d) cross-section at mid-span.

2.2 Non-destructive diagnostics and laboratory tests

Non-destructive tests, including rebound hammer tests and ultrasonic tests, have been conducted on the PC beams to assess the concrete elastic modulus and compressive strength. Laboratory tests have been also carried out on several concrete cores extracted from the beams after full-scale load tests have been performed. The concrete compressive strength has been evaluated with uni-axial compressive tests on cylindrical samples with aspect ratio 1:1 or 1:2 and different diameter (i.e., Ø75, Ø100, and Ø150 mm). The results of the laboratory tests are in good agreement with the results of non-destructive tests based on the SonReb method. Uni-axial compressive strength tests have been also adopted to evaluate complete stress-strain curves. The tensile concrete strength has been evaluated through splitting tensile strength tests (Anghileri et al. 2023). Table 1 summarizes the nominal material mechanical properties evaluated based on the data reported in the available technical documentation complemented by the results of the experimental testing.

Table 1. Nominal material mechanical characteristics of the precast PC I-beams.

Material property	Value
Compressive concrete strength, f_c	-29.94 MPa
Tensile concrete strength, f_{ct}	3.33 MPa
Concrete elastic modulus, E_c	27.22 GPa
Steel bar yielding strength, f_{sy}	450 MPa
Steel bar ultimate strength, f_{su}	540 MPa
Steel bar elastic modulus, E_s	200 GPa
Steel strand yielding strength, f_{py}	1468 MPa
Steel strand ultimate strength, f_{pu}	1722 MPa
Steel strand elastic modulus, E_p	195 GPa

2.3 Full-scale load tests

Full-scale load tests are performed using the testing framework and the four-point loading scheme shown in Figure 2 (Tondolo et al. 2021, Savino et al. 2023). The loading system includes four actuators, two for each point load. The applied load is transferred by two transverse steel beams to the PC beam simply-supported at both ends by the steel reaction frame through bridge bearings. The setup of the experimental sensors installed to monitor the beam structural response during the full-scale load tests is shown Figure 2a (Tondolo et al. 2021, 2022). The reaction steel frame has been designed to allow for variable distance between the applied forces and reproduce the in-service span of the deck beams. Multiple load tests with different shear span ratio $\alpha=all$ are planned to investigate bending and shear failures.

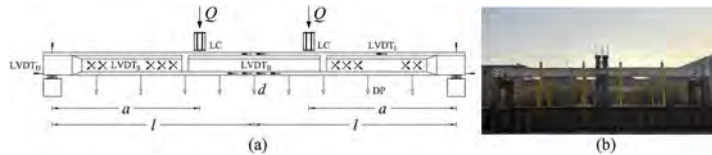


Figure 2. Full-scale load tests. (a) Loading scheme and experimental sensors setup: load cells (LC), transducers to control the bending (LVDT_B) and shear (LVDT_S) behavior, displacement potentiometers (DP), transducers for strand slip and bearing settlements (LVDT_D), and transducer for beam-slab connection (LVDT_I). (b) View of the testing framework with a deck beam ready to be tested.

The testing program is ongoing. In this paper, the results obtained on the first six I-beams in the series are considered. The first four load tests have been carried out with shear span ratio $\alpha \approx 1.00$ (i.e., three-point loading) to favor a pure bending failure. Two additional tests have been performed with $\alpha \approx 0.68$ (i.e., four-point loading). The experimental load protocol consists of a preliminary loading phase up to concrete cracking, a stop under loading for the assessment of the cracking pattern, a subsequent unloading and final reloading up to collapse. The first three PC beams with top RC slab, namely beams #1, #2, and #3, have been tested under a three-point loading. They showed very similar structural behavior with collapse loads $Q_1=156$ kN, $Q_2=161$ kN, and $Q_3=144$ kN, respectively (Tondolo et al. 2022, Savino et al. 2023). In order to investigate the structural capacity of the PC beam only, the beam #4 has been tested after the removal of the top RC slab, leading to a collapse load $Q_4=129$ kN. Finally, beams #5 and #6 have been tested with the top slab under four-point bending with $\alpha \approx 0.68$. The experimental results obtained for these two beams showed a similar structural response with collapse loads $Q_5=244$ kN and $Q_6=254$ kN, respectively (Savino et al. 2023). The six beams exhibited a structural failure which started with full crushing in compression of the top RC slab in the critical regions, i.e., at mid-span or close to the applied loads, and then propagated through the entire PC beam cross-section.

The experimental test on beam #2 covers the entire load protocol and the results of this test are then considered in the following for the numerical validation under three-point bending, along with the results on beam #4 without the top slab and beam #6 under four-point bending.

3 NONLINEAR ANALYSIS AND EXPERIMENTAL VALIDATION

3.1 Finite element modeling

Several finite element formulations for nonlinear analysis of concrete structures have been proposed in literature with distinctive features based on several factors, including element discretization and formulation and solution process. In this paper, a RC/PC beam finite element (BFE) is considered since it allows for a trade-off among multiple factors including robustness of the formulation, accuracy of the solution process, and computational cost. The BFE

assumes the linearity of the cross-sectional strain field and neglects shear failures and bond-slip of steel reinforcement. The formulation accounts for the material nonlinearities associated with the constitutive laws of materials. The structure is discretized into beam finite elements (Figure 3a), the member cross-section is subdivided into four-node isoparametric subdomains, and numerical integration based on the Gauss-Lobatto rule is adopted to handle material nonlinearities (Bontempi et al. 1995).

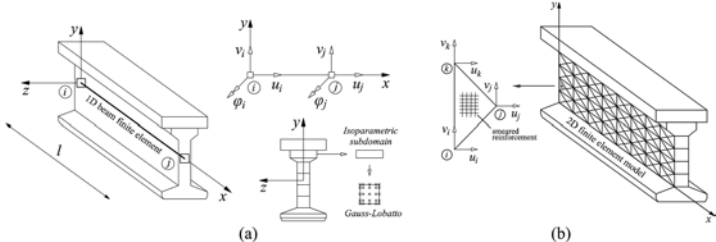


Figure 3. Structural modeling: (a) BFE model: nodal displacements, isoparametric discretization, and Gauss-Lobatto integration scheme; (b) MCFT model: nodal displacements and element discretization.

A plane-stress finite element model, formulated in accordance with the MCFT, is also considered to better account for shear effects and local stress-diffusion phenomena. MCFT allows for a general approach to nonlinear plane-stress analysis of concrete structures (Vecchio and Collins 1986). It is based on a smeared rotating crack approach (i.e., cracks change orientation according to the direction of principal strains) and considers the cracked RC medium as an orthotropic material with its own constitutive laws. Equilibrium, compatibility, and constitutive laws are formulated in terms of average stresses and average strains and principal stresses and strain directions are considered coincident. The structure is discretized into constant strain triangle (CST) finite elements (Figure 3b) with smeared reinforcement (Bontempi et al. 1994).

Detailed information about formulation and modeling criteria adopted for the structural modeling of the tested beams can be found in Anghileri (2022) and Anghileri and Biondini (2022).

3.2 Nonlinear analysis of a PC deck beam without top RC slab

In the construction process of the bridge, the RC slab was cast after the PC beams were already assembled and in place under the effects of beam self-weight and prestressing action. Therefore, the deck beams can be considered as characterized by a composite cross-section (i.e., precast PC beam and cast-in-situ RC slab). In order to investigate the residual capacity of the PC deck beam only, a full-scale load test has been carried out on a PC beam after the removal of the RC top slab.

The BFE-based structural modeling of the PC I-beam exploits the symmetry and it is based on a discretization with 13 elements for the half beam, with one outer element with rectangular cross-section at the support region, one adjacent element with linearly varying width of the beam web, and eleven inner elements with I-shaped cross-section. The beam cross-section is subdivided in nine quadrilateral isoparametric subdomains. Numerical integration is based on a Gauss-Lobatto integration scheme with 8x8 Gauss-Lobatto sampling points. Moreover, eight sampling cross-sections are considered for each finite element. The constitutive laws of the materials are defined based on uniaxial stress-strain relationships. Saenz’s law in compression and elastic-perfectly plastic model in tension are assumed for concrete, while a bilinear hardening model is assumed for both reinforcing and prestressing steel with the material characteristics listed in Table 1.

The MCFT-based structural modeling of the PC I-beam exploits the symmetry and it is based on a discretization with 940 CST finite elements for the half beam. Based on the available technical documentation and results of non-destructive diagnostic test (e.g., pacometer), stirrups with diameter of 8 mm and spacing of 250 mm and 100 mm for the inner I-shaped

cross-section and outer rectangular cross-section, respectively, are considered. Stirrups are modeled as smeared reinforcement over the beam volume. Longitudinal reinforcing steel bars and prestressing strands are modeled as truss elements built over the CST finite element mesh. Constitutive relationships of the materials are defined to link average stresses and average strains based on uniaxial stress-strain relationships with the material characteristics listed in Table 1. For concrete in compression, the stress-strain relationship in the principal directions is the Hognestad parabola with compressive strength f_c related to the transversal principal strain to account for cracking effects. The behavior of concrete in tension is linear up to cracking with a post-cracking softening branch accounting for the tension stiffening effect. A bilinear hardening constitutive law is assumed for both reinforcing and prestressing steel.

The loss of the initial prestressing can be associated to several factors, including elastic shortening at prestress transfer, time-dependent losses, corrosion of steel strands, among others. The role of prestressing is firstly investigated considering different levels of residual prestressing. Figure 4a shows the load Q versus mid-span displacement d (net of the effects of self-weight and prestressing) of the PC deck beam under three-point bending ($\alpha=1.00$) for different prestressing $P=\eta P_0$ ($\eta=1.00, 0.80, 0.60$), where P_0 is the nominal prestressing force as reported in the design technical documentation ($\sigma_{pd}=836$ MPa). As expected, prestressing mainly impacts the serviceability stage. After calibration of the material mechanical characteristics, the numerical results have been compared with the outcomes of the load tests and a residual prestressing level $\sigma_p=614$ MPa has been estimated to best fit the experimental results. It is worth noting that this reduction of prestressing is in line with the ongoing diagnostic measurements on the residual prestressing (Savino et al. 2023).

Figure 4b compares experimental and numerical results obtained with $\sigma_p=614$ MPa based on MCFT. The experimental results consist of a preliminary loading phase up to $Q=107$ kN, a stop under loading for the assessment of the cracking pattern and dynamic testing, a subsequent unloading, and final reloading up to collapse ($Q=129$ kN). The nonlinear finite element analysis is carried out under monotonic loading. The backbone curve of the load versus displacement diagram is reproduced with high accuracy by the MCFT-based structural model. Similar results are obtained with a BFE-based structural model, as shown in Figure 5a. Moreover, Figure 5b indicates high accuracy also in terms of load versus the concrete axial strain at mid-span region recorded through transducers located at the top and bottom slab of the beam.

The close correspondence of the results obtained with BFE and MCFT is mainly due to the pure bending failure of the tested beam. However, significant deviations may occur under four-point bending with reduced shear span ratios because of possible shear failures that the BFE formulation is unable to capture. This will be further investigated in future load tests.

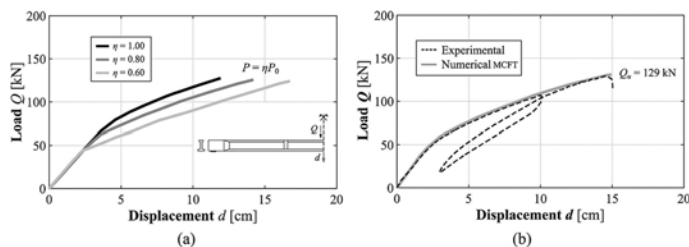


Figure 4. Load Q versus mid-span displacement d of PC deck beam without RC slab (MCFT): (a) Different prestressing levels $P=\eta P_0$ ($\eta=1.00, 0.80, 0.60$); (b) Experimental vs numerical results.

3.3 Nonlinear analysis of PC deck beams with top RC slab

Key factors to be investigated for the PC deck beams are the influence of the construction phases of the viaduct and the actual degree of collaboration between PC I-beam and RC slab. In fact, the RC slab has been cast with the PC deck beams already assembled and in place under

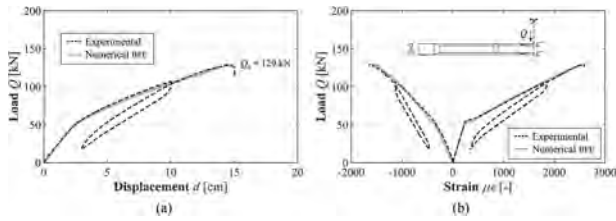


Figure 5. Experimental vs numerical results for the PC deck beam without RC slab (BFE): (a) Load Q vs mid-span displacement d ; (b) Load Q vs axial strain ε at mid-span.

the effects of beam self-weight and prestressing action. Moreover, the shear connectors of the slab to the beam just consist of transverse stirrups extended from the beam web. A steel wire mesh is also placed at the beam-slab interface. Therefore, considering also the type of structural failure, obtained in the experimental tests with full crushing in compression of the top slab and lack of connection between beam and slab at mid-span at incipient collapse, the effects of a possible lack of collaboration between beam and slab should be taken into account.

To this purpose, separate MCFT models are considered for beam and slab and a possible slip at the beam-slab interface is taken into account by means of a set of elastic links. The construction process and load stages are considered in a two-level approach. Beam self-weight and prestressing are applied in a first stage to the beam only and the slab contribution to self-weight and overall structural stiffness is evaluated incrementally in a second stage.

The MCFT-based structural modeling of the PC deck beam with top RC slab exploits the symmetry and is based on a discretization with 1128 CST finite elements for the half beam. Stirrups are modeled as smeared reinforcement over the beam volume. Longitudinal reinforcing bars and prestressing strands are modeled as truss elements built over the CST finite element mesh. Constitutive relationships and material properties are the same as for the PC beam without RC slab. Separate nodal points are considered at the beam-slab interface. The nonlinear structural analysis is based a two-level incremental approach. In a first stage, the beam only is loaded with self-weight and prestressing action. In a second stage, the two separate sets of CST finite elements (i.e., PC beam and RC slab) are connected at each pair of nodal points at the beam-slab interface by rigid links in the direction normal to the beam axis. For what concerns the interaction in the longitudinal direction, the beam-slab connection is modeled by means of a set of longitudinal elastic links to be activated in a second stage only. The link is considered rigid up to concrete cracking. This is confirmed by the results obtained in case of a full collaborating beam-slab system which accurately capture the experimental results in terms of initial stiffness of the uncracked beam (Anghileri and Biondini 2021, Anghileri 2022). After concrete cracking, the links are elastic with stiffness estimated to best fit the experimental results. This modeling strategy is also confirmed by the data recorded by the LVDT located at the beam-slab interface. Based on this structural modeling, the self-weight of the slab and the testing loading are applied incrementally in a second stage. The displacements of the beam nodal points are cumulated over both loading stages, while the displacements of the nodal points of the slab derive from the second stage only.

The experimental results of both three-point loading ($\alpha \approx 1.00$) and four-point loading ($\alpha \approx 0.68$) are considered to validate the finite element formulations and the modeling strategies. Figure 6a compares experimental and numerical results for the three-point bending test ($\alpha \approx 1.00$), in terms of load Q versus mid-span displacement d net of self-weight and prestressing, for the PC beam with and without RC slab. This comparison allows to quantify the role of the top slab in the structural response. For the case of beam with slab, the experimental results show a preliminary loading phase up to $Q=100$ kN, a subsequent unloading and final reloading up to the collapse load $Q=161$ kN. The nonlinear finite element analysis is carried out under monotonic loading. The best-fit stiffness value at beam-slab interface for the three-point loading scheme is $k=3000$ N/mm. Figure 6b compares the results for the four-point bending test ($\alpha \approx 0.68$). The experimental results show a preliminary loading phase up to $Q=134$ kN, a subsequent unloading and final reloading up to the collapse load $Q=254$ kN which occurred with full crushing in compression of the top slab in

the critical in the region close to the applied load. The best-fit stiffness value at beam-slab interface for the four-point loading scheme is $k=11500$ N/mm. Finally, a crack pattern survey has been performed on the tested beams after the load tests. As an example, Figure 7 compares the experimental crack pattern at collapse (line thickness proportioned to crack width) and the numerical crack pattern (half beam) obtained for the three-point loading scheme.

Overall, the good agreement between experimental and numerical results obtained for both BFE and MCFT validates the finite element formulations and related modeling strategies under flexural failures. Further investigations are necessary based on future load tests with reduced shear span ratios to investigate the accuracy of the proposed modeling under shear failures.

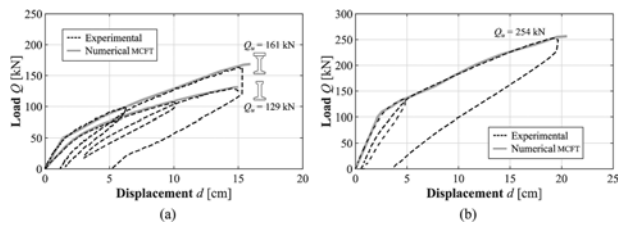


Figure 6. Load Q versus mid-span displacement d of PC deck beam (MCFT): (a) Three-point loading of the I-beam with and without slab; (b) Four-point loading of the I-beam with slab.

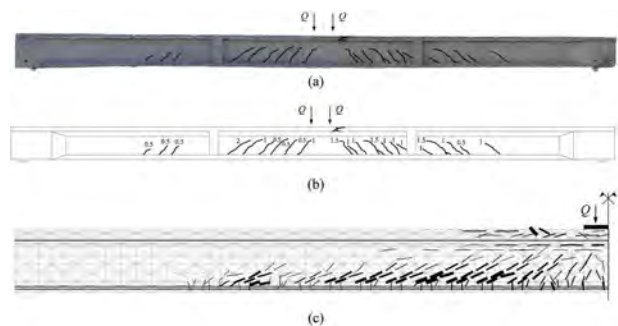


Figure 7. Load test under three-point bending. (a) Digital model; (b) Experimental crack pattern (crack width $\times 10^{-1}$ mm); (c) MCFT-based crack pattern of half beam for load $Q=161$ kN (line thickness proportioned to crack width).

4 CONCLUSIONS

The validation of the finite element models for nonlinear analysis of concrete structures based on BFE- and MCFT-based formulations has been presented through the outcomes of full-scale load tests on the PC bridge deck beams extracted from a dismantled bridge within the BRIDGE|50 research project. The structural and material characteristics and the modeling strategies have been calibrated based visual inspections, non-destructive tests, and laboratory tests. The role of the cast-in-situ RC slab on the structural capacity of bridge deck beams is also investigated considering the structural response of the PC beam with and without the top RC slab with different shear span ratio. The good agreement between numerical and experimental results allows to validate the finite element formulation and the modeling strategies and to support a proper planning of future full-scale load tests.

Future developments will be devoted to further investigate the accuracy of the proposed models to reproduce a shear-dominant structural behavior and failures and to gather additional information about material properties, residual prestressing, degree of collaboration and shear strength at the beam-slab interface, and corrosion damage based on non-destructive testing and laboratory tests on samples from the tested beams.

ACKNOWLEDGMENTS

BRIDGE|50 is a research project based on a research agreement among universities, public authorities, and private companies. Members of the Management Committee: S.C.R. Piemonte (President); Politecnico di Milano (Scientific Coordinator); Politecnico di Torino (Scientific Responsible of the Experimental Activities); Lombardi Engineering (Secretary); Piedmont Region; City of Turin; Metropolitan City of Turin; TNE Torino Nuova Economia; ATI Itinera & C.M.B.; ATI Despe & Perino Piero; Quaranta Group. BRIDGE|50 website: <http://www.bridge50.org>.

REFERENCES

- Anghileri, M. 2022. *Life-cycle structural performance of RC/PC bridges: computational modeling and experimental validation*. PhD thesis. Politecnico di Milano.
- Anghileri, M., Biondini, F. 2021. Nonlinear structural analysis of PC bridge deck beams. *1st Conference of the European Association on Quality Control of Bridges and Structures (EUROSTRUCT 2021)*, August 29 – September 1, 2021, Padua, Italy.
- Anghileri, M., Biondini, F. 2022. Formulation and experimental validation of nonlinear finite element analysis of PC bridge deck beams. *11th International Conference on Bridge Maintenance, Safety and Management (IABMAS 2022)*, July 11 –15, 2022, Barcelona, Spain.
- Anghileri, M., Rosati, G., Biondini, F., Savino, P., Tondolo, F. 2023. Experimental tests for mechanical characterization of prestressed concrete bridge deck beams. *Eighth International Symposium on Life-Cycle Civil Engineering (IALCCE 2023)*, July 2 – 6, 2023, Milan, Italy.
- ASCE 2021. *Report card for America's infrastructure*. America Society of Civil Engineers, Reston, USA.
- Biondini, F., Frangopol, D. M. 2016. Life-cycle performance of deteriorating structural systems under uncertainty: Review. *Journal of Structural Engineering*, American Society of Civil Engineers, 142 (9), F4016001.
- Biondini, F., Frangopol, D. M. 2018. Life-Cycle Performance of Civil Structure and Infrastructure Systems: Survey. *Journal of Structural Engineering*, ASCE, 144 (1),06017008, 1-7.
- Biondini, F., Manto, S., Beltrami, C., Tondolo, F., Chiara, M., Salza, B., Tizzani, M., Chiaia, B., Lencioni, A., Panseri, L., and Quaranta, L. 2021a. BRIDGE| 50 research project: Residual structural performance of a 50-year-old bridge. *Tenth International Conference on Bridge Maintenance, Safety and Management (IABMAS 2020)*, June 28-July 2, 2020 (postponed to April 11-15, 2021), Sapporo, Japan,
- Biondini, F., Tondolo, F., Manto, S., Beltrami, C., Chiara, M., Salza, B., Tizzani, M., Chiaia, B., Lencioni, A., Panseri, L., and Quaranta, L. 2021b. Residual Structural Performance of Existing PC Bridges: Recent Advances of the BRIDGE|50 Research Project. *First Conference of the European Association on Quality Control of Bridges and Structures (EUROSTRUCT 2021)*, August 29 – September 1, 2021, Padua, Italy.
- Bontempi F., Malerba P.G., Romano L. 1994. Il modello M.C.F.T. nell'analisi per elementi finiti di strutture piane in C.A., *Studi e Ricerche*, Scuola di Specializzazione in Costruzioni in Cemento Armato "Fratelli Pesenti", 16, 173–207 (In Italian).
- Bontempi, F., Malerba, P.G., Romano, L. 1995. Formulazione diretta secante dell'analisi non lineare di telai in C.A./C.A.P., *Studi e Ricerche*, Graduate School for Concrete Structures "F.lli Pesenti", Politecnico di Milano, Italy, 16, 351–386 (In Italian).
- Ellingwood, B. R. 2005. Risk-informed condition assessment of civil infrastructure: state of practice and research issues. *Structure and Infrastructure Engineering*, Taylor & Francis, 1 (1), 7–18.
- Savino, P., Quattrone, A., Sabia, D., Chiaia, B., Tondolo, F., Anghileri, M., Biondini, F., Rosati, G. 2023. Large-scale experimental testing of 50-year-old prestressed concrete bridge girder. *Eighth International Symposium on Life-Cycle Civil Engineering (IALCCE 2023)*, July 2 – 6, 2023, Milan, Italy.
- Savino, P., Tondolo, F., Sabia, D., Quattrone, A., Biondini, F., Rosati, G., Anghileri, M., Chiaia, B. 2023. Large-scale experimental static testing on 50-year-old prestressed concrete bridge girders, *Applied Sciences*, MDPI, 13(2), 2023, 1–22
- Tondolo, F., Biondini, F., Sabia, D., Rosati, G., Chiaia, B., Quattrone, A., Savino, P., and Anghileri, M. 2021. Experimental program and full-scale load tests on PC deck beams. *First Conference of the European Association on Quality Control of Bridges and Structures (EUROSTRUCT 2021)*, August 29 – September 1, 2021, Padua, Italy.
- Tondolo, F., Sabia, D., Chiaia, B., Quattrone, A., Savino, P., Biondini, F., Rosati, G., and Anghileri, M. 2022. Full-scale testing and analysis of 50-year old prestressed concrete bridge girders. *11th International Conference on Bridge Maintenance, Safety and Management (IABMAS 2022)*, July 11 –15, 2022, Barcelona, Spain.
- Vecchio, F.J., Collins, M.P. 1986. The modified compression field theory for reinforced concrete elements subjected to shear. *ACI Journal*, 83(2),219–231.

Dynamic response of PC bridge beams under different damages

D. Sabia, A. Quattrone, P. Savino & F. Tondolo

Department of Structural, Geotechnical and Building Engineering, Politecnico di Torino, Italy

ABSTRACT: The present paper describes the dynamic test campaign on prestressed concrete bridge beams taken from a dismantled viaduct in Turin, Italy after a service life of 50 years in the framework of BRIDGE|50 research project. Dynamic measurements were previously performed on the decks from which the 29 beams were taken to characterize the behaviour of the viaduct in service condition. Successively the single beams are tested to analyse and evaluate the effects of the different damage levels on the dynamic properties. The vibration data have been collected before the application of static load, after the first cracking condition and after the maximum load applied on the beam to extract the principal modal components. The results highlight the correlation among the evolution of the damage and the dynamic response of the beam and then the effectiveness of vibration tests to identify the occurrence of damages and follow their evolution. The experimental findings could be used in future works to explore the effects of damages of the single beams on the global response of this bridge typology. This work presents the results of the experimental tests on the first eight beams tested.

1 INTRODUCTION

The progressive obsolescence of infrastructures requires to face challenging issues related to the assessment of their residual performances, the increase of the loading conditions, the extension of their service life and how to monitor the evolution of the health state over the years. Nevertheless, the effectiveness of the monitoring strategies requires to deepen the knowledge of the way the combination of different factors, such as corrosion or deterioration, extreme weather events, increase of loads, material ageing, that may influence the structural reliability.

The BRIDGE|50 research project, started in 2020, aims at deeply investigate the behaviour of aged structural elements approaching the end of their service lives (Biondini et al. 2021). The research activities will be devoted to accurately investigate the structural performances and characterize the material properties of a representative portion of a viaduct dismantled after 50 years of service life, namely 25 prestressed concrete beams, 4 box girders and 2 pier caps. The experimental campaign should represent a great source of information to be used in developing predictive models and calibrating monitoring techniques.

Vibration-based methods are widely applied in structural health monitoring techniques to follow the evolution of structural integrity, due to the direct dependence between the dynamic behaviour and the structural stiffness. Moreover, their appeal has increased due to the ease of managing the continuous streaming of large amount of data and inferring information by means of data mining algorithms (Demarie, Sabia, 2019).

In literature, several studies report the results of experimental dynamic investigations on beam-like prestressed structures, focusing on their use as symptoms of the onset of damage or the evolution of deterioration over time forces (Quattrone et al. 2012, Guiglia et al. 2014). In several cases, the authors have pointed out the low sensitivity of modal parameters to identify the reduction of prestressing. For this reason, tests under controlled conditions on end-of-life structures can contribute to supply more accurate definition of sensitivity limits and the thresholds to be transferred to monitoring systems.

The girders of Bridge|50 project were tested both in their current conditions and after the induction of defined damage steps. The aim is to estimate the contribution of the single beams on the global response of the decks, previously tested before the dismantling, and to investigate the influence of damages of the single beams on the global behaviour.

In this paper the results of the dynamic test campaign on a set of five beams are reported. The beams have the same nominal geometrical and material characteristics but some different damage. The dynamic data have been collected before the execution of the static tests, in cracked state and at the end of static tests, after the application of the ultimate loading condition.

2 THE CORSO GROSSETO VIADUCT

The Corso Grosseto viaduct was built in 1970. It was originally constituted by 80 concrete decks having variable spans, from 16 m to 24 m, and a total length of 1400 m (Figure 1). The structural elements which are investigating in BRIDGE|50 research project belong to the first four decks of the southern part of the viaduct. Each deck was composed of 10 precast prestressed concrete I-beams and 2 external precast prestressed concrete U-beams, simply supported at piers, and completed by two transverse beams at the thirds of the span and the 0.14 m thick upper slab were both casted on site. The dimensions of the I-beams cross section and the on-site casted slab, object of the present work, are shown in Figure 2. A set of 25 prestressed concrete beams constituting the decks have been dismantled and collected in a testing area, where a bench test has been realized to perform both static and dynamic tests.



Figure 1. An historical view of the Corso Grosseto viaduct.

3 STATIC TEST CAMPAIGN

According to the preliminary visual inspection carried out to map the presence of corrosion, cracks, and spalling, the beams have been classified in good structural condition (Table 1). The beams B07 and B08 have been damaged during the dismantling phases, when strands at the bottom flanges were cut. The B07 had two strands cut on both sides of the lower flange, at distances 3.7, 9.6, and 15.5 m from the end section. The B08 girder had two strands cut on one side at distances of 3.8 and 15.5 m.

The static test procedure consists in applying an incremental static load up to the reaching the ultimate load capacity by means of four hydraulic jacks. An intermediate unloading phase was made to evaluate the residual prestressing load and the effects of the opening of the cracks on the dynamic parameters (Savino et al. 2023). The test on B02 beam has been

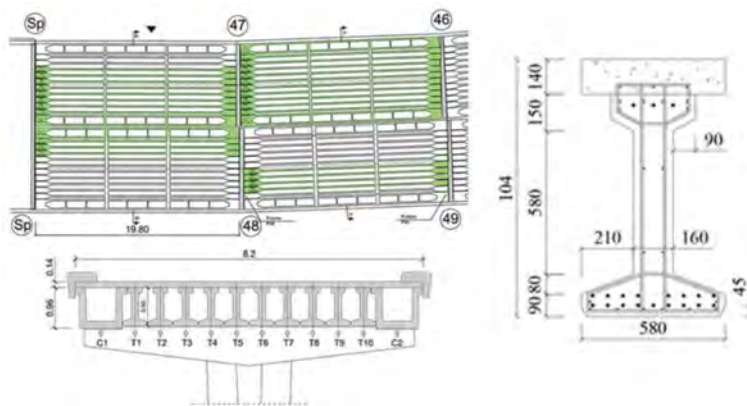


Figure 2. Drawing of the first four decks of the southern part of the viaduct. In green, the beams collected to be tested. On left, the I-shaped beam cross section (measures in mm).

performed in a three-point bending scheme (shear span 9.3 m), whereas a four-point scheme (shear span 6.5 m) was adopted for testing B05 to B08 aimed at investigating the maximum flexural capacity and the shear-bending interaction, respectively. The beams have been loaded up to reach the ultimate condition highlighting a brittle rupture due to the crushing of the upper slab. The principal results are summarized in Table 1. The ultimate flexural strengths M_R take into account the load applied by the hydraulic jacks and the weight of the steel elements used to apply the load to the tested girder.

Table 1. Results of the static tests.

Beam	Position on the deck	Test configuration	M_R (kN m)	Condition
B02	B8 – P47/46	Three Point	1675	Undamaged
B05	B6 – P47/46	Four Point	1656	Undamaged
B06	B6 – Ab/P47	Four Point	1720	Undamaged
B07	B6 – P48/47	Four Point	1445	Damaged (4 strands cut)
B08	B10 – Ab/P47	Four Point	1684	Damaged (2 strands cut)

4 DYNAMIC TEST CAMPAIGN

The description of the test setup is reported in Figure 3. The setup is made of 10 capacitive 1 V/g accelerometers and an instrumented hammer.

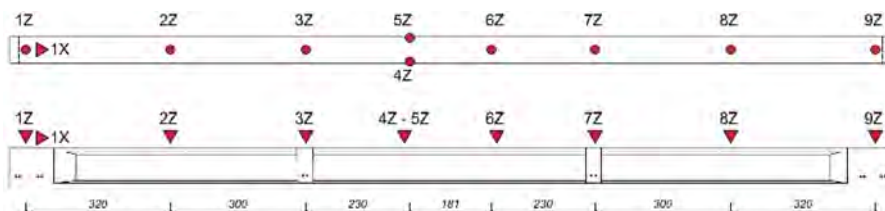


Figure 3. Dynamic test setup.

The accelerometers have been placed on the upper slab along the longitudinal axis of the beam, spaced to get an adequate spatial resolution of the vertical flexural modes. The sensors 1X on the rolling support and the couple of accelerometers 4Z and 5Z placed near the midspan on the edges are used to discriminate the longitudinal and torsional dynamic components.

The acceleration signals were acquired at a 512 Hz sampling frequency for both ambient noise and impact hammer excitations. The impact tests were carried out by hitting the beams with an instrumented hammer in vertical direction in the halfway of two consecutive accelerometers. To replicate as close as possible the onsite supporting conditions of the deck, the bench components lying on the upper slab during the static tests are each time removed.

The dynamic test campaigns have been performed before the static test (Phase 0), after the intermediate unloading cycle (Phase 1) and after the application of the ultimate load (Phase 2).

4.1 Experimental modal analysis

The extraction of the principal modal components is performed evaluating the frequency response function (FRF) matrix with respect of the input given by means of the instrumented hammer. When dealing with experimental or operational modal analysis, the FRF is defined for a linear system by the relationship between the forcing function $\{F(\omega)\}$ and the p structural responses $\{Y(\omega)\}$, usually recorded by accelerometers when measured during in-situ testing. In the frequency domain the FRF matrix $[H(\omega)]$ in described by equation (1):

$$\begin{matrix} \{Y(\omega)\} \\ (p \times 1) \end{matrix} = \begin{matrix} [H(\omega)] \\ (p \times q) \end{matrix} \begin{matrix} \{F(\omega)\} \\ (q \times 1) \end{matrix} \quad (1)$$

The element of FRF matrix $H_{k,j}(\omega)$ maps the input $F_k(\omega)$, applied at the k -th degree of freedom (DOF), and the output Y_j measured at the j -th DOF. In case of acceleration as output signals, the FRF matrix is expressed in the accelerance form (Ljung, 1999). The generic element of the accelerance matrix, expressed in terms of modal properties, is given by:

$$H_{j,k}(\omega) = \frac{\ddot{Y}_j(\omega)}{F_k(\omega)} = -\omega^2 \sum_{r=1}^N \frac{1}{m_r} \frac{\psi_j^r \psi_k}{\omega_r^2 - \omega^2 + 2i\omega\omega_r} \quad (2)$$

The FRF can be estimated by classical H_1 or H_2 estimators, given by the ratio between the cross-spectrum $S_{jy}(\omega)$ of the output $Y(\omega)$ and the input $F_k(\omega)$ and the auto-spectrum of the input $S_{ff}(\omega)$ or of the output $S_{yy}(\omega)$ that can be chosen according to whether the major source of noise is for input or output signals. The FRF is a complex function which amplitude has a maximum at the resonant frequency. The magnitude of the modal coefficient is simply taken as the value of the imaginary part at resonance. The sign is either positive or negative, considering the direction of the peak along imaginary axis. This implies that the phase angle is either 0° or 180° .

Figure 4 shows an example of FRF, magnitude and imaginary part, from the excitation and the time history measured at the position from 1Z to 9Z on the beam.

After a preliminary analysis of the spectral content, the signals were pre-treated by filtering out of the bandwidth [0 - 100 Hz], removing the trends. The FRFs have been estimated basing on each singular impulse acceleration data and then averaged for each hitting position. The first three modal components are clearly identified as shown by the example proposed in Figure 4. The mode shapes associated to these components correspond to the three main flexural modes of the beam. The modal coordinates are estimated by the imaginary part of the FRFs.

5 RESULTS OF THE DYNAMIC IDENTIFICATION

In this paragraph the result of the dynamic identification for each of the five beams for each of the three phases are reported. The tests phases are depicted in Figure 5. The Phase 0 aims at investigating the dynamic properties of the structural elements before the execution of static test, describing the condition after 50 years of service life. The results of the dynamic tests campaign performed on the decks from which the beams have been removed are reported in (Quattrone et al., 2021).

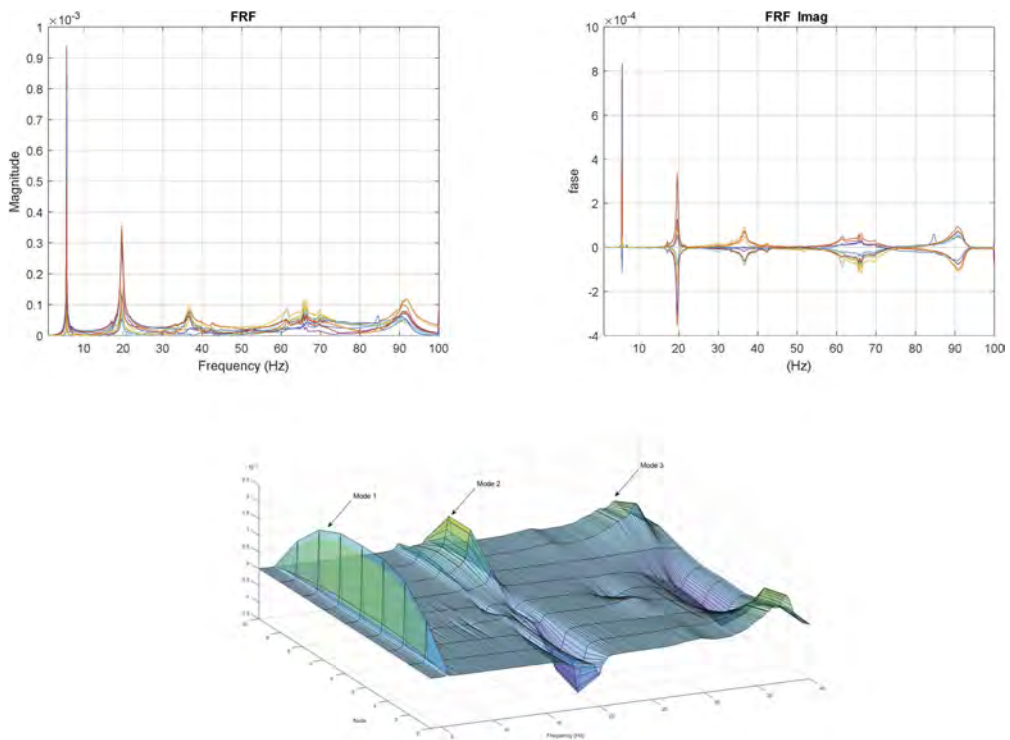


Figure 4. Example of FRF. Left: Magnitude; Right: Imaginary part. Bottom: Mode Shapes.

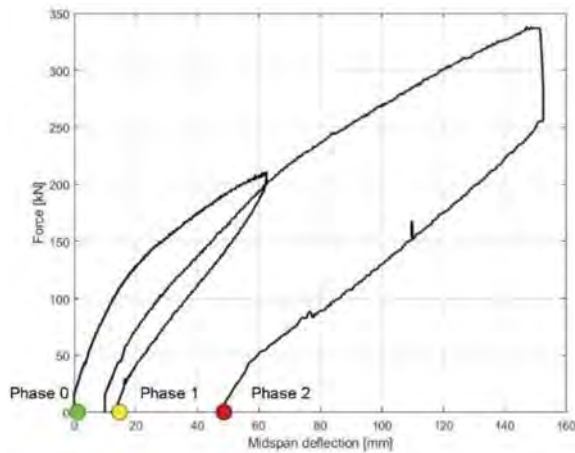


Figure 5. Force – midspan deflection. The dots indicate the phase test.

The Phase 1 corresponds to the unloading condition, subsequent the reaching of the full cracked condition, identified in Table 2 as a fraction of the ultimate bending moment reached during the static tests. The Phase 2 regards the dynamic test on the beams which experienced their ultimate load condition.

Table 2. Damage levels corresponding to Phase 1 tests.

Specimen	M (kNm)	% M_R
B02	1080.7	68.7%
B05	884.0	55.8%
B06	939.9	57.0%
B07	855.7	62.3%
B08	910.7	56.5%

The Table 3 reports the mean values of frequencies and damping estimated at the three phases for each beam.

Table 3. Mean modal frequencies and damping ratios.

		Phase 0			Phase 1			Phase 2		
		mode 1	mode 2	mode 3	mode 1	mode 2	mode 3	mode 1	mode 2	mode 3
B02	f (Hz)	5.49	19.38	36.44	5.28	18.88	36.34	4.78	18.58	32.69
	ξ (%)	0.37	0.84	2.18	0.48	0.81	2.19	0.55	1.00	2.22
B05	f (Hz)	5.47	19.52	36.62	5.31	19.30	35.50	5.05	19.45	33.44
	ξ (%)	0.34	0.80	1.94	0.40	0.74	1.68	0.95	2.16	2.03
B06	f (Hz)	5.60	19.86	37.21	5.47	19.48	36.17	5.01	18.50	33.62
	ξ (%)	0.36	1.30	0.85	0.40	1.33	0.91	0.63	1.06	1.57
B07	f (Hz)	5.58	19.83	35.22	5.48	19.36	34.91	5.01	19.09	33.84
	ξ (%)	0.39	0.65	1.77	0.39	0.68	1.99	0.42	1.30	2.14
B08	f (Hz)	5.61	20.35	38.25	5.41	19.58	37.08	4.83	18.33	33.85
	ξ (%)	0.29	1.46	1.32	0.31	1.04	1.57	0.43	1.06	1.57

The following figures illustrate, as an example, the comparison between the mode shapes at different damage levels (phases 0, 1 and 2) for girder B08. It worth noting that small but noticeable differences can be observed with the increasing of damages. Similar results have been found for the other girders.

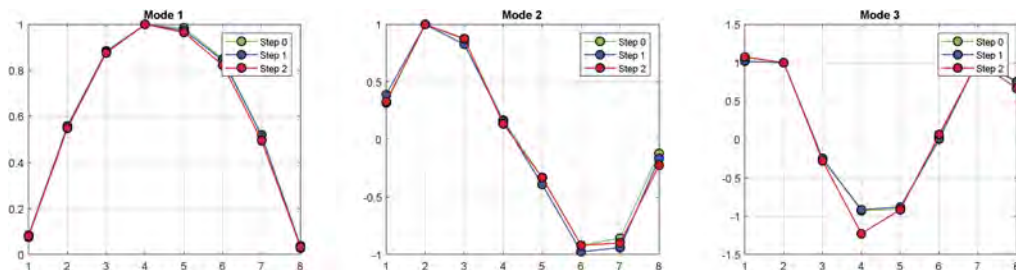


Figure 6. Beam B08 mode shapes at different damage levels.

The Figure 6 shows the distributions of frequencies and damping identified at the different damage levels. It can be noted that at the increase of the damage level correspond the reduction of the modal frequencies and the increasing trend of damping ratios. Moreover, the scattering of both the parameters increase.

The reductions of the frequencies of the first mode vary in range of about 2-4% for Phase 1 tests and about 8-14% for Phase 2. The entities of these reductions are comparable to the findings reported in similar experimental campaign present in literature (Quatrone et al. 2012).

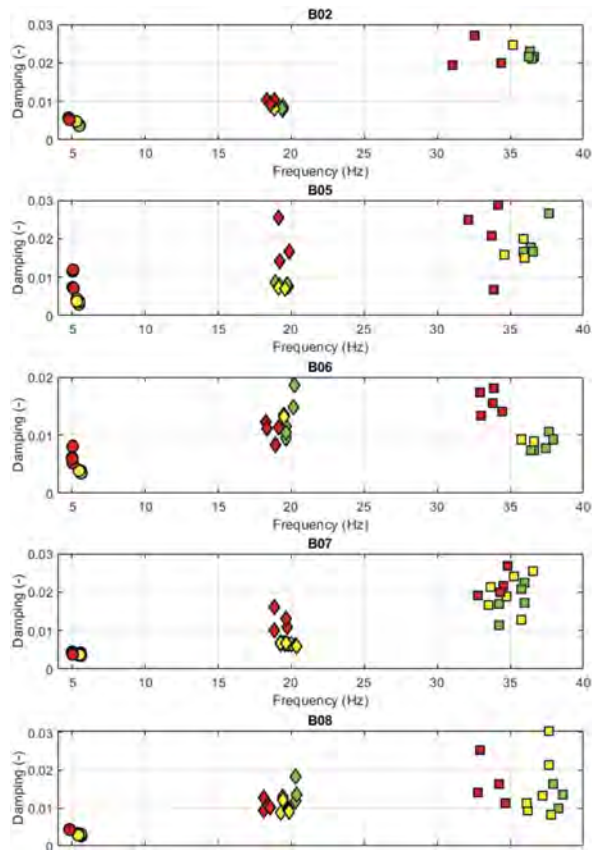


Figure 7. Distribution of frequencies and damping ratios. The colors correspond to the phases as indicated in Figure 4.

6 CONCLUSIONS

This work presents the results of the experimental dynamic campaign performed on a set of bridge girders dismantled after 50 years of service life. The tests are part of the BRIDGE|50 research project.

The girders have been characterized for different damage levels induced by static tests. The variation of the modal parameters have been observed and the results confirm the low sensitivity of modal parameters to the damages for prestressed concrete structures. Albeit the small magnitude, the variations of the structural condition are clearly detectable, confirming the capability of the dynamic structural identification to follow the evolution of damage. The experimental results here presented should be very useful in the field of permanent structural health monitoring. Future works will refine the estimation of damping ratio and the implementation of damage localization and quantification techniques.

ACKNOWLEDGEMENTS

BRIDGE|50 is a research project based on a research agreement among universities, public authorities, and private companies. Members of the Management Committee: S.C. R. Piemonte (President); Politecnico di Milano (Scientific Coordinator); Politecnico di Torino (Scientific Responsible of the Experimental Activities); Lombardi Engineering (Secretary); Piedmont Region; City of Turin; Metropolitan City of Turin; TNE Torino

Nuova Economia; ATI Itinera & C.M.B.; ATI Despe & Perino Piero; Quaranta Group.
BRIDGE|50 website: <http://www.bridge50.org>.

REFERENCES

- Biondini, F., Manto, S., Beltrami, C., Tondolo, F., Chiara, M., Salza, B., et al. 2020 BRIDGE|50 research project: Residual structural performance of a 50-year-old bridge. *Bridge Maintenance, Safety, Management, Life-Cycle Sustainability and Innovations – Proceedings of the 10th International Conference on Bridge Maintenance, Safety and Management (IABMAS 2020)*.
- Demarie G. & Sabia D. 2019. *A machine learning approach for the automatic long-term structural health monitoring*, Structural Health Monitoring, 819–837.
- Guiglia, M. & Taliano, M. 2014 *Experimental analysis of the effective prestress in large-span bridge box girders after 40 years of service life*. Engineering Structures 66 (1), 146–158.
- Quattrone, A., Matta, E., Zanotti Fragonara, L., & Ceravolo, R., 2012. *Vibration tests on dismantled bridge beams and effects of deterioration*, Journal of Physics: Conference Series, 382(1).
- Ljung, L. 1999 *System identification. Theory for users*, Englewood Cliffs, NJ, Prentice Hall.
- Quattrone, A., Sabia, D., Tondolo, F., Capacci, L., Lencioni, A. & Legramandi, C. 2021 *Dynamic tests and modal identification of Corso Grosseto viaduct decks before the dismantling*. Bridge Maintenance, Safety, Management, Life-Cycle Sustainability and Innovations. CRC Press.
- Sabia, D., Quattrone, A., Tondolo, F. & Savino, P. 2021 *Dynamic identification of damaged PC bridge beams*. First Conference of the European Association on Quality Control of Bridges and Structures (EUROSTRUCT 2021), August 29 – September 1, 2021, Padua, Italy.
- Savino, P.; Tondolo, F.; Sabia, D.; Quattrone, A.; Biondini, F.; Rosati, G.; Anghileri, M. & Chiaia, B. 2023. *Large-Scale Experimental Static Testing on 50-Year-Old Prestressed Concrete Bridge Girders*. Applied Sciences 13(834): 1–22.

*SS12: Exploiting digitalization in the intervention planning
for transportation infrastructure*
Organizers: B.T. Adey, S. Moghtadernejad, S. Chuo & H. Mehranfar



Taylor & Francis

Taylor & Francis Group

<http://taylorandfrancis.com>

Decentralized control-based intervention policies for road networks

Y. Nakazato, D. Mizutani & T. Nagae

Tohoku University, Sendai, Miyagi, Japan

ABSTRACT: In the infrastructure management field, the centralized control-based framework is widely applied to the road network management problem to derive network-level intervention policies. However, the optimal network-level intervention policy by the centralized control-based framework is difficult to derive and apply because there is no efficient solution method. In this study, we propose a new framework for the road network management problem, a decentralized control-based framework, where the network is divided into multiple groups and the sub-manager of each group decides the group-level intervention policy according to the aggregated information of all groups. Particularly, we propose a method to decide the groups of links and the solution method for deriving decentralized control-based intervention policies for road networks. Numerical studies demonstrate that the proposed decentralized control-based intervention policy can reduce the life-cycle costs of the road network compared with existing intervention policies.

1 INTRODUCTION

Facilities on road networks stochastically deteriorate due to continuous loading, weather and other uncertain factors. These deteriorated facilities should be repaired for the safety and reliability of the road networks. The repair work is costly and might disturb the traffic; therefore, the road network manager must carefully decide the repair timing of all facilities. In this study, we propose a new framework for such a road network management problem: a decentralized control-based framework.

When the deterioration of facilities is expressed as a stochastic process, a typical road network intervention policy is described as a state-dependent rule that assigns an intervention alternative for each facility corresponding to the condition state (CS) of all facilities. Mathematically, the rule is a mapping from the set of possible CS patterns to the set of possible intervention alternative patterns. For example, suppose a road network comprises 5 links with link id k ($k = a, b, c, d, e$) as shown in Figure 1. Every link has an identical facility, and the CS of each facility is 1 (good), 2 (slightly deteriorated), or 3 (severely deteriorated), whereas the intervention for each facility is either 0 (no repair) or 1 (repair). Let x_k be the CS of the facility on link k and $\mathbf{x} = (x_k)$ be the corresponding CS pattern. The set of the possible CS patterns is then denoted by $\mathcal{X} = \{1, 2, 3\}^5$, whereas the set of possible intervention patterns is $\mathcal{Y} = \{0, 1\}^5$. Then the network intervention policy is denoted by a mapping from $\delta: \mathcal{X} \rightarrow \mathcal{Y}$, whose typical element, $\delta_k(\mathbf{x})$, is the repair alternative of each facility k corresponding to each CS pattern \mathbf{x} . The network intervention policy can also be summarized by the tables as shown in Figure 2, which assign a repair alternative to each facility on link k corresponding to each of the $3^5 = 243$ possible CS patterns, \mathbf{x} .

This typical network intervention policy belongs to a centralized control-based framework because the only manager of the network decides the intervention for all facilities in the network according to the CS pattern. Previous studies using the centralized control-based framework show that other than corrective repair, which means the repair for the facilities severely deteriorated, preventive repair, which means the repair for the facilities slightly deteriorated, can reduce costs because of the interdependence of facilities. However, the intervention policies derived from the centralized control-based framework (i.e. centralized control-based intervention policies) become implausibly complicated as the number of facilities increases, due to the combinatorial explosion of the possible CS patterns. Such complicated intervention policies should be impractical to derive and, even if they are derived, difficult to apply.

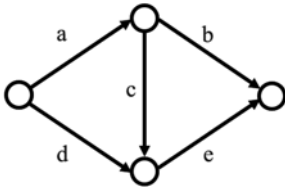


Figure 1. A road network example.

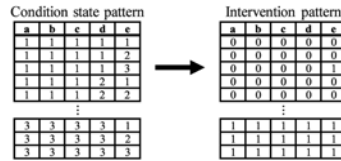


Figure 2. Centralized control-based intervention policy.

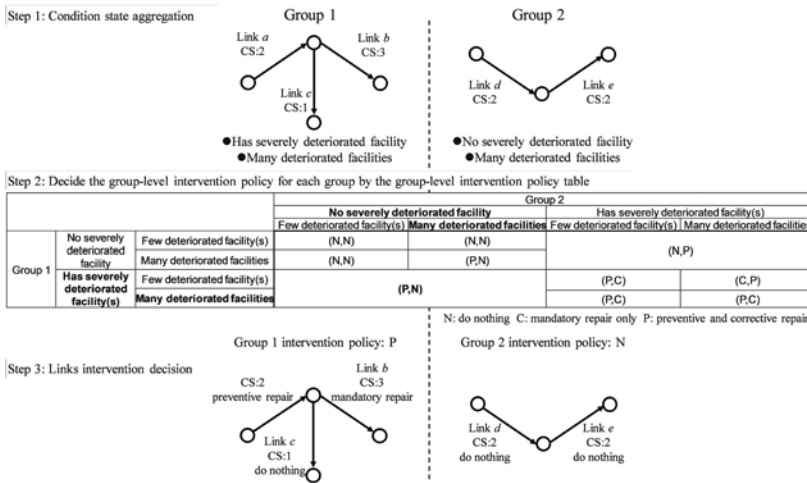


Figure 3. Example of the flow of the intervention decision by the decentralized control-based framework.

In this study, we propose a new framework for the road network intervention policy problem: a decentralized control-based framework. Decentralized control has been employed in many engineering fields other than infrastructure management. Different from the centralized control-based framework, the decentralized control-based framework has multiple sub-managers deciding the intervention policies for part of the network where they are managing. As a result, the intervention policies from the decentralized control framework (i.e. decentralized control-based intervention policies) may have fewer possible CS patterns and hence are relatively easy to derive. Besides, the decentralized control-based framework may be more suitable for real road network management because many road networks are managed by multiple officers.

Figure 3 Shows an example of the flow of the management for the road network shown in Figure 1 by the proposed framework. The road network is divided into 2 groups $G_1 = \{a, b, c\}$ and $G_2 = \{d, e\}$ in advance, and each group is managed by an individual agent (referred to as a “sub-manager”). Each time the decision of intervention is required, there are totally 3 steps to decide the intervention for all links. In Step 1, each sub-manager aggregates the CSs of facilities in each group. Here, the CS of each group is aggregated by 2 criteria: “whether there is severely deteriorated facility(s) in the group” and “whether the network has many deteriorated facility(s)”. This enables the sub-managers to share the least information about CS of each group, while also keeping the complexity of the decision at an considerable level. In Step 2, the group-level intervention policies are decided by the group-level intervention policy table. In this study, we consider 3 types of group-level intervention policies: N, C and P. N means to do nothing, C means to conduct corrective repair to the facilities severely deteriorated (with CS 3) in the network, and P means to conduct preventive repair to the facilities slightly deteriorated (with CS 2) in the network in addition to conduct corrective repair to the facilities severely deteriorated (with CS 3) in the network. In Step 3, each sub-manager decides the intervention for all links managed according to the group-level intervention policies. In the example in Figure 3, to avoid road network

disruptions due to simultaneous repair of links a , d and e , an intervention policy is derived in which the preventive repair is conducted only on link a , not on all links with CS 2.

The centralized control-based intervention policy has exactly $3^5 = 243$ possible CS patterns for the entire network and each CS pattern has $2^5 = 32$ possible intervention alternatives; meanwhile, the decentralized control-based intervention policy have only $4^2 = 16$ possible aggregated CS patterns for the entire network and each aggregated CS pattern has only 3^2 possible intervention alternatives and are hence easier for derivation and application if the group division is given.

In this study, we propose a decentralized control-based framework for road network management. Particularly, we propose (1) a method for deciding the group of links and (2) the solution method for deriving decentralized control-based intervention policy.

2 PREVIOUS STUDIES

To consider the interdependence of facilities managed simultaneously, many centralized control-based studies have targeted network-level management problems. Golabi et al. (1982) proposed an approximate solution method called a randomized policy that assumes that all facilities are homogeneous and decides the facilities to repair stochastically. Smilowitz & Madanat (2000) targeted yearly repair policy problems for road networks considering the yearly budget constraints. However, their solution methods are unsuitable for road networks that have costs highly dependent on the network structure. Lee et al. (2016) considered the repair policy problem by minimizing the LCC of a road network under the green gas emission constraints, using the genetic algorithm (GA). However, the optimal repair policy derived by GA is a large set of network-level situation-dependent rules that contains repair patterns for all combinations of CSs of all links. When the size of the network is large, the result derivation will become extremely difficult and even if the result is derived, it is difficult to interpret and apply. Medury & Madanat (2013) targeted the optimal repair policy by minimizing the LCC of a road network using approximate dynamic programming. They also targeted the derivation of the optimal repair policies for sub-networks. However, they did not consider the interdependence of the multiple sub-networks. Mizutani et al. (2020) considered the optimal repair policy for a road network where economies of scale exist in repair costs, using a heuristic method. But it considers only the repair costs, which is unsuitable for road networks where user costs extremely changes according to the structure. Compared with single-facility-level intervention policies, centralized control-based intervention policies can reduce the costs but have high computational complexity and hence are difficult to derive and apply to real-scale problems. To the best of our knowledge, there is no study considering the decentralized control-based framework for the road network management problem.

In various engineering fields, many studies, such as Bakule (2008), Becker et al. (2004), Chandan et al. (2014), and Sonnenschein et al. (2015), employed the decentralized control-based framework to solve problems. The studies using decentralized control usually target the management problem for a large-scale system, where multiple sub-managers are required to manage the entire system. Each sub-manager makes a decision for the managing group by the simplified information from other sub-manager(s); therefore, the management problem has low computational complexity compared with centralized control.

3 DETERIORATION AND REPAIR PROCESSES OF ROAD NETWORK

In this section, we model the facility deterioration and repair processes of a road network comprising of multiple road links. Each link has only one identical facility. For convenience, the facility of a link is referred to as a link in this study.

Consider a discrete time axis starting at calendar time t_0 , when the road network was constructed. For the road network, the CSs of all links are inspected at the same time interval Δt from t_0 , and based on the inspection results, the manager decides the links to repair. Let z be the positive nature number ($z \in \mathbb{Z}^+$); we define a set \mathcal{T} of inspection and repair times: $\mathcal{T} = \{t_z | \forall z \in \mathbb{Z}^+\}$ where $t_z = t_0 + z\Delta t$.

In this study, the managing network is expressed as a directed graph $\mathcal{G}(\mathcal{N}, \mathcal{A})$. \mathcal{N} is the set of all nodes, whereas \mathcal{A} is the set of all directed links. CS of link $(i, j) \in \mathcal{A}$ is expressed as an M -level discrete variable, $s_{i,j} \in \mathcal{M} = \{1, 2, \dots, M\}$, where $(i, j) \in \mathcal{A}$. \mathcal{M} is the state space of the CS. The larger $s_{i,j}$ is the worse CS is. The CS right after the repair and construction is 1, and the CS M means severely deteriorated. The condition of the entire road network can be expressed as a $|\mathcal{A}|$ -dimensional CS vector: $s \equiv [s_{i,j}] \forall (i, j) \in \mathcal{A}$. The state space of the CS vector is the product of the CSs of all links and can be expressed as $S = \mathcal{M}^{|\mathcal{A}|}$.

We assume that the deterioration process of each link follows the same Markov chain. First, we model the deterioration process of a single link. To identify CS before and after repair, the CS before repair at time $t \in \mathcal{T}$ is expressed as $s^-(t)$, and the CS after repair is expressed as $s^+(t)$. The probability that CS change from $s_{i,j}^a \in \mathcal{M}$ to $s_{i,j}^b \in \mathcal{M}$ from $z(z \in \mathbb{Z}^+)$ th inspection time t_z to t_{z+1} can be expressed as $p_{s_{i,j}^a, s_{i,j}^b} = \text{prob}[s_{i,j}^-(t-1) = a | s_{i,j}^+(t_z) = a]$. In this study, we define the deterioration process of a single link by Markov transition matrix p as $p \equiv [p_{a,b}]$, $\forall a, b \in \mathcal{M}$.

Then we model the deterioration process of the entire road network. In terms of the road network, the probability that the CS vector changes from $s^a \in \mathcal{S}$ at time t_z to $s^b \in \mathcal{S}$ at time t_{z+1} can be expressed as the product of transition probabilities of all links: $P_{s^a, s^b} = \prod_{(i,j) \in \mathcal{A}} p_{s_{i,j}^a, s_{i,j}^b}$.

We only consider reconstruction repair work that changes the CS of the repaired link to 1. At time $t_z \in \mathcal{T}$, the repair for the entire road network can be expressed by an intervention vector consisting of binary variables: $\delta(t_z) \equiv [\delta_{i,j}(t)] \forall (i, j) \in \mathcal{A}$. The change in CS vector s with respect to intervention vector $\delta(t_z)$ can be expressed as $s^+(t_z) = s^-(t_z) - [s^-(t_z) - 1] \circ \delta(t_z)$, where $\delta_{i,j}(t_z) \in \{0, 1\} \forall (i, j) \in \mathcal{A}$. At each time point, the link(s) having CS M (severely deteriorated) must be repaired, i.e.,

$$\delta_{i,j}(t_z) = 1 \quad \text{if} \quad s_{i,j}(t_z) = M \quad (1)$$

4 LIFE-CYCLE COSTS AND INTERVENTION POLICIES FOR THE ROAD NETWORK

4.1 Repair cost, user cost, and life-cycle cost

First, we define the repair costs with the intervention vector $\delta(t_z)$. In this study, we assume that the manager needs to set up a work zone for intervention. Repair costs contain of 2 types of costs: variable and fixed costs. The repair variable cost is proportional to the number of links to repair (i.e. material and labor costs), whereas the fixed repair costs is proportional to the number of continuous work zones (i.e. construction machine and traffic control costs). Assume that the length of link (i, j) is expressed as $l_{i,j}$, the unit price of the repair variable costs is expressed as α , and the unit price of the repair fixed costs is expressed as β , the repair costs $r(\delta(t_z))$ when intervention vector $r(\delta(t_z))$ is implemented can be calculated as follows:

$$r(\delta(t_z)) = \alpha \sum_{(i,j) \in \mathcal{L}} l_{i,j} \delta_{i,j} + \beta \sum_{n \in \mathcal{N}} b_n \quad (2)$$

$$\text{where} \quad b_n = \begin{cases} 0 & \text{if } \delta_{n,j} = 0 \quad \text{and} \quad \delta_{n,i} = 0 \\ 1 & \text{else} \end{cases} \quad \forall (n, j) \in \mathcal{L}, \forall (i, n) \in \mathcal{L} \quad (3)$$

where b_n is the binary variable indicating whether node n is connected to any intervened links.

Then we define the user costs with the intervention vector $\delta(t_z)$. In this study, we consider the traffic demand of the entire road network as constant. K type(s) of traffic demand exists in the network; therefore, the traffic demand $\mathcal{F} \equiv \{(O_k, D_k), f_k\} \forall k \in \mathcal{K}$ $\mathcal{K} \equiv \{1, 2, \dots, K\}$ where O_k denotes the origin node of the k th type of traffic demand, D_k denotes the end node of the k th type of traffic demand, and f_k denotes the amount of the k th traffic demand. The user costs when 1 unit traffic flow passed link $(i, j) \in \mathcal{L}$ for Δt is $c_{i,j}$, max flow in link $(i, j) \in \mathcal{L}$ is $\mu_{i,j}$, k th type of traffic flow in link $(i, j) \in \mathcal{L}$ from time t_z to t_{z+1} is expressed as $y_{i,j,k}(t_{z+1})$.

When a link is intervened at time t_z , the traffic capacity of the link becomes $\gamma(0 < \gamma < 1)$ times until t_{z+1} . If the traffic demand exceeds the network capacity, the excess traffic will use a public

road with a high cost to detour. In this study, we assume that users cannot detour between specific links, and that the public roads have enough capacity for all users to travel. The user costs when 1 unit traffic flow of k th traffic demand passed the public road is C_k , and the traffic cost is $\hat{w}_k(t_z)$.

When intervention vector is $\delta(t_z)$, the user costs $u(\delta(t_z))$ from time point t_z to time point t_{z+1} can be calculated by the following minimum flow problem:

$$u(\delta(t_z)) = \in \left[\min_{\mathbf{w}(t_z), \hat{\mathbf{w}}(t_z)} \sum_{k \in \mathcal{K}} \left(\sum_{(i,j) \in \mathcal{L}} c_{i,j} w_{i,j,k}(t_z) + C_k \hat{w}_k(t_z) \right) \right] \quad (4)$$

$$\text{s.t. } \sum_{(n,j) \in \mathcal{L}} w_{n,j,k}(t_z) - \sum_{(i,n) \in \mathcal{L}} w_{i,n,k}(t_z) = 0 \quad \forall n \in \mathcal{N} \setminus \{\mathcal{O}_k, \mathcal{D}_k\}, \quad \forall k \in \mathcal{K} \quad (5)$$

$$\sum_{(\mathcal{O}_k, j) \in \mathcal{L}} w_{\mathcal{O}_k, j, k}(t_z) + \hat{w}_k(t_z) = f_k, \quad \sum_{(i, \mathcal{D}_k) \in \mathcal{L}} w_{i, \mathcal{D}_k, k}(t_z) + \hat{w}_k(t_z) = f_k, \quad \forall k \in \mathcal{K} \quad (6)$$

$$\sum_{k \in \mathcal{K}} w_{i,j,k}(t_z) \leq \mu_{i,j}(\gamma) \delta_{i,j}(t_z) \quad \forall (i,j) \in \mathcal{L} \quad (7)$$

$$w_{i,j,k}(t_z) \geq 0 \quad \forall (i,j) \in \mathcal{L}, \forall k \in \mathcal{K} \quad \hat{w}_k(t_z) \geq 0 \quad \forall k \in \mathcal{K} \quad (8)$$

\in is the unit cost per time. The objective function of user costs Equation 4 is the sum of the user costs of the road network and the user costs of the public roads. Equation 5 means the total inflow of any node except OD is 0; Equation 6 means the traffic outflow from each O equals each traffic demand, and the traffic inflow to each D equals each traffic demand; Equation 7 means the traffic in each link must not exceed the link capacity; Equation 8 means the non-negative constraint for traffic flow in each link, and the non-negative constraint for traffic flow on each public road.

In this study, the goal of the intervention policy is to reduce LCC Ψ of a newly constructed road network starting from t_0 . The LCC Ψ can be calculated as follows:

$$\Psi(\{\delta(t_z), \forall t_z \in \mathcal{T}\} | s(t_0) = 1) = \sum_{t_z \in \mathcal{T}} \frac{1}{(1+\rho)^{t_z}} E_{s^-(t_z)} [r(\delta(t_z)) + u(\delta(t_z))] \quad (9)$$

ρ is the discount rate, and $E_{s^-(t_z)}[\cdot]$ means the expected value with respect to $s^-(t_z)$.

4.2 Centralized control-based intervention policies

The optimal repair policies can be defined by the following LCC minimizing problem:

$$\min_{\{\delta(t_z), \forall t_z \in \mathcal{T}\}} \Psi(\{\delta(t_z), \forall t_z \in \mathcal{T}\} | s(t_0) = 1) \text{ s.t. (1)} \quad (10)$$

This is an infinite-time Markov decision process, where the optimal intervention vector $\delta(t_z)$ is determined by the CS vector $s(t_z)$ at the time t_z . The optimal intervention policy problem can be defined by the set of the optimal intervention vector Δ , which depends on the CS vector:

$$\min_{\Delta} \Psi(\Delta | s(t_0) = 1) \text{ s.t. (1) where } \Delta \equiv [\delta(s^a)] \quad \forall s^a \in \mathcal{S} \quad (11)$$

The following Bellman equations can be used to calculate the optimal intervention vector $\delta^*(s^a)$ for CS s^a :

$$V(s^a) = r(\delta(s^a)) + u(\delta(s^a)) + \frac{1}{(1+\rho)^{\Delta t}} \sum_{s^c \in \mathcal{S}} P_{s^b, s^c} V(s^c) \quad \text{where } s^b = s^a - [s^a - 1] \circ \delta(s^a) \quad (12)$$

The optimal intervention policy Δ^* is a situation-based pattern of combinations of CSs of all links; therefore, we have to calculate the optimal intervention vector for all patterns of CS vectors simultaneously. To the best of our knowledge, there is no efficient solution method for this problem. One orthodox solution method is full enumeration of all possible intervention policies.

However, in the following numerical study of Sioux Falls, the network has $|\mathcal{A}| = 76$ links and the max CS is $M = 3$, meaning this problem has 76 decision variables, each with 3 possible integer alternatives. As a result, the number of possible intervention policies is 3^{76} , and the optimal intervention policy for such a real-scale road network is impossible to calculate by full enumeration.

4.3 Decentralized control-based intervention policy

The approximate solution method based on the decentralized control in this study does not derive the optimal intervention vectors for all CS vectors but derives the intervention vector at each inspection and repair time. For the observed CS vector s^a , (a) the group of the links $\mathcal{G}_1, \mathcal{G}_2$, (b) the aggregated state for each group $\{\Lambda_1\}, \{\Lambda_2\}$, and (c) repair strategy variables Y_1, Y_2 for each group, are used to derive the group intervention vector $\hat{\delta}(s^a)$.

In this study, we decide the group of links as follows:

$$\min_{\{\delta(t_h), \forall h \in \mathcal{H} = \{1,2\}\}} \sum_{h \in \mathcal{H}} \frac{1}{(1+\rho)^{Mh}} [r(\delta(t_h)) + u(\delta(t_h))] \quad \text{s.t.} \quad \sum_{h \in \mathcal{H}} \delta(t_h) = 1 \quad (13)$$

The group number is 2, and the binary variable $\delta(t_h)$ indicates whether each link belongs to group h . Group $\{\mathcal{G}_h\}$ is decided as follows: $\mathcal{G}_h \equiv \{\mathcal{N}_h, \mathcal{A}_h\}, \forall h \in \mathcal{H}$ where $\mathcal{A}_h \equiv \{(i,j) \in \mathcal{A} | \delta_{i,j}(t_h) = 1\}$, $\mathcal{N}_h \equiv \{\forall n \in \mathcal{N} | \delta_{n,j}(t_h) = 1, \forall (n,j) \in \mathcal{A}\} \cup \{\forall n \in \mathcal{N} | \delta_{i,n}(t_h) = 1, \forall (i,n) \in \mathcal{A}\}$. Equation 15 is a combinatorial optimization problem; in general, it is difficult to obtain an exact solution. In our numerical studies, we find solutions using Gurobi Optimizer (<http://www.gurobi.com/>). However, there is no guarantee that an exact solution to Equation 29 can be easily obtained for any given case. This problem can be interpreted as a “network renewal planning problem within a specific period of time.” This suggests that the Equation 29 may be some approximation to the original intervention policy optimization problem Equation 25 (e.g. a problem that dismisses deterioration), but a rigorous proof is beyond the scope of this study.

The CS of each group is approximated by η_h , a binary variable indicating whether there is any severely deteriorated link in the group, and θ_h , a binary variable indicating whether there are many deteriorated facilities in the group. When the CS vector s^a is observed, the network’s state can be approximated using state aggregation as follows Λ :

$$\Lambda \equiv \{\Lambda_h, \forall h \in \mathcal{H}\} \quad \text{where} \quad \Lambda_h \equiv \{\eta_h, \theta_h\} \quad (14)$$

$$\eta_h = \begin{cases} 1 & \text{if } |\{(i,j) \in \mathcal{A}_h | s_{i,j} = M\}| > 0 \\ 0 & \text{else} \end{cases} \quad \theta_h = \begin{cases} 1 & \text{if } |\{(i,j) \in \mathcal{A}_h | s_{i,j} \geq \bar{M}\}| \geq X_h \\ 0 & \text{else} \end{cases} \quad (15)$$

$\bar{M} = M - 1$ means slightly deteriorated, and links with CS equals to or greater than \bar{M} are assumed to be deteriorated (either slightly or severely). The state space of the solution is $\mathcal{X}_h \equiv \{1, 2, \dots, |\mathcal{N}_h|\}$. When the degradation is progressing in group h (the number of links with CS \bar{M} or higher is equal to or greater than the borderline X_h), $\theta_h = 1$; otherwise, $\theta_h = 0$.

Whether repair is conducted to link (i,j) in group h is decided by the decision variable $Y_h(\Lambda)$ indicating the group-level intervention policy, which is expressed as follows Λ :

$$\hat{\delta}_{i,j}(s^a) = \begin{cases} 1 & \text{if } s_{(i,j)} = M \leq s_{i,j} \\ 1 & \text{if } s_{(i,j)} = M - 1 \text{ and } Y_h(\Lambda) = \text{P} \forall (i,j) \in \mathcal{A}_h \text{ where } Y_h(\Lambda) \in \{\text{N}, \text{C}, \text{P}\} \\ 0 & \text{else} \end{cases} \quad (16)$$

$\hat{\delta}_{i,j}(s^a)$ means whether the link (i,j) is repaired.

$Y_h(\Lambda)$ is a decision variable that indicates the group-level intervention policy for group H . N means to do nothing policy, C means to conduct corrective repair to the facilities severely deteriorated (with CS M) in the network, and P means to conduct preventive repair to the facilities slightly deteriorated (with CS $M-1$) in the network in addition to conduct corrective repair to the facilities severely deteriorated in the network. Because Λ comprises 2 binary variables, there are a total of 16 patterns for the aggregated CS patterns of the network and $Y_h(\Lambda)$ is a 16 - dimensional integer variable; therefore, the state space of the solution is $\mathcal{Y}_h \equiv \mathcal{M} \times \mathcal{M} \times \mathcal{M} \times \mathcal{M}$.

The optimization problem for the decentralized control-based intervention policy $\hat{\Lambda}$ can be written as follows:

$$\min_{\{(X_h, Y_h(\Lambda)), \forall h \in \mathcal{H}\}} \Psi(\hat{\Lambda}(\{(X_h, Y_h(\Lambda)), \forall h \in \mathcal{H}\}) | s(t_0) = 1) \text{ s.t.} \quad (17)$$

where

$$\hat{\Lambda} \equiv [\hat{\delta}(s^a)] \quad \forall s^a \in \mathcal{S} \quad Z \equiv \mathcal{X}_1 \times \mathcal{X}_2 \times \dots \times \mathcal{X}_H \times \mathcal{Y}_1 \times \mathcal{Y}_2 \times \dots \times \mathcal{Y}_H \quad (18)$$

The proposed decentralized control-based intervention policy have 16 decision variables of the group-level intervention policies, each with 3 possible integer alternatives, and 2 decision variables of the borderline, each with $|\mathcal{N}_h|$ possible integer alternatives. Compared with the centralized control-based intervention policy that has 3^{76} possible patterns, the decentralized control-based intervention policy has $3^{16} \times |\mathcal{N}_1| \times |\mathcal{N}_2|$ possible patterns and is possible to calculate by full enumeration.

In this study, the optimal decision variables for the decentralized control-based intervention policy are derived by full enumeration and Monte Carlo simulation. First, all possible combinations of the decision variables for the decentralized control-based intervention policy are listed. Second, the LCCs for decentralized control-based intervention policy with the combinations of decision variables are calculated via Monte Carlo simulation. Finally, the combination of decision variables that has the minimum LCC is chosen as the combination.

5 NUMERICAL STUDY

In the numerical study, we first demonstrate the proposed solution method by applying it to the Sioux Falls network, which is a real-scale road network. Then, we apply an intervention policy by a facility-level solution method, an intervention policy by a centralized control-based solution method, and the derived policy to the Sioux Falls network and compare the costs of the intervention policies by each solution method.

The Sioux Falls network is used in the numerical study, and the parameters of the network are summarized in Table 1. The facility-level intervention policy here does not consider the repair fixed and user costs and hence performs only corrective repair or does nothing to each link. The centralized control-based intervention policy here is from Mizutani et al. (2020), where repair fixed cost are considered but user cost, which changes according to the network capacity, is not considered. To compare these 3 policies, we apply them to the Sioux Falls network from $t = 1$ to $t = 100,000$ and calculate the costs.

All numerical calculations were performed using a machine and a program with the following specifications OS: Windows 10 Pro (64-bit); Processor: Intel(R) Xeon(R) Gold 6258R CPU @ 2.70 GHz; Python version: 3.8.11; Gurobi Optimizer version: 9.1.2 build v9.1.2rc0 (win64).

The grouping result of the proposed solution method is shown in Figure 4, and the optimal decision variables of the proposed intervention policies are listed in Table 2. The optimal borderlines for group 1 and 2 are $X_1^* = 9$ and $X_2^* = 2$, respectively. As an example of Table 2, the (P, C) in the bottom right cell means “If group 1 has severely deteriorated facility(s) (facilities with CS 3) and group 1 has many deteriorated facilities (the number of facilities with CS more than 2 equals to or larger than group1 borderline $X_1^* = 9$); and if group 2 has severely deteriorated facility(s) (facilities with CS 3) and group 2 has many deteriorated facilities (the number of facilities with CS more than 2 equals to or larger than group 2 borderline $X_2^* = 2$), the sub-manager of group 1 should conduct preventive and corrective repair policy (P) and the sub-manager of group 2 should conduct corrective repair policy (C).”

For the sub-manager of group 1, the result of this table can be summarized as follows:

“When group 1 has no severely deteriorated facility and few deteriorated facility(s), implement the do nothing policy (N). When group 1 has no severely deteriorated facility and many deteriorated facilities, if group 2 has no severely deteriorated facility and many deteriorated facilities, implement the preventive and corrective repair policy (P), otherwise, implement the do nothing policy (N). When group 1 has severely deteriorated facility(s) and few deteriorated facility(s), if group 2 has severely deteriorated facility(s) and many deteriorated facilities, implement the corrective repair

Table 1. Parameters for numerical study.

Traffic demand: \mathcal{F}	{((1,20), 2, 500), (2,13), 2,500}		
Ratio of traffic capacity when a link intervened: γ	0		
Public road detour cost: C_k	$C_1 = 300, C_2 = 300$		
Unit repair variable cost: α	10		
Unit repair fixed cost: β	20		
Unit time cost: ϵ	1		
Time discount rate: ρ	0.04		
Markov transition matrix: \mathbf{p}	0.45	0.44	0.11
	0.00	0.64	0.36
	0.00	0.00	1.00

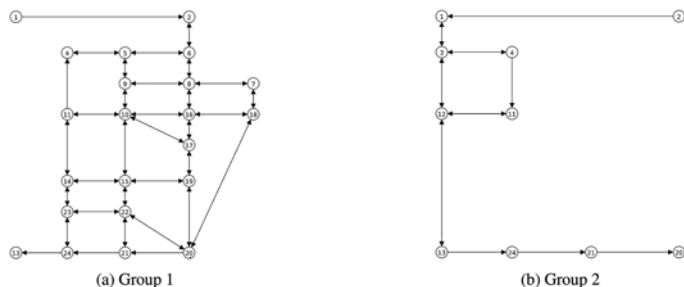


Figure 4. Decentralized control-based intervention policy: Groups of links.

policy (C), otherwise, implement the preventive and corrective repair policy (P).” For the sub-manager of group 2, the result of this table can be summarized as follows:

“When group 2 has no severely deteriorated facility, implement the do nothing policy (N). When group 2 has severely deteriorated facility(s) and few deteriorated facility(s), if group 1 has no severely deteriorated facility, implement the preventive and corrective repair policy (P); if group 1 has severely deteriorated facility(s), implement the corrective repair policy (C). When group 2 has severely deteriorated facility(s) and many deteriorated facilities, if group 1 has no severely deteriorated facility, implement the preventive and corrective repair policy (P); if group 1 has severely deteriorated facility(s) and few deteriorated facility(s), implement the preventive and corrective repair policy (P); if group 1 has severely deteriorated facility(s) and many deteriorated facilities, implement the corrective repair policy (C).”

Table 2. Decentralized control-based intervention policy: group-level intervention policy table.

		Group 2				
		No severely deteriorated facility		Has severely deteriorated facility(s)		
		Few deteriorated facility(s)	Many deteriorated facilities	Few deteriorated facility(s)	Many deteriorated facilities	
Group 1	No severely deteriorated facility	Few deteriorated facility(s)	(N,N)	(N,N)	(N,P)	
		Many deteriorated facilities	(N,N)	(P,N)		
	Has severely deteriorated facility(s)	Few deteriorated facility(s)	(P,N)		(P,C)	(C,P)
		Many deteriorated facilities			(P,C)	(P,C)



Figure 5. Ratio of costs by each policy.

The ratio of the cost of each policy to the cost by the facility-level intervention policy is shown in Figure 5. Compared with the facility-level intervention policy, the centralized control-based intervention policy can target minimizing the repair costs and reduce the annual repair costs by 88%. However, the annual user costs increased, increasing the LCC. The decentralized control-based intervention policy do not significantly reduce the annual repair costs but instead reduce the annual repair costs and annual user costs simultaneously, reducing the LCC. The calculation time for each intervention policy is as follows: the facility-level intervention policy without preventive repair does not require any calculation; the centralized control-based intervention policy that only considers the economies of scale in repair costs requires 30 minutes to 1 hour; and the decentralized control-based intervention policy by the proposed solution method require 2 ~ 3 days.

6 CONCLUSION

In this study, we proposed a decentralized control-based framework for road network management including (1) a method to decide the groups of links and (2) the solution method for deriving decentralized control-based intervention policies for road networks. The decision variables of the decentralized control-based intervention policy, i.e. the variable defining the aggregated CS of all groups and the group-level intervention policies that minimize the LCC, are optimized by full enumeration where the expected LCC is estimated by Monte Carlo simulation. In the numerical study, for comparison, we applied a facility-level intervention policy, a centralized control-based intervention policy, and the proposed decentralized control-based intervention policy. The decentralized control-based intervention policy can reduce the LCC compared with other intervention policies.

ACKNOWLEDGMENTS

This work was supported by the Japan Society for the Promotion of Science (JSPS) KAKENHI [grant number: JP19H00777, JP20H02264, and JP22J22330].

REFERENCES

- Bakule, L. 2008. Decentralized control: An overview. *Annual reviews in control* 32(1).
- Becker, R., Zilberstein, S., Lesser, V., & Goldman, C. V. 2004. Solving transition independent decentralized Markov decision processes. *Journal of Artificial Intelligence Research* 22: 423–455.
- Bellman, R. 1957. A Markovian decision process. *Journal of Mathematics and Mechanics* 6(5): 679–684.
- Chandan, V., & Alleyne, A. G. 2014. Decentralized predictive thermal control for buildings. *Journal of Process Control* 24(6): 820–835.
- Golabi, K., Kulkarni, R. B. & Way, G. B. 1982. A statewide pavement management system. *Interfaces* 12(6): 5–21.
- Lee, J., Madanat, S. & Reger, D. 2016. Pavement systems reconstruction and resurfacing policies for minimization of life-cycle costs under greenhouse gas emissions constraints. *Transportation Research Part B: Methodological* 93: 618–630.
- Medury, A. & Madanat, S. 2013. Incorporating network considerations into pavement management systems: A case for approximate dynamic programming. *Transportation Research Part C: Emerging Technologies* 33: 134–150.
- Mizutani, D., Nakazato, Y., & Lee, J. 2020. Network-level synchronized pavement repair and work zone policies: Optimal solution and rule-based approximation. *Transportation Research Part C: Emerging Technologies* 120(102797).
- Smilowitz, K. & Madanat, S. 2000. Optimal Inspection and Maintenance Policies for Infrastructure Networks. *Computer-Aided Civil and Infrastructure Engineering* 15(1): 5–13.
- Sonnenschein, M., Lünsdorf, O., Bremer, J., & Tröschel, M. 2015. Decentralized control of units in smart grids for the support of renewable energy supply. *Environmental Impact Assessment Review* 52: 40–52.

Efficient early estimates of bridge interventions: Costs, required possession times and associated failure risks

H. Mehranfar, B.T. Adey & S. Chuo

Institute of Construction & Infrastructure Management, ETH Zurich, Switzerland

S. Moghtadernejad

Construction Research Centre, NRC Canada, Ottawa, Canada

ABSTRACT: Due to recent technological advances and the accumulation of historical information related to bridge conditions and bridge maintenance interventions, many managers are in the position to make efficient systematic early estimates of future bridge interventions. If this was possible, it would facilitate communication between different actors within the intervention planning process, e.g., asset managers, production managers, capacity managers, and network developers. Consequently, this paper proposes a methodology to efficiently and systematically make early estimates of bridge interventions, their costs, required possession times and associated risks. The methodology is used in a case study to make early estimates of the possible interventions in different planning periods for a 50m-long masonry bridge located in Switzerland. The results indicate that the methodology has the potential to provide efficient and complete over-views of possible upcoming interventions on all bridges within a bridge portfolio. Once implemented in a digital environment, the methodology is likely to provide bridge managers with an improved way to determine the timing of detailed bridge investigations by engineering offices.

1 INTRODUCTION

Currently, many bridge managers make early estimates of intervention requirements rather qualitatively, meaning that they use inspection reports and discuss with inspectors and engineers as to which interventions may be required on bridges in the future. A downside of the current process is its inability to provide a systematic and efficient overview over all the possible upcoming interventions, and without this systematic estimate it is also difficult to have a good overview of the intervention costs and the required possession times. The lack of a systematic overview may result in interventions being planned earlier or later than they ideally should be, resulting in additional intervention costs and greater than necessary service disruptions. An efficient and systematic approach to estimate the intervention requirements would help bridge managers to reduce costs and service disruptions. The use of digital tools has the potential to support bridge managers in taking advantage of their available data to address this gap in the current intervention planning.

Researchers and asset managers have developed multiple methodologies to improve bridge intervention planning by incorporating different concerns of the bridge managers. For example, (Adey et al., 2015; Adey & Hajdin, 2011) developed methodologies to determine asset-level intervention strategies and estimate financial requirements to execute the interventions. Although such methodologies provide bridge managers with an efficient and systematic overview, they require some improvements before they become useful. The improvements required are more detailed estimates, i.e., no longer focusing on the bridge level but on the component or element level, estimates of risk, and approximations of required track possession times. Examples of methodologies focused on making estimates at the component level include (Kim et al., 2022; Martani et al., 2021; Tserng et al., 2009). Examples of methodologies that have been developed to estimate the risk associated with bridges (Adey et al., 2012).

Examples of studies that make estimates of intervention costs and/or possession times include (Adey & Hajdin, 2011; Burkhalter & Adey, 2022).

This paper fills the identified gaps by proposing an algorithm to estimate the component-level intervention requirements, related costs, and possession times systematically and efficiently for multiple planning periods at the early stages of bridge intervention planning considering:

- the condition evolution over time due to the multiple deterioration processes affecting the components,
- the failure risks as a function of the components being in different condition states,
- the possible preventive interventions on the different components of the bridge, and the associated costs and effects on service through the allocated possession times during their execution.

The methodology enables the use of both qualitative and quantitative information coming from different sources, e.g., results of visual inspections, approximate and detailed estimates of failure risks, and approximate and detailed estimates of the costs and impacts on service of executing interventions on the provided service. The methodology is used to estimate component-level intervention requirements, related costs, and possession times over future planning periods for a masonry arch bridge in Switzerland with a length of 50 m.

2 ALGORITHM

Figure 1 provides an overview of the algorithm for estimating the type, costs, and possession times of interventions that need to be executed over future planning periods.

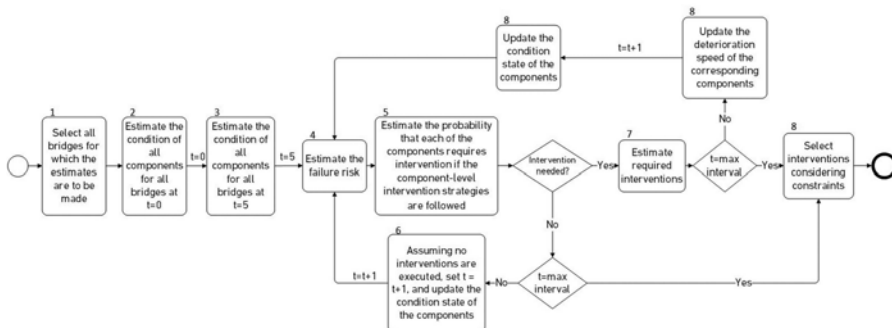


Figure 1. Flowchart for performing the intervention planning process in a digital platform.

Step 1: Select all bridges for which the estimates are to be made. No estimates need to be made for bridges that are already undergoing detailed investigations by engineering offices.

Step 2: Estimate the condition of all components for all bridges at $t=0$.

Step 3: Estimate the condition of all components for all bridges at the start of the planning period to be considered, e.g., $t=5$.

Step 4: Estimate the failure risks at $t=5$.

Step 5: Estimate the probability that each of the components will require intervention if the component-level intervention strategies are followed.

Step 6: Assuming no interventions are executed, set $t = t + 1$ and repeat Steps 3 to 6 until the probabilities of components requiring intervention and the failure risks have been estimated for each of the years in the planning period.

Step 7: Estimate the required interventions: If the probability of requiring an intervention on at least one of the components is higher than a specific threshold value set, or the sum of the failure risks in the planning period is higher than a specific threshold value, it is considered that an intervention is to be executed on the bridge in this period, and indications are given as to which type of interventions are possible and the one that is the most likely, the possessions that are possible and most likely, and the likely intervention costs as a function of the type of intervention and possession times.

Step 8: Propose interventions to postpone if required: If it is known that not all interventions are possible within the planning period, e.g., due to a restricted budget even at this early stage, the indicator of the risk of failure is used to prioritize the bridge interventions, i.e., the bridges exhibiting the highest risk are first on the list. The bridges lowest on the list are postponed until the costs of the interventions included in the list are below the allocated budget.

3 EXAMPLE BRIDGE

The example masonry bridge was constructed in 1926 with a length of 50.8 m. This bridge is located in the canton of Bern, Switzerland and is characterized by three arches made of concrete blocks and resurfaced by rammed concrete (Figure 2).

3.1 Components

The main components of the example masonry bridge are remarked in Figure 2, i.e., foundations, piers, abutments, masonry arches, deck, spandrel walls, and railings and safety walkways.



Figure 2. An overview of different components of the example masonry bridge.

3.2 Condition of components at $t=0$ and $t=5$

Five discrete condition states are defined such that condition state 1 represents a situation with no or insignificant damage, while condition state 5 represents an alarming situation in which safety is at risk. The intermediate states indicate a worsening situation, with an increasing amount of damage. Table 1 shows an example of such definitions for the piers. Similar to the piers such condition states are defined for other bridge components.

Table 1. An example of condition state definition for the piers.

CS	Condition description	Damage description	Damage indicator
1	Good	None/ insignificant	No visible damage; only thin superficial cracks; no sign of corrosion; no or few humid zones.
2	Acceptable	Minor	Visible spot of rust and/or local spalling; thin cracks due to corrosion of the reinforcement; some humid zones; insignificant mechanical damage.
3	Damaged	Significant	Spalling with visible reinforcement; insignificant loss of section, less than 10% than visible reinforcement; cracks and/or humid zones with leaching of the concrete.
4	Poor	Extensive	Spalling of concrete with less than 25% of exposed reinforcement; significant loss of section, more than 10% of visible reinforcement; cracks with significant calcium deposits and/or large humid zones with the leaching of the concrete.
5	Alarming	Safety is endangered	Spalling of concrete with more than 25% of exposed reinforcement; significant loss of section area of the reinforcement; advanced pitting corrosion occurring; large humid zones with the leaching of concrete.

The condition state of all components is then estimated by matching the definition with the physical indicators mentioned in the latest inspection report. According to the records, the

railings and safety walkways are in condition state 1, the foundations and abutments are in condition state 2, and the rest of the components are in condition state 3.

The evolution of the condition states over time is estimated using probabilistic discrete state modelling that approximates the probabilities of the transition of the components from one state to another in each unit of time, similar to the method being used in existing Bridge Management Systems (Mirzaei & Adey, 2015). An example of the transition probabilities for the piers is shown in Table 2. These transition probabilities are for one-year periods, which is the average time between the annual observations. In addition, the deterioration speed is considered as a function of the number of maintenance interventions executed on the component. This assumption is made since the execution of maintenance activities does not necessarily completely improve the physical and chemical properties of the components (Adey & Hajdin, 2011). For example, refilling the cracks in the piers and their rehabilitation can restore the condition state of the piers to condition state 1. There might still be an accumulation of aggregated alkali-silica in the pier, which accelerates the deterioration rate. In this example, it is assumed that following construction and a first maintenance intervention, the deterioration rate increases by 2% after each intervention. The maintenance intervention count resets after the replacement of the components. Similar logic is used to estimate the transition probabilities for other bridge components.

Table 2. An example of the transition probabilities for the piers.

CS	1*					2*				
	1	2	3	4	5	1	2	3	4	5
1	94%	6%	-	-	-	92%	8%	-	-	-
2	-	92%	8%	-	-	-	90%	10%	-	-
3	-	-	83%	17%	-	-	-	81%	19%	-
4	-	-	-	78%	22%	-	-	-	76%	24%
5	-	-	-	-	100%	-	-	-	-	100%

* Maintenance intervention count

An overview of the condition state of all components at $t=5$ is provided in Table 3. These are estimated using the condition states at $t=0$ and multiplying them with the probability of them transitioning from their initial state into the possible future states within 5 years.

Table 3. An overview of the condition state of the components at $t=5$.

Component	CS				
	1	2	3	4	5
Foundations	0%	93%	5%	2%	0%
Piers	0%	0%	48%	35%	17%
Abutments	0%	80%	16%	4%	0%
Masonry arches	0%	0%	46%	36%	18%
Spandrel-walls	0%	0%	50%	34%	16%
Deck	0%	0%	56%	32%	12%
Railing & Safety walkway	35%	56%	8%	1%	0%

3.3 Component-level interventions and intervention strategies

Interventions are executed on components to ensure they continue to function as expected. These interventions are defined individually for each component category in response to the severity of the observed damage. An example of intervention definitions for piers is shown in Table 4, which is defined using two sources (Adey & Hajdin, 2011; VICROADS, 2018). Three generic labels are given, i.e., rehabilitation, renewal, and replacement, to reflect the increasing effort and work required for interventions of each type (Adey & Hajdin, 2011).

Table 4. An example of the intervention definitions for the piers.

Intervention type	Activities
Rehabilitation	Fill out cracks and spalls with mortar or epoxy grouting; concrete protection coating.
Renewal	Renew concrete & reinforcement damaged; strengthen the pier; protection coating.
Replacement	Replacement of part or the whole pier.

The costs associated with these component-level interventions are estimated in terms of the owner and user costs. The owner unit costs are roughly estimated based on the values mentioned in Swiss Construction Price Index (Federal Statistical Office, 2021). The user costs are estimated in terms of the added travel time due to taking alternative connections. It is estimated that the closure of the bridge will increase the travel time by 8 minutes. The unit user cost is estimated based on the average wage, i.e., almost 43 mu/h (Federal Statistics Office, 2020). The total cost associated with an increment in the travel time varies as a function of the number of passengers. The average train occupancy in Switzerland, i.e., 50% occupancy, is considered to estimate the number of affected passengers. The total user costs are estimated as 86'232 mu/day (Equation 1).

$$\text{Daily user costs} = \text{Average number of passengers per day} * \text{average wage}(\mu/h) * \text{added travel time per passenger (h)} \quad (1)$$

An overview of the intervention costs for the piers is shown in Table 5, which indicates, the more advanced and labour-intensive the activity, the more investment is needed. The owner and user costs for other components are estimated as with the pier interventions.

Table 5. An example of intervention costs for piers of the example masonry bridge.

Intervention type	Unit owner cost (mu/m ³)	Volume (m ³)	Duration of the service disturbance (weeks)	Owner cost (mu)	Service disturbance costs (mu)
Rehabilitation	290	11.3	0	3'289	172'465
Renewal	570	11.3	1	6'464	344'929
Replacement	1'100	11.3	2	12'474	603'626

The execution of these interventions does not necessarily restore the condition of the components to a like-new state. The intervention effectiveness for different components is estimated using different sources (Adey & Hajdin, 2011; Martins et al., 2004; VICROADS, 2018).

The intervention strategy selected for the components, along with the effectiveness of the interventions is shown in Table 6. No intervention is needed when the component is in condition state 1 and 2, whereas a replacement is needed when the component is in condition state 5. For condition states 3 and 4, rehabilitation and renewal interventions are carried out respectively, and the values in the table correspond to the effectiveness of these interventions. For example, when a rehabilitation intervention is executed on a component in condition state 3, there is an 85% chance that the component will be in condition state 1 at the beginning of the next year.

Table 6. An example intervention strategy for a bridge component with the effectiveness of interventions.

Condition state	Intervention type	CS1	CS2	CS3	CS4	CS5
1	Do nothing	-	-	-	-	-
2	Do nothing	-	-	-	-	-
3	Rehabilitation	85%	15%	-	-	-
4	Renewal	80%	20%	-	-	-
5	Replacement	100%	-	-	-	-

3.4 Failure risks between $t=6$ and $t=10$ and $t=11$ and $t=15$

As long as the component-level intervention strategies are followed, and there are no changes to the expected loading of the bridge, it can be assumed that failure risks are within the acceptable thresholds that are set by the asset managers, and the consideration of these thresholds can be omitted from the analysis for planning future interventions. If, however, interventions are going to be postponed beyond the time suggested by the component-level intervention strategies the probability and consequences of the bridge not functioning as intended. Two fault trees are developed to approximate the consequences associated with the failure of the bridge to provide the required level of service, while components are in different condition states. The associated top events, i.e., restricted service and interrupted service, are defined based on the severity of the bridge failure which is a function of the severity of component failures. In the former, rehabilitation interventions are executed during night closures, and in the latter, replacement interventions are conducted during a period that includes total closure of the bridge for a certain time. The basic events are defined to include gradual and sudden deterioration events. These events can occur due to a combination of external loads, e.g., traffic loads and excessive loads due to natural hazards.

Figure 3 shows the fault trees developed for the interrupted service.

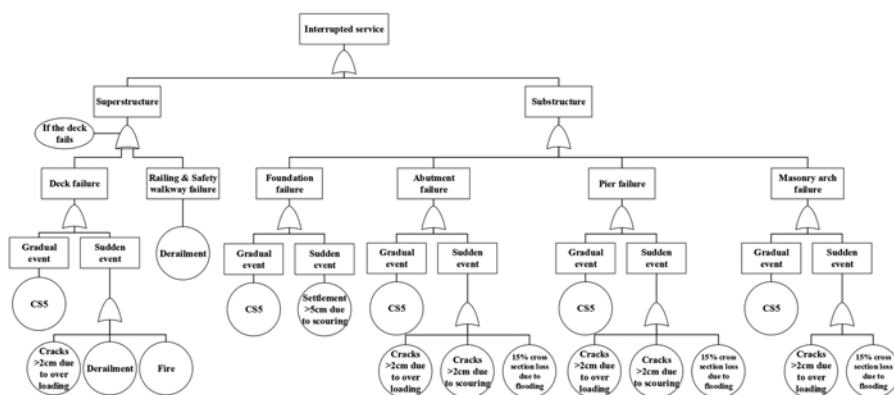


Figure 3. An example fault tree for interrupted service on the masonry bridge.

The probability of failure of each component is estimated as a function of the occurrence probability of each basic event, which in turn is estimated as a function of the probability of imposition of external loads and the resistance of the components. The probability of the imposition of the excessive loads does not depend on the condition state of the components and their annual occurrence probability was estimated using expert opinion. The resistance of the component, however, depends on its geometric and material properties. This resistance changes over time as a function of its condition state. Table 7 shows the considered occurrence probabilities of basic events, where it is less likely that basic events occur when a component is in condition state 1 and it is very likely to occur when the component is in condition state 5. These estimations were used to quantify the probability of failure of each component. The occurrence probability of each top event is estimated using the failure probability of the components.

Table 7. An example of occurrence probabilities of basic events.

Condition state	The annual occurrence probability of each basic event	Assumed probability of occurrence of basic event
1	Very low	0.001%
2	Low	0.01%
3	Medium	0.02%
4	High	0.05%
5	Very high	0.1%

The occurrence of each top event has different consequences. The consequences vary as a function of the amount of work needed to recover the required level of service. The values of required service disruptions and intervention costs are calculated using the information in section 3.3.

The estimates of failure risks as a function of the component behaviour enable the setting of a threshold on the value of additional failure risk that would trigger an intervention, especially in case component-level strategies are for some reason not set. Considering such a threshold also enables obtaining a meaningful overview of the component-level intervention requirements and eliminates the possibility of requiring intervention on different components every year. In this study, the tolerable failure risk threshold was set as the value of failure risks when all components are in CS4. Figure 4 shows the evolution of the failure risks over time for the studied bridge. It is shown how triggering interventions can be dependent on the level of failure risks, given the tolerable failure risk threshold.

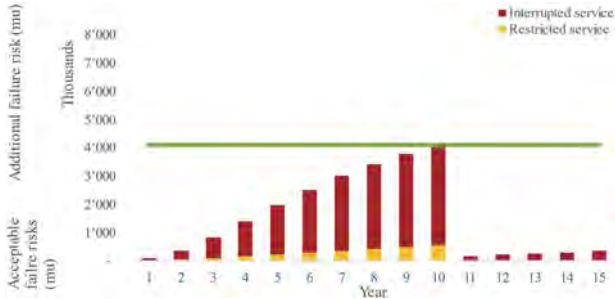


Figure 4. The evolution of the failure risks over time considering a failure risk threshold.

4 MOST LIKELY INTERVENTIONS

The intervention requirements are estimated for the initial phases of the intervention planning process, i.e., 6-15 years ahead of the execution time. Therefore, three planning periods are defined, i.e., 1-5, 6-10, and 11-15, where it is assumed that no interventions are planned for years 1-5 since decisions related to this planning period have already been made. The intervention requirements for the future planning periods are predicted using the intervention strategies determined in section 3.3 and the deterioration rate estimated in section 3.2. Interventions are scheduled to be executed on a component when the failure risks approach the defined failure risk threshold. Table 8 represents detailed information associated with the intervention requirements with the highest probability in the second planning period along with the expected costs and impacts on the service. The execution of this intervention on the

Table 8. The most probable intervention in the future planning periods.

Planning period (expected execution year)	Component	Likelihood of requiring inter- vention (%)	Intervention type	Expected duration	Expected effects on service (weeks) if done alone*			Expected intervention costs (×103 mu)
					None	Restrictions on the traffic	Closure	
11-15 (year 11)	Piers	46	Replacement	51	30	14	7	616
	Abutments	25	Rehabilitation	23	14	7	2	293
	Deck	36	Replacement	64	30	14	20	1'861
	Masonry arches	48	Replacement	57	30	7	20	1'939
	Spandrel-walls	44	Replacement	18	14	4	0	433
	Railings + Side walkway	25	Rehabilitation	3	2	1	0	101

* This table is to serve as a starting point for discussions as to what exactly will be required for the bridge.

piers of this bridge will require 51 weeks to be complete such that the traffic needs to be disrupted for a week, followed by two weeks of service restriction during the execution.

5 CONCLUSIONS

This paper proposed a systematic and digital methodology to make early estimates of future bridge interventions their costs, required possession times and associated risks. The methodology was tested in a case study to provide a detailed overview of intervention requirements for a masonry bridge with a length of 50.88 m in Switzerland. The main novelty of the methodology proposed in this study is in focusing on components instead of assets, and the use of fault trees to estimate the condition state dependent failure risks, since the systematic consideration of failure risks associated with the level of service is missing in existing bridge management systems (Mirzaei et al., 2014). The proposed methodology considers the aspects that are important to bridge managers.

To ensure compatibility with existing practice, the current condition state, the condition evolution, and plausible intervention strategies were estimated to be used in a five-state model with probabilities of transitioning between states over time. The failure risks of the bridge were estimated using fault trees considering two top events associated with the severity of the traffic disturbance. The failure probabilities were estimated as a function of the condition state of the components. The consequences of top events were calculated considering the owner cost of interventions and user costs due to service disruption.

Future studies should focus on the implementation of the proposed methodology to plan the component-level interventions for all assets in a network in both simulated and real planning processes to assess the improvements in efficiency and effectiveness of the proposed digital methodology.

REFERENCES

- Adey, B. T., & Hajdin, R. 2011. Methodology for determination of financial needs of gradually deteriorating bridges with only structure level data. *Structure and Infrastructure Engineering*, 7(7–8), 645–660.
- Adey, B. T., Hajdin, R., & Brühwiler, E. 2015. Optimal intervention strategies for multiple bridges during catch-up periods using age equivalents. In *Advances in Bridge Maintenance, Safety Management, and Life-Cycle Performance, Set of Book & CD-ROM* (pp. 685–686). CRC Press.
- Adey, B. T., Herrmann, T., Tsafatinos, K., Luking, J., Schindele, N., & Hajdin, R. 2012. Methodology and base cost models to determine the total benefits of preservation interventions on road sections in Switzerland. *Structure and Infrastructure Engineering*, 8(7), 639–654.
- Burkhalter, M., & Adey, B. T. 2022. Assessing the Effects of Closure-Free Periods on Railway Intervention Costs and Service. *Journal of Infrastructure Systems*, 28(3).
- Federal Statistical Office. 2021. *Baupreisindex* <https://www.bfs.admin.ch/bfs/de/home/statistiken/preise/baupreise/baupreisindex.assetdetail.20404732.html>
- Federal Statistics Office. 2020. *Swiss Earnings Structure Survey in 2018*. <https://www.bfs.admin.ch/bfs/en/home/statistics/catalogues-databases/press-releases.assetdetail.11927347.html>
- Kim, S., Ge, B., & Frangopol, D. M. 2022. Probabilistic Optimum Bridge System Maintenance Management Considering Correlations of Deteriorating Components and Service Life Extensions. *ASCE-ASME Journal of Risk and Uncertainty in Engineering Systems, Part A: Civil Engineering*, 8(3).
- Martani, C., Adey, B. T., & Wenk, K. 2021. Determining optimal intervention strategies for bridges considering both gradual deterioration and sudden events. In *Life-Cycle Civil Engineering: Innovation, Theory and Practice* (pp. 1071–1076). CRC Press.
- Martins, F., Brito, J., & Branco, F. 2004. *Maintenance Strategies in Stone Masonry Railway Bridges*.
- Mirzaei, Z., & Adey, B. T. 2015. Investigation of the use of three existing methodologies to determine optimal life-cycle activity profiles for bridges. *Structure and Infrastructure Engineering*, 11(11), 1484–1509.
- Mirzaei, Z., Adey, B. T., Klatter, L., Thompson, P. D., & Klatter, L. 2014. Overview of existing Bridge Management Systems, *June 2014*.
- Tserng, H. P., Samuel, Y., Yin, Y.-L., & Chung, C.-L. 2009. Maintenance Strategy for Bridge Components on the Basis of Performance. *Journal of Performance of Constructed Facilities*, 23(4), 234–243.
- VICROADS. 2018. *Bridge Maintenance and Repair Manual*. VICROADS ASSET SERVICES STRUCTURAL TECHNOLOGY AND ASSETS. <https://www.vicroads.vic.gov.au/business-and-industry/technical-publications/bridges-and-structures>

Estimation of bridge component condition states with varying data availability

S. Chuo, B.T. Adey & H. Mehranfar

Institute of Construction and Infrastructure Management, ETH Zürich, Zürich, Switzerland

S. Moghtadernejad

Construction Research Centre, NRC Canada, Ottawa, Canada

ABSTRACT: For computer systems to estimate the type and timing of future interventions on a bridge, and more specifically, on its components, it is important for the bridge managers to understand their current condition states. That information, however, is almost never perfectly available. In this paper, a methodology is developed that accounts for the scenarios of having no or partial inspection data on the bridge components. A Bayesian network is used to estimate the probabilistic condition states of an asset, requiring the utilization of information that is external to an inspection campaign, including the component properties and environment. With partial information available on the bridge and/or component condition state, the Bayesian network takes advantage of the inference capability to draw conclusions on the condition state of interest. The methodology is used to estimate the condition of a railway bridge pier located in Switzerland.

1 INTRODUCTION

Detailed bridge inspections in many countries are usually carried out routinely every five to six years by qualified engineers, where the component condition is described in an inspection report if damages are observed, and an overall bridge condition state is recorded and archived in an internal digital bridge management database. There are two main challenges with using this information to estimate when future interventions might be required: (1) lack of consistencies in the assessment and documentation of condition states for all bridges and their components, such as the information recorded (description of damage vs. numerical condition state) and the platform used (paper-based vs. digital database), and (2) sporadic historical data available through various points in time. This makes it difficult for bridge managers to coordinate activities efficiently and effectively with other stakeholders, including network developers for development interventions, capacity managers for rail traffic scheduling, other asset managers for affected infrastructure objects, and project and production managers for intervention execution. This is especially difficult as the planning of many infrastructure interventions occurs at least 15 to 20 years ahead of time. When the condition state is not known for a bridge component of interest, or there is little confidence in the existing record, bridge managers must request detailed inspection to be performed in order to evaluate the current condition state of the bridge component. Before detailed investigations are ordered it would be useful for bridge managers to be able to make the best estimates of the condition state possible considering all information at their disposition.

With this in mind, this paper contains a methodology to be used to make estimates of the condition state of all bridge components at the current time. The methodology enables the use of different levels of data and can be used to make estimates when no data is available on the condition of the components themselves, but on other explanatory variables. The paper demonstrates how the methodology works by using it to estimate the current condition state of a pier component of a railway bridge in Switzerland. It is an essential component in helping to exploit digitalization in the intervention planning process (Adey 2019, Burkhalter and Adey 2022).

2 OVERVIEW OF METHODOLOGY

The spectrum of data availability to be used to estimate the condition state of bridge components ranges from none to knowing the exact current condition state. There are three levels of condition data availability: (1) no inspection data available on the bridge and on the components of the bridge, (2) partial inspection data available on the bridge and/or on the components of the bridge, and (3) all inspection data available on the condition of the bridge components.

In level 1 where no condition data is available, information that can be used to approximate the condition state needs to be extracted from sources external to those included in an inspection campaign. This information is then used in a Bayesian network to estimate the probable condition states the asset. The Bayesian network makes use of engineering judgment considering design concerns, such that the design variables (e.g., construction year, location, geometry, loading, etc.) serve as explanatory variables (Chang *et al.* 2017). When there is a lack of available inspection data, evident explanatory variables are used as influencing factors to infer the condition state of the component directly. This is different from the use of deterministic physics-based models, which require considerable computation power and simplifying assumptions, and uncertainties are generally not accounted for (Prakash *et al.* 2020). In level 2 where partial data is available, there are several sub-levels which depend on the exact information available. The Bayesian network takes advantage of the updating and inference capability to draw conclusions on the current condition state.

The proposed methodology is demonstrated using an example railway bridge as shown in Figure 1, which consists of the following components: trusses, girders, bearings, abutments, foundations, and the pier. Five condition states are used to describe the different levels of damage of the components, as well as indicators to reflect the specific details that each condition state entails. A condition state of 1 indicates the component is as good as new, with no measurable and observable defects, while condition state 5 suggests that the component has a high probability of requiring an emergency intervention. Structural failure (e.g., collapse) is not considered, as the focus is on serviceability and it is assumed that management teams will detect any problems and request emergency interventions as soon as something alarming is detected, making the probability of structural failure negligible. The methodology is demonstrated in detail using the pier of the example railway bridge.



Figure 1. Illustration of the example railway bridge.

3 ESTIMATION OF CURRENT CONDITION STATE WITH NO CONDITION DATA

3.1 General

In the absence of condition data, estimates have to be made using data that is not normally in an asset management database. This requires the estimation to be based on information coming from either other internal sources (e.g., construction blueprints) or external sources (e.g., traffic frequency). The identification of influencing factors establishes factors and their proxies as indicators to the condition state of the component. These factors may be estimated through regression analysis to model the relationship between dependent and independent variables, to predict based on said relationship, and to infer causality. With lack of sufficient data to support the analysis, expert opinions could be used to provide initial estimation.

For the example bridge pier, the following four influencing factors are identified: pier age, traffic dynamic force, river discharge, and pier geometry. The values of these factors, either

alone or in combination with one another, are likely to be correlated with the condition state of the pier. Together they can be included in a Bayesian network that represent their conditional dependencies as a probabilistic graphical model, as shown in Figure 2.



Figure 2. Bayesian network of pier condition state.

The pier age factor represents the length of time the pier has been in operation since construction. It is correlated with condition because gradual deterioration of the pier materials overtime would lead to worsening condition state. That is to say that without any sudden impact (e.g., boat collision, scour from an extreme flood) in the past and no maintenance interventions throughout its life, the gradual deterioration would ensure that a pier that has been in operation for 60 years would be in a worse condition state than the same pier in an identical environment that has been in operation for only 10 years. This factor does not, however, consider the maintenance history. If maintenance history is known this would be handled in the partial inspection information scenario.

The traffic dynamic force factor represents the repeated axial loading on the pier itself, as trains operate over the bridge carrying passengers and cargo across the river. The effect of cyclic loading on the pier is transferred from the kinetic movement of the trains onto the railway tracks and to the girders beneath, through the bearings, and finally to the substructure including the pier. The stronger and more frequent the loading, the greater damage it would cause to the pier, thus reducing the carrying capacity of the component and the bridge overtime.

The pier in this example is located in the middle of the Aare river in the canton of Bern, Switzerland. In a study that examined over 500 bridge failures between 1989 and 2000, it was found that over 50% of the failures can be attributed to hydraulic factors, which include flood and scour (Wardhana and Hadipriono 2003). As such, scour is identified as a dominant factor that could influence the pier condition state. Scour is a complex process, but can be examined from the perspective of hydraulic, geotechnical, and structural aspects (Wang *et al.* 2017). While the soil bed materials can vary between different parts of a river stream (i.e., upstream and downstream), the bed composition may not be uniform across the cross-sectional depth. Therefore, the geotechnical aspect is not considered, and the hydraulic and structural factors are represented by river discharge and pier geometry, respectively.

In a Bayesian network as shown in Figure 2, the size of the conditional probability table for the child node grows exponentially with increasing number of parent nodes (Diez 1993). For example, in a Bayesian network of five nodes each having three discrete states, with four parent nodes and one child node, a total of 3^5 (i.e., 243) conditional probabilities would need to be defined for the child node. This results in an unrealistic implementation in practice as it requires tremendous cognitive capacity from subject matter experts to provide consistent and dependable results across all possible combinations (Werner *et al.* 2017, Barons *et al.* 2022).

This is a significant challenge given the current structure of the Bayesian network, as the estimation of condition state needs reliable conditional probabilities to infer the component condition state. A comparable problem has been addressed in a methodology that developed a Bayesian network to represent masonry railway bridge condition using bridge components, where the substructure (supports) includes abutments and wing walls, and the bridge deck includes the barrel arch, face rings, parapets, and spandrel walls (Rafiq *et al.* 2015). Their research determined a set of weights to quantify the relative strengths of the influences of the parent nodes (condition states of the bridge components) on the child node (condition state of the bridge), based on the Structures Condition Marking Index (SCMI) developed by Network Rail, the owner and operator of rail infrastructure network across Great Britain. A set of probability

distributions are subsequently assigned to the parent and child nodes to derive the conditional probability table for the child node. While there are similarities between the application of their methodology and this work, their research focused on the estimation of condition state for the bridge while having complete data on the parent nodes, and this work is focused on the estimation of bridge component condition states without complete data on the parent nodes.

The following sections present an objective and efficient process to elicit child node conditional probabilities through an improved methodology for the context of this research, focusing on capturing the expert opinions while maintaining their coherence, as well as generating possible combinations of values using the Monte Carlo simulation. Figure 3 outlines the steps required to develop the final conditional probability table in a Bayesian network.

The first step, which is already complete, is where the Bayesian network is developed for pier condition state based on the four identified influencing factors as explanatory variables, as shown in Figure 2. The description of the remaining steps in the process will use the developed Bayesian network to provide detailed description and direction on the implementation.

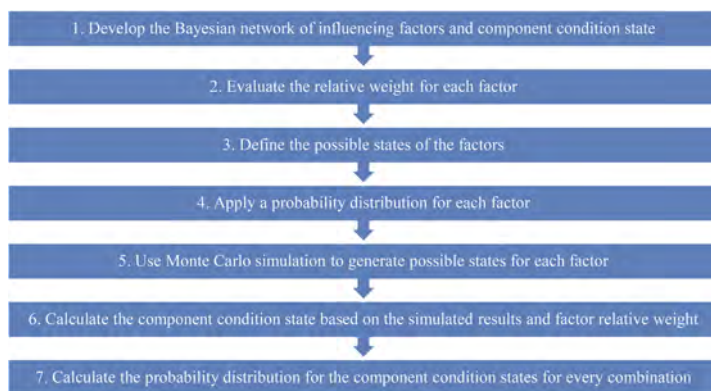


Figure 3. Process to develop the conditional probability table for a Bayesian network child node.

3.2 Relative weights of influencing factors

While the four influencing factors as shown in Figure 2 affect the condition state of the pier either individually or in combination with each other, their scale of impact may be different. This means that certain factors could be more strongly correlated with component condition state than others. To capture the potential difference in influencing factor impact, instead of assuming equal weights for each of the factors, their relative weights are evaluated. Without sufficient data to support regression analysis, which is assumed here the case for illustrative purposes, expert opinion is relied on to facilitate the initial estimation, where the analytic hierarchy process (AHP) is used to quantify the relative weights of the factors through pair-wise comparisons (Saaty 1990). With this approach, two factors are compared with each other at a time, until all possible pairs have been analysed. Table 1 shows the results from the comparisons using the AHP and summarises the final calculated relative weight for each influencing factor. The consistency ratio is 0.0107 (Alonso and Lamata 2006), confirming that the subjective evaluation of the pair-wise comparison is consistent and therefore statistically rational.

Table 1. Pier factor relative weight using the AHP.

Criteria	Pier age	Traffic force	River discharge	Pier geometry	Relative weight
Pier age	1	5	3	7	0.579
Traffic force	1/5	1	1/2	2	0.121
River discharge	1/3	2	1	4	0.233
Pier geometry	1/7	1/2	1/4	1	0.067

3.3 Factor states

The factor states are proxies that describe the different possible input variables that could affect the component condition state. This addresses the problems when (1) there is no quantified value associated with the condition state (e.g., pier geometry), and (2) when there is uncertainty associated with the quantified value of the influencing factor (e.g., traffic force). Similar to how the component condition is classified under five categories of increasingly worse state from 1 to 5, the factors are also classified on an ordinal scale according to their contribution to increasingly worse component condition states. The level of detail for each of the factor is low enough where the differences between each state would not be significant, but high enough where the states can be distinguished from one another.

3.4 Factor probability distribution

In order to simulate different combinations for the possible states of the pier influencing factors (e.g., the pier in the second quartile life, low traffic force, medium discharge level, and bad pier geometry), a probability distribution is assigned to each factor. It is assumed that all four factors are represented by a uniform distribution, meaning all states have an equal likelihood of occurrence. The choice of distribution can be updated when there is supporting data available (Molnar *et al.* 2006, Sobanjo *et al.* 2010). When a random number is generated between 0 and 1, this allows for the classification of the factor state according to the definition of the state itself and the range of values associated with it. Table 2 lists the possible states for each of the influencing factors for the pier, as well as the range for each possible state of the factors on an ordinal scale.

Table 2. Possible states of the pier factors and the ranges of factor states.

Pier life		Traffic force / River discharge		Pier geometry		Pier condition	
States	Range	States	Range	States	Range	States	Range
1 st quart.	0 – 0.25	Low	0 – 0.33	Good	0 – 0.5	1	0 – 0.2
2 nd quart.	0.25 – 0.5	Medium	0.33 – 0.67	Bad	0.5 – 1	2	0.2 – 0.4
3 rd quart.	0.5 – 0.75	High	0.67 – 1			3	0.4 – 0.6
4 th quart.	0.75 – 1					4	0.6 – 0.8
						5	0.8 – 1

3.5 Monte Carlo simulation

In principle, the determination of the component condition state based on various combinations of factor states could be deterministic. However, given the complexity of the model, the Monte Carlo simulation can easily generate random numbers based on the assumed statistical distributions for the component influencing factors, and then compute the resultant condition state without much difficulty. It is important to note that the random numbers are independent for every simulation across the different influencing factors.

3.6 Component condition state

The component condition state is computed based on the pier factor relative weight as determined previously in Table 1. Applying the relative weights from Table 1 where the AHP method was used, Equation 1 is used to determine the final condition state:

$$CS_P = 0.579(S_A) + 0.121(S_T) + 0.233(S_R) + 0.067(S_G) \quad (1)$$

where CS_P is the pier condition state, S_A , S_T , S_R , and S_G represent the state for the pier age, traffic force, river discharge, and pier geometry, respectively. The states from the four influencing factors are the simulated results from the Monte Carlo simulation, where a number between 0 and 1 is randomly and independently generated.

When the pier condition state is computed, its value is transformed to a scale of 1 to 5, where condition state 1 means the component can perform its intended function at full capacity with no structural or cosmetic damage, while condition state 5 means it is no longer safe to continue using the component, thus disrupting the required level of service. A uniform distribution is considered in the conversion of calculated condition state into the linear scale of 1 to 5, as shown in Table 2.

3.7 Component conditional probability table

After running 50,000 simulations, the probability distribution for the component condition state can be evaluated for every possible combination considering the effect of all the influencing factors. This allows for the elicitation of the conditional probability table given that all the combinations are generated through the Monte Carlo simulation. For example, with the combination of having a bad geometry, medium discharge, second quartile life, and low traffic, the probability for the pier condition state from 1 to 5 can be calculated, as summarised in Table 3.

Table 3. Probability distribution of an example pier factor combination.

Combination	Number of results	Probability
B-M-S-L-1	0	0
B-M-S-L -2	22,761	0.455224
B-M-S-L -3	27,239	0.544776
B-M-S-L -4	0	0
B-M-S-L -5	0	0

4 ESTIMATION OF CONDITION STATE WITH PARTIAL INSPECTION DATA

In the database that manages the example bridge, the bridge condition states are recorded as an overall discrete value on a scale from 1 to 5. Despite the inspection reports describing the damages that are observed on the component level, they are not converted into the same numerical scale. This means that when there are partial data available, specifically the availability of the bridge condition state, it can be used in the estimation of the component condition state. This is done by developing another Bayesian network, such that the bridge condition state is a function of the condition state for each of the six components. The structure of the relationship is shown in Figure 4, where the bridge condition state is the child node in the Bayesian network, and the six bridge components are the contributing parent nodes.



Figure 4. Bayesian network of bridge condition state.

In this network, each node contains five discrete states, as such the conditional probability table for the bridge condition state requires a total of 5^7 (i.e., 78,125) conditional probabilities. This Bayesian network is different from the one developed for the component condition state as shown in Figure 2 such that the process to elicit probabilities could be simplified, therefore the methodology is not the same between these two networks. In this case, a policy is put in place to determine the bridge condition state given the combination of the component condition state, where the bridge condition state is the worst condition state out of any of the component condition states. For example, if all the components are in condition state 2 except for the girders which are in condition state 4, then the overall bridge would be in condition state 4 as well. This rationale is in line with the assumption that the failure of any one of the components to provide service would inevitably result in the failure of the bridge to provide service (Faber *et al.* 2000).

In terms of having partial information, there are several possible scenarios that could be evaluated, where they make use of: (1) known condition state of the bridge, (2) known condition state of other bridge components, and (3) external information as described in Section 3. This means the Bayesian network for estimating the current condition state with no inspection data (i.e., Figure 2) would be incorporated into the Bayesian network for estimating the current condition with partial inspection data (i.e., Figure 4). The known information in combination with each other creates a more detailed estimation of the current pier condition state compared to relying only on the known bridge condition state or external information, and this allows for a better planning of future maintenance interventions. For example, five scenarios are considered as outlined in Table 4, and their comparisons are summarised in Table 5, where the pier condition state probabilities are shown given different levels of granularity of known information.

Table 4. Levels of available information.

Scenario	Available information		
	Bridge condition = 3	Abutment condition = 2 Bearing condition = 1	Pier life = 2 nd quartile Traffic = low Geometry = bad Discharge = medium
1	✓		
2	✓	✓	
3			✓
4	✓		✓
5	✓	✓	✓

Table 5. Probability distributions of the pier condition state given known information.

Pier condition state	Scenario 1	Scenario 2	Scenario 3	Scenario 4	Scenario 5
1	0.317	0.292	0	0	0
2	0.317	0.292	0.455	0.42	0.37
3	0.365	0.415	0.545	0.58	0.63
4	0	0	0	0	0
5	0	0	0	0	0

With the fifth scenario using the largest amount of available information out of all the options, its estimation would provide the highest level of confidence given the input data is accurate. This is naturally contingent on the Bayesian network adopting a structure (i.e., relationship between the nodes) and parameters (i.e., weights between the nodes) that adequately reflect the behaviour of the bridge component in estimating its condition state. Nevertheless, the methodology presented heretofore is able to adapt and manifest the level of granularity desired, as well as revise according to the latest understanding of bridge performance and deterioration.

5 CONCLUSIONS

The results of this work help better estimate the current condition states of bridge components based on different levels of inspection data availability, which is essential in using computer software to predict future deterioration and estimate when likely interventions are required on bridges. A Bayesian network is developed that uses information external to an inspection campaign to estimate the probabilistic condition states, where four influencing factors are identified for the example bridge pier. Different combinations of available partial information are also demonstrated, where the condition state of the bridge, condition states of other components of the bridge, and the four influencing factors allow the example bridge pier to be evaluated with

a higher level of confidence compared to the results from any one of the three known available information acting alone. The methodology in this paper supports the existing intervention planning process, where the results would contribute towards the initial estimation of interventions required, which is done 15 to 20 years before planned execution.

There is a couple of limitations in this work that will be addressed in the future. Firstly, given more information could be made available regarding the most likely state for each factor, other probability distributions may be more suitable to reflect the inherent properties of the factors. This would essentially affect the probability that each state would be generated through simulation, and ultimately affect the calculation of the component condition state towards developing the final conditional probability table, as shown through the proposed methodology in Figure 3. Secondly, in this work the bridge condition uses the worst element model, however, risk-based methodology could be implemented for the assessment of bridge condition as a function of the elements that make up the bridge. This means that the structure of the Bayesian network as shown in Figure 4 would remain the same, but the parameters of the component-bridge relationship would need to be updated according to the determined risk class of the bridge element.

ACKNOWLEDGEMENTS

This research project is supported by the ETH Mobility Initiative and the ETH Zurich Foundation.

REFERENCES

- Adey, B.T., 2019. A road infrastructure asset management process: gains in efficiency and effectiveness. *Infrastructure Asset Management*, 6 (1), 2–14.
- Alonso, J.A. and Lamata, M.T., 2006. Consistency in the analytic hierarchy process: a new approach. *International Journal of Uncertainty, Fuzziness and Knowledge-Based Systems*, 14 (04), 445–459.
- Barons, M.J., Mascaro, S., and Hanea, A.M., 2022. Balancing the Elicitation Burden and the Richness of Expert Input When Quantifying Discrete Bayesian Networks. *Risk Analysis*, 42 (6), 1196–1234.
- Burkhalter, M. and Adey, B.T., 2022. Assessing the Effects of Closure-Free Periods on Railway Intervention Costs and Service. *Journal of Infrastructure Systems*, 28 (3), 04022015.
- Chang, M., Maguire, M., and Sun, Y., 2017. Framework for Mitigating Human Bias in Selection of Explanatory Variables for Bridge Deterioration Modeling. *Journal of Infrastructure Systems*, 23 (3), 04017002.
- Díez, F.J., 1993. Parameter adjustment in Bayes networks. The generalized noisy OR-gate. In: D. Heckerman and A. Mamdani, eds. *Uncertainty in Artificial Intelligence*. Morgan Kaufmann, 99–105.
- Faber, M.H., Val, D.V., and Stewart, M.G., 2000. Proof load testing for bridge assessment and upgrading. *Engineering Structures*, 22 (12), 1677–1689.
- Molnar, P., Anderson, R.S., Kier, G., and Rose, J., 2006. Relationships among probability distributions of stream discharges in floods, climate, bed load transport, and river incision. *Journal of Geophysical Research: Earth Surface*, 111 (F2).
- Prakash, G., Yuan, X.-X., Hazra, B., and Mizutani, D., 2020. Toward a Big Data-Based Approach: A Review on Degradation Models for Prognosis of Critical Infrastructure. *Journal of Nondestructive Evaluation, Diagnostics and Prognostics of Engineering Systems*, 4 (2).
- Rafiq, M.I., Chryssanthopoulos, M.K., and Sathananthan, S., 2015. Bridge condition modelling and prediction using dynamic Bayesian belief networks. *Structure and Infrastructure Engineering*, 11 (1), 38–50.
- Saaty, T.L., 1990. How to make a decision: The analytic hierarchy process. *European Journal of Operational Research*, 48 (1), 9–26.
- Sobanjo, J., Mtenga, P., and Rambo-Roddenberry, M., 2010. Reliability-Based Modeling of Bridge Deterioration Hazards. *Journal of Bridge Engineering*, 15 (6), 671–683.
- Wang, C., Yu, X., and Liang, F., 2017. A review of bridge scour: mechanism, estimation, monitoring and countermeasures. *Natural Hazards*, 87 (3), 1881–1906.
- Wardhana, K. and Hadipriono, F.C., 2003. Analysis of Recent Bridge Failures in the United States. *Journal of Performance of Constructed Facilities*, 17 (3), 144–150.
- Werner, C., Bedford, T., Cooke, R.M., Hanea, A.M., and Morales-Nápoles, O., 2017. Expert judgement for dependence in probabilistic modelling: A systematic literature review and future research directions. *European Journal of Operational Research*, 258 (3), 801–819.

State-of-the-art in the use of responsive systems for the built environment

Jiaqi Suo & Claudio Martani

Laboratory for Future-Ready Infrastructure (FuRI Lab), School of Construction Management Technology, Purdue University, West Lafayette, USA

Antoine G. Faddoul, Sneha Suvarna & Venkata K.T. Gunturu

School of Construction Management Technology, Purdue University, West Lafayette, USA

ABSTRACT: The built environment consists of construction and infrastructure that are called to provide the required services for a long stretch of time, often decades. If they fail to do so, the consequences for society can be very severe. Over this time horizon, assets are exposed to variable conditions that influence their performance, e.g. roads are confronted with a volume of traffic that is largely variable both on the short-term, i.e. hourly variation between pick and off-pick times and in the long-term, i.e. trend of demand over decades. Under such variable operation conditions, static construction and infrastructure cannot guarantee an acceptable level of service all the time, e.g., a road with a fixed capacity cannot guarantee to be adequate in peak hours and efficient in off-peak hours. Variable operating conditions require a responsive built environment able to adapt accordingly to provide an effective and efficient response. Recent developments in sensing technologies, actuating systems, and the IoT have explored the potential for the use of responsive systems to optimize the service provided by built environments operating under variable conditions. Some examples include automatically controlled buildings' lighting and fencing, as a function of the outdoor sun exposure, and road line capacities, as a function of the traffic demand. Despite some examples of responsive systems, there is still a lack of systematic analysis of their use in infrastructure and construction. This lack prevents a full understanding of the current capabilities of a responsive built environment is presented. In this work a systematic analysis of the most cutting-edge use of responsive systems for the built environment - in terms of sensing technologies, actuating systems, and triggering logics - and possible future developments are outlined.

1 INTRODUCTION

Infrastructures are built to operate over a long-life span, often decades, under variable conditions. As such it is difficult that assets designed to deliver constant performances are able to provide a satisfactory level of service in the long term. This is due to the fact that assets that deliver constant performances are prone to two types of falls: either they have been designed for a standard operational demand, in which case they are undersized for a non-negligible amount of the time they operate (i.e. they are ineffective), or they have been designed for the maximum demand, in which case they are oversized most of the time they operate (i.e. they are inefficient).

To overcome these limitations and maximize both the effectiveness and the efficiency of the built environment, infrastructure should be made responsive. Responsive infrastructures are those that are able to adjust their performance in real-time to adapt to changing environmental conditions, e.g., buildings with a heating and cooling system that adapt their functioning automatically based on the internal temperature sensed. Responsive infrastructures are equipped with systems characterized by three main components: (i) a sensing technology that monitors the environmental conditions that can influence one or some of the services provided by infrastructure (e.g. temperature, lighting,

number of people in an indoor environment, speed of a vehicle on the highway); (ii) an actuator, or response system, that modifies the characteristic or the performance of the infrastructure according to the condition sensed (e.g. a window that automatically opens and closes according to the indoor air quality and outdoor weather conditions); and (iii) an interface that connects the sensing and the actuators through a triggering logic. These components work together to collect, process, and use a large wealth of information to optimize infrastructure performance.

The recent developments in sensing technology (Kumar et al. 2015), the Internet of Things (IoT) (Tang et al. 2019), machine-to-machine (M2M) communications, artificial intelligence (AI) (Seyedzadeh et al. 2018; Ullah et al. 2020), and robotics (Pan et al. 2018), have created the conditions for the development of several applications of responsive systems. Despite the notorious resistance of the construction industry to the adoption of new technologies (Setaki and van Timmeren 2022), these systems have been recently tested and also used on infrastructure of different kinds (Dong et al. 2019; Valena et al. 2021).

Notwithstanding the numerous recent attempts to use sensing and responding systems to optimize the operation of the built environment, to the best of the authors' knowledge, a systematic analysis of these works has not yet been conducted. The lack of a systematic literature review on the subject prevents the scientific community from gaining a full understanding of the current capabilities, gaps, and future perspectives of responsive systems for the built environment. To address this lack, in this paper a systematic literature review is presented on the current development of responsive infrastructure to chart out a roadmap for how sensing technologies, actuating systems, and triggering logic can be used to improve the effectiveness and efficiency of the built environment.

2 ANALYSIS OF THE STATE-OF-THE-ART IN THE USE OF RESPONSIVE SYSTEMS FOR THE BUILT ENVIRONMENT

In this section, the most cutting-edge works on the use of sensing and responding systems in the built environment are analyzed using a systematic method. In sub-section 2.1, the method used to conduct the analysis is first explained, and then, in section 2.2, the results are presented.

2.1 *Method of the analysis*

To analyze systematically the state of the art of research on responsive infrastructure, the relevant scientific publications on the field have been first selected, then classified, and finally analyzed, according to the following logic. Publications were selected based on three criteria. Works: (1) written within the last ten years; (2) that focused on the use of sensing and responding systems; and (3) applied to the operation and management of the built environment. Each publication selected has then been classified according to: (1) the type of responsive system, classified in: artificial, i.e. where changes on the infrastructure are triggered through a predefined logic based on data sensed, or natural, i.e. where changes on the infrastructure are automatically triggered by environmental variations; the (2) sensing technology, classified in: motion, imaging, light, temperature, humidity, distance, moisture, pressure and other sensors, and Wi-Fi connections; (3) response systems, classified in: information (i.e. where no change in the infrastructure is triggered and the only reaction planned is a data recording on critical situations, alert response, i.e. where only an alert signal is triggered in critical situations, an automatic response, i.e. where only a physical change in the infrastructure is triggered in critical situations, and an alert and automatic response, i.e. where both an alert signal and a physical change in the infrastructure are triggered in critical situations); (4) the triggering logic used, classified in: no triggering (i.e. where the systems work without the need for triggering, explicit triggering, i.e. where the triggering logic is reported, and implicit triggering, where the triggering logic exists but is not explained in the paper); along with (5) the maturity of the technology used (i.e. TRL¹); and (6) the specific infrastructure in object, classified in: buildings,

1. Source: <https://esto.nasa.gov/trl/>

dams and irrigation, transportation, and others (e.g. energy distribution infrastructure). Finally, the classified works have been analyzed to identify frequencies, trends, and gaps in the development of responsive infrastructure. This has been done on two levels. Level 1: the frequency distribution of results for each of the 6 classification characteristics has been investigated, e.g. how many works on responsive infrastructure have been published with a TRL7, 8 and 9. The implementation of the frequency distribution of results has required clustering the results of each classification characteristic into categories. See Table 1. Level 2: an interpolation of the most significant level 1 analysis was made to generate a frequency distribution of results for one classification characteristic versus the others, e.g. how many works on responsive buildings specifically have been published with an automatic responding system and a TRL7, 8, and 9.

2.2 Results

The 51 publications selected for the analysis are reported in Table 1 along with their classification characteristics. The results of the 2 levels analysis are further shown in Figures 1 and 2 and discussed.

Table 1. Classification of the selected research on responsive infrastructure.

Reference	Type of sensing and responding system	Infrastructure	Sensing technology	Actuator	Trigger Logic	TRL
(Ni et al. 2012)	Artificial	Building	Imaging Motion	Alert Response	Explicit	7
(Balaji et al. 2013)	Artificial	Building	Wi-Fi	Automatic Response	Explicit	9
(Saad et al. 2013)	Artificial	Transportation	Light Motion	Automatic Response	Explicit	6
(Peng and Qian 2014)	Artificial	Building	Power	Automatic and Alert Response	Explicit	8
(Öörni et al. 2015)	Artificial	Transportation	NEI	Automatic and Alert Response	Implicit	9
(Orrie et al. 2015)	Artificial	Building	Imaging	Alert Message	Explicit	7
(Suryadevara et al. 2015)	Artificial	Building	Power	Automatic Response	Explicit	7
(Li and Mi 2015)	Artificial	Transportation	Others	Automatic Response	Explicit	9
(Madli et al. 2015)	Artificial	Transportation	Distance	Alert Response	Explicit	7
(Dunlop et al. 2016)	Artificial	Transportation	Motion	Alert Response	Explicit	4
(Lakshminarasimhan 2016)	Artificial	Transportation	Motion	Automatic and Alert Response	Explicit	9
(Lee et al. 2016)	Artificial	Transportation	Imaging	Information	N/A	5
(Kanase and Gaikwad 2016)	Artificial	Building	Light	Alert Response	Explicit	2
(Nellore and Hancke 2016)	Artificial	Transportation	Others	Automatic Response	Explicit	6
(Favoino et al. 2016)	Artificial	Building	Temperature	Automatic Response	Explicit	6
(Biloria 2016)	Artificial	Building	Motion Distance	Automatic Response	Explicit	9
(Sharma and Bedi 2016)	Natural	Others	N/A	Alert Response	N/A	9
(Gultom et al. 2017)	Artificial	Dams & Irrigation	Moisture	Automatic Response	Explicit	6
(Vishwas and Ullas 2017)	Artificial	Building	Motion	Automatic Response	Explicit	7
(Aviv 2018)	Artificial	Building	NEI	Automatic Response	Implicit	6
(De Belie et al. 2018)	Natural	Others	N/A	Automatic Response	Explicit	9

(Continued)

Table 1. (Continued)

Reference	Type of sensing and responding system	Infrastructure	Sensing technology	Actuator	Trigger Logic	TRL
(Khan et al. 2018)	Artificial	Transportation	Distance Motion	Alert Response	Explicit	6
(Yang et al. 2018)	Artificial	Transportation	Power	Alert Response	N/A	9
(Perilla et al. 2018)	Artificial	Building	Temperature Humidity Air Quality Motion	Automatic and Alert Response	Explicit	7
(Al-Yemni et al. 2018)	Artificial	Building	Temperature	Automatic Response	Explicit	8
(Alghamdi and Almagwani 2019)	Artificial	Building	Motion Light Temperature	Automatic Response	Explicit	7
(Asthana et al. 2019)	Artificial	Transportation	Temperature Imaging	Automatic Response	Explicit	1
(Hosseini et al. 2019)	Artificial	Building	Light	Automatic Response	Explicit	3
(Wang et al. 2019)	Natural	Building	N/A	Automatic Response	N/A	7
(Ren et al. 2019)	Artificial	Others	Moisture	Automatic Response	Explicit	4
(Toh et al. 2019)	Artificial	Transportation	Wi-Fi	Automatic Response	Explicit	5
(Daniel et al. 2019)	Artificial	Building	Imaging Pressure	Alert Response	Explicit	7
(Lu et al. 2020)	Artificial	Transportation	Light	Automatic Response	Explicit	9
(Niranjan and Rakesh 2020)	Artificial	Building	Others	Automatic and Alert Response	Explicit	7
(Angdresey et al. 2020)	Artificial	Others	Temperature	Information	Explicit	6
(Liu et al. 2020)	Artificial	Others	Temperature	Alert Response	Explicit	6
(Abdulkareem et al. 2021)	Artificial	Building	Temperature Moisture	Automatic Response	Explicit	6
(Aditya et al. 2021)	Artificial	Dams & Irrigation	Distance Pressure	Automatic and Alert Response	Explicit	4
(Ilham et al. 2021)	Artificial	Building	Air Quality	Automatic Response	Explicit	7
(Jiang et al. 2021)	Natural	Building	N/A	Automatic Response	N/A	7
(Laxman and Jain 2021)	Artificial	Building	Pressure Imaging	Automatic and Alert Response	Explicit	6
(P S et al. 2021)	Artificial	Transportation	Motion	Automatic Response	Explicit	6
(Sai Sri Vastava et al. 2021)	Artificial	Transportation	Motion	Automatic Response	Explicit	9
(Saleem and Hosoda 2021)	Artificial	Transportation	Temperature Light	Automatic Response	Explicit	9
(Brintha et al. 2022)	Artificial	Transportation	Motion Distance	Automatic and Alert Response	Explicit	9
(Gnanavel et al. 2022)	Artificial	Dams & Irrigation	Moisture	Automatic Response	Explicit	9
(He et al. 2022)	Artificial	Building	Temperature	Automatic Response	Explicit	6
(Nicholson et al. 2022)	Artificial	Others	Air Quality Motion Temperature Humidity	Information	N/A	7
(Krishnan et al. 2022)	Artificial	Transportation	Temperature Motion Air Quality	Alert Response	Explicit	8
(Christakis et al. 2022)	Artificial	Building	Temperature Humidity Air Quality	Information	N/A	6
(Soudian and Berardi 2022)	Artificial	Building	Temperature Motion	Automatic Response	Explicit	7

From the level 1 analysis (Figure 1), it is possible to appreciate, in terms of technical characteristics, that: most of the works analyzed are based on types of sensing and responding systems; the deployment of these solutions has affected mainly buildings and transport infrastructure; the sensors used are pressure, motion, and temperature sensors in more than half of cases, while the response systems are largely automatic; and that most of the works reported an explicit triggering logic to control the response. Moreover, it is of interest to notice that in about 70% of the cases, the sensing and responding systems are TRL 7 to 9, which means that the vast majority of the works use technologies that are in an advanced stage of development, if not already commercialized.

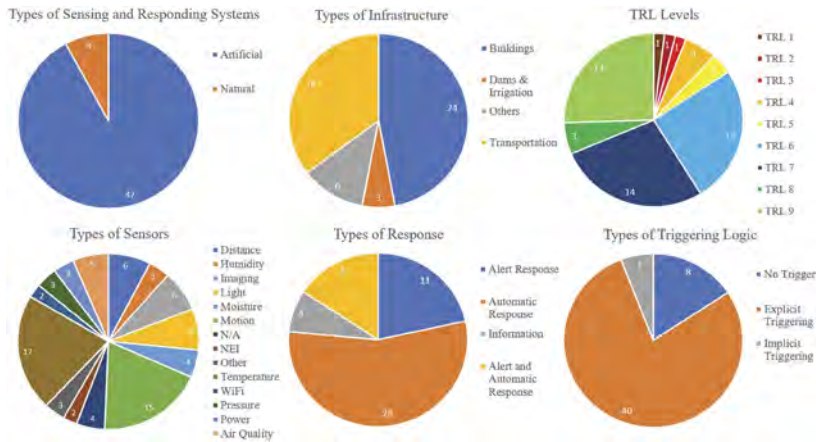


Figure 1. Level 1 analysis of the six classification characteristics.

The level 2 analysis (Figure 2), allows investigating these data deeper, revealing that: (i) in terms of the state of advancement of research, on top of the consolidated technologies, some experimental work, i.e. TRL 1-5 are undergoing mainly to develop alert response and automatic responses on building and transport infrastructure; while (ii) in terms of the type of technology used, the lighting, motion, and temperature sensors, as well as Wi-Fi connections, are largely used mostly in alert and automatic response systems for buildings and transport infrastructure.

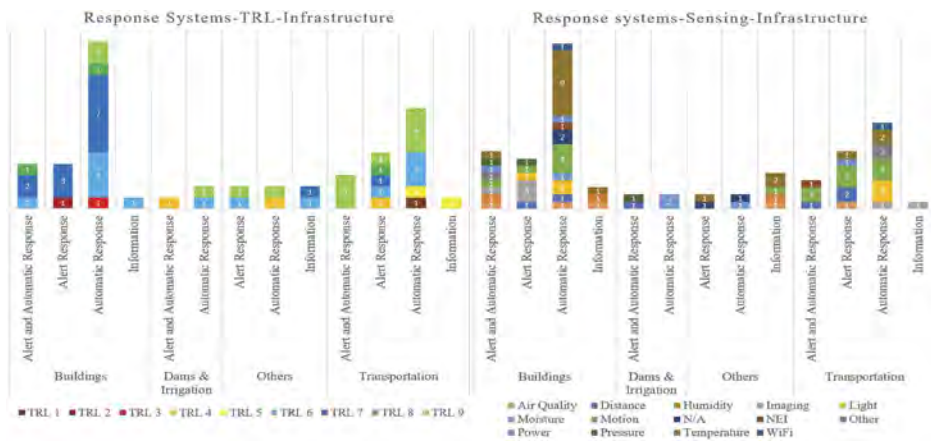


Figure 2. Level 2 analysis of the interpolation between response systems, TRL and infrastructure (left), and response systems, sensing and infrastructure (right).

3 CONCLUSION

A substantial literature exists on the use of sensing and responding systems to optimize the operation of the built environment. The systematic analysis presented in this work shows how the state-of-the-art research in the field has mostly focused on the development of automatic alert response and automatic response systems for buildings and transport infrastructure, although prominent works exist also with respect to dams and irrigation, and other type of infrastructure. This seems to be motivated by the wealth and maturity of the sensing technologies required for optimizing interventions on these assets (i.e. the lighting, motion, and temperature sensors, as well as Wi-Fi connections). Nonetheless, despite the prominent role of the consolidated technologies in the development of a large part of the current applications, some experimental works (i.e. TRL 1-5) are undergoing that use motion, imaging, and distance sensing to develop alert response and automatic response systems, particularly for buildings and transport infrastructure. In the near future, advancements in the use of these environmental and motion sensors are expected to have a high potential for the development of new types of sensing and responding solutions.

REFERENCES

- Abdulkareem, A., T. E. Somefun, V. Oguntosin, and B. O. Adeyemi. 2021. "Design and Construction of a Weather-Based Automatic Sliding Window." *IOP Conf. Ser.: Mater. Sci. Eng.*, 1107 (1): 012179.
- Aditya, V. M. V. S., Ch. T. S. Tanishq, V. C. B. Sai, and S. K. Dhuli. 2021. "IoT and ANN Based Automatic Water Level Monitoring For Dams." *2021 13th International Conference on Computational Intelligence and Communication Networks (CICN)*, 56–60.
- Alghamdi, H., and A. Almagani. 2019. "Smart and Efficient Energy Saving System Using PDLC Glass." 1–5.
- Al-Yemni, A., S. Al-Balam, S. Al-Kulib, and Q. Abu Al-Haija. 2018. "An Arduino based smart faucet design." *Compusoft*, 7: 2752–2754. <https://doi.org/10.6084/ijact.v7i5.718>.
- Angdresey, A., L. Sitanayah, and V. Sampul. 2020. "Monitoring and Predicting Water Quality in Swimming Pools." *EPI International Journal of Engineering*, 3: 119–125.
- Asthana, D., M. Zinaddinov, M. Ushakov, and S. Mil'shtein. 2019. "Cost-Effective Snow Removal from Solar Panels." *2019 IEEE 46th Photovoltaic Specialists Conference (PVSC)*, 1312–1315.
- Aviv, D. 2018. "Adaptive Roof Aperture for Multiple Cooling Conditions."
- Balaji, B., J. Xu, A. Nwokafor, R. Gupta, and Y. Agarwal. 2013. "Sentinel: occupancy based HVAC actuation using existing WiFi infrastructure within commercial buildings." *Proceedings of the 11th ACM Conference on Embedded Networked Sensor Systems, SenSys '13*, 1–14. New York, NY, USA: Association for Computing Machinery.
- Biloria, N. 2016. "Real-time Responsive Spatial Systems: Design Driven Research Experiments in Interactive Architecture." 10.
- Brintha, N. C., C. V. P. Tarun, L. Abhishikth, B. P. K. Rao, and M. T. Reddy. 2022. "Smart Railway Crossing Surveillance System." *2022 International Conference on Computing, Communication, Security and Intelligent Systems (IC3SIS)*, 1–5.
- Christakis, I., G. Hloupis, O. Tsakiridis, and I. Stavrakas. 2022. "Integrated open source air quality monitoring platform." *2022 11th International Conference on Modern Circuits and Systems Technologies (MOCASST)*, 1–4.
- Daniel, O. C., V. Ramsurrun, and A. K. Seam. 2019. "Smart Library Seat, Occupant and Occupancy Information System, using Pressure and RFID Sensors." *2019 Conference on Next Generation Computing Applications (NextComp)*, 1–5.
- De Belie, N., E. Gruyaert, A. Al-Tabbaa, P. Antonaci, C. Baera, D. Bajare, A. Darquennes, R. Davies, L. Ferrara, T. Jefferson, C. Litina, B. Miljevic, A. Otlewska, J. Ranogajec, M. Roig-Flores, K. Paine, P. Lukowski, P. Serna, J.-M. Tulliani, S. Vucetic, J. Wang, and H. M. Jonkers. 2018. "A Review of Self-Healing Concrete for Damage Management of Structures." *Advanced Materials Interfaces*, 5 (17): 1800074.
- Dong, B., V. Prakash, F. Feng, and Z. O'Neill. 2019. "A review of smart building sensing system for better indoor environment control." *Energy and Buildings*, 199: 29–46.
- Dunlop, M. D., M. Roper, M. Elliot, R. McCartan, and B. McGregor. 2016. "Using smartphones in cities to crowdsource dangerous road sections and give effective in-car warnings." *Proceedings of the*

- SEACHI 2016 on Smart Cities for Better Living with HCI and UX*, SEACHI 2016, 14–18. New York, NY, USA: Association for Computing Machinery.
- Favoino, F., F. Fiorito, A. Cannavale, G. Ranzi, and M. Overend. 2016. “Optimal control and performance of photovoltaichromic switchable glazing for building integration in temperate climates.” *Applied Energy*, 178: 943–961.
- Gnanavel, S., M. Sreekrishna, N. DuraiMurugan, M. Jaeyalakshmi, and S. Loksharan. 2022. “The Smart IoT based Automated Irrigation System using Arduino UNO and Soil Moisture Sensor.” *2022 4th International Conference on Smart Systems and Inventive Technology (ICSSIT)*, 188–191.
- Gultom, J. H., M. Harsono, T. D. Khameswara, and H. Santoso. 2017. “Smart IoT Water Sprinkle and Monitoring System for chili plant.” *2017 International Conference on Electrical Engineering and Computer Science (ICECOS)*, 212–216.
- He, Y., H. Zhou, and F. Fahimi. 2022. “Modeling and demand-based control of responsive building envelope with integrated thermal mass and active thermal insulations.” *Energy and Buildings*, 276: 112495.
- Hosseini, S. M., M. Mohammadi, and O. Guerra-Santin. 2019. “Interactive kinetic façade: Improving visual comfort based on dynamic daylight and occupant’s positions by 2D and 3D shape changes.” *Building and Environment*, 165: 106396.
- Ilham, D. N., R. A. Candra, M. S. Talib, M. di Nardo, and K. Azima. 2021. “Design of Smoke Detector for Smart Room Based on Arduino Uno.” *Brilliance: Research of Artificial Intelligence*, 1 (1): 13–18.
- Jia, M., A. Komeily, Y. Wang, and R. S. Srinivasan. 2019. “Adopting Internet of Things for the development of smart buildings: A review of enabling technologies and applications.” *Automation in Construction*, 101: 111–126.
- Jiang, T., X. Zhao, X. Yin, R. Yang, and G. Tan. 2021. “Dynamically adaptive window design with thermo-responsive hydrogel for energy efficiency.” *Applied Energy*, 287: 116573.
- Kanase, P., and S. Gaikwad. 2016. “Smart Hospitals Using Internet of Things(IoT).” 03 (03): 4.
- Khan, T., M. Alam, K. Kadir, Z. Shahid, M. Mazliham, S. Khan, and M. Miqdad. 2018. “Recognizing Foreign Object Debris (FOD): False Alarm Reduction Implementation.” *Indonesian Journal of Electrical Engineering and Computer Science*, 11: 41–46.
- Krishnan, R. S., A. Sangeetha, D. A. Kumari, N. Nandhini, G. Karpagarajesh, K. L. Narayanan, and Y. H. Robinson. 2022. “A Secured Manhole Management System Using IoT and Machine Learning.” *Recent Advances in Internet of Things and Machine Learning, Intelligent Systems Reference Library*, V. E. Balas, V. K. Solanki, and R. Kumar, eds., 19–30. Cham: Springer International Publishing.
- Kumar, P., L. Morawska, C. Martani, G. Biskos, M. Neophytou, S. Di Sabatino, M. Bell, L. Norford, and R. Britter. 2015. “The rise of low-cost sensing for managing air pollution in cities.” *Environment International*, 75: 199–205.
- Lakshminarasimhan, M. 2016. “IoT Based Traffic Management System.”
- Laxman, P., and A. Jain. 2021. “Automation Of Swimming Pools To Prevent Drowning Deaths Using Iot, Sensors And Unique Algorithm.” *Webology*, 5: 2021.
- Lee, S. K., H. R. Kwon, H. Cho, J. Kim, and D. Lee. 2016. “International Case Studies of Smart Cities: Orlando, United States of America.” IADB: Inter-American Development Bank.
- Li, S., and C. C. Mi. 2015. “Wireless Power Transfer for Electric Vehicle Applications.” *IEEE Journal of Emerging and Selected Topics in Power Electronics*, 3 (1): 4–17.
- Liu, W., X. Wang, Y. Song, R. Cao, L. Wang, Z. Yan, and G. Shan. 2020. “Self-powered forest fire alarm system based on impedance matching effect between triboelectric nanogenerator and thermo-sensitive sensor.” *Nano Energy*, 73: 104843.
- Lu, Y., J. Wang, X. Bai, and H. Wang. 2020. “Design and implementation of LED lighting intelligent control system for expressway tunnel entrance based on Internet of things and fuzzy control.” *International Journal of Distributed Sensor Networks*, 16 (5): 1550147720925742. SAGE Publications.
- Madli, R., S. Hebbbar, P. Pattar, and V. Golla. 2015. “Automatic Detection and Notification of Potholes and Humps on Roads to Aid Drivers.” *IEEE Sensors Journal*, 15 (8): 4313–4318.
- Nellore, K., and G. P. Hancke. 2016. “Traffic Management for Emergency Vehicle Priority Based on Visual Sensing.” *Sensors*, 16 (11): 1892. Multidisciplinary Digital Publishing Institute.
- Ni, B., C. D. Nguyen, and P. Moulin. 2012. “RGBD-camera based get-up event detection for hospital fall prevention.” *2012 IEEE International Conference on Acoustics, Speech and Signal Processing (ICASSP)*, 1405–1408. Kyoto, Japan: IEEE.
- Nicholson, S., M. Tomasi, D. Belleri, C. Ratti, and M. Nikolopoulou. 2022. “Greening’ the Cities: How Data Can Drive Interdisciplinary Connections to Foster Ecological Solutions.” *SPOOL*, 9 (1): 5–18. Technical University of Delft.

- Niranjan, D. K., and N. Rakesh. 2020. "Early Detection of Building Collapse using IoT." *2020 Second International Conference on Inventive Research in Computing Applications (ICIRCA)*, 842–847.
- Öörni, R., E. Meilikhov, and T. O. Korhonen. 2015. "Interoperability of eCall and ERA-GLONASS in-vehicle emergency call systems." *IET Intelligent Transport Systems*, 9 (6): 582–590.
- Orrie, O., B. Silva, and G. P. Hancke. 2015. "A wireless smart parking system." *IECON 2015-41st Annual Conference of the IEEE Industrial Electronics Society*, 004110–004114.
- P S M., S. K J, S. Vaishnavi, and S. V G. 2021. "Automatic uplifting of pedestrian crossing platform using congestion monitoring." *2021 Second International Conference on Electronics and Sustainable Communication Systems (ICESC)*, 1532–1536.
- Pan, M., T. Linner, W. Pan, H. Cheng, and T. Bock. 2018. "A framework of indicators for assessing construction automation and robotics in the sustainability context." *Journal of Cleaner Production*, 182: 82–95.
- Peng, C., and K. Qian. 2014. "Development and Application of a ZigBee-Based Building Energy Monitoring and Control System." *The Scientific World Journal*, 2014: 1–13.
- Perilla, F. S., G. R. Villanueva, N. M. Cacanindin, and T. D. Palaoag. 2018. "Fire Safety and Alert System Using Arduino Sensors with IoT Integration." *Proceedings of the 2018 7th International Conference on Software and Computer Applications*, 199–203. Kuantan Malaysia: ACM.
- Ren, Z., Y. Ding, J. Nie, F. Wang, L. Xu, S. Lin, X. Chen, and Z. L. Wang. 2019. "Environmental Energy Harvesting Adapting to Different Weather Conditions and Self-Powered Vapor Sensor Based on Humidity-Responsive Triboelectric Nanogenerators." *ACS Appl. Mater. Interfaces*, 11 (6): 6143–6153. American Chemical Society.
- Saad, M., A. Farij, A. Salah, and A. Abdaljalil. 2013. "Automatic Street Light Control System Using Microcontroller." 6.
- Sai Sri Vastava, S., B. Vandana, M. Bhavana, and R. Gongati. 2021. "Automatic movable road divider using Arduino UNO with Node Micro Controller Unit (MCU)." *Materials Today: Proceedings*.
- Saleem, M., and A. Hosoda. 2021. "Development and testing of glow-in-the-dark concrete based raised pavement marker for improved traffic safety." *JOURNAL OF CIVIL ENGINEERING AND MANAGEMENT*, 27: 278–287.
- Setaki, F., and A. van Timmeren. 2022. "Disruptive technologies for a circular building industry." *Building and Environment*, 223: 109394.
- Seyedzadeh, S., F. P. Rahimian, I. Glesk, and M. Roper. 2018. "Machine learning for estimation of building energy consumption and performance: a review." *Vis. in Eng.*, 6 (1): 5.
- Sharma, S., and M. Bedi. 2016. "Experimental Electromechanical Module (MOSE) for Flood Control in Venice."
- Soudian, S., and U. Berardi. 2022. "Experimental performance evaluation of a climate-responsive ventilated building façade." *Journal of Building Engineering*, 61: 105233.
- Suryadevara, N. K., S. C. Mukhopadhyay, S. D. T. Kelly, and S. P. S. Gill. 2015. "WSN-Based Smart Sensors and Actuator for Power Management in Intelligent Buildings." *IEEE/ASME Transactions on Mechatronics*, 20 (2): 564–571.
- Tang, S., D. R. Shelden, C. M. Eastman, P. Pishdad-Bozorgi, and X. Gao. 2019. "A review of building information modeling (BIM) and the internet of things (IoT) devices integration: Present status and future trends." *Automation in Construction*, 101: 127–139.
- Toh, C. K., J.-C. Cano, C. Fernandez-Laguia, P. Manzoni, and C. T. Calafate. 2019. "Wireless digital traffic signs of the future." *IET Networks*, 8 (1): 74–78. <https://doi.org/10.1049/iet-net.2018.5127>.
- Ullah, Z., F. Al-Turjman, L. Mostarda, and R. Gagliardi. 2020. "Applications of Artificial Intelligence and Machine learning in smart cities." *Computer Communications*, 154: 313–323.
- Valença, G., F. Moura, and A. Morais de Sá. 2021. "Main challenges and opportunities to dynamic road space allocation: From static to dynamic urban designs." *Journal of Urban Mobility*, 1: 100008.
- Vishwas, H. N., and S. Ullas. 2017. "Power efficient automated lights results to security for underground parking space." *2017 International Conference on Inventive Computing and Informatics (ICICI)*, 61–64.
- Wang, C., Y. Zhu, and X. Guo. 2019. "Thermally responsive coating on building heating and cooling energy efficiency and indoor comfort improvement." *Applied Energy*, 253: 113506.
- Yang, H., L. Wang, B. Zhou, Y. Wei, and Q. Zhao. 2018. "A preliminary study on the highway piezoelectric power supply system." *International Journal of Pavement Research and Technology*, In Honor of Professor James S. Lai, 11 (2): 168–175.

Digital twins in construction practice – A use case driven implementation based on existing theory

T. Zinke & C.P. Schimanski

HOCHTIEF ViCon GmbH, Essen, Germany

D. Schäfer

HOCHTIEF PPP Solutions GmbH, Essen, Germany

M. Rowsell & R. Schumann

HOCHTIEF ViCon GmbH, Essen, Germany

ABSTRACT: Digital Twins are a key concept for the industry 4.0 and they are also becoming increasingly important in the construction industry. For the application in construction practice, the paper gives a short introduction of the Digital Twin theory, describes the different elements of a Digital Twin, and discusses the different tasks, which have to be addressed within the life cycle. Based on this, an approach to structure, harmonize, and integrate heterogeneous data is presented. The key element is the definition and exhaustive implementation of a project data structure which is applied to all elements within a 3D-model and all other data sources. This approach allows to “glue” data from multiple sources and to access filtered results. Finally, the paper presents the realization of a Digital Twin. For this purpose a German highway project operated in a public private partnership with a length of 47 km is introduced. The Digital Twin integrates data from different sources like roadway inspections, mobile status monitoring, traffic data, weather data, and 3D model data. All of them are processed for the application in different use cases. A dashboard generated with a Business Intelligence solution provides visually prepared information for the decision making process.

1 INTRODUCTION

Digital Twins (DT) gain more and more attention in the construction industry, both in scientific analyses and practical implementations. The basic concept was created 20 years ago by Michael Grieves and the ongoing digitalization facilitates to bring the concept to life (Grieves 2016). The topic can be classified as a young discipline as shown in Figure 1. Since the year 2016 the number of publications increased significantly and at the same time the internet based search interest rose up.

In Germany, for the implementation of various digitization components in the infrastructure sector the Master Plan BIM Federal Trunk Roads was created, which contains an overarching digitalization strategy (BMVI 2022). The primary focus is on the phased introduction of the BIM method for the planning and erection phase of constructions. This procedure corresponds with the international implementation process of the method Building Information Modeling (BIM), which is currently still accelerating and represents the fundamental basis for an increasing digitalization of the sector (EU BIM 2017).

At the same time, in the masterplan introduces the term “Digital Twin” as a vision for the future, which is primarily aimed at the maintenance and operation of constructions and thus performs its main task in the use phase. This vision provides an important basis for determining which tasks will be assigned to the digital twin in the future. Within the conceptualization of the term Digital Twin a set of various, project-stage depending components that can even exist individually is often associated (Sacks et al. 2020). The components shall be integrated in a holistic information system. However, such holistic information systems are not trivial to build, as the constituting Digital Twin components are often only available fragmented and

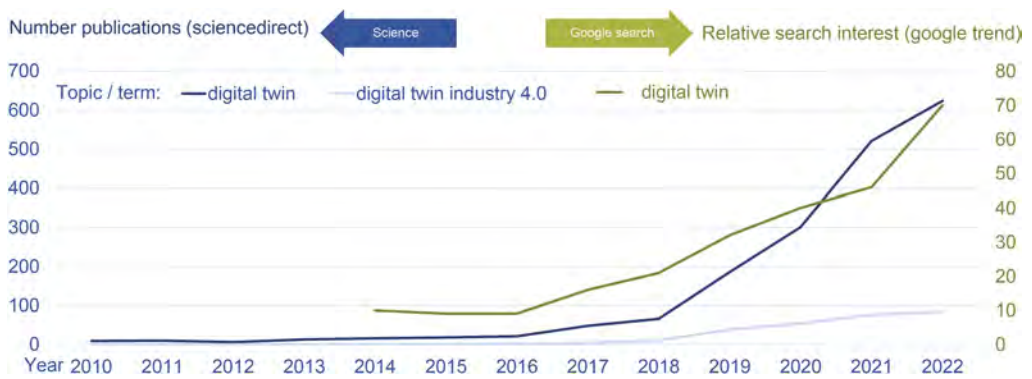


Figure 1. Results for number of scientific publications (left in blue) and relative search interest based on the search engine Google (right in green) for the named topics/terms for the period 2010 to 2022.

semantically disconnected. Addressing these problem statements, this paper suggests practical recommendations for integrating different Digital Twin components as well as the data that they carry, which is usually generated in numerous different data sources. Moreover, this concept is validated by an actual built Digital Twin realization allowing for the implementation of several Digital Twin use cases in practice. The type of use cases from a case study implementation in a German highway operation project are presented in this paper as well.

2 RESEARCH STRATEGY AND IMPLEMENTATION APPROACH

The research strategy presented in this paper is based on a Design Science Research (DSR) approach, which – according to Peffers et al. (2014) – is comprised by the steps of (1) finding a practically relevant problem and describing the motivation, (2) defining the objectives for a solution, (3) designing and developing a potential solution, (4) showing the demonstration, (5) evaluating of the practical applicability of the solution and (6) communication of the results.

While the problem in step (1) has been introduced in the previous section as an increasing importance of Digital Twins and simultaneously existing gap of practically applicable implementations, the next section on related works covers the state-of-the-art of the investigated domain (2). It focusses in particular on the components for theoretical conceptualization of Digital Twins as a main starting point for practical implementation. DSR steps (3) and (4) are addressed in section 4, where it is outlined how different DT components can be semantically connected and how the application of auxiliary artifacts for traceability throughout all data sources can be used. Secondly, section 4 describes how this concept can be transmitted to a practical application. At the example of a case study utilizing an infrastructure project, a short project description and an overview of the implemented use cases is given. Next, in DSR step (5), the practical application is connected to existing DT theory, evaluated and assessed concerning further development activities, also addressing DSR step (6).

3 FRAMEWORK AND OBJECTIVES

Building on the various theoretical considerations of the last 20 years, different definitions can be identified that place different emphases depending on the application domain, target group, or focus on different life cycle phases. However, all definitions have fundamental components in common, which are used in the following as the basic definition of digital twins (Boje et al. 2020):

- a physical component (real asset, asses under construction or actually existing asset),
- a virtual component (digital representation of the real asset or parts of it) and
- a data exchange between the components, which is takes places bidirectional.

As a first objective, a solution for a Digital Twin must be able to address all of the named *three components*. In addition to the physical-virtual components of a digital twin, the differentiation between *construction products and processes* is of particular importance. Leaning on and partly reproducing the fundamental work by Sacks et al. (2020), Table 1 provides examples of components for the product-process dimension representing both the digital and physical twin. It is also indicated what type of information these components can provide when used separately and what type of knowledge this information could lead to when linked (e.g. by means of comparison).

Table 1. Examples for the relation between products and processes in different life cycle phases based on Sacks et al. (2020).

Product	Process	Physical/virtual	Provided information type	Lead to knowledge type
Prototype or mock-up	First run study	physical	Small scale realistic design appearance and constructability facts	Ex-ante knowledge for finding best design alternatives and assessing constructability by considering small scale facts and mapping product to process intent information
3D-Model and documents	4D-Simulation or energy simulation	virtual	Design/process intent information	
Building under construction	Construction process	physical	Construction status perception	Ex-post knowledge gained during construction by comparison of status facts with perception and with ex-ante knowledge (can be used for decision making in current project both for design and construction stage, provided that part of design is still ongoing)
Current As-built model	Progress monitoring data	virtual	Construction status facts	
Finished building	Building in operation	physical	Operation status perception	Ex-post knowledge gained during operation by comparison of facts with perception (can be used for decision making within facility management processes in current operation project, and for design of upcoming projects)
Asset information model	Operational data coming from sensor or forms	virtual	Operation status facts	

It must be emphasized that a purely digital representation of an actually existing structure is not yet a digital twin. A Digital Twin requires a data exchange that both transfers data from the real structure to the digital representation (e.g., inventory of the actual condition of a bridge) and uses the digital representation to perform measures on the real structure, e.g. evaluation of the recorded data and derivation of maintenance measures that are performed manually or automatically (Bittencourt et al. 2021). It must be emphasized that the data combined in the digital representation consist of a *variety of different data types*. These can be, for example, the following data types:

- Measurement data from sensors (traffic load, strain gauges, weather sensors, etc.)
- Data from construction documentation (construction files, construction books, inspection reports, etc.)
- Condition data of structures, components and elements (database)
- Model data (BIM model, GIS model)

As described above, Digital twins can be used for a variety of tasks. Therefore, it is recommended to differentiate between different scopes of application. This is done by defining *Digital Twin use cases* based on existing business processes. These business processes can then be further subdivided if necessary. The advantage of thinking in terms of use cases is that an

overall context can be broken down into individual delimited parts. These can be formulated in detail, for example by writing down the process to be executed with all process steps. Each process step requires data for processing, which in turn can be collected, stored or processed with various software tools. Only when the data required for each use case is known, the implementation of the respective use case can be started.

According to Nieborowski et al. (2023), Digital Twin use cases for traffic infrastructures can be divided into three different subject areas:

- Operational processes, which have to be performed regularly and are necessary for maintenance.
- Maintenance and rehabilitation planning and conduction, which takes place in longer intervals, requires larger measures and is usually carried out by a different groups of people than the operational processes.
- Strategic tasks of life cycle management, through which measures to be carried out in the future, costs, building conditions, etc. are calculated or forecasted.

Based on all aspects described above, a concept for the practical implementation of a Digital Twin can be defined. The developed solutions for a highway project in Germany are presented in the following section.

4 DIGITAL TWIN CONCEPTUALIZATION AND IMPLEMENTATION

4.1 Implementation concept

The definition of a Digital Twin presented above can be combined with the idea of applicability throughout the entire life cycle of structures. A visualization of this concept is given in Figure 2. The first data of a Digital Twin are already generated in the design phase and form the basis for the later application. This can be geometric data, materials, qualities or product descriptions.

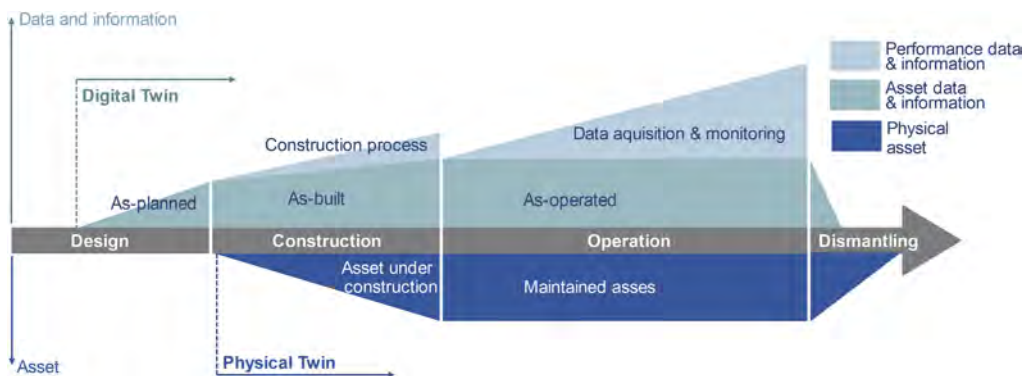


Figure 2. Applied concept of the Digital Twin within its life cycle.

In the manufacturing and construction phase, the component of the physical asset is created for the first time. Especially in the area of construction processes, the exchange of data between the two twins can generate added value. If, for example, the positions of construction equipment on the construction site are known in real time, the deployment planning can be optimized. With regard to the transport routes of materials, such as excavated material, it is possible to minimize transport distances by calculating on a daily basis where sources and sinks exist and to what extent.

Especially in the utilization phase, a large number of possible use cases for digital twins can be identified. The successive recording, storage and processing of data generated during the entire life cycle can support all business processes to be carried out. The most important applications are discussed at the example of the case study in section 4.4.

4.2 Project data structure and data integration

Within software engineering, the term “traceability” refers to the capability of relating data within different artifacts to each other (Unterkalmsteiner & Abdeen 2023). Knowledge of trace links between artifacts allows for semantic reasoning and insights as these artifacts can refer actually to the same “things” in the real world. They may exist on a variety of different abstraction levels, with different appearances as well as with different tools of origination in the virtual world. Insights that are based on these relationships would be more costly to obtain when artifacts are decoupled and no trace links exist.

An example within the domain of software engineering is the connection between requirements and the implemented software features that are supposed to fulfill the requirements. Only when trace links between both artifacts are known, one could decide whether a requirement is fulfilled or not. Unterkalmsteiner & Abdeen (2022) propose to make use of an auxiliary artifact in the form of a domain-specific taxonomy to create this trace links as indirect links instead of associating artifacts directly with each other. In more detail, they propose to apply this concept in the domain of civil infrastructure design and establish trace links between technical project requirements and objects within BIM models by means of a consistent taxonomy, which is comprised of an existing and industry-wide accepted classification system to reduce barriers for adoption. A simplified example of this approach is shown in Figure 3.

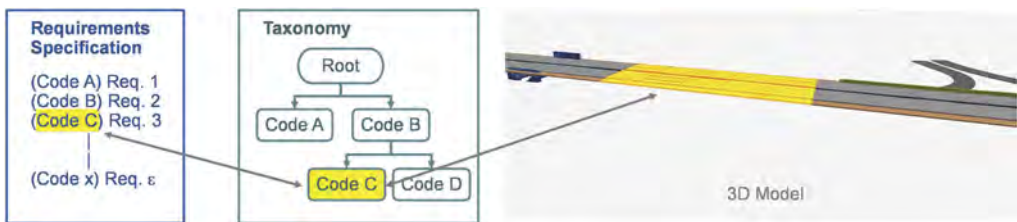


Figure 3. Enabling traceability by means of auxiliary artifacts.

For practical application a multi-hierarchical custom taxonomy is created on a project-specific basis combining location breakdown structures as well as breakdown structures for objects and work activities in a project data structure (PDS). Applying the PDS approach during the project construction and utilization phases allows for data integration, which can be defined as “the problem of combining data residing at different sources, and providing the user with a unified view of these data” (Lenzerini 2002). Data integrated following this approach enables the creation of highly customizable views on that data. Combined views based on both a data-centric representation (table and chart based) and a 3D model representation that are leveraging the PDS concept as data backbone of Digital Twins, see Figure 4.



Figure 4. Applied project data structure (PDS) and key functionalities of the implemented Digital Twin A6.

4.3 Project description

The German highway A6 is one of the most important east-west connections between France and central Europe. A particular section of the A6 in the southwest of Germany, comprising approximately 47 km, is currently highly charged with a traffic load up to 110,000 vehicles per day. With the expansion from four to six lanes, sections of the A6 will be adapted to the growing traffic volumes. For the expansion and the operation of the 47 km long section the HOCHTIEF PPP Solutions GmbH is, inter alia, accountable within a public private partnership project running until the year 2046.

For operation and maintenance, the created Project Information Model (PIM) in line with the terminology in ISO 19650 will continuously be used as part of the Digital Twin of the highway. A wide range of external data is linked to the developed data model leveraging the introduced PDS concept to support numerous Digital Twin use cases comprising the case study in this paper. Key facts of this case study are summarized in the following:

- Length of the route 47,2 km route, thereof 25,4 km expanded and renewed,
- 12 rest areas and parking lots, 7 interchanges,
- 45 rainwater retention or clarification basins,
- 70 bridges, 50 traffic sign bridges, 100 noise barriers and 16 retaining walls.

The A6 operating organization “ViA6West” manages all services and assessments with the help of the digital Twin system developed by HOCHTIEF ViCon and HOCHTIEF PPP Solutions in its day-to-day business. Defined use cases ensure efficient project management and digital, process-supported collaboration between the operating organization, the construction joint venture, construction supervision, the client, and other partners.

4.4 Implemented Digital Twin use cases

The use cases implemented within the scope of this project are mainly related to operational processes, but also to maintenance and rehabilitation planning and execution. The implementation of the use cases in the A6 Digital Twin can be characterized as a first stage of development, which is geared towards the feasibility of the processes set up and not towards the fullest possible integration of all possible use cases. This means that the Digital Twin A6 will be successively developed further by continuously improving processes, integrating additional data sources and implementing new use cases. In addition, data exchange (execution of measures) from the digital twin to the real asset is mainly carried out via manual processes. In the future, the aim is to automate these processes to a greater extent.

The currently implemented use cases are summarized in Figure 5. Depending on the required data, the conversion is carried out on the route, structure or component level.



Figure 5. Implemented use cases of the Digital Twin A6 (buildingSMART award 2022).

4.5 Exemplary presentation of the solution

An example of the implemented frontend for the Digital Twin A6 is shown in Figure 6. Here, different key elements can be used to work with the information provided. The information in the right area are linked to a digital asset model (left) for better orientation. Both a selection of model elements in the building model and the filtering of the results based on this selection can be done, as well as the reverse way of data selection and display of the corresponding building model elements. This is only possible if the project data structure is consistently applied to all data fed into the digital twin.

All data sets required for the underlying knowledge base of the digital twin are captured via mobile apps, external databases and live sensor data (such as weather data, SIB structures, and operating sensor data) or online forms. The digital workflows used for data capturing and processing ensure the high quality and reliability of the information entered. Thus, integrating all information with data from other use cases via the PDS is consistently possible.



Figure 6. Explanation of the key elements in the frontend of the Digital Twin A6.

5 DISCUSSION

The case study A6 introduces a Digital Twin that mainly contains use cases for operational processes, typically carried out by persons of the highway maintenance departments. In addition, various use cases for maintenance planning and execution are integrated. The connection of a 3D asset model is an aid for users to gain better orientation through visualization.

The greatest added value of the A6 Digital Twin lies in the structured storage of data and the resulting processing options. Different data sources are linked with each other and thus made centrally analyzable. In this way, knowledge can be generated that could not be obtained from data stored in data silos. Knowledge is generated by processing data with a Business Intelligence solution and thus generating information that can be used by people for decision support. Harmonizing the PDS across projects, for example by using always a standard classification system for the aspect of system breakdown, would even allow for conducting portfolio analyses on the mid-term and derivation of valuable insights for upcoming projects that have comparable characteristics.

The presented solution is developed for a stand-alone project of a single asset operator. For an application of Digital Twins for a large portfolio of infrastructures possibly operated by different stakeholders, generally accepted and standardized regulations must be generated. They need to cover the description of all data for example by applying taxonomies or ontologies. Based on

this, different technical approaches can be utilized. These are, for example, the usage of a linked data approach and the application of information containers (Hagedorn et al., 2023).

6 CONCLUSIONS

Digital Twins – especially for use in the utilization phase of transport infrastructures – are currently being discussed in many different forms. Due to the comparatively recent history of development, no uniform understanding has yet emerged. However, existing frameworks and first practical examples show that powerful Digital Twins can be built up and a continuous digital information chain can be created with a structured implementation taking into account basic relationships for data linking.

In the future, Digital Twins will gain importance in all areas. A central challenge in the development will be the integration of different existing data sources. In addition, it is desirable for the area of transport infrastructures to develop open linking standards based on ontologies, for example. In this way, different software providers can build on the existing data bases and it will be possible to switch between software solutions.

REFERENCES

- Bittencourt, T. N. & Futai, M. M. & Da Conceição Neto, A. P. & Ribeiro, D. M. (2021). Digital transformation of bridges inspection, monitoring and maintenance processes. In: Hiroshi Yokota/Dan M. Frangopol (Eds.). *Bridge Maintenance, Safety, Management, Life-Cycle Sustainability and Innovations*. CRC Press, 11–30. Doi: 10.1201/9780429279119-2.
- Boje, C. & Guerriero, A. & Kubicki, S. & Rezgui, Y. (2020). Towards a semantic Construction Digital Twin: Directions for future research. *Automation in Construction* 114, 103179. Doi: 10.1016/j.autcon.2020.103179.
- BMDV (2022). Federal Trunk Roads – BIM Masterplan: Digitalization of planning, construction, maintenance and operation in Federal trunk road construction using Building Information Modelling (BIM). Federal Ministry for Digital and Transport, Berlin: English version October 2022. Online available: <https://bmdv.bund.de/SharedDocs/DE/Artikel/StB/masterplan-bim-bundesfernstrassen.html>.
- buildingSMART award (2022). BIM Champions 2022. Online available: <https://www.buildingsmart.de/buildingsmart/aktuelles/die-bim-champions-2022>.
- EU BIM (2017): Handbook for the introduction of Building Information Modelling by the European Public Sector. Strategic action for construction sector performance: driving value, innovation and growth. EU BIM Taskgroup. Online available: <http://www.eubim.eu/handbook/>.
- Grieves, M. (2016). Origins of the Digital Twin Concept. *Working Paper*. Doi: 10.13140/RG.2.2.26367.61609.
- Hagedorn, P. & Liu L. & König M. & Hajdin R. & Blumenfeld T. & Stöckner, M. & Billmaier M. & Grossauer, K. & Gavin, K. (2023). BIM-enabled Infrastructure Asset Management using Information Containers and Semantic Web. *ASCE Journal of Computing in Civil Engineering*, 37 (1). Doi: 10.1061/(ASCE)CP.1943-5487.0001051.
- Lenzerini, M. (2002). Data Integration: a theoretical perspective. *Proceedings of the Twenty-first ACM SIGACT-SIGMOD-SIGART Symposium on Principles of Database Systems*, June 3-5, Madison, Wisconsin, USA. Doi: 10.1145/543613.543644.
- Nieborowski, S. & Windmann, S. & Bednorz, J. & Hindersmann, I. & Zinke, T. (2023). Digitaler Zwilling Brücke im Betrieb. *Bautechnik* 100, H. 2, 86–93. Doi: 10.1002/bate.202200089.
- Peppers, K. & Tuunanen, T. & Rothenberger, M.A. & Chatterjee, S. (2007). A Design Science Research Methodology for Information Systems Research. *Journal of Management Information Systems*, 24:3, 45–77. Doi: 10.2753/MIS0742-1222240302.
- Sacks, R. & Brilakis, I. & Pikas, E. & Xie, H. & Girolami, M. (2020). Construction with digital twin information systems. *Data-Centric Engineering*, 1, E14. Doi:10.1017/dce.2020.16.
- Unterlalmsteiner, M., & Adbeen, W. (2023). A compendium and evaluation of taxonomy quality attributes. *Expert Systems*, 40(1), e13098. Doi: 10.1111/exsy.13098.



Taylor & Francis

Taylor & Francis Group

<http://taylorandfrancis.com>

SS13: Strengthening and rehabilitation of steel bridges
Organizers: X. Jiang, X. Qiang & Z. Lv



Taylor & Francis

Taylor & Francis Group

<http://taylorandfrancis.com>

Numerical analysis of weld throat crack of rib-to-deck reinforced by bonding angle steel

Z.L. Lv, X. Jiang & X.H. Qiang
Tongji University, Shanghai, China

H.L. Wu & J.M. Ding
Tongji Architectural Design, Shanghai, China

ABSTRACT: It is well known that rib-to-deck welded joints are one of the typical fatigue details in the steel bridge decks. The existence of cracks will pose a threat to the safe operation of the bridges. Hence, it is necessary to adopt retrofitting techniques to retard the crack growth. This paper focuses on the failure mode of weld throat cracking of rib-to-deck welds and fatigue improvement of weld throats strengthened by angle steel. Finite element models with repaired and unrepaired specimens were established to investigate the fatigue properties based on linear elastic fracture mechanics. The stress intensity factor (SIF) at the crack front was calculated and the crack propagation trend was predicted. It was demonstrated that out-of-plane bending deformation between the top plate and the U-rib is the main reason for the cracking of the weld throats. The numerical results showed that the fatigue cracks belonged to type I-dominated mixed-mode cracks, and the stress intensity factor increases with the increase of crack depth. However, bonding angle steel can reduce the effective stress intensity factor range to prolong the fatigue life of the cracked weld throats. The stress intensity factor could be reduced by 80% to 97% after repairing. And fatigue crack propagation can be further arrested when strengthening in the early stage of crack initiation. The predicted crack propagation behavior was almost consistent with the experimental results, and the angle between the propagation path and the top plate was between 30° and 45°.

1 INTRODUCTION

Orthotropic steel bridge decks have been universally applied for large-span bridges due to its light weight, high bearing capacity and fast construction speed. However, due to the large number of welds, complex details and the increase of heavy trucks, fatigue damage has become the main problem of orthotropic steel bridge decks. In the previous study (Li et al., 2018, Luo et al., 2020), it was found that the rib-to-deck weld throats of the steel bridge decks built in the early stage are prone to produce fatigue cracks because of the out-of-plane deformation and the influence of welding defects. Therefore, it is urgent to carry out research on fatigue repair of rib-to-deck welds in steel bridge decks.

Several repair methods for damaged steel structures include stop hole method (Fang et al., 2023), welding (Park et al., 2012) and bolting plates (Liu et al., 2022), etc, and these methods are applicable to certain occasions. For the weld throat cracks of rib-to-deck welds, it is difficult to drill a hole at cross weld joints. Welding may introduce residual stress and welding defects. Bolting needs to drill holes and the section strength will be weakened. The use of adhesively bonded steel plates, on the other hand, seems to become a promising strengthening option compared to common repair methods, as the existing structures will not be damaged when repairing by bonding (Abeln et al., 2021, Wang et al., 2018, Teixeira de Freitas et al., 2017). In this paper, the weld throat cracks repaired by

bonding angle steel are investigated by experiments and numerical simulation. At the same time, fatigue failure modes and fatigue assessment of strengthening will be presented.

2 STRENGTHENING TEST

2.1 Specimen fabrication

The notch local specimen was designed to simulate the structure details of a roof and U rib weld, as shown in Figure 1. The deck plate thickness is 14 mm and the rib thickness is 8 mm. Q345qB steel plate was adopted for the fabrication of these specimens. The top plate was connected to the rib by a single-sided groove weld, and the depth of penetration is not less than 0.8 times the plate thickness. Besides, the 4 mm pre-crack was set at the weld root. For strengthened specimens, the angle steel was pasted on the structures after polishing the steel surface. The angle steel was 400 mm in length, 140 mm in width, and 10 mm in thickness. And the thickness of the adhesive was controlled at 5 mm. The strengthened specimens were obtained after curing for seven days, as illustrated in Figure 2.

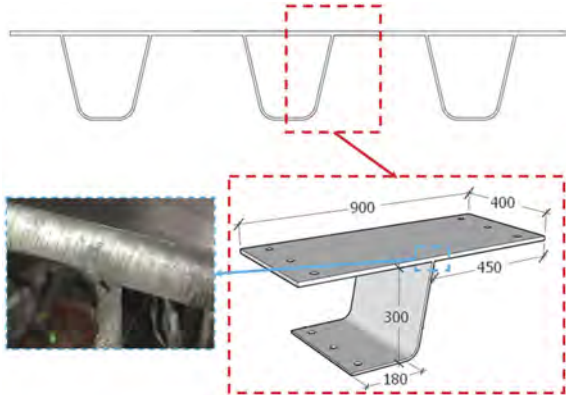


Figure 1. Un-strengthened test specimen (Unit: mm).

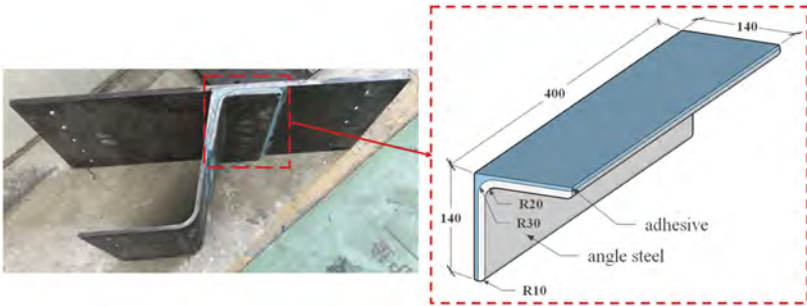


Figure 2. Strengthened test specimen (Unit: mm).

2.2 Experimental test

The fatigue machine was used to test all specimens with repairing or not. The deck plate was fixed to the testing fixture with high-strength bolts. Then the load was directly applied to the rib plate to simulate the relative deformation between the top plate and rib plate. The test set-up is shown in Figure 3, and the loading conditions are listed in Table 1. The fatigue load amplitude was set according to the equivalent stress amplitude of Eurocode. Furthermore, the

deflection of the loading end was measured by deformation gauge during the static test. And the stress distribution along the weld of all specimens was obtained by strain gauges until the cracks were clearly observed.

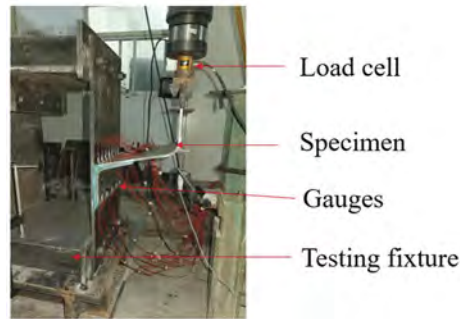


Figure 3. Test set-up.

Table 1. Loading case.

Specimens	Fatigue load/kN	Load amplitude/kN	Loading cycles/ 10^4 times	Cumulative loading cycles/ 10^4 times
RL-1	1-3	2	114.8	114.8
RL-2	1-4	3	68	68
SRL-1	1-3	2	200	200
	1-3	2	100	
	1-4	3	600	
SRL-2	1-6	5	60	953
	2-20	18	150	
	4-40	36	43	

* RL and SRL denote unreinforced specimens and reinforced specimens respectively.

2.3 Test results

Before the fatigue test, the static test was conducted to verify the effectiveness of strengthening angle steel. As shown in Figure 4, the displacement of the rib was significantly reduced after reinforcement, with an average reduction of about 66.8%, and the reinforced angle was very effective in limiting the relative deformation of the rib and top plate. The stress at the weld root of the rib under a static load of 3 kN showed an overall trend of being large in the middle and small at both ends. The average stress at the weld root side of the un-strengthened rib was 177 MPa, while the overall average tensile stress level at the weld root side of the strengthened rib was about 15 MPa, with a reduction of 91.5%, indicating that the angle reinforcement could effectively reduce the tensile stress at the rib weld, thus improving the fatigue resistance of the weld throat. In terms of fatigue failure, as shown in Figure 5, the fatigue crack initiated from the weld root and extended along the weld throat for un-strengthened specimens. For specimens strengthened by angle steel, it was observed that the crack extension to the deck appeared as well as the adhesive layer.

3 FINITE ELEMENT ANALYSIS

3.1 Establishment of FE model

A local model described in the previous experiments was established through ABAQUS software, as depicted in Figure 6. The plane strain CPE8R element was used and collapsed

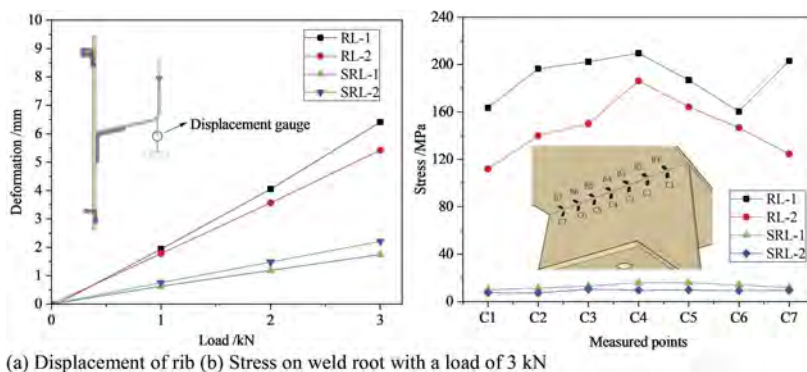


Figure 4. Displacement and stress of specimens under the static load.

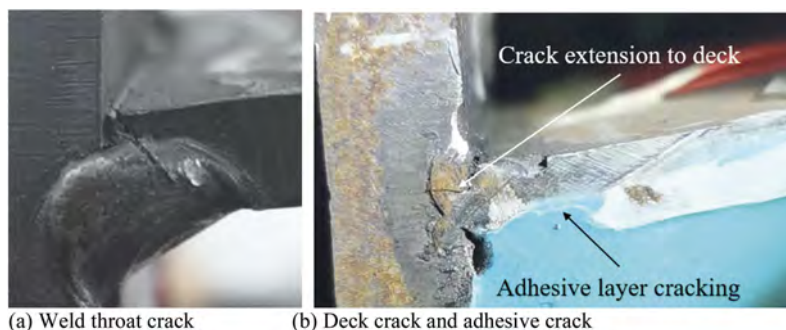


Figure 5. Failure modes of specimens.

triangular singular element was adopted for the crack tip. The global size of the specimen was set at 2 mm, and a refined mesh of 0.1 mm was set around the crack tip. The elastic modulus of steel and the Poisson's ratio were set at 2.06×10^5 MPa and 0.3, respectively. The elastic modulus of structural adhesive was 3500 MPa and the Poisson's ratio was 0.35. "Tie" constraint was set between the steel plate and the adhesive layer. The load was 2 kN.

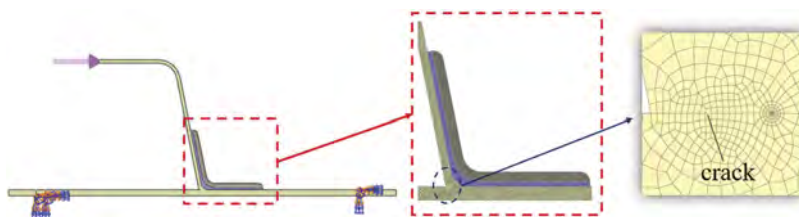


Figure 6. FE model of specimen.

3.2 Crack propagation of un-strengthened weld throat

The amplitudes of the stress intensity factor (SIF) are calculated separately for different crack depths and initial inclined angles, as shown in Figure 7(a). The stress intensity factor amplitude increases with the increase of crack depth. The value of type I is much larger than that of type II, which indicates that the fatigue crack belonged to the type I-dominated composite crack. For planar composite cracking mode cracks, the equivalent stress intensity factor amplitude can be safely calculated according to the following equation (Kuna, 2013)

$$\Delta K_e = \frac{\Delta K_I}{2} + \frac{1}{2} \sqrt{\Delta K_I^2 + 5.336 \Delta K_{II}^2} \quad (1)$$

Where ΔK_I , ΔK_{II} , ΔK_e refer to type I SIF, type II SIF and equivalent SIF respectively.

In linear elastic fracture mechanics, when ΔK_e exceeds the threshold value ΔK_{th} , cracks begin to spread and an unstable forced fracture occurs when the ΔK_e exceeds $(1-R)$ times fracture toughness K_c . And the ΔK_{th} and K_c were set at $63 \text{ MPa}\cdot\text{mm}^{0.5}$ and $110 \text{ MPa}\cdot\text{m}^{0.5}$ according to BS7910 code (BSI, 2019). According to the test, the stress ratio R is equal to 0.3.

Figure 7(b) depicts the variation curve of ΔK_e with crack depth for various initial α . With the increase of crack depth, the equivalent SIF increases, indicating an increase in crack expansion rate. At the same crack depth, the equivalent strength factor increases with the initial inclined angle in the range of 0 to 45° but decreases when greater than 45° . All calculated ΔK_e is greater than the threshold value of $63 \text{ MPa}\cdot\text{mm}^{0.5}$, indicating that the unreinforced specimens will expand under different damage conditions, and crack instability expansion will occur when the crack depth exceeds 9 mm.

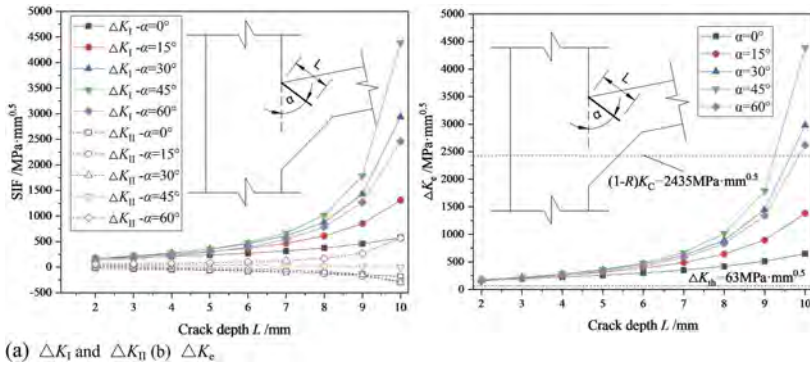


Figure 7. Variation curve of stress intensity factors at different initial angles with crack depths.

The direction of crack initiation can be calculated using the maximum tangential stress criterion. And the crack propagation angle θ can be obtained from the following equation:

$$\theta = \cos^{-1} \left(\frac{3K_{II}^2 + \sqrt{K_I^4 + 8K_I^2 K_{II}^2}}{K_I^2 + 9K_{II}^2} \right) \quad (2)$$

Where K_I and K_{II} refer to type I stress intensity factor and type II stress intensity factor, respectively.

Figure 8 presents the calculated crack propagation angles with different initial angles and crack depths. For the crack at the same depth, with the increase of the initial inclination angle α , the crack extension angle θ gradually changes from positive to negative values, and the absolute values all decrease before increasing. After accounting for the superimposed initial inclination, the angle range $(\theta + \alpha)$ is approximately 30° to 45° , which corresponds to the test results shown in Figure 9.

3.3 Fatigue evaluation of strengthening effectiveness

Take $L=4 \text{ mm}$ as an example, the influence of various angle thicknesses and adhesive thicknesses was investigated. From Figure 10, the equivalent stress intensity factor gradually declines with the increase of thickness, but the amplitude decreases. In contrast, the thickness

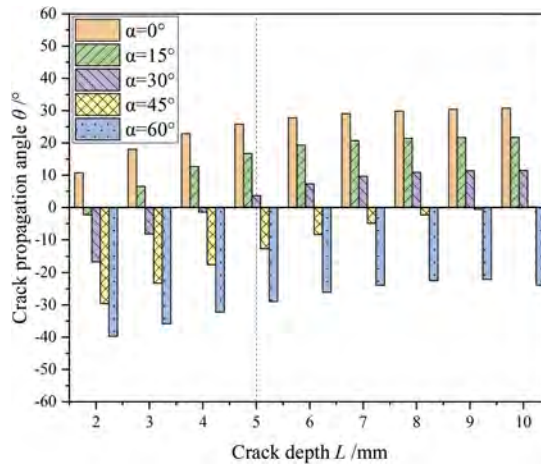


Figure 8. Calculated values of crack propagation angles.

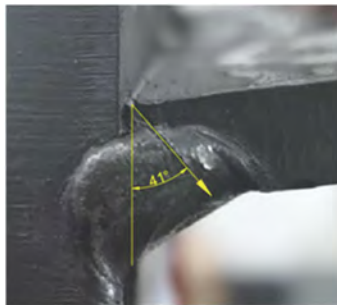


Figure 9. Crack propagation path of test.

of the adhesive layer has few effects on the change of equivalent stress intensity factor. Figure 11 shows the equivalent stress intensity factor of specimens with a 10 mm thick angle steel and a 5 mm thick adhesive. Compared with Figure 7, the equivalent stress intensity factor could be reduced by 80%-97%. And the SIF could be controlled under the extension threshold when the crack depth is less than 7 mm. Therefore, the adoption of bonded angle steel can effectively reduce the stress intensity factor at the crack tip and thus extend the fatigue life of weld details.

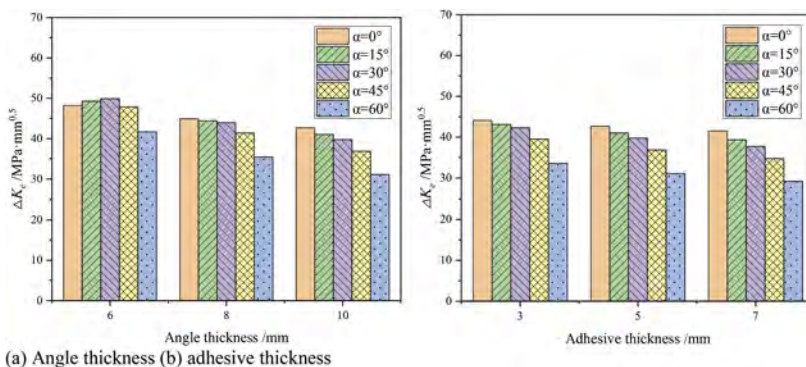


Figure 10. Equivalent stress intensity factors with different strengthening parameters.

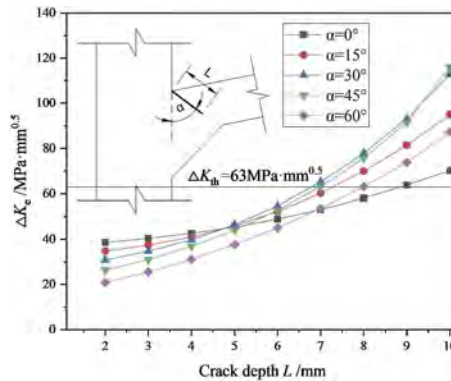


Figure 11. ΔK_c with crack depths after repairing.

4 CONCLUSIONS

- (1) Out-of-plane deformation is the main cause of U-rib weld throat cracking in the top plate. Both experimental and numerical analyses have proved that the reinforced angles can effectively limit the relative deformation and eliminate the risk of fatigue cracking of the weld throat.
- (2) The stress response of weld detail can be reduced by 91.5% in the static test. The strengthened specimens exhibit excellent anti-fatigue performance.
- (3) Weld throat cracks are type I-dominated mixed-mode cracks. The stress intensity factor can be reduced by 80%-97%. The crack propagation angle between the propagation path and the top plate is about 30°-45°.

REFERENCES

- Abeln, B., Gessler, A., Stammen, E., Ilg, F., Feldmann, M., Dilger, K. & Schuler, C. 2021. Strengthening of fatigue cracks in steel bridges by means of adhesively bonded steel patches. *The Journal of Adhesion*, 98(6): 827–853.
- BSI 2019. *Guide to methods for assessing the acceptability of flaws in metallic structures: British standard BS 7910:2019*. London: British Standards Institution.
- Fang, L., Fu, Z., Ji, B. & Fan, J. 2023. Reinforcement Effect of High-Strength Bolts for Stop-Hole under Out-of-Plane Bending Loads. *Journal of Bridge Engineering*, 28(1): 04022129.
- Kuna, M. 2013. *Finite Elements in Fracture Mechanics*, Dordrecht, Springer Netherlands.
- Li, M., Suzuki, Y., Hashimoto, K. & Sugiura, K. 2018. Experimental Study on Fatigue Resistance of Rib-to-Deck Joint in Orthotropic Steel Bridge Deck. *Journal of Bridge Engineering*, 23(2): 04017128.
- Liu, Y., Chen, Z., Zeng, J., Li, C., Peng, H. & Gao, Y. 2022. Study of Secondary Effects of Fatigue Cracks in Cross Partitions of Steel Plate Reinforced Steel Box Girders. *Applied Sciences*, 12(14): 1–19.
- Luo, P., Zhang, Q. & Bao, Y. 2020. Rib loading effects on weld root fatigue failure modes at rib-to-deck welded joint. *Fatigue & Fracture of Engineering Materials & Structures*, 43(7): 1399–1418.
- Park, H.-C., Lee, C.-H. & Chang, K.-H. 2012. Strengthening a damaged steel girder bridge by the replacement repair welding. *KSCE Journal of Civil Engineering*, 16(7): 1243–1249.
- Teixeira de Freitas, S., Kolstein, H. & Bijlaard, F. 2017. Fatigue Assessment of Full-Scale Retrofitted Orthotropic Bridge Decks. *Journal of Bridge Engineering*, 22(11): 04017092.
- Wang, C.-S., Zhai, M.-S., Duan, L. & Wang, Y.-Z. 2018. Cold Reinforcement and Evaluation of Steel Bridges with Fatigue Cracks. *Journal of Bridge Engineering*, 23(4): 04018014.

Flexural behavior of prestressed concrete beams strengthened with external CFRP tendons

L.L. Chen, X.H. Qiang & X. Jiang

College of Civil Engineering, Tongji University, Shanghai, China

P. Liu

Tongji Architectural Design, Shanghai, China

ABSTRACT: The considerable age of many prestressed concrete (PC) bridges conjointly with a steadily increasing amount of traffic and changes in design concepts have made maintenance and retrofitting more and more important over the years. The prestressed carbon fiber reinforced polymer (CFRP) strengthening is an effective reinforcement method for deteriorative bridges. A total of four PC beams with a length of 4300 mm were tested via four-point bending test. One beam was not strengthened and served as the reference beam, and three beams were strengthened by prestressed CFRP tendons with different diameters (7 mm and 10 mm) and initial prestress levels (15%, 30% and 50%). The promising results showed that the self-designed mechanical devices and end anchorage of CFRP tendons worked well. The ultimate load of strengthened beams was increased by 31%, 39% and 54%, respectively, compared with that of reference beam.

1 INTRODUCTION

Prestressed concrete (PC) beam has been extensively used in bridge (Sun et al., 2022). With elongation of service time, increasing traffic load and deterioration of material properties, numerous bridges in service are faced with a variety of problems, such as stiffness degradation, deflection increment and ultimate bearing capacity reduction, which increase collapse risk (Askar et al., 2022). Compared to demolition and reconstruction, strengthening of bridge in service greatly reduces adverse impact on society, environment, and economy (Qiang et al., 2022). Thus, structurally efficient and cost-effective means of reinforcement need to be employed to improve load bearing capacity and prolong service life of bridge (Siwowski et al., 2020).

In recent decades, carbon fiber reinforced polymer (CFRP) materials, including sheet, plate and tendon, have been used in bridge reinforcement due to their high strength, low density, high durability, good corrosion and fatigue resistance (Li et al., 2022; Wu et al., 2022; Hosseini et al., 2019; Michels et al., 2016). Previous research led to the development of the externally bonded (EB) technique (Yang et al., 2022) that non-prestressed CFRP sheets or plates are generally bonded to the tension side of bridge by resin. Debonding, caused by intermediate crack, is the most common failure mode, however, the CFRP sheet is always at a low-level strain and the advantage of the material cannot be fully utilized (Teng et al., 2003).

External prestressing reinforcement is an effective reinforcement system, without the use of structural adhesive bonding. Therefore, it is very convenient to supplement prestress loss and replacement, which are utilized to reinforce existing bridge structures. CFRP tendons are very suitable for external prestressing tendons, because benefits of durability and lightweight.

However, flexural behavior of PC beam strengthened with prestressed CFRP tendons remains unclear. Herein, four PC beams are designed based on a railway prestressed concrete beam in service. One un-strengthened beam plays the role of the reference beam and three beams are strengthened by prestressed CFRP tendons with different diameters and initial prestress levels. The flexural behavior of beams is investigated via four-point bending test.

2 EXPERIMENTAL PROGRAM

2.1 Specimen preparation and material properties

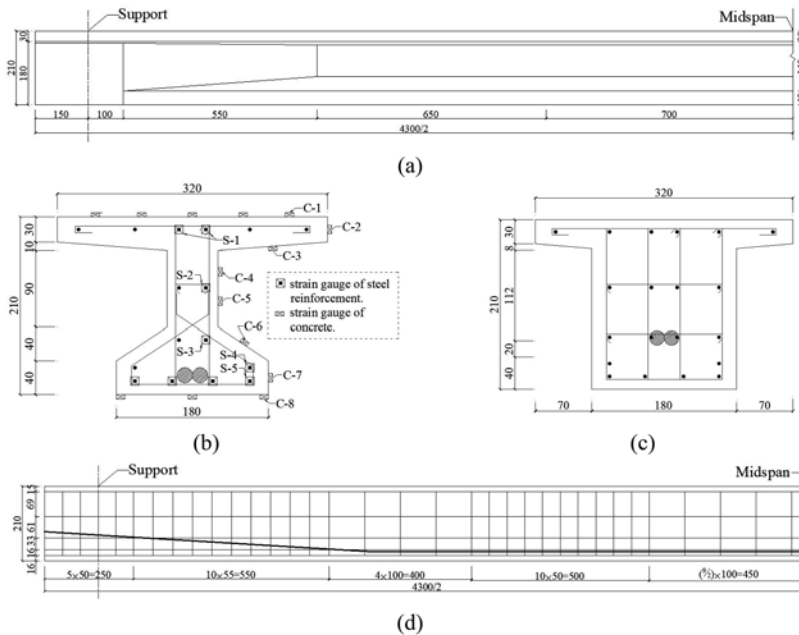


Figure 1. Details of precast concrete beam (unit: mm).

Table 1. Properties of all materials.

Materials	Compressive strength	Yielding strength	Elastic modulus	Ultimate strength
	MPa	MPa	GPa	MPa
Concrete	72.1	-	36.8	-
Steel bar	-	601.4	195.6	751.8
Steel strand	-	-	201	1860
CFRP tendon	-	-	170	2300

Four simply supported PC beams with variable cross-section, designed based on a railway prestressed concrete beam in service, were fabricated. The total length of the beam was 4300 mm, of which calculated span was 4000 mm, and two end supports were 150 mm, as shown in Figure 1a. The dimension and steel reinforcement arrangement of cross-sections at mid-span and support were displayed in Figure 1b and 1c. The mid-span was a π -shaped section. Height of section was 210 mm, and widths of the upper flange, lower flange and web were 320 mm, 180 mm and 60 mm, respectively.

Concrete of beam was Grade C60, and steel reinforcements including longitudinal and transverse reinforcements were HRB335 bars with diameter of 4 mm. The transverse reinforcements of beam were arranged along the full length at a spacing of 100 mm, as presented in Figure 1d. Two unbonded prestressed steel strands with diameter of 15.2 mm were arranged in concrete beam with a folded line shape. Two steel strands were tensioned by 30 T hydraulic jack, and controlled stretching stress of strands were 624 MPa. CFRP tendons with diameters of 7 mm and 10 mm were employed to strengthen PC beam by external prestressing reinforcement. The properties of all material were displayed in Table 1.

2.2 Reinforcement scheme

Four PC beams were tested in this test, including one unreinforced reference beam and three externally reinforced beams with prestressed CFRP tendons. The reinforcement details of specimens were displayed in Table 2. For each reinforced beam, two CFRP tendons were symmetrically arranged on two sides of the beam.

A set of mechanical anchorage was designed independently, including deviation blocks, anchor-roots, and wedge pads, as shown in Figure 2. Each beam was equipped with two anchor-roots and four deviation blocks that were divided into two types according to their installation positions. The wedge pads were used to adjust the angle between CFRP tendon and anchor-roots.

The circular self-locking anchorages were employed to tension and anchor CFRP tendon. Anchorage consisted of external shell, internal clip, nut and gasket, as shown in Figure 3a. The length and diameter of anchorage were 150 mm and 26 mm, respectively. CFRP tendons were stretched by a 30 T hydraulic jacks and pull rods, as shown in Figure 3b.

Table 2. Reinforcement parameters of tested beams.

NO.	Diameter mm	Prestress level %	Prestress MPa	Tension force kN
PCB-U-0	-	-	-	-
PCB-S-1	7	15	345	26.5
PCB-S-2	7	50	1150	88.5
PCB-S-3	10	30	690	108.3

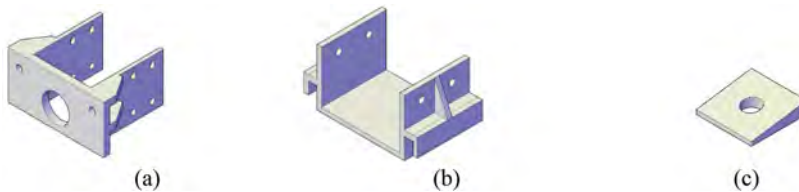


Figure 2. Mechanical anchorage.

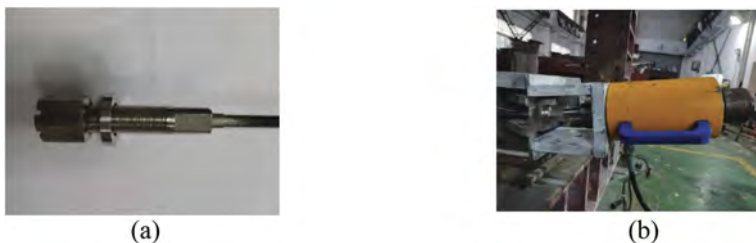


Figure 3. Anchorage and tension of CFRP tendon.

2.3 Test setup and measurement scheme

Four-point bending test was used to investigate the flexural behavior of concrete beams. The external load is applied by a 200 T hydraulic jack and dispersed by distribution beams. The pure bending section between loading points was 1400 mm, and two bending-shear sections on both sides were 1300 mm. The concrete beams were simply supported on the counterforce frame as shown in Figure 4. The loading was controlled by force with rate of 0.1~0.2 kN/s. Every load stage increased 10 kN before cracking and maintained 5 min to check crack. After cracking, the load stage was set to 5kN and maintained 10 min to observe and record the development of crack by black marker pan. All specimens were loaded to failure.

The applied load of hydraulic jack was record by a load cell. The displacements of concrete beam were measured by five displacement meters. The strain development of longitudinal



Figure 4. Test setup for four-point bending test.

reinforcement and concrete at mid-span section were measured by 9 BX120-3AA strain gauges (2 mm×3 mm) and 14 BX120-100AA strain gauges (120 mm×3 mm). The strain gauge distribution was shown in Figure 1b. Each CFRP tendon was divided into five segments by four deviation blocks, and a total of ten BX120-3AA strain gauge (2 mm × 3 mm) were arranged in the middle of each segment.

3 RESULTS AND DISCUSSION

3.1 Failure modes

3.1.1 Reference beam (PCB-U-0)

The deflection of the specimen increased slowly with the increasing of loading, and no crack was observed on the concrete surface in the initial stage of loading. When the load increased to 40 kN, some fine cracks were observed on the low flange of the concrete beam. A main crack with a length of approximately 40 mm appeared near the mid-span section. With the further increase of load, more cracks gradually appeared on the concrete beam.

A sudden drop of external load (about 10 kN) was observed, due to the break of longitudinal reinforcements in low flange. The prestressed steel strand was still work that bears the all the tensile force of beam section, and the deflection at mid-span increased little. The deflection of the beam basically increased linearly with the applied load. The longitudinal reinforcements in upper flange were buckled and deflection suddenly increases. The concrete beam was completely damaged.

3.1.2 Strengthened beams (PCB-S-1, PCB-S-2 and PCB-S-3)

The deformations of strengthened beams linearly increased with the increase of the external load in the initial stage. Cracking loads of three strengthened beams were delayed to 50 kN, 70 kN and 80 kN, respectively. Some small cracks appeared near the mid-span section when the applied load exceeded crack load (P_{crack}). There were a few cracks appear at deviation blocks, which might be due to the limitation of deviation blocks (Sturm et al., 2020). The main crack suddenly increased when width of crack reaches approximately 1 mm. The longitudinal reinforcements in low flange of concrete beam were fractured, which showed plastic characteristics of necking.

The tensile force was borne by prestressed steel strands and CFRP tendons at the cracked section. Therefore, strengthened beams still retained part of load bearing capacity. Finally, the upper flange concrete was crushed and strengthened beams were failure with a loud noise.

CFRP tendons of the three strengthened beams remained intact during loading. It was not observed that fracture or pull-out of CFRP tendons appeared, which indicated that the designed mechanical devices and anchorages were well suited for PC beam reinforcement.

3.2 Load-deflection behavior

The load-deflection relationship of four test beams is illustrated in Figure 5. Each of deflection curve can be divided into three stages: elastic stage, crack stage and fracture stage. Table 3 shows the main experimental results of all beams.

Table 3. Summary of test results of all beams.

NO.	$\frac{P_{crack}}{kN}$	$\frac{P_{fracture}}{kN}$	$\frac{P_{max}}{kN}$	$\frac{\Delta_{crack}^*}{mm}$	$\frac{\Delta_{fracture}^{**}}{mm}$	$\frac{\Delta_{max}}{mm}$
PCB-U-0	40	100	106	6.68	60.17	90.47
PCB-S-1	50	130	139	7.72	67.17	95.38
PCB-S-2	70	140	148	12.33	68.98	97.99
PCB-S-3	80	155	163	13.43	68.92	94.03

* Δ_{crack} is mid-span deflections corresponding to P_{crack} .

** $\Delta_{fracture}$ is mid-span deflections corresponding to $P_{fracture}$.

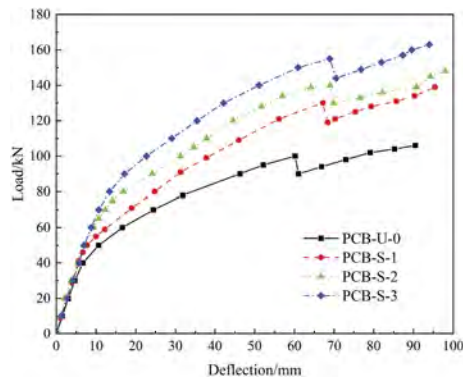


Figure 5. Load and mid-span deflection relation.

Before cracks appearing, the deflection of concrete beam increases linearly with the increase of load. The prestressed CFRP tendons can significantly improve the cracking load of concrete beams. The P_{crack} of three strengthened beams are increased by 25%, 75% and 100%, respectively. When the load reaches P_{crack} , the load-deflection curve begins to deviate from linear.

When the load reaches fracture load ($P_{fracture}$) that longitudinal reinforcements fractured, applied loads are suddenly decreased about 10 kN. The $P_{fracture}$ of strengthened beams are increased by 30kN, 40 kN and 55 kN compared with the unreinforced beam. As the load continues to increase, the deflection of the concrete beam linearly increases. The maximum loads (P_{max}) that corresponds to concrete crush were 106 kN, 139 kN, 148 kN, 163 kN. When beams are completely damaged, the maximum mid-span deflection (Δ_{max}) of strengthened beams increases by 5.38 mm, 7.99 mm and 4.03 mm, respectively.

3.3 Development of concrete strain

Figure 6 shows the development of concrete at the mid-span section during loading. The strain gauges from top to bottom of concrete beam are numbered C-1~C-8, as shown in Figure 1b.

The concrete strain of the upper flange is in compressive state during the whole loading process, as displayed in Figure 6a~6c. The compressive strain of top surface concrete increases linearly with the increase of the external load. The compressive strain of the lower surface of the upper flange increases with the increase of the load. When the load reaches about 0.7 P_{max} , the compressive strain decreases gradually. Figure 6d~6f show the strain development of concrete web. It can be seen from figures that the concrete web is in compression first and then in tension, which is related to the movement of the neutral axis. The lower flange concrete is subjected to tensile stress throughout the loading process, as shown in Figure 6g~6h. When the load reaches 0.50 ~ 0.55 P_{max} , the concrete at the C-7 position is damaged, which indicates that the concrete in C-7 cracked.

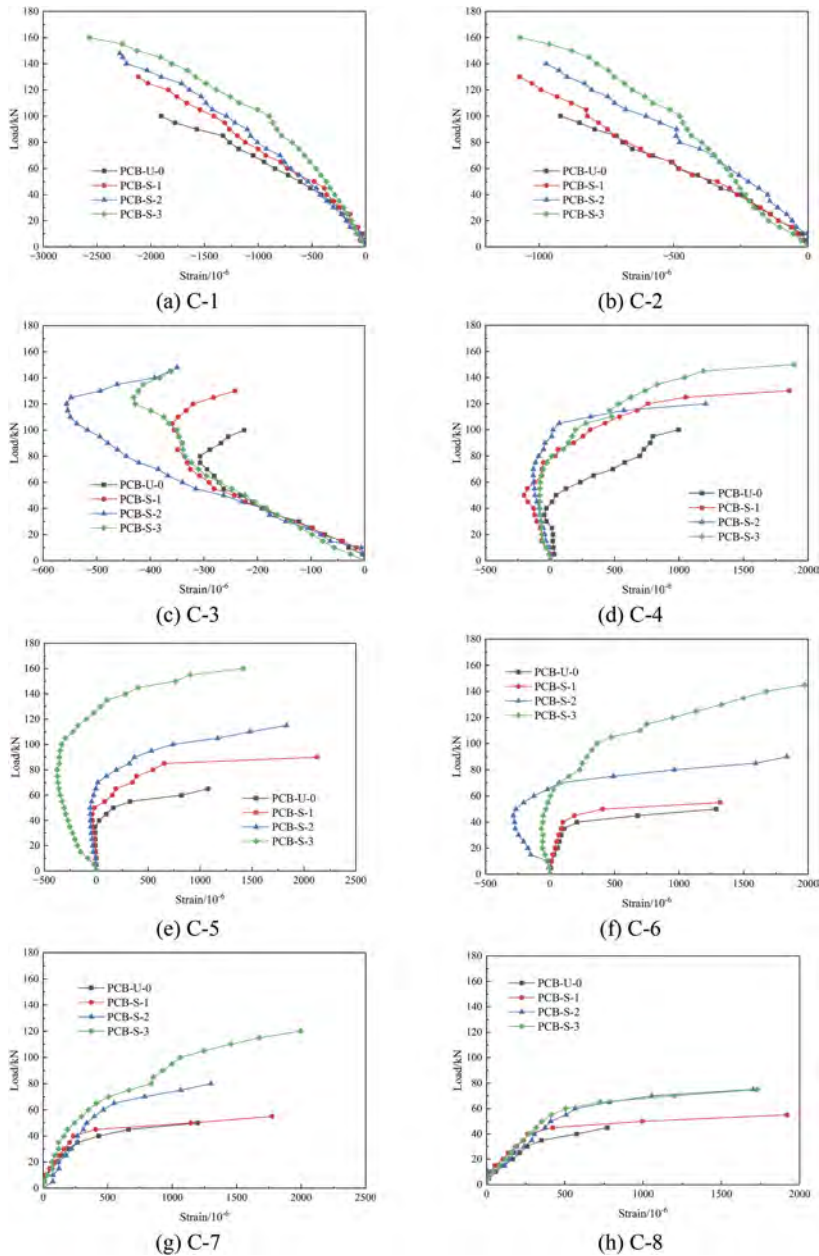


Figure 6. Strain development of concrete.

3.4 Development of steel reinforcement strain

The strain development of longitudinal reinforcements in the mid-span section during loading is shown in Figure 7. The reinforcement in the upper flange is in compressive state and increases linearly with the increase of the load as displayed in Figure 7a. When concrete crushed, the compressive strain of reinforcement is 750~900 ue. Figure 7b shows the development of reinforcement strain in the web. The strain of reinforcement is in compressive state in the initial stage, but change to tensile state when load reaches P_{crack} . The strain development law of reinforcements in lower flange is shown in Figure 9c~9e. Before the cracking load, the reinforcement strain increases linearly with the load. The reinforcements in lower flange are fractured and strain gauges are damaged when load reaches $P_{fracture}$.

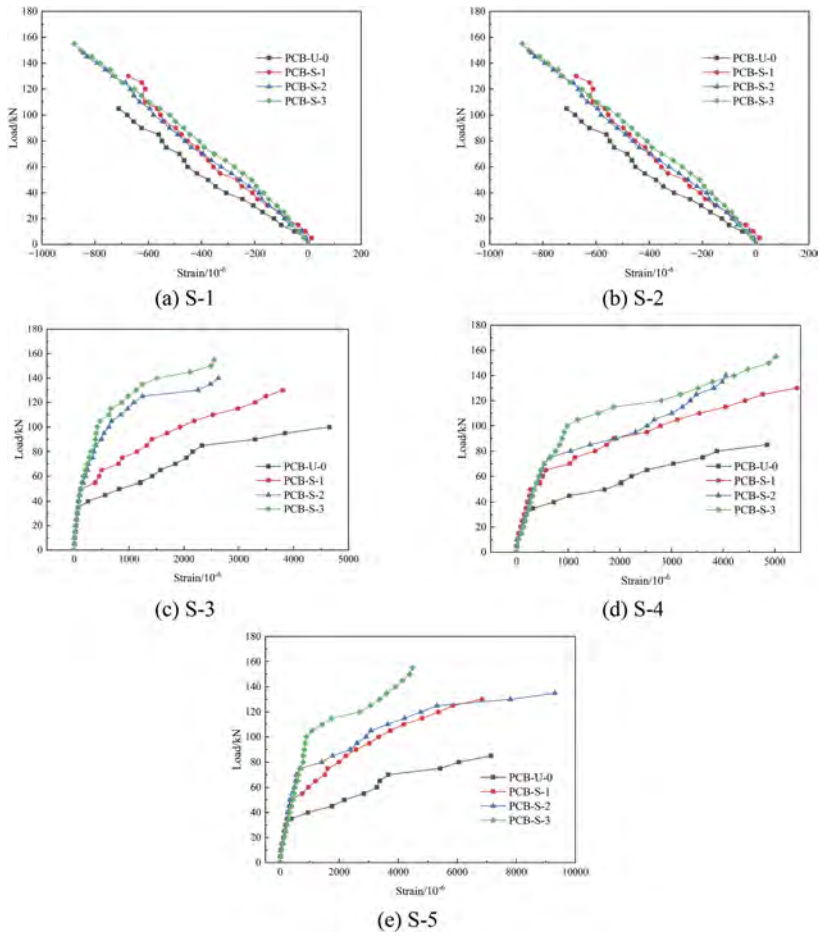


Figure 7. Strain development of reinforcements.

3.5 Development of CFRP tendons strain

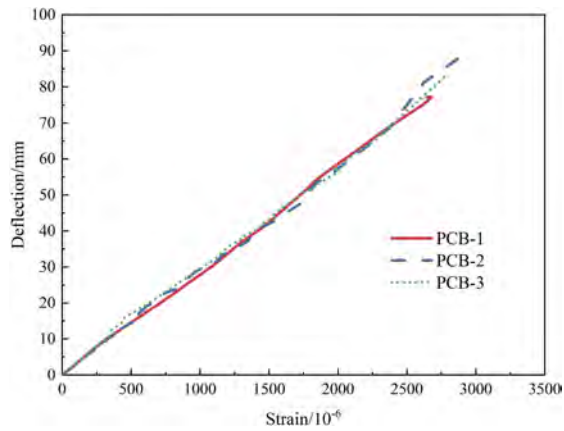


Figure 8. Strain development of CFRP tendons.

Figure 8 shows the relationship between mid-span deflection of beam and strain increment of CFRP tendon. The strain increment of CFRP tendon is basically line with the mid-span deflection during the entire stress process, which is similar to the strain increment low of unbonded prestressed steel strand (Xu et al., 2013). Moreover, curves of the three strengthened specimens are coincident, which indicates that the CFRP tendon strain development is only related to the deflection development of the prestressed beam rather than to the initial prestress level or diameter of CFRP tendon.

4 CONCLUSION

In this study, the flexural behavior of prestressed concrete (PC) beams strengthened by prestressed CFRP tendons with different diameters (7mm and 10mm) and initial prestress levels (15%, 30% and 50%) are investigated. Four beams, including one un-strengthened reference beam and three strengthened beams, are tested via four-point bending test. The following conclusions are drawn:

- 1) The failure mode of strengthened beam is concrete crushing and CFRP tendons remain intact, which is an ideal failure mode. The concrete beams show good plastic performance, and damaged beams does not collapse due to prestressed steel strands and CFRP tendons.
- 2) The concrete beam is in the elastic stage before cracking. Compared with the reference beam, the cracking load of strengthened beams is increased by 25%, 75% and 100% respectively, and ultimate loads is increased by 31%, 39% and 54% respectively.
- 3) The upper flange of the mid-span section including steel and concrete is in compression during loading, while the lower flange is in tension. The strain of steel and concrete at the web shifted from compression to tension, which is related to the upward movement of the neutral axis.
- 4) There is no obvious damage on CFRP tendons, i.e. no fracture or slip, in the whole loading process. The self-designed mechanical devices and end anchorage work well. The strain increment of CFRP tendons has a good correlation with the deflection development of the beam and increases uniformly along the full length during the tension and loading process.

REFERENCES

- Askar, M.K. & Hassan, A.F. & Al-Kamaki, Y.S. 2022. Flexural and Shear Strengthening of Reinforced Concrete Beams Using FRP Composites: A State of The Art. *Case Studies in Construction Materials*, (2022): e01189.
- El-Hacha, R. & Elbadry, M. 2006. Strengthening concrete beams with externally prestressed carbon fiber composite cables: experimental investigation. *PTI journal*. 4.2 (2006): 53–70.
- Hosseini, A. & Ghafoori, E. et al. 2019. Development of prestressed unbonded and bonded CFRP strengthening solutions for tensile metallic members. *Engineering Structures*. 181 (2019): 550–561.
- Li, R.W. & Zhang, N. & Wu, H. 2022. Effectiveness of CFRP shear-strengthening on vehicular impact resistance of double-column RC bridge pier. *Engineering Structures*. 266 (2022): 114604.
- Michels, J. et al. 2016. Prestressed CFRP strips for concrete bridge girder retrofitting: application and static loading test. *Journal of Bridge Engineering*. 21.5 (2016): 04016003.
- Qiang, X.H. & Chen, L.L. & Jiang, X. 2022. Achievements and Perspectives on Fe-Based Shape Memory Alloys for Rehabilitation of Reinforced Concrete Bridges: An Overview. *Materials*, 15.22 (2022): 8089.
- Siwowski, T. & Piąteka, B. et al. 2020. Development and implementation of CFRP post-tensioning system for bridge strengthening. *Engineering Structures*. 207 (2020): 110266.
- Sturm, A.B. & Visintin, P. et al. 2020. Flexural Performance of Pretensioned Ultra-High Performance Fibre Reinforced Concrete Beams with CFRP Tendon. *Composite Structures*, 243(9):112223.
- Sun, B. & Yang, Y. & Li, X. et al. 2022. Full-scale investigation of post-tensioned prestressed concrete bridge girders subjected to frost heaving in cold regions. *Engineering structures*, 2022(250-Jan.1).
- Teng, J.G. & Smith, S.T. et al. Intermediate crack-induced debonding in RC beams and slabs. *Construction and building materials*. 17.6-7 (2003): 447–462.
- Wu, B. et al. 2022. The anti-arch inhibition effect of multispan continuous girder bridge strengthened with prestressed CFRP plates. *Structures*. Vol. 35 2022.
- Xu, L. & Xu, F. et al. 2013. The design and test study on prestressed railway concrete beam bridge strengthened by externally draped CFRP tendons. *Engineering mechanics*. 30(02): 89–95.
- Yang, J.Q. & Feng, P. et al. 2022. Strengthening RC beams with mid-span supporting prestressed CFRP plates: An experimental investigation. *Engineering Structures*. 272 (2022): 115022.

Rehabilitation of cracked diaphragm cutouts in steel bridge using Fe-SMA

Y.P. Wu, X.H. Qiang & X. Jiang

College of Civil Engineering, Tongji University, Shanghai, China

H.L. Wu & J.M. Ding

Tongji Architectural Design, Shanghai, China

ABSTRACT: The Fe-SMA plates covering crack-stop holes method is presented to repair cracks of the diaphragm cutouts in orthotropic steel bridge decks. The activated Fe-SMA plate can increase the local stiffness and introduce precompression in the cracked region of steel plates. The recovery stresses of Fe-SMA with the pretension strain of 4% and activation temperatures of 150, 200, and 250 °C are 192.3, 226.4, and 270.8 MPa respectively, which can meet the requirement of cracking steel plates. The temperature of the non-activated region is maintained below the glass transition temperature of the adhesive during activating, indicating that the activation operation has little effect on the bonding performance between the Fe-SMA plate and the diaphragm. With activating Fe-SMA, compression stresses of 44.2 MPa–63.9 MPa are introduced at the hole edge. The stress at the hole edge is reduced by 66.65% through bonding the Fe-SMA plate.

1 GENERAL INSTRUCTIONS

Orthotropic steel bridge decks are a landmark innovation of modern bridge engineering and have been widely used in long-span bridges (Pfeil & Battista 2005, Freitas et al. 2013). Numerous structural details are prone to fatigue cracking under vehicle-induced vibration and repeated wheel load. Referring to the investigation of cracks distribution in several steel bridges, most fatigue cracks in orthotropic steel bridge decks occur at the arc-shape cutouts of the diaphragm, the connection between the roof plate and the U-rib, and the joint of the U-rib, accounting for about 90% in total (Editorial Department of China Journal of Highway and Transport 2014).

Carbon fiber reinforced polymer (CFRP) has superior mechanical properties, scholars have applied CFRP to strengthen cracked metallic members and studied the repair effect (Jones & Civjan 2003, Colombi & Fava 2015, Lepretre et al. 2018). Many scholars combined NiTi-based shape memory alloys (NiTi-SMA) and CFRP into composite patches to repair cracks in steel plates; specifically, CFRP sheets can increase local stiffness, and activated SMA can introduce precompression (El-Tahan et al. 2015, Abdy et al. 2018, Li et al. 2020).

The crack-stop hole can reduce the stress concentration at the crack tip and noticeably improve the fatigue performance of structures. Moreover, it is convenient in operation and fast in construction, making it especially suitable for the crack repair of orthotropic steel bridge decks involving narrow internal spaces and complex structures (Makabe et al. 2014, Fu et al. 2017). However, the crack-stop hole weakens the cross-section and is prone to secondary cracking (Razavi et al. 2017). Given this, Reddy et al. combined CFRP and crack-stop holes to repair bridge cracks and analyzed the repair mechanism and reinforcement performance (Reddy et al. 2016).

Drawing on the above repair concepts, this study proposes the Fe-SMA plates on the basis of crack-stop holes to repair cracks of the diaphragm cutouts. The stress level of the cracking

region can be effectively reduced by increasing the local stiffness and introducing precompression using the shape memory effect of Fe-SMA. Izadi et al. fixed the Fe-SMA strip on the steel plate using the bolt anchorage and introduced compressive stress of 74 MPa on the steel plate after activating Fe-SMA (Izadi et al. 2018). Wang et al. strengthened the cracked steel plate with the activated Fe-SMA strip, and the fatigue life of the repaired steel plate is 3.51 times higher than that of the unreinforced plate (Wang et al. 2021).

Therefore, this study presents the method of the Fe-SMA plates covering crack-stop holes to repair the cracked diaphragm cutouts in orthotropic steel bridge decks. The material properties of Fe-SMA, strengthening principle, repair scheme, and reinforcement effect are studied.

2 MECHANICAL PERFORMANCE OF FE-SMA

2.1 Mechanical properties

In order to obtain the mechanical properties of Fe-SMA, material specimens were prepared for static tensile tests according to the code of *Metallic materials-Tensile testing-Part 1: Method of test at room temperature* (GB/T228.1-2010, 2010), as shown in Figures 1a, b. In the first loading stage, the strain rate was $3.0 \times 10^{-4} \text{ s}^{-1}$. After the strain reached 0.05, the displacement rate was kept at $2.0 \text{ mm} \cdot \text{min}^{-1}$ until the specimens fractured.

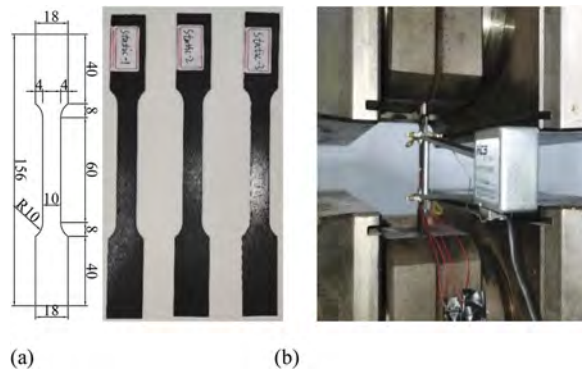


Figure 1. Static tensile test of Fe-SMA: (a) specimens design, (b) test device.

The engineering stress–strain curves of Fe-SMA plates under static tension are shown in Figure 2. The detailed mechanical properties are listed in Table 1. The stress of $\sigma_{y,0.2}$, corresponding to its residual strain of 0.2%, is used to describe the yield strength. The elastic modulus of Fe-SMA plates is determined by the tangent slope of the stress-strain curves in the initial stage, and the calculated average value is 172 GPa, which is close to that of the ordinary

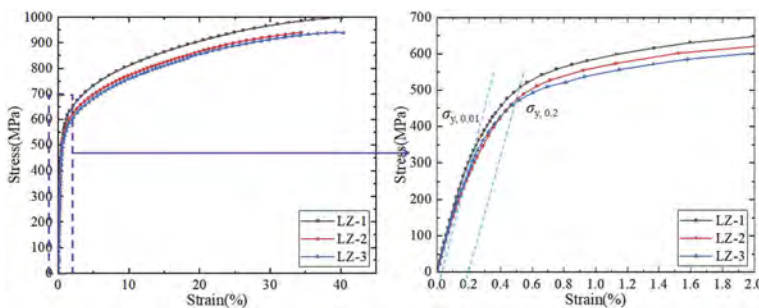


Figure 2. Engineering stress–strain curves of Fe-SMA.

steel. The ultimate strain of the Fe-SMA plates is 38.31%, while the yield strength and ultimate strength are 494 MPa and 960 MPa, respectively.

Table 1. Mechanical properties of Fe-SMA.

Number	Elastic modulus (GPa)	$\sigma_{y,0.2}$ (MPa)	Ultimate strength (MPa)	Ultimate elongation (%)
Static-1	176	519	1000	40.09
Static-2	168	477	940	34.39
Static-3	172	485	939	40.45
Average	172	494	960	38.31

2.2 Activation properties

The Fe-SMA specimens, as shown in Figure 3, are designed to test the activation recovery performance. The total length of the specimens is 326 mm, consisting of 220 mm in the high temperature furnace, and 50 mm for clamping at both ends. Following the pretension strain of 4%, the heating activation was performed at 150°C, 200°C, and 250°C, respectively.

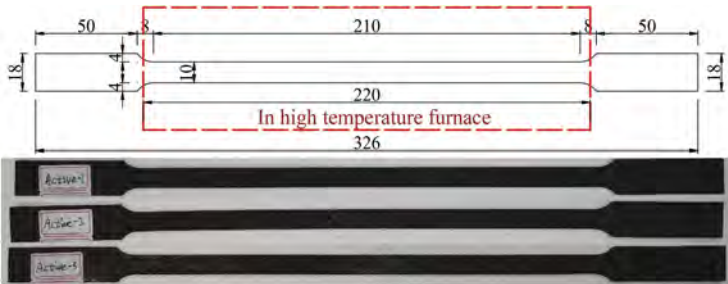


Figure 3. Specimens for activation recovery performance.

Three pairs of thermocouples were arranged on the Fe-SMA specimens’ surface to track the heating temperature, as shown in Figure 4a. An initial tensile stress of 50 MPa was applied to the specimens before activation to prevent buckling in the heating process. the temperature–stress curves in the activation process are depicted in Figure 4b. The internal stress of Fe-SMA specimens decreased initially due to thermal expansion. With the temperature grew, the shrinkage caused by the shape memory effect was dominant, and the internal stress of Fe-SMA specimens gradually increased. After ceasing to heat, the recovery stress of Fe-SMA

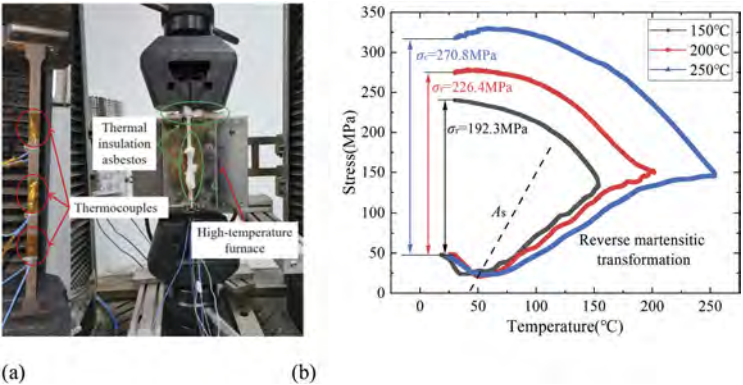


Figure 4. Activation test of Fe-SMA: (a) test device, (b) temperature-stress curves.

continued to increase under the cooling shrinkage effect. The recovery stress of Fe-SMA obtained with the pretension strain of 4% and activation temperatures of 150°C, 200°C, and 250°C are 192.3 MPa, 226.4 MPa, and 270.8 MPa, respectively.

3 REPAIR SCHEME AND TEST SYSTEM

3.1 The diaphragm model

This study intercepts the local model of the diaphragm in orthotropic steel bridge decks to conduct the repair research. The diaphragm cutouts use the Haibach hole type and the interception position of the local diaphragm model is denoted in Figure 5.

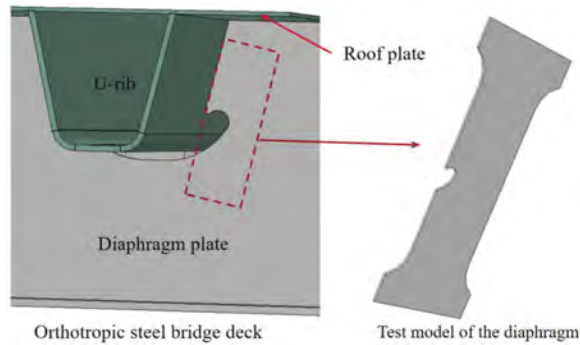


Figure 5. Model selection of the diaphragm specimens.

Figure 6 illustrates the parameters of the diaphragm model: the length of 1000 mm, the center width of 300 mm, and the thickness of 12 mm. An idealized horizontal crack is designed at the minimum section of the diaphragm, with a length of 60 mm. The crack-stop hole schemes with a diameter of 16 mm, whose center is located at the tip of the prefabricated crack. The effective width of the diaphragm section is 175.3 mm.

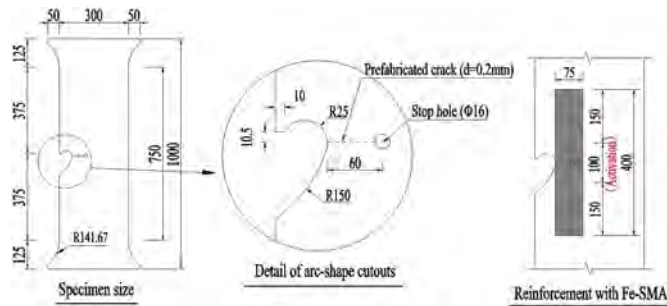


Figure 6. Geometry of diaphragm specimens (Unit: mm).

3.2 Repair scheme of the diaphragm

As shown in Figure 7, five cracked diaphragm specimens were designed, one of which was repaired with the crack-stop hole, and the other four were repaired with the Fe-SMA plates covering crack-stop holes. The fundamental parameters of different reinforcement schemes are listed in Table 2. The cracks and crack-stop holes in steel plates were prefabricated by wire cutting during specimen processing. In the S-FH group, the crack in the diaphragm is adopted as the center, and a 75 mm × 400 mm Fe-SMA plate is bonded on each side of the steel plate.

The thickness of the Fe-SMA plates includes 1.75 mm and 2 mm, and the activation conditions include no-activation, activation at 150°C, and activation at 200°C.

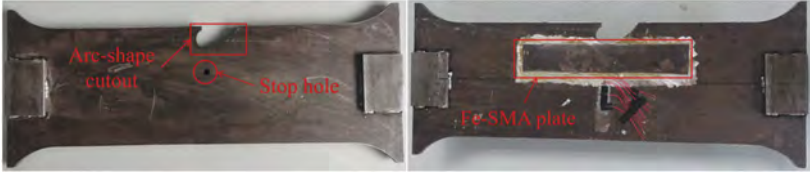


Figure 7. Physical picture of the diaphragm specimens.

Table 2. Specimens design and reinforcement parameters.

Repair method	Name	Stop hole size	Activation temperature	Thickness of Fe-SMA plate
Crack-stop holes	S-H-1	Φ16 mm	None	None
Fe-SMA plates covering	S-FH-1	Φ16 mm	200°C	1.75 mm
	S-FH-2	Φ16 mm	200°C	2 mm
crack-stop holes	S-FH-3	Φ16 mm	150°C	2 mm
	S-FH-4	Φ16 mm	None	1.75 mm

3.3 Test system and measuring points

The specimens were subjected to a static loading process of 0–128.6 kN using the MTS 311.31 S test system, and the load gradient was 20 kN for each grade (as shown in Figure 8a). Six thermocouples were arranged on each side of the diaphragm numbered as denoted in Figure 8b to monitor the temperature on the surface of Fe-SMA and steel plates in the activation. Strain gauges were symmetrically arranged on both sides of the diaphragm along the direction of the prefabricated crack (as shown in Figure 8b). In specimen S-H-1, the center of the strain gauges is 2 mm, 15 mm, 30 mm, 60 mm, and 90 mm away from the hole edge. In the S-FH group, the center of strain gauges is 2 mm, 12 mm, 18 mm, 24 mm, 30 mm, 60 mm, and 90 mm away from the hole edge. The stresses at measuring points with different distances away from the hole edge are denoted from σ_{2mm} to σ_{90mm} , respectively.

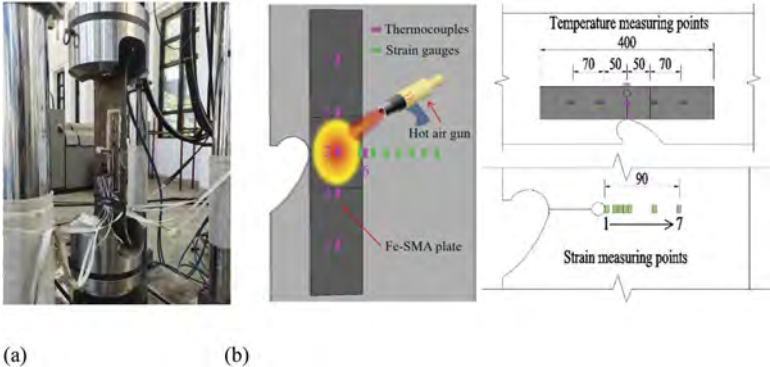


Figure 8. Testing and measuring arrangement: (a) testing device, (b) thermocouples and strain gauges.

3.4 Material properties

The mechanical properties of the steel used in the diaphragms were evaluated in accordance with the Chinese code (GB/T 228.1-2010, 2010). The structural adhesive was provided by Shanghai Horse Construction Co., LTD, and its mechanical properties were tested according

to the code of *Test methods for properties of resin casting epoxy* (GB/T 2567-2008, 2008). The measured mechanical properties of steel and structural adhesive are summarized in Table 3.

Table 3. Specimens design and reinforcement parameters.

Material	Elastic modulus (GPa)	$\sigma_{y,0.2}$ (MPa)	Ultimate strength (MPa)	Ultimate elongation (%)
Steel	208.2	406.39	504.04	16.17
Adhesive	5.892		31.16	0.66

4 RESULT ANALYSIS

4.1 Temperature during activation

The temperature of the repaired diaphragm activated at 200°C is illustrated in Figures 9a, b. Although the instantaneous temperature at the activation boundary (points 2 and 4) exceeded 85°C during the heating procedure of maintaining the Fe-SMA plate center (point 3) at 200°C, it mostly stayed below the glass transition temperature of the structural adhesive (85°C). The temperature farther away from the activation region (points 1 and 5) was maintained under 50°C in the heating process. The temperature at Point 6 on the diaphragm was between 100°C and 120°C, which had no significant effect on the mechanical properties of the steel plate. The temperature on the non-activated surface of the Fe-SMA plate and the diaphragm was maintained at a low level and the maximum value was 60.7°C. Therefore, the temperature in the non-activated region remained at a low level during heating, indicating that the activating operation has little effect on the secure bonding between the Fe-SMA plate and the diaphragm.

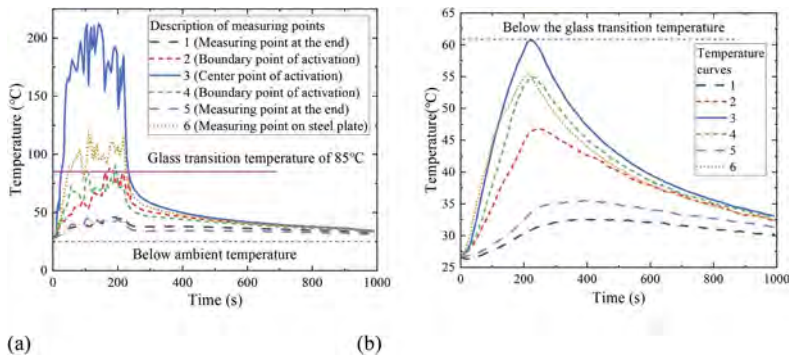


Figure 9. Temperature distribution during activation: (a) activated surface, (b) Non-activated surface.

4.2 Stress comparison

The compressive stresses introduced in the diaphragm after activating the Fe-SMA plates are depicted in Figure 10a. After activating the Fe-SMA plates, compressive stresses of 44.2 MPa–63.9 MPa could be introduced at the edge of crack-stop holes, which could considerably reduce the stress amplitude and stress concentration of the cracking part, and greatly improve the mechanical performance of the diaphragms. At the same activation temperature, the compression stress introduced by the 2 mm Fe-SMA plate at the hole edge was about 9 MPa (16.48%) higher than that of the 1.75 mm Fe-SMA plate. With the same thickness, the compression stress introduced by the Fe-SMA plate activated at 200°C was about 20 MPa (44.59%) higher than that of the Fe-SMA plate activated at 150°C.

As depicted in Figure 10b, the σ_{2mm} of all reinforced specimens increased linearly with the increasing load. For specimen S-FH-4, bonding the Fe-SMA plate significantly reduced stress

concentration and decreased stress at the hole edge from 390.09 MPa to 128.94 MPa, representing a reduction of 66.95%. For specimens S-FH-1, S-FH-2, and S-FH-3, the activation of Fe-SMA makes the stresses of measuring points remain at a low level, and the stresses at the hole edge are reduced by 84.74% in average. The Fe-SMA plate improved the section stiffness of the diaphragm, and the slope of load–stress curves of the S-FH group are obviously reduced compared with specimen S-H-1. Inside the S-FH group, the slope of load–stress curves of specimens S-FH-1 and S-FH-4 is smaller than those of specimens S-FH-2 and S-FH-3 since the thinner thickness of the Fe-SMA plates. Compared with specimen S-FH-4, specimens S-FH-1, S-FH-2, and S-FH-3 achieved considerable results by activating Fe-SMA, which could introduce precompression in the cracking position based on increasing stiffness.

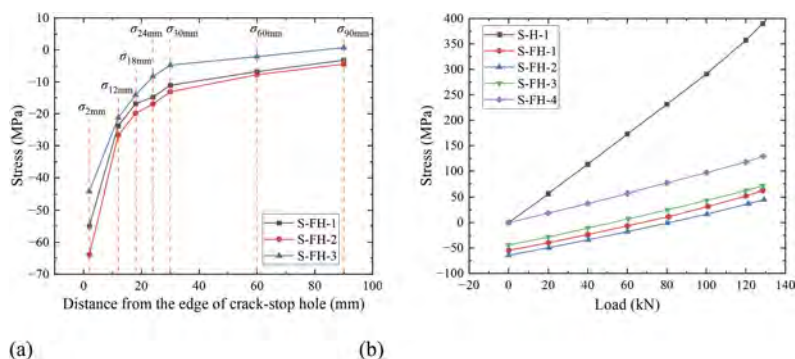


Figure 10. Stress results of repaired diaphragms: (a) compression stress, (b) σ_{2mm} under load.

5 CONCLUSIONS

Based on the crack-stop hole method, the Fe-SMA plate is used to repair cracks of the diaphragm cutouts in orthotropic steel bridge decks. The material properties of Fe-SMA and the reinforcement effect of the proposed method are studied. The operation procedure is introduced and the feasibility is confirmed. The main conclusions are as follows:

- (1) The elastic modulus of Fe-SMA plates is 172 GPa, which is comparable to that of ordinary steels. The yield strength, ultimate strength, and ultimate strain are 494 MPa, 960 MPa, and 38.31%, respectively, indicating its high strength and exceptional ductility. The recovery stresses of Fe-SMA using the pretension strain of 4% and activation temperatures of 150°C, 200°C, and 250°C are 192.3 MPa, 226.4 MPa, and 270.8 MPa respectively, which can meet the repair needs of cracking steel plates.
- (2) During the activation process, the temperature decreases sharply from the activation center to the non-activated region, showing that the activation has little effect on the bonding performance between the Fe-SMA plate and the diaphragm. When Fe-SMA is activated at 200°C, the temperature of the non-activated region is kept below the glass transition temperature of the structural adhesive.
- (3) Activating the Fe-SMA plates can introduce compressive stresses of 44.2 MPa–63.9 MPa at the edge of crack-stop holes, which could considerably reduce the stress amplitude and stress concentration of the cracking diaphragms. The compression stress introduced by the 2 mm Fe-SMA plate is about 9MPa (16.48%) higher than that of the 1.75 mm Fe-SMA plate. In comparison to 150°C, the activation of Fe-SMA at 200°C can raise the compression stress by nearly 20 MPa (44.59%). By bonding the Fe-SMA plate, the stress at the hole edge can be significantly reduced by 66.95%, and the activation of Fe-SMA can further reduce the stresses of measuring points by over 15%.

REFERENCES

- Abdy A.I., Javad H.M. & Riadh A.M. 2018. Fatigue life improvement of steel structures using self-prestressing CFRP/SMA hybrid composite patches. *Engineering Structures* 174: 358–372.
- Colombi P. & Fava G. 2015. Experimental study on the fatigue behaviour of cracked steel beams repaired with CFRP plates. *Engineering Fracture Mechanics* 145: 128–142.
- Editorial Department of China Journal of Highway and Transport. 2014. Review on China's Bridge Engineering Research: 2014. *China Journal of Highway and Transport* 27(05): 1–96. (in Chinese)
- El-Tahan M., Dawood M. & Song G. 2015. Development of a self-stressing NiTiNb shape memory alloy (SMA)/fiber reinforced polymer (FRP) patch. *Smart Materials & Structures* 24(6): 065035.
- Freitas S.T.D, Kolstein H. & Bijlaard F. 2013. Fatigue behavior of bonded and sandwich systems for strengthening orthotropic bridge decks. *Composite Structures* 97: 117–128.
- Fu Z.Q., Ji B.H., Xie S.H. & Liu T.J. 2017. Crack stop holes in steel bridge decks: Drilling method and effects. *Journal of Central South University*, 24(10): 2372–2381.
- GB/T 228.1-2010, Metallic materials-Tensile testing-Part 1: Method of test at room temperature. Beijing: Standardization Administration of China, 2010. (in Chinese)
- GB/T 2567-2008, Test methods for properties of resin casting body. Beijing: Standardization Administration of China, 2008. (in Chinese)
- Izadi M.R., Ghafoori E., Shahverdi M., Motavalli M. & Maalek S. 2018. Development of an iron-based shape memory alloy (Fe-SMA) strengthening system for steel plates. *Engineering Structures* 174: 433–446.
- Jones S.C. & Civjan S.A. 2003. Application of fiber reinforced polymer overlays to extend steel fatigue life. *Journal of Composites for Construction* 7(4): 331–338.
- Lepretre E., Chataigner S., Dieng L. & Gaillet, L. 2018. Fatigue strengthening of cracked steel plates with CFRP laminates in the case of old steel material. *Construction and Building Materials* 174: 421–432.
- Li L.Z., Chen T., Gu X.L. & Ghafoori E. 2020. Heat Activated SMA-CFRP Composites for Fatigue Strengthening of Cracked Steel Plates. *Journal of Composites for Construction* 24(6): 04020060.
- Makabe C., Kaito N. & Ferdous M.S. 2014. Method of arresting crack growth for application at a narrow working space. *Mechanical Engineering Journal* 1(6): 1–12.
- Pfeil M.S. & Battista R.C., Mergulhão A.J.R. 2005. Stress concentration in steel bridge orthotropic decks. *Journal of Constructional Steel Research* 61(8): 1172–1184.
- Razavi S.M.J., Ayatollahi M.R., Sommitsch C. & Moser, C. 2017. Retardation of fatigue crack growth in high strength steel S690 using a modified stop-hole technique. *Engineering Fracture Mechanics* 169: 226–237.
- Reddy S., Jaswanthasai V., Madhavan M. & Kumar V. 2016. Notch stress intensity factor for center cracked plates with crack stop hole strengthened using CFRP: A numerical study. *Thin-Walled Structures* 98: 252–262.
- Wang W.D., Li L.Z., Hosseini A. & Ghafoori E. 2021. Novel fatigue strengthening solution for metallic structures using adhesively bonded Fe-SMA strips: a proof of concept study. *International Journal of Fatigue* 148: 106237 (1–13).

Numerical study on the mechanical behavior of Fe-SMA/steel hybrid joints based on cohesive zone modeling

Y. Shu, X.H. Qiang, X. Jiang & Q.L. Zhang

College of Civil Engineering, Tongji University, Shanghai, China

H.L. Wu

Tongji Architectural Design, Shanghai, China

ABSTRACT: This paper aims to investigate the mechanical behavior of the Fe-SMA/steel hybrid joints. Based on the cohesive zone modeling of software ABAQUS, the numerical model of Fe-SMA/steel hybrid joints is developed, and the parametric analysis on overlap length is carried out. Besides, the damage evolution, failure modes and failure load of hybrid joints under tensile load are evaluated. The proposed model can reasonably simulate the performance of Fe-SMA/steel hybrid joints under tensile load. The results show that the failure load of Fe-SMA/steel hybrid joints increases with the improving overlap length. The existence of the optimal overlap length can ensure good mechanical behavior of Fe-SMA/steel hybrid joints and can reduce the consumption of engineering materials. Furthermore, the failure process of Fe-SMA/steel hybrid joints is firstly the failure of adhesive layers, and finally the bearing failure of the Fe-SMA plates leads to the failure of the whole joint.

1 GENERAL INSTRUCTIONS

Shape memory alloys (SMAs) have both the shape memory effect (SME) and super-elasticity (SE), and there is growing interest in SMAs from almost every industry (Pan et al., 2019). Iron-based shape memory alloy (Fe-SMA) is more and more used in the reinforcement field of civil engineering because of its excellent SME and low price (Hosseini, Michels, et al., 2019; Fritsch et al., 2019). The research has proved the effectiveness of Fe-SMA plates in strengthening steel structures (Fritsch et al., 2019; Izadi et al., 2019; Izadi, Ghafoori, Shahverdi, et al., 2018). In civil engineering, different materials are usually connected by adhesive, welding and bolted joints to repair steel structures. The stress concentration in the bolted joints causes damage and reduces the bearing capacity of structures (Jiang et al., 2013). Although the adhesive joints have a more uniform stress distribution (Jiang et al., 2014), in practical applications, adhesive layers have considerable defects such as bubbles and cracks, and there is peeling stress and stress concentration at the ends. Bolts can prevent sudden fracture of joints, and adhesive layers make the force transfer effective. In order to improve the mechanical performance of joints, hybrid joints are formed by combining the advantages of bolted joints and adhesive joints. Compared with simple bolted joints or adhesive joints, hybrid joints can obtain better static strength and fatigue life (Zhang et al., 2021). Hybrid joints with flexible adhesives can improve the bearing capacity and fatigue life of joints (Kelly, 2006). There are few studies on the mechanical behavior of hybrid joints composed of Fe-SMA plates. Therefore, it is necessary to study the failure load and failure modes of Fe-SMA/steel hybrid joints to optimize the reinforcement design using Fe-SMA plates.

Many studies have investigated the mechanical performance of hybrid joints made of composite materials. A simplified analysis model based on the experimental results of aluminum/aluminum hybrid joints was developed by Paoissien et al. (2017). The model could well capture the mechanical performance of hybrid joints and be adopted to select the optimal adhesive materials. The performance of CFRP/aluminum hybrid joints was evaluated by Chen et al. (2019) through tensile

tests. The results showed that the energy absorption capacity of the hybrid joints was superior. A tensile test of adhesive joints and hybrid joints using digital image correlation was carried out by Sun et al. (2021) to investigate the performance and failure mechanisms of joints. The results demonstrated that CFRP/aluminum hybrid joints had the best mechanical behavior and adhesive layers could reduce the stress concentration around the bolt holes. The stiffness, failure modes and failure progress of CFRP/CFRP hybrid joints were investigated by Jiang et al. (2022) through tensile tests. The results proved that the stiffness of hybrid joints increased considerably. The mechanical performance of FRP/FRP hybrid joints was explored by Mehrabian & Boukhili (2022) using the digital image correlation method. The results indicated that the shear and peeling strains were critical factors influencing the failure of hybrid joints. The influence of temperature on the performance of FRP/FRP hybrid joints was evaluated by Ulus (2022). The failure load of hybrid joints in the temperature range of 20–150°C was better than bolted joints and adhesive joints. However, experimental research is generally costly and time-consuming. In contrast, using the finite element (FE) method to predict the strength and failure modes of hybrid joints is more efficient and conducive to parametric analysis. The FE analysis can also obtain the stress distribution which is difficult to acquire in the experiments, such as the stress distribution and damage evolution process of adhesive layers, to make up for the defects of the experimental results.

The mechanical performance of Fe-SMA/steel hybrid joints requires to be well understood to fulfill the goal of using Fe-SMA plates for strengthening steel structures. In this work, a numerical study is conducted to reveal the damage process and failure mechanisms of Fe-SMA/steel hybrid joints. Based on the previous experimental research, this paper proposes a FE model of Fe-SMA/steel hybrid joints considering the progressive damage model of adhesive layers. Furthermore, the failure load and failure modes of Fe-SMA/steel hybrid joints are investigated based on the B-K energy criterion determining the failure of adhesive layers. A parametric analysis is conducted to reveal overlap length on the performance of Fe-SMA/steel hybrid joints. The optimal design suggestions for Fe-SMA/steel hybrid joints are given.

2 MATERIALS AND DIMENSIONS

2.1 Materials

The adherends employed the Q355 mild steel and Fe-SMA plates were employed in the adherends of hybrid joints. According to the tensile test results of Qiang et al. (2023b) and Qiang et al. (2023a), the material properties of Fe-SMA and Q355 mild steel were implemented, see Table 1. The performance of high strength bolts is listed in Table 1 which obtaining from the Li et al. (2020) and Lyu et al (2021). The preload of high strength bolts is specified in GB50017-2017 (2017), see Equation 1.

$$F_{p,b} = 0.61f_{u,b}A_e \quad (1)$$

Where $F_{p,b}$, $f_{u,b}$ and A_e are preload, ultimate strength and effective area of bolts, respectively, and $A_e = 84.3$ for M12 bolts (GB50017-2017, 2017). In order to describe the change of cross-sectional area during large deformation of Fe-SMA/steel hybrid joints, true strain ε_{true} and true stress σ_{true} are used. ε_{true} and σ_{true} are expressed as:

$$\varepsilon_{true} = \ln(1 + \varepsilon_{nom}) \quad (2)$$

$$\sigma_{true} = \sigma_{nom}(1 + \varepsilon_{nom}) \quad (3)$$

Where ε_{nom} and σ_{nom} are nominal strain and stress, respectively.

For steel plates and bolts, a bi-linear model was implemented in the FE modeling of the hybrid joints.

The adhesive layers are made of Araldite® 2015 structural adhesive, and the mechanical performance of structural adhesive is obtained by Rocha & Campilho (2018) shown in Table 2, which is adopted to develop cohesive zone law in the FE modeling.

Table 1. Mechanical performance of steel (Qiang et al., 2023a; Li et al., 2020; Lyu et al., 2021; Qiang et al., 2023b).

Materials	Elastic modulus E (GPa)	Yielding strength f_y (MPa)	Ultimate strength f_u (MPa)
Q355 steel	211	458	587
Fe-SMA	186	490	894
12.9s bolts	194	1120	1220

Table 2. Mechanical performance of structural adhesive (Rocha & Campilho, 2018).

Property	Araldite® 2015
Elastic modulus, E (GPa)	1.85
Shear modulus, G (GPa)	0.56
Poisson ratio, ν	0.33
Tensile strength, σ_f (MPa)	21.63
Shear strength, τ_f (MPa)	17.9
Tensile fracture toughness, G_{IC} (N/mm)	0.43
Shear fracture toughness, G_{IIC} (N/mm)	4.70

2.2 Dimensions

The dimensions of hybrid joints are presented in Figure 1. $l_0 = 48$ mm, $l_s = 200$ mm and $l_f = 200$ mm are overlap lengths of overlap zone, steel plates and Fe-SMA plates, respectively. $t_f = 1.8$ mm, $t_a = 1$ mm and $t_s = 10$ mm are thicknesses of Fe-SMA plates, adhesive layers and steel plates, respectively. The width of hybrid joints is b , and the diameter of bolts is d_0 . e_1 and e_2 are end and edge distances, respectively. The values of e_1 and e_2 are equal to $2d_0$, which satisfy the requirements of Eurocode 3 Part 1–8 (2005).

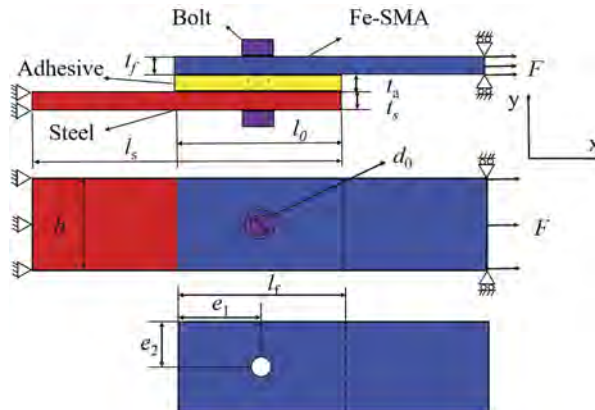


Figure 1. Dimensions of Fe-SMA/steel hybrid joints.

3 NUMERICAL WORK

3.1 FE modeling

Software ABAQUS was employed to investigate the mechanical performance of Fe-SMA/steel hybrid joints. The mixed-mode triangular CZM was employed to simulate the damage behavior of adhesive layers, and COH3D8 elements were adopted to reveal the initial damage, damage evolution and stiffness degradation of adhesive layers.

The diameter of nuts equal to the diameter of washers to improve the efficiency of numerical modeling, and the effects of screw thread were ignored. The simplified method can obtain

the same interaction area when the preload of bolts is applied, and the error caused by simplification can be ignored (Chaudhuri & Xie, 2015). The simplified method considerably reduced the element number in FE models and simulation time.

3.1.1 Boundary and loading conditions

A fixed constraint was applied to one end of hybrid joints and a load was applied to the other end.

3.1.2 Mesh generation

According to the ABAQUS manual (Karlsson & Sorensen, 2021), the $T - \Delta$ relationship to determine the interface failure is based on the relative displacement of the top and bottom of the COH3D8 elements. When the thickness direction of the adhesive layers is divided into two or more layers, the calculation results would be unreliable. Therefore, the thickness direction of adhesive layers was divided into one layer of COH3D8 element, see Figure 2b. C3D8R element was adopted by Fe-SMA plates, steel plates and bolts. The mesh at the overlap zone of the FE model was refined, and the mesh around the holes and the bolts were refined. The mesh generation of Fe-SMA plates, steel plates and bolts is presented in Figure 2.

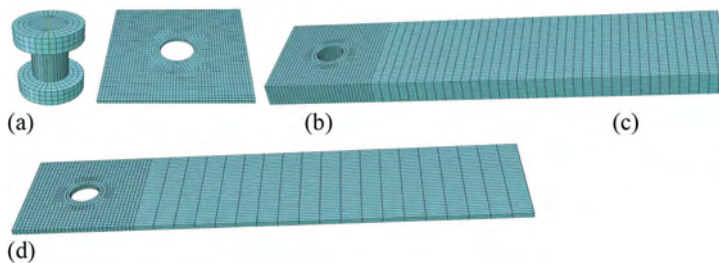


Figure 2. Mesh generation: (a) Bolts, (b) Adhesive layers, (c) Steel plates, (d) Fe-SMA plates.

3.1.3 Interactions and analysis steps

Tie interactions in FE modeling comprise adhesive layers to Fe-SMA plates and adhesive layers to steel plates due to the discretization level of adhesive layers being different from Fe-SMA and steel plates. Surface-to-surface contacts consisted of Fe-SMA plates to bolts and steel plates to bolts, the normal behavior was “hard contact”, and a friction coefficient of 0.3 (Fritsch et al., 2019) was adopted in the tangential direction.

There were five analysis steps in the numerical modeling to reveal the performance of Fe-SMA/steel hybrid joints. First, a temporary fixed boundary was applied to the ends of Fe-SMA plates and adhesive layers, and a 10N force was applied to bolts to establish a stable contact interaction. Second, the temporarily fixed boundary was removed. Third, the corresponding preload was applied to the screw. Fourth, the current length of the bolts was fixed. Fifth, a load was employed at the end of Fe-SMA plates.

3.2 Results

3.2.1 Failure modes

Understanding the failure modes of adhesive and bolted joints is the basis of exploring the failure modes of Fe-SMA/steel hybrid joints. There are four typical failure modes of adhesive joints (Zhao & Zhang, 2007): (i) cohesive failure, (ii) adherend failure, (iii) interface failure and (iv) mixed failure. The adherends of metal adhesive joints generally do not occur yielding, and the adherend failure of composite adhesive joints is generally due to the delamination and rupture of composite materials. The adhesive joints with critical adhesive layers and low adhesive interface strength are prone to cohesive failure and interface failure, respectively.

Net cross-section, shear-out, splitting, bearing, end pull-out and screw shear failure will occur in bolted joints when applying tensile load (Ulus, 2022; He & Wang, 2011). For bolted joints with composite materials, splitting failure will occur when the composite adherend interacts with bolts until cannot bear the load. The zone of adherends tightly contacts with the screw of bolts, when it cannot

bear the shear force, shear-out failure forms in composite adhesive joints. Both shear-out and splitting belong to brittle failure modes, and the bearing capacity of composite bolted joints under brittle failure modes is low. Net cross-section failure occurs when bolted joints with a small edge distance e_2 . For metal bolted joints with thin-walled plates and an appropriate edge distance e_2 , end pull-out failure will occur (Obeydi et al., 2020). Compressive and frictional forces around holes lead to bearing failure of bolted joints. Screw shear failure often occurs in the case of the high load-bearing capacity of adherends, especially if the adherend is a high strength and thick metal material.

The damage distribution and progress of adhesive layers based on the secondary nominal stress criterion (QUADSCRT) in different stages are shown in Figure 3. The Mises stress of Fe-SMA plates, bolts and steel plates are given in Figure 4. After the preload is applied, part of the adhesive layers in contact with the nuts has begun to damage, and as the load is applied until the whole section begins to damage, see Figures 3a, b. At the initial stage of loading, the mechanical behavior of Fe-SMA/steel hybrid joints was the failure of adhesive layers, and the failure propagates from one loading end of Fe-SMA plates in the overlap zone to the inside, see Figure 3. When the adhesive layers failed, the applied load mainly was bore by bolts and Fe-SMA plates of hybrid joints, and the load began to increase. Finally, the bearing failure of Fe-SMA plates around the hole led to a decrease in the bearing capacity of the joints, and the final failure of joints occurred. After the failure of hybrid joints, the overlap zone of Fe-SMA plates generated obvious curling deformation. Curling deformation was also observed in Ref. (Mahmood et al., 2020) when the plates were thin, and curling deformation might lead to bearing failure of hybrid joints due to prevent the shear deformation. When joints failed, the steel plates and bolts almost did not yield and occurred obvious deformation due to the critical parts being the Fe-SMA plates (see Figure 4).

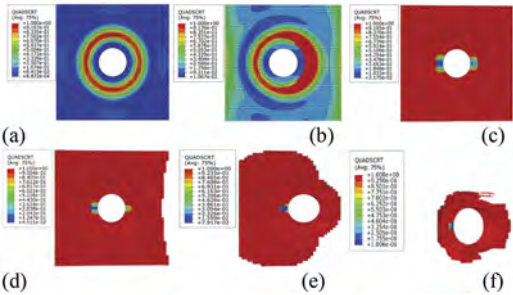


Figure 3. Damage distribution and progress of adhesive layers: (a) Completion of applying preload, (b) Initial stage of applying load, (c) Whole section reached initial damage, (d) Adhesive layer near the loading end began to fail, (e) Adhesive layer away from the loading end began to fail, (f) Adhesive layer completely failed.

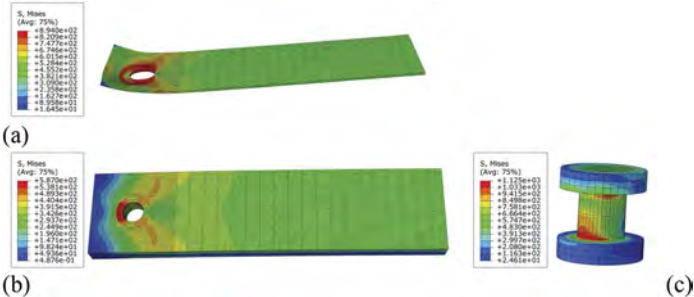


Figure 4. Mises stress of components: (a) Fe-SMA plates, (b) Steel plates, (c) Bolts.

3.2.2 Destruction process of hybrid joints

The tensile load-displacement curve of hybrid joints calculated by FE is given in Figure 5. The first load drop of hybrid joints corresponds to the failure of the adhesive layer, and the load is

46.37 kN. The second load drop corresponds to the bearing failure of Fe-SMA plates, and the failure load of hybrid Fe-SMA/steel joints was 46.85 kN. After the adhesive layer failed, Fe-SMA plates and bolts continued to bear the load, but the ultimate bearing capacity of hybrid Fe-SMA/steel joints did not improve. Three stages of load-displacement curves can be divided. At the first stage of loading, the Fe-SMA plates, the bolts and the adhesive layers bore the load together, and the load-displacement curve was linear. There was no relative sliding between the components and no gap between the bolts and the bolt holes. With the development of adhesive layer damage, the load gradually transferred to the bolts and Fe-SMA plates. The first load drop indicated the failure of adhesive layers. Finally, the bearing failure occurred, the bearing capacity of hybrid joints decreased, and hybrid joints failed.

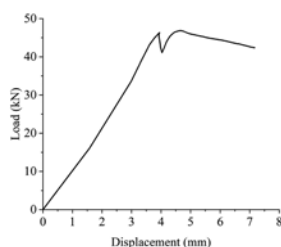


Figure 5. Tensile load-displacement curve of Fe-SMA/steel hybrid joints.

4 PARAMETRIC ANALYSIS

4.1 *Overlap length*

OL series is employed to explore the influence of overlap length on the performance of Fe-SMA/steel hybrid joints, see Table 3. The tensile load-displacement curves of Fe-SMA/steel hybrid joints obtained by the FE modeling are presented in Figure 6. The FE results and failure modes are listed in Table 4.

Table 3. Details of OL series.

ID	Fe-SMA thickness (mm)	Steel thickness (mm)	Adhesive thickness (mm)	Overlap length (mm)
OL1	1.8	10	1	48
OL2	1.8	10	1	60
OL3	1.8	10	1	80
OL4	1.8	10	1	100

It can be seen from Figure 6 that when adhesive layers fail, Fe-SMA/steel hybrid joints can continue to bear the load, and the load-displacement curves of all joints with different overlap lengths are similar. As the overlap length increased, the failure load F_f of hybrid joints improved, but the increasing amplitude gradually decreased. There was an optimal overlap length for Fe-SMA/steel hybrid joints. When hybrid joints reached the optimal length, F_f of Fe-SMA/steel hybrid joints was no longer significantly increased. In practical engineering, the optimal overlap length can be used to save the consumption of materials. Interestingly, when the overlap length was 100 mm, failure modes of hybrid joints changed from bearing failure to net cross-section failure. This might be because adhesive layers could reduce the curling deformation of Fe-SMA plates, with the increase of overlap length. The section along bolts was weakened by openings and became a critical section, resulting in net cross-section failure of Fe-SMA/steel hybrid joints.

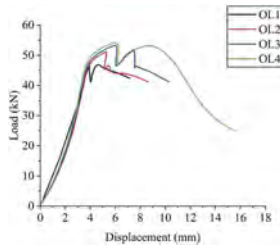


Figure 6. Tensile load-displacement curve of OL series.

Table 4. Mechanical behavior of OL series.

ID	Overlap length (mm)	Failure modes	F_f (kN)
OL1	48	Bearing failure	46.85
OL2	60	Bearing failure	51.14
OL3	80	Bearing failure	53.24
OL4	100	Net cross-section failure	54.06

5 CONCLUSIONS

This paper aims to evaluate the failure modes, failure load and damage process of Fe-SMA/steel hybrid joints based on cohesive zone modeling. The effects of overlap length and overlap width on the mechanical behavior of Fe-SMA/steel hybrid joints are studied. The conclusions are as follows:

- (1) The numerical model can predict the mechanical performance of adhesive layers based on cohesive zone modeling, which provides suggestions for the finite element analysis of Fe-SMA/steel hybrid joints.
- (2) The numerical model of Fe-SMA/steel hybrid joints can reveal the damage mechanism and damage evolution. The numerical model can predict the failure load and failure modes, hence it has good calculation accuracy. At the first stage of loading, the Fe-SMA plates, the bolts and the adhesive layers bear the applied load together. With the development of adhesive layer damage, the load is gradually transferred to the bolts and Fe-SMA plates until the final failure occurs.
- (3) The failure modes of Fe-SMA/steel hybrid joints are related to the overlap length. When the overlap length is 100 mm, Fe-SMA/steel hybrid joints change from bearing failure to net cross-section failure. The adhesive layers could reduce the curling deformation of Fe-SMA plates, with the increase of overlap length.
- (4) The failure load of Fe-SMA/steel hybrid joints improves with the increase of overlap length. The existence of the optimal overlap length can ensure good mechanical behavior of Fe-SMA/steel hybrid joints and can save the use of engineering materials.

REFERENCES

- Abaqus/Standard User's Manual version 2021, Hibbit, Karlsson & Sorensen, Inc. 2021.
- Chaudhuri, R.A. & Xie, M. 2015. On three-dimensional asymptotic solution, and applicability of Saint-Venant's principle to pie-shaped wedge and end face (of a semi-infinite plate) boundary value problems. *Engineering Fracture Mechanics*, 142: 93–107.
- Chen, Y., Yang, X., Li, M., Wei, K. & Li, S. 2019. Mechanical behavior and progressive failure analysis of riveted, bonded and hybrid joints with CFRP-aluminum dissimilar materials. *Thin-Walled Structures*, 139: 271–280.
- EN 1993-1-8, Eurocode 3: Design of steel structures–Part 1–8: Design of joints, CEN, Brussels, 2005.
- Fritsch, E., Izadi, M. & Ghafoori, E. 2019. Development of nail-anchor strengthening system with iron-based shape memory alloy (Fe-SMA) strips. *Construction and Building Materials*, 229: 117042.
- GB50017-2017, Code for design of steel structures, Beijing: China Architecture & Building Press, 2018 (in Chinese).

- He, Y.C. & Wang, Y.C. 2011. Load–deflection behaviour of thin-walled plates with a single bolt in shearing. *Thin-Walled Structures*, 49(10): 1261–1276.
- Hosseini, A., Michels, J., Izadi, M. & Ghafoori, E. 2019. A comparative study between Fe-SMA and CFRP reinforcements for prestressed strengthening of metallic structures. *Construction and Building Materials*, 226: 976–992.
- Izadi, M., Hosseini, A., Michels, J., Motavalli, M. & Ghafoori, E. 2019. Thermally activated iron-based shape memory alloy for strengthening metallic girders. *Thin-Walled Structures*, 141: 389–401.
- Izadi, M.R., Ghafoori, E., Shahverdi, M., Motavalli, M. & Maalek, S. 2018. Development of an iron-based shape memory alloy (Fe-SMA) strengthening system for steel plates. *Engineering Structures*, 174: 433–446.
- JGJ82-2011, Technical specification for high strength bolt connections of steel structures, Beijing: China Standard Press, 2011 (in Chinese).
- Jiang, L., Dong, D., Xiao, S., Chen, D., Yang, B., Yang, G. & Zhu, T. 2022. Experiment and simulation study on bonded, bolted and hybrid bolted/bonded joints of textile CFRP using bimodulus constitutive model. *International Journal of Adhesion and Adhesives*, 116: 103154.
- Jiang, X., Kolstein, M.H. & Bijlaard, F.S.K. 2014. Experimental and numerical study on mechanical behavior of an adhesively-bonded joint of FRP–steel composite bridge under shear loading. *Composite Structures*, 108: 387–399.
- Jiang, X., Kolstein, M.H. & Bijlaard, F.S.K. 2013. Study on mechanical behaviors of FRP-to-steel adhesively-bonded joint under tensile loading. *Composite Structures*, 98: 192–201.
- Kelly, G. 2006. Quasi-static strength and fatigue life of hybrid (bonded/bolted) composite single-lap joints. *Composite Structures*, 72(1): 119–129.
- Li, D., Uy, B., Wang, J. & Song, Y. 2020. Behaviour and design of high-strength Grade 12.9 bolts under combined tension and shear. *Journal of Constructional Steel Research*, 174: 106305.
- Liu, P.F., Peng, X.Q., Guo, Z.Y., Leng, J.X. & Jiao, L. 2019. Viscoelastic bilinear cohesive model and parameter identification for failure analysis of adhesive composite joints. *Composite Structures*, 224: 111016.
- Lyu, Y.F., Li, G.Q., Wang, Y.B., Li, H. & Wang, Y.Z. 2021. Effect of bolt pre-tension on the bearing behavior of high strength steel connections. *Engineering Structures*, 241: 112491.
- Mahmood, M., Elamin, A. & Tizani, W. 2020. Ultimate strength and fracture sequence of bolted connections to thin-walled carbon steel. *Structures*, 23: 646–659.
- Mehrabian, M. & Boukhili, R. 2022. Full-field through-the-thickness strain distribution study of hybrid multi-bolted/bonded single-lap composite joints using digital image correlation. *Composites Part A: Applied Science and Manufacturing*, 163: 107242.
- Obeydi, M., Zeynalian, M. & Daei, M. 2020. New initial stiffness equation for the bearing component of bolted thin-walled steel plates. *Structures*, 24: 791–803.
- Pan, S., Hu, M., Zhang, X., Hui, H. & Wang, S. 2019. A new near-surface-mounted anchorage system of shape memory alloys for local strengthening. *Smart Materials and Structures*, 28(2): 025016.
- Paroissien, E., Lachaud, F., Schwartz, S., Da Veiga, A. & Barrière, P. 2017. Simplified stress analysis of hybrid (bolted/bonded) joints. *International Journal of Adhesion and Adhesives*, 77: 183–197.
- Qiang, X., Shu, Y. & Jiang, X. 2023a. Mechanical behaviour of high strength steel T-stubs at elevated temperatures: Experimental study. *Thin-Walled Structures*, 182: 110314.
- Qiang, X., Wu, Y. & Jiang, X. 2023b. Experimental Investigation on Mechanical Properties and Activation-recovery Performance of Fe-based Shape memory alloys. *Journal of Tongji University (Natural Science)*, (in Chinese).
- Ridha, M., Tan, V.B.C. & Tay, T.E. 2011. Traction–separation laws for progressive failure of bonded scarf repair of composite panel. *Composite Structures*, 93(4): 1239–1245.
- Rocha, R.J.B. & Campilho, R.D.S.G. 2018. Evaluation of different modelling conditions in the cohesive zone analysis of single-lap bonded joints. *The Journal of Adhesion*, 94(7): 562–582.
- Sun, G., Xia, X., Liu, X., Luo, Q. & Li, Q. 2021. On quasi-static behaviors of different joint methods for connecting carbon fiber reinforced plastic (CFRP) laminate and aluminum alloy. *Thin-Walled Structures*, 164: 107657.
- Tvergaard, V. & Hutchinson, J.W. 1996. Effect of strain-dependent cohesive zone model on predictions of crack growth resistance. *International Journal of Solids and Structures*, 33(20–22): 3297–3308.
- Ulus, H. 2022. An experimental assessment of hybrid bolted/bonded basalt fiber reinforced polymer composite joints' temperature-dependent mechanical performances by static and dynamic mechanical analyses. *International Journal of Adhesion and Adhesives*, 114: 103120.
- Valente, J.P.A., Campilho, R.D.S.G., Marques, E.A.S., Machado, J.J.M. & da Silva, L.F.M. 2019. Adhesive joint analysis under tensile impact loads by cohesive zone modelling. *Composite Structures*, 222: 110894.
- Zhang, H., Zhang, L., Liu, Z., Qi, S., Zhu, Y. & Zhu, P. 2021. Numerical analysis of hybrid (bonded/bolted) FRP composite joints: A review. *Composite Structures*, 262: 113606.
- Zhao, X.L. & Zhang, L. 2007. State-of-the-art review on FRP strengthened steel structures. *Engineering Structures*, 29(8): 1808–1823.

Full-scale experimental study on strengthened riveted gusset joints

S. Wang, Q. Su, B. Liu & X. Jiang

Tongji University, Shanghai, China

L. Chen & C. Zhang

Shanghai Municipal Engineering Design Research Institute (Group) Co., Ltd, Shanghai, China

ABSTRACT: Songpu Bridge, a riveted steel truss bridge, was transformed for more traffic, and therefore, the truss members and riveted gusset joints required strengthening. Here, a typical truss joint connecting chords, verticals, and diagonals was focused. The strengthening of the joint included the truss members, gusset plates, and rivets. The tension and compression diagonals were strengthened by bolting additional steel plates and angles to the members, respectively. The gusset plates were strengthened by adding new cover plates, which had a large central opening such that they could be attached to the existing gusset plates without removing the existing rivets. Additional rivets were installed to connect the strengthened members and gusset plates. After strengthening, the riveted gusset joint had a complicated configuration. To evaluate the performance of the joint, a full-scale specimen that simulated one quarter part of the joint was experimentally tested. Failure modes including yielding of gusset plates and diagonal member and shear failure of rivets were observed. An ultimate bearing capacity of 11868 kN was obtained. The experiment aided the designing of the strengthening solution of the riveted gusset joint.

1 INTRODUCTION

Numerous steel structures require strengthening because of aging, corrosion, fatigue, impact damage, or an increase in service loads. Compared with demolition and reconstruction, strengthening is typically a more economical and sustainable solution. For instance, Songpu Bridge, a historical riveted steel truss bridge in Shanghai, was strengthened and transformed (Shao et al., 2019, Su et al., 2019a, Su et al., 2019b).

1.1 Project overview

The superstructure of Songpu Bridge consists of 96 m+112 m two-span continuous riveted steel trusses. Figure 1a shows the diagram of the truss. Songpu Bridge was initially built in 1976 as a highway–railway bridge, of which the upper layer was a two-lane highway and the lower layer was a single-track railway, as shown in Figure 1b.

In recent years, with the road traffic increasing, the highway capacity has been oversaturated; meanwhile, the railway has been disused. In order to improve the transportation capacity across the river, the existing Songpu Bridge is strengthened and transformed. The upper deck is widened from 12m to 24.5m for six vehicle lanes, whereas the lower deck is transformed into bicycle lanes and sidewalks, as shown in Figure 1b. As a result, the truss also requires to be strengthened to undertake the increased service load. The truss members and joints that require strengthening are indicated as red in Figure 1a. For truss members in compression, steel angles are bolted to improve the stability, whereas for truss members in tension, steel plates are bolted (Wang et al., 2022b, Wang et al., 2022a, Wang et al., 2023). For joints, cover plates are attached to the existing joints and more rivets are installed (see more details in Section 1.2).

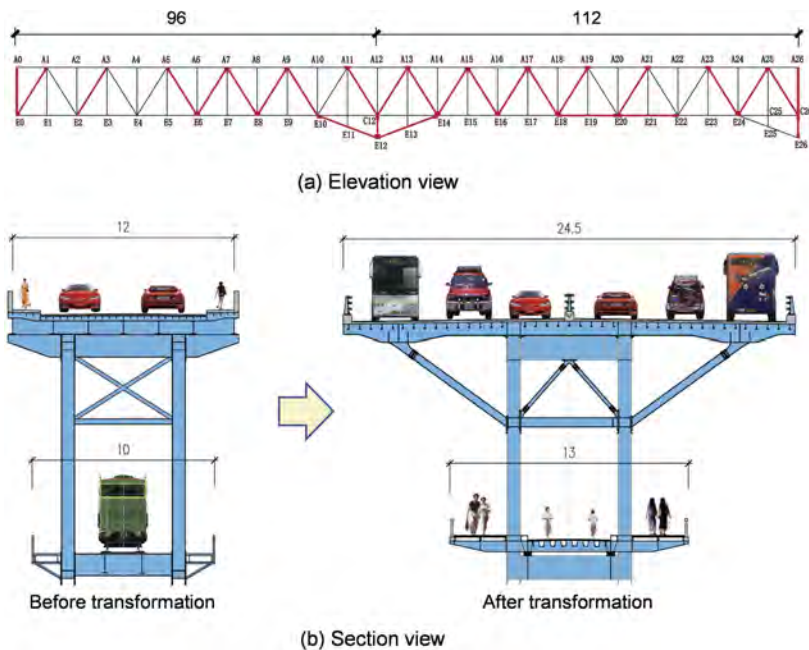


Figure 1. Overview of the strengthening and transformation project of Songpu Bridge (Unit: m).

1.2 Strengthening of truss joints

Taking A17 joint as an example to explain the strengthening solution for joints. The original A17 joint has insufficient horizontal shear resistance and needs to be strengthened. Moreover, the diagonal members connected with A17 joint (i.e., E16A17 and A17E18, in compression and tension, respectively) are strengthened by adding steel angles and steel plates, respectively. The designed strengthening solution of A17 joint is shown in Figure 2, where the strengthening parts are indicated as red. Two cover plates with a big opening are attached to the outside of the original gusset plate, without removing the existing rivets (the opening of the cover plates is for the space of the existing rivets). In addition, splice plates are attached to enhance the connection between the joint and truss members. New rivet groups are added to connect the plates.

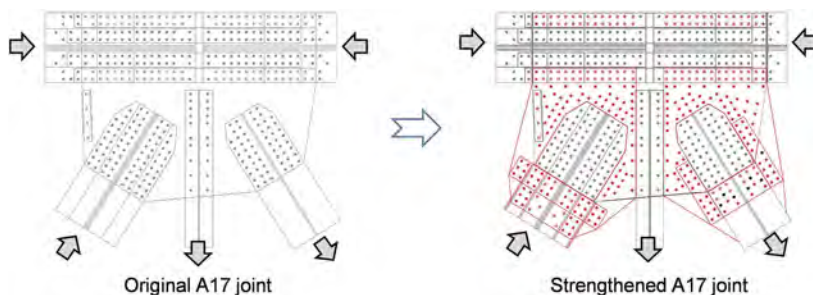


Figure 2. Designed strengthening solution for A17 joint.

1.3 Research significance

After strengthening in-situ, the joint has a complicated configuration, and the load transfer paths and failure modes become unclear. To evaluate the strengthening solution, a full-scale experimental study was conducted.

2 EXPERIMENTAL STUDY

2.1 Specimen

Some researchers conducted full-size tests on gusset joints (Bjorhovde and Chakrabarti, 1985, Turan et al., 2013) and riveted connections (D’Aniello et al., 2011, Collette et al., 2015). To test an entire full-size joint is very costly, which requires a huge reaction frame and multipoint loading devices; on the other hand, it is also difficult to have scaled specimens because of the riveted structure (the manufacturer can only provide a limited range for rivet size). Therefore, a full-scale specimen simulating one quarter structure of the prototype joint was designed, as shown in Figure 3.

The half part connecting with the tension diagonal member A17E18 and the half structure in the z direction was selected. The specimen consisted of 6 plates: original diagonal member ($t=30$ mm, which is equivalent to the area of a flange plate and half web of the H-shaped truss member), cover plate for diagonal ($t=16$ mm), original gusset plate ($t=16$ mm), cover plate for gusset ($t=16$ mm), and two splice plates ($t=16$ mm). The cover plate for diagonal was in the same plane with the original gusset plate, and the cover plate for gusset and the splice plates were on the top surface and bottom surface of these two plates, respectively. The photo of the specimen is shown in Figure 4.

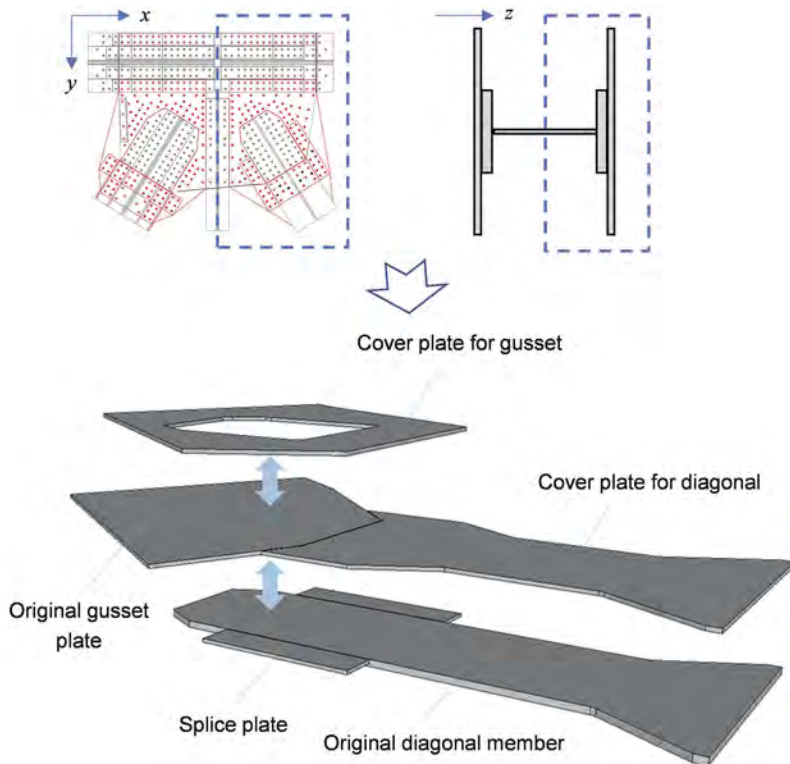


Figure 3. Full-scale joint specimen: one quarter of the prototype joint.

2.2 Test set-up and instrumentations

Figure 5 shows the test set-up that worked as a self-balancing system. The specimen was welded to the two bases. The two bases were customized such that they simulated the boundary

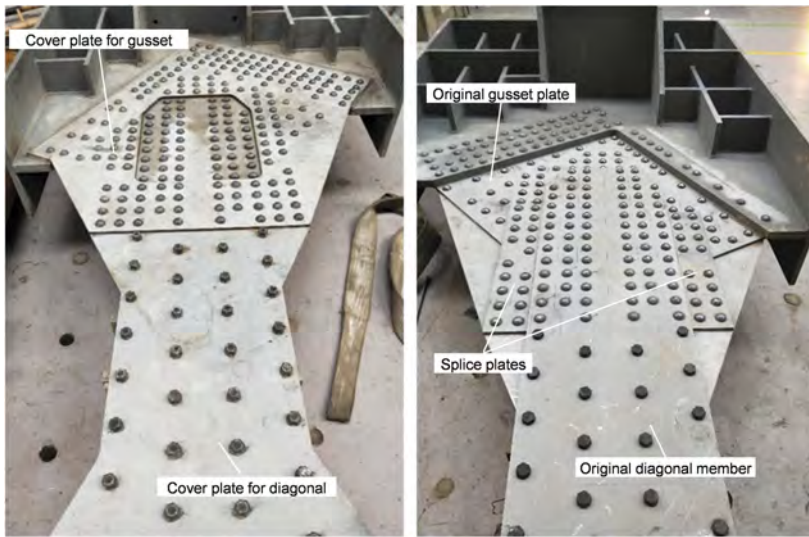


Figure 4. Photo of joint specimen (top and bottom sides).

conditions. Base-1 simulated the chord, vertical member, and the unselected parts of the prototype joint, whereas base-2 simulated the force transfer from the far-end of the tension diagonal A17E18. Two jacks were employed above and under the specimen, respectively. When the upper and lower jacks exerted pressure, the specimen in the middle was pulled. In order to ensure the free deformation of the specimen, rollers were arranged above and below the two bases.

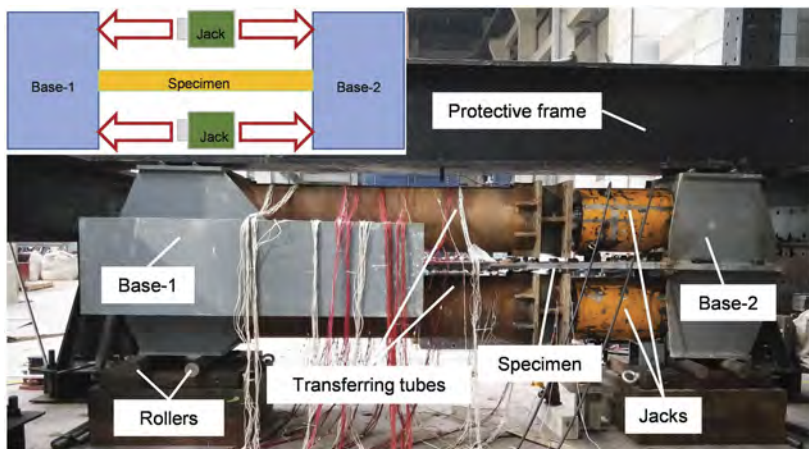


Figure 5. Photo of test set-up.

Eight linear variable differential transducers (LVDTs) were arranged as shown in Figure 6. LVDTs 1~4 were arranged in the plane of the specimen. LVDTs 1~4 measured the deformations in the load direction, of which LVDTs 1~2 and 3~4 measured the deformations of the entire specimen and the joint only, respectively; LVDTs 5~8 were arranged in the direction perpendicular to the plane of the specimen to measure the out-of-plane deformation.

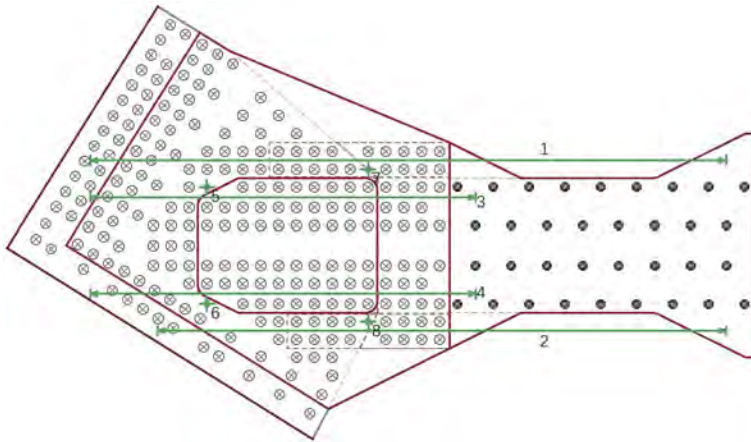


Figure 6. Layout of LVDTs.

3 EXPERIMENTAL RESULTS

3.1 Failure modes

Figure 7 shows the failure modes of the specimen, which included yielding of diagonal member, yielding of gusset plates, and shear failure of rivets.

- (1) Yielding of diagonal member. The original diagonal member and cover plate for the diagonal both yielded, and the bolt holes were elongated whereas bolts were undamaged (Circle A in Figure 7).
- (2) Yielding of gusset plates. Obvious residual deformations were observed at the locations where the cover plate for gusset was connected to the cover plate for diagonal (Circle B in Figure 7) and where the gusset plates were connected to the vertical member (Circle C in Figure 7).
- (3) Shear failure of rivets. The rivet connecting the original gusset plate and the cover plate for gusset, located near the vertical member was sheared to fracture.

3.2 Load–deformation curves

Figure 8a shows the tensile deformation of the entire specimen measured by LVDTs 1–2 and the tensile deformation of the joint measured by LVDTs 3–4, respectively. Both the gusset plates and the diagonal member yielded, resulting in large tensile deformations.

3.3 Ultimate tensile bearing capacity

According to the working conditions of the prototype joint, the required minimum capacity of the specimen is 3500 kN. The test was stopped when the maximum load reached 11868 kN, given that obvious plastic deformation of the specimen was observed, despite that the load could be still increased. The ultimate tensile bearing capacity was therefore taken as 11868 kN, which is 3.39 times of the required one.

4 CONCLUSIONS

An experimental study was conducted on a full-scale joint specimen that simulated one quarter part of a strengthened riveted joint to evaluate the strengthening solution. A novel test set-up was designed and customized to realize the test. Main conclusions are as follows:

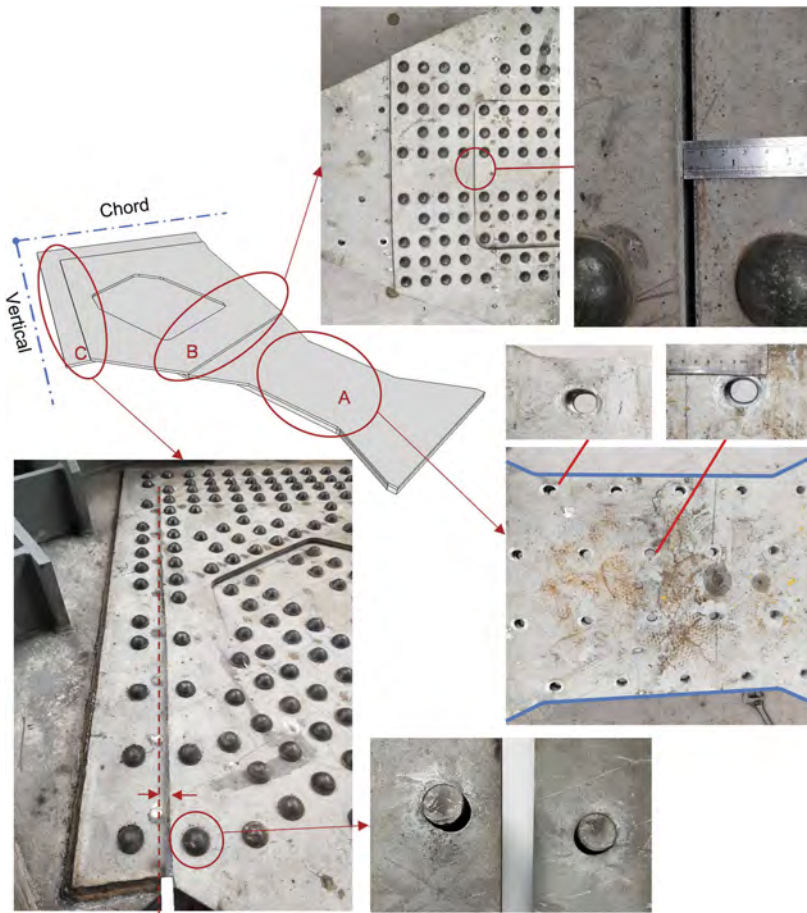


Figure 7. Failure modes.

- (1) The ultimate tensile bearing capacity of the specimen in the test reached 11868 kN, which is 3.39 times of the required minimum capacity, indicating that the strengthening solution of the riveted joint is safe and satisfactory.
- (2) The main failure mode was the yielding of the diagonal member and gusset plates. When the diagonal member yielded, the gusset plates also had obvious yielding deformation.
- (3) Shear failure of a rivet near the vertical member, connecting the original gusset plate and the cover plate for gusset, was observed. Although the failure of one rivet did not cause chain reaction to destroy other rivets around, such rivet failure is undesired. The rivets near the vertical member should be further strengthened.

As a follow-up, the design company optimized the strengthening solution according to the experimental results. An additional cover plate was attached to further strengthen the area near the vertical member.

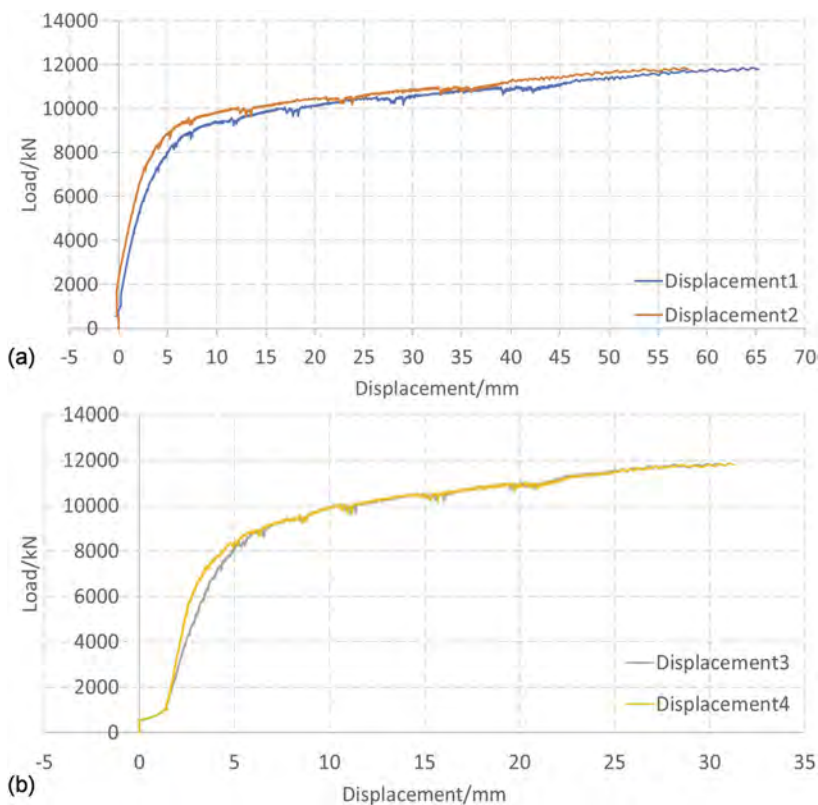


Figure 8. Load–deformation curves of test specimen.

REFERENCES

- Bjorhovde, R. & Chakrabarti, S. K. 1985. Tests of Full-Size Gusset Plate Connections. *Journal of Structural Engineering*, 111, 667–684.
- Collette, Q., Sire, S. & Wouters, I. 2015. Lap shear tests on repaired wrought-iron riveted connections. *Engineering Structures*, 85, 170–181.
- D’aniello, M., Portioli, F., Fiorino, L. & Landolfo, R. 2011. Experimental investigation on shear behaviour of riveted connections in steel structures. *Engineering Structures*, 33, 516–531.
- Shao, C. Y., Yan, H., Chen, L., Xu, Y. & Cao, S. L. 2019. Widening and Strengthening of the Songpu Bridge. *Structural Engineering International*, 29, 354–361.
- Su, Q., Wang, S., Xue, Z., Wang, Q. & Chen, L. 2019a. Reinforcement design of main truss members of existing riveted steel truss bridge in a widening and reconstruction project. *Bridge Construction*, 49, 75–80.
- Su, Q., Wang, S., Xue, Z., Zhang, C., Wang, Q. & Chen, L. 2019b. Influence of unloading degrees on the strengthening effect of the main truss members of steel truss girder bridges. *Engineering Mechanics*, 36, 92-97+105.
- Turan, O. T., Schumacher, T., Higgins, C. & Hafner, A. 2013. Experimental Tests of Truss Bridge Gusset Plate Connections with Sway-Buckling Response. *Journal of Bridge Engineering*, 18, 980–991.
- Wang, S., Su, Q., Jiang, X. & Ghafoori, E. 2022a. Stability of steel columns strengthened under preload: Numerical study with experimental validation. *Journal of Constructional Steel Research*, 197, 107440.
- Wang, S., Su, Q., Jiang, X. & Ghafoori, E. 2022b. Stability of steel columns with bolted strengthening under preload: Experimental study. *Journal of Constructional Steel Research*, 190, 107119.
- Wang, S., Su, Q., Jiang, X. & Ghafoori, E. 2023. Stability of steel columns with bolted strengthening under preload: An analytical model. *Journal of Constructional Steel Research*, 201, 107699.

*SS14: Data management and analysis for predictive
maintenance of aging infrastructure*
Organizers: F. Schmidt, M. Rasol & L.F.M. Sanchez



Taylor & Francis

Taylor & Francis Group

<http://taylorandfrancis.com>

Weather condition effect on the road surface friction: A preliminary assessment based on sensor data

M. Rasol, F. Schmidt & S. Ientile

Université Gustave Eiffel, Champs sur Marne, France

ABSTRACT: Changes in weather condition have a significant influence on the road surface friction. Extreme weather conditions are considered during heavy rains, and ice accumulation or snow-fall for the study of road surface. This could modify the road surface friction, a decrease of the road surface friction due to extreme wet condition, and increase car accident rates. Weather condition related factors usually are water film thickness due to the rain, ice accumulation and major temperatures (pavement, ambient and freezing). Better understanding of the weather condition changes on the road surface friction coefficient considering real-scale data monitoring system is essential to acclaim a reliable maintenance solution for road transport infrastructures. Long term data collection is a key factor for assess the relation between weather conditions, road surface friction coefficient. In the current re-search study, a preliminary assessment of weather condition influence on the road surface friction is elaborated for eighteen months considering data-driven from a novel intelligent road-based passive sensor. Results show that the most extreme weather conditions could impact road surface friction coefficient over time in road transportation system; mostly due to an increase of water film thickness and possibility of ice accumulation on the road surface. In conclusion different friction thresholds are elaborated for traffic management procedures, mainly 0.80 friction coefficient is considered the most stable and standard conditions, 0.60 acceptable, and 0.30 is an urgent condition.

1 INTRODUCTION

1.1 *Main background knowledge*

Road crashes are a major concern and significant problem for highway owners and operators.

There are numerous factors involved in a road accident rate. Friction between tires and pavements is considered one of the factors that could have a partial role in increasing accident rates. Poor friction on the pavement surfaces leads to uncontrolled condition of the driving task, partially this could have an impact on the driver behaviour during the riding. In particular this could be even more dangerous in wet conditions. Friction coefficient is subjected to numerous influential factors, which can be commonly classified into five categories First, tire-related factors (rubber compound, tire properties, rubber tread design and condition, inflation pressure, and tire operation temperature) (Kogbara 2016). Second, the road pavement surface - interrelated factors (pavement type, mix design materials, microtexture and macrotexture, surface temperature and construction age of the pavement) (Srirangam 2015). Third, intervening-substance-related factors (quantity particulate matter, and oil contaminants). Fourth, driver behavior related factors (stopping sight distance, driver health condition, speed control and knowledge of the surface pavement friction) (Plati, 2020). and, the fifth category is weather conditions factors which can influence the friction between vehicle tires and road surface pavement (van Bijsterveld, 2016).

The study of weather conditions influences on the friction force generated between tires and road surface pavement is a key to advance knowledge on the road surface in order to provide an appropriate solution for traffic management procedures. On the other hand, an appropriate traffic management procedure depends on the relation between the road surface friction and weather condition. Weather conditions have significant influence on the driving task considering both on the road surface pavement which directly affect the driving operation and the climate weather which is an important factor being able to modify the driving task in the road network system (van Bijsterveld, 2016) . Combination of both cases could make an impact to the roadway system and in extreme cases, temporary closing roads is recommended. Weather conditions affects can be from various weather changes factors such as ambient temperature, pavement temperature, ice temperature on the road surface during extreme winter condition (Rasol, 2021). On the other hand, under specific conditions, changes in weather condition can produce ice layer, water film. This could need an action which is commonly considered to decrease ice possibility (%) on road surface by means of a de-icing salt procedure. However, de-icing salt action could also affect the road surface when the deterioration is already on the pavement, independently of pavement materials (cement concrete or asphalt). These factors are essential to advance the knowledge on road surface friction coefficient which can partially (directly or indirectly) be involved in the increase of the accident crashes.

A complete traffic management procedure requires an adequate friction coefficient of the road surface pavement based on a specific minimum friction coefficient in a specific region considering changes in weather conditions. A steady minimum required friction of the roadway surface is mandatory. For this reason, an advanced understanding of the weather conditions which can affect the steady level of the friction is crucial to avoid obstacles in driving task operation on roadway. Weather condition data collection is a challenging task for infrastructure assessors specifically in real-time monitoring, and continues data acquisition. Different studies on the influence of the weather condition on road surface and friction has been conducted. Mainly water film thickness and air temperature are considered. In several studies a significant influence of the pavement temperature on friction is identified. In addition, mentioned research studies are based on data-driven from models or/and commonly used techniques such as Finite Element based models. Although, some researches present insignificant or low influence of temperature on road surface friction. Current methodologies are still in use for the purpose of the weather daily data collection on road pavements, a challenge is how accurate and efficient data are taken in term of daily data acquisition. In this study a novel weather sensor is applied to automatically monitoring big data in the daily form or monthly form related to weather changes and factors influencing road pavement surfaces.

In recent works, the use of intelligent road-based passive sensor is highly recommended due to the advantages of ability of big dataset storage, invasive technique, contactless, environmentally approachable and the real time automated data acquisition considering similar interval-time of adverse parameters.

1.2 Objectives and contribution

During the last decades various researches have been conducted by considering diverse techniques in order to define the effect of the weather conditions related parameters on road surface friction. This work focuses on a real case study of the eighteen months data-driven based on a commercially developed intelligent road-based passive sensor. Thus, weather data are collected considering time-interval and location of data acquisition station for current research case study.

The **main objective** of this research study is to present preliminary findings and results of a medium-size number of monitoring data on a real-case roadway system, and link to the followings highlighted points:

- Main objective: To monitor the road surface related data including weather condition and Friction coefficient of road surface on the real scale site based on the data driven from ice sensor in long term database,

- Sub-objective: Decision making tool to support road owners for the purpose of the traffic management procedures. To check with the minimum thresholds,
- The main link between weather condition factors influence on the traffic management procedures and friction coefficient thresholds.

The contribution of this work to the current knowledge is to understand how the consideration of the weather-related parameters can influence the friction stability. In order to provide a safe and reliable traffic management system it is crucial that the future friction measurement models take into account weather parameters.

2 CASE STUDY AND DATA COLLECTION

Intelligent road-based passive sensor is one of the innovative technologies to monitor the meteorological factors in the traffic road pavements. This sensor is installed towards the vehicle moving direction.

Data acquired for this research work is conducted for the purpose of the enhancing the resilience of the road transport infrastructure in the framework of the European project called PANOPTIS; aimed at increasing the resilience of the road transport infrastructures and remaining in safer and robust conditions during unfavorable conditions (Panoptis 2021). Data are acquired for eighteen months (starting December 2019 until June 2021) using intelligent road-based passive sensor.

This case study is conducted in the Spanish on-site highway located in Guadalajara province which connects Madrid city to Barcelona city. The length of the highway is about 77.5 kms (See Figure 1) with four lanes (two each traffic direction). Weather condition in mentioned zone can be severe and long winter session (temperature is commonly decreasing by $\sim 3^{\circ}\text{C}$) and hot and dry summer session (temperature is commonly increase to $\sim 50^{\circ}\text{C}$). The selection of this case study is based on three main reasons:

- The importance of the A2 Highway between two main and largest Spanish cities (Madrid and Barcelona).
- Diverse weather conditions.
- Road transport infrastructure age, and current health condition concern to public.

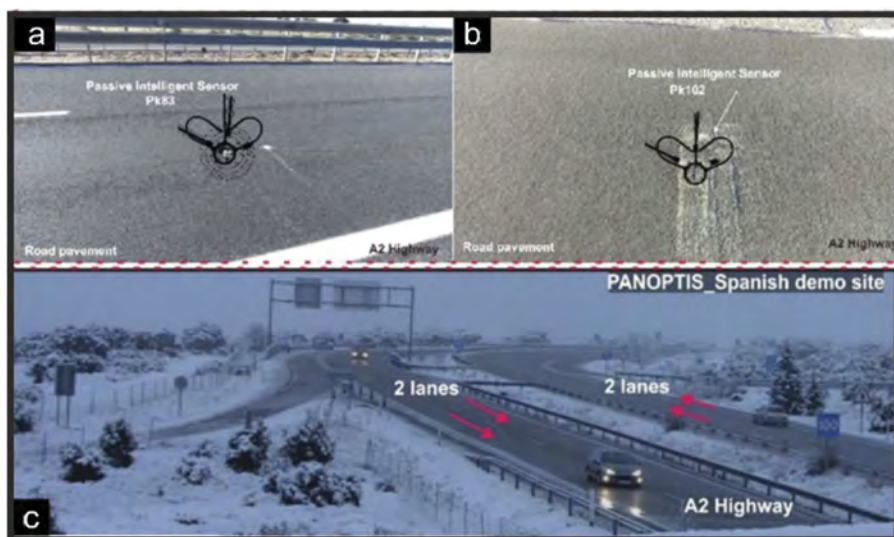


Figure 1. View of the case study in Spain; (a) Intelligent road-based passive sensor at station PK83, (b) Intelligent road-based passive sensor at station PK102, and (c) Spanish case study (adapted from previous work of authors [30]).

3 INFLUENCE OF WEATHER CONDITIONS ON ROAD SURFACE FRICTION

3.1 The relation between road surface friction and weather-related parameters

Safe highway pavement to serve a reliable transportation of humans and goods is crucial for further economy growth. Understanding the pavement friction and factors affecting the operation of surface pavement texture is key in order to provide a safe, comfortable path for transportation operations. In this section, weather conditions factors are investigated by means of weather intelligent road-based passive sensor.

Weather data are collected during eighteen months in a selected A2 highway case study in Spain (see Section 2) for better understanding the influence of weather factors (e.g., ambient temperature, pavement temperature, ice temperature, ice possibility, water film thickness and road conditions) on pavement friction functionality and to further explore influence of each parameter individually on pavement friction. Various minimum thresholds are considered in the literature for a safe friction coefficient operation in road pavements. Generally, a safe and optimal standard friction coefficient is considered in a range of 0.80 in normal conditions (Rasol 2020), and these range is also considered by Spanish authorities in this case study. Figure 3 presents the influence of (ambient or (in another meaning is air temperature and pavement temperature) on the pavement friction. Ambient temperature alone could have slight influence on the friction of the road surface as shown a group of measurements in the square, which friction keeps in a normal range. In addition, during winter season with a decrease in ambient temperature in-between (0 - 10 °C), pavement friction decreases up to 0.58 according to the data collected in this case study this could be not only because of the ambient temperature but interaction with other weather condition for example the presence of temperature of ice layer/ice temperature or water on the road surface (see Figures 2a and 3a, b). On the other hand, Figure 3. b presents a similar reduction in pavement friction during winter season when pavement temperature reaches a low range of (0 - 10 °C) This could be also partially related to the possibility of ice and rainfalls due to the accumulation of water on road surface.

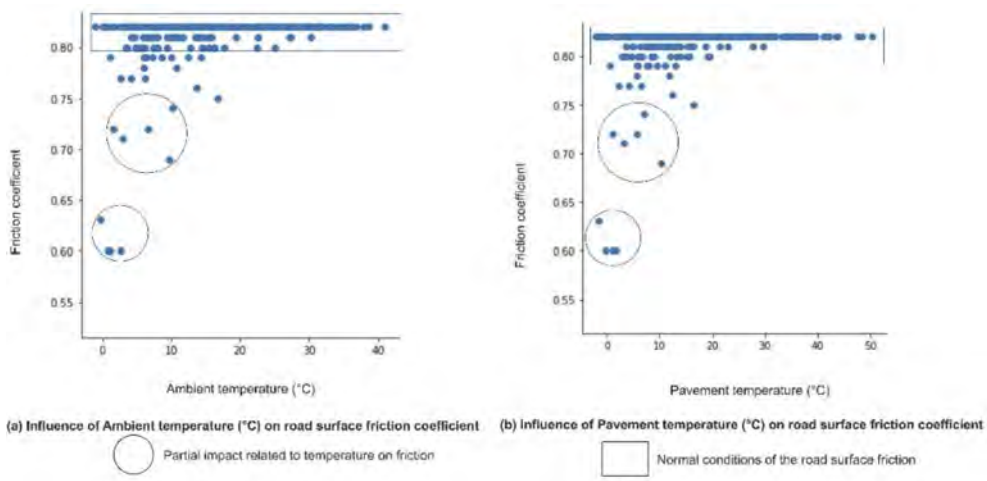


Figure 2. Influence of temperature on road surface friction: (a) Ambient temperature (°C), and (b) Pavement temperature (°C).

Figure 2 presents the data collecting related to two other main weather factors, namely ice temperature and possibility of ice on the surface pavement. In respect of the low ice temperature the friction coefficient decreases up to 0.6. (see Figure 3a). However, the existence of ice possibility (ice layer distribution percentage) on the surface pavement lead to a significant dropping of the friction. For instance, in the winter when ice possibility reaches

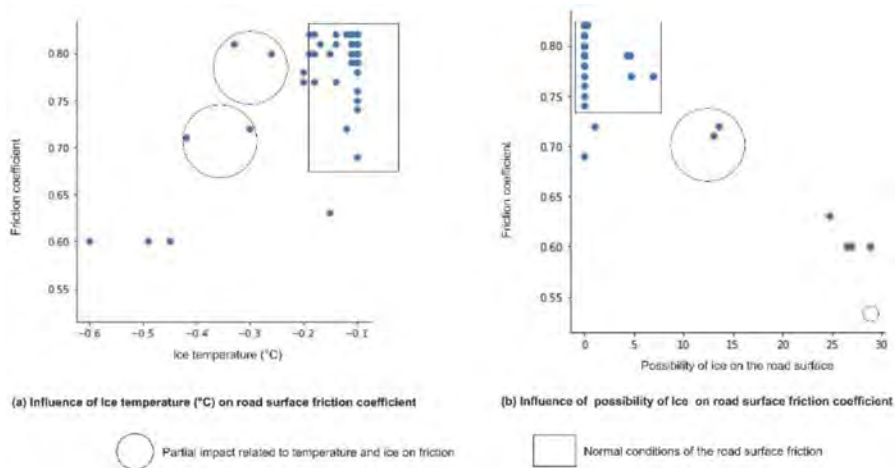


Figure 3. Influence of (a) Ice temperature (°C), and (b) Ice possibility on road surface (%) on road surface friction.

to 30% the friction decreases to 0.24, which is unacceptable threshold according to different standards. For this reason, in similar cases usually de-icing and de-salting plans (Trenouth 2015) are employed in order to guarantee road user's safety (see Figure 4b, small circle in the right).

Water film thickness is one of the main weather conditions factors occurring after a rainfall, which can significantly influence the reliable functionality of the road pavement friction. An increase of water film thickness could cause a decrease in the road surface friction. Figure 3a show the increase in water film thickness would cause decrease in pavement friction coefficient: when water film thickness reaches 1250 (μm) surface pavement friction decrease up to 0.55. Additionally, road conditions (e.g., dry, moist, damp, ice covered, snow and chemically wet) can influence the reliable transportation of goods and people in road pavements. Figure 3b shows during damp (moist) and wet road condition (coding represents in-between 20-255, which is a mix of water and conditions of ice, which is considered wet condition), this is the most frequent condition when friction decreases. In a case of chemically wet or contaminated road pavement surface (see Figure 4b, horizontal axis 35) friction dramatically reaches unsafe value which is 0.24, this could be also partially related to the existence of possibility of ice (Figure 2b).

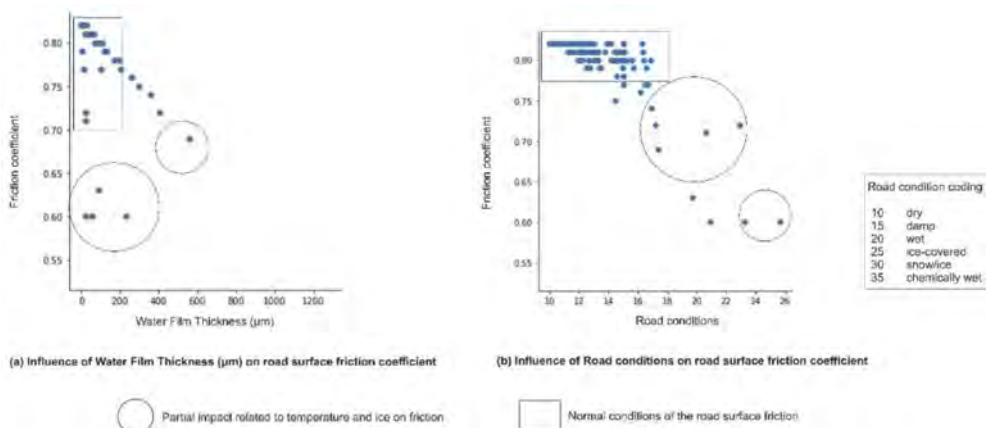


Figure 4. Influence of (a) Water Film Thickness (μm), and (b) Road conditions on road surface friction.

Table 1 shows some critical condition in the different periods of the year including winter and summer season, the relevant and partial influence or more precisely the interaction between two parameters can be observed. For instance, in the point 4 (P4) during winter ice possibility is around 24.76 and water film thickness is 88.49 μm which decreases friction coefficient to 0.63. Here, probably the interaction between ice and water influences the road surface friction. More researches are needed in order to find the interaction between parameters and their influence on the friction.

Table 1. Critical weather conditions for some specific points (not all data) on the Spanish case study.

No.	Time	Season	Friction coefficient	Water Film thickness (μm)	Possibility of ice on road surface	Road condition (see Table 3)
P1	2019/12/20 00:00 - 2019/12/20 23:59	Winter	0.69	559.45	0.00	17.36
P2	2020/03/31 00:00 - 2020/03/31 23:59	Winter-Spring	0.72	403.39	1.00	22.90
P3	2020/05/31 00:00 - 2020/05/31 23:59	Spring-Summer	0.53	1275.32	0.00	20.00
P4	2021/01/08 00:00 - 2021/01/08 23:59	Winter	0.63	88.49	24.76	19.70

3.2 Pre-assessment thresholds and possible action of road surface friction

According to the current procedure, the friction coefficient is monitored in a non-steady basis to ensure the good state of the road surface for drivers, but it does not consider the effect of climatic conditions. This study introduces the effect of the climatic condition on friction coefficient.

Even though the road surface should remain in a good state according to the squid resistance standards, but it is useful to be aware about the effect of climatic conditions in instantaneous friction coefficient. In order to use this valuable information as input when making decisions on instantaneous traffic management (e.g., control of maximum velocity).

For this reason, defining possible thresholds of road surface friction value with potential actions based on different condition is essential. As a consequence of this study and considering local authorities' thresholds for traffic management system, three main thresholds are defined for this specific case study taking into account the global standards of the most stable friction coefficient.

Table 2 presents thresholds of the friction with possible actions of monitoring of road pavement associated to thresholds of friction coefficient.

Table 2. Thresholds of the friction with possible actions of monitoring of road pavement associated to thresholds of friction coefficient.

No.	Thresholds (Friction coefficient)	Conditions	Possible actions	Monitoring level
1	0.30	Critical	An urgent action is needed (e.g., maintenance)	Intervention level [20]
2	0.60	Acceptable low	Frequent monitoring and traffic management plan (TMP) e.g. control of maximum velocity	Intervention level [20]
3	0.80	Optimal	Normal TMP	Investigatory level [20]

Table 3. Summary results of the influence of the critical weather conditions on road surface friction.

No.	Road surface	Weather conditions	Critical values	Surface friction	Friction Reduction Percentage (%)	Figure
1	Temperature	Ambient (°C)	-3	0.59	26.25	3.a
		Pavement (°C)	-2	0.58	27.5	3.b
		Ice (°C)	-0.5	0.58	27.5	4.a
2	Conditions	Possibility of ice on surface	80	0.24	70.00	4.b
		Water film thickness (µm)	1250	0.55	31.25	5.a
		Road conditions	35	0.24	70.00	5.b

4 CONCLUSIONS AND FUTURE WORKS

Reliable road pavement is dominant infrastructure for both human safe transportation and economy growth, specifically with a vast growth in the traffic management system in Europe and worldwide. In order to provide a comprehensive knowledge on road system network various factors should be taking into account (e.g., weather conditions, pavement texture, human behavior, lighting and visibility, signals and road marking, safety instructions). In this research paper, the influence of weather conditions on road surface friction is investigated by means intelligent road-based passive sensor. This work concludes that the relation between several weather condition related factors on the road surface friction in real scale case study. The final remarks for this preliminary study are:

- The use of intelligent road-based passive sensor for 18 months weather condition data related recorded in a real scale case study in Spain. The relation between weather condition, road surface friction is presented in this work. Results show that the most reliable friction coefficient thresholds alarms are considered by Spanish authority, and previous knowledge is 0.80 optimal friction coefficient, which is considered standard condition. On the other hand, a frequent monitoring of the road surface is essential when the friction coefficient decrease to less than 0.60, and less than 0.30 could be considered an urgent condition (see Table 2), and in this case an urgent maintenance of the road surface is needed, specifically in case of extreme weather condition such as ice or snow.
- The most extreme weather condition factors (the weather factors which can influence the road surface friction stability) have significant impact on road surface friction are the increase of ice-percentage and water film thickness on the road surface (see Table 3).
- Ambient (air) and pavement temperatures have slightly similar influence on road surface friction. Which can be considered as an in-direct factors or partially influence the road surface friction and accident rates.
- Beside other intervention factors can also affect the friction stability, which are age, texture depth, abrasion and other macro texture properties. This study has considered a preliminary finding of the main relation between road surface friction and weather condition related factors.
- This study provides a decision-making support tool for end-users, and owners/operators in charge of the operation of the road network. This model has been integrated to the holistic novel platform of the PANOPTIS project funded by European Union in order to increase resilience of road transport infrastructure.
- This work will be extended for future/and on-going project by using machine learning approaches. In the context of machine learning application for forecasting prediction of friction coefficient and use of real-time monitoring of friction coefficient.

ACKNOWLEDGMENT

This project has received funding from the European Union's Horizon 2020 research and innovation program under grant agreements No. 769129.

REFERENCES

- Kogbara R.B., Masad E.A., Kassem E., Scarpas A., and Anupam K., A state-of-the-art review of parameters influencing measurement and modeling of skid resistance of asphalt pavements, *Constr. Build. Mater.*, vol. 114, pp. 602–617, 2016, doi: 10.1016/j.conbuildmat.2016.04.002.
- Panoptis, 'PANOPTIS Horizon 2020 project (Grant No. 769129). <http://www.panoptis.eu/>', 2021.
- Plati C., Pomoni M., and Georgouli K., Quantification of skid resistance seasonal variation in asphalt pavements', *J. Traffic Transp. Eng. (English Ed.)*, vol. 7, no. 2, pp. 237–248, 2020, doi: 10.1016/j.jtte.2018.07.003.
- Rasol M, Schmidt F, Ientile S, Adelaide L, Nedjar B, Kane M, Chevalier C. Progress and Monitoring Opportunities of Skid Resistance in Road Transport: A Critical Review and Road Sensors. Remote Sensing. 2021; 13(18):3729. <https://doi.org/10.3390/rs13183729>
- Srirangam S.K., Anupam K., Kasbergen C., Scarpas A., and Cerezo V., Study of Influence of Operating Parameters on Braking Friction and Rolling Resistance, *Transp. Res. Rec. J. Transp. Res. Board*, vol. 2525, no. 1, pp. 79–90, 2015, doi: 10.3141/2525-09.
- Trenouth W. R., Gharabaghi B., Perera N., Road salt application planning tool for winter de-icing operations, *J. Hydrol.*, vol. 524, pp. 401–410, 2015, doi: 10.1016/j.jhydrol.2015.03.004.
- Van Bijsterveld W., del Val M.A., Towards quantification of seasonal variations in skid resistance measurements, *Road Mater. Pavement Des.*, vol. 17, no. 2, pp. 477–486, 2016, doi: 10.1080/14680629.2015.1090909.

Prediction of recovery time of infrastructure functionalities after an earthquake using machine learning

B. Derras

University of Tlemcen and University of Saida, Tlemcen, Algeria

N. Makhoul

Politecnico di Milano, Milan, Italy

ABSTRACT: The recovery time (RT) is one of the essential components of infrastructure seismic resilience analysis. This seismic infrastructure resilience is crucial to keep the functionality of critical infrastructure and recover them quickly during strong earthquakes. It is necessary to ensure that the RT is estimated beforehand. This RT depends on some factors (Derras & Makhoul 2022). We develop machine-learning empirical models for estimating the RT based on earthquake damage data to achieve that goal. Firstly, a dataset of earthquake damage was established. This dataset contains the metadata (explanatory factors), such as earthquake magnitude (M), Ground-Motion Intensity Measures (IM), as well as the recovery time (target). Using the more famous machine learning algorithms, we establish empirical models to predict the RT of a given system (gas, power, water, and Telecommunications). The best model must represent well the resilience curve with an optimal aleatory variability. The estimate early of the recovery time (here by machine learning approach) is essential information for authorities and a primary step in the infrastructure seismic resilience assessment.

1 INTRODUCTION

Prediction of recovery time of infrastructure functionality refers to the process of estimating how long it will take for infrastructure, such as roads, bridges, buildings, and utilities, to be repaired and restored to full functionality after an earthquake or other disaster (Cao et al. 2022). The recovery time prediction is based on various factors, including the earthquake severity, the infrastructure condition before the earthquake, and the availability of resources for the recovery effort.

There are several reasons why predicting the recovery time of infrastructure after an earthquake is essential: 1) It helps emergency responders and decision-makers allocate resources and plan for the response and recovery efforts more effectively. 2) It allows affected communities and individuals to better prepare for the disruption and plan accordingly. 3) It informs the prioritization of repair efforts, ensuring that essential services, such as electricity and water, are restored as quickly as possible. 4) It helps identify potential bottlenecks or challenges in the recovery process, allowing for proactive planning to address these issues. 5) It can aid in the development of contingency plans in case the recovery takes longer than expected.

Several methods (Cremen et al. 2020) can be utilized to predict the recovery time of infrastructure after an earthquake, including: a) Statistical models: Statistical models can be used to analyze data on past earthquakes and the recovery time of infrastructure in order to identify trends and patterns that can be utilized to make predictions about future recovery times. b) Expert judgment: Experts in earthquake engineering and infrastructure recovery can use their knowledge and experience to make informed estimates about the recovery time of different types of infrastructure. c) Machine learning algorithms: Machine learning algorithms can analyze a range of data, including data on the severity of the earthquake, the condition of the infrastructure before the earthquake, and the availability of resources for the recovery effort (Derras & Makhoul 2022) and (Durante & Rathje 2021). By training a model on data from past earthquakes, it may be possible to make more accurate predictions about the recovery time for future earthquakes.

Statistical models present several potential disadvantages to predicting the recovery time of infrastructure after an earthquake: i) Limited data: Statistical models rely on data to make predictions. However, there may be a limited amount of data available on past earthquakes and the recovery time of infrastructure. This can make it difficult to predict recovery times for future earthquakes accurately. ii) Assumptions: Statistical models often rely on certain assumptions about the data and the underlying relationships between variables. If these assumptions are not met, the predictions made by the model may not be accurate. iii) Limited flexibility: Statistical models are designed to identify patterns and trends in data and may not be able to accurately capture more complex relationships or unusual events. This can limit the accuracy of the predictions made by the model. iv) Black box approach: Statistical models can be difficult to interpret, making it difficult to understand why a particular prediction was made. This can make it challenging to identify any potential biases or errors in the model.

On the other side, there are several potential disadvantages to using expert judgment to predict the recovery time of infrastructure after an earthquake: α) Limited knowledge: Experts can only provide predictions based on their knowledge and experience. They may not be aware of all relevant factors that could impact the recovery time. β) Limited objectivity: Expert judgment is subject to personal biases and opinions, which can impact the accuracy of the predictions. γ) Limited scalability: Relying on the expert judgment can be time-consuming and may not be practical in situations where a large number of infrastructure systems need to be evaluated. δ) Dependence on a single source: Relying on a single expert for predictions can be risky, as the expert may not be available or may make an error in their evaluation.

Considering these inconveniences, we are choosing, in this study, machine learning algorithms as a powerful tool for predicting the recovery time of infrastructure after an earthquake, and they can provide a range of benefits in certain situations. There are numerous advantages to using machine learning algorithms to predict the recovery time of infrastructure after an earthquake: 1) Ability to handle large amounts of data: Machine learning algorithms can analyze a large amount of data, including data on the severity of the earthquake, the condition of the infrastructure before the earthquake, and the availability of resources for the recovery effort. This can help to identify patterns and trends which may not be visible to the human eye and can improve the accuracy of the predictions. 2) Ability to make accurate predictions: When trained on sufficient data, machine learning algorithms can make highly accurate predictions. This can be particularly helpful in situations where the recovery time of infrastructure is critical, as it can help to ensure that the necessary resources are allocated, and the recovery process is planned effectively. 3) Ability to continuously improve: Machine learning algorithms can be trained on new data as it becomes available, which can help to improve the accuracy of the predictions over time. 4) Automation: Machine learning algorithms can automate the prediction process, saving time and reducing the potential for human error. Overall, machine learning algorithms can be a powerful tool for predicting the recovery time of infrastructure after an earthquake and can provide a range of benefits in certain situations.

For example, researchers at the University of Texas at Austin and the Texas Advanced Computing Center used machine learning to assess the effectiveness of four common algorithms in predicting earthquake-induced damage grade and rehabilitation intervention in residential buildings (Sajan et al. 2023). The researchers used a dataset of 549251 buildings collected after the 2015 Nepal earthquake (Sajan et al. 2023). In addition, machine learning has been used to predict earthquakes in four different seismic zones (Japan, Turkey, Greece, and Indian Subcontinent) (Hoque et al. 2020). Researchers have also published data, models, and methods related to their research on natural hazards (Dubrow 2021), which can be used to refine machine learning models for predicting the recovery time of infrastructure functionalities after an earthquake.

The roadmap used in this study that allows estimating the downtime caused by an earthquake is summarized in the following: 1) Determine the scope of the analysis: First, you should determine the specific systems or infrastructure that you are interested in analyzing, as well as the time frame over which you want to estimate the downtime. 2) Collect data: Next, you will need to collect data on the location and magnitude of earthquakes, as well as information about the types and conditions of the systems or infrastructure that you are analyzing. This may include data on the material, design, and construction of the systems or infrastructure, as well as any past damage

or repairs. 3) Analyze the earthquake's impact: Using the data you have collected, you should assess the earthquake's potential impact on the systems or infrastructure that is of interest to you.

This may involve analyzing the damage that the systems or infrastructure are likely to sustain, as well as the time needed for repair or replacement. 4) Estimate the downtime: Based on the earthquake's impact on the systems or infrastructure, you should estimate the downtime the earthquake will cause. This may involve calculating the time needed for repair or replacement and any additional time required to implement contingency plans or bring the systems or infrastructure back to full capacity. 5) Validate your results: To ensure the accuracy and reliability of your estimates, it is essential to validate them by comparing them to real-world data or by using other methods to estimate the expected downtime due to an earthquake. This will help you confirm your analysis validity and identify areas for improvement.

2 DATA

2.1 *Initial dataset and basic evaluation model*

The dataset used herein is based on (Kammouh et al. 2018) dataset from 32 earthquakes all over the world (around 28% in USA, 31% in Japan, 3% in Africa, 6% in Oceania, 18% in South America, and 12% in Southern and Eastern Asia). The selected earthquakes occurred between 1960 and 2014 and has a magnitude ranging between 6 and 9. The affected lifelines are the power, water, gas, and telecom, and the downtime (DT) is reported for those infrastructures. The dataset detailed in (Kammouh et al. 2018), is an empirical dataset, and it was completed using (AI methods) and will be developed further for article (Derras & Makhoul 2024). In this article we consider the downtime DT in number of days similarly as the T_{AB} time needed for the infrastructure or here the lifeline to recover (Cimellaro et al. 2006) and (Bruneau et al. 2003). The Downtime DT is similar to the recovery time RT. The evaluation model with the initial dataset is very simplistic one and it rows with sophistications as we add additional input factors.

2.2 *Adding additional factors to improve data quality.*

Adding estimation factors as inputs to the machine learning model can help improve its performance by providing the additional information from which the model can learn. This process is called feature engineering, and it's an iterative process where different features are tested, and the most informative ones are selected for the final model. Before adding the estimation factors to the inputs, it is essential to understand how they relate to the output variable and if they can add value to the model. It's also important to preprocess the data and handle any missing or outliers' values. Once the estimation factors are added to the inputs, the model can be re-trained using the new data. The model's performance can be evaluated using metrics such as square correlation coefficient R^2 (in the cross-validation phase) and Root Mean Square Error (RMSE). If the performance improves, the new features are considered beneficial and kept in the final model.

The initial dataset has three factors system, magnitude, and PGA. Here we add and test four strong factors: Joyner-Boore distance (RJB), cumulative absolute velocity (CAV), EMS-98 (European Macro-seismic Scale), and global recovery time by country from the GEM platform. We use the neural networks technic as a reference model (B. Derras et al. 2012). As discussed in (Derras & Makhoul 2022), many other variables need to be considered such as the region wealth, man-power, season of the earthquake occurrence, the localization within a country etc. The first model here is a simplification and the full assessment is considered in (Derras & Makhoul 2024).

2.2.1 *Joyner-Boore distance (RJB)*

The relationship between Joyner-Boore distance and downtime after an earthquake is generally inversely proportional. The greater the Joyner-Boore distance, the less intense the ground motion is likely to be, and the less severe the damage to the structure or building is expected to be. This means that structures or buildings farther away from the earthquake's epicenter will have a shorter downtime after the event. Conversely, structures or buildings closer to the epicenter will experience stronger ground motion and are more likely to sustain severe damage, leading to a longer downtime.

2.2.2 Cumulative Absolute Velocity (CAV)

Cumulative Absolute Velocity (CAV) is a metric (that accounts for the amplitude, frequency, and time) used in seismic engineering to measure the total amount of ground shaking that occurs during an earthquake. CAV is a good indicator of an earthquake's damage potential, so that it might add and test in the current study.

There is a relationship between CAV and downtime after an earthquake, as a higher CAV value generally corresponds to more significant damage and longer downtime. The more damage an infrastructure sustains, the more repairs will be needed and the longer the downtime will be. Infrastructure exposed to higher levels of ground shaking will typically sustain more damage than those exposed to lower levels, which can result in a longer downtime (Figure 1).

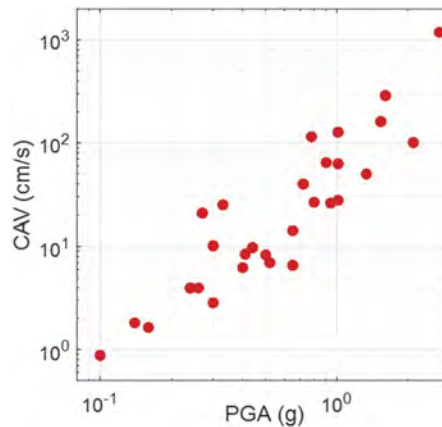


Figure 1. The RJB function of peak ground acceleration (PGA) for an RSME equals 0.23.

2.2.3 EMS-98 (European macro-seismic scale)

The European Macro-Seismic Scale (EMS-98) is a scale used to measure the intensity of ground shaking during an earthquake. It denotes how strongly an earthquake is felt and the associated damage it causes. It is used to evaluate seismic intensity in European countries. It ranges from 1 to 10, with 10 being the highest level of intensity. There is a correlation between EMS-98 and ground-motion parameters such as peak ground acceleration (PGA, CAV). Still, there is no direct relation between EMS-98 and downtime after an earthquake: This is what we show next.

However, theoretically, there is a relationship between the EMS-98 and downtime after an earthquake, as a higher EMS-98 value generally corresponds to greater damage and longer downtime. Buildings and infrastructure that experience a higher level of intensity of ground shaking will typically sustain more damage than those exposed to lower levels, which can result in a longer downtime. The more damage an infrastructure sustains, the more repairs will be needed and the longer the downtime will be. It is worth noting that the EMS-98, potentially, is a good indicator of the damage potential of an earthquake with other factors, such as the ground intensities measured (PGA, CAV). (Zanini et al., 2019) suggested the following expression:

$$ESM_{98} = 2.03 + 2.28 * \log_{10}(PGA); \% \text{ PGA in gal} \quad (1)$$

2.2.4 Global recovery level

The Recovery/Reconstruction Potential Map is closely aligned with the concept of disaster resilience. Enhancing a country's resilience to earthquakes is to improve its capacity to anticipate threats, reduce its overall vulnerability, and allow its communities to recover from adverse impacts from earthquakes when they occur. The measurement of recovery and reconstruction potential includes capturing inherent conditions that will enable communities within a country to absorb the impacts and cope with a damaging earthquake event, such as the density of the built environment,

education levels, and political participation. It also encompasses post-event processes that facilitate a population’s ability to reorganize, change, and learn in response to a damaging earthquake.

3 METHODOLOGY

The correct prediction of downtime T_{AB} is crucial for evaluating the resilience of a system (The parameter systems are the considered lifelines (i.e., power, water, gas, and telecom)). that has been disturbed by an external force. T_{AB} is closely related to functionality Q , which is, in turn, dependent on various social, economic, and intensity measures of the earthquake and structural factors. A supervised machine learning model ((Derras et al. 2012), (Derras & Makhoul 2022)) can be used to establish a correlation between these factors and the T_{AB} . This can be done by using the factors as inputs and training the model to output predictions for T_{AB} . However, it is essential to state that the accuracy of this model will depend on the quality of data and the complexity of the model used. Preprocessing the data and adequately selecting the model architecture will help to improve the predictions. It is also essential to consider the factors that influence T_{AB} and to take them into account when building the model.

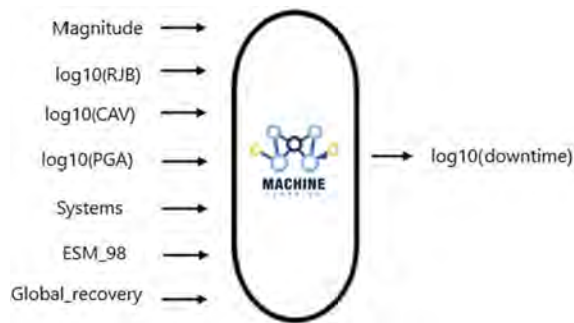


Figure 2. The Input and output factors of the machine learning final model.

3.1 Machine learning algorithms

The concept of Machine Learning (ML) was first introduced in 1959 by IBM scientist Arthur Samuel. ML is considered a subset of the broader field of Artificial Intelligence (AI), and it allows computers to learn and improve their performance without being explicitly programmed. ML algorithms can be divided into different categories based on their purpose. One category of particular interest is supervised learning, which involves training a model to map inputs to outputs based on example input-output pairs. In earthquake engineering, various ML algorithms are commonly used to extend classical regression techniques and eliminate the need for pre-defined functional forms. The following section presents some of this field’s most widely used ML algorithms.

4 COMPARISON BETWEEN SEVERAL MACHINE LEARNING APPROACHES

The correlation coefficient and Root Mean Squared Error (RMSE) are commonly used metrics to evaluate the performance of different machine learning algorithms. We can use these metrics to compare the performance of different machine learning algorithms like Tree Decision, SVM, Boosted tree, Gaussian-Process Regression, and Neural Networks. A higher correlation coefficient and lower RMSE indicate a better model fit to the data and better algorithm performance.

- **Linear Regression:** Linear regression is a supervised machine learning algorithm for predicting a continuous target variable based on one or more input features. It finds the line of best fit through the data points and uses it to make predictions. It’s a simple algorithm that can be useful when the relationship between the input and output is linear.

- **Decision Tree (DT):** A decision tree is a supervised machine learning algorithm that creates a tree-like model of decisions and their possible consequences. It's commonly used for classification and regression problems. It's simple to understand, interpret and visualize.
- **Support Vector Machines (SVM):** The SVM is a supervised machine learning algorithm. SVM can be utilized for classification and regression problems. It's effective in high-dimensional spaces and can be used with a non-linear boundary using the kernel trick. It finds the best boundary between different classes by maximizing the margin, i.e., the distance between the closest data points of each class and the boundary.
- **Boosted Tree:** Boosted tree is a supervised machine learning algorithm combining multiple decision trees to improve the model's overall performance. It iteratively adds decision trees to the model and adjusts the weights of the trees to minimize the overall error. It's a powerful algorithm that can handle large datasets and complex relationships between inputs and outputs.
- **Gaussian-Process Regression:** Gaussian Process Regression (GPR) is a supervised machine learning algorithm based on the theory of Gaussian processes. It's a non-parametric approach that can model any continuous function and makes predictions by computing the probability distribution of the function's values at any point. GPR is useful for problems with small datasets or complex relationships between inputs and outputs.
- **Neural Network:** Neural network is a supervised machine learning algorithm that is inspired by the human brain structure and function. It's composed of layers of interconnected nodes, called neurons, that process information. Neural networks can be used for various tasks, natural language processing, including image and speech recognition, and time series forecasting. They are particularly useful for handling large and complex datasets.

4.1 *Boosted tree ensemble method.*

The Boosted Regression Trees (BRT) is a combination of two techniques: decision tree algorithms and boosting methods (Sajan et al. 2023). Boosting is an ensemble meta-algorithm used in machine learning to reduce errors in predictive data analysis (Sajan et al. 2023) and (Dubrow 2021). It generates multiple weak learners and combines their predictions to form one strong classifier (Hoque et al. 2020) and (BCCVL 2021). In the case of BRT, each tree is dependent on prior trees (Dubrow 2021). The Boosted Trees Model makes predictions by combining decisions from a sequence of base models (BCCVL 2021). When to use a boosted trees model? It is useful when you have a large number of variables concerning the number of observations (Sajan et al. 2023) and (BCCVL 2021). Whereas decision tree algorithms are supervised learning approaches used in statistics, machine learning and data mining (Sajan et al. 2023). They use multiple algorithms to decide to split a node into two or more sub-nodes, increasing the homogeneity of each node (Dubrow 2021). Decision trees are an easy way to understand and interpret, require little data preparation, and have a low cost of predicting data (Hoque et al. 2020). Example of decision tree is where each leaf node corresponds to a class label, and branches to attributes (BCCVL 2021).

4.2 *Hyperparameter optimization*

Hyperparameter optimization for boosted trees involves tuning parameters such as the learning rate, the minimum number of leaves, and the number of learners to improve the model's performance. This is done here by (popular method) using Bayesian optimization techniques (BOT), which uses a probabilistic model to guide the search for the optimal set of hyperparameters. By using this technique, a probabilistic model guides the search for the optimal set of hyperparameters. We have obtained the following values: Minimum leaf size = 1, Number of learners = 1000, and Learning rate = 0.1. Moreover, we keep 20 % of all data for the validation phase to avoid an overfitting problem.

5 RESULTS

The results are presented briefly in Section 5.1 for the predictor importance and the final improved estimation using a machine-learning techniques (Section 5.2).

5.1 Predictor importance

The predictor importance (PI) chart aims to indicate the relative importance of every predictor in the model estimation. The sum of all the predictors relative values is 1.0 (or 100%). The PI does not express the model accuracy but reflects the importance of the predictors in prediction making. For the DT Machine Learning model we suggested, we obtained as show in Figure 3 that the systems (i.e., lifelines) are the most important predictors (around 60%), followed by CAV (15%), and the least important is EMS₉₈ with 0% relative value.

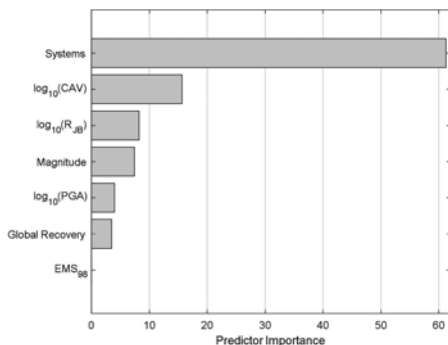


Figure 3. The predictor importance for the DT machine learning model.

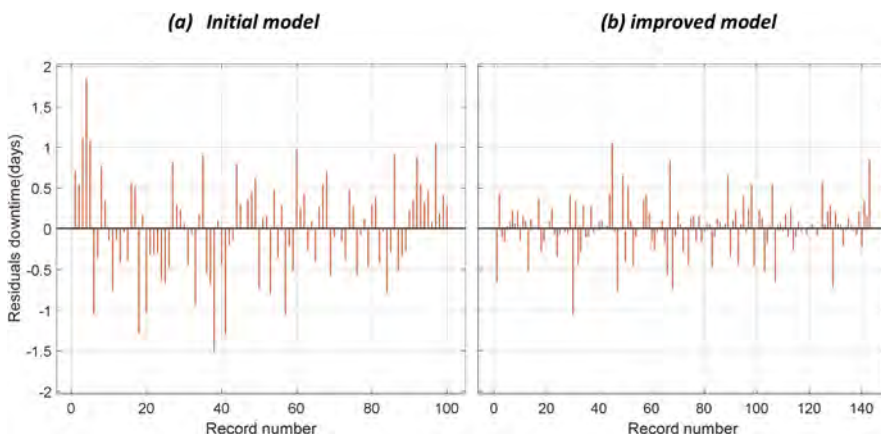


Figure 4. The residual downtime in days for: a) initial model and b) improved model.

5.2 Improve estimation by using a machine-learning technique.

To show how the machine-learning technique improved the DT estimation model, in Figure 4 the residual downtime in days is computed and compared for the initial model and the improved model. The residual downtime varied between -1.5 and 1.5 for the initial model and between -1 and 1 for the improved model, which is a noticeable improvement.

We also report in Table 1 the values of the simple metrics RSME and R². Namely, for the original model ((Kammouh et al. 2018) data and the improvement model ((Kammouh et al.

Table 1. Values of the simple metrics RSME and R².

Metrics (validation phase)	Initial model	improved model	improvement (%)
RMSE in log10	0.59	0.29	51
R ² in log10	0.07	0.53	757

2018) data + boosted data for this study). We can clearly see that it is a significant improvement of 51% (RMSE) and 757% when we consider R^2 .

6 CONCLUSIONS

The recovery time (RT) or its counterpart the downtime DT is an essential components of seismic resilience analysis of infrastructure. Thus, it is crucial to keep the functionality of critical infrastructure and recover them quickly during strong earthquakes.

In this article, we developed machine-learning empirical models for estimating the DT based on an earthquake damage dataset to predict the DT of the gas, power, water, and telecommunications lifelines. The machine-learning models used the most renowned machine learning algorithms. The model was increasingly, improved by adding additional factors such as RJB, CAV, etc. It was deduced that those factors can improve the DT model and that that the lifelines systems are the most important predictors followed by the CAV.

ACKNOWLEDGEMENT

We thank Politecnico di Milano for funding this research through the Seal of Excellence project, CYBERES. We thank the University of Tlemcen and University of Saida.

REFERENCES

- BCCVL. 2021. *Boosted Regression Tree*. BCCVL Knowledge Base. <https://support.bccvl.org.au/support/solutions/articles/6000083202-boosted-regression-tree>
- Bruneau, M., Chang, S.E., Eguchi, R.T., Lee, G.C., O'Rourke, T.D., Reinhorn, A.M., Shinozuka, M., Tierney, K., Wallace, W.A. & von Winterfeldt, D. 2003. A Framework to Quantitatively Assess and Enhance the Seismic Resilience of Communities. *Earthquake Spectra*, 19(4), 733–752. <https://doi.org/10.1193/1.1623497>
- Cao, Q.D., Miles, S.B. & Choe, Y. 2022. Infrastructure recovery curve estimation using Gaussian process regression on expert elicited data. *Reliability Engineering & System Safety*, 217, 108054. <https://doi.org/10.1016/j.ress.2021.108054>
- Cimellaro, G., Reinhorn, A. & Bruneau, M. 2006. Quantification of seismic resilience. *Proceedings of the 8th U.S. National Conference on Earthquake Engineering*.
- Cremen, G., Seville, E. & Baker, J.W. 2020. Modeling post-earthquake business recovery time: An analytical framework. *International Journal of Disaster Risk Reduction*, 42, 101328. <https://doi.org/10.1016/j.ijdr.2019.101328>
- Derras, B., Bard, P.-Y., Cotton, F. & Bekkouche, A. 2012. Adapting the Neural Network Approach to PGA Prediction: An Example Based on the KiK-net Data. *Bulletin of the Seismological Society of America*, 102(4), 1446–1461. <https://doi.org/10.1785/0120110088>
- Derras, B. & Makhoul, N. 2022. An overview of the Infrastructure seismic resilience assessment using Artificial Intelligence and machine-learning algorithms. *ICONHIC2022-3rd International Conference on Natural Hazards & Infrastructures*.
- Derras, B., & Makhoul, N. 2024. Machine Learning a tool for Prediction of Earthquake Recovery Time of Infrastructure Functionalities. *Forthcoming*.
- Durante, M.G. & Rathje, E.M. 2021. An exploration of the use of machine learning to predict lateral spreading. *Earthquake Spectra*, 37(4), 2288–2314. <https://doi.org/10.1177/87552930211004613>
- Dubrow, A. 2021. Machine learning aids earthquake risk prediction. *ScienceDaily*. University of Texas at Austin, Texas Advanced Computing Center. <https://www.sciencedaily.com/releases/2021/06/210623130649.htm>
- Hoque, A., Raj, J., Saha, A. & Bhattacharya, P. 2020. *Earthquake Magnitude Prediction Using Machine Learning Technique* (pp. 37–53). https://doi.org/10.1007/978-3-030-66763-4_4
- Kammouh, O., Cimellaro, G.P. & Mahin, S.A. 2018. Downtime estimation and analysis of lifelines after an earthquake. *Engineering Structures*, 173, 393–403.
- Sajan, K. C., Bhusal, A., Gautam, D. & Rupakhety, R. 2023. Earthquake damage and rehabilitation intervention prediction using machine learning. *Engineering Failure Analysis*, 144, 106949.
- Zanini, M.A., Hofer, L. & Faleschini, F. 2019. Reversible ground motion-to-intensity conversion equations based on the EMS-98 scale. *Engineering Structures*, 180, 310–320.

Condition assessment and management protocols for concrete infrastructure affected by internal swelling reactions: Challenge and research needs

R. Medeiros, A. Bergmann & L.F.M. Sanchez
University of Ottawa, Ottawa, Canada

ABSTRACT: Internal swelling reactions (ISR) are amongst the most harmful deterioration mechanisms affecting the durability, serviceability, and overall performance of critical concrete infrastructure around the globe. Over the years, several approaches have been developed worldwide to assess the condition and manage ISR-affected structures. However, several challenges have still been faced in the proper selection and efficiency of laboratory and field tools to assess the condition, along with rehabilitation strategies and management protocols to mitigate effects and extend the service life of affected infrastructure assets. This paper aims to conduct a thorough literature review on the topic, showing the recent developments and current challenges faced by engineers, infrastructure owners and researchers dealing with ISR-affected structures. In addition, it will highlight current research needs and future opportunities.

1 INTRODUCTION

Despite its limitations, concrete durability has been highlighted as one of the main reasons for being the world's most widely used construction material. Yet, a combination of factors such as design and severe exposure conditions may trigger deterioration, resulting in aesthetic, functional, and structural issues. Billions of dollars have been invested in maintaining and replacing critical concrete infrastructure worldwide. For instance, in North America, Canadian, US infrastructure requires a minimum investment of \$50 and \$70.9 billion, respectively (Hajjalizadeh et al. 2017; Omar & Nehdi, 2018). Thus, concrete infrastructure maintenance has been a topic of interest in many research investigations from both civil engineering material and structural perspectives; for example, the Robert-Bourassa/Charest overpass (Fournier et al. 2015) and Champlain bridge (Cartier Bridge, 2019).

Different distress mechanisms may affect critical concrete infrastructure; these mechanisms may be generated by external sources (e.g., fire, static overload, impact, chloride ingress, and carbonation) and internal sources (e.g., free and thaw, internal sulfate attack, alkali-aggregate reaction) (Blight & Alexander 2011). Although both sources may develop extremely aggressive damage in concrete and require expertise to be dealt with, it is agreed in the scientific community that deterioration caused by external sources is easier to manage since a) one may rapidly identify the occurrence of deterioration, b) there are several past literature works on the topic and, c) one may reproduce the deterioration process (and forecast future behavior) through accelerated tests in the laboratory that display quite acceptable outcomes. Nevertheless, the external sources may be considered well understood since they have been further investigated due to the possibility of rapidly identifying the damage mechanism, reproducing it in laboratories and advancing in numerical models to forecast the behavior.

On the other hand, internal sources of distresses are more complicated to assess since the first signs (i.e., surface cracking) may be influenced by several factors, such as the type and abundance of reactive aggregate present in the reaction (i.e., alkali-aggregate reaction - AAR) or the amount of sulfate and water available (i.e., delayed ettringite formation - DEF). Alkali content of the concrete, geometry of members, presence and arrangement of reinforcement, exposure condition, load and stress applied, and presence of other distressing mechanisms are also parameters that

may corroborate on initiating or maintaining internal damaging mechanisms. In addition, ISR mechanisms have been identified as distressing structures worldwide (Sims & Poole, 2017). Since its cause is intrinsic to concrete, there is no specific affected region that can be cleaned and protected or strengthened as per the protocols of corrosion and overloading. Hence, the management of ISR-affected critical infrastructures is vital for the structure owners in order to maintain the serviceability of pavements, dams, bridges, overpasses, and railroads. In this sense, to enhance the safety of the structure once distressed by ISR, at least two questions must be addressed: a) Which mechanism(s) is the main cause(s) of deterioration? b) what is the extension of the current deterioration? c) Is it possible to foresee the future of the structure?

In this context, a significant amount of work has been dedicated to diagnosing and prognosing ISR-affected structures, and few management protocols have been proposed. This paper focuses primarily on the management protocols proposed for critical concrete infrastructure in general purpose, with the aim of synthesizing current knowledge, demonstrating the current perspective of the topic, and then drawing attention to infrastructure management once distressed by ISR. Finally, the gaps in the state-of-the-art of ISR management infrastructures protocols are explored.

2 MANAGEMENT OF CRITICAL CONCRETE INFRASTRUCTURE

Several evaluation and management protocols are used worldwide for critical infrastructure, including bridges, culverts, tunnels, ferry berths, retaining walls, highways, pavements, and quays. Although each country has its management system adjusted to particular conditions, the protocols are based on fundamental concepts and follow a general framework.

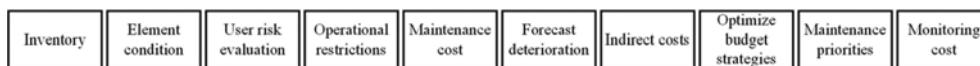


Figure 1. General framework of a management system of critical infrastructure.

As seen in Figure 1, the management system structured into ten streams enhances the oversight of the information for each structure by gathering design drawings, calculations, material data, delivery protocols, former inspection protocols and reports, special investigations, repairing, strengthening measures, and available photographic documentation throughout the lifetime of the structure. In addition, this management system structure supports the planning and schedule of condition and structural assessment, deterioration prediction, lifecycle cost, and effectiveness of maintenance optimization. However, Helmerich et al. (2008) discuss the need for improvements in current management protocols, particularly early assessment of deterioration progress so that the cause can be appropriately identified. Accordingly, Sanchez (2014) establishes that diagnosis must consider the cause of the deterioration process (i.e., what has triggered the damage) and its extent (i.e., the point where the damage has escalated).

Figure 2 presents the management system, rating scale, and inspection frequency for distinct countries. One can notice that inspections are usually performed in fixed intervals. Moreover, Helmerich et al. (2008) comment that performing regular inspections of the most critical concrete infrastructure is sufficient.

Country	Canada	Denmark	United Kingdom	Japan	Germany	South Africa	USA	Norway	France
Rating scale	1 - 9	0 - 5	3 categories	4 categories	1 - 4	4 categories	0 - 9	1 - 4	1 - 3
Inspections frequency	1 - 2 years	5 years	6 years	5 years	6 years	3 - 5 years	2 years	5 years	3 years

Figure 2. Critical concrete infrastructure management systems for different countries (modified from (FHWA, 2005).

Generally, critical infrastructures are rated into three categories, which might be further split into nine subcategories: poor, adequate (fair), and good, based on the structure components' condition and functionality. The structure assessment is usually based on inspection results performed in

a specific frequency, ranging from 1 to 6 years. The inspections currently commence performing a visual routine inspection and depending on the results obtained, the frequency and approaches may change. The countries suppressed in this paper usually appraise critical infrastructure following a few approaches, such as visual inspection, non-destructive testing (NDT), structural health monitoring (SHM), and numerical modelling (Finite element - FEM).

Visual inspection: Visual inspection is the primary step of all existing critical infrastructure management protocols regarding assessment. Visual inspection relies solely on the inspector's experience, and this approach usually provides qualitative results and external structure characteristics (Hsien-Ke et al., 2017). Even though it is only the first step in managing critical infrastructure, visual inspection results have been the input parameters in deterioration models, such as damage description, photography, dimension of the elements under evaluation, and cracking pattern. Additionally, ISR signs, such as cracking propagation and orientation, discoloration, and presence or not of secondary products, shall be easily noticed at moderate damage degree.

Non-destructive testing (NDT): In the early stages of deterioration, non-destructive techniques may be used to correlate concrete properties with possible deterioration mechanisms. Also, stiffness and strength may be assessed, the moisture content may be examined, and hidden defects may be detected. Some management protocols recommend NDT during periodic surveys or when visual inspections indicate irregularities. The most used NDT tools to assess concrete infrastructure are chain drag and hammer sounding. Despite their convenience to be performed, they are not entirely reliable due to inherent subjectivity (Kot et al. 2021). Advanced NDT techniques can provide improved reliability, such as acoustic techniques (i.e., impact echo, ultrasound pulse velocity, surface wave), electro-magnetic techniques (i.e., ground penetration radar), electro-chemical techniques (i.e., half-cell potential, electrical resistivity, polarization resistance), thermal techniques (i.e., infrared thermography), and digital imaging (i.e., 3D optical evaluation, remote viewer camera, digital image correlation). However, these techniques have been questioned regarding their accuracy in evaluating ISR-distressed structures.

Structural health monitoring (SHM): Embedded sensors have been used to monitor structural response and detect anomalous behavior. Critical infrastructure maintenance systems may be assisted by these devices, which capture a variety of physical measurements related to loads, environmental conditions, and structural responses. Further, laser scanning may help monitor infrastructures' health and damage, and laser point clouds may be used to develop a condition rating system. Structural health monitoring systems can rate structural capacity or assess specific structural performance aspects (e.g., corrosion) over long periods (Güemes et al., 2020). Regarding ISR distressed structures, it is expected to monitor at least the internal temperature and humidity of the concrete, the deformations and cracking propagation.

Numerical modelling (Finite element - FEM): FEM may provide a more accurate structural response and condition representation than traditional methods of assessing structure health. In developing robust FEM models, the construction method, material properties, geometric accuracy, cracking, and creep in concrete are crucial factors (Gorga et al., 2020). In addition, by calibrating FEM with digital image correlation, critical infrastructures that display unusual behavior, such as defects caused by ISR, can be assessed long-term. The ISR FEM models are expected to provide the future behavior of the swelling process, along with, the displacement, and mechanical properties reduction.

3 MANAGEMENT OF CRITICAL CONCRETE INFRASTRUCTURE AFFECTED BY INTERNAL SWELLING REACTIONS

In North America, there are a few guidelines for managing critical infrastructure when affected by internal swelling reactions; due to the frequency of occurrence, these guidelines are more specific for alkali-silica reactions. In addition, the US department of transportation – Federal Highway Administration (FHWA) issued the Alkali-silica reactivity field identification handbook in 2011. This handbook refers to the CSA A864 (2000).

Although it has been applied to manage critical infrastructures in North America, this approach is solely a general descriptive step-by-step procedure to evaluate a structure distressed by ASR. Yet, it neither presents any threshold concrete properties or structural performance to determine

whether the structure is safe nor takes into consideration past experiences of affected structures to propose future recommendations.

3.1 Bérubé et al. (2005) management protocol

Bérubé et al. (2005) developed an extensive experimental campaign involving parallel field and laboratory investigations. As a result, they proposed a protocol for assessing and managing structures affected by ASR in Quebec (Canada). This protocol emphasizes that concrete expansion is the main criterion for determining whether action should be taken in a structure affected by ASR. Additionally, they established that the elastic limit of the reinforcement is reached when the concrete expands by 0.20%. Thus, the decision-making in this protocol lies in the expansion achieved, the current rate of expansion, and the number of years remaining before the reinforcing steels are yielded. The investigation strategy includes the following steps.

Visual inspection of ASR-affected critical infrastructure (Step 1): The first inspection must determine if the ASR is present in the studied structure. It may be determined based on the visible defects generally associated with this reaction.

Once ASR is probably the mechanism distressing the critical infrastructure, the investigation must move to step 2.

Crack readings and estimating the expansion attained (Step 2): For each component, surveys should be conducted on the most exposed areas since they are the spots where surface cracking will provide the closest estimates of volumetric expansion. For instance, barriers located under overpasses expanded more slowly than those directly exposed to the weather in the Quebec City region. It is recommended that the first crack readings be performed in the middle of summer and preceded by at least two days of sunshine. The crack measurements shall be separated by structural member type (e.g., column, slabs, and beam). Further, the direction of the surface accessed may reveal appreciable comparisons on the expansion development throughout the structure. The main criterion of whether an intervention is required lies in the expansion already achieved by the concrete, estimated either from the surface cracking (i.e., the sum of the crack opening per unit of length) or from the mechanical test, such as Stiffness damage test (SDT) carried out on specimens cored under the reinforcement.

Calculation of current expansion rate - %/year (Step 2): The calculation of the current expansion rate (i.e., expansion (%)/year) is based on the expansion achieved to date (i.e., in %/age - in years) and the ratio between the measured expansion rate (studs) and the estimated expansion rate from surface cracking.

Calculation of the number of years before yielding (Step 2): The present step consists of estimating the years the structure expansion may take to reach 0.20% at the current expansion rate estimated before, which may follow Equation 1. This expansion level (i.e., 0.20%) can be considered as the steel reinforcements have reached their elastic limit.

$$\text{years before 0.20\%} = \frac{0.20\% - \text{expansion achieved (\%)}}{\text{expansion rate} \left(\frac{\%}{\text{year}} \right)} \quad (1)$$

Analysis of the results and follow-up: In order to continue the evaluation, it is necessary to evaluate the results obtained in the previous step. Three possibilities are considered based on the age of the structure and the number of years that can elapse before there is yielding: (a) 15 years → Monitoring program I. (b) 5 to 15 years → Stage 3A and follow-up monitoring program II. (c) <5 years → Stage 3B and follow-up monitoring program II.

When the crack opening exceeds 0.3 mm, and corrosion is still limited, the following intervention is required: sand blasting the element surface and applying silane based penetrant sealants. Under these conditions, corrosion and degradation of the reinforcements will be prevented while the progression of ASR will be reduced. Additionally, if there is an imminent risk to the safety of the users of a structure, action must be taken.

Monitoring program I: When an expansion of 0.20% is not expected to be reached before 15 years, the follow-up program I shall be applied. It includes regular visual inspections every 5 years and cracking readings at the same spots.

Plot and minimum coring (Step 3A): Stage 3A consists of installation of studs, reading distances between plots, and minimum coring with petrographic examination and specific mechanical tests.

Metallic studs should be installed on the same sections as those used for the crack surveys (see step 2) but also on less exposed sections. In this stage, the concrete volumetric expansion is also of interest beyond the deterioration of the surface, leading to coring demands. Therefore, at least three specimens of 100 mm diameter and 300 mm length in the components showing signs of ASR must be cored from the most exposed places. Samples must be used for detailed petrographic examination and mechanical evaluation involving the stiffness damage test (SDT).

Following step 3A, monitoring includes an annual visual inspection, along with cracking and expansion surveys, at least three times a year. If necessary, other cores may be taken for physical (i.e., porosity) and chemical (i.e., alkalis, chlorides) analyses, as well as for specific mechanical tests (including pure tensile test) and expansion residual.

Plot and greater coring (Step 3B): Step 3B applies when an expansion of 0.2% is expected within five years. This step, which can be started immediately after steps 1 and 2, requires the coring of specimens to perform SDT, pure tensile strength, and residual expansion (i.e., at least one specimen kept at 38°C, >95% RH, soaked in 1N NaOH and two specimens kept at 38°C, >95% RH only in at humid air) for a minimum of 1 year. The monitoring, the petrographic evaluation, and the mechanical tests support the re-adjustment of the expansion rate; likewise, the residual expansion test estimates the expansion's plateau.

3.2 *Saouma et al. (2014) management protocol*

Saouma & Hariri-Ardebili (2014) extensively reviewed available public documents from the Seabrook nuclear power plant (NPP) located in the US once the structure has been reported to be suffering from ASR. Based on the available data and the knowledge of the essence of ASR (i.e., the behavioral monitoring records of existing structures affected ISR, and the laboratory testing experience up-to-date), the authors addressed the following management protocol.

Structural tests: Because of the differences between laboratory tests conducted on small samples and field tests and monitoring, structural tests are highly recommended. For instance, the Seabrook NPP was assessed by laboratory tests on structural elements designed to represent the real members affected by ASR. Along these tests, the affected elements were evaluated regarding their mechanical behavior and reaction development. In addition, laboratory testing was used to validate the numerical model.

Field measurements: In the authors' view, surface cracking measurements are of minimal significance since member confinement and reinforcement greatly influence ISR cracking. Hence, it is suggested that long-term monitoring of the dynamic elastic properties through an appropriate technique (i.e., pulse velocity, frequency resonant, and impact echo), the strains in the rebars (i.e., by simply scraping the concrete surface to install strain gauges), and surface deformation (i.e., using laser measurements) shall be performed. Further, the internal relative humidity and temperature measurements may support the accuracy of reaction propagation modelling.

Material testing: Regarding the material testing, it is suggested to conduct residual expansion according to Saouma (2013) to obtain the magnitude (i.e., plateau of the reaction) and the kinetics (i.e., the time required to reach a certain expansion level). The mechanical tests suggested are the tensile strength, modulus of elasticity, and fracture energy GF. If the mechanism identified is ASR, it is recommended that the compressive strength may be disregarded since it is the less affected concrete mechanical property.

Nonlinear finite element: The serviceability and safety of the structure shall be of the primary interest. Thus, the structural modelling must consider the deformation and crack, giving proper attention to the members' mechanical solicitation and correctly identifying if the member is under shear, tensile, or compressive. Moreover, the code must be validated before evaluating serviceability and safety. It is crucial to gain a holistic understanding of permanent deterioration displayed by the ISR mechanism, which may be obtained by correlating materials testing, structural testing, field measurements, and nonlinear finite element simulations. It is considered a dynamic process and, as such, must be updated every few years up until the lifespan of the structure is achieved.

The authors highlighted the complexity of evaluating ASR-affected structures and the demand for further understanding and managing critical infrastructure affected by ISR. Therefore, they suggested consulting available literature before conducting an affected structure assessment.

Furthermore, the authors emphasized that a proper structural evaluation must be carefully performed, considering the particularity of each type of structure. Finally, it was stated that ISR mechanisms present particular kinetics and just considering the worst-case scenario without modelling the affected structure behavior is no longer satisfactory. Hence, proper modelling and testing must be performed so that the safety and serviceability of the investigated structure may be estimated.

4 DISCUSSION

4.1 *Comparison of the management protocols*

Helmerich et al. (2008) and Omar & Nehdi (2018) noted that non-destructive testing (NDT) is not incorporated into most routine inspection procedures proposed for general evaluations. Even though these tools are very effective for monitoring deformation and differential displacement, there is no NDT technique available to diagnose ISR in the field, although some researchers suggest that they have proven to be reliable indicators for ISR progression (Swamy & Al-Asali, 1988; Saint-Pierre et al., 2007; Sargolzahi et al., 2009). However, most management protocols recommend that the structure evaluation starts with a visual inspection. It is suggested that the structural members be inspected closely, but the tools recommended first involve tapping the structural members with a hammer or making measurements by hand (MTO, 2008; CSA, 2019).

Aside from that, no consideration is given to diagnosing the mechanisms causing the damage to critical concrete infrastructure in any protocol of general purposes management. It is solely recommended to perform a visual inspection routine where critical concrete infrastructures are classified into three categories, purely qualitative and heavily subjected to the inspector's experience and point of view. Additionally, inspection frequency is insufficient in some countries to detect mechanisms, such as ISR (in some conditions), that can rapidly escalate and significantly distress structures. The recommendation, in the case of a structure deemed substandard or unsafe, is a local repair or strengthening.

On the other hand, the management protocols proposed for internal swelling reactions begin with a field investigation; however, there is no agreement about approaching the structure. Bérubé et al. (2005) recommend that the crack opening must be taken as one of the primary references to estimate the damage extent. In contrast, Saouma & Hariri-Ardebili (2014) suggest that the cracking measurement is doubtful since reinforcement and member confinement geometry heavily influence cracking from ISR. While Bérubé (2005) does not recommend any NDT test, Saouma & Hariri-Ardebili (2014) suggest using pulse velocity, frequency resonant, and impact echo. Moreover, the use of NDT is recommended by a few researchers (Swamy & Al-Asali, 1988; Saint-Pierre et al., 2007; Sargolzahi & Rivard, 2009), whereas their accuracy in appraising ISR-distressed structures is questioned (Sanchez, 2014; Sanchez et al., 2016). The first protocol (item 3.1) specific for ISR suggested that 0.20% concrete expansion is the safe threshold of the structure since the reinforcement yields at this deformation point. The second protocol (item 3.2) argued that ISR-induced tension might damage the reinforcement. Nevertheless, it is essential to highlight that a proper bond loss must be assessed since the ISR swelling takes place on a tridimensional scale, which is yielded by the reinforcement. Therefore, a bond loss is supposed to occur, releasing the rebars rather than over-stressing them.

Both ISR protocols suggest that residual expansion must be conducted, and the mechanism propagation rate shall be reassessed and updated over time. The first protocol suggests that the expansion rate may be estimated through the overtime surface cracking measurements. However, this rate is just a fragment of the real swelling since ISR mechanisms behave as explained by a sigmoid curve divided into four phases (Sanchez et al., 2014; De Grazia et al., 2021). It means that the expansion rate may increase or decrease depending on where the structure is on the expansion curve.

Apart from that, it is essential to mention that the approaches presented by the protocols used worldwide are descriptive and, at best, deterministic. However, it is well known that the structure behavior must be assessed and foreseen by robust deterministic or stochastic approaches, which is still not the case. With a deterministic model, future events can be calculated precisely without the involvement of randomness. However, to be precise, it requires a heavy amount of data, and different scenarios must be simulated and validated prior to implementation into the model. Further data

must be collected in order to be able to predict the outcome with certainty. However, stochastic models are capable of handling uncertainties in the inputs that are to be applied. In addition, stochastic models have the inherent property that their output will fluctuate based on the parameter values and the initial conditions. For example, the same initial conditions will produce a range of different outcomes depending on the parameter values and the initial conditions. This range of outcomes may enhance more timely decision-making compared to weak deterministic models.

4.2 *Research needs and opportunities*

Based on an overview of existing literature, it is clear that some research findings related to critical concrete infrastructure management protocols still require research and further development. For instance, there remains a significant gap between recent research and the protocols currently used to assess structures, as well as a lack of comprehensive investigations of applying the recently developed tools to appraise concrete structures distressed by internal swelling reactions. However, some of them have already been validated in the field. In addition, the relationship between the laboratory test used to assess ISR-affected concrete in the scale of laboratory and the behavior observed in the field has still needed to be adequately investigated to date. These highlighted gaps might be addressed by stochastic approaches, using the current data obtained in the inspections already carried out in critical concrete structures worldwide.

Stochastic approaches to managing critical concrete infrastructure involve using probabilistic methods to assess and mitigate risks associated with the structural integrity of the infrastructure. These approaches can be used to evaluate the likelihood of different types of failures or degradation, such as ISR mechanism, and to identify the most effective maintenance and repair strategies based on the likelihood and consequences of different failure scenarios. They can help decision-makers understand the likelihood of different outcomes and make informed choices about how to manage best and maintain the infrastructure. Some common stochastic techniques used in critical concrete infrastructure management may include:

- Monte Carlo simulation: This involves generating many random samples based on the factors that could affect the performance of the infrastructure, such as its age, design, environmental conditions, and presence of a distressing mechanism. The simulation helps to estimate the probability of different outcomes and can be used to evaluate the risks and benefits of different courses of action.
- Fault tree analysis: This uses logical reasoning to identify the various ways in which a system could fail and can be used to evaluate the risks associated with different courses of action.
- Reliability analysis: This involves estimating the probability of failure for different components of the infrastructure and can be used to identify vulnerabilities and prioritize maintenance and repair efforts.
- Risk assessment: This involves identifying, analyzing, and evaluating the potential risks associated with the infrastructure and developing strategies for mitigating or managing those risks.

With these and other stochastic techniques, decision-makers can make more informed choices about managing critical concrete infrastructure.

5 CONCLUSIONS

The main objective of the literature review investigation carried out in this study was to review the current protocols available to assess critical concrete infrastructure worldwide from a general perspective and those focused on internal swelling reaction distressed structures. The main conclusions of the above investigations are:

- Most general-purpose management protocols rely on unaided visual inspections based on qualitative rating classification of the structural condition;
- The general-purpose management protocols consulted do not address the diagnosis of the mechanism distressing critical concrete infrastructure;
- The ISR protocols do not agree on whether the cracking measuring supports the ISR field assessment;

- Modern NDT techniques may address the purpose of measuring the cracks to understand the swelling process. The embedded sensors and the laser scanning may replace the studs installed on the distressed structure surface. It would ensure the reliability of the results and strengthen structural health monitoring. Furthermore, using these techniques would enable the evaluation of the influence of the reinforcement on the tridimensional swelling, accurately identifying the yielding phenomena. In addition, valuable data for the modeling of ISR propagation, such as internal concrete humidity and temperature, may be monitored over time by embedded sensors;
- The lab tests and field tests must be combined to provide more correlatable results, which would increase the reliability of the monitoring process, and the results would converge in the same direction;
- Mathematical modeling must be on top of any management protocol since it is a powerful tool able to evaluate the structure's condition and foresee future behavior quickly. However, the models still need to be further enhanced;
- The descriptive qualitative rating systems and weak deterministic approaches must be improved by some stochastic approaches to strengthen the reliability of critical infrastructure management.

REFERENCES

- Bérubé, Marc-André, Nizar Smaoui, Benoit Bissonnette, and Benoit Fournier. 2005. *Outil d'évaluation et de Gestion Des Ouvrages d'art Affectés de Réactions Alcalis-Silice (RAS)*. Québec: ministère des Transports du Québec.
- Blight, Geoffrey E, and Mark G Alexander. 2011. *Alkali-Aggregate Reaction and Structural Damage to Concrete*. Canadian Standard Association (CSA). 2019. *Canadian Highway Bridge Design Code. S6:19*. Toronto: Canadian Standard Association (CSA).
- Canadian Standards Association (CSA). 2000. *Guide to the Evaluation and Management of Concrete Structures Affected by Alkali-Aggregate Reaction*. Toronto.
- Cartier Bridge, Jacques. 2019. *En Un Coup d'oeil At a Glance*.
- Federal Highway Administration U.S. Department of Transportation (FHWA). 2005. *Bridge preservation and maintenance in Europe and South Africa*.
- Fournier, B., Sanchez, L, Beauchemin, S.. 2015. *Outils d'investigation de La Réactivité Alcalis-Granulats Dans Les Infrastructures En Béton Rapport Final Par*.
- Gorga, R. v., L. F. M. Sanchez, B. Martín-Pérez, P. L. Fecteau, A. J. C. T. Cavalcanti, and P. Silva N.. 2020a. *Finite Element Assessment of the ASR-Affected Paulo Afonso IV Dam*. Journal of Performance of Constructed Facilities 34 (4): 04020065. [https://doi.org/10.1061/\(asce\)cf.1943-5509.0001456](https://doi.org/10.1061/(asce)cf.1943-5509.0001456).
- Hajjalizadeh, D., OBrien EJ, and O'Connor A.J.. 2017a. *Virtual Structural Health Monitoring and Remaining Life Prediction of Steel Bridges*. Canadian Journal of Civil Engineering 44 (4): 264–73. <https://doi.org/10.1139/cjce-2016-0286>.
- Hsien-Ke, L, M Jallow, Y Nie-Jia, J. M. Yi, H Jyun-Hao, S Cheng-Wei, and C. Po-Yuan. 2017. *Comparison of Bridge Inspection Methodologies and Evaluation Criteria in Taiwan and Foreign Practices*. In 34th International Symposium on Automation and Robotics in Construction (ISARC 2017).
- Kot, Patryk, Magomed Muradov, Michaela Gkantou, George S. Kamaris, Khalid Hashim, and David Yeboah. 2021. *Recent Advancements in Non-Destructive Testing Techniques for Structural Health Monitoring*. Applied Sciences 11 (6): 2750. <https://doi.org/10.3390/app11062750>.
- Omar, Tarek, and Moncef Nehdi. 2018. *Condition Assessment of Reinforced Concrete Bridges: Current Practice and Research Challenges*. Infrastructures 3 (3): 36. <https://doi.org/10.3390/infrastructures3030036>.
- Saint-Pierre, François, Patrice Rivard, and Gérard Ballivy. 2007. *Measurement of Alkali-Silica Reaction Progression by Ultrasonic Waves Attenuation*. Cement and Concrete Research 37 (6): 948–56. <https://doi.org/10.1016/j.cemconres.2007.02.022>.
- Sanchez, Leandro F.M. 2014. *Contribution to the Assessment of Damage in Aging Concrete Infrastructures Affected by Alkali-Aggregate Reaction*, PhD., 377. <http://citeseerx.ist.psu.edu/viewdoc/download?doi=10.1.1.723.8765&rep=rep1&type=pdf>.
- Saouma, Victor E., and Mohammad A. Hariri-Ardebili. 2014. *A Proposed Aging Management Program for Alkali-Silica Reactions in a Nuclear Power Plant* Nuclear Engineering and Design 277 (October): 248–64. <https://doi.org/10.1016/j.nucengdes.2014.06.012>.
- Sargolzahi, M., and Rivard P. 2009. *Evaluation of Residual Reactivity of Concrete Cores from ASR-Affected Structures by Non-Destructive Tests*. NDTCE'09, Non-Destructive Testing in Civil Engineering.
- Sims, I. Poole, A. B. *Alkali-aggregate reaction in concrete: A world review*. CRC Press. 2017.

The efficiency of laboratory test procedures for assessing field performance of concrete against Alkali-Aggregate Reaction (AAR)

A. Bergmann, R. Medeiros & L.F.M. Sanchez
University of Ottawa, Ottawa, Canada

ABSTRACT: Alkali-aggregate reaction (AAR) is among the most harmful deterioration mechanisms affecting concrete infrastructure worldwide, impacting more than 50 countries. Over the last decades, numerous laboratory tests have been developed to evaluate the reactivity of aggregates and the effectiveness of supplementary cementitious materials (SCMs) to mitigate AAR. Among them, the accelerated mortar bar test (AMBT) and the concrete prism test (CPT) stand out and are used around the globe nowadays. However, in recent years, some discrepancies have been found between laboratory results (i.e., AMBT or CPT, especially AMBT) and concrete mixture performance in the field. Yet, these discrepancies have never been quantified. This work aims to critically review current laboratory methods for assessing AAR-induced development, followed by a comparison of performance (i.e., laboratory versus field) at distinct scales (i.e., laboratory specimens vs. field blocks and structures) and quantification of the risk associated with these tests to forecast AAR in the field.

1 INTRODUCTION

As one of the more harmful deterioration mechanisms affecting concrete infrastructures worldwide, the alkali-aggregate reaction (AAR) has been reported in over 50 countries. In hardened concrete, both types of AAR, alkali-silica reactions (ASR) and alkali-carbonate reactions (ACR), occur when dissolved alkali hydroxides react with unstable mineral phases (Fournier & Bérubé, 2000; Nixon & Sims, 2016). In order to evaluate the potential and avoid AAR in the field, several approaches and recommendations have been developed based on the three main reasons for its development: reactive aggregates, high alkali hydroxide, and moisture (Borchers et al., 2022; Fournier et al., 2018; Kawabata & Yamada, 2017; Oberholster & Davies, 1986).

Among the several testing methods developed in laboratories to assess aggregate reactivity and the effectiveness of supplementary cementitious materials (SCMs) in mitigating AAR, the accelerated mortar bar test (AMBT) and the concrete prism test (CPT) are among the most used around the globe (Fournier & Bérubé, 2000; Sims & Nixon, 2003). Based on these results, aggregates are then classified as non-, moderately, highly, and very highly reactive (ASTM C1778, 2022; CSA A23.2-27A, 2019). Nevertheless, a number of discrepancies have been documented in the past few years between the laboratory results (i.e., AMBT or CPT) and the actual performance of concrete mixtures in the field (Borchers et al., 2022; Custódio et al., 2022). Although the magnitude of these discrepancies has not been quantified, the amount of data regarding outdoor exposure sites has significantly increased (Borchers et al., 2022; Custódio et al., 2022; Fournier et al., 2016; MacDonald et al., 2012, 2012).

By studying parameters that have been identified in the literature as influencing the testing performance, it is possible to investigate several factors in depth, such as type of aggregates and binders, mix design aspects, pre-storage circumstances, and sample exposure conditions (Lindgård et al., 2012). In spite of this, current descriptive and, at best, basic deterministic approaches (ASTM C1260, 2022; CSA A23.2-27A, 2019) are not sufficient to predict the potential behavior of alkali-reactive aggregates since the field outcomes are influenced by several factors. Using stochastics and artificial intelligence methods may therefore lead to a faster diagnosis and

prognosis of AAR-affected structures. Further, it can accelerate the understanding of the risks associated when incorporating specific aggregates into new structures.

In this scenario, this work aims to critically review current laboratory methods for assessing AAR-induced development, followed by a comparison of performance between laboratory specimens and field blocks and quantification of the risk associated with current tests to forecast AAR in the field.

2 ALKALI AGGREGATE REACTION (AAR) AND TEST PROCEDURES

AAR is a destructive process in concrete, causing premature distress and resulting in serviceability reduction of concrete-affected structures. To initiate and sustain AAR in concrete, three conditions are required: reactive aggregate, high concentration of alkali hydroxides in the concrete pore solution, and sufficient moisture. It is recommended, however, to avoid AAR deterioration when designing new concrete, especially in critical infrastructure, by (a) establishing an adequate alkaline pore solution in the concrete; (b) acquiring the critical amount of reactive silica; and (c) defining the sufficient supply of water (Fournier & Bérubé, 2000; Nixon & Sims, 2016). Alkali-silica reaction (ASR) and alkali-carbonate reaction (ACR) are two types of AAR.

According to Fournier & Bérubé (2000), ASR occurs in poorly crystalline or metastable silica minerals and quartz-bearing rocks incorporating fine-grained quartz. In which alkali hydroxides attack the microcrystalline particles within the fine and/or coarse aggregates, transforming them into a viscous reaction product: ASR gel. By causing localized differences in free energy, water and ionic species diffuse into the gel. Internal tensile stresses increase with gel expansion, and cracking is displayed when localized pressure exceeds the tensile strength of concrete components. The result is extensive microcracking, allowing the gel to spread freely and gradually lose its expansive properties due to ion exchange with the paste's hydrates. Thus, concrete tensile strength and modulus of elasticity are significantly reduced by ASR, whereas compressive strength remains relatively unaffected until high expansion occurs (Sanchez et al., 2018).

There is an entirely different and still not fully understood damage pattern for ACR (Scaglione & Piercey, 2016), which produces cracks most frequently at cement paste and adjacent aggregate locations without the presence of secondary products (Alexander, 2011; Sanchez et al., 2015). As per some researchers, ACR expansion is a consequence of the dedolomitization process, more specifically due to the brucite ($Mg(OH)_2$) crystallization (Alexander, 2011; Fournier & Bérubé, 2000). In contrast, it has also been suggested that swelling may be caused by water adsorbing from intergranular clay materials in the matrix and new clay released in the dedolomitization (Beyene et al., 2013; Grattan-Bellew & Katayama, 2017). Nevertheless, ACR-susceptible aggregates are more concentrated in the southern edge of the Canadian Shield in the southern Ontario (Alexander, 2011; Fournier & Bérubé, 2000). Thus, ASR has been studied more among AARs.

In such context, the addition of supplementing cementitious materials (SCM) (e.g., fly ash, slag) has proven to mitigate ASR concrete expansion (De Souza et al., 2022; Lindgård et al., 2012; Thomas, 2011) since they reduce the pore solution alkali concentration to safe levels (Duchesne & Bérubé, 1994). Besides rate and amount (Swamy, 1991), the effectiveness of SCMs depends on their composition, aggregate reactivity, Portland cement alkalis, exposure conditions, and criticality of the structures (Thomas, 2011). Contrary to ASR, SCM is ineffective at mitigating ACR (Grattan-Bellew & Katayama, 2017; Scaglione & Piercey, 2016).

Nevertheless, new and existing aggregate sources must often be assessed for their suitability prior to use in concrete. In the past, it was believed that petrographic examination was enough to assess the alkali-reactivity potential when conducted by an experienced petrographer (Fournier & Bérubé, 2000). However, it has been explored that petrography examination may be used only as a first step to determine whether an aggregate presents AAR potential and further testing is required (CSA A23.2-27A, 2019; Nixon & Sims, 2016). In cases where silica and/or carbonate are identified, rapid screening tests (e.g., AMBT and Concrete Microbar Tests (CMBT)) are recommended to determine whether the aggregate is non-reactive, reactive, or potentially reactive. In addition, concrete expansion through Concrete Cylinder Test (CPT) is necessary if an aggregate is potentially reactive. While there are a few different test methods to assess AAR potential in aggregates, only the most used ones (Nixon & Sims, 2016) are summarized in Table 1.

Other tests have also been conducted, which usually are modifications of the methodologies presented in Table 1. Danish mortar bar tests, or TI-B51, are variants of the AMBT in which samples are stored at 50°C, and expansions are monitored for 52 weeks. Another variant is the Danish Chatterji method, which measures the degree of reaction between silica and KCl by checking the alkalinity with a non-reactive standard. Moreover, for concrete tests, the Norwegian concrete prism method (NCPM), which is similar to RILEM AAR-3, varies the concrete prisms' sample size (e.g., 100×100×450 mm³). AAR-4 Alt is a variation of RILEM AAR-4, with wrapped samples. German concrete method (GCM) suggests the evaluation of concrete prisms (e.g., 100x100x450 mm³) and cubes (300x300x300 mm³) stored at 40°C in a fog chamber for nine months. Finally, the Texas DOT CCT considers cylinder samples, typically used for compressive strength (e.g., 100x200 mm). The test can be conducted under different temperatures, 38°C, 50°C, and 60°C, and measurements are taken until 730 days. This method has shown that final expansion values in the 15th week are comparable to those in the 1-year CPT (Stacey et al., 2016).

Table 1. Laboratory test procedures for evaluating AAR development in concrete.

Procedure	Description
Petrographic examination (RILEM AAR-1)	Petrographic examinations can be conducted in fine-grained rock types and fine and coarse aggregate particles with the following objectives: (a) determine physical and chemical characteristics of the sample, (b) determine and classify sample constituents, (c) quantify sample constituents, and (d) compare aggregate samples from new sources with aggregate samples from other databases (ASTM C295/C295M, 2019). In general, the test depends on the nature of the aggregate and can be conducted by hand, under microscope, or by preparing thin sections.
Accelerated Mortar Bar Test – AMBT (RILEM AAR-2)	The purpose of AMBT is to quickly determine (e.g., 14 days) if aggregates are alkali-reactive through the expansion of mortar bars (i.e., AAR-2.1: 25x25x285 mm ³ or AAR-2.2: 40x40x160 mm ³) immersed in NaOH solution at 80° C. First, mortar prisms using 1:2.25:0.47 proportions of cement, aggregate, and water by mass are cast. After 24 ± 2 hours, the prisms are demolded, stored in moist rooms (20 ± 1 °C and RH≥90%) and initial length is measured. The specimens are placed in a sealed container coated with a 1M NaOH solution for 14 days at 80°C. Regular measurement of the specimens' length reveals information regarding the reaction's kinetics (Nixon & Sims, 2016).
Concrete Prism Test – CPT (RILEM AAR-3)	This method aims to assess the potential for alkali-aggregate reaction by regularly measuring concrete prism (e.g., 75x75x250 mm ³) expansion stored in warm (38°C) and high humid conditions (RH>95%) for 12 months. The method may be performed for two purposes: AAR-3.1 to assess the potential for alkali-aggregate reactive and AAR-3.2 to appraise the alkali threshold of a combination of aggregates. For AAR-3.1, prisms are made with high content of cement and the alkali content must be adjusted to 5.5kg/m ³ in order to promote further any potential for reaction. Further, pessimum effects should be assessed by either combining reactive fine and coarse aggregates or by combining the aggregate of interest with a non-reactive aggregate. For AAR-3.2 the alkali content may be adjusted between 2-5 kg/m ³ (Sims & Nixon, 2003).
Accelerated Concrete Prism Test – ACPT (RILEM AAR-4)	This method is a shorter version (e.g., 20 weeks) of conventional CPT, in which concrete prism (e.g., 75x75x250 mm ³) specimens are stored in a harsh environment to rapidly trigger the development of the ASR. To promote the potential for ASR development, the alkali content of the concrete also must be adjusted to 5.5kg/m ³ . Now the storage conditions must be 60°C of temperature and high humid condition (RH>95%). The swelling of the specimens must be monitored periodically for 20 weeks (Sims & Nixon, 2003).
Concrete Microbar Test – CMBT (RILEM AAR-5)	The ACR potential test method was proposed based on the AAR-2 method, for concrete bars (e.g., 40x40x160 mm ³) immersed in 1M of NaOH solutions at 80°C. Then, the kinetics of the reaction is monitored by regular measurements of the specimens' lengths over 14 days.
Field measurements	Cubes of concrete (e.g., usually 300x300x300 mm ³) are exposed to the outside environment. It is possible to measure the sample expansion by placing studs into the surface over a period. A crack width analysis is also performed on field samples.

3 CORRELATION BETWEEN LABORATORY METHODS AND FIELD RESULTS

In the last few decades, outdoor exposure sites have clarified the correlation between laboratory test methods and the performance of AAR-affected field concrete. Researchers have mainly evaluated the alkali-reactivity of concrete aggregates (Borchers et al., 2022; MacDonald et al., 2012) and investigated SCMs and lithium-based admixtures and supplementary cementing materials as mitigation approach for AAR (Custódio et al., 2022; Fournier et al., 2016; MacDonald et al., 2012).

Borchers et al. (2022) have conducted an extensive study evaluating the alkali-reactivity potential of thirteen aggregates, covering most types of reactive aggregates found in Europe. Field specimens (e.g., concrete cubes) were exposed for 15 years to eight different field sites; their expansions and maximum cracks were compared with laboratory specimen expansions tested according to currently used methods (AMBT RILEM AAR-2.1, AMBT RILEM AAR-2.2, CPT RILEM AAR-3, CPT RILEM AAR-4.1, GCM, NCPT, Danish mortar bar test TI-B51, Danish Chatterji).

In general, highly reactive aggregates expanded within the first six years, while moderately reactive aggregates expanded considerably slower. No cracking or expansion was observed in cubes containing non-reactive aggregate. When compared with the laboratory results, both AMBT versions (RILEM AAR-2.1 and AAR-2.2) reliably differentiated between non- and highly reactive aggregates and could identify moderately reactive aggregates in most cases. Conversely, CPT (RILEM AAR-3 and AAR-4.1) effectively distinguished between non-reactive and highly reactive aggregates. Yet, the RILEM test method AAR-4.1 was found to be more accurate than AAR-3 in detecting moderately reactive aggregates. Yet, the authors suggested assessing the samples after 20 instead of 15 weeks and agreed with RILEM's proposal to change the acceptance limit to 0.03%.

Moreover, in the study, the GCM did not identify moderately reactive aggregates properly, probably because of the fog chamber's higher alkali leaching rate. Compared with AAR-3 and GCM, NCPT showed the strongest correlation with cube performance. The effectiveness of NCPT would be related to the samples' size, which is slightly larger than the adopted by AAR-3, consequently due to less alkali-leaching. Lastly, the Danish mortar bar test TI-B51 proved to be successful for non-reactive and highly reactive aggregates but underestimated moderately reactive aggregates. Yet, the Danish Chatterji method produced equivocate results regarding the reactivity of aggregates.

Additionally, for over 30 years, Canadian researchers have implemented a very relevant comparative field and laboratory research program (Fournier et al., 2016). In 1991, it was initiated at CANMET to evaluate the efficacy of laboratory tests for reliably evaluating the potential alkali-reactivity of concrete aggregates and the efficacy of SCMs in preventing ASR. This study found that the CPT and AMBT reliably identified alkali-reactive aggregates. In the performance evaluation of concrete incorporating SCMs, it was found that the correlation between CPT and expansion of exposure blocks decreases over time, possibly due to alkali leaching and local environmental conditions at the exposure site. It was also found that by exposing the laboratory test prisms to alkalis and/or storing them at higher temperatures, correlations improved in some cases.

Another relevant project, a combination of the Norwegian R&D project and the RILEM TC 258-AAA activities, was launched in 2015 to correlate the results of field and laboratory investigations against ASR in concrete (Custódio et al., 2022). A total of 85 concrete cubes were manufactured and placed at ten different outdoor exposure sites situated in Europe and North America for the purpose of monitoring long-term expansion and cracking.

A high-alkali cement and a normal cement were used in this project, along with three coarse aggregates: an extremely alkali-reactive polymictic gravel from the USA, a highly alkali-reactive crushed aggregate from Norway, and a non-reactive crushed limestone from Portugal. Furthermore, selected concrete mixtures incorporated Fly ash Type F and Category A to evaluate SCMs' effectiveness in preventing ASR development. In addition to the concrete blocks, prism specimens were tested and evaluated with RILEM AAR-3.1 and AAR-4.1 over 205 and 28 weeks, respectively.

Regarding the study conducted by Custódio et al. (2022), current approaches graphically correlate the laboratory test results (Expansion 38°C CPT, in %) and field performance (Expansion field site cube, in %). One can notice different clusters and behavior among the different aggregates when performed in two different environments: laboratory and field. The three methods (NCPT, CCT, RILEM AAR 3.1) show similar behavior despite a few discrepancies between them. In the AAR-3.1 test method, expansion was higher than in CCT and

NCPT. However, it should be noted that the AAR-3.1 testing was conducted at a different laboratory than NCPT and CCT. Furthermore, air-entraining admixtures were not added to the concrete mixes performed at SINTEF. Overall, both laboratories obtained almost identical classification results using the same test procedure, RILEM AAR-4.1, despite using concrete mixtures with (LNEC) and without (SINTEF) air entrainment. This project is still in progress, and further results should be available soon.

4 CURRENT PROTOCOLS FOR ASSESSING THE POTENTIAL ALKALI-REACTIVITY OF AGGREGATES

Current approaches to determine the potential alkali-aggregate reactivity are proposed by CSA A23.2-27A (2019), ASTM C1778 (2022), and RILEM AAR-0 (Sims & Nixon, 2003). For all protocols, descriptive flowchart procedures are used either to validate the use of aggregates or suggest preventative measures. CSA A23.2-27A (2019) decision-making process starts with a geological examination of the aggregate, including rock type, formation, quarry name, and petrographic composition. Additionally, the first acceptance process relies on the aggregate meeting the CSA A23.1 (2019) specifications, specifically aggregate grading limits, uniformity, color, and particle shapes. Upon failure to meet these requirements, the aggregate must be rejected for use, further investigation must be conducted, or corrective measures must be adopted.

The following step in the Canadian standard, corresponding to ASTM C1778's (2022) starting point, involves evaluating the field history of the desired aggregate. The aggregate may be accepted if its performance in the field is satisfactory within the imposed parameters. To be more specific, the following items need to be considered: the cement and alkali contents in the field concrete must be the same or higher than the proposed new structure, exposed concrete must be at least ten years old, exposure conditions of the evaluated concrete must be as severe as defined for the proposed structure, the petrographic analysis must reveal that aggregates are identical in the existing and new structures, SCM implementation must be considered, and water to cementitious material ratio must be noted. When the desired aggregate lacks a history of field use or previous satisfactory performance but has differences between existing and new structures, a petrographic examination should be conducted in accordance with all the mentioned protocols.

A petrographic examination, the first step of RILEM AAR-0 (Sims & Nixon, 2003), can identify silica and/or carbonates in aggregates and classify them as follows: (a) Class I: very unlikely to be alkali-reactive, meaning the sample does not contain known alkali-reactive minerals or rock types, (b) Class II: alkali-reactivity uncertain, meaning neither Class I nor III is applicable, and (c) Class III: very likely to be reactive, meaning the sample contains alkali-reactive minerals or rock types in sufficient quantities to cause damage. Although RILEM AAR-0 (Sims & Nixon, 2003) indicated no further tests for Class I aggregates, it has been suggested that using solely petrographic results may be insufficient (CSA A23.2-27A, 2019; Nixon & Sims, 2016).

For both CSA A23.2-27A (2019) and ASTM C1778 (2022), the presence of carbonate rocks indicates that chemical analysis (e.g., CaO, MgO, and Al₂O₃ contents) are required. After comparing the limits with CSA 23.2-26A (2019) and confirming the possible expansion due to alkali-carbonate reaction, it is recommended to perform CPT. If the CPT expansion is within the established limits (e.g., 0.04% for CSA and ASTM after one year), aggregate can be used without preventative measures. The ASTM C1778 (2022) recommends avoiding aggregates when their alkali-silica reactivity exceeds standard limits, while CSA A23.2-27A (2019) states that aggregates should be classified as moderately (0.04% to 0.12%) or highly (>0.12%) reactive. For CSA A23.2-27A (2019), if ACR has not contributed to the expansion, the aggregate can be accepted; however, if the contribution has been confirmed, its extent should be determined by someone with experience in this type of reaction and further testing must be conducted, such as the CMBT.

If petrographic examinations do not reveal carbonated rocks, but ARS-potential exists, two options must be considered: (a) the aggregate may be accepted without further testing, but preventative measures should be taken considering an extremely reactive aggregate, or (b) further test, such as AMBT, must be performed. The aggregate can be accepted without AAR preventative measures if AMBT results in lower expansion than the established limits (e.g., 0.15% and 0.10% for CSA and ASTM, respectively). If AMBT is not satisfactory, CPT must be conducted.

In cases where standard limits are not exceeded, the aggregate can be directly used; otherwise, preventative measures are required.

5 RESEARCH NEEDS AND OPPORTUNITIES

Extensive experience has been gained using CPT in various forms, which has established it as a reference test nowadays (Sims & Nixon, 2003). For reliable results, CPT needs a longer evaluation period, up to 1 year, so other tests have been used, like AMBT, to provide results earlier, in 14 days. However, it has been observed that AMBT and CPT can show contradictory results when compared to each other (De Souza, 2022). Figure 1a illustrates the uncertainty when defining aggregates as reactive or not, based on ASTM C1778 (2022) limits of 0.04% and 0.1%, for CPT and AMBT, respectively. Since the proposed approaches may provide doubtful interpretations in this scenario, the reliability of test outcomes is questionable.

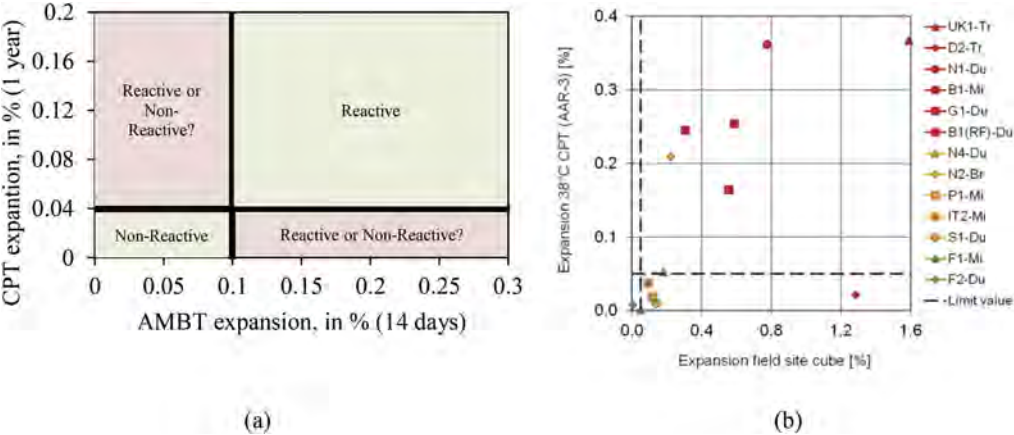


Figure 1. (a) Comparison between CPT and AMBT results (Authors, 2023). (b) Preliminary results from the Norwegian R&D project and the RILEM TC 258-AAA activities: correlation between field and laboratory investigations against ASR in the concrete (Custódio et al., 2022).

As seen in Figure 1b, field and laboratory results are presented comparing both observed expansions. Again, a proper correlation between short-term results (i.e., laboratory) and long-term field performance has not yet been demonstrated. Nevertheless, current approaches interpreting the extensive amount of data generated by outdoor fields are still descriptive and are not explored to predict future behavior nor explored to understand particular contributions of each variable in the final expansion.

As such, implementing anything other than a descriptive approach requires a large research effort with the aim of elaborating accurate predictions based on currently established methodologies. In this sense, the representation of laboratory tests may become more reliable in representing field conditions even though many variables interfere the outcomes. As a final improvement consideration, stochastic and artificial intelligence approaches can be used to enhance prediction and reduce the risk of false non-reactive results.

6 STOCHASTIC AND ARTIFICIAL INTELLIGENCE AS PROPOSED APPROACHES

Stochastic methodologies and artificial intelligence (AI) are being implemented in various fields, including civil engineering. Yet, lacking information technology (IT) human resources with a civil engineering background is related to a slow process of implementing such powerful tools to interpret data inputs (Pregolato et al., 2022).

In this sense, a few solutions can be explored to incorporate stochastic and AI approaches to enhance prediction and reduce the risk of false non-reactive results, such as using probabilistic

modeling, implementing Monte Carlo simulations, developing machine learning (ML) algorithms, and utilizing active learning tools such as Artificial Neural Networks (ANN).

By implementing probabilistic modeling, the outcomes would explore the probability of the occurrence of aggregate reactivity. It would better capture uncertainties regarding the risk of field AAR development that is dependent on the above-mentioned variables. Moreover, Monte Carlo simulations would be a useful tool for generating random samples in the probabilistic distribution, which would allow analyzing more variable combinations to better predict the AAR development on the field. Next, using current laboratory and field data would be sufficient to train machine learning algorithms and evaluate the risk of occurrence of AAR; this process would lead to better predictions and accurate decision-making. It could be implemented by decision analysis, such as decision trees or sensitivity analysis, by evaluating the variable's impacts. Moreover, active learning models, as the case of ANN, can be extremely suitable for pattern recognition and prediction. In this way ANN can be trained to identify a common pattern in data collected from laboratory methods and field measurements regarding AAR.

7 CONCLUSION

The main objective of the literature review investigation carried out in this study was to critically review current laboratory methods for assessing AAR-induced development and understand the context in which laboratory specimens and field blocks are being evaluated to quantify the risk associated with current tests to forecast AAR. The main conclusions of the above investigations are:

- It has been stated that it is necessary to consider not only the potential of an aggregate for AAR but also an assessment of the conditions under which the aggregate might still be used in an actual structure. Therefore, an outdoor exposure site is necessary to validate the effectiveness of performance laboratory tests used to select long-term prevention measures against ASR in concrete infrastructure in different environments.
- It has been observed that AMBT and CPT can show contradictory results when compared to each other. Therefore, complementary methods can be implemented to evaluate the data and propose accurate limits when correlating both tests.
- A proper correlation between laboratory methods and long-term field performance has not yet been demonstrated. Nevertheless, current extensive data on outdoor exposure sites are valid for implementing stochastic and AI to better understand and predict the future behavior of AAR development.

REFERENCES

- Alexander, M. (2011). *Alkali-Aggregate Reaction and Structural Damage to Concrete: Engineering Assessment, Repair and Management*. CRC Press. <https://doi.org/10.1201/b10773>
- ASTM C295/C295M. (2019). *Guide for Petrographic Examination of Aggregates for Concrete* (p. 9). ASTM International. https://doi.org/10.1520/C0295_C0295M-19
- ASTM C1260. (2022). *Test Method for Potential Alkali Reactivity of Aggregates (Mortar-Bar Method)* (p. 5). ASTM International. <https://doi.org/10.1520/C1260-22>
- ASTM C1778. (2022). *Guide for Reducing the Risk of Deleterious Alkali-Aggregate Reaction in Concrete*. ASTM International. <https://doi.org/10.1520/C1778-22>
- Beyene, M., Snyder, A., Lee, R. J., & Blazkiewicz, M. (2013). Alkali Silica Reaction (ASR) as a root cause of distress in a concrete made from Alkali Carbonate Reaction (ACR) potentially susceptible aggregates. *Cement and Concrete Research*, 51, 85–95. <https://doi.org/10.1016/j.cemconres.2013.04.014>
- Borchers, I., Lindgård, J., & Müller, C. (2022). Evaluation of laboratory test methods for assessing the alkali-reactivity potential of aggregates by field site tests. *Materiales de Construcción*, 72(346), e286. <https://doi.org/10.3989/mc.2022.17221>
- CSA A23.2-27A. (2019). *Standard Practices to identify degree of alkali-reactivity of aggregates and to identify measures to avoid deleterious expansion in concrete*. In *CSA Standards A23.1–09/A23.2–09 Concrete materials and methods of concrete construction/Test methods and standard practices for concrete* (13th edition, pp. 594–610). CSA Group.

- Custódio, J., Lindgård, J., Fournier, B., Santos Silva, A., Thomas, M. D. A., Drimalas, T., Ideker, J. H., Martin, R.-P., Borchers, I., Johannes Wigum, B., & Rønning, T. F. (2022). Correlating field and laboratory investigations for preventing ASR in concrete – The LNEC cube study (Part I – Project plan and laboratory results). *Construction and Building Materials*, 343, 128131. <https://doi.org/10.1016/j.conbuildmat.2022.128131>
- De Souza, D. J., Antunes, L. R., & Sanchez, L. F. M. (2022). The evaluation of Wood Ash as a potential preventive measure against alkali-silica reaction induced expansion and deterioration. *Journal of Cleaner Production*, 358, 131984. <https://doi.org/10.1016/j.jclepro.2022.131984>
- Duchesne, J., & Bérubé, M. A. (1994). The effectiveness of supplementary cementing materials in suppressing expansion due to ASR: Another look at the reaction mechanisms part 2: Pore solution chemistry. *Cement and Concrete Research*, 24(2), 221–230. [https://doi.org/10.1016/0008-8846\(94\)90047-7](https://doi.org/10.1016/0008-8846(94)90047-7)
- Fournier, B., & Bérubé, M.-A. (2000). Alkali-aggregate reaction in concrete: A review of basic concepts and engineering implications. 27.
- Fournier, B., Chevrier, R., Bilodeau, A., Nkinamubanzi, P.-C., & Bouzoubaa, N. (2016). COMPARATIVE FIELD AND LABORATORY INVESTIGATIONS ON THE USE OF SUPPLEMENTARY CEMENTING MATERIALS (SCMs) TO CONTROL ALKALI-SILICA REACTION (ASR) IN CON-CRETE. 15th International Conference on Alkali-Aggregate Reaction (ICAAR), Brazil.
- Fournier, B., Lindgård, J., Wigum, B. J., & Borchers, I. (2018). Outdoor exposure site testing for preventing Alkali-Aggregate Reactivity in concrete – a review. *MATEC Web of Conferences*, 199, 03002. <https://doi.org/10.1051/mateconf/201819903002>
- Grattan-Bellew, P. E., & Katayama, T. (2017). So-Called Alkali-Carbonate Reaction (ACR). In *Alkali-Aggregate Reaction in Concrete* (p. 26). CRC Press. <https://doi.org/10.1201/9781315708959>
- Kawabata, Y., & Yamada, K. (2017). The mechanism of limited inhibition by fly ash on expansion due to alkali-silica reaction at the pessimum proportion. *Cement and Concrete Research*, 92, 1–15. <https://doi.org/10.1016/j.cemconres.2016.11.002>
- Lindgård, J., Andiç-Çakır, Ö., Fernandes, I., Rønning, T. F., & Thomas, M. D. A. (2012). Alkali-silica reactions (ASR): Literature review on parameters influencing laboratory performance testing. *Cement and Concrete Research*, 42(2), 223–243. <https://doi.org/10.1016/j.cemconres.2011.10.004>
- MacDonald, C. A., Rogers, C., & Hooton, R. D. (2012). THE RELATIONSHIP BETWEEN LABORATORY AND FIELD EXPANSION – OBSERVATIONS AT THE KINGSTON OUTDOOR EXPOSURE SITE FOR ASR AFTER TWENTY YEARS. 14th International Conference on Alkali-Aggregate Reaction (ICAAR), Austin, Texas, USA.
- Nixon, P. J., & Sims, I. (Eds.). (2016). *RILEM Recommendations for the Prevention of Damage by Alkali-Aggregate Reactions in New Concrete Structures* (Vol. 17). Springer Netherlands. <https://doi.org/10.1007/978-94-017-7252-5>.
- Oberholster, R. E., & Davies, G. (1986). An accelerated method for testing the potential alkali reactivity of siliceous aggregates. *Cement and Concrete Research*, 16(2), 181–189. [https://doi.org/10.1016/0008-8846\(86\)90134-1](https://doi.org/10.1016/0008-8846(86)90134-1).
- Pregolato, M., Gunner, S., Voyagaki, E., De Risi, R., Carhart, N., Gavriel, G., Tully, P., Tryfonas, T., Macdonald, J., & Taylor, C. (2022). Towards Civil Engineering 4.0: Concept, workflow and application of Digital Twins for existing infrastructure. *Automation in Construction*, 141, 104421. <https://doi.org/10.1016/j.autcon.2022.104421>.
- Sanchez, L. F. M., Drimalas, T., Fournier, B., Mitchell, D., & Bastien, J. (2018). Comprehensive damage assessment in concrete affected by different internal swelling reaction (ISR) mechanisms. *Cement and Concrete Research*, 107, 284–303. <https://doi.org/10.1016/j.cemconres.2018.02.017>.
- Sanchez, L. F. M., Fournier, B., Jolin, M., & Duchesne, J. (2015). Reliable quantification of AAR damage through assessment of the Damage Rating Index (DRI). *Cement and Concrete Research*, 67, 74–92. <https://doi.org/10.1016/j.cemconres.2014.08.002>.
- Scaglione, N. J., & Piercey, P. L. (2016). ACR and ASR of a Carbonate Coarse Aggregate in Missouri. In D. Cong & D. Broton (Eds.), *Advances in Cement Analysis and Concrete Petrography* (pp. 65–88). ASTM International. <https://doi.org/10.1520/STP161320180009>.
- Sims, I., & Nixon, P. (2003). RILEM Recommended Test Method AAR-0: Detection of Alkali-Reactivity Potential in Concrete—Outline guide to the use of RILEM methods in assessments of aggregates for potential alkali-reactivity. *Materials and Structures*, 36(7), 472–479. <https://doi.org/10.1007/BF02481527>.
- Stacey, S., Folliard, K., Drimalas, T., & Thomas, M. D. A. (2016). AN ACCELERATED AND MORE ACCURATE TEST METHOD TO ASTM C1293: THE CONCRETE CYLINDER TEST. 15th International Conference on Alkali-Aggregate Reaction (ICAAR), Brazil.
- Swamy, R. N. (1991). Role and effectiveness of mineral admixtures in relation to alkali-silica reaction. In *The Alkali-Silica Reaction in Concrete* (1st Edition, p. 288). CRC Press. <https://doi.org/10.4324/9780203036631>.
- Thomas, M. (2011). The effect of supplementary cementing materials on alkali-silica reaction: A review. *Cement and Concrete Research*, 41(12), 1224–1231. <https://doi.org/10.1016/j.cemconres.2010.11.003>.

Digital twins for civil infrastructure: A case study on the Clifton suspension bridge (Bristol, UK)

M. Pregnotato, S. Gunner, E. Voyagaki, R. De Risi, G. Gavriel, P. Tully, N. Carhart, T. Tryfonas & C. Taylor

Department of Civil Engineering, University of Bristol, Bristol, UK

ABSTRACT: Validated digital Twins support the optimisation of the performance, life-extension, maintenance, design and full-life costs of infrastructural assets; however, in the Civil Engineering sector their actual application and technology is still largely at the development stage. This study advanced a framework for using Digital Twins for civil infrastructure, which could be applied to various assets. This paper applied the framework to the historic Clifton Suspension Bridge in Bristol (UK). This aim was achieved through the following objectives: (i) proposing a working framework applicable to various assets; (ii) applying the framework and developing the physical-virtual architecture for the case study of the Clifton Suspension Bridge (Bristol); (iii) reflecting and drawing lessons from the application. The novelty of this work consists in illustrating the step-by-step framework of twinning, which is not limited to a methodological perspective nor to a particular asset of civil infrastructure. In addition to the theoretical contribution, this work's importance also includes the case study itself, which ultimately offers a needed demonstration of the concept of digital twinning.

1 INTRODUCTION

The smooth running of modern cities is hugely dependent on our national and local infrastructure. Buildings, roads and bridges are key elements of communities and economies, affecting immediate through to very long-term performance and investment. However, climate change, aging and societal changes (e.g. urbanization) are threatening the functionality and integrity of these structures (Pregnotato, 2019). The risks involved are also exacerbated by disjointed infrastructure data and ad-hoc maintenance that often does not address a problem until it becomes a very costly fix, or a structural failure. As part of the UKCRIC (UK Collaboratorium for Research in Infrastructure and Cities) programme (<https://www.ukcric.com/>), this study explores how to ensure the resilience of infrastructure in the face of increasingly severe hazards, proposing an entirely new way of managing all kinds of infrastructure around the world: Digital Twins (DTs).

Digital twinning is the process of digitally replicating all the facets and features of a real-world object in a 3D computational model, whilst integrating real-world data such that it has an effect on that object (CDBB, 2020; Jones et al., 2020). This technique supports the forecasting of outcomes over broad timescales and the exploration of different performance improvement scenarios safely on a computer, rather than navigating the risks that would come with doing so in real life (Figure 1). Digital twinning has already seen widespread application in the manufacturing sector in the creation and design of new products, but it has been limitedly applied to civil infrastructure (Lamb, 2019; Pregnotato et al., 2022; Voyagaki et al. 2022).

Dang et al. (2018) suggested a 3D DT model for improving the maintenance of typical bridge structures, combining 3D, FE and damage models. Similarly, Ye et al. (2019) studies two railway bridges and the relative capabilities required for developing

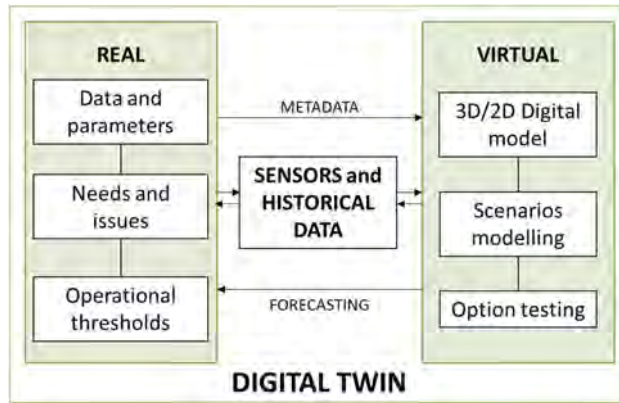


Figure 1. Digital Twin diagram.

a DT for structural health monitoring purposes. Also, Shim et al. (2019a) presented a DT-based model concept for bridge maintenance and more reliable decision-making; this work progressed into Shim et al. (2019b), who offered a DT model for a suspension bridge and stiffening girders, applied to a pilot for maintenance and automatic damage detection in Korea. Lu and Brilakis (2019) adopted cloud-to-cloud distance-based metrics to advance the automation of digital twinning for existing reinforced concrete bridges, using ten highway bridges around Cambridgeshire (UK). In the same geographical area, Lu et al. (2019, 2020a) developed a DT-enabled anomaly detection system for built asset monitoring to support operation and maintenance. They developed a process flow and a pilot for circulating pumps in a building's HVAC (heating, ventilation, and air conditioning) system, which was further extended by Lu et al. (2020b). Others have investigated the incorporation of real-time sensor data into BIM-like bridge models, such as Davila Delgado et al. (2017 and 2018).

This paper re-proposed the methodology of Pregnotato et al. (2022) (which is under a Creative Commons license), using the Clifton Suspension Bridge in Bristol (UK) as proof-of-concept (Figure 2). This work was developed in collaboration with the Clifton Suspension Bridge Trust and the engineering firm COWI.



Figure 2. The Clifton Suspension Bridge in Bristol (UK).

2 METHODOLOGY

The proposed methodology combines the DT “maturity spectrum” presented in Evans et al. (2020) and the five layers of Lu et al. (2020b). A framework of five actionable steps is advanced (Figure 3) and outlined below (Pregnotato et al., 2022).

(1) *Data and need acquisition.* This step consists of an enquiry into the ‘real’ structure, that elicits the information required for building and calibrating the virtual model. This step generates information about the operational processes used to manage a structure, clearly identifying the objectives and decisions that the DT will support, as well as the actions that provide the feedback between the DT and structure.

(2) *Digital modelling.* This step involves the creation of a ‘virtual’ ‘physics-based model that simulates, visualises, controls and models the behaviour of the structure (either in 2D or 3D). Depending on the purpose of the DT, multiple compatible models may be required. Open and well-documented interfaces must be created if the model is to become part of a federated ecosystem of connected DTs, and these should be considered during the design stage. The DT must be able to combine models and data (e.g. for calibration, validation, updating, etc.), requiring suitable model interfaces.

(3) *Sensor data transmission.* The collection of sensor data is the other element of the ‘real’ component of a DT. Suitable sensors (or observations) enable model validation and updating, while the data management elements facilitate automatic retrieval and processing. The sensing and transmission system must collect, transfer and store data, presenting it and its metadata through open interfaces for use by the integration framework. The necessary data quality (e.g. resolution and sample rate) depends on the requirements of the application and have an impact on the sensing and communications technology that can be used. The adoption of industry standards, both in technology and process, is also strongly advised as this will reduce design time and improve functionality.

(4) *Data/model integration.* A DT’s peculiarity is the link between the real and virtual. An interoperability architecture guarantees this connection, which should be flexible and agile (through open platforms and a modular design) to accommodate advances in technology and society. At a systems-of-systems level (where outputs from one DT become inputs to another), a scalable federation requires the adoption of yet-to-be-created standards, as well as governance frameworks that clarify issues of data ownership and service level agreements.

(5) *Operation.* To inform and enable effective and efficient asset management, actions should drive the purpose of a DT. A DT informs operational decisions when its outputs flow into the decision-making process, i.e. essentially by allowing comparison between the potential outcomes of a set of available actions, based upon available information.

The detailed five-step framework provides a process to create a DT by considering each of its components. The framework is applied to the case study of the Clifton Suspension Bridge (monitoring of the tower saddles) in Section 3.

3 RESULTS

The Grade I listed Clifton Suspension Bridge (Figure 2) in Bristol (UK) spans the river Avon and was completed in 1864, based on a design by I. K. Brunel. It constitutes an excellent example of legacy infrastructure, with obvious ageing and maintenance issues (Mitchell-Baker and Cullimore, 1988; Anderson, 2013) and no BIM data. The Clifton Suspension Bridge Trust (CSBT) is responsible for managing and maintaining the bridge; one of their concerns is the operation of the tower saddles, seizure of which may impair the bridge’s safety. Currently, sensor information about the saddles is presented to the bridgemanter in the form of periodic reports, whereas a system able to detect real-time changes in the friction of these saddles would allow managers to better quantify risk factors and select appropriate, safety and cost effective, actions. This demonstration focuses on this operational need.

(1) *Data and need acquisition.* Without BIM data to rely on, enquiry into the current state of the structure has included examining historical drawings and operational records from archives and site visits to inspect specific details in person. For this study, the Trust and the bridge consultant COWI facilitated data, the definition of needs, and the model validation. The tower rollers minimise the horizontal forces on the towers and land saddles from the chains, which would otherwise result from changes due to changes in loads and temperature, but this is only possible while the rollers move freely. If they seized, large forces could be



Figure 3. The five-step framework to develop a Digital Twin (e.g. for a bridge) (from Pregnolato et al., 2022).

transferred to the towers, which could significantly increase the stresses in the rock abutment. This abutment is a natural structure, so exact operational stress thresholds are not easy to identify. There is, therefore, an operational imperative to ensure that the frictional coefficient of the saddles is kept low. Understanding the change in the friction coefficient over time allows bridge management to schedule preventive maintenance and actions, e.g. lubricant application, or even bridge closure. The expansion and contraction of the chains due to changes in temperature were identified as providing the cause of the largest contribution to impact on the force applied to the saddles; thus, the bridge was instrumented with appropriate sensors (Figure 4). Temperature sensors measure the temperature of chain links while displacement transducers (located on each saddle, two in each tower) measure the saddle displacements. The strain on the chain links of one saddle in the East tower is measured by a single strain gauge. Finally, two weather stations and two weigh-in-motion machines, for measuring vehicle weights, are also in place.

(2) *Digital modelling.* A 3D FEM (Finite Element Model) of the bridge has been developed by the authors to numerically simulate the response of the structure under the loading conditions of interest (Figure 4). The software Midas Gen (Midas, 2020) was selected for initial FE modelling. The model has been calibrated and validated against two previous numerical models: the NODLE model (COWI, 2010); and 3D FEM model developed in ANSYS (Yeung and Smith, 2005). Comparisons against experimental results of some selected symmetric load cases presented by Flint and Pugsley (1955) generally show reasonable agreement. Modal analysis results show good agreement when comparing the vibration modes to available experimental data (Macdonald, 2008; BEELAB, 2003) using the Modal Assurance Criterion (MAC) (Allemang, 2003; mean MAC=0.973). Modelling and validation details are available in Pregnolato et al. (2022) and Voyagaki et al. (2022).

(3) *Sensor data transmission.* For this case study, the deployment is limited to the tower tops, where wired communications are provisioned. Regarding the strain gauges fitted to each

of the bridge side chain links, analogue to digital converters encapsulate the sensor measurements and publish them via IP to a server located at ground level in one of the nearby toll houses. The displacement transducers are functional to calculate the friction coefficient; the strain gauge provides the data necessary to calculate the friction estimation. A WSN (Wireless Sensor Network) deployment removes the need for provisioning wired power and communications on-site by relying on battery power and wireless communications technologies. The WSN gateway will receive the temperature readings and publish them to the local server hosting an InfluxDB time-series database instance. There are two layers at which the model and data interface: (1) the software layer, i.e. the model software's interface through which parameters can be modified, and the model invoked; and (2) the application layer, i.e. the interface at which the link "understands" the received input measurement (e.g. a temperature reading) and send back information about how to adjust the model eventually. Layer 1 enables the functionality of Layer 2. At a software layer, real-time integration between the model and sensors requires each functional block to have a set of computing interface (APIs) through which it can be interacted with. Technical details include that the sensors' API is provided by an MQTT message broker (MQ Telemetry Transport protocol), to which the ADCs and WSN gateway will publish their data. The DT software will subscribe to this data stream and so be passed any measurements received by the broker. The specific software package used for this purpose was the Lord MicroStrain MSCL Python API.

(4) *Data/model integration.* Different types of sensor data are present and need to be integrated. To enable this range of functionality, the model requires a sophisticated set of APIs. The DT software must be able to update the FEM by modifying the parameters of interest. For example, data from the chain strain measurements due to temperature change will inform the friction coefficient at the saddles. Features of interest are returned as software variables that the DT software can access. This study is currently at the exploratory stage and uses a simple software (Midas GEN); however, a more sophisticated software package, such as the OpenSeesPy library, allows models to be build and run in a Python environment. Before producing any output, the DT compares the modelled strain values with the recorded value to help provide confidence that the model parameters are correct. This comparison allows the system to generate an uncertainty value for the modelled output. Consistent or systematic discrepancy between the modelled and verified and validated measured values require the model to be updated. This updating is based on all the available information since any measurement (or set of similar measurements) could give huge uncertainty, especially for short records. The DT then combines the strain values with the relevant recorded displacement values to calculate the coefficient of friction for each saddle, which is the feature of interest. These coefficients are recorded in an InfluxDB time-series database so that historical trends can be created and values be presented to the infrastructure management.

(5) *Operation.* Historical records could enable the definition of operational thresholds, i.e. in this case the operational limit of the saddles friction of coefficient. Thus, engineering judgement is used to estimate what is a maximum safe strain on the back-span chains, and so at what value of friction a particular course of action must be taken. The DT can then report real-time and historic friction values and present rates of change, presenting the data through a dashboard. When the operational threshold is reached, a set of pre-defined actions or alerts are triggered, e.g. for maintenance or inspection of the rollers. For example, if the friction coefficient increases linearly over time, the validated DT information would prompt the infrastructure managers and operators to adjust maintenance schedule accordingly. On the other hand, more complicated scenarios can arise. For example, cold weather could increase the value of the friction coefficient since low temperatures affect the performance of the lubricant. In this scenario, weather forecasting data would allow the DT to predict what value of friction might be expected for those temperatures and allow maintenance when temperatures are mild and access is straightforward.

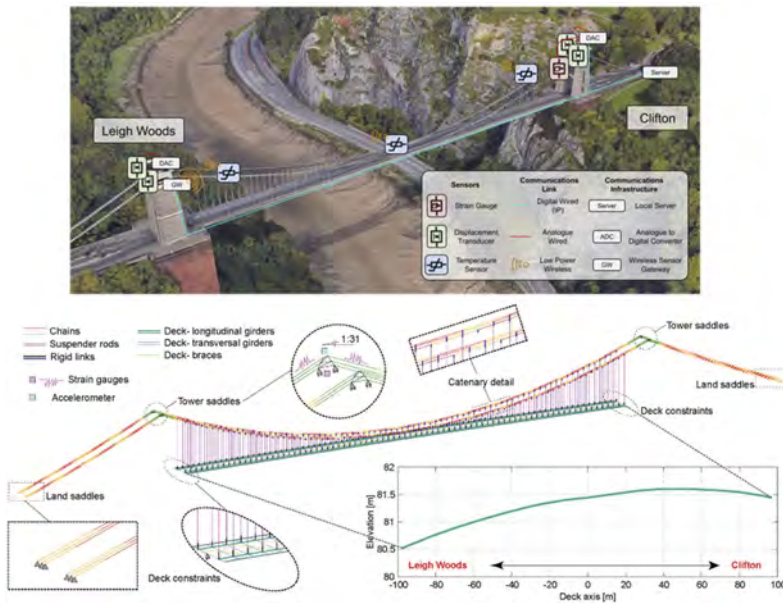


Figure 4. Top: an illustration of sensor deployment required for a DT which would serve for saddle monitoring (base photograph from Google Earth) for the Clifton Suspension Bridge. Bottom: the 3D FEM developed using Midas Gen platform.

4 DISCUSSION AND FUTURE RESEARCH

Digitalisation, and digital twinning in particular, will play a fundamental role in future infrastructure management, by driving the business case for investment and ultimately making structures safer and cost effective. However, DTs are heavily reliant on data. Data management and sharing is a delicate process due to privacy issues, and policies are needed to set standards and share data confidently. As owner and manager of the bridge, the Trust must sign a Data Transfer Agreement (DTA) which defines data and DT ownership, exchange and governance, e.g. stating explicitly which sorts of data belong to which organisation. This agreement relates to the contingency of academic research and, thus, also underpins any wider dissemination of data (e.g. via publication, presentation). In other contexts (e.g. industry), a DT would be run for and by (or under a contract for) the owner or operator, who decides on any agreements they make with any other organisations. Although infrastructure data is unlikely to contain any personal data (so not under the remit of regulations such as the EU's GDPR), it can still be extremely sensitive and not liable to open access. However, if the data are structured on *open standards* frameworks (which does *not* imply *open access*), they can be more readily integrated with other similarly structured data sets and be processed by tools that can ingest these structures, thereby opening up new, controllable, value creation pathways for the data owners and the data processors.

This study started to explore how valuable digital twinning can be in the built environment by developing a DT framework for civil infrastructure and applying it to the Clifton Suspension Bridge. More case studies are needed to demonstrate the viability of digital twinning, and the potential benefits. Future works could look into applying the framework to other structures, such as buildings or wind turbines. In the medium-term, there is also a clear scope for the integration of artificial intelligence and machine learning into the platform, which could help researchers identify novel threats or those forecast within a timeframe outside the usual monitoring period. In the longer-term, it is evident that no single DT will be sufficient for modern complex cities: in a smart city

scenario, independent validated DTs of various assets will need to communicate and cooperate, providing feedback to a central decision making “hub” or city-level decision makers. For example, the DT of a particular asset (e.g. a bridge) could be federated with the DTs of other related assets (e.g. roads). Finally, the fundamentals of the proposed workflow could be combined with other elements related to human health, safety and well-being, environmental sustainability and disaster/climate resilience. For example, a DT of an asset of interest (e.g. a building) could be used in relation to users’ health and wellbeing, by means of immersive reality and other tools.

5 CONCLUSIONS

The concept of Digital Twins (DTs) could potentially change the design, production, maintenance, and life-extension of civil infrastructural assets; however, more research is needed in order to accelerate this digital transformation. This paper has advanced a five-step framework for developing DTs for existing structures, which comprised: data and need acquisition (1), digital modelling (2), dynamic data transmission (3), data/model integration (4) and operation (5). The framework was applied to the Clifton Suspension Bridge (Bristol, UK), which was adopted as a case study. In the future, machine learning and AI could provide the DT with autonomous decision-making; in the longer-term, this bridge DT could be federated with the DTs of other bridges or related assets (e.g. roads). Some challenges were identified in the development and adoption of DTs, such as its transferability to other structures (e.g. wind turbines), data management and the business proposition (cost vs benefits) behind it. This paper’s importance resides in the knowledge challenge, value proposition and operation dictated by developing a DT framework for civil infrastructure, as well as the demonstration for an exemplary bridge which ultimately represents a relevant use case.

ACKNOWLEDGEMENTS

This work was supported by the Engineering and Physical Sciences Research Council (EPSRC) Fellowship (EP/R00742X/2); UK Collaboratorium for Research in Infrastructure & Cities (UKCRIC): Urban Observatories (EP/P016782/1); UKCRIC City Observatory Research platform for iNnovation and Analytics (CORONA) (EP/R013411/1). The authors gratefully acknowledge: the Clifton Suspension Bridge Trust and the Bridgemaister Trish Johnson, COWI, and AMP Electrical.

REFERENCES

- Allemang, R.J. (2003). The Modal Assurance Criterion - Twenty Years of Use and Abuse. *Sound and Vibration* 37(8): 14–21. <http://www.sandv.com/downloads/0308alle.pdf> (accessed 12/05/22)
- Anderson, D. (2013). Maintenance of the Clifton Suspension Bridge an Historic and Iconic Grade 1 listed structure. In: *ICSBOC (8th International Cable Supported Bridge Operators’ Conference)*, Edinburgh, 3-5 June 2013, CRC press. ISBN 9781482208450
- BEELAB (2003). *Dynamic behaviour of the Clifton Suspension Bridge: Modal behaviour in light winds and response to crowd loading*. Report No. CSB703/REP/1 (Personal communication)
- CDBB, Centre for Digital Built Britain (2020). *The Approach to Delivering a National Digital Twin for the United Kingdom* [online]. https://www.cdbb.cam.ac.uk/files/approach_summaryreport_final.pdf (accessed 1/06/2020)
- Dang, N-S., Kang, H-R., Lon, S. & Shim, C-S (2018). 3D Digital Twin Models for Bridge Maintenance. In: *Proceedings of 10th International Conference on Short and Medium Span Bridges*, Quebec, Canada, July 31-August 3. ISBN 9781617389900
- Davila Delgado, J. M., Butler, L. J., Brilakis, I., Elshafie, M. Z. E. B & Middleton, C. (2018). Structural Performance Monitoring Using a Dynamic Data-Driven BIM Environment. *Journal of Computing in Civil Engineering* 32(3). [https://doi.org/10.1061/\(asce\)cp.1943-5487.0000749](https://doi.org/10.1061/(asce)cp.1943-5487.0000749).

- Davila Delgado, J. M., Butler, Gibbons, N., Brilakis, I., Elshafie, M. Z. E. B & Middleton, C. (2017). Management of Structural Monitoring Data of Bridges Using BIM. *In: Proceedings of the Institution of Civil Engineers: Bridge Engineering* **170**(3). <https://doi.org/10.1680/jbren.16.00013>.
- Evans, S., Savian, C., Burns, A. & Cooper, C. (2020). Digital twins for the built environment [online]. *The IET (Institution of Engineering and Technology)*: London. <https://www.theiet.org/impact-society/sectors/built-environment/built-environment-news/2019-news/digital-twins-for-the-built-environment/> (accessed 12/05/2022)
- Flint, A.R. & Pugsley, A.G. (1955). Some experiments on Clifton Suspension Bridge. *The Institution of Civil Engineers*. Preliminary volume: 124–134. London. <https://www.icevirtuallibrary.com/doi/abs/10.1680/cotcbcaosadisfv.45071.0002>
- Jones, D., Snider, C., Nassehi, A., Yon, J. & Hicks, B. (2020). Characterising the Digital Twin: A systematic literature review. *CIRP Journal of Manufacturing Science and Technology* **29**(A): 36–52. <https://doi.org/10.1016/j.cirpj.2020.02.002>
- Lamb, K. (2019). *Principle-Based Digital Twins: A Scoping Review* [online]. https://www.cdbb.cam.ac.uk/files/scopingreview_dec20.pdf (accessed on 5/5/2020)
- Lu, Q., Xie, X., Parlikad, A. & Schooling, J.M. (2020a). Digital twin-enabled anomaly detection for built asset monitoring in operation and maintenance. *Automation in Construction* **118**: 103277. <https://doi.org/10.1016/j.autcon.2020.103277>
- Lu, Q., Parlikad, A. K., Woodall, P., Don Ranasinghe, G., Xie, X., Liang, Z., Konstantinou, E. and Schooling, J.M. (2020b). Developing a Digital Twin at Building and City Levels: Case Study of West Cambridge Campus. *Journal of Management in Engineering* **36**(3): 05020004. [https://doi.org/10.1061/\(asce\)me.1943-5479.0000763](https://doi.org/10.1061/(asce)me.1943-5479.0000763)
- Lu, R. & Brilakis, I. (2019). Digital twinning of existing reinforced concrete bridges from labelled point clusters. *Automation in Construction*, **105**: 102837. <https://doi.org/10.1016/j.autcon.2019.102837>
- Macdonald, J. H. G. (2008) Pedestrian-induced vibrations of the Clifton Suspension Bridge, UK. *Proceedings of the Institution of Civil Engineers: Bridge Engineering* **161**(BE2): 69–77. <https://doi.org/10.1680/bren.2008.161.2.69>
- Midas (2020). Midas Gen Manuals and Tutorials [online]. <https://globalsupport.midasuser.com/helpdesk/KB/View/32609792-midas-civil-manuals-and-tutorials> (accessed on 5/5/2020)
- Mitchell-Baker, D. & Cullimore, M. S. G. (1988). Operation and maintenance of the Clifton Suspension Bridge. *Proceedings of the Institution of Civil Engineers* **1**(84): 291–308. <https://doi.org/10.1680/iicep.1988.63>
- Pregolato, M., Gunner, S. D., Voyagaki, E., Gavriel, G., Carhart, N. J., Macdonald, J. H. G., Tryfonas, T. and Taylor, C. A. (2022). Towards Civil Engineering 4.0: concept, workflow and application of Digital Twins for existing infrastructure. *Automation in Construction* **141**: 104421. <https://doi.org/10.1016/j.autcon.2022.104421>
- Pregolato, M. (2019). Bridge safety is not for granted - A novel approach to bridge management. *Engineering and Structures* **196**: 109193. DOI: <https://doi.org/10.1016/j.engstruct.2019.05.035>
- Shim, C.S., Kang, H.R. & Dang, N.S. (2019a). Digital twin models for maintenance of cable-supported bridges. *In: Proceedings of the International Conference on Smart Infrastructure and Construction (ICSIC 2019)*. <https://doi.org/10.1680/icsic.64669.737>
- Shim, C-S., Ngoc S-D, Sokanya, L., & Chi H-J. (2019b). Development of a Bridge Maintenance System for Prestressed Concrete Bridges Using 3D Digital Twin Model. *Structure and Infrastructure Engineering* **15**(10): 1319–1332. <https://doi.org/10.1080/15732479.2019.1620789>
- Voyagaki, E., De Risi, R., Gunner, S., Pregolato, M., Macdonald, J.H.G., Carhart, N., Gavriel, G., Tryfonas, T., Taylor, C.A. (2022). Towards a Digital Twin Prototype for the Clifton Suspension Bridge (UK). *ICOSSAR 2021-2022 13th International Conference on Structural Safety and Reliability*, Shanghai, China, 13-17 September 2022.
- Ye, C., Butler, L., Calka, B., Iangurazov, M., Lu, Q., Gregory, A., Girolami, M., & Middleton, C. (2019). A Digital Twin of Bridges for Structural Health Monitoring. Structural Health Monitoring 2019: Enabling Intelligent Life-Cycle Health Management for Industry Internet of Things (IIOT) - *Proceedings of the 12th International Workshop on Structural Health Monitoring* **1**: 1619–1626. <https://doi.org/10.12783/shm2019/32287>
- Yeung, W.T. and Smith J.W. (2005) Damage detection in bridges using neural networks for pattern recognition of vibration signatures. *Engineering Structures* **27**(5): 685–698. <https://doi.org/10.1016/j.engstruct.2004.12.006>

SHM analysis for damage detection using time series analysis methods

F. Schmidt & F. Chabi

Université Gustave Eiffel, MAST-EMGCU, France

J.-F. Bercher

Université Gustave Eiffel, LIGM, France

ABSTRACT: SHM is generally performed using continuous vibration or deformation monitoring. These signals correspond then to time series, whose evolution can be predicted based on their past history. This paper presents such a study on the Austerlitz bridge in Paris: it is a steel bridge, built during the 19th century, and carries the Parisian metro since then. The monitoring is therefore important to detect anomalies in its behavior. For that, it has been instrumented by 24 strains sensors (optic strands) and 4 temperature sensors, which record the corresponding signals during train passages at a 100Hz frequency. The individual passage signals have been extracted, the corresponding data has been gathered (data fusion) and cleaned. Finally, the evolution of the monitoring signals has been predicted based on their evolution with time and temperature. Machine Learning algorithms of type VARMAX have been used to realize the time prediction. The anomalies, defined as differences between the prediction and measured signals, have been identified. This paper will explain the context and the research questions, the work that has been realized and to finish the still-open points.

1 INTRODUCTION

1.1 Background

In France, 10% of the value of the road heritage comes from the engineering structures that are existing in the country (estimated at 200,000 to 250,000 bridges) (Patrick, 2019). This road network is used a lot since it ensures 88% of all trips for freights and people travels, which is why it plays an essential role in the communication and the economy of the country. However, a survey by the IPSOS institute has highlighted an increase in the rate of dissatisfaction of the French people, which has risen from 17% to 22% in two years (Patrick & Michel 2019). This follows the collapse of the Morandi bridge in Genoa in 2018, which revived the debate on the safety of engineering structures and the memory of the Mont Blanc tunnel disaster in 1999. This feeling may be justified when we know that a third of the bridges managed by the French State require repair, according to the Ministry of Ecological Transition and Solidarity in 2018, and that all metal bridges are in non optimal health condition. This leads to traffic restrictions or closures, which is detrimental to economic activity, the environment and the mobility.

This ageing of the French road network is perfectly normal and expected, since the theoretical lifespan of a bridge structure is estimated at 100 years. However, many bridges were built before the year 2000 and the introduction of European standards (Eurocodes, Eurocodes 1992), which means that their lifespan is less than the expected 100 years and tends to be around 70 years. Indeed, a large proportion of the structures were built in the post-war period, in the 1950s and 1960s, and should therefore reach the end of their life very soon and at the same time. This lifespan varies according to several factors such as the type of bridge but also global warming and environmental conditions which can lead, for example, to corrosion (see for example Île de Ré bridge), conditions of use (with the increase in road traffic, some advice of GPS to use the secondary network to avoid slowing down while it has been not designed to receive such loads), or the quality and regularity of maintenance.

The last point tends to be lacking as the inventory of bridges in France is complicated since the managers of some of them are not always known. Moreover, the monitoring of deterioration is only visual, which is far from sufficient to identify certain types of pathologies, such as corrosion, which develops inside the materials. There is therefore a need to address the problem further upstream. However, under-investment and lack of technical skills are a problem as small municipalities do not always have the means and skills to check the condition of their structures and maintain them. It is therefore necessary that the tools used are adapted to all, including local managers, since this emergency management of assets is not good maintenance practice and is neither sustainable nor economically viable in the long term.

A solution which is nowadays widely proposed is the intensive monitoring of structures, also called Structural Health Monitoring. Nevertheless, this monitoring may sometimes lead to (big) amount of data, which may therefore be difficult to be treated. More precisely, it might be difficult to extract pertinent information which would help the infrastructure manager to take decisions related to maintenance, repair, or strengthening actions (Tripura, 2000), (Salawu, 1997), (Seo, 2015).

1.2 *State-of-the-art*

Damage detection is traditionally done through vibration analysis, see (Burgos, 2020), (Lakhdar, 2013) for some examples in the civil engineering domain. Nevertheless, these methods are of various natures, depending on the focus they make, namely on eigenvalues (Belmokhtar, 2022) or eigenmodes, or the mathematical/algorithmic procedures for dealing with the fact that the actions on the structure are unknown (Sadhu, 2017), (Bandara, 2014). Nevertheless, it may be quite difficult to propose or use some criteria to decide if changes/damage in the structure have occurred (Jayasundara, 2019).

Therefore, with the development of bigger data volumes, new ways of detecting damages have been proposed (Rasol, 2023) (Wang, 2022): while some works use supervised learning methods (Zhou, 2013), some others propose unsupervised methods (Entezami, 2020). In particular, neural networks are used to predict future time series, and assess the deviation between this predicted data with the “real”, measured one (Manzini, 2021) (Xu, 2015). Changes can then be detected, also via pattern recognition (Yeung & Smith 2005).

It should be noted that other Machine Learning methods are sometimes proposed, like random forests (Zhou, 2013) and XG-Boost (Wang, 2022).

This paper proposes to predict the time series of strain sensors, using the theory of ARMA processes and comparing the predicted values with the measured ones.

2 THE AUSTERLITZ VIADUCT AND ITS MONITORING SYSTEM

2.1 *A steel arch bridge*

The Austerlitz viaduct allows metro line 5 to cross the Seine between the Austerlitz station and the quai de la Rapée (Figure 1).



Figure 1. Photo of Austerlitz bridge.

The viaduct consists of two arches of 20 metres in span with three joints, one at the top of the arch and two at the abutments. This system creates an underpinning at the supports, the span of the arch is thus reduced from CC' to RR' , which is equivalent to going from 140

metres to only 107 metres. In addition, the ball-and-socket joint at the top allows the height of the arches to be reduced considerably.

Two masonry abutments are placed at the end of the arches, which are then cantilevered by 16.4 metres. The two ends of the half-arches are joined by a lattice brace on each side of the keystone.

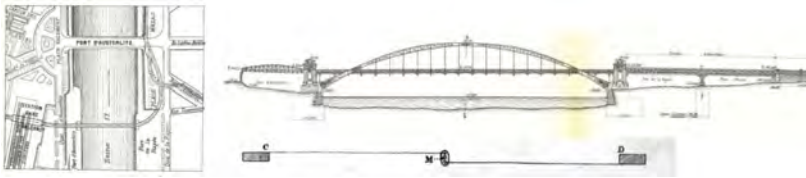


Figure 2. Drawings of the Austerlitz bridge.

Today the Austerlitz viaduct is facing three major pathologies whose origins are still unknown. The first was reported in November 1998: a central hanger oscillated abnormally, by 7 or 8 cm laterally, while all the other lines had remained completely inert. This phenomenon was observed by technicians working on the track. The second pathology would impair the proper behavior of the bridge. Indeed, the male-female connections and the central connecting rod seem to be blocked. Finally, inspections of the bridge revealed the presence of numerous cracks at the attachment nodes of various lines.

2.2 Monitoring based on optical strands

The structure is inspected every five years with a gondola mounted on a train and visited by foot every year to prevent pathologies.

Since 2010, several types of structural elements are monitored using fiber strands sensors: these sensors and the corresponding data are denoted by S1, S2, S3, S4, S5, S6, S7, S8, S9, S10, S11, S12, S13, and S14 (in Figure 3) and listed in Table 1. In all, 14 strain sensors and 3 temperature probes have been installed. It is noted that among these 14 strain sensors, 8 sensors are installed at the level of the bridge deck, 2 sensors are at the level of the hanger, and 6 sensors are fixed at the level of the arch of the bridge.

Also, for any two nearby structures, stain sensor have been duplicated: This aims to see if these nearby structures have the same strain behavior as a function of time, when the metro passes.

The general conclusions while studying this data are:

- The support beams become longer because they are located under the deck, so they tend to bend.

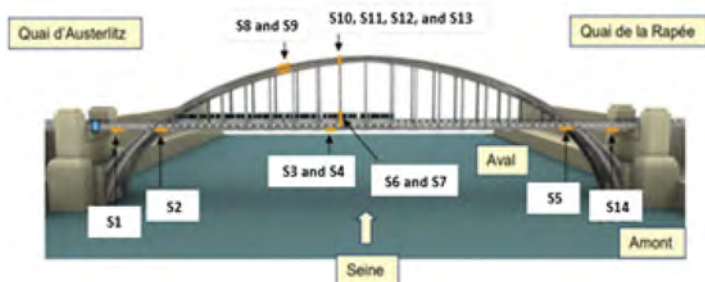


Figure 3. Scheme of Austerlitz bridge, and the installed sensors.

- The anchor beam on the Austerlitz side lengthens because it tends to sag, whereas the anchor beam on the Rapée side shortens because it tends to lift.

Table 1. Name of sensors and corresponding structural elements.

Name of sensor	Monitored structural element
S1	Anchoring beam Austerlitz
S2	Braking tie-rod Austerlitz
S3	Upstream side beam
S4	Downstream side beam
S5	Braking tie-rod Rapée
S6	Inside bottom hanger
S7	Outside bottom hanger
S8	Lower arch
S9	Upper arch
S10	Low diagonal brace
S11	Transverse brace
S12	Diagonal brace Austerlitz
S13	Diagonal brace Rapée
S13	Anchoring beam Rapée

- The tie rods behave in the opposite way to the opposite to the anchor beams. The tie rod on la Rapée side becomes longer while the tie beam on the Austerlitz side undergoes a shortening.

The characteristics of these sensors in term of period and frequency of acquisition and number of the total data that are recorded by each sensor are various:

- For the strain sensors that are installed on structures S1, S2, S3, S4, S5, S6, S7, S8, S9, S10, S11, S12, and S13, the acquisition period starts from 01/09/2020 and ends 23/09/2021, which means that a whole year of measurement is available. For the sensor installed at S14, the acquisition started on 25/01/2021, which has as consequence that we will not be consider this sensor in the analysis. The acquisition of these sensors is triggered when the subway passes, and the acquisition frequency is 100 Hz. During the acquisition period, each of the 13 strain sensors recorded around 500 million points of data. It is noted that as the acquisition is done at the subway crossings, the recording is not continuous, therefore there exists missing data.
- For the 3 temperature probes, the acquisition started on the 01/09/2020 and ended on 23/09/2021, with one acquisition for 10 minutes. Each temperature probe recorded 56285 pints of data. They are installed on structures S8, S1 and S7, and denoted T1, T2 and T3 respectively.

Data processing has been performed with Python language, in Jupyter notebook, using libraries Numpy, Pandas, Scipy, Sklearn, seaborn and matplotlib. In this article, the study is focused initially on the analysis of data from different types of sensors (strain, and temperature) in order to understand how the different structures of the bridges behave in terms of strain when the subway passes.

3 DATA ANALYSIS AND TIME SERIES PREDICTION

3.1 Data analysis

Looking now at the evolution of the strain within the structures that are close (in space), we see that the trend is the same. The correlation matrix (Figure 4) shows that the strain correlation between:

- S1 and S2 is 0.88,
- S3 and S4 is 0.98,
- S6 and S7 is 0.91,
- S8 and S9 is 0.62,
- S10, S11, S12 is between 0.88 and 0.93. However, S13 is less correlated with S10, S11, and S12 with a correlation between 0.57 and 0.64.



Figure 4. Correlation matrix between all sensors (strain and temperature).

As the evolution of the deformation is the same when the structures are close, we have therefore selected to use only the data from the sensors S1, S3, S5, S6, S9, and S10 for the rest of the analysis.

3.2 Time effect removal

The strain within the majority of bridge structures is temperature dependent. It is therefore necessary to correct this effect of temperature, to see the other factors which can influence the deformation of the structures. To eliminate the effect of temperature, the proposed method is as follows:

- Calculate the correlation between strain and temperature values. If the correlation coefficient between the two parameters is close to 1, this means that there is a linear relationship between the two parameters (see Equation (1)):

$$\tilde{\epsilon} = A \times T + B \quad (1)$$

- Apply the Linear Regression prediction model to find the values of A and B of Equation (1) which gives the prediction line, i.e. the predicted strain values $\tilde{\epsilon}$.
- Calculate the difference between the real values of strain ϵ and the predicted one $\tilde{\epsilon}$ to obtain the time evolution of the strain values corrected ϵ_{corr} with no temperature effect.

Figure 5 shows the relation between the real values of the strain of structure S1 and the temperature at the same time: the relationship is linear, which confirms the value of the coefficient of correlation of 0.96 found by the correlation matrix (see Figure 4). The red line in Figure 1 is the predicted strain values $\tilde{\epsilon} = 0.077 \times T - 0.29$. Figure 6 shows the strain time evolution with temperature effect (right graph) and with no temperature effect (left graph): the measured strains are more stable (in amplitude) along time.

3.3 Time series prediction

For temporal signals, we can use ARMA, or ARIMA type models when the signal has to be derived as input. In our case, we have multivariate data for which we wish to use and explore the inter-sensor dependencies. We can then consider multivariate VARMA (Vector Autoregressive Moving Average) extensions. We propose here a variation around these models. We note $x(t)$ the vector of dimension d collecting all the measurements of the d sensors at time t . The model takes the form:

$$x(t) = A_0 x(t) + \sum_{k=1}^p A_k x(t-k) + c + \epsilon(t), \quad (2)$$

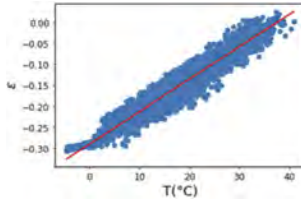


Figure 5. Relationship between strain at S1 and temperature values.

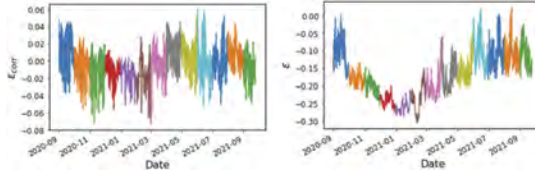


Figure 6. Time strain evolution at structure S1: measured value of strain (right), and corrected strain values with no temperature effect (left).

where matrices have dimension $d \times d$, c is a vector of offsets, and where matrix A_0 is constrained to have zeros on its diagonal. The role of A_0 is to take into account dependencies between signals (sensors) at the same time t . A LASSO regularization is used to stabilize the method and has the interesting property of forcing the coefficients of non-active variables to zero.

A prediction of $x(t)$ can be done according to:

$$\hat{x}(t) = A_0 x(t) + \sum_{k=1}^p A_k x(t-k) + c, \quad (3)$$

where $\epsilon(t)$ is the error or prediction residual. This means that a component j is computed as:

$$\begin{aligned} \hat{x}_i(t) &= \sum_{i=0, i \neq j}^d [A_0]_{i,j} x_i(t) \\ &+ \sum_{i=0}^d \sum_k k = 1^p [A_k]_{i,j} x_i(t-k) + c_j. \end{aligned} \quad (4)$$

A value at time t will be estimated as a function of the outputs of other sensors at the same time, and of all sensors outputs at previous timestamps.

For our experiment, we learn the model, i.e. we determine the coefficients, on a part of the data and compute the residuals on the whole data, which allows us to test the predictive capacity on data that have not been used for learning. The data are thus split into a learning part (from September 2 to May 17: two thirds of the data) and a test part (the last third, from May 18 to September 23, 2021). In order to test the capacity of the model to detect anomalies, we have introduced:

- An attenuation of 0.97 on AMPL-AS between the first and 14 of July,
- A factor of 1.05 on AMPL-TFR between 12 and 20 August.

For $p = 0$, the model only explores the interactions between sensors at the same time. In other words, the output of a sensor is only computed from the outputs of the other sensors at the same time. The coefficients of the sensors, and thus the dependencies they reveal, are given in Figure 7.

The residuals are computed, and we note that the introduced anomalies are correctly detected (the “boundaries”, related to the derivation, appear clearly between July 1 and 14 for AMPL-AS and on several other sensors, and from August 12 to 20 for AMPL-TFR). Other points are detected around February 10, when an exceptional freezing period is known to have occurred.

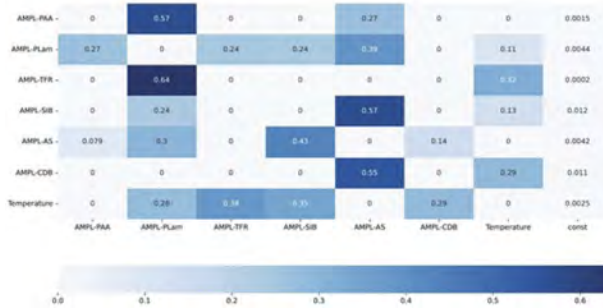


Figure 7. Coefficients of sensors for $p = 0$.

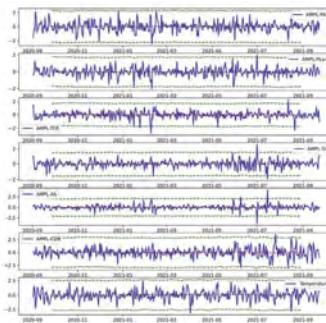


Figure 8. Residuals of prediction for $p = 6$.

For $p > 0$, the results are very similar. The coefficients associated with the time lags are small, and the improvement in the residuals remains tenuous (Figure 8). This indicates that there is in fact little temporal dependence between the samples; or at least that it has been removed by the initial derivation operation.

The predictions obtained show that the model allows to correct the effect of the artificially introduced defects (see Figure 9).

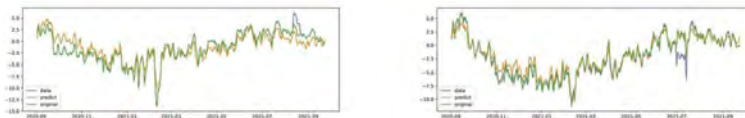


Figure 9. Prediction obtained for a defect on TFR and AS, for $p = 0$.

4 CONCLUSIONS

This work has shown a simple and yet effective method, using time series prediction, to detect changes in behaviour of structures. For that, the time series are analysed and simplified, first by considering only data which is non- (or less) correlated with other, then by removing the effect of temperature which is a big issue in civil engineering.

By experimenting on these data and introducing artificially anomalies into the measurements – which would simulate either a true structural anomaly or a sensor anomaly; we show that the regularised VAR statistical model learned on a portion of the data, is able to (a) detect anomalies on the unseen portion of the data, (b) correct the effect of these anomalies on the data; thus being able to compensate for a deficient sensor.

Future work are on the possibility to introduce physical/mechanical calculations in the analysis, especially for structures like Austerlitz bridge which are quite easy to model.

REFERENCES

- Bandara, R., Chan, T. & Thambiratnam, D. 2014. Structural damage detection method using frequency response functions. *Structural Health Monitoring*. **13**, 418–429.
- Belmokhtar, M., Schmidt, F., Chevalier, C. & Savadkoochi, A. 2022. Vibration-based method for structural health monitoring of a bridge pier subjected to environmental loads. *Experimental Vibration Analysis For Civil Engineering Structures*. pp. 73–82.
- Burgos, D., Vargas, R., Pedraza, C., Agis, D. & Pozo, F. 2020. Damage identification in structural health monitoring: A brief review from its implementation to the use of data-driven applications. *Sensors (Switzerland)*. **20**.
- Entezami, A., Shariatmadar, H. & Mariani, S. 2020. Fast unsupervised learning methods for structural health monitoring with large vibration data from dense sensor networks. *Structural Health Monitoring*. **19**, 1685–1710.
- EN 1992-1-1Eurocode 2: Design of concrete structures - Part 1-1: General rules and rules for buildings EN CEN, (2015).
- Jayasundara, N., Thambiratnam, D., Chan, T. & Nguyen, A. 2019. Vibration-based dual-criteria approach for damage detection in arch bridges. *Structural Health Monitoring*. **18**, 2004–2019.
- Lakhdar, M., Mohammed, D., Boudjemâa, L., Rabiâ, A. & Bachir, M. 2013. Damages detection in a composite structure by vibration analysis. *Energy Procedia*. **36** pp. 888–897.
- Manzini, N., Mar, N., Schmidt, F., Bercher, J., Orcesi, A., Marchand, P., Gazeaux, J. & Thom, C. 2021. An automated machine learning-based approach for structural novelty detection based on SHM. *Proceedings Of The 1st Conference Of The European Association On Quality Control Of Bridges And Structures EUROSTRUCT 2021*. pp. 1180–1189.
- Patrick, C. & Michel, 2019. D. Sécurité des ponts: éviter un drame, <https://www.senat.fr/rap/r18-609/r18-6091.pdf>
- Rasol, M., Schmidt, F., Ientile, S., Santos-Assunção, S. & Pomoni, M. 2023. Construction and Building Materials FriC-PM: Machine Learning-based Road Surface Friction Coefficient Predictive Model Using Intelligent Sensor Data Powered by Editorial Manager® and ProduXion Manager® from Aries Systems Corporation. *Construction And Building Materials*.
- Sadhu, A., Narasimhan, S. & Antoni, J. 2017. A review of output-only structural mode identification literature employing blind source separation methods. *Mechanical Systems And Signal Processing*. **94** pp. 415–431.
- Salawu, O. 1997. Detection through changes: a review. *Engineering Structures*. **19** pp. 718–723.
- Seo, J., Asce, M., Jong,., Hu, W., Asce, A. & Lee, J. 2015. Summary Review of Structural Health Monitoring Applications for Highway Bridges.
- Tripura, T., Bhowmik, B., Pakrashi, V. & Hazra, 2020. B. Real-time damage detection of degrading systems. *Structural Health Monitoring*. **19**, 810–837.
- Wang T., Reiffsteck P., Chevalier C., Zhu Z., Chen C.-W., Schmidt F. 2022. A novel extreme gradient boosting algorithm based model for predicting the scour risk around bridge piers: application to French railway bridges, *European Journal of Environmental and Civil Engineering*.
- Xu, Z., Zeng, X. & Li, S. 2015. Damage Detection Strategy Using Strain-Mode Residual Trends for Long-Span Bridges. *Journal Of Computing In Civil Engineering*. **29**.
- Yeung, W. & Smith, J. 2005. Damage detection in bridges using neural networks for pattern recognition of vibration signatures. *Engineering Structures*. **27**, 685–698.
- Zhou, Q., Ning, Y., Zhou, Q., Luo, L. & Lei, J. 2013. Structural damage detection method based on random forests and data fusion. *Structural Health Monitoring*. **12**, 48–58.

*SS15: Reinforced concrete-to-concrete interfaces:
experiments and modelling*
Organizers: V. Palieraki & S. Cattaneo



Taylor & Francis

Taylor & Francis Group

<http://taylorandfrancis.com>

Effect of size on the shear strength between old to new concrete interface

S. Cattaneo & M. Scamardo

Department of Architecture, Built Environment and Construction Engineering, Politecnico di Milano, Milan, Italy

ABSTRACT: The retrofitting of the existing RC structures with added concrete layer crossed by post installed rebars is strongly related to the behavior of the interface between the new and the old concretes. The overall strength of the connection depends on several mechanisms such as friction and dowel action between the two concrete layers as well as the type of loading. In the past, attention was given to understand these mechanisms considering several types of specimens, usually characterized by small dimensions. Nevertheless, it is well known that size effect is often crucial in concrete elements. In this paper, with reference to a specimen geometry already employed for assessing the shear strength between old to new concrete interface, the influence of the size effect on the overall response is analyzed. Based on the results of an experimental campaign, a numerical model is adopted and validated. Therefore, specimens with three different dimensions were numerically analyzed to define the suitable specimen size.

1 INTRODUCTION

Connections between concrete layers with different ages are very common in both existing buildings (i.e. repairing or strengthening) and in new buildings (e.g. connecting pre-cast elements) (Júlio et al. 2005). To ensure a reliable functioning of these connections, a quantifiable amount of shear strength at the interface must be mobilized.

The shear transfer mechanism between two concrete layers is a very complex phenomenon influenced by several interacting parameters (Mattock et al. 1975, Bass et al. 1989, Júlio et al. 2005, 2010, Santos & Júlio 2012, Cattaneo et al. 2021, Palieraki et al. 2021): (1) the quality, the strengths and also the thickness of the two layers (new and old); (2) the surface of the old concrete that could be smooth or artificially roughened; (3) the diameter of the reinforcement crossing the interface; (4) the reinforcement ratio crossing the interface; (5) the embedment length into old/new concrete; (6) external actions on the structure; (7) type of actions (monotonic/cyclic and the amplitude of the displacement); (8) the size of the shear interface. For these reasons, several research campaigns have been carried out in the past (Mattock et al. 1975, Bass et al. 1989, Júlio et al. 2005, 2010, Santos & Júlio 2012, Cattaneo et al. 2021, Palieraki et al. 2021) to evaluate the effect of each parameter and their interactions. Most of the studies were based on monotonic loading experimental tests, while in actual cases (i.e. bridge decks, jacketed columns) structures undergo reversal cyclic loading, e.g., due to fatigue or seismic actions.

For this reason, recently the European Organization for Technical Assessment (EOTA) introduced a new European Assessment Document (EAD) (EOTA 2021) that allows to evaluate the shear strength both under monotonic and cyclic actions. The EAD defines an experimental set-up to assess the shear strength (considering also reversal cyclic loads) that was designed to reduce the perturbative effects of the boundary conditions and of parasitic bending moments. Although the proposed set-up seems to be the most reliable (Cattaneo et al. 2021), the parasitic effects are not eliminated, and the specimen dimensions are relatively of large size with respect to the most common dimensions which usually range between 50 and 100 cm (with length from 30 cm) (Wieneke 2019), and require a significant experimental

effort. Nevertheless, it is well known that concrete is a quasi-brittle material, because the size effect could play a crucial effect in assessing the real shear strength (Biolzi et al. 2000).

The aim of this paper is to investigate the influence of the specimen size on the overall behavior. A numerical model of the specimen defined in the EAD (EOTA 2021) was developed and validated on the basis of experimental result. Two additional models were made considering reduced length of the specimen with respect to the length of the reference specimen (ratio between interface area/reference area 1:0.5:0.25).

2 EXPERIMENTAL RESEARCH

2.1 Test specimen and test set-up

An experimental campaign aimed at assessing the shear strength according to EAD (EOTA 2021) was carried out (Cattaneo et al. 2021), considering the geometry shown in Figure 1. The specimens were realized in two phases: the green block, casted first, simulates the existing concrete, while the grey block, casted at a second stage, represents the added concrete. The concrete strengths were evaluated at the time of testing on cubes (side 150 mm). The average compressive strength of the old concrete was about 28.4 MPa and of the new concrete was 32.1 MPa. The interface (area 200 mm x 500 mm) was crossed by three concrete screws (diameter 14 mm, length 150 mm, $f_{yk} = 690$ MPa). After three months from the first casting, the interface surface (500 x 200 mm) was artificially roughened with the use of an electric chisel by employing different bits. The average roughness of the interface was 2.98 mm, measured with the sand-patch method according to (EN 13036-1:2010 2010). In the roughened area three concrete screws (Figure 1, in red) were installed with a spacing of 170 mm, and with an embedment depth in the old concrete of 85 mm (65 mm in the new concrete). Overall, 4 specimens were tested.

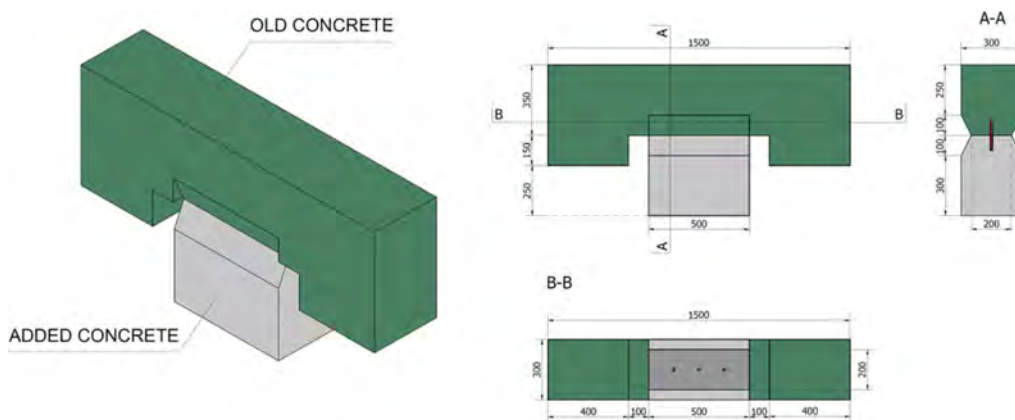


Figure 1. Specimen geometry.

Figure 2 shows the test set-ups. The specimen was set on the strong floor and restrained on both sides (front and back) with two stiff supports connected to the strong floor. The load was applied at the interface level with two plates and four rods that connected the specimen to the hydraulic jack (with capability of 500 kN equipped with a load cell of 500 kN).

Two additional orthogonal restraints were added to allow the sliding of the “old concrete block”, preventing rotations. Four steel cylinders (two on both side of the specimen) were added at the bottom to support the specimen. Similarly, on the top of the specimen, four steel cylinders support two steel plates that were connected to the strong floor to prevent the rotation of the specimen. A Teflon sheet was placed between steel cylinders and concrete surface to reduce friction. The slip between the old and the new concrete block was measured with four LVDTs (gage length 10 mm) placed close to the interface. All measurements were acquired with the MOOG system. The tests were displacement controlled with monotonic loading.



Figure 2. Experimental test set-up.

2.2 Test results

The average shear strength was 3.7 MPa with a coefficient of variation of about 9.5%. A typical load-displacement curve is shown in Figure 3, in which distinct phases are clearly identifiable: the elastic branch (up to point A), the cracking of the interface between the two concrete castings (between points A and B), the friction and dowel action effect (associated to the plateau starting from point B). This curve was used to calibrate the parameters of the numerical model.

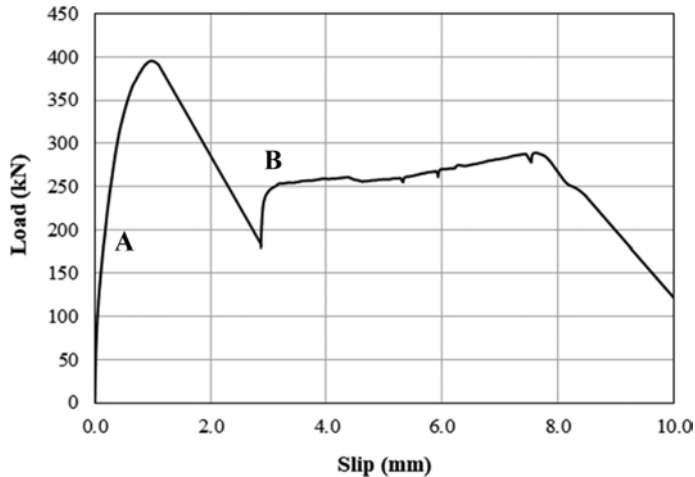


Figure 3. Load-displacement curve.

3 NUMERICAL ANALYSES

Three different specimens were modeled with the software ABAQUS (Dassault Systèmes 2017) to assess the influence of the size effect on the overall mechanical response. The reference specimen size was assumed according to EAD (EOTA 2021) as in Figure 1, with a shear interface area of 500 mm x 200. The scaled specimens (Figure 4) had the same thickness and reduced length and height (1:0.5:0.25), resulting in shear interface areas of 250 mm x 200 mm and 125 mm x 200 mm. A higher reinforcement percentage has been adopted in the scaled specimens with respect to the reference one (0.61% vs. 0.46%) in order to have an integer number of connectors.

The mesh was created using an automatic tool with some manual refinement (Figure 5, left). The interface between the concrete parts was modelled as a concrete layer with a thickness of 10 mm (Cattaneo et al. 2021). The top and bottom concrete blocks, the interface layer and the anchors were modeled with linear hexahedral elements (type C3D8). The element size ranges from approximately 1.5 mm in regions that require more refinement, such as near the anchors, to around 20 mm in regions that allow a rougher mesh (far from stress concentration). The reinforcement used for the cage of the specimen according to (EOTA 2022) (diameters 8 mm

and 12 mm) was modeled as 1D elements (linear line elements of type B31). As these elements do not require much refinement, their meshes reach element sizes up to 50 mm.

The boundary conditions were defined with the aim to reproduce the experimental settings (Figure 5, right). The new concrete block was fixed on the lateral surfaces of the specimen. Orthogonal constraints were considered at the top of the old concrete, to prevent the rotations and to allow the sliding of the old/new concrete blocks. The top and bottom surfaces of the interface layer were tied to the old and new concrete, respectively (no relative motion allowed). A perfect bond was considered between the anchors and the surrounding concrete, defined as surface-to-surface contact with tangential behavior (friction coefficient $\mu=0.8$) and normal behavior (hard contact). The horizontal displacement was applied on the side of the old concrete block.

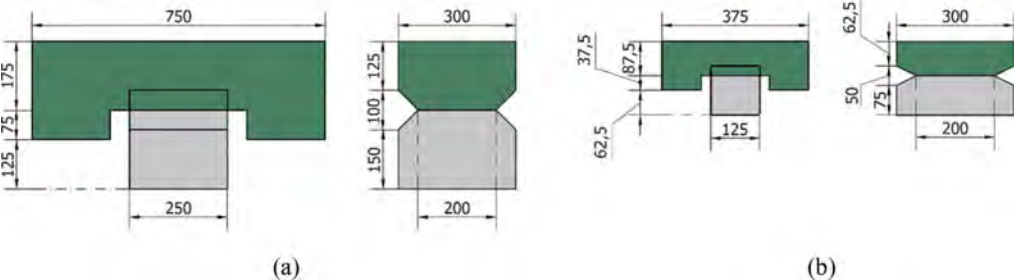


Figure 4. Scaled specimens geometry: (a) size II and (b) size III.

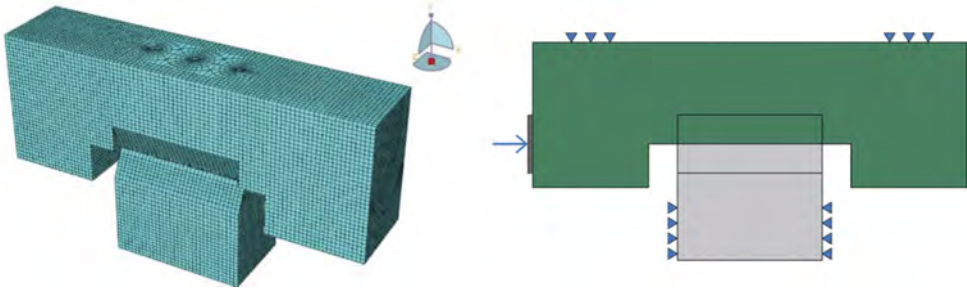


Figure 5. FEM mesh (left) and boundary conditions (right).

3.1 Model validation

The validation of the numerical model was performed by comparing the numerical results of the reference specimen with the experimental results (Cattaneo et al. 2021). The nonlinear behavior of the concrete was taken into account by assuming the Concrete Damaged Plasticity (CDP) model (Lubliner et al. 1989, Dassault Systèmes 2017) as constitutive law. The elastic modulus E_c was assumed equal to 31 GPa (C20/25) and 32 GPa (C28/35) for the old and the new concrete, respectively. The adopted Poisson’s ratio had a value of 0.18 for both materials. A lower value of elastic modulus was chosen for the interface ($E_c = 1$ GPa), as proposed in other researches (Cattaneo et al. 2021).

The parameters adopted for the CDP are summarized in Table 1 where Ψ is the dilation angle, e is the eccentricity, f_{b0}/f_{c0} represents the ratio between strengths in biaxial compression and in uniaxial compression, K represents the ratio between deviatoric stresses in uniaxial tension and compression (in absolute values) and μ represents the viscosity. The values were calibrated on the experimental results and according to typical values proposed in the scientific literature (Lubliner et al. 1989). Figure 6 shows the good agreement between the experimental and the numerical load-displacement curves comparison.

Table 1. CDP Parameters.

$\Psi(^{\circ})$	e	f_{b0}/f_{c0}	K	μ	
				C25/30	C28/35
15	0.1	1.16	0.667	0.006	0.00205

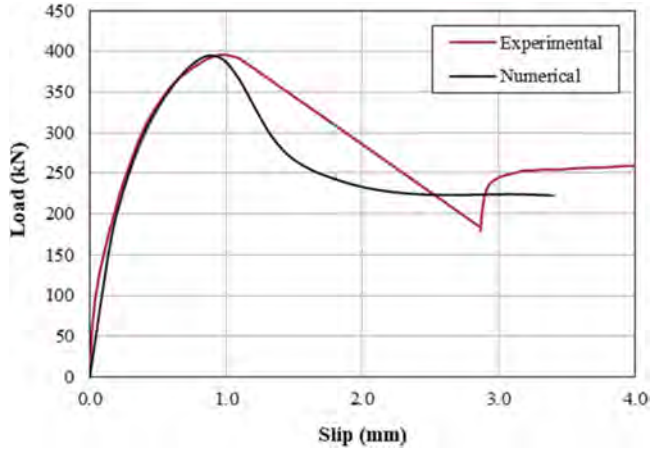


Figure 6. Numerical and experimental load-displacement curves.

3.2 Numerical results

The load-displacement curves for the three considered sizes are shown in Figure 7a together with the experimental outcome. Figure 7b shows the variation of the average shear strength for the different contact area of the three specimens.

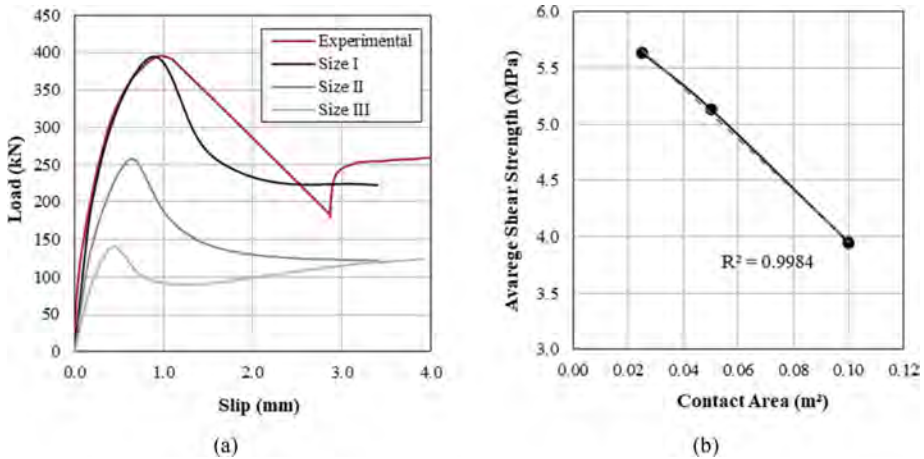


Figure 7. (a) Load-slip curves of different sizes and (b) variation of the average shear strength.

Table 2 summarizes the peak load and the associated displacement, together with the shear strength evaluated assuming a uniform stress distribution over the interface surface. As expected, the nominal shear strength decreases with increasing size, and a softer post-peak branch is observed in small specimen. These two observations confirm that this type of test is strongly size dependent (Biolzi et al. 2000).

Table 2. Size effect: main results.

	Contact Area [mm x mm]	Peak Load [kN]	Displacement associated to Peak Load [mm]	Average Shear Strength [MPa]
Size I	500 x 200	394.81	0.878	3.95
Size II	250 x 200	256.77	0.617	5.14
Size III	125 x 200	140.96	0.438	5.64

It should be observed that to consider feasible specimens, 3 2 and 1 anchor were used respectively for the different sizes. This implies that the larger specimen has a lower geometric reinforcement ratio than the other two specimens in which the ratio is constant. Nevertheless, the higher reinforcement ratio affects mainly the dowel action (i.e. post peak behavior). Indeed, the size effect is noted also for the two specimens (II and III) with the same reinforcement ratio (Figure 7b).

4 DISCUSSION

The numerical results make possible to add further considerations to the experimental issues. By considering the distribution of the tensile damage at the peak load in a section at a quarter of the width (Figure 8), it is possible to observe that the reference specimen (a) and the medium specimen (b) show non-uniform damage distribution, while the smaller specimen (c) shows a more uniform damage distribution. This is probably due to the fact that, in the bigger specimens, the eccentricity between the applied load (that acts at the interface level) and the respective horizontal reaction force (that is located on the new concrete part at a distance of about 25 cm) is higher than in the smaller specimen. Indeed, on the side of the reaction (Figure 8a) a certain damage appears close to the support reaction.

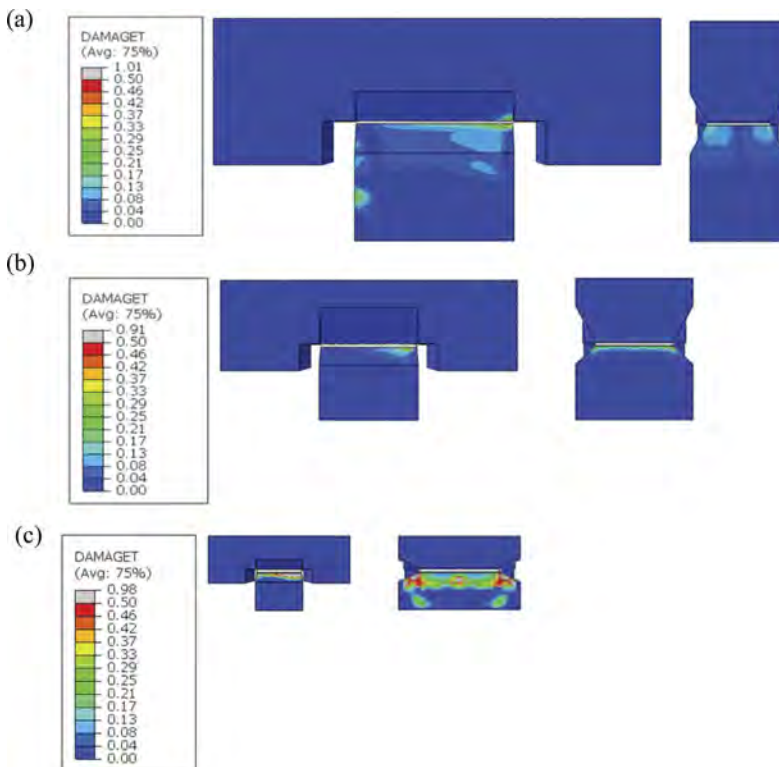


Figure 8. Distribution of tensile damage for (a) size I, (b) size II and (c) size III models.

Looking at the shear stress distribution (Figure 9), it is interesting to observe that all sizes exhibit similar distribution with a concentration of stresses close to the loaded edge, high stresses close to the anchor position which drop in the anchor section. Although the trend is similar, in the reference specimen there is a high stress concentration close to the edge of the specimen and then, in the intermediate section, there is a nearly uniform stress distribution. The smaller specimen shows the higher stress close to the edge, while the intermediate size has the lower stress close to edge. Overall, the stress distribution of the intermediate specimen does not show steep changes, although there is not an area with constant stress (as shown in the central portion of the reference specimen).

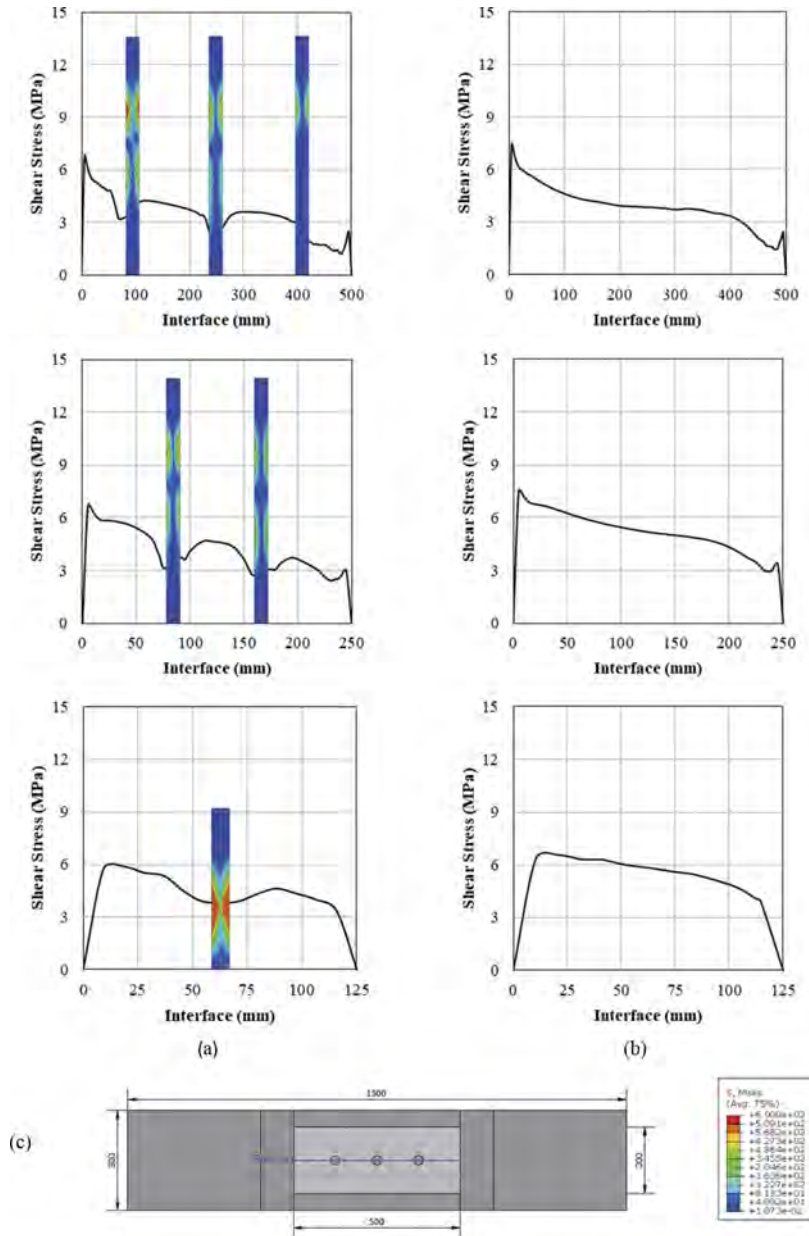


Figure 9. Shear stress distribution in path a (a) and in path b (b) for the three different sizes, with Von Mises Stresses in the anchor. In (c) section scheme with anchor stresses legend.

Based on the obtained results, it is evident how stress and damage distributions are strongly influenced by the size of the specimen and higher stress gradients are found when the size effect is more pronounced. In any case, at the interface, a non-uniform stress distribution is manifest with a mixed-mode stress field which affects the damage evolution and the experimental results (Biolzi 1990). Although the smaller specimen leads to the highest strength and thus it is not on the safe side, it shows a more uniform stress distribution. The intermediate specimen leads to higher strength with respect to the reference specimen, and, although the stress distribution is not uniform, it does not present steep changes. The reference specimen allows to evaluate the shear strength on the safe side.

5 CONCLUSIONS

The numerical analyses conducted highlight that the assessment of the shear strength is strongly affected by the size effect both in terms of shear stress distribution, strength and ductility.

The reference specimen seems a suitable specimen size for a safer evaluation of the shear strength. The intermediate specimen could be considered to assess the shear strength, since the stress distribution along the interface does not show steep changes. In this case, a suitable reduction coefficient should be applied to account for the size effect and a proper experimental validation is needed. The smaller specimen does not seem suitable to assess the shear strength, since it is strongly affected by the size effect. Moreover, the fact that the new cast part resulted strongly damaged suggests that secondary effects could be involved in the strength evaluation.

REFERENCES

- Bass, R.A., Carrasquillo, R.L., & Jirsa, J.O., 1989. Shear transfer across new and existing concrete interfaces. *ACI Structural Journal*, 86 (4).
- Biolzi, L., 1990. Mixed mode fracture in concrete beams. *Engineering Fracture Mechanics*, 35 (1–3).
- Biolzi, L., Cattaneo, S., & Guerrini, G.L., 2000. Fracture of Plain and Fiber-Reinforced High Strength Mortar Slabs with EA and ESPI Monitoring. *Applied Composite Materials*, (7), 1–12.
- Cattaneo, S., Zorzato, G., & Bonati, A., 2021. Assessing method of shear strength between old to new concrete interface under cycling loading. *Construction and Building Materials*, 309.
- Dassault Systèmes, 2017. ABAQUS/CAE Documentation.
- EN 13036-1:2010, 2010. *Road and airfield surface characteristics - Test methods - Part 1: Measurement of pavement surface macrotexture depth using a volumetric patch technique*.
- EOTA, 2021. *EAD 332347-00-0601-v01: Connector for strengthening of existing concrete structures by concrete overlay: behavior under seismic action*.
- EOTA, 2022. *EAD 330076-01-0604-v01: Metal injection anchors for use in masonry under seismic actions*. Brussels, Belgium.
- Júlio, E., Branco, F., & Silva, V., 2005. Reinforced concrete jacketing - Interface influence on monotonic loading response. *ACI Structural Journal*, 102 (2).
- Júlio, E., Dias-da-Costa, D., Branco, F., & Alfaiate, J., 2010. Accuracy of design code expressions for estimating longitudinal shear strength of strengthening concrete overlays. *Engineering Structures*, 32 (8).
- Lublinter, J., Oliver, J., Oller, S., & Oñate, E., 1989. A plastic-damage model for concrete. *International Journal of Solids and Structures*.
- Mattock, A.H., Johal, L., & Chow, H.C., 1975. Shear transfer in reinforced concrete with moment or tension acting across the shear plane. *J Prestressed Concr Inst*, 20 (4).
- Palieraki, V., Vintzileou, E., & Silva, J.F., 2021. Behavior of RC interfaces subjected to shear: State-of-the art review. *Construction and Building Materials*.
- Santos, P.M.D. & Júlio, E.N.B.S., 2012. A state-of-the-art review on shear-friction. *Engineering Structures*.
- Wieneke, K.M., 2019. Horizontal Shear Design of Concrete Interfaces in Beam and Slab Structures. *PhD Thesis*.

Experimental behavior of interfaces with anchors to thin overlays

E. Oikonomopoulou, V. Palieraki & E. Vintzileou

National Technical University of Athens, Athens, Greece

G. Genesisio

Hilti AG, Liechtenstein

ABSTRACT: The behavior of interfaces created between existing and added concrete when applying intervention techniques, strongly affects the efficiency of the intervention in terms of stiffness, bearing and deformation capacity. To contribute to the investigation of key parameters related to those interfaces, the current work focuses on cases where the available thickness of the concrete members is limited, thus allowing for small embedment depths for the dowels. Previously performed tests on interfaces reinforced with reinforcing bars or industrial steel screws have shown that a very short embedment depth in the added concrete may ensure substantial interface resistance, thus suggesting that they might offer a solution in case of thin concrete overlays added to existing members. The results of tests performed with the purpose of exploring the behavior of interfaces with limited thickness of the added concrete, where the anchorage conditions of the connectors are unfavorable, are presented herein.

1 INTRODUCTION

Interventions to existing reinforced concrete (RC) structures are a field of growing significance worldwide. In most of the frequently applied techniques (e.g. flexural and shear strengthening of beams, column jacketing, filling of RC frame spans with RC shear walls, etc.), reinforced interfaces occur between the existing and the added concrete layer or element. The efficiency of the intervention techniques, in terms of stiffness, bearing and deformation capacity strongly depend on the behavior of interfaces.

The experimental evidence on the cyclic behavior of RC interfaces is rather limited compared to the significance of the topic. To contribute to the investigation of key parameters related to interfaces between concretes cast at different times and subjected to seismic actions, series of experimental programs were carried out at the Laboratory of Reinforced Concrete, National Technical University of Athens (Palieraki et al., 2021, Vintzileou et al., 2020a, Vintzileou et al., 2020b). The current work focuses on cases where the available thickness of the concrete members is limited, thus allowing for small embedment depths for the interface reinforcement. The behavior of beams or slabs reinforced with an overlay of limited thickness has been investigated by many researchers (indicatively, Seible & Latham 1990, López-Carreño et al. 2020). The test results on specimens with an interface between concretes cast at different times, subjected to direct shear, is very limited. Choi et al. 1999 have tested specimens with an overlay of 145mm, and Randl 1997 has investigated specimens with overlay thickness equal to 200mm. The failure of the overlay is not commented, as in both cases the focus is oriented towards the pullout of the reinforcement from the old concrete part. Millard & Johnson 1984, Papanicolaou & Triantafillou 2002, Dimitriadou et al. 2005 and Costa et al. 2018, have investigated the behavior of specimens with thickness of both the old and the new concrete equal to 125mm, 100mm, 150mm and 100mm respectively. Given that the thickness of both parts was the same, the authors do not comment on the influence of the limited thickness

of the overlay. Finally, Waweru et al. 2018, have performed tests on typical push-off specimens, 254mm thick in total (127mm thick on each side). The anchorage of the reinforcement in the new concrete varied between 50.8mm and 101.6mm. In the case of very short anchorage, the specimens experienced an explosive pullout failure from the new concrete, whereas this failure was not so pronounced in the case of longer anchorage.

Previously performed tests on interfaces reinforced with reinforcing bars or industrial steel screws (Vintzileou et al., 2020a) have shown that a very short embedment depth in the added concrete may ensure substantial interface resistance, thus suggesting that they might offer a solution in case of thin concrete overlays added to existing RC members. To further investigate this possibility, specimens with geometry identical to that of specimens used in previous tests (Vintzileou et al., 2020a) were prepared. The only difference is the limited thickness (50mm) of the RC block simulating the added concrete. In the current paper, the results of the tests performed with the purpose of exploring the behavior of such interfaces (with limited thickness of the added concrete), where the anchorage conditions of the interface reinforcement are unfavorable, are presented and commented upon.

2 EXPERIMENTAL PROGRAM

2.1 The experimental program incentive

In most of the cyclic tests performed up to now by the authors, the main interest of the research was focused on the old part of the specimen, where the (post-installed) connectors were provided with a limited embedment length. Nevertheless, a small number of previously conducted experiments (Figure 1) have shown that alternative connectors (steel screws) provided with a very short embedment depth (2.5d) in the added concrete may ensure substantial interface resistance, thus suggesting that they might offer a solution in case of thin concrete overlays added to existing RC members (e.g. slabs in residential buildings). One of the frequently used solutions in such cases is that of reinforcing bars with a bent at their end into the added thin layer. This paper presents the results of a preliminary investigation performed with the purpose of exploring the behavior of such interfaces, where the anchorage conditions of the interface reinforcement in the new layer of concrete are very unfavorable.

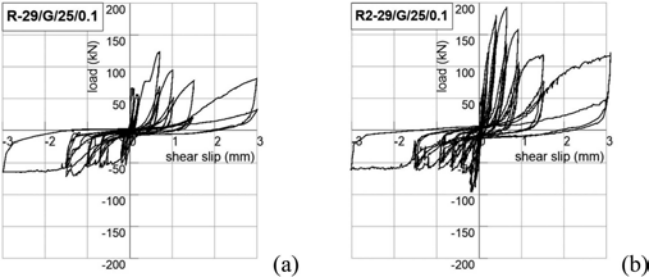


Figure 1. Hysteresis loops of previously conducted tests on specimens with thick overlays, with very short embedment depth (2.5d) in the added concrete part.

2.2 Characteristics of specimens

Figure 2 shows the specimens tested in the context of this experimental program. Their overall geometry was identical to that of specimens used in the previously presented tests (Vintzileou et al., 2020a). The only difference was that, before casting the added concrete, a 50mm thick layer of polyethylene was placed in the molds to limit the thickness of the added layer to the desired value of 50mm.

The type of interface reinforcement was the only investigated parameter within this experimental program. Each specimen (Table 1) was reinforced using either three 12mm reinforcing bars

with a 90° hook (two specimens) or three 10mm concrete screws (two specimens). The embedment length in the old concrete was either 10d (for the reinforcing bars – which is considered adequate for their anchorage) or 6.7d (for the screws - as defined by the Manufacturer), d being the connector diameter. Finally, one specimen was reinforced with three 12mm reinforcing bars embedded 10d into the old concrete block, with a shaped head into the new concrete block. Comparisons between the behavior of interfaces reinforced with the described screws and rebars can be drawn, as the reinforcement parameter, namely ρf_{sy} (ρ being the geometrical reinforcement ratio and f_{sy} denoting the yield strength of steel) is similar for those cases (~163 MPa and ~178MPa respectively).

All 12mm rebars were embedded into the old concrete block using injectable epoxy mortar and the anchorage into the new concrete block was achieved by means of concrete bond. For the interfaces crossed by screws, the anchorage in the old part was mechanical interlock, whereas in the new part both mechanical interlock anchorage (due to the screw’s head) and anchorage provided by concrete bond along the shaft was present as well.

After casting the portion of the specimen simulating the existing concrete, the interface was artificially roughened (chipped with pickaxe). In order to make possible the comparison among the specimens, the same value of medium (~2.00mm) roughness was reached in all five tested interfaces. The standardized “Sand Patch” Test (ASTM E965-96) was applied to measure the interface roughness.

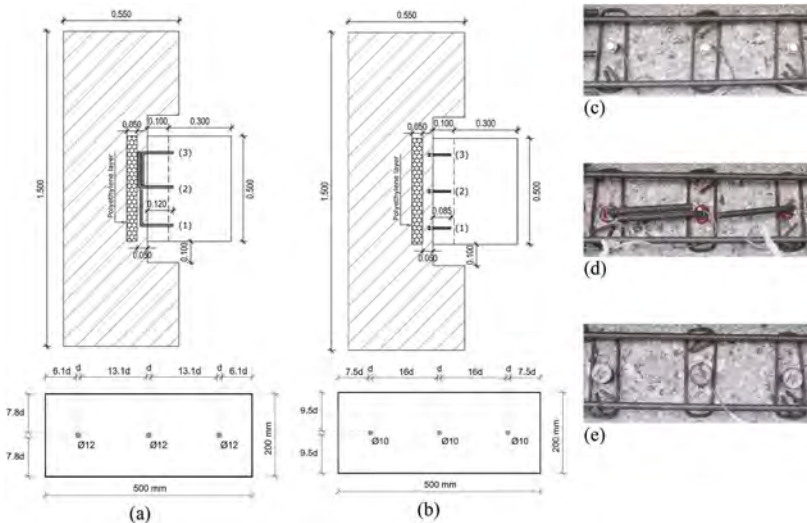


Figure 2. Geometry of specimens simulating thin overlays reinforced with: (a) diameter 12mm rebars with a hook, (b) diameter 10mm screws. The diagonally hatched parts depict the new concrete block. Photos of interfaces reinforced with: (c) diameter 10mm screws, (d) diameter 12mm rebars with a hook, (e) diameter 12mm rebars with a head.

Ready-mixed limestone coarse aggregate concrete was used for the construction of all specimens. For each batch of concrete, conventional cylindrical specimens (diameter 150mm, height 300 mm) were cast. The cylinders were tested (Table 1) to failure the day of testing the respective specimens. The C16/20 concrete of the old part contained aggregates of conventional maximum dimension (32mm), whereas for the new part, C25/30 quality was used, with aggregates of smaller maximum dimension (16mm).

2.3 Test setup and instrumentation

The setup used for testing is illustrated in Vintzileou et al., 2020a. In all tests, there was no external compressive normal stress acting on the interface. Tests were performed under cyclically

imposed shear slip at low speed (i.e., quasi-static conditions); three cycles were carried out at each displacement value with increasing amplitude.

Shear slip along the interface was measured by means of four displacement transducers (two per face of the specimen), placed in close proximity of the interface, whereas in total six displacement transducers placed perpendicular to the interface measure the width of the crack at the interface. In addition, two electrical strain gauges glued on each connector are used to measure the strains developed in the dowels during the test. The strain gauges are positioned close to the interface, at a distance of approximately 1.5 diameters, oriented along the direction of loading.

Table 1. Characteristics of thin-overlay specimens and main test results.

	Thin-R- 33/G/25/0.1	Thin-R- 35/G/25/0.1	Thin-Re- 38/E/10/0.1	Thin-Re- 35/E/10/0.1	Thin-Re- 38/H/10/0.1
f_{sy} (MPa)	690	690	524	524	524
ρ (%)	0.236	0.236	0.339	0.339	0.339
$L_{emb,old}/d$	6.7d	6.7d	10d	10d	10d
$L_{emb,new}/d$	2.5d	2.5d	3d	3d	3d
R (mm)	1.98	2.29	2.04	2.30	1.95
$f_{c,old}$ (MPa)	33	35	38	35	38
$f_{c,new}$ (MPa)	47	50	50	50	50
τ_u (MPa)	0.65	0.76	0.71	1.11	0.88
s_u (mm)	0.40	0.40	0.40	0.80	0.80
τ_{u1+}/τ_{u1-}	5.99	4.30	1.23	6.15	4.57

Notation:

R: mechanical anchorage at rough interface, Re: anchorage by means of epoxy resins at rough interface.

The first number indicates the compressive strength of the weaker concrete block (in MPa).

E: specimens with three bars 12 mm in diameter, G: specimens with three screw anchors 10 mm in diameter, H: specimens with three bars 12 mm in diameter, with shaped head. All dowels are post-installed.

The second number indicates (a) the embedment depth in the old part for the rebars normalized to the bar diameter (b) the embedment length in the new part for the screws, in mm.

The third number indicates the magnitude of the cyclic shear slip imposed during the first set of cycles in mm.

Characteristics of specimens:

The yield stress of the connectors (f_{sy}), the geometrical reinforcement ratio of the interfaces (ρ), the embedment length into the old ($L_{emb,old}$) and the new concrete part ($L_{emb,new}$), the roughness (R) and the concrete strength of the old ($f_{c,old}$) and the new concrete part ($f_{c,new}$) are given.

Test results:

τ_u (MPa) is the maximum shear resistance of the interface, given as the average value between the two loading directions for the first cycle.

s_u (mm) is the shear slip value corresponding to the mobilization of the maximum capacity of the interface, given as the average value between the two loading directions for the first cycle.

τ_{u1+}/τ_{u1-} is the absolute value of the ratio between the maximum resistance at the first loading direction and the second loading direction, at s_u shear slip.

3 TEST RESULTS

3.1 Failure mode and hysteretic behavior

As shown in Figure 3a-c, typical of all thin overlay specimens, the interfaces exhibited a concrete breakout failure: a crack parallel to the interface has occurred, at a distance from the interface approximately equal to the embedment length of the connectors into the new block (25mm-40mm). After the termination of the test, the two concrete parts were easily separated, and the dowels remained into the old concrete block.

The hysteresis loops for all specimens are presented in Figure 4. In addition to the typical characteristics of shear-sensitive behavior, the specimens exhibited extremely pronounced asymmetry in the two loading directions, as depicted in the hysteresis loop envelopes for the first and the third cycle (Figure 5a, b). Moreover, an intense response degradation (of 30% up to 70%) due to cycling is illustrated in Figure 5c. This is attributed to the pullout of joint reinforcement in the first loading direction, confirmed by the shear slip – dilatancy curves

shown in Figure 6, where at first semi-cycle of 0.40mm shear slip there is an abrupt increase of crack opening. Pullout damage cannot be reversed during unloading, thus, not allowing for substantial interface resistance to be mobilized in the second loading direction.

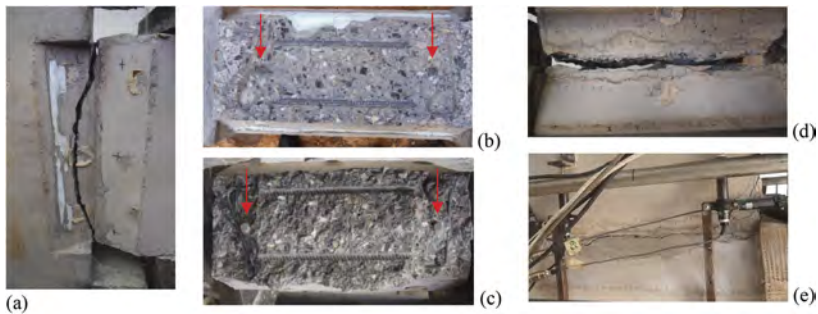


Figure 3. Specimens with thin overlays after the termination of the test: (a) Before the separation of the two blocks. (b) New concrete block: imprints of the two screws near the edges (see arrows), (c) Old concrete block: heads of the two screws near the edges (see arrows). Specimens with thick overlays after failure, reinforced with: (d) screws, (e) reinforcing bars.

In the diagrams presented in Figure 4, it is noted that the interfaces could not withstand shear slips larger than 0.8mm. From then on, the tests were either terminated or were continued monotonically. Specimens reinforced with screws reached their maximum resistance at a slip value of 0.40mm, whereas specimens reinforced with bars reached a slightly higher load, and at a slip value of 0.40mm or 0.80mm. No significant difference in the behavior could be identified between the specimens reinforced with screws and those reinforced with rebars (with hook or shaped head). However, although the number of specimens is limited and may not allow for final conclusions, a more similar behavior is noticed for duplicate interfaces reinforced with screws, compared to those with rebars.

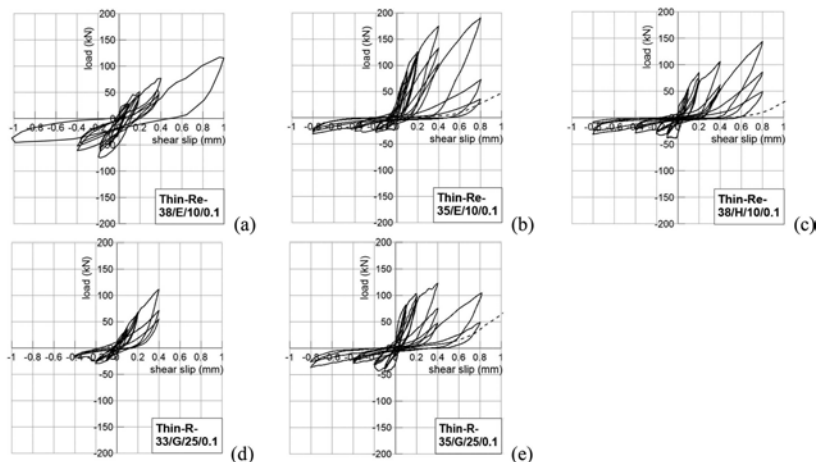


Figure 4. Hysteresis loops for all specimens.

Regarding the steel strain measurements, as observed in Figure 7, the maximum measured tensile strains did not reach the connector yield strain. This is due to the premature brittle concrete failure of the specimens, which occurred at small shear slip and, in turn, at a small interface crack opening, limiting the maximum steel strains to values lower than 1‰, for

specimens reinforced with rebars and screws. When larger embedment length is provided, the reinforcement is more efficiently exploited as steel strains much higher than the strain corresponding to yielding (as high as 4‰) are recorded, so the interfaces can take profit from the yield strength of the reinforcement (Vintzileou et al., 2020b).

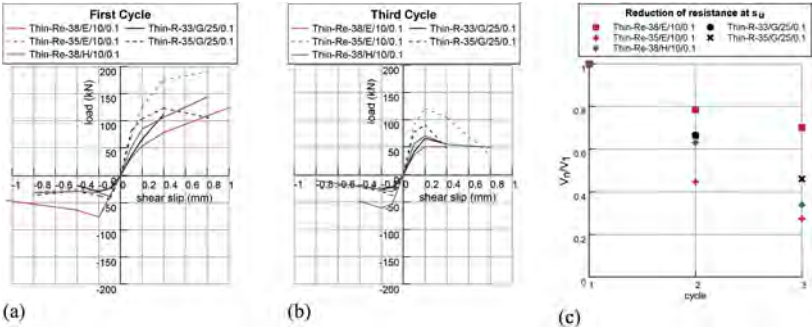


Figure 5. (a) Hysteresis loop envelopes for first cycle and (b) third cycle. (c) Reduction of the resistance during cycling at s_u shear slip for all specimens.

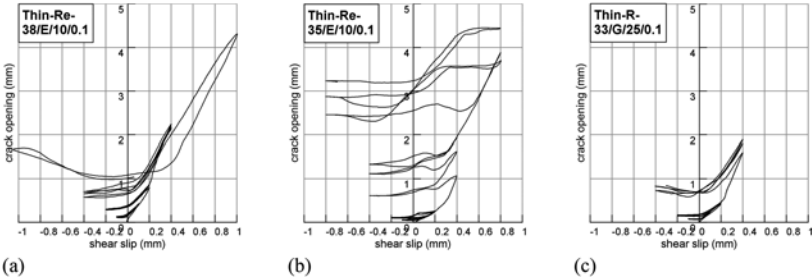


Figure 6. Typical shear slip versus crack opening (lateral dilatancy) curves.

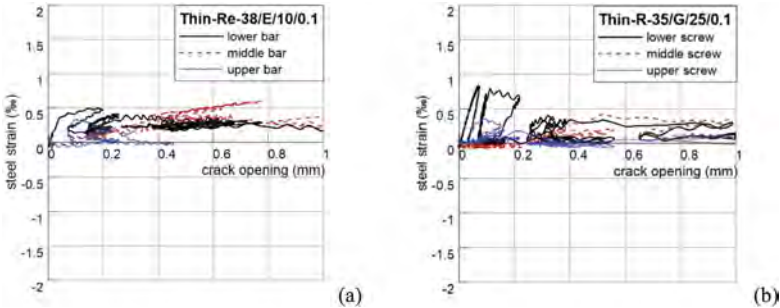


Figure 7. Steel strains versus crack opening (lateral dilatancy) curves. The vertical axis maximum value (2‰) corresponds to the yield strain of the reinforcing bars.

3.2 Comparison with specimens with thick overlays

Table 2 presents the characteristics and the main test results for specimens with similar features, but with thick (400mm) overlay, whereas in Figure 8 the hysteresis loop envelopes for the first cycle for comparable specimens reinforced with bars and screws are provided.

At first, a significant difference of the failure mode could be observed for interfaces with thick overlays, compared to those with thin overlays. The specimens with thick overlays and rough interfaces crossed by screws (Figure 3d) exhibited failure along the interface. After the tests, the two parts of the specimens could be easily separated, due to the wide crack along the

interface, and the imprint of the screwhead could be observed in the new part. The specimens with thick overlays and rough interfaces crossed by reinforcing bars (Figure 3e) exhibited failure along the interface with diagonal crack in the new part or with the formation of a crack at the end of the embedment of the bars into the old block, but without concrete cone failure.

Table 2. Characteristics of thick-overlay specimens and main test results.

	R-29/G/25/0.1	R2-29/G/25/0.1	Re-24/E/10/0.1	Re-31/E/10/0.1	Re2-31/E/10/0.1
f_{sy} (MPa)	690	690	524	524	524
ρ (%)	0.236	0.236	0.339	0.339	0.339
$L_{emb,old}/d$	6.7d	6.7d	10d	10d	10d
$L_{emb,new}/d$	2.5d	2.5d	29d	29d	29d
R (mm)	6.23	5.46	2.50	1.80	1.70
$f_{c,old}$ (MPa)	29	29	24	33	33
$f_{c,new}$ (MPa)	40	40	31	31	31
τ_u (MPa)	0.91	1.28	2.10	2.60	2.04
s_u (mm)	0.70	0.65	0.40	0.40	1.20
τ_{u1+}/τ_{u1-}	2.13	3.08	0.83	1.52	2.94

Thin-overlay interfaces crossed by screws have slightly lower maximum resistance compared to thick-overlay interfaces, a fact that could be attributed also to the significantly larger roughness of the latter. Nevertheless, the difference is obvious for specimens reinforced with bars. In this case, thick-overlay interfaces undertake significantly larger load compared to thin-overlay interfaces, a result imputed to the sufficient protruding length of the bars into the thick overlay.

In general, thick-overlay specimens, in contrast to the thin-overlay ones, do not fail prematurely, so they can withstand larger shear slip values. It is underlined that they are characterized by a more symmetric behavior along the two loading directions, as appears both in the shape of the loop envelopes (Figure 8) and the τ_{u1+}/τ_{u1-} ratio (Table 1 compared to Table 2 values), which acquires values up to 3, approximately.

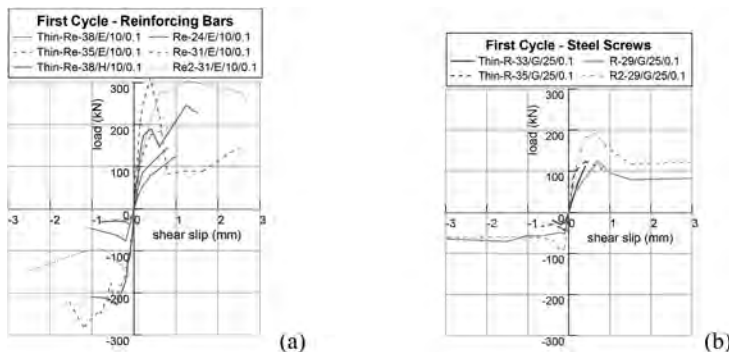


Figure 8. Hysteresis loop envelopes for first cycle for comparable interfaces reinforced with: (a) bars, (b) screws.

4 CONCLUSIONS

On the basis of this preliminary investigation on interfaces crossed by very short dowels, the following conclusions can be drawn:

- All three types of alternative anchors embedded to thin concrete overlays were able to activate interface resistance, which may be sufficient for some applications where very limited deformations are expected (e.g. diaphragm slabs). No remarkable difference could be

identified for interfaces reinforced with conventional bars and the interface crossed by bars with shaped head.

- Compared to the behavior of thick-overlay specimens, thin-overlay interfaces fail at an earlier stage, without reaching large shear slip values, and have typically lower maximum resistance at both loading directions.
- Additionally, the pronounced asymmetry of the hysteresis loops and the degradation of the resistance to minimal values suggest that this small protruding length for either type of reinforcement (bars and screws) is not adequate for applications where cycling of loads is to be addressed.
- Therefore, the use of any type of anchor in seismic conditions needs to be supported by adequate experimental evidence in application tests.

ACKNOWLEDGEMENTS

The authors gratefully acknowledge Hilti AG for funding this research project. Opinions, conclusions and recommendations expressed in this paper are those of the authors, and do not necessarily reflect those of the funding organization.

REFERENCES

- ASTM. 2006. Standard test method for measuring pavement macrotexture depth using a volumetric technique. *Designation: E 965-96*.
- Choi, D. U., Jirsa, J. O., & Fowler, D. W. 1999. Shear transfer across interface between new and existing concretes using large powder-driven nails. *Structural Journal*, 96(2), 183–192.
- Costa, H., Carmo, R. N. F., & Júlio, E. 2018. Influence of normal stress and reinforcement ratio on the behavior of LWAC interfaces. *Construction and Building Materials*, 192, 317–329.
- Dimitriadou, O. Kotsoglou, V. N., Thermou, G. E., Savva, A., & Pantazopoulou, S. J. 2005. Experimental Study of Concrete Interfaces in Sliding Shear, *Tech. Chron. Sci. J. TCG*, V. I, No. 2-3, pp. 123–136. (in Greek)
- López-Carreño, R. D., Carrascón, S., Aguado, A., & Pujadas, P. 2020. Mechanical Connectors to Enhance the Interfacial Debonding of Concrete Overlays. *Applied Sciences*, 10(11), 3876.
- Millard, S. G., & Johnson, R. P. 1984. Shear transfer across cracks in reinforced concrete due to aggregate interlock and to dowel action. *Magazine of concrete research*, 36(126), 9–21.
- Palieraki, V., Vintzileou, E., Oikonomopoulou, E., Genesio G., & Piccinin R. 2021 Design of Interfaces Between Concretes Cast at Different Times Subjected to Cyclic Loading. *In Proceedings of the FIB Symposium 2021: Concrete Structures: New Trends for Eco-Efficiency and Performance*. June 14-16, 2021, Lisbon, Portugal.
- Papanicolaou, C. G., & Triantafyllou, T. C. 2002. Shear transfer capacity along pumice aggregate concrete and high-performance concrete interfaces. *Materials and Structures*, 35(4), 237–245.
- Randl, N. 1997. Untersuchungen zur Kraftübertragung zwischen Alt-und Neubeton bei unterschiedlichen Fugenrauigkeiten, PhD thesis, Universität Innsbruck, Innsbruck, Austria, 379 pp.
- Seible, F., & Latham, C. T. 1990. Horizontal load transfer in structural concrete bridge deck overlays. *Journal of Structural Engineering*, 116(10), 2691–2710.
- Vintzileou, E., Genesio, G., Oikonomopoulou, E., & Palieraki, V. 2020a. Alternative Connectors for Seismic Interface Shear Applications. *In Proceedings of the 17th World Conference on Earthquake Engineering*.
- Vintzileou, E., Palieraki, V., & Oikonomopoulou, E. 2020b. Reinforced concrete interfaces: contribution of the two shear mechanisms based on measured steel strains. *In Proceedings of the 17th World Conference on Earthquake Engineering*.
- Waweru, R. N., Palacios, G., & Chao, S. H. 2018. Strength of interface shear reinforcement with limited development length. *ACI Structural Journal*, 115(4), 983–996.

Calculation of the interface resistance in RC construction using different codes

V. Palieraki & E. Vintzileou

National Technical University of Athens, Athens, Greece

S. Cattaneo

Politecnico di Milano, Milan, Italy

ABSTRACT: The need for the assessment of interface shear strength in reinforced concrete construction arises in conjunction with a wide variety of structural details. Several design codes (e.g., EC2, ACI 318, MC 2010) provide guidance on the design of interfaces, assuming full anchorage of the interface dowels. As dowels, cast-in reinforcing bars, are typically assumed. Nevertheless, in case of repair and strengthening of structures, the interface dowels are usually post-installed in the existing concrete member, while their embedment length may be limited. The European Organization for Technical Assessment has issued a design Guideline (EOTA TR 066 2019), allowing to design interfaces with connectors of limited anchorage. To cover the cyclic behavior of interfaces, an extension of the guidelines, amended in 2020, was introduced. In the current paper, the equations for the prediction of interface resistance, included in the codes and guidelines are compared with experimental results, are evaluated, and commented upon.

1 INTRODUCTION

Interfaces being loaded in shear, occur along crack surfaces that develop at points of maximum shear, in cold joints resulting from construction sequencing and between precast elements. The calculation of the interface resistance is particularly relevant for repair and strengthening of structures, where, because of geometrical limitations of existing elements and added overlays, the embedment of the interface reinforcement may be limited. For example, the thickness of an existing slab is limited, in most cases not exceeding 10-12cm, while also the thickness of the added overlay is limited, in order to avoid the excessive increase of the self-weight of the structure.

Several design codes (e.g., EC2 2004, ACI 318 2019, MC 2010 and various National Codes) provide guidance on the design of interfaces. The codes provide equations for the calculation of shear resistance, for interfaces that are smooth, rough or very rough. No guidance is offered regarding the way in which the interface roughness should be measured, except than in MC 2010, which proposes the sand patch method (Kaufmann 1971). It is though noted that this method cannot be used in case of non-horizontal interfaces. Additionally, these design provisions typically assume full anchorage of the dowels crossing the interface, i.e., their anchorage length is sufficient to allow the interface reinforcement to develop its yield strength. As dowels, cast-in reinforcing bars, perpendicular or inclined to the interface, are typically assumed. Nevertheless, strengthening measures in most cases require installation of the dowels in the existing reinforced concrete member, thus making a cast-in solution unfeasible. Last but not least, the codes do not cover the case of cyclic loading of the interfaces. Experimental investigations (Bass et al. 1989, Valluvan et al. 1999, Cattaneo et al. 2021, Palieraki et al. 2023) have shown that the interface resistance is reduced due to cyclic loading, while the amount of the reduction depends on various parameters, such as the concrete strength, the roughness of the interface, the type of the interface reinforcement, the embedment depth and the amplitude of the applied shear slip.

The European Organization for Technical Assessment has issued a design Guideline (EOTA TR 066 2019), which allows to design interfaces with shear connectors provided with an anchorage length smaller than the one required for full anchorage and considering the properties of engineered connectors in terms of material ductility, cross section geometry and pullout resistance. In order to cover the cyclic behavior of interfaces crossed by different types of connectors, an extension of the EOTA guidelines was recently introduced (EOTA TR 066 2019, amended 2020).

In the current paper, the equations for the prediction of the interface resistance, included in codes, and technical documents are compared with experimental results, they are evaluated and commented upon.

2 CODE PROVISIONS

The equations included in some of the current design codes, are presented in Table 1. In those equations the interface resistance is expressed in terms of interface shear stress (MPa).

Table 1. Design codes equations for the calculation of interface resistance.

Code	Equation
EC2 (2004)	$\tau_{calc} = c \cdot f_{ctd} + \mu \cdot \sigma_n + \rho \cdot f_{yd} (\mu \cdot \sin \alpha + \cos \alpha) \leq 0.5 \cdot v \cdot f_{cd}$
ACI 318 (2019)*	$\tau_{calc} = \rho \cdot f_y (\mu \cdot \sin \alpha + \cos \alpha)$
MC 2010 (2010)	$\tau_{calc} = c_r \cdot f_{ck}^{1/3} + \mu \cdot \sigma_n + \kappa_1 \cdot \rho \cdot f_{yd} (\mu \cdot \sin \alpha + \cos \alpha) + \kappa_2 \cdot \rho \cdot (f_{yd} \cdot f_{cd})^{1/2} \leq \beta_c \cdot v \cdot f_{cd}$

*Upper limits are proposed for the ACI 318 equation, depending on the roughness of the interface

where,

τ_{calc} = interface resistance, calculated using the equations proposed in the codes or guidelines

f_{ctd} = design tensile strength of concrete

f_{ck}, f_{cd} = characteristic and design compressive strength of concrete, correspondingly

f_y, f_{yd} = nominal and design yield strength of steel, crossing the interface, correspondingly

α = angle of the reinforcement with the perpendicular to the interface

σ_n = stress caused by the minimum external normal force across the interface (positive for compression)

ρ = percentage of the interface reinforcement

v, β_c = coefficients related to the concrete strength, described in EC2 (2004), MC2010 (2010)

$c, c_r, \mu, \kappa_1, \kappa_2$ = factors which depend on the roughness of the interface

In the equations of Table 1, there are common terms, corresponding to the mechanism of shear friction, namely, the friction coefficient, μ , the percentage of the interface reinforcement, ρ , and the yield strength of steel, f_{yd} . The remaining terms are met in one or more equations and they refer to the adhesion along the interface and/or to the dowel action of the interface reinforcement. It is noted that in almost all equations, an upper limit is set for the interface resistance, equal to a percentage of the compressive strength of concrete. In ACI 318 (2019), this upper limit depends on the roughness of the interface, while there is an additional upper limit, a fixed value of the interface resistance, which depends again on the interface roughness.

The provisions of equations included in the codes and the guidelines, were compared to the experimental results included in a database (Palieraki et al. 2021). The data were obtained from testing interfaces within monolithic specimens, as well as cold joints, i.e., interfaces between concretes cast at different times. In the current paper, the data on cold joints, in total 868 test results, are analyzed.

The database covers a wide range of parameters. The compressive strength of the weaker concrete varies between 6MPa and 120MPa, while the most common values are between 12MPa and 60MPa. The yield strength of the reinforcement ranges between 300MPa and 700MPa, with the higher value being exceeded in a very small number of tests. The reinforcing bars are anchored in the concrete by means of bond, or by means of adhesive material. In a limited number of tests,

special reinforcement is used (screws or bolts). The reinforcement may be in the form of closed hoops, thus, allowing for the assumption of full anchorage to be made, it may be straight and fully anchored, or it may be of limited length, which does not allow yielding of the reinforcement. In most of cases, rough or very rough interfaces are tested, while the specimens with smooth or very smooth interface, as defined in the fib Model Code (MC 2010), do not exceed the 15% of the total number of specimens.

As already mentioned, the design provisions included in the codes, typically assume full anchorage of the reinforcement crossing the interface. Nonetheless, in the fib Model Code (MC 2010), it is stated that the tensile force to be anchored may be assumed equal to a percentage, κ , of the force required for the tensile stress to be fully developed (Paragraph 6.3.5, Equ. 6.3-8).

For the assessment of the various equations, the database is divided into two parts: (a) Tests in which the reinforcement is anchored to a length that allows the development of its yield strength (605 tests). This category includes specimens reinforced with closed hoops, cast-in reinforcing bars with a bonded length larger than $20d_b$ in either side of the interface, and post-installed reinforcement, with a bonded length (in epoxy material) greater than $10d_b$, and (b) Tests on interfaces (189 specimens), where the reinforcement does not fall into one of the cases of category (a).

The plots of Figure 1 prove that even in case of interfaces reinforced with fully anchored bars, the predictions of the equations included in Table 1 are not always conservative. It is noted that the equations were applied without any safety factor on the properties of the materials. Nonetheless, even when safety factors relevant to each code are used (Figure 2), there is still a small percentage of cases, for which the equations remain unconservative. The most significant statistical values resulting from the application of the code equations are reported in Table 2.

In case of interfaces crossed by short reinforcement, which cannot reach yielding, the comparison between experimental and predicted interface resistances is expected to yield unconservative results in a significant number of cases. This is confirmed by Figure 3, where in the calculated interface resistances safety factors are accounted for.

The codes that are assessed in this work are not meant for use in seismic design. Nonetheless, they are evaluated for this case as well, because ACI 318 (2019) is used in practice for seismic design of interfaces as well, while EC8 (2005) (its Part 3 included) refers to the EC2 (2004) equation for the design of interfaces. Finally, in the fib Model Code (MC 2010), there is a provision exclusively for unreinforced interfaces, penalized with a reduction factor of 0.50. In Figure 4, the code provisions are plotted against experimental values obtained from cyclic tests on interfaces. It is noted that in those plots, the reduction due to cycling interface resistance is accounted for. Both the plots of Figure 4 and the statistical data of Table 2 prove that the current code provisions cannot cover in a conservative way the design of interfaces subjected to seismic actions.

3 CHANGES TO THE TR 066 FOR CYCLIC LOADING

As analyzed in the previous section, the evaluated code provisions are not adequate, especially for interfaces with reinforcement of limited anchorage, as well as for the design of interfaces subjected to cyclic loading. Thus, in the framework of EOTA, the equation of the fib Model Code (MC 2010) was modified as per TR 066 (2019) (Table 3). The main difference between the two equations, lies in their third term: The compressive stress, σ_c , used for the calculation of the friction coefficient, μ , i.e. the stress due to clamping effect, is calculated as $\sigma_c = \rho \sigma_s$, σ_s being the tensile stress of the reinforcement crossing the interface and calculated using the following equation: $\sigma_s = l_{emb} * f_{yd} / l_b$, where $l_b = f_{yd} * d_b / (4 * f_{bd})$.

Therefore, the tensile stress of the reinforcement is not assumed to be equal to the yield strength of steel, but it is calculated on the basis of the available anchorage length of the interface reinforcement, and it is associated to the relevant failure mode. In case of post-installed reinforcing bars or industrial connectors, the value of τ_{Rd} (bond strength) provided by the respective manufacturer (based on evaluation tests) is used in the abovementioned Equation in lieu of f_{bd} . When interfaces are crossed by short post-installed bars (embedment length between $6d_b$ and $10d_b$), to predict their reduced bearing capacity, the verification for concrete cone breakout capacity is also required. The results of the application are presented in

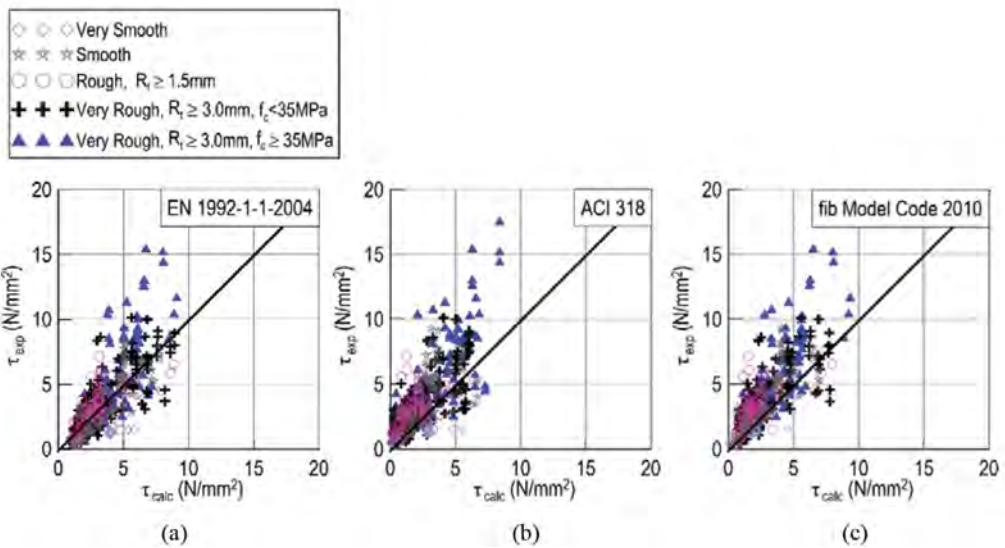


Figure 1. Specimens crossed by sufficiently anchored reinforcement: Comparison between experimental interface resistances and (a) Eurocode 2 (EN 1992-1-1-2004), (b) ACI 318 (2019) code, (c) fib Model Code (MC 2010). No safety factors are used.

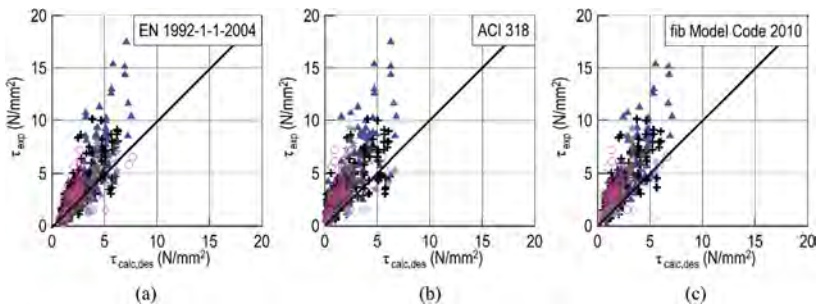


Figure 2. As Figure 1, with the use of relevant safety factors, namely, 1.15 and 1.50 for steel and concrete, respectively, for (a) and (c), and global safety factor $\phi=0.75$ in (b).

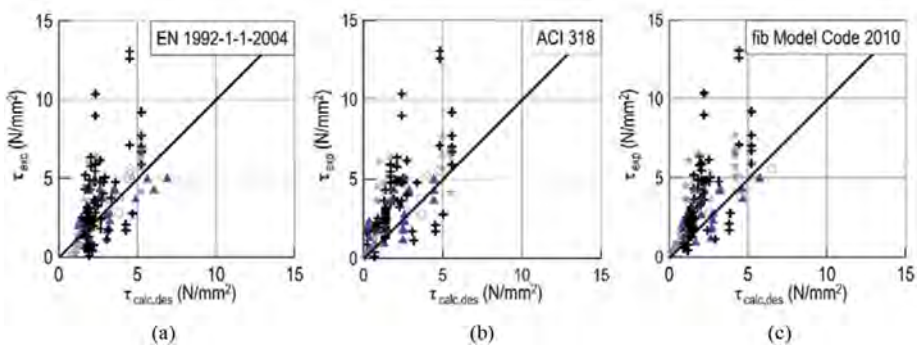


Figure 3. Specimens crossed by reinforcement with limited anchorage length: Comparison between experimental interface resistances and (a) Eurocode 2 (EN 1992-1-1-2004), (b) ACI 318 (2019), (c) fib Model Code (MC 2010). For the calculations relevant safety factors are used.

Table 2. Comparison between experimental interface resistances and code provisions. Statistical data.

Reinforcement	Bars that may yield			Bars of limited length			Cyclic loading		
	τ_c/τ_{exp} Average Values	$\tau_{c,des}/\tau_{exp}$ Average Values	$\tau_{c,des}/\tau_{exp} > 1.0$ Uncons. Values	τ_c/τ_{exp} Average Values	$\tau_{c,des}/\tau_{exp}$ Average Values	$\tau_{c,des}/\tau_{exp} > 1.0$ Uncons. Values	τ_c/τ_{exp} Average Values	$\tau_{c,des}/\tau_{exp}$ Average Values	$\tau_{c,des}/\tau_{exp} > 1.0$ Uncons. Values
EC2 (2004)	1.161	0.954	193	1.578	1.254	52	2.299	1.852	106
CoV (%)	55.3	55.5		142.2	141.8		70.8	67.7	
ACI 318 (2019)	0.777	0.598	66	0.850	0.677	17	1.456	1.121	65
CoV (%)	57.5	58.6		88.7	85.7		57.8	60.6	
MC 2010 (2010)	0.771	0.670	76	0.795	0.672	19	1.522	1.442	65
CoV (%)	43.8	43.7		55.3	57.1		73.6	66.0	
TR 066 (2020)				0.689	0.586	11	0.889	0.606	13
CoV (%)				52.3	56.0		44.1	48.2	

Uncos. Values stands for Unconservative Values

τ_c (τ_{calc}) is the value of the interface resistance calculated without the use of relevant safety factors

$\tau_{c,des}$ is the value of the interface resistance calculated with the use of relevant safety factors

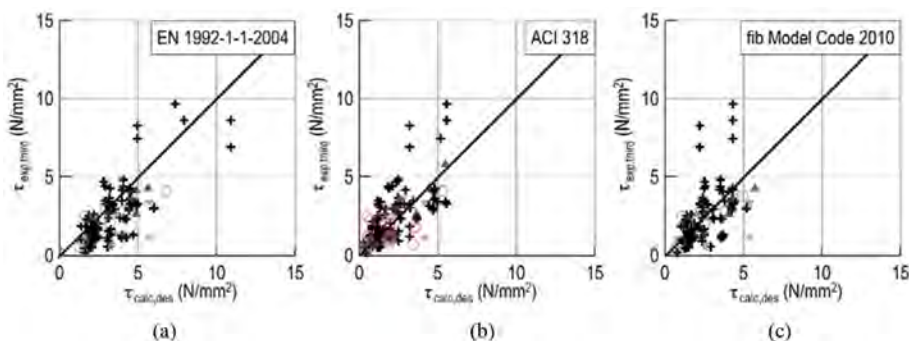


Figure 4. Interfaces subjected to cyclic actions. Comparison between experimental interface resistance measured during the third cycle, and values calculated according to (a) Eurocode 2 (EN 1992-1-1-2004), (b) ACI 318 (2019), (c) fib Model Code (MC 2010). For the calculations, relevant safety factors are used.

Figure 5 a, b. It is noted that the information regarding the exact values of f_{bd} or τ_{Rd} are not available for the reinforcement of all tested specimens, therefore the value of σ_s is calculated as: $\sigma_s = l_{emb} \cdot f_{yd} / 20d_b$, in case of cast-in reinforcement and $\sigma_s = l_{emb} \cdot f_{yd} / 10d_b$, in case of post-installed reinforcement. The prediction is more conservative, and a limited number of data points is unconservative.

Table 3. The equations included in TR 066 (2019), and version amended in 2020.

Technical Report	Equation
TR 066, 2019	$\tau_{calc} = c_r \cdot f_{ck}^{1/3} + \mu \cdot \sigma_n + \mu \cdot \kappa_1 \cdot \alpha_{\kappa 1} \cdot \rho \cdot \sigma_s + \kappa_2 \cdot \alpha_{\kappa 2} \cdot \rho \cdot (f_{yd} \cdot f_{cd})^{1/2} \leq \beta_c \cdot v \cdot f_{cd}$
TR 066, amended 2020	$\tau_{calc} = a_{seis} \cdot [c_r \cdot f_{ck}^{1/3} + \mu \cdot \sigma_n + \mu \cdot \kappa_1 \cdot \alpha_{\kappa 1} \cdot \rho \cdot \sigma_s + \kappa_2 \cdot \alpha_{\kappa 2} \cdot \rho \cdot (f_{yd} \cdot f_{cd})^{1/2}] \leq \beta_c \cdot v \cdot f_{cd}$

In the equations of Table 3, c_r , κ_1 , $\alpha_{\kappa 1}$, κ_2 , $\alpha_{\kappa 2}$ and a_{seis} , are factors depending on the roughness of the interface, on the type of the product used as interface reinforcement, as well as on the type of loading, namely monotonic or cyclic.

The equation of TR 066 (2019) does not account for reduced interface resistance due to cyclic loading. This was made possible by the additional provisions of the amended version of TR 066 (2020). It is noted that the method described in the Technical Report TR 066, both versions, deals with the design of connections realized using products covered by an ETA based on EAD 332347-00-0601 (2019) or EAD 332347-00-0601-v01 (2020).

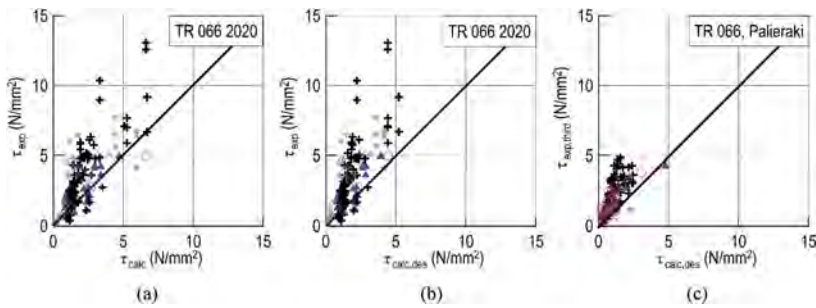


Figure 5. Specimens crossed by reinforcement with limited anchorage length: Comparison between experimental interface resistances and TR 066, for monotonic loading. For the calculations relevant safety factors (a) are not used, (b) are used, (c) Prediction for cyclic loading, using TR 066, in combination with α_{seis} , as proposed in Palieraki et al., 2022.

The equations included in the two versions of the Technical Report TR 066, are similar, in the sense that they account for both mechanisms of shear transfer along reinforced interfaces, namely, friction (due to external normal stress and due to clamping effect of the connectors) and dowel action. Both equations set the same limiting value for the resistance of the interface (the failure of concrete strut). It is noted that the equation in the amended version, is based upon the model presented in Palieraki et al. (2022). The main modifications of the amended version of TR 066 (2020), applicable to interfaces subjected to seismic actions, are the following:

- (a) Interfaces characterized as “very smooth” are excluded, given that their resistance is very small even under monotonic loading, and, thus, they are inadequate for use under seismic conditions.
- (b) The term of adhesive bond resistance/aggregate interlock, added to the resistance due to friction and to dowel action in the current equation is neglected in the new version of the equation. Indeed, in case of seismic actions, under the application of cyclic shear slips at values that exceed those (extremely small) needed for the mobilization of the adhesive bond resistance/aggregate interlock, this mechanism is not any more active. Additionally, another major change is needed, as explained herein:
- (c) In the equation included in the TR 066 (2019), for static loading, conservative (safe for the design) friction coefficient values are adopted. Those values depend exclusively on the roughness of the interface. Although it is well known that the friction coefficient is not constant, as it depends on the normal stress acting on the interface, it is understood that the need for a simple and safe calculation of the shear resistance of interfaces led to the adoption of friction coefficients independent of the value of the normal stress.

On the contrary, and due to the fact that the embedment length of the post-installed anchors is, in most cases, smaller than the one required for full development of the yield strength of the steel, the normal (compressive) stress on the interface is expected to be in several cases rather limited in value. For this frequent case, constant friction coefficient values (depending on the roughness of the interface), in combination with the reduction factors that account for the cyclic behavior, would lead to overconservative (unrealistically small) design values for the resistance of interfaces. Thus, on the basis of the available experimental data (taken from the international literature), a simple equation is proposed for the calculation of the friction coefficient, depending on the normal stress acting on the interface normalized to the compressive strength of the concrete. The friction coefficient is calculated using the following equation:

$$\mu = c \cdot \sqrt[3]{\left(\frac{f_{cd}}{\sigma_c + \sigma_n}\right)^2} \quad (1)$$

where the factor c , depends on the roughness and the concrete strength.

- (d) Last but not least, when the interface is under the adverse condition of cyclic actions, there are four phenomena that lead to the reduction of the maximum shear resistance (taken into account through the coefficient $\alpha_{seis} = \alpha_{seis,1} \cdot \alpha_{seis,2} \cdot \alpha_{seis,3} \cdot \beta_{seis}$, Figure 6), namely: (i) the maximum shear resistance under cyclic actions is smaller than the one corresponding to monotonic action ($\alpha_{seis,1}$), (ii) there is an asymmetry of behavior in the two loading directions, and in most cases, the load along the second loading direction is smaller ($\alpha_{seis,2}$), (iii) the shear resistance is decreased due to cycling ($\alpha_{seis,3}$), while (iv) larger scatter is associated with the seismic behavior of interfaces (β_{seis}). Thus, compared to the static resistance of an interface, its cyclic resistance is decreased by a significant percentage (depending, of course, on the specific anchor, on the roughness of interface, etc.).

For the equation included in the amended version of the TR 066, the coefficient α_{seis} should be calculated, according to tests, as described in the EAD 332347-00-0601-v01 (2020). Nevertheless, such tests are not available for the results reported in the literature, the calculations are performed based on Palieraki et al. (2022), using a reduction factor equal to 50%. The results are presented in Figure 5c and Table 2. The equation is quite conservative, while also the coefficient of variation is high, but this is expected to be corrected, when the values of α_{seis} calculated according to the test results are used.

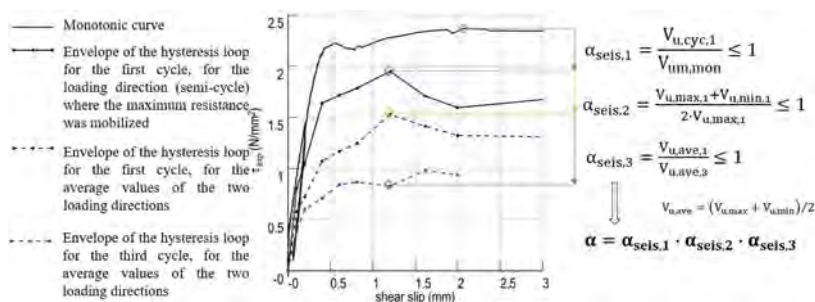


Figure 6. Typical curves reported for monotonic and cyclic loading, for the first, second and third cycle. The reduction factors due to cyclic loading, $\alpha_{seis,1}$, $\alpha_{seis,2}$, $\alpha_{seis,3}$ are shown in the relative curves.

4 CONCLUSIONS

The current paper provides a comparison of interface shear experimental results on cold joints, with shear resistance values calculated according to the EC2 (2004), ACI 318 (2019) and fib Model Code (MC 2010) provisions, as well as to the two versions of the design Guideline (EOTA TR 066 2019 and amended version, 2020).

The comparison shows that the calculations according to the equations of the assessed current codes, are in most cases conservative, leading at the same time to the overestimation of the results of part of the tests. This conclusion is valid for interfaces provided with reinforcement anchored to allow yielding. In case of interfaces provided with reinforcement of limited embedment length, or interfaces subjected to cyclic loading, the calculated resistance values are in average larger than the experimental resistances. Furthermore, in all cases, the scatter of the ratio between predicted and calculated values of interface resistances, expressed by the coefficient of variation, is very high.

An alternative equation is proposed as an improvement over the current interface shear provisions of fib Model Code (MC 2010) and is included in the Technical Report TR 066 (2019), for the calculation of the shear resistance of interfaces reinforced with post-installed reinforcement of limited length. This formulation accounts for the shear friction and the dowel action, while the tensile stress of the reinforcement, which is taken into account for the calculation of the friction term, is considered reduced, corresponding to the available embedment length. The alternative equation is more conservative and leads to a reduced number of points on the unconservative side.

In addition to the inaccuracy of the code equations in case of bars of limited length, the reduced shear resistance due to cyclic loading is not accounted for. Nonetheless, the provisions used in practice for seismic conditions as well, lead to unconservative results. The amended in 2020 version of the TR 066, provides a modified equation for the calculation of this reduced resistance. The application of the modified equation has proven its satisfactory performance in predicting the shear resistance of cold joint interfaces, subjected to cyclic loading.

REFERENCES

- ACI Committee 318. 2019. *Building Code Requirements for Structural Concrete (ACI 318-19) and Commentary (ACI 318R-19)*. American Concrete Institute, Farmington Hills, MI, 2019, 624pp.
- Bass, R.A., Carraquillo, R.L. & Jirsa, J.O. 1989. Shear Transfer across New and Existing Concrete Interfaces. *ACI Structural Journal* 86(4): 383–393.
- Cattaneo, S., Zorzato, G. & Bonati, A. 2021. Assessing method of shear strength between old to new concrete interface under cyclic loading. *Construction and Building Materials* 309.
- EAD 332347-00-0601. 2018. *Connector for strengthening of existing concrete structures by concrete overlay*. European Organisation for Technical Assessment (EOTA), Brussels.
- EAD 332347-00-0601-v01. 2021. *Variant: Connector for strengthening of existing concrete structures by concrete overlay: behavior under seismic action*. European Organisation for Technical Assessment (EOTA), Brussels.
- EN 1992-1-1-2004. 2004. *Eurocode 2: Design of Concrete Structures – Part 1-1: General rules and rules for buildings*. European Committee for Standardisation (CEN), Brussels.
- EN 1998-1-3-2005. 2005. *Eurocode 8: Design of structures for earthquake resistance – Part 3: Assessment and retrofitting of buildings*. European Committee for Standardisation (CEN), Brussels.
- EOTA TR 066. 2019. *Design and requirement for construction works of post-installed shear connection for two concrete layers*. European Organization for Technical Assessment (EOTA), Brussels.
- EOTA TR 066. Amended November 2020. *Design and requirement for construction works of post-installed shear connection for two concrete layers*. European Organization for Technical Assessment (EOTA), Brussels.
- fib Bulletin 65. 2010. *Model Code 2010 - Final draft*. Fédération Internationale du Béton (fib), Lausanne, Switzerland.
- Kaufmann, N. 1971. Das Sandflächenverfahren (The sand-patch method). *Straßenbautechnik*, 24(3): 131–135 (in German).
- Palieraki, V., Oikonomopoulou, E., Genesio, G. & Vintzileou, E. 2023. Concrete Interfaces with post-installed reinforcing bars and alternative connectors. *Structural Concrete*, in press.
- Palieraki, V., Vintzileou, E. & Silva, J.F. 2021. Behavior of RC interfaces subjected to shear: State-of-the-art review. *Construction and Building Materials* 306:124855.
- Palieraki, V., Vintzileou, E. & Silva, J.F. 2022. Modeling Reinforced Interfaces-Cold Joints Subjected to Cyclic Shear. *ACI Structural Journal* 119(4): 225–238.
- Valluvan, R., Kreger, M.E. & Jirsa, J.O. 1999. Evaluation of ACI 318-95 Shear-Friction Provisions. *ACI Structural Journal* 96(4): 473–481.

Performance-based design of new concrete walls for building seismic rehabilitation

S.M. Alcocer & B. Moctezuma

Institute of Engineering, UNAM, Mexico City, Mexico

ABSTRACT: In the aftermath of the September 19, 2017 earthquake, several hundred buildings were rehabilitated in Mexico City. Based on a research project jointly developed by UNAM and The University of Texas at Austin, addition of new reinforced concrete walls was found to be the most widely used rehabilitation technique. Different configurations were recorded. In cases where building sides were readily accessible, walls were built eccentric to the existing frame structure. Most walls were concentric with the frame axes. Some concentric walls were infilled so that the vertical and horizontal wall reinforcement was not continuous across the building height and width, respectively. In other cases, vertical wall reinforcement was made continuous through the floor system. To develop analysis and design recommendations, aimed at applying performance-based design rules, a dataset of tests on the addition of RC walls was assembled. Emphasis was given to identify the distinct modes of failures, including those related to connections and interface shear transfer between wall edges and existing frame members. Most significant results of the analysis of the dataset are discussed. Comments related to connection modeling and design are presented.

1 INTRODUCTION

Seismic rehabilitation of buildings by adding new reinforced concrete (RC) walls is one of the most used techniques worldwide. The addition of walls has been suitable for buildings with deficient stiffness and strength, as well as for buildings with torsional effects, flat slabs and/or weak stories. In Mexico City, in the aftermath of the 19 September 2017 earthquake, most buildings that exhibited inadequate performance were retrofitted with new RC walls. Distinctly different wall configurations have been observed in the field. Many of them have been tested in the laboratory. Most specimens tested are scaled models, typically with one or two stories. Some specimens have studied the effect of openings in the new added RC walls. Experimental data from those tests have been used to develop analysis and design recommendations. A detailed analysis of experiments studied may be found elsewhere (Moctezuma 2022). In this paper, tests with failure at the connections are primarily discussed. Emphasis is given to the calculation of connection strength and to the effect of connection failure type on backbone curves for performance-based design.

1.1 *Addition of RC walls in buildings rehabilitates after the earthquake of 2017*

After the earthquake of 2017, different configurations of RC walls were observed in the 94 rehabilitated buildings that were studied: wing walls (wall segments connected to existing columns), concentric walls (walls with a collinear axis with the frame and continuous vertical reinforcement), eccentric walls (walls built against the exterior face of the building), infill walls, and thickening of existing walls (building a concrete shell against the wall). The most widely used configuration were concentric walls, used in 46% of buildings analyzed. Three types of connections between floor system and concentric walls were observed (Figure 1). An opening with a width equal to the new wall thickness was made in the beam or slab, without damaging existing reinforcement, to allow concrete casting and for the continuity of the new wall vertical reinforcement. In one building, holes through the slab were made to pass the new wall vertical

reinforcement. In four other buildings, an opening was created in the floor system only where boundary elements next to columns were to be built. This procedure permitted new wall vertical reinforcement at the edges to be continuous while the vertical reinforcement of the new wall web was anchored to the floor system with epoxy resin. When concentric walls were built adjacent to columns, wall connection consisted of anchoring wall horizontal reinforcement to the RC column jacket or by overlapping wall horizontal reinforcement with epoxied dowel bars. For eccentric walls, connection to the floor system consisted of epoxy grouted dowels with a 90-degree standard bent. When infill walls were used, the connection with the original frame was made with epoxy grouted post-installed anchors or dowel bars.



Figure 1. Connection of concentric walls with floor system: a) opening in the slab along the wall; b) holes to allow placement of vertical reinforcement; and c) openings at wall edges adjacent to columns.

2 DATASET OF RC FRAMES REHABILITATED WITH RC WALLS

A dataset of experiments on RC frames rehabilitated with RC walls was assembled. A total of 93 specimens of different countries, including Greece, Japan, Türkiye, and USA, were studied (Altin et al. 1992, Anil & Altin 2007, Aoyama et al. 1984, Canbay et al. 2003, Chrysostomou et al. 2012, Gaynor 1988, Hayashi et al. 1980, Higashi et al. 1980, Jiménez 1988, Kara & Altin 2006, Moretti et al. 2014, Papatheocharis et al. 2019, Sonuvar et al. 2004, Strepelias et al. 2014, Teymur et al. 2014). Wall configuration included: bare frames, monolithic walls where the infill wall was cast together with the frame, full infill walls, partial infill walls (wing walls or wall panels located at the center of the bay), infill walls with openings and eccentric walls. Most specimens (86.0%) were designed to a 1:3 scale. The following frame configurations were observed: one story and one bay (59.1% of specimens), two stories and one bay (33.3% of tests), four stories and one bay (3.2% of models), two stories and three bays (2.2% of specimens) and four stories and three bays (2.2% of tests).

Different configurations of connections between new walls and existing frames have been tested (Figure 2). The most widely connection studied consists of post-installed anchors with epoxy resin. Other types of connections include expansive anchors, shear keys, wall reinforcement welded to existing column reinforcement and anchoring of the horizontal wall reinforcement in the concrete jacket of the columns. In the specimen with an eccentric wall, the connection with the beam consisted of epoxy grouted anchors and the horizontal reinforcement of the wall was anchored in the RC column jacket. Another variable included in the experiments is the location and distribution of anchors, either by placing anchors along the entire wall perimeter or only along the upper beam and the foundation. In one specimen, anchors were placed only along the wall interface with the upper beam. In three specimens, no special connection detailing was provided between wall and frame. Surface roughness of the old concrete along the wall-column and wall-beam interfaces was also included in the dataset. In 31.9% of the retrofitted frames, surface roughness along the wall interface was purposely increased. No surface preparation was found in 14.5% of the specimens; no data about surface roughening was available for 53.6% of the tests.

3 STRENGTH OF SPECIMENS WITH A FAILURE MECHANISM AT THE CONNECTION

Three methods were compared to evaluate the resistance of the specimens that exhibited a failure mechanism controlled by the connection between the infill wall and the beam or the

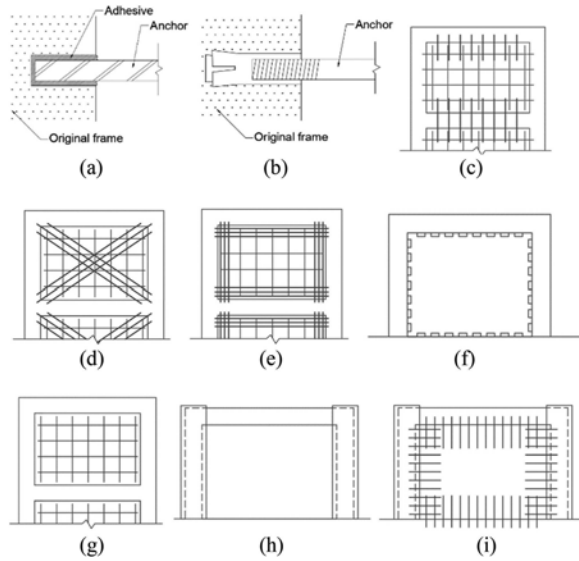


Figure 2. Connection between new wall and original frame: a) post-installed anchors with epoxy resin and epoxied dowel bars; b) expansion anchors; c) epoxied dowel bars in beams and horizontal reinforcement welded to existing column reinforcement; d) diagonal reinforcement welded to column reinforcement; e) wall bars concentrated at wall edges welded to the frame reinforcement; f) shear keys connected to the frame with epoxy; g) no connection of wall reinforcement nor intended surface preparation; h) RC column jacketing cast monolithically with RC infills without anchors; and i) epoxied dowel bars and RC jacketing of columns.

foundation. Models with this failure mechanism without anchors along the connection with the foundation and the beam were not included. The first method (JBDPA method) is that proposed by the Japan Building Disaster Prevention Association (JBDPA 2001) in Equation 1:

$$Q_{Wsu} = Q_j + Q_{pc} + \alpha \cdot Q_c \quad (1)$$

where Q_j = the sum of the shear resistance of each anchor in the connection with the beam; Q_{pc} = direct shear strength at the top of the column; α = reduction factor depending on the type of failure of the column (1.0 in case of shear failure and 0.7 for flexural failure); and Q_c = lesser value between the column shear resistance and the shear force at column yielding. In the second method, a new model was proposed to estimate the strength of the specimens using the design equations of the Mexico City Concrete Standards -NTC-Concrete- (Gobierno 2017) for shear friction and the strength of the columns. The shear strength of the connectors below the beam was calculated with ACI 318-19 Chapter 17 design equations. ACI 318-19 was used because no design requirements for anchors are yet provided in NTC-Concrete. Strength of specimens was estimated with Equation 2:

$$V_{calc} = V_j + V_{Fr} + \alpha \cdot V_c \quad (2)$$

where V_j = shear strength of the connection calculated as the lesser between the sum of the steel strength of each connector in shear V_{sa} (Equation 3) and the nominal concrete pryout strength of the group of connectors in shear V_{cpg} (Equation 4); V_{Fr} = shear friction strength in the upper end of the column calculated as the lesser of the Equations 5, 6 and 7; α = reduction factor according to the column failure type (1.0 in case of shear failure and 0.7 for flexural failure); and V_c = lesser value of the column shear strength and the shear force at flexural strength of the other column, according to NTC-Concrete.

$$V_{sa} = 0.6A_{se}f_{uta} \quad (3)$$

where: $A_{se,v}$ = effective cross-sectional area of an anchor in shear, mm^2 ; and f_{uta} = specified tensile strength of the connector steel, .

$$V_{cpg} = k_{cp}N_{cpg} \quad (4)$$

where: $k_{cp} = 1.0$ for $h_{ef} < 63.5 \text{ mm}$; $k_{cp} = 2.0$ for $h_{ef} \geq 63.5 \text{ mm}$; h_{ef} = effective embedment depth of the connector; in the case of adhesive anchors N_{cpg} was the lesser of the nominal bond strength in tension of the group of connectors N_{ag} (Equation 17.6.5.1b of ACI 318-19) and the nominal concrete breakout strength in tension of the group of connectors N_{cbg} (Equation 17.6.2.1b of ACI 318-19); in the case of expansion anchors N_{cpg} was the nominal concrete breakout strength in tension of the group of connectors N_{cbg} (Equation 17.6.2.1b of ACI 318-19).

$$V_{Fr} = F_R\mu(A_{vf}f_y + N_u) \quad (5)$$

$$V_{Fr} = F_R[1.4A + 0.8(A_{vf}f_y + N_u)] \quad (6)$$

$$V_{Fr} = F_R0.25f'_c A \quad (7)$$

where: F_R = strength factor (to evaluate the strength of the specimen a $F_R = 1.0$ was used); f_y = specified yield strength of the longitudinal reinforcement, N/mm^2 ; f'_c = compressive strength of the frame concrete, N/mm^2 ; A_{vf} = total area of the longitudinal reinforcement of the column, mm^2 ; A = cross-sectional area of the column, mm^2 ; N_u = axial load in the column, N ; and μ = friction coefficient ($\mu = 1.4$ for monolithic concrete).

In the third method, the strength of the connection V_j was studied considering two interface shear mechanisms: a) the friction between old and new concrete along the interface; and b) the dowel mechanism. The total strength was computed with the Equation 8 proposed by Palieraki et al. (2022):

$$\tau_u = \beta_d\tau_d + \beta_f\tau_f \quad (8)$$

where β_d = contribution factor of the dowel action; $\beta_d = 0.7$ was used for dowels with a minimum embedment length of $8d_b$ (this factor was multiplied by an additional 0.5 to consider the degradation of the dowel action due to cycling); τ_d = strength of the dowel mechanism using Equation 9; β_f = contribution factor of the friction mechanism ($\beta_f = 0.40$ for mechanically roughened interface with normal strength concrete, cyclic loading and an embedment length between $6d_b$ and $12d_b$ or $\beta_f = 0.20$ for smooth interface); and τ_f = strength for the friction mechanism calculated with Equation 10.

$$\tau_d = \left(1.3nd_b^2\sqrt{f_c f_y}\right)/A_c \quad (N/mm^2) \quad (9)$$

where n = number of reinforcing bars across the connection; d_b = diameter of reinforcement across the connection mm ; f_c = the lesser value of the compressive strength of concrete of the frame and the wall, N/mm^2 ; f_y = yield strength of the reinforcement across the connection, N/mm^2 ; and A_c = area of the interface, mm^2 .

$$\tau_f = 0.44\sqrt[3]{f_c^2\sigma_c} \quad (N/mm^2) \quad (10)$$

where f_c = the lesser value of the compressive strength of concrete of the frame and the wall; $\sigma_c = f_c A_s/A_c$ (this value can be adjusted to consider the degree of anchorage of the reinforcement across the connection. This adjustment was not included in this analysis because the bond strength was not available), N/mm^2 ; f_y = yield strength of the reinforcement across the connection, N/mm^2 ; A_s = total area of reinforcement in the connection, mm^2 ; and A_c = area of the interface, mm^2 .

The strength of each specimen was obtained by replacing the connection strength V_j in the Equation 2 (obtained using ACI 318) with the total connection strength computed with the method proposed by Palieraki et al. (2022). In Figure 3 the ratio of experimental strength V_{exp}

to calculated strength V_{calc} for each specimen for the three methods is shown. For tests AO 7, HA 5, HA 6, PA 7, MO 1, MO 2 and MO 3 (Aoyama et al. 1984, Hayashi et al. 1980, Moretti et al. 2014, Papatheocharis et al. 2019), results for the first two methods were comparable. With the JBDPA method, calculated strengths for all specimens were closer to the experimental strength (e.g., the ratio was closer to 1) compared to those computed using the method that combined ACI 318 and NTC-Concrete. The connection strength computed ACI 318-19 Chapter 17 was significantly lower than that calculated using the JBDPA method. It is apparent that strengths calculated with the combined method by NTC-Concrete and ACI are too conservative. ACI 318 design equations provide a more comprehensive analysis of the connection by considering, among other variables, the steel anchor shear resistance, connectors effective depth, connector spacing, and the effect of the distance of anchors to the edge of the element. In the JBDPA model, steel anchor shear strength of the steel is also considered, but the other variables in ACI 318 are not. Although ratios obtained with both methodologies were conservative (e.g., larger than 1.0), ratios for the JBDPA method were closer to 1.0 and with a smaller coefficient of variation, CV (0.29 and 0.21 for ACI 318 and JBDPA methods, respectively). Only for specimen MO 3, V_{exp}/V_{calc} was less than 1.0 (actual ratio was 0.92).

With the third method, which used the Palieraki et al. approach, lowest V_{exp}/V_{calc} ratios were calculated. In this method, roughness along the interface was an important parameter in calculating specimens' strength. In models where surface of the old concrete at the connection was roughened (specimens AO 6, AO 7, AO 9 and PA 7) calculated strength was conservative. In effect, V_{exp}/V_{calc} was greater than 1.0, with an average of 1.31 and CV=0.15. For tests where no additional roughness was provided (specimens PA 4, PA 5, MO 1, MO 2 and MO 3), calculated strength was conservative only for the specimen PA 5. In Figure 6, V_{exp}/V_{calc} for tests PA 4, PA 5, MO 1, MO 2 and MO 3, was 0.90 on the average, with a CV=0.11. The strength of the specimens HA 5 and HA 6 was not calculated with this method because no specimens with an embedment length smaller than $6d_b$ were included in the database used to calibrate the proposed method.

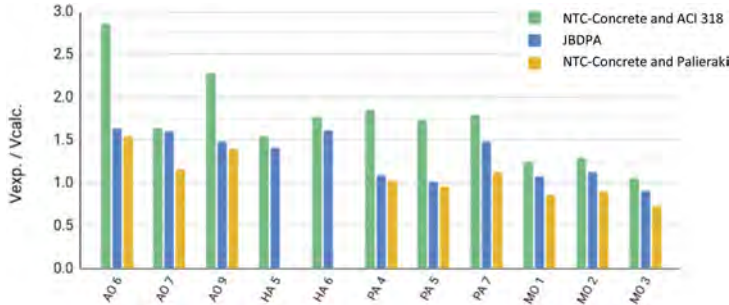


Figure 3. Ratio of experimental to calculated strength of the specimens with a failure mechanism at the connection.

4 BACKBONE CURVES FOR PERFORMANCE-BASED SEISMIC DESIGN

Performance-based seismic design of new and rehabilitated buildings requires modelling of the structure and its components to large deformations. Aimed at providing guidance on the modelling of RC frames rehabilitated by the addition of new RC walls, backbone curves were developed. Backbone curves of specimens with a failure mechanism at the connection between the infill wall and the upper beam and/or the foundation are shown in Figures 4 and 5. Backbone curves for other failure mechanisms, outside the scope of this paper, have been developed and may be found elsewhere (Moctezuma 2022). The behaviour was different among tests although a “connection failure” was reported. Based on this observation, the envelope curves of the specimens were divided into four different types. Each type corresponded to a specific mode of failure within the connection. Envelopes were obtained by digitizing the published hysteresis

loops or, when available, envelope curves (Rohatghi 2021). The curves were normalized by the shear friction strength computed as the product of the connection transverse area (infill wall and columns) and the reported yield strength of the reinforcement across the connection (either expected or measured yield strength) (Equation 11).

$$V_N = V / [(A_C + A_w)f_y] \tag{11}$$

where: V_N = the normalized lateral force; V = measured lateral force N , A_c = sum of the cross-sectional area of each column mm^2 ; A_w = cross-sectional area of the wall, mm^2 ; and f_y = yield strength of the connectors, N/mm^2 .

In general, curves exhibit a trilinear or tetra-linear form. The first linear elastic branch ends at cracking; the second branch is limited by the strength, while the third represents the descending portion of strength in the experiment. When at large drift angles a residual strength was identified, a fourth horizontal branch was used in the model. The backbone curves obtained from the envelopes of the specimens HA 6 and HA 7 are presented in Figure 4a. In these specimens, the connectors were sheared off resulting in the failure of the retrofitted frame; once strength was reached, loss of resistance and stiffness was observed. For PA 4 and PA 5 (Figure 4b), failure was due to a combination of shearing of the dowel bars at the connection with the foundation with shear failure at the column base. In this case, the backbone curve could be approximated as a curve with a yielding plateau.

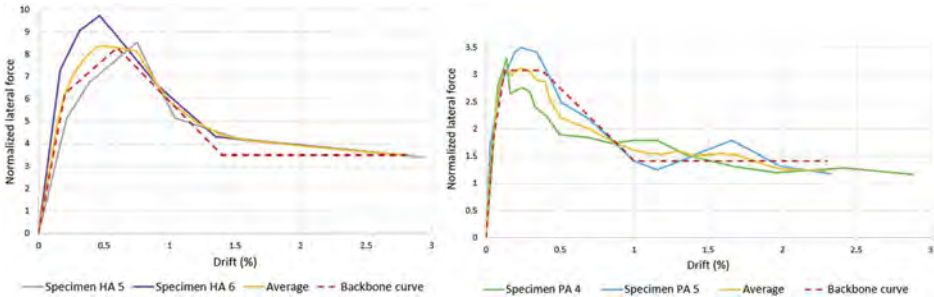


Figure 4. Backbone curves of specimens: a) HA 5 and HA 6 (Higashi et al. 1980); b) PA 4 and PA 5 (Papatheocharis et al. 2019).

In specimen PA 7 (Figure 5a), columns of the existing frame were retrofitted with a RC jacket. At yielding, strength was maintained prior to loss of strength and stiffness, following a linear degradation. Failure of PA 7 was attributed to shearing of the connectors from the beam and shear failure at the top of the columns. In specimens MO 1 and MO 3 (Figure 5b), failure at the connection was credited to shearing of the dowel bars of the connection with the foundation. For these tests, the backbone curves feature three branches.

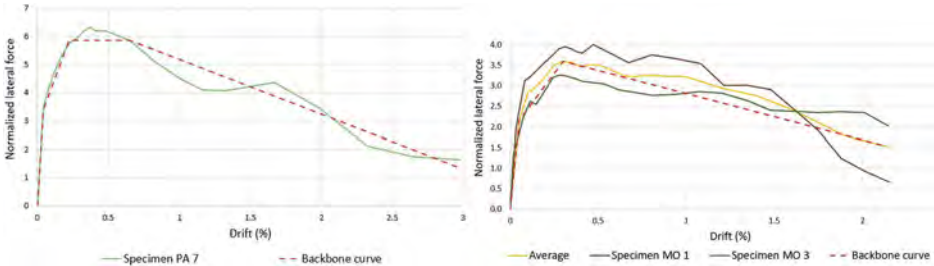


Figure 5. Backbone curves of specimens: a) PA 7 (Papatheocharis et al. 2019); b) MO 1 and MO 3 (Moretti et al. 2014).

PA 4 and PA 5, PA 7, MO 1 and MO 3 exhibited significant slip between the wall and the frame led to the failure of the specimens and a conspicuous strength and stiffness decay. From the graphs, it is apparent that normalized peak strength and drift at strength depended on the characteristics of the failure mechanism.

5 CONCLUSIONS

Addition of RC walls to rehabilitate RC frames is a very widely used technique. To develop analysis and design guidelines for building rehabilitation, test results of different wall configurations and its connections to the frame were studied. Experimental investigations on infills, wing walls, concentric and eccentric walls, and on walls with window and door openings were gathered and revised. A dataset of tests was assembled. Different failure modes were observed; details may be found elsewhere (Moctezuma 2022). In this paper, tests with a failure at the connections between the new wall and the existing frame elements have been discussed. Experimental strength was compared to calculated strengths using three methods: a) the Japanese approach (referred to as JBDPA method); b) a combination of the Mexico City Concrete Standards (NTC-Concrete) design equations and the ACI-318-19 Chapter 17 requirements; and c) a combination of the design equation of NTC-Concrete and the interface shear model proposed by Palieraki et al. (2022). Additionally, backbone curves for other different types of failure mechanism at the connection were developed but are not presented here. Based on the analysis of data, the following conclusions were drawn:

Addition of new RC walls for frame rehabilitation is a very common technique. In the aftermath of the 2017 earthquake in Mexico City, concentric walls (walls with a collinear axis with the frame and the vertical reinforcement is continuous) were the most used configuration.

Strength of the connection depended on the type of detailing used. Superior behaviour was observed where surface roughness along the connection interface was implemented and sufficient amount of properly anchored reinforcement was placed across the connection.

From the three methods used to calculate connection strength, the JBDPA methodology and the combination of NTC-Concrete and the ACI 318-19 Chapter 17 requirements led to conservative estimations. Strength estimations with the JBDPA method were closer to experimental strength and with lower coefficient of variation than those calculated using the combination NTC-Concrete/ACI 318-19. With the third method, that considers friction along the interface and dowel action, strength calculations were conservative where intentionally roughened interface surface was implemented. When the surface was not prepared, results were unconservative, but close to experimental values (average measured-to-calculated strength ratio of 0.90).

REFERENCES

- ACI Committee 318. 2019. Building Code Requirements for Structural Concrete (ACI 318-19), *ACI*.
- ACI Committee 369. 2022. Standard Requirements for Seismic Evaluation and Retrofit of Existing Concrete Buildings and Commentary (ACI 369R-1.22), *ACI*.
- Altin S., Ersoy U., and Tankut T. 1992. Hysteretic Response of Reinforced-Concrete Infilled Frames, *ASCE Journal of Structural Engineering* 118 (8): 2133–2150.
- Anil. O., and Altin. S. 2007. An Experimental Study on Reinforced Concrete Partially Infilled Frames, *Engineering Structures* 29 (3): 449–460.
- Aoyama H., Kato D., Katsumata H., and Hosokawa Y. 1984. Strength and Behaviour of Postcast Shear Walls for Strengthening of Existing Reinforced Concrete Buildings, in Vol. 1 of *Proc. 8th World Conf. on Earthquake Engineering*, 485–492, San Francisco, California.
- ASCE. 2017. Seismic Evaluation and Retrofit of Existing Buildings, *ASCE/SEI*, Reston, Virginia.
- Canbay E., Ersoy U., and Ozebe G. 2003. Contribution of Reinforced Concrete Infills to Seismic Behavior of Structural Systems, *ACI Structural Journal*, 100 (5): 637–643.
- Chrysostomou C. Z., Kyriakides N., Kotronis P., Poljanšek M., Taucer F., Roussis P., and Kosmopoulos A. 2012. Seismic Retrofitting of RC Frames with RC infilling, *15th World Conf. on Earthquake Engineering*, Lisboa, Portugal.

- Gaynor P. 1988. The Effect of Openings on the Cyclic Behaviour of Reinforced Concrete Infilled Shear Walls, Master Thesis, The University of Texas at Austin.
- Gobierno de la Ciudad de México. 2017. Normas Técnicas Complementarias para Diseño y Construcción de Estructuras de Concreto (NTC-Concreto) (in Spanish).
- Hayashi T., Niwa H., and Fukuhara M. 1980. The Strengthening Methods of the Existing Reinforced Concrete Buildings”, in Vol. 4 of *Proc. 7th World Conf. on Earthquake Engineering*, Vol 4, pp. 89–96, Istanbul, Türkiye.
- Higashi Y., Endo T., Ohkubo M., and Shimizu Y. 1980. Experimental Study on Strengthening Reinforced Concrete Structure by Adding Shear Wall, in Vol 7 *Proc. 7th World Conf. on Earthquake Engineering*, Vol 7, pp. 173–180, Istanbul, Türkiye.
- Jiménez L. R. 1989. Strengthening of Reinforced Concrete Frame Using an Eccentric Wall, Master Thesis, The University of Texas at Austin, 67 pp.
- Kara M. E., and Altin S. 2006. Behavior of Reinforced Concrete Frames with Reinforced Concrete Partial Infills, *ACI Structural Journal* 103 (5): 701–709.
- Moctezuma B. 2022. Rehabilitación sísmica de edificios mediante la adición de muros de concreto reforzado (in Spanish), B.Sc. Thesis, National Autonomous University of Mexico, UNAM, Mexico City, 154 pp. https://tesiunam.dgb.unam.mx/F/HIQIKL1X7V64VATAX7DQ66JJP4M2FPFEBJULIMYVMF367VGKE-12803?func=full-set-set&set_number=024459&set_entry=000001&format=999, last accessed 2023/02/01
- Moretti M. L., Papatheocharis T. and Perdikaris P. C. 2014. Design of Reinforced Concrete Infilled Frames, *ASCE Journal of Structural Engineering*, 140 (9).
- National Institute of the School Building Infrastructure (INIFED) (2021). Technical guide – Seismic rehabilitation of school building infrastructure (in Spanish), Mexico City, Mexico, http://www.resilienciassismica.unam.mx/normas_guias.html, last accessed 2023/02/01
- Palieraki V., Vintzileou E. and Silva J. F. 2022. Interface Shear Strength under Monotonic and Cyclic Loading, *ACI Structural Journal*, 119 (3): 17–28.
- Papatheocharis T., Perdikaris P. C., and Moretti M. L. 2019. Response of RC Frames Strengthened by RC Infill Walls: Experimental Study, *ASCE Journal of Structural Engineering*, 145 (11).
- Rohatghi, A. 2021. Webplotdigitalizer: versión 4.5, <https://automeris.io/WebPlotDigitizer>.
- Sonuvar M. O., Ozcebe G., and Ersoy U. 2004. Rehabilitation of Reinforced Concrete Frames with Reinforced Concrete Infills, *ACI Structural Journal* 101 (4): 494–500.
- Strepelias E., Palios X., Bousias S. N., and Fardis M. N. 2014. Experimental Investigation of Concrete Frames Infilled with RC for Seismic Rehabilitation, *ASCE Journal of Structural Engineering* 140 (1).
- Teymur P., Yuksel E., and Pala S. 2014. Behaviour of Reinforced Concrete Frames Retrofitted with Shotcrete Panels Connected Only to the Beams, *Arab J Sci Eng*, 39 (3): 1531–1546.
- The Japan Building Disaster Prevention Association, JBDPA. 2001. *Guidelines for Seismic Retrofit of Existing Reinforced Concrete Buildings*.

Composite action in tunnel linings by use of shear connectors in concrete interfaces

K. Mitroulis

Dr Sauer & Partners Ltd, London, UK

N. Mellios & P. Spyridis

TU Dortmund University, Dortmund, Germany

K. Bergmeister

University of Natural Resources and Life Sciences, Vienna, Austria

ABSTRACT: The standard construction method of the sprayed concrete lining (SCL) in soft ground tunnelling comprises a temporary primary lining of sprayed concrete, a permanent cast-in-situ or sprayed secondary lining and a waterproofing membrane interface between them. In the last twenty years, a novel design philosophy suggests the primary lining to be part of the permanent structure contributing to the long-term structural response of the tunnel's SCL system. Also, if the sheet membrane is substituted with a sprayed one, some bond and shear capacity can be assumed between the concrete linings. This could lead to a composite behaviour and load sharing between the linings, potentially reducing the secondary concrete lining thickness and improving the overall system's efficiency, e.g., by reducing excavation volumes and lining material consumption. This paper presents research for this composite configuration by use of mechanical shear connection in relation to the tunnel's geometry. This is further compared to the boundary situations with frictionless interfaces and full monolithic bond. This paper delivers first insights on this novel concrete lining philosophy aiming to significantly improve the overall sustainability and life-cycle load bearing performance of critical underground infrastructure assets.

1 INTRODUCTION

In soft ground tunnelling, the standard construction method of a sprayed concrete lined tunnel (SCL) includes a temporary primary lining of sprayed concrete, a permanent cast-in-situ or sprayed secondary and a sheet waterproofing membrane between them. Over the last two decades, an innovative tunnel design philosophy has been established considering the traditionally primary lining as part of the long-term structure. According to (Spyridis 2014), a long service life for primary lining sharing the loading with the secondary lining can lead to a material reduction of 40-45% for tunnel construction, while the savings in concrete consequently result in additional savings in excavation volumes. Moreover, the use of a new sprayed membrane material as a structural bonding connection between the concrete linings has been introduced leading to a composite bonded action of the two lining layers. This denotes the ability of the concrete linings to transmit shear stresses within them leading to a composite action of the whole tunnel's SCL system. Several experimental investigations have been conducted in recent years (Nakashima et al. 2015; Johnson et al. 2016; Su & Bloodworth 2016, Vogel et al. 2017), including both laboratory and on-site testing procedures, in order to evaluate the degree of the bond and the shear transfer between the linings. Detailed studies on the sustainability performance of such lining configurations on the basis of Global Warming Potential (GWP) metrics are presented in (Spyridis & Bergmeister 2023a; Spyridis & Bergmeister 2023b).

Besides, the topic of the shear transfer between concrete interfaces in general has gained a lot of scientific interest for more than 60 years (Palieraki et al. 2021). This is reflected in the amount of existing experimental investigations and the number of design provisions that have been published throughout the years covering this specific topic. Significant recent paradigms include references to the ACI 318 (Palieraki et al. 2022), fib Model code 2010 (Randl 2013) and the EOTA TR 066 (EOTA 2019). More profound information regarding composite structures can be found in (Johnson 2018). In addition, (Palieraki et al. 2021) (Randl 2013) deliver a thorough description of the design recommendation of the fib model code 2010 and the theory behind them, alongside the summary of more than a thousand experiments from the last 60 years.

There are many ways to introduce a composite behaviour between the interface of concrete constructions that were cast in separate time frames. One of the most efficient methods due to its applicability and fast implementation is with post installed anchors that behave as shear connectors. These post installed anchors are commonly used with success for repairing or strengthening applications considering both static and life-cycle actions (recurring and extreme loads); examples can be seen in (Vintzileou & Palieraki 2007) and (Kwon et al. 2010). Particularly the latter indicates that post installed anchors have a significantly higher performance than the corresponding conventional shear studs. (Palieraki et al. 2021) suggests a new modified design formula for monotonic and cyclic actions based on investigations and verification accounting for more than 1240 previous experiments on post-installed dowels. In the same spirit, (López-Carreño et al. 2020) and (Heinrich et al. 2019) conducted a series of real-scale experimental investigations on the performance of post-installed anchors as shear connectors between concrete elements. In both studies, the performance of the dowels is tested under both static and cyclic long-term loading. The results proved that the performance of mechanical post-installed anchors has a very satisfactory behaviour in terms of shear load transfer.

The main focus of the present study is to provide preliminary insights into an innovative approach for composite sprayed concrete linings (SCL). By means of post-installed dowels as shear connectors, the overall thickness of the concrete linings can be reduced while increasing the sustainability of this construction methodology. The performance of post-installed dowels as a shear transfer mechanism has been well established but still, there is no sufficient research on how they operate in conjunction with the tunnel geometry and SCL linings. Moreover, this study aims to highlight the influence of the shear connectors' geometrical distribution throughout the length of the tunnel linings. For the purpose of the present study, two different finite element (FE) software are used. Rocscience2 (RS2) as exclusively geotechnical FE software is utilized to evaluate the loading conditions at a shallow tunnel's linings caused by the ground in long term conditions. Subsequently, the critical tunnel's cross sections derived, are designed in ANSYS FE with interface shear connectors and the system's overall structural performance is assessed.

2 GROUND – STRUCTURE INTERACTION SIMULATION

2.1 *Geotechnical model*

In order to simulate the long-term geotechnical conditions and the construction sequence of a shallow tunnel (20m below ground level), a multi-stage model is demanded. RS2 as a geotechnical finite element (FE) software is able to simulate the tunnelling process step by step assuming full-face excavation. The model of the present study consists of the following four stages:

- Initial ground conditions
- Ground relaxation, to simulate unloading and convergence prior to lining installation
- Full-face excavation and installation of the concrete lining
- Long-term ground conditions in interaction with the tunnel

In RS2, a rectangular block is designed to represent the geological model of the study. The tunnel's cross section is placed at a distance of 5 tunnel diameters from the block's edges. Based on research of available geotechnical information in relevant publications (Spyridis et al. 2016), this geological model is assumed to represent a typical London clay soil with an initial drained Young's modulus (E_{clay}) equal to 300 MPa and Poisson's ratio equal to 0.3.

Two tunnel geometries were chosen for the present study. The first one has a height/width ratio < 1 and is referred to as a wide (long) tunnel shape. The second one has a height/width ratio > 1 and is referred to as a tall tunnel shape. Both of them, have an excavation area equivalent to a typical circular tunnel with 8m diameter. All the geometries were designed in AutoCAD software and imported to RS2. The numerical models implement 2D plane strain analyses following the Mohr Coulomb failure criterion. The ground is modelled by 3-noded triangular solid elements, and the concrete lining is modelled by the Timoshenko-standard beam elements. The lining is assumed 0.6 m thick and is modelled by an elastic concrete material with Young's modulus of 25000 MPa and Poisson's ratio of 0.2. The support configuration assumes two separate 0.3 m thick linings with a fully bonded contact between them, representing a monolithic connection. The mesh of the model for the indicative long shape cross section is shown in Figure 1. The model block is simply supported at the two sides allowing the vertical displacement. The bottom of the block is simply supported allowing the horizontal displacement while the bottom corners are considered fixed. The upper limit serves as the free surface of the ground. Underneath the tunnel's cross section, there are three soil regions with different properties compared to the surrounding ground. The yellow layers have a drained Young's modulus equal to 600 MPa ($2 \times E_{\text{clay}}$) and the green one has a drained Young's modulus equal to 900 MPa ($3 \times E_{\text{clay}}$). The basic purpose of this consideration was to achieve better results regarding the ground's unloading heave at the tunnels' invert. During the excavation sequence, the anticipated heave at the invert has a ratio of approximately 1/3 of the settlement at the crown. In general, this consideration aims to account for a stiffer ground response during unloading phase. Hence the material properties of the surrounding ground are modified in the fourth stage, except for the unloading layers which remain unaffected. Specifically, there is a reduction in Young's modulus value which is equal to 140 MPa (E'_{clay}) and an increase in Poisson's ratio value which is equal to 0.45. With this, the geotechnical conditions are simulated more accurately in interaction with the tunnel structure at the final stage, after the lining's installation.

2.2 Probabilistic model – Stochastic input parameters

The geotechnical conditions play a primary role in tunnels designing. Due to their inherent uncertainty and spatial variability, a probabilistic analysis is needed. A 1000-point sample of unput parameters is populated using a Latin Hypercube simulation in order to assess the variability of the lining section because of the uncertainty of the surrounding ground. The selected stochastic parameters are assumed to follow a normal distribution. The same 1000-point sample is used in the FE analyses of the cross sections. The ground's Young's modulus (E_{clay}) and the lateral earth coefficient (K_o) are the stochastic parameters while the material properties of the concrete are kept deterministic. Table 1 provides an overview of the geotechnical input parameters of the probabilistic analyses.

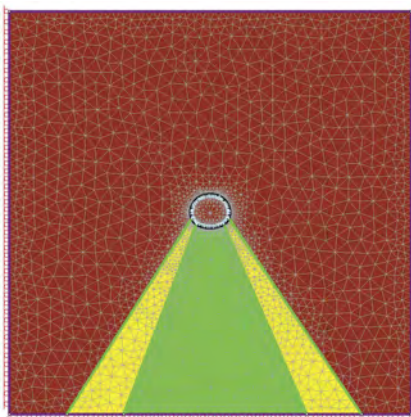


Figure 1. RS2 finite element model of the wide shape tunnel.

Table 1. Geotechnical stochastic input parameters.

Soil Property	Units	Mean value	Standard deviation
E_{clay}	MPa	300	75
E'_{clay}	MPa	140	35
Soil layer (2x E_{clay})	MPa	600	150
Soil layer (3x E_{clay})	MPa	900	225
K_o	-	1	0.1
Unit weight	MN/m ³	0.02	-
Peak friction angle	°	25	-
Peak cohesion	MPa	0.1	-

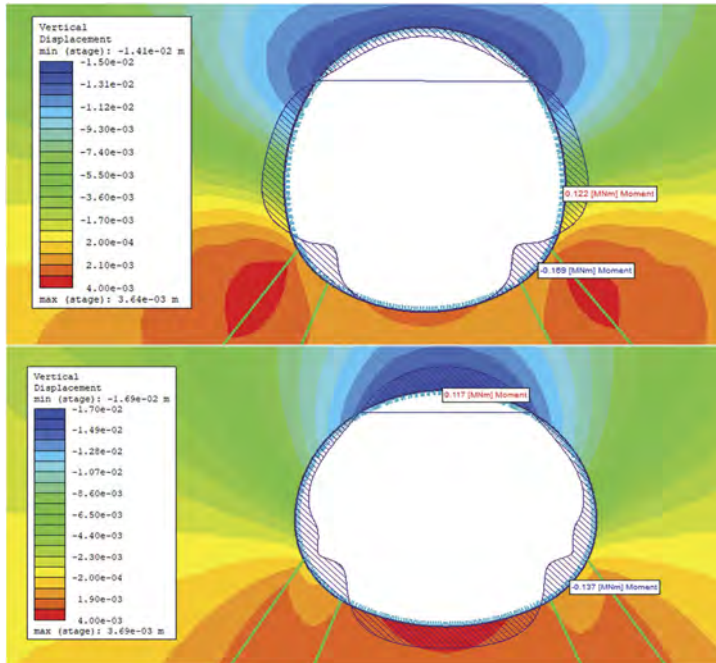


Figure 2. Vertical displacement – Bending moment diagrams of wide cross section (top) and tall cross section (bottom) in RS2.

2.3 RS2 Probabilistic analyses results

The results of the probabilistic analyses, under gravity load, confirm that the expected ground's heave occurs only underneath the tunnel's cross section while the expected settlement occurs at the crown respectively. Hence for both the cross sections, the heave/settlement ratio in long-term ground conditions is approximately equal to 1/3, proving the initial theoretical assumption about ground stiffer unloading response. According to the bending moment diagrams displayed at cross sections circumference (Figure 2), two curvatures for each tunnel shape are obtained and are utilized as study cases in Ansys structural analyses. The points where the bending moment is equal to zero at tunnel's crown define the cross section that is used subsequently in Ansys software assumed as an approximate location of hinge support (see horizontal line in Figure 2). The selected curvature is considered as the most critical for the function of the whole tunnel structure. The vertical displacement at the crown is 17 mm and 14 mm for the wide and tall cross section geometry respectively. Based on these values, the load conditions in Ansys are back-analysed accordingly in order to achieve the same displacements.

3 STRUCTURAL FINITE ELEMENT SIMULATION

3.1 *Simulation design process*

In the present study, the Static Structural system of Ansys workbench (Version 2020 R1) is utilized for the finite element analysis (FEA), as the most suitable for the investigation of the behaviour of tunnel concrete linings with interface shear connectors. The two cross sections extracted from the RS2 bending moment diagrams are designed accordingly in Ansys design modeler. The curvature for both cross sections is different due to the different bending moment diagrams in RS2 as a result of the unlike tunnel shape. The wide shape's cross section length is 5m while the tall shape's length is 5.7m respectively. 2D plain strain analyses are implemented. The two tunnel linings are 0.3m thick and are modelled with a bilinear material law for concrete with yield stress equal to 50 MPa. The steel Young's modulus is equal to 25000 MPa and the Poisson's ratio is equal to 0.2. The mesh is modelled by triangular-rectangular linear elements with a size of 0.05m. Each lining is supported by nodal supports at the middle of their thickness for both edges. Rotational movement is permitted by the left nodal support while horizontal displacement is allowed by the right one.

In order to achieve the RS2 crown displacement in Ansys, several preliminary parametric analyses were carried out. The scope of these parametric analyses was to identify the load which causes the same crown displacement indicated by Table 2. For both cross sections, the interface's contact was considered fully bonded, assuming a system thickness of 0.6m, and a uniform load was applied at the upper surface of the primary lining. Nodal supports were selected at the mid-span of the system's thickness allowing rotational displacement on the left side and horizontal movement on the right one. The concrete material was kept elastic with Young's modulus of 25000 MPa and Poisson's ratio of 0.2. Indeed, this led to identical crown displacements for both cross sections and the estimated uniform load was used subsequently for the FE structural analyses of the two concrete linings with mechanical interface shear connection.

3.2 *Specifics of modelling of dowel interface reinforcement*

As mentioned before, the scope of the present study is to report investigations on the novel theory of connecting tunnel concrete linings with shear connectors, e.g., dowels, which potentially may lead to composite behaviour. Given the complexity of the problem, a series of assumptions were adopted. In construction, the shear connectors are spatially dispersed throughout the entire length of the tunnel. Considering the two-dimensional design of the simulations, the diameter of the shear connectors was intentionally increased in order to correspond to one-meter investigation length. The total cross-sectional amount of steel was 36 cm². In total two configurations of shear connectors were investigated. The first configuration consists of 2 shear connectors placed at a distance of 1/4 of the linings' total length from the supports. The second configuration consists of 4 shear connectors that are placed at an even distance of 1/4 of the linings' length from each other, thus allowing a clearance of 1/8 of the total length from the supports (see Figure 3). The shear connectors in both configurations have a length of 0.3m and are placed in such a way in order to bridge the two concrete linings forming the interface connection between them. Each lining is penetrated equally by 0.15 m shear connectors length. In the configuration of the two shear connectors, the 2D width of each is equal to 0.060 m while in the four shear connectors configuration, the 2D width of each is equal to 0.030 m. The shear connectors were modelled by surface elements with a typical elastic material of steel with Young's modulus of 200000 MPa and a Poisson's ratio of 0.2. For the simulation of the interface between the concrete linings and the shear connector, a perfectly bonded contact was applied. The slip of the shear connectors was considered to be outside of the scope of this study. The interface between the concrete linings was considered frictionless in order to highlight the contribution of the shear connectors to the performance of the whole system. Two extreme cases without shear connectors were additionally evaluated, that of two concrete linings with frictionless interface and a fully bonded one. These two served as benchmarks in order to estimate the influence of the shear connectors on the system's structural response. The study cases in conjunction with the number of shear connectors and the concrete linings interface are summarized below:

- Case study 1: No shear connectors, frictionless interface
- Case study 2: Two shear connectors, frictionless interface

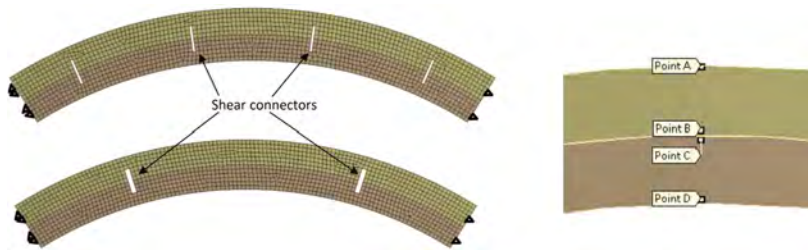


Figure 3. Wide shape cross section mesh in conjunction with shear connectors and boundary conditions (left); locations of interest/points of data extraction for the structural assessment (left).

- Case study 3: Four shear connectors, frictionless interface
- Case study 4: No shear connectors, fully bonded interface

3.3 Simulation results of arch with advanced interface configuration

For both cross sections, the most critical area is at the mid span where the maximum vertical displacement occurs. Two study points for each lining were chosen, one at the upper part of the lining and one at the bottom part. All the study points were aligned vertically at the centre of the linings mid-span. Vertical displacements, stresses and strains are the structural parameters which are evaluated by the structural analyses. Figure 3 shows the four investigating points. For these four locations, both strains and stresses are recorded while the vertical displacement is recorded only for the bottom points i.e., Points B and D. This differentiation is due to the fact that the vertical displacements at both points of each lining have insignificant differences.

From the first sight of the vertical displacement results, it can be seen that the concrete linings geometry plays a significant role. This becomes more evident when there is no means of shear transfer at the interface of the two linings i.e. frictionless interface. The frictionless case is the worst study case scenario in terms of maximum displacement and the most uneconomical design methodology (Figure 4). In these figures, it can be observed that there is a significant difference in distribution of the vertical displacement. The most uniform case is that of the two fully bonded linings which proves that they perform as a composite system. For both cross sections, the case with the four shear connectors exhibits a very similar behaviour to that of the fully bonded linings. On the other hand, the study case with the two shear connectors presents a unique vertical displacement distribution where the secondary lining has a greater deformation than the primary lining. This phenomenon becomes more obvious in the case of the tall cross section. Such a differential displacement between the primary and the secondary lining can potentially pose a threat to the performance of the waterproofing membrane and overall system's safety..

In Figure 5, the distribution of the stresses within the concrete layers is presented by the contour plots. Like in the case of the vertical displacement, the geometry, the interface connection and the combination of them impact the stresses distribution within the concrete linings. The frictionless case exhibits the highest stresses for both cross sections. It can be seen that in both linings there are both compression and tension zones. This proves that the two concrete linings work as two discrete bodies. On the contrary, for the bonded scenarios, there is clearly one single compression and tension zone indicating that the concrete linings work together as one body. The more evenly installed shear connectors can lead to a behaviour closer to that of the fully bonded. A high concentration of normal stresses is observed around the area of the shear connectors. This phenomenon is more intense in the case of the two shear connectors. Furthermore, it becomes evident that the shear connectors perform under shear loading conditions. The further the distance of the shear connectors installation position from the mid -span of the cross sections, the greater the induced load. In the case of two connectors, further insight is provided by the stress distribution regarding the phenomenon of differential vertical displacement. In the upper lining, compressive stresses are mostly observed, while the bottom lining works under significant tensile stresses. This indicates that between the two connectors, the linings behave as a truss system. Where the upper lining operates as a compression element and the bottom part as a tensile element. As

mentioned above, the material law for the concrete linings is that of a bilinear perfectly plastic material with a yield stress of 50 MPa. Therefore, some significantly high tensile stresses that are unrealistic for concrete elements can be seen, especially for the frictionless case.

4 CONCLUSIONS

This study investigates the ability of dowels (considered here predominantly as post-installed anchors) to act as structural fastening to reinforce the interface between the primary and secondary sprayed and cast concrete tunnel linings. The composite performance of such a system is examined in relation to the tunnel geometry and the dowels' spatial arrangement. In total, two different cross sections are simulated based on a combination of geotechnical and structural FE software.

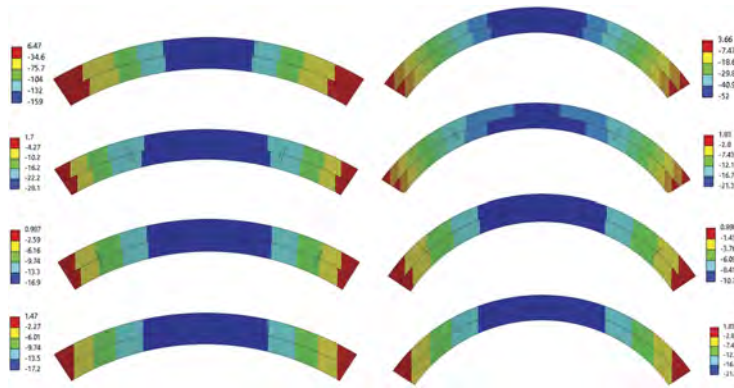


Figure 4. Vertical displacement (mm) contour plots of the wide cross section (left) and the tall cross section (right) for every case (top down view: frictionless, 2 shear connectors, 4 shear connectors and bonded).

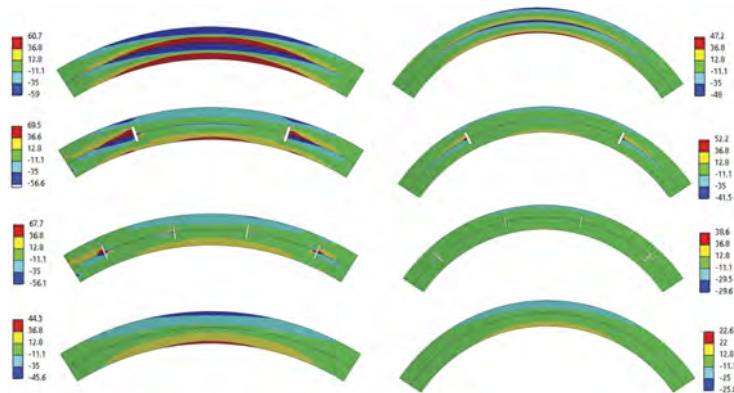


Figure 5. Stress (MPa) distribution contour plots of the wide cross section (left) and the tall cross section (right) for every case (top down view: frictionless, 2 shear connectors, 4 shear connectors and bonded).

For each configuration, two scenarios of dowels' arrangement are assumed and compared with two extreme cases of interface connection. Besides two types of ovalized cross sections (long and tall) are considered. According to the findings, the cross sections geometry plays a significant role in the structural behaviour of concrete linings with any type of combined or composite action in the long-term. The most influential factor though is the ability to transfer shear through the interface between the concrete linings. Particularly, the configuration with the four shear connectors, for both cross sections, tends to acquire a composite behaviour identical to the one with a fully bonded interface. On the other hand, the configuration which consists of two shear connectors allows some slippage between the linings: a relative displacement between the secondary and the primary lining is observed which could potentially lead to higher bending resistance requirements

Table 2. Concentrated strain values for the study points A to D.

Type	Case	Primary lining		Secondary lining	
		Point A	Point B	Point C	Point D
Wide shape cross section	Frictionless	-2.1	2.1	-2.1	2.1
	2 dowels	-1.3	0.2	-1.0	1.8
	4 dowels	-1.2	0.0	-0.4	1.3
	Bonded	-1.7	-0.1	-0.1	1.6
Tall shape cross section	Frictionless	-1.7	1.2	-1.6	1.8
	2 dowels	-0.6	0.0	-0.5	0.8
	4 dowels	-0.5	-0.1	-0.2	0.6
	Bonded	-1.0	-0.2	0.0	0.9

and hence additional material consumption (concrete/steel) and, accordingly, excavation volumes, with immediate impacts on the overall system's structural as well as sustainability performance. This highlights the necessity to consider the geometrical particularities of such systems and optimise them in terms of curvature and fasteners distribution. Further investigations on the application of post-installed dowels between sprayed/cast concrete tunnel linings can lead to enhanced reliability in the composite lining behaviour of the system and open the ways for more sustainable design solutions by reducing the concrete lining thickness and overall life-cycle requirements for materials.

REFERENCES

- EOTA TR 066:2019-04 – EOTA Technical Report, *Design and requirements for construction works of post-installed shear connection for two concrete layers*, April 2019
- Heinrich, J., Zenk, T., & Maurer, R. 2019. Bewehrte Beton-Beton-Verbundfugen bei nachträglicher Verstärkung: Statische Tragfähigkeit. *Bauingenieur*, 94(11).
- Johnson, R. P., Swallow, F. E., & Psomas, S. 2016. Structural properties and durability of a sprayed waterproofing membrane for tunnels. *Tunnelling and Underground Space Technology*, 60, 41–48.
- Johnson, R.P. 2018. Composite Structures of Steel and Concrete: beams, slabs, columns and frames for buildings. John Wiley & Sons.
- Kwon, G., Engelhardt, M. D., & Klingner, R. E. 2010. Behavior of post-installed shear connectors under static and fatigue loading. *Journal of Constructional Steel Research*, 66(4),532–541.
- López-Carreño, R. D., Carrascón, S., Aguado, A., & Pujadas, P. 2020. Mechanical Connectors to Enhance the Interfacial Debonding of Concrete Overlays. *Applied Sciences*, 10(11), 3876.
- Nakashima, M., Hammer, A. L., Thewes, M., Elshafie, M., & Soga, K. 2015. Mechanical behaviour of a sprayed concrete lining isolated by a sprayed waterproofing membrane. *Tunnelling and Underground Space Technology*, 47, 143–152.
- Palieraki, V., Vintzileou, E., & Silva, J. F. (2022). Interface Shear Strength under Monotonic and Cyclic Loading. *ACI Structural Journal*, 119(3).
- Palieraki, V., Vintzileou, E., & Silva, J. F. 2021. Behavior of RC interfaces subjected to shear: State-of-the-art review. *Construction and Building Materials*, 306, 124855.
- Randl, N. (2013). Design recommendations for interface shear transfer in fib Model Code 2010. *Structural Concrete*, 14(3),230–241.
- Spyridis, P. 2014. Adjustment of tunnel lining service life through appropriate safety factors. *Tunnelling and underground space technology*, 40 (2014), 324–332.
- Spyridis, P., Bergmeister K. 2023a. Life cycle and sustainability impact of composite and combined concrete tunnel linings. In: *IALCCE – 8th Internatioanl Symposium on Life-Cycle Civil Engineering 2023, Milan (in press)*
- Spyridis, P., Bergmeister K. 2023b. Optimizing the climate impact of tunnel structures by advanced numerical simulations In: *Proceeings of the World Tunnel Conference 2023, Athens*
- Spyridis, P., Konstantis, S., & Gakis, A. 2016. Performance indicator of tunnel linings under geotechnical uncertainty. *Geomechanics and Tunnelling*, 9(2),158–164.
- Su, J., & Bloodworth, A. 2016. Interface parameters of composite sprayed concrete linings in soft ground with spray-applied waterproofing. *Tunnelling and Underground Space Technology*, 59, 170–182.
- Vintzileou, E., & Palieraki, V. 2007. Shear transfer along interfaces in repaired/strengthened RC elements subjected to cyclic actions. *Beton-und Stahlbetonbau*, 102(S1), 60–65.
- Vogel, F., Sovják, R., & Pešková, Š. (2017). Static response of double shell concrete lining with a spray-applied waterproofing membrane. *Tunnelling and Underground Space Technology*, 68, 106–112.

SS16: Risk-informed life-cycle management of bridges
Organizers: I. Venanzi, M.P. Limongelli & U. Alibrand



Taylor & Francis

Taylor & Francis Group

<http://taylorandfrancis.com>

SHM-informed management of bridges in a life-cycle perspective

L. Ierimonti, F. Mariani, I. Venanzi & F. Ubertini

University of Perugia, Perugia, Italy

ABSTRACT: Recent bridge failures highlighted that bridges are key elements for guaranteeing the functionality of transportation systems. The main causes of bridge's deterioration are the exposure to environmental conditions and the steadily increase of traffic volume. Hence, timely maintenance interventions are crucial to guarantee adequate performance levels. To the purpose, the actual practice is mainly based on visual inspections. Recently, the "Guidelines for risk classification and management, safety assessment and monitoring of bridges" issued in 2020 by the Italian Ministry of Sustainable Mobility promoted the use of Structural Health Monitoring (SHM) systems. Hence, the goal of the present work is to develop a general framework able to evaluate the costs and benefits of different SHM-based strategies in a life-cycle perspective. The results highlight the twofold potentiality of the proposed framework in quantifying and updating in a unified manner the bridge's lifetime expenses, and in comparing different alternatives of SHM systems.

1 INTRODUCTION

The extensive use of SHM on real-world structures is strongly limited because of the difficulty in quantifying the benefit of monitoring systems, which have non negligible installation and maintenance costs. Recently, probabilistic-based framework are developed with the main objective of quantifying the value of SHM in a life-cycle costs perspective (Thöns 2018, Kamariotis et al. 2023). Indeed, Life Cycle Cost Analysis (LCCA) is commonly considered an important technique for assisting investment decisions, since it allows to compute, in a probabilistic setting, the total lifetime cost, accounting for all the possible cost sources like initial costs, repair and maintenance costs, inspection costs, SHM-related expenses, downtime costs and, eventually, disposal costs. The main idea is to assist decision making in allocating economic resources according to the best cost-benefit performance criteria. The LCCA is a widely used methodology in earthquake engineering (Wang et al. 2015) and in wind engineering (Ierimonti et al. 2019) and it is currently spreading in bridges applications (Frangopol et al. 2017, Venanzi et al. 2019, Torti et al. 2022). As underlined in (Biondini & Frangopol 2016) there is the need to further investigate the field of life-cycle performance of bridges under uncertainty in order to fill the gap between theory and practice by incorporating life-cycle concepts in structural design.

In order to gather the slowly evolving deterioration processes over the lifetime of a bridge it can be appropriate to collect relevant data continuously over time, and incorporate the extracted information into a time-dependent reliability analysis (Kim & Song 2021). In light of this, an important parameter for the buildings safety evaluation is the deflection. The inclinometers can be used as simple and inexpensive method to control the deflection during the construction life-cycle. Indeed, the measured data can be processed by analytical functions that link the values of the rotation angle with the deflection curve (Lan et al. 2019, Hou et al, 2005).

In recognition of the above mentioned needs, a LCCA-based approach in conjunction with the use of a continuous SHM system is proposed, with the aim to highlight the advantage of the use of an SHM system. The main novelty of the approach is that the structural reliability is automatically evaluated and updated continuously over time as a support to visual inspections, accounting for real time SHM data related to different Damage Limit States (DLS).

Moreover, the use of a LCCA-based framework allows to quantify in a unified manner the bridge's lifetime expenses and to perform a quantitative comparison between different alternatives of SHM systems, in terms of life-cycle costs.

The feasibility of the method is explored through numerical simulations aimed at controlling the span deflection during the years of a post-tensioned single-span concrete bridge including bridge's damage over time, environmental noise and instrumental errors.

The rest of the paper is organized as follows. Section 2 gives an overview of the theoretical background. Section 3 presents the proposed framework. Section 4 illustrates the case study. Section 5 highlights some preliminary results and Section 6 concludes the paper.

2 THEORETICAL BACKGROUND

The concepts of LCCA with a general formulation for the evaluation of the expected life-cycle is presented in (Wen & Kang 2001). According to LCCA approach, the life-cycle cost can be computed as follows:

$$E[C(T)] = C_I + \sum_{t=1}^T \left[\frac{E[C_M(t)] + E[C_F(t)]}{(1+r)^t} \right] \quad (1)$$

where $E[\]$ is the expected value, C_I is the initial cost which can be defined as the sum of the initial construction cost and the cost of the SHM system $C_I = C_0 + C_{SHM}$, C_M is the maintenance cost at time t , C_F is the cost of failure at time t , T is the bridge's lifetime, and r is the discount rate. The cost of failure C_F depends on the analyzed DLS and can be formulated as:

$$E[C_F(t)] = \sum_{s=1}^S \sum_{x=1}^K P_{f,s,x}(t) n_s c_{R,s} \quad (2)$$

where S is the total number of independent DLS s ; K is the total number of relevant sections x along the structural members; $P_{f,s,x}(t)$ is the time-dependent probability of failure evaluated for the s -th limit state at section x ; $c_{R,s}$ is the repair cost for limit state s for unit element, and n_s is the number of unit elements subjected to limit state s .

In order to compute the failure probability $P_{f,s,x}(t)$ in Equation (2), for each considered limit state and for each section, the Hasofer-Lind procedure is adopted. Probabilities of failure are calculated considering stochastic independence between all the involved random variables and treating them as normally distributed. In this way, the probability of failure is related to the well-known reliability index, which represents the shortest distance of the selected limit state function from the origin of the reference system in the space of normal standard random variables.

$$P_{f,s,x}(t) = \Phi\left(-\beta_{j,k}(t)\right), \quad (3)$$

3 THE PROPOSED FRAMEWORK

The proposed methodology consists of the steps presented in Figure 1 and summarized as follows:

1. Select possible DLS which can be monitored through the available SHM system. The sensors located along the structures allow to monitor one or more DLS.
2. Perform data analysis and pre-processing. In this phase environmental effects must be removed from original signals by means of statistical models after analyzing the time series of ambient and material temperature measurements during a training period, typically 1 year ensures the optimal calibration of the statistical models.
3. For each selected j -th DLS (such as bridge deflection) perform the reliability analysis as follows:

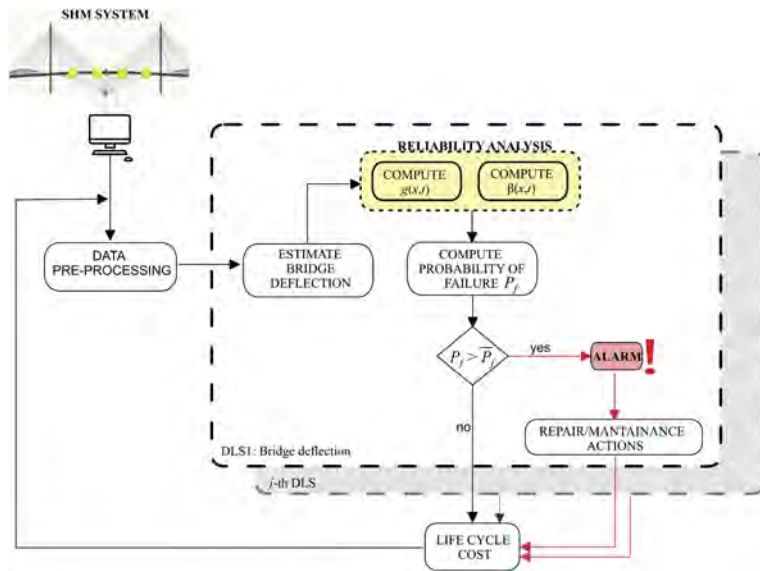


Figure 1. The proposed methodology.

DLS: BRIDGE DEFLECTION

- online estimation of bridge deflection $w(x, t)$, where x indicates the position along the bridge and t stands for time;
 - definition of limit state function $g(x, t)$;
 - online evaluation of reliability index $\beta(x, t)$;
 - evaluation of the corresponding Probability of failure P_f ;
 - if P_f exceeds a pre-defined threshold \bar{P}_f an alarm is activated and further actions are needed, then go to step 5;
 - if P_f does not exceed the threshold \bar{P}_f go to step 5.
-

4. Repeat step 3 for each DLS;
5. Evaluate the LCC and go back to step 1.

4 THE CASE STUDY

A simply supported, post-tensioned single-span concrete bridge is considered as a case study. The concrete slab, with a thickness of 0.2m is supported by 3 beams with a I-shaped cross section, modified in rectangular sections in correspondence of the supports, as represented in Figure 2. Each beam is supported by 2 gravity abutments. The total span of the bridge l is 32 m. The post-tensioning system consists of a total of 5 cables characterized by different strands. Each strand has a diameter Φ of 7 mm. Cables no. 1 and 2 at the beam extrados are composed by 32 strands, while the remaining cables (no. 3, 4 and 5) have 42 strands.

For the numerical simulations, only the permanent loads q and the pre-stress loads $q_{p,eq}$ are included in the model. The value of q is determined considering the influence area of each supporting beam as: $q = q_d + q_s + q_p + q_e$, where q_d is the beam's dead load equal to 15.8 kN/m; q_s is the upper slab load equal to 14.30 kN/m; q_p is the pavement's load equal to 3.26 kN/m; q_e refers to the superstructure's equipment and it is equal to 2 kN/m.

The equivalent pre-stress loads $q_{p,eq}$, evaluated as a uniformly distributed load, is calculated as: $q_{p,eq} = \frac{8Ne_0}{L^2}$, where N is the total axial force applied to the tendons, e_0 is the distance between the section center of gravity and tendons at the middle-span and L is the length of the tendons.

For the analyzed case study $q_{p,eq}$ is equal to 36 KN/m.

Table 1. Properties of inclinometers used in case study [Huseynov et al. 2020].

Type	Measurement Range [°]	Precision [°]	Resolution [°]	Sampling Rate [Hz]
1	±85	±3·10 ⁻²	3·10 ⁻³	100
2	±1	±4·10 ⁻³	1·10 ⁻⁴	125

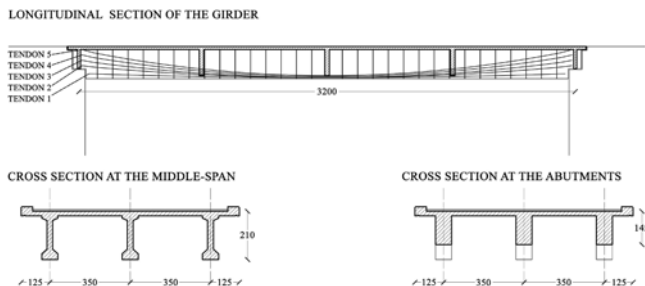


Figure 2. The case study: Longitudinal and cross sections of the bridge.

4.1 SHM system

In order to demonstrate the feasibility of the proposed framework, a monitoring system is considered installed along the structure consisting of 5 inclinometers (Figure 3), which is commonly considered the minimum number of sensors to accurately reconstruct the bridge's deflection (Lan et al. 2019). Then, monitoring data (rotations) θ^* are artificially simulated as follows:

$$\theta^* = \theta_0^*(1 + \epsilon), \quad (4)$$

where θ_0^* is the analytically measured nodal rotation at each inclinometers' position and ϵ represents the noise coefficient which accounts for measurement uncertainty associated with sensors precision.

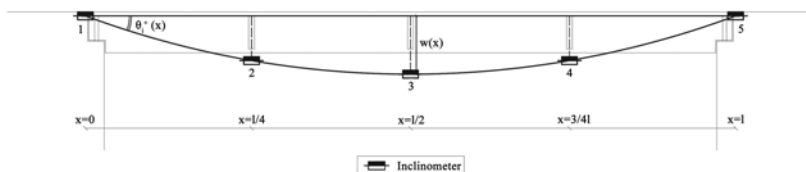


Figure 3. SHM system consisting of 5 inclinometers installed along the beam of the bridge.

For this application, two different types of inclinometer, designated as type 1 and type 2, with a different precision level are selected. Sensor's properties are summarized in Table 2 (Huseynov et al. 2020).

4.2 Degradation model

For the numerical simulations, a degradation model is adopted to reproduce the progressive decrease of concrete elastic modulus due to damage. For the purpose, a simplified degradation model is selected (Venzani et al. 2019, Biondini & Marchiondelli 2008): $E(t) = [1 - \delta(t)]E_0$ where E_0 is the nominal value and $\delta(t)$ is evaluated according to (Venzani et al. 2019).

4.3 Reliability analysis

In order to perform the reliability analysis continuously over time t , the bridge deflection is selected as a DLS and the following limit state equation is defined.

$$g_w(x, t) = \frac{L}{250} - w(x, t), \quad (5)$$

where $w(x, t)$ is the bridge's deflection that can be evaluated by means of analytical methods under predefined assumptions ($w_0(x, t)$) or experimentally using SHM data ($w^*(x, t)$). Analytically, the deflection can be evaluated according to the well known Euler-Bernoulli beam theory as follows:

$$w_0(x, t) = \left[\frac{(q(t) - q_{p,eq(t)})x}{24E(t)J(t)} \right] (l^3 - 2lx^2 + x^3) \quad (6)$$

where E_c is the concrete elastic modulus; J is the moment of inertia; l is the span of the bridge; q and $q_{p,eq}$ are defined in Section 4. Deriving Equation (6) it is possible to evaluate the rotation at the position x as follows:

$$\frac{\delta w_0(x, t)}{\delta x} = \theta_0(x, t) = \left[\frac{(q(t) - q_{p,eq(t)})}{24E(t)J(t)} \right] (l^3 - 6lx^2 + 4x^3). \quad (7)$$

According to (Lan et al. 2019), assuming that a certain number of inclinometer N are installed along the bridge, it is possible to reconstruct the bridge's deflection based on inclinometer data by means of an appropriate polynomial function:

$$w^*(x, t) = A(x) [a_1(t)x^3 + a_2(t)x^2 + a_3(t)x + a_4(t)] \quad (8)$$

where $A(x)$ is a function that respects the boundary conditions of a simply supported beams, defined as $A(x) = x(x - L)$; the terms $a_i(t)$ ($i = 1, \dots, 4$) are the unknown coefficients to be calibrated through experimental data at each time step t . Deriving Equation (8) the rotation angle function is obtained:

$$\theta^*(x) = A'(x) [a_1(t)x^3 + a_2(t)x^2 + a_3(t)x + a_4(t)] + A(x) [3a_1(t)x^2 + 2a_2(t)x + a_3(t)] \quad (9)$$

It is clear that an accurate reconstruction of the bridge deflection require at least 5 or more inclinometers (Hou et al, 2005).

A group of optimal solutions for coefficients $a_i(t)$ can be obtained by using the least square method (Lan et al. 2019) consisting in minimizing the following objective function:

$$J(a_1, a_2, a_3, a_4, t) = \sum_{j=1}^N (\theta^*(x_j, t) - \theta_j(t))^2 \quad (10)$$

where $\theta^*(x_j, t)$ is evaluated according to Equation (9) while $\theta_j(t)$ is the inclinometer's measurement recorded at position x_j .

Once the limit state function is defined, the reliability analysis can be performed and the corresponding probability of failure $P_{f,s,x}(t)$ can be evaluated, according to Equation (3). Table 1 summarizes the parameters of the probabilistic distribution of random variables (mean values and co-variance CoV) that have been used in this study (Joint Committee on Structural Safety 2000).

Table 2. Reliability analysis: the selected random variables.

No.	Variable	Symbol	Mean Value	CoV
1	Concrete Elastic modulus	E_c	32600 MPa	0.15
2	Permanent load	pp	nominal value	0.04
3	Equivalent prestress load	$q_{p,eq}$	nominal value	0.04
4	Measured deflection type 1	$\theta^*(x)$	daily measured value	0.3
5	Measured deflection type 2	$\theta^*(x)$	daily measured value	0.2

Without loss of generality the following cases are analyzed and compared in the numerical simulations: (1) case a), without SHM (w/o SHM), i.e., without the use of monitoring data (selected no. variables 1,2 and 3);(2) case b), with SHM type 1 (selected no. variable 4); (3) case c), with SHM type 2 (selected no. variable 5).

4.4 Life-cycle cost analysis

Total expected life-cycle cost is computed according to Equations (1)-(2) where a discount rate $r = 0.05$ is adopted. Preliminary, in order to demonstrate the potential benefit of the proposed framework, initial costs C_I and maintenance costs C_M are neglected. The repair cost is defined according to (Zhang et al.2022): $c_R = 2 \cdot 10^2 \text{ €}$.

5 PRELIMINARY RESULTS

This section summarizes preliminary results and observations from the LCC-based analyses conducted on the selected case study.

Preliminary, in order to study the influence of the CoV values presented in Table 2, a parametric analysis is carried out by varying CoV from 0.02 to 0.2 for E , q and $q_{p,eq}$. Results illustrated in Figure 4 highlight that index β is strongly influenced on CoV variations of E , meaning that adopting different CoV values for q and $q_{p,eq}$ would not significantly affect the results.

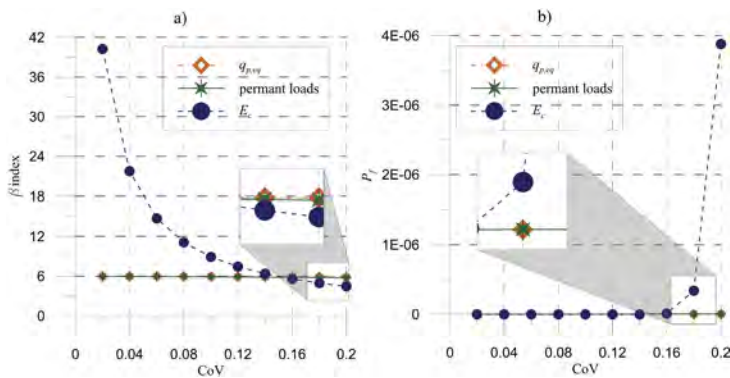


Figure 4. Parametric analysis for the case w/o SHM carried out by varying CoV from 0.02 to 0.2 for E , q and $q_{p,eq}$: a) minimum value of β ; b) corresponding values of P_f .

Then, SHM data are simulated according to Equation (4) with $T = 182500$ days, i.e. 50 years, on a hourly basis. The simulation accounts for the possible concrete degradation, e.g. time-dependent reduction of the Elastic modulus, as reported in Section 4.2. The simulated θ values are averaged on a daily basis.

In Figures 5a)-b) can be depicted some realizations of the bridge's deflection, numerically reconstructed from the simulated SHM data considering type 1 and type 2 inclinometers for a time period $t=35$ days with 1 realization per day. From the figure it can be noted that type 1 results (Figure 5a) have a higher dispersion, due to the lower precision of the selected sensor (see Table 1).

Finally, Figures 6a)-b) summarize the minimum values of β for the cases w/o SHM, with SHM type 1 and with SHM type 2 for the E -related degradation model. It can be observed that the degradation model has a non negligible influence on the reliability index, whose values decreases with time. Moreover, it can be observed the use of a SHM allows to dramatically reduce the intrinsic uncertainty related to the reliability analysis, thanks to the increased level of knowledge, providing higher values of β , which correspond to almost null values of the probability of failure during the analyzed bridge's lifetime (50 years). In addition, the different precision of the sensors type 1 and type 2 leads to a percentage difference of about 25 % in the evaluation of β . It is worth noticing that the values of β obtained in the cases with SHM entail very small values of $E[C_F]$,

due to the very small values of the associated probability of failure. Table 3 summarized the percentage of $E[C_F]$ evaluated at $t=100$ years. For instance, the cost $E[C_F]$ evaluated for the case w/o SHM has an increment of $1.15 \cdot 10^3$ % for the case with SHM type 1 and of $5.3 \cdot 10^{13}$ % for the case with SHM type 2, while type 1 has a percentage increment of $4.6 \cdot 10^{10}$ % with respect to type 2. Without loss of generality, these preliminary results highlight the benefit related to the use of SHM systems in terms of reliability and the potential benefit in terms of LCC, considering the fact that a complete LCCA needs accounting for all the possible DLS and cost components along the bridge's lifetime.

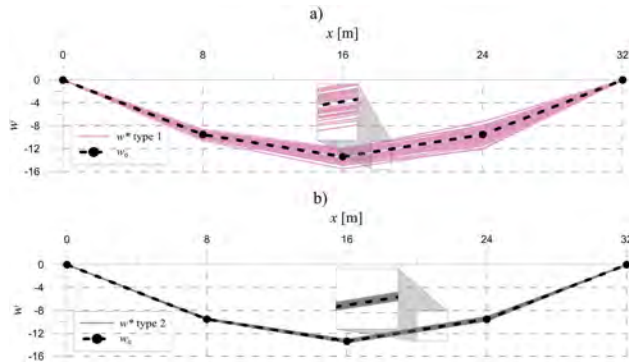


Figure 5. Realizations of simulated deflections (in mm) using type 1 (a) and type 2 (b) inclinometers.

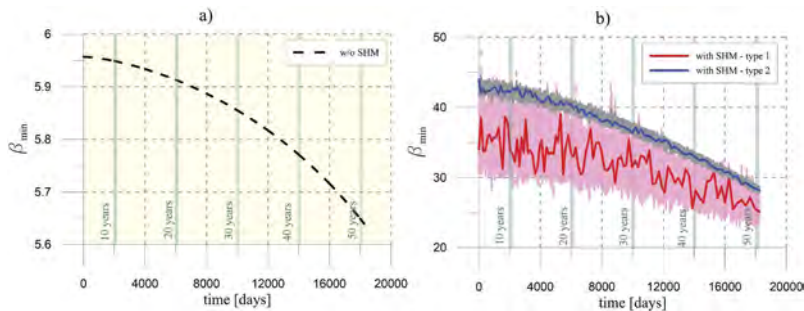


Figure 6. β index over time: a) w/o SHM; b) with SHM type 1 and type 2.

Table 3. Percentage difference (increment) for the total repair cost $E[C_F]$ at $t=100$ years evaluated considering type 1 and type 2 cases with respect to the case w/o SHM and type 1 vs type 2.

	w/o SHM vs type 1	w/o SHM vs type 2	type 1 vs type 2
Increment [%]	$1.15 \cdot 10^3$	$5.3 \cdot 10^{13}$	$4.6 \cdot 10^{10}$

6 CONCLUSIONS

The present paper has proposed an automatic framework for the life-cycle cost analysis of bridges. The feasibility of the method is explored through numerical simulations aimed to control the span deflection during the years of a post-tensioned single-span concrete bridge, including damaging and pres-tress losses, environmental noise and instrumental errors suffered by the measurements. The procedure accounts in a simplified manner for material degradation by introducing the dependency on time of a damage-dependent parameter. Preliminary results confirm that the use of SHM systems allow to reduce the probability of failure and, consequently, the LCC over time, due to the higher knowledge acquired on the structural condition.

The framework facilitates the estimation of the benefits associated with continuous SHM information in order to optimize the SHM strategies before implementation. The procedure is general and can be easily populated with different DLS. The idea is to develop an efficient and adaptive strategy including other types of DLS in conjunction with different sources of information (such as visual inspections and so on) in order to firstly identify the best SHM strategy and then optimize maintenance works over the service life of a deteriorating structure under changing environments.

ACKNOWLEDGMENTS

The Authors would like to acknowledge the support of the project “Study and methodological analysis of the instrumental monitoring procedures of infrastructural works, with particular attention to the cost aspects and benefits in the bridges life-cycle (bridge life-cycle cost analysis - BLCCA)” funded by the FABRE consortium, a research consortium for the assessment and monitoring of bridges and viaducts and other structures.

REFERENCES

- Thöns, S. 2018. On the Value of Monitoring Information for the Structural Integrity and Risk Management. *Computer-Aided Civil And Infrastructure Engineering* 33: 79–94.
- Kamariotis, A., Chatzi, E. & Straub, D. 2023. A framework for quantifying the value of vibration-based structural health monitoring. *Mechanical Systems And Signal Processing* 184: 109708
- Wen, Y. & Kang, Y. 2001. Minimum building life-cycle cost design criteria. I: Methodology. *Journal Of Structural Engineering New York, N. Y.* 127: 330–337
- Wang, C., Zhai, M., Li, H., Ni, Y. & Guo, T. 2015. Life-cycle cost based maintenance and rehabilitation strategies for cable supported bridges. *Advanced Steel Construction*. 11(3): 395–410
- Ierimonti, L., Venanzi, I., Caracoglia, L. & Materazzi, A. 2019. Cost-Based Design of Nonstructural Elements for Tall Buildings under Extreme Wind Environments. *Journal Of Aerospace Engineering*. 32 (3): 04019020
- Frangopol, D., Dong, Y. & Sabatino, S. Bridge life-cycle performance and cost: analysis, prediction, optimisation and decision-making. 2017 *Structure And Infrastructure Engineering*. 13(10): 1239–1257
- Venanzi, I., Castellani, R., Ierimonti, L. & Ubertini, F. 2019. An Automated Procedure for Assessing Local Reliability Index and Life-Cycle Cost of Alternative Girder Bridge Design Solutions. *Advances In Civil Engineering*.
- Torti, M., Sacconi, S., Venanzi, I. & Ubertini, F. 2022. Monitoring-Informed Life-Cycle Cost Analysis of Deteriorating RC Bridges under Repeated Earthquake Loading. *Journal Of Structural Engineering (United States)*. 148(9):04022145
- Biondini, F. & Frangopol, D. 2016. Life-cycle performance of deteriorating structural systems under uncertainty: Review. *Journal Of Structural Engineering (United States)*. 142(9): F4016001
- Kim, J. & Song, J. 2021. Time-Dependent Reliability Assessment and Updating of Post-tensioned Concrete Box Girder Bridges Considering Traffic Environment and Corrosion. *ASCE-ASME Journal Of Risk And Uncertainty In Engineering Systems, Part A: Civil Engineering*. (7)4: 04021062.
- Lan, R., Wang, Y. & Chi, Q. 2019. Reconstitution of Static Deflections of Suspension Bridge Based on Inclinometer Data. *IOP Conference Series: Earth And Environmental Science*.
- Hou, X., Yang, X. & Huang, Q. 2005. Using inclinometers to measure bridge deflection. *Journal Of Bridge Engineering*.
- Huseynov, F., Brownjohn, J. M.W., O'Brien, E. J., Kim, C., Chang, K.C. & Hester, D. 2020. Bridge damage detection using rotation measurements—Experimental validation. *Mechanical Systems and Signal Processing*.
- Joint Committee on Structural Safety, 2000. Joint Committee on Structural Safety, Probabilistic Model Code, Chap. Part 3: Material Properties.
- Biondini, F. & Marchiondelli, A. 2008. Evolutionary design of structural systems with time-variant performance. *Structure and Infrastructure Engineering*. 4(2): 163–176.
- Zhang, W., Qin, J., Lu, D., Thöns, S. & Faber, M. 2022. VoI-informed decision-making for SHM system arrangement. *Structural Health Monitoring*. 21: 37–58.
- European Committee for Standardization, 2005. Basis of structural design, Eurocode 0: EN 1990, Brussels, Belgium.

Integration of MCDM-based regional flood hazard indexing with the Cerema guidelines for risk assessment of riverine bridges

M. Loli

Grid Engineers, Athens, Greece

G. Kefalas

International Hellenic University, Thessaloniki, Greece

S. Dafis

National Observatory of Athens, Athens, Greece

Data4Risk, Paris, France

S.A. Mitoulis

University of Birmingham, UK

F. Schmidt

Université Gustave Eiffel, Champs-Sur-Marne, France

ABSTRACT: Due to their location, across rivers and streams, bridges often interact with torrential, erosive flows, suffering (1) transient loads of high magnitude, due to flow obstruction, and (2) loss of support, due to scour. To take both components (1) and (2) into account, hazard evaluation is here based on the introduction of an integrated indicator of flood hazard intensity (IFHI). This is an extension of the existing Flood Hazard Index, which is increasingly used to map flood inundation. IFHI is appropriate for the evaluation of bridge susceptibility because it embeds the key parameters of flow velocity, flow obstruction, and sediment characteristics, in addition to inundation height. IFHI is found useful for streamlining the application of the scour hazard indicators recently included in the French guidelines (CEREMA, 2019). Combined with a high-level vulnerability model, it is implemented for a prediction of flood-induced bridge damages across the road and rail network of the Karditsa county in Central Greece. The region was the hot spot of large-scale flooding after a Mediterranean cyclone in September 2020. Comparison between predicted and observed response for 16 bridges, which were inspected after the same flood, allowed validation of the framework's predictive accuracy across the entire range of damage levels, from minimal damage to complete failure. Results verify that IFHI is a suitable hazard indicator yielding reasonably accurate predictions of bridge response to flood hazard impacts, for engineering applications.

1 INTRODUCTION

The Multi-Criteria Decision-Making (MCDM) method is the most popular empirical approach to flood hazard assessment (e.g.: Arabameri et al., 2019; Dodangeh et al., 2020; Kazakis et al., 2015; Papaioannou et al., 2015; Tripathi et al., 2022). It relies on the expert judgment of a decision-maker for the identification and ranking of a set of conditioning criteria (flood controlling parameters).

To the authors' best knowledge, the MCDM framework has been used to date for the characterization of flood hazard only in terms of a location's susceptibility to inundation,

parametrized by floodwater height (h_w). The approach is useful when the main concern is functionality loss due to the submergence of land or infrastructure. However, h_w alone is not adequate to describe the impact of flooding on bridges, because structural failure is influenced by flow – soil – structure interaction mechanisms. The latter are critically dependent on flow velocity (U), which affects the magnitude of hydrodynamic loads as well as scour penetration. Therefore, incorporation of U in the description of flood hazard intensity is key for the evaluation of flood impacts on bridges, especially as they often interact with high-velocity, torrential flows, depending on the type of flood and on the environment.

Here, it is advocated that the AHP-based MCDM method, as implemented in the relevant literature, can be adopted for mapping the spatial variation of U , as well as h_w , provided that the controlling parameters are ranked and evaluated appropriately (as detailed in Loli et al., 2022b). This enables a more comprehensive assessment of hydraulic actions for bridge-specific analysis of flood risk.

The MCDM framework is implemented for the evaluation of the impact of flooding on bridges, through an approach that considers the mechanisms governing flow–structure interaction. The endeavor relies on the extension of the existing methodology, currently used to evaluate the height of floodwater, to simultaneously consider the spatial variation of flow velocity. A new index, namely the Index of Flood Hazard Intensity (IFHI), is introduced combining both components in one measure of flood hazard intensity. IFHI fits squarely in the risk-based framework for the assessment of scour risk, recently included in the French guidelines (CEREMA, 2019; Durand et al., 2018). This paper provides a synopsis of a recent study (Loli et al., 2022b), setting a roadmap for use of a bridge-specific flood risk assessment framework, focusing on the realistic prediction of bridge damage in intense flood events.

2 METHODOLOGY

Figure 1 displays the methodological framework. It includes three core modules, where hazard, vulnerability, and consequences are assessed independently. Assessment of damage is carried out at the asset scale integrating hazard (through the IFHI) with a simple, but reliable, vulnerability model, fused with basic engineering parameters relevant to the design, construction, and maintenance characteristics of the structure. By contrast, a systemic perspective is adopted for the assessment of consequences. The three components are integrated via interaction matrices. The classification of hazard and vulnerability in three classes from 1– 3, i.e., from low to high, allows the construction of a 3x3 damage prediction matrix, which yields the predicted DL of the specific asset.

C is the key to the scaling-up of the analysis from asset level to the system level. It is evaluated based on parameters that correlate bridge damage with the associated impact on the transport network and its users. Considering C in conjunction with DL yields an estimate of Risk (R), on a scale from of 1 to –5.

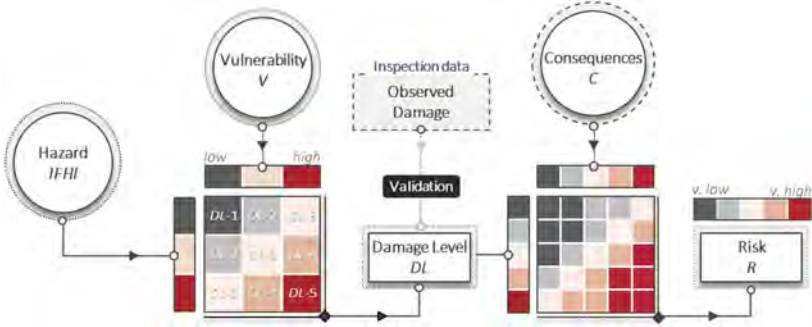


Figure 1. The methodological framework for the assessment of flood-induced bridge damage and the associated system (network) risk.

The framework is implemented to study flood risk in the county of Karditsa, (Central Greece), a flood-prone area which suffered widespread devastation, including tens of failed bridges, after the passage of a catastrophic cyclone in September 2020 (known as Medicane Ianos, Loli et al., 2022a,b; Zekkos et al., 2020). The analysis of this case study offered an opportunity for verification of the method based on a comparison of predicted bridge damage with damage observed in the field.

2.1 Index of Flood Hazard Intensity (IFHI) for bridges

The two main factors of flood-induced damage on bridges, namely the hydrodynamic loads and scour, are essentially dependent on the magnitude of flow velocity (U), as well as water height (h_w). Importantly, high values of U are generally expected in steep terrains, while, on the contrary, increased water heights are expected on flat grounds. Owing to this antithesis, assessment of bridge response to flooding on the basis of h_w alone can lead to misleading, even unsafe, predictions, although h_w is broadly used as a flood intensity measure, suitable for problems where functionality loss due to accumulation of water volumes is the main concern.

Here, U and h_w were considered in the evaluation of hazard by introduction of a combined indicator, namely the Index of Flow Intensity (IFI). As shown in Figure 2, IFI can be evaluated at regional scale after classification and synthesis of qualitative maps of the expected water height (represented by the Water Height Index, WHI) and the expected flow velocity (according to the Water Velocity Index, WVI). As presented in detail in Loli et al. (2022b), layers of WHI and WVI can be produced using MCDM analysis of geomorphological, meteorological, hydrological, and land use/cover data, based on the exploitation and processing of satellite images and relevant global datasets in GIS.

To also account for scour, *IFI* is integrated with a set of indicators (namely $A1$, $A2$, and $A3$) which represent susceptibility to scour (general scour, contraction scour, and local scour, respectively). To this end, the scoring method for scour hazard assessment proposed by the CEREMA guidelines is adopted, as summarized in Table 1.

Then, *IFHI* is introduced as an indicator that incorporates all the above components in one index of flood hazard intensity:

$$IFHI = (A1 + A2 + A3) IFI \quad (1)$$

Table 1. Indicators of scour susceptibility.

Symbol	(Sub)Indicator of	Scoring
A1.1	Flow conditions	=1, if U = very low; 2, if U = low; 3, if U = medium; 4, if U = high; 5, if U = very high.
A1.2	Riverbed	=0, for rock; 1, for blocks; 1.6, for gravel; 2.8, for cohesive soil; 3.5, for sands.
A1	General scour susceptibility	= 2A1.1A1.2-5
A2	Contraction scour susceptibility	=0.5 for $l/W < 0.1$; 1, for $0.1 \leq l/W < 0.2$; 2.5, for $0.2 \leq l/W < 0.3$; 4, for $0.3 \leq l/W < 0.4$; 6, for $l/W \geq 0.4$, where l is the bridge length and W is the channel width.
A3.1	Indicator of local scour susceptibility	=0 for $B/W < 0.02$; 1.5, for $0.02 \leq B/W < 0.1$; 2.5, for $0.1 \leq B/W < 0.2$; 3.5, for $B/W \geq 0.4$, where B is the width of the widest support obstructing the flow.
A3.2	Support Alignment/ Shape effects	=0 for symmetric supports and well aligned with the flow; 2, for oblong supports; 3. For highly skewed supports.
A3.3	Riverbed morphodynamics	=1.1 for a fixed riverbed; 1.3 for riverbeds with dunes/mobile sandbags.
A3.4	Sub-indicator: Riverbed	=0, for rock; 0.4, for blocks and gravel; 1, for soil.
A3	Indicator of local scour susceptibility	= 1.2 A3.1A3.2A3.3 A3.4A1.1

2.2 Scoring of bridge vulnerability to flood impacts

The predisposition of a structure to be adversely affected by a flood of standard magnitude is viewed as a function of the structure’s physical characteristics and assessed based on a simple but reliable model, fused with basic engineering parameters relevant to the design, construction, and maintenance properties of the structure, using the indicators that are summarized in Table 2.

Following the CEREMA guidelines, vulnerability (V) is defined as the total of three components: the vulnerability of the foundations (V1), the vulnerability of the superstructure (V2), and the sensitivity of the deck to the movements of its supports (V3).

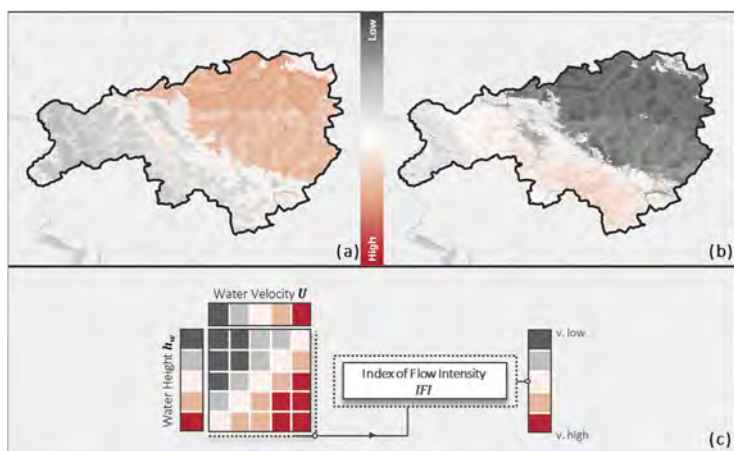


Figure 2. Flood hazard assessment integrating (a) prediction of water height (WHI) and (b) prediction of water velocity (WVI) for estimation of (c) flow intensity (IFI).

Table 2. Indicators of bridge vulnerability.

Symbol	(Sub)Indicator of	Scoring
V1.1	Construction age	= -1, for structures constructed after 2000; 1, for constructions dating from 1985 – 1999; 3, for constructions dating from 1955 – 1984; 5, for constructions dating before 1954.
V1.2	Foundation type	= 2, for piles and deep caissons; 5, for embedded foundations; 6, for RC surface footings; 10, for masonry or wooden foundations.
V1.3	Surveillance level	= 0, if surveillance data exist showing good condition; 4, in case that no surveillance information is available.
V1	Indicator of foundation vulnerability	$V1 = V1.1 + V1.2 + V1.3$
V2.1	Construction material	= 1, for metal/RC in good condition; 2, for metal/RC in bad condition; 3, for masonry structures.
V2.2	Pier shape	= 0, for sharp cutwater; 0.5, for cylindrical support or circular cutwater; 1, for rectangular supports.
V2	Indicator of superstructure vulnerability	$V2 = V2.1 + V2.2$
V3	Indicator of deck stability	= 2, for culverts of truss-bridges; 4, for other cases.

3 INSPECTION OF BRIDGE DAMAGES AFTER AN EXTREME FLOOD EVENT

On 17 September 2020, the “Ianos” Mediane struck Greece causing heavy precipitation that exceeded in various locations the mean annual precipitation. It was an extreme weather event, classified as one of the most powerful Mediterranean Cyclones recorded since 1969 (Zekkos et al., 2020; Lagouvardos et al., 2021). It affected a relatively wide area, extending from the Ionian islands to the eastern coast of the mainland. The maximum daily accumulated values,

as measured by the network of automatic meteorological stations of the National Observatory of Athens, reached up to 317 mm (peak recorded in Pertouli) and were among the highest recorded in Greece during the past decade.

The severity and spread of destruction were unprecedented. In the mountainous regions, the catastrophic consequences of flash flooding included numerous landslides, debris flows, and erosion, impacting buildings, transportation infrastructure, and powerlines. In the low-lying areas of the Thessaly Plain, large scale flooding with the inundation of over 400 km² of agricultural and urban land, caused widespread disruptions to communities and severe effects on the economic activity, especially in the city of Karditsa. The town of Mouzaki was harshly impacted. Flash flooding and overflowing of Pamissos river led to widespread erosion of its gabion-protected riverbanks, sweeping away roads, cars (causing one fatality), and riverside structures.

The reconnaissance of damage in the aftermath of Ianos offered a wealth of field evidence on the response of bridges to flood-associated impacts. Tens of bridges suffered substantial damage or complete failure, several of which were inspected during the field surveys carried out a few days after the event (Zekkos et al., 2020). Later, selected cases were also mapped in detail by employing aerial imagery captured by UAVs, as reported in Loli et al. (2022c). In the area of interest, a total of 16 bridges were inspected between 3 – 15 October 2020 (i.e., up to one month after the passage of the Medicane). Figure 3 shows a selection of representative photographs.



Figure 3. Photos of bridges in the lowlands of Karditsa: (a) No.3; (b) No. 4; (c) No. 6; and in the mountainous region W and NW of the city: (d) No. 7; (e) No. 8; (f) No. 9; (g) No. 10; (h) No. 11; (i) No.12.

Failures were dominated by extreme hydrodynamic loading of structures, due to flow obstruction, often facilitated by scour. A general shortcoming of hydraulic sections (bridge openings) was observed resulting in overflowing of rivers and streams and failure of bridge supports in locations where flow velocity was high enough to produce loads that transiently exceeded the capacity of load-bearing elements. This was the case along the Pamissos river, where torrential water flow caused partial or complete failure of five bridges (e.g., Figure 3d – 3h). On the contrary, the bridges in the Plain area were found structurally unscathed (Figure 3b – 3c). Out of the seven bridges inspected in the lowlands, none showed evidence of considerable structural displacements, despite the reports of their inundation and the abundant evidence of overflowing in their perimeter. Nevertheless, substantial debris masses were found concentrated upstream of bridges, especially those having in-stream piers. It is anticipated that the lowland bridges owe their survival to the flat ground morphology which, naturally, reduced flow velocities and hence the magnitude of erosive actions. This observation has guided the development of the Index of Flood Hazard Intensity (IFHI), as a bridge-specific indicator of flood hazard.

3.1 Bridge Damage Levels (DL)

Five bridge performance states have been defined and associated with relevant damage levels (DL), as follows:

- DL-1 implies no impact on the structural integrity and/or the functionality of the bridge. Figure 2b shows an indicative example of this category.
- DL-2 is equivalent to minimal damage, such as minor spalling, and functional loss due to debris built-up (Figure 2c), which poses no threat to the stability of the structure and the operability of the network.
- DL-3 is assigned in cases of moderate damage necessitating repair works which, however, did not result in complete closure of the bridge with at least one lane remaining operational (Figure 2d).
- DL-4 refers to cases of significant, albeit repairable damage, where temporary closure of the bridge is deemed necessary (examples shown in Figure 2e – g).
- DL-5 is the ultimate failure state, associated with complete collapse or unreparable damage, as is the case for the structures shown in Figure 2h – j, where replacement of the entire or large part of the asset would be required.

Table 3 lists the coordinates of inspected structures summarizing observations and damage levels (DL).

Table 3. Summary of observed damage to bridges after the Ianos Medicanе.

No.	Lat., Lon. (WGS 84)	DL	Damage description
1	39.25381, 21.71591	4	Scour at abutments and backfill wash-away. Collapse of approach roadway with no structural damage.
2	39.32248, 21.79625	4	Erosion and scour. Partial, repairable abutment failure.
3	39.34473, 21.89406	1	Signs of overflowing with no damage.
3A	39.34474, 21.89400	2	Signs of overflowing with no damage. Debris built-up.
4	39.34858, 21.90459	2	Overflowing and debris built-up.
5	39.34652, 21.92067	2	Overflowing and debris built up.
6	39.34506, 21.92634	2	Overflowing and debris built up.
7	39.42734, 21.92634	4	Scour and erosion at the abutment. Collapse of approach roadway with no structural damage to the bridge.
8	39.42580, 21.66623	5	Settlement of mid-pier. Erosion of abutment backfills. Severe, non-repairable structural damage.
9	39.40610, 21.66315	5	Abutment scour and backfill erosion. Collapse due to fracture of concrete walls.
10	39.40184, 21.66842	3	Abutment erosion and partial collapse of roadway.
11	39.40117, 21.65286	5	Collapse of consecutive piers and deck segments due to excessive scouring, hydrodynamic loads, and debris.
12	39.30350, 21.68657	5	Erosion of backfill and collapse of approach roadway.
13	39.30956, 21.71081	4	Abutment erosion with partial collapse of roadway and partial wash-away of masonry abutment. No damage to the RC part.
14	39.09779, 21.87822	1	Overflowing with no damage.
15	39.47911, 21.84343	1	Overflowing with no damage.

4 PREDICTION OF BRIDGE DAMAGE: RESULTS AND VALIDATION

Figure 4a Shows the spatial distribution of the hazard index (IFHI), as calculated at the location of every bridge in the area of study (Karditsa county), considering an inventory of 117 bridges, for the rainfall produced by Medicanе Ianos. Despite the severity of the event, calculations show that over 60% of the bridge stock (79 out of 117) faces a relatively low-intensity hazard. Only 18 structures are exposed to high hazard levels. Unsurprisingly, all are in the western (mountainous) area of the county, where steep topography amplifies flow intensity.

Figure 4b reveals the county's highly vulnerable bridge stock, showing that 56 moderately vulnerable and 35 highly vulnerable structures are randomly distributed across the region. Prediction of damage (in terms of DL) is carried out at the asset scale, according to Figure 1. DL predictions for Medicane Ianos are plotted against actual (observed) DL in Figure 5a, for the 16 bridges that were inspected during the post-flood reconnaissance study (the inspected sample equals to 14% of the entire inventory). A very satisfactory correlation ($R^2 = 0.71$; $p < 0.05$) is achieved. This is largely thanks to the introduction of IFHI, as a combined indicator of flood water depth and flow velocity, as indicated by the significantly poorer comparison between observed and predicted DL in Figure 5b. In the latter image, damage prediction has been based on the same method, but using only h_w as an indicator of hazard intensity, i.e., ignoring flow velocity (U).

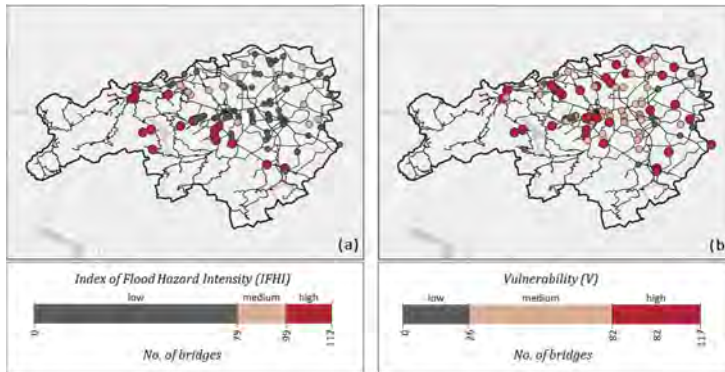


Figure 4. Analysis of the impact of Medicane Ianos on the bridges of the Karditsa county: spatial variability (a) of the IFHI, (b) V.

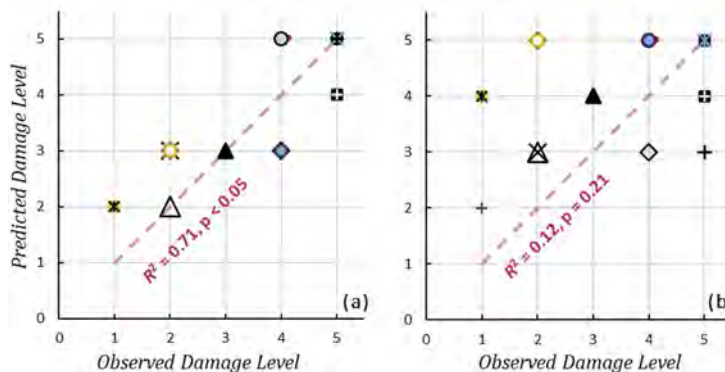


Figure 5. (a) Predicted damage against damage observed in the field; compared to (b) DL results when hazard is evaluated solely based on flood water depth (h_w).

5 CONCLUSIONS

The developed flood risk assessment framework is appropriate for the prediction of bridge susceptibility to flooding. It has been supported by a combination of field-based and theoretical research into the parameters that control the intensity of hydraulic actions on stream-crossing bridges. All of them have been incorporated, either directly or indirectly, into the proposed, bridge-specific Index of Flood Hazard Intensity (IFHI). Of major importance has been the recognition that U is a primary contributor to the flood-induced bridge distress. The generation of

a regional-scale prediction of U , albeit qualitative, has been decisive for the accurate prediction of bridge damage, as judged by the comparison against field observations after a severe flooding event (Figure 5a – 5b). Importantly, high values of U are generally expected in steep terrains, while, on the contrary, increased water heights (h_w) are expected on flat grounds. Owing to this antithesis, assessment of bridge response to flooding based on h_w (following the current state of the art) can lead to misleading, even unsafe, predictions. Indeed, as illustrated in Figure 5b, prediction of DL using only h_w as the indicator of flood hazard intensity, leads to unrealistic results that compare poorly with the recorded damages (as per Table 3).

The use of an empirical classification-based approach by MCDM analysis is the reason for the qualitative nature of the proposed framework. Although quantitative estimates would be possible, if the results of hydraulic analysis of flood propagation in the basin of interest became available to provide quantitative estimates of h_w and U , the developed MCDM-based framework has the advantage of being easily and relatively rapidly implementable, requiring the use of a comparatively reduced amount of data

ACKNOWLEDGEMENT

This study has been funded by the European Union H2020-Marie Skłodowska-Curie Research Grants Scheme MSCA-IF-2019 (grant agreement No 895432: ReBounce-Integrated resilience assessment of bridges and transport networks exposed to hydraulic hazards).

REFERENCES

- Arabameri, A., Rezaei, K., Cerdà, A., Conoscenti, C., & Kalantari, Z. (2019). A comparison of statistical methods and multi-criteria decision making to map flood hazard susceptibility in Northern Iran. *Science of the Total Environment*, 660, 443–458.
- CEREMA. (2019). Analyse de risque des ponts en site affouillable. CEREMA.
- Durand, Edouard & Davi, D. & Delgado, J. . (2018). AROSA: A new French guideline for scour at bridges risk-based analysis. In *Scour and Erosion IX* (Issue October, pp. 671–671). Taylor & Francis. doi: 10.1201/9780429020940-97.
- Dodangeh, E., Choubin, B., Eigdir, A. N., Nabipour, N., Panahi, M., Shamshirband, S., & Mosavi, A. (2020). Integrated machine learning methods with resampling algorithms for flood susceptibility prediction. *Science of the Total Environment*, 705.
- Kazakis, N., Kougias, I., & Patsialis, T. (2015). Assessment of flood hazard areas at a regional scale using an index-based approach and Analytical Hierarchy Process: Application in Rhodope-Evros region, Greece. *Science of the Total Environment*, 538, 555–563.
- Lagouvardos, K., Karagiannidis, A., Dafis, S., Kalimeris, A., & Kotroni, V. (2021). Ianos - A hurricane in the Mediterranean, *Bulletin of the American Meteorological Society*, 10.1175/BAMS-D-20-0274.1
- Loli, M., Mitoulis, S. A., Tsatsis, A., Manousakis, J., Kourkoulis, R., & Zekkos, D. (2022a). Flood characterization based on forensic analysis of bridge collapse using UAV reconnaissance and CFD simulations. *Science of The Total Environment*, 822, 153661.
- Loli M., Kefalas G., Dafis S., Mitoulis S.A., Schmidt F. (2022b). Bridge-specific flood risk assessment of transport networks using GIS and remotely sensed data. *Science of the Total Environment*, 850, 1157976
- Loli, M., Manousakis, J., Mitoulis, S.A., Zekkos, D. (2022c). UAV-enabled flood damage assessment and recovery monitoring of bridges following Medicane Ianos. *Proceedings of the 11th International Conference on Bridge Maintenance, Safety and Management, IABMAS*.
- Papaoiannou, G., Vasiliades, L., & Loukas, A. (2015). Multi-Criteria Analysis Framework for Potential Flood Prone Areas Mapping. *Water Resources Management*, 29(2), 399–418.
- Tripathi, G., Pandey, A. C., & Parida, B. R. (2022). Flood Hazard and Risk Zonation in North Bihar Using Satellite-Derived Historical Flood Events and Socio-Economic Data. *Sustainability*, 14(3), 1472.
- Zekkos D., Zalachoris G., et al. (2020). The September 18–20 2020 Medicane Ianos Impact on Greece Phase I Reconnaissance Report Geotechnical Extreme Events Reconnaissance Association.

Assessment as to the best strategies for the maintenance of existing bridges

A. Contardi & G. Pasqualato

SINA S.p.A. – ASTM GROUP, Milan, Italy

ABSTRACT: According to the new Italian standards, all existing bridges that have been declared not compliant with the current applicable rules (Norme Tecniche 2018) shall be subject to assessment in the next years. Due to the high number of non-compliant bridges, the Administrations and the infrastructural managers are asked to choose the appropriate maintenance activities to be performed. The question as to how to schedule a long-term planning for the interventions still remains unanswered. The managers are not only asked to assess an order of priority for the works to be done – which simply allows to decide the bridges to be restored – but also to conduct a more complete assessment so as to define the type of the restoration works needed and the relevant timeframe. By carrying out a complete risk analysis for each bridge, the best maintenance strategy appears to be the one that entails the lowest possible effort, such cost for each bridge expressed not only as the sum of the construction costs but including also all possible damages of the structure multiplied by their probability of occurrence (calculated with respect to a reference time period). By treating the probability of collapse or damage to the structure over time as a living cost, the manager will have the most efficient and reliable rational tools to determine the best maintenance strategy to follow.

1 INTRODUCTION

1.1 Requirements

The new Italian standards (Existing Bridge Guidelines), based on a multilevel risk analysis (the “**Italian Guidelines**”)¹, require “*de facto*” infrastructural managers to restore historical and aged bridges characterized by:

- significant degradations or high defect level;
- structural critical elements (such as “Gerber” support or bearings) deteriorated;
- girders with criticalities due to post-stressed precompression cables;
- high risk exposure from a social or economic standpoint.

Restoration works of so-called “accessible” (*transitabili*) bridges (the worst one) are required to be implemented in a very limited timeframe (5 years, as possibly extended to 10 years in case a long term monitoring activity thereon is pending). For all the other structures denominated “operational” (*operative*) – characterized by limited non-compliance with the applicable standards and quite good conditions – representing the vast majority, managers can choose the maintenance activity to be conducted in a long term timeframe (maximum 30 years).

1. Ref. is to Ministerial Decree 1 July 2022, No. 204, *Linee guida per la classificazione e gestione del rischio, la valutazione della sicurezza ed il monitoraggio dei ponti esistenti*

The need for some structures to comply with the requirements of the 2018 standards² arises from the recent guidelines. This said, the question for managers now is how to implement an effective Bridge Management System (BMS), that is, how to schedule a long-term planning of such maintenance works, with the purpose of achieving the maximum level of safety in a best cost benefit approach.

1.2 *Current tools*

Chapter 7.7 the Italian Guidelines introduces the new structural reliability index **R**, without providing for an explanation as to the relevant calculation method, its variation over time and the determination of the attention threshold above which the procedure for securing the structure should be triggered. To this end, the legislation seems to suggest the adoption of the sum of the relative defects $D_R = \sum Gk_1k_2$, obtained through normal visual inspection activities, where, for every defect, *G* means the weight, *k*₁ means the extension and *k*₂ the relevant intensity. However, this parameter is indicative of the condition of the bridge only for structures with very low and limited levels of deterioration and it is not suitable for highlighting more serious problems that may concern the safety of the bridge.

Conversely, it would be possible to use the classic reliability index **β** as **R**, a direct expression of the probability of collapse, estimated by calculating the safety factor with respect to the rules for new structures and taking into account all the calculation uncertainties; in this case, instead, the index reflects the degree of safety of the bridge but does not give any indication as to need to conduct the ordinary maintenance works to be implemented to prevent future emergency situations that are not yet detectable.

To date, managers are essentially working on defining two simple classifications of bridges in parallel, one category to be targeted with ordinary maintenance works and the other one with extraordinary maintenance works:

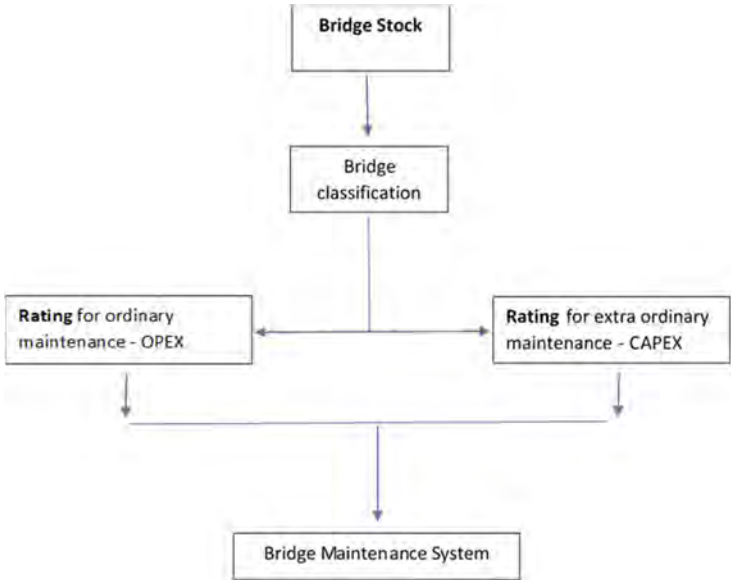


Figure 1. Flowchart of BMS application.

2. Ref. is to Ministerial Decree 17 January 2018, *Aggiornamento delle 'Norme tecniche per le costruzioni'*

- the first category, by collecting degradation data in order to address a continuous maintenance to guarantee a standard level of functionality (in general, this applies to bridges in a good level of condition or not presenting structural problems);
- the second category, on the basis of the safety factors obtained by an accurate assessment compliant with Eurocodes (Level 4 procedures of the Italian Guidelines) applying to aged bridges that have a lack of structural functionality.

It should be noted that managers' need is not to be provided with a simple order of priority for works, that just allows to decide which bridges are to be restored, but with a more complex and complete system that permits to define also the type of the needed restoration works and the relevant timeframe.

The following paragraphs provide for a calculation method aimed at planning the maintenance of the bridges by targeting a predetermined time frame and, at the same time, obtaining a single order of priority for the interventions to be carried out in the near future.

2 GENERAL “BMS” METHOD FORMULATION

Consider a reference time period t_{ref} during which it is necessary to ensure the safety and operation of the bridges of an infrastructure, e.g. 50 years. Throughout the time span considered, maintenance is carried out on each bridge by performing a certain number of activities. Each of these activities can be categorised as follows:

1. ordinary maintenance intervention aimed at increasing the durability of the bridge, without any increase in its resistant capacity;
2. repair intervention through which the individual structural elements can be modified in order to increase the resistant capacity of the bridge;
3. reconstruction of the deck or of the entire bridge.

The basic idea of the following method, based on what is indicated in Bulletin FIB 80 “*Partial factor methods for existing concrete structures*”, chapter 3.2.2., is that the preferable maintenance strategy is the one which involves the lowest possible total cost for the community, where for each bridge the total cost is expressed by the following formula:

$$C_{tot} = \sum C_i + \sum D_j P_j \quad (1)$$

where:

- C_i means total cost of the i -th intervention on the bridge in question.
- D_j means total damage caused by exceeding the j -th limit state.
- P_j means probability of exceeding the j -th limit state, calculated with respect to the time interval considered, as a function of the pre-selected maintenance actions.

As far as possible, the limit states should be chosen and treated so that they are statistically independent.

For example, those that could typically be adopted for a medium-sized viaduct are the following:

- collapse of a beam (and therefore of an entire part of the deck) due to vertical traffic loads;
- collapse of a slab mirror due to a concentrated vertical load;
- collapse of a pile or a group of bearing devices (and therefore of an entire part of the deck) due to a seismic event, wind or braking on the deck;
- collapse of the entire structure or part of it due to a hydrogeological event.

A maintenance strategy that contemplates a series of demanding interventions will involve very high costs and therefore will maximize the first addendum of the formula, but at the same time it will allow to reduce the probability of collapse and therefore to minimize the second term. Conversely, a strategy with much less invasive interventions (at least even

one that envisages doing nothing for the entire reference period) will make it possible to eliminate costs but will also lead to the maximum probability of collapse.

The indicated formula, although quite simple from a conceptual point of view, cannot be used yet due to the unavailability in current literature of practical procedures allowing the calculation of all the indicated parameters without uncertainties. In particular, while the costs of the interventions could be easily estimated in a parametric way even without carrying out preliminary complete projects, it would be important to develop two lines of research, described below, relating to the calculation of the probability of collapse and of economic and social costs and damages.

3 ESTIMATION OF THE PROBABILITY OF COLLAPSE “ P_j ”

The total probability of exceeding a limit state P_j shall mean the probability that limit state can be exceeded in the period t_{ref} depending on all actions taken.

The total probability could be calculated directly by assessing the structure applying Eurocodes as if it were new and considering the current level of degradation, as it is normally done in the first part of the safety checks. However, the result would not be correct since, for a historic structure, deterioration can evolve much more rapidly than for a new structure and in the period of time considered the probability of collapse could be considerably underestimated.

The most convenient way to proceed is to estimate preliminarily the probability of collapse p_j relating to a single year. As is known, p_j is not constant in the reference period but increases very slowly at first, then increasing rapidly following the progress of the deterioration phenomena. Simplifying the formula, it is possible to calculate the total probability as the sum of the probabilities of the individual years:

$$P_j = 1 - \prod_i^{t_{ref}} (1 - p_j(t_i)) \cong \sum_i^{t_{ref}} p_j(t_i) \quad (2)$$

It is therefore advisable to proceed according to the methodology described in the following paragraphs. For the sake of conciseness, further elaborations have been omitted and will be the subject of next studies.

3.1 First year probability

The structure is verified considering the current degradation and using, only for accidental and exceptional loads, reduced safety factors which reflect the fact that the structure is no longer verified with respect to a useful life of 50 years but considering only one year.

For example, for traffic loads the values indicated by the Eurocodes, since they refer to a return time of 1000 years, in this analysis are no longer related to the 5% exceedance but to 0.1% and for this reason the safety factor should be much lower. For traffic loads, it is suggested to use a coefficient equal to 1.0.

The safety factor of a structure with respect to the j -th limit state is defined as the ratio $S_{Fj} = R_{dj}/E_{dj}$ between the resistance (calculated as if the structure were new, but also considering the reductions in bearing capacity due to degradation) and the effect of external loads at the point of the structure under consideration. The safety factors can be conveniently used as the final result of the structural analysis carried out with the reduced partial coefficients of the loads. It should be noted that this information can be obtained with both in-depth FEM analyses and with simplified analyses (Level 4 or 3 of the mentioned Italian Guidelines).

More in detail, it is possible to estimate the reliability index β_j , which is linked to the probability of collapse by the relation $p_j = \Phi(-\beta_j)$, assuming a log-normal statistical distribution for the safety factor and therefore using the following formula:

$$\beta_j = \beta_1 + \ln(SF_j)/\sigma_j \quad (3)$$

A very similar formulation has already been proposed in a study conducted by the University of Trento referred to under a circular from the Ministry of Infrastructure³.

Parameter β_1 is constant for all limit states and for all structures. The standard deviation σ_j , on the other hand, is different for each structure and for each limit state and can normally be calculated only using the data available in literature.

However, for all limit states dependent on traffic loads, it is proposed to use a simpler and more transparent approach in order to obtain results in full compliance with Italian current standards. In fact, it is possible to obtain the value of the two parameters by directly imposing that a structure respects the following two conditions:

1. according to the Eurocode, the minimum reliability index of new structures correctly designed in consequence class CC3 is equal to 3.8, i.e. the maximum collapse probability over 50 years of a correctly designed bridge is $\Phi(-3.8) = 7 \cdot 10^{-5}$. Assuming for simplicity that the probability does not change over time, over one year it is possible to introduce the following parameter:

$$\beta_{EC} \triangleq \beta_1 + \ln(SF_{EC})/\sigma_j = -\Phi^{-1}\left(1 - (1 - \Phi(-3.8))^{\left(\frac{1}{50}\right)}\right) = 4.7 \quad (4)$$

2. A structure - which in the safety verification is on the threshold between Operativo and Transitable - has a reliability index of 2.8 over 50 years.

$$\beta_{OP} \triangleq \beta_1 + \ln(SF_{OP})/\sigma_j = -\Phi^{-1}\left(1 - (1 - \Phi(-2.8))^{\left(\frac{1}{50}\right)}\right) = 3.9 \quad (5)$$

Therefore, estimating the indexes SF_{EC} and SF_{OP} for one year and replacing the values in (3), the followings apply

$$\sigma_j = \ln(SF_{EC}/SF_{OP})/(\beta_{OP} - \beta_{EC}) \quad (6)$$

$$\beta_1 = \beta_{EC} - \ln(SF_{EC})/\sigma_j \quad (7)$$

For example, if the effect of dead loads and live loads is very similar, which is often the case with historical reinforced concrete structures, the safety factors are $SF_{EC} = 1.16$ and $SF_{OP} = 1.00$ and therefore $\sigma_j = 0.18$ and $\beta_1 = 3.87$.

The value of σ_j should then be appropriately modified considering, with respect to the design of a new structure, the additional factors of uncertainty that influenced the performed analysis. Typically, in the structural analysis these factors are the effect of degradation and the resistance of the materials obtained through laboratory tests; moreover, in simplified analyses it would be advisable to consider also the greater uncertainties inherent in the type of analysis. These calculations can be found in a PIARC paper in course of publication⁴.

3.2 Evolution of probability over time

In this historical moment, the subject matter of research should be the estimation of the evolution over time of the probability p_j . As is known, this changes over the years according to the age of the bridge and the progress of the deterioration phenomena.

3. Ref. is to Ministero delle infrastrutture e dei trasporti – 29 November 2019, *Criteri di priorità e programma delle manutenzioni autostradali*

4. Ref. is to PIARC ITALY National Committee – Technical Committee 4.2 – Bridges – 2019-2023 cycle, *Bridge safety monitoring and classification - State of the art and operational recommendations*

The causes of material degradation over time can be several and often coexist. The most evident phenomena are usually linked to the action of water and the salts it contains which encounters the surfaces of the structures due to malfunctions in the platform water disposal system or expansion joints. However, these problems in most cases are due to carelessness and can be solved through relatively simple and cheap repairs. Some degradation phenomena occur above all in the first years of the bridge's life, such as shrinkage and movements of the ground, or are due to construction defects, such as the failure to inject the sheaths of the post-tension cables; other phenomena are difficult to predict, such as shocks or fires.

For the purpose of calculating $p_j(t)$ it is advisable to focus attention on the phenomena that are inevitable and therefore easily predictable, such as carbonation for concrete and oxidation for steel.

With respect to reinforced concrete, it is necessary to correlate the reduction of the safety factors SF_j with the progress of the carbonation as a function of the quality of the concrete and the steel of the reinforcements and the thickness of the concrete cover. Since these features can be known *a priori*, it is possible to construct the resistance reduction curve of each section. Similar reasoning applies to the oxidation of steel.

The curves obtained should then be updated according to the inspection results. If phenomena of crumbling and detachment of the concrete surfaces appear in a bridge earlier than expected, the carbonation progress curve should be corrected accordingly.

Finally, the probabilities must consider the actions taken by the maintainers. Each of the three types of interventions presented in chapter 2 modifies the $p_j(t)$ curve in one of the following ways:

1. In case of ordinary maintenance intervention, the function remains continuous but - at least in the first period - constant, then it returns to increase within a relatively short time.
2. In case of repair, the function is discontinuous as p_j is lowered to a target value (usually the probability corresponding to β_1). In the first period it is also constant, and then it returns to rise in a relatively slow time.
3. In case of renovation, the function is discontinuous since from the instant of the intervention onwards $p_j(t)$ is the characteristic of the new structures.

4 DAMAGE ESTIMATION “ D_j ”

The most delicate and most complex part of the method is the determination of D_j , since the uncertainties involved are many and the values of these parameters may significantly impact on the final results of the calculation. Each damage can be estimated as the sum of the following contributions:

- Cost of replacing the collapsed structural part.
- Cost of infrastructure disruption for the managing company. Economic damage in term of missing payment (applicable to the toll road).
- Economic losses due to non-availability or malfunction of the structure for the whole community. In this case, it shall be considered that from the date of the collapse to the date of the reopening of the bridge, users must take an alternative route, thus taking longer to reach their destination. This damage is usually calculated assuming an hourly amount for light vehicles and one for heavy vehicles. The greater accident rate of the routes, due to the presence of road construction sites, must also be considered. If material, other costs to the regional economy are also taken into account.
- Social consequences (costs of injuries and fatalities) and unfavourable environmental effects. Bulletin FIB 80 contains a very simple formula to estimate the probability of casualties as a function of the length of the collapsed structural part. For the average compensation for a victim, the Italian *Decreto Dirigenziale* No. 189 dated 24 September 2012 by *Ministero delle Infrastrutture e dei Trasporti* provides the figure to be used. The damage caused to the areas underlying the bridge must be considered on a case-by-case basis, since these can be extremely variable. In the case of viaducts passing through uninhabited areas, only

environmental damage should be considered. Conversely, if the bridge crosses urbanized areas or near houses, the damage will obviously be much greater and must be carefully evaluated.

- Psychological effects (loss of reputation). This damage could be more significant for a private concessionary company, exposed to the financial market. To value this item, which could be extremely remarkable, a reliable estimate could be provided by calculating the immediate decrease in value of the shares suffered by companies that have had incidents with a certain media coverage in the past.

It should be noted that each limit state is assigned its own economic impact, which can be very different from that of the other limit states. For example, the damages associated with the breakage of a part of slab is much less than those related to the breakage of a girder.

It is important to remember that Bulletin FIB 80 also stated that in developed countries it is not accepted that the probability of becoming the victim of a structural failure could be larger than the normal probability of dying as a result of an accident (chapter 3.3). This requirement (not considered by the Italian Guidelines) could be respected by this method simply properly calibrating the damage estimation.

It is important to notice also that the vast majority of the damages involves the community and not the managing company.

The greater the importance and exposure of the bridge, the greater the damage will be. It should also be emphasized that this estimate is also a function of the *robustness* of the structure since many damages are more or less proportional to the length of the deck that collapsed as a result of the crisis.

5 BMS RATING

The search for the minimum value of C_{tot} (referring to the formula $C_{tot} = \sum C_i + \sum D_j P_j$) must be carried out bridge by bridge to determine which is the most effective maintenance strategy in the time t_{ref} . However, since for all the structures for which a type 3 intervention - i.e. the complete renovation - is convenient, the investment is always cheaper if made as soon as possible, but if all the maintenance plans were carried out all together as established, it could be unsustainable from an economic and traffic management point of view on the infrastructure due to huge number of construction site on the road.

It is therefore advisable to immediately focus on the most significant interventions and postpone the less important interventions to the next planning moment. For this reason, having discarded all the bridges for which it is not convenient to carry out interventions, it is suggested to order the maintenance giving priority to the structures for which the cost of the postponement C_p is maximum:

$$C_p = \sum D_j p_j \quad (8)$$

It should be noted that the indicated probability is the initial annual one.

The costs of the construction site should then be added to the costs due to the postponement of some urgent interventions, in terms of traffic diversion and lower efficiency of the infrastructure and greater accidents, this to penalize a choice of isolated and distant structures versus a set of interventions involving construction sites with less impact and therefore fewer problems with road traffic.

This rating procedure cannot be adopted without taking into account the considerations made in the previous chapters. The optimal maintenance strategy must always be determined at first instance and only afterwards the rating shall be calculated to establish which interventions shall be implemented in the short term. Once these interventions have been carried out, the overall calculation shall be updated with respect to the most recent inspection results of the bridges.

6 CONCLUSION

The methodology proposed in this paper is supposed to potentially integrate to the procedures proposed by the current Italian Guidelines, as it could suggest the implementation of a single classification of interventions to be put in place, without making distinctions between safety issues and durability problems. For sure, the next step of this research could be a test application on a case study bridge stock.

Maintenance policy which privileges more limited interventions would entail a lower cost in the first term in (1) and higher costs in the second one. On the other hand, the complete reconstruction of the bridge with a new one entail high costs (first term) but a much more significant risk limitation. By treating the probability of collapse or damage to the structure over time as a living cost, the Administrations and the managers will be provided with the most efficient and reliable rational tools for determining the maintenance strategy to be implemented.

ACKNOWLEDGEMENTS

PIARC ITALY National Committee – Technical Committee 4.2 – Bridges – 2019-2023 cycle

REFERENCES

- Bulletin FIB 80, *Partial factor methods for existing concrete structures*.
Decreto Dirigenziale No. 189 dated 24 September 2012 by Ministero delle Infrastrutture e dei Trasporti.
Ministerial Decree 17 January 2018, *Aggiornamento delle 'Norme tecniche per le costruzioni'*.
Ministerial Decree 1 July 2022, No. 204, *Linee guida per la classificazione e gestione del rischio, la valutazione della sicurezza ed il monitoraggio dei ponti esistenti*.
Ministero delle infrastrutture e dei trasporti – 29 November 2019, *Criteri di priorità e programma delle manutenzioni autostradali*.
PIARC ITALY National Committee – Technical Committee 4.2 – Bridges – 2019-2023 cycle, *Bridge safety monitoring and classification – State of the art and operational recommendations*.
Zonta, D. Zandonini, R. & Bortot, F. 2009. *A Tool for Planning the Future of Regional Infrastructure*. Zurich, Switzerland: IABSE Symposium, 2009.

The possibility of data integration of drive-by monitoring and direct bridge monitoring

M. Miyagi

School of Science and Engineering, University of Tsukuba, Japan

R. Shin & E. Mudahemuka

Graduate School of Science and Technology

K. Yamamoto

Institute of Systems and Information Engineering/Center for Artificial Intelligence Research, University of Tsukuba, Japan

ABSTRACT: The VBISI (Vehicle-Bridge Interaction System Identification) method is a drive-by monitoring method that measures and collects a large amount of vibration and route data from a group of vehicles, and simultaneously identifies the mechanical parameters of each vehicle and the bridges. The identification process randomly assumes the mechanical parameters of each vehicle and bridge, and solves two processes, namely the vehicle IEP (Input Estimation Problem) and the bridge DRS (Dynamic Response Simulation) to estimate the road unevenness. Bridge DRS is not required if bridge vibration data is available. However, if the bridge DRS is replaced by the measured value, the identification accuracy tends to decrease. Therefore, this study proposes a method to obtain the maximum likelihood value of bridge vibration from DRS-estimated values and measured values using sequential processing.

1 BACKGROUND

1.1 *Social demand for SHM*

Bridges are usually inspected by visual inspection and hammering. This is the most popular and reliable method, but it is costly because inspectors often have to carefully look at, tap and evaluate every component of the bridge. In other words, the bridge inspection is still a tough business. Even today, the total length of roads continues to grow and the number of bridges continuously increases. As building more bridges, the total cost of regular inspections also become more of a burden for governments. The biggest problem is the need for more veteran engineers who can properly inspect bridges. Bridges should be classified based on the probability of damage, and detailed inspections should be carried out with priority given to bridges with a high likelihood of damage, thereby reducing maintenance costs.

1.2 *Previous studies*

Bridge monitoring based on vehicle vibration data has been proposed in previous studies to estimate the damage probability. For example, Y.B. Yang et al. (2004) measured the vibration of vehicles travelling on bridges and estimated the natural frequencies of bridges from their power spectra. This method can be used to evaluate a large number of bridges at low cost, without the need to install sensors on the bridges. Wang et al. (2019) estimated the first-order natural frequencies of bridges with relatively good accuracy by fixing a smartphone to

a standard car and driving it over a real bridge, which also increases the potential for bridge damage detection. Yang et al. (2009) have also shown analytically that the natural frequencies of bridges can be extracted from vehicle vibrations. In addition to natural frequencies, some studies use mode shapes for damage assessment. Yamamoto et al. (2021) proposed a method for estimating bridge mode shapes using towing vehicles and confirmed its effectiveness numerically. Yang et al. (2022) also estimated the bridge first-order mode shape using two towing vehicles in a real environment. However, health assessments based on vibration indices such as natural frequencies and mode shapes require values prior to damage. In situations where ageing has already progressed, there is also a need for a method to directly estimate the existing performance. Nagayama et al. (Xue, 2020 and Zhao, 2019) proposed a method for simultaneously estimating vehicle dynamics parameters (mass, damping and stiffness) and road unevenness from vehicle vibration. This method assumes a random vehicle system and applies a Kalman filter to the vehicle vibration data to obtain the road unevenness as a system input. When the vehicle passes over a bridge, the system input includes a bridge vibration component. Acquiring the bridges' state by Drive-by Monitoring method will make bridge inspections more efficient. However, the drive-by method has low accuracy. A way to improve accuracy is required while maintaining efficiency.

Therefore, this research proposes drive-by monitoring using bridge vibration in addition to vehicle vibration. Specifically, the VBISI (Vehicle-Bridge Interaction System Identification) method proposed by Yamamoto et al. (2022) is extended. The VBISI method is a drive-by monitoring method that measures and collects large amounts of vibration and route data from fleets of vehicles and simultaneously identifies mechanical parameters of each vehicle and bridge. The identification process randomly assumes the mechanical parameters of each vehicle and bridge and solves two processes: vehicle IEP (input estimation problem) and bridge DRS (dynamic response simulation) to estimate road unevenness. Bridge DRS is not required if bridge vibration data is available. However, replacing the bridge DRS with the measured value tends to reduce the identification accuracy. In this study, we propose a method to obtain the maximum likelihood value of bridge vibration from the DRS estimated value and the measured value by sequential processing. This research is limited to proposing the basic mathematics, and numerical simulation is a future topic. In addition, since Yamamoto et al. (2022) have already explained the mathematical formula for the VBISI method, this study only describes the extension of the Kalman filter.

1.3 The purpose of the study

Therefore, it is considered to perform vibration measurement on vehicles and some bridges and to perform high-accuracy vehicle and bridge identification using vehicle and bridge vibration data. Although this scheme is applied to some bridges, the accuracy improvement effect may spread to the surrounding area of the monitoring bridges when the vehicles identified with high accuracy pass through other bridges. Therefore, this study constructs the theory of the VBISI method using simultaneous vehicle-bridge vibration measurement data.

2 NUMERICAL EXPERIMENT

2.1 Finite element model for the bridge

According to Yamamoto et al. (2022), the finite element formula of a bridge is expressed as follows.

$$\mathbf{M}_b \ddot{\mathbf{y}}(t) + \mathbf{C}_b \dot{\mathbf{y}}(t) + \mathbf{K}_b \mathbf{y}(t) = \mathbf{L}_v(t) \mathbf{P}(t) \quad (1)$$

$$\mathbf{M}_b = \left[\int_0^L \rho A \mathbf{N} \mathbf{N}^T dx \right] \quad (2)$$

$$\mathbf{C}_b = \alpha_c \mathbf{M}_b + \beta_c \mathbf{K}_b \quad (3)$$

$$K_b = \left[\int_0^L EI \frac{\partial^2 \mathbf{N}}{\partial x^2} \frac{\partial^2 \mathbf{N}^T}{\partial x^2} dx \right] \quad (4)$$

$$\mathbf{L}_v = [N(x_1) \ N(x_2)] \quad (5)$$

$$\mathbf{P} = \{P_1 \ P_2\}^T \quad (6)$$

where $\mathbf{y}(t)$ is the numerical solution vector of bridge vibration, $N(x)$ is the basis function vector, EI is flexural rigidity, ρA is mass per unit length, x_1 and x_2 are the position of front and rear axle of the vehicle, and P_1 and P_2 are the contact force due to the front axle and rear axle of the vehicle.

2.2 Rigid-body-spring model for vehicle

According to Yamamoto et al. (2022), the rigid-body-spring model for vehicle is expressed as follows.

$$\mathbf{M}_v \ddot{\mathbf{z}} + \mathbf{C}_v \dot{\mathbf{z}} + \mathbf{K}_v \mathbf{z} = \mathbf{f}_v \quad (7)$$

where $\mathbf{z}(t)$ is vehicle vibration vector, \mathbf{f}_v is input vector. In this model, m_s is the mass of the vehicle body and c_{si} , k_{si} , d_i , m_{ui} and k_{ui} represent the suspension damping, the suspension stiffness, the distance from the gravity point, the unsprung mass, and the tire stiffness of i -th axle, respectively. The system parameter matrices and input/output vectors of the vehicle can be given by

$$\mathbf{z} = \{z_{s1} \ z_{s2} \ z_{u1} \ z_{u2}\}^T \quad (8)$$

$$\mathbf{f}_v = \{0 \ 0 \ k_{u1}u_1 \ k_{u2}u_2\}^T \quad (9)$$

$$\mathbf{M}_v = \begin{bmatrix} \frac{d_1 m_s}{d_1 + d_2} & \frac{d_1 m_s}{d_1 + d_2} & & \\ \frac{d_1 m_s}{d_1 + d_2} & \frac{d_1 m_s}{d_1 + d_2} & & \\ & & m_{u1} & \\ & & & m_{u2} \end{bmatrix} \quad (10)$$

$$\mathbf{C}_v = \begin{bmatrix} c_{s1} & c_{s2} & -c_{s1} & -c_{s2} \\ c_{s1}d_1 & -c_{s2}d_2 & -c_{s1}d_1 & c_{s2}d_2 \\ -c_{s1} & & c_{s1} & \\ & -c_{s2} & & c_{s2} \end{bmatrix} \quad (11)$$

$$\mathbf{K}_v = \begin{bmatrix} k_{s1} & k_{s2} & -k_{s1} & -k_{s2} \\ k_{s1}d_1 & -k_{s2}d_2 & -k_{s1}d_1 & k_{s2}d_2 \\ -k_{s1} & & k_{s1} + k_{u1} & \\ & -k_{s2} & & k_{s2} + k_{u2} \end{bmatrix} \quad (12)$$

Each system parameter corresponds to the Figure 1.

2.3 The contact force

According to Yamamoto et al. (2022), the contact force matrix $\mathbf{P}=[P_1 \ P_2]^T$ is expressed as:

$$\begin{aligned} \mathbf{P} &= \begin{bmatrix} -m_{s1}(g + \ddot{z}_{s1}) - m_{u1}(g + \ddot{z}_{u1}) \\ -m_{s2}(g + \ddot{z}_{s2}) - m_{u2}(g + \ddot{z}_{u2}) \end{bmatrix} \\ &= -\mathbf{M}_p \ddot{\mathbf{z}} - \gamma \mathbf{g} \end{aligned} \quad (13)$$

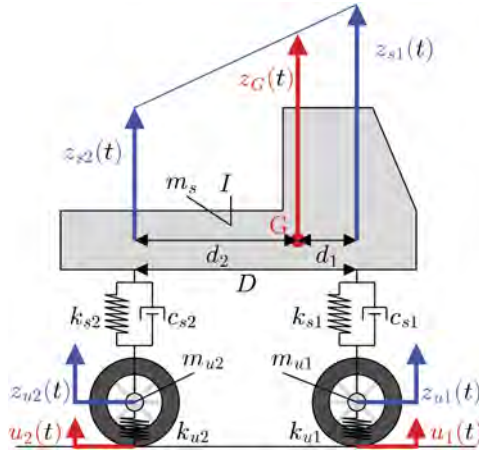


Figure 1. Rigid-Body-Spring model for the vehicle.

where

$$\mathbf{M}_p = \begin{bmatrix} m_{s1} & 0 & m_{u1} & 0 \\ 0 & m_{s2} & 0 & m_{u2} \end{bmatrix} \quad (14)$$

$$\boldsymbol{\gamma} = \begin{bmatrix} m_{s1} + m_{u1} & 0 \\ 0 & m_{s2} + m_{u2} \end{bmatrix} \quad (15)$$

$$\mathbf{g} = [g \quad g]^T \quad (16)$$

g is the acceleration of gravity.

3 STATES ESTIMATION METHOD

Numerical experiments were carried out using the Newmark Beta and Newton-Raphson methods, following previous studies (Yamamoto et al., 2022). The numerical experiment simulates the measured data. The proposed method estimates the vehicle vibration $\mathbf{z}(t)$, the bridge vibration $\mathbf{y}(t)$, and the road profile $\mathbf{r}(t)$.

3.1 Observation equation

Let $w_i(t)$ be the displacement of the bridge sensor at $x = x_i$,

$$\mathbf{w} = \mathbf{L}_b^T \mathbf{y}(t) \quad (17)$$

where

$$\mathbf{w} = \{w_1 \quad w_2 \quad \cdots \quad w_m\}^T \quad (18)$$

$$\mathbf{L}_b = [N(x_1) \quad N(x_2) \quad \cdots \quad N(x_m)] \quad (19)$$

3.2 State space model

The state space model of the vehicle and bridge can be given by the following equations. The state variable $\mathbf{X}(t)$ is composed of the vehicle vibrations $\mathbf{z}(t)$ and $\dot{\mathbf{z}}(t)$, the bridge vibrations $\mathbf{y}(t)$

and $\dot{\mathbf{y}}(t)$, and the input profiles $\mathbf{u}(t)$ and $\dot{\mathbf{u}}(t)$. The observation variable $\mathbf{s}(t)$ consists of the bridge vibrations $\dot{\mathbf{w}}(t)$ and $\mathbf{w}(t)$ which is delivered by numerical integration.

$$\dot{\mathbf{X}}(t) = \mathbf{A}(t)\mathbf{X}(t) + \boldsymbol{\omega}(t) \quad (20)$$

$$\mathbf{s}(t) = \mathbf{B}(t)\mathbf{X}(t) + \boldsymbol{\epsilon}(t) \quad (21)$$

where

$$\mathbf{X}(t) = \{ \mathbf{z}^T \quad \dot{\mathbf{z}}^T \quad \mathbf{y}^T \quad \dot{\mathbf{y}}^T \quad \mathbf{r}^T \quad \dot{\mathbf{r}}^T \quad \mathbf{g}^T \}^T \quad (22)$$

$$\mathbf{s}(t) = \{ \dot{\mathbf{z}}^T \quad \mathbf{z}^T \quad \dot{\mathbf{w}}^T \quad \mathbf{w}^T \quad \mathbf{g}^T \}^T \quad (23)$$

$$\mathbf{M}_A(t) = \mathbf{M}_b^{-1} \mathbf{L}_v(t) \mathbf{M}_p \mathbf{M}_v^{-1} \quad (24)$$

$$cA(t) = \begin{bmatrix} \mathbf{O}_{4 \times 4} & I_{4 \times 4} & \mathbf{O}_{4 \times 2n} & \mathbf{O}_{4 \times 2n} & \mathbf{O}_{4 \times 2} & \mathbf{O}_{4 \times 2} & \mathbf{O}_{4 \times 2} \\ -\mathbf{M}_v^{-1} \mathbf{k}_v & -\mathbf{M}_v^{-1} \mathbf{C}_v & \mathbf{M}_v^{-1} \mathbf{F}_v \mathbf{L}_v^T & \mathbf{O}_{4 \times 2n} & \mathbf{M}_v^{-1} \mathbf{F}_v & \mathbf{O}_{4 \times 2} & \mathbf{O}_{4 \times 2} \\ \mathbf{O}_{2n \times 4} & \mathbf{O}_{2n \times 4} & \mathbf{O}_{2n \times 2n} & \mathbf{I}_{2n \times 2n} & \mathbf{O}_{2n \times 2} & \mathbf{O}_{2n \times 2} & \mathbf{O}_{2n \times 2} \\ \mathbf{M}_A \mathbf{k}_v & \mathbf{M}_A \mathbf{C}_v & -\mathbf{M}_A \mathbf{F}_v \mathbf{L}_v^T - \mathbf{M}_b^{-1} \mathbf{k}_b & -\mathbf{M}_b^{-1} \mathbf{C}_b & \mathbf{M}_A \mathbf{F}_v & \mathbf{O}_{2n \times 2} & -\mathbf{M}_b^{-1} \mathbf{L}_v \boldsymbol{\gamma} \\ \mathbf{O}_{2 \times 4} & \mathbf{O}_{2 \times 4} & \mathbf{O}_{2 \times 2n} & \mathbf{O}_{2 \times 2n} & \mathbf{O}_{2 \times 2} & \mathbf{O}_{2 \times 2} & \mathbf{O}_{2 \times 2} \\ \mathbf{O}_{2 \times 4} & \mathbf{O}_{2 \times 4} & \mathbf{O}_{2 \times 4} & \mathbf{O}_{2 \times 2n} & \mathbf{O}_{2 \times 2n} & \mathbf{O}_{2 \times 2} & \mathbf{O}_{2 \times 2} \\ \mathbf{O}_{2 \times 4} & \mathbf{O}_{2 \times 4} & \mathbf{O}_{2 \times 2n} & \mathbf{O}_{2 \times 2n} & \mathbf{O}_{2 \times 2} & \mathbf{O}_{2 \times 2} & \mathbf{O}_{2 \times 2} \end{bmatrix} \quad (25)$$

$$\mathbf{B}(t) = \begin{bmatrix} -\mathbf{M}_v^{-1} \mathbf{k}_v - \mathbf{M}_v^{-1} \mathbf{C}_v & \mathbf{M}_v^{-1} \mathbf{F}_v \mathbf{L}_v^T & \mathbf{O}_{4 \times 2n} & \mathbf{M}_v^{-1} \mathbf{F}_v & \mathbf{O}_{4 \times 2} & \mathbf{O}_{4 \times 2} \\ \mathbf{I}_{4 \times 4} & \mathbf{O}_{4 \times 4} & \mathbf{O}_{4 \times 2n} & \mathbf{O}_{4 \times 2n} & \mathbf{O}_{4 \times 2} & \mathbf{O}_{4 \times 2} \\ \mathbf{L}_b^T \mathbf{M}_A \mathbf{k}_v \mathbf{L}_b^T \mathbf{M}_A \mathbf{C}_v - \mathbf{L}_b^T (\mathbf{M}_A \mathbf{F}_v \mathbf{L}_v^T + \mathbf{M}_b^{-1} \mathbf{k}_b) & -\mathbf{L}_b^T \mathbf{M}_b^{-1} \mathbf{C}_b & -\mathbf{L}_b^T \mathbf{M}_A \mathbf{F}_v & \mathbf{O}_{m \times 2} & -\mathbf{L}_b^T \mathbf{M}_b^{-1} \mathbf{L}_v \boldsymbol{\gamma} \\ \mathbf{O}_{m \times 4} & \mathbf{O}_{m \times 4} & \mathbf{L}_b^T & \mathbf{O}_{m \times 2n} & \mathbf{O}_{m \times 2} & \mathbf{O}_{m \times 2} \\ \mathbf{O}_{2 \times 4} & \mathbf{O}_{2 \times 4} & \mathbf{O}_{2 \times 2n} & \mathbf{O}_{2 \times 2n} & \mathbf{O}_{2 \times 2} & \mathbf{O}_{2 \times 2} \end{bmatrix} \quad (26)$$

The discretized model of Eq. (39) and Eq. (40) can be expressed as

$$\mathbf{X}_k = \mathbf{A}_k \mathbf{X}_{k-1} + \boldsymbol{\omega}_k \quad (27)$$

$$\mathbf{s}_k = \mathbf{B}_k \mathbf{X}_k + \boldsymbol{\epsilon}_k \quad (28)$$

Eq. (50) and (51) are discretized by Δt .

$$\mathbf{X}_k = \mathbf{X}(k\Delta t) \quad (29)$$

$$\mathbf{s}_k = \mathbf{s}(k\Delta t) \quad (30)$$

$$\boldsymbol{\omega}_k = \boldsymbol{\omega}(k\Delta t) \quad (31)$$

$$\boldsymbol{\epsilon}_k = \boldsymbol{\epsilon}(k\Delta t) \quad (32)$$

$$\mathbf{A}_k = \exp(\mathbf{A}(k\Delta t)\Delta t) \quad (33)$$

$$\mathbf{B}_k = \mathbf{B}(k\Delta t) \quad (34)$$

The covariance matrix of model error $\boldsymbol{\omega}_k$ and observation error $\boldsymbol{\epsilon}_k$ is \mathbf{Q}_k and \mathbf{R}_k .

$$\mathbf{E}[\boldsymbol{\omega}_k \boldsymbol{\omega}_k^T] = \mathbf{Q}_k \quad (35)$$

$$\mathbf{E}[\boldsymbol{\epsilon}_k \boldsymbol{\epsilon}_k^T] = \mathbf{R}_k \quad (36)$$

where $E[\]$ denotes an expected value.

3.3 Karman filter

The observability matrix of the state-space model is

$$\mathbf{O} = \begin{bmatrix} \mathbf{B}^T & \mathbf{A}^T \mathbf{B}^T & (\mathbf{A}^T)^2 \mathbf{B}^T & \dots & (\mathbf{A}^T)^{n-1} \mathbf{B}^T \end{bmatrix}^T \quad (37)$$

where N is the degrees of freedom of the state vector, which in this study is $N = 12 + 4n$. A necessary and sufficient condition for a system to be observable is that the observable matrix must satisfy $\text{rank}(\mathbf{O}) = N$. The initial values of the posterior state estimate $\hat{\mathbf{X}}_k$ and the posterior error covariance matrix $\hat{\mathbf{P}}_k$ are

$$\hat{\mathbf{X}}_0 = E[\mathbf{X}_0] \quad (38)$$

$$\hat{\mathbf{P}}_0 = E[(\mathbf{X}_0 - E[\mathbf{X}_0])(\mathbf{X}_0 - E[\mathbf{X}_0])] \quad (39)$$

The prior state estimate $\hat{\mathbf{X}}_{k+1}^-$ and the prior error covariance matrix $\hat{\mathbf{P}}_{k+1}^-$ are

$$\hat{\mathbf{X}}_{k+1}^- = \mathbf{A}_k \hat{\mathbf{X}}_k \quad (40)$$

$$\hat{\mathbf{P}}_{k+1}^- = \mathbf{A}_k \hat{\mathbf{P}}_k \mathbf{A}_k^T + \mathbf{Q}_k \quad (41)$$

where \mathbf{Q}_k is the process noise variance-covariance matrix. The Kalman gain \mathbf{G}_{k+1} , the posterior state estimate $\hat{\mathbf{X}}_{k+1}$ and the posterior error variance-covariance matrix $\hat{\mathbf{P}}_{k+1}$ at step $k+1$ is

$$\mathbf{G}_{k+1} = \hat{\mathbf{P}}_{k+1}^- \mathbf{B}_{k+1}^T \left(\mathbf{B}_{k+1} \hat{\mathbf{P}}_{k+1}^- \mathbf{B}_{k+1}^T + \mathbf{R}_{k+1} \right)^{-1} \quad (42)$$

$$\hat{\mathbf{X}}_{k+1} = \hat{\mathbf{X}}_{k+1}^- + \mathbf{G}_{k+1} \left(\mathbf{s}_{k+1} - \mathbf{B}_{k+1} \hat{\mathbf{X}}_{k+1}^- \right) \quad (43)$$

$$\hat{\mathbf{P}}_{k+1} = (\mathbf{I} - \mathbf{G}_{k+1} \mathbf{B}_{k+1}) \hat{\mathbf{P}}_{k+1}^- \quad (44)$$

3.4 Results and discussion

In order to verify the theoretical best performance of the state estimation algorithm, noise-free and correct dynamics parameters are substituted into the state equation. The bridge length is 30 [m] and the vehicle speed is constant at 10.0 [m/s]. When $t = 1.0$ [s], the front wheels enter the bridge, and the bridge begins to forced vibration. Then at $t = 4.4$ [s] the rear wheels exit the bridge. After that, the bridge is in the state of free vibration. Figure 2 shows the simulated and estimated values of the bridge's displacement vibration at the center of the bridge.

According to Figure 2, the estimated and simulated bridge vibration are different. In Figure 3, there is an error between the simulated and the estimated values between times $t = 1$ [s] to 4.4 [s]. because the vehicle is on the bridge.

Figure 3 shows the simulated and estimated road profile of the front wheel. From Figure 3, the road profile when the vehicle is not on the bridge matches the simulation. However, the estimation accuracy of the road profile of the front wheels decreases when the vehicle is on the bridge. The reason for the error is thought to be that the estimated value of bridge vibration contains an error.

In this study, the Newmark- β method is used to simulate bridge vibrations. However, in the state estimation algorithm, bridge vibrations are calculated by the difference method. It can be said that the estimation error is accumulated due to this difference and the accuracy of the bridge vibration estimation decreases.

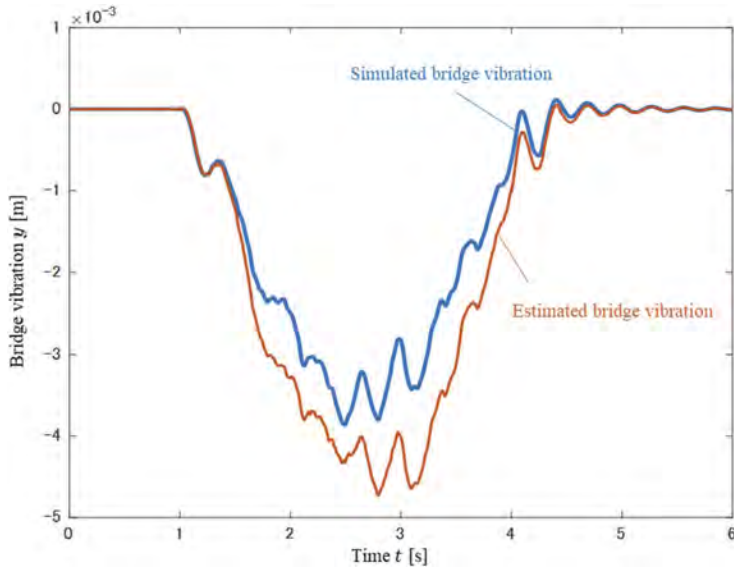


Figure 2. Simulated bridge vibration and Estimated bridge vibration.

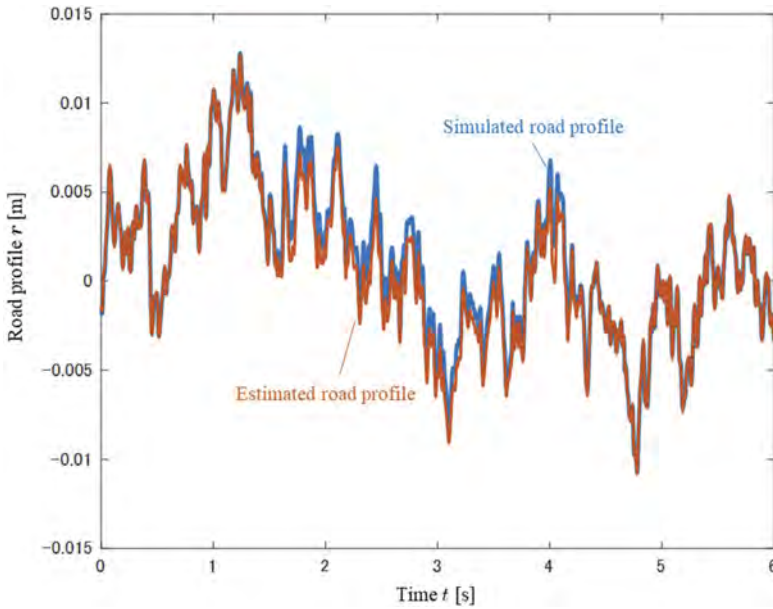


Figure 3. Simulated road profile and Estimated road profile.

Figure 4 shows the estimated road unevenness at the front and rear axles. The bridge section is $x = 0$ to 30 [m]. The road unevenness estimated by the front and rear axles are different. In the VBISI method, the road unevenness estimated by the front and rear wheels must match when the dynamic parameters are correct. Therefore, the VBISI method could not be applied with the proposed state estimation algorithm.

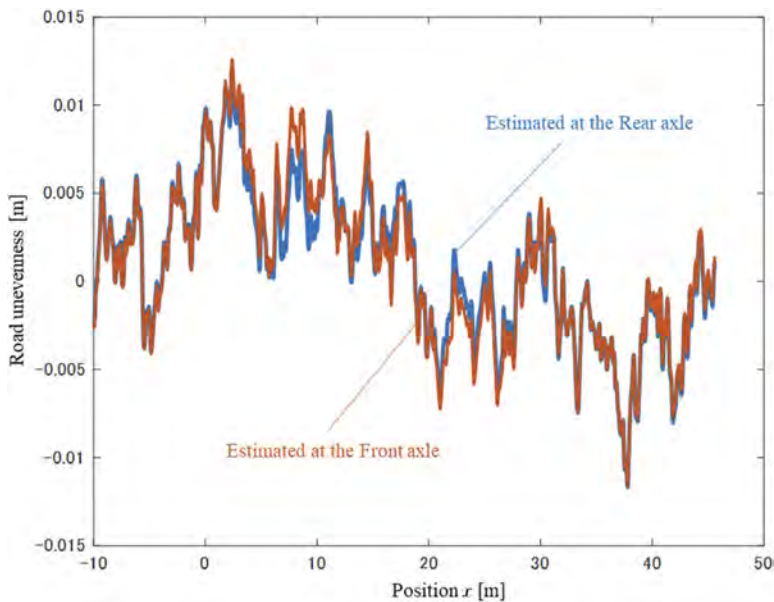


Figure 4. The estimated road unevenness.

4 CONCLUSION

In this paper, a new scheme to apply vehicle and bridge vibration data to Drive-by Bridge Monitoring, when vibration data of some bridges is obtained. However, it is expected that the proposed method cannot identify the bridge system because the estimation accuracy of the state variables is still low. Future works are to identify the error sources and to improve the estimation accuracy of state variables.

REFERENCES

- Wang, H., Nagayama T. & Su, D., 2019. Estimation of dynamic tire force by measurement of vehicle body responses with numerical and experimental validation. *Mechanical Systems and Signal Processing*, 123, 369–385.
- Xue, K., Nagayama, T. & Zhao, B. 2020. Road profile estimation and half-car model identification through the automated processing of smartphone data, *Mechanical Systems and Signal Processing*, 142, 106722.
- Yamamoto, K., Fujiwara, S., Tsukada, K., Shin, R. & Okada, Y. 2022. Numerical Studies on Bridge Inspection using Data obtained from sensors on vehicle, *Proc. of 13th International Workshop on Structural Health Monitoring, Stanford University, 7-9 December 2021*. CA: USA.
- Yamamoto, K., Murakami, K., Shin, R., Okada, Y. 2022. Application of Particle Swarm Optimization method to Drive-by Monitoring for estimating Vehicle-Bridge Interaction System
- Yang Yang; Huicheng Lu; Xiaokun Tan; Hwa Kian Chai. 2022. Ruiqiong Wang; Yao Zhang. Fundamental mode shape estimation and element stiffness evaluation of girder bridges by using passing tractor-trailers, *Mechanical Systems and Signal Processing*, 169, 108746.
- Yang, Y.B., Lin, C.W. & Yau, J.D. 2004. Extracting bridge frequency from the dynamic response of a passing vehicle. *Journal of Sound and Vibration*, 272, 471–493.
- Yang, Y.B. & Chang, K.C. 2009. Extracting the bridge frequencies indirectly from a passing vehicle, Parametric study. *Engineering Structures*, 31, 2448–2459.
- Zhao, B., Nagayama T. & Xue, K. 2019. Road profile estimation and its numerical and experimental validation by smartphone measurement of the dynamic responses of an ordinary vehicle, *Journal of Sound and Vibration*, 457, 92–117.

*SS17: BIM-based sustainability considerations
in infrastructure construction
Organizer: M. König*



Taylor & Francis

Taylor & Francis Group

<http://taylorandfrancis.com>

Potential of holistic asset information management

A. Buttgercit

Jade University of Applied Sciences Oldenburg, Germany

M. Block

Ruhr University Bochum, Germany

D. Gogolin

Engineering Company PTM Dortmund mbH, Germany

S. Gomolluch

City of Münster, Germany

ABSTRACT: Road construction is a major contributor to CO² emissions, but it also plays a crucial role in connecting people and enabling economic growth. Municipal road construction must consider not only ecological factors such as resource efficiency and mobility change, but also economic factors such as costs and depreciation, as well as socio-cultural factors. To manage these factors, sustainable asset information management (AIM) is needed, which involves using modern procedures and efficient data systems to manage asset information at strategic, tactical, and operational levels. This paper aims to identify the factors that influence sustainable AIM and translate them into requirements for the maintenance management of the city of Münster. By recording trends and changes in the municipal organisation, the paper provides insights into the structured management of AIM to ensure a sustainable road construction in the future.

1 INTRODUCTION

The majority of our road infrastructure was built during reconstruction or was rebuilt or expanded to meet actual needs. Thus the political focus was on new construction, reconstruction and expansion. While in the area of trunk roads, the constantly growing heavy traffic and the increasing axle loads have been causing an ever-increasing need for maintenance and considerable costs for years, in the subordinate network of municipalities, which comprises about 2/3 of the total road network in Germany (Knoll 2012), there has been a constantly growing need for maintenance and financing for years. However, our modern way of life is no longer possible without a demand-oriented and well-maintained transport infrastructure. Further constraints on such an infrastructure result, for example, from changing mobility, digitisation and the increasingly clear consequences of climate change. These aspects are associated with major financial burdens and personnel expenses for the public sector and considerable restrictions for the public due to the increasing interventions in municipal infrastructure. From a fiscal policy perspective, transportation infrastructure represents an enormous fixed asset that must be maintained on a sustainable basis. Failure to maintain it as needed threatens major financial risk. Qualified comprehensive maintenance management is required to avoid this.

Entrepreneurial thinking and methods have already found their way into German municipal administrations. Citizens are seen as stakeholders or customers for whom services or products are provided. The provision of transport infrastructure represents a product and, in order to provide it, the necessary infrastructure must be built and maintained. The infrastructure already in place had to be accurately recorded and monetised as a fixed asset. In addition to the technical view, the commercial view and life cycle cost considerations were also incorporated into the maintenance management.

The goal of the municipalities should be to carry out the necessary interventions in the road infrastructure in proper time, to proceed in a coordinated manner and to minimise the total number. In this way, the available financial resources can be used optimally to achieve the useful lives, to ensure that the value of the fixed assets is maintained and to realise the new requirements for the infrastructure. This requires a suitable management tool, such as municipal asset management (AM). Using the example of the municipal maintenance management in the Office for Mobility and Civil Engineering of the City of Münster, it will be shown how such an AM can be realised. Furthermore, the potentials emerging due to current changes and the relevance of integrating additional data and information into the existing AM will be presented.

2 MUNICIPAL ASSET MANAGEMENT

2.1 *What is the additional value of AM?*

AM is a tool to support leadership and management tasks. While quality management describes the process flow for task completion, AM in this context comprises coordinated, multidisciplinary processes within an organisation that deploys resources in the form of personnel, equipment and finances for tangible assets throughout their life cycle in order to achieve defined performance and cost targets at an acceptable level of risk, taking into account the relevant legal, geopolitical, economic, social, technological and environmental framework conditions (Ruitenburg et al. 2014). It is used for task- and result- or target-oriented management. Which assets represent a value contribution depends on the organisation (ISO 2014b). In the maintenance management of the city of Münster, for example, the assets sewer, road, bridge, traffic control and parking guidance systems (Buttgereit et al. 2021) are combined to form the asset portfolio.

Internationally, AM in civil engineering is a well-researched and practicable discipline (Abdirad and Dossick 2020), but in Germany in particular, there is a lack of comprehensive and integrated use, especially at the municipal level. Thus, it is the authors' intention to develop a long-term strategy to accelerate the implementation of AM in German municipalities. In contrast to Asset Management Systems (AMS), many municipalities still use Pavement Management Systems (PMS), which are technical data repositories of information for road maintenance, but focus primarily on economic evaluations, i.e. the monetary valuation of assets, and do not cover the life cycle.

2.2 *What are the limits of strategic PMS in municipalities?*

For decades, systematic maintenance planning has been searching for efficient solutions to determine, for example, the operational and strategic financial requirements. So far, a PMS supports the municipality in the preparation of the operational construction program and provides indications for the development of condition values with a limited budget (budget scenario) (Maerschalk et al. 2013).

Since the complexity is many times higher in urban areas than in non-urban areas, algorithms were initially developed for non-urban roadways and included in the regulations (FGSV 2001), which, for example, calculate maintenance programs for the next 3-5 years on the basis of systematic condition surveys and assessments of the roads (mainly the carriageways) using forecast functions for the expected development of the road condition (operational maintenance management) or attempt to estimate the financial requirements in the longer term (strategic maintenance management). In the vast majority of cases, the approaches and models used are condition-driven, whether based on simple thresholds that elicit an appropriate maintenance action or based on highly complex simulations of condition development. These condition-driven approaches can be described as "reactive" processes that allow for short-term to at most medium-term maintenance planning. Already obtaining the data of suitable quality required for the maintenance management of non-urban roads is a major challenge.

For municipal roads, it is usually many times more difficult, as there are no uniform or even standardised assessment procedures for the majority of municipal surfaces such as ancillary facilities to date. In addition, there are municipal peculiarities and requirements, e.g. complex forecasts of traffic load or heavy traffic as well as lack of forecasting function for the condition development

of municipal roads. In the same way, paved areas, such as work by utility companies and third parties, have so far been left out of the PMS and thus also left out of the determination of financial requirements. These aspects, on the other hand, can be indirectly represented in an AMS, if necessary. In parallel, a further development of a computer-aided municipal maintenance system should take place, which supports the engineer and the financial expert in his decisions in the AM.

2.3 *How can AM be structured?*

From the management function circle, namely the continuous sequence of goal definition and planning, decision, implementation and monitoring, management models for road maintenance can be developed in an analogous manner, in which the diverse tasks for safety and performance, construction and maintenance of road pavements are combined and linked. Different organisational forms are conceivable depending on the management structure, task definition, task weighting and standards. The foundations of an AM are outlined in ISO 55000 (ISO 2014b). The requirements are part of ISO 50001 (ISO 2014a). The AM is thus described as an international standard. However, it has not yet been transferred to the German regulations of the FGSV or specifically for road maintenance management. The systematics of asset management corresponds well with the life cycle considerations and can be used for orientation when setting up an AM system.

The basis of systematic road maintenance in Germany is a condition-based target system with target criteria to be defined individually. For this purpose, the current condition of the road pavements must be known, i.e. recorded and evaluated in consideration of the target criteria. At the same time, a forecast of the condition to be expected if a measure is not taken is to be estimated (deterioration). On the basis of the condition assessment, the measures to be implemented are then planned on the basis of a listed selection of measures, an order of urgency and the preparation of a program of measures with the budgetary resources required for implementation (financial requirements). In a next step, the individual measures are planned in more detail. In addition, possible alternatives with regard to the design and dimensioning of the pavements as well as alternative maintenance strategies must be identified and evaluated before a measure is then implemented. After completion of the construction measure, the basic data of the measure, such as the time of execution, the road structure, the results of quality assurance and the materials used must be recorded in a road database.

The management of road maintenance is therefore a special planning task in which, on the one hand, strategic decisions on maintenance measures or measure strategies are made network-wide (FGSV 2019). On the other hand, the preparation of a construction program and the preparation and implementation of maintenance measures are carried out object-by-object. The road network recorded in a road database forms the basis for this planning. In order to better incorporate financial aspects into construction decisions, a road database should be linked to information from asset accounting, such as residual book value and remaining useful life. This is usually no longer part of the PMS, but the step towards AM. In order to be able to control efficiently in terms of AM, it is necessary to define targets, metrics for target achievement as well as associated key figures. Based on the defined goals and key figures, long-term or short-term control options can be developed. Long-term management (strategic level) should create inter-generational equity, i.e. not burden future generations, or be sustainable. To this end, it is necessary (in the medium term) to achieve a balance between resource consumption and resource generation. Depreciation and provisions must be earned in the respective year. This would ensure the long-term performance of a municipality (Buttgereit et al. 2021). Short-term control (operational level) is primarily concerned with achieving a balanced annual result, i.e. the resource consumption of the financial year is covered by the resource revenue of the same financial year. Performance control can be carried out, for example, by time comparisons, operational comparisons or by target/actual comparisons. Short-term control of the budget should be carried out with the help of target agreements within the framework of contract management. The prerequisite for this is that product information is known about monetary variables, quantities and qualities, which are mapped and controlled in a management system (Figure 1).

Compared to PMS, AM focuses on maintaining the value of the assets over their life cycle. Synergies can be achieved through appropriate maintenance strategies for the respective assets as well as a coordinated maintenance strategy for the assets (especially sewers and roads). This

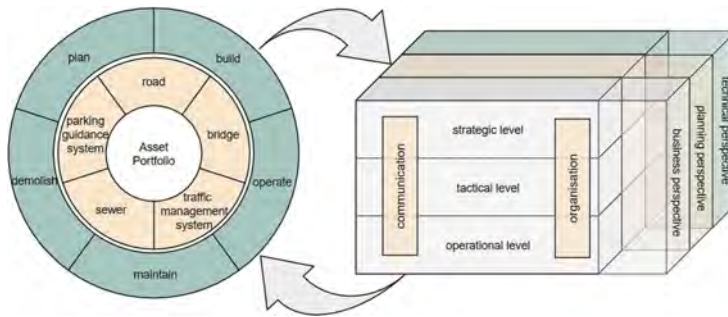


Figure 1. Continuous effect of the maintenance management organisation (right) on the asset portfolio to be managed depending on the respective life cycle phase (left).

ensures that the available financial resources are used economically and that the environmental impact and the impact on road users are kept to a minimum.

2.4 What is the additional value of information management respective BIM?

Infrastructure data, which is collected successively during the life cycle and also comes from different sources, is often subject to errors (Hajdin et al. 2022). However, different stakeholders also frequently provide data whose depth of content and accuracy deviates from the real information needs of maintenance management. To correct this deficiency, the use of the BIM method lends itself. Through the clear and also contractually secured definition of information exchange processes and the Level of Information Need (EN 2020), the information quality is ensured and thus represents an excellent supplement for asset information management. For the exchange of model data, the open exchange format Industry Foundation Classes (IFC) is used, which is also mandatory to be requested by public clients. Current further developments of buildingSmart, such as IFCalignment or IFCroad, will in the future also cover specific object classes from the infrastructure sector more precisely in the future. Garramone et. al. name frequent advantages present in the literature that can be achieved by BIM in AM (Garramone et al. 2022). In terms of information management, BIM allows information to be mapped throughout the asset life-cycle (Abdirad and Dossick 2020). In this regard, it is recommended that BIM models be used from the beginning of the project. In addition, differentiation support for both strategic and operational action planning is cited. Precise geometric information greatly facilitates the planning of maintenance measures, but strategic decisions in particular are often linked to network-level issues. The integration of BIM and GIS is a particular focus of attention here (Bradley et al. 2016). Moreover, many municipal road databases have already been implemented on the basis of GIS systems and are thus already an integral part of AMS. One concrete integration option is the conversion of IFC files into shape format, which can then in turn be transferred into the GIS system (Zhu et al. 2018). Among many other approaches to integrate both domains (Celeste et al. 2022), there are efforts by the Open Geospatial Consortium and buildingSMART International to develop a Common BIM/GIS Data Standard (OGC 2020). Another integration option may be to link external data sources in the prevailing system (Bradley et al. 2016), such as using information containers to map BIM data into the AMS (Hagedorn et al. 2022). Although this potential has not yet been fully exploited in Münster, various pilot projects are being carried out.

3 METHODOLOGY: FACTORS OF PESTEL

With the help of the PESTEL analysis, a conceptual framework is created in which the requirements for holistic asset information management can be ascertained in a structured manner. The PESTEL analysis is a strategic tool that is used to identify external influencing factors (Haynes and Nunnington 2010). PESTEL is to be understood as an acronym.

- Political includes the consideration of current government policy decisions and regulations that have an impact on the organisation or its sphere of influence.
- Economical factors look at monetary influences, such as price of building materials.
- Social cultural considers factors related to people and the way they live together.
- Technological encompasses factors that enable organisations and employees to leverage existing technologies and innovations and ensure future viability.
- Ecological includes energy efficiency, recycling and sustainability.
- Legal looks at the regulatory framework in which an organisation operates. For example, it examines the general legal certainty, the expression of guidelines as well as the approval procedures for new products or services.

The PESTEL analysis focuses primarily on external trends or mega trends, but also looks at external factors that are changing to a particular extent. As an example, road safety has always been a relevant topic in transport planning, but due to the increase in traffic, this topic now also plays an increasing role in maintenance management, thus changing the requirements accordingly.

4 INFLUENCING FACTORS AND REQUIREMENTS ON ASSET INFORMATION MANAGEMENT

4.1 *Results from PESTEL and requirement analysis*

An excerpt of the results of the PESTEL analysis is shown in 1 and 2. The focus of the analysis here is on the sphere of influence of the organisation that conducts maintenance management. The structure of the table is to be seen from left to right in logical consequence. External trends or changes in the organisational environment often result in positive or negative consequences that have an impact on maintenance management. In the next instance, this results in concrete requirements that are to be implemented by the AM, or already from the external factor if no assessable consequences can be derived.

4.2 *The need of asset information management*

One way of meeting these requirements and taking the above-mentioned future aspects into account is to set up an AIM. This can be understood as a digitally supported system that enables all management levels of an organisation to have an overview of the current situation, to make decisions based on facts, and to recognize and implement optimizations in the course of quality assurance, effectiveness control, and continuous improvement. Flanked by risk management, decisions can be weighed up in terms of relevance, among other things. In addition, in the case of planned and unplanned changes, an analysis should be carried out at short notice and corrective decisions made if necessary. There is already good experience from road construction technology as well as from environmental issues, which can be supplemented by the new challenges. The further development and limits of an existing AMS into a system that is capable of answering holistic questions can be illustrated below using the use case of the city of Münster.

5 CLIMATE CHANGE INFLUENCE ON THE MATERIAL

An increased risk in the course of climate change is the increase of future extreme weather events (heat, floods, storms) and the general expansion or shift of the temperature range of the service temperature range of asphalt surfaces. This results in changed and stronger physical loads on the infrastructure in terms of deformation or relaxation behavior. Consequently, the determination of weather data and the structural substance recording are of fundamental importance (determination of the actual condition). The resulting assessment of the infrastructure in terms of resilience must be integrated into a risk management system and opened up for forecast calculations (response to potential climatic changes). The results of the assessment are to be taken into account proactively in future action planning and supported by regular monitoring of the structural substance during the service life (sensor technology).

The road maintenance including bridge construction and traffic engineering of the city of Münster is the first in Germany to be certified according to ISO 55000 since April 2018. The

Table 1. Identified external factors, their consequences and concrete requirements for the organisational maintenance management.

External factors	Consequences	Requirements
Political		
- digital administration	- more transparency, data access for citizens, high implementation costs	- adapt network, hardware and software, train employees, security concepts
- federal and state level committed to the use of BIM	- provide human and IT resources and structures	- mutual integration of BIM and asset database
- citizen involvement and participation	- demand for more transparency, higher acceptance	- train employees, provide finances, present information appropriately, define information security needs
- transformation of mobility	- reallocation of land, redefinition of urban development standards, adaptation of maintenance management, increase in cycling	- prioritisation of construction measures (motorised individual traffic to individual traffic), potential analysis, decision-making basis for long-term strategy
- consolidation of finances	- savings in personnel and material resources, ...	- coordinated construction site management across all assets, dealing with short-term changes in the budget plan, sustainable value preservation of the infrastructure
Economical		
- shortage of building materials	- refurbishment backlog increases, delays in project plan	- resource-efficient construction, detection of sources of recyclable material, dynamic adjustment of system variables
- inflation	- loss of value exceeding regular asset degradation, deviations from the budget plan	- consideration of inflationary trends
- energy prices	- deviations from budget	- long-term energy savings, use of low-consumption technology (e.g. adaptive lighting), retrofitting measures
- out- or in-sourcing	- change in "business model", changes in responsibilities, changed need for coordination	- changes in the management system (personnel and competencies, information flows, etc.)
- refurbishment backlog	- action deadlines are exceeded, isolated decommissioning of assets, structural damage	- optimisation of the programme of measures, rapid awarding and approval, dynamic prioritisation
Socio-cultural		
- mobility participation and accessibility	- reallocation of space, redefinition of urban development standards, adaptation of maintenance management	- potential analysis, identifying obstacles, adapting infrastructure (e.g. traffic lights, bus stops) etc.
- demographic change	- such as mobility participation and accessibility, additional threat of loss of knowledge within the organisation, more difficult acquisition of personnel	- such as mobility participation and accessibility, ensuring knowledge transfer, more efficient processes, municipality as an attractive employer
- changes in urban planning	- change of land use, e.g. development of new building areas, shortage of capacities in supply and disposal security	- strategic alignment of the action plan, increase asset capacity or change in asset use
- increase in traffic	- traffic jam, impaired traffic safety due to spatial constriction, noise emissions, air pollutants, increased strain on transport infrastructure, faster material exhaustion	- reduce traffic disruption, use improved methods and materials (e.g. low-noise pavements), expand public transport, ensure health protection, coordinated construction site management across all assets
Technical		
- technological development of building materials and processes	- technological innovation, improvement and savings potentials, regulations and state of the art change	- technical recording of new information
- automation of machines and processes	- changing demands on personnel and hardware and software	- retraining and advanced training for employees, consider new apprenticeship professions
- increasing amounts of data	- IT infrastructure of public administrations reach their limits	- IT infrastructure must be improved
- artificial intelligence	- potentials for e.g. forecasting possibilities arise	- information systems should be usable by AI services in the long term

(Continued)

Table 1. (Continued)

External factors	Consequences	Requirements
Ecological		
- climate change	- risk of extreme weather (heat, flood, storm), risk of material expansion, shift in temperature ranges (service temperature range), hanging physical load on infrastructure	- consolidation of weather data, opening the system for forecasts, inclusion of risk management, assessment of the structural substance of the existing infrastructure with regard to resilience, result-based proactive action planning, monitoring of the structural substance during the useful life (sensor technology)
- resource-efficient construction	- more recycling and reuse, less primary building materials, life cycle material passport	- integration of new relevant developments, technical collection of new information, training of staff, asset consideration in the entire life cycle
- concept of the "Sponge City"	- more infiltration-capable traffic areas, increase proportion of green spaces, delayed water runoff	- potential analysis, circular water management concept, adaptation of the regulatory framework, designation in the development plan
Legal		
- environmental protection laws (e.g. Water Framework Directive)		- continuous consideration of all applicable legal requirements
- EU taxonomy		
- EU Construction Products Directive		
- changes in procurement and contracting		
- EU-MAK values (occupational health and safety in construction)		

AM is a task-oriented management tool for the management levels for strategic decision support in the context of generation-oriented, target- or result-oriented maintenance management over the entire life cycle of the assets.

In order to respond adequately to the aforementioned use case, it must be possible to integrate new data sources into the AM of the city of Münster. The DaRkSeit project is investigating the extent to which existing traffic monitoring data can be combined with available climate data and material data from existing road sections in order to make more precise statements about the progress of degradation and the remaining useful life (BMDV 2021). For sustainable maintenance management and to achieve the goal of climate neutrality, the RekoTi project is investigating, among other things, new alternative, resource-efficient construction methods and construction methods, approaches for efficient material flow management by means of information on the type, location, quantity and quality of resources used, as well as examining integration options for LCA data (Maibaum et al. 2022, Flamme et al. 2022). If the evaluation is positive, the knowledge of these projects gained will be transferred to the city's AM.

6 CONCLUSION

The holistic view in an Asset Information Management (AIM) means infrastructure management in the sense of responsibility for the entire infrastructure over the entire life cycle by combining the technical and commercial aspects with the goal of generational equity.

According to the authors, AM is a useful tool, also in public administration. AM helps, for example, both in the development of investment decisions and in safeguarding services of general interest. At the same time, it gives the opportunity to make quick forecasts and thus enables the administration to react to current political topics or issues. Likewise, future relevant topics can be better analyzed with the help of AM and implemented in the existing work environment. The same applies to the consideration of new technologies.

In order to be able to answer questions in the context of global (climate change, mobility transition) or national trends (digital administration), it is increasingly necessary to obtain new or supplementary information and to make it available to relevant interest groups in a quality-checked manner. This effort is often shied away from, with the result that more complex questions are not answered at all or are dealt with on the basis of insufficient information at considerable additional expense. At this point, a conscious turn towards Asset Information Management should take place. By combining AM and BIM as well as risk management towards an AIM, the decision makers of the municipality are supported in their work for more sustainability, also in infrastructure.

In Münster, strategies and concepts have already been developed to complement the existing regulatory framework, and some have already been tested and implemented in pilot projects. The potential identified in the process is enormous. The successive realignment of individual processes, the courage to carry out pilot projects, and the will to innovate and consistently develop further will enable Münster to meet future challenges.

REFERENCES

- Abdirad, H. and Dossick, C.S. 2020. Rebaselining Asset Data for Existing Facilities and Infrastructure. *Journal of Computing in Civil Engineering*, 34 (1)
- BMDV 2021. Datenbasierte Bewertung der Resilienz kommunaler Straßeninfrastruktur – DaRkSeit. Available from: tinyurl.com/dpba8j45 [Accessed 01 Nov 2022]
- Bradley, A., et al. 2016. BIM for infrastructure: An overall review and constructor perspective. *Automation in Construction*, 71, 139–152.
- Buttgereit, A., et al. 2021. Erhaltungsmanagement - Ein Baustein im Asset Management in Münster (Teil 2). *Straße und Autobahn* (1.2021), 33–39.
- Celeste, G., et al. 2022. Innovating the Construction Life Cycle through BIM/GIS Integration: A Review. *Sustainability*, 14 (2), 766.
- EN 2020. Building Information Modelling – Level of Information Need: Part 1: Concepts and principles, 35.240.67 (17412-1).
- FGSV 2001. RPE-Stra 01: Richtlinien für die Planung von Erhaltungsmaßnahmen an Straßenbefestigungen FGSV-Nr.: 488.
- FGSV 2019. M FinStraKom: Merkblatt über den Finanzbedarf der Straßenerhaltung in den Kommunen FGSV-Nr.: 986. Köln.
- Flamme, S., et al. 2022. Lösungsansätze für einen ressourceneffizienten Tiefbau: Ressourcenplan kommunaler Tiefbau: RekoTi. *Deutsches Ingenieurblatt*, 48–49.
- Garramone, M., et al. 2022. A multi-scale BIM/GIS framework for railways asset management. *The International Archives of the Photogrammetry, Remote Sensing and Spatial Information Sciences*, XLVI-5/W1-2022, 95–102.
- Hagedorn, P., et al. 2022. BIM-Enabled Infrastructure Asset Management Using Information Containers and Semantic Web. *Journal of Computing in Civil Engineering*, 37 (1).
- Hajdin, R., et al. 2022. Approaches for data exchange and exploitation to combine Asset Management Systems and BIM: AMSFree.
- Haynes, B.P. and Nunnington, N. 2010. *Corporate real estate asset management: Strategy and implementation*. Kidlington, Oxford, Burlington, MA: EG Books.
- ISO 2014a. *Asset management – Management systems – Requirements*. 2014th ed. (55001).
- ISO 2014b. *Asset management - Overview, principles and terminology*. 2014th ed. (55000).
- Knoll, E., ed. 2012. *Der Elsner*. Dieburg: Elsner.
- Maerschalk, G., et al. 2013. *Daten und Methoden für ein systematisches Erhaltungsmanagement innerörtlicher Straßen*. Forschung Straßenbau und Straßenverkehrstechnik 1079. Bonn.
- Maibaum, J., et al. 2022. Resource indicator-oriented building information modeling for the management of infrastructure.
- OGC 2020. OGC and buildingSMART International publish discussion paper on the integration of BIM and GIS. Available from: <https://www.ogc.org/pressroom/pressreleases/3187> [Accessed 23 Nov 2022].
- Ruitenburg, R.J., et al. 2014. A Multidisciplinary, Expert-based Approach for the Identification of Lifetime Impacts in Asset Life Cycle Management. *Procedia CIRP*, 22, 204–212.
- Zhu, J., et al. 2018. An Assessment of Paths for Transforming IFC to Shapefile for Integration of BIM and GIS. 26TH INTERNATIONAL CONFERENCE ON GEOINFORMATICS.

Towards environmental design decision-making for infrastructure planning using parametric BIM

J. Hofmeyer, K. Forth, S. Esser & A. Borrmann

Technical University of Munich, Munich, Germany

ABSTRACT: The AEC industry is responsible for 32% of the global greenhouse gas (GHG) emissions. The greatest potential to reduce the environmental impacts of infrastructure projects has been identified to be in the early design stages, where trailblazing decisions of the road corridor and the construction type must be made. We propose a methodology for an automated calculation of embodied and traffic emissions based on Building Information Models (BIM) of infrastructure assets. Our approach supports decision-makers in identifying optimal road corridors not only by means of design aspects but also by taking environmental impacts into consideration. Hence, we introduce predefined, parametric LCA profiles including cut-and-fill considerations, various road profiles, and structural assets like tunnels and bridges. The bill of quantities is automatically derived from the BIM model for the subsequent LCA calculation. Finally, the resulting GHG emissions of different routing variants can be automatically calculated and compared for holistic design decision-making.

1 INTRODUCTION & MOTIVATION

In terms of climate change and the scarcity of resources, it is necessary for the AEC sector to sufficiently evaluate and justify the decision-making for construction projects. In addition to building construction, this is also of utmost importance for infrastructure projects. For the continuous reduction of CO₂ emissions, the embodied and traffic emissions of different routing alternatives should be considered at an early design stage (Liljenström 2021, Sauer 2016).

For the calculation of the embodied and traffic emissions over the entire lifecycle, the methodology of life cycle assessment (LCA) is used. LCA is a standardized approach to calculate the environmental performance of products and processes and “can be used to identify the highest points of concentration of emissions and analyze which actions can be taken to achieve their reduction more efficiently” (de Oliveira et al. 2021).

The greatest opportunity to reduce the environmental impacts of a road design is located in the early design stage where the choice of the road corridor and the construction type is made (Liljenström et al. 2021). However, the required information for conducting an LCA, such as the quantity of construction material, is hardly available and time-consuming to collect in an early planning stage. The relevant information becomes available in later design stages when fewer opportunities exist to reduce the environmental impacts.

A possibility to balance the conflicting objectives is the application of BIM methods to accelerate the time-consuming data collection and design evaluation of different routing alternatives. The BIM methodology shifts the design efforts into earlier design stages as semantic 3D models are developed and their relevant information is collected to conduct analyses. Therefore, the evaluation of different design possibilities can be conducted earlier where changes have greater effectiveness and possible conflicts can be resolved in time which improves the design quality (Borrmann et al. 2018).

The objective of this research is the development of an integrated evaluation system that provides end-users with a quick assessment of different routing alternatives by considering emissions caused by constructing and operating the infrastructure assets in question.

The rest of the article is structured as follows. Section 2 provides an overview of related research activities and motivates the identified research gap. Section 3 introduces the conceptual approach and elaborates on the assumptions made to implement a holistic yet flexible approach for LCA considerations in the early design stages of civil infrastructure projects. The proposed workflow has been tested in a case study, which is summarized in section 4. Section 5 concludes the findings and discusses future improvements.

2 BACKGROUND & RELATED WORKS

Currently, the environmental impacts of built assets are mostly considered within the framework of a rating system in the context of a sustainability assessment. The ecological aspects of sustainability are thereby determined with the help of an LCA. For example, a proposal for an indicator system by Schmellekamp (2016) evaluates the different sustainability aspects with a degree of fulfillment depending on a point system. Even though, no evaluation system for the sustainability of infrastructure projects has been officially introduced (Zinke et al. 2021).

Sustainability tools are mostly developed for end-product evaluation. The design phase must be completed to a certain extent in order to be able to carry out a sustainability assessment. However, decisions that have the highest impact on the environmental effects need to be made during the early design stages as the choice of the road corridor. For conducting an LCA for the choice of the road corridor, a simplified LCA is required (van Eldik et al. 2020). A European research project about Life Cycle Consideration in EIA of Road Infrastructure (LICER) addressed this issue. They developed an LCA tool in Microsoft Excel to calculate the annual energy use and related annual GHG emissions over the life cycle of the infrastructure project (Brattebø et al. 2013). However, it is still necessary to enter the data manually from the road model to the LCA model.

In a simplified LCA, traffic as well as embodied emissions should be considered. Traffic emissions are the emissions emitted by vehicles due to fuel consumption in the operation phase. Embodied emissions are associated with the life cycle of an infrastructure asset and include the construction, operation, maintenance, and demolition of the engineering constructions such as the superstructure of roads, bridges, and tunnels. According to Sauer (2016), the construction of a tunnel in mountainous regions might reduce GHG emissions as a smaller longitudinal gradient is achieved. The emissions from the reduced traffic will compensate for the higher emissions during the construction phase after several years.

The implementation of a BIM-based LCA has rarely been performed so far in infrastructure projects. The consideration of traffic emissions and the combination of road superstructures and civil engineering assets has not yet been carried out. In previous studies, only the embodied emissions were evaluated for different engineering constructions. Differences in previous studies exist in the functional unit, the consideration of different life cycle stages, different environmental indicators, and the integration process of BIM and LCA. Slobodchikov et al. (2019) and Maibaum & Block (2022) both conducted a BIM-based LCA for calculating the embodied emissions of the superstructure of a road. Van Eldik et al. (2020) evaluated the environmental impacts of a bridge in a cradle-to-grave consideration. As part of the Integridge research project, a BIM-based LCA has been developed for steel bridges. In addition to the ecological aspects, the other two dimensions of sustainability are also taken into account (Zinke et al. 2022).

The literature overview has unveiled deficiencies in BIM-based LCA calculations that consider the construction process as well as the operation phase of infrastructure assets. Therefore, the next section introduces a comprehensive framework that aims to close the gap identified.

3 METHODOLOGY FOR ENVIRONMENTAL DESIGN DECISION-MAKING

The objective of our proposed methodology is the automated assessment of different routing alternatives regarding their environmental impact with the help of BIM models in the early planning stages. Thereby, the routing alternatives consist of the road corridor and engineering constructions such as bridges and tunnels. The overall structure is illustrated in Figure 1.

In the first step, the LCA objectives, functional unit and system boundaries are defined as goal and scope. The functional unit of the conducted LCA is set as:

GWP [kg CO₂ e] over the life cycle of 100 years of different infrastructure routing alternatives enabling traffic between the same start and end point.

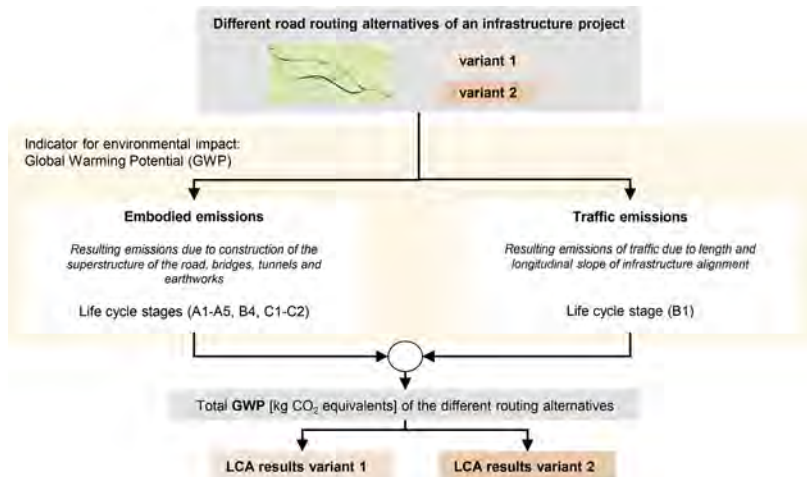


Figure 1. Defined goal and scope of the life cycle assessment.

Since engineering structures are designed for 100 years (EN 1990 2010), the same period is assumed here for LCA calculation. For the superstructure materials of a road, differentiated life cycles are accumulated over the period of 100 years. The different service life cycles depend on the type of material, which is divided into an asphalt and a concrete superstructure, and influence the replacement of components (B4) in the maintenance stage. For example, the service life for the top layer of asphalt superstructure is set to 10 years, and for concrete superstructure 60 years (according to Liljenström et al. 2021). As depicted in Figure 1, LCAs are conducted for each routing alternative of a road infrastructure project. The global warming potential (GWP) is selected for evaluation as the environmental indicator. The indicator is evaluated for both, the embodied and traffic emissions of the infrastructure asset in question. To oversee the infrastructure project over its entire life cycle, the embodied emissions of the product stage (A1-A3), transport to site (A4), construction process (A5), replacement of components (B4), and end-of-life stage (C1-C2) must be considered in the calculation. The traffic emissions are relevant for comparison with the embodied emissions (Sauer 2016), and therefore included and assumed here as the use stage (B1) for an infrastructure project. The final LCA result is the total GWP of each routing alternative created over the defined period.

3.1 Proposed workflow

In order to carry out a BIM-based LCA in an early planning stage, the parametric BIM models on the one hand and the predefined LCA profiles on the other hand are required. Their interactions are depicted in Figure 2.

Due to existing uncertainties in early design stages, BIM models mainly consist of sparse information and typically include information about the envisioned axes, terrain information, and assumed cross sections that are positioned along the envisioned track. Furthermore, many design decisions in early project phases build upon standards and regulations that take the expected traffic load into consideration. These guidelines enable resilient assumptions about the overall shape of the road body, the number of lanes per direction, and the envisioned overall width of the road. Furthermore, the analysis of the terrain information provides the basis for the axis design including the horizontal and the gradient layout. Subsequently, supporting structures like bridges or tunnels can be placed accordingly and are included in the resulting BIM models at least in a low level of detail.

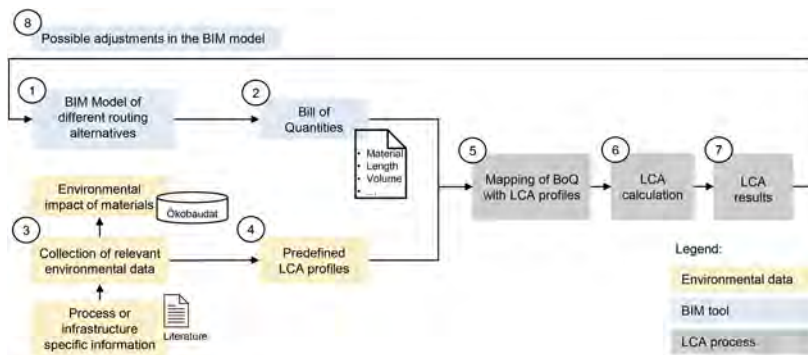


Figure 2. Overview of the proposed methodology including model preparation, calculation, result assembly, and impact evaluation.

After creating the BIM models, all information relevant to the subsequent LCA calculation is collected in the bill of quantities (BoQ). This includes, for example, the type of material such as concrete or asphalt for the superstructure and the associated volumes of the different layers. In the next step, the BoQ is automatically mapped with the LCA profiles.

For compiling suitable LCA profiles, different kinds of sources are considered. The first and main source is the ÖKOBAUDAT which is a German database with verified data quality and uniform data formats (Brockmann et al. 2019). Unfortunately, the ÖKOBAUDAT does not provide all information relevant to the evaluation of civil infrastructure assets yet. Therefore, missing information, such as transport distances caused by the location of the construction site and environmental coefficients for fuel consumption must be gathered from other sources. These sources consist of results from different research studies, which are explained in more detail in the following subsection.

Finally, the LCA calculation can be conducted using the predefined LCA profiles and the information extracted from the BIM models. The calculation of the LCA (indicated as step 6 in Figure 2) reports the GWP for each routing alternative (step 7). Depending on the results, the BIM model can be adjusted to optimize the routing alternative and iterate through steps 1, 2, and 5 to 8 until a sufficient design option is reached.

3.2 LCA profiles for the early planning stage

As outlined before, it is essential to choose suitable LCA profiles that are capable of representing environmental indicators for the different road features.

According to the data typically available in early-design BIM models, assumptions for the material choices and its specific service life cycles of the road superstructure must be taken. Furthermore, indicators for cut-and-fill considerations and engineering structures like bridges and tunnels are required.

For the superstructure of a road, the corresponding environmental indicators are compiled from the ÖKOBAUDAT for the life cycle stages A1-A3, A5, and C1-C2. For an asphalt superstructure, data concerning the different road layers are represented. However, the LCA data quality in the ÖKOBAUDAT for concrete road layers is incomplete. Therefore, it was necessary to compile different materials for individual layers. Since these were not available for all life cycle stages, a comparison at this point is not completely representative. Next to modules C3 and C4, data for the construction installation process (A5) of a concrete superstructure are missing.

In order to roughly estimate the GWP for the early planning phase of a tunnel, estimations developed by Sauer (2016) are utilized. These results in length factors (per tunnel meter) that depend on the selected standard cross-section and the type of excavation. Next to the construction, length factors for the annual GWP, resulting from the use phase, were determined. Thereby, a distinction is made between operation and maintenance. The emissions in the operational phase result from the electricity consumption for lighting and operating technology. Maintenance and servicing of the tunnel structure lead to emissions during maintenance.

The LCA profile for bridges contains area factors for the resulting GWP. These consist of an upper and lower limit value to address the level of uncertainty. As a lower limit, the assumption of Sauer is stored with a GWP of 1000 kg CO₂e/m² bridge area. For the upper limit, a reference value of 1370 kg CO₂/m² is applied which was determined in research projects for uniform sustainability criteria for infrastructure projects (Mielecke et al. 2016). The different life cycle stages are considered with a percentage share for production, maintenance, and end of life.

The amount of traffic emissions depends on the type of cross-section which determines the annual average daily traffic (AADT), the length of the route, and the type of vehicle. The latter is distinguished by car or truck, and both of them are powered by diesel or petrol.

The consideration of electric cars and the changing electricity mix are not part of this framework. In the LCA profiles, the GWP depending on the longitudinal slope for cars and trucks is stored. The associated factors are based on the assumptions of Fischer et al. (2012).

3.3 Required data from BIM model

For the proposed methodology, the information listed in Table 1 needs to be extracted from the BIM model. It is distinguished between information needed to calculate the embodied and traffic emissions. For the embodied emissions, the BoQ is needed which includes mostly the geometric information as volumes and quantities of the construction project. Whether the length, area, or volume of the road structure element is needed, is determined by the associated unit in the LCA profile. To estimate the traffic emissions, the length sections with a continuous longitudinal gradient are required from the BIM model.

Table 1. Required information to extract from the BIM model.

	Required information from BIM model
Embodied emissions	Road corridor with its superstructure layers Volumes of the different layers Cut and fill volumes of road corridor Kind of road structure element Tunnel length and corresponding cross-section type Bridge area
Traffic emissions	Length sections Corresponding longitudinal slope

4 CASE STUDY, IMPLEMENTATION & RESULTS

4.1 Prototypical implementation

A prototypical implementation has been made using well-established software tools. The model preparation takes place in Autodesk Civil 3D (version 2022), where the BoQ and all other relevant information can be extracted using the visual programming application Dynamo for Civil 3D. In addition, the predefined LCA profiles prepared in Excel are imported into Dynamo and linked with the data of the BIM model. The subsequent calculation of the LCA is directly performed in Dynamo and its results are exported to Excel.

The use of existing LCA tools for the calculation process was not possible as not all of the necessary data is available there. Data concerning environmental indicators for tunnel or bridge construction are for example missing. Therefore, as suggested by van Eldik et al. (2020) and Maibaum & Block (2022), visual programming language (VPL) is used for the integration and calculation process. In case of new aspects to consider in the future, visual programming tools offer high adaptability.

4.2 Case study project

In order to validate the presented methodology and its implementation, a case study was carried out. The case study evaluates different routing alternatives located at the Irschenberg in Bavaria and its results can be partially compared and validated with those of Sauer (2016).

Within the framework of a master’s thesis (Bracher 2010), several different routing variants of the motorway A8 in the area of Irschenberg were developed. The new variants should lead to a more optimal routing thus coping better with the considerable amount of traffic and reducing the number of accidents that occur.

Due to the difficult topography, there is a different need for engineering structures such as bridges and tunnels. In order to demonstrate the balancing of the GWP for tunnels, bridges, and roads, two variants are investigated in the following which is both adjusted to the same starting and end point. The alignment of the first variant mainly consists of a 4.3 km long tunnel that passes under the Irschenberg with a longitudinal gradient of 1%. Variant 2 consists of three bridges with a total length of 1.5 km additionally to the road corridor.

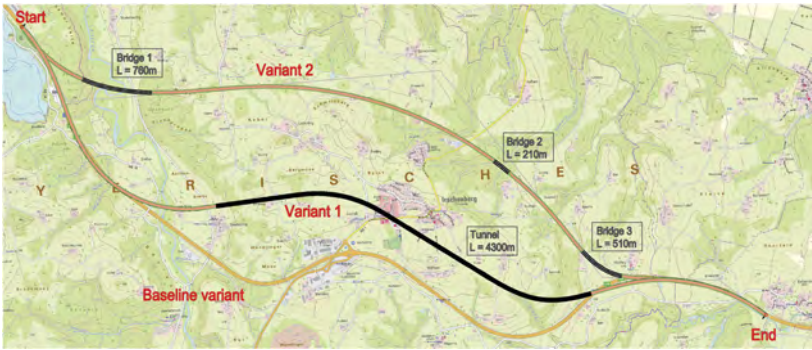


Figure 3. Overview of the case study project consisting of the different road routing alternatives.

4.3 LCA results

The LCA results are exported from Dynamo in an Excel file for each respective routing alternative. The results of the GWP-related emissions are provided in individual worksheets for the different infrastructure elements and the traffic emissions. A comparison over 100 years indicates the dominance of traffic-related emissions. The question arises, after how many years the embodied emissions are compensated by the relatively lower traffic emissions in comparison to the baseline variant. To assess this, the respective cumulative emissions of the different variants are considered over time. In order to assess the traffic emissions of the baseline variant, the results obtained by Sauer (2016) are applied. Exemplarily, only the results of the asphalt superstructure are presented in Figure 4. More detailed results can be found in an extended version (Hofmeyer 2022). The emission results of each

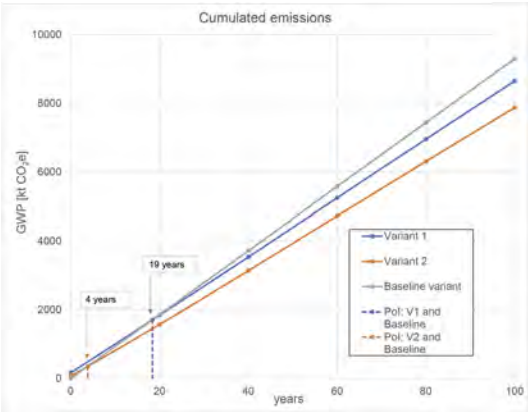


Figure 4. Cumulated emissions over a time period of 100 years of the different variants and its point of intersection (PoI) with the baseline variant.

variant were calculated and visualized cumulatively over the construction life cycle period of 100 years considering all LCA stages, such as production stage (A1-A5), usage (B1) and maintenance (B4) and End of Life (C1-C2). The replacement effects of the LCA results are hardly visible due to the dominating traffic emissions.

The construction of the tunnel in variant 1 results in the highest embodied emissions which leads to the largest GWP of this variant after the construction is completed (year 0). The baseline variant starts with the lowest GWP as no construction measures were applied. Since the baseline variant yields the highest traffic emissions, this approach displays the steepest slope. As a result of the construction of variant 2 and the reduced traffic emissions, the point of intersection (PoI) with the baseline variant is already reached after 4 years. For variant 1, the intersection with the baseline variant occurs after approximately 19 years. With regard to the GWP, the construction of variant 1 or 2 is an improvement over the baseline variant. When comparing variants 1 and 2, variant 2 performs better, as both embodied and traffic emissions are lower.

5 CONCLUSIONS

In the early design stage, only limited information regarding the rough construction parameters of infrastructure projects is available and can be represented in the BIM model. Nevertheless, the choice of different routing variants has a big influence on the environmental impacts of infrastructure projects. Hence, we propose a methodology for an automated calculation of embodied and traffic emissions based on BIM models reflecting infrastructure assets. The LCA results of the applied case study confirm that traffic emissions are responsible for the largest share of the GWP over a lifespan of 100 years. Therefore, it is important to raise awareness in the construction industry that fuel-efficient construction of infrastructure projects can significantly reduce the GWP impacts.

Since the designs for engineering structures, such as bridges and tunnels, have not been detailed at that early planning stage, length factors depending on the required cross-section or area factors are applied for determining the embodied GWP emissions of engineering structures.

As the implementation has shown, all relevant information can be extracted from the BIM model, including the volume of the individual road layers, the cut and fill volumes, the area of the bridge structures, and tunnel lengths. The manual, time-consuming process of calculating the BoQ can thus be reduced in time and increased in quality simultaneously.

The limiting factor in the presented methodology is the missing datasets specifically for infrastructure materials and construction processes. While comprehensive indicators for building construction are already available in the ÖKOBAUDAT, this is unfortunately not the case for infrastructure components. For example, datasets for the different layers of a concrete superstructure are not sufficient or fully missing.

For the future, the presented methodology can be extended due to limitations, which were initially made in order to limit the scope of the present work. The scope of the performed LCA only considers the GWP as an environmental indicator. If the availability of other indicators gets better in the future, the scope can be extended accordingly. At the sustainability level, only the environmental aspects have been evaluated. However, the economical and social dimensions could be extended for a BIM-based decision-making process. Another limitation is the type of traffic mode as only roads have been considered so far. An extension for railway systems would therefore be feasible and is also highly dependent on sufficient LCA data. Therefore, the enrichment of standardized and officially validated life cycle databases for infrastructure projects should be aimed for. In addition to material-specific environmental impacts, more information regarding the lifespan of the materials and transport distances is required. Since the highest embodied emissions in road construction occur during the maintenance phase, the applied maintenance cycles and lifespans are of great consequence. Another open research question considers the dynamic aspect of the LCA profiles and datasets. Different traffic scenarios, the development of fuel efficiency, and the share of electric, hydrogen, or petrol-powered cars lead to dynamic changes in the datasets rather than static ones. Data

from the ÖKOBAUDAT should also vary over time, as different energy sources and mixes change dynamically, too. These changes will lead to a different ratio of embodied and traffic emissions but will give a more realistic prediction of the overall environmental emissions of infrastructure projects.

REFERENCES

- Borrmann, A. & König, M. & Koch, C. & Beetz, J. 2018. *Building Information Modeling - Technology Foundations and Industry Practice*. Springer International Publishing.
- Bracher, B. 2010. *Varianteuntersuchung zum Ausbau der A8 Ost im Bereich Irschenberg*. Master thesis. Munich: Technical University of Munich.
- Brattebø, H. & O’Born, R. & Miliutenko, S. & Birgisdóttir, H. & Lundberg, K. & Toller, S. & Potting, J. 2013. LICCER Model Technical Report: Account of technical backgrounds of the LICCER model: Report No. 4.2 (final report).
- Brockmann, T. & Figl, H. & Huemer-Kals, V. & Kusche, O. & Kerz, N. & Rössig, S. (Eds.) 2019. ÖKO-BAUDAT: Grundlage für die Gebäudeökobilanzierung. *Bundesinstitut für Bau- Stadt- und Raumforschung im Bundesamt für Bauwesen und Raumordnung*. 09 (2).
- de Oliveira, J. A. & Lopes Silva, D. A. & Puglieri, F. N. & Saavedra, Y. M. B. 2021. *Life Cycle Engineering and Management of Products*. Springer International Publishing.
- EN 1990. 2010. Eurocode 0: Basis of structural design.
- Fischer, O. & Sauer, J. & Freudenstein, S. & Xalter, S. 2012. *Ganzheitliche Beurteilung der Nachhaltigkeit und Energieeffizienz bei der Planung und dem Bau von Infrastrukturprojekten: Abschlussbericht*. Munich: Technical University of Munich.
- Hofmeyer, J. 2022. *Evaluating environmental impacts of road routing alternatives using Building Information Modeling*. Master thesis. Munich: Technical University of Munich.
- Liljenström, C. 2021. *Life cycle assessment of transport systems and transport infrastructure: Investigating methodological approaches and quantifying impacts at project and network levels*. Stockholm: KTH Royal Institute of Technology.
- Liljenström, C. & Miliutenko, S. & O’Born, R. & Brattebø, H. & Birgisdóttir, H. & Toller, S. & Lundberg, K. & Potting, J. 2021. Life cycle assessment as decision-support in choice of road corridor: case study and stakeholder perspectives. *International Journal of Sustainable Transportation* 15(9): 678–695.
- Maibaum, J., & Block, M. 2022. BIM-basierte Ressourceneffizienzberechnung mittels LCA-Integration anhand parametrischer Infrastrukturmodelle. *Proceedings of 33. Forum Bauinformatik*: 282–289.
- Mielecke, T. & Kistner, V. & Graubner, C. & Knauf, A. & Fischer, O. & Schmidt-Thrö, G. (Eds.). 2016. *Entwicklung einheitlicher Bewertungskriterien für Infrastrukturbauwerke im Hinblick auf Nachhaltigkeit*. B 126. Bremen: Fachverlag NW.
- Potrč Obrecht, T. & Röck, M. & Hoxha, E. & Passer, A. 2020. BIM and LCA Integration: A Systematic Literature Review. *Sustainability* 12(14): 5534.
- Sauer, J. 2016. *Ökologische Betrachtungen zur Nachhaltigkeit von Tunnelbauwerken der Verkehrsinfrastruktur*. Dissertation. Munich: Technical University of Munich.
- Schmellekamp, C. (Ed.). 2016. *Weiterentwicklung von Verfahren zur Bewertung der Nachhaltigkeit von Verkehrsinfrastrukturen*. B 129. Bremen: Fachverlag NW.
- Slobodchikov, R.; Lohne Bakke, K. & Ragnar Svennevig, P. & O’Born, R. 2019. Implementing climate impacts in road infrastructure in the design phase by combining BIM with LCA. *IOP Conference Series: Earth and Environmental Science* 323(1): 012089.
- van Eldik, M. & Vahdatikhaki, F. & dos Santos, J. & Visser, M. & Doree, A. 2020. BIM-based environmental impact assessment for infrastructure design projects. *Automation in Construction* 120: 103379.
- Zinke, T. & Müller, M. & Ummerhofer, T. 2021. Ganzheitliche Analyse und Bewertung von Infrastrukturprojekten: 257-270. In: Hauke, B. (Ed.) *Nachhaltigkeit, Ressourceneffizienz und Klimaschutz*. Berlin: Ernst und Sohn.
- Zinke, T. & Müller, M. & Hermann, M. 2022. Integrale und ganzheitliche Planung von Straßenbrücken auf Basis von hierarchischen Modellen. *IntegBridge*: 1281.

BIM-based EPD adaption in the context of ecological sustainability and municipal infrastructures

J. Maibaum, M. Block & M. König
Ruhr University Bochum, Bochum, Germany

A. Wachsmann
Hochschule Karlsruhe, University of Applied Sciences, Karlsruhe, Germany

ABSTRACT: Municipal infrastructure projects are mostly awarded, planned and financed at the municipal level. The quantities, materials, construction processes and construction equipment used in these projects are currently only recorded and linked to a limited extent. Therefore, it is presently not possible to record the entire inventory and environmental impacts in detail. Environmental product declarations (EPDs), which can be used for this purpose, are also incomplete at present, particularly for the infrastructure sector. To make progress in this field, a method has been developed to investigate, compare, validate and adapt digital EPDs. In addition, integration with the BIM methodology is being undertaken to enable a model-based life cycle approach for typical municipal road infrastructure structures. The methodology is based on existing EPDs and allows the inclusion of additional life cycle phases through data input options. In order to include the LC phases transportation, O&M and recycling, a generic and continuously extensible application was implemented.

1 INTRODUCTION

The construction of infrastructure is reported to be one of the most resource-intensive sectors and is responsible for a substantial amount of energy consumption, greenhouse gas emissions, and the high-demand binding and leveraging of raw materials (Backes Taverso 2021). In the context of the increasing awareness of sustainable and resource-conserving construction, various challenges emerge. The climate protection law passed in Germany for example demands, a significant reduction of emissions and the consumption of resources and energy. Simultaneously, recycling rates should be increased and material cycles closed, with the public sector client acting as a role model. The provision and maintenance of public infrastructure are key factors in considering sustainability. According to this, the public administration is responsible for the awarding of contracts, planning, maintenance, renovation, and demolition, and, if necessary, also for the execution of construction work. To enable the public administration to consider sustainability analyses in these processes, it needs reliable and consistent information management. This can be ensured by using Building Information Modeling (BIM). The fundamental assumption of BIM to comprehensively map the building life cycle in terms of information technology also coincides with the definition of the circular economy “an industrial economy that is restorative or regenerative by intention and design” (MacArthur 2012).

To provide circular information management, quantities, volumes, and conditions of infrastructure must be adequately quantified. Based on this, a comparison of financial requirements and ecological impact becomes feasible. The ecological impact can finally be assessed by using environmental product declarations (EPD). These can currently be used as a basis for a subsequent ecological evaluation of materials and, to a minor extent, processes (compare section 3.1). The contribution provides an approach for ecological sustainability considerations of municipal construction measures via the adaption of relevant EPD data sets.

2 RESEARCH FOUNDATION

In terms of sustainability in the field of infrastructure, the municipality is a player that has received little attention so far, even though it is responsible for more than two-thirds of the entire road network in Germany. The challenges listed are now being explored in the scope of a municipality, multi-criteria sustainability assessment, and the digital working method BIM to provide the scientific foundation and context for the EPD-related approach.

2.1 *Sustainability in municipal asset management*

Asset management (AM) is the organizational process of allocating human, equipment, and financial resources to physical assets throughout their life cycle to achieve defined performance and cost objectives at acceptable levels of risk, taking into account the relevant political, economic, social and technological context (Ruitenburg et al. 2014). In infrastructure AM, depending on the organizational orientation, road, road installations and equipment, parking guidance system, bridge, and sewer are understood as assets (Buttgereit et al. 2021). However, AM currently focuses primarily on safety and economic efficiency (Staubli et al. 2017). In the long term, sociocultural requirements such as generational equity and ecological aspects such as resource-efficient construction and efficient recycling management must also be included in this process. In this development, municipal AM in particular has a special social task. Currently, construction projects are often awarded solely on the basis of economic factors, with the result that quality and sustainability criteria only have a reduced impact on project awards. As a result of the transformation of the construction industry towards greater resource efficiency and sustainability mentioned in section 1, criteria such as these must also be increasingly taken into account when awarding contracts. In addition to numerous international assessment procedures, national assessment systems such as the Assessment System for Sustainable Building (BNB) and German Sustainable Building Council (DGNB) can also be used for building construction. For infrastructure construction, no assessment system is so far legally binding at the national level. The Federal Highway Research Institute (BAST) provides an assessment system for the infrastructure systems road, bridge, and tunnel, which equally takes into account ecological and socio-cultural criteria in addition to economic criteria (BAST 2016).

2.2 *Ecological sustainability assessment - Life Cycle Assessment (LCA)*

In terms of ecological assessment, the LCA method can be applied. It is specified in ISO 14040 and ISO 14044. Concerning these standards, the method follows a four-step iterative process (ISO 2006a, ISO 2006b). This process consists of the definition of the objective and scope, the Life Cycle Inventory (LCI), the Life Cycle Impact Assessment (LCIA), and the interpretation of the LCIA. The first step is to collect relevant data and quantify input and output flows. Next, direct environmental impacts are recorded based on the inventory. Linked to this, the total environmental impacts recorded are categorized, characterized, and finally interpreted and evaluated. LCI and LCIA data are generated for a material unit and, to a lesser extent, for a process unit as an EPD and stored in an EPD database. LCA data sets can be specified as the smallest modeling unit in a life cycle model. In the process, each of these data sets incorporates different inputs (resources) and outputs (emissions and waste products) (Pasetto et al. 2017). Several of these data sets are combined into one life cycle model. Data sets can be subdivided into cradle-to-gate, cradle-to-grave, and cradle-to-cradle data collections (Olivier et al. 2016). A cradle-to-gate data set covers the environmental impacts from extraction to the end of production. Cradle-to-grave also includes the impact of product disposal, and cradle-to-cradle additionally contains the impact when returning the product to the use phase. As a current challenge in the application of LCA Dossche et al. (2017) state that LCA provides a global framework, but not an exact technique to calculate environmental impacts. This makes it possible to perform LCA in different ways as various boundary conditions are applicable. LCA research is a fragmented state which makes a comparison challenging.

In general, several commercial and non-commercial LCA tools are available that can be used to determine the life cycle impact of road infrastructure (e.g. asPECT (British), ECORCE-M (France) PaLATE (USA)). For the building construction sector, several BIM-LCA-tools like Tally and One Click LCA which attempt to take the BIM method into account

are existing. For the infrastructure sector, however, this approach is still only feasible to a very limited extent. In particular, the non-transparent calculation methods, as well as the lack of certain LC phases, the poor comparability, and additionally the less implemented EPD product range, are to be seen as disadvantages (dos Santos et al. 2017). By integrating LCA into the BIM methodology, different challenges can be addressed. The work from Hausschild et al. (2018) points the challenges of the integration of LCA into BIM out by stating to focus on the digital and transparent quantification and calculation of environmental impacts, which leads to objective benchmarks. Despite the continuous progress of digitization and the application of the building information modeling (BIM) method in road construction, its dissemination is currently still limited. Furthermore, the integration of LCA into the BIM methodology is also still in the early stages (Dalla Mora et al. 2020). The heterogeneous software landscape is also cited as challenge in integrating LCA with BIM, which leads to incomplete BIM models. Moreover, it is stated that currently, no explicit data structure exists for the integration of environmental and BIM data (van Eldik et al. 2020).

When it comes to technical implementation Slobodchikov et al. (2019) showed a simplified possibility of linking LCA calculations in the BIM methodology using a generic approach as an example. The project uncertainties or the availability of data turned out to be a major challenge here. A first approach of BIM-based multi-criteria sustainability analysis is provided by Lammers and Forth (2022) by combining the methods of LCA and LCC with the BIM method. For this purpose, they use related databases and the IFC format in order to automatically evaluate the sustainability of buildings over their life cycle in early planning phases on the basis of the available data and calculation methods.

2.3 *Environmental product declarations - EPD*

Based on LCA, EPDs represent a standardized format for reporting LCA outcomes in a third-party audited and certified document. Within the European Union, the EN 15804 standard contains the core category rules for product EPDs in the building and construction sector as well as a subdivision of the life cycle into information modules (EN 2012).

An EPD database should provide uniform naming, comprehensive input/output flows for data sets, a consistent modeling approach, and documentation. The aggregation of process and inventory is done either individually or grouped depending on the database (Olivier et al. 2016, Pagnon et al. 2020, Takano et al. 2014). Databases such as GaBi and Ecoinvent provide mostly reference data, EPD platforms such as EcoPlatform EPD, IBU, INIES, ÖKOBAUDAT, and the international EPD system also offer ready-made EPDs.

In Germany BNB offers ÖKOBAUDAT, an open-source and -access web-based EPD database, and with eLCA, an online EPD analysis tool is available. The tool is launched and managed by the German Federal Institute for Research on Building, Urban Affairs and Spatial Development (BBSR). The motivations for the digitization of the LCA infrastructure under the BNB were to enhance all data-related workflows, to ensure independence, and to reduce the cost of preparing LCAs for buildings (Brockmann et al. 2019). At the European level, with InData, a working group exists that aims to establish an open, web-based, international data network for EPD/LCA data using a common data format and open-source software. The main objective is to establish best practices for providing digitized EPD as a quality source of verified EPD/LCA data for BIM, as well as for construction LCA and other relevant uses. Globally, about 6000 registered EN 15804-compliant EPDs are currently available. Another reason for working on this topic is the high demand for linking EPD data with BIM-based building models (Brockmann et al. 2019).

Lasvaux et al. (2015) note that on the database level, the EPD values vary depending on the LCIA indicators and the building materials. The discrepancies are caused by the fact that in mixed EPD databases, different background data are used in the same EPD database, and, for certain construction materials, specific procedures created by the manufacturers in the national context are applied. Stapel et al. (2022) determined in their qualitative analysis of EPD data sets, that a large proportion of EPDs include a full life cycle with End-of-Life (EoL) options. However, nearly 45% of the data sets only consider phases A1-A3 (Production). This proportion is expected to change in the transition to EN15804+A2, when C1-C4

(EoL) and D (Recycling) will be included in the data set (c. f. 1). Thus, the study highlights the importance of transparency and more consistent guidelines for publishing data in the process of supporting LCA. According to the authors, collective EPDs or generic data from public databases are a valid instrument.

Nevertheless, when it comes to comparing alternatives in the bidding phase, a specific EPD from the manufacturer of the product to be installed is appropriate and should be required. For each project, a specific LCA should be performed at every design and construction phase based on data from product-specific EPDs adjusted to project-specific assumptions (ArcellorMittal 2022).

In contrast, the approaches of Palumbo et al. (2020) and Carstens et al. (2021) focus on a better understanding of existing EPD data sets. The first named quantified in terms of different types of EPDs that there have been limitations in matching impacts generated in Modules A4 to D (resulting from the boundaries of the LCA system). This is due to the lack of consistency between the different data granularities (generic versus specific). To meet this problem the authors generate safety factors and benchmarks. Further Carstens et al. (2021) also used various benchmark methods to make the results of EPDs more accessible to non-experts. They establish reference values through statistical analysis and develop single result benchmarks based on EPDs for better comprehension.

It should be concluded that the analysis and evaluation of EPD data sets and their background processes are already partially part of the research. However, especially for the infrastructure sector and the special features mentioned, the path to valid EPDs is currently still long.

3 METHODOLOGY AND CONCEPT

An approach has been developed that aims to address the current difficulties in using EPD databases and data sets at a technical level. Our implementation is based on the problems identified in section 2. In particular, the rudimentary availability of EPDs for the infrastructure sector leads to short-term assessments and cannot be used beneficially as in the municipal AM. The focus of the implementation is currently on the determination of the ecological impact of a construction measure in relation to the road infrastructure asset.

Table 1. Illustrative comparison of EPDs data sets from various databases for the main used infrastructure material asphalt (Selection); Grey: LC phases that currently receive low to no coverage in the available EPD data sets; Enclosed dots indicate that isolated data sets exist in the respective LC phase and database.

Database und dataset comparison for the infrastructure construction product ASPHALT				LC phase																		
				Production			Design			Use					End-of-Life			RC				
Data set publisher	Country	Amount datasets	Total Amount	Data format	A1	A2	A3	A4	A5	B1	B2	B3	B4	B5	B6	B7	C1	C2	C3	C4	D	
Ökobaudat	DE	6 (EN 15804+A1)	1085	csv, xml	●	●	●		●									●	●	●	●	●
Ökobaudat	DE	6 (EN 15804+A2)	668	csv, xml	●	●	●		●									●				●
epddanmark	DK	1 (EN 15804+A1)	271	PDF	●	●	●	●														
epddanmark	DK	3 (EN 15804+A2)	74	PDF	●	●	●	●										(●)	(●)	(●)	(●)	(●)
International EPD-System	SWE	36	3603	PDF (other)	●	●	●											(●)	(●)	(●)	(●)	(●)
Eco Plattform	BEL	15	4353	csv, xml	●	●	●	(●)										(●)	(●)	(●)	(●)	(●)
IBU	DE	2	1731	PDF (other)	●	●	●	(●)	(●)									(●)	(●)	(●)	(●)	(●)
asphaltEPD	US	340	340	PDF	●	●	●															

3.1 Proof-of-concept assessment of EPDs

As described in section 2 environmental product declarations are essential for being able to define ecology in the sustainability evaluation of municipal infrastructures and used to determine the environmental impact of materials and reduced construction processes. Furthermore, some of the production, transportation and construction processes are mapped indirectly in material EPDs, since the material EPDs are based on specific manufacturing processes. The

identified inventory and calculated environmental impact can be aggregated and incorporated into the ecological sustainability assessment of a planned construction measure. Economic and socio-cultural data are not included, so only a subset of the overall sustainability assessment is highlighted, which is relevant for the municipal AM.

An analysis and evaluation of the EPD availability were carried out as an example for the construction object asphalt surface course. An overview of the identified data sets, their completeness, and their source is shown in Table 1. Further, the table illustrates that the data sets are not valid for the complete life cycle. Especially the operation & maintenance phase as well as the phase of installation, demolition, and reuse are not accurately represented.

In addition, it should be inserted that the automated use of the data sets is only possible to a limited extent. Thus, it is necessary to implement an intermediate database in order to have a clear foundation for the subsequent integration of the LCA into the BIM methodology.

3.2 *Components of the implementation*

The contribution primarily provides a concept for the rational extension of existing EPD data sets and also offers the basis for the extension of economic and socio-cultural sustainability aspects. The example of asphalt pavement is used as a representative example to show existing EPD availability and which LC phases are included or not included so far. In national terms, asphalt road pavements account for the vast majority of road pavement types. Furthermore, it was quantified that the availability of asphalt EPDs is the highest compared to other infrastructure construction materials. In addition to the amount of EPD data sets, Table 1 also shows EPD data sets provided by organizations and individual companies in document format.

Especially in the case of EPDs provided in document format, automated use and linking with a BIM model is not directly applicable. An intermediate step has to be taken via a database to prepare the data for use in a machine-readable format and the ILCD structure. Subsequently, the data is imported and - if needed - adapted via an EPD editor. Our focus hereby lies on mapping the environmental impact of measures via EPDs in terms of certain resources and indicators. It is possible to adjust or add indicator data for individual LC phases. This is essential due to the special characteristics of infrastructure structures mentioned in section 1, since, as shown in Table 1, it is mainly the LC phases O&M that have to be mapped in a reliable and proper way. In addition to the adaptation of material EPDs, available EPDs of construction processes can also be adapted or extended accordingly. This is done - analogously to the EPDs - for individual LC phases. The interaction and aggregation of materials and processes are essential for the planning of measures.

Following this, the adapted EPDs are linked to the BIM model. This is realized via material or GUID matching, assigning the individual material layers of the BIM model to the material data of the EPDs. Based on this, a BIM-integrated determination of the LCI (life cycle inventory) and LCIA (life cycle impact assessment) data can be performed. The determined environmental data can be visualized via graphs or further used in a model-based way in the form of a property set. A high level of expertise in the planning, construction, and maintenance of individual infrastructure structures is required. The knowledge base for various procedures will be supplemented and the implicit knowledge, which is often contained in domain experts or documents, will be made machine-readable, graph-database driven, and retrievable. A clear illustration of the individual processes and sub-processes is provided in Figure 1.

3.3 *Technical implementation and proof of concept*

From a technical point of view, Autodesk products were used for the implementation and the open-source environment Dynamo was applied for visual programming. Dynamo is already integrated as a plug-in in the Autodesk software at installation. It can be observed that visual programming tools like Dynamo are being predominantly and increasingly applied for the integration of LCA into BIM methodology (Collao et al. 2021). This is in part due to the fact that Dynamo and other visual programming tools provide an intuitive and user-friendly interface for designers and analysts to seamlessly integrate LCA considerations into the design process.

In the first step of the implementation EPDs had to be partly converted manually from the documents into a structured data template. For this purpose, the guideline for the BIM-compliant use of data templates of EPDs for building products was used as a reference (ISO 22057). The EPD database is accessed via a Dynamo script and can be addressed in a user-defined way in order to first import and then customize the relevant data sets. This is accomplished via the integrated user interface of the EPD editor. Next, by implementing geometric and mathematical operations, both life cycle inventory data (LCI) and impact assessment data (LCIA) are transparently determined in the LCA implementation step. For the modeling of three-dimensional road infrastructure models Civil 3D was used. The infrastructure information model (IIM) is based on two-dimensional parametric road cross sections, to which the LCA property data sets are attached. In a final implementation step, relevant LCA data were linked to the model via a Dynamo script. Since there is currently no adequate application programming interface (API), the data sets were imported from Excel and finally exported again.

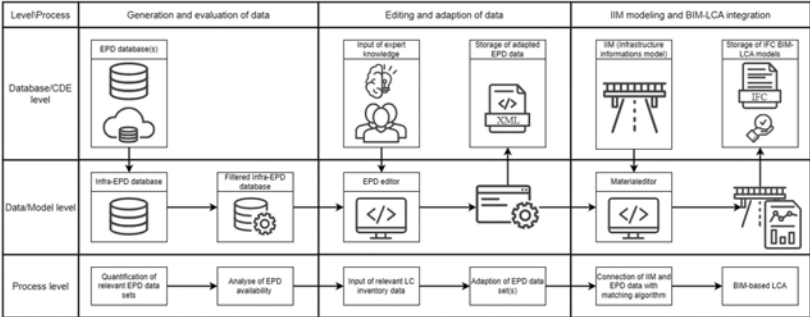


Figure 1. Implementation processes from data generation, adaptation and following the integration of LCA into BIM methodology classified into the database, data, and process level.

4 USE-CASE

The described methodological approach will be exemplified by a generic use case. A standardized parametric IIM, which is based on the national German building regulations, serves as a basis. The EPD adjustment and subsequent BIM-based LCA execution are subsequently performed for the main road construction material asphalt. Asphalt data sets shown in Figure 1 provide the data foundation for this. For this purpose, a typical construction measure in a municipal context is simulated with a renewal of a fictitious asphalt pavement. On the one hand, the material is relevant and, on the other hand, the renewal process of the construction. The material EPDs include the LC phases of production (A1-A3), transport (A4, C2), and demolition (C1) of the new road layer. The process EPD, meanwhile, contains data for the construction process (A5) of the layer. Operational, O&M (B1 -B7), and other LC phase data do not exist and can be added to the data set accordingly via the EPD editor (c.f. 2). The LCA results for a construction measure are subsequently composed of the partial LCA results of the material and construction process. The as-built measure LCA values can then be compared for various construction implementations. Thus, it is possible to derive conclusions about the environmental sustainability of infrastructure structures. The aim here was to show the sequence and execution of the implementation and to illustrate the potential of the method created.

5 CONCLUSIONS

The critical summary of the paper is intended to present the current implementation status, and identify problem areas and force future extensions and connecting factors that can be anticipated. In a nutshell, an approach for transparent, expandable EPD use was developed.



Figure 2. Left: Input of measure relevant material and process data to complete or adapt the existing EPD database for certain LC phase; Right: Linking of LCA data to IIM; At the edges: Relevant inputs and outputs for the implementation approach.

For this purpose, in a preliminary phase, available EPDs were quantified, considered, and finally qualitatively checked for completeness. By means of a low-threshold and modular EPD tool, the EPDs can be adapted for the respective use case and finally linked to the IIM for sustainability assessment. The approach currently focuses on the ecological aspects of sustainability assessment but suggests that economic and socio-cultural factors could also be included in the future. In particular, comprehensive sustainability assessment is important in the context of municipal asset management, particularly when it comes to planning and implementing infrastructure construction measures. For the digital tool-based implementation, the knowledge of domain experts is currently necessary, which will be countered in the future by the creation of a knowledge database, whereby the approach and implementation of the coherent holistic sustainability assessment within a digital transparent BIM-based application can be helpful in decision-making support for measures.

Currently, the existing EPD data sets and the linked properties of EPDs are not useful for the holistic sustainability assessment of infrastructure constructions and measures due to the lack of material EPDs and LC phases. Also the lack of transparency is a current drawback. In addition, only some EPDs exist in machine-readable formats and can be addressed via APIs. To address this, initial tools are emerging that allow EPDs to be edited, such as BNB's EPD Editor and the EPD-Analyzer. In particular, BIM-based approaches to EPD editing have not yet been part of the research. In addition, the current benefit of integrating the LCA methodology into the BIM methodology, especially for the municipal asset management of infrastructure construction assets, is to be assessed as rather low. The purely ecology-oriented sustainability survey is often insufficient here.

The approach presented in this paper also provides a number of conceivable methodological extensions and additional technical implementations. In the first step, the current structure can be extended by a database that can store and query highly interconnected data. The structure of graph databases is suitable for this purpose, as it can be used to map complex relationships, as for infrastructure construction measures. In the mid to long term, the current focus on quantifying ecological impact should at least be supplemented by the area of economics. An additional extension of the socio-cultural and technical domain would be useful to achieve a more comprehensive assessment of sustainability. Finally, it can be assumed that in the future, the holistic consideration of environmental impact aspects will become increasingly relevant, especially for municipal infrastructure construction projects. However, at present, there are neither BIM-integrated LCA tools nor a wide-ranging and reliable amount of environmental product declarations (EPDs) for infrastructure materials and processes defined.

ACKNOWLEDGMENT

The research project *RekoTi – Ressourcenplan kommunaler Tiefbau* created the context for this paper. It is funded by the German Federal Ministry of Education and Research (BMBF) [grant number 033R264] under the scientific program *Ressourceneffiziente Kreislaufwirtschaft – Bauen und Mineralische Stoffkreisläufe (ReMin)* and supported by the *Research for Sustainability (FONA)* platform. The authors are responsible for the content of this publication.

REFERENCES

- ArcelorMittal Commercial RPS - Sheet piling - Luxembourg. 2022. Implementation of environmental criteria in civil engineering (infrastructure).
- Backes, J. & Taverso, M. 2021. Application of Life Cycle Sustainability Assessment in the Construction Sector: A Systematic Literature Review. In *Processes*.
- BAST (Bundesanstalt für Strassenwesen). 2016. Conceptual estimates for the sustainability assessment in the life cycle of elements of the street infrastructure. Heft B 126 (and B 125, S 97). In Fachverlag NW.
- Brockmann, T. 2019. Digitalization of building LCA and international activities – in the context of German assessment system for sustainable building. In *IOP Conference Series: Earth and Environmental Science*.
- Buttgereit, A. et al. 2021. Erhaltungsmanagement - Ein Baustein im Asset Management in Münster (Teil 2). *Straße und Autobahn* (1.2021), 33–39.
- Carstens, A. et al. 2021. Deriving Benchmarks for Construction Products Based on Environmental Product Declarations. In *Advances and New Trends in Environmental Informatics*.
- Collao, J. et al. 2021. BIM Visual Programming Tools Applications in Infrastructure Projects: A State-of-the-Art Review. In *Applied Sciences*.
- Dalla Mora, T. et al. 2020. Key Parameters Featuring BIM-LCA Integration in Buildings: A Practical Review of the Current Trends. In *SUSTAINABILITY*.
- dos Santos, J. M. O. et al. 2017. Comparison of Life-Cycle Assessment Tools for Road Pavement Infrastructure. 28–38. In *Transportation Research Record: Journal of the Transportation Research Board*.
- Dossche, C. et al. 2017. Use of Life Cycle Assessments in the Construction Sector: Critical Review. In *Procedia Engineering*.
- Hauschild, M. et al. 2018. Life cycle assessment: Theory and practice. In *SpringerLink*.
- EN. 2012. EN 15804: Sustainability of construction works - Environmental product declarations - Core rules for the product category of construction products. In *European Committee for Standardization*.
- ISOa. 2006. ISO 14040: Environmental management - Life cycle assessment - Principles and framework. In *International Organization for Standardization*.
- ISOb. 2006. ISO 14044: Environmental management - Life cycle assessment - Requirements and guidelines. In *International Organization for Standardization*.
- Lammers, B. & Forth, K. 2022. IFC-based variant analysis considering multi-criterial sustainability analysis of buildings. In *Proceedings of 33. Forum Bauinformatik*.
- Lasvaux, S. et al. 2015. Comparison of generic and product-specific Life Cycle Assessment databases: application to construction materials used in building LCA studies. 1473-1490. In *The International Journal of Life Cycle Assessment*.
- Ellen MacArthur Foundation. 2012. *TOWARDS THE CIRCULAR ECONOMY - Economic and business rationale for an accelerated transition*.
- Olivier, J. et al. 2016. *Environmental life cycle assessment*. In *CRC Press*.
- Pagnon, F. et al. 2020. A review of online sources of open-access life cycle assessment data for the construction sector. In *IOP Conference Series: Earth and Environmental Science*.
- Palumbo, E. et al. 2020. How to Obtain Accurate Environmental Impacts at Early Design Stages in BIM When Using Environmental Product Declaration. A Method to Support Decision-Making. In *SUSTAINABILITY*.
- Pasetto, M. et al. 2017. Life-Cycle Assessment of road pavements containing marginal materials: comparative analysis based on a real case study. In *Pavement Life-Cycle Assessment*.
- Ruitenburg, R.J., et al. 2014. A Multidisciplinary, Expert-based Approach for the Identification of Lifetime Impacts in Asset Life Cycle Management. In *Procedia CIRP*, 22, 204–212.
- Slobodchikov, R et al. 2019. Implementing climate impacts in road infrastructure in the design phase by combining BIM with LCA. In *IOP Conference Series: Earth and Environmental Science*.
- Stapel, E. et al. 2022. Environmental Product Declarations - an extensive collection of availability, EN15804 revision and the ILCD+EPD format. In *IOP Conference Series: Earth and Environmental Science*.
- Staubli, R. et al. 2017: *Werterhaltung von Straßen - Ein Leitfaden für Gemeinden und Städte*. Hg. v. Organisation Kommunale Infrastruktur (OKI), Schweizerischer Gemeindeverband (SGV), Schweizerischer Städteverband (SSV).
- Takano, A. et al. 2014. Comparison of life cycle assessment databases: A case study on building assessment. 20–30. In *Building and Environment*.
- Trunzo, G. et al. 2019. Life Cycle Analysis of Road Construction and Use. In *SUSTAINABILITY*.
- van Eldik, M. A. et al. 2020. BIM-based environmental impact assessment for infrastructure design projects. In *AUTOMATION IN CONSTRUCTION*. 10.1016/j.promfg.2015.07.483.

Element approach for BIM-based life-cycle modeling of bridges

M. Müller

Karlsruhe Institute of Technology, Karlsruhe, Baden-Wuerttemberg, Germany

T. Zinke

HOCHTIEF ViCon, Essen, North Rhine-Westphalia, Germany

T. Ummenhofer

Karlsruhe Institute of Technology, Karlsruhe, Baden-Wuerttemberg, Germany

ABSTRACT: In order to establish a sustainable bridge assessment within a practical planning routine, it is necessary to reduce the calculation effort by applying automated algorithms. Information generated by the application of Building Information Modeling (BIM) can be used as project-specific input data for this purpose. For the method of life cycle assessment (LCA), the approach of linking the materials of the BIM-model with environmental data sets to calculate the ecological impacts has become widely established. This material-based approach provides sufficiently accurate results for an ecologic assessment in late planning phases. For early planning phases it is not directly applicable and the approach is not transferable to the application of the calculation methods life cycle costing and macroeconomic cost calculation.

The approach presented in this paper introduces a framework that can be used to calculate the life cycle impacts of a bridge by linking the objects of a BIM-model with the content of a hierarchically structured catalogue of elements. To establish this catalogue, individual items are pre-balanced and combined to generate base elements. To represent the entire life cycle of a bridge, follow-up elements, which occur after a specific time interval within the use and dismantling phase, are additionally defined. The individual base elements are combined into generalized major and macro elements into which the individual base elements are included with statistical shares. By applying the different element types, it is possible to use BIM-bridge models with different levels of detail for a holistic assessment and to include all impacts that occur during the complete life cycle.

1 INTRODUCTION

The sustainability assessment of bridges requires the application of different assessment methods. Some methods are based on qualitative and subjective evaluations and are therefore difficult or impossible to automate. For some quantitative assessment methods, Building Information Modeling (BIM) can be used to (partly) automate the calculation procedures and therefore reduce the manual effort significantly. This reduction is necessary to implement sustainability assessment as a method in everyday infrastructure planning. For life cycle assessment, a material-based approach using the volumes of BIM-objects and multiplying the derived material quantities with environmental impact datasets has been implemented in several software products. This paper discusses the shortcomings of such material-based approaches and introduces an element approach which can be used to calculate life cycle costs, ecological impacts and macroeconomic costs.

2 SUSTAINABILITY ASSESSMENT

In the following, the methodological principles and standards for the quantitative methods of life cycle assessment, life cycle costing and macroeconomic costing are shortly described. For these methods the element approach can be used to calculate the impacts of a bridge using data generated by Building Information Modelling as project specific input data.

2.1 *Life cycle assessment*

Life cycle assessment (LCA) is a method for quantifying the potential environmental impacts of product systems over their entire life cycle. The calculation is standardized since 1996. DIN EN ISO 14040 (2021) and DIN EN ISO 14044 (2021) provide the methodological basis. A specification for the building product level is made in DIN EN 15804 (2022). Framework conditions at the building level are given in DIN EN 15643 (2021). The calculation methodology is specified for buildings in DIN EN 15978-1 (2021) and for infrastructures in DIN EN 17472 (2022). All material and energy flows within the specified temporal and spatial system boundaries must be recorded by default to fulfill the requirements of the standards. This surveyed life cycle inventory is translated into a life cycle impact assessment using characterization factors. As a result, the potential environmental impacts within different impact categories are provided.

2.2 *Life cycle costing*

Life cycle costing (LCC) is a method for quantifying the costs incurred within firmly defined system boundaries for a product system. The method is standardized by DIN EN 17472 (2022) and ISO 15686-5 (2017). Costs that occur during the use phase and dismantling phase are discounted to the year of construction using a discounting rate.

2.3 *Macroeconomic costing*

Most construction, repair and maintenance measures on bridges result in an impact on traffic flow. Due to construction sites the capacity of adjoining roadways is reduced. This leads to traffic jams and therefore large time losses, especially on highly frequented routes, for the general public. In addition, the emission of pollutants from cars increases significantly in a stop-and-go mode of driving. All mentioned effects can be monetized which means that impacts are transferred into monetary units. For example, time lost due to traffic disruption can be monetized by a macroeconomic hourly rate. As a result, the calculated macroeconomic costs can be compared with the direct construction-related costs. It is noticeable that these macroeconomic costs can exceed the direct building-related costs by a far extend (Zinke 2016). The calculation is part of whole-life costing (WLC) according to ISO 15686-5 (2017) and DIN EN 17472 (2022). The calculation rules for different impact categories are based on state-of-the-art descriptions in different national and international studies, for example Axhausen et al. (2014).

2.4 *BIM-based life cycle analysis*

Most existing calculation approaches within a BIM-based sustainability assessment use a material-based methodology (Alvarez Antón & Diaz 2014) and they mainly refer to the method of life cycle assessment. The calculation process is normally designed as follows: The BIM-model is transferred from the authoring software to an environmental assessment software via an IFC-interface or a plug-in. In the environmental assessment software, an environmental product declaration (EPD)-dataset is assigned to each geometric BIM-object based on the assigned materials in the BIM-model. The selection should always be checked manually. The multiplication of the EPD-datasets with the material quantity of the geometric objects delivers the result in the single environmental impact categories.

An assessment applying a material-based approach leads to sufficiently accurate results in later planning phases for calculating the ecological impacts of the main materials used to erect a bridge. However, if the entire life cycle is to be considered, the problem arises that building materials used

in different elements possess different service lives and undergo different measures during the life cycle. The concrete which is part of a bridge edge beam, for example, is renewed on average every 33 years, while the concrete of the abutment survives the 100-year service life of a bridge. Accordingly, an assignment of specific life cycle measures to single materials is not appropriate.

Sustainability analyses in early phases can create great benefits as in these phases the greatest leverage for influencing the later impacts exists. However, BIM-models, especially in early planning phases, do not have the necessary level of detail for an analysis on a material basis. For example, connection details are usually not modelled within the design planning. Corrosion protection systems are often not represented as geometric objects at all and are therefore they are not considered in the material-based methodology.

Furthermore, depending on the selected system boundaries and calculation methods used, the material-based methodology can result in significant inaccuracies. This can be explained at the example of corrosion protection systems. While for LCA focusing on building products (equivalent with the modules A1-A3 defined in DIN EN 15643) the neglect of the materials used in the corrosion protection systems is partly understandable due to the relatively small quantities of coating. Significant effects arise in the energy-intensive application of coatings (A5), as well as the repair measures (B2) and renewal processes (B4, B5) during the life cycle. For the methods life cycle costing and macroeconomic costing, these components cannot be neglected due to the costly scaffolding and significant traffic disruptions.

3 ELEMENT APPROACH

The element approach comprises that instead of focusing on materials, elements are used for the different life cycle-oriented assessment methods. These elements consist of all the items needed to fully compose an element. As an exemplary element the organic corrosion protection for steel beams is described. For this element, different items consisting of materials (e.g. coating materials) and processes (blasting the surface, coating the surface, etc.) are used. For all items, the resulting costs, environmental impacts and traffic impacts are pre-balanced.

3.1 Considering different levels of detail

In early planning phases and sometimes also in later planning phases shear studs or coatings are normally not represented in BIM-Models as specific geometric objects. To enable an analysis in early planning phases, pre-balanced items are added to base elements which are combined to major and macro elements (see Figure 1). The quantities of the pre-balanced base elements are allocated in the major and macro elements with statistical shares.

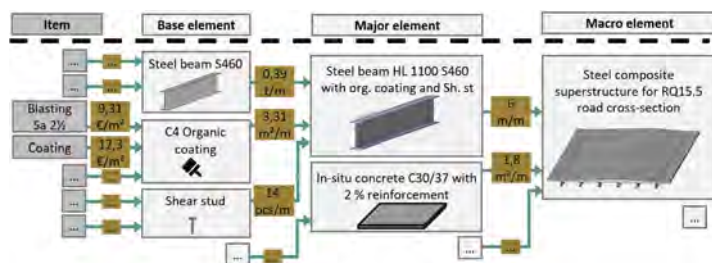


Figure 1. Composition of base, major and macro elements using statistical shares (Müller 2023).

The workflow foresees that macro elements and major elements (depending on the detailing of the BIM-model) are used in early planning phases. Accordingly, results can already be created in early planning phases in which all non-modelled components are represented by statistical shares in the composed elements. In the course of planning, the major and macro elements are

replaced by base elements and thus the statistical shares are replaced by project-specific quantities which increases the accuracy of the calculation (see Figure 2).

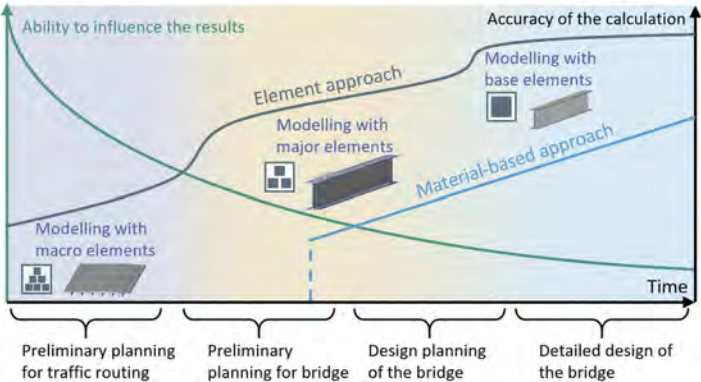


Figure 2. Life cycle dependent usage of different types of elements mapped with the corresponding accuracy of the calculations.

3.2 Life cycle maintenance measures

Base elements represent all bridge construction parts containing all potential impacts occurring in the production and erection phase. In order to represent all measures during the use and dismantling phase, follow-up elements are defined. Follow-up elements, like base elements, are composed of pre-balanced items, but only occur after a maintenance strategy-dependent time interval during the life cycle. In order to represent different measures, a distinction is made between measure specific types of follow-up elements. Maintenance and repair elements are elements, that occur during the service life of a base element. Selective dismantling and renewal elements occur after the underlying base element has reached the end of its service life. Once the service life on a structural level has been reached, a dismantling element occurs which represents the demolition of the complete structure. Figure 3 illustrates the interactions of base and follow-up elements.

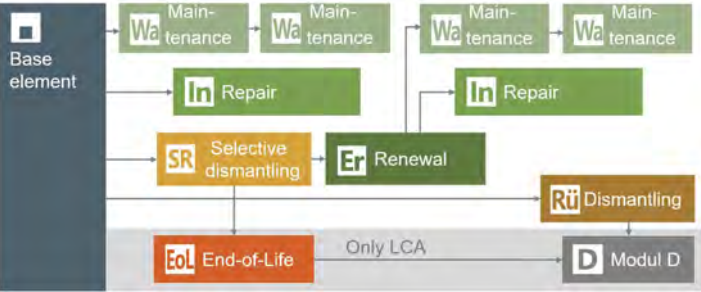


Figure 3. Interaction between base elements and follow-up elements (Müller et al. 2023).

4 LINKED BIM-MODEL APPROACH

All pre-balanced items as well as the base, major, macro and follow-up elements are stored in an element-database. To additionally use BIM-models as input data for calculations, the pre-balanced elements must be linked to the geometric objects of the BIM-model. An automated assignment based on the materials is not possible, because firstly, the elements are sometimes composed of several materials and secondly, elements made of the same material can have

completely different properties (costs, degree of traffic impact, service life). An example is described above for edge beams and abutment concrete.

For an automated linkage of BIM-objects with base-elements, the IFC-classes could be used. Thus, based on the entity IFCBEAM with IFCBeamtype: Edgebeam, it can be determined that a linkage to an element “edgebeam” has to be established. However, it cannot be completely automatically determined whether for the calculation a base element (only the edgebeam) or a major element (edgebeam with sealing and curbstone) should be used.

In order to enable a mapping between the BIM-objects and the element-database, each pre-balanced element of the element-database is given a unique label. This unique label must be attributed to every BIM-object that is modelled in the authoring software. How the attribute is integrated into the BIM-model is workflow dependent. The labels of all available elements can be exported from the database as a classification file and loaded into a BIM authoring software. Here, the elements can be linked to the BIM-objects depending on the level of detail. The next step is the transfer of the attributed object with its quantities into a software for impact calculation which is labeled here as evaluation software. In the evaluation software the quantities of the BIM-models are combined with the specific impacts of the different elements to calculate the economic, ecological and macroeconomic impacts of a bridge (see Figure 4).



Figure 4. Workflow to use a BIM-model for a holistic evaluation.

5 CASE STUDY

The presented framework is exemplarily implemented using a steel composite bridge. To reduce the complexity for this paper only one steel girder is covered in this case study. The evaluation takes place during the comparison of different bridge variants and uses a BIM-model with the appropriate level of detail (no explicitly modeled connection details).

5.1 BIM-model classification

To use the BIM-model as input for a sustainability calculation, each geometric object must be linked to a pre-balanced element of the database. This can be done, for example, via the classification manager in the authoring software Revit (see Figure 5).

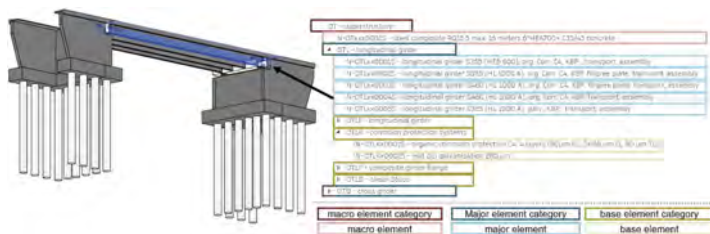


Figure 5. Assigning a label to each BIM-object for the holistic evaluation in the authoring software Revit.

Depending on the level of detail of the model, a major or fine element must be selected for the assignment. Since in this case the corrosion protection system and the shear studs are not modelled, a major element “*Longitudinal girder S460 HL 1000A, with organic coating C4 and shear studs*” is used.

5.2 Calculation of impacts

To use the classified BIM-model for a sustainability assessment, an evaluation software as explained and prototypical implemented in (Müller et al. 2023) has to be used. When the IFC-File with the linked BIM-objects is transferred to the evaluation software, the corresponding sub-elements and follow-up elements with their corresponding items are loaded from the element-database into the evaluation software automatically. In this case a beam with the length of 36 meter was assigned with the label for a major element. In the evaluation software this steel beam is split up into 119 m² organic coating, 504 shear studs and 14 tons of steel profile (see Figure 6).

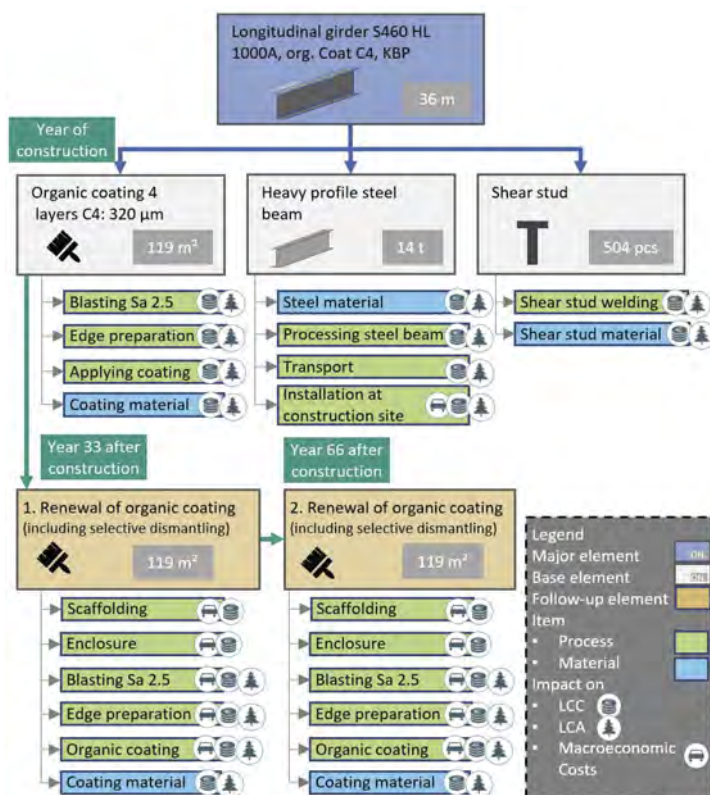


Figure 6. Elements and items used to calculate the impact of one steel beam.

For the steel profile and shear studs no measures occur during the complete life cycle of the bridge. The organic coating only has a service life of 33 years. Therefore, in the year 33 and 66 the selective dismantling and renewal elements of organic coating for 119 m² are used for the calculations. Each element consists of process and material items which can have an impact on LCC, LCA or macroeconomic costs. For example, the “Blasting SA 2.5” and “Applying coating” of the base element organic coating have an influence on LCA and LCC but not on macroeconomic costs since the coating is applied inside the production plant and therefore no traffic disruption occurs during the production. For the renewal of the organic coating the traffic must be disrupted and therefore these items lead to macroeconomic costs.

5.3 Comparison of results

Macroeconomic costs cannot be calculated when applying a material-based approach. For life cycle costs, the material-based approach is also generally not applied due to the poor interrelation between costs and pure material quantities. Nevertheless, this approach is often used for a BIM-based life cycle assessment. The deviations that arise with this approach compared to the introduced element approach are shown in the following.

When applying the material-based approach, the weight of the steel beam is multiplied with the values of a corresponding EPD-dataset. For the subsequent calculation the average data set for open rolled sections in Germany is utilized (bauforumstahl 2018). Therefore, the steel beam of 14 tons create a Global Warming Potential of 15.795 tons CO₂-eqv. (see first row of Table 1).

For the element approach, the same emissions result for the material of the steel beam. In addition, minor emissions for the welded head plate and end anchorage result in 0.175 t CO₂-eqv. The emissions for the 504 head bolt anchors lead to 0.280 t CO₂-eqv.

For the production of the organic corrosion protection system, emissions for the steel girder amount to 1.906 t CO₂-eqv. This results in additional emissions of 15% in the manufacturing phase. The major difference arises within the use phase. Bridge steel girders and head bolt anchors usually reach the 100-year service life. The corrosion protection must be replaced twice during this period. This results in high costs due to the required scaffolding and enclosure during the execution of the measures, as well as in high ecological impacts due to the energy-intensive blasting and application of the renewed coating. The ecological impacts for the renewal of the organic coating are higher than the ones of the initial organic coating applied in the production plant, due to the lower efficiency and higher overspray content of the processes on the construction site. In this case study, the emission calculated with a material approach underestimates the emissions by 30 % due to the neglected coatings and measures within the use phase.

Table 1. Comparison of LCA impacts calculated with a material and element approach.

Element	Quantity per functional unit	Year of Con. [t CO ₂ -eqv.]	Year 33 [t CO ₂ -eqv.]	Year 66 [t CO ₂ -eqv.]	Total [t CO ₂ -eqv.]
Steel beam (material approach)	14 t	15.795	-	-	15.795
Steel beam with shear studs and org. Coating (element approach)	36 m	18.161	2.169	2.169	22.498
- Steel beam with processing	14 t	15.970	-	-	-
- Shear Studs	504 pcs	0.283	-	-	-
- Organic coating production	119 m ²	1.906	-	-	-
- Renewal of organic coating	119 m ²	-	2.169	2.169	-

6 CONCLUSIONS

The introduced element approach allows to support a BIM-based sustainability assessment in different planning phases. Especially in early planning phases, in which an assessment can lead to major changes of the design, the element approach facilitates to create meaningful results. This is in particular the case when the underlying BIM-model do not have a level of detail with which a precise quantity takeoff can be performed. With an element approach, only the actual modeled content can be taken into account for an assessment and therefore the calculated potential impacts will be regularly underestimated.

6.1 Limitations

To apply the element approach to a specific structure, the corresponding elements and their items must be pre-balanced for all components of which the bridge consists of. This requires

large preparatory works. In addition, the required items for an element depend on many boundary conditions. For example, a huge difference regarding the results of the macroeconomic costs calculation arises depending on the chosen construction process. If the corrosion protection system on a valley bridge is renewed using a hanging scaffold, the traffic below the bridge is not disturbed. If for a motorway overpass a standard scaffold is applied, a partial closure of the lower roadway is necessary. Accordingly, two different elements must be pre-balanced for the same organic corrosion protection under different boundary conditions and stored in the element database. Users must consider for which boundary conditions the elements were pre-balanced when assigning a label to an element in the BIM-model.

6.2 Further steps

For a large-scale implementation, many elements must be pre-balanced representing different bridge types, different spans and different construction processes. All pre-balanced results must be kept up to date. Especially for costs a yearly update should be provided. This can be realized by using accounted and already realized bridge projects as input for the database. Ecologic background data as well as input for macroeconomic cost calculation can be update within a longer period (2 to 3 years). The continuous support should be ensured by implementing a foster home.

REFERENCES

- Alvarez Antón, L.; Diaz, J. 2014. Integration of Life Cycle Assessment in a BIM Environment. In: *Procedia Engineering*, 26–32.
- Axhausen, K; Ehreke, I; Glemser, A; Hess, S; Jödden, C; Nagel, K; Sauer, A; Weis, C. 2014 FE-Projekt-Nr. 96.996/2011: Ermittlung von Bewertungsansätzen für Reisezeiten und Zuverlässigkeit auf der Basis eines Modells für modale Verlagerungen im nicht-gewerblichen und gewerblichen Personenverkehr für die Bundesverkehrswegeplanung.
- bauforumstahl e.V. 2018. Umwelt-Produktdeklaration: Offene Walzprofile und Grobbleche Deklarationsnummer EPDBFS20180116IBG2DE Herausgeber: Institut Bauen und Umwelt e.V.
- DIN EN ISO 14040. 2021. Environmental management– Life cycle assessment – Principles and framework.
- DIN EN ISO 14044. 2021. Environmental management - Life cycle assessment - Requirements and guidelines.
- DIN EN 15804. 2022. Sustainability of construction works - Environmental product declarations - Core rules for the product category of construction products.
- DIN EN 15643. 2021. Sustainability of construction works - Framework for assessment of buildings and civil engineering works.
- DIN EN 15978-1. 2021. Sustainability of construction works - Methodology for the assessment of performance of buildings - Part 1: Environmental Performance.
- DIN EN 17472. 2022. Sustainability of construction works - Sustainability assessment of civil engineering works - Calculation methods.
- ISO 15686-5. 2017. Buildings and constructed assets - Service life planning - Part 5: Life-cycle costing.
- Müller, M; Zinke, T; Herrmann, M; Ummenhofer, T. 2023. Integral and Holistic Planning of Road Bridges based on Hierarchical Models FOSTA project P1281 IntegBridge. Düsseldorf: Forschungsvereinigung Stahlanwendung e.V. (not yet published).
- Müller, M 2023. Vorläufiger Titel: Ganzheitliche Brückenbewertung mit digitalen und BIM-gestützten Methoden. Karlsruhe, Karlsruher Institut für Technologie, Dissertation. (not yet published).
- Zinke, T. 2016. Nachhaltigkeit von Infrastrukturbauwerken – Ganzheitliche Bewertung von Autobahnbrücken unter besonderer Berücksichtigung externer Effekte. Karlsruhe, Karlsruher Institut für Technologie, Dissertation.

*SS18: Optimization of inspection, monitoring and maintenance
strategies for existing concrete structures*
Organizers: R. Caspeele, W. Botte, G. Lombaert & A. Strauss



Taylor & Francis

Taylor & Francis Group

<http://taylorandfrancis.com>

Inspection and assessment of PT structures: Results from application to an existing bridge

Isabella Mazzatura, Silvia Caprili & Walter Salvatore

Department of Civil and Industrial Engineering (DICI), University of Pisa, Pisa, Italy

Joan R. Casas

UPC-BarcelonaTech, Barcelona, Spain

Massimo Gammino, Filippo Ferrari & Andrea Piscini

SINA S.p.A, Milan, Italy

ABSTRACT: Pre-stressed concrete with post-tensioned (PT) cables historically represented an attractive alternative to ordinary reinforced concrete (RC). A wide portion of the world-wide existing concrete bridges was PT. As the nominal service life of those structures expires, several collapses occurred, highlighting the problem of the inspection. The main issue is that PT cables may be affected by relevant corrosion phenomena related to the presence of air or water inside the ducts: such ‘hidden’ defects need to be determined through reliable testing methodologies. This paper presents the in-progress research aiming to quantify the influence of the damage of the single cable on the entire structure. The case study is an Italian viaduct composed of simply supported beams connected by an upper slab. An extensive investigation campaign was carried out to locate and quantify the damage. Starting from the data collected on-site a series of damage conditions of cables can be simulated.

1 INTRODUCTION

Prestressed concrete bridges with post-tensioned (PT) cables represent a relevant percentage of the infrastructural heritage worldwide. The rise of this constructive technology coincided, especially in Italy, with the economic boom in the 60ties-70ties: most of the bridges and viaducts along the main infrastructure system own a PT system, since several advantages – among them the achievement of long spans, the use of less material and the partial prefabrication - were provided in comparison to Reinforced Concrete (RC) ones. Nevertheless, several issues became to appear with the decades: the constituting materials gradually degraded and recent events (see for instance the collapse of the Morandi bridge in Genoa in 2018), highlighted how urgent the assessment of PT structures is today.

The inspection of the PT structure is a very complex issue because of the impossibility to use the same test methods as for the RC structures and the inherent conformation of the PT cables, located within the concrete section and ducts. Indeed, the defectiveness of these structures can be visible or completely hidden. Visible defects can be worrying if localized on the cable itself, for instance when the wires or strands are exposed to the air due to loss of the concrete cover and corrosion of the duct, or they may appear less severe if they affect only the concrete or ordinary reinforcements. However, the less severe defectiveness may be symptomatic of a dangerous hidden situation, for instance dark spots following the trace of a cable may occur because of the actual presence of water within the ducts. Anyway, the worst scenario happens when defects are not visually detectable but there is

hidden defectiveness. One of the most dangerous situations for PT structures is the loss of bearing capacity due to the corrosion of the cables, which could lead both to the embrittlement of the steel and/or to the reduction of the cross-section and loss of bonding properties of the wires or the strands. This situation occurs frequently if the cable is not protected, therefore when the grouting is not efficient and air, or, in the worst cases, water can be within the voids between duct and cable due to an inaccurate grouting of the ducts after tensioning. Because of that, a large part of the testing proposed and employed in the assessment of PT structures aims to locate voids and the presence of air or water inside the ducts. Other important information about the conservation condition of a PT beam can be derived from the estimation of the remaining tension acting through the cables and/or through the concrete cross-sections. By investigating the actual acting tension in steel, it is possible to assess the efficacy of the post-tensioning in the single cable; by investigating the tensional state of a cross-section of the concrete, it could be possible to have an idea about the efficacy of the post-tensioning on all the cables. To achieve this information, several non-destructive (ND) and semi-destructive (SD) test methodologies were proposed. The present work aims to estimate the state of conservation of a PT bridge located in the North of Italy by the execution of SDTs and NDTs and their critical elaboration. Starting from the data collected on-site and verifying their mutual compatibility, as well as their compatibility with the design data, a series of damage conditions of cables will be simulated, and the corresponding width of the cracks computed.

2 A REVIEW OF TEST METHODOLOGIES

The assessment of PT bridges is a complex issue due to the inherent nature of the PT system. Whereas for reinforced concrete (RC) structures a visual inspection can give a general idea of the state of conservation, for PT bridges this is not sufficient. Furthermore, it is not possible to apply the same test methodologies as for RC, because the objectives of the investigation are different. The *Classification, risk management, safety evaluation, and monitoring guidelines of the existing bridges* (MIT CSLP, 2020) represent a useful tool for planning and designing the experimental test to be performed on PT structures. The Italian Guidelines require the execution of the so-called *Special Inspections* for PT bridges, providing necessary information about the layout of the cables, the location of the defects and their quantification. The tensional state of the concrete cross-section and the tension acting in the cables shall be investigated as well, thus providing relevant information about the efficiency of the PT system and/or to warn on the likely presence of damage. However, the Italian Guidelines give little information about the test's methodologies to follow and the instrumentation to use. Over the years, many non-destructive techniques have been proposed to investigate the PT system, proving more or less effective depending on the specific objective. For the location of ducts and defects, the most common available techniques are the Ground Penetrating Radar (GPR), the Ultrasonic Tomography (UT) and the Impact Echo (IE) (Giannopoulos et al., 2002; Sławski et al., 2016; Terzioglu et al., 2018; Wai-Lok Lai et al., 2018). The evaluation of the tensional state of the section can be performed by the investigation of the tension through the steel cables and/or by the determination of the tensional state of the concrete cross-section. Regarding the first issue, a promising NDT is the X-Ray diffraction method, historically employed to determine the residual stresses deriving from metal manufacturing processes in the field of the quality control and even applied to PT wires/strands (Brauss et al., 1998; Carfagno et al., 1995; Morelli et al., 2021; Zanini et al., 2022). The other possibility is to determine the tensional state acting through the concrete section, by using, for instance, the drilled-hole or the saw-cut method (Bagge et al. 2017, Kral'ovanec, Bahleda, et al., 2021; Kral'ovanec, Moravčík, et al., 2021). A quick revision of the test's methodologies relating to the specific objective is given, focusing in particular on the techniques employed in the present research work.

2.1 Identification of cables' layout

Cables' tracing is fundamental for checking the correspondence of the actual layout with the design documentation (if available) determining the eventual presence of substantial differences

which may need to be further investigated. Besides, since the in-depth investigation shall be focused on the cable itself, it is necessary to know its location. The GPR is a technique frequently used to identify the thickness of road pavement, tunnels, the presence and the trace of utilities, the reinforcements' location in the concrete structures and the trace of PT cables (Terzioglu et al., 2018). GPR technique is very sensitive to presence of metallic bodies, since it elaborates the echoed signals derived from the emission of high frequency electromagnetic pulses.

2.2 Identification of voids

Having reconstructed the cables' trace, it is possible to proceed with the identification of voids inside the ducts. A combination of ND and SD testing methodologies can be reliably used: the basic idea is to investigate the large part of the cables through NDT (e.g. ultrasonic tomography – UT), focusing the SDT (e.g. endoscopic investigations) mainly on the areas notified as defective by the previous testing. UT is frequently used to estimate the thickness of elements or layer and for the individuation of reinforcement in concrete, of voids (cracks, honeycomb, delamination) or water defects, ducts, tendons' location (Martin et al., n.d.; Muldoon et al., 2007; Shickert, 2002; Terzioglu et al., 2018). The endoscopic investigations shall be performed along the trace of the cable, both in the areas warned by UTs and in random areas. The results given by the two test methodologies can be combined, providing an overall idea of the accuracy of the UTs and reliable information about the presence of defects along the cables.

2.3 Assessment of remaining prestressing force

The definition of the actual prestressing tension in steel cables is a relevant information to evaluate a structure under both service and fatigue limit states. To obtain this information, it is possible to directly investigate the tension acting in the individual wire, and/or to check the tensional state of the concrete cross-section and to obtain the actual tension in the cables, since the actual permanent loads are known, and it is possible to estimate the losses.

The X-ray diffraction technique is classically employed as NDT to determine residual stresses in metals; it can investigate a very shallow region (10 μm) and can be applied to assess stresses in the wire. From a practical point of view, it estimates the inter-plane distance between planes of the crystal lattice and, assuming linear elastic distortion and knowing the inter-plane distance at zero stress, the acting stress can be derived. The saw-cut method, on the other hand, is based on a very simple principle: by isolating a concrete area and by recording its deformation, assuming a linear relation between stresses and strain, and knowing the Elastic Modulus, it is possible to obtain the acting stress. The tests can be carried out on-site, but normally it is not possible to employ strain gauges with a measuring base major of 30 cm, since the cuts would have become too deep. These tests are usually carried out in the mid-span section of the simply-supported beam since the tensional state there is the simplest (i.e. no shear under uniformly distributed load).

3 THE CASE OF STUDY

The viaduct is along the highway Turin-Savona in Savona Province. It is a one-way viaduct with 14 spans for a total length of around 600 m. Single spans have variable lengths of 45, 34, and 40 m; the large part (11 on 14) presents 45 m spans. Each deck is composed of 4 PT simply supported beams and 4 reinforced concrete (RC) cross members equidistant from each other, 14.16 m apart; the two extremes' members are at the heads of the beams. The 13 piers have a RC frame structure of variable height. The beam cross-section has a variable shape, tapering from the head to the mid-span cross-section and with a constant height equal to 2,40 m (Figure 1).

From the original documentation, the cables' layout for each type of beam and information about the mechanical properties of the materials used are known; however, there was no data on the initial prestressing force. The inspections focused on the 45 m beams, being the most common ones. The results of the in-situ experimental tests are presented below, distinguishing them according to their purpose.

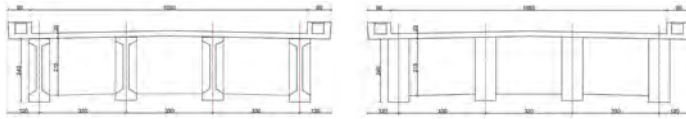


Figure 1. Cross section of the viaduct.

3.1 Identification of cables' layout

The tests for determining cables' trace were carried out on 7 beams belonging to 3 different spans; each beam was examined in all areas where it was possible to perform the test, excluding consequently the head areas of the beam, due to the massive presence of ordinary steel and the large concrete cover, and the areas where the cables lie within the bulb. The GPR technique was adopted, and comparison between the design trace and as derived from the in-situ tests was performed (Figure 2). The results obtained on all beams were similar.

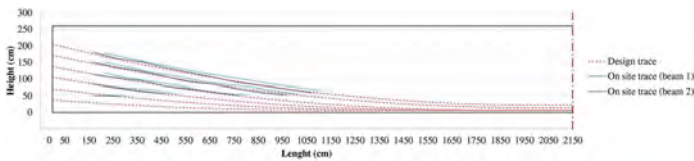


Figure 2. On site trace of two beams and comparison with the design.

Figure 3 summarizes the errors achieved for all measuring locations and tested beams: the average error was of 3.28 cm, but this error is probably due to how the measurements were carried out on-site and the errors in the cable deployment during construction rather than a systematic error of the instrument. The shape of the histogram is quite like a Gaussian distribution with average of 3.28 cm and a standard deviation of 3.37 cm. The associated coefficient of variation is about 1, therefore the variability of the results is huge. However, considering the present application, the probable error of ± 3.4 cm is negligible, considering that the height of a PT beam is usually within 1.75÷2.50 m. The results of the tests state the efficacy of the GPR measurements, even if a larger sample would be desirable.

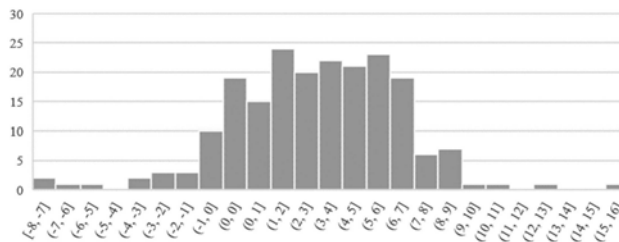


Figure 3. Distribution of the GPR error.

3.2 Tests for identification of voids

Tests for the identification of voids are performed, as said, by combining NDT with endoscopic tests (SDT). The choice was to have a comparison between the results of NDT, which are inherently more uncertain, and those of SDT. Some direct essays are performed in all areas that cannot be detected either through UTs or endoscopies. The tests were performed on the same 7 beams inspected by GPR, since the trace of the cable is known; for each beam 2 cables were investigated in the areas considered as riskiest i.e. (Trejo et al., 2009): the beam head, the change of curvature, and the mid-span intrados zone (Figure 4).



Figure 4. Location of the tests. In blue are the tested cables; the red line indicates the riskiest zones.

The UT tests were performed in all detectable areas of the cables: it was not possible to test the intrados region, due to the strong presence of ordinary steel, and the beam head, due to the thicker concrete cover resulting from the tapering. The tests were executed by choosing a pitch of 10 cm and positioning the instrument in the transverse direction of the cable.

The calibration was performed by imposing the shear wave velocity, which is estimated by the relation $c_s t = \sqrt{(E/\rho \cdot 1/(2 \cdot (1 - \nu)))} = \sqrt{(G/\rho)}$ (Krautkrämer & Krautkrämer, 1990) and assuming a certain density (ρ) and shear modulus (G). The goodness of these assumptions was then verified by performing some scans in areas where no cables were present, calculating the estimated thickness of the beam, knowing the time t required for the wave to return, and comparing it with the actual thickness of the beam. Other important input parameters (analog and digital gain) were chosen by performing scans in areas with two or more cables where voids were less likely to be present, so that the displayed scan was not completely saturated. Both linear (Figure 5a) and matrix (Figure 5b) scans were performed: linear scan means that the 16 dry-point contact sensor of the instruments works in groups composed of 4 sensors; matrix scans means that each sensor works by itself (ACS Group, 2021). The presence of voids is considered probable when the visualized output is strongly saturated, for instance as happen for the scans (a) and (b) in Figure 5. The duct is considered fully grouted when is visualized as in Figure 5c.

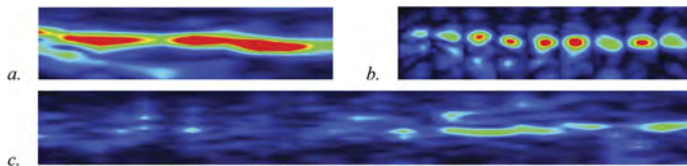


Figure 5. Outputs of some UTs. a) is a linear UT which shows a probable void defect and b) show the same area but the test was performed through the matrix mode. The UT in c) shows a cable probably fully grouted.

The endoscopies were performed by drilling holes with a diameter of 20 mm both in areas warned as “defective” by the UTs and in random areas of the cables. Some outputs of the endoscopies are reported in Figure 6: 6.a show a fully grouted duct, while 6.b shows the presence of a void within the duct and the concrete matrix, and 6.c a not grouted duct. On a total of 56 endoscopies, 26 were executed in random areas of the cables and 30 in the areas warned by UTs. 63% of the tests in the warned areas reported the presence of voids; however, some of these voids are not located inside the duct but outside of it. The tests in random areas reported voids in 23% of the cases. No oxidized or corroded wires were found. These results prove that it is desirable to employ more than one NDT/SDT to investigate a structure.



Figure 6. The endoscopy in a. shows a fully grouted duct, the one in b. a void between the duct and the concrete matrix, the one in c. an ungrouted duct.

3.3 Tests for the definition of actual prestressing tension

The tests were carried out on 3 of the 7 beams inspected with the previous methodologies.

The X-Ray Diffraction (XRD) tests were performed in the intrados area of the beams at mid-span region, being here easier to locate the instrument; on each beam at least 4 measurements on the same cable were executed. The average value of acting tension ranges from 569 to 686 MPa depending on the tendon (Table 1). It can be noticed that both on the same cable and on the same wire consistent deviations of maximum 110 MPa (beam 3 of span 3) were observed, probably due to the variability in residual stresses induced by the operation of stressing (Carfagno et al., 1995). By assuming an initial stress in the cables equal to the 65% of the ultimate tensile stress of the steel (i.e. 1570 MPa) and by estimating the friction and the long-term losses (resulting equal to the 22% of the initial tension), it was obtained an acting tension of 776 MPa. Therefore, the XRD measurements seem to indicate major losses, around the 27%, or the presence of compressive residual stresses deriving from the manufacturing processes (Carfagno et al., 1995). The results obtained are aligned to other recent applications of the XRD (Zanini et al., 2022).

Table 1. XRD measurements.

Span	Beam	Wire	Measure 1	Measure 2	Measure 3	Mean	CoV
			[MPa]	[MPa]	[MPa]	[MPa]	
3	1	A	631	/	/	648	7%
		B	685	/	/		
		C	688	588	/		
3	3	A	708	742	726	686	6%
		B	704	678	/		
		C	634	665	630		
6	3	A	550	525	/	569	6%
		B	611	559	601		

In addition, the saw-cut method was used for the estimation of the tension acting through the concrete. The test was carried out in the mid-span cross-section of the 3 selected beams. These sections were chosen due to the supposed simpler tensional state in the simply supported static scheme (no shear influence). Three measuring points in the single beam (Figure 7b) were selected. The test was carried out by posing strain gauges of 30 mm base of measure in the longitudinal direction and by performing two cuts in the transversal direction. The choice of these measuring bases comes from the necessity to not deepen the cuts more than 30-40 mm. Figure 7c shows the comparison between the measurements and the ideal behavior. It was necessary to discard all the data of the E2 point, as un-reliable values were obtained. In general, the on-site results are very far from the theoretical ones assuming an elastic and linear behavior of

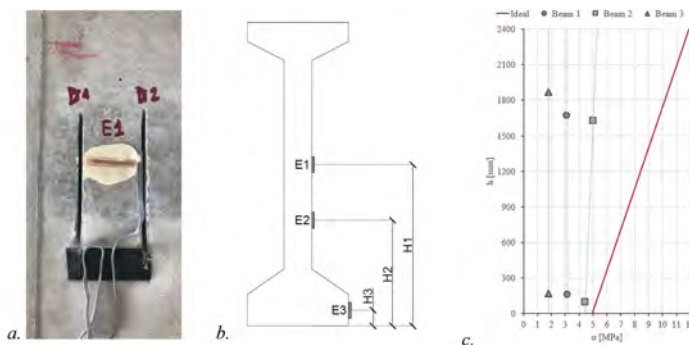


Figure 7. Execution of the saw-cut test: *a.* configuration of the cuts, *b.* location of measurements and *c.* comparison between theoretical acting tension (red) and experimental ones.

the material. It can be noticed that E3 measuring points are more reliable than the others, but still not enough to be employed in the assessment of the stress state.

4 SIMULATION OF DAMAGE SCENARIOS AND CORRESPONDING PERFORMANCE

By performing inspections according to the methodologies described above, information concerning the cables' layout, the possible presence of voids related to the activation of corrosion phenomena and an estimation of the tensional state of the beam can be derived. Since voids in the ducts could lead to a favourable environment for deterioration, it is worth to investigate the possible presence of these phenomena by the estimation of the width of the cracks. During the present campaign, no corrosion of the cables was ever found; since not a reasonably large number of endoscopies were performed and since the UTs investigated only the presence of voids, it would be reasonable to search for the condition in which cracking started to occur. For this reason, a series of damage scenarios will be considered, and the relative width of the cracks accordingly computed. The dimensions of the beam, the ordinary reinforcement, the mechanical properties of materials and the PT cables were known by the design documentation; only permanent loads were considered. Since the dimensions of the beam were verified on-site, the self-weight was considered in its actual value, while the weight of the road surfacing was considered in its characteristic upper value. Damage scenarios account for the loss of a certain amount of cross-sectional area of one or more cables are selected; in this case, corrosion was assumed to affect the lower cables, as this condition is more feasible since these cables present lower cover. Table 2 shows the considered damage scenarios, the value of the associated decompression (M_{dec}) and cracking moment (M_{crack}), the ratio between this last and the design value of acting moment (M_{sd}/M_{crack}), and the width of the cracks (w_k). The acting moment is equal to 10'608 kNm. It can be noticed that the loss of cross section in cable 1 or 2 (see Figure 8) leads to a serious situation in comparison to the loss of cross section in cable 3 or 4, as biaxial bending occurs. These results show that the presence of serious corrosion in the cables (or alternatively the loss of prestressing) can be easily visualized by cracks of considerable width. In some cases (scenario a., d., e., g. in Table 2) the cracking moment is higher than the acting moment. However, it is important to notice that for each of the considered damage scenarios, the safety at the ULS is still verified (M_{sd}/M_{rd} in Table 2). The calculations were performed adopting a rectangle parabola constitutive law for the concrete and an elastic-perfectly plastic behavior for both reinforcing and prestressing steels.

Table 2. Damage scenarios.

Damage scenario	M_{dec}	M_{crack}	M_{sd}	w_k	M_{sd}
	[kNm]	[kNm]	M_{crack}	[mm]	M_{rd}
a. Loss of 30% section in cable 1 or 2	9'185	10'900	0.97	-	0.69
b. Loss of 50% section in cable 1 or 2	8'440	10'140	1.05	0.44	0.70
c. Loss of 100% section in cable 1 or 2	6'595	8'250	1.29	0.47	0.71
d. Loss of 30% section in cable 3 or 4	9'658	11'380	0.93	-	0.69
e. Loss of 50% section in cable 3 or 4	9'225	10'950	0.97	-	0.70
f. Loss of 100% section in cable 3 or 4	8'146	9'830	1.08	0.48	0.71
g. Loss of 30% section in cable 1 and 2	9'258	10'975	0.97	-	0.70
h. Loss of 50% section in cable 1 and 2	8'558	10'260	1.03	0.48	0.71
i. Loss of 30% section in cable 1, 2, 3, 4	8'207	9'900	1.07	0.50	0.72
l. Loss of 50% section in cable 1, 2, 3, 4	6'806	8'465	1.25	0.53	0.76

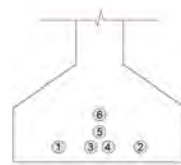


Figure 8. Bulb's cross section.

5 CONCLUSION

The current research can be considered the starting point of a more articulated project aiming to define a reliable methodology for the inspection of PT bridges and to translate the results of these inspections in numerical terms for the evaluation of the residual capacity and remaining service life. Several NDTs were selected and adopted on a case-study bridge located in Italy. As

visible, several tests are promising: for instance, the GPR is very effective in the location of the cables and the XRD method is able to give a very reliable value of the acting tension through the PT cables. The UTs work quite well but results are affected by a big issue: it is impossible to know if the inspected void is inside or outside the duct; moreover, by an on-site test campaign it is not possible to know where voids effectively are and, therefore, there are no sufficient data to estimate the sensitivity of the UT tests. At the moment, results provided by the saw-cut method needs to be improved, but in any case, it is desirable to extend the samples for each test's methodology and carry out tests in controlled conditions, such as the laboratory, to quantify their effectiveness and accuracy. On the other hand, it is necessary to assess how the results of the tests may affect the overall structural performance. In the present work, the proposal has been to transpose the presence of corrosion/oxidation in the loss of the cables' cross-section and the equivalent prestressing loss and ultimate capacity. Only the width of the cracks is preliminarily computed in correspondence with a hypothesized damage condition. These preliminary results show how serious damage is often associated with a considerable width of the cracks that can be easily assessed by visual inspection. By having an idea about the expected loss of cross-section on the tendons, it would be possible to estimate the corresponding loss of performance of the single beam and, therefore, the related effect on the span and the whole structure.

REFERENCES

- ACS Group. (2021). *A1040 MIRA 3D Operation manual Ultrasonic low-frequency tomograph*.
- Brauss, M. E., Pineault, J. A., Belassel, M., & Teodoropol, S. I. (1998). *Nondestructive, quantitative stress characterization of wire rope and steel cables*. <http://proceedings.spiedigitallibrary.org/>
- Carfagno, M. G., Noorai, F. S., Brauss, M. E., & Pineault, J. A. (1995). Extending the Lifespan of Structures. In *IABSE Reports* (Vol. 73). <http://proceedings.spiedigitallibrary.org/>
- Giannopoulos, A., Macintyre, P., Rodgers, S., & Forde, M. C. (2002). *GPR DETECTION OF VOIDS IN POST-TENSIONED CONCRETE BRIDGE BEAMS*.
- Krautkrämer, J., & Krautkrämer, H. (1990). Ultrasonic Testing of Materials. In *Ultrasonic Testing of Materials*. Springer Berlin Heidelberg. <https://doi.org/10.1007/978-3-662-10680-8>
- Martin, J., Broughton, K. J., Giannopolous, A., Hardy, A., & Forde, M. C. (n.d.). *Ultrasonic tomography of grouted duct post-tensioned reinforced concrete bridge beams*. www.elsevier.com/locate/ndteint
- MIT CSLP. (2020). *Linee Guida per la classificazione e gestione del rischio, la valutazione della sicurezza ed il monitoraggio dei ponti esistenti*.
- Morelli, F., Panzera, I., Piscini, A., Salvatore, W., Chichi, F., Marconi, G. P., Maestrini, D., Gammino, M., & Mori, M. (2021). X-ray measure of tensile force in post-tensioned steel cables. *Construction and Building Materials*, 305. <https://doi.org/10.1016/j.conbuildmat.2021.124743>
- Muldoon, R., Chalker, A., Forde, M. C., Ohtsu, M., & Kunisue, F. (2007). Identifying voids in plastic ducts in post-tensioning prestressed concrete members by resonant frequency of impact-echo, SIBIE and tomography. *Construction and Building Materials*, 21(3), 527–537. <https://doi.org/10.1016/j.conbuildmat.2006.04.009>
- Shickert, M. (2002). Ultrasonic NDE of concrete. *Proceedings of the IEEE Ultrasonics Symposium*, 1, 739–748. <https://doi.org/10.1109/ultsym.2002.1193506>
- Slawski, L., Kosno, L., & Świt, G. (2016). Evaluation of Precast Pre-post-tensioned Concrete Bridge Beams with the Use of GPR Method. *Procedia Engineering*, 156, 443–450. <https://doi.org/10.1016/j.proeng.2016.08.319>
- Terzioglu, T., Karthik, M. M., Hurlebaus, S., Hueste, M. B. D., Maack, S., Woestmann, J., Wiggenghauser, H., Krause, M., Miller, P. K., & Olson, L. D. (2018). Nondestructive evaluation of grout defects in internal tendons of post-tensioned girders. *NDT and E International*, 99, 23–35. <https://doi.org/10.1016/j.ndteint.2018.05.013>
- Trejo, D., Pillai, R., Beth, M., Hueste, D., & Gardoni, P. (2009). Parameters Influencing Corrosion and Tension Capacity of Post-Tensioning Strands. *ACI Materials Journal*, 106, 144–153. <https://www.researchgate.net/publication/289723918>
- Wai-Lok Lai, W., Dérobert, X., & Annan, P. (2018). A review of Ground Penetrating Radar application in civil engineering: A 30-year journey from Locating and Testing to Imaging and Diagnosis. *NDT and E International*, 96, 58–78. <https://doi.org/10.1016/j.ndteint.2017.04.002>
- Zanini, M. A., Faleschini, F., & Pellegrino, C. (2022). New trends in assessing the prestress loss in post-tensioned concrete bridges. *Frontiers in Built Environment*, 8. <https://doi.org/10.3389/fbuil.2022.956066>

Non-destructive and partially destructive test locations in RC structures: A combined spatial optimisation and Bayesian updating approach

S. Karmakar & S. Ghosh

Structural Safety, Risk & Reliability (SSRR) Lab, Department of Civil Engineering, Indian Institute of Technology Bombay, Mumbai, India

D. Saha

Bhabha Atomic Research Centre, Mumbai, India

S.A. Faroz

Infrastructure Risk Management (IRM), Mumbai, India

ABSTRACT: Non-destructive (NDT) and partially destructive (PDT) tests are conducted for assessing present health of reinforced concrete structures. An improved understanding from this is possible by the judicious fusion of NDT and PDT results. Though international standards provide guidelines for NDT/PDT, a scientific approach for the selection of NDT/PDT locations is missing from literature. The selection of location is particularly critical for PDT, because of their limited number, additional distress to the structure and higher costs. Quantitative decision criteria for maximising the information collected through NDT/PDT, while incorporating constraints of cost, accessibility, functional restrictions and criticality of locations can be very useful. The proposed approach attempts to capture the actual spatial variability of concrete strength through judicious choice of NDT locations, executed under multiple constraints. This is subsequently augmented with Bayesian updating for the selection of PDT locations, based on the prior knowledge of deterioration and NDT results. The proposed approach is demonstrated with case studies.

1 THE CHALLENGE OF SELECTING NDT AND PDT LOCATIONS

Reinforced concrete structures – nearing the end of design life, requiring functional modifications, showing potential distresses, or demanding re-qualification as per latest codes – need to be scientifically evaluated to decide upon their repair, rehabilitation, retrofitting or demolition. The present-day characteristic compressive strength of concrete in the structure is one of the crucial elements in this decision-making. Where underestimation of strength can lead to unnecessary costly repairs, overestimation may compromise safety and lead to unforeseen losses.

Though some of the past research works on NDT and PDT had identified that the selection of test locations is a challenge (Faroz, Ghosh, & Faroz 2023), till today, no standardised method has been developed that a practising engineer can follow specially for NDT. Many of the practical projects (Pfister, Tundo, & Luprano 2014; Alwash, Breyse, & Sbartaï 2017) have carried out selection of NDT locations primarily based on experience and/or ease of testing. Sometimes core tests too are performed without using NDT test results (Dauji & Karmakar 2022), that might lead to gross mis-representations of concrete properties. Of the various approaches tried so far, experience-based approaches (Dauji & Karmakar 2022) may involve bias, site feasibility-based approaches (Faroz, Ghosh, & Faroz 2023) may not be truly representative, and uniform random distribution of test locations (Pfister, Tundo, & Luprano 2014) can be good only when conducted in large numbers. The major limitation of such applications is an improper representation of the in-situ spatial variability of the concrete strength and consequent underestimation of associated uncertainty (McCann & Forde 2001). Codes, standards, and

guidelines (FEMA 2000; CEN 2005; BSI 2019) generally suggest a combined application of NDT and PDT to overcome the limitations of each, and advise selecting locations for PDT based on NDT results. The same philosophy has been implemented by some researchers (Pfister, Tundo, & Luprano 2014; Alwash, Breyse, & Sbartaï 2017; Saleh, Tarawneh, Dwairi, & AlHamaydeh 2022) using various techniques, such as, proportional stratified random sampling, and guided/conditioned coring which uses NDT test results to arrive at PDT locations.

The research gaps existing today in literature would include: (i) non-inclusion of domain knowledge in identifying the possible zones of concrete homogeneity across a structure (Breyse 2012; Breyse & Luis 2014; BSI 2019); (ii) not performing a thorough statistical analysis of NDT and core sample distribution across different elements in the structure (Pfister, Tundo, & Luprano 2014); and (iii) not including cost as one of the criteria for selection of location (Sbartaï, Alwash, Breyse, Romão, & Luprano 2021; Faroz, Ghosh, & Faroz 2023). The ideal objective for optimisation of selection of NDT/PDT locations, therefore, is to capture the true variability of concrete strength and to extract maximum information on its distribution with cost consideration.

This article proposes a step-wise procedure for the selection of NDT, PDT locations for existing reinforced concrete buildings first; then it demonstrates the proposed approach with a real-life case studies. This proposed method is expected to result in a better statistical inference of the structural condition from NDT, by enhancing the spatial variability captured using domain knowledge. Further, a process of selection of PDT locations based on Bayesian updating, using the combination of NDT results and prior knowledge of similar buildings, is also presented in this work.

2 FRAMEWORK FOR THE SELECTION OF NDT LOCATIONS

2.1 Methodology for the selection of NDT locations

2.1.1 Global importance fraction (\mathcal{G}_i) to define immediate effects of failure

This particular fraction is applicable for different types of members (slab, beam, column, etc.). The objective of defining this parameter is to quantify the immediate possible effects (not cascading effects) of failure of each structural member as elaborated here:

- Effect of a slab failure: Adjacent 4 slabs (for internal slabs), adjacent 3 slabs (for peripheral slabs), adjacent 2 slabs (for corner slabs).
- Effect of a beam failure: 8 elements for internal beams (2 beams + columns of 2 floors at two ends + 2 slabs), 7 elements for peripheral beams (2 beams + columns of 2 floors at two ends + 1 slab), 6 elements for corner beams (1 beam + columns of 2 floors at two ends + 1 slab).
- Effect of a column failure: 10 elements for internal columns wall (below and above column + 4 slabs + 4 beams), 7 elements for peripheral columns (below and above column + 2 slabs + 3 beams), 5 elements for corner columns (below and above column + 1 slab + 2 beams).

A beam failure would result in a column failure when its failure converts a short column to a long column and demand exceeds capacity. Therefore, only a 50% contribution is taken in these cases. Hence, considering internal elements, failure of 1 slab will affect 4 structural elements; failure of 1 beam will affect $(2+2 \times 2 \times 0.5+2) = 6$ structural elements; and failure of 1 column will affect $(2+4+4) = 10$ structural elements. The ratio of effects of failure of different internal elements failures (slab : beam : column) thereby becomes 4 : 6 : 10, which is normalised to make the sum unity, to arrive at global importance fractions. Thus, $\mathcal{G}_i = 0.20, 0.30$ and 0.50 for (internal) slabs, beams and columns, respectively. Similarly, for others $3 : 5 : 7 = 0.20 : 0.33 : 0.47$ (peripheral), and $2 : 4 : 5 = 0.18 : 0.36 : 0.46$ (external). Here, $i = 1, \dots, m$ counts the member types (for example, $m = 3$ for structures comprising of beam, column and slab).

2.1.2 Local importance factors (\mathcal{L}_{ijk})

This factor is applicable for subcategories of a member type for a floor. Depending on the functionality and exposure conditions of each structural members, first a factor I_{ik} is obtained for each individual elements all across the building. This I_{ik} is obtained by multiplying \mathcal{I}_{ik} (Equation 1) which depends on the influence area, L_{ik} i.e., the load applied, and \mathcal{E}_{ik} which is

the exposure factor that quantifies the effect of exposure to deteriorating environment as shown in Equation 2. However, this leaves a scope of further refinement in the future with more controlling factors.

$$I_{ik} = \mathcal{I}_{ik} L_{ik} \mathcal{E}_{ik} \quad (1)$$

$$\mathcal{E}_{ik} = 1 + \frac{\text{Number of exposed surfaces to the environment, or in moisture zones}}{\text{Number of available surfaces}} \quad (2)$$

Here, $k = 1, \dots, f$ counts the number of floors. The whole range of I_{ik} is divided into n subcategories for each member types, with equal intervals of I_{ik} values. For each of the n subcategories, the average of all I_{ik} values, $\mathcal{I}_{m_{ijk}}$ is obtained. Here, $j = 1, \dots, n$ counts the member subcategories. The value of n may be 3 to 5 depending upon the size of building. Afterwards, the local importance factor is calculated by normalising these $\mathcal{I}_{m_{ijk}}$ values:

$$\mathcal{L}_{ijk} = \frac{\mathcal{I}_{m_{ijk}}}{\min_{i,j,k \in \text{all}} \{ \mathcal{I}_{m_{ijk}} \}} \quad (3)$$

2.1.3 Member-wise floor importance fraction (\mathcal{M}_{ijk})

In this step global importance fraction (\mathcal{G}_i), local importance factors (\mathcal{L}_{ijk}) are combined to obtain member-wise floor importance fraction (\mathcal{M}_{ijk}) to be used for multi constraint problem for optimisation of spatial variability. Member-wise floor importance fractions \mathcal{M}_{ijk} , is defined as the floor-wise fractions for each subcategory of members in different floors as given in Equation 4.

$$\mathcal{M}_{ijk} = \frac{\mathcal{G}_i N_{ijk} \mathcal{L}_{ijk}}{\sum_{i=1}^m \sum_{j=1}^n \sum_{k=1}^f \mathcal{G}_i N_{ijk} \mathcal{L}_{ijk}} \quad (4)$$

Where, N_{ijk} is total numbers of elements in each subcategory.

2.1.4 Multi-constraint problem and solution algorithm

The constraints for the given problem are:

1. The total number of NDTs (N) for the building is considered to be limited by budget:

$$N = \sum_{i=1}^m \sum_{j=1}^n \sum_{k=1}^f \mathcal{N}_{ijk} \quad (5)$$

2. The number of test samples for each floor is proportional to the sum of $\mathcal{G}_i \times \mathcal{L}_{ijk}$ of all elements.
3. The number of samples for each subcategory across all floors is proportional to the sum of ($\mathcal{G}_i \times \mathcal{L}_{ijk}$) of the that subcategory across all floors.

In Equation 4, member-wise floor importance fractions \mathcal{M}_{ijk} are obtained for each sub-category, member type, and floor. The challenge is to arrive at whole numbers (\mathcal{N}_{ijk}) from these fractions (\mathcal{M}_{ijk}), so that the constraints are satisfied. The systematic approach is proposed as follows:

1. Multiply all \mathcal{M}_{ijk} with the overall sample size (N) to obtain \mathcal{S}_{ijk} :

$$\mathcal{S}_{ijk} = N \times \mathcal{M}_{ijk} \quad (6)$$

2. Round off \mathcal{S}_{ijk} to the nearest integer value:

$$\mathcal{I}_{R_{ijk}} = \text{round}[\mathcal{S}_{ijk}] \quad (7)$$

where $\text{round}[\cdot]$ represents the nearest integer value.

3. The problem is to solve (fmn) unknowns with available ($f + mn$) number of equations.
4. Find the following summations:

$$C_{IR_{ij}} = \sum_{k=1}^f \mathcal{I}_{R_{ijk}} \text{ and } C_{IR_k} = \sum_{i=1}^m \sum_{j=1}^n \mathcal{I}_{R_{ijk}} \quad (8)$$

5. Round off after carrying out the summations as given below:

$$\mathcal{S}_{C_{ij}} = \text{round} \left[\sum_{k=1}^f \mathcal{S}_{ijk} \right] \text{ and } \mathcal{S}_{R_k} = \text{round} \left[\sum_{i=1}^m \sum_{j=1}^n \mathcal{S}_{ijk} \right] \quad (9)$$

6. Find the sum of all rounded off values (\mathcal{C}_{SC} and \mathcal{C}_{SR}):

$$\mathcal{C}_{SC} = \sum_{i=1}^m \sum_{j=1}^n \mathcal{S}_{C_{ij}} \text{ and } \mathcal{C}_{SR} = \sum_{k=1}^f \mathcal{S}_{R_k} \quad (10)$$

7. Ideally, \mathcal{C}_{SC} and \mathcal{C}_{SR} should be equal to the actual sample size (N). But in most practical cases it will vary due to rounding off operations. In such cases, some adjustments are necessary. If \mathcal{C}_{SC} and/or \mathcal{C}_{SR} are less than actual sample size (N), the sample needs to be added (in integers) with $\mathcal{S}_{C_{ij}}$ and \mathcal{S}_{R_k} values, based on the following priority.

- i. Groups with lower value of $\mathcal{S}_{C_{ij}}$ or \mathcal{S}_{R_k} (including zero),
- ii. If $\mathcal{S}_{C_{ij}}$ or \mathcal{S}_{R_k} values are the same for two groups, the groups with the higher fractional values $\left(\left[\sum_{k=1}^f \mathcal{S}_{ijk} \right], \left[\sum_{i=1}^m \sum_{j=1}^n \mathcal{S}_{ijk} \right] \right)$.

If \mathcal{C}_{SC} and/or \mathcal{C}_{SR} are greater than the actual sample size, additional sample needs to be removed (in integers) based on priority list given below:

- i. Groups with higher value of $\mathcal{S}_{C_{ij}}$ or \mathcal{S}_{R_k}
- ii. If $\mathcal{S}_{C_{ij}}$ or \mathcal{S}_{R_k} values are the same for two groups, the groups with the lower fractional values $\left(\left[\sum_{k=1}^f \mathcal{S}_{ijk} \right], \left[\sum_{i=1}^m \sum_{j=1}^n \mathcal{S}_{ijk} \right] \right)$.

This step will update the $\mathcal{S}_{C_{ij}}$ values to $\mathcal{M}_{SC_{ij}}$ and \mathcal{S}_{R_k} values to \mathcal{M}_{SR_k} .

8. Find the difference \mathcal{D}_{ij} of updated values of $\mathcal{M}_{SC_{ij}}$ (Step 7) and $\mathcal{C}_{IR_{ij}}$ (Step 4).

$$\mathcal{D}_{ij} = \mathcal{M}_{SC_{ij}} - \mathcal{C}_{IR_{ij}} \quad (11)$$

9. Follow an iterative process until all \mathcal{D}_{ij} becomes 0 as enumerated below:

- i. Due to the rounding off operations, some $\mathcal{I}_{R_{ijk}}$ would become zero and some will remain zero in case \mathcal{S}_{ijk} equals to zero. Hence, at first mark $\mathcal{I}_{R_{ijk}}$ which corresponds to \mathcal{S}_{ijk} equal to zero, called forbidden locations. These elements will not participate in subsequent steps.
- ii. Exchange $\mathcal{I}_{R_{ijk}}$ in between (ij)s corresponding to maximum positive and minimum negative values of \mathcal{D}_{ij} . These operations will be done $\min[\max(\mathcal{D}_{ij}), |\min(\mathcal{D}_{ij})|]$ times. The selection of (k)s for exchange of $\mathcal{I}_{R_{ijk}}$ will be determined by random number generation to avoid any bias in the choice.
- iii. Iterate this process until all the differences carry same sign or zero. In the iterations, if multiple $\max(\mathcal{D}_{ij})$ or $|\min(\mathcal{D}_{ij})|$ is encountered, one of these shall be selected through random number generation. After this step $\mathcal{C}_{IR_{ij}}$ and \mathcal{C}_{IR_k} will also get updated. Find the difference \mathcal{D}_k of updated values.

$$\mathcal{D}_k = \mathcal{M}_{SR_k} - \mathcal{C}_{IR_k} \quad (12)$$

- iv. After arriving to the same final sign of all \mathcal{D}_{ij} or exceptional cases as mentioned in the previous point, addition or deletion shall be done only in those cells where $\mathcal{D}_k \neq 0$ and $|\mathcal{D}_k|$ reduces with alteration. At the end of this step, all \mathcal{D}_{ij} and \mathcal{D}_k will become zero. This will update few/all $\mathcal{I}_{R_{ijk}}$ to the final desired \mathcal{N}_{ijk} .

It is worth mentioning that above mentioned method can give multiple solutions due to the process of random number generation. However, solutions will be devoid of bias in overall due to application of domain knowledge, step wise solution with random selection in conflicting cases.

2.2 Execute survey for site feasibility

A field survey should be conducted to identify feasible locations for NDT, for each sub-category of elements. It is suggested that the number of such locations should be at least five times the required numbers for each sub-category, to avoid bias in the optimisation process.

2.3 Mathematical optimisation for spatial variability with member wise floor importance and site constraints

Samples from nearby locations tend to be more alike than ones farther apart (Warrick & Myers 1987). Using this concept, it is assumed here that the optimal selection of locations – for capturing maximum information on spatial variability and distribution of concrete strength – should contain the farthest among feasible NDT locations. This should also be satisfying \mathcal{N}_{ijk} in various sub-categories. An optimisation method for capturing maximum spatial variability is developed in this study based on this, by maximising minimum distance between sampling locations.

1. All distances between the locations derived from site feasibility study are calculated.
2. For each floor, the sampling location(s) yielding the minimum distance is/are iteratively eliminated provided options are still available for selection of \mathcal{N}_{ijk} in each sub-categories from truncated set of available choices for each subcategory that was initially derived from site feasibility study in Section 2.2. Otherwise, the location/s are retained in the selection.
3. The set of locations obtained in the end would be the optimal set of NDT locations for capturing maximum spatial variability under given constraints.

3 FRAMEWORK FOR THE SELECTION OF PDT LOCATIONS

Prior knowledge on the structure and/or other structures with similar background has not been considered so far in improving PDT locations. This can be especially useful in case of clusters of buildings with similar features (age, design considerations, environmental exposure, construction, soil, and maintenance strategies). This can be used for defining prior distribution of NDT parameters. Using likelihood function obtained from rebound hammer (RH) tests on structure, Bayesian updating is employed on prior distribution of parameters, to obtain posterior distribution.

3.1 Methodology for selection of PDT locations

The likelihood function (\mathcal{L}) of RH values is assumed to be lognormally distributed:

$$\mathcal{L}(R | \mu_{R_m}, \sigma_{R_p}) = \prod_{t=1}^{N_t} \frac{1}{R_t \sigma_{R_p} \sqrt{2\pi}} \exp \left[-\frac{(\ln R_t - \mu_{R_m})^2}{2\sigma_{R_p}^2} \right] \quad (13)$$

where, R is the result of RH test on the building with counter t , μ_{R_m} = mean value of natural logarithm of a RH population m , σ_{R_p} = standard deviation of natural logarithm of a RH population p , N_t = total number of RH tests carried out for the present building. The prior distributions of μ_{R_m} and σ_{R_p} are a derivation of knowledge from surrounding buildings. In the absence of any significant correlation between the prior parameters, the bi-variate joint distribution of mean and standard deviation can be obtained by simply multiplying the individual probabilities. Using likelihood (Equation 13) and prior, posterior distribution of RH parameters is obtained:

$$\mathbb{P}(\mu_{R_m}, \sigma_{R_p} | R) = \frac{\mathcal{L}(R | \mu_{R_m}, \sigma_{R_p}) \mathbb{P}(\mu_{R_m}, \sigma_{R_p})}{\sum_{m=1}^{p_1} \sum_{p=1}^{q_1} \mathcal{L}(\mathcal{R} | \mu_{R_\downarrow}, \sigma_{R_\downarrow}) \mathbb{P}(\mu_{R_\downarrow}, \sigma_{R_\downarrow})} \quad (14)$$

where, p_1 and q_1 are the number of subgroups in prior mean and standard deviation distribution. The posterior predictive distribution of \bar{R} is then obtained using likelihood function (Equation 13) and posterior distribution of RH parameter (Equation 14). Afterwards, the core samples of each cluster/identified groups are divided according to the fractional weightage in approximate proportion to the posterior predictive distribution.

$$\mathbb{P}(\tilde{R}/R) = \sum_{m=1}^{p1} \sum_{p=1}^{q1} \frac{1}{\tilde{R}\sigma_{R_p}\sqrt{2\pi}} \exp\left[-\frac{(\ln\tilde{R} - \mu_{R_m})^2}{2\sigma_{R_p}^2}\right] \mathbb{P}(\mu_{R_m}, \sigma_{R_p} | R) \quad (15)$$

4 DEMONSTRATION ON TWO MULTI-STOREY RC BUILDINGS

4.1 Building description

Buildings considered for selection of NDT and PDT locations are G+13 storey commercial and G+2 storey residential building, located on coast of Arabian Sea, India. To set up the prior for PDT case study, NDT data are acquired from adjacent buildings having similar environmental exposure, design grade of concrete and reinforcement, subsoil, seismic zone, and age group.

4.2 Test results for the selection of NDT locations

The office building has two typical floor plans: (a) ground to 9th (Area: 510 m²/ floor) and (b) above 9th (Area: 360 m²/ floor). The pre-specified number of NDT locations are divided as per varying plan area: 200 (ground to 9th floors) and 60 (floors above). The structural members are column, beam (primary and secondary) and slab; each of which are subdivided using local importance factors (shown in Figure 1b for ground to 9th floors) into three subcategories. Hence, total of nine subcategories are used, three each for columns (C1, C2, C3), beams (B1, B2, B3), and slabs (S1, S2, S3). The bar charts of different groups with respect to frequency and local importance factors (\mathcal{S}_{ijk}) are shown in Figure 1 for one typical case (applicable for ground to 9th floor).

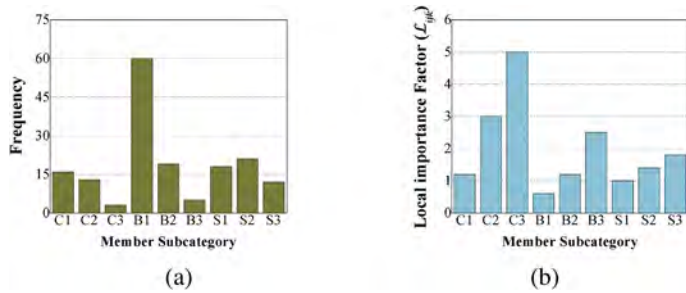


Figure 1. (a) Frequency and (b) local importance factor of each subcategory from ground to ninth floor.

Number of samples in each subcategory (\mathcal{S}_{ijk} and \mathcal{N}_{ijk}) is shown in Figure 2. Possible locations for NDT of each subcategory are obtained by site survey and proposed optimisation is performed to finalise NDT locations. Distribution of NDT locations in ground floor is presented in Figure 3.

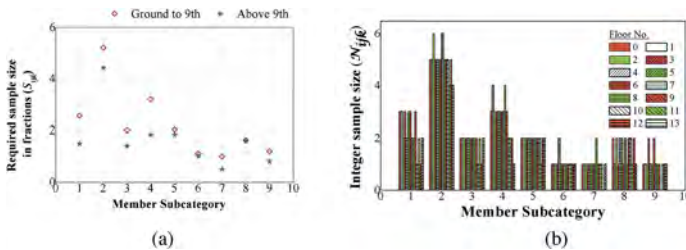


Figure 2. (a) \mathcal{S}_{ijk} (Fractional) and (b) \mathcal{N}_{ijk} (Integer) for each floor (0th to 13th) and different subcategory.

4.3 Test results for the selection of PDT locations

This work proposes an additional measure prior applying conditioned/guided coring approach adopted in various past publications (Pfister, Tundo, & Luprano 2014; Alwash, Breyse, & Sbartaï

2017; Faroz, Ghosh, & Faroz 2023). This novel modification is achieved by employing observed RH data-set as likelihood for updating prior RH parameters (shown in Figure 4a) to posterior predictive distribution (shown in Figure 4b). The posterior predictive distribution of RH parameters is found using Equations 13-15. Inclusion of likelihood in prior knowledge reduces the associated uncertainty of the RH parameters i.e., lesser spread of RH parameters as shown in Figure 4(b).

For the fractional weightage of different ranges of RH values, the prior predictive distribution, obtained test results and posterior predictive distribution are computed, and are presented in Figure 5. The slight unevenness of the observed data is moderated with prior predictive distribution (Figure 5a) to obtain a smooth posterior predictive distribution (Figure 5b). This posterior predictive distribution can later be used as a guiding criterion in the conditioned/guided coring.

4.3.1 Multi-constraint problem and optimisation of sampling location

Within the limited scope of this paper, selection of PDT locations is implemented on the overall building RH data using proportional stratified random sampling (Pfister, Tundo, & Luprano 2014). Same approach can be integrated with the other conditioned/guided coring applications. At first, the total number of samples should be divided into columns and beams, based on their global importance fractions (since coring from slabs is generally not recommended), in proportion to the posterior predictive distribution, i.e. Figure 5(b). Next, a random selection needs to be applied, following a stratified pattern with respect to floor and member type. The selection criteria will follow a way such that any new sample should not be from same floor or same type of subcategory until a complete cycle of floor and subcategory is incorporated. However in optimisation part the only difference over here is that the Euclidean distance needs to be calculated in the 3-D space, in contrast to the earlier 2-D plans used in NDT location optimisation.

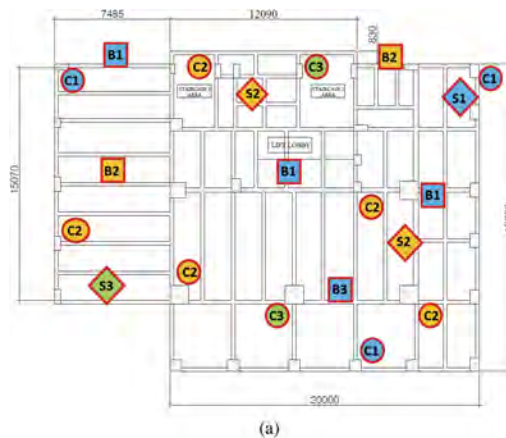


Figure 3. Proposed locations for NDT on Ground floor.

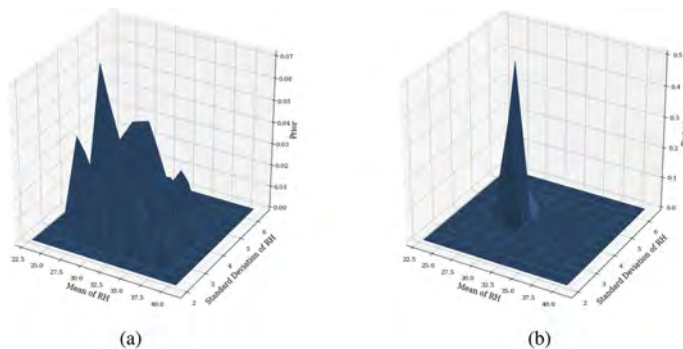


Figure 4. (a) Prior distribution, (b) Posterior distribution of RH parameters.

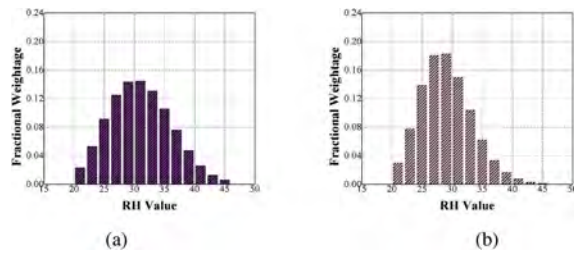


Figure 5. (a) Prior predictive, (b) Posterior predictive distribution of RH value.

5 CONCLUSIONS

The prevalent methods for the selection of NDT and PDT locations have inherent limitations as exemplified in the relevant literature. This study proposes the selection of such test locations with the following additions: (i) application of domain knowledge (NDT) with a multi-constraint solution and (ii) the use of prior knowledge from similar buildings (PDT). For a limited number of test locations, proposed optimisation methodology is another novelty of the paper. Further, additional aspects such as the nature of an element, type of a member, and the importance of a member – so far not considered in NDT/PDT testing plan – are incorporated in the approach. The proposed practicable methodology is demonstrated through two sample case studies, wherein the objective of capturing the true spatial variability of concrete strength from a given number of tests is achieved. Future works in this direction should be oriented towards the evaluation of the proposed approach in comparison with existing approaches from the perspective of robustness.

REFERENCES

- Alwash, M., D. Breyse, & Z. M. Sbartai (2017). Using Monte-Carlo simulations to evaluate the efficiency of different strategies for nondestructive assessment of concrete strength. *Materials and Structures* 50, 90.
- Breyse, D. (2012). Nondestructive evaluation of concrete strength: An historical review and a new perspective by combining ndt methods. *Construction and Building Materials* 33, 139–163.
- Breyse, D. & F.-M. J. Luis (2014). Assessing concrete strength with rebound hammer: Review of key issues and ideas for more reliable conclusions. *Materials and Structures* 47.
- BSI (2019). Assessment of *In-Situ Compressive Strength in Structures and Precast Concrete Components (BS EN 13791)*. The British Standards Institution, London, UK.
- CEN (2005). *Eurocode 8: Design of Structures for Earthquake Resistance (EN 1998:3) – Part 3: Assessment and Retrofitting of Buildings (Draft n. 6)*. Comité Européen de Normalisation, Brussels, Belgium.
- Dauji, S. & S. Karmakar (2022). Estimating Concrete Strength From Nondestructive Testing With Few Core Tests Considering Uncertainties. *ASCE-ASME J Risk and Uncert in Engrg Sys Part B Mech Engrg* 8(4), 041102.
- Faroz, S. A., S. Ghosh, & A. M. Faroz (2023). Tri-level framework for realistic estimation of concrete strength using Bayesian data fusion of UPV and guided coring. *Journal of Nondestructive Evaluation* 41, 78.
- FEMA (2000). *Prestandard and Commentary for the Seismic Rehabilitation of Buildings (FEMA 356)*. Federal Emergency Management Agency, Washington D.C., USA.
- McCann, D. & M. Forde (2001). Review of NDT methods in the assessment of concrete and masonry structures. *NDT&E International* 34(2), 71–84.
- Pfister, V., A. Tundo, & V. A. M. Luprano (2014). Evaluation of concrete strength by means of ultrasonic waves: A method for the selection of coring position. *Construction and Building Materials* 61, 278–284.
- Saleh, E., A. Tarawneh, H. Dwairi, & M. AlHamaydeh (2022). Guide to non-destructive concrete strength assessment: Homogeneity tests and sampling plans. *Journal of Building Engineering* 49, 104047.
- Sbartai, Z.-M., M. Alwash, D. Breyse, X. Romão, & V. A. M. Luprano (2021). Combining the bi-objective approach and conditional coring for a reliable estimation of on-site concrete strength variability. *Materials and Structures* 54, 104047.
- Warrick, A. & D. Myers (1987). Optimization of sampling locations for variogram calculations. *Water Resources Research* 23, 496–500.

FL decision system to choose the best maintenance strategy depending on condition

F. Binder & N. Hlebec

Asfinag Baumanagement GmbH, Vienna, Austria

U. Schneck

CITec Concrete Improvement Technologies GmbH, Dresden, Germany

A. Strauss

University of Natural Resources and Life Sciences, Institute of Structural Engineering, Vienna, Austria

ABSTRACT: For a highway operator, such as ASFiNAG, bridges are very important assets. Despite all regular maintenance measures, these structures are strongly subjected to ageing and degradation, because of their exposure. Thus, leading to high maintenance expenditures. The optimal time for rehabilitation is therefore a decisive factor in the cost and measure planning of an infrastructure operator.

To find this optimal point in time and condition, it is important to have a simple index-based method for declaring an accurate condition status. Often the input for the method is gained in the course of regular bridge inspections.

The aim of this paper is to determine condition and degradation (condition indices) by using objective indicators, like humidity, electrical resistivity, and corrosion potential. For the purpose of objectivity and the demand of an exact determination of the condition state, an overall performance index (CDI) is derived from the condition indices by using an analytic hierarchy process (AHP). The challenge of assessing corrosion relevant data – especially when doing this in an automated process – is the influence of many factors on the measurement values in unknown extent (e.g. concrete humidity on corrosion potentials), which doesn't allow an explicit, fixed interpretation as it can be done with e.g. concrete strength data.

Hence, this assessment methodology is Fuzzy-Logic (FL), which treats and combines input data in not clear-cut borderlines to choose an optimal maintenance measure. A case study will proof the method to deal with lack of knowledge and uncertainty in this fuzzy decision process.

1 INTRODUCTION

A large number of components of road infrastructure are exposed to increased degradation due to various damaging effects. Exposure of concrete surfaces to chlorides is a major factor and driver of degradation. In many cases, the amount at the rebar level is the determining indicator of deterioration here. Degradation of the reinforcement in the concrete is triggered at a threshold level of chlorides that the concrete can no longer absorb. Over time, other indicators of degradation develop, such as cracking, visual appearance of the concrete surface, or a drop in the electrochemical potential of the reinforcement.

The aim of the paper is to show those examinations that were used to provide an objective assessment of the degradation of the reinforced concrete member. The results of the survey provide information about the condition of the object. All common indicators of degradation that can be recorded visually or simply non-destructively are addressed and assigned to a four-part damage class. The classification of the degradation indicators into damage classes is based on relevant standards and guidelines as well as on published literature.

Finally, the classified degradation indicators are transferred into an overall Condition index (CDI) by using the AHP process. This index serves as an input parameter for the Fuzzy logic decision algorithm to propose the optimal maintenance measure.

2 METHODOLOGY

Condition assessments are mostly regulated by national standards or internal guidelines. Primarily, condition surveys are performed on a visual basis. This procedure is informative, fast and, when performed by experienced engineers, sufficiently accurate.

Nevertheless, the obtained data are discrete in time and covers only a small section of possible data for condition assessment. Condition surveys are mostly governed by national standards or internal guidelines. Nowadays Europe-wide efforts are undertaken in standardization of indicators obtained during principal inspections, through a visual examination, a non-destructive test or a temporary or permanent monitoring system (Casas & Matos, 2017). It should be noted that currently the majority of condition assessments are based purely on visual inspections. At the same time, this means that damage tends to be detected too late, because it is not sufficiently apparent by visual inspection, and thus the danger of systematically underestimating the condition is present. An objective condition assessment with easy-to-handle preliminary inspection techniques should support in this case and help to reduce the gap between visual assessment and actual condition.

Prerequisite for a successful and sustainable repair of reinforced concrete structures is an exact knowledge of the condition based on a detailed visual assessment of the components, as well as results of performed material tests. All preliminary examinations together have the goal of showing as complete and exact a picture as possible of the current condition of the existing structure. In addition, it should be possible to use the condition analysis to predict future development in terms of a forecast of an optimal time for maintenance.

The scope of the condition analysis must always keep in mind the overall objective. In addition, the actual condition state also plays a major role, e.g., in the selection of suitable condition surveys methods.

There are many different Non-Destructive Testing (NDT) methods used to identify and evaluate the deterioration of reinforced concrete. However, there is no single NDT method capable of identifying all aspects of reinforced concrete deterioration. For this reason, a multimodal NDT approach is a more effective one in terms of condition assessment. A multimodal approach provides a more complete condition assessment because it can identify different deterioration states simultaneously (see Figure 1).

Figure 1 shows the efficiency of condition survey techniques as a function of the condition state. For example, a determined investigation for a specific problem, such as half-cell potential mapping, does not provide more accurate information about the state of preservation until parts of the reinforcement are already affected by corrosion and the concrete components can be therefore already in the damage phase. Furthermore, the figure shows an important insight for the engineer, that with single visual condition assessment, damage is detected very late. Therefore, it is of enormous importance to know when and how accurate a possible degradation can be detected.

The examination techniques mentioned in Figure 3.1 are established procedures and allow one to obtain acceptable good and quantitatively sufficient results with sufficient monetary expenditure. It is always important that the procedures enable and support the increase of knowledge of the overall objective of the condition analysis.

As already mentioned, it is difficult to determine the true dimension of damage only based on visual appearance of the concrete component. Nevertheless, different condition survey techniques are available depending on the stage of degradation (see Figure 1).

2.1 *Indicators for corrosion*

The condition, which is initially determined mainly visually, as well as the development of damage due to corrosion over time, is serving as the basis for decisions regarding the time and intensity of repair. A simple and objective method for assessing the condition of concrete structures is of decisive economic interest.

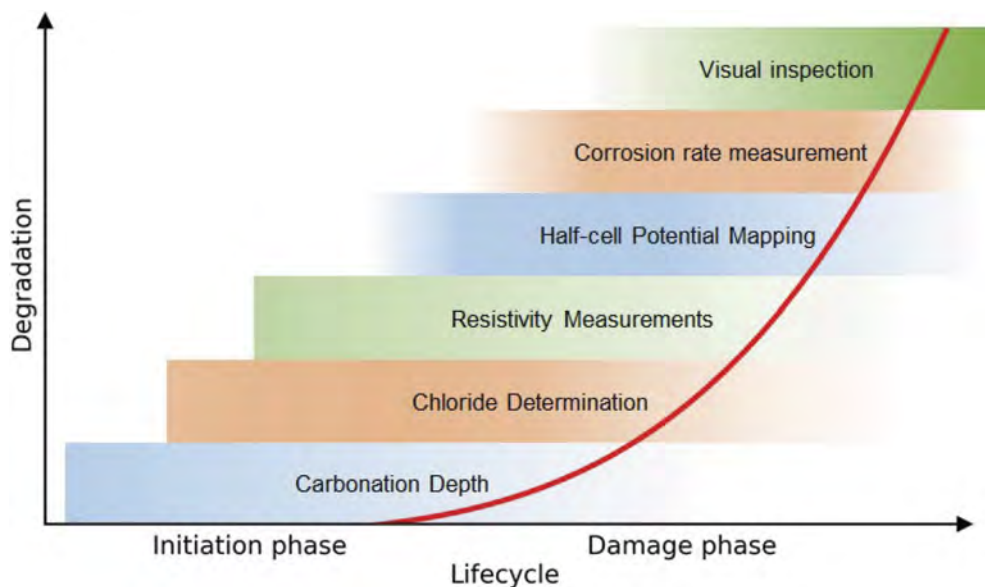


Figure 1. Effectiveness of different condition survey methods for condition assessment depending on the state of degradation based on (Pailes & Gucunski, 2015).

Based on all available results from preliminary examinations, the condition of the structural element should be determined simply and objectively. The primary basis in the procedure for objectifying and standardizing the results of condition assessment is a thorough and, above all, complete inspection, which thus makes it possible to take further steps towards classification and indexing of the results obtained. The indicators obtained individually from the various preliminary inspections are of varying degrees of importance for degradation. Therefore, the indicators were subjected to weighting via an analytical hierarchy process (AHP) before being synthesized into a condition index.

Additionally, the results of condition assessments are often not clearly interpretable, as they also contain a subjective perspective. This results in unclear decisions regarding the maintenance strategy. Therefore, a fuzzy logic expert system is introduced which can deal with this vague decision space.

Table 1. Indicator for degradation and their levels.

Degradation Ind.	Akr.	Unit	Degradation indicator level			
			1	2	3	4
			Negligible	Low	Moderate	High
Visual appearance	Vis	[mm]	< 1	≥ 1 - 4	≥ 4 - 10	≥ 10
Carbonation depth	X _{CO}	[mm]	0% C	≤ 75% C	> 75% C	≥ C
Chloride content	X _{Cl}	[m%]	≤ 0,2	0,2 - 0,6	0,6 - 1,0	> 1,0
Concrete resistivity	ρ	[Ωm]	> 1000	500 - 1000	100 - 500	< 100
Corrosion potential ¹	E _{corr}	[mV]	> -200	-200 - -350	-350 - -500	< -500
Corrosion state	KG	[-]	0 < 1	≥ 1 - 2	≥ 2 - 3	≥ 3 - 4

¹ using Cu/CuSO₄ reference electrode C means thickness of the concrete cover

2.2 Condition index

For the determination of a condition index, all available results from preliminary investigations at the evaluation time, such as carbonation depth and chloride content at the reinforcement level, are divided into classes. From these, information is obtained that can provide

information on the current state, respectively the intensity of the damage due to corrosion. The index is divided into four classes as follows:

1. = no damage and negligible or no corrosion,
2. = minor damage and low corrosion,
3. = moderate damage and moderate corrosion,
4. = high damage and high corrosion.

The corrosion damage index (CDI) is obtained by first transferring measured values to Corrosion indicator levels, see Table 1. These scenarios represent common evaluation approaches which have to be proven and possibly up dated in practical use. The mean of the corrosion indicator levels results in the “Corrosion Damage Index”:

$$CDI_{Mean} = \sum_i^n \frac{Degradation\ indicator\ level_i}{n} \quad (1)$$

here n is the number of corrosion indicators used, according to Table 1.

The mean value is calculated for simplification purposes. In principle, it is possible to assign more importance to individual indicators.

A weighting can be based on the type of measurement on the one hand and on the significance of the indicator on the other. The indicators carbonation, visual appearance, chloride content at reinforcement level and cracks are all indicators that provide indirect information about the degradation, whereas potential, corrosion rate or cross-section loss of the rebar represent direct measured values related to the corrosion of the reinforcement and may therefore weighted stronger. A method for determining the weights, the analytical hierarchy process (AHP) (Saaty, 1977). The calculation of the condition index when weighted indicators are used is as follows:

$$CDI_{AHP} = \sum_i^n Degradation\ indicator\ level_i \cdot w_i \quad (2)$$

where w_i is the weighting factor for the particular degradation indicator used.

The method enables transparent traceability of how prioritization was calculated and, thus, strengthens the understanding and acceptance in decision making. Thus, a comprehensible and expert-based weighting is achieved. The approach of the method is to simplify the problem by breaking it down into a hierarchical system and to form a systematic procedure to structure and solve the decision processes. Which indicators are used in particular and how they are ranked and prioritized can be seen in Table 2. Therefore, the corrosion indicator chloride content is two times more important than the corrosion potential (X_{CI}) and seven times more influential than the carbonation depth (X_{CO}). This additional information is processed in the AHP algorithm and derives the weighting in percent, which is given in the last column of Table 2 labeled as priority.

Table 2. Weights of the degradation indicators to determine the condition index

Degradation indicator DI	Rank	Importance						w_i [%]
		1	2	3	4	5	6	
Chloride content	1	1	3	4	5	7	8	43,7
Corrosion potential	2	1/2	1	2	3	6	7	23,9
Concrete resistivity	3	1/3	1/2	1	2	5	6	15,7
Corrosion state	4	1/4	1/3	1/2	1	4	5	10,3
Carbonation depth	5	1/7	1/6	1/5	1/4	1	2	3,8
Visual appearance	6	1/8	1/7	1/6	1/5	1/2	1	2,7

The CDI is thus a measure of the direct quantifiable damage due to corrosion the reinforcement has undergone, combined with the expected corrosion progress. The result is therefore a measure that provides information about damage already caused and describes the current status of the degradation. The level of the index (CDI) shows the extent of the damage that has already occurred. The higher the damage index, the greater the damage and extent of the degradation. By using AHP

the decision problem is decomposed into a hierarchy of more easily comprehensible sub-problems, which can be analyzed independently. Once the hierarchy is built, the process consists of systematically evaluate the elements and determine their interrelations and by comparing them to each other with respect to their impact on an element above them in the hierarchy. In making the comparisons, concrete data about the elements can be used to enhance the judgments about the elements' relative meaning and importance. The AHP converts these evaluations to numerical values that can be processed and compared over the entire range of the proposed problem. Finally, a numerical weight or priority is derived for each element of the hierarchy, allowing diverse and often incommensurable elements to be compared in a rational and consistent way. After incorporating these judgments this yields to a set of overall priorities for the hierarchy. With every kind of pairwise comparison, inconsistencies can also occur. For the examination of these inconsistencies a so called Consistency Ratio (CR) is used, where $CR < 10\%$ is considered to be acceptable. For the examination of these inconsistencies a so called Consistency Ratio (CR) is used, where $CR < 10\%$ is considered to be acceptable (Saaty, 1990).

2.3 Fuzzy-logic decision support system

It is indeed difficult to perform a quantitative evaluation of the effectiveness of repairs. This problem has many sources. They include environmental influences, time pressure during implementation, lack of root cause analysis, price wars among repair companies and poor execution quality.

It is not possible to evaluate the effectiveness of repair procedures quantitatively. Complex tests on site and in the laboratory are required for realization.

It is more appropriate to use an expert system so that knowledge can be made available to experts. A rule-based expert system (RES) models an expert who can handle the system instead of the system to be operated. This makes the expert knowledge accessible to non-experts, who can thus make decisions with the help of the RES. Furthermore, the conception of a RES enables the knowledge of the experts, which is intuitive and empirical, to be readable and processable by computers.

Fuzzy RES are based on qualitative (fuzzy) expert statements and thus on (fuzzy) stored qualitative knowledge. In addition to the use of linguistic variables and operators, an essential concept is the method of defuzzification. In this paper, it is shown how the effectiveness of individual repair measures can be estimated as a function of the damage classes or corrosion indicators using the fuzzy logic approach.

The simplest form of a fuzzy logic application is a fuzzy controller. This takes input, then performs calculations and finally provides an output value. Fuzzy sets were first applied by (Zadeh, 1965). The following steps must be gone through:

- Setting the input and output values as linguistic variables,
- Definition of the fuzzy sets of input and output values,
- Converting the input values into fuzzy values (fuzzyfication),
- Formulation of the rules and store in the knowledge base,
- Applying the rules to the fuzzy values (inference),
- Convert obtained statements into numerical form (defuzzyfication).

Figure 2 illustrates the basic structure of a fuzzy logic expert system with focus of the presented problem.

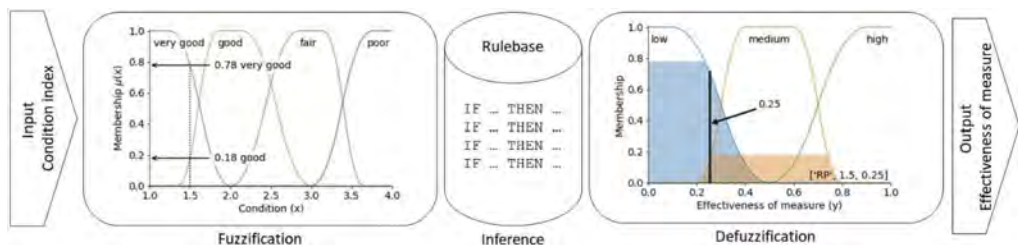


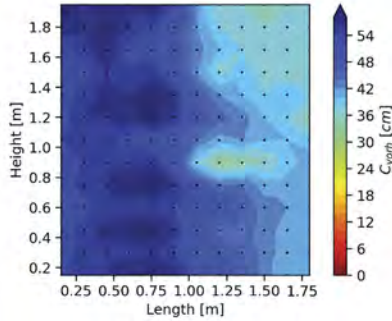
Figure 2. Illustration of the fuzzy logic process to determine the effectiveness of repair measure based on the condition index (CDI = 1.5).

3 FIELD STUDY

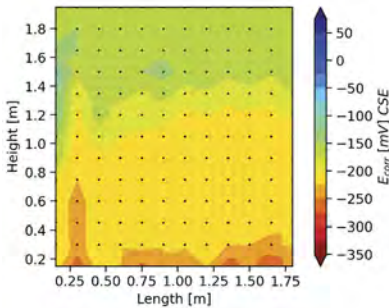
The survey was undertaken on a retaining wall situated in Vienna at the Austrian motorway network of ASFiNAG. The retaining wall is 3.80 m beside the motorway lane. The wall is 133 m long and between 0.5 m and 5.90 m of height. It is retaining a slope before an overpass. Taking into account that the surveyed structure is 38 years old, the evaluation of the conditions shows already degradation phenomena, like delamination, cracks and particularly corrosion of the reinforcement. The preliminary survey shows a mean carbonation depth of 2.4 cm and chloride contamination over 1 % Chloride per mass binder up to approximately 4 cm in the concrete surface (see Figure 3).



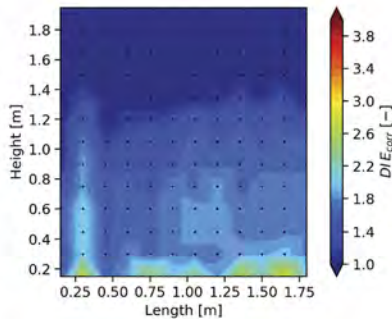
a) Visual appearance of the component.



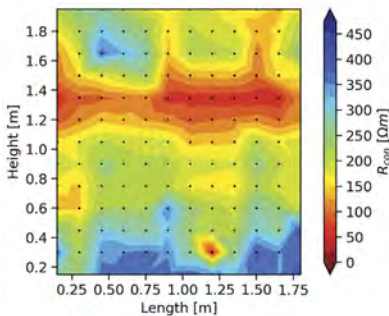
b) Concrete cover C_{exg} represented as surface plot.



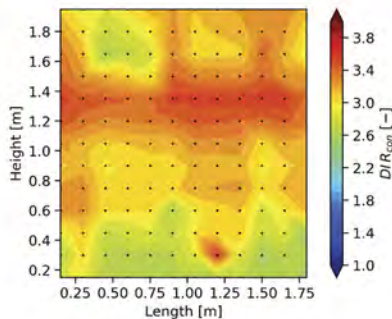
c) Measurement results of the potential measurement.



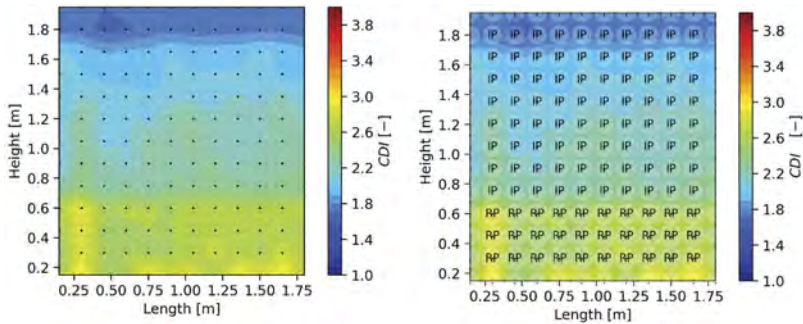
d) Representation of the corrosion potential as Degradation indicator ($DI E_{corr}$).



e) Measurement results of the concrete resistivity



f) Representation of the concrete resistivity as Degradation indicator ($DI R_{con}$).



g) Representation of the condition indicator (CDI). h) Representation of the condition indicator (CDI) including the by the FL-algorithm proposed repair measure.

Figure 3. Representation of the in-situ measurements from the preliminary surveys and their degradation indicators to obtain the overall condition indicator (CDI) which is serving as an input parameter to derive the optimal repair measure by using the developed Fuzzy Logic algorithm.

4 CONCLUSIONS

The paper presented a methodology to assess the condition of concrete components. The condition is determined from real and therefore objective values which are suitable to indicate degradation. The obtained data is mainly derived from condition surveys and may also monitoring data, like humidity, electrical resistivity, and corrosion potential.

The demand of an exact as possible determination of the condition state is a key mission for the asset management to decide which maintenance measure is the best for a certain condition at certain time. This is considered by using objective indicators (degradation indices) to derive an overall performance index. This condition indicator (CDI) is handled through an analytic hierarchy process (AHP) for the sake of objectivity and comprehensibility.

The AHP was utilized in this paper to develop a useful tool for determining the corrosion damage condition of a reinforced concrete bridge component based on different corrosion indicators. AHP method was used to help determine weight factors for different indicators relative to the determination of the final corrosion condition. AHP method can reduce the influence of certain expert's mistakes in the judgment by using pairwise comparison method. A final and more accurate CDI value can be obtained.

The condition index has been transformed into a fuzzy logic system. An overview of the whole fuzzy logic process for determining the effectiveness of repairs based on the condition index CDI was given. A simple expert-based decision rule regime was used to determine the effectiveness of individual repair principles.

At first, membership functions of the sharp input, here condition index, and output variables, here theoretical effectiveness of repair, are conceived. Fuzzy ranges of values are created. These values are related in the inference via a rule database, which was designed empirically and based on expert knowledge. After defuzzification, the effectiveness of the respective maintenance principle is the output to the corresponding condition index CDI.

In Figure 3.h) it can be seen that the effectiveness of a certain maintenance measure is not completely ineffective or fully effective in any of the cases. The developed decision algorithm can reliably represent the state of knowledge of experts in the field of repair of reinforced concrete structures. The structure of the system is deliberately kept simple and the reconstruction of the decisions is also clearly comprehensible.

In addition, the fuzzy logic expert system can be extended with respect to the degradation indicators forming the condition index. Furthermore, the developed system is machine-readable, therefore simultaneously applicable to a collective of reinforced concrete components or even entire infrastructure networks.

The methodology was evaluated, proofed, and demonstrated within the case study. If enough data from the condition assessment is available, it can provide a more accurate condition overall and so serve for more profound input for the Fuzzy Logic expert system to choose an optimal repair measure.

The strict rely on only visual inspection data for condition assessment to manage repair measures is considered as critical by the authors.

The paper presents a comprehensive methodology for structural monitoring with the aim of showing how directly usable results from monitoring can be, obtained in the long term for service life prognosis, asset management and maintenance with acceptable effort.

In addition, with the application of this approach on a larger, representative building stock, the perspective of an even more reliable service life prognosis will take place. Therefore, the data already acquired, but also future data, can be described as valuables. In the future better forecasts will be possible based on more precise condition assessments. An important point is that uncertainties on both the impact and the resistance side can be concretized or reduced through dense NDT in time and space, or monitoring.

5 OUTLOOK

The transfer of damage to reinforced concrete components into damage classes can be extended to include indicators for freeze-thaw attack or sulfate attack. Also, such damage classifications can be applied to other materials, such as steel by extension. The application of the degradation indicators allows an objective representation of the state and contributes to the homogenization of the data.

With this more accurate data, at the structure level, the fuzzy logic algorithm can serve as a decision support tool in choosing the optimal repair method. In addition, the fuzzy logic expert system can be extended with regard to the degradation indicators forming the condition index. In addition, the developed system is also applicable to a collective of components, structures or even entire infrastructure networks.

At the network level, the fuzzy logic algorithm can provide more accurate results when calculating the budget requirements of future maintenance activities. This allows to take full advantage of the optimal rehabilitation at the optimal time and so effectiveness of financial resources.

REFERENCES

- Casas, J.R., Matos, J.C. e, 2017. Standardization of quality control plans for highway bridges in Europe: COST Action TU 1406. IOP Conf. Ser.: Mater. Sci. Eng 236. <https://doi.org/10.1088/1757-899X/236/1/012051>
- Pailes, B.M., Gucunski, N., 2015. Understanding Multi-modal Non-destructive Testing Data Through the Evaluation of Twelve Deteriorating Reinforced Concrete Bridge Decks. *J Nondestruct Eval* 34, 14. <https://doi.org/10.1007/s10921-015-0308-6>
- Saaty, T.L., 1990. How to make a decision: The analytic hierarchy process. *European Journal of Operational Research* 48, 9–26. [https://doi.org/10.1016/0377-2217\(90\)90057-I](https://doi.org/10.1016/0377-2217(90)90057-I)
- Saaty, T.L., 1977. A scaling method for priorities in hierarchical structures. *JMP* 15, 234–281–234–281. [https://doi.org/10.1016/0022-2496\(sci77\)90033-5](https://doi.org/10.1016/0022-2496(sci77)90033-5)
- Zadeh, L.A., 1965. Fuzzy sets. *Information and control* 8, 353. [https://doi.org/10.1016/S0019-9958\(65\)90241-X](https://doi.org/10.1016/S0019-9958(65)90241-X)

Probability-based service life design of repair mortar overlay in case of chloride-induced depassivation risk

K. Van Den Hende, S. Helderweirt, W. Botte, S. Matthys & R. Caspee

Department of Structural Engineering and Building Materials, Ghent University, Ghent, Belgium

G. Lombaert

Structural Mechanics, Civil Engineering Department, KU Leuven, Leuven, Belgium

ABSTRACT: Chloride ingress is one of the most important causes of reinforcement corrosion. To assess the risk of chloride-induced corrosion, a frequently used technique is to measure the concrete cover and chloride profile in order to map the chloride ingress process and associated risk for depassivation of the rebars. Based on the results of the analysis, a range of different repair solutions can be proposed, among which a repair mortar applied to the concrete surface to increase the quality and thickness of the concrete cover, such to lower the risk of forthcoming depassivation. Unfortunately, modelling of the migration process of chlorides after such an intervention becomes more complex as two different materials with varying diffusion coefficients are combined. Here, a novel framework is proposed in order to determine the minimal thickness of the repair mortar applied to the surface, ensuring that the probability of depassivation stays below a predefined threshold.

1 INTRODUCTION

Chloride migration in reinforced concrete is one of the main reasons why reinforcement starts to corrode. When chlorides penetrate the concrete, the chloride concentration at the reinforcement level rises to the point where it may exceed a critical chloride concentration and the steel is depassivated, i.e. it may start to corrode. Fortunately, extensive research has been done in the past and consensus has been achieved regarding the modelling of the time to corrosion initiation, considering uncracked concrete structures subjected to chloride ingress (fib Bulletin 34, 2006). In case of performance-based design of new structures, generally the required concrete cover is determined as to ensure the probability of depassivation stays below 10% throughout the structure's lifetime (CROW 2018). However, for existing structures a different threshold might be appropriate due to the limited remaining lifetime and considering the corrosion propagation phase. To make sure this threshold is not exceeded during the structure's remaining or extended lifetime, a repair intervention might be needed.

A possible intervention could be to apply an additional repair mortar layer on top of the concrete surface. The effect of this compact mortar layer is twofold: (1) it will slow down the migration of new chlorides into the concrete, and (2) part of the chlorides in the already contaminated concrete can diffuse into the mortar layer. Solving the differential equation for two materials with different diffusion coefficients has been done in the past, when studying the so-called skin-effect (Andrade, 1997). However, in order to take into account the previously diffused chlorides which have migrated into the concrete substrate before the application of the repair mortar, the differential equation is numerically solved by discretizing in time and space using the finite difference method.

This numerical approximation is complex and impractical for practicing engineers and hence an objective way to determine an appropriate repair mortar strategy is still lacking. In this work, a framework is proposed for the development of easy-to-use nomograms to determine the required thickness for a repair mortar overlay for a specific situation. The influence of several input parameters on the proposed repair strategy is investigated first, in order to select the main parameters to be used in the nomograms.

2 MODELLING THE MIGRATION PROCESS OF CHLORIDES INTO CONCRETE

2.1 Modelling diffusion of chlorides

The one-dimensional transport of chlorides through the concrete substrate is described by the diffusion law (Saetta 1993, Crank 1979):

$$\frac{\partial C}{\partial t} = \frac{\partial}{\partial x} D \frac{\partial C}{\partial x} \quad (1)$$

where C [m%*cement*] is the chloride concentration at time t and location x and D [mm²/s] is the diffusion coefficient of the substrate material. Considering that chlorides are migrating through a single material with a time-invariant diffusion coefficient, no initial chlorides were present in the substrate and a constant chloride concentration is maintained at the surface, the solution of the differential equation becomes:

$$C(x, t) = C_s \left[1 - \operatorname{erf} \left(\frac{x}{2\sqrt{Dt}} \right) \right] \quad (2)$$

where C_s [m%*cement*] is the surface chloride concentration which follows from the environmental conditions, and $\operatorname{erf}(x)$ the Gauss error function. When the diffusion coefficient and surface concentration are known, this equation allows to determine the chloride concentration at any time and location. However, in case a repair mortar is applied to the concrete surface, a new material with a different diffusion coefficient is introduced. Consequently, the diffusion coefficient in equation (1) varies with the depth of the substrate, and the single material solution given by equation (2) does not apply anymore. To solve the chloride migration problem, the differential equation can be solved numerically. In the work of Petcherdchoo (2018), the following numerical scheme is proposed based on the finite-difference principle of Crank-Nicolson (William, 2007):

$$\frac{c_{i,j+1} - c_{i,j}}{\Delta t} = \frac{1}{2} \left(\frac{D_{i+\frac{1}{2}}(c_{i+1,j+1} - c_{i,j+1}) - D_{i-\frac{1}{2}}(c_{i,j+1} - c_{i-1,j+1})}{(\Delta x)^2} + \frac{D_{i+\frac{1}{2}}(c_{i+1,j} - c_{i,j}) - D_{i-\frac{1}{2}}(c_{i,j} - c_{i-1,j})}{(\Delta x)^2} \right) \quad (3)$$

where $c_{i,j}$ is the chloride concentration at mesh point i and timestep j . Diffusion coefficients $D_{i+\frac{1}{2}}$ and $D_{i-\frac{1}{2}}$ are located in between two mesh points and determined by taking the average of the diffusion coefficients of their neighbours.

2.2 Time-dependent diffusion coefficient

Conflicting with the assumptions previously made, the diffusion coefficient and chloride concentration at the surface may change over time (Andrade, 2011). First of all, the diffusion coefficient changes due to a change in the porosity of the concrete as it ages, and binding of the chlorides to the substrate material instead of migrating further. Secondly, the surface chloride concentration is in reality not constant due to the varying exposure conditions. These

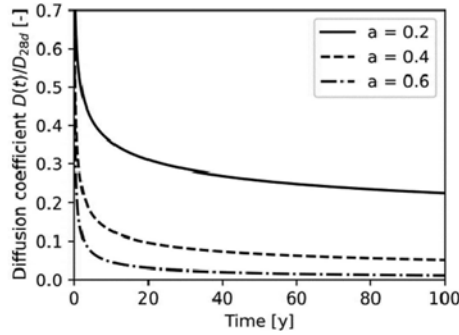


Figure 1. Apparent diffusion coefficient over time.

effects are taken into account by defining an averaged diffusion coefficient over the period considered, the so-called apparent diffusion coefficient D_{app} , defined in the *fib* Model Code for Service Life Design (2006):

$$D_{app}(t) = k_e \cdot D_{RCM,0} \cdot k_t \cdot \left[\frac{t_0}{t} \right]^a \quad (4)$$

where k_t [-] is the transfer variable which is equal to 1 by default and a [-] the ageing exponent describing the time-dependent behaviour of the diffusion coefficient. k_e [-] is the environmental transfer variable considering the outside temperature's influence. This value is assumed to be equal to 1 in the subsequent analyses, i.e. the temperature of the concrete element under consideration is equal to a reference temperature of 20°C. $D_{RCM,0}$ is the diffusion coefficient at a reference time t_0 of 28 days measured by the Rapid Chloride Migration (RCM) method.

Equation (4) is based on multiple diffusion measurements of the same concrete substrate over time. However, when applying a repair mortar to the concrete surface, the time-dependent processes influencing the diffusion coefficient, such as the ageing of concrete, might be altered. Figure 1 shows the evolution of the diffusion coefficient D_{app} over time for different values of the ageing exponent, indicating that the diffusion coefficient more or less stabilizes after a period of 20 to 30 years. In most practical cases, an intervention is required only for existing structures with a considerable age and thus the application of the repair mortar will not alter the time-dependent behaviour of the concrete diffusion coefficient much. Hence, the use of the apparent diffusion coefficient D_{app} in combination with equation (3) to simulate the progression of chlorides through the concrete substrate and mortar layer is appropriate. About the time-dependent behaviour of repair mortars, little research has been executed and in this work the diffusion coefficient of the repair mortar is assumed to be described by equation (4) as well.

2.3 Mesh properties and incremental time step

To numerically approximate the multi-material diffusion process by means of equation (3), a discretization in time and space is required. Therefore, the mesh point size Δx , depth of 1D space x_{limit} and incremental time step Δt , need to be determined. Increasing Δx and Δt and decreasing x_{limit} reduces the computation time, but at the expense of numerical accuracy and therefore an appropriate choice should be made. First of all, based on the recommendations of Petcherdchoo (2018), Δx is taken equal to 1 mm. Secondly, the considered depth x_{limit} of 1D space should be large enough to ensure that the assumption $C(x=+\infty; t)=0$ is satisfied. Here, the value for x_{limit} is determined based on the analysis of a single material diffusion process, where the analytical solution of equation (2) can be compared to the numerical solution according to equation (3). The results are shown in Figure 2 for an extreme set of parameters compared to the values included in *fib* Bulletin 76 (2015) ($C_s = 2$ m% cement,

$D = 50 \text{ mm}^2/\text{y}$, $t = 150 \text{ y}$, $\Delta t = 0.1 \text{ y}$ and $\Delta x = 1 \text{ mm}$). It appears that $x_{limit} = 200$ and 300 mm lead to an acceptable prediction of the chloride concentration at the level of the reinforcement, typically located around 20 to 70 mm from the boundary. Therefore, x_{limit} is chosen equal to 300 mm.

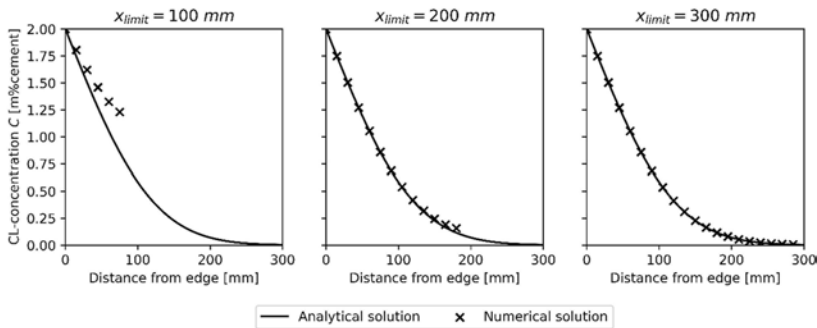


Figure 2. Influence of depth of 1D space on the numerical approximation of the diffusion process.

Finally, Δt is an important parameter because it has a significant influence on the computation time. This is because the chloride concentration needs to be iteratively determined for every time step, compared to the spatial characteristics which can be vectorized. In the work of Petcherdchoo (2018), Δt is chosen equal to 0.08 y (1 month) to ensure a smooth transition of the chlorides into the two-material substrate. In Figure 3, the problem statement as described previously is solved for different values of Δt , considering the application of a repair mortar of 20 mm after 50 years. The graphs represent the results at respectively 5, 20 and 50 years after application of the repair mortar. It is clear that the smaller Δt , the more smooth the chloride migration process is simulated and especially for larger values, the chloride concentration at the boundary between the concrete and the repair mortar is not well simulated. However, the chloride concentration at the level of the reinforcement, which is typically around 20 to 70 mm from the original surface (+20 mm to mortar surface), seems to be predicted well by all values of Δt . To increase the efficiency of the algorithm and still maintain a reasonable approximation of the chloride concentration at the materials' interface, the value of Δt is set equal to 1y in this work.

3 FRAMEWORK FOR DETERMINATION OF THE REPAIR STRATEGY FOR REPAIR MORTAR OVERLAY

3.1 Description of the general framework

The framework which is developed in this contribution allows to assemble practical nomograms which indicate the appropriate repair mortar solution for a set of input parameters. In the *fib* Model Code for Service Life Design (2006) and *fib* Bulletin 76 (2015), the probabilistic characteristics of the parameters describing the diffusion process have been characterised. For a given concrete composition and mortar type (diffusion coefficients of both materials), exposure condition (chloride concentration) and concrete cover, it is possible to derive nomograms that indicate the most appropriate repair strategy (usefulness of repair mortar overlay and its thickness), taking into account a maximum threshold for the probability of depassivation and age of the structure.

Using Latin Hypercube Sampling (Ollson 2003), first the probability of depassivation P_{dep,t_0} at the time of intervention t_0 is determined. If P_{dep,t_0} already exceeds the threshold probability P_{lim} , a repair mortar overlay solution is not advised and a more drastic repair strategy is needed, e.g. removing and repairing the contaminated concrete. If P_{dep,t_0} did not

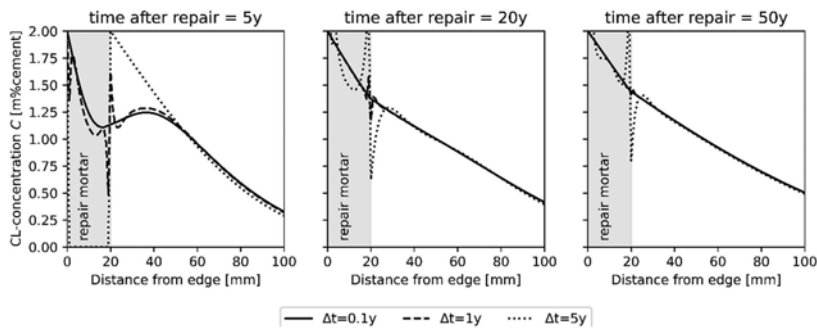


Figure 3. Influence of the incremental time step on the numerical approximation of the diffusion process.

exceed P_{lim} yet, the probability of depassivation $P_{dep,t1}$ at the end of the structure's intended lifetime t_1 is determined. In case $P_{dep,t1}$ is still below P_{lim} , no repair mortar is needed at all. If $P_{dep,t0}$ is below P_{lim} and $P_{dep,t1}$ is above P_{lim} , a repair mortar overlay solution might be possible and the repair mortar thickness is increased step by step by 5 mm until $P_{dep,t1}$ is below P_{lim} . The maximum repair mortar thickness is considered to be 50 mm.

3.2 Reference nomogram

Consider a concrete composed of fly-ash cement combined with a water/cement ratio of 0.4 located in environmental class XD2 (wet, rarely dry). Based on this information, further to that of a polymer-cement based (PCC) repair mortar, the input parameters and probabilistic characteristics are given in Table 1. Note that the parameters that were defined in literature as normally distributed are defined as lognormally distributed in order to exclude negative values. The characteristics of the repair mortar correspond to a commercially available repair mortar. Due to the absence of probabilistic information about the properties of the repair mortar, the ageing exponent a_m is considered deterministic and the coefficient of variation of the diffusion coefficient $D_{RCM,0,m}$ is considered to be equivalent to the corresponding value of the original concrete, and hence $V_{RCM,0,m}$ is considered equal to 0.2. The calculation is done for different ages of mortar application (between 20 to 70 years) and concrete covers (between 30 and 60 mm). Furthermore, the desired remaining lifetime is considered to be 50 years, the probability of depassivation threshold is 10% and 10 000 Latin Hypercube Samples are used.

The resulting nomogram is given in Figure 4, where three different regions are visualized: a region where no repair mortar overlay is needed (green), a region where a repair mortar overlay could be applied (blue) and a region where no repair mortar overlay solution is possible (red), either due to the probability of depassivation being already exceeded at the time of intervention or the need for an excessive mortar overlay thickness.

Within the region where a repair mortar overlay could be applied, the required thickness of the repair mortar layer increases by 5 mm in a stepwise manner indicated by the dotted lines, starting from 0 mm at the most right boundary. For example, for the reference nomogram in Figure 4, a mean concrete cover of 40 mm combined with a time of application of 40 years gives a required repair mortar layer thickness of 10 mm to prevent the probability of depassivation from going over the threshold of 10%.

The region where a repair mortar can be applied is rather narrow, indicating that a repair mortar overlay solution would only be feasible in a limited amount of cases. Also, the largest thickness of repair mortar needed is 20 mm. This indicates that in situations where the threshold would be exceeded (yet where depassivation of the reinforcement was not yet reached at time of intervention), a relatively thin layer of additional repair mortar can be enough to stay below the required threshold probability.

Table 1. Probabilistic distribution of parameters influencing the migration of chlorides.

Variable	Distribution	μ	V	σ	a^*	b^{**}
Ageing exponent concrete $a_c[-]$	Beta	0.6	0.2	0.12	0	1
Ageing exponent mortar $a_m[-]$	Deterministic	0.5	/	/	/	/
Diffusion coefficient concrete $D_{RCM,0,c}[10^{-12}m^2/s]$	Lognormal	5.6	0.2	1.12	/	/
Diffusion coefficient mortar $D_{RCM,0,m}[10^{-12}m^2/s]$	Lognormal	1.27	0.2	0.25	/	/
Concrete cover $c[mm]$	Lognormal	Varying	σ/μ	8	/	/
Surface concentration $C_s[m\%cement]$	Lognormal	3	0.75	2.25	/	/
Critical concentration $C_{crit}[m\%cement]$	Beta	0.6	0.25	0.15	0.2	2.0

a^* : lower bound of Beta distribution
 b^{**} : upper bound of Beta distribution

4 INFLUENCE OF PARAMETERS ON NOMOGRAMS

To derive nomograms for different diffusion coefficients, surface concentrations etc., it is important to consider the influence of these parameters on the proposed repair mortar overlay solution. The influence of the mean value of four parameters from the reference nomogram in Figure 4 will be investigated: the ageing exponent and diffusion coefficient of the concrete, the surface concentration and the remaining lifetime. The uncertainty of the characteristics of the repair mortar is not varied as currently information on these properties is rather scarce and should be investigated more in-depth in further work. The results are given in Figure 5, where only the indicated variable is changed compared to the reference nomogram, while the other value remain as indicated in Table 1.

It can be seen that the nomograms change significantly compared to the reference case, which indicates the importance of each of the varied parameters. Moreover, increasing the desired remaining lifetime increases the feasibility of a repair mortar overlay strategy.

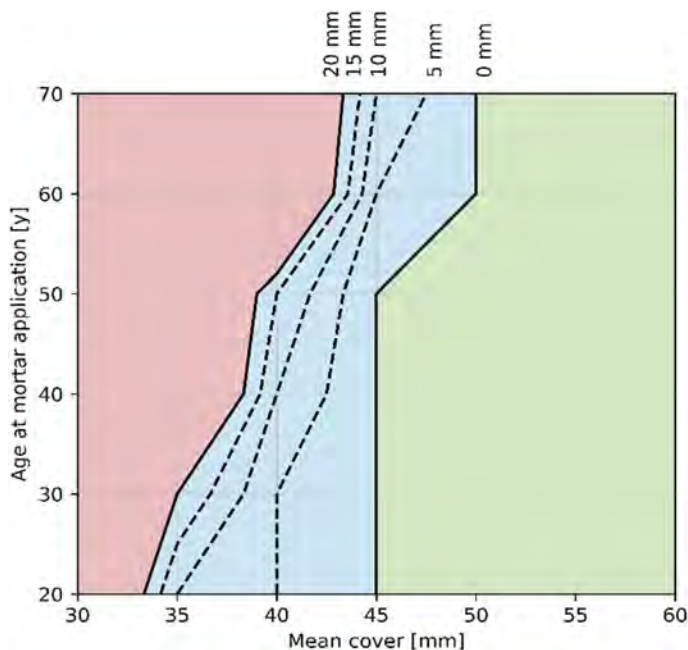


Figure 4. Reference nomogram.

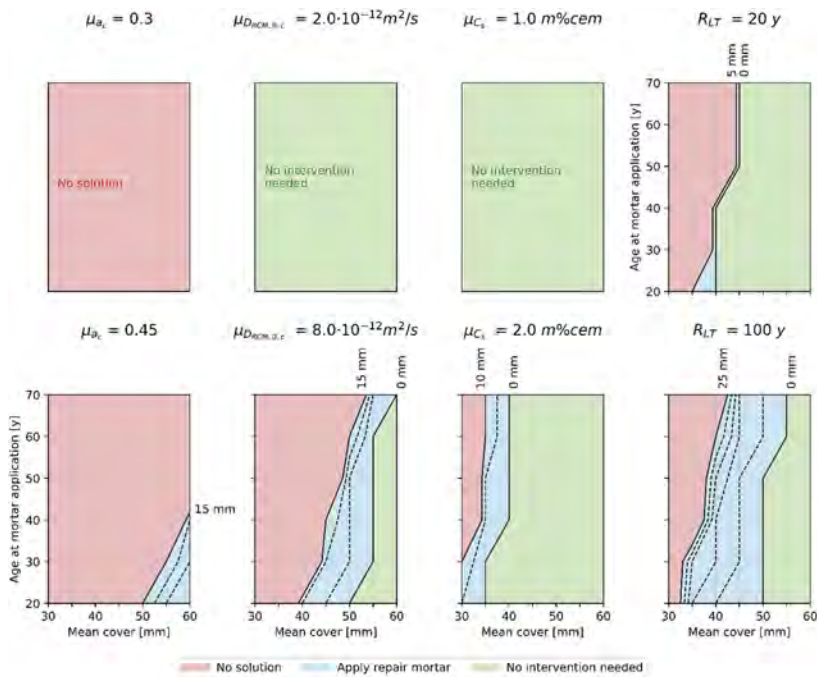


Figure 5. Influence several parameters on nomogram.

5 CONCLUSIONS AND FURTHER WORK

In this work, a framework was proposed to determine the minimal thickness of repair mortar overlay that needs to be applied to the concrete surface to slow down the chloride ingress and make sure the probability of depassivation stays below a certain predefined threshold. This framework can be used to construct easy-to-use nomograms for different types of concrete compositions and environmental conditions, using the probabilistic characteristics defined in the fib Model Code for Service Life Design (2006) and fib Bulletin 76 (2015). Generally, only a limited repair mortar thickness is required to make sure the threshold of depassivation probability is not exceeded. However, the required thickness of the mortar overlay increases when the desired remaining lifetime increases.

In order to generate different nomograms, it is important to determine the parameters which have a significant influence on the final repair solution. It was found that the mean values of the ageing exponent, diffusion coefficient, surface concentration and remaining intended lifetime significantly influence the resulting nomograms. However, it is important to note that the influence of the properties of the repair mortar has not been considered here and possibly has also a large influence on the final nomograms. Further work includes investigating the influence of the repair mortar properties and also the influence of the uncertainty on the parameters involved.

ACKNOWLEDGEMENTS

This research was performed within the framework of FWO SBO project lifeMACS “Multi-layer Bayesian life-cycle Methodology for the Assessment of existing Concrete Structures”, supported by FWO-Flanders (FWO-SBO project S001021N).

REFERENCES

- Andrade, C et al. 1997. Mathematical Modeling of a Concrete Surface “Skin Effect” on Diffusion in Chloride Contaminated Media. *Advanced Cement Based Materials* 6: 39–44.
- Andrade, C. 2011. Measurement of ageing effect on chloride diffusion coefficients in cementitious matrices. *Journal of Nuclear Materials* 412: 209–216.
- Crank, J. 1979. *The Mathematics of diffusion*. Oxford University Press.
- CROW. 2018. *CUR-Aanbeveling 121:2018*. Delft: CROW.
- Ferreira, M. et al. 2015. *Fib Bulletin 76: Benchmarking of deemed-to-satisfy provisions in standards: Durability of reinforced concrete structures to chlorides*. FIB.
- Ollson, A. et al. 2003. On Latin Hypercube Sampling for Structural Reliability Analysis. *Structural Safety* 25: 47–68.
- Petcherdchoo, A. 2018. Probability-based Sensitivity of Service Life of chloride-Attacked Concrete Structures with Multiple Cover Concrete Repairs. *Advances in Civil Engineering*.
- Saetta, A. et al. 1993. Analysis of Chloride Diffusion into Partially Saturated Concrete. *Materials Journal* 90(5): 441–451.
- Schiessl, P. et al. 2006. *Fib Bulletin 34: Model code for service life design of concrete structures*. FIB.
- William, H. et al. 2007. *Numerical recipes 3rd edition: The art of scientific computing*. Cambridge University Press.

Early detection of corrosion in reinforced concrete using ultrasonic-guided waves

N. Habbaba

Department of Civil and Environmental Engineering, American University of Beirut, Beirut, Lebanon

S. Mustapha

Department of Mechanical Engineering, American University of Beirut, Beirut, Lebanon

Y. Lu

Department of Civil Engineering, Monash University, Melbourne, Victoria, Australia

ABSTRACT: Reinforced Concrete is one of the most widely used composite materials in the modern construction industry, but corrosion has become a significant problem worldwide, resulting in exceptionally high maintenance costs. To maintain structural integrity and safety, robust non-destructive techniques are required. Ultrasonic-guided wave (UGW) based monitoring has proven to be sensitive to a wide range of flaws, since they can propagate for long distances to inspect larger areas. Corrosion causes delamination between the reinforcing steel and concrete interface, which affects the wave propagation characteristics. In this study, we aimed at detecting early corrosion in steel-reinforced concrete by relying on UGW. Hence, UGW propagation in steel bars embedded in concrete and the inspection of leaked energy from one bar to another through propagating in the concrete medium was investigated. Since natural corrosion is a slow process, an accelerated corrosion setup was used to induce artificial corrosion using the impressed voltage approach.

1 INTRODUCTION

Reinforced Concrete (RC) is one of the most widely used composite materials in the modern construction due to its robustness, availability, relatively low cost, ease of casting and fire resistance. The actual cause of concrete failure is rarely visible, where only symptoms are visible due to accumulated internal stresses. These stresses may end up in many types of failure that can trigger partial or full collapse of the structure. One of these failures could be due to the stresses generated as a result of rust accumulation since corrosion not only reduces the strength of the reinforcement, but its by-product, iron oxide, expands where this expansion causes stresses in the surrounding concrete, which eventually leads to cracking, delamination, spalling, and may reach a complete loss of serviceability (Sharma et al., 2018).

One of the major contributors to the corrosion of steel reinforcement is chloride attack as a result of the use of chloride-contaminated components, or diffusion into the concrete from the surrounding environment, particularly in coastal regions with high chloride concentrations (Sharma et al., 2018, Luković et al., 2017). Chloride attack is special because it acts primarily on corroding the steel reinforcement, and the surrounding concrete is only damaged because of the corrosion process (Luković et al., 2017).

Non-destructive testing (NDT) is the process of evaluating components, materials, or systems without affecting their serviceability. However, even if they involve invasive procedures, non-destructive testing techniques are those that do not compromise a component's future usefulness (Ivanchev, 2022). To avoid being late in corrosion detection, the initiation of corrosion should be recognized as early as possible to select appropriate protective measures to control subsequent deterioration (Gjørv, 2011). Hence, structural health monitoring (SHM) has been intensively

investigated in recent years because of its feasibility and importance in early non-destructive monitoring and damage detection, where the literature reported a variety of techniques that were suitably employed for monitoring and assessment of concrete health (Tan et al., 2016). Structural and civil engineers used different nondestructive techniques to monitor and assess concrete structures. One of the most promising active techniques for monitoring corrosion-related damage in reinforcing bars has been ultrasonic guided wave (UGW) monitoring (Su and Ye, 2009). This approach makes use of ultrasonic waves that travel over an extended structure while being directed by its boundaries and then observing waves transmission. The steel bar embedded in concrete serves as a waveguide, aiding in the transmission of wave packet where the transmitted wave properties will vary when the bar deteriorates due to corrosion (Sharma et al., 2015). The modes propagating a cylindrical structure are the longitudinal, torsional, and flexural modes, labeled with L, T, and F, respectively and they are frequency dependent modes (Su and Ye, 2009).

Some of the studies reported the use of UGW as a method for corrosion detection where the delamination was studied using both low frequency (100 kHz) and high frequency (1 MHz) signals. It was concluded that the low frequency fundamental mode excited at 100 kHz was less attenuative and it is a surface sensitive mode capable of detecting corrosion's debonding action. However, the $L(0, 7)$ mode at 1 MHz is a core sensitive with low attenuation and minimal leakage into the surrounding concrete (Luković et al., 2017). Moreover, the UGW technique was adopted to monitor the damage evolution due to corrosion of 20 mm steel rebar embedded in concrete. Based on the dispersion curves, the $L(0, 1)$ mode was selected at an excitation frequency of 40 kHz where in this study, the amplitude of first wave packet was only observed where it showed a gradual decrease as the corrosion process proceeded (Li et al., 2014). Another study investigated the effect of debonding levels between steel bar and concrete on the transmitted wave using a 120 kHz excitation frequency and a five-cycle sinusoidal wave (Miller et al., 2013). Before pouring concrete, PVC pipes were wrapped around the steel to simulate delamination. $L(0, 1)$ is the first wave in the received signal since it has the highest velocity, so the first peak was studied for different delamination lengths. Wave propagation was examined along the rebar with and without simulated corrosion introduced by partial removal of the concrete surrounding the rebar (Mustapha et al., 2014). The time reversal of wave signal was experimentally used to detect damage in rebar without relying on previous benchmark signals, which are typically impacted by external factors. The signals were generated using piezoelectric ceramics at one end of the rebar, received from the other end, time-reversed in the time domain, and then resent to be captured by the original piezoelectric ceramic. It was concluded that the time reversal process can detect damage of different lengths in rebar embedded in reinforced concrete since the damage size will ultimately modify the actuated signal.

This work focuses on the investigation of UGW propagation in steel bars embedded in concrete and the inspection of leakage behavior of the guided waves where the waves will be captured and monitored from different bars when actuating at a single bar. Also, it aims at active monitoring and early detection and propagation of corrosion of steel reinforcement embedded in concrete using UGW technique. To verify the proposed approach, an impressed voltage technique was used for accelerating corrosion of steel reinforcement in RC specimen. The response of the specimens will be monitored to detect the wave characteristics and correlate it with corrosion phases.

2 METHODOLOGY

2.1 Reinforced concrete specimen preparation

In this experiment two test specimens were first prepared using ordinary Portland cement (P.O 42.5), water, coarse aggregates, standard sand, and reinforcing steel. The water to cement ratio was 0.5 and the mix proportion of concrete is presented in Table 1. Each of the specimens prepared was of 400 mm long, 400 mm wide and 200 mm high and reinforced with five deformed rebar of 10 mm diameter and 600 mm length of which 400 mm centered embedded length in concrete and 100 mm was outstretched outside the concrete from each side. The properties of the steel bar are shown in Table 1. Before preparing the specimen, the reinforcing bars were cleaned, then fresh concrete was poured into the molds and cured for two days before demolding the specimen, then subsequently put in a normal curing chamber for 28 days. Concrete cylinders have been tested after 7 and 28 days

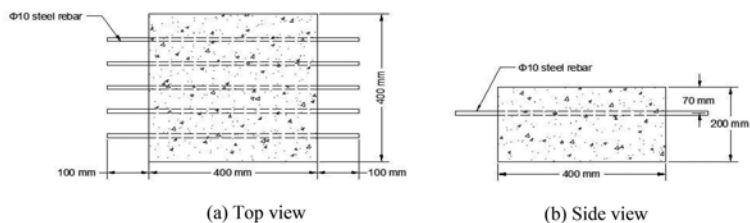


Figure 1. Reinforced concrete specimen detailing; (a) Top view, (b) Side view.

Table 1. Concrete and steel properties used.

Concrete Mix	Water	Cement	Fine Aggregates	Coarse Aggregates	
Proportions (kg/m ³)	200	400	700	1150	
Steel bar	Diameter	Length	Density	Young's modulus	Poisson ratio
properties	10 mm	600 mm	7850 kg/m ³	210 GPa	0.28

respectively and the average final compressive strength is 21 and 24.8 MPa, respectively. Specimen detailed dimensions are presented in Figure 1.

2.2 UGW monitoring setup

To facilitate the attachments of PZTs, both ends of the steel rebars were smoothed. The rectangular PZTs (PI Ceramics, Lederhose, Germany) 20 mm x 5 mm x 1 mm were then glued 550 mm apart on both ends of the rebar where one end PZT will serve as an actuator and the other end PZT will serve as a sensor. A typical ultrasonic testing setup for ultrasonic guided wave monitoring is used consisting of a Keysight 33500B signal generator, where the wave packet is produced, an EPA-104 Piezo System Inc voltage amplifier, and a keysight Inc. InfiniiVision DSO-X-3024A oscilloscope, which enables the data collection from the PZTs. The experimental setup with the generation and acquisition systems are shown in Figure 2 with the actuators and sensors connected to the amplifier and oscilloscope devices, respectively. The input signal is a five-cycle sine pulse in a Hanning window. The voltage peak-peak was set to about 200 volts.

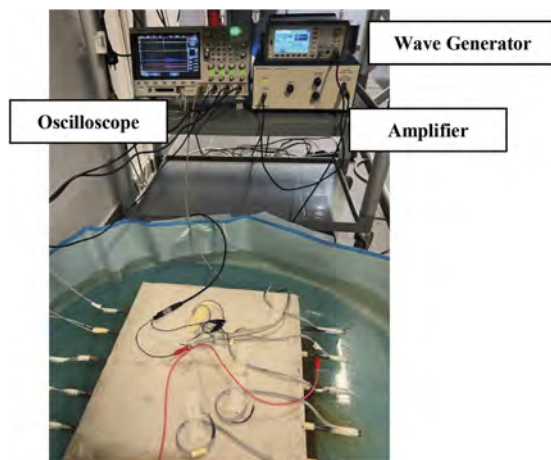


Figure 2. Experimental setup of the concrete specimen.

In the set-up, the change in the transmitted signal compared to a healthy signal due to the degradation of the steel bars resulting from the corrosion was monitored. Moreover, the steel

rebar may be considered as a smooth cylinder when the diameter to length ratio is less than 0.4, which is the case in this experiment where the diameter to length ratio is 0.018 where the effect of ribs is neglected (Ervin et al., 2006).

3 RESULTS AND DISCUSSION

3.1 Excitation frequency and wave mode selection

The responses to various excitation frequencies were studied varying from 25 kHz to 150 kHz. The work suggests that the optimum results with the clearer waveforms of the first longitudinal mode and highest amplitude values were obtained with an excitation frequency of 75 kHz.

3.2 Wave analysis in a healthy concrete

3.2.1 UGW through the steel bars embedded in concrete

Figure 3 represents the sensor numberings and distribution over the bars. In this section, the guided wave through the rebar will be investigated on a healthy concrete.

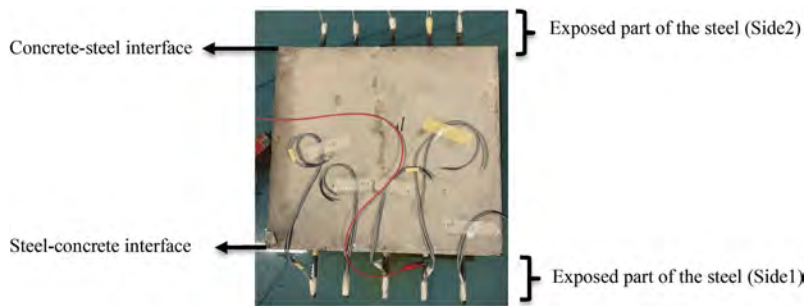


Figure 3. Sensor distribution and specimen main parts allocation.

So, actuation was conducted the rebar subjected to corrosion where PZT attached at one end of the rebar will serve as an actuator and the PZT attached to the other end will serve as a sensor so the waves will be guided within the steel bar boundaries. Thus, PZT2 will act as an actuator and PZT7 will acts as a sensor.

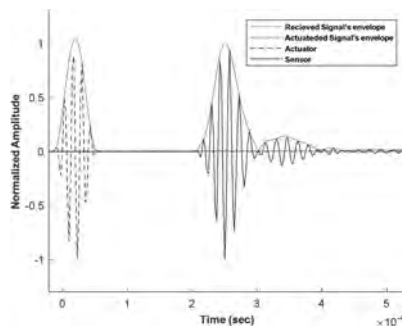


Figure 4. Waveforms actuated and sensed along bar2 embedded in a healthy concrete at 75 kHz.

Figure 4 represents the results of guided wave and its envelope showing the actuated and received signals where amplitudes are normalized for better visualization of actuated and received signal on the same graph. The signals of the UGW propagation in steel surrounded by concrete were quite complicated, as shown Figure 4, but the signals of the first received

wave packet were very significant. The guided wave's reflection and refraction at the steel rebar's end and in the steel rebar's contact with the concrete cause the modes to change which increases the complexity of the received waves, so low amplitude wave packets noticed will be attributed to boundary reflections.

In this research, the first wave packet was explored by evaluating the velocity and amplitude that are main features of the signals, so the collected data will serve as a benchmark. Based on the literature, the predominant mode propagating may be attributed to the longitudinal mode $L(0, 1)$.

3.2.2 Wave leakage investigation

Guided-wave structures may experience wave leakage throughout propagation. Wave leakage is highly influenced by a variety of factors such as structural geometry, fill materials, surrounding conditions, and simulation frequency. The leaky behavior of GWs will be explored in this part, where PZT2 attached to the bar subjected to corrosion, will be an actuator and PZT6, PZT9, and PZT10 from the facing side will be sensors (see Figure 3). Once the wave is sent, it will propagate through the exposed part of the steel in side 1 shown in Figure 3 then at the steel-concrete interface, part of the wave will leak into the surrounding concrete where it will propagate in the concrete and then at the concrete-steel interface part of the wave will be guided again through the exposed part of the steel from side 2.

3.2.2.1 Actuating by PZT2 and receiving by PZT6

The received wave packets are complicated, with no clearly separable modes; this might be attributable to the fact that concrete is a heterogeneous material made up of randomly distributed aggregates of various sizes and shapes. Peaks were selected visually, and the amplitude and velocity of these peaks were determined as shown in Figure 5. The peaks were referred to mode1, mode2, and mode3 since the wave is propagating through different mediums (steel and concrete) and different body sections (cylindrical and rectangular). However, since we are exploring the leakage behavior, the amplitude the dominant mode propagating through the rebar will be monitored which corresponds to the highest peak shown in Figure 5.

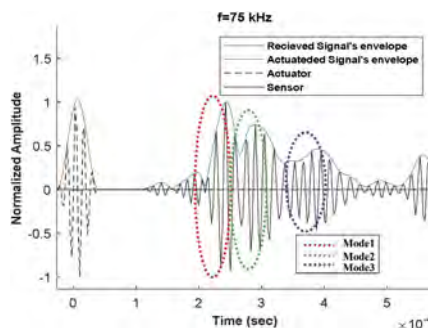


Figure 5. Actuated and received waveforms at 75 kHz (PZT6).

3.2.2.2 Actuating by PZT2 and receiving by PZT9

Similar results were shown in Figure 6 with clearer wave packets. It is shown here that the highest peak corresponds to the dominant mode propagated along the rebar. The amplitude of this peak which is 6.34% of the amplitude received by PZT7 with a velocity of 2375 m/s.

3.2.2.3 Actuating by PZT2 and receiving by PZT10

The wave captured by PZT10 is presented in Figure 7. Although the wave is propagating larger distance in the concrete, the dominant mode guided along the rebar is still appearing and the dominant mode with the highest amplitude. Since one mode with the highest peak was detected by all sensors, this will allow the monitoring of corrosion effect by monitoring this dominant mode.

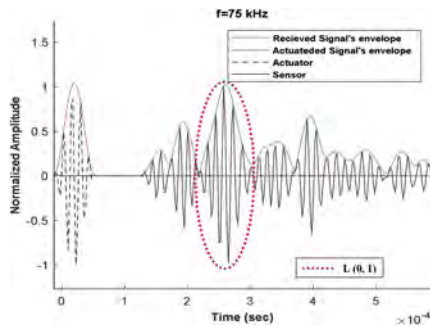


Figure 6. Actuated and received waveforms at 75 kHz (PZT9).

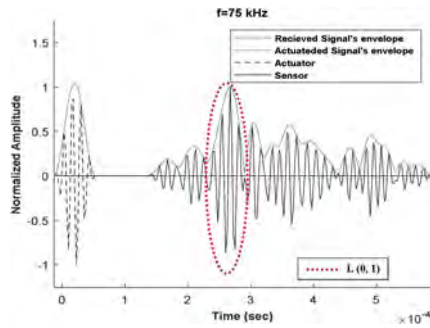


Figure 7. Actuated and received waveforms at 75 kHz (PZT10).

3.3 Effect of corrosion on UGW

The ultrasonic pulse transmission signals were recorded on a regular basis in the RC specimen undergoing corrosion. Despite the complexity of the signals received, L(0, 1) mode signals were highly significant, and amplitude fluctuation was clearly detectable throughout various corrosion days. The corrosion phases will be related to amplitude variation; an increase or decrease in amplitudes will correspond to one of the corrosion phases that are corrosion initiation following the entry of chloride solution, corrosion propagation and rust accumulation, and finally diameter reduction as progression takes place.

3.3.1 UGW through the steel bars during different phases of corrosion

The changes in amplitude for the waves guided in bar 2 subjected to corrosion are presented in Figure 8. Since corrosion was started at bar 2, a change in amplitude was noticed in rebar 2 at day 3, where a drop of 37.02% of the initial amplitude was detected and was attributed to the corrosion

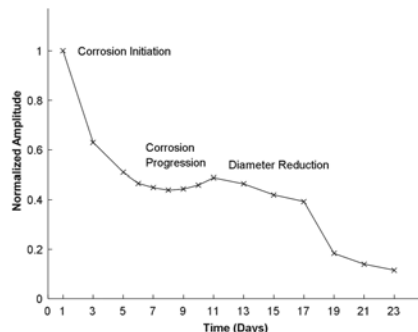


Figure 8. Variation in the amplitude of the dominant mode in bar2 with the progress of corrosion.

initiation. So, the start of corrosion results in an increase in the rebar's diameter where the initiation of corrosion is indicated by the reduced amplitude due to the increase in bonding strength between the concrete and steel, thus increasing the energy released to the surrounding concrete.

The amplitude gradually decreases until it started to increase at day 9 (Figure 8). The rise in signal is due to debonding of the rebar from the surrounding concrete due to rust buildup and formation of internal cracks that will weaken the bonding between concrete and steel which leads to the reduction in the energy leakage, indicating that the progression phase is detected. The specimen was left in the corrosion setup for further days so that the visible changes may be correlated with received waves signals. In this phase, there is a decrease in amplitude referring to the diameter reduction after corrosion progression and it continued to decrease until day 23.

3.3.2 Wave leakage during different phases of corrosion

The initiation and evolution of flaws in steel and concrete will be reflected by UGW since the wave is propagating in both mediums between the sending and receiving points, making the received signal more complicated. However, as indicated in previous sections, monitoring the leakage of L (0, 1) will reveal the presence of defects or changes in the RC specimen.

3.3.2.1 Actuating by PZT2 and receiving by PZT6

According to Figure 9, the amplitude of the received waves was decreasing between day 1 and 9 then it showed a slight increase between day 11 and 17 where a sharp increase started to appear after day 17 after the beginning of diameter reduction phase of bar2 which started at day 15.

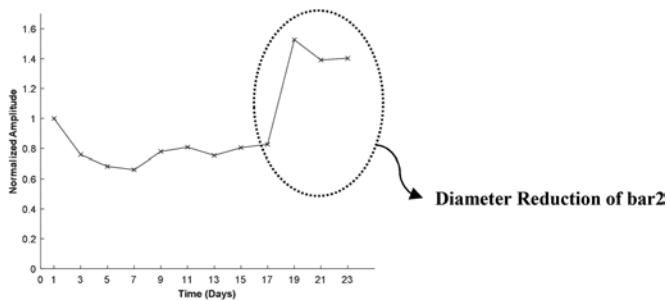


Figure 9. Amplitude variation of the dominant mode received by PZT6 with the progress of corrosion.

3.3.2.2 Actuating by PZT2 and receiving by PZT9

Starting day 11, no signals were received by PZT9. This could be attributed to an internal major crack along the path of the wave.

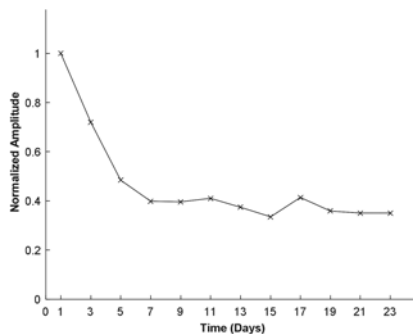


Figure 10. Amplitude variation of the dominant mode received by PZT10 with the progress of corrosion.

3.3.2.3 Actuating by PZT2 and receiving by PZT10

The amplitude of L (0, 1) was monitored from PZT10 signals. The amplitude showed a continuous decrease with a slight increase at day 17. From Figure 10, it is shown that the amplitude is highly affected by the stresses generated due to corrosion initiation and progression. However, at day 17 the increase in amplitude was very small compared to the jump in amplitude captured by PZT6. This could be referred to two reasons. One of them is the large distance covered by the wave in concrete medium which is a dispersive material for wave propagation so waves will lose its energy while propagating. Another reason may be the formation of the internal crack along the path of wave to PZT9 which may affect the strength of the received signals by PZT10.

4 CONCLUSIONS

In this work, it was shown that ultrasonic guided waves can identify corrosion phases and detecting corrosion of steel bars embedded in concrete before symptoms appearance. The assessment of guided wave propagation in steel bars embedded in healthy concrete has been examined. Following that, the impressed voltage technique was used to accelerate the corrosion of the steel bars, as corrosion is normally slow and takes a long time. Also, the leakage behavior of UGW was investigated on a healthy concrete and during different phases of corrosion. Because corrosion activity was the only variable in the experiment, the change in the collected UGW amplitudes of the dominant mode attributed to the first longitudinal mode L (0, 1) in the corroding and adjacent bars over the exposure time is assigned to corrosion activity.

UGW demonstrated a high sensitivity to the initiation and propagation of corrosion even when monitored away from the source of corrosion, and the proposed methodology is a potential NDT technique for use in RC members.

ACKNOWLEDGMENTS

The author would like to acknowledge the financial support from the Middle East Partnership Initiative- Tomorrow's Leaders Graduate program at the American University of Beirut provided to Ms. Nura Habbaba with the following award number: SNEAAC19CA0037

REFERENCES

- Eervin, B. L., Bernhard, J. T., Kuchma, D. A. & Reis, H. 2006. Estimation of general corrosion damage to steel reinforced mortar using frequency sweeps of guided mechanical waves. *Insight-Non-Destructive Testing and Condition Monitoring* 48(11): 682–692.
- Gjørø, O. E. 2011. Durability of concrete structures. *Arabian Journal for Science and Engineering* 36(2): 151–172.
- Ivanchev, I. 2022. Investigation with Non-Destructive and Destructive Methods for Assessment of Concrete Compressive Strength. *Applied Sciences* 12(23): 12172.
- Ii, D., Zhang, S., Yang, W. & Zhang, W. 2014. Corrosion monitoring and evaluation of reinforced concrete structures utilizing the ultrasonic guided wave technique. *International Journal of Distributed Sensor Networks* 10(2): 827130.
- Luković, M., Šavija, B., Ye, G., Schlangen, E. & Van Breugel, K. 2017. Failure modes in concrete repair systems due to ongoing corrosion. *Advances in Materials Science and Engineering* 2017: 9649187.
- Miller, T. H., Kundu, T., Huang, J. & Grill, J. Y. 2013. A new guided wave-based technique for corrosion monitoring in reinforced concrete. *Structural Health Monitoring* 12(1): 35–47.
- Mustapha, S., Lu, Y., Li, J. & Ye, L. 2014. Damage detection in rebar-reinforced concrete beams based on time reversal of guided waves. *Structural Health Monitoring* 13(4): 347–358.
- Sharma, A., Sharma, S., Sharma, S. & Mukherjee, A. 2015. Ultrasonic guided waves for monitoring corrosion of FRP wrapped concrete structures. *Construction and Building Materials* 96: 690–702.
- Sharma, A., Sharma, S., Sharma, S. & Mukherjee, A. 2018. Investigation of deterioration in corroding reinforced concrete beams using active and passive techniques. *Construction and Building Materials* 161: 555–569.
- Su, Z. & Ye, L. 2009. *Identification of damage using Lamb waves: from fundamentals to applications*. Berlin. Springer Science & Business Media.
- Tan, C., Shee, Y., Yap, B. & Adikan, F. M. 2016. Fiber Bragg grating based sensing system: Early corrosion detection for structural health monitoring. *Sensors and Actuators A: Physical* 246: 123–128.

The use of corrosion rates for the identification of damaged zones in a football stadium and efficacy of surface inhibitors as repair method

C. Andrade

International Center of Numerical Methods in Engineering (CIMNE)-Madrid, Madrid, Spain

J.J. Muñoz

SAFECOR Engineering and Polytechnical University of Madrid (UPM), Madrid, Spain

J.R. Rosell

Polytechnical University of Catalonia-Barcelona (UPC), Barcelona, Spain

ABSTRACT: For the assessment of the condition of a large structure suffering reinforcement corrosion, it is necessary first to have a strategy for the inspection for collecting the appropriate parameters for appraisal of its present condition and the prediction of its residual life. In present communication very briefly the procedure followed for identifying the corroding zones of a football stadium will be described and how the efficacy of corrosion inhibitors has been evaluated for their repair. In each selected zone the corrosion rate was measured through the Polarization Resistance technique using a modulated confinement to delimit the polarized area.

1 INTRODUCTION

Corrosion of reinforcement is the most common deterioration mechanism that unfortunately shortens the service life of structural concrete. Reinforcement corrosion impairs the structural capacity by reducing the steel cross section and inducing cover cracking. When the corrosion is visible through the identification of rust spots or cracks/spalling appear, inspections are necessary to characterize the condition and the level of corrosion. Numerous administrations and owners have issued maintenance rules (ACI 222R, JSJC no.17), which consider procedures and guidance to perform such inspections when the reinforcement corrosion has started. However, in spite the corrosion rate is a key parameter to characterize the present condition and to predict the evolution of the corrosion process (Andrade et al.1978, Contecvet 2001), this parameter is neither measured or used. The lack of the key parameter related to the deterioration rate evolution limits very much the possibility to quantify the structural consequences of the corrosion.

In present paper the procedure is presented to quantify the level of corrosion and the measurement of the corrosion rate in the case of a football stadium and additionally also for evaluating the efficacy of corrosion inhibitors (Berke 1987, Page et al. 2000) that were selected as the least invasive method to stop the corrosion process. Their efficiency including the economic cost is out of the scope of the present study. The main first interest of the owners is the incorporation of an auxiliary structure, hanging on the beams to carry all the cabling allowing the new technologies transmission. This new structure will be metallic but its weight plus that of the cables and instruments demanded a structural recalculation.

2 EXPERIMENTAL

The structure is around 50 years old. It is framed structure with columns and beams as Figure 1 shows. The bleachers of the stadium are exposed to the atmosphere and rain (Figure 2) because most of them are not covered. The aim of the inspection was focused on identifying if the structural elements to support the new auxiliary structure are corroding and if so, which is their level of degradation. Additionally, the aim was to inspect all the main structural elements and the bleachers.

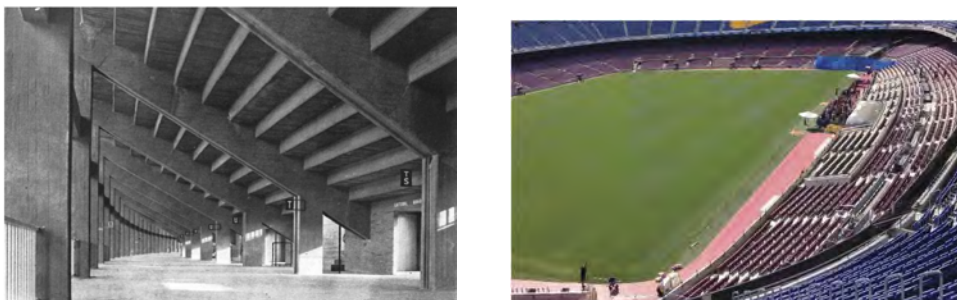


Figure 1. Aspect of the bottom parts of the bleachers. Figure 2. The bleachers are exposed to rain.

The procedure of inspection and reporting was:

1. Visual observations
2. Grouping the elements and zones in lots by: a) structural function, b) apparent degradation level and c) exposure class.
3. Performing of corrosion rate measurements in each lot
4. Analysis of results and issuing of first step Report

The grouping in lots was made after the visual inspection. It was decided to make the groups by structural elements in; columns, beams and slabs, all placed in the interior protected from rain. Another lot was the bleachers that are exposed to rain. As an example, only the tests performed in the cores drilled from the columns will be commented. Figure 3 shows where the selected columns were located. The test types were: compression strength, ultrasound velocity, porosity, density, cover depth, carbonation depth and chloride profile. Besides the drilled cores were, corrosion measurements were performed to obtain the corrosion potential, resistivity and corrosion rate.

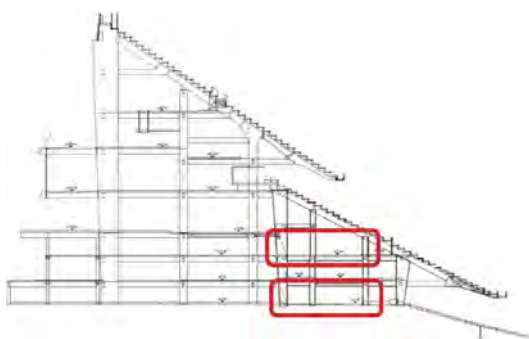


Figure 3. Zones where the cores were drilled in several places of the stadium.

The measurement of the corrosion rate was made using the Polarization Resistance (R_p) technique following (Andrade et al. 1978, Andrade et al. 2004, Feliu et al. 1990) using the portable corrosimeter Gecor10 which used a modulated confinement of the current applied in

order to delimit the area of the bar that is polarized. Thus, R_p and I_{corr} are obtained from the equations (Andrade et al. 1978):

$$R_p = \left[\left(\frac{\Delta E}{\Delta i} \right)_{\Delta E \rightarrow 0} - R_{oh} \right] \quad \text{and} \quad I_{corr} = \frac{B}{R_{ps}}$$

Where Δi is the galvanostatic pulse applied, ΔE is the shift in potential produced, R_{oh} is the ohmic drop produced by the concrete, B is a constant with an averaged value of 26 mV and R_{ps} is the value of the Polarization resistance multiplied by the polarized area. The units are: R_p [Kohm], R_{ps} [Kohm·cm²] and I_{corr} [μ A/cm²]. The measurement was made through a corrosion meter with a modulated confinement of the current (Figures 4 and 5).



Figure 4. Measuring the corrosion in a column.

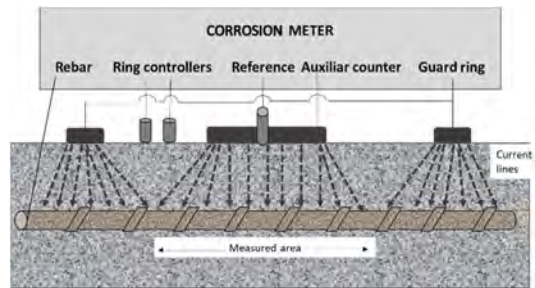


Figure 5. Corrosion-meter to measure in large elements by means of the modulated confinement of the current.

2.1 Inhibitor efficacy

After the assessment of the condition of the concrete elements, corrosion inhibitors were applied in selected zones for comparing their effects. The steps of the phase of studying the efficacy of corrosion inhibitors were:

1. Selection of zones where the trial with inhibitors was to be performed
2. Measurement of corrosion rates in each trial zone before application
3. Application of inhibitors by the different producers. Survey of the works
4. Post application measurement of corrosion rates in each trial zone
5. Analysis of the results and comparison of efficacy
6. Issuing of definitive Report with the categorization of inhibitor efficacy (only technical comparison)

For the trial 5 different commercial inhibitors were selected. Two zones were also selected having a similar corrosion level (Figure 6): one was a wall and the other a beam. In both a grid was made (see Figure 6) for the different inhibitor suppliers.

In each of the zones of the grid a different inhibitor was applied by each supplier with their own operator and methodology (Figure 7). The corrosion rate was measured before and after the application in all the zones treated. Figure 7 shows some examples of preparation of the surface before the application of each inhibitor and two different manners of application with a spray and a roller.

3 RESULTS

From the first visual inspection it could be realized that the different types of defects were very slight and superficial taking into account the age of the structure. Thus, some delamination in the bottom of the columns (Figure 8) or in some slabs as well as some leaking places (Figure 9) from the bleachers were localized.

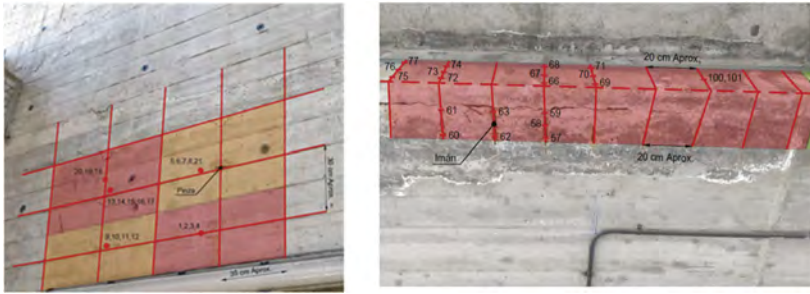


Figure 6. Aspect of the two selected zones for the trials and the grid made for each inhibitor.



Figure 7. Examples of preparation of the surface before the application of each inhibitor and two different manners of application with a spray and a roller.

The results of the tests in the columns are given in Table 1. In general, the strength is relatively low, typical of the age when the stadium was built coherent with the high values of porosity, however the ultrasound velocity is relatively high and the density is also above 2.1 g/cm^3 . The carbonation depth was deeper than the cover depth of the bar and there is a certain content of superficial chlorides because the stadium is located in a town besides the sea, but with negligible concentration of chlorides at the rebar level.

The values of the Polarization resistance technique enabled to have the corrosion potential, ohmic resistance and corrosion rate (Table2). From them it was possible to identify that, in spite the carbonation front was deeper than the position of the bar, the corrosion rates were relatively low because the columns were not affected by the rain, except in two places, as shown in Figure 10 (in red color), where the values recorded were shown along the sketch of the stadium. The green captions mean corrosion rates below $0.1 \mu\text{A/cm}^2$ indicative of negligible corrosion following (5) and the red color captions mean corrosion rates above such threshold value.

3.1 Inhibitor efficacy

For the repair, the treatment by corrosion inhibitors was selected as the corrosion level and rate (shown in Table 2) (5) was small enough for not having produced cover cracking or spalling except in few places of the stadium.

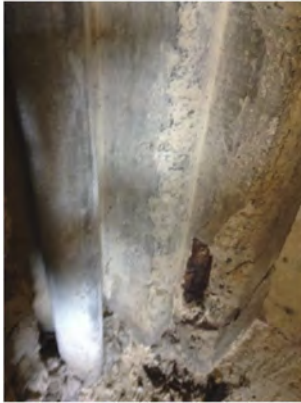


Figure 8. Delamination in the bottom of a column.



Figure 9. Leaking places underneath the bleachers.

Table 1. Results of the tests performed in the cores drilled from the columns.

	Column 96B	Column 85B	Column 75C	Column 67A	Column 52B	Column 44B	Column 30A	Column 26A
Compression strength (MPa)	19.0	-	23.7	-	14.9	-	20.1	-
Ultrasound velocity (m/s)	4143	4123	4472	4308	4621	3883	4505	3846
Porosity (%)	21.4	-	15.0	-	18.7	-	17.5	-
Density (g/cm ³)	2.14	-	2.25	-	2.21	-	2.19	-
Cover depth (cm)	2.8	2.5	1	2.5	2.5	2.5	1	2
Carbonation depth (cm)	5	> 2.5	2.5	> 2.5	5	3.5	3	4
Surface Chloride conc. by cement (%)	0.32	-	0.17	-	0.16	-	0.40	-
Chloride conc at rebar level (%)	0.08	-	<0.08	-	<0.08	-	0.16	-
Corrosion Potential (E _{corr} - mV)	137	-755	3.4/71	-	45	187	-227	151
Resistivity (KOhm-cm)	670	0	769/454	-	835	912	155	387
Corrosion rate (I _{corr} - μA/cm ²)	0,04	0,08	0,03	0,01	0,04	0,04	0,003	0,30

Table 2. Levels of corrosion rates and condition of the bar (5).

Corrosion level	μA/cm ²	μm/year	Rebar condition
Negligible	< 0.1	< 1	Passive
Low	0.1 – 0.5	1 – 5	Depassivated, low humidity concrete
Moderate	0.5 – 1	5 – 10	Active corrosion, medium humidity
High	1 - 10	10-100	Large areas corroding in wet concrete
Very high	>10	>1000	Very corroded all around

To compare the several corrosion inhibitors available in the market, it was decided to make a pre-application trial. As soon as the trial zones were selected, the corrosion measurements were also made in each of the zones where the inhibitors will be applied. The previous level is shown in Figure 11. The letter F means the number given to the particular supplier. Five different inhibitors were applied. The color of each supplier indicates the level of corrosion prior the application.

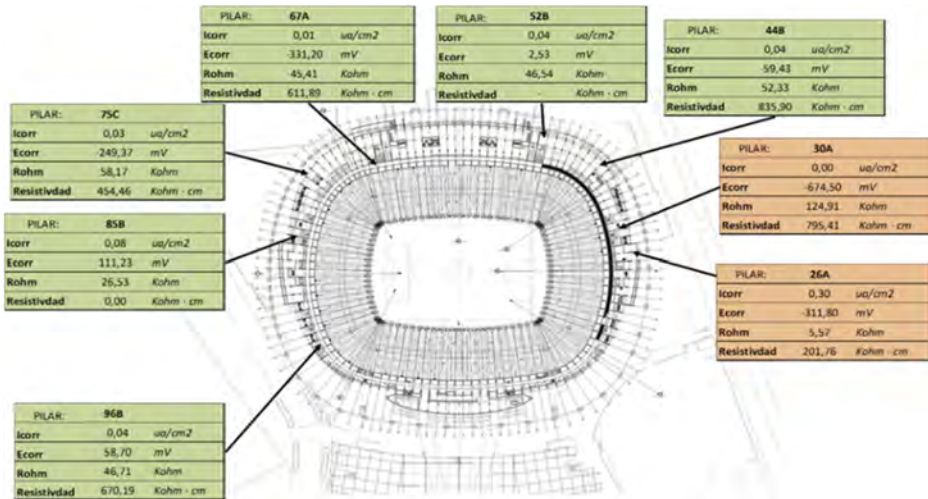


Figure 10. Values of the corrosion parameters measured in the columns in different zones of the stadium.

Element	ZONE				
	A	B	C	D	E
G3.1	F2	F1	F3	F5	F4
G3.2	F1	F2	F3	F4	F5
G3.3	F3	F4	F5	F1	F2
G3.4	F1	F2	F3	F4	F5
G2.1	F4	F5	F1	F2	F1
G2.1	F2	F3	F4	F5	F3

Legend

	not measured
	high corrosion
	moderate corrosion
	no corrosion

Figure 11. Levels of corrosion found in the trial sites before application of inhibitors.

The criteria for comparing the efficacy were based on the decrease of the corrosion rate and with less importance, as well the shift in the values of corrosion potential and electrical resistance in each of the zones treated. Table 3 shows the relative weight from 1 to 4 given.

Table 3. Criteria based on the corrosion rate for comparing efficacy of inhibitors.

Decrease of corrosion rates	1	2	3	4
Achieving values below $< 0,10 \mu\text{A}/\text{cm}^2$.	Any zone has achieved a lowering in the corrosion rate	Less than half of the points	More than half of the points	All points have achieved passivity

Figure 12 shows the weight achieved by each of the measurement points grouped by type of element. Figure 13 shows the results by inhibitor supplier (F1 to F5). From this Figure 13 it is possible to deduce that there was an element in which any of the inhibitors in that particular place were good enough, as the weight reached by them was very low. In the rest of places several inhibitors were effective.

With this technical information, and the cost of each inhibitor treatment, the designer of the repair technique selected the best option for the different zones of the stadium.

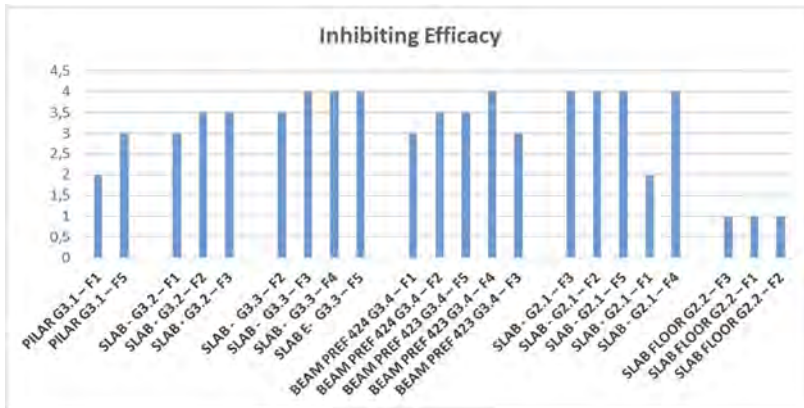


Figure 12. Relative weight by element treated.

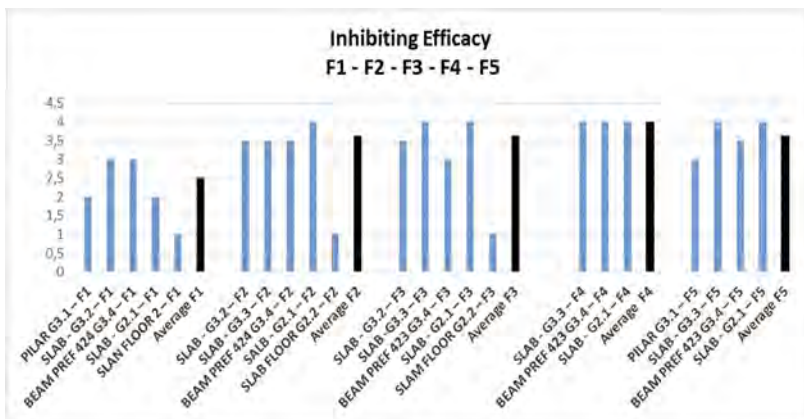


Figure 13. Relative weight by type of inhibitor (1 is the worst and 4 the best efficacy).

4 DISCUSSION

There are numerous structures all around the world that are inspected because they are corroding due to the progressive aging and contamination of concrete. In these inspections, in spite corrosion is the main reason of the damage its level and rate is not measured. Just corrosion is noticed and reported but its level is not accounted for. This lack of quantification is an important goal for the correct link between the corrosion level of the bars and the loss in structural performance. It is essential that in naturally corroding elements the degree of corrosion is measured in order to have a database for the future improvements of the methods to assess corroding elements. For the measurement of the corrosion degree two main techniques are available: the direct measurement of the loss in bar cross section through a capiler and the electrochemical measurement of the corrosion rate with approprita corrosio-meters (3,6). The first gives the accumulated corrosion (P_{corr}) until the time of the inspection, while the electrochemical measurement informs on the instantaneous rate (I_{corr}) that needs to be integrated back from the moment that corrosion could have started. The extrapolation back is made using the carbonation depth (7) which informs on the time of initiation and then enables to know the number of years since when the corrosion started on the bar surface.

For the comparison of the efficacy of the inhibitors (the efficiency is taking into account the cost as well) a pre-application trial was performed because this repair method is not yet

well established and there were doubts on the time after application needed by the product to show its inhibitor effect and also on the long term duration of it. For that long term effect it was suggested to measure again after 5 years for the continuity verification of the inhibiting ability.

5 CONCLUSIONS

The main aim and conclusion of the work was to show the advantages for a quick and reliable assessment of the degree and rate of corrosion by using electrochemical techniques and direct visual inspection of the bar aspect.

This practice is seldom used in the numerous inspections made in the world in corroding structures where the corrosion is noticed but not accounted for and even less a link to the relative loss of structural performance.

A systematic recording of both corrosion loss (P_{corr}) and corrosion rate (I_{corr}) are needed for the statistical link between the material and the structural degradation.

REFERENCES

- ACI 222R 2001. Protection of metals against corrosion.
- JSCE no.17. Japanese Standard Specifications for concrete structures 2007- Maintenance.
- Andrade, C. and González, J.A., 1978. Quantitative measurements of corrosion rate of reinforcing steels embedded in concrete using polarization resistance measurements- *Werkstoffe und Korrosion*. 29, pp. 515.
- CONTECVET 2001. A validated user's manual for assessing the residual life of concrete structures, DG Enterprise, CEC, (The manual can be downloaded from the web site of https://www.ietcc.csic.es/wp-content/uploads/1989/02/manual_contecvet_ingles.pdf).
- Berke, N. S. 1987. The Effects of Calcium Nitrite and Mix Design on the Corrosion Resistance of Steel in Concrete (Part 2, LongTerm Results). Proc., *Corrosion-87 Symposium on Corrosion of Metals in Concrete, NACE*, Houston, pp. 134–144.
- Page C.L., Ngala V.T., Page M.M. 2000. Corrosion inhibitors in repair systems. *Magazine of Concrete Research*, vol. 52, no.1 Feb, pp.25–37
- Andrade C, Alonso C, Gulikers J, Polder R, Cigna R, Vennesland Ø, Salta M, Raharinaivo A, Elsener B. 2004. "RILEM TC 154-EMC: Electrochemical Techniques for Measuring Metallic Corrosion. Recommendations Test methods for on-site corrosion rate measurement of steel reinforcement in concrete by means of the polarization resistance method." *Materials & Structures* 37 (273): 623–643
- Feliú S., González J.A., Feliú S. Jr., and Andrade, C., 1990. "Confinement of the electrical signal of in-situ measurement of Polarization Resistance in Reinforced concrete," *ACI Mater. J.*, 87, pp 457.

SS19: Sustainability of steel production chain
Organizers: H. Gervasio & M.M. Sesana



Taylor & Francis

Taylor & Francis Group

<http://taylorandfrancis.com>

Net-zero and lightweight steel technologies for the construction sector: Overview and case studies in Italy

M.M. Sesana

DICATAM Department, Fondazione Promozione Acciaio Commissione Sostenibilità, University of Brescia, Brescia, Italy

ABSTRACT: The construction industry is responsible for approximately 25% of global emissions, about a third of which are associated with the construction process, being a voracious steel consumer, accounting to 50% of global demand. Given these impacts, there is an urgent need for the construction steel chain to define a realistic decarbonization path. In this context, the paper focuses on a promising technology, the Light-weight Steel Frame (LSF), providing an overview coupled with real applications. LSF and drywall techniques have been shown around the world to result in cost-effective and sustainable buildings under different aspects: fast in construction, seismically resistant, high levels of thermal and acoustic performance, energy efficient, and aesthetic value. The publication also addresses a review of the latest regulations and methodologies for sustainability and carbon neutrality assessment, to clarify challenges and contributions that the steel company can provide to the construction sector in terms of sustainability and circularity.

1 INTRODUCTION

From houses to bridges, hospitals, and skyscrapers, the construction industry is responsible for approximately 37 percent of CO₂ global emissions, about a third of which are associated with the construction process, and for around 34% of total energy consumption (United Nations 2022). Therefore, the reduction of energy consumption and the use of energy from renewable sources in the building sector constitute important measures needed to reduce the European Union's energy dependency and to reach carbon neutrality by 2050, as defined in the European Green Deal, in 2019 (European Commission 2021a). To achieve this ambitious goal, it is urgent to drastically reduce harmful emissions in the construction sector, improve its efficiency and complete its circular transition, which is still struggling to become a consolidated and stable mechanism. For this change to take place, however, it must be conceived not only as an environmental or economic project but as a new cultural project for Europe, capable of triggering a real systemic change with its aesthetics, combining design and sustainability. Sustainable construction is a relatively new subject with which many of those involved in planning and construction are not familiar. It has been covered in numerous publications, but a limited number of them present specific measures for implementing sustainability in the steel building and construction industry.

Light Steel Frame (LSF) solutions are becoming increasingly popular in construction practice in response to the need to work on a heterogeneous and energy-intensive building stock and to meet the new demands of the construction market in a flexible, versatile, industrialized, and sustainable manner. Off-site industrialization, reduced construction time and costs, and aesthetic and performance quality are the strengths of cold-formed profile solutions for the building industry. These technologies provide flexible and aesthetically expressive constructions both from a morphological-architectural point of view and in terms of room adaptability, allowing the design of tailor-made solutions that meet people's needs. This publication aims to review the latest regulations and methodologies for sustainability and carbon neutrality assessment, to clarify

challenges, opportunities, and prominent contributions that the steel company can provide to the construction sector in terms of sustainability and circularity, thanks to lightweight steel technologies.

After the introduction in section one, the second section sets the scene by discussing the latest regulations and standards for the construction sector in Europe and also providing an overview of methods and tools to assess and evaluate sustainability in buildings. Section 3 presents the steel industry's reply to the European New Green Deal, with a focus on LSF solutions as a suitable construction technology to reach the current energy efficiency requirements and targets of the construction sector. Section 4 presents the results of applied research on case studies realized in LSF to verify the level of implementation into the practice of this technology, with a focus on an Italian residential case study. Finally, Section 5 provides conclusions and inputs for improvements and further works in order to complete the framework of challenges and opportunities of the steel construction industry to reach the carbon neutrality target and to realize sustainable buildings.

2 SUSTAINABILITY AND CARBON NEUTRALITY FOR CONSTRUCTION SECTOR

2.1 *Regulations and standards for certification and assessment*

Energy production and consumption significantly impact climate change due to their contribution to atmospheric emissions of CO₂ resulting from fossil fuels. Decarbonization and sustainability have been since decades the key points of the European regulation frameworks, in particular, the reduction of energy demand in buildings through the adoption of an energy efficiency policy is a key pillar of the European Union (EU) climate and energy strategy.

In the European Union (EU), energy production and use is responsible for 80% of all GHG emissions, accounting for about 40% of EU's final energy and 36% of CO₂ emissions, buildings are associated with a significant untapped energy saving potential due to outdated construction practices, use of inefficient systems or appliances and lack of effective technical control systems, even if there are already in the market various passive and active solutions that can limit this energy waste in buildings. (Camarasa et al. 2019).

In the EU, buildings have been an integral part of the EU energy and climate policy for several years. Energy efficiency policies for buildings can take the form of regulatory or control instruments, building codes, consumer information campaigns, and economic or financial incentives.

The "SAVE" Directive (93/76/EEC) of 1993 represents the first major EU policy on energy efficiency. The Directive required the Member States to draw up and implement programs to improve energy efficiency, with the aim to limit CO₂ emissions and to promote the rational use of energy. Since 2000 the Commission has published several Energy Efficiency Action Plans laying out its strategic vision and proposing actions such as new policies or strengthened existing measures. In 2006 the European Commission published its second Energy Efficiency Action Plan (Fawcett et al. 2019) with the scope to control and reduce energy demand and to take targeted action on consumption and supply with the intention to save 20% of the annual consumption of primary energy by 2020 compared to baseline energy consumption forecasts for 2020. This objective corresponded to achieving approximately a 1.5% saving per year up to 2020.

The first cohesive European legal act on energy policy in buildings was the Energy Performance of Buildings Directive (EPBD, 2002/91/EC) which introduced a joint energy performance calculation methodology for buildings. Since its adoption, the EPBD has been closely connected with the EU climate targets and has been aligned to reflect their progressive evolution. In this context, the core aim of the directive – to systematically enhance the energy performance of buildings and to increase the level of renovations – has remained unchanged since its introduction.

In 2009 the European Commission presented the recast of the EPBD (2010/31/EC, EPBD Recast) with the aim to strengthen some original EPBD provisions and capture additional energy savings and introduced for the first time the concept of nearly zero energy building (NZEB), defined as a building of very high energy performance, where the nearly zero or very low amount of energy required should be covered to a very significant extent by energy from renewable sources produced on-site or nearby.

Later, a targeted revision of the EPBD (2018/844/EU, EPBD) was launched as part of the clean energy for all Europeans package and adopted in 2018 (European Parliament 2018). This new

Directive came into force introducing targeted amendments to the previous EPBD version aimed at accelerating the cost-effective renovation of existing buildings, with the aim of a decarbonized building stock by cutting its net CO₂ emissions by at least 55% by 2030, compared to the 1990 levels, and to become climate neutral by 2050. To reach these goals, the EU then adopted a new strategic agenda for 2019-2024, including the European Green Deal (EGD), a package of strategic initiatives. The EGD is the environmental plan of the European Union divided into 116 points, in which all the Member States (MS) declare their commitment to undertake urgent and ambitious interventions to tackle climate change and environmental challenges to limit global warming to 1.5°C and further biodiversity losses. The main objective of this ambitious climate regulation is the achievement of the legally binding national target of achieving zero emissions by 2050, as well as the 2030 interim target of a 55% reduction in emissions compared to levels of 1990. The EGD is not limited to outlining environmental policy but rather uses environmental protection as a pretext to define and promote attention to a wide range of sectors: from transport to construction and from agriculture to industry (European Commission 2019b).

In this framework, the EU Commission launched in October 2020 the Renovation Wave initiative with the intention to double the European renovation rate of buildings by 2030 and to maintain it in the following years. This strategy highlights several points of intervention with a precise timeline to make existing buildings energy efficient by reducing the consumption of energy and resources, with the use of circular economy approaches, low environmental impact strategies to improve the quality of indoor environmental and air quality, and the buildings' comfort for end users and it can be summarized in the following four main priorities: (i) decarbonization of heating and cooling systems; (ii) tackling energy poverty and inefficiency; (iii) renovation of public buildings such as schools, hospitals and offices; (iv) application of holistic approach throughout the building lifecycle, from project design and financing to completion and subsequent maintenance.

The Renovation Wave strategy aims to reach the target of doubling up the renovation rate of the built environment by 2030, applying existing measures such as energy performance certificates, long-term strategies, financial incentives, and technological innovations but also introducing some new instruments, such as mandatory minimum energy performance standards and the development of a roadmap to 2050 to reduce carbon emissions throughout the buildings' life cycle. In December 2021, the Commission has proposed to align the rules for the energy performance of buildings with the European Green Deal and decarbonize the EU's building stock by 2050 (European Parliament 2021). To achieve this, it is necessary to promote a rapid energy conversion of the building stock, favoring deep renovations and transformation into "nearly zero energy buildings" (nZEB). In the same year, the EC launched, as part of the Green New Deal package, also the New European Bauhaus, to foster spaces for discussion and experimentation around the theme of physical spaces, a creative and interdisciplinary movement to rethink European cities, making them more functional and accessible to all. The program of the new European Bauhaus is divided into three phases: collective design, realization, and dissemination. The first design phase ended in June 2021 with the identification of the first five sites where the program has to be applied, representing the beginning of the second phase of realization. The aim is to make methods and solutions available to designers and the community that can be shared and replicated on a large scale. From January 2023, the third and final phase of Bauhaus will begin, in which space will be given to disseminating and sharing good practices to as wide an audience as possible, including outside Europe.

At the Italian level, the Italy Tomorrow Plan (Piano Nazionale di Ripresa e Resilienza - PNRR) approved in April 2021, foresees reforms and investments to be implemented in the span of the next five years in key sectors. The plan is developed around three strategic axes shared at the European level: digitalization and innovation, ecological transition, and social inclusion, and is divided into 16 components, grouped into 6 missions. Relevance has been set for the construction sector in Component 3 (Energy Efficiency and Renovation of Buildings) of Mission 2 (Green Revolution and Ecological Transition) with which energy efficiency can be strengthened by increasing the efficiency of buildings, which suffers from a building stock more than 60% of which is over 45 years old, both in public and private Italian buildings. The measures included in the PNRR aim to provide a boost to the economy and employment and to promote social resilience by improving comfort, energy saving, and seismic risk prevention of buildings (Sesana 2022a).

2.2 Methodologies and tools framework

Besides the regulations, also the tools for the analysis of the sustainability levels of buildings play a fundamental role in their application, as it required particular care to align them. An overview of such instruments is presented in this section, to better understand the methodologies currently in use and the new initiatives with high potential to support the carbon neutrality goal.

The implementation of the regulations outlined in the previous section, especially in relation to buildings, led to the need to define energy-environmental assessment and certification systems as an essential method to improve energy efficiency, minimize energy consumption and enable greater transparency regarding energy use. To provide a complete overview of such methodologies and tools, this subsection focuses on compulsory tools, as required by current regulations, and those that are voluntary or in the process of being defined, for sustainable nZEB design with practical indications and recent updates for their use.

Over the years, the EPBD has employed a diverse set of policy tools, but the most well-known mandatory one for buildings is the energy performance certificate (EPC). The EPC was introduced at the European level by Directive 2010/31/EU and the recent EPBD 2018/844 strengthened the certification system for existing buildings with the inclusion of a mandatory recommendations report listing improvement measures and their priorities (European Parliament 2010).

The Italian version of the EPC, the so-called *Attestato di Prestazione Energetica* (APE), is considered mainly as an informative document that certifies the energy performance of a building using a rating scale from A4 to G, which provides general recommendations for energy efficiency improvements. If properly drafted, the APE certification could become a powerful market tool for creating demand for energy efficiency in buildings by providing recommendations for cost-effective, time- and cost-optimized improvements (Sesana 2022a).

Complementary to the EPC and structured according to a long-term renovation roadmap outlining intervention measures for the improvement of energy performance based on quality criteria, the Building Renovation Passport (BRP) was introduced for the first time in the revision of Directive 2018/844/EU (Toth et al 2022). The purpose of this tool was then detailed in the Renovation Wave strategy, as a support tool for owners and investors to better understand and plan interventions, providing a clear roadmap for gradual renovation over the lifetime of a building. According to this, the Building Passport can be described as a repository of relevant building-related information covering the physicality, management, financing, valuation and ownership of buildings with the structure defined by two key elements: a data archive part, usually called a logbook, and a renovation roadmap for identifying the actions to be implemented for a deep renovation in terms of time, cost and building technologies to be used.

Alongside experiences with building passports, there have also been initiatives related to establishing digital passports for single material or products in general (Digital Product Passport, DPP). The implementation of such tool could facilitate tracking and tracing materials and compiling information in one unique database. It is supposed to deliver information on the origin, composition, repair, and dismantling options of a product, as well as on its handling at the end of its service life. However, there are several open questions regarding the DPP's final design and its implementation. For instance, any future DPP information requirements should be ideally designed in a way that manufacturers, which are the most important source of product information, and other stakeholders perceive them as an advantage and not as an additional burden, to create business models and intrinsic motivation. Therefore, implementation options for digital product passports need to be evaluated to allow a circular flow of materials through the active engagement of all the actors involved (Sesana 2022a).

An important contribution to the issue of tools and methodologies for construction in the field of efficiency and sustainability has been made by the voluntary environmental assessment and certification developed worldwide over the past twenty years with different approaches: some with prerequisites to gain optional credits in relation to the specific context, others with prescriptive approach or performance-based requirements according to building types. As a result, it can be difficult and time-consuming in terms of time and quality to determine which standards, certifications, and assessment programs are most reliable and applicable to a particular building being various per building types or goals' project. For this reason, the EC within the EGD initiative

launched a common framework for assessing the sustainability performance of buildings: Level(S) (European Commission 2019), with the aim to create a common approach based on the integration of current certification tools with a whole life cycle approach. This system relies on existing standards and circularity principles using a limited number of indicators to measure the effects of carbon, materials, water, health, and comfort. Although Level(s) is not a certification scheme, its simple structure aims to facilitate existing schemes to use the same language and facilitate assessment methods and data comparison between projects (Ferrari et al 2022).

3 THE STEEL INDUSTRY REPLIES TO THE EUROPEAN NEW GREEN DEAL

Steel is one of the most important engineering and construction materials. However, the industry now needs to cope with the pressure to reduce its carbon footprint from both environmental and economic perspectives. Currently, the steel industry is among the three biggest producers of carbon dioxide, with emissions being produced by a limited number of locations; steel plants are therefore a good candidate for decarbonization.

For this reason, the European steel industry has set itself the main goal of investing in research and development to rethink its production processes and achieve substantial reductions in emissions to remain competitive and contribute to the achievement of carbon neutrality by 2050.

Steel is a sustainable material, and in some cases, the most sustainable choice, since it is a circular material, being reusable and recyclable repeatedly and allowing a long service life.

In response to the EGD, the more feasible option for the steel sector is to move to a much more circular system by 2050, replacing 30 Mt of the current 92 Mt of primary steel production with secondary production and reducing emissions by 57 Mt CO₂ per year by mid-century to meet the targets (EUROFER 2021).

Conceiving steel management as much as possible from a perspective of sustainability and circularity means intervening in the process of production, use, and end-of-life of this material whose properties allow theoretically infinite recycling. However, given this characteristic, a complementary path to increase the level of sustainability of the material is to optimize its use, minimize processing waste, or facilitate the recovery of components to be sent for recycling. It is necessary to rethink on one hand the technologies in use in Europe to produce steel, but at the same time also to encourage the use of scrap, instead of producing a virgin product, with a circular approach. It follows, however, that the efforts required to implement these changes must be supported by all sectors that use steel either as a base material or as a component of other products. The annual volumes recorded in 2019 of the steel demand are distributed percentage-wise between construction and infrastructure (42% of demand), followed by the transportation sector (31%), machinery (16%), and finally a range of other steel products (11%).

Although recycling steel for production not from virgin material is advantageous, particularly in terms of preserving materials and reducing the extraction of raw materials, there is another lower-impact option that is gaining popularity not only in research but also in practice: the reuse of the steel materials and components themselves. From this perspective, the built environment can thus be seen as a veritable bank of materials including the stored energy and carbon emissions in building materials, components, and structures. Their targeted separation and recovery during demolition can avoid the passage of more than 70% of materials from landfills in addition to contributing to the circular economy goals should such materials, components, or structures be reused in new construction. Compared to other recycling options, therefore, it offers additional environmental and economic benefits but often requires higher initial investment costs. Recent research conducted on the technical feasibility of this type of reuse in both quantitative and qualitative terms has confirmed the possibility of achieving the goals that the steel industry has set for itself but has also identified the barriers that currently limit the spread of this practice.

In the case of steel-based structural steelwork and building components, reuse avoids the negative impacts associated with scrap recycling in steel production. Avoided scrap can come from individual fabricated components or entire steel assemblies or steel parts separated by composite elements (McKinsey Global Institute 2022). The market for recycled steel building products is still small because the effort associated with their reconditioning and CE marking often makes the process more expensive than recycling the materials. In addition, reusing

individual structural steel components is more difficult because they are generally optimized and manufactured for a specific building project. Therefore, most successful reuse projects are whole building relocations, repairs and renovations or extensions of steel structures, or on-site reuse. The overall benefit of building steel reuse depends on the widespread adoption of this approach in design and construction practices by all stakeholders in the building process. Designers should understand how to incorporate reclaimed materials into new design applications and how to optimize their designs for deconstruction and reuse, while manufacturers should consider reclaimed steelwork as a possible source of materials. Of course, there are also some technical challenges associated with this issue that would require the integrated design to avoid increased deconstruction costs and time.

3.1 *Light steel frame solutions*

The importance of steel in the building construction industry derives from the combination of lightness and loadbearing capacity but also from factors like prefabrication, fast construction time, and 'dry' building site. These aspects, in addition to their lightness and performance, make steel a sustainable building material with great potential for the future. In the last 20 years, Light Steel Frame used as a structural material have become a widely used solution for residential and industrial buildings, especially due to the main advantages that offer in comparison with traditional building materials (Martins et al 2013). The lightness of the system implies the use of less material, facilitates the transportation phase to the construction site, and offers benefits in terms of time construction phase by offering preassembled solutions and demonstrating their great potentialities in terms of circularity. All the main advantages that the technology offers, make LSF the main competitor for traditional structural construction systems (Abou Hamad et al 2019).

In Italy, prefabrication and dry construction are a long tradition in commercial, industrial and public construction, but have been less frequently applied to residential construction, however, recently the benefits of this building technique have opened many interesting opportunities for application in residential buildings. The dry construction system is based on the prefabrication and mechanical assembly of several functional layers made up of elements that are supplied to the worksite certified and ready to be assembled on a light and resistant framework made of steel, wood, and reinforced concrete. In the past, the idea of prefabrication was associated with a limited catalog of building components to combine to form a complete building, characterized by modular rigidity. This aspect was thus seen as a limitation to customization and design creativity and as the reason for the simplicity and seriality of low architectural and technological quality buildings.

Nowadays prefabrication foresees elements manufactured with the precision of industrial production for beams, pillars, uprights, cross-pieces, walls, floors, roofs, unique works or works that can be repeated on a large scale and the architecture/industry nexus, which felt impossible for a long time, has found a real possibility for development. Moreover, the LFS can provide a high level of adaptability to different architectural solutions; high energy and acoustic performance and safety in case of earthquake and fire; industrialization of the system, and the lightness of dry solutions combined with the great durability of steel constructions.

In literature, the LSF is defined as a construction system based on structures composed of cold-formed steel elements, produced by cold-forming or press-bending thin steel sheets (Lawson 1999). The intrinsic characteristics of the construction system, make it competitive compared to traditional systems, this is because the LSF represents a clear point of contact between construction and industry, through the standardization of products, processes, and design. the purely industrial approach of this construction system has proven effective in terms of economic advantages and sustainable performance: compared to traditional construction techniques, the most obvious advantage of LSF is the lightness of the system.

It is estimated that the weight of an LSF building can weigh up to ten times less than a building made with traditional techniques. The physical properties of cold-formed steel make it an exceptionally sustainable material: resilient, durable, and adaptable, steel allows it to operate in a wide range of buildings and environments. For example, its ductility, strength, and lightweight make it a suitable material for construction in windy and seismic locations. The ability to treat steel

against corrosion phenomena, for example with zinc coating, provides the material with durability properties that exceed even one hundred years. Steel also does not emit volatile organic compounds and is 100% recyclable, a feature that significantly reduces life cycle costs.

The advantages of the LSF system are not limited to the peculiarities of the production technique and the material; but benefits vary depending on the project site, the complexity of the work, and the quality of the result. In recent years there has been a progressive increase in the number of catalog solutions offered by companies producing cold-formed profiles, and their diffusion is increasing not only for new constructions but also for renovations (Sesana 2022b).

4 AN ITALIAN RESIDENTIAL CASE STUDY WITH LIGHT STEEL FRAME SYSTEM

A study was conducted in 2021, in collaboration with Fondazione Promozione Acciaio (FPA), Italian promotion and communication entity of steel in construction, on a selection of recent mostly residential case studies, mainly located in Italy and some outside the European Union, meeting the above-mentioned regulations and methodologies with LSF solutions.

In this section, one case study in Italy, as representative of the study, is presented as a proof of concept of the LSF feasibility construction and to underline its potentialities in terms of efficiency and sustainability for buildings.

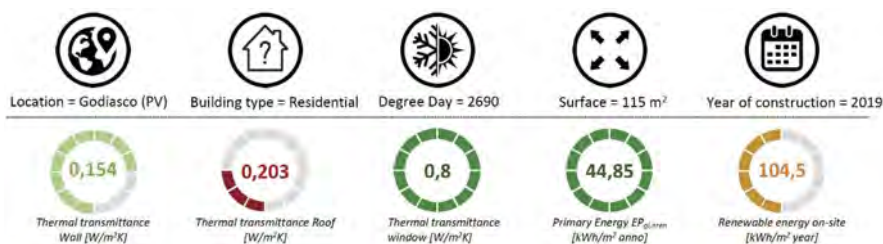


Figure 1. Graphical summary of the main data of the residential case study realized in LSF in Italy.

Slash House is the name of the high-energy-efficient residential building realized in 2019 in Godiasco Salice Terme (PV).

The main data about the location, the climatic context, the year of construction, and geometry are summarized in the first line of the graphical summary (Figure 1), while in the second row, there are represented both the envelope performance in terms of thermal transmittance for wall, roof, and window and the main KPIs for energy (Primary energy and Renewable energy produced on-site). The load-bearing structure is separate from the curtain wall structure: thus the insulating capacity of the walls, curtain wall, and windows and doors was optimized. For the walls, a drywall construction system constituted by C profiles in LSF was used with an outer cladding of reinforced concrete slabs and an inner cladding of gypsum plasterboards. The high-performance envelope is completed with the installation of triple-glazed windows, including the curtain wall, with Argon gas in the double-glazing units and selective low-emissivity treatment. Strategies for optimizing envelope performance include flat roofs with hanging greenery that provide excellent performance in both summer and winter due to the inertia provided by the soil.

In order to achieve nearly zero energy consumption, the system plant foresees efficient summer-winter air conditioning, both in the generation and distribution of heating or cooling fluid, supplemented by mechanical ventilation with heat recovery.

The air-conditioning system is an air-to-air heat pump with internal splits, supplemented by a controlled mechanical ventilation system with total heat recovery and all of the house and system is managed by automatic control.

The house is not connected to the gas grid; electricity is produced by the photovoltaic system composed by 24 modules of about 6 kW, integrated in the roof.

The house, with a total non-renewable primary energy requirement of 44.85 kWh/m² per year, reached an energy performance class of A4 and reach its target of nearly-zero energy building covering the overall energy demand with the renewable energy produced on-site.

5 CONCLUSIONS

The paper presents an overview of the major role of the steel construction sector in making sustainable and efficient buildings for the future and reducing the environmental impact of the construction sector in order to achieve the European goal of climate neutrality by 2050.

From the analysis of the presented work, it emerged that despite the effort of the steel industry to adapt their products and building systems to the European goal of carbon neutrality, there is an urgent to identify: (i) the most suitable methodology to design net-zero energy buildings; (ii) commons tools to manage, share and calculate data in a digitalized way; (iii) a common data framework to evaluate the energy performance of the building using the LCA methods.

The LSF solutions implemented in the case study represent a valuable solution to reach the NEB goals thanks to the described potentialities and advantages in comparison with traditional solutions. The LSF systems in fact offer more flexibility compared, for example, to concrete and brick walls and are, therefore, less sensitive to dynamic stress and it is also suited to earthquake-proof designs. The “dry” and “light” aspects, therefore, seem to address all the requirements of modern living, from design to comfort, taking their place in the environment with a light footprint.

REFERENCES

- AbouHamad, M. & Abu-Hamd, M. 2019. Framework for construction system selection based on life cycle cost and sustainability assessment. *Journal of Cleaner Production* 241.
- Camarasa, C., Nägeli, C., Ostermeyer, Y., Klippel, M. & Botzler, S. 2019. Diffusion of energy efficiency technologies in European residential buildings: a bibliometric analysis. *Energy and Buildings* 202.
- EUROFER 2021. *We are ready – are you? Making a success of the EU Green Deal*. Brussels.
- European Commission 2019a. *Level(s), Tacking Action on the total impact of the construction sector*. Luxembourg: Publications Office of the European Union.
- European Commission 2019b. *The European Green Deal*. Brussels.
- European Commission 2021a. *European Green Deal: Commission proposes transformation of EU economy and society to meet climate ambitions*. Brussels.
- European Parliament 2010. Directive 2010/31/EU of European Parliament and of the Council of 19 May 2010 on the energy performance of buildings (recast). *Official Journal of the European Union* L.153: 13–35.
- European Parliament 2018. Directive (EU) 2018/844 of European Parliament and of the Council of 30 May 2018 amending Directive 2010/31/EU on the energy performance of buildings and Directive 2012/27/EU on energy efficiency. *Official Journal of the European Union* L.156: 75–91.
- European Parliament 2021. Regulation (EU) 2021/1119 of the European Parliament and of the Council of 30 June 2021 establishing the framework for achieving climate neutrality and amending Regulations (EC) No 401/2009 and (EU) 2018/1999. *Official Journal of the European Union* L.243: 1–17.
- Fawcett, T., Rosenow, J. & Bertoldi, P. 2019. Energy efficiency obligation schemes: their future in the EU. *Energy Efficiency* 12: 57–71.
- Ferrari, S., Zoghi, M., Blazquez, T. & Dall’O’, G. 2022. New Level(s) framework: Assessing the affinity between the main international Green Building Rating Systems and the European scheme. *Renewable and Sustainable Energy Reviews* 155.
- Lawson, R.M., Grubb, P.J., Prewer, J. & Trebilcock, P.J. 1999. *Modular Construction using Light Steel Framing: An Architect’s Guide*. Ascot: Steel Construction Institute Publication.
- Martins, C., Santos, P. & Simões da Silva, L. 2013. Lightweight Steel Framed Construction System. *Proceedings of the International Conference Portugal SB13: contribution of sustainable building to meet EU 20- 20-20targets 1*: 395–402.
- McKinsey Global Institute 2022. *Net-zero steel in construction: The way forward*. Mission Possible Partnership.
- Sesana, M.M. 2022a. *Progettare e costruire edifici sostenibili con profili in acciaio sagomati a freddo: l’innovazione tecnologica delle soluzioni in light steel frame per l’edilizia*. Palermo: D. Flaccovio.
- Sesana, M.M. 2022b. Sustainable buildings with Light Steel Frame structure: challenges and potentialities. *Colloqui.AT.e 2022 Convegno Artec, Genova, 7-10 September 2022*.
- Toth, Z., Volt, J. & Steuwer, S. 2022. *Roadmap to climate-proof buildings and construction: how to embed whole-life carbon in the EPBD*. Brussels: Buildings Performance Institute Europe.
- United Nations Environmental Programme 2022. *2022 Global Status Report for Buildings and Construction: Towards a Zero-emission, Efficient and Resilient Buildings and Construction Sector*. Nairobi.

Life-cycle assessment of light steel frame buildings: A systematic literature review

G. Marrone & M. Imperadori

Architecture, Built Environment and Construction Engineering Department, Politecnico di Milano, Milan, Italy

M.M. Sesana

DICATAM Department, University of Brescia, Brescia, Italy

ABSTRACT: Light Steel Frame structures (LSF) have become one of the main competitors of traditional construction systems. The optimized material use, its lightness, and the timesaving in the construction phase, show the potential of this technology to reduce environmental impacts. The purpose of this study is to review and analyse the current literature on the application of the Life Cycle Assessment (LCA) methodology to LSF buildings and identify related gaps. A systematic literature review has been performed to query Web of Science and Scopus databases, highlighting methods, limitations, trends, and tools used to address LCA applied to LSF buildings. Although many efforts have been made to evaluate LSF buildings in comparison with other construction solutions, a gap persists in performing whole LCA. Considering the potential disassembly and reuse offered by LSF and the recyclability of steel, there is a need for future research focusing beyond the end-of-life stage.

1 INTRODUCTION

Climate breakdown, resource scarcity, ecological collapse, as well as economic uncertainties make the next years crucial to shape the conversion to a carbon-neutral construction sector. Considering the increasing number of net-zero energy buildings and the consequent optimization of the operational energy emissions, within the next years, the building's embodied energy is likely to become fundamental towards the accomplishment of sustainability goals (Gervásio *et al.* 2010).

The European Green Deal (European Commission 2020) aims to eliminate greenhouse gas emissions through the introduction of circular economy principles in energy-intensive industries (i.e. steel, cement) enhancing the secondary use of materials, components and products (European Commission 2014). In this context, the steel industry plays an important role, since the largest amount of steel produced worldwide is used in construction, material efficiency is necessary. In reducing embodied energy, weight plays an important role (Mateus *et al.* 2013). Therefore, new lightweight building systems such as Light Steel Frame (LSF) have emerged as a promising solution for low-rise buildings.

In the last 20 years, there has been growing interest in LSF both for residential and industrial applications due to the main advantages offered compared to traditional construction techniques (Grubb *et al.* 1999, Abouhamad and Abu-Hamd 2019). LSF is an offsite construction system which relies on the optimization of the shape in favour of the lightness, thus facilitating the transportation and construction phases. Furthermore, the possibility to preassemble the profiles in panels and volumes offers construction time benefits. Moreover, as a dry construction system, it also has a great potential for circularity and recyclability.

Even though there is a general understanding of the cause-and-effect link between a building's environmental performance and its energy needs, the same link is not immediate for embodied

energy. Hence, is necessary to provide benchmarking values also for the embodied energy (Gervasio *et al.* 2018). In recent years, many researchers have focused on building performance calculation within a life-cycle perspective, investigating and comparing different types of buildings, construction materials, and techniques. Life Cycle Assessment (LCA) is a quantitative approach to measure and analyse products and processes' environmental impacts. According to ISO 14040/44:2006, the LCA methodology usually consists of four main steps: (i) goal and scope definition, (ii) life cycle inventory (LCI), (iii) life cycle impact assessment (LCIA), (iv) interpretation of results. EN15978 regulates the application of LCA in construction works considering environmental, economic, and social aspects of sustainability.

Besides some review articles have been published concerning LCA applied to LSF buildings, they usually followed the traditional review approach. Therefore, a shared and recognized methodology to perform the review is needed. Considering the growing reputation of offsite construction systems and particularly LSF both in the scientific community and in the construction market as a reliable system in terms of environmental impacts and sustainability assessment (Smith and Quale 2017, Buzatu *et al.* 2020, Tavares, Soares, *et al.* 2021, Thirunavukkarasu *et al.* 2021) the purpose of this work is to give an overview and interpretation of the existent literature.

Through a systematic literature review, the studies on LCA methodology applied to LSF buildings are investigated, understanding methods, highlighting limitations, tools, and trends, thereby enabling practitioners and researchers to gain knowledge on the already researched areas and identifying existent literature gaps. The paper is organized as follows: the second section presents the research questions and the process followed for the systematic literature review. The third section introduces the review of the selected works, highlighting the methodological choices in performing LCA. The paper concludes with a discussion of the main findings in the fourth section, identifying literature gaps and suggesting future research directions.

2 METHODOLOGY

This study contributes to the existing literature by synthesising previous scientific works about the application of LCA methodology to LSF buildings through a systematic literature review. Xiao and Watson (2019) recognise the need to perform a systematic literature review to find the current state and gaps of the topic through the breadth and deep analysis of the existing high-quality literature. In this paper, the systematic review follows the methodology found in the literature, which consists of four main steps: the definition of the scope and research questions, the definition of inclusion and exclusion criteria and a synthesis of the findings.

Once the scope of the work has been defined, the authors designed three research questions: 'What are the methodological choices made to perform an LCA of LSF buildings?' and 'What is the environmental performance of LSF buildings?', 'What promising opportunities for future research can be identified?'. To answer the research questions, the authors queried two frequently used databases – Scopus and Web of Science. To gather and analyze a significant and high-quality sample of papers, different spelling (i.e. cold-formed" OR "coldformed" OR "cold formed") and different terms (i.e. cold formed, light steel frame, light gauge) have been used. The search string and the inclusion and exclusion criteria are shown in Table 1.

Table 1. Construction of the search string and criteria used for the articles' selection.

Search string	Inclusion criteria	Exclusion criteria
<ul style="list-style-type: none"> – Keywords: ("cold-formed" OR "cold-formed" OR "cold formed" OR "light steel" OR "LSF" OR "light gauge") – AND ("Life cycle" OR "LCA" OR "Environmental impact") – Search in: title, abstract, keywords – Document type: articles and review articles (Peer-reviewed) 	<ul style="list-style-type: none"> – Articles/review articles investigating the building sector – Articles/review articles investigating environmental LCA of LSF buildings 	<ul style="list-style-type: none"> – Full text not available – Articles not published in peer-reviewed journals – Articles not written in English

The databases' query was executed on 18 December 2022. The literature identification process retrieved 49 articles from SCOPUS and 42 articles from Web of Science, a total of 91 articles. After removing 34 duplicate articles, 57 articles remained for the abstract screening phase.

Through the abstract reading, the relevance of each article within the search objectives has been evaluated with the inclusion and exclusion criteria. Accordingly, 28 articles were out of scope and related to other disciplines (i.e. metallurgy, chemistry, structural engineering) thus leaving 31 articles for full-text analysis. Once the full-text reading has been completed, the criteria have been applied again: 3 articles were not readable, while 10 articles were investigating LSF buildings but environmental LCA. Since the 10 articles don't meet the criteria, they were not included in the deep review. The remaining 18 articles were analysed to identify the methodological choices made in performing LCA on LSF buildings, considering the first three phases of LCA according to ISO 14040/44:2006. A schematization of the methodology used to narrow down the number of articles from 91 to the final sample of the 18 deeply reviewed papers is presented in Figure 1.

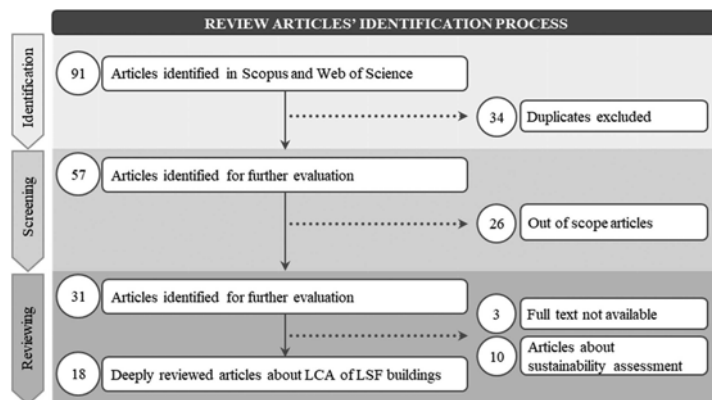


Figure 1. Flow chart for the identification of the reviewed articles according to inclusion/exclusion criteria.

The papers have been analysed to identify methodological choices in performing LCA on LSF buildings to enable researchers and practitioners to gain insights into previously researched areas and identify research gaps. The data have been collected in a comprehensive table divided according to the first three steps of the LCA.

3 LIFE CYCLE ASSESSMENT OF LIGHT STEEL FRAME BUILDINGS

With the rapid growth of LCA studies in the building sector, also review papers have been published to summarize the progress. Although, the review articles published concerning LCA applied to LSF buildings follow a traditional reviewing approach. In this section, the results of the systematic literature review of the 28 identified articles are presented to address the search objectives. Among the 28 reviewed articles, 18 works are related to the application of environmental LCA to LSF buildings; the remaining articles are not concerning the specific topic, although they are considered relevant for the reviewed literature body. Within these 10 works identified, Soares et al. (2017) published a traditional literature review highlighting key advantages and drawbacks of LSF in terms of energy efficiency and thermal performance. Many studies focused on Life Cycle Energy Assessment, Gervásio et al. (2010) published a parametric study on different insulation levels of a residential LSF building, confronting operational and embodied energy. The study highlighted that in 16 years the operational energy can overcome the embodied one. On the same page, Santos et al. (2014), focused on the LSF operational energy by optimization of thermal bridges and improvement of thermal inertia, thus addressing "life-cycle design". Other works focused on the calculation of Life Cycle Cost or the adoption of multidimensional methods, acting on the life cycle's risks (Zeynalian et al. 2013, Çelik and Kamali 2018, Abouhamad and Abu-Hamd 2019, Sen et al. 2021, Noorzai et al. 2022). Also considering the structural performances, Lu (2016) and Usefi et al. (2021) addressed the sustainability assessment of LSF.

Considering the 18 articles related to the application of LCA to LSF buildings, the analysis follows the first three main steps of the methodology suggested by ISO 14040/44:2006. The main methodological choices described in the reviewed papers in performing LCA have been synthesized in Table 2. First, the goal and scope definition is presented, highlighting the type of building, the type of study performed, the lifespan, the geographical location, the functional equivalent/unit and the system boundaries. Then, the tools and databases used to create the inventory of input and output flows (LCI) have been highlighted: we found that there isn't a harmonized inventory data collection methodology. Lastly, the choices about the environmental impact assessment (LCIA) are reported. According to this structure, the results are presented in the following paragraph.

3.1 Goal and scope definition in the reviewed literature

Within the body of reviewed literature, two types of studies have been identified (i) a baseline study (non-comparative) used to assess individual project performances, (ii) a comparative study to compare the environmental performances of different construction systems. On one hand, some methodological choices are shared across the literature, but many others are different and need to be deepened. There is a general agreement on the selection of 50 years lifespan of the building, only one study proposes 90 years. Among the 18 works, the residential building is the most investigated. Considering the building locations, many areas of the world have been covered. Some studies addressed the buildings' environmental impacts in different scenarios and locations (Tavares *et al.* 2019, Tavares, Gregory, *et al.* 2021).

In performing LCA, the definition of the life cycle stages included in the system boundaries is fundamental and can affect the results. According to EN15978, the life cycle stages are: (i) product stage (A1-A3), which includes the provision of materials, products and energy; (ii) construction (A4-A5), which includes transport to the building site and installation; (iii) use (B1-B7) includes also maintenance, repair, replacement, refurbishment and operational energy and water use; (iv) end-of-life (EoL)(C1-C4), includes deconstruction/demolition, transport to waste processing and disposal; (v) benefits and loads beyond the system boundaries (D), this module allows to take into account the net impacts and benefits of reuse, recovery or recycling after demolition.

Considering the non-comparative approach, both a whole case study building and a single component have been analysed. Both Tuca *et al.* (2012) and Zygomalas and Baniotopoulos (2014) focused on a whole building, one calculating the impact of the maintenance process and the other highlighting the type of environmental impact caused by LSF, which mainly affects natural resources and human health. In the last years, Liu *et al.* (2022) addressed a new demountable and modular LSF wall, highlighting the environmental impact advantages of a reusable module. Highlighting the benefits associated with recycling and reuse, Abouhamad and Abu-Hamd (2020) included in the analysis also the module D, finding that Global Warming Potential (GWP) is reduced by 15.4% while the embodied primary energy is reduced by 6.22%, accordingly, the environmental impacts of LSF are considerably lower than conventional construction systems. Using the same case study building, Abouhamad and Abu-Hamd (2021) proposed a new framework to facilitate the decision-making process in selecting sustainable design alternatives.

Recycled steel is used in the production of new steel thus, the relevance of module D in steel buildings is confirmed by many comparative studies. Vitale *et al.* (2018) calculated that LSF has a better environmental performance than reinforced concrete and brick wall buildings, considering the profiles' recovery the performance can increase up to 24%. On the same page, Dani *et al.* (2022) published a comparative study in New Zealand between LSF and timber frame buildings. Using a cradle-to-cradle approach, the authors showed that when module D is considered, LSF has lower emissions: the difference is 1.69 kg CO₂ eq/m²/year.

Many comparative studies showed the environmental advantages of timber frames in different applications and locations when module D is excluded (Gong *et al.* 2012, Rodrigues and Freire 2014, Crafford *et al.* 2017, Li *et al.* 2021). Broadly speaking, the literature agrees on the better environmental performance of LSF among traditional construction systems. For example, some studies highlighted the environmental advantages of LSF when compared to masonry buildings (Iuorio *et al.* 2019, Bianchi *et al.* 2021, de Oliveira Rezende *et al.* 2022).

Table 2. Analysis and synthesis of the reviewed literature.

N.	Author(s)	Goal and Scope definition				System Boundaries							LCI	LCIA		
		Case study	Type of study	Lifespan	Location	Functional Equivalent/Unit	P	C	U	EoL	BLC	Databases			Tools	Environmental impacts
1	Gong et al. (2012)	R	CS of 3 systems	50 years	Beijing, China	Building designs, same function and design plan	•	•	•	•	•	Ecoinvent; SinoCenter; CAI; data manufacturers/ literature EU databases	SimaPro; Designer's simulation Toolkits	PE and CO ₂ emissions		
2	Tuca et al. (2012)	R	NCS	50 years	Timisoara, Romania	Whole building	•	•	•	•	•	EU databases	SimaPro	According to Eco-Indicator 99		
3	Rodrigues and Freire (2014)	R	CS of 3 systems	50 years	Coimbra, Portugal	1 m ² of living area over a period of 50 years	•	•	•	•	•	Tool's database; data from manufacturers and literature	SimaPro 7; Energy Plus	Non-renewable life-cycle PE, CC, OD, TA, FE, ME		
4	Zygomalas and Baniotopoulos (2014)	R	NCS	50 years	Greece	1 m ² of living area over a period of 50 years	•	•	•	•	•	Ecoinvent; ETH-ESU 96; manufacturers' data	-	According to Eco-Indicator 99 and CML 2 baseline 2000		
5	Craftford et al. (2017)	R	CS of 3 systems	50 years	Cape Province, South Africa	Quantity of materials required to build the roof	•	•	•	•	•	Ecoinvent 3.1	openLCA 1.4.2	According to CML baseline impact assessment method version 4.4		
6	Vitale et al. (2018)	R	CS of 2 systems	50 years	Vaicano, Italy	The total floor area of the building: 130 m ²	•	•	•	•	•	Ecoinvent 3.0.1; data from manufacturers	SimaPro 8.0.2; Epix7	Respiratory inorganics, Global warming, Non-renewable energy		
7	Johnston et al. (2018)	I	CS of 2 systems	-	Malaysia	-	•	•	•	•	•	ICE database; Ecoinvent; manufacturers' data	-	Embodied energy, CO ₂ emissions		
8	Iuorio et al. (2019)	R	NCS; CS of 2 systems;	50 years	Naples, Italy	25m ² ; 1 m ² for the comparison.	•	•	•	•	•	Data from SimaPro 7.3; Ecoinvent 3.0.1; EPDs; manufacturers' data	SimaPro 7.3	GWP, OPD, POCP, AP, EP, NRE		
9	Tavares et al. (2019)	R	CS of 4 systems	-	Different scenarios	One inhabitant (hab); 1 m ² of gross floor area.	•	•	•	•	•	ICE 2.0; Manufacturers' data	-	Embodied energy and greenhouse gas emissions		
10	Abouhamad and Abu-Hamd (2020)	E	NCS	50 years	Cairo, Egitto	1 m ² of building area per year	•	•	•	•	•	Tool's database	Athena Impact Estimator v5.04-0100; eQUEST	GWP, AP, OPD, EP, HHP, POCP, PE and fossil fuel consumption		
11	Tavares, Gregory, et al. (2021)	R,O	CS of 4 systems	30 years	Lisbon, Berlin, Stockholm	m ² of built area; total building stock.	•	•	•	•	•	Ecoinvent 3	-	non-renewable energy and global warming		
12	Tavares, Soares, et al. (2021b)	R	CS of 4 systems	50 years	Portugal	U-value	•	•	•	•	•	Ecoinvent 3; Market data	SimaPro V8.0	AD, ADFF, GW, OD, PO, AC, EU and Non-renewable energy (NRE) CO ₂ emissions		
13	Li et al. (2021)	R	CS of 5 systems	50 years	China	kg CO ₂ eq/m ²	•	•	•	•	•	-	-	CO ₂ emissions		
14	Bianchi et al. (2021)	R	CS of 3 systems	-	Brazil	1 m ²	•	•	•	•	•	Tally database	Autodesk Revit, Tally	GWP, AP, OPD, EP, SFP, PED, NRE, RE		
15	Abouhamad and Abu-Hamd (2021)	E	CS of 3 systems	50 years	Cairo, Egitto	-	•	•	•	•	•	EPDs	-	Use of non-renewable primary energy resources, GWP		
16	de Oliveira Rezende et al. (2022)	R	CS of 2 systems	-	Brazil	GWP Performance of the whole structural frame	•	•	•	•	•	Ecoinvent 3.6; site observation data; previous know-how	openLCA v.1.7	GWP		
17	Liu et al. (2022)	M	NCS	-	-	Specimen 90-60-90	•	•	•	•	•	Ecoinvent database	SimaPro 9.0	GWP and non-renewable energy		
18	Dani et al. (2022)	R	CS of 2 systems	90 years	Auckland, New Zealand	kg CO ₂ eq/m ² /year.	•	•	•	•	•	LCAQuick database	LCAQuick V3.4.4	GWP		

M: Module; R: Residential, I: Industrial, O: Office and E: Educational; CS: Comparative study, NCS: Not Comparative Study; P: Production, C: Construction, U: Use, EoL: End of Life, BLC: Beyond Life Cycle.

Also, the comparison between hot-rolled steel and LSF in a portal frame of industrial buildings performed by Johnston et al. (2018) highlighted the better economic and environmental performances of LSF, which allows 33% of steel savings.

Besides the comparison with different construction materials, the potential of LSF as a prefabricated construction system has been addressed by Tavares, Soares, et al. (2021): prefabricated construction has a lower environmental impact (except for abiotic depletion for LSF) compared to conventional construction systems. The comparative studies analysed, in summary, show that LSF represents a good alternative to traditional construction systems.

3.2 *Life cycle inventory in the reviewed literature*

The uncertainty of LCA results occurs also when the inventory phase is performed because of the missing foreground data. Addressing the LCI phase, it must be highlighted the complexity of the data collection of the material flows through the system boundaries. Most of the studies gathered data with the help of well-known databases, such as EcoInvent or databases already included in the LCA tools used to perform the analysis. In some contributions also Environmental Product Declarations (EPDs) have been used as a data source.

Many studies contributed to the LCA literature through primary data collection directly from manufacturers. In performing an LCA, different calculation tools are used to address the environmental impacts. From the literature, it can be observed that in the first publications, the main tool used is SimaPro while in the last years, the increasing sensitivity on the topic allowed the spread of new simplified tools specialized in building applications, often connected with BIM instruments.

3.3 *Life cycle impact assessment in the reviewed literature*

In all the studies analysed, the environmental impacts calculated and considered are different. Among others, the entire body of reviewed literature focused on the calculation of the GWP. Although, as many parametric studies highlighted, when performing an LCA it is appropriate to give a complete overview of the performances in all the impact categories, especially in comparative studies. Highlighting a better or worst performance between different materials considering only one specific environmental impact category can lead to misleading conclusions.

4 CONCLUSIONS

This systematic literature review has provided an overview of the key methodological choices made by researchers in performing environmental LCA on LSF buildings. In this section, some observations on the reviewed literature are made and research gaps are identified, thus providing guidelines for future research that can contribute to the progress of the scientific debate on the topic. The following propositions mirror the main conclusions of our analysis:

- The review has shown that there is a lot of effort invested in comparative studies. Although, they are not performed considering the same boundary conditions (i.e. different building layouts). In some cases, critical information in goal and scope definition is completely absent;
- The results obtained by different studies are not comparable because they have been conducted with different methodologies, also considering the location. Concerning this, there is a need to develop georeferenced and structured data related to the specific construction system;
- The calculations may vary significantly depending on the data collection, geographical location, scope, and methodology used. These items should not be used to compare results between buildings out of the same scope;
- The comparative studies aim to demonstrate the better environmental performance of a construction technology compared to another. In doing so, some fundamental features of LSF such as recyclability and durability are often not considered;
- In comparative studies, different assets of the system boundaries lead to different results. According to the potential recyclability, further developments are needed to assess the LCA of LSF buildings with a cradle-to-cradle approach which also considers module

- D. The potential recyclability of structural elements is fundamental in net-zero buildings since they contain up to 60% of the total embodied energy (Berggren *et al.* 2013). Therefore, the cradle-to-gate analysis should be revised considering also the new European policies on the minimum recycled content;
- Further experimental studies with realistic data and coherent methods are needed to implement and develop reliable and georeferenced benchmarking in different scenarios.

Considering the above, generical statements about the use of specific materials based on not harmonized methodologies and not related to a specific scenario should be revised. Nonetheless, the construction market, asks the scientific community for guidance and comparisons between different construction materials using the right KPIs. In response to this need, the authors are investigating an embryonic project (ARCADIA - ENEA) developed at the Italian level on some material supply chains focused also on the construction of a materials database. In conclusion, the authors want to turn the reader's attention to three main future research directions, LSF durability, its potential use in recladding applications and the need to perform the whole LCA.

Steel durability is rarely considered in comparative studies, especially when steel is compared to wood. In this regard, the authors consider it fundamental to deepen the LCA of LSF through the exploration of different end-of-life scenarios considering that the lifespan of steel is higher than the building's one. The matrix of the scenarios should be recalibrated with meticulous work of sensitivity analysis.

According to the authors' experience, future research in the application of LCA to LSF buildings can be done considering the potential application in buildings' recladding. The authors believe that the application in this context could highlight the LSF benefits among other solutions. Lastly, few studies addressed the potential of LSF also in terms of economic sustainability. Given the advantages of this construction technology, further research is suggested in developing multicriterial methods to perform a whole LCA of LSF, addressing all the various aspects of sustainability.

REFERENCES

- Abouhamad, M. and Abu-Hamd, M., 2020. Life cycle environmental assessment of light steel framed buildings with cement-based walls and floors. *Sustainability (Switzerland)*, 12 (24), 1–17.
- Abouhamad, M. and Abu-Hamd, M., 2021. Life cycle assessment framework for embodied environmental impacts of building construction systems. *Sustainability (Switzerland)*, 13 (2), 1–21.
- Abouhamad, M. and Abu-Hamd, M., 2019. Framework for construction system selection based on life cycle cost and sustainability assessment. *Journal of Cleaner Production*, 241, 118397.
- Berggren, B., Hall, M., and Wall, M., 2013. LCE analysis of buildings - Taking the step towards Net Zero Energy Buildings. *Energy and Buildings*, 62.
- Bianchi, P.F., Yepes, V., Vitorio, P.C., and Kripka, M., 2021. Study of alternatives for the design of sustainable low-income housing in Brazil. *Sustainability (Switzerland)*, 13 (9).
- Buzatu, R., Muntean, D., Ciutina, A., and Ungureanu, V., 2020. Thermal performance and energy efficiency of lightweight steel buildings: A case-study. *IOP Conference Series: Materials Science and Engineering*, 960 (3).
- Çelik, T. and Kamali, S., 2018. Multidimensional comparison of lightweight steel and reinforced concrete structures: A case study. *Tehnicki Vjesnik*, 25 (4), 1234–1242.
- Crafford, P.L., Blumentritt, M., and Wessels, C.B., 2017. The potential of South African timber products to reduce the environmental impact of buildings. *South African Journal of Science*, 113 (9–10), 1–8.
- Dani, A.A., Roy, K., Masood, R., Fang, Z., and Lim, J.B.P., 2022. A Comparative Study on the Life Cycle Assessment of New Zealand Residential Buildings. *Buildings*, 12 (1), 1–16.
- European Commission, 2014. Communication from the Commission - Towards a circular economy: A zero waste programme for Europe. *European Commission*, 398.
- European Commission, 2020. European green deal: Circular economy action plan for a cleaner and more competitive Europe. *European Union*.
- Gervasio, H., Dimova, S., and Pinto, A., 2018. Benchmarking the life-cycle environmental performance of buildings. *Sustainability (Switzerland)*, 10 (5), 1–30.
- Gervásio, H., Santos, P., Da Silva, L.S., and Lopes, A.M.G., 2010. Influence of thermal insulation on the energy balance for cold-formed buildings. *Advanced Steel Construction*, 6 (2), 742–766.

- Gong, X., Nie, Z., Wang, Z., Cui, S., Gao, F., and Zuo, T., 2012. Life cycle energy consumption and carbon dioxide emission of residential building designs in Beijing: A comparative study. *Journal of Industrial Ecology*, 16 (4), 576–587.
- Grubb, P.J., Lawson, R.M., Prewer, J., and Trebilcock, P.J., 1999. Modular Construction using Light Steel Framing: An Architect's Guide SCI PUBLICATION P272. *Steel Construction Institute*, 272.
- Iuorio, O., Napolano, L., Fiorino, L., and Landolfo, R., 2019. The environmental impacts of an innovative modular lightweight steel system: The Elissa case. *Journal of Cleaner Production*, 238, 117905.
- Johnston, R.P.D., McGrath, T., Nanukuttan, S., Lim, J.B.P., Soutsos, M., Chiang, M.C., Masood, R., and Rahman, M.A., 2018. Sustainability of Cold-formed Steel Portal Frames in Developing Countries in the Context of Life Cycle Assessment and Life Cycle Costs. *Structures*, 13 (October 2017), 79–87.
- Li, H., Luo, Z., Xu, X., Cang, Y., and Yang, L., 2021. Assessing the embodied carbon reduction potential of straw bale rural houses by hybrid life cycle assessment: A four-case study. *Journal of Cleaner Production*, 303.
- Liu, C., Mao, X., He, L., Chen, X., Yang, Y., and Yuan, J., 2022. A new demountable light-gauge steel framed wall: Flexural behavior, thermal performance and life cycle assessment. *Journal of Building Engineering*, 47 (December 2021), 103856.
- Mateus, R., Neiva, S., Bragança, L., Mendonça, P., and Macieira, M., 2013. Sustainability assessment of an innovative lightweight building technology for partition walls - Comparison with conventional technologies. *Building and Environment*, 67.
- Noorzai, E., Gharouni Jafari, K., and Moslemi Naeni, L., 2022. Lessons Learned on Selecting the Best Mass Housing Method Based on Performance Evaluation Criteria in Iran. *International Journal of Construction Education and Research*, 18 (2), 123–141.
- de Oliveira Rezende, M., Saade, M.R.M., Nunes, A.O., da Silva, V.G., Moris, V.A.S., and Silva, D.A.L., 2022. A Lean and Green approach for the eco-efficiency assessment on construction sites: description and case study. *Clean Technologies and Environmental Policy*, 24 (5), 1535–1552.
- Rodrigues, C. and Freire, F., 2014. Integrated life-cycle assessment and thermal dynamic simulation of alternative scenarios for the roof retrofit of a house. *Building and Environment*, 81, 204–215.
- Santos, P., Martins, C., and Simões Da Silva, L., 2014. Thermal performance of lightweight steel-framed construction systems. *Metallurgical Research and Technology*, 111 (6).
- Sen, R., Bhattacharya, S.P., and Chattopadhyay, S., 2021. Are low-income mass housing envelopes energy efficient and comfortable? A multi-objective evaluation in warm-humid climate. *Energy and Buildings*, 245, 111055.
- Smith, R.E. and Quale, J.D., 2017. *Offsite architecture: Constructing the future*. Offsite Architecture: Constructing the Future.
- Soares, N., Santos, P., Gervásio, H., Costa, J.J., and Simões da Silva, L., 2017. Energy efficiency and thermal performance of lightweight steel-framed (LSF) construction: A review. *Renewable and Sustainable Energy Reviews*, 78 (May), 194–209.
- Tavares, V., Gregory, J., Kirchain, R., and Freire, F., 2021. What is the potential for prefabricated buildings to decrease costs and contribute to meeting EU environmental targets? *Building and Environment*, 206.
- Tavares, V., Lacerda, N., and Freire, F., 2019. Embodied energy and greenhouse gas emissions analysis of a prefabricated modular house: The “Moby” case study. *Journal of Cleaner Production*, 212, 1044–1053.
- Tavares, V., Soares, N., Raposo, N., Marques, P., and Freire, F., 2021. Prefabricated versus conventional construction: Comparing life-cycle impacts of alternative structural materials. *Journal of Building Engineering*, 41.
- Thirunavukkarasu, K., Kanthasamy, E., Gatheeshgar, P., Poologanathan, K., Rajanayagam, H., Suntharalingam, T., and Dissanayake, M., 2021. Sustainable performance of a modular building system made of built-up cold-formed steel beams. *Buildings*, 11 (10).
- Tuca, I., Ungureanu, V., Ciutina, A., and Dubina, D., 2012. Life-cycle assessment of a steel framed family house. *Pollack Periodica*, 7 (1), 15–26.
- Vitale, P., Spagnuolo, A., Lubritto, C., and Arena, U., 2018. Environmental performances of residential buildings with a structure in cold formed steel or reinforced concrete. *Journal of Cleaner Production*, 189, 839–852.
- Xiao, Y. and Watson, M., 2019. Guidance on Conducting a Systematic Literature Review. *Journal of Planning Education and Research*, 39 (1), 93–112.
- Zeynalian, M., Trigunaryah, B., and Ronagh, H.R., 2013. Modification of Advanced Programmatic Risk Analysis and Management Model for the Whole Project Life Cycle's Risks. *Journal of Construction Engineering and Management*, 139 (1), 51–59.
- Zygomalas, I. and Baniotopoulos, C., 2014. Life cycle assessment environmental data for structural steel construction in Greece. *International Journal of Sustainable Engineering*.

Building life-cycle assessment considering different structural materials

J.H. de Paula Filho

ArcelorMittal Global R & D, Esch-sur-Alzette, Luxembourg

M. Charlier

Steligen ArcelorMittal, Esch-sur-Alzette, Luxembourg

M. D'Antimo

Steligen ArcelorMittal, Milan, Italy

ABSTRACT: To date, most of the efforts to reduce the environmental impact of the construction sector were mainly focused on operational carbon. However, due to the decarbonization of the energy sector, embodied carbon has been recognized as the dominant climate impact driver. In response, countries are currently accelerating their efforts to comply with climate change commitments and regulations, pressure grows for the construction sector to reduce its impact rapidly. Life-cycle assessment (LCA) of buildings is an important tool in this process. Building LCA is a science-based methodology for quantifying the lifetime environmental impacts of buildings. It is used to measure and reduce the embodied, operational, and whole-life carbon of buildings. This paper presents the comparative results of a building LCA of a structure in Luxembourg. The work presented here compares three structural systems: a steel frame, a prefabricated reinforced concrete frame, and a timber frame.

1 INTRODUCTION

The building and construction sector is responsible for around 40% of global carbon emissions and if improvement is not made in short term this impact will probably double in the next 20 years (Khan S.A, 2022). Sustainability of the built environment and the need to stem the climate crisis are topics that have gained great popularity thanks to many public awareness actions. In response to this grow of attention, several countries have aligned their policy to meet the goals of the Paris agreement, encouraging and supporting environmental policies at various levels. Recently, the European Green Deal set a goal to achieve zero net emission by 2050, a key sector is the building construction and renovation. This sector has become more efficient in terms of energy consumption, but a lot is still needed for reducing overall emissions. Some European countries have introduced policies to reduce whole-life carbon emissions from buildings and construction. While a common EU policy on whole-life carbon is still in the making, Denmark, the Netherlands, and France have introduced CO_{2eq} limits for a large share of new buildings, while Finland and Sweden have plans to do so. Germany, the UK, and Switzerland have life cycle assessment requirements for certain public buildings; Belgium is planning similar requirements.

In a building, part of emissions is coming from the so-called “embodied carbon”, associated with materials and all the construction process during the whole life cycle. The carbon emission of a building can be grouped in different stage of its lifetime, from the material extraction until the end of life (EOL), considering the material processing and component manufacturing, the construction and assembly, the operation and service, and all the emission related to transport (i.e., from manufacturing to site). Given the need to rapidly decarbonise the energy

supply chain, embodied carbon will soon be the main source of emissions in the built environment, and for this reason, the topic is attracting considerable attention.

Reducing the carbon embedded in a structure involves evaluating each design choice using a whole life-cycle approach and seeking to minimize upfront carbon impacts (e.g., low carbon materials), as well as taking steps to avoid future embodied carbon during the end of life (e.g., circularity). Low carbon solutions do not only rely on selecting low embodied carbon materials, but also on an efficient structural design where engineers and architects play an important role.

To assess the carbon emissions of a building, a procedure called LCA (Life Cycle Assessment), is generally used. This procedure is a science-based and standardized (AEN/CTN 198, ISO 14044) methodology for quantifying and reporting on environmental impacts. It can be used to give insights on how to reduce the carbon emissions of buildings over their life cycle: before the use of the building, during the use of the building and the EOL of the building. Even if an LCA can be performed at any stage of the design processes, LCA performed at the earliest possible can maximise the optimization of the solution (Hauke B., 2016). Emissions from materials and products must be addressed by LCAs to ensure that the buildings designed and built today are optimized for minimizing emission over lifetime. This involves evaluating each design choice using a whole life-cycle approach seeking to minimize upfront carbon impacts (e.g., efficient design, low carbon materials), as well as taking steps to avoid future embodied carbon during the end- of-life. Low carbon solutions do not only rely on selecting low embodied carbon products and materials, but also on an efficient structural design where engineers and architects play an important role. A proper and optimized design positively influences the overall sustainability of the project, for example, reducing the material quantity by selecting a proper structural grid and using high strength materials can have a significant impact on global emissions. There are additional choices that can further improve a building's carbon footprint like the reuse of existing elements and low carbon materials.

1.1 *Life Cycle Assessment (LCA)*

LCA is a scientific and quantitative method for determining and assessing environmentally relevant processes. It was first developed for assessing products, but it is also used today to assess industrial processes, services, behavioural patterns, and complete buildings. Buildings have different life-cycle stages such as: product, construction, use, end-of-life, and benefits beyond the system boundary. These stages correspond to specific standardized modules (from A1 to D). The LCA procedure is defined by the ISO norm 14,040 series (ISO 2006a; ISO 2006b) and the steps to follow are: goal and scope definition, life cycle inventory analysis (LCI), life cycle impact assessment (LCIA), and interpretation of the results. At the building level, the EN 15978 (2011) *Sustainability of construction works - Assessment of environmental performance of buildings - Calculation method*, provides calculation rules for the assessment of the environmental performance of new and existing buildings based on a life cycle approach. It is intended to support the decision-making process and documentation of the assessment of the environmental performance of a building. LCA assesses several environmental impact categories, with Global Warming Potential (GWP) being the most widely recognized. When only GWP is measured, the assessment is known as a carbon footprint. During LCA, emissions are converted into environmental impacts potentials. The impacts are expressed in quantities of a substance that can cause environmental harm, such as greenhouse gas emissions, and known as midpoint indicators. They do not represent the actual harm, known as endpoint indicators, for example sea level rise. The Building LCA is based on the following stages (Figure 1): (modules A1-A3), construction process (modules A4-A5), end-of-life (module C), and the benefits and loads beyond the system boundary (module D).

1.2 *Objective of the work*

This paper presents the comparative results of a building LCA of a typical office building located in Luxembourg with 50 years of service life. Three structural systems are compared:

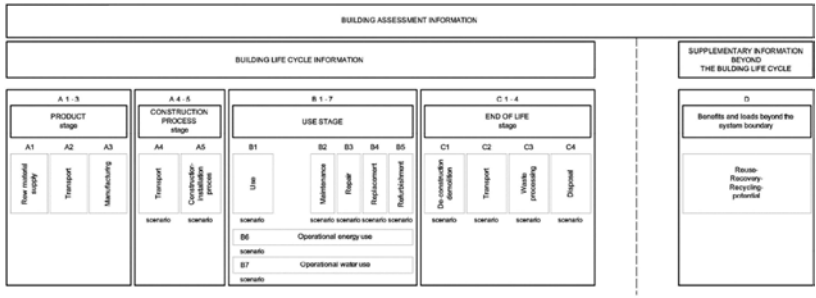


Figure 1. Display of modular information for the different stages of the building assessment.

a steel frame, a prefabricated reinforced concrete frame, and a timber frame. To ensure that the structural alternatives were functional equivalent, the same life-cycle scenario and assumptions are used in this work. To assess the impact of all the material and product used in the comparison environmental product declarations (EPDs) published according to the EN 15804+A1 and the EN 15978 are used. LCA studies are performed using the commercial software One Click LCA*. The Building LCAs, presented in this work, have as final objective the comparison and the potential benefits of different materials for the building structural frame application. This building LCA focuses on the following modules: A1-A5, B4, C3-4, D.

2 STUDIED EXAMPLE

2.1 Generalities of the office building

This paper presents the comparative results of a building LCA of a typical 9-storey office building located in Luxembourg (2018) with 50 years of service life. To define a representative office building for the Luxemburgish construction context, a market analysis was performed by the company TBC. The selected office building type was configured in an “L” shape (Figure 2) and the most significant dimensions are listed in Table 1.

Table 1. Significant office building dimensions.

Building depth [m]	13,60
Building length [m]	78,15
Superstructure the number of levels	R+8
Infrastructure number of levels	2
Free height on the ground floor [m]	3,5
Free height on the intermediate floors [m]	2,7



Figure 2. Typical floor layout.

2.2 Structural options

Three structural systems are compared: a steel concrete composite frame, a prefabricated reinforced concrete frame, and a timber frame. Two grid options were adopted based on the best performance of the different structural options and materials: 8,1m by 13m (clear span) for the steel concrete composite steel option, 8,1m by 5m +8m (with intermediate columns) for the prefabricated reinforced concrete option, and finally 5,4m by 5m + 8m (with intermediate columns) for the timber options (Figure 3a, b and c). All the structural options assessed were designed and verified according to the Eurocode's rules by independent design offices. Also, Table 2 shows a summary of the structural options analysed in this work.

Table 2. Structural options.

Reinforced concrete	
Frame	Prefab Concrete principal beams 8m + 5m span Prefab Concrete façade beams 8,1m span
Floor	Pre-stressed concrete hollow slabs 8,1m span
Composite steel	
Frame	ArcelorMittal Angelina® 13m span S460 Hot rolled steel sections 8,1m span S460
Floor	ArcelorMittal Cofraplus® 60 composite floor 2,7m span
Timber	
Frame	Glulam GL24h beams 8m + 5m span Glulam GL24h façade beams 5,4m span
Floor	CLT GL24h panel 5,4m span

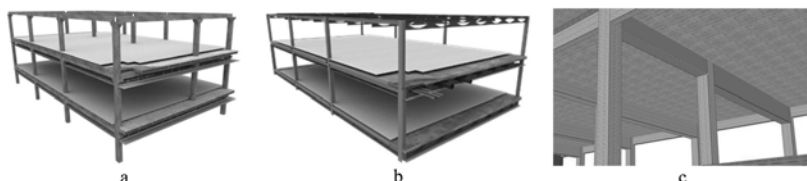


Figure 3. Structural options: a. Reinforced concrete; b. Composite; c. Timber.

2.3 Goal and scope definition

The first step of the analysis consists in choosing a functional unit and defining a level of detail. All the modules that can be included in a LCA are shown in Figure 1. The goal of the present building LCA is to quantify the environmental performance of equivalent structural options, composed of different materials, of an office building located in Luxembourg. This comparative study can support the different construction chain players (e.g.: engineers, architects, real estate developers, etc.) in the decision-making process by providing comparisons of the environmental performance of different design options and by indicating the potential for environmental performance improvement. As mentioned above, this building LCA focuses on the following modules: A1-A5, B4, C3-4, D.

2.3.1 Product Stage A1-A2

These modules are covering resource extraction (A1), transport of the resourced (A2) the manufacturing process, and completion of the finished products at the factory gate (A3). Material and product quantities were extracted from construction drawings, bills of quantities, and BIM models as delivered by designers. Net quantities were used in this work.

2.3.2 Construction Process Stage (A4-A5)

Transportation of building materials and products from the factory to the construction site (A4), and the actual construction/assembly on-site (A5). Transportation scenarios from One

Click LCA were used and represent regionally typical transportation distances and methods. Wastage quantities were estimated by default values of One Click LCA based on different materials and accounted for in module A5.

2.3.3 Use stage – Replacement (B4)

Due to the purpose of the building LCA, the only relevant life-cycle stage during the use of the building was module B4. Service life determines how long the product is used before being replaced. Values for the different products and materials were taken from the respective EPDs.

2.3.4 End of life stage (C3-C4)

Waste processing (C3) relates to structural elements and building materials that can be reused, recycled, or used otherwise (e.g., for energy recovery) (C3), and Disposal (C4) relates to structural elements and building materials that must be disposed/landfilled (C4) life-cycle stages were considered in the building LCA analysis. Table 3 presents the end-of-life (EOL) scenarios adopted for the different materials:

Table 3. EOL assumptions.

Material	Landfill %	Re-use %	Recycling %	Incineration with energy recovery %	Source
Structural steel	1	11	88		EPD
Steel reinforcement bars	10		90		EPD
Reinforced concrete	25		75		BETie
Timber scenario 1				100	One Click LCA
Timber scenario 2	100				EPD

The EOL assumptions are taken from the considered EPDs and One Click LCA’s database (see Table 3). They reproduce the current practices for deconstruction and treatment of the Construction Demolition Waste (CDW) of the location where the building is situated. Since the EPD used for wood elements declares several EOL scenarios, two are proposed: landfilling and incineration with energy recovery since often timber CDW is subjected to different practices. It is assumed that the amount of CO₂ absorbed during the photosynthesis and stored within wood during its life cycle is equal to that released at the EOL and thus there is no net impact on emissions. This assumption is commonly adopted for wood-based products in LCA (Morris F., 2021), however, a focus on biogenic carbon is presented in the next chapter.

2.3.5 Benefits and loads beyond the system boundary (D)

Based on decisions taken at the EOL, potential benefits related to the substitution of primary resources are accounted for. Module D is considered in the building LCA analysis characterizing it as a cradle-to-cradle LCA. For the end-of-life scenario Timber scenario 1, where the energy recovered by incineration is substituted in the energy mix, the District Heat, Luxembourg profile IEA2019 was selected.

2.4 Life cycle inventory

The life cycle inventory (LCI) is composed of construction environmental product declarations (EPDs) published according to the EN 15804+A1 and the EN 15978. EPDs provide quantified information on environmental impacts and aspects of products and services for use in a building LCA. The main EPDs and environmental data used in the building LCA are presented in Table 4 together with their embodied carbon impacts (A1-A3) in terms of their functional unit (FU).

Table 4. EPDs and environmental data.

Data source	Material	FU	GWP [kg CO ₂ eq./FU]
EPD XCarb™ Recycled and renewably produced Structural steel sections and merchant bars ArcelorMittal Europe	Structural steel sections	kg	0,33
EPD Structural steel sections in HISTAR grades ArcelorMittal	Structural steel sections	kg	0,52
EPD XCarb™ Reinforcing steel in bars ArcelorMittal Europe	Steel reinforcement bars	kg	0,3
EPD Reinforcing steel in bars ArcelorMittal	Steel reinforcement bars	kg	1,23
One Click LCA	Ready-mix concrete C30/37	m ³	270,88
One Click LCA	Ready-mix concrete C40/50	m ³	355,83
One Click LCA	Ready-mix concrete C50/60	m ³	429,00
EPD Cross-laminated timber (X-Lam) Studiengemeinschaft Holzleimbau e.V.	CLT	m ³	187,23
EPD binderholz Glulam - binderholz Bois lamelle-colle BSH - Legno lamellare BSH binderholz - binderholz BSH glulam	Glulam	m ³	205,53

3 RESULTS AND DISCUSSION

The Building LCA presented focuses on global warming potential (GWP) to describe the environmental impact. For the office building designed in composite steel structural solution, two building LCA analyses were made. The first is referred to as “Steel Composite usual AM’s structural steel” to highlight the environmental results of ArcelorMittal’s electric arc furnace (EAF) process of structural steel making. The second is referred to as “Steel Composite XCarb®” to highlight the benefits achieved using 100% recycled steel (scrap) and 100% renewable energy during the process of steel-making. Results of all the analysed options are plotted in terms of the total gross floor area (GFA) of the office building for the two wood EOL scenarios: 100% incineration with energy recovery (Figure 4a) and 100% landfilling respectively (Figure 4b). Similarly, Figure 5 (a, b) show results of the GWP by GFA highlighting the contribution of each structural building part.

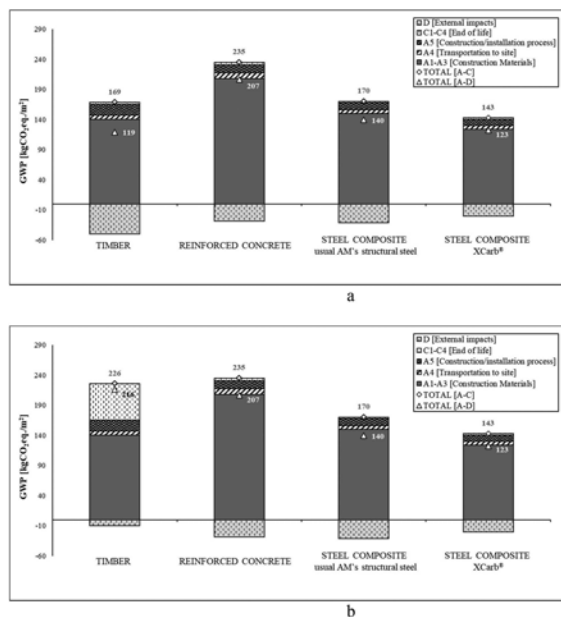


Figure 4. GWP [kgCO₂eq./m²] results by life cycle stages, 100% wood incineration with energy recovery (a); 100% wood landfilling (b).

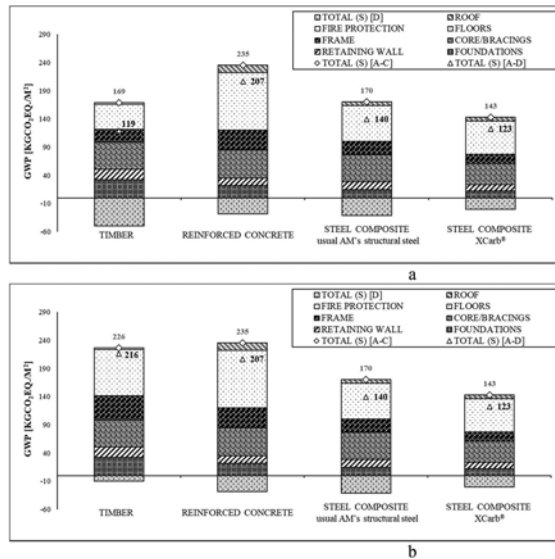


Figure 5. GWP [kgCO₂eq./m²] results by structural building parts, 100% wood incineration (a) and 100% wood landfilling (b).

3.1 Results & comparison

Regardless of the structural option, the product life-cycle stage (A1-A3) is the most contributing to the GWP. In terms of CO₂_{eq} emissions, the steel frame outperforms the reinforced concrete frame by reducing by 32% the overall GWP for the usual structural steel scenario (Figure 4). A greater reduction is achieved using XCarb® steel frame scenario where the overall GWP can be reduced by up to 41%. The timber frame when compared to the steel frame scenarios: usual structural steel and the XCarb®, is outperformed by 43% for the 100% landfill EOL scenario and performs equally for the 100% incineration with energy recovery, EOL scenario.

For all the structural options, the building part that contributes the most to the overall GWP is the floors (Figure 5). Steel composite floors outperform prefabricated reinforced concrete hollow core slabs by 37% and 42% for the usual structural steel and XCarb® steel frame scenarios respectively. It is seen that for the timber option, the floors are greatly impacted by the choice of EOL scenarios: 82 kgCO₂_{eq}/m² and 45 kgCO₂_{eq}/m² for the 100% landfill and 100% incineration with energy recovery scenarios respectively. Timber EOL has an important influence on the overall GWP, this will be discussed further in the next paragraph.

3.2 Focus on biogenic carbon

To understand the difference between the scenarios considered in this work for the timber option it is important to recognize the role played by Biogenic carbon. All the biological materials accumulate during their life carbon dioxide subtracted to the atmosphere (process known as sequestration). This carbon is released back to the atmosphere in form of biogenic CO₂, CO and CH₄ because of the oxidation and/or reduction of biomass by means of its transformation or degradation (e.g., combustion, digestion, composting, landfilling) (Hoxha E., 2020). Methane is a gas that contributes to the GWP, it causes 25 times more warming over 100 years compared to 1kg of CO₂, and so methane has a GWP of 25 (Forster P., 2007).

In the 100% landfill scenario for wood EOL, it is assumed that the landfill is a large modern Type 3 facility with CH₄ collection. The methane uptake partially substitutes natural gas in heat production as a benefit in module D. The non-collected CH₄ is released and accounted for GWP in module C. This explains the variation of results of the timber frame option

between both EOL scenarios. It also explains the reason why the timber frame module C, for the 100% landfill EOL assumption is the highest compared to the other structural options. According to the current practices, most of the wood (58%) is being landfilled in its EOL.

When it is assumed the 100% incineration with energy recovery scenario, the energy created in the combustion process is harnessed for electricity generation. In consequence, the life-cycle stage module D represents the benefit of avoiding energy production and not the benefit of avoiding raw material extraction (the harvesting of virgin wood) to produce timber structural elements. According to the current practices of wood as a CDW, just the minority (6%) is being incinerated with energy recovery in its EOL. When accounting for biogenic carbon, neglecting some phase of the LCA can lead to a misleading result (Hoxha E., 2020), for example if only modules A are considered in the LCA only the positive effect if the biogenic carbon is included without including the release at end of life.

4 CONCLUSIONS

The purpose of this building LCA application is two-fold: to quantify the environmental performance of equivalent structural options with materials and, based on the first, to guide the different construction chain players the decision-making process of different structural design options.

In this study, an R+8 multi-story office building representative of the Luxembourgish market with an RSL of 50 years is analysed. Three structural systems are considered: a steel frame, a prefabricated reinforced concrete frame, and a timber frame. A cradle-to-cradle Building LCA is performed to quantify the overall GWP of each building's structural system.

The steel frame outperforms the reinforced concrete frame reducing by 32% the overall GWP for the usual AM's structural steel scenario. For the XCarb® steel frame scenario, the overall GWP can be further reduced by 41%. The overall GWP of the timber frame is very sensitive to the wood EOL assumptions. When compared to the XCarb® steel frame scenario, the timber frame with the EOL assumption: 100% incineration with energy recovery, performs equivalently concerning the overall GWP. On the other hand, when 100% landfilled, the timber frame is outperformed by the XCarb® steel frame scenario by 43%. To conclude, steel frame option profits from a high-recycled material content, greatly reducing the embodied carbon from steel products. In addition, XCarb® environmental performance is enhanced using 100% renewable energy in steel production, lowering, even more, the embodied carbon.

REFERENCES

- AEN/CTN 198, "EN 15978:2012 - Sustainability of construction works - Assessment of environmental performance of buildings - Calculation method," Brussels, 2012.
- B. Hauke, M. Kuhnhenne, M. Lawson, and M. Veljkovic, *Sustainable Steel Buildings: A Practical Guide for Structures and Envelopes*, First Edit., no. 2016. John Wiley & Sons, Ltd, 2016.
- EN 15804:2012 + A1:2013. Sustainability of construction works - Environmental product declarations - Core rules for the product category of construction products, CEN, Brussels.
- EN 15978:2011. Sustainability of construction works - Assessment of environmental performance of buildings - Calculation method, CEN, Brussels.
- Forster, P.; Ramaswamy, V.; Artaxo, P.; Berntsen, T.; et al. (2007), *Climate Change 2013: The Physical Science Basis. Contribution of Working Group I to the Fourth Assessment Report of the Intergovernmental Panel on Climate Change*.
- Freya Morris, Stephen Allen, Will Hawkins, *On the embodied carbon of structural timber versus steel, and the influence of LCA methodology*, *Building and Environment* 206 108285. 2021
- Hoxha, E., Passer, A., Saade, M. R. M., Trigaux, D., Shuttleworth, A., Pittau, F., Habert, G. (2020). Biogenic carbon in buildings: a critical overview of LCA methods. *Buildings and Cities*, 1(1),504–524. DOI: <http://doi.org/10.5334/bc.46>.
- ISO, "14044: Environmental management—Life cycle assessment—Requirements and guidelines," International Organization for Standardization, vol. 14044. 2006.
- Khan, S.A.; Alam, T.; Khan, M.S.; Blecich, P.; Kamal, M.A.; Gupta, N.K.; Yadav, A.S. Life Cycle Assessment of Embodied Carbon in Buildings: Background, Approaches and Advancements. *Buildings* 2022, 12, 1944. <https://doi.org/10.3390/buildings12111944>.

Optimised steel structures for a low carbon future

M. D'Antimo

Steligen[®] ArcelorMittal, Milan, Italy

ABSTRACT: The construction sector is responsible for a considerable share of global CO₂ emissions. With the growing trend of the world population and the world's building stock, the share of emissions of the built environment is bound to increase dramatically in the coming years. Embodied carbon of structural materials will be soon the major source of emissions in constructions. The most promising construction material to help reducing building emissions and enhancing circularity is certainly steel. Even if the steel industry has the stigma of being among the highest-emitting industries, the carbon footprint of its manufacturing process is rapidly decreasing, and today low carbon steel products are cutting emissions faster than before. In this work the decarbonization journey of the steel industry will be addressed and simplified embodied carbon calculations will be presented and discussed for different material solutions in structural applications.

1 INTRODUCTION

1.1 *The Climate crisis*

The construction industry is the largest consumer of raw materials and the built environment alone accounts for about 25 and 40 percent of total carbon emissions in the world. The sector is also responsible for nearly 40% of raw material use annually and around 39% of the total primary energy use. In the coming years with the increase of world population will also increase the need to build/renovate structures and infrastructures; almost 75 percent of the infrastructure that will exist in 2050 has yet to be built, in fact, the world's building stock is expected to double by 2060, this will add 100-200 gigatons of embodied carbon coming only from construction materials. In this framework, the construction industry is only expected to expand, and with it the associated emissions, however, this will provide a significant opportunity to improve its efficiency and transition toward a low-carbon future (Carbon Pricing Leadership Coalition, 2018).

Embodied carbon of structural materials will be soon the major source of emissions in constructions. Operational carbon, which today is the major source of buildings emissions, is expected to decrease in time thanks to the ongoing decarbonisation strategies of the energy sector. The journey towards decarbonization of construction materials must speed up to reach the carbon neutrality targets. The most promising construction material in terms of low emissions and increasing circularity is steel.

Although the steel industry has the stigma of being among the highest-emitting industries (about 7% of global carbon dioxide emissions), the carbon footprint of its manufacturing process has decreased by 37 percent per ton since 1990 (Carbon Pricing Leadership Coalition, 2018), and today new low carbon alternatives are cutting emissions faster than before. The circularity of steel, enhanced by the possibility to upcycle, unlike other materials, and its low carbon alternatives have encouraged its use in ambitious projects driven by sustainability and facilitated higher ratings than would otherwise have been possible. The decarbonisation journey of production chains must go together with a change of paradigm in the way a project is conceived, design should be approached in a holistic way considering sustainability as an added value and not a burden. The first step is to approach an efficient design process, reducing the use of material by avoiding over-design, reducing impact of renovation and maintenance, allowing easy reversion of spaces, and only at the end of this process select low carbon alternatives for the traditional materials.

The increase in popularity of environmental issues has certainly led to a growth in awareness but it has also led to an exponential increase in often contradictory information. It is

more and more difficult to understand what can be practically done in design to reduce the emissions of construction in general. Starting from this consideration, this work tries to give a brief and surely non-exhaustive overview on decarbonization journey of the steel production and ultimately to present an easy way to estimate the embodied carbon of structural elements.

1.2 *Sustainability in construction and materials*

Materials and technologies play a fundamental role in cultural and social transformation, not only for technological development, but also in urbanization and in stemming the climate crisis.

Manufacturers and construction industry have engaged to reach net zero carbon within 2050, in line with the European and international strategic objectives. In response to the growing demand for green, sustainable, and low-carbon constructions, the industry is making efforts to address emissions of construction materials. Investors increasingly require the industry to meet standards of energy efficiency and sustainability (RE 2020 in France, LETI Guide in England, CAM in Italy...), green building rating systems (like LEED and BREEAM), responsible resource management, together with resilience and high-performance requirements for buildings and infrastructure. In this framework the journey towards decarbonisation of construction industry must speed up to meet the Paris Agreements.

To date the only scientific way to compare structural solutions in term of sustainability is the standardized methodology called LCA “life cycle assessment”. This technique is used for assessing the potential environmental impacts associated with a product or a service not only related to construction world. LCA is an objective method to evaluate and quantify the environmental loads, and potential impacts along the entire life cycle, from the acquisition of raw materials to the end of life (“from the cradle to the grave”) and beyond (“cradle to cradle”). The tool can be used at different “scales”: for the single product (steel, cement, etc.), for a solution (steel beam, composite flooring) or for a building, a group of buildings or even a city. Designers can use LCA to choose between alternative solutions, while manufacturers use LCA to define the impact of a product, in both cases, it is a useful tool to address and reduce the environmental impacts.

The relevance of the LCA technique lies mainly in its approach which consists of evaluating all the phases of a production process as related and dependent. The use of the LCA method is defined and regulated by the technical committee CEN TC 350 (in particular, EN 15978: Sustainability of construction works – Assessment of environmental performance of buildings – Calculation method). Several indicators are used in the assessment, but the current focus is on the Global Warming Potential (GWP), which expresses the contribution of a gas to the greenhouse effect in relation to the effect of CO₂, whose reference potential is equal to 1. It is expressed in units of CO_{2e}, where the “e” stands for equivalent.

LCA also breaks down the impacts into stages and modules that represent the magnitude of the impacts throughout each life stage – see Figure 1. An important aspect of carrying out an LCA is to define the goal and scope, and which boundaries are included in the analysis, for example, the analysis can be “cradle to gate”, “cradle to practical completion” or “cradle to cradle” (i.e., including module D) (Swann, 2021).

These aspects are crucial when different products or structural solutions are compared, the give comprehensive information to select a more sustainable option. If all the stages of the LCA are not included, the comparison could be inconsistent and therefore misleading. It is worth emphasising that conclusions reached on a cradle to gate analysis could be different to those on a cradle to grave or cradle to cradle. At European level, LCA supports the development of Environmental Labelling schemes, which provide information about a product or service in terms of its overall environmental benefits, such as the recyclability of its packaging, or the absence of noxious ingredients. Three type of labels exists: Type I (ecolabel), Type II (Ricoh Recycle Label) and Type III (EPD- Environmental Product Declaration). Type III environmental declarations (EPD), quantify the environmental information for the life cycle of a product and represent the most reliable and transparent data to develop an LCA assessment at the scale of the building (GBC Italy, 2019). To ensure consistency and to compare functionally equivalent products or services, these are classified into well-defined groups following a specific Product Category Rules (PCR), manufacturers must comply with it when conducting LCA for EPD evaluation. For construction products the reference, updated to 2020 is the EN 15804+A2.

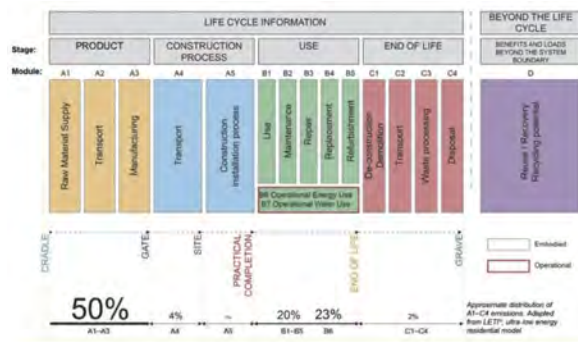


Figure 1. BS EN 15978 Life cycle stages LCA stages.

Reducing embodied carbon in a project is not a linear process often there are no general rules and assumptions that apply in all cases.

Designers should be able to compare in a simple but coherent way different solutions and environmental impacts, with the aim of choosing the most appropriate one for their project. Reducing emission implies first to use less material, refurbish instead of built, use a life cycle approach, minimize upfront embodied carbon (lean construction, low carbon materials, low carbon process, etc.), but also thinking about end of life. This last point is quite crucial in modern design, and answer to the question: what will happen to a building behind its life span? Building must be flexible, have a low embodied carbon (including renovation and maintenance), allow for adaptation and reconversion of spaces, include circular materials, and account for demountability, etc.

The approach to sustainable design and life cycle thinking is a complex process and it has to involve all the actors of the construction process: producers, and their engagement in decarbonization; investor, designer, and construction companies, with the need of having more sustainable option and a clear path to include sustainability in their daily practice.

2 STEELMAKING AND SUSTAINABILITY

Referring to building emissions, the highest impact on the emissions is given by the energy consumption (operation carbon), followed by construction process and materials and their production processes (embodied carbon). However, the energetic impact, which seems to be predominant today, can be reduced designing energy efficient buildings with well-designed insulation, efficient HVAC systems, photovoltaic roofing, etc. Additionally, considering the effort of the energy supply in shifting to clean energy, one can assume that this impact will decrease in the next 30 years.

Briefly, energy efficiency and clean production will drastically reduce operational carbon. On the contrary, the material impact remains unchanged and over time will be the major source of CO₂ emissions in the construction sector (D'Antimo, 2022). In this section the emissions of the steel industry will be addressed and the ongoing decarbonisation path will be presented.

2.1 Steel circularity

As stated, steel is a key material for technological evolution and in the circular economy. Many advances are currently taking place in the steel industry, increasing the rate of recycling (and potential reuse), implementation of decarbonization strategies (ArcelorMittal, 2021), industry standards and certification programs, such as ResponsibleSteel, improved productivity and efficiency of process (from energy efficiency to increased use of scrap).

Steel recycling is a well-established and efficient practice with capture rates as high as 99% at end of life (Figure 2) and steel production from scrap is already a mature steelmaking process. However, the predicted increase in global steel demand, means a transition to

steelmaking entirely based on scrap will not be possible for some time and so there will still be a need for primary steelmaking, and an urgent need to decarbonise the primary production too. The circularity of steel, enchanted by the possibility to upcycle, unlike other materials, and its low carbon alternatives have encouraged the use of this material in ambitious projects driven by sustainability and helped them to obtain better ratings in green certifications.

Steel is a perfect material to help designer in their approach to a more sustainably way of designing constructions and reducing usage of material. For example, approximately 75% of modern steels have been developed in the past 20 years. This means that, if the Eiffel Tower were to be rebuilt today, with the new steel types, it could be built with one-third of the steel that was originally used. This is true not only in construction but in all the sectors where steel is a key material, modern cars are built with new steels that are stronger and up to 35% lighter than in the past (WBCSD, 2003).

Over the past decades, technology, knowledge, and research have led to a more efficient use and exploitation of steel and materials in general. In a nutshell, this means that the first rule to cut emissions is to use is to “use less stuff”. If manufacturers are engaged in the decarbonization process to reduce the carbon footprint of production, designers have an important role to play in the transition. It is no longer enough to simply design efficiently, it is also necessary for designers to understand and engage with the supply chain and be aware of the latest developments and the available alternatives with lower embodied carbon, if they are to successfully deliver low impact buildings.

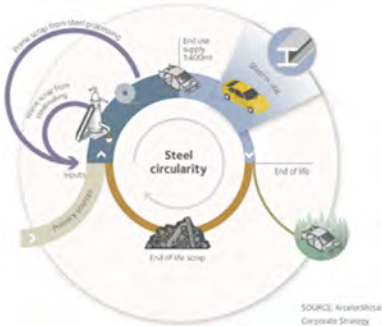


Figure 2. Steel circularity from (ArcelorMittal, 2020).




2.2 Decarbonization of the steel industry

There are currently three main technologies to produce steel:

- Primary steel making or Blast Furnace – Basic Oxygen furnace route (BF-BOF), where carbon coke is used to reduce the iron ore to make iron, the direct CO₂ emissions are the result of this chemical reaction in the furnace (Table 1). After iron is produced steel can be made in a Basic oxygen furnace by injecting oxygen.
- Secondary steel making from scrap (with Electric Arc Furnaces), where emissions are coming from the used electricity.
- Direct Reduced Iron (DRI) where a sponge iron is produced from the direct reduction of iron ore (in the form of lumps, pellets, or fines) into iron using reducing gasses (CO and H₂) derived from natural gas (CH₄). Then the sponge iron is melted in an electric arc furnace. The two reducing gasses, carbon monoxide and hydrogen, contribute to the reduction process in roughly equal amounts, resulting in respective emissions of CO₂ and H₂O. This illustrates one of the potential transition pathways to carbon neutral steelmaking, 100% hydrogen reduction using hydrogen from the electrolysis of water using 100% renewables (Swann et al, 2021).

3As presented in Table 1, different steel production routes have different sources of emissions and therefore require completely different technological efforts and decarbonization strategies to reach emission reduction targets. EAF steel is already relatively low in carbon.

Table 1. Steelmaking routes and emissions.

Blast Furnace (BF/BOF)	Direct Reduced Iron (DRI)	(c) Electric Arc furnace (EAF)
		
Source of CO ₂ e: Coke and electricity	Source of CO ₂ e: CH ₄ and electricity	Source of CO ₂ e: Electricity

When the feedstock is 100% scrap, the main source of emissions are those indirect emissions due to electricity generation. Over time, as the proportion of renewable electricity in the grid mix increases, the impacts of scrap-EAF steel will reduce.

Different strategies are needed for the primary steelmaking journey toward carbon neutral steel. Among these, green hydrogen can be used to completely replace the use of natural gas in DRI-EAF manufacture bringing the process close to carbon neutrality. Green hydrogen can only be produced with clean energy and the infrastructure to support this shift is not yet ready, however, the steel industry is already moving in this direction (ArcelorMittal, 2021). To summarise, the strategies being implemented for the decarbonisation of the steel supply chain are based on five major millstones: (i) Steelmaking transformation, from coal to natural gas as a precursor to green hydrogen DRI; (ii) Energy transformation (including green hydrogen, circular forms of carbon and carbon capture usage and storage technologies); (iii) Increased use of scrap; (iv) Sourcing clean electricity; and (v) Offsetting residual emissions.

3 EMBODIED CARBON ASSESSMENTS

3.1 *Build with less embodied carbon*

A structure built today needs to reduce its environmental impact as much as possible, in the next 50 years there will be many changes that the planet and the construction world will have to face. The approach to sustainable design and life cycle thinking is a complex process and involves all the actors of the construction process, producers, and their engagement in decarbonization, investor, designer, and construction companies. Reducing emission also means investing more in renovation more than new buildings, design using a life cycle approach, minimizing upfront embodied carbon (lean construction, low carbon materials, low carbon process, etc.), but also thinking about end of life. This last point is crucial in modern design, buildings must be flexible, reduce the embodied carbon for renovation and maintenance, adaptation and reconversion of spaces, circularity of materials, including demountability of the whole structure or some elements. More holistically, flexibility and end of life are an old-new way to approach construction. Flexibility in design and space allows for better utilization of the building potential and can be realized using long spans to create clear spaces that can easily accommodate change of use, allowing for demountable solutions, which allow possible reuse of elements and ensuring a life of the structure far behind the service life. A project and its impacts must always be analysed using a life cycle approach, otherwise there is a risk of missing all the benefits that some sustainable choices bring to the design. For example, the benefits of reducing the weight of structural elements does not only bring a direct benefit (less material = less CO₂) but also many indirect benefits. Among these, less impact due to transportation of materials (therefore less CO₂ from transport and less cost), less weight in the foundations (therefore less material, less excavations, lower cost in construction), lower impact of the construction site (in terms of duration, size, and cost), etc. This simple example explains how without considering the whole picture (LCA) it is not possible to make informed choices and compare solutions or alternatives in terms of sustainability. A project and its impacts must always be analysed using a whole life cycle approach, this is the principle on which the LCA approach is based.

3.2 Reducing embodied carbon of a beam element

Embodied carbon is important through the entire design process. To calculate it, the quantity of material is multiplied by carbon factor (in kgCO₂ per kg of material), as shown below:

$$\text{Embodied carbon (EC)} = \text{quantity} \times \text{carbon factor} \quad (1)$$

The carbon factor varies for the different LCA modules. The quantities, especially in early-stage evaluation or feasibility study, might be approximate. However, it is still a good way to assess impact (Orr et al, 2020). In this work, only emissions covering the production processes [A1-A3] (cradle to gate) are considered for the comparison of five alternative column solutions of a tall building. The column type (CT) elements compared are subjected to the same design assumptions, same length (4m) and, although it is a theoretical exercise, the methodology can be used for different cases and structural solutions. The column types compared, are as follows:

1. CT1: Circular reinforced concrete Φ 850 c40/50
2. CT2: Circular steel hollow section 508/30
3. CT3: Open welded profile (400 x 287)
4. CT4: Hot-rolled profile (HD 400 x 287- Histar®)
5. CT5: Hot-rolled & low carbon steel profile (HD 400 x 287- XCarb® recycled and renewably produced)

To estimate the value of equation (1), embodied carbon factors (ECF) from relevant EPD can be used or other equivalent sources. Attention must be paid in the calculation because the same materials, from different manufacturers, can have different environmental impacts. For example, the A1-A3 factor for structural steel section varies from 2.45 (British steel EPD) to 0.33 (ArcelorMittal XCarb® recycled and renewably produced EPD for sections and merchant bars). In Table 2 the EPD used in this work are reported with the ECF for [A1-A3], which, when multiplied by the material quantity gives an estimate of the embodied carbon.

Table 2. Used EPD and values.

EPD	Producer/publisher	Units	ECF [A1-A3]
Concrete	ICEv3-[C40/50-100% OPC	tCO ₂ e/m ³	0.42
Reinforcing steel bar	ArcelorMittal/IBU	tCO ₂ e/ t	1.23
Tubular	ArcelorMittal/IBU	tCO ₂ e/ t	2.27
Steel plate	ArcelorMittal/IBU	tCO ₂ e/ t	2.6
Steel profile	ArcelorMittal/IBU	tCO ₂ e/ t	0.524
Low carbon (XCarb®)	ArcelorMittal/IBU	tCO ₂ e/ t	0.333

For example, for CT1 the calculation according to (1) accounting for the contribution of the concrete and the steel rebars is as follows:

$$EC_{\text{concrete}} + EC_{\text{RBars}} = 0.42 \text{ tCO}_2\text{e/m}^3 \times 0.57 \text{ m}^2 + 0.135 \text{ t/m} \times 1.23 \text{ t CO}_2\text{e/ t} = 405 \text{ kgCO}_2\text{e/m} \quad (2)$$

While for CT4, a hot rolled steel profile with high strength steel S460 (HISTAR®), the embodied carbon is as follows:

$$EC = 0.287 \text{ kg/m} \times 0.524 \text{ t CO}_2\text{e/ t steel} = 151 \text{ kgCO}_2\text{e/m} \quad (3)$$

To make comparison easy, the embodied carbon in this case is expressed in kg per m of column. Quantities can be representative of the functional unit considered, however, when confronting different functional units, the coherence of results must be ensured. All the inputs and the results for the analysed cases are reported in Table 3.

In the reference project, the initial studied solutions were CT1 and CT2 (BF/BOF production) with an associated embodied carbon of 405 kgCO₂e/m and 807 kgCO₂e/m. However, to

Table 3. EC Results.

Case #	CT1	CT2	CT3	CT4	CT5
Dimensions	Φ 850	CHS 508/ 30	400 x 287	HD 400 x 287	HD 400 x 287
Material	Concrete/Rebars	S355	S460	S460 Histar [®]	S460 XCarb [®]
Quantity	0.57m ² /135 kg/m	354 kg/m	287 kg/m	287 kg/m	287 kg/m
EC	405 kgCO ₂ e/m	807 kgCO ₂ e/m	746 kgCO ₂ e/m	151 kgCO ₂ e/m	95 kgCO ₂ e/m

optimize the design, an open rolled profile in high-strength steel was proposed (CT4), which led to a considerable reduction in weight and dimensions and to a reduction of 80% in embodied carbon compared to CT2. To optimize further, an alternative low carbon material is added (case CT5) and a total reduction of 651 kgCO₂e/m (87%) can be obtained. For comparative purposes also CT1 and CT3 (welded profile) are presented in the Table 3.

3.3 Flooring

Following the same approach presented in the previous paragraph, different flooring solutions are compared estimating the EC associated with each solution. For the sake of brevity, the compared solutions are schematically presented in Table 4: (a) flat slab, (b) flooring composed of a cellular or smart beam and steel composite deck and (c) a slim floor beam (SFB) with additive steel floor.

For each element of the solution, an EPD or equivalent database (namely [13] for the concrete) have been used to establish a relevant ECF and summed to obtain the total embodied carbon.

Contrary to the previous column comparison, here the functional unit is expressed in m² (and not in m) thus the EC will be expressed in kgCO₂e/m². Two scenarios are considered: ordinary steel elements which give the EC (1) value and low-emission steel from the XCarb[®] family which returns the EC (2) value of the solution (b) and (c), nothing changes for (a).

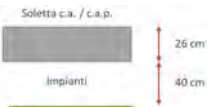
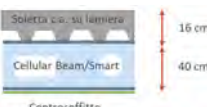
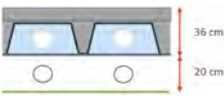



For the sake of consistency, reinforcing rebars are the same in all solutions (EPD: Arcelor-Mittal with an ECF of 1.23 tCO₂e/t) For case (a) cellular or smart beams with steel deck, using equation (1) for all the elements comprising the flooring solution, it is possible to obtain the embodied carbon following the procedure presented in the previous paragraph and more details can be found in (D'Antimo et al., 2022). Using low carbon steel, case EC (2), for solutions (b) and (c) can bring a reduction of about 30-33% of the embodied carbon. Comparing the same cases with the flat slab option where rebars are kept the same (EC of 139.5 kgCO₂e/m² is constant) embodied factor can be reduced of 55 % passing from (a) to (b) while the reduction is 41% passing from (a) to solution (c).

4 CONCLUSIONS

This work provides a brief overview of the decarbonization pathways of the steel industry, some considerations on the future of the construction industry and its emissions are examined. The main purpose of the work is to provide easy way to assess embodied carbon in projects at early stage, and how to effectively compare different solutions in terms of sustainability. A project or a solution must always be analysed using a life cycle approach, and the usual conception of a structure might be revised. The first step is to adapt instead of building (renovate); the second step is checking the design process to reduce the material and the primary resources used; paying attention to use the right material in the right place; at this stage low carbon alternatives can help further reducing the emissions. The conception of a structure must go behind the end of life, including possible scenarios (dismountability, reuse of space, reconversion), this can be achieved with flexible, clear spaces that are easy to convert, and using demountable solutions with circular materials.

Using a life cycle approach together with low carbon specifications can drastically reduce the carbon footprint of the built environment and help to meet sustainability targets. Low carbon alternatives and a more conscious choice of material sourcing have been proven to reduce the embodied carbon emissions, but this reduction can be even greater if coupled with an efficient lean design of high-performance buildings.

Table 4. Embodied Carbon factor (EC) for different flooring solutions.

	(a) Flat slab	(b) Beam and composite deck	(c) SFB additive flooring
Flooring type			
Example of application			
Elements	Concrete C40/50 and mesh Reinforcing steel in bars ArcelorMittal ICE v 3 - 10 Nov 2019 C40/50 100% OPC (420 kg/m ³)	Steel beam + Cofraplus® 60 Reinforcing steel in bars ArcelorMittal ICE v 3 - 10 Nov 2019 C32/40 100% OPC (355 kg/m ³)	Slimfloor beam + Cofraplus® 220 Reinforcing steel in bars ArcelorMittal ICE v 3 - 10 Nov 2019 C32/40 100% OPC (355 kg/m ³)
Materials/EPD		1) HISTAR Steel Sections ArcelorMittal 2) XCarb® recycled and renewably produced 1) Hot dip galvanized steel zinc coating (Z275) ArcelorMittal 2) XCarb® green steel certificate	1) HISTAR Steel Sections ArcelorMittal 2) XCarb® recycled and renewably produced 1) Hot dip galvanized steel zinc coating (Z275) ArcelorMittal 2) XCarb® green steel certificate
EC (1)	139.5 kgCO ₂ e/m ²	89.5 kgCO ₂ e/m ²	122 kgCO ₂ e/m ²
EC (2)	139.5 kgCO ₂ e/m ²	63 kgCO ₂ e/m ²	81.7 kgCO ₂ e/m ²

REFERENCES

- ArcelorMittal. *Climate Action Report 2*. Luxembourg, July 2021
- Carbon Pricing Leadership Coalition; International Finance Corporation. 2018. *Construction Industry Value Chain: How Companies are Using Carbon Pricing to Address Climate Risk and Find New Opportunities*. International Finance Corporation, Washington, DC. © World Bank. <https://openknowledge.worldbank.org/handle/10986/31055> Li-cense: CC BY-NC-ND 3.0 IGO.
- D'Antimo Marina, Marion Charlier, Walter Swann, Olivier Vassart. Proc. *Why optimised steel structures will help reducing embodied carbon*. C.T.A. XXVIII Giornate italiane della costruzione Metallica, Francavilla a Mare, 29 September -1 October 2022. Pescara
- GBC Italia Position paper: Life Cycle Assessment in edilizia – 2019.
- Orr J, Gibbons O, Arnold W. *A brief guide to calculating embodied carbon*. The Structural Engineer July 2020. <https://www.istructe.org/ISTRUCTE/media/Public/Resources/istructe-how-to-calculate-embodied-carbon.pdf>
- Swann, Walter 2021. Developing a low carbon circular economy for steel. The Structural Engineer 99 (4), pp. 18–19.
- Swann, Walter & Hanus, François & Vassart, Olivier & Knight, Alan. (2021). *Steel: friend or foe in the face of the climate emergency?* 175–182. 10.2749/ghent.2021.0175.
- World Resources Institute, World Business Council for Sustainable Development, *The Greenhouse Gas Protocol*, WRI, WBCSD, 2003.

The contribution of low carbon steel to the decarbonization of the building sector

H. Gervasio & L. Simões da Silva

ISISE, University of Coimbra, Coimbra, Portugal

M. D'Antimo

Stelligence ArcelorMittal, Milano, Italy

ABSTRACT: The building sector is responsible for about 40% of carbon emissions, in which about 11% are related to embodied carbon emissions. Therefore, buildings play an important role to the carbon neutrality of the construction sector, and the use of low-carbon materials is an added-value towards this goal. This paper aims to highlight the contribution of low-carbon steel buildings to the reduction of embodied carbon emissions in the building sector. The study entails a comparative life cycle assessment of a steel building using standard carbon steel and a building made of low-carbon steel. The comparative analysis entails the complete life cycle of the building, from the construction stage to the recycling stage, including Module D. As expected, the results show that the low-carbon steel has a lower impact in the production stage when compared with the standard steel. However, in the end-of-life stage, the result is the opposite as the net credits allocated in Module D are in this case a burden. Nevertheless, in terms of the whole LCA result, the life cycle result of the low-carbon steel is about 24% lower when compared with the standard carbon steel.

1 INTRODUCTION

The increase of atmospheric CO₂ and other greenhouse gases, mainly as result of anthropic activities, induced an increase in global air temperature (about 1°C compared to the preindustrial era) (IPCC, 2021), and has been leading to climate changes. These changes, which are effecting the entire planet, are unequivocal according to the United Nations Intergovernmental Panel on Climate Change (IPCC, 2021).

Across EU there is a broad agreement that decarbonization of the economy to net-zero by 2050 is required to avoid an increase of global temperature by more than 1.5°C or 2°C, above pre-industrial levels, complying with the Paris Agreement (UNFCCC, 2015).

However, decarbonization of the EU economy requires the engagement of all economic sectors, and the construction sector must play its role towards climate-neutrality. In fact, the construction sector has a huge contribution towards the increase in carbon emissions: the building sector alone is responsibility for about 40% of carbon emissions, in which about 11% are related to embodied carbon emissions (Worldgbc, 2019). Therefore, the construction sector is a priority under the umbrella of the European Green Deal (COM(2019) 640) and related initiatives, such as the Circular Economy Action Plan (COM(2020) 98), the Industrial Strategy for Europe (COM(2020) 102), the Renovation Wave for Europe (COM(2020) 662) and the New European Bauhaus (COM(2021) 573).

The steel industry is very energy intensive and therefore, it is also responsible for a significant share of carbon emissions. Nevertheless, over the years, different strategies have been implemented in order to reduce the consumption of energy for steel production, and consequently reduce carbon emissions.

In this context, this paper aims to highlight one of such strategies, the production of low-carbon steels and its contribution to the reduction of embodied carbon emissions in the building sector. The analysis will be carried out based on a comparative life cycle assessment of a steel structure. The paper is organized into the following sections. After this introductory section, in Section 2, a brief overview is provided on the main strategies for the decarbonization of the building sector, given emphasis on the production of steel for the construction sector, and its application to buildings. Then the adopted approach for life cycle analysis is described in Section 3, focusing on the modelling of steel production and end-of-life stages. In Section 4, this approach is applied in the comparative life cycle analysis between a steel structure of a building using standard carbon steel and the same structure made of low-carbon steel. The comparative analysis entails the complete life cycle of the structure, from the construction stage to the recycling stage, thus allowing to discuss the adopted allocation approach for Module D, which takes into account the use of recycled material in the production of steel and the recycling of steel at the end-of-life of the structure. Final conclusions are drawn by the end of the paper, in Section 5.

2 DECARBONIZATION OF BUILDINGS

Despite the investments in the energy efficiency of buildings, the energy consumption and related carbon emissions of the building sector have increased after the post-pandemic crisis. In 2021, the emissions of CO₂ related to the consumption of energy increased about 5% in relation to 2020 (UNEP, 2022). Unfortunately, this means that the gap between the climate performance of the building sector and the decarbonization target is widening.

Moreover, with the world economic grow, the global consumption of raw materials may double by 2060 (OECD, 2019). To reduce overall emissions, the building and construction sector should keep investing in energy and material efficiency, promoting materials' circularity and materials with low embodied carbon. For instance, the implementation of material efficiency strategies, such as the use of recycling materials, may reduce greenhouse gas emissions of residential buildings by over 80% in 2060 (UNEP, 2022).

Steel is one of the most popular construction materials in the world. The steel industry has a strategic importance to the EU economy, employing about 330000 people and creating around 29 billion euros of added value (Somers, 2021). At the same time, the production of steel is very energy intensive, being responsible for about 5% of CO₂ emissions at the EU level and 7% at the global level (IEA, 2020).

The emission of CO₂ from the production of steel has a wide variability as it depends on the production route. Steel is produced mainly from two distinct routes: the blast furnace or blast oxygen furnace (BF/BOF), and the electric arc furnace (EAF). The former is known as the primary (integrated) route, in which iron ore is reduced by coke and injection of coal to achieve the required (high) temperature. On the other hand, in the EAF, steel is produced mainly by melting recycled steel scrap, and therefore it is usually known as the secondary route. In the latter case, the process is almost fully electrified, and the emission of CO₂ is much smaller when compared with the BF/BOF route. To illustrate this, Figure 1 provides the values of Global Warming Potential (GWP) and Primary Energy (PE) for the production of 1 kg of steel products, with different inputs of steel scrap in the production stage. It is noted that data displayed in Figure 1 is global generic data from GaBi database (Thinkstep, 2017).

The production of steel in 2020 is illustrated in Figure 2, by country and respective steelmaking process. China is one of the main steel producers, and in 2020 it was responsible for about 45% of the world's steel (Somers, 2021). This steel was produced mainly through the BOF route.

On the other hand, in Europe, the production of steel is more balanced, although the BOF route has a slightly higher share than the EAF route. It is noted that another route is indicated in Figure 2 for Ukraine and Russia. This other route, the open hearth furnace (OHF), is an older and less efficient process to produce steel.

Although not as popular as the two previous routes, an alternative way to produce steel is through the Direct Reduced Iron (DRI) process. In this case, iron ore is directly reduced in its

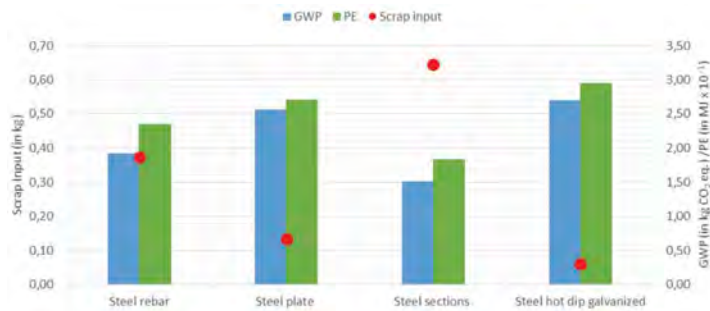


Figure 1. GWP and PE in the production of 1 kg of different steel products (Gervásio and Dimova, 2018).

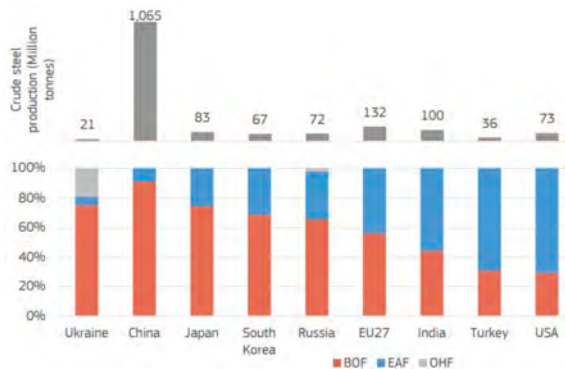


Figure 2. Stages considered in the analysis [extracted from Somers (2021)].

solid state to produce sponge iron, which in turn is melted and refined into steel, often with the addition of scrap in a EAF. The reduction gases in this process are hydrogen and carbon monoxide generated from natural gas or coal, thus avoiding the use of a blast furnace. Steel produced through this route accounts for a minor share (around 5%) (WorldSteel, 2019). However, this production route is currently increasing.

To be in line with EU's climate targets, new low-carbon technologies have to be adopted and/or developed within the near future.

From the above, one important lever for decarbonization of the steel industry is to maximize the recycling of steel, although virgin material will still be required. Other strategies currently being exploited by the steel industry to cut CO₂ emissions, although with completely levels of development, include the replacement of fossil fuels by low-carbon energies, carbon capture and storage, the use of hydrogen to reduce iron-ore (Hydrogen DRI), among others. These latter solutions are beyond the scope of this paper, and in the following, the focus is given to the production of low carbon steel, made through the EAF route and relying on the use of renewable energy.

3 METHODOLOGY FOR LCA

3.1 General framework

The adopted model for the Life Cycle Assessment (LCA) of buildings is based on the standardized framework for LCA developed by CEN TC 350 for the sustainability assessment of construction works (Gervásio and Dimova, 2018). Two main standards will be herein addressed: EN 15804:2012 for the assessment at the product level and EN 15978:2011 for the assessment at the building level. This model was implemented into GaBi (Thinkstep, 2017), a professional software for LCA.

The model takes into account the complete life cycle of the building, from the product stage to the end-of-life stage. According to the above standards, a modular concept is considered for the definition of the system boundaries of the LCA. In this case, the potential impacts occurring at each stage are allocated to a different module, as illustrated in Figure 3.

In the following case study, all modules were taken into account except Modules A4 to A5 and B1 to B7. It is considered that these modules do not depend on the structural system of the building and therefore, they are not considered in the scope of the analysis.

In the following paragraphs, a brief description of the most relevant modules is provided.

Product stage			Process stage		Use stage							End-of-life stage				
A1	A2	A3	A4	A4	B1	B2	B3	B4	B5	B6	B7	C1	C2	C3	C4	D
Raw material supply	Transport	Manufacturing	Transport	Construction	Use	Maintenance	Repair	Replacement	Refurbishment	Operational energy use	Operational water use	Deconstruction	Transport	Waste processing	Disposal	Reuse-recycling-recover
x	x	x	-	-	-	-	-	-	-	-	-	x	x	x	x	x

Figure 3. Stages considered in the analysis.

Modules A1 to A3 – Include the production of all buildings materials that are used in the foundations and structure of the building, until the gate of the factory. Data for these modules is usually provided from the Bill of Materials (BoM) of the building.

Module C1 – C4 – These modules include all relevant data from decommission of the structural system of the building to the stage in which the end-of-waste state is reached by all the structural materials. This includes the use of equipment and machinery for the deconstruction of the building structure, sorting of materials and transport of the resulting materials to their final destination. This data should be based on scenarios.

Module D – This module allocates net benefits due to the reuse, recycling and recover of materials. Data for this module should be based on scenarios taking into account the average available technology, current practices and current rates of recycling, reuse and recover of materials.

Since the case study herein provided is focused on a steel structure, in the following subsection a brief description is provided for the life cycle of steel products.

3.2 Life cycle of steel products

As previously indicated, steel is usually produced either by BF/BOF or EAF. The main difference between these two routes is the percentage of scrap introduced into the steelmaking process. In the BOF route the input of scrap may be up to 35%, while in the EAF route the input is close to 100% (WorldSteel, 2017).

After the steel making process, the downstream processes of casting and rolling are the same, independently of the upstream route. According to the WorldSteel (2017), all products can be produced through both routes, depending on the plant in which they are produced.

Hence, the life cycle of steel products has to consider both possibilities as illustrated in Figure 4. In addition, since there might be an input of steel scrap (in the production stage) and an output of scrap in the end-of-life (steel sent for recycling or reuse), an appropriate allocation procedure has to be adopted to cope with the credits due to the input and output of steel scrap.

The adopted allocation procedure is based on the model developed by WorldSteel (2017). In this case, Module D is given by:

$$Module\ D = \sum_i (RR_i - S_i) (X_{EAF,i} - X_{BF,i}) Y_i \tag{1}$$

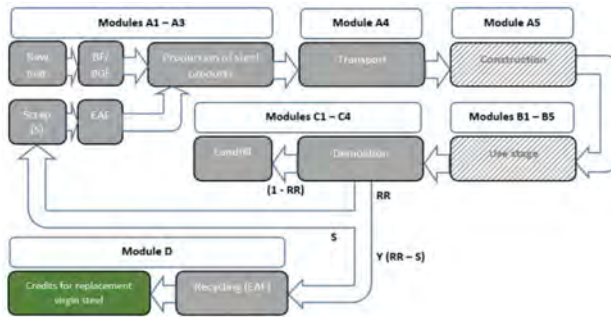


Figure 4. Model for life cycle analysis of steel (Gervasio and Dimova, 2018).

Where, RR is the recovering and recycling rate at the end-of-life stage; S is the recycled content in the production stage; $(X_{EAF,i} - X_{BF,i})$ represents the ‘potential savings’ achieved through recycling (or reuse) relative to primary (BF/BOF) production; and Y is a yield factor representing the efficiency of the steelmaking process.

It is noted that according to expression (1), Module D takes into account only ‘net flows’, given by the difference between output and input flows.

For example, the production of 1 tonne of steel sections, from GaBi database, has a scrap input (S) of 731 kg. Assuming that the recycling rate (RR) at the end-of-life stage is 80%, then the credit allocated in module D corresponds to $800 - 731 = 69$ kg of steel. In this case, Module D has a negative sign, and the complete life cycle of steel sections is given by the values indicated in Table 1:

Table 1. GWP for 1 tonne of steel from a generic database.

Modules A1-A3	Module D	Total LCA
1653 kg CO ₂ eq	-163 kg CO ₂ eq	1480 kg CO ₂ eq

It is worth noting that when the amount of steel leaving the system (scrap to be recycled) is lower than the amount of steel entering the system (scrap input), then the value in Module D is positive, and in this case it represents a burden.

4 COMPARATIVE LIFE CYCLE ASSESSMENT

4.1 Goals of the case study

This case study aims to demonstrate the contribution of low carbon steels in the life cycle analysis of steel buildings. Hence, a comparative life cycle analysis is carried out using two steels with the same grade (S355) but with different values of embodied carbon.

The analysis is focused on a demonstration building to be built in the framework of the project DREAMERS (2021 – 2025), and based on the results of a previous research project: FREEDAM - *Free from damage steel connections* (2015 – 2018).

As the goal of the analysis is to compare different types of steel, the analysis is limited to the load-bearing structure of the building, as all other components would be the same independently of the material of the structure. Further details of the case study are provided in the following sub-section.

4.2 Description of the case study

The demonstration building developed in DREAMERS aims to show the applicability and the increased seismic performance achievable by using innovative friction connections. Hence, the case study hereby presented is focused on a seismic resilient two-storey building, with about 800 m², which is currently being built in the University Campus of Salerno, Italy. It is noted that the following life cycle analysis was carried out based on the preliminary design of the building, considering a total of 93.7 tonnes of steel S355JR.

The building is characterized by a 15 m x 25 m plan, and 2 storeys with a total height of about 10 m. The building will be used for offices and classrooms, and therefore it offers wide internal spaces that allow flexible use of the areas as lecture rooms or open space offices.

The load-bearing structure of the building is composed of twelve columns made with HEB 500 profiles and slim composite floors (CoSFB), with HE300A+500x25 beams, developed by Arcelor Mittal, as illustrated in Figure 5.

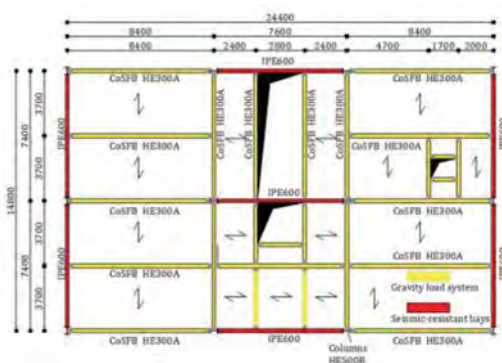


Figure 5. Floor layout of the structure of the building [DREAMERS (2021 – 2025)].

This free from damage structure will be equipped with beam-to-column friction joints, developed in FREEDAM project, which are made by friction pads coated by friction material located in the middle of a vertical sliding plates connected by high strength bolts to the bottom flange of the beams (Latour et al., 2022). These joints are assumed to be installed in both buildings so that the structural performance of both buildings may be assumed to be equivalent.

4.3 Life cycle analysis of the building structure

The life cycle analysis herein provided is based on the model previously described. In this case, the environmental data for steel production was retrieved from Environmental Product Declarations (EPD) available online from the platform IBU (<https://ibu-epd.com/>), all the remaining data was from GaBi database. In both cases, the LCA was carried out according to EN 15804:2012.

Two different analysis were carried out: the first analysis took into account a steel produced through the two main routes and a standard energy mix; while, the second analysis takes into account a low carbon steel produced from recycled material and renewable energy. The former analysis is hereafter denominated with standard carbon steel.

Hence, the first analysis took into account a steel produced in both the integrated route BOF (26%) and the electric arc furnace (EAF) route (74%) (bauforumstahl, 2018). The analysis took into account modules A1-A3, C1-C4 and D, and the results are illustrated in Figure 6. The end-of-life scenario assumed 11% reuse, 88% recycling and 1% landfill. The calculation of module D followed the procedure described above.

On the other hand, using a low-carbon steel, considering the production from the EAF (100%) with 100% renewable energy (Arcelor, 2021). In this case, the analysis took into account modules A1-A3, C1-C4 and D. The end-of-life scenario and the allocation procedure considered for

module D are the ones considered for the standard carbon steel. The results of this analysis are compared with the results of the previous one in Figure 6, in terms of Global Warming Potential (in kg CO₂ eq./ton). It is noted that the scenarios considered for modules C1-C4 were the same for both analysis and therefore, the results are not indicated in Figure 6.



Figure 6. Comparative LCA of both steel structures.

As expected, in the case of steel production (modules A1 – A3) the value of the low carbon is much lower than the value of the standard steel (about 2/3 lower). On the other side, in module D the value of the low carbon steel is positive, thus representing a burden (i.e. the net balance between the output and input is negative); while, in the case of the standard steel the result is negative, as the output of scrap is higher than the input. Nevertheless, in terms of the whole LCA result, the life cycle result is about 24% lower when compared with the value obtained by the standard carbon steel.

5 CONCLUSIONS

Despite the investments over time in energy and material efficiency of buildings, the emissions of CO₂ are still rising, widening the gap between the climate performance of buildings and the decarbonization target. Steel is one of the most popular construction materials in the world, but its production is also very energy demanding, thus having an important contribution towards carbon emissions.

To be in line with EU's climate targets, low-carbon materials and technologies have to be considered. Hence, this paper highlighted the contribution of low-carbon steel buildings to the reduction of embodied carbon emissions in the building sector. The study entailed a comparative life cycle assessment of a steel building using standard carbon steel and a building made of low-carbon steel. The results of the life cycle analysis, in terms of Global Warming Potential, showed that the use of the low-carbon steel allowed to reduce in about 24% the value obtained with the other carbon steel.

ACKNOWLEDGEMENTS

This research work has received funding from the European Community's Research Fund for Coal and Steel (RFCS) under grant agreement no. RFSR-CT-2020-101034015.

This paper reflects only the author's views and the Community is not liable for any use that may be made of the information contained therein.

REFERENCES

- Arcelor. 2021. XCarb Recycled and renewably produced structural steel sections and merchant bars, Environmental Product Declaration EPD-ARC-20210132-CBB1-EN (valid until 18/ 07/2026).
- bauforumstahl. 2018. Structural steel: Sections and Plates, Environmental Product Declaration EPD-BFS-20180116-IBG2-EN (valid until 24/ 10/2023).
- COM(2019) 640 final. Communication from the Commission to the European Parliament, the European Council, the Council, the European Economic and Social Committee and the Committee of the Regions: The European Green Deal.
- COM(2020) 102 final. Communication from the Commission to the European Parliament, the European Council, the Council, the European Economic and Social Committee and the Committee of the Regions: A New Industrial Strategy for Europe.
- COM(2020) 662 final. Communication from the Commission to the European Parliament, the Council, the European Economic and Social Committee and the Committee of the Regions: A Renovation Wave for Europe - greening our buildings, creating jobs, improving lives.
- COM(2020) 98 final. Communication from the Commission to the European Parliament, the Council, the European Economic and Social Committee and the Committee of the Regions: A new Circular Economy Action Plan For a cleaner and more competitive Europe.
- Dreamers (2021-2025): Design REsearch, implementation And Monitoring of Emerging technologies for a new generation of Resilient Steel buildings. Fund for Coal and Steel, Grant Agreement No RFSR-CT-2020-101034015.
- EN 15804:2012 + A1:2013. Sustainability of construction works - Environmental product declarations - Core rules for the product category of construction products, CEN, Brussels.
- EN 15978:2011. Sustainability of construction works - Assessment of environmental performance of buildings - Calculation method, CEN, Brussels.
- FREEDAM (2015-2018): FREE from DAMAge Steel Connections. Fund for Coal and Steel, Grant Agreement No. RFSR-CT-2015-00022.
- Gervasio, H. and Dimova, S. 2018. Model for Life Cycle Assessment (LCA) of buildings, EUR 29123 EN, Publications Office of the European Union, ISBN 978-92-79-79974-7 (print); 978-92-79-79973-0 (pdf), doi:10.2760/10016 (online),10.2760/789069 (print), JRC110082.
- International Energy Agency (IEA). 2020. Iron and Steel Technology Roadmap Towards more sustainable steelmaking, available online: https://iea.blob.core.windows.net/assets/eb0c8ec1-3665-4959-97d0-187ceca189a8/Iron_and_Steel_Technology_Roadmap.pdf.
- IPCC. 2021. Summary for Policymakers. In: Climate Change 2021: The Physical Science Basis. Contribution of Working Group I to the Sixth Assessment Report of the Intergovernmental Panel on Climate Change [MassonDelmotte, V., P. Zhai, A. Pirani, S.L. Connors, C. Péan, S. Berger, N. Caud, Y. Chen, L. Goldfarb, M.I. Gomis, M. Huang, K. Leitzell, E. Lonnoy, J.B.R. Matthews, T.K. Maycock, T. Waterfield, O. Yelekçi, R. Yu, and B. Zhou (eds.)]. Cambridge University Press, Cambridge, United Kingdom and New York, NY, USA, pp. 3–32, doi:10.1017/9781009157896.001.
- Latour, M., Santos, F., Santiago, A., Cavallaro, G., Piluso, V. 2022. Component modelling of low-damage beam-to-column joints equipped with friction dampers, Structures 46(3), pp. 1561–1580.
- Somers, J. 2021. Technologies to decarbonise the EU steel industry, EUR 30982 EN, Publications Office of the European Union, Luxembourg, ISBN 978-92-76-47147-9 (online), doi:10.2760/069150 (online), JRC127468.
- Thinkstep AG. 2017. Leinfelden-Echterdingen GaBi software-System and Database for Life Cycle Engineering 1992-2017 (version 8.1.0.29).
- UNEP - United Nations Environment Programme. 2022. 2022 Global Status Report for Buildings and Construction: Towards a Zero-emission, Efficient and Resilient Buildings and Construction Sector. Nairobi.
- UNFCCC. 2015. Paris Agreement. <https://unfccc.int/process-andmeetings/the-paris-agreement/the-paris-agreement>.
- World Green Building Council. 2019. Bringing embodied carbon upfront, available online: https://worldgbc.s3.eu-west-2.amazonaws.com/wp-content/uploads/2022/09/22123951/WorldGBC_Bringing_Embodied_Carbon_Upfront.pdf.
- WorldSteel Association. 2017. Life Cycle Inventory Methodology Report, Life cycle inventory methodology report for steel products, Brussels.
- WorldSteel Association. 2019. Total Production of crude steel. Steel Statistical Yearbook 2019, 1. <https://www.worldsteel.org/steel-by-topic/statistics/steel-statistical-yearbook.html>.

SS20: Advances in performance and life-cycle design of green structural materials for a more sustainable environment
Organizers: B. Belletti, P. Bernardi & A. Sirico



Taylor & Francis

Taylor & Francis Group

<http://taylorandfrancis.com>

Use of coarse recycled concrete aggregates and vitrified MSW ash in eco-concrete design

P. Plaza & C. Medina

Department of Construction, School of Engineering, University of Extremadura, Institute for Sustainable Regional Development (INTERRA), Cáceres, Spain

A. Sirico, B. Belletti & P. Bernardi

Department of Engineering and Architecture, University of Parma, Parma, Italy

J. Sánchez

Eduardo Torroja Institute (IETcc-CSIC), Madrid, Spain

ABSTRACT: Concrete industry is responsible for 8% of CO₂ emissions (primarily related to cement production) and for about 20 billion tons of natural aggregate consumption. On the other side, it is worth noticing that around 35% of waste generated in Europe is Construction and Demolition Waste (CDW). To reduce the amount of waste generated and prevent raw material consumption, coarse recycled concrete aggregates (CRCA) are a smart solution that can replace natural aggregates without affecting mechanical performance significantly. Furthermore, incineration of municipal solid waste (MSW) is a good option to reduce the volume of waste and generate electric energy in the process. However, this process produces ash that needs to be disposed of, and usually includes heavy metals and toxic organic components. A feasible way to treat ash is vitrification, which allows using it as supplementary cementitious material (SCM) without risks to humans and the environment. In this research, CRCA and vitrified ash from municipal solid waste incineration (MSWI) were used as coarse aggregate (25 and 50%) and cement (10%) replacement, respectively, and then an experimental analysis of fresh state properties and mechanical performance of the developed eco-concretes is presented.

1 INTRODUCTION

Concrete is the second most-used material by mass just after water, with an estimated annual production of 30 billion tons (Monteiro et al., 2020). This massive amount of concrete requires large quantities of components, resulting in particular in 4.17 billion tons of cement used in 2020 (Cembureau, 2021), and converting cement into the largest manufactured product by mass (Scrivener et al., 2018).

The use of by-products created with different types of waste is a viable solution to reduce environmental impact and greenhouse gas emissions in concrete production. According to Eurostat (European Commission, 2020), 798 Mt of construction and demolition waste (CDW) were produced only in Europe. Almost 100% of this waste can be reused in the construction sector as raw material for new elements. Concrete and masonry wastes are the best components that can be used as recycled aggregates to reduce the amount of natural resources exploited in the construction sector, and also reduce energy consumption and waste disposal (Kisku et al., 2017). Several Authors tested concrete with coarse and fine recycled aggregates to check if strength and durability properties were significantly affected. Among others, Hassan et al. (2021) tested full recycled aggregate concrete, analysing coarse and fine fractions alone and together. All mixes had compressive and tensile strength losses, up to 40% in case of full substitution of aggregates by recycled concrete. However, test results by Vinay Kumar

et al. (2018) showed that concrete with recycled aggregates could be even stronger than natural aggregate concrete. This behaviour is depending on the amount of old mortar attached to recycled aggregates. In particular, Duan & Poon (2014) pointed out that voids and cracks in old cement paste can cause more absorption and a weak granular skeleton.

Furthermore, to reduce CO₂ emissions, the use of supplementary cementitious materials (SCM) is the most common option to reduce both the Portland cement consumption and waste generated in some valorization activities. Municipal solid waste (MSW) has increased significantly during the last decades. One common strategy adopted to treat this waste while generating energy is incineration. However, in this thermal process, combustion residues are generated, namely bottom and fly ash, which usually contains toxic compounds for human health and the environment, mainly consisting of heavy metals and toxic organic components. Moreover, the presence of dangerous compounds, such as soluble salts, which could worsen the performance of cementitious materials makes the use of ash without any treatment not advisable. A possible way to treat ash so to make it chemically inert is vitrification. In this way, MSW incineration ash can be used safely as SCM, because of its pozzolanic activity, as highlighted in previous research in the literature (Saccani et al., 2005), (Ferraris et al., 2009), (Sharifikolouei et al., 2020).

In the present study, concrete containing coarse recycled concrete aggregates (CRCA) and municipal solid waste incineration (MSWI) vitrified bottom ash as partial cement replacement was tested. The combined use into concrete of these two kind of waste was never explored before. After raw materials characterization, concrete containing 25% and 50% CDW as aggregate replacement and 10% MSWI vitrified ash as cement replacement was cast and cured in water. Fresh state (slump, fresh density) and hardened state (compressive and flexural strength and fracture energy) were evaluated to determine if these types of concrete could be used as structural material.

2 MATERIALS AND METHODS

2.1 *Materials*

The natural aggregates used were divided into two fractions: river sand (RS) and natural gravel (NG). All materials had around 70-80% SiO₂, containing also low contents of Al₂O₃, CaO, and Fe₂O₃. Recycled concrete aggregates were supplied by ARAPLASA, a CDW management plant located in the Spanish province of Cáceres. This recycled gravel (RG), which consisted only of crushed concrete, was characterised by almost the same particle size distribution of natural gravel.

Municipal solid waste incineration (MSWI) ash used in this experimental campaign came from a plant located in the North of Italy. To apply vitrification, this ash was subjected to temperature increase by starting at 1100°C and then reaching 1450°C (Ferraris et al., 2009). This thermal treatment aims to convert ash into a stable and homogeneous glassy solid material by melt quenching (Colombo et al., 2003) and also to incorporate heavy metals in a stable form inside the glass matrix, combusting, by the way, toxic organic components as dioxins. In this study, after vitrification, the glassy material was ground to obtain powder for cement replacement, with a maximum particle size of 70 µm. Portland cement chosen was CEM II/A-LL 42.5 R according to EN 197-1:2011 standard. Finally, to obtain good workability while maintaining a low w/c ratio, a superplasticizer (Mapei Dynamon Xtend W202R) was used.

2.2 *Mix design*

The six different mixes studied were batched as summarized in Table 1. Reference concrete (RC) contained 100% natural aggregate and no cement replacement, while five different mixes were defined by considering two replacement levels for coarse aggregate and one for cement. In more detail, two mixes (C25 and C50) were obtained by replacing natural aggregates with 25% and 50% of recycled gravel, respectively; one mix (V), by replacing 10% of cement with MSWI vitrified ash and finally, two mixes (VC25 and VC50) were studied with both aggregate and cement replacement. For RC mix, cement, sand, gravel, and water were used in the proportion of 1:2.75:1.375:0.5 by weight. For eco-concrete, the percentage of replacement of natural gravel was computed by volume, while MSWI vitrified ash partially replaced cement by mass.

It is worth noticing that the amount of aggregates (natural and recycled) and water reported in Table 1, refers to the saturated-surface-dry (SSD) condition for the aggregates, so indicating the effective water of the mix. During mixing, all the aggregates were used in dry state, so properly adjusting the amount of required water by considering aggregate absorption (i.e. 0.79%, 0.86%, 5.40%, for RS, NG and RG, respectively).

Table 1. Mix batching.

Concrete components kg/m ³							
Mix	River Sand RS	Natural Gravel NG	Recycled Gravel RG	Cement C	MSWI Vitrified Ash	Water W	Superplasticizer SP
RC	1138.98	567.34	0.00	400.00	0.00	200.00	2.60
C25	1138.98	425.51	134.31	400.00	0.00	200.00	2.60
C50	1138.98	283.67	268.63	400.00	0.00	200.00	2.60
V	1138.98	567.34	0.00	360.00	40.00	200.00	2.34
VC25	1138.98	425.51	134.31	360.00	40.00	200.00	2.34
VC50	1138.98	283.67	268.63	360.00	40.00	200.00	2.34

2.3 Experimental campaign

All mixes were cast using a drum-type mixer following the same procedure. i) dry aggregates were poured inside the mixer with the inner drum surface wet; ii) ~50% of required water was added and mixed for 3-4 minutes; iii) binders (cement and ash) and ~25% of water were added and mixed for about 2-3 minutes; iv) remaining water and superplasticizer were poured and mixed for 3 minutes until concrete components were homogeneous. In all cases, no segregation and bleeding problems were found.

To obtain the same consistence class, defined as S5 according to EN 206:2013, superplasticizer content was modified in the mixes with vitrified ash, reducing the content from 0.65% of cement weight, for RC, C25 and C50 mix, to 0.585% for V, VC25 and VC50 mix.

For each mix, 2 different types of moulds were used for casting according to EN 12390-1:2021: 100 x 100 x 100 mm cubes for compressive strength and fresh density tests and 100 x 100 x 400 mm prisms for three-point bending test and fracture energy. Then, the specimens were cured in water at 20°C ±2°C until testing.

3 RESULTS

3.1 Aggregate characterization

Figure 1 reports particle size distributions of aggregates (river sand, natural and recycled gravel), which were tested according to EN 933-1:2012. Fines content resulted in any case low, because all natural aggregates were washed. In the case of recycled gravel, fines content was below 1.5% according to the standards. Comparing natural to recycled gravel, particle size distribution was almost the same, even if recycled aggregates had sharp edges while natural gravel had smooth edges.

In case of recycled gravel, classification test for the constituents according to EN 933-11:2009 was performed. Results are listed in Table 2. Composition of recycled gravel was almost concrete and unbound particles (Rc+Ru), that must be over 95% to classify this type of aggregate as concrete aggregate.

Coarse aggregate properties are listed in Table 3. Density of recycled gravel was lower than that of natural gravel, with a 10% decrease. Furthermore, water absorption of recycled gravel was nearly 6.2 times higher compared with that of natural gravel. The remaining properties were similar, so this kind of RG can be used in partial replacement of NG in the ratio allowed by the standards for structural concrete. The lower density and higher absorption of recycled

gravel were caused by the attached mortar from old concrete. This old mortar had a lot of voids and cracks, allowing water to enter the pores and increase absorption.

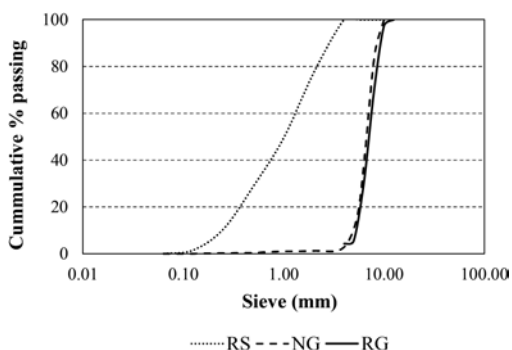


Figure 1. Grading curves.

Table 2. Classification of recycled gravel constituents.

Type	Code	Amount wt%
Concrete, concrete products, mortar	Rc	38.28
Unbound mortar, natural stone	Ru	59.90
Masonry	Rb	0.73
Asphalt	Ra	0.00
Floating particles	FL	0.03
Other (metal, plaster)	X	0.06
Other + Glass	X+Rg	0.06

Table 3. Coarse aggregate properties.

Type	Density Mg/m ³	Absorption wt%	Flakiness index wt%	Water-soluble chlorides wt%	Acid-soluble sulfates wt%	Total sulfates wt%
NG	2.64	0.86	<15	0.0013	<0.2	<1
RG	2.37	5.40	16.08	<0.01	<0.002	<0.001

3.2 Fresh concrete properties

Slump values of all mixes are listed in Table 4. All the values, obtained by following EN 12350-2:2020 standard, were very similar, and equivalent to a S5 consistency according to EN 206:2013, as expected. These findings confirm that recycled aggregates have no influence on workability if the effective w/c ratio is constant. Moreover, C, C25 and C50 mix also had the same SP content.

The experimental data are consistent with the results reported by other Authors replacing up to 100% of coarse (Zhang et al., 2022) or up to 50% of fine natural aggregates with recycled concrete aggregates (Plaza et al., 2021).

On the contrary, it was observed that MSWI vitrified ash increased slump values if w/c ratio and SP content were kept constant. So, in this study, to adjust workability and work with the same consistency in all mixes, SP content was modified for all mixes which included MSWI vitrified ash, resulting in a low amount of SP for mix V, VC25 and VC50 (Table 1). This behaviour was already described by Sirico et. al. (2022) using the same type of vitrified waste material.

Figure 2 plots fresh density obtained for all the mixes, divided into two groups: i) mixes where only CEM II/A-LL 42.5 R is used (denoted as V0, and including RC, C25 and C50 mix,

with a RG percentage equal to 0%, 25% and 50%, respectively) and ii) mixes where MSWI vitrified ash was used as partial (10%) cement replacement (denoted as V10, and including V, VC25 and VC50 mix, with a RG percentage equal to 0%, 25% and 50%, respectively). Density, which was measured according to EN 12350-6:2020, was observed to decline with the increasing of recycled aggregates content, with a linear relationship ($R^2 > 0.99$) between replacement ratio and density. The lower density of recycled aggregates caused a decrease in density, but differences were lower than 2% in all the cases. Xiao et. al. (2005) found slightly higher losses (between 2.4 and 5%) using the same types of aggregates. For MSWI, there was no significative difference by keeping constant the content of recycled aggregates.

Table 4. Slump values obtained for all the concrete mixes.

Mix	RC	C25	C50	V	VC25	VC50
Slump (cm)	22.50	23.25	24.00	23.50	23.00	23.50

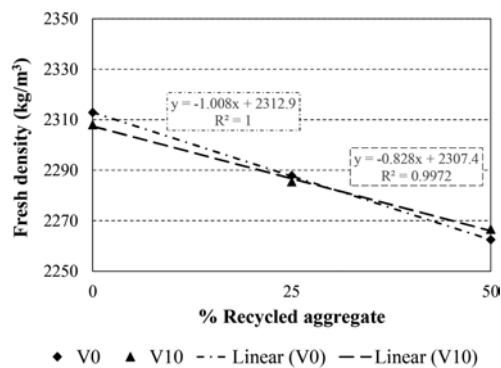


Figure 2. Fresh density for mixes without (V0) and with (V10) vitrified ash.

3.3 Hardened concrete properties

3.3.1 Compressive strength

Compressive strength values for all mixes at 7 and 28 days were measured according to EN 12390-3:2020, by means of a testing machine METROCOM PV P30. The results, which represent the mean values obtained on three cubes, together with the related standard deviations, are plotted in Figure 3.

As can be noted, 7-day compressive strength was lower in mixes including MSWI ash (V10), inducing variations between 8.54% (V mix) to 17.53% (VC50 mix). However, at 28 days strength was slightly higher compared with RC mix (0.32% for V mix) or presented comparable values to the corresponding mix without vitrified ash (the maximum reduction, which was registered for VC25 with respect to C25, is less than 3.5%). By comparing 7 and 28 day-strength, it can be argued that MSWI vitrified ash has pozzolanic activity, improving long-term strength by sealing pores due to CaCO_3 obtained by pozzolanic reaction. These results confirm the trend already recognized in literature (Saccani et al., 2005), (Ferraris et al., 2009), (Sharifikolouei et al., 2020).

7 and 28 day-strength was higher for 25% replacement ratio of recycled aggregates (0.78% and 3.45% variation for 7 and 28 days). For 50% replacement, compressive strength decreased by 8.93% at 7 days and 6.49% at 28 days. Chang et al. (2022) observed similar behaviour at 7 days for C25 and similar losses for C50 at 28 days. A higher volume of macropores induced a loss in load transfer capacity due to the presence of mortar in recycled aggregates (Pedro et al., 2017).

3.3.2 Flexural strength and fracture energy

Flexural strength $f_{ct,flex}$ and fracture energy G_f were evaluated by performing three-point bending tests on notched specimens according to the Japan Concrete Institute Standard

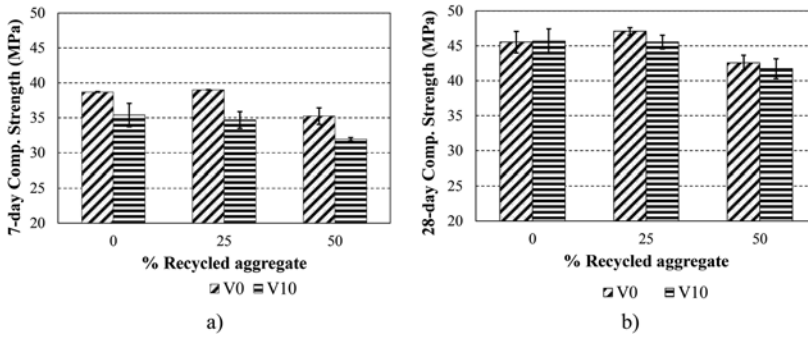


Figure 3. Compressive strength for mixes without (V0) and with (V10) vitrified ash including an increasing percentage of recycled aggregates at: a) 7 days; b) 28 days.

JCI-S-001-2003, which enables to get the load F – Crack mouth Opening Displacement ($CMOD$) curve. The notch was cut in the middle of each beam at the bottom, after 28 days of curing, and its height d and thickness t were equal to 30 mm and 5 mm, respectively. The tests were performed by using an INSTRON 8862 machine, under $CMOD$ control.

Flexural strength, which represents an indirect measure of the tensile strength of the material starting from the peak load of F – $CMOD$ curve (F_{max}), was computed as:

$$f_{ct,flex} = F_{max} \frac{3S}{2B(D-d)^2} \quad (1)$$

where D and B are the height and the width of the cross section (equal to 100 mm), and S is the span (equal to 300 mm).

Fracture energy G_f , a parameter that describes the ability of the material to resist fracture, and related to the area W_0 under the P – $CMOD$ curve, was evaluated as:

$$G_f = \frac{0.75W_0 + W_1}{B(D-d)} \quad (2)$$

where W_1 takes into account the work done by the deadweight of specimen and testing equipment.

The results in terms of $f_{ct,flex}$ and G_f , which were evaluated as the mean values obtained on three specimens for each mix, together with the related standard deviations, are shown in Figure 4.

Considering the standard deviations of the different mixes, it can be stated that the replacement of 10% cement with vitrified ash does not significantly modify the flexural behaviour of concrete in terms of both flexural strength and fracture energy, as already stated by Sirico et al. (2022). This effect is due to the pozzolanic reaction that MSWI vitrified ash develops in combination with Portland cement, as already recognized in this work for compressive strength.

However, concrete with recycled aggregates showed higher values for flexural strength, with similar values for 25% and 50% of replacement. This behaviour is not the most common, but some Authors found similar strength when good quality recycled aggregates are used (Kenai et al., 2002). Furthermore, Jayasuriya et al. (2021) analysed statistically more than 2200 data and found that flexural strength can be from 0.5% higher to 9.3% lower in concrete including partial or total replacement of recycled aggregates.

4 CONCLUSIONS

This work presents the results of an extensive experimental program concerning the development of eco-concrete incorporating recycled concrete aggregates (CRCA) and vitrified municipal solid waste from incineration (MSWI) ash, used as partial replacement of natural aggregates and cement, respectively. The novelty of this study concerns both this use of MSWI vitrified ash as SCM, which was scarcely explored in previous research, and the combined use of these two kind of waste into concrete, which was never been explored before.

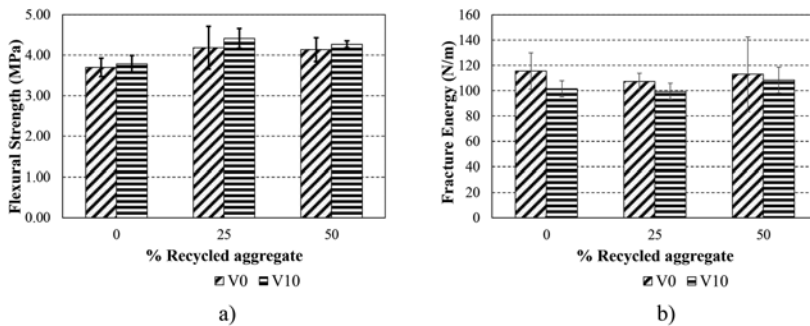


Figure 4. Results for mixes without (V0) and with (V10) vitrified ash including an increasing percentage of recycled aggregates in terms of: a) flexural strength; b) fracture energy.

By analysing the physical and mechanical behaviour of the developed eco-concrete, it can be concluded that the partial substitution of natural gravel and cement with these two types of waste can be successfully adopted for concrete production. These replacements indeed do not cause a significant worsening of the main properties of concrete, but provide undeniable environmental benefits in terms of saving natural resources and reducing CO₂ emissions. Based on the experimental results, the following conclusions can be asserted:

- CRCA have lower density and higher absorption than natural aggregates, but, especially for a replacement up to 25%, all the main physical and mechanical properties of concrete are not negatively affected.
- Recycled concrete aggregates have no influence in workability, whereas MSWI vitrified ash increases slump values.
- Fresh density is not significantly affected by the presence of CRCA or MSWI vitrified ash. More in detail, fresh density is slightly lower when recycled aggregate replacement ratio increases, but in all cases, losses were below 2%.
- Compressive strength is negatively affected by MSWI vitrified ash at 7 days but at 28 days, thanks to its pozzolanic activity, this effect disappears, so obtaining almost the same values as reference. Replacing 25% natural aggregates with CRCA does not worsen the compressive behaviour both at 7 and 28 days, while 50% replacement leads to a reduction equal to 6.49% at 28 days.
- Flexural and fracture energy are not negatively affected by both CRCA or MSWI vitrified ash.

ACKNOWLEDGEMENTS

This research was granted by University of Parma through the action “Bando di Ateneo 2021 per la ricerca” co-funded by MUR-Italian Ministry of Universities and Research - D.M. 737/2021 - PNR - PNRR - NextGenerationEU. Moreover, this study benefitted from the Spanish Ministry of Universities mobility grant (ETS22/00702) awarded in connection with pre-doctoral university professor scholarship FPU19/06704, under which Pablo Plaza Caballero participated in the research at the University of Parma.

Authors gratefully acknowledge Cementirossi SpA and Mapei SpA for providing cement and superplasticizer for concrete preparation.

REFERENCES

- Cembureau 2021. 2021 Activity report.
- Chang, Y. C., Wang, Y.-Y., Zhang, H., Chen, J. & Geng, Y. 2022. Different influence of replacement ratio of recycled aggregate on uniaxial stress-strain relationship for recycled concrete with different concrete strengths. *Structures*, 42, 284–308.

- Colombo, P., Brusatin, G., Bernardo, E. & Scarinci, G. 2003. Inertization and reuse of waste materials by vitrification and fabrication of glass-based products. *Current Opinion in Solid State and Materials Science*, 7, 225–239.
- Duan, Z. H. & Poon, C. S. 2014. Properties of recycled aggregate concrete made with recycled aggregates with different amounts of old adhered mortars. *Materials & Design*, 58, 19–29.
- European Commission 2020. Waste statistics.
- EN 933-11:2009/AC:2009. Tests for geometrical properties of aggregates. Part 11: Classification test for the constituents of coarse recycled aggregate.
- EN 197-1:2011. Cement, Part 1: Composition, specifications and conformity criteria for common cements.
- EN 933-1:2012. Test for geometrical properties of aggregates. Part 1: Determination of particle size distribution. Sieving method.
- EN 12350-2:2020. Testing fresh concrete. Part 2: slump test.
- EN 12350-6:2020. Testing fresh concrete. Part 6: Density.
- EN 12390-3:2020. Testing hardened concrete. Part 3: Compressive strength of test specimens.
- EN 206:2013+A2:2021/IM:2022. Concrete. Specification, performance, production and conformity.
- EN 12390-1:2021. Testing hardened concrete. Part 1: Shape, dimensions and other requirements for specimens and moulds.
- Ferraris, M., Salvo, M., Ventrella, A., Buzzi, L. & Veglia, M. 2009. Use of vitrified MSWI bottom ashes for concrete production. *Waste Management*, 29, 1041–1047.
- Hassan, R. Y., Faroun, G. A. & Mohammed, S. K. 2021. Withdrawn: Mechanical properties of concrete made with coarse and fine recycled aggregates. *Materials Today: Proceedings*.
- JCI-S-001: 2003. Method of test for fracture energy of concrete by use of notched beam.
- Jayasuriya, A., Shibata, E. S., Chen, T. & Adams, M. P. 2021. Development and statistical database analysis of hardened concrete properties made with recycled concrete aggregates. *Resources, Conservation and Recycling*, 164, 105121.
- Kenai, S., Debieb, F. & Azzouz, L. Mechanical properties and durability of concrete made with coarse and fine recycled concrete aggregates. *Challenges of Concrete Construction: Volume 5, Sustainable Concrete Construction: Proceedings of the International Conference held at the University of Dundee, Scotland, UK on 9–11 September 2002, 2002*. Thomas Telford Publishing, 383–392.
- Kisku, N., Joshi, H., Ansari, M., Panda, S. K., Nayak, S. & Dutta, S. C. 2017. A critical review and assessment for usage of recycled aggregate as sustainable construction material. *Construction and Building Materials*, 131, 721–740.
- Monteiro, P. J., Miller, S. A., & Horvath, A. 2017. Towards sustainable concrete. *Nature materials*, 16, 698–699.
- Pedro, D., DE Brito, J. & Evangelista, L. 2017. Structural concrete with simultaneous incorporation of fine and coarse recycled concrete aggregates: Mechanical, durability and long-term properties. *Construction and Building Materials*, 154, 294–309.
- Plaza, P., Sáez Del Bosque, I. F., Frías, M., Sánchez De Rojas, M. I. & Medina, C. 2021. Use of recycled coarse and fine aggregates in structural eco-concretes. Physical and mechanical properties and CO₂ emissions. *Construction and Building Materials*, 285, 122926.
- Saccani, A., Sandrolini, F., Andreola, F., Barbieri, L., Corradi, A. & Lancellotti, I. 2005. Influence of the pozzolanic fraction obtained from vitrified bottom-ashes from MSWI on the properties of cementitious composites. *Materials and structures*, 38, 367–371.
- Scrivener, K. L., John, V. M. & Gartner, E. M. 2018. Eco-efficient cements: Potential economically viable solutions for a low-CO₂ cement-based materials industry. *Cement and Concrete Research*, 114, 2–26.
- Sharifikolouei, E., Canonico, F., Salvo, M., Bairo, F. & Ferraris, M. 2020. Vitrified and nonvitrified municipal solid wastes as ordinary Portland cement (OPC) and sand substitution in mortars. *International Journal of Applied Ceramic Technology*, 17, 573–583.
- Sirico, A., Bernardi, P., Sciancalepore, C., Milanese, D., Ferraris, M. & Belletti, B. 2022. Fracture behavior of concrete containing MSWI vitrified bottom ash. *Procedia Structural Integrity*, 39, 494–502.
- Vinay Kumar, B. M., Ananthan, H. & Balaji, K. V. A. 2018. Experimental studies on utilization of recycled coarse and fine aggregates in high performance concrete mixes. *Alexandria Engineering Journal*, 57, 1749–1759.
- Xiao, J. Z., LI, J. B. & Zhang, C. 2005. Mechanical properties of recycled aggregate concrete under uniaxial loading. *Cement and Concrete Research*, 35, 1187–1194.
- Zhang, H., Xiao, J., Tang, Y., Duan, Z. & Poon, C.-S. 2022. Long-term shrinkage and mechanical properties of fully recycled aggregate concrete: Testing and modelling. *Cement and Concrete Composites*, 130, 104527.

Vitrified beads as aggregate replacement for sustainable cementitious materials

B. Belletti, P. Bernardi, S. Ravasini, A. Sirico, D. Milanese & C. Sciancalepore
Department of Engineering and Architecture, University of Parma, Parma, Italy

M. Malavasi & A. Cortese
ITEA spa, Sofinter Group, Gallarate, Italy

ABSTRACT: This work aims at the experimental investigation of cementitious materials that incorporate recycled waste, in order to boost the transition of the building industry towards a sustainable path and for the development of a circular economy. More in detail, vitrified beads, which represent the by-products obtained by an innovative industrial plant that produces low-cost energy (steam and electricity), are used as partial aggregate replacement in mortars. Vitrified beads are inserted into the mixes in two different forms: “as they are”, i.e. without any pre-treatment, and after grinding, by replacing in both cases 15% of natural aggregates. The performance of the cementitious mortars with vitrified beads is assessed both on fresh and hardened samples, by means of density and consistence measurements, as well as by performing compressive and three-point bending tests. The obtained experimental results show that this by-product could be a promising waste to be recycled into construction cementitious materials.

1 INTRODUCTION

Nowadays, due to global urbanization, the demand for concrete, and in general for cementitious materials, is increasing, with a level of production reaching more than 30 billion tons each year (Monteiro et al. 2017). This results in high environmental impacts, especially in terms of carbon dioxide emissions (CO₂) and consumption of raw materials. For this reason, in the last years, there has been an increased focus on mitigation strategies, including the use of recycled materials as substitutes for non-renewable resources. The aim is to reduce the environmental impact of the concrete industry and decrease the amount of waste to be disposed of in landfills, so promoting a circular economy. Depending on the chemical composition, the recycled waste can be inserted in the formulation of cementitious materials as filler, cement replacement, or aggregate replacement. Limiting the attention to this latter case, different kinds of industrial by-products or waste have been studied during the last decades; among others, plastics (Saikia & De Brito 2012), glass (Shi & Zheng 2007), fly (Shanmugasundaram et al. 2010) and bottom (Kim et al. 2021) ash, granulated blast furnace (Sandanayake et al. 2020) or steel (Anastasiou et al. 2014) slag, biomass (Thomas et al. 2021), construction and demolition waste (Tam et al. 2018).

The use of waste materials for the concrete industry follows the new trends promoted by the European Green Deal related to sustainability and circular economy, as well as the European actions of Green Public Procurement (GPP). At national level, within GPP policy, the Minimum Environmental Criteria (CAM), which represent mandatory environmental requirements for public procurement in Italy, prescribe that at least 5% by weight of dried product, for both cast-in-situ and precast concrete, should be represented by recycled materials. However, finding suitable recycled materials, which do not compromise the performance of concrete and can be considered safe for the human health and the environment, is still often not easy for concrete producers.

Focusing the attention on ash derived from power plants, furnaces or incinerators, different treatments were proposed in the literature to assure its safety, before inserting it as fine aggregate replacement in cementitious materials. Among them, Revasol process (Aubert et al. 2004), stabilization by a cement-lime process (Collivignarelli & Sorlini 2002), sintering process (Mangialardi 2001), or vitrification process (Sharifikolouei et al. 2019, Ferraris et al. 2009) can be cited. This latter represents a thermal treatment allowing obtaining a glassy solid material with a strongly reduced metal content and organic components compared to the original ash, since the toxic products are volatilized or remain trapped in a stable form.

Few works in the literature have investigated the use of the vitrified product as aggregate replacement. Sharifikolouei et al. (2019) found that the replacement of sand up to 20% in mortars can be adopted without compromising excessively the strength. Ferraris et al. (2009) stated that a sand replacement of more than 25% in mortars leads to unsatisfactory results, whereas the replacement of coarse aggregates (4-10 mm and 10-20 mm) up to 50% replacement by volume allows maintaining almost the same compressive strength as reference concrete with only natural aggregates.

Within the context of finding waste materials suitable for the building industry, in this work the use into concrete of an industrial by-product represented by vitrified beads is investigated. The beads were at first chemically analyzed to check their safety, and then used as partial aggregate replacement in mortars, as a first step for analyzing concrete. Vitrified beads, in which incombustible ash are fixed in a glassy structure, represents a kind of waste coming from an industrial plant that produces energy. The aim of the experimental program was to check the feasibility of developing an eco-concrete that incorporates the vitrified beads: i) without any treatment, ii) after grinding, in both cases as replacement of fine aggregates. The influence of the use of vitrified beads on main properties of the developed mortars were explored in the present study in terms of valuation of density, workability, compressive strength, flexural strength, and fracture energy.

2 MATERIALS AND METHODS

2.1 *Vitrified beads*

The vitrified beads used in this experimental campaign are by-products obtained from an innovative industrial plant that produces low-cost energy (steam and electricity) by using low-rank fuels, such as municipal solid waste, industrial waste, heavy oils, flare gas, pet coke, and poor carbon. In more detail, the plant is based on the “ISOTHERM®” technology, and the process can be summarized as follows. The material to be treated, which in the present research was represented by municipal waste, is introduced into the reactor in the form of a slurry suspension, together with technical oxygen (title 88-94%). In the reactor, slightly under pressure and at a uniform temperature between 1300 and 1500°C, the “ISOTHERM®” process takes place, in a completely different way from traditional combustion. No flame forms and the oxidation reactions of the material occur homogeneously throughout the entire reactor chamber, in a predictable and controllable manner, with a production of only CO₂ and water vapor. In the reactor, the incombustible fraction present in the material to be treated is brought to molten state. Then, it is collected and discharged on the bottom of the reactor, by pouring it into a current of water that causes its instantaneous solidification into inert pearls with a glassy structure, i.e. the vitrified beads.

These beads, which fix incombustible fraction in a glassy structure, are totally amorphous, carbon-free, and do not release unburnt pyrolytic compounds or metals, so being perfectly compatible with the production of building materials, without posing risks to the health and safety of people and environment, as demonstrated by the leaching analysis performed according to EN 12457-2:2004 and EN ISO 11885:2009. The results are reported in Table 1. For this reason, the vitrified beads are respective of the “end of waste” regulation for the reuse of by-products. XRF (X-ray fluorescence) was performed on the vitrified beads, highlighting the presence of oxygen (O), silicon (Si), calcium (Ca), aluminium (Al) in quantities greater than 40%, 25%, 10% and 5%, respectively. Moreover, the amount of chlorine (Cl) and sulphur (S), which can be harmful for cementitious composites, is less than 0.05%. The vitrified beads were used without any treatment (Figure 1a), or after grinding (Figure 1b), as partial replacement of fine aggregates in mortars.

Table 1. Analytical results of the leaching test (in mg/l).

Sb	As	Ba	Cd	Cr	Mo	Ni	Pb	Cu	Se	Zn
<0.003	<0.001	0.002	<0.001	0.005	0.003	<0.01	<0.01	0.002	<0.003	<0.01

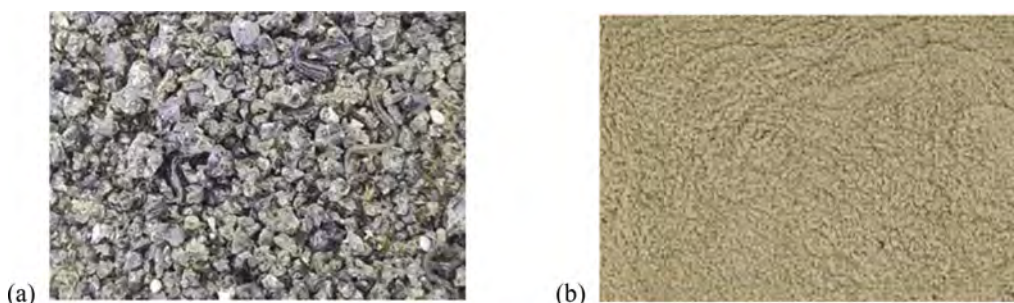


Figure 1. Vitrified beads: a) as obtained from the plant; b) after grinding (roll crushing) process.

2.2 Preparation of specimens

To study of the effect of vitrified beads on concrete, mortar mixes were defined with the aim of reproducing a typical concrete for precast elements, by using the “method of concrete equivalent mortar” (MBE), which was originally developed by the Technical Laboratory of Italcementi France (Schwartzentruber & Catherine 2000) and adapted on purpose for this study, on the basis of previous research (Sirico et al. 2020). MBE was adopted to realize tests on mortars, so saving materials (since the smaller size of specimens), but at the same time performing reliable tests able to approximate the behaviour of concrete. Hence, aggregates with maximum diameter of 6 mm were adopted and their quantity with respect to the other components of the mix was adjusted based on MBE. More in detail, this method implies using the same water/cement ratio and the same sand (or very fine gravel) of the reference concrete, while excluding the amount of gravel.

The grain size distribution of natural aggregates used in this study is reported in Figure 2, while the amount of all the components needed for casting are reported in Table 2. All the mixes were prepared by using cement II A-LL 42.5 R, and with a water/cement ratio of 0.45. Moreover, a superplasticizer, Mapei Dynamon Xtend W202R, was used to reach the desired consistency. It is worth noticing that the amount of aggregates and vitrified beads reported in Table 2, refers to the saturated-surface-dry (SSD) condition for them; hence, the amount of water in Table 2 refers to the effective water of the mix. The absorption of natural aggregates and vitrified beads was equal to 0.80% and 0.35%, whereas density was equal to 2.7 g/cm³ and 2.6 g/cm³, respectively.

Table 2. Mix design (in g).

Mix	Cement	Water	Aggregates	Vitrified beads “as they are”	Vitrified beads “grounded”	Superplasticizer
R	391	176	1315	-	-	3.46
V	391	176	1116	196	-	3.46
GV	391	176	1116	-	196	3.46

Vitrified beads were inserted “as they are” (V mix), so without any pre-treatment, and also after grinding (GV mix), in order to highlight the influence both of the waste material and the pre-treatment with respect to the properties of the reference mix (R). R mix contained 100% natural aggregates, while both V and GV mixes contained 15% of vitrified beads, by computing this percentage of replacement by volume of natural aggregates. Vitrified beads “as they are” or grounded were substituted to the corresponding sieve part of natural aggregates, so to obtain about the same size distribution curve for all the mixes, as can be seen in Figure 2.

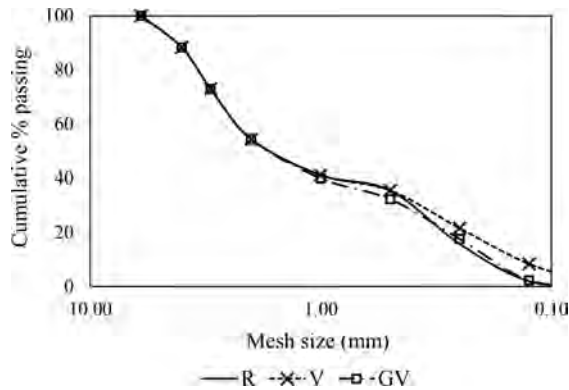


Figure 2. Comparison between the three mixes in terms of grading curves.

All the mixes were cast by using a fully automatic mortar mixer. At first, the bowl was wet, then all the aggregates (natural/vitrified beads) and half of the total water were added and mixed for 120 s at low speed. After 90 s of stop, cement was added and the components were mixed for 60 s at low speed, and then the remaining water and the superplasticizer were added. After 60 s of mixing at high speed, the mixer was stopped for other 90 s, while the edge of the bowl was scraped, and finally, the components were mixed at high speed for 30 s. Then, the admixtures were cast into 40 mm × 40 mm × 160 mm prisms, and compacted by means of a jolting table, by applying 60 jolts per minute for each layer, as described in EN 196-1 (2016). Polythene sheets were put on the molds for the next 24 hours until demolding, and then the specimens were cured in water at 20°C ± 2°C until the day of testing (i.e. 28 days after casting).

2.3 Experimental set-up and methods

Properties at both fresh and hardened state of mortars were analyzed, by means of density and consistence measurements, as well as by performing compressive and three-point bending tests.

Bulk density of fresh mortars was obtained by following EN 1015-6 (2007) standard; whereas consistence was measured as the mean diameter of the test sample, in the two perpendicular directions, placed on a flow table, after shaking the flow table 15 times at a constant rate of about one shot per second, according to EN 1015-3 (2007).

For the measure of flexural strength, each 40 mm × 40 mm × 160 mm prism was subjected to three-point bending, over a net span S of 120 mm. Before testing, a notch a , which was equal to 0.3 times the depth d of the sample, was made at the middle of the specimen by following JCI-S-001 (2003) standard. Three-point bending tests were performed under Crack Mouth Opening Displacement (CMOD) control by using an Instron 8862 machine, by following JCI-S-001 (2003) standard. CMOD was acquired by a clip-gage mounted across the notch, while the load was measured through a load cell with a capacity of 100 kN. Flexural tensile strength $f_{ct,fl}$ was determined as:

$$f_{ct,fl} = 1.5 \frac{P_{max} S}{b(d-a)^2} \quad (1)$$

where b is the width of the cross section and P_{max} represents the peak load of P - CMOD curve.

By performing three-point bending tests, it is also possible to evaluate the fracture energy G_f , since it is related to the ratio between the area W_0 under the load-CMOD curve and the area of the nominal ligament A_{lig} by also taking into account the work done by the deadweight of specimen and loading equipment W_1 . The equation proposed in the JCI-S-001 (2003) standard is adopted herein:

$$G_f = \frac{0.75 W_0 + W_1}{A_{lig}} \quad (2)$$

where $A_{lig} = b(d-a)$.

Compression tests were then performed on the two halves of the broken prisms, previously subjected to three-point bending test (3PBT), by using an Instron 5882 testing machine working under loading control with a loading rate of 2400 N/s, according to EN 196-1 (2016).

3 RESULTS

3.1 Properties on fresh state

As regards bulk density, as expected, no significant differences are recorded for the mixes with vitrified beads (V and GV) compared to the control one (R), as shown in Figure 3a. The density of natural aggregates and vitrified beads presents indeed almost the same values (i.e. 2.7 g/cm³ and 2.6 g/cm³, respectively).

Consistence values, obtained by using the same w/c ratio and superplasticizer (SP) content for all the mixes, are reported in Figure 3b. Since the experimental values for all mixes are between 140 and 200 mm, the mortars can be considered of plastic consistency. By examining Figure 3b, it can be stated that the presence of vitrified ash without pre-treatment (V mix) does not change the consistency of mortar, whereas the use of the grounded material (GV mix) causes a reduction of 19% in the obtained value.

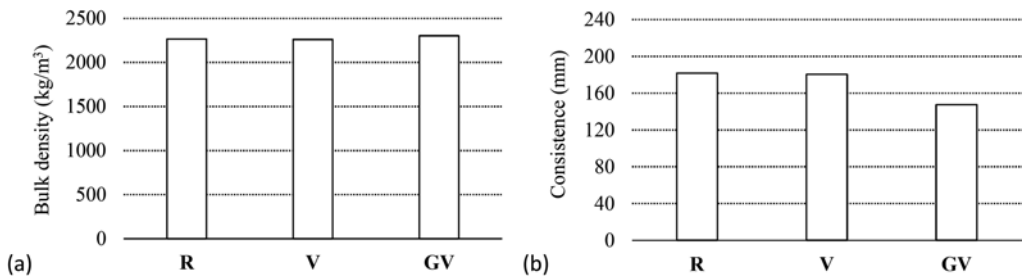


Figure 3. Comparison between the three mixes in terms of: a) bulk density; b) consistency (by flow table).

3.2 28-day mechanical properties

As concern the flexural behaviour, Figure 4 reports the results of three-point bending tests. It can be seen that the replacement of 15% natural aggregates with vitrified beads, grounded or not, does not lead to a significant difference with respect to control, since the same flexural behaviour in terms of stress σ – CMOD, can be recognized for all the admixtures.

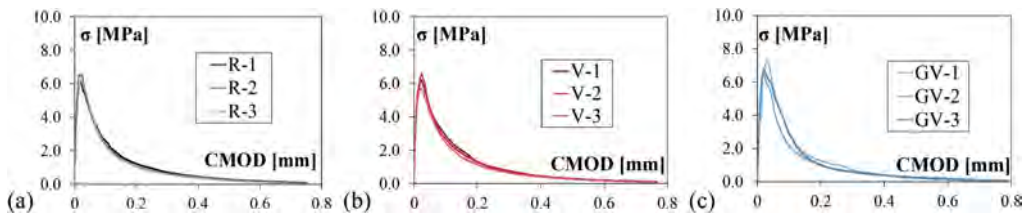


Figure 4. Stress σ – CMOD curves as obtained from three-point bending tests for: a) reference mix (R); b) mix with vitrified beads without pre-treatment (V); c) mix with grounded vitrified beads (GV).

More in detail, the average values in terms of flexural strengths and fracture energy computed on three specimens for each mix, as well as the corresponding standard deviations, are reported in Figure 5. Flexural strengths in Figure 5a are analysed by ANOVA statistical test, by adopting a level of significance of 5%, which implies a 95% probability of the use of vitrified beads being significant. Since $F_{\text{calculated}}$ is less than F_{critical} , the null hypothesis is accepted,

which means that there is no statistically significant effect among the averages of the considered mixes. The same ANOVA analysis is performed also on the results of fracture energy reported in Figure 5b, so confirming that there is no statistically significant variation in fracture energy values when vitrified beads are used as partial aggregate replacement.

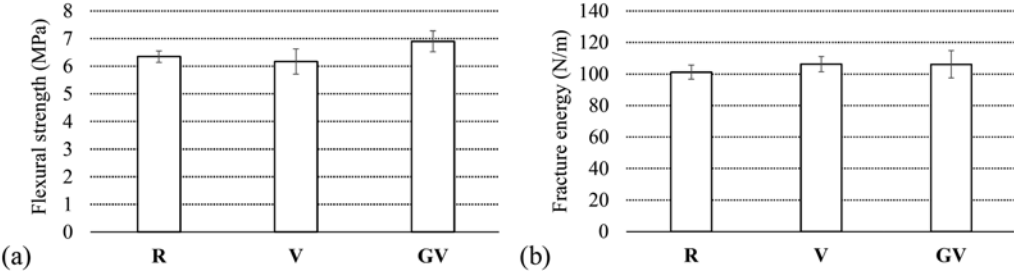


Figure 5. Comparison between the three mixes in terms of average: a) flexural strength, and b) fracture energy, together with the corresponding standard deviations.

Figures 6a and b report the images of one-half of the broken prism for mix V and GV, after three-point bending test. As can be seen, the vitrified beads are well distributed along the whole height of the sample, so confirming at hardened state the high homogeneity of the mixture, which was seen also during mixing, without any segregation or bleeding.

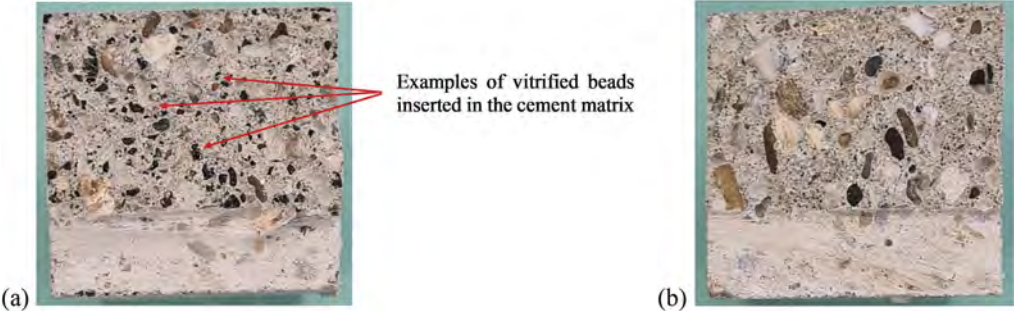


Figure 6. Broken specimens from 3PBT: a) V mix with vitrified beads without any treatment; b) GV mix with grounded vitrified beads.

Each of the two halves of the prisms broken under flexure were then tested under compression. Figure 7 reports the average compressive strength computed on the six resulting specimens for each mix, together with the corresponding standard deviations. As can be seen, the replacement of 15% fine aggregates with the vitrified beads, without pre-treatment or after grinding, does not worsen the compressive behaviour. The ANOVA analysis confirms indeed that there is no significant variation between the experimental values of the three mixes.

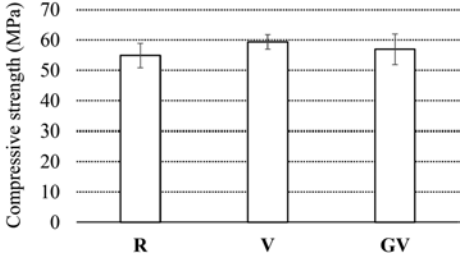


Figure 7. Comparison between the three mixes in terms of average compressive strength together with the corresponding standard deviations.

4 CONCLUSIONS

In this work, the mechanical behavior of mortars that incorporated vitrified beads was experimentally investigated, so to assess if the use of this by-product coming from an innovative industrial plant that produces low-cost energy, could be promising for the development of eco-friendly and sustainable cementitious materials.

The vitrified beads were included in the mixes both “as they are” and grounded. The substitution of 15% aggregates by volume with vitrified beads without pre-treatment enables reducing the environmental impact of mortars (by saving natural resources), without diminishing their physical and mechanical performance. 28-day compression strength resulted slightly enhanced, while the observed flexural behavior was almost the same then that of the reference mortar. Similarly, the use of grounded vitrified beads leads to the same mechanical properties as reference, but a significant reduction of flowability was observed. Since in this case also an additional energy consumption is needed for grinding, it can be argued that the more favorable option for the use of these vitrified beads into concrete is without any pre-treatment.

So, based on the experimental results, it can be concluded that this vitrified material without pre-treatment seems an excellent substitute for fine aggregates, since its use allowed maintaining unaltered all the analyzed properties of the mortars: density, consistence, compressive and flexural behavior. Given the promising results obtained from this first experimentation, the use of this by-product into concrete could be further explored, also by considering increasing percentages of aggregate substitution. Moreover, in order to better clarify the actual environmental benefits related to the recycling of this material, the study should be completed by a Life Cycle Assessment analysis able to quantify the overall sustainability of this eco-concrete.

REFERENCES

- Anastasiou, E., Georgiadis Filikas, K. & Stefanidou, M. 2014. Utilization of fine recycled aggregates in concrete with fly ash and steel slag. *Construction and Building Materials* 50: 154–161.
- Aubert, J.E., Husson, B. & Vaquier, A. 2004. Use of municipal solid waste incineration fly ash in concrete. *Cement and Concrete Research* 34(6): 957–963.
- Collivignarelli, C. & Sorlini, S. 2002. Reuse of municipal solid wastes incineration fly ashes in concrete mixtures. *Waste Management* 22(8): 909–912.
- EN 1015-3:2007. Methods of test for mortar for masonry. Part 3: determination of consistency of fresh mortar (by flow table).
- EN 1015-6:2007. Methods of test for mortar for masonry. Determination of bulk density of fresh mortar.
- EN ISO 11885:2009. Water quality - Determination of selected elements by inductively coupled plasma optical emission spectrometry (ICP-OES).
- EN 12457-2:2004. Characterisation of waste - Leaching - Compliance test for leaching of granular waste materials and sludges - Part 2: One stage batch test at a liquid to solid ratio of 10 l/kg for materials with particle size below 4 mm (without or with size reduction).
- EN 196-1:2016. Methods of testing cement - Part 1: Determination of strength.
- Ferraris, M., Salvo, M., Ventrella, A., Buzzi, L. & Veglia, M. 2009. Use of vitrified MSWI bottom ashes for concrete production. *Waste Management* 29(3): 1041–1047.
- JCI-S-001-2003. Method of test for fracture energy of concrete by use of notched beam.
- Kim, Y.H., Kim, H.Y., Yang, K.H. & Ha, J.S. 2021. Effect of concrete unit weight on the mechanical properties of bottom ash aggregate concrete. *Construction and Building Materials* 273: 121998.
- Mangialardi, T. 2001. Sintering of MSW fly ash for reuse as a concrete aggregate. *Journal of Hazardous Materials* 87(1–3): 225–239.
- Monteiro, P.J.M., Miller, S.A. & Horvath, A. 2017. Towards sustainable concrete. *Nature Materials* 16 (7): 698–699.
- Saikia, N. & De Brito, J. 2012. Use of plastic waste as aggregate in cement mortar and concrete preparation: A review. *Construction and Building Materials* 34: 385–401.
- Sandanayake, M., Bouras, Y., Haigh, R. & Vrcelj, Z. 2020. Current sustainable trends of using waste materials in concrete—a decade review. *Sustainability* (Switzerland) 12(22): 1–38.
- Schwartzentruber, A. & Catherine, C. 2000. La méthode du mortier de béton équivalent (MBE)—Un nouvel outil d'aide à la formulation des bétons adjutants. *Materials and structures* 33(8):475–482.

- Shanmugasundaram, S., Jayanthi, S., Sundararajan, R., Umarani, C. & Jagadeesan, K. 2010. Study on utilization of fly ash aggregates in concrete. *Modern Applied Science* 4(5): 44–57.
- Sharifikolouei, E., Canonico, F., Salvo, M., Bairo, F. & Ferraris, M. 2019. Vitrified and nonvitrified municipal solid wastes as ordinary Portland cement (OPC) and sand substitution in mortars. *International Journal of Applied Ceramic Technology* 17 (2): 573–583.
- Shi, C. & Zheng, K. 2007. A review on the use of waste glasses in the production of cement and concrete. *Resources, Conservation and Recycling* 52(2): 234–247.
- Sirico, A., Bernardi, P., Belletti, B., Malcevschi, A., Delcanale, E., Domenichelli, I., Fornoni, P., & Moretti, E. 2020. Mechanical characterization of cement-based materials containing biochar from gasification. *Construction and Building Materials* 246: 118490.
- Tam, V.W.Y., Soomro, M. & Evangelista, A.C.J. 2018. A review of recycled aggregate in concrete applications (2000–2017). *Construction and Building Materials* 172: 272–292.
- Thomas, B.S., Yang, J., Mo, K.H., Abdalla, J.A., Hawileh, R.A. & Ariyachandra, E. 2021. Biomass ashes from agricultural wastes as supplementary cementitious materials or aggregate replacement in cement/geopolymer concrete: A comprehensive review. *Journal of Building Engineering* 40: 102332.

Mechanical strength and environmental sustainability of EAF concrete

F. Faleschini, D. Trento, M.A. Zanini & C. Pellegrino
University of Padova, Padova, Italy

V. Ortega-López
University of Burgos, Burgos, Spain

A. Santamaria
University of Basque Country, Leioa, Biscay, Spain

ABSTRACT: The use of recycled materials in concrete members has gained a significant attraction in the last years. In this context, the possibility of including metallurgical slags in concrete has been explored by several research works, among them it is worth citing the ones carried out in the last 15 years by the research groups of the University of Padova, University of Burgos and University of Basque Country. In this contribution, a review of the main features of Electric Arc Furnace slag (EAF) concrete is made, focusing on the improvements observed in the properties of this concrete compared to the reference realized with natural aggregates only. Furthermore, two examples of real-scale applications in reinforced concrete (RC) structures are shown. Lastly, a life cycle analysis (LCA) has been applied to one of the above-mentioned cases, demonstrating the gains in terms of reduced environmental impacts that can be achieved using this material.

1 INTRODUCTION

During the last years, many efforts have been made to develop sustainable concretes containing recycled materials, thanks to the policies related to the sustainable development goals (SDGs) asked by United Nations. The possibility of using industrial waste as aggregate in concrete has been widely studied. Some research groups primarily studied Basic Oxygen Furnace (BOF) slags and Blast Furnace (BF) slags (Douglas et al. 1997, Jelidi & Bouslama 2015, Reddy et al. 2006). In Italy and Spain, however, the production of steel occurs mainly in Electric Arc Furnaces (EAF), and thus EAF slag is much more abundant than the others. Particularly, EAF slag is formed during the refining process of the molten steel bath, thanks to the addition of some materials such as limestone, lime and fluorspar. Nowadays, about 40% of global steel production is carried out properly in EAF plants, and every year, more than 10 million tons of this slag are produced all over Europe, with some peaks in North-Eastern Italy and in Northern Spain. Recall indeed that from one ton of steel produced in an EAF, approximately 100–150 kg of electric arc furnace slag is obtained.

For this reason, a consistent literature was provided by authors from these two regions, to find suitable recycling potentials for this material. Among the others, the contributions from University of Padova in Italy and University of Burgos and Basque Country in Spain are worth mentioning, both for their consistency and abundance of experimental data.

In the past, the partial and total substitution of natural aggregates with EAF slags was investigated by the authors. Since aggregates represent about 70% of total concrete volume, they significantly affect the properties of the fresh and hardened conglomerate. As an indicative data, the permanent growing of raw material consumption is principally due to building industry according to OECD (OECD 2018). At the end of 2021, US construction aggregate

producers closed the year with shipments totaling 1.54 billion tons of crushed rock and 1 billion tons of sand and gravel (Concrete News 2022). According to the principle of circular economy, the possibility to employ EAF slags in concrete allows to reduce raw material consumption and the amount of slag to be disposed of.

Several research works have been developed to test both mechanical properties and durability of concrete containing EAF slag. In most cases, EAF concrete shows similar, and even superior, mechanical properties than Natural Aggregate Concrete (NAC). Promising results were obtained about the adoption of this concrete for structural applications, as observed testing different real-scale elements, such as RC beams under flexure-shear (Faleschini & Pellegrino 2013), RC beam-columns joints under cyclic reversed lateral loading with flexural-shear failure (Faleschini et al. 2017a,b). Some recent results highlighted that, both under gravity loads (Zanini 2019) and seismic solicitation (Faleschini et al. 2019), the use of EAF concrete allows attaining the same, or even higher structural reliability than NAC. Additionally, even in the production of self-compacting concrete (Santamaria et al. 2020) and high-strength concrete (Faleschini et al. 2015), EAF slag seems to be employable in substitution of natural aggregates.

To better understand which are the main features that characterize EAF concrete, a first review of the main outcomes from more than 15 years of past research studies are shown here. Then, two examples of real-scale applications of EAF concrete in reinforced concrete (RC) structures are presented. Lastly, the environmental performance of this kind of concrete is discussed, through the application of a life cycle analysis (LCA) to one of the above-mentioned cases.

2 EAF SLAG PROPERTIES

The properties of EAF slag, and in turns, those of EAF concrete, depend on multiple variables that can be summarized as: the type of furnace, the type of steel to be produced, the type of additions, the operating conditions of the furnace, the management operations carried out during and after the slag cooling. Focusing on the EAF-C type only, i.e., the slag produced from carbon steel production, and on the most common type of cooling processes (based on slow air-cooling) and slag treatments (weathering and crushing, sieving, magnetic separation), it can be said that typically this material is reused as an aggregate for bituminous and hydraulically bound mixtures (Kumar & Varma 2021) or for cement-based materials (Lee et al. 2019). This slag type appears as a dark grey/black rock (Figure 1), sometimes with some white spots (associated to the presence of limited quantity of free CaO, when the slag is not properly weathered), and it has a crystalline nature.



Figure 1. EAF slag particles (coarse fraction).

The above-mentioned variables may influence significantly the physical, chemical and micro-structural properties of the slag: in fact, non-negligible differences may be found when comparing slags obtained from different facilities. For instance, Santamaria et al. (2017) compared two slag

types, one coming from Zerocento Srl, a company located in Italy, and from Hormor-Zestoa in Spain, demonstrating that the two slags have different compositions (e.g. the iron oxides content varied more than 10%). Different phases were observed through the X-Ray Diffraction (in the former case, the most abundant phases were wustite, larnite, ghelenite and magnetite, whereas in the latter wustite, ghelenite and kristenite), and also the physical properties differed. Particularly, the Spanish slag was characterized by a higher porosity and lower density compared to the Italian one, with a difference, for this last property, of more than 10%. Additionally, the treatment operations may affect significantly the expansion potential of a slag: dimensional stability is a feature of paramount importance for a safe use in concrete materials, and it should be limited below 0.5% according to some recent indications (Santamaria et al. 2018). The same authors highlighted how the pretreatment operations, and specifically cooling and weathering type and duration, have a significant impact to reduce slag swelling potential.

A dataset collected by some of the authors (Pellegrino & Faleschini 2016), continuously updated during time, allows to provide the range of variations of some main features of the EAF-C slag type, that can be summarized as shown in Table 1. Data refer to average values from aggregates having both fine (0-4 mm) and coarse (> 4 mm) particle size.

Table 1. Range of variations of the physical properties of EAF slag from carbon steel production.

Property	Unit	Average Value
Density	kg/m ³	2840 – 4020
Bulk density	kg/m ³	1480 – 1900
Water absorption	%	0.1 – 10.0
Volumetric expansion	%	0.1 – 3.5
Pore dimensions	mm	0.2 – 8000
Porosity	%	2 – 42
Los Angeles Loss	%	10 – 35
Crushing Value	%	10 – 22
Shape Index	%	1 – 10
Flakiness Index	%	1 - 10

3 EAF SLAG CONCRETE PROPERTIES

EAF slag has been used to cast both concretes with normal strength (NSC) and ordinary features, but, as already mentioned, also high strength concrete (HSC) and self-compacting mixes (SCC) could be achieved using this material as an alternative aggregate. Here the effects of aggregates partial or total substitution on NSC are discussed only for sake of brevity, recalling that the introduction of the EAF slag in a mix affects the properties both in the fresh and hardened states.

EAF concrete is generally characterized by a worse workability than NAC, and the decrease of this property is proportional to the amount of the substitution. In general, the highest deterioration of the slump value is observed when also the fine fraction of the aggregates is substituted. The reasons of this low performance at the fresh state depend on the particles shape, which is typically very angular due to the crushing process (Pellegrino et al. 2013), and this has an impact on both the viscosity and yielding stress characterizing the flow of a viscoplastic fluid. Further, some slags are characterized also by high water absorption, thus altering the water demand of the mix. However, the adoption of water reducing admixtures (fluidifying, plasticizers, air entrainers) is able to limit this effect and to allow to cast EAF concrete mixes with comparable fluidity of NAC.

In terms of density, EAF concretes exhibit higher values of this property, but the increase depends significantly on the slag density itself, and on the slag replacement ratio. As discussed in Section 2, depending on the slag type, this property may vary a lot. EAF concretes density may vary between 2500 and 3100 kg/m³, and even more. However, in general terms, an EAF concrete can be seen as a high-density concrete, and thanks to this feature, several works attempted to investigate its ability to shield the radiations, obtaining successful results (Papachristoforou & Papayianni

2018, Pomaro et al. 2019). Accordingly, EAF concrete can be used as a sustainable alternative to concretes made with barite, limonite, hematite, etc.

Concerning the mechanical strength, the main parameters that are investigated in literature are compressive, tensile and flexural strength, other than the strength gain in time. All the three main strength properties are generally positively influenced by the addition of the slag, especially when it is used in the coarse fraction. The beneficial effect associated to the EAF slag use is linked to several co-causes, among which is worth mentioning the high strength of the slag itself (recall that the composition is made by iron oxides in large amount), the good bond with the cementitious matrix thanks to the slag shape, and lastly, a good interfacial transition zone (ITZ) quality (Arribas et al. 2015). The strength enhancement depends also on the slag type: in fact, when porous slags are used, this beneficial effect is less visible. However, in average, Faleschini et al. (2019) estimated that the average increase is about 35-40% on the compressive strength value. Concerning the latter feature, i.e., the strength development in time, this is not influenced by the slag use in the concrete mix.

The elastic modulus of EAF concrete is also affected, but also in this case two main cases may be observed, depending on the slag porosity: when low-porosity slags are adopted, the elastic modulus increases even by 30% compared to that of NAC; instead, for porous slags, such increase is much more limited, and, in some cases, even less stiff concretes may be obtained compared to their natural counterparts.

In terms of durability-related properties, the number of available experimental evidences decrease significantly in literature, which however are sufficient to depict a trend of the expected behavior of this kind of concrete in the longtime. In fact, similarly to what already observed for the mechanical strength and elastic properties, properties such as water absorption, chlorides penetration, freezing/thawing and wetting/drying resistance are all affected depending on the slag features, and particularly, on its porosity. Better behavior is displayed by those concretes made with non-porous EAF slag, with improvements in the above properties until 10-20%, whereas when porous slags are used, generally no enhancement (but either, no deterioration) is obtained. A special mention has to be done about two properties: carbonation and high temperature resistance. For the former property, non-conclusive results are available in literature: some authors reported a better behavior of EAF mixes (Andrade et al. 2021, Sosa et al. 2022), some others an increase of the carbonation depth that could reach six times higher than that observed in NAC (González-Ortega et al. 2019). The latter property is instead investigated in Beaucour et al. (2020): EAF concrete is more stable with regard to linear expansion and contraction, it does not display appreciable signs of aggregates spalling even when the heating rate is more critical, and its strength loss at high temperatures (until 600°C) is more limited than in NAC.

Table 2 provides a brief summary of the effects of EAF slag introduction in concrete, in qualitative terms when no quantitative average indications can be provided. Recall that these data refer to average values considering both the most and least porous slags that may be found in the market.

Table 2. Average variations of EAF concrete properties compared to those of NAC.

Property	Unit	Average Variation (%)	Average Effect
Workability	mm	-	Slightly decrease
Density	kg/m ³	+ 15% (up to + 30%)	Increase
Compressive strength	MPa	+ 20% (up to + 30%)	Increase
Tensile strength	MPa	+ 15% (up to + 30%)	Increase
Flexural strength	MPa	+ 15% (up to + 30%)	Increase
Strength gain in time	MPa	-	Not affected
Secant Elastic Modulus	GPa	+ 15% (up to + 40%)	Increase
Water absorption	%	-	Decrease
Carbonation depth	mm	-	Increase or decrease
Chlorides penetration	mm	-	Decrease
Freezing/thawing resistance	-	-	Slightly increase
Wetting/drying resistance	-	-	Slightly increase
High temperature resistance	-	-	Increase

4 EAF SLAG CONCRETE: APPLICATIONS IN REAL SCALE STRUCTURES

Here, two applications in real structures of EAF slag concretes are shown, one from the Spanish and one from the Italian context. The first case-study deals with the construction of the Kubik building, owned by Tecnia, and located in Zamudio, in the Basque Country (Figure 2). The building, with an overall surface of 500 m² distributed in an underground floor, a ground floor and up to two story, was inaugurated in 2010 and currently it is in its full operation. The main walls and the foundations of this building were casted with two different concrete mixes including large amounts of EAF slag (Chica et al. 2011). For instance, to cast the foundation slabs, about 150 m³ of EAF concrete were used: the mix was based on a limestone cement with rapid strength development, a relatively low w/c ratio, whereas the 80% of the coarse aggregates and 100% of the fine ones were made by EAF particles. The overall recycled constituents of this mix reached about 76% on the total compounds. The average compressive strength of the concrete at 28 days of curing was 47 MPa and 53 MPa for the walls and the foundation slabs, respectively.



Figure 2. Kubik building from Tecnia (courtesy of Prof. Manuel Manso, University of Burgos).

The second case-study deals with the rehabilitation works of a military infrastructure (owned by the North Atlantic Treaty Organization - NATO) located in Vicenza, Italy, where Heidelberg Cement Groups casted about 11455 m³ of EAF concrete for varying structures. The works were carried out in 2009. Among them, they produced concretes characterized by different strength classes, varying from $f_c = 10$ to 32 MPa, which were employed both in non-structural elements and for the foundation elements, including the slabs and piles. The mix design, in this case, includes a slag cement with rapid strength development, and the overall content of EAF slag was about 10% on the overall constituents of the mixes (Zecchini 2019).

5 ENVIRONMENTAL FOOTPRINT OF EAF CONCRETE

The most common tool to assess the environmental impacts associated to a product is the Life Cycle Assessment (LCA), which is a methodology for quantifying environmental impacts and burdens associated with an item over its entire life (ISO 14040, 2006). LCA is often applied even in the field of construction materials and more generally, in civil engineering (Knoeri et al. 2013, Faleschini et al. 2014), to quantify and compare different scenarios related to the adoption of one material (i.e., the natural) or another (i.e., in the present case, the EAF slag concrete). Depending on the system boundaries, the analysis is carried with a cradle-to-gate or cradle-to-cradle approach: in the former case, the analysis simply stops when the material is released in the market, whereas in the latter it integrates all the life phases of the structure, i.e., material manufacture,

construction, maintenance and operation, and lastly the end of life, with its alternative solutions being dismantling and landfilling or materials recovery and recycling.

Here, LCA is carried out with reference to the first case-study, i.e., the casting of the RC slab of the Kubik building, comparing the current scenario to that of having adopted natural aggregates only. LCA is made by four mandatory phases: (i) the goal and scope definition; (ii) the inventory analysis (LCI); (iii) the impact assessment (LCIA); and finally (iv) the interpretation. The simplified procedure followed here assumes that first only the aggregates' impacts are analyzed; once the aggregate emissions estimation has been performed, the assessment of the environmental impacts of the experimental concrete mixes of NAC and EAF concrete is carried out. This means that in this case, only the impacts related to production of the materials are considered, thus neglecting both transportation and manufacturing of concrete, which are assumed to be similar both in case of NAC and EAF concrete.

Concerning the first step, the aim of the study is to define the environmental emissions of the products "1 slab made with NAC" and "1 slab made with EAF concrete", and compare the main results together. For this scope, it is necessary to define the system boundaries related to the aggregates production, with a cradle-to-gate approach, where the major processes included are the extraction of raw materials, manufacturing and transportation. Concerning the EAF slag, particularly, the "zero burden assumption" (Ekvall et al. 2007) is adopted, meaning that the slag does not carry any of the steel production upstream burdens into the waste-management system. This choice is due to the fact that still in most cases the slag is not considered as a product, but for a steel-plant, it is considered a waste only. The choice is also supported by the enormous difference in the final price to the market of 1 ton of steel and 1 ton of slag (economic principle).

All the supporting data are taken from Faleschini et al. (2014), where an exhaustive analysis was already carried out using inventory data collected from real plants of natural aggregates extraction and slag management. Particularly, in that work, the Life Cycle Inventory (LCI) phase was carried out to collect the data for each unit process, quantifying all relevant input and output elements of the products systems, both for NA and EAF slag. Cement impacts are still taken from the same publication, whereas the impacts related to the admixtures are not considered due to the small amount of them in the mixes. The impacts related to the steel reinforcement are instead neglected, assuming that the same reinforcement details are used both for the project with EAF concrete and NAC, given the same strength class of the two mixes.

The impact assessment is carried out following a problem-oriented methodology, thus allowing to calculate the environmental impacts associated with climate change, eutrophication, acidification, human toxicity, eco-toxicity, etc. In order to evaluate the environmental burdens for the systems of NA and EAF slag, the evaluation procedure is performed in all the production phases, and it is based on the basic categories of CML 2002 Method (Guinée et al. 2002). A limited set of mid-point indicators will be shown here for sake of brevity, which are Global Warming Potential (kg CO₂ eq.), Acidification (kg SO₂ eq.) and Eutrophication (kg PO₄ eq.).

The interpretation phase follows with a comparison of the two identified scenarios, i.e., the production of 1 slab made with 150 m³ of NAC and 1 slab made with 150 m³ of EAF concrete. Particularly, two mix designs are considered, that correspond both to the same strength class with $f_{ck} = 30$ MPa. The two mixes are shown in Table 3, whereas the calculated impacts are shown in Table 4 for each of the analyzed impact categories.

Table 3. Mix details (in kg/m³).

Compound	NAC	EAF concrete
Cement II-B-M(V-L-S) 42.5R	400	385
Natural sand	723	-
Natural Coarse Aggregate	1085	271
EAF Slag Sand	-	958
EAF slag Coarse Aggregate	-	1091
Water	172	173
Admixtures (%)	0.6	1.2

Table 4. Total environmental emissions for the analyzed categories, for 1 slab of RC with 150 m³.

Compound	NAC	EAF concrete	Saved Emissions
Climate change (kg CO ₂ eq.)	23597	21795	- 8%
Acidification (kg SO ₂ eq.)	78.8	71.2	- 10%
Eutrophication (kg PO ₄ eq.)	8.2	7.8	- 5.3%

6 CONCLUSIONS

The following conclusions can be drawn from this study:

- EAF slag is a very hard, black, stony-like recycled material coming from steelmaking industry as by-product; its properties depend on multiple variables, but generally it is characterized by lower porosity and higher density compared to NA.
- The concrete containing EAF slag shows similar mechanical properties, or even better, compared to traditional counterparts in terms of compressive, tensile and flexural strength. In terms of durability, the properties are typically enhanced, too.
- Real-structures applications confirmed that EAF concrete can be suitably used without compromising the serviceability, functionality and the behavior at the ultimate state.
- Casting a RC element with EAF concrete, instead with NAC with the same strength class, allows to reduce the environmental emissions in terms of CO₂, SO₂ and PO₄.

REFERENCES

- Andrade, H.D. et al. 2021. Mechanical performance and resistance to carbonation of steel slag reinforced concrete. *Construction and Building Materials* 298: 123910.
- Arribas, I. et al. 2015. Electric arc furnace slag and its use in hydraulic concrete. *Construction and Building Materials* 90: 68–79.
- Beaucour, A. L. et al. 2020. Influence of elevated temperature on properties of radiation shielding concrete with electric arc furnace slag as coarse aggregate. *Construction and Building Materials* 256: 119385.
- Chica, J. A. et al. 2011. KUBIK: Open building approach for the construction of an unique experimental facility aimed to improve energy efficiency in buildings. *Open house international* 36(1): 63–72.
- Concrete News 2022. Concrete Products. [Online] Available at: <https://concreteproducts.com/index.php/2022/04/12/construction-aggregates-shipments-near-30-billion-watermark/> [Accessed 16 April 2022].
- Douglas, E. et al. 1997. Alkali activated ground granulated blast-furnace slag concrete. Preliminary investigation. *Cement and Concrete Research* 21(1): 101–108.
- Ekvall, T. et al. 2007. What life-cycle assessment does not do in assessment of waste management. *Waste Management* 101: 113–121.
- Faleschini, F. & Pellegrino, C. 2013. Experimental Behaviour of Reinforced Concrete Beams with Electric Arc Furnace Slag as Recycled Aggregate. *ACI Materials Journal* 110(2): 197–205.
- Faleschini, F. et al. 2014. Recycled concrete containing EAF slag: environmental assessment through LCA. *European Journal of Environmental and Civil Engineering* 18(9): 1009–1024.
- Faleschini, F. et al. 2015. High performance concrete with electric arc furnace slag as aggregate: Mechanical and durability properties. *Construction and Building Materials* 101: 113–121.
- Faleschini, F. et al., 2017a. Experimental behaviour of beam-column joints made with EAF concrete under cycling loading. *Engineering Structures* 139: 81–95.
- Faleschini, F. et al. 2017b. Experimental and numerical investigation on the cyclic behaviour of RC beam column joints with EAF slag concrete. *Engineering Structures* 152: 335–347.
- Faleschini, F. et al. 2019. Seismic reliability assessment of code-conforming reinforced concrete buildings made with electric arc furnace slag aggregates. *Engineering Structures* 195: 324–339.
- González-Ortega, M.A. et al. 2019. Durability of concrete with electric arc furnace slag aggregate. *Engineering Structures* 195: 324–339.
- Guinée, J.B. & Lindeijer, E. 2002. *Handbook on life cycle assessment: operational guide to the ISO standards* (7). Cham, Switserland:Springer.

- ISO 14040. 2006. Environmental management — Life cycle assessment — Principles and framework.
- Jelidi, A. & Bouslama, S. 2015. Use effects of blast furnace slag aggregates in hydraulic concrete. *Materials and Structures* 48(11): 3627–3633.
- Knoeri, C. et al. 2013. Comparative LCA of recycled and conventional concrete for structural applications. *The international journal of life cycle assessment* 18(5): 909–918.
- Kumar, H. & Varma, S. 2021. A review on utilization of steel slag in hot mix asphalt. *International Journal of Pavement Research and Technology* 14: 232–242.
- Lee, J.Y. et al. 2019. Comparing properties of concrete containing electric arc furnace slag and granulated blast furnace slag. *Materials* 12(9): 1371.
- Manso, J. M. et al. 2004. Electric arc furnace slag in concrete. *Journal of Materials in Civil Engineering* 16(6): 639–645.
- Monosi, S. et al. 2016. Electric arc furnace slag as natural aggregate replacement in concrete production. *Cement and Concrete Composites* 66: 66–72.
- OECD 2018. *Global Material Resources Outlook to 2060 - Economic drivers and environmental consequences*. Paris: OECD Publishing.
- Papachristoforou, M. & Papayanni, I. 2018. Radiation shielding and mechanical properties of steel fiber reinforced concrete (SFRC) produced with EAF slag aggregates. *Radiation Physics and Chemistry* 149: 26–32.
- Pellegrino, C. et al. 2013. Properties of concretes with black/oxidizing electric arc furnace slag aggregate. *Cement and Concrete Composites* 37: 232–240.
- Pellegrino, C. & Faleschini, F. 2016. *Sustainability Improvements in the Concrete Industry: Use of Recycled Materials for Structural Concrete Production*. Cham, Switzerland: Springer.
- Pomaro, B. et al. 2019. Gamma-ray shielding properties of heavyweight concrete with Electric Arc Furnace slag as aggregate: an experimental and numerical study. *Construction and Building Materials* 200: 188–197.
- Reddy, A. et al. 2006. Utilization of basic oxygen furnace (BOF) slag in the production of a hydraulic cement binder. *International Journal of Mineral Processing* 79(2): 98–105.
- Santamaria, A. 2017. A comparison between European electric arc furnace slags. *Proc. intern. symp., Metz, 11-13 October 2017*. Metz, France.
- Santamaria, A. et al. 2018. Dimensional stability of electric arc furnace slag in civil engineering applications. *Journal of Cleaner Production* 205(20): 599–609.
- Santamaria, A. et al. 2020. The study of properties and behavior of self compacting concrete containing Electric Arc Furnace Slag (EAFS) as aggregate. *Ain Shams Engineering Journal* 11:231–243.
- Sosa, I. et al. 2022. Durability of high-performance self-compacted concrete using electric arc furnace slag aggregate and cupola slag powder. *Cement and Concrete Composites* 127: 104399.
- Zanini, M. A. 2019. Structural reliability of bridges realized with reinforced concretes containing electric arc furnace slag aggregates. *Engineering Structures* 188: 305–319.
- Zecchini, A. 2019. Materiali per l'Edilizia e le Infrastrutture Sostenibili: Gli Aggregati Riciclati. L'Esperienza Italcementi e Calcestruzzi nella valorizzazione dei materiali derivanti da altri processi. *HeidelbergCement presentation, 26 February 2019*.

Sustainable design of lightened reinforced concrete flat slabs in coastal environment

A.J. Sánchez-Garrido, I.J. Navarro & V. Yepes
Universitat Politècnica de València, Valencia, Spain

ABSTRACT: The construction industry has a significant impact on the environment, particularly in the residential building sector, due to high resource consumption. To reduce environmental impact in the construction, service, and end-of-life phases of buildings, scholars prioritize adopting Modern Methods of Construction (MMC) to optimize material consumption and minimize the life cycle impact of buildings. This study assesses the sustainability of reinforced concrete flat slabs using a hollow structural body system, especially in environments that trigger concrete corrosion. The analysis focuses on seven design alternatives for a beachfront hotel structure, using the VIKOR technique to aggregate five sustainability criteria. The most cost-effective and environmentally beneficial option is using 10% silica fume concrete, which reduces life-cycle costs by 87% and impacts the base design by 67%. However, considering economic and environmental sustainability criteria led to better sustainable designs, such as a more extensive concrete cover for bottom reinforcing bars resulting in a 46% better sustainability index.

1 INTRODUCTION

Around half of the non-renewable resources consumed by humanity come from the construction industry, making it one of the less sustainable sectors in the world (Yepes & Lopez, 2021). If this trend continues, energy efficiency and the transition to renewable energy will no longer be enough. Against this alarming backdrop, the newly established European Green Deal aims to overcome the challenges posed by climate change by, among other objectives, the firm intention of achieving no net greenhouse gas emissions by 2050. The fact that one-third of the investments from the NextGenerationEU Recovery Plan are intended to finance the European Green Deal shows the commitment of the European Commission to achieve climate neutrality. This is only one of the many initiatives slowly trying to materialize the Sustainable Development Goals established in 2015.

In this context, the search for sustainable buildings and other infrastructures arises as a critical requirement to achieve the abovementioned carbon-neutral horizon we aspire to (Lei et al., 2021; Chan et al., 2022). Recently, research has been conducted on the sustainability assessment of several infrastructures (Navarro et al., 2020), building structures (Sánchez-Garrido et al., 2022b) or constructive elements (Pons et al., 2018; Balasbaneh & Marsono, 2020). A conclusion that is recurrently reached in recent research is that the impacts related to the maintenance of buildings and other types of structures play an essential role in the life cycle-related sustainability performance of the designs. Consequently, more and more studies focus on optimizing maintenance activities (Frangopol et al. (2017); García-Segura et al., 2017) or analyzing different material alternatives to increase the durability of conventional designs (Biondini & Frangopol, 2017; Navarro et al., 2018), trying

to reach conclusions on the best practices to achieve sustainable structures and buildings along their service lives.

Such impacts are particularly relevant in aggressive environments, where the maintenance demands can be significant. Such is the case for coastal regions, where concrete structures are affected by chlorides (Petcherdchoo, 2015). Consequently, studies on the performance of different design alternatives in such scenarios are essential to achieve both durable and sustainable solutions.

The present communication aims to evaluate the life cycle impacts of seven improved design alternatives on a particular type of MMC, namely “Unidome” slabs. MMCs are postulated as economically preferable alternatives to conventional construction methods and a powerful way to reduce life cycle environmental impacts by optimizing material consumption. These alternatives are intended to increase the durability of the base design, thereby reducing maintenance requirements over the life cycle of use and maintenance of the structural solution. Several economic and environmental criteria are considered to evaluate each design’s sustainability.

2 MATERIALS AND METHODS

2.1 *Goal and scope definition*

This work aims to analyze the sustainable performance of different alternatives based on the reference design for the structure of a hotel building located on the coast of Chiclana, Cadiz (Spain). The reference design (hereafter REF) comprises a module of rooms between expansion joints that, with three floors and repeated longitudinally, represents more than 80% of the built area of the hotel. Structurally, the module consists of a mat foundation and three slab levels (Figure 1), designed with an innovative MMC. The system consists of reinforced concrete flat slabs lightened with hollow structural bodies (hereafter referred to as “Unidome slabs”).

One of the attacks that most affect the durability of concrete is the penetration of chlorides from seawater, with varying degrees of severity. The design alternatives considered base their durability strategy on extending the service life of the concrete structure. For this purpose, different response mechanisms against chloride-induced corrosion are used, such as improving the resistance of the concrete to external aggressions, its thickness, the inhibitory protection, or the type of steel. Six alternative designs are analyzed here, along with the REF design, for comparison. Three design options are based on reducing the permeability of concrete. One way is to modify the base mix using cement with 10% silica fume (hereafter, SF-C) or adding admixtures such as 20% fly ash (hereafter, FA-A). Another way is to achieve a very compact and well-vibrated concrete by reducing the water-to-cement ratio from 0.60 in the base mix to 0.50 (W/C alternative). The duration of the protective effect of the concrete on the reinforcement can be extended over time by increasing, at most, the concrete cover from 3 cm in the baseline option to 4.5 cm (CC45 alternative). Applying a hydrophobic corrosion inhibitor impregnation (HCII) to protect the exposed surface of the slabs is also a suitable option. Using corrosion-resistant steels is also an excellent way to increase corrosion durability. In our case, we replaced conventional carbon steel reinforcing bars with galvanized steel reinforcing bars (GSR). Stainless steel is not valued because its cost for building construction is so high that, except in very justified cases, it is economically unsustainable.

In order to compare the life cycle impact assessment, it is necessary to base it on the same functional unit, according to ISO 14040. This analysis considers 1 m² built based on a hotel module composed of three levels of rooms and 2132 m² built of structure and foundations. To assess the impacts derived from both construction and maintenance activities, a “gate to gate” approach has been considered. Construction and maintenance activities are included for a nominal service life of 50 years, as required by national codes (Fomento, 2008).

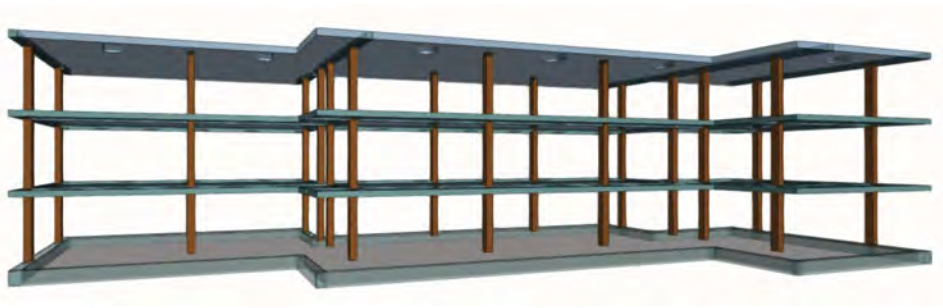


Figure 1. 3D model of the baseline (REF) structure.

2.2 Reliability-based maintenance requirements

A deterioration model will be chosen to determine the impact of maintenance on each of the design alternatives to be compared. A durability model has been chosen for chloride corrosion processes versus carbonation since the former is a much faster attack in a marine exposure environment such as the one in question. Concrete deterioration begins when chloride ions penetrate the concrete cover and reach the reinforcing bars at a concentration capable of triggering the steel corrosion process. This concentration is known as the critical chloride content (C_{cr}), whose reach time depends on the properties of the concrete cover. Under normal conditions, a value of 0.6% of the weight of cement is adopted according to the Spanish concrete code. The propagation stage is completed when an unacceptable steel section loss occurs, or cracks appear in the concrete cover. A two-dimensional version of the Fickian model suggested in Fib Bulletin 34 (2006), subsequently refined by Navarro et al. (2019), to evaluate the progression in chloride concentration in concrete as a function of time is used. The chloride concentration C at any time t (in years) and any depth (in mm) in the x and y directions of the analyzed cross-section can be calculated as:

$$C(x, y, t) = C_s \left[1 - \operatorname{erf} \frac{x}{2\sqrt{D_{0,x} \cdot \left(\frac{t}{t_0}\right)^\alpha \cdot t}} \cdot \operatorname{erf} \frac{y}{2\sqrt{D_{0,y} \cdot \left(\frac{t}{t_0}\right)^\alpha \cdot t}} \right] \quad (1)$$

where C_s = surface chloride concentration (wt%/binder); $\operatorname{erf}(\cdot)$ = the Gaussian error function; D_0 ($\times 10^{-12}$ m²/s) is the chloride diffusion coefficient (mm²/year); α = age factor, assumed 0.5 according to the Spanish codes; $t_0 = 0.0767$ years (28 days).

Table 1 shows the value of the parameters used to characterize the measures analyzed and the maintenance cycles required during the structure's service life (50 years) according to the durability obtained for each alternative. After each maintenance cycle, the structure is assumed to recover its original state (Stewart et al., 2004).

Table 1. Characterization of the durability of the preventive alternatives studied.

Parameter	REF	SF-C	FA-A	W/C	CC45	HCH	GSR
C_{cement} (kg/m ³)	275	225*	200**	300	275	275	275
C_{cr} (%)	0.6	0.6	0.6	0.6	0.6	0.6	1.2
erf	0.853580	0.931932	0.977853	0.812476	0.869583	0.849931	0.524771
C_s (%)	2.62	3.20	3.60	2.40	2.74	2.62	2.62
x (mm)	30	25	25	30	45	45***	30
D_0 ($\times 10E-12$ m ² /s)	25	3.4	5	15.8	25	25	25
t (years)	2	36.7	14	6.1	9.4	10.3	14
No. of repairs	25	1.36	3.57	8.20	5.32	4.85	3.57

*+10% Silica fume; **+20 Fly ash; ***effective coating increase 50%

2.3 Impact assessment

Two sets of criteria have been considered to assess the impacts generated along the life cycle of each of the design alternatives under study. The first set, containing economy-related criteria, includes two impacts: the costs associated with the construction of the above-described functional unit and the costs associated with the use and maintenance life cycle stage.

The second set of criteria includes the three endpoint assessment criteria associated with the environmental assessment methodology called ReCiPe: damage to human health, ecosystems, and resource availability. ReCiPe methodology converts the emissions of any activity into 18 so-called midpoint indicators, which include impacts such as an increase in various types of diseases (respiratory, cancer, and others), damage to different types of species (terrestrial marine and freshwater), and also the effects of the increasing scarcity of natural resources. These midpoint impacts are then adequately grouped and converted into the abovementioned endpoint indicators. On the one hand, the damage to human health is measured in DALYs, which stands for Disability-Adjusted Life Years. This metric takes into consideration the living years which are lost due to premature death or due to illnesses of different types.

The damage to ecosystems is measured in PDF, which stands for Potentially Disappeared Fraction. It evaluates the species that are potentially lost yearly due to the effects of anthropogenic activities occupying or converting their habitats. In addition, the PAF is also considered to evaluate the impacts on the ecosystems, which stands for Potentially Affected Fraction. This metric measures the percentage of species exposed to unbearable toxic substances. The last assessment criterion is related to the contribution of each of the alternatives under study to the scarcity of natural resources. According to the ReCiPe assessment methodology, this impact considers the energy surplus required to extract mineral resources or fossil fuels.

Finally, the subjective weightings of each criterion are determined using the Analytic Network Process (ANP) through a group of experts (Sánchez-Garrido et al., 2022c). Once the relevance is assigned to each criterion, a distance-based MCDM technique, namely VIKOR, is applied to find the design alternative with the maintenance interval that maximizes the sustainability of the structure's life cycle.

2.4 Inventory analysis

The material quantities associated with each alternative will be defined to evaluate the above impacts. The costs are summarized in Table 2 and include materials, labor, equipment and machinery, and direct ancillary costs. The material costs assumed in this analysis have been collected from specific and recognized Spanish construction databases developed by "CYPE Ingenieros", updated to 2022, and specific supplier data.

Table 2. Construction and repair costs considered in LCCA.

Parameters of design alternatives	Cost	Unit
Mat foundation 60 cm (25 Mpa) + steel 60 Kg/m ³	196.22	€/m ³
Concrete slab 25cm (25 Mpa) + steel 104 Kg/m ³	116.76	€/m ³
Concrete slab 30cm (25 Mpa) + steel 73.33 Kg/m ³	112.19	€/m ³
UNIDOME XS-D420 (470)	7.13	€/m ²
UNIDOME XS-120 (150)	6.85	€/m ²
UNIDOME XS-160 (190)	8.56	€/m ²
Mat foundation 60 cm +10% SF* (25 Mpa) + steel 60 Kg/m ³	321.80	€/m ³
Concrete slab 25cm +10% SF* (25 Mpa) + steel 104 Kg/m ³	191.49	€/m ³
Concrete slab 30cm +10% SF* (25 Mpa) + steel 73.33 Kg/m ³	183.99	€/m ³
Mat foundation 60 cm +20% FA** (25 Mpa) + steel 60 Kg/m ³	237.43	€/m ³
Concrete slab 25cm +20% FA** (25 Mpa) + steel 104 Kg/m ³	141.28	€/m ³

(Continued)

Table 2. (Continued)

Parameters of design alternatives	Cost	Unit
Concrete slab 30cm +20% FA** (25 Mpa) + steel 73.33 Kg/m ³	135.75	€/m ³
Mat foundation 60 cm (30 Mpa) + steel 60 Kg/m ³	219.96	€/m ³
Concrete slab 25cm (30 Mpa) + steel 104 Kg/m ³	121.40	€/m ³
Concrete slab 30cm (30 Mpa) + steel 73.33 Kg/m ³	117.67	€/m ³
Corrosion-inhibiting hydrophobic impregnation	33.81	€/m ²
Galvanizing bath for reinforcing bars + transport <10 km	0.90	€/Kg
Repair of the reinforced concrete slab edge (27cm average)	58.46	€/m
Structural concrete surface preparation, with manual means	43.08	€/m ²
Preparation of the surface of the reinforcement	8.23	€/m ²
Structural repair of concrete with polymer-modified cement mortar	88.78	€/m ²

*SF= Silica fume; **FA= Fly ash

Table 3 presents the different concrete mixes for each design alternative considered in the LCA, both for the construction and use and maintenance phases. The Ecoinvent 3.2 environmental database was used to collect the inventory data for the environmental assessment of each alternative under study.

Table 3. Materials assumed in each design option for the LCA of the construction phase and repair cycles.

Materials (per m ² of structure)	REF	SF-C	FA-A	W/C	CC45	HCII	GSR
Cement (Kg)	86.14	70.48	62.65	93.97	90.24	86.14	86.14
Water (l)	51.68	50.90	50.90	46.98	54.14	51.68	51.68
Sand (Kg)	213.00	213.00	213.00	213.00	223.13	213.00	213.00
Gravel (Kg)	439.31	439.31	439.31	428.97	460.20	439.31	439.31
Rebar steel B-500S (Kg)	27.52	27.52	27.52	27.52	27.52	27.52	-
HD-PE* (m ³)	2.158E-05	2.158E-05	2.158E-05	2.158E-05	2.158E-05	2.158E-05	2.158E-05
Silica fume (Kg)	-	7.83	-	-	-	-	-
Fly ash (Kg)	-	-	15.66	-	-	-	-
Silane-based impregnation (l)	-	-	-	-	-	0.66	-
Galvanized steel (Kg)	-	-	-	-	-	-	28.48
Trichloroethylene solvent (l)	2.91	0.16	0.42	0.95	0.62	0.56	0.42
Aluminosilicate abrasive (Kg)	101.77	5.55	14.54	33.37	21.65	19.76	14.54
Cement (Kg)	6.11	0.33	0.87	2.00	1.30	1.19	0.87
Cement 75 N/mm ² (Kg)	313.88	17.11	44.84	102.91	66.78	60.95	44.84
Cement 40 N/mm ² (Kg)	900.00	49.05	128.57	295.08	191.49	174.76	128.57
Water (l)	191.54	10.44	27.36	62.80	40.75	37.19	27.36

*HD-PE= Recycled high-density polyethylene

3 RESULTS AND DISCUSSION

3.1 LCCA results

Figure 2 reproduces the results obtained in the life cycle economic assessment for the seven design options analyzed. It includes the costs associated with construction per square meter of structure and those related to maintenance over 50 years. Repair costs are calculated based on the reactive maintenance cycles required for each alternative, depending on the strategy adopted to extend the structure's service life.

The lower construction cost is attributed to the REF option because it is the baseline option that does not incorporate any preventive strategy. This economic reading will be distorted if the whole life cycle is not considered. By incorporating the maintenance phase, the total cost becomes a ruin by requiring 25 repairs in 50 years. However, designs such as W/C and CC45, with minimum increases of 6% over the reference cost, achieve a drastic reduction in repair frequency and, therefore, the maintenance cost of 68% and 75%, respectively.

Finally, the design option based on silica fume cement (SF-C) resulted in the lowest life-cycle costs, followed by adding fly ash (FA-A) and galvanized reinforcing bars. Their results represent cost reductions of 87%, 80%, and 79%, respectively, over the total economic impact associated with the reference design.

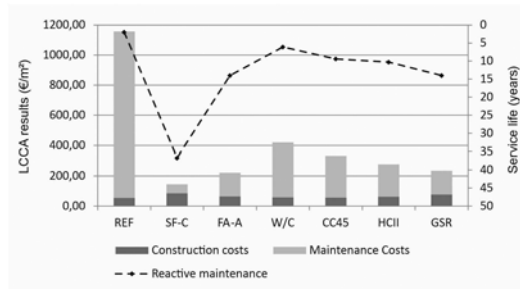


Figure 2. Results of the Life Cycle Cost Assessment (LCCA).

3.2 LCA results

The impacts resulting from the environmental life cycle assessment of the six alternative designs are presented in Figure 3. The endpoint approach has been adopted with three oriented damage indicators: human health, ecosystems, and availability of natural resources. The graphs highlight the most relevant environmental impacts affecting human health, followed by resource depletion, which is very similar in all the alternatives analyzed, except in the case of the REF, which is disproportionate. The options with silica fume (SF-C) and fly ash (FA-A) added to the concrete mix provide the best environmental performance by reducing REF impacts by 67% and 60%, respectively. In general, it is concluded that the greater the durability of the preventive maintenance strategy, the lower the frequency of reactive maintenance, which will reduce the resulting impact on the environment.

3.3 LCCA-LCA sustainability assessment

The relevance of each criterion was obtained through an expert seminar to evaluate the sustainability of each design presented. Table 4 shows the weights assigned by the group to each of the five impact categories defined.

From the obtained crisp weights, the VIKOR technique (Sánchez-Garrido et al., 2022a) is applied to aggregate the five different impact categories into a single sustainability score ($0 \leq Q_j \leq 1$) for each design option to be compared. In this case, Q_j is better the closer to 0. Figure 4 shows the results for each design alternative, considering the interval in years leading to the

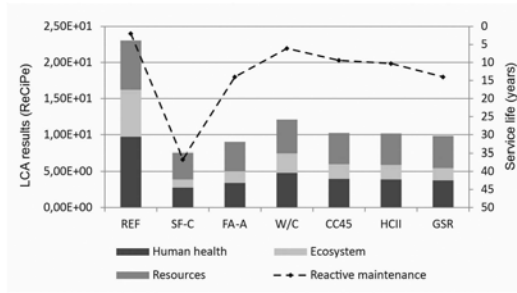


Figure 3. Results of the Life Cycle Assessment (LCA).

Table 4. Results of the weighting of criteria.

Criteria	Definition	Weight
C1	Construction Costs	0.1971
C2	Service life Costs	0.1529
C3	Human health impact	0.3059
C4	Ecosystem impact	0.0986
C5	Resources	0.2455

first maintenance and, therefore, to the repair of the cover concrete to prevent the propagation of corrosion in the reinforcement.

From a sustainability standpoint, the optimal preventive maintenance design is CC45, with an overall score of 98.3%, followed closely by FA-A with 97.6% and HCII with 95.7%. It is worth noting that the SF-C alternative, which was the best in the LCA and LCA, obtained an intermediate performance in the final sustainability evaluation, with a discrete 67.1%. On the other hand, design strategies that did not stand out in the individual evaluations have turned out to have superior performance when aggregated into a sustainability score. This has been the case for the CC45 and HCII alternatives, first and third in the ranking, with virtually equal maintenance intervals. Only FA-A, second in the ranking, has performed well economically and environmentally.

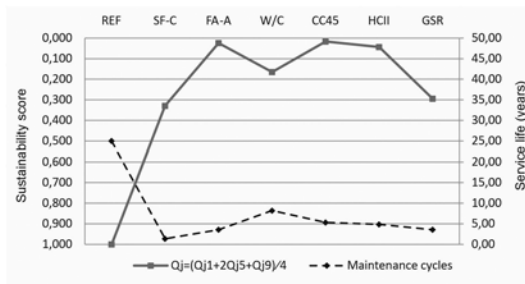


Figure 4. Results of the Sustainability Life Cycle Assessment.

4 CONCLUSIONS

The present communication shows the different durability performances over the life cycle of a concrete structure, based on MMC, exposed to aggressive environments. Several alternatives are evaluated that base the durability strategy on using different base concrete mixes, increasing the bottom cover of the slab with corrosion inhibitor impregnation, and substituting the type of reinforcing steel.

From the results, the evaluation of economic and environmental impacts by a one-dimensional life cycle analysis does not guarantee that a design is optimal from a sustainability point of view. Sustainability is a complex issue that tries to solve a multi-criteria decision-making problem, so it must be approached from a holistic perspective, simultaneously considering all the dimensions involved in the evaluation associated with the design of the structure.

ACKNOWLEDGEMENTS

Grant PID2020-117056RB-I00 funded by MCIN/AEI/ 10.13039/501100011033 and by “ERDF A way of making Europe”. The authors would also like to thank the companies that provided some of the data and information necessary for this study (UNIDOME Deutschland GmbH).

REFERENCES

- Balashbaneh, A.T. & Marsono, A.K.B. 2020. Applying multi-criteria decision-making on alternatives for earth-retaining walls: LCA, LCC, and S-LCA. *International Journal of Life Cycle Assessment* 25: 2140–2153.
- Biondini, F. & Frangopol, D.M. 2017. Time-variant redundancy and failure times of deteriorating concrete structures considering multiple limit states. *Structure and Infrastructure Engineering* 13(1): 94–106.
- Chan, M., Jin, H., van Kan, D. & Vrcelj, Z. 2022. Developing an innovative assessment framework for sustainable infrastructure development. *Journal of Cleaner Production* 368: 133185.
- Frangopol, D.M., Dong, Y. & Sabatino, S. 2017. Bridge life-cycle performance and cost: analysis, prediction, optimisation and decision-making. *Structure and Infrastructure Engineering* 13(10): 1239–1257.
- Fib. Fib Bulletin 34: Model Code for Service Life Design. Fib, Lausanne, 2006.
- Fomento. 2008. EHE-08 Instrucción del Hormigón Estructural.
- García-Segura, T., Yepes, V., Frangopol, D.M. & Yang, D.Y. 2017. Lifetime reliability-based optimization of post-tensioned box-girder bridges. *Engineering Structures* 145: 381–391.
- Lei, H., Li, L., Yang, W., Bian, Y. & Li, C-Q. 2021. An analytical review on application of life cycle assessment in circular economy for built environment. *Journal of Building Engineering* 44: 103374.
- Navarro, I.J., Yepes, V., Martí, J.V. & González-Vidosa, F. 2018. Life cycle impact assessment of corrosion preventive designs applied to prestressed concrete bridge decks. *Journal of Cleaner Production* 196: 698–713.
- Navarro, I.J., Martí, J.V. & Yepes, V. 2019. Reliability-based maintenance optimization of corrosion preventive designs under a life cycle perspective. *Environmental Impact Assessment Review* 74: 23–34.
- Navarro, I.J., Yepes, V. & Martí, J.V. 2020. Sustainability assessment of concrete bridge deck designs in coastal environments using neutrosophic criteria weights. *Structure and Infrastructure Engineering*, 16 (7): 949–967.
- Petcherdchoo, A. 2015. Environmental impacts of combined repairs on marine concrete structures. *Journal of Advanced Concrete Technology* 13(3): 205–213.
- Pons, J.J., Penadés-Plà, V., Yepes, V., & Martí, J.V. 2018. Life cycle assessment of earth-retaining walls: An environmental comparison. *Journal of Cleaner Production* 192: 411–420.
- Sánchez-Garrido, A.J., Navarro, I.J. & Yepes, V. 2022a. Multi-criteria decision-making applied to the sustainability of building structures based on Modern Methods of Construction. *Journal of Cleaner Production* 330: 129724.
- Sánchez-Garrido, A.J., Navarro, I.J. & Yepes, V. 2022b. Evaluating the sustainability of soil improvement techniques in foundation substructures. *Journal of Cleaner Production* 351: 131463.
- Sánchez-Garrido, A.J., Navarro, I.J., García, J. & Yepes, V. 2022c. An Adaptive ANP & ELECTRE IS-based MCDM Model Using Quantitative Variables, *Mathematics* 10(12): 2009.
- Stewart, M. G., Estes, A. C., & Frangopol, D. M. 2004. Bridge deck replacement for minimum expected cost under multiple reliability constraints. *Journal of Structural Engineering* 130(9).
- Yepes, V., Lopez, S. 2021. Knowledge management in the construction industry: Current state of knowledge and future research. *Journal of Civil Engineering and Management* 27(8): 671–680.

*SS21: Durability of reinforced concrete structures and infrastructures
under changing climate conditions
Organizers: S. Kessler, F. Marsili, P. Croce & F. Landi*



Taylor & Francis

Taylor & Francis Group

<http://taylorandfrancis.com>

Exploratory analysis of the impact of natural hazards on road infrastructure in the Philippines

M. Adarne, A. Amir & M. Henry

Shibaura Institute of Technology, Kotou-ku, Tokyo, Japan

ABSTRACT: The Philippines is in the Golden age of Infrastructure development, where roads and bridges are currently being constructed to interconnect the cities and provinces. However, these infrastructures are susceptible to the adverse effects of climate change, as the Philippines ranked 8th on the risk index among the countries with the highest exposure to disaster. Natural hazards may temporarily or permanently interrupt the normal operation of road infrastructures resulting in the need to adopt a sustainable risk management approach for road networks exposed to natural disasters. The research aimed to find the impact of natural hazards in the shape of damages to the road network by performing statistical analysis on the natural hazards data of the year 2021. The results may help in understanding and visualizing risks and damages to road networks under natural hazards and provide effective safety management practices when a disaster occurs.

1 INTRODUCTION

Infrastructure can be the deciding factor in determining whether or not the situation becomes a disaster when extreme natural hazards occur (World Risk Report, 2016). Road infrastructure is an integral part of the country's economy and is most prone to these hazards. Natural hazards may temporarily or permanently interrupt the normal operation of road infrastructures; however, they provide access to quickly supply relief aids to affected communities but if they become the first affected by the disaster, the entire region can be cut off.

In recent years, the Philippines has been focusing on infrastructure development in which roads and bridges are being constructed to overcome the limitations provided by its outdated and inadequate infrastructure. The country has started the "Build Build Build" Program in which roads and bridges are being constructed to interconnect the country's cities and provinces (Malindog-Uy, 2020). However, at the same time, these infrastructures are prone to natural disasters and calamities as the Philippines ranked 8th on the risk index with a score of 21.39 and placed 9th among countries with the highest exposure to disaster (World Risk Report, 2021). The country faces a variety of natural hazards, including geophysical disturbances like earthquakes and volcanic eruptions, meteorological and hydrological events like typhoons and floods, and slow-onset disasters like droughts that affect the infrastructure (Iuchi et. al., 2019), specifically the transport infrastructure to larger extent and resulting in damages and significantly affecting the economy and livelihoods of the country. Unlike the development of a proper scheduled plan for the timely completion of these infrastructures, natural disasters and ensuing damage to these infrastructures cannot be planned for in the same way. However, it is possible to prepare in advance for such events to some extent through the development of a mitigation plan (Shibayama, 2017). With the evolution of data analytics, it is now possible to analyze historical data in terms of understanding the impact of past events or past patterns, and by conceptualizing what transpired, a future mitigation strategy can be developed. May Haggag et. al. employed data analytics and machine learning techniques on the disaster data of New York state to investigate the relationship between different climate-induced disasters and infrastructure performance and then developed the performance prediction framework for the infrastructure (Haggag et. al., 2021). Similarly, the database of high-impact weather events that

occurred in Greece was developed, and a descriptive impact analysis was performed for the period 2001-2011 (Papagiannaki et. al., 2013).

In this study, data on natural disasters that caused damage to infrastructure in the Philippines in the year 2021 obtained from the Bureau of Maintenance (BOM), Department of Public Works and Highways (DPWH) were analyzed. First, the occurrences of natural hazards in the different regions at different times were examined. Then the damages that occurred to road infrastructures in different regions in the Philippines were studied. Finally, the combined effect of disasters on the road infrastructure was studied by performing an Odds Ratio (OR) analysis to obtain an idea of the relative impact a natural event may have on road infrastructure as compared to other natural disasters. The study can be utilized in the future for the development of mitigation planning by sorting out the critical structure based on natural disasters.

2 RESEARCH METHODOLOGY

2.1 Research data

The data was collected from DPWH which included 1,305 damage events of various disaster types that occurred in the country in 2021. The BOM, DPWH gathered information from District offices that report data immediately after the occurrence of natural disasters. The condition of the structure prior to the natural disaster is usually not determined, however, the damages that occurred due to the natural disaster are collected and reported. Five variables were used in the study, i.e., year of occurrence, types of natural disasters, region of the affected area, types of infrastructures, and types of damages. Data cleaning was done, and it was observed that 936 damage events are associated with transportation infrastructures such as roads and bridges, with 64% and 8% of the total damages, respectively. The remaining 369 damage events are associated with flood control and public building infrastructures, with 21% and 7% of the total damages, respectively, as shown in Figure 1. Damages related to transportation infrastructure were classified into road and bridge damage groups based on the type of infrastructure affected by natural disasters. The damages to the roads and bridges were subsequently subdivided into three groups based on the importance and traffic conditions during repairs. In addition, the data were grouped by affected regions and month of occurrence to determine the distribution of damages and affected areas during natural disasters.

2.2 Natural disaster

The data obtained from the department consisted of various natural disasters that occurred in the year 2021 and caused damages to infrastructures. It was observed that among nine natural disasters that caused damage to infrastructures, eight disasters were related to damage to the transportation infrastructure (roads and bridges). The percentage of damage caused by each natural disaster is depicted in Figure 2. It was found that typhoons caused the majority of road and bridge infrastructure damages (42%), followed by tropical storms (41% and 15%, respectively).

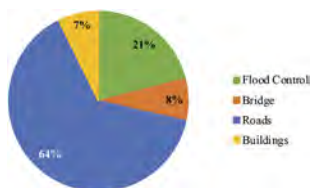


Figure 1. Total number of damages to infrastructure the year 2021.

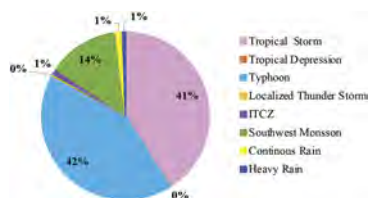


Figure 2. Percentage of Natural disasters cause in damages.

2.3 Roads and bridges damages

The data consisted of 138 types of damages to roads and bridges in 2021 caused by natural disasters, with a total of 936 incidents of damage to roads and bridges. Figure 3 shows the

percentage of damages to the transportation infrastructures in the year 2021. Roads were the most affected by disasters as they got the highest percentage of damages as compared to the bridge infrastructure in 2021. Similarly, 50% of damages were received by the road structures group, which shows that they were most impacted during the climatic events in the year 2021, followed by road protection structures and road-associated structures.



Figure 3. Corrosion Damage States (CDSs) probabilities for structural components over the structural lifetime.

2.4 Odds Ratio (OR) analysis

Odds Ratio (OR), a statistical analysis that was done to measure the strength of the association between natural disasters and infrastructure damage. OR Analysis measures the probability that an outcome (infrastructure damage) will occur given a specific exposure (natural disaster). It can determine if a certain exposure is a risk factor for a certain outcome and compare the size of different risk factors for that outcome. (Szumilas, 2010). The OR can be defined as the ratio between the odds values where odds are the probability that an event will occur divided by the probability that the event will not occur, as shown by the formula.

$$OR = \frac{\text{odds that an outcome occur in particular exposure}}{\text{odds that an outcome occur in the absence of exposure}} \quad (1)$$

where $OR=1$, exposure does not affect the odds; $OR>1$, exposure associated with higher odds of an outcome; $OR<1$, exposure associated with lower odds of an outcome

In this research, the exposure is the natural disaster that caused damages to transport infrastructures in the year 2021, while the outcome was the damages that occurred during the natural disaster. Hence, the OR was performed to find the probability that infrastructure damage will occur in the presence of a specific disaster.

3 RESULTS AND DISCUSSION

3.1 Region and month of disaster occurrence

Table 1 shows the total natural disaster events that affected transportation infrastructure in 2021 per region by disaster type, as well as the percentage of individual natural events in each region that affected roads and bridges. Typhoon has caused the highest number of infrastructure damages among the eight natural disasters, with 393 occurrences, followed by tropical storms with 383 occurrences, and southwest monsoon with 129 occurrences. In addition, typhoons caused infrastructure damage in most regions, with region VII being one of the worst affected areas.

Table 1 also depicts that the Cordillera Administrative Region (CAR) has the highest incidence of infrastructure-damaging events compared to other regions, with 53.8% of damaging events attributed to tropical storms and 53.5% attributed to the southwest monsoon. CAR might possibly be experiencing these infrastructure-damaging events because the region has two distinct seasons, the dry season from November to April and the wet season for the rest of the year. But from the last few years, the regions also experienced the effect of climate

change due to which sometimes there is no dry season but there is maximum rainfall in November and December (Philippine Statistic Authority 2020) thus causing a greater number of events of infrastructure damage. According to Hugen et al., the typhoon events seem to indicate a gradual shift towards the end of the year, such that the number of typhoons in the rainy season, which run from June to November, has decreased while the number of typhoons in December has increased in the Philippines (Hugen et al., 2006).

Table 2 indicates the month-wise infrastructure damages caused by different natural disasters. Typhoons caused the most infrastructure damage in the month of December (91.6%), followed by September (8.4%). According to Philippine Atmospheric, Geophysical, and Astronomical Services Administration (PAG-ASA), the agency for assessing and forecasting weather in the Philippines, the peak season of typhoons is from July through October, when nearly 70% of the typhoon develop (Department of Science and Technology 2022), however, by analyzing the data, it was observed that the typhoons in the month of December were more disastrous to the road and bridges infrastructure.

Table 1. Percentage of occurrence per region when natural events cause damage to infrastructure.

Region	Total events per region	Tropical storm	Tropical depression	Typhoon	Southwest monsoon	ITCZ	Continous rain	Localized thunder storm	Heavy rain
	No. events	383	1	393	129	10	12	3	5
NCR	10	0.0	0.0	0.0	7.8	0.0	0.0	0.0	0.0
CAR	297	51.2	0.0	5.3	51.5	0.0	0.0	33.3	0.0
I	54	12.5	0.0	0.0	4.7	0.0	0.0	0.0	0.0
II	26	3.7	0.0	3.1	0.0	0.0	0.0	0.0	0.0
III	26	0.0	0.0	0.0	20.2	0.0	0.0	0.0	0.0
IV-A	16	0.0	0.0	0.0	12.4	0.0	0.0	0.0	0.0
IV-B	50	9.7	0.0	2.8	1.6	0.0	0.0	0.0	0.0
V	47	11.7	0.0	0.5	0.0	0.0	0.0	0.0	0.0
VI	38	0.3	0.0	9.4	0.0	0.0	0.0	0.0	0.0
VII	201	4.2	100.0	0.0	0.0	0.0	0.0	0.0	0.0
VIII	84	2.3	0.0	19.1	0.0	0.0	0.0	0.0	0.0
IX	1	0.0	0.0	0.0	0.0	10.0	0.0	0.0	0.0
X	20	0.0	0.0	4.1	0.0	0.0	16.7	0.0	40.0
XI	5	0.0	0.0	0.0	0.0	0.0	16.7	0.0	0.0
XII	11	0.0	0.0	0.0	0.0	90.0	0.0	66.7	0.0
XIII	50	1.8	0.0	8.9	0.0	0.0	66.7	0.0	0.0

Table 2. Percentage of occurrence of natural disaster per month.

Region	Total events per month	Tropical storm	Tropical depression	Typhoon	Southwest monsoon	ITCZ	Continous rain	Localized thunder storm	Heavy rain
	No. events	383	1	329	119	10	12	3	5
January	0	0.0	0.0	0.0	0.0	0.0	0.0	0.0	0.0
February	18	4.7	0.0	0.0	0.0	0.0	0.0	0.0	0.0
March	0	0.0	0.0	0.0	0.0	0.0	0.0	0.0	0.0
April	0	0.0	0.0	0.0	0.0	0.0	0.0	0.0	0.0
May	9	0.0	0.0	0.0	0.0	90.0	0.0	0.0	0.0
June	23	6.0	0.0	0.0	0.0	0.0	0.0	0.0	0.0
July	108	0.0	0.0	0.0	83.7	0.0	0.0	0.0	0.0
August	29	0.0	0.0	0.0	16.3	0.0	66.7	0.0	0.0
September	93	15.1	0.0	8.4	0.0	0.0	16.7	0.0	0.0
October	288	74.5	100.0	0.0	0.0	10.0	8.3	33.3	0.0
November	7	0.0	0.0	0.0	0.0	0.0	8.3	33.3	100.0
December	361	0.0	0.0	91.6	0.0	0.0	0.0	33.3	0.0

Figure 4 shows the percentage of damaged roads and bridges across the country, with CAR experiencing the highest level of road damage (32.25%) compared to other regions, while Region VII experienced the highest level of bridge damage (38.5%), which also the highest percent of bridge damage compared to other regions.

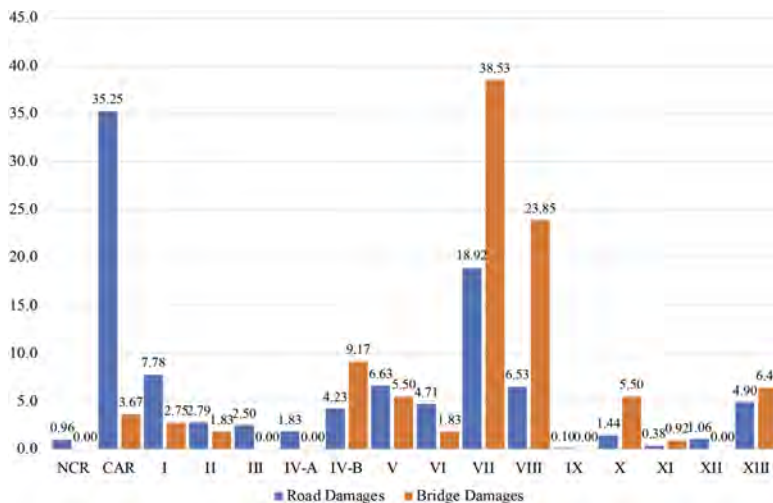


Figure 4. Percentage of road and bridge damages per region.

3.2 Types of damage caused by natural disasters.

The percentage of infrastructure damages (roads and bridges) caused by natural events in each region is shown in Table 3. It was observed that CAR and region VII experienced the highest portion of total damages, as shown in Figure 4. Among the road damages and bridge damages groups, the road group experienced more numbers of damages, with a total of 581 damages to the road structure, and 39.6% of total road structure damages occurred in CAR. Whereas the bridge protection work was worst affected by natural disasters in a bridge damages group, with a total of 46 incidents causing damages to bridge structures and 45.7% of these damages occurred in Region VII. CAR is susceptible to more damage may be due to its geophysical and astrological condition, mountainous topography comprised of towering peaks, plateaus, and intermittent valleys, and 71 percent of the region’s land area has slopes of 30 degrees or more. The soil characteristics of this area also contributed to the greater numbers of damages, as it consists of various types of soil, primarily mountain soil and clay loam. The most common type of soil degradation is soil erosion. According to the Department of Environmental and National Resources (DENR), 36 percent of the region’s land area is susceptible to moderate erosion, and most of the region’s land area is susceptible to slight erosion (36%) (Philippine Statistic Authority 2020). In Region VII, the potential for damage may be due to the presence of major islands, one smaller island, and several outlying islands. The Visayan Sea borders to the north, the Camotes Sea and Camiguin Channel to the east, Negros Island to the west, and the Mindanao Sea to the south. The interior of the provinces of Region VII is dominated by highlands, with narrow strips of arable land lining the coast, and most of the province’s land area is hilly and mountainous (62% of total land), while the remainder is flat and rolling (32% of land) (Arkipelago, 2016).

Table 4 indicates the month-wise natural disasters that caused damage to the roads and bridges infrastructure. It was observed that most of the infrastructure damaging events occurred in the months of July, October, and December, with the maximum number of damages in the month of December as shown in Figure 5. Among various infrastructure damages in the year 2021, the maximum number of road structures were damaged in October, whereas the majority of bridge protection structures were affected in December due to natural disasters.

3.3 Odds Ratio (OR) analysis

After analyzing the disasters and damages separately, OR analysis was conducted on the data to determine the likelihood of the association between infrastructure damages and natural disaster events. Table 5 shows the result of the OR analysis. The zero and no values in the table are due to the minimal exposure or outcome that cannot be calculated.

Table 3. Percentage of infrastructure damages that occurred per region.

Region	Total events per region	Road Damages			Bridge Damages		
		Road structure	Road associated structures	Road Protection	Bridge substructure	Bridge superstructure	Bridge protection
	No. damages	581	174	286	18	45	46
NCR	10	1.7	0.0	0.0	0.0	0.0	0.0
CAR	371	39.6	28.7	30.4	0.0	4.4	4.3
I	84	2.9	9.8	16.4	0.0	4.4	2.2
II	31	1.5	4.6	4.2	0.0	4.4	0.0
III	26	3.8	1.7	0.3	0.0	0.0	0.0
IV-A	19	1.9	2.3	1.4	0.0	0.0	0.0
IV-B	54	5.0	4.0	2.8	5.6	6.7	13.0
V	75	6.0	8.0	7.0	5.6	2.2	8.7
VI	51	2.9	16.1	1.4	0.0	0.0	4.3
VII	239	23.6	11.5	14.0	44.4	28.9	45.7
VIII	94	1.2	6.9	17.1	11.1	46.7	6.5
IX	1	0.0	0.0	0.3	0.0	0.0	0.0
X	21	1.5	0.6	1.7	11.1	2.2	6.5
XI	5	0.7	0.0	0.0	5.6	0.0	0.0
XII	11	1.0	0.6	1.4	0.0	0.0	0.0
XIII	58	6.5	5.2	1.4	16.7	0.0	8.7

Table 4. Percentage of infrastructure damages that occurred per month.

Months	Total events per month	Road Damages			Bridge Damages		
		Road structure	Road associated structures	Road Protection	Bridge substructure	Bridge superstructure	Bridge protection
	No. damages	581	174	286	18	45	46
January	0	0.0	0.0	0.0	0.0	0.0	0.0
February	30	1.9	0.6	3.8	16.7	0.0	8.7
March	0	0.0	0.0	0.0	0.0	0.0	0.0
April	0	0.0	0.0	0.0	0.0	0.0	0.0
May	9	0.7	0.6	1.4	0.0	0.0	0.0
June	24	2.4	3.4	0.0	11.1	2.2	2.2
July	119	13.9	5.7	9.8	0.0	0.0	0.0
August	32	4.1	1.1	2.1	0.0	0.0	0.0
September	124	10.8	13.2	10.5	5.6	4.4	10.9
October	375	32.9	36.8	36.7	0.0	13.3	19.6
November	9	0.9	0.6	0.7	5.6	0.0	0.0
December	428	32.4	37.9	35.0	61.1	80.0	58.7

It was observed that tropical storms, typhoons, and continuous rains were the events that caused most of the damage to the transportation infrastructure in the year 2021. The results of OR analysis showed that when tropical storms occur, it is 28.5 % more likely to cause damage to road structures, 62% more likely to cause damage to road-associated structures, and 36.3% more likely to cause damage to road protection structures than any other types of natural disaster. Conversely, in the case of typhoons, it is 120.5% more likely to cause damage to bridge structures, 498.3% more likely to cause damage to bridge superstructures, and 103.5% more likely to cause damage to bridge protection works than any other type of natural event.

However, continuous rainfall was found to be associated with damage to both roads and bridges. The analysis revealed that if it is continuous rainfall, it is 583.2% more likely to cause road structure damages and 385% more likely to cause bridge substructure damages than any other natural disaster.

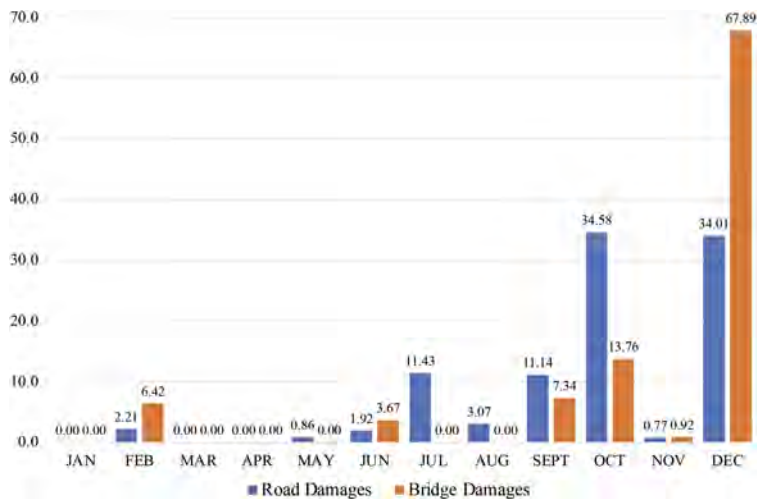


Figure 5. Percentage of road and bridge damage per month.

Table 5. Odds Ratio Analysis results show the relative risk of damages to the infrastructure in case of natural disasters that cause damages to road infrastructure.

Natural Disaster		Road Damages			Bridge Damages		
		Road Structure	Road Associated Structure	Road Protection	Bridge Substructure	Bridge Superstructure	Bridge Protection
Tropical storm	odds	1.3	1.6	1.4	0.7	0.3	1.0
	%	28.5	62.0	36.3	-28.2	-65.4	1.7
Tropical depression	odds	-	-	0.0	0.0	0.0	0.0
	%	-	-	-	-	-	-
Typhoon	odds	0.5	1.1	0.9	2.2	6.0	2.0
	%	-46.8	8.8	-13.7	120.5	498.3	103.5
Southwest monsoon	odds	2.0	0.4	0.8	0.0	0.0	0.0
	%	102.3	-59.2	-21.2	-	-	-
ITCZ	odds	0.4	0.5	2.3	0.0	0.0	0.0
	%	-59.7	-51.6	129.5	-	-	-
Continous rain	odds	6.8	0.0	0.0	4.9	0.0	0.0
	%	583.2	-	-	385.0	-	-
Localized thunderstorm	odds	-	2.2	1.1	0.0	0.0	0.0
	%	-	119.7	13.7	-	-	-
Heavy Rain	odds	2.5	0.0	0.6	0.0	0.0	0.0
	%	145.4	-	-43.3	-	-	-

4 CONCLUSION

Considering the significant adverse effect of natural events on transportation infrastructures, the current work aimed to 1) specify the region-wise disasters that are prone to transportation infrastructure, 2) categorize the damages of road and bridge infrastructure due to natural events, and 3) to find the impact of each natural disasters on road and bridge infrastructure in different regions. The results of the analysis of the disaster showed that CAR and Region VII were the most affected regions in the case of road and bridge infrastructure damages, thus, raising the need to give special attention to the transport infrastructure in these regions.

However, most of the transport infrastructure damaging events occurred in the months of September, October, and December due to tropical storms and typhoons therefore, the concerned departments need to take this into consideration during the development of a mitigation plan. The results of the odds ratio analysis concluded that typhoons caused maximum numbers of damage to bridges while tropical storms were found to be most devastating for roads. However, continuous rains were found to cause damage to both roads and bridges. Therefore, road authorities need to consider these disasters during the designing stage of roads and bridges to reduce the effect of disasters on the transport infrastructure.

Conclusively, the work tries to indicate awareness and knowledge of transportation infrastructure damages in case of natural disasters. However, the research needs to extend to more previous years' data in order to study the complete pattern of damages to transportation infrastructure during natural disasters, which may enable to develop the mitigation plan for the transportation infrastructure.

ACKNOWLEDGEMENT

The Authors would like to thank the Japan International Cooperation Agency (JICA) for their support through the Road Asset Management Platform (RAMP), the Shibaura Institute of Technology (SIT) for providing the environment for the research, the Department of Public Works and Highways Philippines (DPWH), for sharing the data and information needed, and the Unified Project Management Office (UPMO), DPWH for their warm support.

REFERENCES

- Aleksandrova, M., 2021. *World Risk Report 2021*
- Bureau of Maintenance, Department of Public Works and Highways 2021, *Calamity Damage Infra-Report 2021*
- Department of Budget and Management 2022, dbm.gov.ph, <https://www.dbm.gov.ph/index.php/dbcc-matters/macro-economic-assumptions-and-fiscal-targets/182nd-dbcc-meeting>
- Department of Science and Technology 2022, pagasa.dost.gov.ph, <<https://www.pagasa.dost.gov.ph/climate/tropical-cyclone-information#:~:text=With%2520the%2520average%2520of%252020,70%2525%2520of%2520a%2520typhoon%2520develop.>>
- Garschagen, M., Hagenlocher, M., Comes, M., Dubbert, M., Sabelfeld, R., Lee, Y.J., Grunewald, L., Lanzendorf, M., Mucke, P., Neuschäfer, O. and Pott, S., 2016. *World risk report 2016*.
- George, A., Stead, T.S. and Ganti, L., 2020. What's the risk: differentiating risk ratios, odds ratios, and hazard ratios?. *Cureus*, 12(8)
- Haggag, M., Yorsi, A., El-Dakhkhni, W. and Hassini, E., 2021. Infrastructure performance prediction under climate-induced disasters using data analytics. *International journal of disaster risk reduction*, 56: 102121.
- Huigen, M.G. and Jens, I.C., 2006. Socio-economic impact of super typhoon Harurot in San Mariano, Isabela, the Philippines. *World Development*, 34(12): 2116–2136.
- International Monetary Fund 2020, <https://www.imf.org/en/News/Articles/2020/02/06/na020620the-philippines-a-good-time-to-expand-the-infrastructure-push>
- Iuchi, K., Jibiki, Y., Solidum Jr, R. and Santiago, R., 2019. Natural hazards governance in the Philippines. In *Oxford Research Encyclopedia of Natural Hazard Science*.
- Kapuluang ng Pilipinas 2016, kapuluangpilipinas.wordpress.com, <https://kapuluangpilipinas.wordpress.com/2016/05/16/region-vii-central-visayas/>
- Malindog-Uy, A., 2020. 'Build Build Build' Program Amid a Pandemic. *The ASEAN Post*, September 13.
- Philippines Statistic Authority 2020, rssocar.psa.gov.ph, <<http://rssocar.psa.gov.ph/environment-statistics/RCES%20Component%201%3A%20Environmental%20Conditions%20and%20Quality%20Physical%20Conditions>>
- Shibayama, T. (2017). Japan's transport planning at national level, natural disasters, and their interplays. *European transport research review*, 9(3): 1–18.
- Szumilas, M., 2010. Explaining odds ratios. *Journal of the Canadian academy of child and adolescent psychiatry*, 19(3): 227
- Taghizadeh-Hesary, F., Yoshino, N., Mortha, A. and Sarker, T., 2019. *Quality infrastructure and natural disaster resiliency* (No. 991). ADBI Working Paper Series.
- The Asean Post 2020, <<https://theaseanpost.com/article/build-build-build-program-amid-pandemic>

Prediction of R.C. bridge deterioration under changing environmental conditions

F. Landi & P. Croce

Department of Civil and Industrial Engineering, University of Pisa, Italy

F. Marsili & S. Kessler

Helmut-Schmidt-University/University of the Federal Armed Forces Hamburg, Hamburg, Germany

ABSTRACT: Climate change affects the reliability and durability of r.c. structures both increasing the magnitude and the frequency of extreme events and accelerating the rate of degradation processes such as carbonation and corrosion. In the paper, bridge deterioration models are presented and discussed with the aim to extend their application to structures exposed to changing environmental conditions over their life cycle. The evaluation of transition probabilities in Markov and semi-Markov model, which is generally carried out by means of inspection data, is integrated with data derived by mechanistic-empirical models describing the deterioration of r.c. structures. Existing models for chloride induced corrosion, corrosion propagation and cracking are considered, introducing in the analysis the expected variations of temperature and atmospheric humidity. Results in terms of predicted deterioration curves are presented and discussed for a case study highlighting the influence of the expected changes in environmental conditions under different climate change scenarios.

1 INTRODUCTION

The degradation of structures and infrastructures is a major challenge for the coming decades with significant implications in terms of safety and costs (Stewart et al. 2012, Forzieri et al. 2018). Evaluating the performance and the remaining service life of aging bridges is of great concern to the asset owners and is the subject of several researches in civil engineering (van Noortwijk and Frangopol, 2004, Ellingwood, 2005, Thomas and Sobanjo, 2016). Numerous infrastructures are approaching the end of their design service life and at the same time a combination of environmental factors, operating conditions and delayed or ineffective maintenance accelerate deterioration (Ellingwood, 2005, Croce et al 2020).

In this context, specific attention should be devoted to the potential impact of climate change on the environment to which the structure is exposed. In fact, climate change will affect the reliability and durability of structures and infrastructures both increasing the magnitude and the frequency of extreme events and accelerating the rate of degradation processes such as carbonation and corrosion (Croce et al., 2019, Sousa et al., 2020).

Environmental conditions significantly influence the durability of r.c. structures, and the current increase of CO₂ concentrations, with the associated temperature and humidity variations increase degradation rate (Stewart et al. 2011, Sousa et al., 2020, Nasr et al. 2022, Zhang et al. 2022). For example, the rise of CO₂ concentration and the alternation of dry and wet conditions will increase the risk of carbonation-induced corrosion, while temperature increases directly affects corrosion rates due to the decrease of electrochemical resistances in the system.

In bridge maintenance management systems, the deterioration of reinforced concrete elements is generally predicted based on statistical models, such as Markov and semi-Markov

models, where transition probabilities are evaluated using the results of time-ordered visual inspections (Thomas and Sobanjo, 2016, Lethanh et al., 2017). However, scarce inspection data series complicate the evaluation of transition probabilities. In these situations, the infrastructure managers can rely only on expert opinion and mechanistic empirical models to predict the degradation (Mizutani et al., 2017). These models refer to a combination of a mechanistic model, which describes the physical behavior of the elements, and an empirical model, which is based on direct observations and measurements. A mechanistic empirical model is used in (Thomas and Sobanjo, 2016) to develop the transition probabilities for r.c. bridge elements affected by chloride-induced corrosion.

In the paper, the use of mechanistic empirical models is proposed to evaluate transition probabilities in a changing environment. The expected variations of climatic variables, such as temperature and relative humidity, are included in the implementation of the model for chloride-induced corrosion and their influence on transition probabilities and deterioration curves is assessed.

2 METHODOLOGY

The general methodology can be summarized in the following steps:

- Selection or development of mechanistic-empirical models, to describe the degradation of the investigated bridge elements;
- Definition of condition states for the bridge, associating them to chemical and physical parameters obtained from the mechanistic-empirical models;
- Simulation of condition indicators over time, considering uncertainties in the parameters of the mechanistic-empirical models and the expected variations of climate variables;
- Aggregation of condition states in each time interval and estimation of transition probabilities for the different condition states;
- Evaluation of expected condition and derivation of deterioration curves over time.

In the following sub-sections, details about each step of the procedure are provided.

2.1 Mechanistic-empirical model for chloride induced corrosion

The deterioration models of r.c. elements are mostly based on the outcomes of the DuraCrete project (DuraCrete, 2000), which formed the basis for the probabilistic durability design of r. c. structures and for several research in the field (Choe et al., 2008, Stewart et al., 2011, Thomas and Sobanjo, 2016, Nasr et al., 2022, Zhang et al. 2022). In this work, the initiation and propagation models proposed by DuraCrete are adopted as well, and the effect of climate change is quantifiable through time-dependent parameters.

Focusing on the deterioration of r.c. elements induced by chlorides, the first phase is the chloride penetration which is described by mechanistic-empirical models based on Fick's second law of diffusion. The chloride concentration C_{cl} at depth x at time t is obtained as:

$$C_{cl}(x, t) = C_s \left[1 - \operatorname{erf} \left(\frac{x}{2\sqrt{k_e k_t k_c f_t(t) f_{RH}(t) D_0 \left(\frac{t_0}{t}\right)^n t}} \right) \right] \quad (1)$$

Where C_s is the surface chloride concentration; k_e is the environmental factor; k_t is the test method factor; k_c is the execution parameter; D_0 is the empirical chloride diffusion coefficient; t_0 is the reference time in years, i.e. 0.0767 years corresponding to 28 days; n is the age factor; and $f_t(t)$ is the temperature effect on diffusion coefficient which can be obtained according to Stewart et al. (2011) by:

$$f_T(t) = \exp \left(\frac{E}{R} \left(\frac{1}{293} - \frac{1}{273 + T_{av}(t)} \right) \right) \text{ and } T_{av}(t) = \frac{\sum_{i=t_1+1}^t T(t)}{t - t_1} \quad (2)$$

with $E = 40$ kJ/mol is the activation energy of the diffusion process; $R = 8.314 \times 10^{-3}$ kJ/mol K is the gas constant; $T(t)$ is the average temperature for year t ; and t_1 is the year of construction. In a similar way, the influence of relative humidity on diffusion coefficient can be considered by means the coefficient $f_{RH}(t)$

$$f_{RH}(t) = \exp\left(1 - \frac{(100 - RH_{av}(t))^4}{(100 - 75)^4}\right)^{-1} \text{ and } RH_{av}(t) = \frac{\sum_{i=t_1+1}^t RH(t)}{t - t_1} \quad (3)$$

The surface chloride concentration depends on the exposure category of the structural element, i.e. submerged, splash, tidal, and atmospheric zone, and is described as a function of the water to cement ratio w/c and an error term ε_{cl} (DuraCrete, 2000, Choe et al., 2008)

$$C_s = A_{cl} \frac{w}{c} + \varepsilon_{cl} \quad (4)$$

where A_{cl} = regression coefficient associated to the exposure category.

Once the chloride concentration C_{cl} reaches critical values C_{cr} , corrosion of steel rebar is initiated. Corrosion of the reinforcement leads to the formation of corrosion products which occupies a larger volume than the original steel rebar, thus causing cracks in the concrete cover and eventually spalling. The crack width is evaluated according to the mechanistic-empirical model defined by the DuraCrete project (DuraCrete, 2000) as

$$w(t) = w_0 + b[p(t) - p_0] \quad (5)$$

where w_0 is the initial width of the visible crack in mm; b is the parameter which controls the propagation and depends on the position of the rebar in mm/ μ m; p_0 is the value of the corrosion penetration necessary to produce a crack in μ m; $p(t)$ is the corrosion penetration at time t in μ m. The corrosion penetration needed to open a crack p_0 can be derived from the following expression

$$p_0 = a_1 + a_2 \frac{x}{\phi} + a_3 f_{ct} \quad (6)$$

where a_1, a_2, a_3 are regression parameters; x is the concrete cover depth in mm; ϕ is the diameter of the steel rebar in mm; f_{ct} is the concrete tensile strength in N/mm². The corrosion penetration at time t , $p(t)$, is evaluated as

$$p(t) = i_{corr}(t) w_t (t - t_i) \quad (7)$$

Where w_t is the relative time of wetness; t_i is the time to corrosion initiation; $i_{corr}(t)$ is the corrosion rate at time t in mm/year, which depends on temperature and is estimated starting from the value at 20 °C ($i_{corr,20}$) as

$$i_{corr}(t) = i_{corr,20} [1 + K(T(t) - 20)] \quad (8)$$

in which K is the factor that describes the dependency of conductive with temperature T .

Reference values of the parameters in Equations (1) to (7) are provided in the final report of the DuraCrete project (DuraCrete, 2000) depending on the location and exposure zone of the structure, together with their probabilistic models which are summarized in Table 1.

2.2 Definition of bridge condition states

In bridge maintenance management systems, the condition states are mainly described qualitatively based on visual inspection and there is still little connection from these condition states and the structural behavior of the elements.

Table 1. Probabilistic models for the parameters of the mechanistic empirical model.

Parameter	Mean	St. Dev.	Distribution	Unit
x	x^c	10	LogNormal	[mm]
A_{cl} (atmospheric)	2.565	0.356	Normal	[%] relative to binder
ε_{cl} (atmospheric)	0	0.405	Normal	[%] relative to binder
k_e (atmospheric)	0.676	0.114	Gamma	[-]
A_{cl} (splash)	7.758	1.36	Normal	[%] relative to binder
ε_{cl} (splash)	0	1.05	Normal	[%] relative to binder
k_e (splash)	0.265	0.045	Gamma	[-]
k_t	0.832	0.024	Normal	[-]
k_c	1	-	Deterministic	[-]
D_0 ($w/c=0.5$)	473	43.2	Normal	[mm ² /year]
t_0	0.0767	-	Deterministic	[year]
n	0.3	0.12	Beta	[-]
w_0	0.05	0.005	Normal	[mm]
b	0.0086	0.0048	Normal	[mm/ μ m]
a_1	74.4	3.2	Normal	[μ m]
a_2	7.3	0.06	Normal	[μ m]
a_3	-17.4	5.7	Normal	[μ m/MPa]
f_{ct}	$0.53\sqrt{f_c}$	$0.08\sqrt{f_c}$	Normal	[MPa]
w_t	0.75	0.20	Normal	[-]
i_{corr}	0.03	0.02	Weibull	[mm/year]
$K(T > 20^\circ C)$	0.073	0.015	Normal	[-]
$K(T < 20^\circ C)$	0.025	0.005	Normal	[-]

A relationship between bridge condition states and the physical quantities described by the chloride induced corrosion model is here established. For the corrosion process, the condition states from CS1, where the structure is considered without any damage, to CS5 where the structure is severely damages, are generally used (Lethanh et al., 2017).

Examples of the relationship between condition states and analytical models for corrosion process can be found in Roelfstra et al. (2004) and Lethanh et al. (2017).

In this work, the definition proposed in Lethanh et al. (2017) is adopted with some slight modifications as reported in Table 2.

Table 2. Definition of bridge condition states based on the chloride content and crack width.

Condition state	Description	Criteria
1	New concrete contaminated	$0 \leq C_{cl}(x, t) < 0.24\%$
2	Increase in chloride content up to critical values	$0.24\% \leq C_{cl}(x, t) < 0.48\%$
3	Corrosion initiation, no visible cracks	$C_{cl}(x, t) > 0.48\% \cup w(t) < 0.25\text{mm}$
4	Visible cracks	$C_{cl}(x, t) > 0.48\% \cup 0.25\text{mm} \leq w(t) < 1\text{mm}$
5	Corrosion damage, severe cracks	$C_{cl}(x, t) > 0.48\% \cup w(t) > 1\text{mm}$

2.3 Generation of bridge condition indicators over time

The probabilistic models in Table 1 are adopted to perform Monte Carlo simulations and generate values of condition indicators, $C_{cl}(x, t)$ and $w(t)$, in each year t for a 100-year period according to the mechanistic-empirical model defined in Section 2.1.

In the simulations, the variation of climate parameters, annual temperature $T(t)$ and relative humidity $RH(t)$, are estimated considering an ensemble of climate projections provided by high-resolution Regional Climate Models (RCMs) based on different emission scenarios. Climate projections of temperature and relative humidity over several regional domains all over the world can be obtained from the Copernicus Data Store.

For Europe, the climate projections provided by the EURO-CORDEX initiative represents the most updated input for climate change impact studies (Jacob et al., 2014) and will be considered in this study. The data series cover the period 1951– 2100 and are split in two parts: a control period from 1951 until 2005 (Historical Experiment), and a future period depending on the emission scenario 2006–2100 (RCP Experiment).

Among the four available scenarios RCPs (van Vuuren et al., 2011), RCP4.5 and RCP8.5 are the most used in climate risk studies, and for them most climate projections are available. They correspond to medium and maximum concentration pathways, and they have been adopted in the present study as well. A probabilistic description of variations in temperatures and relative humidity is thus obtained enlarging the ensemble of climate projections by means of the use of weather generation techniques (Croce et al., 2021).

Once generated the time series of condition indicators, $C_c(x,t)$ and $w(t)$, condition states are evaluated according to the definitions in Table 2.

2.4 Evaluation of transition probabilities

The series of bridge condition indicators can be used to develop statistical models for bridge management. Markov and semi-Markov chain models can be set-up where changes from one state to another are evaluated in accordance with a set of transition probabilities defined analyzing the generated series of condition indicators.

Transition probabilities P_{ij} for the Markov process can be evaluated making use of the restricted least-squares transition probability estimator as illustrated in Lethanh et al.(2017), while for the semi-Markov, transition probabilities $P_{ij}(t)$ are estimated from the distribution of sojourn time in each condition state (Thomas and Sobanjo, 2016).

2.5 Expected bridge condition ratings and deterioration curves

Finally, the vector of bridge condition states at any time t , $CS(t)$, is predicted as the product of the estimated transition probability matrix $P_{ij}(t)$ and the initial condition vector $CS(t = 0)$

$$CS(t)^T = CS(t = 0)^T \times P_{ij}(t) \quad (9)$$

where $CS(t = 0)^T = [1 \ 0 \ 0 \ 0 \ 0]$ is a vector collecting the probability or proportion of the bridge to be in each state at time $t = 0$. Starting from the rating vector, $RATING^T = [1 \ 2 \ 3 \ 4 \ 5]$, the bridge expected condition state at any time t , $EXPCS(t)$, is evaluated by

$$EXPCS(t) = CS(t)^T \times RATING \quad (10)$$

3 RESULTS

The implementation of the presented methodology is demonstrated here focusing on a reinforced concrete bridge exposed to chloride-induced corrosion. For illustration purposes the following assumptions are made:

- the bridge is located in Italy, close to Pisa (lat. 43.6839, lon. 10.3927, alt.82 a.s.l.)
- the bridge was built in 2000
- a Portland cement with a water-cement ratio of 0.5 was used
- the curing time was 7 days
- two exposure category, atmospheric and splash zone, are considered for the element
- a concrete cover depth $x^c = 35$ mm is considered

First, climate data for the location of the bridge are collected considering historical observations at Pisa weather station, and an ensemble of climate projections provided by the EURO-CORDEX initiative (Jacob et al., 2014) for the historical experiment (period 1951-2005) and the two scenarios RCP4.5 and RCP8.5 (period 2006-2100).

The climate projections at the grid cell corresponding to the weather station are extracted and compared with the observations for the historical period. Changes in yearly average

temperatures are estimated from the analysis of climate model ensemble and then applied to the observations following the factor of change approach (Maraun, 2016). In Figure 1, the variations of annual temperature and relative humidity are shown for the period 2000-2100.

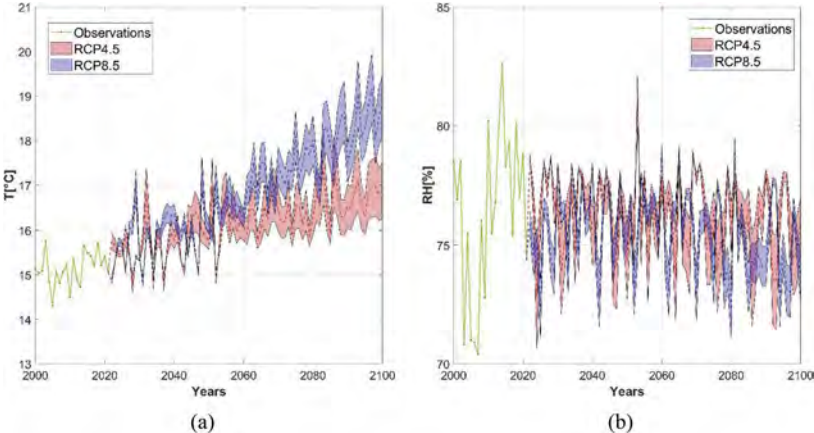


Figure 1. Expected variations of temperature (a) and relative humidity (b) according to different scenarios.

Significant changes are expected for temperature levels, with an average increase of 2.6°C (RCP4.5) and 4.5°C (RCP8.5) at the end of the century with respect to the period 1951-2000, while no clear trend is detected for relative humidity.

The analyses are then carried out considering three different scenarios: a stationary climate referring to the average temperature and relative humidity observed in the period 1951-2000 before the construction of the bridge, two changing climate conditions according to RCP4.5 and RCP8.5 concentration pathways.

Time series of condition indicators for chloride-induced corrosion, $C_{cl}(x,t)$ and $w(t)$, are generated implementing the mechanistic-empirical model described in previous section and adopting the probabilistic models in Table 1. Condition states are then defined according to the criteria established in Table 2 and transition probabilities are evaluated.

In Figure 2, the bridge expected condition states over time are shown for the investigated climate scenarios: stationary climate in black, RCP4.5 in red and RCP8.5 in blue.

Looking at the curves, it can be noticed that the impact of climate change becomes more and more relevant over time, thus affecting the time at which critical conditions are reached.

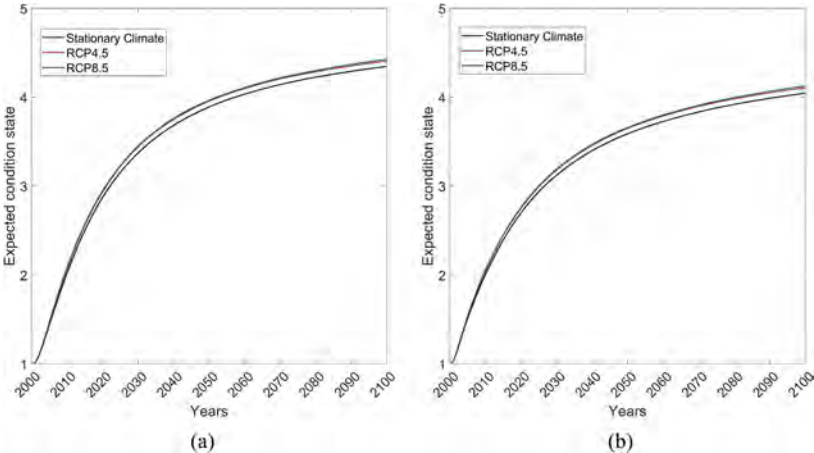


Figure 2. Expected condition ratings under stationary climate, (a) splash zone (b) atmospheric zone.

Moreover, for the investigated case study no significant differences are detected for the RCP4.5 and RCP8.5 scenario. For a structural element in splash zone, condition state 4 is expected to be reached after 58, 53, and 52 years under stationary climate, RCP4.5 and RCP8.5 respectively; while for a structural element in atmospheric zone, condition state 4 is expected to be reached after 93, 83, and 81 years.

The accelerated degradation due to climate change is confirmed by the results shown also in Figure 3 and 4, in which the predicted deterioration curves for atmospheric and splash zone are presented, respectively. Figures 3a and 4a refer to stationary climate conditions, while Figure 3b and 4b illustrate the deterioration curves corresponding to the RCP8.5 scenario but very similar results are obtained for the RCP4.5. In these Figures, the age of the bridge associated with a 50% probability to move to a worse condition state is highlighted by means of black dashed lines.

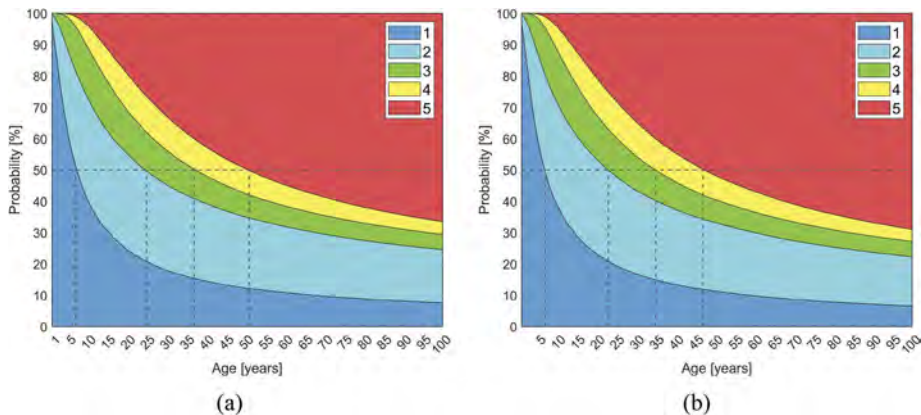


Figure 3. Deterioration curves for r.c. element in atmospheric zone: stationary climate (a) and RCP8.5 scenario (b).

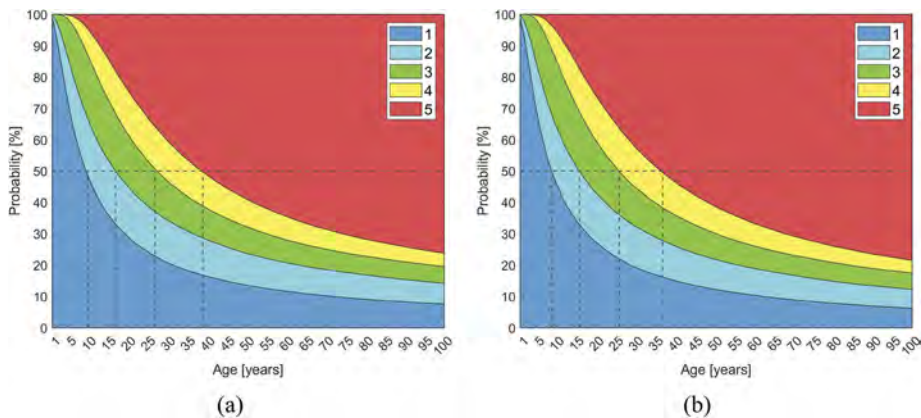


Figure 4. Deterioration curves for r.c. element in splash zone: stationary climate (a) and RCP8.5 scenario (b).

4 CONCLUSION

A methodology to predict the deterioration of r.c. bridge elements affected by chloride induced corrosion is presented in the paper, considering the influence of changing environmental conditions over the life cycle.

The procedure, which is based on mechanistic empirical models, can support the prediction of bridge condition states in bridge management systems supplementing the information

collected during inspections and evaluate the acceleration of the corrosion processes due climate change as shown for a case study of r.c. bridge in Italy.

The procedure is general and can be applied to different degradation processes once the mechanistic-empirical model is established. However, it is important to notice that models for the prediction of corrosion initiation and propagation, although widely used in civil engineering community, are rough approximations, and still there is a need for improved models, allowing a better estimation of time-dependent effects and including improved knowledge about climate parameters such as temperature or humidity. Further studies will be thus devoted to improving the prediction of corrosion initiation and propagation as a function of time-dependent exposure climate.

REFERENCES

- Bastidas-Arteaga, E., Schoefs, F., Stewart, M.G., Wang, X. 2013. Influence of global warming on durability of corroding RC structures: A probabilistic approach. *Engineering Structures* 51: 259–266.
- Choe, D.E., Gardoni, P., Rosowsky, D., Haukaaset T. 2008. Probabilistic capacity models and seismic fragility estimates for RC columns subject to corrosion. *Reliability Engineering and System Safety* 93: 383–393.
- Croce, P., Formichi, P., Landi, F. 2019. Climate change: Impacts on climatic actions and structural reliability. *Applied Sciences* 9:5416.
- Croce, P., Formichi, P., Landi, F. 2020. Influence of Reinforcing Steel Corrosion on Life Cycle Reliability Assessment of Existing R.C. Buildings. *Buildings* 10(6):99.
- Croce, P., Formichi, P., Landi, F. 2021. Enhancing the output of climate models: A weather generator for climate change impact studies. *Atmosphere* 12, 1074.
- DuraCrete. 2000. *Statistical quantification of the variables in the limit state functions. Dura-Crete-Probabilistic performance-based durability design of concrete structures*. EU-brite EuRam III. Contract BRPR-CT95-0132. Project BE95-1347/R9. January 2000. p. 130.
- Ellingwood, B. 2005. Risk-informed condition assessment of civil infrastructure: state of practice and research issues. *Structure and Infrastructure Engineering* 1: 7–18.
- Forzieri, G., Bianchi, A., Batista e Silva, F.B., Herrera, M.A.M., Leblois, A., Lavallo, C., Aerts, J.C.J.H., Feyen, L. 2018. Escalating impacts of climate extremes on critical infrastructures in Europe. *Glob Environ Chang.* 48:97–107.
- Jacob D., et al. 2014. EURO-CORDEX: New high-resolution climate change projections for European impact research. *Reg. Environ. Chang.* 14, 563–578.
- Lethanh, N., Hackl, J., Adey, B.T. 2017. Determination of Markov Transition Probabilities to be Used in Bridge Management from Mechanistic-Empirical Models. *J. Bridge Eng.* 22(10): 04017063.
- Maraun, D. 2016. Bias Correcting climate change simulations—A critical review. *Curr. Clim. Chang. Rep.* 2, 211–220.
- Mizutani, D., Lethanh, N., Adey, B.T., Kaito, K. 2017. Improving the Estimation of Markov Transition Probabilities Using Mechanistic-Empirical Models. *Front. Built Environ.* 3:58.
- Nasr, A., Honfi, D., Ivanov, O.L. 2022. Probabilistic analysis of climate change impact on chloride-induced deterioration of reinforced concrete considering Nordic climate. *J Infrastruct Preserv Resil.* 3:8.
- Roelfstra, G., Hajdin, R., Adey, B., Bruhwiler, E. 2004. Condition Evolution in Bridge Management Systems and Corrosion-Induced Deterioration. *J. Bridge Eng.*, 9(3): 268–277.
- Sousa, M.L., Dimova, S., Athanasopoulou, A., Rianna, G., Mercogliano, P., Villani, V., Nogal, M., Gervasio, H., Neves, L., Bastidas-Arteaga, E., Tsionis, G. 2020. *Expected implications of climate change on the corrosion of structures*. EUR 30303 EN, Publications Office of the European Union, Luxembourg.
- Stewart, M.G., Wang X., Nguyen, M.N. 2011. Climate change impact and risks of concrete infrastructure deterioration. *Engineering Structures* 33: 1326–1337.
- Stewart, M.G., Wang X., Nguyen, M.N. 2012. Climate change adaptation for corrosion control of concrete infrastructure. *Structural Safety* 35: 29–39.
- Thomas, O., Sobanjo, J.O. 2016. Semi-Markov Models for the Deterioration of Bridge Elements. *J. Infrastruct. Syst.* 22(3): 04016010.
- van Noordwijk, J.M., Frangopol, D.M. 2004. Two probabilistic life-cycle maintenance models for deteriorating civil infrastructures. *Probabilistic Engineering Mechanics* 19: 345–359.
- van Vuuren, D.P., et al. 2011. The representative concentration pathways: An overview. *Climatic Change* 109, 5–31.
- Zambon, I., Vidovic, A., Strauss, A., Matos, J. 2019. Condition Prediction of Existing Concrete Bridges as a Combination of Visual Inspection and Analytical Models of Deterioration. *Appl. Sci.* 9:148.
- Zhang, Y., Ayyub, B.M., Fung, J.F. 2022. Projections of corrosion and deterioration of infrastructure in United States coasts under a changing climate. *Resilient Cities and Structures* 1:98–109.

Life-cycle assessment of R.C. bridge components based on cluster analysis and stochastic process

F. Marsili & S. Keßler

Helmut-Schmidt-University/University of the Federal Armed Forces, Hamburg, Germany

F. Landi

University of Pisa, Pisa, Italy

ABSTRACT: This article proposes an approach to assess the life-cycle of reinforced concrete bridge components by applying a cluster algorithm and a stochastic model for damage evolution. The k-means algorithm is used to identify families of bridge components that deteriorate at similar rates. A measure of performance, i.e., silhouette width, supports the choice of the optimal number of clusters. Once the cluster model is defined, a gamma process is fitted to the data on the evolution of the conditions that belong to each family. By simulating the gamma process, the cumulative distribution function of time to failure is calculated for each cluster of components. The procedure applies to reinforced concrete bridge components in Switzerland, whose inspection and maintenance data is collected in the KUBA-DB database. This approach ensures that the expected service life of bridge components can be predicted with limited uncertainty.

1 INTRODUCTION

The management of existing infrastructure and its maintenance is an increasingly topical and relevant issue for the well-being of our societies. While, on the one hand, and as a result of a period strongly marked by new construction, physical infrastructure assets are aging and increasingly in need of maintenance, on the other hand, investment in maintenance is insufficient and even declining. Keeping infrastructures in good condition is therefore a challenge, requiring highly advanced approaches that can significantly improve maintenance efficiency. Remaining useful life should be understood as the time remaining before the infrastructure reaches a critical condition and maintenance is required to ensure safety, serviceability, or durability. However, and despite the fact that physical assets are ageing, only in few cases the condition has been judged critical, so that little information is available concerning the time when a critical condition is reached.

With the scope to increase maintenance efficiency, many infrastructure operators have undertaken a digitization process, which has led to the development of digital systems for managing infrastructure and its maintenance. Condition databases collect the results of periodic visual inspections and special tests, which are represented by digital data of different types, such as images, and qualitative and quantitative information on the progress of degradation. An important information is the qualitative judgment issued at the end of each inspection which regards the criticality of damage, as well as the condition of the component and the object as a whole, which is also linked to the urgency of the maintenance intervention.

A maintenance intervention is deemed necessary when the safety, durability or serviceability of the component and therefore possibly also of the object are jeopardized by the deterioration process. The judgment is expressed through an increasing condition index: the more significant the damage, the higher the index. The condition index can thus be interpreted as a measure of damage accumulation. The objects whose information is contained in these databases were built in different periods and therefore have different ages. As a result, not all the objects have already reached a critical condition. In addition to that, the objects have different characteristics, which affect their

robustness against aging in different ways. Since the information relating to objects in satisfactory condition are predominant over those in critical condition, the database is affected by the well-known problem of data imbalance, and information about the time in which the critical condition is reached cannot be directly derived from the database in most of the cases.

The evaluation of the time in which the damage reaches a critical condition is subject to uncertainties that can significantly influence the maintenance planning and therefore must not be neglected. One way to consider the uncertainties affecting the prediction of the remaining service life is to model damage evolution through probabilistic models such as Markov process or gamma process (Frangopol et al., 2004). Markov process is currently the most commonly used approach in bridge maintenance models. However, it has some drawbacks: first, it does not provide any reliability estimation, making it also difficult to link life-cycle analysis to structural reliability assessment; secondly, it is a condition model suitable for incorporating information from visual inspections, but not for predicting the attainment of conditions that have not already been observed. This represents a major problem in the case of imbalance data such as condition data. Gamma processes have so far been less applied, but do not have these drawbacks. The gamma process is suitable to model gradual damage monotonically accumulating over time, such as wear, fatigue, corrosion, crack growth, erosion, consumption, creep, swell, a degrading health index (van Noortwijk, 2009), as in the case of damage affecting civil infrastructures and reinforced concrete bridges. A gamma process can be fitted to available degradation data and used to assess the probability of reaching a critical condition as a function of time. Gamma processes have been already used for modelling fatigue damage evolution (Guida and Penta, 2015), deterioration of coating systems (Nicolai et al., 2007), and corrosion in reinforced concrete structures (Zhang et al., 2023). Modelling the deterioration as a gamma process is also suitable when visual inspections are involved and summarized into a condition index, provided that the condition index can be interpreted as a measure of damage accumulation (Edirisinghe et al., 2013).

Although uncertainties are inevitable, it is necessary to assess the probability of reaching a critical condition and consequently to predict the remaining service life as precise as possible. In other words, it is necessary to identify groups of objects, or objects components, which show similarities in terms of condition evolution paths. Unsupervised learning techniques and cluster algorithms are data mining techniques suited for finding patterns in big data sets. A review of the application of these techniques to life-cycle assessment can be found in Ghoroghi et al. (2022). Cluster analyses have been already applied to identify spatial clusters of structurally deficient bridges (Amin et al., 2020), to identify damage patterns affecting bridges (Chang and Chi, 2019), to develop bridge deterioration models (Moscoso et al., 2022). Although a grouping of objects based on similar condition evolution paths has already been theorized and proposed by infrastructure operators (Marsili et al., 2018), this result has never been pursued in a completely empirical way, by applying cluster algorithms to condition databases for infrastructure management.

The objective of this paper is to assess the life-cycle of aging reinforced concrete (r.c.) bridge components by combining a cluster analysis with a stochastic process. The k-means algorithm is implemented to cluster bridge components with similar degradation paths. Once the families of bridge components with similar condition evolution have been identified, the gamma process is fitted to the data characterizing each cluster. This approach makes it possible to predict the service life of bridge component with higher precision and construct the cumulative distribution of time to reach an undesired condition, which can be referred to as time to failure, for each identified group of components. The paper is organized as follows: Section 2 gives some background information about the methods at the basis of the proposed approach, Section 3 presents the case study at which the procedure has been applied and Section 4 draws some conclusion.

2 METHODS

2.1 *Gamma process*

van Noortwijk (2009) presents a survey of gamma processes in maintenance. By following its presentation of gamma process, a random quantity X has a gamma distribution with shape parameter $v > 0$ and scale parameter $u > 0$ if its probability density function (PDF) is given by

$$\text{Ga}(x|v, u) = \frac{u^v}{\Gamma(v)} x^{v-1} \exp(-ux) I_{0,\infty}(x) \quad (1)$$

where $I_A(x) = 1$ for $x \in A$ and $I_A(x) = 0$ for $x \notin A$ and $\Gamma(a) = \int_{z=0}^{\infty} z^{a-1} e^{-z} dz$ is the gamma function for $a > 0$. Furthermore $v(t)$ is a non-decreasing, right continuous, real valued function for $t \geq 0$ with $v(0) = 0$. The gamma process with shape function $v(t) > 0$ and scale parameter $u > 0$ is a continuous time stochastic process $X(t), t \geq 0$ with the following properties:

- $X(0) = 0$ with probability one;
- $X(\tau) - X(t) \sim \text{Ga}(v(\tau) - v(t), u), t \in [0, \tau]$;
- $X(t)$ has independent increments.

$X(t)$ represents the deterioration at time $t, t \geq 0$. Its probability density function is given by

$$f_{X(t)}(x) = \text{Ga}(x|v(t), u) \quad (2)$$

in which

$$E(X(t)) = \frac{v(t)}{u}, \quad (3)$$

$$\text{Var}(X(t)) = \frac{v(t)}{u^2} \quad (4)$$

are the expectation and the variance, respectively.

Assuming H_0 as the initial value of the damage accumulation index, failure occurs when the damage accumulation index $H(t) = H_0 - X(t)$ reaches the critical level H_{crit} . The time at which failure occurs is especially called T_{crit} , which is also referred to as the first hitting time of the critical level H_{crit} . Then the cumulative distribution function (CDF) of time to failure can be written as

$$F(t) = \Pr\{T_{\text{crit}} \leq t\} = \Pr\{X(t) \geq H_{\text{crit}}\} = \int_{x=H_{\text{crit}}}^{\infty} f_{X(t)}(x) dx = \frac{\Gamma(v(t), uH_{\text{crit}})}{\Gamma(v(t))}, \quad (5)$$

where $\Gamma(a, x) = \int_{z=x}^{\infty} z^{a-1} e^{-z} dz$ is the incomplete gamma function for $x \geq 0$ and $a \geq 0$.

2.2 Parameter estimation for the gamma process

Let us assume to model the temporal variability in the deterioration with a gamma process. Empirical studies show that the expected deterioration at time t is often proportional to a power law

$$E(X(t)) = \frac{v(t)}{u} = \frac{ct^b}{u} \quad (6)$$

in which $c > 0$ and $b > 0$ are constant. The gamma process is called stationary if the expected deterioration is linear in time, i.e., when $b = 1$, and non-stationary when $b \neq 1$.

Let us consider a typical data set of inspection times $t_i, i = 1, \dots, n$, where $t_0 < t_1 < \dots < t_n$, and corresponding observations of the cumulative amounts of deterioration $x_i, i = 1, \dots, n$, where $0 = x_0 \leq x_1 \leq \dots \leq x_n$. The parameter b can be determined based on engineering experience or estimated from data, according to a least square method (Hu et al., 2022)

$$b = \frac{n \sum_{i=1}^n (\log t_i)(\log x_i) - (\sum_{i=1}^n \log t_i) (\sum_{i=1}^n \log x_i)}{n \sum_{i=1}^n (\log t_i)^2 - (\sum_{i=1}^n \log t_i)^2}. \quad (7)$$

The parameters c and u can be estimated according to different approaches such as method of maximum likelihood, method of moments, method of Bayesian statics. According to the method of moments (Hu et al., 2022)

$$c = \frac{x_n^2 \left[1 - \sum_{i=1}^n \left(\frac{\Delta t_i}{t_n} \right)^2 \right]}{t_n S_Y^2}, \quad (8)$$

$$u = \frac{x_n \left[1 - \sum_{i=1}^n \left(\frac{\Delta t_i}{t_n} \right)^2 \right]}{S_Y^2} \quad (9)$$

in which S_Y^2 is given by

$$S_Y^2 = \sum_{i=1}^n (\Delta x_i - \bar{Y} \Delta t_i)^2, \quad (10)$$

and

$$\bar{Y} = \frac{\sum_{i=1}^n \Delta x_i}{\sum_{i=1}^n \Delta t_i} = \frac{x_n}{t_n}. \quad (11)$$

2.3 The k-means algorithm

The k-means is one of the simplest and most efficient as well as most widely used partitional clustering algorithms. The algorithm starts by choosing K representative points as the initial centroids. Each point is then assigned to the closest centroid based on a proximity measure, usually the Euclidean distance metric. Once the clusters are formed, the centroids for each cluster are updated. The algorithm then iteratively repeats these two steps until a convergence criterion is met and the centroids do not change anymore. In particular, the objective function employed by k-means is the Sum of Squared Errors (SSE).

Given a set of m observation $\mathbf{z}_1, \mathbf{z}_2, \dots, \mathbf{z}_m$ in which each observation is a d-dimensional real vector, k-means clustering aims to partition the m observations into $k \leq m$ sets $\mathbf{D} = \mathbf{D}_1, \mathbf{D}_2, \dots, \mathbf{D}_k$ so as to minimize the SSE (Aggarwal and Reddy, 2014)

$$\underset{\mathbf{D}}{\operatorname{argmin}} = \sum_{k=1}^K \sum_{\mathbf{z}_j \in \mathbf{D}_k} \|\mathbf{z}_j - \mathbf{d}_k\|^2, \quad (12)$$

$$\mathbf{d}_k = \frac{\sum_{\mathbf{z}_j \in \mathbf{D}_k} \mathbf{z}_j}{|\mathbf{D}_k|}, \quad (13)$$

in which \mathbf{d}_k is the centroid of cluster \mathbf{D}_k and $|\mathbf{D}_k|$ is the size of \mathbf{D}_k .

The major factors that can impact the performance of the k-means algorithm are the following: 1) Choice of the initial centroids; 2) Estimation of the number of clusters K. Several methods are proposed in the literature to tackle these factors. In this work, the k-means++ algorithm is applied to select the initial centroids. According to this technique, the first cluster center is chosen uniformly at random from the data set. The next centroid is chosen randomly from the remaining data points with probability proportional to its distance from the point's closest existing cluster center. The problem of estimating the correct number of clusters is addressed by calculating the silhouette coefficient. This performance measure is based on the calculation of the intra- and inter-cluster distances. For a given point \mathbf{z}_j , first the average of the distances to all points in the same cluster is calculated. This value is set to e_j . Then for each cluster that does not contain \mathbf{z}_j , the average distance of \mathbf{z}_j to all the data points in each cluster is computed. This value is set to f_j . Using these two values the silhouette coefficient of a point is estimated. The average of all the silhouettes in the dataset is called the average silhouette width

$$P = \frac{\sum_{j=1}^m \frac{f_j - e_j}{\max(f_j, e_j)}}{m}, \quad (14)$$

and the larger its value, the higher the quality of clustering.

3 CASE STUDY

3.1 KUBA-DB

The Federal Roads Office (ASTRA) is the Swiss authority for road infrastructure management. In the context of the maintenance of ASTRA's engineering structures, inspection is of primary importance in order to detect damage at an early stage and to assess the current condition of the structure or the individual parts of the structure. Three different types of inspection can be carried out: primary, intermediate and special. The findings of primary and intermediate inspections are damage processes and information collected during the inspection is collected in the database KUBA-DB. A set of homogeneous damage processes within the same segment of the structural member and having the same effects on the functionality of the component forms a damage group. Each damage group is assigned to a condition class, which describes the condition of a relevant area of the structural element. Five condition classes have been defined, from "good condition" class to "alarming condition" class, with which a condition index from 1 to 5 is associated. Then, an assessment of the condition of the whole structural component is made, based on the damage groups and their effect on the safety and on the functionality of the component. This information is then aggregated at higher level to determine the condition of the whole object.

3.2 Description of the procedure

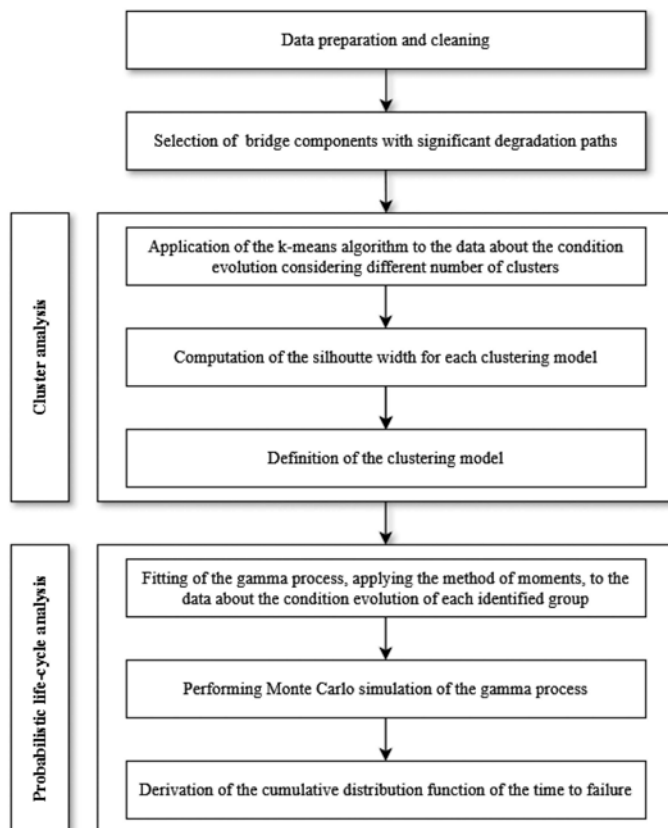


Figure 1. Flow chart summarizing the applied procedure.

Figure 1 summarizes the applied procedure for the analysis of the data. The first step is to prepare the data for analysis. In this step, data affected by inconsistencies due to human errors in their recording are removed, such as typing error. The data are cleaned and transformed into an appropriate format to perform the analysis. In a second step, the data for each structural component are selected, focusing on those structural components that show significant deterioration in their condition, i.e., those for which the condition index has experienced at least an increase from 1 to 2 and from 2 to 3. Such components are able to provide relevant information on the development of their condition, which will allow the fitting of a gamma process. Then, cluster analysis is performed, considering a variable number of clusters and calculating for each cluster model the performance measure. In general, it is possible to identify between two and three families of components that show similar condition development. More families can be identified only if a larger data set is available. The performance measure, i.e., silhouette width, supports the choice of the optimal number of clusters and is supplemented with a visual inspection of the identified clusters. Once the cluster model has been defined, a gamma process is fitted to the data belonging to each identified cluster. The parameters of the gamma process are determined based on Equations 7, 8, 9. Their definition allows a Monte Carlo simulation of the gamma process and the derivation of the mean time to failure as well as its CDF.

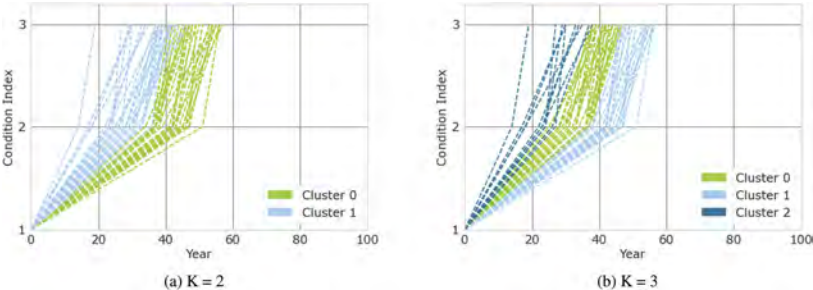


Figure 2. Results of k-means clustering for two and three centers.

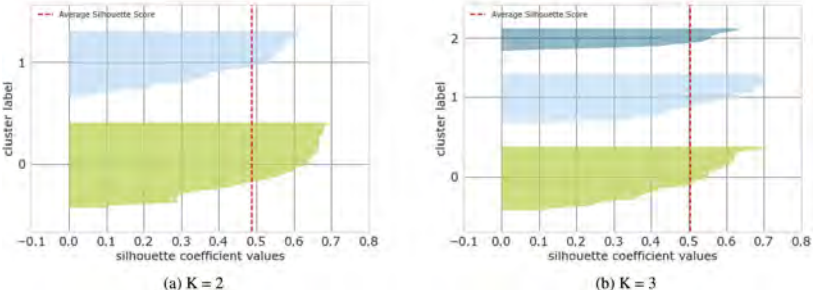


Figure 3. Silhouette plot of k-means clustering for 64 samples and two and three centers.

3.3 Results

For illustrative purposes, the results for a single component, namely the deck slab of reinforced concrete bridges, are reported. In a total of $m = 64$ cases, the condition of the deck slab deteriorate significantly over time, and the condition index increases from 1 up to 3.

The cluster analysis with the k-means algorithm is performed considering the evolution of the condition index over time of the selected elements. Figure 2 shows the clusters identified in the case where $K = 2$ and $K = 3$. For each cluster model the average silhouette width is calculated (Figure 3). Results reveal that the silhouette width of the model characterized by three clusters ($P(K = 3) = 0.505$) is higher than the silhouette width of the model characterized by

two clusters ($P(K = 2) = 0.488$). For this reason, the optimal number of clusters is three, and this model is assumed and considered in the subsequent analysis. The cluster analysis identifies three families of bridge deck slab that show markedly different condition evolution, which can be referred to as slow (cluster 1), normal (cluster 0) and fast (cluster 2). The next step is to fit the gamma process to the data characterizing each cluster, that is, to statistically estimate the parameters b , c , and u for each family of bridge deck slab. The results of the inspection, namely the condition index, must be first adjusted to obtain an index representing the accu-

Table 1. Estimated parameters of the gamma process and average time to failure resulting from its simulation for each cluster.

	b	u	c	Average time to failure (year)
Cluster 0	1.7027	1.3333	0.0069	52.4
Cluster 1	2.3245	1.3333	0.0004	60.2
Cluster 2	1.0930	1.3333	0.0935	43.6

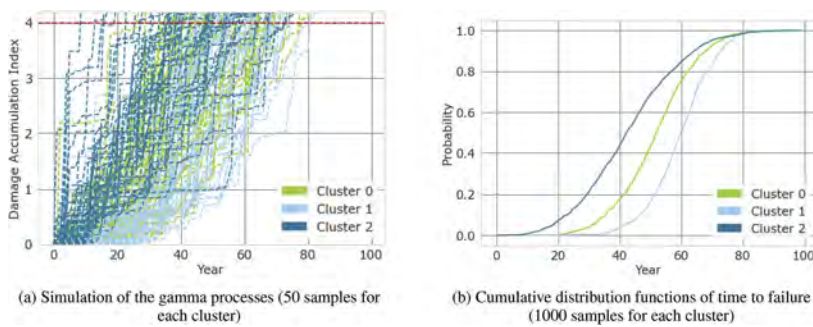


Figure 4. Probabilistic models for life-cycle assessment.

mulation of deterioration over time. Hence, the condition index is transformed into a damage accumulation index through the following equation

$$\text{Damageaccumulationindex} = \text{Conditionindex} - 1, \quad (15)$$

which is considered to fit the gamma process.

It is assumed that the critical damage accumulation level is 4, which corresponds to the condition index value 5, which is the critical value at which the component no longer fulfills a function (safety, serviceability, durability).

After that the parameters of the gamma process have been estimated (Table 1), a Monte Carlo simulation is performed (Figure 4). The Monte Carlo simulation allows the derivation of the average time to failure (Table 1) and the time to failure CDF for each identified cluster, which is shown in Figure 4. The CDF describes the trend of the failure probability as a function of time, which is directly related in statistical terms to the service life of the component. The average time to failure especially represents the expected service life of the component. Based on this result, it can be concluded that the group of components having a fast rate of deterioration has an expected service life of 43.6 years, the normal one of 52.4 years, and the slow one of 60.2 years.

4 CONCLUSIONS

The assessment of the remaining service life, understood as the service life before a degradation process reaches a critical level for which a maintenance intervention is deemed urgent, is an important step in improving the management of physical assets of infrastructure. Conscious of

this, this article proposes an approach to assess the life-cycle of reinforced concrete bridge components by applying an unsupervised learning technique and a stochastic process. A cluster analysis based on the k-means algorithm is applied to identify families of bridge components that degrade with similar rates. A gamma process is fitted to the data concerning the evolution of the degradation that characterizes each family. By simulating the gamma process, the average expected service life of each family of components can be estimated. The simulation also allows the estimation of the time-dependent probability of damage exceeding a threshold level, called the probability of failure. An application of this approach to the case of reinforced concrete bridges in Switzerland, whose inspection results are contained in the KUBA-DB database, is developed. In particular, condition data related to the deck slab of reinforced concrete bridges is analyzed with the described procedure. Results reveal that three families of components whose condition evolves in a similar way can be identified. A performance measure, namely the silhouette width, supports the choice of the optimal number of clusters. Finally, it can be said that through this approach the service life of components can be predicted with reduced uncertainties.

ACKNOWLEDGMENT

This research study is funded by the FFG project “ENDURE - Estimation of the remaining service life of bridges through the development and testing of hybrid models”, whose aim is to improve bridge life-cycle assessment analysing the infrastructure management databases of the D-A-CH countries.

REFERENCES

- Aggarwal, C. C. and Reddy, C. K. (2014), *Data Clustering, Algorithms and Applications*, Taylor Francis Group.
- Amin, R., Kocak, S., Sevil, H., Peterson, G., Hamilton, J., Rivera, B. and Barraco, T. (2020), ‘A spatio-temporal cluster analysis of structurally deficient bridges in the contiguous usa’, *Developments in the Built Environment* **4**, 100034.
- Chang, K. and Chi, S. (2019), ‘Bridge clustering for systematic recognition of damage patterns on bridge elements’, *Journal of Computing in Civil Engineering* **33**(5), 04019028.
- Edirisinghe, R., Setunge, S. and Zhang, G. (2013), ‘Application of gamma process for building deterioration prediction’, *Journal of Performance of Constructed Facilities* **27**(6), 763–773.
- Frangopol, D. M., Kallen, M.-J. and Noortwijk, J. M. V. (2004), ‘Probabilistic models for life-cycle performance of deteriorating structures: review and future directions’, *Progress in Structural Engineering and Materials* **6**(4), 197–212.
- Ghoroghi, A., Rezgui, Y., Petri, I. and Beach, T. (2022), ‘Advances in application of machine learning to life cycle assessment: a literature review’, *The International Journal of Life Cycle Assessment* **27**(3), 433–456.
- Guida, M. and Penta, F. (2015), ‘A gamma process model for the analysis of fatigue crack growth data’, *Engineering Fracture Mechanics* **142**, 21–49.
- Hu, C., Fan, H. and Wang, Z. (2022), *Gamma Process-Based Degradation Modeling and Residual Life Prediction*, Springer Singapore, Singapore, pp. 77–97.
- Marsili, F., Bödefeld, J., Croce, P. and Landi, F. (2018), Bayesian approaches to lifetime prediction, in ‘Safety and reliability - safe societies in a changing world, proceedings of the 28th International European Safety and Reliability Conference (ESREL 2018)’, Trondheim, Norway.
- Moscoso, Y. F. M., Rincón, L. F., Leiva-Maldonado, S. L. and e Matos, J. A. S. C. C. (2022), ‘Bridge deterioration models for different superstructure types using markov chains and two-step cluster analysis’, *Structure and Infrastructure Engineering* **0**(0), 1–11
- Nicolai, R. P., Dekker, R. and van Noortwijk, J. M. (2007), ‘A comparison of models for measurable deterioration: An application to coatings on steel structures’, *Reliability Engineering System Safety* **92** (12), 1635–1650. Special Issue on ESREL 2005.
- van Noortwijk, J. (2009), ‘A survey of the application of gamma processes in maintenance’, *Reliability Engineering System Safety* **94**(1), 2–21. Maintenance Modeling and Application.
- Zhang, Z., Ren, X., Niu, Q., Zhang, Y. and Zhao, B. (2023), ‘Durability degradation simulation of rc structure based on gamma process considering two-dimensional chloride diffusion and life probabilistic prediction’, *Structures* **48**, 159–171.

Corrosion effects of RC bridges considering the climate change impact

M. Zucca, M.L. Puppio & F. Mistretta

University of Cagliari, Cagliari, Italy

F. Landi, P. Formichi & P. Croce

University of Pisa, Pisa, Italy

ABSTRACT: Climate change is associated with significant variations of temperature, atmospheric humidity, and carbon dioxide concentration levels. These changes potentially produce a double negative effect on the safety and the life cycle of civil engineering structures: increased climatic actions and rate of material degradation. In fact, changes in these variables affect the service life of reinforced concrete and steel structures by acting on the rate of carbonation and corrosion. Corrosion has a detrimental effect especially on the seismic vulnerability influencing strength, ductility and affecting the dynamic response and consequently the failure of reinforced concrete structures. Particularly bridges, as structures directly exposed to the weather effects, are more susceptible to these phenomena. In this paper, a framework to quantitatively account for the effects of climate change on carbonation-induced corrosion is proposed, focusing on the loss of concrete passivity, and thus widespread corrosion. Different scenarios for the expected variations in CO₂ concentrations and temperature are analyzed and seismic risk indexes are evaluated through a real case study of bridge located in the province of Massa-Carrara (Italy).

1 INTRODUCTION

Corrosion has a detrimental impact on life cycle and on the seismic performance particularly of reinforced concrete structures. The effects of corrosion are more significant on strength than on ductility (Berto et al., 2012). Typically, reinforced concrete bridges, in which all the structural elements are exposed to the environmental conditions, are more prone to corrosion than steel bridges, where the possibility of inspection and maintenance are more effective, and buildings, where the structure is fully protected (Biondini et al. 2014).

Existing reinforced concrete bridges can be interested by damaging or collapse due to aging, design errors and usually the deterioration can be exacerbated by lack of maintenance and climate change impacts. The main failures are due to steel corrosion producing loss of prestress and a wide of brittle failure, especially diffused in the Gerber type bridges (Sassu et al. 2023).

Climate changes strickles existing structures and infrastructures with several effects. Rain-storms or tropical cyclones threaten the stability of bridges, particularly the one of reduced spans, producing erosion or additional actions (Sassu et al. 2017) (Puppio et al. 2021). Maintenance and visual inspections, joined with modern strategy of vulnerability assessment and refurbishment, are key action in the prevention of bridge failures (Mistretta et al. 2015) (Stochino et al 2018)(Pucci et al 2021)(Coni et al. 2021) (Hasa et al 2022).

The effects of climate change on civil engineering structures are now recognized and investigated into international context, considering different models and scenarios (Stewart et al., 2011) (Bastidas-Arteaga et al., 2013) (Croce et al., 2019). The Joint Research Center of the European Commission produced new international guidelines on the expected implications of climate changes on the corrosion of structures (Sousa et al., 2020). The report highlighted the impact of the increase of CO₂ levels and temperature levels on corrosion processes of r.c. structures thus calling for adaptation strategies guaranteeing that the corrosion damage probability will be not compromised from future climate.

The topic is of strategic concerns in Italy particularly considering the huge diffusion of r.c. bridges, the seismic exposure of the environments and the current state of maintenance. The paper proposes a method of investigation to consider the effects increase of temperature on seismic vulnerability of r.c. bridge and considering a real case of study in the province of Massa Carrara.

2 EFFECTS OF GLOBAL WARMING ON CORROSION RATE

The durability of reinforced concrete structures is affected by climate change mainly entailing the variations of three environmental parameters: temperature, relative humidity, and carbon dioxide (CO₂) concentration levels. In this work, the attention is focused on the impact of temperature increase on corrosion rate i_{corr} .

Future climate is predicted based on assumptions about future trends in socio-economic dynamics, future concentrations of greenhouse gasses, variations in land use and land cover. These assumptions lead to an increase in radiative forcing, i.e. the change in energy flux, in the year 2100 equal to 2.6, 4.5, 6.0 and 8.5 W/m² compared to the preindustrial era and define the so-called Representative Concentration Pathways (RCPs) (van Vuuren et al., 2011). The scenarios which are mostly considered in climate risk studies are RCP4.5 and RCP8.5, for which most climate projections are available. They correspond to medium and maximum pathways, and they have been adopted in the present study as well. Expected changes in climate parameters are thus estimated by the analysis of climate projections provided by high-resolution Regional Climate Models according to RCPs scenarios (Jacob et al., 2014). The limited number of climate projections can be then increased to provide a probabilistic description of temperature variations by means of the use of weather generation techniques such as that presented in (Croce et al., 2021). In Figure 1, the variations of yearly average temperature are shown for the location of the bridge, which will be investigated in the following sections, Massa in Italy (lon=10.141; lat=44.025).

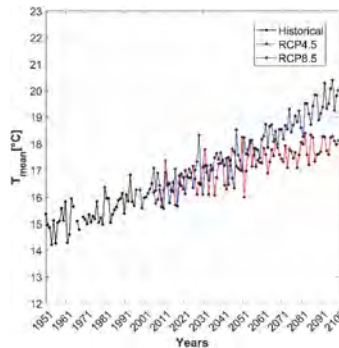


Figure 1. Historical and future variation of yearly average temperature at Massa (Italy).

Temperature raises are associated with an increase of corrosion rate, which is generally described by the model developed by (DuraCrete, 2000):

$$i_{corr}(t) = i_{corr,20}[1 + K(T(t) - 20)] \quad (1)$$

where $i_{corr,20}$ is the corrosion rate at 20°C, which depends on the environmental exposure, and K is a factor can be assumed $K = 0.025 \text{ } ^\circ\text{C}^{-1}$ if $T(t) < 20 \text{ } ^\circ\text{C}$ and $K = 0.073 \text{ } ^\circ\text{C}^{-1}$ if $T(t) > 20 \text{ } ^\circ\text{C}$. Assuming $i_{corr,20} = 0.345, 0.172$, and $0.431 \text{ } \mu\text{A}/\text{cm}^2$, average values given in (Stewart et al., 2011) for exposure class C2 - Wet-rarely dry (unsheltered), C3 - Moderate humidity (sheltered), and C4 -Cyclic wet-dry (unsheltered), variation of corrosion rate i_{corr} with time are evaluated. Different outcomes, are obtained starting from the reference values $i_{corr,20}$ given in (DuraCrete, 2000) for slight, moderate, and high exposure: 0.1,1, and $5 \text{ } \mu\text{A}/\text{cm}^2$. Another model which is commonly used to describe temperature effects on corrosion rate is the one based on the Arrhenius Law (Pour-Ghaz et al., 2009):

$$i_{corr}(t) = i_{corr,20} \exp\left(\frac{E}{R} \left(\frac{1}{293} - \frac{1}{273 + T(t)}\right)\right) \quad (2)$$

where E is the activation energy of the diffusion process (40 kJ/mol) and R is the gas constant (8.314×10^{-3} kJ/mol K). In this case, the percentage of variations will be higher than the previous one, leading to increases up to 30% at the end of the century. Variation of corrosion rate i_{corr} with time are again evaluated considering the same reference values of $i_{corr,20}$ given in (Stewart et al., 2011) and (DuraCrete, 2000).

3 STRUCTURAL MODELLING AND ANALYSIS METHOD

To evaluate the corrosion effects due to carbonation on the seismic performance of existing RC bridges, the approach proposed by (Crespi et al., 2022) has been considered, based on the implementation of simplified 3D Finite Element Models (FEMs) using MIDAS Civil commercial software. The piers, the pier caps and the deck have been modelled with beam elements, while the elastomeric bearings have been schematized through elastic links having rotational and translational stiffnesses calculated according to EN 1337-3:2005. To guarantee the connection between the beam elements and the elastic links, a series of rigid links have been applied (Crespi et al., 2022). The abutments have been considered as perfect restrains and the non-structural elements have been implemented in the FEM as uniform distributed beam loads (Zucca et al., 2023).

To obtain the correct dynamic behavior of the bridge, the reduction of the bending stiffness of the piers due to the concrete cracking has been introduced through specific scale factors applied to the concrete gross-section elastic stiffness of each pier, calculated starting from the moment-curvature ($M-\chi$) diagrams of the gross-section of the piers according to EN 1998-3:2005. On the contrary, the stiffness of the deck is not scaled (Chen & Duan, 2000) and the traffic load has been neglected according to as reported in (Decreto Ministeriale, 2018).

Two different failure mechanisms are taken into consideration for each pier: the ductile and the brittle collapse mechanism. In particular, the ductile collapse mechanism is related to the moment-curvature diagram of the cross-section of the pier, and it is characterized by an initial elastic branch followed by a large strain hardening plastic trend while the brittle failure mechanism presents a linear load-displacement trend until reaching the ultimate shear resistance. The ductile collapse mechanism is regulated by the rotational capacity of the plastic hinge while the brittle collapse mechanism depends on the shear strength of the monitored structural element.

The non-linear behavior of the concrete and of the of the steel reinforcement bars has been considered using, respectively, Kent and Park model (Kent & Park, 1971) and Park Strain Hardening constitutive law (Park & Paulay, 1975). The two different verification criteria considered in this work are the following: for the ductile mechanism the achievement of $\frac{3}{4}$ of the ultimate rotation θ_u while for the brittle failure mechanism the achievement of the shear resistance of the monitored structural element, calculated considering the cyclic shear resistance reported in EN 1998-2, 2005. The corrosion effects due to carbonation have been considered in the FEM through a simplified analytical model related to the progressive reduction of the steel reinforcements diameter and where the penetration law in a generic concrete volume follows a parabolic trend:

$$s = k \cdot t^n \quad (3)$$

where s = thickness of the carbonated layer of concrete; k = penetration rate coefficient; and t = time. For existing RC bridges built around 1970's, it is possible to assume the parameter n equal to 2 because they were realized using normal compacted concrete (Saetta & Vitaliani, 2004).

As mentioned before, the existing RC bridges considered in this work were built around the 1970's and they have been designed without considering the seismic action. For this reason, the proposed approach directly considers the influence of the steel reinforcements area reduction on the seismic capacity of the bridges, according to Equations 4 and 5

$$d(t) = d_0 - 2P(t) = d_0 - 2i_{corr}k(t-t_1) \quad (4)$$

$$A_{s(t)} = \frac{\pi [d_0 - 2i_{corr}(t-t_i)]^2}{4} \quad (5)$$

Equation 4 considers the variation of the diameter of the steel reinforcement d as a function of the corroded thickness $P(t)$ while Equation 5 is related to the variation of cross-section area $A_{s(t)}$.

As mentioned in previous Sections, three different corrosion scenarios have been considered: slight, moderate and high. For these scenarios two different assumptions were made for the evaluation of i_{corr} value. In the first assumption, the value of i_{corr} has been obtained considering the average values given in (Stewart et al., 2011) which indicates values of i_{corr} equal to 0.172, 0.345, and $0.431 \mu\text{A}/\text{cm}^2$, respectively for slight, moderate and high corrosion level. In the second case, the values of i_{corr} have been calculated according to as reported in (DuraCrete, 2020) that is 0.1, 1 and $5 \mu\text{A}/\text{cm}^2$ respectively for slight, moderate and high corrosion scenario.

The reduction of the steel reinforcements diameter has been evaluated considering the difference between the initial steel reinforcements diameter d_0 and the actual one $d(t)$. The following values of the other parameters are taken into consideration: water/cement ratio (w/c) = 0.6, the compressive strength of the concrete $f_{ck} = 28 \text{ MPa}$, the penetration rate coefficient $k = 0.0116$ and the steel rebar ultimate deformation $\varepsilon_{u,0} = 9 \%$ are considered as constant for the different corrosion levels analysed. The initiation time t_i is assumed constant and equal to 13.5 years as in (Berto et al., 2009), disregarding the effect of climate change, especially the increase of CO_2 levels and temperatures, on the diffusion process. In this work, the corrosion effects are evaluated at different times (construction time and after 13.5, 50, 75 and 100 years of bridge service life) to obtain the variation of the seismic performance of the bridge over time. To evaluate the seismic behaviour of the bridges, multi-modal pushover approach has been chosen considering the Capacity Spectrum Method (CSM) for the determination of the performance point (ATC-40, 1996). Several capacity curves have been obtained and for each of them, corresponding to a vibration mode shape with a participating mass greater than 1% and a modal loading profile, the performance point is calculated considering the relevant seismic demand spectrum. For each vibration mode, the internal actions acting on the monitored structural element have been determined in correspondence to the performance point obtained by the intersection of the capacity curve and the demand spectrum in ADRS plane. The internal actions obtained for each capacity curve are combined through the complete quadratic combination (CQC) rule, for the safety verification purposes. Further detail about modelling can be found in (Zucca et al., 2023).

4 CASE STUDY

The procedure described in previous Section has been applied to a one existing RC bridge located in the province of Massa-Carrara and built around the 1970's. The main seismic parameters which characterize the site are the following: soil type C and PGA equal to 0.156 g. The analyzed bridge is characterized by the presence of two adjacent and independent carriageways, consisting in a sequence of four simply supported 40.40 m spans. The planimetric and altimetric layout is rectilinear. The overall width of the roadway is equal to 9.86 m and each span is realized by a precast concrete girder of three longitudinal prestressed I beams and five transverse beams. The bridge deck consists in a 20 cm concrete slab. Each span is supported by 2 x 3 elastomeric bearings located into the hammer cap. The deck is supported by three hexagonal hollow RC piers characterized by a height ranging between 5.06 m and 15.51 m (Figure 2). Table 1 reports the main characteristics of the piers. The first three fundamental periods which characterize the dynamic behaviour are $T_1 = 2.73 \text{ s}$, $T_2 = 2.56 \text{ s}$ and $T_3 = 2.41 \text{ s}$.

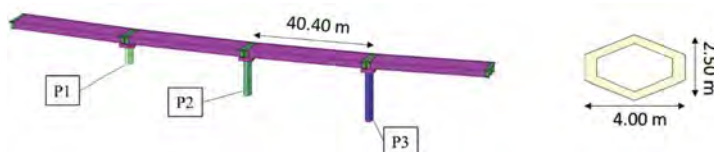


Figure 2. The analyzed bridge.

Table 1. Piers main characteristics.

Piers [n°]	Cross-section dimensions [m]	Height [m]	Longitudinal steel reinforcement [-]	Transverse steel reinforcement [-]	Piers thickness [m]
1	4.0 x 2.5	5.06	148Ø14	Ø10/20	0.35
2	4.0 x 2.5	10.84	148Ø14	Ø10/20	0.35
3	4.0 x 2.5	15.51	148Ø14	Ø10/20	0.35

Tables 2 and 3 summarize the results of the corrosion effects on the steel reinforcements expressed in terms of diameter and area reductions as a function of the age of the bridge considering, respectively, the reference values of i_{corr} suggested by (Stewart et al., 2011) and (DuraCrete, 2020). It is important to highlight that the reduction of the steel rebar ultimate deformation $\epsilon_{u,0}$ has been calculated according to (Lee & Choo, 2009). On the contrary, considering the i_{corr} values suggested by (DuraCrete, 2020) significant steel reinforcements area reductions can be observed as early as 50 years after the construction of the structure for the high corrosion scenario characterized by $i_{corr} = 5 \mu\text{A}/\text{cm}^2$. Considering the high corrosion level, it is possible to notice that, after 100 years from the construction of the bridge the transverse steel reinforcements appear completely corroded. As a result a slight increase of the natural periods of the bridge can be observed especially for the first vibration modes.

Table 2. Corrosion effects on steel reinforcements (Stewart et al., 2011).

t [years]	Slight Corrosion $i_{corr} = 0.172 [\mu\text{A}/\text{cm}^2]$				Moderate Corrosion $i_{corr} = 0.345 [\mu\text{A}/\text{cm}^2]$				High Corrosion $i_{corr} = 0.431 [\mu\text{A}/\text{cm}^2]$			
	d_0 [mm]	d [mm]	ΔA_s [%]	ϵ_u [%]	d_0 [mm]	d [mm]	ΔA_s [%]	ϵ_u [%]	d_0 [mm]	d [mm]	ΔA_s [%]	ϵ_u [%]
0-13.5	10.00	10.00	0.00	9.00	10.00	10.00	0.00	9.00	10.00	10.00	0.00	9.00
	14.00	14.00	0.00	9.00	14.00	14.00	0.00	9.00	14.00	14.00	0.00	9.00
50	10.00	9.85	1.46	8.79	10.00	9.71	2.92	8.59	10.00	9.64	3.65	8.36
	14.00	13.85	1.04	8.85	14.00	13.71	2.09	8.70	14.00	13.64	2.61	8.54
75	10.00	9.75	2.45	8.57	10.00	9.51	4.92	8.14	10.00	9.39	6.15	7.92
	14.00	13.75	1.75	8.69	14.00	13.51	3.52	8.38	14.00	13.39	4.39	8.23
100	10.00	9.65	3.45	8.39	10.00	9.31	6.92	7.78	10.00	9.14	8.65	7.48
	14.00	13.65	2.47	8.57	14.00	13.31	4.95	8.13	14.00	13.14	6.18	7.92

Table 3. Corrosion effects on steel reinforcements (DuraCrete, 2020).

t [years]	Slight Corrosion $i_{corr} = 0.1 [\mu\text{A}/\text{cm}^2]$				Moderate Corrosion $i_{corr} = 1 [\mu\text{A}/\text{cm}^2]$				High Corrosion $i_{corr} = 5 [\mu\text{A}/\text{cm}^2]$			
	d_0 [mm]	d [mm]	ΔA_s [%]	ϵ_u [%]	d_0 [mm]	d [mm]	ΔA_s [%]	ϵ_u [%]	d_0 [mm]	d [mm]	ΔA_s [%]	ϵ_u [%]
0-13.5	10.00	10.00	0.00	9.00	10.00	10.00	0.00	9.00	10.00	10.00	0.00	9.00
	14.00	14.00	0.00	9.00	14.00	14.00	0.00	9.00	14.00	14.00	0.00	9.00
50	10.00	9.92	0.85	8.88	10.00	9.15	8.47	7.80	10.00	5.77	42.34	1.57
	14.00	13.92	0.60	8.91	14.00	13.15	6.05	8.15	14.00	9.77	30.24	3.69
75	10.00	9.86	1.43	8.75	10.00	8.57	14.27	6.50	10.00	2.87	71.34	1.17
	14.00	13.86	1.02	8.82	14.00	12.57	10.19	7.21	14.00	6.87	50.96	2.33
100	10.00	9.80	2.01	8.65	10.00	7.99	20.07	5.48	10.00	0.00	100.00	0.00
	14.00	13.80	1.43	8.75	14.00	11.99	14.33	6.48	14.00	3.97	71.67	1.01

To complete the evaluation of the seismic behaviour of the analysed bridge, multi-modal push-over analyses have been carried out considering an iterative process. Once the determination of the peak ground acceleration which leads to the collapse of the first structural elements (PGA_C) it is possible to calculate the risk indices which characterize the bridge for the different corrosion scenarios analysed through Equation 6, where PGA_D = design peak ground acceleration:

$$RI_{PGA} = \frac{PGA_C}{PGA_D} \quad (6)$$

Values of risk indices close or greater than one concern cases of safe bridges, whereas values smaller than one indicate structures with a high risk of seismic failure. Tables 4 and 5 summarize the values of the risk indices obtained for the investigated corrosion scenarios, i_{corr} determined as reported in (Stewart et al., 2011) and in (DuraCrete, 2020), and where X indicates the direction along the longitudinal axis of the bridge and Y the transverse direction.

The reduction of the risk indices is more evident considering the moderate and high corrosion scenarios characterized by i_{corr} values suggested by (DuraCrete, 2020). It is possible to notice that after 100 years from the construction of the bridge, taking into consideration a value of $i_{corr} = 5 \mu\text{A}/\text{cm}^2$, the reduction of the risk indices reaches 80% for the ductile collapse mechanism and exceeds 90% for the brittle collapse mechanism while for $i_{corr} = 1 \mu\text{A}/\text{cm}^2$ there is a significant reduction of the brittle failure mechanism risk index in Y direction which slightly exceeds 75%. Important reduction of the risk indices is also highlightable after 75 years of the construction of the structure.

Table 4. Risk indices values considering i_{corr} given in (Stewart et al., 2011).

Corrosion scenario		Ductile mechanism					
		50 years		75 years		100 years	
		X	Y	X	Y	X	Y
RI_{PGA}	Slight	5.342 (0.00%)	3.936 (0.00%)	5.342 (0.00%)	3.936 (0.00%)	5.231 (-2.08%)	3.851 (-2.16%)
	Moderate	5.262 (-1.50%)	3.888 (-1.22%)	5.201 (-2.64%)	3.866 (-1.79%)	5.171 (-3.20%)	3.815 (-3.07%)
	High	5.231 (-2.08%)	3.851 (-2.16%)	5.171 (-3.20%)	3.815 (-3.07%)	5.100 (-4.20%)	3.799 (-4.14%)
		Brittle mechanism					
RI_{PGA}	Slight	1.379 (0.00%)	0.959 (0.00%)	1.379 (0.00%)	0.959 (0.00%)	1.257 (-8.46%)	0.889 (-7.30%)
	Moderate	1.313 (-4.79%)	0.913 (-4.80%)	1.297 (-5.94%)	0.901 (-6.04%)	1.221 (-11.45%)	0.836 (-12.82%)
	High	1.257 (-8.46%)	0.889 (-7.30%)	1.221 (-11.45%)	0.836 (-12.82%)	1.144 (-17.04%)	0.632 (-34.09%)

Table 5. Risk indices values considering i_{corr} given in (DuraCrete, 2020).

Corrosion scenario		Ductile mechanism					
		50 years		75 years		100 years	
		X	Y	X	Y	X	Y
RI_{PGA}	Slight	5.342 (0.00%)	3.936 (0.00%)	5.342 (0.00%)	3.936 (0.00%)	5.342 (0.00%)	3.936 (0.00%)
	Moderate	5.100 (-4.20%)	3.799 (-4.14%)	5.083 (-4.84%)	3.801 (-3.43%)	4.537 (-15.01%)	3.004 (-23.68%)
	High	4.968 (-7.00%)	3.782 (-4.56%)	3.194 (-40.21%)	2.348 (-40.35%)	1.114 (-79.15%)	0.876 (-77.74%)
		Brittle mechanism					
RI_{PGA}	Slight	1.379 (0.00%)	0.959 (0.00%)	1.379 (0.00%)	0.959 (0.00%)	1.379 (0.00%)	0.959 (0.00%)
	Moderate	1.144 (-17.04%)	0.632 (-34.09%)	1.003 (-27.26%)	0.413 (-56.93%)	0.829 (-39.88%)	0.222 (-76.85%)
	High	0.937 (-32.05%)	0.299 (-68.82%)	0.442 (-67.95%)	0.241 (-74.87%)	0.123 (-91.08%)	0.054 (-94.37%)

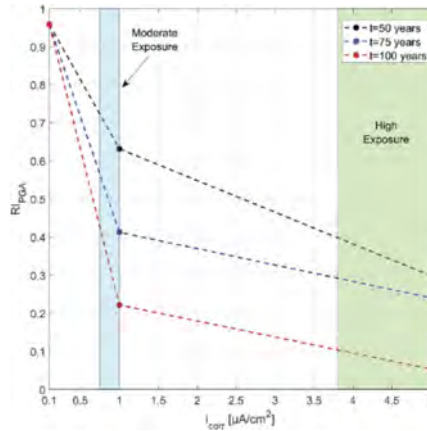


Figure 3. Variation of seismic risk index with i_{corr} .

The results for moderate and high exposure in Y direction are summarized in Figure 3. The results presented above are obtained considering constant reference values of i_{corr} , and can be used to assess the impact of global warming on seismic risk when different i_{corr} values are expected as illustrated in Section 2. Looking at R_{lPGA} for brittle mechanism in Y direction, the range of values of i_{corr} for the location of the bridge predicted in section 2 for moderate and high exposure lead to the variation of seismic risk indexes highlighted by the shaded colored areas in Figure 3.

5 CONCLUSIONS

In this work a framework to considers the effects of the increase of temperature on the corrosion of steel reinforcement in r.c. structures are presented and applied to a case of study in the province of Massa Carrara (Italy). The analyses considered both extreme as well as verisimilar scenarios; the results are definitely affected by the limited availability of data for corrosion rate i_{corr} . In any case, the situation at 100 years of age appears deserving of attentions, even considering numerous uncertainties and the fact that the method should be subject to successive refinements.

In any case, it should be considered that as at today the investigate viaduct has already 50 years of service life and that projections to 100 years are to be referred to 2070. Since most of the national heritage is built in the 50-70s an improvement of the framework could be to consider the current state of corrosion for numerical analyses. This, coupled with experimental i_{corr} knowledge and specific to that area, allow an improvement in the reliability of the numerical analysis. Considering the corrosion scenarios characterized by i_{corr} values suggested by (Stewart et al., 2011), a significant reduction of the risk indices values occurs only in the case of high corrosion level ($i_{corr} = 0.431 \mu A/cm^2$) for the brittle collapse mechanism. The slight corrosion scenario does not lead to significant reductions of risk indices values for the considered collapse mechanisms due to the small reduction of the steel reinforcements area that characterizes such a corrosion level. Different conclusions can be drawn from the i_{corr} values suggested by (DuraCrete, 2000), where more significant reduction of the risk indices is obtained with reduction up to 80% for the ductile collapse mechanism and exceeds 90% for the brittle collapse mechanism. Further refinement of the method and the introduction of other kind of degradation due to the environmental actions are expected as subsequent development of the works.

ACKNOWLEDGEMENTS

The authors would like to thank the RELUIS bridges project for financial support.

REFERENCES

ATC-40:1996. Seismic Evaluation and Retrofitting of Concrete Buildings. Applied technology council, 8.1–8.66, Redwood City, CA.

- Bastidas-Arteaga, E., Schoefs, F., Stewart, M.G., Wang, X. 2013. Influence of global warming on durability of corroding RC structures: A probabilistic approach. *Engineering Structures* 51: 259–266.
- Berto, L., Vitaliani, R., Saetta, A.V. & Simioni, P. 2009. Seismic assessment of existing RC structures affected by degradation phenomena. *Structural Safety* 31(4): 284–297.
- Berto, L., Saetta, A., Simioni, P. 2012. Structural risk assessment of corroding RC structures under seismic excitation. *Construction and Building Materials* 30: 803–813.
- Biondini, F., Camnasio, E., Palermo, A. 2014. Lifetime seismic performance of concrete bridges exposed to corrosion. *Structure and Infrastructure Engineering*, Vol. 10, No 7, 880–900.
- Chen, W.F. & Duan, L. 2000. *Bridge engineering – seismic design*. CRC press, Boca Raton, FL.
- Coni, M., Mistretta, F., Stochino, F., Rombi, J., Sassu, M., Puppio, M. L. 2021. Fast falling weight deflectometer method for condition assessment of rc bridges. *Applied Sciences*, 11(4),1–19.
- Crespi, C., Zucca, M., Valente, M., Longarini, N. 2022. Influence of corrosion effects on the seismic capacity of existing RC bridges. *Engineering Failure Analysis* 140: 106546.
- Croce, P., Formichi, P., Landi, F. 2019. Climate change: Impacts on climatic actions and structural reliability. *Applied Sciences* 9:5416.
- Croce, P., Formichi, P., Landi, F. 2021. Enhancing the output of climate models: A weather generator for climate change impact studies. *Atmosphere* 12, 1074.
- Decreto Ministeriale 17/01/2018, Ministero delle Infrastrutture e dei Trasporti, G.U. Serie Generale n.42 del 20/02/2018–S.O.8.
- DuraCrete. 2000. *Statistical quantification of the variables in the limit state functions. Dura-Crete-Probabilistic performance-based durability design of concrete structures*. EU-brite EuRam III. Contract BRPR-CT95-0132. Project BE95-1347/R9. January 2000. p. 130.
- Hasa, L., Corsini, G., Diani, M., Battagliere, M.L., Sassu, M., Puppio, M.L. Territorial scale monitoring of civil infrastructures through remote sensing. *Proceedings of the International Conference on Natural Hazards and Infrastructure 2022 3rd International Conference on Natural Hazards and Infrastructure, ICONHIC 2022 Athens, 5-7 July 2022 Code 282299*.
- Jacob D., et al. 2014. EURO-CORDEX: New high-resolution climate change projections for European impact research. *Reg. Environ. Chang.* 14, 563–578.
- Kent, D.C. & Park, R. 1971. Flexural members with confined concrete. *Journal of the Structural Division* 97: 1969–1990.
- Lee, H.S. & Cho, Y.S. 2009. Evaluation of the mechanical properties of steel reinforcement embedded in concrete specimen as a function of the degree of reinforcement corrosion. *International Journal of Fracture* 157(1): 81–88.
- Mistretta, F., Piras, M. V., Fadda, M. L. 2015. A reliable visual inspection method for the assessment of r.c. structures through fuzzy logic analysis. Paper presented at the Life-Cycle of Structural Systems: Design, Assessment, Maintenance and Management - Proceedings of the 4th International Symposium on Life-Cycle Civil Engineering, IALCCE 2014, 1154–1160.
- Park, R. & Paulay, T. 1975. *Reinforced Concrete Structures*. John Wiley and Sons, New York.
- Pour-Ghaz, M., Burkan Isgor, O., Ghods P. 2009. The effect of temperature on the corrosion of steel in concrete. Part I: Simulated polarization resistance tests and model development. *Corrosion Science*, 51, 415–425.
- Pucci, A., Puppio, M. L., Sousa, H. S., Giresini, L., Matos, J. C., Sassu, M. 2021. Detour-impact index method and traffic gathering algorithm for assessing alternative paths of disrupted roads. *Transportation Research Record*, 2675(12), 717–729
- Puppio, M. L., Novelli, S., Sassu, M. 2018. Failure evidences of reduced span bridges in case of extreme rainfalls the case of Livorno. *Frattura Ed Integrità Strutturale*, 12(46), 190–202.
- Saetta, A.V. & Vitaliani, R. 2004. Experimental investigation and numerical modelling of carbonation process in reinforced concrete structures: Part I: Theoretical formulation. *Cement and Concrete Research* 34(4): 571–579.
- Sassu M., Doveri F., Ferrini M., Mistretta, F., Puppio M. L. Time and cost-effective intervention strategy for r.c. bridges with Gerber beams: methodology and a real case study, Sustainable and Resilient Infrastructure, preprint version.
- Sassu, M., Giresini, L., Puppio, M. L. 2017. Failure scenarios of small bridges in case of extreme rainstorms. Sustainable and Resilient Infrastructure, 2(3), 108–116.
- Sousa, M.L., et al. 2020. *Expected implications of climate change on the corrosion of structures*. EUR 30303 EN, Publications Office of the European Union, Luxembourg.
- Stochino, F., Fadda, M. L., Mistretta, F. 2018. Assessment of RC bridges integrity by means of low-cost investigations. *Frattura Ed Integrità Strutturale*, 12(46), 216–225.
- Stewart M. G., Wang X., Nguyen M. N. 2011. Climate change impact and risks of concrete infrastructure deterioration. *Engineering Structures*, 33, 2011, 1326–1337.
- van Vuuren, D.P., et al. 2011. The representative concentration pathways: An overview. *Climatic Change* 109, 5–31.
- Zucca, M., Crespi, P., Stochino, F., Puppio, M.L. Coni, M. 2023. Maintenance interventions period of existing RC motorway viaducts located in moderate/high seismicity zones. *Structures* 47: 976–990.

SS22: Life-cycle and sustainability of precast concrete structures
Organizers: B. Dal Lago, H. Rodrigues & P. Negro



Taylor & Francis

Taylor & Francis Group

<http://taylorandfrancis.com>

Seismic response analysis of precast structures retrofitted with dissipation devices, including qualitative assessment of environmental impact

F. Cavalieri & D. Bellotti

European Centre for Training and Research in Earthquake Engineering (EUCENTRE), Pavia, Italy

M. Caruso

University of Pavia, Pavia, Italy

R. Nascimbene

University School for Advanced Studies (IUSS), Pavia, Italy

ABSTRACT: Reinforced concrete precast industrial buildings can attain a performance enhancement and extend their nominal service life through seismic retrofitting strategies. This work investigates the behaviour of two seismic dissipation devices designed for retrofit of precast buildings, with the aim of testing their effectiveness in improving the seismic response of this construction system, as well as qualitatively assessing their life cycle environmental impact. With reference to a single-storey case study building, a comparative analysis of the seismic response of the structure before and after the retrofit with the two proposed devices was undertaken. Two numerical models of the building, with and without the retrofit, were created in OpenSees and subjected to nonlinear static analyses. The obtained results provided reassurance on the efficacy of the proposed solutions in improving the seismic performance of existing and new precast industrial buildings. Moreover, the potentials of environmental impact reduction of the proposed retrofitting solutions showed that they are attractive under a sustainable viewpoint as well.

1 INTRODUCTION

Italian reinforced concrete (RC) precast industrial buildings, especially those not specifically designed to resist seismic actions, suffered from extensive damage following the recent earthquakes that struck Italy (Abruzzo 2009, Emilia-Romagna 2012 and Central Italy 2016-2017). The seismic response of these buildings can be generally improved by imposing the dissipation of an appropriate amount of energy. In the last decade, a large body of literature has been devoted to the development and the application of dissipation devices that can be used for precast structures, to enhance their seismic performance and extend their nominal service life. The practical issues that have been considered include the possibility to use the devices for both existing and new precast structures, the possibility to examine the devices from close up, the replaceability after a seismic event, the dry installation without the use of mortar, and the compatibility with the techniques adopted for the construction of typical precast buildings, for instance in the case of structures with monolithic columns and pin-ended beams (Belleri et al. 2010). The devices typically employed for these structures can dissipate energy through friction or by hysteresis and be combined with elements having the function to increase the initial stiffness; in this way, they prevent or mitigate the second order effects and excessive displacements at the serviceability limit state, which often drive the design of flexible structures.

While several works in the current literature explored the feasibility of energy dissipative cladding panel connection systems, the focus in this work is on dissipation devices designed for beam-to-column connections of precast industrial buildings, as well as dissipative bracing systems. Several researchers to date proposed retrofitting solutions that are applicable to frictional beam-to-column connections (e.g. Santagati et al. 2012, Belleri et al. 2017, Magliulo et al. 2017, Hu et al. 2020, Belleri & Labò 2021, Bai et al. 2022), or that make use of dissipative braces (e.g. Dal Lago et al. 2021). However, despite the relevance of sustainability issues related to the reduction of economic and environmental impacts (in terms of earthquake-induced losses) allowed by the retrofit, the benefit of dissipation devices to the life cycle seismic performance of precast structures, as well as their own life cycle environmental impact, have not been fully investigated yet.

This paper aims to test the effectiveness of energy dissipation devices in improving the seismic response of precast industrial buildings, while also qualitatively assessing their environmental impact reduction potentials: the latter include the impact of each device life cycle phase, as well as the consequent reduction of earthquake-induced losses during the service life of the structure. With reference to a single-storey case study building, a comparative analysis was undertaken on the seismic response of the structure before and after the retrofit with two proposed dissipation devices, namely a friction rotation damper for beam-to-column connections and a bracing system with dissipative sacrificial elements. The advantages deriving from the use of such devices include not only the reduction of global lateral displacements and resisting forces in the main structural elements, and the increase of the building’s lateral strength, but also their replaceability after a seismic event. Two three-dimensional numerical models of the case study building, with and without the retrofit, were created in OpenSees (McKenna et al. 2000) and subjected to nonlinear static (pushover) analyses in both the main directions. In Section 5, for each life cycle phase of the employed devices, their potentials of impact reduction are explored using a Life Cycle Thinking (LCT) indicator, showing that the proposed retrofitting solutions are expected to be environment-friendly under a life cycle perspective.

2 CASE STUDY BUILDING AND ADOPTED DISSIPATION DEVICES

The case study considered for this endeavour, depicted in Figure 1, is a single-storey precast structure representative of the Italian construction period of the ‘70s, located in Naples and designed on the base of gravity loads only.

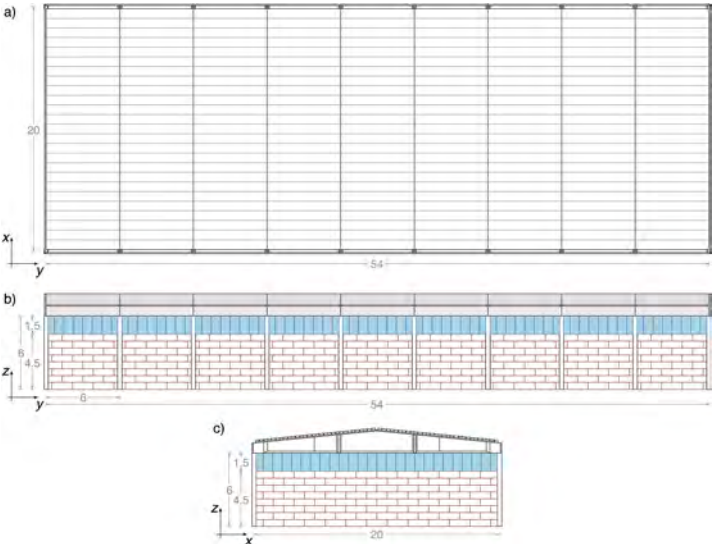


Figure 1. a) Top, b) side and c) frontal view of the case study building (Units: m).

The geometry consists of a single span with total plan size of $20 \times 54 \text{ m}^2$. The columns have a $0.35 \times 0.35 \text{ m}^2$ cross-section and a 6 m height. The prestressed main beams in the transverse (x) direction have a span length of 20 m and a double slope (10% inclination) with an I-section variable in both height and thickness. The secondary beams (or girders) in the longitudinal (y) direction are 6 m long with a tee cross-section. The connections of the main beams to the columns only rely on friction and are characterised by the presence of neoprene pads on the column top allowing for beam seating. On the other hand, the girders are fastened to the columns by steel dowels. The roof is composed of double-tee prestressed elements, rigidly jointed to the main beams by reinforcement stirrups protruding from the beams, additional steel bars between the elements and a finishing concrete casting. The external closure is present on all sides of the building and is constituted of masonry infill panels, creating a ribbon window of a 1.5 m height.

2.1 Dissipation devices

The first dissipation device considered herein is a friction rotation damper (see Figure 2), conceived to be applied at beam-to-column connections. The device is able to dissipate energy (thus increasing the system damping) through the friction generated by the relative rotation of steel plates with interposed brass discs. The interposition of brass discs, softer than the connected steel plates, guarantees smoothness during relative rotations (Belleri et al. 2017). The increase of the device activation moment is accomplished by incrementing the number of sliding surfaces (four in Figure 2b). The steel plates are fixed to the mounting frame by bolts placed in slotted holes, thus transferring the external tightening force to the brass discs. Cup springs are introduced on the main bolt for a better control of the tightening load acting on the brass discs. For each beam-to-column connection, the device works in a three-hinge scheme, where sliding surfaces are applied only at one hinge, whilst the remaining two hinges are left free to rotate. In the current study, this first retrofitting solution encompasses the use of the rotation damper coupled with steel profiles and passing holes hosting steel pins, which allow for relative rotations but prevent joint sliding. Also, given the presence of secondary beams, with no specific structural function, in the perimeter portal frames along the longitudinal direction, it was decided to install the rotation dampers only at the beam-to-column frictional connections in the ten portal frames that include the main beams, along the transverse direction. The size of the devices allows some clearance between them and the masonry infills, which are thus left intact.

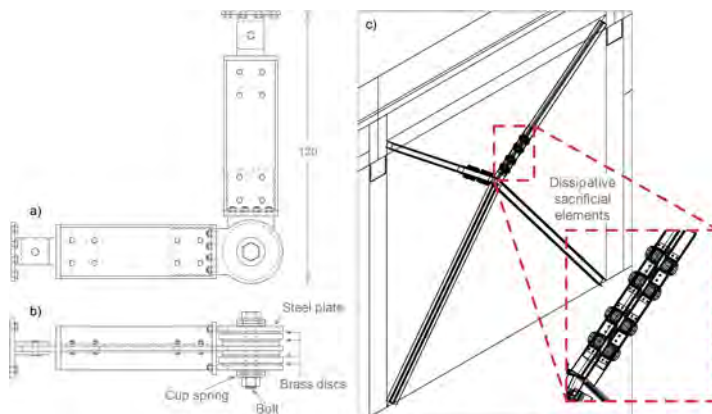


Figure 2. a) Side and b) bottom view of the adopted friction rotation damper (Units: cm); c) Diagonal steel braces, with a close-up on the dissipative sacrificial elements.

The second dissipation solution adopted in this work entails the use of non-traditional diagonal steel braces, characterised by the inclusion of dissipative sacrificial elements, as well as the presence of a junction in the middle, which allows the upper and lower portions of the braces to be off-axis (Resilio system 2017). This system is able to channel the ingoing seismic energy towards predefined points in the vicinity of the junction, where the sacrificial elements are located (see Figure 2c): the latter are pushed in the nonlinear field and dissipate energy by hysteresis, thus preserving the rest of the structure. A crucial property of this system is its immediate activation during an earthquake, something that prevents the occurrence of strong bending moments at the base of the columns. The elements may be easily replaced after a seismic event. Moreover, the global static scheme of the structure remains unchanged. In the current study, given the relevant width (i.e. 20 m) of the portal frames along the transverse direction, the braces are installed only along the longitudinal direction, and in particular within the central bay of the perimeter portal frames (see Figure 1b). The braces are connected to the bottom and the top portions of the columns, thus occupying the entire clearance below the girders: consequently, the central field of masonry infill must be removed and the glazing of the correspondent ribbon window dismounted; then, after the retrofitting intervention, lightweight infills made of green or sustainable materials are put in place only for closure purposes, and the glazing is just remounted.

3 NUMERICAL MODELLING

Two 3D numerical models of the case study building, with and without the retrofit, were created in OpenSees. In both building models, a concentrated plasticity approach with a plastic hinge at the base of the columns was used to describe the global structural nonlinear behaviour; in the adopted model, the stiffness of the entire element is obtained by connecting in series the stiffness of the rotational spring and the one of the column element. The plastic hinge model was defined using the *ModIMKPeakOriented* material, as implemented in OpenSees, whose mechanical parameters were assigned according to Bosio et al. (2023). A rigid link was introduced on top of each column so as to properly account for the eccentricity between the column and the main beam axis. Beam-to-column frictional connections were modelled by means of the *flatSlider-Bearing* element of OpenSees, which allows for the translation in both the main horizontal directions at the attainment of the friction force computed following the Coulomb model. The friction coefficient was evaluated according to the model proposed by Magliulo et al. (2011) for neoprene-concrete friction, as a function of the normal stress acting on the sliding surface. On the other hand, pinned connections (i.e. pure hinges) were introduced to model the beam-to-column dowel connections for the girders. The properties of the roof system, as described in Section 2, justify the adopted assumption of rigid diaphragm for the roof: in particular, the roof elements were explicitly introduced as elastic elements, rigidly connected to the beams. The masonry infills were modelled following the work by Liberatore et al. (2018), based on the equivalent strut approach. With reference to the Italian “double-UNI” infill masonry, with a thickness of 24 cm, the stress and strain values provided by Bosio et al. (2023) were adopted herein. Such values were introduced in OpenSees using the *Concrete01* material. For each field of masonry infill, two *twoNodeLink* elements with the latter material and embedding the infill’s mass were employed to model two diagonal compression-only connecting struts. Given the presence of a ribbon window on all sides of the case study building, an additional lumped plastic hinge was introduced, through a *zeroLength* element, at the intersection between the upper end of the equivalent strut and the column, so as to model the behaviour of the upper part of the column (i.e. the squat or short column), failing in flexure.

The friction rotation dampers were introduced in the retrofitted structural model adopting the following strategy. First, in order to simulate the presence of steel profiles that allow for relative rotations but prevent joint sliding along both the main directions, the beam-to-column frictional connections, modelled by means of *flatSliderBearing* elements in the unretrofitted model, were replaced with pinned connections; it is important to note that rotations are allowed only in the in-plane (transverse) direction and prevented in the out-of-plane direction, as well as about the axis

of the main beams. Then, within the three-hinge scheme described above, the two lateral hinges that are left free to rotate were modelled as pinned connections by means of *zeroLength* elements with sufficiently low rotational stiffness. On the other hand, the central hinge where sliding surfaces are applied was introduced in OpenSees as a *zeroLength* element characterised by a rigid-plastic behaviour only in the rotational degree of freedom of interest; in particular, an elastic-perfectly plastic behaviour was assigned (using the *MultiLinear* material of OpenSees), with “large” initial stiffness and moment capacity equal to 40 kNm: the latter value was selected for this application among the three values of moment of activation considered by Santagati et al. (2012), namely 40, 80 and 120 kNm, related to the properties of the cup springs (see Figure 2b). The three *zeroLength* elements are connected to each other, as well as to the column and the main beam, by rigid links. It is noteworthy that the horizontal rigid link connecting one of the lateral hinges to the column is attached to the upper node of the *zeroLength* element (i.e. the plastic hinge) introduced at the base of the short column adjacent to the ribbon window: with this configuration, the formation of the plastic hinge and the consequent occurrence of the “squat column” effect is somehow hampered, though not prevented.

Coming to the second retrofitting solution, firstly the *twoNodeLink* elements that model masonry infills in the central bay of the perimeter portal frames along the longitudinal direction were removed. Then, the junction was modelled with one central node plus four additional lateral nodes along the directions of the upper and lower portions of the braces; four *zeroLength* elements with very low rotational stiffness (i.e. pure hinges) were then introduced between the deriving four couples of nodes. The lower portions of the braces were modelled as elastic elements having the properties of HEA200 profiles with S275 steel, with one end node attached to the correspondent node of the junction, and the second end node attached to the base node of the column (i.e. beneath the base plastic hinge). On the other hand, the entire upper portions of the braces were modelled with two *twoNodeLink* elements, representing the dissipative sacrificial elements, with one end node attached to the correspondent node of the junction, and the second end node attached to a *zeroLength* element (a pure hinge), itself connected to the lower node of the rigid link introduced on top of each column. A *BoucWen* hysteretic material in OpenSees was calibrated against experimental results related to a single sacrificial element of class 60, constituted of 60×4 mm S355 steel lamellas. To model the presence of four sacrificial elements arranged according to the scheme in Figure 2c, four identical calibrated *BoucWen* materials were created, each couple was combined in parallel (using the *Parallel* material of OpenSees) and then the two derived parallel materials were combined in series (through the *Series* material of OpenSees), obtaining a material with an axial force capacity of nearly 30 kN; subsequently, the *MinMax* command of OpenSees was employed in order to simulate the failure of the system when the demand displacement falls below or above certain minimum and maximum threshold values, fixed at -0.06 m and 0.06 m herein, based on the experimental behaviour. The resulting material was finally assigned to each *twoNodeLink* element, only along its axial direction, whilst a rigid elastic behaviour was applied in the other directions. The numerical model featuring both the adopted retrofitting solutions is characterised by an increased global stiffness, reflected in a reduction of the fundamental period from 1.45 s to 0.45 s; this is mainly caused by the presence of the friction rotation dampers and the pinned connections, which lead the model to exhibit a different static scheme with respect to the unretrofitted case.

4 ANALYSES AND RESULTS

This Section presents the results of the pushover analyses carried out along both the main directions, on both the unretrofitted and retrofitted models (see Figure 3). Given the regularity in plan of the building, the latter may be considered to behave independently along the two directions: therefore, the two adopted retrofitting solutions play a role only along the direction in which they are applied, namely the transverse direction for the rotation dampers and the longitudinal direction for the diagonal braces. However, the pinned connections representing steel profiles introduced along the transverse direction do provide a stiffening effect also along the longitudinal direction.

Since the employed dissipation devices can dissipate the ingoing seismic energy only in dynamic conditions, with static analyses it is possible to only capture the increase in lateral stiffness, strength and ductility due to the installation of the devices, not their dissipation capabilities.

From Figure 3a, it is readily gathered that the unretrofitted structure (curve in blue) has a quite low capacity along the transverse direction, owing to the occurrence of the “squat column” effect: a plastic hinge, indicated by a change of slope in the pushover curve, is formed in the short columns adjacent to ribbon windows, only at the four corner columns that enclose infills. In the retrofitted structure, the “squat column” effect does still occur, although for a much higher base shear value (curve in red). However, thanks to the presence of a total of 20 rotation dampers that can withstand a moment capacity of 40 kNm, as well as steel profiles preventing joint sliding, the building exhibits a significant (nearly fourfold) increase in lateral stiffness and strength.

Coming to the longitudinal direction, Figure 3b shows that the unretrofitted model (curve in blue) has a base shear limited to a value of around 400 kN, due to the attainment of the friction force in the frictional beam-to-column connections: in the latter condition, the pushover curve becomes flat, indicating that the beam freely slides until loss of support. On the other hand, the retrofitted building exhibits an increased lateral stiffness and a much larger resistance (curve in red), as expected. It was observed that the latter increase in lateral resistance is mainly due to the presence, in the ten portal frames along the transverse direction, of pinned connections preventing rotations about the axis of the main beams (see Section 3): the relevant role of the diagonal steel braces embedding the Resilio devices will be much better highlighted by undertaking dynamic analyses on the investigated case study building, which will be the object of future work. It is finally interesting to note that in the retrofitted model, given that the masonry infills do not collapse and the lower (main) parts of the columns do not yield, the “squat column” effect occurs again, with the formation of a plastic hinge (indicated by a change of slope in the pushover curve) in the short columns adjacent to ribbon windows.

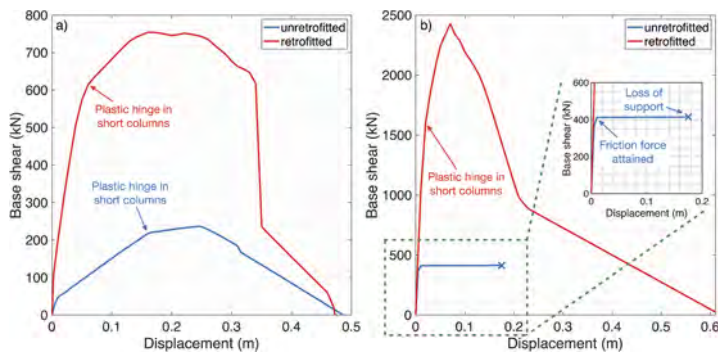


Figure 3. Results of the nonlinear static analyses for both models, along a) the transverse (x) direction, and b) the longitudinal (y) direction, with close-up on the blue curve for the unretrofitted model.

5 ENVIRONMENTAL IMPACT ASSESSMENT OF THE ADOPTED DEVICES

LCT is a holistic approach for the evaluation of environmental, social, and economic impacts of products through each of their life cycle stages, where there is the potential to reduce resources consumption and improve operational performance (Passoni et al. 2022). In this Section, preliminary LCT-based evaluations are carried out to qualitatively assess the sustainability of the considered devices, accounting for the life cycle impacts of the retrofit components themselves.

The main stages that are typically considered throughout a given product’s life cycle are: (i) the production phase, including raw materials extraction, transportation, and manufacturing; (ii) the construction phase, including transportation and installation; (iii) the use phase, including use, maintenance, repair, refurbishment, replacement, energy and water use; and (iv) the end-of-life phase, including demolition, transportation, processing and disposal of waste

materials. An additional stage is represented by the so-called beyond-life stage, which considers possible reuse, recycle and recovery of salvaged materials.

Specific LCT performance targets can thus be assigned to each of the above life cycle phases, with a view to minimise all the potential related impacts. The LCT qualitative targets evaluated herein, based on those discussed in much more detail in Passoni et al. (2022), are the following:

- in the production phase, the choice of eco-efficient materials (e.g. recycled/reused materials or renewable biomaterials) for retrofitting could be useful to avoid/minimise the impacts of extraction and manufacturing, and preferring local materials could limit transportation distances and fossil fuel consumption to reach production plants;
- in the construction phase, easy assemblage and/or prefabrication of the retrofit components could reduce duration of works, costs, emissions of air pollutants, and disturbance to buildings' occupants, whereas the use of components of reduced size could limit the impacts of transportation to the construction site (while also optimising the use of materials);
- in the use phase, the adopted materials and techniques should allow for easy reparability, durability, maintenance, adaptability and flexibility to future needs (e.g. dry techniques), while also ensuring the suitable level of indoor comfort and safety against seismic hazard;
- in the end-of-life phase, retrofitting solutions conceived for easy deconstruction/demountability, recyclability and/or reusability of materials and/or retrofit components should be preferred.

Figure 4 summarises, through a LCT indicator (LCTI), the potentials of environmental impact reduction at each life cycle phase of the considered dissipation devices, the latter being compared to traditional retrofitting techniques for precast structures, e.g. concrete or steel jacketing of structural members. The green leaf and warning symbol indicate an expected better and worse performance, respectively, given the provided description, whilst a white box indicates no significant improvement (or similar performance) with respect to traditional interventions. The A3 module only was assigned a warning symbol in this qualitative assessment (given the relevant impact of structural steel manufacturing, as discussed in Gervasio & Dimova 2018), whilst three of the four white boxes are related to not applicable phases. It can be thus concluded that the retrofitting solutions discussed herein for precast industrial buildings are expected to be environment-friendly at most of the applicable life cycle phases, while also guaranteeing a high level of seismic protection to the building itself, thus reducing operational building's impacts due to potential seismic damage repair activities, as shown in Section 4.

	LIFE CYCLE PHASE	LCTI	DESCRIPTION
PRODUCTION	A1 Raw material supply	🌿	Recycled/reused materials, material optimization
	A2 Transport	🌿	Local materials, material optimization
	A3 Manufacturing	⚠️	Impactful production of steel components
CONSTRUCTION	A4 Transport	🌿	Reduced size of components
	A5 Construction/Installation	🌿	Prefabrication, reduced emissions of air pollutants, dry technique
USE	B1 Use	☐	Non-toxic materials, as in traditional interventions
	B2 Maintenance	🌿	Durable materials, dry technique
	B3 Repair	🌿	Durable materials, dry technique, low seismic damage
	B4 Refurbishment	☐	Not applicable
	B5 Replacement	🌿	Durable materials, dry technique, low seismic damage
	B6 Operational energy use	☐	Not applicable
	B7 Operational water use	☐	Not applicable
END OF LIFE	C1 Deconstruction/demolition	🌿	Easy disassembly, reduced size of components, dry technique
	C2 Transport	🌿	Reduced size of components
	C3 Waste processing	🌿	Reduced size of components, dry technique
	C4 Disposal	🌿	Recyclable/reusable materials
	BEYOND LIFE – Reuse, recovery, recycling	🌿	Recyclable/reusable materials

Figure 4. Qualitative LCT-based evaluation of the considered seismic dissipation devices.

6 CONCLUSIONS

It is known that the seismic response of reinforced concrete precast industrial buildings can be generally improved by imposing the dissipation of an appropriate amount of energy. Given that the benefit of dissipation devices to the life cycle seismic performance of precast structures has not been fully explored, this paper investigated the effectiveness of energy dissipation devices in improving the seismic response of precast buildings, while also qualitatively assessing their potentials of life cycle environmental impact reduction. Seismic retrofitting with two dissipation devices was considered herein, namely a friction rotation damper and a bracing system with dissipative sacrificial elements. Two three-dimensional numerical models of a case study building representative of the Italian building stock in the '70s, with and without the retrofit, were created in OpenSees and subjected to pushover analyses in both the main directions. Although with static analyses it is possible to only capture the increase in lateral stiffness and strength due to the installation of the devices, not their dissipation capabilities, the obtained pushover results provided reassurance on the efficiency of the proposed retrofitting solutions in improving the seismic performance of existing and new precast industrial buildings. Lastly, it was concluded that such retrofitting solutions are expected to be environment-friendly at most of their life cycle phases, owing to the use of recycled/recyclable, local and durable materials, the reduced size of components, the dry installation and disassembly processes, as well as the high level of seismic protection.

REFERENCES

- Bai, J., He, J., Li, C., Jin, S. & Yang, H. 2022. Experimental investigation on the seismic performance of a novel damage-control replaceable RC beam-to-column joint. *Engineering Structures* 267: 114692.
- Belleri, A. & Labò, S. 2021. Displacement-based design of precast hinged portal frames with additional dissipating devices at beam-to-column joints. *Bulletin of Earthquake Engineering* 19(12): 5161–5190.
- Belleri, A., Marini, A., Riva, P. & Nascimbene, R. 2017. Dissipating and re-centring devices for portal-frame precast structures. *Engineering Structures* 15: 736–745.
- Belleri, A., Riva, P., Bolognini, D. & Nascimbene, R. 2010. Metodi di protezione sismica di strutture prefabbricate mediante dispositivi di dissipazione. *Proc. of 18^o Congresso CTE, Brescia (Italy), 11-13 November 2010* (in Italian).
- Bosio, M., Di Salvatore, C., Bellotti, D., Capacci, L., Belleri, A., Piccolo, V., Cavalieri, F., Dal Lago, B., Riva, P., Magliulo, G., Nascimbene, R. & Biondini, F. 2023. Modelling and Seismic Response Analysis of Non-residential Single-storey Existing Precast Buildings in Italy. *Journal of Earthquake Engineering* 27(4): 1047–1068.
- Dal Lago, B., Naveed, M. & Lamperti Tornaghi, M. 2021. Tension-only ideal dissipative bracing for the seismic retrofit of precast industrial buildings. *Bulletin of Earthquake Engineering* 19(11): 4503–4532.
- Gervasio, H. & Dimova, S. 2018. Model for Life Cycle Assessment (LCA) of Buildings. Publications Office of the European Union: Copenhagen, Denmark.
- Hu, G., Huang, W. & Xie, H. 2020. Mechanical behavior of a replaceable energy dissipation device for precast concrete beam-column connections. *Journal of Constructional Steel Research* 164: 105816.
- Liberatore, L., Noto, F., Mollaioli, F. & Franchin, P. 2018. In-plane response of masonry infill walls: Comprehensive experimentally-based equivalent strut model for deterministic and probabilistic analysis. *Engineering Structures* 167: 533–548.
- Magliulo, G., Capozzi, V., Fabbrocino, G. & Manfredi, G. 2011. Neoprene–concrete friction relationships for seismic assessment of existing precast buildings. *Engineering Structures* 33(2): 532–538.
- Magliulo, G., Cimmino, M., Ercolino, M. & Manfredi, G. 2017. Cyclic shear tests on RC precast beam-to-column connections retrofitted with a three-hinged steel device. *Bulletin of Earthquake Engineering* 15(9): 3797–3817.
- McKenna, F., Fenves, G.L. & Scott, M.H. 2000. OpenSees: Open System for Earthquake Engineering Simulation. *Software*, University of California, Berkeley, USA. Available at: <http://opensees.berkeley.edu> (last accessed 23 February 2023).
- Passoni, C., Palumbo, E., Pinho, R. & Marini, A. 2022. The LCT challenge: defining new design objectives to increase the sustainability of building retrofit interventions. *Sustainability* 14(14): 8860.
- Resilio system 2017. Website: <https://www.sistemiresilienti.it/resilio-la-differenza/> (in Italian) (last accessed 23 February 2023).
- Santagati, S., Bellotti, D., Bolognini, D. & Brunesi, E. 2012. Seismic Response Comparisons between RC Precast Structures with Dissipation Devices on Beam-Column Connections. *Proc. of 15WCEE 2012, 15th World Conference on Earthquake Engineering, Lisbon (Portugal), 24-28 September 2012.*

Aggregates for innovative use in precast concrete panels: State of the Art and perspectives

M.L. Puppio, F. Coccu, A. Usman, M. Valdés, A. Frattolillo & M. Sassu

Department of Civil and Environmental Engineering (DICAAR), University of Cagliari, Cagliari, Italy

L. Casali

Manini Prefabbricati S.p.A., Santa Maria Degli Angeli, Perugia, Italy

ABSTRACT: The use of lightweight and/or recycled aggregates for concrete elements in industrial applications for Civil and Industrial Engineering is strongly increased in recent years. Starting from classical use of pumice and other lightweight aggregates, the industry production of expanded clay and perlite offers interesting mix design that can optimize structural and energy performances of cladded panels. The authors illustrate recent experiences of research projects on the recycling of stone aggregates from demolition of r.c. structures in which mechanical properties are compared with natural aggregates. Several mix designs based on expanded perlite are also investigated in terms of mechanical and thermal performances optimizing both aspects: they are especially dedicated to full unit masonry walls and to create insulating-reinforcing panels to be coupled with masonry walls. Finally, is referred an experimental investigation with a concrete mix design of recycled aggregates, coming from collapsed buildings in central Italian area hit by earthquake 2016.

1 INTRODUCTION

This work presents the first result of an experimental campaign on the use of recycled aggregates in cladding panels. Cladding panels appears, in the context of precast concrete constructions, one of the most challenging elements for the application of recycled concrete. This because of the significant volume of material involved (on average 1/3 of the concrete of the whole concrete structure) and of the function of this elements (structural and thermal performances). Generally, from 70% to 80% of the volume of concrete is made up of natural aggregates.

It is estimated that 40% of the total energy and 50% of the total natural resources are used in construction activities. Nowadays, the construction sector is producing a significant amount of demolition waste and such waste constitutes the largest volume of all waste (Cheng et al., 2015). Construction and demolished wastes account for 25% to 30% of the whole waste that is being produced in Europe. The central part of Italy is prone to earthquake and has severely affected by earthquakes in the past 20 years (Rovida et al., 2016, Hofer et al., 2016). Post-disaster waste is an area of main concern and the debris can be recycled and used in the construction of new structures (Andreini et al, 2014) (Faleschini et al., 2017). Here the recycled waste obtained from the 2016 Earthquake in Italy will be employed for recycled concrete in the precast construction industry.

From this, the strategic relevance to use recycled aggregates in precast panels. In this work a mix design of concrete with fully recycled aggregates is proposed and studied aiming to compare the structural and thermal performances with respect to standard plain concrete currently used in production chain of Manini Prefabbricati.

2 STATE OF THE ART

At the State of the Art the innovative use of concrete, using special aggregates or additive to obtain best structural and thermal performance and to have more sustainable production chain is a very significant challenge. The walls constitute the total weight of the structure, hence reducing the weight of the walls results in the reduced size of the foundation. The lightweight concrete panels also make it easy to move and mount these components in an easier way (Cavaleri et al., 2003). Precast concrete structures, with heavy self-weight, should be optimized for construction because they inevitably require heavier equipment, which makes transportation more challenging and necessitates the use of stronger bearing and support elements, especially considering the seismic action, and this could increase the overall cost of the project (Yardim et al., 2013).

Adopting lightweight concrete (LWC) reduces dead weight (Sajedi and Shafigh, 2012). Moreover, concrete with light-weight particles can have less thermal conductivity improving the energetic performance of the building. Typically, several Lightweight Aggregates (LWA) materials, including expanded glass (EG) aggregates, expanded clay (EC), pumice aggregate and plastic bottles, can be used to produce LWC. However, with these materials, the strength of the concrete generally decreases, so the application of these materials has its own limitations in terms of the mechanical response of the concrete (Adhikary et al., 2020). Several attempts are made to make LWC using some natural and artificial lightweight materials including shale, pumice, expanded clay, glass, etc., (Divya Bhavana et al., 2017, Kurpinska and Kuřak, 2019, Singh, 2016).

The use of the steel fibres and the LWC based on the fly ash aggregates were investigated and it was found that these fly ash lightweight aggregates can produce some concrete with a compressive strength of 40 MPa (Longarini et al., 2014). The addition of the steel fibers in the lightweight aggregate concrete will increase the compressive strength and the tensile strength of the LWC (Güneyisi et al., 2015). (Mboya et al., 2019) investigated the effects of the scoria and pumice on the performance response of the concrete. They found that natural scoria and pumice binders can be substituted up to 10% without compromising the mechanical properties including permeability, modulus of rupture and the compressive strength of the concrete .

It is found that by using volcanic pumice, a concrete that is 30 to 40% lighter than typical concrete and has good insulation and structural strength properties can be produced (Campione et al., 2001, Hossain, 1999). Khankhaje, et al. used oil palm kernel shell (OPKS) as a partial replacement of the coarse aggregate in concrete mixes and concluded that OPKS amount had adverse effects on the mechanical properties of the concrete. The shape of the OPKS particles was round that disturbing the micro arrangements of the concrete resulting in inferior mechanical properties including the strength of the concrete (Khankhaje et al., 2016). This is just an example of construction materials based on bio natural aggregates. (Sassu et al., 2016) used the bio natural aggregate i.e., hemp shives and cork granules in concrete and recommended such material for non-load bearing structural components or combined with other structural elements. The experimental study evaluated the effects of these materials on the flexural and compressive response of concrete and found that the cork granules showed better mechanical performance. Such materials are recommended to use in insulating wall panels.

University of Cagliari has been starting work about production, performance and durability of recycled aggregates and recycled aggregate concretes since 2009. The most recent research project, “Materials for Sustainable Building and Infrastructure - Recycled Aggregates” (MEISAR), funded by Regione Sardegna, has aimed at developing an eco-sustainable chain of concrete constructions by enhancing recycled aggregates (Pani, L. et al., 2019, Pani, L. et al., 2021). The study featured several applications, including the substitution of recycled aggregates (instead of natural aggregates) in reinforced concrete. Seven different concrete mixtures were casted: one mix control made with only natural aggregates, and six mix made with recycled coarse aggregates from the demolition and crushing of the concrete structures (beams and foundation blocks) of the Sant’Elia Stadium in Cagliari. The samples are differentiated by the origin of the recycled aggregates and by the different percentages of replacement of the recycled coarse aggregate (introduced in place of natural aggregate). A production of compounds made with 30%, 50% and 80% recycled coarse aggregates instead of natural ones, was provided. In this case, no substantial differences in compressive and in splitting tensile strengths between the different

mixtures have been observed. In fact, in some cases the recycled concrete samples showed slightly higher strengths with respect to the natural mix control samples (Pani, L. et al., 2020).

Additional tests were also carried out on blocks with recycled aggregates obtaining quite similar results and slightly lower compressive strength at 70% replacement rate and an almost unchanged strength for lower replacement rates. Further tests performed on structural elements such as plinths and columns at life (or at a smaller scale) showed similarly encouraging results. (Pani, L. et al., 2022).

The history of structural concrete highlights a non-negligible problem: the significance of mixing process (segregation of aggregates) and effectiveness of the casting that can produce a variable mechanical behaviour of concrete and so in the structural response. (Puppio et al., 2017, Puppio et al., 2019) investigated the impact of the material variability on global and local seismic response of the structure. (Crespi et al., 2022, Puppio et al., 2017) also proposed a simplified method to consider the material irregularity while performing the seismic assessment. The mechanical properties of the concrete i.e., effective compressive strength greatly affects the response of the structural elements in case of seismic activity. Three material strengths were considered during the study to check the global response and seismic performance (De Stefano et al., 2020).

The use of recycled aggregate has become an alternative material to the natural aggregate in construction industry worldwide. It will directly control the accumulation of the waste along with saving the natural resources (Noguchi et al., 2015, Quattrone et al., 2014, Fauzi et al., 2021). (Attri et al., 2021) used the recycled aggregates to prepare concrete paver blocks and found that the 45 % of the coarse aggregate and 40% fine aggregate can be replaced without compromising the strength of the structural elements (Ruslan et al., 2021) replaced the natural aggregates with recycled aggregates in the precast wall panels mix. The researcher found that by replacing the 50 % natural aggregate can enhance the effectiveness of the wall panels by 179.5% compared with the wall panels prepared with the natural aggregates only. Moreover, using the wall panels with 50 % recycled aggregate can have 203.26 kN higher ultimate load capacity compared with the wall panels with 0 % and 100 % natural aggregate samples.

As discussed, lightweight or recycled aggregates represent an interesting application in the building of cladding panels. Recycled aggregates from Assisi'2016 earthquake is a 0km-resource for the Manini's production in Bastia Umbra, but it also has a high symbolic value for what the Assisi Earthquake represented for Umbria and for Italy. For all the explained reason the strategic role of this experimental campaign.

3 METHOD

The standard production of precast prototypes is based on a proprietary concrete mix that optimizes the available natural resources and the mixture processing. The mix design *B* (mdB) is used by Manini for the construction of ordinary structural member, and it represents the base mix for the integration of the recycled aggregates (mix design *A* - mdA). The only difference between mdB and mdA is in the coarse aggregates: natural in the first case and recycled in the second case.

The mix designs are both based on the same concrete quantity and water to concrete ratio and an experimental structural and thermal characterization has been achieved according to the following European Standards:

- Shape, dimensions and other requirements for specimens and moulds: UNI EN 12390-1 (Table 1).

Table 1. Specimens.

Tests	Dimensions [mm]			n.
Compression - mdA	150	150	150	5
Tension - mdA	150	150	150	5
Elastic modulus - mdA	cylinders $\phi=150$			3
Thermal conductivity - mdA	100	100	50	10
Thermal conductivity - mdB	100	100	50	10

- Making and curing specimens for strength tests: UNI EN 12390-2.
- Uniaxial compression tests: UNI EN 12390-3 (5 specimens).
- Indirect tension tests: UNI EN 12390-6 (5 specimens).
- Secant modulus of elasticity in compression: UNI EN 12390-13 (3 specimens).
- Thermal conductivity: UNI EN 12664 (10 specimens for each mix design) (Table 1).

4 EXPERIMENTAL CAMPAIGN

4.1 Test set up

Uniaxial compression tests and tensile splitting tests are carried out by applying an increasing force until the specimen's failure. The uniaxial compression tests are carried out, according with UNI EN 12390-3, applying a quasi-static force throughout rigid steel plates. Tensile strength is determined according to the recommendations of UNI EN 12390-6, through the application on the cubic specimen of a linearly distributed load on a narrow region along its length. In this case failure is obtained due to orthogonal tensile stress generated in the diametral plane. The modulus of elasticity is measured under compression on cylindrical specimens, according to UNI EN 12390-13 (Method B). The test is based on three stress cycles. Load application starting from a non-zero-base stress to the upper stress; every loading condition is maintained for a period not exceeding 20 seconds, following which the strain is recorded by means of a couple of electrical strain gauges 50mm length glued on each of two diametral opposite measurement lines. The stabilized secant modulus of elasticity $E_{C,S}$ is defined as:

$$E_{C,S} = \frac{\Delta\sigma}{\Delta\varepsilon_S} = \frac{\sigma_a^m - \sigma_b^m}{\varepsilon_{a,3} - \varepsilon_{b,2}} \quad (1)$$

where:

$\Delta\sigma$ Difference between measured upper and lower compression stress.

$\Delta\varepsilon_S$ Difference between average strain at upper stress on loading cycle 3 and at lower stress on loading cycle 2.

The test machines used for the experimental campaign above are illustrated in Figures 1 and 2.

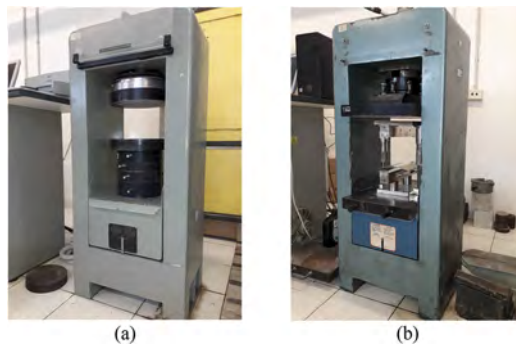


Figure 1. Testing machine for compression tests on cubical specimens (a); testing machine for splitting tensile tests on cubical specimens and for modulus of elasticity in compression on cylinder specimens (b).

Thermal conductivity tests are performed by means a heat flow meter measuring device, model Taurus TCA300, at three different mean specimen temperature: 10 °C; 20 °C; 30 °C. The thermal flow is generated by a temperature gradient (ΔT) of 20 K between the heating and the cooling plates. The thermal flow Q propagating in the unit time on the surface of section A in the thickness direction, is connected to the conductive properties of the material and to the other measured quantities by the:

$$\dot{Q} = \frac{\lambda \cdot A \cdot \Delta T}{s} \quad (2)$$

Thermal conductivity λ is calculated from Equation 2, known the thermal flow Q . The device Taurus TCA300 is in Figure 2 while the scheme for the thermal conductivity test is showed in Figure 3.



Figure 2. Thermal conductivity measuring device, model Taurus TCA 300.

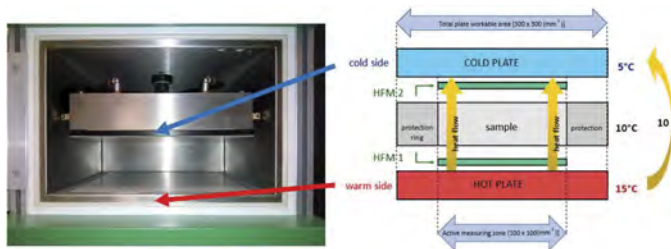


Figure 3. Inside view of the heat flux measuring device and scheme for the thermal conductivity test at the temperature of 10°C.

4.2 Tests

Tests are performed at the Material Testing Laboratory and at the Technical Physics Laboratory of the Department of Civil, Environmental Engineering and Architecture (DICAAR) of the University of Cagliari.

Both mechanical and thermal stress are carried out after a 28-day curing period. The specimens are classified by means of progressive numbers, NP:xx as Figure 4 shows. Dimensions, weight, and density are resumed in Table 2. In the case of specimens for thermal tests, the specimens with recycled aggregates are labelled by the letter *A* while the plain concrete by Manini is identified by the letter *B*. The labels of the specimens are showed in Figure 3.

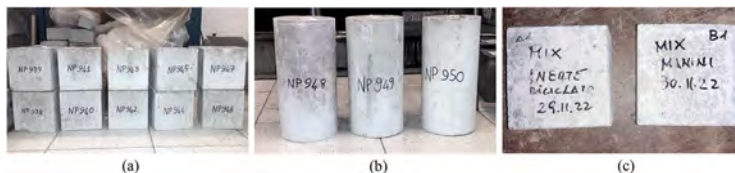


Figure 4. Labels of the specimens: cubic specimens for uniaxial compression and indirect tension tests (a); cylindrical specimens for the elastic modulus (b); two samples of specimens for thermal tests (c).

Mechanical tests carried out by Manini Prefabbricati on the original mix design (after 28 days of aging) highlight the following average values:

- Density 2387 kg/m³;
- Cubic compressive strength 48.4 N/mm²;

Figure 4 shows some pictures of the tests already performed.

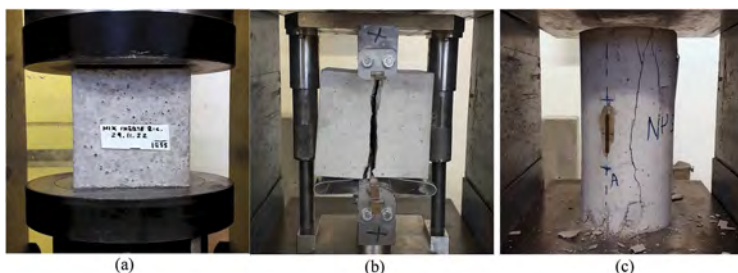


Figure 5. Mechanical tests: uniaxial compression test (a); splitting tensile test (b); determination of secant modulus of elasticity in compression and uniaxial compression test (c).

The specimens tested for thermal conductivity were previously milled to regularize their faces from any surface roughness. The thermal conductivity test has been carried out according to the following procedure: the specimen is equipped by a sheep wool side heat guard to generate a one-dimensional heat flow through the transverse direction of s width and then placed within the heat flow meter measuring device between the heating and the cooling plate. Each individual established temperature range value is maintained for 180 minutes, while the average parameters are acquired and updated every 3 minutes; each test takes approximately 9 hours.

4.3 Results

Main geometry of the specimens for mechanical testing is summarized in Table 2. Data obtained from tests are:

- Density 2239 kg/m^3 ;
- Cubic compressive strength 47.0 N/mm^2 ;
- Splitting tensile strength 3.0 N/mm^2 ;
- secant modulus of elasticity gives the values of 32.7 GPa .

Main results of the thermal conductivity tests are summarized in Figure 6. The average thermal conductivity is:

- $0,493 \pm 0,04 \text{ W/mK}$ for the concrete with recycled aggregates (mdA).
- $0,502 \pm 0,05 \text{ W/mK}$ for plain concrete (mdB).

Table 2. Main data of the specimens with recycled aggregates.

P.N.	Dimensions			Density
	[mm]			D [kg/m^3]
938	149	150	149	2270.2
939	152	150	151	2175.6
943	148	149	149	2233.9
950	148		300	2276.7
940	150	150	150	2269.6
941	151	149	149	2240.2
942	151	150	149	2254.9

5 CONCLUSIONS

The thermal conductivity of the specimens obtained by recycled concrete does not change significantly. The compression strength of recycled concrete specimens seems to be satisfactory for structural uses (mean value of 47 MPa) showing the (97% of the strength of the original mix design). The density of the specimens is 2239 kg/m^3 (94% of the density of the original

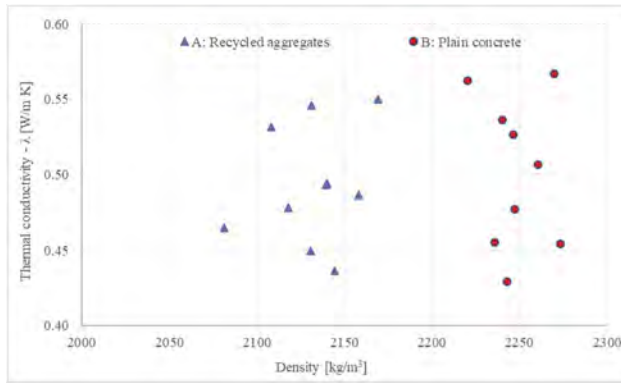


Figure 6. Determination of thermal conductivity for specimens with recycled aggregates (mdA), and with plain concrete by Manini (mdB).

mix design). The experimental campaign should be enforced to ensure statistical significance of the results, anyway the first data are encouraging. In this perspective, the use of recycled aggregates on concrete structures can ensure the following advantages:

1. Recycled aggregates obtained by demolition of damaged buildings from seismic prone areas reduces the environmental and economic impact of the reconstruction phases.
2. Satisfactory compression strength permits the structural use for panels or other precast elements.
3. The use of recycled aggregates on precast elements reduced the critical issue of ensuring quality control, respect to onsite casting elements: the uncertainty of recycled elements can be better managed in precast element layout respect to onsite works.

Further tests at the scale of material should be arranged to best investigate the above performances as well as the material compatibility with tradition reinforcing bars. Moreover, tests at the element scale (panels, beams, columns) can better assess the feasibility of the described idea.

ACKNOWLEDGEMENT

The Authors would like to sincerely thank the Material Testing Laboratories of Manini Prefabbricati in Bastia Umbria (which also manufactured the samples) and the and the Laboratories of DICAAR of University of Cagliari for their availability to perform the test campaign in a short time with effective cooperation.

REFERENCES

- Adhikary, S. K., Rudzionis, Ž. & Vaičiukynienė, D. 2020. Development of flowable ultra-lightweight concrete using expanded glass aggregate, silica aerogel, and prefabricated plastic bubbles. *Journal of Building Engineering*, 31, 101399.
- Andreini, M., De Falco, A., Giresini, L., & Sassu, M. 2014. Structural damage in the cities of Reggiolo and Carpi after the earthquake on May 2012 in Emilia Romagna. *Bulletin Of Earthquake Engineering*, 12(5), 2445–2480. doi:10.1007/s10518-014-9660-7
- Attri, G. K., Gupta, R. & Shrivastava, S. 2021. Impact of recycled concrete aggregate on mechanical and durability properties of concrete paver blocks. *Materials Today: Proceedings*, 42, 975–981.
- Campione, G., Miraglia, N. & Papia, M. 2001. Mechanical properties of steel fibre reinforced lightweight concrete with pumice stone or expanded clay aggregates. *Materials and Structures*, 34, 201–210.
- Cavaleri, L., Miraglia, N. & Papia, M. 2003. Pumice concrete for structural wall panels. *Engineering structures*, 25, 115–125.
- Crespi, P., Zucca, M., Valente, M. & Longarini, N. 2022. Influence of corrosion effects on the seismic capacity of existing RC bridges. *Engineering Failure Analysis*, 140, 106546.
- CEN 2000. Testing hardened concrete-Part 2: Making and curing specimens for strength tests.

- Cheng, J. C., Won, J. & Das, M. Construction and demolition waste management using BIM technology. 23rd Ann. Conf. of the International Group for Lean Construction, Perth, Australia, 2015. 381–390.
- De Stefano, M., Tanganelli, M. & Viti, S. 2020. Effect of the Mechanical Properties of Concrete on the Seismic Assessment of RC Irregular Buildings. *Seismic Behaviour and Design of Irregular and Complex Civil Structures III*. Springer.
- Divya Bhavana, T., Kumar, R. K., Nikhil, S. & Sairamchander, P. 2017. Study of light weight concrete. *International Journal of Civil Engineering and Technology*, 8, 1223–1230.
- EN, B. 2000. 12390-1 Testing hardened concrete–Part 1: Shape, dimensions and other requirements for specimens and moulds. European Committee for Standardization, 2.
- Faleschini, F., Zanini, M. A., Hofer, L., Zampieri, P. & Pellegrino, C. 2017. Sustainable management of demolition waste in post-quake recovery processes: The Italian experience. *International journal of disaster risk reduction*, 24, 172–182.
- Fauzi, M. A., Arshad, M. F. & Nor, N. M. 2021. Statistical models to develop optimised controlled low-strength materials with wastepaper sludge ash. *Construction and Building Materials*, 286, 122816.
- Güneyisi, E., Gesoglu, M., Özturan, T. & Ipek, S. 2015. Fracture behavior and mechanical properties of concrete with artificial lightweight aggregate and steel fiber. *Construction and Building Materials*, 84, 156–168.
- Hofer, L., Zanini, M. A. & Faleschini, F. 2016. Analysis of the 2016 Amatrice earthquake macroseismic data. *Annals of Geophysics*.
- Khankhaje, E., Salim, M. R., Mirza, J., Hussin, M. W. & Rafeizonooz, M. 2016. Properties of sustainable lightweight pervious concrete containing oil palm kernel shell as coarse aggregate. *Construction and Building Materials*, 126, 1054–1065.
- Kurpinska, M. & Kulak, L. 2019. Predicting performance of lightweight concrete with granulated expanded Glass and Ash aggregate by means of using Artificial Neural Networks. *Materials*, 12, 2002.
- Longarini, N., Crespi, P., Zucca, M., Giordano, N. & Silvestro, G. 2014. The advantages of fly ash use in concrete structures. *Inzynieria Mineralna*, 15, 141–145.
- Mboya, H. A., Njau, K. N., Mrema, A. L. & King'ondo, C. K. 2019. Influence of scoria and pumice on key performance indicators of Portland cement concrete. *Construction and Building Materials*, 197, 444–453.
- Noguchi, T., Park, W.-J. & Kitagaki, R. 2015. Risk evaluation for recycled aggregate according to deleterious impurity content considering deconstruction scenarios and production methods. *Resources, conservation and recycling*, 104, 405–416.
- Pani, L., Francesconi, L., Rombi, J., Naitza, S., Balletto, G., Mei, G. 2019. Recycled Aggregates, Mechanical Properties and Environmental Sustainability Conference: INPUT aCADemy 2019 24–26 June 2019 Cagliari - Sardinia – Italy
- Pani, L., Francesconi, L., Rombi, J., Mistretta, F., Sassu, M. & Stochino, F. 2020. Effect of parent concrete on the performance of recycled aggregate concrete, *Sustainability*, 12 (22), 1–17
- Pani; L., Francesconi, L., Rombi, J., Salis, M. & Stochino F., 2021. Circular Economy Strategy in the Construction Sector: The Use of Recycle Aggregates in the Sardinian Island ICCSA 2021: Computational Science and Its Applications, 33–43.
- Pani; L., Francesconi, L., Valdes, M. Stochino, F., 2022. Structural performances of recycled aggregates concrete foundation plinths Italian Concrete Conference 2022, 53–58.
- Puppio, M., Giresini, L., Doveri, F. & Sassu, M. 2019. Structural irregularity: The analysis of two reinforced concrete (rc) buildings. *Engineering Solid Mechanics*, 7, 13–34.
- Puppio, M. L., Pellegrino, M., Giresini, L. & Sassu, M. 2017. Effect of material variability and mechanical eccentricity on the seismic vulnerability assessment of reinforced concrete buildings. *Buildings*, 7, 66.
- Quattrone, M., Angulo, S. C. & John, V. M. 2014. Energy and CO₂ from high performance recycled aggregate production. *Resources, Conservation and Recycling*, 90, 21–33.
- Rovida, A. N., Locati, M., Camassi, R. D., Lolli, B. & Gasperini, P. 2016. CPTI15, the 2015 version of the Parametric Catalogue of Italian Earthquakes.
- Ruslan, A. K., Nor, N. M., Kamar, M. S. H., Zainal, M. Y., Saliyah, S. N. M., Ismail, S. & Ibrahim, A. 2021. The Utilisation of Recycled Concrete Aggregate as Partial Sand Replacement in Wall Panel Production.
- Sajedi, F. & Shafiqh, P. 2012. High-strength lightweight concrete using leca, silica fume, and limestone. *Arabian journal for Science and engineering*, 37, 1885–1893.
- Sassu, M., Giresini, L., Bonannini, E. & Puppio, M. L. 2016. On the use of vibro-compressed units with bio-natural aggregate. *Buildings*, 6, 40.
- Singh, N. 2016. Effective uses of light weight concrete. *J Civil Eng Environ Technol*, 3, 208–211.
- Yardim, Y., Waleed, A., Jaafar, M. S. & Laseima, S. 2013. AAC-concrete light weight precast composite floor slab. *Construction and Building materials*, 40, 405–410.

Environmental impact reduction of precast multi-storey buildings by crescent-moon seismic dampers hidden in beam-column joints

L. Casali

Manini Prefabbricati S.p.a., S. Maria degli Angeli (PG), Italy

B. Dal Lago

Università degli Studi dell'Insubria, Varese/Como, Italy

A. Fulco & M. Mezzi

University eCampus, Como, Italy

ABSTRACT: The growing demand of sustainable precast structures for multi-storey constructions is often driven by the optimisation of cross-sections and reinforcement volumes of the structural elements. The present paper describes a real building recently designed and assembled with the installation of crescent-moon hysteretic dampers in the beam-column joints, recently proposed and patented. The joint continuity allows for an optimisation of the lateral load resisting system, reducing the size of the columns with respect to the classical precast frame structural arrangement with hinged joints, whilst protecting columns and beams from the large actions deriving from the classical moment-resisting cast-in-situ or partially precast technological solutions. After the complete detailed design of the case study building employing the 3 solutions described above, the precast dissipative one being designed with dynamic non-linear analysis, the results of an environmental impact analysis are compared and discussed, confirming a reduced environmental impact for the dissipative solution, with respect to both precast with hinged beam-column joints and moment-resisting cast-in-situ alternatives.

1 INTRODUCTION

The demand of precast structures for the construction of multi-storey buildings is growing, mainly due to the advantages offered by pre-stressing technology, speed of assemblage, robust performance, quality checks, etc. The most economical and typical beam-to-column joints in such buildings are hinged, which however makes the structure not always compatible with the requirements of drift limitation and reasonable column cross-sections. This issue becomes critical in zones of medium/high seismicity. Moreover, the adoption of wall panel or coupled wall/frame structures often results not compatible with architectural requirements. In typical cast-in-situ concrete frames, the stiffness and resistance of the spatial frame structure relies on moment-resisting beam-to-column joints. Such a solution is accompanied by large bending moments insisting on the joints, both in static and seismic load combinations. Indeed, combining this with the capacity design principle of strong column/weak beam for ductile seismic design, the dimensions of the elements also typically become large.

Emulative precast structures with wet-completed full moment-resisting joints typically become too complex if spans larger than the usual for cast-in-situ structures are employed. Recently, dry-assembled precast frame structures with hinged joints adaptable to clamped after dead loads are transferred was proposed by Dal Lago et al. (2018) thanks to the late activation of mechanical couplers, thus optimising the bending moment insisting on the joints.

This paper presents an alternative solution consisting in equipping the beam-to-column joints with crescent-moon steel hysteretic dissipative devices with elastic-plastic behaviour, allowing to control the degree of rotational stiffness of the joints, whilst thresholding the moments after yielding of the devices is attained. Such devices are conceived as structural seismic fuses, to be replaced after possible heavy use after strong earthquakes. This detail was recently proposed and patented by Manini Prefabbricati S.p.A. with deposit No. 102019000025459.

The efficacy of this joint is shown through a real case study building located in an Italian university campus, designed following dynamic non-linear analysis. An axonometric view and a picture of the case-study building made by 3 floors for a total height of 15 m and a total built surface near 3.000 m², are shown in Figure 1. The optimisation of the cross-sections of structural elements attained thanks to the proposed joint is also accompanied by enhanced environmental sustainability, typically mined for reinforced concrete structures by the components of reinforcing/insert steel and cement.

The main strategies currently tackled to reduce the environmental impact of structures can be essentially framed in two. The first strategy, object of wide research activities in the last decades, consists in partially or totally replacing the most impacting components with green alternative ones, such as sulfoaluminate cement instead of Portland (Coppola et al. 2018), or composite material rebars instead of steel (Dal Lago et al. 2017). Such replacements, on the basis of the current knowledge, are generally accompanied with a reduction of the structural performance and/or cost competitiveness of the structure. The second strategy, less extensively tackled in literature, consists in reducing the consumption of material volume, following the adoption of sophisticated technologies (e.g. pre-stressing and highly-technological moulds for precast structures) associated with a process of structural optimisation.

Recent research (Bonamente et al. 2014, Lamperti Tornaghi et al. 2018, Abey & Anand 2019, Wang et al. 2020, Baldoigrani et al. 2022, Dal Lago et al. 2022b, Nagireddi et al. 2022) demonstrated that precast structures, although employing more performing and impacting materials with respect to traditional cast-in-situ concrete structures, allow for a strong reduction of total volume of material employed for the construction, which results prevailing in the sustainability balance, and much more efficient than replacing cement or steel with green alternative materials (Baldoigrani et al. 2022, Dal Lago et al. 2022b). Such a balance tends to even more pend towards precast structures if analysing the sustainability in the framework of a Life-Cycle Analysis (LCA – Rodrigues et al. 2018), where additional factors contribute, including higher durability due to the adoption of high-quality concrete, absence of cracks in service due to pre-stressing, demountability, enhanced resilience, etc. Counter-balancing effect include the consumptions of precast production plants, and the transportation of the elements.

With the aim to quantify the advantages of the proposed dissipative solution in terms of environmental sustainability, the same structure was designed according to the following solutions:

1. precast frame with beam-to-column joints equipped with dampers;
2. precast frame with hinged beam-to-column joints;
3. cast-in-situ frame with moment-resisting beam-to-column joints.

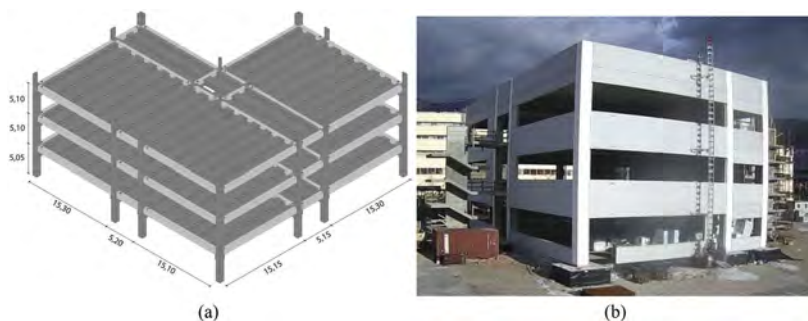


Figure 1. Structure at study: (a) axonometric view with main structural elements and geometry; (b) picture of the building near completion.

The present paper tackles the sustainability analysis with reference to the prime material consumption only, leaving to further publications currently ongoing extensions of the research in terms of wider LCA.

2 DESIGN OF THE STRUCTURAL FRAMES

2.1 Precast frame with beam-to-column joints equipped with dampers

Due to the highly non-linear and dissipative behaviour of the hysteretic crescent-moon dampers, and to the difficult framing of such original system in the classical seismic force-based design with response spectrum analysis, non-linear dynamic analysis was employed to check the previously proportioned structural members. The Finite Element Method (FEM) numerical model employed to this aim, shown in Figure 2, is made with linear beam elements for all frame members, since all non-linearities are expected to be concentrated in the joints. In particular, the column base was equipped with non-linear spring elements to which moment-rotation bi-linear diagrams were attributed (Figure 3), and the beam-to-column joints were modelled with a saddle combination of rigid links and non-linear spring elements provided with Bouc-Wen hysteretic behaviour calibrated on the basis of experimental qualification tests (Figure 4). The floor decks, made with adjacent pre-stressed elements making a double-flat hollow cross-section (similarly to the one described in Dal Lago et al. 2022a) after steel sheets are placed in the open central core of the elements and in-situ concrete topping is cast, were modelled with semi-rigid diaphragm, simulating the effective in-plane floor stiffness. Cladding panels were introduced as masses without stiffness, thanks to the adoption of special sliding connectors decoupling their motion from that of the frame (Toniolo & Dal Lago 2017).

Design resistance was considered for concrete class C45/55, rebars mild steel grade B450C, and 7w-strand pre-stressing steel fp1860.

The design process followed these steps: (a) evaluation of the structural performance under first-phase static loads without dissipative devices; (b) activation of the dissipative devices; (c) application of second-phase static loads; (d) non-linear dynamic time history analysis for different hazard scenarios encompassing limit states of Operability (OLS), Damage (DLS), Life-Safety (LSLS), and Collapse (CLS).

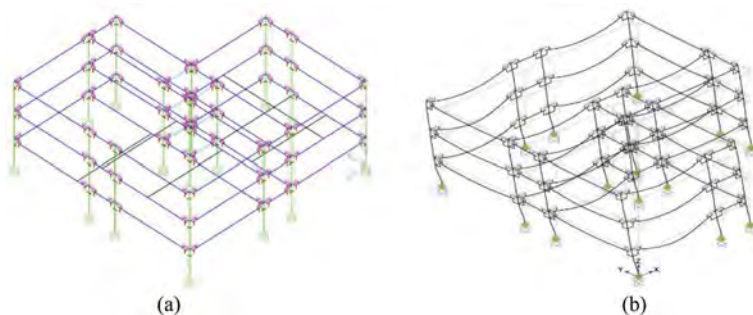


Figure 2. Deformed shape and activated plastic hinges (green dots) at the end of one of the dynamic NL analyses at collapse limit state.

For each limit state, the response under 7 triplettes (X,Y,Z) of artificially-generated EC8-spectrum-compatible accelerograms was evaluated (EN 1998-3:2005). The stationary part of the accelerograms was assumed to be 10s long. The pseudo-stationary time window of the accelerograms followed a 2s time interval with accelerations of increasing amplitude starting from zero, and was set to be followed by a tail of 13 s with accelerations of decreasing amplitude. Thus, the whole duration of a single ground motion is 25 s. The mean of the maximum values evaluated through the 7 triplettes for each limit state was considered for the checks.

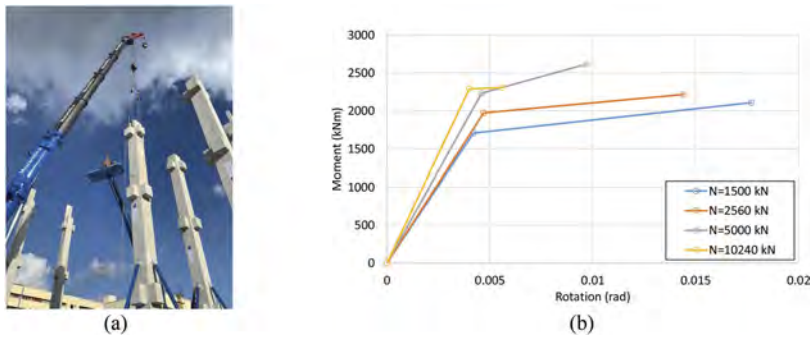


Figure 3. Column elements: (a) picture during assemblage; (b) bi-linear moment-rotation curves attributed to the base spring.

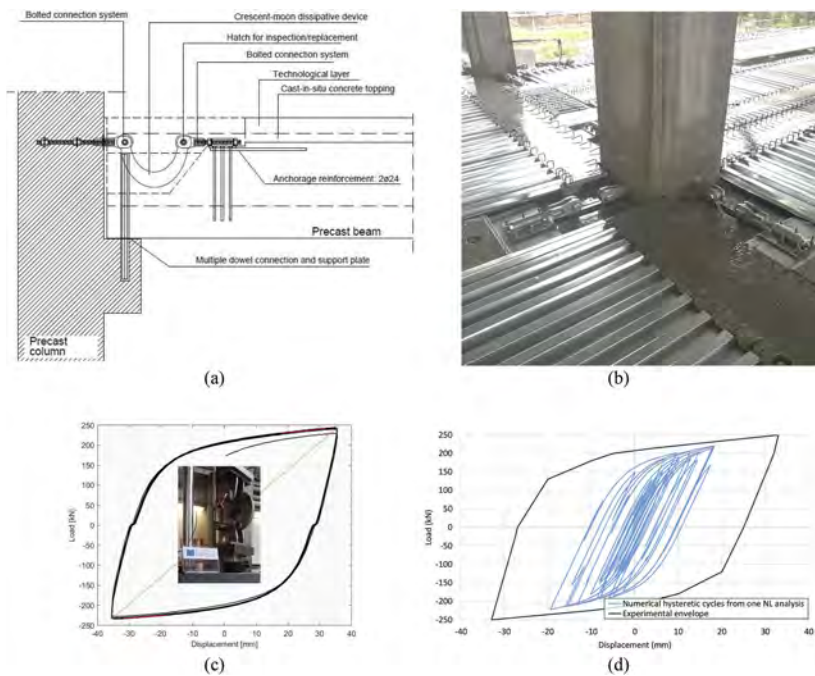


Figure 4. Dissipative beam-column joint with hidden crescent-moon hysteretic dampers: (a) schematic description; (b) picture from real building; (c) experimental hysteresis of crescent-moon damper; (d) non-linear force-displacement diagram attributed to spring elements in the model.

Figure 2b shows the deformed shape of the frame structure and the activation of the column base plastic hinges after an analysis related to CLS. The exemplificative hysteretic response of a crescent-moon device under the same analysis is shown in Figure 4d.

On the basis of the analysis results, it was observed that the column base attained a minimum capacity over demand ratio (C/D) of 2.39, evaluated based on the ultimate rotation capacity. Critical for the design resulted indeed the interstorey drift of the last storey in OLS, equal to 0.331% versus a maximum value which, according to the class of use III of the building, was equal to 0.333%.

In order to synthetically estimate the hysteretic contribution of the dissipaters, acting in parallel with the contribution of the column bases, further analyses were run assuming a perfect elastic response of the dissipative devices considering an equivalent secant stiffness associated to the mean local device displacement obtained in the first series of NLTHA for each LS.

The comparison with the first series of analyses allows to compute the reduction factor β associated with the displacement reduction due to the hysteresis of the dissipative crescent-moon devices. The spectral demand reduction due to the added dissipation effect may be expressed in terms of added equivalent viscous damping (e.g. within the capacity spectrum method – Dal Lago & Molina 2018) or by increasing the force reduction (behaviour) factor q (e.g. within the force-based design method – EN 1998-3:2005), within the assumption of equivalent anelastic displacement for flexible structures. Considering Eq. (1):

$$q_D = \beta \times q_{lim} \quad (1)$$

where

q_{lim} is the limit behaviour factor in the context of modal analysis with response spectrum, assumed equal to 2.0 for the considered case study;

q_D is the behaviour factor to be attributed to the presence of the dissipative devices.

The value of the behaviour factor of the dissipative structure q_D is calculated as 2.56 following a β coefficient of 1.28 for LSLS, and as 2.78 following a β coefficient of 1.39 for CLS, respectively. It is highlighted that the above values are directly referred to the case study analysis, based on a conservative limit behaviour factor assumed in the design phase, where even at CLS the full deformation capacity of frame structure and dissipative devices was far to be attained, and hence these values could potentially be extended.

With the aim to validate the estimation carried out with the above method, further linear dynamic analyses with response spectrum were carried out utilising a CLS spectrum and adopting the behaviour factor q_D determined as above. The total base shear obtained in the two main directions (3009 kN and 2934 kN in X and Y directions, respectively) resulted close to the peak values of the NLTHA (3121 kN and 3321 kN in X and Y directions, respectively).

The contribution of the proposed dissipative joint led to large benefits in the proportioning of the column cross-section, which was set to be square with 80 cm of side, assumed constant along the height. The bending moment transmitted by the joint, thresholded by yielding of the hysteretic dissipative devices, attained a maximum contained in 189 kNm at LSLS. Hence, the partial continuity of beams and columns did not lead to additional reinforcement for all frame members in seismic load combinations with respect to that calculated for gravity load combinations, and the typical details requested to ensure ductility around beam ends for typical cast-in-situ members resulted indeed not necessary.

The foundations were made with footing RC plates supported on 4 piles of diameter 0.60 m and length of 20 m.

2.2 Precast frame with hinged beam-to-column joints

Within this solution, representative of the typical precast solution for this typology of buildings, the design was carried out assuming columns cantilevering from their clamped base and perfectly hinged beam-column joints. Since this structural typology is framed in the current normative, a traditional design process was carried out following modal analysis with response spectrum on the basis of a force reduction (behaviour) factor q equal to 2.0.

Figure 5 shows the envelope of bending moments on the columns in direction X. A maximum base bending moment per single column of 2879 kNm was evaluated at LSLS. This led to the adoption of square cross-sections of side 1.10 m.

The foundations were evaluated to be similar to the previous case.

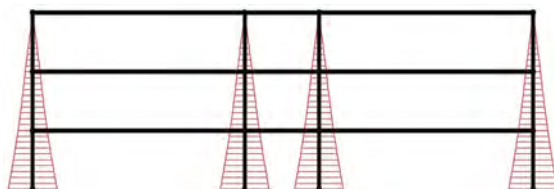


Figure 5. Precast frame with hinged beam-to-column joints: envelope of bending moments on columns.

2.3 Cast-in-situ frame with moment-resisting beam-to-column joints

The design of the cast-in-situ frame was carried out assuming a traditional “shear-type” frame structure, on the basis of modal analysis with response spectrum assuming a force reduction (behaviour) coefficient equal to 2.76. Figure 6 shows the resulting bending moment envelopes on both column and beam elements.

Maximum bending moments equal to 3317 kNm and 3634 kNm were evaluated at LSLS for individual column and beam members, respectively. This led the cross-sections to be designed as square with side of 1.20 m and T-shaped with height of 1.40 m and thickness of 0.60 m for column and beam members, respectively.

Foundations were designed to be very similar to the previous cases, except for a slight increase of pile length to 22.5 m.

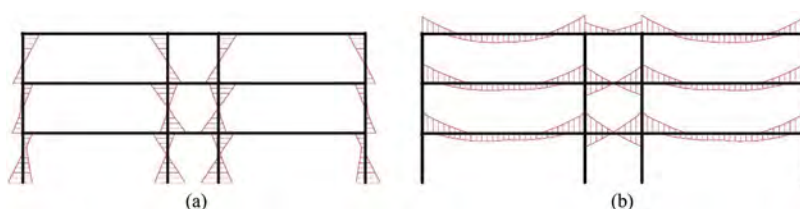


Figure 6. Cast-in-situ frame with moment resisting beam-to-column joints: envelope of bending moments on (a) columns; (b) beams.

3 ENVIRONMENTAL IMPACT ANALYSIS

The environmental impact of the structural organism of the case study building designed according to the 3 different technological solutions described above is analysed with reference to the contribution of primary structural materials. In order to quantify environmental impact, reference was made to the ponderation indexes of Global Warming Potential (GWP) relative to the different materials employed, and to their single components. Such indexes have been taken from Environmental Product Declarations (EPD) spontaneously issued on a voluntary basis by Italian producers (where present) following the procedure described in EN:15804:2012+A2:2019 and UNI EN ISO 14025:2010. Global indexes (sum of items A+B+C) were considered, since mostly relevant to quantify the impact deriving from the use of primary structural materials.

The GWP values utilised in the computation are reported in Table 1 expressed in terms of equivalent carbon dioxide (eqCO₂) referred either to unity of mass or volume of material. The summation of the concrete components for different concrete grades were evaluated based on actual mix designs employed by Manini Prefabbricati S.p.A.

On the basis of the complete quantity list of materials employed for each designed solution, the balance of environmental sustainability was evaluated, as synthetically reported in Figure 7. It is noted that the impact of about 600 tons of eqCO₂ related to the foundations is practically equivalent for all solutions, with slight increase in the case of the cast-in-situ frame due to the longer piles employed.

Differently, it can be observed a relevant difference related to the superstructure, ranging in between 835 and 1100 tons of eqCO₂. Referred to the built surface of the building, these values range in between 278 and 367 kgeqCO₂/m². The results shown in Table 2 demonstrate that the more sustainable solution is the proposed one with dissipative beam-to-column joints, where the additional impact related to the physical steel devices and anchorage systems is more than balanced by the reduction of concrete and reinforcement in columns with respect to the traditional precast solution with hinged beam-to-column joints (+12% of eqCO₂), and in both columns and beams with respect to the cast-in-situ frame (+31% of eqCO₂).

Table 1. GWP weighted indexes for the different materials and composites employed.

MATERIAL	DENSITY (ton/m ³)	GWP (kg Co ₂ eq/ton)	GWP (kg Co ₂ eq/m ³)
CEMENT CEM I 52,5 R	3.15	910	2866.5
CEMENT CEM IV 32,5 N	3.15	588	1852.2
AGGREGATES	1.5	20.7	31.1
SUPERPLASTICISER	1.1	1888	2076.8
WATER	1	-	-
LEAN CONCRETE C12/15	1.8	109	196.7
CONCRETE C25/30	2.4	116	279.4
CONCRETE C28/35	2.4	122	293.6
CONCRETE C32/40	2.4	162	388.8
CONCRETE C40/50	2.4	167	401.8
CONCRETE C45/55	2.4	226	542.2
POLYSTYRENE	0.02	5436	108.72
INSERT STEEL	7.85	1130	8870.5
REBAR STEEL B450	7.85	924	7253.4
STRAND fy1860	7.85	2530	19860.5

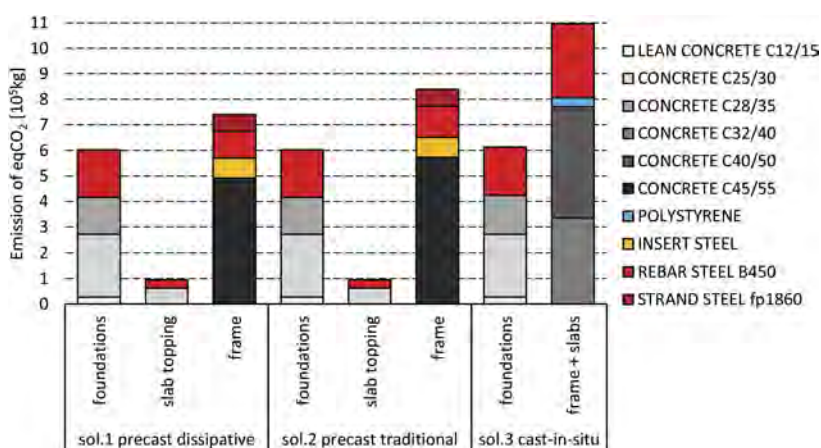


Figure 7. Equivalent CO₂ emission for the different structural components of each solution.

Table 2. Total equivalent CO₂ emission for the different structural solutions analysed.

Emission of eqCO ₂ for the superstructure [10 ⁵ kg]		
sol.1 precast dissipative	8.35	-
sol.2 precast traditional	9.34	(+11.9%)
sol.3 cast-in-situ	10.96	(+31.3%)

4 CONCLUSIONS

The non-linear time history analysis of the real case study building provided with semi-rigid beam-column joints with dissipative crescent-moon hysteretic dissipaters installed showed a seismic behaviour characterised by a good balance between the requisites of (a) limitation of drift, and (b) member strength according to the different limit states analysed. This behaviour is associated with the hysteretic added damping provided to the structural assembly by the dissipaters through flexural stiffening, energy dissipation, and thresholding of the actions on the frame structures after attainment of yielding. The alternative design of the same building

with either ordinary precast with hinged beam-column joints or traditional cast-in-situ with clamped joints, led to larger cross-sections and reinforcement volume. The environmental impact analysis of the 3 alternative solutions classified the precast dissipative one as the more sustainable due to the following reasons: with respect to the ordinary precast, the contribution of the metallic dampers and their anchoring systems more than balanced the larger column cross-section of the ordinary precast solution, with 12% equivalent CO₂ emission less for the super-structure; with respect to the traditional cast-in-situ solution, the contribution of the use of more performing though impacting materials much more than balanced the larger volumes of concrete and reinforcement of the less optimised traditional cast-in-situ solution, with 31% equivalent CO₂ emission less for the superstructure. It is currently under development an extension of the environmental impact analysis herein presented which includes factors other than the consumption of prime materials, following a more general LCA approach.

REFERENCES

- Abey, S.T. & Anand, K.B. 2019. Embodied energy comparison of prefabricated and conventional building construction. *Journal of The Institution of Engineers (India): Series A* 100(4): 777–790.
- Bahramian, M. & Yetilmezsoy, K. 2020. Life cycle assessment of the building industry: An overview of two decades of research (1995–2018). *Energy and Buildings* 219: 109917.
- Baldograni, G., Binaglia, M., Casali, L., Dal Lago, B., Fusco, A. & Mezzi, M. 2022. Role of crescent-moon hysteretic dampers employed in beam-column joints on the environmental impact of a real precast multistorey building. *Italian Concrete Conference 2022 (ICC22)*, Naples, Italy, 137–144.
- Bonamente, E., Merico, M.C. Rinaldi, S., Pignatta, G., Pisello, A.L., Cotana, F. & Nicolini, A. 2014. Environmental impact of industrial prefabricated buildings: Carbon and energy footprint analysis based on an LCA approach. *Energy Procedia* 61: 2841–2844.
- Coppola, L. *et al.* 2018. Binders alternative to Portland cement and waste management for sustainable construction—part 1. *Journal of Applied Biomaterials & Functional Materials*, 16(3): 186–202.
- Dal Lago, B., Martinelli, L. & Foti, F. 2022a. Slender precast voided slabs under walking-induced vibration. *Structural Concrete* 23(6): 3416–3443.
- Dal Lago, B. & Molina, F.J. 2018. Assessment of a capacity spectrum design approach against cyclic and seismic experiments on full-scale precast RC structures. *Earthquake Engineering and Structural Dynamics* 47(7): 1591–1609.
- Dal Lago, B., Negro, P. & Dal Lago, A. 2018. Seismic design and performance of dry-assembled precast structures with adaptable joints. *Soil Dynamics and Earthquake Engineering* 106: 182–195.
- Dal Lago, B., Taylor, S.E., Deegan, P., Ferrara, L., Sonebi, M., Crosset, P. & Pattarini, A. 2017. Full-scale testing and numerical analysis of a precast fibre reinforced self-compacting concrete slab pre-stressed with basalt fibre polymer bars. *Composites Part B: Engineering* 128: 120–133.
- Dal Lago, B., Ferronato, N. & Torretta, V. 2022b. Comparison of the environmental impact of similar supermarket structures built with cast-in-situ and precast reinforced concrete. *Italian Concrete Conference 2022 (ICC22)*, Naples, Italy, 291–297.
- European Committee for Standardization (CEN). 2005. EN 1998-3:2005 – Eurocode 8: Design of structures for earthquake resistance, Part 3: Assessment and retrofitting of buildings; Brussels, Belgium.
- European Committee for Standardization (CEN). 2010. EN ISO 14025:2010 – Labels and environmental declarations – general principles; Brussels, Belgium.
- European Committee for Standardization (CEN). 2012+2019. EN 15804:2012+A2:2019 - Sustainability of construction works – Environmental product declarations – Core rules for the product category of construction products; Brussels, Belgium.
- Lamperti Tornaghi, M., Loli, A. & Negro, P. 2018. Balanced evaluation of structural and environmental performances in building design. *Buildings* 8(52): 1–24.
- Nagireddi, J., Gedela, S.K., Shaik, M.S. & Sundaram, B. 2022. Environmental Performance and Cost Assessment of Precast Structural Elements for Cleaner Construction Solutions: LCA Approach. *Journal of Hazardous, Toxic, and Radioactive Waste*, ASCE, 26 (2): 04021052.
- Rodrigues, V., Martins, A.A., Nunes, M.I., Quintas, A., Mata, T.M. & Caetano, N.S. 2018. LCA of constructing an industrial building: focus on embodied carbon and energy. *Energy Procedia* 153: 420–425.
- Toniolo, G. & Dal Lago, B. 2017. Conceptual design and full-scale experimentation of cladding panel connection systems of precast buildings. *Earthquake Engineering and Structural Dynamics*, 46(14), 2565–2586.
- Wang, H., Zhang, Y., Gao, W. & Kuroki, S. 2020. Life cycle environmental and cost performance of prefabricated buildings. *Sustainability* 12(7): 2609.

Life-cycle assessment of coal mining wastes upcycling

S. Muller & F. Lai
BRGM, Orléans, France

M. Nucci & E. Segù
NTS, Casale sul Sile, Italy

R. Crane & W. Nash
University of Exeter, Exeter, UK

A. Wrana
GIG, Katowice, Poland

B. Bezak
PGG, Katowice, Poland

L. Ferrara
Politecnico di Milano, Milan, Italy

ABSTRACT: Coal extraction generates coal mining wastes (CMW) that lead to additional environmental burdens. This study assesses the potential environmental benefits of using these CMW as secondary materials in the production of precast concrete cladding panels. Potential environmental impacts are measured using life cycle assessment (LCA). The system under assessment is a multi-functional system, including both the management of CMW and the production of concrete panels. Company data have been used to perform the assessment. Preliminary results show, for the business-as-usual (BAU) scenario, that the main impacts associated with wastes management are due to diesel consumption and direct emissions to groundwater. For the concrete panel production, the impacts are primarily induced by cement production. This BAU scenario will be compared to a recycling scenario where CMW are incorporated into concrete production. Based on this comparative LCA, recommendations as to the use of CMW into construction products will be provided.

1 INTRODUCTION

In order to meet the Paris agreement, governments and stakeholders of the civil society call for phasing down or transitioning away from coal as an energy source. Yet, according to the International Energy Agency in 2021, coal fired power generation reached 769 TWh, a level higher than before resulting in record levels in terms of CO₂ emissions as well (IEA, 2022a). Thermal coal accounted for 78% of the total coal consumption, which reached almost 8 billion tons in 2022 (IEA, 2022b).

This coal is extracted from various mine sites leading to important volumes of coal mining wastes (CMW). Some authors report that for each ton of coal produced, 0.4 to 0.5 ton of waste is generated (Pactwa et al., 2020). In Poland, for example, around 35 million tons of CMW is generated every year (Warcholik et al., 2014). Wastes associated with hard coal extraction and processing can lead to environmental and social issues when stored. Storage of

coal mining waste can lead to soil and/or water pollution depending on the sulfur or heavy metals content of the wastes. Fire hazard is also a risk associated with the storage of CMW that can lead to atmospheric pollution (Pactwa et al., 2020).

Apart from environmental and social concerns, handling and storing mining wastes also has an economic cost for mining companies and the society. Direct costs for mining companies include for example the workforce, equipment and fuel needed to handle the wastes from the production plant to the waste storage area. Given the social and environmental issues, monetized externalities can also be associated with CMW costs. As per Wang et al. (2020), the costs associated with the waste storage in terms of land function loss and use sum up to 3.57 USD/t.

To limit the amount of CMW stored and the associated economic, social and environmental costs, solutions to use them as secondary raw materials are being explored. One of their use as secondary raw materials could be as geomaterials in the construction sector (Vo et al. 2022). The research project MINRESCUE is exploring this pathway by assessing the inclusion of CMW as raw materials for the production of precast concrete panels to be used in industrial buildings. In order to assess the potential environmental benefits associated with this solution, a comparative life cycle assessment (LCA) has been performed considering, on the one hand, a *business-as-usual* (BAU) scenario representing how CMW are today handled and, on the other hand, a *recycling* scenario where these CMW are used as secondary materials for concrete panel productions. In this work, an emphasis is put firstly on the modelling of the BAU scenario and its resulting environmental impacts (Section 2) and secondly on the key parameters to focus on in the modelling of the *recycling* scenario (Section 3).

2 LIFE CYCLE ASSESSMENT OF THE BUSINESS-AS-USUAL SCENARIO

Over the last decades, LCA has gained interest as a decision-support tool to assess the environmental performance of products and services to support company or policy decision-making. LCA considers a so-called life cycle perspective, covering all life cycle stages in a cradle-to-grave perspective (i.e. from raw materials extraction to end-of-life disposal). It accounts for both direct and indirect impacts, in a multi-criteria framework that includes various impact categories (e.g. carbon footprint, toxicity-related issues, resource consumption). In particular, LCA enables i) the identification of environmental hotspots; ii) the comparison of different scenarios to identify the best performing scenario and potential burden-shifts from one impact category/life cycle stage to another. The implementation of LCA is framed by ISO standards (14040 and 14044) and follows four different steps, as hereafter detailed (see Sections 2.2, 2.3 and 2.4).

2.1 Definition of the BAU scenario

This study focuses on two different industrial activities in their current functioning:

- i) Coal mining, with focusing on waste management operations and considering currently operating mine sites in Poland in particular, the BAU scenario considers current on-site operations, where part of the mining waste is reused (e.g. in roadbed) while the remaining part is disposed of through on-site stockpiling.
- ii) Precast concrete elements production, focusing on pre-cast concrete panels currently produced by the NTS company in Italy. The BAU scenario in particular entails considering the current concrete mix (i.e. including cement, sand, gravel, filler, additive and water) as used by the NTS company.

2.2 Goal and scope

The product system here under study can be considered a multifunctional system providing two different functions: i) the management of solid wastes resulting from coal processing; ii) the production of pre-cast concrete panels.

It is decided to capture both functions in the functional unit of this study, rather than privileging one over the other. In this context, the functional unit is defined as:

The management of 1 ton of solid wastes resulting from coal processing, and the production of 1 pre-cast concrete panel.

The system boundaries include: i) the production and consumption of reagents, ancillary materials, energy and water; ii) the direct emissions to the environment generated by the operations under study; iii) the transport of raw materials; and iv) the production of the infrastructure and equipment.

Moreover, these boundaries cover all unit operations associated with:

- The processing of wastes prior to their final disposal or reuse;
- The final disposal or reuse of the wastes;
- The production of concrete;
- The casting of concrete into pre-cast panels.

The upstream coal mining and processing operations have been here excluded from the boundaries.



Figure 1. System boundaries for the BAU scenario.

The environmental impacts have been calculated using the Simapro LCA software, considering the European life cycle impact assessment method (EF method 3.0; Fazio et al. 2018). This method, established by the Joint Research Centre (JRC) of the European Commission (EC), encompasses 16 impact categories recommended by the JRC in the context of the European Product and Organization Environmental Footprint (PEF/OEF), which aims to establish a common method to measure and communicate the life cycle environmental performance of products and organizations in the EU.

2.3 Life Cycle Inventory (LCI)

The foreground system (i.e. all processes for which specific data have been collected and used in the modelling) has been modelled primarily using data provided by companies. These data were completed with generic data (e.g. from the ecoinvent LCI database) and assumptions in cases of data gaps.

The compiled inventory encompasses data about:

- Energy consumption, including the electricity necessary to concrete mixing and casting into pre-cast panel as well as the diesel necessary to fuel the machinery operating the coal waste storage area. Data about electricity consumption were obtained from calculations based on technical specifications related to the used equipment. As for data on fuel consumption, the latter were drawn from the ecoinvent LCI database, in the absence of data specific to the machinery implemented on-site.
- Raw materials and chemicals consumption, in particular for manufacturing concrete, which requires various constituents such as concrete, sand, gravel and other additives. This concrete mix is based on the actual mix as used by the NTS company for manufacturing of its precast concrete products.
- Water consumption, for concrete production.
- Transport, especially regarding the supply of concrete constituents to the NTS manufacturing plant.

- Infrastructure, considering the concrete mixing plant as a whole. In particular, it is assumed that the plant is solely made of “low-alloyed” steel, with deriving the total weight of the plant from technical specifications.
- Equipment, necessary to handling waste and operating the coal waste storage area (e.g. conveyor belt, stackers, bulldozers). In the absence of specific information regarding each piece of equipment implemented on-site, generic data drawn from the ecoinvent LCI database were used as a proxy for modelling some pieces of equipment.
- Land occupation, considering the superficial land occupation and transformation induced by the coal waste storage area.
- Emissions to the environment, in particular considering potential long-term emissions of substances to groundwater, resulting from the waste storage area. The quantification of these emissions is based on a geochemical model, as currently implemented in the widely used LCI database ecoinvent. The model is adapted by using specific on-site data obtained from one mine site. These data encompass the coal tailings composition, the characteristics of the waste storage area and specific data regarding the climatic conditions.

2.4 *Life cycle impact assessment and interpretation*

In a life cycle perspective, the management of 1 ton of solid wastes resulting from coal processing, and the production of 1 pre-cast concrete panel potentially induces a total of 607 kg CO₂-eq (climate change), 0.197 CTUh (human toxicity, non-cancer effects) and 0.192 kg P-eq (eutrophication, freshwater). The complete list of impacts, considering the 16 impact categories from the EF method 3.0, is detailed in Table 1.

Overall, the production of concrete panels stands for the main contributor to the environmental impacts, as it dominates the impacts for 15 impact categories out of 16 (with contributions ranging from 84.1% to 100%; Table 1). Coal wastes management only stands out in the case of freshwater eutrophication, as it accounts for 69.4% of the impacts.

With reference to the production of concrete panels, the use of cement stands out as the main environmental hotspot as it accounts for the largest share of impacts with respect to all impact categories (more than 60% of the impacts for all categories excepting water use, for which cement represents about 40% of the impacts – Figure 2). Aside from cement, the use of electricity (in particular for the casting process) appears to have a relatively modest contribution to the impacts, regarding the “ozone depletion”, “ionizing radiation”, “land use”, “water use” and “resource use, fossils” impact categories (more than 10% of the impacts).

The impacts induced by coal waste management are essentially driven by the machinery operating on-site as well as direct emissions to environment (Figure 3). In particular, the diesel consumed by the machinery is responsible for the most significant part of the impacts with respect to 11 impact categories out of 16, with bulldozers and ZGOT stackers respectively accounting for about 60% and 40% of these impacts. Four impact categories, namely toxicity-related categories and freshwater eutrophication, direct emissions of substances to groundwater account for the largest share of the impacts (more than 90% of the impacts). Finally, impacts relative to “land use” are due to the land occupation and transformation as induced by the coal waste storage area.

3 MODELLING THE RECYCLING SCENARIO

3.1 *Definition of the product system*

Regarding the recycling scenario, the boundaries of the system cover the same functional reality as the BAU scenario (cf. Section 2.2). In comparison with the BAU scenario, this recycling scenario includes unit operations associated with the preparation of waste and its transport to the concrete panel production site.

Table 1. Resulting impacts for the functional unit under assessment and contribution of each part of the functional unit considering 16 impact categories from the EF method 3.0.

Impact category	Unit	Concrete panel production	Waste management
Climate change	kg CO2 eq	6.04E+02 99.47%	3.21E+00 0.53%
Ozone depletion	kg CFC11 eq	2.40E-05 97.26%	6.75E-07 2.74%
Ionising radiation	kBq U-235 eq	1.97E+01 99.01%	1.98E-01 0.99%
Photochemical ozone formation	kg NMVOC eq	1.43E+00 98.94%	1.53E-02 1.06%
Particulate matter	disease inc.	1.36E-05 98.79%	1.67E-07 1.21%
Human toxicity, non-cancer	CTUh	1.97E-01 100.00%	1.81E-07 0.00%
Human toxicity, cancer	CTUh	2.07E-07 91.24%	1.99E-08 8.76%
Acidification	mol H+ eq	1.86E+00 99.26%	1.38E-02 0.74%
Eutrophication, freshwater	kg P eq	8.13E-02 30.61%	1.84E-01 69.39%
Eutrophication, marine	kg N eq	5.42E-01 99.10%	4.95E-03 0.90%
Eutrophication, terrestrial	mol N eq	5.89E+00 99.09%	5.41E-02 0.91%
Ecotoxicity, freshwater	CTUe	8.24E+03 84.10%	1.56E+03 15.90%
Land use	Pt	2.67E+03 88.54%	3.46E+02 11.46%
Water use	m3 depriv.	8.40E+01 99.91%	7.44E-02 0.09%
Resource use, fossils	MJ	3.38E+03 98.73%	4.35E+01 1.27%
Resource use, minerals and metals	kg Sb eq	3.02E-03 99.95%	1.49E-06 0.05%

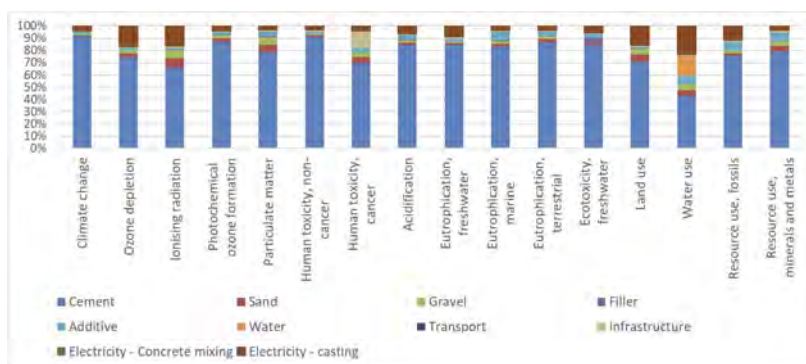


Figure 2. Contributions to the environmental impacts of concrete panel production, considering 16 impact categories from the EF method 3.0.

As the project is still on-going, the actual mix-design to produce a concrete panel with the incorporation of CMW is not yet fully finalized. Once crushed at the right granulometry, the CMW would be mixed with natural aggregates in a proportion yet to be quantified (cf.

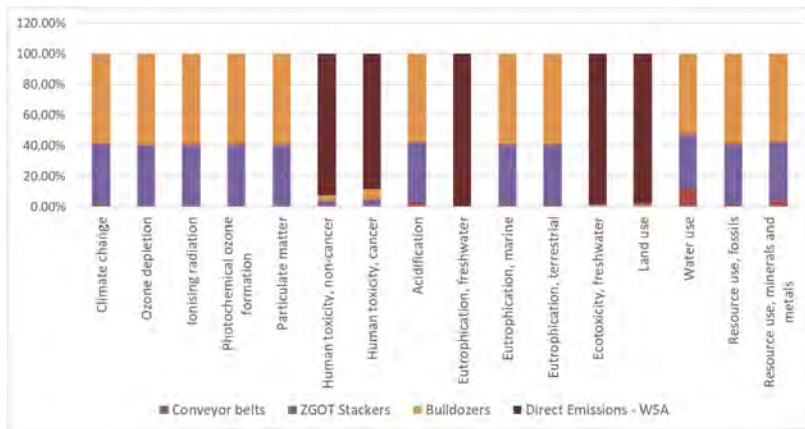


Figure 3. Contributions to the environmental impacts of coal wastes management, considering 16 impact categories from the EF method 3.0.

Section 3.2) to obtain the concrete to be used in the panel production. CMW would replace both a fraction of fine and coarse natural aggregates in the concrete production.



Figure 4. System boundaries for the recycling scenario.

3.2 Accounting for recycled products durability

In the framework of the MINRESCUE project a comprehensive investigation has been performed by the last author's group on the performance of concrete containing recycled CMWGs from different sources, with preliminary results reported in detail in (del Galdo et al., 2022). The investigation has considered compressive and flexural strength, fracture energy and shrinkage and has confirmed, as from some exemplary results on compressive strength shown in Figure 5, that, while the mechanical properties suffer some reduction because of the replacement of natural aggregates with CMWGs, when the latter are employed to replace fine aggregates or a combination of fine and coarse aggregates, an overall set of mechanical performance can be obtained which still complies with those required by several engineering applications.

This, on the one hand, paves the way for a valorization of CMWGs in the construction industry and on the other hand, strengthens the motivation for this study, corroborating first of all the possibility that the intended precast structural elements can be produced with concrete incorporating CMWGs as a recycled aggregate in partial replacement of natural ones and furthermore that the expected service life could be comparable, though quantitative assessment of durability performance for the aforesaid concretes is still on-going.

3.3 Differences expected against the business as usual scenario

Given the results presented in Section 2.4 and the product system presented in Section 3.1, some results of the comparison of the recycling scenario against the BAU scenario could be

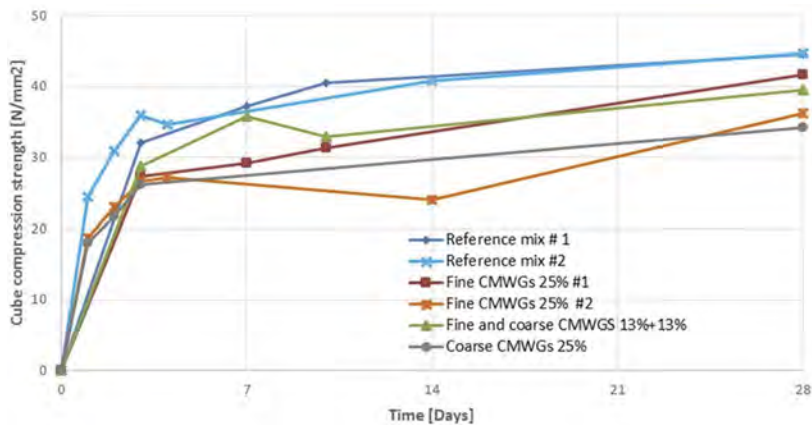


Figure 5. Evolution of cube compressive strength for mixes incorporating different types and replacement percentages of CMWGs.

anticipated. Firstly, for the BAU system, the concrete panel production is the higher contributor for a large majority of the impact categories and in this concrete panel production, cement production is the highest contributor. In the envisioned recycling scenario, CMW will replace sand and gravel but not cement; those impacts won't so not be diminished by the inclusion of CMW in the concrete mix.

However, recycling of CMW will have a direct effect on different impact categories. It will firstly diminish all impacts associated with on-site CMW management and in particular, the impact for which the direct emissions are the greatest contributor (Figure 3). Among these impacts, the category "Eutrophication freshwater" will be the most affected by the consideration of the recycling scenario (cf. Table 1).

If the recycling scenario will directly lower some of the impact categories, its specific unit process will however have other impacts. It is the case of the waste processing unit process that consists of an energy consumption to obtain the desired wastes granulometry. It is also the case of the waste transport from the mining site to the plant producing the concrete panels. The type of energy used and the transportation distance could be parameters that have strong influence on the resulting comparison. Given this fact, sensitive and scenario assessments will be performed on those parameters in order to find the tipping point where the recycling scenario may no longer be more environmentally friendly than the BAU scenario.

4 CONCLUSIONS

In order to conclude this study, work still needs to be done. In particular, durability performance of the concrete panel containing CMW should be quantified, the mix between primary and secondary materials for the recycling scenario should be defined and finally, the LCA of the recycling scenario should be performed to compare the results against the ones obtained for the BAU scenario.

Results of the comparison between the BAU and the recycling scenario would lead to recommendations for both the mine operators and the concrete panel producers on the development of an optimized scenario regarding different parameters such as the distance between the mine site and the producer of the concrete panels. This optimized scenario should minimize the environmental impacts associated with the inclusion of CMW into concrete production moving from linear to circular economy.

ACKNOWLEDGEMENTS

This project has received funding from the Research Fund for Coal and Steel under Grant Agreement No. 899518 MINRESCUE “From Mining Waste to Valuable Resource: New Concepts for a Circular Economy”. GIG research activities were co-funded also by Polish Ministry of Education and Science.

REFERENCES

- del Galdo, M., Albertini, L. and Ferrara, L. 2022. Mechanical characterization of concrete with recycled aggregates from coal mining wastes. In « Concrete Innovation for Sustainability», S. Stokkeland, H.C. Braarud eds. *Proceedings of the 6th fib International Congress 2022*, Oslo, 12-16/6/2022 pp. 834–841, ISBN 9782940643158.
- Fazio, S. Castellani, V. Sala, S., Schau, EM. Secchi, M. Zampori, L., 2018. Supporting information to the characterisation factors of recommended EF Life Cycle Impact Assessment methods, EUR 28888 EN, European Commission, Ispra, ISBN 978-92-79-76742-5, doi:10.2760/671368, JRC109369
- IEA 2022a. Coal-Fired Electricity, IEA, Paris <https://www.iea.org/reports/coal-fired-electricity>, License: CC BY 4.0
- IEA 2022b. Coal 2022 Analysis and Forecast to 2025, IEA, Paris <https://iea.blob.core.windows.net/assets/91982b4e-26dc-41d5-88b1-4c47ea436882/Coal2022.pdf>, License: CC BY 4.0.
- Pactwa K, Woźniak J, Dudek M 2020. Coal mining waste in Poland in reference to circular economy principles. *Fuel* 270:117493. <https://doi.org/10.1016/J.FUEL.2020.117493>
- Vo TL, Nash W, Del Galdo M, et al 2022. Coal mining wastes valorization as raw geomaterials in construction: A review with new perspectives. *J Clean Prod* 336:130213. <https://doi.org/10.1016/J.JCLEPRO.2021.130213>
- Wang, X.; Wang, L.; Chen, J.; Zhang, S.; Tarolli, P. 2020. Assessment of the External Costs of Life Cycle of Coal: The Case Study of Southwestern China. *Energies* 13, 4002. <https://doi.org/10.3390/en13154002>
- Warcholik, W., Dolnicki, P., & Gawor, Łukasz. 2014. Possibilities of exploitation of secondary deposits (post mining dumping grounds) as an example of changes in extractive industry. *Studies of the Industrial Geography Commission of the Polish Geographical Society*, 27, 256–266. <https://doi.org/10.24917/20801653.27.16>

*SS23: Shaping development planning processes for infrastructure
systems under future uncertainty*
Organizers: B.T. Adey, A. Elvarsson & O. Román



Taylor & Francis

Taylor & Francis Group

<http://taylorandfrancis.com>

The value of accelerating the infrastructure planning process

A.B. Elvarsson, B.T. Adey & O. Roman

Chair of Infrastructure Management, ETH Zürich, Switzerland

ABSTRACT: Infrastructure planners strive to ensure that infrastructure meets the needs of stakeholders in the short, medium and long-term. This is a challenging task because there is considerable uncertainty associated with future stakeholder needs, and the infrastructure built to meet these needs has a life-time spanning decades, if not centuries. Additionally, the planning of either new infrastructure or the modification of existing infrastructure usually requires years, or even decades, meaning that stakeholder needs often change during the planning process itself.

Planners' responsiveness, i.e., how quickly planners can adjust to changing stakeholder needs, depends on the planning processes in which the planners are embedded. The relationship between improving responsiveness (in this paper the time taken to increase rail capacity to acceptable levels) and its impact on stakeholder needs (in this paper the unmet demands for acceptable travel comfort) is investigated using three fictive but realistic infrastructure planning process alternatives. The planning decision enabling the capacity increase is the expansion of the tracks from single to double track between Uster and Aathal in the Canton of Zürich, Switzerland. The responsiveness and travel comfort are modelled given an uncertain population growth.

The results show that the responsiveness of infrastructure planners (1) plays a role in the ability to meet stakeholder needs, (2) can be measured and (3) provides argument that in developing planning processes, considering planner responsiveness could be worthwhile. The specific example shows that being more responsive outperforms acting early in approximately 90% of the scenarios modelled.

1 INTRODUCTION

Infrastructure systems are planned to meet stakeholder needs. In the planning of these systems, the ability to meet stakeholder needs is quantified through the service provided to stakeholders, i.e. the benefits of providing a service (e.g. travelling by rail for commute) or costs due to a lack in service (e.g. not having a seat during commute). The planning phase starts with the decision to engage in planning, often triggered by the identification of stakeholder needs. The time that it takes for planning decisions to take effect to meet stakeholder needs is to be explored so that it can be considered more explicitly in decision-making in practice. The planner's ability to provide stakeholder needs more quickly is named 'responsiveness'; a more responsive planner will be able to improve the service level to an adequate state more quickly than a less responsive planner.

In this paper, the authors propose to assess the impact of responsiveness of planners when making a decision and compare it to making a decision earlier. For an example of the rail service in the corridor Dübendorf-Hinwil at times of a growing population, an intervention of a double-track between Uster and Aathal is to be realized in the face of an uncertain population growth. Two fictitious approaches to reduce the negative impacts of stakeholder needs are compared: (1) a more responsive planner with a shorter time from decision to realisation is compared to (2) acting earlier, by lowering the threshold at which an intervention is made. We compare the net benefits experienced by users in overcrowded trains and the effect that a time reduction in the infrastructure planning process has on the net benefits.

In this paper we find that responsiveness (1) plays a role in the ability to meet stakeholder needs, (2) can be measured and (3) provides argument that in developing planning processes, considering planner responsiveness could be worthwhile.

2 BACKGROUND

In the field of long-term planning decision-support, there have been advances made with a focus on including uncertainty in an explicit manner in decision-support models. This field has been referred to as adaptive planning and has two major branches.

On the one side, there has been a focus of efforts on methods to ensure robust-decision making. Central to this paradigm is the idea of finding a dynamically robust plan (Kwakkel et al., 2015). Numerous approaches and tools have been developed to adapt dynamically to one or more uncertain factors to develop pathways to ensure that an end-goal objective (e.g., climate neutrality by 2050) can be reached (Haasnoot et al., 2012, 2013; Herman et al., 2015; Ranger et al., 2013).

On the other side, there has been a focus of efforts on the flexible design of engineering structures. The implementation of the flexibility in engineering structures was elaborated in the work of de Neufville and Scholtes (Neufville & Scholtes, 2011). To better evaluate engineering variants under uncertainty, these flexibilities are treated as an option to intervene so that the methods of real options can be applied to systems under uncertainty. The triggering of these options enables the adaptive planning of systems (Cardin et al., 2013; Elvarsson et al., 2021; Martani et al., 2022; Neufville & Scholtes, 2011; Neufville & Smet, 2019). The implementation of the flexibility is one way to reduce the downside of uncertainty, or maximise the impact of potential upsides, generally leading to lower total costs or higher net benefits (Neufville & Scholtes, 2011).

What unites both branches is that engineers ensure adaptiveness of planning processes, so that engineers remain flexible to adjust and ensure that they can meet the needs that do arise over time and are not stuck in a suboptimal system state.

However, as the value framework concerning planning decisions not only consists of construction costs, but increasingly considers environmental, social and economical costs beyond the decision-maker, we find that our processes become increasingly time-sensitive. This is particularly true for transportation infrastructure, which are socially important with demand increasing as population grows and long duration planning processes persist (Saxe et al., 2021). In Switzerland, the expansion step until 2035 in rail infrastructure was legally decided on approximately 17 years in advance (Schweizerische Bundesrat, 2018a), whereas the expansion step for road was decided on approximately 5 years in advance until 2023 (Schweizerische Bundesrat, 2018b). While the time since decision to plan until realization can have many benefits through increased stakeholder interaction & coordination and the possibility of improved solutions through detailed studies, the added value of being more responsive and its impact on decision-making is less explored.

3 METHODS

First, a scenario is generated providing the expected growth in population and therefore in demand. The sample of population growth scenarios is generated via the Latin hypercube sampling method (McKay et al., 1979). The population grows annually.

Given a current state of the network, the scenario's demand is compared to the supply every year of a simulation. The service provided to users is then quantified and summed over the entire planning period. The service provided depends on the compared three alternatives of the planning process. The alternatives differ in the time taken to operationalize the planned change after an intervention is carried out.

If the supply is sufficient, no action is taken. If the supply is insufficient, based on the trigger condition defined by each planning process, a capacity expansion is proposed once the trigger condition is met. If the decision to intervene is made, the improved capacity is only realized a specified amount of time after the decision is made.

The comparison of the different alternatives is performed with the methods of Engineering options analysis, a decision-support tool for decision-making under uncertainty (Neufville et al., 2019; Neufville & Scholtes, 2011). Since the population growth is uncertain, 500 Monte Carlo simulations are run to explore the impact of differing futures on the outcome of the net benefits.

4 CASE STUDY

The rail service in the corridor between Dübendorf and Hinwil connects people of the Glattal region to Zürich, the main regional hub. The corridor is connected to Zurich through the north via Wallisellen to Zürich-Oerlikon and through the East via tunnel through Stettbach to Zürich-Stadelhofen. The railway corridor is illustrated in Figure 1.

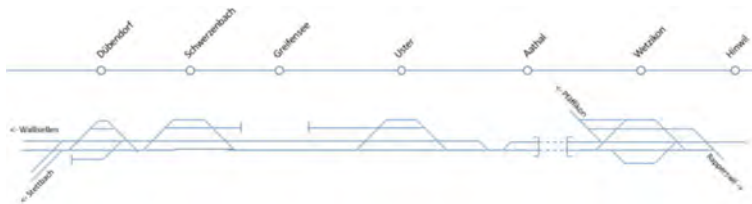


Figure 1. An illustration of the railway network between Dübendorf and Hinwil. Not to scale.

The provision of rail service to meet the demand is currently hampered by rail network bottlenecks, i.e., the limited supply of infrastructure, specifically due to a single-track segment between Uster and Aathal. To enable a capacity development, an infrastructure planner will respond by having a second track built on the 4 km segment. The impact of differing planning alternatives focusing on the time taken to operationalize planned changes was modelled, and the three alternatives consisted of either triggering the intervention (1) when peak hour demand levels reach 3.5 times the seat capacity or, (2) acting earlier, at 3.1 times the seat capacity. Alternatively, the planner could be (3) more responsive by reducing the planning time from 20 years to 8 years. The first planning process alternative we name “Reference”, the second “Early action” and the third “More responsive”.

The built infrastructure defines the capacity of the service, quantified in the number of seats provided per peak hour. The railway service on the infrastructure is provided by the Federal Railway Company (SBB) and the Zurich Transportation Agency (ZVV). The capacity is defined by the service planned before and after the track expansion (Schweizerische Bundesrat, 2018a; Stadtrat Uster, 2019).

While it is already decided that in the network development step until 2035, the Federal government funds the construction of a second track on the 4 km long stretch between Uster and Aathal for 180 million CHF (Schweizerische Bundesrat, 2018a, 2018c). It is assumed that this decision has not yet been made. Instead, a fictitious triggering condition is determined, which, when met, triggers the decision to develop the single track between Uster and Aathal to a double track. Subsequently after the track can be operationalized, capacity gains are made.

For the modelling of the system, the corridor is split into three parts (from now on sub-regions), based on the locations of the single track bottlenecks, from Dübendorf to and including Uster (DÜB-UST) from Uster to Wetzikon (UST-WTZ) and then to Hinwil (WTZ-HIN). The population of the different sub-regions and the portion of the population assumed to travel via rail in a peak hour to Zürich are reported in the following Table 1. The share of population travelling in the peak hour reduces as distance from Zürich increases. Consequently, the rail demand is assumed to be the highest between Dübendorf and Uster as the train will carry the passengers from the other sub-regions travelling into Zürich.

The population growth is uncertain. It is expected to grow annually between 0.5% and 2.5%. For each of the 500 scenarios generated, a single value in this range is generated for the average population growth over 40 years from 2021 to 2060. The growth rate is assumed consistent across all sub-regions.

Table 1. Assumptions to evaluate the demand for each sub-region.

Demand	Sub-regions		
	DÜB-UST	UST-WTZ	WTZ-HIN
Population in 2020	86'931	26'113	11'117
Assumed share of population travelling to Zürich in peak hour	14%	12%	8%

In the following Table 2, the supply of rail services is summarized. The number of seats provided from each of the sub-regions to Zürich in an hour, assuming 350 seats per wagon with two wagons per line service. The lines S3, S9, S14 and S15 travel in the corridor every half hour each, where S9 has an end station in Uster and S14 is the only line to travel from Wetzikon to Hinwil (SBB, 2020).

After the double-track between Uster and Aathal will be realized, it will not only increase the capacity of rail timetable slots between Uster and the east of the valley, but also free up space in the Uster train station as the S9 normally blocks one of the tracks and respective platform before heading in the opposite direction since it can be relocated to elsewhere or the service expanded to go further into the corridor (Stadtrat Uster, 2019). Therefore, it is assumed there will be an overall increase in capacity throughout the corridor. Hinwil will still be constrained by the single track segment between Wetzikon and Hinwil (Bundesamt für Verkehr (BAV), 2017; Schweizerische Bundesrat, 2018a).

Table 2. Assumptions to evaluate the supply for each sub-region.

Supply	Sub-regions		
	DÜB-UST	UST-WTZ	WTZ-HIN
Frequency of the service to Zürich in peak hour	8	6	2
Seat capacity in peak hour			
-> before the development	5600	4200	1400
-> after the development	8400	5600	1400

The demand is simulated over time. It grows with the population and the assumed share of the population travelling to Zürich in the peak hour is assumed unchanged. In peak hours, people will not only sit, but also stand. It is assumed that the infrastructure planner will see it necessary to intervene once the peak demand between Dübendorf and Uster is higher or equal to 3.5 times the seat capacity on the rail service. Once the trigger condition has been met, the duration of planning the pre-defined intervention and realizing it is assumed to be 20 years. This is considered the reference alternative.

To improve the service provided to stakeholders over the planning period, the planners generate solutions to better meet stakeholder needs. On the one hand planners can act early and change their triggering condition to 3.1 times the seat capacity to more preventively offset the lead time. Generating simulations with the different trigger conditions leads to the empirical cumulative probability distribution curves for reaching the triggering condition over time as shown in the following Figure 2.

By reducing the triggering condition to 3.1 instead of 3.5, the condition is met between 5-24 years earlier, depending on the scenario. In all scenarios, the triggering condition was met by 2060. In reality, the need to intervene is not determined in such a discrete manner by being triggered at such a particular value, as resources and budget also constrain the creation of intervention programs. However, it is assumed in this paper for modelling purposes.

On the other hand, planning processes could be enable planners to be more responsive. In this example, the time that it takes to modify the system so that it provides an adequate level

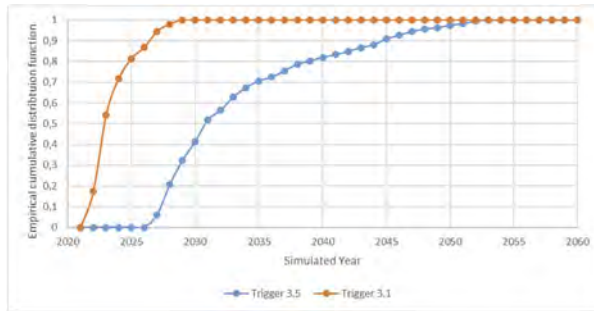


Figure 2. The probabilities of meeting triggering condition for two different values, 3.1 and 3.5.

of service is reduced, albeit with an unchanged triggering condition. The ‘reference’ time from decision until realization is set at 20 years. This is similar to the time horizon defined by the Expansion Step Rail 2035 (Schweizerische Bundesrat, 2018a). It is assumed that this can be reduced from 20 years to 8 years to model the impact of being able to meet stakeholder needs more quickly, i.e., planners being more responsive.

The different planning process alternatives that planners would follow to improve the service provision as discussed above are summarized in the following Table 3. The early-action alternative triggers an intervention at a lower threshold, whereas the responsive alternative will take less time to implement the planned change.

Table 3. Assumptions to evaluate the infrastructure supply for each sub-region.

Supply	Alternative		
	Reference	Early-action	Responsive
Time since triggering until realization	20	20	8
Triggering condition	3.5	3.1	3.5

For all passengers who do not have a seat once the train is travelling between Uster and Dübendorf towards Zürich in the morning peak hour a discomfort cost is calculated. We assume that all standing passengers have a value of discomfort of 7 CHF per trip. The value was chosen as it is approximately the opportunity cost of choosing the train as a mode. It corresponds approximately to the fuel cost if the stretch were travelled by the private car at single occupancy. We furthermore assume 3 equal peak hours per day and 250 workdays per year as well as a 2% discount rate. The total discomfort costs are simulated for each of the process alternatives for all scenarios. Dependent on the population growth, the costs will differ.

Figure 3 shows the resulting empirical cumulative distribution functions of the discounted discomfort costs over the forty years. Both the responsive (dashed orange line) and early-action (dotted green line) alternative have consistently lower costs than the reference case.

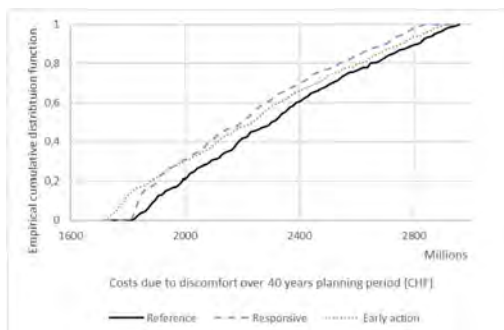


Figure 3. Discomfort costs over the forty year planning period in million CHF.

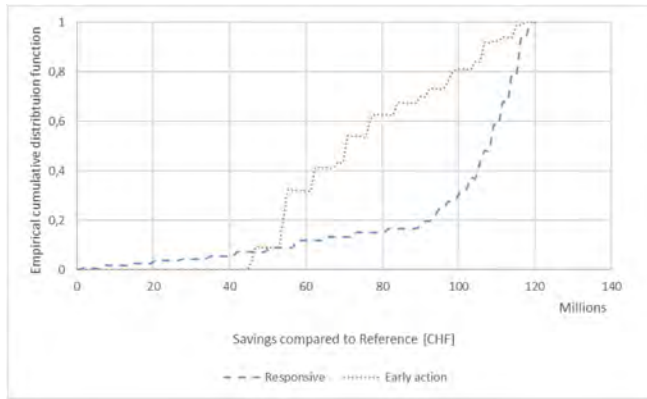


Figure 4. Savings per planning variant relative to the reference variant, in million CHF.

The modelled discomfort costs differ per process alternative and by scenario and range from approximately 1700 million CHF to 3000 million CHF over the 40 year planning period.

In Figure 4, the savings per scenario are put in relation to the reference case. The figure shows the results of the difference in costs of the more responsive alternative and the reference case (the blue dashed line) and the difference between the early-action alternative and the reference case (the orange dotted line). By comparing the two lines, one can see the distribution of the scenarios for which it would be beneficial to choose to be more responsive or act earlier. The benefit of the responsive alternative becomes apparent: A planner acting more responsively will yield higher savings (i.e., reduction in discomfort costs) in about 95% of scenarios. Simply put, this is because the more responsive planner acts quickly to a need that is arising as opposed to the planner acting early in case the need will arise. Due to the uncertain population growth, the need will not always arise as quickly as expected. However, in 100% of the scenarios, the early-action planner provides savings over about 43 Million CHF in comparison to the reference case. This is because of the comfort savings by acting earlier. The highest savings yielded by an early-action or a responsive planner in a specific scenario are about 120 Million CHF over the forty year planning period from 2021 to 2060. In about 90% of the scenarios, the responsive alternative will yield more than 60 Million CHF savings compared to the reference case. These results of the distribution of the savings relative to the reference are also summarized in Table 4.

Table 4. Savings per alternative compared to the reference alternative.

Savings in Mio CHF	Savings per alternative compared to reference	
	Early-action	Responsive
Expected value	75.9	98.0
Percentiles		
5th	45.7	34.6
20th	53.2	91.1
80th	97.7	113.7
95th	115.1	117.8

The question remains under what circumstances the early action planner reaps higher benefits than the responsive planner. The early action planner will reap the most benefits when the population growth is slow enough, so that during the 20 years time until the planned changes come into effect, the costs do not outweigh the comparative alternative of acting later, but faster. The responsive planner provides more benefits with increased growth.

Figure 5 compares the savings observed plotted over the differing growth percentages, which is considered the uncertain variable. If over 1% annual population growth is expected, it makes sense to prefer this particular responsive planning process over the modelled early action process.

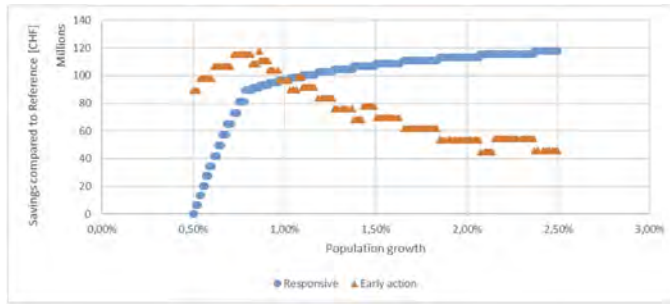


Figure 5. Savings per planning alternative compared to the population growth rate.

5 DISCUSSION

In this paper the perceived discomfort costs due to an uncertain increasing demand in rail services is modelled. The model is set up in a simplistic manner to illustrate the quantification of the costs linked to the responsiveness of planners. The more responsive alternative outperforms the early-action alternative in most scenarios. Simply put, this happens because a planner acts responsively to a need that is arising as opposed to acting early in case the need will arise. In high growth scenarios, being responsive yields higher comfort cost savings than having acted earlier. This is due to the costs inflicted on the users during the time which the early action planned change is being realized (taking 20 years), which the responsive planner manages to overcome more responsively (in 8 years).

In reality, the planning process cannot be easily shortened. The planning process generally includes stakeholder engagements, budgeting negotiations, land acquisition processes and other constraints requiring more time. Furthermore, given that the shortening of the processes is possible, it is very possible that this expediation will bear some costs that should be considered in the evaluation process.

Having established the potential to focus on responsiveness of planners, the outlook on future research based on this work not only addresses the need for better models for the planning of complex infrastructure systems incorporating the value framework of the relevant stakeholders. The conversion of these attributes into costs and benefits is vital to be able to make an objective appraisal between planning alternatives or competing planning visions.

Based on the above, the next steps include the mapping of planning processes and to what extent they could be adapted to better meet uncertain stakeholder needs. Further research is also required on appraisal tools, how they may consider costs during the planning time and explicitly consider future uncertainty.

6 CONCLUSIONS

A responsive planning process alternative is analyzed for a fictitious, but realistic case study. The results show that more responsive planners are better able to reduce the travel discomfort experienced by users and provide additional savings in comparison to an early-action planner, who triggers interventions at a lower triggering condition. The results illustrate that being more responsive can be of value and that infrastructure planners should be mindful of the time duration of planning processes from the time of decision to plan until the implementation of the planned change.

Furthermore, it is shown that the responsiveness of infrastructure planners (1) plays a role in the ability to meet stakeholder needs, (2) can be measured and (3) provides argument that in developing planning processes, considering planner responsiveness could be worthwhile.

ACKNOWLEDGEMENTS

This research was conducted at the Future Cities Lab Global at ETH Zurich. Future Cities Lab Global is supported and funded by the National Research Foundation, Prime Minister's Office, Singapore under its Campus for Research Excellence and Technological Enterprise (CREATE) programme and ETH Zurich (ETHZ), with additional contributions from the National University of Singapore (NUS), Nanyang Technological University (NTU), Singapore and the Singapore University of Technology and Design (SUTD).

REFERENCES

- Bundesamt für Verkehr (BAV). (2017). *Netznutzungskonzept zum Ausbauschnitt 2025 der Eisenbahninfrastruktur Ausgangslage*. 1–50.
- Cardin, M. A., Ka-Ho Yue, H., Jiang, Y., Deng, Y., & Santhanakrishnan, D. (2013). Empirical evaluation of flexible design concept generation procedures: A study in emergency services. *Proceedings of the International Conference on Engineering Design, ICED, 7 DS75-07*(May 2014), 1–10.
- Elvarsson, A. B., Martani, C., & Adey, B. T. (2021). Considering automated vehicle deployment uncertainty in the design of optimal parking garages using real options. *Journal of Building Engineering, 34*. <https://doi.org/10.1016/j.jobe.2020.101703>.
- Haasnoot, M., Kwakkel, J. H., Walker, W. E., & ter Maat, J. (2013). Dynamic adaptive policy pathways: A method for crafting robust decisions for a deeply uncertain world. *Global Environmental Change, 23*(2), 485–498. <https://doi.org/10.1016/j.gloenvcha.2012.12.006>.
- Haasnoot, M., Middelkoop, H., Offermans, A., van Beek, E., & van Deursen, W. P. A. (2012). Exploring pathways for sustainable water management in river deltas in a changing environment. *Climatic Change, 115*(3–4), 795–819. <https://doi.org/10.1007/s10584-012-0444-2>.
- Herman, J. D., Reed, P. M., Zeff, H. B., & Characklis, G. W. (2015). How Should Robustness Be Defined for Water Systems Planning under Change? *Journal of Water Resources Planning and Management, 141*(10), 04015012. [https://doi.org/10.1061/\(asce\)wr.1943-5452.0000509](https://doi.org/10.1061/(asce)wr.1943-5452.0000509).
- Kwakkel, J. H., Haasnoot, M., & Walker, W. E. (2015). Developing dynamic adaptive policy pathways: a computer-assisted approach for developing adaptive strategies for a deeply uncertain world. *Climatic Change, 132*(3), 373–386. <https://doi.org/10.1007/s10584-014-1210-4>.
- Martani, C., Eberle, S., & Adey, B. T. (2022). Evaluating highway design considering uncertain mobility patterns and decision flexibility. *Infrastructure Asset Management, 9*(3), 135–155. <https://doi.org/10.1680/jinam.21.00018>.
- McKay, M. D., Beckman, R. J., & Conover, W. J. (1979). A comparison of three methods for selecting values of input variables in the analysis of output from a computer code. *Technometrics, 21*(1), 293–245. <https://doi.org/10.1080/00401706.2000.10485979>.
- Neufville, R. De, & Scholtes, S. (2011). *Flexibility in Engineering Design*. MIT Press.
- Neufville, R. De, & Smet, K. (2019). Decision Making under Deep Uncertainty. In *Decision Making under Deep Uncertainty*. Springer International Publishing. <https://doi.org/10.1007/978-3-030-05252-2>.
- Neufville, R. De, Smet, K., Cardin, M., & Ranjbar-bourani, M. (2019). Decision Making under Deep Uncertainty. In *Decision Making under Deep Uncertainty*. Springer International Publishing. <https://doi.org/10.1007/978-3-030-05252-2>.
- Ranger, N., Reeder, T., & Lowe, J. (2013). Addressing 'deep' uncertainty over long-term climate in major infrastructure projects: four innovations of the Thames Estuary 2100 Project. *EURO Journal on Decision Processes, 1*(3–4), 233–262. <https://doi.org/10.1007/s40070-013-0014-5>.
- Saxe, S., Dean, M., Raghav, S., Durrant, D., & Siemiatycki, M. (2021). Timelines of transportation infrastructure delivery 2000 to 2018 in toronto, canada and london, uk. *European Journal of Transport and Infrastructure Research, 21*(3), 82–105. <https://doi.org/10.18757/ejtir.2021.21.3.5515>.
- SBB. (2020). *Kursbuch*.
- Schweizerische Bundesrat. (2018a). *Botschaft zum Ausbauschnitt 2035 des strategischen Entwicklungsprogramms Eisenbahninfrastruktur*. 7321–7436.
- Schweizerische Bundesrat. (2018b). *Botschaft zum Zahlungsrahmen Nationalstrassen 2020 – 2023, zum Ausbauschnitt 2019 für die Nationalstrassen und zum Verpflichtungskredit*. 1–107.
- Schweizerische Bundesrat. (2018c). Bundesbeschluss über den Ausbauschnitt 2035 für die Eisenbahninfrastruktur. *Botschaft Des Bundesrates*, 3747–3750. <http://www.admin.ch/opc/de/federal-gazette/2018/7321.pdf>.
- Stadtrat Uster. (2019). *Antwort des Stadtrates zur Anfrage 517/2018* (Issue 517). https://www.uster.ch/_docn/2002448/517_AntwortStadtrat.pdf.

Stakeholder inclusive port development planning for an uncertain future

M. Eskafi

EFLA Consulting Engineers, Reykjavik, Iceland

G.F. Ulfarsson

Faculty of Civil and Environmental Engineering, University of Iceland, Reykjavik, Iceland

ABSTRACT: Ports have always been evolving to satisfy stakeholders' new or changing demands. The long design lifetime of a port system calls for uncertainty considerations in the planning process. A structured framework is presented to deal with opportunities and vulnerabilities derived from uncertain developments. A three-dimensional decision surface is presented to quantify the salience of stakeholders. A problem structuring method and a fuzzy multi-attribute group decision-making method are integrated to define the success of the plan. Salient stakeholders are engaged to identify uncertainties. SWOT analysis is conducted to recognize opportunities and vulnerabilities. Effective actions are planned to seize opportunities and manage vulnerabilities in a projected lifetime. Port authorities and decision makers can strategically implement the actions in the face of uncertainty that emerges in the planning horizons. The results indicate that the uncertainties mainly present opportunities in the short-term horizon, while during the middle-term horizon the port is confronted with vulnerabilities.

1 INTRODUCTION

A port is a complex set of functions, as it has emergent and nonlinear behavior in which multiple interactions between different components are possible. Port sectors are in a state of radical change, and the main challenge in port planning is to deal with uncertainties. Dealing with uncertainties in the planning process increases the success of projects (Taneja 2013). Analytical and quantitative tools, even those that model dynamic decision making, cannot deal with the qualitative nature of uncertainty. Forecast models have uncertainties associated with input data and models (Eskafi et al. 2021a). Scenario planning, as an alternative approach, may not seize opportunities offered by transitions in port planning projects. Scenarios cannot capture trend-break /breakthrough developments. In this vein, Walker, Haasnoot, and Kwakkel (2013) emphasized that a static optimal plan using a single most likely future may fail if another future materializes. Instead of investing efforts to reduce uncertainties, different methods at different time horizons should be applied to coexist with and benefit from uncertainties (Herder et al. 2011), just as the framework in the present study offers. In the context of uncertainty and complexity, policymaking (setting a course of action) to deal with uncertainty in projects works better than relying only on predictions (Lempert and Popper 2005). Furthermore, Adey et al. (2022) stated that management flexibility facilitates dealing with uncertainty in investment decision making.

In this study, a framework is developed based on four components to identify the uncertainties that are manifested during the projected lifetime of the plan and deal with them in the planning process. The components are: 1- stakeholder analysis to a) identify port stakeholders, b) define the success of port planning, c) identify uncertainties around stakeholders' activities and objectives, and d) determine different planning horizons; 2- different methods to systematically address uncertainties; and 3- SWOT analysis to identify opportunities and vulnerabilities derived from uncertainties; 4) effective actions to seize opportunities and manage vulnerabilities and thus deal with uncertainties. Decision makers can strategically implement the actions in the face of uncertainty that emerges in the projected lifetime of the port.

2 BACKGROUND AND METHODS USED

A single-issue focus of dealing with uncertainties, including opportunities and vulnerabilities, is no longer sufficient. To deal with uncertainties against projected, probable, plausible, possible futures, a framework is developed and adapted to port planning as shown in Figure 1.

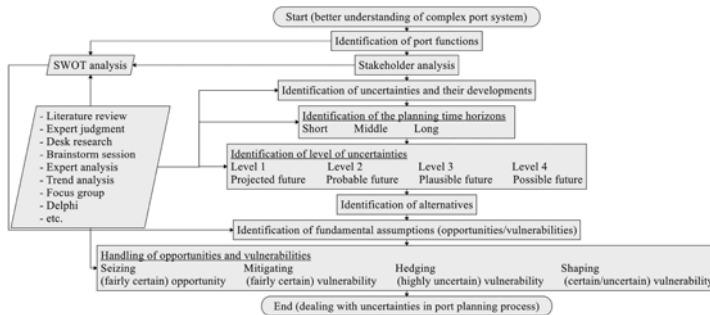


Figure 1. A framework of dealing with uncertainty in the port planning process, (Eskafi et al. 2021b).

2.1 Identification of port functions

The main functions of a port represent the main purposes for which the port is used. Prior to the planning and design of ports, it is necessary to determine their functions (Ligteringen 2017). The functions of a port play important roles in decision making for greenfield and brownfield port development plans. To determine the port functions and port activities, information was obtained through the literature, port visits, and interviews with the Port Authority.

2.2 Stakeholder analysis

A port system involves a variety of stakeholders with a broad spectrum of involvement. Stakeholder analysis is often ad-hoc and relinquishes the spatial and temporal changing attributes of stakeholders. Therefore, a framework is presented to map stakeholders' salience using a fuzzy logic 3-dimensional (3D) decision surface for their effective and timely engagement in the planning process. The framework is depicted in Figure 2.

2.2.1 Identification of stakeholders

Stakeholder identification and their engagement in a project is an important task. Although focus groups, expert interviews, etc., can be used for stakeholder identification, these methods only develop an initial list of stakeholders. A project manager or a group may not have the skill to identify all stakeholders. A snowball technique is a suitable method for stakeholder identification as it benefits from the knowledge of networks. It assures a variety of suggestions from different perspectives to identify stakeholders (Colvin, Witt, and Lacey 2016).

2.2.2 Engagement of stakeholders

Decision making can be enriched by engaging stakeholders. In this study, stakeholders are engaged first by email and phone calls to provide general information about the project. Then face-to-face interviews are conducted to gather information about their objectives. Furthermore, a written survey is developed to aggregate input data for stakeholder salience measurement. A survey has several advantages in comparison to other methods of data gathering from stakeholders. A survey engages stakeholders in a task-oriented manner, encourages stakeholders to express their thought, and gives privacy to stakeholders for independent information sharing.

2.2.3 Differentiation and grouping of stakeholders

In this study, stakeholders are categorized into groups based on similarities in their contributions, interests, and influence. Stakeholders in a group can be viewed with a common area of

interest and power to the port planning. The groups can be unbundled in several sub-groups based on the overarching nature of engagement undertaken and their interrelations together and or to the port planning. To group stakeholders, a literature review on stakeholders' categorization is carried out.

2.2.4 Identification of stakeholders' objectives

Interviews can provide valuable information about stakeholders' objectives. To ensure the validity of data gathering, it is important to consider the education and experience of interviewees. In this study, to identify stakeholders' objectives, interviews are conducted with the widest possible range of stakeholders who are well informed about the interests, and influence of their activities into the planning. To identify objectives of port planning, the Value Focused Thinking (VFT) method is used. The VFT method provides a systematic approach for identification of values (e.g., idea), categorizing these values, converting them to the means objectives (i.e., what stakeholders wish to achieve), recognizing the relationships among objectives, prioritizing the means objectives to achieve the fundamental objective (i.e., the definition of success) (Keeney 1996).

2.2.5 Stakeholder mapping

To ensure in-depth consideration of the power, interest, and salience of stakeholders in decision making, stakeholders are mapped based on fuzzy logic. The Fuzzy Inference System (FIS) is applied to implement fuzzy logic. The FIS relates input (power, interest) and output (salience) variables, to develop the decision surface. Using the fuzzy logic approach, the stakeholders receive a degree of membership instead of a discrete class. A 3D decision surface for stakeholder salience measurement is developed by using the Fuzzy Logic Toolbox in MATLAB.

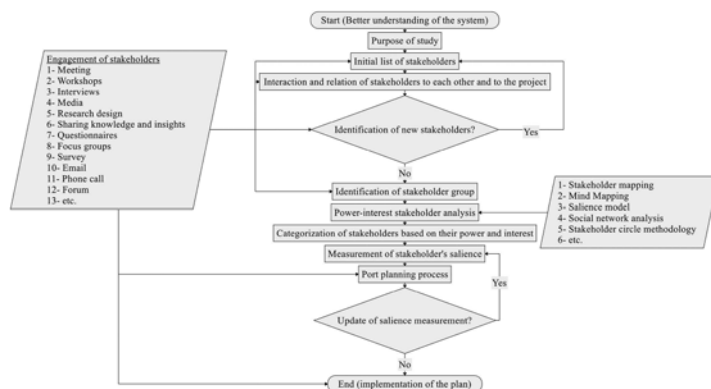


Figure 2. Steps in stakeholder salience analysis and prioritization, (Eskafi et al. 2019).

2.3 Definition of success

To discover the importance of identified means objectives (see subsection 2.2.4) and to properly prioritize them in the plan, separate meetings were held with the representatives of key stakeholders. The selection of the representatives is based on their short-, middle-, and long-term roles in port planning and development. In the meetings, they are asked to prioritize the means objectives.

2.3.1 Fuzzy multi-attribute group decision-making method

To define the maximum level of agreement among the stakeholders' preferences regarding the fundamental objective, the fuzzy multi-attribute group decision-making method is used. The method reveals the highest level of agreement on the means objective among the key stakeholders with a multiplicity of objectives. Therefore, the method facilitates reaching consensus among stakeholders on the success of the plan and may reduce holding meetings with all stakeholders that might be time consuming and conflicting.

2.4 *Identification of uncertainties and their developments*

One of the best ways to deal with uncertainties is to understand the sources, amount, and quality of information available (Uusitalo et al. 2015). Aven (2008) stated that uncertainty identification is a qualitative procedure using expert opinion, literature review, brainstorming sessions, group discussions, and interviews with stakeholders. In this study, to identify uncertainties, separate in-depth face-to-face interviews were conducted with representatives of key stakeholders. Separate interviews allowed each key stakeholder a more comfortable and honest information sharing, a high possibility of participation, and providing valuable input (Vu, Grant, and Menachof 2019).

2.5 *Identification of the planning time horizons*

Describing uncertainty propagation over time provides more complete information about the planning processes (Brier 2005). Nordlund (2012) stated that there is not a generally accepted standard to demarcate short-, middle-, and long-term horizons from the present time to the future. Masini (1993) asserted that time horizons vary and closely depend on the subject under consideration. In this study, a planning time horizon is defined as the farthest time that uncertain developments are addressed. The main drivers of uncertain developments related to the stakeholders' activities and objectives are examined to distinguish a time horizon.

2.6 *Identification of level of uncertainties*

Handling uncertainties based on their level is an appropriate approach. These levels express the severity of uncertainties and range from complete certainty to total ignorance. They are addressed based on the four levels of uncertainties (Walker, Haasnoot, and Kwakkel 2013). Van Dorsser et al. (2018) linked the four levels of uncertainties to different disciplines of the future field. Level 1 uncertainty is addressed by deterministic forecasting. Level 2 uncertainty is handled by probabilistic forecasting. Level 3 uncertainty is considered by (strategic) foresight. Level 4 uncertainty accounts for visualization of any possible future. The levels are recognized by gaining insight from the key stakeholders and a group of multidisciplinary experts.

2.7 *Identification of alternatives and fundamental assumptions*

In the presence of uncertainty, generating alternatives is a successful approach in planning (Walker, Haasnoot, and Kwakkel 2013). In response to the uncertain developments, several alternatives are developed over different time horizons, and consequently, their fundamental assumptions were explored. If a fundamental assumption moves the plan toward its success, it is an opportunity, and if it causes the plan to fail achieving its success it is a vulnerability (Haasnoot et al. 2013). To identify the opportunities and vulnerabilities, a port SWOT analysis was carried out.

2.8 *Handling of opportunities and vulnerabilities*

To handle fundamental assumptions, effective actions are planned to either seize opportunities or manage vulnerabilities. Taneja (2013) distinguished actions to deal with opportunities and vulnerabilities. The actions are mitigating, hedging, shaping, and seizing actions. Mitigating actions are in response to fairly certain vulnerabilities and reduce their potential adverse effects. Hedging actions spread and reduce highly uncertain adverse effects of vulnerabilities. Shaping actions affect certain and uncertain vulnerabilities to change their nature, prevent their development, and direct them toward a preferred plan. Seizing actions take advantage of fairly certain opportunities.

3 RESULTS AND DISCUSSION

3.1 *Study area and the port functions*

This study was carried out for the Ports of Isafjordur Network, which includes the Ports of Isafjordur, Sudureyri, Flateyri, and Thingeyri, in Iceland (Figure 3).



Figure 3. The Ports of Isafjordur Network. The study area is shown on the map of Iceland.

The Port of Isafjordur is the biggest container port in the Westfjords region and the distribution center for the network. The port network is the third busiest port of call for cruise ships in Iceland. By coastal shipping and road transportation, the network is connected to its hinterland.

The main functions of the port network are: 1- Transfer and storage of containerized and non-containerized cargo; 2- Industrial value-added activities, including marine productions; 3- Recreational activities, including servicing expedition and cruise ships, and sailing boats.

3.2 Stakeholder analysis

Using snowball sampling stakeholders were identified (Eskafi et al. 2019). Five port stakeholder groups were defined including: internal stakeholder, external stakeholder, legislation and public policy stakeholder, community stakeholder, and academic stakeholder. Fifty-one face-to-face interviews were conducted resulting in 314 values being elucidated from the interviews. From these values, a set of 8 means objectives were determined, namely: increasing competitiveness, increasing effective and efficient use of land, increasing safety and security, increasing hinterland connectivity, increasing financial performance, better environmental implications, creating flexibility and increasing positive economic and social impacts (Eskafi et al. 2020). To map stakeholders on the 3D surface, a survey was conducted between stakeholders. Figure 4 shows the results of the dynamic stakeholder mapping. The decision surface indicates the internal stakeholder group possesses a high degree of salience and is placed on the flat area of the decision surface. This indicates a stable role by this group in port planning. The acute slope of the decision surface (i.e., fuzzy area) indicates a rapid changing of the degree of membership in the attributes. Placement of a stakeholder group in this area means that small changes in their attributes (i.e., interest, power) lead to a rapid change in their salience. Figure 4 shows that the legislation and public policy, the external, and community stakeholder groups are placed on the steep slope.

3.3 Definition of success

Using the fuzzy multi-attribute group decision-making method, the highest level of agreement among the representatives of key stakeholder groups on the means objectives was ordered as: increasing competitiveness, increasing effective and efficient use of land, increasing safety and security, increasing hinterland connectivity, increasing financial performance, creating flexibility, better environmental implications, increasing positive economic and social impacts. This order is defined as the definition of success (i.e., fundamental objective) (Eskafi et al. 2020).

3.4 Identification of uncertainties and their developments

The outcome of interviews with the key stakeholders and literature review indicates that fishing and aquaculture activities are growing quickly to win markets. Export of farmed and wild,

frozen and fresh, and processed and unprocessed fish are expected to be the most sustainable cargo. Containers will continue to be attractive to transport cargo. Vessel size is increased to utilize economies of scale. Furthermore, expedition and cruise vessel calls are expected to increase. The increase in expedition and cruise vessel calls will grow coastal excursions and tourism activities.

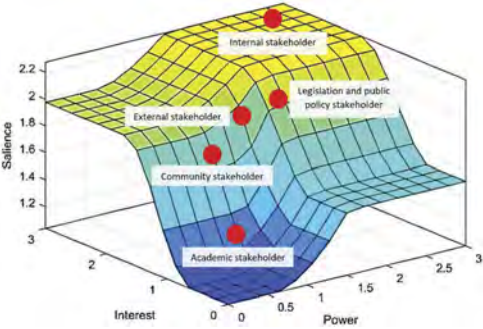


Figure 4. A 3D decision surface for the relationship between power and interests of the stakeholder groups.

3.5 Identification of the planning time horizons

Five years (2020-2025) and 25 years (2025-2050) were considered as the short- and middle-term horizons, respectively. Five years was chosen as the short-term horizon because the Port Authority wants to develop the Port of Isafjordur within the next five years to meet the expected rapid and changing demands of fishing, aquaculture, and cruise activities. Also, this time horizon covers the Icelandic Road and Coastal Administration’s policy from 2020 to 2025 (Icelandic Road and Coastal Administration 2019). Furthermore, this five-year time horizon is in line with the short-term horizon indicated in the literature (e.g., Masini 1993). The ports’ users, including fishing, aquaculture, and transportation companies, are developing their commerce in the port network. A 25-year middle-term horizon would capture their development projects. A 25-year time horizon fulfills the middle-term horizon cited in the literature (e.g., Masini 1993).

3.6 Identification of level of uncertainties

In the short-term horizon, the uncertain developments around marine production can adequately be described and thus have level 1 uncertainty. The materialization of these developments can reasonably be explained by expert judgment. However, in the middle-term horizon, the size and probability of these developments cannot be estimated as they are faced with multiple influencing (political, societal, environmental, and financial) factors. Therefore, they have level 3 uncertainty in the middle-term horizon. At this level of uncertainty, foresight should be used to cover a range of plausible futures. The uncertain developments around the cargo flow and relevant activities can be projected in the short-term horizon. These uncertain developments have level 1 uncertainty. Thus, a reliable forecast provides the future state of the cargo flow. However, in the middle-term horizon, the level of uncertain developments increases as there is less information about the flow. These uncertain developments, therefore, have level 2 uncertainty and a probabilistic forecast can be used. The uncertain developments around expedition and cruise markets have level 2 uncertainty in the short-term horizon due to the COVID pandemic. At this level of uncertainty, the probabilistic forecast can be used. However, this market is expected to grow in the middle-term horizon and have level 1 uncertainty. To provide insight into these uncertain developments, expert judgment and reliable forecasts can be conducted.

3.7 *Identification of alternatives and fundamental assumptions*

To respond to the uncertain developments, different alternatives were generated to meet planning objectives in the short- and middle-term horizons. In the short-term horizon, uncertain developments lead to many opportunities. This is because the port network has a competitive position in the Westfjords region. However, in the middle-term horizon, the port network is confronted with a multiplicity of vulnerabilities. These vulnerabilities are mainly due to a lack of infrastructure and land in the port network for satisfying the increasing number of port users' demands.

3.8 *Handling of opportunities and vulnerabilities*

In the short-term horizon, as the port network has a competitive position, the Port Authority can seize opportunities by attracting cruise expeditions and cruise markets and increasing the storage and flow of cargo and containers, and the number of vessel calls. In the middle-term horizon, in response to the vulnerabilities derived from the volume of container/cargo flow, and the size and number of vessels, shaping and hedging actions can be used. These actions include the improvement of infrastructure in the port network including the small ports. The full list of actions for the port functions is presented by Eskafi (2021).

4 CONCLUSIONS

A structured framework was presented to facilitate the identification of uncertainties that manifest during the projected lifetime of the plan and deal with them in the planning process. The framework was applied to the Ports of Isafjordur Network in Iceland, to demonstrate its potential use in practice. A fuzzy logic 3D decision surface was used to identify the salient stakeholders and effectively and timely engage them in the planning. To reach a consensus among the key stakeholders on a definition of success for the plan, a fuzzy multi-attribute group decision-making method was applied. The highest level of agreement on the objectives among the key stakeholders was identified as prioritizing increasing competitiveness of the port. Uncertain development and their level were determined from the interviews with the key stakeholders. Opportunities such as increase in container and cargo flows, increase in marine traffic (e.g., container and cruise ships), and increase in aquaculture activities, and vulnerabilities such as climate change impacts, and lack of infrastructure for digitalization, automation, utilization of renewable energy were identified. The main results indicated that uncertainties mainly present opportunities in the short-term horizon, while in the middle-term horizon the port network is confronted with multiple vulnerabilities due to lack of infrastructure. To seize opportunities and manage vulnerabilities derived from uncertainties, effective actions were planned. The value of this framework lies in the nonlinearity of dealing with uncertainties in different time horizons. The theoretical contribution of this study is to meaningfully identify uncertainties that manifest during the projected lifetime of the plan and deal with them in the port planning process. Thus, inevitable changes become part of a recognized process and the plan is not forced to be remade repeatedly on an ad hoc basis. The managerial contribution enables decision makers to choose a preferred course of action and strategically implement the plan in the face of uncertainty.

ACKNOWLEDGMENTS

This study was supported in part by the doctoral grants of the University of Iceland Research Fund, the Municipality of Isafjordur, and the Icelandic Road and Coastal Administration Research Fund.

REFERENCES

Adey, B.T., Martani, C., Hackl, J., 2022. "Investing in water supply resilience considering uncertainty and management flexibility." *Proceedings of the Institution of Civil Engineers - Smart Infrastructure and Construction*. 175, 104–115. <https://doi.org/10.1680/jsmic.21.00005>

- Aven, Terje. 2008. *Risk Analysis: Assessing Uncertainties Beyond Expected Values and Probabilities*. 1st ed. Wiley, Chichester.
- Brier, David J. 2005. "Marking the Future: A Review of Time Horizons." *Futures* 37 (8): 833–48. doi:10.1016/j.futures.2005.01.005.
- Colvin, R. M., G. Bradd Witt, and Justine Lacey. 2016. "Approaches to Identifying Stakeholders in Environmental Management: Insights from Practitioners to Go beyond the 'Usual Suspects.'" *Land Use Policy* 52 (March): 266–76. doi:10.1016/j.landusepol.2015.12.032.
- Eskafi, Majid, Reza. Fazeli, Ali. Dastgheib, Poonam. Taneja, Gudmundur. F. Ulfarsson, Ragnheidur I. Thorarinsdottir, and Gunnar. Stefansson. 2019. "Stakeholder Salience and Prioritization for Port Master Planning, a Case Study of the Multi-Purpose Port of Isafjordur in Iceland." *European Journal of Transport and Infrastructure Research* 19 (3): 214–60. doi:10.18757/ejtir.2019.19.3.4386.
- Eskafi, Majid, Reza Fazeli, Ali Dastgheib, Poonam Taneja, Gudmundur F. Ulfarsson, Ragnheidur I. Thorarinsdottir, and Gunnar Stefansson. 2020. "A Value-Based Definition of Success in Adaptive Port Planning: A Case Study of the Port of Isafjordur in Iceland." *Maritime Economics & Logistics* 22 (3): 403–31. doi:10.1057/s41278-019-00134-6.
- Eskafi, Majid, Milad Kowsari, Ali Dastgheib, Gudmundur F. Ulfarsson, Gunnar Stefansson, Poonam Taneja, and R. I. Thorarinsdottir. 2021a. "A Model for Port Throughput Forecasting Using Bayesian Estimation." *Maritime Economics and Logistics* 23 (2): 348–68. doi:10.1057/s41278-021-00190-x.
- Eskafi, Majid, Ali Dastgheib, Poonam Taneja, Gudmundur F. Ulfarsson, Gunnar Stefansson, and Ragnheidur I. Thorarinsdottir. 2021b. "Framework for Dealing with Uncertainty in the Port Planning Process." *Journal of Waterway, Port, Coastal, and Ocean Engineering* 147 (3). American Society of Civil Engineers: 05021003. doi:10.1061/(ASCE)WW.1943-5460.0000636.
- Eskafi, Majid. 2021. *Framework for Dealing with Uncertainty in the Port Planning Process: An Icelandic Case of the Ports of Isafjordur Network*. University of Iceland. ISBN: 978-9935-9579-9-3. <https://opin.visindi.is/handle/20.500.11815/2615>
- Haasnoot, Marjolijn, Jan H. Kwakkel, Warren E. Walker, and Judith ter Maat. 2013. "Dynamic Adaptive Policy Pathways: A Method for Crafting Robust Decisions for a Deeply Uncertain World." *Global Environmental Change* 23 (2): 485–98. doi:10.1016/j.gloenvcha.2012.12.006.
- Herder, Paulien M., Jeroen de Joode, Andreas Ligtvoet, Sigrid Schenk, and Poonam Taneja. 2011. "Buying Real Options – Valuing Uncertainty in Infrastructure Planning." *Futures, Special Issue: Flexible infrastructures*, 43 (9): 961–69. doi:10.1016/j.futures.2011.06.005.
- Keeney, R. 1996. "Value-Focused Thinking: identifying decision opportunities and creating alternatives." *European Journal of Operational Research* 92 (3): 537–49. doi:10.1016/0377-2217(96)00004-5.
- Lempert, R. J, and S.W Popper. 2005. "High-Performance Government in an Uncertain World." In *High Performance Government: Structure, Leadership, and Incentives*, edited by R Klitgaard and P Light. Santa Monica, CA: RAND Corporation.
- Ligteringen, Han. 2017. *Ports and Terminals*. 2nd ed. Delft: Delft Academic Press.
- Masini, Eleonora. 1993. *Why Futures Studies?* London: Grey Seal Books.
- Nordlund, Göran. 2012. "Time-Scales in Futures Research and Forecasting." *Futures* 44 (4): 408–14. doi:10.1016/j.futures.2012.01.002.
- Uusitalo, Laura, Annukka Lehtikoinen, Inari Helle, and Kai Myrberg. 2015. "An Overview of Methods to Evaluate Uncertainty of Deterministic Models in Decision Support." *Environmental Modelling & Software* 63 (January): 24–31. doi:10.1016/j.envsoft.2014.09.017.
- Taneja, P. 2013. "The Flexible Port" Delft, the Netherlands: Delft university of technology. doi:10.4233/uuid:a9f0c128-d4c3-41a2-8790-13aec89dca63.
- Van Dorsser, J.C.M, Warren E. Walker, Poonam Taneja, and Vincent A. W. J. Marchau. 2018. "Improving the Link between the Futures Field and Policymaking." *Futures* 104 (December): 75–84. doi:10.1016/j.futures.2018.05.004.
- Vu, Thao Phuong, David B. Grant, and David A. Menachof. 2019. "Exploring Logistics Service Quality in Hai Phong, Vietnam." *The Asian Journal of Shipping and Logistics*, December. doi:10.1016/j.ajsl.2019.12.001.
- Walker, Warren E., Marjolijn Haasnoot, and Jan H. Kwakkel. 2013. "Adapt or Perish: A Review of Planning Approaches for Adaptation under Deep Uncertainty." *Sustainability* 5 (3): 955–79. doi:10.3390/su5030955.

Probabilistic circular economy assessment for infrastructures considering time-variant influencing factors

H. Lei, W. Wang & C.Q. Li

RMIT University, Melbourne, Victoria, Australia

W. Yang

The University of Melbourne, Melbourne, Victoria, Australia

ABSTRACT: Circular economy (CE) is increasingly used to accelerate the transition of infrastructure towards circularity and sustainability. However, a practical and accurate assessment procedure considering the stochasticity of influencing factors for CE implementation in infrastructures has not yet been fully developed. This paper first develops a CE index and models for predicting the CE performance of infrastructure over time based on functional circularity, embodied carbon and embodied energy. Time-dependent reliability theory is then employed to account for the randomness of factors, such as structural degradation rates, embodied impact coefficients, recycling rates and recycling efficiency. The proposed methods are demonstrated through a case study of three concrete structures with design for disassembly (DfD) and different recycled aggregate substitution rates. Results of the case study suggest that the structure with DfD and natural aggregate has a lower probability of unsatisfactory CE performance. The results will guide the future implementation of CE in infrastructures.

1 INTRODUCTION

Infrastructure currently emits 39.5 billion tons of greenhouse gas (GHG) emissions annually, which is about 79% of global emissions (UNOPS 2021). While infrastructure has played a crucial role in meeting the increasing service demands due to population growth and urbanization process worldwide, sustainable and circular development of infrastructures is in great need to overcome the significant environmental burdens. Thus, circular economy (CE) is adopted as a potential solution to reduce GHG emissions and increase the circularity throughout the value chains of infrastructures. CE is a systematic approach that focuses on narrowing, slowing and closing resource loops by implementing various regenerative and restorative strategies to benefit the environment, economy and society (Geissdoerfer et al. 2017). Design for disassembly (DfD) is an important CE strategy to be implemented in infrastructures and it focuses on reversible designs and reusing structural components (Sanchez et al. 2020). However, the successful implementation of CE strategies, e.g. DfD, relies on effective assessment procedures that comprehensively evaluate CE performance from different aspects.

CE performance can be assessed from two aspects, namely circularity and sustainability (Corona et al. 2019). Circularity assessment involves the quantification of the alignment degree of a system with the CE principles, i.e. narrowing, slowing and closing loops (Morsetto 2020). Sustainability assessment relies on life cycle assessment (LCA), in which the environmental impact of a system needs to be determined from various aspects, such as climate change, human health and fossil resource depletion (Potrč et al. 2021). There are many studies conducted on categorizing existing CE indicators according to their applicability to different assessment objectives and criteria, such as Kravchenko et al. (2019) and Saidani et al. (2019). In comparison, probabilistic CE assessments are relatively rare. Most existing CE indicators only focus on a single aspect, i.e. either circularity or

sustainability, which results in an incomplete evaluation of CE performance (Moraga et al. 2019). Furthermore, these indicators exclude time dimension and ignore the impact of durability on circularity performance (Figge et al. 2018). The uncertainty embedded in the life cycle of infrastructures, e.g. the structural degradation and uncertain environmental impacts of structural components with DfD in complex product, reuse and end-of-life treatment processes, are often ignored and the CE performance may not meet the CE assessment criterion (Lei et al. 2022). A thorough review of literature shows that a comprehensive and probabilistic CE assessment considering time-variant influencing factors for infrastructures has not been fully developed.

Some attempts have been observed to apply reliability theory to LCA, however, the circularity aspect of CE performance was not considered, such as Wei et al. (2016) and Shahtaheri et al. (2019). Lei et al. (2022) developed probabilistic CE assessment methods and an overall CE index to evaluate material circularity and environmental sustainability of building materials. Multiple uncertain variables in different end-of-life scenarios were considered, but the stochasticity of time-variant influencing factors, e.g. the structural degradation affects the long-term CE performance of reusable components, was ignored. It is well acknowledged that the degradation of concrete structures significantly influences the durability and environmental impacts of infrastructure. Considering the long life span of concrete components with DfD, structural degradation will reduce their ability to be reused directly after deconstruction. Therefore, integrating time-dependent reliability theory into CE assessment will further increase the accuracy of probabilistic CE assessment method in predicting long-term CE performance under the impact of time-variant influencing factors.

This work aims to develop CE assessment methods for infrastructures based on time-dependent reliability theory. Different time-variant influencing factors are considered, such as structural degradation rates, embodied impact coefficients, recycling rates and recycling efficiency. The objectives of this work include: 1. Develop a CE index for infrastructure based on time-dependent reliability theory; 2. Develop models for computing circularity and sustainability indexes considering time-variant influencing factors and their stochasticity; 3. Demonstrate the feasibility of developed methods by predicting the long-term CE performance of concrete structures. This work will help practitioners to understand the long-term CE performance of infrastructure, in particular, the time-dependent CE performance of reusable concrete structural components with different recycled aggregate substitution rates. The results of probabilistic CE assessment will guide the future adoption of CE strategies in infrastructure.

2 METHODOLOGY

2.1 Basics of time-dependent reliability methods

In the time-dependent reliability analysis, two critical elements need to be identified: the stochastic process $X(t)$ and the limit state function $G(X,t)$ which changes with time (Li and Yang 2022). In this study, circularity and sustainability are modelled as stochastic process $X(t)$. The limit state function $G(X,t) = G(X_p, X_b, t)$ is used as the assessment criteria that describes the relation between the performance of circularity and sustainability at time t , denoted by $X_p(X,t)$ and the corresponding threshold, denoted by $X_b(t)$ of the target system. The safe domain, i.e. satisfactory performance zone, can be determined as $G(X,t) \leq 0 = [X_p(X,t) - X_b(t) \leq 0]$. For example, the embodied carbon performance is influenced by different time-variant factors, such as the structural degradation rates, embodied carbon coefficients and recycling rates after the deconstruction of components. The satisfactory embodied carbon performance thus represents the circumstance that embodied carbon is less than the threshold at time t . The unsatisfactory performance therefore depends on the time that the stochastic process $X_p(X,t)$ crosses out the safe domain for the first time, i.e. embodied carbon is larger than emission threshold at time t . The probability of the first occurrence of such outcrossing, is known as ‘first passage’ probability (Breitung and Rackwitz 1982) and is considered as the probability of unsatisfactory performance, or failure, as denoted by $p_f(t)$. Then, the rice formula can be adopted to determine the solution of the first passage probability as follows (Li and Yang 2022)

$$p_f(t) = P[X_p(\mathbf{X}, t) \geq X_b(t)] \leq p_f(0) + \int_0^t u dt \quad (1)$$

where $p_f(0)$ is the probability of unsatisfactory performance at $t = 0$ and u is the upcrossing rate. The detailed calculation process of upcrossing rate u is omitted here due to page limitation and can refer to Melchers and Beck (2017) and Li and Yang (2022).

2.2 Formulation of circular economy index

Based on the formulation of time-dependent reliability index, i.e. Equation (1), circularity assessment criteria can be developed as follows,

$$p_{f_{CR}}(t) = P[\mathbf{G}_{CR}(\mathbf{X}, t) \geq 0] = P[CR_p(\mathbf{X}, t) \geq CR_b(t)] \quad (2)$$

where $p_{f_{CR}}(t)$ is the probability of unsatisfactory circularity performance; $\mathbf{G}_{CR}(\mathbf{X}, t)$ is circularity assessment criteria, i.e. the limit state function for circularity; $CR_p(t)$ is circularity performances; $CR_b(t)$ is the corresponding circularity thresholds at time t . The sustainability assessment criteria can be determined analogously.

A new CE index therefore is developed based on these circularity and sustainability assessments criterion. Three components of CE were selected to be assessed in this study: functional circularity, embodied carbon and embodied energy, to represent the assessment criterion from circularity and sustainability aspects. The probability of failure for CE performance can be assessed in series, parallel or hybrid systems. A series system is modelled to consider three CE components equally, i.e. if one of these criteria is not met the overall CE performance requirement is not met. The probability of system failure $p_{f_{CE}}(t)$, i.e. unsatisfactory CE performance at time t , can be determined as follows (Melchers and Beck 2017)

$$p_{f_{CE}}(t) = P[F_{CR}(t) \cup F_{EC}(t) \cup F_{EE}(t)] \quad (3)$$

where $\mathbf{P}(\cdot)$ is the probability operator and $F_{CR}(t)$, $F_{EC}(t)$ and $F_{EE}(t)$ represent the event of unsatisfactory functional circularity, embodied carbon and embodied energy performances at time t , respectively. Thus, the time-dependent reliability index, i.e. CE index, is obtained as follows

$$\beta_{CE}(t) = -\Phi^{-1}[p_{f_{CE}}(t)] \quad (4)$$

where $\beta_{CE}(t)$ is the CE index at time t , $\Phi^{-1}(\cdot)$ is the inverse function of cumulative distribution function of standard normal variable. Therefore, a probabilistic CE assessment is formulated.

3 MODELLING OF FUNCTIONAL CIRCULARITY

The modelling of circularity assessment criteria, i.e. $\mathbf{G}_{CR}(\mathbf{X}, t)$, involves the determination of performance, i.e. $GR_p(\mathbf{X}, t)$, and related threshold, i.e. $GR_b(t)$, Hatzfeld et al. (2022) developed a functional circularity indicator (FCI) based on modelling functionality of products over use-time. Through measuring the integral surface of functionality over the use-time, FCI can be used to demonstrate multicyclic longevity, upcycling and downcycling effects and disruptive changes in circularity performance of product. A cross-functional circularity indicator (CFCI) was also developed to measure the time when the functionality of a product is reduced by half. In this study, FCI and CFCI are selected to model the circularity performance and threshold, respectively. Furthermore, CFCI is modified to represent half of the integral surface of functionality over the predicted service life of infrastructure. Therefore, $GR_p(\mathbf{X}, t)$ and $GR_b(t)$ can be determined as follows (Hatzfeld et al. 2022)

$$CR_p(\mathbf{X}, t) = FCI(t) = \int_{t_0}^t f(t) dt \quad (5)$$

$$CR_b(t) = CFCI(t) = \frac{1}{2} \int_0^{T_b} f(t) dt \quad (6)$$

where t_0 is the used time of components in previous use cycles; t is the use time in the current cycle; $f(t)$ is the functionality at time t ; T_b is the baseline service life of structures.

The structural degradation of concrete components is considered as a key factor leading to the loss of functionality in infrastructure. Thus, the changes in structural degradation rate, denoted by $D(t)$, can be used to model functionality over use-time. Concrete carbonation is a critical factor leading to the degradation of concrete structures. Thus, it is assumed that the structural degradation rate corresponds to concrete carbonation depth, which is approximately proportional to the square root of carbonation time (Xia et al. 2020). It is worth noting that the real degradation process of structural performance is affected by complex mechanisms and structural state factors, which is out of the scope of this study. The $FCCI(t)$ can be determined as follows

$$FCCI(t) = \int_0^t [I - D(t)] dt = \int_0^t \left(I - \frac{\sqrt{t_0 + t} - \sqrt{t_0}}{\sqrt{T_c}} \right) dt \quad (7)$$

where T_c is the predicted service life of structure; $t_0 + t \leq T_c$ to ensure structural safety. The inclusion of predicted service life of structures T_c in Equation (7) provides the opportunity to incorporate durability in circularity assessment criteria. Lognormal distribution is selected to model predicted service life. The mean value μ_{T_c} and standard deviation σ_{T_c} of predicted service life T_c to produce the lognormal distribution can be obtained from the literature. Through adopting different durability improvement technologies, predicted service life may change accordingly. The probability of unsatisfactory circularity performance $p_{fCR}(t)$ thus can be determined by Equation (2), in which the event of remaining functionality reduces to less than half of its original functionality is considered unsatisfactory.

4 MODELLING OF ENVIRONMENTAL SUSTAINABILITY

Environmental sustainability, such as embodied carbon and embodied energy, is modelled by following a similar procedure for functional circularity. LCA is commonly used in quantifying the environmental impact of infrastructures and thus is selected to formulate the sustainability assessment criterion. The modelling procedure follows related standards, e.g. ISO 14044/14040. This study only considers embodied carbon and embodied energy as two critical environmental impacts to be analyzed. Other environmental impacts, such as resource depletion and human health, can be easily included in the model by following the procedure outlined below.

Embodied carbon is the cumulative carbon emissions across all life cycle stages of infrastructures except for the energy and water use phases (Wolf et al. 2017). It can be further divided into initial embodied carbon, recurrent embodied carbon and demolition carbon. Initial embodied carbon represents the carbon emissions released in the product and construction stages. Recurrent embodied carbon consists of carbon emissions due to maintenance, replacement and reuse during the use stage of infrastructures. Demolition carbon is net carbon emissions that integrate all emissions, including potential avoided carbon emissions, of waste flow treatments in one single module.

For structures with DfD, the allocation of life cycle impacts between their multiple life cycles needs to be considered. Three common life cycle impact allocation methods, i.e. cut-off allocation (100:0), recyclability (0:100) and distributed (50:50) methods, either underestimate the benefits of CE practices or ignore the material quality degradation between life cycles (Lei et al. 2021). This study allocates life cycle impacts according to the structural degradation rate to address these gaps in using structural components with DfD.

The embodied carbon performance $EC_p(X_{(i)}, t)$ is determined as follows

$$EC_p(X_{(i)}, t) = EC(X_{(i)}) \times D(t) = EC(X_{(i)}) \times \frac{\sqrt{t_0 + t} - \sqrt{t_0}}{\sqrt{T_c}} \quad (8)$$

$$EC(\mathbf{X}_{(i)}) = f(IC_{(i)}, C_{(i)}, E_{(i)}) = \sum_{i=1}^n Q_{(i)} [IC_{initial(i)} + IC_{reuse(i)} + IC_{recycling(i)} \times CR_{(i)} \times ER_{(i)} + IC_{landfill(i)} \times (1 - C_{R(i)} \times E_{R(i)})] \quad (9)$$

where $EC(\mathbf{X}_{(i)})$ is the embodied carbon function based on variable $\mathbf{X}_{(i)}$; $\mathbf{X}_{(i)}$ are the vector carbon emission coefficients (kg CO₂-eq/kg) for product and construction, reuse, recycling and landfill processes ($IC_{(i)}$), the fractions of material mass being collected for recycling ($C_{R(i)}$) and the fractions of material loss during recycling process ($E_{R(i)}$); $Q_{(i)}$ is the mass (kg) of the material labelled i obtained from the bill of quantities.

According to the Paris Agreement, global carbon emissions need to be reduced by 30% to 60% by 2050 to achieve the 2-degree target. The Australian government has proposed a 43% emission reduction target by 2030. Based on these targets, the embodied carbon threshold $EC_b(t)$ can be determined as follows

$$EC_b(t) = EC_0 \times (1 - \alpha_{EC})^{t_0+t} \quad (10)$$

where EC_0 is the baseline embodied carbon (kg CO₂-eq) of analyzed infrastructure, e.g. total embodied carbon of concrete structure; α_{EC} is the annual emission reduction rate, which can be determined based on emission reduction targets obtained from related literature and government reports.

The embodied energy performance $EE_p(\mathbf{X}_{(i)}, t)$ and threshold $EE_b(t)$ can be determined by replacing $IC_{(i)}$ with embodied energy coefficients ($IE_{(i)}$) in Equations (8) to (10).

Then the probability distributions of identified basic variables, e.g. $IC_{(i)}$, $C_{(i)}$ and $E_{(i)}$, need to be determined. Due to the limited data and characteristics of previously identified rates and coefficients, normal distribution and lognormal distribution are selected to model different basic variables. Normal distribution is selected for embodied impact coefficients ($IC_{(i)}$ and $IE_{(i)}$) and lognormal distribution is selected for recycling rate and related efficiency coefficient ($C_{R(i)}$ and $E_{R(i)}$). The mean value and standard deviation of distributions for these variables can be obtained by conducting statistical analysis of data from, such as, ICE material inventory database (Hammond and Jones 2019) and national waste reports (DAWE 2020a, 2020b). After the probability distributions of basic variables are defined, Monte Carlo simulation can be carried out to obtain, for example, the mean μ_{EC} and standard deviation σ_{EC} of $EC(\mathbf{X}_{(i)})$. According to the central limit theorem, $EC(\mathbf{X}_{(i)})$ follows the Gaussian distribution if the number of variables is larger than say 5 (Johnson 2004). After the probability of unsatisfactory circularity and sustainability performances are determined, the result of the probability of unsatisfactory CE performance and CE index can be computed by Equations (5) and (6).

5 CASE STUDY

Three concrete structures with DfD are selected from the literature (Xia *et al.* 2020). Different recycled aggregate substitution rates are observed in three reusable concrete structures, i.e. natural aggregate concrete (NAC) with no recycled content, recycled aggregate concrete (RAC0.5) with a 50% substitution rate and recycled aggregate concrete (RAC1) with a 100% substitution rate. The concrete cover depth for three structures is identical, i.e. 25mm. This study defines 1 m³ concrete structure as the functional unit. Each functional unit consists of 1.03 m³ of concrete and 144.79 kg of steel bars. The material loss during the component pre-fabrication process and the increased material consumption due to adopting DfD are considered. For concrete structures with recycled aggregate, the service life will be shorter due to faster carbonation progress compared to the natural one. Thus, the predicted service life spans for three concrete structures are different, which are 91.56, 88.66 and 86.12 for NAC, RAC0.5 and RAC1, respectively (Xia *et al.* 2020).

In this study, three concrete structures are in their first use cycle, i.e. $t_0 = 0$. The reuse of structural components includes deconstruction, transport and construction processes. Deconstruction is considered as a reverse construction process. After one reuse cycle, three concrete structures are no longer suitable for direct reuse and therefore are deconstructed and sent to

recycling or landfill facilities. It is assumed that different recycled aggregate substitution rates will not affect the end-of-life process and all end-of-life materials travel the same distance from the demolition site to the recycling plant or landfill. The embodied carbon and embodied energy coefficients for each material are obtained from the EPD Australasia database and the ICE material inventory database (Hammond and Jones 2019). The fractions of different materials to be recycled and landfilled are obtained from Australian government reports. According to the national waste report, 81% of masonry and 90% of metal are recycled (DAWE 2020a). Recycling efficiency coefficients for concrete and steel are 80% and 90%, respectively, due to the material loss during collection, sorting and recycling (DAWE 2020b). An average coefficient of variance $CoV = \sigma/\mu$ and the autocovariance $C(t_i, t_j) = \sigma^2 \exp(\theta t_i t_j)$, where $CoV = 0.1$ and $\theta = -1 \times 10^5$, are assumed for all variables due to the absence of data.

The mean value and standard deviation of embodied carbon and embodied energy are computed using a simulation number of 1×10^6 based on the convergence study. Table 1 summarizes the characteristics of embodied carbon and embodied energy involved in probabilistic CE assessment. The mean values of embodied carbon for NAC, RAC0.5 and RAC1 are 645, 637 and 630 kg CO₂-eq/m³, respectively. In addition, the mean values of embodied energy for three concrete structures are 5567, 5482 and 5398 MJ/m³, respectively. A decrease in the embodied carbon and embodied energy of concrete structures are observed when the recycled aggregate substitution rate is increased. Then, the annual reduction rate for embodied carbon and energy is assumed as 0.00865 to achieve a 50% emission reduction by 2100. Therefore, the example results of the probability of unsatisfactory CE performance and CE index are computed and illustrated in Figure 1.

Table 1. Mean and standard deviation of embodied carbon and embodied energy for three concrete structures based on Monte Carlo simulation.

Probabilistic circular economy assessment variables		NAC	RAC0.5	RAC1	Distribution type
Embodied carbon (kg CO ₂ -eq/m ³)	Mean μ_{EC}	645	637	630	Normal
	Standard deviation σ_{EC}	79	78	78	
	Coefficient of variation ($\pm\%$)	12.2%	12.3%	12.4%	
Embodied energy (MJ/m ³)	Mean μ_{EE}	5567	5482	5398	Normal
	Standard deviation σ_{EE}	802	800	799	
	Coefficient of variation ($\pm\%$)	14.4%	14.6%	14.8%	

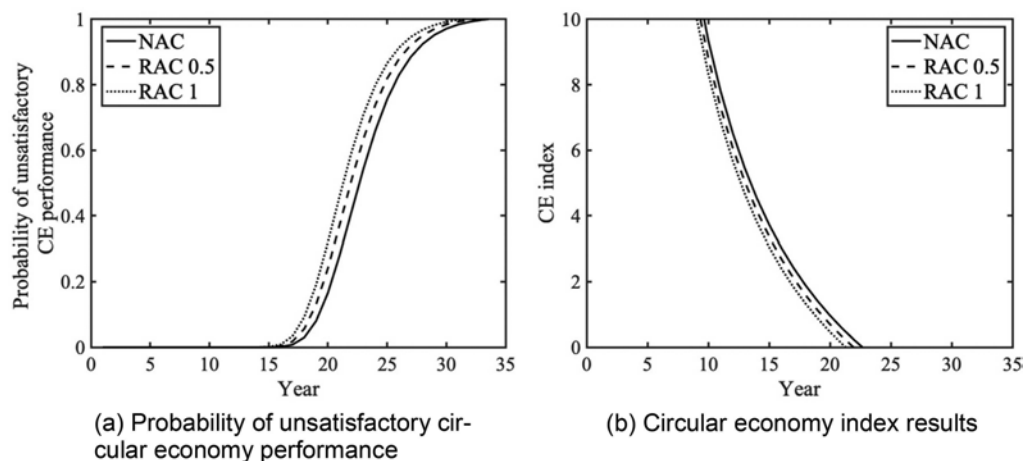


Figure 1. Probabilistic circular economy assessment results for three concrete structures.

6 DISCUSSION

A probabilistic CE assessment considering time-variant influencing factors is developed and tested on reusable concrete structures with different recycled aggregate substitution rates. According to the results, two reusable concrete structures with recycled aggregate, i.e. RAC0.5 and RAC1, have lower CE index results and higher probabilities of unsatisfactory CE performance than natural aggregate concrete, i.e. NAC, throughout the time. For example, in year 20, the probabilities of unsatisfactory CE performance of RAC0.5 and RAC1 are 22.9% and 30.2%, respectively, while that for NAC is only 16%. The CE index results of RAC0.5 and RAC1 are 0.74 and 0.52, respectively. At the same time, the CE index of NAC is 0.99. Therefore, the durability of reusable concrete structures has significant impacts on functional circularity and environmental sustainability. Without additional durability improvement actions, the input of recycled aggregates increases the probability of unsatisfactory CE performance of concrete structures with DfD.

It is worth noting that the mean values of embodied carbon and embodied energy of RACs are lower than that of NAC. This is because the use of recycled aggregate in RACs avoids the extraction and production of natural aggregates. However, the environmental benefit of recycled aggregate is limited due to cement being the largest source of embodied carbon and energy in concrete production. Furthermore, recycled aggregate accelerates the degradation process compared to natural aggregate in the same environment and carbonation time. Therefore, when combining different CE strategies, such as reuse and recycling, the trade-off between functional circularity and environmental sustainability needs to be carefully evaluated.

Different from most existing CE indicators, the developed CE index in this study has considered a wide range of time-variant influencing factors and their stochasticity to comprehensively evaluate the long-term CE performance. In circularity assessment, FCI is adopted to model the loss of functionality due to structural degradation of infrastructure during use. By defining different functionalities, FCI can be applied to various infrastructures that provide different services. In sustainability assessment, environmental impacts, i.e. embodied carbon and embodied energy, are allocated according to structural degradation rate. The structural degradation allocation method not only accounts for material degradation between multiple use cycles but also facilitates design for durability of reusable components. The implementation of probabilistic CE assessment can provide practitioners with decision-making confidence where the level of details in CE strategies is uncertain.

The limitations of present study need to be acknowledged. For example, only normal and lognormal distributions are considered in modelling the uncertain variables. Using different probabilistic distributions may result in different mean and standard deviation values for the circularity and sustainability performances of three concrete structures. Other distributions, e.g. gamma and triangular, need to be considered in future studies for comparing the effect of probabilistic distributions on the results. Also, in this study, a simplified structural degradation process is considered with focus on the carbonation only. It is acknowledged that the material degradation of concrete structures can be influenced by other factors, e.g. chloride ions, temperature and humidity. Future studies should also include these structural degradation factors to improve the accuracy of CE assessment.

7 CONCLUSIONS

A CE index has been developed for probabilistic CE assessment of infrastructures considering time-variant influencing factors in this paper. The time-variant models for FCI, embodied carbon and embodied energy have been established. The proposed CE index has been tested on three example concrete structures with DfD and different recycled aggregate substitution rates. Multiple uncertain and time-variant variables, such as structural degradation rates, environmental impact coefficients, recycling rates and recycling efficiency, are considered. It has been found that the combination of reuse and recycling strategy by sacrificing durability can lead to higher probabilities of unsatisfactory CE performance of infrastructures in the long term. It can be concluded that the CE index can integrate time-dependent reliability methods into CE assessment effectively. The developed methods and results provide a comprehensive understanding of CE performance and will guide the future adoption of CE in infrastructures.

REFERENCES

- Breitung, K. and Rackwitz, R., 1982. Nonlinear combination of load processes. *Journal of Structural Mechanics*, 10(2), pp.145–166.
- Corona, B., Shen, L., Reike, D., Carreón, J.R., and Worrell, E., 2019. Towards sustainable development through the circular economy—A review and critical assessment on current circularity metrics. *Resources, Conservation and Recycling*, 151, 104498.
- Department of Agriculture, Water and the Environment (DAWE), 2020a. Waste Account, Australia, Experimental Estimates, Waste generation, management and economic response by industry and household in alignment with System of Environmental-Economic Accounts (SEEA). <https://www.abs.gov.au/statistics/environment/environmental-management/waste-account-australia-experimental-estimates/latest-release>
- Department of Agriculture, Water and the Environment (DAWE), 2020b. National Waste Report 2020. <https://www.awe.gov.au/sites/default/files/env/pages/5a160ae2-d3a9-480e-9344-4eac42ef9001/files/national-waste-report-2020.pdf>
- Figge, F., Thorpe, A.S., Givry, P., Canning, L., and Franklin-Johnson, E., 2018. Longevity and Circularity as Indicators of Eco-Efficient Resource Use in the Circular Economy. *Ecological Economics*, 150, 297–306.
- Geissdoerfer, M., Savaget, P., Bocken, N.M.P., and Hultink, E.J., 2017. The Circular Economy – A new sustainability paradigm? *Journal of Cleaner Production*, 143, 757–768.
- Hammond, G., and Jones, C., 2019. The ICE Database. V3.0, *Circular Ecology*. <https://circularecology.com/embodied-carbon-footprint-database.html>
- Hatzfeld, T., Backes, J.G., Guenther, E., and Traverso, M., 2022. Modeling circularity as Functionality Over Use-Time to reflect on circularity indicator challenges and identify new indicators for the circular economy. *Journal of Cleaner Production*, 134797.
- Johnson, O., 2004. *Information theory and the central limit theorem*. World Scientific.
- Kravchenko, M., Pigosso, D.C., and McAloone, T.C., 2019. Towards the ex-ante sustainability screening of circular economy initiatives in manufacturing companies: Consolidation of leading sustainability-related performance indicators. *Journal of Cleaner Production*, 241, 118318.
- Lei, H., Li, L., Yang, W., Bian, Y., and Li, C.Q., 2021. An analytical review on application of life cycle assessment in circular economy for built environment. *Journal of Building Engineering*, 44, 103374.
- Lei, H., Yang, W., Wang, W. and Li, C.Q., 2022. A new method for probabilistic circular economy assessment of buildings. *Journal of Building Engineering*, 57, p.104875.
- Li, C.Q., and Yang, W., 2022. Time-dependent Reliability Theory and its Applications. Elsevier, London.
- Lindgreen, E.R., Salomone, R., and Reyes, T., 2020. A Critical Review of Academic Approaches, Methods and Tools to Assess Circular Economy at the Micro Level. *Sustainability*, 12 (12), 4973.
- Melchers, R.E. and Beck, A.T., 2018. *Structural reliability analysis and prediction*. John Wiley & sons.
- Moraga, G., Huysveld, S., Mathieux, F., Blengini, G.A., Alaerts, L., Acker, K.V., Meester, S. de, and Dewulf, J., 2019. Circular economy indicators: What do they measure?. *Resources, conservation, and recycling*, 146, 452–461.
- Morseletto, P., 2020. Targets for a circular economy. *Resources, Conservation and Recycling*, 153, 104553.
- Potrč, O., Tajda, Sabina, J., Andraž, L., Mendes, S., Marcella Ruschi, and Alexander, P., 2021. An LCA methodology for assessing the environmental impacts of building components before and after refurbishment. *Journal of Cleaner Production*, 327, 129527.
- Saidani, M., Yannou, B., Leroy, Y., Cluzel, F., and Kendall, A., 2019. A taxonomy of circular economy indicators. *Journal of Cleaner Production*, 207, 542–559.
- Sanchez, B., Rausch, C., Haas, C., and Saari, R., 2020. A selective disassembly multi-objective optimization approach for adaptive reuse of building components. *Resources, Conservation and Recycling*, 154, 104605.
- Shahtaheri, Y., Flint, M.M., and Garza, J.M. de la, 2019. A multi-objective reliability-based decision support system for incorporating decision maker utilities in the design of infrastructure. *Advanced Engineering Informatics*, 42, 100939.
- UNOPS, 2021. Infrastructure for climate action. University of Oxford. https://content.unops.org/publications/Infrastructure-for-climate-action_EN.pdf
- Wei, W., Larrey-Lassalle, P., Faure, T., Dumoulin, N., Roux, P., and Mathias, J.-D., 2016. Using the Reliability Theory for Assessing the Decision Confidence Probability for Comparative Life Cycle Assessments. *Environmental Science & Technology*, 50 (5), 2272–2280.
- Wolf, C.D., Pomponi, F., and Moncaster, A., 2017. Measuring embodied carbon dioxide equivalent of buildings: A review and critique of current industry practice. *Energy and Buildings*, 140, 68–80.
- Xia, B., Ding, T., and Xiao, J., 2020. Life cycle assessment of concrete structures with reuse and recycling strategies: A novel framework and case study. *Waste Management*, 105, 268–278.

Data-driven infrastructure systems design for uncertainty, sustainability, and resilience

M.-A. Cardin

Dyson School of Design Engineering and Centre for Systems Engineering and Innovation, Imperial College London, London, UK

A. Mijic

Department of Civil and Environmental Engineering and Centre for Systems Engineering and Innovation, Imperial College London, London, UK

J. Whyte

School of Project Management, University of Sydney, Sydney, Australia

ABSTRACT: There are currently many discussions around the need to design infrastructure systems that are more resilient and sustainable in the future, especially considering growing uncertainties from climate change, pandemics, geopolitical conflicts, and cyber/physical terrorism. It is widely recognized that infrastructure systems provide vital functions for society e.g., power generation, transportation, water management, and that they face much uncertainty and variability over their operating lifetime (+20 years). Yet, standard engineering methods provide limited guidance on how to best design such systems to make them more adaptable, evolvable, and reconfigurable to deal with future uncertainty and risks. The field of *Flexibility in Engineering Design* that emerged from the theory of real options provide systematic and innovative computational tools, algorithms, and digital processes to help designers and engineers better account for uncertainty and risks in early conceptual design activities. This paper provides an overview of the latest developments and future directions in this rapidly growing field. It discusses how flexibility provides the foundations for a unifying conceptual framework to create infrastructure systems that are both more sustainable and resilient. It introduces cutting edge techniques to support the design process based on principles from stochastic programming, robust optimization, deep reinforcement learning, and simulation games, including examples in energy and transportation systems.

1 INTRODUCTION

Infrastructures are complex engineered systems that play crucial roles for society and the world. They support power generation, resource production, healthcare, transportation, and allow us to explore our planet and beyond. Such systems typically operate for decades and face a wide range of uncertainty and risks during their operations, which are exacerbated by ongoing climate change, increasing likelihood of pandemics, geo-political tensions, as well as cyber and physical terrorism. Yet, such systems are often designed to accommodate projected capacity and are therefore often not adaptable to the impacts of changing conditions in markets, environments, regulations, and technology.

This paper presents recent research efforts to develop a data-driven framework leveraging concepts and techniques from machine learning, real options analysis, and flexibility in engineering design to improve the economic performance, sustainability, and resilience of future infrastructure systems operating under uncertainty. It is motivated in part by the fact that many countries

around the world, such as the UK, have set targets to decarbonize their economy by 2050, which will require massive investments in infrastructures, in the order of ~\$10 billion each year for the next 28 years (Krishnan et al., 2022). The research is motivated by climate change, which imposes further requirements for infrastructures to be more sustainable and resilient in the future.

The world is constantly witnessing the deployment of mega-infrastructure projects. For example in the UK, HS2, a railway system costed at £55 billion in 2015, is currently deployed to connect the Northwest and Southeast regions, stopping at major cities such as Manchester, Birmingham, and London (High Speed 2 Ltd., 2022). The development of electric vehicle take-off and landing (EVTOL) capabilities will soon require the deployment of new vertical airport (or vertiport) infrastructures and complex transportation networks. These are just two examples of complex engineered systems that will require careful design and capacity planning over time and space. HS2 provides an exciting research opportunity to revisit original designs and understand what could have been done differently, with an eye towards the remaining phases of the project. Vertiports present an opportunity to consider the design and operations of new infrastructures from scratch. Both systems will operate for decades and witness important changes in terms of demographics and needs, markets, regulations, and technology, especially as the world moves toward decarbonization and net zero. They will need to be sustainable by design and make best use of limited resources, but also be resilient, in view of the inevitable impacts of climate change. All such considerations call for the development of new thinking and methodological approaches to design complex engineered systems of the futures.

2 MOTIVATION

This paper is motivated by the realization that standard methods to assess the economic performance of complex infrastructure projects (e.g., net present value analysis or NPV) do not account well for uncertainty, and most likely mis-calculate the true future costs and benefits (Cardin and Cherian, 2022). This may significantly impact investments into achieving net zero by 2050. For instance, the HS2 project has been delayed severely with massive cost increases for several reasons that were largely foreseen (de Castilla and Westcott, 2013). Development of new vertiports is also subject to high uncertainty in terms of future demand, usage patterns, and technology development. Such development is cited by Uber as the main barrier to the future EVTOL transportation systems (Uber Technologies Inc., 2022). Another motivation is that standard design methods e.g., V-model in systems engineering (INCOSE, 2015) do not account systematically for intelligent management and adaptation strategies to deal with changing conditions and risks. Infrastructure mega-projects are often designed and optimized for a certain capacity, which often leads to rigid systems and plans that are costly to change if the future turns out different.

Ongoing research efforts builds upon the paradigm of *Flexibility in Engineering Design* (de Neufville and Scholtes, 2011). This paradigm has emerged from real options theory (Trigeorgis, 1996), and aims at designing systems that are adaptable, reconfigurable, and changeable in a cost-effective manner in the face of uncertainty and risks (Cardin et al., 2022b). Examples of flexibility include modular, multi-stage development projects, where deployment of subsequent phases is contingent on fulfilling certain socio-economic objectives, or the ability to reconfigure a system after an important disruption. One example of flexibility is the 25 de Abril bridge connecting Lisbon to the municipality of Almada in Portugal. Originally designed in the 1960s to carry four car lanes, the bridge was further designed to accommodate more car lanes if needed in the future and a railway on its lower platform. Decades later, this capacity expansion flexibility was exercised to accommodate growing traffic between the two shores. Growing demographic and changing economic patterns warrant full use of the six car lanes and two-railroad tracks infrastructure that exist today. Countless other studies have shown that flexibility improves expected economic value routinely by 10-30%, sometimes up to 80%, as compared to standard system design outcomes (Cardin, 2014, de Neufville and Scholtes, 2011). This is significant for investments in the order \geq £100 million. This value typically comes at an upfront cost early on, which is often much less than the future costs of adapting later, when operating conditions have changed.

The research efforts build upon the idea that flexibility is an important enabler of sustainability. Flexibility enables better value for systems that are already sustainable by providing contingencies to reduce exposure to downside risks (e.g., abandoning a project doomed to fail), and by helping systems to capitalize on upside opportunities (e.g., expanding capacity to capture higher demand). It promotes sustainability by enabling capacity deployment when needed, which reduces costs in NPV terms, and makes better use of limited resources by avoiding unnecessary deployments and reducing pollution. This contrasts with the approach to “build big” to maximize benefits from economies of scale, which irrevocably commits large resources at the start of a project, and where those may neither be needed, nor appropriately up-to-date when the time comes (Cardin and Hu, 2016). Flexibility also enables resilience, because it enables systems to reconfigure quickly after an unexpected shock, and to regain quickly pre-disruption performance levels. The NHS Nightingale hospital deployed in just nine days over the ExCel London Centre to increase critical care treatment capacity during COVID is an excellent example of how flexibility enabled resilience in a critical healthcare situation (Hospital Times, 2020).

Given that the complexity of designing and deploying future infrastructure systems is ever so increasing, this paper sets as vision to develop a much-needed computational paradigm for *Data-Driven Systems Design for Uncertainty, Sustainability, and Resilience*. The proposed vision is to exploit recent developments in machine learning and important principles from flexibility in design and real options theory to expand our ability to explore the computational design and decision spaces¹ than currently feasible with existing methods and practices. The goal is to find better design and operations solutions, quantify potential improvements in terms of economic, sustainability, and resilience metrics, and importantly to “close the loop” and understand how the solutions can be used by system designers and engineers in a realistic operational environment. This work will support engineers in their ability to provide better advise to policymakers and business leaders on important infrastructure design decisions, in line with the view shared by the Royal Academy of Engineering (2020).

3 RESEARCH DIRECTIONS

Sections 3-4 as well as Figures 1-2 below are reproduced with permission from the book chapter by Cardin et al. (2022a)².

The field of flexibility in engineering systems design is highly multi-disciplinary. It is still relatively new (by academic standards!) and therefore still has much to offer in terms of future research directions and opportunities. An interesting aspect is that, given its nature, it often benefits from new developments in different disciplines. For instance, recent developments in artificial intelligence, machine learning, and data science are widely applicable in this field, with considerably untapped potential. The same goes for developments in digital twin modelling and virtual reality as more tools to support the design and decision-making process emerge. Although not exhaustive, this section provides an overview of ongoing and future directions for research and applications.

3.1 Flexibility as enabler of sustainability and resilience

With much uncertainty about the future, and ongoing threats from climate change, cyber-physical terrorism, and pandemics, infrastructure systems are exposed to massive risks in the coming decades. Such risks may disrupt global financial, urban, economic and political landscapes, as seen recently through the COVID crisis.

Ongoing research shows that flexibility can play a crucial role as a core, enabling paradigm to sustain and improve value in infrastructure systems design and make systems more resilient.

1. The computational design space is defined as the abstract mathematical space containing all the feasible design and operational solutions for a particular engineering system considering uncertainty.

2. The book chapter is accessible at https://link.springer.com/referenceworkentry/10.1007/978-3-030-46054-9_35-1

Flexibility can help provide actionable strategies to mitigate risks and secure a better future. Flexibility enables sustainability – defined by the United Nations as “developments that meet the needs of the present without compromising the ability of future generations to meet their own needs” – by generating better value for systems that are already sustainable (e.g., renewable technologies), and by enabling system operators to deploy capacity and resources *if and when* needed. For example, a recent formulation exploiting decision rules captures intelligent management strategies based on uncertainty realizations in the form of *if-then-else* statements, which emulate the decision-making process in operations. Decision rules are connected to the design in the sense that the flexibility must be designed *a priori* for it to be used in operations. Those can be optimized stochastically using advanced mathematical techniques like stochastic programming and/or robust optimization (Caunhye and Cardin, 2017, Cardin et al., 2017). The solutions are dynamic in nature, intuitive from a managerial standpoint, and typically consist of an initial design plan augmented by a set of rules that will guide future expansions and system operations given uncertainty realizations. Flexibility in design enables better resilience in infrastructure systems, because it promotes “the ability of a system, community or society exposed to hazards to resist, absorb, accommodate to and recover from the effects of a hazard in a timely and efficient manner, including through the preservation and restoration of its essential basic structures and functions” (United Nations). It provides important properties like adaptability and reconfigurability after an unexpected shock, to regain quickly pre-disruption performance.

An important opportunity in research is to develop a systematic, unified agile design framework that helps address ostensible confusion and indecisiveness in design practice that exist due to wide ranging and diverse views on sustainability and resilience. One benefit from systematic design activities focusing on flexibility is to provide a unifying framework to enable both system concepts simultaneously, while enabling engineers to focus on their design efforts. Indeed, despite the many facets to the problems of designing for sustainability and resilience (Chester and Allenby, 2019, Wied et al., 2020, Naderpajouh et al., 2018), flexibility is often discussed in both communities as an important enabling system property. This property can help further develop new frameworks to help generations of future engineers better quantify the added value from sustainability and resilience, whether using economic (e.g., profits, costs) or social metrics (e.g., environmental, social, and governance or ESG) (Schroders, 2020). The study by Caputo et al. (2023) provides an example where the value of flexibility in dynamic mobile micro-grid systems is quantified both in terms of expected costs and CO₂ emissions.

3.2 *Data-driven flexibility and real options*

Up until recently, there has been very little work aiming at leveraging the power of data science and machine learning in the context of flexibility and real options analysis. For example, flexibility strategies still rely in most parts on generic real option strategies (e.g., abandonment, capacity expansion, investment deferral) with exercise rules that are defined through human creativity (e.g., decision rules), and/or through Bellman’s expected reward maximization principles (e.g., maximize expected discounted cash flow). Large datasets that are produced or used by infrastructure systems may provide new combinations or rules, timing, and strategies that may not be intuitive to human designers, but that could very well complement existing approaches, by providing unexplored value-enhancing solutions and reconfiguration policies. For example, one could specify the moves that are allowed for a system to adapt and reconfigure (e.g., deploy new phase, expand or contract capacity, abandon the project) based on certain criteria (e.g., decision rules or policies, timings) and let the system combine these in different ways through a heuristic process to learn valuable strategies from the data. In this context, techniques such as deep reinforcement learning show tremendous potential as demonstrated in early research (Caputo and Cardin, 2022), and also generate other exciting new computational and mathematical problems (e.g., how to design optimal rules in a live, data-driven setting). The availability of large datasets also enables generation of better predictive models that can be used to improve scenario modelling in simulations. Overall, there is a new, largely unexplored field for the development of a new data-driven formulation for flexibility and real options in infrastructure systems design.

3.3 Simulation games and empirical studies

Another important direction for future research is to understand through empirical studies designers' and decision-makers' thinking and process during design activities and operations. Much research has been done where methods are demonstrated through applications in one or a few case studies. This may not be enough to fully validate a new design method.

Empirical studies enable collecting data on design and decision-making behaviors, describe, and make inferences based on statistical analysis. For example, one may devise "treatments", i.e., different methods to train designers on how to make best use of a decision rule or deep reinforcement learning policy to flexibility analysis. The effect of the different treatments can be assessed as compared to a baseline, or control treatment, along different performance indicators, i.e., dependent variables, such as the number of times the decision rules are used, quantitative performance assessment, etc. While such studies are usually conducted in a controlled environment that may not exactly correspond to the real world, this approach is nonetheless complementary to case study research since it relies on statistical main and interaction effects, as opposed to case study evidence that takes longer to generate, and in smaller sample sets.

Combined with simulation games (also known as *serious games*), empirical studies provide a valuable environment to test different design methods and procedures statistically. Inspired from military simulation games – *Kriegsspiel* being considered one of the oldest – they emulate an environment where behavior and decision-making can be studied more thoroughly (see Figure 1). A few studies have taken an empirical approach to study flexibility in complex systems design (Cardin et al., 2013, Cardin et al., 2015, Jiang et al., 2018, Gil et al., 2015), but many more are needed to thoroughly validate new computational methods, algorithms, and innovative digital processes emerging from research.



Figure 1. Example of simulation game to study a decision rule formulation to real options analysis in design and operations of resilient and sustainable power systems. (Reproduced by permission for academic use only, "Development of a Simulation Game Platform for Flexible Generation Expansion Planning and Design of Power Grid Systems" in Proceedings of the 2018 Annual Conference, Institute of Industrial and Systems Engineers).

3.4 Decision support systems, digital twins, and metaverse technologies

There is a need to develop and evaluate new computational aided engineering tools to support the design and decision-making process in industry. Many of the methods developed through research take the form of algorithms or equations that are difficult to visualize for end users in practice. There is a need to embed the research output into relevant software tools that can be used in a practical setting to support decision and policymaking.

This work is currently taking place at different scales. As mentioned before, recent developments in data science and machine learning provide wide ranging opportunities to make better use of increasingly accessible datasets on engineering systems. For example in the UK, the Data Analytics Facility for National Infrastructures (DAFNI) provides datasets, models, and algorithms on infrastructures for research development (STFC et al., 2020). At a project and portfolio scale, work is ongoing to develop a control room for construction (Farghaly et al., 2021). Figure 2 shows another example through an integrated data-driven decision support system for designing large-scale complex engineered systems. The system integrates data visualization and analytics capability, optimization input and output visualization, as well as visualization of the optimization outputs in a 3D virtual environment. It overlays an optimization model developed for design and planning of waste-to-energy systems in Singapore (Kuznetsova et al., 2019). This kind of system provides designers and decision-makers with a tangible environment for training and decision-making, in a more intuitive setting than complex models and equations.

The ideas above are in line with recent developments in digital twin modelling, where complex high-fidelity models are developed and improved over time from large datasets, as well as metaverse technologies such as augmented and virtual reality (AR/VR) for digital project delivery (Nikoli et al., 2019, Whyte et al., 2019, Sacks et al., 2020). Such technologies are useful to support visualization, optimization, planning, and design decision-making under uncertainty in a highly immersive environment. They have been, however, largely unexplored in the context of flexibility in design. They have the potential to enhance significantly design activities, as well as training, and decision-making. By closely emulating a real-world environment and changing environmental and operational conditions, such system can be used to quickly prototype system design alternatives, stress-test their performance in a simulated environment, and find optimal configurations. It can be used to train operators to operate the systems and determine when it is appropriate for the system to adapt, reconfigure, or evolve, which is especially useful for systems operating in a harsh

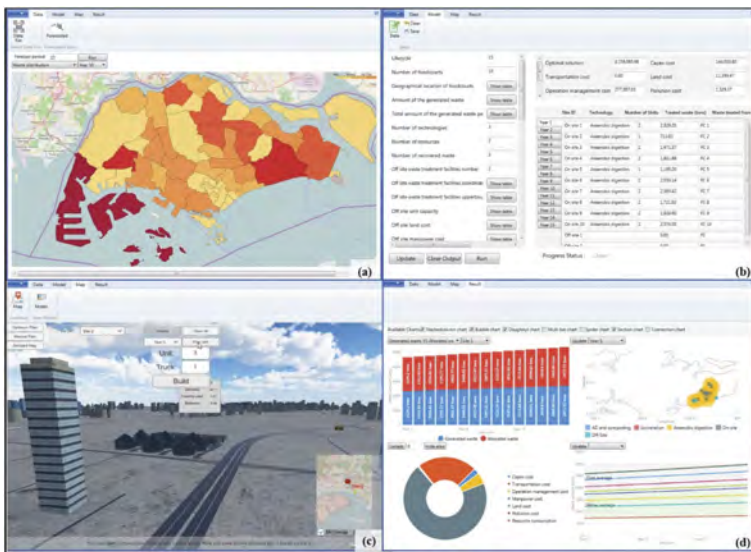


Figure 2. Example of integrated data-driven decision support system for example waste-to-energy systems. (a) Data analytics and visualization. (b) Optimization variable and parameter input definition. (c) 3D virtual environment. (d) Optimization output visualization.

environment, e.g., mining, drilling, and space (Malone et al., 2022). New knowledge on explainable AI (XAI) is particularly well suited to enhance the quality of design and operational decision-making. Overall, digital twin modelling, complemented by metaverse technology, XAI and decision-support systems yield very high potential for future research developments.

4 CONCLUSION

At a time where infrastructure systems face significant threats from climate change, pandemics, and terrorism, there is a need to change our approach to infrastructure systems design, management and operations (Lethanh and Adey, 2015). There is a need to consider uncertainty explicitly early in the design process, to extract better value for society, through improved economic performance, sustainability, and resilience. Designing infrastructure systems for flexibility is of utmost importance for future generations of systems designers and operators, policymakers, and business leaders. It prepares systems for change, adaptation, reconfiguration, and evolution in ways that ensure not only better survivability, but also better value in the long term. While the field of flexibility in design emerged in part from real options analysis, it is now evolving on its own, and at a steady accelerating pace. Researchers continually develop and evaluate novel design methods and computational procedures to enable flexibility, as a systematic value enhancement mechanism. The community is growing, as seen by the expanding volume of literature on the topic. This paper provides an overview of such evolution over recent decades, motivated by an important need in industry and policymaking. The overview exposes the multi-disciplinarity of the field, which involves finance, systems engineering and design, optimization, statistics, and uncertainty modeling, with applications in many relevant sectors such as aerospace, automotive, energy, real estate, transportation, space, and water systems. The research overview paves the way to exciting and applied new opportunities, much needed in industry practice and academia. Such opportunities involve a unifying paradigm for sustainability and resilience by design, data-driven flexibility analysis, empirical studies and simulation games, as well as AI and machine learning for decision support, digital twin modelling, and virtualization.

REFERENCES

- Caputo, C., Cardin, M.-A., Ge, P., Teng, F., Korre, A. & Antonio Del Rio Chanona, E. (2023) Design and planning of flexible mobile Micro-Grids using Deep Reinforcement Learning. *Applied Energy*, 335, 120707.
- Caputo, C. & Cardin, M. A. (2022) Analyzing real options and flexibility in engineering systems design using decision rules and deep reinforcement learning. *ASME Journal of Mechanical Design*, 144.
- Cardin, M.-A. (2014) Enabling Flexibility in Engineering Systems: A Taxonomy of Procedures and a Design Framework. *ASME Journal of Mechanical Design*, 136, 1–14.
- Cardin, M.-A. & Cherian, J. (2022) Flexibility is key: Costly net zero projects require innovative valuation and financing options. *Asia Asset Management*.
- Cardin, M.-A. & Hu, J. (2016) Analyzing the Tradeoffs Between Economies of Scale, Time-Value of Money, and Flexibility in Design Under Uncertainty: Study of Centralized vs. Decentralized Waste-to-Energy Systems. *ASME Journal of Mechanical Design*, 138, 011401-011401-11.
- Cardin, M.-A., Jiang, Y., Yue, H. K. H. & Fu, H. (2015) Training Design and Management of Flexible Engineering Systems: An Empirical Study Using Simulation Games. *IEEE Transactions on Systems, Man, and Cybernetics: Systems*, 45, 1268–1280.
- Cardin, M.-A., Kolfshoten, G. L., Frey, D. D., Neufville, R., Weck, O. L. & Geltner, D. M. (2013) Empirical Evaluation of Procedures to Generate Flexibility in Engineering Systems and Improve Life-cycle Performance. *Research in Engineering Design*, 24, 277–295.
- Cardin, M.-A., Mijic, A. & Whyte, J. (2022a) Flexibility and Real Options in Engineering Systems Design. IN Maier, A., Oehmen, J. & Vermaas, P. E. (Eds.) *Handbook of Engineering Systems Design*. Cham, Springer International Publishing.
- Cardin, M.-A., Xie, Q., Ng, T. S., Wang, S. & Hu, J. (2017) An approach for analyzing and managing flexibility in engineering systems design based on decision rules and multistage stochastic programming. *IJSE Transactions*, 49, 1–12.

- Cardin, M. A., Mijic, A. & Whyte, J. (2022b) Flexibility and real options in engineering systems design Handbook of Engineering Systems Design. Springer.
- Caunhye, A. M. & Cardin, M.-A. (2017) An Approach based on Robust Optimization and Decision Rules for Analyzing Real Options in Engineering Systems Design. *IISE Transactions*, 49, 753–767.
- Chester, M. V. & Allenby, B. (2019) Toward adaptive infrastructure: flexibility and agility in a non-stationarity age. *Sustainable and Resilient Infrastructure*, 4, 173–191.
- De Castella, T. & Westcott, K. (2013) HS2: 20 reasons why it can take 20 years to build a railway. *BBC*.
- De Neufville, R. & Scholtes, S. (2011) *Flexibility In Engineering Design*, Cambridge, MA, United States, MIT Press.
- Farghaly, K., Soman, R. & Whyte, J. (2021) Visualizing real-time information through a construction production control room. *European Conference on Computing in Construction (EC3)*.
- Gil, N., Biesek, G. & Freeman, J. (2015) Interorganizational Development of Flexible Capital Designs: The Case of Future-Proofing Infrastructure. *IEEE Transactions on Engineering Management*, 62, 335–350.
- High Speed 2 Ltd. (2022) What is HS2?
- Hospital Times (2020) How Flexible Healthcare Infrastructure can be Crucial to Fighting Covid-19. Hospital Times.
- Incese (2015) *INCOSE Systems Engineering Handbook: A Guide for System Life Cycle Processes and Activities, 4th Edition*, Wiley.
- Jiang, Y., Caunhye, A. M. & Cardin, M.-A. (2018) Development of a Simulation Game Platform for Flexible Generation Expansion Planning and Design of Power Grid Systems. *IISE Conference and Expo*. Orlando, FA, United States.
- Krishnan, M., Samandari, H., Woetzel, J., Smit, S., Pachod, D., Pinner, D., Nauc ler, T., Tai, H., Farr, A., Wu, W. & Imperato, D. (2022) The net-zero transition: What it would cost, what it could bring. McKinsey and Cie.
- Kuznetsova, E., Cardin, M.-A., Diao, M. & Zhang, S. (2019) Integrated Decision-Support Methodology for Combined Centralized-Decentralized Waste-to-Energy Management Systems Design. *Renewable & Sustainable Energy Reviews*, 103, 477–500.
- Lethanh, N. & Adey, B. T. (2015) A real option approach to determine optimal intervention windows for multi-national rail corridors. *Journal of Civil Engineering and Management*, 22, 38–46.
- Malone, L., Cardin, M.-A., Cilliers, J. J. & Hadler, K. (2022) Development of a Comprehensive Lunar Mining Simulator to Study Design and Decision-Making under Uncertainty. *International Astronautical Congress*. Paris, France.
- Naderpajouh, N., Yu, D. J., Aldrich, D. P., Linkov, I. & Matinheikki, J. (2018) Engineering meets institutions: an interdisciplinary approach to the management of resilience. *Environment Systems and Decisions*, 38, 306–317.
- Nikoli, D., Maftei, L. & Whyte, J. (2019) Becoming familiar: how infrastructure engineers begin to use collaborative virtual reality in their interdisciplinary practice. *Journal of Information Technology in Construction*, 24, 489–508.
- Royal Academy of Engineering (2020) COVID 19: Engineering a Resilient Future - From Ideas and Insights to Collective Engineering Advice.
- Sacks, R., Brilakis, I., Pikas, E., Xie, H. S. & Girolami, M. (2020) Construction with digital twin information systems. *Data-Centric Engineering*, 1, e14.
- Schroders (2020) ESG and Infrastructure Finance.
- Stfc, Epsrc, Innovate Uk & Ukcric (2020) Data Analytics Facility for National Infrastructures - Bridging the Gap Between Academic Research, Data Analysis, and Strategic Infrastructure Planning IN Ukcric (Ed.
- Trigeorgis, L. (1996) *Real Options: Managerial Flexibility and Strategy in resource Allocation*, Cambridge, MA, United States, MIT Press.
- Uber Technologies Inc. (2022) The future of urban mobility.
- Whyte, J., Chen, L., Gamble, C., Genes, C., Pierce, K., Fitzgerald, J., Coca, D., Mayfield, M., Babovic, F., Pedro, A. & Shah, N. (2019) Analysing Systems Interdependencies Using a Digital Twin. *2018/19 General Project funded by CDBB, Final Report*.
- Wied, M., Oehmen, J. & Welo, T. (2020) Conceptualizing resilience in engineering systems: An analysis of the literature. *Systems Engineering*, 23, 3–13.

Evaluating design modifications on a building portfolio considering future uncertainty and multiple stakeholders

Claudio Martani

Laboratory for Future-Ready Infrastructure (FuRI Lab), School of Construction Management Technology, Purdue University, West Lafayette, USA

Nicholas Calen & Bryan T. Adey

Infrastructure Management Group (IMG), Institut für Bau- und Infrastrukturmanagement (IBI), ETH Zürich, Zürich, Switzerland

ABSTRACT: The optimization of interventions for urban regeneration projects is a complex task that involves substantial investments and impacts the service provided to stakeholders over a long period. Part of the complexity of optimizing interventions on large building portfolio is that they are typically financed by a subset of the affected stakeholders, i.e., the owners or building developers who are understandably inclined to maximize their own interests and not those of the wider community. Another part is the need to account for uncertainty in future market demand across a portfolio of buildings, e.g., the possible future large-scale use of remote working, makes it questionable whether the current fixed configurations of many buildings (e.g., offices that have been dimensioned for a fixed demand, and residential units without proper places to work) will enable an optimal use of space, affecting the service provided to multiple stakeholders. This problem is particularly acute in urban areas. In recent years, the possibility has been put forward to use the real options method for optimizing the design and management of assets considering future uncertainty. The method, however, has never been used to determine optimal design of multiple buildings for multiple stakeholders. In this paper a general methodology is presented to evaluate design modifications for a building portfolio considering future uncertainty and the interests of multiple stakeholders. The methodology makes explicit that there is a need to consider the effects of regulations and incentives in to encourage owners to select design modifications that are in the best interest of all stakeholders.

1 INTRODUCTION

The optimization of design modifications on large real estate portfolios, which is common in urban regeneration projects, is a task that involves substantial investments and impacts the service provided to stakeholders over a long period. The repurposing of several buildings in an urban area modifies the service provided in these areas, in economic, social and environmental terms. Part of the complexity of determining the design modifications is that they are typically financed by a subset of the affected stakeholders, i.e., the owners or building developers who are understandably inclined to maximize their own interests and not those of the wider community. Another part is the need to account for uncertainty in future market demand across a portfolio of buildings, e.g., the possible disposal of a large amount of office space in the future due to the expanding use of remote working, and the possible disposal of retail spaces due to the continued rise of e-commerce.

Despite the fact that the economic, social and environmental impacts of urban regeneration projects can be large, and they are subject to considerable uncertainty, there has been little effort to try to optimize the required design modifications. This is largely due to the fact that comparing the impacts of all possible design modifications over a sufficiently representing set of future scenarios is a computationally intense task, that also requires quantifying the impact of each loss of service with the consensus of all involved stakeholders. Tackling such a problem requires being able to: (i) estimate the consequences of alternative design modifications on the provided services, (ii) take into account the future uncertainty affecting the provision of services (e.g., changes in population, technological developments), and (iii) quantify the needed incentives and regulations to align the interests of the investors with these of the wider community.

In recent years, the possibility has been put forward to use the real options method for optimizing the design and management of assets considering future uncertainty (De Neufville & Scholtes, 2011). Despite the undoubted merit of having extended the time dimension in the evaluation of the design of construction and infrastructure, the real options method has so far been focused on the design of single assets mainly, and always with the objective to use flexibility to maximize the economic interests of the owner. No attempt has been made yet to evaluate the designs of building portfolios considering future uncertain demand and the interests of multiple stakeholders. The first step in being able to do so requires adapting a methodology designed to use the real options method to allow the mapping the building portfolio for the characteristics that influences the market demand as well as costs and possibilities of design modification, the estimation of the impact of alternative sets of design modifications on the services provided over the investigated time period, and quantifying the needed incentives and regulations to align the interests of the investors with those of the other stakeholders (Martani et al., 2021). In this paper, an adaptation to the methodology proposed by Esders et al., 2020 is presented to cover the current gaps and enable optimizing the designs of building portfolios considering future uncertainty and the interests of multiple stakeholders.

2 LITERATURE REVIEW

Several attempts have been made in the past to optimize decisions on building designs considering future uncertainty. Examples are shown in Table 1, along with the uncertain future trends and stakeholder interests considered. It can be observed from Table 1 that all the works except one (i.e., Geltner & Neufville, 2018) have focused on single assets. Moreover, all the works have focused on maximizing only the economic interests of the owner. Indeed, despite a wider set of interests (i.e., economic, social and environmental) and stakeholders (i.e. owner, users, directly and indirectly affected people) have been considered in the design optimization of other types of constructions, e.g., highways (Martani et al., 2022), this has never been the case for buildings. As a consequence of the predominant focus on the economic interests of the owners, none of the works have considered the incentives and regulations required to align the interests of the owners (i.e. the investors) with these of the wider community.

3 METHODOLOGY

The outline of a general methodology to evaluate the possible designs of a building portfolio (i.e. either the design of new buildings, or the design modification of existing ones) considering future uncertainty and the interests of multiple stakeholders is presented in Figure 1. The methodology is an extension of that presented in (Esders et al., 2020) to optimize the designs of single buildings. The steps added are highlighted in grey. The methodology consists of 13 steps over 5 main areas, color coded in Figure 1: (1) Boundaries and objective definition, (2) Portfolio characterization, (3) Uncertainty recognition and modelling, (4) Design definition, and (5) Results generation, analysis and verification. The five following sub-chapters describe the steps in each area.

Table 1. Examples of research investigating flexible designs using the real options method.

Infrastructure	Source	Future uncertainty considered
Hospitals and clinics	de Neufville et al., 2008	Changes in demographics, changes in patterns, causes and effects of health and disease, changes in medical technology
Heating and cooling systems in office buildings	Eswers et al., 2019, 2020	Change in patient demand
	Martani et al., 2015, 2016	The prices of gas and electricity, heating and cooling loadings and performances of the systems
Building façades	Eswers et al., 2016	Operating costs
Buildings	Menassa, 2011	Changes in performance of materials and components
Military barracks	Eswers et al, 2015	Space demand
Buildings	Fawcett & Chadwick, 2007; Fawcett & Rigby, 2009	Demand of working space
Building ground floors	Ellingham & Fawcett, 2007	Commercial rents
Office buildings	Guma A. & de Neufville, 2008	Future cash flows (rents), and demand for office space
Ground floor ceilings in buildings	Martani et al., 2018	Use change rate
Buildings	Ashuri et al., 2011	Energy price
Multi-level parking facilities	De Neufville et al., 2006; De Neufville & Scholtes, 2011; Elvarsson et al., 2021	Number and types of parking plots required
Buildings portfolio	Geltner & Neufville, 2018	Real estate demand for destination of use

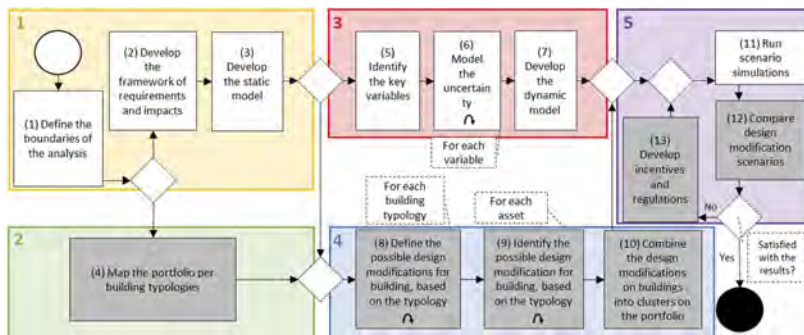


Figure 1. Methodology to evaluate the designs of multiple buildings in a building portfolio considering future uncertainty and the interests of multiple stakeholders.

3.1 Boundaries and objective definition

Step 1 - Define the boundaries. The first step is to conduct a context analysis to define the boundaries of the study. This includes defining the assets and stakeholders to be considered, as well as the time horizon of the analysis. This is crucial because the optimal combination of building designs in a portfolio is dependent on the boundaries. In other words the optimal designs for a portfolio over one time period may not be the same another portfolio or the same portfolio but another time period (as in Elvarsson et al., 2021).

Step 2 - Develop the framework of requirements and impacts. The second step is to specify the requirements of each of the stakeholders, e.g. for the tenant of a commercial unit one key requirement is the ability to operate their business for the working hours of each business day,

along with an estimate of the unit reduction of each of these services, e.g. the loss of profit if the commercial unit is unable to operate one day. Examples of extensive lists of the services provided by other types of assets are given in (Adey et al., 2020).

Step 3 - Develop the static model. The static model is the mathematical formulation of the objective of the stakeholders (also known as objective function) and it is developed to enable quantification of the expected impacts on the different stakeholders. The static model depends on different constant or fixed parameters (Esders et al., 2020).

3.2 *Portfolio characterization*

Step 4 - Map the portfolio per building typologies. The buildings defined in step 1 are here characterized by typology, i.e., for the main features that have an influence on the demand per use, as well as the type of design modifications that can be made and their costs. For example: (i) location (e.g., urban-central, urban-periphery, rural), (ii) size, and (iii) predominant use of the area (e.g., residential, office, commercial and mix use). This is done assuming that, the repurposing of each building is conditional on all three aspects, e.g., the possibilities for repurposing a small building in a peripheral residential area are different than these to repurpose a large building in a central mixed area.

3.3 *Uncertainty recognition and modelling*

Step 5 - Identify the key variables. Once the static model has been developed, the parameters within it whose values have a non-negligible probability of changing in a way that will affect the provision of level of service are identified. These parameters are typically contextual conditions that do not depend by the physical characteristics of the buildings but influence their service and their market, e.g., the demand for small studio units in central urban areas.

Step 6 - Model the uncertainty. After the variable parameters within the static model have been identified, the long-term uncertainties associated with each of these has to be modelled. These include, the demand for space, which is highly variable depending on demographic and economic developments, the demand for energy, parking space and level of utilities automation, which are subject to technological developments, the demand for delivery spaces, which is dependent on the development of e-commerce, etc. The uncertainty associated with these aspects makes it difficult for any portfolio of residential buildings to guarantee a satisfactory level of service, e.g. enough parking spaces. In this step, the probability distribution over all possible values that an uncertain variable can take are estimated over time based on the best current knowledge of the modeler on the future evolution of each variable (e.g. as in Martani et al., 2015, 2016). This is done by collecting information on future trends of the key parameters to gain insight into which possible future scenarios may occur and with what likelihood. Analyze their past evolution and changes in trends when data is available. Solicit expert opinion when necessary. Use the information collected to model the uncertainty of the key parameters.

Step 7 - Develop the dynamic model. In this step the static model is extended to consider the variations in the key parameters, the interactions between them and their influence on the system. Evaluate the effect of variations in the values of the key parameters on future benefit. An example of how this is done can be seen in (Elvarsson et al., 2021).

3.4 *Design modifications definition*

Step 8 - Define the possible design modifications per building typology. Following up with the mapping of the portfolio of assets (step 4), the set of all possible design modifications that can be executed for each typology, i.e., according to their characteristics (e.g., location, size and predominant use of the area), is defined. This is done to create a catalog of all the plausible modifications to be considered for each specific building based on its characteristics and location. Amongst the possible design modifications there should be a “do nothing” design

modification, since it cannot be taken for granted that implementing a design modification is always a good idea, i.e. any modification requires a consistent upfront investment. If these are not compensated by long-term benefits, it is preferable not to make any modification. This requires considering the interest of the owners, and analyzing the marked demand for destination of use per area and size. Moreover, for each of the design modifications defined, a unit cost (e.g. €/ sq. mt.) of execution is estimated to later (in step 9) allow estimating the cost of modifications for specific buildings based on their dimensions.

Step 9 - Identify the possible design modifications for buildings based on the typology. Once the building typologies (i.e., location, size and predominant use of the area) have been mapped (step 4), and the set of possible design modifications have been identified for each building typology (step 8), the extent of the design modifications are identified for each specific building. For each specific design modification on a building the cost is estimated by multiplying the unit cost of the design modifications as from step 8 for the dimension of the specific building.

Step 10 - Combine the design modifications on buildings into clusters on the portfolio. After the possible design modifications have been identified for all buildings these are grouped into all the possible combinations for all buildings in the portfolio. This is done considering external constraints in order to filter the clusters of modifications and avoid considering unrealistic ones, e.g., if in an area the number of residential units cannot exceed 70% of the buildings, all combinations of design modifications that do not respect this are excluded.

3.5 *Results generation, analysis and control*

Step 11 - Run scenario simulations. With all above conditions defined, multiple design modification scenarios, i.e. long-term scenarios generated by each of the interventions proposed to modify the existing building, are simulated using the Monte Carlo method, to estimate their impact on the objective function in light of future uncertainty. Through this technique, the stochastic scenarios are developed considering the evolution of all variables through time according to the uncertainty modeled as in Martani et al., 2018. At this stage the total risks on requirements are estimated for all design modification scenarios.

Step 12 - Compare design modification scenarios. In this step the design modification scenario that provides the minimal estimated negative impact on the objective function is selected as the optimal one among these considered and, if it is considered satisfactory (i.e., if the optimal cluster of design modifications is also the one that minimize the negative impact for the owners), the process is finished. Otherwise, the incentives and/or regulations need to be introduced to align the interests of the investors with these of the objective function.

Step 13 - (if needed) develop incentives and regulations. If the design modification scenario that minimizes the negative impact on the objective function is not the same as the one that minimizes the negative impact on the owners of the buildings, consideration has to be given as to the regulations and/or incentives that can be introduced to persuade the owners of the buildings to make the design modifications that have the best chance of reducing the risk on the interests of multiple stakeholders. This action is not solely at the planners' prerogative, but requires the cooperation of the planners with the legislative and executive government to implement any of the policies, regulations or incentives deemed useful. An example incentive is tax benefits that encourage the renewal of existing buildings instead of the demolition and construction of new buildings or using heating from renewable energy sources. Example regulatory constraints are forcing the use of a minimum share of recycled material during the modifications. The development of incentives and regulations needs to continue until the impact on the requirements of the objective function are considered satisfactory.

4 CONCLUSIONS

In this paper a general methodology is presented to evaluate design modifications for a building portfolio considering future uncertainty and the interests of multiple stakeholders. The methodology makes explicit that there is a need to consider the effects of regulations and incentives in to encourage owners to select design modifications that are in the best interest of all stakeholders. It also calls for the use for the first time of the real options methodology beyond the traditional scope of evaluating the design of single buildings. The use of the proposed methodology requires a high level of interdisciplinary integration as it combines skills that are typical in architecture, i.e., classifying buildings in techno-typological clusters, skills that come from the field of urban studies, i.e., GIS spatial mapping of buildings as a function of their characteristics, and engineering skills, such as uncertainty modelling and scenario simulation, as well as an understanding of the market dynamics, which are more traditionally economic skills.

The methodology presented is expected to provide guidance to individuals who are evaluating possible design modifications on building portfolios while accounting for future uncertainty and aiming to ensure that interests of a wide set of stakeholders are met as best possible both now and in the future. It will be tested in the near future on a case study repurposing of 12 bank branches in Zurich where the best assets repurposing intervention is to be determined, finding the optimal point of equilibrium between the owner's interest of maximizing the revenues, and all the social, environmental and economic implications for the directly and indirectly affected citizens

REFERENCES

- Adey, B. T., Burkhalter, M., & Martani, C. (2020). Defining road service to facilitate road infrastructure asset management. *Infrastructure Asset Management*, 7(4), 240–255. <https://doi.org/10.1680/jinam.18.00045>
- Ashuri, B., Kashani, H., & Lu, J. (2011). An investment analysis framework for energy retrofit in existing buildings. *47th ASC Annual International Conference*.
- de Neufville, R., Lee, Y. S., & Scholtes, S. (2008). Using flexibility to improve value-for-money in hospital infrastructure investments. *Infrastructure Systems and Services: Building Networks for a Brighter Future (INFRA)*, 2008 First International Conference On, 1–6.
- De Neufville, R., & Scholtes, S. (2011). *Flexibility in engineering design*. MIT Press.
- De Neufville, R., Scholtes, S., & Wang, T. (2006). Real options by spreadsheet: Parking garage case example. *Journal of Infrastructure Systems*, 12(2), 107–111.
- Ellingham, I., & Fawcett, W. (2007). *New generation whole-life costing: Property and construction decision-making under uncertainty*. Routledge.
- Elvarsson, A. B., Martani, C., & Adey, B. T. (2021). Considering automated vehicle deployment uncertainty in the design of optimal parking garages using real options. *Journal of Building Engineering*, 34, 101703. <https://doi.org/10.1016/j.jobbe.2020.101703>
- Edsers, M., Adey, B. T., & Lethanh, N. (2016). Using real option methods as a tool to determine optimal building work programs. *Structure and Infrastructure Engineering*, 12(11), 1395–1410.
- Edsers, M., Adey, B. T., & Martani, C. (2019). Evaluating Initial Building Designs Considering Possible Future Changes: The Example of the New Pet Centre of the University Hospital of Zurich. In *International Conference on Smart Infrastructure and Construction 2019 (ICSIC)* (pp. 35–41). ICE Publishing. <https://doi.org/10.1680/icsic.64669.035>
- Edsers, M., Martani, C., & Adey, B. T. (2020). Evaluating initial building designs considering possible future changes and decision flexibility: The example of the new PET Centre of the University Hospital of Zurich. *International Journal of Architecture, Engineering and Construction*, 9(4), 12020021.
- Fawcett, W., & Chadwick, A. (2007). Space-time management and office floorspace demand: Applied experience and mathematical simulations. *Journal of Corporate Real Estate*, 9(1), 5–24.
- Fawcett, W., & Rigby, D. (2009). The interaction of activity, space and cost variables in office workstation sharing. *Journal of Corporate Real Estate*, 11(1), 38–51.
- Geltner, D., & Neufville, R. de. (2018). *Flexibility and Real Estate Valuation under Uncertainty: A Practical Guide for Developers*. John Wiley & Sons.

- Guma A., & de Neufville, R. (2008). *Real option analysis of a vertically expandable real estate development*. MIT.
- Martani, C., Cattarinussi, L., & Adey, B. T. (2018). A new process for the evaluation of the net-benefit of flexible ground-floor ceiling in the face of use transition uncertainty. *Journal of Building Engineering*, 15, 156–170.
- Martani, C., Eberle, S., & Adey, B. T. (2022). Evaluating highway design considering uncertain mobility patterns and decision flexibility. *Infrastructure Asset Management*, 9(3), 135–155. <https://doi.org/10.1680/jinam.21.00018>
- Martani, C., Jin, Y., Soga, K., & Scholtes, S. (2015). *A New Model for Evaluating the Future Options of Integrating Ground Source Heat Pumps in Building Construction*.
- Martani, C., Jin, Y., Soga, K., & Scholtes, S. (2016). Design with Uncertainty: The Role of Future Options for Infrastructure Integration. *Computer-Aided Civil and Infrastructure Engineering*, n/a–n/a. <https://doi.org/10.1111/mice.12214>
- Martani, C., Talamo, C., Paganin, G., Campioli, A., Adey, B.T., Baum, A (2021). *A new methodology for promoting a sustainable regeneration of the European residential building stock, considering future uncertainty*. In: Kvanvik, S. H. (2021). *Book of abstracts. Contradictions Shaping Urban Futures. EURA Conference 2021. Oslo*.
- Menassa, C. C. (2011). Evaluating sustainable retrofits in existing buildings under uncertainty. *Energy and Buildings*, 43(12), 3576–3583.

Exploratory modelling for transport infrastructure planning under future uncertainty

O. Roman, A.B. Elvarsson & B.T. Adey

Chair of Infrastructure Management, ETH Zürich, Switzerland

ABSTRACT: Planning transport infrastructure is particularly difficult due to infrastructure's long-lived nature, unpredictable technological progress and changing mobility trends in society. In complex systems facing major uncertainties, exploratory modelling can help define salient system characteristics and discover potential risks and opportunities by evaluating large ensembles of potential conditions during the planning process. This paper demonstrates how exploratory modelling can provide planning support for a federal highway from Dübendorf to Hinwil in Zürich, Switzerland. We model the future traffic flows at peak hours considering uncertainty in urban development, jobs distribution and future modal share. Current road infrastructure and further potential capacity expansions and reallocations are then tested on their robustness to provide adequate performance (in terms of travel delays) in multiple future scenarios. We use quantitative methods to identify the subset of scenarios representing risks and opportunities for the infrastructure system. The visualization of such subset of scenarios in uncertainty maps can help target interventions only when needed.

1 INTRODUCTION

Transport infrastructure planning is particularly difficult due to its long-lived nature, unpredictable new technologies, changing trends in society, and environmental change effects. Furthermore, transport infrastructure has widespread economic, environmental and social impacts and therefore numerous stakeholders, with different interests and value frameworks, are involved in the decision-making process. The difficulty of estimating the future, the complexity of how infrastructure systems work and the uncertain valuations that can be put into infrastructure outcomes by different stakeholders make decision-making particularly challenging. Therefore, transport infrastructure planning often involves making decisions under deep uncertainty.

When dealing with complex systems under deep uncertainty, the assumption that we can identify a “best-guess” future condition might no longer be appropriate. Instead, the projection of multiple plausible future scenarios is increasingly seen as an alternative even when those scenarios cannot be ranked in terms of their likelihood (Maier et al., 2016). A wide exploration of many potential alternatives is warranted to gain a better understanding of the system and identify decision-relevant scenarios (e.g. scenarios that could result in high risks or valuable opportunities). This approach is commonly known as Exploratory Modelling (Bankes, 1993) and includes the use of quantitative techniques such as Feature Selection (Kwakkel, 2017) and Scenario Discovery (Bryant & Lempert, 2010). To measure system performance under multiple scenarios, robustness is often the preferred metric as it rewards plans that perform satisfactorily under many future conditions instead of focusing on isolated predictions (Maier et al., 2016). Common robustness metrics include regret metrics (e.g., quantification of performance in each scenario in comparison with a baseline) and satisficing metrics (e.g. quantification of the number of scenarios that meet certain requirements) (Herman et al., 2015).

Despite the increasing recognition that transportation systems face deep uncertainty, traditional methods for transport planning are inadequate to deal with this level of uncertainty

(Lyons & Davidson, 2016; Wall et al., 2015). Most research efforts have focused on increasing the granularity and complexity of models to gain accuracy, which further impedes a wide exploration of scenarios (Milkovits et al., 2019).

This paper uses a macroscopic transportation model to simulate a wide range of future scenarios and quantify robustness. Exploratory modelling techniques are used to identify the most relevant uncertain factors and subsets of decision-relevant scenarios. Furthermore, we show how the identification of such scenarios, through the development of uncertainty maps, can inform transport infrastructure planning by targeting interventions, such as road expansions only when needed, and road space reallocations, only when feasible. As an example, we use the road infrastructure between Dübendorf and Hinwil and their potential expansions and modifications in the future. Travel times on the corridor are estimated as a measurement of the level of service provided by the infrastructure. Future changes in travel times and potential delays are modelled annually to evaluate system performance’s adequacy in multiple plausible futures.

2 STUDY AREA AND MODEL

The corridor Dübendorf-Hinwil extends from the Zürich city border between the Pfannenstiel and the Zurich Highlands. Table 1 shows the population (Statistisches Amt des Kantons Zürich, 2022a) and jobs (Statistisches Amt des Kantons Zürich, 2022b) in each of the towns within the corridor, being Zurich the major urban centre. Different population projections for the Canton of Zurich vary between 0.5% and 1.1% per year (Bundesamt für Statistik, 2020) which might also drive growth in job opportunities and further changes in the region.

Table 1. Population and jobs within the corridor in 2020.

Town	Population	Jobs
Zurich	420'891	495'223
Dübendorf	29'854	19'362
Schwerzenbach	24'034	14'169
Uster	35'295	17'370
Seegräben	1'423	593
Wetzikon	25'038	14'088
Hinwil	11'344	7'150

The A15 federal highway (4 lanes) is a main component in the corridor connecting Dübendorf to Uster. After Uster, a cantonal road (2 lanes) continues to connect Uster to Hinwil. The Federal government has given the green light to the extension of the A15 from Uster to Hinwil but it is still not clear when the expansion will be realized. These expansion plans are being discussed and considered at both the cantonal and federal levels.

In this paper, the corridor is modelled as a simple linear link-node network as illustrated in Figure 1. The road infrastructure capacity along the corridor is estimated to be approximately 100 lane-km, including the federal highway and the cantonal road. To calculate the number of trips originating and ending in each of the towns, a gravity model is used with the population and jobs generating travel demand from each of the node pairs (de Dios Ortúzar & Willumsen, 2011). The generalized costs of travelling between the nodes, which are used to distribute the trips in the corridor model, are assumed to be related to the distance between each node pair. The modal share of cars in the canton of Zürich is estimated at 25% according to the 2015 Microcensus (Bundesamt für Statistik, 2017) and was used in the generation of trips.

Zürich, as the largest city, is a regional hub that serves and influences multiple networks in its surroundings, including the corridor from Dübendorf to Hinwil. Jobs in Zürich attract people living in the corridor, and people living in Zürich are also attracted by jobs in the corridor, both generating more trips. Several model parameters were calibrated to fit the traffic levels at peak hours for the traffic measuring points in the corridor (Kanton Zurich, 2019) including the portion of Zurich generating trips along the corridor which was estimated as 10%.

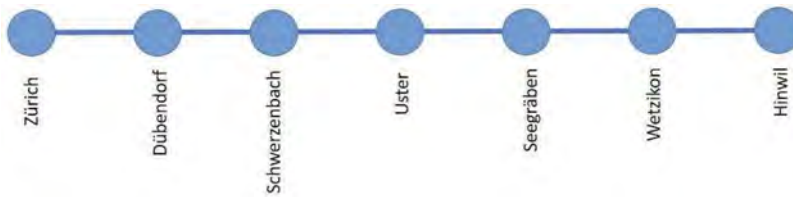


Figure 1. Simplified illustration of the corridor zürich-dübendorf-hinwil.

In the corridor model, as the population and jobs grow, the traffic volume is expected to grow. Increasing population leads to increased travel demand and potentially, to increased travel delay, particularly when demand is closer to the road capacity.

The average traffic flow at peak hours in the corridor is modelled using a Macroscopic flow model (de Dios Ortúzar & Willumsen, 2011). The input variables are the travel demand (expected traffic flow) and the infrastructure supply (road capacity available). We use a fundamental diagram of traffic flow to estimate the relationship between speed, flow and density in the model as shown in Figure 2.

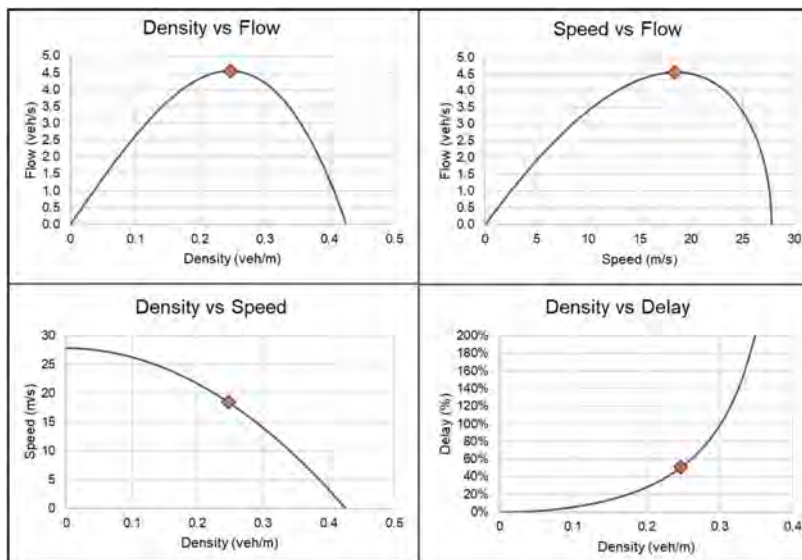


Figure 2. Fundamental diagram of traffic flow for the corridor. The critical density is shown in orange, i.e. the number of cars, as a ratio of the supply of lane-km available, that generates the maximum flow in the road. This will result in a certain speed being travelled on average across the system.

Besides classical flow-density, flow-speed and speed-density curves, Figure 2 also shows an estimation of the travel delay-density curve. Travel delay (in percentage) is estimated, as the additional travel time with respect to the free flow travel time (i.e. the travel time at the maximum allowed speed on the road). The calibrated model estimates that current delays are about 5% in the corridor. Figure 2 shows that reaching the critical density (orange diamond) generates a delay of about 50%.

For the evaluation of the ensemble of future scenarios, robustness was calculated by defining satisficing criteria (i.e. the level of performance considered adequate). For the satisficing criteria in this paper, we defined a delay of 20% as tolerable if it is not permanent. Therefore the first satisficing criterion is to not reach more than 20% of delay for more than 5 years until 2050 (one-sixth of the time). Additionally, reaching a delay of 50% (i.e. reaching road capacity and entering the congestion phase) is considered inadequate. The corridor performance will be simulated until 2050 under multiple scenarios and will be considered adequate if both

satisficing criteria are met. The satisficing criteria set for this paper reflects the need to avoid severe delays (e.g. the congestion state) and also assume the ability of infrastructure managers to act when delays reach 20% and consequently improve the performance in a reasonable time. Satisficing criteria can also be based on planning instruments, historic performance or elicited from stakeholders (Hadjimichael et al., 2020).

3 EXPLORATORY MODELLING

The model was used to evaluate the corridor performance under multiple future scenarios. Exploratory modelling was then carried out to identify the most relevant uncertain factors and the subset of decision-relevant scenarios (risks and opportunities). A scenario is defined as a particular combination of uncertain factors. Risk scenarios are the ones in which current capacity will not meet the satisficing criteria, indicating that expansions are needed. Opportunity scenarios are the ones in which reduction of road capacity (50% of the A15 federal highway) will still meet the satisficing criteria, indicating that road space can be reallocated to other uses (e.g. bike paths or bus priority lanes).

When scenarios are developed to represent a broad range of future conditions, their generation is usually done using numerical modelling and/or sampling (Kwakkel et al., 2015; McPhail et al., 2020). Key uncertain factors are first selected based on literature (Kwakkel et al., 2012; Milkovits et al., 2019; Wall et al., 2015) and during the process of model calibration (selecting the factors with bigger impact on performance). The selected uncertain factors were: 1) population growth, 2) job growth, 3) the change in the modal share of cars, and 4) the change on the influence of the city of Zurich in the corridor. Table 2 provides a short description of the factors along with their respective ranges of uncertain values. We develop an ensemble of future scenarios by sampling within the ranges using the Latin hypercube sampling method (McKay et al., 1979).

Table 2. Uncertain factors considered to generate future scenarios.

Uncertain Factor	Short Description	Range
Population Growth	Annual population growth rate in each town	(0%, +3%)
Job Growth	Annual job growth rate in each town	(0%, +3%)
Change in the influence of Zurich	Annual change in the portion of Zurich population and jobs that generates trips within the corridor	(-1%, +1%)
Change in Modal Share - Cars	Annual change in the proportion of trips done by car	(-1%, +1%)

As the gravity model works by generating trips based on population and jobs, they were selected as key uncertain factors for the future. Population growth forecasts for the canton of Zurich range between 0.5% and 1.1% per year (Bundesamt für Statistik, 2020). In this paper, we expand the potential range of population growth from 0% to 3% in order to explore a wider set of future scenarios. We use the same range for jobs growth as specific job projections are not available.

During the calibration of the model, the most sensitive parameters were the proportion of Zurich influence on the corridor and the car share, therefore, they were selected as key uncertain factors of the model. The proportion of Zurich influence on the corridor in the future will depend on regional dynamics which are uncertain. Future mode share is also uncertain as societal preferences (e.g., towards active mobility or automated vehicles) can drastically change mobility patterns. We selected a plausible but wide range of potential change of $\pm 1\%$ per year for each factor (i.e., ranging between -26% and $+35\%$ by 2050).

We generated 500 equally plausible scenarios (i.e. without assigning probability distributions) using the Exploratory Modeling Workbench (Kwakkel, 2017). For each of the 500 scenarios generated, a single value in the range was selected and applied to each modelled year until 2050. The factors were assumed to be consistent across all sub-regions. As part of the exploratory modelling, we identified the most relevant uncertain factors by applying feature

selection techniques which are typically used to rank and prioritize the input variables in a model. Table 3 shows the results of the feature selection over the 500 modelled scenarios by using two common algorithms: an extra trees and a random forest algorithm. As a higher score means a higher influence of the factor with respect to meeting the satisficing criteria (as defined in Chapter 2), Job growth and the Change in modal share are the most relevant uncertain factors for the corridor model.

Table 3. Feature selection scores to identify the most relevant uncertain factors.

Uncertain Factor	Algorithm	
	Extra Trees	Random Forest
Population Growth	0.098	0.076
Jobs Growth	0.49	0.54
Change in the influence of Zurich	0.12	0.093
Change in Modal Share - Cars	0.28	0.28

Figure 3 shows the uncertainty map of the performance of the road system over the 500 modelled scenarios for the road infrastructure along the corridor. As the robustness metric, we calculate the fraction of scenarios that meet the satisficing criteria (Herman et al., 2015; Schneller & Sphicas, 1983). In Figure 3, each point represents one scenario as a combination of the uncertain factors. Dark diamonds (48% of the total) indicate adequate performance of the current infrastructure by 2050. Red circles (14% of the total) indicate inadequate performance of the current infrastructure by 2050 (i.e. risk scenarios). Blue squares (38%) indicate adequate performance by 2050 with a reduced road capacity (i.e. opportunity scenarios). The two most relevant uncertain factors, identified in Table 3, are used as the axes of the graph so it is possible to visualize the combination of uncertain factors that generate risks and opportunities. A high increase in mode share for cars and high jobs growth represent high likelihood of inadequate performance with the current infrastructure. On the other hand, decreases in car share and low jobs growth represent high likelihood of adequate performance with reduced road capacity.

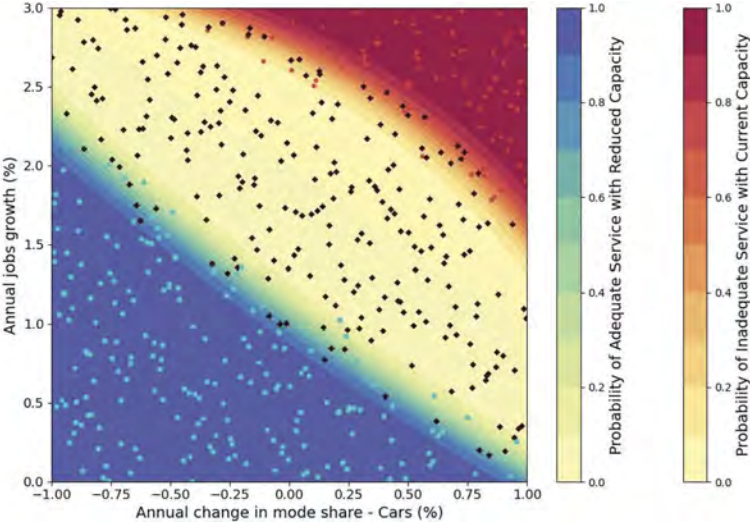


Figure 3. Uncertainty map and scenario discovery results for the future performance of the road infrastructure along the corridor.

Scenario discovery is used to estimate the boundaries of the adequate/inadequate performance regions of the uncertainty map. Some common algorithms for scenario discovery are

Patient Rule Induction Method (PRIM) and Classification and Regression Trees (CART), however, one limitation of them is that they divide the space with boundaries orthogonal to the axes (Reed et al., 2022). Given that the adequate/inadequate boundary in our case study shows a non-orthogonal and non-linear shape, we use logistic regression, as the classification algorithm, for the scenario discovery (Hadjimichael et al., 2020). Figure 3 shows the classification as colored regions according to the probability of obtaining risk and opportunity scenarios in the uncertainty map.

Exploratory modelling techniques help identify likely risk and opportunity regions of the uncertainty map and therefore, shed light on which combinations of uncertain factors require particular attention of infrastructure planners. For this paper, we use the expansion of the road infrastructure capacity as the only intervention to reduce delays and meet the satisficing criteria in the risk regions. We use the reallocation of road capacity (i.e., for others uses) as an intervention in the opportunity regions. The model was rerun by targeting expansions and reallocations to be deployed in the risk and opportunity regions in Figure 3. As road expansions have a considerable time from planning decisions to implementation (assumed to be 4 years in this case), planners need to decide well in advance of reaching inadequate performance (e.g., congestion). The triggering of expansions is modelled as a simple decision rule of expanding 10 lane-kms of capacity (approx. a double lane road between any two nodes in the corridor) every time the corridor reaches 75% of road capacity (i.e., the maximum flow in the fundamental diagram). The triggering of road reallocations is also modelled as a simple decision rule of reallocating 10 lane-kms of capacity when the road capacity use is lower than 60%. The decision rules are implemented as function of the traffic flow as the traffic flow is an easily measurable indicator given that several real-time traffic monitoring stations function along the corridor.

The implementation of decision rules to trigger road expansions and reallocations conditional to traffic flows will produce different number and timing of interventions for different future scenarios. Higher travel demands will produce more frequent expansions while lower demands will produce sporadic expansions only, in the risk regions. Higher travel demands will produce sporadic reallocations while lower demands will produce more frequent reallocations, in the opportunity regions Figure 4 shows the uncertainty map for the 500 modelled scenarios with the targeted interventions. Dark diamonds (97% of the total) and red circles (3% of the total) indicate an adequate or inadequate performance by 2050, respectively. Figure 4 shows that the targeted implementation of the expansions greatly increases robustness (i.e. the number of scenarios with adequate performance). The residual number of scenarios with inadequate performance can be tackled by additional targeted interventions or just left untreated if stakeholders consider such a combination of uncertain factors as unlikely to happen. The absence of blue squares indicate that the decision rule was able to reallocate road space in all opportunity scenarios.

4 DISCUSSION

In this paper, we present a simple macroscopic flow model for the road infrastructure in the Dübendorf-Hinwil corridor. The model estimates the number of trips originated and attracted by each town, depending on the population and job numbers, and calculate the average flows, densities and speeds on the road. The model is used to evaluate the robustness of the road in an uncertain future (i.e., the provision of adequate performance under multiple future scenarios). While current performance indicators for transportation planners are numerous including carbon emissions, sustainable development indicators, accessibility or economic impacts, we focus on travel times only as an example. Similar techniques can be applied to evaluate multiple performance indicators and the trade-offs between them in an exploratory manner. Furthermore, while we assume arbitrary satisficing criteria for robustness evaluation purposes, this can be established in planning guidelines or directly elicited from stakeholders.

The model developed in this paper is able to capture some non-linear dynamics between supply of and demand for infrastructure through the fundamental diagram of traffic flow. However, the model can be further expanded to better represent the complexity of the road system along the corridor. For example, the model could be expanded to capture network effects in the region, to consider the different travel modes explicitly, or to include a broader

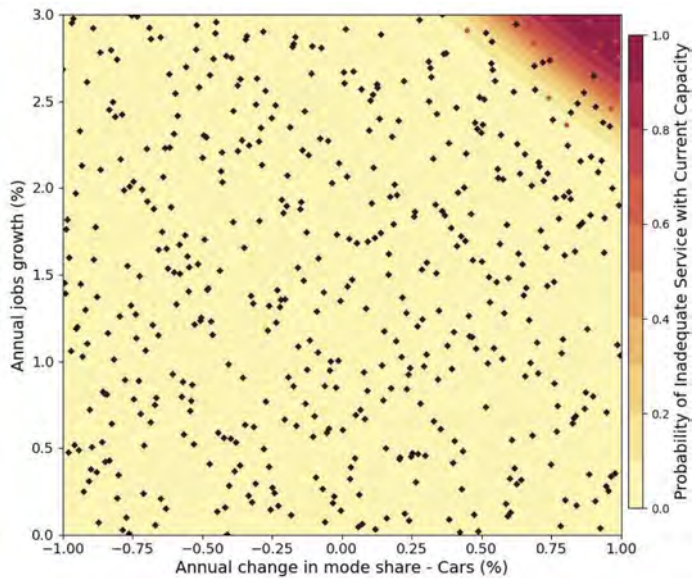


Figure 4. Uncertainty map and scenario discovery results for the future performance of the road infrastructure by targeting expansions and road space reallocations.

range of interventions such as further modifications of the current infrastructure, demand management and other transport policies. Modelling efforts can also be directed to include endogenous feedbacks such as induced travel demand and spatial dynamics in the region.

The paper showcases the importance of considering a wide spectrum of future scenarios when planning transport infrastructure. The set of uncertain factors used in this paper can be further expanded and the development of future trends can be refined for more detailed results. It is the belief of the authors that further refinements and expansions of the modelling side will only bolster the value of the techniques presented in this paper, as exploratory modelling is particularly suitable to navigate complexity and uncertainty.

5 CONCLUSIONS

This paper demonstrates that the use of simulations and quantitative techniques, when displayed in an interpretable way, can provide valuable planning support in infrastructure planning. We produce uncertainty maps in which decision-makers can visually identify risk and opportunity regions. Furthermore, we implemented simple decision rules for expansion and reallocation interventions targeted to the risk and opportunity regions, respectively, on the uncertainty map to increase the robustness of the road.

The results show that the current road infrastructure capacity in the corridor might not be able to provide adequate service (risk) in 14% of the scenarios. Furthermore, 38% of the scenarios can provide an adequate level of service even if the road capacity is reduced by 50% in the A15 federal highway (opportunity). Feature selection and Scenario discovery methods helped identifying the combination of uncertain factors that result in risk and opportunity regions. Therefore, the techniques shown here can help decision-makers to target efforts only in a subset of scenarios. In this case, the implementation of targeted interventions result in the seizing of opportunities and a reduction of the risk scenarios to only 3% of the uncertainty map.

ACKNOWLEDGEMENT

This research was conducted at the Future Cities Lab Global at ETH Zurich. Future Cities Lab Global is supported and funded by the National Research Foundation, Prime Minister's

Office, Singapore under its Campus for Research Excellence and Technological Enterprise (CREATE) programme and ETH Zurich (ETHZ), with additional contributions from the National University of Singapore (NUS), Nanyang Technological University (NTU), Singapore and the Singapore University of Technology and Design (SUTD).

REFERENCES

- Bankes, S. (1993). Exploratory Modeling for Policy Analysis. *Operations Research*, 41(3), 435–449. <https://doi.org/10.1287/opre.41.3.435>
- Bryant, B. P., & Lempert, R. J. (2010). Thinking inside the box: A participatory, computer-assisted approach to scenario discovery. *Technological Forecasting and Social Change*, 77(1), 34–49. <https://doi.org/10.1016/j.techfore.2009.08.002>.
- Bundesamt für Statistik. (2017, May 16). *Verkehrsverhalten der Bevölkerung, Kenngrößen—Schweiz—2015 | Tabelle*. Bundesamt für Statistik. <https://www.bfs.admin.ch/asset/de/2004970>.
- Bundesamt für Statistik. (2020, May 28). *Szenarien zur Bevölkerungsentwicklung der Kantone der Schweiz 2020-2050—Ständige Wohnbevölkerung nach Kanton gemäss 3 Szenarien—2020-2050 | Tabelle*. Bundesamt für Statistik. <https://www.bfs.admin.ch/asset/de/12107013>.
- de Dios Ortúzar, J., & Willumsen, L. G. (2011). *Modelling transport* (4th ed.). John Wiley & Sons.
- Hadjimichael, A., Quinn, J., Wilson, E., Reed, P., Basdekas, L., Yates, D., & Garrison, M. (2020). Defining Robustness, Vulnerabilities, and Consequential Scenarios for Diverse Stakeholder Interests in Institutionally Complex River Basins. *Earth's Future*, 8(7), e2020EF001503. <https://doi.org/10.1029/2020EF001503>.
- Herman, J. D., Reed, P. M., Zeff, H. B., & Characklis, G. W. (2015). How Should Robustness Be Defined for Water Systems Planning under Change? *Journal of Water Resources Planning and Management*, 141(10), 04015012. [https://doi.org/10.1061/\(ASCE\)WR.1943-5452.0000509](https://doi.org/10.1061/(ASCE)WR.1943-5452.0000509).
- Kanton Zurich. (2019). *Strassenverkehrszählung, Oberland-Autobahn (A53) Daten 2019*. <https://maps.zh.ch/>.
- Kwakkel, J. H. (2017). The Exploratory Modeling Workbench: An open source toolkit for exploratory modeling, scenario discovery, and (multi-objective) robust decision making. *Environmental Modelling and Software*, 96, 239–250. <https://doi.org/10.1016/j.envsoft.2017.06.054>.
- Kwakkel, J. H., Haasnoot, M., & Walker, W. E. (2015). Developing dynamic adaptive policy pathways: A computer-assisted approach for developing adaptive strategies for a deeply uncertain world. *Climatic Change*, 132(3), 373–386. <https://doi.org/10.1007/s10584-014-1210-4>.
- Kwakkel, J. H., Walker, W. E., & Marchau, V. A. W. J. (2012). Assessing the Efficacy of Dynamic Adaptive Planning of Infrastructure: Results from Computational Experiments. *Environment and Planning B: Planning and Design*, 39(3), 533–550. <https://doi.org/10.1068/b37151>
- Lyons, G., & Davidson, C. (2016). Guidance for transport planning and policymaking in the face of an uncertain future. *Transportation Research Part A: Policy and Practice*, 88, 104–116. <https://doi.org/10.1016/j.tra.2016.03.012>.
- Maier, H. R., Guillaume, J. H. A., van Delden, H., Riddell, G. A., Haasnoot, M., & Kwakkel, J. H. (2016). An uncertain future, deep uncertainty, scenarios, robustness and adaptation: How do they fit together? *Environmental Modelling & Software*, 81, 154–164. <https://doi.org/10.1016/j.envsoft.2016.03.014>.
- McKay, M. D., Beckman, R. J., & Conover, W. J. (1979). A Comparison of Three Methods for Selecting Values of Input Variables in the Analysis of Output from a Computer Code. *Technometrics*, 21(2), 239–245. <https://doi.org/10.2307/1268522>.
- McPhail, C., Maier, H. R., Westra, S., Kwakkel, J. H., & van der Linden, L. (2020). Impact of Scenario Selection on Robustness. *Water Resources Research*, 56(9), e2019WR026515. <https://doi.org/10.1029/2019WR026515>.
- Milkovits, M., Copperman, R., Newman, J., Lemp, J., Rossi, T., & Sun, S. (2019). Exploratory Modeling and Analysis for Transportation: An Approach and Support Tool - TMIP-EMAT. *Transportation Research Record*, 2673(9), 407–418. <https://doi.org/10.1177/0361198119844463>.
- Reed, P. M., Hadjimichael, A., Malek, K., Karimi, T., Vernon, C. R., Srikrishnan, V., Gupta, R. S., Gold, D. F., Lee, B., Keller, K., Thurber, T. B., & Rice, J. S. (2022). *Addressing uncertainty in multi-sector dynamics research*. Zenodo. <https://doi.org/10.5281/zenodo.6110623>.
- Schneller, G. O., & Sphicas, G. P. (1983). Decision making under uncertainty: Starr's Domain criterion. *Theory and Decision*, 15(4), 321–336. <https://doi.org/10.1007/BF00162111>.
- Statistisches Amt des Kantons Zürich. (2022a). *Bevölkerungsbestand und -wachstum des Kantons Zürich*. Kanton Zürich. <https://www.zh.ch/de/soziales/bevoelkerungszahlen.html>.
- Statistisches Amt des Kantons Zürich. (2022b). *Gemeindeporträt*. Kanton Zürich. <https://www.zh.ch/de/politik-staat/gemeinden/gemeindeportraet.html>.
- Wall, T. A., Walker, W. E., Marchau, V. A. W. J., & Bertolini, L. (2015). Dynamic Adaptive Approach to Transportation-Infrastructure Planning for Climate Change: San-Francisco-Bay-Area Case Study. *Journal of Infrastructure Systems*, 21(4), 05015004. [https://doi.org/10.1061/\(ASCE\)IS.1943-555X.0000257](https://doi.org/10.1061/(ASCE)IS.1943-555X.0000257).



Taylor & Francis

Taylor & Francis Group

<http://taylorandfrancis.com>

SS24: Functional end-of-life framework applied to hydraulic structures
Organizers: E.J. Hamerslag, E. van Baaren & A. Bakker



Taylor & Francis

Taylor & Francis Group

<http://taylorandfrancis.com>

Embedding functional performance in asset management of hydraulic structures

E.J.F. Hamerslag

Ministry of Infrastructure and Water Management, Utrecht, The Netherlands

A.M.R. Bakker

Ministry of Infrastructure and Water Management, Utrecht, The Netherlands

Delft University of Technology, Delft, The Netherlands

ABSTRACT: In the coming decades, the storm surge barriers in the Netherlands will reach their end of the designed life time of 100 years. Therefore, the Dutch storm surge barriers are preparing for major renovations. Next to this, as a result of the expected sea level rise, the hydraulic loads and the number of necessary closures will exceed the original design requirements. This gives urgency to look further than an one-to-one replacement or conservation and it a good moment to include changes in functional requirements. The functional end of life is, however, typically surrounded by large uncertainties. Since storm surge barriers bear multiple functions (e.g. hydraulic safety, the environment, shipping and road traffic infrastructure connection), changes in conditions can lead in several ways to the *functional* end of life. In this paper we explore what aspects should be added to current asset management strategy to include the functional performance of our hydraulic structures.

1 INTRODUCTION

The Netherlands has a long history of protecting the hinterland against high water by building dikes and dams. After the flood disaster of 1953, by far the largest Dutch natural disaster of the 20th century, the Delta works were built to defend the ‘provinces Zeeland’ and ‘Zuid Holland’ for the high tide from the sea. This was done, in addition to the reinforcement of the dikes, by constructing dams and storm surge barriers to close the estuaries and reduce the length of the high water defense system. The complete system consists of five storm surge barriers, two locks and six dams. The first storm surge barrier was built in 1958: the ‘Hollandsche IJsselkering’. The last, the Europort barrier, consists of the ‘Maeslantkering’ and the ‘Hartelkering’, was finished in 1997.

Most barriers were designed for 100 years with the sea-level rise expectations set during construction. These predictions were conservative at that time but are rapidly caught up and under-rated by the latest predictions. This implies that the storm surge barriers may reach their functional end of life well before the originally anticipated date. Therefore, it is important to also include the functional end of life the strategic asset management of the storm surge barriers.

This paper wants to answer the question if the current risk-based inspection method in combination with the Statutory Assessment of water safety is sufficient to determine the end-of-life of storm surge barriers.

2 DUTCH MAINTENANCE AND SAFETY ASSESMENTS

The infrastructure of the Netherlands that is maintained by Rijkswaterstaat (Rijkswaterstaat is part of the Dutch Ministry of Infrastructure and Water Management and responsible for

the design, construction, management and maintenance of the main infrastructure facilities in the Netherlands) has a great diversity. It ranges from floodplains and road(side)s to tunnels, pumping stations and storm surge barriers. To make the right choices risk-driven maintenance is introduced. This is done, depending on the complexity and the consequence of the objects, by qualitative or (semi)quantitative risk analyses. Separately from the risk-driven maintenance, the Dutch water act prescribes its own system for the periodic safety assessments of the main flood defenses. The two systems complement each other in the sense that the one focusses on technical and the other on functional aspects. Yet, both systems are not coordinated with each other. In this section of the paper we give a brief overview of the main aspects of both systems.

2.1 *Risk based asset management*

For the risk based asset management in the Nederland's line objects (roads and waterways) an initial risk analysis is made on which the maintenance is based. And in order to maintain the quality level and to determine the maintenance requirements of all the different objects every six years a technical inspection of all the infrastructural object is made. With the results of this technical inspection the financial reservation for the maintenance and a prediction for the end of life is made. With the prediction for the end of life, major replacement and renovation projects are started in a separate project with separate budgeting. The starting point of the end of life determination is this technical inspection. Afterward the economical choices are made with the option of renovation or replacement. In this process the new functions are combined in a new design or renovation plan. This is an organic and logical way to work with the majority of the infrastructural objects. For the more critical objects it's better to look at the different lifespans separately.

2.2 *The Dutch Water Act*

Since December 22, 2009, the Dutch Water Act merges eight previous water management laws, several water pollution laws and which we will discuss further here the law on flood defenses. The Dutch water act provides two types of standards for each dike trajectory. The lower limit is the actual standard and the (stricter) signaling level is established as an alert for when to take action. According to the Water Act, the flood defenses must be assessed if they meet the safety standards once every 12 years. This is elaborated in the Statutory Assessment Instruments (Van Waal 2018), which states that the uncertainties in load and strength are included in the assessment of the flood defenses.

When the dike or object meets the requirements for signaling value the barrier is approved. If the signaling requirements are not met, a plan must be drawn up to meet them. This signaling value is typically a factor 3 higher than the lower limit. In this way, the sea level rise is implicitly anticipated for.

If the barrier meets the requirement of the signaling value, it has to be proved it will stay that way through good management, translated from Dutch it is called 'duty of care'. This can be done by a good maintenance plan for dikes and simple structures. For more critical structures by the substantiation of the reliability based maintenance, with the aim that everything remains in good condition until the end of its life.

2.3 *The National Delta Program*

Besides the management and the Dutch Water Act, the Delta Program is a national program of the Dutch government that describes how to maintain a the climate-resilient and water-robust design of the Netherlands. How do we protect the Netherlands against flooding and how do we ensure sufficient freshwater? And how do we ensure a water-robust and climate-proof design. The Delta program provides qualitative and quantitative information about

Table 1. Overview of the rating categories of the WBI.

Cat.	Designation of test assessment category per subject per test track	Limit category $P_{f,dsn}$ = probability of failure per section (section or structure) [1/year] $P_{eis;sig}$ = signaling value [1/year] $P_{eis;ond}$ = lower boundary [1/year] $P_{eis;sig;dsn}$ = probability of failure [1/year]
I _v	Sufficiently wide of the signaling value	$P_{f,dsn} < 1/30 P_{eis;sig;dsn}$
II _v	Meets the signaling value	$1/30 P_{eis;sig;dsn} < P_{f,dsn} < P_{eis;sig;dsn}$
III _v	Meets the lower limit and possibly the signaling value	$P_{eis;sig;dsn} < P_{f,dsn} < P_{eis;ond;dsn}$
IV _v	May meet the lower limit and/or the signaling value	$P_{eis;ond;dsn} < P_{f,dsn} < P_{eis;ond}$
V _v	Does not meet the lower limit	$P_{eis;ond} < P_{f,dsn} < 30 P_{eis;ond}$
VI _v	Well below the lower limit	$P_{f,dsn} > 30 P_{eis;ond}$
VII	No judgment yet	

climate, water systems, water use and land use in different scenarios. With the purpose of a robust nation resilient to water related challenges in 2050 and 2100. The Delta Scenarios are based on the IPCC predictions which now predict stronger increases than were initially expected (Wolters). The Delta Scenarios will be updated in 2023 on this basis.

With the help of the scenarios and the forecast of the IPCC, the delta program has come to realize that the functional end of life of the storm surge barriers may be reached before 2050. The delta program has therefore initiated a study into the functional end-of-life of the Maeslant barrier, no results of this study have been produced yet.

2.4 Discussion current asset management and assessment strategies

The current asset management process does not pro-actively include changes in functional and performance requirements. The functional requirements are only assessed when the technical state requires renovation or replacement. This seems adequate for relatively simple, non-critical structures, as temporarily reduced performance has only manageable consequences for the greater network. For critical structures, however, replacements may take much more time and their reduced performance may have large consequences for the overall functioning of the network.

For flood defenses, potential future changes in the safety requirements or hydraulic loadings are implicitly accounted for by the introduction of the signaling safety level. The 12 year assessment cycle is likely to be sufficient for dams and dikes. For critical hydraulic structures this is however questionable, since they typically bear many other functions and their replacement can take several decades.

3 END OF LIFE INFRATRUCURAL OBJECTS

For the determination of the end of life of the objects, Rijkswaterstaat has identified three different ways for an object to reach its end of life, corresponding with the used asset management. These are:

Functional, this is determent by the answer to the question if the object still fulfills the functional demands

Economical, this is determent by the costs to retain the object

Technical, this is determent by the initial expected end of life and the condition of the object
 The definitions Rijkswaterstaat uses are given in Table 2.

Table 2. Definitions for three categories of lifespans.

Technical lifespan
The time period until an asset is no longer able to fulfill its functions according to the original functional requirements due to deterioration of non-replaceable components or the use of outdated technologies.
Economical lifespan
The time period over which the costs of owning and operating an asset are still less than the costs of equivalent alternatives. With equal functional requirements
Functional lifespan
The time period during which an asset complies with the functional requirements. The end of the functional life could be reached due to changing physical conditions, societal developments, or altering functional requirements.

For a timely anticipation of the end of life of critical hydraulic structures requires the combined assessment of all types of end of life.

3.1 Procedure technical end of life

The technical end of life of an object will be predicted by its designed lifespan and will eventually be determined by the inspection of the object. When the end of life is imminent the actions that can be taken are threefold:

- (1) The functionality of the object can be reduced, for instance a reduction of the load on a bridge or the reduction of the speed limit on a highway.
- (2) Or one could strengthen the bridge with an emergency solution or with an renovation program.
- (3) And the last option is a replacement of the object.

The choice for renovation and the replacement of the object is re-evaluated after each inspection. Inspections help plan the necessary work and there will be time to take the appropriate action.

Actually for the technical end of life can be prolonged with an technical solution and this can be done endlessly, there is always a technical solution. The boundary here is not defined by the technical possibilities but by the economic value or changed desires.

3.2 Procedure economical end of life

The economical end of life will submerge when the costs of maintaining will rise to a point that it is not justifiable anymore to maintain the structure with the required expenses. For the Dutch infrastructure after each technical inspection, the EELI 'Economical End of Life Indicator' is automatically determined by the results of the inspection. The Economic End of Life Indicator (EELI) is determined by the sum of the cost of future periodic replacement and current maintenance costs of the object divided by the sum of the costs of a new construction and maintenance costs of the new object 'formula 1' (Bakker 2016).

$$EELI = \frac{\text{future periodic replacement} + \text{current maintenance costs}}{\text{new construction} + \text{periodic replacement} + \text{maintenance costs new object}}$$

Formula 1 determination of the EELI

An EELI of 0,8 to 1,0 indicates that its becomes uncertain if the object is economically sustainable. With this indicator it's easy to make a first selection what objects will be reviewed with a more in-depth study to decide if maintaining the object is still economically justified. As already mentioned, the technical end of life can be prolonged endlessly, but with the technical information the economic end of life can be determined. With this information the schedule of the major structural project can be made.

3.3 Procedure functional end of life

The functional end of life is determined by changes in the functional and performance requirements of the network and other demanded functional changes, like changes of the law. All the Dutch objects have, in addition to all building standards, functional requirements which are usually set for an agreed capacity, availability and reliability. A change in the agreed capacity, availability and reliability, is a decision for change of network functionality, this is almost always a political choice. If the choice is made to change the requirements of a network link all the objects must comply with these requirements and all the objects reach their end of functional life. Although the objects still comply with the original technical requirements.

For instance, the road network is overcrowded, the functional requirements has changed overtime. Here there is a choice if we want to fulfill the new requirements or exempt more traffic jams, which is a political choice. If the politics want to reduce the traffic congestion, the traffic links have to be studied with the accompanying objects. In this case it is a political decision to improve the function.

This is the case with road networks and waterways. This will not be the case with high water safety objects. This is because of the Dutch water act that prescribes safety requirements, so that the technical requirements automatically grow along with the hydraulic loads. A flood defense can therefore be in perfect condition to withstand the original design loads, but still no longer meet the unchanged statutory safety requirements because the design loads have increased.

For instance a dike is in perfect condition but the waves pounding on the dike are increased. The dike can't fulfill its safety water safety task and has to be strengthened. This is in the Nederland's obliged by the water act and must be carried out.

The storm surge barriers are specials in this case and will be discussed in chapter 4.

4 END OF LIFE FOR STORM SURGE BARRIERS

Storm surge barriers are special objects for the reason that the decision to build a storm surge barrier is not only made to ensure water safety. If the storm surge barrier had no other function than high water safety the building of a dam would be sufficient. There are always other aspects that come into play. Some of these aspects for example are, an open passage for shipping, the preservation of an ecological system or the accessibility of an island. This has to be taken in account by determining the end of life of the object. Although the results of the determination of technical and the economical end of life give similar results as the other objects, for the functional end of life of the storm surge barriers this is different.

First thing is that the hydraulic conditions change and will become greater than the initial predicted conditions. The effect will be on all the functions the storm surge barriers end of life. The consequence of this is that the end of life of a storm surge barrier isn't one end of life point but for every function there will be an end of life. Choices what function requirements are mandatory and which one not have to be determent and choices eve to be made.

For example a storm surge barrier has a functional description to close with a chance of failure of 1/1000 years and has to close at a certain high water level. In the design stage the prediction is that this would only occur in the winter, the storm period. Maintenance is done in the summer when there is no risk of high water. While in maintenance the barrier will be secured and fixated by a beam, while not obstructing the waterway (one of the design requirements) and the maintenance work can be done. This way in the summer the chance of failure will be greater than 1/100 years, this is no problem because no summer storm is expected. Till the end of the technical life cycle there are no problems to be expected. Unfortunately sea level rise is accelerated and the chance of closing in the summer period is imminent. The normal procedure of blocking the barrier while maintaining is not possible any more. The structure is still strong enough in this example the functional requirement change is dominant.

The above example suggest there is no other option and the life cycle of the storm surge barrier can't be extended, this is true if not all functional requirements are reevaluated. By

reassessing all the functional requirements and reevaluating all the consequence of not only the object but of the whole system affected by the storm surge barrier. And mitigating measures can be made were is has the best result, see Figure 1(Klatter 2019).



Figure 1. Overview of scenarios consequences of storm surge barrier functionality due to sea level rise.

As can be seen in Figure 1 a sea level rise can have several direct consequences, with the several subsequent functional consequences with the mitigating measures, this also implies that there is not one solution but multiple and the options are not only found in improving the object.

If we continue with the previous example, in the summer there is not a storm free period anymore. This influence has functional consequences for instance in the functions of shipping, aging and maintenance. And one must define the consequences is the safety of the hinterland. The consequences of a summer storm can be less than the winter storms. For example only buildings outside the dike could be flooded. Are there hinterland mitigating preventive or corrective measurements possible. An evacuation plan can be made and dikes can be strengthened.

We now only look at the function water safety, the key can be in the other functions the storm surge barrier has. We return design of the storm surge barrier, what were the functions and are they still of importance. For instance the storm surge barrier is built with the base of an open waterway. With the progress of time, the settings change. The reasons of the open waterway can be diverse, in this case we take only shipping. It must be determined all requirements are still opportune. For instance shipping can be less important than originally expected or a detour is possible. We could also be that the open waterway also has an ecological need. And it has to be researched if the waterway has to be opened all the way or can be closed for a longer time. These options open opportunities to maintain the storm surge barrier for a longer time.

The example shows that the functional requirements can't be viewed separately and a functional end of life can't be given on one of the functional requirement. It's a combination of the different requirements. With the example you can also conclude that the different requirement are also not of the same importance and with all the functional requirements you have to take all the functional requirements and the influence for the hinterland into account.

Commissioned by Rijkswaterstaat an end of life study of the 'Hollandsche IJssel' storm surge barrier is made(Vader). This study states the following: 'The Hollandsche IJssel storm surge barrier is designed to last another 40 years, but replacement or renovation may be needed sooner than anticipated due to factors such as climate change and societal developments'. The study indicates that with various sea level rise projections and the combination of the performance levels expressed the remaining life of the Hollandsche IJssel barrier were obtained. The study found that the end of life of the storm surge barrier was significantly shorter than originally designed. The study concluded that even with a moderate sea level rise scenario, there is a significant probability that the end of life of the barrier could be reached within 20 years. The storm surge barrier is technic and economical not for long at its end of

life. With this study mitigating measures have to be re researched in the coming years to ensure the safety of the hinterland.

5 CONCLUSION

The end of life of most objects is determined by technical factors which often can be solved technically. The main factor is the technical solution is still financially viable. Therefore the economic factors become leading and the economic lifespan is decisive for predicting the end of life. The EELI is a good indicator to use in these cases.

For storm surge barriers the functional lifespan is a main factor for the determination of the end of life. The acceleration of the high water level rise is the main factor of the end of life of the storm surge barriers, and can significantly shorten the life span of all storm surge barriers.

The statutory assessment of flood defenses is a good instrument for a test whether it meets the requirements and a guarantee that the quality remains guaranteed with the maintenance.

As observed the water level rise can have surprisingly functional consequences. Due to the complexity of the functional consequence and the different mitigating measures, it will need time to get to an acceptable solution.

As indicated, the end of the life of barriers depends on the functional requirements of the barrier, it has to be clear whether all requirements, that were initially established, are still valid and whether the water system has not changed compared to the period of construction. It is therefore recommended to verify all functional requirements of the barriers at regular intervals, my proposal is to carry this out every 12 years in parallel with the safety assessments. And it need to be studied if the signaling value is sufficient for the storm surge barriers and other constructions that are hard to replace which have major consequences in case of failure.

REFERENCES

- Bakker, J, 2016 Life-Cycle of engineering Systems: Emphasis on Sustainable Civil Infrastructure, Proceedings of the Fifth International Symposium on Life-Cycle Civil Engineering (IALCCE 2016), Delft, Balkema
- Klatter, L. Prognoserapport 2019, 2019, Utrecht, Netherlands Rijkswaterstaat
- Vader, H. Assessing the remaining life of the Hollandsche IJssel storm surge barrier, 2021, Delft, TUDelft
- Van Waal, H. Basisrapport WBI 2017, 2018, Delft, Deltares
- Wolters, H, Deltascenario's voor de 21^e eeuw hoofdrapport, 2018, Utrecht, Deltares

Assessing the functional end of life of critical hydraulic structures in The Netherlands

A.M.R. Bakker

Ministry of Infrastructure and Water Management, Utrecht, The Netherlands
Delft University of Technology, Delft, The Netherlands

E.S. van Baaren

Deltares, Delft, The Netherlands

E.J.F. Hamerslag

Ministry of Infrastructure and Water management, Utrecht, The Netherlands

C.J.J. Bodelier

Delft University of Technology, Delft, The Netherlands

ABSTRACT: Next decades, many hydraulic structures in the Netherlands will reach their end of life. Timely mitigation requires accurate estimates of the end of life. This appears however hard since many external drivers and multiple functions may lead in many plausible combinations to insufficient technical or functional performance. As a consequence, a complete integrated assessment is rather labour intensive and time consuming. This study shows a quick-scan of the end of life of five storm surge barriers and three other critical hydraulic structures in the Netherlands. The quick-scan reveals that sea-level rise is the major driver for the end of life of most coastal hydraulic structures since it impacts both the free discharge capacity and the flood protection function. Yet, the strategy to adapt the river delta to climate change may be even more important. Future developments are however such uncertain that the life time assessments may prove especially useful for the exploration of adaptive asset management strategies and to a lesser extent as an accurate planning tool.

1 INTRODUCTION

The Netherlands are currently preparing for a major replacement and renovation of large parts of their aging infrastructure as many objects are approaching their technical or economic end of life.

The planning and management of this massive replacement task ideally builds on accurate estimates of the end-of-life. For hydraulic structures, the decision to replace may also be triggered by changes in requirements or loadings as a result of socio-economic developments and/or climate change (Klatter et al. 2019, Bredeveld & Kramer 2019). In those cases, it is the (perceived) insufficient functional performance that determines the end of life.

Critical hydraulic structures typically bear multiple functions such as protecting against flooding, facilitating navigation and enabling the discharge of rivers and precipitation. The performance of these functions might be affected by divergent external drivers. End of life assessments therefore require a systematic approach that ensures that all pathways that might lead to the end of life are assessed (Vader et al. in press, Van Baaren et al. 2019).

Recently, Vader et al. (in press) proposed a four step ‘top-down’ approach for the systematic assessment of the end of life of storm surge barriers in order to identify the dominant pathways. First, clear and unambiguous definitions of the different life span concepts (technical, economical

and functional) should be set to avoid confusion in the subsequent steps. Second, a functional analysis and physical decomposition are performed. Third, the relevant external drivers and their impacts on the technical state and the different functions are listed. And fourth, the most important external drivers and pathways that may lead to the end of life are identified.

The usefulness of the framework is convincingly demonstrated by means of a case study with the oldest storm surge barrier in the Netherlands, the Hollandsche IJssel barrier (HIJK). Yet, the framework is rather labour intensive and a full assessment of all Dutch storm surge barriers and other critical hydraulic structures may require considerable time. Therefore, this paper presents a quick-scan in order to explore to what extent end of life assessments of different hydraulic structures reveal common pathways to the end of life that deserve more attention. The quick-scan assesses the end of life of five storm surge barriers, a discharge sluice, a flood gate and a pumping station by loosely applying the framework of Vader et al. (in press).

2 METHOD

In this study we adopt the same life time concepts as defined by Vader et al. (in press).

- The technical life is the time period over which an asset is able to fulfil its functions according to the original requirements before it must be replaced due to deterioration of non-replaceable components or the use of outdated technologies.
- The functional life is the time period during which an asset complies with the functional requirements, such as the exceedance frequency of the critical water level or the acceptable number of closures.
- The economic life is the time period over which the costs of owning and operating an asset are still lower than the costs of equivalent alternatives.

Since this quick-scan mainly focusses on the functional end of life, the system analysis is restricted to a functional analysis (see section 3). Furthermore, explicit performance requirements are not determined as the purpose of this assessment is only to identify the most threatened functions and the major drivers that may cause insufficient functional performance. Instead, it is assumed that the structures more or less comply with the current requirements and can be adjusted for small changes in requirements or loads.

The analyzed physical drivers are based on Vader et al. (in press) complemented by a recent, first interpretation of the Sixth Assessment Report of the IPCC (2021) for the Netherlands by the Royal Netherlands Meteorological Institute (KNMI, 2021). For the socio-economic developments this study uses the four principle adaptation strategies to sea-level rise as recently presented by the Dutch Delta Program (Van Alphen 2022, Haasnoot & Diermanse 2022).

3 SYSTEM ANALYSIS OF HYDRAULIC STRUCTURES

In this study we assess the end of life of five storm surge barriers, one major discharge sluice, a flood gate and a pumping station (Table 1 and Figure 1). Storm surge barriers are partly movable barriers that only close at extreme storm surges to keep the water levels behind within acceptable/safe limits and such to protect the hinterland against flooding (Mooyart & Jonkman, 2017). The Netherlands count five storm surge barriers that were constructed between 1954 and 2002. The Hollandsche IJssel barrier (HIJK), the Eastern Scheldt barrier (OSK), Maeslant barrier (MK) and the Hartel barrier (HK) protect the southwestern delta against extreme storm surges from the North sea and the Ramspol barrier (RK) protects an area in the eastern part of the Netherlands against surges from Lake IJssel.

The Haringvliet sluices (HV) also play an important role in the flood protection of the South-western delta. At low tide, they enable the free discharge of the Rhine and Meuse rivers into the North Sea, while they prevent the water of the North Sea to flow back during high tide.

Floodgate Ravenswaaij (FGR), is a 80m wide vertical lift gate in between the Lek (one of the Rhine branches in the Netherlands) and a reach of the Amsterdam-Rijn Canal. Like storm

Table 1. Main characteristics of the assessed hydraulic structures.

Structure name (abbreviation)	Type	Gate/pump type	Design life
Hollandsche IJssel barrier (HIJK)	Storm surge barrier	Double lift gate (80m)	1958-2058
Haringvliet sluices (HV)	Discharge sluices	17 Tainter gates (56.5m)	1971-2071
Eastern Scheldt barrier (OSK)	Storm surge barrier	62 lift gates (42m)	1986-2136
Maeslant barrier (MK)	Storm surge barrier	2 floating sector gates (360m)	1997-2097
Hartel barrier (HK)	Storm surge barrier	2 lift gates (98m, 48m)	1997-2097
Ramspol barrier (RK)	Storm surge barrier	3 inflatable rubber gates (80m)	2002-
Floodgate Ravenswaaij (FGR)	Flood gate	Lift gate (80m)	1978-2078
Pump-weir complex IJmuiden (PWIJ)	Pump	4 Stork pumps (40m ³ /s)	1975-2025
		2 Nijhuis pumps (50m ³ /s)	2004-2054
	Weir	7 movable weirs	2040-

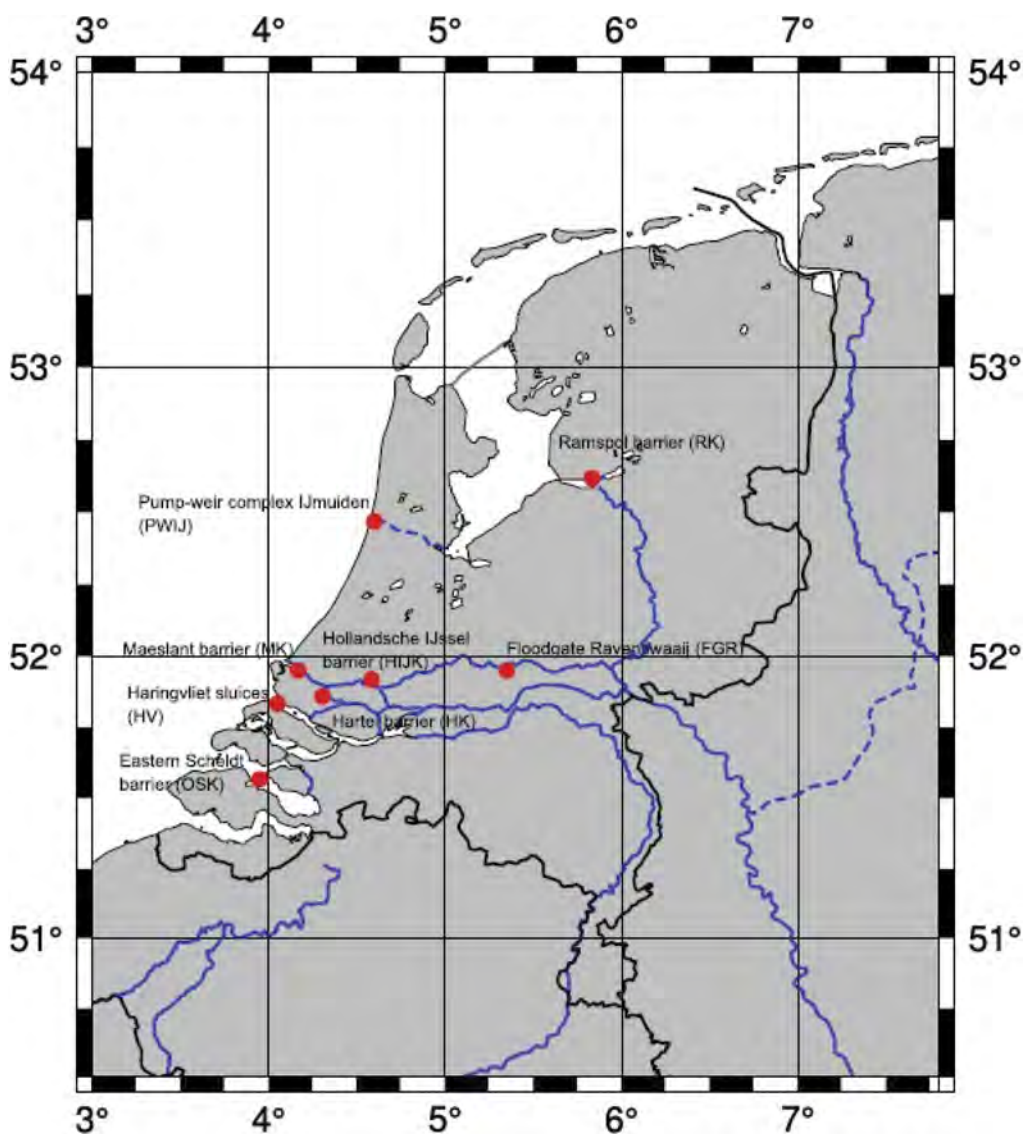


Figure 1. Overview of the assessed hydraulic structures.

surge barriers, the floodgate is open under normal conditions and only closes in case of extreme river water levels to protect the hinterland from flooding.

The main function of Pump-weir complex IJmuiden (PWIJ) is to manage the water level and quality in the North Sea Canal and Amsterdam-Rijn Canal. The complex separates the canal system from the North Sea, discharges precipitation and excessive water from the surrounding polders and regulates the salt intrusion.

Besides the water management functions, the assessed structures all bear several other functions (Table 2). Navigation is facilitated at or near all structures. The Hollandsche IJssel barrier, Floodgate Ravenswaaij and the Hartel barrier allow free passage under normal conditions and by means of adjacent navigation locks when closed. The Maeslant barrier and the Ramspol barrier only allow free passage of ships under normal condition and at Pumping-weir complex IJmuiden, the Haringvliet sluices and the Eastern Scheldt barrier ships can only pass through nearby navigation locks. Furthermore, the structures have ecological, monumental/iconic and road functions.

Table 2. Main functions of assessed hydraulic structures.

Function*	HIJK	FGR	HV	GSIJ	OSK	MK	HK	RK
Retain extreme water levels	x	x	x		x	x	x	x
Facilitate navigation	x	x				x	x	x
Provide discharge capacity for polders	x	x	x	x				x
Allow (natural) river discharge			x					x
Provide fresh water	x							
Prevent salt intrusion	x		x	x				
Allow tidal flow	x		x		x			
Provide corridor for fish migration			x		x			x
Provide road connection	x	x	x		x			
Provide iconic/monumental value	x		x		x	x		

* Functions of adjacent and nearby navigation locks are not taken into account

4 FIRST ORDER EFFECTS PHYSICAL DRIVERS

Analysis of the identified functions leads to the same short-list of potentially relevant physical drivers (Table 3.) as found by Vader et al. (in press). This seems logical as the assessed structures are located in nearby and comparable areas and together only serve two additional functions with respect to the Hollandsche IJssel barrier (allow natural river discharge and provide corridor for fish migration).

Careful analysis reveals that sea level rise is *the* dominant driver for changes in the functional performance of the assessed hydraulic structures. Sea level rise will directly increase the exceedance probability of critical levels. It is estimated that a rise of 50-75 cm will increase the exceedance probabilities roughly with a factor 10 and a rise of 100-150 cm with a factor 100 (e.g. Haasnoot et al. 2020). Without adaptation, this has a direct impact on the required reliability (operational, structural and height) and on the number of closures (and consequently on the hindrance for navigation).

Moreover, sea level rise will substantially decrease the capacity and time window for free discharge because the levels at low tide will also rise. For pumping-weir complex IJmuiden it is for instance estimated that 30 cm sea level rise might reduce the free discharge capacity by 90%, which needs to be compensated by sufficient pumping capacity (Van Gijzen & Bakker 2023). For the Haringvliet sluices it will be way more challenging to replace the free discharge capacity by pumps as it needs to discharge the rivers Rhine and Meuse.

Next to sea level rise, precipitation and drought deserve some attention. Precipitation extremes are expected to increase substantially, but this especially concerns local, relatively

Table 3. Identified potentially physical drivers.

Driver	General consequence
Temperature	Extreme temperatures can temporarily reduce the operational reliability. The impact on the hydraulic performance is considered minor since extreme temperatures do typically not occur in stormy conditons.
Precipitation	Increased precipitation extremes may result in higher pump volumes from polders.
Land subsidence	Lowering of the crest height of dikes. Foreseen subsidence is however small compared to projected sea level rise.
Sea level rise	Increase in exceedance probability of critical water levels. Higher number of storm closures. Decrease in free discharge capacity.
High river discharges	Higher volumes to be discharged
Low river discharges	Reduction of (navigation) depth and fresh water availability
Drought	Salt intrusion Dike instability Increase in fresh water demand
CO ₂ concentration	no impact on requirements, use or loads
Wind	minor changes in wind regime expected (KNMI 2021)

short term precipitation (KNMI 2021). Increases in larger scale, multi-day events that are more determinant for the necessary discharge capacity will be more moderate. Also more frequent droughts may urge for substantial system adaptations and potentially increase the importance of the fresh water retention function of the Haringvliet sluices and the Pump-weir complex IJmuiden. However, the direct impacts of sea level rise on the functional performance may be several orders of magnitude and will dwarf the potential effects of the other physical drivers.

5 EFFECTS OF SYSTEM ADAPTATION TO CLIMATE CHANGE

Next to physical drivers, socio-economic developments can seriously affect the functional performance of a hydraulic structure. In the decades to come, the functional performance is likely to be dominated by the chosen strategy to adapt to sea level rise.

Recently, the Dutch Delta Program presented four principal adaptive strategies to (accelerated) sea level rise (Van Alphen 2022, Haasnoot & Diermanse 2022). The first strategy ‘Protect-open’ basically is a continuation of the current policy. First and second line flood defenses will be strengthened in line with the changing hydraulic loads while maintaining an open connection with the sea. The second strategy ‘Protect-closed’ focusses on the strengthening of the first line of defense and will close the connection with the sea to prevent higher levels and salinization of the inland water bodies. This strategy will however require enormous pump capacity to drain the rivers Rhine and Meuse (see also section 4). The third strategy ‘Advance’ advocates to extend the present coastline seawards to be able to build more robust flood defenses and create new land and water storage. The fourth strategy ‘Accommodate’ proposes to accept changes and prepare for the ‘living with water’ concept and/or retreat.

The studies argue that the current policy ‘Protect-open’ may be continued up to 1m sea level rise, maybe 2m if the closure levels of the storm surge barriers are heightened. This may, however, require substantial adaptation or even replacement of the current storm surge barriers. For instance, the Maeslant barrier was originally designed for only 25cm sea level rise during its entire design life time and the Maeslant barrier is currently already struggling to meet the strict requirements for the operational reliability and the gradually shrinking time window for maintenance.

In 2014, a group of six experienced Dutch engineers led by Frank Spaargaren proposed to replace the Maeslant barrier by a closed dam with navigation locks, watering sluices and a pumping station in order to anticipate the sea level rise induced challenges (e.g. Dokter et al. 2016). This potential first step towards ‘Protect-closed’ would imply the end of life of the Maeslant barrier, but also substantially impact the remaining life of other hydraulic structures. The Hollandsche IJssel barrier, for instance, is located behind the Maeslant barrier. The replacement of the Maeslant barrier by a closed dam would significantly reduce the impact of sea level rise which could imply the elongation of the functional life. Yet, severe reduction of the extreme water levels could also nullify the flood protection function which would imply the economic end of life. On the other hand, heightening of the target water levels in the southwestern Delta in order to longer benefit from free discharge would immediately increase the functional relevance of the Hollandsche IJssel barrier again.

In contrast to a closed dam, the sea level rise induced challenges of the Maeslant barrier could also be tackled by ‘Advancing’. A recent study of Mooyaart et al. (in review) suggests that a second sea ward storm surge barrier could be cost effective at sea level rise beyond 0.45m. This second, redundant barrier would actually elongate rather than end the remaining life of the Maeslant barrier.

It is clear, that every step in the system adaptation can have enormous impact on the remaining functional and economic life of hydraulic structures. It is however impossible to predict which adaptation step will be implemented first as this is a political decision. This means that accurate functional end of life estimates are actually impossible for more than several decades ahead.

6 CONCLUSIONS

The quick-scan presented in this paper suggests that sea-level rise is *the* determinant factor for the functional end of life of coastal hydraulic structures. It is not expected that a more thorough assessment will identify other physical drivers as the potential effect of sea level rise can be several orders of magnitude larger.

The large uncertainties in future sea-level rise projections also make the functional end of life estimates intrinsically uncertain. Maybe more important are the uncertainties in the exact adaptation pathway to sea level rise (and maybe drought). Many plausible adaptation options exist. Yet, which adaptation option is implemented when is a political choice and the impact on the functional and economic end of life really depends on the implementation details.

Accurate estimates of the functional end of life for more than several decades ahead are not possible under rapidly, but uncertain changing circumstances. Nevertheless, functional end of life assessments may prove very useful for the exploration of detailed adaptation pathways.

REFERENCES

- Breedevelde, J. & Kramer, N. 2019. *Kennisprogramma Natte Kunstwerken Functionele levensduur (final)* Report No. 11200741-079-HYE-0001. Delft: Deltares.
- Dokter, J., Botterhuis, T., Kok, M., & Van Waveren, H. (2016). Adaptation with small steps or a big step? A probabilistic approach of flood risk reduction in the Dutch Delta. In L. Walls, M. Revie and T. Bedford (eds) *Risk, reliability and safety: innovating theory and practice – Proceedings of the 26th European Safety and Reliability Conference, ESREL 2016 (Glasgow, Scotland, 25-29 September 2016)*. Leiden: CRC Press/Balkema.
- IPCC, 2021. *Climate Change 2021: The Physical Science Basis. Contribution of Working Group I to the Sixth Assessment Report of the Intergovernmental Panel on Climate Change* [Masson-Delmotte, V., Zhai, P., Pirani, A., Connors, S.L., Péan, C., Berger, S., Caud, N., Chen, Y., Goldfarb, L., Gomis, M.I., Huang, M., Leitzell, K., Lonnoy, E., Matthews, J.B.R., Maycock, T.K., Waterfield, T., Yelekçi, O., Yu, R. & Zhou, B. (eds.)]. Cambridge University Press, Cambridge, United Kingdom and New York, NY, USA.

- Klatter, H.E., Roebbers, H., Slager, J. & Hooimeijer, H. 2019. *Prognoserapport Vervanging en Renovatie (VenR) 2019*. Utrecht: Rijkswaterstaat.
- KNMI 2021. *KNMI Klimaatsignaal'21: hoe het klimaat in Nederland snel verandert*. De Bilt, KNMI.
- Mooyaart, L.F. & Jonkman, S.N. 2017. Overview and Design Considerations of Storm Surge Barriers. *Journal of Waterway, Port, Coastal, and Ocean Engineering* 143(4): 06017001.
- Mooyaart, L.F., Bakker, A.M.R., Van den Bogaard, J.A., Rijcken, T. & Jonkman, S.N. in review. Economic Optimization of Coastal Flood Defence Systems including Storm Surge Barrier Closure Reliability. *Journal of Flood Risk Management* in review.
- Vader, H., Bakker, A.M.R., Jonkman, S.N., Van den Boomen, M., Van Baaren & E., Diermanse, F.L.M. in press. A framework for assessing the remaining life of storm surge barriers. *Structure and Infrastructure Engineering* in press
- Van Baaren, E., De Jong, M., De Bel & M., Bredeveld, J. 2022. *Raamwerk beslismomenten VenR Stormvloedkeringen – Gecombineerde functionele en technische prestatie en economische afweging met case Hollandsche IJsselkering* Report No. 11206063-000-HYE-0002. Delft: Deltares
- Van Gijzen, L. & Bakker, A.M.R. 2023. Determining the future functional requirements of a pumping station with the help of data analysis. In IALCCE2023 (eds), IALCCE 2023 proceedings (in press)

Framework functional performance hydraulic structures

E.S. van Baaren, J. Breedevelde, N.J.M. ten Harmsen van der Beek, T. O'Mahoney & N. Kramer

Deltares, Delft, The Netherlands

H. Berger & A. Barneveld

Ministry of Infrastructure and Water management, Utrecht, The Netherlands

ABSTRACT: In the life-cycle of infrastructure assets, distinction can be made between technical, economical and functional performance. When the performance does not meet the requirements anymore, end-of-lifetime is reached. By considering functional aspects of hydraulic structures -like meeting the requirements on flood protection, navigation, water availability or ecology- an integral analysis for the life-cycle can be performed. The framework functional performance assesses the impact of climate and socio-economic changes and (future) policy decisions on the functional performance of hydraulic structures in time. This framework can be applied to systematically 1. Identify the current functional performance; 2. Identify end-of-life tipping points and 3. Assess renewal and renovation options. It was applied to one of the steps in the preparation process for the renewal of the weirs in the Dutch part of the river Meuse. Since functional lifespan is rarely quantified, our next step is the development of (rapid assessment) tools to quantify the functional performance in time for other structures, drivers and functions in order to fill the framework and make it applicable for policy analysis.

1 INTRODUCTION

Physical infrastructure is vital for a society. As in many countries, much of this infrastructure in the Netherlands was built in the 20th century. Since then, the performance of the infrastructure required to keep our country safe, accessible, and habitable has been maintained by means of intensive management and maintenance.

In the coming decades, the loads and demands on infrastructure networks, particularly in delta areas such as the Netherlands, are expected to change dramatically. Nevertheless, existing components such as structures in the current infrastructure constitute an excellent basis for ongoing construction (even in uncertain future scenarios). However, long-term exposure to degradation has rendered components outdated. As a result, the parts with the longest lifespan will soon be reaching the end of their service life. Moreover, the networks are being used more intensively and are already being affected by developments in the fields of climate (adaptation), sustainability and social-economics. This means that simply maintaining the current performance level will require extra effort from managing authorities.

To make a well-considered and substantiated investment decision about immediately renewing (or first extending the lifespan) of infrastructure components, asset managers require essential information about its current condition and the risks involved in different decisions. Methods are needed to support the asset managers regarding complex decisions on renewal and renovation of infrastructure components, as part of a strategy towards a future-resilient network. The objective of this paper is to provide a framework how to consider functional performance of hydraulic structures in an integral and structured way.

In the life-cycle of infrastructure assets, distinction can be made between technical, economical and functional performance (how well a structure fulfills its requirements). When the performance does not meet the requirements anymore, end-of-lifetime is reached. Slightly different definitions are used for the technical, functional and economical end-of-lifetime, for example Hermans (1999), Hertogh et al. (2018) and Vader et al. (2023). Here, we consider technical end-of-lifetime as the moment that an asset is no longer able to fulfill its functions due to deterioration of non-replaceable components or the use of outdated technologies. Functional end-of-lifetime is considered as the moment that an asset does not meet the functional requirements, such as the exceedance frequency of the critical water level or the acceptable number of closures. End of technical lifetime thereby always leads to end of functional lifetime. Economic end-of-life is the moment that the costs of owning and operating an asset are higher than the costs of equivalent alternatives.

Technical end-of-life is often taken into consideration in the Netherlands, and almost always at least a theoretical value is available (Klatter et al. 2022). Technical performance of structures is monitored regularly. Functional lifespan is something which is rarely quantified, and functional performance is rarely monitored. By considering functional aspects of hydraulic structures -like meeting the requirements on flood protection, navigation, water availability or ecology- an integral analysis for the life-cycle can be performed for existing and to-be-build hydraulic structures.

Although this paper focuses on structures in the water infrastructure – in other words, hydraulic structures, retaining walls (e.g. quay walls) and the associated structural parts - the method functional performance must also be applicable to decision-making for other infra-structural components.

2 METHOD FUNCTIONAL PERFORMANCE

2.1 *Functional lifetime*

Various studies have already been carried out in the Netherlands into tipping points in the system and the infrastructure (eg Kwadijk et al., 2010). The study for the Thames Barrier is an international example of these tipping points (Hall et al., 2019). The method of using decision points or tipping points has been further developed in recent years for hydraulic structures, often within large, multi-year programs such as VONK (Iv-Infra/HKV, 2014; HKV, 2015), ROBAMCI (Risk and Opportunity Based Asset Management for Critical Infrastructures with various case studies; Robamci.nl) and the Knowledge Program on Hydraulic Structures (Dutch abbreviation KpNK, Bredeveld & Kramer, 2019). Functional lifespan had been included in a limited amount of policy documents, the IMA (including lock capacity bottlenecks in various scenarios, Rijkswaterstaat (2021)) is one of the examples.

An exploratory study into the functional lifespan of hydraulic structures has been carried out in KpNK. Discussions in that context about a (practical) method for determining end of functional life have led to an inventory of available knowledge, models and information (KpNK, 2018).

KpNK (2018) argues that the need to define a generic transparent Functional Lifetime Method to determine the end of functional lifespan. Subsequently, there was a need for a practical, preferably generic, working method in which the relationship between the (future) functional performance(s) of an object and the subsystem of which it is part is included. To this end, the Toolbox Functional Lifespan has been drawn up (Bredeveld & Kramer, 2019).

This Toolbox is intended to facilitate the estimation of the end of functional life for individual structures and groups of structures at various levels of detail. The least detailed level concerns an elaboration of the Functional Lifespan-light (MFL-light) Method, which is a simplified qualitative assessment based on expert judgment that can be used to determine the points of attention for a more detailed assessment of end-of-functional life. This further analysis can take place based on existing information (medium) or by performing additional calculations with prediction models (heavy).

2.2 Framework functional performance

In Bredeveld & Kramer (2019) the Toolbox Functional Lifetime was developed to select the main drivers (sea level rise, changes in precipitation etc.) for the set of functions of a hydraulic structure. This methodology was applied to several cases to identify the end-of-functional-lifetime based on expert judgement.

In (Van Baaren et al 2022a; Van Baaren et al 2022b) this research continued into the development of the Framework Functional Performance (Figure 1). Instead of indicating a fixed end of lifetime, functional performance, defined as how well a structure fulfills its functions, can change in time. The framework functional performance assesses the impact of climate and socio-economic changes and (future) policy decisions (drivers in Figure 1) on the functional performance of hydraulic structures in time (number 4 in Figure 1). Information at structure and system level about the functions, acreage and requirements are needed to derive this performance (number 3 in Figure 1). If the functional performance in time does not meet the requirements, bottlenecks can be identified. Which can lead to new alternatives for Renewal and Renovation (number 2 in Figure 1) or a change in guiding principles or requirements (number 3 in Figure 1). Translation of the functional performance into input for the economic assessment can be used for an economic assessment. In case of Renewal and Renovation of infrastructure we foresee several iterations from the first end-of-life signal towards a system analysis towards the planning phase for the new infrastructure. Depending on the answers needed in that phase, the Method Functional Performance light, medium or heavy can be used. Every step is a selection of relevant parameters (drivers, functions, options), so the number of functions and drivers decreases from light towards medium towards heavy.

Drivers can influence the functional performance, so this performance is not (always) constant over time. For each function, the future functional performance could be described, provided requirements or goals are described for the hydraulic structure for that function.

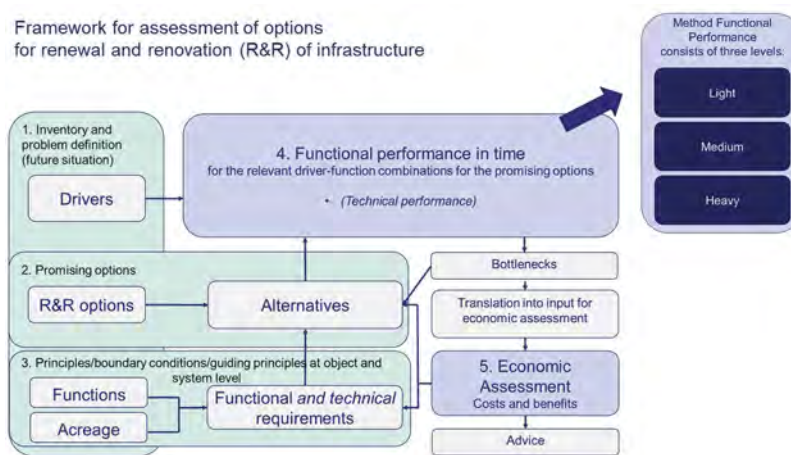


Figure 1. Framework for assessment of options for renewal and renovation (R&R) of infrastructure.

2.3 Applications

This framework can be applied to systematically:

1. Identify the current functional performance of hydraulic structures

For each function, the functional performance could be described, provided requirements or goals are described for the hydraulic structures for that function. The functional performance can be measured at object level, but there is also a wish (Klatter et al., 2022) to add (elements of) the functional lifespan of hydraulic structures to the analysis of the (residual) lifespan. In this application the number of promising options (see step 2 in Figure 1) is limited to one (only the current situation).

2. Determine decision moments for Renewal and Renovation

Decrease in the functional performance can lead to decision moments at which the functional performance of hydraulic structures decreases to such an extent that:

- The end of the functional lifespan of the structure reached; or
- Large investments in management or renovation must be made to maintain the functional performance of the structure at a sufficient level; or
- Large decrease in benefits in the system arise due to a decrease in the functional performance of the structure.

The method is applied to a storm surge barrier are in Van Baaren et al. 2022a and Vader et al. 2023. In this application the number of promising options (see step 2 in Figure 1) is limited to one (only the current situation).

3. Assess renewal and renovation options

After reaching end-of-life of hydraulic structures, assessment of renewal and renovation options is carried out. By quantifying the functional performance for different Renewal and Renovation options, options can be compared. The differences in functional performance between the options can then be translated into benefits in a cost benefits analysis. Requirements for the functional performance are desirable, but without wishes the options can still be compared by translating the differences in functional performance into benefits. See chapter 3.

3 APPLICATION TO THE ASSESSMENT OF OPTIONS FOR RENEWAL

The framework was applied to one of the steps in the preparation process for the renewal of the weirs in the Dutch part of the river Meuse (Van Baaren et al. 2022b). These weirs will soon reach their end-of-technical lifetime.

3.1 Case description

There are 7 weirs in the Meuse in the Netherlands (Borgharen, Linne, Roermond, Belfeld, Sambeek, Grave and Lith) that were built at the beginning of the 20th century. The design life of these weirs is around 100 years. Monitoring and inspections show that the weirs Linne, Roermond, Belfeld, Sambeek and Grave will soon reach their end of life. These five weirs, with outdated Poirée techniques, will have to be replaced. The regional analysis of the Meuse weirs concluded that the current guiding principles, namely water drainage and shipping, will continue to be leading in the future, and that new weirs are required for this. The forthcoming replacement and renovation assignment of the seven weirs on the Meuse is based on the preservation of seven weirs, which will be located at approximately the same location as now.

Most of the time, the weir is closed, and ships pass through the lock. In the case of high river discharge, the weir is opened, and shipping can choose to pass the weir complex via the weir or via the lock. If the river discharge increases even further, the water level will rise further, also on the upstream side of the complex. At a certain point, the water will flow over the lock gates and the lock operation must be stopped. At even higher discharges, the water will partly flow via the floodplains. Ships then only have the option of passing through the weir complex until the river is found to be unnavigable.

3.2 Application framework functional performance

An important question when designing the new weirs is whether they should be navigable at high water, as is currently the case with the weirs at Roermond, Belfeld, Sambeek, Grave and Lith. This is a choice to be made at the system level. However, this does not necessarily mean that the same choice must be made for all weirs. This choice provides a precondition for the design of the weirs in the Meuse. Navigability during high water is one of the important

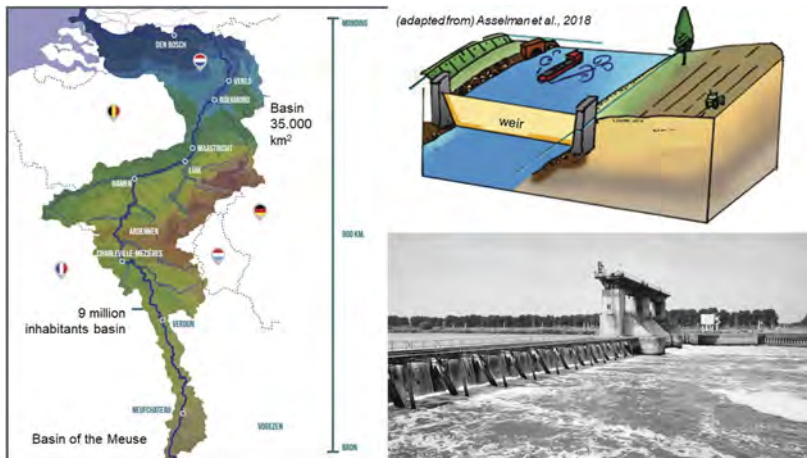


Figure 2. The basin of the Meuse with 7 weirs in the Netherlands (not shown in the map).

decisions that policy must take in the initial phase, a decision that must take into account existing policy documents. This is number 1 in Figure 1, the ‘inventory and problem definitions (future situation)’.

The Knowledge Program for Hydraulic Structures has addressed and answered a number of questions regarding the mapping of current shipping intensities at the various river discharges and future navigability. The developed framework for assessment of options for renewal and renovation (R&R) of infrastructure (Figure 1) was applied to this case study to systematically assess the differences between the alternatives for the new weirs for all functions.

The research conducted focused on 3 alternatives, (number 2 in Figure 1):

1. A navigable weir
2. An impassable weir
3. An impassable weir, combined with an elevation of the lock



Figure 3. Three alternatives for the weirs on the Meuse: a. a navigable weir; b. an impassable weir; c. an impassable weir combined with an elevation of the lock.

The study started with an inventory of the functions of the weir complexes (the weir including the lock, fish passage, bridge and so on) and the underlying requirements/ambitions/ desires for the functions (number 3 in Figure 1). Then the underlying drivers that influence the extent to which these functions will be fulfilled in the future were identified (number 1 in Figure 1). Together with several stakeholders the Method Functional Performance ‘Light’ was applied to this case study, identifying the effects of drivers on the functions of the various alternatives. This was done by means of several workshops and specific interviews with asset owners, hydraulic engineers responsible for the new design, and experts on specific functions. The systematic approach followed shows that whether weirs are navigable or not also influences other functions, which should therefore also be considered in the policy decision on navigability. However, a supported prioritized set of requirements is still lacking, and is very important for an integral analysis of all functions.

Since navigability was one of the priority functions, the functional performance for navigation under the driver climate change was quantified (Method Functional Performance

'Medium' in Figure 1). The focus was on high river discharges because the analysis in the Method Functional Performance 'Light' showed a large distinction in functional performance for this driver between the different alternatives for the weirs. The least and most extreme future climate change scenarios (WH and GL, Dutch scenarios for national climate change) for 2050 and 2085 of KNMI (2014) and a reference scenario for the current climate in the Netherlands were considered, and a translation of these climate change scenarios to a representative dataset of river discharges made by Deltares (2016) was used to quantify the number of navigable days per alternative.

An analysis based on IVS90 shipping data shows that, in the current situation, once the weir has been opened, a large proportion of shipping prefers to pass through the weir rather than passing through the lock that is still operational (more than 90%). The benefits of a weir that can be passed through for shipping partly depend on climate developments and socio-economic developments. Due to a changing climate, the number of days with higher discharge increases, and therefore the number of days per year that a weir is open will increase, which means that the benefits of a navigable weir will also increase. And with an increase in the total value of the ship's cargo, the benefits will also increase. Based on the available scenarios, estimates have been made about the number of days and the duration that shipping can benefit from the navigability. Future (policy) decisions have additional influence on the benefits, but these are so uncertain that they have not been quantified.

4 CONCLUSIONS

Currently, functional performance of hydraulic structures is mainly used to identify the system's tipping points. More detailed information and knowledge on the hydraulic structures and application of the Method Functional Performance can lead to more insights in the renewal and renovation process of hydraulic structures in three settings:

1. Identify the current functional performance of hydraulic structures;
2. Determine decision moments for Renewal and Renovation
3. Assess renewal and renovation options.

A major task of studies awaits Renewal and Renovation of infrastructure. Therefore, a systematic approach is needed that can facilitate the Renewal and Renovation. The approach from this study takes functions, requirements/ambitions/wishes, drivers into account and – through objective analyzes of a combination of datasets – leads to insight into the differences between the alternatives for Renewal and Renovation in a transparent manner. It is recommended to test this data-driven methodology for other (more diverse) alternatives to the weirs and other cases. It is also recommended to further elaborate the functional performance of hydraulic structures for other functions and drivers, and to translate this information into decision information. This creates a data-driven toolbox for functional performance analysis, in order to arrive at a systematic elaboration of alternatives for the major Renewal and Renovation challenge. Since functional lifespan is rarely quantified, our next step is the development of (rapid assessment) tools to quantify the functional performance in time for other structures, drivers and functions in order to fill the framework and make it applicable for policy analysis.

A supported set with prioritized requirements/ambitions/wishes/principles is the basis for deriving the differences between the alternatives. This set is often not available at the level of the structures. Translation from system expectations into structure requirements is challenging and not constant in time. It is important, in the context of traceability and stackability of analysis and decisions, to also keep items with a (at first apparently) low priority. After all, the priority can change during the process.

It is recommended that a good climate change data series will be drawn up and translated into local discharges, water levels and possibly salinity for large bodies of water in the Netherlands as a result of rising sea levels and changing discharges. So that datasets are available with clear user conditions for all situations – dry, average, high and extreme situations. Substantiating the Renewal & Renovation task with data provides insights, clarity and substantiation.

REFERENCES

- Asselman, N., Barneveld, H., Klijn, F., van Winden, A. 2018. Het verhaal van de Maas, De Maas uit balans?.
- Breedevelde, J. & Kramer, N. 2019. *Kennisprogramma Natte Kunstwerken Functionele levensduur (final)* Report No. 11200741-079-HYE-0001. Delft: Deltares.
- Deltares. 2016. Kramer, N., Mens, M. Methode voor het afleiden van een 100-jarige toekomstige afvoerrreeks voor Lobith en Monsin. Memo-kenmerk: 1230078-000-BGS-0001.
- Hall JW, Harvey H and Manning LJ. 2019 'Adaptation thresholds and pathways for tidal flood risk management in London' *Climate Risk Management*, 24, pp.42–58
- Hermans, M. H. 1999. *Building performance starts at hand-over: The importance of life span information*. In M. A. Lacasse & D. J. Vanier (Eds.), *Durability of building materials and components 8: Service life and durability of materials and components* (pp. 1867–1873). NRC Research Press.
- Hertogh, M. J. C. M., Bakker, J., Van der Vlist, M., & Barneveld, A. 2018. Life cycle management in upgrade and renewal of civil infrastructures. *Organization, Technology and Management in Construction: an International Journal*, 10(1), 1735–1746.
- HKV Lijn in Water & Iv-Infra b.v. 2014. Gevoeligheidstest natte kunstwerken (VONK). Rapportage 'methodiek gevoeligheidstest natte kunstwerken'.
- HKV Lijn in Water 2015. Gevoeligheidstest Natte Kunstwerken: Methode Functionele Eindelevensduur. Kwaliteit en toepasbaarheid FLSA-methode.
- Klatzer, H.E. et al 2022. *Vervanging en Renovatie. Prognose voor de periode 2023 tot en met 2050*. Utrecht: Rijkswaterstaat.
- KNMI. 2014. KNMI'14: Climate Change scenarios for the 21st Century – A Netherlands perspective. De Bilt, Version 26 May 2014, KNMI WR 2014-01.
- KpNK. 2018, Kennisprogramma Natte Kunstwerken – Functionele levensduur, Deltares kenmerk 11200741-020, versie concept, januari 2018;
- Kwadijk, J.C.J., Haasnoot, M., Mulder, J.P.M., Hoogvliet, M.M.C., Jeuken, A.B.M., van der Krogt, R. A.A., van Oostrom, N.G.C., Schelfhout, H.A., van Velzen, E.H., van Waveren, H. and de Wit, M.J. M. 2010. Using Adaptation Tipping Points to Prepare for Climate Change and Sea Level Rise: A Case Study in the Netherlands. *Wiley Interdisciplinary Reviews: Climate Change*, 1, 729–740. <https://doi.org/10.1002/wcc.64>
- Rijkswaterstaat Water Verkeer en Leefomgeving (WVL). 2021. Achtergrondrapportage Vaarwegen Integrale Mobiliteitsanalyse 2021.
- Vader, H., Bakker, A.M.R., Jonkman, S.N., Van den Boomen, M., Van Baaren. E. & Diermanse, F.L. M. 2023. A framework for assessing the remaining life of storm surge barriers. *Structure and Infrastructure Engineering*
- Van Baaren, E.S., De Jong, M., De Bel M., Breedevelde, J. 2022a. *Raamwerk beslismomenten VenR Stormvloedkeringen – Gecombineerde functionele en technische prestatie en economische afweging met case Hollandse IJsselkering* Report No. 11206063-000-HYE-0002. Delft: Deltares
- Van Baaren, E.S., Breedevelde, J., Ten Harmsen van der Beek, N.J.M., Kramer, N., O'Mahoney T., Barneveld, A., Berger, H., Helmer, J., Ligtenberg, J. 2022b. *Analyse naar de doorvoerbaarheid van de toekomstige Maasstuwen*. Report No. 11208384-002-HYE-0001 Kennisprogramma Natte Kunstwerken.

Determining the future functional requirements of a pumping-weir station with the help of data-analysis

L. van Gijzen & A.M.R. Bakker

Technische Universiteit Delft, Delft, The Netherlands
Rijkswaterstaat, Utrecht, The Netherlands

ABSTRACT: The pumping-weir complex at IJmuiden plays an important role in the drainage of excess water in the Western Netherlands. Multiple pumps need replacing as 4 out of 6 pumps near their end-of-life term. The optimal replacement strategy critically hinges on the future required pumping capacity. Yet, currently available models are not suited to assess the effect of sea level rise or extremer precipitation events as they ignore certain complexities of the water system. Preliminary data analysis in this paper showed the sensitivities of the system. The required pumping capacity is sensitive to the ability of free discharging during extreme water events. Yet, it is less susceptible to extremer precipitation events. Further research will aim at including more of the water system's complexity in the model. Due to the node-like structure and high availability of data, a neural network modelling approach will probably be suitable.

1 INTRODUCTION

The pumping-weir complex located at IJmuiden functions as a separator between the complex water system of the Amsterdam Rhine Channel - North Sea Channel and the North Sea. Most pumping stations are found in sewage systems or in prevention against urban floods due to heavy rainfall. Yet, not often are they found at the end of a channel system with over 200 access points such as weirs, sluices and local pumps.

The water system situated in the Western Netherlands has been the result of efforts over the last centuries to protect the land from the sea and facilitate navigation at the same time. The result is a channel from the Rhine, via Amsterdam to IJmuiden (North Sea), into which the surrounding low-lying polders excess water (Figure 1). The channel from Amsterdam to IJmuiden was officially opened in 1876, with locks separating the channel from the North Sea. In 1940 the weirs were constructed, through which excess water was discharged and they are still part of the complex today. By 1975 four pumps were added to the complex, to be able to closer regulate the channel's water level and to be able to discharge the water to the North Sea during high tide. Two extra pumps were added in 2004 to increase the discharge capacity. By now, the 4 oldest pumps in the complex are nearing their technical end-of-lifetime and need to be replaced.

The new pumps will need to meet their functional requirements for at least 30 years into the future. Therefore the predicted sea level rise along the Dutch coast plays an important role in determining those future functional requirements. For as the sea level rises, the window for regular discharging through the weirs will get shortened and more volumes will need to be disposed of by means of pumping

Additionally, the extreme rainfall events are expected to get more intense (KNMI, 2014). In terms of precipitation a distinction can be made between the area precipitation and peak rainfall. The area precipitation is expected to increase by 2.5-5.5 % depending on the scenario, which will lead to a similar increase of volumes that will need to be pumped out of the ARC-NSC system. Earlier research has concluded that the current pump capacity will suffice to process this increase



Figure 1. Left) System overview of the NSC-ARC (in dark blue). The catchment area is pictured in green (direct) and yellow (indirect), adapted from (Rijkswaterstaat, 2019). Top right) Pumping-weir complex at IJmuiden (NGS, 2022). Bottom right) Location of the 6 pumps (red) and 7 weirs (yellow).

as the volumes are averaged out over time (van Veen, 2022). Yet, an increase in extreme peak rainfall events might require extra pump capacity in the future. Therefore new functional requirements need to be determined for the pumps. Due to the complex nature of the system, the more traditional methods of designing a pumping station are likely not feasible in this case.

The most important questions for the pump set-up are: How much pump capacity will be required, how often will it be required and with what reliability during its proposed lifetime? These questions are difficult to answer at this moment, as the current available models are not suitable to estimate the required future capacity. A long sequence of historical operational data of the pumps is available at Rijkswaterstaat. Presumably, a lot can be learned from the historical data, which can help estimating the future requirements of the pumps.

This paper shows that historical data analysis can indeed provide various useful insights, which helps estimating the future required pump capacity. Additionally, the sensitivities of the system can be identified based on the conducted data analysis. Following this new information, new methods will be suggested to improve the estimation of the required pump capacity for the pump-weir complex in future studies.

Due to the difficult acquisition of data, the outcomes in this paper are preliminary results. Therefore, the goal of this paper is not to provide precise and direct answers on the required pump capacity and reliability. It is the goal to showcase the complexity of the system, show the sensitivities and propose subsequent steps that can be taken to determine the required capacity.

2 SYSTEM OVERVIEW

The water system North Sea Channel - Amsterdam Rhine Channel (NSC-ARC) fulfils an important role in navigation and draining the surrounding low-lying areas of excess water, thereby it prevents flooding events in the Western Netherlands. The water level in the system is highly regulated as all incoming water sources except for precipitation are regulated by pumping stations, sluices or weirs. The system provides drainage of an area of approximately

2300 km² (Rijkswaterstaat, 2020), which includes highly developed regions surrounding Amsterdam and Utrecht (Figure 1). The target water level is NAP¹ -0.40 m for the entire channel system, but the margins for variations are small. An increase of 10 cm can lead to importunity in the low-lying surrounding polders, a decrease of 10 cm can harm navigation by going below the required navigation depth. The ‘alarm’ water level of NAP -0.30 m was only exceeded for 10 days in the last 10 years and the water level of NAP -0.20 m was never reached . Numerous smaller pumping stations excess water into the water system, with a maximum combined discharge of 360 m³/s. Yet, the largest and most important pumping station is located at IJmuiden, which discharges all water to the North Sea.

The North Sea Channel - Amsterdam Rhine Channel guides the excess water of the surrounding regions (Figure 1) towards IJmuiden like a funnel, where the largest portion of water exits the system through the pumping-weir complex to the North Sea. The pumping station has 3 main functions: 1) Regulating the daily water level (max NAP -0.30/min NAP -0.55), 2) Prevention of extreme water levels, 3) Salt/freshwater regulation.

The pumping station at IJmuiden consists of 6 pumps and 7 weirs with each different discharge capacities (Table 1). At this moment about 50% of the water is discharged through the weirs and 50% is pumped out of the system (Vermeulen et al., 2021). Discharging through weirs is always preferred as this requires no energy, except for lowering the weir doors. The pumps 1-4 were constructed in 1975 and need replacement in the near future.

Table 1. Characteristics of the pumps and weirs.

	capacity	unit	operational head	unit	quantity	since
Pumps 1-4	40	m ³ /s	0 – 2.3	m	4	1975
Pumps 5-6	50	m ³ /s	-0.2 – 2.7	m	2	2004
Weirs	72	m ³ /s	-0.12 and lower	m	7	1940
Total pumps	260	m ³ /s				
Total weirs*	500	m ³ /s				

* The preferred flow rate under normal circumstances is 300 m³/s. Under extreme circumstances 700 m³/s is possible but undesirable.

** Head difference between sea and channel when the pumps can operate.

3 DATA COLLECTION & METHOD

3.1 Data collection

Operational pump data of the time period 1984-2018 was obtained from Rijkswaterstaat where the data quality is internally assessed. The following variables are entered manually: date, start time of operation [HH:MM], end time of operation [HH:MM], discharged volume [m³] and the number of activated pumps. The discharge of the pumps is determined based on measurements with pressure sensors, but their accuracy is uncertain as additional information could not be obtained at this point in time.

To analyse the relation between pumped volumes and the historical data of surrounding stations was obtained from the KNMI (Royal Dutch Meteorological Institute) (KNMI, 2022a). The data is collected at the so called precipitation stations where the daily sum of precipitation is measured. It concerns the precipitation from 08:00 UTC on the previous day to 08:00 UTC at the mentioned date. The quality of that data is guaranteed by the internal control service of the KNMI. There is no data available on the freely-discharged volumes via the weirs for the 1984-2018 period. Data will likely be obtained in a later stage, when it will be incorporated in the analysis.

¹ NAP = Dutch Ordnance Datum, which approximately corresponds to mean sea level

3.2 Analysing the outgoing discharge volumes during extreme events

First, a trend-analysis was conducted by analysing the annual daily maxima and averages. After that, the general characteristics of the usage of the pump will be determined. To assess the required outgoing discharge capacity, a simple water balance is assumed (Figure 2).

In section 4 the return period of daily pumped volumes during extreme events will be determined based on historical data. The current free-discharged volume (Q_{weirs}) is assumed to be equal to the pumped volume (Q_{pumps}) (Vermeulen et al., 2021).

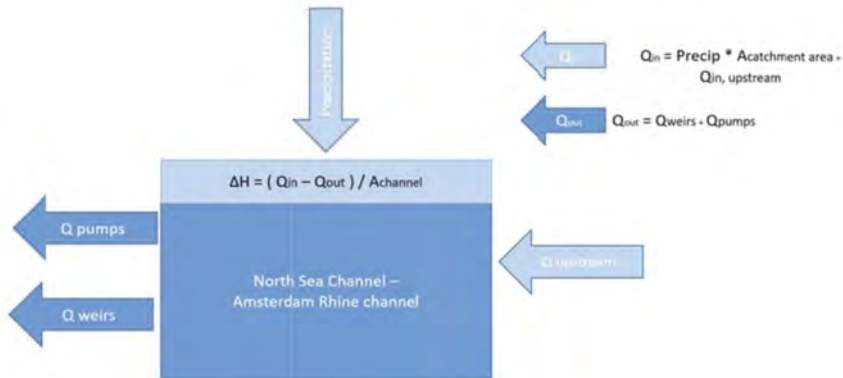


Figure 2. Conceptual scheme of the simplified water balance of the water system.

3.3 Assessment of the future requirements

The future Q_{in} is assumed to increase as the precipitation increases. Additionally, the distribution between Q_{weirs} and Q_{pumps} will likely change as the window for free-discharging is reduced due to sea level rise. Therefore, the required Q_{pumps} would increase with sea level rise. An estimation of the required pump capacity during future extreme events is made by adding the lost capacity of Q_{weirs} to the required Q_{pumps} . Possible future rainfall sequences were generated with the KNMI Transformator (Bakker, 2015) to assess the effect of more extreme rainfall events on the required Q_{pumps} . The newly calculated return periods will provide an indication if the more extreme rainfall events requires more pump capacity.

4 ANALYSIS OF HISTORICAL DATA

Historical pump data is available from 1984, which allows for analysing long-term trends. Both the annual average daily volume per year and the annual maximum daily volume were calculated and have been depicted in Figure 3. The daily maximum shows a clear jump since 2004, which coincides with the installation of 2 extra pumps. Therefore the historical sequence will be divided in two different periods for further analysis: 1984-2003 when 4 pumps were available and 2004-2018 when 6 pumps were available.

The pumps have been activated about +/- 30 % of the time since 1991. Figure 3 shows that most of the time only 1 or 2 pumps are activated, so the pumps are mainly used to regulate the daily variations to maintain the target water level of NAP -0.40 m. The older pumps are operated at full capacity (40 m³/s), but a varying discharge amount can be used at the 2 newer pumps (max. 50 m³/s). If 5-6 pumps are activated, it can indicate that the pumps are used to prevent extreme water levels in the channel, with a maximum capacity of 260 m³/s. This is the case for 3.8 % of the time. However, the 'alarm' water level of NAP -0.30 m was only exceeded for 10 days in the last 10 years and the critical water level of NAP -0.20 m was never reached. Insufficient data is available to identify so called pump-stops due to high tide, while it was required due to high water levels in the channel.

The return periods of daily pumped volumes during extreme events are shown in Figure 4 do not include Q_{weirs} . Different analyses were conducted for a 1-day sum, multi-day sum, weekly sum and a monthly sum. In all sub-plots the pumped volumes seems to approach its maximum asymptotically as the return period increases, which can be explained by the finite

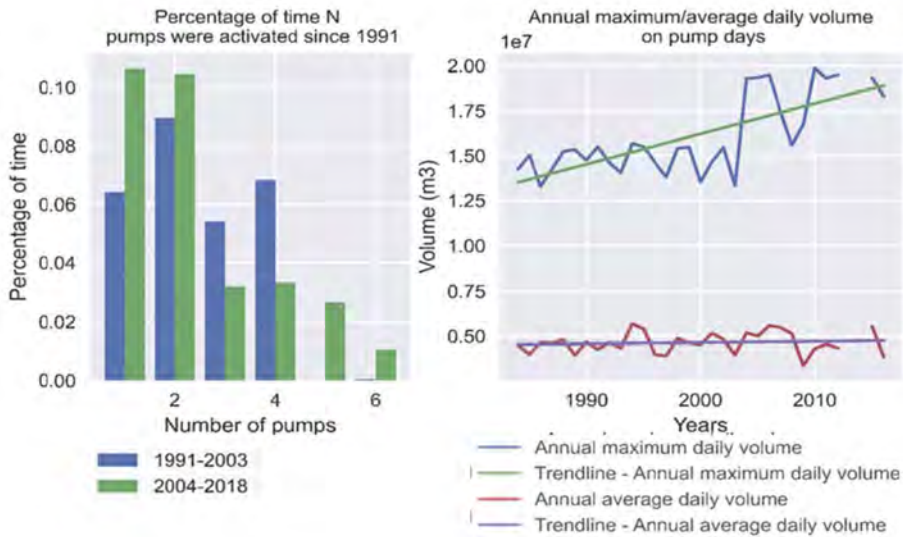


Figure 3. Left) An overview of the usage of the pumps. A distinction is made between the time periods 1991-2003 and 2004-2018. Right) The daily maximum pumped volume each year in blue and the yearly averaged daily pumped volume. The data from 2013, 2014, 2017 and 2018 was excluded from the analysis due to large gaps in the data sequence.

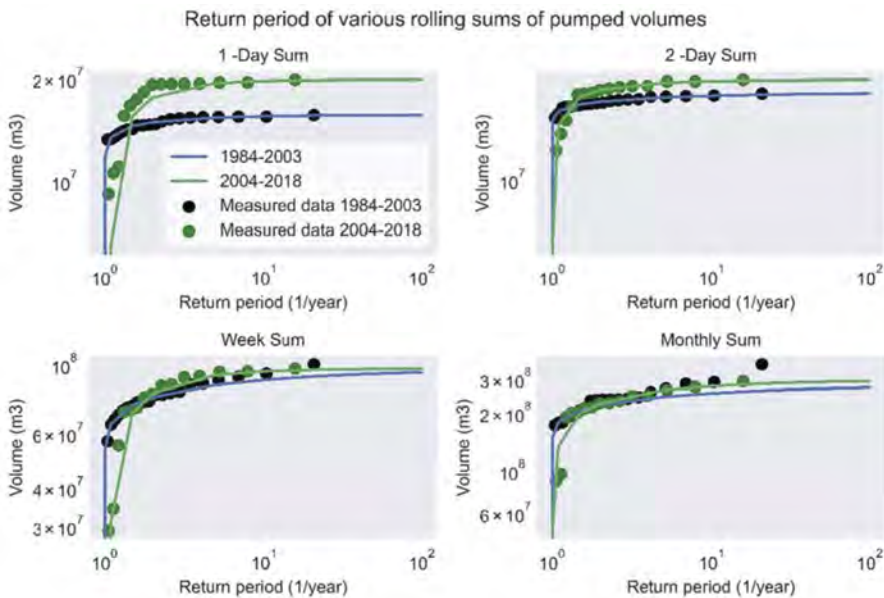


Figure 4. Depiction of the return period of the daily pumped volumes (Q_{pumps}). The total sequence was divided into the period of 1984-2003 when there were two pumps in the complex and 2004-2018 when two extra pumps were added. These volumes do not include Q_{weirs} .

capacity of the pumps. Higher extremes are found in the 1-day sum. Yet, the 2-day sum subplot shows a reduced difference between the extremes. This indicates that not all 6 pumps were required during 2 consecutive days. This difference decreases even further when the weekly sum and the monthly sum are concerned.

5 FUTURE EXPECTATIONS

5.1 Reduction of free-discharge as a result of sea level rise

For the ARC-NSC system we are interested in the absolute sea level rise, as a fixed target water level is maintained and the surrounding dikes can be heightened (Vermeulen et al., 2021). In this paper the following quantities of absolute sea level rise will be considered, it is yet uncertain when these will occur: 10 cm, 30 cm and 80 cm SLR.

Currently, the distribution of discharging through pumps and weirs is approximately 50 \%/50%. The reduction of free-discharging capacity (Q_{weirs}) due to sea level rise was determined by (Vermeulen et al., 2021) and can be found in Table 2. To approximate the required pumping capacity in the future (Q_{pumps}), the reduction of Q_{weirs} will be added to Q_{pumps} , keeping Q_{out} constant. Simultaneously the effect of 2 possible mitigation measures will be assessed: 1) increasing the target water level from NAP -0.40 m to NAP -0.20 m, 2) introducing an extra pump (50 m³/s). Figure 4 (right) shows the new return periods of pumped volumes for several amounts of SLR. The current maximum daily pumping capacity is indicated in yellow, which is exceeded for every scenario. If an extra pump is added the maximum daily capacity will increase, which is depicted in the dashed blue line. In that cases, the maximum daily capacity is exceeded with 80cm SLR. In Figure 4 (right) the target level is increased to NAP -0.20 m, which will result a lower reduction of free-discharging capacity. This results in different return periods than the left, especially for 0.30 cm SLR.

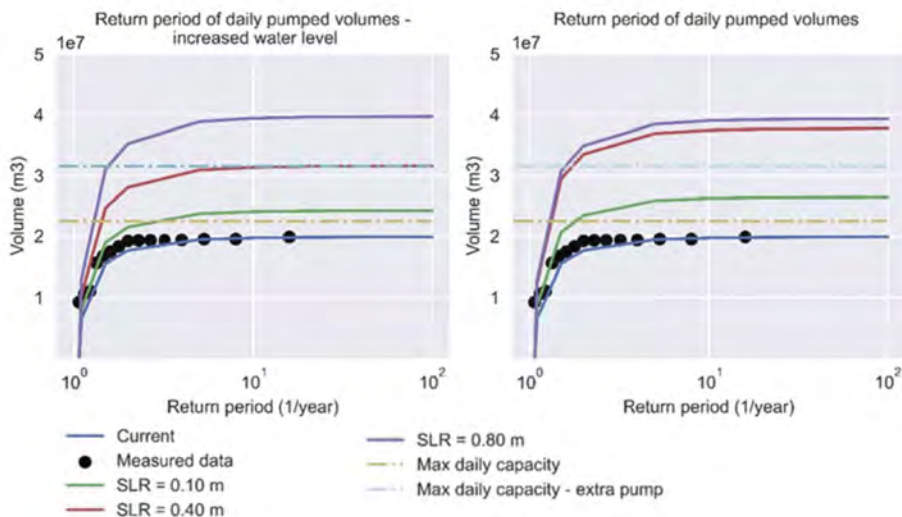


Figure 5. Return period of the daily pumped volumes of the historical data (black) which was fitted in blue with the generalized extreme value distribution. The return periods for 0.10 cm, 0.30 cm and 0.80 cm SLR are depicted in green red and purple. The new return periods were determined by adding the reduction of Q_{weirs} to Q_{pumps} . Left) The new return periods can be compared to the current maximum pump capacity (dashed yellow) and if an extra pump is added (dashed light-blue). Right) In this subplot target water level is increased with 0.20 cm, so less free discharge capacity is lost. This results in different return periods than the left, especially for 0.30 cm SLR.

Table 2. Reduction of volumes to be freely discharged as the sea level rises for 10 cm, 30 cm, 80 cm. Calculated for a target level of NAP-0.40 m and NAP-0.20 m, from (Vermeulen et al., 2021).

SLR	Reduced free-discharge volume	
	Target level	Target level
	NAP 0.40 m	NAP 0.20 m
10 cm	33 %	22 %
30 cm	90 %	59 %
80 cm	99 %	98 %

5.2 Precipitation patterns

In this section the effect of an increased Q_{in} during extreme rainfall events on the required pump capacity is analysed, while Q_{out} and Q_{weirs} remain constant. Possible future precipitation sequences were generated with the KNMI Transformer (Bakker, 2015) for 2030, 2050 and 2080 (Figure 6, left) conform the WI scenario.

The return period of extreme rainfall events are shown in Figure 6. Even for an 1/100 year extreme rainfall event in 2080, it will only result for a 10 cm increase of the water level. This will not result in many issues, as the 10 cm lie between the regulatory margins and the extra volume can be disposed of by the current pump capacity (van Veen, 2022). However, it's difficult to determine how the effects of both sea level rise and extreme rainfall events will coincide with current modelling. The higher volumes of precipitation may not lead to an extension of the complex, but they are likely to lead to a higher required Q_{out} over multiple days. If such a period would coincide with a period when little to no free-discharging is possible, extra pump capacity might be required.

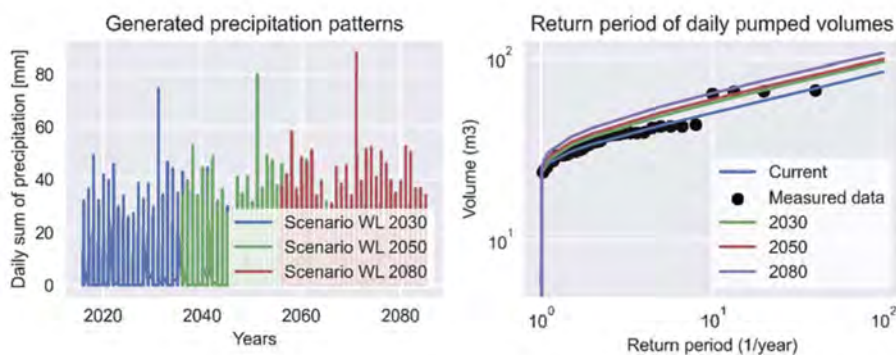


Figure 6. Left) Generated sequences of daily precipitation with the KNMI transformation tool (KNMI, 2022b), with “real” historical data in blue. Precipitation station: Wijk aan Zee. Right) Extreme value analysis of the daily sum of precipitation of the historical data from the weather station Wijk aan Zee and the generated sequences from the right figure.

6 CONCLUSIONS

The analyses in the previous sections provide an indication of the effect of climate change on the return periods of pumping volumes during extreme events. Additionally, they show the sensitivities in the system. The system seems to be dependent on the capacity of free-discharging during extreme water events, which will likely reduce as sea level rises. The system seems to be less sensitive to more extreme precipitation events.

In reality, the system is more complex and several crude assumptions were necessary in this analysis. Most importantly, the change of the capacity of free discharging was calculated by uniformly adding the sea level rise to the water levels of an one-year historical time sequence, not taking into account the impact on tides. Secondly, the assumption of a current 50%/50% distribution between pump and weir discharging is quite straightforward, as it varies under seasonal trends and differs for daily and extreme conditions. Though the free-discharging data is currently not available, it will most likely be in the future.

Additionally, the maximum pump capacity could be lower than displayed in Figure 6, as the pumps cannot operate during low tide or very high water levels. Therefore the exact maximum pumping capacity varies per extreme event, which was not included in this general analysis. However, if the real maximum capacity was overestimated due to a long period of low water levels, it is likely that free-discharging is possible. Discharging via the weirs has a higher discharge capacity than the pumps themselves, which can compensate the overestimation of the pump capacity.

Finally, the influence of the failure probability of the pumping station has not been included in this analysis. The interaction between failure probability of the pumps and the water system is not included in this paper, but it is very important to include this in the future. Malfunctions of the pumps can influence the return period of exceedance of the critical water level. If a malfunction coincides with an extreme water event, more pumping capacity will be necessary to maintain a constant return period of exceedance of the critical water level.

The complexities of the system cannot be included in a straightforward analysis. Therefore a different approach will be explored in the future. Modelling the system with neural networks will probably be a feasible for this problem due to the node-like structure of the channel and the high availability of data. This method has already been applied successfully in the field of water management (Palmitessa et al., 2022). Additionally, more research is required on the effect of sea level rise on tidal harmonics and storm surges. Recent studies predict that tidal amplitudes in the North Sea may increase (Deltares, 2020, Idier et al., 2017), so the window for free-discharging might not decrease as much as was assumed in Vermeulen et al. (2021). Due to the sensitivity of the system to free-discharging, it is important to provide a more detailed estimation in the future.

REFERENCES

- Bakker, A. 2015. Time series transformation tool version 3.1 Description of the program to generate time series consistent with the KNMI'14 climate scenarios.
- Deltares 2020. Effect van SLR op getij Nederlandse kust definitief. Deltares.
- Idier, D., Paris, F., Cozannet, G. L., Boulahya, F., Dumas, F. & 2017. Sea-level rise impacts on the tides of the European Shelf. *Continental Shelf Research*, 137, 56–71.
- Knmi 2014. KNMI14 - Klimaatscenario's.
- Knmi. 2022a. *Klimatologie - Metingen en waarnemingen* [Online]. Available: <https://www.knmi.nl/nederland-nu/klimatologie-metingen-en-waarnemingen> [Accessed 8-1-2023].
- Knmi. 2022b. *KNMI: Climate Explorer* [Online]. Available: http://climexp.knmi.nl/scenarios_knmi14_form.cgi [Accessed 10-1-2023].
- Ngs, N. G. S. 2022. *Rijksgemaal IJmuiden* [Online]. Available: <http://www.gemalen.nl/> [Accessed 08-01-2023].
- Palmitessa, R., Grum, M., Engsig-Karup, A. P. & Löwe, R. 2022. Accelerating hydrodynamic simulations of urban drainage systems with physics-guided machine learning. *Water Research*, 223.
- Rijkswaterstaat 2019. *Water management in the Netherlands*, Utrecht.
- Rijkswaterstaat 2020. Watersystemen - Amsterdam Rijn Kanaal - Noordzeekanaal.
- Van Veen, J. 2022. Onderzoek naar de uitbreiding pompcapaciteit gemaal IJmuiden.
- Vermeulen, C., Honingh, D. & 2021. TB ARK/NZK-Effecten zeespiegelstijging op pomp-en spuicapaciteit. HKV Lijn in Water.



Taylor & Francis

Taylor & Francis Group

<http://taylorandfrancis.com>

SS25: The process of decarbonization: from ideation to specification
Organizers: D. Shook & M. Sarkisian



Taylor & Francis

Taylor & Francis Group

<http://taylorandfrancis.com>

Resilience through superelasticity

D. Shook & M.P. Sarkisian

Skidmore, Owings & Merrill, San Francisco, USA

C. Horiuchi

Skidmore, Owings & Merrill, San Francisco, USA (formerly)

ABSTRACT: To reduce the impact of climate change we must incorporate carbon-reducing materials while increasing the resiliency of buildings and infrastructure. Shape memory alloys (SMAs) offer a unique opportunity to achieve these goals. SMAs are unique materials which experience phase changes due to stress allowing large, fully recoverable deformations, energy dissipation, and significant restoring forces. This is particularly helpful in regions of high seismicity. The SMA properties allow for a fully elastic seismic force resisting system. This stands in contrast to traditional steel moment frames which have significantly higher embodied carbon and buckling restrained braces (BRBs) which have a known tendency to have residual drift – rendering the building unusable. Moment frames and BRBs systems cannot achieve the combined goals of carbon reductions and resiliency. Component, prototype, and large-scale shake table testing has been conducted to validate this approach.

1 A NEW ERA OF RESILIENCE

1.1 Growing environmental risks

Rapid decarbonization is critical considering the time-value of carbon (CLF, 2017). The world is seeing promising near-term advancements of common high-volume building materials such as concrete, timber, and steel. New concrete alternatives such as algae-based cements (Prometheus, 2023) and ground glass pozzolans (Sioneer, 2023) are creating local, circular economies. Timber is being more widely used with increased code acceptance, and embodied carbon of steel is being mitigated with wider use of electric arc furnaces on cleaner electrical grids. As whole building life-cycle assessments of buildings and urban environments have shown, these common high-volume materials must decarbonize to meet the carbon reduction needs.

Many new building materials are being used as carbon storage vaults to lock up harmful carbon from emitting back into the atmosphere. For example, CO₂ is being injected into concrete for enhanced properties and long-term storage (CarbonCure, 2023), expanded use of mass timber, and other new carbon sequestering technologies are emerging rapidly. The importance of protecting these structures has expanded from one of life-safety to one of vital environmental consequence. This is of particular importance in areas of moderate to high seismic risk where a single event can emit mass quantities of carbon into the atmosphere due to the initial damage and during the subsequent carbon-intensive repair and rebuild.



Figure 1. Resiliency.

Thus, the need for resilience in buildings is growing as buildings become carbon sinks addressing climate change. This is especially true for buildings located in regions of seismically activity. Thus, a new era of resilience is here which expands beyond its traditional definition to include the carbon stored in the built environment.

1.2 *Urgency for fully recoverable seismic systems*

Nearly all seismic force resisting systems in today's building code are fundamentally based on controlled damage resulting in hysteretic damping and energy dissipation. The damping and energy dissipation are vital to reduce the seismic demands to manageable levels. Concrete shear walls, eccentric braced frames, and steel/concrete moment frames are used in nearly every building construction throughout the world and all of them work on this principle. While this approach, when detailed and constructed correctly, has been shown to be reliable for life-safety in a single large earthquake (Maffei, 2014), they have also been shown to require significant repairs or entire replacement after a large seismic event.

The development of cost-effective seismic force resisting systems which can be easily repaired or require no repair at all are vital to the protection of life during an earthquake, minimization of repair/replacement after an earthquake, and long-term protection of carbon storage in buildings. The use of non-traditional materials which meet these needs is required. These materials must be rigorously developed, tested, and smartly deployed to be effective.

1.3 *Shape memory alloys*

Shape Memory Alloy (SMA) materials such as Nitinol (nickel-titanium) have been used in niche applications since the 1970s, but in recent years it has become widely used in medical devices such as heart stents, aerospace components, and deep space applications due to their reliable performance, high corrosion resistance, while reducing material costs.

SMA are metallic alloys typically composed of multiple metallic elements including nickel-titanium ("Nitinol"), copper-zinc-aluminum, and iron-manganese-silicon-chromium-nickel (Ozbulut, 2011). While not the lowest cost, nitinol is the most widely used SMA type due to its favorable performance at a wide range of temperatures and high-corrosion resistance. Copper-based SMA are typically the lowest cost and have similar performance in many regards to nitinol, but Copper-based SMA have lower-stiffness than nitinol and do not share nitinol's corrosion resistance. Iron-based SMA are stiffer, but do not share the wide performance range of nitinol. While copper-based and iron-based SMA have potential for further development in seismic-force resisting systems, nitinol is ready for immediate application and considered for this investigation.

SMA are complex materials whose physical response to deformation depends on the magnitude of strain and material temperature. Also, as described above there are a wide variety of SMA material types. To describe their behavior for this investigation the following focus on superelastic nitinol at a material temperature range of 0C to 40C (32F to 104F).

1.4 *Traditional steel and SMA behavior under deformation*

Steel used in building applications is ductile. This ductility stems from the crystalline structure of common structural steels which have numerous slip planes. The high number of slip planes allow for numerous successive slips to occur under increasing deformation. Each new slip plane allows for further and further elongation which structural engineers call ductility. As described above, ductility allows for energy dissipation which is fundamental to traditional seismic force resisting systems.

SMA have few slip planes. Typically, this is not favorable for building applications because materials with few slip planes tend to crack or rupture because the crystalline structure cannot slip along multiple planes. Instead of moving along slip planes the SMA material undergoes a stress-induced or temperature-induced phase change between a stiffer austenite phase and a softer martensite phase which can experience significant deformations without forming slip

planes. A phase change due to temperature change is typically termed the ‘shape memory effect’ and a phase change due to stress is typically termed ‘superelasticity’. Since slip planes are not created, only phase changes are occurring, the deformation is fully recoverable.

To control and fine tune the behavior of SMAs at common temperature ranges an SMA is produced to be either a shape memory SMA or a superelastic SMA. Both types can be nitinol-based but their exact metallurgy and resulting behaviors are fine tuned for specification applications.

The ‘movement’ of SMAs is due to the current phase ‘wanting’ to shift to a lower energy state. For shape memory SMAs this is commonly seen when applied heat changes the lowest energy state causing the material to change phase and therefore ‘move’ to a prior ‘trained’ geometry. For superelastic SMAs this is commonly seen when applied stress changes the phase, but the new phase is not the lowest energy state causing the material to ‘pull’ back to its prior geometry as the applied stress is reduced.

2 RECOVERABLE MATERIALS

2.1 Behavior of single SMA wire

Superelastic SMA is used for this application. The material can be composed into a wide range of geometries including wire, bar, spring, washer, etc. SMA wires can be commercially procured ranging from 0.02mm to nearly 2mm. For this application 1mm wires are used.

The stress-strain relationship of superelastic nitinol material is well represented by a single wire. Below is the stress strain relationship for a superelastic nitinol wire. Several common terms are defined below and described in Figure 2:

- UPS: Upper Plateau Stress
- LPS: Lower Plateau Stress

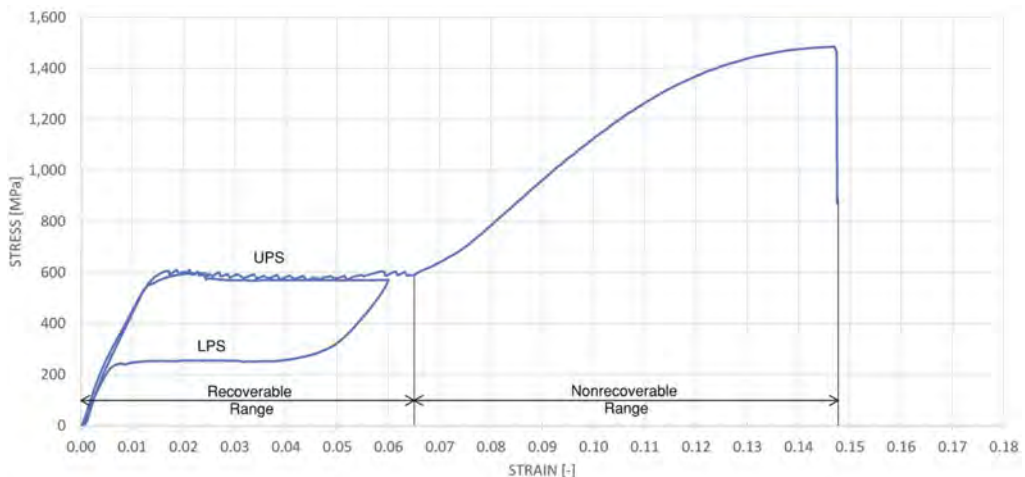


Figure 2. Stress vs strain of single nitinol wire.

For the nitinol used in this investigation the UPS is 483 MPa (70 ksi) and the LPS is 138 MPa (20 ksi). The UPS and LPS plateaus are generally flat in their martensite phase within their recoverable range. Beyond 6% strain permanent deformation occurs. At the strain a peak stress of 1,241 MPa (180 ksi) is observed. It is noted that these properties appear change when composed into a wire rope, but that is a result of geometry, as discussed later.

As can be observed, the hysteresis is fully recoverable up to 6% strain which is quite remarkable considering traditional structural steel is only fully recoverable (elastic) up to about 0.2% strain.

As a comparison of single superelastic SMA Nitinol wire and traditional structural steel (A592 Grade 50 ksi (350 MPa)), a stress versus strain relationship is shown below. As evident in the Figure 3, steel has a much higher initial elastic stiffness. Also, the yield stress of steel is between the upper and lower plateau of nitinol. Beyond 6% strain the nitinol stress ramps up quickly while steel remains relatively constant. This relationship will change for different steel and SMA materials, but the general trends are important for building designers to understand.

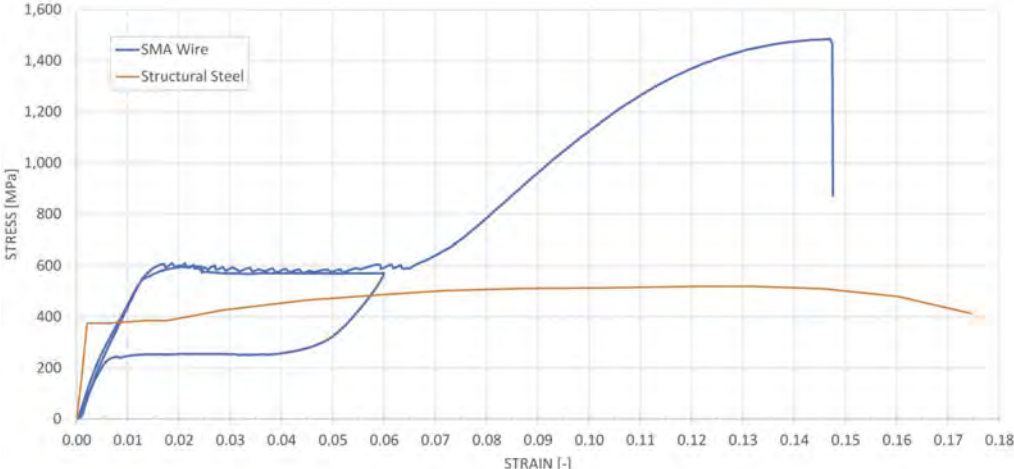


Figure 3. Stress vs strain for SMA nitinol wire and structural steel.

2.2 Behavior of SMA wires composed as a rope

The behavior of wires composed into a rope is different than a single wire. This is due to several factors, but perhaps most predominate is the differential elongation of each individual wire in the rope. If the rope has a uniform strain, each wire will have different strain magnitudes due to the different lengths of each individual wire.

For this application a 7x7 wire arrangement is used with 1 mm diameter wires. The total 49 wires act as a single unit, but the stress strain behavior differs from that of a single wire as shown below. The upper and lower plateaus are sloped compared to a single wire and the energy dissipation is slightly less. In Figure 4 below the solid blue line shows testing within the fully recoverable range of 6%, beyond 6% some of the individual wires will strain beyond their fully recoverable limit while the remainder are fully recoverable. Even up to 7% strain enough of the 49 wires remain fully recoverable such that the residual strain is negligible.

Several key studies considering strain rate effect (Ozbulut & Hurlebaus, 2010), corrosion (McCarty, 2006), and other key factors (Ozbulut et al., 2011) have been reported on by prior researchers.

2.3 Analytical representation of SMA wire or rope

This numerical representation of SMA wire or rope is a unique challenge for structural engineers since most seismic components with established numerical models are based on traditional structural steel with plastic/permanent deformations. The fully recoverable ‘flag’ shaped hysteresis of SMA is unique. Domenico & Gandelli (2021) proposed a novel modeling method which can be used in traditional structural analysis software such as ETABS and SAP2000. This method has been successfully adopted for the current investigation as demonstrated below comparing laboratory testing results and numerical modeling in ETABS.

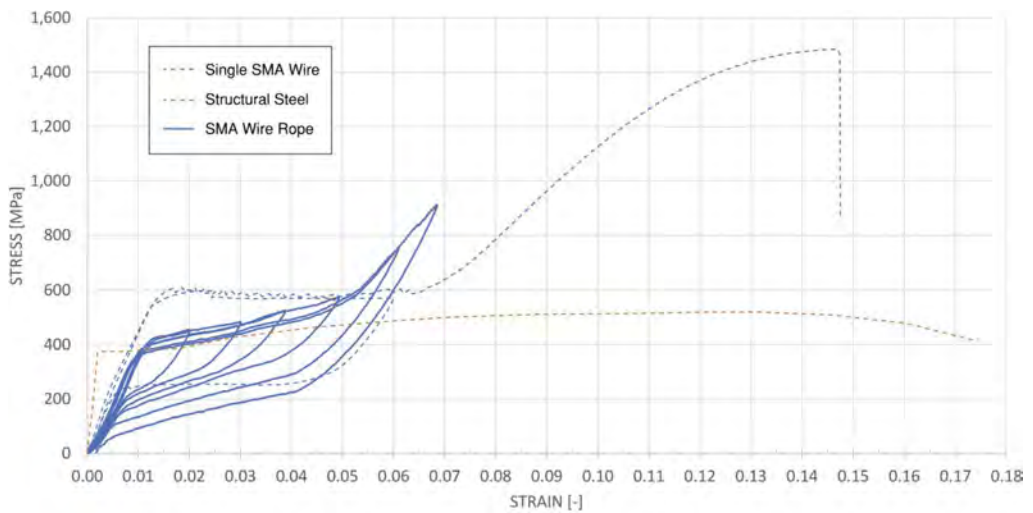


Figure 4. Stress vs strain of nitinol wire rope used in this investigation.

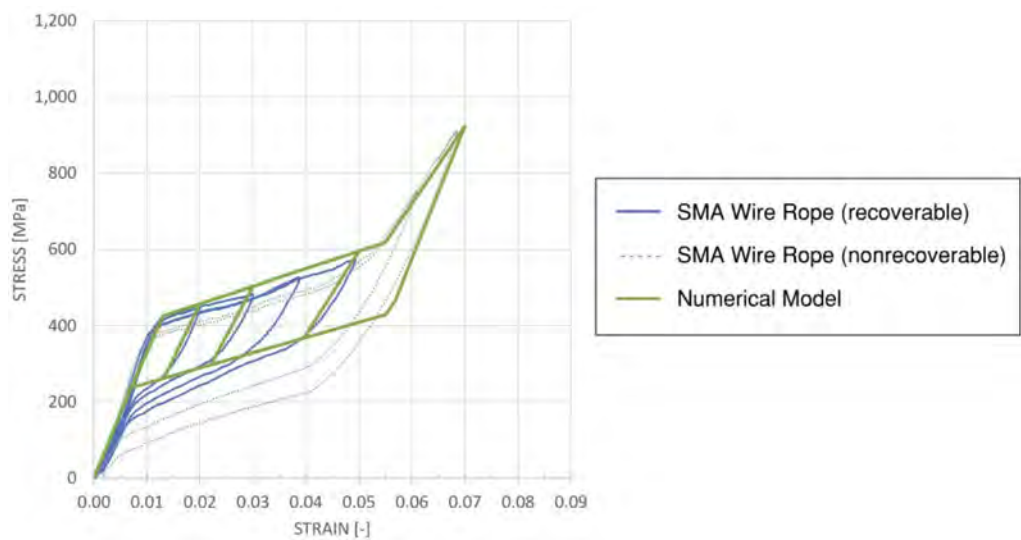


Figure 5. Numerical modeling of SMA wire rope.

3 CONNECTING TO BUILDING FRAMES

3.1 Swaged connection

Studies conducted by Ozbulut et al. (2011) reviewed prior works and explored the potential of a wire rope swaged connection with favorable results. Prior efforts with rods and threaded connections were unable to develop the full material strength and elongation due to localized concentrations of strain. The swaged connection was able to develop the material's full potential of 13.5% strain at wire rope failure. This is very similar to a single wire showing the connection develops the potential of the wire rope without stress concentrations. Also, the failure was within the gage length and not in the connection.



Figure 6. SMA wire rope swaged connection.

Investigators tested SMA wire rope swage connections produced from several traditional swaging companies in blind testing, and all showed similar results to that found by Shi et al (2021).

3.2 Swage to tension rod

The swaged connection must be composed into a building frame to resist seismic forces of the building. Investigators elected to use a novel connection that concentrically develops the force of multiple wire ropes. When composed into a tension-only bracing system a simple, yet effective bracing system is conceived which is termed SMA Tension Rod System. This system could be used in a variety of configurations including “X”, “V”, and inverted “V”. A key advantage of this system is the revival of tension-only braces as a seismic force resisting system which is generally not permitted for large structures in moderate to high seismic zones. The use of tension only bracing can allow new opportunities for structural and architectural designers to incorporate slender and minimal exposed systems into building architecture instead of relegating it to non-visible locations.

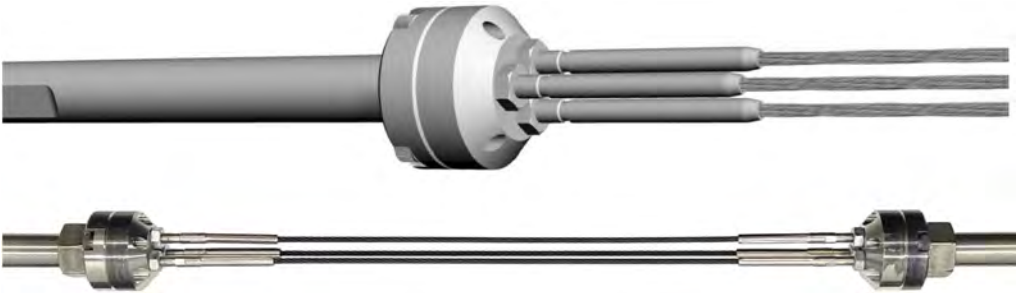


Figure 7. SMA connection to tension rod render (top) and photo (bottom).

4 SHAKE TABLE TESTING

4.1 Shake table testing description

To better understand the dynamic behavior of the SMA Tension Rod System and its sub-assemblies in a building frame, shake table testing was conducted by the investigators in a large-scale testing frame with three floors at the Pacific Earthquake Engineer Research (PEER) Center. Detailed instrumentation included floor displacement, floor acceleration, overall tension rod axial displacement, device axial displacement, tension rod force, and other key recordings. The beam-column connections were fixed, thus the lateral force resisting system was the SMA tension rod system and an elastic moment frame. Numerous ground motions were scaled from 20% to 100% of the original recording. Strains in the devices went up to 8% for select ground motions. Even though some ground motions exceed the anticipated recoverable limit of the devices, they continued to perform well in subsequent testing. This demonstrates the robust nature of the SMA tension rod system.



Figure 8. Shake table frame on table (left) and enlarged elevation of level 1 (right).

4.2 Shake table testing results

After the shake table testing the obtained data was reviewed and post-processed to better understand the numerical model prediction of the SMA Tension Rod System force response. In general, the experimental results align well with the numerical prediction in comparison to shake table testing of traditional seismic force resisting systems. It is noted that the acceptable accuracy of numerical prediction in a shake table test compared to pseudo-static testing is different. For shake table testing results, it is determined that the results of numerical prediction are acceptable when compared to other similar testing of steel and concrete energy dissipation components.

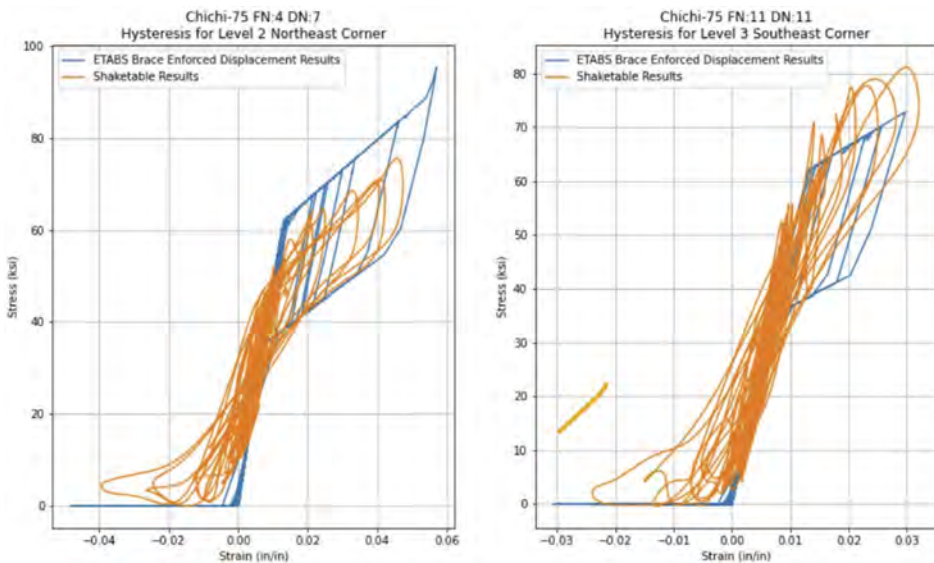


Figure 9. Numerical prediction vs shake table results.

5 CONCLUSION

With the increasing acceptance of carbon storage in as a means to mitigate climate change, a new era of resilience is here. The implementation of fully recoverable seismic force resisting systems is vital to the increased protection of our environment. As shown through this investigation, the use of shape memory alloys composed in a SMA tension rod system can be an important part of the resiliency of our urban fabric. The numerical and experimental testing results of this system demonstrate that SMA wire ropes composed into a SMA tension rod system are ready for full-scale deployment in buildings in regions of moderate and high seismic risk.

REFERENCES

- CarbonCure, 2023, <https://www.carboncure.com/>
- Domenico, D. & Gandelli, E. 2021. Advanced Modeling of SMA Flag-Shaped Hysteresis for Nonlinear Time-History Analysis in SAP2000, *American Society of Civil Engineering Journal of Structural Engineering* 147(11).
- McCarty, D. 2006. Durability of Nitinol for Structural Applications. *University of Auburn*.
- Maffei et al., 2014, Recommendations for Seismic Design of Reinforced Concrete Wall Buildings Based on Studies of the 2010 Maule, Chile Earthquake, *NIST GCR 14-917-25*.
- Ozbulut, O. & Hurlebaus, S. 2010. Neuro-fuzzy Modeling of Temperature and Strain Rate dependent Behavior of NiTi Shape Memory Alloys for Seismic Applications, *Journal of Intelligent Materials and Systems and Structures* 21: 837–849.
- Ozbulut, O. et al. 2011. Seismic Response Control Using Shape Memory Alloys: A Review, *Journal of Intelligent Material Systems and Structures* 22: 1531–1549.
- Prometheus Materials, 2023, <https://prometheusmaterials.com/>
- Shi, F., et al, 2021. Development and Experimental Validation of Anchorage Systems for Shape Memory Alloy Cables, *Engineering Structure* 228.
- Sioneer, 2023, <https://www.sioneer.com/>
- Strain, L. 2017. Time Value of Carbon, *Carbon Leadership Forum* pgs 1–10.

Design of the urban sequoia tower

M.P. Sarkisian, E. Long, A. Beghini, K. Micallef & S. Jaberansari
Skidmore Owings & Merrill, San Francisco, CA, USA

ABSTRACT: What if builds were more like trees and cities were more like forests? The concept of Urban Sequoia combines optimized structural design with low embodied carbon materials, efficient construction, and carbon-capturing technologies to transform carbon producers into carbon consumers. These carbon-capturing approaches allow buildings to start their service life with an ultra-low embodied carbon and sequester additional carbon over time, becoming net carbon negative. The structural approach to Urban Sequoia incorporates nature-based, living materials that embody far less carbon than conventional structural solutions while absorbing additional carbon over time. When combined with non-structural systems such as exterior wall systems that incorporate biomass and algae and technologies including Direct Air Capture (DAC), tall buildings could absorb three to five times the amount of carbon emitted at the time of construction. Urban Sequoia includes ideas that can be applied to buildings at all scales and uses. The floor framing system, for example, could be used in a building with only a few floors or one that has a hundred floors. The strength of the concept is enhanced when buildings that make up a city combine to become a source of biofuel that can be used to power heating systems, automobiles, and aircrafts and create bioprotein. An even broader impact could include using carbon byproducts for infrastructure.

1 INTRODUCTION

The concept of Urban Sequoia (Figure 1) combines optimized structural design with low embodied carbon materials, efficient construction, and carbon-capturing technologies. These carbon-capturing approaches allow buildings to start their service life with an ultra-low embodied carbon and sequester additional carbon over time, becoming net carbon negative. The structural approach to Urban Sequoia incorporates nature-based, living materials that embody far less carbon than conventional structural solutions while absorbing additional carbon over time. When combined with non-structural systems such as exterior wall systems that incorporate biomass and algae and technologies including Direct Air Capture (DAC), tall buildings could absorb three to five times the amount of carbon emitted at the time of construction. Urban Sequoia includes ideas that can be applied to buildings at all scales and uses. The floor framing system, for example, could be used in a building with only a few floors or one that has a hundred floors. The strength of the concept is enhanced when buildings that make up a city combine to become a source of biofuel that can be used to power heating systems, automobiles, and aircraft and create bioprotein. An even broader impact could include using carbon byproducts for infrastructure.

2 LOW EMBODIED CARBON

The initial embodied carbon in a structure must be driven to absolute minimums to go beyond carbon neutrality. Materials and construction are vital components in a building's initial embodied carbon assessment. Materials must have low embodied carbon, high strength-to-weight ratios,

components with injected carbon, and components that have already sequestered carbon. The construction process must require minimal time to build and include alternative processes such as robotics. Before conceptualizing the structural design of Urban Sequoia, available low-carbon materials and emerging technologies needed to be understood and a construction process curated for them.



Figure 1. Urban Sequoia concept applied at a city scale.

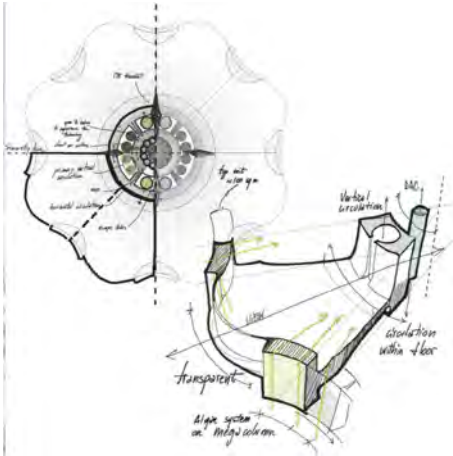


Figure 2. Urban Sequoia concept plan and diagram.

3 ADVANCED MATERIAL INCLUDING THOSE THAT ABSORB CARBON

High strength materials combined with optimization analyses that carefully assess the placement of materials for given loadings are an essential initial basis for design to reduce embodied carbon. However, this approach alone is not nearly enough. Advancing existing materials to lower their embodied carbon and developing new building materials which absorb carbon is also essential to success.

Portland cement is currently responsible for more than 5% of global CO₂ emissions. Therefore, low embodied carbon products used to replace part or all of the portland cement content in concrete like fly ash or slag can directly impact and significantly reduce global carbon emissions. An alternative Supplementary Cementitious Material (SCM) is recycled ground glass.

Low-carbon concrete made with carbon-neutral portland cement and other cementitious materials could become an environmentally friendly material that yields similar or superior performance characteristics to traditional portland cement and has a low carbon impact. An emerging technology, for example, allows for the extraction of lime (CaO), which is used to produce ordinary portland cement, from calcium silicate (Ca₂SiO₄) rather than limestone (CaCO₃); thus eliminating the CO₂ emission due to traditional lime extraction. Furthermore, as a waste byproduct of this process, magnesium hydroxide (Mg(OH)₂) can absorb CO₂ from the air resulting in magnesium carbonate (CMgO₃) that permanently sequesters CO₂. The overall process reduces the CO₂ emissions associated with portland cement production by up to 60%, which, combined with the sequestration from magnesium hydroxide, renders the final produced cement net-zero or even net negative carbon.

High-strength recycled steel typically contains up to 70% recycled content. Strengths of available structural steel and reinforcing steel for concrete continue to increase along with increasing fire and corrosion resistance. Ultra-high-strength reinforcing materials such as carbon fiber offer an excellent alternative to conventional reinforcing in concrete and can also replace high-strength reinforcing steel commonly used for prestressing.

Structural materials which sequester and store carbon over their life include algae-based concrete, hempcrete, timber, Mycelium, and carbon sequestering fillers and aggregate. algae-based concrete, developed at the University of Colorado, Boulder, is a Living Building Material (LBM) created by combining a sand-hydrogel scaffold with *Synechococcus* sp. PCC 7002, a photosynthetic cyanobacterium. The algae-based concrete are essentially made of food-based products and use biology to provide a structural binder to any aggregate type. When using fine sand without coarse aggregate, the structural material strength of the algae-based concrete is comparable to common concrete masonry units, with the advantage that the tensile strength of the material is considerably higher, offering a potentially wide range of applications where some tension demands exist.

Hempcrete is a biocomposite material that is a mixture of hemp shives (the woody inner portion of the hemp stalk broken into pieces), water, lime, and sand or cement binder. The strength of the material is limited, so the use is typically appropriate for non-structural components.

Carbon sequestration of timber-based products occurs when atmospheric CO₂ is sequestered in the production of biomass through photosynthesis. The trees emit oxygen in return and permanently store the carbon until the material is combusted for fuel or decays in a landfill. Bamboo and other fast-growing grasses, including straw, are considered one of the best carbon-sequestering materials because of the rate at which it grows. For example, *Guadua Angustifolia* bamboo sequesters as much carbon in 6 years as douglas fir does in 34 years.

Mycelium consists of a mass of thread-like branching fungus and is typically combined with natural fibers to increase its strength characteristics. Although overall material strengths are low, Mycelium has an excellent strength-to-weight characteristic and are used in non-structural components (e.g., insulation).

Finally, emerging technologies have resulted in carbon sequestering aggregates that can sequester carbon from the atmosphere. For example, through the process of mineralization, carbon is captured from natural gas-fired or similar fossil fuel-generated energy facilities and permanently stored in synthetic limestone.

4 DESIGN FOCUSED ON CONSTRUCTION

A significant amount of carbon is emitted during the construction process, in some cases accounting for up to 25% of a building's embodied carbon. The carbon associated with site construction includes emissions from machinery required to build, materials shipped from disparate locations, transportation of personnel required, and the like. Given the known properties of low carbon materials, how do we design for construction differently? What properties does low Portland Cement or even low-carbon concrete have, and how do we address them via the construction process, such as setting time? What type and size of steel are available from electric arc furnaces fueled with renewable energy? The answers to these questions should inform structural design.

As a widely used material for building structures, concrete has known embodied carbon associated with the construction process primarily centered around formwork and the number of days per floor in the construction cycle. Optimizing cores and columns for ease of vertical forming systems and floor plate geometry (for ease of horizontal forming systems) can help reduce floor-to-floor cycles from 7 days to 5 days to even 3 days. A common characteristic of low portland cement and low-carbon concrete is low early strength and extended time to gain higher design strengths. While this seems at odds with the desire to achieve fast floor-to-floor cycles, the construction process could involve precast to allow the material to reach necessary strength off-site and be quickly erected on-site, still achieving fast floor-to-floor cycles. Another approach is to provide formwork systems that are part of the permanent structural design such as algae-based concrete masonry unit or similar carbon-neutral materials from emerging technologies. These formwork systems are not removed, allowing the low-carbon concrete to have extended time to reach design strength. These approaches to the construction process lead to the pre-assembly of major building components to minimize construction time, waste, and associated carbon.

5 STRUCTURAL SYSTEM

The Urban Sequoia Tower is conceptually organized around a tubular geometry integrating systems of vertical circulation, movement of air to the Direct Air Capture system, and movement of biomass and algae around the perimeter of the program space. The programmatic space is organized into eight petals around the tubular core (Figure 2). The structural system is directly integrated into this tubular geometry. It is articulated in a central structural core, perimeter gravity columns, and a floor framing system spanning between the core and the perimeter columns.

The low-carbon concrete core is considered a circular tube divided into four quadrants. Each quadrant contains two circular shafts forming the basis of the precast concrete module. Elevators can occupy a circular shaft, or two shafts could be combined to create a stair shaft. The shafts are lined with a recycled steel liner that extends above the top of the precast, serving as a shear key between precast units. The precast units are vertically tied together with vertical post-tensioned recycled steel strands and linked horizontally with a link beam element (Figure 3).

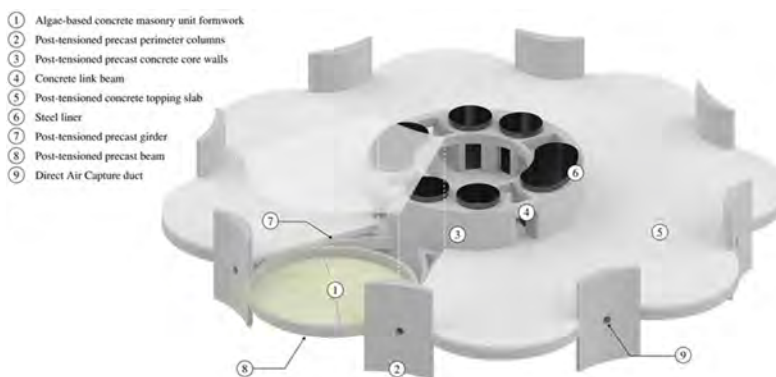


Figure 3. Urban Sequoia structural system overview.

Perimeter precast columns with low-carbon concrete are located in the inner concave portions of the petals geometry. The horizontal framing system is similarly organized around the eight programmatic floor spaces directly connecting the perimeter columns to the center core. The low-carbon precast beam framing is curved in plan around each petal, leaving an open circular floor space in the center of each petal (Figure 3). The precast beams incorporate prefabricated ducts for post-tensioned strands and large diameter air ducts to directly capture outside air from the perimeter and channel it to the central tubes inside the core using the naturally occurring positive and negative air pressures from wind. The precast columns are also laced together with post-tensioned strands made with recycled steel.

The circular floor space between post-tensioned precast beams is infilled with leave-in-place algae-based concrete masonry unit formwork panels cast into eight pie-shaped elements and an octagonal (or circular) centerpiece. The pie-shaped segments are vaulted to keep the material in pure compression and minimize the thickness required. The flooring system is completed with a low-carbon concrete topping slab that works compositely with the formwork (Figure 3).

6 COMPARISON OF URBAN SEQUOIA TO A BENCHMARK BUILDING

The continuously growing industry of residential high-rise construction provides a meaningful basis to evaluate the carbon emission reduction potential of the Urban Sequoia Tower. The Benchmark Tower project is a high-performing 42-story, 420-foot-tall, 450,000-square-foot

reinforced concrete residential tower recently designed and constructed in San Francisco (Figure 4a). The structural system for the tower includes a core-only lateral load-resisting system and perimeter gravity columns with post-tensioned flat slabs for the gravity system. The typical tower floor plan and size of structural elements are illustrated in Figure 5a. This project is located in a high seismic hazard zone and was designed with particular attention to seismic resilience and environmental sustainability.

The tower considered was designed using a performance-based design process and was highly optimized in terms of structural material utilization compared to other structures of similar height, geometry, and site characteristics. This approach led to a reduction in structural embodied carbon by more than 20% compared to a similar building.

The total embodied carbon equivalent intensities associated with A1-A3 (Cradle-to-Gate) Life-cycle stages, according to the EN 15804 standard for the primary structural components for the Benchmark Tower, are reported in Table 1 for reference.

Table 1. Benchmark Tower A1-A3 embodied carbon intensities.

Structural Element ¹	Concrete ² (lb.CO ₂ e/sf)	Post-Tensioning Tendon ³ (lb.CO ₂ e/sf)	Steel Reinforcement ⁴ (lb.CO ₂ e/sf)
Shear wall core	10.0~11.0	0	5.5~6.5
R/C columns	1.5~2.0	0	1.0~1.5
PT slabs	20.0~21.0	2.2~2.7	2.5~3.0

Notes:

1- Embodied carbon metrics of the miscellaneous structural elements are not listed in the table.

2- Embodied carbon metrics are taken as 708~928 lb.CO₂e/cy depending on type of concrete based on the NRMCA, Member Industry-Average EPD For Ready Mixed Concrete.

3- Embodied carbon metrics are taken as 2.27 lb.CO₂e/lb based on the ICE, Industry average: Steel, Wire rod.

4- Embodied carbon metrics are taken as 0.98 lb.CO₂e/lb based on the CLF, 2021 Material Baselines.

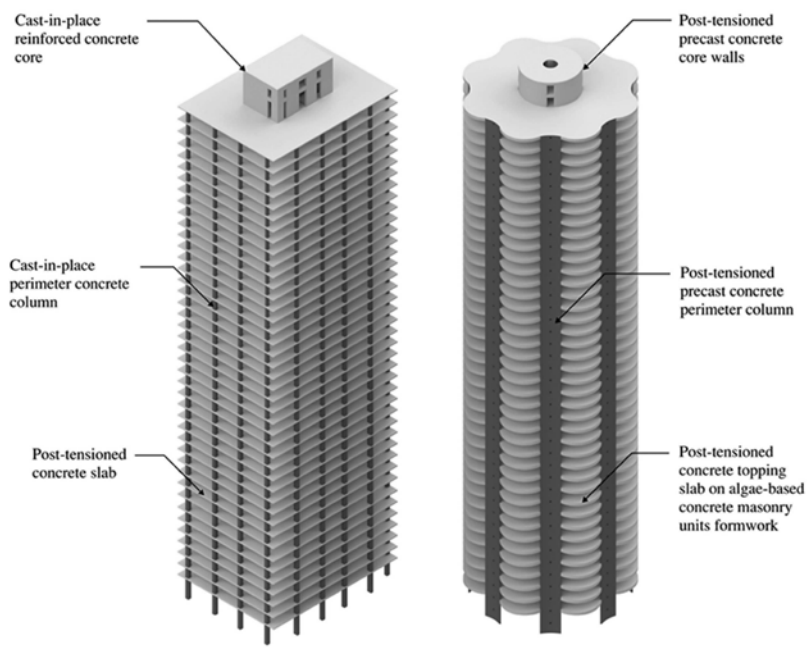


Figure 4. Axonometric view of the Benchmark Tower (a) and Urban Sequoia Tower (b).

The Urban Sequoia Tower represents the next generation of residential buildings with excellent opportunities to reduce embodied carbon and become net negative carbon over its operational life. For example, considering an Urban Sequoia Tower of equivalent floor and the total area to the Benchmark Tower results in an overall tower diameter of 126 feet (Figure 5b) with the same typical 10-foot floor-to-floor height, number of stories, and total tower height.

The precast cellular core has wall thicknesses varying from 24 inches at the base to 14 inches at the top and utilizes low-carbon concrete with a strength of 8,000 psi at the bottom two-thirds of the tower and 6,000 psi in the top one-third of the tower. The crescent-shaped precast columns vary from 170 by 30 inches at the base to 170 by 20 inches at the top. The columns utilize low-carbon concrete with a strength of 8,000 psi in the bottom two-thirds of the tower and 6,000 psi in the top one-third of the tower.

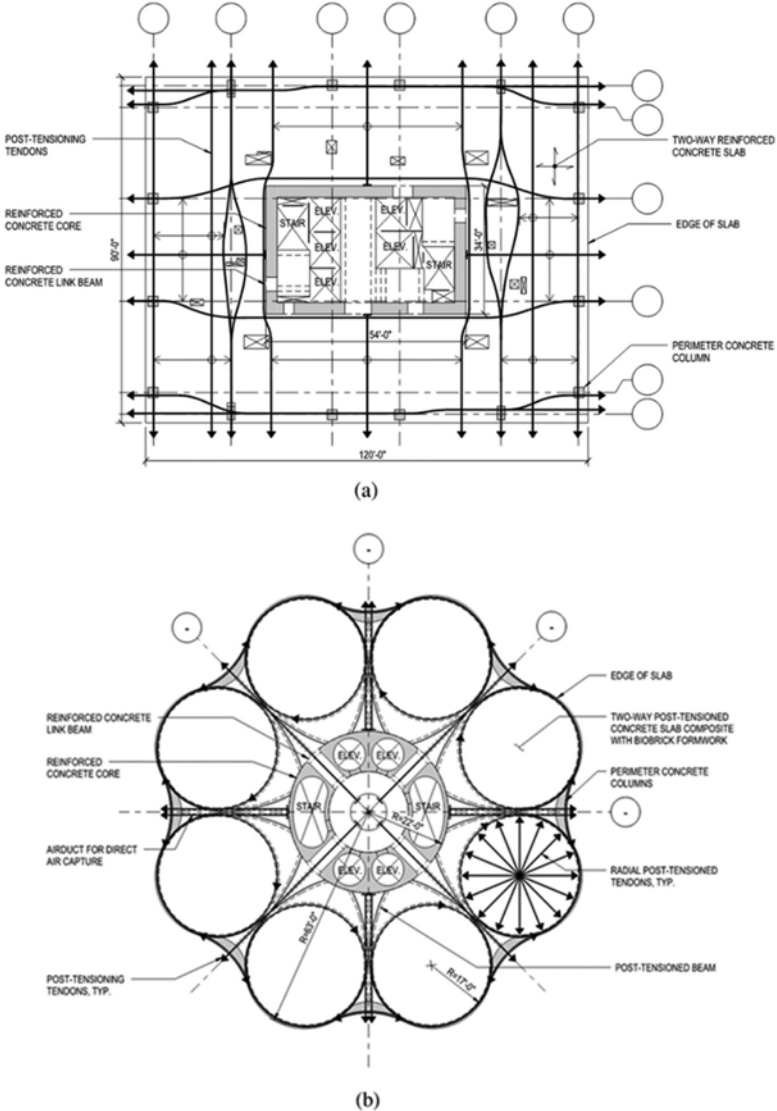


Figure 5. Structural plan of Benchmark Tower (a) and Urban Sequoia Tower (b).

The total embodied carbon equivalent intensities associated with the primary structural components for the Urban Sequoia Tower are summarized in Table 2.

Table 2. Urban Sequoia Tower A1-A3 embodied carbon intensities.

Structural Element	Concrete ² (lb.CO ₂ e/sf)	Post-Tensioning Tendon ³ (lb.CO ₂ e/sf)	Steel Reinforcement ⁴ (lb.CO ₂ e/sf)	Steel Plate ⁵ (lb.CO ₂ e/sf)
Precast shear wall core	1.2~1.4	1.7~1.9	1.4~1.7	0
Precast columns	0.3~0.4	0.7~0.9	0.7~1.0	0
Precast beams & girders	1.2~1.4	0.9~1.1	0.2~0.4	0
Algae-based concrete masonry unit ⁶ formwork	~0.0	0	0	0
Topping slab	1.4~1.6	0.9~1.1	0.4~0.6	0
Steel liner	0	0	0	0.5~0.7

Notes:

1- Embodied carbon metrics of the miscellaneous structural elements are not listed in the table.

2- Embodied carbon metrics are taken as 106~139 lb.CO₂e/cy based on the NRMCA, Member Industry-Average EPD For Ready Mixed Concrete and modified for Low-Carbon Concrete emerging technologies.

3- Embodied carbon metrics are taken as 2.27 lb.CO₂e/lb based on the ICE, Industry average: Steel, Wire rod.

4- Embodied carbon metrics are taken as 0.49 lb.CO₂e/lb based on the Nucor Recycled Steel Rebar EPD.

5- Embodied carbon metrics are taken as 1.26 lb.CO₂e/lb based on the CLF, 2021 Material Baselines.

6- Material alone yields net carbon absorption (net-zero with the current assembly process).

The total A1-A3 structural embodied carbon of the Benchmark Tower adds 9,500~11,700 tons of CO₂e, while the Urban Sequoia Tower contains only 2,800~3,400 tons of CO₂e, representing more than 70% reduction in CO₂e. This extremely low starting point for structural embodied carbon is achieved by employing technologies available today or otherwise close to commercialization. Further embodied carbon reduction will be achieved by replacing low carbon concrete with biogenic materials opening up avenues to structural embodied carbon neutrality. For example, with the current developments of the algae-based concrete material, it is anticipated that the material and related assembly process will yield net carbon absorption. Nevertheless, the low embodied carbon based on today's technologies combined with the additional carbon absorption enabled by the algae façade and Direct Air Capture technologies renders Urban Sequoia Tower in Figure 4b can absorb 39,000 tons of CO₂e over a 60-year life span, where 25% of operational carbon sequestration comes from the algae façade and Direct Air Capture technologies sequester the remaining 75%.

7 CONCLUSIONS

The urban sequoia concept combines a broad range of sustainable design thinking, including emerging technologies, and applies them at scale in a tower. By combining optimized structural design resulting in minimal materials and integrating biomaterials, biomass concepts, and carbon-capturing technologies into an integrated system, the urban sequoia can achieve substantially more carbon reductions than using these techniques separately. Combining these systems in a typical residential tower based on today's technologies can result in the sequestration of as much as 650 tons of carbon per year, equivalent to 31,500 full-grown trees each year.

REFERENCES

- Altair Engineering Inc. (2021) SimSolid. (Version 2021.1.1). [Computer Software]. www.altair.com.
<https://www.altair.com/simsolid/>
- Altair Engineering Inc. (2021) SimSolid. (Version 2021.1.1). [Computer Software]. www.altair.com.
<https://www.altair.com/simsolid/>
- Arrigoni, A., Pelosato, R., Melià, P., Ruggieri, G., Sabbadini, S., & Dotelli, G. (2017). Life cycle assessment of natural building materials: The role of carbonation, mixture components and transport in the

- environmental impacts of Hempcrete blocks. *Journal of Cleaner Production*, 149, 1051–1061. <https://doi.org/10.1016/j.jclepro.2017.02.161>
- Boden, T.; Marland, G., Andres, R. J. (1999). *Global, Regional, and National Fossil-Fuel CO2 Emissions (1751-2014)* (V. 2017). Carbon Dioxide Information Analysis Center (CDIAC), Oak Ridge National Laboratory (ORNL), Oak Ridge, TN (United States), ESS-DIVE repository. Dataset. doi:10.3334/CDIAC/00001_V2017 accessed via https://data.ess-dive.lbl.gov/datasets/doi:10.3334/CDIAC/00001_V2017 on 2022-04-10
- Carbon Leadership Forum. (2021). 2021 Material Baselines. (Baseline Report v2). <https://carbonleadershipforum.org/2021-material-baselines/>
- Clippinger, J., & Davis, R. (2019). Techno-economic analysis for the production of algal biomass via closed photobioreactors: Future cost potential evaluated across a range of cultivation system designs. <https://doi.org/10.2172/1566806>
- Computer & Software Inc. (2021) ETABS. (Version 19.1.0). [Computer Software]. csiamerica.com. <https://www.csiamerica.com/products/etabs/enhancements/19>
- Elfordy, S., Lucas, F., Tancret, F., Scudeller, Y., & Goudet, L. (2008). Mechanical and thermal properties of lime and hemp concrete (“hempcrete”) manufactured by a projection process. *Construction and Building Materials*, 22(10),2116–2123. <https://doi.org/10.1016/j.conbuildmat.2007.07.016>
- Finke, C.E., Leandri, H. (2020). Process to make calcium oxide or ordinary portland cement from calcium-bearing rocks and minerals. (U.S. Patent No.US20210070656A1). U.S. Patent and Trademark Office.
- Inventory of Carbon & Energy. (2019). Industry average: Steel, Wire rod [Version 3.0 Beta]
- Jayasinghe, A., Orr, J., Ibell, T., & Boshoff, W. P. (2022). Minimizing embodied carbon in reinforced concrete flat slabs through parametric design. *Journal of Building Engineering*, 50, 104136. <https://doi.org/10.1016/j.jobte.2022.104136>
- Jones, R. J., Delesky, E. A., Cook, S. M., Cameron, J. C., Hubler, M. H., & Srubar, W. V. (2022). Engineered living materials for construction. *Engineered Living Materials*, 187–216. https://doi.org/10.1007/978-3-030-92949-7_7
- Jones, M., Mautner, A., Luenco, S., Bismarck, A., & John, S. (2020). Engineered mycelium composite construction materials from fungal biorefineries: A critical review. *Materials & Design*, 187, 108397. <https://doi.org/10.1016/j.matdes.2019.108397>
- Nath, A. J., Lal, R., & Das, A. K. (2015). Managing Woody Bamboos for carbon farming and carbon trading. *Global Ecology and Conservation*, 3, 654–663. <https://doi.org/10.1016/j.gecco.2015.03.002>
- National Ready Mixed Concrete Association. (2020). Member Industry-Average EPD For Ready Mixed Concrete. <https://www.nrmca.org/wp-content/uploads/2020/02/EPD10080.pdf>
- Nucor Steel Seattle, Inc. (2017). Environmental product declaration, steel concrete reinforcing bar, and merchant bar products. <https://www.nucor.com/certifications/>
- Prentice, D., Mehdipour, I., Falzone, G., Raab, S., Simonetti, D., & Sant, G. (2022). Field demonstration of the REVERSA™ mineral carbonation process using coal and natural gas flue gas streams. *The Minerals, Metals & Materials Series*, 589–594. https://doi.org/10.1007/978-3-030-92563-5_62
- Rippmann, M., & Block, P. (2018). Computational tessellation of Freeform, cut-stone vaults. *Nexus Network Journal*, 20(3),545–566. <https://doi.org/10.1007/s00004-018-0383-y>
- Terlouw, T., Treyer, K., Bauer, C., & Mazzotti, M. (2021). Life cycle assessment of direct air carbon capture and storage with low-carbon energy sources. *Environmental Science & Technology*, 55 (16),11397–11411. <https://doi.org/10.1021/acs.est.1c03263>
- Yiping, L.; Yanxia, L.; Buckingham, K.; Henley, G.; Guomo, Z. *Bamboo and Climate Change Mitigation*; International Network for Bamboo and Rattan (INBAR): Beijing, China, 2010; p. 126645

Achieving net zero embodied carbon: The SE2050 program and its impact on structural design

C. Horiuchi

Skidmore, Owings & Merrill, San Francisco, USA (formerly)

M. Stringer

Holmes US, San Francisco, USA

N. Wang

Skidmore, Owings & Merrill, San Francisco, USA

ABSTRACT: The SE2050 program is sponsored by the Structural Engineering Institute (SEI) of the American Society of Civil Engineers (ASCE) with the aim to reach net-zero embodied carbon of structural materials by the year 2050. This goal is based on global carbon targets for building materials required to limit to a 1.5-degree temperature increase per the Paris Climate Agreement. Approximately 100 independent design firms across the U.S. have joined this program. Firms committing to join the program follow four steps: sustainable practice education, embodied carbon tracking on projects, embodied carbon reduction in designs over time and advocacy for change with architects, contractors and owners. SE2050 is building a structural embodied carbon database for U.S. projects to establish carbon benchmarks and track industry-wide carbon emissions towards a net-zero future.

Engineers looking at the bigger picture should think holistically about limiting environmental impacts. This paper explores this program in comparison to other global industry efforts for embodied carbon reduction. The structural design process impacts are explored, presenting resources provided to designers and how firms incorporate carbon calculations into practice.

1 INTRODUCTION

The SE 2050 Commitment Program is a collection of US-based structural engineering firms who have committed to reducing the embodied carbon of the structural materials in their designed buildings by 2050. This paper will present an overview of the program, including its development and current status at the national scale. To understand how this commitment program affects the work of individual firms, a summary of specific items from Skidmore, Owings & Merrill (SOM), an early member of the program, will be provided.

2 TIMELINE OF SE 2050

The SE 2050 Commitment Program originated in grassroots style from structural engineers who recognized the necessity of the structural engineering profession to engage more actively in conversations surrounding sustainability. Upon the announcement of the American Institute of Architects (AIA) 2030 commitment program in 2009, several structural engineers began to formulate a program that would specifically address the embodied carbon of structures. These early conversations occurred predominantly within the Carbon Leadership

Forum (CLF) community, a US-based organization of engineers, architects and other designers interested in addressing embodied carbon in buildings. In collaborating with key national organizations, including the American Society of Civil Engineers Structural Engineering Institute (ASCE-SEI), the AIA and the United States Green Building Council (USGBC), the CLF created a commitment program focused on embodied carbon reduction, This SE 2050 Challenge was presented and endorsed by the SEI Board of Governors.

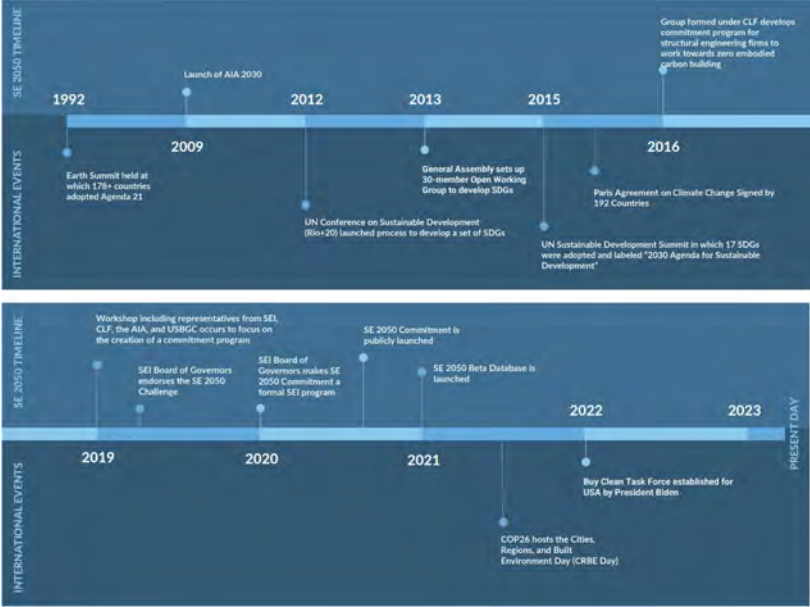


Figure 1. SE 2050 Timeline.

After endorsing the SE 2050 Challenge, SEI officially launched the SE 2050 Commitment as a subcommittee of the SEI Sustainability Committee in 2020. The SE 2050 subcommittee has gained over 30 dedicated members and the support of nearly 100 engineering firms across North America. In mid-2021, SE 2050 launched its beta database in which firms submit life cycle assessment (LCA) data on their projects. Still in the early stages of its existence, SE 2050 continues its focus on advocacy for sustainable structural design, growth of firm commitments, and refinement of the database. Figure 1 (TOP) highlights key moments of SE 2050 to this point.

It is important to recognize how SE 2050 fits into the broader landscape of sustainability-focused movements. To demonstrate, Figure 1 (BOTTOM) additionally displays notable conferences and governmental commitments related to international cooperation on addressing the climate crisis.

Such a timeline shows how international declarations spur on conversations within industry. Between the Launch of AIA 2030 in 2009 and the SE 2050 Challenge of 2019, ten years of international work on developing the United Nations Sustainable Development Goals (SDGs) took place. These SDGs are widely considered the most comprehensive assessment on the meaning of sustainability, and they act as goal posts for both governments and the private sector. Indeed, the UN SDGs are referenced within several of the ECAPs submitted to SE 2050 (read more in Section: ECAPS). The Figure 1 timeline shows that within half a decade of governments signing the Paris Agreement on Climate Change, the recognized importance of establishing sustainability within the built environment grew significantly. This is exemplified by COP21 at which an entire day was labeled Buildings Day. This day studied the operation and embodied carbon of buildings and put specific items on the international agenda as they

relate to the embodied carbon of buildings. COP21 was the first time an inter-governmental event on climate action has dedicated such a significant amount of time to buildings.

As sustainability movements related to structural systems continue to grow, SE 2050 aims to use the momentum of international movements as well as its own recent history of influence and transform them into education and action across the structural engineering industry.

3 SE 2050 ENGAGEMENT: ADVOCACY & EDUCATION

Since officially launching at the Greenbuild International Conference & Expo in November 2020, SE 2050 has sought to increase industry engagement in the embodied carbon conversation through education and advocacy.

Over the past two years, subcommittee members of SE 2050 have presented at building conferences and conventions across North America. Members have presented at notable building conferences such as Greenbuild International Conference & Expo (2020), Structures Congress (2020), the International Association for Bridge and Structural Engineering (IABSE, 2021), the Structural Engineering Association of California (SEAOC, 2021), and the Net Zero Conference (NZT, 2022).

In addition to speaking at large-scale conventions, SE 2050 has targeted smaller audiences through presentations at local CLF meetings, seminars for students at high schools and colleges, and by providing presentations to firms who are interested in joining the SE 2050 program and/or are new to the embodied carbon conversation and have questions.

More recently, SE 2050 has been called upon to develop seminar series to provide guidance in performing life cycle assessments (LCAs) on structural systems. SE 2050 members have developed several documents on best practice methodologies for specific structural systems, which can be found at the SE 2050 website. Developing educational tools is particularly noteworthy for, while the definitions and methodologies for such practices continue to take new form, establishing common principles amongst practitioners is crucial to validation. Therefore, SE 2050 acting as a common thread amongst firm sustainability education is an important new phase of the program.

Taken together, these advocacy and education actions highlight the reach that SE 2050 has attained since its launch. Dedicated SE 2050 members have spoken and advocated data-driven sustainability goals to hundreds, if not thousands, of structural engineers. It is now common for subcommittee members to be attendees at seminars in which SE 2050 is referenced as a key industry movement. Presenting to industry professionals has been crucial to SE 2050's growth and such presentations continue as a key aspect of the program's net zero strategy.

4 SE 2050 COMMITTED FIRMS

The SE 2050 program is premised on volunteered firm engagement. As such, both the level of engagement the number of committed firms are primary attributes of the program's achievements.



Figure 2. SE 2050 Committed Firms.

SE 2050 is proud of the steady growth in firm commitments over the past 2 years. Through advocacy of the program and education on the cause, SE 2050 has successfully garnered the commitment of about 100 firms within two years.

Additional to the remarkable speed at which structural engineering firms have committed to the SE 2050 program, is the demographic range of these firms. As shown in Figure 2, firms are committed across all Northern America. It is worth noting, that pegged locations represent the original “signed on” firm such that firms with multiple offices are represented with only one peg. Therefore, Figure 2 conservatively visualizes the office locations that are working to achieve the SE 2050 stated program goals. As a note, multiple offices are captured in the SE 2050 program requirements—for example, a multi-office firm is currently required to submit two LCAs per office (though not required to submit more than five LCAs across offices).

In addition to office location, the number of employees of committed firms ranges considerably. Firm size is an important aspect of how the SE 2050 Subcommittee continues to discuss and formulate future program requirements. As a program, inclusivity and representation across the full range of structural engineering firms is considered critically important to achieving carbon reduction goals (read more in Section on Future Goals).

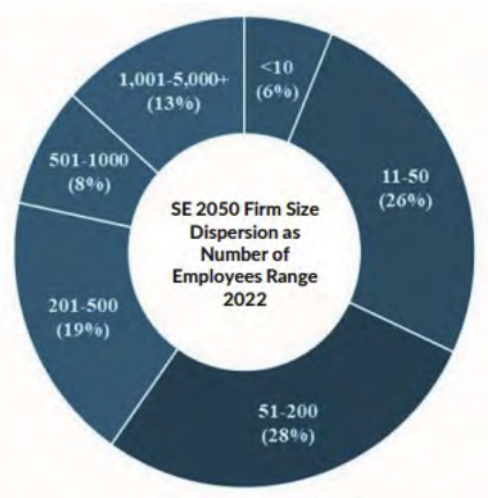


Figure 3. SE 2050 Firm Types.

5 EMBODIED CARBON ACTION PLANS

Embodied Carbon Action Plans (ECAPs) are central to firms’ engagement with SE 2050 and the path to net zero embodied carbon structures. The ECAP articulates how a firm will Educate, Report, Reduce, and Advocate for the sustainability of building structures. When firms engage with SE 2050, they are referred to the SE 2050 Program Requirements Guidance Document. In addition to other program requirements, this document provides details on ECAP deliverables which can be summarized in the following actions:

- Provide an outline of your firm’s strategy to educate employees about embodied carbon and advocate for net zero embodied carbon structures
- Provide an outline of your firm’s embodied carbon reduction work to report externally
- Specify measurable goals to assess your firm’s process in reducing embodied carbon in project work

ECAPs are to be submitted yearly and published on the SE 2050 website. Currently, 65 firms have published their ECAP. Several firms have already submitted an updated ECAP for their second committed year.

The collection of ECAPs that SE 2050 has aggregated is a unique and encompassing data set in and of itself. For this paper, all submitted ECAPs were assessed. The outcome of the study revealed common goals, actions, and statements of firms as they relate to sustainability. Additionally, this study shows the general status of data collection capabilities as well as embodied carbon reduction strategies.

5.1 Educate and advocate

Embodied Carbon Action Plans (ECAPs) are central to each firm’s engagement with SE 2050 and the path to net zero embodied carbon structures. The ECAP articulates how a firm will Educate, Report, Reduce, and Advocate in its commitment to SE2050.

From the 65 unique firm ECAPs, it is apparent that the structural engineering industry acknowledges their role in the management of embodied carbon and supports the SE 2050 mission to achieve net zero embodied carbon for structures by 2050. In the ECAPs, all firms state a repeating educational event for sustainability. More specifically, 60% of ECAPs showed the creation of internal working groups for embodied carbon reduction as separate from a general sustainability team.

Most ECAPs refer to the AIA 2030 Commitment and several go on to explain the relationship between operational carbon versus embodied carbon. Noted here is the chart demonstrating the in-step relationships carbon reductions on both fronts should attain (SEI Sustainability Committee, 2018).

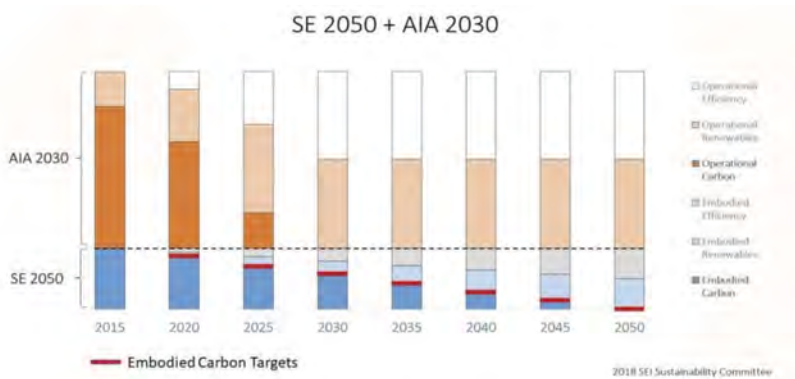


Figure 4. SE 2050 Firm Types.

In addition to AIA 2030, ECAPs demonstrate that most firms engage with several sustainability-related organizations and movements. In fact, 65% of ECAPs list their partnerships with other “green” organizations (e.g., CLF, USGBC, LEED, NCSEA, Green Globes, IStructE, etc.). Less common, but of interest, is that 23% of firm ECAPs state the firm’s interest in driving policy and/or code requirements as related to sustainability structural systems. SE 2050 is itself explicitly partnered with CLF, IStructE, and NCSEA and believes that the combined influence of like-minded organizations is important to achieving net zero.

A common set of statements amongst firm ECAPs surrounds advocacy of processes that would better facilitate sustainable design. As a percentage of ECAPs: 65% stated the need to onboard the client as an initial or highly important step, 60% referenced the benefit of greater access to product specific EPDs and their desire to use them in specifications, and 46% stated a high benefit in engaging across disciplines and stakeholders early in the design process for sustainability goals.

5.2 Report

As stated, firm reporting is integral to the success of SE 2050. Therefore, ECAPs are required to explain how a firm will collect and report its LCA data. As such, 72% of firms explicitly listed the LCA tool they are using. Most firms are using external tools like Tally, OneClick, or Athena, but 22% of firms reported that they are developing internal tools to conduct LCAs. Currently, these tools are shown to have significant differences in GWP evaluation. As explain in the SE 2050 Database Section, one input parameter for the SE 2050 database is the LCA tool used. Understanding how outcomes differ across tools will be important in refining the LCA process.

With the need for tool refinement in mind, it is unsurprising that 72% voiced the need for more data prior to establishing reduction targets. This signals a clear need for the database that SE 2050 is developing. While SE 2050 is working to establish program requirements related to year-by-year reductions, 11% of firms studied have already established their own internal reduction targets ranging 5% - 30% over the next few years. Oppositely, 14% of firms state limited resources availability to establish baselines making reduction targets difficult to establish.

5.3 Reduce

While reporting and setting clear reduction goals is important to achieving net zero, there are many actions firms can take now to reduce the embodied carbon of their designs. Many firms recognize this and list actions for reduction in their ECAP. The most common action being taken is editing General Notes/Specifications. Sixty percent of firms state they will be implementing requirements related to material GWP values and product-specific EPDs. These contractual requirements will (1) serve to both reduce a project's total GWP via materials selection and (2) spur on manufacturers to produce products more sustainably and document the outcome via creating product-specific EPDs.

Other means of reducing embodied carbon relate to firms' goals to design with materials known as being more sustainable and/or to incorporate sustainable methodologies into design outcomes. For example, 38% of firms stated they aim to increase designs featuring biogenic construction materials. Additionally, another 12% of firms stated their goal to design for adaptive reuse and/or regenerative design.

6 SE 2050 DATABASE - OVERVIEW

An acknowledged limitation to setting embodied carbon reduction targets for structural systems is the current lack of knowledge/confidence in baseline data that structural systems will embody. As such, the SE 2050 database will be a powerful tool for embodied carbon reduction. While still in the beta stage, SE 2050 is focused on ensuring smooth processes of data collection as well as increasing the quantity of data collected.

The SE 2050 Database anonymizes and aggregates firm submitted LCA data for structural systems. To date, firms have collectively submitted 100+ LCAs. There exists no other cross-firm database on embodied carbon that has such widespread support in North America. The requested data inputs include, but are not limited to, the following (*note: published data differs from this list and is currently limited to Total GWP, Project Sq Ft, and Height):

- project zip code
- primary building use type (public assembly, education, retail, etc.)
- construction type (new construction, major renovation, etc.)
- gross square footage
- build height, number of stories above and below grade
- typical column grid by spacing
- risk category and other seismic/wind classifications
- material of primary gravity system

- material of primary lateral system
- geotechnical attributes such as allowable soil bearing pressure and foundation system type (piles, shallow footings, etc.)
- LCA tool used (Tally, OneClick, Athena, hand calculated, etc.)
- Total GWP in kg-CO₂eq

As outlined in the SE 2050 Program Requirements Guide, firms are currently required to submit two LCAs per year, which inform the database. For firms with multiple office locations, the requirement states that two LCAs are to be submitted per office, but that a firm is not required to submit more than five LCAs in total. This data is not public and only signatory firms can access the database viewer.

New project LCAs are being added to the SE 2050 database each week. This data will provide new insights into GWP baselines for a variety of structural design. As such, one of SE 2050's primary upcoming goals is the analysis and reporting of the anonymized data.

7 SOM'S COMMITMENT TO SE 2050

SOM's commitment to SE 2050 is part of the firm's climate action plan to reduce resource usage and taking the lead toward a zero-carbon economy. As an interdisciplinary design practice, SOM is also a signatory of the AIA 2030 Commitment, the Architecture 2030 China Accord and World Green Building Council Bringing Embodied Carbon Upfront. Structural designers are active in groups such as the SOM Climate Action Group, working to reduce carbon across urban planning principles, material usage and research, and building construction.

The SOM SE 2050 champions organize activities to implement the Embodied Carbon Action Plan. The Structural Life Cycle team develops the workflow used for LCA and internal reporting efforts for all structural projects at all design phases. All structural designers are encouraged to participate in the firmwide discussion about the principles of embodied carbon and its reduction, and project case studies are presented to share innovations for and setbacks to successful embodied carbon reduction that can be applied to on-going and future projects. Structural designers also collaborate with industry partners to bring research to market for implementation into built projects and advocate for best practices in sustainable design both internally and in professional practice groups outside the firm. Furthermore, advocacy with both clients and builders aligns design and development interests to implement appropriate sustainable goals for all projects.

REFERENCES

- ICBO, 1997, Uniform Building Code, Structural Engineering Provisions, Vol. 2, 1997 edition, pp. 2-161 to 2-163, International Conference of Building Officials, Whittier, California.
- "SE 2050 Challenge." Carbon Leadership Forum, 17 Oct. 2021, carbonleadershipforum.org/se-2050-challenge/.
- "Sustainable Development History." United Nations: Department of Economic and Social Affairs, Sustainable Development, 2022, sdgs.un.org/goals.
- Graham, Genevieve, et al., "Reaching Net-Zero Structures - SE 2050 Commitment Program Status and Vision for the Future", Proceedings of the SEAOC Convention, 2022.

Quantifying and specifying decarbonization in buildings

N. Wang & D. Shook

Skidmore, Owings and Merrill LLP, San Francisco, CA, USA

K. Chang

Skidmore, Owings and Merrill LLP, Los Angeles, CA, USA

E. Leung

Skidmore, Owings and Merrill LLP, New York, NY, USA

ABSTRACT: As designers, efficient material use to achieve a certain design is a well-established principle that is evolving to be centered around the whole building decarbonization. From early design to construction to operation and end of life, calculating the embodied carbon of building structures based on a bill of materials helps to quantify the impact of design decisions and build a database of design-specific carbon values that can be used to improve a design and to benchmark across different building types and structural systems. Ultimately, decarbonization will require the specification of low-carbon material technologies and the establishment of material- or product-specific global warming potential (GWP) limits, used to better qualify the embodied carbon of a specific design.

Quantifying embodied carbon takes different forms at the various stages of design, with all tools sharing a central repository of industry-wide carbon factors. As the industry works toward carbon reduction, designs can specify project-specific low-carbon materials, which will refine the calculation to include product-specific carbon factors. Alternatively, for some building materials, accounting for and reducing the use of carbon-intensive ingredients, in addition to collaboration with industry partners early in design to create and select materials based on performance and project goals, will drive decarbonization over the next few decades.

Attendees will learn about the calculation of embodied carbon of building designs, the use of material specifications to realize project-specific design goals and the feedback loop from carbon quantification and specification efforts to future building design.

1 RESILIENCE AND CARBON

1.1 *Whole building decarbonization*

To address the climate emergency, the spotlight on carbon emissions has shifted from a focus not only on operational carbon emissions but also on embodied carbon emissions, among other environmental impact factors relating to whole-building life cycle assessment (LCA). Agencies like LETI and IStructE have established guidelines on recommended embodied carbon targets relative to building area based on building program or height. In addition, other pathways to limiting global warming potential (GWP) per unit weight or volume in specific building materials come from policymakers by way of new provisions such as Buy Clean California and the Marin County Low Carbon Concrete code. Other groups like SE2050 aim to collect an industry-wide database of structural embodied carbon for its membership's designed projects that will report on the current state of the industry and provide the basis for specific embodied carbon targets.

Decarbonization is not possible without continued advancements in the building material industry. In recent years, cement production with lower emissions and energy usage coupled with low-carbon alternatives to cements have been directed at the heavy-hitting Portland cement, known to be an intensive-carbon building material. The use of carbon-sequestering materials such as timber allow for the storage of carbon in building materials until the building is demolished and technologies such as bioenergy with carbon capture and storage (BECCS) can permanently remove the EC.

1.2 *Embodied carbon*

Embodied carbon (EC) refers the carbon dioxide (CO₂) emissions emitted during the raw material extraction, transportation and manufacturing of building materials; during the construction and use of buildings; and at the building end of life. Through detailed design EC calculations, it is common to consider mainly the product and construction stages, as most environmental product declarations (EPDs), for a building material product, report environmental impact factors for LCA modules A1, A2 and A3 (EN 15978). When designing for long-term resilience, it is important to also consider the building use and end of life stages, for example, where buildings are not designed for immediate occupancy and limited repair after design-level seismic events. The consideration of carbon-sequestering building materials also allows for carbon storage over the building service life that factors into strategies for reducing upfront embodied carbon.

1.3 *Carbon accounting to achieve decarbonization*

To align the discussion on embodied carbon, industry-wide carbon accounting through calculation and specification is needed. By understanding and limiting the carbon emitted in construction today, this accounting can provide important justification for low-carbon materials and pave the way for net zero embodied carbon buildings.

EC calculations provide the cornerstone for benchmarking the industry and setting up future policies to achieve net-zero embodied carbon goals in the next three decades. Through standardization and automation of these calculations, the database has increased consistency and facilitates comparison across many building types regarding material efficiency. Establishing these benchmarks will allow for a clear pathway to EC reduction in building structures.

The building design forms the basis of the embodied carbon calculation. During the building design phases, the designer determines the best reduction strategies given the design space. The specifications then implement those reduction strategies, working with industry partners such as the contractor and material suppliers to achieve those EC reductions. Post-construction LCA is also a reliable tool for ensuring the design meets the intended EC goals.

2 CALCULATIONS AND CARBON DATABASE

2.1 *Building carbon calculations*

Each building structure is a function of design constraints based on parameters including project site and architectural program. The database of carbon values for each building design includes these parameters which give the database dimensionality for the establishment and selection of appropriate benchmarks to be used for future designs. Recording data at each design phase tracks the change associated with design decisions and development and its relative impact on EC. As a designer, many of the construction, use and end of life stage LCA modules may be estimated, but the contributions of these stages may vary in the final project delivery. Thus, current calculations consider LCA modules A1-A3, also known as measuring “cradle-to-gate”, to align data across different projects.

An example structural carbon calculation is developed in the following sections for a six-story cultural center project in Northern California, from the bill of materials to the carbon factors associated with local material procurement to the final summary of structural embodied carbon.

2.2 Establishing the bill of materials

Effective material use for decarbonization depends on how the material is used in the building structure. To quantify the impact of the building structure, it is important to categorize the building materials based on location in the building superstructure/substructure/foundation, structural element type, general material category, specific material type, etc.

All structural materials are categorized as defined in the material specifications. The structural steel, reinforcement and connection tonnages and the concrete and timber material volumes can be calculated and sorted into a clear bill of materials based on the categorization.

Alignment on the definition of structural material quantities is important to the development of the EC database. Automation and standardization of the quantity takedown from all design and documentation tools and software ensure consistent calculations, ensuring that all project EC is calculated. During early design phases, estimated quantities are based on prior experience and architectural design models. During later design phases, structural analysis models and BIM documentation models form the basis for the bill of materials. A post-construction bill of materials validates the design phase assumptions.

Depending on the design phase, different structural models may be used to establish the bill of materials by assigning products or material properties to specific modeled elements. These properties include, but are not limited to, structural element type, material strength, material density, material composition and region of production. In earlier phases, analysis models are used to validate and approximate the material quantities associated with in-progress designs. In later phases, building information modeling (BIM) allows for a detailed accounting of model elements and their assigned materials aligned with the level of development during design – accounting that can be verified in collaboration with the general contractor during construction.

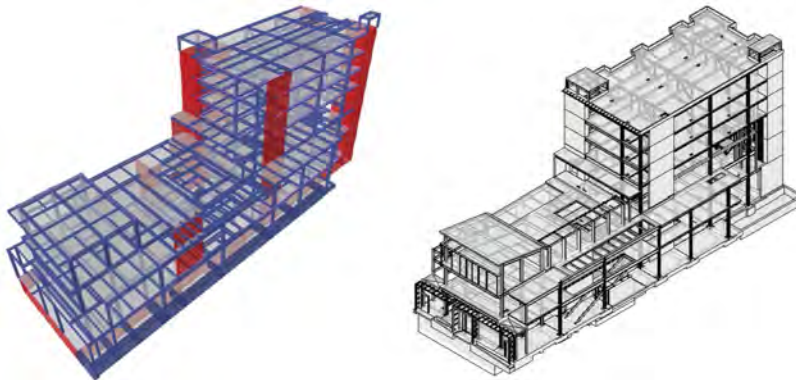


Figure 1. The bill of materials can be established from both early-phase and later-phase models, including structural analysis models (left) and BIM models (right).

2.3 Selecting carbon factors

EC factors are dependent on the construction market, as different factors including, but not limited to, the energy used during the project stage, the raw and recycled materials available and the transportation from the production facility to the construction site are region-specific. Regions such as North America and Europe/UK have more robust environmental product declaration (EPD) databases (*Standard for building carbon emission calculation*, GB/T 51366-2019, provides Chinese code-based EC factors), but other regional markets may rely on databases such as the Inventory of Carbon and Energy (ICE) for building materials with a shortage of EC information. Where the information is available or limits are defined separately, each LCA module (e.g. A1, A2 and A3) has its own EC factor.

For materials such as timber, biogenic carbon may be considered a negative value (carbon removal) in LCA module A1 and added as a positive value in modules C3/C4 at the end of life

stage when the timber waste after demolition releases the carbon emissions where the LCA study measures beyond cradle-to-gate (A1-A3). Based on product-specific EPDs collected, NRMCA has published a member national and regional LCA benchmark report, used to develop a range of concrete EC factors for the project workbook study and the specification GWP limits. Concrete mixes are made of carbon-intensive materials such as cement with EPDs. Since the use of supplementary cementitious materials (SCMs) lowers the GWP impact of concrete, some LCA tools and industry-wide EPDs allow for more granularity in the concrete carbon factors based on the aggregate type, concrete strength or material grade and the percentage of cement replacement.

The A1-A3 EC factors for the example project are selected based on an average factor for steel and reinforcement produced and fabricated in the United States; and on average factors for concrete of a specific strength and supplementary cementitious material (SCM) replacement typical for concrete mixes supplied in the Pacific Southwest region.

2.4 Calculating embodied carbon

To benchmark and show improvements to the building's embodied carbon, the designer calculates the impact of building materials from earlier concept phases through later design phases. Early estimation tools such as the assumptions included in the Environmental Analysis Tool™ developed by SOM allow for EC calculations when the building has not yet developed a bill of materials, with minimal inputs including building area, program and site conditions. In the proposed embodied carbon workflow, an engineer inputs project information and structural material quantities based on the bill of materials in the project workbook. This workbook is linked to (1) an EC factor database with information generally from industry-wide EPDs and (2) a project database backend that compiles all the information stored for each project based on the final summary at the end of a design phase (e.g. Schematic Design, Design Development, Construction Documents, etc.). As the structural material quantities are associated with specific material types and market regions, the embodied carbon is calculated and summarized automatically. Where coordination with other designers is required, LCA tools such as One Click LCA® are used for a more comprehensive study.

The A1-A3 embodied carbon in units of carbon dioxide equivalent (CO₂e) is calculated based on applying the EC factor in kg CO₂e per weight of metal material or per volume of concrete or wood material. With proper segmentation, the calculated embodied carbon can be associated with a specific structural system, structural object or element or structural material, allowing for further analysis and comparison between different building structures in the database.

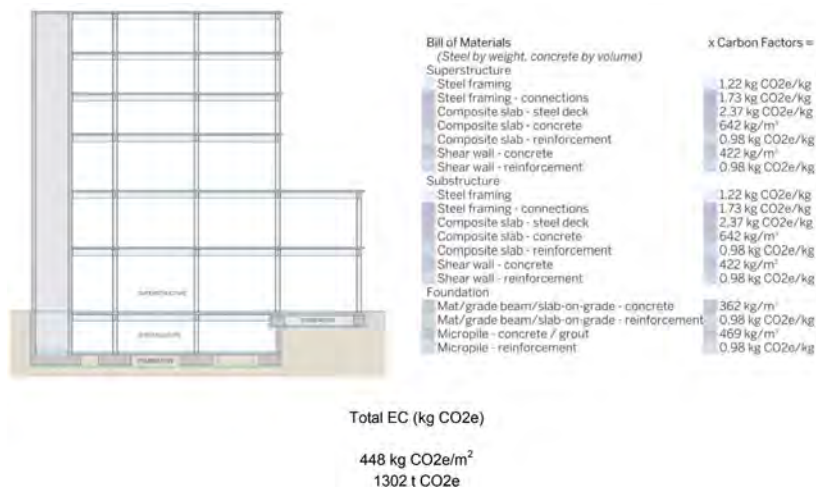


Figure 2. Summary of the baseline embodied carbon calculation for the project-specific and design-specific bill of materials.

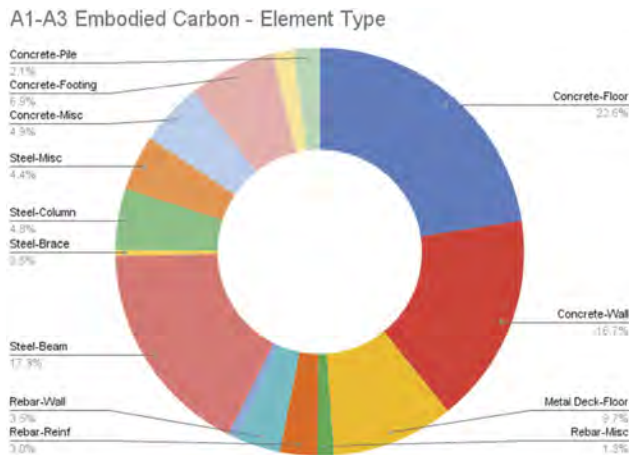


Figure 3. Summary of the baseline embodied carbon calculation by element type.

The following figure summarizes the structural embodied carbon study for 90 current and recent projects. Active studies include categorization of building structure parameters such as architectural height and EC targets based on current data trendlines that evolve between the years 2025 and 2040.

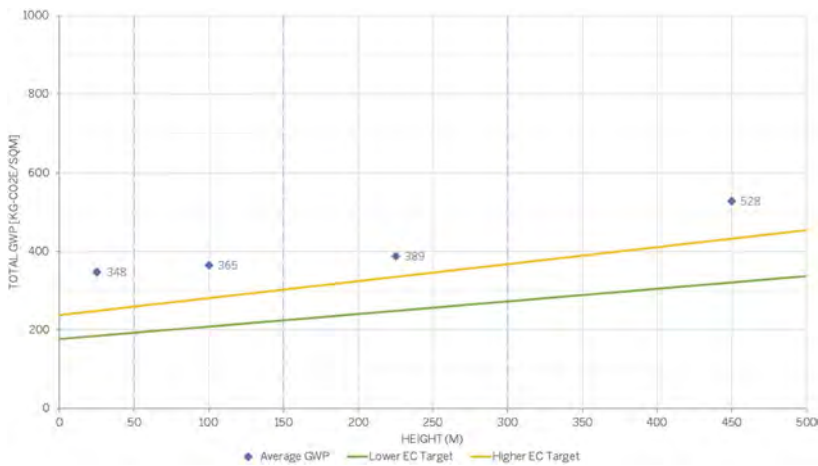


Figure 4. Graphical investigation of embodied carbon data for 90 current and recent projects from the Project Workbook database.

3 SPECIFYING MATERIALS

3.1 Understanding the market

To meet carbon emissions reduction targets by way of the Paris Agreement, low-carbon codes are being adopted, imposing GWP limits on some building materials. Buy Clean California set GWP limits for eligible materials such as unfabricated structural steel sections and concrete reinforcing steel. Marin County’s Low Carbon Concrete policy limits cement usage and embodied carbon by concrete mix or by project. These code-based limits will increase industry awareness, shifting the focus from client- and designer-driven GWP limits through specifications to industry-wide reduction of building material carbon emissions. These policy changes are needed as the industry move toward net-zero carbon building construction.

Carbon emission reductions are best achieved by understanding the regional construction practices and material availability. Some market regions may be able to reduce the carbon emissions associated with cement and have high availability of concrete mix components, whereas some market regions produce steel with high recycled content. These market factors should impact the structural system selection and the material specifications.

3.2 *Tuning material specifications to achieve project-specific targets*

Structural materials are a large component of the whole-building embodied carbon emissions, particularly the upfront carbon released by the end of construction. The material specifications implement the EC factors assumed during an LCA study, or design-phase carbon accounting, forming an important basis for the construction and material procurement.

Electric arc furnaces (EAF) melt recycled or scrap steel whereas blast furnaces can also melt raw iron ore for steel production. The energy intensity and the carbon emissions produced with EAF steel production allow for significantly lower GHG emissions. For concrete reinforcing and structural steel, an average recycled content should be specified to reduce the GWP impact. If the project is in a region where EAF is prevalent, limiting the structural steel sections specified based on availability so structural steel can be locally milled also lowers the EC.

For concrete materials, the material specification allows for two conformance paths that demonstrate the GWP limits for the project can be met. Compliance Method A - Total Carbon Budget relies on the contractor to account for the concrete supplied on the project with a final report showing the EC across all concrete supplied for the project. Compliance Method B - Individual Mix Carbon Limits relies on the concrete supplier to deliver mixes that meet individual limits and the designer to set limits that meet the overall project EC target. In addition, cement usage can be reduced where concrete mixes can achieve the compressive strength requirements beyond 28 days as defined by ACI 318 where slower strength gain is an acceptable structural performance criterion. Concrete cementitious replacement can be specified or limited, and limits can be developed from EN 15978-compliant LCA tools.

Table 1. Example Individual Mix Carbon Limits for projects using Compliance Method B.

Typical Application of Concrete Class/Mix Design	Design Strength (psi)	Maximum GWP per EPD (kg/m ³)
Footings, Pile Caps and Grade Beams	5,000	295
Slabs-on-grade	5,000	295
Basement Walls (Shotcrete)	5,000	337
Shear Wall (CIP)	See Elev.	312
LWC Fill on Metal Deck	4,000	466
NWC Fill on Meta Deck	4,000	288
Curbs, Pads, Column Encasements and Miscellaneous	4,000	288

3.3 *Allowing for material technology adoption*

Net-zero carbon construction relies not only on the carbon optimization of current building materials, but also on the development of new materials that can be specified as structural materials. An example is carbon dioxide mineralization, where mineralized CO₂ is introduced as an admixture, sequestering carbon in the concrete mix. Performance-based specifications also allow for these available and upcoming materials such as recycled concrete aggregates, carbon-sequestered aggregates and pozzolan cements.

4 CONCLUSIONS

Environmental impacts of building structures must be minimized. First, policy makers, developers, contractors and designers continue to work carbon accounting and reduction strategies

as a common part of the design and construction process. Second, establishing an EC benchmark or target pushes the industry to reduce material usage and explore new material technologies. Third, designers specifying more efficient material usage and new material technologies will expedite their adoption into the coming generation of building structures. Fourth, this cyclical process continues with each generation of buildings until structures are net-zero embodied carbon from cradle-to-grave.

REFERENCES

- LETI. 2021. Embodied Carbon Target Alignment.
- The Institution of Structural Engineers. 2020. Setting carbon targets: an introduction to the proposed SCORS rating scheme.
- CarbonCure. 2023. <https://www.carboncure.com/>.
- EN 15978: 2011, Sustainability of construction works.
- ISO 21930: 2017, Sustainability in buildings and civil engineering works — Core rules for environmental product declarations of construction products and services.
- M. Sarkisian, D. Shook, C. Horiuchi & N. Wang. 2020. Embodied Carbon-Based Design: Incorporating Estimations of Carbon Reduction into Building Design Decisions.
- NRMCA. 2022. NRMCA Member Industry-average EPD For Ready Mixed Concrete.

Carbon optimization of hybrid material structures

M.P. Sarkisian, D. Shook & A. Zha
Skidmore, Owings & Merrill, San Francisco, USA

C. Horiuchi
Skidmore, Owings & Merrill, San Francisco, USA (formerly)

ABSTRACT: It is commonly known that the structural materials included in building construction contribute significantly to global emissions due to the associated carbon required with their extraction, production, and transportation. The most common structural materials, concrete and steel, can also have the greatest impact in part due to their high volume of usage. However, with requirements of fire protection, vibration, seismic detailing and constraints of constructability, it is not feasible to simply eliminate all concrete and steel from our buildings. Instead, structural engineers can look to make intelligent replacements of carbon-intensive materials with low carbon, fiber-based materials such as timber. In this way, engineers can make noticeable reductions in buildings immediately and not wait until codes catch up with new structural systems. This topic has been explored by the authors with a variety of materials and geometries. Recently the authors designed a built hybrid mass timber and steel structure in a height seismic zone. In each case the use of timber is expanded and therefore overall embodied carbon incrementally reduced.

1 HYBRID SOLUTIONS

1.1 *Rethinking design and construction with hybrid solutions*

Traditional construction methods are on the cusp of rapid change. The architectural, engineering, and construction (AEC) communities are seeing a significant realignment fueled by the urgency of climate change. In a market controlled by costs, governments are raising the standards to reduce embodied carbon. The industry will likely continue to be a cost-driven sector, but reconsideration of past assumptions is needed to efficiently meet the needs of the pending climate crisis.

To reduce carbon quickly and efficiently the use of mass timber must be expanded. A key short coming of mass timber are the larger structural dimensions required. Also, spans are typically reduced resulting in less flexible spaces. To ensure that building remain flexible in the future, selective use of steel and concrete can create a balance between significant carbon reductions while maintaining flexible spaces.

1.2 *Evolving requirements from designers, owners, and governments*

The past 5 to 10 years have seen numerous US design organization such as the American Institute of Architect (AIA), Structural Engineers Association, nearly every major consumer market company (e.g. Google, Ford, Lendlease), and several regional governments (e.g. States of California, Oregon & Washington) all adopt a wide range of commitments and requirements pertaining to reducing embodied carbon. As a signatory of SE 2050, Skidmore, Owings & Merrill (SOM) has committed to bringing meaningful carbon reductions to a wide spectrum of buildings.

1.3 *How these changes will affect structural system construction and design*

As the two above changes unfold (increased use of low-carbon materials and AEC commitments) it is likely that general contractors will rethink how they can have more sub-contractors internally self-perform key tasks such as mass timber fabrication/installation. There is already precedent in the industry of this with concrete, drywall, cabinetry, etc. Alternatively, traditional concrete and steel sub-contractors may seek to have more trades under their control such as mass timber. The second is a potentially beneficial realignment with sub-contractors finding best ways to adopt low-carbon materials complimented by their traditional work. This hybrid option could greatly expand the use of low-carbon materials to a wider range of buildings.

2 EXPLORATIONS OF MASS TIMBER HYBRID STRUCTURES

While the number of commonly used structural materials is limited: concrete, steel & timber, their combinations can be composed in a wide variety of ways. The following outlines several explorations, incrementally increasing the use of mass timber, seeking material and cost efficiency balanced with performance and aesthetics.

2.1 *Floor system explorations*

Floor systems compose 35% to 45% of the total embodied carbon of most mid-rise and high-rise structural systems, based on data collected internally by SOM, making them the largest single culprit of embodied carbon. Thus, their decarbonization is vital. The structural frame of floor systems typically also provides acoustic and fire separation between floors. While traditional steel and concrete have found effective methods for these separations, mass timber will require its own solutions. Acoustic separation is typically provided by an acoustic mat and a minimum of 50mm (2") of concrete (Johnson, 2021). The concrete may or may not be part of the structural system but must be included. An early exploration by SOM utilized a concrete slab supported by glulam beams, see Figure 1, at the United Nations Office at Geneva. This was complimented by the façade system aesthetic to create a unique and efficient building composition.



Figure 1. Example of built hybrid floor systems.

In parallel, SOM also considered the potential of composite behavior of cross-laminated timber (CLT) panels with the concrete topping already required for acoustics. This was found through full scale testing to be highly effective in controlling deflection over a 7.3m (24'-0") span (Johnson, 2017a).



Figure 2. Hybrid composite floor system full scale testing (Johnson, 2017a).

Further explorations of hybrid floor systems considered steel beams with composite CLT panels spanning between composite steel beams, see Figure 3. This efficient system also had the benefit of a flat soffit which has numerous benefits from MEP coordination to aesthetics.

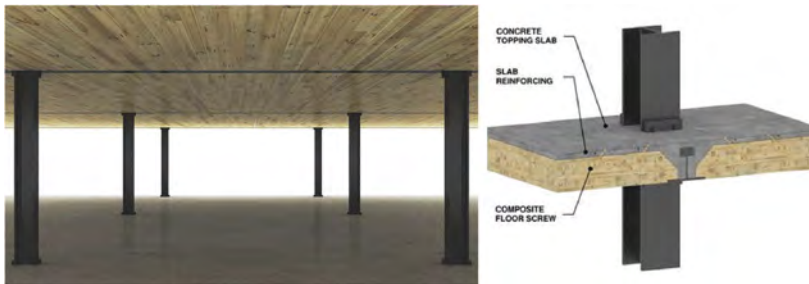


Figure 3. Hybrid floor system concept (Johnson, 2017b).

2.2 Building system explorations

As part of a total building exploration of mass timber it was found that select regions enhanced with reinforced concrete would be important in achieving the long gravity framing spans and lateral strength common in high-rise construction (Johnson, 2014).

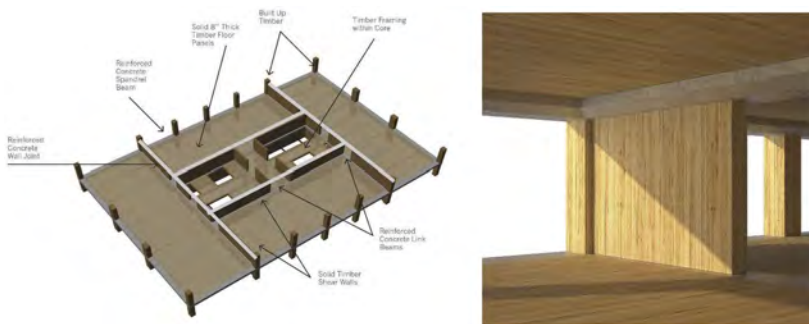


Figure 4. Timber tower systems (Johnson, 2014).

3 PROTOTYPE OFFICE BUILDING

3.1 Mass timber in a cost-focused building

In what follows, a recently constructed office building shows how designers can work effectively with all trades, contractors, and owners to achieve a cost-effective, low-carbon solution meeting the dynamic needs of our urban fabric.



Figure 5. COB3 building rendering.

The COB3 building will redefine the San Mateo County Government Center with an iconic, forward-looking design that reflects the values of the community. With a mass timber/CLT structural system, ultra-low carbon footprint, and net zero energy goal - the design sets a new standard for sustainable, generational, civic buildings beyond the Bay Area. The 5-story mass timber building totaling 19,325sqm (208,000sqft) is in downtown Redwood City and surrounded by existing county buildings, including the San Mateo Superior Court. The building configuration features a north and south public plaza linked by a transparent building lobby creating a connection between the downtown Redwood City Theater District and the San Mateo County buildings. The building houses the main public functions at the ground level, including the Board of Supervisors Chamber.

The project is being developed by the Project Development Unit, with SOM as the architect and structural engineer and Truebeck Construction as the general contractor. Scheduled for completion in late 2023, with the goal of both net-zero energy and a significantly reduced embodied carbon footprint, SOM's structural engineering design team responded to the challenges of the nation's first net-zero energy mass timber civic building.

3.2 Building structural systems

Designed in conformance with the 2018 International Building Code (IBC, 2018) with State of California Amendments (CBC 2019), the civic building is assigned to Category II per occupancy load limits of 2019 CBC Table 1604.5. The structure is classified as a Type IV HT (Heavy Timber) construction per fire-resistance rating requirements of 2019 CBC Table 601. The building is located not only in a high seismic region, with a seismic design category D, but also in a region highly susceptible to liquefaction with a seismic site class F.

COB3 is characterized by its H-shaped layout with the gravity system consisting of glue-laminated (glulam) timber beams and columns with a cross-laminated timber (CLT) floor system. The plan dimensions of the building are typically 85m by 60m (280ft by 195ft).

Distinctly, glulam beams are utilized only in a single direction: a pair of glulam beams, each measuring 22cm by 65cm (8¾-inch by 25½-inch), span 10.7m and 9.1m (35ft and 30ft) bays. The long spans were achievable with relatively shallow beam depths by having beams continuous over the center supporting column.



Figure 6. COB3 hybrid structural frame with steel (Grey) and timber (Brown).

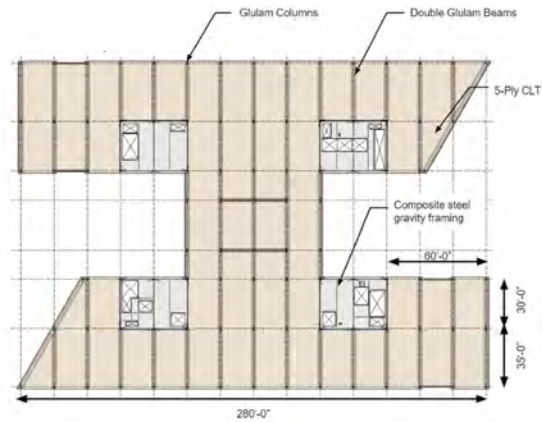


Figure 7. COB3 hybrid structural frame with concrete (Grey) and timber (Brown).

All glulam columns are of consistent width perpendicular to the beam spans to allow for a continuous beam configuration with the beams running past the side faces of the rectangular columns. A unique connection system is utilized to secure the glulam beams at column supports while also acting as the splice connection for the columns. Having a repeatable dual-purpose connection system, combined with off-site fabricated, allowed for an efficient erection schedule by reducing the number of picks that needed to be made on-site as well as reducing the overall steel material quantities. Only simple screw-type connections are needed on-site, in pre-drilled holes, to secure the structural elements. As part of the HT classification, all timber connections are hidden from view with a nominal layer of timber for fire protection.

Because timber beams only occur in one direction, the 17cm (6 7/8in)-thick 5-ply CLT slab system acts predominantly as a one-way spanning system spanning the 6.1m (20ft) bays. Therefore, no additional spandrel beam is required around the perimeter of the building. CLT panels are nominally 2.6m (8'-6") wide, and 12.2m (40ft) long. The length of the panels provides a double span condition over the center supports, reducing the deflection of the panels, which is critical to achieving the large span-to-depth ratio of the panel.

The composition of the CLT was optimized for cost and performance. The CLT outer plies comprise a strong Structural Select grade of Douglas fir, while the inner three layers are of a weaker but stiff Coast Sitka spruce. This composition allowed the exposed CLT layers to match the similarly exposed glulam beams and columns while providing the strength required of the panel. The weaker but stiff inner CLT plies significantly reduced the panels' costs while providing the required stiffness to limit deflection and floor vibrations, often an issue in long-span timber buildings.

The structure consists of four separate cores located at the reentrant corners of the building. The cores are supported between W14 (36cm) columns with floors comprised of composite steel beams. The composite steel slab system generally consists of 11cm (4½in) normal-weight concrete fill over 8cm (3in) metal deck. The cores also provide the lateral force-resisting system for the building. Buckling-restrained-braced frames (BRBF) are provided on all four sides of each core. Forces are developed into the BRBF system through the CLT diaphragm. CLT panels are spliced together using plywood splines and screw connectors, allowing in-plane shear transfer. Panels are also connected to each other and to the steel cores through steel straps and screws forming chords and collectors, creating a load path into the braced frames.

The deep foundation system consists of 46 cm (18in)-diameter auger cast-in-place displacement piles supported on pile caps that resist superstructure gravity and lateral load reactions at the base of the building. A total of 300 piles extends 22.8m (75ft) into the soil below. Grade beams interconnect pile caps with a 30cm (12in) pile-supported suspended slab on grade at the first-floor level.



Figure 8. COB3 Construction showing steel frames in mass timber construction.

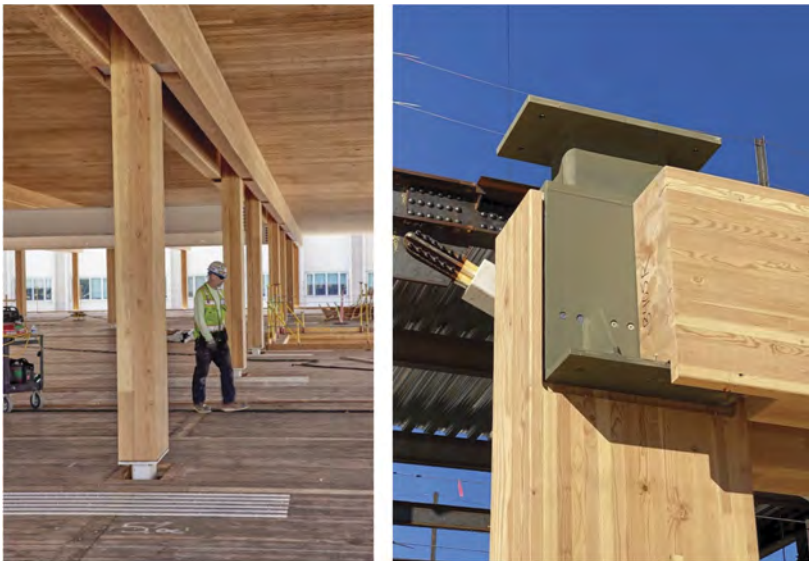


Figure 9. COB3 Steel column and steel diaphragm connections.

3.3 *Net zero energy and embodied carbon*

The COB3 design team focused on passive design strategies. With narrow floor plates, a balance between daylighting and solar heat gain to lower the lighting power density could be achieved. This also enabled the configuration of the floorplates to allow natural ventilation for night cooling to reduce loads. The design optimized the active systems, tailoring the mechanical equipment to its use, leveraging efficient hydronic fan coil units at the perimeter and VAV air distribution at the interior core spaces. The interior design strategically places the engineering systems within centrally located cores to minimize distribution distances for the most effective

services. The exterior windows have automated window shades that reduce solar heat gain and reduce glare. Once the design loads were reduced, the energy required to operate the building was offset by on-site renewable energy generated by photovoltaics on the project’s roof and the roof of the nearby parking garage, making it a net-zero operational energy building.

In addition to being net-zero operational energy, the project has reduced its embodied carbon by 70% primarily by using advanced structural technologies, including Cross Laminated Timber slabs, with Glued Laminated Timber beams and columns. The below embodied carbon life-cycle assessment was conducted using OneClick LCA regional average values.

To reduce the embodied carbon footprint of a building, the starting point should be the structure, as it is the largest contributor. While using mass timber instead of a steel or concrete structure yields significant savings in the embodied carbon of any project, additional savings through engineering design and close collaboration with architecture and other trades can be had.

Optimal bays and column spacings considering modules based on office spaces, the layout of mechanical systems, fire sprinklers, and lighting, among other items, all in conjunction with the quantity, size, and thicknesses of glulam beams and CLT required for each configuration, were considered. In addition, the pieces and connections could be priced in real-time with the contractor’s help. The solution was ultimately to reduce the number of beams and have them run in only one direction, leading to a reduced number of pieces and connections, creating an efficient bay size that works well with the office layouts.

By running beams continuously over supports, long spans could be achieved with relatively shallow beams, saving overall timber quantities compared to traditional post-and-beam timber framing systems. In addition, by running the beams in only one direction, a more efficient ceiling/floor structure is achieved by integrating the MEP distribution parallel with the beam direction, which reduces the typical floor-to-floor height and the overall building height. Subsequently, with a reduced floor-to-floor height, the overall enclosure volume could be significantly reduced, saving further on the embodied carbon.

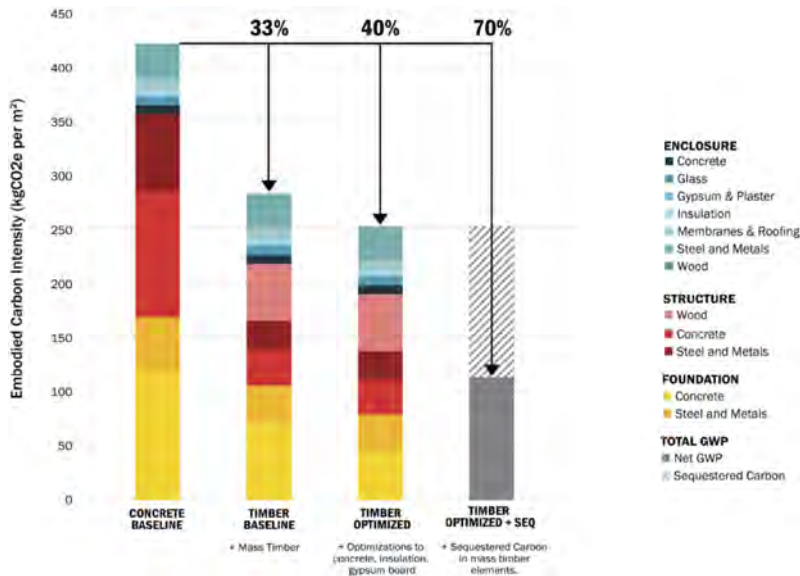


Figure 10. COB3 embodied carbon summary of options.

Setting an example of sustainability for the district, the new County Office Building will be an iconic and symbolic addition to Redwood City’s built environment. The material selection, structural optimization, and collaborative approach achieve enhanced performance, reduced embodied carbon impacts, net-zero energy, and a LEED Platinum rating.

4 CONCLUSION

The COB3 structural material selection facilitated significant cost and carbon reduction in non-structural systems such as ceilings, walls, and façade. While this project's general contractor utilized separate steel and timber fabricators and installers, the commonly perceived cost and coordination issues of having multiple large structural sub-contractors was successful. In the future, it is likely that the mass timber work could be under a single steel or concrete sub-contractor that could unlock improved design and construction efficiencies.

REFERENCES

- California Building Code (CBC), 2019.
International Building Code (IBC), 2018.
Johnson, B. 2014. *Timber Tower Research Project-System Report #1*. SOM.
Johnson, B. 2017a. *Timber Tower Research Project-Physical Testing Report #1*. SOM.
Johnson, B. 2017b. *AISC Steel & Timber Research for High-Rise Residential Buildings*. SOM.
Johnson, B. 2021. *Acoustic Testing of CLT Composite Floor Assemblies for TMBR Minneapolis*. SOM.

*SS26: Structural resilience in bridge engineering: Method,
theory, and practice*
Organizers: A. Chen, X. He & X. Ruan



Taylor & Francis

Taylor & Francis Group

<http://taylorandfrancis.com>

A study on the mutual effect on fatigue damage of orthotropic steel decks and pavements

B. Wang, D.L. Wang, R. Ma & A.R. Chen
Tongji University, Shanghai, China

ABSTRACT: The fatigue issue on orthotropic steel decks (OSDs) is closely related to the mechanical property of pavements. On the other hand, the fatigue cracks on OSDs can lead to local deteriorations of the supporting conditions of pavements, and therefore accelerates the fatigue damage evolution. This paper attempts to investigate the mutual effects on the OSD-Pavement system with existing cracks. Firstly, the finite element model of the OSD with penetrating cracks on the rib-to-deck welded joint is established. By obtaining the stress intensity factors along the crack front, the fatigue crack growth behavior is analyzed. The fatigue damage evolution on pavement is then studied using a continuum damage model in terms of the first principal strain range. According to the results, it can be addressed that the mechanical performance of pavements may help to resist growth of penetrating cracks on rib-to-deck welded joints on OSDs. On the other hand, the cracks will accelerate the fatigue damage on pavements as well. For a crack that reaches $0.75t$ (t as the deck plate thickness), the damage initiation on the pavement can be accelerated by about 16%. The results can be helpful in the decision making for the pavement maintenance of bridge, as well as the retrofitting works on OSDs, which may further benefit the life-cycle performance of the bridge.

1 INTRODUCTION

Fatigue cracks are commonly observed on orthotropic steel decks (OSDs). Different types of cracks are addressed at welded joints and their vicinities. Among them, the crack that grows to penetrate the deck plate is quite unfavorable. Since this type of crack may initiate at the weld root of the rib-to-deck joint, it is quite difficult to detect and consequently, to prevent the growth in early-stages. On the other hand, penetrating cracks on an OSD can reduce its local stiffness, and alter the boundary conditions of pavements, ultimately resulting in premature damage of pavements. Studies have shown that the weld defects, specifically the lack-of-penetration (LOP) and the coarse-grained heat-affected zone, are the key to penetrating cracks on OSDs (Wang et al., 2019; Wang et al., 2021).

Figure 1 demonstrates an example of a bridge that suffers from this issue, in which the cracks can be observed by removing the pavements. Although there are only a few cracks observed on the deck top, the corrosion seems more severe by covering rusts in a large range longitudinally. These sites follow the location of the rib-to-deck joints, indicating the early damage site on the waterproof layer of the pavement. Other similar examples are provided by the reports in the Netherlands (Maljaars et al., 2012) and Japan (Yamada & Samol, 2008).

By any measure, it is irrational to deem the OSD as a failure upon the occurrence of fatigue cracks. Hence, it introduces the serviceability concern on an OSD with fatigue issues, which is even more important to the structural safety concern due to the high redundancy of such large-scale engineering works. For the problems presented above, it is crucial to prioritize the



Figure 1. Fatigue cracks on actual OSDs and the corruptions due to pavement damage.

coupling effect between the OSD and the pavement during the fatigue process. The possible premature damage of pavements, which is induced by the cracked OSD, should be noted.

On the other hand, it is also necessary to address the benefit from the pavement to keep the OSD from cracking. Though the mechanical performances are often ignored in the designing phase, the pavement can be a significant factor in realistic projects, according to the practices on actual bridges (Rao & Ji, 2019).

This paper aims to investigate the fatigue damage on OSDs and pavements, namely the OSD-pavement system, which may enable the proposal of more specific fatigue failure criteria and maintenance approaches. For the first step, the effect from the pavement on the fatigue crack growth on OSDs is given. Afterwards, the pavement damage induced by a cracked OSD is investigated by considering typical crack positions and sizes. According to the results, the conclusions are drawn.

2 FATIGUE CRACK GROWTH ON A PAVED OSD

2.1 *FE model of the cracked OSD*

The FE model of a typical section of OSD is built using ANSYS 19.0, as shown in Figure 2. It consists of five trapezoidal ribs and three diaphragms. With consideration of the computational intensity, the 4-node shell element, i.e. SHELL181, is used for the majority of the model, and the 8-node solid element, i.e. SOLID185, is used in the region of interest. The two parts are connected by applying the multi-point constraint (MPC) in the model. The fatigue crack at the rib-to-deck welded joint is modeled by FRANC3D, a fracture mechanics based software that enables to embed the crack in the ANSYS model. The boundary condition of the model is applied by fixing the vertical displacements of the bottom flange of the diaphragms, and the displacements on the lateral and the longitudinal directions on the respective edges.

Also, a 70-mm-thick pavement layer is modeled by solid elements, and the bonding contact is applied, meaning an ideal connection between the OSD and the pavement. The material of the OSD part is steel, whose elastic modulus is 206 GPa and the Poisson's ratio is 0.3. The material of the pavements is the asphalt concrete, whose elastic modulus and Poisson's ratio are 1.5 GPa and 0.25, respectively. Considering the symmetry of the structure, it is applied a symmetric load of a 5-ton-weighted wheel with the size of 300mm×200mm, resulting in a pressure on the OSD-pavement system of 0.82 MPa.

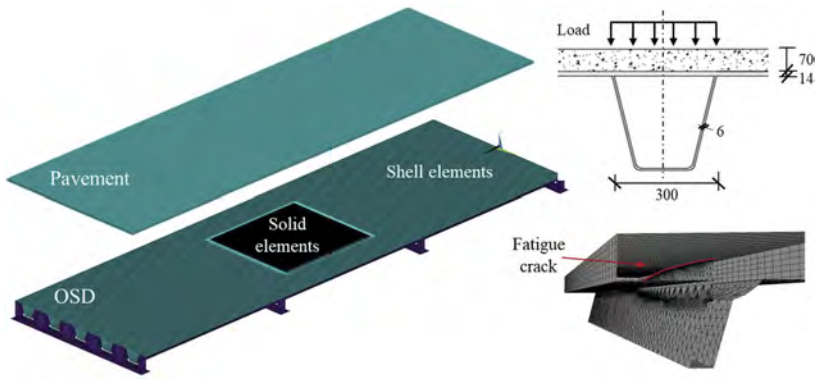


Figure 2. FE model of the cracked OSD.

2.2 Fatigue crack growth behavior based on SIF ranges

By the FE model of the cracked OSD, the crack growth can be predicted based on the SIF ranges along the crack front. For a contrastive analysis, the FEA is firstly conducted using the OSD model by removing the pavements, and both the root crack (RC) and the toe crack (TC) are considered. With respect to the commonly-accepted fatigue failure criteria of OSD, the crack depth of half thickness ($a = 0.5t$) and 3/4 thickness ($a = 0.75t$) of the deck plate is assumed.

For OSDs, the Mode-I cracking behavior is often dominant. The results from the OSD model with a root crack are provided in Figure 3, which shows that the value of K_I is larger than K_{II} and K_{III} by an order of magnitude. Consequently, the SIF range, i.e. ΔK , is generally the same as the range of K_I .

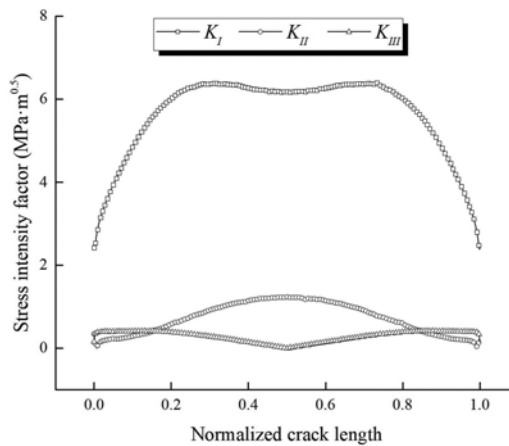


Figure 3. Comparison of the three-mode SIFs ($a = 0.75t$).

By comparing SIF ranges of RC cases and TC cases, it can be addressed that the two groups of results are quite close, except for the slight difference when the crack depth is $0.75t$, as shown in Figure 4. It means that the crack at the rib-to-deck joint, regardless of the specific site of weld root or weld toe, will grow in a similar rate. Therefore, the effect of pavement on SIF ranges is investigated based on RC cases only.

The results, as shown in Figure 4, depict the important effect of the pavement when ideally connected to the OSD. Even for a conventional asphalt concrete overlay, it may reduce the SIF range by about 70~80%. In terms of fatigue crack growth rate (CGR), it can be quite low as the SIF ranges along the crack front are mainly in the near-threshold region.

On the other hand, the distribution of SIF ranges along the crack front indicate that the maximum SIF range can be at the crack tip when the crack depth is $0.5t$ or smaller. While as the crack propagates, the location of the maximum value will shift laterally, indicating a larger tendency for the crack to grow in length. Combining with the low CGR, it implies the difficulty for the crack to penetrate through the deck plate, and also explains the few cracks observed on the deck top as shown above.

Therefore, it can be inferred that when the pavement and OSD behave in a composite structural way, the growth of the typical cracks (i.e. $a = 0.5t$ & $0.75t$) is slow, and can hardly reach the unstable fracture stage. It further implies the possibility of using an overlay with a higher mechanical performance to retrofit the cracked OSD, though further discussions are required on various aspects, including the contact effect to the cracked OSD, the viscoelasticity, and the temperature stability.

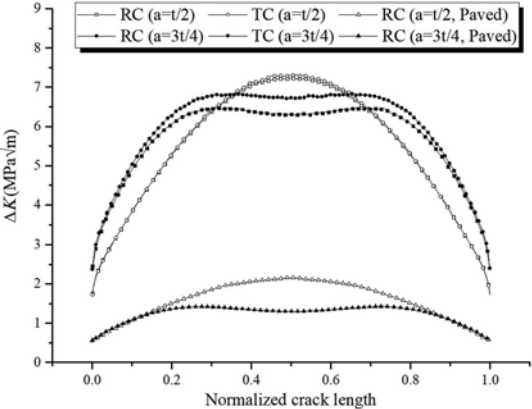


Figure 4. SIF ranges along the crack front by the OSD-pavement model.

3 PAVEMENT DAMAGE EVOLUTION ON A CRACKED OSD

3.1 Model description

Considering the high cycle fatigue damage induced by axle loads, the damage on pavements is evaluated using continuum damage mechanics. For a linear-elastic study, the damage evolution model can be given as follows (Jin, 2015),

$$\frac{dD}{dN} = \alpha \left[E(\varepsilon - \varepsilon_{th}) \sqrt{1 - D} \right]^m \tag{1}$$

where D is the damage index of the pavement, α and m are the material properties, N is the cycle count, E is the Young's modulus, ε is the range of first principal strain, ε_{th} is the threshold strain range for the fatigue limit.

The damage evolution is then simulated for part of the pavements, namely a region of $1m \times 2m$. Without loss of generality, the value of α is set as 1605.63, m equals 2.69, and ε_{th} equals zero, adapted from the ε - N curve provided in (Sun, 2013). For the sake of the computational efficiency, the damage evolution process is calculated for 10 steps, with the step size that the maximum damage index increases by 0.1.

3.2 Damage evolution

By assuming different crack conditions, the effect of promoting the fatigue damages on pavements can be obtained by comparison. The results of pavement damage evolution on the uncracked OSD are given as the benchmark. Figure 5 presents the damage for the first two steps. The corresponding results obtained by the case with a crack, whose depth is $0.75t$, is shown in Figure 6.

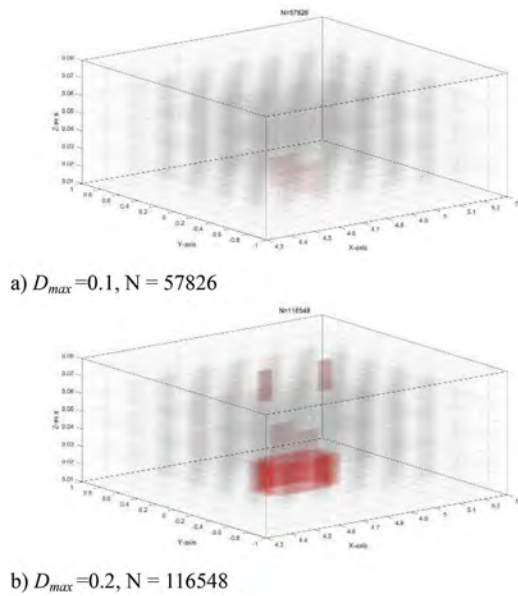


Figure 5. Early stage damage for the pavement on the uncracked OSD.

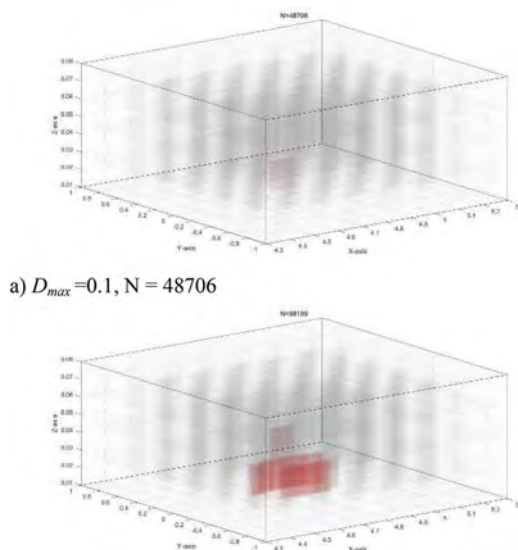


Figure 6. Early stage damage on the pavement on cracked OSD ($a = 0.75t$).

Accordingly, it is clear that the damage evolution is symmetric if no crack is embedded. While it is no longer symmetric for the cracked case, and the damage initiation site is right above the cracked RD joint. Meanwhile, the cycle count to reach $D_{max} = 0.1$ for the uncracked case is 57826, and that for the OSD with cracks are prominently smaller. The count for crack with a depth of $0.5t$ and of $0.75t$ are 51726 and 48706, respectively. The former indicates the 11% faster in pavement damage evolution, and the percentage for the latter is 16%.

On the other hand, the difference in damage distribution when D_{max} reaches 1 is not as significant, as shown in Figure 7. Generally, the damage on the lower side is always severe, as can be expected by using first principle strain in the damage evolution model. Hence, the damage index is always kept in a low level for the area that directly compressed by the wheel load. In terms of the cycle count, the case of the crack with the depth of $0.75t$ is smaller by about 14%.

The damage evolution in the early stage seems to be more affected by the penetrating cracks. Yet, it should be noted that the connection between the pavement and the OSD is assumed stable during the fatigue progress. In reality, the increment on shear strain may lead to the failure of the connection layer. When the damage initiates at the bottom layer of pavements, it accompanies the deterioration on the connection to the OSD, and is highly possible to result in a worse result thereafter. A reasonable consideration should be given to understand the behavior of the partially or completely detached pavement to the OSD in the future.

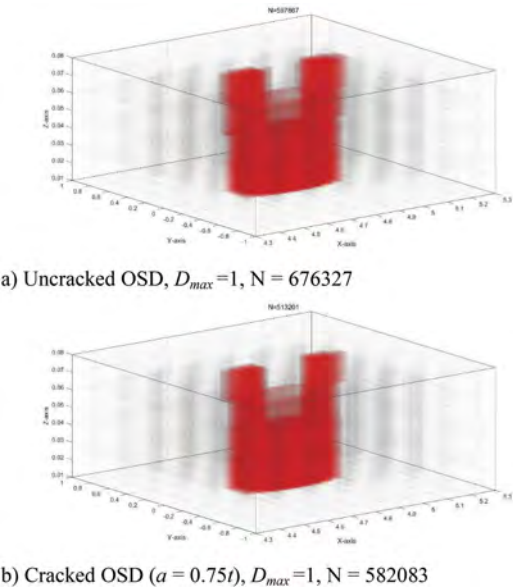


Figure 7. Fatigue damage on the pavement when $D_{max} = 1$.

4 CONCLUSIONS

With respect to the fatigue problem on OSDs and the subsequent effects on pavements, the fatigue crack growth behavior of penetrating cracks at the rib-to-deck joint on OSDs and the damage evolution on pavements are studied. The following conclusions are drawn.

1. The benefit from the pavement on resisting crack growth on OSDs is significant when the connection between them is kept in good shape. Even for a conventional asphalt concrete overlay, it may reduce the SIF range by about 70~80%.
2. The growth of the penetrating cracks is not likely to reach the unstable fracture stage under ordinary traffic loads on OSDs. And according to the distribution of SIF ranges along the crack front, it will rarely go through the deck plate.
3. By conducting damage evolution analysis on pavements on OSDs with cracks in different depths, the crack does promote the premature pavement damage. The damage initiation is 11% faster when the penetrating crack depth is $0.5t$, and the percentage for the crack with a depth of $0.75t$ is 16%. For a comprehensive understanding of this effect, further consideration of the possible deterioration of the connection between the OSD and the pavement is still required.

REFERENCES

- Jin, G. 2015. *Numerical Analysis of Fatigue Crack Growth in Asphalt Pavement Based on Extended Finite Element Method* (in Chinese). Nanjing: Southeast University.
- Maljaars, J., van Dooren, F., & Kolstein, H. 2012. Fatigue assessment for deck plates in orthotropic bridge decks. *Steel Construction*, 5(2), 93–100.
- Rao, J., & Ji, B. 2019. *Report on maintenance and operation of Jiangyin Yangtze river bridge (1999-2019)* (in Chinese). Beijing: China Communications Press.
- Sun, L. 2013. *Behaviors of Asphalt Pavement Structures* (in Chinese). Shanghai: Tongji University Press.
- Wang, B., Nagy, W., De Backer, H., & Chen, A. 2019. Fatigue process of rib-to-deck welded joints of orthotropic steel decks. *Theoretical and Applied Fracture Mechanics*, 101, 113–126.
- Wang, D., Xiang, C., Ma, R., Chen, A., & Wang, B. 2021. Experimental study on the root-deck fatigue crack on orthotropic steel decks, *Materials and Design*, 203, 109601
- Yamada, K., & Samol, Y. 2008. Plate bending fatigue tests for root crack of trough rib of orthotropic steel deck. *Journal of Structural Engineering*, A, 54A, 675–684.

Modeling of coarse aggregate based on 3D point cloud and spherical harmonics

J.J. Zhang & Z.C. Pan

College of Civil Engineering, Tongji University, Shanghai, China

ABSTRACT: Aggregate morphology is an important part of concrete at meso-scale. In this study, a numerical method is proposed to model the coarse aggregate based on 3D point cloud and spherical harmonics. A total of 200 aggregates, including 100 pebbles and 100 crushed-stones, are collected by using the 3D point cloud technology. The aggregate is constructed by the spherical harmonics using 3D point cloud data. A typical example of a crushed-stone is presented to verify the feasibility of the proposed method. The distortion coefficient is defined to measure the similarity between the modeled and real aggregates. The effects of the sampling point number and calculation order on the accuracy of modeling the aggregate are investigated. The results show that proposed method has a promising application to establish a huge database of real aggregate shapes.

1 INTRODUCTION

The corrosion of reinforcement has a significant influence on the durability of reinforced concrete. Therefore, the initiation corrosion time of steel bars is an important index to predicting the life of RC Structures. Some studies have shown that the index can be affected signally by mass transport processes, such as chloride ion erosion in the chloride salt environment, CO₂ diffusion in the atmospheric environment, etc. Thereby, the resilience of RC structures under long-term environmental effects can be characterized by the transport properties of these masses. Some studies have shown that the meso-scale model of concrete has a noticeable effect on the properties of concrete (Thai et al., 2021, Mehdipour and Khayat, 2018). At the meso-scale, the transport path of the mass will be affected by the impermeability of aggregates (Pan et al., 2016), which is known as the tortuosity effect. The tortuosity effect is largely determined by the shape and distribution of aggregates. Thus, it is necessary to build meso-scale models of realistic concrete.

At meso-scale, concrete can be considered as a composite material consisting of aggregate, cement mortar, and interfacial transition zone (ITZ) (Chen et al., 2016). In this case, the cement mortar is a homogeneous material. ITZ is a special microstructure attached to the aggregate surface, whose thickness is related to factors such as cement particle size and curing conditions (Chen et al., 2004). Hence, the essence of modeling the concrete at meso-scale is to simulate the shape and distribution of aggregates in the cement mortar.

At present, there are two typical methods to model aggregate shapes. The first one is the pixel-based or voxel-based method (Kroener and Dornenech Carbo, 2013, Cheng et al., 2020). This method discretizes the aggregate into voxels and models the aggregate by storing the coordinates of each voxel. In this method, the accuracy of the aggregate model depends on the number of voxels. Thus, a huge amount of the storage space is required to ensure the accuracy (Tong et al., 2011). Duris et al. (2016) analyzed the two-dimensional shape features of particles based on pixels and evaluate the effect of the number of pixel points on shape parameters.

The other method is based on mathematical model (Melinska et al., 2017, Wei et al., 2018, Zhao et al., 2017, Xu et al., 2010). This method is to store the shape of the aggregate surface through a mathematical function. The coordinates of aggregate surface points will be calculated when modeling the aggregate. Compared with the voxel-based method, this method requires less

storage space but the modeling process is more complex. (Garboczi, 2002, Kiryati and Maydan, 1989). Shi et al. (2016) analyzed the two-dimensional shape parameters of real aggregates based on complex Fourier analysis and reconstructed the aggregate. Recently, to improve the refinement of aggregate models, modeling methods based on real aggregate have gradually become a research hotspot. Sun et al. (2020) and Li et al. (2021) used 3D point cloud techniques to extract several characteristic parameters and shape indicators such as isometric ratio, flake ratio, and sphericity of aggregates. Fu Ru et al. (2018) carried out a quantitative analysis of the shape parameters such as sphericity, roundness, and elongation of sand by spherical harmonics. At present, the modeling method based on real aggregate usually uses the CT scan to obtain aggregate data. This method needs to combine the scanned images, and the process is complicated. Moreover, the extant research scantily discusses how to select the number of data points for modeling and the calculation order of spherical harmonics for preservation. In this study, three-dimensional point cloud technology, which is a convenient method to collect aggregate information, is used to construct the aggregate model. The selection method of data points number for modeling and the calculation order of spherical harmonics is discussed.

This paper proposes a modeling method for constructing coarse aggregates which combines 3D point cloud with spherical harmonics. Firstly, the basic principles of 3D point cloud technology and spherical harmonics is expounded, and the accuracy of the aggregate model is evaluated by distortion coefficient.; Secondly, the modeling method proposed in this paper is validated with an example of a crushed-stone. Finally, the influence of the sampling point number and calculation order on the accuracy of aggregate is investigated.

2 MODEL AND METHOD

2.1 Point cloud obtained by 3D laser scanner

Firstly, a 3D laser scanner was used to obtain point cloud data of the aggregate shape. The basic principle is that a laser is emitted from the scanner to the aggregate, and the distance between the surface of the aggregate and the scanner is measured according to the phase difference between the emitted laser and the returned laser. The horizontal angle and vertical angle of each point are recorded Combined with the angle measurement system in the scanner. then the 3D coordinates of each point on the surface of the aggregate are obtained. Secondly, the resulting point cloud data is subjected to the necessary post-processing. Due to factors such as surface roughness and lighting conditions, some data points will deviate significantly from the surface of the aggregate. Thus, methods such as Gaussian filtering are used to denoise the initial point cloud. Finally, the coordinates of the sampling points are obtained by differencing the coordinates of the data points in the point cloud.

2.2 Aggregate model constructed by spherical harmonics

There are two requirements when modeling aggregates using the spherical harmonics. Firstly, anyone ray from the center of mass of the aggregate can only have a unique intersection with the surface of the aggregate. Secondly, the aggregate cannot have internal voids. The essence of the spherical harmonics is to solve the Laplace equation in the spherical domain. To do this, the Cartesian coordinates of the point cloud are converted to spherical coordinates. The origin of the spherical coordinates coincides with the quality center of the aggregate, using the top angle (θ), azimuth angle (φ), and distance (r) to characterize the position of the point, as shown in Figure 1. The coordinate transformation equations are shown in Eqs. (1)-(3).

$$x = r\sin(\varphi) \sin(\theta) \quad (1)$$

$$y = r\cos(\varphi) \sin(\theta) \quad (2)$$

$$z = r\cos(\theta) \quad (3)$$

The general form of the spherical harmonics is given by:

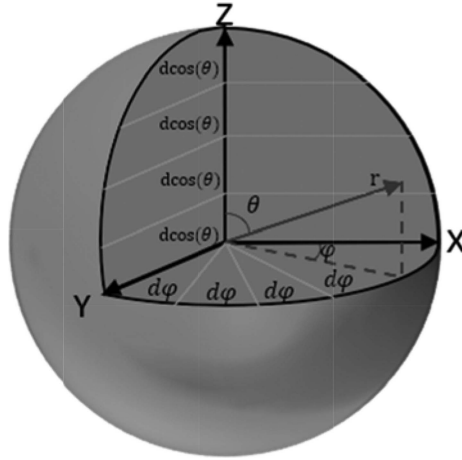


Figure 1. Schematic of spherical coordinate and position of sampling point.

$$r(\theta, \varphi) = \sum_{n=0}^{\infty} \sum_{m=-n}^n a_{n,m} Y_{n,m}(\theta, \varphi) \quad (4)$$

where the $a_{n,m}$ is the spherical harmonic coefficient. $Y_{n,m}(\theta, \varphi)$ is the real spherical harmonics ($0 \leq \theta \leq \pi, 0 \leq \varphi \leq 2\pi$), which is given by:

$$Y_{n,m}(\theta, \varphi) = \begin{cases} (-1)^m \sqrt{2} \sqrt{\frac{2n+1}{4\pi} \frac{(n-|m|)!}{(n+|m|)!}} P_n^{|m|}(\cos \theta) \sin(|m|\varphi) & m < 0 \\ \sqrt{\frac{2n+1}{4\pi}} P_n^m(\cos \theta) & m = 0 \\ (-1)^m \sqrt{2} \sqrt{\frac{2n+1}{4\pi} \frac{(n-m)!}{(n+m)!}} P_n^m(\cos \theta) \sin(m\varphi) & m > 0 \end{cases} \quad (5)$$

where n and m represent the order of the spherical harmonics. P_n^m is the Associated Legendre polynomial, which is the solution of the Associated Legendre Equation.

The $a_{n,m}$ in Eq. (4) is the coefficient to be solved according to the following definition:

$$a_{n,m} = \int_0^{2\pi} \int_0^{\pi} r(\theta, \varphi) Y_{n,m}(\theta, \varphi) \sin(\theta) d\varphi d\theta \quad (6)$$

The corresponding discrete format is given by:

$$a_{n,m} = \frac{4\pi \sum_{i=0}^N r_i Y_{n,m,i}}{N} \quad (7)$$

where N is the number of sampling points, r_i is the distance from sample point i to the origin of the coordinates, $Y_{n,m,i}$ is the value of the spherical harmonics for the sampling point i corresponding to the order n and degree m .

Note that the theoretical value range of n in Eq. (4) is $[0, \infty)$. Eq. (4) can be expanded to a sum of infinite numbers. Therefore, it is necessary to truncate at order n_0 (hereafter referred to as the calculation order), to use the spherical harmonic coefficients of the first n_0 orders for aggregate modeling. The value of n_0 has a significant influence on the accuracy of the aggregate model.

The data points need to be sampled uniformly over the surface of the aggregate to calculate $a_{n,m}$ by Eq. (7). Otherwise, it may lead to distortions in local areas. As shown in Figure 1, φ and $\cos(\theta)$ are each divided into k equal parts. The number of sampling points N is k^2 . The r_i corresponding to any combination of φ_i and $\cos(\theta_i)$ will be obtained by interpolating the coordinates of the data points.

There are three steps to construct an aggregate model by spherical harmonics:

- (1) The value of the spherical harmonics $Y_{n,m}(\theta, \varphi)$ is calculated for each sampling point on the aggregate surface and each combination of n and m by Eq. (5).
- (2) $a_{n,m}$ is calculated by Eq. (7).
- (3) The shape of the aggregates is described based on $a_{n,m}$ and Eq. (4).

2.3 Distortion coefficient

When determining the number of sampling points and the calculation order, it is necessary to design an index to quantitatively characterize the similarity between the aggregate model and the actual aggregate shape. In some research, average error of the distance from the coordinate origin to the surface of the figure was used to measure the similarity between the two-dimensional figures (Tang et al., 2009), as shown in Figure 2, this paper uses the difference between the distance from the actual aggregate surface point to the coordinate origin (\bar{r}_i) and the distance from the aggregate model surface point to the coordinate origin (r_i) to define the distortion coefficient of the aggregate model:

$$\sigma = \sum_{i=1}^N \frac{|\bar{r}_i - r_i|}{N \cdot \max(\bar{r}_i, r_i)} \quad (8)$$

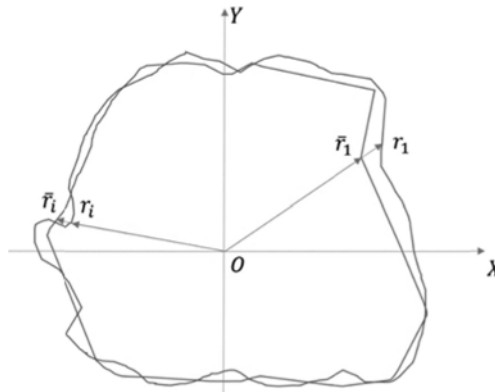


Figure 2. Schematic of distortion coefficient.

3 VERIFICATION

To verify the correctness of the method, a crushed-stone was modeled in this paper using different numbers of sampling points and calculation orders. The actual shape of the aggregate and the



Figure 3. Shape of aggregate used in typical case study.

simulation result are shown in Figure 3 and Figure 4, respectively. It can be seen from Figure 4 that when n_0 is constant, the aggregate model gradually approaches the true shape and then no longer appears to change significantly as N increases. When N is constant, the aggregate model first gradually changes to the real shape as n_0 increases. But when n_0 exceeds a critical value, the aggregate model shows significant local distortions that affect the overall realism of the model. Therefore, it is necessary to determine the reasonable values for N and n_0 during aggregate modeling.

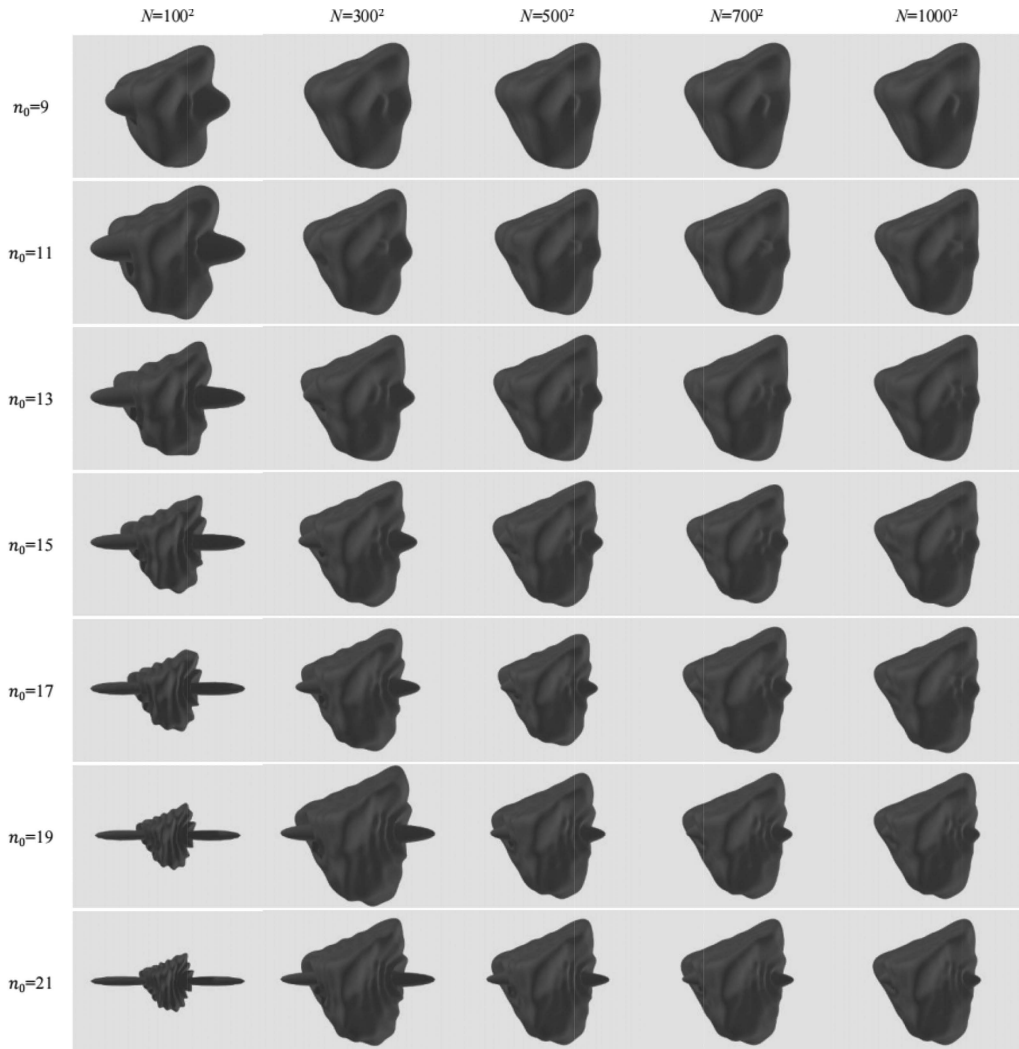


Figure 4. Effects of N and n_0 on aggregate model.

The σ under various simulation results are shown in Figures 5 (b)-(f). According to Eq. (8), it can be seen that with the σ value close to 0, the aggregate model is gradually accurate.

4 EFFECT OF SAMPLING POINT NUMBER AND CALCULATION ORDER

4.1 Sampling point number

To determine a reasonable value for the number of sampling points, a statistical analysis of the distortion coefficients of 100 pebbles and 100 crushed-stones was carried out using

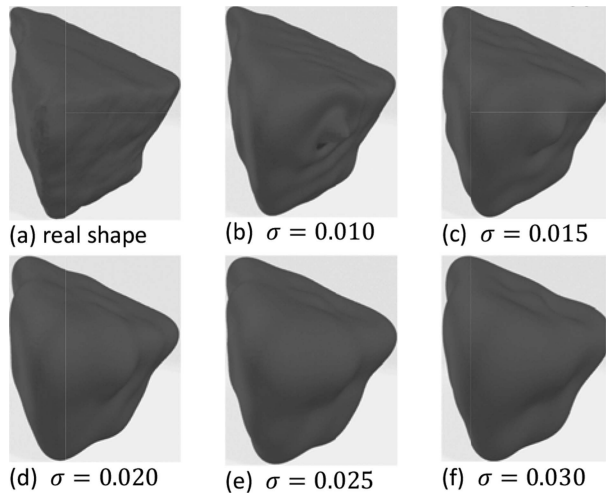


Figure 5. Schematic to distortion coefficient of aggregate model.

different sampling points and calculation orders. The results are shown in Figure 6, it can be found that for pebbles and crushed-stone aggregates, the distortion coefficient decreases monotonously with the increase of sampling points. It can be seen from Eq. (7) that the increase in sampling points will lead to a decrease in modeling efficiency. In this paper, sampling points of $N = 400^2$ and $N = 500^2$ are used for pebble and crushed-stone, respectively. Compared with pebble, crushed-stone need more sampling points to express surface texture.

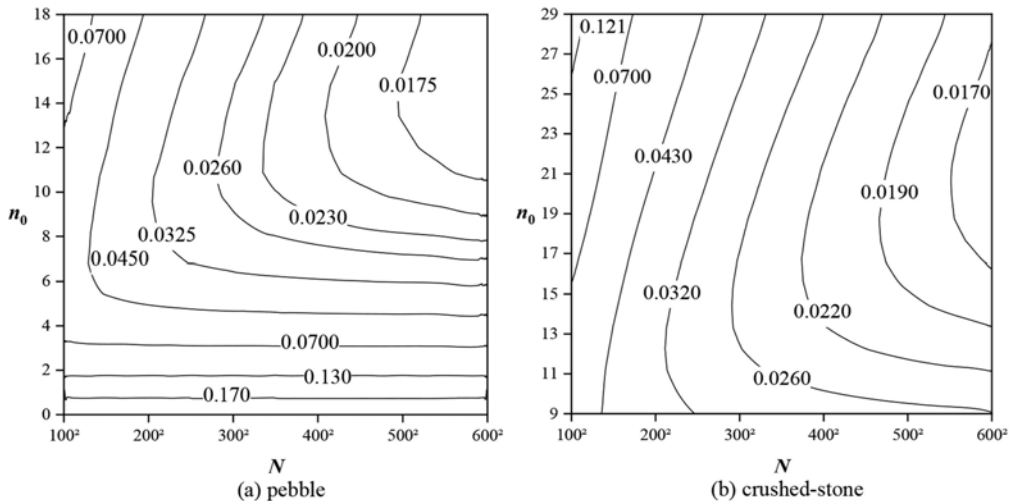


Figure 6. Plot of distortion coefficient of aggregate model as a function of N and n_0 .

4.2 Calculation order

As shown in Figure 4, when the calculation order is too large, the local area of the aggregate model will appear obvious distortion. Due to the characteristics of the spherical harmonics, this distortion generally occurs at the intersection of the aggregate model and the Z axis. Therefore, The most appropriate calculation order is determined by monitoring the distance between the two intersections of the aggregate model and the Z-axis in this paper to establish the aggregate model. This method can avoid the distortion of the aggregate model caused by excessive calculation order. The specific process is shown in Figure 7.

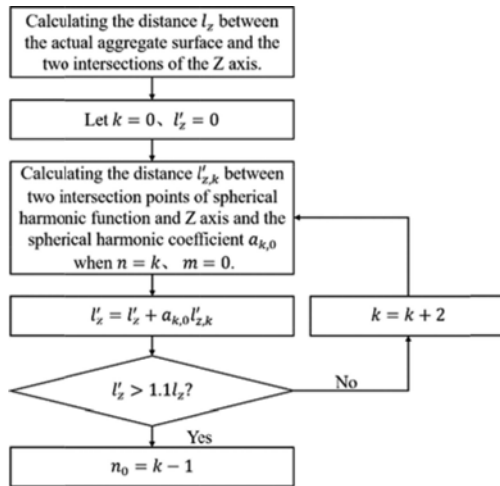


Figure 7. Procedure to determine optimized calculation order.

The optimal calculation order of each aggregate is calculated for 100 pebbles and 100 crushed-stone studied in this paper, as shown in Figure 8. It can be seen that for most pebbles and crushed-stone, the optimal calculation order is between 11 ~ 13 and 11 ~ 15, respectively.

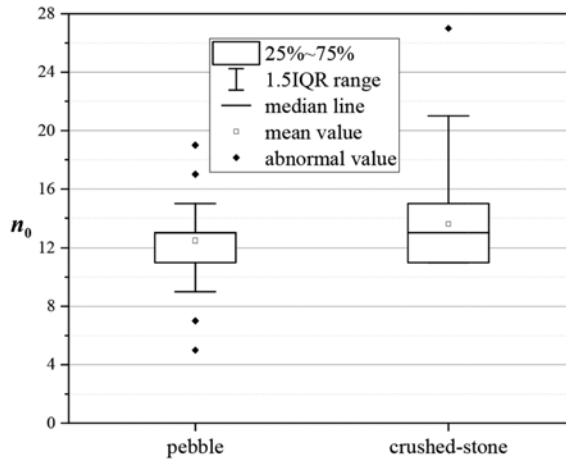


Figure 8. Optimized calculation order of pebble and crushed-stone.

5 CONCLUSION

In this paper, a coarse aggregate modeling method combining 3D point cloud technology with spherical harmonics is proposed. By this method, 200 aggregates are modeled. The accuracy of the aggregate model was evaluated by distortion coefficient. Effect of sampling coefficient and calculation order on distortion coefficient is evaluated. The determination process of aggregate sampling point number and optimal calculation order of spherical harmonics is proposed. According to the research of this paper, the following conclusions can be drawn:

- (1) Using the spherical harmonics, the three-dimensional point cloud data of aggregate which is easy to collect can be transformed into the function which is easy to store. In this process, the shape characteristics of aggregate can be retained.

- (2) An optimal calculation order determination method based on Z-axis local distortion monitoring of the aggregate model is proposed. Under the condition of the same number of sampling points, the aggregate model can be more accurate.

ACKNOWLEDGMENTS

This research project was financially supported by the National Natural Science Foundation of China under the Grant No. 52238005.

REFERENCES

- Chen, A.R., Pan, Z.C., Ma, R.J. & Wang, D.L. 2016. New development of mesoscopic research on durability performance of structural concrete in bridges. *China Journal of Highway and Transport*, 29: 42–48.
- Chen, H.S., Sun, W. & Stroeven, P. 2004. Interfacial transition zone between aggregate and paste in cementitious composites (II): Mechanism of formation and degradation of interfacial transition zone microstructure, and its influence factors. *Journal of the Chinese Ceramic Society*.
- Cheng, Q., Sun, P., Yang, C., Yang, Y. & Liu, P.X. 2020. A morphing-based 3D point cloud reconstruction framework for medical image processing. *Computer Methods and Programs in Biomedicine*, 193: 105495.
- Duris, M., Arsenijevic, Z., Jacimovski, D. & Radoicic, T. K. 2016. Optimal pixel resolution for sand particles size and shape analysis. *Powder Technology*, 302: 177–186.
- Fu, R., Hu, X.I., Zhou, B., Wang, H.B. & Wang J.F. 2018. A quantitative characterization method of 3D morphology of sand particles. *Rock and Soil Mechanics*, 92: 483–490.
- Garboczi, E.J. 2002. Three-dimensional mathematical analysis of particle shape using X-ray tomography and spherical harmonics: Application to aggregates used in concrete. *Cement and Concrete Research*, 32: 1621–1638.
- Thai, H.N., Kato, A., Nguyen, H.G., Nguyen, T.D., Tong, T.K., Nguyen, V.T., Uchimura, T., Maki, T., & Kawamoto, K. 2021. Effects of particle size and type of aggregate on mechanical properties and environmental safety of unbound road base and subbase materials: A literature review. *Geomate Journal*, 20(78): 148–157.
- Kiryati, N. & Maydan, D. 1989. Calculating geometric properties from fourier representation. *Pattern Recognition*, 22: 469–475.
- Kroener, S. & Carbo, M.T.D. 2013. Determination of minimum pixel resolution for shape analysis: Proposal of a new data validation method for computerized images. *Powder Technology*, 245: 297–313.
- Li, L., Guo, M. & Zeng, C. 2021. Study on the Accurate Measurement and Quantitative Evaluation Methods of Aggregate Surface Roughness. *Advances in Materials Science and Engineering*, 2021: 1–12.
- Mehdipour, I. & Khayat, K.H. 2018. Understanding the role of particle packing characteristics in rheo-physical properties of cementitious suspensions: A literature review. *Construction and Building Materials*, 161: 340–353.
- Melinska, A.U., Romaszkiwicz, P., Wagel, J., Antosik, B., Sasiadek, M. & Iskander, D.R. 2017. Statistical shape models of cuboid, navicular and talus bones. *Journal of Foot and Ankle Research*, 10: 1–8.
- Pan, Z.C., Fang, X.R. & Chen, A.R. 2022. Effect of aggregate morphology on physical tortuosity of chloride diffusive path at meso-scale of concrete. *Construction and Building Materials*, 323: 126215.
- Shi, C., Bai, J.S., Yu, S.Y. & Wang, W. 2016. Mesostructural characteristic and random reconstruction of soil-rock particles based on plural Fourier analysis. *Rock and Soil Mechanics*, 37: 2780–2786.
- Sun, Z., Wang, C., Hao, X., Li, W. & Zhang, X. 2020. Quantitative evaluation for shape characteristics of aggregate particles based on 3D point cloud data. *Construction and Building Materials*, 263: 120156.
- Tang, L.L., Li, Q.Q. & Yang, B.S. 2009. Shape Similarity Measuring for Multi-resolution Transmissi on of Spatial Datasets over the Internet. *Acta Geodaetica et Cartographica Sinica*, 38: 336–340.
- Tong, S., Xu, X.G., Yi, C.T. & Shao, C.Y. 2011. Overview on vision-based 3D reconstruction. *Application Research of Computers*, 28: 2411–2417.
- Wei, D., Wang, J. & Zhao, B. 2018. A simple method for particle shape generation with spherical harmonics. *Powder Technology*, 330: 284–291.
- Xu, W., Chen, H. & Lv, Z. 2010. A 2D elliptical model of random packing for aggregates in concrete. *Journal of Wuhan University of Technology-Materials Science Edition*, 25: 717–720.
- Zhao, B.D., Wei, D.H. & Wang, J.F. 2017. Particle shape quantification using rotation-invariant spherical harmonic analysis. *Geotechnique Letters*, 7: 190–196.

Bridge tower aesthetic assessment using convolutional neural network

D.L. Wang, Y. Ning, C. Xiang & A.R. Chen

College of Civil Engineering, Tongji University, Shanghai, China

ABSTRACT: With the rapid social and economic development and social progress, bridges are no longer purely to meet traffic demand. The huge span, strong body-shape expression, and extraordinary scale of the bridge may even reshape the urban or terrestrial landscape. Therefore, it is urgent to pay more attention to bridge aesthetics in the process of bridge design. In this paper, a neural network for assessing bridge tower aesthetics is proposed, which can classify a bridge tower into low or high aesthetic quality automatically, and better serve the bridge aesthetic design. Firstly, 150 cable-stayed bridges and 118 suspension bridges with the highest spans in the world were selected. For each bridge, several high-quality images were screened from the Internet, and the standard bridge tower diagram of each bridge was obtained through semantic segmentation and projection mapping. Then, a WeChat Mini Program for bridge tower aesthetic assessment was constructed and released, and the aesthetic assessments of the above bridge towers from different groups of people were obtained. Finally, the bridge tower aesthetic assessment network (BTAANet) was trained with the above standard bridge tower diagram and the corresponding assessment label, and the aesthetic quality can be obtained automatically with the well-trained BTAANet. The proposed method can provide an important reference for bridge design and promote the implementation of bridge aesthetics.

1 INTRODUCTION

Aesthetics is a manifestation of human evolution toward advanced civilization and the pursuit of a higher spiritual world, permeating the entire vein of human civilization. Bridge aesthetics is also a hot issue in contemporary bridge construction, especially in the stage of conceptual design and scheme selection of bridge, so the fusion of bridge aesthetics thought and innovative technology is a new direction of bridge development (Liang *et al.* 2020).

In recent years, deep learning methods have been widely applied in computer vision tasks, such as image recognition, object detection, automatic driving, and image classification (Arman *et al.* 2021). Convolutional neural networks (CNN) have also been applied to image aesthetic assessment and significantly contributed to the development of image aesthetic assessment due to their powerful feature extraction and image-based decision-making capabilities. (Lu *et al.* 2015) implemented image global and local feature capture by constructing and training a two-column CNN network to support heterogeneous inputs. (Xin *et al.* 2016) introduced a CNN to solve the problem of image aesthetic classification, that is, automatically classifying the aesthetic quality of images into low-quality and high-quality. (Tan *et al.* 2016) used a CNN photo aesthetic classifier with both depth and breadth to achieve fine-grained aesthetic quality prediction. (Li 2018) proposed a two-channel CNN image aesthetic quality assessment method based on semantic information, which can extract aesthetic features from both the whole and part of the image, thereby improving the accuracy of image aesthetic quality assessment. (Dou *et al.* 2018) developed an automatic quantitative assessment method of webpage aesthetics using CNN, and the performance of the model is improved by transferring the knowledge from the image style recognition task into the proposed network.

Although the deep learning method has been widely used in the field of image aesthetic assessment, the above studies are mostly based on traditional neural network (TNN) with large amounts of parameters and high computational cost, which does not conform to the trend of lightweight development of neural network and the development demand of mobile applications. Therefore, a lightweight neural network (LNN) for bridge tower aesthetic quality assessment is proposed in this paper, which realizes the automatic assessment of bridge tower form aesthetic quality and improves the efficiency of aesthetic assessment.

The remainder of this article is organized as follows. Section 2 introduces the process of generating standard bridge tower diagrams and assessment labels, and the training of BTAANet based on TNNs and LNN. Section 3 compares and evaluates the performance of the two types of networks from the perspective of precision and complexity. Section 4 concludes this article.

2 BRIDGE TOWER ASSESSMENT

2.1 *Standard bridge tower dataset*

The supervised learning model is used to achieve intelligent assessment of bridge towers due to the lack of mathematical definition in bridge aesthetics. The performance of the model depends on the quality of the dataset, so it is crucial to construct a high-quality training dataset. To help better reflect the current situation of bridge design and makes the tower data more representative, the tower data in this paper is selected from the built large-span bridges worldwide. A total of 150 cable-stayed bridges with a span larger than 400m and 118 suspension bridges with a span larger than 500m were selected as the source bridge tower data.

The images adapted in computer vision research often have various distortions that affect the quality of the images. Perspective distortion is one of the most common kinds of image distortion, which occurs when the image plane of the shooting equipment is not balanced with the plane of the shooting object. This kind of distortion is common in the pictures we collected from the Internet. To make use of such images in the neural network, it is first corrected to eliminate the perspective distortion, as shown in Figure 1(a) and (b). The contour of the bridge tower is then extracted to eliminate the environmental background of the corrected bridge tower image, as manifested in Figure 1(c).

During the training of the neural network, the images that are fed into the network need to be the same size. Therefore, the obtained bridge tower contour is further standardized with a size of 128*256. The height of the bridge tower is scaled to 256, the width is scaled in equal proportion, and the excess is filled with 0.

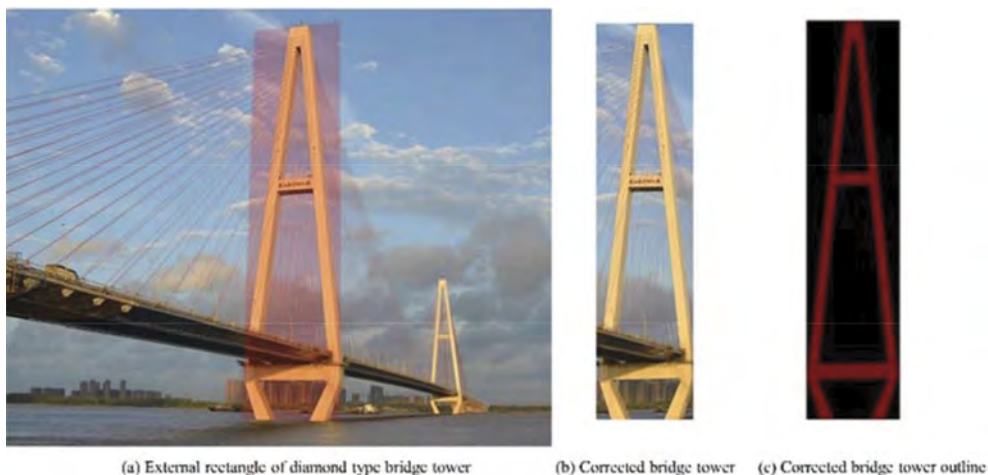


Figure 1. Perspective distortion correction of the bridge tower images.

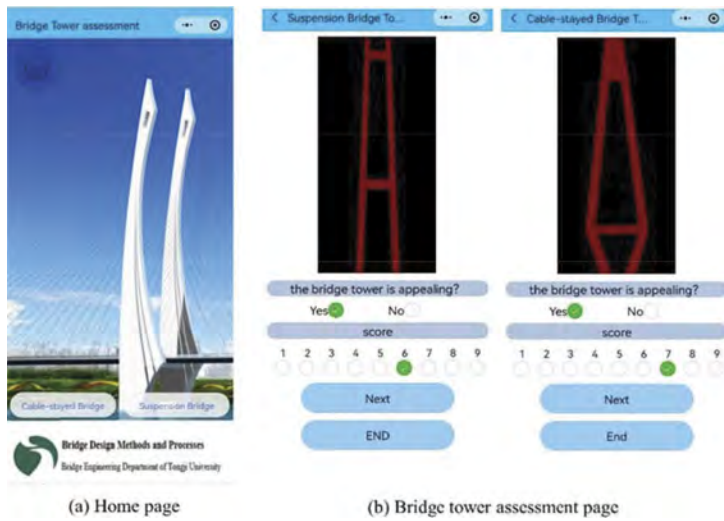


Figure 2. WeChat Mini Program for bridge tower assessment.

Supervised learning should work with labeled data, and the label of whether the bridge tower form is appealing or not is obtained by questionnaire survey. This paper develops an HBuilder X-based bridge tower assessment WeChat Mini Program to efficiently implement questionnaires and obtain the labeled data applicable to the BTAA Net. The applet in this paper contains three main pages: home page, cable-stayed bridge tower assessment, and suspension bridge tower assessment, as shown in Figure 2.

To make sure the credibility of the assessment results, a sufficient number of samples is required when performing the questionnaire survey. Here, a total of 44 complete evaluation results were collected through the applet, including 32 people majoring in civil engineering and the rest were not, and 20 people with master's degrees or above. Relevant studies (Liao *et al.* 2021, Loos *et al.* 2022, Lima and Grasse 2022) show that 44 assessment results can meet the requirements of aesthetic assessment. Some assessment results of the bridge towers can be found in Figure 3.

In determining whether the bridge tower form is appealing or not, increasing the difference in assessment criteria can improve the accuracy of aesthetic classification in some ways (Xin *et al.* 2016, Tan *et al.* 2016). Therefore, in this research, when more than 55% of people (24) give a positive evaluation for the bridge tower form, it is assigned the label 1, otherwise, the tower is assigned the label 0. Moreover, the size of the training dataset is expanded by using a data enhancement method that flips the image horizontally and uses the same evaluation labels as the original image. In this way, a total of 550 samples are generated in the bridge tower aesthetic assessment dataset (BTAA Dataset), and they are randomly divided into the training set, validation set, and test set with a ratio of 8:1:1.

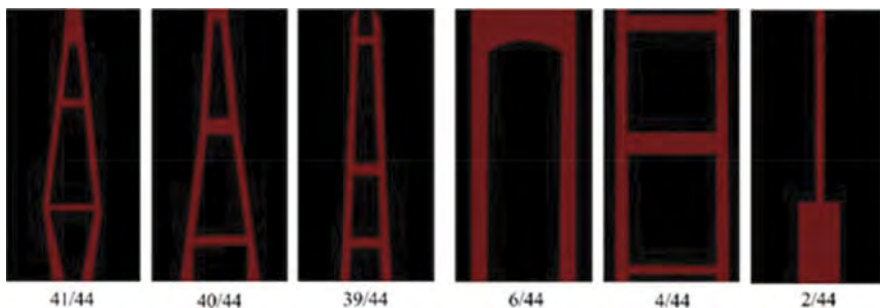


Figure 3. Assessment results of some bridge towers (a/44, a is the number of appealing results).

2.2 The proposed BTAA Net

Taking into account the richness of image information, the size of the BTAA Dataset, and the complexity of the bridge tower form aesthetic classification problem, TNN, like VGGNet, GoogleNet as well as ResNet, and recently proposed LNN, including the MobileNet, SqueezeNet, and ShuffleNet were tested to find the most appropriate base model for BTAA Net. For TNN, they usually possess a large number of parameters, which leads to expensive computational costs. In comparison, in LNN, the number of parameters is significantly reduced due to the operations like depthwise separable convolution, deep compression, and channel shuffle, so that the size of the model is also reduced dramatically, which significantly improves the efficiency of the model and facilitates model saving and transferring. For instance, ShuffleNet significantly reduces the number of parameters and the computational cost by changing the data flow direction using channel shuffle, as shown in Figure 4.

Besides, deep learning usually requires a large amount of high-quality data. To improve the performance of the model, the strategy of transfer learning is adopted (Lu et al. 2015, Xin et al. 2016, Talebi and Milanfar 2018), that is, the model is pre-trained on the ImageNet, and then the model weight is transferred to the bridge tower assessment task, as shown in Figure 5. Models that use transfer learning strategy are followed by -TL.

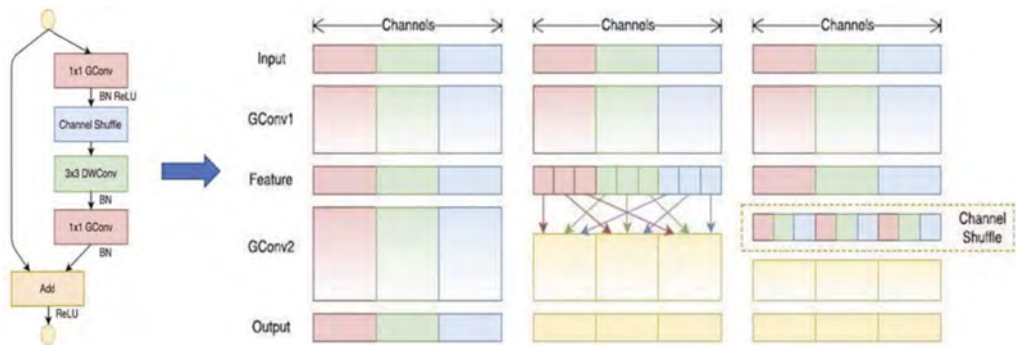


Figure 4. The unit architecture of ShuffleNet.

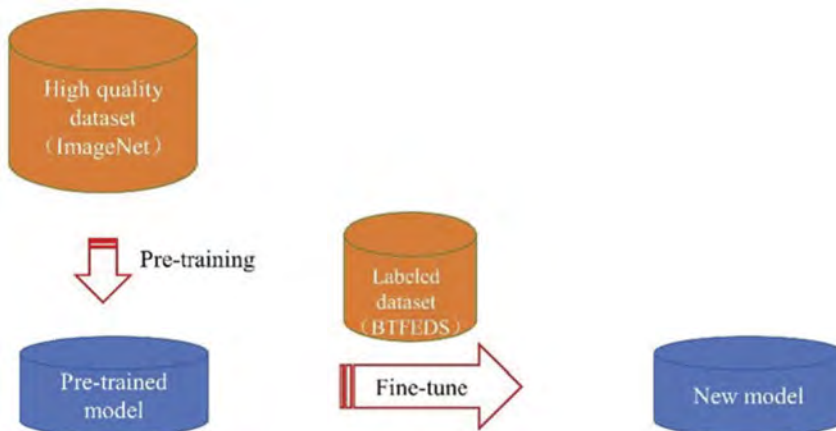


Figure 5. Transfer learning for bridge tower assessment based on ImageNet.

2.3 Training the neural network

All models mentioned in Section 2.2 were trained and tested on a computer with an Intel[®] Core[™] i7-8700k CPU and an NVIDIA GeForce GTX1080 Ti GPU using the Keras framework.

The Adam was used to determine the optimal weights of the networks, and the loss function adopted CrossEntropy Loss. During training, the initial learning rate was 0.0001. When the validation accuracy does not increase for 10 epochs, the learning rate will decay by 0.1 times and the training will stop when the validation accuracy does not increase for 30 epochs.

2.3.1 Traditional neural networks

Table 1 illustrates all TNN models and the corresponding validation accuracy. The number of fully connected units (4096, 512, 256) and dropout ratios (0.2, 0.5) was modified for the top layer of the network in the VGG16 model. Inception V1 and Inception V3 models were selected under the inception architectures, and ResNet34, ResNet50, and ResNet101 models were selected under the ResNet architectures. In addition, transfer learning is performed for the above models.

Under these three architectures, the one that performs the best on the validation set were all trained by the transfer learning method, and the validation accuracy of VGG16-TL, Inception V1-TL, and ResNet101-TL model was 90.74%, 90.70%, and 92.59%, respectively.

Table 1. TNN model and validation accuracy.

Architecture	VGG	Inception	ResNet
Model (validation accuracy)	VGG16-1 (77.80%)	Inception V1 (85.20%)	ResNet34 (83.33%)
	VGG16-2 (87.04%)	Inception V1-TL (90.70%)	ResNet34-TL (87.04%)
	VGG16-3 (83.30%)	Inception V3 (87.04%)	ResNet50 (83.33%)
	VGG16-4 (79.60%)	Inception V3-TL (88.89%)	ResNet50-TL (83.33%)
	VGG16-5 (77.80%)		ResNet101 (74.07%)
	VGG16-TL (90.74%)		ResNet101-TL (92.59%)

2.3.2 Lightweight neural networks

Table 2 shows all the LNN models and the corresponding validation accuracy, where MobileNet V1~V3 were selected under the MobileNet architectures, SqueezeNet1_0 and SqueezeNet1_1 were selected under the SqueezeNet architectures, and under the ShuffleNet architectures ShuffleNet_v2_x0_5 and ShuffleNet_v2_x1_0 were chosen. In addition, the transfer learning method is also used here.

Figure 6 shows the loss and accuracy variation during the training of the shuffle-net_v2_x0_5-TL model. The validation loss decreased and converged to about 0.35, and the validation accuracy of the model reached a maximum of 92.59% at the 69th epoch.

Similar to the TNN models, the LNN models with the best performance on the validation set were all trained by the transfer learning method, and the validation accuracy of MobileNet V3-TL, SqueezeNet1_0-TL, and ShuffleNet_v2_x1_0-TL was 92.59%, 94.44%, and 96.30%, respectively.

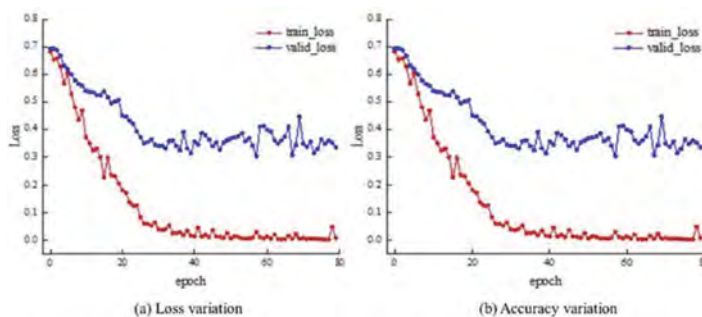


Figure 6. Loss and accuracy variation during training of shuffle-net_v2_x0_5-TL model.

Table 2. LNN model and validation accuracy.

Architecture	MobileNet	SqueezeNet	ShuffleNet
Model (validation accuracy)	MobileNet V1 (90.74%)	SqueezeNet1_0 (90.74%)	ShuffleNet_v2_x0_5 (87.04%)
	MobileNet V1-TL (88.89%)	SqueezeNet1_0-TL (94.44%)	ShuffleNet_v2_x0_5-TL (92.59%)
	MobileNet V2 (80.36%)	SqueezeNet1_1 (87.04%)	ShuffleNet_v2_x1_0 (83.33%)
	MobileNet V2-TL (90.74%)	SqueezeNet1_1-TL (94.44%)	ShuffleNet_v2_x1_0-TL (96.30%)
	MobileNet V3 (85.19%) MobileNet V2-TL (92.59%)		

3 EVALUATING THE NEURAL NETWORK

3.1 Prediction of the neural network

The trained neural network in Section 2.3 was used to predict the aesthetic quality of the bridge tower images in the test set, and some prediction results of the ShuffleNet_v2_x1_0-TL model are shown in Figure 7. The one-hot form was used to encode the label in the dataset, the first value is the probability of not appealing and the second value is the probability of appealing, and whichever value is greater is the final classification result.

Table 3 shows the test accuracy of the model with the highest validation accuracy under different architectures. It found that both kinds of networks can handle the bridge tower aesthetic assessment task well, but LNN better in terms of validation accuracy and test accuracy. The three kinds of LNN achieved the same test accuracy, but ShuffleNet had the highest validation accuracy, followed by SqueezeNet and MobileNet. Therefore, from the perspective of model accuracy, the ShuffleNet_v2_x1_0-TL model performs best in the bridge tower aesthetics assessment task, followed by Squeezenet1_0-TL, and MobileNet V3-TL.

Table 3. Test accuracy of the model with the highest validation accuracy.

Type of neural network	Model	Validation accuracy	Test accuracy
TNN	VGG16-TL	90.74%	87.50%
	Inception V1-TL	92.59%	82.14%
	ResNet101-TL	92.59%	85.71%
LNN	MobileNet V3-TL	92.59%	89.29%
	SqueezeNet1_0-TL	94.44%	89.29%
	ShuffleNet_v2_x1_0-TL	96.30%	89.29%

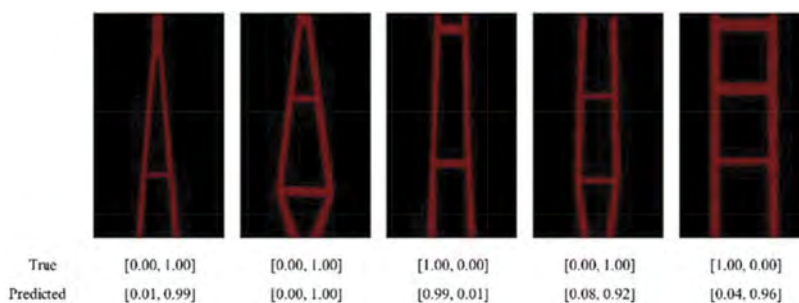


Figure 7. Part of the predicted results.

3.2 Complexity evaluation of the neural network

To comprehensively evaluate the performance of TNN and LNN, the complexity of the six models in Table 3 was further evaluated by the following indexes: model size, number of parameters, floating point of operations (Flops), multiply-add operations (MADD), memory required for node reasoning (Memory) and memory usage of graphics card (MemR+W). The results for each model complexity are shown in Table 4.

Table 4. Complexity results for each model.

Model	Model size/ MB	Number of parameters	Flops	MADD	Memory/ MB	MemR+W/ MB
VGG16-TL	512.0	1.34×10^8	10.2 G	20.3 G	71.5	655.4
Inception V1-TL	21.5	5.60×10^6	984.0 M	2.0 G	19.6	67.8
ResNet101-TL	162.0	4.25×10^7	5.12 G	10.2 G	105.6	373.8
MobileNet V3-TL	16.2	4.20×10^6	148.8 M	293.3M	31.5	71.7
SqueezeNet1_0-TL	2.82	7.36×10^5	474.2 M	940.2 M	21.9	47.4
ShuffleNet_v2_x1_0-TL	4.95	1.26×10^6	97.7 M	193.1 M	13.6	32.8

The complexity of the LNN is significantly smaller than that of the TNN. In terms of model size and parameter, the SqueezeNet1_0-TL model has the smallest size of 2.82 MB and the least number of parameters of 7.36×10^5 , while that of VGG16-TL and ResNet101-TL are 1-2 orders of magnitude larger than those of the LNN. For the indexes of MADD, Flops, Memory, and MemR+W, the shufflenet_v2_x1_0-TL model has the smallest values for each of these metrics, and the values for the TNN are all much greater than those of the LNN. Therefore, comparing the complexity indexes of all models, the Shufflenet_v2_x1_0-TL model has the lowest complexity, and the Squeezenet1_0-TL and MobileNet V3 large-TL show similar complexity.

In summary, taking into account both model accuracy and complexity, the LNN perform better than the TNN and Shufflenet_v2_x1_0-TL performs is the most ideal network architecture for the bridge tower aesthetic assessment task with the highest accuracy and lowest complexity.

3.3 Comparison with similar studies

To verify the applicability of the proposed method, some comparisons are made between that of similar studies. The results can be found in Table 5, which shows the accuracy achieved by the proposed method is only second to the model obtained by (Dong *et al.* 2015). Admittedly, the model of the neural network obtained by training with the different datasets is not rigorous enough, but it also reflects the feasibility of the proposed method.

Table 5. Accuracy of relevant study models.

Model	Dataset	Accuracy
(Lu <i>et al.</i> 2015)	AVA dataset	75.42%
(Kong <i>et al.</i> 2016)		77.33%
(Talebi and Milanfar 2018)		81.51%
(Dong and Tian 2015)		83.52%
(Hou <i>et al.</i> 2022)		83.10%
(Tan <i>et al.</i> 2016)	Dpchallenge dataset	87.10%
(Schwarz <i>et al.</i> 2018)	AROD dataset	75.83%
(Dong <i>et al.</i> 2015)	CUHKPQ dataset	90.76%
The proposed model	BTFE dataset	89.29%

4 CONCLUSION

In this study, a BTAANet based on the LNN is proposed to realize efficient and accurate automatic evaluation of the aesthetic quality of the bridge tower forms. A BTAA Dataset was constructed combined with the standard bridge tower contour image and the evaluation results obtained through the applet. With the BTAA Dataset, TNN models and LNN models were trained. The trained models were then used for aesthetic quality prediction of bridge tower images in the test set, and the prediction accuracy and complexity of these models were evaluated.

The results show that the bridge tower aesthetic assessment is efficiently and accurately implemented using the trained neural networks, and the BTAANet that takes ShuffleNet_v2_x1_0-TL as the base model, not only has the highest accuracy but also the lowest model complexity, which performs best in the bridge tower aesthetics assessment task. In addition, a comparison with similar studies revealed the high accuracy and feasibility of the method in this paper. The proposed method provides an important basis for designers in the design process of bridge towers and promotes the development of bridge aesthetics.

ACKNOWLEDGMENT

This work was supported by the National Natural Science Foundation of China(No. 52078365).

REFERENCES

- Arman, S., Mohammad, A. & Saman, S. 2021. A Comprehensive Review of Deep Learning Architectures for Computer Vision Applications, *American Scientific Research Journal for Engineering, Technology, and Sciences (ASRJETS)*77 1.
- Dong, Z. & Tian, X. 2015. Multi-level photo quality assessment with multi-view features, *Neurocomputing* 168.
- Dong, Z., Shen, X., Li, H. & Tian, X. 2015. Photo quality assessment with DCNN that understands image well., Springer.
- Dou, Q., Sam, Z., Tongfang, S. & Pheng-Ann, H. 2018. Webhetics: Quantifying Webpage Aesthetics with Deep Learning, *International Journal of Human - Computer Studies* 124.
- Hou, J. W., Ding, H. H., Lin, W. S., Liu, W. D. & Fang, Y. M. 2022. Distilling Knowledge From Object Classification to Aesthetics Assessment, *IEEE TRANSACTIONS ON CIRCUITS AND SYSTEMS FOR VIDEO TECHNOLOGY*32 11:7386–7402.
- Kong, S., Xiaohui, S., Zhe, L., Radomír, M. & Charless, C. F. 2016. Photo Aesthetics Ranking Network with Attributes and Content Adaptation., *CoRR*abs/1606.01621.
- Liao, W., Lu, X., Huang, Y., Zheng, Z. & Lin, Y. 2021. Automated structural design of shear wall residential buildings using generative adversarial networks, *Automation in Construction* 132.
- Lima, A. L. D. S. & Gresse, V. W. C. 2022. Assessing the Visual Esthetics of User Interfaces: A Ten-Year Systematic Mapping, *International Journal of Human–Computer Interaction* 38 2.
- Loos, S., Wolk, S. V. D., Graaf, N. D., Hekkert, P. & Wu, J. 2022. Towards intentional aesthetics within topology optimization by applying the principle of unity-in-variety, *Structural and Multidisciplinary Optimization* 65 7.
- Lu, X., Lin, Z., Jin, H., Yang, J. & Wang, J. Z. 2015. Rating Image Aesthetics Using Deep Learning, *IEEE transactions on multimedia* 17 11.
- Schwarz, K., Wieschollek, P. & Lensch, H. 2018. Will People Like Your Image? Learning the Aesthetic Space.
- Talebi, H. & Milanfar, P. 2018. NIMA: Neural Image Assessment., *IEEE transactions on image processing: a publication of the IEEE Signal Processing Society*.
- Tan, Y., Pengjie, T., Yimin, Z., Wenlang, L., Yongping, K. & Guangyao, L. 2016. Photograph aesthetical evaluation and classification with deep convolutional neural networks, *Neurocomputing* 228.
- Xin, J., Jingying, C., Siwei, P., Yulu, T., Chaochen, Y. & Xiaodong, L. 2016. Deep Image Aesthetics Classification using Inception Modules and Fine-tuning Connected Layer. *CoRR*abs/1610.02256.
- H, Li. 2018. Image Aesthetic Quality Assessment based on Convolutional Neural Networks and Composition Rules., Xidian University.
- Y, Liang., W, He. & M, Tang. 2020. State-of-the-art review of bridge aesthetics in 2019, *Journal of Civil and Environmental Engineering* 42 05:213–222.

Influence of different curing condition on seismic performance of reinforced concrete bridge piers

Qiang Peng Wen, Liang Lu Wen, Lin Li Feng & Dong Tang Ya

School of Civil Engineering and Architecture, Beijing Jiaotong University, Beijing, China

Feng Xu Lin

Beijing Municipal Design Institute Co., Ltd., Beijing, China

ABSTRACT: In order to explore the influence of different curing conditions on the seismic capacity of reinforced concrete (RC) piers in construction, the mechanical properties of concrete under different curing conditions were tested. Based on the experimental data of concrete mechanical properties and numerical simulation method, the finite element models of RC piers under different curing conditions are established. The quasi-static analysis method is used to compare and analyze the influence of different curing conditions on the seismic performance of RC piers. The results show that the elastic modulus of C50 fine stone concrete is lower than that of cube compressive strength and axial compressive strength, but increases rapidly after 14 days of curing. The basic shape and development trend of the hysteresis curve of RC piers under different curing conditions are similar. The fullness of the hysteresis curve of the same curing temperature and humidity increases with the increase of age. When the curing temperature and humidity are the same, the yield load, ultimate load and ultimate displacement of RC piers increase with the increase of age, and the yield displacement decreases slightly with the increase of age. The curves of cumulative displacement ductility coefficient of RC bridge piers under different curing conditions are similar, and the maximum cumulative displacement ductility coefficient increases with the age when the curing temperature and humidity are the same. Before the horizontal displacement of RC pier top reaches yield displacement under different curing conditions, the change of viscous damping coefficient is small, and the viscous damping coefficient increases sharply after reaching yield displacement. When the curing time is the same, the difference in seismic performance of RC piers between standard curing and natural curing is small; when the curing temperature and humidity are the same, the seismic performance of RC piers at different ages varies greatly.

1 INTRODUCTION

The gradual hardening and strength growth of concrete is the result of cement hydration, which requires certain humidity, temperature and time, and when the construction site temperature and humidity do not meet the curing requirements, the concrete needs to be maintained manually. Differences in curing conditions can lead to significant effects on the mechanical properties of the concrete structure. The precast and cast-in-place concrete structures may not reach the expected strength within the specified time, and the mechanical properties of bridge piers as load-bearing members are more obviously affected by the curing conditions.

Many scholars have conducted a lot of research on the seismic damage of bridges in the construction phase and the seismic performance of bridge piers in the operation phase. Zheng Yuguo (Zheng & Yuan 2013a, b) analyzed the seismic response spectrum of three different pier-shaped large-span continuous girder bridges during the whole construction process, and obtained the change law of seismic response of piers during the whole cantilever construction

process. Tong, Dawei (Tong et al. 2022) considered analytically the effect of construction process and different backfill compaction qualities on the seismic response of prestressed steel barrel concrete pipes. Shi Yan (Shi & Xiong 2013a, Shi & Zhang 2020b) proposed an equivalent load calculation formula for the internal forces of main girders and main piers based on the equivalent load method applicable to the construction phase of continuous rigid frame bridges, and obtained the seismic susceptibility curves of the bottom and top of main piers and the root of main girders by means of finite element software. Yang Cheng (Yang & Chen, et al. 2016) proposed a vulnerability index for bridge construction process with a vulnerability model considering the construction process. Many other scholars (Bai 2019; Jia 2022; Guo 2022; Cao 2021; Lu 2021; Shao 2022; Cheng 2017; Li 2011) have also studied the seismic performance of different bridge piers in the operation phase.

In this paper, the mechanical properties of C50 concrete under different curing conditions were analyzed through tests, and the seismic performance of RC piers under different curing conditions was analyzed based on the test data and using OpenSees finite element software.

2 CONCRETE MECHANICAL PROPERTIES TEST

2.1 Specimen material

The mass ratio of raw material composition of C50 fine stone concrete is: $w(\text{cement}):w(\text{water}):w(\text{sand}):w(\text{stone}):w(\text{Silicafume}):w(\text{admixture}) = 1:0.36:1.81:2.72:0.2:0.014$. Among them, the cement is P-O42.5 cement; the stone is 5-25 continuous grained gravel; the sand is river sand with maximum particle size of 3.2mm; the water is natural water; the fly ash with fineness of 9.4% is chosen as the compound material; the water reducing agent is polycarboxylic acid water reducing agent with water reduction rate of 29%, and the specific ratio is shown in Table 1.

Table 1. Material dosage of C50 fine stone concrete.

Material dosage (kg/m ³)					
cement	water	sand	stone	Silica fume	admixture
400	147	726	1088	83	5.9

2.2 Specimen preparation and curing

Prepare 16 groups of 100mm × 100mm × 300mm prismatic specimens, 3 groups of 100mm × 100mm × 100mm cubic specimens, 8 groups of prismatic specimens and 4 groups of cubic specimens into the curing room for standard curing condition (temperature (20±2)°C, humidity ≥95%), the rest of the specimens are placed in the precast concrete workshop (average daily temperature (18±2)°C, humidity ≥65%) for natural curing condition.

2.3 Test results

The average values of cubic compressive strength f_{cu} , axial compressive strength f_c and modulus of elasticity E_c were determined under different curing conditions up to 7, 14, 28 and 45 days, as shown in Table 2.

3 RC BRIDGE PIER FINITE ELEMENT

3.1 RC bridge pier finite element model

Based on the OpenSees, the Concrete02 material model is selected to simulate the concrete constitutive relationship, and the compressive stress-strain curve is shown in Figure 1(a), where f_{pc} is the compressive strength of concrete; The strain generated when *eposco* concrete reaches its compressive strength; f_{pcu} is the residual compressive strength, for unconfined zone

Table 2. Mechanical properties of C50 fine stone concrete at different curing conditions.

Curing conditions	age/day	f_c /MPa	f_{cu} /MPa	E_c /GPa
Standard Curing	7	43	56	30.4
	14	46.5	61.3	34.7
	28	53.2	68.3	44.1
	45	59.3	71.2	46.6
Natural Curing	7	39.2	50.9	26.4
	14	43.3	56.6	30.2
	28	51.1	62	39.4
	45	53.6	65.3	43.4

concrete take $f_{pcu} = 0.2f_{pc}$; For the core concrete principal structure constrained by hoop reinforcement using the Mander model for calculation, the compressive strength of concrete in the core area of the rectangular section constrained by hoop reinforcement is calculated as:

$$f'_{cc} = f'_c(1 + k_1\bar{x}) \quad (1)$$

In the formula: $k_1 = [0.1 + \frac{0.9}{1+B\bar{x}}]$; f'_c is the cylindrical compressive strength of concrete; A and B are parameters for the increase in concrete strength due to hoop restraint, and the specific values are taken with reference to the literature (Chang & Mander 1994); $\bar{x} = \frac{f'_{11} + f'_{12}}{2f'_c}$, $r = \frac{f'_{11}}{f'_{12}}$, $f'_{11} > f'_{12}$, f'_{11} and f'_{12} are two directional restraint stresses in concrete.

The longitudinal reinforcement tensile stress-strain curve is shown in Figure 1(b). Where f_y is the tensile yield stress; f_u is the tensile ultimate stress; E_s is the tangential modulus in the elastic phase; E_{sh} is the initial tangential modulus in the strengthening phase; ϵ_{sh} is the initial strain in the strengthening phase; ϵ_{su} is the strain when the stress reaches its peak.

Bond slip model of pier bottom reinforcement using Bond_SP01 material model. The skeleton curve is shown in Figure 1(c). Where K is modulus of elasticity of reinforcement; F_y is yield stress of reinforcing steel; F_u is ultimate stress of reinforcing steel; S_y is yield slip of reinforcement; S_u is ultimate slip of reinforcement. In addition, when setting the model parameters, the values of the stiffness reduction factor b and the pinch factor R should be considered, In this paper, the numerical simulation b takes the value of 0.4, R takes the value of 0.8, and each parameter takes the value of reference (Zhao & Srtharan 2007).

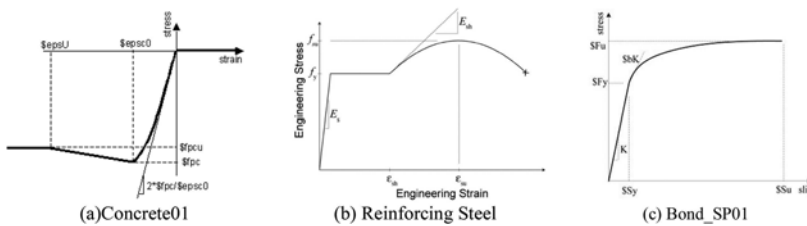


Figure 1. Constitutive relation curve of material model.

3.2 RC bridge pier finite element model reliability verification

In order to test the reliability of the numerical simulation method of RC piers, the simulation of reduced-scale RC concrete solid piers carried out by Fang Lin (Fang. 2016) of Southwest Jiaotong University was examined, in the test, the vertical force at the top of the RC bridge pier was constant, and the horizontal direction was subjected to reciprocal cyclic loading. The concrete grade of RC bridge pier is C40, the longitudinal reinforcement is HRP400 and the stirrup is HRB335, and the parameters of the specimen are shown in Table 3.

From Figure 2, it can be seen that both the experimental and simulated hysteresis curves show pinching phenomenon, the morphology and size of both hysteresis loops are similar. The yield loads and yield displacements obtained using Park (Park,R. 1989) method are

Table 3. Specimen parameters.

Number	Size/m	Height/m	Axial pressure ratio	Reinforcement rate	Stirrup spacing	Stirrup ratio
B1	0.5×0.5	2.95	0.5	1.79%	70	2.44%
B2	0.5×0.5	2.95	0.5	1.79%	140	1.22

shown in Table 4. As can be seen from Table 4, the relative errors of yield load and yield displacement obtained from the test and simulation are less than 5%, indicating that the finite element model established in this paper is highly reliable.

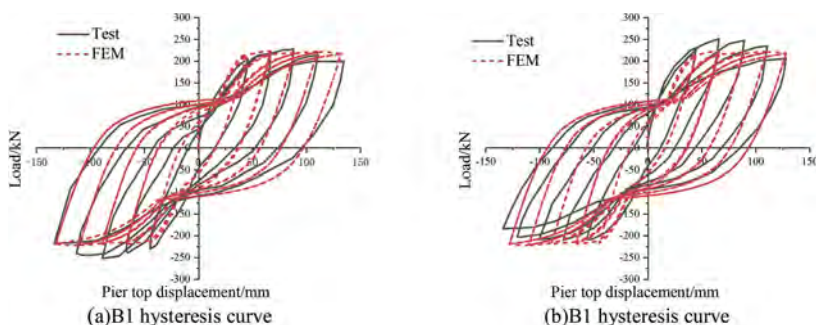


Figure 2. Comparison of test and FEM results.

Table 4. Specimen parameters.

Number	Yield load(kN)			Yield displacement(mm)		
	Test	Simulation	Relative Error	Test	Simulation	Relative Error
B1	210	201	4.29%	40.63	39.5	2.78%
B2	206	198	3.88%	37.72	36.3	3.76%

4 SEISMIC PERFORMANCE OF RC BRIDGE PIERS

4.1 Hysteresis curve

In this paper, the numerical simulation adopts the variable displacement loading system, and the loading level is divided into 9mm, 18mm, 27mm, 36mm, 45mm, 54mm, 63mm, 72mm, 81mm, 90mm, 100mm, 110mm, 120mm及140mm. The hysteresis curves of RC piers under different curing conditions were obtained by numerical simulation once per loading cycle, as shown in Figure 3. From Figure 3, the basic shape and development trend of the hysteresis curve of RC piers under different curing conditions are similar, and the fullness of the hysteresis curve grows with the age when the curing temperature and humidity are the same.

4.2 Skeleton curve

To further compare the seismic performance of RC piers under different curing conditions, the skeleton curves were extracted, as shown in Figure 4. From Figure 4, the horizontal ultimate bearing capacity of the top of the pier grows with the growth of curing time, Standard curing 7 days, 14 days, 28 days and 45 days of the top of the pier horizontal limit bearing capacity of 246.6kN, 250.8kN, 257.6kN and 262kN respectively. The horizontal ultimate bearing capacity of the top of pier for 7 days, 14 days, 28 days and 45 days of natural curing are 241.4kN, 247.1kN, 255.6kN and 257kN respectively.

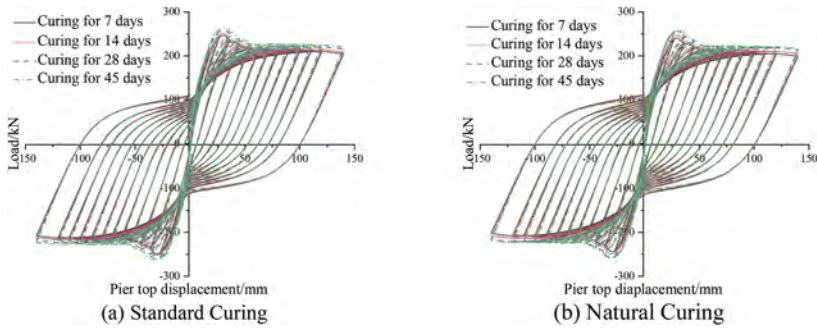


Figure 3. Hysteresis curves of RC piers under different curing conditions.

Park method is used to calculate the yield displacement of RC piers under different curing conditions, and take the pier top horizontal bearing capacity down to 85% of the ultimate bearing capacity. Yield load f_y , yield displacement Δ_y , ultimate load f_u and ultimate displacement of RC piers under different curing conditions Δ_u are shown in Table 4.

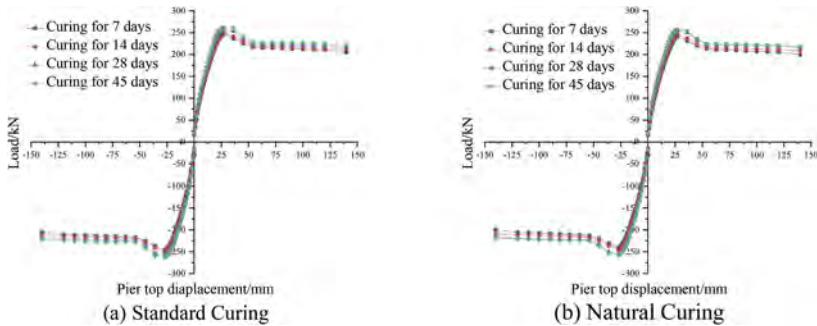


Figure 4. Skeleton curves of RC piers under different curing condition.

Table 5. Numerical simulation results of RC bridge piers under different curing conditions.

Curing conditions	Age/day	f_y /kN	Δ_y /mm	f_u /kN	Δ_u /mm
Standard Curing	7	211.1	20.2	209.6	126
	14	223.9	19.8	213.2	130
	28	229.2	19.2	218.9	135
	45	233.4	18.7	223.1	140
Natural Curing	7	216.1	20.6	204.9	122
	14	221.8	20.2	210.1	126
	28	221.2	19.3	217.3	128
	45	229.1	19	219.2	136

Note: f_y is the yield displacement; Δ_y is the yield displacement; f_u is the ultimate load; Δ_u is the ultimate displacement.

4.3 Cumulative displacement ductility factor

In order to analyze the deformation capacity of RC piers under different curing conditions, the cumulative displacement ductility factor N_Δ is used to analyze its deformation capacity.

N_Δ is calculated as:

$$N_\Delta = \sum_{i=1}^n \frac{\Delta_i}{\Delta_y} \quad (2)$$

in the formula: Δ_i —The average value of positive and negative peak displacement of the i -th cycle loading; Δ_y — Yield displacement; n —The number of cycles loaded in the current state.

The N_Δ variation curves of RC concrete piers under different curing conditions are shown in Figure 5. From Figure 5, the curves of cumulative displacement ductility coefficients of RC piers under standard curing conditions and natural curing conditions have similar trends, and the cumulative displacement ductility coefficients increase with the increase of curing age. The ratio of the maximum cumulative displacement ductility coefficient of 7, 14 and 45 days of standard curing to 28 days of curing is 0.945, 0.964 and 1.02; the ratio of the maximum cumulative displacement ductility coefficient of 7, 14 and 45 days of natural curing to 28 days of curing is 0.936, 0.955 and 1.01. RC bridge pier ductility performance increases with curing time. When the curing time is the same, the difference between standard curing and natural curing RC pier cumulative displacement ductility coefficient maximum value are less than 3%.

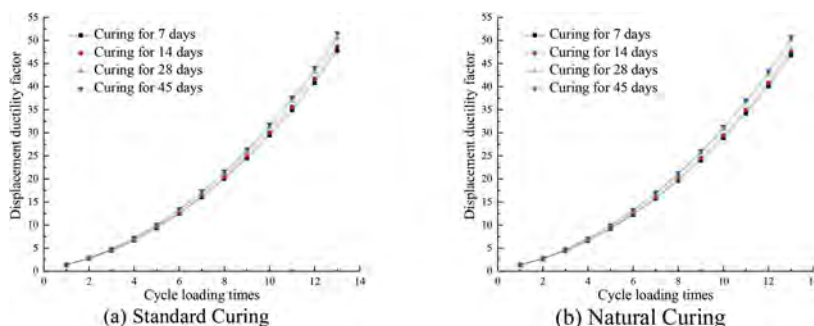


Figure 5. Cumulative displacement ductility coefficient of RC under different curing conditions.

4.4 Viscous damping coefficient

In order to analyze the energy dissipation of RC piers under different curing conditions, the viscous damping coefficient ζ_{hys} is used to analyze their energy dissipation capacity. ζ_{hys} is calculated as:

$$\zeta_{hys} = \frac{1}{2\pi} \frac{E_{hys}}{E_{els}} \quad (3)$$

In the formula: E_{hys} —Total energy dissipated during the complete hysteresis cycle; E_{els} —Elastic strain energy corresponding to the maximum displacement in the hysteresis cycle.

The variation curves of ζ_{hys} of RC concrete piers under different curing conditions are shown in Figure 6. From Figure 6, it can be seen that the variation of ζ_{hys} curve under standard and natural conservation conditions is similar. The horizontal displacement of the top of the pier reaches 27mm when the RC piers of different ages have yielded, so that the ζ_{hys} of the RC piers of different ages increase sharply when the next level of loading is carried out. When the horizontal displacement of the top of the pier is less than 64 mm, the ζ_{hys} curves of RC piers at different ages basically overlap, and the ζ_{hys} decreases slightly with the growth of age when the horizontal displacement of the top of the pier is greater than 64 mm, which is due to the growth of both E_{hys} and E_{els} with the growth of age, but the growth rate of E_{els} is slightly greater than E_{hys} resulting in a slight decrease of ζ_{hys} with the growth of age. The maximum values of ζ_{hys} for 7, 14, 28 and 45 days of standard curing were 0.334, 0.325, 0.32 and 0.318, respectively; the maximum values of ζ_{hys} for 7, 14, 28 and 45 days of natural curing were 0.339, 0.328, 0.321 and 0.32, respectively. When the curing time is the same, the difference between the maximum value of viscous damping coefficient of standard curing and natural curing RC piers is less than 2%.

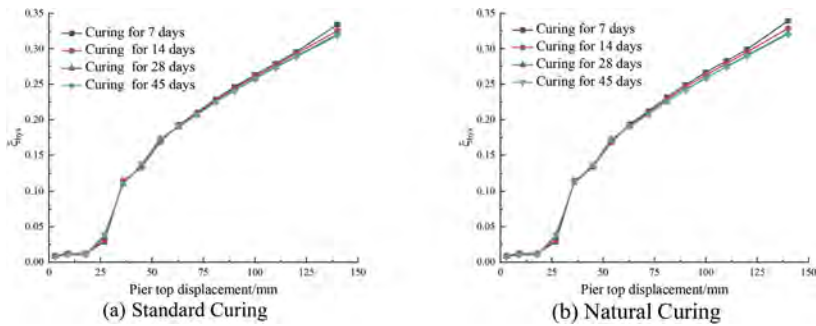


Figure 6. Viscous damping coefficient of RC under different curing conditions.

5 CONCLUSIONS

This paper investigates the seismic performance of RC piers at different ages using the proposed static analysis method based on the results of C50 fine stone concrete mechanical performance tests and the verification of the reliability of the numerical model. The study concluded as follows:

- (1) The basic shape and development trend of RC pier hysteresis curves under different curing conditions are similar, and the degree of fullness grows with the age; The yield load, ultimate load and ultimate displacement of RC piers all increase with age, and the yield displacement decreases with age.
- (2) The curves of cumulative displacement ductility coefficients of RC piers under different curing conditions have similar trends, and the maximum cumulative displacement ductility coefficients of RC piers under the same curing conditions increase with the growth of age.
- (3) Before the horizontal displacement of pier top reaches the yield displacement of RC pier, the change of ζ_{hys} is small; After the horizontal displacement of pier top reaches the yield displacement of RC pier, ζ_{hys} surge; When the horizontal displacement of pier top is less than 81mm, the ζ_{hys} curves of RC piers of different ages basically overlap; ζ_{hys} decreases with age when the horizontal displacement of pier top is greater than 81mm.
- (4) When the curing time is the same, the difference in seismic performance of RC piers with standard curing and natural curing is small; When the curing conditions are the same, the seismic performance of RC piers varies greatly at different ages.

ACKNOWLEDGEMENTS

The authors gratefully acknowledge supports from the Key Project of Beijing Construction Engineering Group (RGA501020200001).

REFERENCES

- Bai & Wang, et al. 2019. Seismic capacity assessment of corroded reinforced concrete bridge piers. *Journal of Hunan University of Science and Technology (Natural Science Edition)*: 34(04): 58–66.
- Cao & Li. 2021. Experimental study on seismic performance of defective fabricated concrete beam-column joints. *Engineering Mechanics*: 38 (11):134-146+159.
- Cheng & Li, et al. 2017. Seismic performance analysis of reinforced concrete bridge piers considering corrosion and bond degradation. *Engineering Mechanics*: 34(12):48–58.
- Chang & Mander J.B. 1994. Seismic energy based fatigue damage analysis of bridge columns: part 1 evaluation of seismic capacity. *New York: State University of New York*.
- Fang. 2016. Experimental study on seismic performance of reinforced concrete hollow piers. *Southwest Jiaotong University*.

- Guo & Yao. 2022. Experimental study on residual seismic performance of reinforced concrete columns damaged by earthquakes. *Journal of Hunan University(Natural Science Edition)*: 49(09):1–8.
- Jia & Tan, et al. 2022. Seismic performance analysis of self-resetting prefabricated RC bridge piers based on OpenSees simulation. *Chinese Journal of Applied Basic and Engineering Sciences*: 30(02):328–340.
- Lu & Chen, et al. 2021. Research on Simplified Model for Seismic Calculation of Railway Gravity Piers. *Vibration and Shock*: 40(09):71–76.
- Li & Wang, et al. 2011. Seismic performance analysis of reinforced concrete bridge piers based on OpenSees. *Journal of Huazhong University of Science and Technology (Natural Science Edition)*: 39(08): 49-52+71.
- Park,R. 1989. Evaluation of Ductility of Structures and Structural Assemblages from Laboratory Testing. *Bulletin of the New Zealand National Society for Earthquake Engineering*: Vol.22.No3. September.1989.
- Shi & Xiong, et al. 2021. Seismic Vulnerability Analysis of Continuous Rigid Frame Bridges Considering Internal Forces in Typical Construction Stages. *Vibration and Shock*: 40 (24):136-143+179.
- Shi & Zhang, et al. 2020. Seismic damage analysis of high-pier and long-span continuous rigid frame bridges during typical construction stages: *Vibration and Shock*: 39(22):89–95.
- Shao & Qi Qi-ming, et al. 2022. Experimental study on ductile seismic performance of rectangular concrete hollow piers. *Journal of Southwest Jiaotong University*: 57 (01):129-138+157.
- Tong & Wang et al. 2022. PCCP seismic response analysis considering the influence of construction process. *Journal of Hohai University (Natural Science Edition)*: 50(02):76–82.
- Yang & Chen, et al. 2016. Vulnerability analysis of bridge construction process in aftershock areas. *Engineering Mechanics*: 33(S1):251–256.
- Zheng & Yuan. 2013. Earthquake Response Spectrum Analysis During Cantilever Construction of Typical Large-span Continuous Girder Bridges. *Journal of Hunan University of Science and Technology (Natural Science Edition)*: 28(03):59–65.
- Zheng & Yuan. 2013. Seismic safety evaluation of typical long-span girder bridge construction process based on CDR. *Chinese Journal of Safety Science*: 23(07):73–78.
- Zhao & Srtharan. 2007. Modeling of strain penetration effects in fiber-based analysis of reinforced concrete structures. *ACI Structural Journal*: 104(2):133–141.



Taylor & Francis

Taylor & Francis Group

<http://taylorandfrancis.com>

SS27: Practical applications and value of advanced computational and probabilistic modelling in life-cycle engineering
Organizers: P. Bocchini, A. Strauss & H. Sousa



Taylor & Francis

Taylor & Francis Group

<http://taylorandfrancis.com>

Semi-probabilistic assessment of concrete bridge exploiting additional data from experiments and numerical analysis

L. Novák & D. Novák

Faculty of Civil Engineering, Brno University of Technology, Brno, Czech Republic

M. Cao

Department of Engineering Mechanics, Hohai University, Nanjing, China

R. Pukl

Cervenka Consulting, Prague, Czech Republic

ABSTRACT: The paper presents an application of the novel methodology for the assessment of structures using a semi-probabilistic approach exploiting advanced probabilistic modeling and experimental results. The selected existing bridge is represented by a costly finite element model, which reflects the non-linearity of concrete and the construction process. Due to a significant computational burden of each simulation, it is not feasible to perform a Monte Carlo simulation and a semi-probabilistic approach was thus adopted. In this study, we investigate the possibility of a Gram-Charlier expansion described by the first four central moments efficiently obtained directly from Polynomial Chaos Expansion metamodel together with the uncertainty quantification of input random variables described by a joint probability distribution obtained from experimental data combined with prior assumptions from codes. Obtained results are compared to the standard approach assuming a Lognormal probability distribution of structural resistance.

1 INTRODUCTION

Mathematical models of real structures, e.g. bridges, are typically analyzed by computationally expensive non-linear finite element method (NLFEM) reflecting material and geometrical non-linearity. Non-linear models are not compatible with standard partial safety factors (PSF) implemented in Eurocode (CEN 2002) and advanced probabilistic methods should be employed. Nonetheless, standard probabilistic design or assessment of structures represented by computational models solved by NLFEM is extremely time-consuming and it is usually necessary to use semi-probabilistic methods developed for NLFEM. The paper focuses on the semi-probabilistic assessment of concrete structures using simplified methods.

In the semi-probabilistic approach (Val et al. 1997, Novák & Novák 2021), the resistance of structure R is separated (similarly is in PSF by sensitivity factor α), and the design value R_d that satisfies safety requirements is evaluated, instead of the direct calculation of failure probability. The whole process represents the estimation of a quantile satisfying the given safety requirements under the prescribed simplifying assumptions. The given task is thus simplified to statistical analysis of target probability distribution of resistance (output of the model) – its mean value μ , coefficient of variation (CoV) etc. Safety requirements are given by codes in form of the target reliability index β dependent on consequence classes, e.g. β for the ultimate limit state, moderate consequences of failure and a reference period of 50 years is set at $\beta = 3.8$ according to the Eurocode 1990 (CEN 2002). In this paper, we investigate the role of simplifying assumptions regarding the probability distribution of input variables and resistance (output variable).

The procedure is a combination of the following steps:

- development of NLFEM finite element model of structure (high-fidelity model, computationally very expensive);
- stochastic model based on prior knowledge for input random variables;
- Bayesian approach - based on experimental data updating statistics of input random variables;
- development of surrogate model using Polynomial Chaos Expansion (PCE – low fidelity model, computationally cheap);
- determination of design value of resistance based on statistical moments of resistance directly obtained from PCE or estimated by Monte Carlo using surrogate model using Gram-Charlier expansion.

2 ASSUMPTIONS IN SEMI-PROBABILISTIC APPROACH

Existing simplified semi-probabilistic methods were developed for an estimation of CoV using very low number of samples (ECoV methods), e.g. ECoV by Červenka (Červenka 2013), Taylor Series Expansion (Novák & Novák 2020) or recently developed Eigen ECoV (Novák & Novák 2021). These methods are based on very strict assumptions, which allow to use simple formulas together with a few numerical simulations (e.g. 2 for ECoV by Červenka or 3 for Eigen ECoV) for an estimation of the first two statistical moments. The mean value μ and variance σ^2 are further used to describe an assumed 2-parametric probability distribution of resistance, typically Lognormal distribution or Gaussian distribution. Lognormal distribution is moreover recommended as a typical distribution for modeling of resistance in codes (fib 2013, CEN 2002, JCSS 2001). This has well-justified rationale: Lognormal distribution is non-negative (reflecting reality) and it is fully-described by the first two statistical moments (computational efficiency). However, this paper presents methodology for semi-probabilistic approach for medium-size experimental design (ED) 10-100 samples. In that case, it is possible to construct a surrogate model sufficiently accurate for an estimation of higher statistical moments. Additionally it will be shown that it is beneficial to use Bayesian updating of input variables to estimate a realistic R_d incorporating real data obtained from material experiments for input random variables.

2.1 Standard approach

The standard formula for the estimation of R_d , assuming a Lognormal distribution of R , is

$$R_d = \mu_R \cdot \exp(-\alpha_R \beta v_R), \quad (1)$$

where μ_R is the mean value, v_R is the coefficient of variation (CoV) and α_R represents sensitivity factor derived from First Order Reliability Method (FORM); the recommended value is $\alpha_R = 0.8$ according to Eurocode 1990 (CEN 2002). In this case, it is necessary to estimate only the first two statistical moments μ and σ^2 . Estimation of statistical moments using ECoV methods is based on numerical simulations with specific quantile of input random variables, e.g. mean values and characteristic values of material parameters. Although such an approach is extremely efficient, it is also very limited to assumed Lognormal distribution of resistance. There are many studies investigating this approach and comparing various ECoV methods (Schlune et al. 2011, Bagge 2020, Novák et al. 2022). Although ECoV methods are well-suited for extremely computational expensive numerical models, their limitations could lead to inaccurate results as probability distribution of resistance can differ from Lognormal distribution significantly in some cases (eg. high non-linearity). Thus the further paragraphs describe a methodology based on Polynomial Chaos and Gram-Charlier Expansions used for estimation of higher statistical moments and construction of an artificial probability distribution for structural resistance.

2.2 Polynomial chaos and gram-charlier expansions

An approximation of cumulative distribution function (CDF) F_R of structural resistance R by Gram-Charlier expansion (G-C) is a completely determined by the first four statistical

moments obtained here efficiently from Polynomial Chaos Expansion (PCE). Assuming that it is possible to write probability distribution of R as a perturbation of Gaussian Gaussian probability distribution function (PDF) ϕ . Once the R is normalized to be zero-mean and unit-variance, it is possible to write the Gram-Charlier approximation of CDF in the terms of its higher central moments (skewness γ_Y and kurtosis κ_Y) as:

$$F_R = \Phi(r) - \left[\frac{\gamma_Y}{3\sqrt{2!}} H_2(r) + \frac{\kappa_Y - 3}{4\sqrt{3!}} H_3(r) \right] \phi(r). \quad (2)$$

where $H_n(r)$ are probabilists' Hermite polynomials of n -th order and $\Phi(r)$ represents standard Gaussian CDF.

It is typically not feasible to get higher statistical moments by crude Monte Carlo simulation due to its computational demands, moreover the moments estimated from samples are highly sensitive to outliers. Fortunately, it is possible to get statistical moments analytically in case of PCE, which represents the output variable R as a function g^{PCE} of an another random variable ξ called the germ with given distribution and representing the original computational model $R = g(X)$ via polynomial expansion. A set of polynomials, orthonormal with respect to the probability distribution of the germ, are used as a basis of the Hilbert space of all real-valued random variables of finite variance. In the case of X and ξ being vectors containing M random variables, the polynomial $\Psi(\xi)$ is multivariate and it is built up as a tensor product of univariate orthogonal polynomials:

$$R = g(X) = \sum_{\alpha \in \mathbb{N}^M} \beta_\alpha \Psi_\alpha(\xi), \quad (3)$$

where $\alpha \in \mathbb{N}^M$ is a set of integers called the multi-index corresponding to polynomial orders in each term of PCE, β_α are deterministic coefficients and Ψ_α are multivariate orthogonal polynomials. Coefficients β_α can be usually obtained by ordinary least squares.

Once a PCE approximation is created, it is possible to obtain statistical moments of R analytically, which represents an enormous advantage with respect to this study, as will be shown in computationally expensive numerical example. Specifically, the first statistical moment (mean value) is equal to the first deterministic coefficient of the expansion

$$\mu_R = \langle Y^1 \rangle = \beta_0. \quad (4)$$

Further the variance $\sigma_Y^2 = \langle Y^2 \rangle - \mu_Y^2$ is obtained as a sum of all squared deterministic coefficients except the intercept, which represents the mean value:

$$\sigma_R^2 = \sum_{\substack{\alpha \in A \\ \alpha \neq 0}} \beta_\alpha^2. \quad (5)$$

Higher statistical central moments, skewness γ_R (3^{rd} moment) and kurtosis κ_R (4^{th} moment), can be similarly obtained analytically for Legendre and Hermite polynomials (Novák 2022).

2.3 Bayesian approach

Given some experimental data \mathcal{D} for input model parameters, a parameterized model for the data (likelihood function) $p(\mathcal{D}|\theta)$, and a prior probability density $p(\theta)$ for the model parameters, the posterior probability density function (PDF) $p(\theta|\mathcal{D})$ of the model can be identified by Bayesian theorem:

$$p(\theta|\mathcal{D}) = \frac{p(\mathcal{D}|\theta)p(\theta)}{p(\mathcal{D})}. \quad (6)$$

Although Bayes' rule looks simple, its efficient evaluation is still challenging and it must be calculated numerically, and thus Markov Chain Monte Carlo sampling (MCMC) is employed in this paper. For numerical calculation, we use existing algorithm implemented in UQPy package for Python (Olivier et al. 2020). Such an approach allows updating prior knowledge about the material characteristics (Rózsás et al., 2022). In this study, Bayesian approach is employed for updating of materials' statistics (mean and variance) obtained from codes combining prior knowledge and results obtained from laboratory experiments. Obtained updated statistics of input random variables together with prescribed probability distribution function were further used in Monte Carlo simulation using surrogate model in form of PCE. Note that evaluation of PCE is very fast even for very large number of simulations used for estimation of higher statistical moments. Estimated statistical moments were ultimately used for G-C expansion and an estimation of R_d as described in section 2.2.

3 NUMERICAL APPLICATION: POST-TENSIONED CONCRETE BRIDGE

The proposed methodology is applied for the existing post-tensioned concrete bridge with three spans. The super-structure of the mid-span analyzed by NLFEM is 19.98 m long with total width 16.60 m. In transverse direction, each span is constructed from 16 prefabricated bridge girders KA-61 commonly used in Czech Republic. Load is applied according to national annex of Eurocode for load-bearing capacity of road bridges by exclusive loading (by six-axial truck).

3.1 Finite element model

The numerical model is created in software ATENA Science based on theory of non-linear fracture mechanics (Červenka & Papanikolaou 2008). In order to reflect complex behavior of the bridge, the numerical model contains three construction phases as illustrated in Figure 1. The NLFEM consists of 13,000 elements of hexahedra type in the major part of the volume and triangular 'PRISM' elements in the part with complicated geometry. Reinforcement and prestressing tendons are represented by discrete 1D elements with geometry according to original documentation. The numerical model is further analysed in order to investigate the ultimate limit state (ULS) (peak of a load-deflection diagram) in order to determine the load-bearing capacity of the bridge. Load-deflection diagram from simulation using mean values of input random variables can be seen in Figure 2 together with typical crack pattern and highlighted 3 limit states: decompression, the first occurrence of cracks and ULS represented by collapse of the bridge.

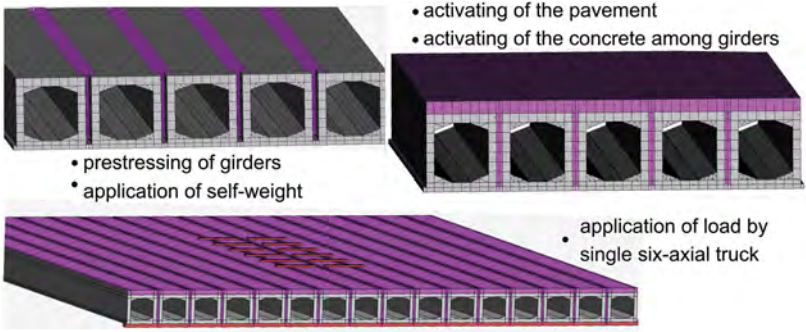


Figure 1. Three construction phases of the bridge mid-span analysed by NLFEM.

3.2 Stochastic model

The stochastic model contains 4 random material parameters of concrete C50/60: Young's modulus E ; compressive strength of concrete f_c ; tensile strength of concrete f_{ct} and fracture

energy G_f . Characteristic values of E , f_{ct} , G_f were determined from f_c according to formulas implemented in the fib Model Code 2010 (fib 2013) – G_f , E , and prEN 1992-1-1: 2021 (CEN 2021) – f_{ct} . The last random variable P represents prestressing losses according to JCSS: Probabilistic Model Code (JCSS 2001). The stochastic model is summarized in Table 1. Mean values and coefficients the of variation were obtained according to prEN 1992-1-1: 2021 (Annex A) for adjustment of partial factors for materials. Statistical correlation among random variables was not considered in this study.

Table 1. Stochastic model of the numerical example.

Var.	Mean	CoV [%]	Distrib.	Units
f_c	56	16	Lognormal	[MPa]
f_{ct}	3.64	22	Lognormal	[MPa]
E	36	16	Lognormal	[GPa]
G_f	195	22	Lognormal	[Jm2]
P	20	30	Normal	[%]

3.3 Results

Once the stochastic model was defined and computational model was developed in ATENA Science, it was possible to create 30 realizations of input random vector generated by Latin Hypercube Sampling (Iman & Conover 1980, Novák et al. 2014, 2022), which covers the whole design domain, and thus it is suitable technique for construction of ED for surrogate modeling. Note that each simulation takes approximately 24 hours using standard hardware. The PCE is created with maximum polynomial order $p = 5$. The whole algorithm of adaptive construction of PCE connecting state of art techniques into stand-alone software tool can be found in (Novák & Novák 2018). The design values of resistance R_d are determined as a quantile of distribution of R with identified statistical moments and target reliability indices $\beta_{ULS} = 3.8$ according to EN 1990. Additionally, design values are reduced by global safety factor reflecting model uncertainties $\gamma_{R_d} = 1.06$ introduced originally in fib Model Code 2010. Note that we compare three design values obtained by described semi-probabilistic approach: i) standard approach assuming Lognormal distribution of R parameterized by the first two statistical moments obtained by PCE; ii) R_d as a quantile of artificial probability distribution constructed by G-C parametrized by the first four statistical moment obtained by PCE and iii) combination of G-C expansion of R and Bayesian updating of input parameters.

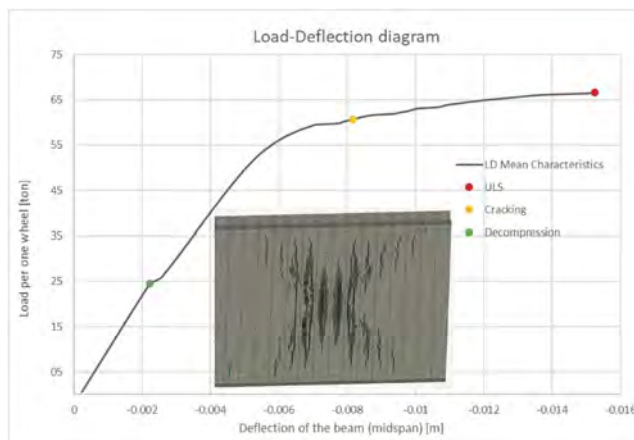


Figure 2. Design values of resistance obtained by semi-probabilistic approach determined by the described methods together with corresponding PDFs.

Bayesian updating is performed using artificially generated data: 20 experiments of concrete specimens. Note that artificially generated data have realistic CoVs of material parameters, which were identified in the previous experimental campaigns (Slowik et al. 2021). Prior distribution of material characteristic was assumed to be Uniform and likelihood distribution is selected according to Table 1, i.e. distributions provided in codes. Obtained results can be found in Figure 3: each row corresponds to a specific material characteristic, the first column shows estimation of mean value and the second column shows estimation of standard deviation. Both columns, the first and second, show also prior and posterior distribution identified by Bayesian approach. Vertical solid lines corresponds to values assumed by codes, obtained directly from experiments by statistical processing and the Bayesian estimation identified as a mean value of posterior distribution. The very last column shows 5000 samples used in MCMC for estimation of posterior distributions. Note that the identified values are significantly different in comparison to recommended values by codes, but this is dependent on real-life experimental results.

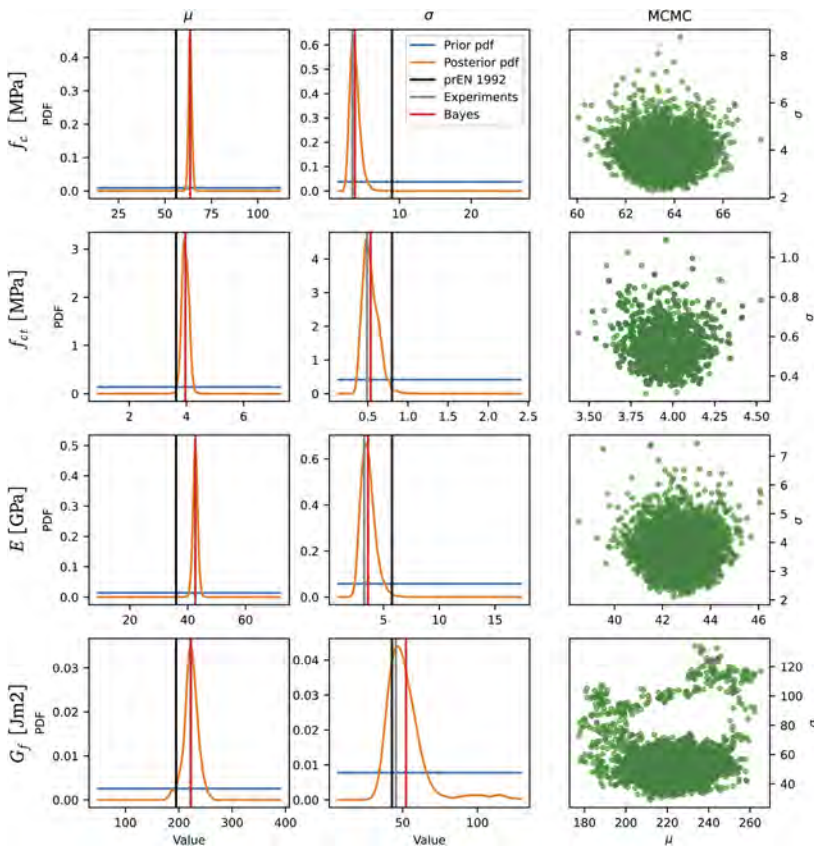


Figure 3. Bayesian estimation of mean μ and standard deviation σ of concrete material characteristics. Solid vertical lines show values determined by codes, experiments and Bayesian approach.

Once the PCE was created, it was possible to analytically derive statistical moments used for Lognormal (first two statistical moments) and G-C expansion (first four statistical moments). The difference between these two design values (corresponding to the identical percentile) is caused by higher statistical moments. Further, the created PCE was employed as computationally cheap surrogate model for crude Monte Carlo simulation with 106 realizations of input random variables identified by Bayesian approach. So Bayes G-C expansion was based on estimation of first four statistical moments needed for Gram-Charlier expansion by Monte Carlo simulation. Comparison of identified PDFs together with determined design values of resistance R_d can be found in 4.

4 CONCLUSIONS

The paper described the advanced semi-probabilistic methodology based on G-C and PCE for estimation of higher statistical moments and an approximation of probability distribution of structural resistance. Additionally, estimation was further improved by Bayesian estimation of input random variables combining likelihood distributions from codes with material experiments. The whole methodology was applied for an estimation of design value of resistance of existing post-tensioned concrete bridge. It can be seen from comparison of determined design values, that is beneficial to include additional information on structural parameters (Bayesian approach) as well as higher statistical moments (G-C expansion). Methodology was shown using concrete bridge example, exploiting additional experimental data and Bayesian approach resulted in less conservative design value here.

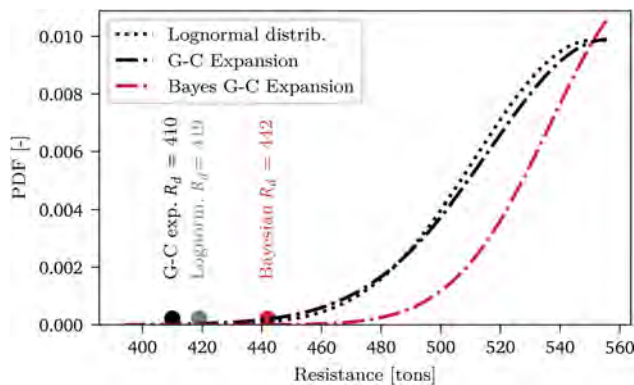


Figure 4. Design values of resistance obtained by semi-probabilistic approach determined by the described methods together with corresponding PDFs.

ACKNOWLEDGEMENTS

This research was funded by Czech Science Foundation under project MAPAB, No. 22-00774S. Numerical results were partially obtained by the software developed with support of Technology Agency of the Czech Republic under project BRIHIS, No. TM04000012. The third author is supported by the Jiangsu International Joint Research and Development Program under project No. BZ2022010.

REFERENCES

- Allaix, D.L.; Carbone, V.I. & Mancini, G. 2013. *Global safety format for non-linear analysis of reinforced concrete structures*. Structural Concrete 14: 29–42.
- Bagge, N. 2020. *Demonstration and examination of a procedure for successively improved structural assessment of concrete bridges*. Structural Concrete 21(4): 1321–1344.
- Comité Européen de Normalisation (CEN) 2002. *EN 1990: Eurocode: Basis of Structural Design*. Brussels, Belgium.
- Comité Européen de Normalisation (CEN) 2004. *EN 1992: Eurocode 2: Design of concrete structures*. Brussels, Belgium.
- Comité Européen de Normalisation (CEN) 2021. *prEN 1992- 1-1 Eurocode 2: design of concrete structures – Part 1-1: general rules – rules for buildings, bridges and civil engineering structures*. Brussels, Belgium.
- Červenka, V. 2013. *Reliability-based non-linear analysis according to fib Model Code 2010*. Structural Concrete 14: 19–28.
- Červenka, J. & Papanikolaou, V. K. 2008. *Three dimensional combined fracture-plastic material model for concrete*. International Journal of Plasticity: 2192–2220.

- fib - federation internationale du beton 2013. *fib Model Code for Concrete Structures 2010*. Berlin: John Wiley & Sons. ISBN: 9783433030615.
- Iman, R.L. & Conover, W.J. 1980. *Small sample sensitivity analysis techniques for computer models with an application to risk assessment*. Communications in Statistics - Theory and Methods 9(17): 1749–1842.
- JCSS - Joint Committee on Structural Safety 2001. *fJCSS Probabilistic Model Code*. JCSS. ISBN: 978-3-909386-79-6
- Novák, D., Vořechovský, M. & Rusina, R. 2022. *FReET v.1.6 – program documentation. User's and Theory Guides*. Červenka Consulting s.r.o., Brno, Czech Republic, <http://www.freet.cz>.
- Novák, D., Vořechovský, M. & Teplý, B. 2014. *FReET: Software for the statistical and reliability analysis of engineering problems and FReET-D: Degradation module*. Advances in Engineering Software 72, 179–192.
- Novák, L. 2022. *On distribution-based global sensitivity analysis by polynomial chaos expansion*. Computers & Structures 267: 106808. DOI: 10.1016/j.compstruc.2022.106808
- Novák, L. & Novák, D. 2018. *Polynomial chaos expansion for surrogate modelling: Theory and software*. Beton- und Stahlbetonbau 113: 27–32. DOI: 10.1002/best.201800048
- Novák, L. & Novák, D. 2020. *On Taylor Series Expansion for Statistical Moments of Functions of Correlated Random Variables*. Symmetry 12(8): 1379. DOI: 10.3390/sym12081379
- Novák, L. & Novák, D. 2021. *Estimation of coefficient of variation for structural analysis: The correlation interval approach*. Structural Safety 92: 102101. DOI: 10.1016/j.strusafe.2021.102101
- Novák, L.; Červenka, J.; Červenka, V.; Novák, D. & Sýkora, M. 2022. *Comparison of advanced semi-probabilistic methods for design and assessment of concrete structures*. Structural Concrete. DOI: 10.1002/suco.202200179
- Olivier, A.; Giovanis D.G.; Aakash, B.S.; Chauhan M.; Vandanapu L. & Shields, M. D. 2020. *UQpy: A general purpose Python package and development environment for uncertainty quantification*. Journal of Computational Science 47: 101204. DOI: 10.1016/j.jocs.2020.101204.
- Schlune, H.; Plos, M. & Gylltoft, K. 2011. *Safety formats for nonlinear analysis tested on concrete beams subjected to shear forces and bending moments*. Engineering Structures 33 (8): 2350–2356.
- Slowik, O.; Novák, D.; Novák, L. & Strauss, A. 2021. *Stochastic modelling and assessment of long-span precast prestressed concrete elements failing in shear*. Engineering Structures 228: 111500. DOI: 10.1016/j.engstruct.2020.111500
- Rózsás, A.; Slobbe, A.; Martini, G. & Jansen, R. 2022. *Structural and load parameter estimation of a real-world reinforced concrete slab bridge using measurements and Bayesian statistics*. Structural Concrete 23: 3569–3600. DOI: 10.1002/suco.202100913
- Val, D.; Bljoger, F. & Yankelevsky, D. 1997. *Reliability evaluation in nonlinear analysis of reinforced concrete structures*. Structural Safety 19 (2): 203–217.

Probabilistic structural assessment of RC bridges under corrosion based on efficient simulation methods

F. Padovani

Amplia Infrastructures, Milan, Italy

L. Capacci & F. Biondini

Politecnico di Milano, Milan, Italy

ABSTRACT: The life-cycle assessment of structural reliability and seismic vulnerability of aging bridges is a key issue for optimal management of critical components of transportation systems. Predictive models of the structural performance should be able to integrate uncertainties associated with material properties and environmental stressors. In a life-cycle context, simulation-based methods relying on time-consuming non-linear structural analyses may require unfeasible computational efforts, especially when mechanical non-linearities are involved in structural response of deteriorating members. This paper presents a computational approach for lifetime structural reliability assessment of deteriorating Reinforced Concrete (RC) structures. The life-cycle numerical estimate of failure probability is evaluated over time based on suitable adaptation of Importance Sampling considering a Stationary Proposal distribution to efficiently select the sample structural models. The proposed methodology is investigated for seismic fragility assessment of a RC bridge pier under corrosion based on non-linear static pushover analysis.

1 INTRODUCTION

The performance of infrastructure networks depends on the structural integrity of stand-alone components, such as bridges in transportation networks (Capacci and Biondini 2020). In life-cycle analysis of civil structures and infrastructure systems, the random variability of basic input parameters can be exacerbated by aging and structural deterioration processes, such as fatigue and corrosion (Biondini and Frangopol 2016). In this context, life-cycle probabilistic frameworks adopted for the structural assessment of seismic capacity evolving over time need not only accurate analytical models properly calibrated by experimental data, but also effective numerical tools to accurately estimate statistical descriptors and failure probabilities. Numerical methods based on Monte Carlo Simulation (MCS) often lack efficiency, since the probabilistic assessment of structural systems typically involving small failure probabilities would require huge samples, leading to unfeasible computational efforts (Melchers and Beck 2018).

Variance reduction techniques have been formulated in the past decades to improve the efficiency of simulation methods by minimizing the structural samples needed to obtain sufficiently accurate estimates of failure probabilities. Importance Sampling (IS) exploits a proposal density to simulate basic random variables in proximity of the most relevant portions of the failure region. The main issue of IS approaches lies in the appropriate selection of the important density (Au and Beck 1999, Neal 2001, Rubinstein and Kroese 2004) and in their inefficiency when a large number of basic random variables are involved, i.e., the curse of dimensionality (Au and Beck 2003). Subset simulation exploits Markov-chain Monte Carlo procedures to provide a probability estimate as the product of conditional probabilities (Au and Beck 2001). Directional simulation (Ditlevsen et al. 1986, Bjerager 1988) and line sampling methods (Schuëller et al. 2004) deal with a reformulated version of the reliability

problem transforming basic RVs and evaluating the limit state function in polar coordinates. Failure regions in the sample space can be a-priori excluded in the simulation process by censor sampling techniques (Grooteman 2008, Thedy and Liao 2021). The sample space can be efficiently mapped also by means of data reduction techniques such as clustering algorithms (Capacci and Biondini 2022a) and by functional quantization (Miranda and Bocchini 2015). Simulation procedures can be enhanced at the sample generation stage adopting Latin hypercube sampling techniques (Helton and Davis 2003). Finally, surrogate models are adopted to enhance the efficiency of the reliability estimate by suitably calibrating approximate limit state functions (Kaymaz and McMahon 2005, Dubourg et al. 2011).

This paper presents an IS methodology tailored for life-cycle reliability problems by adopting a Stationary Proposal (SP) distribution. The basic concepts and implementation strategies of the proposed SP-IS approach are briefly illustrated. Potentialities and limitations of the proposed simulation procedure are hence investigated and discussed with reference to time-variant pushover analyses conducted on a four-span highway bridge under severe chloride-induced corrosion of the hollow core Reinforced Concrete (RC) piers.

2 STRUCTURAL RELIABILITY AND SIMULATION

2.1 Failure probability of deteriorating structures

The failure probability is associated with the failure region F in the sample space of the Random Variables (RVs) collected in a vector \mathbf{X} and characterized by the joint Probability Density Function (PDF) $f_{\mathbf{X}}(\mathbf{x})$. The boundaries of failure and safety regions are expressed by a limit state surface $g(\mathbf{X})=0$. The failure probability is conveniently expressed as the expectation of the indicator function I , which is unitary in the failure region (i.e., $\mathbf{X} \in F$) and null in the safety region (i.e., $\mathbf{X} \notin F$):

$$P_F = \int_{\mathcal{Z}} I[g(\mathbf{X}) = 0] \cdot f_{\mathbf{X}}(\mathbf{x}) d\mathbf{x} \quad (1)$$

Uncertainties in environmental hazard parameters, such as concentration of aggressive chemical agents and permeability of structural materials, may exacerbate the fragility of the structural system over time. Indeed, deterioration processes involves the evolution of the basic random variables described by the time-variant joint PDF $f_{\mathbf{X}}(t)$ and, in turn, will lead to a progressive decay of structural reliability.

2.2 Monte Carlo Simulation (MCS)

Simulation methods are robust and intuitive approaches to solve structural reliability problems with adequate accuracy. Traditional MCS provides an unbiased probability estimator through the artificial generation of a set of samples \mathbf{x}_i based on the actual distribution $f_{\mathbf{X}}(\mathbf{x})$ of the RVs:

$$p_{MCS} = \frac{1}{N} \sum_{i=1}^N I[g(\mathbf{x}_i) \leq 0] \quad (2)$$

The accuracy of the MCS estimate can be quantified by the Coefficient of Variation (CoV) of the failure estimator (Melchers and Beck 2018):

$$\text{CoV}[p_{MCS}] = \frac{\sqrt{p_{MCS} \cdot (1 - p_{MCS})}}{p_{MCS} \sqrt{N}} \approx \frac{1}{\sqrt{p_{MCS} \cdot N}} \quad (3)$$

For small values of the target failure probability P_f , the estimate CoV is inversely proportional to both sample size N and estimated probability p_{MCS} . Therefore, small failure probabilities require a significant computational effort, which would be unfeasible for complex non-linear

structural systems and time-consuming analysis methods. Nonetheless, such computational cost is further increased in life-cycle reliability problems, in which the reliability of the investigated structure is deemed to be estimated over a timeframe spanning its entire service life.

2.3 Stationary Proposal Importance Sampling (SP-IS)

The proposed SP-IS methodology relies on the selection of a convenient time-invariant density ψ to simulate samples of the basic RVs. An unbiased probability estimate is provided weighting the indicator function by the time-variant coefficient $W(\mathbf{x}|t)$ given by the ratio between the actual time-variant density $f_{\mathbf{x}}(t)$ and the proposal distribution ψ :

$$p_{IS}(t) = \frac{1}{N} \sum_{i=1}^N I[g(\mathbf{x}_i) \leq 0] \cdot W(\mathbf{x}|t) \quad (4)$$

Therefore, the reliability estimates are computed by weighting each failed sample based on the actual distribution of the stochastic processes describing the probabilistic evolution of structural damage throughout the system lifetime. A quantitative measure of the probability estimator accuracy can be expressed based on its variance estimate, as presented in Capacci and Biondini (2023):

$$\sigma_{IS}^2(t) = \frac{1}{N-1} \left\{ \frac{1}{N} \sum_{i=1}^N [I[g(\mathbf{x}_i) \leq 0] \cdot w_i^2(t)] - p_{IS}^2(t) \right\} \quad (5)$$

3 CASE STUDY

3.1 Four-span viaduct with RC piers exposed to chloride-induced corrosion

The life-cycle seismic reliability of the four-span RC viaduct shown in Figure 1 is investigated (Franchin et al. 2023). An isometric view representative of the structural model is shown in Figure 1a. RC bridge piers are composed by two bents with hollow-core rectangular cross-sections connected on top by a pier cap, as shown in Figure 1b. Along the longitudinal direction x , the static scheme of the bridge piers is similar to a vertical cantilever, whereas, in the transversal direction y , exhibits a frame type resisting mechanism. The steel-concrete composite deck is moderately free to slide in the longitudinal direction over both the outer joints at the abutments and the pier P1 whereas fixed-type bearings prevent the relative transversal displacements of the deck over the abutments and all piers. Figure 1c shows the geometry and the reinforcement layout of a single-bent base cross-section (pier P3). The wall thickness at the base of the tallest piers (P2 and P3) is 0.65 m over a length of 10 m and then reduced to 0.40 m. The wall thickness of the pier P1 is 0.40 m. The net concrete cover is 75 mm. The piers are considered exposed to a chloride concentration C_0 over external and internal surfaces of the hollow-core cross-sectional profile.

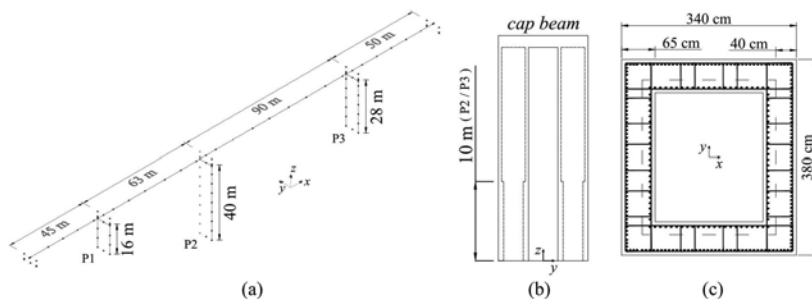


Figure 1. Highway bridge: (a) Structural model; (b) Transverse sectional view of a bridge pier; (c) single-bent cross-section at the base of pier P3.

3.2 Corrosion damage modeling

Chloride attack reduces the resisting area of steel reinforcement (Biondini et al. 2004):

$$A_s = [1 - \delta_s(t)]A_{s0} \quad (6)$$

where A_{s0} is the area of the undamaged reinforcement and $\delta_s(t) \in [0,1]$ is a dimensionless damage index representative of the percentage of steel mass loss. In addition, a progressive reduction in time of steel ductility ε_{su} is considered as proposed in Biondini and Vergani (2015).

$$\varepsilon_{su}(t) = \begin{cases} \varepsilon_{su0} & 0 \leq \delta_s \leq 0.016 \\ 0.1521 \cdot \varepsilon_{su0} \cdot [\delta_s(t)]^{-0.4583} & 0.016 \leq \delta_s \leq 1 \end{cases} \quad (7)$$

where $\varepsilon_{su0}=0.075$ is the initial steel strain elongation capacity. Corrosion is also responsible for the onset of expansion products inducing splitting cracks up to spalling over the concrete surrounding the reinforcement. This phenomenon is modelled applying a reduction of the concrete strength f_c over the concrete cover according to Coronelli and Gambarova (2004) based on the modelling strategy presented in Biondini and Vergani (2015).

Corrosion initiates at time t_{cr} when chlorides reach a critical mass concentration C_{cr} , i.e., $C(t_{cr})=C_{cr}$. In the damage propagation phase, the damage index δ_s is related to the concentration $C=C(t)$ of the aggressive agent by assuming a linear relationship (Biondini et al. 2004):

$$\frac{\partial \delta_s(t)}{\partial t} = q_s C(t) \quad (8)$$

where q_s is a damage rate coefficient.

The one-dimensional Fick's diffusion equation is often used to define the profile in time of the chloride concentration $C(x_c, t)$ at a given depth x_c with diffusivity D :

$$C(x_c, t) = C_0 \left[1 - \operatorname{erf} \left(\frac{x_c}{2\sqrt{Dt}} \right) \right] \quad (9)$$

This simplified approach is considered in this paper. However, it is worth noting that for structural members with complex geometry and non-uniform chloride concentration exposure the diffusion process should be more accurately described by two- or three-dimensional patterns of concentration gradients (Biondini et al. 2004, Titi & Biondini 2016).

3.3 Modelling of uncertainties

Uncertainties can be associated to mechanical properties of the pristine structure, such as concrete and steel strengths, as well as the governing parameters of the degradation phenomenon. Such variability is addressed by modeling the following parameters as statistically independent random variables: unconfined concrete strength f_{c0} , steel yielding strength f_y , concrete diffusivity D , surface chloride concentration C_0 , critical chloride concentration C_{cr} , damage rate q_s . Distribution type and statistical descriptors are reported in Table 1 for each random variable.

3.4 Structural modeling and non-linear static analysis

The three-dimensional structural model of the bridge is implemented in OpenSees (Mazzoni et al 2009). The deck is modeled with elastic beam elements. Elastic connections and rigid offsets are adopted to model the deck-to-abutment and deck-to-pier connections between the end nodes of the elements. A bilinear model with effective stiffness applies for the expansion joints at the abutments and a uniaxial viscous damper is also considered at one end. The pier bents are modeled with force-based fiber beam-column elements considering both material and geometrical non-linearities and taking into account the actual distribution of steel reinforcement over the height of the piers. More in detail, a trilinear model for the generalized shear stress-strain relationship is integrated within the force-based formulation to account for the post-elastic

Table 1. Probability distributions.

Random Variable	Distribution Type	Mean μ	CoV
Concrete strength f_{c0} [MPa]	Lognormal	40.02	12.50%
Yielding strength f_y [MPa]	Lognormal	487.58	6.15%
Diffusivity D [m ² /sec]	Normal*	15.8×10^{-12}	20.00%
Surface concentration C_0 [wt. %/c]	Normal*	3.0	30.00%
Critical concentration C_{cr} [wt. %/c]	Beta**	0.6 wt. %/c	25.00%
Damage rate q_s [1/(wt. %/c yrs)]	Normal*	1/(C_0 50 yrs)	30.00%

* Truncated positive.

** Bounded distribution $\in [0.2, 2.0]$ wt. %/c.

shear behaviour of the piers. A stress-strain model in compression with strength f_{c0} (Table 1), peak strain $\epsilon_{cc} = -0.002$, ultimate strain $\epsilon_{cu} = -0.0035$, and zero tensile strength is considered for unconfined concrete fibers. For confined concrete fibers, the concrete strength f_{cc} and the other constitutive parameters of the stress-strain model in compression are related to the transversal reinforcement ratio ρ_s according to Mander et al. (1989), with tensile strength $f_t = -0.1f_{cc}$ and spalling strain $\epsilon_{sp} = 0.007$. A bilinear elastic-plastic model is assumed for steel reinforcement with yielding strength f_y (Table 1), elastic modulus $E_s = 206$ GPa and post-yielding modulus $0.15E_s$. Further information about structural modeling of the bridge can be found in Padovani (2022).

Non-linear static pushover analysis represents an effective way to explore the seismic capacity of RC bridges as an alternative to computationally demanding non-linear time-history analysis (Petronijević et al. 2018, Isaković and Fischinger 2011, Biondini et al. 2014). Figure 2 shows the results of deterministic non-linear static analyses of the bridge performed in both longitudinal direction x (Figure 2a) and transversal direction y (Figure 2b) at different time instants ($t=0, 30$, and 50 years) by assuming mean values in Table 1 as nominal values and a load pattern consistent with the first modal shape. The capacity curves in terms of total base shear of the piers vs drift of pier P2 highlight the detrimental impact of corrosion in terms of stiffness, strength, and ductility. The reduction in terms of stiffness and strength is similar in both directions, while reduction of ductility is particularly critical in the longitudinal direction. Moreover, in the transversal direction the failure mode of the critical regions at the base of the piers is changing over time since structural capacity is attained with concrete failure at $t=0$ and 30 years and steel failure at $t=50$ years.

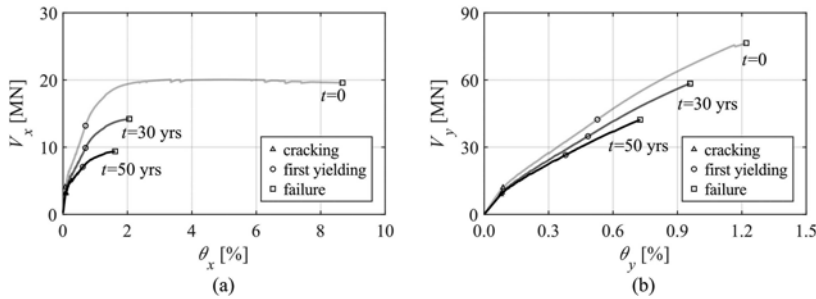


Figure 2. Nominal capacity curves in terms of total base shear of the piers vs drift of pier P2 at different time instants ($t=0, 30$, and 50 years): (a) Longitudinal direction; (b) Transversal direction.

3.4 Life-cycle probabilistic seismic analysis

The effects of uncertainties on the corrosion damage and seismic response are taken into account. Figure 3 shows the empirical CDF of the corrosion damage index δ_s every 10 years up to 50 years of lifetime based on MCS with sample size $N=10000$. The severity of the damage scenario is indicated by the large likelihood of corrosion initiation after 10 years, i.e., $P[\delta_s(10 \text{ yrs}) > 0] \approx 95\%$, and the probability of occurrence of extensive damage conditions progressively increases in time.

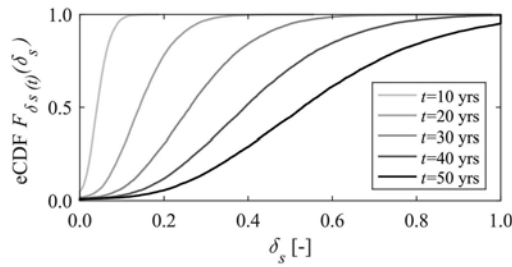


Figure 3. Empirical cumulative distribution function of the damage index.

Figure 4 shows the results of non-linear static analyses in the longitudinal direction based on a sample of 1000 realizations. The capacity curves in terms of total base shear of the piers vs drift of pier P2 in pristine conditions (Figure 4a), as well as after 30 years (Figure 4b) and 50 years (Figure 4c), highlight the impact of randomness of material properties in the structural response over time, that is particularly evident on stiffness, strength, and ductility. Random variability of concrete strength mainly influences the cracking capacity, whilst steel strength significantly influences both yielding and ultimate capacities. In the early loading stage, the stiffness is mildly affected in the elastic range by damage and spalling of concrete cover. Also, strength and ductility drastically reduce over time respectively due to steel mass loss and reduction of steel ultimate strain capacity. The significant correlation between displacement capacity and damage index can be informative for the selection of effective simulation densities in the SP-IS methodology.

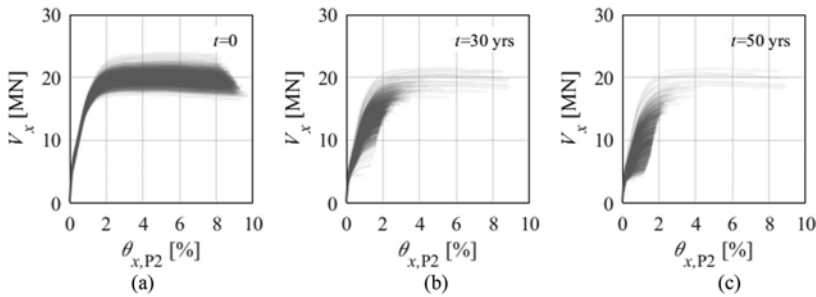


Figure 4. Capacity curves in terms of total base shear of the piers vs drift of pier P2 based on a sample of 1000 realizations: (a) $t=0$; (b) $t=30$ years; and (c) $t=50$ years.

3.5 Life-cycle structural reliability and comparison of simulation methods

Time-variant failure probabilities are investigated with respect to damage limitation associated to the attainment of prescribed drift threshold values described by the following limit state function:

$$\{g_s(\mathbf{X}) \leq 0\} \equiv \{\theta_x^{ult}(f_c, f_y, D, q_s, C_0, C_{cr}) \leq \theta_x^{lim}\} \quad (10)$$

Two damage limitation conditions are considered, with limit state g_1 associated to drift limit $\theta_x^{lim}=1\%$ and limit state g_2 with $\theta_x^{lim}=2\%$. The estimate of the time-variant occurrence probabilities is obtained by MCS. The reliability index $\beta_{MCS}(t)=\Phi^{-1}[1-p_{MCS}(t)]$ is shown in Figure 5a. The related CoV versus the sample size is shown in Figure 5b. The reliability estimates are only available for a limited range of time instants from 20/30 years on, when failure tends to occur with a minor ultimate displacement due to structural deterioration. From Figure 5b is clear that more than 10000 samples would have been necessary to estimate with sufficient accuracy the reliability associated to limit state g_1 at 30 years, which is higher than 3.0. This emphasizes the need of effective variance reduction techniques, such as SP-IS, for life-cycle reliability problems.

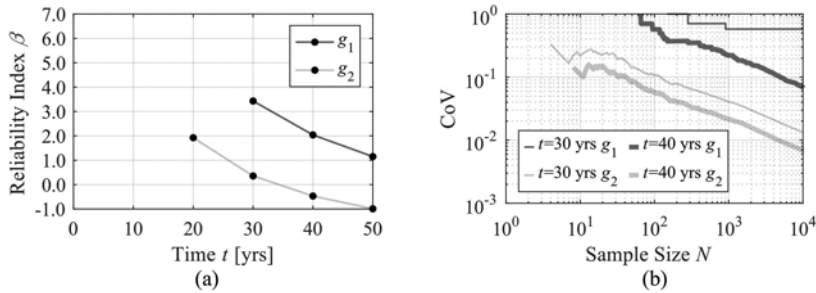


Figure 5. Time-variant reliability assessment based on MCS: (a) Reliability index and (b) CoV.

An intuitive choice for the SP-IS density function for the damage index is the distribution obtained at 50 years Figure 3. The actual time-variant PDFs of the damage index are analytically unknown. Therefore, the time-variant weighting coefficients w_i in the SP-IS framework can only be evaluated in an approximate way. They can be quantified either based on the calibration of suitable analytical distributions or by numerically estimating the empirical PMFs indicator over suitable statistical bins within the damage index sample space (Capacci 2020).

Figure 6a shows the SP-IS time-variant estimates of the reliability index β_{SP-IS} in comparison with the results obtained with MCS. The results of both methods are comparable, yet SP-IS allows to evaluate the reliability estimates for a denser set of time instants (i.e., every 5 years rather than 10) due to the minimal computational effort required by the evaluation of the weighting coefficients w_i in place of carrying out time-consuming structural analyses. Nonetheless, SP-IS can also provide reliability estimates at early time instants in which small failure probabilities are deemed to be estimated. Better accuracy for early time instants could be further achieved by establishing an SP-IS density also for the material strengths. Finally, the comparison between the CoVs of reliability estimates versus the sample size N shown in Figure 6b further consolidates that SP-IS outperforms MCS in terms of accuracy for limit state g_1 at 30 and 40 years.

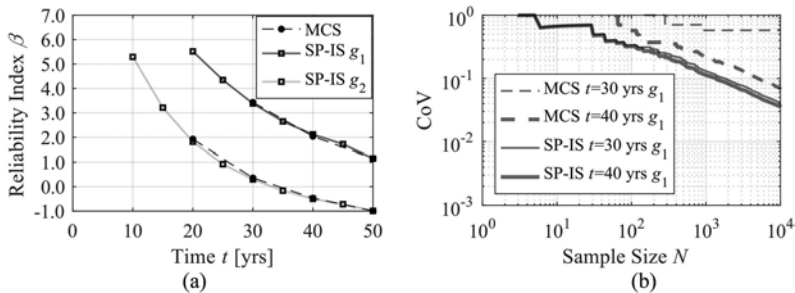


Figure 6. Stationary-proposal importance sampling reliability index of displacement capacity limit states (a) and related convergence of the estimate (b). Monte Carlo results are reported with dashed-lines.

4 CONCLUSIONS

Efficient numerical strategies for probabilistic structural assessment represent valuable tools to aid design and assessment, maintenance and repair, emergency management and resources prioritization under uncertainties of resilient infrastructure facilities such as bridges and viaducts. This paper discusses simulation-based approaches typically adopted in structural reliability analysis and raises the issue of efficiently estimating the time-variant failure probability of deteriorating structures. To this purpose, a novel methodology is formulated to extend basic variance reduction techniques, such as IS, to structural reliability problems with a life-cycle perspective. The method relies on the selection of a SP simulation density to efficiently sample structural systems accounting for time-variant modeling uncertainties typical of life-cycle reliability problems.

The proposed methodology can thrive when time-consuming analyses are required to assess the structural response of systems characterized by a limited number of time-variant constitutive parameters. The proposed SP-IS framework has been applied to probabilistic assessment of a RC bridge with two-bent piers exposed to chloride-induced corrosion. The results show that SP-IS can outperform traditional MCS approaches when a suitable proposal density is adopted.

Further research is currently ongoing to establish optimal criteria for the selection of the sampling distribution based on cross-entropy minimization methods for reliability problems extended to a life-cycle perspective as well as seismic risk assessment of vulnerable infrastructure lifelines (Capacci and Biondini 2023). Advances are necessary to address the feasibility limitations in high-dimensional reliability problems with complex deterioration patterns. The investigation of other potential fields of application of the proposed methodology should include calibration of time-variant seismic fragility curves of aging bridges (Capacci and Biondini 2022b), reliability analysis of structural systems under climate change considering non-stationary climate conditions (Nava et al. 2023), and reliability-based life-cycle design optimization, among others.

REFERENCES

- Au, S.K., Beck, J.L. (1999). A new adaptive importance sampling scheme for reliability calculations. *Structural Safety*, 21(2):135–158.
- Au, S.K., Beck, J.L. (2001). Estimation of small failure probabilities in high dimensions by subset simulation. *Probabilistic Engineering Mechanics*, 16(4):263–277.
- Au, S.K., Beck, J.L. (2003). Important sampling in high dimensions. *Structural Safety* 25(2):139–163.
- Biondini, F., Bontempi, F., Frangopol, D.M., Malerba, P.G. (2004) Cellular automata approach to durability analysis of concrete structures in aggressive environments. *Journal of Structural Engineering*, ASCE, 130(11):1724–1737.
- Biondini, F., Camnasio, E., Palermo, A. (2014). Lifetime seismic performance of concrete bridges exposed to corrosion. *Structure and Infrastructure Engineering*, 10(7):880–900.
- Biondini, F., Vergani, M. (2015). Deteriorating beam finite element for nonlinear analysis of concrete structures under corrosion. *Structure and Infrastructure Engineering*, 11(4):519–532.
- Biondini, F., Frangopol, D.M. (2016). Life-cycle performance of deteriorating structural systems under uncertainty: review. *Journal of Structural Engineering*, ASCE, 142(9):1–17.
- Bjerager, P. (1988). Probability integration by Directional Simulation. *Journal of Engineering Mechanics*, ASCE, 114(8):1285–1302.
- Capacci, L. (2020) *Life-cycle seismic resilience of aging bridges and infrastructure networks*. PhD Thesis, Politecnico di Milano, Milan, Italy.
- Capacci, L., Biondini, F. (2020). Probabilistic life-cycle seismic resilience assessment of aging bridge networks considering infrastructure upgrading. *Structure and Infrastructure Engineering*, 16(4): 659–675.
- Capacci, L., Biondini, F. (2022a). Efficient sampling techniques for simulation-based life-cycle structural reliability and seismic fragility assessment. *13th International Conference on Structural Safety and Reliability (ICOSSAR 2022)*, September 13–17, 2022, Shanghai, China.
- Capacci, L., Biondini, F. (2022b). Stationary Proposal Importance Sampling (SP-IS) for life-cycle resilience-based seismic risk assessment of deteriorating bridge networks. *3rd European Conference on Earthquake Engineering and Seismology (ECEES 2022)*, September 4–9, 2022, Bucharest, Romania.
- Capacci, L., Biondini, F. (2023). Cross-Entropy-based Stationary Proposal Importance Sampling for life-cycle structural reliability and seismic risk assessment. *14th International Conference on Application of Statistics and Probability in Civil Engineering (ICASP14)*, July 9-13, 2023, Dublin, Ireland.
- Coronelli, D., Gambarova, P. (2004). Structural assessment of corroded reinforced concrete beams: modeling guidelines. *Journal of Structural Engineering*, ASCE, 130(8): 1214–1224.
- Ditlevsen, O., Olesen, R., Mohr, G. (1986). Solution of a class of load combination problems by directional simulation. *Structural Safety*, 4(2):95–109.
- Dubourg, V., Deheeger, F., Sudret, B. (2011). Metamodel-based importance sampling for the simulation of rare events. *11th International Conference on Applications of Statistics and Probability in Civil Engineering (ICASP11)*, August 1–4, 2011, ETH Zurich, Switzerland
- Franchin, P., Baltzopoulos, G., Biondini, F., Callisto, L., Capacci, L., Carbonari, S., Cardone, D., Dall’Asta, A., Flora, A., Gorini, D.N., Iervolino, I., Marchi, A., Noto, F., Perrone, G. (2023). Seismic reliability of Italian code-conforming bridges, *Earthquake Engineering and Structural Dynamics* (submitted).

- Grooteman, F. (2008). Adaptive radial-based importance sampling method for structural reliability. *Structural Safety*, 30(6):533–542.
- Helton, J. C., Davis, F. J. (2003). Latin hypercube sampling and the propagation of uncertainty in analyses of complex systems. *Reliability Engineering & System Safety*, 81(1):23–69.
- Isaković, T., Fischinger, M. (2011). Applicability of pushover methods to the seismic analyses of an RC bridge, experimentally tested on three shake tables. *Journal of Earthquake Engineering*, 15(2):303–320.
- Kaymaz, I., McMahon, C.A. (2005). A response surface method based on weighted regression for structural reliability analysis. *Probabilistic Engineering Mechanics* 20(1):11–17.
- Mander, J.B., Priestley, M.J.N., Park, R. (1989). Theoretical Stress-Strain Model for Confined Concrete. *Journal of Structural Engineering* 114(8):1804–1826.
- Mazzoni, S., McKenna, F., Scott, M. H., and Fenves, G. L. (2009). *OpenSees: Open System for Earthquake Engineering Simulation*. Pacific Earthquake Engineering Research Center, University of California, Berkeley, CA, USA.
- Melchers, R. E., Beck, A. T. (2018). *Structural Reliability Analysis and Prediction*. Wiley, 3rd Edition.
- Miranda, M. J., Bocchini, P. (2015). A versatile technique for the optimal approximation of random processes by functional quantization. *Applied Mathematics and Computation*, 271:935–958.
- Neal, R.M. (2001). Annealed importance sampling. *Statistics and Computing* 11(2):125–139.
- Nava G., Capacci, L., Biondini, F., Casti, L. (2023). Life-cycle structural reliability of RC bridge piers under corrosion in a changing climate. *8th International Symposium on Life-Cycle Civil Engineering (IALCCE 2023)*, July 2–6, 2023, Milan, Italy.
- Padovani, F. (2022). *Advanced Simulation Methods for Life-Cycle Seismic Assessment of RC Bridges*. Master Thesis, Politecnico di Milano, Milan, Italy.
- Petronijević, M., Marjanović, M., Milojević, D. (2018). Pushover analysis for seismic assessment of RC Nišava Bridge. *16th European Conference on Earthquake Engineering (16ECEE 2018)*, June 18–21, 2018, Thessaloniki, Greece
- Rubinstein, R.Y., Kroese, D.P. (2004). The cross-entropy method: a unified approach to combinatorial optimisation, Monte-Carlo simulation and machine learning. *Technometrics* 48(1):147–148.
- Schuëller, G.I., Pradlwarter, H.J., Koutsourelakis, P.S. (2004). A critical appraisal of reliability estimation procedures for high dimensions. *Probabilistic Engineering Mechanics* 19(4):463–474.
- Thedy, J., Liao, K.W. (2021). Multisphere-based importance sampling for structural reliability. *Structural Safety*, 91, 1–16.
- Titi, A., Biondini, F. (2016). On the accuracy of diffusion models for life-cycle assessment of concrete structures. *Structure and Infrastructure Engineering*, 12(9):1202–1215.

Life-cycle assessment of Tunnel Boring Machine (TBM) segments of a new tunnel: Carbonation attack and sulfate attack

F.T. Torabian, I. Vangelisti & C. Beltrami
Lombardi Ingegneria s.r.l., Milan, Italy

ABSTRACT: The life cycle of TBM segments of a new tunnel were assessed considering two main degradations for the side exposed to ambient air and for the side exposed to the ground. The two degradations were carbonation attack and sulfate attack, respectively. In order to numerically model these two degradations, Full-Probabilistic Approach (FPA) was employed, using fib34 and FEM model, respectively. To calibrate the model for the carbonation simulation, inverse carbonation resistance $R_{acc,0}^{-1}$ of the concrete mix (40% slag, w/c=0.35, cement = 467 kg/m³) used for TBM segments, was examined in the laboratory. The relative humidity values were also acquired from the nearest weather station in the area. To calibrate the FEM model for the sulfate attack, the chemical composition of the ground and groundwater was acquired from the nearest geological boreholes. The results showed that the carbonation penetration after 100 years of service life in term of 95th percentiles of normal distribution is 14 mm. The carbonation penetration depth in comparison to 50mm concrete cover of the TBM segment does not seem to be problematic and results in <0.1% failure probability. Moreover, thickness loss due to decalcification of CSH by sulfate attack in terms of 95th percentiles of normal distribution is 7.22mm. The thickness loss does not seem to be problematic for the extrados of the TBM segments, comparing to the 50mm concrete cover and to 14.5mm depth of embedded anchor of sealing gaskets. The findings imply that the sulfate attack does not result in loosening of the sealing gasket.

1 INTRODUCTION

Tunnel Boring Machine (TBM) concrete segments are prefabricated reinforced concrete segments which are in contact to ground on extrados and to ambient air on intrados for new tunnels. Therefore, depending on the chemistry of the ground and condition of the ambient air, several degradations might occur. For sake of this study, two degradations are identified for the concrete segments in the new tunnel under study.

Carbonation attack reduces the alkalinity of the concrete cover and if the carbonation front reaches the rebar, it results in onset of reinforcement corrosion in presence of the humidity. This degradation occurs on the intrados of the concrete segments.

Sulfate attack may occur if the ground and/or groundwater contain sulfate bearing elements and may cause disintegration of the concrete cover. If the disintegration front reaches the depth of rebar, the reinforcement becomes exposed.

In addition, in concrete segments, the EPDM gaskets are installed to seal the interior of the tunnel. The gaskets are maintained in their positions with an anchor embedded in the concrete (see Figure 1). If the disintegration front reaches the mid-depth of the anchor sealing (based on the recommendation of the manufacturer), the performance of the gasket will be compromised.

The mechanism of the carbonation attack and its consequences on the reinforced concrete have been extensively investigated in literature [Bertolini et al. 2012, “Corrosion of Steel in Concrete”].

The sulfate attack mechanism is developed in the following.

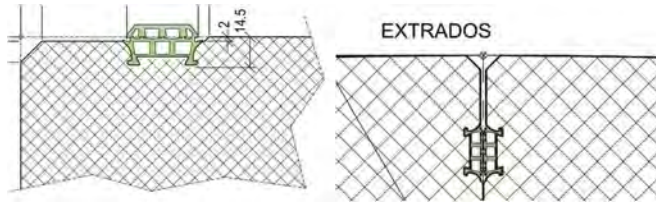


Figure 1. EPDM Gasket details.

1.1 Mechanism of sulfate attack

The main hydration products are calcium silicate hydrate (CSH), calcium hydroxide or Portlandite (CH), ettringite ($C_6AS_3H_{32}$), calcium monosulfoaluminate ($C_4AS_3H_{12}$), hydrogarnet (C_3AH_6), etc.

When sulfate ions penetrate a cement-based structure, a series of reactions take place [Sarkar et al. 2010]. Sulfate ions react with Portlandite to form gypsum and some calcium aluminate phases to form ettringite (as shown by the light arrows in Figure 2). Then gypsum reacts with calcium aluminate phases (as shown in the box in Figure 2), if present, to form ettringite (as shown in bold arrows in Figure 2).

Initially the calcium ions are supplied by Portlandite. When Portlandite is not available, CSH dissociates into silica gel, releasing calcium ions (as shown by the dashed arrow in Figure 2) for ettringite formation. Therefore, one of the consequences of the sulfate attack is dissociation of the CSH, that is the main hydration product in concrete.

Another consequence of sulfate attack is expansion of concrete, thus cracking (exfoliation) of the concrete cover. The main expansive products formed as a result of the reactions are ettringite and gypsum [Sarkar et al. 2010].

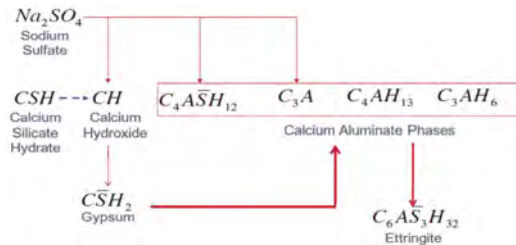


Figure 2. Schematic diagram of the chemical reactions due to sulfate ingress [Sarkar et al. 2010].

The change in volume due to the chemical reactions is obtained by subtracting the total volume of the products from the total volume of the reactants. The change in volume leads to volumetric strain if the volume of the products is greater than the volume of the reactants. The strain developed exerts pressure on the surrounding cement matrix. The structure starts cracking when the stress exceeds the tensile strength of the material.

As it was said above, the calcium silicate hydrate dissociation into calcium hydroxide and silica gel results in loss of strength because silica gel is not cohesive. Thus, the net effects of sulfate attack are expansion, cracking and strength loss.

1.2 Research significance

In TBM tunnels design nowadays, the durability of the concrete segments is receiving high attention between the contractors in construction industry. The contractors nowadays are very interested in mathematical calculations of the service life of the TBM tunnels subjected to degradations. So, providing the tools of service life calculation of executive projects is becoming important in construction industry. In this study, it was tried to employ the existing mathematical models of the service life calculations and to link the mathematical calculations to

executive projects, through some laboratory tests for calibrating the mathematical models. The measured environmental conditions are imposed as the degradation source.

In this article as a case study, degradation mechanisms of the TBM concrete segments of a new tunnel are studied. The advancement of each degradation in time is numerically modelled and the service life of the concrete segments is evaluated. The design of the concrete segments is adopted to the durability assessment, so that the concrete segment can fulfill its design life. The reference design life of the new tunnel under study is 100 years.

2 EXPERIMENTAL METHODS

2.1 Materials

The mix design of the TBM segment is shown in Table 1. The thickness of the segment is 380mm and nominal design concrete cover is 50mm.

For measuring the inverse carbonation coefficient, two samples are fabricated following the recommendations of fib34. The results of inverse carbonation coefficient measurement are shown in the following table with normal distribution with mean value and standard deviation.

Table 1. Mix designs examined for the TBM concrete segments.

Portland cement (Kg/m ³)		280
Slag (Kg/m ³)		187
Slag %		40
Total binder content (Kg/m ³)		467
Compressive strength (MPa) of 6 hr		10.0
Water(mls/m ³)		163.6
Water/Cement	ratio	0.35
Slump (AS1012.3.1)	mm	110
$R_{ACC,0}^{-1}((m^2/s)/(kg/m^3)) \times 10^{-11}$	mean value	0.40
	Std. dev.	0.34

2.2 Test procedure

Two approaches are used to simulate the carbonation attack on the concrete segment: deterministic approach and full-probabilistic approach. For sulfate attack, the full probabilistic approach is used to simulate the advancement of the degradation in time.

2.2.1 Carbonation attack

For carbonation modelling, the deterministic approach was performed by CARBUFF model. The full-probabilistic approach followed fib34 model code.

The limit state for the carbonation attack is when the carbonation front reaches the rebar depth. To estimate the service life of the TBM tunnel, the laboratory experiments were performed to calibrate the model and correctly estimate the service life. The inverse carbonation coefficient, $R_{acc,0}^{-1}$, is measured for various concrete mix designs based on the recommendations of fib34 (see Table 1). The target probability of failure, regarding the importance of the project is set at 1% equivalent to reliability index (β) if 2.3. The reliability index relates to the probability of depassivation of the steel and ultimate limit state.

2.2.2 Sulfate attack

For sulfate attack modelling, the full-probabilistic approach is performed by FEM model by STADIUM software. When sulfate attack is developing, the Calcium Silicate Hydrate (CSH) content reduces because of the dissociation. CSH dissociates to form ettringite in the last stages of the sulfate attack, after portlandite is consumed. Therefore, the thickness loss due to sulfate attack is consider the depth of the concrete, where the CSH content reaches 5%.

To calibrate the sulfate attack simulation, sulfate content of ground and groundwater were measured and collected from boreholes located close to the chainage of the tunnel.

The limit state for the sulfate attack is when the thickness loss due to sulfate attack reaches 7.25mm. When the thickness loss reaches the mid depth of the hook of the sealing gasket, $14.5/2 = 7.25\text{mm}$ (based on the recommendation of the manufacturer, see Figure 1), the sealing ability of the gasket is compromised. The full-probabilistic approach has been employed for the FEM model for sulfate attack. Thus, the thickness loss values due to sulfate attack, which were calculated through FEM model, was fit to a lognormal distribution and as a convention, 95th percentiles of the distribution is reported. To calibrate the FEM model for calculating the thickness loss due to sulfate attack, total void volume of concrete is measured by ASTM C642 for two samples. The results are shown in Table 5.

2.3 Environmental input data

2.3.1 Carbonation

The environmental data for carbonation simulation, was collected from closest weather station to the tunnel portal. The environmental data is as follows. The relative humidity is fitted by Beta distribution with a mean value of 73.6% relative humidity as follows.

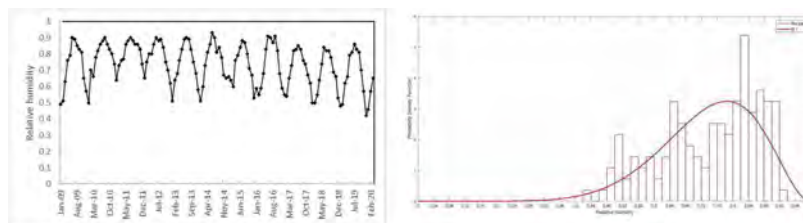


Figure 3. (Left) Relative humidity of the tunnel portal from worldwetheronline.com from 2009 to 2020. (Right) Probability Density Function curve of the relative humidity data from 2009 to 2020, fitted by Beta distribution with $\alpha=8.85$, $\beta=3.16$ and mean value of 0.736.

2.3.2 Sulfate attack

The environmental data for the sulfate attack were collected from the perforated boreholes close to the tunnel chainage. The ground chemistry and groundwater chemistry are presented in Tables 2 and 3, respectively.

2.3.2.1 Ground data

The ground chemistry data are shown in the following table. Sulfate content of the rock, chloride content of the rock, and pH values for different boreholes are collected and are statistically analysed. Mean value and standard deviation of the abovementioned values are reported in the table below.

Table 2. A summary of the ground chemistry: sulfate content, chloride content and pH values extracted from series of boreholes located close to the tunnel chainage.

Parameter	pH	Sulfate content (by AS1289 4.2.1) (mg/kg)	Chloride content (mg/kg)
Mean	9.25	18.7	89,7
Median	9.3	17.9	57,6
Std. Dev.	0.27	10.6	112,4
Kurtosis	0.24	3.2	9,9
Skewness	-0.04	1.4	3,1
Minimum	8.3	6.2	8,9
Maximum	10	52	115.2
Count (n)	427	23	23

2.3.2.2 Groundwater data

The groundwater data are reported in the following table.

Table 3. Groundwater chemistry data measured from the boreholes.

Borehole designation	pH	electrical conductivity (µS/cm)	Eh (mV)	pe	T (°C)	Ca (mg/L)	Alk (as HCO ₃ /L)	SO ₄ (mg/L)	Cl (mg/L)	NH ₄ (mg/L)	NO ₃ (mg/L)	Langelier Saturation Index (L _i)
1	7.44	1902	-132.5	-2.3	15.3	56	158.5	608	52	0.006	0.04	0.8
2	7.36	1860	-164.2	-2.9	11	58	180.5	720	49	0.077	0.02	0.8
3	7.76	2082	-138.4	-2.5	11.3	54	202.4	798	49	0.006	0.02	1.2
4	7.59	1963	-202.9	-3.6	10.2	62	214.6	721	51	0.006	0.02	1.1
5	7.83	1906	-189.4	-3.4	10.2	60	250	826	54	0.026	0.02	1.4
6	7.68	2157	-139.5	-2.5	8.6	65	264.6	656	52	0.003	0	1.3
7	7.92	2117	-150	-2.7	9	64	293.8	817	63	0.003	0	1.6
8	8.04	1923	-224.2	-4	9.4	61	317	753	52	0.003	0.02	1.7
9	7.86	2131	-140.4	-2.5	8.8	60	352.4	648	57	0.003	0.03	1.6
10	7.64	1603	-157.6	-2.8	9.6	57	356	648	46	0.003	0.01	1.3
11	7.8	2045	-139.1	-2.5	11.2	65	435.3	848	54	0.024	0.03	1.6

Statistical analysis was performed on the groundwater data and are shown in the following table. Thus, for groundwater data for pH, chloride content and sulfate content, 95th percentiles of the data series are considered as the representative of the data set.

Table 4. Sulphates content, chloride content and pH for groundwater.

parameter	N	%	Mean	Median	Std. Dev.	90° p	95° p	99° p
pH	70	12.2	5.17	5.29	5.24	4.88	4.76	4.54
Chloride (mg/L)	6	2.9	191	191	14.5	210	216	227
Sulfate (mg/L)	12	10.9	729	725	80.7	835	869	937

Comparing the results of Table 4 with Table 2, the sulfate content of groundwater is more critical than the ground sulfate content. Therefore, for the sulfate attack simulation, the sulfate content of the groundwater is considered as the sulfate content of the aggressive media.

3 RESULTS

3.1 Carbonation attack

3.1.1 Deterministic approach

The input parameters for CARBUFF simulation are the following.

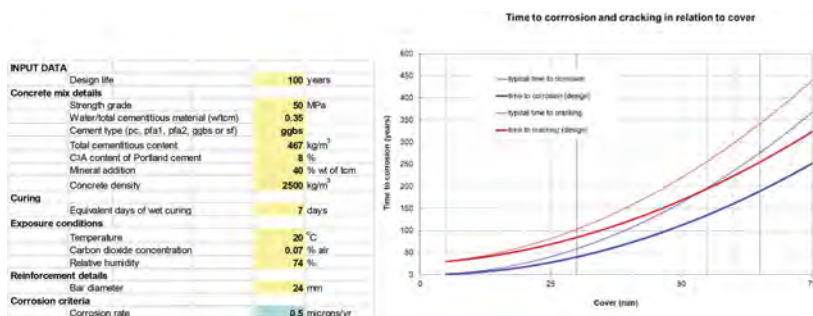


Figure 4. Input parameters and the results of the CARBUFF simulation.

The results of the carbonation modelling based on the concrete cover is shown in Figure 4. The results are obtained by CARBUFF model using a deterministic approach. The results shows that the time to corrosion (as for limit state for carbonation) for a concrete cover of 50mm is 112 years.

3.1.2 Probabilistic approach

The input table for the full-probabilistic carbonation simulation is reported below. The nominal concrete cover as per design is 50mm. The carbon dioxide content in each year is elevated based on the current global trend of carbon dioxide increase.

The carbonation depth calculated by full-probabilistic approach is fit by a normal distribution with mean values 12mm and standard deviation of 4.3mm.

The figure above shows that the carbonation depth does not overlap with the concrete cover. This means that the probability of failure is <0.1%.

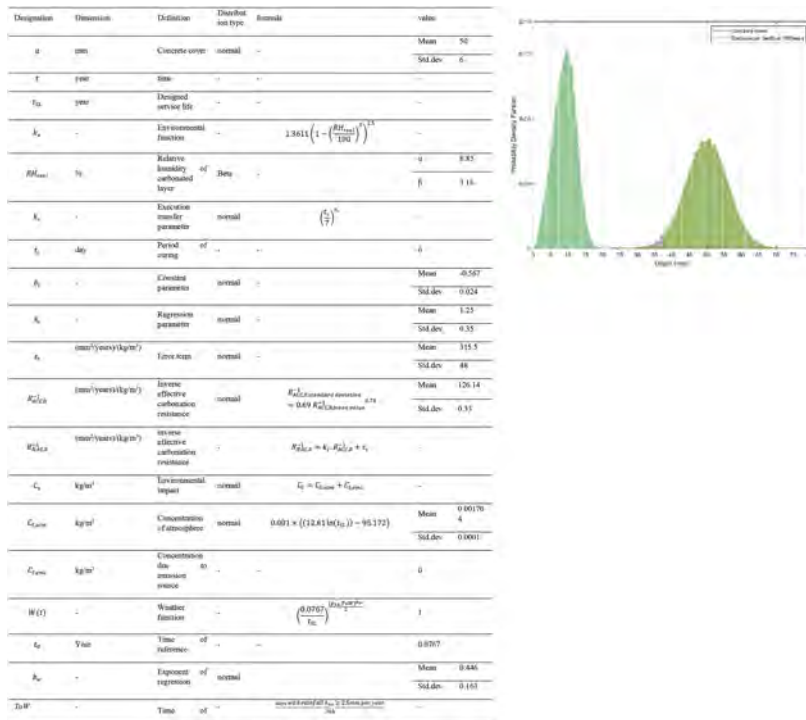


Figure 5. Description of all parameters with their values considered in the full-probabilistic approach. Probability density function for carbonation depth at 100 years and concrete cover of 50mm. The depth is considered from the segment intrados.

3.2 Sulfate attack

The input parameters for the FEM modelling of sulfate attack are reported in the following table.

The thickness loss due to sulfate attack is reported in the figure below a lognormal distribution for 25, 50, 75, 100, 125 and 150 years of service life.

Figure 6 shows the 95th percentiles of the thickness loss distributions as a function of time shown in Figure 6. Each data point in this figure is 95th percentiles of the relevant distribution as per the convention in this study.

The thickness loss after 100 years is equal to 7.22mm. Please note that as per convention in this study, the thickness loss value is equal to 95th percentiles of a lognormal distribution.

Table 5. Input parameters for sulfate attack simulation through full-probabilistic FEM model.

Transport properties					
			considered in simulation		Measured in lab
porosity	ave.		0.098		
	st. dev.		0.0049	m ³ /m ³	ASTM C642
			normal distribution		Sample A: 0.0119 Sample B: 0.0117
SO ₄ effective diff. Coef.	ave.		0.96	m ² /s	ASTM C1202
	st. dev.		0.144		
			normal distribution		
permeability	ave.		0.42	m ²	ASTM C1792
	st. dev.		0.105		
			normal distribution		
aging function (deterministic)	A(t)	a	0.58		
		c	0.0041/day		

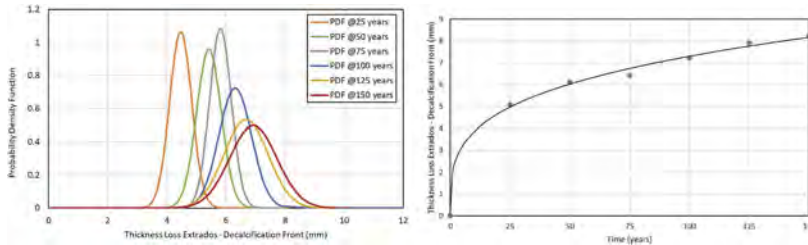


Figure 6. (Left) Probability density function of thickness loss distribution for different period of time. (Right) Thickness loss due to sulfate attack as a function of time.

Table 6. Summary of the tools for service life prediction of TBM new tunnels with required laboratory tests.

exposure condition	ambient air				ground			
Relevant degradation	carbonation attack				sulfate attack			
approach	deterministic		probabilistic		probabilistic			
mathematical model for degradation	Carbuff		fib34		STADIUM (FEM model)			
laboratory tests required for calibration of model	parameter	reference	parameter	reference	min number of samples required	parameter	reference	min number of samples required
	mix design	literature data	Inverse carbonation coefficient test	fib34	2	Porosity	ASTM C642	2
			humidity	weather station	period of 1 year	diffusion coefficient	ASTM C1202	2
			temperature	weather station	period of 1 year	permeability	ASTM C1792	2

4 DISCUSSIONS

4.1 Carbonation

The results of carbonation modelling by either deterministic approach or full probabilistic approach show that the designed concrete cover of 50mm for TBM concrete segments fulfills the service life of the project that is 100 years.

By comparison between deterministic modelling and full-probabilistic modelling of carbonation phenomena, it can be inferred that the deterministic modelling is more conservative than the full-probabilistic approach.

One of the drawbacks of the deterministic modelling is that it is not calibrated by the laboratory results of the actual concrete mix by which the segments are going to be fabricated. In addition, the ternary mixes cannot be simulated by deterministic approach because this approach uses the predefined carbonation resistance data from literature for binary mixes.

The results above conclude that by calibrating the carbonation modelling with the laboratory results, more realistic life cycle assessment could be performed. Therefore, the full-probabilistic approach possibly can provide more accurate evaluation of the service life for the concrete structure subjected to carbonation attack than the deterministic approach. It should however be noted that the current fib34 does not consider the propagation time rather it considers only the initiation time of corrosion.

4.2 Sulfate attack

The results of sulfate attack simulation show that the performance of the sealing gasket in TBM segment is not compromised by the sulfate attack. The thickness loss due to sulfate attack after 100 years (7.22mm) does not reach the mid-depth of the gasket hook that is 7.25mm. Therefore, stability of gasket after 100 years of sulfate attack is confirmed and the sealing effect could be maintained.

5 CONCLUSIONS

The results above conclude that:

A thorough environmental investigation shall be performed during the design phase of concrete infrastructures to identify the main degradation mechanisms.

Full-probabilistic approach could be utilized for the numerical modelling of any degradation mechanism, which could be mathematically formulated by Fick's 1st & 2nd laws.

By performing simple and cheap laboratory experiments to calibrate the numerical models of degradation mechanism prior to the execution of the project, the durability of the concrete structures during the design service life of the project could be ensured.

To compare the carbonation depth calculated by fib34 with the nominal concrete cover, 95th percentiles of a normal distribution carbonation depth distribution, calculated by fib34, could be a suitable representative of the normal distribution of the carbonation depth.

Table 6 shows a guideline for the durability assessment of the segments of TBM tunnel. For each exposure condition, the relevant degradation is shown. Each degradation shall be numerically modelled and the approach for the modelling is categorized. The model shall be calibrated by means of several parameters. The relevant parameters are reported in the table, with associated reference and adequate number of samples.

ACKNOWLEDGEMENTS

The authors would like to acknowledge the technical support of SIMCO by providing the FEM simulation of the sulfate attack using full-probabilistic approach through STADIUM software.

REFERENCES

- AS 1289.4.2.1—1997, Methods of testing soils for engineering purposes Method 4.2.1: Soil chemical tests — Determination of the sulfate content of a natural soil and the sulfate content of the groundwater— Normal method.
- Bertolini et al., 2012, "Corrosion of Steel in Concrete", Wiley-VCH publication.
- CARBUFF, "Enhancing reinforced concrete durability", by P.B. Bamforth, Concrete Society Technical Report No. 61.
- Fib34 Model code for service life design, 2006.
- Sarkar S., Mahadevan S., Meeussen J.C.L., van der Sloot H., Kosson D.S., "Numerical simulation of cementitious materials degradation under external sulfate attack", *Cement & Concrete Composites* 32 (2010) 241–252.
- Simco Durability Engineering, STADIUM® SERVICE-LIFE MODELING & ANALYSIS OF CONCRETE STRUCTURES. (www.simcotechnologies.com).

Holistic assessment-framework for railway noise barrier constructions

M.F. Granzner & A. Strauss

University of Natural Resources and Life Sciences, Vienna, Austria

M. Reiterer

REVOTEC gmbh, Vienna, Austria

ABSTRACT: The high safety requirements for railway infrastructures are a basic demand that the railway user places on the railway operator. Noise barriers that are erected along high-speed railway lines are loaded by aerodynamic pressure and suction waves due to the passing trains. Noise barriers are an integral part of railway infrastructures, and their level of safety must be maintained throughout their entire lifetime. This concept paper discusses deterministic and probabilistic-based approaches for condition assessment and prognosis of remaining service life of railway noise barriers, embedded in a safety concept that takes damage consequence classes into account. These approaches are combined into a holistic assessment concept, in other words a progressive four-stage model in which the information content increases with each model stage and thus successively increases the accuracy of the determined structural conditions at the time of observation and the forecast for the remaining service life of the structure. The analytical methods used in the first stage of the developed holistic framework are based on common static calculations used in the engineering practice and, together with expert knowledge and large-scale fatigue test results of noise barrier constructions, form the basis for the subsequent stages. Linking routines that combine the condition assessments from the common executed visual inspections and additional information from permanent monitoring systems applied to failure-critical elements with the analytical methods of the first stage are implemented in the second stage of the holistic framework. With application of numerical finite element methods in the third stage and finally the probabilistic approaches in stage four, the highest degree of determination accuracy of the noise barrier condition at the time of observation and prediction accuracy of the remaining lifetime shall be achieved. Depending on how far the degradation of the considered noise barrier has already progressed, the corresponding stage of the holistic assessment concept is activated, which enable infrastructure managers to plan their future investments regarding maintenance, retrofit or rebuilt of noise barriers more economically. The aim is to integrate the project results into a supranational framework, which is established through orientation towards Europe-wide preliminary projects.

1 INTRODUCTION

Noise barriers (NB) are erected alongside railway lines, and they are exposed to high aerodynamic loading by passing trains. Due to the current increasing train frequencies and train speeds material fatigue becomes important for all construction parts of NB like the steel posts, fastening elements and the foundations. Hence, NB must be maintained at a level of safety and reliability specified by politics and society throughout their entire lifetime. This is basically the task of infrastructure managers, who, in addition to the safe and reliable

functionality of the infrastructure, must also manage its availability, maintainability, environmental compatibility and the necessary financial capital and workforce. Assessment of existing NB structures is nowadays often based on the subjective visual evaluation of the examiner or the responsible consulting engineer. However, designing and evaluating the design of new and existing NB structures as it is done with common engineering methods, doesn't yet include all the relevant information needed to predict the structural behaviour over time. The inclusion of information from visual inspections as well as information which, due to the technical progress of monitoring systems, is feasible but is not yet done regularly, has great potential to improve the accuracy of condition assessments and forecasts of the remaining service-life for NB constructions.

2 BACKGROUND RESEARCH

To plan the necessary maintenance measures for NB constructions in a resource-efficient way, concepts based on building/component conditions and minimum threshold values for maintenance are used in many European countries. Although there is no uniform supranational definition for these maintenance concepts. These throughout Europe varying maintenance concepts, condition-state definitions and lower limits of maintenance strategies are presented, discussed and compared in Strauss et al. (2022a). The management process of life cycles of individual objects or even entire infrastructure networks includes not only the inspection, i.e. the survey of the condition, and the assessment of the structural performance, but also the evaluation of the maintenance strategies. These management systems are usually based on deterministic performance prediction models to describe degradation processes of the considered structures. Increasing experience in the use of up-to-date measurement technology and rapid developments in computer processing power and storage capacity have caused a trend towards data-based approaches to condition monitoring. Identifying and implementing key performance indicators plays a major role here. The characterisation and systematisation of performance indicators for bridges and tunnel systems and how to link them to data-based performance assessment methods and inspection and monitoring concepts is another important point which is discussed in Strauss et al. (2022b). Incorporating practical condition monitoring systems into the safety concepts of existing standards at a national and European level is a step that is currently being taken and is urgently needed in order to make appropriate decisions about conservation and safety. Strategies to fill this gap are proposed in Strauss et al. (2022c). In developing the holistic model presented here, care was taken to ensure the best possible incorporation into the proposed supranational concepts. The linking of information from currently applied purely visual condition inspections, as well as new monitoring methods with existing expert knowledge from tests and calculations, based on artificial intelligence methods and the subsequent integration into a safety concept, which is based on a hybrid and model-based reliability index, has already been shown in preliminary projects on this topic (Reiterer et al., 2021). The condition prediction models developed from this, consisting of four model levels, provide the expected service life of the engineering structure under consideration, taking into account the corresponding damage consequence classes. These approaches are exemplarily applied to the highly aerodynamically stressed NB.

NB installed alongside the tracks of railway lines are exposed to air pressure waves caused by passing trains. These air pressure waves create a sinusoidal dynamic loading consisting of a pressure and a suction load. The size of the dynamic loading depends on the aerodynamic shape of the trains, the speed of the train, the shape of the structure as well as on the distance between the axis of track and the surface of the noise barrier (Figure 1). The dynamic amplification may become a factor of 6.6 in the most unfavourable case (Reiterer et al., 2020). Until 2005, train-induced aerodynamic loading has not been adequately considered in the design of NB as well as in the applied calculation methods (pure static analysis) and in the relevant normative specifications given in Eurocode. Causes for the resulting fatigue damage have been investigated by Hoffmeister (2007) and Hertle & Näfl (2005), among other things by investigating unfavourable structural responses of the NB, and the design of new NB constructions.

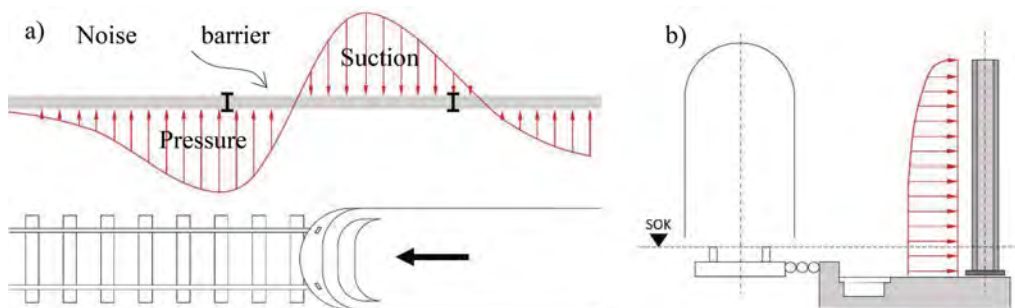


Figure 1. A) Aerodynamic loading situation in the longitudinal direction of the noise barrier during train passage. b) Aerodynamic loading situation over the height of the noise barrier during train passage.

The determination of the train-induced aerodynamic loading as regulated in the standards and guidelines currently in use was carried out and compared by Reiterer et al. (2017). The results of the current applied calculations were finally compared with the results from a permanent measuring point of the considered NB. In addition to the aerodynamic pressure-suction loads that occur when trains pass by, the corresponding dynamic reaction of the NB construction was also measured. As can be seen from the experimental investigations and evaluations of Reiterer (2019), NBs exhibit increased material fatigue especially at the welded seam connections between the steel post and the steel base plate and even more decisive at the threaded connection bolts between the concrete edge beam and the NB steel post (Figure 2), whereby the fatigue at the welded seams does not lead to a complete failure of the NB construction and is therefore not considered here. The more critical case is the fatigue failure of the fastening elements, i.e. threaded bolts installed to the concrete edge beam, which lead to an instant collapse of the NB construction. The experiments in Reiterer (2019) were carried out in form of fatigue tests with up to 5 million load cycles, which were simultaneously recorded by a measurement system. Different installation conditions of the steel post with different degrees of execution deficiencies, i.e. variation of preload, were investigated within the fatigue tests. The aim of the tests was to study the influence of execution deficiencies on the durability of NB constructions.



Figure 2. Exemplary photographs of the fastening situation of NB on the concrete edge beam.

One of the most important execution deficiencies is the fastening of the NB posts to the concrete edge beam with an insufficient preload. In further experiments, published by Reiterer (2019), the preload behaviour was investigated and evaluated, from which a procedure instruction for the nut-side prestressing could finally be derived (Reiterer et al., 2020). The behaviour of prestressed bolt-nut-connections is also shown in Alt et al. (2007), where settlement is observed after applying the preload and the beginning of rupture when fatigue tests are

conducted. In addition, the influence of superimposed tensile and bending stress on the fatigue behaviour was investigated.

3 HOLISTIC FOUR-STAGE MODEL

In the concept of the holistic four-stage model presented here, state-of-the-art safety concepts, as well as monitoring concepts and systems, are to be combined with time-honoured condition assessment methods in such a way that infrastructure operators can manage structural safety and track availability in the most economically and ecologically efficient way.

The core elements of the four-stage model are the currently applied standard methods of visual inspection with its resulting condition classes (ZK_v) and fatigue calculations according to RVE 04.01.01 currently carried out only in the design processes of NB. Figure 3 shows the individual model stages of the proposed holistic four-stage model, which are successively activated with ongoing degradation of NB. The activation of the respectively following model stage happens when a certain condition-state threshold is reached. With each model stage, the precision of the condition-state determination and prognosis of remaining lifetime is increased, whereby an increased monetary expenditure must also be expected. In a later paragraph of this chapter, the individual model stages are explained.

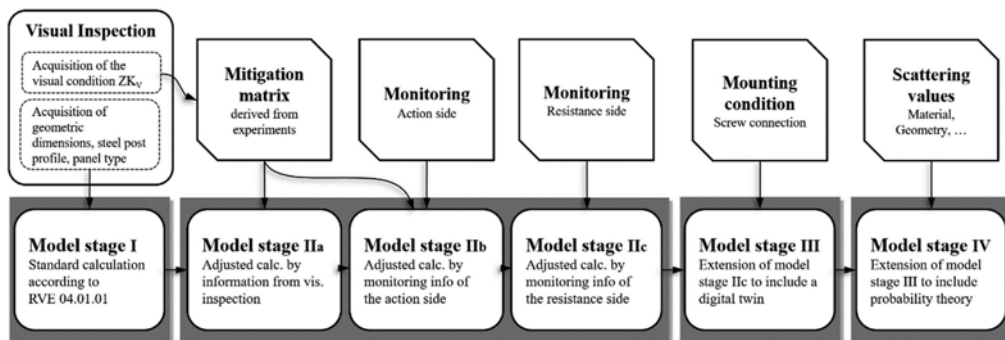


Figure 3. Scheme of the proposed holistic four-stage model.

By transferring/embedding the conducted calculations for the current conditions and forecasts of the technical service-life of NB into the reliability index β according to ÖNORM EN 1990, damage consequence classes can be considered. Based on the consequence class corresponding to the structure under consideration, in the case of noise barriers along railways its CC2, mechanical condition classes can be defined. In analogy to the visual condition classes (ZK_v), mechanical classes (ZK_m) are additionally defined in a kind of school grading system with class 1 for a good mechanical condition and class 5 for a bad mechanical condition. The mechanical condition describes the state of fatigue in a deeper level of detail, which is not or barely detectable in a purely visual inspection. To make another comparison visual condition classes contain visually detectable information, which is strongly dependent on the inspector's experience and knowledge, on the other hand the mechanical condition classes combine visual and monitoring information, information from experiments, applied standard calculations, and digital twins, from which a more stable and accurate solution is expected.

Figure 4 shows an example of the calculated end-of-lifetime of NB for four different cases and the linear progression of the mechanical condition classes in the reliability index space. The four cases have the same input parameters except for the visual condition class. The loading situation, which is 50 RailJets per day, with the train speed of 230 km/h, is as well the same for all cases.

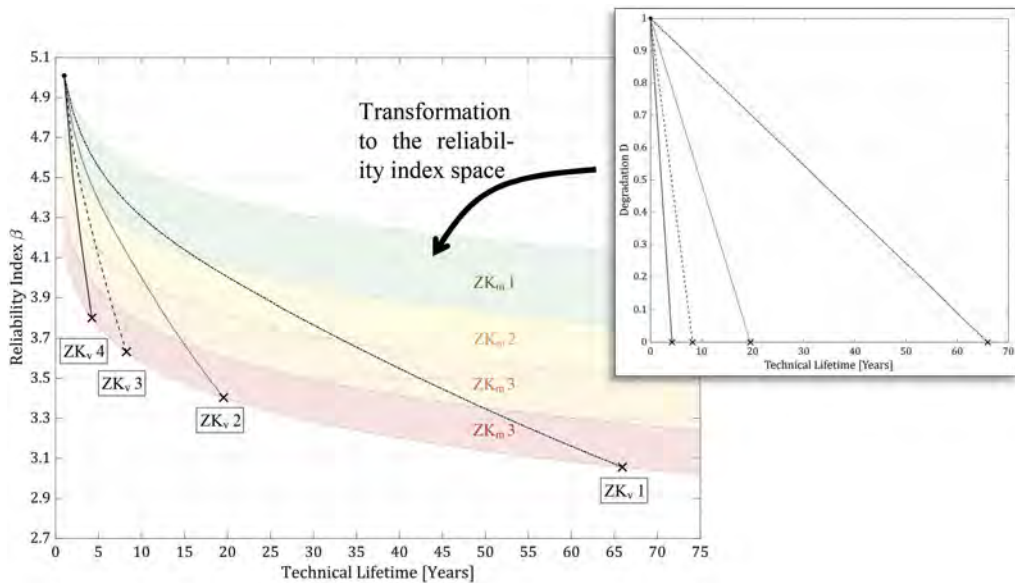


Figure 4. End-of-life prediction of NB for four different cases in a reliability index framework.

The following section describes the proposed individual model stages of the previously introduced holistic four-stage model which is depicted in Figure 3.

Visual Inspection – The inspection of the NB construction, which takes the first position, is carried out by the expert/personnel of the operator. In this step, the structural conditions are recorded, which include the geometric dimensions, type of steel post, NB panel type/material, as well as the visually recognisable and assessable condition of the construction, components, and execution details. The data recorded during the visual inspection serve as input values for the standard calculation of the service life according to RVE 04.01.01, on which the first two model stages are based.

Model Stage I – Calculation according to current standards – The first and simplest model stage is based purely on a common applied standard durability calculation. For this project in particular, the calculations are carried out according to RVE 04.01.01, which refers to NBs on bridges and concrete supporting walls with the executed edge beam types 2.1 and 4.0 (Figure 1b) according to ÖBB regulations. The input parameters are the geometric dimensions of the NB structure, type of steel post, type of NB panel, load effect, etc., which were recorded during the visual inspection. The output of the calculations is a forecast of the technical service life, which in a further step is converted into a reliability index β (Figure 4).

Mitigation matrix – In the mitigation matrix, the visual condition classes from visual inspection are assigned to the corresponding reduction factors, which are included in the calculation of model stage IIa and IIb. The reduction factors, which are derived from experimental fatigue tests, are intended to consider the reduction of the stress vibration range in the mechanical fasteners caused by the applied preload, which is not considered in the common applied standard calculation.

Model Stage IIa – Enhanced calculation according to standards through visual inspection – By incorporating information from visual inspections, the next level of the four-stage model is reached. The normative fatigue calculation on which model stage I is based also forms the basis for model stage IIa, but here the condition classes assigned in the course of the visual inspection are also taken into account. The reduction factor is used in order to come closer to the actual effective stress vibration width in the fastening element of the NB.

Monitoring action-side – Monitoring of the action side takes place at check points on the tracks along the rail network, where the axle loads of passing trains are measured. By

subsequently analysing the data, the train type, train speed and number of trains per day can be precisely determined.

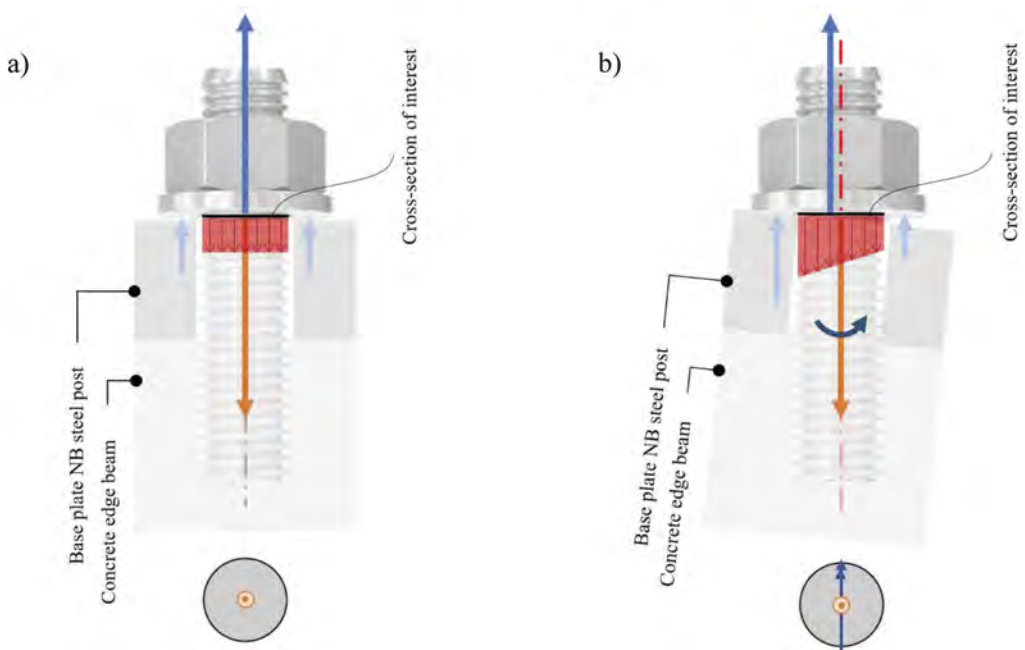


Figure 5. A) Ideal installation condition of threaded bolt. b) Faulty installation condition of threaded bolt.

Model Stage IIb – Enhanced calculation according to standards through monitoring load side – In addition to the correction of the stress variation range, which is carried out in model stage IIa by taking into account the visual condition classes, monitoring on the action-side is incorporated in model stage IIb, thus the degree of accuracy of the condition determination and prognosis is further increased.

Monitoring resistance-side – The preload and stress variation range in the threaded bolts is measured directly by means of a measuring nut.

Model Stage IIc – Enhanced calculation according to standards through monitoring resistance-side – Contrary to model stage I - IIb, in model stage IIc the entire calculation from the load action via the NB construction into the fastening elements is bypassed by resistance-side monitoring and thus also the associated uncertainties. Using the rainflow-method, the number and amplitude of the measured stress variations can be analysed precisely, which significantly increases the accuracy of the calculation of the partial damage.

Mounting conditions – The most prominent faulty mounting conditions are defined together with experts. Faulty installation conditions of the bolted joint can introduce bending moments in addition to the preload.

Model Stage III – Digital twin – In the previous model stages, the influence of the installation condition was broken down to one factor derived from visual information, and the monitoring system proposed offers only a limited possibility of recording the influence of the installation condition. This still clearly existing discrepancy between these highly simplified models and reality is to be further reduced in model stage III. For this purpose, various “faulty” installation conditions (Figure 5) are defined and modelled by means of a digital twin. An ideal installation condition has a constant normal stress in the cross-section under consideration (Figure 5a), whereas faulty installation conditions cause a moment, which results in an additional bending component in the normal stress (Figure 5b). By investigating

the influence of faulty installation conditions on the stress amplitude, the calculations can be calibrated and thus the influence on the fatigue behaviour can be determined.

Model Stage IV – Probabilistic Approach – In this stage probabilistic approaches are employed to model the degrading process over time. In these considerations, the observations, information, and methods of the previous stages can be included in relation to the boundary securities according to their significance.

4 CONCLUSIONS

The proposed holistic four-stage model has great potential to improve the accuracy of condition-state assessments and forecasts of remaining lifetime of NB constructions along railway lines by combining time-honoured condition assessment methods with state-of-the-art safety concepts and monitoring concepts and systems. This allows infrastructure operators to manage structural safety and availability of the railway tracks in a more economic and ecologic way. By investigating different installation conditions more or less favourable situations can be identified and avoided in future.

ACKNOWLEDGEMENT

The authors thank the FFG for funding the KI-LEB Research Project. The authors also thank the ÖBB Infra for discussions and support.

REFERENCES

- Alt, A., Mertens, H., Arz, U., Blessing, L., Berger, C. 2007. Schwingfestigkeit von Schraube-Mutter-Verbindungen. *Materialwissenschaft und Werkstofftechnik* 38, 402–409.
- Hertle, R., Näßl, A. 2005. Aerodynamische Anregung von Schutzwandkonstruktionen an schienengebundenen Hochgeschwindigkeitsstrecken. *Bauingenieur* 80, 151–161.
- Hoffmeister, B. 2007. Lärmschutzwände an Hochgeschwindigkeitsstrecken der Bahn – eine Herausforderung für den Leichtbau. Presented at the D-A-CH Tagung der Österreichischen Gesellschaft für Erdbebeningenieurwesen und Baudynamik, Österreichischen Gesellschaft für Erdbebeningenieurwesen und Baudynamik.
- Reiterer, M. 2019. Experimentelle Untersuchung von Lärmschutzwandstehern und deren Befestigung auf Kunstbauten, Teil 1 - Ermüdungsverhalten. *Stahlbau* 88, 988–1003.
- Reiterer, M., Lachinger, S., Kari, H. 2017. Lärmschutzwände entlang von Hochgeschwindigkeitsstrecken: Normung – Berechnung – Messung/Noise barriers on high speed railway lines: Codes – Calculation – Measurement. *Bauingenieur* 92, 39–49.
- Reiterer, M., Stranghöner, N., Jungbluth, D. 2020. Experimentelle Untersuchung von Lärmschutzwandstehern und deren Befestigung auf Kunstbauten, Teil 2 - Vorspannverhalten. *Stahlbau* 89, 164–178.
- Reiterer, M., Strauss, A., Kari, H. 2021. Ansätze zur performancebasierten Zustandsbeurteilung und Lebensdauerprognose von Ingenieurkonstruktionen. *Beton- und Stahlbetonbau* 116, 170–182.
- Strauss, A., Vliet, A.B., Daró, P., van Meerveld, H. 2022a. Condition-states and low limit maintenance thresholds of transport infrastructures in a European Context. Presented at the fib Symposium, pp. 2713–2723.
- Strauss, A., Vliet, A.B., Rodríguez, A.S., Daró, P., Granzner, M., Bergmeister, K. 2022b. Performance indicators for an objective assessment and through-life management of bridges and tunnels. Presented at the fib Symposium, pp. 2702–2712.
- Strauss, A., Bergmeister, K., Daró, P., Mancini, G., Sattler, F., Bigaj-van Vliet, A. 2022c. Monitoring and data informed approaches for the assessment of existing structures. Under Review
- RVE 04. 01.01 Assessment of the Acoustic Durability of Noise Barrier Elements, Panels, Gates and Doors. Österreichische Forschungsgesellschaft Straße – Schiene – Verkehr
- ÖNORM EN 1990 Eurocode – Basis of structural design

SS28: Use of SHM and NDE for decision making
Organizers: N.M. Apaydin, F.N. Catbas & B. Briseghella



Taylor & Francis

Taylor & Francis Group

<http://taylorandfrancis.com>

The state-of-the-art in health monitoring of long-span cable supported bridges in Turkey

O. Çetindemir & A.C. Zülfikar

Gebze Technical University, Kocaeli, Turkey

N. Memişoğlu Apaydın

Istanbul University-Cerrahpasa, Istanbul, Turkey

ABSTRACT: Long-span cable-supported bridges are one of the most important links in the transportation network of a city. This is why their structural health during construction and in operation is very vital and should be monitored. Especially over the last two decades due to safety concerns and to reduce costs, Structural Health Monitoring (SHM) systems have become extremely useful tools for making well-informed decisions regarding the operation and management of bridge structures. Numerous experts in SHM have identified and summarized the challenges and future trends of health monitoring for civil infrastructure. However, the field is extremely dynamic and rapidly evolving, so visions should be updated in a timely manner. Therefore, this work aims to provide the current status of long-span cable-supported bridges' health monitoring in Turkey by introducing SHM systems and their design considerations for eight long-span bridges. In addition, since these bridges are exposed to both strong seismic excitations and wind incidents due to the geographical locations where they are built, such extreme events may create critical load conditions on the bridges. For this reason, these events recorded by SHM systems are also provided in this work. It is believed that this study will be beneficial to bridge management authorities in order to extent their knowledge on the SHM and its potential use.

1 INTRODUCTION

Long-span bridges are one of the most vital lifelines in nations where they are built, as they shorten transportation by allowing passage of major waters such as rivers, canals, dams, and seas. Turkey is a critical transcontinental country between Asia and Europe because of its geographical location. In Turkey, where long-span bridges are subject to significant traffic and seismic risks, it is essential to monitor their structural health and execute maintenance in a timely and cost-efficient manner. Due to their size, these bridges are challenging to maintain. Periodic bridge inspections are usually planned every two to six years to examine the structure's condition (Kromanis, 2020). Nevertheless, inspections may be subjective and are still uncommon. Therefore, the most reliable technique for monitoring the structural state of such bridges in service is to install structural health monitoring (SHM) systems because of their high towers and difficult-to-access cables (Memisoglu Apaydin et al., 2022). This paper focuses on a concise overview of SHM systems for long-span cable-supported bridges in Turkey. In addition, experienced extreme events and the benefits of the SHM system are presented to help improve current systems and inform interested owners and users of such health monitoring systems.

The remaining sections of this paper are organized as follows: Section 2 represents a general description of long-span cable-supported bridges in Turkey. Section 3 provides essential information on the structural health monitoring of the bridges. In Section 4, extreme cases recorded through SHM systems on the bridges are provided. Section 5 concludes the paper by presenting the beneficial effects of the SHM system and sharing insightful recommendations.

2 LONG-SPAN CABLE-SUPPORTED BRIDGES IN TURKEY

The First Bosphorus Bridge was the 4th longest bridge in the world when it was completed in 1973. This bridge is currently the 40th longest suspension bridge in the world. The aerodynamic box section is utilized for a deck in order to require less maintenance than conventional truss systems, to decrease wind effect by one-third, and to use less materials to produce a lighter and more cost-effective solution. The main span length of the bridge is 1074 meters, and there are two approach viaducts (see Figure 1). The main span is suspended by hangers, whereas the viaducts' bases are supported by columns of varying heights. Additionally, they are simply supported on the ground near the anchors. After constructing a new beltway (O-2) in Istanbul known as the Trans-European Motorway (TEM), it became imperative to construct a second bridge over the Bosphorus Strait. The Fatih Sultan Mehmet (FSM) Bridge was the fifth longest suspension bridge in the world when it was completed in 1988; it is currently rated 36th. The FSM bridge is a long-span suspension bridge made of steel. The towers of the bridge are supported at ground level. Since the ends of the bridge's deck are on the same level as the tower's base, there is no approach span on the bridge. The main span length of the bridge is 1090 meters, while the width and height of the deck's aerodynamic box section are 39.40 and 3.00 meters, respectively. The bridge tower is a rectangular box with a total height of 110 meters. The mid-span deck is 64 meters above mean sea level. The length of the bridge is 1510 meters, with two 210-meter side spans (see Figure 2).

The Yavuz Sultan Selim (YSS) Bridge is a hybrid cable-stayed suspension bridge enabling rail and motor vehicle passage across the Bosphorus Strait. The YSS Bridge's construction started in 2013 and opened to traffic in 2016. It is located 5 kilometers north of the First Bosphorus Bridge at the entrance to the Bosphorus Strait and relatively close to the Black Sea. The YSS Bridge is among the widest suspension bridges, with a 59-meter-wide deck. It was the second-tallest bridge in the world after the Millau Viaduct in France, with a structural height of 322 meters; it is currently rated fifth. With a main span length of 1,408 meters, this bridge is the world's longest suspension bridge with a railway system. At a particular location, the stay cables and hanger cables of the YSS Bridge overlap a transitional section. Figure 3 illustrates the bridge's general layout. The Osman Gazi Bridge (OGB) was built at the narrowest point of Izmit Bay on the eastern side of the Marmara Sea. The OGB is the only bridge at Izmit Bay. Thus, it is a crucial transportation network between the Istanbul Motorway and the Izmir Motorway, reducing travel time by six times. Construction of the bridge began in 2013 and opened to traffic in 2016. With a primary span of 1550 meters, it is the 7th-longest suspension bridge in the world. It has two 566-meter-long side spans and a 1550-meter-long main span (see Figure 4). In addition, the bridge features two 120-meter transition spans at the anchorage blocks at the end of each side span. The bridge's entire span length is 2922 meters. Underwater concrete foundations support the towers, and their height is 252 meters. The approach spans are suspended using hangers rather than ground-based supports. The construction of the 1915 Çanakkale bridge began on March 18, 2017, and was recently opened to traffic on March 18, 2022. It is the longest mid-span suspension bridge in the world, with a length of 2023 m, exceeding the Japanese Akashi Kaiky Bridge. A 318-meter-tall H-shaped bridge tower is constructed as a rectangular hollow section, and the tower's foundation is 40 meters below sea level. As shown in Figure 5, the base and top tower sections have dimensions of 11.00 m by 10.50 m and 8.00 m by 7.50 m, respectively. 318 m is the elevation of the intersection point of the main cable, which is essential for design, actual tower height considering the tower top enclosure, is 334 m. This makes the bridge 2nd tallest bridge in the world. The deck is an orthotropic steel with three lanes in each direction, a height of 3.50 meters, and a width of 45.06 meters. The bridge's side spans (each 770 m) connect approach viaducts supported at the base of each side, measuring 385 m on the European side and 680 m on the Asian side.

The Agin (Karamağara) cable-stayed bridge is part of a provincial route that spans the Keban Dam reservoir lake. The bridge's construction began in 2001. Due to modifications to the project, construction was delayed, but work resumed on January 10, 2012, and the opening took place on October 26, 2015. The route connects Elazığ and Arapgir. The 520-meter-long cable-stayed bridge has spans of 120 + 280 + 120 meters and is supported by two 55-meter-tall

steel towers on concrete piers. The main deck comprises a 13-meter-wide orthotropic steel box section supported by stay cables in a central plane. The layout of the bridge is shown in Figure 6a (Megaba, 2016). The Nissibi cable-stayed bridge was erected on the Atatürk Dam Reservoir across the Euphrates River in Southeast Anatolia and opened to traffic in May 2015. The main and total lengths of the bridge are 400 m and 610 m, respectively. It is now the longest cable-stayed bridge in Turkey. The side spans of the prestressed concrete box section deck have a length of 2x105 m and a width of 24.50 m. The main span was designed as a steel box section deck with a width of 22.90 m and a height of 2.70 m. The bridge's plan is depicted in Figure 6b. The pylon foundations are 50 m x 20 m x 5 m rectangular spread footings, whereas the usual pier foundation is 13.3 m x 6 m x 1.5 m, and the abutment foundation is 28.7 m x 12.2 m x 1.5 m. The New K m rhan Bridge is a cable-stayed bridge that connects the Elazığ-Malatya Highway D.300 over the Karakaya Dam Lake on the Euphrates River in eastern Turkey. The bridge is located on the shortest route between Malatya and Elazığ and has no alternate route. Construction began in 2014, and the new bridge was officially opened on January 2, 2021. The New K m rhan Bridge replaced an older box-girder bridge built between February 23, 1983, and April 8, 1986, by the STFA Group. The total length of this 168.5 m tall cable-stayed bridge is 660 m, and its widest span is 380 m. With its 380-meter center span, it is ranked as the world's 4th longest single-pylon cable-stayed bridge. The cables connect to the bridge deck in the middle of the bridge on a single plane. The 21 cables that support the 380 m long main span are stabilized with the same number of cables anchored onto the 180 m long foundation block on the land side. The bridge's layout are shown in Figure 6c.

3 HEALTH MONITORING OF LONG-SPAN CABLE-SUPPORTED BRIDGE IN TURKEY

Petrovski et al. (1974), Tezcan et al. (1975), Erdik and Uckan (1988), and Brownjohn et al. (1989) completed prior research for the establishment of a health monitoring system on the First Bosphorus Bridge. The significance of a permanent SHM system was highlighted by these primary investigations that utilized a temporary SHM system with portable sensors. In 1993, the bridge was equipped with an essential permanent SHM system consisting of three subsystems: a sensor, data acquisition, and recording station. After a severe wind event in 2004, the national authority decided to extend the SHM system. The total sensor quantity is 168 and consists of various sensor types, including 12 force transducers, 19 accelerometers, 15 tiltmeters, 70 strain gauges, 6 weather stations, 8 laser displacements, 33 thermocouples, and 5 GPS. Figure 2a depicts the SHM system of the First Bosphorus Bridge. In 2001, based on the research by Apaydin (2002), Apaydin and Erdik (2001), a permanent SHM system was first built on the FSM Bridge, as well as the primary monitoring studies (Brownjohn et al., 1991, Brownjohn et al., 1992a, Brownjohn et al., 1992b). 12 accelerometers, 4 displacement meters, 2 seismometers, 2 GPS, a weather station, and a thermometer were installed on the FSM Bridge as an initiative SHM system. Before the YSS Bridge was built, the FSM Bridge was subject to significant truck traffic. Therefore, the traffic load was heavier than the First Bosphorus Bridge. Since the design specifications require high expansion joint movement capacity, all displacement sensors on the bridge are installed at the expansion joints. At ground level, four seismometers are installed on support points of backstay anchorages and tower legs. Later, KGM decided to conduct a preliminary study for enhancing the FSM Bridge's permanently installed SHM system. Among the most notable new planned sensors are on cable components, expansion joints, and anchorage locations. Figure 2 shows current and planned SHM system of the FSM Bridge.

The KGM prepared a comprehensive report on the primary objectives, requirements, and monitoring parameters of the SHM system to be installed on the YSS, based on the experience gained from the First and the Second Bosphorus (the FSM) Bridges regarding the optimal design and installation of an SHM system (KGM, 2014b). 18 triaxial, 56 biaxial, and 2 uniaxial accelerometers, 5 GPS sensors, 5 biaxial tiltmeters, 22 displacement meters, 5 wind sensors (speed and direction), 1 weather station, and 12 temperature sensors were utilized in consideration of the bridge's dynamic characteristics and critical points. Due to the importance of the

stress-strain history and cable vibration for long-span bridges, strain gauges, and force transducers are instrumented to monitor the reaction. At the tower top-saddle of the bridge, strain gauges are installed to monitor the high load and stress concentration. In addition, the width of the deck makes it more susceptible to torsional rotation and tilting. Therefore, accelerometers and tiltmeters have been mounted in the two corners of the deck. After analyzing the behavior of the bridge during extreme events, it is planned to improve its SHM system. Figure 3 shows current sensor configuration of the YSS Bridge. The SHM system of the OGB has six essential purposes: (1) wind monitoring, (2) road monitoring, (3) dynamics monitoring, (4) temperature monitoring, (5) stress/strain monitoring, and (6) fatigue stress monitoring (KGM, 2014a). In total, 386 sensors are utilized to understand the bridge's response to extreme events and environmental conditions. Those are 160 fiber optic strain measurements, 84 steel temperature sensors, 49 accelerometers (2D and 3D), 16 humidity sensors (external), 12 force transducers (LVDT), 8 GPS sensors, 8 mono-strand loadcells, 8 sonic distance sensors, 6 main cable surface temperature sensors, 6 pavement temperature sensors, 6 hanger temperature sensors, 4 pyranometers, 4 weather stations, 3 air temperature sensors, 3 static inclinometers, 2 dynamic inclinometers, 2 rain gauges, 2 weight in motion (WIM) stations, 2 load measuring pins, and road wear. Figure 4 depicts the general layout and current sensor configuration of the OGB. The SHM system employed in the 1915 Çanakkale Bridge is the most advanced in Turkey in terms of sensor variety and quantity. In total, 1049 sensors are installed, including 508 dynamic strain gauges, 103 accelerometers (1D, 2D, and 3D), 88 static strain gauges, 74 biaxial inclinometers, 64 displacement sensors, 52 steel temperatures, 36 corrosion sensors, 34 data acquisition units, 26 GPS receivers, 16 load cells, 8 asphalt temperatures, 6 weather stations, 4 air temperatures, 4 barometric pressures, 4 cable thermometers, 4 sensors in the damper, 4 humidity, 4 road weather measurement stations, 2 sensors in the buffer, 2 clearance-sonic distance sensors, 2 weight in motion system, 2 pyrometers, and 2 seismic stations. The general layout and sensor configuration on the bridge can be seen in Figure 5.

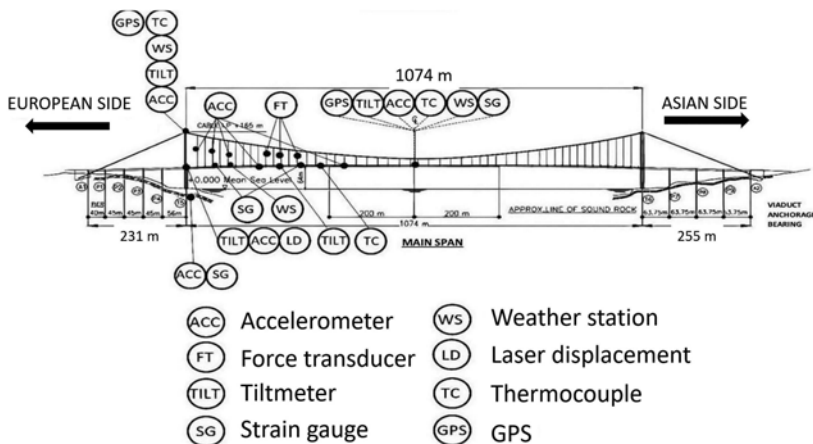


Figure 1. The general layout and sensor configuration of the First Bosphorus Bridge.

The SHM system of Ağın Cable-stayed Bridge is comprised of 40 sensors and 68 channels situated on the abutments, deck, pylons, and cables, including 16 accelerometers (2D and 3D), 10 structural temperature, 4 displacement meters of bearings (longitudinal and uplift), 3 video cameras, 2 wind sensors (3D ultrasonic), a solar radiation, 2 air temperature, and 2 air humidity sensors. Figure 6a illustrates the bridge's general and sensor layouts (VCE, 2012). Nissibi Euphrates Cable-stayed Bridge's SHM system has 29 sensors and 59 channels in total including 8 cable load cells, 16 accelerometers (1D, 2D, 3D), 2 wind sensors (3D ultrasonic), a solar

radiation, an air temperature, and an air humidity sensor. The SHM configuration are shown in Figure 6b. K m rhan Cable-stayed Bridge was equipped with a permanent monitoring system by VCE. This monitoring system comprises 56 sensors with 86 measuring channels. All measurement data are automatically evaluated and visualized in the password-protected BRIMOS web-user-interface and provided to clients. The bridge was equipped with a variety of sensors, including 2D and 3D accelerometers, strain gauges (for steel and concrete), load cells, GPS, weather stations (wind speed, temperature, and humidity), and pyranometers. Figure 6c illustrates the sensor configurations installed on the bridge (VCE., 2020).

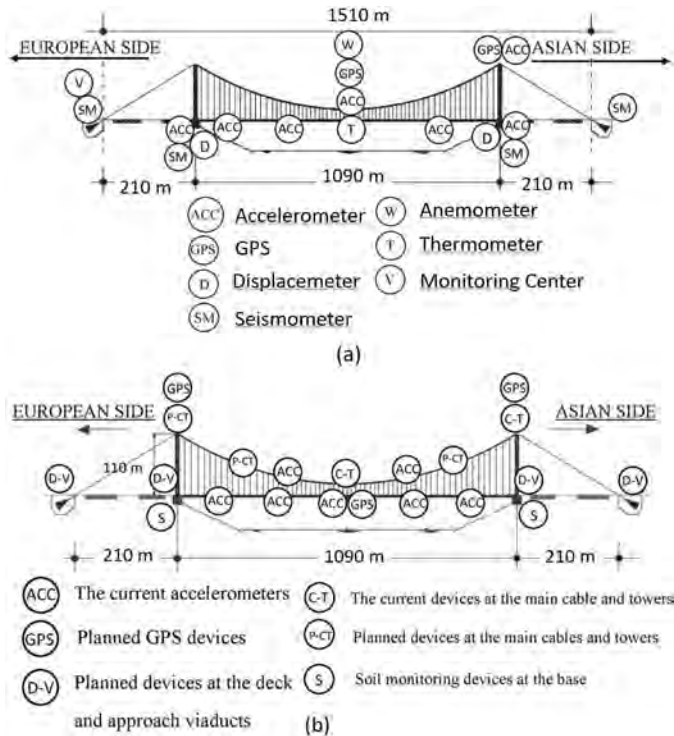


Figure 2. The general layout and sensor configuration of the Second Bosphorus Bridge (the FSM Bridge): (a) the current SHM system, (b) the planned SHM system.

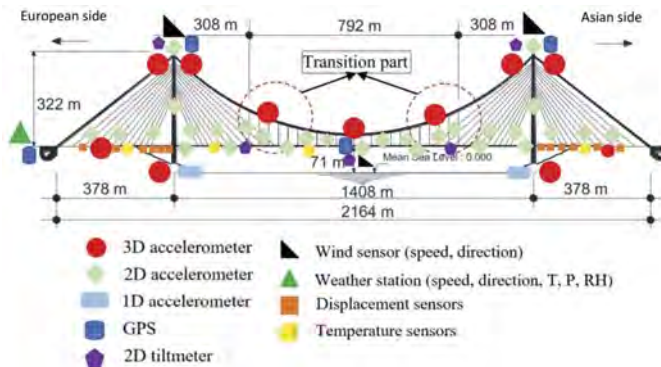


Figure 3. The general layout and sensor configuration of the Third Bosphorus Bridge (the Yavuz Sultan Selim Bridge).

4 EXTREME CASES RECORDED THROUGH SHM SYSTEMS ON BRIDGES

Using a SHM system, the structural and functional performance of a bridge can be examined in response to extreme events such as earthquakes, heavy traffic, strong winds, and human-induced loads. As a result, essential actions can be performed immediately. Extreme events recorded through SHM systems are presented as listed in Table 1.

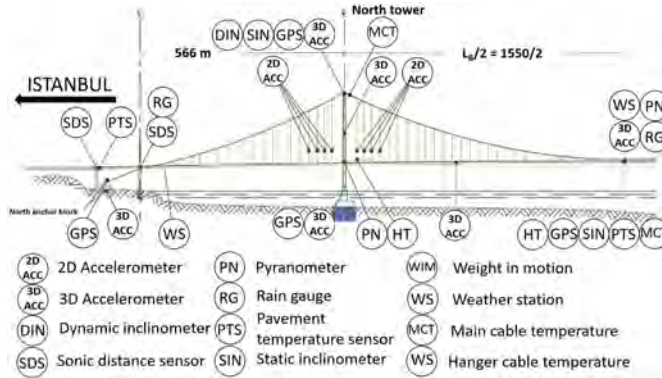


Figure 4. The general layout and sensor configuration of the Osman Gazi Bridge (the İzmit Bay Bridge).

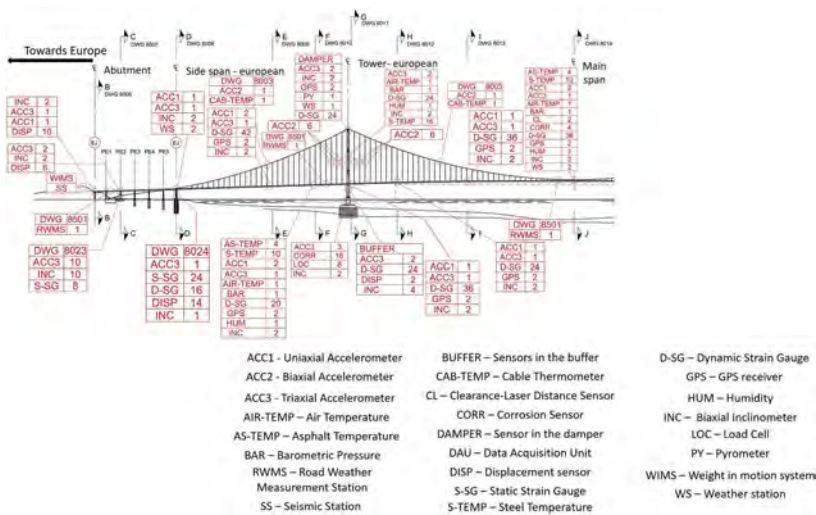


Figure 5. The sensor configuration of the 1915 Çanakkale Bridge (Dardanelles Bridge).

Table 1. Extreme events experienced on the bridges (N/A: not available).

Event	Date	Location	SHM data	Damage	Notes
Marathon	17Sep2010	Istanbul	The 1st bridge	No	SHM system improved
Wind	18Apr2012		The 2nd	damage	Hanger replacement
Protest	19Sep2013		bridge (FSM)		Extreme eccentric truck load
Earthquake	26Sep2019				The recorded data is analyzed by Memisoglu Apaydin et al. (2022)

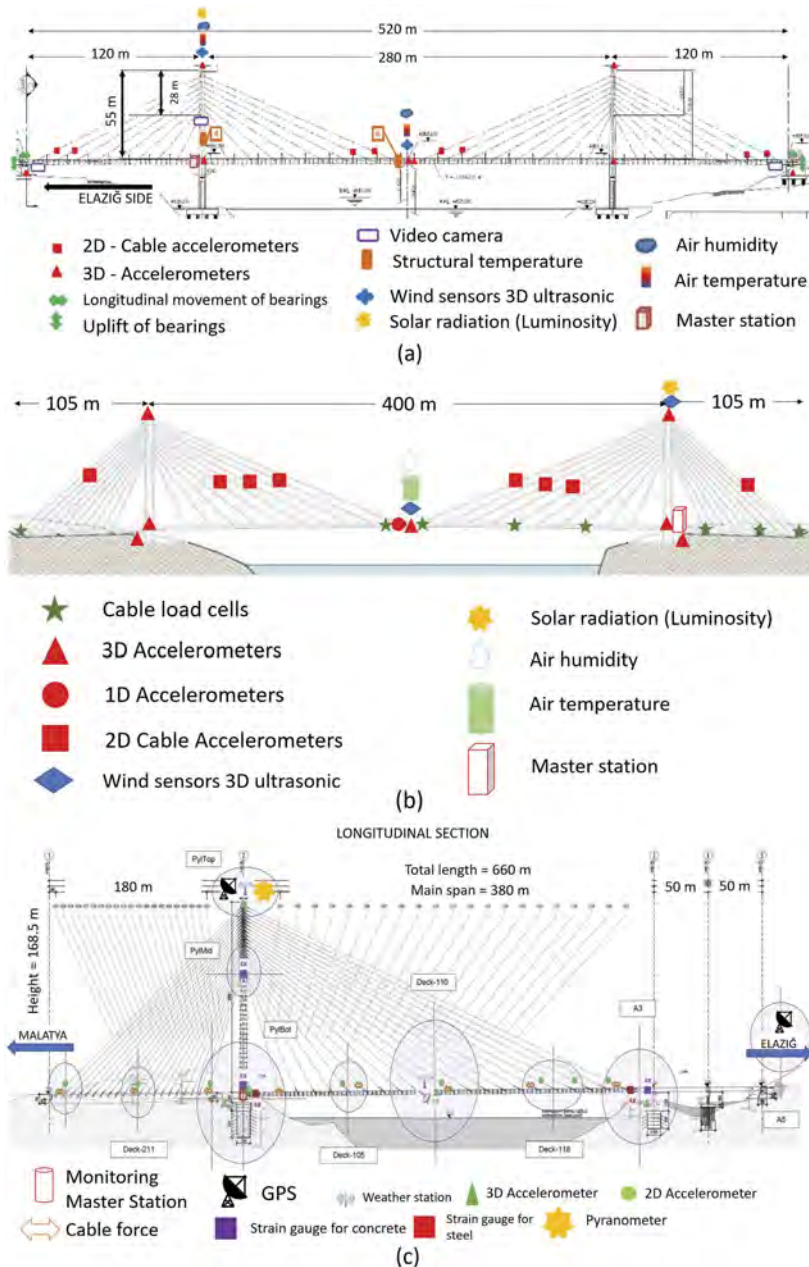


Figure 6. The general layout and sensor configuration: (a) the Ağın Bridge (Karamağara Bridge), (b) the Nisibi Euphrates Cable-stayed Bridge, (c) the New Kömürhan Bridge.

5 CONCLUSIONS

This paper can be concluded as follows: (1) Lessons learned from the first applications of structural health monitoring (SHM) systems and extreme events experienced on the long-span bridges in Turkey provide valuable knowledge for implementing more comprehensive SHM systems on recently constructed bridges, (2) it was observed that SHM systems allow for rapid and

continuous health monitoring of the bridges. However, sometimes, the damage of some structural and/or non-structural elements may not be clearly understood as a result of SHM data analysis since they do not cause major changes in the dynamic properties of the structure. Therefore, although it may be difficult due to their large structural elements, field inspections might also be needed to verify analyses results, (3) the vast amount of different sensors assists in understanding the traffic condition in depth for the efficient management of bridge structures. Therefore, for especially recent SHM applications in Turkey, these new types of sensors provide the overall system with additional information on an autonomous basis, (4) The essential components of the SHM system to be built are the general structural elements such as the main cable, hangers, deck, and towers. A simple system is always the best option for the initial application when installing an SHM. Later, it would be the appropriate approach to establish a more complex SHM system in light of the data obtained from the first employed system. In conclusion, this state-of-the-art paper will contribute to the innovative efforts of SHM systems for users in general and provide invaluable insight and recommendations for scholars.

REFERENCES

- Apaydin, N. 2002. Seismic analysis of Fatih Sultan Mehmet suspension bridge. Ph. D Thesis, Department of Earthquake Engineering, Bogazici University.
- Apaydin, N. & Erdik, M. 2001. Structural vibration monitoring system for the Bosphorus suspension bridges. *Strong motion instrumentation for civil engineering structures*. Springer.
- Brownjohn, J., Dumanoglu, A. & Severn, R. 1991. Fatih Bridge: Part II: Ambient vibration survey.
- Brownjohn, J., Dumanoglu, A. & Severn, R. 1992a. Ambient vibration survey of the Fatih Sultan Mehmet (Second Bosphorus) suspension bridge. *Earthquake engineering & structural dynamics*, 21, 907–924.
- Brownjohn, J., Dumanoglu, A., Severn, R. & Blakeborough, A. 1989. Ambient vibration survey of the Bosphorus suspension bridge. *Earthquake engineering & structural dynamics*, 18, 263–283.
- Brownjohn, J., Severn, R. & Dumanoglu, A. 1992b. Full-scale dynamic testing of the second Bosphorus suspension bridge. *Proceedings of the Tenth World Conference on Earthquake Engineering*. AA Balkema Rotterdam.
- Erdik, M. & Uckan, E. 1988. Ambient vibration survey of the Bogazici Suspension Bridge. *Istanbul: Department of Earthquake Engineering, Kandilli Observatory and Earthquake Research Institute, Bogazici University, Turkey*.
- Kgm 2014a. A preliminary technical report on structural health monitoring system for The Osman Gazi Bridge. Ankara: General Directorate of Turkish State Highways.
- Kgm 2014b. A preliminary technical report on structural health monitoring system for The Third Bosphorus Bridge. Ankara: General Directorate of Turkish State Highways.
- Kromanis, R. 2020. Health monitoring of bridges. *Start-up creation*. Elsevier.
- Megaba 2016. Project information-Agin Bridge, Turkey.
- Memisoglu Apaydin, N., Zulfikar, A. & Cetindemir, O. 2022. Structural health monitoring systems of long-span bridges in Turkey and lessons learned from experienced extreme events. *Journal of Civil Structural Health Monitoring*, 1–38.
- Petrovski, J., Paskalov, T., Stojkovich, A. & Jurokovski, D. 1974. Vibration studies of Istanbul Bogazici suspension bridge. *Report OIK*, 74.
- Tezcan, S., Ipek, M., Petrovski, J. & Paskalov, T. 1975. Forced vibration survey of Istanbul Bogazici bridge. *Proceeding of the 5th ECEE*, 2.
- Vce 2012. Bridge monitoring system.
- Vce. 2020. Bridge monitoring system.

Informed assessment of structural health conditions of bridges based on free-vibration tests

M. Mazzeo, D. De Domenico & R. Santoro

Department of Engineering, University of Messina, Messina, Italy

G. Quaranta

Department of Structural and Geotechnical Engineering, Sapienza University of Rome, Rome, Italy

ABSTRACT: A consolidated procedure for the evaluation of current structural health conditions in bridges consists in the comparison between estimated modal features from in-situ tests and numerical values. This strategy allows making informed decisions for existing bridge structures to ensure structural safety or serviceability. Free vibration tests are common in bridges monitoring since they allow a quick and cost-effective determination of dynamic information about the structure, using a sparse network of few sensors and avoid long-lasting monitoring campaigns. Exploiting an identification method based on a tuned version of Variational Mode Decomposition and an area-ratio based approach, modal parameters are determined from free vibration tests. This technique is applied to the dynamic identification of cables in a stay-cabled bridge assumed as case study: the obtained results prove reliability of the adopted method as a useful tool for objective dynamic identification purposes, with focus on the structural health conditions of bridges.

1 INTRODUCTION

Modal parameters are key structural properties in characterization of dynamic behaviour of constructions: the comparison between experimental values obtained from the identification process and theoretical ones represents a significant tool to investigate the state of health in an existing structure as well as to identify possible defects. Particularly in large-scale civil structures such as bridges, the dynamic characterization via free vibration tests is becoming quite popular: the advantages are the use of a temporary network made up of a limited number of sensors, the possibility of carrying out a complete monitoring campaign in a relatively short time frame and the cost effectiveness.

Li et al. (2014) estimated the modal damping ratios of the cables of a cable-stayed bridge from their free vibration response. Both Clemente et al. (1998) and Tomaszewicz et al. (2022) dealt with the dynamic identification of cable-stayed bridges using free vibrations produced by a truck moving over a step fixed on the paving.

The identification of modal parameters in a multi-degree-of-freedom structure may be carried out prior to selection of significant components from dynamic response: this can be achieved using adaptive decomposition methods.

This study presents the results of a monitoring campaign in which free vibration tests were performed on the cables of a stay-cable bridge to investigate their actual condition via dynamic identification. The single-degree-of-freedom modal components are isolated using a variational decomposition framework. Modal frequencies are compared with estimation obtained from practical formulas whereas estimated modal damping ratios are compared with the ones obtained from ambient vibration.

2 IDENTIFICATION PROCEDURE

In this section a procedure for modal identification of structures such as existing bridges based on free vibration tests is recalled. This methodology combines a tuned version of the Variational Mode Decomposition (VMD) to isolate each modal mono-component signal and its correspondent natural frequency with an area ratio-based approach. An important feature of the method is its automatic implementation which averts user's subjective choices in the selection of VMD parameters. The adopted method has already been tested on benchmark signals and existing deck bridges (Mazzeo et al. 2023) proving its reliability in the dynamic identification of modal parameters.

2.1 Tuned Variational Mode Decomposition

Variational Mode Decomposition algorithm (Dragomiretskiy et al. 2014) achieves an adaptive decomposition of a multi-component target signal considering a variational framework in which the bandwidth associated to each modal component, called Intrinsic Mode Function (IMF), is assessed looking for the optimal solution of a constrained variational problem.

The optimization process is carried out in the frequency domain: each mode is iteratively obtained as the signal produced by a narrow-band Wiener filter applied to the signal estimation residual of all other modes. The assessment of the bandwidth for each mode is carried out calculating the associated analytical signal via Hilbert-Huang Transform, shifting its spectrum to baseband due to multiplication for a proper exponential function and subsequently calculating the H_1 Gaussian smoothness of demodulated signal:

$$\mathbf{BW}_k = \left\| \partial_t \left\{ \left[\left(\delta(t) + \frac{j}{\pi t} \right) * v_k(t) \right] e^{-j\omega_k t} \right\} \right\|_2^2 \quad (1)$$

Based on these steps, the following constrained variational problem is obtained:

$$\min_{\substack{v_1(t), \dots, v_K(t) \\ \omega_1, \dots, \omega_K}} \left\{ \sum_{k=1}^K \left\| \partial_t \left[\left(\delta(t) + \frac{j}{\pi t} \right) * v_k(t) \right] e^{-j\omega_k t} \right\|_2^2 \right\} \text{ s.t. } \sum_{k=1}^K v_k(t) = v(t) \quad (2)$$

where ∂_t is the gradient operator and $\|\cdot\|_2$ the L^2 -norm operator. By using a quadratic penalty term and the Lagrange multipliers technique to enforce the constraints, the search for the solution of this variational problem leads to the following augmented Lagrangian function:

$$\begin{aligned} L(v_1(t), \dots, v_K(t), \omega_1, \dots, \omega_K, \lambda) = & \alpha \sum_{k=1}^K \left\| \partial_t \left[\left(\delta(t) + \frac{j}{\pi t} \right) * v_k(t) \right] e^{-j\omega_k t} \right\|_2^2 \\ & + \left\| v(t) - \sum_{k=1}^K v_k(t) \right\|_2^2 + \left\langle \lambda, v(t) - \sum_{k=1}^K v_k(t) \right\rangle \end{aligned}$$

where α is the quadratic penalty factor, λ is the Lagrangian multiplier and $\langle \cdot, \cdot \rangle$ is the L^2 -inner product. The solution of the governing constrained problem is thus equivalent to the evaluation of the saddle point of the augmented Lagrangian function. This can be achieved using alternating direction method of multipliers, which solves two parallel sub-optimization problems which provide an estimation of the k -th IMF $v_k(t)$ and the center frequency ω_k , the latter is correspondent to the modal frequency in the adopted identification framework.

The performance of the VMD technique is highly dependent on the proper tuning of two main parameters, namely the number of IMFs to be extracted K and the penalty factor α . Therefore, a suitable procedure for the choice of this parameter is implemented to significantly limit the subjectiveness of the results. This tuning method evaluates the optimal K and α

separately: the selection for number of modes K starts considering a range of possible values $\tilde{K} \in [K_{\min}, K_{\max}]$ and for each one of them exploits the mean correlation measure $\rho_{k,k+1}$ between each two consecutive sampled IMFs:

$$K = \underset{K_{\min} \leq \tilde{K} \leq K_{\max}}{\operatorname{arg\,min}} \left\{ \frac{1}{\tilde{K} - 1} \sum_{k=1}^{\tilde{K}-1} \rho_{k,k+1} \right\} \quad (4)$$

Repeating this procedure for each value of α in a fixed range $[\alpha_{\text{start}}, \alpha_{\text{end}}]$, a stabilization diagram is built from each couple (α, K) and the number of IMFs is sought in the range $[\alpha_{\min}, \alpha_{\max}] \subseteq [\alpha_{\text{start}}, \alpha_{\text{end}}]$ in which K remains stable.

The estimation of the optimal penalty factor starts calculating for each value of $\tilde{\alpha} \in [\alpha_{\min}, \alpha_{\max}]$ two parameters called Power spectrum information entropy $\text{PSIE}_k(\tilde{\alpha})$ and uncorrelation factor $\text{UC}_k(\tilde{\alpha})$ defined as in literature (Yang et al. 2020). The optimal value of the penalty factor is obtained as:

$$\alpha = \underset{\alpha_{\min} \leq \tilde{\alpha} \leq \alpha_{\max}}{\operatorname{arg\,min}} \{ \overline{\text{PSIE}}(\tilde{\alpha}) + \overline{\text{UC}}(\tilde{\alpha}) \} \quad (5)$$

where $\overline{\text{PSIE}}(\tilde{\alpha})$ and $\overline{\text{UC}}(\tilde{\alpha})$ represent the dimensionless averaged values of the two parameters with respect to the selected number of modes K .

2.2 Modal damping ratios estimation

For each modal component the correspondent modal damping ratio can be obtained using an area-based approach (Huang et al. 2007). Under the assumptions that the k -th modal component can be seen as the free vibration response of the correspondent k -th SDOF modal oscillator and that it has $2N_k+1$ zero-crossing points, it is possible to relate the modal damping ratio with the $2N_k$ areas $S_{i,k}$ enclosed between the response function and the time axis as follows:

$$\zeta_k = \frac{1}{\sqrt{1 + (2N_k\pi/A_k)^2}} \quad (6)$$

being A_k the area ratio evaluable with any quadrature method and defined as:

$$A_k = \ln \left[\frac{\sum_{i=1}^{N_k} S_{i,k}}{\sum_{i=N_k+1}^{2N_k} S_{i,k}} \right] \quad (7)$$

The advantage of using this method for damping estimation is due its robustness against the noise: the area evaluation is less affected from local distortions due to noise in the signal which on the contrary may significantly influence the estimation of local maxima used in traditional logarithmic decrement method.

3 CASE STUDY: BRIDGE OVER GARIGLIANO RIVER

The case study herein analysed is the cable-stayed bridge over the Garigliano river (see Figure 1), part of the highway infrastructures connecting the cities of Naples and Rome (Italy). The structure consists of two spans of equal length for a total of 180 m and the deck consists of precast multicell block girders in prestressed reinforced concrete assembled in situ with height 2.45 m and width 26.1 m (see Figure 2). Both spans are simply supported at one end and constrained to a central pylon at the other one.



Figure 1. Overview of cable-stayed bridge over Garigliano river.

Each span is sustained by 9 couples of cables, each couple is spaced 1.7 m. The cables and have a variable number of 0.6" galvanized sheathed high-strength prestressing steel strands, from 45 to 55, and a variable length from 23 m to 87.5 m. The pylon is made up of three parts: the first 5 m are in reinforced concrete with a linearly variable transversal section from 4.6 m x 2.5 m to 4 m x 2.5 m, the second part, from height 5 m to 10 m, is a steel box linearly variable up to a section of 2.9 m x 2.5 m, and the last part, from height 10 m to 25 m, has constant hollow section made of steel. The central pier on which the deck and the pylon are connected is 8.4 m high and it has a 10 m x 2.5 m reinforced concrete rectangular section with rounded corners with radius of 1.25 m.

A monitoring campaign was conducted to monitor the state of health of the structure cables and, because of their large number, a suitable solution consisted in free vibration tests which are less expensive and require a minimal equipment. For each stay-cable, the test setup consisted of two piezoelectric uniaxial accelerometer (sensitivity 10 V/g) positioned at a medium height of 3.8 m from the bridge deck extrados.

Each couple of accelerometers was mounted on both faces of a steel angle as in to record both horizontal and vertical accelerations. The steel angle was connected to the stay-cable using nylon tightening straps. The stay-cables were excited with an impulsive load applied to the bridge in its service conditions, i.e., concurrent with environmental vibrations due to wind and traffic in both directions. By the application of a vertical impulsive load, both the accelerations in vertical and horizontal direction were recorded and are herein labelled V/V and V/H respectively; similarly applying a horizontal impulsive load, the acceleration in the horizontal direction is labelled H/H whereas the one in vertical direction H/V.

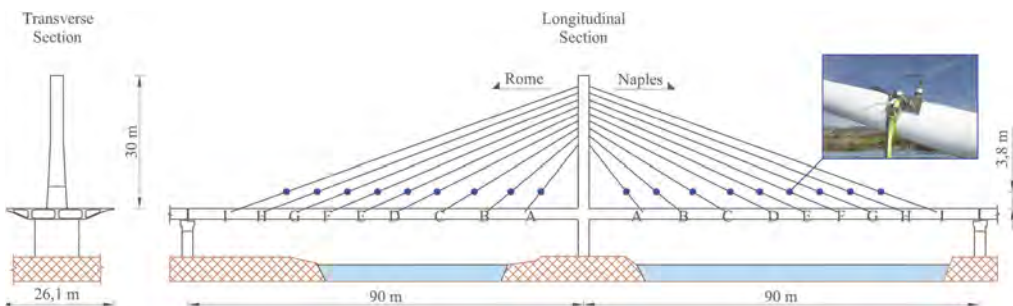


Figure 2. Bridge geometry and sensor layout of stay cables.

The selected ranges for VMD parameters are $K \in [2, 8]$ and $\alpha \in [1, 10000]$ respectively. In Figure 3, the IMFs retrieved for the stay cable B in Rome direction for the acceleration recording V/V are shown: the ideal number of IMFs is $K=3$ and the evaluation of the

quadratic penalty factor α must be executed in the narrower range $\alpha \in [1, 8500] \subset [1, 10000]$ and it leads to $\alpha = 76$.

An estimation of the natural frequencies is obtained by means of practical formulas which relates them to the correspondent cable force obtained under the assumptions that prestressing steel has a Young Modulus equal to 198,000 MPa, the linear weight for strands and PHED sheath are 1.305 kg/m and 5.68 kg/m respectively and the density of the grout filling equal is 1,440 kg/m³. The identified frequencies are compared with the obtained from practical formulas (Zui et al. 1996) for the first mode: data points focus on the quadrant bisector line showing a nice agreement between experimental and predicted values (see Figure 4). Predicted values of frequencies are slightly higher with respect to the experimental ones with differences under 7%. Missing outputs are dependent on the corruption of the related recordings.

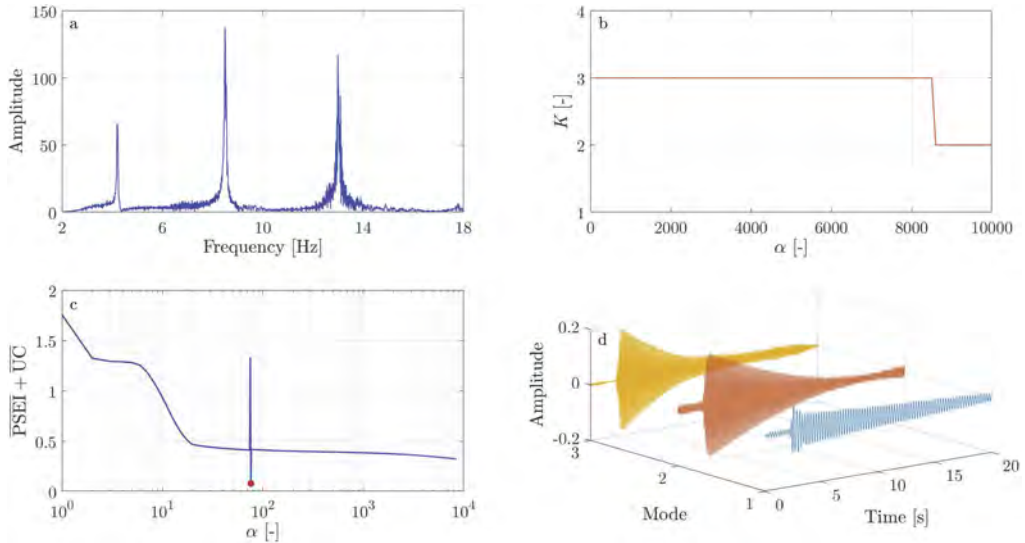


Figure 3. Elaborations on the signal V/V - Cable B in Rome direction: a) Fourier Transform, b) Stabilization diagram for K , c) Evaluation of optimal α and d) VMD of the signal with $K=3$ and $\alpha=76$.

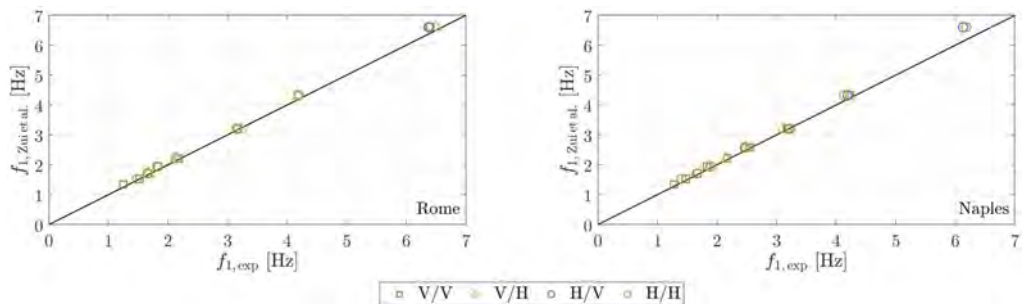


Figure 4. Comparison between experimental and predicted frequencies for the first mode of cables in both the road directions.

For each stay cable, the considered identification method also allows the estimation of modal damping ratios from the free vibration response (see Figure 5). All modal damping ratios fall within the range 0-0.8% with an average value of 0.25%; these results are consistent with literature studies on cable modal damping ratios in cable-stayed bridges (Chen et al. 2019). The estimations for the first mode are compared with results obtained interpreting

ambient vibration tests executed on the same cables by means of the Natural Excitation Technique (James III et al. 1993) in Figure 6: consistent values can be observed between the two set of results obtained from two kind of vibration test with limited scattering.

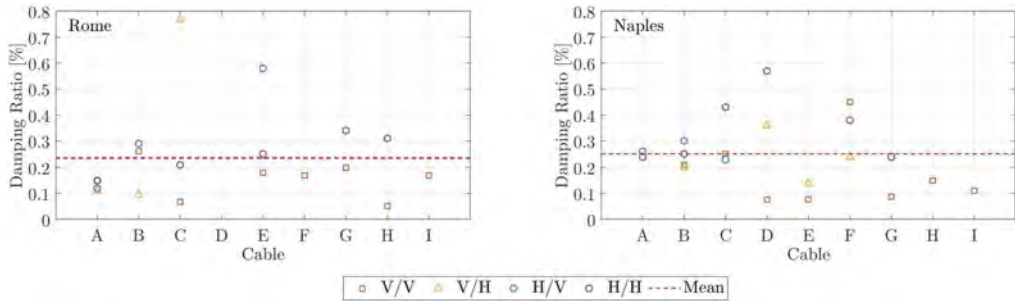


Figure 5. Identified Modal Damping Ratio for the first mode in both the road directions.

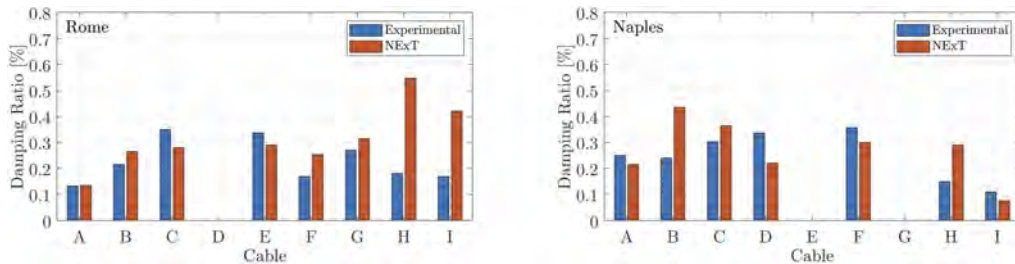


Figure 6. Comparison of modal damping ratios identified from free vibration tests (experimental) and ambient vibration tests (NExT).

4 CONCLUSIONS

In this contribution, the modal identification of cables in a stay-cabled bridge has been addressed. Using a tuned version of the VMD the modal acceleration components have been isolated and modal frequencies have been identified: comparing the latter to the ones obtained from theoretical formulations, good agreement has been achieved. Exploiting an area-ratio based approach, the modal damping ratio for the first mode of each cable has been evaluated. The estimations have been corroborated by the comparison with results from elaboration of ambient vibration data, showing good correspondence and reduced data scattering. The adopted decomposition method appears reliable also in case of cable-stayed bridges and the comparison between the parameters numerically identified and the theoretical ones may allow to make informed decisions for existing bridge structures in terms of eventual repair actions needed to ensure structural safety or serviceability.

REFERENCES

Chen, C.C., Wu, W.H., Yu, S.T. & Lai, G. 2019 Investigation of modal damping ratios for stay cables based on stochastic subspace identification with ambient vibration measurements. *Advances in Structural Engineering*, vol. 22, no. 16, pp. 3444–3460.

Clemente, P., Marulo, F., Lecce, L. & Bifulco, A. 1998. Experimental modal analysis of the Garigliano cable-stayed bridge. *Soil Dynamics and Earthquake Engineering*, vol. 17, no. 7-8, pp. 485–493.

Dragomireskiy, K. & Zosso, D. 2013. Variational mode decomposition. *IEEE Transactions on Signal Processing*, vol. 62, no. 3, pp. 531–544.

- Huang, F.L., Wang, X.M., Chen, Z.Q., He, X.H. & Ni, Y.Q. 2007. A new approach to identification of structural damping ratios. *Journal of Sound and Vibration*, vol. 303, no. 1-2, pp. 144–153.
- James III, G.H., Carne, T.G. & Lauffer, J.P. 1993. The natural excitation technique (NExT) for modal parameter extraction from operating wind turbines. *Tech. Rep., Sandia National Labs.* Albuquerque, NM (USA).
- Li, X.-l., Sum, L.-m., Cheng, W. & Xia, Y. 2014. Damping analysis on steel strand cables of a cable-stayed bridge based on field tests. In: *Proceedings of the 2014 World Congress on Advances in Civil, Environmental, and Materials Research*, Techno-Press.
- Mazzeo, M., De Domenico, D., Quaranta, G., Santoro, R. 2023. A Novel Procedure for Damping Ratio Identification from Free Vibration Tests with Application to Existing Bridge Decks. In: *European Workshop on Structural Health Monitoring. EWSHM 2022. Lecture Notes in Civil Engineering*, vol. 270. Springer, Cham.
- Tomaszkiewicz, K., Owerko, T. 2022. Estimation of the bridge damping decrement for in-situ recorded signal with unusual features. In: *Bridge Safety, Maintenance, Management, Life-Cycle, Resilience and Sustainability*, pp. 501–508, CRC Press.
- Yang, X.M., Yi, T.H., Qu, C.X., Li, H.N. & Liu, H. 2020. Modal identification of high-speed railway bridges through free-vibration detection. *Journal of Engineering Mechanics*, vol. 146, no. 9, p. 04020107.
- Zui, H., Shinke, T. & Namita, Y. 1996. Practical formulas for estimation of cable tension by vibration method. *Journal of Structural Engineering*, vol. 122, no. 6, pp. 651–656.

The effect of road roughness on vehicle-bridge interaction modeling

A. Aloisio & R. Alaggio

University of L'Aquila, L'Aquila, Italy

A. Contento & B. Briseghella

Fuzhou University, Fuzhou, China

ABSTRACT: The study of the bridge response under moving loads is commonly investigated with two alternative approaches. One approach represents the vehicle as a moving load, the other with sprung mass models. This study is aimed to compare the two approaches and evaluate the difference in their accuracy to assess if there are cases where vehicle bridge-interaction modelling (i.e. the use of sprung mass models) is needed to accurately estimate the bridge response. For this purpose, both a moving load model and a one degree of freedom sprung mass model have been implemented and used to compare the bridge response under different road roughness. The probabilistic distributions of two indicators, used to compare the bridge displacement responses in three roughness scenarios with variable velocity and different vehicle mass and dynamics, are derived through Montecarlo simulations. It is found that an increasing level of road roughness modelled according to ISO-8608 increases the differences between the predictions of the models.

1 INTRODUCTION

Vehicle-bridge interaction (VBI) problems were extensively studied for several reasons that include the growing interest in the safety assessment of infrastructures. Additionally, the interest in vibration-based approaches for structural health monitoring (SHM) of infrastructures further fed the research in VBI modelling.

Additionally VBI models can be either coupled or uncoupled. In the coupled models, the moving vehicle contributes to the bridge vibration, whereas in the uncoupled models vehicle dynamics does not affect the bridge response. Uncoupled models are often preferred due to their relatively simple implementation, reduced computational cost, and robustness against numerical instability. However, the assumptions of the uncoupled approach cannot always be acceptable. In many cases the accurate modelling of VBI is essential for precisely predicting fatigue phenomena occurring when a structure is subjected to repeated load cycles, like bridges under vehicular traffic. The accurate prediction of the fatigue life is fundamental for the structure's life-cycle assessment (LCA). Thus, VBI modelling is necessary component of the mathematical framework needed for the LCA of infrastructure.

To the authors' knowledge, a few papers are attempting to understand the trade-off between model complexity and accuracy in VBI problems (González et al., 2022). Additionally, several investigations lack experimental validation and focus on the modal parameters, i.e. estimating the time-variance of the bridge response in terms of instantaneous frequency, damping and mode shape. Experimental investigations are generally based on time-frequency analyses using vibration data in terms of velocity or acceleration (Li et al., 2022; Quqa et al., 2022). Recently, Gonzalez (González et al., 2022) attempted to quantify the modelling error in predicting the bridge response under moving vehicles using uncoupled methods. However, his attempt lacks experimental validation and focuses on a few scenarios.

Within this framework, this paper's ultimate goal is to clarify when the assumptions of the uncoupled model are reasonable or not and to highlight the role of road roughness in the differences between the two approaches. For this purpose, the authors used a moving load

model and a one degree of freedom sprung mass model to simulate the bridge response under the effect of a running vehicle and performed Montecarlo simulations varying three parameters describing the vehicle dynamics (velocity, mass and natural frequency) and the roughness level according to the ISO:8608. The outcomes of the analyses lead to a probabilistic model to describe the difference between the two modelling approaches. Since the accuracy of the two models depends on the quantity being predicted (e.g. use the midspan deflection to estimate the maximum load effect and the time-history of a dynamic system), the authors select two discrepancy indicators (i.e. error estimates): the relative variation in the maximum deflection and (ii) the modal assurance criterion. The former is relevant for safety problems, where the primary intent is to assess the maximum load effect on the structure. The latter is essential for those researches where the bridge time-history is involved in the analyses. The elements of novelty can be summarised in

1. estimating the error gap between coupled and uncoupled approaches using mathematical models validated against experimental results;
2. developing a computationally efficient Finite-Difference (FD) formulation of the VBI problem;
3. fitting the discrepancy indicators with suitable probability density functions that can be used to estimate the modelling error when using concentrated load models.

2 VEHICLE-BRIDGE INTERACTION MODEL

The randomness of the road surface roughness can be represented with a periodic modulated random process. In ISO-8608 (ISO/TC et al., 1995) specifications, road surface roughness and vehicle speed are related through the relation between velocity power spectral density (PSD) and displacement PSD. The general expression for the displacement PSD of the road surface roughness is $S_d(n) = S_d(n_0) \cdot (n/n_0)^{-a}$, where $n_0 = 0.1$ cycles/m is the reference spatial frequency, a is an exponent of the PSD, and n is the spatial frequency (cycles/m). The classification of the road roughness is based on a constant vehicle velocity PSD by taking $a = 2$. The road roughness profile can be generated through the following equation:

$$r(x) = \sum_{i=1}^Q d_i \cos(n_i x + \Theta_i). \quad (1)$$

In the equation, n_i is the i -th spatial frequency, Θ_i is the random phase angle, and d_i is the i -th amplitude computed as $d_i = \sqrt{2S_d(n)\Delta n}$ with Δn denoting the sampling interval of the spatial frequency.

The dynamic equilibrium equation of the vehicle mass m_v can be written as follows:

$$m_v(\ddot{w}_v + \ddot{r} + \ddot{w}_b) + c_v \dot{w}_v + k_v w_v = 0, \quad (2)$$

where m_v , c_v , and k_v are respectively the sprung mass, the damping coefficient, and the stiffness of the vehicle. The absolute displacement of the vehicle mass is written as the summation of three terms: w_v , r , and w_b . Namely, w_v indicates the relative displacement between the road surface and the center of gravity of the vehicle mass, r indicates the road roughness, and w_b is the beam deflection measured from the line axis of the bridge. The contact force due to the vehicle oscillation f_c does not include the weight of the sprung-mass system and can be written as

$$m_w(\ddot{r} + \ddot{w}_b) + f_c - c_v \dot{w}_v - k_v w_v = 0, \quad (3)$$

where m_w is the mass of the wheel.

The bridge can be described as an Euler-Bernoulli beam. The EB beam has a constant mass per unit length $\rho_c A_c$ (where ρ_c is the specific mass of concrete and A_c is the cross-section area of the beam) and A_c constant flexural rigidity $E_c I_c$ (where E_c is the Young's modulus of concrete and I_c the cross-section inertia of the beam). The vertical displacement $w_b(x, t)$ of the bridge is governed by the following partial differential equation (Fryba, 2013):

$$\rho_c A_c \ddot{w}_b(x, t) + E_c I_c w_{r,xxxx}(x, t) = \delta(x - ct)(f_c + m_w g + m_v g) \quad (4)$$

where δ is the Dirac delta. The left and right boundary conditions for a pinned-pinned beam are

$$\text{Left : } w_b(0, t) = 0 \quad w_{b,xx}(0, t) = 0; \quad \text{Right : } w_b(L, t) = 0 \quad w_{b,xx}(L, t) = 0. \quad (5)$$

The VBI equations (Equations 2 and 4) can be written in matrix form by discretizing the beam into n elements with a Δx length. The spatial discretization is obtained using the finite difference method that leads to the following coupled system of equations:

$$\begin{aligned} & \begin{bmatrix} \rho_c A_c \Delta x \mathbf{I} + m_w \delta \otimes \delta^T & \mathbf{0} \\ m_v \delta^T & m_v \end{bmatrix} \begin{Bmatrix} \dot{\mathbf{w}}_b(t) \\ \dot{\mathbf{w}}_v(t) \end{Bmatrix} + \begin{bmatrix} E_c I_c \mathbf{D}_4 & -\delta k_v \\ \mathbf{0} & k_v \end{bmatrix} \begin{Bmatrix} \mathbf{w}_b(t) \\ w_v(t) \end{Bmatrix} + \\ & + \begin{bmatrix} \mathbf{C} & -\delta c_v \\ \mathbf{0} & c_v \end{bmatrix} \begin{Bmatrix} \dot{\mathbf{w}}_b(t) \\ \dot{\mathbf{w}}_v(t) \end{Bmatrix} + \begin{Bmatrix} \delta[-m_v g + m_w(\ddot{r} - g)] \\ m_v \ddot{r}(t) \end{Bmatrix} = 0. \end{aligned} \quad (6)$$

In Equation 6, \mathbf{I} and $\mathbf{0}$ are the identity and null matrices, respectively, and $\mathbf{D}_4^{\{n \times n\}}$ is the approximate fourth matrix derivative. Additionally, δ is the discretization of the Dirac function, $\mathbf{w}_b(t)$ collects the vertical deflection of the bridge discretized in N segments, and \mathbf{C}_r is the damping matrix. The damping matrix is estimated using the Rayleigh approximation and is assumed proportional to the mass and stiffness matrices following the Rayleigh approach (Chopra, 1975). The i -th term of the discretized Dirac function (δ_i) is

$$\delta_i = \begin{cases} 1, & \text{if } i = \left[\frac{ct}{\Delta x} + 0.5 \right] \wedge i = 1 \\ \frac{|ct - i\Delta x|}{\Delta x}, & \text{if } i = \left[\frac{ct}{\Delta x} + 0.5 \right] \wedge i > 1 \\ 1 - \frac{|ct - i\Delta x|}{\Delta x}, & \text{if } i = \left[\frac{ct}{\Delta x} + 0.5 \right] - 1 \wedge i > 1 \\ 0, & \text{else} \end{cases}, \quad (7)$$

where $[\cdot]$ denotes the rounding function. Equation 6 can be solved using the Dormand-Prince method based on an explicit Runge-Kutta temporal discretization (Dormand and Prince, 1980).

3 EXPERIMENTAL TESTS AND MODEL CALIBRATION

The bridge span under investigation belongs to the Italian motorway network. It is a simply-supported, prestressed concrete girder. The girder has the trapezoidal cross-section shown in Figure 1. The cross-section is 2.3m high, with two cantilevered wings 3.85m wide, and prestressed by bonded post-tensioned tendons. A pair of piers, whose centre distance is about 40m, sustains each bridge span.

3.1 Experimental setups

The response of the considered bridge span is measured in terms of acceleration and displacement of the mid-span. The setup for the accelerations consists in two rows of seven equally-spaced Force Balance Accelerometers (FBA); the experimental equipment for the displacements consists of an easel supporting a laser sensor. The dynamic tests are carried out under the excitation of a moving two-axes vehicle with mass 3860kg (Jin et al., 2022). The modal parameters are estimated using the covariance-driven Stochastic Subspace Identification (SSI) method (Peeters and De Roeck, 2001). For each setup, the data are sampled at a 200Hz rate and used for SSI and subsequent modal analysis to derive eigenfrequencies, damping ratios, mode shapes, covariances of the modal parameters, and, as a consequence, the bending stiffness of the beam model.

3.2 Model calibration

In the analysis, the vehicle velocity and its characteristic in terms of mass and stiffness are assumed known, as well as the area of the cross section A_c , the weight per unit of volume of

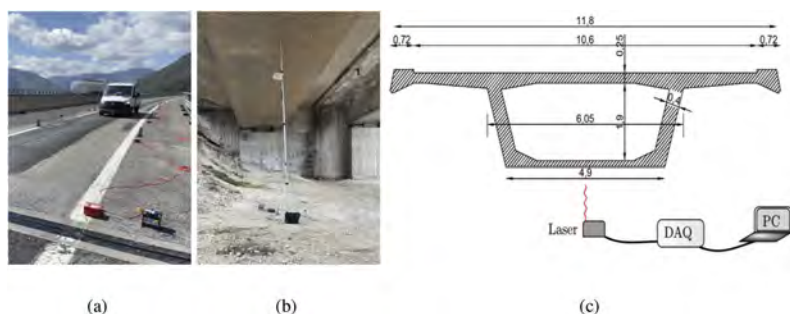


Figure 1. (a) View of the bridge with the accelerometers, view (b) and scheme (c) of the experimental setup.

concrete ρ_c , and the natural frequency of the first bending mode, estimated from output-only dynamic identification, are also used as input parameter to further constraint the optimization problem. The bridge spatial discretization is assumed equal to 0.2m, approximately equal to the wheel footprint, while the sampling frequency equal to 100Hz. The remaining unknown parameters of the VBI model are the bending stiffness EI , the equivalent viscous damping of the bridge ξ_b , and the roughness level $S_d(n_0)$. The viscous damping is included in the VBI model optimization because its dynamic identification could be unreliable due to its possible underestimation (Frizzarin et al., 2010). The authors follow a three-step approach for estimating the three unknown parameters:

1. the bending stiffness (EI) is estimated from the first bending mode of the considered bridge span;
2. the bridge damping (ξ_b) is estimated from experimental displacement response using the VBI model without road roughness;
3. the bridge roughness ($S_d(n_0)$) is estimated from experimental displacement response using the VBI model with road roughness.

The first mode closely resembles that of a pinned-pinned beam. Such bending mode can be reasonably used (in terms of mode shapes and natural frequencies) to estimate the bending stiffness EI of an equivalent beam model. To estimate EI , the authors solve a nonlinear least-squares problem (He et al., 2021) that which leads to find a global minimum of the objective function for $E \approx 1.575 \text{Nm}^2$.

Conversely, the experimental displacement data are used to calibrate the bridge damping and the road roughness. The calibration is performed by using a genetic optimization algorithm (Sirrotti et al., 2021). The genetic algorithm performs iteration of parameters with the goal of minimizing the integral of the difference between experimental and simulated displacement. As anticipated, the authors assume the value of the bending stiffness EI to further constrain the optimization problem that provided $\xi_b = 0.02$ and $S_d(n_0) = 2 \cdot 10^{-5}$ as optimum values of the parameters. The damping value is consistent with that of concrete structures, while the roughness level corresponds to a profile class A, according to the ISO:8608 classification.

Figure 2 plots the experimental displacement response of the bridge span against the predictions of the moving load (labelled load-smooth) and VBI models (labelled mass-smooth). The experimental data refer to the transit of a two-axes vehicle with a 3860kg mass, moving at constant velocity approximately equal to 80km/h. Such data reveal a significant noise level. However, the maximum beam deflection is low, and close to the sensor resolution ($\approx 10^{-2} \text{mm}$). The maximum deflection is approximately equal to 0.08mm. The model predictions are in good agreement with the experimental data, especially in the first part of the response and after the vehicle has crossed the bridge. Two significant aspects arise from the observation of Figure 2:

- in case of no or negligible roughness, there is no substantial difference between the VBI and moving load models. Therefore, the two responses are almost indistinguishable.
- even a minor level of road roughness (road profile A) leads to differences between the two models because the road roughness activates a VBI phenomenon, which is evident in the second part of the transit (shaded red rectangle). The VBI model (in red) can closely

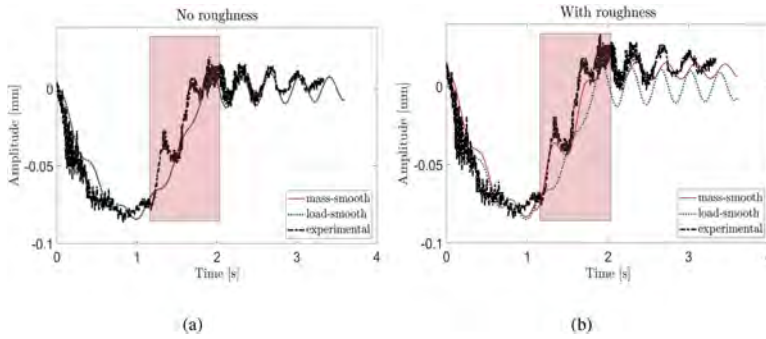


Figure 2. Experimental validation of the VBI and the concentrated force models in case of constant velocity (a) without and (b) with roughness ($S_d(n_0) = 2 \cdot 10^{-5}$).

follow the experimental data, especially the peaks arising in this part of the response. Conversely, the moving load model is not significantly influenced by the road roughness. The two models do not lead to noteworthy differences in maximum deflections, but the difference manifests as additional peaks due to the vehicle dynamics.

4 PARAMETRIC ANALYSES AND DISCREPANCY INDICATORS

A parametric analysis is performed to assess how the vehicle dynamics affects the bridge response under different roughness conditions. The parameters varied in the analyses are the vehicle velocity c , in the range 50–150 [km/h], the vehicle mass m_v , in the range 1–50 [ton], and the viscous damping coefficient of the vehicle, in the range 0.15–0.30. Such ranges reasonably represent the variation related to the variability of the vehicular traffic. Additionally, the values of $S_d(n_0)$ for the considered road roughness profiles according to ISO 8608 are $S_d(n_0) = 16 \cdot 10^{-6} \text{m}^3/\text{cycle}$ for Profile Class A, $S_d(n_0) = 64 \cdot 10^{-6} \text{m}^3/\text{cycle}$ for Profile Class B, and $S_d(n_0) = 256 \cdot 10^{-6} \text{m}^3/\text{cycle}$ for Profile Class C. The three-dimensional parameters' space is sampled following the Latin hypercube sampling scheme (Iman and Conover, 1979). The number of samples is set equal to 10000, which allowed to obtain a value of the COV ($< 0.1\%$). The authors used two discrepancy indicators to quantify the differences between the two predictions, one referred to the maximum displacement and the other to the cross-correlation, following the definition of the modal assurance criterion. Such indicators read

$$\delta = \frac{\max(|w_{vbi}|) - \max(|w_{cl}|)}{\max(|w_{cl}|)}; \text{MAC} = \frac{|w_{vbi} \cdot w_{cl}^T|^2}{(w_{vbi} \cdot w_{vbi}^T)(w_{cl} \cdot w_{cl}^T)}; \quad (8)$$

where w_{vbi} and w_{cl} collect the bridge responses from the VBI and concentrated load models. Given the roughness level, the road roughness is randomly varied in each run of the two models.

The results of the parametric analyses in terms of δ and MAC are first used to estimate the Sobol sensitivity indexes (Sobol, 1993).

Table 1. Sobol sensitivity indicators for the effects of weight, damping, and velocity of the vehicle.

Parameter	δ	MAC	δ	MAC	δ	MAC
	Class A		Class B		Class C	
Weight	0.53	0.67	0.63	0.57	0.50	0.49
Damping	0.25	0.25	0.26	0.27	0.23	0.44
Velocity	0.21	0.24	0.30	0.28	0.42	0.45

Table 1 shows the Sobol sensitivity indicators, which estimate the effects of the weight, damping, and velocity of the vehicle on δ and MAC for the three roughness classes. The weight has a dominant effect on values of δ and MAC obtained for the three road classes ($> 50\%$),

whereas, the effects of damping, and velocity are almost equal and range between 20 and 30%. Increments in the road roughness, from class A to C, cause an increment in the effects of damping and velocity on the chosen discrepancy indicators.

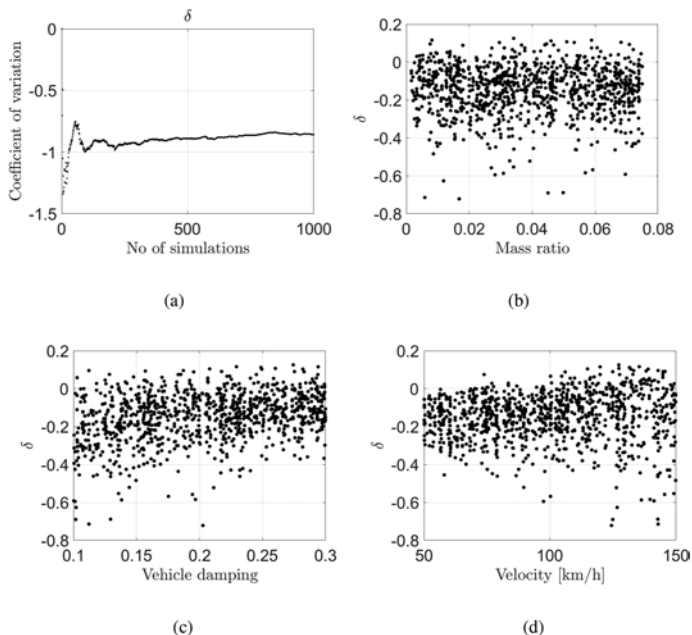


Figure 3. (a) Coefficient of variation of δ (Equation 8) as a function of the number of simulations. (b)-(d) Comparison between coupled and uncoupled models in terms of δ in Equation 8 as a function of the mass ratio, vehicle damping, velocity given a roughness class A.

Figure 2 shows the plots of δ as a function of the mass ratio (vehicle mass divided by the bridge mass), velocity and damping of the vehicle. Using these results the authors derived the probability density functions of the δ and MAC parameters as functions of the mass, damping, and velocity of the vehicle.

5 PROBABILISTIC DENSITY FUNCTIONS OF THE DISCREPANCY INDICATORS

The parameters δ and MAC obtained from the parametric analyses (Table 2) are fitted by suitable probability density functions. Specifically, it is assumed that

$$Z_i = T(Y_i) \sim N(\mu_i, \sigma_i^2), \quad (9)$$

where $T(\cdot)$ is the two-parameters Box-Cox transformation, $Y_i \in \{\delta, \text{MAC}\}$ are random variable associated to two parameters, and μ_i and σ_i^2 are unknown parameters ($i = \{\delta, \text{MAC}\}$). The posterior distribution of the parameters $\Theta = \{\mu_i, \sigma_i\}$ is derived by means of the Bayes' rule in closed form assuming a prior of the joint distribution of μ_i and σ_i^2 in the form $p(\Theta) \propto 1 \cdot \sigma_i^{-2}$. The two posterior marginal distributions are a t distribution for μ_i

$$\mu_i \sim t(\bar{z}_i, s_i^2/n, n-1), \quad (10)$$

and an Inverse-Gamma distribution for σ^2

$$\sigma^2 \sim IG((n-1)/2, s_i^2(n-1)/2). \quad (11)$$

In Equations (10) and (11), \bar{z}_i is the mean value of the realizations of the transformed random variables, s_i is the correspondent corrected sample standard deviation, and $n = 1000$ is the number of realizations of z_i . The values of \bar{z}_i and s_i^2 for the δ and MAC indicators related to each roughness class can be found in Table 5.

Table 2. Posterior statistics of the fitting probability density functions δ .

Roughness class	Descriptive parameter	λ_1	λ_2	Sample mean \bar{z}_i	Sample standard deviation s_i
A	δ	1.800	0.722	-0.344	0.006
	MAC	3.400	0.0	-0.057	0.001
B	δ	1.800	1.459	0.110	0.059
	MAC	1.700	0.000	-0.202	0.009
C	δ	1.800	3.086	1.780	0.607
	MAC	1.700	0.000	-0.622	0.065

6 ANALYSIS OF THE RESULTS

Figure 4 shows the histogram plots of the δ and MAC functions. The road roughness plays a crucial role in magnifying the VBI effects because it activates the vehicle dynamics, which interacts with the bridge significantly, especially for frequency ratios close to 1. Consequently, an increase in road roughness entails increasing the difference between the VBI and moving load models. The moving load model is not conservative: the percentage of underestimation of the beam deflection rises from nearly 14% to almost 90% as the road roughness increases from Class A to Class C. Such results shows that there are cases, and in particular those with high road roughness, where the effects of VBI cannot be neglected. Consequently, to use moving load models, which are usually easier to implement, it is necessary to separately account for the additional effect of VBI that can be estimated using the fitted probability density functions of δ .

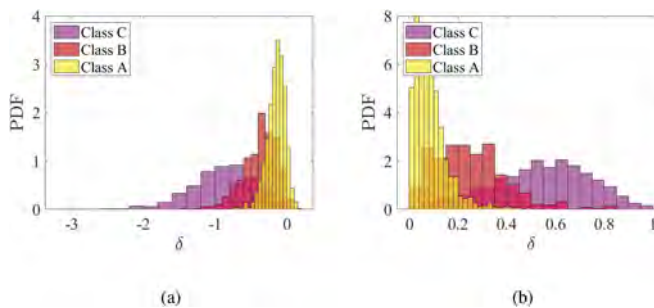


Figure 4. Histograms of δ and 1-MAC for the considered roughness classes.

In mid-span bridges, like the one considered in this paper, especially those belonging to high-level road networks, the road roughness belongs to class A and the increase of deflection due to VBI is, on average, 14%. In design, the potential underestimation of the load effects due to moving load models is compensated by including safety factors and load values corresponding to high fractiles of given probability distributions according to national and international standards.

7 CONCLUSIONS

This paper quantifies the effect of road roughness on vehicle bridge interaction (VBI) in a mid-span prestressed concrete bridge response. The bridge is modelled as a pinned-pinned Euler

Bernoulli beam, while two vehicle models are compared to simulate the vehicle transit: a concentrated load and a sprung-mass model. The first model does not include the mutual interaction between the bridge and the vehicle dynamic. It is used as a reference model to estimate the modelling error related to the lack of VBI effects. The differences between the two models are quantified in terms of relative error (δ) and correlation (MAC) between time histories. The governing equations are solved numerically after temporal and spatial discretization. It is found that the roughness triggers VBI phenomena and leads to higher discrepancies between the VBI and load models. Averagely, the load model underestimates the load effect by 14%, 37% and 90% in roughness classes A, B, and C, respectively. Future research papers will extend this study to different bridge typologies by varying the frequency ratio, i.e. the ratio between the vehicle and bridge natural frequency and more detailed VBI models. Additionally, the authors will extend the analyses further to include the effect of roughness in VBI due to vehicle braking.

REFERENCES

- Aloisio, A., Pasca, D. P., Alaggio, R., and Fragiaco, M. (2020). Bayesian estimate of the elastic modulus of concrete box girders from dynamic identification: A statistical framework for the a24 motorway in Italy. *Structure and Infrastructure Engineering*, pages 1–13.
- Chopra, A. K. (1975). Dynamics of structures.
- Dormand, J. R. and Prince, P. J. (1980). A family of embedded runge-kutta formulae. *Journal of computational and applied mathematics*, 6(1):19–26.
- Frizzarin, M., Feng, M. Q., Franchetti, P., Soyoz, S., and Modena, C. (2010). Damage detection based on damping analysis of ambient vibration data. *Structural Control and Health Monitoring*, 17(4):368–385.
- Fryba, L. (2013). *Vibration of solids and structures under moving loads*, volume 1. Springer Science & Business Media.
- González, A., Covián, E., and Casero, M. (2022). Verifying the suitability of uncoupled numerical methods for solving vehicle-bridge interaction problems. *Structure and Infrastructure Engineering*, pages 1–18.
- He, L., Castoro, C., Aloisio, A., Zhang, Z., Marano, G. C., Gregori, A., Deng, C., and Briseghella, B. (2021). Dynamic assessment, fe modelling and parametric updating of a butterfly-arch stress-ribbon pedestrian bridge. *Structure and Infrastructure Engineering*, pages 1–12.
- Iman, R. L. and Conover, W. J. (1979). The use of the rank transform in regression. *Technometrics*, 21(4):499–509.
- ISO/TC, T. C., Vibration, M., Measurement, S. S. S., of Mechanical Vibration, E., and as Applied to Machines, S. (1995). *Mechanical Vibration—Road Surface Profiles—Reporting of Measured Data*, volume 8608. International Organization for Standardization.
- Jin, N., Dertimanis, V. K., Chatzi, E. N., Dimitrakopoulos, E. G., and Katafygiotis, L. S. (2022). Sub-space identification of bridge dynamics via traversing vehicle measurements. *Journal of Sound and Vibration*, page 116690.
- Li, H., Wang, T., and Wu, G. (2022). A bayesian deep learning approach for random vibration analysis of bridges subjected to vehicle dynamic interaction. *Mechanical Systems and Signal Processing*, 170:108799.
- Lotfi, B. and Huang, L. (2016). An approach for velocity and position estimation through acceleration measurements. *Measurement*, 90:242–249.
- Peeters, B. and De Roeck, G. (2001). Stochastic system identification for operational modal analysis: a review. *Journal of Dynamic Systems, Measurement, and Control*, 123(4):659–667.
- Quqa, S., Giordano, P. F., and Limongelli, M. P. (2022). Shared micromobility-driven modal identification of urban bridges. *Automation in Construction*, 134:104048.
- Sirotti, S., Pellicciari, M., Di Trapani, F., Briseghella, B., Carlo Marano, G., Nuti, C., and Tarantino, A. M. (2021). Development and validation of new bouc-wen data-driven hysteresis model for masonry infilled rc frames. *Journal of Engineering Mechanics*, 147(11):04021092.
- Skolnik, D. A. and Wallace, J. W. (2010). Critical assessment of interstory drift measurements. *Journal of structural engineering*, 136(12):1574–1584.
- Sobol, I. M. (1993). Sensitivity estimates for nonlinear mathematical models. *Mathematical modelling and computational experiments*, 1(4):407–414.

Influence of different debonding gap types on mechanical performance of axially compressed CFST stub columns with same debonding arc-length ratio

J.Q. Xue, J.P. Huang, L.Q. He, B. Briseghella & A. Contento

College of Civil Engineering, Fuzhou University, Fuzhou, China

Joint International Research Laboratory of Deterioration and Control of Coastal and Marine Infrastructures and Materials, Fuzhou University, Fuzhou, China

ABSTRACT: The mechanical properties of concrete-filled steel tubular (CFST) members are influenced by the possible debonding gap between the steel tube and concrete core. To investigate this phenomenon, finite element models (FEMs) of the CFST columns with different debonding types, such as the circumferential debonding gap (CDG) and spherical-cap debonding gap (SDG), were established by using ABAQUS. The accuracy of the FEMs was verified comparing the obtained results with experimental ones. The verified FEMs were used to analyze the influence of different debonding types on the mechanical performance of the axially compressed CFST stub columns with the same debonding arc-length ratio (R_D). The results showed that with an increase in R_D , the ultimate load-bearing capacity (N_u) of CFST columns decreased. However, a critical R_D (R_{D-cr}) was found, in fact when the R_D was less than or equals to the R_{D-cr} , the influence of different debonding types on the N_u and failure modes of CFST columns were basically the same. When the R_D was larger than the R_{D-cr} , with an increase in R_D , the N_u of SDG CFST columns decreased linearly, however, the N_u of CDG CFST columns decreased nonlinearly with gradually reduced decrease rates. Finally, it was found that the overall bending, inward and outward buckling in SDG CFST columns were more serious than those in CDG CFST columns.

1 INTRODUCTION

According to the inspections made in arch bridges, debonding gaps can be found between the steel tube and concrete core, which can weaken the combined effect of two materials in CFST (concrete-filled steel tube) structures (Han et al. 2016, Shen et al. 2022, Xue et al. 2010, 2012). Two different types of debonding gaps could be found, which are the circumferential debonding gap (CDG) (Figure 1a) and spherical-cap debonding gap (SDG) (Figure 1b) (Contento et al. 2022, Han et al. 2016, Shen et al. 2022, Xue et al. 2021a).

The main parameters of CDG or SDG are shown in Figures 1a, b, respectively, including the debonding thickness (T_D : T_{CDG} or T_{SDG}), debonding arc-length ratio (R_D : R_{CDG} or R_{SDG}) and debonding length (L_D : L_{CDG} or L_{SDG}). T_{CDG} or T_{SDG} is the maximum distance between the outer surface of the concrete core and the inner surface of the steel tube within the range of CDG or SDG. R_{CDG} or R_{SDG} is the ratio of the arc-length of CDG or SDG to the perimeter of the section ($\theta_{CDG}/2\pi$ or $\theta_{SDG}/2\pi$), where the θ_{CDG} or θ_{SDG} is the angle of CDG or SDG. L_{CDG} or L_{SDG} is the length of CDG or SDG along the direction of the specimen length (L).

Some experimental tests done to investigate the influence of CDG on the mechanical performance of CFST columns have been carried out by choosing the R_{CDG} as the key parameter ($R_{CDG} = 0, 0.25, 0.5$ and 0.75 (Xue et al. 2012), $R_{CDG} = 0$ and 0.25 (Xue et al. 2020, 2021b), $R_{CDG} = 0$ and 0.5 (Shao et al. 2018), $R_{CDG} = 0, 0.5$ and 1 (Xie. 2018), and $R_{CDG} = 0$ and 1 (Liao et al. 2011, Han et al. 2016)). It can be found that, with an increase in R_{CDG} , the ultimate load-bearing capacity (N_u) of CFST columns decreased, and the influence of R_{CDG} on the N_u

also decreased. Regarding the failure mode, with an increase in R_{CDG} , the number of local buckling in the range with debonding gap (DG range) increased, the outward local buckling in the range without debonding gap (NDG range) at the mid-height and the elephant-foot shaped buckling near both ends were more obvious (Liao et al. 2011, Han et al. 2016, Xue et al. 2012).

Experimental tests on the influence of SDG on the mechanical performance of CFST columns have been also carried out by choosing the gap ratio of SDG ($\chi_{SDG} = T_{SDG}/D$) as the key parameter. It can be concluded that, with an increase in χ_{SDG} , the N_u of CFST columns linearly decreased. With an increase in χ_{SDG} , the axially compressed CFST columns exhibited clearly local buckling in DG range at failure, and the number of outward local buckling increased at the mid-height; the failure mode of the eccentrically compressed CFST columns changed from inward bending to wavy inward local buckling in DG range. In the literature, there is no research on the influence of R_{SDG} on the mechanical performance of CFST columns.

The influence of CDG or SDG on the mechanical performance of CFST stub columns was analyzed separately in some references (Han et al. 2016, Liao et al. 2011, Shen et al. 2022, Xue et al. 2021). However, the results of CDG or SDG were not compared with each other in the same research. The influence of different debonding gap types on mechanical performance of axially compressed CFST stub columns with the same debonding area was studied by Xue et al. (2022). The results showed that the mechanical performance of CDG or SDG CFST columns with the same debonding area were different.

It is difficult to measure the T_D in real applications. The most accurate detection technology for the T_D is to drill holes on the steel tube, which may damage the steel tube. The knocking method is a nondestructive detection method which can be used to measure the approximate range of debonding gaps to calculate the R_D . Therefore, the R_D should be considered as the key parameter in CFST columns with CDG or SDG. However, there is few research on the influence of different debonding gap types on mechanical performance of axially compressed CFST stub columns with the same R_D based on the knowledge of authors. In this paper, the influence of CDG or SDG on the N_u and failure modes of CFST stub columns with the same R_D were analyzed.

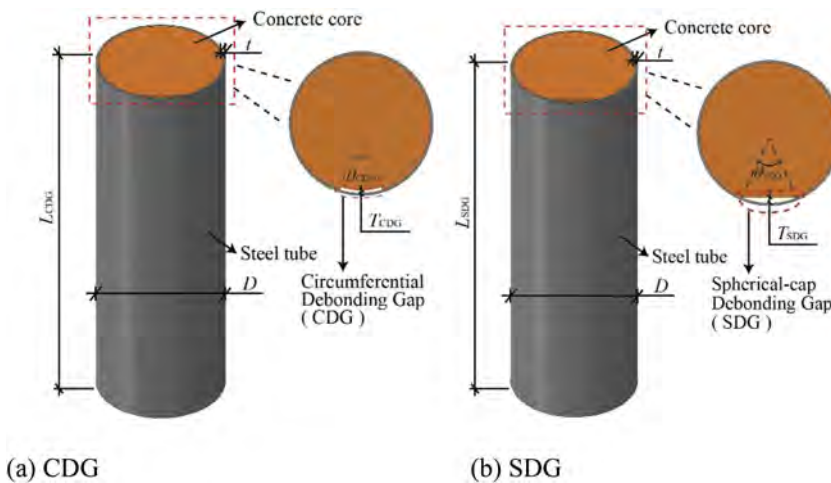


Figure 1. Parameters of debonding gaps.

2 FINITE ELEMENT SIMULATION

2.1 Finite element modelling

The steel tube was simulated by shell elements (S4R). The core concrete was simulated by solid elements (C3D8R). The end plates were simulated by discrete rigid elements (R3D4).

The steel tube was simulated by an elastic-plastic model using a stress-strain relation that consists of five stages with Von Mises yield criterion (Han et al. 2007). The damage plasticity model

was used for modelling concrete by using the equivalent stress-strain model proposed by (Han et al. 2007). For concrete in tension, the tensile softening behaviour was set by using the fracture energy model specifying the post failure stress as a tabular function of cracking displacement.

Both the bond and friction actions were considered in the interface modeling between the steel tube and concrete core. For the interface of the cross-sectional area in NDG range, the normal behaviour was simulated with hard contact; the friction coefficient was taken as 0.6 (Xue et al 2022). For the cross-sectional area in DG range (CDG or SDG shown in Figures 1a, b, respectively), both normal contact pressure and tangential shear stress were taken as zero at the beginning. When the inner surface of the steel tube contacted with the outer surface of the concrete core due to the inward buckling in the steel tube, the normal and tangent behaviours of the interface was simulated as the same as the interface of the cross-sectional area in NDG range.

The loading history was applied by using vertical downward displacement in the z-axis at the top end plate, as illustrated in Figure 2.

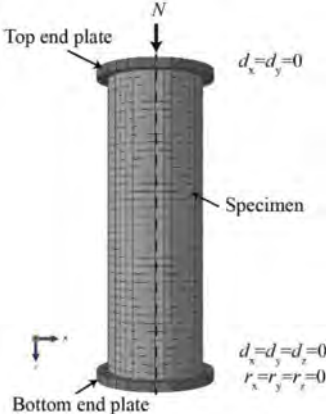


Figure 2. Load applications and boundary conditions.

2.2 Verification of finite element models

The FEMs of CDG and SDG CFST stub columns information were listed in Table 1.

3 INFLUENCE OF DIFFERENT DEBONDING GAP TYPES WITH SAME RD

3.1 Parameters selection

According to GB 50923-2013 (MOHURD 2013), when the R_{CDG} is larger than 0.2 or the T_{CDG} is larger than 3 mm, it is recommended to drill holes on the steel tube in DG range and grout. Therefore, in this research the maximum R_D was set at 0.2 and T_{CDG} was set as 3 mm. T_{SDG} was changed from 0 to 21 mm with an increment of 1 mm, and the corresponding χ_{SDG} changed from 0 to 9.1%. The corresponding R_{SDG} could be calculated according to the known T_{SDG} . The D of 219 mm, t of 4 mm, L of 657 mm were chosen. The cross-sections of SDG and CDG CFST columns with $R_{SDG} = R_{CDG}$ were shown in Figure 3. For the material properties of steel, a yield strength (f_y) of 345 MPa. For the material properties of concrete, a characteristic strength (f_{ck}) of 32.4 MPa, cylinder strength (f'_c) of 41.5 MPa.

3.2 Ultimate load-bearing capacity

In order to understand the influence of debonding gap on N_u , a reduction coefficient of N_u ($K_D = N_{u-D}/N_{u-N}$) was defined (Xue et al. 2012). The N_{u-D} was the N_u of specimens with debonding gap (CDG or SDG specimen) and N_{u-N} was the N_u of specimen without debonding gap (NDG specimen).

Table 1. Experimental and numerical results of CFST stub columns with CDG or SDG.

Debonding gap type	Literature	Label	N_u (kN)		
			N_{u-EXP}	N_{u-FEM}	N_{u-FEM}/N_{u-EXP}
CDG	Xue et al. (2012)	N3-0-A	2647	2705	1.02
		D3-1-A	2433	2431	0.99
		D3-2-A	2306	2358	1.02
		D3-3-A	2281	2345	1.02
		N4-0-A	2896	2965	1.02
		D4-1-A	2602	2625	1.00
		D4-2-A	2538	2554	1.00
		D4-3-A	2503	2532	1.01
	Han et al. (2016)	N-1	1559	1428	0.92
		N-2	1544		0.92
		C1.1-1	1143	1164	1.02
		C1.1-2	1113		1.05
SDG	Liang (2008)	PX-0-0	3400	3385	0.99
		PX-0-2	3130	3010	1.04
		PX-0-5	3010	3022	1.00
	Guo et al. (2020)	A0C0	5582	5809	1.04
		A0C6.42	5476	5236	0.96
	Zhang et al. (2019)	C0-0-0a	1779	1708	0.96
		C0-0-0b	1722		0.99
		CS-6-0a	1569	1467	0.93
		CS-6-0b	1518		0.97

The N_u obtained by experimental tests (N_{u-EXP}) and FEMs (N_{u-FEM}) were compared, as listed in Table 1. The mean value of N_{u-FEM}/N_{u-EXP} was 1.001 and the standard deviation was 0.045. Therefore, the finite element simulation method could be used to simulate the mechanical performance of CDG and SDG CFST stub columns.

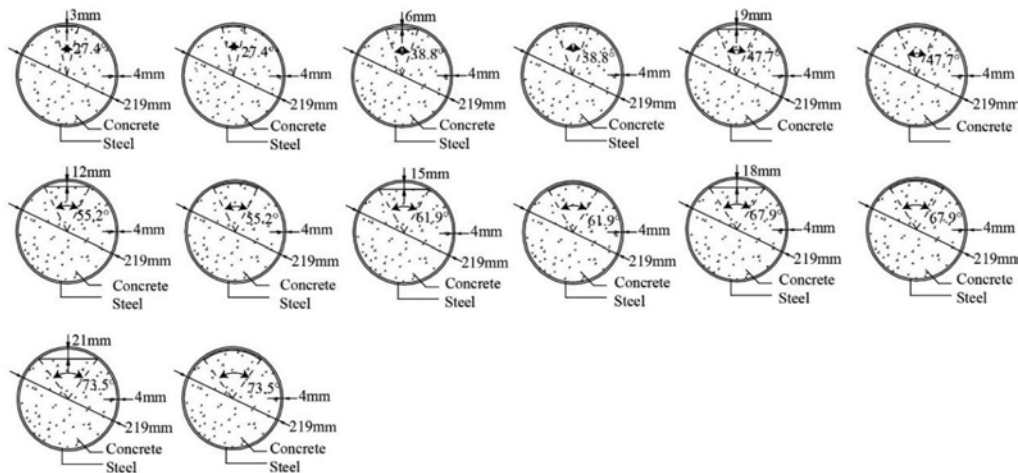


Figure 3. Cross-sections of SDG and CDG specimens with same R_D .

The influence of different debonding types with the same R_D on the N_u , K_D and the decrease rate of K_D are shown in Figure 4. It can be found that with an increase in R_D , the N_u and K_D of CDG or SDG specimens decreased. A critical R_D (R_{D-cr}) (0.12) can be found. When $R_D \leq R_{D-cr}$, with an increase in R_D , the influence of different debonding types on N_u and K_D was negligible, and the minimum K_D was 0.94. When $R_D > R_{D-cr}$, with an increase in

R_D , the influence of different debonding types on N_u and K_D was different; the N_u and K_D of SDG specimens decreased linearly, however, the N_u and K_D of CDG specimens decreased nonlinearly with gradually reduced decrease rates, as shown in Figure 4a. When $R_D = 0.2$, for CDG specimen, the N_u decreased from 3005 kN to 2674 kN and the K_D decreased to 0.89; for SDG specimen, the N_u decreased from 3005 kN to 2597 kN and the K_D decreased to 0.86. With an increase in R_D , the decrease rate of K_D for CDG or SDG specimens increased firstly until the R_D reached 0.09 and the maximum decrease rate of K_D was 0.014; when $R_D > 0.09$, the decrease rate of K_D for CDG or SDG specimens decreased, as showed in Figure 4b, the decrease ratio of K_D of CDG specimen reduced faster than that of SDG specimen.

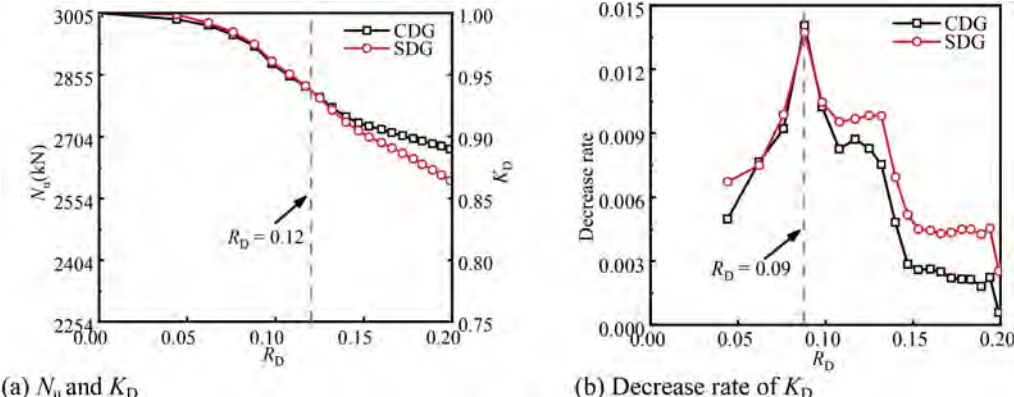


Figure 4. Influence of different debonding gap types on N_u , K_D , and decrease rate of K_D .

3.3 Axial load-axial displacement curves

The comparisons of the axial load (N)-axial displacement (Δ) relationship curves of different NDG or DG specimens (CDG and SDG specimens) are shown in Figure 5. It can be found that when $R_D = 0.12$, the influence of different debonding gap types on the N_{u-D} and the curves was negligible. When $R_D = 0.2$, the difference of $N-\Delta$ relationship curves of CDG or SDG specimens was the descending stage after N_{u-D} . For CDG specimen, the N decreased until nearly $A_s f_y + A_c f_c'$; for SDG specimen, the descending branch of the $N-\Delta$ relationship curves was longer than that of CDG specimen, and the N decreased to a value less than $A_s f_y + A_c f_c'$. It is because even the R_D was the same (0.2), the T_{CDG} (3 mm) was less than the T_{SDG} (20 mm). Therefore, the inward buckling in CDG specimen can easier let the steel tube and concrete core in DG range contact and provide contact stress to partial concrete core in DG range from the steel tube than that of SDG specimen.

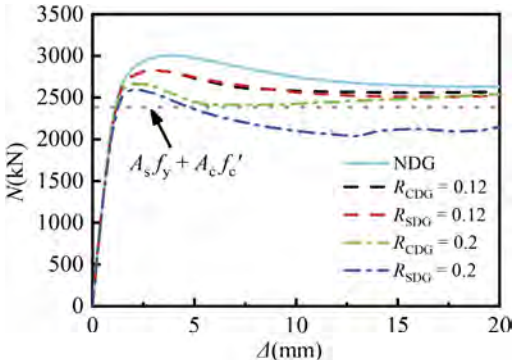


Figure 5. Comparisons of $N-\Delta$ relationship curves of NDG or different DG specimens.

3.4 Failure mode

The CDG or SDG range and NDG range in the cross-section of the specimen were defined in Figure 6.

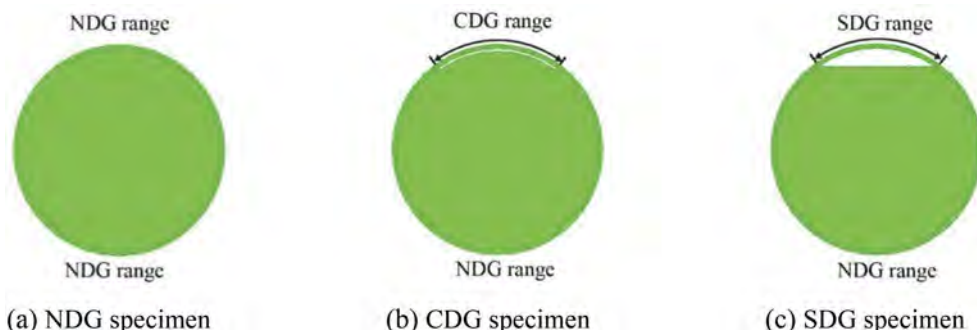


Figure 6. Debonding or non-debonding ranges in cross-section.

The failure modes of axially compressed CDG or SDG CFST stub columns with the same R_D were showed in Figure 7. When $R_D = 0.12$, the inward buckling in DG range (CDG and SDG range), overall bending in NDG range, and lightly elephant-foot shape buckling at both ends were observed in CDG or SDG specimens, as shown in Figures 7a, b. When $R_D = 0.2$, the overall bending in NDG range and elephant-foot shape buckling at both ends can be observed in CDG or SDG specimens; however, in DG range, the inward buckling was observed in CDG specimen, while wavy inward and outward local buckling was observed in SDG specimen, as shown in Figures 7c, d.

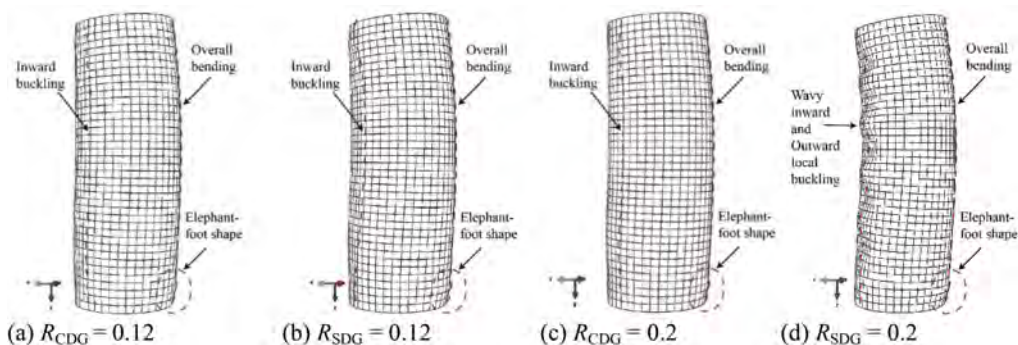


Figure 7. Failure modes of SDG and CDG specimens with same R_D .

The lateral deflection (U) curves along the L of different specimens corresponding to N_u were illustrated in Figures 8a, c. The $R_D = 0.12$, $R_D = 0.2$ and NDG specimens were compared. The U away from the center of the specimen was defined as the positive and the U towards the center of the specimen was defined as the negative. The NDG and DG range in the specimen were illustrated in Figure 8b, where the NDG range is in the right and the DG range (DG specimen) or NDG range (NDG specimen) is in the left.

By comparing the U of DG specimens and NDG specimen, the overall bending toward to DG range can be found in DG specimen, and the outward buckling can be found in NDG specimen.

By comparing the U at the $L/2$ in DG range ($U_{L/2-D}$) of different specimens (Figure 8a), it could be found that when the R_{CDG} increased from 0.12 to 0.2, the $U_{L/2-D}$ decreased from 0.66 to 0.51 mm (by 0.15 mm). When the R_{SDG} increased from 0.12 to 0.2, the $U_{L/2-D}$ slightly increased from 0.65 to 0.70 mm (by 0.05 mm). When $R_D = 0.12$, the $U_{L/2-D}$ of CDG or SDG specimens

were nearly the same, therefore, the influence of different debonding gap types on the $U_{L/2-D}$ is small. When $R_D = 0.2$, the $U_{L/2-D}$ of CDG specimen was smaller than that of SDG specimen, it is because that the inward buckling in SDG specimen was more serious than that in CDG specimen.

By comparing the U at the $L/2$ in NDG range ($U_{L/2-N}$) of different specimens (Figure 8c), it could be found that with an increase in R_D , the $U_{L/2-N}$ decreased. When the R_{CDG} increased from 0.12 to 0.2, the $U_{L/2-N}$ decreased from 0.65 to 0.35 mm (by 0.3 mm). When the R_{SDG} increased from 0.12 to 0.2, the $U_{L/2-N}$ slightly decreased from 0.64 to 0.53 mm (by 0.11 mm). When $R_D = 0.12$, the $U_{L/2-N}$ of CDG or SDG specimens were nearly the same, therefore, the influence of different debonding gap types on the $U_{L/2-N}$ was small. When $R_D = 0.2$, the $U_{L/2-N}$ of CDG specimen was smaller than that of SDG specimens, therefore, the overall bending in SDG specimen was more serious than that in CDG specimen.

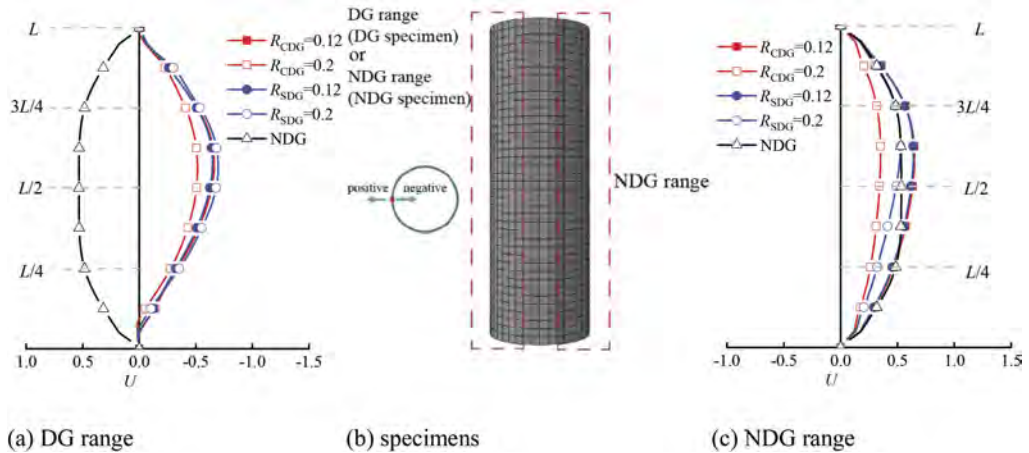


Figure 8. Lateral deflections corresponding to N_u .

4 CONCLUSIONS

Based on the finite element analyses, the following conclusions can be drawn:

- (1) With an increase in debonding parameters, the ultimate load-bearing capacity of axially compressed CFST stub columns decreased. The critical value of debonding arc-length ratio could be obtained. When the debonding arc-length ratio was less than the critical value (0.12), the influence of different debonding types on load bearing capacity was negligible. When the debonding arc-length ratio was greater than the critical value (0.12), the load bearing capacity of SDG specimen decreased linearly, however, CDG specimen decreased nonlinearly with gradually reduced decrease rates.
- (2) When the debonding arc-length ratio was 0.12, the influence of different debonding gap types on the load-displacement curve was negligible. When the debonding arc-length was 0.2, the descending stage after N_u in SDG specimen was longer than CDG specimen.
- (3) When the debonding arc-length ratio was less than the critical value (0.12), the influence of different debonding gap types on the failure mode was negligible. The failure modes of steel tubes shows that the inward buckling in debonding range, and overall bending in non-debonding range. When the debonding arc-length ratio reached 0.2, the failure mode had no obvious change in CDG specimen, but the wavy inward and outward local buckling could be observed in SDG specimen.
- (4) When the debonding arc-length ratio was less than the critical value (0.12), the influence of different debonding gap types on the lateral deflections was negligible. However, when debonding arc-length ratio was 0.2, both inward buckling in DG range and overall bending in NDG range of SDG was more serious than CDG, wavy inward and outward local buckling could be observed in DG range of SDG specimen.

- (5) The constraint effect between steel tube and concrete was the key to influence the ultimate bearing capacity of CFST axially compresses stub columns. The next step of the research is to analyze the influence of different debonding types on the constraint effect between steel tube and concrete.

ACKNOWLEDGEMENTS

This research was supported by the National Natural Science Foundation of China (grant numbers 51508103 and 51778148), the Open Project of Fujian Provincial Key Laboratory on Multi-Disasters Prevention and Mitigation in Civil Engineering (MPMC-2022-4) and the Open Project Fund of the Sustainable and Innovative Bridge Engineering Research Center of Fujian Province University, Grant No. SIBERC 202203.

REFERENCES

- Chen, S.M. & Zhang, H.F. 2012. Numerical analysis of the axially loaded concrete filled steel tube columns with debonding separation at the steel-concrete interface. *Steel Composite Structures* 13(3): 277–293.
- Contento, A., Aloisio, A., Xue, J.Q., Quaranta, G., Briseghella, B. & Gardoni, P. 2022. Probabilistic axial capacity model for concrete-filled steel tubes accounting for load eccentricity and debonding. *Engineering Structures* 268: 114730.
- Guo, C. & Lu, Z. 2020. Air void and cap gap composite defects of concrete-filled steel-tube arch bridge transverse brace. *Journal of Performance of Constructed Facilities* 34(4): 04020073.
- Han, L.H., Ye, Y. & Liao, F.Y. 2016. Effects of core concrete initial imperfection on performance of eccentrically loaded CFST columns. *Journal of Structural Engineering* 142(12): 04016132.
- Liang, K.F. 2008. *Effect of debonding on mechanical properties of concrete-filled steel tube*. Changsha: Hu'nan University.
- Liao, F.Y., Han, L.H. & He, S.H. 2011. Behavior of CFST short column and beam with initial concrete imperfection: Experiments. *Journal of Constructional Steel Research* 67(12): 1922–1935.
- Liao, F.Y., Han, L.H. & He, S.H. 2011. Behavior of CFST stub column with initial concrete imperfection: Analysis and calculations. *Thin-Walled Structures* 70:57–69.
- Ministry of Housing and Urban-Rural Development of the People's Republic of China (MOHURD). 2013. *Technical specification for concrete-filled steel tube arch bridges*. Beijing: China Planning Press.
- Schnabl, S. & Planinc, I. 2018. Circumferential gap and partial debonding effects on buckling loads and modes of slender CFST circular columns. *Acta Mechanica* 230: 909–928.
- Shao, Z.X., Ren, G.F. & Fang, Y.X. 2018. Reinforce technical analysis of concrete-filled steel tube with cementation deviating. *Journal of Guangxi University (Natural Science Edition)* 43(1): 126–131.
- Xie X. 2020. *Effect of Core Concrete Defects on Mechanical Properties of Ordinary Circular Steel Tube Concrete Axial Compression Components*. Sichuan, China: Southwest University of Science and Technology.
- Xue, J.Q., Briseghella, B. & Chen, B.C. 2012. Effects of debonding on circular CFST stub columns. *Journal of Constructional Steel Research* 69(1): 64–76.
- Xue, J.Q., Chen, B.C. & Briseghella, B. 2010. Experimental research on debonding in concrete-filled steel tubes columns subjected to eccentric loading. *IABSE Symposium Report 2010*: 40–47. Switzerland: IABSE.
- Xue, J.Q., Fiore, A., Liu, Z.H., Briseghella, B. & Marano, G.C. 2021a. Prediction of ultimate load capacities of CFST columns with debonding by EPR. *Thin-Walled Structures* 164: 107912.
- Xue, J.Q., Huang, J.P., Briseghella, B. & Huang, F.Y. 2022. Influence of different debonding gap types on mechanical performance of axially loaded CFST stub columns. *IABSE Congress Nanjing 2022 Report*: 1600–1608. Switzerland: IABSE.
- Xue, J.Q., Liu, Z.H., Zhang, Y.F., Briseghella, B., Chen, B.C. & Wei, J.G. 2021b. Experimental research on influence of debonding on circular CFST long columns subjected to eccentric load. *IALCCE2020*: 1481–1485. Florida: CRC Press.
- Xue, J.Q., Zhang, Y.F., Briseghella, B. & Chen, B.C. 2020. Experimental Research on Effects of Debonding on Circular CFST Columns with Different Slenderness Ratios. *Proceedings of ARCH 2019*: 369–377. Switzerland: Springer.
- Zhang, K.K., Liao, F.Y. & Huang, Z.W. 2019. Study on axial compression behavior of CFRP reinforced short concrete-filled steel tube (CFST) columns with spherical-cap debonding. *Journal of Building Structures* 40(S1): 227–232.

Dynamic assessment of a stress-ribbon CFST arch bridge with SHM and NDE

J.P. Huang, L.Q. He, J.Q. Xue, S.N. Zhou & B. Briseghella

Sustainable and Innovative Bridge Engineering Research Center & Joint International Research Laboratory of Deterioration and Control of Costal and Marine Infrastructures and Materials, College of Civil Engineering, Fuzhou University, Fuzhou, China

C. Castoro & A. Aloisio

Department of Civil, Construction-Architectural and Environmental Engineering, University of L'Aquila, L'Aquila, Italy

G.C. Marano

Department of Structural, Environmental and Geotechnical Engineering, Polytechnic University of Turin, Turin, Italy

Joint International Research Laboratory of Deterioration and Control of Costal and Marine Infrastructures and Materials, College of Civil Engineering, Fuzhou University, China

ABSTRACT: Vibration-based structural health monitoring is an efficient technique for dynamic assessment of the structures. Based on the identified dynamic characteristics, the condition of a bridge can be assessed by means of structural identification through the finite element model updating procedure. The modal parameters are generally the indicators that reflect the changes of the global performance of the bridges. As the supplement, non-destructive evaluation methods can be employed to provide more detailed information about the local condition of the structure. In this study, operational modal analysis was performed on a butterfly-arch pedestrian bridge at Fuzhou University, which was based on an innovative design concept, known as the stress-ribbon bridge. The uncertain model parameters of the structure were identified by updating the refined FE model in reference to the experimental modes. The ultrasonic instruments and rebound hammers were used to determine the debonding condition of the concrete-filled steel tubular sections of the main arches and the elastic modulus of the concrete slabs, respectively. Both of them play an important role to influence the dynamic behaviour of the bridge. The key structural parameters that were identified by the FE model updating procedure are compared to the nondestructive testing results. It's found that the nondestructive testing methods provide important supplementary information to the SHM for condition assessment of the structure.

1 INTRODUCTION

In vibration-based structural health monitoring (VBM), operational modal data is usually extracted by ambient vibration tests (AVT) to investigate the initial state of the bridges and structures. On the basis, the baseline model can be built by model calibration for long-term monitoring of the structure with good accuracy and high fidelity. The modal information (e.g., natural frequencies and mode shapes) are however the indicators of global dynamic characteristics of the structure, which sometimes have difficulties to reflect minor structural degradation or localized deterioration of the materials (Aktan et al. 2000). On the other hand, non-destructive evaluation (NDE) technique focuses on the local condition of the structures. Verma et al. (2013) provided a comprehensive review of nondestructive testing methods for condition monitoring of concrete structures. It's concluded that NDE methods have been used for more than three decades for monitoring concrete structures, which has currently

reached a mature status for condition evaluation of existing RC structures. However, as the local approach of structural evaluation the application of the NDE on site can be very time-consuming and require heavy labour works. The advantages and disadvantages of the SHM and NDE suggest that both approaches can be supplementary to each other. Aldrin et al. (2016) presented a comprehensive approach that integrates the VBM and NDE under the framework of probability of detection (POD) evaluation procedure for aerospace structures. By using a model-based method, they discovered that justification of the underlying assumptions of the statistical model choices was the key to the success of condition-based maintenance for the real applications. In this regard, development of a comprehensive approach of SHM and NDE is highly anticipated by civil engineers. Patil & Reddy (2020) presents a combination of the vibration-based method and non-destructive method for damage assessment of carbon composite fiber reinforced structure. Changes of the frequency response functions are used as the damage indicator to distinguish the intact and damaged specimens. Following that, the ultrasonic C-scanning method is used to locate and quantify the damage in the specimen. Vandecruys et al. (2022) presents a case study of acoustic emission and vibration-based monitoring of locally corroded reinforced concrete beams. Their findings suggested that the local (NDE) and global (VBM) monitoring techniques supplemented each other. The proposed comprehensive approach increased the sensitivity and efficiency of damage detection method in different phases of corrosion damage progress.

In the current study, an onsite investigation of an arch pedestrian bridge is performed by using VBM and NDE. The current study follows a previous research work on the same structure (He et al. 2022). The local defects of the main arches, known typically as debonding/void of the concrete core is the focus of the current work. Ultrasonic testing was implemented to assess the condition of the Concrete-Filled Steel Tubular (CFST) composite sections. In addition, the deck system of the bridge, known as the stress ribbon, is composed of several precast concrete segments. Evaluation of the compressive strength and hardness of the concrete slab is conducted by the rebound hammer testing. The results of structural identification obtained by the FE model updating method are then presented. Fidelity of the updating results will be addressed in reference to the findings of NDE for the identified model parameters.

2 EXPERIMENTAL PROGRAM

2.1 *Description of the bridge*

As shown in Figure 1, the stress-ribbon deck of the pedestrian bridge is supported by the cross beams between the outward inclined CFST arches, also known as the butterfly arches. Since the stress ribbons were anchored to the abutment where the springs of the arches were rooted, the whole structure consists of the self-anchored system, which loads the foundations mainly in the gravity direction. The span of the main arches is 25 meters with the rise of 5.5 meters. See Figure 2. They are made of the 42.6cm-diameter steel pipes with the thickness of 1.6 cm. The angle between the inclined arches and the ground is 60 degrees. The span of the secondary arches is 16.8 meters. They are made of the 37.7cm-diameter steel pipes with the thickness of 1.6 cm. The connections between the main and the secondary arches are welded. They are also interconnected by seven rigid hangers on each side. The stress-ribbon deck was assembled from the precast concrete segments by using two pre-stressed tendons. Each of the precast segment is 6 meters in width, 1.15 meters in length and 14 cm in thickness. The tendons are formed by two bundles of 12×Φ15.2mm monostrands grouted inside the galvanized steel pipes. The middle part of the bridge deck simply rests on the cross beams, whereas the side parts of the bridge deck are supported by the pre-stressed tendons. See Figure 3.

2.2 *Ultrasonic testing*

2.2.1 *Working principle*

Debonding is the common structural defect of the CFST members in an arch bridge (Chen et al. 2022). They can usually be assessed by using the ultrasonic testing method. Shown in Figure 4 is a typical sound wave transmission detector for quality testing of the CFST construction.



Figure 1. A stress-ribbon CFST arch pedestrian bridge at Fuzhou university.

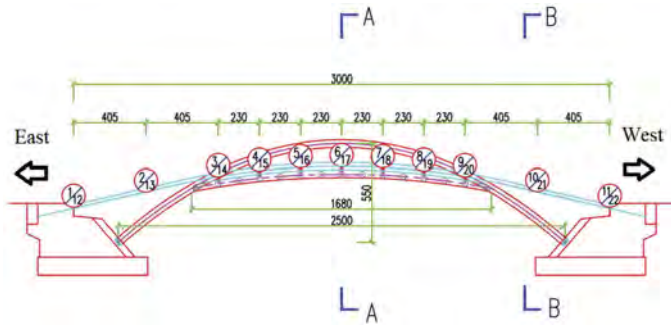


Figure 2. Front view of the bridge with the measurement nodes of AVT labeled (units in mm).

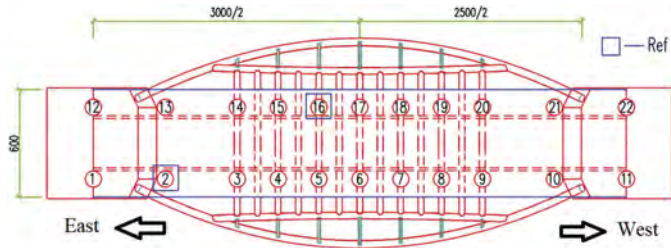


Figure 3. Top view of the bridge with the measurement nodes of AVT labeled (units in mm).

The propagation speed of ultrasonic waves in solid is a function of the Young's modulus E and the density ρ of the materials, $V_{solid} = f(E/\rho)$. The ultrasonic wave speed in steel and concrete is generally 4000–6000 m/s (Li et al. 2020). Under a certain ambient condition, the following relationship applies for the ultrasonic wave speeds,

$$\frac{V_s}{V_c} = p_c \quad (1)$$

where V_s = the wave speed in steel; V_c = the wave speed in concrete; and p_c = a constant to be determined. For a CFST section without defects, the ultrasonic time-of-flight T_f equals to,

$$T_f = \frac{2 \cdot t}{V_s} + \frac{D - 2 \cdot t}{V_c} \quad (2)$$

where t = the thickness of steel pipe; D = the diameter of steel pipe. Once p_c is obtained by the CFST specimen tests, both V_s and V_c can be obtained by solving Equation (2). On the basis, for the CFST sections with debonding/void, the ultrasonic time-of-flight T_f can be estimated by



Figure 4. Ultrasonic instrument: WE-520 sound wave transmission detector (operating at 50 kHz).

$$T_f = \frac{2 \cdot t}{V_s} + \frac{D - 2 \cdot t - \Delta h}{V_c} + \frac{\Delta h}{V_a} \quad (3)$$

where Δh = the thickness of void or debonding in the concrete core on the path of the wave passage and V_c = the wave speed in air, which can be assumed as a constant of 340m/s.

2.2.2 Testing scheme

As shown in Figure 5, on each cross section of the CFST the ultrasonic tests were repeated in four different directions. They were equally distributed around the perimeter and all go through the center of the cross section. The values of the ultrasonic time-of-flight T_f were read from the device. And the thickness of debonding Δh can be determined by Equation (3). A linear interpolation is then applied to the discrete values of Δh along the perimeter of the section to estimate the total debonding area at the concrete core. On the main arches, eleven cross sections were tested at each side. See Figure 6. In addition, before the ultrasonic testing, the traditional testing method of hammer impacts was also applied in order to quickly evaluate the severity of the debonding condition. The results of the hammer impact tests were indicated by the quality number N_q . For instance, $N_q=10$ for the arc-length ratio of debonding $R_d < 5\%$, $N_q=9$ for $R_d = 5\sim 10\%$, $N_q=8$ for $R_d = 10\sim 20\%$, and $N_q=7$ for for $R_d = 20\sim 30\%$ (Xue et al. 2012).

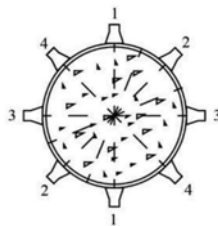


Figure 5. Placement of the probes at the cross section in the ultrasonic testing.

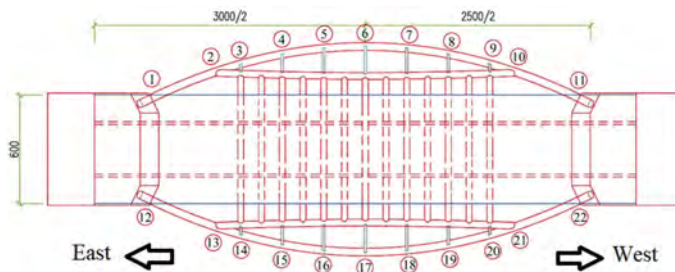


Figure 6. Top view of the bridge with the cross sections of ultrasonic testing labeled (units in mm).

2.3 Rebound hammer testing

2.3.1 Working principle

A rebound hammer is a handheld device for non-destructive testing of concrete. It helps determine the compressive strength and hardness of concrete by measuring the rebound height of a steel ball dropped onto the surface. The relevant technical specification (MOHURD 2011) in China provides the detailed requirements and process to perform the rebound hammer testing. In particular, the depth of the carbonation at the concrete surface has to be identified, which influences the results of the rebound hammer tests. To convert the cubic strength of concrete $f_{cu,k}$ to the corresponding Young's modulus of concrete $E_{c,s}$, the Chinese Code for design of concrete structure (MOHURD 2015) suggests the following formula:

$$E_{c,s} = \frac{10^5}{2.2 + \frac{34.7}{f_{cu,k}}} \text{ (MPa)} \quad (4)$$

The values $E_{c,s}$ above are however the static elastic modulus of concrete. Memory et al. (1995) suggests the following equation to calculate the dynamic elastic modulus of concrete $E_{c,d}$:

$$E_{c,s} = 1.25E_{c,d} - 19 \text{ (GPa)} \quad (5)$$

2.3.2 Testing scheme

Since the concrete deck is fully covered with the ceramic pavement, the rebound hammer tests were only applied from underneath the bridge. By considering the accessibility, the two segments of the precast concrete slab next to the east and west abutments were tested.

2.4 Ambient vibration testing

Ambient vibration tests were performed for twenty-two measurement nodes distributed on the bridge deck across the span. The acquisition system consisted of four wireless accelerometers. The signals of three-dimensional records were highly synchronized. As shown in Figure 3, the nodes No. 2 and No. 16 were the reference nodes, which are used to glue the separate mode shape vectors from each individual testing setups. In detail, the tests included 11 setups.

System and modal parameters are extracted from the ambient data with the output-only reference-based stochastic subspace identification algorithm (Peeters et al. 1999). The reference channels were those of the reference sensors. Data processing and system identification process was accomplished by using the MACEC toolbox (Reynders et al. 2014).

3 EXPERIMENTAL RESULTS

3.1 Ultrasonic testing

By the tests of the CFST specimens in laboratory, p_c in Equation (1) is found to be 1.18. Correspondingly, $V_s = 7,778$ m/s and $V_c = 4,896$ m/s by solving Equation (2). On the basis of the working principle in Section 2.2.1, the debonding/void rate k_d can be obtained, which defines the ratio between the debonding/void area and the circular area of the concrete core at the CFST cross section. On the basis of the formulas to calculate the design values of the compressive and flexural stiffness of the CFST members (Chen et al. 2022), the following equation is proposed herein for the equivalent stiffness of the CFST members:

$$(EA)'_{\text{equivalent}} = E_s A_s + k E_c A_c \quad (6)$$

$$(EI)'_{\text{equivalent}} = E_s I_s + 0.6 k E_c I_c \quad (7)$$

where the subscripts s and c stand for the steel pipe and concrete core, respectively. The reduction factor of 0.6 to the flexural stiffness of the concrete core $E_c I_c$ takes into account the cracking of the concrete core under tension (Chen et al. 2022). By considering the effects of debonding, the

values of the compressive and flexural stiffness of the CFST section can be modified by introduction of the reduction factor $k (= 1 - k_d)$. The experimental results of the ultrasonic testing are given in Figure 7 in terms of the k factors. The mean values of k are similar of the two main arches, around 0.98. The minimum values of k are found at the springs of the arches, around 0.97. In particular, the experimental results obtained from the ultrasonic testing are usually in agreement with the findings of the hammer impact tests. The crown sections are labeled by 10, suggesting an almost zero debonding rate. And the spring sections are labeled by $N_q=7$, suggesting the most severity of the debonding condition.

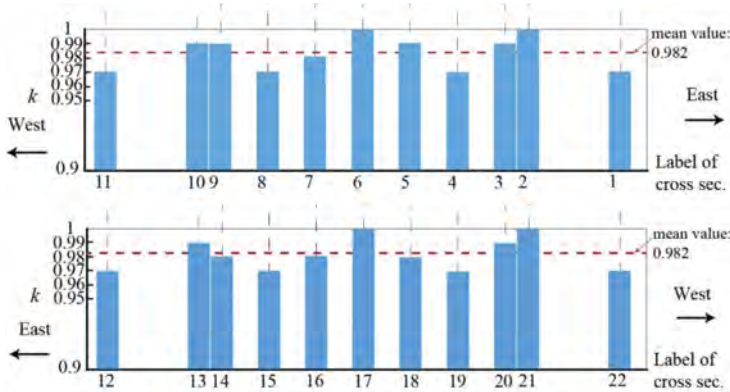


Figure 7. Stiffness reduction factors k identified at the CFST cross sections by ultrasonic testing.

3.2 Rebound hammer testing

Totally 16 rebound hammer tests shall be repeated on an individual test area (MOHURD 2011). In Table 1, the results of the hammer tests are provided in detail. The two deck segments being tested are, repetitively, next to the east and west abutments. The cubic strength of the concrete was obtained in reference to the specification. The static elastic modulus of concrete $E_{c,s}$ is then estimated by Equation (4). Finally, the dynamic elastic modulus of concrete $E_{c,d}$ is obtained by Equation (5). Figure 8 illustrates the variation of the rebound values on each test area for the 4 by 4 test points in the gray colour scale.

Table 1. Results of rebound hammer testing.

Test area	Rebound value (mm)				Average value (mm)	Carbonization depth (mm)	Cubic strength (MPa)	Static $E_{c,s}$ (MPa)	Dynamic $E_{c,d}$ (MPa)
East side	52	52	58	49	54.1	3.0	57.8	35,709	43,767
	56	42	57	57					
	54	58	54	46					
West side	56	56	52	52	45.4	1.5	46.6	33,960	42,372
	44	45	36	47					
	46	48	39	46					
	42	46	48	45					
	52	63	44	54					

3.3 Ambient vibration testing

The results of the ambient vibration tests were provided in Table 2 concerning the identified experimental modes. They included five vertical bending modes and three torsion modes. No lateral modes were identified under the current ambient vibration conditions. The identified damping ratios were generally around 1% except of the second mode. Significant modal deformation was observed in the 2nd mode for the main arches, whereas the other bending or torsion modes were

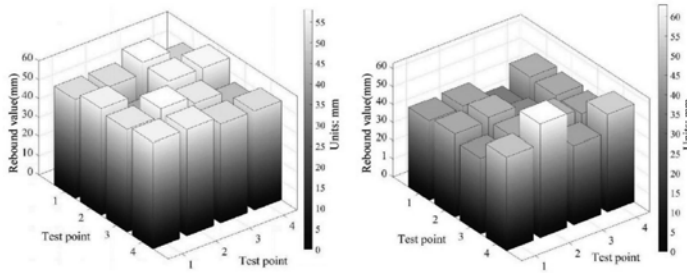


Figure 8. Rebound values at the slabs of the west side (left) and east side (left).

characterized with the deformation mainly for the slab. The composite action of CFST cross sections is considered to influence the energy dissipation mechanism for the the 2nd vibration mode.

Table 2. The identified experimental modes.

No.	Nature frequency f (Hz)	Damping ratio ξ	Type of the vibration modes
1	3.59	0.7%	1st Vertical bending mode
2	5.28	3.9%	2nd Vertical bending mode
3	6.91	1.6%	1st Torsion mode
4	7.79	1.2%	3rd Vertical bending mode
5	9.17	1.1%	2nd Torsion mode
6	10.98	1.0%	3rd Torsion mode
7	14.45	0.8%	4th Vertical bending mode
8	14.92	0.6%	5th Vertical bending mode

4 RESULTS OF MODAL-BASED FE MODEL UPDATING

Structural identification was performed by using parametric updating of the refined reference model of the bridge (He et al. 2022). In the refined FE model, the bridge deck was modeled with the shell elements. Four rigid links were introduced between the anchors of the prestressed tendons and the springs of the main arch to simulate the abutments. The numerical solution process of the FE model updating was formulated into the nonlinear least square problem, which intends to minimize the relative differences between the experimental and numerical natural frequencies. The stiffness of the soil springs at the abutments, the elastic modulus of the concrete deck E_C and the elastic modulus of the tendons E_t were chosen as the updating parameters for a total of eight parameters. Under the optimal solution, E_C of the concrete deck is identified as 57,598 MPa. E_C of the concrete core of the CFST sections is 42,000 MPa and the E_s of the steel pipe of CFST is 210,000 MPa. In particular, both of them were not included into the updating parameters and kept as the constants in the updating process.

5 DISCUSSION

The results of ultrasonic testing show that the average debonding/void rate k_d is 2% for all the 22 cross sections along the main arches. Xue et al. (2012) found that if the debonding/void rate k_d is less than 1.2%, its influence on the ultimate load capacity and stiffness of CFST columns can be neglected. Therefore, for the current CFST bridge, it might be necessary to consider the uncertainty of E_C of the concrete core of the CFST main arches by taking it as one of the updating parameters. In addition, with respect to the variation of k (Figure 6), the assumption for a uniform value of E_C for the main arches is acceptable. Besides, both hammer impact tests and ultrasonic tests found almost zero debonding rate on the secondary arches. Therefore, the stiffness of the secondary arches need not be updated, since the initial estimation of the material properties are sufficiently accurate.

The results of rebound hammer testing showed the variation of E_C of the concrete deck between the selected two segments. The absolute value of the relative difference is 3.2%. In this regard, it is reasonable to assume a constant E_C of the concrete deck in the FE model updating. The identified value by FE model updating is found to be almost 30% greater than those identified by NDE. The non-structural elements, including the hand-rails and ceramic pavement should contribute to the increased value of E_C , as well as the influence of pre-stressing forces at the tendons. Nevertheless, further investigation remains open for any future research.

6 CONCLUSION

In this study, a butterfly-arch pedestrian bridge was investigated by both VBM and NDE methods. The uncertain model parameters of the structure were identified by updating the refined FE model in reference to the experimental modal data. The ultrasonic instruments and rebound hammers are used to determine the debonding condition of the CFST members of the main arches and the elastic modulus of the concrete slabs, respectively. Both of them play an important role to influence the dynamic performance of the self-anchored structural system. Accuracy and variability of the key structural parameters that were identified by the FE model updating process is investigated in comparison to the NDE results. It is found that the NDE methods serve as an important supplementary technique to the SHM technique for condition assessment of the studied structure.

REFERENCES

- Aktan, A.E., Catbas, F.N., Grimmelsman, K.A. & Tsikos, C.J. 2000. Issues in infrastructure health monitoring for management. *Journal of Engineering Mechanics*, 126(7): 711–724.
- Aldrin, J.C., Annis, C., Sabbagh, H.A. & Lindgren, E.A. 2016, February. Best practices for evaluating the capability of nondestructive evaluation (NDE) and structural health monitoring (SHM) techniques for damage characterization. *42ND ANNUAL REVIEW OF PROGRESS IN QUANTITATIVE NONDESTRUCTIVE EVALUATION: Incorporating the 6th European-American Workshop on Reliability of NDE*. AIP Publishing LLC.
- Chen, B., Liu, J. & Wei, J. 2022. *Concrete-Filled Steel Tubular Arch Bridges*. Beijing: China communication press: Springer.
- Ministry of Housing and Urban-Rural Development of the People's Republic of China (MOHURD). 2015. *Code for design of concrete structures*. Beijing: China Architecture & Building Press.
- He, L., Castoro, C., Aloisio, A., Zhang, Z., Marano, G.C., Gregori, A., Deng, C. & Briseghella, B. 2022. Dynamic assessment, FE modelling and parametric updating of a butterfly-arch stress-ribbon pedestrian bridge. *Structure and Infrastructure Engineering* 18: 1–12.
- Ministry of Housing and Urban-Rural Development of the People's Republic of China (MOHURD). 2011. *Technical specification for inspecting of concrete compressive strength by rebound method*. Beijing: China Architecture & Building Press.
- Li, H., Yan, P., Sun, H. & Yin, J. 2020. Axial compression performance and ultrasonic testing of multicavity concrete-filled steel tube shear wall under axial load. *Advances in Civil Engineering*, 2020(1): 1–19.
- Memory, T.J., Thambiratnam, D.P. & Brameld, G.H. 1995. Free vibration analysis of bridges. *Engineering Structures*, 17(10): 705–713.
- Patil, S. & Reddy, D.M. 2020. Impact damage assessment in carbon fiber reinforced composite using vibration-based new damage index and ultrasonic C-scanning method. *Structures* 28: 638–650.
- Peeters, B. & De Roeck, G. 1999. Reference-based stochastic subspace identification for output-only modal analysis. *Mechanical systems and signal processing* 13(6): 855–878.
- Reynders, E., Schevenels, M. & De Roeck, G. 2014. *MACEC 3.3: A Matlab Toolbox for Experimental and Operational Modal Analysis*. Katholieke Universiteit: Leuven.
- Vandecruys, E., Martens, C., Van Steen, C., Nasser, H., Lombaert, G. & Verstryngne, E. 2022. Preliminary results on acoustic emission and vibration-based monitoring of locally corroded reinforced concrete beams. *The International Symposium on Nondestructive Testing in Civil Engineering* 27
- Verma, S.K., Bhadauria, S.S. & Akhtar, S. 2013. Review of nondestructive testing methods for condition monitoring of concrete structures. *Journal of construction engineering* 2013(2008): 1–11.
- Xue, J.Q., Briseghella, B. & Chen, B.C. 2012. Effects of debonding on circular CFST stub columns. *Journal of Constructional Steel Research* 69(1): 64–76.

Bridge maintenance prioritization by using multi-criteria decision analysis

H. Silimanotham & M. Henry

Shibaura Institute of Technology, Tokyo, Japan

ABSTRACT: Bridges are one of the essential components of road infrastructure, however, if they are not maintained, their rehabilitation causes huge burdens on the country's economy. In Lao PDR, due to the absence of a maintenance management plan, the prioritization of the bridges for the maintenance plan does not depend on technical factors, due to which the important structure gets neglected. The research explores the application of Fuzzy-Analytic-Hierarchy-Process (FAHP) and Linear-Aggregation methods (LAM), the multi-criteria-decision-making techniques, on a database obtained from the Ministry of Public Works and Transport, to solve bridge maintenance prioritization problems. Both methods involved determining the weight of criteria on the three bridge characteristics i.e., condition, aging, and maximum loading. FAHP was found suitable if the bridge prioritization can be done relative to the characteristics of all the other bridges, whereas LAM can be applied if the priority is determined just by the characteristics of the bridge itself.

1 INTRODUCTION

Efficient road transport is the backbone of a country's economy, and bridges are one of the essential components of road infrastructure. However, bridges deteriorate with the passage of time due to a variety of factors that include traffic loading, aging, and various environmental impacts. Special attention should be given to the maintenance plan of these expansive structures (Leonovich & Kashevskaja, 2007). If their maintenance is ignored due to any reason, the rehabilitation of these structures becomes a huge burden on the country's economy.

Lao PDR has 3,580 bridges with 6 classifications i.e., national, provincial, district, urban, rural, and specific road bridges. However, the Ministry of Public Works and Transport (MPWT) has only 1 percent of the road budget for the bridges' maintenance which also includes site inspection and surveying. Due to the absence of a maintenance management strategy in Lao PDR, the selection of a bridge for the maintenance plan is normally determined by coordination meetings between relevant agencies without considering and evaluating technical factors. Due to this, the maintenance budget is usually spent on urgent cases only and routine and periodic maintenance is generally ignored. Yet, there is no proper bridge maintenance management system exists to deal with such a problem. There is a need to develop the bridge maintenance system for prioritizing the bridge to be included in the maintenance plan.

Over the last few decades, a lot of research has been made to develop the technique for assessing the bridge condition for prioritizing it for the maintenance plan. It includes the deterministic approach (Frangopol et. al., 2001), the stochastic approach (Val & Melchers, 1997), and the fuzzy logic-based approach. Tee et. al. (1988) suggested a fuzzy approach for the evaluation of bridges, and Sasmal et. al. (2006) suggested the fuzzy AHP approach for the condition rating of existing concrete bridges. This research was focused to utilize the existing data of bridges with MPWT for developing and comparing the weighted rating criteria for bridge prioritization, based on Linear Aggregation Method (LAM), and the Fuzzy Analytic Hierarchical process (FAHP). However, the data obtained from MPWT was incomplete due

to the lack of bridge characteristics and year of construction for some of the bridges. Therefore, the research was focused on bridge maintenance prioritization on small scale in a Luang Prabang province that belongs to the national road and has complete data.

2 METHODOLOGY

2.1 *Data and evaluation criteria*

The data for the research was collected from the MPWT. It was observed that most of the bridges were located on the national road, followed by provincial, district, urban, rural, and specific roads. The national road network consists of around 34% of the total bridges (3580). However, the research was focused on one road section of the national road network i.e., road number 13th North section in Luang Prabang province. This road section has around 671,700 meters of road distance and has 21 bridges. The bridge's characteristics are shown in Table 1. Due to data limitations, the analysis was done based on three bridge characteristics i.e., bridge condition, bridge aging, and bridge capacity in terms of maximum loading. The bridge conditions were classified into 5 categories in the data obtained, with 1 showing "no damage" to the 5 representing the "severe damage" of the bridge. Two Multi-Criteria Decision Making (MCDM) techniques i.e., Fuzzy Analytic Hierarchy Process (FAHP), and Linear Aggregation Method (LAM) were applied to the data. The weight criteria for prioritization were selected as equal weighting, in which the three bridge characteristics (criteria) were considered equally important, and strong importance for each characteristic individually (condition strongly more important, aging strongly more important, and maximum loading strongly more important as shown in Table 2) for both methods (FAHP, LAM). The first step for both the methods involved categorization of the bridges. The bridges were classified into 5 categories based on bridge aging data by following the Laos MPWT bridge maintenance frequency and on the maximum loading data following the concept proposed by Paeglitis (Paeglitis & Paeglitis, 2010).

Table 1. Actual bridge characteristics of 21 bridges.

Bridges no.	Condition	Aging	Maximum Loading
B1	2	50	40
B2	2	50	40
B3	2	50	40
B4	2	28	40
B5	2	28	40
B6	1	3	40
B7	1	28	40
B8	1	3	40
B9	1	3	40
B10	1	3	40
B11	2	28	40
B12	1	3	40
B13	2	28	40
B14	2	28	40
B15	4	28	40
B16	3	28	40
B17	2	28	40
B18	3	28	40
B19	2	28	40
B20	2	28	40
B21	2	28	40

2.2 *Fuzzy Analytic Hierarchy Process (FAHP)*

The Analytic Hierarchy Process (AHP) is one of the methods of Multi-Criteria Decision Making (MCDM) that is applied to decision-making problems with different evaluation criteria

and conditions for assisting in decision-making by using a pairwise comparison matrix. Saaty elaborated in detail on the basic principles and stages of decision-making (Saaty, 1980; Laarhoven & Pedrycz, 1983). Many researchers propose this method as an easy approach that can be used for decision-making. However, the AHP has some limitations, i.e., the dependence of the AHP model on its main input, or when an expert perception is subjective. Triangular Fuzzy Numbers (TFN) and linguistic variables can overcome the weaknesses of the AHP method in determining priorities from the decision-making of vague decision-makers (Yossysfra et al., 2019). Therefore, the research utilizes Fuzzy Analytic Hierarchy Process (FAHP) for decision-making for prioritizing the bridges for the maintenance plan (Zadeh et al., 1965). The method of FAHP assists in avoiding decisions that are detrimental to the surroundings (Pan, 2008). The structure of FAHP is the combination of AHP and the Fuzzy concept that elaborate the standard AHP method into the fuzzy domain by utilizing the fuzzy number instead of the real number for calculations (Petkovic et al., 2012). The process starts with data normalization. Once the data is normalized, the weightage of all the criteria is determined by using a fuzzy number. Therefore, based on the Chang scale, the intensity of criteria importance was transformed into the TFN comparison scale (Fuzzy number) that consisted of three values i.e., l (lowest value), m (middle value), and u (highest value) (Chang, 1996) as shown in Table 2. Once the weightage for all the criteria was established, the geometric mean and local weight for all the criteria were calculated. Then the bridge maintenance prioritization by using a pair-wise comparison matrix was developed and finally, the bridges were ranked for maintenance prioritization by averaging the three fuzzy numbers (l, m, and u). The results of FAHP were then compared with the Linear Aggregation Method. The stepwise equations for the FAHP process are mentioned below for bridge maintenance prioritization (Guzman, 2001).

$$\text{Inverse triangle fuzzy: } (l, m, u)^{-1} = \left(\frac{1}{u}, \frac{1}{m}, \frac{1}{l}\right) \tag{1}$$

$$\text{Fuzzy multiplication: } (l_1, m_1, u_1) \times (l_2, m_2, u_2) = (l_1 \times l_2, m_1 \times m_2, u_1 \times u_2) \tag{2}$$

$$\text{Geometric mean of criteria i: } g_i = \left(\prod_{j=1}^n r_{ij}\right)^{\frac{1}{n}} \tag{3}$$

$$\text{Local weight of criteria i: } W_i = g_i / \sum_{i=1}^n g_i \tag{4}$$

$$\text{Final priority weight of bridge i: } PW_i = \sum W_{overall} \times W_{local} \tag{5}$$

Where g_i is the geometric mean of criteria, r_{ij} is the pair-wise comparison matrix, $W_{overall}$ is the weight per criteria, and W_{local} is the local weight of criteria.

Table 2. Definition and membership function of fuzzy number.

Intensity of importance	Definition	Fuzzy number (l, m, u)
1	Equally important	(1,1,2)
3	Moderately more important	(2,3,4)
5	Strongly more important	(4,5,6)
7	Very strongly more important	(6,7,8)
9	Extremely more important	(8,9,9)

2.3 Linear Aggregation Method

The Linear Aggregation Method (LAM) is one of the methods of MCDM for decision-making that uses the relations between the criteria and the weighting of criteria from the decision-makers' perceptions for finding the highest priority criteria (Yager, 2009). The Linear Aggregation Method (LAM) was applied to the same data to prioritize bridge maintenance by comparing the bridge characteristics in four different weightings. LAM analyzes the bridge priority weight by combining LAM and FAHP as the local weight of all criteria via equation 6 (Yager, 2008). The first step for performing LAM is to normalize data for calculating the linear aggregation. Then the data normalization was done based on the range from 0 to 1 scale for calculating the

linear aggregation for all criteria. Once the data were normalized, the local weights of FAHP for all the criteria were used to calculate the LAM. Finally, the bridge ranking was done for maintenance prioritization. The following equations were used for the LAM process.

$$\text{Linear aggregation: } LAM = \sum C_i \times W_i \quad (6)$$

Where C_i is the criteria data (condition, age, and maximum loading), and W_i is the local weight of all criteria from FAHP in 4 weighting cases (equal weighting, condition strongly important, aging strongly important, and maximum loading strongly important).

3 RESULTS AND DISCUSSIONS

3.1 Effect of weighting

3.1.1 Fuzzy Analytic Hierarchy Process

The results of the FAHP are shown in Table 3 which illustrated the bridge maintenance prioritization weight by using a pairwise comparison matrix for all 21 bridges for equal weighting, and for each bridge characteristic individually i.e., condition strongly more important, aging strongly more important, and maximum loading strongly more important. The results obtained prioritized the 21 bridges in 6 categories of ranking in 4 different weights (equal weight, condition, aging, and maximum loading). It was observed that bridge B15 has the highest priority (rank 1) on the equal weight, the bridge condition strongly more important, and the maximum loading strongly more important criteria, but it has 2nd priority in case of aging strongly more important for the maintenance plan. On the other hand, bridges B1, B2, and B3 are the highest priority for the bridge maintenance plan on the aging strongly more important criteria. They are the second rank for bridge maintenance on equal weighting and maximum loading strongly more important and the third rank on condition strongly more important. On the contrary, bridges B6, B8, B9, B10, and B12 are the least ranked or lowest priority bridges for the maintenance plan.

Table 3. Result of Fuzzy Analytical Hierarchy Process.

Bridge No	Equal weight		Condition strongly more important		Aging strongly more important		Max_Load strongly more important	
	Weight	Rank	Weight	Rank	Weight	Rank	Weight	Rank
B1	0.059	2	0.052	3	0.073	1	0.053	2
B2	0.059	2	0.052	3	0.073	1	0.053	2
B3	0.059	2	0.052	3	0.073	1	0.053	2
B4	0.048	4	0.047	4	0.049	4	0.048	4
B5	0.048	4	0.047	4	0.049	4	0.048	4
B6	0.034	6	0.033	6	0.027	6	0.042	6
B7	0.043	5	0.037	5	0.047	5	0.046	5
B8	0.034	6	0.033	6	0.027	6	0.042	6
B9	0.034	6	0.033	6	0.027	6	0.042	6
B10	0.034	6	0.033	6	0.027	6	0.042	6
B11	0.048	4	0.047	4	0.049	4	0.048	4
B12	0.034	6	0.033	6	0.027	6	0.042	6
B13	0.048	4	0.047	4	0.049	4	0.048	4
B14	0.048	4	0.047	4	0.049	4	0.048	4
B15	0.066	1	0.085	1	0.056	2	0.055	1
B16	0.057	3	0.066	2	0.052	3	0.052	3
B17	0.048	4	0.047	4	0.049	4	0.048	4
B18	0.057	3	0.066	2	0.052	3	0.052	3
B19	0.048	4	0.047	4	0.049	4	0.048	4
B20	0.048	4	0.047	4	0.049	4	0.048	4
B21	0.048	4	0.047	4	0.049	4	0.048	4

3.1.2 Linear Aggregation Method (LAM)

The results of linear aggregation methods are presented in Table 4 for the bridge maintenance priority weight for all 21 bridges in four weighting cases. The LAM results ranged between 0 and 1, with higher values signifying higher priority and lower values signifying lower priority.

Table 4. Result of Linear Aggregation Method.

Bridge No	Equal weight	Rank	Condition strongly more important	Rank	Aging strongly more important	Rank	Max_Load strongly more important	Rank
B1	0.733	1	0.544	3	0.885	1	0.771	1
B2	0.733	1	0.544	3	0.885	1	0.771	1
B3	0.733	1	0.544	3	0.885	1	0.771	1
B4	0.600	3	0.487	4	0.600	4	0.713	3
B5	0.600	3	0.487	4	0.600	4	0.713	3
B6	0.400	5	0.287	6	0.287	6	0.627	5
B7	0.533	4	0.344	5	0.571	5	0.685	4
B8	0.400	5	0.287	6	0.287	6	0.627	5
B9	0.400	5	0.287	6	0.287	6	0.627	5
B10	0.400	5	0.287	6	0.287	6	0.627	5
B11	0.600	3	0.487	4	0.600	4	0.713	3
B12	0.400	5	0.287	6	0.287	6	0.627	5
B13	0.600	3	0.487	4	0.600	4	0.713	3
B14	0.600	3	0.487	4	0.600	4	0.713	3
B15	0.733	1	0.771	1	0.658	2	0.771	1
B16	0.667	2	0.629	2	0.629	3	0.742	2
B17	0.600	3	0.487	4	0.600	4	0.713	3
B18	0.667	2	0.629	2	0.629	3	0.742	2
B19	0.600	3	0.487	4	0.600	4	0.713	3
B20	0.600	3	0.487	4	0.600	4	0.713	3
B21	0.600	3	0.487	4	0.600	4	0.713	3

Table 4 shows that bridges B1, B2, and B3 have the first rank for maintenance prioritization in equal weight strongly more important, aging strongly more important, and maximum loading strongly more important characteristics. However, for condition strongly more important, these bridges ranked 3rd for prioritization. While bridge B15 also ranked 1st for prioritization based on equal weight, a condition strongly more important and maximum loading strongly more important but ranked 2nd for aging strongly more important. But the same bridges i.e., B6, B8, B9, B10, and B12 that were ranked lowest with FAHP were also observed to be ranked lowest in LAM. It was observed that among four different weights of criteria, the most critical weight of criteria were condition strongly more important, and aging strongly more important in the LAM process because the ranks for the bridges were found highly changing than other weights of criteria.

3.2 Comparison of the results of FAHP and LAM

For comparison purposes, the results of FAHP were multiplied by 10 and the graphs were generated for both methods for all criteria.

3.2.1 Equal weighting

Figure 1 shows the comparison of equal weighting for both cases (FAHP, LAM). The results of the two methods were found slightly different. In LAM, the highest priority weight (ranking) was found for four bridges i.e., B1, B2, B3, and B15 but for the FAHP, only one bridge i.e., B15 was found the top-ranked bridge for prioritization for equal weighting cases. B1, B2, and B3 were the oldest bridges (50 years old) with insignificant damages (condition-2) and with a maximum loading capacity of 40 tons. However, bridge B15 was found 28 years old, with severe damage (bridge condition-4) and 40 tons maximum loading as shown in Table 1. It shows that in LAM, the bridge ranking was done by taking the combined effect of aging, condition, and maximum loading

individually for each bridge but in FAHP, the bridge characteristics were involved separately in bridge ranking among all 21 bridges.

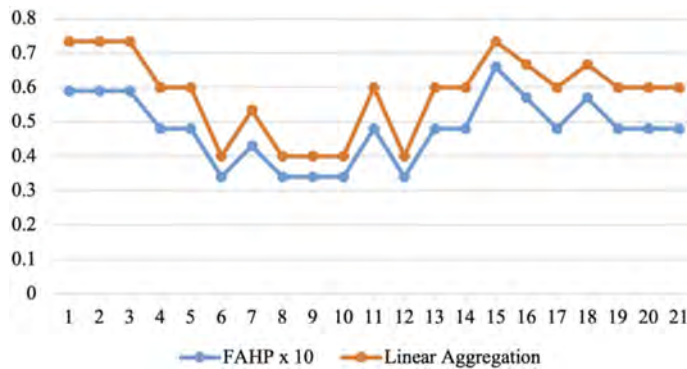


Figure 1. The results comparison of equal weighting between FAHP and LAM.

3.2.2 Maximum loading strongly more important

Figure 2 shows the comparison of the results of FAHP and LAM for the maximum load characteristic strongly more important for the 21 bridges. In LAM, four (4) bridges B1, B2, B3, and B15 were found highest rank for the prioritization for maintenance planning in case of maximum loading strongly important but for FAHP, only one bridge B15 was found the top ranking. From Table 1, it was observed that the maximum loading was found similar for all bridges (40 tons) but the ranking was done based on the other characteristics i.e., condition and aging.

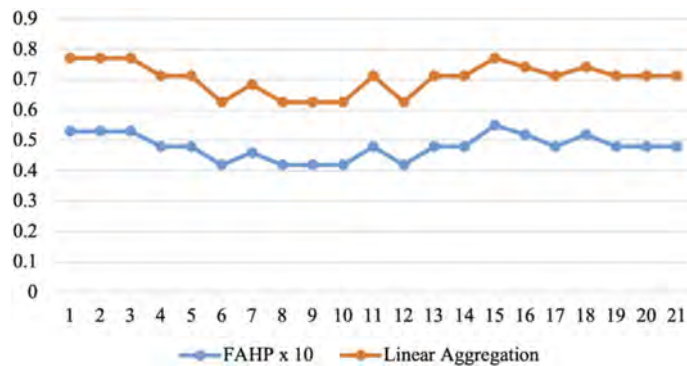


Figure 2. The results comparison of maximum loading strongly more important between FAHP and LAM.

3.2.3 Bridge condition strongly more important

Figure 3 shows the results comparison of the LAM and FAHP for the bridge condition strongly more important characteristic only. It was observed that for both methods the bridge ranks are similar for prioritization based on bridge condition strongly more important for the maintenance plan. Bridge B15 was found the first rank for both the methods (LAM, and FAHP) having severe damage (condition-4) whereas bridges B6, B8, B9, B10, and B12 were having the least rank for prioritization by both methods having condition-1 (No damage).

3.2.4 Aging strongly more important

The comparison of the result of both methods for aging strongly more important are shown in Figure 4. The results show that bridges' ranks are similar for both methods (LAM and FAHP) for considering the aging characteristic only. Three bridges B1, B2, and B3 were

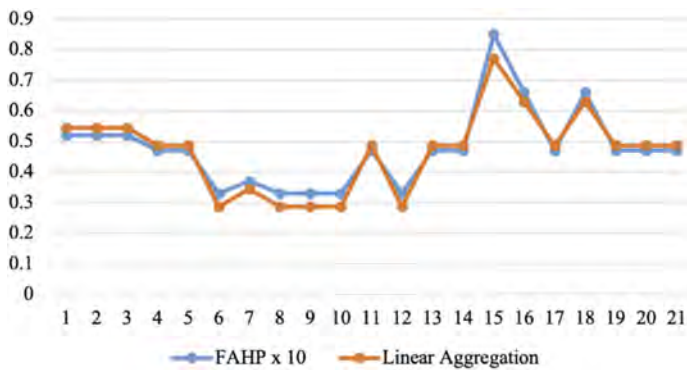


Figure 3. The results comparison of condition strongly more important between FAHP and LAM.

found with the highest rank having maximum age (50-years old) and bridges B6, B8, B9, B10, and B12 having age 3-years old were found the least important to be consider for prioritization for the maintenance plan based on aging strongly more important as shown in Table 1.

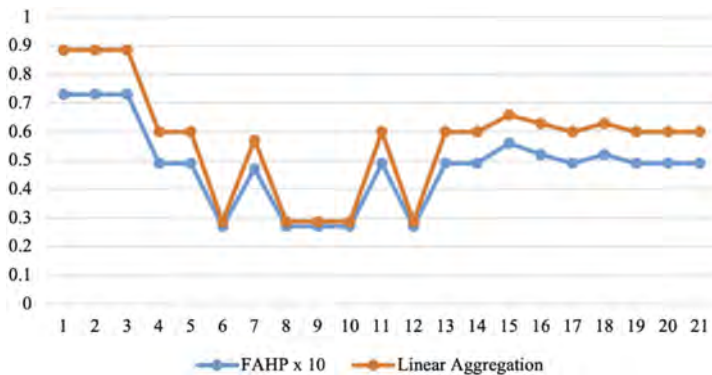


Figure 4. The results comparison of aging strongly more important between FAHP and LAM.

4 CONCLUSIONS

The research was carried out to develop the method for bridge maintenance prioritization based on the available data with MPWT in Luang Prabang province of Laos. Two different methods of the MCDM technique i.e., Linear Aggregation Method (LAM) and Fuzzy Analytic Hierarchy Process (FAHP) were applied to the four different weighting selection criteria for prioritizing the bridges for the maintenance plan. The results of both methods were analyzed and compared. It was found that for prioritizing the bridge for the maintenance plan, the rankings of the bridges were found similar in the case of bridge condition as strongly more important and aging strongly more important for both the methods (FAHP, LAM).

From the bridge maintenance perspective, both methods were found useful for bridge maintenance planning. However, if the road agency has to select the bridges for prioritization based on bridge characteristics individually for each bridge, the LAM may be the better approach. However, if the bridge selection is to be done among the number of bridges, then FAHP can be the suitable approach for the prioritization of the maintenance plan. The LAM approach was also found easier and can be useful in case of time constraints as it does not need much detail analysis as compared to FAHP which is a deep detail analysis.

ACKNOWLEDGEMENT

The Authors would like to extend their gratitude to Mr. Azam AMIR for helping me with the paper writing, to Japan International Cooperation Agency (JICA) for their support through the Road Asset Management Program, to Shibaura Institute of Technology (SIT), Tokyo for providing the environment for the research, and to Ministry of Public Works and Transport (MPWT) in Lao PDR, for sharing the data and information needed.

REFERENCES

- Angelia, N. and Mazni, D.I., 2019, August. Determining the priority criteria and ranking of provincial bridge maintenance in West Sumatra using a combination of the Fuzzy Analytical Hierarchy Process and VIKOR-Modification methods. In *IOP Conference Series: Materials Science and Engineering* (Vol. 602, No. 1, p. 012105). IOP Publishing.
- Chang, D.Y., 1996. Applications of the extent analysis method on fuzzy AHP. *European journal of operational research*, 95(3), pp.649–655.
- Frangopol, D.M., Kong, J.S. and Gharaibeh, E.S., 2001. Reliability-based life-cycle management of highway bridges. *Journal of computing in civil engineering*, 15(1), pp.27–34.
- Guzman, L.M., 2001. Multi-criteria decision making methods: a comparative study. Applied optimization. Evangelos Triantaphyllou. Kluwer Academic Publishers, 288 pp.
- Leonovich, I. and Kashevskaja, E., 2007. Selection of criteria for process monitoring at the operative level of road quality management. *Technological and Economic Development of Economy*, 13(2), pp.144–152.
- Paeglitis, A. and Paeglitis, A., 2010. Simple Classification Method for the Bridge Capacity Rating. *Construction Science*, 11.
- Pan, N.F., 2008. Fuzzy AHP approach for selecting the suitable bridge construction method. *Automation in construction*, 17(8), pp.958–965.
- Petkovic, J., Sevarac, Z., Jaksic, M.L. and Marinkovic, S., 2012. Application of fuzzy AHP method for choosing a technology within service company. *Technics technologies education management-ttem*, 7(1), pp.332–341.
- Saaty, T., 1980, November. The analytic hierarchy process (AHP) for decision making. In *Kobe, Japan* (Vol. 1, p. 69).
- Sasmal, S., Ramanjaneyulu, K., Gopalakrishnan, S. and Lakshmanan, N., 2006. Fuzzy logic based condition rating of existing reinforced concrete bridges. *Journal of Performance of Constructed facilities*, 20(3), pp.261–273.
- Tee, A.B., Bowman, M.D. and Sinha, K.C., 1988. A fuzzy mathematical approach for bridge condition evaluation. *Civil Engineering Systems*, 5(1), pp.17–24.
- Val, D.V. and Melchers, R.E., 1997. Reliability of deteriorating RC slab bridges. *Journal of structural engineering*, 123(12), pp.1638–1644.
- Van Laarhoven, P.J. and Pedrycz, W., 1983. A fuzzy extension of Saaty's priority theory. *Fuzzy sets and Systems*, 11(1-3), pp.229–241.
- Yager, R.R., 2008. Prioritized aggregation operators. *International Journal of Approximate Reasoning*, 48(1), pp.263–274.
- Yager, R., 2009. Prioritized OWA aggregation. *Fuzzy Optimization & Decision Making*, 8(3).
- Zadeh, L.A., 1965. Fuzzy sets. *Information and control*, 8(3), pp.338–353.



Taylor & Francis

Taylor & Francis Group

<http://taylorandfrancis.com>

*SS29: Durability and structural assessment of fiber reinforced
strengthening materials and strengthened structures*
Organizers: F. Micelli, C. Papanicolaou, B. Ghiassi & M. Leone



Taylor & Francis

Taylor & Francis Group

<http://taylorandfrancis.com>

Freeze/thaw effects on the performances of FRCM strengthened reinforced concrete beams

S. Verre

Università eCampus, Novedrate (CO), Italy

M. Guglielmi

Department of Civil Engineering, University of Calabria, Arcavacata di Rende, Italy

ABSTRACT: Nowadays, the use of FRCM (Fabric Reinforced Cementitious Mortar) systems is largely adopted in the field of structural retrofitting. Nonetheless, the durability issue is a lightly investigated phenomenon, even if it is important for the long-term effects on external reinforcement effectiveness. This paper presents the results of freeze/thaw cycles and low temperature on the mechanical response of concrete members strengthened with a PBO-FRCM system consisting of Polyparaphenylenebenzo-bisoxazole fiber meshes embedded into an inorganic mortar. In particular, the experimental investigation was performed on small RC-beams (1000 mm long), on FRCM specimen and FRCM-concrete joints. Test results were reported and discussed in the paper.

1 INTRODUCTION

New techniques based on the use of innovative materials, commonly known as Fabric Reinforced Cementitious Matrix (FRCM) or Textile Reinforced Mortars (TRM), have been developed in the last decades for strengthening existing masonry or concrete structures. This alternative strengthening method uses fiber grids embedded in cement-based mortars; the function of the fibers is to bear the tensile stresses, while the mortar should be able to contain and protect the textile also providing to the stress transfer from the substrate to the fiber. This phenomenon is accomplished through the bonding between the substrate and the mortar and the mechanical interlocking between the fabric and the mortar. The use of FRCM reinforcements has the following main advantages: *i*) less sensitivity to debonding phenomena because of the lower stress concentrations related to the larger bonded area of the grid; *ii*) simplicity of application; *iii*) workability assured in a wide range of temperatures and *iv*) less sensitivity to modified environmental conditions. These features make the use of FRCM effective in the strengthening of concrete structures (Awani et al. 2017). As for tensile behavior, the bond behavior of FRCM systems is also influenced by cracking of the cement-based matrix and friction phenomena between rovings and mortar. It was demonstrated that the treatment of the substrate surface and the use of a matrix with controlled shrinkage reduced the possibility of reinforcement detachment even if several aspects are involved, such as the arrangement of the fibers in the fabric mesh, the matrix impregnating capacity and the non-uniform distribution of the stress among the fibers. Moreover, several experimental tests (Carozzi & Poggi 2015) showed that for FRCM materials, different debonding mechanisms also involving the fiber–matrix interface may occur in addition to the “telescopic” tensile failure of the fibers. The well-known benefits of these materials have to be balanced with the sensitivity of such a strengthening technique to debonding phenomena and to environmental conditions different from the standard ones. Because of the inorganic origin of the mortar, FRCM systems seem to be less sensitive to modified environmental conditions. Although the mechanical characterization and the effectiveness of FRCMs as externally bonded reinforcement systems have been deeply investigated (Koutas et al. 2018), their ability to withstand the

exposure to service environments is relatively unknown. At present, very few works concerning the performance of FRCM systems under various environmental exposure conditions have been conducted. Moreover, the long-term behavior of FRCM systems also concerns all the degradation mechanisms typical of cementitious materials. For example, alkali aggregate reaction, sulphate attack and freeze–thaw cycles represent chemical-physical conditions that may promote the formation of expansive compounds usually responsible for crumbling or spalling of cementitious materials. The decay of mechanical properties due to freeze–thaw cycles and salt attack is more noticeable in matrices with high porosity and low strength (Verre 2021). Thus, in the case of FRCM systems made of lime-based matrices, the effects of artificial exposure could be more compromising than in the case of cementitious matrices. Recent guidelines (CNR-DT 215 2020; ACI549.4R 2013), provide durability tests to evaluate the residual mechanical properties of FRCM systems after being subjected to different environmental exposures. These tests include aging in water vapor, immersion in saltwater and alkaline solution at 23°C up to 3000h, freezing–thawing cycles, fuel resistance and thermal tests. These guidelines provide for mechanical tests on FRCM coupons, constituted by the coupling of fabric reinforcement and inorganic matrix. However, beside the importance of investigating the effect of different aging protocols, a deep understanding of the factors affecting the durability of FRCM composite systems should also consider the behavior of each of its components subjected to environmental stresses. In this study, the effects of freeze/thaw cycling exposure on the mechanical properties of an FRCM system constituted by a bidirectional fabric, made of PBO (short for Polyparaphenylenebenzo-bisoxazole) fibers coupled with a cement-based matrix have been investigated. Experimental tests have been conducted on the individual materials (PBO fiber fabrics, matrix) and on FRCM coupons, in order to assess the structural efficiency of the whole composite system subjected to the detrimental environmental actions of freeze–thaw cycles from 18°C to +38°C. The number of cycles, the exposure time and temperature/exposure time before the conditioning were the investigated parameters. In detail, single bundles and dry textile mechanical properties were evaluated in accordance to different guidelines, while both flexural tensile and compressive strength were considered for the mortar. A total of six direct tensile (DT) tests were carried out on PBO-FRCM coupons to evaluate the mechanical response of the composite systems, according to CNR-DT 215 (2020). Moreover, six direct single-lap shear tests (DS) were performed on PBO-FRCM concrete joints following the recommendations of CNR-DT 215 (2020) in order to provide further insights on their bond properties. Since information about the long-term behavior of concrete elements bonded with FRCM systems and exposed to temperatures and a wet environment corresponding to serviceability conditions are lacking, the experimental program presented in this paper is aimed to partially fill such a gap. In order to investigate the effect of low temperature and freeze/thaw cycles on the mechanical response of concrete members strengthened with the PBO-FRCM system, all the tests were carried out in a chamber able to replicate the same values of temperature applied during the conditioning phases.

2 EXPERIMENTAL INVESTIGATION

The experimental investigation was performed on four rectangular RC beams, six FRCM specimen and six FRCM-concrete joints subjected to freeze–thaw cycles and freeze temperature. All the beams had a cross section of 150x150 mm and a length of 1000 mm. The geometry and the internal reinforcement of the beams were reported in Figure 1a. The internal reinforcement was composed by two steel bars (dia. 8 mm) on the tension side of the beams, two steel bars (dia. 8 mm) on the compression side of the beams and five steel stirrups (dia. 8 mm). The concrete cover adopted with respect to the transversal reinforcement was equal to 20 mm for all sides. All the beams were tested as simply supported in symmetrical three-point bending. All concrete prisms had a rectangular cross section equal to 200x150 mm and a height of 400 mm (Figure 1b). Three beams were strengthened, and one un-strengthened beam used as the reference beam (called B-Control). All the specimens were named according to the following notation: B (DT or DS)-FRCM-U (FT or T)- η L-Z, where B indicates beam specimen, DT and DS indicates the FRCM and FRCM-concrete joint, respectively, FRCM is used to

identify the strengthened beam, U indicates the unconditioned specimen, FT and T indicate the Freeze/Thaw or low temperature conditioning, respectively, ηL indicates the number of fiber layers (1 layer in this study) and Z is the specimen number.

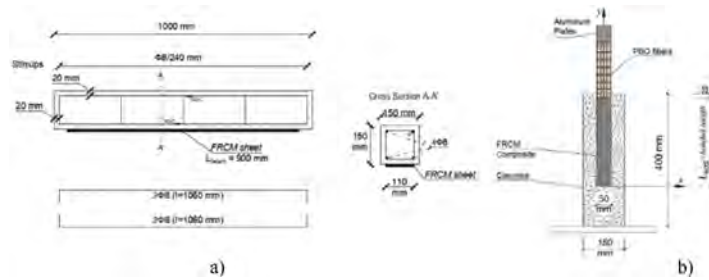


Figure 1. Geometry: a) for the RC beam with internal reinforcement and b) DS specimen.

2.1 Materials

The compressive strength f_{cm} of the ready-mix concrete evaluated at 28 days after the casting (evaluated on three specimens) was equal to 30.5 MPa (CoV=0.01). The mechanical properties of the longitudinal rebar and the stirrups were evaluated under the tensile test. For the 8-mm bars, the yielding and ultimate strength obtained on three specimens were 525.5 MPa (CoV= 0.01) and 628.5 MPa (CoV= 0.02), respectively. The fabric mesh adopted in the FRCM system presents a bi-directional development of fiber bundles and different fiber density; in particular, the fiber bundles along two orthogonal directions was unbalanced ($70\text{-}18 \text{ g/m}^2$). The mechanical properties of the PBO fibers in terms of the tensile strength, ultimate strain and elastic modulus, evaluated according to CNR-DT 215 (2020) guidelines, were 3375 MPa (CoV= 0.04), 2.5 % (CoV= 0.09) and 211 GPa (CoV.= 0.05), respectively. The mortar was a stabilized mono-component inorganic cementitious matrix (Ruregold 2022). Three specimens were tested, the load was applied with a rate equal to 100 N/s and 500 N/s for the flexural tensile and compressive test, respectively, in accordance to UNI 1015 (2007). The mechanical properties (compressive and flexural strength) in terms of average values were equal to 43.11 (CoV= 0.03) and 6.73 (CoV= 0.05), respectively.

2.2 Specimen preparation

The technique adopted in the application of the composite strips for the single-lap direct shear (DS), direct tensile (DT) specimens and the strengthening beams is similar, and it is organized in three steps. The first step consists of the realization of a formboard of 3 mm thickness, attached on the concrete surface and a wood planer, respectively. The shape used to strengthen the RC-beam of the formboard, having a bonded length (L_{beam}) of 900 mm and a width of 100 mm, was cut out of the in order to accommodate the composite strips (Figure 2a). Each composite strip was made individually and it was applied along the centerline of the tension for RC beams, while for the DS specimen, shape of the formboard having a bonded length ($L_{b,DS}$) of 260 mm and 50 mm, respectively. Lastly, the shape of the formboard used to for the DT specimens having a bonded length ($L_{b,DT}$) of 500 mm and 50 mm, respectively. The DT specimens were casted on the wood planer surface to ensure the planarity of the surface. In the second step, the mortar (called the internal layer) was applied by mold with light pressure and subsequently the textile was placed on the internal layer. However, the second step is the most critical one, where the perfect alignment of the fibers and impregnation with the matrix must be ensured (Figure 2b). Finally, in the third step the same operation as in step one is repeated (Figure 2c). During the casting of the strengthened beams, K-type thermocouples (0.3 mm of conductor diameter) were glued to the concrete-internal mortar layers and fiber interfaces. In all applications of the composite strips on the DS specimens, the bonded area was started at 20 mm of the edge of the top face of the concrete prism, while for the strengthened beams the bond area was centered with respect to the middle of the beam (Figure 1b). Finally, all specimens were stored and cured in laboratory for 28 days, while for the

DT specimens were demolded from the respective formboards after about 7 days. Specimens were all left to cure at room condition (temperature $T=20^{\circ}\text{C}$ and relative humidity $\text{RH}=65\%$).

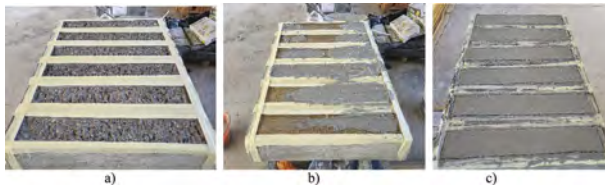


Figure 2. Specimen preparation: a) apply the formboard and internal layer of mortar, b) PBO-fibers and c) external matrix layer.

2.3 Freeze/Thaw protocol (FT) and Low Temperature (LT)

All the specimens subjected with the Freeze/Thaw regime were conditioned in a chamber for one week at a relative humidity of 90% and a temperature of $38^{\circ}\text{C} \pm 2^{\circ}\text{C}$. Subsequently, the specimens were subjected to freeze-thaw cycles (20 in total). Each cycle consisted of 4 hours at $-18^{\circ}\text{C} \pm 2^{\circ}\text{C}$, then, 12 hours at 90% humidity and a $38^{\circ}\text{C} \pm 2^{\circ}\text{C}$ temperature, in accordance with CNR-DT 215 (2020). In Figure 3 the environmental conditioning regime was reported.

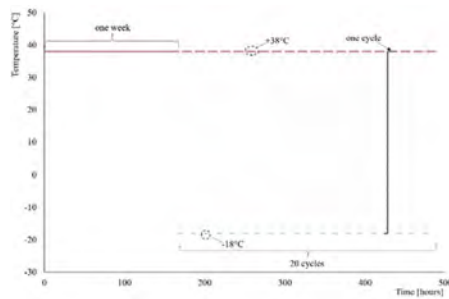


Figure 3. Environment conditioning regime.

The B-FRCM-T-1L-1 was cooled at a temperature of $-18^{\circ}\text{C} \pm 2^{\circ}\text{C}$ in a chamber until the fiber interface reaches the same temperature present in the climatic chamber, in order to evaluate the effects of freeze.

2.4 Direct Tensile (DT), single lap Direct Shear (DS) and flexural test protocol

Direct tensile tests carried out on six FRCM specimens (three unconditioned and three subjected to conditioning). The test setup adopted is shown in Figure 4a. The gauge length and the tabs used were 300 mm in length and 100 mm in width. The strain measurements between the ends of the tab were acquired by LVDT a and b, that were fixed lengthwise at the side of the specimen by aluminum supports. Six FRCM-concrete joints specimen (control and subjected to conditioning) were tested by single-lap direct shear test set-up using the push pull configuration (Carloni et al. 2022). The test setup used (Figure 4b) is the classic push pull configuration. The steel frame was bolted by four steel bars to the machine used for the test. In addition, the shape of the steel frame was realized to restrain the movement of the concrete prism during the test and to allow the composite strip to be housed on the sides of the prism not involved in the test.

The load was applied through a couple of aluminum tabs glued by thermosetting epoxy on the dry fiber at the top of the fibers. An L shape aluminum plate was attached to the dry fiber at the top of the concrete prism near the bonded area. The reaction of the latter was measured by two linear variable displacement transformers (LVDTs) attached at both sides of the composite strip, called LVDT “a” and “b”.

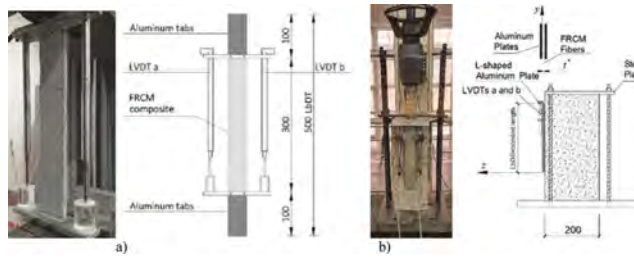


Figure 4. Test setup adopted for: a) tensile test for DT and (b) single-lap shear test for specimen.

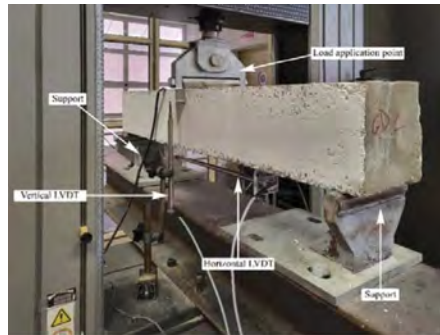


Figure 5. Test setup adopted for reinforced concrete beam.

All the beams were tested in symmetric three-point bending under displacement control. The midspan displacements were measured through the LVDTs positioned on both sides at the middle of the beams and in correspondence of the load point (Figure 5). On the longitudinal internal bar, two strain gauges were attached close the applied load point. All the tests were conducted under displacement control using the rate of 0.2 mm/min; this loading rate value was already used for RC beams strengthened with FRCM composites (Sneed et al. 2016).

3 RESULTS AND DISCUSSION

3.1 Direct Tensile (DT), single lap Direct Shear (DS) and flexural test protocol

After FT treatment, the majority of the FRCM composites didn't show any crack patterns on the surface of the specimens or at the matrix-to-substrate interface. After the FT treatment, the flexural and compressive strength of the mortar were 7.59 MPa (CoV= 4%) and 46.09 MPa (CoV= 3%), respectively. Therefore, after the FT treatment, there was a slight increase of the mechanical properties of the mortar; with reference to the initial values, the flexural strength and the compressive strength increase of 13%, and 7%, respectively. The results of the DS tests are reported in Table 1 in terms of peak load P^* , average value of P^*_{avg} evaluated for each group of specimens (unconditioned and conditioned) and the ratio between the average value of unconditioned and conditioned specimen Δ^* .

Table 1. Experimental results of DS specimens.

	P^* (kN)	P^*_{avg} (kN)	Δ^*
DS-FRCM-U-1L-1	4.60		
DS-FRCM-U-1L-2	4.70	4.62	-
DS-FRCM-U-1L-3	4.56		
DS-FRCM-FT-1L-1	4.61		
DS-FRCM-FT-1L-2	4.83	4.74	1.03
DS-FRCM-FT-1L-3	4.78		

For all tested specimens, the debonding failure at the fiber–matrix interface was observed. The experimental curves applied load-global slips of the unconditioned and conditioned specimens are reported in Figure 6a. It should be noted that, after the FT treatment, the peak load values of strengthened specimens increased slightly (3%) with respect to the untreated specimens. In addition, all conditioned specimens showed an initial stiffness increment due to the environment conditioning. In Figure 6b the stress-strain curves for both unconditioned and conditioned specimens subjected to tensile test are reported.

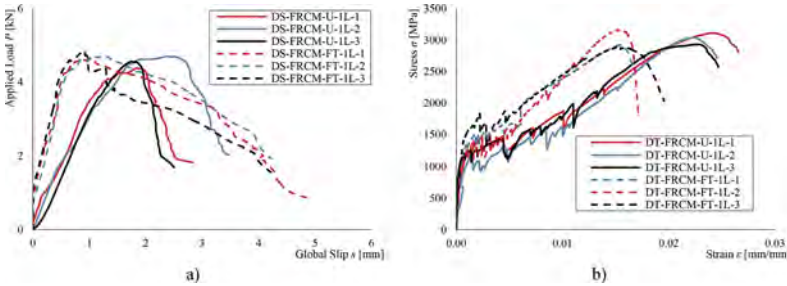


Figure 6. Comparison between experimental curves (unconditioned and conditioned): a) DS specimen and b) DT specimens.

Table 2 reports the values of the ultimate stress (σ), the corresponding strain (ϵ) and the cracked modulus of elasticity (E) for all tested specimens. The analysis of the results evidences a small increase of the ultimate stress for conditioned specimens with respect to the unconditioned one. Comparing the experimental curves shown in Figure 6b, the global behavior in the cracked stage of the conditioned specimens shows similar stress values but a smaller strain range. The cracked elasticity modulus of conditioned specimens increases of 6.8% with respect to that of the unconditioned one.

Table 2. Experimental results of DT specimens.

	σ (MPa)	ϵ (‰)	E (GPa)
DT-FRCM-U-1L-1	3111.30	26.6	108.9
DT-FRCM-U-1L-2	3041.72	24.5	121.7
DT-FRCM-U-1L-3	2931.57	24.6	119.9
DT-FRCM-FT-1L-1	2920.58	16.7	122.6
DT-FRCM-FT-1L-2	3155.39	17.1	126.6
DT-FRCM-FT-1L-3	2899.08	19.6	125.0

The increase of the capacity in terms of ultimate stress and modulus of elasticity should be attributed to an extended curing time of one week at relative humidity of 90% and a temperature of $38^{\circ}\text{C} \pm 2^{\circ}\text{C}$ in the conditioned environment. Furthermore, the compatibility of the mortar with the substrate (concrete), high strength (mortar), and the low permeability of the materials (concrete and mortar) contributed to the increase of performance of the reinforcement (Arboleda et al. 2014). Table 3 reports the results obtained in the flexural tests

Table 3. Summary of the results obtained in the flexural tests of RC beams.

	P_{yie} (kN)	δ_y (mm)	P_{max} (kN)	δ_{max} (mm)	δ_{max}/δ_y (-)	ϵ_{frcm} (-)	$P_{max}/P_{max-B-control}$ (-)
B-Control	28.19	3.32	34.20	13.06	3.93	-	-
B-FRCM-U-1L-1	33.52	4.10	42.30	11.21	2.73	0.015	1.24
B-FRCM-FT-1L-1	41.93	5.03	47.43	9.62	1.91	0.016	1.39
B-FRCM-T-1L-1	45.56	5.32	45.06	7.61	1.43	0.014	1.32

on the strengthened and un-strengthened reinforced concrete beams in terms of yielding load (P_{yie}), yielding displacement, δ_y , maximum load, P_{max} , maximum displacement, δ_{max} , the ductility index δ_{max}/δ_y , the strain at failure in the FRCM system ϵ_{frcm} and the ratio $P_{max}/P_{max-B-control}$ of the ultimate load between strengthened beam and B-control were summarized.

The experimental load-midspan deflection curves reported in Figure 7 can be divided in three stages: (i) linear elastic, followed by a second stage (ii) almost linear branch, in which the concrete starts cracking and then (iii) a non-linear ascending branch corresponding to the post-yielding stage until reaching the peak load. The beam B-FRCM-U-1L reached a higher ultimate applied load (P_{max}), with an increment equal to 24% with respect to the B-Control.

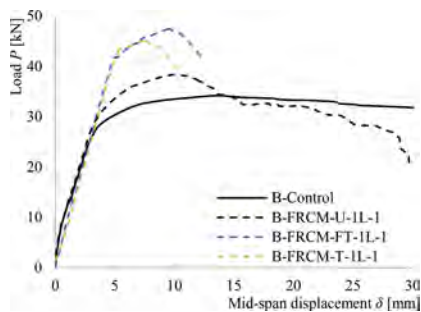


Figure 7. Load– midspan displacement response of beam specimens.

The conditioned beams showed an increase between 32 and 39% in terms of P_{max} , while the initial stiffness was unchanged. The conditioning effect, as reported for the DT and DS specimens, is evident in the post peak behavior of the beams where the midspan displacement is reduced compared to the B-FRCM-U-1L-1.

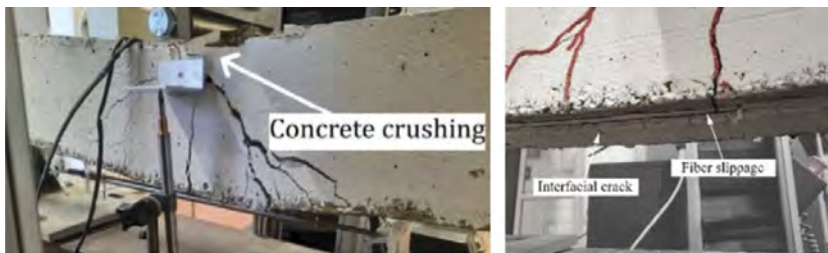


Figure 8. Typical failure mode for the strengthening beams.

The un-strengthened beam (B-Control) exhibited the typical flexural behavior of a flexure-dominant with the gradual occurrence and progression of flexural and flexure-shear cracks and a significant amount of deflection. For the strengthened beams, the flexural cracks first appeared near the applied load point and progressed in length and number with increasing load. Flexural and flexure-shear cracks also appeared within the shear span regions on each end of the beam. The cracks in the concrete beam extended through the thickness of the matrix and were observed on the external surface of the composite. Interfacial cracks formed within the composite at the level of the fibers between the load point and the support at the localized locations of flexural cracks as shown in Figure 8.

4 CONCLUSIONS

The paper presented the results of the experimental investigation on the effect of the Freeze/Thaw and low temperature FRCM composite systems. Based on the results, the following conclusion can be drawn:

- The mechanical characteristics of the mortar in terms of flexural tensile and compressive strength showed an increase of 13 and 7% for the specimens subjected at Freeze/Thaw;
- The Freeze/Thaw environment had no significant influence on the behavior of the FRCM composite;
- The DS conditioned specimens showed an increase of initial stiffness and in terms of peak load;
- The behavior of DT conditioned specimens in the third stage showed an increase in terms of tensile modulus equal to 6.8%;
- The beams strengthened unconditioned and conditioned showed an increment between the 24 and 32% to 1.32 with to respect the conditioned beam.

Additional studies are needed to better understand the role of F-T cycles and low temperatures on the mechanical properties of PBO-FRCM systems.

REFERENCES

- ACI 549.4R. 2013. Design and Construction of Externally Bonded Fabric-Reinforced Cementitious Matrix (FRCM) Systems for Repair and Strengthening Concrete and Masonry Structures; ACI: Farmington Hills, MI, USA.
- Arboleda, D., Babaeidarabad, S., Hays, C.D.L., Nanni, A. 2014. Durability of fabric reinforced cementitious matrix (FRCM) composites. 7th International Conference on FRP Composites in Civil Engineering in Proceedings of the CICE 2014, Vancouver, Canada.
- Awani, O., El-Maaddawy, T., Ismail, N. 2017. Fabric-reinforced cementitious matrix: A promising strengthening technique for concrete structures, *Construction and Building Materials*, 132: 94–111.
- Carlioni, C., Verre, S., Sneed, L.H., Ombres, L. 2022. Open issues on the investigation of PBO FRCM-Concrete debonding. *Composite Structures* 299–116062.
- Sneed, L.H., Verre, S., Carlioni, C., Ombres, L. 2016. Flexural behavior of RC beams strengthened with steel-FRCM composite, *Engineering Structures*, 127, 686–699.
- Carozzi, F.G. & Poggi, C. 2015. Mechanical properties and debonding strength of Fabric Reinforced Cementitious Matrix (FRCM) systems for masonry strengthening, *Composites Part B: Engineering*, 70: 215–230.
- Koutas, L.N., Tetta, Z., Bournas, D.A., Triantafyllou, T.C. 2018. Strengthening of Concrete Structures with Textile Reinforced Mortars: State-of-the-Art, *Review. J. Compos. Constr.* 2019, 23, 03118001.
- National Research Council. Guide for the design and construction of externally bonded fibre reinforced inorganic matrix systems for strengthening existing structures. CNR-DT 215/2018. Rome, Italy, CNR, 2020.
- Ruregold, 2022. Available online: <https://www.ruregold.com/it>.
- UNI EN 1015-11: 2007. Methods of Test for Masonry Units—Part 11: Determination of Flexural and Compressive Strength of Hardened Mortar.
- Verre, S. 2021. Effects of different environments conditioning on the debonding phenomenon in Fiber-Reinforced Cementitious Matrix-Concrete joints, *Materials* 2021, 17, 7566.

Interface experimental behavior between basalt-FRCMs and natural stones

G. Bramato, M. Leone & M.A. Aiello

Department of Engineering for Innovation, Campus Ecotekne, University of Salento, Lecce, Italy

ABSTRACT: The issue of environmental sustainability is central to several areas of research; in fact, the reduction of polluting emissions and concentration of CO₂ in the atmosphere is a key objective for both private and public institutions. In structural engineering, the sustainability goal involves the design stage, the construction technologies and materials, the maintenance. Specifically referring to structural materials, the research effort is very relevant, as the production of many materials currently used is particularly energy intensive. In the last years, innovative materials have been developed by replacing some components with recycled ones or from industrial processing waste. For example, innovative geopolymers mortars are made with lightweight components, blast furnace or fly ashes (a residue from coal combustion in electricity generation) that replace traditional binder. This new kind of materials can be used as inorganic matrix in case of FRCM (Fiber Reinforced Cementitious Matrix) applications to restore and strengthen existing buildings. The object of the experimental campaign, whose results are reported in this paper, is to study the shear-bond behavior between basalt-FRCM reinforcement system and masonry varying the binder in the mortar: two traditional (cement and lime-based, both with short fibers inside) and an innovative geopolymer matrixes. Two different types of substrates representative of the historical and artistic heritage of Southern Italy are also used: a compact calcareous stone, called *Pietra Leccese*, and a porous calcareous stone, called *Calcarenite*. The results obtained evidenced that the mechanical properties of inorganic matrix always influence the shear bond behavior of the samples, similar conclusion cannot be drawn referring to the mechanical properties of substrates.

1 INTRODUCTION

The Kyoto Protocol was adopted in December 1997 by the Conference of Countries to the United Nations Convention on Climate Change and entered into force in February 2005, following its ratification by the 55 countries responsible for 55% of carbon dioxide emissions. It aims to reduce emissions of six gases (carbon dioxide, nitrous oxide, methane, hydrofluorocarbons, perfluorocarbons and sulphur hexafluoride) considered to be the main causes of climate change and promotes, with the same scope, the protection and expansion of forests to absorb carbon dioxide. Following the entry into force of the Protocol, different solutions have been sought in several areas, including electricity generation, transport, agriculture, waste management and productions of building materials. In fact, the manufacturing of materials like cement, bricks, ceramics, etc. is particularly energy intensive. In addition, with the advent of Environmental Criteria, building materials must have a variable percentage of recycled components and the reuse of materials must be encouraged. Taking all this into account, in the last years new materials have been developed replacing some components with waste from industrial processes. Longo et al (2020) developed a new *Geopolymer Matrix* (GPM) made of dry binders (fly ash and metakaolin), alkali activators and LWA (i.e., expanded glass aggregate). This innovative inorganic matrix therefore involves the use of recycled components (waste from the processing of a coal-fired power plant) and also has further energy benefits in

terms of conductivity, as it results lower than that of a traditional mortar. Nonetheless, the proposed GPM has proper mechanical characteristics for being used in FRCM systems to restore existing building. FRCMs are composite materials made by inorganic matrix and dry fibers meshes. The composite is an externally bonded system, so its effectiveness is influenced by stress transfer mechanisms between fibre mesh and inorganic matrix and between composite and substrates. With the aim of investigating the parameters most influential on the shear bond behavior, Raof et al (2016) analyzed different aspects: the bond length, the number of layers, the concrete surface preparation, the substrate compressive strength. Eighty shear bond concrete samples reinforced with carbon fibers different kinds of matrix were fabricated and tested under double-lap direct shear. The results evidenced that:

- increasing the bond length, the bond capacity increases in a non-proportional way for all the number of layers;
- increasing the number of layers for the same bond length, the bond capacity increases in a non-proportional way;
- the number of layers has a significant effect on the failure mode;
- different concrete surface preparation methods did not influence the bond characteristics between TRM and concrete; the use of lower concrete compressive strength marginally affected the bond strength of the TRM to concrete.

In Askouni et al (2019) et al the bond between (AR) glass FRCM and solid clay bricks was studied testing 37 specimens under double lap shear configuration. The matrix of the reinforcement was polypropylene fiber-reinforced cement-based mortar. The chosen variable parameters were bond length, bond width, number of layer and number of yarns. The results evidenced that the maximum axial stress increases almost linearly with the bond width because of the transversal yarns provide improved anchoring conditions for the longitudinal yarns and improved mechanical interlocking between mortar and meshes. Moreover, different textile configurations exhibit different shear bond behaviors.

The present work aims to investigate the stress transfer mechanism between Basalt FRCMs and masonry substrates typical of Southern Italy. Three different kind of mortar (two traditional, cementitious and lime-based, and the new GPM) and two types of substrates (Calcarenite – a calcareous porous stone - and Pietra Leccese – a calcareous compact stone) were considered.

2 EXPERIMENTAL PROGRAM AND SET-UP

The work is part of a research project, whose first results can be found in Bramato et al (2022). The experimental program discussed in the present paper is reported in Table 1 and included 18 samples divided into 6 series of 3 samples made by varying the type of substrate and matrix.

Table 1. Experimental program.

	#	Substrate	Matrix	Fibre
<i>PL_B_R</i>	3	Pietra Leccese	Lime-based	Basalt
<i>PL_B_M</i>	3		Cementitious	
<i>PL_B_G</i>	3		Geopolymer	
<i>C_B_R</i>	3	Calcarenite	Lime-based	
<i>C_B_M</i>	3		Cementitious	
<i>C_B_G</i>	3		Geopolymer	

The used nomenclature *W_X_Y_Z* indicated: W the type of substrate (C=Calcarenite, PL=Pietra Leccese), X the type of dry mesh (B=Basalt), Y the kind of inorganic matrix (R=lime-based, M=cementitious and G=Geopolymeric) and Z the progressive number of samples (i.e. 1 to 3). The mechanical properties of the constituent materials were reported in previous papers – Longo et al (2020) and Bramato et al (2022) - and the utilized geopolymer

matrix was developed in Longo et al (2020). The experimental mechanical strength (compressive and flexural strength) for the traditional mortars (lime-based and cementitious) are those reported in manufacturer technical sheet Bramato et al (2022). In Longo et al (2020) the characteristics of the innovative GPM are reported in terms of energetic and mechanical properties. Comparing the GPM with an equivalent traditional NHL mortar, better performance in terms of conductivity but worse mechanical properties were found. The Geopolymeric matrix exhibited 73% lower values of conductivity if compared with a traditional NHL according to the experimental data reported in Longo et al (2022).

The substrate used is a calcareous compact stone called *Pietra Leccese*, and a calcareous porous stone called *Calcarenite*. The mechanical properties of the natural stones were evaluated according to the current guidelines in terms of flexural and compressive strength and discussed in Bramato et al (2022).

All the tests were performed in displacement control with a rate of 0.2 mm/min by using the same universal machine and test set-up (Figure 1) reported in Bramato et al (2022).

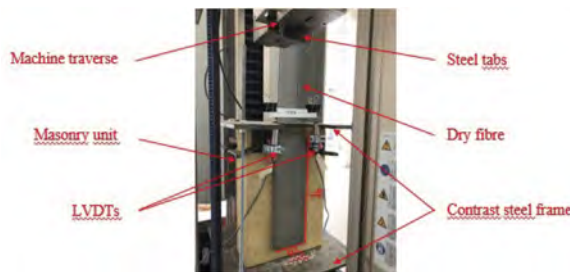


Figure 1. Test set-up.

2.1 Experimental results

The experimental results are reported in Table 2 in terms of peak axial force, exploitation rate and global displacement average values. The exploitation rate was calculated as the ratio between the peak axial stress obtained by the shear bond test and the tensile strength of the dry mesh, while the global displacement was set equal to the relative shift of the universal machine transverses, in the following called “global displacement”. The peak axial stress (σ_{\max}), was calculated according to the following equations.

$$\sigma_{\text{peak}} = F_{\text{peak}} / (A_{\text{y}} * n) \quad (1)$$

where:

σ_{peak} = Peak axial stress [MPa];

F_{peak} = Peak axial load [N]

A_{sy} = Single yarn section area [equal to 0.23 mm², according to data sheet provided by the supplier]

n = Number of yarns [equal to 15]

Table 2. Average experimental results.

Label	F_{peak} [kN]	$\sigma_{\max} / f_{\text{tf}}$ [%]	s [mm]	Label	F_{peak} [kN]	$\sigma_{\max} / f_{\text{tf}}$ [%]	s [mm]
<i>C_B_R</i>	3269.85	72.24	10.98	<i>PL_B_R</i>	2897.04	64.00	7.78
<i>C.o.V.</i>	5.48%	5.48%	6.58%	<i>C.o.V.</i>	20.74%	20.74	20.20%
<i>C_B_M</i>	4167.35	92.07	9.79	<i>PL_B_M</i>	4738.64	104.69	10.16
<i>C.o.V.</i>	11.69%	11.69%	11.55%	<i>C.o.V.</i>	7.77%	7.77	10.20%
<i>C_B_G</i>	1037.63	22.92	4.67	<i>PL_B_G</i>	1513.54	53.68	2.65
<i>C.o.V.</i>	11.66%	11.6%	25.22%	<i>C.o.V.</i>	-	-	-

Three different kinds of failure mode were observed and reported in Figure 2:

- FM type “C”: debonding at the matrix-fibre interface;
- FM type “F”: widespread tensile failure of the dry fibre at the unbonded zone of the reinforcement;
- FM type “F*”: tensile failure of the dry fibre at the fibre-reinforcement interface.

In case of samples reinforced with lime-based mortar, about 83% of the specimens failed for debonding at the matrix-fibre interface, while half of the samples reinforced with cementitious matrix failed for debonding at the matrix-fibre interface, the other half failed because of a diffuse tensile failure at the unbonded zone of the reinforcement. All samples reinforced with geopolymer matrix were characterized by a tensile rupture at the dry fibre-reinforcement interface.

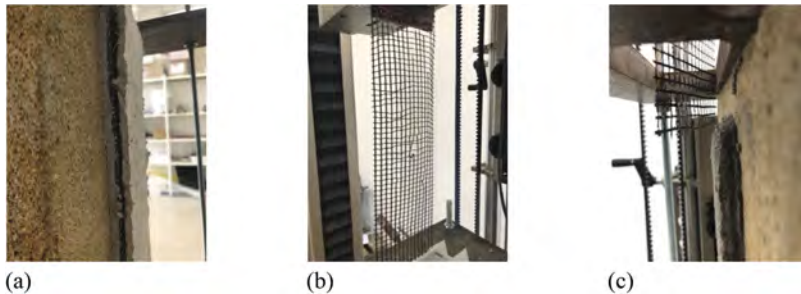


Figure 2. Typical Failure Modes observed: (a) Type “C”; (b) Type “F”; (c) Type “F*”.

For samples reinforced with geopolymeric mortar, the exploitation rate is very low even if a fibre rupture was observed. It seems that there is a possible compatibility problem between the basalt mesh utilized and the innovative geopolymer matrix. With the aim to understand these experimental results, a deep microscopic analysis of the tested specimens has been performed, that evidenced the absence of fibre damage or matrix cracking. Moreover, the lower values of coefficient of variation of both series confirmed the absence of possible experimental error. However, further tests are suggested for validating the data obtained and deepen the problem of the fibre-geopolymeric matrix compatibility. In fact, different studies evidenced that basalt fibers have good chemical stability, chemical resistance, corrosion resistance and water resistance [6-10], however studies devoted to the compatibility between Basalt fibers and geopolymeric matrix are still limited.

Figure 3 shows the average curves axial stress-displacement and the variability range for each of the six series of tested specimens. It can be observed that the variability range is very small as confirmed by the values of the coefficient of variation reported in Table 2. All the average curves show a similar trend and almost the same slope of the first phase (except for C_B_G series), even if the average peak axial stress obtained by samples reinforced with the innovative geopolymer mortar is lower with respect to that obtained in case of traditional mortar. The comparison between the experimental average curves, shown in the Figure 4, evidences and confirms that the mechanical properties of the inorganic matrix influenced the results in terms of peak axial force for both type of substrates (i.e. PL and C stone). In fact, based on this experimental data, increasing the compressive strength of inorganic matrix the maximum axial stress increases as well. In particular, comparing data obtained in case of cementitious and based-lime mortar an increase of 27% and 63% has been registered in case of *Calcarenite* and *Pietra Leccese* samples, respectively.

Figure 5 evidences the effect of substrate on the experimental results. The average curves and the relative scatter areas of series reinforced with lime-based (a), cementitious (b) and geopolymer (c) mortar are drawn. It can be observed that experimental results in terms of average peak axial stress of samples reinforced with lime-based mortar are influenced by the kind of substrates. In this case, the mortar and both the substrates have similar mechanical properties. Contrariwise, in case of cementitious samples, the influence of substrates seems negligible,

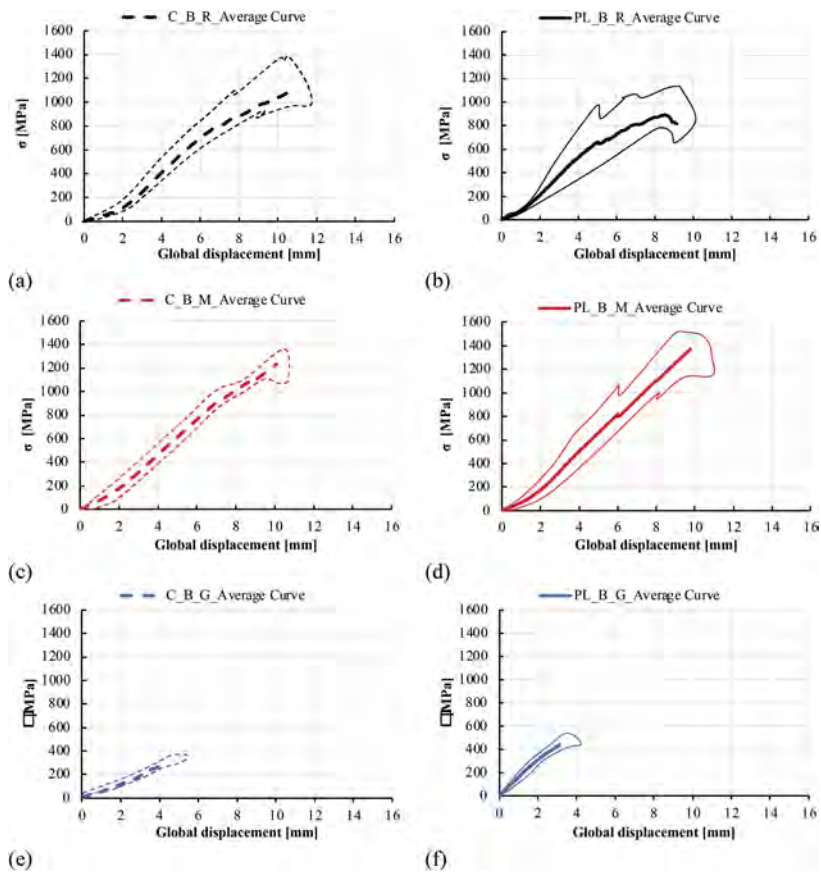


Figure 3. Shear bond specimens global displacement-stress curves: a) C_B_R series; b) PL_B_R series; c) C_B_M series; d) PL_B_M series; e) C_B_G series; f) PL_B_G series.

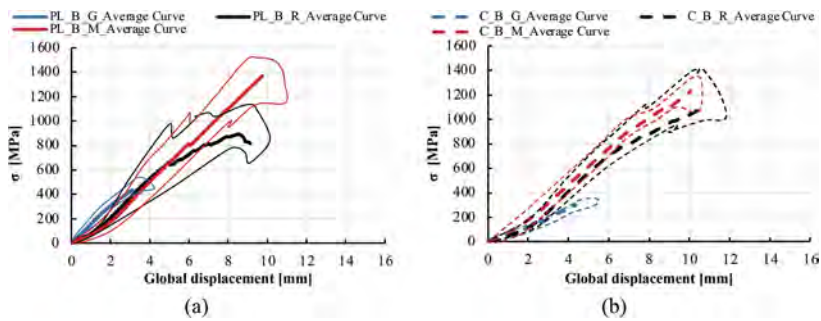


Figure 4. Shear bond specimens global displacement-stress curves: a) *Pietra Leccese* substrates; b) *Calcarenite* substrates.

probably because, the mortar has flexural and compressive strength higher than both the substrates. The analysis is still in progress to understand if the recorded percentage difference could be also attributed to the physical properties of the substrates. In case of samples reinforced with geopolymer matrix, a reduction of the slope of the curve was observed passing from *Pietra Leccese* to *Calcarenite*. A reduction in average peak axial force was also recorded. However, this data are still under investigation.

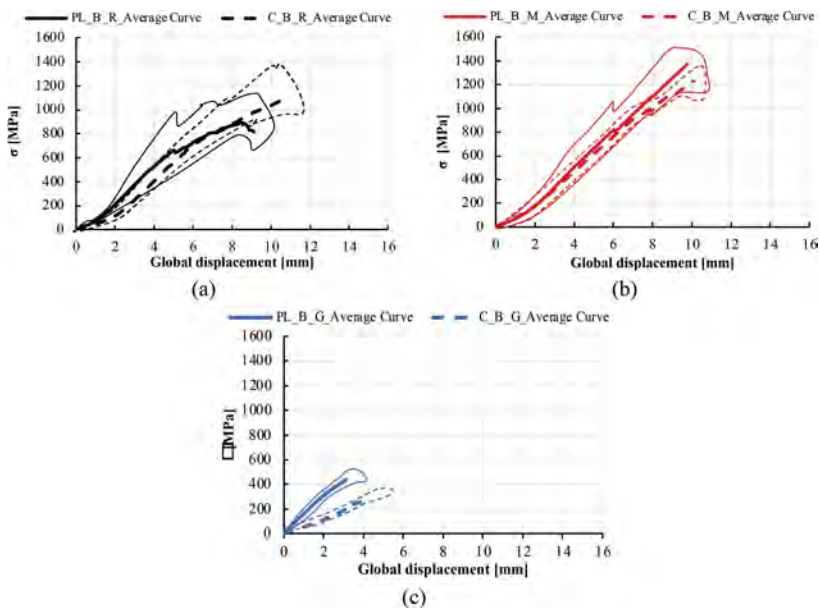


Figure 5. Shear bond specimens global displacement-stress curves: a) C_B_R series; b) PL_B_R series; c) C_B_M series; d) PL_B_M series; e) C_B_G series; f) PL_B_G series.

Billotta et al (2017) tested 10 clay bricks prisms with mechanical properties similar to natural stone used in the reported investigation and reinforced with almost the same Basalt open grid dry mesh and matrix. In detail, a natural hydraulic lime mortar with short fibers inside was used. In this case, an average peak axial force equal to 4.6 kN was recorded, a value 41% and 58% higher than in case of C_B_R and PL_B_R series, respectively. Two different failure mode were observed: tensile failure at unbonded zone of the reinforcement and a mix of tensile failure at unbonded zone of the reinforcement and slippage between fibre and matrix without matrix cracking.

Lignola et al (2017) carried out a large experimental campaign in order to investigate the performance of Basalt FRCMs in retrofitting applications by making single lap shear bond test. Some samples made had geometry and mechanical properties of fibre, substrate and matrix similar to those reports in this paper. In detail, 16 coupons were realized with clay bricks prisms with compressive strength equal to 14.6 MPa reinforced with lime-based mortar with 15 MPa compressive strength and almost the same open grid dry mesh. The results obtained was average peak axial force equal to 3.75 kN, a value 15% and 29% higher than in case of C_B_R and PL_B_R series, respectively. Moreover, Lignola et al recorded two different types of Failure Mode: type “E” – slippage between fibre and matrix with mortar cracking; type “F” – tensile failure of fibre at unbonded zone of the reinforcement.

The diversity of the results obtained in terms of axial peak strength and failure mode highlights the need to further deepen the experimental and theoretical investigation.

3 CONCLUSION

The present paper reports the main experimental results of shear bond tests on masonry samples reinforced with different Basalt-FRCM systems. In detail, three different mortars (lime-based, cementitious and an innovative geopolymer mortar) were used with the same Basalt open mesh grid. Two different substrates typical of Southern Italy were considered. The following conclusions can be drawn:

- The types of substrates influence the experimental results when their mechanical properties are similar to those of inorganic matrix;
- The mechanical properties of inorganic matrix strongly influenced the experimental results. In fact, increasing the mortar strength, a higher experimental peak stress was found;
- A possible compatibility problem between the basalt mesh and the innovative geopolymer matrix utilized in the reported investigation was observed. The progress of the research aims to deepen this issue.

ACKNOWLEDGEMENTS

The study object of this test was founded by the Italian Ministry of Education, University and Research in the framework of PRIN 2017 – SURMOUNT (Innovative systems on inorganic mortar non-metallic reinforcement for the upgrade of masonry structures and non-structural elements). The authors would acknowledge also Mapei s.p.a for materials supply.

REFERENCES

- Askouni, P. D., & Papanicolaou, C. C. G. (2019). Textile Reinforced Mortar-to-masonry bond: Experimental investigation of bond-critical parameters. *Construction and Building Materials*, 207, 535–547.
- Bilotta, A., Ceroni, F., Lignola, G. P., & Prota, A. (2017). Use of DIC technique for investigating the behaviour of FRCM materials for strengthening masonry elements. *Composites Part B: Engineering*, 129, 251–270.
- Bramato, G., Leone, M., & Aiello, M. A. (2022). Experimental investigation on bond behaviour between Basalt-FRCMs and natural stones. The 15th International Conference on Fibre-Reinforced Polymers for Reinforced Concrete Structures (FRPRCS-15) & The 8th Asia-Pacific Conference on FRP in Structures (APFIS-2022) 10-14 December 2022, Shenzhen, China
- E. UNI, 1015-11. Metodi di prova per malte per opere murarie - Determinazione della resistenza a flessione e a compressione della malta indurita, 2007. [In Italian]
- Lignola, G. P., Caggegi, C., Ceroni, F., De Santis, S., Krajewski, P., Lourenço, P. B., ... & Zuccarino, L. (2017). Performance assessment of basalt FRCM for retrofit applications on masonry. *Composites Part B: Engineering*, 128, 1–18.
- Longo, F., Lassandro, P., Moshiri, A., Phatak, T., Aiello, M. A., & Krakowiak, K. J. (2020). Light-weight geopolymer-based mortars for the structural and energy retrofit of buildings. *Energy and Buildings*, 225, 110352.
- Militký, J.; Kováčic, V.; Rubnerová, J. Influence of thermal treatment on tensile failure of basalt fibers. *Eng. Fract. Mech.* 2002, 69, 1025–1033
- Monaldo, E.; Nerilli, F.; Vairo, G. Basalt-based fiber-reinforced materials and structural applications in civil engineering. *Compos. Struct.* 2019, 214, 246–263.
- Raof, S. M., Koutas, L. N., & Bournas, D. A. (2016). Bond between textile-reinforced mortar (TRM) and concrete substrates: Experimental investigation. *Composites Part B: Engineering*, 98, 350–361.
- Sim, J.; Park, C.; Moon, D.Y. Characteristics of basalt fiber as a strengthening material for concrete structures. *Compos. Part B Eng.* 2005, 36, 504–512.
- Singha, K.A. Short review on basalt fiber. *Int. J. Text. Sci.* 2012, 1, 19–28.
- Smarzewski, P. Flexural toughness evaluation of basalt fibre reinforced HPC beams with and without initial notch. *Compos. Struct.* 2020, 235, 111769.

Tensile behavior of a glass FRCM composite with textile lap splice exposed to freeze-thaw cycles

A.S. Calabrese, V. Bertolli, P. Colombi, T. D'Antino & C. Poggi

Department of Architecture, Built environment and Construction engineering, Politecnico di Milano, Milan, Italy

ABSTRACT: Fiber-reinforced cementitious matrix (FRCM) composites represent a valid alternative to fiber-reinforced polymer (FRP) composites for the strengthening of existing reinforced concrete and masonry members. FRCM composites are comprised of high strength textiles embedded within inorganic matrices and can be either applied with a discontinuous (i.e., discrete strips) or continuous layout, such as in the case of masonry elements with large surfaces (e.g., walls and vaults). Continuous applications require textile lap splices to guarantee the continuity of the composite mechanical performance. Recent investigations of the long-term behaviour of FRCM composites showed that aggressive conditions can affect the stress-transfer mechanism between fiber and matrix, determining possible reductions of the composite mechanical properties. This issue can be particularly critical in the lap splice zone due to the complex stress-transfer mechanism. Thus, the behavior of FRCM with textile lap splice under the effect of aggressive environments should be properly investigated. In this paper, the tensile behavior of a glass FRCM with continuous and overlapped textiles is studied using clamping-grip tensile tests. The effect of freeze-thaw cycles on the mechanical properties of the FRCM composite with textile lap splice is studied by comparing the results of specimens exposed to 20 freeze-thaw cycles with those of corresponding control specimens. The results obtained are analyzed in terms of maximum stress, corresponding strain, and slope of the axial stress-axial strain curve.

1 INTRODUCTION

Inorganic-matrix composites have been increasingly employed as externally bonded reinforcement (EBR) for concrete and masonry members due to their advantages with respect to organic-matrix composites (Peled et al. 2017). Among inorganic-matrix composites, fiber-reinforced cementitious matrix (FRCM) (ACI Committee 549 2020 549, Consiglio Nazionale delle Ricerche 2019 215), also referred to as textile-reinforced mortar (TRM) (Papanicolaou et al. 2008), are particularly attractive to reinforce masonry members, where the compatibility of the matrix with the masonry substrate and the reversibility of the application make these systems a valid alternative to traditional reinforcing techniques (Ferrari 2019). FRCMs comprise high strength open-mesh fiber textiles, usually made with carbon, glass, basalt, polyparaphenylene benzobisoxazole (PBO), or steel fibers, embedded within an inorganic matrix, usually a cement- or a lime-based mortar. Each FRCM composite has peculiar mechanical properties, which depend, among others, on the textile and matrix physical and mechanical properties, textile layout, and bond between matrix and fibers. Acceptance criteria are available in Italy (CSLLPP - Servizio Tecnico Centrale 2022) and in the United States (International Code Council Evaluation Service (ICC-ES) 2018) to assess the tensile behavior of FRCM composites using clamping-grip (Calabrese et al. 2020) and clevis-grip (Focacci et al. 2022) tensile tests, respectively. In addition, the Italian acceptance criteria require bond test to determine the maximum load that can be transferred between the externally bonded FRCM and a certain substrate (Bertolli and D'Antino 2022).

When applied to large surfaces, such in the case of masonry walls and vaults, textile lap splices are needed to ensure continuity of the FRCM reinforcement. Thus, both the Italian and US

acceptance criteria require tensile tests on FRCM coupons including textile lap splice, where the lap splice length l_s shall be sufficient to obtain the same tensile strength in coupons with continuous textile and with textile lap splice. Limited studies regarding the stress-transfer between lap spliced textiles in FRCM composites can be found in the literature. In (Thermou et al. 2018), steel reinforced grout (SRG) coupons with textile lap splice and different l_s were tested, observing a clear influence of l_s on the tensile strength obtained with clamping-grip tests. Carbon and glass FRCM coupons tested in (Truong et al. 2019) and (Donnini et al. 2019), respectively, using the clevis-grip test showed failure due to textile rupture. Corresponding FRCM coupons with textile lap splice showed the same failure mode and tensile strength when a lap splice length equal to 200 mm and 150 mm, respectively, was adopted. Based on numerical results of a PBO FRCM composite with textile lap splice tested using the clevis-grip set-up, a method to estimate the minimum lap splice length needed to obtain the composite load carrying capacity (or debonding load P_{deb}), i.e., the effective lap splice length $l_{s,eff}$, was proposed in (D'Antino et al. 2022). This method was then validated and confirmed comparing experimental results of PBO FRCM coupons with five different l_s with corresponding non-linear numerical models that accounted for the non-linear behavior of matrix and matrix-fiber interface (D'Antino et al. 2023).

Although these studies helped improving the state of knowledge regarding the stress-transfer mechanism between lap spliced textiles, no information is available regarding the long-term behavior of FRCM coupons with textile lap splice. In fact, exposure of FRCM composites to aggressive environments could affect their physical and mechanical properties (Ceroni et al. 2018, Calabrese et al. 2022b) and this effect could be even more important where textile lap splice are located, due to the reduced thickness of the embedding matrix that also works as a textile protection (Signorini and Nobili 2021, Ombres et al. 2020).

In this paper, the tensile behavior of a glass FRCM composite with textile lap splice under the effect of aggressive environments is investigated using clamping-grip tensile tests. Nine FRCM coupons with three different lap splice lengths are subjected to 20 freeze-thaw cycles and their response is compared with that of corresponding control, i.e., not conditioned, specimens. The effect of freeze-thaw cycles on the maximum stress, corresponding strain, and slope of the cracked portion of the axial stress-axial strain curve are analyzed and discussed.

2 EXPERIMENTAL STUDY

In this study, FRCM coupons with three different lap splice lengths (l_s) were subjected to clamping-grip tensile tests after being exposed to 20 freeze-thaw cycles. The lap splice lengths were $l_s=120$ mm, 180 mm, and 200 mm. For each l_s , three specimens were not conditioned and tested as control while three were subjected to the freeze-thaw cycles protocol, which resulted in 18 tensile tests. The tensile behavior of the glass FRCM considered in this study was previously investigated by the authors testing five specimens with a single continuous textile layer (Calabrese et al. 2022a). In (Calabrese et al. 2022a), the effect of the same freeze-thaw cycles protocol considered in this paper on the FRCM tensile behavior was also investigated.

The 18 specimens presented in this study were named following the notation $LT_{xxx}_L_W_{NC(or F/T)}_n$, where LT (=lap tensile) is the type of test, xxx (=120, 180, or 200) is the lap splice length (in mm), L and W are the specimen length and width (in mm), respectively, NC (=control) or F/T (=freeze/thaw) indicate control and conditioned specimens, and n is the specimen number.

2.1 Materials

The mechanical properties of the alkali-resistant (AR) glass FRCM composite investigated in this study and those of its constituent materials are reported in Table 1. The open-mesh bidirectional AR glass textile was coated with a styrene butadiene rubber (SBR) and had yarns spaced at 17 mm on center in both directions (Sika Italia SpA 2020). Its mechanical properties were experimentally obtained by testing textile strips comprising 3 longitudinal yarns (i.e., aligned with the load direction), according to (CSLLPP - Servizio Tecnico Centrale 2022). The AR glass FRCM properties reported in Table 1 were experimentally obtained in

(Calabrese et al. 2022a) by testing rectangular FRCM coupons with nominal dimensions equal to 450 mm (length) \times 50 mm (width) \times 10 mm (thickness), comprising one textile layer, including 3 longitudinal yarns, embedded within two 5 mm thick cementitious mortar layers. The mechanical properties of the cement-based matrix employed for the FRCM composite were declared by the manufacturer (Sika Italia SpA 2021).

Table 1. Mechanical properties of the FRCM and its components.

Property	AR glass textile	Cement matrix	FRCM
Tensile strength f_f	756 [MPa]	-	-
Elastic modulus E_f	52 [GPa]	-	-
Yarn area A_f	1.05 [mm ²]	-	-
Tensile strength σ_u	-	-	828 [MPa]
Ultimate strain ε_u	-	-	1.75 [%]
Cracked-stage slope E_3	-	-	51 [GPa]
Matrix cracking stress σ_{T1}	-	-	128 [MPa]
Compressive strength f_c	-	22* [MPa]	-
Elastic modulus E_c	-	7.6* [GPa]	-
Flexural strength f_r	-	6.0* [MPa]	-

*Declared by the manufacturer (Sika Italia SpA 2021).

2.2 Specimen geometry and test set-up

Figure 1a shows the geometry of lap splice specimens considered in this study. The FRCM coupons were comprised of two textile layers and three matrix layers and had an overall nominal thickness of 10.5 mm. Each textile layer included 3 longitudinal yarns, resulting in an overall fiber cross-sectional area $A=3.15 \text{ mm}^2$. Textile layers were overlapped in the specimen central portion considering a lap splice length l_s equal to 120 mm, 180 mm, and 200 mm. The clamping-grip tensile test set-up adopted in this study is shown in Figure 1b. The specimen ends were reinforced with epoxy-bonded GFRP tabs of dimensions 80 mm (length) \times 50 mm (width), which were clamped by the machine wedges applying an adequate clamping pressure to minimize matrix-fiber slippage at the specimen ends. Tests were conducted in displacement control, according to the indications of (CSLLPP - Servizio Tecnico Centrale 2022), monotonically increasing the machine stroke at a rate of 0.2 mm/min. A 200 mm gauge length extensometer was applied to the central portion of the specimen to measure the longitudinal strain, as provided by the Italian acceptance criteria (CSLLPP - Servizio Tecnico Centrale 2022).

2.3 Freeze-thaw cycles

The freeze-thaw cycles protocol adopted in this study followed the indications of (CSLLPP - Servizio Tecnico Centrale 2022). It comprised first 7 days of exposure to 92% RH and 38 °C and then 20 freeze-thaw cycles, each consisting of 4 hours at -18 °C followed by 12 hours at 92% RH and 38 °C. A 2.5 °C/min heating and cooling rate was adopted for the freeze-thaw cycles.

3 RESULTS AND DISCUSSION

3.1 Control specimens

Figures 2a,b, and c provide the axial stress σ – axial strain ε responses of control specimens, where σ is computed as $\sigma=P/A$, being P and A the load applied by the testing machine and the overall fiber cross-sectional area, respectively. Since for most of the specimens tested matrix cracks occurred outside the extensometer gauge length (see Figure 2d), the strain measured by the extensometer represents and underestimation of the actual specimen longitudinal strain. Accordingly, for all specimens considered in this paper the axial strain ε was computed as $\varepsilon=\delta/L_0$, being δ and L_0 the machine stroke and the length of the specimen portion included between the machine wedges (referred to as the specimen free length), respectively.

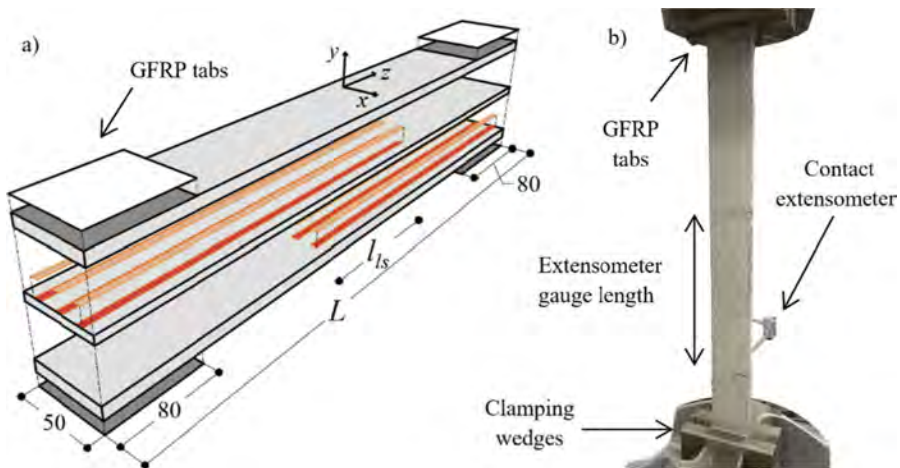


Figure 1. Specimen geometry (a) and test set-up (b).

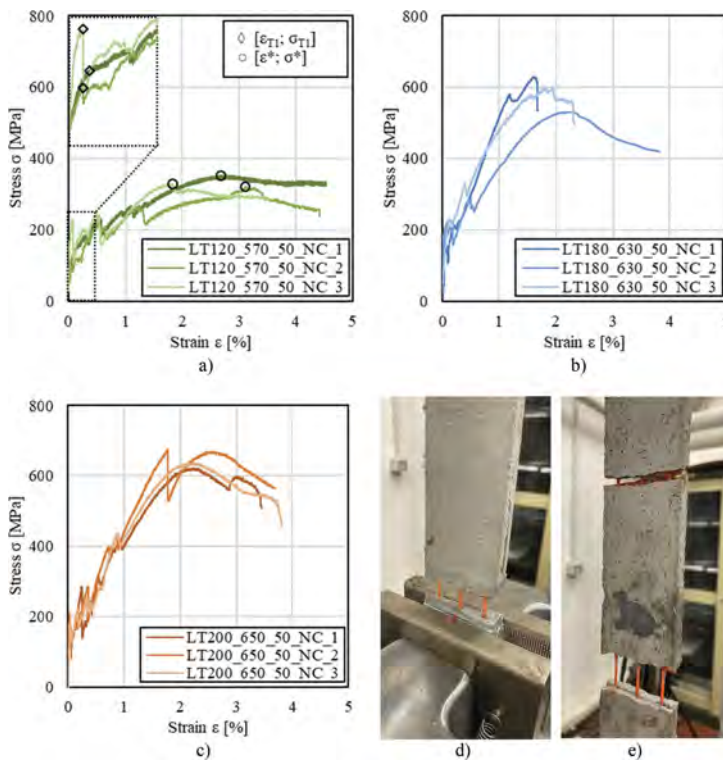


Figure 2. Stress-strain responses of control specimens: a) specimens LT120_570_50_NC; b) specimens LT180_630_50_NC; and c) specimens LT200_650_50_NC. Representative failure modes: d) specimen LT180_630_50_NC; and e) specimens LT120_570_50_NC.

As shown in Figure 2a, b, and c, the σ - ϵ response of control specimens was characterized by an initial linear branch associated with the specimen uncracked stage. This stage ended when the matrix tensile strength was reached (stress σ_{T1} in the σ - ϵ curve, see Figures 2a). Beyond this point, matrix cracks progressively occurred and widened with increasing the machine stroke δ (cracking stage). Matrix cracks occurred in different places in the three groups of specimens,

with LT120_570_50_NC specimens showing cracks at the edges of the lap splice length (see Figure 2e), whereas for specimens of groups LT180_630_50_NC and LT200_650_50_NC cracks occurred both at the edges of the lap splice length and close to the specimen gripped portion (see Figure 2d). When no further matrix cracks occurred, the specimen cracked stage began. During this stage, specimens of group LT120_570_50_NC ($l_s=120$ mm) were characterized by a non-linear response associated with the relative slippage between fiber and matrix along the lap splice length. For specimens LT180_630_50_NC and LT200_650_50_NC, the cracked stage response was initially characterized by an approximately linear branch associated with the elastic behavior of textile. With increasing the machine stroke, relative slippage between textile and matrix occurred and the response became non-linear. The transition from the linear to the nonlinear branch was recognizable in some specimens by a stress drop in the σ - ϵ response, which could be associated with the onset of debonding at the matrix-fiber interface. For some specimens (e.g., LT180_630_50_NC_1 and LT200_650_50_NC_2), the extent of the linear branch was more pronounced, which was attributed to the randomly distributed matrix-fiber interface properties and to a more uniform stress distribution among the textile yarns with respect to that of other specimens. In all specimens the maximum stress σ^* was attained during the cracked stage and was associated with the strain ϵ^* . Specimen failure eventually occurred due to the wide opening of one of the matrix cracks due to high relative slippage between fiber and matrix. In specimens LT120_570_50_NC, textile slippage occurred within the lap splice length (see Figure 2e), whereas for specimens LT180_630_50_NC and LT200_650_50_NC it occurred close to the specimen end and was eventually followed by textile rupture (Figure 2d).

Significant test response parameters of control specimens are reported in Table 2, alongside with corresponding average values and coefficient of variation (CoV). These parameters include the peak stress σ^* and corresponding strain ϵ^* , the matrix cracking stress σ_{T1} and corresponding strain ϵ_{T1} , and the post-cracked stage secant slope K , computed according to Equation 1.

$$K = \frac{\sigma^* - \sigma_{T1}}{\epsilon^* - \epsilon_{T1}} \quad (1)$$

Parameters reported in Table 2 (except K) are shown in Figure 2a for specimens LT120_570_50_NC. The maximum stress exhibited by specimens LT120_570_50_NC was on average 43% and 48% lower than that of specimens LT180_630_50_NC and LT200_650_50_NC, respectively (Table 2). This was attributed to the higher lap splice length of the latter specimens ($l_s=180$ mm and 200 mm), which prevented the textile slippage along the lap splice length, thus guaranteeing the reinforcement continuity. However, ϵ^* was 31% and 21% higher for specimens with

Table 2. Test response representative parameters of control specimens.

Specimen	σ^*	ϵ^*	σ_{T1}	ϵ_{T1}	K
	[MPa]	[%]	[MPa]	[%]	[MPa/%]
LT120_570_50_NC_1	352	2.68	146	0.11	80
LT120_570_50_NC_2	320	3.11	113	0.08	68
LT120_570_50_NC_3	330	1.83	228	0.08	58
Average	334	2.54	162	0.09	69
CoV	0.048	0.256	0.363	0.222	0.158
LT180_630_50_NC_1	629	1.61	169	0.04	294
LT180_630_50_NC_2	529	2.25	208	0.03	145
LT180_630_50_NC_3	597	1.95	229	0.12	202
Average	585	1.93	202	0.06	213
CoV	0.087	0.167	0.150	0.809	0.353
LT200_650_50_NC_1	622	2.25	186	0.03	197
LT200_650_50_NC_2	674	1.78	210	0.02	265
LT200_650_50_NC_3	639	2.24	209	0.04	195
Average	645	2.09	202	0.03	219
CoV	0.041	0.130	0.066	0.299	0.182

$l_s=120$ mm compared to that of specimens with $l_s=180$ mm and 200 mm, respectively, due to the higher textile slippage occurred along their lap splice length, which also resulted in 68% and 69% lower K values, respectively.

3.2 Specimens subjected to freeze-thaw cycles

All specimens exposed to freeze-thaw cycles provided the same failure modes of corresponding control specimens, which indicated that the conditioning protocol did not affect the specimen failure mode. The σ - ε responses of conditioned specimens are shown in Figure 3 where the envelopes of corresponding control specimens are also provided for comparison. Conditioned specimens provided σ - ε responses consistent with those of control specimens, as they were characterized by three subsequent stages: uncracked, cracking, and cracked stages. It should be noted that specimen LT120_570_50_F/T_2 prematurely failed due to improper fabrication and is not shown in Figure 3. Calabrese et al. (2022) investigated the effect of the same freeze-thaw cycles protocol on the tensile behavior of single textile layer coupons of the same AR glass FRCM considered in this study, observing a 12.4% reduction of the average tensile strength after conditioning. This reduction was attributed to the possible degradation of the textile SBR coating due to temperature cycles, which in turn altered the matrix-fiber stress-transfer mechanism and thus the conditioned specimen tensile capacity.

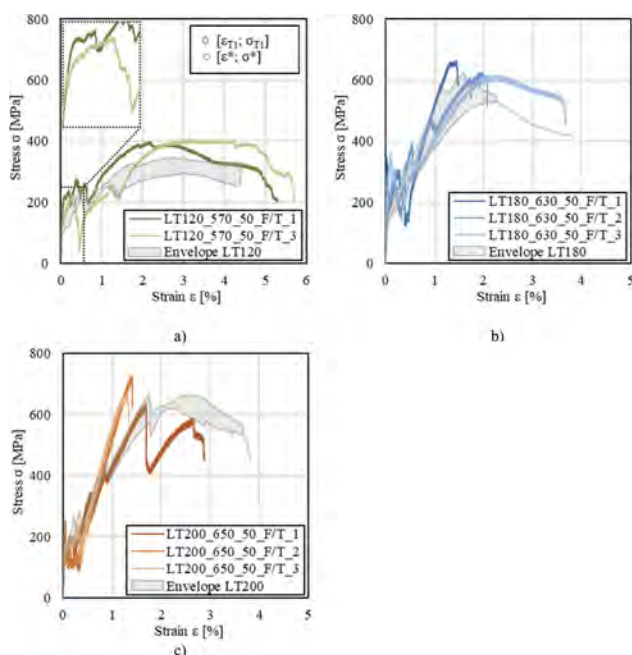


Figure 3. Stress-strain responses of specimens subjected to freeze-thaw cycles: a) specimens LT120_570_50_F/T; b) specimens LT180_630_50_F/T; and c) specimens LT200_650_50_F/T.

Table 3 collects the relevant parameters of the σ - ε response for all conditioned specimens, alongside with average values, CoV, and percentage of average retained stress, strain, and secant modulus, with respect to the corresponding average parameters provided by control specimens (Table 2). As inferred by Table 3, σ_{T1} was between 4% and 63% higher for conditioned specimens in comparison with that of control specimens. This was attributed to the specimen exposure to a high moisture environment, which promoted the continuous curing of the cement-based matrix. A similar finding was reported by (Calabrese et al. 2022a, Calabrese et al. 2022b) on cement-based matrix composites subjected to various ageing protocols.

Despite of a same failure mode, the σ^* of conditioned specimens was on average 5% to 20% higher than that of corresponding control specimens. It can be postulated that the prolonged matrix curing improved the matrix-fiber stress-transfer mechanism resulting in a higher tensile strength of conditioned than of control specimens. Furthermore, 2% and 30% lower ϵ^* average values were recorded on specimens of groups LT180_630_50_NC and LT200_650_50_NC, respectively. The different matrix-fiber stress-transfer is also confirmed by specimens showing a long linear branch in the cracked stage.

Table 3. Test response representative parameters of conditioned specimens.

Specimen	σ^*	ϵ^*	σ_{T1}	ϵ_{T1}	K
	[MPa]	[%]	[MPa]	[%]	[MPa/%]
LT120_570_50_F/T_1	398	2.19	213	0.08	87
LT120_570_50_F/T_2	†	-	-	-	-
LT120_570_50_F/T_3	405	3.15	161	0.08	79
Average	401	2.67	187	0.08	83
CoV	0.012	0.253	0.197	0.001	0.068
Retained	120%	105%	115%	88%	121%
LT180_630_50_F/T_1	664	1.44	344	0.04	227
LT180_630_50_F/T_2	625	1.97	280	0.02	177
LT180_630_50_F/T_3	614	2.27	360	0.10	117
Average	634	1.90	328	0.05	174
CoV	0.041	0.222	0.130	0.785	0.317
Retained [%]	108%	98%	163%	88%	81%
LT200_650_50_F/T_1	634	1.69	250	0.05	234
LT200_650_50_F/T_2	725	1.40	203	0.01	376
LT200_650_50_F/T_3	664	1.29	174	0.05	392
Average	675	1.46	209	0.04	334
CoV	0.069	0.140	0.184	0.572	0.261
Retained [%]	105%	70%	104%	109%	153%

†Premature failure.

4 CONCLUSIONS

This paper investigated the effect of freeze-thaw cycles on the tensile behavior of AR glass FRCM specimens with textile lap splice. Three different lap splice lengths were considered, namely $l_s=120$ mm, 180 mm, and 200 mm. The results showed that low a lap splice length led to high slippage at the matrix-fiber interface along the lap splice length, which in turn resulted in 43% and 48% lower average tensile strength of specimens with $l_s=120$ mm with respect to that of specimens with $l_s=180$ mm and 200 mm, respectively. The freeze-thaw cycles protocol considered in this study did not affect the specimens failure mode. The average cracking stress of conditioned specimens resulted higher than that of control specimens, which was attribute to the continuous matrix curing. Similarly, matrix curing improved the matrix-fiber stress-transfer mechanism, determining a slight ϵ increase in the specimen tensile strength after conditioning.

REFERENCES

- ACI Committee 549 2020. Guide to Design and Construction of Externally Bonded Fabric-Reinforced Cementitious Matrix and Steel-Reinforced Grout Systems for Repair and Strengthening of Concrete Structures. ACI 549.4R-20 Farmington Hills, 48331 MI.
- Bertolli, V. and D'Antino, T. 2022. Modeling the behavior of externally bonded reinforcement using a rigid-trilinear cohesive material law, International Journal of Solids and Structures 111641.

- Calabrese, A.S., D'Antino, T., Colombi, P., Carloni, C. and Poggi, C. 2020. Fatigue Behavior of PBO FRCM Composite Applied to Concrete Substrate, *Materials (Basel)* 13,.
- Calabrese, A.S., D'Antino, T., Colombi, P. and Poggi, C. 2022a. Durability of a Glass Fabric-Reinforced Cementitious Matrix Composite under Different Environmental Conditions, *Key Engineering Materials* 916, 35–42.
- Calabrese, A.S., D'Antino, T., Colombi, P. and Poggi, C. 2022b. Long-Term Behavior of PBO FRCM and Comparison with Other Inorganic-Matrix Composites, *Materials* 15, 3281.
- Ceroni, F., Bonati, A., Galimberti, V. and Occhiuzzi, A. 2018. Effects of Environmental Conditioning on the Bond Behavior of FRP and FRCM Systems Applied to Concrete Elements, *J Eng Mech* 144, 04017144.
- Consiglio Nazionale delle Ricerche 2019. Istruzioni per la Progettazione, l'Esecuzione ed il Controllo di Interventi di Consolidamento Statico mediante l'utilizzo di Compositi Fibrorinforzati a matrice inorganica. CNR-DT 215/2019 Rome, Italy.
- CSLLPP - Servizio Tecnico Centrale 2022. Linee guida per la identificazione, la qualificazione ed il controllo di accettazione di compositi fibrorinforzati a matrice inorganica (FRCM) da utilizzarsi per il consolidamento strutturale di costruzioni esistenti Rome, Italy.
- D'Antino, T., Calabrese, A.S., Colombi, P. and Poggi, C. 2022. Numerical Study of the Effective Lap-Splice Length of FRCM Composites, in A. Ilki, M. Ispir and P. Inci (eds), 10th International Conference on FRP Composites in Civil Engineering (Lecture Notes in Civil Engineering) Cham 213–23.
- D'Antino, T., Calabrese, A.S., Colombi, P. and Poggi, C. 2023. Experimental and numerical investigation on the tensile behavior of PBO FRCM composites with textile lap splice, *Constr Build Mater* 363, 129437.
- Donnini, J., Chiappini, G., Lancioni, G. and Corinaldesi, V. 2019. Tensile behaviour of glass FRCM systems with fabrics' overlap: Experimental results and numerical modeling, *Comp Struct* 212, 398–411.
- Ferrari, L. 2019. First-Aid and Provisional Devices in Historical Structures with Collapse Risk after Seismic Shock, *Key Eng Mater* 817, 301–8.
- Focacci, F., D'Antino, T. and Carloni, C. 2022. Tensile testing of FRCM coupons for material characterization: discussion of critical aspects, *J Compos Constr* 1–20.
- International Code Council Evaluation Service (ICC-ES) 2018. Acceptance criteria for masonry and concrete strengthening using fabric-reinforced cementitious matrix (FRCM) and steel reinforced grout (SRG) composite systems. AC434 Whittier, CA.
- Ombres, L., Mazzuca, P. and Verre, S. 2020. Durability Under Thermal Actions of Concrete Elements Confined with an Inorganic Matrix Fiber-Reinforced Composites, in J. Sena-Cruz, L. Correia and M. Azenha (eds), *Proceedings of the 3rd RILEM Spring Convention and Conference (RSCC 2020) (RILEM Bookseries)* Cham 99–108.
- Papanicolaou, C.G., Triantafyllou, T.C., Papathanasiou, M. and Karlos, K. 2008. Textile reinforced mortar (TRM) versus FRP as strengthening material of URM walls: out-of-plane cyclic loading, *Mater Struct* 41, 143–57.
- Peled, A., Mobasher, B. and Bentur, A. 2017. Repair and retrofit with TRC, in *Textile Reinforced Concrete (1st edn)* London 28.
- Signorini, C. and Nobili, A. 2021. Comparing durability of steel reinforced grout (SRG) and textile reinforced mortar (TRM) for structural retrofitting, *Mater Struct* 54, 131.
- Sika Italia SpA 2020. SikaWrap®-340 G Grid AR Technical Sheet. April 2021. Available at: https://usa.sika.com/content/dam/dms/us01/t/sikadur_-30.pdf [Accessed: 9 May 2021].
- Sika Italia SpA 2021. Sika MonoTop®-722 Technical Sheet. April 2021.
- Thermou, G., de Felice, G., De Santis, S., Alotaibi, S., Roscini, F., Hajirasouliha, I. and Guadagnini, M. 2018. Mechanical characterization of multi-ply steel reinforced grout composites for the strengthening of concrete structures, in *Proc. of the 9th International Conference on Fibre-Reinforced Polymer (FRP) Composites in Civil Engineering, CICE 2018 Paris, France* 298–305.
- Truong, G.T., Park, S.-H. and Choi, K.-K. 2019. Tensile Behaviors of Lap-Spliced Carbon Fiber-Textile Reinforced Mortar Composites Exposed to High Temperature, *Materials* 12.

Effect of salt crystallization on the bond behavior of glass FRCM-masonry joints

V. Bertolli, A. Cagnoni, A.S. Calabrese, P. Colombi & T. D’Antino

Department of Architecture, Built environment and Construction engineering, Politecnico di Milano, Milan, Italy

ABSTRACT: The use of fabric-reinforced cementitious matrix (FRCM) composites for reinforcement of existing masonry members has attracted an increasing interest in recent years. FRCM composites are particularly suitable for masonry strengthening and retrofitting due to their ease of installation, reversibility, excellent compatibility with the substrate and vapor permeability. Tensile mechanical properties and bond behavior of FRCM composites were extensively studied. However, limited information is available regarding the durability of FRCM and FRCM-strengthened members, which may represent a critical issue for the effectiveness of the strengthening system. Indeed, existing masonry structures suffer from the presence of moisture, which can come from rising damp, condensation, infiltration of rainwater, etc. Water is often responsible for the presence of salt within the element, which represents a major cause of masonry damage. When the salt crystallization takes place at the interface between the FRCM and the substrate, a possible reduction of the FRCM bond capacity can be observed.

In this paper, the effect of salt crystallization on the bond behavior of an FRCM applied onto a masonry substrate is experimentally investigated. The FRCM composite employed comprises a glass open mesh reinforcing textile and a cementitious matrix. FRCM-masonry joints were conditioned in a saline solution to induce salt crystallization in the FRCM, i.e., within the composite strips and at the FRCM-masonry interface. The bond behavior of the FRCM composite before and after the conditioning is investigated with single-lap direct shear tests. The results obtained provide information on the long-term behavior of the glass FRCM composite considered.

1 INTRODUCTION

Fabric-reinforced cementitious matrix (FRCM) composites have gained large popularity in recent years as externally bonded reinforcement (EBR) for masonry (Carozzi and Poggi 2015) and reinforced concrete (RC) structures (Täljsten and Blanksvärd 2007), where they proved to be effective as in-plane (de Felice et al. 2014) and out-of-plane (Papanicolaou et al. 2008) reinforcement for walls and flexural, shear, and torsional reinforcement for RC beams (Bencardino et al. 2018, Triantafyllou and Papanicolaou 2006, Alabdulhady et al. 2017). They comprise different high strength fibers arranged in open-mesh textiles embedded within inorganic matrices. FRCMs overcome some of the main drawbacks related to the use of fiber-reinforced polymers (FRP) composites, such as irreversibility of the application and absence of vapor permeability (Ombres 2015, Del Prete et al. 2015). Furthermore, recent studies on FRCM long-term behavior showed that these inorganic matrix composites have better resistance to high temperatures (Ferretti et al. 2022) and to aggressive environments (Franzoni et al. 2019, Al-Lami et al. 2021) than FRPs (Trapko 2013, Tedeschi et al. 2014). However, the inorganic matrix of FRCMs is not able to uniformly impregnate fiber filaments as the organic resin of FRP composites does, due to the dimension of the components of the mortar matrix. In FRPs, an even stress distribution among fiber filaments can be assumed thanks to the use of organic resins and this leads to different resisting mechanism developing in FRP and FRCM when subjected to external loads. FRCM mechanical properties are determined with tensile tests (i.e., clamping- (CSLLPP 2022) or clevis-grip (International Code Council Evaluation Service (ICC-

ES) 2018) tests) and single- or double-lap direct shear tests (European Organization for Technical Assessment (EOTA) 2018), which allows for assessing the composite tensile strength and the FRCM-substrate interface debonding mechanism, respectively (Focacci et al. 2022). When failure occurs due to debonding, direct shear tests provide information on the bond behavior of the interface where debonding occurs and allow the evaluation of the bond capacity and cohesive material law (CML) of this interface (Bertolli and D'Antino 2022, D'Antino et al. 2020).

Moreover, durability of FRCMs is a fundamental aspect to be considered when dealing with their application on external surfaces of existing structures, where they can be exposed to humidity, rainfall, and to saline and alkaline environments (Al-Lami et al. 2020). Among different detrimental effects of atmospheric processes, salt attack is the most common cause of weathering in masonry structures (Donnini 2019). There are limited studies in the literature focused on the effects of aggressive saline environment on the mechanical behavior of FRCM composites. Long-term tensile behavior of FRCM was evaluated by Arboleda (2014) and the results indicated a slight increase in tensile capacity of FRCM conditioned in saline and alkaline solution and with freeze-thaw cycles. Similarly, Nobili (2016) assessed FRCM durability against alkaline and saline environments through tensile tests on alkali-resistant (AR) glass FRCM coupons. The saline solution employed comprised 3.5 wt% of sodium chloride (NaCl). Even though not as high as that obtained for the alkaline solution, a reduction of the peak stress attained by the specimen conditioned in saline environment was observed. Tensile behavior of FRCM conditioned in saltwater was also investigated by Donnini et al. (2020), in which it is shown that the tensile strength slightly increased after conditioning, due to curing of the mortar matrix.

Long-term bond behavior of FRCM was investigated by Franzoni et al. (2017), which carried out direct shear tests on steel reinforced grout (SRG) composites aimed at defining an accelerated conditioning procedure able to reproduce the actual environmental conditions to which FRCM are subjected in real applications. The conditioning consisted in four wet-dry cycles, composed of 2-day wetting phase in a sodium chloride (NaCl, 2 wt%) and sodium sulfate decahydrate ($\text{Na}_2\text{SO}_4 \cdot 10\text{H}_2\text{O}$, 8 wt%) solution, followed by a 3-day drying phase in a ventilated oven at 60 °C. The duration of wetting and drying phases was selected to allow for water saturation and evaporation, respectively. Moreover, to avoid possible effects due to the presence of water within the specimen (i.e., water saturation effect (Franzoni et al. 2015)) on the bond behavior of the specimens (Franzoni et al. 2018), they were oven dried at 60 °C for 2 days before testing. This accelerated procedure was modified by Franzoni et al. (2018), where six wet-dry cycles were performed on SRG-masonry joints. Then, the same conditioning procedure was performed in Franzoni et al. (2019), where different mortar matrices were adopted to investigate the matrix role on the bond behavior of SRG composites. Results showed a reduction of the peak stress attained in direct shear tests in all the conditioned specimens, with lower strength reduction for specimen with cement-based matrix. In Donnini (2019), the same saline solution of Franzoni et al. (2019) was employed for the conditioning of 12 glass FRCM DS test specimens that were subjected either to 1000 hour immersion in saline solution or to wet-dry cycles. Results showed higher strength reduction for the specimens immersed in the saline solution. The effect of salt crystallization on FRCM-masonry joints was also investigated by Garavaglia et al. (2020) by means of pull-off tests. The conditioning procedure was selected according to (RILEM TC 127-MS 1998), and the specimens were inserted in a dry gravel layer filled with water saturated with a 10 wt% of Na_2SO_4 solution for 11 months. Pull-off test showed strong reduction on the bond strength (ASTM International 2004) of conditioned specimens.

The number of studies available in the literature assessing the long-term bond behavior of FRCM is quite limited. US and Italian acceptance criteria (AC 434-13 2013, CSLLPP 2022) evaluate FRCM durability by means of clamping- or clevis- grip tensile tests on specifically conditioned specimens. For example, (International Code Council Evaluation Service (ICC-ES) 2018) prescribes conditioning procedure for 1000 or 3000 hours in water, saltwater (immersion in a solution at 22 °C), alkaline solution, and freezing and thawing cycles. However, as also evidenced in (Franzoni et al. 2019), a common conditioning procedure for the evaluation of the effect of salt crystallization on the bond behavior of different FRCM composites is not yet defined.

In this paper, the effect of salt crystallization on the bond behavior of FRCM-masonry joints is investigated considering a coated glass FRCM embedded within a cement-based

mortar matrix. Four specimens were exposed to three wet-dry cycles in saline solution and then tested using a single-lap direct shear test set-up. The results obtained were compared with those of four corresponding control (i.e., unconditioned) specimens highlighting the detrimental effect of the conditioning procedure on the FRCM bond behavior.

2 MATERIALS AND METHODS

2.1 *Materials*

To evaluate the effect of salt crystallization on the bond behavior of FRCM-masonry joints, an experimental campaign was carried out on eight FRCM composite strips applied to masonry wallettes, tested with a push-pull single-lap direct shear set-up. Four out of eight specimens were subjected to an accelerated conditioning procedure whereas the remaining four were used as control specimens.

The FRCM composite comprised a coated glass open-mesh textile and a cementitious matrix. The textile employed was made with alkali-resistant glass fibers arranged in discrete bundles, each coated with styrene butadiene rubber (SBR). The textile was embedded within a commercial M20 (EN 998-2 2016) cementitious matrix (Sika Italia SpA 2021). The textile cross-sectional area was determined by the calcination method (EN 1172 1999) on eight bundle specimens and was $A^*=1.05 \text{ mm}^2$ (CoV 0.8%) for a single longitudinal bundle (warp direction) and $A_t^*=0.99 \text{ mm}^2$ (CoV 0.4%) for a single transversal bundle (weft direction). The equivalent thickness of the textile in longitudinal direction was $t_f=0.063 \text{ mm}$. Tensile tests of nine bare textile strips (i.e., not impregnated with the mortar) including 3 longitudinal bundles provided a tensile strength, ultimate strain, and modulus of elasticity of 756 MPa (CoV 6.1%), 1.48% (CoV 15.6%) and 52 GPa (CoV 6.1 %).

Each masonry wallette was made of seven solid clay UNI bricks and six 10 mm-thick mortar joints. The masonry wallettes total height was 480 mm, and their width and depth 240 and 110 mm, respectively. The bricks had nominal dimensions 240×110×60 mm and compressive strength ranging from 15 to 25 MPa, according to information provided by the manufacturer (Danesi srl 2020). The mortar used for the joint was a commercial pre-mixed mortar (Fassa Bortolo srl 2020, EN 998-2 2016). The FRCM strips were applied to the 240 mm-wide side of the wallettes with the loaded end placed 30 mm below the upper edge of the masonry wall. The strips had bonded width $b_f=50 \text{ mm}$ and bonded length $L=300 \text{ mm}$ (CSLLPP 2022). The specimens were cast with the following procedure:

- A first 5 mm-thick layer of mortar was applied to the surface of the wallette using a mold to accurately control the strip geometry.
- The open-mesh textile, which comprised $n=3$ bundles longitudinal bundles, was gently pressed onto the first mortar to assure proper impregnation. A portion of the textile with length 270 mm was left bare beyond the loaded end.
- A second 5 mm-thick layer of mortar was applied as finishing layer. Thus, the total thickness of the FRCM strip was 10 mm.

2.2 *Accelerated conditioning procedure*

After being left to cure for at least 28 days, four FRCM-masonry joints were subjected to an accelerated weathering procedure. The conditioning comprised three wet-dry cycles in which the specimens were first immersed in a saline solution for 48 hours and then dried in a controlled environment characterized by a $23 \pm 2 \text{ }^\circ\text{C}$ temperature and a $50 \pm 10 \%$ relative humidity for 72 hours. As reported by (Franzoni et al. 2017), at least 8h immersion is necessary to obtain a complete saturation of masonry walls by capillarity adsorption. However, the amount of time required depends on the type of brick and mortar employed and 48 hours were selected in this work for the wetting phase. During the 72 hours drying phase, specimens were stored at room conditions and water evaporated from the masonry substrate, promoting salt crystallization. Dry conditions of the specimens were essential to guarantee the absorption of saline solution during the following cycle.

During the wetting phase, the specimens were partially immersed in a 20 mm-head Na_2SO_4 (10 wt%) solution for 48 hours, to allow capillary absorption of the saline solution. In each cycle, during the first 24 hours the specimen was immersed in the solution on one 480×110 mm side and then was turned and immersed on the opposite side for the remaining 24 hours (Figure 1a). During immersion, the masonry wallettes were placed on a composite grid to promote a homogeneous solution absorption. Duct tape was applied to every side of the masonry wall (except for the two alternatively immersed in the solution), including the side where the composite strip was applied, to induce salt crystallization through the FRCM strip. The level of the solution was kept constant through the cycles. At the end of the conditioning procedure, a considerable amount of salt crystallized in the free (i.e., not covered by the duct tape) surfaces of the masonry wallettes. Salt crystallization was also observed in the FRCM strip, with most of the crystallized salt located on the strip sides and in correspondence of the mortar joints (Figure 1b). At the end of the conditioning cycles, the duct tape around the wallettes was removed and the specimens were left to cure for additional 48 hours before testing (Figure 1c).

The conditioning applied in this work was an accelerated procedure (see (Franzoni et al. 2018)) aimed at inducing a realistic damage in a relatively short period of time without changing the masonry deterioration process. The end of the conditioning procedure was determined by visual inspection when a remarkable amount of efflorescence was obtained on the wall free surfaces.

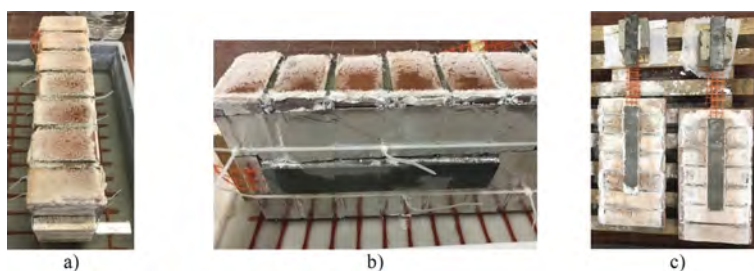


Figure 1. A) Specimen immersed in salt solution during the second wet-dry cycle. b, c) Specimens 48 hours after the end of the conditioning procedure.

2.3 Direct shear tests

After the conditioning procedure, single-lap direct shear tests were performed on control and conditioned specimens to study the debonding mechanism of the glass FRCM composite. Experimental tests were carried out in displacement control at a rate of 0.0034 mm/s using a servo-hydraulic testing machine. GFRP tabs (with dimensions 50×80 mm) were epoxy bonded at the end of the bare textile beyond the loaded end to promote uniform stress distribution among the bundles and allow for clamping by the testing machine. During the test, fibers were pulled whereas the masonry wallette was restrained with a steel frame (Figure 2a, b).

Two linear variable displacement transducers (LVDTs) with measurement range of 200 mm were employed to measure the relative displacement, i.e., slip, between the masonry wallette and the textile. They were attached to the masonry surface at the loaded end and reacted off of an aluminum L-shaped plate fixed to the bare fibers immediately outside the FRCM strip. The average of the measurements of the two LVDTs (*LVDTa* and *LVDTb*) was named global slip g in this paper. During the test, the applied load, P , and the stroke of the testing machine, δ , were recorded with a frequency of 5 Hz. The stress in the textile, σ , was obtained as the ratio between the load recorded by the testing machine, i.e., the applied load P , and the textile cross-sectional area in warp direction, $A_f = t_f b_f = n A^* = 3.15 \text{ mm}^2$.

3 RESULTS AND DISCUSSION

Specimens were named DS_X_Y_C_S_N, where DS = direct shear (type of test), X = bonded length [mm], Y = bonded width [mm], C = clay brick masonry (type of support), S (if present) =

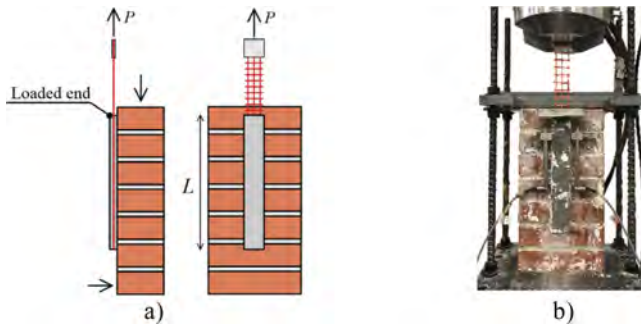


Figure 2. Single-lap direct shear test set-up: a) sketch and b) specimen DS_300_50_C_S_1 before testing.

indicates the salt conditioned specimens, and N = specimen number. The applied stress σ – global slip g curves for the FRCM-masonry joints studied are reported in Figure 3a, b for control and conditioned specimens, respectively. All specimens failed due to rupture of the fibers at the loaded end, either inside the FRCM strip or immediately outside it. Failure occurred first in one bundle and then in the remaining, which indicated the non-uniform stress distribution among the different bundles in the FRCM strip (see Figure 4a, b). However, fibers within each bundle failed approximately at the same time (i.e., no telescopic behavior (Hegger et al. 2006) was observed) due to the presence of the SBR coating that promoted the uniform distribution of stresses among fibers within the bundle.

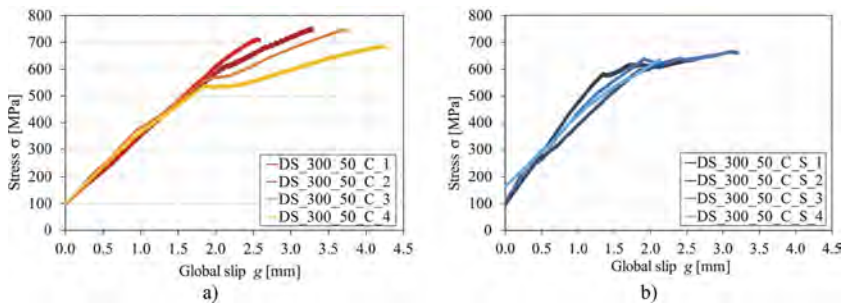


Figure 3. Applied stress σ – global slip g curves for a) control and b) conditioned specimens.

The main parameters obtained by direct shear tests on control and conditioned specimens are reported in Table 1. P^* is the peak load, σ^* the corresponding peak stress, and g^* the global slip associated with the peak stress. Average values and coefficient of variations of nominally equal specimens are also reported. The average peak stress of control specimens was $\sigma^* = 742$ MPa, while that of conditioned specimen was $\sigma^* = 645$ MPa. Thus, an average reduction of 13.1% was observed for specimens subjected to the conditioning procedure. Moreover, a reduction of 11.8% in the average value of the global slip associated with the peak stress, g^* , was also observed for conditioned specimens.

Figure 4c shows the comparison between the envelope curves of control and conditioned specimens. The conditioning procedure caused a modest decrease in the peak stress attained in direct shear tests and had no influence in the failure modes of the specimens. It is worth noting that a direct evaluation of the effects of the salt crystallization on the bond behavior of the FRCM-masonry joints could not be performed since failure was attained right outside the FRCM strip. Indeed, the only conclusion that could be drawn is that the bond behavior of the joint was not adversely affected enough by the conditioning procedure to induce failure at the matrix-substrate or matrix-fiber interfaces before fiber rupture occurred (due to hierarchy of interface failures (Carloni et al. 2018)). Moreover, visual observation of the crystallized salts suggested a lower porosity of the cementitious matrix employed with respect to the masonry

bricks or mortar layers (salt crystallized mostly in correspondence of the mortar joints and on the FRCM strip sides). Thus, salt crystallization could be expected at the FRCM-masonry interface. These aspects will be clarified with the investigations on porosity and salt migration pattern of the different materials involved in the bond behavior.

Table 1. Results of direct shear tests on control and conditioned specimens.

Samples Name	P^* [kN]	σ^* [MPa]	g^* [mm]	Samples Name	P^* [kN]	σ^* [MPa]	g^* [mm]
DS_300_50_C_1	2.39	759	2.96	DS_300_50_C_S_1	2.03	643	2.66
DS_300_50_C_2	2.26	717	2.09	DS_300_50_C_S_2	1.98	627	2.26
DS_300_50_C_3	2.36	749	3.63	DS_300_50_C_S_3	2.11	670	3.14
DS_300_50_C_4	2.18	691	4.14	DS_300_50_C_S_4	2.01	639	2.12
Avg	2.34	742	2.89	Avg	2.03	645	2.55
CoV [%]	2.4	2.4	21.9	CoV [%]	2.8	2.8	18.0

It is worth noting that a clear conditioning procedure for the evaluation of the effect of salt crystallization on FRCM-masonry joints is not yet defined in the literature. Further experimental results are needed to improve our knowledge on the joint bond behavior of conditioned specimens and to define a shared conditioning procedure.

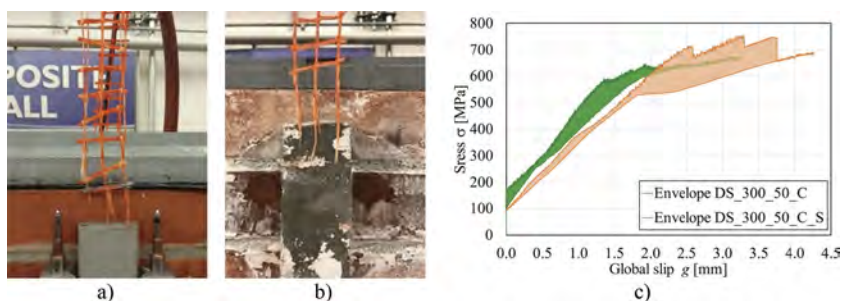


Figure 4. A) Failure modes of representative a) control and b) conditioned specimens; c) comparison between average applied stress σ – global slip g curves of control and conditioned specimens.

4 CONCLUSIONS

In this paper, an accelerated conditioning procedure was performed on direct shear test specimens to evaluate the effect of salt crystallization on the bond behavior of glass FRCM-masonry joints. The FRCM comprised a cementitious mortar and a coated glass fiber textile. The results obtained for conditioned specimens were compared with those of corresponding control specimens and allow for drawing the following conclusions:

- the detrimental effect of the conditioning procedure performed resulted in a slightly lower average peak stress attained by conditioned than by control specimens;
- all specimens tested failed due to tensile rupture of the textile either inside the FRCM strip or right outside it;
- physical and chemical investigations on the microstructure of the materials and interfaces will provide additional information on the long-term behavior of the FRCM reinforcement and of FRCM-masonry joints;
- considering the limited number of tests performed and available in the literature, more investigation is needed to clarify the effect of salt crystallization on the behavior of FRCM-

masonry joints. To this aim, a commonly accepted conditioning procedure should be defined for the determination of the salt crystallization resistance of FRCM composites.

REFERENCES

- AC 434-13 2013. Acceptance Criteria for Masonry and Concrete Strengthening Using Fabric-Reinforced Cementitious Matrix (FRCM) Composites.
- Alabdulhady, M.Y., Sneed, L.H. and Carloni, C. 2017. Torsional behavior of RC beams strengthened with PBO-FRCM composite – An experimental study, *Engineering Structures* 136, 393–405.
- Al-Lami, K., Calabrese, A.S., Colombi, P. and D’Antino, T. 2021. Effect of Wet-Dry Cycles on the Bond Behavior of Fiber-Reinforced Inorganic-Matrix Systems Bonded to Masonry Substrates, *Materials* 14, 6171.
- Al-Lami, K., D’Antino, T. and Colombi, P. 2020. Durability of Fabric-Reinforced Cementitious Matrix (FRCM) Composites: A Review, *Applied Sciences* 10, 1714.
- Arboleda, D. 2014. Fabric Reinforced Cementitious Matrix (FRCM) Composites for Infrastructure Strengthening and Rehabilitation: Characterization Methods, PhD Thesis, Miami.
- ASTM International 2004. Standard Test Method for Tensile Strength of Concrete Surfaces and the Bond Strength or Tensile Strength of Concrete Repair and Overlay Materials by Direct Tension (Pull-off Method). *ASTM C 1583-04* West Conshohocken, PA, United States.
- Bencardino, F., Carloni, C., Condello, A., Focacci, F., Napoli, A. and Realfonzo, R. 2018. Flexural behaviour of RC members strengthened with FRCM: State-of-the-art and predictive formulas, *Composites Part B: Engineering* 148, 132–48.
- Bertolli, V. and D’Antino, T. 2022. Modeling the behavior of externally bonded reinforcement using a rigid-trilinear cohesive material law, *International Journal of Solids and Structures* 248, 111641.
- Carloni, C., D’Antino, T., Sneed, L.H. and Pellegrino, C. 2018. Three-Dimensional Numerical Modeling of Single-Lap Direct Shear Tests of FRCM-Concrete Joints Using a Cohesive Damaged Contact Approach, *J. Compos. Constr.* 22, 04017048.
- Carozzi, F.G. and Poggi, C. 2015. Mechanical properties and debonding strength of Fabric Reinforced Cementitious Matrix (FRCM) systems for masonry strengthening, *Composites Part B: Engineering* 70, 215–30.
- CSLLPP 2022. Linee guida per la identificazione, la qualificazione ed il controllo di accettazione di compositi fibrorinforzati a matrice inorganica (FRCM) da utilizzarsi per il consolidamento strutturale di costruzioni esistenti, Rome, Italy.
- Danesi S.r.L. 2020. Technical datasheet of Solid Brick 11. 6.24. Available at: <https://www.danesilaterizi.it/product/mattone-pieno-11-6-24-mattoni-pieni-prezzo/>.
- D’Antino, T., Focacci, F., Sneed, L.H. and Carloni, C. 2020. Relationship between the effective strain of PBO FRCM-strengthened RC beams and the debonding strain of direct shear tests, *Engineering Structures* 216, 110631.
- Del Prete, I., Bilotta, A. and Nigro, E. 2015. Performances at high temperature of RC bridge decks strengthened with EBR-FRP, *Composites Part B: Engineering* 68, 27–37.
- Donnini, J. 2019. Durability of glass FRCM systems: Effects of different environments on mechanical properties, *Composites Part B: Engineering* 174, 107047.
- Donnini, J., Bompadre, F. and Corinaldesi, V. 2020. Tensile Behavior of a Glass FRCM System after Different Environmental Exposures, *Processes* 8, 1074.
- EN 998-2 2016. Specification for mortar for masonry.
- EN 1172 1999. Textile-glass-reinforced plastics - Determination of the textile-glass and mineral-filler content - Calcinations methods.
- European Organisation for Technical Assessment (EOTA) 2018. Externally-bonded composite systems with inorganic matrix for strengthening of concrete and masonry structures. *EAD 340275-00-0104* Brussels, Belgium.
- Fassa Bortolo S.r.L. 2020. Technical datasheet of MS 5. Available at: https://www.fassabortolo.it/documenti/10179/536572/FASSA_STE_IT_MS-20_2022-02.pdf/cc9149c0-653d-469c-9d45-0382089046d8.
- de Felice, G. et al. 2014. Mortar-based systems for externally bonded strengthening of masonry, *Mater Struct* 47, 2021–37.
- Ferretti, F., Tilocca, A.R., Incerti, A., Mazzotti, C. and Savoia, M. 2022. Tensile Behavior of FRCM Coupons under Thermal Stresses, *KEM* 916, 50–57.
- Focacci, F., D’Antino, T. and Carloni, C. 2022. Tensile Testing of FRCM Coupons for Material Characterization: Discussion of Critical Aspects, *Journal of Composites for Construction* 26, 04022039.

- Franzoni, E., Gentilini, C., Graziani, G. and Bandini, S. 2015. Compressive behaviour of brick masonry triplets in wet and dry conditions, *Construction and Building Materials* 82, 45–52.
- Franzoni, E., Gentilini, C., Santandrea, M. and Carloni, C. 2018. Effects of rising damp and salt crystallization cycles in FRCM-masonry interfacial debonding: Towards an accelerated laboratory test method, *Construction and Building Materials* 175, 225–38.
- Franzoni, E., Gentilini, C., Santandrea, M., Zanotto, S. and Carloni, C. 2017. Durability of steel FRCM-masonry joints: effect of water and salt crystallization, *Mater Struct* 50, 201.
- Franzoni, E., Santandrea, M., Gentilini, C., Fregni, A. and Carloni, C. 2019. The role of mortar matrix in the bond behavior and salt crystallization resistance of FRCM applied to masonry, *Construction and Building Materials* 209, 592–605.
- Garavaglia, E., Valluzzi, M.R., Perego, S. and Tedeschi, C. 2020. Probabilistic damage evolution in masonry strengthened with FRCM subjected to aggressive environment, *Construction and Building Materials* 239, 117718.
- Hegger, J., Will, N., Bruckermann, O. and Voss, S. 2006. Load-bearing behaviour and simulation of textile reinforced concrete, *Mater Struct* 39, 765–76.
- International Code Council Evaluation Service (ICC-ES) 2018. Acceptance criteria for masonry and concrete strengthening using fabric-reinforced cementitious matrix (FRCM) and steel reinforced grout (SRG) composite systems. *AC434* Whittier, CA.
- Nobili, A. 2016. Durability assessment of impregnated Glass Fabric Reinforced Cementitious Matrix (GFRCM) composites in the alkaline and saline environments, *Construction and Building Materials* 105, 465–71.
- Ombres, L. 2015. Analysis of the bond between Fabric Reinforced Cementitious Mortar (FRCM) strengthening systems and concrete, *Composites Part B: Engineering* 69, 418–26.
- Papanicolaou, C.G., Triantafillou, T.C., Papathanasiou, M. and Karlos, K. 2008. Textile reinforced mortar (TRM) versus FRP as strengthening material of URM walls: Out-of-plane cyclic loading, *Materials and Structures/Materiaux et Constructions* 41, 143–57.
- RILEM TC 127-MS 1998. MS-A.1 Determination of the resistance of wallettes against sulphates and chlorides, *Mat. Struct.* 31, 2–9.
- Sika Italia SpA 2021. Sika MonoTop®-722 Technical Sheet. April 2021.
- Täljsten, B. and Blanksvärd, T. 2007. Mineral-based bonding of carbon FRP to strengthen concrete structures, *Journal of Composites for Construction* 11, 120–28.
- Tedeschi, C., Kwiecień, A., Valluzzi, M.R., Zajac, B., Garbin, E. and Binda, L. 2014. Effect of thermal ageing and salt decay on bond between FRP and masonry, *Mater Struct* 47, 2051–65.
- Trapko, T. 2013. The effect of high temperature on the performance of CFRP and FRCM confined concrete elements, *Composites Part B: Engineering* 54, 138–45.
- Triantafillou, T.C. and Papanicolaou, C.G. 2006. Shear strengthening of reinforced concrete members with textile reinforced mortar (TRM) jackets, *Materials and Structures* 11.

On the behaviour of FRCM fibres in saturated alkaline solution

M. Canestri, F. Ferretti, E. Sassoni & C. Mazzotti

DICAM Department, University of Bologna, Bologna, Emilia Romagna, Italy

ABSTRACT: The main objective of this work was to study the behaviour of fibre grids, usually employed in FRCM (Fibre Reinforced Cementitious Matrices) systems, when exposed to an alkaline solution. Three basalt and a glass fibre textiles were conditioned in a saturated solution of calcium hydroxide and distilled water at 23°C. The total exposure time was chosen equal to 1000h. To monitor the conditioning process, alkalinity levels were periodically controlled for the whole exposure time. Subsequently, tensile tests were conducted on textile samples, including multiple longitudinal strands. A series of preliminary SEM (Scanning Electron Microscopy) analyses was also conducted to verify the integrity of the organic coating applied to the fibres. The coating, indeed, has the fundamental role of preventing or delaying the degradation process. The obtained results are discussed in terms of ultimate strength and elastic modulus reductions, showing significant detrimental effects of the alkaline environment especially for the basalt fibres.

1 INTRODUCTION

In recent years, retrofitting systems such as FRCMs (Fibre Reinforced Cementitious Matrices) have been extensively applied to recover damages caused by earthquakes or to improve the structural capacity of existing constructions. These externally bonded solutions have shown excellent mechanical performances and a good compatibility with the masonry substrates. Many authors have already proven the retrofitting potential and efficiency of these composite materials in several experimental studies, where the behaviour of strengthened elements was compared with the behaviour of unreinforced ones (Feo et al. 2016, Angiolilli et al. 2020, Garcia Ramonda et al. 2021, Ferretti et al. 2021a,b). However, still limited studies have examined their behaviour when exposed to temperature variations (Ferretti et al. 2022a, b), freeze and thaw cycles, or to aggressive environmental actions.

Composite systems can be affected by alkaline and saline environments, which can have significant effects on their mechanical properties, as demonstrated by recent studies. Nobili (2015) studied the effect of 1000h of exposure in saline and alkaline environment on the two components characterising a glass-FRCM system, i.e., fibres and mortar, both showing reduced strength values after the conditioning process. Hristozov et al. (2016) organised a large experimental campaign, with 490 samples in total, to study the effect of four environmental conditions (dry heat, distilled water, salt water and alkaline) for 4 total durations (500, 1000, 2000, 3000h) on flax and glass fibers. Tensile properties of both fibre typologies significantly decreased with the conditioning process, with flax composite showing slightly higher strength retention rates. Donnini et al. (2020) examined the effects of saline, alkaline environments and freeze thaw cycles on the mechanical properties of carbon and AR (Alkali Resistant) glass fibres. Alkaline exposure was demonstrated to be the most detrimental condition for glass yarns, characterised by a final strength reduction of about 25%. Micelli & Aiello (2019) focused their work on examining the residual mechanical properties of glass, basalt, PBO (polyparaphenylene benzo-bisoxazole) and steel fibers when exposed to alkaline environment. They carried out an interesting literature review, leading to the definition of four different aging aqueous solutions, aiming at representing the spectrum of

different possible combinations of inorganic matrix. Tests demonstrated that fibers were more susceptible to cementitious environments than to lime-based ones, especially in the case of glass and basalt materials, with strength loss up to 86% and full deterioration achieved in some cases. Some of the aging protocols defined in this experimental work were then reproduced and used (Rizzo et al. 2020, Micelli et. al. 2021) to further demonstrate the efficiency of the methodology and its effectiveness in studying the deteriorating effect on glass fibres based FRCM systems.

The objective of this research is the study of the behaviour of different types of fibre grids, when exposed to an alkaline solution. Conditioning protocols, such as solutions and exposure time, were selected considering the indications found in the cited literature, as will be specified in the following.

2 MATERIALS AND METHODS

2.1 Materials

In this experimental campaign, four different textiles, adopted as reinforcements in lime-based FRCM systems, were conditioned in alkaline solutions and then tested to verify material degradation. According to the manufacturer's indications, geometrical and technical specifications of the investigated reinforcing fibres are the following:

- B1 (Figure 1a): a balanced bidirectional basalt grid, characterised by a total weight density of 304 g/m², a bundle spacing of 20 mm and an equivalent thickness of 0.035 mm. As a result, an area of 0.7 mm² was considered for each bundle;
- B2 (Figure 1b): a balanced bidirectional basalt grid, characterised by a total weight density of 210 g/m², a bundle spacing of 16 mm and an equivalent thickness of 0.034 mm. As a result, an area of 0.544 mm² was considered for each bundle;
- B3 (Figure 1c): a balanced bidirectional basalt grid, characterised by a total weight density of 200 g/m², a bundle spacing of 17 mm and an equivalent thickness of 0.032 mm. As a result, an area of 0.544 mm² was considered for each bundle;
- G1 (Figure 1d): a balanced bidirectional glass grid, characterised by a total weight density of 240 g/m², a bundle spacing of 25 mm and an equivalent thickness of 0.036 mm. As a result, an area of 0.9 mm² was considered for each bundle.

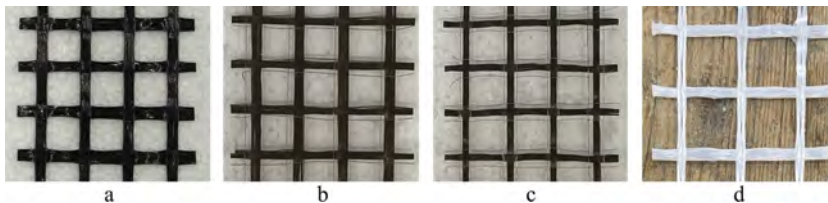


Figure 1. Reinforcing textiles: (a) B1; (b) B2; (c) B3; (d) G1.

2.2 Conditioning protocols

Experimental tests to investigate the potential capacity reduction of textiles or FRCM systems when exposed to alkaline environments are usually carried out without shared and recognised procedures or standards to be followed, both in terms of type of solutions in which samples should be immersed, temperature levels and exposure times. However, based on the experimental works currently available in the literature, some of which are reported in Section 1, one possibility is to simulate the alkaline environment, which can be potentially found in lime-based mortars, by dissolving a specific content of calcium hydroxide (Ca(OH)₂) in distilled water. In this research, the 0.16% content, in weight, of Ca(OH)₂ was adopted to obtain a saturated solution with a pH approximately equal to 12. The solution was poured inside High-Density PolyEthylene (HDPE) tanks. Subsequently, the grid samples were submerged

inside the solution at 23°C for a total exposure time equal to 1000h. To control the conditioning process, the alkalinity level was periodically monitored through a standard pH sensor, while the temperature stability was ensured by means of a room with a controlled temperature and humidity environment. The values of the registered pH levels are reported in Figure 2b.

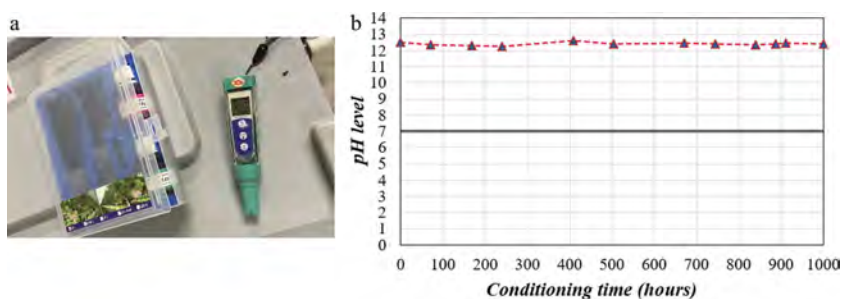


Figure 2. pH sensor (a) and pH level of the alkaline solution for 1000h (b).

A mean pH value of 12.4 was found during the 1000h of the conditioning process, while its value was almost constant with minimal variation (i.e., ± 0.2). As a result, the quality of the conditioning setup, achieved after a series of preliminary tests, was confirmed. In fact, one of the main issues that can occur is the undesired reaction of the calcium hydroxide with the carbon dioxide (CO_2) contained in the air, which could potentially lead to the precipitation of calcium carbonate (CaCO_3) and, consequently, to the reduction of the pH, therefore nullifying the conditioning process. In order to avoid this effect, airtight tanks were used with a high height-to-width ratio, to minimize the free surface of the solution, where this reaction could take place, and reduce the air intake.

2.3 Tensile test setup

The preparation of the specimens was performed following the indications and prescriptions provided by the *Italian Guidelines for the identification, qualification and acceptance control of FRCM composites to be used for the structural strengthening of existing constructions* (2018). In particular, 500 mm long textile samples were cut out of rolls, including 4 longitudinal bundles for the three basalt-based systems and 3 for the glass one (Figure 1). A total of 6 specimens for each grid type were prepared, half of which were directly tested. The remaining ones were conditioned as described in Section 2.2 and tested afterwards. The extremities of the samples were reinforced with $7 \times 7 \text{ cm}^2$ GFRP (Glass Fibre Reinforced Polymer) tabs, applied to the textiles by means of a bi-component epoxy resin. This solution was adopted to avoid an uneven stress distribution between the longitudinal bundles during the tensile tests. The tests were performed using a servo-hydraulic testing machine (Figure 3), equipped with a 0.5 load cell, with a maximum load capacity of 100 kN. Particular attention was paid to ensure the verticality of the samples inside the testing apparatus to avoid potential parasitic effects. Subsequently, all the tests were conducted under displacement control, with a constant rate of 0.5 mm/min. Strain values were recorded alongside load ones by means of an extensometer, which was firmly clipped to the central part of the specimens, with a gauge length of 100 mm.

3 EXPERIMENTAL RESULTS AND DISCUSSION

3.1 Stress vs strain curves

The results of the tensile tests are reported in this section both for the unconditioned and the conditioned samples. A total of 24 tests were carried out, considering the 4 fibre grid types analysed. Samples are identified in the following by the notation “TT_XX_AK_n”, where the

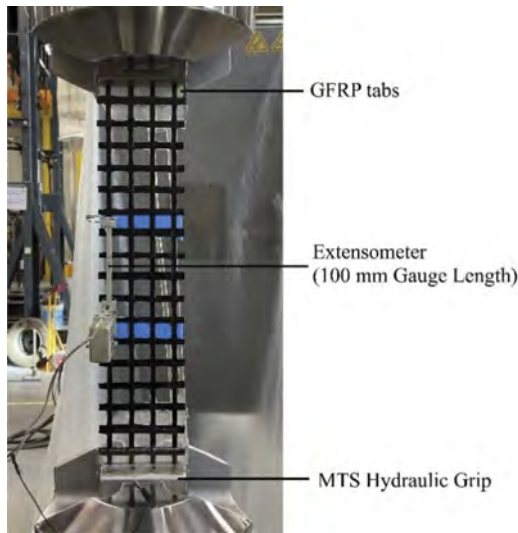


Figure 3. Setup of the direct tensile tests.

first two letters indicate the test type (Tensile Test), XX the material, AK the alkaline conditioning process (when applicable), and n is the specimen number. The obtained results are shown in Figures 4-7 in terms of axial stress *vs* strain. Stress values were derived from the axial load ones by dividing them for the cross-section area of the textiles, as indicated in Section 2.1. Deformation values were derived by dividing the registered displacement values by the gauge length of the extensometer, equal to 100 mm.

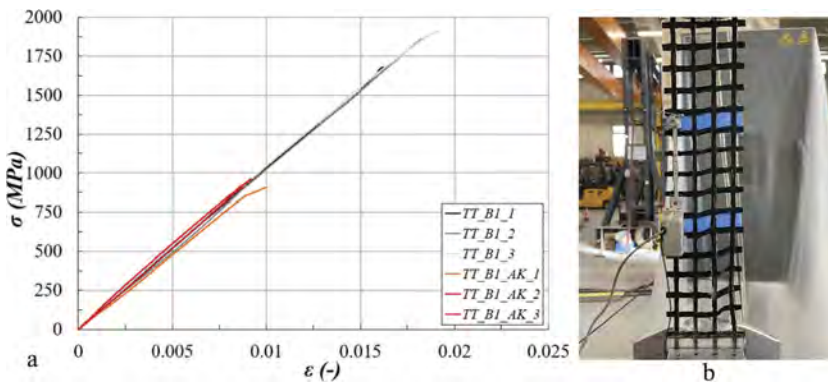


Figure 4. Stress *vs* strain curves for material B1 (a) and representative failure mode obtained for the sample TT_B1_1 (b).

The stress *vs* strain behaviour observed in all the tests was linear elastic up until the failure, which occurred due to fibres rupture inside the free length of the samples in all cases. This was detected for both material types (basalt or glass) and for both the unconditioned and the alkaline conditioned samples. In addition, for B1 and B3 materials, the rupture always occurred locally along the bundles of the textile, with minimal diffusion in the length of the specimens. On the other hand, for B2 specimens, the failure developed involving longer portions of material, with a complete shattering of the yarns (Figure 5). G1 samples showed a progressive failure and detangling of the strands that form the single bundles (Figure 7). Finally, it is worth highlighting that the exposure in the aggressive environment did not affect the obtained failure modes.

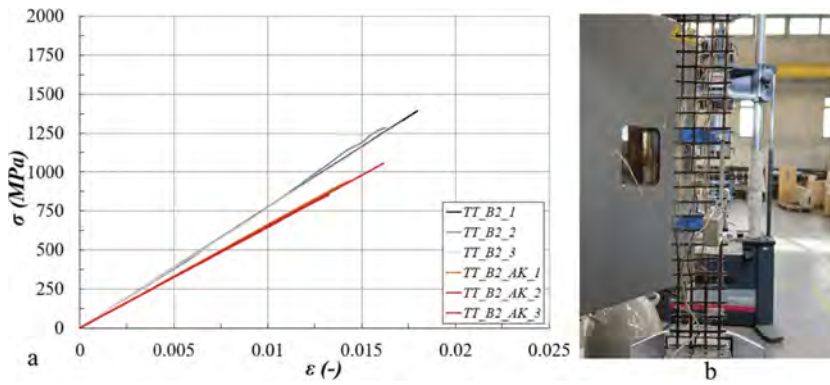


Figure 5. Stress vs strain curves for material B2 (a) and representative failure mode obtained for the sample TT_B2_3 (b).

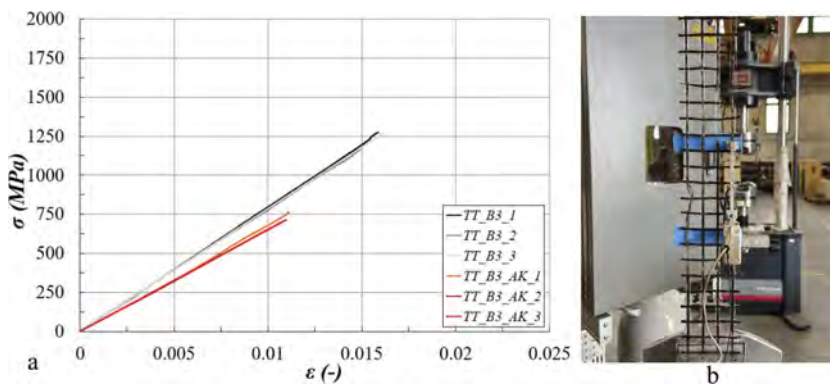


Figure 6. Stress vs strain curves for material B3 (a) and representative failure mode obtained for the sample TT_B3_2 (b).

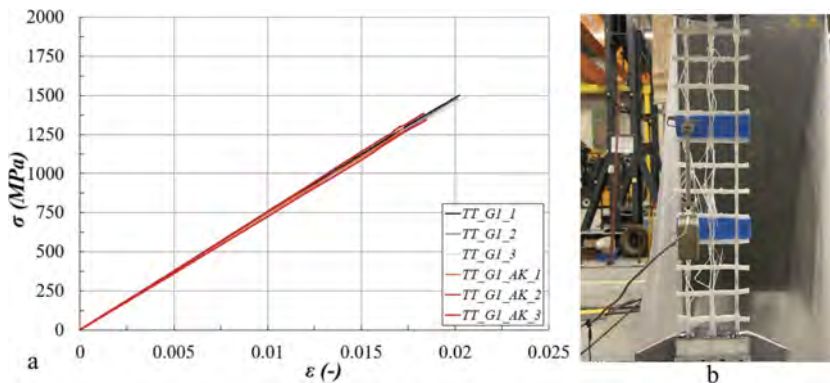


Figure 7. Stress vs strain curves for material G1 (a) and representative failure mode obtained for the sample TT_G1_2 (b).

3.2 Mechanical properties and capacity retention rates

The mechanical properties obtained from the 24 tensile tests are reported in Table 1: mean values of the maximum tensile strength σ_{uf} are displayed alongside the corresponding ultimate

strain values ε_{uf} and the elastic modulus E_f (evaluated in a range of 20%-50% of the tensile capacity). Moreover, following the indication of the International standard ISO10406-1, capacity retention rates were evaluated for the tensile strength (R_σ) and the elastic modulus (R_E), according to the following expressions:

$$R_\sigma = \left(\frac{\sigma_{uf,AK}}{\sigma_{uf,0}} \right) \cdot 100 \quad (1)$$

$$R_E = \left(\frac{E_{f,AK}}{E_{f,0}} \right) \cdot 100 \quad (2)$$

where $\sigma_{uf,AK}$ and $E_{f,AK}$ are the tensile capacity and elastic modulus of the conditioned specimens, respectively, while $\sigma_{uf,0}$ and $E_{f,0}$ are the corresponding reference values for unconditioned ones.

Table 1. Mechanical properties obtained from the tensile tests.

Specimen	σ_{uf} MPa	ε_{uf} %	E_f GPa	R_σ %	R_E %
TT_B1	1817 (6.74)	1.79 (8.26)	103.42 (1.22)	100.0	100.0
TT_B1_AK	924 (3.31)	0.93 (7.33)	103.00 (7.45)	50.9	99.6
TT_B2	1333 (4.10)	1.7277.15 (4.95)	100.0 (0.37)	100.0	TT_B2
TT_B2_AK	951 (10.7)	1.46 (10.0)	65.42 (1.25)	71.3	84.8
TT_B3	1244 (3.70)	1.57 (3.37)	78.81 (0.86)	100.0	100.0
TT_B3_AK	724 (5.17)	1.09 (2.43)	64.93 (0.72)	58.2	82.4
TT_G1	1490 (0.78)	2.03 (1.37)	73.91 (0.98)	100.0	100.0
TT_G1_AK	1339 (3.69)	1.80 (3.72)	74.34 (2.20)	89.9	100.6

(CoV % values are reported in parenthesis)

A strong reduction in terms of tensile capacity was clearly observed in all the basalt fibres systems (B1-B2-B3), with retention rates varying from 50.9% to 71.3%. On the other hand, the effect of the alkaline environment on the tensile behaviour of glass fibres was less prominent, with a retention rate equal to 89.9%. At the same time, elastic modulus values remained almost unchanged for the B1 and G1 materials; conversely B2 and B3 specimen showed affected retention values of 84.8% and 82.4%, respectively.

3.3 SEM analyses

Considering the results obtained in the tensile tests, a series of SEM analyses was carried out using a Tescan Mira 3 FEG-SEM, trying to explain the experimental outcomes and the degradation experienced by the conditioned materials. For this purpose, during the specimen preparation phase, additional textile samples of B1 and G1 materials (denoted as B1_AK and G1_AK in the following) were prepared and cured inside the same conditioning tanks. Subsequently, after making both unconditioned and conditioned samples conductive by sputtering with graphite, they were examined at 100x of magnification.

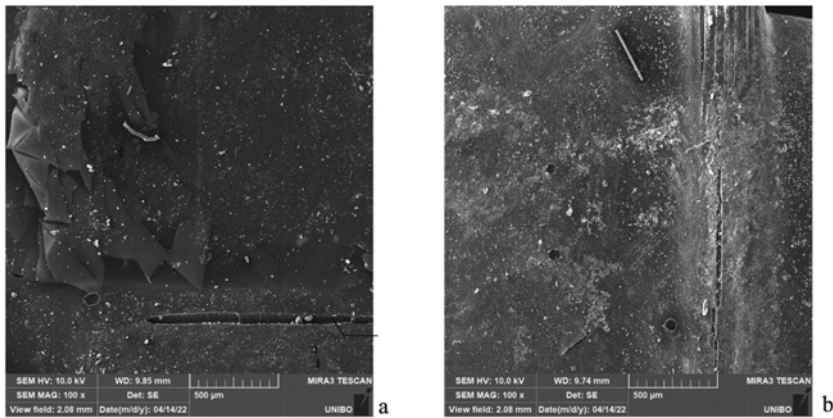


Figure 8. SEM images of B1 sample at 100x (a) and B1_AK sample at 100x (b).



Figure 9. SEM images of G1 sample at 100x (a) and G1_AK sample at 100x (b).

For the B1 sample, the images (Figure 8a) clearly show that the external coating was already fractured in multiple positions and evident cracks were already present. In these positions, the aggressive attack of the alkaline environment could concentrate its major effects (Figure 8b), causing widespread damage also to the nearby intact surface. This observation can explain the reason why the basalt fibres showed the lowest retention rates after 1000h of conditioning time. On the contrary, the organic coating covering the glass fibres in the unconditioned G1 samples (Figure 9a) seemed almost intact, with some small holes which started developing on the G1_AK sample only (Figure 9b). For this reason, the detrimental effect of the alkaline environment on the glass fibres was mitigated, with medium-high level of capacity retention rate from the tensile tests after 1000h.

4 CONCLUSIONS

In this work, an experimental study was presented on the mechanical behaviour of fibres, commonly used in FRCM systems, when exposed to an alkaline solution. After a series of preliminary tests, the aging solution was chosen and prepared introducing 0.16% of calcium hydroxide, in weight, in distilled water at 23°C. Then, samples made of three different basalt and one glass textiles were cut and immersed inside the solution. The level of alkalinity was controlled periodically to monitor the conditioning process. Tensile tests were then executed,

following standard setup configuration from Italian Guidelines, both on conditioned samples and unconditioned ones, used as reference. A comprehensive comparison was reported, in terms of stress vs strain curves, failure modes and retention rates of strength and deformability values. The strongest effects due to alkaline exposure were observed in the basalt fibres specimens, with reduced capacity retention rate up to 50.9%. On the other hand, glass fibres were less affected and showed higher retention rates after the detrimental exposure. SEM observation of the samples suggested the pivotal role of the coating integrity in influencing the degradation process.

ACKNOWLEDGMENTS

The financial support of the Italian Department of Civil Protection (ReLUIS 2022-24 Grant - WP14) is gratefully acknowledged. The technical staff of the Interdepartmental Centre for Industrial Research (CIRI Buildings & Construction) is gratefully acknowledged for the work during the setup of the tests.

REFERENCES

- Angiolilli, M., Gregori, A., Pathirage, M., Cusatis, G. 2020. Fiber reinforced cementitious matrix (FRCM) for strengthening historical stone masonry structures. *Engineering Structures* 224: 111102.
- Donnini, J., Bompadre, F., Corinaldesi, V. 2020. Tensile Behavior of a Glass FRCM System after Different Environmental Exposures. *Processes* 8(9): 1074.
- Feo, L., Luciano, R., Misseri, G., Rovero, L. 2016. Irregular stone masonries: analysis and strengthening with glass fibre reinforced composites, *Composites Part B: Engineering* 92: 84–93.
- Ferretti, F., Incerti, A., Tilocca, A.R., Mazzotti, C. 2021. In-Plane Shear Behavior of Stone Masonry Panels Strengthened through Grout Injection and Fiber Reinforced Cementitious Matrices. *International Journal of Architectural Heritage* 15: 1375–1394.
- Ferretti, F., Mazzotti, C. 2021. FRCM/SRG strengthened masonry in diagonal compression: experimental results and analytical approach proposal. *Construction and Building Materials* 283:122766.
- Ferretti, F., Canestri, M., Mazzotti, C. 2022. Effect of temperature variations on the bond behavior of FRCM applied to masonry. *Materials and Structures* 55(6): 166.
- Ferretti, F., Tilocca, A.R., Incerti, A., Mazzotti, C., Savoia, M. 2022. Effects of thermal variations on the tensile behavior of FRCM strengthening systems. *Journal of Composites for Constructions* 26(5): 04022067.
- Garcia-Ramonda, L., Pel'a, L., Roca, P., Camata, G. 2021. Cyclic shear-compression testing of brick masonry walls repaired and retrofitted with basalt textile reinforced mortar, *Composite Structures* 283: 115068.
- Hristozov, D., Wroblewski, L., Sadeghian, P. 2016. Long-term tensile properties of natural fibre-reinforced polymer composites: Comparison of flax and glass fibres. *Composites Part B: Engineering* 95:82–95.
- Micelli, F., Aiello, M.A. 2019. Residual tensile strength of dry and impregnated reinforcement fibres after exposure to alkaline environments. *Composite Part B: Engineering* 159: 490–501.
- Micelli, F., Rizzo, V., Bonati, A., Aiello, M.A. 2022. Mechanical Behaviour of Glass Fibers FRCM and CRM Systems after Ageing in Alkaline Environments. *Key Engineering Materials* 916: 58–65.
- Nobili, A. 2015. Durability assessment of impregnated Glass Fabric Reinforced Cementitious Matrix (GFRCM) composites in the alkaline and saline environments. *Construction and Building Materials* 105: 465–471
- Rizzo, V., Micelli, F., Leone, M., Bonati, A., Aiello, M.A. 2020. Residual Strength and Durability of Glass fiber FRCM and CRM Systems Aged in Alkaline Environments. <XV International Conference on Durability of Building Materials and Components DBMC 2020.

Durability of CRM reinforcements

F. Micelli

Department of Innovation Engineering, UniSalento, Lecce, Italy

A. Franco

CNR ITC, San Giuliano Milanese (MI), Italy

R. Greppi

TCS srl, Montichiari (BS), Italy

M.A. Aiello

Department of Innovation Engineering, UniSalento, Lecce, Italy

ABSTRACT: The use of inorganic matrix fiber-reinforced systems has been investigated and promoted in the last years for the structural repair and rehabilitation of historical masonry constructions. Fabric Reinforced Cementitious Matrix (FRCM) and Composite Reinforced Mortar (CRM) are the two families of materials that have been studied and put into practice. The high physical-mechanical compatibility with masonry and ease of installation are the key points that made these systems suitable for structural engineering practice. Durability issues related to the presence of an alkaline matrix and aggressive agents in harsh environments are the actual frontier of the research in the field. This experimental study allowed to investigate the mechanical behavior and durability of a Glass Fiber Reinforced Polymer (GFRP) grid and GFRP pultruded bar used respectively as reinforcement and connectors in a new CRM system. Tensile tests were performed before and after aging consisting of separate exposure to moisture, alkaline solutions, freeze-thaw cycles, and marine water. Different exposure times were investigated. Pull-out from different substrates and lap splice tests were also performed on the GFRP connectors. Measurements of the glass transition temperature and electronic microscopy completed the experimental protocol. The results in terms of mechanical comparison between the control and aged specimens are provided and discussed in the paper.

1 INTRODUCTION

Composite materials, constituted by fibers of various nature (carbon, steel, basalt, glass, aramid, PBO or natural fiber) embedded in a matrix constitute a modern generation of strengthening systems widely used in civil engineering. In this scenario two families of fiber reinforced materials are used: FRP (Fiber Reinforced Polymers) that have an organic matrix, and inorganic matrix composites. The materials used in existing masonry are called FRCM (Fabric Reinforced Cementitious Matrix) or CRM (Composite Reinforced Mortar). FRCM and CRM systems are successfully used in masonry construction because of their mechanical compatibility with masonry substrates and the high vapor permeability of mortar. Unfortunately only few works are available in literature on the durability of FRCM and CRM materials. The first studies were related to the use of carbon fibers (Nobili & Signorini 2017; Donnini et al. 2017) and AR-Glass FRCM (Nobili 2016), and others include the study of the durability of the constituent materials, fibers (Micelli & Aiello 2017) and mortar (Nobili 2016). A recent work (Arczewska et al. 2021) put in evidence the essential role of the resin in Glass FRP products, as a protection against the ingress of alkaline

fluids. In this perspective the matrix has also an important role to prevent degradation in terms of inter-laminar shear strength (Pan & Yan 2021; Yu et al. 2021). Another recent study (Wang et al. 2022) illustrated that a small drop in the pH values from 13 to 11 could significantly reduce the alkali-induced fiber erosion and thereby greatly alleviate the tensile strength degradation of conditioned GFRP. In this study the mechanical properties and the durability of the GFRP reinforcements and connectors of a CRM system were investigated. Short and long-term properties were measured and compared by performing different ageing protocols that include immersion in artificial seawater (saline solution), high humidity and alkaline solutions. Connectors were also tested in lap splice and pull-out configurations. The obtained results, in terms of residual mechanical properties are discussed in the paper in order to highlight the influence of potential aggressive environments on the engineering properties of the tested specimens.

2 EXPERIMENTAL PROGRAMME

2.1 Materials and specimens

A new GFRP grid made by glass fibers and epoxy matrix was investigated, named MR44, with a spacing of 40x40 mm. Transversal connectors made by GFRP bars having a nominal diameter of 7 mm were also tested. The GFRP grids were tested under direct tensile force in the two directions, as illustrated in Figure 1. The two directions show a different configuration of the fibers: twisted and flat. Twisted bars are named “warp”, while the flat bars are called “weft”. Specimens were cut from the grid and tested according to ISO 10406-1:2015, as same as done for the connectors that have a cross-section area of 52.28 mm², obtained from experimental tests by weighting. Lap splice tests were also performed for the connectors, by using an overlap length of 100 mm. GFRP connectors were also tested for measuring the highest pull-out force causing the extraction of the connector from a substrate. Four different substrates were used, concrete, limestone masonry, clay bricks masonry and hard stone blocks masonry. An embedded length of 100 mm was used. In Figure 2 the geometry of the specimens is shown: LxBxH are 250x250x350 mm (concrete), 380x380x270 mm (clay), 370x350x230 cm (limestone), 340x250x260 cm (hard stone). In addition to tensile tests, joint-shear tests were performed on specimens that are shown in Figure 2.

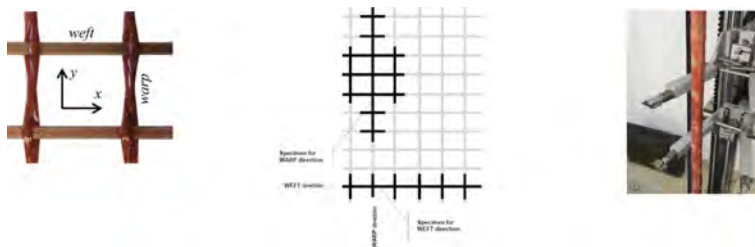


Figure 1. GFRP grids and geometry of the tensile specimens - GFRP rebar connector.

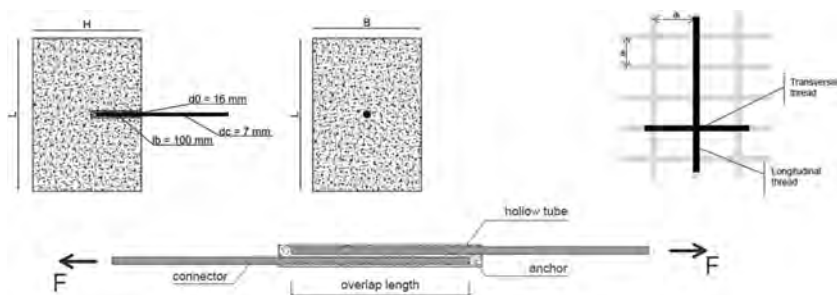


Figure 2. Pull-out connectors specimens – joint shear test specimens - lap splice specimens.

2.2 Ageing and test set-up

The durability of the composites materials described above (grids and connectors) was investigated by using protocols of accelerated ageing. Freeze and thaw cycles: the samples were conditioned in a humid chamber for one week (RH > 90%, T= 38±2°C); then they were subjected to 20 cycles of freezing and thawing. Each cycle includes four hours at -18±1 °C, followed by 12 hours in a humid chamber (RH > 90%, T= 38±2°C). Humid environment: conditioning was carried out for 1000 and 3000 hours by immersing the samples in chemically inert water at a temperature of 38±2°C assuring a relative humidity > 90% (ASTM D 2247-11, ASTM E104-02). Saline environment: the conditioning was carried out for 1000 and 3000 hours by immersing the samples in a solution made of 245 g of NaCl and 40.94 g of Na₂SO₄ per 10 liters of distilled water, at a temperature of 23±2 °C (ASTM D1141-98, ASTM C581 -03). Alkaline environment: conditioning was carried out for 1000 and 3000 hours by immersing the samples in a solution composed of Ca(OH)₂ (0.83 g/litre) and distilled water with pH=12.5 (periodically monitored by pH-meter), at a temperature of 23± 2°C.

In Table 1 the total number of specimens and tests are shown.

Table 1. Experimental tests.

Test type	Specimen type and repetitions		
	grid MR44 warp	grid MR44 weft	Connector
Tensile Control specimens	15	15	10
Tensile Freeze-thaw	5	5	5
Tensile Humidity 1000 hrs	5	5	5
Tensile Humidity 3000 hrs	5	5	5
Tensile Saline 1000 hrs	5	5	5
Tensile Saline 3000 hrs	5	5	5
Tensile Alkaline 1000 hrs	5	5	5
Tensile Alkaline 3000 hrs	5	5	5
Pull-out from four substrates	-	-	20
Lap splice	-	-	3
Joint strength	10	10	-

During the ageing period small specimens of GFRP grids were immersed in water at 40°C and the increase of weight was measured twenty times in a period of 2000 hours.

3 TEST RESULTS AND DISCUSSION

All the composites specimens that were subjected to tensile tests until failure exhibited a linear elastic behaviour, as expected from theory. In the following sub sections the results will be presented for each type of material. The values of the elastic modulus reported herein were those measured in the range between 20% and 50% of the ultimate load.

3.1 GFRP grids MR 44

Failure modes of warp and weft specimens were caused by fibers breakage. There were not significant differences in failure modes observed for control and conditioned specimens. The typical circumstances described above are illustrated in Figure 3.

The average values of the tensile strength and elastic modulus are reported in the following Table 2, where A_n is the cross-section area. When the residual properties of conditioned specimens, after ageing, exceed the reference specimens (due to the statistical error), they are reported as 100%.

As reported in the Table 2 the ageing in the different environments did not produce severe reduction of the engineering properties such as ultimate strength and longitudinal stiffness (modulus E).

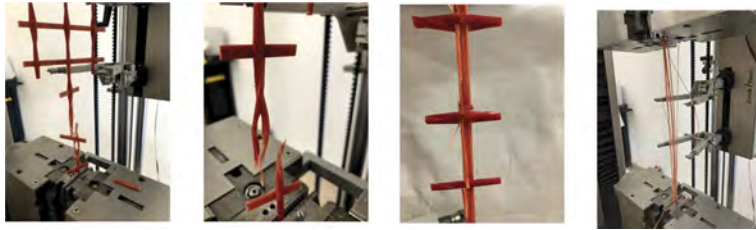


Figure 3. Typical failure modes of MR 44 grid after tensile tests.

Table 2. Experimental results - GFRP grid MR44.

MR44-warp-ref ($A_n=9.70\text{mm}^2$)	F_u	σ_u	ϵ_u	E	MR44-weft-ref ($A_n=9.58\text{mm}^2$)	F_u	σ_u	ϵ_u	E
	kN	MPa	%	GPa		kN	MPa	%	GPa
Average value	4.52	465.79	1.03	45.06	Average value	7.79	813.34	1.39	58.72
Standard dev	0.19	20.08	0.04	0.98	Standard dev	0.73	76.26	0.14	1.00
COV %	4.3%	4.3%	4.2%	2.2%	COV %	9.4%	9.4%	9.8%	1.7%
MR44-warp-freeze-thaw	F_u	σ_u	ϵ_u	E	MR44-weft- freeze-thaw	F_u	σ_u	ϵ_u	E
	kN	MPa	%	GPa		kN	MPa	%	GPa
Average value	4.34	447.09	1.00	44.67	Average value	7.07	738.27	1.25	59.22
Standard dev	0.21	21.25	0.04	1.17	Standard dev	0.70	72.70	0.13	0.54
COV %	4.8%	4.8%	4.4%	2.6%	COV %	9.8%	9.8%	10.3%	0.9%
% residual	-	96.0%	-	99.1%	% residual	-	90.8%	-	100%
MR44-warp-humidity 1000hrs	F_u	σ_u	ϵ_u	E	MR44-weft- humidity 1000hrs	F_u	σ_u	ϵ_u	E
	kN	MPa	%	GPa		kN	MPa	%	GPa
Average value	4.38	451.46	1.01	44.50	Average value	8.47	883.99	1.49	59.41
Standard dev	0.46	47.53	0.10	0.94	Standard dev	0.97	101.23	0.15	1.55
COV %	10.5%	10.5%	10.0%	2.1%	COV %	11.5%	11.5%	10.1%	2.6%
% residual	-	96.9%	-	98.7%	% residual	-	100%	-	100%
MR44-warp-humidity 3000hrs	F_u	σ_u	ϵ_u	E	MR44-weft- humidity 3000hrs	F_u	σ_u	ϵ_u	E
	kN	MPa	%	GPa		kN	MPa	%	GPa
Average value	4.27	439.79	0.98	44.88	Average value	7.44	776.33	1.30	59.75
Standard dev	0.33	34.05	0.09	1.99	Standard dev	1.26	132.04	0.22	0.36
COV %	7.7%	7.7%	9.0%	4.4%	COV %	17.0%	17.0%	16.9%	0.6%
% residual	-	94.4%	-	99.6%	% residual	-	95.4%	-	100%
MR44-warp-Saline 1000hrs	F_u	σ_u	ϵ_u	E	MR44-weft- Saline 1000hrs	F_u	σ_u	ϵ_u	E
	kN	MPa	%	GPa		kN	MPa	%	GPa
Average value	4.65	479.75	1.05	45.60	Average value	7.48	780.65	1.31	59.41
Standard dev	0.18	18.70	0.06	1.51	Standard dev	1.05	109.59	0.17	1.68
COV %	3.9%	3.9%	6.1%	3.3%	COV %	14.0%	14.0%	13.1%	2.8%
% residual	-	100%	-	100%	% residual	-	96.0%	-	100%
MR44-warp-Saline 3000hrs	F_u	σ_u	ϵ_u	E	MR44-weft- Saline 3000hrs	F_u	σ_u	ϵ_u	E
	kN	MPa	%	GPa		kN	MPa	%	GPa
Average value	4.36	449.92	1.02	44.25	Average value	7.79	813.13	1.39	58.59

(Continued)

Table 2. (Continued)

Standard dev	0.35	35.71	0.08	1.91	Standard dev	1.10	115.11	0.19	0.80
COV %	7.9%	7.9%	7.7%	4.3%	COV %	14.2%	14.2%	13.7%	1.4%
% residual	-	96.6%	-	98.2%	% residual	-	100%	-	99.8%
MR44-warp-Alkali 1000hrs	F_u	σ_u	ϵ_u	E	MR44-weft- Al kali 1000hrs	F_u	σ_u	ϵ_u	E
	kN	MPa	%	GPa		kN	MPa	%	GPa
Average value	4.25	438.21	0.97	45.00	Average value	7.29	760.52	1.25	60.71
Standard dev	0.28	28.53	0.07	1.01	Standard dev	0.57	59.21	0.09	1.03
COV %	6.5%	6.5%	7.2%	2.2%	COV %	7.8%	7.8%	7.1%	1.7%
% residual	-	94.1%	-	99.9%	% residual	-	93.5%	-	100%
MR44-warp-Alkali 3000hrs	F_u	σ_u	ϵ_u	E	MR44-weft- Al kali 3000hrs	F_u	σ_u	ϵ_u	E
	kN	MPa	%	GPa		kN	MPa	%	GPa
Average value	4.46	460.10	1.04	44.02	Average value	7.31	763.26	1.27	60.32
Standard dev	0.36	37.38	0.04	2.34	Standard dev	1.64	171.56	0.30	2.63
COV %	8.1%	8.1%	3.5%	5.3%	COV %	22.5%	22.5%	23.4%	4.4%
% residual	-	98.8%	-	97.7%	% residual	-	93.8%	-	99.8%

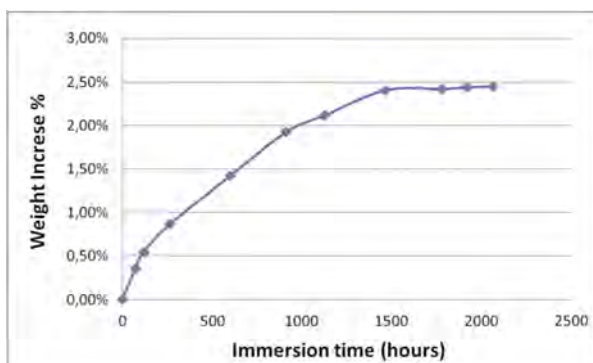


Figure 4. Absorption curve after 2000hrs in hot water for MR 44 GFRP grid.

This results was observed either after 1000 hours or 3000 hours of immersion. The specimens after ageing were covered by a white film made of solid particles produced by deposition, but at the same time no microcracks or detachments were visible on the matrix surface.

The most important result is that related to the ageing in alkaline environment, since it was potentially the most detrimental condition for glass fibers. It is well known in fact that alkaline attack may produce a chemical degradation of the fibers which causes a physical dissolution due to the hydrolysis. Different degradation mechanisms were observed in literature in presence of alkaline solutions, they include: an effect of the $(OH)^-$ ions which produce corrosion of the fibers; a second effect due to the precipitation of hydration products, which may reduce the flexibility of the fibers and change the behavior at the interface with the inorganic matrix; the presence of chemical products which cause a densification of the matrix at the interface level which may produce a bending effect in the fibers. These effects are avoided by using alkali resistant glass and at the same time when the physical protection provided by the matrix is able to strongly reduce the penetration of fluids also at the interlaminar level. In the case studied herein it was measured that the presence of the alkaline solutions did not produce any effect on the tested GFRP grids, in both directions. In Figure 4 the absorption diagram is shown for the GFRP specimens immersed in hot water for 2000 hours, after twenty weight measurements. From the diagram it is observed that at the early stages

the weight increase follows a pseudo linear trend, which is typically described by the Fick's law. After 1500 hours a knee-point is visible, where the slope of the curve lies in a horizontal branch, which indicates that absorption process is almost complete and the weight increase is not expected to develop in a significant way. The weight increase remained lower than 2.5% which is a measure of the very low permeability of the epoxy resin used as matrix in the studied reinforcement. This confirms the high values of the retained strength after ageing in the moist environments used for the studied durability protocols. The tests performed to measure the joint shear strength on MR 44 grid revealed a maximum load of 2.08 kN and 0.99 kN, as average values respectively for warp and weft specimens. Coefficient of variations were respectively 7.7% and 13.1%, thus the results can be considered free from significant experimental errors. The high difference between the two directions is due to the different technology used to join the two filaments, as visible in Figure 1. The warp filament is glued to the weft filament which is inserted into a sort of buttonhole created inside the warp filament. This produced a sort of mechanical interlock along the warp direction under tensile forces. While along the weft direction the failure is due to the sliding of the weft filament inside the buttonhole. Three DSC tests (Differential Scanning Calorimetry) were performed on the epoxy resin before and after ageing in hot water. The control specimens have shown an average glass transition temperature of 75.3 °C which was almost the same for the aged specimens. This confirmed that no significant changes were produced at the matrix level. In order to detect possible damages on the glass fibers scanning electronic microscopy (SEM) was applied to MR 44 specimens aged after 3000 hours in alkaline bath. A SEM view of the aged fibers is shown in Figure 5. Some solid precipitates are visible on the surface of the glass fibers, but no damage is detectable. This confirms the good durability of the composite reinforcement, as measured through the mechanical tests.

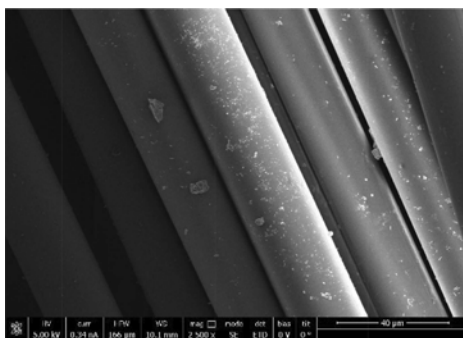


Figure 5. SEM microscopy after ageing in alkaline solution (3000 hrs) - GFRP grid MR44.

3.2 GFRP connectors

GFRP connectors are made by GFRP pultruded bars, by using the same glass fibers and resin of MR 44 grids. The alignment of the fibers and good impregnation are the most important technological parameters that may assure a good mechanical response in terms of engineering properties. When subjected to tensile forces up to the ultimate strain value, the failure modes of GFRP connectors were characterized by fiber rupture far from the gripping area, which was accompanied, in some cases, to an intralaminar failure inside the resin or at the fiber/matrix interface. Typical failure modes of the tested GFRP rods are shown in Figure 6. In this kind of specimens the failure of aged specimens evidenced in more cases a failure mode characterized by the presence of a delamination mechanism, accompanying the fiber breakage, as evident in the last picture of Figure 6.

The results of the tensile tests on GFRP connectors are reported in Table 3.

Freeze-thaw cycles did not produce a reduction of the engineering properties that could be considered meaningful for design applications. The same conclusion can be addressed to the aged specimens in saline solution, after 1000 hours. A reduction of about 12% in ultimate strength was observed after 3000 hours of immersion in saline solution. The aged rods demonstrated to be more sensitive in presence of humidity and alkaline solutions, especially after 3000 hours. The reduction in ultimate strength was respectively about 12% and 18% after ageing in humid and alkaline bath.

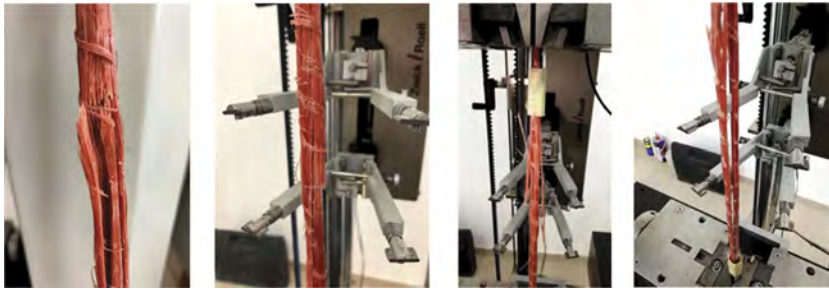


Figure 6. Tensile failure of GFRP connectors.

Table 3. Experimental results - GFRP connectors.

GFRP connector-ref ($A_n=52.28\text{mm}^2$)	F_u	σ_u	ϵ_u	E	GFRP connector-freeze-thaw	F_u	σ_u	ϵ_u	E
	kN	MPa	%	GPa		kN	MPa	%	GPa
Average value	30.19	577.43	1.32	44.00	Average value	28.82	551.31	1.25	44.38
Standard dev	1.42	27.18	0.15	3.73	Standard dev	1.40	26.80	0.08	3.18
COV %	4.7%	4.7%	11.0%	8.5%	COV %	4.9%	4.9%	6.1%	7.2%
% residual	-	-	-	-	% residual	-	95.5%	-	100%
GFRP connector-humidity 1000hrs	F_u	σ_u	ϵ_u	E	GFRP connector-humidity 3000hrs	F_u	σ_u	ϵ_u	E
	kN	MPa	%	GPa		kN	MPa	%	GPa
Average value	26.45	505.84	1.11	45.61	Average value	25.50	487.73	1.09	45.02
Standard dev	1.74	33.27	0.10	1.01	Standard dev	1.16	22.12	0.10	3.39
COV %	6.6%	6.6%	8.7%	2.2%	COV %	4.5%	4.5%	9.5%	7.5%
% residual	-	87.6%	-	100%	% residual	-	84.5%	-	100%
GFRP connector-Saline 1000hrs	F_u	σ_u	ϵ_u	E	GFRP connector-Saline 3000hrs	F_u	σ_u	ϵ_u	E
	kN	MPa	%	GPa		kN	MPa	%	GPa
Average value	29.92	572.26	1.22	46.87	Average value	26.72	510.99	1.13	45.17
Standard dev	1.75	33.48	0.07	1.98	Standard dev	2.19	41.87	0.09	0.56
COV %	5.8%	5.8%	5.5%	4.2%	COV %	8.2%	8.2%	7.9%	1.2%
% residual	-	99.1%	-	100%	% residual	-	88.5%	-	100%
GFRP connector-Alkali 1000hrs	F_u	σ_u	ϵ_u	E	GFRP connector-Alkali 3000hrs	F_u	σ_u	ϵ_u	E
	kN	MPa	%	GPa		kN	MPa	%	GPa
Average value	28.33	541.81	1.18	46.08	Average value	24.79	474.23	1.07	44.54
Standard dev	2.39	45.80	0.12	1.12	Standard dev	2.97	56.82	0.12	2.16
COV %	8.5%	8.5%	10.5%	2.4%	COV %	12.0%	12.0%	11.2%	4.8%
% residual	-	93.8%	-	100%	% residual	-	82.1%	-	100%

Three DSC tests (Differential Scanning Calorimetry) were performed on the epoxy resin of the connectors before and after ageing in hot water. Aged and unaged specimens have shown the same behavior (average $T_g=77.1$ °C). The tensile tests on the lap splice configuration, with a superposition of 100 mm, exhibited an ultimate force that was about 5 times lower than the average ultimate tensile force. A maximum force of 6.51 kN was recorded as average value of the tested bars, corresponding to a maximum tensile stress of 124.53 MPa. The maximum force of extraction from different substrates varied, in relationship to the single material that was considered. This because the mechanical properties of the substrates were very different from each other. The compressive strength of the four substrates was measured by performing uniaxial compression tests that

evidenced the following average values: $f_m=12.2$ MPa for clay bricks masonry with cement mortar joints; $f_c=34.3$ MPa for concrete; $f_m=4.8$ MPa for masonry made with soft limestone squared blocks and lime based mortar; $f_m=4.8$ MPa for blocks of hard stone and lime based mortar. In this last case failure was governed by cracks along the irregular mortar joints. The test typical failure modes of the pull-out tests are shown in Figure 7.



Figure 7. Set-up and failure modes of pull-out tests.

Concrete elements with embedded GFRP did not present any crack, and the failure was due to tensile breakage of the fibers at an average ultimate load of 27.9 kN which is fully comparable to the values of the tensile tests. Therefore the length of 100 mm inside concrete provided a full anchorage of the bar. For GFRP connectors glued inside soft limestone masonry blocks, the pull-out load was the lowest (average value equal to 12.9 kN), respect to the other substrates. In this case the failure was caused by an adhesive debonding, as visible in Figure 7. For hard stone and clay bricks the failure modes were similar (splitting failure), as visible in Figure 7. The ultimate load for clay bricks was 21.2 kN, higher than hard stone that recorded an average ultimate load of 16.4 kN.

4 CONCLUSIONS

An experimental study has been presented on GFRP reinforcements and connectors used in a Composite Reinforced Mortar system, commonly applied for the structural strengthening of masonry construction. The mechanical properties have been investigated in the short term, and after ageing in different aggressive solutions. The results confirmed that the presence of a good polymeric matrix can act as a protective agent for the impregnated fibers. The residual mechanical properties after ageing were very high in all cases. The maximum reduction of 18% for GFRP connectors was observed after immersion in alkaline solutions for 3000 hours.

REFERENCES

- Arczewska P., Polak, M.A. & Penlidis, A. 2021. Degradation of glass fiber reinforced polymer (GFRP) bars in concrete environment. *Construction and Building Materials* (293): 123451.
- Donnini, J., De Caso, F., Corinaldesi, V., Lancioni, G., & Nanni, A. 2017. Fabric-Reinforced Cementitious Matrix Behavior at High-Temperature: Experimental and Numerical Results. *Composites Part B* (108): 108–21.
- Micelli, F. & Aiello, M.A. 2017. Residual Tensile Strength of Dry and Impregnated Reinforcement Fibres after Exposure to Alkaline Environments. *Composites Part B: Engineering* (159): 490–501.
- Nobili, A. 2016. Durability Assessment of Impregnated Glass Fabric Reinforced Cementitious Matrix (GFRCM) Composites in the Alkaline and Saline Environments. *Construction and Building Materials* (105): 465–71.
- Nobili, A., & Signorini, C. 2017. On the Effect of Curing Time and Environmental Exposure on Impregnated Carbon Fabric Reinforced Cementitious Matrix (CFRCM) Composite with Design Considerations. *Composites Part B* (112): 300–313.
- Pan, Y. & Yan, D. 2021. Study on the durability of GFRP bars and carbon/glass hybrid fiber reinforced polymer (HFRP) bars aged in alkaline solution. *Composite Structures* (261): 113285.
- You, Y., Liu, S., Pan, Y., Miu, X. & Liu, J. 2021. Durability of glass fiber-reinforced polymer bars in water and simulated concrete pore solution. *Construction and Building Materials* (299): 123995.
- Wang, P., Ke, L., Wu, H., Leung, C.K.Y. 2022. Lowering exposure pH for durability enhancement of glass fiber reinforcement polymer (GFRP) rebars. *Construction and Building Materials* (354): 129131.



Taylor & Francis

Taylor & Francis Group

<http://taylorandfrancis.com>

*SS30: Durability of sustainable reinforced concrete for civil
engineering structures*
Organizers: M. Carsana & E. Redaelli



Taylor & Francis

Taylor & Francis Group

<http://taylorandfrancis.com>

Performance and environmental analysis of Reclaimed Asphalt Pavement (RAP) concrete produced in industrial environment

G. Masi, A. Michelacci, S. Manzi, A. degli Esposti, B. De Pascale, A. Bonoli & M.C. Bignozzi

Department of Civil, Chemical, Environmental and Materials Engineering, University of Bologna, Bologna, Italy

ABSTRACT: This study aims at evaluating the performances of reclaimed asphalt pavement (RAP) as concrete aggregate replacement in terms of mechanical and physical properties and environmental analysis. RAP concrete production was scaled up and it occurred in an industrial environment (CTI, Imola, Italy) by preparing a 3.5 m³ concrete casting. A partial aggregate replacement of 40% of RAP was fixed to ensure acceptable workability and mechanical performance. For comparison's sake, the same concrete mix with 100% natural aggregates was also tested. Concrete performances in terms of mechanical and physical properties were checked initially after 7 and 28 days of curing. Environmental analysis of RAP concrete was also carried out using Life Cycle Assessment (LCA) analysis applying a “cradle-to-gate” approach. All the realistic input data collected from the industry plant were considered. Durability tests are ongoing and freezing-thawing resistance and exposure to salt spray chamber on unreinforced and reinforced concrete specimens will be evaluated. As main outcomes, even if inferior mechanical properties were obtained in terms of compressive, tensile strength and elastic modulus values, a relevant reduction (average value of 15%) of environmental impacts was found especially related to global warming potential, terrestrial ecotoxicity, human non-carcinogenic toxicity and fossil resource scarcity. This study is set in the framework of “Sustainable concrete made with recycled asphalt pavement (RAPCON)” project (2020–2023), funded by Cariplo Foundation under the “Circular Economy for a sustainable future” call (2019).

1 INTRODUCTION

In order to improve the environmental sustainability of concrete, several routes have been and are currently investigated. Mainly the use of supplementary cementitious materials (SCMs) or alkali activated binders as cement replacement or the recycling of construction and demolition waste (CDW) as aggregate replacement, as well as the combination of these strategies, have shown promising results (Boobalan *et al.*, 2022). As aggregates usually represent about the 80% of a concrete mix and are the mostly used materials after water, using recycled aggregates from CDW is a promising route to improve concrete sustainability (de Brito and Kurda, 2021). Among the others, reclaimed asphalt pavement (RAP) has been widely studied as potential concrete aggregate from CDW (Debbarma, Selvam and Singh, 2020; Nandi and Ransinchung, 2021). RAP consists of natural aggregates covered by a bituminous layer and dust film, and it is derived from demolition and milling processes during asphalt pavement maintenance (Singh, Ransinchung and Kumar, 2017). A recent study has highlighted the suitability of RAP as recycled concrete aggregate thanks to its good dimensional stability and freezing and thawing resistance (Masi *et al.*, 2022). However, the presence of the bituminous layer can hinder the overall performances of concrete at the fresh and hardened state.

Increasing the RAP content in concrete mix induces a decrease in the mechanical performance due to moderate adhesion between the bituminous layer and the cement binder (Huang, Shu and Li, 2005; Al-Oraimi, Hassan and Hago, 2009; Hossiney, Tia and Bergin, 2010; Brand and Roesler, 2017). Other studies have highlighted the negative effect of RAP in the workability of fresh concrete (Huang, Shu and Burdette, 2006; Al-Oraimi, Hassan and Hago, 2009). Thus, a preliminary characterization protocol of RAP as concrete aggregate is fundamental to ensure the final concrete performance (Masi *et al.*, 2022). On the other hand, the use of RAP as concrete aggregate can improve some mechanical and durability properties, such as toughness and freezing and thawing resistance, respectively, due to different pore size distribution and the presence of the bituminous layer (Huang, Shu and Li, 2005; Huang, Shu and Burdette, 2006; Abraham and Ransinchung, 2019). The limited use of this type of CDW as recycled concrete aggregate is surely related to the lack of specific guidelines and standards and also to limited systematic information related to the environmental sustainability of RAP when used as concrete aggregate replacement (i.e., life cycle assessment (LCA)). Few studies are currently available in literature reporting LCA analyses and are mainly related to specific applications such as concrete slab production (Shi, Mukhopadhyay and Zollinger, 2018), precast concrete blocks (Nandi and Ransinchung, 2021) and cement-based pavement layers (Bressi, Primavera and Santos, 2022).

So, this study investigates the mechanical performances (i.e., compressive, tensile strength and elastic modulus) and their correlation with some physical properties (i.e., geometric density and open porosity) of a concrete mix produced by 40% RAP as replacement for concrete aggregates. A reference concrete mix (with 100% natural aggregates) was also prepared and tested for comparison purpose. All concrete mixes were prepared in a real industrial environment (CTI, Imola, Italy) by formulating 3.5 m³ for each investigated mix. In addition, the main environmental impacts for both the investigated concrete are studied using LCA analysis, applying a “cradle-to-gate” approach and considering 3.5 m³ concrete mix as the functional unit. All the input data for the LCA analysis have been kindly provided by CTI industrial plant, so as to build a realistic case study that well simulates the production of RAP-based concrete. This study reports the first results of the task related to the “validation in industrial relevant environment” of the project “Sustainable concrete made with recycled asphalt pavement” (RAP-CON, 2020-2023) granted by Fondazione Cariplo (“Circular Economy for a sustainable future” call, 2019).

2 MATERIALS AND METHODS

2.1 Materials

For preparing concrete mixes, CEM III/A 42.5 R was used together with superplasticizer (MasterEase 7007, Master Builder solution) as admixture. Natural siliceous aggregates were used with a maximum diameter of 16 mm. The applied RAP was kindly provided by CTI with a maximum diameter of 16 mm. Figure 1 reports images of RAP stored in the CTI plant and their particle size distribution.

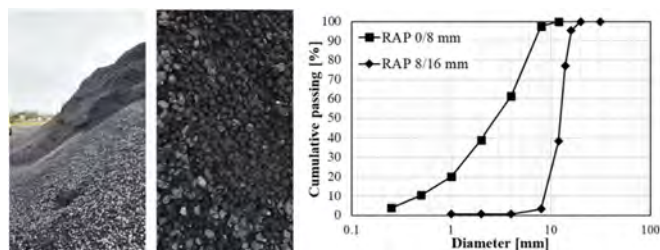


Figure 1. Images of RAP in the industrial plant and particle size distribution of the used RAP.

2.2 Mix design and sample preparation

Concrete mixes were prepared in CTI industrial plant located in Imola (Bologna, Italy). Two different concrete mixes were formulated by using 100% natural aggregates (CNAT used as reference mix) and a 40% RAP replacement (CRAP). Both these mixes were prepared in order to produce 3.5 m³ concrete using the mix design reported in Table 1. The material dosage was designed in order to produce both CRAP and CNAT characterized by C32/40 strength class and a S4 slump class. For both the mixes, the water (considering both the added water and the humidity of the aggregate) to cement ratio (W/C) was kept constant and equal to 0.448. After mixing procedures, slump test was carried out to validate the targeted slump class (S4) and values of 170 and 185 mm were measured for CRAP and CNAT, respectively. Then, fresh concrete was cast in sample holders and compacted by using concrete vibrator. Lastly, curing was performed for 7 and 28 days at 20 °C with a relative humidity of 95%. For this study, the following samples were used for each mix and curing time: 10 cubic samples (with the edge of 150 mm) for compressive strength and geometric density measurements, 3 cylindrical sample (with 150 mm diameter and 300 mm height) for tensile strength and other 3 cylindrical samples (with the same dimensions) for elastic modulus determination.

Table 1. Mix design for producing 1 m³ of concrete.

	Material dosages (kg/m ³)					
	Cement	Water	Additives	Gravel	Sand	RAP
CNAT	375	127	3.86	971	840	-
CRAP	380	137	3.58	461	628	696

2.3 Characterization

Geometric density was calculated by dividing the dry mass of cubic sample by its geometric volume. The reported results are an average of at least 3 repeated measurements.

Mechanical performances of CRAP and CNAT samples were evaluated in terms of compressive, tensile splitting strength and elastic modulus measurements. Compressive strength was determined in accordance with the EN 12390-3 standard (*EN 12390-3 Testing hardened concrete: compressive strength of test specimens*, 2019) as the ratio of the maximum load at failure and cross-sectional area of the cubic specimen. The reported results are the average of 10 measurements on cubic samples (L=150 mm). Tensile splitting strength was performed on 2 cylindrical samples (D=100 mm and H=200 mm) according EN 12390-6 standard (*EN 12390-6 Testing hardened concrete: tensile splitting strength of test specimens*, 2009). Elastic modulus was measured in accordance with EN 12390-13 (*EN 12390-13 Testing hardened concrete: determination of secant modulus of elasticity in compression*, 2013) on 3 cylindrical samples (D=150 mm and H=300 mm).

Lastly, to determine the open porosity and the average pore diameters of the two concrete mixes at the different curing time, mercury intrusion porosimetry (MIP) using Pascal 140 and 240 instruments (Thermo Fisher Scientific). MIP analyses were performed onto concrete samples of about 1 cm³ (avoiding external surfaces) in triplicate.

2.4 Life Cycle Assessment (LCA)

LCA analysis was carried out using Simapro 9.2 software in accordance with ISO 14040 standard series (*ISO 14040 Environmental management - life cycle assessment - principles and framework*, 2006th ed., 2020). The objective of the analysis is the evaluation of the environmental impact of a cement mix produced in an industrial scenario applying 40% RAP as replacement for natural aggregate, compared with a control mix made with 100% natural aggregate. The system boundary is set on a “cradle-to-gate” approach (i.e., from materials extraction/production to concrete production at the batching plant). In details, the RAP

production phases take into account the impacts related to the treatments (crushing and screening) at the CTI plant, while milling and transportation to the CTI plant of asphalt waste are not considered in the analysis because they are part of the previous product system (Santos, Flintsch and Ferreira, 2017; Vandewalle *et al.*, 2020). The functional unit (FU) used in the present study is 3.5 m³ of concrete. Data on the impacts generated by extraction/production of materials commonly used in concrete (i.e., cement, water, natural aggregates, and plasticizers) were obtained from the Ecoinvent 3.8 database available on the SimaPro software. The transportation conditions considered for each material are based on CTI suppliers. Materials were modeled starting from the inventory data and some specific data were implemented using information from CTI, as reported in Table 2.

Table 2. Materials used in investigated concrete mixes and their transportation distances considered in the analysis.

Material	Material dataset	Origin	Destination	Transportation dataset	Distance (km)
CEM III/A 42.5 R	Cement, blast furnace slag 36-65%	Cement supplier	CTI Batching plant	Transport, freight, lorry	60
Water	Tap water	-	CTI Batching plant	-	-
Plasticizer	Polycarboxylates, 40% active substance	Supplier	CTI Batching plant	Transport, freight, lorry	214
Gravel	Gravel, crushed	Quarry	CTI Batching plant	Transport, freight, lorry	18
Sand	Sand	Quarry	CTI Batching plant	Transport, freight, lorry	18

Since CTI also operates in the field of pavements, the company directly recovers waste generated from the milling of pavements following maintenance work. Waste is crushed and screened with a diesel-powered machinery (CAMS CENTAURO 100/32) consuming 0.325 L/t_{RAP} of diesel under conditions of high productivity. The processed waste is known as RAP, ready to be used as recycled aggregate. Both RAP processing and concrete production take place in the CTI plant. To enhance the use of RAP as natural aggregate replacement for concrete production, a credit for the designed system has been considered (Pantini, Borghi and Rigamonti, 2018) as shown in Table 3. More specifically, the use of 40% of RAP in concrete mixture avoids not only the use, but also the production of 2356 kg of natural aggregate (1614 kg of gravel and 742 kg of sand) for 3.5 m³ of concrete and its transportation from the quarry to the CTI plant.

A mixing plant working with about 10 kWh for 3.5 m³ of concrete was considered as the last step in concrete production. The method used for the analysis is ReCiPe 2016 at the mid-point level in hierarchist (H) perspective, which addresses 18 impact categories.

3 RESULTS AND DISCUSSION

3.1 Concrete properties

First results of mechanical performance and physical properties of CRAP and CNAT after 7 and 28 days of curing are reported in Table 3.

In general, CRAP exhibits inferior mechanical properties in terms of compressive, tensile strength and elastic modulus compared to CNAT. This is related to the porosity of the samples, as shown by the reduction in geometric density related to the use of RAP as aggregate replacement. On the other hand, considering the different curing time, while CNAT reaches compressive strength slightly higher than 40 MPa (the strength target of the mix design)

Table 3. Mechanical and physical properties of concrete made with natural and RAP aggregates after 7 and 28 days of curing.

Sample	Geometric density (ρ , g/cm ³)	Compressive strength (R_c , MPa)	Elastic modulus (E_d , GPa)	Tensile strength (f_t , MPa)	Open porosity (%)	Median pore diameter (μ m)
CNAT-7	2.21±0.04	41±2	29.2±0.5	3.2±0.2	10.9±0.5	0.025±0.001
CRAP-7	2.03±0.01	25±2	21.6±0.1	2.6±0.3	19±4	0.17±0.06
CNAT-28	2.20±0.03	52±3	43±3	2.9±0.4	9.8±0.2	0.021±0.001
CRAP-28	2.02±0.01	34±1	26±5	2.3±0.2	18±2	0.09±0.06

already after 7 days of curing, CRAP shows slightly lower values than expected even after 28 days. This result is also partly related to a small addition of water (about 30 L for the whole 3.5 m³ mix) during the concrete preparation for workability reasons even if the overall W/B ratio (considering both the added water and aggregate humidity) does not change. More in detail, while tensile strength values can be considered constant for both the concrete mixes and considered curing time, compressive strength and elastic modulus values exhibit a significant increase for both CRAP and CNAT passing from 7 to 28 days of curing: CRAP exhibits a compressive strength of 25 MPa after 7 days and 34 MPa after 28 days, representing an increase of 36%, and an elastic modulus of 22 GPa and 26 GPa after 7 and 28 days, respectively, representing a 20% increase. CNAT shows compressive strength values of 41 and 52 MPa for 7 and 28 days, respectively (a correspondent increase of 27%) and elastic modulus values of 29 GPa after 7 days and 43 GPa after 28 days, representing a 47% increase. These inferior mechanical performances measured for this mix where 40% RAP has been used are quite expected results based on the literature analysis (Huang, Shu and Li, 2005; Al-Oraimi, Hassan and Hago, 2009; Hossiney, Tia and Bergin, 2010).

More interestingly, Table 3 also reports the outcomes of the MIP measurements in terms of open porosity and median pore diameters. For both 7 and 28 days of curing, open porosity measured for CRAP is higher than the ones measured for CNAT. These results well highlight that CRAP is more porous and characterized by larger pores. This difference in pore size distribution is an important key in terms of durability. In fact, pore size distribution towards larger pores induces a decrease in the crystallization pressure of water or salts when samples are exposed to freezing and thawing or salt crystallization cycles (Scherer, 1999). Therefore, these results are quite encouraging regarding durability tests in terms of frost resistance that are currently ongoing, indicating that probably CRAP will show good durability performance in this regard (Thomas, Fellows and Sorensen, 2018). However, due to the fact that RAP is partially replaced as concrete aggregate and is distributed more or less evenly throughout the concrete, a dedicated investigation is currently ongoing to validate the durability performance in terms of frost resistance.

3.2 LCA analysis

The environmental impacts related to both the analyzed mixes are reported in Table 4.

Four categories show significant impact values: global warming potential (GWP), terrestrial ecotoxicity (TE), human non-carcinogenic toxicity (HNCT) and fossil resource scarcity (FRS). CRAP exhibits variations equal to -5% in GWP, -18% in TE, -15% in HNCT and -12% in FRS compared to CNAT. Generally, the production of 3.5 m³ of CRAP shows lower values than CNAT for each of the considered impact categories, with an average reduction of about 15%. Thus, the 40% of RAP in the concrete mix brings significant benefits, as remarked in Figure 2.

The impact related to each input data was evaluated for both CNAT and CRAP for the 4 categories in which concrete is most impactful (Figure 3): raw material production, power consumption (electricity) for concrete mixing, all the considered transportation phases and the credits related to avoided use of natural aggregates.

Table 4. Results of LCA analysis in terms of the 18 impact categories addressed by the Recipe midpoint (H) method for 3.5 m³ of concrete made with natural aggregate (CNAT) and concrete containing 40% of RAP in mixture (CRAP).

Impact category	Unit	CNAT	CRAP
Global warming potential (GWP)	kg CO ₂ eq	7.71×10 ²	7.33×10 ²
Stratospheric ozone depletion (SOD)	kg CFC11 eq	1.30×10 ⁻⁴	1.09×10 ⁻⁴
Ionizing radiation (IR)	kBq Co-60 eq	4.23×10 ¹	3.67×10 ¹
Ozone formation - Human health (OF1)	kg NO _x eq	1.49×10 ⁰	1.30×10 ⁰
Fine particulate matter formation (FPMF)	kg PM2.5 eq	6.40×10 ⁻¹	5.60×10 ⁻¹
Ozone formation - Terrestrial ecosystems (OZ2)	kg NO _x eq	1.51×10 ⁰	1.32×10 ⁰
Terrestrial acidification (TA)	kg SO ₂ eq	1.67×10 ⁰	1.51×10 ⁰
Freshwater eutrophication (FE)	kg P eq	1.50×10 ⁻¹	1.30×10 ⁻¹
Marine eutrophication (MEu)	kg N eq	1.00×10 ⁻²	1.00×10 ⁻²
Terrestrial ecotoxicity (TE)	kg 1.4-DCB	1.77×10 ³	1.45×10 ³
Freshwater ecotoxicity (FE)	kg 1.4-DCB	1.24×10 ¹	1.06×10 ¹
Marine ecotoxicity (MEc)	kg 1.4-DCB	1.70×10 ¹	1.45×10 ¹
Human carcinogenic toxicity (HCT)	kg 1.4-DCB	2.05×10 ¹	1.50×10 ¹
Human non-carcinogenic toxicity (HNCT)	kg 1.4-DCB	3.10×10 ²	2.65×10 ²
Land use (LU)	m ² a crop eq	1.24×10 ¹	9.90×10 ⁰
Mineral resource scarcity (MRS)	kg Cu eq	3.93×10 ⁰	3.72×10 ⁰
Fossil resource scarcity (FRS)	kg oil eq	1.04×10 ²	9.12×10 ¹
Water consumption (WC)	m ³	8.65×10 ⁰	5.24×10 ⁰

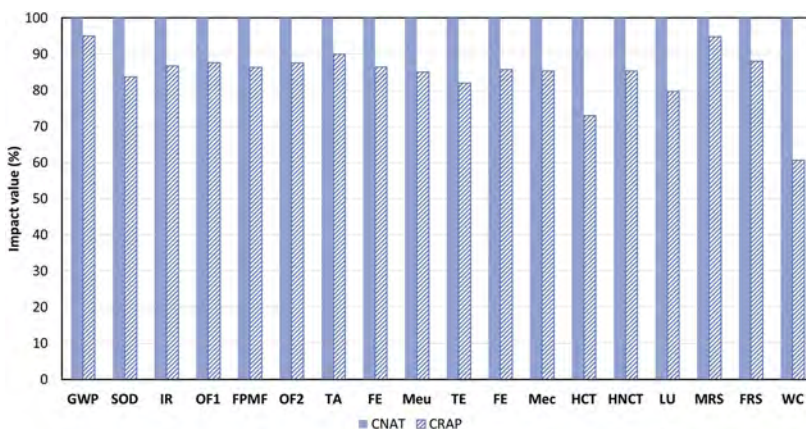


Figure 2. Impact categories addressed by the Recipe midpoint (H) method for 3.5 m³ of concrete made with natural aggregate (CNAT) and concrete containing 40% of RAP in mixture (CRAP). Results are shown according to internal normalization.

Firstly, cement production is the most critical stage for most of the total impact of each category: it is responsible of about the 90% of CO₂ emissions for both concrete mixes, where a 5% reduction of GWP category was measured in CRAP due to RAP incorporation. Transportation is the most relevant stage after cement production. Thus, a unique RAP processing and concrete batching plant is a favorable condition (as in the considered industrial plant). In addition, the advantage associated with the reduction of natural aggregate in mixture is greatly appreciated in TE category. In HNCT and FRS categories, natural aggregate production follows cement in impact. Water and RAP production exhibit almost no impact, but they were still reported for completeness. Lastly, the registered impact reduction for CRAP is mainly due to the avoided use of natural aggregates (Pantini, Borghi and Rigamonti, 2018).

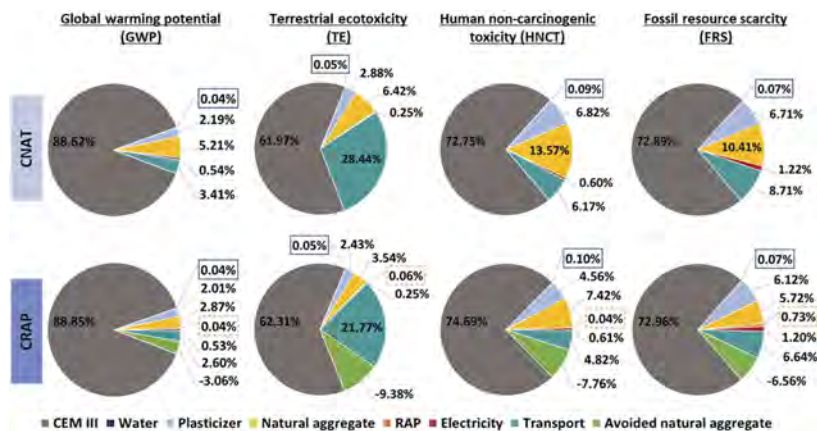


Figure 3. Impact assessment for each input data: CEM III (blast furnace slag cement), water (framed with a continuous blue line), plasticizer, natural aggregate (sand and gravel), RAP (framed with an orange dotted line), electricity for concrete mixture, transport (as the total transport of all materials involved in concrete production) and the avoided natural aggregate (due to the use of RAP as recycled aggregate).

4 CONCLUSIONS

This study reports preliminary results in terms of mechanical and physical properties, as well as the environmental assessment by life cycle analysis (LCA) of concrete mixes prepared in a real industrial environment by partially replacing natural aggregates with Reclaimed Asphalt Pavement (RAP). In this study, a 3.5 m³ concrete mix with a replacement of 40% RAP has been evaluated. The main results can be drawn as follows:

- concrete with 40% RAP exhibits inferior mechanical properties in terms of compressive, tensile strength and elastic modulus for both 7 and 28 days compared to concrete with 100% natural aggregate (reference mix). These findings are mainly related to higher porosity of the mix with RAP incorporation as highlighted by the lower geometric density and MIP analysis results. In addition, incorporation of RAP as concrete aggregates also induces higher average pore diameters of one order of magnitude for both considered curing times.
- The incorporation of RAP (40%) induces a beneficial effect in terms of environmental impacts, as highlighted by LCA analysis. Especially for the most significant impact categories for concrete production, such as global warming potential, terrestrial ecotoxicity, human non-carcinogenic toxicity and fossil resource scarcity, a relevant reduction has been measured of an average value of 15%. Surely, increasing the RAP replacement a more significant reduction in the environmental impacts can be measured. However, higher RAP amount can strongly hinder the mechanical performances of resulting concrete. Thus, a complete characterization in terms of materials and environmental performance is a fundamental approach for sustainable building materials designing.

ACKNOWLEDGEMENTS

This study was carried out in the framework of RAPCON (“Sustainable concrete made with recycled asphalt pavement”) project (2020–2023), under the “Circular Economy for a sustainable future” call (2019) funded by Cariplo Foundation. The authors would like to acknowledge Eng. Luca Guardigli (CTI, Imola) and Mr. Paolo Carta (University of Bologna) for their precious help in preparing and testing concrete samples.

REFERENCES

- Abraham, S. M. and Ransinchung, G. D. R. N. (2019) 'Pore Structure Characteristics of RAP-Inclusive Cement Mortar and Cement Concrete Using Mercury Intrusion Porosimetry Technique', *Advances in Civil Engineering Materials*, 8(3), p. 20180161. doi: 10.1520/acem20180161.
- Al-Oraimi, S., Hassan, H. F. and Hago, A. (2009) 'Recycling of reclaimed asphalt pavement in Portland cement concrete', *Journal of Engineering Research*, 6(1), pp. 37–45. doi: 10.24200/tjer.vol6iss1pp37-45.
- Boobalan, S. C. *et al.* (2022) 'Studies on green concrete – A review', *Materials Today: Proceedings*. Elsevier Ltd, 65, pp. 1404–1409. doi: 10.1016/j.matpr.2022.04.392.
- Brand, A. S. and Roesler, J. R. (2017) 'Bonding in cementitious materials with asphalt-coated particles: Part I – The interfacial transition zone', *Construction and Building Materials*. Elsevier Ltd, 130, pp. 171–181. doi: 10.1016/j.conbuildmat.2016.10.019.
- Bressi, S., Primavera, M. and Santos, J. (2022) 'A comparative life cycle assessment study with uncertainty analysis of cement treated base (CTB) pavement layers containing recycled asphalt pavement (RAP) materials', *Resources, Conservation and Recycling*, 180. doi: 10.1016/j.resconrec.2022.106160.
- de Brito, J. and Kurda, R. (2021) 'The past and future of sustainable concrete: A critical review and new strategies on cement-based materials', *Journal of Cleaner Production*. Elsevier, 281, p. 123558. doi: 10.1016/j.jclepro.2020.123558.
- Debbarma, S., Selvam, M. and Singh, S. (2020) 'Can flexible pavements' waste (RAP) be utilized in cement concrete pavements? – A critical review', *Construction and Building Materials*. Elsevier Ltd, 259, p. 120417. doi: 10.1016/j.conbuildmat.2020.120417.
- EN 12390-13 *Testing hardened concrete: determination of secant modulus of elasticity in compression* (2013).
- EN 12390-3 *Testing hardened concrete: compressive strength of test specimens* (2019).
- EN 12390-6 *Testing hardened concrete: tensile splitting strength of test specimens* (2009).
- Hossiney, N., Tia, M. and Bergin, M. J. (2010) 'Concrete containing RAP for use in concrete pavement Mitigation of Cracking in Concrete View project Concrete Containing RAP for Use in Concrete Pavement', *International Journal of Pavement Research and Technology*, 3(5), pp. 251–258. Available at: <https://www.researchgate.net/publication/290031177>.
- Huang, B., Shu, X. and Burdette, E. G. (2006) 'Mechanical properties of concrete containing recycled asphalt pavements', *Magazine of Concrete Research*, 58(5), pp. 313–320. doi: 10.1680/macr.2006.58.5.313.
- Huang, B., Shu, X. and Li, G. (2005) 'Laboratory investigation of portland cement concrete containing recycled asphalt pavements', *Cement and Concrete Research*, 35(10), pp. 2008–2013. doi: 10.1016/j.cemconres.2005.05.002.
- ISO 14040 *Environmental management - life cycle assessment - principles and framework, 2006th ed.* (2020).
- Masi, G. *et al.* (2022) 'Assessment of reclaimed asphalt pavement (RAP) as recycled aggregate for concrete', *Construction and Building Materials*. Elsevier Ltd, 341(February), p. 127745. doi: 10.1016/j.conbuildmat.2022.127745.
- Nandi, S. and Ransinchung, G. D. R. N. (2021) 'Performance evaluation and sustainability assessment of precast concrete paver blocks containing coarse and fine RAP fractions: A comprehensive comparative study', *Construction and Building Materials*. Elsevier Ltd, 300, p. 124042. doi: 10.1016/j.conbuildmat.2021.124042.
- Pantini, S., Borghi, G. and Rigamonti, L. (2018) 'Towards resource-efficient management of asphalt waste in Lombardy region (Italy): Identification of effective strategies based on the LCA methodology', *Waste Management*. Elsevier Ltd, 80, pp. 423–434. doi: 10.1016/j.wasman.2018.09.035.
- Santos, J., Flintsch, G. and Ferreira, A. (2017) 'Environmental and economic assessment of pavement construction and management practices for enhancing pavement sustainability', *Resources, Conservation and Recycling*. Elsevier B.V., 116, pp. 15–31. doi: 10.1016/j.resconrec.2016.08.025.
- Scherer, G. W. (1999) 'Crystallization in pores', *Cement and Concrete Research*, 29(8), pp. 1347–1358. doi:10.1016/S0008-8846(99)00002-2.
- Shi, X., Mukhopadhyay, A. and Zollinger, D. (2018) 'Sustainability assessment for portland cement concrete pavement containing reclaimed asphalt pavement aggregates', *Journal of Cleaner Production*. Elsevier Ltd, 192, pp. 569–581. doi: 10.1016/j.jclepro.2018.05.004.
- Singh, S., Ransinchung, G. D. and Kumar, P. (2017) 'An economical processing technique to improve RAP inclusive concrete properties', *Construction and Building Materials*. Elsevier Ltd, 148, pp. 734–747. doi: 10.1016/j.conbuildmat.2017.05.030.
- Thomas, R. J., Fellows, A. J. and Sorensen, A. D. (2018) 'Durability analysis of recycled asphalt pavement as partial coarse aggregate replacement in a high-strength concrete mixture', *Journal of Materials in Civil Engineering*, 30(5), pp. 1–7. doi: 10.1061/(ASCE)MT.1943-5533.0002262.
- Vandewalle, D. *et al.* (2020) 'Assessment of eco-friendly pavement construction and maintenance using multi-recycled rap mixtures', *Recycling*, 5(3), pp. 1–21. doi: 10.3390/recycling5030017.

Life extension of existing steel reinforced structures by simple cathodic protection techniques for sustainable durability

G. Sergi

Vector Corrosion Technologies Ltd, West Midlands, UK

ABSTRACT: The most successful technique for controlling reinforcement corrosion of structural elements is Cathodic Protection (CP) which became well-established and acceptable over the last decades. Long-term maintenance of impressed current cathodic protection systems (ICCP), however, started to be seen as a burden to most structure owners and managers as it involves additional and continual costs. A requirement arose, therefore, for simpler CP systems to be made available which will involve less maintenance and monitoring requirements. As a first stage to simpler systems, galvanic cathodic protection anodes were developed in the 1990's, first, only to protect steel reinforcement immediately around patch repairs but subsequently to control reinforcement corrosion over wider areas where corrosion risk was found to be high. It was the combination of ICCP and galvanic anode systems, however, that set the benchmark for a simpler alternative long-term method for corrosion control of steel reinforcement. This paper attempts to follow the development of all galvanic CP systems utilised for atmospherically exposed steel reinforced structural elements and looks at recently developed simpler cost-effective systems and methodologies that would likely form the future of the CP industry and improve durability and sustainability of existing structures and buildings.

1 BACKGROUND

Concrete can be a very durable material. There are many examples of concrete structures that have remained serviceable for millennia such as the Pantheon in Rome. A greater risk for deterioration of concrete structures was created when steel reinforcement was introduced for improved tensile strength. Fresh and relatively new concrete normally contains an alkaline pore liquid phase which protects embedded steel from corrosion by allowing a highly dense passive oxide film to develop on its surface when oxygen is available. This form of protection can be lost, however, if the concrete undergoes either carbonation or chloride contamination in the vicinity of the steel. Such effects can lead to cracking and spalling of the cover concrete. There have been too many structures where corrosion was allowed to continue until they were no longer serviceable and led to their demolition and replacement.

Although modern standards (EN 1990) look for 100-year designs for monumental and historical structures, bridges and other civil engineering structures, it is still the case that deterioration occurs often within 20-30 years of construction. In most cases, the issue is corrosion of the steel reinforcement. This has been recognised by the Strategic Highway Research Programme in the USA (SHRP 2) who published a document which deals not only with the design of bridges for 100 or more years service life but, more appropriately, with the extension of the service life of existing bridges to beyond 100 years.

Cement production is now seen as a major issue with a massive carbon dioxide footprint. It is estimated that one tonne of cement produces 900 kg of CO₂ and globally cement production represents around one billion tonnes of CO₂ release annually. If manufacture of aggregate, steel reinforcement and transport of the products is taken into account, the carbon footprint rises to 1.5 billion tonnes of CO₂ per year. It makes perfect sense, therefore, to extend the surface life of structures to as long as realistically possible rather than demolish and reconstruct even if the structure requires downgrading or a change of use. As steel reinforcement corrosion is one of the most common deterioration processes of structures, developing and improving steel reinforcement protection techniques is of the utmost importance.

1.1 Cathodic protection

Cathodic protection has been established as the most successful process for controlling corrosion of the steel reinforcement. A major development in steel protection since the early 1990's has been the introduction and establishment of galvanic anodes. They were originally used to control the formation of incipient anodes, often described as the 'ring effect', around the periphery of patch repairs (Sergi & Page 1999), simply by attaching galvanic anodes to the exposed steel around the perimeter of patch repairs prior to the application of the repair material (Figure 1a). Subsequently, more and more applications of continuously improving galvanic anodes have been established (Sergi & Seneviratne, 2014) with anodes placed in a grid formation for more general corrosion control (Figure 1b) or along the exposed steel reinforcement where applicable (Figure 1c)



Figure 1. Alkali activated galvanic anodes, (a) as in inset, attached to steel reinforcement prior to the application of the repair material, (b) as in inset, inserted in a grid formation in drilled holes and (c) as 'rods' positioned along steel reinforcement in an expansion joint prior to the placing of the repair mortar.

That galvanic anodes control steel reinforcement adequately was demonstrated elegantly in large slabs in India (Krishnan et.al. 2019). These had dimensions of 1 m x 1 m x 0.25 m. Some had nine galvanic anodes attached to the steel members in a 3 x 3 grid configuration and some were cast with no anodes. All had 2% chloride by weight of cement additions in the mix water, a level that would normally cause significant corrosion of the steel reinforcement. After 10 years of exposure in the outdoor warm and humid conditions of Mumbai, the slabs containing the anodes remained intact while the slabs with no anodes had suffered from severe corrosion and cracking of the concrete cover (Figure 2).



Figure 2. Slab protected by galvanic anodes (left) and corroded slab without anode protection (right) showing extent of cracking of the concrete caused by steel corrosion after exposure to outdoor warm and humid conditions for over 10 years.

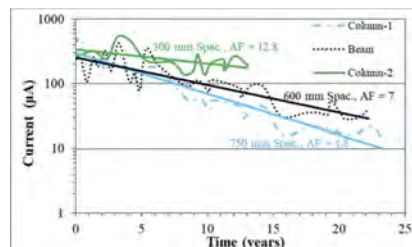


Figure 3. Reduction of mean current output of galvanic anodes embedded in structural elements of a bridge in the UK. Notice the variability caused by temperature.

2 LESSONS OBSERVED FROM LONG-TERM DATA

A major discovery with regard to galvanic anodes has been made from their long-term monitoring. Results from a 23-year field trial in the UK has indicated that the current output of alkali-activated galvanic anodes diminished approximately exponentially.

What is striking from Figure 3, is the different rates of exponential decay of the anode sets, described here as an Aging Factor (AF), in the three different structural elements. AF is the time it takes for the current output to be halved. The halving is repeated over the same period as would be expected in a half-life decay. Even though the anodes in the beam and in Column-1 are identical and were installed at the same time, the observed Aging Factor of each set is very different. Current output for the beam approximately halved over a 7-year period compared to a 4.8-year period for Column-1. As both structural elements are part of the same structure, concrete quality and steel density are expected to be comparable. The environment and concrete resistivity have been consistently similar over the whole exposure period. Only the spacing between adjacent anodes was different. In the beam the anodes were set at a spacing-on-centre of 600 mm whereas in Column-1 the spacing was 750 mm. The early current output of the anodes (Figure 3) was clearly affected by the anode spacing. In the beam the first mean maximum current output of individual anodes was of the order of 300 μA but in Column-1 this was in excess of 500 μA . This high current in Column-1 at the beginning was induced by the greater steel surface area that each anode in the set was required to protect. Consequently, the current output diminished more rapidly in Column-1.

In Column-2 of the same bridge but installed 10 years later, anodes of higher surface area, which were capable of delivering higher currents, were set out at only 300 mm centres so were not pushed to deliver current at the high rates of the earlier anodes resulting in a much-improved Aging Factor of 12.8 years. The reason why there is a diminishing performance when the anodes were forced to deliver a very high current early on is because the corrosion products, initially soluble zincate ions, are less likely to migrate away from the zinc/mortar interface before precipitating as solid zinc oxide hence blocking the pore system around the interface and reducing the volume of current paths.

By studying long term results from over a dozen monitored sites of alkali-activated anodes, the values determined for the Aging Factor were found to vary between 5 and 14 years. This compares very favourably with halide activated anodes (chloride, bromide) which achieve an Aging Factor of less than 3.8 years (Sergi & Seneviratne, 2021, Whitmore & Sergi, 2021).

In a strong alkali-activating medium, as is the case with the anode encasing mortar used for the above-mentioned anodes, zinc, following its dissolution, exists as soluble zincate ions which are able to migrate within the pore structure of the encasing mortar. When supersaturation of zincate gradually occurs, it precipitates out as zinc oxide (Sergi & Seneviratne, 2021, Sergi et. al., 2021). The fast early production of zincate ions in the case of Column-1 would have restricted their migration further into the encasing mortar pores as supersaturation occurred so zinc oxide would have formed close to the zinc/mortar interface reducing the immediate porosity around the zinc metal and slowing down further dissolution of the metal. The lower early current of the anodes in the beam and, particularly of the larger anodes in Column-2, ensured a gentler zinc dissolution, which permitted the zinc corrosion products to migrate further into the mortar pore structure allowing a more open path for electrolytic current flow (Sergi & Seneviratne, 2021).

The importance of the Aging Factor in the design of galvanic CP systems is considerable as the current density at a future time can be accurately estimated in order to design for long-term protection. Figure 4 demonstrates this elegantly. An alkali-activated anode set is, in this case, required to achieve a specific current density of 0.4 mA/m^2 at 20 years. For an Aging Factor of 11.5 years, the anode layout would need to be designed to deliver an early current density of around 2 mA/m^2 . Furthermore, the design will maintain a current density above 0.2 mA/m^2 even beyond 30 years. A typical halide anode set would require an initial current density of around 800 mA/m^2 in order to achieve the required 0.4 mA/m^2 at 20 years, clearly an improbability.

The current density was also found to vary with concrete temperature. Analysis of data sets of current output of galvanic anodes in relation to the concrete temperature had shown that the level of current output is related to the reciprocal of the absolute temperature according to the Arrhenius equation (Equation 1) as depicted in Figure 5.

$$k = Ae^{-\frac{Ea}{RT}} \quad (1)$$

Where, k = Rate constant, A = Frequency factor, Ea = Activation energy, R = Universal gas constant, T = Absolute temperature (K)

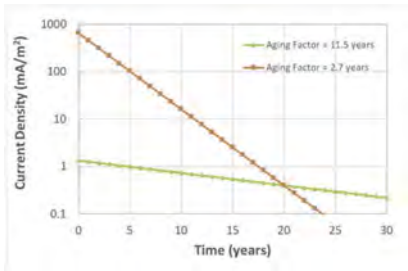


Figure 4. Anode current density vs time for two types of anode with different Aging Factors such that both anodes provide a current density of 0.4 mA/m² at 20 years.

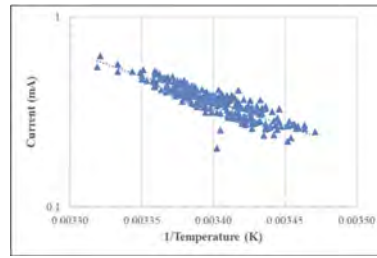


Figure 5. Relationship between the reciprocal of the concrete temperature in K and the logarithm of current output of the anode.

A form of the equation (Emran, 2016) relates the corrosion rate, i.e. the current output from the zinc, to the reciprocal of temperature (Equation 2).

$$\text{Log}i_{corr} = \log A - \left(\frac{\Delta E_a}{2.303RT} \right) \quad (2)$$

Where, i_{corr} = Corrosion current of zinc metal, ΔE_a = Apparent activation energy of the corrosion process.

The relationship shown represents a doubling of current density every 10-15°C increase in temperature over ambient conditions. The same variation of current output with temperature was seen in all monitored galvanic CP installations (see, for example, Figure 3). This knowledge allows a better calculation of the required current density for particular climatic conditions, for example, a higher current output will be expected in tropical conditions compared to cooler climates.

3 THE NEED FOR SIMPLER ICCP SYSTEMS

There is no doubt that ICCP of steel reinforced concrete has, over the last decades, become a well-established technique for controlling reinforcement corrosion of structural elements. The expectation of long-life protection has, however, been somewhat reduced as some anode systems fail, monitoring equipment become antiquated, and lack of adequate maintenance makes the systems inoperable with the average service life of any CP system falling to 15 years (Polder et. al., 2014). Inevitable additional costs are involved in maintaining and prolonging correct operation of the system. It appears that there is a requirement by structure managers and owners for simpler CP systems which will involve less maintenance and monitoring requirements.

ISO EN 12696:2022 has clear performance criteria that need to be continuously satisfied to ensure that the system is working. A much-used criterion is that a depolarisation potential of 100 mV should be achieved when the system is temporarily turned off for a period of 24 hours. The standard also defines that a successful CP system either passivates the steel or reduces the corrosion rate of the steel reinforcement which implies, correctly, that achieving 100 mV of polarisation does not necessarily mean that corrosion has been arrested short-term. Nonetheless, it has been shown in several cases that if a CP system is running for an extended period, e.g. 5 years, and is then turned off, corrosion of the steel does not reinitiate over a significant time period (Christodoulou et. al., 2010). This phenomenon is believed to be caused by some secondary effects, primarily, the increase in alkalinity and reduction in chloride concentration at the steel/concrete interface (Sergi & Seneviratne, 2014), which in effect reduces the $[\text{Cl}^-]/[\text{OH}^-]$ ratio considerably below the critical ratio for initiation or maintenance of corrosion. It has also been suggested that realisation of the acidified pits occurs which allows steel repassivation within them (Glass & Davison, 2010).

3.1 A two-stage corrosion control system

It was soon realised that a system that can arrest steel corrosion relatively early and can then switch to cathodic prevention mode over the longer term is realistically possible. It was important, however, to identify the desired current density and overall charge delivery to the

steel reinforcement for successful corrosion arrest to occur before the current density is reduced to the lower cathodic prevention current density levels (0.4-2 mA/m²) which have been shown to be easily achieved by galvanic anodes (Sergi, 2011).

To develop a viable Stage-1 procedure in which corrosion arrest of corroding steel can be achieved, a series of experiments were conducted, the results of which are published elsewhere (Rathod et. al., 2018). What was discovered was very interesting. At two constant current levels, 30 mA/m² and 50 mA/m², the corrosion of pre-corroded steel plates in mortars containing increasing doses of chloride by weight of cement as NaCl, was arrested after a length of time under polarisation. The required charge (current in amps multiplied by time in seconds) delivered to the steel until passivation of the steel was achieved increased with the level of chloride but was lower at the higher current density of 50 mA/m², as summarised in Table 1. Passivity of the steel was assumed when the 24-hour depolarised potential had reached -150mV vs Ag/AgCl, 0.5M KCl as indicated in EN 12696:2022.

Table 1. Cathodic Charge required to passivate steel at the chloride levels and current densities shown.

Current Density (mA/m ²)	30		50	
% Cl in Mortar	2	3	2	4
Cathodic Charge (kC/m ²)	120	190	74	108

Work in Italy (Pedferri, 1996) and USA, (Presuel-Moreno et. al., 2005) had demonstrated that passivity of the steel can be maintained in a corrosive environment for considerable periods, by a process they termed Cathodic Prevention, by applying a current density of 0.4-2 mA/m². Even constant exposure to highly corrosive environments could not initiate corrosion at a current density of 1 mA/m². Once corrosion is arrested, it would appear reasonable to suggest that a second stage of a process, based on Cathodic Prevention, is likely to protect the steel from further corrosion. Thus, a CP system based on a Two-Stage process appears to be a viable corrosion mitigation method.

This understanding formed part of a process that has enabled the recent development of a simple to install and operate Two-Stage Corrosion Mitigation system (Arnesen et. al., 2018, Whitmore et. al. 2019) as illustrated in Figure 6. A trial was set up on a column of a bridge in Leicester, UK, where six anodes were set up at an approximate spacing of 500 mm on-centre around a repaired area where corrosion and spalling was caused by chlorides up to a concentration of about 2% by weight of cement (Sergi et. al., 2022). The ICCP element of the anodes had passed a current to the steel reinforcement over a range of 20-35 mA/m² of steel density over a period of several months ensuring a total of around 200 kC/m² of charge was delivered to the steel reinforcement. Once the battery-operated Stage-1 was completed, current was subsequently delivered from the galvanic anode at a level of 0.9-1.5 mA/m², sufficient for preventing corrosion long-term.

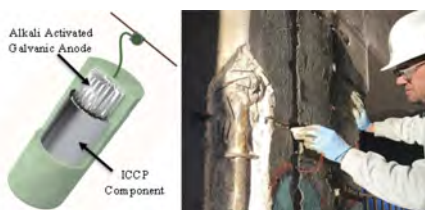


Figure 6. Two-Stage anode system and schematic of its operation and installation of the anodes in pre-drilled holes at a spacing of 500 mm around the affected area.

The potential of the steel within the repaired area was monitored at two positions using embeddable silver/silver chloride electrodes, 0.5 M KCl, and confirmed that the early high charge delivery over the first 120 days was sufficient to passivate the steel. The subsequent cathodic prevention current maintained passivity of the steel with 24-hour depolarised potentials remaining higher than -150 mV (vs Silver/silver chloride) as depicted in Figure 7. Depolarisation potentials during Stage-1 of high current delivery was of the order of 150-200 mV. Subsequently, during Stage-2, depolarisation was of the order of 50-70 mV (Whitmore et. al., 2023).

A second structure in Wales was also repaired using the Two-Stage technique (Whitmore et. al., 2023). Two piers and a crossbeam of a bridge had suffered from corrosion from chlorides in excess of 2% by weight of cement with cracking and spalling. Chains of up to 20 anodes were installed in several zones. The anodes were spaced out at 500 mm on centre in a grid configuration, designed to deliver a minimum of 300 kC/m² of charge during Stage-1. This was achieved over a period within 100 days (Figure 8). The current density was 30-80 mA/m². As in the Leicester column above, the high current density resulted in depolarised potentials during Stage-1 of the order of 180-230 mV, well above 100 mV suggested by the standards for cathodic protection. The high current density was required to achieve passivation of the steel which was achieved within Stage-1 with 24-hour depolarised potentials considerably higher than -150 mV vs silver/silver chloride, 0.5 M KCl.

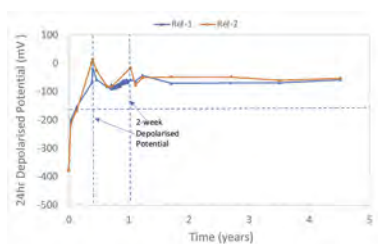


Figure 7. Change of potential of steel reinforcement (vs silver/silver chloride) around the repaired zone 24-hours after depolarisation, including two sets of potentials following depolarisation over a two-week period within the first year.

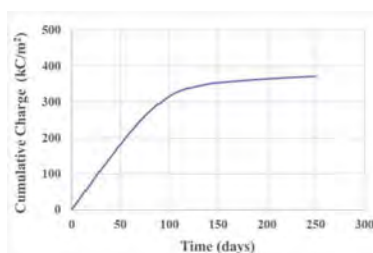


Figure 8. Cumulative charge delivered to the steel in one zone indicating a sharp delivery of over 300 kC/m² over a period about 100 days.

3.2 Surface applied anodes

Galvanic anodes encased in an activating mortar need to be embedded in the concrete to at least the depth of the steel reinforcement so that the moisture level, when high enough to maintain corrosion of the steel reinforcement, is also sufficient to maintain current delivery from the galvanic anode. Because of this fact, attempts to position anodes on the surface of the concrete, instead of the normal practice of embedding the anodes beyond the cover depth, were generally unsuccessful. This was owing to their inability to maintain sufficient current owing to drying which resulted in moisture content around the anode much lower than at the depth of the steel. To overcome this problem and to allow the moisture level around the anode to be maintained to the level experienced by the steel reinforcement, long galvanic anodes were designed and were covered on the outermost end by an impermeable surface, wide enough to ensure that the distance of the centrally positioned anode rod from either edge of the impermeable surface is at least equal to the depth of cover of the reinforcement.

A schematic of the anode and a field trial installation on a cross beam of a bridge in the USA are shown in Figure 9. The steel reinforcement had suffered from corrosion caused by chlorides seeping through a joint above. The current output of the anodes delivered to the steel beneath was 3-20 mA/m², equivalent to an ICCP installation and was dependant primarily on the ambient temperature (Figure 10). As described in Section-2 the current output is governed by the Arrhenius relationship (Equation 1) so is expected to be lower over the winter months. The level of depolarisation on Day-60 was just short of 100 mV at 24 hours but was still rising up to 48 hours when the anodes were reconnected to the steel, reaching around 140 mV suggesting a high level of protection of the steel reinforcement.

3.3 The future of cathodic protection

Judging by advancements in the last 5-10 years, it is inevitable that further developments will occur in the field of cathodic protection of steel reinforcement. It is likely that reliable and greatly simplified cathodic prevention systems will become more of a norm in new construction where corrosion prevention would be considered more desirable and cost-effective than eventual corrosion mitigation and

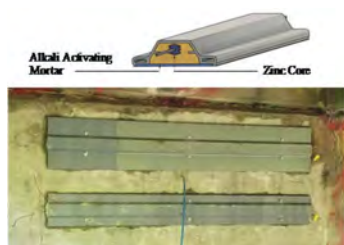


Figure 9. Schematic of the new surface anode design and installed anodes on a cross beam in a field trial in USA.

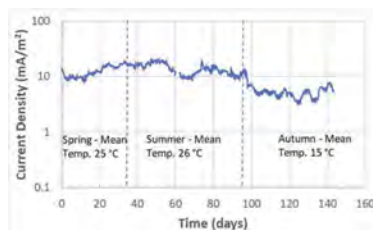


Figure 10. Current density by area of steel over a period of around 140 days showing variation with mean ambient temperature.

repair or even replacement of the structure. Considerably less power would be required to drive cathodic prevention systems as the current density does not need to exceed 1-2 mA/m² but more importantly, disruptions and added expenses for subsequent repair can be eliminated. Such low levels of current density can be easily achieved by well-designed galvanic anode systems. Furthermore, intelligent monitoring systems may be set up to predict when steel reinforcement corrosion initiation risk increases and activate an already installed cathodic prevention system. A move in that direction will be driven by the requirement for more environmentally acceptable procedures for structure management. Such a need will make the replacement of existing structures, buildings and infrastructure in general, environmentally very costly, so maintenance of existing structures and their conversion to new use is likely to become standard practice. For steel reinforced structural elements, extensive repairs to reinstate corroded areas would have to be reduced and cathodic protection would be a prime candidate for maintaining the structure to a safe condition with minimal repairs. For the same environmental reasons, low emission power generation will start to proliferate and self-powered localised CP systems, i.e. driven by solar and wind energy or rechargeable components, will likely become the norm.

The concept of cathodic protection would likely also evolve as a two-stage process similar to what was described in Section 3.1. Allowing a higher than what is currently considered to be a normal long-term cathodic current density of less than 10 mA/m² will inevitably arrest corrosion owing to the rapid build-up of alkali ions and the depletion of the aggressive chloride ions after which cathodic prevention would again be viable. As an example of power use, the long-term charge required to achieve 30-year protection with an ICCP system at a mean current density of, for example, 6 mA/m² to maintain a minimum of 100 mV depolarisation as required by standards, is estimated to be of the order of 5,500 kC/m² of steel area. An equivalent 2-stage CP system where an early current density of 25 mA/m² for 2 months is applied to arrest corrosion and a long-term current density of 1 mA/m² up to 30 years to maintain steel passivity would use just 1,000 kC/m², achieving a substantial saving in power consumption.

The continual development of galvanic anodes would likely increase the Aging Factor to well beyond 20 years by a combination of better design of the metallic sacrificial element and of the encasing activating mortar. This would allow a much longer service life of galvanic anodes at designable current densities for specific environmental conditions and particularly, ambient temperature.

4 CONCLUSIONS

The Carbon Footprint of cement manufacture in combination with steel and aggregate production is very large so demolition of structures and their replacement is non-sustainable. Better initial design with in-build cathodic protection or prevention capabilities should be the norm for new construction. Maintenance of aging structures with sustainable cathodic protection techniques should always be preferred as an environmentally friendly alternative to replacement of the structures.

Cathodic Protection or Prevention methodologies have been improving over the years and new developments, clear understanding of anode behaviour and improved performance of galvanic anodes have given rise to better long-term steel reinforcement protection. For example,

an Aging Factor, describing the diminishing exponential current output of galvanic anodes and the Arrhenius relationship of current to temperature are critical predetermined parameters that must be used to aid in the design of the galvanic system.

A 2-Stage cathodic protection method involving early high current delivery by an ICCP component to arrest corrosion followed by prevention using a second galvanic anode has been successfully developed and tested and offers great promise for sustainable long-term cathodic protection systems.

The development of functioning surface applied galvanic anodes allows flexibility and ease of use whilst providing substantial protection equivalent to ICCP systems.

REFERENCES

- Arnesen, T., Beaudette, M., Simpson, D., Sergi, G. 2018. Modular Corrosion Protection System for Mitigating Corrosion of Reinforced Concrete Structures. *Engineering 8th Congress - Forging Forensic Frontiers*.
- Christodoulou, C., Glass, G., Webb, J., Austin, S. and Goodier, C. 2010. Assessing the long term benefits of Impressed Current Cathodic Protection. *Corrosion Science*, 52 (8), pp. 2671–2679.
- Emran, K. M. 2015. Effects of concentration and temperature on the corrosion properties of the Fe–Ni–Mn alloy in HCl solutions, *Research on Chemical Intermediates* 41, pp. 3583–3596
- EN 1990, Eurocode - Basis of structural design
- Glass, G.K, Davison, N. 2006 Pit Realkalisation and its Role in the Electrochemical Repair of Reinforced Concrete. *J Corros Sci Eng*, 9, 10
- Krishnan, N., Kamde, D., Pillai, R., Sergi, G., Shah, D. & Velayudham, R. 2019. 8-year performance of cathodic protection systems in reinforced concrete slabs and life-cycle cost benefits. *Proc. Int. Conf. Sustainable Materials, Systems and Structures RILEM (SMSS2019)*, 20-22 March 2019 – Rovinj, Croatia pp. 611–618
- Pedefferri, P. 1996. Cathodic protection and cathodic prevention. *Constr Build Mater*, 10, pp. 391–402.
- Polder, R.B., Leegwater, G., Worm, D., Courage, W. 2014. Service life and life cycle cost modelling of cathodic protection systems for concrete structures. *Cem Concr Compos*, 47 pp. 69–74.
- Presuel-Moreno, F.J., Sagues, A. 2005. Steel Activation in Concrete Following Interruption of Long-Term Cathodic Polarization. *Corrosion*, 61, pp. 428–36.
- Rathod, N., Slater, P.R., Sergi, G., Seneviratne, G. 2018. A Suggestion for a Two-Stage Corrosion Mitigation System for Steel Reinforced Concrete Structures. *EUROCORR 2018*, 102036, Kraków, 9 September 2018
- Sergi, G. and Page, C. L. 1999. Sacrificial anodes for cathodic protection of reinforcing steel around patch repairs applied to chloride-contaminated concrete' *Proc. EUROCORR'99 European Corrosion Congress*, Aachen, Aug-Sept 1999.
- Sergi, G. 2011. Ten-year results of galvanic sacrificial anodes in steel reinforced concrete. *Mater. Corros*, 62, pp. 98–104.
- Sergi, G., Seneviratne, G. 2014. A two-stage cathodic protection system for steel reinforced concrete. Cathodic Protection and Associated Coatings, Theory and Applications On-land, Seawater, Concrete and Inner surfaces. *EFCC Event n° 363, 6th Journees Protection Cathodique*, Palais des Congrès d'Antibes Juan-les-Pins (24-26 June 2014),
- Sergi, G., Seneviratne, G. 2014. Extending residual service life of steel reinforced structures by the use of galvanic anodes. *Proc. of the RILEM International workshop on performance-based specification and control of concrete durability*, pp. 385–92.
- Sergi, G., Seneviratne, G. 2021 Improved design considerations for steel reinforcement corrosion control with galvanic anodes following performance evaluation from analysis of site data. *Struct. Faults & Repair*, Edinburgh, UK,
- Strategic Highway Research Program 2: Project R19A. Bridges for Service Life Beyond 100 Years: Innovative Systems, Sub-Systems and Components
- Whitmore, D., Sergi G. 2021. Long-term Monitoring Provides Data Required to Predict Performance and Perform Intelligent Design of Galvanic Corrosion Control Systems for Reinforced Concrete Structures. *NACE Corrosion*, Paper No. 16712
- Whitmore, D., Simpson, D., Sergi, G. 2023. A Two-Stage Cathodic Protection System Combining ICCP of Reinforced Concrete Structures with Long-Term Galvanic Anode Protection. *AMPP Annual Conf. & Expo.*, Paper No. 18868
- Whitmore, D., Simpson, D., Beaudette, M and Sergi, G. 2019 'Two-Stage, Self-Powered, Modular Electrochemical Treatment System for Reinforced Concrete Structures' *Corrosion & Materials*, August 2019, pp 28–32
- Sergi, G., Seneviratne, G. and Simpson, D. 2022. Long term control of corrosion of steel reinforcement by a two-stage cathodic protection method. *Concrete Solutions*, MATEC Web of Conferences 361, 0 <https://doi.org/10.1051/mateconf/202236102004>

Corrosion of rebars in concrete: Comparison of preventative measures

F. Bolzoni, A. Brenna, S. Beretta, M. Ormellese, M.V. Diamanti & M.P. Pedferri

Dipartimento di Chimica, Materiali e Ingegneria Chimica “Giulio Natta”, Politecnico di Milano, Milan, Italy

ABSTRACT: Prevention of rebar corrosion is achieved in the design and construction phases, by means of suitable mix design, casting and curing, and adequate cover depth; this approach has been introduced in international standards (EN 206) and design codes (Eurocode 2). Preventative measures (cathodic protection, stainless steel or galvanised rebars, corrosion inhibitors, concrete coatings) can be used in very aggressive environments, especially in presence of chlorides, or when increased service life is required. In this work, a performance-based approach, based on Monte Carlo simulation, has been used to evaluate the service life (initiation time of corrosion) in chloride containing environments.

1 INTRODUCTION

In concrete pore solution, due to the high alkalinity (pH>13 in general), carbon steel reinforcements are protected from corrosion by a passive film. Corrosion initiation can occur due to: 1) carbonation of concrete that reduces its pH and 2) presence of chlorides in concentration superior to a critical threshold (CEB 1982; Bertolini et al. 2013; Pedferri 2018). In this article, we do not consider hydrogen embrittlement of high-strength reinforcements and stray current corrosion; in particular, the latter is not frequent in concrete.

Corrosion prevention must be addressed during design and construction, with proper concrete composition, sufficient cover thickness, and proper placement and curing of concrete. Additional corrosion protection methods may be useful in aggressive environments, especially in presence of chlorides, or when a high service life is required (Bertolini et al. 2013; Pedferri 2018).

In this work, performance based approach is used. Analytical solution of 2nd Fick's law of diffusion is used to evaluate corrosion initiation time (limit state) and its probabilistic distribution is calculated by Monte Carlo method. Some of the results were presented in (Bolzoni et al 2022d).

2 PREVENTION OF CORROSION IN CONCRETE

2.1 *Durability and service life*

The evolution of the corrosion phenomenon is interpreted by Tuutti's model, introduced in the '80s, which considers two periods: corrosion initiation and propagation (Bertolini et al. 2013).

In case of chloride induced corrosion, corrosion initiation occurs when at the rebar surface chloride concentration reaches a critical threshold. Moreover, chloride transport into concrete occurs mainly by non-stationary diffusion, that follows 2nd Fick's law. Under specific boundary and initial conditions, 2nd Fick's law has an analytical solution (Equation 1) first applied to chloride diffusion in concrete in 1972 by Collepardi and co-authors (Collepardi 2002):

$$C_x = C_s \cdot \left(1 - \operatorname{erf} \frac{x}{2\sqrt{D_{app}t}}\right) \quad (1)$$

Where erf is the error function, t is time, C_s and C_x are chloride concentration at the surface (constant over time) and at distance x from the surface, respectively, D_{app} is the apparent chloride diffusion coefficient, constant in space (homogeneous concrete) and time. The approach is valid considering a semi-infinite domain. An additional assumption for the Equation 1 is that the initial concentration of chlorides in concrete is zero. The assumptions underlying equation, i.e. constancy of C_s and D_{app} and the absence of other transport mechanisms are not always verified in practice (Bertolini et al. 2013). Despite this, experience has shown that experimentally measured profiles can be interpolated with good approximation with Equation (1).

The first protection against corrosion is represented by a sufficient thickness of cover and low porosity concrete (Colleparidi 2002, Bertolini et al. 2013). These concepts have been implemented, since the 1990s, in European standards, with limits on concrete composition (water/cement ratio), minimum concrete cover thickness and structures execution (curing) depending on the environment (EN 206, EN 1992-1-1). Compliance with these regulations would eliminate the vast majority of corrosion cases for usual service lives of 50 to 75 years, and even longer in the case of carbonation-induced corrosion.

There are some situations, characterized by high environmental aggressiveness, or when the required service life is longer than usual, in which preventative methods can be useful. In these situations, it would also be necessary to use a performance-based approach, to properly evaluate the influence of these methods on service life. deterministic or probabilistic. Deterministic methods are limited because they provide only an “average” value without information on the distribution. Therefore, in the last 20 years there has been a tendency towards the use of probabilistic methods. One example is FIB Model Code for Service Life design (FIB 2006): the service life of structures affected by reinforcement corrosion is approached by using Tuutti model, and the corrosion initiation time in case of chlorides-induced corrosion is calculated with a modified version of the Equation 1.

2.2 Preventative methods

Before dealing with preventative methods, it is fundamental to recall the effect of different types of concrete. In particular, since we focus on corrosion due to chlorides, the reduction of the diffusion of chlorides resulting from the use of a pozzolanic and blast furnace cement, if concrete is properly cured, has been known for long time (Bertolini et al. 2013; Colleparidi 2002).

Preventative methods can be effective on both corrosion initiation and propagation time, although the effect on the initiation time is generally the most important (Bertolini et al. 2013). Only techniques for which there is established experience are considered in the paper: cathodic protection, corrosion resistant reinforcements, corrosion inhibitors and concrete coatings. The effect of preventative methods on critical chloride content and chloride diffusion coefficient will be only briefly recalled in chapter 3. More details about their performances can be found in (Bertolini et al. 2013; Nurnberger 1994; Elsener 2001; Bolzoni et al. 2022a, b) and in literature cited herein. Cathodic prevention, if properly designed and monitored, is able to ensure a service life of at least 50 years without extraordinary maintenance even in presence of chloride content above the threshold (Pedefferri 1996; Bertolini et al 2013, Polder & Peelen 2019).

3 METHODS - ASSESSMENT OF SERVICE LIFE

3.1 Concrete and rebar properties

Environmental exposure was chosen in agreement with EN 206 standard: marine atmospheric (XS1) and splash zone/areas (XS3). Concrete with w/c ratio 0.45, according to EN 206 was selected. Three types of cement are considered: CEM I (Portland), CEM IV (pozzolanic, in particular with fly ash) and CEM III (blast furnace slag) according to the European standard EN 197.

Cover thickness (Table 1). The normal distribution was chosen according to the FIB Model Code with mean values for each exposure class equal to the minimum reported in the Euro-code (EN 1992-1-1) (Table 1); the standard deviation was 10 mm (Lollini et al 2015).

Surface concentration of chlorides (Table 1): the distribution (lognormal), mean values and standard deviation were chosen according to the literature in the case of exposure class XS3 (Lollini et al. 2015). For class XS1 the mean value and standard deviation were reduced by 50%, having not found indications in the literature. In presence of the coating applied on concrete cast with CEM I, surface concentration was reduced by 40% (Brenna et al. 2020).

Chloride diffusion coefficient (Table 2): values referred to long-term exposures were considered (Bertolini et al. 2013). In presence of concrete coating, when CEM I is used, a value reduced by 30% was considered (Brenna et al. 2020). The distribution is lognormal (FIB 2006).

Critical chloride concentration (Table 3). Values were chosen for carbon steel in accordance with the Model Code (FIB 2006). Preventative methods are: corrosion inhibitors, concrete coatings, use of stainless steel type 1.4307 (containing 18% Cr and 8%Ni, similar to the well-known AISI 304L). The critical chloride content for preventative methods was based on literature (Bertolini et al. 2013; Lollini et al. 2015; Ormellese et al. 2008; Bolzoni et al. 2022c) in absence of specific indication in (FIB 2006).

Table 1. Surface chloride content (Cs, % vs cement mass) and cover (d, mm).

	Distribution	Marine (XS1)		Tidal splash (XS3)	
		Mean	St. dev.	Mean	St. dev.
Cs no coating	Lognormal	2.5%	1%	5%	2%
Cs with coating	Lognormal	1.5%	0.6%	3%	1.2%
d (mm)	Normal	35	10	45	10

Table 2. Chloride diffusion coefficient (D_{app}).

D_{app} ($10^{-12} \text{ m}^2 \text{ s}^{-1}$)	Distribution	Mean	St. dev	Mean*	St. dev*
w/c 0.45 CEM I	Lognormal	1	0.2	2	0.4
w/c 0.45 CEM I + coating	Lognormal	0.7	0.14		
w/c 0.45 CEM IV	Lognormal	0.5	0.1		
w/c 0.45 CEM III	Lognormal	0.2	0.04	0.25	0.05

* values used only for the comparison with FIB 2006

Table 3. Critical chloride content (C_{cr}).

C_{cr} vs cement mass	Distribution	Mean	St. dev.
Carbon steel	Beta	0.6%	0.15%
Stainless steel 1.4307	Beta	5%	1.25%
Carbon steel + inhibitor	Beta	1.2%	0.3%
Carbon steel + inhibitor (“high dosage”)	Beta	1.8%	0.45%

3.2 Service life evaluation

In the case of chloride-induced corrosion, there is agreement among most researchers to consider the service limit state corresponding to corrosion initiation; in fact, localized corrosion propagation can lead to unacceptable cross section reduction in a short time (Bertolini et al. 2013). Corrosion initiation (t_i) occurs when at cover thickness ($x = d$), the chloride content C_{x,t_i} is equal to the critical value C_{cr} ; time for corrosion initiation can be evaluated inverting Equation (1), see Equation 2, in which erf^{-1} is the inverse of the error function and the other parameters have been already defined:

$$t_i = \frac{1}{D_{app}} \left\{ \frac{d}{2 \left[\text{erf}^{-1} \left(1 - \frac{C_{cr}}{C_s} \right) \right]} \right\}^2 \quad (2)$$

In the deterministic method, average values of the input variables, chloride surface concentration (C_s), concrete cover (d), apparent chloride diffusion coefficient D_{app} , critical chloride concentration (C_{cr}) are used (Tables 1, 2 and 3). In the probabilistic method, corrosion initiation time is evaluated by means of 4 independent extractions of random numbers and the following procedure is used:

- a random number ranging from 0 to 1 is extracted;
- this number is entered in the Y axis of the relevant cumulative probability curve (Figure 1);
- the value of the variable is determined on the X axis of the same graph.

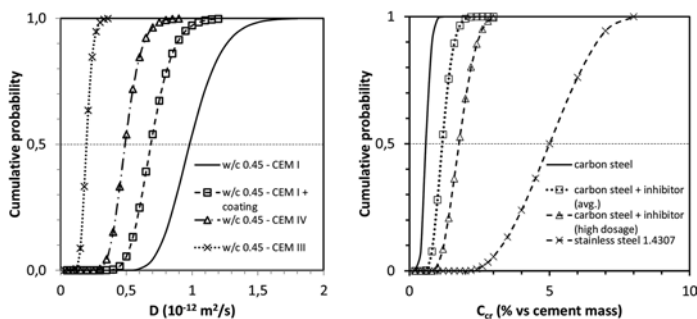


Figure 1. Cumulative probability for apparent chloride diffusion coefficient D_{app} (left), critical chloride concentration C_{cr} (right).

Once all values have been evaluated for one simulation, the value of corrosion initiation time is calculated by means of Equation 2 and this value is stored. The simulation is repeated 1000 times according to previous experience (Cheldi et al. 1997) and the distribution of corrosion initiation time is plotted. The simulation was performed by using a datasheet (Excel©) with a modified macro used in a previous work (Cheldi et al. 1997).

4 RESULTS AND DISCUSSION

4.1 Deterministic evaluation of service life

Under severe exposure conditions (XS3), the use of carbon steel reinforcements in concrete with water/cement ratio 0.45 cast with CEM I is not a reliable option: service life is about 13 years with concrete cover 45 mm (Figure 2). In practice, the prescriptive approach based on EN 206 and Eurocode is not conservative. Service life 50 years is not reached even with 80 mm cover.

The use of different cement types, CEM IV or CEM III, can help to exceed 50 years service life (Figure 2) by the proper concrete cover.

In marine atmospheric exposure (XS1), the situation is less severe but considering the suggestions of EN 206 (cover 35 mm) and Eurocode the performance of carbon steel is not satisfactory: service life results at least 50 years only by selecting a concrete cover higher than 65 mm.

A sensitivity analysis relative to the critical chloride concentration was performed (Figure 3). In an aggressive environment (XS3) with 45 mm cover, there is a significant increase in the corrosion initiation time if the critical chloride content is at least 2.5% vs. cement mass. These values can be exceeded only by using stainless steel reinforcements. Less performing solutions can be used only in combination with low porosity concrete, cast with CEM III.

4.2 Probabilistic evaluation of service life

Results obtained using the probabilistic approach are represented in Figures 4 and 5. They should be considered as an indication of a trend. In real cases, the behavior of reinforcement, concrete, and/or the environment may vary depending on design and execution.

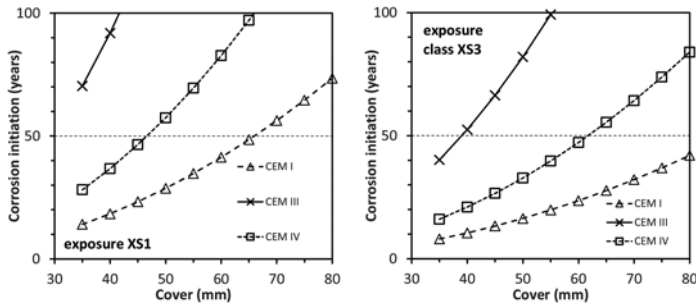


Figure 2. Time for corrosion initiation (service life) evaluated with deterministic method for carbon steel reinforcements (C_{cr} 0.6% by cement mass), with concrete w/c 0.45 and different type of cements in exposure class XS1 (left) and XS3 (right).

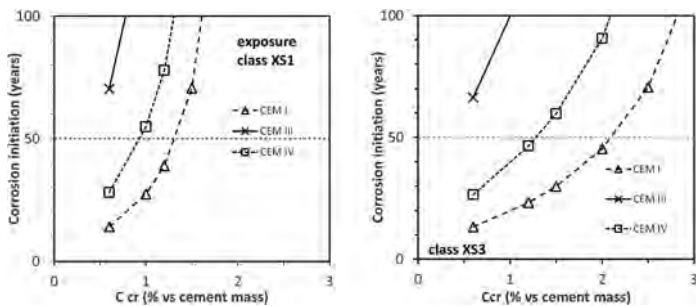


Figure 3. Time for corrosion initiation (service life) evaluated with deterministic method: sensitivity analysis on critical chloride threshold. Concrete w/c 0.45 and different type of cements in exposure class XS1 with cover 35 mm (left) and XS3 with cover 45 mm (right).

In the two graphs, a horizontal dashed line was drawn at a value equal to 10% of the probability of failure (Pf), defined as the probability of reaching the limit state (corrosion initiation). The value is considered a minimum target (FIB 2006). A vertical line is drawn at 50 years, the expected service life for common buildings according to Eurocode 2, while 100 years corresponds to a minimum service life for important structures.

In conditions of high aggressiveness, exposure class XS3 (Figure 4), it is clear that a concrete with w/c ratio 0.45 (as suggested by EN 206) and cast with CEM I and concrete cover 45 mm (Eurocode) is not a reliable solution, for. Considering a service life of 50 years, the probability of corrosion initiation is 90% or higher. In this severe exposure conditions, the technical solution that can guarantee at least 50 years service life with a probability of corrosion initiation equal to 10% are:

- Stainless steel rebar, independently on the concrete cover or cement type.
- Corrosion inhibitor, only if they are combined with low porosity concrete as the concrete cast with CEM III (blast furnace slag cement); the reliability of this technical solution depends on the maintenance of corrosion inhibitor concentration for long time, i.e. absence of leaching (for example in correspondence with cracks).

In less severe exposure (XS1), the surface concentration of chlorides is lower with respect to class XS3, as well as the minimum cover thickness recommended by the Eurocode (35 mm). These two factors have an opposed influence on the corrosion initiation. The overall results are more favorable in the less severe environment but the trends identified in the more severe exposure class are confirmed.

4.3 Comparison with FIB Model code for service life design

The results have been compared with those obtained by the FIB Model code for service life design (FIB 2016), reported in (Lollini et al. 2015). The same input data were used for critical chloride content, concrete cover and surface chloride content (Tables 1 to 3).

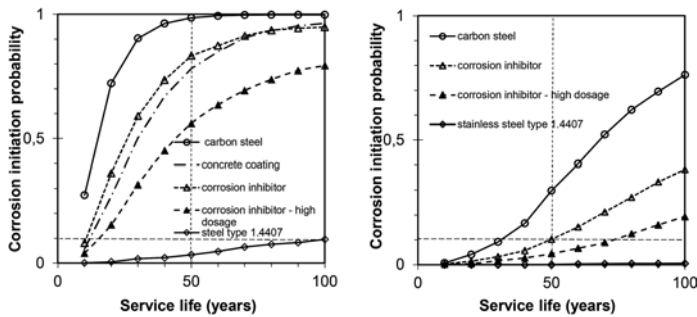


Figure 4. Cumulative distribution of the service life: exposure class XS3, mean cover 45 mm, concrete w/c ratio 0.45, cement type EN 197 CEM I (left) CEM III (right).

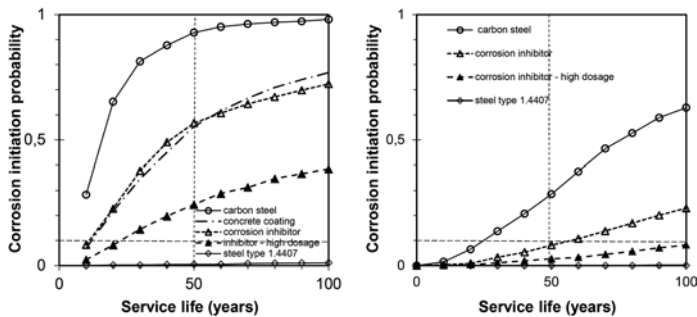


Figure 5. Cumulative distribution of the service life: exposure class XS1, mean cover 35 mm, concrete w/c ratio 0.45, cement type EN 197 CEM I (left) CEM III (right).

The situation is different for chloride diffusion coefficient: FIB model code suggest to evaluate the apparent chloride diffusion coefficient D_{app} with this formula:

$$D_{app} = k_c \cdot DRCM \cdot k_t \cdot \left(\frac{t_0}{t}\right)^a \quad (3)$$

where DRCM is an experimental value measured with accelerated testing (DRCM) at time t_0 (generally 28 days) or estimated according the annex B in (FIB 2006), k_c is related to the temperature, k_t a transfer parameter and a is the aging exponent, mean value 0.3 for CEM I and 0.45 for CEM III. The ratio between the values of D_{app} , calculated after 1 year and 100 years is around 8 for CEM III, and 5 approximately for CEM I.

The results of the two approaches are in agreement, especially in the case of concrete manufactured with CEM I (Figure 6). Significant differences can be observed in the case of concrete with CEM III, and this can be related to the higher change of the chloride diffusion coefficient through the exposure time considered in the FIB model code.

These results confirm that in service life models, i.e. the FIB model code, some factors require further research work, as already stated in (Lollini et al. 2011; Lollini et al. 2015). In particular more information is needed on traditional and new materials, regarding chloride transport and chloride threshold levels for different types of rebars or preventative methods: these last currently are not included in the FIB Model Code (FIB 2006).

4.4 Life cycle considerations

Life-cycle cost (LCC) analysis has not been explored in this article, but some considerations can be made by comparison with the literature.

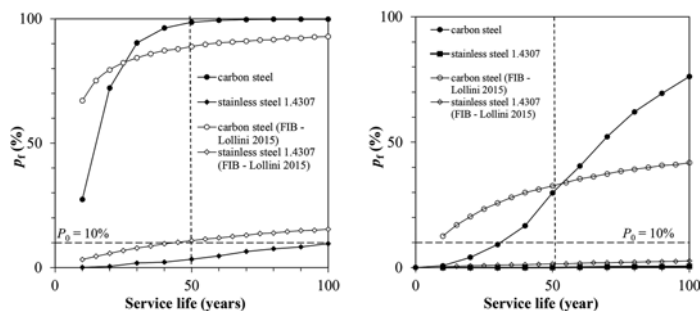


Figure 6. Cumulative distribution of the service life: exposure class XS3, mean cover 45 mm, concrete cast with w/c ratio 0.45, cement type EN 197 CEM I (left) or CEM III (right). Open marks: data evaluated by FIB Model Code for service life design (Lollini et al 2015), filled marks: present work.

A preliminary life-cycle cost assessment was performed for a bridge slab exposed to aggressive environments due to chloride-containing de-icing salts in the work (Polder et al. 2016).

Different corrosion prevention solutions were compared by deterministic Life Cycle Cost, and it was shown that the use of stainless steel reduces the life cycle cost, similarly to water repellent coatings; the cost of cathodic prevention is slightly higher, while the cost of conventional repair, a solution still often used today, is significantly higher. Indirect costs (traffic disruption, etc.) were not considered in the cited article (Polder et al. 2016); if they were considered, stainless steels and cathodic prevention would become more cost effective.

Corrosion inhibitors, concrete coatings and galvanized reinforcements are less expensive and less effective in delaying corrosion, and they can reduce maintenance and rehabilitation costs vs the solution without any preventative measure. This achievement is conditioned by the durability of the preventative method, related to the stability of the coating in time (without disbonding for example) and the maintenance of the inhibitor concentration in concrete, i.e. absence of leaching.

The environmental impact of the different solutions has not been analyzed in the paper, but it can be argued that extending the service life can reduce the overall impact of the structure on the environment and the withdrawal of resources from it (Matthews 2020; Coppola et al. 2018). This is even more important for more durable solutions like stainless steels or cathodic prevention.

5 CONCLUSIONS

Performance based approaches have been applied to evaluate preventative methods against rebar corrosion due to chlorides. Considering the limitations of the analysis, some trend can be identified.

In concrete cast with Portland cement (CEM I) with w/c 0.45 and concrete cover (mean value) 45 mm, as suggested by EN 206 and Eurocode, only stainless steel rebars and cathodic prevention can guarantee more than 50-year service life in severe conditions, as in splash/tidal zone of marine structures (XS3). The use of corrosion inhibitors and coatings delay corrosion initiation, but the 50-year service life could be reached only if they are combined with low porosity concrete, i.e. manufactured with CEM III. These solutions can reduce maintenance and rehabilitation costs vs the absence of preventative measures, provide that their durability is guaranteed.

To improve the reliability of the prediction by means of service life models, is necessary to collect more data, mainly concerning critical chloride concentration for different preventative methods, not indicated in the FIB Model Code, and chloride transport with different concrete type.

REFERENCES

- Bertolini, L., Elsener B., Pedferri P., Redaelli E. & Polder R. 2013. Corrosion of steel in concrete – prevention, diagnosis, repair, 2nd ed. Weinheim: Wiley VCH.
- Bolzoni, F., Ormellese, M., Pedferri, MP. & Proverbio, E. 2022a. Big milestones in the study of steel corrosion in concrete. *Structural Concrete*. 1–12. <https://doi.org/10.1002/suco.202200315>
- Bolzoni F., Brenna A. & Ormellese M. 2022b. Recent advances in the use of inhibitors to prevent chloride-induced corrosion in reinforced concrete, *Cement and Concrete Research* 154 106719. <https://doi.org/10.1016/j.cemconres.2022.106719>
- Bolzoni, F., Brenna, A., Beretta, S., Diamanti, M.V., Ormellese, M., & Pedferri, M. 2022c. Long term performance of corrosion inhibitors in concrete. American Concrete Institute, ACI Special Publication, SP-354, pp. 193–208
- Bolzoni, F., Brenna, A., Beretta, S., Ormellese, M., Diamanti, M.V. & Pedferri, M. 2022d. Evaluation of Preventative Methods against Rebar Corrosion in Concrete, *Key Engineering Materials*, 919 KEM, pp. 132–142. <https://doi.org/10.4028/p-9yww6l>
- Brenna, A., Beretta, S., Berra, M., Diamanti, MV., Ormellese, M., Pedferri, MP., Pastore, T. & Bolzoni F. 2020. Effect of polymer modified cementitious coatings on chloride-induced corrosion of steel in concrete. *Structural Concrete*. 21: 1810–1822.
- Cheldi, T., Cavassi, P., Lazzari, L. & Pezzotta L. 1997, Use of decision tree analysis and Montecarlo simulation for downhole material selection, *Proc. Of Corrosion/97 Conference*, Nace International, Houston, TX, Paper 97018.
- CEB Comité eurointernational du beton. Durable Concrete Structures. Bulletin n. 148 (1st ed.) 1982; bulletin n. 182 (2nd ed.) 1989.
- Colleparidi M. 2002. The new concrete. Villorba (TV) Italy: Tintoretto.
- Coppola, L. et al 2018 Binders alternative to Portland cement and waste management for sustainable construction part 1 and 2, *J Appl. Biomater. Funct. Mater.* 16 (3) 186–202; 16 (4) 207–221.
- Elsener, B. 2001, Corrosion inhibitors for steel in concrete - an EFC state of the art report. European Federation of Corrosion, Number 35. London: Institute of Materials and EFC.
- EN 197 Composition, specifications and conformity criteria for common cements. European Committee for Standardisation
- EN 206 Concrete – Specification, performance, production and conformity, European Committee for Standardisation
- EN 1992-1-1 Eurocode 2: Design of concrete structures – Part 1-1: general rules and rules for buildings. European Committee for Standardisation
- FIB 2006. Model code for service life design. Bulletin n. 34, Lausanne: International Federation for Structural Concrete.
- Lollini, F., Carsana, M., Gastaldi, M., Redaelli, E. & Bertolini, L. 2011. Durability design of reinforced concrete structures, *Proc. of the Institution of Civil Engineers, Construction Materials* 164 (2011), Issue CM6: 273–282.
- Lollini, F., Carsana, M., Gastaldi, M., Redaelli, E. & Bertolini, L. 2015. The challenge of the performance-based approach for the design of reinforced concrete structures in chloride bearing environment, *Constr. and Build. Mat.* 79: 245–254
- Matthews, S., 2020. FIB Model Code 2020, life-cycle management of existing concrete structures and the potential benefits of building as little as possible, *Proc. of the FIB Workshop Capacity Assessment of Corroded Reinforced Concrete Structures*, 1st- 4th December 2020, 15–29.
- Nurnberger, U. 1994. Stainless steel in concrete. State of the art report, European Federation of Corrosion Working Party WP11, July 1994.
- Ormellese M., Bolzoni F., Lazzari L. & Pedferri P. 2008, Effect of corrosion inhibitors on the initiation of chloride-induced corrosion on reinforced concrete structures, *Mater Corros*, 59 (2): 98–106.
- Pedferri, P. 1996. Cathodic protection and cathodic prevention, *Construction and building materials*, 10: 391–402.
- Pedferri, P. 2018. Corrosion science and engineering, ed L Lazzari and MP Pedferri. Cham, Switzerland: Springer Nature.
- Polder, R., Pan, Y., Courage, W. & Peelen, W. 2016. Preliminary study of life cycle cost of preventive measures and repair options for corrosion in concrete infrastructure, *Heron* 61 (1), 1–13.
- Polder R. & Peelen W. 2019. Cathodic protection of reinforcement in concrete – experience and development over 30 years, *MATEC Web Conf.*, 289 (2019) 03006. <https://doi.org/10.1051/mateconf/201928903006>.

Role of concrete and reinforcement characteristics to increase the service life of structures

M.C. Alonso

Institute of Construction Science Eduardo Torroja (IETcc-CSIC), Madrid, Spain

ABSTRACT: The advantages of reducing the transport of aggressive agents through the concrete cover, either through the use of cements with lower carbon footprint, incorporating supplementary cementitious materials (SCM) or using high performance concrete (HPC) to increase its density, are proven technologies to extend the service-life of concrete structures.

Another challenge is to delay the initiation of corrosion by using systems capable of increasing the corrosion resistance of reinforcement. The incorporation of additives in the concrete matrix with corrosion-inhibiting properties to improve the interaction between reinforcement and concrete at the interface. Inhibitors encapsulation is a promising technology that follows a controlled release of the inhibition part and at the same time is effective in capturing chloride. On the other hand, there is the use of new types of reinforcement, such as stainless steel, which significantly increase the critical chloride content to prevent the initiation of corrosion during the service-life.

1 INTRODUCTION

The guarantee of a high durability of concrete structures and, consequently, a longer service-life are increasingly demanding requirements in the increasingly challenging environmental conditions as a result of climate change.

The cost associated with repair work in Europe is estimated to be equivalent to half of the annual construction budget spent on the renovation and remediation of the existing structures to extend their service-life, Cailleux & Pollet (2009). Furthermore, although European Standards consider that any concrete structure must have a service-life of at least 50 years, contractors are generally liable for damages only up to 10 years, Silva et al (2015).

Reinforcement corrosion is the main cause of degradation and loss of service-life of concrete structures. The carbonation of the concrete cover and the presence of chlorides are the two main aggressive agents responsible for deterioration of concrete structures that operate in extreme environmental conditions. The ever increasing demand in the construction industry to build structures with long service-life necessarily leads to evaluating the incorporation of new technologies and methods of protection against corrosion in current engineering projects. The particular focus is to achieve the goal of the sustainability of construction and at the same time allow to reduce the maintenance in operation of the structures and the related costs.

2 SERVICE LIFE PREDICTION FOR CORROSION OF REINFORCEMENTS

The thermodynamic model proposed by Tuutti (1982) is the most accepted framework for the prediction of corrosion of reinforcements and after 40 years its basic concept is maintained. Tuutti's model considers two successive periods for the corrosion process of reinforcement in concrete identified as initiation (t_i) and propagation (t_p) periods

The end of the service-life of a reinforced concrete structure is usually associated with the durability limit state of corrosion initiation, preventing the propagation of corrosion, Browne

(1982), Funahashi (1990), Maage et al (1995). For this reason, special attention has been devoted to the quantification of the initiation period, differentiating two stages, one associated to the assessment of the transport of the aggressive agent and another focused on the determination of the critical concentration of the aggressive agent that accumulates on the rebar and causes the initiation of corrosion. These two stages in the initiation period are differentiated in the Figure 1-left, also reflecting the variability associated to the parameters involved in their determination.

Most of the research advances with this model have been dedicated to the quantification of the two stages that intervene in the initiation period ($t_i = t_{\text{transp}} + t_{\text{dep}}$), the transport of the aggressive, (t_{transp}) and the depassivation of the rebar (t_{dep}).

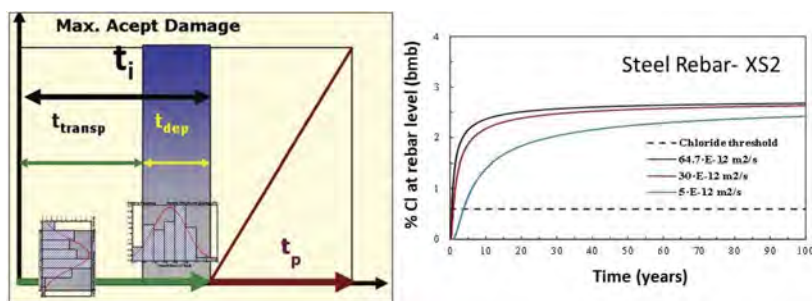


Figure 1. Left) Modified Tuutti's diagram differentiating two stages during the initiation period (t_i): 1) transport of aggressive agents (t_{transp}) and 2) rebar depassivation (t_{dep}). Right) effect of D_{app} decrease on the prediction of % of Cl accumulation at the rebar level in a Conventional Concrete (CC) and time to onset of corrosion at Cl threshold (dash line).

In the case of chloride-contaminated environments, t_i focuses primarily on determining the two critical parameters involved, the Cl diffusion coefficient (D_{app}) and the corrosion resistance of the reinforcement until a critical level of Cl accumulates on the rebar surface that causes the initiation of corrosion, the chloride threshold (C_{crit}).

The entry of chloride into reinforced concrete structures is complex since it depends on random parameters that are related to transport and characteristics of the concrete, resulting in high variability values. These variations raise the need for statistical approaches to assess the risk of corrosion initiation due to chloride ingress, Kiese et al (2020).

Song et al (2008) analyzed data reported in the literature on the evolution of diffusion coefficient (D_{app}) and surface content of chloride, C_s , of concrete structures and specimens exposed to marine environments. Several factors were found to influence the chloride transport in terms of D_{app} and C_s , such as concrete mix characteristics (water/binder ratio, binder type or air void content), curing methods, the external environment and proximity to seawater. The type of cement has a significant effect on the variability of D_{app} for similar concrete characteristics.

Kiese et al (2020) used sensitivity analysis to identify the influence of input parameters on the critical time period before the onset of corrosion predicted by the Cl diffusion model. The results showed that the corrosion initiation time was more sensitive to the effective diffusion coefficient of chloride, D_{eff} , a parameter more controllable by the stakeholders than C_s , which is an uncontrollable parameter that depends on surrounding conditions.

Furthermore, the micro and macro structural features at the steel/concrete interface are generally recognized as the most important factors influencing the chloride induced corrosion and threshold values, Angst et al (2017 & 2019). Regarding the critical chloride that can induced corrosion onset, in the reviews of the literature by Ann& Song (2007), Alonso & Sanchez (2008) and Angst et al (2009) a high variability was found. This large scatter in the literature data is associated with different experimental conditions, different definitions and methods and with the numerous factors that affect the critical chloride content suggested by Angst et al (2009).

Stochastic models have been used for the prediction of critical chloride concentration for the depassivation of reinforcements to statistically analyse the variability of the chloride

threshold. Izquierdo et al (2004) applied a normal distribution to the chloride threshold values obtained by the potentiostatic method using different types of cement; the 95% probability of depassivation of the reinforcement gave values from 0.62% to 0.77% for total chlorides; with a minimum value for the 5% depassivation risk of 0.32%.

Alonso & Sanchez (2008), based on a large collection of chloride threshold values, performed a statistical analysis of the variability. The frequency distribution of chloride threshold data are around 1% for total chloride.

To predict the service-life of concrete structures exposed to chloride environments it is necessary to know parameters such as, D_{app} , C_s and chloride threshold (C_{crit}), according to the Equation 1, considered in the Model Code (2006):

$$C_{crit} = C(x = a, t) = C_0 + (C_{s,\Delta x} - C_0) \cdot \left[1 - \operatorname{erf} \frac{a \cdot \Delta x}{2 \cdot \sqrt{D_{app,C} \cdot t}} \right] \quad (1)$$

Where

- C_{crit} : critical chloride content for rebar corrosion initiation [wt.-%c]
- $C(X,t)$: content of chlorides in the concrete at a depth x (structure surface $x = 0$ m) and a time t [wt.-%c]
- C_0 : initial chloride content of the concrete [wt.-%c]
- $C_s, \Delta x$: Chloride content at a depth Δx and a certain point of time t [wt.-%c]
- x : depth with a corresponding content of chlorides $C(X,t)$ [mm]
- a : concrete cover [mm]
- Δx : depth of the convection zone (concrete layer, up to which the process of chloride penetration differs from Fick's 2nd law of diffusion) [mm]
- D_{app}, C : apparent coefficient of chloride diffusion through concrete [mm^2/year]
- t : time [years]
- erf: error function

Figure 1-right shows the result of the prediction of accumulation of Cl at the level of the reinforcement with a conventional concrete (CC) using equation 1. The time to reach the chloride threshold for the onset of corrosion (end of service-life) is marked with a dashed line. The D_{app} used in the calculation were obtained from experiments performed in Luna et al (2018). The D_{app} was determined by Cl diffusion tests in concrete samples fabricated with OPC (CEM I type) using 380kg/m^3 and $w/c=0.6$. As chloride threshold (C_{crit}) the value of 0.6% of total Cl by mass of binder (bmb) was used. Figure 1-right shows that the time to reach the Cl threshold is less than 10 year. The effect of reducing chloride diffusion, D_{app} , increases the time to reach the Cl threshold for corrosion initiation but remain below 10 years.

The increase in the thickness of concrete cover depending on the aggressiveness of the environment, as prescribed in some standards, EN1992-1-1(2004), as a way of delaying the arrival of the aggressive agent at the rebar level, has a structural limit in design and increases costs.

The growing demand in the construction industry to build structures with long service-life, necessarily of at least 50 years, leads to evaluating the incorporation of corrosion protection methods in current engineering projects. Two tendencies are followed to extend the service-life of concrete structures, the action on the concrete matrix or on the reinforcement. That is, affecting the transport process of aggressive agents by modifying the concrete cover or improving the resistance to corrosion by changing the chemical characteristics of the reinforcement.

3 INTERVENTION ON THE CHARACTERISTICS OF THE CONCRETE COVER TO EXTEND THE SERVICE-LIFE OF STRUCTURES

A specific action to extend the transport period is to retard the penetration of the aggressive agent by manufacturing high density and less permeable concrete matrices, such as using high performance concrete (HPC) or ultra-high performance fibre reinforced concrete (UHPC). Also by using binders with a smaller footprint, that incorporate SCM capable of increasing

the binding of chloride ions, thus delaying the transport of chloride. These forms for corrosion prevention through concrete cover actions is being contemplated in standards based on the exposure class of the structure and the relationship with aspects of durability of reinforcement, ENV 206-100 (2022).

The type of cement, in terms of the incorporation of mineral additions has been revealed as one of the most influential factors in the resistance of concrete to the penetration of chlorides, Paiva et al (2016), Luna et al (2018). SCM lead to a denser microstructure and decrease the pore size distribution to more refined net-pore as found by Luna et al (2018) in concrete with 35% of Blast Furnace Slag (BFS) compared with Ordinary Portland Cement (OPC), using the same $w/b = 0.6$.

A clear decrease of the non-steady state diffusion coefficient, D_{app} , have been measured with BFS compared with OPC concrete in Luna et al (2018), plotted in Figure 2-left. The positive effect of BFS in reducing the chloride transport is attributed to reduced porosity and the Cl binding capacity, Leng et al (2000), Moon et al (2006), Song et al (2006), Luna et al (2018). Furthermore, the pore structure can be reduced by increasing the binder content and reducing the w/b ratio, Alonso at al (2021). Porosity reduction has a clear effect on chloride transport, as can be appreciated in Figure 2-right for $D_{app mig}$ and different concrete porosities. Porosities less than 6% leads to reduction in $D_{app mig}$ from 10^{-11} , for a CC, to $10^{-13} \text{ m}^2 \cdot \text{s}^{-1}$, with HPC and UHPFRC.

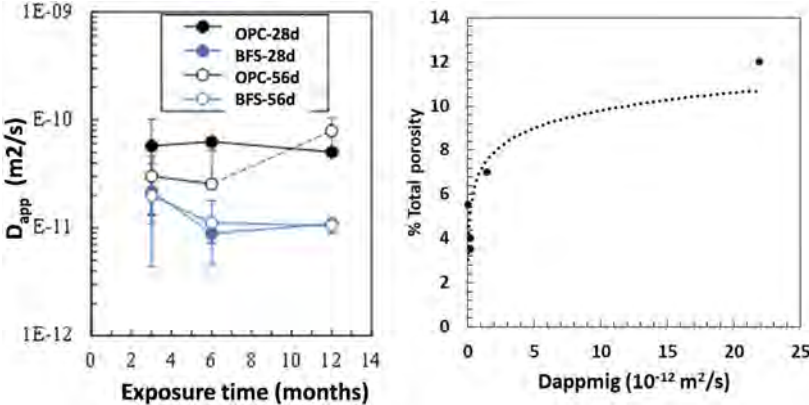


Figure 2. Left, Effect in Cl diffusion, D_{app} , for concretes with OPC and BFS (Luna Et al 2018). Right, Concrete total porosity vs $D_{app mig}$.

The chemical composition of the binder affects the pH of the pore solution and its microstructure, which would be important when considering the interaction of steel and concrete for the development of the passive layer. Those types of binders that contain pozzolanic properties, such as fly ash and silica fume, lower the pH of the pore solution and the tolerable amount of chlorides can be affected. Large amounts of pozzolan additions (above 30%) have been found to reduce the threshold value of chloride from 0.5 to 0.3%, Reddy et al (2002). In recent studies by Alonso et al (2021) Cl threshold values were found to vary from 0.5 to 0.35 % total chloride in HPC and 0.1 to 0.2 in UHPFRC.

The importance of the characteristics of the concrete cover in the service-life of the structures is significant, since it affects both the transport of the aggressive agent and the process of depassivation for the rebar corrosion initiation. The evaluation of both stages and their incorporation into the models will allow to more rigorous predictions of service-life of concrete structures and the benefits derived from considering the characteristics of the cover.

The positive effect of a CC with BFS in the prediction of time for chloride accumulation at the rebar level from Equation 1 has been plotted in Figure 3-left using in the calculation the experimental data of D_{app} obtained in Luna et al (2018) and chloride threshold. Reducing CC chloride transport by BFS can extend the service life of a concrete structure above 50 years. In addition, the use of HPC and UHPFRC also have significant beneficial effect in the span of

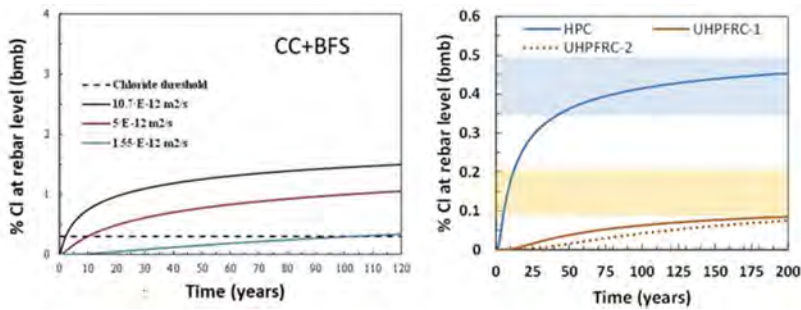


Figure 3. Left, Prediction of Chloride accumulation at rebar level with BFS concrete. Right, Influence of high density concretes: HPC and UHPFRC.

service-life due to the important reduction of the porosity and the drastic effect on the chloride transport given in Figure 2-right, which allow a significant delay in accumulation of chlorides at the rebar level, shown in Figure 3-right. The dashed lines indicate the chloride thresholds determined for corrosion initiation.

4 INTERVENTION ON THE REINFORCEMENT CHARACTERISTICS TO EXTEND THE SERVICE-LIFE OF CONCRETE STRUCTURES

Another challenge to take into account in order to increase the service-life of the concrete structures is based on the use of protection measures for reinforcements that increase the time to corrosion onset. Systems that modify the form of the interaction of the reinforcement with the concrete and at the same time improve the corrosion resistance in presence of the aggressive agents.

Protection methods incorporated into the concrete matrix, as the case of corrosion inhibitors additives. The most recent advances in this protection method are the encapsulation of corrosion inhibitors that modify the interaction at the steel/concrete interface through a controlled release of the inhibition part to improve the passive layer resistance; but at the same time, affecting the cover of the concrete by being efficient with the capture of chloride.

The role of corrosion inhibitors is to modify the surface passive layer of the steel bar to hinder the corrosion process. Calcium nitrite has been used extensively in concrete and is very affective in mitigating chloride-induced corrosion of reinforcement, reducing the corrosion rate and increasing the time to corrosion initiation, Ann et al (2006), Berke & Hicks (2004). The chloride threshold for this protection method has been reported primarily as the $[\text{NO}_2^-]/[\text{Cl}^-]$ mole ratio when calcium nitrite has been used, because it indicates the amount of corrosion inhibitor required to inhibit chloride-induced corrosion. For concrete, the inhibitive efficiency of nitrite is often considered to be in the range 0.5-1, Gonzalez et al (1998).

Corrosion inhibitor encapsulation is gaining increasing interest as a new promising technology for incorporating corrosion inhibitors in concrete. Layered double hydroxides (LDH) have a layered structure; three layers are the most common. The ion exchange capability of LDH is the most important property with respect its application in concrete. Mg-Al hydrotalcites have a large surface area, high anion exchange capacity, such as chloride ions, and if charged with an anion that has inhibitory ability they can prevent corrosion of reinforcement, Tedim et al (2012). In the case of LDH loaded with an inhibitory anion, the inhibitory response mechanism is based on ion exchange between free chloride ions and the inhibitory anion intercalated in the hydrotalcite matrix and simultaneous release of the inhibitor. The corrosion inhibition efficiency associated with the LDH released inhibitor has been demonstrated in mortar. Cao et al (2017) found a longer corrosion onset and decreased Cl transport when adding MgAlNO_2 and NO_3^- , more efficient with the first. The basic mechanism for corrosion inhibition and long-term delay of corrosion onset in LDH-Inh is attributed to simultaneous superposition actions, the decrease of Cl in the pore solution due to LDH anion exchange, the increase of pH due to the release of LDH hydroxides and the contribution of the released LDH inhibitor modifying the passive layer.

The positive effect of encapsulated inhibitors can be seen in Figure 4, from recent studies carried out by the author in concrete with and without of LDH inhibitor added in 1% by mass of binder. A positive effect on Cl transport and corrosion inhibition of reinforcement has been found. Chloride diffusion tests in Figure 4-left showed that the D_{app} can be decreased with the addition of LDH. But the most relevant effect found with LDH addition is the delay of the onset of corrosion of the bars due to the inhibition of the corrosion process, as shown in Figure 4-right. For this study reinforced concrete samples were immersed in 3% NaCl solution and the rebar corrosion was monitored for more than three years. A clear delay of more than three times in the onset of corrosion have been observed, values of $i_{corr} < 0.1 \mu A/cm^2$ indicative of a passive state of the rebar. In Figure 4-right after 400 days in REF samples corrosion has started, while after 1400 days of exposure the concretes with LDH do not showed sign of corrosion initiation.

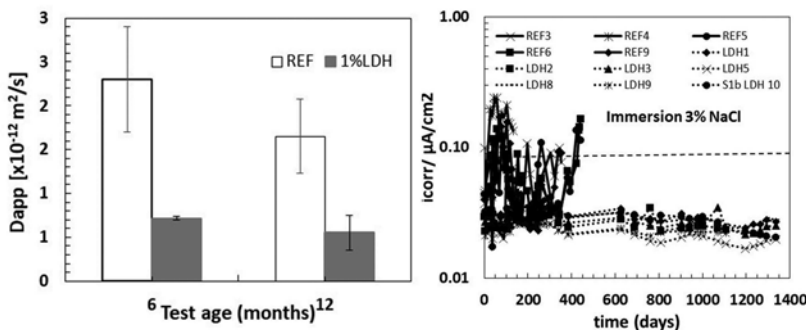


Figure 4. Left, Chloride diffusion tests in REF vs. LDH concretes. Right, Retardation of corrosion initiation of reinforcement as i_{corr} ($\mu A/cm^2$) vs immersion time in NaCl solution.

Regarding the reinforcement, two types of actions are considered, on the one hand, the protection of conventional reinforcement with some type of coating that acts as a protective barrier of the bare steel, as well as an organic type through the application of epoxy coating. In addition, hot-dip galvanizing, highlighting this last technique over the other due to the metallic bond created between the galvanized coating and the bare steel. On the other hand, the replacement of conventional reinforcing steel by new type of reinforcements, such as stainless steel, which significantly increases the chloride threshold.

Stainless steel reinforcements (SSR) have been used for decades and have demonstrated their ability to prevent reinforcement corrosion damage for a long time in aggressive environments, both in laboratory and in field exposure, Castro et al (2002). Therefore, the use of stainless steel reinforcements is now considered a very reliable method to ensure the long-term durability of reinforced concrete structures when exposed to extremely aggressive environments.

Most of the research with SSR has concentrated on evaluating the increase of corrosion resistance in chloride environments. The high corrosion resistance of stainless steel in alkaline media is mainly attributed to the high resistance passive film that forms on its surface, being determined by the composition of the stainless steel alloy type, Abreu et al (2004). Austenitic SS and duplex SS show the highest resistance to chloride induced pitting corrosion, Garcia-Alonso et al (2007), Alonso et al (2019).

Figure 5 shows the chloride threshold values obtained with different duplex SSR in concrete, Alonso et al (2019). Values between 3 to 13% Cl (bmb) in OPC and BFS are shown in Figure 5-left. The variations depends on the quality of the SS, such as the Mo content, and the type of cement. Lower Cl threshold values were found for the concrete with high BFS. The high Cl thresholds with SS reinforcement allow the prediction of large extension of service-life. Long times are predicted to reach the accumulation of the Cl threshold at the level of the reinforcement, as represented in Figure 5-right, even with concretes that have high chloride transport, such as those in Figure 2-right considered in this calculation.

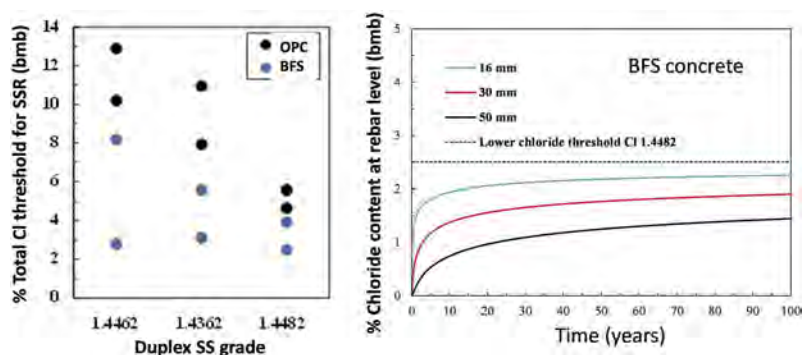


Figure 5. Left, Chloride threshold values for Duplex SSR, Alonso (2019). Right, Cl prediction at rebar level for BFS concrete, influence of cover thickness.

5 CONCLUSIONS

To face the challenge of sustainability through the extension of the service-life of concrete structures, it is necessary to act in the development of new products and technologies, guaranteeing the performance in operating conditions, as well as to facilitating the incorporation of the advances in the building codes.

Take advantages of materials and products that reduce the transport of the aggressive agents by modifying the concrete cover, using binders with smaller footprint incorporating SCM or with high-density concretes, such as HPC or UHPFRC. Both are technologies that have shown great influence on the extension of service-life of concrete structures.

Facilitate the use of reinforcement protection measures that increase the time to initiation of reinforcement corrosion. Protection methods such as new encapsulated corrosion inhibitor technology or the use of stainless steel reinforcement have been shown to increase the chloride threshold and contribute to extend the service-life. Technologies, such as SSR, for protection of reinforcement are well supported with extensive laboratory and field applications, but are not yet considered in the building codes.

REFERENCES

- Abreu, C. Cristóbal, M.J. Losada, R. Nóvoa, X.R. Pena, G. & Pérez, M.C. 2004. High frequency impedance spectroscopy study of passive films formed on AISI 316 stainless steel in alkaline medium. *J. Electroanalytical Chemistry*, 572: 335
- Alonso, M.C. & Sanchez, M. 2008. Analysis of the variability of chloride threshold values in the literature. *Materials and Corrosion*, 60: 8631–637.
- Alonso, M.C. Luna, F.J. & Criado, M. 2019. Corrosion behaviour of duplex stainless steel reinforcement in ternary binder concrete exposed to natural chloride penetration. *Construicio & Building Materials*, 199: 385–395.
- Alonso, M.C., Giménez, M., Menendez, E., Soto, J., Gandía, M., Serna, P., Roig M., Ferrara, L., Cuenca E., Schröfl, C, Reichardt, M, Peled, A. & Regev, O. 2021. D 5.4 Understanding the durability performance of UHDC-XS and UHDC-XA. *RESHEALIENCE project*. <https://cordis.europa.eu/project/id/760824/results>.
- Ann, K.Y. Jung, H.S. Kim, H.S. Kim, S.S. & Moon, H.Y. 2006. Effect of Calcium nitrite-based corrosion inhibitor in preventing corrosion of embedded steel in concrete, *Cement & Concrete Research* 36 520–525.
- Ann, K.Y. & Song H.W. 2007. Chloride threshold level for corrosion of steel in concrete, *Corrosion Science*, 49: 4113–4133.
- Angst, U., Elsener, B. Larsen, C.K. & Vennesland, Ø. 2009. Critical chloride content in rein-forced concrete. review, *Cement and Concrete Research* 39: 1122–1138. Press/ Balkema, The Netherlands, 149.
- Angst, U. M. Geiker, M. R. Michel, A. Gehlen, C. Wong, H. Isgor, O. B. . . & Polder, R. 2017. The steel–concrete interface. *Materials and Structures*, 50(2), 143.

- Angst U.M. Geiker, M.R. Alonso M.C. Polder, R. Elsener, B. Isgor, O.B. Wong, H. et al. 2019. The effect of the steel-concrete interface on chloride-induced corrosion initiation in concrete. A critical review by RILEM TC 262-SCI. *Materials and structures*: 52–88.
- Berke, N.S. & Hicks, M.C. 2004. Predicting long-term durability of steel reinforced concrete with calcium nitrite corrosion inhibitor, *Cement & Concrete Composites*, 25: 439–449.
- Browne R. 1982. Design prediction of the life for reinforced concrete in marine and other chloride environments. *Durability Building Materials*, 1:113–25.
- Cailleux, E. & Pollet, V. 2009. Investigations on the development of self-healing properties in protective coatings for concrete and repair mortars. *Proceedings of 2nd International Conference on Self-Healing Materials*, Chicago, IL, USA.
- Cao, Y. Dong, S. Zheng, D. Wang, J. Zhang, X. Du, R. Song, G. & Lin, C. 2017. Multifunctional inhibition based on layered double hydroxides to comprehensively control corrosion of carbon steel in concrete. *Corrosion Science*, 126: 166–179.
- Castro, P. Troconis, O. Moreno, E. Torres-Acosta, A. Martínez-Madrid, M. & Knudsen, A. 2002. *Materials Performance NACE* 41 (10): 50–55
- ENV 206-100 2022. Exposure resistance classes (ERC).
- EN 1992- 1-1 2004. Eurocode-2: Design of concrete structures - Part 1: General rules and rules for buildings, Brussels, Belgium: CEN (European Committee for Standardization).
- Funahashi, M. 1990. Predicting corrosion free service life of a concrete structure in a chloride environment. *ACI Materials Journal*, 87: 581–7.
- Garcia-Alonso, M.C. Escudero, M.L. Miranda, J.M. Vega, M.I. Capilla, F. Correia, M.J. Salta, M. Bennani A. & González, J.A. 2007. Corrosion behaviour of new stainless steels reinforcing bars embedded in concrete. *Cement & concrete Research* 37: 1463.
- González, J.A. Ramírez, E. & Bautista, A. 1998. Protection of steel embedded in chloride-containing concrete by means of inhibitors, *Cement & Concrete Research*, 28: 577–589.
- Izquierdo, D. Alonso, C. Andrade, C. & Castellote C. 2004. Potentiostatic determination of chloride threshold values for rebar depassivation: Experimental and statistical study. *Electrochimica Acta*, 49: 2731.
- Kiesse, T.S. Bonnet, S. Amiri, O. & Ventura, A., 2020. Analysis of corrosion risk due to chloride diffusion for concrete structures in marine environment. *Marine Structures*, 73, 102804.
- Leng, F. Feng, N. Lu, X. 2000. An experimental study on the properties of resistance to diffusion of chloride ions of fly ash and blast furnace slag concrete. *Cement & Concrete Research*, 30: 989–92. [https://doi.org/10.1016/S0008-8846\(00\)00250-7](https://doi.org/10.1016/S0008-8846(00)00250-7).
- Luna, F.J., Fernandez, A. & Alonso, M.C. 2018. The influence of curing and aging on chloride transport of concrete with ternary cements. *Materiales de Construcción*, 68(332),eL71. <https://doi.org/10.3989/mc.2018.11917>.
- Maage, M, Helland, S. & Carlsen, J. 1995. Practical non-steady chloride transport as a part of a model for predicting the initiation period. In: Nilsson LO, Ollivier J, editors. *Chloride Penetration Into Concrete.*, 398–406.
- Model Code for Service Life Design, 2006. Bulletin 34, FIB, 116 pages, ISBN 978-2-88394-074-1.
- Moon, H.Y. Kim, H.S. & Choi, D.S. 2006. Relationship between average pore diameter and chloride diffusivity in various concretes. *Construction and Building Materials*, 20: 725–32. <https://doi.org/10.1016/j.conbuildmat.2005.02.005>
- Paiva, H. Velosa, A. Cachimb, P. & Ferreira V.M. 2016. Effect of pozzolans with different physical and chemical characteristics on concrete properties. *Materiales de Construcción*, 66: 1–12. <http://dx.doi.org/10.3989/mc.2016.01815>.
- Reddy, B. Glass, G.K. Lim, P.J. & Buenfeld, N.R. 2002 On the corrosion risk presented by chloride bound in concrete. *Cement & Concrete Composites*, 24,1–5.
- Silva, F.B. Boon, N. De Belie N. & Verstraete, W. 2015 Industrial application of biological self-healing concrete: challenges and economical feasibility. *J. Commercial Biotechnology*, 21(1): 31–37. <https://doi.org/10.5912/jcb662>.
- Song, H.W. & Saraswathy, V. 2006. Studies on the corrosion resistance of reinforced steel in concrete with ground granulated blast-furnace slag-An overview. *J Hazard Materials*, 138:226–33. <https://doi.org/10.1016/j.jhazmat.2006.07.022>.
- Song, H.W. Lee, C.H. & Ann, K.Y. 2008. Factors influencing chloride transport in concrete structures exposed to marine environments. *Cement & Concrete Composites* 30: 113–121.
- Tedim, J. Kuznetsova, A. Salak, A.N. Montemor, F. Snihirova, D. Pilz, M. Zheludkevich, M.L. & Ferreira, M.G.S. 2012. Zn–Al layered double hydroxides as chloride nanotraps in active protective coatings. *Corrosion Science*, 55:1–4.
- Tuuti, K. 1982. Corrosion of Steel in Concrete, *PhD*, Swedish Cement and Concrete Research Institute (CBI). 4–82, Stockholm.

Durability performance indicators for service life analysis and quality control

F. Moro

Hagerbach Test Gallery, Flums, Switzerland

R.J. Torrent

Materials Advanced Services, Buenos Aires, Argentina

ABSTRACT: Durability Performance Indicators (DPIs), measurable in relatively short time, are proposed to assess the durability performance of concretes under risk of chloride-induced corrosion. The suitability of these DPIs is validated against results of a comprehensive experimental investigation, conducted on 18 concrete mixes of two w/b ratios (0.40 and 0.65) and binder contents (280 and 380 kg/m³), made with nine different Portland clinker-based binders including two OPCs, Silica Fume, Fly-Ash, Blast-Furnace Slag and Limestone Filler. The mixes were evaluated for compressive strength and also by several DPIs: Coefficient of Chloride Migration (EN 12390-18), Rapid Chloride Permeability (ASTM C1202), Coefficient of air-permeability kT (Swiss Standard SIA 262/1 and Argentine IRAM 1892) and Electrical Resistivity (AASHTO T358 and UNE 83988-2). The validity of the proposed DPIs and their potential usefulness for Service Life design and quality control is discussed. The unsuitability of w/b ratio and compressive strength as durability indicators is confirmed.

1 INTRODUCTION

1.1 *Service life prediction in chloride-rich environments*

The prediction of service life (SL) of reinforced concrete structures exposed to a chloride-rich environment is a challenging endeavor. The main cause of deterioration is the degradation of the embedded steel due to the strong localized pitting corrosion of the metal by an electrochemical process, despite the passivating high pH environment of the concrete.

In the case of structures directly in contact with sea or salty water, the complexity of the chlorides accumulation into concrete involves several mechanisms governing the transport of matter through concrete (Hunkeler, 2000, Torrent et al, 2022). The complexity of the problem is aggravated by the fact that concrete transport properties, strongly associated to the pore structure and ionic composition of the pore solution of the material, evolve during the exposure time and are affected by chemical influences, like the chemical binding of chlorides.

In general, SL prediction models focus on the initiation/incubation phase, trying to predict the time at which the chloride concentration at the level of the steel reaches the critical level that will trigger the corrosion process.

Although there are more complex models, e.g. (Conciatori et al, 2008), the most spread ones (Duracrete, 2000; Life-365, 2019) introduce a simplification by considering that the penetration of chlorides follows a purely, non-steady diffusion process, based on the 2nd Fick's law of diffusion. The associated differential equation finds an explicit solution (Eq. 1) in the case of constant D (coefficient of chloride-diffusion through concrete) and constant C_s (concentration of chlorides at the concrete surface).

$$C(x, t) = C_0 + (C_s - C_0) \cdot \left[1 - \operatorname{erf}\left(\frac{x}{\sqrt{4 \cdot D \cdot t}}\right) \right] \quad (1)$$

where C is the concentration of chlorides at depth x and time t and C_0 is the initial concentration of chlorides (contributed by the concrete constituents).

Often, a mathematical manipulation is introduced to account for the strong decay of D with time, of the form:

$$D(t) = D_0 \left(\frac{t_0}{t} \right)^n \text{ for } t \leq t_d \quad (2)$$

where $D(t)$ is the coefficient of chloride diffusion averaged over a period of time t and D_0 is the coefficient of chloride diffusion measured at time t_0 (typically 28 days). Exponent n is a material property, called aging factor, which is a critical parameter in SL prediction (Gulikers, 2006; Torrent, 2018).

As a consequence, Eq. 1 becomes:

$$C(x, t) = C_0 + (C_s - C_0) \cdot \left\{ 1 - \operatorname{erf} \left[\frac{x}{\sqrt{4 \cdot D_0 \cdot (t_0/t)^n \cdot t}} \right] \right\} \quad (3)$$

The corrosion initiation time t_i is reached when:

$$C(d, t_i) = C_{cr} \quad (4)$$

where d is the cover thickness of the steel and C_{cr} is the (also elusive) critical concentration of chlorides capable of initiating the corrosion process.

1.2 Codes' classical approach to deal with chloride-induced corrosion

Reference is made to the two most influential codes worldwide: ACI 318 and European Standards EN 206 and EN 1992-1-1 (Eurocode 2), where the resistance to chloride-induced corrosion is based on specifying a minimum cover thickness d_{min} and a minimum concrete quality in terms of a maximum water/cement ratio w/c_{max} and a minimum concrete strength $f'c_{min}$.

Table 1 presents a comparison of the requirements specified by ACI for concrete structures exposed to chlorides (C2 exposure class) and those of EN for concretes under the most insidious chloride exposure classes XD3 (parts of bridges exposed to spray containing chlorides) and XS3 (parts of marine structures in the tidal, splash and spray zones). The cover thickness from EN 1992-1-1 corresponds to 50 years SL; for 100 years SL, the value has to be increased by 10 mm, which is not correct (Torrent, 2018).

Table 1. Codes' requirements for non-prestressed, cast on site concrete structures.

Requirement	Code/Exposure Class	
	ACI 318/C2	EN/XD3 & XS3
w/c_{max} (-)	0.40	0.45
$f'c_{max}$ (MPa) at 28 d. (cylinder)	35	35
d_{min} (mm)	54 or 40 (walls & slabs)	45
Expected SL (years)	not defined	50

The way SCM, added to the concrete mix, are considered as "cement" is different for both codes

There are two problems associated with w/c ratio as quality indicator: firstly, that for the same w/c ratio, the performance of the concrete depends on the quality of the constituents, chiefly the cement characteristics. Secondly, that so far it is not possible to accurately control the w/c ratio during production nor to measure it reliably on delivery for compliance purposes (Torrent, 2018). Therefore, specifying a characteristic that cannot be controlled is futile and may lead to unfair competition and fraudulent practices.

ACI 318 Section R19.3.2 explains that compressive strength is introduced as an indirect (surrogate) test to cope with the impossibility of accurately checking the w/c ratio by standard tests.

2 DURABILITY PERFORMANCE INDICATORS

The following definition of Durability Performance Indicator (DPI) has been proposed by one of the Authors (Torrent, 2022): *Characteristic of the concrete structure (e.g. cover thickness) or materials' property that is essential to or bear a significant role in the service life of a structure under its specific exposure conditions. A Durability Indicator should:*

- *be meaningful, i.e., as closely connected as possible to the relevant physical, chemical and/or electrochemical deterioration mechanisms that govern the performance of the structure*
- *be measurable, preferably in a reasonably short time (say one week), through well-defined, standardized methods of test or analysis*
- *allow conformity assessment with specified requirements based on tests conducted at suitable, well defined, sampling points (production plant, delivery point, placement point, in situ, in service)*
- *preferably be directly or indirectly (e.g., via robust correlations) included as parameters of existing performance prediction models*

2.1 Coefficient of chloride-diffusion as DPI

In the case of chloride-induced corrosion, as discussed in 1.1, the most relevant DPI of a given concrete would be its coefficient of chloride diffusion D_0 . There are standard test methods to measure it (ASTM C 1556 and EN 12390-11, both quite similar) which consist in immersing a concrete sample with an unsealed face in contact with a high NaCl concentration solution for a time that ranges between 35 and 91 days and in measuring the resulting chloride profile by analytical methods. The best fit of Eq. 1 to the obtained chlorides' profile $C(x)$ yields the value of D_0 . The problem is that the test is costly and time-consuming, therefore inadequate as practical DPI.

2.2 Chloride-migration as DPI

To overcome those limitations, good use has been made of Nernst-Planck Equation (Eq. 5), that describes the flow of ions in a fluid where an electric field is superimposed.

$$-J = D \left(\frac{\partial C}{\partial x} + C \frac{z.F}{R.T} \frac{\partial E}{\partial x} \right) \quad (5)$$

where:

J = flux of ions or molecules ($\text{g}/\text{m}^2/\text{s}$). The minus indicates that the flux is opposite to the gradients

z = electric charge of the ion (-)

C = ion concentration in the fluid (g/m^3)

F = Faraday constant = $96,485 \text{ J.V}^{-1}.\text{mol}^{-1}$

R = universal gas constant = $8.3144598 \text{ J.mol}^{-1}.\text{K}^{-1}$

T = absolute temperature (K)

$\partial C/\partial x$ = gradient of ion concentration (g/m^4)

$\partial E/\partial x$ = gradient of electric potential across the element (V/m)

The first term within the parenthesis in Eq. 5 corresponds to the component of the flow of ions driven by the concentration gradient (diffusion) and the second term by the electric potential gradient. This second component is known as migration. Notice that, according to Eq. 5, both diffusion and migration are, in theory, governed by the same property of concrete D . This opens the possibility of measuring D_0 much faster, by applying a convenient electrical field.

Two test methods have been standardized, based on forcing the penetration of chlorides into a concrete sample by applying an electrical field. Both consists in placing a fully saturated concrete disc in contact with two different solutions, one of them containing NaCl and forcing the penetration of Cl^- ions by applying an electrical field – during a certain period - through electrodes immersed in the solutions. The outcome of the ASTM C1202 test is directly the amount of electrical charge Q (Coulombs) passed after 6 hours under 60 V. In the EN 12390-18 test, after subjecting it during up to 168 h to 10-30 V, the specimen is removed, split and the penetration

depth of chlorides is measured colorimetrically on the split surface. This allows to yield, as test result, the coefficient of migration M , expressed in m^2/s , same units as for D_0 .

Relations have been established for both Q (Olek et al, 2002) and M (Li, 2016; Ren et al, 2021) with D_0 , of the form:

$$D_0(Q) = 0.4 + 0.002 \cdot Q \quad \text{with } D_0(Q) \text{ in } 10^{-12} m^2/s \text{ and } Q \text{ in Coulomb} \quad (6)$$

$$D_0(M) = M/2 \quad (7)$$

Migration tests are much faster than Diffusion tests but the duration is still considerable and the number of samples that can be tested simultaneously is limited by the amount of cells available.

2.3 Surface electrical resistivity as DPI

This test method consists in placing, on the tested concrete surface, a linear arrangement of four electrodes, the tips of which are moistened to ensure electrical contact. A current of intensity I is applied between the two external electrodes and the resulting potential U , established between the two internal electrodes, is measured. The surface electrical resistivity ρ is calculated as:

$$\rho = 2 \cdot \pi \cdot a \cdot G \cdot \frac{U}{I} \quad (8)$$

where

ρ = surface electrical resistivity ($\Omega \cdot m$)

I = intensity of applied current (A)

U = measured potential (V)

a = separation of the electrodes (m)

G = geometric factor (-); $G=1$ for application on a semi-infinite surface; (see Table 3)

The method has been standardized in the USA (AASHTO T358) and in Spain (UNE 83988-2) for use in the laboratory. The electrodes are applied on the surface of a fully saturated concrete specimen, yielding a result in a couple of minutes.

Its potential for site application is limited by the sensitivity of ρ to: degree of saturation, temperature, vicinity of steel bars, etc. To the authors' knowledge, there is no standard for site application of this test.

A relation between D_0 and the saturated surface electrical resistivity ρ has been proposed in (Torres-Acosta et al, 2019), of the form:

$$D_0(\rho) = 400/\rho^{0.908} \quad \text{with } D_0(\rho) \text{ in } 10^{-12} m^2/s \text{ and } \rho \text{ in } \Omega \cdot m \quad (9)$$

2.4 Coefficient of air-permeability as DPI

This test method measures, non-destructively, the coefficient of air-permeability kT of concrete by the double-chamber vacuum cell technique, and is standardized in Switzerland (SIA 262/1) and Japan (NDIS 3436-2) for site testing and in Argentina (IRAM 1892) for both lab and site testing. A relation has been established between D_0 and kT of the form (Torrent et al, 2022):

$$D_0(kT) = 10 \cdot \sqrt[3]{kT} \quad \text{with } D_0(kT) \text{ in } 10^{-12} m^2/s \text{ and } kT \text{ in } 10^{-16} m^2 \quad (10)$$

The vacuum cell is applied on the plane surfaces of 150 mm cubes or cylinders, or directly on structural elements *in situ*, which have to be relatively dry, yielding a result in up to 6 minutes.

3 EXPERIMENTAL VALIDATION OF DPIS

The validity of the proposed DPIS, briefly described in 2.1 to 2.4 was investigated on a series of concrete mixes, as described below. The Coefficient of Diffusion $D_0(M)$, obtained from the coefficient of migration M (Eq. 7) is taken as reference, given the closer relation between D and M , expressed by Eq. 5, also supported by experimental evidence (Vivas et al, 2007).

3.1 Concrete mixes

A total of 18 concrete mixes, nine with water/binder ratio $w/b=0.40$ and 380 kg/m^3 of binder and nine with $w/b=0.65$ and 280 kg/m^3 of binder, were prepared (Moro & Torrent, 2016).

3.2 Binder types

Each pair of mixes ($w/b = 0.40$ and 0.65) was prepared with a different industrial binder, covering a wide range of compositions, as described in Table 2.

Table 2. Binders used in the concrete mixes.

Code	Composition
OPCA	OPC (Clinker A)
MS8	92% OPCA + 8% Silica Fume
S22	Portland-slag Cement (22% GBFS, Clinker A)
S43	Portland-slag Cement (43% GBFS, Clinker A)
S69	Portland-slag Cement (69% GBFS, Clinker A)
OPCB	OPC (Clinker B)
L22	Portland-limestone cement (22% L. Filler, Clinker B)
FA25	Portland-fly ash cement (25% Fly Ash, Clinker B)
FA33	Portland-fly ash cement (33% Fly Ash, Clinker B)

3.3 Properties measured and test procedures

Table 3 presents a summary of the relevant properties measured on the 18 concrete mixes, the test methods applied and the specimen type and preconditioning employed. All specimens were cured under water (20°C) for 28 days prior to testing.

Table 3. Properties measured and test procedures.

Property	Test Method	Specimens and Preconditioning
Chloride Migration Q	ASTM C1202	$\text{Ø}100 \times 50$ mm discs, drilled and saw-cut from
Chloride Migration M	SIA 262/1-B (EN 12390-18)	150 mm cubes, water saturated
Surface Electrical Resistivity ρ	AASHTO T358; UNE83988-2	120x120x360mm saturated prism; electrodes spacing = 38 mm; $G = 0.8$ (Haldor Topsøe, 1968)
Air-Permeability kT	SIA 262/1-E – IRAM 1892	$\text{Ø}150 \times 50$ mm discs cut off cast $\text{Ø} 150 \times 300$ cylinders. Prior to testing, 6 d. oven-drying at 50°C .
Compressive strength f_c	EN 12390-3	150 mm cubes*

* Converted into 150×300 mm cylinder strength as described in (Moro & Torrent, 2016)

3.4 Test results

Table 4 summarizes the results obtained for the 18 mixes tested. Regarding the DPIs, instead of the test results, already the estimates of D_0 obtained from them (Eqs. 6, 7, 9 and 10) are reported.

Taking as reference the estimate $D_0(M)$, the standard error ξ_e of the other estimates is reported in the last row of Table 4.

3.5 Analysis of the results

Figure 1 shows the results of $D_0(M)$ for the 9 binders investigated, differentiating the concretes with w/b ratios of 0.40 and 0.65. As reference, the classification after [Tang, 1996] is shown: P (Poor), N (Normal), G (Good) and VG (Very Good).

Figure 1 shows that, for the same low $w/b = 0.40$, a large variety of performances are achieved with the different binders. Very Good chloride-resistance is achieved for binders containing 8% silica fume and 69% of GBFS. The two OPCs show a Good chloride-resistance, same as the

cements with 22 and 43% GBFS and 25% and 33% of fly ash, whilst the limestone-filler cement achieves just a Normal chloride-resistance. It can be seen also that a Good chloride-resistance can be achieved, at $w/b = 0.65$, with the binders containing 8% Silica Fume and 43 and 69% of GBFS.

Table 4. Compressive strength and estimated values of D_0 (Eqs. 6, 7, 9, 10).

Concrete mix		D_0 (10^{-12} m ² /s) estimated from				Mean strength*
w/b	Binder	Q	M	ρ	kT	f_{cm} (MPa)
0.40	OPCA	4.3	2.1	5.3	3.1	57.4
	MS8	1.2	0.6	1.3	1.3	66.5
	S22	2.8	1.5	3.9	2.7	65.2
	S43	2.5	0.5	2.6	2	51.5
	S69	1.2	0.2	1.3	1.4	48.5
	OPCB	6.2	3.6	6.9	2.9	65.1
	L22	6.4	5.4	7.7	4.9	32.7
	FA25	3.6	3.2	5.1	2.4	45.7
	FA33	1.9	2	2.8	2.2	49.4
0.65	OPCA	10.5	7.0	10.1	7.9	24.5
	MS8	2.9	2.0	3.2	2.6	30.2
	S22	6.9	4.7	8.5	4.9	25.5
	S43	3.4	2.0	4.1	3.5	23.3
	S69	1.7	0.3	1.7	3.4	19.7
	OPCB	11.2	9.3	12.5	9.2	31.8
	L22	14.4	14.1	12.4	8.5	15.2
	FA25	9.1	11.1	8.5	6.0	15.8
	FA33	3.5	5.9	4.6	3.6	17.0
\bar{s}_e (10^{-12} m ² /s)		1.8	—	2.3	2.2	*cylinder

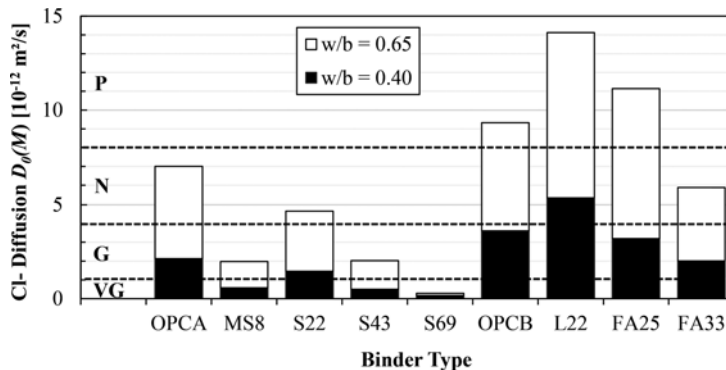


Figure 1. Effect of binder type and w/b ratio on $D_0(M)$.

The results of Figure 1 confirm the unsuitability of the w/c or w/b ratio to specify resistance of concrete to chlorides, since the performance depends strongly on the binder type used. On one extreme, a concrete with $w/b = 0.40$ may not display enough chloride resistance for certain applications, whilst on the other, the required performance could be achieved with higher w/b ratios (and less binder content), with the consequent extra cost and reduced sustainability.

Figure 2 shows the results of $D_0(M)$ for the 18 mixes investigated, plotted as function of the mean cylinder compressive strength, measured at 28 days, with the same classification as for Figure 1.

It can be seen that all the mixes complying with the minimum requirement of 35 MPa (Table 1) of specified strength (say, 40 MPa of mean strength) present $D_0(M)$ values within the Good and Very Good chloride-resistant classes. Therefore, from the durability point of view, these limits look adequate. There are three mixes having strengths below the minimum requirements that, yet, show a Good performance, corresponding to the mixes ($w/b = 0.65$) made with 8% Silica Fume and 43

and 69% of GBFS. These three performing mixes, with just 280 kg/m³ of binder, are more sustainable and, yet, would be rejected due to lack of compliance with the specified $f'_{c_{min}}$.

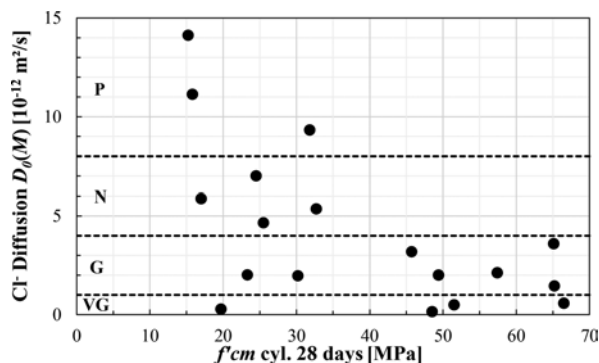


Figure 2. Relation between $D_0(M)$ and mean compressive strength f'_{cm} of the 18 mixes tested.

Figure 3 compares the estimates of D_0 , obtained from the measured values of Q , ρ and kT , applying Eqs. 6, 9 and 10, respectively, with the adopted reference values of $D_0(M)$, obtained from the measured values of M , through Eq. 7.

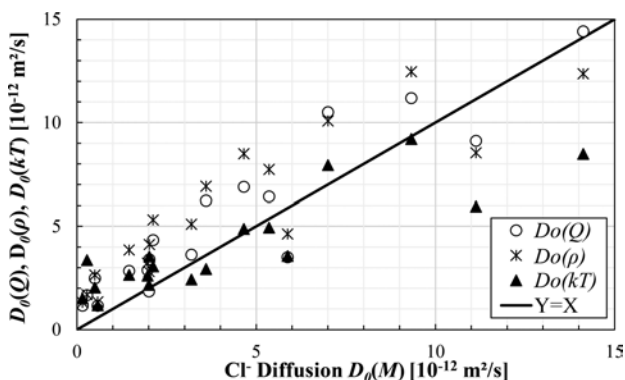


Figure 3. Relation between $D_0(M)$ and D_0 values estimated from Q , ρ and kT test results of 18 mixes.

Figure 3 shows a visible trend that higher values of D_0 , estimated from the measured values of Q , ρ and kT , generally correspond to higher values of $D_0(M)$. This suggests that all the DPIs are, in principle, suitable to detect concretes of higher or lower chloride diffusivities.

In what concerns accuracy, quite accurate estimates of $D_0(M)$ are obtained, with a tendency to overestimate it, especially for low values, i.e., on the safe side. This is visible in Figure 3, but also from the low standard error of estimates \hat{s}_e shown in Table 4.

4 CONCLUSIONS

The investigation reported in this paper produced results that yield the following conclusions:

- The unsuitability of the w/c or w/b ratio as mix parameter to judge the resistance to chlorides of a concrete mix has been confirmed, because its true performance is strongly affected by the binder used. In addition, no standard method exists to measure it accurately. It should be substituted or complemented in Codes by suitable DPIs
- The minimum compressive strength specified in ACI and EN Codes seems adequate to ensure that chloride-resistant concretes are used. Yet, mixes not complying with the $f'_{c_{min}} = 35$ MPa may still be suitable, the rejection of which affects cost and sustainability of concrete structures

- w/c or w/b and $f^c_{c_{min}}$ cannot be associated with SL models and, therefore, the requirements cannot be tuned to SLs beyond the one expected by the Codes (typically 50 years)
- The evaluated DPIs, namely Chloride Migration (M and Q), Electrical Resistivity (ρ) and Air-Permeability (kT), show a good potential to assess the chloride-resistance of concrete mixes
- The more direct estimate of the Coefficient of Chloride-Diffusion D_0 is provided by the EN 12390-18 test for Coefficient of Chloride Migration (M)
- The problem with that test is its duration and the need to use special cells to conduct it, features shared with the ASTM C1202 “RCPT” (Q), which limits the testing capacity of a laboratory
- Both the Electrical Resistivity (ρ) and Air-Permeability (kT) tests present the advantage of being non-destructive, applied directly on specimens and lasting few minutes
- For lab applications, Electrical Resistivity (ρ) has the advantage of being measured on the same saturated specimens used for strength, whilst Air-Permeability (kT) requires a pre-drying
- Air-Permeability (kT) can be measured by standard procedures directly on site, thus providing a more realistic picture of the true quality of the end-product than cast specimens
- All DPIs provide an estimate of the Coefficient of Chloride-Diffusion D_0 , which is a key input for Service Life analysis. The accuracy of the estimates, based on M , Q , ρ and kT test results is quite consistent. Taken into consideration the strong effect of exponent n (Equations 2 and 3) on the SL prediction, the accuracy of the estimates of D_0 seems adequate
- The requirements of concrete mixes in terms of D_0 can be fine-tuned to the expected service life t_s , cover thickness d and aggressivity of the exposure C_s (Equation 3). This D_0 limiting values can be converted into limiting values of M , Q , ρ and kT through Equations 6, 7, 9 and 10, properties on which the routine quality control can be exercised

REFERENCES

- Conciatori, D., Sadouki, H. & Brühwiler, E. (2008). “Capillary Suction and Diffusion Model for Chloride Ingress into Concrete”. *Cem. & Concr. Res.*, 38 (12): 1401–1408.
- Duracrete (2000). Probabilistic Performance based Durability Design of Concrete Structures. *The European Union–Brite EuRam III*, BE95-1347/R17, CUR, Gouda, The Netherlands.
- Gulikers, J. (2006). Considerations on the reliability of service life predictions using a probabilistic approach. *J. Phys. IV France*, 136: 233–241.
- Haldor Topsøe (1968). Geometric factors in four point electrical resistivity measurement. *Semiconductor Div.*, Vedbæk, Denmark, 2nd Ed., 64p.
- Hunkeler, F. (2000). Corrosion in reinforced concrete: processes and mechanisms. In *Corrosion in reinforced concrete structures*, H. Böhni (ed.), CRC Press, Cambridge, UK, pp. 1–45.
- Li Kefei (2016). *Durability Design of Concrete Structures*. 1st Ed., John Wiley & Sons, Singapore, 280 p.
- Life-365 (2019). Service Life Prediction Model and Computer Program for Predicting the Service Life and Life-Cycle Cost of Reinforced Concrete Exposed to Chlorides. *Life 365 Consortium II*, 80 p.
- Moro, F. & Torrent, R. (2016). Testing *fib* prediction of durability-related properties. *fib Symposium 2016*, Cape Town, South Africa, 21-23 Nov.
- Olek, J., Lu, A., Feng, X. & Magee, B. (2002). Performance-related specifications for concrete bridge superstructures, vol. 2: High-performance concrete. *Purdue Univ. – Joint Transportation Research Program Technical Report Series*, 215 p.
- Ren, F., Li, L., Wang, W. & Zhou, C. (2021). Transport properties of surface layers from full-scale reinforced concrete member. *Struct. Concr.*, v22 (Suppl.1): E1062–E1073.
- Tang, L. (1996). Chloride Transport in Concrete - Measurement and Prediction. *PhD thesis*, Chalmers Univ. of Technology, Sweden, October, 104 p.
- Torres-Acosta, A.A., Presuel-Moreno, F. & Andrade, C. (2019). Electrical Resistivity as Durability Index for Concrete Structures. *ACI Mater. J.*, 116(6), 245–253.
- Torrent R.J. (2018). Bridge durability design after EN standards: present and future. *Structure and Infrastructure Engineering*, DOI: 10.1080/15732479.2017.1414859, 13 p.
- Torrent, R. (2022). Durability Indicators: Definition, Requirements and Swiss Standards’ Example. *fib Workshop : Definition of Durability Indicators*, 25 October
- Torrent, R., Neves, R. & Imamoto, K. (2022). *Concrete Permeability and Durability Performance – From Theory to Field Applications*. CRC Press, Boca Raton, FL, USA and Abingdon, Oxon, UK, 570 p.
- Vivas, E., Boyd, A. & Hamilton III, H.R. (2007). Permeability of Concrete – Comparison of Conductivity And Diffusion Methods. *Univ. of Florida, Final Report*, 238 p.

*SS31: Structural health monitoring and
asset management of infrastructures
Organizers: S. AlSanad & J. Parol*



Taylor & Francis

Taylor & Francis Group

<http://taylorandfrancis.com>

Measuring heavy traffic using alternative systems in an urban environment

M.L. Soudijn & S. van Rossum

Engineering office - City of Amsterdam, Amsterdam, The Netherlands

A. de Boer

Engineering office - City of Amsterdam, Amsterdam, The Netherlands

Ane de Boer Consultancy, Arnhem, The Netherlands

ABSTRACT: By recombining available traffic load data with local traffic measurements we aim to determine a more accurate traffic load model. The model we obtain should help verify more precisely which bridges and quay walls can still withstand current traffic loading and which need strengthening or replacing. The current assessment on structural safety of existing structures uses the national standards for traffic loads based on WIM-ROAD highway traffic measurements. WIM-ROAD is sub-optimal for urban environments because bumpy roads and traffic behaviour, e.g. proximity to traffic lights, can negatively impact measurement accuracy. Therefore, we investigate alternatives to get accurate and reliable measurements. We discuss combinations of sound-radar, advanced counting traffic hoses, ANPR cameras coupled to national vehicle databases and our own WIM-ROAD measurements within a semi-urban environment. We show the accuracy and reliability of these different measurement systems and the potential in coupling their measurements.

1 INTRODUCTION

The city of Amsterdam faces a large infrastructural challenge. About 830 historic bridges and 200 km of quay walls, loaded by motorized traffic, were built two or even three centuries ago on wooden pile foundations. An estimate is that a substantial number of these structures is in a poor state of repair due to a combination of (too much) heavy traffic and overdue maintenance. The challenge Amsterdam faces is huge because simply replacing or strengthening all the structures in need of maintenance at once is not an option. Apart from the enormous cost and time needed, the city would become uninhabitable by such an enterprise. Additionally, the exact numbers of which structures need replacing or strengthening are unknown, which is why investigations are underway to determine their current state: the (material) strength of the structures, the allowable traffic load and the actual current traffic loads. Here not only the traditional models are used but these are supplemented with experimental research. Overall it is essential to find a way that can help the city of Amsterdam improve planning this enormous challenge.

Simply checking current structures according to the current - relatively conservative - standards is insufficient, as it is expected that many structures will be rejected, possibly on unjust grounds. Particularly, with the introduction of the Dutch National Annex to the Eurocode (Steenbergen et al. 2012, NEN-EN 2019) in 2012 the traffic load models gave rise to a large increase compared to the Dutch traffic load models that were previously in use, especially for urban environments, such as Amsterdam. Taking into account these increased traffic loads combined with the situation in Amsterdam would undoubtedly lead to a mass rejection of bridges. However, the National Annex also leaves room for using the actual traffic loads to determine a local traffic load model. This requires accurate and reliable measurements of the local traffic loads. In this paper the traffic load measurements are described that were performed for the City of Amsterdam with the goal of

setting up a local traffic load model. Even though high accuracy Weigh-in-Motion (WIM) measurements were performed in a semi-urban environment, including Automatic Number (or License) Plate Recognition (ANPR) cameras and a sound-radar system (Soudijn et al. 2021, Soudijn et al. 2022), additional measurements are required to relate these WIM measurements to the inner city areas for which the aim is to set up our load model(s).

Using WIM systems in the inner city area is not preferable because bumpy roads and proximity to crossings lead to decreased measurement accuracy, due to erratic vehicle behaviour, rendering such measurements useless. The question remains however, how one can achieve accurate load measurements in an inner city environment. The approach to this challenge is trying to map the expected weights throughout the inner city of Amsterdam. The aim is to use a “resampling” method which uses both the urban WIM measurements as well as alternative measurement methods such as advanced counting pneumatic tubes, sound-radar detectors and ANPR cameras, whichever provides the most useful and accurate information. Both sound-radar (Ch. 2.2) as well as ANPR cameras (Ch. 2.3) were used at our WIM location (Ch. 2), and alternatively the advanced pneumatic tubes can detect similar vehicle classes as WIM. The goal is to investigate the method that will work best to relate the types of vehicles to particular WIM traffic load measurements and thus build up a traffic load spectrum through the “resampling” method. Furthermore, the municipality of Amsterdam decided in 2020 to enhance existing vehicle limitations to inner city areas. The precise limits are 10 m for the vehicle length and 75 kN for the vehicle mass. Permanent permits can be given to transport vehicles up to 300 kN or a longer vehicle length. These constraints give an alternative or additional way to correlate our measurements.

2 MEASUREMENT METHODS FOR HEAVY TRAFFIC

Various measurement systems were used at the WIM location in the western harbour district of Amsterdam at the location “Westpoortweg”. Both a WIM-ROAD and WIM-BRIDGE system were installed (based on COST 323 2002 & OIML 2006) at the pilot location in the western harbour district of Amsterdam as shown in Figure 1a. The WIM-ROAD system, which is the main system used in this paper (Ch. 2.1), consists of 8 lineas-quartz sensors (Kistler) per lane, as shown in Figure 1b, to achieve a high measurement accuracy. The WIM-BRIDGE measurements are still under evaluation, however, a sound-radar system was part of this setup from which measurements are used in this paper (Ch. 2.2). As part of the setup (Figure 1a) 4 ANPR cameras and 2 line-scan cameras were installed. The ANPR cameras were placed to detect both front and back license plates in order to include details of semi-trolley trucks from the Dutch Vehicle Authority (RDW) database. The line-scan cameras were used to detect lifted axle’s and special vehicles as shown in Figure 1c. A more detailed description of the WIM setup used in this research and its preliminary results are described in more detail in Soudijn, van Rossum & de Boer (2021 & 2022).

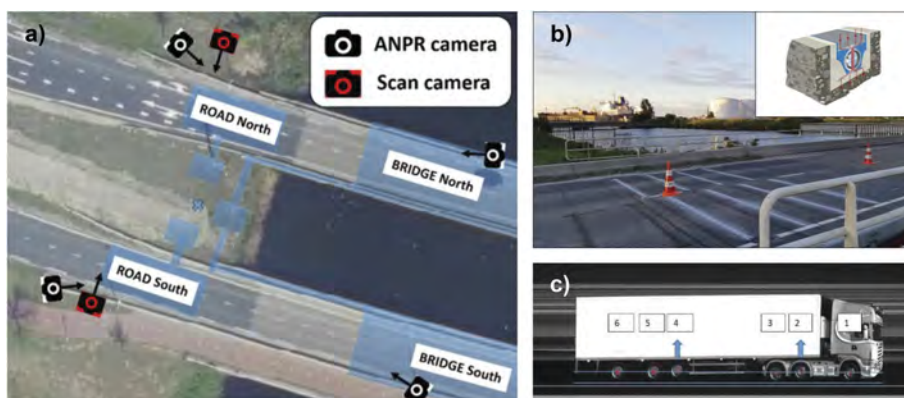


Figure 1. a) Location Westpoortweg: WIM systems and camera setup as indicated. b) WIM-ROAD North system: 8 Lineas-quartz sensors (inset) per lane. Induction loop detectors detect each vehicle. c) A vehicle ‘side-scan’ image where two lifted axles are visible.

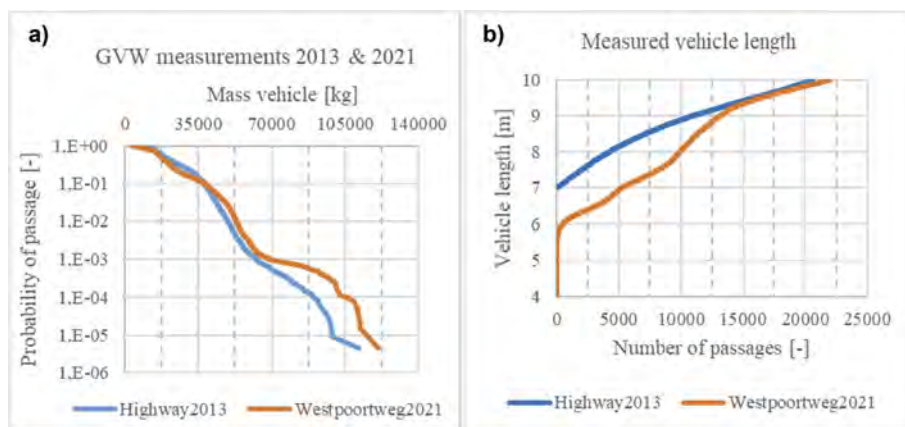


Figure 2. a) Heavy traffic measurements: GVW > 3.5 kN. b) Vehicle length versus occurrence numbers. For both figures a comparison is made between the 2013 highway and 2021 Westpoortweg measurements.

2.1 Relevant measurement results from the WIM-ROAD system at Westpoortweg

An overview of the heavy traffic vehicle passages from our own Westpoortweg WIM-ROAD system (one month, 95,000 passages) and of the relevant Dutch highway system in 2013 (Eurocode evaluation, one month, 220,000 passages) (Steenbergen et al, 2018) are shown in Figure 2a.

Figure 2a shows the Gross Vehicle Weight (GVW) occurrence with some more passages in the lower GVW region at the Westpoortweg than in the highway measurements. But at the Westpoortweg there are more heavier passages above the 60,000 kg vehicle mass than on the highway. The Westpoortweg lies within an industrial area of Amsterdam and forms a regional connection between the city and west side of the province, so both observations are realistic.

The highway 2013 measurements show only vehicles with a minimum length of 7 m, however this lower limit is too high when considering inner city areas. The Westpoortweg measurements show a minimum vehicle length of around 4 m. This is a more realistic lower limit in case of the inner city heavy traffic, where the narrow streets and tight corners constrain vehicle lengths. Figure 2b shows the relation between the length of the vehicles versus the occurrence numbers.

During the measurement period at the Westpoortweg the City of Amsterdam introduced enhanced restrictions on the maximum vehicle length and GVW for the inner-city area. The maximum length is now 10 m and the existing maximum GVW of 75 kN is enforced more seriously through camera surveillance. Permanent permits are given to vehicles with a GVW vehicle up to 300 kN with inner-city destinations. Single day permits with a prescribed route are given to transport firms who carry unmovable loads that go above a GVW of 300 kN or require a vehicle length of more than 10 m.

These limits and the registration of these permits can provide insight on the expected traffic loads in the inner city of Amsterdam. Figure 3a shows what a 10 m cap on length would mean for the amount of vehicles to consider for the inner city. As a first order approximation a GVW up to 300 kN can be assumed, however, an overload of 30% should be included as a safety margin. As an initial indication, Figure 3b shows the effect on the probability of passages derived from 5 months of Westpoortweg data using these GVW and length constraints. Comparing the overall measurements and the derived restriction measurements both curves show a very continuous probability of passages. An almost log linear function is seen from a mass of 3500 kg up to 45,000 kg for the 10 m length restriction and up to 35,000 kg for both restrictions.

In addition to the GVW measurements it is important to evaluate the single axle loads and the tandem/tridem axle configuration loads as well, especially for the more localized loads and when considering short span bridge structures. Figure 4a shows the probability of single axle load passages based on the 5 months of vehicle data including the inner-city restrictions as mentioned.

Near the probability of 10^{-5} in Figure 4a, a difference in axle weight of 25 kN is shown. Both curves show high maximum values regarding the legal axle load limit of 115 kN. Still

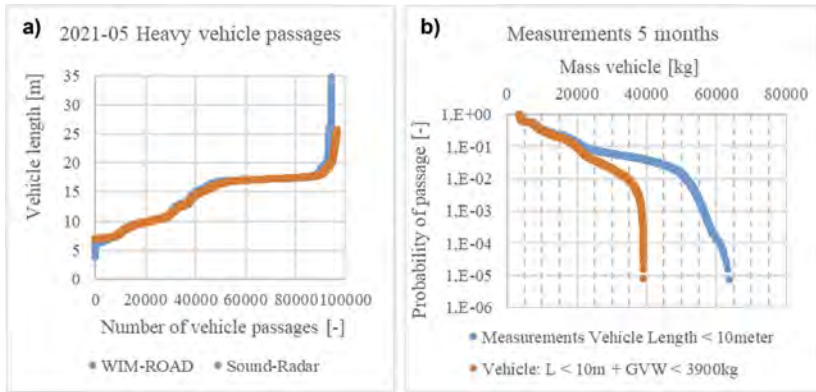


Figure 3. a) Vehicle length as function of heavy vehicle passages, results from WIM-ROAD and sound-radar system compared. b) GVW measurements with inner city restrictions to the vehicle length and GVW.

there is no asymptotic limit in the measurements and thus extrapolation to a maximum axle load limit is not possible from only 5 months of data. A whole year (2021) of measurements are available, but not properly checked yet for erroneous measurements at this time. The maximum measured axle load, however, is 230 kN, which is far below the 300 kN given by the Load Model 1 Eurocode or the 400 kN of Load Model 2 Eurocode. This is not a guarantee, but a good indication that a lower load limit can be found.

Finally, in Figure 4b we show the WIM-ROAD measurements in terms of the probability of passages of the tandem and tridem axle configurations. Only 4 quad axle configurations were measured in total, which is insufficient for a figure. These quads belong to vehicles with 6 or more axles and the restricted measurement set has a negligible number of 3 vehicles with 6 axles.

Both curves in Figure 4b show an asymptotic behaviour which means that an estimate tandem or tridem load limit can be made based on this data. Including the extra uncertainty factor of 10^{-4} in the Eurocode, the tandem axle load limit comes down to an estimate of 330 kN at a probability level of 10^{-8} . The tridem axle load limit could, by extrapolation, go to 375 kN at a probability level of 10^{-7} . This estimate for the tandem load limit is far below the standard Eurocode limit of 600 kN for the tandem axle configuration and also far below the Dutch reduced limit for regional areas, which is 480 kN. Thus far, the conclusion that can be drawn

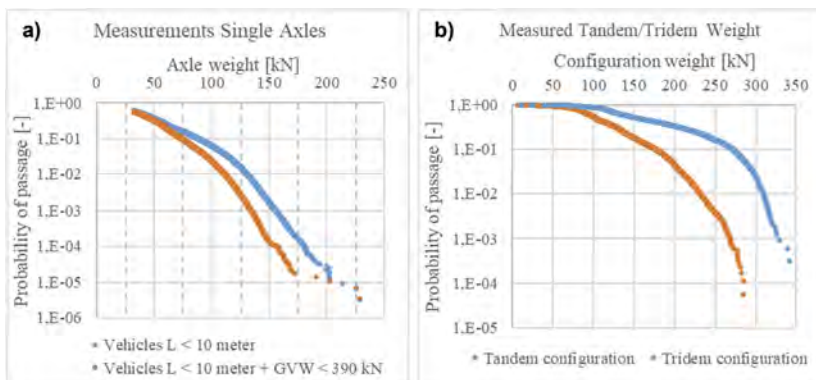


Figure 4. a) Probability of single axle load vehicles including the inner city restrictions. b) Probability of passages of tandem and tridem axle configurations for the inner city.

from our WIM measurement data for vehicles and axles is that the inner city load model, given the restrictions on vehicle length of 10 meter and GVW of 390 kN, could potentially be reduced substantially compared to the current Eurocode.

2.2 Sound-radar measurements

At the Westpoortweg pilot location, as part of the WIM-BRIDGE setup, a sound-radar system was installed to detect vehicle passages. The output of this sound-radar system is: a timestamp per vehicle, vehicle length, vehicle category, speed, number of axles, noise of the vehicle, lane number and the distance between the system and the passing vehicle. In Figure 3a we compare the number of heavy vehicles passages between the WIM-ROAD and the sound-radar systems.

There are some differences in the lower and higher region of the vehicle lengths, but compared to the expected inner city traffic flow, there is only a difference in the lower region of the vehicle length. For most passages up to the 10 m vehicle length restriction for the inner city a sufficient agreement is found when comparing the sound-radar with the WIM-ROAD data.

2.3 Camera measurements

The ANPR camera measurements of the front and backside of the vehicles make it possible to match the license plates of the vehicles with the Vehicle database of the Dutch Vehicle Authority (RDW). That means that additional information about the vehicle parameters can be included in the measurements. First these parameters can be used to check if the measured data of the passing vehicle is correct, which allows to ‘clean’ the WIM measurements. The possible overload of the passing vehicles can also be derived and estimates for the expected overload in the inner city can be made. The scan camera shows a photo of the side of the passing vehicle. With this photo it can be checked if a vehicle has one or more of its axles lifted (as shown in Figure 1c). This aspect is also a part of the information of the Dutch Vehicle database, so an additional check can be made. At this moment, work is still in progress on accurate automatic coupling of the camera data to the WIM measurement data (Ch. 3.2).

2.4 Vehicle distributions

The above measurement systems all have a means of detecting the number of axles for each vehicle. In Table 1 the different distributions from each of the systems are shown, by count and by percentage, for the Westpoortweg measurements during the same month (May 2021).

The camera system which, in this case, uses only the front license plate, detects relatively more 3-axle vehicles than the other systems. While the other systems detect more vehicles with > 3 axles. This is done to get an idea of what the camera system in the inner city – which has only front view cameras – would detect (Ch. 4.2). The reason can probably be found in a large quantity of 3-axle vehicles being part of a truck-trailer combination at the location, where the trailer is only detected by the back-camera (which is not coupled for this particular comparison).

Table 1. Vehicle distribution by axle for vehicles ≤ 10 m and > 10 m respectively.

Vehicle type	Vehicle length ≤ 10 m						Vehicle length > 10 m					
	Radar		WIM-ROAD		Camera		Radar		WIM-ROAD		Camera	
	[#]	[%]	[#]	[%]	[#]	[%]	[#]	[%]	[#]	[%]	[#]	[%]
2-axles	372522	80.4	467911	84.8	405560	94.2	13270	2.9	8342	1.5	4423	1.0
3-axles	4310	0.9	4093	0.7	12336	2.9	6009	1.3	5398	1.0	2171	0.5
4-axles	2914	0.6	4180	0.8	3123	0.7	25318	5.5	25905	4.7	425	0.1
5-axles	1447	0.3	1455	0.3	1785	0.4	30746	6.6	29654	5.4	792	0.2
6-axles	610	0.1	113	0.0	NA	0.0	4312	0.9	3723	0.7	3	0.0
> 6-axles	688	0.2	35	0.0	NA	0.0	1113	0.2	908	0.2	2	0.0
Total	382491	82.6	477787	86.6	422804	98.2	80768	17.4	73930	13.4	7816	1.8

For the inner city it is expected that the trailer data will be less relevant and thus the camera system may still be sufficient to get a good estimate of the vehicle distribution by axle count. The aim is to verify this assumption through traffic tube measurements.

3 MEASUREMENT ACCURACY & RELIABILITY

3.1 Comparison WIM-ROAD, sound-radar & cameras

The rough WIM-ROAD database can be ‘cleaned’ by checking and matching the measurements against the other 2 systems. This initially shows that there are a limited number of vehicles from outside the Netherlands. By using the optimal WIM-ROAD setup with 8 lineas-quartz sensors per lane (Ch. 2) a small amount of outliers in the heavy traffic vehicles can be seen. Table 1 shows the overall vehicle passages including the personal cars. The ratio between sound-radar, WIM-ROAD and the camera overall passages is 463:552:501. The results of the camera system shows about 90% coverage of the WIM-ROAD system and the sound-radar is at about 80% coverage. Several reasons can be found for these differences. The first one is that the cameras have a relatively high miss-rate as the trigger is ‘recognition’ of a license plate. Also, one camera covers two lanes, which can cause shielding (another vehicle is in front of the license plate). Additionally not every vehicle is well documented in the Dutch Vehicle database, losing some of the vehicle information. The heavy traffic vehicles show on average 100,000 passages every month for both directions, which is comparable with the periodic counting of vehicles (including type), also performed by the municipality of Amsterdam. Nevertheless, both installed systems show an 80-90% coverage compared to the WIM-ROAD system, which is acceptable for checking of vehicle passage types and numbers. Because of the importance of the camera systems in the inner city, this is discussed in the next section.

3.2 Coupling camera and WIM-ROAD measurements

To verify measurements and get a more accurate measure of overloading the goal was to couple the WIM-ROAD measurements to the camera data. As part of the camera data, vehicle characteristics were collected from the “RijksDienst voor het Wegverkeer” (RDW; the Dutch Vehicle Authority). The WIM-ROAD and camera datasets were matched by traffic lane and nearest time, with a correction for the mean difference in time between a vehicle passing the WIM-ROAD sensors and a vehicle being detected by the cameras.

Sometimes a picture was coupled to more than one WIM-ROAD measurement and vice versa. In those cases conditions were added by which the most relevant match should be made: the measured gross vehicle weight should be less than twice the allowed maximum weight; and the measured gross weight should be more than half the empty weight of the vehicle. Lastly, the duplicates are deleted, by first ruling out the duplicates that could not meet both conditions; and then ruling out the ones that had a bigger time difference.

Table 2. Detailed example of the coupling result.

WIM-ROAD	Camera/RDW	WIM-ROAD		RDW database		
StartTimeStr	StartTimeStr	Length [m]	Gross weight [kg]	Length [m]	Empty weight [kg]	Allowed weight [kg]
	13:12:28.602			3.84	953	1530
13:12:32.631		4.27	1220			
	13:12:37.880			9.70	13565	29000
13:12:41.998	13:12:41.880	9.59	19410	0	1110	1655
	13:12:43.160			3.56	840	1290
13:12:46.039		4.28	1330			
13:12:47.256		3.95	930			

Figure 5a shows the difference between the WIM-ROAD time and the camera time after the initial correction over the period of one week (delta_T). It is seen that the systems go out of sync during the day and at certain points, as indicated by the red lines, they get corrected, which happens at apparently random moments.

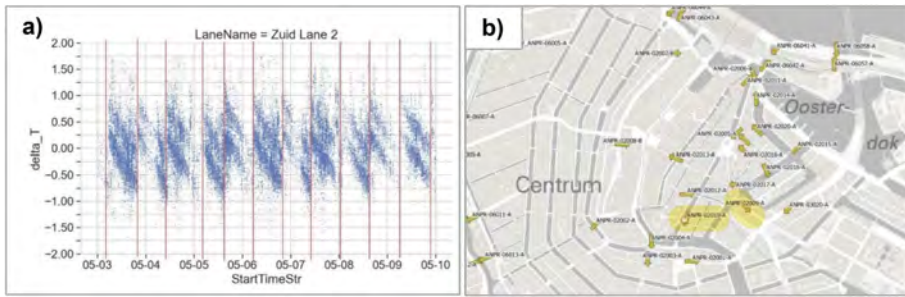


Figure 5. a) Timedrift between camera and WIM-ROAD data; the vertical axis shows the difference between the WIM-ROAD time and the camera time after the initial correction as described in the text. b) Selected cameras (yellow oval marking) for the zones of interest within the inner city of Amsterdam.

To check whether the coupling was done correctly the coupling is verified by looking for data with a big relative difference between the allowed weight as registered in the RDW database and the measured weight by our WIM-ROAD system. An example of a non-matched vehicle that should have been matched is shown in grey in Table 2. But the other vehicles shown are also wrong matches.

It can be seen that at this point in the dataset, the ΔT is about 4 s, which is significantly bigger than we found in Figure 5a. However, most of the time, by looking at samples of the data, the matching seems to be done correctly. It was not possible to accurately get numbers on how often and when the ΔT gets too big. A solution is yet to be found.

In conclusion it is recommended that for future measurements when data needs to be coupled; it needs to be coupled by a trigger cable between the WIM-ROAD and camera measurements. We cannot rely on their passing times being always in sync. Using the same process in the inner city it should be much easier to couple the measurements by the lower number of passages.

4 SETUP MEASUREMENTS CITY CENTER

4.1 General

Little to no reliable measurements are known within the inner city regions and it is often too expensive to set up a WIM measurement system like above for a small scope of bridges and quay walls; while also technically challenging due to the number of traffic lights and side roads in the inner city. A solution that we are currently exploring is to count and classify vehicles in the inner city with cameras, sound-radar or advanced pneumatic tubes.

4.2 Cameras – traffic research results inner city

Amsterdam is already full of ANPR-cameras that are used for enforcing restrictions on environmentally unfriendly vehicles in the inner city, which could help in this research. The cameras were selected based on their location and highlighted in Figure 5b. These cameras are most relevant for the next set of bridges and quay walls to be verified for their structural reliability.

In Table 3 the distribution of vehicles is shown by their number of axles as registered by the RDW and related to only the front license plate. They are divided in 2 categories: vehicles > 10 m and vehicles ≤ 10 m. This is done because the drivers need a permit to drive vehicles longer than 10 m in the inner city. Disadvantage of the camera method is that currently there are barely any back ANPR-cameras. So when a vehicle is pulling a heavy trailer, the unique license plate of the trailer will not show up in the data.

Table 3 shows no vehicles with over 4 axles. Which can be caused by the low total number of vehicles, but also by the restriction of the zone for vehicles over 30,000 kg which requires a more specific permit for a single route.

Table 3. Vehicle distribution by axle count and their allowed weight as counted during a month by 2 ANPR-cameras for vehicles smaller than or equal to 10 m in length (and greater than 10 m in length).

Axle count	Vehicle Count	Percentage of occurrences [%]	Mean of the maximum allowed weights [kg]	Standard deviation of the maximum allowed weights [kg]
2	643 (10)	56.1 (0.9)	14,769 (18,218)	4175 (1678)
3	451 (4)	39.3 (0.4)	25,032 (28,447)	2473 (415)
4	30 (9)	2.6 (0.8)	36,905 (37,278)	940 (2718)

As stated earlier, it is not known whether certain vehicles pulled heavy trailers while driving through the inner city. Though it might be assumable that those are exceptions, in which case we would like to verify this by other means of measurements or back-side cameras.

5 CONCLUSIONS

1. The WIM-ROAD measurement database gathered at the Westpoortweg location is a valuable and useful resource which is a good starting point for a ‘resampling’ approach to determine an adjusted traffic load model for the inner city of Amsterdam.
2. The various measurement methods that were introduced and partly researched (cameras, advanced pneumatic tubes, etc.) to determine the vehicle ‘spectrum’ for the inner city, each have their merits and their challenges. However, by using one or more of these systems together with WIM measurements, a usable traffic load model should be achievable.
3. Our expectation is that an early stage of this model should be presentable during the IALCCE conference in Milan 2023.
4. The next steps are to verify this model in cooperation with the Dutch recommendation organisation TNO-research and get acceptance of the model by the Dutch authorities.

ACKNOWLEDGEMENTS

The authors wish to express their gratitude and appreciation to the Programme Bridges and Quay Walls of the Engineering Office of the City of Amsterdam for support of the pilot project “Traffic load measurements”. Thanks also goes to all members of the team for their contributions.

REFERENCES

- COST 323, 2002. Weigh-in-Motion of Road Vehicles: Final Report of the COST 323 Action. Jacob, B., OBrien, E.J., Jehaes, S. (Eds.), Paris: LCPC.
- NEN-EN 1991-2+C1:2015/NB:2019 nl, 2019, National Annex to NEN-EN 1991-2+C1 Eurocode 1: Actionson structures – Part 2: Traffic Loads on Bridges [Dutch], Delft: NEN
- OIML, 2006. R134-1: Automatic Instruments for weighing Road Vehicles in Motion and Axle Load measuring. Part 1: Metrological and technical requirements – Tests. Paris: OIML.
- RDW, Dutch Vehicle database, <https://www.rdw.nl/>
- Soudijn, M., van Rossum, S., de Boer, A., (2021, September 22-24). Measuring heavy traffic with WIM-ROAD and WIM-BRIDGE systems in an urban environment [Paper presentation], IABSE Congress Ghent 2021: *Structural Engineering for Future Societal Needs*, Ghent, Belgium, Congress Proceedings p.331–340, ISBN: 978-3-85748-176-5.
- Soudijn, M., van Rossum, S., de Boer, A., (2022, November 10). Traffic load measurements with WIM-ROAD and WIM-BRIDGE systems in an urban environment [Dutch, Paper presentation], *CROW Infradagen 2022*, Boskalis, Rotterdam, The Netherlands
- Steenbergen, R.D.J.M., Morales Napoles, O., Vrouwenvelder, A.C.W.M. 2012, General safety overview and modelling of road traffic load for bridge constructions [Dutch], TNO-060-DTM-2011-03695-1814 Endreport, Delft: TNO
- Steenbergen, R.D.J.M., Allaix, D.L., la Gasse, L.C. & Vervuurt, A.H.J.M. 2018, Traffic load model for traffic bridges in the underlying road network without yearly permit [Dutch], TNO-2017-R10614, Delft: TNO.

Improving the resolution and accuracy of low-cost Arduino-based accelerometers

S. Komarizadehasl, G. Ramos & J. Turmo

Department of Civil and Environment Engineering, Universitat Politècnica de Catalunya, BarcelonaTech

J.A. Lozano-Galant

Department of Civil Engineering, Universidad de Castilla-La Mancha

V. Torralba

Tunnel and Bridge Technologies, S.L

M. Haiying

Department of Bridge Engineering, Tongji University

ABSTRACT: An increasing number of researchers are working on Structural Health Monitoring (SHM) applications. However, the high price of traditional commercial accelerometers is known to be one of the significant drawbacks of SHM methods. On the one hand, to apply SHM applications to structures with a lower budget dedicated for their health and safety assessments, development of low-cost sensors can be an answer. On the other hand, low-cost sensors are known to have lower accuracy and resolution compared with those of traditional commercial accelerometers. For the first time in the literature, this paper represents a methodology for improving the resolution and accuracy of low-cost, low-resolution accelerometers. To do so, this paper proposes averaging the outputs of several aligned synchronized low-cost accelerometers.

The validity of the proposed methodology has been examined through a series of laboratory experiments. These experiments tested accelerometers made from one, two, three, four and five combined MPU9250 chipsets on a shaking table. Moreover, two commercial accelerometers (393A03 and 356B18) were used to validate the accuracy of the developed solutions.

1 INTRODUCTION

Structural Health Monitoring (SHM) systems are composed of sensors that measure the structural response (such as accelerations, rotations, strains, or deflections) over time. This information can be used to estimate changes in the structural performance of infrastructures (Gómez, Casas, & Villalba, 2020). The time variation of some environmental factors (such as temperature or humidity) that could produce crack opening (Komarizadehasl & Khanmohammadi, 2021), rotations, settlements, corrosion and other pathologies is so slow that they can be considered quasi-static or static (Baraccani et al., 2017)(Turmo, Lozano-Galant, Mirambell, & Xu, 2015). However, some events (such as the wave response due to earthquake ground motion, traffic-induced vibrations, or ambient activities) need to be accounted for for the dynamic nature of the structural response they induce. To observe and control them, dynamic SHM Systems are required (Chae, Yoo, Kim, & Cho, 2012). The modal parameters needed for SHM application are acquired mainly by accelerometers (Feng & Feng, 2015). MEMS (micro electro mechanical system) accelerometers are silicon-based micromachined devices that traditionally incorporate an accelerometer sensor and a signal conditioning

circuitry (Khandpur, 2020)(Komarizadehasl, Lozano, Lozano-Galant, Ramos, & Turmo, 2022). The low-cost MEMS accelerometers have found their way to various industrial applications due to their significant ongoing technology developments (Behnam Mobaraki et al., 2022). Some of these accelerometers offer low-cost alternatives compared with traditional applications (Looney, 2014)(J. A. Lozano-Galant & Turmo, 2014). Information on various MEMS accelerometers from various structural health monitoring applications is summarized in Table 1. This Table has been ordered by the price of the accelerometers.

Table 1. Summary of the characteristics of the accelerometers commonly used in the literature.

N ^{o1}	Name ²	Price (€) ³	Spectral noise (μg/√Hz) ⁴	Operation Temperature (C°) ⁵	Structural Type ⁶
1	3713B112G (PCB Piezotronics, 2012)	2070.0	22.90	[-54, +121]	Wind Turbine (Botz, Oberlaender, Raith, & Grosse, 2016)
2	3711B1110G (PCB Piezotronics, 2015)	870.0	107.90	[-54, +121]	Railroad Bridges (A. Ozdagli, Liu, & Moreu, 2019)
3	ADXL335 (Analog Devices, n.d.)	10.7	300.00	[-40, +85]	Bridges (Grimmelsman & Zolghadri, 2020)
4	LIS344ALH (ST, 2008)	12.0	50.00	[-40, +85]	Steel beam (Girolami, Zonzini, De Marchi, Brunelli, & Benini, 2018)
5	MPU9250 (Aguero, Ozdagli, & Moreu, 2019)	5.8	300.00	[-40, +85]	Steel Pile and Column (Chatterjee et al., 2017)
6	MPU6050 (InvenSense, n.d.)	5.4	400.00	[-40, +85]	Building Model (Varanis, Silva, & Mereles, 2018)

The analysis of Table 1 shows that low-cost sensors generally have higher noise density. This high noise density results in a lower resolution in comparison with expensive MEMS accelerometers.

Arduino is an open-source electronics platform based on easy-to-use hardware and software. The Arduino Due is a microcontroller board based on the Atmel SAM3X8E ARM Cortex-M3 CPU. Unlike most Arduino boards, the Arduino Due board runs at 3.3V. The maximum voltage that the I/O pins can tolerate is 3.3V. Applying voltages higher than 3.3V to any I/O pin could damage the board (Blum, 2013) (Komarizadehasl, Komary, et al., 2022). In fact, many of the MEMS sensors can interact directly with an Arduino microcontroller (Man & Chang, 2016). Sensors 2 to 6 from Table 1 are low-cost MEMS accelerometers. They need an external power supply and could work with Arduino (B. Mobaraki, Komarizadehasl, Pascual, & Lozano-Galant, 2020). The low-cost sensors in the literature are primarily dedicated to projects with low frequencies and strong acceleration amplitude (A. I. Ozdagli, Liu, & Moreu, 2018)(Mobaraki*, Komarizadehasl, Pascual, & Galant, 2021) as they do not have enough resolution to read low amplitude acceleration.

The literature review shows no solutions for improving the resolution of low-cost accelerometers. To fill this gap, this work investigates the increasing number of aligned accelerometers located in the exact location for measuring the same vibration is beneficial. In fact, individual sensors' individual noise density can better be detected by a Fast Fourier Transformation (FFT)

1. Sensor number.

2. Sensor name.

3. Sensor price: the prices are obtained from retailers (VAT excluded).

4. Spectral Noise: the power spectral density of noise per unit of bandwidth (1 Hz).

5. Operational temperature: temperature range where the sensor works accurately.

6. Structural type: where the sensors are used.

when the average results of a few sensors are evaluated (Jose Antonio Lozano-Galant, Nogal, Turmo, & Castillo, 2015)(Farré-Checa, Komarizadehasl, Ma, Lozano-Galant, & Turmo, 2022).

To validate the performance of the proposed device on laboratory conditions, five accelerometers (MPU9250) were aligned and tested on a hydraulic jack. The jack induced a number of low-amplitude vibrations, and the increasing benefit of accelerometers for decreasing the noise density of the whole system was evaluated (Komary et al., 2023)(Atencio, Komarizadehasl, Lozano-Galant, & Aguilera, 2022).

This paper is organized as follows: In section 2, the proposed system for validating the proposed theory is introduced. Then, in section 3, the laboratory test is used to validate the proposed methodology, and the obtained results are detailed. Finally, the main conclusions are drawn in Section 4.

2 ACQUISITION SYSTEM

In this section, the used equipment for making a vibration acquisition system is illustrated.

Five MPU9250 accelerometers were attached to an Arduino by a multiplexer. It is essential to report that although the sensors are not synchronized, the lag is known.

When the code is executed, the Arduino opens the library and uses the information to get the acceleration from the first sensor, and after the second one, and so on. The lag between each sensor-print is about 2.2 milliseconds. As the lag is known, the average of the measurement (information given by the proposed accelerometer) can also be located in time.

In a nutshell, the proposed accelerometer is working with the average value of the sensors. Therefore, this lag would not interfere with the needed information or the process as the FFT application, which is the heart of this system, and only requires amplitudes and frequency sampling. Frequency sampling is the number of acquired outputs in one second.

3 LABORATORY TESTS

This section compares the sensitivity, ND, and resolution of a single MPU9250 accelerometer. This section studies the performed experiments on the proposed accelerometer in laboratory conditions.

For validating the beneficial effect of using several sensors, an experiment on a hydraulic jack was performed. This jack (INSTRON 8803 (INSTRON, 2017)) is located at the Structural Laboratory Lluís Agulló of Technical University of Catalonia (Spain).

A sinus signal has been programmed with a dynamic jack, and the accelerometer has saved the vibrations. This jack can vibrate its lower jaw as was programmed. The hydraulic jack's instructions were to make a wave with a fixed frequency of 0.5 hertz (one complete wave in two seconds). The jack's movement was to go up to 0.1 millimeters up and -0.1 millimeters down from its null axis to make a sinus wave. With a two-time elementary differential, the acceleration equation could be calculated.

$$y = d * \sin(\omega * t + \varphi) \quad (1)$$

$$\omega = 2 * \pi * f \quad (2)$$

In the above equations, y is the displacement in time t , d is the maximum allowed movement of the jack in each cycle, ω is the angular frequency, and f is the set frequency, which equals 5Hz, and φ is the phase constant. On Eq.3, acceleration has been calculated from Eq.1. This was done by getting the second-order derivative of Eq.1. By putting all the data in Eq.3, the Input Acceleration (IA) was calculated as $0.1006 \text{ g} * 10^{-3} \text{ m/s}^2$.

$$a = (d^2 * y) / (dt^2) = \ddot{y} = -d * \omega^2 * \sin(\omega * t + \varphi) \quad (3)$$

4 EFFECT OF THE NUMBER OF SENSORS

In this section, the beneficial effects of adding an increasing number of averaged sensors are studied.

In Figure 1, estimated errors obtained for a different number of sensors in are compared. The Max and the Min in each graph represent the enveloped error for all the possible sensor selections from the five available accelerometers (the proposed accelerometer represents the proposed kit with five sensors). The results of the increasing number of sensors are presented in Figures 1, 1.a (one sensor), 1.b (two sensors), 1.c (three sensors), 1.d (four sensors). In all these figures, the horizontal axis presents the frequency of the experiment, and the vertical one illustrates the MA error in percentage. The MA for 0.5 Hz is not presented in Figure 1.a and b because the system resolution for acquiring low acceleration amplitudes was insufficient.

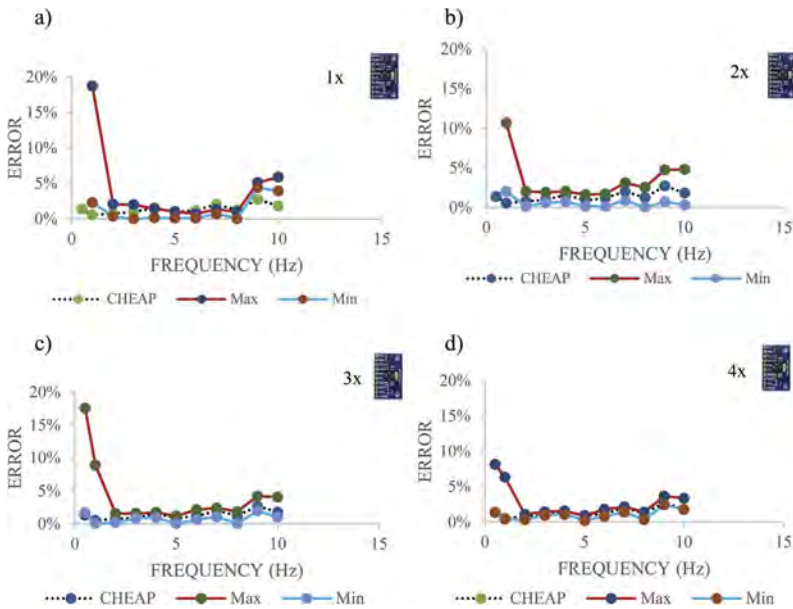


Figure 1. Estimated measured amplitude acceleration (MA) error for different number of sensors: one sensor (a), two sensors (b), three sensors (c), four sensors (d).

The analysis of Figure 1 shows that, as expected, the error depends to a greater extent on the number of sensors and the analyzed frequency. The experienced error for one, two, three, four and five (the proposed accelerometer) were at the worst-case scenario, 18.67%, 20.12%, 17.58%, 8.17%, and 1.55%, respectively. Therefore, it can be concluded that lower errors are obtained when the number of accelerometers is increased, especially on the tests with lower acceleration amplitude (less than 0.4 milli-g). Results in Figure 1 also show that the part of the experiment that had the lowest frequency (0.5 Hz) could be considered the most important one for the following reasons. Firstly, the highest experienced error appears there. Secondly, the lowest acceleration amplitude (0.1022 milli-g) is in this part of the experiment. In a nutshell, locating this low-level acceleration amplitude (MA) from the FFT evaluation was an opportunity to compare the resolution and accuracy of the proposed accelerometer with a different number of sensors.

For a single MPU9250 accelerometer, the resolution for this part of the experiment was not enough. The resolution of the kit with a single accelerometer appeared to be at least 0.19 Milli-g. The amplitude of the needed signal was less than this resolution. As a result, finding and reporting this signal from the FFT output was not possible. The resolution for the kit of sensors with two MPU9250 accelerometers was not entirely clear either. This resolution was

at least 0.13 milli-g, which is still 0.03 milli-g higher than the value of the captured signal. The resolution for the kit of sensors with three MPU9250 was about 0.10 milli-g. As a result, finding the amplitude of this part of the experiment was still impossible. The analysis of the same experiment with four MPU9250 accelerometers shows that the resolution of the system is slightly less than 0.08 Milli-g. This resolution made locating the needed signal from the FFT output diagram possible. This test reports the MA of the signal as 0.10384 Milli-g, which has a 3.22% error from the IA. On the other hand, the analysis of the kit of sensors with five MPU9250 (the proposed accelerometer) provides a resolution of around 0.06 Milli-g. In addition, it was deduced that the proposed accelerometer had an error of 1.55% from the IA.

5 CONCLUSION

In order to determine maintenance applications, minimize the reparation costs, and guarantee the safety of the structures, Structural Health Monitoring (SHM) systems are required. For applying the SHM application to structures with a lower budget for assessing their health state, this paper presents a novel method for enhancing the accuracy of low-cost accelerometers.

Adding an increasing number of averaged sensors is investigated to have beneficial effects on the resolution and accuracy. For example, it was seen on an experiment with a frequency of 0.5 Hz that a kit of sensors with four MPU 9250 had a resolution of about 0.08 Milli-g while with five accelerometers (the proposed accelerometer), the resolution became around 0.06 Milli-g.

In conclusion, the proposed methodology can solve the low resolution and high noise density of low-cost accelerometers. However, further research for implementing this idea on bridges and structures is needed.

REFERENCES

- Aguero, M., Ozdagli, A., & Moreu, F. (2019). Measuring reference-free total displacements of piles and columns using low-cost, battery-powered, efficient wireless intelligent sensors (LEWIS2). *Sensors*, 19(7), 1549–1566. <https://doi.org/10.3390/s19071549>
- Analog Devices. (n.d.). ADXL 335 data-sheet. Retrieved August 1, 2020, from <https://www.sparkfun.com/datasheets/Components/SMD/adxl335.pdf>
- Atencio, E., Komarizadehasl, S., Lozano-Galant, J. A., & Aguilera, M. (2022). Using RPA for Performance Monitoring of Dynamic SHM Applications. *Buildings* 2022, Vol. 12, Page 1140, 12(8), 1140. <https://doi.org/10.3390/BUILDINGS12081140>
- Baraccani, S., Palermo, M., Azzara, R. M., Gasparini, G., Silvestri, S., & Trombetti, T. (2017). Structural Interpretation of Data from Static and Dynamic Structural Health Monitoring of Monumental Buildings. *Key Engineering Materials*, 747, 431–439. <https://doi.org/10.4028/www.scientific.net/KEM.747.431>
- Blum, J. (2013). *Exploring Arduino: tools and techniques for engineering wizardry*. Retrieved from https://books.google.com/books?hl=en&id=8QUeAAAQBAJ&oi=fnd&pg=PT7&dq=Blum,+J.,+Exploring+Arduino:+tools+and+techniques+for+engineering+wizardry.+2013:+John+Wiley+%26+Sons.&ots=qxY4PnjdqI&sig=9jIMNwsBAK_W-3Q61QoZ7PIcezM
- Botz, M., Oberlaender, S., Raith, M., & Grosse, C. U. (2016). Monitoring of wind turbine structures with concrete-steel hybrid-tower design. In *EWSHM -8th European Workshop on Structural Health Monitoring* (Vol. 3). Retrieved from <http://www.ndt.net/?id=19909>
- Chae, M. J., Yoo, H. S., Kim, J. Y., & Cho, M. Y. (2012). Development of a wireless sensor network system for suspension bridge health monitoring. *Automation in Construction*, 21(1), 237–252. <https://doi.org/10.1016/j.autcon.2011.06.008>
- Chatterjee, G., Latorre, L., Maily, F., Nouet, P., Hachelef, N., & Oudea, C. (2017). Smart-MEMS based inertial measurement units: gyro-free approach to improve the grade. *Microsystem Technologies*, 23(9), 3969–3978. <https://doi.org/10.1007/s00542-015-2741-y>

- Farré-Checa, J., Komarizadehasl, S., Ma, H., Lozano-Galant, J. A., & Turmo, J. (2022). Direct simulation of the tensioning process of cable-stayed bridge cantilever construction. *Automation in Construction*, 137, 104197. <https://doi.org/10.1016/J.AUTCON.2022.104197>
- Feng, D., & Feng, M. Q. (2015). Model Updating of Railway Bridge Using in Situ Dynamic Displacement Measurement under Trainloads. *Journal of Bridge Engineering*, 20(12), 04015019–04015031. [https://doi.org/10.1061/\(ASCE\)BE.1943-5592.0000765](https://doi.org/10.1061/(ASCE)BE.1943-5592.0000765)
- Girolami, A., Zonzini, F., De Marchi, L., Brunelli, D., & Benini, L. (2018). Modal Analysis of Structures with Low-cost Embedded Systems. *International Symposium on Circuits and Systems, 2018-May*, 1–4. <https://doi.org/10.1109/ISCAS.2018.8351705>
- Gómez, J., Casas, J. R., & Villalba, S. (2020). Structural Health Monitoring with Distributed Optical Fiber Sensors of tunnel lining affected by nearby construction activity. *Automation in Construction*, 117, 103261–103279. <https://doi.org/10.1016/j.autcon.2020.103261>
- Grimmelsman, K. A., & Zolghadri, N. (2020). Experimental evaluation of low-cost accelerometers for dynamic characterization of bridges. *Conference Proceedings of the Society for Experimental Mechanics Series*, 145–152. https://doi.org/10.1007/978-3-030-12115-0_19
- INSTRON. (2017). 8802 (250 kN) Fatigue Testing System. Retrieved August 1, 2020, from <https://www.instron.co.hu/-/media/literature-library/products/2013/10/8803-servo-hydraulic-fatigue-testing-system.pdf?la=hu-HU>
- InvenSense. (n.d.). MPU6050 data-sheet. Retrieved August 1, 2020, from 2013 website: <https://www.invensense.com/wp-content/uploads/2015/02/MPU-6000-Datasheet1.pdf%0A>
- Khandpur, R. S. (2020). accelerometer. In *Compendium of Biomedical Instrumentation*. <https://doi.org/10.1002/9781119288190.ch1>
- Komarizadehasl, S., & Khanmohammadi, M. (2021). Novel plastic hinge modification factors for damaged RC shear walls with bending performance. *Advances in Concrete Construction*, 12(4), 355–365. <https://doi.org/10.12989/ACC.2021.12.4.355>
- Komarizadehasl, S., Komary, M., Alahmad, A., Lozano-Galant, J. A., Ramos, G., & Turmo, J. (2022). A Novel Wireless Low-Cost Inclinometer Made from Combining the Measurements of Multiple MEMS Gyroscopes and Accelerometers. *Sensors 2022, Vol. 22, Page 5605*, 22(15), 5605. <https://doi.org/10.3390/S22155605>
- Komarizadehasl, S., Lozano, F., Lozano-Galant, J. A., Ramos, G., & Turmo, J. (2022). Low-Cost Wireless Structural Health Monitoring of Bridges. *Sensors 2022, Vol. 22, Page 5725*, 22(15), 5725. <https://doi.org/10.3390/S22155725>
- Komary, M., Komarizadehasl, S., Tošić, N., Segura Pérez, I. S., Lozano-Galant, J. A., & Turmo, J. (2023). Low-Cost Technologies Used in Corrosion Monitoring. *Sensors 2023, Vol. 23, Page 1309*, 23(3), 1309. <https://doi.org/10.3390/S23031309>
- Looney, M. (2014). An Introduction to MEMS Vibration Monitoring. In *analog dialog* (Vol. 48). Retrieved from <https://www.mouser.com.gt/pdfdocs/intro-to-mems-vibration-monitoring.pdf>
- Lozano-Galant, J. A., & Turmo, J. (2014). An algorithm for simulation of concrete cable-stayed bridges built on temporary supports and considering time dependent effects. *Engineering Structures*, 79, 341–353. <https://doi.org/10.1016/j.engstruct.2014.08.018>
- Lozano-Galant, Jose Antonio, Nogal, M., Turmo, J., & Castillo, E. (2015). Selection of measurement sets in static structural identification of bridges using observability trees. *Computers and Concrete*, 15(5), 771–794. <https://doi.org/10.12989/cac.2015.15.5.771>
- Man, S. H., & Chang, C. C. (2016). Design and performance tests of a LED-based two-dimensional wireless crack propagation sensor. *Structural Control and Health Monitoring*, 23(4), 668–683. <https://doi.org/10.1002/stc.1802>
- Mobaraki*, B., Komarizadehasl, S., Pascual, F. J. C., & Galant, J. A. L. (2021). Open source platforms for monitoring thermal parameters of structures. In *Bridge Maintenance, Safety, Management, Life-Cycle Sustainability and Innovations* (pp. 3892–3896). <https://doi.org/10.1201/9780429279119-532>
- Mobaraki, B., Komarizadehasl, S., Pascual, F., & Lozano-Galant, J. (2020). Environmental Monitoring System Based on Low-Cost Sensors. *XV International Conference on Durability of Building Materials and Components. EBook of Proceedings*. <https://doi.org/10.23967/dbmc.2020.201>
- Mobaraki, Behnam, Komarizadehasl, S., Javier, F., Pascual, C., Lozano-Galant, A., & Soriano, R. P. (2022). A Novel Data Acquisition System for Obtaining Thermal Parameters of Building Envelopes. *Buildings 2022, Vol. 12, Page 670*, 12(5), 670. <https://doi.org/10.3390/BUILDINGS12050670>
- Ozdagli, A. I., Liu, B., & Moreu, F. (2018). Low-cost, efficient wireless intelligent sensors (LEWIS) measuring real-time reference-free dynamic displacements. *Mechanical Systems and Signal Processing*, 107, 343–356. <https://doi.org/10.1016/j.ymsp.2018.01.034>

- Ozdogli, A., Liu, B., & Moreu, F. (2019). Real-time low-cost wireless reference-free displacement sensing of railroad bridges. *Conference Proceedings of the Society for Experimental Mechanics Series*, (213429), 103–109. https://doi.org/10.1007/978-3-319-74642-5_12
- PCB Piezotronics. (2012). 3713B112G data-sheet. Retrieved August 1, 2020, from https://www.pcb.com/contentstore/docs/PCB_Corporate/Vibration/Products/Manuals/3713B112G.pdf
- PCB Piezotronics. (2015). 3711B1110G data-sheet. Retrieved August 1, 2020, from https://www.pcb.com/contentstore/docs/PCB_Corporate/Vibration/Products/Manuals/3713B1110G.pdf
- ST. (2008). LIS344ALH data-sheet. Retrieved August 1, 2020, from <https://www.st.com/resource/en/data-sheet/lis344alh.pdf>
- Turmo, J., Lozano-Galant, J. A., Mirambell, E., & Xu, D. (2015). Modeling composite beams with partial interaction. *Journal of Constructional Steel Research*, 114, 380–393. <https://doi.org/10.1016/j.jcsr.2015.07.007>
- Varanis, M., Silva, A. L., & Mereles, A. G. (2018). On mechanical vibration analysis of a multi degree of freedom system based on arduino and MEMS accelerometers. *Revista Brasileira de Ensino de Fisica*, 40(1), e1304–e1314. <https://doi.org/10.1590/1806-9126-RBEF-2017-0101>

Preventive SHM for asset management: A case study on the Mont-Blanc tunnel

F.B. Cartiaux & B. Prudhomme
OSMOS Group SA, Paris, France

ABSTRACT: The Mont-Blanc Tunnel is an infrastructure of strategic importance for Europe, linking France and Italy under the highest summit of the Alps. The tunnel was opened in 1965 and is a 11.6 km long single tube structure with 8.6m diameter. The road inside the tunnel is carried by a reinforced concrete slab, which is supported by two concrete linear walls, separating three service ducts. In the general scheme of preventive maintenance for this asset, this concrete slab is undergoing replacement works to build it new after nearly 60 years of operation. Before and during these works, planned over a few years, an exhaustive Structural Health Monitoring (SHM) system based on strain measurements on the lower face of the slab has been in operation. This paper describes the SHM strategy implemented since 2016 and its results for the asset manager. A first phase was achieved from 2016 to 2018 before the beginning of the slab works with 56 wireless optical strand sensors on a 555m long zone. Then, from 2019 to 2022, the SHM system was removed from the initial zone undergoing replacement works, and extended to next zones before and after, with a total of 117 sensors on 1200m along the tunnel. Starting from 2022, the wireless system has been replaced by a fully integrated wired solution, allowing the gathering of more volume of relevant data and an instantaneous dataflow while the works are going on. Long-term evolutions reflecting the effect of ageing, as well as short records at 100 Hz sampling rate for assessing the effect of the traffic loads on the concrete slab, are combined to give a synthetic stability index of each monitored location on the slab and check the health of the structure in real time throughout the duration of the works.

1 INTRODUCTION

Tunnels are transportation assets of great importance as they often stand as the shortest convenient way to cross significant obstacles, like wide sea channels, dense urban areas, and high mountains. They are sensitive to various phenomena induced by the soil conditions and the traffic throughout their life cycle, which deserve attention to be able to anticipate any anomaly before it becomes critical. Thus, they are usually monitored by their operator, at least with traditional means like regular visual inspection and periodic convergence assessment.

However, continuous monitoring of tunnels with a dedicated set of sensors and the associated means for data collection, transmission, management, and analysis are not widely spread. Experiments of continuous monitoring for durations over a few months have been documented on tunnels under current exploitation, for example with wireless tiltmeters in China (Zhang, 2017), and with strain measurements in Belgium (Maes, 2021). Specific tunnel installations like the one of the CERN near Geneva, very sensitive to soil movements, are monitored continuously as well (Cunningham, 2023).

This paper documents a recent and long-lasting SHM operation with continuous strain measurements, on the concrete slab of the Mont-Blanc tunnel under the Alps between France

and Italy. It focuses on the sensor and data management technologies and on the use of the SHM data for preventive asset management.

2 DESCRIPTION OF THE ASSET AND CONTEXT OF THE SHM IMPLEMENTATION

2.1 *The Mont-Blanc tunnel and its concrete slab*

Opened in 1965, the Mont-Blanc tunnel is a 11.6 km long single tube road tunnel with two lanes for traffic in opposite directions. The concrete tube has a diameter of 8.6 m and its cross-section is divided into four ducts. The main duct is located over a horizontal concrete slab which carries the road. Under the concrete slab, three service ducts are separated by two linear walls. One of them called “AV” is used for exhausting stale air and is not usually walkable. The two other ducts called “AF3” and “AF4” are used as service ducts.

The tunnel is divided into longitudinal portions called “fiches”, each one around 30 m long. This division allows an easy naming for specific zones along the tunnel to facilitate maintenance operations. Figure 1 shows a schematic view of the ducts and displays two “fiches” (nb 206 and 207), with the location of some of the long-basis strain sensors used for the SHM operation.

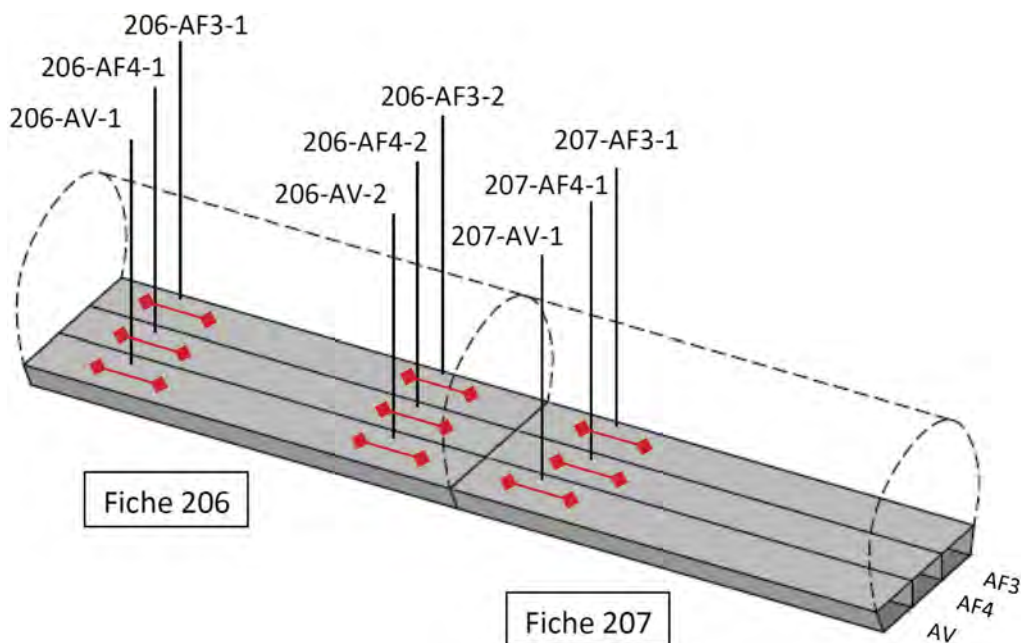


Figure 1. Schematic view of a portion of the tunnel, with two “fiches” and nine sensors.

2.2 *Motivation for the implementation of a SHM system*

The concrete slab which carries the road suffers from the usual effects of ageing for a concrete structure with almost sixty years of operation under a significant heavy traffic. Frequent visual inspections are carried out by the GEIE Tunnel du Mont Blanc, in charge of the asset, to check any default affecting the concrete, especially on the lower face of the slab. Because of some evidence of rebar corrosion and risk of spalling coverage concrete, and in prevention for potential harder damages due to the age of the structure in the future, the concrete slab is now undergoing reconstruction works, starting at a central portion of the tunnel and expanding towards the two ends.

Before, and during these reconstruction works, the remaining portions of the structure located in the vicinity of the works zone deserve a specific attention. The visual inspections enable a regular exhaustive report of damages, but in the period between two inspections, no information is available. Thus, it was decided to complement the monitoring of the concrete slab with sensors continuously measuring the strain in the slab, to get a quantified assessment of the evolutions of the structure, and eventually to be able to configure automatic real-time alerts in case of a critical situation.

3 STRUCTURAL HEALTH MONITORING OPERATION

3.1 *Optical strand technology*

The sensors chosen for the SHM operation on the concrete slab of the Mont-Blanc tunnel are fiber-optic based strain sensors called Optical Strands. They use the principle of the light intensity modulation through micro-bending of the fiber optic. In the case of Optical Strands, the micro-bending is generated by braiding three fibers together inside a coating duct.

The Optical Strands were chosen because of their robustness, sensitivity, and longevity. This type of strain sensor has indeed been used already for various applications linked to the SHM of civil works, including continuous assessment of both static and dynamic behavior over long durations (Cartiaux, 2019, 2021b) and Weigh-In-Motion on road bridges (Cartiaux, 2023).

The Optical Strands are available as wireless or wired sensors, and both options have been used in the case of the Mont-Blanc tunnel. The wireless option (Figure 2) offers an easier installation and does not require power supply but has a limited capacity for the data storage between data retrievals. The wired option requires cable pulling and power supply, but offers real-time transfer of the data on the internet, and both synchronicity and exhaustivity for the recording of dynamic effects on several sensors.



Figure 2. One wireless Optical Strand set under the concrete slab of the Mont-Blanc tunnel.

3.2 *Phases of the SHM of the Mont-Blanc tunnel*

The SHM of the concrete slab of the Mont-Blanc tunnel first started in November 2015 and went through successive different phases, distinguished by the number and type of sensors used (i.e. wireless or wired solutions) and by their location along the tunnel:

Table 1. Phases of the SHM of the Mont-Blanc tunnel.

Phase	Start	End	Type of sensors	Number of sensors	Length of SHM zone
Preliminary	11/2015	05/2016	Wireless	20*	420 m*
Before works	11/2016	03/2018	Wireless	56	555 m
Works Phase 1	02/2019	07/2022	Wireless	117	1200 m
Works Phase 2	08/2022	08/2026	Wired	74	720 m

* Rolling zones of 60 m with half of the 20 sensors moved every month

The average ratio is one sensor for 10 m length along the tunnel, which allows a dense sampling of the monitoring locations. The first phase in 2015 and 2016, called preliminary, is an exception to this rule: a stock of 20 sensors was used on rolling zones of 60 m, each zone being monitored for two months, and 10 sensors moved from one zone to the next one every month, to finally cover a 420 m long zone. This preliminary phase allowed to define priorities before the switch to permanent monitoring on well-chosen locations.

From November 2016 to March 2018, 56 wireless sensors monitored a 555 m long zone on which the first phase of works was scheduled. Then, from February 2019 to July 2022, while this first zone was totally rebuilt, 117 wireless sensors were set on next zones before and after, covering a total length of 1200 m. Finally, part of this second zone is currently undergoing replacement works while 74 sensors remain, after a switch to the wired solution.

3.3 Data flow and processing

The strain measurements are performed continuously with one point every hour for the wireless option, and one point every ten minutes for the wired option (customizable up to one point every second). In addition, dynamic records with a high sampling rate of 50 points every second (up to 100 points every second for the wired option) are automatically triggered in the case of rapid variations of the strain, including in the case of heavy vehicles driving on the slab.

The data flow has been organized through different means depending on the monitoring phases, as follows:

Preliminary phase (2015 to 2016): each month, half of the 20 wireless sensors are moved from one zone to the next one. At this occasion, the data of all sensors is retrieved manually through a radio modem connected to the operator's laptop on site.

Before works (2016 to 2018): six gateways are installed along the tunnel. These are industrial computers, connected to the tunnel's optical fiber network, and including a radio modem for the wireless communication with each wireless sensor in their vicinity. Every month, the data is retrieved remotely from the OSMOS office (or elsewhere) through the internet, by establishing a secured connection to the gateways.

During works phase 1 (2019 to 2022): to keep the monitoring data flow independent from the tunnel network again, the data retrieval is performed on site by an operator, every month.

During works phase 2 (2022, planned until 2026): the switch to the wired system allows a real-time transfer of the data on the internet, through a dedicated additional fiber optic network that has been installed on purpose along the tunnel.

Once the measurement data is retrieved (for the wireless option) or automatically sent every minute (for the wired option), it is received and organized on a remote cloud in a MongoDB database, from which the raw data is available for release on a dedicated web interface or through API routes. Every day, a dedicated algorithm gathers all available data to compute a synthetic stability index which is released on the same web interface.

4 MAIN RESULTS OF THE SHM

4.1 Stability index and anomaly detection

The first aim of the SHM operation is to keep an updated overview of the stability of the concrete slab, for every monitored location. This is achieved by the automatic release of a stability index, as one unique value for each location, which summarizes the general evolution of the strain in the concrete for each sensor (Figure 3). This index is computed every day on the cloud (if updated data is available), instantly released on the web interface as a color code for each location, from green to red, and summarized in monthly formal reports (Cartiaux, 2021a).

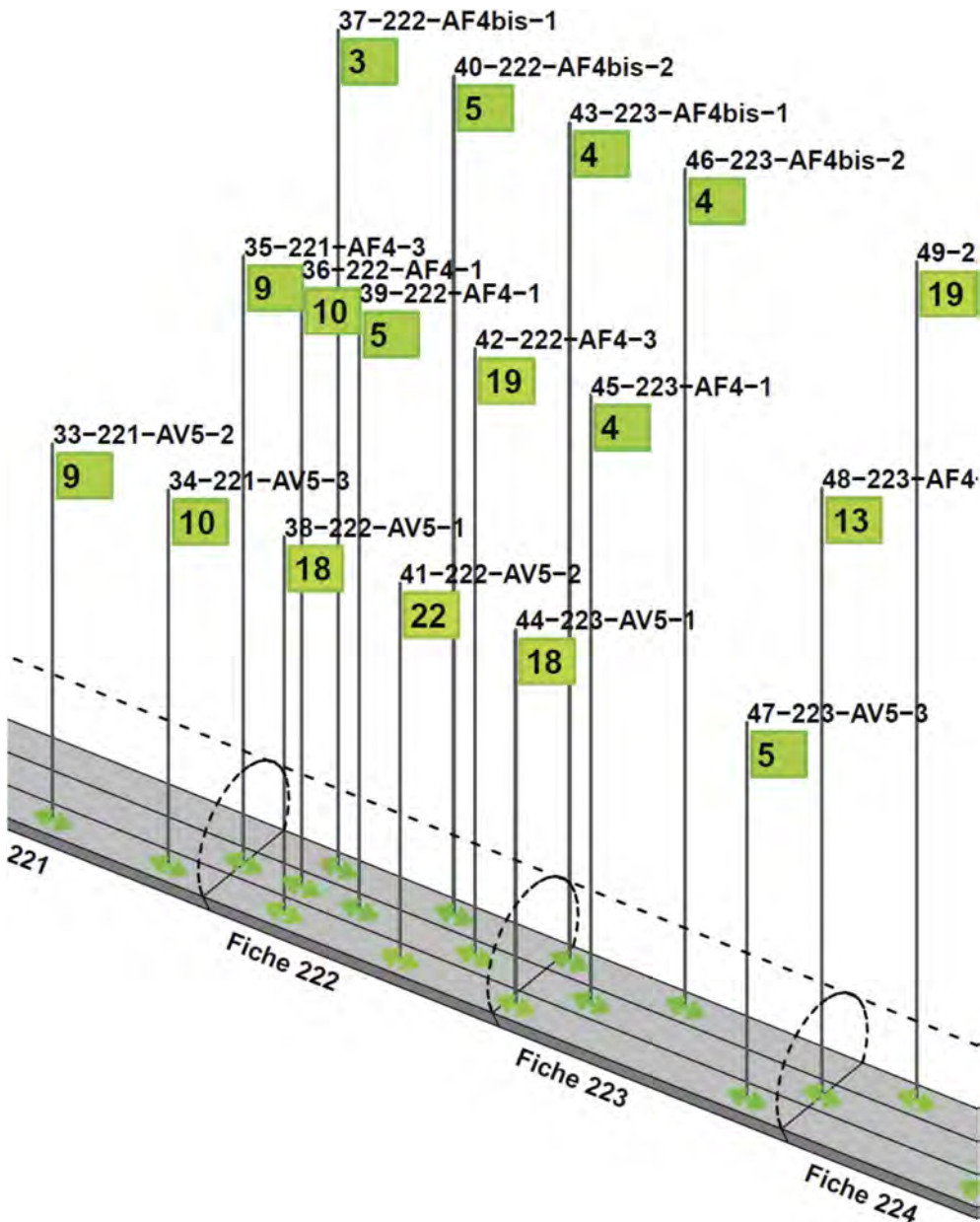


Figure 3. Synthetic release of stability indices on a sample of monitored locations.

The stability index processing gathers all available static data, i.e., one measurement every hour for the wireless option and one every ten minutes for the wired option. In parallel, it also gathers temperature measurements taken at the same sampling period by the monitoring system at different locations along the tunnel.

Even if the temperature variations are usually smooth inside the tunnel, a correction of the effects of the temperature is performed on the strain data. These effects are automatically learned by the algorithm through an analysis of the correlation between strain and temperature on limited periods of time (learning periods). The law linking strain and temperature identified by this analysis is then applied to the whole set of temperature data, to estimate the part of strain variations due to the temperature effects. Then, the raw strain data is corrected from this effect to obtain residual strain evolution without the incidence of temperature.

Once the strain data is corrected from temperature effects, its variations are analyzed to assess the stability of the concrete slab under quasi-permanent effects only. With no damages appearing, these variations are supposed to remain near to zero, and the stability index keeps a low value and remains in the “green zone”.

When damages occur in the concrete on the monitored locations, the loss of material induces a loss of rigidity, and additional tension under quasi-permanent loads. This evolution is pointed out with increasing values of the stability index, first corresponding to the opening of crack patterns (average tension strain around 0.5 mm/m for example) and eventually to concrete spalling (more than 2 mm/m, which is the “red zone”).

The automatic update of the index every day allows, first, an always updated overview of the evolution of strain in the concrete slab (corrected from potential temperature effects), and secondly, an early warning about potential damages, to schedule reparation works before they become critical.

4.2 Assessment of the effects of the traffic on the concrete slab

In addition to the synthetic stability index which summarizes long-term evolutions of the strain in the concrete slab, the monitoring system also detects rapid variations of the strain and releases them as dynamic records with a high sampling rate of up to 100 points every second.

Usually, this feature allows to detect and assess the effect of the heaviest vehicles driving on the road carried by the concrete slab. The sensitivity of the strain measurement is sufficient to get a very clear record of the local bending of the slab under the effect of each axle load (Figure 4). The customizable detection thresholds are set to optimize the volume of useful data, with not more than a few dozens of vehicles recorded each day, what is however enough to perform a statistical analysis on the amplitude of the strain due to the traffic, and to monitor potential changes of rigidity with this additional parameter.

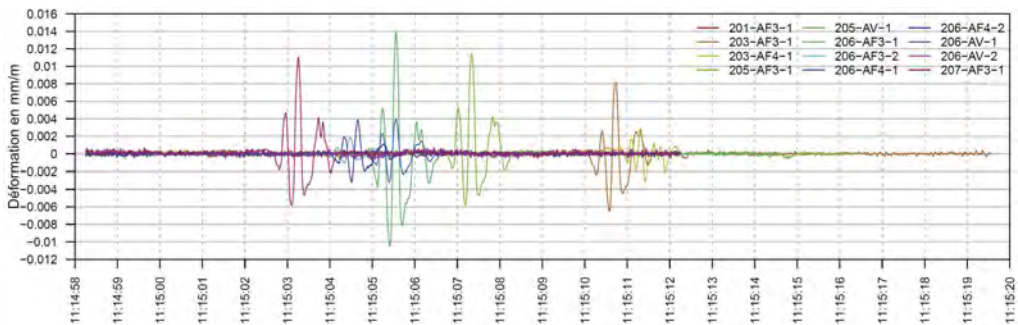


Figure 4. Example of recorded passage of one truck by sensors on different locations.

4.3 Monitoring during works on the slab

While the concrete slab is undergoing replacement works, the monitoring system remains in operation on zones next to the location of the works. This enables to include the potential effect of the works on the remaining – or newly built in the case of works phase 2 – parts of the concrete slab as part of the stability assessment.

For example, the works require to use vehicles that are uncommon compared to the usual traffic loads in the tunnel, and the effect of these exceptional loads are assessed to check the amplitude of strain and the return to the initial state of the slab after their passage (Figure 5). The pattern of the strain measurements shows that these vehicles are driving very slow compared to usual traffic, and the induced strain is approximately the double of the strain due to common vehicles. However, the order of magnitude remains acceptable (up to 0.03 mm/m) and the slab always reaches its initial state back, showing that these passages do not have any consequence in terms of new damages.

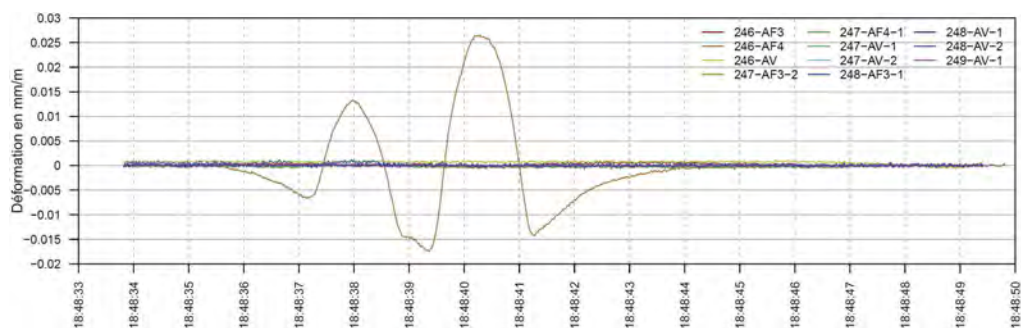


Figure 5. One unusual vehicle recorded by an optical strand.

In addition, an automatic notification feature is activated for the works phase 2, which releases instantaneous messages by SMS and e-mail in the case of exceedance of some thresholds on the measured values, following two different modalities:

- Static threshold if the raw static measurement value becomes out of an acceptable range,
- Dynamic threshold if the range (maximum minus minimum) of the strain over four seconds exceeds a threshold value.

In both static and dynamic cases, the threshold values are learnt from the past data and customized for each sensor, to alert in case of an abnormal situation only.

5 CONCLUSION

Strategic tunnels supporting an intense heavy traffic deserve monitoring solutions which go beyond the usual visual inspections, in the frame of an optimized preventive maintenance. The Mont-Blanc tunnel is an interesting case study, which shows the applicability of SHM through continuous strain measurements at a wide scale in an operational context, including heavy maintenance works operations on the concrete structure of the slab supporting the road.

Measurements remotely available in real-time on a web interface, and daily updated synthetic stability indices for each monitored location along the tunnel, allow an efficient overview of the evolution of the concrete slab and help to intervene at the right place and at the right time in the case of a new damage. Moreover, the continuity of the measurements enables to anticipate further evolutions before they induce visible consequences like concrete spalling. In addition, threshold-triggered records at a high sampling rate of 100 Hz are used for the

assessment of the response of the structure to the traffic loads, including specific exceptional vehicles used for the works.

The SHM operation, which started in 2015 before the first reconstruction works of the concrete slab, is still going on and planned until 2026, to perform a continuous check of the stability of the structure during the works and to automatically notify in the case of abnormal evolutions.

ACKNOWLEDGEMENTS

The authors wish to thank the GEIE Tunnel du Mont-Blanc for its support in the release of this publication.

REFERENCES

- Cartiaux, F.-B., Pelletier, P. & Semiao, J. 2019. Traffic and Temperature Effects Monitoring on Bridges by Optical Strands Strain Sensors. *5th Conference on Smart Monitoring, Assessment and Rehabilitation of Civil Structures*. http://data.smar-conferences.org/downloads/SMAR_2019_Proceedings.zip
- Cartiaux, F.-B. 2021a. Surveillance en continu de la dalle du tunnel du Mont-Blanc par mesures de déformation. *Academic Journal of Civil Engineering*, 38, 2 (May 2021), 188–191.
- Cartiaux, F.-B., Le Corvec, V., Cachot, E., Vayssade, T., Servant, C. 2021b. Continuous Static and Dynamic Strain Measurements on Civil Infrastructures: Case Study on One Pier of the Millau Viaduct. In: Rizzo, P., Milazzo, A. (eds) *European Workshop on Structural Health Monitoring. EWSHM 2020. Lecture Notes in Civil Engineering, vol 127*. Springer, Cham. https://doi.org/10.1007/978-3-030-64594-6_23
- Cartiaux, F.-B., Fort, V., Pelletier, P.M., Jacob, B., Brouste, A. 2023. Combined Bridge Weigh-In-Motion and Structural Health Monitoring on Road Bridges: Case Study on the Salso Viaduct (Italy). In: Rizzo P., Milazzo A. (eds) *European Workshop on Structural Health Monitoring. EWSHM 2022. Lecture Notes in Civil Engineering, vol 254*. Springer, Cham. https://doi.org/10.1007/978-3-031-07258-1_8
- Cunningham, R., Osborne, J.A., Perez-Duenas, E., O'Brien, D., Li, Z. 2023. Tunnel Asset Management at CERN. In: Rizzo P., Milazzo A. (eds) *European Workshop on Structural Health Monitoring. EWSHM 2022. Lecture Notes in Civil Engineering, vol 254*. Springer, Cham. https://doi.org/10.1007/978-3-031-07258-1_34
- Maes, K., Stijn, F., Salesn, W., Feremans, G., Segher, K. 2021. The application of black-box modeling in long-term tunnel deformation monitoring. In: *IABSE Congress Ghent 2021, Structural Engineering for Future Societal Needs, Congress Proceedings*, Eds. H.H. Snijders, B. De Pauw, S.F.C. van Alphen & P. Menges, .pp. 580-587. IABSE, Zürich, 2021.
- Zhang, J., Zhao, M. 2017. A Method to Monitor the Circular Deformation of Metro Shield Tunnels in Soft Soils. In: *Proceedings of the 11th International Workshop on Structural Health Monitoring 2017*. DEStech Publications, Lancaster, PA, USA, 2017.

Characteristics of ultrasonics guided waves in timbers under moisture and temperature

R. Yassine & S. Mustapha

Laboratory of Smart Structures and Structural Integrity (SSSI), Department of Mechanical Engineering, American University of Beirut, Beirut, Lebanon

ABSTRACT: The application of ultrasonic guided waves (GWs) in evaluating the structural integrity of timber utility poles has shown high potential in detecting and assessing various types of defects. Yet, the effects of temperature and moisture content (MC) on the propagation of GWs are not well-understood and the uncertainty that may influence the results is not well-investigated. This study aims to scrutinize the effect of MCs (0% to 24%) and temperatures (-20° till 100°C) on the propagation characteristics of bulk wave, longitudinal and circumferential GWs in-cylinder timbers excited at 10-20kHz. The results showed that at 0% MC the velocity change is insignificant due to absence of water. As MC increases below the Fiber Saturation Point (FSP), the difference in mode velocities is 20% at -20°C, 50% at 100°C, and 40% upon varying the timber's temperatures. Above FSP, the difference was less than 2% at fixed temperatures and 58% under temperatures variations.

1 INTRODUCTION

1.1 Overview

Timber has long been used in various applications such as utility poles, as it is attributed to ease in production and adaptability in customized fabrications. The use of timbers as embedded utility poles for supporting overhead power electrical and communication lines, expose them to critical external factors affecting its mechanical characteristics (Bandara et al., 2021). At high moistures, the timbers become a favorable region for fungus and termite attacks yielding to complete material degradation with no exterior visible signs (Bandara et al., 2021). Accordingly, yearly inspections are employed on utility poles, which in some cases is unnecessary since the timbers might be healthy and serviceable (Bandara et al., 2021). Therefore, maintenance times should be scheduled based on continuous monitoring of timber poles and data assessment to ensure their safety, reduce maintenance cost, and prolong its lifetime by early damage detection.

Condition assessment of timber poles includes destructive, semi-destructive, and non-destructive techniques (NDT) (Rose, 2014). Destructive and semi-destructive testing apply a load and drilling on the structure, respectively, and assess its material properties based on its response. Sound poles will have higher resistance to load and drilling, and it decreases with material degradation. However, these techniques yield to permanent damage effect and provide discontinuous information about the structural health. From that ground NDT comes as a sufficient technique for structural health assessment based on its response to an input excited along the structure as waves or vibrations with no permanent effect (Rose, 2014). As stress waves propagate within the timber, any change in the applied loading, boundary conditions, material properties, are observed and detected as a change in the wave characteristics (Bandara et al., 2021). These methods are used frequently as they provide crucial information about the health of the structure and the effect of the surrounding environment while using simple and economical tools (Bandara et al., 2021).

Much research effort over the years employed stress waves on in-service utility poles to determine its embedment length, identify damages for health assessment, and investigate the effect of surrounding environment on the GWs in timbers. Subhani et al. (Subhani et al., 2013) used sonic stress waves to investigate the effect of timber's mechanical behavior (transversely isotropic vs. isotropic) on detecting its boundary conditions. Isotropic material assignment of timbers was not able to detect any change in the GW due to the surrounding soil, whereas transversely isotropic the GW velocity was greatly shifted. El Najjar and Mustapha (El Najjar and Mustapha, 2020), investigated the timber's embedded length and the presence of defects using GW reflections numerically and validated experimentally. The GWs are actuated using Macro Fiber Composites (MFC) (Smart Material Corp., 2017) transducers, where they studied MFC usage on rough curved surfaces as timbers. The authors aimed to improve the propagation of longitudinal modes by designing a ring of MFC actuators, which enhances the GW sensitivity to damage.

1.2 *Effect of moisture content and temperature on the propagating modes*

Timber's material can significantly degrade due to the surrounding temperature and MC which influence the propagation of the ultrasonic wave. The literature shows a decrease in the wave velocity as MC increases in all timber's orientations but at different rates (Bandara et al., 2021). Full saturation of water in the wood cells occurs at Fiber Saturation Point (FSP), where the timber's material changes negligibly, and consequently the GWs velocity remain constant. The FSP for Pine wood is 20% (Sakai et al., 1990). A work by Oliveira et al. (Oliveira et al., 2005) emitted GWs along the longitudinal and transverse timber's directions under MC variations from 6% to 60%. The longitudinal wave velocity of the BW dropped by 11.4% as MC varied, while the transverse wave velocity reduced by 7.6%. Acoustic waves were also used in the literature for assessing the effect of MC from 10 to 170% on propagating waves in the timber (Moreno Chan et al., 2011). The stress waves were emitted and received using a microphone. The work observed a rapid linear decrease in the BW velocity as MC varied below FSP at temperatures from -71° C to 59° C. Above FSP and at freezing temperatures, the BW velocity increased slightly and then decreased similarly to the other temperatures. At high MCs, the effect of high temperatures was larger than the velocity reduction at low temperatures from -71° C to -3° C.

This work evaluates the propagation of ultrasonic GWs (bulk, flexural and longitudinal) in Western White Pine timber pole actuated at various frequencies upon varying its temperature and MC. The work is studied numerically for a tapered timber pole model with transversely isotropic properties in COMSOL Multiphysics (Multiphysics, 1998). The ultrasonic waves are actuated and sensed using composite transducers (MFCs), which are mounted on curved the timber. The work scrutinizes the GW modes based on the dispersion curves obtained from DISPERSE (Pavlakovic and Lowe, 2003) as MC changes from 0% (dry condition) to values larger than the FSP, and temperature ranges from -20° C to 100° C excited at 10, 12.5, and 20 kHz.

2 METHODOLOGY

2.1 *Guided waves in solid circular structures*

The propagation of ultrasonics in cylindrical structures were studied and modeled extensively in the literature, whereby the longitudinal and flexural guided waves were strongly affected by the structure's health and hence can play as an important health indicator. The family of propagating modes are Torsional modes $T(n, m)$, Longitudinal modes $L(n, m)$ and Flexural modes $F(n, m)$ (Rose, 2014). Propagating modes are denoted by (n, m) , where the circumferential order (n) determines the symmetry of the solutions in the azimuthal direction and m is the branch number (Seco and Jiménez, 2012). Longitudinal and Torsional modes are axisymmetric with n denoted by zero $L(0, m)$, whereby non-axisymmetric flexural modes have $n > 0$ denoted by $F(1, m)$. The bulk longitudinal wave (BW) is constant at all exciting frequencies where m is denoted by 0, while the guided flexural and longitudinal modes depend on the exciting frequency. The first propagating modes are called Fundamental branches $L(0, 1)$ and $F(1, 1)$. The relation between the frequency and the group wave velocity is developed using the wavenumber of propagating GWs, which generates the dispersion curves for the longitudinal, and first-order

flexural modes (Rose, 2014). In this study, the dispersion curves for 22 cm diameter timber pole are generated using the DISPERSE software for transversely isotropic material properties (Table 1) (Green et al., 1999, Pavlakovic and Lowe, 2003).

Table 1. Material properties of the transversely isotropic white western Pine used in this study.

Material Property	Modulus of Elasticity			Shear Modulus of Elasticity			Poisson's ratio			Density
	E_L	E_R	E_T	G_{LR}	G_{LT}	G_{RT}	ν_{LR}	ν_{LT}	ν_{RT}	d
	GPa	GPa	GPa	GPa	GPa	GPa				kg/m^3
Value	11.11	0.866	0.866	0.577	0.577	0.0533	0.329	0.344	0.41	380

2.2 Numerical work

2.2.1 Material properties and characterization of timber poles

Timber is anisotropic, heterogeneously layered, and is mostly affected by the temperature and MC. Relevant studies in the literature states that an increase in timber's temperature yields to a decrease in the stiffness modulus ((Dinwoodie, 2000, Olsson and Salmén, 1997)). The range of MC in timbers that most influence its material properties are dry, below FSP, and after FSP conditions. Timbers under 0% MC have witnessed very low stiffness variation (6%) upon varying its temperature, and the variation increases to 40% at 20% MC (Dinwoodie, 2000). As more water is introduced to the timber, its material properties will vary until reaching full saturation, known as FSP = 20% (Sakai et al., 1990). Saturated timbers at elevated temperatures (>50° C) have observed the most loss in its properties (Olsson and Salmén, 1997). The stiffness is related to the temperature and MC through statistical analysis and empirical formulas derived from data collected under various temperature and moisture conditions. The stiffness-T-MC model that is applied in this work to find the mechanical properties of the timber numerical model under the three studied ranges of MC is shown in Equations (1) and (2) (Subhani et al., 2013). The tangential and radial E values are computed based on orthotropic relations with the longitudinal stiffness (Table 1) (Green et al., 1999).

$$E_a = E_0 (0.475 - 0.0038T) \quad (1)$$

$$(E_L - E_g)(E_L - E_0 + 5(E_0 - E_g)MC) = E_g^2 / 1000 \quad (2)$$

Where E_0 : stiffness at 0% MC, E_a : stiffness at instant T, and E_L is at a given temperature and MC.

2.2.2 Finite element analysis model

Finite element analysis (FEA) using COMSOL Multiphysics is employed in evaluating the effect of temperature and MC on the ultrasonic wave propagation (Multiphysics, 1998). Solid Mechanics and Electrostatics physics are used to model the piezoelectric devices. The actuation and sensing of GW by the piezoelectric transducer (PZT) is modeled using the Electrostatics physics module, and the particle displacement due to wave propagation is modeled using Solid Mechanics physics module. The numerical model is simulated on an Intel® Xeon® 2.10 GHz virtual machine with 64 GB RAM and 300 GB disc space. The FEA model is a 2 m tapered timber pole (Figure 1). The material is transversely isotropic (check Table 1) assigned using Equation (2) and the orthotropic relations for longitudinal, radial, and tangential stiffness as a function of temperature and MC (Green et al., 1999). The study covers timber's temperature of -20, 0, 20, and 100° C, and MC of 0, 12, 20 and 24%. The GWs are generated using MFCs as PZT placed 1 m apart. MFCs have the malleable ability to couple well on curved structures. The FEA model of the MFCs is modeled as a solid isotropic PZT of type PZT-5A despite its composite nature. The timber pole is singly actuated with the MFC emitting a 5-cycle Hanning window sine wave at 10, 12.5, and 20 kHz, and the MFC sensor is grounded with zero voltage sensing axial propagations. The exciting frequency should be set

in objective of tuning the propagating modes, and according to the dispersion curves high mode dispersion was seen at low frequencies. Hence, a frequency range of 10 to 20 kHz is considered where both longitudinal and flexural modes show relative stability. The GWs along the timber will be characterized based on their time of flight (ToF) from the actuator to the sensor. The model is discretized using a mesh size of 6 to 10 elements per wavelength (Marburg, 2002) resulting with 311408 as the total number of elements. This study explores the combination of the various factors including temperature, MC, and excitation frequency on the wave propagation characteristics.

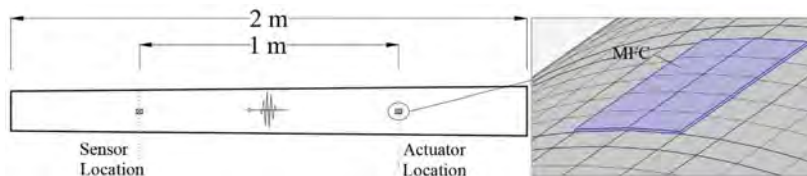


Figure 1. Numerical model of the timber pole, a top view sketch of traction free timber pole and close view of the generated mesh showing the curved MFCs acting as an actuator and as a sensor.

3 RESULTS AND DISCUSSION

The temperature and MC conditions affect the timber's material properties which varies the propagating GW characteristics. This effect is studied numerically, and the results are discussed in this section. Finite element analysis (FEA) tool is used to model the GWs propagation in the timber pole and its varying surrounding conditions, which is COMSOL Multiphysics. The timber pole is modeled as tapered with traction free boundary conditions, considering no embedment since it has minimal effect on the direct wave propagation characteristics unlike its effect on the wave reflections (El Najjar and Mustapha, 2020). The effect of temperature and humidity on the GW characteristics propagating in the timber pole is studied at the following exciting frequencies: 10, 12.5, and 20 kHz. The data collected from the sensor was assessed and modes are identified by the group velocities obtained from the dispersion curves generated by DISPERSE (Pavlakovic and Lowe, 2003).

3.1 Effect of moisture content

The effect of timber's MC varying from 0% to 24% on the ultrasonic GW at 0° C excited at 12.5 kHz is displayed in Figure 2. The increase in MC yielded to modes arriving at longer times, and it was observed at all temperatures but displayed for 0° C only. The BW is the first arriving mode with a group velocity of 5000 m/s (El Najjar and Mustapha, 2020), after which the sensor receives the first order flexural mode F(1, 1) and the longitudinal mode L(0, 1) with 1498 m/s and 1226 m/s, respectively. As MC increases to 24%, the BW velocity is reduced by 27%, and F(1, 1) and L(0, 1) by 18%. The F(1, 1) and L(0, 1) modes propagated at similar speeds, and hence were difficult to be distinguished. The F(1,2) and L(0, 2) modes showed less dispersion upon varying the timber's temperature and MC. The F(1, 2) mode arrives in a distinctive wave packet with a speed of 1932 m/s at 0% MC and decreased till 1360 m/s at 24% MC. The L(0, 2) observed a 26% reduction in the velocity arriving with 1039 m/s at 0% MC and dropped to 769 m/s at 24% MC. The reduction in the wave velocities for F(1, 2) was higher with 29.6%. The increase in MC affected the second branch modes more than the first branches. Identifying the F(1, 3) was intricate and the mode peak observation and tracing was ambiguous with 36% difference in the wave velocity as MC varied. The received wave signals at FSP and beyond (MC \geq 20%) have the same shape and hence their characteristics are preserved as MC increases beyond FSP (Figure 2). The difference in the wave velocities beyond FSP at fixed temperatures is less than 2%.

3.2 Effect of temperature

The effect of varying timber's temperature from -20°C to 100°C on the ultrasonic GW at 0% MC excited at 12.5 kHz is displayed in Figure 3. At 0% MC, the observations from the results show that the GW signal has preserved its velocity and amplitude. This observation draws a conclusion that at complete absence of water (MC=0%) under varying temperatures the variation in the material stiffness is negligible since all wave velocities are maintained. Figure 4 validates this assumption upon plotting the variation of the material's stiffness at different temperatures and MCs. In Figure 4(a), the stiffness variation at varying MCs with respect to temperature variations is plotted, and Figure 4(b) presents the percentage difference of difference in stiffness along the temperature range as per the following relation $E_{\text{variation}} = E_{\text{at } -20^{\circ}\text{C}} - E_{\text{at } 100^{\circ}\text{C}}$. At 0% MC from -20°C to 100°C , the stiffness varied insignificantly with 0.07% difference with a value of 16 GPa (Figure 4(a)), while the literature computed a 6% stiffness difference within the temperature range of -20°C and 60°C (Dinwoodie, 2000). The stiffness slope varied in an increasing manner as MC increases with increasing temperature, which has led to a 40% velocity difference at MCs below FSP (MC=12%) and has increased to 58% at MCs above FSP (MC \geq 20%). The difference in stiffness modulus at fixed temperatures shows large difference as MC increases which led to large velocity variations, with 20% at -20°C , 50% at 100°C . Figure 4(b) shows that the percentage of stiffness difference between -20°C and 100°C increases from 0% at low MCs to 82.6% at higher MCs, however, a 40% reduction in stiffness is recorded in the literature at temperatures from -20°C till 60°C (Dinwoodie, 2000). At high MC values (\geq 20%), the material's stiffness plots are the same showing the highest variation (Figure 4(a)), by which the percentage difference became constant with 82.7% from -20°C to 100°C (Figure 4(b)) which explains the constant wave velocities (Dinwoodie, 2000, Sakai et al., 1990, Seco and Jiménez, 2012). The negligible difference in stiffness at high MCs in Figure 4(b) validates the observation that the material will not experience any further change beyond FSP due to full saturation (20% for Pine) (Sakai et al., 1990). Figures 5 and 6 present the wave propagation at 0°C under varying MC conditions excited by 10 kHz, and 20 kHz. At 10 kHz exciting frequency (Figure 5), and under dry conditions ($T=0^{\circ}\text{C}$ and MC=0%), the labeled modes propagate in indistinct wave packets. Mode peaks are packed closely, while only the trace of the second branch modes is apparent. As the exciting frequency is increased to 20 kHz (Figure 6), at 24% MC all modes are

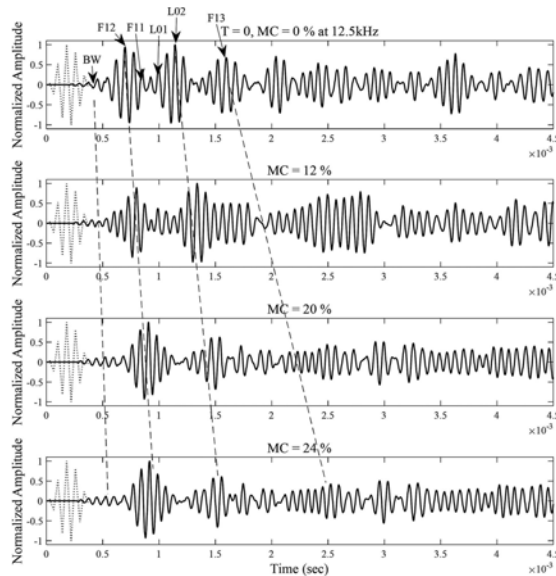


Figure 2. Raw signals of GW propagating at $T=0^{\circ}\text{C}$ with varying MCs: 0%, 12%, 20% and 24%, excited at $f=12.5\text{ kHz}$. The dotted lines show the shift to the right as MC increases.

distinctive and clearly traced upon changing the MC. However, at 12.5 kHz, the wave packets are less dispersive and maintained the shape of the 5-peak packet input signal. This was also seen in a work by El Najjar and Mustapha on a similar setup which was validated experimentally (El Najjar and Mustapha, 2020). MFCs have proved to be effective in acting as a transducer for stress GWs in timber poles due to their malleable ability to couple on curved surfaces. This work can distinctively identify and trace the BW and the second branch flexural and longitudinal modes as MC increases from 0% to 24% at constant temperatures.

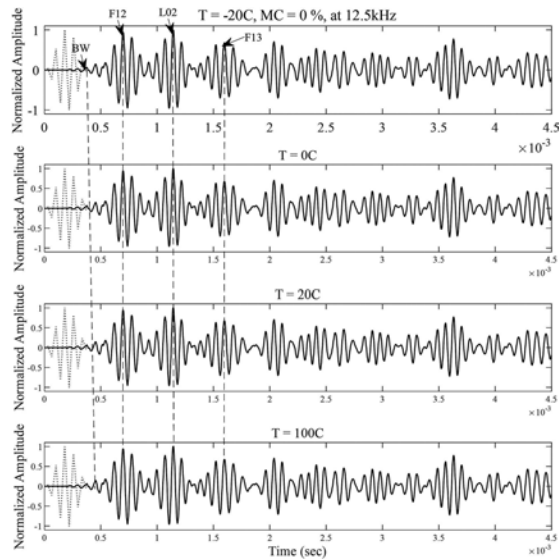


Figure 3. Raw signals of GW propagating at various temperatures, a MC=0 % and excited at $f=12.5$ kHz. The tracing of wave packets shows no shift in time as temperature varies in dry wood.

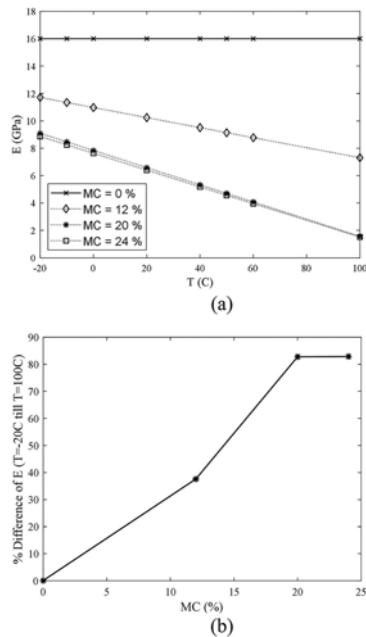


Figure 4. (a) Variation of modulus upon varying MC and temperatures, and (b) percentage difference of stiffness variation with respect to MCs between $T=-20^{\circ}$ C and $T=100^{\circ}$ C.

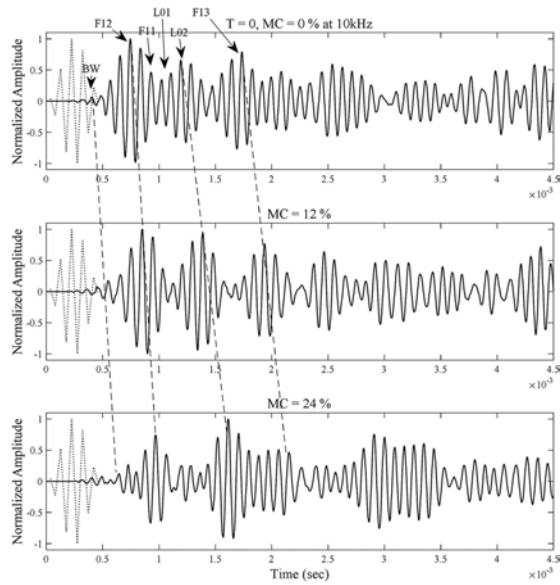


Figure 5. Raw signals of GW propagating at $T=0$ °C with varying MCs excited at $f=10$ kHz. The tracing of wave packets shows a shift to the right as MC increases.

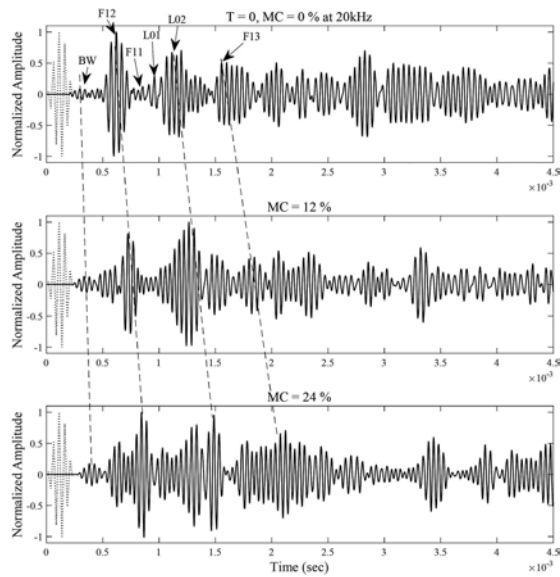


Figure 6. Raw signals of GW propagating at $T=0$ °C with varying MCs excited at $f=20$ kHz. The tracing of wave packets shows a shift to the right as MC increases.

4 CONCLUSIONS

Timber poles should be continuously monitored to ensure safe and proper performance. Ultrasonic guided waves (GWs) have proven that it can indicate the health of the structure as it is sensitive to various types of defects, material degradation, and surrounding temperature and moisture content (MC) conditions. This work studies the behavior of

ultrasonic GWs in transversely isotropic timber pole using COMSOL Multiphysics under varying temperature and MC. Microfiber Composite (MFC) transducers are coupled to the curved timber pole to actuate and sense the GWs to achieve proper propagation. The GWs velocities decrease due to the reduction of timber's stiffness as temperature and MC increase, and the drop is compatible with the literature. Temperature's effect on the GWs characteristics is insignificant at low MCs and prominent at high MCs, consequently affecting the GWs characteristics. At 0% MC, the timber's stiffness changes insignificantly as temperature varies, and hence the wave maintains its characteristics. The reduction in GW velocities is larger upon increasing MC below the Fiber Saturation Point (FSP). The full saturation in timber cells abstain any further variations in the stiffness, hence, the GW velocities decrease negligibly above FSP at constant temperatures. The modes that are able to characterize the timber's material and be visually distinguished and identified are the BW, F(1,2) and L(0,2).

ACKNOWLEDGMENTS

We acknowledge the financial support from the American University of Beirut by providing a PhD scholarship to the first author. We further acknowledge the support from the University Research Board at the American University of Beirut for their Award #103780.

REFERENCES

- Bandara, S., Rajeev, P. & Gad, E. 2021. Structural health assessment techniques for in-service timber poles. *Structure and Infrastructure Engineering* 40:1–21.
- Dinwoodie, J. M. 2000. *Timber: its nature and behaviour*. NewYork: CRC Press.
- El Najjar, J. & Mustapha, S. 2020. Understanding the guided waves propagation behavior in timber utility poles. *Journal of Civil Structural Health Monitoring* 10: 793–813.
- Green, D. W., Winandy, J. E. & Kretschmann, D. E. 1999. Mechanical properties of wood. *Wood handbook: wood as an engineering material*. Madison, WI: USDA Forest Service, Forest Products Laboratory, 1999. General technical report FPL; GTR-113: 4.1-4.45.
- Marburg, S. 2002. Six boundary elements per wavelength: Is that enough? *Journal of computational acoustics* 10(01): 25–51.
- Moreno Chan, J., Walker, J. C. & Raymond, C. A. 2011. Effects of moisture content and temperature on acoustic velocity and dynamic MOE of radiata pine sapwood boards. *Wood Science and Technology* 45: 609–626.
- Multiphysics, C. 1998. Introduction to COMSOL Multiphysics_ COMSOL Multiphysics. Burlington, MA, accessed Feb 9:2018.
- Oliveira, F. G. R. D., Candian, M., Lucchette, F. F., Salgon, J. L. & Sales, A. 2005. Moisture content effect on ultrasonic velocity in *Goupia glabra*. *Materials research* 8: 11–14.
- Olsson, A.-M. & Salmén, L. 1997. The effect of lignin composition on the viscoelastic properties of wood. *Nordic Pulp & Paper Research Journal* 12(3): 140–144.
- Pavlakovic, B. & Lowe, M. 2003. Disperse Software Manual Version 2.0. 1 6B. Imperial College, London, UK.
- Rose, J. L. 2014. *Ultrasonic guided waves in solid media*. NewYork: Cambridge university press.
- Sakai, H., Minamisawa, A. & Takagi, K. 1990. Effect of moisture content on ultrasonic velocity and attenuation in woods. *Ultrasonics* 28(6): 382–385.
- Seco, F. & Jiménez, A. R. 2012. Modelling the generation and propagation of ultrasonic signals in cylindrical waveguides. *Ultrasonic waves* 7:1–28.
- Subhani, M., LI, J. & Samali, B. 2013. A comparative study of guided wave propagation in timber poles with isotropic and transversely isotropic material models. *Journal of civil structural health monitoring* 3: 65–79.

Asset management – Towards adaptive resilient infrastructures

Shaikha AlSanad & Jafarali Parol

Kuwait Institute for Scientific Research, Kuwait City, Kuwait

ABSTRACT: In middle eastern countries, investment in infrastructure is at an all-time high. This also means that a large number of decisions are being made now that will affect the patterns of development for future generations. It is worth noting that infrastructure can also create harmful social and environmental impacts, increase vulnerability to natural disasters and leave an unsustainable burden of debt. Interestingly, these investments in the infrastructures are intended to increase economic prosperity and employment. It is possible to achieve the necessary economic, social, and environmental results within the framework of sustainable development goals by the creation and use of sustainable infrastructure. Disruptions in infrastructure services in the event of blackouts, road closures, water services, etc make us realize the importance of these assets in our day-to-day living. Therefore, we should manage infrastructure in the best possible way to ensure that they are resilient or can withstand extreme events, continue to provide service, and are affordable to users. Although a new discipline, IAM is evolving and attracting the attention of many agencies that own infrastructure. Due to the high cost of infrastructure in terms of money and time to build, governments and organizations managing infrastructure would want to maximize its value by extending the life of their assets.

1 INTRODUCTION

Infrastructure is one of the key components of the United Nations Sustainable Development Goals (SDG). Careful planning, designing, implementing, and operating of the infrastructures are necessary to create a sustainable infrastructure, and to achieve target economic, social, and environmental goals within the framework of the sustainable development goals. Infrastructure systems provide essential services such as energy, water, waste management, transport, and telecommunications. The infrastructures are sustainable if they ensure economic, social, environmental, and institutional sustainability throughout the entire life cycle. Infrastructures form the backbone of every society. Infrastructure projects are projects that have high public benefits with a large cost that ranges from one hundred million to several billions of Dollars, mostly planned or administered by a government to bring an important outcome such as economic development and social needs in accordance to a State's development program (Eberts, 2014; Buhr, 2003). They are distinctive by strategic importance, dynamic complexity, adaptability and extensive impacts as they play an important role in the contribution to economic and social growths, however, such characteristics make them vulnerable to crisis (Flyvbjerg, 2014). For instance, Infrastructure projects require a huge amount of capital and other resources, such as technology, equipment, and labor. The decision-making criteria at the initiation stage is critical during infrastructure planning to ensure an efficient allocation of resources and risk mitigation. Infrastructure projects include a wide range of service projects like public utilities projects such as power plants, gas projects, water projects, sanitation and sewage, cable systems; or it could public works projects such as roads, airports, urban transport, ports, oil and gas fields development, museums, concert halls, convention centers and city parks (Wang *et al*, 2020).

According to Choguill (1996) infrastructure is an essential element if urban sustainability is to be achieved. They suggested programs that involve progressive improvement of such infrastructure in a more efficient way and cost-effective manner. The objectives of this study were (1) a literature review of all kinds of existing infrastructure, (2) developing a model for the progressive improvement of the infrastructure in a sustainable manner, (3) demonstrating the sustainability of the model in terms of cost, maintenance, and level of technology, and (4) suggesting management structures to attain the sustainability of such infrastructure. It is emphasized that government, non-government organizations, and local communities must work together to design a system to build, operate, and maintain from the ground-up toward sustainable infrastructure. A white paper reported published by Randall Elberts, (2014) focusing on transportation infrastructure and its contribution to the economy was a 3-year effort to review methods used to estimate the value of transportation infrastructure. Part of this review is to provide what statistical information should be generated at the national level to the decision-makers. This review also includes alternative strategies for using statistical data, relative strengths and weaknesses of methods used, and potential benefits of improved methods and data.

Qureshi (2016) examined the environmental effects on the sustainability of infrastructure have been thoroughly studied. It is mentioned that public policy plays an important role in the development of a country's economy once infrastructure investment is initiated. To boost infrastructure sustainability and resiliency, some specific public policies required more detailed, prioritized, and sequenced to be tailored to country-specific needs. The public policies for sustainable infrastructure should be publicized in overall projects and country investment and growth strategies.

It is observed that systematic, holistic, and sustainable asset management in developing countries is not adequately established despite the huge financial issues in funding infrastructure projects (Tafazzoli, 2017). This is mainly because of the lack of cost-effective management and long-term strategies for operating, maintaining, and upgrading of infrastructure projects. It was suggested that the essence of changes over the conventional methods for managing the development of the infrastructure. This can be achieved by providing a data collection system and up-to-date tools to analyze those data. Such an approach will make informed infrastructure investment decisions easily accessible to the private sector/partners.

The importance of designing and planning the construction has been evaluated by establishing a well-defined predictive sustainability assessment method called multi-criteria decision analysis (Ek et al, 2019). This method is supposed to increase the positives and decrease the negatives of sustainability impacts in infrastructure projects. It was recommended to use this method in the procurement stage of the infrastructure project. However, it was suggested for more future sustainability assessments due to limited information, and should comply with some international standards mentioned in this study.

2 ASSET MANAGEMENT OF INFRASTRUCTURES

Buildings and bridges are the two important civil infrastructures. These infrastructures are key elements of a city's development and social fabric. In Particular, bridges are critical to the operation of any city's road networks. Therefore, proper maintenance of bridge infrastructures is essential in order to ensure safety and minimize associated risks and more accurate short and long-term financial planning. Structural health monitoring technology is an important tool that allows city planners to collect data from the bridge infrastructures and to ensure safety and performance.

It is important to note that the resilience of infrastructures is the primary parameter of asset management. The data should be collected from all the bridges in the city in order to prepare an effective asset management plan. Individual bridges are seen as parts of wider networks and bridge risk and criticality assessment emphasize bridge failure or underperformance risk in the network context. It is therefore necessary to integrate the SHM system into the city's asset management plan. SHM has an important too in bridge asset management. An SHM system implemented in Kuwait as a pilot project is depicted in Figure 1.

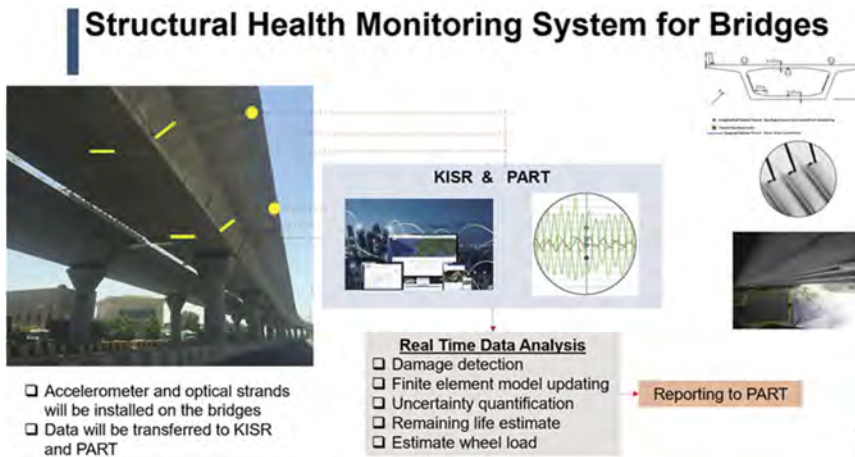


Figure 1. SHM system implemented in a concrete Highway bridge in Kuwait.

In the bridge SHM system implemented in Kuwait, we have used accelerometers, strain-measuring optical strands, inclinometers, and temperature sensors. The data collected from the sensors are used to obtain an evolution score showing the behavior of the bridge structure, at every important location (based on data measuring location). The structural stability is then represented using the scale in Figure 2.

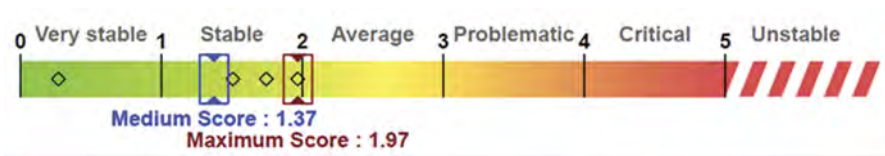


Figure 2. Stability Index used in the bridge SHM system in Kuwait.

The indicator can be used for planning maintenance, repair, retrofiting, etc. Therefore, this is an important indicator of the ecomanagement. If the SHM system is installed at several bridge networks, such a stability index can be prepared for each bridge and the city planners can use the indicators for the asset management plan. A sample of measured data from the bridge SHM system that is an important input for asset management is shown in Figure 3.

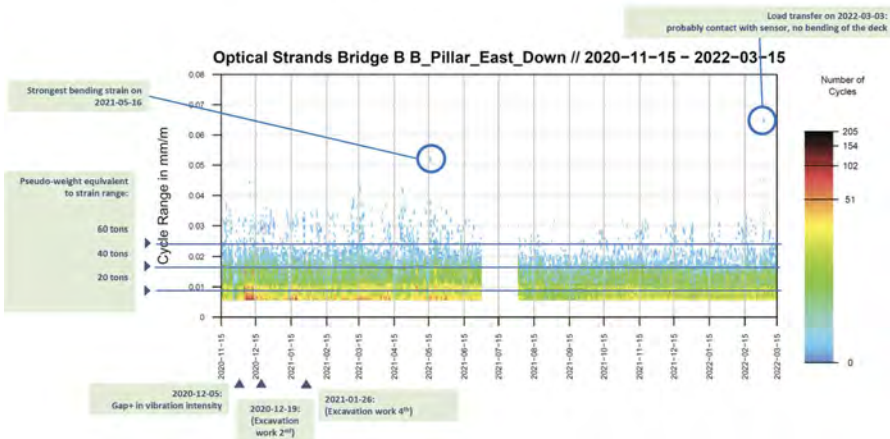


Figure 3. Measured strain from a typical optical strand (2 years of data).

We have implemented weigh-in-motion so that the weight of the truck can be estimated and connected to the bridge response. The entire life cycle events can be connected in a single window (Figure 4), which is quite handy for asset management. The resilience of the bridge infrastructure significantly improves if a proper asset management plan is in place based on the actual measured data.



Figure 4. Single window access to life cycle event.

Our experience is that SHM data is quite vital for major and regular maintenance, life estimation, etc, and, in general, asset management of infrastructures. Such a system also improves infrastructure resilience.

3 SUMMARY AND CONCLUSION

Although modern-day infrastructure is designed to ensure that large and complex structures perform safely in harsh environments under various loading conditions, deterioration and damage can occur during their operational life. Consequently, the protection, maintenance, and repair of infrastructure assets are crucial. Achieving optimal asset management is challenging, as the life-cycle costs of these activities must be minimized while ensuring that infrastructure performance and reliability related to the asset's condition, serviceability, safety, and capacity are adequately addressed. SHM is a technology that, if used strategically, can help to address these challenges. Currently, SHM technologies are used to assess structural performance, detect damage and continuously monitor the condition of a structure. These technologies have enabled data collection to support comprehensive asset management analysis and evaluation processes. However, SHM has not been explicitly designed to provide actionable information to assist asset management decision-making. With many infrastructure assets nearing their end of life, mainly those nearing their end of design service life, the management process focuses on the later stages of the asset's (infrastructure) life to prolong its usefulness through maintenance, rehabilitation, and replacement. We have briefly shared our experience in asset management of bridge infrastructures in Kuwait and how it can enhance infrastructure resilience.

REFERENCES

- Buhr, W., 2003. What is infrastructure? (No. 107-03). Volkswirtschaftliche Diskussionsbeiträge.
 Choguill, C.L., 1996. Ten steps to sustainable infrastructure. *Habitat International*, 20(3), pp. 389–404.
 Eberts, R.W., 2014. White paper on valuing transportation infrastructure.

- Ek, K., Mathern, A., Rempling, R., Rosén, L., Claeson-Jonsson, C., Brinkhoff, P. and Norin, M., 2019. Multi-criteria decision analysis methods to support sustainable infrastructure construction. In Proceedings of the IABSE Symposium.
- Flyvbjerg, B., 2014. What you should know about megaprojects and why: An overview. *Project management journal*, 45(2), pp .6–19.
- Qureshi, Z., 2016. Meeting the challenge of sustainable infrastructure: The role of public policy.
- Tafazzoli, M., 2017, October. Strategizing sustainable infrastructure asset management in developing countries. In *International Conference on Sustainable Infrastructure* (pp. 375–387).
- Wang, A. and Pitsis, T.S., 2020. Identifying the antecedents of megaproject crises in China. *International Journal of Project Management*, 38(6), pp .327–339.

*SS32: Corrosion-induced structural damage and prevention
measures for reinforced concrete infrastructure
Organizers: S. Yang, F. Tang & W. Zhang*



Taylor & Francis

Taylor & Francis Group

<http://taylorandfrancis.com>

Corrosion and bond behavior of silicate dioxide particle modified enamel coated steel bar

F. Tang, Y. Kuang & H. Cui

School of Civil Engineering, Dalian University of Technology, Dalian, China

Z. Lin

Department of Civil, Construction and Environmental Engineering, North Dakota State University, Fargo, USA

ABSTRACT: Protective coating is considered to be one of the most economical and effective methods to protect steel from corrosion, as it can establish a physical barrier between the steel and the corrosive environment. In this study, silicate dioxide particle modified enamel (SDPME) coating is proposed for improved corrosion resistance and enhanced bond strength of steel bars in concrete structures. Plain steel bars with a diameter of 12 mm were used. Enamel slurry was made by mixing enamel frits with tap water, and silicate dioxide particle with an average size of 0.50 mm was added. The silicate dioxide particle is 10 wt.% of the enamel frits. The steel bars were dipped into the enamel slurry for 2 minutes and moved out, and then placed in a furnace at 800°C for 5 minutes, and finally cooled down to room temperature to produce SDPME-coated steel bars. The corrosion resistance of the SDPME-coated steel bar was tested by immersing in saturated calcium hydroxide solution containing 3.5 wt.% NaCl with open circuit potential, linear polarization resistance and electrochemical impedance spectroscopy. The bond strength was determined by using pull-out tests of SDPME-coated steel bar when embedded in concrete specimens. For comparison, both the corrosion resistance and bond strength of uncoated and pure enamel coated steel bars were also tested. Electrochemical corrosion results show that the corrosion resistance of SDPME-coated steel bar is ~300 times higher than that of the uncoated one. Pull-out tests demonstrate that the bond strength of SDPME-coated steel bar is 3.63 times greater than that of the uncoated steel bar. Therefore, SDPME coating increases both the corrosion resistance and the bond strength of steel bar.

1 INTRODUCTION

Concrete is a porous construction material, and the aggressive chemicals in the environment such as chloride can penetrate through the concrete cover to reach the surface of steel rebar and results in steel rebar corrosion (Angst, 2018). Corrosion of steel rebar causes cross-sectional area loss, concrete cover cracking, bond degradation, and consequently a reduction in the carrying capacity of both structural members and system (Li & Yang, 2011; Zhao et al, 2022; Tang et al, 2022). Application of rebar coatings is considered to be one of the most effective and economical methods to protect steel rebar from corrosion attack. The most widely used steel rebar coating is fusion bonded epoxy (FBE) coating, however, a major side effect of applying the FBE coating is the considerable reduction in the bond strength between steel bars and the surrounding concrete (Choi et al, 1991). Besides, under-film corrosion is prone to occur due to weak adherence of FBE coating with substrate steel (Tang et al, 2016).

Enamel coating, which is made by firing powdered glass on the surface of metal at temperature between 750 and 850 °C, is widely used in industry container or household application

(Jones, 1995). The enamel coating has many advantages, such as chemical inertia, corrosion resistance, flexible properties, and therefore has been used as a coating material for steel rebar (Tang et al, 2012a, 2012b, 2013; Yan et al, 2012). Previous studies show that enamel coating improves the corrosion resistance of steel rebar and enhances the chemical adherence with the steel substrate, and therefore prevents under-film corrosion (Tang et al, 2012a). As the enamel coating has a shining and smooth surface, silicate calcium has been added in the enamel frit during the firing process to manufacture chemically reactive enamel coating, which can chemically bond with the surrounding concrete. This chemically reactive enamel coating increases the bond strength with concrete (Yan et al, 2012). However, the corrosion resistance decreases due to presence of connected channels in the coating (Tang et al, 2012b, 2013). Therefore, it is necessary to modify the enamel coating for increase in both corrosion resistance and bond strength.

In this study, a silicate dioxide particle modified enamel (SDPME) coating, which is made by adding silicate dioxide particle in the pure enamel coating, is proposed for improved corrosion resistance and enhanced bond strength of steel bars in concrete structures. The corrosion performance is characterized by immersing in saturated calcium hydroxide solution containing 3.5 wt.% NaCl with electrochemical techniques including open circuit potential, linear polarization resistance and electrochemical impedance spectroscopy. The bond strength with concrete is determined through pull-out tests.

2 EXPERIMENTAL DETAILS

2.1 Specimen preparation

Table 1 shows the chemical composition of pure enamel (PE) coating. Plain steel bars with a diameter of 12 mm were used. Enamel slurry was made by mixing enamel frits with tap water, and silicate dioxide particle with an average size of 0.50 mm was added. The silicate dioxide particle is 10 wt.% of the enamel frits. The steel bars were dipped into the enamel slurry for 2 minutes and moved out, and then placed in a furnace at 800°C for 5 minutes, and finally cooled down to room temperature to produce silicate dioxide particle modified enamel (SDPME) coated steel bars. The yield strength and ultimate strength of the uncoated steel bars were 531.60 MPa and 613.01 MPa, respectively.

Table 1. Chemical composition of enamel coating.

Composition	Content(%)
SiO ₂	37.8
Al ₂ O ₃	15.8
B ₂ O ₃	14.6
KCO ₃	6.7
Li ₂ CO ₃	5.4
MnO ₂	5.2
NaNO ₃	4.8
CaF	3.6
TiO ₂	2.7
NaCO ₃	1.7
NiO	1.2
CoO	0.5

Figure 1 shows the dimensions of the steel bar specimens for electrochemical corrosion tests. The SDPME-coated steel bars were cut into a piece of 60 mm long, and one end was soldered with a copper wire for electrochemical corrosion tests. To limit the coated surface exposed to the test solution, the two ends of the steel bar were encased in PVC pipes filled with epoxy resin. Therefore, the length of steel bar is 40 mm and the surface area is approximately 15.08 cm² as

shown in Figure 1. For comparison, both pure enamel (PE) coated and uncoated steel bar specimens are also prepared and tested.

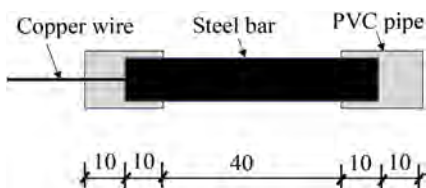


Figure 1. Steel rebar specimen for electrochemical corrosion test (unit: mm).

Figure 2 shows the concrete block specimen design for pull-out tests. The side length of the concrete block specimens is 120 mm. A 60 mm bonded length was used to achieve a relatively uniform bond stress distribution. Polyvinyl Chloride (PVC) pipes were used to create the unbonded regions in the specimens to prevent cone-type failure of the concrete at the loaded end.

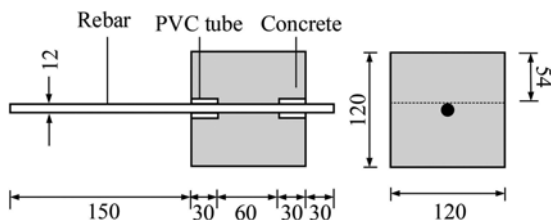


Figure 2. Detail of pull-out test specimen (unit: mm).

The mix proportion of concrete is presented in Table 2. Three 150×150×150 mm concrete cubes were prepared and the average compressive strength at 28 days was 43.05 MPa.

Table 2. Mixture proportion of concrete.

Target concrete grade	w/c	Mix proportions (kg/m ³)				Mean compressive strength (MPa)
		Cement	Water	Sand	Coarse aggregate	
C30	0.47	350	165	719	1173	43.05

2.2 Electrochemical corrosion test

The steel rebar specimen including uncoated, PE-coated and SDPME-coated was first immersed in saturated calcium hydroxide solution for one week and then 3.5 wt.% NaCl powder was added. Electrochemical corrosion tests including open circuit potential (OCP), linear polarization resistance (LPR) and electrochemical impedance spectroscopy (EIS) were performed after three days of the addition of NaCl powder. The three-electrode system was used as shown in Figure 3: the steel bar worked as the working electrode, a platinum sheet with 20 mm ×20 mm×0.2 mm served as the counter electrode, and saturated calomel electrode (SCE) was the reference electrode. All of them are connected with Gamry reference 600 plus for data acquisition. LPR was conducted from -15 mV to +15 mV around the OCP with a scan rate of 0.167 mV/s. EIS was performed by applying a sinusoidal potential 10 mV around the OCP from 100 kHz to 5 mHz with a rate of 5 points per decade.

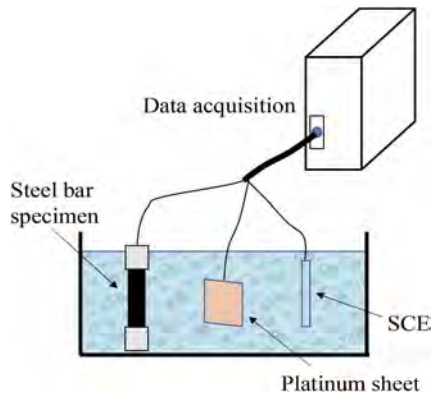


Figure 3. Electrochemical corrosion test setup.

2.3 Pull-out test

Figure 4 shows the pull-out test setup. A material testing machine with a capacity of 100 kN was used through displacement control. The loading rate used was 0.06 mm/s. Each specimen was installed with two Linear Variable Differential Transformers (LVDTs) at the end of the loaded and the free end of the concrete block specimen, respectively. The test terminated when the recorded free end displacement reached 20 mm. Test data were collected by IMC dynamic measurement system.



Figure 4. Pull-out test setup.

3 RESULTS AND DISCUSSION

3.1 Bond strength

Assuming a uniform distribution of bond stresses along the bonded length of the bar, then the average bond stress (τ) was calculated as follows:

$$\tau = \frac{P}{\pi dl} \quad (1)$$

where P is the pullout force, d is the nominal diameter of the rebar, and l is the bonded length.

Figure 5 compares the maximum bond stress (bond strength) of uncoated, pure enamel (PE) coated, and SDPME-coated steel bar. It can be observed that the bond strength of uncoated plain steel bar is 3.2 MPa, and the bond strength of enamel coated steel bar increases up to 4.29 MPa. The bond strength of SDPME-coated steel bar is 11.62 MPa, which is 3.63 and 2.17 times greater than the uncoated and PE-coated steel bar, respectively. The significant increase in the bond strength for SDPME-coated steel bar is attributed to the increase of the surface roughness of enamel coating after addition of silicate dioxide particles.

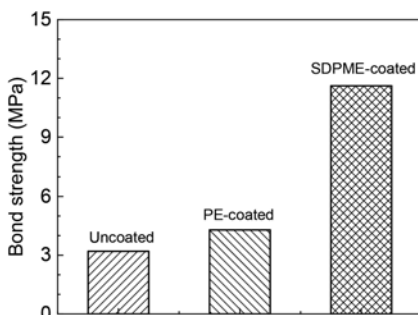


Figure 5. Comparison of bond strength.

3.2 Corrosion resistance

Figure 6a shows that comparison of open circuit potential (OCP) of uncoated, PE- and SDPME-coated steel bars immersed in saturated calcium hydroxide solution with 3.5 wt.% NaCl. The OCP of uncoated steel bar is -651 mV/SCE, which is more negative than those of PE- and SDPME-coated steel bars. The OCP of SDPME-coated steel bar is -547 mV/SCE, which is greater than the OCP of PE-coated steel bars (i.e., -574 mV/SCE). The corrosion current density obtained from the linear polarization resistance is shown in Figure 6b. The uncoated steel bar has a corrosion current density of $0.17 \mu\text{A}/\text{cm}^2$, which is lower than the typical active corrosion rate of steel bar (Tang et al, 2012b). This is because the majority of the steel bar is covered with a passive film and only small pitting corrosion occurred, and the corrosion current density is average by the entire surface area of the steel bar. The corrosion current density of PE- and SDPME-coated steel bar is $0.84 \text{ nA}/\text{cm}^2$ and $0.39 \text{ nA}/\text{cm}^2$, respectively, which is almost 1000 times lower than the uncoated steel bar. Therefore, SDPME-coating significantly increases the corrosion resistance of steel bar.

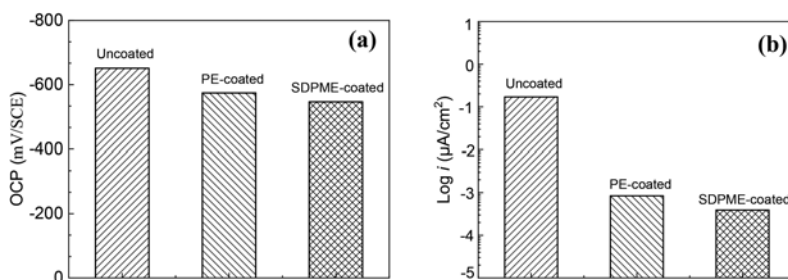


Figure 6. Comparison of (a) OCP, and (b) corrosion current density.

Figure 7 shows the impedance spectrum of uncoated, PE- and SDPME-coated steel bar immersed in saturated calcium hydroxide solution containing 3.5 wt.% NaCl solution in the format of both Nyquist and Bode plots. The impedance was fitted by using electrical circuit as shown in Figure 8: model (a) is used for uncoated steel bar and model (b) was used for PE- and SDPME-coated steel bar. In these models, R_s is the solution resistance, R_c is the coating

resistance, CPE_c represents the nonideal capacitive behavior of coating, R_{ct} is the charge transfer resistance, and CPE_{dl} represents the non-ideal capacitance behavior of the double layer at the interface where corrosion occurs between the solution and the steel bar.

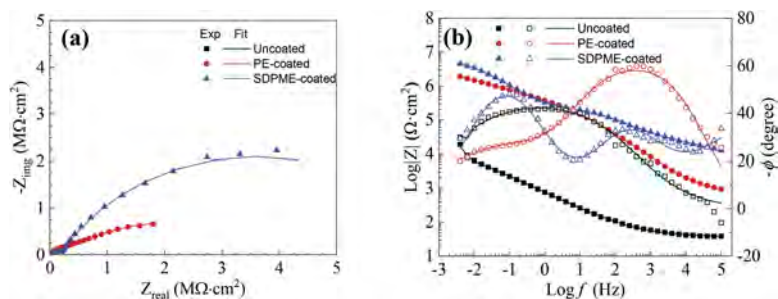


Figure 7. EIS in the format of (a) Nyquist, and (b) Bode plots.

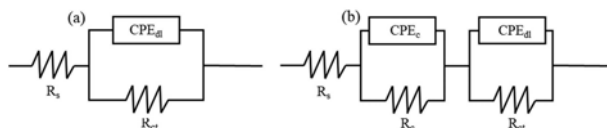


Figure 8. Equivalent electrical circuit for (a) uncoated, and (b) PE- and SDPME-coated steel bar.

Figure 9 shows the charge transfer resistance of uncoated, PE- and SDPME-coated steel bars extracted from the impedance spectrum in saturated calcium hydroxide solution containing 3.5 wt.% NaCl. The charge transfer resistance of uncoated steel bar is $22.15 \text{ k}\Omega\text{cm}^2$. The charge transfer resistance of PE- and SDPME-coated steel bar is $4.15 \text{ M}\Omega\text{cm}^2$ and $6.79 \text{ M}\Omega\text{cm}^2$, respectively. The charge transfer resistance of SDPME-coated steel bar is ~ 300 times greater than that of the uncoated steel bar. Therefore, the SDPME coating dramatically enhances the corrosion resistance of steel bar.

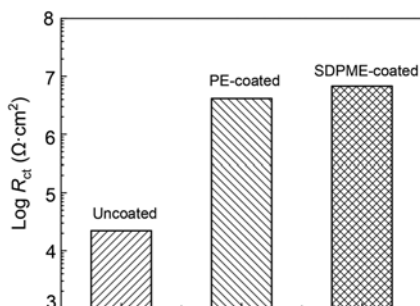


Figure 9. Comparison of charge transfer resistance.

4 CONCLUSIONS

The bond strength and corrosion resistance of silicate dioxide particle modified enamel (SDPME) coated steel bar are experimentally investigated in this study. Pull-out was conducted to determine the bond strength. Linear polarization resistance and electrochemical impedance spectroscopy were used to quantify the corrosion resistance of SDPME-coated steel bar in saturated calcium hydroxide solution containing 3.5 wt.% NaCl. For comparison,

uncoated and pure enamel coated steel bar specimens are also prepared and tested. Based on the results and discussion, the following conclusions can be drawn:

- (1) Both pure enamel and silicate dioxide particle modified enamel improve the bond strength of steel bar with concrete. The bond strength of PE and SDPME-coated steel bar is 1.34 and 3.63 times greater than that of the uncoated steel bar.
- (2) The corrosion current density of PE- and SDPME-coated steel bars is 0.84 nA/cm² and 0.39 nA/cm², respectively, which is almost 1000 times lower than the uncoated steel bar.
- (3) The charge transfer resistance of SDPME-coated steel bar is 6.79 MΩcm², which is ~300 times greater than that of the uncoated steel bar.

REFERENCES

- Angst, U.M., 2018. Challenges and opportunities in corrosion of steel in concrete. *Materials and Structures* 51(4): 1–20.
- Choi, C.C., Hadje-Ghaffari, H., Darwin, D., & McCabe, S.L. 1991. Bond of Epoxy-Coated Reinforcement: Bar Parameters. *ACI Materials Journal* 88(26): 207–217.
- Jones, D.A. 1995. Principle and prevention of corrosion. 2nd edition, Pearson, NJ, United States.
- Li, C., Yang, S. 2011. Prediction of concrete crack width under combined reinforcement corrosion and applied load. *ASCE Journal of Engineering Mechanics* 137(11): 722–731.
- Tang, F., Chen, G., Brow, R. K., Volz, J. S., & Koenigstein, M. 2012a. Corrosion resistance and mechanism of steel rebar coated with three types of enamel. *Corrosion Science* 59: 157–168.
- Tang, F., Chen, G., Volz, J. S., Brow, R. K., & Koenigstein, M. 2012b. Microstructure and corrosion resistance of enamel coatings applied to smooth reinforcing steel. *Construction and Building Materials* 35: 376–384.
- Tang, F., Chen, G., Volz, J. S., Brow, R. K., & Koenigstein, M. 2013. Cement-modified enamel coating for enhanced corrosion resistance of steel reinforcing bars. *Cement and Concrete Composites* 35(1): 171–180.
- Tang, F., Chen, G., Brow, R. K. 2016. Chloride-induced corrosion mechanism and rate of enamel- and epoxy-coated deformed steel bars embedded in mortar. *Cement and Concrete Research* 82: 58–73.
- Tang, F., Lin Z., Qu, H., Chen, G. 2022. Investigation into corrosion-induced bond strength degradation between concrete and steel rebar with acoustic emission and 3D laser scan techniques. *Journal of Infrastructure Preservation and Resilience* 3: 1–18.
- Yan, D., Reis, S., Tao, X., Chen, G., Brow, R. K., & Koenigstein, M. 2012. Effect of chemically reactive enamel coating on bonding strength at steel/mortar interface. *Construction and Building Materials* 28 (1):512–518.
- Zhao, L., Tang, F., Verstryngge, E., Ren, L., Li, H. 2022. Experimental and numerical investigation into corrosion-induced mortar/concrete cracking with distributed optical fiber sensors. *Journal of Civil Structural Health Monitoring* 12: 943–960.

Non-destructive investigation of corrosion in reinforced concrete structures and modelling the structural degradation

S.T. Yang, F. Zhang & Z. Yin
University of Strathclyde, Glasgow, UK

X. Xi
University of Science and Technology Beijing, Beijing, China

ABSTRACT: Corrosion-induced concrete cracking is a significant durability problem for reinforced concrete structures. Conventional method of examining corrosion progression is upon crushing the corroded samples which led to inaccurate or in some cases misleading estimation. This has hindered the development of rational corrosion models as reliable experimental data are rather limited. In this research, the chloride-induced corrosion progression of the steel bar in concrete was investigated by X-ray Computed Tomography (i.e., XCT). 3D XCT images were obtained and processed to characterize the different material phases. It has been found that pitting corrosion is prone to appear around the voids close to the steel bar, mainly due to the pre-existing supply of oxygen and moisture. In addition, a distinct transverse crack has been identified which is caused by non-uniform corrosion along the reinforcing steel bar. A non-uniform corrosion model was then parameterized based on the XCT results. It can be concluded that the combination of the use of wetting and drying cyclic corrosive environment and the XCT scanning can provide a new method to the non-destructive investigation of corrosion process, rust distribution and corrosion-induced concrete cracking in the reinforced concrete structures.

1 INTRODUCTION

Corrosion of the reinforcement in concrete structures is arguably the most significant durability problem, affecting the serviceability and safety of civil engineering structures and infrastructures. Corrosion can cause cracking of concrete and de-bonding between the reinforcement and concrete, which may destroy the integrity of concrete cover, reduce the reliability of concrete and lead to premature failure of the structures and infrastructures. Under the climate change, the aging infrastructure will face exacerbated deterioration which warrants new research in understanding the corrosion in civil engineering.

Over the last few decades, considerable researches have been conducted in understanding the corrosion mechanism (Česen et al. 2013; Angst and Elsener 2017), predicting the structural effect (Bazant 1979; Yang et al. 2018), preventing the corrosion initiation and propagation (Melchers and Li, 2009), etc. In particular, a variety of experiments have been carried out in understanding the corrosion phenomena of the reinforcement and the corrosion-induced concrete cracking (González et al. 1995; Andrade et al. 1993; Mullard and Stewart 2011). To understand the corrosion development of the reinforced concrete structures, the traditional method is to employ destructive means, i.e., cutting the samples to physically expose the cross section and then analysing the corrosion progression between the steel bar and the concrete. It was usually followed by crush of the samples for weighing the mass of the corroded steel to calculate of corrosion degree. This approach has been widely used to help understand the rust properties and distributions, the corrosion effect on the steel-concrete interface and the

corrosion products expansion behaviour coupled with digital optical microscope, scanning electron microscope (SEM) and energy-dispersive X-ray spectroscopy (EDS). However, the microstructures of the reinforced concrete samples are very likely to be affected or interfered by the cutting, grinding and polishing processes. Moreover, the technician skills, processing procedure and measuring method are likely to affect the results.

Using non-destructive imaging method, e.g., XCT, has become a promising approach to investigate the corrosion behaviour of the reinforced concrete structures. The distinct advantage of XCT test on corrosion of reinforced concrete is the corrosion development, e.g., initiation, propagation and rust distribution, can be imaged without any physical cut or smash. Beck (2007) perhaps first applied the XCT method to investigate the corrosion process of the reinforcing steel in a mortar cylinder with a height of 90 mm and a diameter of 40 mm. Michel et al. (2011) employed XCT to study the corrosion products and the formation and propagation of cracks in a reinforced mortar prism sample with a resolution of 75 μm . Šavija et al. (2014) investigated the corrosion induced cover cracking in a mortar cylindrical specimen with a diameter of 34.1 mm by XCT scanning with a resolution of 16 μm . Dong et al. (2017) observed the development of steel corrosion, corrosion products formation, as well as the subsequent initiation and propagation of corrosion-induced cracks by XCT. Itty et al. (2014) compared the difference in morphology of corrosion deterioration in the case of carbon steel or stainless steel reinforcement in mortar cylinders.

This paper attempts to investigate the corrosion progression of the reinforced concrete structure by XCT test, under the accelerated wetting and drying cyclic corrosion. High resolution XCT images are obtained and then processed by in-house scripts, to reliably characterize the different material phases, consisting of, steel bar, mortar, corrosion products and voids/cracks. The corrosion products expansion behaviors are analysed and discussed; the corrosion degree and the maximum and average radial losses of steel bar along the longitudinal direction are then evaluated. Further, the corrosion progression data obtained from analyzing the XCT results are used to parameterize a non-uniform corrosion model. This non-uniform corrosion model can then be applied to modelling the corrosion-induced concrete cracking problems with confirmed accuracy.

2 NONDESTRUCTIVE XCT ASSESSMENT

2.1 *Image processing and segmentation*

Figure 1 shows the reconstructed images of the specimen exposed to the corrosive environment for 112 days. The XCT attenuation value is quantified on a grey value scale with 65,536 levels (i.e., 16-bit image), which provide higher quality presentation than 256 levels (8-bit image). In the meantime, the 16-bit image data is much larger than an 8-bit image. Since steel, corrosion products, mortar and voids or cracks have different densities, the attenuation of X-ray will produce different grey values, in a wide range, as illustrated in Figure 1.

Depending on the densities of the materials, the XCT pictures show different grey value for each of the material phases; the denser material shows the brighter in the XCT image and has the higher grey value. In this study, we used trial and error approach coupled with manual check-up to identify the phases at some suspicious points. Once the thresholds are determined, they are then used for segmentation of the raw images. By using the segmentation thresholds, the 3D images of the corroded reinforced mortar sample can be separated and recognized in terms of the mortar, steel bar, corrosion products and voids/cracks. Figure 2 shows the 3D images of (a) mortar, (b) steel bar after corrosion, (c) distribution of corrosion products and (d) distribution of voids and cracks around the corner. In Figure 2(a), clearly, there are 2 longitudinal cracks presenting; most interestingly, a transverse crack close to the bottom of the sample also appears. The transverse crack takes place where the most corrosion products are accumulated along the longitudinal direction. This changes our usual understanding that corrosion induced concrete cracking is normally longitudinal cracking, whilst transverse cracks can also be induced by reinforcement corrosion. Moreover, it has been found that the transverse crack initials from the concrete surface and propagates towards the steel bar. From Figure 2(b) it can

be seen the corrosion of the steel bar is non-uniform along both the longitudinal and the circumferential directions. Figure 2(c) shows the accumulation of corrosion products along the reinforcing bar; it should be noted that the thickness of the cylindrical wall significantly varies, though it cannot be clearly observed from this figure and especially the current viewing angle. Figure 2 (d) illustrates the pore voids and cracks due to corrosion expansion.

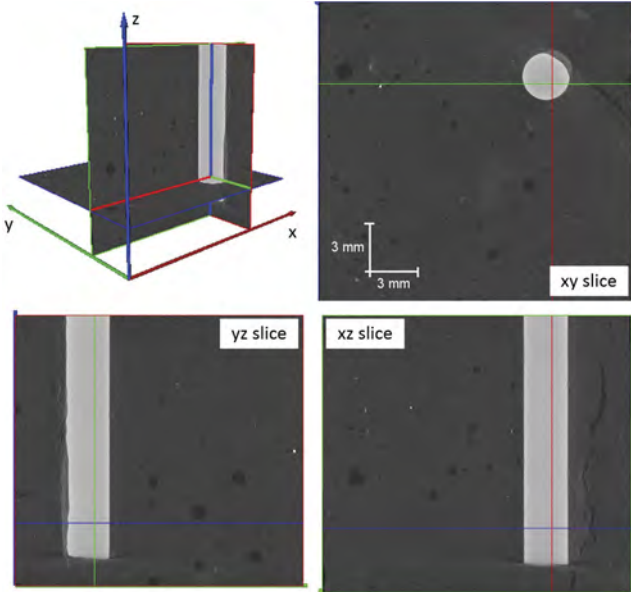


Figure 1. Geometrically processed images.

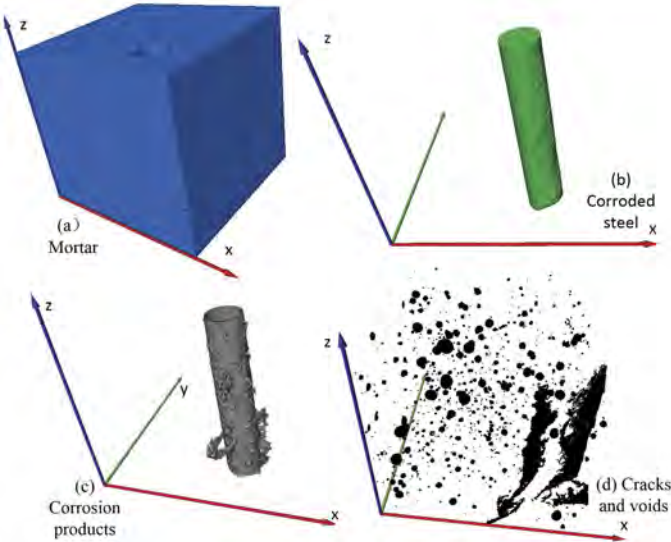


Figure 2. Three-dimensional views of (a) mortar, (b) corroded steel, (c) corrosion products and (d) cracks and voids.

To better analyze the spatial distribution of corrosion, the 3D structure of the corroded sample is cut vertically (i.e., cross section) and longitudinally at a number of locations. Figure 3 shows three typical cross section images around the steel bar at different locations. Some useful

observations have been obtained, i.e., (i) pitting corrosion was initiated around voids (Figure 3 (a)), (ii) corrosion products penetrated or flowed into the cracks (Figure 3(b)) and (iii) corrosion rust layer was separated (Figure 3(c)). Given abundant supply of oxygen and water which were pre-existed in the voids, corrosion was more prone to occur at the location of the steel bar in contact with large voids. Moreover, the corrosion products had penetrated into the cracks and/or voids during the accumulation process of the rust. Figure 3(c) presents the image for a slice taken from the 3D structure where there was minor corrosion compared with other locations in the same sample at the same time. In this slice, corrosion rust layer separation is observed. Such a separation phenomenon of rust is caused by the stronger expansion in adjacent places.

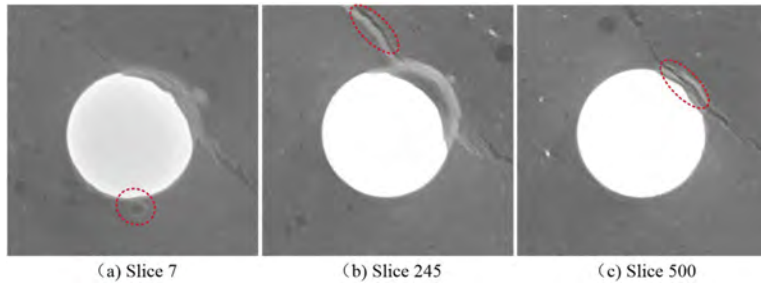


Figure 3. Typical cross section images around the steel bar.

2.2 Quantification of the corrosion loss

By measuring the residual area of the steel bar after corrosion, corrosion degree of the steel bar at any given location can be calculated as follows:

$$\eta = \frac{W_0 - W_r}{W_0} \times 100\% \quad (1)$$

where W_0 is the original mass of the steel for any given cross section and W_r is the residual mass of the steel for the same cross section of the reinforcing bar.

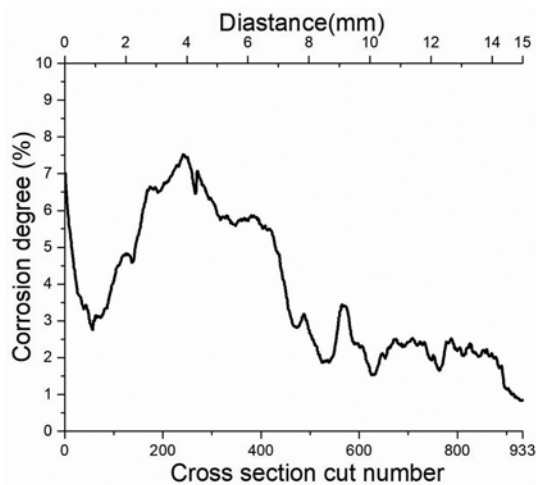


Figure 4. Corrosion degree of the steel bar along the longitudinal direction.

Figure 4 illustrates the corrosion degree along the longitudinal direction of the steel bar, calculated from 933 slices cut from the 3D CT reconstructed structure. 15mm length structure was chosen for analysis. Clearly, the corrosion degree of the steel bar varies along the reinforcement.

The maximum corrosion degree is 7.5% while the minimum corrosion degree is only about 1%. It should be noted that, because the diameter of the steel bar is only 2.94 mm and thus W_0 is quite small, the corrosion degree to concrete cracking should become very high.

The residual cross section of the steel bar significantly influences the failure probability of corroded RC members. The maximum and average radial losses of steel bar for any cross sections can reflect the non-uniform or pitting corrosion nature along the longitudinal direction. The maximum radial loss can be obtained as follows:

$$R_{ml} = \max_{\theta \in [0, 2\pi]} \{1 - R_{re}(\theta)\} \quad (2)$$

where R_{ml} is maximum radial loss of the steel bar; R_{re} is residual radius of the steel bar; θ is the polar angle within the cross section of the steel bar which varies from 0° to 360° by the increment of 1° .

In addition, the average radial loss can be calculated as follows:

$$R_{av} = \frac{\sum_{\theta=0}^{2\pi} (1 - R_{re}(\theta))}{2\pi} \quad (3)$$

Figure 5 illustrates that the maximum and average radial loss along the reinforcement. The maximum radial loss considerably varies along the longitudinal direction. The maximum value of R_{ml} is 0.22 mm while the corresponding average radial loss is only 0.05mm which reflects severe non-uniformity. According to the definition, the average radial loss has a linear relationship with corrosion degree. Generally, the average radial loss and the maximum radial loss keep the same trend of change.

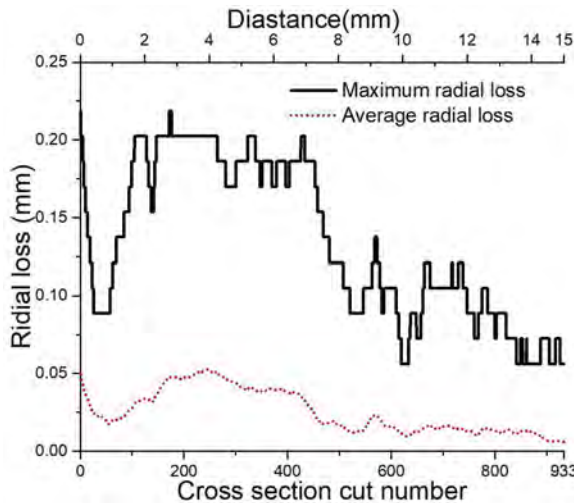


Figure 5. Maximum and average radial losses of the steel bar along the longitude direction.

2.3 Rust distribution

The processed binary images were used for rust thickness measurement. As shown in Figure 6, a polar coordinate system was built with its origin located in the centre of the steel bar. The rust thickness was calculated by measuring the distance between the first two points at the black and white boundaries along the radial line. This radial line was rotating against the origin for 360° to obtain the thickness for the whole circumference of the steel bar. The measurement approach was achieved by an in-house script written in Python. It should be noted that the corrosion products flowed into the surrounding cracks were not counted. This measurement approach can provide an effective and accurate way to analyze the rust distribution.

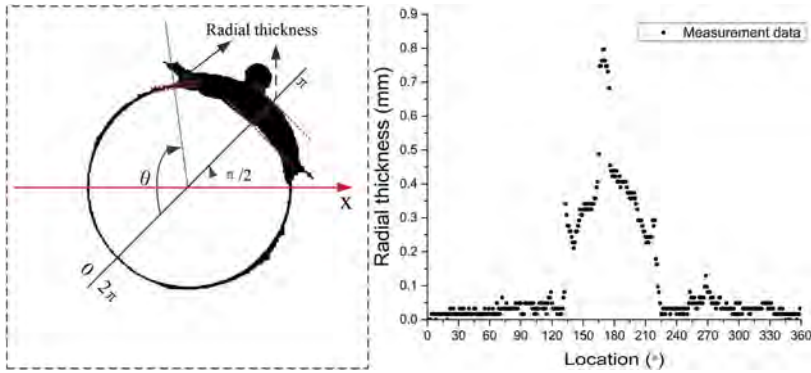


Figure 6. Radial thickness measurement of the rust along the circumference of the steel bar.

3 CT-INFORMED CORROSION MODEL

A non-uniform corrosion model has recently been developed by the authors based on von Mises distribution which is a continuous probability distribution on a circle (Xi et al. 2018). This model describes the non-uniform distribution of corrosion rust around the steel bar as a modified function of von Mises distribution. The model is simply composed of three parameters including the corrosion degree indicator λ , the non-uniform coefficient k and the location of the maximum thickness of the corrosion layer μ . In this paper, the non-uniform corrosion model is parameterised by the experimental data obtained from the novel X-CT analysis. The corrosion rust layer thickness around the reinforcing steel bar is formulated as follows:

$$T_{cl}(\theta) = \lambda \frac{e^{k \cos(\theta - \mu)}}{2\pi I_0(k)} \quad (4)$$

where λ is a corrosion degree indicator, μ is the location where the maximum thickness of corrosion layer appears, k is the non-uniform corrosion coefficient, $I_0(k)$ is the modified Bessel function of order 0.

After the regression analysis of the von Mises corrosion model fitted with the XCT data, we have fitted the corrosion model for all the cross sections along the longitudinal direction of the sample which has 933 slice cuts. Figure 7 shows the fitted parameters k and λ along the longitudinal direction. The maximum value of k is about 10.6 and the minimum value of k is about 2.0 and k significantly varies along the reinforcing steel bar. k in a range of 3-4.5 accounts for 64% of the total cut cross sections. The number of cross sections with k larger

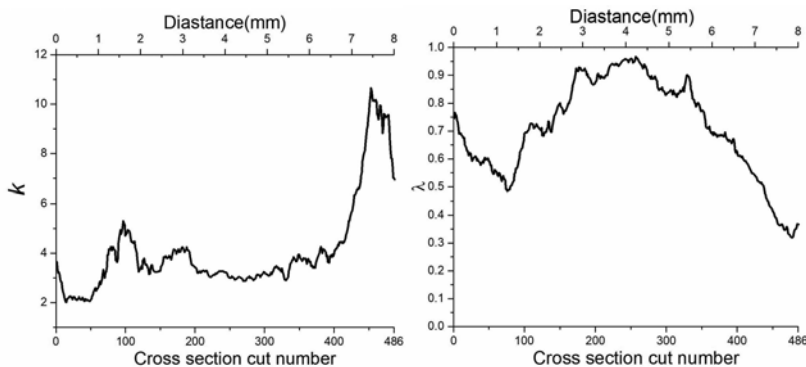


Figure 7. Parameter fitting for von Mises non-uniform corrosion model.

than 5 is very small. This finding suggests that the non-uniform corrosion coefficient k might fall within a small realistic range, affected by chloride content, geometry of the RC structures, corrosion degree and surface crack of concrete. More experimental study would be necessary to clarify the effects of different underlying parameters on k and ideally to formulate an analytical function for k . The experimental results and the parameterised von Mises corrosion model can be applied to civil engineering practice in predicting the corrosion induced concrete cracking problems.

4 CONCLUSIONS

In this paper, the corrosion of corner-located steel bar in mortar was non-destructively examined through XCT scanning. 3D images were obtained and segmented in terms of concrete, steel bar, corrosion products and voids or cracks. It has been found that pitting corrosion is prone to appear around voids close to steel bar because the pre-existing supply of oxygen and moisture. Moreover, corrosion has been found varying considerably along both the longitudinal direction of the sample and the cross sections. Also, the ratio of maximum to average radial loss of the steel bar differs from about 4 to 13 along the reinforcing bar. The rust distribution in the cross sections obtained has been used to parameterise the von Mises corrosion model. The non-uniform coefficient which represents the non-uniformity of the rust distribution has been found tending to fall in the range of 3 – 4.5. The experimentally validated non-uniform corrosion model can be applied to corrosion induced concrete cracking problems with good accuracy.

REFERENCES

- Andrade, C. Molina, F.J. & Alonso, C. 1993. Cover cracking as a function of rebar corrosion: Part 1-experiment test, *Materials and Structures* 26: 453–454.
- Angst, U.M. & Elsener, B. 2017. The size effect in corrosion greatly influences the predicted life span of concrete infrastructures, *Science Advances* 3(8): e1700751.
- Bazant, Z.P. 1979. Physical model for steel corrosion in concrete sea structures - theory, *Journal of the Structural Division-ASCE* 105(6): 1137–1153.
- Beck, M., Goebbels, J. & Burkert, A. 2007. Application of X-ray tomography for the verification of corrosion processes in chloride contaminated mortar, *Mater. Corros.* 58(3): 207–210.
- Česen, A., Kosec, T. & Legat, A. 2013. Characterization of steel corrosion in mortar by various electrochemical and physical techniques, *Corrosion Science* 75: 47–57.
- Dong, B., Fang, G., Liu, Y., Dong, P., Zhang, J., Xing, F. & Hong S. 2017. Monitoring reinforcement corrosion and corrosion-induced cracking by X-ray microcomputed tomography method, *Cement and Concrete Research* 100: 311–321.
- González, J.A., Andrade, C. Alonso, C. & Feliu, S. 1995. Comparison of rates of general corrosion and maximum pitting penetration on concrete embedded steel reinforcement, *Cement and Concrete Research* 25(2): 257–264.
- Itty, P.A., Serdar, M., Meral, C., Parkinson, D., MacDowell, A.A., Bjegović, D., Monteiro, P.J.M. 2014. In situ 3D monitoring of corrosion on carbon steel and ferritic stainless steel embedded in cement paste, *Corrosion Science* 83: 409–418.
- Michel, A., Pease, B.J., Geiker, M.R., Stang, H. and Olesen, J.F. 2011. Monitoring reinforcement corrosion and corrosion-induced cracking using non-destructive x-ray attenuation measurements, *Cement and Concrete Research* 41(11): 1085–1094.
- Melchers, R.E. & Li, C.Q. 2009. Reinforcement corrosion initiation and activation times in concrete structures exposed to severe marine environments, *Cement and Concrete Research* 39(11): 1068–1076.
- Mullard, J.A. & Stewart, M.G. 2011. Corrosion-induced cover cracking: new test data and predictive models, *ACI Structural Journal* 108(1): 71–79.
- Šavija, B., Luković, M., Hosseini, S.A.S., Pacheco, J. & Schlangen, E. 2014. Corrosion induced cover cracking studied by X-ray computed tomography, nanoindentation, and energy dispersive X-ray spectrometry (EDS), *Materials and Structures* 48(7): 2043–2062.
- Xi, X., Yang, S. & Li, C.Q. 2018. A non-uniform corrosion model and meso-scale fracture modelling of concrete, *Cement and Concrete Research* 108: 87–102.

Chloride transport properties of Portland cement and limestone systems

Z.L. Jiang, Z. Dong & C.Q. Fu

College of Civil Engineering, Zhejiang University of Technology, Hangzhou, China

Y.J. Pan & Y.C. Wang

Guangdong Provincial Key Laboratory of Durability for Marine Civil Engineering, College of Civil and Transportation Engineering, Shenzhen University, Shenzhen, China

ABSTRACT: Limestone powder has been used to replace part of Portland cement because of environmental and economic benefits. The durability of the cement-based materials is important to consider the performance of concrete structures under a long-term service life. Under a marine environmental condition, the chloride-induced corrosion is the main mechanism for the degradation of reinforced concrete structures. In this study, the effects of limestone addition on the pore structure, chloride binding capacity and apparent chloride diffusivity of Portland cement paste were investigated. The porosity and pore size distribution were obtained by mercury intrusion porosimetry, focused ion beam/scanning electron microscopy and X-ray computed tomography. The chloride binding isotherms and the binding kinetics of cement paste with different limestone addition were studied. The apparent chloride diffusivity was obtained by a ponding test. The MIP results showed that the addition of limestone powder led to a coarser pore structure, especially when more limestone powder was added or coarser limestone powder was used. Limestone powder accelerated the rate of chloride ion binding at first and then the binding rate slowed down as the absorption time increased. The bound chloride amount was larger as the particle size of limestone powder was smaller. The result also showed that cement paste containing 5% replacement of limestone powder had positive effect in resisting chloride ion penetration before 14 d of diffusion. For a longer diffusion time, the apparent chloride diffusivity of cement paste was greater with greater limestone powder content or larger limestone powder size.

1 INTRODUCTION

In order to reduce the emission of carbon dioxide and the consumption of natural resources, fly ash, slag, silica fume and other supplementary cementitious materials are used to partially replace cement with commonly 20% replacement (Scrivener et al., 2018). However, the supply of these industrial by-products is relatively limited with non-uniform regional distribution. Therefore, it is necessary to find supplementary cementitious materials that can partially replace cement without significantly affecting the performance and are also rich in resources. Limestone powder is an industrial by-product produced when crushing limestone to produce manufactured sand in quarries. It is not only inexpensive and stable in composition, but also can partially replace cement as a supplementary cementitious material, effectively reducing carbon emissions in the cement production process. So far, many studies have been carried out on the mechanism of limestone powder in cement-based materials, including filling effect, nucleation effect, chemical effect and dilution effect (Aqel and Panesar, 2016). The research results showed that when the content of limestone powder is less than 5% - 10%, the diffusivity of chloride ions in cement-based materials will be reduced to some extent. However, with the increase of limestone powder content, due to the dilution effect, the chloride diffusivity of cement-based materials increases (Meddah et al., 2014).

Chloride ions in seawater transport into the concrete through its pore structure. Therefore, the pore structure characteristic of concrete is a direct factor affecting the chloride transport. The transport properties of chloride ions in cement-based materials are highly dependent on the pore network. At present, many methods have been used to characterize the pores of cement-based materials. The indirect method detects the response of the measured material under external stimulus and converts it to the pore structure parameters by a proper model. The direct method images the material microstructure directly and characterizes the three-dimensional pore network in the material intuitively. X-ray computed tomography (XCT) is a non-destructive imaging method. However, the resolution of conventional CT scanning system generally stays at the micron level, so that most of the nano-scale pores in cement-based materials cannot be observed. XCT is more suitable for characterizing the large pores and cracks of cement-based materials at the micron level. Compared with XCT, focused ion beam/scanning electron microscopy (FIB/SEM) can obtain images at nanometer scales. Song et al. (2018) used FIB/SEM to characterize the three-dimensional pore structure of high performance concrete, and the pore size range studied was between 10 and 600 nm. The permeability of cement-based materials was predicted by combining the FIB/SEM results with the Katz-Thompson model. However, the dimension of the observed volume in FIB/SEM is only tens of microns, which leads to insufficient representativeness of the volume. Jiang et al. (2022) used XCT and FIB/SEM to characterize the three-dimensional pore structure of cement paste, indicating that these two methods have significant advantages in measuring characteristic pore parameters such as pore connectivity and tortuosity. In addition, the hydraulic tortuosity values measured by the two methods are similar and close to the calculated values of Archie's law tortuosity.

This paper investigates the effect of limestone powder on chloride transport and pore structures in cement-based materials. Three pore characterization methods, i.e., mercury intrusion porosimetry (MIP), FIB/SEM and XCT, were used to obtain the pore characteristic parameters of cement paste containing limestone powder with different fineness and addition. The chloride binding isotherms and binding kinetics of cement paste were tested. The effect of limestone powder on the chloride ion diffusion performance of cement paste was studied under different fineness and addition of limestone powder.

2 MATERIALS AND METHODS

2.1 Materials and specimen preparation

Portland cement, natural limestone powder with different fineness and deionized water are used for cement paste. The chemical composition of the cement and limestone powder is determined by X-ray fluorescence analysis (XRF), and the results are shown in Table 1. The median particle sizes of cement, fine limestone (FL) and coarse limestone (CL) are 13.68, 1.71 and 19.97 μm , respectively. The mix proportion of each cement paste group is shown in Table 2. The water-binder ratios of all groups are 0.45. The cement pastes with 5%, 10%, 15% and 20% replacement of fine limestone are designated as 5FL, 10FL, 15FL and 20FL, respectively, and those with 10% and 20% replacement of coarse limestone are designated as 10CL and 20CL, respectively. After mixing the binder with deionized water, the cement paste was cast into $40 \times 40 \times 160$ mm and $100 \times 100 \times 100$ mm molds and they were vibrated for 60 seconds. The molds were demoulded after 24 hours and cured at 20 °C and relative humidity (RH) of 95% for 28 days.

Table 1. Chemical composition of cement and limestone powder (% in weight).

	CaO	SiO ₂	Al ₂ O ₃	SO ₃	Fe ₂ O ₃	MgO	Other	LOI
Cement	64.46	20.37	5.04	2.93	2.69	1.02	0.67	2.37
Limestone	55.45	0.35	0.18	-	0.10	0.27	0.12	43.50

2.2 Pore structure characterization

2.2.1 Mercury Intrusion Porosimetry (MIP)

Small cylinders with a diameter of 3 mm and a height of 5 mm were cored at the center part of the cured $40 \times 40 \times 160$ mm specimens. The cored samples were soaked in isopropanol solution for 7 days to stop hydration, and then they were vacuum dried at 40°C until the equilibrium mass was reached. The samples' pore structures were measured by mercury porosimeter (Auto Pore IV 9500 produced by Micromeritics). The samples were subjected to step-by-step increasing pressures with the maximum pressure at 3.0×10^4 psia. The relation between the pore size and the implied pressure is obtained by Washburn's equation (Washburn and E., 1921):

$$d = -\frac{4\gamma\cos\theta}{P} \quad (1)$$

where d is the pore diameter, P is the implied pressure, γ is the surface tension of the mercury and θ is the contact angle between mercury and pore walls.

Table 2. Mix proportion of each cement paste group (kg/m^3).

Groups	Water	Cement	Fine limestone	Coarse limestone
PC	586	1302	—	—
5FL	586	1237	65	—
10FL	586	1172	130	—
10CL	586	1172	—	130
15FL	586	1107	195	—
20FL	586	1042	260	—
20CL	586	1042	—	260

2.2.2 Focused Ion Beam/Scanning Electron Microscopy (FIB/SEM)

Thin slices with dimensions of $5 \times 5 \times 5$ mm were cut from the cured cement paste specimens. After being soaked in isopropanol solution to stop hydration, the samples were impregnated with a low-viscosity epoxy in a vacuum chamber. The sample surfaces were mechanical ground and then polished by argon ion beam. The polished samples were dried at 40°C before the test. The instrument crossbeam 540 (produced by Carl Zeiss, Germany) was used to observe the microstructure of the cement paste. The imaging process was conducted as follows:

- (1) The polished samples were sprayed by a layer of gold and then was fixed on the sample stage. After the sample chamber was vacuumed, the sample surface was observed in a scanning electron mode, and the target area of about $11 \times 10 \mu\text{m}$ which was away from the anhydrous cement particles and microcracks was selected.
- (2) The sample stage was rotated by 54° so that the sample surface was perpendicular to the electron beam. A positioning mark was made near the selected target area for image alignment correction. Platinuma was then plated on the surface of the target area to reduce damage to the area during ion beam etching.
- (3) The areas surrounding the target area were etched by the ion beam and the imaging surface was finely cut by a small beam of ion. The ion beam cut every 10 nm, and the electron beam was used to image the freshly cut surface. The working voltage of gallium ion beam is 30 kV and the working current is 700 Pa. The working voltage of the electron beam is 1.5 kV and the working current is 500 pA. The FIB/SEM system can automatically perform subsequent repeated cutting and imaging to obtain 1048 two-dimensional sequence images with a resolution of 5 nm/voxel.

2.2.3 X-ray Computed Tomography (XCT)

Cylinder samples with a diameter of 2 mm and a height of 2 mm were cored for the XCT test. A high-resolution X-ray CT instrument SkyScan2211 (Brook, produced in Germany) was used. A voltage of 80 kV and a current of 280 μA were used. The samples were scanned using

4032 × 2688 pixel CCD detector. The distance between radiation source and sample was 9.7 mm, and the distance between radiation source and detector is 146.8 mm. The three-dimensional internal structure of the cement paste was reconstructed with a resolution of 0.60 μm/voxel.

2.3 Chloride binding test

Crushed cement paste samples of sizes between 0.25 to 2 mm were collected for the dynamic chloride binding tests. The crushed samples were vacuum-dried at 25 °C for 2 days, and then they were dried at a 11% RH until mass balance in a desiccator with saturated LiCl solution for 7 days. After drying, 20 g sample was collected and soaked in 60 g 6% NaCl solution. At a given soaked time from 1 h to 28 d, 2 mL supernatant of the standing solution was taken and then the potentiometric titrator was used for titration by 0.1 mol/L AgNO₃.

The crushed samples were also collected for the chloride binding isotherms. The dried sample was soaked in 60 g of sodium chloride solution with different concentrations from 0.0125 to 1.829 mol/L. Tang and Nilsson (1993) pointed out that the chloride binding for the crushed cement paste samples reached equilibrium at about 10 d. To ensure sufficient binding, we tested the bound chloride content at 14 d as the equilibrium binding. The bound chloride content at equilibrium is obtained by:

$$c_b = M_{Cl} \times V \times \frac{c_0 - c}{w_d} \quad (2)$$

where c_b is the bound chloride content at equilibrium (mg/g), c_0 is the initial concentration of NaCl solution (mol/L), c is the free chloride ion concentration in solution (mol/L), V is volume of NaCl solution (mL), M_{Cl} is the molar mass of chloride (g/mol), and w_d is the mass of the dry sample which is calculated by

$$w_d = w_{11}(1 - \xi_{11}) \quad (3)$$

where w_{11} is the sample at 11% RH (g) and ξ_{11} is the evaporable water content at 11% RH.

2.4 Chloride diffusion test

For the chloride diffusion tests, 100 × 100 × 100 mm cement paste cubes were used. The first 5 mm layer of the specimen was removed and the freshly cut surface was used as exposure surface. The specimen was vacuum-saturated by saturated calcium hydroxide solution and then the specimen surfaces were sealed by epoxy resin except the exposure surface. The sealed specimens were immersed in 6% NaCl solution in a container. The container was shaken and the solution was replaced regularly to keep the solution concentration unchanged. After the immersion for 7, 14, 28, and 60 days, cement paste powder was obtained by layered grinding from the exposure surface to the inner part of the specimen. The total chloride content in each layer was measured through potentiometric titration by 0.02 mol/L AgNO₃ solution.

3 RESULTS AND DISCUSSION

3.1 Pore structure parameters

The porosity and pore size distribution (PSD) of different specimen groups measured by MIP are shown in Figure 1. The results show that the total porosity increases with the increase of limestone powder content. Under the same limestone replacement, the porosity of cement paste with coarse limestone is greater than that with fine limestone. The addition of limestone powder reduces the amount of small capillary pores (10 – 50 nm), and increases the amount of medium (50 - 100 nm) and large (0.1 - 10 μm) capillary pores. The proportion of large capillary pores in the cement paste is greater with more limestone powder addition. The critical pore size is closely related to the permeability and ion diffusivity of the material (Halamickova et al., 1995). The PSD measured by MIP shows that the PSD gradually shifts to the large pores and the critical pore size gradually increases as the limestone powder content increases.

Even 5% replacement of limestone powder leads to coarser pore structure, and the pore coarsening becomes more obvious when limestone powder with larger replacement or larger particle size is used.

Based on the three-dimensional pore structure measured by FIB/SEM and XCT, the simulated MIP (SMIP) PSD was obtained by simulating the mercury intrusion process from the low-Z surface of the sample. The PSD results by SMIP are shown in Figure 2. The PSD of all groups obtained based on FIB/SEM is between 10 and 300 nm, while the PSD based on XCT is between 600 nm and 15 μm . The results of FIB/SEM show that the peak pore size of PSD includes 20, 40 and 80 nm. In Figure 2(b), the PSDs of different specimens based on the XCT show a single peak distribution. Due to the difference in resolution between FIB/SEM and XCT, the obtained PSD is different. The PSD for FIB/SEM is different from that by MIP, because the samples tested in MIP are millimeter-scale, which is more representative than FIB/SEM samples which are micrometer-scale. MIP samples contain multi-scale pore structures with pore diameters ranging from a few nanometers of gel pores to tens of microns of macropores, while FIB/SEM samples are mainly concentrated in capillary pores in hydrated matrix.

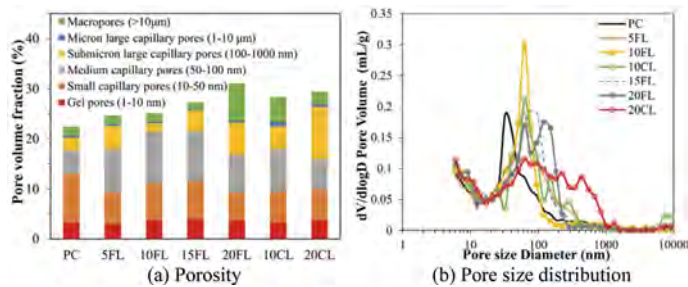


Figure 1. Pore structure parameters of cement paste measured by MIP.

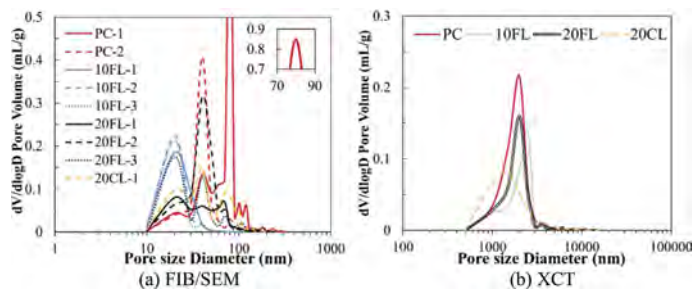


Figure 2. Pore size distribution by simulating mercury intrusion based on FIB/SEM and XCT images.

3.2 Chloride binding behavior

3.2.1 Binding kinetics

Figure 3 shows the change of bound chloride amount in different cement paste groups as soaking time increases. At 24 h, the chloride binding reached more than 70% of the equilibrium amount. After that, the binding gradually slows down, and the binding equilibrium is basically reached at 14 d. The results are consistent with the results of Feng et al. (2018) on the binding kinetics of chloride ions in cement paste. The results in Figure 3 also show that the addition of limestone powder accelerates the chloride binding within 4 h, and the accelerating effect is more obvious as the addition increases. After 8 h, the dilution effect of limestone powder gradually reduced the binding rate of chloride ions.

For solid-liquid adsorption, Equation 5 for the pseudo-first-order kinetic (Boparai et al., 2011) and Equation 6 for the pseudo-second-order kinetic equation (Yu and Zhang, 2017) are

used to analyze the binding kinetics. In general, pseudo-first-order kinetics is related to physical adsorption (Page and Vennesland, 1983), and chemical adsorption (Boparai et al., 2011) is expressed by pseudo-second-order kinetics with more required energy.

$$\lg(q_e - q_t) = \lg q_e - \frac{K_1 t}{2.303} \quad (4)$$

$$\frac{t}{q_t} = \frac{1}{K_2 q_e^2} + \frac{t}{q_e} \quad (5)$$

where t is the binding time (h), q_t is the bound chloride content at time t (mg/g), q_e is equilibrium bound chloride content (mg/g), K_1 is quasi-first-order kinetic adsorption rate constant (1/h), and K_2 is quasi-second-order kinetic adsorption rate constant, (g/(mg·h)).

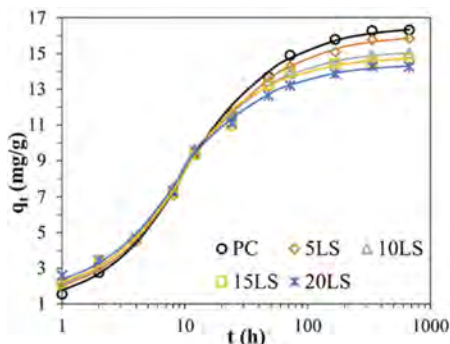


Figure 3. Bound chloride amount of cement paste at different absorption time.

Based on Equations 4 and 5, the fitting results are shown in Figure 4. the chloride ion binding in the cement paste conforms to the quasi-first-order kinetics within 12 h, and it conforms to the quasi-second-order kinetics after 24 h. The results indicate that the chloride binding is mainly controlled by physical action at first and then the chemical binding dominates. The addition of limestone powder accelerates the chloride binding and shortens the time to reach binding equilibrium.

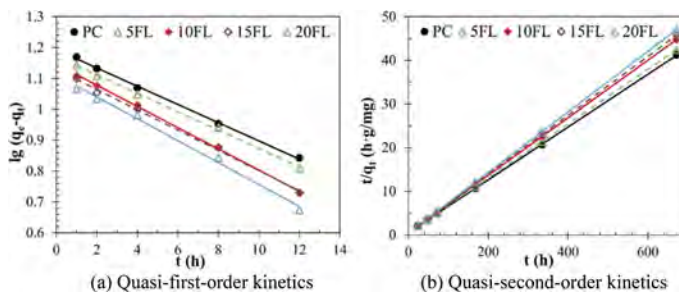


Figure 4. Chloride binding kinetic model fitting.

3.2.2 Chloride binding isotherms

Figure 5 shows the chloride binding isotherms of cement paste containing limestone powder with different addition and fineness. The relationship between the amount of bound chloride ion c_b and the free chloride ion concentration c in the solution is nonlinear. The binding isotherms are fitted by Freundlich's equation (Tang et al., 1993).

$$c_b = K_F c (Cl^-)^{1/n} \quad (6)$$

where K_F (mL/mol) and $1/n$ are two parameters for the Freundlich's equation.

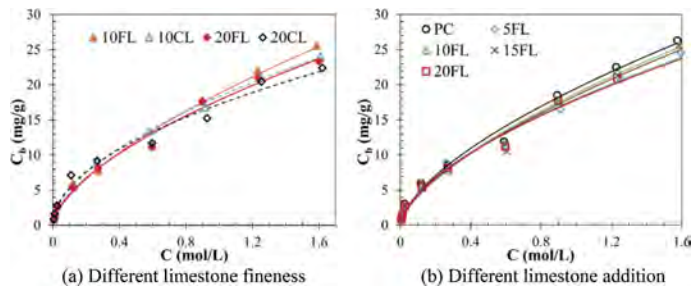


Figure 5. Chloride binding isotherms of cement paste.

The results in Figure 5 show that the bound chloride amount decreases with the increase of limestone powder content. Similarly, Ipavec et al.'s results (2013) showed that the replacement of 10% limestone powder would slightly reduce the chloride binding capacity of the cement paste. The results in Figure 5 also show that under the same limestone powder content, the amount of chloride ion adsorbed by the fine limestone group is greater than that of the coarse limestone group. This is because the smaller the particle size of limestone powder, the more obvious the filling effect and the nucleation effect. The formation and precipitation of hydration products (Bentz, 2006) is accelerated, thereby increasing the chloride binding through physical adsorption of C-S-H.

3.3 Apparent chloride diffusivity

Figure 6 shows a comparison of apparent chloride ion diffusivity for different specimen groups. The results show that the apparent diffusivity for PC and fine limestone groups decreases with the increase of soaking time, while the diffusivity of coarse limestone group increases from 7 to 14 d and then decreases gradually. When the soaking time is 7 d and 14 d, the diffusivity of 5FL group is slightly smaller than that of PC group, indicating that a small amount of limestone powder at the beginning of diffusion has a positive effect to resist chloride ion penetration. As the diffusion time increases, the diffusivity for 5FL is larger than that for PC because of the dilution effect. At 28 d and 60 d, the apparent chloride diffusivity in the 5FL, 10FL and 15FL groups are close to each other. For the convenience of comparison, the specimens were further divided into four groups: no limestone powder NL (PC group), a small amount of fine limestone powder SL (5FL, 10FL and 15FL groups), a large amount of fine limestone powder ML (20FL), and coarse limestone powder CL (10CL, 20CL). In general, the apparent chloride diffusivity of ML group is larger than that of NL and SL groups. Under the same limestone addition, the smaller the particle size of the limestone powder, the smaller the apparent chloride diffusivity of the cement paste.

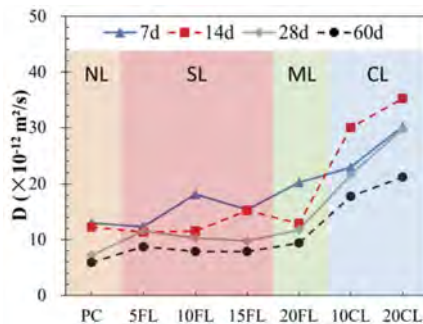


Figure 6. Apparent chloride diffusivity of cement paste at different diffusion time.

4 CONCLUSIONS

In this paper, the pore structure of cement paste containing limestone powder was studied by different test methods. The effects of limestone powder content and fineness on chloride binding and chloride diffusivity of cement paste were investigated. Based on the test results, the following conclusions can be drawn:

- (1) The MIP results show that the addition of limestone powder makes the pore structure of the paste coarser, especially when more limestone powder is added or coarser limestone powder is used.
- (2) At the adsorption time of 4 h, limestone powder accelerates the rate of chloride ion binding. After that, due to the dilution effect, the binding rate of chloride ions slows down and the total adsorption capacity decreases. The bound chloride amount is larger as the particle size of limestone powder is smaller, because of the limestone powder's filling effect and nucleation effect.
- (3) Cement paste containing 5% replacement of limestone powder has positive effect in resisting chloride ion penetration before 14 d of diffusion. For a longer diffusion time, the apparent chloride diffusivity of cement paste is greater with greater limestone powder content or larger limestone powder size.

REFERENCES

- Aqel, M. & Panesar, D.K. 2016. Hydration kinetics and compressive strength of steam-cured cement pastes and mortars containing limestone filler. *Construction and Building Materials* 113: 359–368.
- Bentz, D.P. 2006. Modeling the influence of limestone filler on cement hydration using CEMHYD3D. *Cement and Concrete Composites* 28(2): 124–129.
- Boparai, H.K., Joseph, M. & O'Carroll, D.M. 2011. Kinetics and thermodynamics of cadmium ion removal by adsorption onto nano zerovalent iron particles. *Journal of Hazardous Materials* 186(1): 458–465.
- Feng, W., Xu, J., Chen, P., Jiang, L., Song, Y. & Cao, Y. 2018. Influence of polycarboxylate superplasticizer on chloride binding in cement paste. *Construction and Building Materials* 158: 847–854.
- Halamiczkova, P., Detwiler, R.J., Bentz, D.P. & Garboczi, E.J. 1995. Water permeability and chloride ion diffusion in portland cement mortars: Relationship to sand content and critical pore diameter. *Cement and Concrete Research* 25(4): 790–802.
- Ipavec, A., Vuk, T., Gabrov Ek, R. & Kau I, V. 2013. Chloride binding into hydrated blended cements: The influence of limestone and alkalinity. *Cement and Concrete Research* 48: 74–85.
- Jiang, Z., Pan, Y., Lu, J. & Wang, Y. 2022. Pore structure characterization of cement paste by different experimental methods and its influence on permeability evaluation. *Cement and Concrete Research* 159: 106892.
- Meddah, M.S., Lmbachiya, M.C. & Dhir, R.K. 2014. Potential use of binary and composite limestone cements in concrete production. *Construction and Building Materials* 58: 193–205.
- Page, C.L. & Vennesland. 1983. Pore solution composition and chloride binding capacity of silica-fume cement pastes. *Matériaux et Construction* 16(1): 19–25.
- Scrivener, K.L., John, V.M. & Gartner, E.M. 2018. Eco-efficient cements: Potential economically viable solutions for a low-CO₂ cement-based materials industry. *Cement and Concrete Research* 114: 2–26.
- Tang, L. & Nilsson, L.O. 1993. Chloride binding capacity and binding isotherms of OPC pastes and mortars. *Cement and Concrete Research* 23(2): 247–253.
- Washburn & E., W. 1921. Note on a method of determining the distribution of pore sizes in a porous material. *Proceedings of the National Academy of Sciences of the United States of America* 7(4): 115–116.
- Song, Y., Davy, C.A., Troadec, D. & Bourbon, X. 2018. Pore network of cement hydrates in a High Performance Concrete by 3D FIB/SEM — Implications for macroscopic fluid transport. *Cement and Concrete Research* 115: 308–326.
- Yu, Y. & Zhang, Y.X. 2017. Coupling of chemical kinetics and thermodynamics for simulations of leaching of cement paste in ammonium nitrate solution. *Cement and Concrete Research* 95: 95–107.

Simplified analytical method for moment-curvature response of corroded prestressed concrete beams

S. Ravasini, L. Franceschini & B. Belletti

Department of Engineering and Architecture, University of Parma, Parma, Italy

ABSTRACT: Nowadays, the corrosion phenomenon is recognized as one of the main causes of deterioration of reinforced and prestressed concrete (*PC*) structures. Several experimental and numerical investigations have been proposed in the literature for the flexural and shear response of reinforced concrete structures. However, the lack of simplified yet accurate analytical models have been outlined, especially concerning the residual mechanical response of corroded prestressed concrete members. To this aim, the present work focuses on the proposal of a simplified analytical model for the flexural resistance of prestressed concrete beams - subjected to chloride-induced corrosion - in terms of moment-curvature response. Firstly, the basic assumptions of the approach and the validation against un-corroded *PC* beams are described by adopting a novel stress-strain relationship for corroded strands previously proposed by the authors. Secondly, the effect of the corrosion level on the moment-curvature response of deteriorated *PC* beams is investigated. Finally, outcomes are provided concerning: (i) the expected flexural failure mode, (ii) the evaluation of useful parameters for the assessment of flexural and shear resistances - the latter referring to the current formulation provided in the Model Code 2010.

1 INTRODUCTION

The corrosion phenomenon is one of the most investigated topics in the engineering community since it affects the durability and residual capacity of existing structures. During the years, studies were conducted aimed to the assessment of prestressed concrete (*PC*) structures (Vereecken et al., 2021). Different authors investigated the performance of corroded pre-tensioned (Dai et al., 2020; Wang et al., 2018) and post-tensioned (Jeon & Shim, 2020; Zhang et al., 2017) beams. In addition, experimental pull-out tests on the bond-slip behaviour between prestressing strands and concrete (Wang et al., 2017b; Wang et al., 2017a) and prestress loss due to corrosion (Dai et al., 2020) were conducted. Belletti et al. (2020) and Vecchi et al. (2020) experimentally investigated the performance of naturally corroded pre-tensioned concrete beams without shear reinforcement. Thereafter, the same authors studied in detail the pit morphology of the prestressing strands relieved from the mentioned beams (Vecchi et al., 2021). Coronelli et al. (2022) recently investigated both pre- and post-tensioned beams subjected to natural corrosion. Despite the availability of studies on corrosion effects on prestressed concrete members, simple yet reliable analytical approaches are rare in the current literature.

In this context, a recent novel stress-strain relationship for corroded prestressing strands has been developed (Franceschini et al., 2022), which provided good agreement against experimental tensile tests on corroded strands. On this basis, this paper deals with the proposal of an analytical method for the flexural performance of pre-tensioned beams. Firstly, a piecewise moment-curvature response is proposed and validated. Secondly, the corrosion effect was applied on such response to investigate the capacity reduction in terms of both resistance and ductility. Finally, useful insights for the sectional assessment of flexural and shear resistance of *PC* members are provided.

2 THE MOMENT-CURVATURE RESPONSE

In the following, the simplified analytical approach of the moment-curvature response, $M-\chi$, for prestressed concrete sections is described.

2.1 Main assumptions and failure cases

The constitutive laws for concrete and un-corroded prestressing strands are shown in Figure 1(a) and (b), respectively. The strands' stress-strain is based on a recent publication by Franceschini et al. (2022), where the main points are highlighted as "a" ($\varepsilon_{pp,0}; f_{pp,0}$), "b" ($\varepsilon_{py,0}; f_{py,0}$) and "c" ($\varepsilon_{pu,0}; f_{pu,0}$). The stresses, $f_{pp,0}$ and $f_{py,0}$, are assumed equal to $0.7 \cdot f_{pu,0}$ and $0.882 \cdot f_{pu,0}$, respectively, while the strains, $\varepsilon_{pp,0}$ and $\varepsilon_{py,0}$, are assumed equal to $f_{pp,0}/E_p$ and 0.01, respectively.

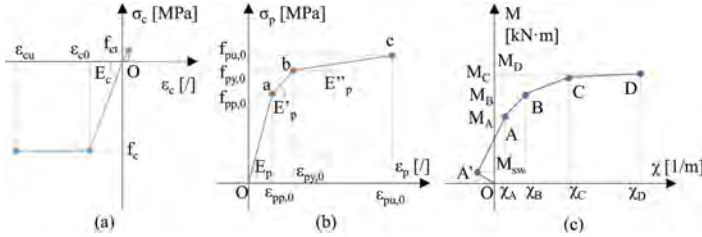


Figure 1. (a) Stress-strain of concrete in compression and in tension, (b) stress-strain of un-corroded prestressing strands (Franceschini et al., 2022), and (c) piecewise moment-curvature response.

The assumed piecewise moment-curvature response is shown in Figure 1(c). The main events are related to the achievement of: (A') the negative curvature at prestress with eventually the moment due to self-weight, M_{sw} , (in the following, this contribution is neglected), (A) the cracking moment, (B) the point "a", (C) the point "b" of the strands' relation and (D) the first occurrence of concrete crushing or strands' fracture.

The basic assumptions are:

- The centre of gravity, G , is located at the mid-height of the cross section and the eccentricity of the strands, e , is $e = d_p - h/2$, where d_p is the effective depth of strands.
- The concrete tensile strength is used to evaluate the cracking moment. The tensile strength and the elastic modulus of concrete, f_{ct} and E_c , are calculated according to the Model Code 2010 (fib, 2013). The tension-stiffening is roughly considered by connecting the events A , B .
- A Euler-Bernoulli behaviour is assumed, where the strain compatibility condition between concrete in compression, ε_c , and strands in tension, ε_p , is expressed with the Equation (1):

$$\varepsilon_c = \frac{\Delta\varepsilon_p x}{(d_p - x)} \quad (1)$$

where x is the neutral axis depth, $\varepsilon_{p,0}$ is the prestressing strain of strands, calculated as the ratio $\varepsilon_{p,0} = \sigma_{p,0}/E_p$ and $\Delta\varepsilon_p = \varepsilon_p - \varepsilon_{p,0}$.

The limitations of the model are:

- It is limited to rectangular pre-tensioned cross sections.
- The ordinary rebars are neglected.

The geometrical features are shown in Figure 2 and the failure cases are:

- "1": the section is under-reinforced. The failure mode is associated to the achievement of the maximum strength of the strand, while concrete may behave elastically.
- "2": the section is balanced. The failure mode is attributed to concrete crushing, while strands are yielded (beyond the point "b" of the strands' stress-strain response).
- "3": the section is over-reinforced. The failure mode is due to concrete crushing, while strands are not yielded.

The failure case "3" will not be described since: (i) it is quite rare in practice and (ii) the corrosion effects on reinforcement leads to ductile-to-brittle failure (from failure case "2" to "1").

The mechanical reinforcement ratio, ω_p , is calculated with the Equation (2):

$$\omega_p = \frac{n_p A_{1p,0} f_{py,0}}{f_c b d_p} = \frac{A_{p,0} f_{py,0}}{f_c b d_p} \quad (2)$$

where $A_{1p,0}$ and n_p are the area of a single strand and the number of strands, respectively.

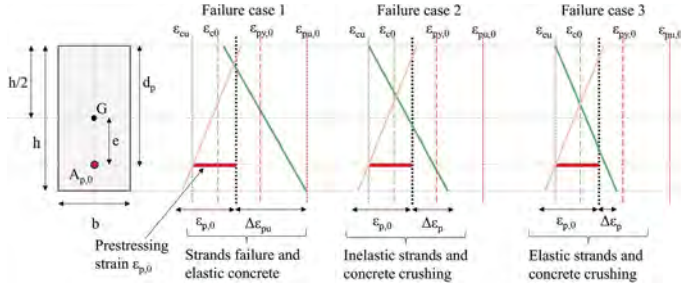


Figure 2. Failure cases for prestressed concrete beam sections.

The previous value must be compared with threshold limits depending on strain distribution of each failure case. The threshold limit between failure cases “1” and “2”, ω_{21} , is:

$$\omega_{21} = \frac{\lambda \varepsilon_{cu}}{(\varepsilon_{pu,0} - \varepsilon_{p,0} + \varepsilon_{cu})} \frac{f_{pu,0}}{f_{py,0}} \quad (3)$$

The threshold limit between failure cases “2” and “3”, ω_{23} , is:

$$\omega_{23} = \frac{\lambda \varepsilon_{cu}}{(\varepsilon_{py,0} - \varepsilon_{p,0} + \varepsilon_{cu})} \quad (4)$$

where λ is the “stress-block” parameter, assumed equal to 0.8. Finally, the expected failure case is identified as follows: (i) if $\omega_p \leq \omega_{21}$, the expected failure case is “1”, (ii) if $\omega_{21} < \omega_p < \omega_{23}$, the expected failure case is “2” and (iii) if $\omega_p \geq \omega_{23}$, the expected failure case is “3”.

2.2 Piecewise moment-curvature response for un-corroded members

The events of the sectional moment-curvature response are described herein. The events A' and A are related to linear elastic behaviour and the steps are the same for all the failure cases.

2.2.1 Events A' and A

The curvature at event A' is calculated by assuming a linear elastic calculation, Equation (5):

$$\chi_{A'} = \frac{M_{p,0}}{E_c I_i} = \frac{N_{p,0} e}{E_c I_i} = \frac{(-A_{p,0} \sigma_{p,0}) e}{E_c I_i} \quad (5)$$

Where $N_{p,0}$ is assumed as negative. The terms I_i are the second moment of inertia and A_i is the gross section area. The strands' strain is calculated with a linear elastic calculation. The mid-height strain of the section, $\varepsilon_{x,A'}$, is evaluated by considering the superimposition of effects:

$$\varepsilon_{x,A'} = \frac{N_{p,0}}{E_c A_i} \quad (6)$$

The event A corresponds to the achievement of the cracking moment (i.e., a stress equal to f_{ct} is reached at bottom of the beam section), M_A , and is calculated with the Equation (7):

$$M_A = \frac{2I_i}{h} \left[f_{ct} - \frac{N_{p,0}}{A_i} - \frac{M_{p,0} h}{I_i} \right] \quad (7)$$

The strain at strands' level is calculated with usual linear elastic calculation. In this case, the curvature is positive and is evaluated with the Equation (5) by substituting the numerator with M_A of the Equation (7). The mid-height strain is calculated with the Equation (6).

2.2.2 Event B

This event corresponds to the point “a” ($\varepsilon_{pp,0}; f_{pp,0}$) of the stress-strain relation of strands.

Regarding the failure case “1”, the concrete is assumed linear elastic, and the equilibrium is:

$$0.5bx_{1,B}\varepsilon_c E_c = A_{p,0}f_{pp,0} \quad (8)$$

By adopting the equilibrium and the compatibility in Equation (1) for ε_c , the neutral axis depth is:

$$x_{1,B} = \frac{A_{p,0}f_{pp,0} \left(-1 + \sqrt{1 + \frac{2bE_c\Delta\varepsilon_{pp,0}d_p}{A_{p,0}f_{pp,0}}} \right)}{bE_c\Delta\varepsilon_{pp,0}} \quad (9)$$

where $\Delta\varepsilon_{pp,0} = \varepsilon_{pp,0} - \varepsilon_{p,0}$. The moment and the curvature are evaluated with Equations (10) and (11):

$$M_{1,B} = A_{p,0}f_{pp,0} \left(d_p - \frac{x_{1,B}}{3} \right) \quad (10)$$

$$\chi_{1,B} = \varepsilon_c / x_{1,B} \quad (11)$$

If the concrete strain, ε_c , is greater than ε_{c0} , the first trial of the failure case “2” must be used.

Regarding the failure case “2”, as first trial, the neutral axis is calculated by using the equilibrium in Equation (12) by considering the concrete compressive strength, f_c , and the stress block formed:

$$x_{2,B} = \frac{A_{p,0}f_{pp,0}}{0.8bf_c} \quad (12)$$

If the corresponding concrete strain in compression, ε_c , is greater than ε_{c0} , the moment results:

$$M_{2,B} = A_{p,0}f_{pp,0}(d_p - 0.4x_{2,B}) \quad (13)$$

Otherwise, the concrete remains linear elastic and the neutral axis depth, $x_{2,B}$, and the moment, $M_{2,B}$, are evaluated as the previous case with the Equations (9) and (10) while the curvature, $\chi_{2,B}$, is calculated with the Equation (11). As stated by the Model Code 2010 (fib, 2013), for shear resistance verification, the longitudinal strain is calculated at half of the effective shear depth, z . This latter is assumed equal to $z = z_p = 0.9d_p$. Based on geometrical features, ε_x is calculated with the Equation (14). The same formulations can be applied to the events *C* and *D*.

$$\varepsilon_{x,2,B} = \chi_{2,B}(0.55d_p - x_{2,B}) \quad (14)$$

2.2.3 Event C

This event corresponds to the achievement of the point “b” ($\varepsilon_{py,0}; f_{py,0}$) of the stress-strain relation of strands. For both the failure cases “1” and “2”, the formulations and steps of the paragraph 2.2.2 are still valid.

2.2.4 Event D

Regarding the failure case “1”, the equilibrium is expressed with the Equation (12), where $f_{pp,0}$ is replaced by $f_{pu,0}$ and the check on concrete strain is done. The moment, the curvature, the concrete strain and the longitudinal strain are calculated by adopting the same steps of the paragraph 2.2.2.

Regarding the failure case “2”, the concrete crushing ($\varepsilon_{cu}; f_c$) is reached, and the equilibrium is expressed with the Equation (12) where $f_{pp,0}$ is substituted by $[f_{py,0} + E_p''(\varepsilon_p - \varepsilon_{p,0})]$. Thus, the neutral axis depth (with $f_{p,2,D}^* = [-f_{py,0} + E_p''(\varepsilon_{cu} + \Delta\varepsilon_{py,0})]$) and the moment are calculated as:

$$x_{2,D} = \frac{-A_{p,0}f_{p,2,D}^* + \sqrt{\left(A_{p,0}f_{p,2,D}^*\right)^2 + 3.2bf_cA_{p,0}E_p''\varepsilon_{cu}d_p}}{1.6bf_c} \quad (15)$$

$$M_{2,D} = A_{p,0}\left(f_{py,0} + E_p''(\varepsilon_p - \varepsilon_{p,0})\right)(d_p - 0.4x_{2,D}) \quad (16)$$

The longitudinal strain, $\varepsilon_{x,2,D}$, is calculated with the Equation (14) where the curvature, $\chi_{2,D}$, is:

$$\chi_{2,D} = \varepsilon_{cu}/x_{2,D} \quad (17)$$

The proposed approach is validated against some experimental tests (Billet, 1953) on moment-curvature of un-corroded beams. The analytical results in Figure 3 show good agreement with the tests, although a slight overestimation of the ultimate curvature is detected.

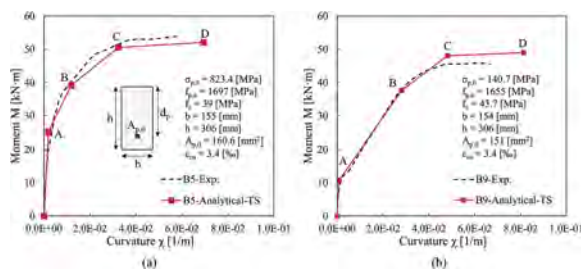


Figure 3. Comparisons between analytical and experimental moment-curvature responses.

2.3 Corrosion effects on the moment-curvature response

To the best authors' knowledge, experimental campaigns aimed to the moment-curvature response of corroded prestressed concrete members are not available. The experimental campaign by Belletti et al. (2020) and Vecchi et al. (2020) is taken as reference, where three- and four-points (“3p” and “4p”) tests on corroded pre-tensioned concrete beams without stirrups were carried out. The following corrosion levels were estimated on strands relieved from beams, based on probabilistic analyses of the maximum pit depth of the most corroded wire, $P_{max,sect}$: (i) $P_{max}=0.05$ mm; $P_{max}/r_{outer}=0.023$ (ii) $P_{max}=1.13$; $P_{max}/r_{outer}=0.531$, (iii) $P_{max}=1.75$; $P_{max,sect}/r_{outer}=0.822$, where r_{outer} is the radius of exterior wires. The ultimate stress and strain of un-corroded strands were 1901.75 MPa and 5.1%, while the concrete compressive strength was 45.4 MPa. By considering long-term effects, the prestressing stress, $\sigma_{p,0}$ was estimated equal to 1171 MPa. According to Franceschini et al. (2022), the corroded strand' stress-strain relation can be evaluated as:

- Calculate the ultimate corroded strain of the most corroded wire, $\varepsilon_{pu,cor}$ based on its maximum pit depth $P_{max,sect}$, which corresponds to the conventional failure of the strand.
- Calculate the average pit depth $P_{av,sect}$ of the remaining wires and the corroded areas of each wire $A_{w,cor}$ and finally the remaining strand's area, $A_{p,cor}$. The section loss is $\mu = A_{p,cor}/A_{p,0}$.
- Calculate the ultimate stress at failure, $f_{pu,cor}$, and the stress-strain relation is completed.

For details refer to Franceschini et al. (2022). The reduced concrete compressive strength was not considered herein since the reinforcement ratio of compressive bars was negligible. In addition, the concrete spalling may be considered for high corroded members (Franceschini et al., 2021).

Concerning the $M-\chi$ response, the failure case is evaluated by updating the equations from (2) to (4), by substituting the corroded properties of prestressing strands ($\varepsilon_{p0,cor}$; $\sigma_{p0,cor}$) and ($\varepsilon_{pu,cor}$; $f_{pu,cor}$). The reduction of the bond between strands and concrete, induced by corrosion, is $\sigma_{p0,cor} = R\sigma_{p0}$ (Dai et al., 2020). The coefficient R was estimated by Wang et al. (2017b) on tests on specimens failing by pull-out. In another work (Wang et al., 2017a), specimens failing by splitting failure mode were tested and, in this paper, a related reduction coefficient R is proposed.

Table 1. Features of some *PC* beams (Belletti et al., 2020; Vecchi et al., 2020) and corrosion data.

<i>PC</i> beam	L, a^* [mm], [mm]	$A_{p,0}$ [mm ²]	$b \times h$ [mm ²]	$P_{max,sec}/r_{outer}$ [-]	$A_{p,cor}$ [mm ²]	μ [%]	$R, \sigma_{p,0,cor}$ [-, MPa]
<i>PBN3P1</i> (3p)	5040, 2520	201	150x300	0.0	201	0.0	1, 1171
<i>PBN4P2</i> (4p)	5040, 1680	(2 ϕ 12.9)		0.0	201	0.0	1, 1171
<i>PB3P11</i> (3p)	4710, 2520			0.822	166	8.08	0.14, 167
<i>PB4P5</i> (4p)	4260, 1420			0.531	185	17.24	0.40, 470

* a is equal to $L/2$ and $L/3$ for 3p and 4p, respectively

The corrosion level was not constant along the beams and the failure was governed by the most corroded strand in the sections in proximity of the loads. In these zones, the corresponding corrosion levels were considered for the comparisons, reported in Table 1 with the features of some of the *PC* beams analysed and the corroded prestress level, $\sigma_{p,0,cor}$. The resulting stress-strain relations of corroded strands are shown in Figure 4(a). The coefficients R are shown in Figure 4(b) (note that $P_{max}/r_{outer}=0$ is the un-corroded case).

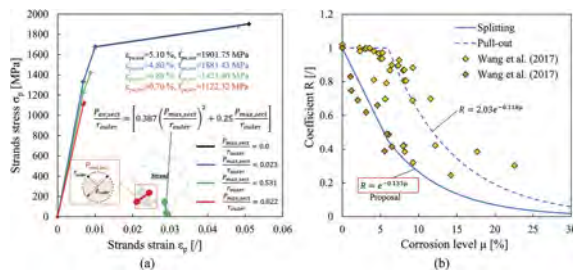


Figure 4. (a) Corroded stress-strain relations for strands, (b) coefficient R for bond reduction.

The formulations of the previous paragraph are still valid by using the corroded properties for the $M-\chi$ response of corroded *PC* members. It is worth mentioning that, the un-corroded strands area is adopted, since the corrosion effect is implicitly considered in the stress-strain relation by Franceschini et al. (2022). The moment-curvature responses are reported in Figure 5(a), where the reduction of both ultimate moment and curvature, as well as the cracking moment, is observed. Figure 5(b) shows both strands and concrete strains at failure, where it is evident the failure mode's transition from concrete crushing to steel fracture with increasing corrosion level.

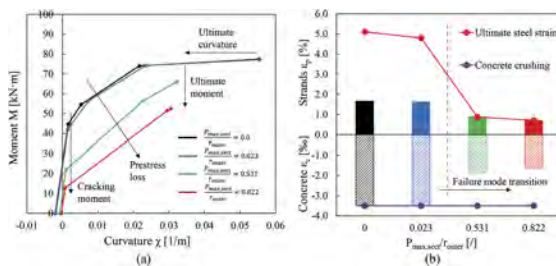


Figure 5. (a) Corroded $M-\chi$ responses, (b) strands and concrete strains vs corrosion levels.

3 FLEXURAL VS SHEAR RESISTANCES

The flexural resistance of a three- and four-point *PC* beam is calculated with the Equation (18):

$$P_{Rd} = 2M_{Rd}/a \quad (18)$$

where M_{Rd} is the ultimate moment calculated in the previous section. The shear resistance is calculated with the *LoA II* of Model Code 2010 (fib, 2013), Equation (19):

$$V_{Rd} = k_v \frac{\sqrt{f_{ck}}}{\gamma_c} z b_w = \left[\frac{0.4}{1 + 1500 \varepsilon_x} \frac{1300}{1000 + k_{dg} z} \right] \frac{\sqrt{f_{ck}}}{\gamma_c} z b_w \quad (19)$$

where $\gamma_c=1$ and $k_{dg}=1$ is assumed, and the average concrete strength, f_{cm} , is used for the comparisons. The longitudinal strain is established with (i) the proposed analytical model, $\varepsilon_{x,an}$, and (ii) the formulation of the Model Code 2010, modified to account for corrosion Equation (20):

$$\varepsilon_{x,mod} = \frac{1}{2(z_p E_p A_{p,cor}/z)} \left[\frac{(M_{Ed0} + N_{p,cor} e)}{z} + V_{Ed0} + N_{p,cor} \frac{(z_p - e)}{z} \right] \quad (20)$$

where $N_{p,cor} = -A_{p,cor} \sigma_{p0,cor}$ is the prestress level of corroded strands. As suggested in *MC 2010* (fib, 2013), the shear verification is conducted at a distance equal to d_p from the loads (or, at a distance $(a - d_p)$ from the support), where M_{Ed0} and V_{Ed0} are the corresponding moment and shear demands, depending on the applied loads. In addition, $z=z_p=0.9d_p$ is assumed.

The comparisons between analytical and experimental results in terms of failure loads and failure modes (flexural, *I*, and flexural-shear, *II*) are shown herein. To consider the shifting of moment diagram and the shear demand, the proposed analytical strain is amplified by a factor $(1+\beta)$:

$$\varepsilon_{x,an}^{MV} = \varepsilon_{x,an} [1 + \beta] = \varepsilon_x \left[1 + \frac{V_{Ed0} z}{M_{Ed0} 2} (\cotg(\theta) + \cotg(\alpha)) \right] \quad (21)$$

Since in the reference work no stirrups were provided, $\theta=45^\circ$ and $\cotg(\alpha)=0$ is assumed. Figure 6(a) shows the longitudinal strain vs bending moment for the beams *PBN3P1* (black lines, $P_{max,sect}/r_{outer}=0$) and *PB3P11* (red lines, $P_{max,sect}/r_{outer}=0.822$). For un-corroded members, the positive strains are similar for both approaches till the event *C*, where the strands' yielding starts. The upper limit strain from *MC 2010* is also assumed. For corroded members, the proposed approach provides lower strain compared with the Equation (20). Figure 6(b) shows the shear demand and capacity by using the proposed analytical procedure. The shear capacity was calculated by adopting the longitudinal strain of Equation (21) and substituted in Equation (19). The flexural-shear failure occurs if the shear capacity intersects the shear demand, leading to the onset of a shear crack.

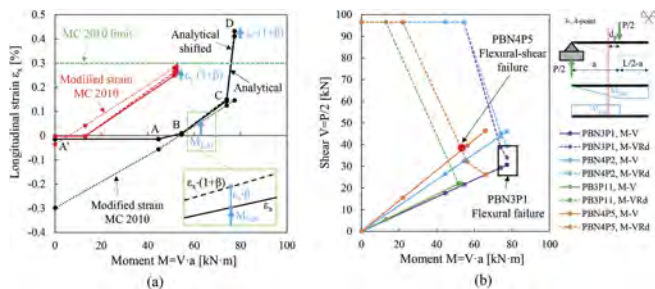


Figure 6. (a) Longitudinal strain, (b) demand vs capacity for the different *PC* beams.

Table 2 shows the obtained results, where the proposed model tends to provide better predictions for corroded *PC* members compared with the modified formulation of Model Code

Table 2. Summary of results in terms of failure loads and modes.

<i>PC</i> beam	M_{Rd} [kN·m]	$P_{fail,exp}$ [kN]	$P_{fail,mod}$ [kN]	β [%]	$P_{fail,an}$ [kN]	$P_{fail,exp}^I / P_{fail,mod}^I$ [I]	$P_{fail,exp}^{II} / P_{fail,an}^{II}$ [II]	Failure mode exp./an./mod.
<i>PBN3P1</i>	77.4	70.1	61.4	4.9	61.4	1.14	1.14	I/I/I
<i>PBN4P2</i>	77.4	98.5	89.2	7.8	89.2	1.12	1.10	II/II/II
<i>PB3P11</i>	52.4	62.0	42.8	5.3	44.0	1.45	1.41	I/II/II
<i>PB4P5</i>	65.9	90.2	70.0	9.6	75.1	1.28	1.20	II/II/II

2010. The coefficient β increases with loading configuration (from “3p” to “4p”) and seems also with the corrosion level. Failure modes are well captured except for the beam *PB3P11*.

4 CONCLUSIONS

In this paper, an analytical method for the sectional moment-curvature response of corroded pre-tensioned beams is proposed. The following conclusions can be drawn:

- The effects of corrosion are investigated through a simplified moment-curvature response, based on a novel stress-strain relationship of prestressing strands. The proposed method can predict the failure mode of the section and the loss of both resistance and ductility. Future improvements concern the role of ordinary rebars and the extension to post-tensioned beams.
- The proposed sectional approach was then used to predict the failure load of available experimental tests on *PC* beams, showing good yet conservative results in terms of failure load.
- Further experimental campaigns should be aimed to the evaluation of: (i) corrosion patterns and spatial variability of reinforcement pit depths, (ii) the bond-slip behaviour of full-scale beams, and its effects on the prestress level and on the capacity and ductility of such members.

ACKNOWLEDGMENTS

The presented study is part of a program of activities funded by the Italian “Consiglio Superiore dei Lavori Pubblici”.

REFERENCES

- Belletti, B., Rodríguez, J., Andrade, C., Franceschini, L., Sánchez Montero, J., & Vecchi, F. (2020). Experimental tests on shear capacity of naturally corroded prestressed beams. *Structural Concrete*, 21(5), 1777–1793.
- Billet, D. F. (1953). *Study of prestressed concrete beams failing in flexure* (Issue April). PhD thesis, University of Illinois.
- Coronelli, D., Mircea, C., Rogers, R., Rosati, G., & Consiglio, A. N. (2022). Structural assessment of prestressed beams with natural corrosion. *Structural Concrete*, November, 1–15.
- Dai, L., Bian, H., Wang, L., Potier-Ferry, M., & Zhang, J. (2020). Prestress Loss Diagnostics in Pretensioned Concrete Structures with Corrosive Cracking. *Journal of Structural Engineering*, 146(3).
- fib. (2013). *fib Model Code for Concrete Structures 2010*.
- Franceschini, L., Belletti, B., & Calcavecchia, B. (2021). Capacity assessment of existing RC columns taking into account bi-axial shear failure. *Proceedings of the CACRCS DAYS 2021*, 30 November-3 December, 1, 173–176.
- Franceschini, L., Belletti, B., Tondolo, F., & Sanchez, J. (2022). A simplified stress-strain relationship for the mechanical behaviour of corroded prestressing strands: the SCPS-model. *Structural Concrete*, May.
- Jeon, C. H., & Shim, C. S. (2020). Flexural behavior of post-tensioned concrete beams with multiple internal corroded strands. *Applied Sciences*, 10(22), 1–17.
- Vecchi, F., Belletti, B., Franceschini, L., Andrade, C., Rodriguez, J., & Montero, S. J. (2020). Flexural Tests on Prestressed Beams Exposed to Natural Chloride Action. In *Proceedings of the 2nd CACRCS Workshop*.
- Vecchi, F., Franceschini, L., Tondolo, F., Belletti, B., Sánchez Montero, J., & Minetola, P. (2021). Corrosion morphology of prestressing steel strands in naturally corroded PC beams. *Construction and Building Materials*, 296, 123720.
- Vereecken, E., Botte, W., Lombaert, G., & Caspeele, R. (2021). Assessment of corroded prestressed and posttensioned concrete structures: A review. *Structural Concrete*, 22(5), 2556–2580.
- Wang, L., Yi, J., Zhang, J., Floyd, R. W., & Ma, Y. (2018). Bond behavior of corroded strand in pretensioned prestressed concrete beams. *ACI Structural Journal*, 115(6), 1803–1812.
- Wang, L., Yi, J., Zhang, J., Jiang, Y., & Zhang, X. (2017a). Effect of corrosion-induced crack on the bond between strand and concrete. *Construction and Building Materials*, 153, 598–606.
- Wang, L., Zhang, X., Zhang, J., Yi, J., & Liu, Y. (2017b). Simplified Model for Corrosion-Induced Bond Degradation between Steel Strand and Concrete. *Journal of Materials in Civil Engineering*, 29(4), 04016257.
- Zhang, X., Wang, L., Zhang, J., Ma, Y., & Liu, Y. (2017). Flexural behavior of bonded post-tensioned concrete beams under strand corrosion. *Nuclear Engineering and Design*, 313, 414–424.

Structural behavior of PC beams under simultaneous corrosion and sustained loads

F.F. Bico, M. Bartoli, F. Di Carlo, A. Meda, F. Molaioni & Z. Rinaldi

Department of Civil Engineering and Computer Science Engineering, University of Rome “Tor Vergata”, Rome, Italy

ABSTRACT: The paper presents an experimental study for the evaluation of the flexural response of prestressed concrete beams subjected to simultaneous sustained loads and corrosion. The tested beam features a 200 x 300 mm rectangular cross section, a total length of 3700 mm and a clear span of 2700 mm. In the performed four-point bending test, the beam was subjected to about 60% of the ultimate load of an identical undamaged reference beam, and to a simultaneous accelerated corrosion process of the strands. The flexural response of the tested element was monitored over a period of 70 days, up to failure, shown to be highly dependent on the localization of the corrosion phenomena affecting the strands, especially when coinciding with the maximum bending moment position. The obtained results confirm the importance of accounting for the combined effect of reinforcement corrosion and loading when assessing the structural performance of prestressed concrete beams.

1 INTRODUCTION

The assessment of degraded prestressed concrete (PC) existing structures is nowadays a topical problem. In this framework, corrosion of internal reinforcements represents one of the main causes of long-term deterioration. Potential consequences can be extremely serious, even more serious than those in reinforced concrete (RC) structures, as witnessed by recent cases worldwide, in which severe damages can lead to unexpected structural crisis. A crucial aspect for the structural safety consists in the combined effect of corrosion-induced sectional reductions and wires rupture failures. Despite the need to deepen the knowledge of the influence of corrosion on the behavior of PC elements, not many research documents are available in literature. Experimental tests have been performed on rectangular-shaped [Rinaldi et al. 2010] and T-shaped [Menoufy & soudki 2014] PC beams in four-point bending, varying the corrosion level. The results of cyclic loading tests on T-shaped corroded PC beams are discussed in [ElBatouny et al. 2015]. The fatigue behavior of pre-tensioned partially pre-stressed concrete beams with corroded prestressing wires or rebars is studied in [Zhang et al. 2016]. Post-tensioned concrete beams with corroded strands were tested in bending by [Zhang et al. 2017]. Studies regarding the possible relationship between the prestressed concrete cracking induced by strand corrosion and the corrosion itself can be found in [Dai et al. 2016, Dai et al. 2020]. Finally, experimental tests on PC beams [Mircea et al. 1994, Belletti et al. 2020] and actual bridge PC beams [Pape and Melchers 2011, Rogers et al. 2012, Rogers 2012] subjected to natural corrosion are also available.

Nevertheless, much of these works are based on laboratory procedure in which the artificial corrosion and loading processes are considered as two distinct and sequential phases. Actually, corrosion affects the steel reinforcement of a real structure simultaneously with the application of the sustained load. This results in an increase of the deterioration state of the structure since cracks due to the formation of the corrosion products are widened by the applied loads and vice versa. In this way, a greater diffusion of oxygen and water takes place, resulting in a more rapid corrosion process. Many studies on the coupled effect of sustained load and corrosion on the

long-term behavior of RC beams exists in literature (Yoon et al. 2000, Ballim et al. 2001, Ballim and Reid 2003, Malumbela et al. 2009a). A critical review of the studies carried out to investigate the effects of simultaneous load and steel corrosion on the rates of corrosion and the behavior of RC structures is performed in Malumbela et al. (2009b). Hariche et al. (2012) investigate the effect of reinforcement corrosion on the serviceability behavior of RC beams under load. Further studies regarding the influence of simultaneous loading and reinforcement corrosion on the structural performance of RC beams can be found in (Du et al. 2013, Zhu et al. 2013, Dong et al. 2017, Li et al. 2018, Zhang et al. 2018). On the contrary, with reference to PC elements, not many research documents are available in literature on the coupled effect of sustained load and corrosion on the long-term behavior. An experimental investigation based on a set of six PC beams simultaneously corroded and subjected to a sustained load is reported in Yang et al. (2020).

In the present paper, an experimental study for the evaluation of the flexural response of PC beams, subjected to the simultaneous effect of sustained loads and corrosion of the strands, is presented. Section 2 describes the experimental campaign, giving an insight on the geometry and material properties of the specimen and on the test set-up, realized ad-hoc to allow the simultaneous execution of the two processes of artificial corrosion and loading. The main outcomes in terms of cracking pattern and load-dependent and time-dependent deflections of the PC beam are shown in Section 4.

2 EXPERIMENTAL CAMPAIGN

A wide experimental survey for the evaluation of the flexural response of corroded RC (Di Carlo et al. 2022a) and PC beams has been planned and conducted at the Laboratory of the University of Rome “Tor Vergata”, within the framework of an Italian PRIN project. The research program is based on a set of twelve RC and twelve PC beams, that have been subjected to artificial corrosion processes and to four-point bending tests up to failure. One of the aims of the research consists in the comparison of the results obtained through different test methods. The first and most currently used method for the assessment of the effects of corrosion of the steel reinforcement on the behavior of a RC and/or PC element, is based on the execution of two distinct and sequential phases, consisting in the artificial corrosion process and bending test. Nevertheless, the above test method is clearly not able to faithfully represent the actual condition of the element within the real structure, in which these two phases cannot be considered as separate, since reinforcement corrosion naturally occurs together with the application of loads. For this reason, an alternative test method can be adopted, considering the artificial corrosion and loading as two simultaneous processes.

This paper, starting from the outcomes related to five PC beams tested within the same research project with the usual Laboratory procedure (Di Carlo et al. 2022b), presents a more realistic experimental test procedure of PC beam corroded under loading.

2.1 *Geometry and materials of the specimens*

The experimental campaign includes at the present the execution of six four-point bending tests, of which one performed on a beam kept uncorroded (PC-UC) for reference, four adopting the usual test method (PC-C1 to PC-C4) – the four specimens were subjected before testing to accelerated corrosion, with different corrosion levels of the prestressing reinforcement (Di Carlo et al. 2022b) – and one with simultaneous corrosion (PC-CL1), better described in the following. All beams feature a 200×300 mm rectangular cross section and a total length of 3700 mm. The longitudinal reinforcement is made of three $\frac{1}{2}$ -inch seven wires strands, two placed at the bottom of the section and one at the top, and four $\text{Ø}10$ mm ordinary rebars. $\text{Ø}8$ mm bars are adopted for the stirrups, with a spacing of 100 mm and 200 mm in the outer (1450 mm) and inner (800 mm) zones of the beams, respectively. The concrete cover is equal to 20 mm. Figure 1 shows the geometry and reinforcement details of the specimens.

Concrete with a mean compressive strength equal to 52.6 MPa – value measured on 100 mm side cubes - has been used, while the ordinary rebars are characterized by yielding and ultimate strengths equal to 510 MPa and 630 MPa, respectively. The initial wire prestressing stress is equal to 1300 MPa, corresponding to about 70% of the ultimate strength equal to 1860 MPa.

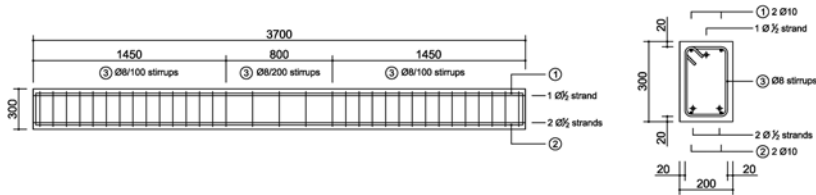


Figure 1. Geometry and reinforcement details of the PC beam.

For further details about the accelerated corrosion process and the set-up of the four-point bending test of the specimens tested with the usual Laboratory procedure see Di Carlo et al. 2022b. A full list of all the performed tests is reported in the following table, together with the correspondent nominal corrosion level, expressed as percentage mass loss and evaluated after the tests by cleaning (ASTM G1-90 2002) and weighing the strands extracted from each specimen. The experimental values of the maximum loads are also summarized.

Table 1. List of the performed tests nominal corrosion level and maximum load.

N	Beam	Mass loss %	Maximum Load [kN]
1	PC-UC	-	241
2	PC-C1	1.6	232
3	PC-C2	9.03	124.5
4	PC-C3	19.15	40.5
5	PC-C4	27.48	47.2

2.2 Test set-up

This section is devoted to the description of the test set-up of the PC-CL1 specimen, designed ad-hoc to allow the simultaneous execution of the two processes of artificial corrosion and loading. The testing procedure foresees in fact the application of two vertical 75 kN point-loads on a scheme of simply supported beam – corresponding to about 60% of the ultimate load of the uncorroded reference beam – and the implementation of a corrosion process of the two bottom longitudinal strands at the same time.

The artificial corrosion is provided with an accelerated process through electrolytic cells, by dipping the beam within a 3% saline solution, up to half of the height of the cross section. To this aim, a wooden box, coated with a waterproof membrane and two plastic sheets, has been realized, fully embedded with the loading system. Only the two lower longitudinal ½-inch strands are connected to the positive pole of the power supply (anode), while the cathodes are realized with two Ø10 diameter steel bars soaked in the saline solution. A current intensity equal to 0.65 A has been applied. Some images of the artificial corrosion set-up are shown in Figure 2.



Figure 2. Artificial corrosion set-up.

The vertical load is applied through two hydraulic 300 kN jacks, connected to a 700 bar hydraulic pump for the automatic pressure recovery, ensuring the maintenance of the pre-set load during all the test period, with a deviation lower than $\pm 5\%$. The contrast frame, made with

steel beams, is anchored to the laboratory strong floor by means of two pre-tensioned high strength rebars, running outside the wooden box. The two supports are realized with two rotating cylinders, resting on the bottom panel of the wooden box and connected with each other by means of two C-shaped steel profiles. Figure 3 shows some images of the overall test set-up.



Figure 3. Details of the experimental test set-up.

A scheme of the experimental test-set, with superimposed the type and location of all measuring instruments, is shown in Figure 4. The span of the PC beam during the test is equal to 2700 mm, while the shear length is 900 mm, corresponding to one third of the total span length. The vertical load is measured with a load transducer, while five potentiometer transducers have been used to measure the vertical displacements at the midspan (P1), under the two point-loads (P2 and P3) and at the support point (P4 and P5). Furthermore, five 2-axes MEMS clinometer (T1 to T5) are placed on the extrados of the beam to measure the tilting of the specimen throughout the entire test period (Figure 4).

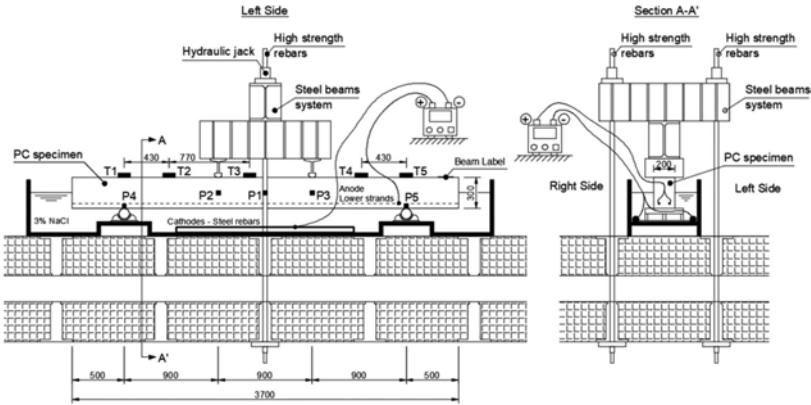


Figure 4. Scheme of the set-up with superimposed the measuring instruments.

3 EXPERIMENTAL RESULTS

This section presents the main experimental results in terms of cracking pattern, load-dependent and time-dependent deflections of the PC beams under simultaneous loading and corrosion of the two bottom longitudinal strands. Figure 5a shows the cracking pattern detected during the entire period of execution of the test, up to failure. The first cracks occurred in the central portion of the beam between the two point-loads. During the test, a wide spread of cracks developed towards the longitudinal middle axis of the beam and the two supports. A view of the beam failure condition is shown in Figure 5b. It is worth to highlight that the evaluation of a corrosion index based on the estimation of the percentage mass loss of the strands is not applicable in this specific test, since the corrosion of the reinforcement results to be highly concentrated in the middle section of the beam.

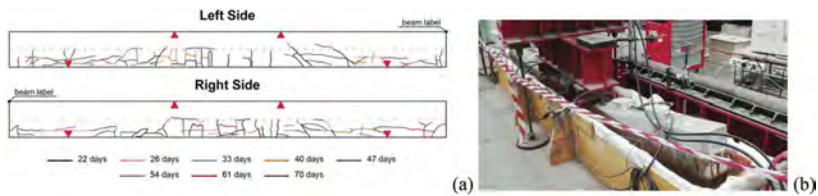


Figure 5. (a) Cracking pattern detected during the execution of the test. (b) Beam failure.

Figure 6 shows the trend of the beam deflection measured by the five potentiometers. The displacements measured at locations P1, P2 and P3 are corrected for the support settlement (even if almost negligible), measured by the potentiometers P4 and P5. In particular, Figure 6a refers to the entire test period, while Figure 6b shows a detail at the beginning of the test, up to 0.1 day, from which the initial loading history to reach the pre-set load of 150 kN can be observed. Superimposed in the same graphs with a dashed black line is the trend of the load during the test. It can be noted that the applied vertical load has been properly maintained during all the test period.

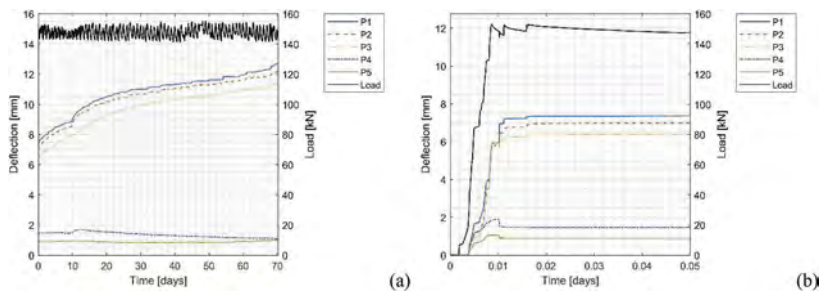


Figure 6. Trend of the beam deflections and load with time: (a) entire test period (b) detail at the beginning of the test.

The experimental results of the tested beam are summarized in Figure 7 in terms of Load-Deflection graph. In particular, Figure 7a refers to the entire test period, while Figure 7b shows a detail related to the end of the test. The failure, shown in Figure 5b, occurred in a brittle way, due to the breakage of the two bottom longitudinal strands in their middle section, corresponding to the section characterized by the maximum bending moment.

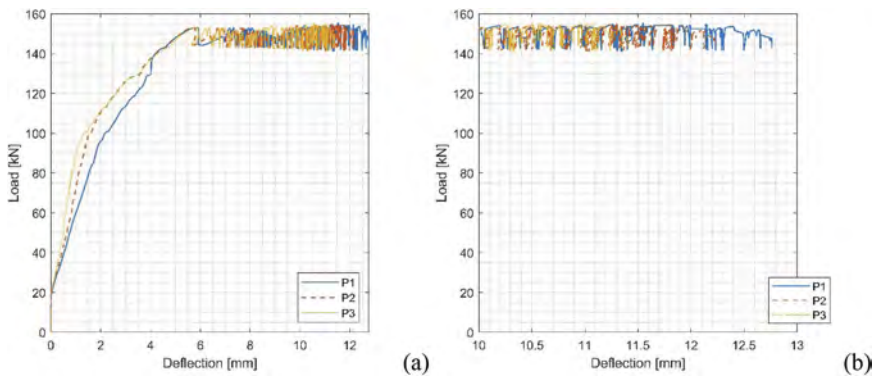


Figure 7. Load-deflection curves: (a) entire test period (b) detail at the end of the test.

For the sake of clarity, Figure 8 summarized the load and displacement measurements over the entire test period through the use of a three-dimensional graph.

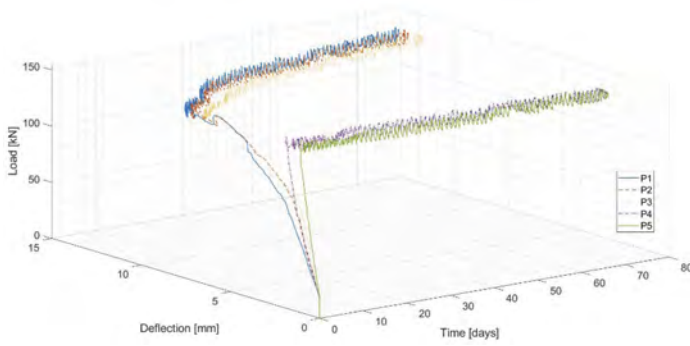


Figure 8. Three-dimensional graph: trend of load and displacement over the entire test period.

Figure 9 shows the trend of the tilting of the beam measured by the five 2-axes MEMS clinometer. In particular, Figure 9a refers to the entire test period, while Figure 9b shows a detail at the beginning of the test, up to 0.1 day, from which the initial loading history to reach the pre-set load of 150 kN can be observed. Superimposed in the same graphs with a continuous black line is the trend of the load during the test.

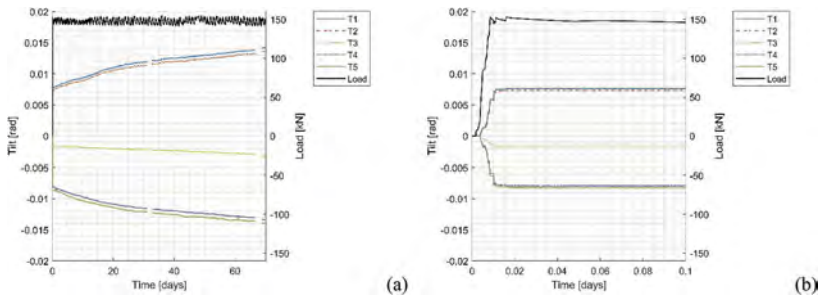


Figure 9. Trend of the beam tilting and load with time: (a) entire test period (b) detail at the beginning of the test.

Finally, a comparison of the displacement and tilting measurements of the tested beam is carried out in Figure 10. As it can be noted, the two different measurements are in good agreement over the entire test, showing their effectiveness in catching the structural response of the element.

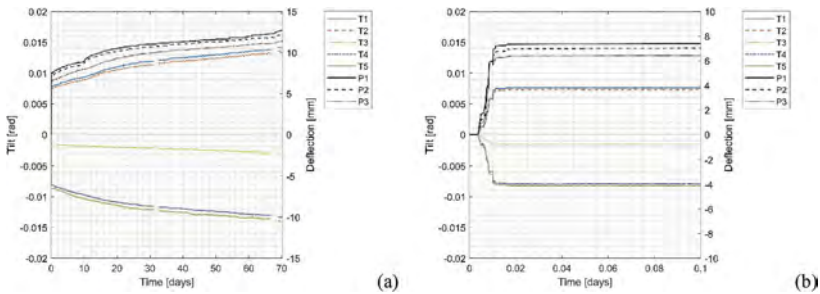


Figure 10. Comparison of the displacement and tilting measurements: (a) entire test period (b) detail at the beginning of the test.

4 CONCLUSIONS

The experimental campaign described in the paper provides an important reference to deepen the knowledge about the evolution of the corrosion process in PC elements. A more realistic test method has been adopted to investigate the flexural response of corroded PC beams, in order to overcome the limits of traditional laboratory procedures. Current test methods, considering the artificial corrosion and loading processes as two distinct and sequential phases, are not able to faithfully reproduce the actual behavior of the element within the real structure. Reinforcement corrosion phenomena occurring simultaneously with sustained loads, are in fact responsible for an increase of the deterioration state of a real element, due to the widening of corrosion-induced cracks because of applied loads and vice versa. Aiming to improve the understanding of the effect of corrosion of the steel reinforcement on the behavior of PC elements, the adoption of a test method considering the simultaneous action of sustained loads and corrosion is therefore fundamental. The described test method has been applied to a 3700 mm long PC beam, subjected to two vertical 75 kN point-loads on a scheme of simply supported beam and to a corrosion process of the two bottom longitudinal strands at the same time. As a result, the collapse of the PC beam occurred after 70 days in a brittle way, due to the failure of the two bottom longitudinal strands in their middle section, corresponding to the maximum bending moment section. It is worth to highlight that the evaluation of a corrosion index based on the estimation of an average percentage mass loss of the strands is not applicable in this specific test, since reinforcement corrosion results to be highly concentrated in the middle section of the beam. The flexural response is shown to be highly dependent on the morphology and localization of the corrosion phenomena affecting the strands, especially when coinciding with the maximum bending moment position. A good agreement between displacement and tilting measurements is found, highlighting the importance and usefulness of implementing a proper monitoring system, in order to constantly control the response of the structure. The obtained results confirm the importance of accounting for the combined effect of reinforcement corrosion and loading when assessing the structural performance of prestressed concrete beams.

ACKNOWLEDGEMENTS

The research presented in this paper is supported by the PRIN 2017 grant, from the Italian Ministry of University and Research, within the project “Life-long optimized structural assessment and proactive maintenance with pervasive sensing techniques”.

REFERENCES

- ASTM G1-90. 2002 Practise for preparing, cleaning and evaluating corrosion test specimens. ASTM International, West Conshohocken, Pa.
- Ballim, Y., Reid, J.C. & Kemp, A.R. 2001. Deflection of RC beams under simultaneous load and steel corrosion. *Magazine of Concrete Research* 53(3): 171–181.
- Ballim, Y. & Reid, J.C. 2003. Reinforcement corrosion and the deflection of RC beams—an experimental critique of current test methods. *Cement & Concrete Composites* 25: 625–632.
- Belletti, B., Rodríguez, J., Andrade, C., Franceschini, L., Sánchez Montero, J. & Vecchi, F. 2020. Experimental tests on shear capacity of naturally corroded prestressed beams. *Struct Conc* 21(5): 1777–1793.
- Dai, L., Wang, L., Zhang, J. & Zhang, X. 2016. A global model for corrosion-induced cracking in prestressed concrete structures. *Engineering Failure Analysis* 62: 263–275.
- Dai, L., Bian, H., Wang, L., Potier-Ferry, M. & Zhang, J. 2020. Prestress Loss diagnostics in pre-tensioned concrete structures with corrosive cracking. *Journal of Structural Engineering* 146(3): 04020013.
- Di Carlo, F., Meda, A. & Rinaldi, Z. 2022a. Structural performance of corroded R.C. beams. *Engineering Structures* 115117.
- Di Carlo, F., Isabella, P., Rinaldi, Z. & Meda A. 2022b. Structural performance of corroded prestressed concrete beams. *NBSC 2022, The New Boundaries of Structural Concrete, Lecce, Italy*, 8-9.11.2022.
- Dong, J., Zhao, Y., Wang, K. & Jin, W. 2017. Crack propagation and flexural behaviour of RC beams under simultaneous sustained loading and steel corrosion. *Construction and Building Materials* 151: 208–219.

- Du, Y., Cullen, M. & Li, C. 2013. Structural performance of RC beams under simultaneous loading and reinforcement corrosion. *Construction and Building Materials* 38: 472–481.
- ElBatanouny, M.K., Nanni, A., Ziehl, P.H. & Matta, F. 2015. Condition Assessment of Pre-stressed Concrete Beams Using Cyclic and Monotonic Load Tests. *ACI Structural Journal* 112(1): 81–90.
- Hariche, L., Ballim, Y., Bouhicha, M. & Kenai, S. 2012. Effects of reinforcement configuration and sustained load on the behaviour of reinforced concrete beams affected by reinforcing steel corrosion. *Cement & Concrete Composites* 34: 1202–1209.
- Li, H., Li, B., Jin, R., Li, S. & Yu, J. 2018. Effects of sustained loading and corrosion on the performance of reinforced concrete beams. *Construction and Building Materials* 169: 179–187.
- Malumbela, G., Moyo, P. & Alexander, M. 2009a. Behaviour of RC beams corroded under sustained service loads. *Construction and Building Materials* 23: 3346–3351.
- Malumbela, G., Alexander, M. & Moyo, P. 2009b. Steel corrosion on RC structures under sustained service loads - A critical review. *Engineering Structures* 31: 2518–2525.
- Menoufy, A.E. & Soudki, K. 2014. Flexural behavior of corroded pretensioned girders repaired with CFRP sheets. *PCI Journal* 59(2): 129–143.
- Mircea, D., Ioani, A., Filip, M. & Peparar, I. 1994. Long-term durability of reinforced and pre-stressed elements in aggressive environments. *Materials Journal* 91(2): 135–140.
- Pape, T.M. & Melchers, R.E. 2011. The effects of corrosion on 45-year-old pre-stressed concrete bridge beams. *Structure and Infrastructure Engineering* 7(1-2): 101–108.
- Rinaldi, Z., Imperatore, S., & Valente, C. 2010. Experimental evaluation of the flexural behavior of corroded P/C beams. *Construction and Building Materials* 24(11): 2267–2278.
- Rogers, R., Wotherspoon, L., Scott, A.N. & Ingham, J.M. 2012. Residual strength assessment and destructive testing of decommissioned concrete bridge beams with corroded pretensioned reinforcement. *PCI Journal* 57(3): 100–118.
- Rogers, R. 2016. Assessing pre-tensioned reinforcement corrosion within the New Zealand concrete bridge stock”, Doctoral Dissertation, Dep. of Civil and Environmental Engineering, University of Auckland.
- Yang, J., Guo, T. & Li, A. 2020. Experimental investigation on long-term behavior of pre-stressed concrete beams under coupled effect of sustained load and corrosion. *Advances in Struct Eng* 23(12): 2587–2596.
- Yoon, S., Wang, K., Weiss, W.J. & Shah S.P. 2000. Interaction between Loading, Corrosion, and Serviceability of Reinforced Concrete. *ACI Materials Journal* 97(6): 637–644.
- Zhang, W., Liu, X. & Gu, X. 2016. Fatigue behavior of corroded prestressed concrete beams. *Construction and Building Materials* 106: 198–208.
- Zhang, X., Wang, L., Zhang, J., Ma, Y. & Liu, Y. 2017. Flexural behavior of bonded post-tensioned concrete beams under strand corrosion. *Nuclear Engineering and Design* 313: 414–424.
- Zhang, W., Zhang, H., Gu, X. & Liu, W. 2018. Structural behavior of corroded reinforced concrete beams under sustained loading. *Construction and Building Materials* 174: 675–683.
- Zhu, W., François, R., Coronelli, D. & Cleland, D. 2013. Effect of corrosion of reinforcement on the mechanical behaviour of highly corroded RC beams. *Engineering Structures* 56: 544–554.

Random field analysis of corrosion of steel in the artificial marine atmosphere

Weiping P. Zhang, Xianglin L. Gu, Qianqian Q. Yu & Jinping Chen
Department of Structural Engineering, Tongji University, Shanghai, China

ABSTRACT: This paper presents a study on the surface morphology of corroded steel in the artificial marine atmosphere. Three groups of specimens in three different supported angles were obtained in the environmental cabinet. The 3D scanner was used to digitalize the corrosion surface. The geometry characteristics contributing to the random field model of the corrosion surface were studied statistically. Results show that the corrosion depth obeys the normal distribution as corrosion proceeds and the corrosion surface random field can be regarded as a weak stationary random field. The better fitting model for autocorrelation function is cosine exponential model and the distribution of parameter correlation length l_c is related to the supported angles.

1 INTRODUCTION

Corrosion is a widespread problem for steel structures during service. The reduction in material leads to a deterioration of the structural component, thus raising the probability of structural failure. Exposed to higher salinity and humidity, steel structures in the marine environment are more susceptible to corrosion, resulting in a more rapid rate of degradation than those in the normal environment. Since 1985 in Switzerland (Ortega & Bisgaard 2000), a certain number of collapses of steel swimming pools have been reported worldwide, in the Netherlands in 2001 (Heselmans & Vermeij 2013), in Perm, Russia in 2005 and China in recent years. Reports suggest that the cost of corrosion amounts to about 3% of the gross global domestic product, leading to an estimated worldwide direct cost exceeding \$1.8 trillion (Schmitt et al. 2009). From the point of view of structural safety and socio-economic benefits, scholars are increasingly focused on assessing the load capacity of corroded steel structures in the marine environment.

The geometry of the corroded component determines its mechanical properties, implying that the remaining load capacity of the component can be estimated by the corrosion degree approximately. Corrosion depth, the most common geometric representation of corrosion on steel, was statistically normal, log-normal or mixed-normal (Kim et al. 2013; Paik et al. 2004; Rivas et al. 2008; Tang et al. 2014) in distribution meanwhile the maximum corrosion depth shown to obey the extreme value distribution (Rivas et al. 2008). The ratio of width to depth of the visible corrosion pits was also adopted to represent the shape of corrosion geometry (Nakai et al. 2004). As the width-to-depth ratio is not enough to present a corrosion geometry. The relation between corrosion surface characteristic parameters and the corrosion degree was statistically studied in the surface geometry evolution (Qin et al. 2016). For the reason the corroded steel bars and steel plates tend to fail at the minimum cross-section under tensile load, the factor R (the ratio of the average cross-sectional area to the minimum one) was put forward to quantify the longitudinal non-uniformities of corrosion (Cairns et al. 2005; Zhang et al. 2014). Those statistical works allow us to predict the mechanical properties of components with different corrosion geometries. However, these predictions can be defective for the overall corrosion shape cannot be captured to obtain specific mechanical properties, leaving the prediction at the probabilistic analysis stage. In some assumed corrosion models, such as

randomly shaped corrosion pits set into steel plates, there is a lack of consideration in expressing the continuity of the corroded surface. Teixeira considered to represent distributions of the thickness of the corroded plate by random fields and demonstrated the importance of using random field models (Teixeira & Soares 2008), though the correlation length was chosen as 0.3m subjectively. A latent Gaussian random field was applied as a useful tool to characterize the corrosion depth on the external surface of buried steel oil and gas pipelines (Bao & Zhou 2021).

This study aims to analyze and simulate the surface morphology of corroded steel in the marine atmosphere. Three groups of specimens in three different supported angles were obtained in the environmental cabinet. The 3D scanner was used to digitalize the corrosion surface. The geometry characteristics contributing to the random field model of the corrosion surface were studied statistically. The main parameter correlation length l_c was estimated by cosine exponential model to represent the corrosion surface.

2 MATERIALS AND METHODS

2.1 Specimen and preparation

A survey by the China Steel Structure Association showed that the proportion of Q235 steel and Q345 steel in the production of steel stood at 31% and 62% respectively in 2010 (Li et al. 2013). The Q345 steel plates with a thickness of 6mm were used in the study. The size of the specimen is 950mm × 500mm × 6mm. To retain the uncorroded surface as a reference, layers of epoxy were wrapped around the four edges of the steel plates after recording the original mass m_0 . The specimens were to be placed in the environmental chamber at 0°, 45° and 90° angles. Figure 1a shows that wooden frames and spacers were used to support the specimens inside the environmental chamber to ensure that the steel plates are insulated from each other. The solution, pH, RH and fog rate in the environmental chamber conditions were 5±1% NaCl solution, 6.5~7.2, 95%~98% and 1~2mL/h·80cm² respectively (ASTM 2019). The parameters and numbering of the specimens are listed in Table 1. Three specimens at each of the three angles were taken out every four months. The corrosion products were removed from the surface of the specimens according to ISO standard (ISO 2009). Figure 1b shows an example of specimens before and after the removal of corrosion products. Then the mass of the specimen m_1 was measured to quantify the mass corrosion degree η_m . Each corrosion surface point cloud data were captured by a ZEISS COMET scanner as shown in Figure 1c. Geomagic Studio 12 was adopted to optimize point cloud data by removing data points exclusive from steel bars, processing filtering and removing noise to improve the signal-to-noise ratio.

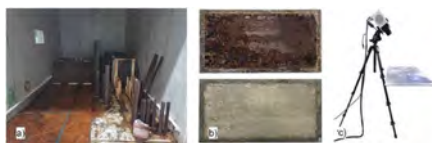


Figure 1. a) Placement of specimens inside the environmental chamber b) Before and after removal of corrosion products c) 3D optical scanning of the specimen.

Table 1. The parameters and numbering of the specimens.

No.	Angle	Corrosion duration	η_m
H1	0°	4 months	0.0274
H2	0°	8 months	0.0543
S1	45°	4 months	0.0523
S2	45°	8 months	0.0574
V1	90°	4 months	0.1110
V1	90°	8 months	0.0897

After coordinate system alignment, the 3D coordinates of equally spaced points with 1mm were exported from PolyWorks.

In the paper, the suffixes '-1' and '-2' after the specimen number represent the two faces of the specimen.

2.2 Detrending of point cloud data

As steel plates inevitably warp during manufacture and transport, the surfaces are not ideal planes and the 3D data need to be de-trended before corrosion depth statistics. Taking the area covered by epoxy resin as a reference, the 3D coordinate data of the area were extracted first and fit the surface using the fifth-order polynomial. Based on the initially fitted surface equation, the corrosion depth of the corroded area on the surface was then adjusted. Although the goodness of fit was greater than 0.98, the fitted surfaces were not the true warped surfaces and part of the adjusted corrosion depth was less than zero, which means that the fitted surfaces needed further modification. With the fitted corrosion depth data, the points above the fitted surface in the z-direction were obtained and re-fitted by incorporating them into the sample points used in the previous fit, repeating this process to obtain the corrosion depth data after several cycles of the fitting under condition that the percentage of corrosion depth less than zero is less than 5%. By comparison with the measured mass corrosion rates, the set of cyclically adjusted data closest to the actual average corrosion depth was chosen as the sample to be analyzed. The flow chart for de-trending using S1-1 as an example is shown in Figure 2. The volume corrosion degree η_v was obtained from the adjusted corrosion depth and was also compared with the mass corrosion degree η_m obtained from weighing in Figure 2. It can be seen from the figure that the processing errors using this rule are relatively small and the adjusted corrosion depths obtained are truly representative of the mass corrosion degree.

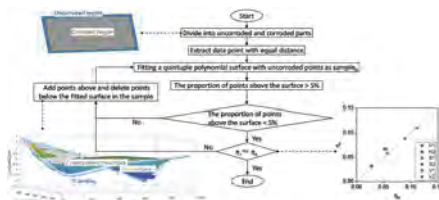


Figure 2. The flow chart of de-trending of the point cloud and the the volume corrosion degree η_v obtained from the adjusted corrosion depth and the mass corrosion degree η_m obtained from weighing.

2.3 Analysis of the corrosion random field

In the paper, the corrosion on the steel surface was taken as a random field. Spatial data distributed on a regular grid was extracted from the cloud point. The sample set X contains point sets on 12 faces of 6 specimens. Each distribution was characterized by parameters mean μ and standard deviation σ . The covariance function (Hristopulos 2020), which was defined by the expectation of the product of the field values at two different points minus the product of the respective mean functions at the same points, is introduced to describe the correlation between two locations s_1 and s_2 in the field. The spatial correlation between two locations s_1 and s_2 with distance τ was characterized by autocorrelation function defined as:

$$\hat{\rho}(\tau) = \frac{\hat{C}(s_1, s_2)}{\hat{\sigma}^2} \quad (1)$$

Before performing parameter estimation of the corrosion random field autocorrelation function, a stationarity and statistical homogeneity analysis was carried out in later sections. A weakly stationary random field should meet two conditions: the mean is constant and the covariance function is a function of τ . In the paper, the correlation length was estimated in two ways: i) fitting the theoretical model to the sample autocorrelation function, ii) evaluating

the distance (Jaksa 1995) the sample autocorrelation function first intersects Bartlett's upper limit r_B given in Equation (2). The common used theoretical autocorrelation models and the corresponding correlation lengths l_c are listed in Table 2.

$$r_B = \pm \frac{1.96}{\sqrt{N}} \quad (2)$$

where N is the dataset size.

Table 2. Theoretical autocorrelation models and the correlation length.

Model	Markovian	Gaussian	Cosine exponential	Second-order autoregressive
ACF	$\rho(\tau) = e^{-\frac{ \tau }{a}}$	$\rho(\tau) = e^{-\left(\frac{ \tau }{a}\right)^2}$	$\rho(\tau) = e^{-\left(\frac{ \tau }{a}\right)^2} \cos\left(\frac{ \tau }{b}\right)$	$\rho(\tau) = \left[1 + \frac{ \tau }{a}\right] e^{-\left(\frac{ \tau }{a}\right)^2}$
l_c	$2a$	$\sqrt{\pi}a$	a	$4a$

3 RESULTS AND DISCUSSION

3.1 Distribution of the corrosion depth

The mean and standard deviation of the adjusted corrosion depth on the surfaces of each specimen is shown in Figure 3. The figure first shows that the standard deviation of the corrosion depth is approximately linear to the mean value. As corrosion develops, the inhomogeneity of the corrosion surface increases. Secondly, the corrosion rates were different for different exposure conditions at the same supported angle. The discrepancy between the two faces (solid dots and hollow dots) of the specimens taken out of the second batch in the figure is larger than that of the first batch (solid and hollow square dots). Finally, it can be seen that the corrosion rate and dispersion of the horizontally placed specimens are the smallest under the three angles, followed by the vertically placed slightly less than the obliquely placed.

The observed and adjusted corrosion depth distribution according to Section 2.2 for each specimen surface is given in Figure 4. The figure also gives the percentage of corrosion depth less than zero (shaded bars) before and after adjustment. Noticeably, the corrosion depth distribution on each surface follows a bell-shaped shape. The normal distribution was used to fit the corrosion depth, and the distribution parameters μ_N and σ_N of the fitted results are listed in each subplot. To ensure data accuracy, portions of the corrosion depth that are less than zero were included in subsequent analyses.

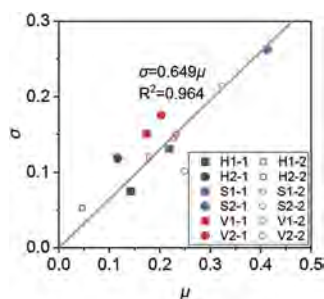


Figure 3. The mean and standard deviation of the adjusted corrosion depth of the specimens.

3.2 Stationarity and statistical homogeneity analysis

In this section, the statistical properties of the mean and correlation functions of the corrosion random field are analyzed based on the definition of stationary.

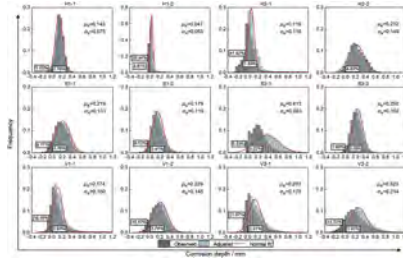


Figure 4. The distribution of corrosion depth of the specimens before and after de-trending.

3.2.1 Changes of the mean value function with position

To investigate the change in the mean value of the random field with position, the corrosion depth at each cross-section was counted individually and compared to the corrosion depth of the entire surface. The Kullback-Leibler divergence (Csiszár & Shields 2004) (Equation (3)) was employed to measure the similarity between the distributions of individual cross sections and the whole surface for analyzing the translation invariance of the mean corrosion depths of the cross sections.

$$D_{KL}(P \parallel Q) = \sum_{\delta \in \Delta} p(\delta) \log \frac{p(\delta)}{q(\delta)} \quad (3)$$

where $p(\delta)$ and $q(\delta)$ are respectively the statistical frequencies at corrosion depth δ for the whole surface and for a single cross-section.

The value of D_{KL} being equal to zero means that the two distributions are identical. It is an approximation in the calculation in relation to the statistical spacing division; the smaller the statistical spacing, the closer D_{KL} is to the true value. The lower bound of D_{KL} (Nishiyama 2019) (Equation (4)) is also used to assess the similarity between the distributions. Figure 5a gives the similarity between the corrosion depth distribution at cross-section $x = 300$ mm and the corrosion depth distribution over the whole surface with statistical spacing division of 0.05mm, using S1-1 as an example.

$$D_{KL}(P \parallel Q) \geq \frac{(A - 2V_P)}{D} \tanh^{-1} \frac{D}{A} + \frac{1}{2} \log \frac{V_P}{V_Q} \quad (4)$$

where $A = (E_Q - E_P)^2 + V_P + V_Q$, $D = \sqrt{A^2 - 4V_P V_Q}$,

E_P, E_Q and V_P, V_Q denote $E_P[f], E_Q[f]$ and $V_{arP}(f), V_{arQ}(f)$, respectively.

Figure 5b gives the empirical distribution function of D_{KL} for the 12 corroded surfaces of the six specimens and the lower bound of D_{KL} . It can be observed that the lower bound of D_{KL} for all surfaces except H2-1 and H2-2 is approximately within 0.2 at 70% guarantee and the mean value of the lower bound of D_{KL} for all surfaces is approximately 0.35 at 90% guarantee. This indicates that the mean values of the corroded surfaces are fairly translational invariant.

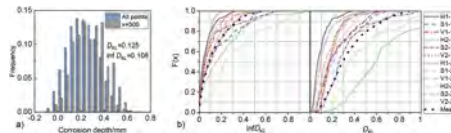


Figure 5. A) An example of determining D_{KL} and lower bound of D_{KL} b) The empirical distribution function of D_{KL} and the lower bound of D_{KL} .

3.2.2 Changes of the sample autocorrelation function in two directions

Examining the second condition for the weakly stationary random field: the covariance function is a function of τ . Since the autocorrelation function and the covariance function are related. The positional correlation and anisotropy of the random field are discussed through the statistical autocorrelation function. Taking H-1 as an example, the corrosion depth data at each cross-section was extracted along two vertical directions within a square domain (400mm×400mm) and

a rectangular domain (850mm×400mm) of the plate (Figure 6a) and the autocorrelation function was separately calculated at different sections (Figure 6b). The autocorrelation coefficients for the different sections in the other direction were counted according to the distance and autocorrelation coefficient interval of 5mm and 0.05 respectively (Figure 6c). The intensity of the coefficients on the whole surface (rectangular area with 850mm×400mm) is represented in the form of a planar heat map in Figure 7.

The intensity heat maps of the autocorrelation coefficients for the surfaces of the twelve specimens are shown in Figure 7. It can be observed that except for V1-1, the autocorrelation functions are all around a statistical average, concentrated around the dotted line of the mean in the figure, which means that the autocorrelation functions of the surfaces along that direction can be seen to vary to a small extent. It can be assumed that the corrosion surface is a weakly stationary random field. Regarding the method proposed by Jaksa (Jaksa 1995) for estimating the correlation length. The autocorrelation lengths obtained by Bartlett’s upper limit method for each section along both directions were counted separately on square domain. The two-sample K-S tests on the two direction sets of estimated autocorrelation length on square domain from specimen H1-2, S1-2 and H2-2 are not significantly different at the level of 0.05. It is difficult to completely confirm or deny the isotropic nature of the corrosion surfaces, but the results of the two-sample K-S test suggest that there shows less directional variability in the surface of specimens laid horizontally. More research is necessary on the directional variability of corrosion surfaces.

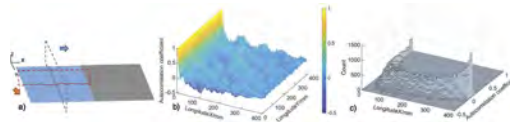


Figure 6. The calculation process of intensity heat maps of the autocorrelation function: a) obtain the corrosion depth at each cross section, b) autocorrelation function map, c) histogram of autocorrelation coefficients along longitude x.

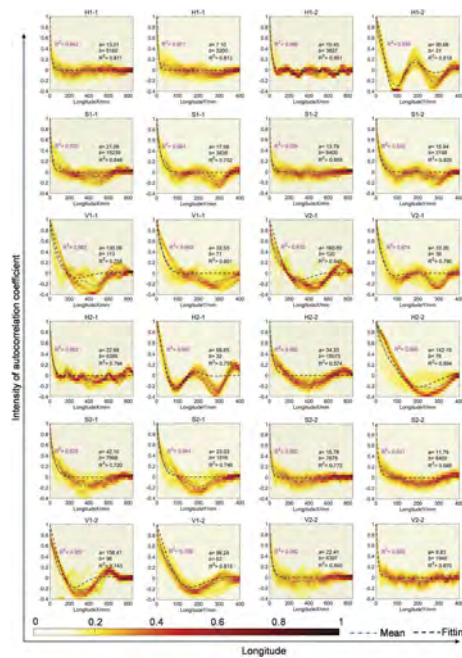


Figure 7. The intensity heat maps of the autocorrelation coefficients of the specimens in the rectangular sample domain (400mm×850mm) and the parameter fitted results of the mean of the coefficients (in black) as well as the R^2 of the function greater than Bartlett’s limit (in magenta).

3.2.3 Model fitting and parameter statistics

As the estimated correlation length l_c depends on the sampling domain length (Christodoulou et al. 2021; Fenton 1999), the main analysis adopted in this paper is the long-edge direction of the specimen surface. A preliminary estimate of the autocorrelation length in both directions is likewise carried out for the entire plate surface (400mm×850mm) according to the steps in Figure 6. In order to choose a suitable correlation function model, the goodness-of-fit of the four models fitting to the mean of sample autocorrelation function are plotted in Figure 8a. The cosine exponential model and the Markovian model in the graph show similar goodness of fit. Observation can be found in Figure 7 that the sample autocorrelation function decreases mainly in the shape of the cosine exponential. The cosine exponential model is used for the parameter fitting to preserve the information in the latter part of the sample autocorrelation function.

Figure 7 also shows the statistical results of the sample autocorrelation function for each specimen surface and the fitting of the cosine exponential model based on the mean value of the sample autocorrelation function. As Uzielli et al. recommended that only the theoretical autocorrelation model with the goodness of fit of the sample function before Bartlett's limit is greater than 0.9 is accepted (Uzielli et al. 2006), the R^2 of the function greater than Bartlett's limit is also shown in the figure in magenta. Apart from two samples less than 0.5 and five less than 0.9, all other seventeen R^2 for sample autocorrelation function before Bartlett's limit are greater than 0.9.

As the correlation length is related to the parameter a in cosine exponential, the statistical result of a in two directions is shown in Figure 8b and c. There is a certain similarity in the distribution of a in two directions. Pearson correlation coefficients of 0.065 and -1.397 indicate that there is no relationship between the corrosion degree and the correlation length along the x and y directions. In contrast, the mean and standard deviation of parameter a have linear relationships at different placement angles. Regression analysis suggests that the dispersion of autocorrelation lengths is greatest for horizontally placed specimens, followed by obliquely placed specimens and least for vertically placed specimens. This may be associated with the fact that the adhesion of the aerosol is influenced by gravity. On the surface of a vertically placed steel plate, the salt spray will condense into water droplets and then flow down in clumps due to gravity. On the contrary, on the surface of a horizontally placed steel plate, the salt spray adheres to the surface and merges with other tiny liquid droplets in the vicinity by tension, showing greater randomness. Comparing the results in two directions shows that the dispersion of the statistical parameters is lower in the shorter sample domain (y direction), which is caused by the fact that the sample domain is not large enough to cover five times (Christodoulou et al. 2021) of the length of the autocorrelation.

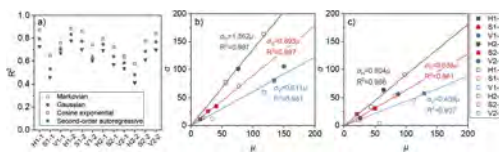


Figure 8. A) The goodness-of-fit of the four models fitting to the mean of sample autocorrelation function, b)-c) relationship of the standard deviation and of the parameter a of the specimens at different supported angles along longitude x and longitude y respectively.

4 CONCLUSION

- 1) The corrosion depth obeys the normal distribution as corrosion proceeds. There is a linear relationship between the mean and standard deviation of the corrosion depth. The corrosion rate and dispersion of the horizontally placed specimens are the smallest under the three angles, followed by the vertically placed slightly less than the obliquely placed.
- 2) The lower bound of D_{KL} for most specimen surfaces is approximately within 0.2 at 70% guarantee and the mean value of the lower bound of D_{KL} for all surfaces is approximately 0.35 at 90% guarantee. The mean values of the corroded surfaces are fairly translational invariant.

- 3) The autocorrelation functions are all around a statistical average, suggesting that the corrosion surface is a weakly stationary random field.
- 4) The better fitting model for autocorrelation function is cosine exponential model and the distribution of parameter correlation length l_c is related to the supported angles.

REFERENCES

- ASTM B117–19: Standard Practice for Modified Salt Spray (Fog) Testing., Pub. L. No. G85–19 (2019)
- Bao, J., & Zhou, W. 2021. A random field model of external metal-loss corrosion on buried pipelines. *Structural Safety* 91(August 2020): 102095.
- Cairns, J., Plizzari, G.A., Du, Y., Law, D.W., & Franzoni, C. 2005. Mechanical properties of corrosion-damaged reinforcement. *ACI Materials Journal* 102(4): 256–264.
- Christodoulou, P., Pantelidis, L., & Gravanis, E. 2021. A Comparative Assessment of the Methods-of-Moments for Estimating the Correlation Length of One-Dimensional Random Fields. *Archives of Computational Methods in Engineering* 28(3): 1163–1181.
- Csiszár, I., & Shields, P.C. 2004. Information theory and statistics: A tutorial. *Foundations and Trends® in Communications and Information Theory*, 2004, 1(4): 417–528. 1(4): 417–528.
- Fenton, G.A. 1999. Random Field Modeling of CPT Data. *Journal of Geotechnical and Geoenvironmental Engineering* 125(6): 486–498.
- Heselmans, J., & Vermeij, P. 2013. Fatal accident in Dutch swimming pool caused by environmentally cracked bolts. *CORROSION* 2013.
- Hristopulos, D. 2020. *Random Fields for Spatial Data Modeling*. Springer Netherland.
- ISO 8047: Corrosion of metals and alloys - Removal of corrosion products from corrosion test specimens, (2009).
- Jaksa, M.B. 1995. *The influence of spatial variability on the geotechnical design properties of a stiff, over-consolidated clay*. [Overconsolidated Clay].
- Kim, I.T., Lee, M.J., Ahn, J.H., & Kainuma, S. 2013. Experimental evaluation of shear buckling behaviors and strength of locally corroded web. *Journal of Constructional Steel Research* 83: 75–89.
- Li, G., Wang, Y., Chen, S., & Sun, F. 2013. State-of-the-art on research of high strength structural steels and key issues of using high strength steels in seismic structures. *Jianzhu Jiegou Xuebao/Journal of Building Structures* 34(1): 1–13.
- Nakai, T., Matsushita, H., & Yamamoto, N. 2004. Effect of pitting corrosion on local strength of hold frames of bulk carriers (2nd Report) - Lateral-distortional buckling and local face buckling. *Marine Structures* 17(8): 612–641.
- Nishiyama, T. 2019. *A New Lower Bound for Kullback-Leibler Divergence Based on Hammersley-Chapman-Robbins Bound*. 1–8.
- Ortega, I., & Bisgaard, S. 2000. Quality improvement in the construction industry: Three systematic approaches. *Total Quality Management* 11(4–6): 383–392.
- Paik, J.K., Thayamballi, A.K., Park, Y. II, & Hwang, J.S. 2004. A time-dependent corrosion wastage model for seawater ballast tank structures of ships. *Corrosion Science* 46(2): 471–486.
- Qin, G. chong, Xu, S. hua, Yao. qiang, & Zhang, Z. xing. 2016. Study on the degradation of mechanical properties of corroded steel plates based on surface topography. *Journal of Constructional Steel Research* 125: 205–217.
- Rivas, D., Caleyó, F., Valor, A., & Hallen, J.M. 2008. Extreme value analysis applied to pitting corrosion experiments in low carbon steel: Comparison of block maxima and peak over threshold approaches. *Corrosion Science* 50(11): 3193–3204.
- Schmitt, G., Schütze, M., Hays, G.F., Burns, W., Han, E., Pourbaix, A., & Jacobson, G. 2009. Global Needs for Knowledge Development in Materials Deterioration and Corrosion Control. *Federal Highway Administration FHWA-RD-01(May)*: 1–44.
- Tang, F., Lin, Z., Chen, G., & Yi, W. 2014. Three-dimensional corrosion pit measurement and statistical mechanical degradation analysis of deformed steel bars subjected to accelerated corrosion. *Construction and Building Materials* 70: 104–117.
- Teixeira, Á.P., & Soares, C.G. 2008. Ultimate strength of plates with random fields of corrosion. *Structure and Infrastructure Engineering* 4(5): 363–370.
- Uzielli, M., Vannucchi, G., & Phoon, K.K. 2006. Random field characterisation of stress-normalised cone penetration testing parameters. *Risk and Variability in Geotechnical Engineering: The Institution of Civil Engineers I* 3–20.
- Zhang, W., Zhou, B., Gu, X., & Dai, H. 2014. Probability distribution model for cross-sectional area of corroded reinforcing steel bars. *Journal of Materials in Civil Engineering* 26(5): 822–832.

SS33: Life-cycle and sustainability performance of fastenings
Organizers: P. Spyridis, G. Muciaccia, K. Bergmeister,
T. Pregartner, R. Piccinin & T. Sippel



Taylor & Francis

Taylor & Francis Group

<http://taylorandfrancis.com>

Installation, structural, and sustainability characteristics of direct fastening in textile reinforced concrete plates

P. Spyridis & J. Orłowsky

TU Dortmund University, Dortmund, Germany

K. Bergmeister

University of Natural Resources and Life Sciences, Vienna, Austria

ABSTRACT: Currently, the construction sector is experiencing a wider development of different sustainable concrete types, such as thin concrete plates with fibre reinforced polymer textiles in an effort to reduce the energy and material related carbon footprint of building materials and structures whilst enhancing durability of built assets. One of the aims of the structural engineering community at this stage is to confirm the applicability of such beneficial materials and techniques for existing needs in the building industry. Textile reinforced concrete (TRC) has seen radical development in the recent years as a high-performance laminar material for various applications such as lightweight shell structures, sacrificial load bearing formwork, strengthening and facade components. Fastenings on this type of material have scarcely been researched, although structural connections are an essential part for many components of structural and non-structural systems. Direct fastening by use of powder actuated nail-type fasteners is also an established connection method for non-structural applications in common concrete, since it brings along several benefits in terms of energy and material consumption, site safety, welfare and labour skills, time and costs in construction logistics, which reflect aspects environmental, social and economic sustainability. This paper presents first experimental results on direct fastenings to thin TRC plates, and discusses the practical applicability of this technique.

1 STATE-OF-ART AND SUSTAINABILITY ASPECTS

1.1 *Textile reinforced concrete*

Textile reinforced concrete (TRC) has seen radical development in the recent years as a high-performance laminar material for various applications such as lightweight, modular or 3D printed structures, sacrificial formwork, strengthening layers, noise barrier and facade components (Beckmann et al., 2021; Ivaniuk et al., 2023; Brameschuber et al., 2008; Thomoglou et al., 2020; Flansbjerg et al., 2018; Orłowsky et al., 2021; Orłowsky et al., 2023). A decisive advantage of this composite construction material, as described by Curbach and Jesse (2009), is the possibility to minimise the dimensions of structural components and thus their self-weight, compared to typical reinforced concrete elements. The carbon fibre-based textile reinforcement used instead of steel has a substantially smaller cross-section. It is not affected by corrosion and it poses a much higher durability than steel reinforcement. Consequently, a minimal concrete cover is required (both for bond and corrosion resistance purposes) and structural elements can be dimensioned with a thickness of even 10 mm. Such composite components can then lead to up to 86% reduction of material resources in relation to conventional concrete and much lower total CO₂-equivalent emissions than steel reinforced concrete over the entire life cycle of comparable building components (Orłowsky et al., 2021; Haist et al., 2022). On the example of a pedestrian bridge deck exclusively built with TRC, Kulas et al. (2012) predicts a reduction in terms of material related CO₂-equivalent glasshouse gas emissions in the order of 25% for reinforcement and 30% in terms of concrete, besides maintenance and transportation gains due to high durability and reduced component weights. Laiblová et al. (2019) perform a comparative investigation of TRC (with glass, carbon and basalt fibres) and steel reinforced facade

panels based on a series of environmental impact indices and lean to the conclusion that TRC scores overall better than steel reinforced concrete, although they highlight drawbacks of the fibre materials and particularly carbon in regards to abiotic and ozone depletion. Scope et al. (2020) perform a series of comparative analyses between steel reinforced concrete and carbon concrete for sandwich wall elements based on an innovative combination of environmental and social life cycle assessments, life cycle costing, as well as circularity opportunities and conclude that the latter have a superior performance in all aspects of sustainability.

1.2 *Direct fastenings*

The very special nature of the material requires the re-examination of conventional fastening systems or the development of new methods. One approach to improving sustainability can be to minimise the material volume and production complexity of fastening products and at the same time the energy resources of the fastening process itself. One such efficient methodology is the direct fastening of nails. Further positive characteristics of this fastening method are the very fast – virtually instant – installation and the overall reduced labour time, reduced noise/absence of dust and vibrations (compared to e.g. hammer drilling), and the independence from weather conditions, specially trained and qualified labour, and power supply on site, which reflect aspects environmental, social and economic sustainability as well as potentials for automatization.

On the other side, the highly dynamic installation characteristics may lead to a substantial variability of the load resistance as discussed by Patzak (1979) and demonstrated on the basis of probabilistic analyses by Mellios et al. (2022). Nails for use in concrete may have a diameter and embedment depth of up to approximately 5 and 40 mm respectively. The fact that concrete is quite inhomogeneous at this scale, and considering that the nail encounters a hard region during the setting procedure (typically a tough large aggregate or weak spots and microcracks in the cement matrix) can lead to a dislocation and distortion of the nail, to local spalling and then possibly to a significant reduction in the load-bearing capacity or even to a setting failure. Therefore, design of direct fastenings typically relies on redundancy approaches by use of multiple fixing locations with the possibility of load redistribution among the participating fasteners. Such are prescribed already in standards (CEN 2019) for other types of lightweight concrete fixings. Applications of setting bolts are accordingly non-structural – but often safety critical – systems such as pipe and electrical conduits, suspended ceilings, partition walls, architectural finishes, auxiliary temporary works elements (Hilti 2019). Further applications in load-bearing structures have been proposed in research, particularly for attachment of strengthening materials such as steel plates, shape memory alloys, or fibre reinforced polymers to allow a fast retrieval of load bearing and as such to enhance the resilience of damaged concrete structures – see (Shan et al. 2020), (Michels et al., 2018), (Lamanna et al, 2004).

1.3 *Previous investigations and scope of the study*

One of the first areas of application for TRC is facade construction. An officially approved system is specified with the following fastening requirements (DIBt 2019): Four internally threaded sleeves are cast into the back of the panel for later assembly using special screws. The special screws are fastened to the substructure using support profiles or agraffes. An alternative approved fastening method for the same type of panels is achieved by means of a shallow post-installed undercut anchor (DIBt, 2021a). The building system approval specifies, among other things, that the fastening is realised by use of four anchor points, and an M6 threaded connector must be inserted at a depth of at least one diameter in the panel to ensure the anticipated bearing conditions. Another possible system that is available in the market specially approved for fastening thin facade plate elements, including TRC panels is also a cast-in element integrated to the substructure with a mechanical connection system for a board typology of external walls (DIBt, 2021b).

Curbach and Speck (Curbach and Speck, 2008) carried out extensive experimental investigations on the use of dowels in glass-fibre-reinforced plates. Headed steel anchors were cast into the slab and tested with axial tension load. Based on these investigations, basic influences between the applied load and the concrete failure mechanism and resistance were established. It has been found that the flexural strength of the test specimen is strongly related to

the load-bearing capacity of the anchor. At the same time, the failure mode was found to be more brittle, due to a lower participation of the reinforcement. An increasing of reinforcement ratio in the specimen also led to an increase in load-bearing capacity of the anchor. It was also noted that, although additional layers of reinforcement do not have a positive effect on the load capacity, the failure is more ductile when several textile layers are used. As a reference for the study herein, tests with an anchor embedment depth of about 9 mm at a diameter of 20 mm in a 16 mm thick, single-layer reinforced slab, pull-out forces of around 2 kN could be achieved.

In addition to the previously mentioned examples of insertion installation, post-installation methods are also common in concrete construction in principle. For the application in TRC, investigations were carried out by Höpfner et al (Hoepfner et al, 2021) with undercut anchors and bonded anchors in embedment depths between 10 and 25 mm were tested. The resulting range of anchor tensile resistance was between 2.0 and 6.0 kN, with a strong dependence on the embedment depth.

TRC is characterised by a relatively fine concrete matrix (Beßling et al., 2022), while the tension bearing reinforcement is more uniformly distributed with the matrix. Hence, the use of direct fastenings in TRC is a promising solution also in terms of load bearing reliability, which forms the motivation of the study reported herein. The aim of the work is first of all to establish the practical feasibility of direct fastenings in TRC plates. The study presents the most promising results out of large exploratory testing campaign carried out at the Technical University of Dortmund (Langenbeck 2022; Langenbeck et al, 2023). These refer to TRC panels with a quadratic arrangement of uniform fibre quantities in both directions. Based on these results, an applicability spectrum but also the limits of the TRC and direct fastening system are disclosed for the first time in international scientific literature. The following presented experimental investigations and results are part of the cited study. In this article the most promising results will be presented in detail and discussed regarding sustainability. Thereupon the limits of practical application are to be explored.

2 EXPERIMENTAL CONFIGURATION

2.1 *Materials*

In the experimental campaign, two strength levels were used, namely 40 and 80 MPa in accordance with DIN EN 12390-2, i.e. measured on a cube with an edge length of 150 mm (DIN, 2019). As part of the mix development, prisms were produced and tested following DIN EN 196-1 with varying mixing process (DIN, 2016). The conversion of the cube compressive strength from a cube with an edge length of 40 mm to a cube with an edge length of 15 cm is carried out by means of the factor 0.86, based on previous experience at the TU Dortmund. The bending tensile strength is derived from 3-point bending tests of 40x40x160 mm prisms according to (DIN, 2016). The TRC plates were produced through a horizontal casting process with short vibration intervals and keeping the textile clamped at the edges of the formwork. Spacers were deliberately omitted in order to be able to safely exclude a possible influence on the nail setting, which led to a slight waviness in the finally cast reinforcement placement. A set of material tests prisms was produced and stored in the same process as the plates, and another one was produced following the above-mentioned standards. The latter specimens were subjected to immersed and climate chamber curing. The TRC plates and the similarly produced set of prisms were placed together in the non-conditioned indoor environment of the laboratory, covered with a canvas until stripping and then wrapped in a wet canvas and tarpaulin.

The specimens included styrene-butadiene impregnated carbon fibre textile reinforcement, commercially identified as HTC 21/21-40 (Hitexbau, 2022), placed in three parallel layers within a plate thickness of 40 mm at two different strength classes of nominal strength at 40 MPa and 80 MPa respectively. For the series with 40 MPa strength which showed the most promising results regarding reliability of the system, a second test set of the same parameter combination was retroactively conducted for confirmation. Also, a test series with a predrilled pilot hole was conducted as explained below. The used fastener was the Hilti X-U 27 P8, made of high-strength steel with 4 mm diameter and 27 mm shank length. Table 1 presents the constituents of the concrete mix and Figure 1 basic details of the specimen preparation and textile reinforcement. An overview of the test series is given in Table 2.

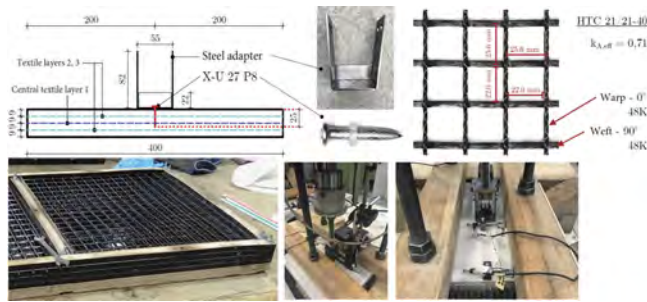


Figure 1. Specimen geometry and textile layout (top) and casting and testing configuration (bottom).

Table 1. Concrete mix compositions of the used specimens.

Ingredients/Properties	Class 40 MPa	Class 80 MPa
Cement	CEM I 32.5: 501.57 g	CEM I 42.5: 527.16 g
Water	275.84 g (w/c =0.55)	210.85 g (w/c =0.40)
Superplasticizer MasterGlenium ACE 460	0.80 g (0.16% wt.)	4.23 g (0.80% wt.)
Rhine sand 0-2 mm	1323.96 g	1391.55 g
Limestone powder Millsil W12	137.93 g	212.72 g

Table 2. Test series description.

Test series	Compressive strength Standard/Plain curing [MPa]	Flexural strength Standard/Plain curing [MPa]	No. of tests, remarks
A-40-21/21-3-0	39.8 / 38.1	8.0 / 5.1	N = 6
A-80-21/21-3-0	80.9 / 74.3	12.1 / 7.5	N = 6, high strength
A-40-21/21-3-0_WH	37.7 / 36.0	8.8 / 4.5	N = 6, repetition series
A-40-21/21-3-7	36.1 / 36.2	8.7 / 4.7	N = 6, predrilling

2.2 Setting and pull-out process

Observing the installation and pull-out test results, a comparison of the different substrate configuration is made in terms of safety and the most efficient combination of fastening parameters is determined with respect to TRC strength, as well as the implementation of a pilot pre-drilling hole. A comparative evaluation of the nail setting performance and the respective load bearing capacity of the nail is also carried out. The specimen and test set-up are shown in Figure 1.

Pre-drilling was of a 4 mm diameter and 7 mm depth and it was carried out for one of the test series by use of a rotating drill bit without percussion; otherwise the nail fasteners were directly set on the formwork-free side of the plate. Setting was performed with the Hilti DX 5-F8 powder-actuated setting tool at an approximate setting energy of 150-200 Joules depending on the concrete strength and pre-drilling (Hilti 2021). The specimen is placed on a 1 cm thick elastomer with a hardness of 65 +/- 5 at the Shore A scale. A 2 mm thick metal adapter with a 4 mm hole was designed and laser-cut to simulate a realistic fixture element and also to attach the load adapter.

The load capacity of the nails was tested in terms of axial tensile load. The load cell is placed centrally on the wooden frame construction which also acts as a resistance boundary for the load. When the plate is pressed under the wood girders due to the tensile load, an approximately symmetrical line support of the plate is created on two sides. The installation of the plate is always done in such a way that the plate is subjected to bending in a 90° direction. The metal adapter is connected to the cylinder's piston, with two through-pins which resist rotation. The tensile force is introduced into the nail connection by a displacement-controlled upward movement, at 0.02 mm per second. The applied load and the displacement of the nail head in relation to the concrete surface are measured hydraulically on the load cell and by use of LVDT's respectively.

3 RESULTS AND DISCUSSION

3.1 Nail setting performance

Once the nails were installed according to the procedure described above, the setting quality was recorded regarding cracking and spalling on both sides of the plates, so called the fastening side and the fixture-free side. The general setting quality respecting these two defect characteristics is evaluated by a visual classification in 4 categories (defect classes 0 - 3) as described in Table 3 and shown in Figure 2. Invisible spalling under the metal adapter is neglected. By spreading a water solution on the panel surfaces the maximum visible crack width was measured by means of a crack loupe magnifier with an accuracy of 0.02 mm. Additionally two different crack patterns characterized as follows were identified, namely (A) Crack paths perpendicular to the panel edges, with one significant large crack quasi-parallel to the panel edge, and (B) Radial cracks starting from the nail and running in different angles towards the edges of the panel, with crack width uniform distribution. Settings without any visual damage only occurred occasionally and only on the fastening side of the panel – this was, however, also the case for severe spalling. Besides this, the defect classes of the two panel sides did not necessarily correlate or coincide. This may indicate a plate thickness influence, but possibly also an interruption of the failure progress between the different concrete layers separated by the textile reinforcement. With regard to the herein presented testing series the following observations can be summarized:

- Defect class 1 in general dominates for all test series on the fastening side as well as on the fixture-free side in test series A-40-21/21-3-0 (40 MPa concrete).
- The most severe damage (defect class 3 on both panel sides) only occurs in series A-80-21/21-3-0 (80 MPa concrete).
- Crack pattern B occurs in 83% of the settings.
- The measured maximum crack width at setting ranges in between 0,02 mm and 0.12 mm. The average maximum crack width within one parameter combination is highest on both panel sides in series A-80-21/21-3-0 (80 MPa concrete). The lowest average crack width could be obtained on the fastening side by the application of an additional pre-drilling in series A-40-21/21-3-7 (also lowest strength concrete). The fixture-free side of the latter test set shows slightly higher defect classes and crack widths compared to the sets without pre-drilling.

Table 3. Defect class description.

Defect class	Fastening side of the panel	Fixture-free side of the panel
0	No damage	No damage
1	Cracking	Cracking
2	Cracking, spalling but firm fastening	Linear and circular cracking
3	As above but loose parts	As above but with surface spalling/flaking-off

3.2 Load resistance

A summary of the load resistance characteristics is given in Figure 3 and more details on the results can be found in (Langenbeck et al. 2023). As regards the maximum load, it is evident that the overall highest average and maximum loads of 5.43 kN are observed in A-80-21/21-3-0 plates. The absolute highest load capacity of a nail within this test series is 7.29 kN, and the standard deviation of the test series is 1.56 kN (variation coefficient CoV = 28.7 %). The smallest scatter of results was achieved when using the lower strength concrete without additional pre-drilling (A-40-21/21-3-0 and A-40-21/21-3-0-WH). The average pull-out load of the latter series was 4.92 kN with a standard deviation of 0.17 kN (CoV = 3.5 %). The repetition series A-40-21/21-3-0_WH reached a mean load of 4.37 kN and a standard deviation of 0.52 kN (CoV = 11.9 %). Summarizing the results of these two sets, an average load of 4.64 kN and a standard deviation of 0.47 kN (CoV = 10.1 %) is reached. The tests A-40-21/21-3-7 (with pre-drilling) did not exhibit an influence of the mean load or scatter significantly. Figure 4 presents all L-D curves of the test sets showing a significant variance. A rough distinction can be made between a linear load drop and a stepwise failure. This indicated a brittle failure which is more frequent in series

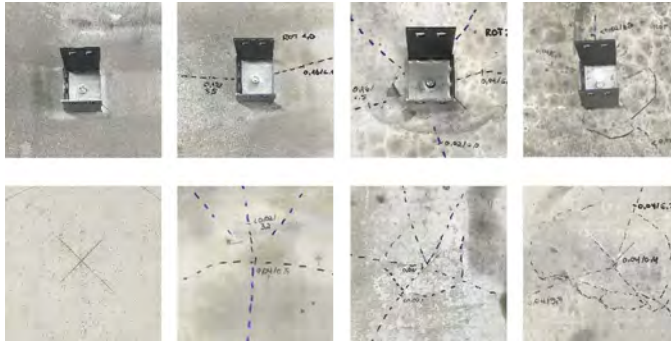


Figure 2. Damage images of classes 0 (left), 1 (centre-left), 2 (centre-right) and 3 (right) on both the fastening (top) and the fixture-free side (bottom).

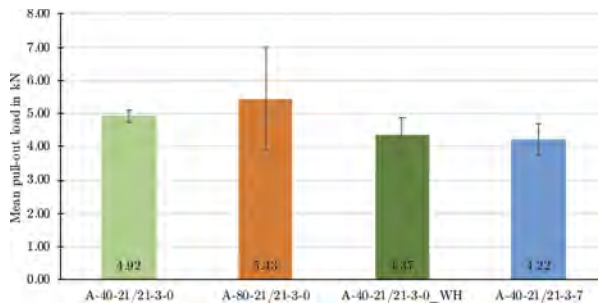


Figure 3. Overview of the average values and standard deviations of the fastening load capacities.

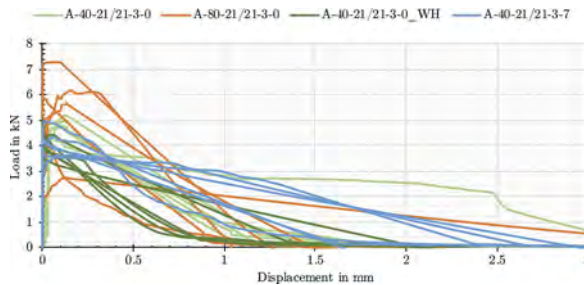


Figure 4. Load-Displacement curves.

A-80-21/21-3-0, and a quasi-brittle failure, which slightly more pronounced in other series, respectively.

4 CONCLUDING REMARKS

This paper presents experimental investigations of nail fastenings in carbon textile reinforced concrete panels. Test parameters include the concrete strength (40 and 80 N/mm²), and the installation with or without pre-drilling of a pilot hole. The feasibility of this structural system is evaluated and confirmed for the first time in international literature. Focus is drawn on the load bearing capacity of the fastenings, the associated uncertainty, and the visual quality that can be achieved during installation. Some minor cracking in the panel could not be avoided completely. Furthermore, the pilot hole pre-drilling which is proven of benefit in previous concrete applications (both in research and practice) did not indicate significant benefits on load or damage characteristics in the presented tests. Although TRC is often used for visible concrete applications

(such as e.g. facades), the virtually unavoidable defects in the conducted tests can only render the application of the system for outdoor facade construction as rather debatable. The use of a 40 MPa concrete class is associated with significantly less spalling and crack width damage compared to 80 MPa concrete, while a noteworthy load bearing capacity remains, moreover with even minor scattering of results (i.e. high structural reliability). Therefore, the new system still seems to be promising regarding use cases with subordinate visual requirements or indoor applications.

As discussed above the combined materials and structural techniques of TRC and direct fixings may come with several advantages in terms of sustainable construction. Toward a sustainable solution the following principles should be particularly addressed when future practical applications are considered. This also leads to the potential of future research in the field.

- The tests carried out have certain limitations: the tests samples are relatively few to allow safe conclusions or design recommendations, while the size of the tested panels may still need to be increased to eliminate boundary effects and adequately assess the damage potential of the installation. This damage potential needs to also be investigated and optimised with respect to the supporting conditions of the plate. Additional evaluations need to be carried out in order to identify optimal configuration of the system in terms of concrete and its constituents, textile reinforcement, fastener and pre-drilling properties and dimensions. Local strengthening in fastening locations may also be considered, by local thickening and/or enhanced reinforcing elements such as short fibres or additional textile layers.
- The durability and service life of the fastenings should meet the ones of the TRC substrate to allow full exploitation of both components. Respective investigations need to be carried out among others in terms of load and crack cycling as well as concrete creep effects.
- The nail and textile reinforcement should be separable from each other but also other construction elements as for example the substructure or the plates. One advantage of the use of direct fastening is the small shape of the nails which saves valuable materials and eases removal and reuse or recycling at the end of the lifecycle. Besides, the use of exclusively mineral components for the TRC plates (e.g. cement based impregnation and mineral fibre textiles) may enhance the recycling potential of the system.
- Promising current applications of TRC that might benefit of the new system could be lightweight and shell structures, sacrificial formworks or TRC-retrofitting.

ACKNOWLEDGEMENTS

The textiles used in the experimental investigations were kindly provided by Hitexbau GmbH. The fastening tools and consumables were offered by Hilti Corporation. The laser cutting of the metal sheet adapters was delivered by the laboratory of the Institute of Forming Technology and Lightweight Components of the TU Dortmund. Ms A.D. Langenbeck has conducted a major part of the experimental research in the frame of her MSc studies at the TU Dortmund. M. Bessling and L. Walter of the TU Dortmund also assisted in the experimental research. The authors express their strong appreciation for this support and contributors.

REFERENCES

- Beckmann, B., Bielak, J., Bosbach, S., Scheerer, S., Schmidt, C., Hegger, J. & Curbach, M., 2021. Collaborative research on carbon reinforced concrete structures in the CRC/TRR 280 project. *Civil Engineering Design*, 3(3), pp.99–109.
- Beßling, M. and Orlowsky, J., 2022. Quantification of the Influence of Concrete Width per Fiber Strand on the Splitting Crack Failure of Textile Reinforced Concrete (TRC). *Polymers*, 14(3), p.489.
- Brameshuber, W., Koster, M., Hegger, J. & Voss, S., 2008. Integrated formwork elements made of textile-reinforced concrete. *American Concrete Institute, Special Publication*, 250-03, pp.35–48.
- CEN - European Committee for Standardization. 2019 DIN CEN/TR 17079. Design of anchorage of fastening systems in concrete - Redundant non-load-bearing systems. Berlin: Beuth Verlag.
- Curbach, M. & Jesse, F. 2009. Eigenschaften und Anwendung von Textilbeton. *Beton- und Stahlbetonbau*, 104(1):9–16.
- Curbach, M. & Speck, K. 2008. *Konzentrierte Lasteinleitung in dünnwandige Bauteile aus textilbewehrtem Beton*. German Committee for Reinforced Concrete, (571).

- DIBt - Deutsches Institut für Bautechnik. 2019. *abZ+aBG Nr. Z-10.3-814*. (Rückseitige Befestigung von betoShell-Fassadenplatten mittels fischer Zykon-Plattenanker FZP II auf Unterkonstruktionen).
- DIBt - Deutsches Institut für Bautechnik. 2021a. *aBG Nr. Z-21.9-2072*. (Rückseitige Befestigung von betoShell-Fassadenplatten mittels fischer Zykon-Plattenanker FZP II auf Unterkonstruktionen).
- DIBt - Deutsches Institut für Bautechnik. 2021b. *abZ+aBG Z-21.8-2067* (HALFEN Fassadenplattenankersystem FPA SL30 zur Verankerung von Fassadenplatten).
- DIN - Deutsches Institut für Normung. 2019. *Prüfung von Festbeton - Teil 2: Herstellung und Lagerung von Probekörpern für Festigkeitsprüfungen*. DIN EN 12390-2
- DIN - Deutsches Institut für Normung. 2016. *Prüfverfahren für Zement - Teil 1: Bestimmung der Festigkeit*. DIN EN 196-1.
- Flansbjer, M., Williams Portal, N., Vennetti, D. and Mueller, U., 2018. Composite behaviour of textile reinforced reactive powder concrete sandwich facade elements. *International Journal of Concrete Structures and Materials*, 12(1), pp.1–17.
- Haist, M., Bergmeister, K., Curbach, M., Forman, P., Gaganelis, G., Gerlach, J., Mark, P., Moffatt, J., Müller, C., Müller, H.S. & Reiners, J., 2022. Nachhaltig konstruieren und bauen mit Beton. In Bergmeister, K., Fingerloos, F., and Wörner, J.-D., (eds) *BetonKalender 2022: Nachhaltigkeit, Digitalisierung, Instandhaltung*, pp.421–531.
- Hilti Corporation. 2021. Direct Fastening Technology Manual. Schaan. www.hilti.de (19.12.2022).
- Hitexbau GmbH. 2022. Technical sheet “Art. 279136 - HTC 21/21-40”. www.hitexbau.com (02.12.2022).
- Hoepfner, M., Spyridis, P., Bessling, M., & Orlowsky, J. 2021. Experimental investigations of shallow mechanical and bonded anchors in textile reinforced concrete. In Chen, A., Ruan, X., & Frangopol, D., (eds) *Life-Cycle Civil Engineering: Innovation, Theory and Practice*, pp. 1046–1053. CRC, London.
- Ivaniuk, E., Eichenauer, M.F., Tošić, Z., Müller, S., Lordick, D. and Mechtcherine, V., 2022. 3D printing and assembling of frame modules using printable strain-hardening cement-based composites (SHCC). *Materials & Design*, p.110757.
- Jesse, F. & Curbach, M. 2009. Verstärken mit textilbeton. In Bergmeister, K., Fingerloos, F., and Wörner, J.-D., (eds), *BetonKalender 2010: Brücken, Betonbau im Wasser*, pp. 457–565.
- Kulas, C., Hegger, J., Goralski, C. and Karle, R., 2012. Design and sustainability of a prestressed and precast pedestrian bridge made of textile-reinforced concrete. In *PCI Convention and National Bridge Conference, Nashville* (Tennessee), USA (Vol. 29, No. 02.10).
- Laiblová, L., Pešta, J., Kumar, A., Hájek, P., Fiala, C., Vlach, T. and Kočí, V., 2019. Environmental impact of textile reinforced concrete facades compared to conventional solutions - LCA case study. *Materials*, 12(19), p.3194.
- Lamanna AJ, Bank LC, Scott DW. 2004. Flexural strengthening of reinforced concrete beams by mechanically attaching fiber-reinforced polymer strips. *Journal of composites for construction*, 8(3):203–10
- Langenbeck A.D., Spyridis, P., Bessling, M., & Orlowsky, J. (2023). Experimental investigations of power actuated fastenings in TRC (*Developments in the Built Environment - in review*)
- Langenbeck A.D. (2022). Experimentelle und analytische Untersuchungen von Direktbefestigungen in faserbewehrtem Beton im Hinblick auf innovative Konstruktionslösungen für den Fassadenbau. (supervisors: Spyridis P., Orlowsky J.) Master thesis, Technical University of Dortmund
- Mellios, N., Mustafa, B., Yousef, A., Spyridis, P. 2022. Probabilistic finite element investigation of direct fasteners in concrete with discrete aggregates. In: Di Prisco, M., Meda, A., Balázs, G.L. (eds) *Proceedings of the 14th fib PhD Symposium, Rome, Italy, 5-7 September 2022*.
- Michels, J., Shahverdi, M., Czaderski, C. 2018. Flexural strengthening of structural concrete with iron-based shape memory alloy strips. *Structural Concrete*, 19(3), pp.876–891.
- Orlowsky, J., Beßling, M. and Kryzhanovskiy, V., 2023. Prospects for the Use of Textile-Reinforced Concrete in Buildings and Structures Maintenance. *Buildings*, 13(1), p.189.
- Orlowsky, J., Maurer, R., Heeke, G., Beßling, M. and Bettin, M., 2021. Ressourcenschonende Lärmschutzelemente aus Textilbeton als Alternative für konventionelle Stahlbetonfertigteile. *Beton- und Stahlbetonbau*, 116(12), pp.947–957.
- Patzak, M. 1979. Zur Frage der Sicherheit von Setzbolzenbefestigungen in Betonbauteilen. *Betonwerk und Fertigteil-Technik*, 45(5):308–314
- Scope, C., Guenther, E., Schütz, J., Mielecke, T., Mündecke, E., Schultze, K. and Saling, P., 2020. Aiming for life cycle sustainability assessment of cement-based composites: A trend study for wall systems of carbon concrete. *Civil Engineering Design*, 2(5-6), pp.143–158.
- Shan, Z. W., Looi, D. T. W., Su, R. K. L. 2020. A novel seismic strengthening method of RC columns confined by direct fastening steel plates. *Engineering Structures*, 218, 110838
- Thomoglou, A.K., Rousakis, T.C., Achillopoulou, D.V. & Karabinis, A.I., 2020. Ultimate shear strength prediction model for unreinforced masonry retrofitted externally with textile reinforced mortar. *Earthquakes and Structures*, 19(6), pp.411–425.

Redundancy of concrete fastenings under combined fatigue and corrosion – A probabilistic study on catenary system installations

S. Kessler

Helmut-Schmidt-University, Hamburg, Germany

N. Mellios

TU Dortmund University, Dortmund, Germany

A. Takriti

Helmut-Schmidt-University, Hamburg, Germany

P. Spyridis

TU Dortmund University, Dortmund, Germany

ABSTRACT: Fastenings to concrete are implemented in a wide variety of statistically indeterminate structures such as suspended ceilings. In contrast to statistically determinant systems, failure of one fastener does not lead to direct collapse but to a redistribution of the load to adjacent fasteners. This concept can serve well in situations of high uncertainty and variance at the failure time, particularly with some level of tolerance for states of limited damage – an example is non-structural safety-critical suspended installations. Such systems can be subjected to sustained or dynamic loading. This can result in very brittle failures without any prior signs throughout the system's life-cycle, making the safety evaluation crucial. The present study focuses on the evaluation of safety in redundant fastening systems with fatigue and corrosion effects. A computational probabilistic model is used to evaluate the life-cycle performance of a redundant installation to showcase the feasibility of this approach. The virtual system consists of anchor groups and a fatigue-relevant load in each group is determined and distributed among the anchors. Degradation of the system is also implemented by randomly assigning corrosion damage to individual elements and by reducing annually the level of prestress in the anchors. Failure of a single anchor leads to redistribution and possible progressive collapse of the system. The year of failure is collected from multiple realizations and it is evaluated statistically. The resulting probable year of element and system failure for the entire system are calculated accounting for stochastic degradation processes, and it subsequently provides the basis for inspection and maintenance plans.

1 INTRODUCTION

Fastening to concrete is gaining a lot of ground in the last decades in everyday construction for various building, industrial and infrastructure applications such as attaching necessary equipment and other non-structural architectural details. These connections are typically realised through precast or post-installed steel anchor bolts. The installations are often statically indeterminate by use of multiple anchor points and with significant stiffness and strength of the fixture. In such systems failure of a single element does not necessarily lead to a collapse of the system but to a redistribution of the load to adjacent elements, a so-called alternative load path.

The static indeterminacy alone, however, cannot provide information about the system reserves in the event of a loss. It must be known where the reserves are present in the system and where damage cannot be tolerated due to a lack of alternative load paths. The excess of load-bearing elements combined with the ability of a system to transfer residual loads from failed

elements to alternative paths is expressed by the term “redundancy” (Frangopol & Curley 1987; Biondini et al. 2008; Spyridis & Strauss 2020). Apart from accidental actions, particular life-cycle risks can be considered in conjunction to damage to the load-bearing structure due to deterioration processes, which are governed by significant uncertainties and hidden defects. This renders the evaluation of their structural performance and safety a daunting task.

In this article, the research approach to provide a method for the structural evaluation of redundant fastening systems is presented. Emphasis is given to failure caused by deterioration factors, namely cyclic fatigue which can also be accelerated by corrosion. To showcase the benefits of a probability-based approach, a virtual case study of a redundant fastening system is investigated. The system is assumed to replicate a tunnel (or broadly speaking a linear infrastructure) catenary system. The installation of the catenary is formed by groups of anchors in two parallel lines. Each group consists of four anchors. In the case of a local failure i.e. anchor or group, the load can be redistributed among anchors of a group or adjacent groups respectively. To account for the inherent uncertainty of defects, material properties, and loading conditions, a probabilistic approach with random sampling is implemented yielding multiple failure scenarios. All calculations are integrated in an optimized object-oriented algorithm. The aim is to propose a more sophisticated design approach that accounts for both element and system properties, providing a safer and more economical result. These models can also be implemented to facilitate decision-making as regards the life-cycle management of an existing system as a performance-based design paradigm (Urban et al. 2012), (Strauss et al., 2016). A similar analysis but without account for accelerated degradation from corrosion effects is presented by Mellios et al. (2021).

2 FATIGUE AND CORROSION OF ANCHOR BOLTS IN CONCRETE

Designing a fastener against steel fatigue failure is based on the specific properties of the corresponding product derived from an experimental assessment carried out at the TU Dortmund. The current state of assessing anchors against fatigue cyclic loading in combination with or without quasi-static load is described by EOTA (2018). Fatigue cyclic loading can be caused by pulsating tension load or alternating shear load or combinations of both. The reasons that can cause the dynamic loading vary, but they are typically imposed by weather/climate phenomena, vehicle traffic, or machinery effects, and load actions are considered harmonic or periodic for simplicity. Assessment of a specific fastening product against fatigue relies on the product specific S-N design curve where the load amplitude is represented as a continuous function of the load cycles. As simplified assumption for the case study, one cycle stands for the static resistance of the fastener and fatigue limit resistance stands for an infinite number of cycles (see Figure 1). For a load range smaller than the fatigue limit range the anchor does not suffer any deterioration due to fatigue, which can e.g. rely on the design provisions of EN 1992-4 (CEN 2018). Experimental S-N curves for product specifications are derived for anchors without prestressing since this is an onerous case and it is known that prestressed anchors subjected to cyclic loading can gradually lose the torque at the nut, they become unfirm, and the fatigue effects are magnified.

Outside of pure dynamic loading, another deteriorating factor that can also threaten the fasteners structural performance is also present. In particular, corrosion, like fatigue, is also a time-dependent process, which acts on the steel surface leading to degradation in its mechanical properties and consequently effects the fatigue behaviour. This alteration in fatigue properties appears in two different forms on the S-N curve. In order to understand this, a distinction between corrosion fatigue and fatigue of pre-corroded steel (e.g. due to accelerated corrosion) is necessary. The latter case is relatively straightforward. Here, corrosion causes cross-sectional loss combined with surface irregularities like formation of notches, leading to decreased mechanical resistance and shorter fatigue life (see Figure 1 – left – green line) (Apostolopoulos & Michalopoulos 2007). In case of corrosion fatigue, the situation is different. Here, both electrochemical and mechanical attacks act simultaneously leading to mutual impacts on each other. Unlike artificially corroded steel, long-time corrosion impacts the steel surface more inhomogeneously causing a gradual decline in fatigue life over time (Zhang et al. 2012). Thus corrosion fatigue appears on the S-N curve as a decline in the fatigue limit which is anticipated to appear only in the absence of corrosion fatigue (see Figure 1 – left – red line) (Gehlen et al. 2016).

3 CASE STUDY OF ROBUSTNESS ASSESSMENT

3.1 Overview

For the analysis in this study, a simplified S-N curve was assigned to every anchor, formed by two points, i.e. the static resistance at $N=1$ and the fatigue limit resistance that stands for a stochastically assigned amount of cycles (Figure 1 – right). Initially, the same static resistance of 128 kN is assumed and deterministic assigned to all anchors. The assignment of the second point corresponds to a fully random value between 900,000 and 1,100,000 cycles. A further step was taken here to account for both the beneficial effect of the prestress in anchors and the negative effect of unfirm installation. The correct prestress level was assumed at $F_{pre}=60$ kN, and the fatigue limit of each anchor is set equal to this prestress load. Finally, the two points are connected linearly in logarithmic scale of the horizontal axis to form the fatigue resistance curve, described by a bilinear function (see green curve in Figure 1-right). To consider the installation inaccuracies, 5% of the anchors are considered insufficiently torqued. Additionally, a deterioration rate for the prestress load is assigned and gradually anchors lose their prestress with a time-dependent rate. Loose elements are then randomly assigned a new prestress load between 30 and 60 kN and their S-N curve is updated.

The deterioration due to corrosion is assigned to the individual anchors at a subsequent phase of the algorithm. After each anchor is stochastically assigned a unique S-N curve and installation defect status, corrosion effects are added. Initially a percentage of anchors afflicted by corrosion is predefined and randomly tagged to individual elements. The predefined percentages that were investigated range between 0 % and 100 % of the anchors. Furthermore, four deterioration levels are parametrically considered, i.e. 0 %, 20 %, 40 %, and 60 % resistance loss from the initial fatigue resistance, reflected by an inclination of the deteriorated S-N line (see red lines in Figure 1-right). Consequently, corroded anchors experience a reduction of the total number of load cycles that they can sustain as well as an elimination of their fatigue limit state, considering that the material cannot sustain a load infinitely, whilst being under progressive corrosion.

3.2 Geometrical characteristics

The multiple fastening system (catenary fixture) consists of anchor groups positioned in two parallel lines. Each group is formed by four individual anchors. Anchors within groups are considered to be connected by a rigid plate. Each line of anchor groups consists of 120 groups. In total, the system contains 960 individual anchors. All groups are considered to be connected with a rigid beam or truss system as sketched in Figure 2. Possible failure of the fixture elements outside the anchors is neglected. The exact geometrical dimensions and properties of the truss system and anchor connection plate were considered to be unnecessary for explicit simulation, but it was assumed that adequate tying of the fixture elements is achieved, allowing for the creation of alternative load paths. Therefore, instead of explicitly designing the truss system, failure scenarios are examined and corresponding predefined alternative load paths are assigned.

3.3 Load and progressive failure simulation

The system is considered to be loaded only under cyclic tension, with a harmonic pulsating load of a constant period. The frequency of the pulsating load was kept constant throughout the entire analysis, at ten thousand cycles per year (10,000 c/y). Each group of anchors is initially loaded with a deterministic load i.e. 240 kN, which is then stochastically distributed among the anchors of each group. The element load distribution is updated within a group in the event of failure of a single anchor (when the fatigue resistance of an anchor is exceeded) or in adjacent groups in the event of full group failure. At the initiation time of the calculation, the maximum possible load for a single anchor is 96 kN and the minimum is 24 kN, so no failure is considered. Based on the individual load and S-N curve of each anchor the estimated life expectancy is evaluated. The status of the anchors (algorithm loop) is evaluated on a yearly basis, namely after every 10000 load cycles. Degradation of the anchors due to loosening is based on a rate that increases yearly to represent the increment of the degradation rate seen in existing application (Equation 1) and respectively the new prestress load is assigned.

$$r = 1 - (1 - 0.002)^y \tag{1}$$

with: r the degradation rate and
 y the number of years in service.

If two anchors in a group fail then the entire group is considered to have failed. The load of the group is redistributed among adjacent groups. Through this interaction between the adjacent groups, alternative load paths can be achieved in a group failure event. To account for the system's material and geometric properties implicitly, predefined load paths were assigned based on deliberate assumptions of load transfer as depicted in Figure 2. Two main redistribution scenarios were identified subject to the boundaries of the system. The first (general) failure scenario is covering

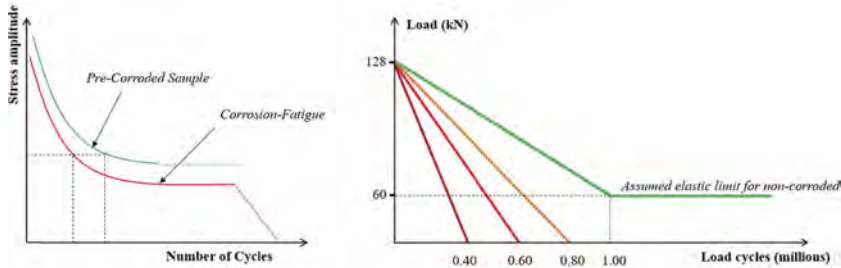


Figure 1. Effect of corrosion on fatigue properties. Left: S-N curve of uncorroded steel (green line); S-N curve of corroded steel (red line); declination of fatigue limit due to corrosion fatigue (dotted lines). Right: Simplified assumed S-N Curve used in the analyses for different levels of corrosion.

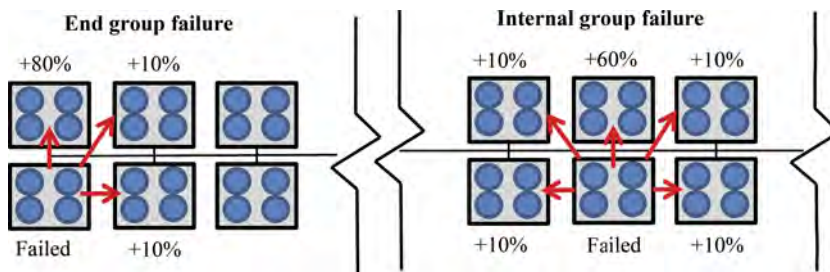


Figure 2. Geometry of the investigated system, each rectangle represents a group and each circle an individual anchor.

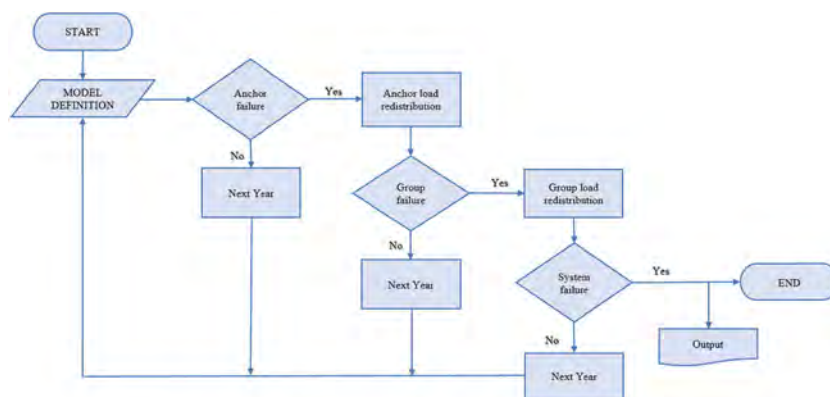


Figure 3. Graphical representation of the algorithm for the calculation of the system performance.

the internal groups of the system and the second one the two groups at each end of the system. The alternative load paths here are defined as percentages of the load of the failed group.

These percentages are corresponding to the distance that the load has to be transferred. The load is only redistributed to groups that are in the immediate circumference of the failed group. This corresponds to five groups in the case of the internal group failure and three groups in the case of edge failure. This discrepancy between these two cases, caused by the geometry of the system, results in a higher concentration of load in the case of end failure and it is more bound to lead to progressive failure. The total system failure is considered when two adjacent groups have failed. In this event, the concentration of the load on the remaining anchors leads to instantaneous failure under static load and it is considered to be the initiation of a progressive collapse. The year that this failure occurs and the total amount of failed anchors per year form the model output. For this example, it was decided to run 100,000 different combinations by use of random input property generators. The conceptual algorithm flow is shown graphically in Figure 3.

4 RESULTS AND DISCUSSION

Indicative results from the evaluation of structural performance with regard to redundancy are presented below. They can be separated into two categories, the ones describing the entire system performance and the ones regarding the individual anchors, both providing insights into the behaviour of the investigated type of redundant systems. The reference case is considered to be on the one hand side the case without corrosion effects, achieving an average service life of 100 years and on the other, the average situation with 20% of all anchors afflicted by corrosion, as listed in Table 1. In this Table, it can already be seen that the uncorroded situation achieves by far higher service life thresholds, more than double the one of extensive corrosion affecting all anchors in the system, i.e. nearly 100 years compared to 40 years or less for different confidence quantile levels. Moreover, the uncorroded case exhibits relatively narrow variation, which maintains also the quantile confidence levels at relatively high values (90 % to 93 % for typical quantile levels in engineering structures). On the contrary, comparing these design thresholds for corroded systems, it is made evident that a redundancy-based design service life converges to approximately 40-50 years even from just a 4 % of the anchors being affected by corrosion.

This is correspondingly evident in the representation of Figure 4, which depicts the development of individual anchor failure per year. In this case, it is seen that, for the same corrosion

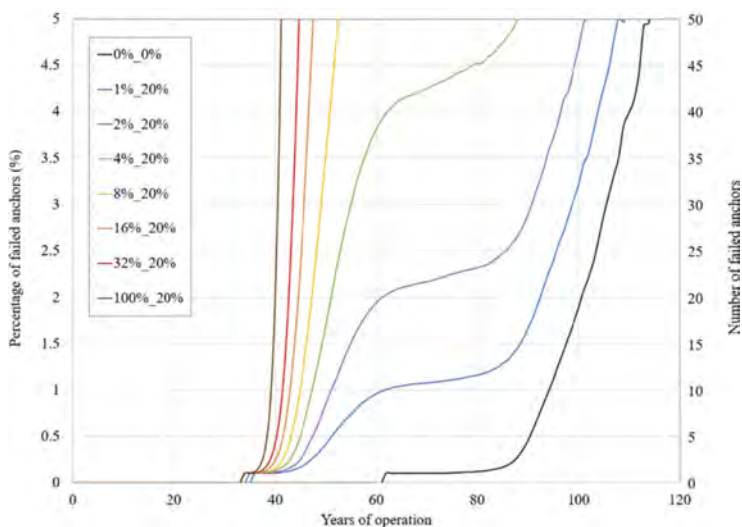


Figure 4. Mean percentage and total number of failed anchors per year of operation, assuming a 20 % material corrosion rate and various extends of corrosion afflicted anchors.

Table 1. Model results for reference case of 20% of all anchors afflicted by corrosion.

Anchors afflicted by corrosion (%)	Mean failure time (years)	Standard deviation (years)	Coefficient of variation (-)	1% Quantile (years)	5% Quantile (years)
0%	101.5	5.3	0.05	90.0	93.0
1%	90.9	10.8	0.12	52.5	69.0
2%	84.4	11.9	0.14	50.0	61.5
4%	72.0	12.7	0.18	48.0	51.0
8%	54.4	7.4	0.14	44.5	46.0
16%	46.3	2.1	0.04	42.0	43.0
32%	43.1	1.4	0.03	40.0	40.0
100%	40.0	0.9	0.02	38.0	39.0

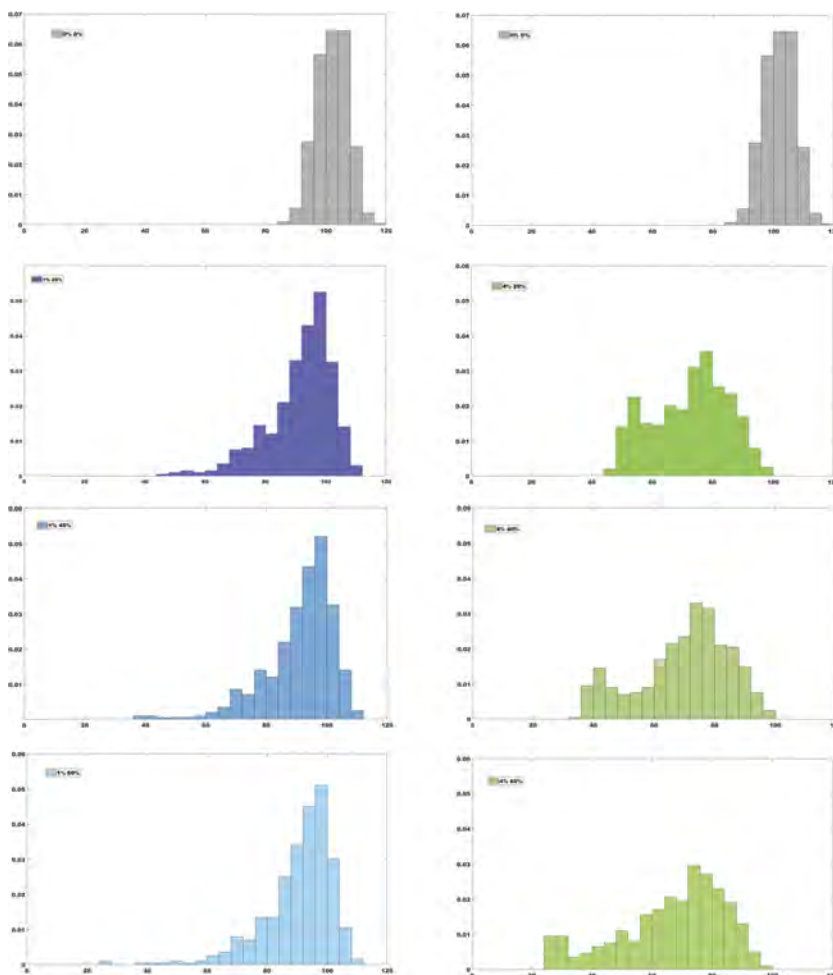


Figure 5. Failure year/life expectancy probability density functions for various parameters (extend of corrosion afflicted anchors and material corrosion rate).

rate at material level of 20 %, a 4 % of the anchors is expected to fail within the first 40 to 60 years of operation. Conversely, if the corrosion is restricted to 2 % of the anchors (e.g. if the corrosive agent is contained only in one small region of the system), the same anchor failure

rate is expected to occur only after the 90th year of operation, which approaches the system without corrosion effects. The analyses indicate also an abrupt increase of system failure after failure of a 5 % of the individual anchors regardless of the corrosion rate – this is discernible in the instabilities of the curves in the upper right area of the graph in Figure 4.

The life expectancy of the entire system is presented for various values of material corrosion rate under two different extents of corrosion afflicted anchors, namely 1 % and 4 %, as illustrated in Figure 5 on the basis of probability density functions. The left column (blue) represents the corrosion extend of 1 % in the total individual anchors, this being 4 % for the right (green) column. The first (grey) graphs are the same and they reflect the uncorroded situation. Here it is also made obvious that a relatively small extend of corroded anchors influences the catenary systems service life forecast only to a minor extend. The mean value is at 100 years and the minimum-to-maximum range is mostly at 90 to 110 years for the uncorroded case. This becomes 90 years at mean value and ranges at roughly 60 to 110 years, independently to the material corrosion susceptibility. However, already at a small increase of the corrosion extend to 4 %, the mean value drops to approximately 70 years and the minimum values are at 25 to 45 years, subject to the material corrosion resistance.

5 CONCLUSIONS

This study examines the feasibility to assess the redundancy and associate service life of fastening systems with multiple anchors using probability-based methods with integrated deterioration models. Degradation mechanisms due to fatigue and deficient prestressing in combination with corrosion are identified and investigated in conjunction with the beneficial effect of alternative load paths. The aim is to demonstrate a methodology that can realistically calculate the performance of redundancy in structural systems under multiple uncertainty agents. To this end, an object-oriented algorithm is coded with explicit definitions of both the alternative load paths and the degradation of the system during its life cycle. A virtual tunnel catenary – or broadly speaking linear infrastructure installation – is investigated. The results highlight the sensitivities of the system to the extent of corrosion along the structural system in terms of a ratio of anchors afflicted and the anchor material susceptibility to corrosion in terms of fatigue resistance degradation rate. It further calculates a service life expectancy in terms of probabilistic distribution, which enables risk-based decisions and planning with respect to life cycle management activities, such as inspection and maintenance exercises. With increasing computational power, and automated monitoring of degradation agents and processes, such an assessment approach can be implemented to design against various disruptive events and provide a life time performance profile for this and similar engineered systems.

ACKNOWLEDGEMENTS

The authors express their appreciation to Dr. Kleidi Moisi and Dr. Jakob Kunz of Hilti AG and for their technical input and Dr. Stefan Lachinger of the Austrian Institute of Technology for his expert advice in developing the case study and load redistribution algorithm.

REFERENCES

- Apostolopoulos, C.A., & Michalopoulos, D. 2007. Mechanical Properties of Reinforcing Steel and Fatigue Behavior in Corrosive Environment. *Materials Engineering and Performance* 16(5):559–66.
- Biondini, F., Frangopol, D.M. & Restelli, S., 2008. On structural robustness, redundancy, and static indeterminacy. In *Structures Congress 2008: Crossing Borders* (pp. 1–10).
- CEN (European Committee for Standardization). 2018. *EN 1992-4:2018 Eurocode 2 – Part 4, Design of concrete structures. Design of fastenings for use in concrete*. CEN/TC 250 Brussels
- EOTA (European Organisation for Technical Approvals). 2018. *EOTA TR061, Design method for fasteners in concrete under fatigue cyclic loading*, EOTA, Brussels

- Frangopol, D.M. & Curley, J.P., 1987. Effects of damage and redundancy on structural reliability. *Journal of Structural Engineering*, 113(7),pp.1533–1549.
- Gehlen, C., Osterminski K. & Weirich, T. 2016. High-Cycle Fatigue Behaviour of Reinforcing Steel under the Effect of Ongoing Corrosion. *Structural Concrete* 17(3):329–37.
- Mellios, N., Lachinger, S., & Spyridis, P., 2021. Feasibility study on probabilistic evaluation of redundant fastening systems in concrete. In: *18th fib Symposium Proceedings*, Lisbon 14-16 June 2021.
- Spyridis, P. and Strauss, A., 2020. Robustness assessment of redundant structural systems based on design provisions and probabilistic damage analyses. *Buildings*, 10(12), p.213.
- Strauss, A., 2016. Numerical and monitoring based Markov Chain approaches for the fatigue life prediction of concrete structures. *Engineering Structures*, 112, pp.265–273.
- Urban, S., Strauss, A., Macho, W., Bergmeister, K., Dehlinger, C. & Reiterer, M., 2012. Concrete structures under cyclic loading-robustness and redundancy considerations for residual lifetime optimization. *Bautechnik*, 89(11),737–752.
- Zhang, Weiping, Xiaobin Song, Xianglin Gu, & Shibin Li. 2012. Tensile and Fatigue Behavior of Corroded Rebars. *Construction and Building Materials* 34:409–17.

Long term assessment of bonded anchors with two different methods, Findley extrapolation vs. time-to-failure approach

I. Boumakis

fischer Austria GmbH, Traiskirchen, Austria

K. Nincevic & R. Piccinin

Hilti Corp., Schaan, Principality of Liechtenstein

R. Wan-Wendner

Ghent University, Ghent, Belgium

T. Pregartner

fischerwerke GmbH & Co. KG, Waldachtal, Germany

K. Bergmeister

University of Natural Resources and Life Sciences, Vienna, Austria

ABSTRACT: The recent research developments regarding the utilization of time-to-failure testing as an assessment tool for the long-term behavior of bonded fasteners under sustained load raise the question of the link between the current assessment procedure (so called Findley extrapolation method) with the time-to-failure approach. The two methods are using data from tests loaded at different relative load levels. Nevertheless, both methods require sustained load tests which are analyzed with the objective of deriving the ultimate long term bond resistance. Although both methods use the same type of tests, they differ with respect to (i) the actual result of the tests (failure/no failure), (ii) the measured quantities during the tests, and (iii) the analysis. These essential differences make a direct comparison of the two approaches rather challenging. However, the link between the two methods and ultimately a comparison of the assessment that they provide is feasible when some assumptions that are supported by the literature are considered. This contribution presents a detailed comparison of the two assessment methods using the same datasets of experimental data of bonded anchors with two different adhesive mortars. The current contribution establishes a clear link between the two assessment methods. Additionally, it confirms the conservatism of the currently used approach. Finally, an optimized approach is proposed based on time-to-failure tests, which could serve as an optimized and yet still sufficiently conservative assessment method for the long-term behavior of bonded anchors under sustained loads.

1 INTRODUCTION

Fastening technology plays a key role in structural engineering. As a matter of fact, their role is the connection of different structural elements, assemblage of precast elements, and the attachment of non-loading bearing components. The previous can be done during construction, as well as during strengthening and retrofitting. The adhesive anchors are post-installed fastening systems which ensure the connection of the steel member with the concrete substrate in terms of bond through a layer of adhesive agent (Cook, Kunz, Fuchs, & Konz, 2006). In general, all fastening systems need to go through rigorous tests which assess their performance under the influence of various environmental conditions, loading direction, concrete class, and condition in order to obtain an approval for a lifetime of 50 years (ACI Committee 318, 2019;

EAD 330499-01-601, 2018). Additionally, the international standards require the performance assessment of bonded anchors under sustained load (EN 1992-4:2018, 2018).

The long-term performance of bonded fasteners is assessed on experimental data from sustained load tests in a confined configuration and the Findley approach for extrapolating the creep displacements. As a matter of fact, following this assessment method the anchors are installed in the concrete member and, after the required curing time has passed, are loaded to a target load, typically ~30-40% of the ultimate bond resistance, $\tau_{R,k}$. Then the load is kept constant for a certain period, usually 2.000 hours and the displacements at the top of the anchor are measured. After the target testing time has passed the anchors are unloaded and tested in a confined configuration to characterize the residual resistance. The measured displacements are analyzed and a power function (see Equation 1) is fitted on the last points of the measured displacements in course of time.

$$s = s_0 + \alpha t^n \quad (1)$$

with s the time dependent displacement, s_0 the initial displacement after the target load has been reached, t the time and α , n the power law parameters to be fitted.

Then the power function is extrapolated to a time of 50 years and the corresponding displacement is predicted. Finally, the latter displacement is compared with the displacement at loss of adhesion, $s_{adh\ loss}$ which is typically the displacement at the ultimate pull-out resistance obtained in a confined pull-out test (EAD 330499-01-601, 2018). In case the extrapolated displacement is below the critical displacement $s_{adh\ loss}$ then the anchor passes the test and the long-term characteristic resistance, $\tau_{Rk, L}$ as well as the sustained load factor ψ_{sus} as it is imposed by the EN 1992-4 are calculated (EN 1992-4:2018, 2018).

Despite its simplicity the Findley approach has also some limitations. Its main problem is that it fails to provide an expected failure time and thus an expected life-time for a given load level. The assessment furthermore needs to be repeated to assess the influence of elevated temperature on the long-term characteristic bond resistance. Additionally, it shows significant sensitivity on the initial displacement as well as on the selected data for fitting, the measurement frequency, and the testing time range (Stierschneider, Tamparopoulos, McBride, & Bergmeister, 2021). An alternative assessment approach, the stress vs. time-to-failure, has been proposed by Cook et al. (Cook & Davis, 2009) to overcome the aforementioned limitations. Following this approach, the anchors are tested again under sustained loads. However, the load levels are selected such that they result in failure within a reasonable time range, typically between few seconds and weeks/months. The failure times are recorded and plotted against the corresponding load level. Finally, a logarithmic function (see Eq. 2) is fitted on the data and its extrapolation reveals the long-term bond resistance of a bonded anchor system.

$$N_{sus}/N_u = \alpha \cdot \ln t_f + b \quad (2)$$

where N_{sus} the sustained load, N_u the ultimate bond resistance, t_f the failure time and α , b parameters to be fitted.

This approach has the advantage of fitting and extrapolating actual failure. Nevertheless, the selected logarithmic function has the problem of resulting in failure time even for zero or negative load level when it is extrapolated. Therefore, it has no physical interpretation, and it should be considered as a purely empirical regression model. Additionally, the logarithmic function is unnecessarily conservative since it fails to capture the transition to an asymptotic behaviour which is a typical characteristic of the stress vs. time-to-failure curve (Blochwitz, 2019). Recent research advances have proposed alternative assessment equations which overcome the problem of the physical interpretation. As it has been derived in (Boumakis, Nincevic, Vorel, & Wan-Wendner, 2019) the stress vs. time-to-failure can be considered as a combination of creep rate failure criterion (Monkman & Grant, 1956) and the widely used Prandtl creep model (Prandtl, 1928). This study reveals a reduction of the time-dependent behavior until a critical load level below which no more time-dependent failure is expected.

Furthermore, an empirical sigmoid function (see Eq. 3) derived from experimental and numerical studies of time-to-failure of concrete specimens has been adopted and successfully evaluated for the time-to-failure tests of bonded anchors (Ninčević, Boumakis, Meissl, & Wan-Wendner, 2020).

$$N_{sus}/N_u = (1 - L) + L \cdot [1/(1 + bt_f)]^n \quad (3)$$

where N_{sus} the sustained load, N_u the ultimate bond resistance, t_f the failure time, $0 \leq L \leq 1$, b , and n parameters to be fitted, with $(1-L)$ defining the load level for infinitive failure time. Eq. 3 results into an asymptotic behavior of the stress vs time-to-failure curve which is theoretically supported by the findings of (Boumakis, Nincevic, Vorel, & Wan-Wendner, 2019) while it has the advantage of controlling the asymptotic value of the load level, ensuring that always a conservative assessment has been obtained. However, a comparison of the long-term assessment with the Findley approach and the stress vs. time-to-failure method cannot be directly derived and therefore still misses.

This contribution formulates a failure criterion based on the Findley approach and compares the long-term assessment obtained by the two approaches on experimental data of bonded anchor systems with two different adhesive agents, an epoxy based adhesive mortar (P1) and a vinylester based adhesive mortar (P2). The experimental data have been obtained by the literature (Boumakis, Nincevic, Vorel, & Wan-Wendner, 2019; Ninčević, Boumakis, Meissl, & Wan-Wendner, 2020) and are based on tests with anchor rods with a nominal diameter of 16 mm and an embedment depth, $h_{ef} = 75$ mm.

2 DESCRIPTION OF THE ANALYSIS METHODS

2.1 Time-to-failure

The time-to-failure analysis is performed on the reported failure times vs. load. This manuscript uses a modified version of the Eq. 3 by having as dependent variable the load expressed in terms of bond strength τ_{sus} calculated by a uniform bond model. Thus, the assessment equation becomes

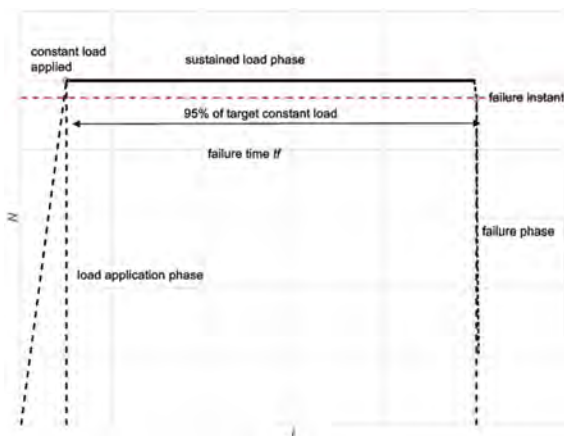


Figure 1. Failure time definition.

$$\tau_{sus} = (\tau_u - a) + a \cdot [\tau_u / (\tau_u + bt_f)]^n \quad (4)$$

with τ_u the ultimate bond resistance, $0 \leq a \leq \tau_u$ a parameter to be fitted with $\tau_\infty = \tau_u - a$ and b , and n parameters to be fitted. The conversion of the sigmoid function into the form of Eq. 4 allows directly collecting the long-term bond resistance at 50 years. Moreover, for the purpose of the analysis the asymptotic value can be fixed at 40% and 0% of the ultimate bond resistance by having $\alpha=60\% \tau_u$ and $\alpha = \tau_u$ respectively.

Note that for this method the failure times are defined as the time interval from the instant when the load is fully applied until the instant that the load drops instantaneously. Therefore, the failure time does not include the duration of the loading. In order to have a consistent criterion for all different cases the failure instant is defined when the instantaneous drop of the load is larger than 5% of the sustained load as it is illustrated in Figure 1.

2.2 Times based on the displacement criterion

The main obstacle for the realization of the comparison between the Findley and the time-to-failure (ttf) method is that the Findley approach does not provide any estimate of failure time (t_f) for a given sustained load (τ_{sus}). The present contribution overcomes this problem by defining failure times which are determined from the displacement criterion used in the Findley method. Therefore, a specimen is considered as failed when the total displacement $s(t)$ under sustained load exceeds the critical displacement at the loss of adhesion ($s_{adh loss}$), as it is calculated according to (EAD 330499-01-601, 2018). Then the failure time noted in this manuscript as “Findley failure time” is the time when the displacement at loss of adhesion has been reached. The Findley failure time is obtained either by actual data or in the case that the displacement has not reached the critical displacement $s_{adh loss}$ by following the fit and the extrapolation scheme that is imposed in the EAD (EAD 330499-01-601, 2018). The calculation of the Findley failure times is shown in Figure 2. Note that the failure times obtained by the displacement criterion are always shorter than the actual failure times if failure has occurred. That is expected since the failure displacement in the time-to-failure tests is always larger than the displacement at the ultimate capacity and it tends to follow the descending post-peak branch of the short-term load-displacement curve (Muciaccia, Consiglio, & Rosati, 2017; Boumakis, Di Luzio, Marcon, & Vorel, 2018).

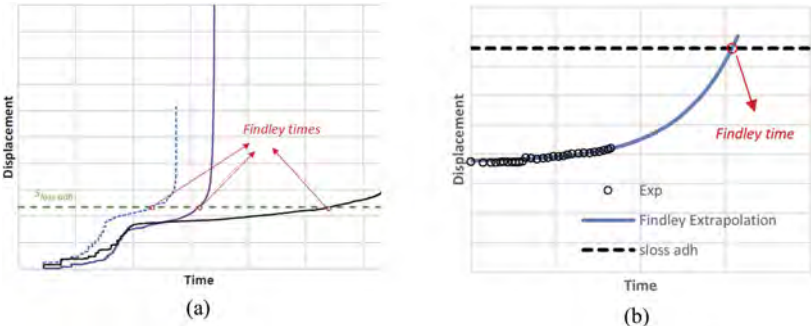


Figure 2. Examples of Findley failure times calculation.

Following this approach all the sustained load data (also the failed ones) can be considered in the analysis. Then the data are analyzed in terms of stress vs time-to-failure and Eq. 4 is fitted on them.

3 ANALYSIS AND RESULTS

First the stress vs. time-to-failure model is fitted on the experimental data of both products. The failure times and the corresponding load levels are shown in Table 1 for the epoxy based

P1 and in Table 2 for the vinyl ester based P2, respectively. As it can be seen many of the specimens have already exceeded the critical displacement during the loading phase. Therefore, the corresponding Findley failure time is zero. However, and in order to be also used in the analysis a fictitious failure time of 10^{-10} hours is assigned to them.

Table 1. Failure times and Findley failure times for P1.

Load [MPa]	Failure time [h]	Findley time [h]
39.644	0.003	0
39.644	$8.24 \cdot 10^{-5}$	0
39.644	$8.42 \cdot 10^{-4}$	0
35.471	0.003	0
35.471	0.008	0
35.471	0.004	0
31.298	0.252	0.155
31.298	0.060	0
31.298	0.311	0
31.298	0.016	0
27.125	15.620	0
27.125	23.729	1.89
27.125	2568	0
25.036	1296	0.98
25.036	1296	0.003
25.036	4290	26
25.036	-	9.2
12.52	-	$2.54 \cdot 10^{25}$
12.52	-	$1.80 \cdot 10^5$
12.52	-	$4.77 \cdot 10^8$

Table 2. Failure times and Findley failure times for P2.

Load [MPa]	Failure time [h]	Findley time [h]
25.20	0.05	0
25.20	0.004	0
25.20	0.002	0
23.72	2.20	0
23.72	0.16	0
23.72	0.50	0
22.23	0.44	0
22.23	0.52	0.002
22.23	0.96	0.003
20.75	41.72	0
20.75	-	0.003
20.75	-	0.10
19.27	25.75	0.09

Then the different datasets are expressed in terms of stress vs. time-to-failure and Eq. 4 is fitted on them. Figure 3 and Figure 4 present the different stress vs. time-to-failure datapoints obtained as actual failure times (blue points) and by the displacement for the two different bonded anchor systems.

Nevertheless, this is expected since the failure displacement under sustained loads is usually larger than the displacement at loss of adhesion (Muciaccia, Consiglio, & Rosati, 2017). Therefore, this preliminary analysis indicates that a three domain stress vs. time-to-failure curve which can be approximated by a sigmoid function is not only suitable for results from time-to-failure tests but also for sustained load tests that exhibit no actual failure assuming as failure time the

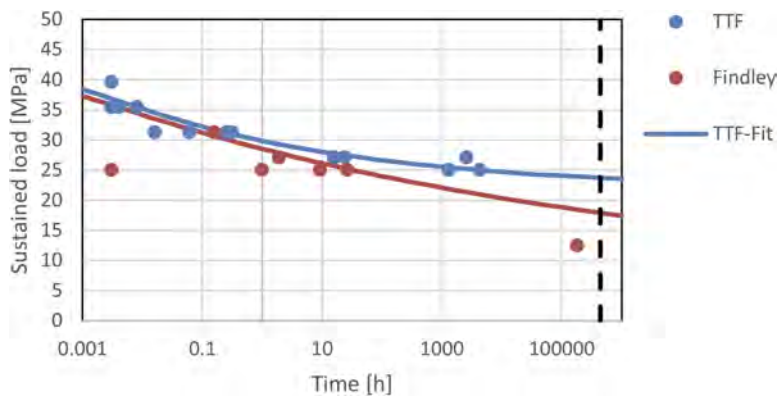


Figure 3. Stress vs time-to-failure of P1 on failure times and on times obtained from the displacement criterion.

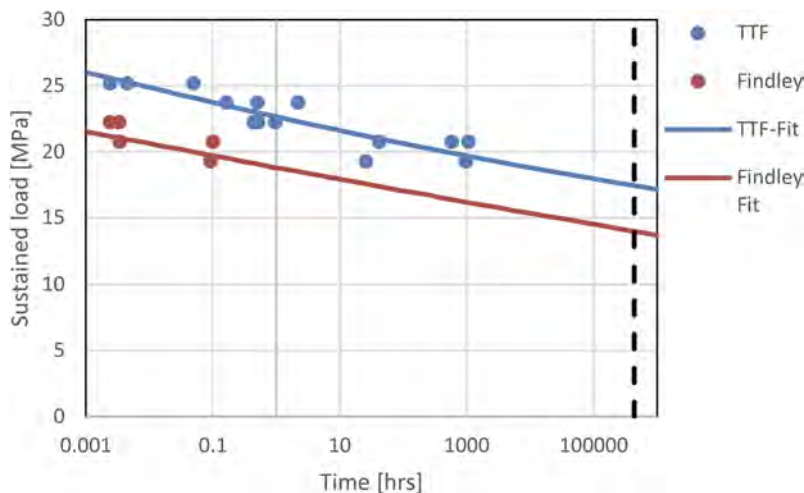


Figure 4. Stress vs time-to-failure of P2 on failure times and on times obtained from the displacement criterion.

time when the displacement at loss of adhesion is reached. Based on the analysis the long term bond resistance obtained by the extrapolation of the stress vs. times when the displacement criterion is exceeded (Findley) found to be 70% and 75% of the long term bond resistance obtained by the extrapolation on the time-to-failure data for P1 and P2, respectively.

Finally, when the 5% prediction bound of the stress vs. time-to-failure based on the actual failure times is calculated and compared to the assessment curve based on the displacement criterion, as it is shown for P2 in Figure 5, a relatively good agreement is observed. Thus, the time-to-failure method could serve as an alternative more physical and less conservative assessment method for the characteristic long term bond resistance for combined pull-out and concrete cone failure and the calculation of the ψ_{sus} as it is imposed in EAD 330499-01-0601 (EAD 330499-01-601, 2018) and in EN 1992-4:2018 (EN 1992-4:2018, 2018).

The current European assessment approach (EAD 330499-01-601, 2018) results to the calculation of the long-term characteristic bond resistance from the sustained load that passes the displacement criterion after extrapolation. As a matter of fact, the sustained load, N_{sus} that leads to displacement with an extrapolated value at 50 years lower than the critical displacement at loss of adhesion, $s_{50} < s_{adh loss}$ is converted to sustained load in terms of bond according to Eq. 5.

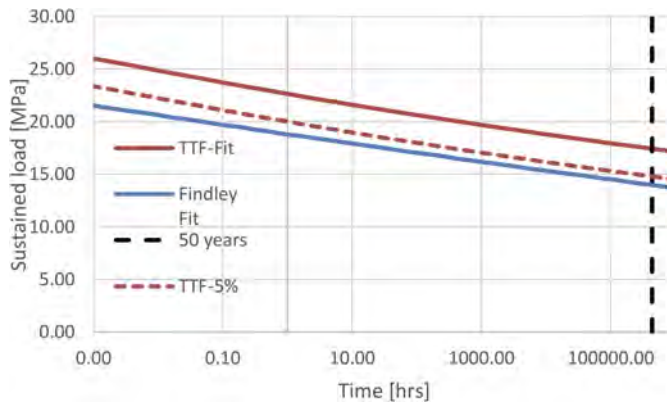


Figure 5. Comparison of the 5% prediction percentile of stress vs time-to-failure with the extrapolation based on the displacement criterion for P2.

$$\tau_s = \frac{N_{sus}}{\pi \cdot d \cdot h_{ef}} \cdot \min\left(1; \frac{a}{0.9}\right) \quad (5)$$

where α reduction factor based on the residual capacity of the sustained load specimens. Then the basic characteristic long-term bond resistance τ_{Rk}^0 is defined as $\tau_{Rk}^0 = \tau_{sus}$. Finally, the characteristic long-term bond resistance is calculated as $\tau_{Rk} = \tau_{Rk}^0 \cdot a_3 \cdot a_4 \cdot a_{setup} \cdot k_{sus} \cdot \min\beta_{CV}$, with α_3 , α_4 reduction factors for the effect of the maximum short temperature and of high alkalinity and sulphurous atmosphere, $a_{setup} = 0.75$ the reduction factor for uncracked concrete, $k_{sus} = 1.1.35$, and $\min\beta_{CV}$ the minimum of the β_{CV} factors related to the scatter represented by the coefficient of variation. Finally, the factor ψ_{sus} is calculated as $\psi_{sus} = \tau_{Rk} / \tau_{Rk,ucr} \cdot 1.15$ where $\tau_{Rk,ucr}$ the short-term characteristic bond resistance for combined pull-out and concrete cone failure.

Based on the results of the present comparison the long term sustained load for a service lifetime of 50 years can be directly obtained by the stress vs time-to-failure curve. The advantage would be that the long-term bond resistance is obtained by the fit on actual time dependent failure tests. A conservative assessment approach would be to consider the 5% prediction bound $\tau_{5\%}$ for the determination of the τ_{sus} . Then all the other steps of the calculation of the ψ_{sus} could stay the same. Therefore, based on that the calculation of the ψ_{sus} based on time-to-failure data could follow the scheme below:

- i. fit Eq. 4 on the time-to-failure data
- ii. calculate the 5% prediction bound $\tau_{5\%}$ and extrapolate
- iii. calculate the sustained load as $\tau_{sus} = \tau_{5\%} \cdot \min(1; a/0.9)$, where a reduction factor as it is determined in clause 2.2.2.6.2 of EAD 330499-01-0601 (EAD 330499-01-601, 2018).
- iv. take the characteristic bond resistance τ_{Rk}^0 as $\tau_{Rk}^0 = \tau_{sus}$.
- v. Apply the reduction factors of EAD 330499-01-0601 (EAD 330499-01-601, 2018) and calculate $\tau_{Rk} = \tau_{Rk}^0 \cdot a_3 \cdot a_4 \cdot a_{setup} \cdot k_{sus} \cdot \min\beta_{CV}$.
- vi. Calculate ψ_{sus} as $\psi_{sus} = \tau_{Rk} / \tau_{Rk,ucr} \cdot 1.15$ where $\tau_{Rk,ucr}$ the short-term characteristic bond resistance for combined pull-out and concrete cone failure.

4 CONCLUSIONS

This contribution explores the link of two different methods for the assessment of the long-term behaviour of bonded anchors under sustained loads. The comparison of the long-term bond resistance for an epoxy based and a vinylester based bonded anchor system calculated based on time-to-failure tests found to be 1.25-1.30 of the corresponding value based on the

displacement criterion (Findley approach). The analysis, even in a preliminary state, indicates that the stress vs. time-to-failure curve can be well described by a sigmoid function which imposes a critical sustained load below which no failure is expected under sustained load in course of time. Furthermore the 5% prediction bound of the stress vs. time-to-failure curve and its extrapolation shows no significant difference compared to the extrapolated curve obtained by the displacement criterion. Therefore, the stress vs. time-to-failure method using a sigmoid function could be used as an assessment method in the corresponding EAD without violating the necessary conservatism.

REFERENCES

- ACI Committee 318. (2019). *Building Code Requirements for Structural Concrete (ACI 318-9) and Commentary (ACI 318R-19)*. Farmington Hills, MI, USA: American Concrete Institute.
- Blochwitz, R. (2019). *Verbunddübelssysteme unter dauerhafter Lasteinwirkung*. Stuttgart, Germany: Universität Stuttgart.
- Boumakis, I., Di Luzio, G., Marcon, M., & Vorel, J. W.-W. (2018). Discrete Element Framework for modeling tertiary creep of concrete in tension and compression. *Engineering Fracture Mechanics*, 200 (6), S. 263–282.
- Boumakis, I., Nincevic, K., Vorel, J., & Wan-Wendner, R. (2019). Creep rate based time-to-failure prediction of adhesive anchor systems under sustained load. *Composites Part B: Engineering*, 178(1), S. 107389.
- Cook, R. A., Kunz, J., Fuchs, W., & Konz, R. (2006). Behavior and design of adhesive bonded anchors. *ACI Structural Journal*, 103(6).
- Cook, R. D., & Davis, T. (2009). *NCHRP Report 7639: Adhesive Anchors in concrete under sustained loading conditions*, Tech. rep. Washington, D.C.
- EAD 330499-01-601. (2018). *Bonded Fasteners for use in concrete*. EOTA.
- EN 1992-4:2018. (2018). *Eurocode 2 - Design of Concrete Structures -Part 4: Design of Fastenings for Use in Concrete*. Brussels, Belgium: European Committee for Standardization.
- Monkman, F., & Grant, N. (1956). An empirical relationship between creep rupture life and minimum creep rate in creep rupture tests. *Proceedings ASTM*, 56.
- Muciaccia, G., Consiglio, A. N., & Rosati, G. (2017). Creep Behavior of Bonded Anchor Under High Sustained Loading at Long Term Temperature. In *High Tech Concrete: Where Technology and Engineering Meet*. Springer.
- Ninčević, K., Boumakis, I., Meissl, S., & Wan-Wendner, R. (2020). Consistent Time-to-Failure Tests and Analyses of Adhesive Anchor Systems. *Applied Sciences*, 10(4), S. 2076–3417.
- Prandtl, L. (1928). Ein Gedankenmodell zur kinetischen Theorie fester Körper. *Zeitschrift für Angewandte Mathematik und Mechanik*, 8(2).
- Stierschneider, E., Tamparopoulos, A. E., McBride, K. E., & Bergmeister, K. (2021). Influencing factors on creep displacement assessment of bonded fasteners in concrete. *Engineering Structures*, 241, S. 112448

Impact of concrete age and aggregate type on anchor load performance

K. Nincevic & R. Piccinin

Hilti Corp., Schaan, Principality of Liechtenstein

I. Boumakis

fischer Austria GmbH, Traiskirchen, Austria

T. Pregartner

fischerwerke GmbH & Co. KG, Waldachtal, Germany

R. Wan-Wendner

Ghent University, Ghent, Belgium

ABSTRACT: Fastening systems have become essential elements in civil engineering constructions as the field of application of modern fastening technique is expanding. In recent years, the construction industry saw a shift towards rehabilitation and modular construction to address the growing demand for faster construction on one side and the change in usage and sustainability on the other side. Consequently, efficient design and utilization require a thorough understanding of all involved materials and their changes throughout their lifetime. Considering the potential damage and consequences due to anchorage failure, it is obvious that such products must undergo rigorous approval tests. Practice has shown that for the same concrete class and anchor type load capacities can vary, especially when the results are compared between different laboratories in a worldwide scope. There are several different possible reasons that can cause such differences, and for some of these limited restrictions are given (e.g., only the minimum concrete age is specified). This contribution presents an experimental campaign investigating two potential influence factors on the concrete cone capacity: (i) age and curing, and (ii) the aggregate effect. The investigation comprises full material characterization for each aggregate and concrete, and structural pull-out tests on mechanical anchors performed at two ages. Finally, the experimentally obtained data is used to check the current design codes in an attempt to evaluate the predictive quality of the investigated models and their sensitivity with regard to the discussed influence factors.

1 INTRODUCTION

Over the last years, fastening systems became an essential component in the business that deals with the designing, planning, and construction. The rapid growth in construction engineering is ensured by relatively “user-friendly” products with a high ability to fulfil all demands in modern design and fast modular construction. Currently, various fastener types can be found on the market, usually grouped by the working principle (mechanical or bonded anchors), and by installation time (pre- or post-installed), see Eligehausen (2006). Fastener classifications, working principles, load scenarios, and failure mechanisms were in-depth discussed many times in the past. Therefore, all relevant references are provided in the manuscript, while deeper discussion would exceed the scope of this paper. In general, fasteners are mostly steel components made to mechanically join or affix two or more objects together (e.g., load-bearing structural members, installation of equipment). As such, these products must meet the two most important requirements: (i) high performance and safety requirements through the most rigorous testing and development methods, and (ii) to ensure innovative solutions supported by easy installation procedure and relatively simple design.

In many applications, fasteners are typically installed in a concrete base material, which became one of the most used structural materials. Concrete is a well-known cementitious material made of cement, aggregates, and water. As widely known, concrete properties improve over time. With the highest portion of space in concrete, aggregates are one of the most important mix design parameters. Their shape, size and surface roughness highly influence the fresh concrete workability, and the mechanical concrete properties (e.g., compressive, and tensile strength). Because concrete is used worldwide, it is obvious that the used cement and aggregate types can vary significantly, thus influencing the concretes' performance. Naturally, different local concrete properties in a structure will affect crack propagation and consequently failure mode. Following the current design guidelines, concrete is typically characterized in terms of 28-day compressive strength only (Eurocode 2 Part 1-1 (2009), fib Model Code for Concrete Structures (2010)). The same approach is also followed by fastening related approvals (e.g., EOTA (1997), EOTA (2002)) and design standard (EN 1992-4 (2018)). Here, the concrete compressive strength is the only material parameter used to describe the anchor load capacity, regardless of the curing condition, cement type, mix-design, and the failure mechanism.

In the last few decades, many different studies on fastening systems (see Ballarini (1986), Bazant (1985), Bazant (1989), Eligehausen (1985), Eligehausen (1989), Eligehausen (2006), Fuchs (1995), Krenchel (1985), Ottosen (1981), Ozbolt (1990), Stone (1983)) were performed to experimentally determine the load capacities for different fastener types, and to develop simple “user-friendly” predictive models. These contributions aimed to not only derive the predictive equations, based on the best fit of the experiments, but also to understand the anchor behavior, and the different failure mechanisms. In the present study, the focus was merely on only one failure mechanism, most known in the anchor community as concrete cone breakout, as shown in Figure 1. It is a typical failure mode for mechanical anchors under pure tensile loading, determined by the crack initiation at the anchor head as soon as the concrete tensile strength is exceeded and subsequent propagation.



Figure 1. Considered failure mechanism: concrete cone failure.

After several basic studies, Fuchs (1995) proposed an empirical model to calculate the load capacity for anchors under tensile loading. This method is known as the Concrete Cone Capacity Design (CCD) method. The mean concrete cone failure load of a single anchor loaded in tension is given by Equation 1 and is currently used in design to predict concrete cone capacity:

$$N_{u,c} = k \cdot \sqrt{f_c} \cdot h_{ef}^{1.5} \tag{1}$$

where k is calibrated factor; f_c = concrete compressive strength; h_{ef} = embedment depth.

Following this approach, the concrete cone capacity is a function of a dimensional $[N^{0.5}/mm^{0.5}]$ anchor dependent calibration factor k (in case of considered headed studs is proposed to be 15.5), the concrete cube compressive strength f_c [MPa] measured on a 200 mm side cube, and the anchor embedment depth h_{ef} [mm]. As introduced above, the predictive equation assumes that all possible differences in the concrete mix-design and the curing conditions are captured by the compressive strength, and such no additional effect on the anchor performance is expected. In other words, regardless of the cement type, water to cement ratio, aggregate to cement ratio, aggregate type, and curing condition, the concrete compressive strength is the only material

input required to predict the anchor load capacity in any point in time. Of course, simplified empirical models supported by limited numerical investigations cannot be experimentally validated for all possible scenarios, due to time and costs restrictions. However, they are an essential tool for design purposes and can, if necessary, be improved. In some cases, limited guidelines are provided and can contribute inconsistencies between different research groups attributing it to one effect rather than the other. For instance, current anchor related codes specify minimum requirements for the aggregate type, specifically it is suggested to use aggregates of medium hardness only. Furthermore, merely a minimum age of the tested concrete member is given, while no upper limit specified (only in the case of bond tests an upper limit of 18 months is given). However, situations may exist where different laboratories test anchors installed in concrete with different ages or different maturity depending on the history of environmental boundary conditions, and as a result, might obtain differences which are not attributed to the effect anticipated to study (e.g., aggregate type effect).

Based on the above-mentioned facts, the motivation of systematically carried out experimental investigations was to quantify (i) the influence of the concrete age, and (ii) the possible effect of different aggregate types on the concrete cone capacity. The experimentally obtained data is normalized to remove the known functional dependencies using the current predictive equation and to compare the results. Due to the paper limits, this contribution is limited to the most relevant information summarizing the work of two recent publications (Nincevic (2019) and Nincevic (2019)). In the original referenced manuscripts, more detailed discussions with corresponding details and figures are provided.

2 EXPERIMENTAL DESIGN

2.1 Overview

The present work attempts to determine how the used aggregate type and the concrete age affect the concrete cone capacity by normalizing the pull-out loads by the corresponding compressive strength. The experimental program comprises the characterization of both aggregates and concretes identifying the most practically relevant mechanical properties. The properties of the used coarse aggregates were determined by grid-indentation and standard abrasive Los Angeles Tests. Concretes were fully characterized by means of compressive strength, tensile strength, elastic modulus, and fracture properties. In parallel to the material tests, structural tests were performed on cast-in headed studs under tensile loading. Both concrete and structural tests were performed at two different ages: 28- and 70-days. In total 12 slabs were used for anchor tests, together with 70 cylinders, 90 cubes and 24 prisms.

2.2 Concrete mix design and selected aggregate types

Three different concrete mix designs were considered, with the aim to keep all mix-design parameters the same but varying the aggregate type. Therefore, all three concretes have the same cement type CEM II 42.5N and are following the sieve curve according to the ETAG guidelines (ETAG (2012)). Table 1 shows the exact values and differences among the used concretes. As can be seen, the water to cement (w/c), and the aggregate to cement (a/c) ratios were very similar. Even though the aim was to keep all parameters the same, it is important to note that basalt aggregates in case of the E3 batch could not be delivered with a maximum coarse aggregate size of 16 mm and in round shape. Therefore, broken aggregates with a maximum coarse aggregate size of 22 mm were used for concrete E3.

Table 1. Concrete mix design.

Concrete ID	Cement type	Aggregates		Max. size [mm]	w/c ratio [-]	a/c ratio [-]
		Type	Shape			
E1	CEM II 42.5N	Quartz	Round	16	0.63	6.93
E2	CEM II 42.5N	Limestone	Round	16	0.6	7.27
E3	CEM II 42.5N	Basalt	Broken	22	0.58	7.19

2.3 Material characterization tests

2.3.1 Aggregate characterization tests

The selected coarse aggregate types are grouped as quartz, limestone, and basalt type. These groups are based on a mineralogical analysis performed by the X-ray powder diffraction method (XRD). For each representative coarse aggregate type, mechanical properties such as modulus and hardness were obtained by nanoindentation tests (Doerner (1986), Fischer-Cripps (2002), Oliver (1992)). Additionally, standard abrasion tests, so-called Los Angeles (L.A.) tests, were carried out to identify the coefficient of abrasion (BS EN 1097-2:2010-03). Those properties are listed in Table 2. It can be seen that quartz aggregates are by far the softest among the three considered types. The expected trend is confirmed with the L.A. results, where the softest aggregate resulted in the highest coefficient of abrasion.

Table 2. Experimentally obtained aggregate mechanical properties.

Aggregate type	L.A. coefficient [-]	Hardness [GPa]	Modulus [GPa]
E1 - Quartz	26	0.5	11.4
E2 - Limestone	22.6	1.4	37.5
E3 - Basalt	15	2.3	45.6

2.3.2 Concrete characterization tests

The standard concrete characterization tests were carried out to identify the most important concrete mechanical properties. Since the current design approach considers the concrete compressive strength only, also in this contribution merely the compressive strength data is used to perform the analysis of the anchor load capacities. The extended analysis that includes all the other concrete properties (e.g., Young's modulus, tensile strength, fracture energy) and discusses correlations between aggregates/concretes/anchor load capacities are reported in Nincevic (2019).

Concrete related codes require the concrete specimens for the material characterization to be stored in "lime-saturated" water or in high humidity conditions (> 95%) prior to testing, ensuring that the constant water supply needed for the hydration process is guaranteed.

In contrast, anchor related codes require no specific storage conditions for concrete specimens and structural members. They may be stored inside or outside the laboratory exposed to the environmental relative humidity and temperature. It is only required to store specimens (both test members and concrete specimens) indoor for the first seven day, and after can be stored outdoor, ensuring they are protected from frost, rain, and direct sun deterioration (ETAG – Annex A (2012)). The concrete compressive strength used to predict the concrete cone capacity using Equation 1 needs to be obtained from concrete specimens undergoing the same temperature and humidity histories as the structural member.

In this study, one set of specimens was stored inside the laboratory at an ambient temperature of 23°C in "lime-saturated" water after being in the moulds for the first 24 h. Those specimens were following the concrete-related codes and are named "moist-in cured" specimens. The second set of specimens stored according to the anchor related codes. Those specimens are named "dry-cured" specimens. An additional set of specimens followed the moist curing conditions but were stored outside at variable ambient temperature. The results of the outside stored moist specimens are not further discussed in this contribution, see in Nincevic (2019) for further details and results.

Table 3 contains all experimentally obtained mechanical properties at two ages for the "moist-in cured" specimens (following the concrete-related codes). The cube compressive strength results were obtained from 150 mm side cube ($f_{c, cu}$) following EN 12390-3 guidelines. The results show that the concrete with the limestone and the basalt aggregate type resulted in a similar strength class, while the concrete with quartz aggregate has the lowest compressive strength. As expected, the results are following the same trend for the second age. Additional material properties are reported in Table 3, such as the compressive strength obtained from cylindrical specimens ($f_{c, cyl}$), the modulus (E), and the indirect tensile strength properties ($f_{t, sp}$). More details about the testing procedure, followed standards and specimen geometries are reported in Nincevic (2019).

Table 3. Experimentally obtained concrete mechanical properties for moist-in cured specimens.

Concrete ID	$f_{c, cu}$ [MPa]	$f_{c, cyl}$ [MPa]	$f_{t, spl}$ [MPa]	E [GPa]
E1-28d	34.3 ± 6.2%	32.3 ± 7.7%	3.0 ± 20.8%	30.6 ± 8.1%
E2-28d	40.3 ± 4.2%	33.9 ± 9.7%	4.1 ± 3.3%	31.4 ± 11.2%
E3-28d	42.1 ± 4.9%	36.3 ± 6.7%	3.4 ± 2.0%	31.8 ± 4.0%
E1-70d	38.7 ± 7.6%	36.5 ± 2.9%	3.4 ± 8.6%	31.2 ± 7.5%
E2-70d	45.6 ± 4.3%	44.8 ± 6.4%	4.4 ± 4.2%	42.2 ± 6.4%
E3-70d	46.7 ± 9.6%	39.4 ± 6.2%	3.5 ± 9.1%	34.4 ± 5.6%

2.4 Structural tests on cast-in headed stud anchors

Structural anchor tests were performed on cast-in headed studs loaded in tension with concrete cone failure. The anchors were made of M20 hex-bolt anchors with the head of 40 mm (2 x size of anchor rod diameter) with 12.9 steel grade design to avoid potential steel failure. Only one embedment depth of 100 mm was investigated (h_{ef} =100 mm). The tests were performed in displacement control mode under quasi-static loading on concrete slabs with dimensions of 250 x 100 x 30 cm. The anchors were spaced such that the splitting of the concrete member or influences by adjacent anchors are avoided. All tests were carried out in a so-called “unconfined configuration” using a circular steel ring with an inner diameter of 400 mm. The exact anchor design, slab layout and test setup, as well as the testing procedure are reported in Nincevic (2019). The experimentally obtained mean concrete cone capacities based on four tests each are listed in Table 4 together with the corresponding coefficient of variation (CoV). Additionally, the mean “dry-cured” cube compressive strengths based on 4 tests each following the anchor related code are shown.

Table 4. Experimentally obtained pull-out load capacities with corresponding cube strength with required curing conditions (“dry cured”).

Concrete ID	N_{exp} [kN]	$f_{c, cu}$ [MPa]
E1-28d	111.2 ± 8.3%	29.1 ± 5.0%
E2-28d	136.6 ± 9.6%	35.3 ± 3.4%
E3-28d	124.4 ± 1.2%	35.0 ± 6.3%
E1-70d	143.4 ± 4.9%	30.6 ± 5.5%
E2-70d	183.4 ± 7.0%	40.0 ± 6.7%
E3-70d	173.9 ± 5.6%	39.7 ± 8.0%

Considering the mean concrete cone capacity as a function of compressive strength, the expected trend is confirmed for E1 concrete which showed the lowest compressive strength and as well resulted in the lowest cone capacity, while the other two concretes have similar cube strengths and also cone capacities.

3 RESULTS AND DISCUSSION

In order to facilitate the comparison of different concrete batches, the results are presented in terms of normalized values. The most basic approach given by Equation 2 defines the ratio (α) between the experimentally obtained (N_{exp}) and the predicted pull-out load capacities (N_{uc}) according to Equation 1. That means that for all concretes and all ages the results are individually normalized using the cube compressive strength for the given concrete batch and age.

$$\alpha(t) = \frac{N_{exp}}{N_{u,c}} = \frac{N_{exp}(t)}{k \cdot \sqrt{f_c(t)} \cdot h_{ef}^{1.5}} \quad (2)$$

Ideally, the normalized values (α) should be equal to 1.0, or closely scattering around that value, indicating that the predictive equation based on the concrete compressive strength is

able to accurately predict the load capacity for any given age, regardless of the concrete aggregate type, and any other mix-design parameter.

3.1 Age effect

The main interest here is to answer the question whether there is an additional age effect on the concrete cone capacity that is not captured by the current predictive model formulated in terms of the compressive strength. In other words, if the concrete compressive strength is a sufficiently good material parameter to predict the concrete cone capacity at any point in time. As a first check, the experimentally observed evolution of concrete compressive strength obtained with moist-in cured specimens following the concrete-related codes is checked using the ageing law suggested by codes BS-EN-1992-1-1:2009. Evaluating the ageing law based on the experimentally obtained 28-day values, the 70-day predictions are in very good agreement with the experiments, underestimating the actual results by 4.5% for E1, 4.8% for E2, and 2.9% for concrete E3. A more detailed analysis is reported in Nincevic (2019). This confirms that all three tested concretes showed the expected strength evolution for the considered time window.

Figure 2 shows the normalized load capacities by the concrete compressive strength obtained on dry-cured specimens (as suggested by the anchor-related codes) for all tested concretes and both ages. The normalization is performed according to Equation 2, using the coefficient $k = 15.5 \text{ (N}^{0.5}/\text{mm}^{0.5}\text{)}$, as proposed by the codes for the given anchor type.

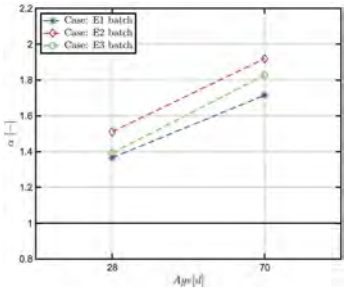


Figure 2. Normalized load capacities using Equation 2 and “dry cured” specimens.

As can be seen, the results indicate a significant offset from the target value at 28 days, indicating that the calibration factor k is approximately 40% higher than proposed for this specific anchor type and geometry. Additionally, it can be clearly seen that there is a significant difference between the normalized 28- and 70-day values. In study reported by Nincevic (2019) is shown that the same trend is observed for all three concretes regardless of the curing protocol of the concrete specimens used to obtain the concrete compressive strength.

These results might indicate that the small cubical specimens do not fully represent the material properties of a larger structural member in some cases. Additionally, it shows that the current predictive equation captures insufficiently well the ageing phenomenon, where the 70-day predictions are approximately 25% more conservative than the predictions at 28 days.

3.2 Aggregate effect

The presence of an aggregate effect on concrete cone capacity is evaluated based on the above introduced normalized values and the variability (CoV) among all the concretes. Figure 3 shows the normalized pull-out load capacities for all three concretes tested at an age of a) 28 and b) 70 days. The red markers represent the mean normalized values using the concrete compressive strength obtained from “dry-cured” cubes, while the blue markers represent the “moist-in cured” concrete specimens. As can be seen, the relative difference among the concretes/markers is relatively small compared to the standard scatter observed in this type of experiments (~10%).

The results clearly show that the current predictive model is able to predict the concrete cone capacity regardless of the considered coarse aggregates used in this study. In both cases,

using either “dry-cured” or “moist-in cured” compressive strength, the relative difference is still much lower than 10%. Therefore, from a practical point of view, no significant aggregate effect on concrete cone capacity can be assumed. The effect of coarse aggregate type is reflected in the concrete mechanical properties. Beyond that, no significant deviations in the relationship between concrete compressive strength and concrete cone capacity can be observed. A systematic analysis including other predictive energy-based models and correlations between material properties and load capacities are reported in Nincevic (2019).

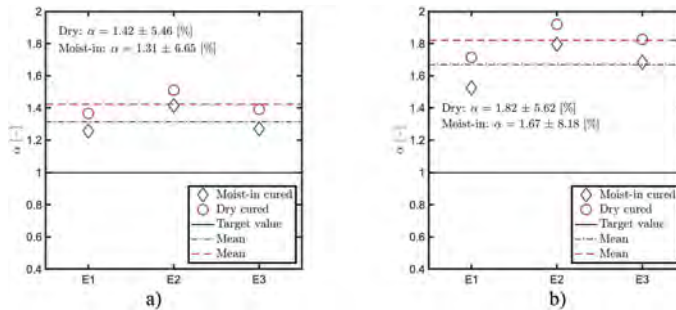


Figure 3. Normalized load capacities using Equation 2 with “dry” and “moist-in cured” specimens for a) 28 days, and b) 70 days results.

3.3 Age and aggregate effect on the cone shape and size

Finally, a photogrammetric analysis was performed to reconstruct 3D models of the concrete fracture surface (concrete cones) to analyse potential correlations between concrete age and aggregate effect on one side, and shape and size of concrete cones on the other side. The analysis showed neither a significant effect of the concrete age nor of the aggregate type on the mean cone profiles and sizes (more details and result reported in Nincevic (2019)). Additionally, all concrete cones were localized at the circular steel support with an inner diameter of 400 mm, corresponding to four times the embedment depth ($d=4 \cdot h_{ef}$). It must be noted here that the anchor-related code requires a circular support with an inner diameter of minimum three times the embedment depth ($d=3 \cdot h_{ef}$) to avoid influences of the boundary conditions on the peak load.

4 CONCLUSIONS

In the present contribution, a comprehensive and systematically carried out experimental investigation on cast-in mechanical anchors comprising three concretes tested at two different ages is presented with the aim to investigate the effect of age and aggregate type on the concrete cone capacity. In parallel to the structural anchor tests, the analysis involves full material characterization tests on concrete specimens following different curing protocols. Based on the presented results of the experimental investigations, the following conclusions are drawn.

1. Three investigated concretes tested at two ages showed the expected evolution of concrete compressive strength. The evolution of the material properties is in good agreement with the concrete-related codes suggested ageing law. The predictions at 70 days deviate only 2-5% from the experimentally observed values.
2. The concrete cone capacities predicted using the current predictive model based on the concrete compressive strength underestimates the experimental results. This indicates a very conservative choice of the calibration factor k used in the equation for the investigated hex bolt anchor type.
3. For the investigated concretes and anchor type, a clear age effect is revealed, where the 70-day concrete cone capacity predictions are approximately 25% more conservative than the predictions at 28 days.

4. The currently established predictive model captures and accounts for the effect of different coarse aggregate type. The results based on normalized pull-out load capacities showed an insignificant remaining aggregate effect, typically smaller than the experimental scatter of 5% - 10% in anchor pull-out tests.
5. A photogrammetric analysis was performed on the extracted concrete cones geometrical properties and showed no significant age and aggregate effect on the cone shape and size.

ACKNOWLEDGEMENTS

Marco Marcon and Lisa-Marie Czernuschka are gratefully acknowledged for their contribution performing the concrete characterization tests, and Stefan Meißl for his support in performing the anchor pull-out tests and the data post-processing. Gabriel Pfuner is acknowledged for his support performing the photogrammetric analysis and detailed documentation. The financial support by the Austrian Federal Ministry of Economy, Family and Youth and the National Foundation for Research, Technology and Development is gratefully acknowledged.

REFERENCES

- Ballarini R, Shah SP, Keer LM., 1986, Failure characteristics of short anchor bolts embedded in a brittle material. *Proc Roy Soc Lond A: Math Phys Eng Sci* 1986;404(1826):35–54.
- Bazant ZP, Planas J., 1998, Fracture and size effect in concrete and other quasi brittle materials. Boca Raton, Florida: CRC Press
- Bazant ZP., 1985, Size effect in blunt fracture: concrete, rock, metal. *J Eng Mech ASCE* 1984;110:518–35.
- British Standard Institutes, BS EN 1097-2:2010-03. Tests for mechanical and physical properties of aggregates, Part 2: Methods for the determination of resistance to fragmentation. British Standard Institution, London.
- CEB-FIB. Model Code for Concrete Structures 2010. Ernst & Sohn; 2010.
- CEN. Eurocode 2: Design of concrete structures – Part 1–1: General rules and rules for buildings, volume BS-EN-1992-1-1:2009. European Committee for Standardization; 2009.
- Doerner MF, Nix WD., 1986, A method for interpreting the data from depth-sensing instruments. *J Mater Res* 1986;1:60–9.
- Eligehausen R, Malle R, Silva J., 2006, Anchorage in concrete construction. Berlin: Ernst & Sohn
- Eligehausen R, Sawade G, 1985, Verhalten von Beton auf Zug (Behavior of Concrete in Tension). *Betonwerk und Fertigteil-Technik* 5 und 6, 1985;51(5):315–22
- Eligehausen R, Sawade G. 1989, A fracture mechanics based description of the pull-out behavior of headed studs embedded in concrete. *Fract Mech Concr Struc*. <https://doi.org/10.18419/opus-7930>.
- EN 1992-4:2018 Eurocode 2 - Design of concrete structures- Part 4: Design of fastenings for use in concrete
- ETAG 001: Metal Anchors for Use in Concrete – Annex A: Details of tests, European Organisation for technical Approvals (EOTA); 2012.
- European organisation for technical approvals (EOTA). Guideline for European technical approval of metal anchors for use in concrete. Part One: Anchors in general; Brussels, Belgium, volume ETAG 001; 1997.
- Fischer-Cripps Anthony C., 2002, Nanoindentation. New York: Springer-Verlag New York, Inc.;
- Fuchs W, Eligehausen R, Breen JE., 1995, Concrete capacity design (CCD) approach for fastening to concrete. *ACI Struct J* 1995;92:73–94.
- Guideline for European technical approval of metal anchors for use in concrete. Part Five: Bonded Anchors; European Organisation for Technical Approvals: Brussels, Belgium, volume ETAG001; 2002.
- Krenchel H, Shah SP., 1985, Fracture analysis of the pullout test. *Mater Struct* 1985;18(6):439–46.
- Nincevic, K., Boumakis, I., Marcon, M., Wan-Wendner, R., 2019, Aggregate effect on concrete cone capacity, *Engineering Structures* 191 (2019) 358–369.
- Nincevic, K.; Czernuschka, L.; Marcon, M.; Wan-Wendner, R., 2019. Age and Cure Dependence of Concrete Cone Capacity in Tension. *ACI Struct. J.* 2019, 116.
- Oliver WC, Pharr GM., 1992, An improved technique for determining hardness and elastic modulus using load and displacement sensing indentation experiments. *J Mater Res* 1992;7:1564–83.
- Ottosen NS. 1981, Nonlinear finite element analysis of pull-out test. *J Struct Div ASCE*;107(4):591–603.
- Ozbolt J, Eligehausen R. 1990, Numerical analysis of headed studs embedded in large plain concrete blocks. In: Bicanic N, Mang H (Herausgeber), editors. *Computer aided analysis and design of concrete structures*. London: Pineridge Press
- Stone WC, Carino NJ., 1983, Deformation and failure in large-scale pullout tests. *ACI J Proc* 1983;80(6).

Impact of end-of-life stage in cradle-to-cradle LCA analysis of timber and timber-hybrid buildings

L. Corti & G. Muciaccia

Politecnico di Milano, Milan, Italy

ABSTRACT: Timber and hybrid timber buildings are very-well known for their properties of optimizing structural performances through a forward-looking combination of timber with other materials. These types of structures are also more sustainable from environmental perspective if compared to traditional RC buildings, especially considering the End-Of-Life stage (stage C) and Beyond System Boundary Stage (stage D) of Life Cycle Assessment (LCA) analysis where timber members contribute to the reduction of e.g., Global Warming Potential, given their very low – or even negative – values in terms of released kg CO₂ eq.

Two main issues have been identified by the authors concerning assessment of that topic, as first of all no standard methods are available for stage D impact evaluation; this problem is exacerbated by data shortage, given that this stage is currently not compulsory in the development of LCA analysis. In order to standardize this phase with the goal of spreading its importance, the authors investigated different case studies. Analysed previous studies are also needed for the second issue development, as a point of primary importance is the building structural scheme, with particular focus on fastening technology. Considering re-use, recovery or recycling potential of a building part or member, a key issue is the disassembling simplicity: this characteristic should be definitely taken into account in a cradle-to-cradle LCA analysis as this is the unique way to design the building in sustainable terms.

Reducing number of steps from building dismantling to the new building construction and minimizing amount of materials destined for disposal become measures of the building ability to reverse CO₂ emissions to zero or negative values with stages C and D detailed assessment.

1 INTRODUCTION

Nowadays global attention is focused on environmental impact of every product and process, with special careful on emissions of each phase of the life cycle, starting from the raw material extraction to the end-of-life, possibly including re-use, recovery or recycling procedures. This special care is needed as the current situation is the result of the last decades continuously increasing harmful emissions which are leading to irreversible damaging of the planet (Solomon, Plattner, & Knutti, 2009). The issue is complex as several problems can be identified, apart from already mentioned matter of emissions quantities; resources exploitation by the most developed countries is no more compatible with the Earth's capacity to regenerate these resources. This unbalance reflects in every aspect of human life, from the economical, to the social and health aspects (Lenton, et al., 2019) (Markkanen & Anger-Kraavi, 2019). In Figure 1 two indicators of the gravity of the situation are represented.

Climate change has been treated for years as a slow process which implications would have been far away in time: this assumption is proven to be wrong, just considering sudden temperature growth. This laxity has placed both changes observations and mitigation measures in a secondary position that lead to even more severe consequences that nowadays are visible to everyone. Another issue that draws the attention on the topic is the irreversibility of some processes, such surface's temperature increase that continues growing even though CO₂ emissions are reduced to zero, following a hysteretic path behaviour delayed in time (Soong-Ki, et al., 2022).

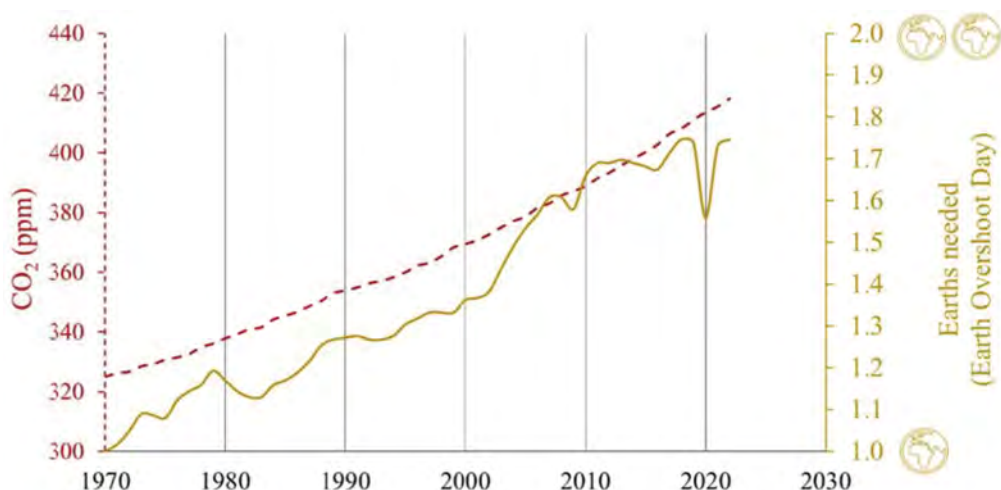


Figure 1. Carbon dioxide concentration in part per million (https://gml.noaa.gov/webdata/ccgg/trends/co2/co2_mm_mlo.txt) and Earth Overshoot Day starting from 1970 (<https://www.overshootday.org/newsroom/past-earth-overshoot-days/>). Year 2020 drop of the Earth Overshoot Day is caused by pandemic lockdown effects.

Considering that building and construction sector is responsible for almost 40% of the emissions (Jahan, et al., 2022) (taking into account both energy usage and processes related) and that the building stock is growing in order to accommodate increasing population especially in urban areas, a special effort is required. Considering annual reports delivered by the Global Alliance for Buildings and Construction (GABC) that started monitoring the sector under consideration from the COP21, some mild improvements have been noticed, as the increase of green building certifications (Global Status Report for Buildings and Construction: Towards a Zero-emission, Efficient and Resilient Buildings and Construction Sector, 2021) Considering on the other hand the building sector emissions, last two years data – in particular year 2020 – have recorded significant decrease, which is again a pandemic effect that hides the fact that building decarbonization is not on track.

This fact claims for new solutions and greater attention in terms of sustainability actions for new and existing buildings. Considering new buildings, the sustainability perspective is imperative and of primary importance; on the other hand, also existing buildings should be considered. These buildings will contribute to waste generation once reached their end-of-life, which treatment contribute to soil consumption, power usage and greenhouse gases emissions (Alsheyab, 2022), even though applying a waste management hierarchy significant mitigation of impacts is granted (Sasitharan, et al., 2012). Amount of waste generated by construction and demolition (C&D) contributes worldwide for about 25% of the total generated waste, even though discrepancies are recorded for different countries (Nunes & Mahler, 2020), which again establishes an alarming datum. Reuse, recycling and recovery must be always hierarchically considered to guarantee a sustainable management, as sketched in Figure 2.



Figure 2. Waste management sustainability, adapted from Sasitharan, et al., 2012.

In a holistic approach to guarantee sustainability, it turns crucial to monitor each phase of the building's life by Life Cycle Assessment (LCA) analysis. This is a worldwide-accepted method whose main outcomes are classified with a tree-model of impacts. Considering e.g.,

carbon dioxide (CO₂) emissions, the resulting effect is interpreted in terms of climate change which is part of the macro category of harmful effects on the ecosystem. In this way a methodological approach is available for evaluation and comparison of different technologies, even though some shortages are noticed; the main issues are linked with phases C (End-of-Life stage) and D (Benefits and Loads beyond the System Boundary) of LCA. First of all these stages are intrinsically affected by indelible uncertainties due to their non-immediate applications, as they are expected to be involved some decades later than building design phase. Moreover, given that stage D is nowadays not mandatory, low level of standardization and short amounts of data are available in literature (Delem & Wastiels, 2019).

Considering a sustainable building, an interesting solution lies in Timber-Concrete Composite (TCC) buildings, which optimize timber in an engineered perspective and reduce concrete volumes. In more general terms, engineered timber products like CLT, Glulam, LVL... are characterized by low values of carbon footprint thanks to a low-energy consumption production process (Khorsandnia, Valipour, Schänzlin, & Crews, 2016), reduced construction times compared to traditional RC buildings (Mirdad, Daneshvar, Joyce, & Chui, 2021), lower values of density-to-strength ratio and reduced thermal conductivity (Khorsandnia, Valipour, & Bradford, 2018); moreover the concept of disassembling simplicity is more readily enforceable with members made by timber-based products (Bertino, et al., 2021). In this way e.g., deconstructable connections facilitate dismantling and recycling processes, leading to lower waste amounts (Derikvand & Fink, 2021), which imply less material destined to landfilling, a reduction of dismantling times and preservation of natural resources (Hradil, et al., 2014). Almost all of the current studies on connectors accurately focus on their performances (Mirdad, Khan, & Chui, 2022), without explicitly considering the fact that they may hinder building deconstruction and saving of the greatest possible quantity of materials, so without carrying out environmental considerations.

The authors suggest an overview of today's practices concerning the End-Of-Life management of TCC buildings, with a focus on fastenings technology and their disassembling simplicity, range of expected scenarios (Quéheille, Ventura, & Saiyouri, 2022), convergence towards a cradle-to-cradle approach and waste minimization through reuse, recycling and recovery. Nowadays most widespread approaches are cradle-to-grave (from stage A to stage C of LCA) and no or limited alternative scenarios are generally considered (Allan & Phillips, 2021). Moreover, given the actual difficulty in finding literature where the issue of scenarios concerning End-Of-Life stage is assessed considering also disassembling simplicity, an innovative perspective towards a closed loop in terms of LCA is suggested.

The paper is organized as follows. Section 2 presents the method applied for literature selection. Results of such phase are presented in Section 3, identifying main strategies for stages C and D of LCA and detecting common disassembling procedures. Finally, Section 4 provides discussion of results and conclusions.

2 METHOD

The methodology adopted for this study consists of different steps sorted in this way:

- i. Identification of literature concerning End-Of-Life and Benefits and Loads beyond the System Boundary stages with focus on timber or timber-hybrid buildings. The reason of the emphasis on buildings with timber members lies in the fact that accurate scheduling of dismantling phase should be foreseen; otherwise, environmental advantages of using timber-based products is – at least partially – missed. This first step pursues the aim of creating a photograph of current considerations of such phases.
- ii. Analysis of widespread scenarios for End-Of-Life stage. The aim of this step is highlighting importance of accurate considerations taking into account uncertainties that naturally occur due to long terms and deficiency of real-cases data.
- iii. Detection of fastenings common technologies and analysis of disassembling procedures with identification of common patterns. Disassembling simplicity always guarantees the

most efficient solution in terms of sustainability; by observing Figure 2, it is clear that apart from comparisons of the solutions at the opposite ends, also consecutive approaches bring different levels of emissions. Comparing e.g., reuse and recycling, the second solution includes some manufacturing processes that generate Greenhouse Gases (GHG), while the first one does not need any working process.

- iv. Proposal of a flow chart in order to facilitate the transition from the current most widespread cradle-to-grave approach to the more forward-looking and sustainable cradle-to-cradle one, where the concepts defined in points ii. and iii. are assessed together.

The suggested method starts from a literature review in order to offer an innovative methodological approach, especially designed for timber-hybrid buildings.

3 RESULTS

Literature retrieved during the review is formerly subdivided in three categories, according to the topics addressed in the work. Considering the issues of End-of-Life scenarios and of disassembling simplicity, the following classes of papers are identified:

- a. Articles with focus on strategies for LCA's stages C and D and without consideration of connectors role in disassembling procedures. The following papers are identified: Quéheille, Ventura, & Saiyouri, 2022, Tam & Tam, 2006, Mirdad, Khan, & Chui, 2022, Jahan, Zhang, Bhuiyan, & Navaratnam, 2022, Nunes & Mahler, 2020, Younis & Doodoo, 2022, Lukić, Premrov, Passer, & Žegarac Leskovar, 2021, Bertino, et al., 2021, Hart & Pomponi, 2020, Niu, Rasi, Hughes, Halme, & Fink, 2021, Alsheyab, 2022, Condotta & Zatta, 2021, Hradil, et al., 2014, John & Buchanan, 2013. The most widespread scenarios are: 1) reuse of timber-based materials panels; 2) recycling of timber-based panels with production of microchips and production of new panels without usage of virgin resources; 3) energy recovery through incineration and reduction of natural gas use; 4) landfilling, which is substantially a non-development of stage D.
- b. Articles addressing the connectors role in disassembling procedures and not focusing on strategies for LCA's stages C and D. The following papers are identified: Derikvand & Fink, 2021, Khorsandnia, Valipour, & Bradford, 2018, Derikvand & Fink, 2020, Khorsandnia, Valipour, Schänzlin, & Crews, 2016. These studies present experimental and numerical results of different TCC connections, with comparisons between permanent and deconstructable solutions. In general terms, even though some quantitative predictable differences, failure modes are comparable according to some expedients as insertion of internal threads in the PVC plug (Derikvand & Fink, 2020) or different angles of connectors insertion and different timber joists thickness (Khorsandnia, Valipour, Schänzlin, & Crews, 2016).
- c. Articles dealing both with the connectors role in disassembling procedures and with strategies for LCA's stages C and D. The following papers are identified: Hafner, Ott, Bodemer, & Winter, 2014, Cristescu, et al., 2020, O'Grady, Minunno, Chong, & Morrison, 2021.

In class a. 14 papers are collected, while just 4 articles are included in b. class; on the other hand, 3 articles consider both topics of classes a. and b., populating class c. Considering aforementioned literature, Table 1 lists recurrent topics for classes a. and b., thus common best practices and widespread investigated issues are detected.

Considering subjects listed in Table 1, they clearly reflect the current approach that still struggles to reach a circular economy outline, as detected best-researched topics are strongly related to a two-track view; thereby a flow chart with an innovative methodological approach is suggested in. The role of this original perspective arises from the necessity to take into account together structural and environmental requirements, as nowadays – as confirmed by literature review outcomes – the trend is closer to a separated approach, with some serious practical and methodological shortcomings. The proposed tool is a methodological and theoretical support which recommends some best practices which mainly lead to structural and environmental advantages: disassembling simplicity significantly reduces dismantling times, with dropping of GWP gases emissions and greater reuse rates of e.g., timber-based products panels.

Table 1. Recurrent topics for two literature categories identified.

Strategies for LCA's stages C and D	Connectors role in disassembling procedures
<ul style="list-style-type: none"> • Development of different scenarios • Waste management: assessment accuracy as a function of the country's sensitivity to environmental issues • Overview of recycling technologies • Importance of comparative LCA • Rising importance of circular economy • Critical considerations of unavoidable uncertainties linked with broad temporal perspective 	<ul style="list-style-type: none"> • Comparative failure analysis of permanent and deconstructable shear connectors • Investigation of different alternatives with comparisons of waste at the End-of-Life stage of the building • Disassembling simplicity before and after load application • Identification of obstacles in disassembling procedures that hinder timber re-use

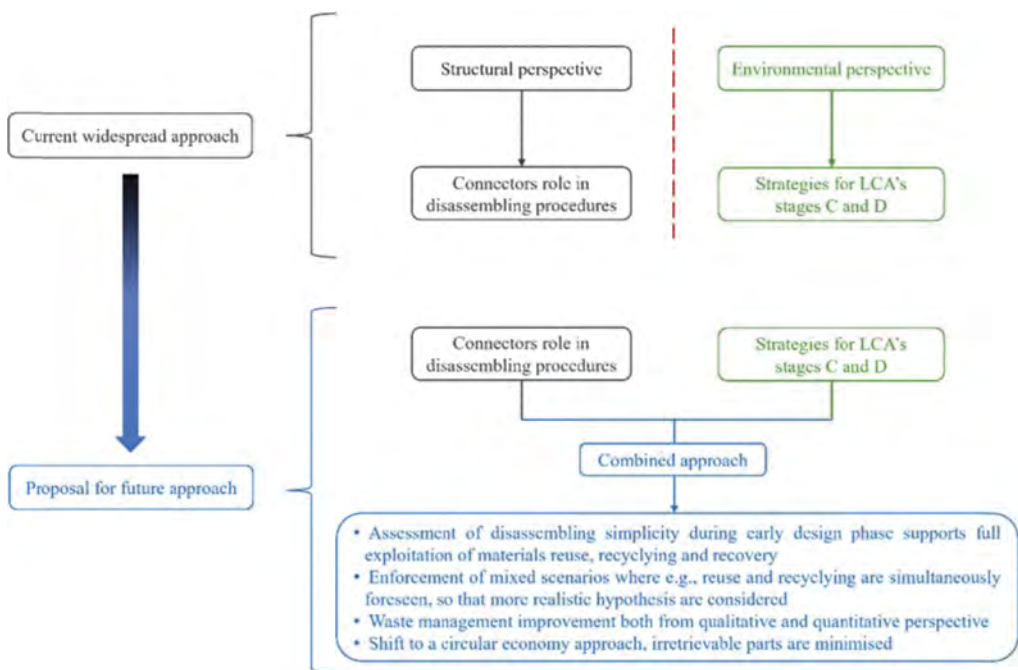


Figure 3. Flow chart with authors' original proposal concerning the combination of structural and environmental requirements.

One of the issues nowadays scarcely considered is the possibility to foresee different scenarios, as e.g., considering just a reuse hypothesis may be limiting, even if this is the most preferable from a sustainability perspective.

Unexpected events and damages experienced and encountered during the dismantling phase may hinder a “total reuse” scenario, so it is worth providing one or more alternative chances where damaged parts are not directly destined for landfilling, but recycling is scheduled, chips are produced, and virgin material is not used for panels manufacturing. This example represents how a combination of both structural and environmental points of view is extremely favourable, even though up-cycling is not always totally practicable. Moreover, this approach reduces wastes both from physical (materials) and organisational (times and costs) sides. An example of applicability of a mixed scenario is presented in Figure 4, where firstly reuse of suitable parts is carried out and recycling of portions probably damaged during dismantling is suggested.

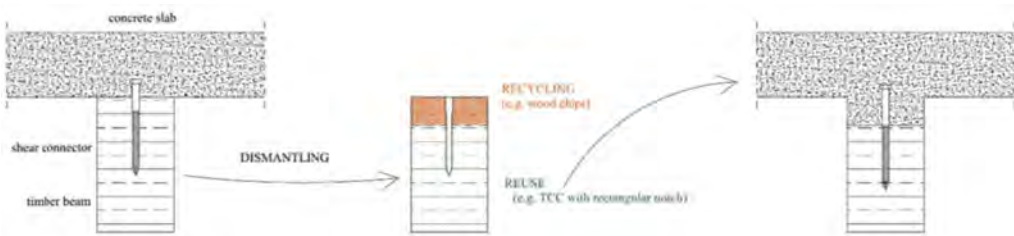


Figure 4. Example of reuse and recycle of a timber beam from a TCC slab.

4 DISCUSSION AND CONCLUSIONS

The literature review acknowledged that environmental and structural fields still suffer of a communication problem; the fact that environmental issues linked to the building sector have been realised in recent years, while the structural side is obviously the core of this field, produced some gaps that still need to be filled.

This work first proposes as a preliminary methodological research which findings are mainly:

- i. Identification of research shortcomings, mainly detected in the missing relationship between structural and environmental requirements.
- ii. Dismantling procedures are generally not accounted for during building design phase, so at the End-of-Life many uncertainties that increase times and costs should be faced.
- iii. Planning of building End-of-Life is becoming widespread from a theoretical point of view, such that a plurality of scenarios is always more frequently suggested.

In addition to such methodological observations, the paper proposes an innovative outlook concerning simultaneous consideration of structural and environmental requirements. First of all, the novelty introduced by the flow chart presented in is the concomitant mention to connectors and their role in building dismantling, stages C and D of LCA, sustainable waste management and consequently reasonings towards a circular economy approach. An example of such approach is reported in Figure 4, where a TCC solution is conceived according to a reuse and recycle scenario.

Finally, the proposed approach paves the way to future developments, where considering buildings impact on climate change is everyday more urgent; it is expected that building environmental standards will become more stringent, so a close link between structural and environmental requirements is no longer deferrable; this cooperation is intended as an optimization on both sides, with an accurate design of connectors in order to guarantee the maximum rate of material to be reused in a cradle-to-cradle approach.

REFERENCES

- Allan, K., & Phillips, A. R. 2021. Comparative cradle-to-grave life cycle assessment of low and mid-rise mass timber buildings with equivalent structural steel alternatives. *Sustainability*, 13(6). <https://doi.org/10.3390/su13063401>
- Alsheyab, M. A. T. 2022. Recycling of construction and demolition waste and its impact on climate change and sustainable development. *International Journal of Environmental Science and Technology*, 19(3): 2129–2138. <https://doi.org/10.1007/s13762-021-03217-1>
- Bertino, G., Kisser, J., Zeilinger, J., Langergraber, G., Fischer, T., & Österreicher, D. 2021. Fundamentals of building deconstruction as a circular economy strategy for the reuse of construction materials. *Applied Sciences*, 11(3). <https://doi.org/10.3390/app11030939>
- Condotta, M., & Zatta, E. 2021. Reuse of building elements in the architectural practice and the european regulatory context: Inconsistencies and possible improvements. *Journal of Cleaner Production*, 318. <https://doi.org/https://doi.org/10.1016/j.jclepro.2021.128413>
- Cristescu, C., Honfi, D., Sandberg, K., Sandin, Y., Shotton, E., Walsh, J., Cramer, M., Ridley-Ellis, D., Risse, M., Ivanica, R., Harte, A., Ui Chulain, C., De Arana-Fernandez, M., Llana, D. F., Iniguez-Gonzalez, G., Barbero, M. G., Nasiri, B., Hughes, M., & Krofl, Z. 2020. Design for deconstruction and reuse of timber structures – state of the art review. <https://doi.org/10.23699/bh1w-zn97>

- Delem, L., & Wastiels, L. 2019. The practical use of module D in a building case study: Assumptions, limitations and methodological issues. *IOP Conference Series: Earth and Environmental Science*, 323. <https://doi.org/10.1088/1755-1315/323/1/012048>
- Derikvand, M., & Fink, G. 2020. Deconstructable timber-concrete composite connectors. Paper presented at the Proceedings of the 63rd Society of Wood Science and Technology International Convention: 98–105. <https://www.scopus.com/inward/record.uri?eid=2-s2.0-85104395402&partnerID=40&md5=4dd41b3a7817c27f1df87debc7396454>
- Derikvand, M., & Fink, G. 2021. Deconstructable connector for TCC floors using self-tapping screws. *Journal of Building Engineering*, 42. <https://doi.org/https://doi.org/10.1016/j.jobbe.2021.102495>
- Hafner, A., Ott, S., Bodemer, E., & Winter, S. 2014. A case study for end of life reuse and recycling survey methodologies: The höllentalanger cottage. *Journal of Civil Engineering and Architecture*, 10: 1211–1220. <https://doi.org/10.17265/1934-7359/2014.10.001>
- Hart, J., & Pomponi, F. 2020. More timber in construction: Unanswered questions and future challenges. *Sustainability*, 12(8). <https://doi.org/10.3390/su12083473>
- Hradil, P., Talja, A., Wahlström, M., Huuhka, S., Lahdensivu, J., & Pikkuvirta, J. 2014. Re-use of structural elements; environmentally efficient recovery of building components. <https://doi.org/http://dx.doi.org/10.13140/2.1.1771.9363>
- Jahan, I., Zhang, G., Bhuiyan, M., & Navaratnam, S. 2022. Circular economy of construction and demolition wood Waste. A theoretical framework approach. *Sustainability*, 14(17). <https://doi.org/10.3390/su141710478>
- John, S., & Buchanan, A. 2013. Review of end-of-life options for structural timber buildings in new zealand and australia. University of Canterbury. Civil and Natural Resources Engineering. <http://hdl.handle.net/10092/10296>
- Khorsandnia, N., Valipour, H., Schänzlin, J., & Crews, K. 2016. Experimental investigations of deconstructable Timber–Concrete composite beams. *Journal of Structural Engineering*, 142(12). [https://doi.org/http://dx.doi.org/10.1061/\(ASCE\)ST.1943-541X.0001607](https://doi.org/http://dx.doi.org/10.1061/(ASCE)ST.1943-541X.0001607)
- Khorsandnia, N., Valipour, H., & Bradford, M. 2018. Deconstructable timber-concrete composite beams with panelised slabs: Finite element analysis. *Construction and Building Materials*, 163: 798–811. <https://doi.org/https://doi.org/10.1016/j.conbuildmat.2017.12.169>
- Lenton, T. M., Rockström, J., Gaffney, O., Rahmstorf, S., Richardson, K., Steffen, W., & Schellnhuber, H. J. 2019. Climate tipping points — too risky to bet against. *Nature*, 575: 592–595. <https://doi.org/10.1038/d41586-019-03595-0>
- Loss, C., Piazza, M., & Zandonini, R. 2016. Connections for steel–timber hybrid prefabricated buildings. part II: Innovative modular structures. *Construction and Building Materials*, 122: 796–808. <https://doi.org/10.1016/j.conbuildmat.2015.12.001>
- Lukić, I., Premrov, M., Passer, A., & Žegarac Leskovar, V. 2021. Embodied energy and GHG emissions of residential multi-storey timber buildings by height – A case with structural connectors and mechanical fasteners. *Energy and Buildings*, 252. <https://doi.org/https://doi.org/10.1016/j.enbuild.2021.111387>
- Markkanen, S., & Anger, A. 2019. Social impacts of climate change mitigation policies and their implications for inequality. *Climate Policy*, 19: 1–18. <https://doi.org/10.1080/14693062.2019.1596873>
- Mirdad, A. H., Daneshvar, H., Joyce, T., & Chui, Y. H. 2021. Sustainability design considerations for timber-concrete composite floor systems. *Advances in Civil Engineering*, 2021, 1–11. <https://doi.org/10.1155/2021/6688076>
- Mirdad, M. A., Khan, R., & Chui, Y. H. 2022. Analytical procedure for Timber–Concrete composite (TCC) system with mechanical connectors. *Buildings*, 12(7). <https://doi.org/10.3390/buildings12070885>
- Niu, Y., Rasi, K., Hughes, M., Halme, M., & Fink, G. 2021. Prolonging life cycles of construction materials and combating climate change by cascading: The case of reusing timber in finland. *Resources, Conservation and Recycling*, 170. <https://doi.org/https://doi.org/10.1016/j.resconrec.2021.105555>
- Nunes, K. R. A., & Mahler, C. F. 2020. Comparison of construction and demolition waste management between Brazil, European Union and USA. *Waste Manag Res*, 38(4): 415–422. <https://doi.org/10.1177/0734242X20902814>
- O’Grady, T. M., Minunno, R., Chong, H., & Morrison, G. M. 2021. Interconnections: An analysis of disassemblable building connection systems towards a circular economy. *Buildings*, 11(11). <https://doi.org/10.3390/buildings11110535>
- Quéhelle, E., Ventura, A., Saiyouri, N., & Taillandier, F. 2022. A life cycle assessment model of end-of-life scenarios for building deconstruction and waste management. *Journal of Cleaner Production*, 339. <https://doi.org/10.1016/j.jclepro.2022.130694> <https://www.sciencedirect.com/science/article/pii/S095965262200333X>
- Sasitharan, N., Ismail, A. R., Ade, A., Aftab, M., Latif, I., & Bux, Q. 2012. Issues on construction waste: The need for sustainable waste management. <https://doi.org/10.1109/CHUSER.2012.6504333>

- Solomon, S., Plattner, G., Knutti, R., & Friedlingstein, P. 2009. Irreversible climate change due to carbon dioxide emissions. *Environmental Sciences*, 106(6): 1704–1709. <https://doi.org/https://doi.org/10.1073/pnas.0812721106>
- Soong-Ki, K., Jongsoo, S., Soon-Il, A., Hyo-Jeong, K., Nari, I., Shang-Ping, X., Jong-Seong, K., & Sang-Wook, Y. 2022. Widespread irreversible changes in surface temperature and precipitation in response to CO₂ forcing. *Nature Climate Change*, 12(9): 834–840. <https://doi.org/10.1038/s41558-022-01452-z>
- Tam, V. W. Y., & Tam, C. M. 2006. A review on the viable technology for construction waste recycling. *Resources, Conservation and Recycling*, 47(3): 209–221. <https://doi.org/https://doi.org/10.1016/j.resconrec.2005.12.002>
- United Nations Environment Programme. 2021. Global status report for buildings and construction: Towards a zero-emission, efficient and resilient buildings and construction sector. <https://globalabc.org/resources/publications/2021-global-status-report-buildings-and-construction>
- Worrell, E., Price, L., Martin, N., Hendriks, C., & Ozawa-Meida, L. 2001. Carbon dioxide emission from the global cement industry. *Annual Review of Energy and the Environment*, 26: 303–29. <https://doi.org/10.1146/annurev.energy.26.1.303>
- Younis, A., & Doodoo, A. 2022. Cross-laminated timber for building construction: A life-cycle-assessment overview. *Journal of Building Engineering*, 52. <https://doi.org/10.1016/j.jobe.2022.104482>

GENERAL SESSIONS
Organizers: F. Biondini & D.M. Frangopol



Taylor & Francis

Taylor & Francis Group

<http://taylorandfrancis.com>

Shear strength assessment of FRP pre-tensioned concrete beams

A. Marí, E. Oller, J. Murcia-Delso, J.M. Bairán & N. Duarte

Universitat Politècnica de Catalunya, Barcelona, Spain

ABSTRACT: The low susceptibility to corrosion of fiber reinforced composite materials (FRP) has led to considering their use for prestressing reinforcement, as an alternative to steel. However, the effects of FRP fragility, low elastic modulus, and low bond with concrete, when compared to usual prestressing steel, must be accounted for in the design of structures. This paper presents a theoretical model for predicting the shear strength of FRP prestressed pre-tensioned concrete beams, extending a previously developed model (CCCM), to account for the properties of FRP as active reinforcement, and to capture reductions in shear strength caused by bond loss in the FRP tendons. The model has been validated by comparing the theoretical predictions with the results of shear tests available in the literature. Good accuracy has been obtained in predicting the shear capacity and also in identifying those cases where shear failure is associated to loss of anchorage bond.

1 INTRODUCTION

Fibre reinforced polymers might be a suitable alternative to conventional steel reinforcement to avoid corrosion of prestressing reinforcement, which is one of the main causes of deterioration of concrete structures. Although the use of FRP as passive reinforcement has been studied in depth during the last decades, the level of knowledge of FRP prestressed concrete structures is much lower, and there are few design guidelines or recommendations.

Up to date, few analytical models have been proposed to assess the ultimate shear strength of FRP prestressed beams. Kueres et al. (2020) and Küres (2019) extended a variable strut inclination model to determine the shear strength of non-prestressed FRP reinforced beams with shear reinforcement to consider the beneficial effects of prestressing on the shear strength. ACI440.4R-04 (ACI 2004), CSA S806-12 (CSA 2012) and JSCE (Astuhiko Machida 1997) consider that the ultimate strength is provided by the concrete, by the shear reinforcement and by the beneficial vertical component given by the prestressing force, with different provisions for each component.

The aim of this paper is to present an extension of the Compression Chord Capacity Model (CCCM) (Cladera et al. 2016), previously developed by the authors together with Cladera and Ribas from the University of Balearic Islands (UIB), to predict the shear strength of prestressed concrete beams with FRP tendons and FRP passive shear reinforcement. This model includes the effects of loss of anchorage of the FRP tendons. The performance of this model is assessed by comparing the theoretical predictions for the ultimate shear strength to the experimental ultimate values of 43 FRP pre-tensioned beams.

2 DESCRIPTION OF THE DEVELOPED SHEAR STRENGTH MODEL FOR CONCRETE MEMBERS PRESTRESSED WITH FRP TENDONS

2.1 *The Compression Chord Capacity Model for steel reinforced and prestressed concrete members*

It is generally accepted that the shear strength in a RC beam is provided by the contribution of the un-cracked concrete chord V_{cc} , the shear transferred along the cracks, V_{cw} , due to

aggregate interlock and the residual tensile forces transferred across the crack, the shear resisted directly by the transverse reinforcement, V_s , crossing the critical crack, and the shear resisted by the longitudinal reinforcement, V_l , so called dowel action. However, the relative contribution of each shear transfer action change along the loading process since, as the loading and the critical shear crack width increase, the shear transferred by aggregate interlock and the residual stresses crossing the crack tend to reduce as well as the dowel action. Then, shear stresses redistribute, increasing in the region of the uncracked compression chord; which becomes the most relevant shear transfer action until failure takes place under a biaxial stress state. To account for this experimental evidence, the Multi-action Shear Model (Mari et al. 2014) which included the four shear transfer actions, was simplified, into the Compression Chord Capacity Model (CCCM) (Cladera et al. 2016). In this model, the critical shear crack typically involves two branches, as shown in Figure 1. The opening of the first branch of the critical crack is assumed to be the result of a rotation around its tip. The compression zone above the tip prevents any meaningful contribution of shear slip along the crack interface, thus the contributions of aggregate interlock and dowel action are small, considered as constant values and incorporated into the contribution of the uncracked concrete chord.

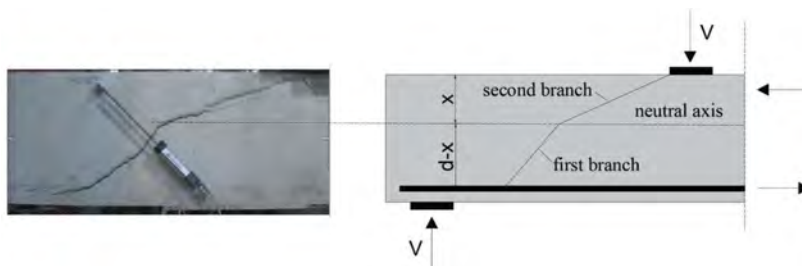


Figure 1. Assumed shape of the critical shear crack; internal forces equilibrium.

The most relevant assumptions of the CCCM are:

- The shear stresses are concentrated in the uncracked compression chord, concrete tensile strength is neglected and the normal compressive concrete stresses distribution is linear.
- The critical shear crack starts at a section where at shear failure, the bending moment reaches the cracking moment of the section. The horizontal projection of the critical shear crack is $0.85d$, based on experimental observations.
- The weakest section subjected to a combined shear-bending failure is considered to be located at the tip of the first branch of the critical crack, where it reaches the flexural neutral axis
- Failure is assumed to take place when the pair of principal stresses reach the Kupfer's Biaxial Failure Envelope (Kupfer & Gerstle 1973).
- For usual values of $ald=MI(V \cdot d)$, the critical point inside the compression chord, is located at a vertical distance from the neutral axis $z=0.425c$, being c the neutral axis depth.

The key equation to obtain the contribution of the concrete chord V_c , is the following:

$$V_c = \int_0^c \tau(z)b(z)dz = K_\tau \zeta b c \sigma_1 \sqrt{1 - \frac{\sigma_x + \sigma_y}{\sigma_1} + \frac{\sigma_x \sigma_y}{\sigma_1^2}} \quad (1)$$

where $\tau(z)$ = shear stress at a point of the uncracked chord at a distance z of the neutral axis; c = neutral axis depth given by Eq (11b) of Table 1; b = rectangular section width; σ_1 = principal tensile stress; σ_x = normal longitudinal stress due to bending; σ_y = normal vertical stress; K_τ = integration constant of value 0.682, and ζ = size effect factor given by Eq. (10) of Table 1.

Relating the normal stresses with the internal forces, and setting the equilibrium conditions Eq. (1) can be expressed as a function of the internal forces and the components of the shear

transfer actions, see Figure 2. Once solved, Eq (1) provides a solution in which the contribution V_c is almost a linear function of c/d , including the effects of the confining stresses in the concrete generated by the stirrups.

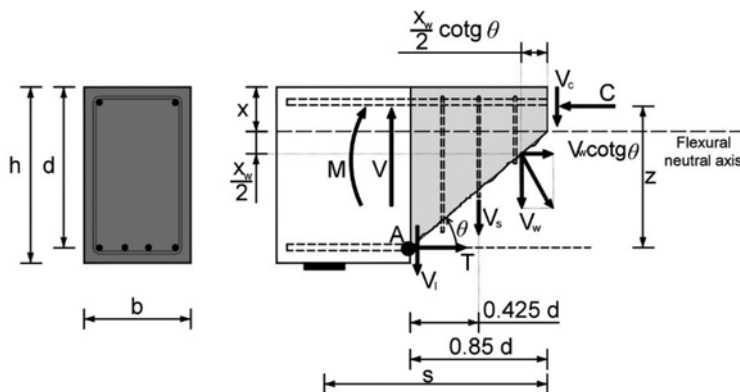


Figure 2. Internal forces and stress resultants considered in the shaded free body equilibrium.

The CCCM shear model, initially derived for reinforced concrete members with rectangular cross section, was extended to T sections, in which a non-negligible contribution of the flanges to the shear strength exists. This and other effects produced by the differences in section shape were incorporated by using an effective shear flanges width $b_{v,eff}$, as detailed in Cladera et al. (2016).

The CCCM was also extended to incorporate the effects of longitudinal prestressing of a beam in the shear strength (Marí et al. 2015). The increment of the neutral axis depth due to the axial compressive force, the reduction of inclination angle of the cracks and the increment of the cracking moment and, therefore, of the position of the critical shear crack were accounted for. For inclined tendons, the vertical component of the prestressing force $V_p = P \cdot \sin \alpha$, is deducted from the shear force due to external actions.

For simplicity reasons, the effects of confinement of the concrete chord due to stirrups, initially included into V_c , were incorporated into V_s . These changes and extensions gave place to the following expressions for the concrete and steel reinforcement contributions to the shear strength in reinforced and prestressed concrete beams with rectangular T and I section, in which, for design purposes, the tensile strength was replaced by an equivalent term in terms of the concrete compressive strength:

$$V_{cu} = 0.3 \zeta \frac{c}{d} f_{cd}^{2/3} b_{v,eff} d \leq V_{cu,min} = 0.25 \left(\zeta K_c + \frac{20}{d_0} \right) f_{cd}^{2/3} b_w d \quad (2)$$

$$V_{su} = 1.4 \frac{A_{sw}}{s} f_{yw} (d_s - x) \sin \alpha (\cot \theta + \cot \alpha) \quad (3)$$

where $K_c = cd \geq 0.2$; $d_0 = d \geq 100$ mm; and $b_{v,eff}$ = shear effective web width, which accounts for the flanges contribution, given by Eqs. (12a) and (12b) of Table 1. The neutral axis depth in prestressed concrete sections c is approached by a linear interpolation between the state with zero prestressing ($c = c_0$) and the decompression state ($c = h$), given by Eq (11a) in Table 1.

2.2 Extension of CCCM for beams reinforced with FRP bars as prestressing and transverse reinforcement, without anchorage loss of prestressing reinforcement

Due to the elastic-brittle nature of FRP, the contribution of the shear reinforcement to the shear strength must be modified. As no yielding occurs in FRP reinforcement, the stirrups behave elastically until failure and their individual stress is not constant along the shear crack, but it depends on their deformation. Therefore, the vertical shear force provided by the

stirrups (V_f) can be estimated using an average value of their stress along the critical crack (Oller et al. 2015), resulting for vertical stirrups ($\alpha=90^\circ$):

$$V_f = 0.85 \frac{A_{fw}}{s} \sigma_{fw,m} d_s (1 + \Delta V_{cu}) = 0.85 \rho_{fw} \cdot E_f \cdot \varepsilon_{fw,m} \cdot d_s (1 + \Delta V_{cu}) \quad (4)$$

where A_{fw}/s = area of FRP stirrups per unit length of the beam; $\sigma_{fw,m}$ = mean stress of the stirrups at shear failure, $\varepsilon_{fw,m}$ = mean strain of the stirrups at shear failure; E_f = modulus of elasticity of the FRP bars; and ΔV_{cu} = effect of confinement due to stirrups given by Eq. (14) of Table 1.

The mean strain of the FRP stirrups at failure ($\varepsilon_{fw,m}$) is obtained assuming a linear variation of the stirrups strains along the crack length (Figure 3), as recommended by Oller et al. (2015). The stirrup that fails is assumed to develop a strain of $0.45 \varepsilon_{fw,u}$, where the 0.45 factor is derived from the strength limit of bent FRP bars proposed in JSCE (Astuhiko Machida 1997) assuming a bent radius of 3 bar diameters and $\varepsilon_{fw,u}$ is the ultimate strain of the FRP stirrup. This results in an average stirrup strain along the shear crack of $0.225 \varepsilon_{fw,u}$. As a result, the shear force resisted by the stirrups in a length equal to the horizontal projection of the crack until the neutral axis, $0.85 d_s$, is:

$$V_f = 0.85 \rho_{fw} 0.225 \varepsilon_{fw,u} d_s (1 + \Delta V_{cu}) \approx 0.191 \rho_{fw} E_f \varepsilon_{fw,u} d_s (1 + \Delta V_{cu}) \quad (5)$$

Table 1 summarizes the proposed formulation for predicting the shear strength of prestressed concrete beams with or without FRP stirrups, assuming that no anchorage failure takes place.

Table 1. Proposed shear strength formulation.

Strength parameter	Equation	Eq. #
Shear strength	$V_{Rd} = V_{cu} + V_f \leq V_{Rd,max}$	(6)
Shear strength limit (diagonal compression)	$V_{Rd,max} = \alpha_{cw} b_w z v_{fd} \frac{\cot\theta + \cot\alpha}{1 + \cot^2\theta}$	(7)
Concrete contribution	$V_{cu} = 0.3 \zeta \frac{c}{d} K_{ad} f_{cd}^{\frac{3}{2}} b_{v,eff} d$	(8a)
	$V_{cu} \not\leq V_{cu,min} = 0.25 \left(\zeta K_c + \frac{20}{d_0} \right) f_{cd}^{2/3} b_w$	(8b)
Shear reinforcement contribution	$V_{frp} = 0.191 \rho_{fw} E_f \varepsilon_{fw,u} d_s (1 + \Delta V_{cu})$	(9)
Size and slenderness effect	$\zeta = \frac{2}{\sqrt{1 + \frac{d_0}{200}}} \left(\frac{d}{a} \right)^{0.2} \not\leq 0.45$; $d_0 = d \geq 100 \text{ mm}$	(10)
Relative neutral axis depth	$\frac{c}{d} = \frac{c_0}{d} + \left(\frac{h-c_0}{d} \right) \left(\frac{d}{h} \right) \frac{\sigma_{cp}}{\sigma_{cp} + f_{cm}}$; $\sigma_{cp} = \frac{P}{A_c}$; $A_c = \text{Section Area}$	(11a)
	where $\frac{c_0}{d} = \alpha_e \rho_l \left(-1 + \sqrt{1 + \frac{2}{\alpha_e \rho_l}} \right)$; $\rho_l = \rho_s + \rho_p$	(11b)
Effective flange width	if $c \leq h_f \rightarrow b_{v,eff} = b_v = b_w + 2h_f \leq b$	(12a)
	if $c > h_f \rightarrow b_{v,eff} \approx b_w + (b_v - b_w) \left(\frac{h_f}{c} \right)^{3/2}$	(12b)
Crack inclination	$\cot\theta = \frac{0.85d_s}{d_s - c} \leq 2.5$	(13)
Stirrup confinement factor	$\Delta v_{cu} = 0.5 \zeta \frac{c}{d} \left(1 + \frac{b}{b_v} \right) \frac{b_{v,eff}}{b}$	(14)

2.3 Shear strength considering anchorage loss of FRP prestressing bars (shear-bond failure)

As evidenced by experimental tests, premature shear failures may occur due to slip of the prestressing tendons at the critical shear crack. This type of failure occurs when the available bonded length between the critical shear crack and the free end of the beam (l_{av} in Figure 4a) is smaller than the anchorage length (l_{req}) required to develop the tensile force of the prestressing reinforcement at the cracked section. The shear-bond failure mode can be considered by computing l_{av} and l_{req} based on the position of the critical shear crack.

The available bonded length is equal to the sum of the beam offset (e) and the distance between the centre of the support and the critical crack (s_{cr}):

$$l_{av} = e + s_{cr} = e + \frac{M_{cr}}{V_u} \quad (15)$$

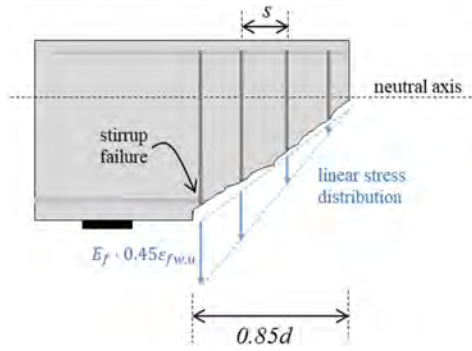


Figure 3. Idealized tensile stress distribution for stirrups crossing the critical shear crack.

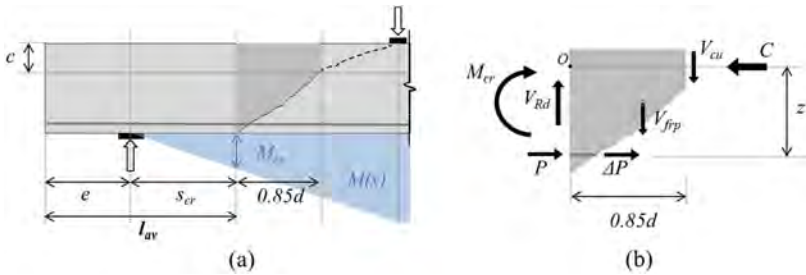


Figure 4. Available bonded length and forces acting in critical section.

The required anchorage length can be computed based on equilibrium of the tensile force and bond forces acting on the FRP reinforcement:

$$l_{req} = \frac{F_p}{u \cdot \tau_{max}} \quad (16)$$

where F_p = tensile force of prestressing reinforcement at the critical crack; τ_{max} = average bond strength along the anchorage length; and u = total perimeter of prestressing reinforcement. The value of F_p is obtained by studying moment equilibrium at the critical crack. Based on the moment equilibrium at point O of the free body diagram shown in Figure 4b:

$$F_p = \frac{M_{cr} + V_c \cdot \beta \cdot d + 0.5V_t \cdot \beta \cdot d}{z} = \frac{M_{cr} + V_c \cdot 0.85 \cdot d + 0.5V_t \cdot 0.425 \cdot d}{z} \quad (17)$$

Assuming no bond failure will occur, the shear strength and critical section can be initially estimated using the equations in Table 1. The available bonded length and required anchorage length are then calculated using Eqs. (15) and (16), respectively, given the position of the critical section. If $l_{av} \geq l_{req}$, the prestressing reinforcement is capable of developing the tension force at the shear crack (no bond loss) and the development of the full shear strength is confirmed. If $l_{av} < l_{req}$, a bond failure will occur prior to reaching the required tension force at this critical section, which implies that a reduced prestressing force (P_{red}) is acting at the instant of failure. The reduction of the prestressing force results in a smaller shear strength and a shorter distance to the critical section (s_{cr}). Bond failure has to occur for the value of P_{red} that satisfies $l_{av} = l_{req}$. The shear strength for bond loss ($V_{Rd,B}$) is obtained using the equations in Table 1 for $P = P_{red}$. The values of P_{red} and $V_{Rd,B}$ are obtained by iteration since both l_{av} and l_{req} depend nonlinearly on P .

3 VERIFICATION OF THE PROPOSED MODELS

A database of shear tests on FRP prestressed concrete beams reported in the literature has been compiled in order to assess the accuracy of the proposed model. The database includes 43 tests on FRP pre-tensioned beams, with and without FRP shear reinforcement. The tests correspond to studies conducted by Grace et al. (2015), Kueres et al. (2020), Nabipay & Svecova (2014), Park & Naaman (1999), Preinstorfer et al. (2021), and Whitehead & Ibell (2005). Table 2 provides the list of beam tests included in the database and their key geometrical and reinforcement characteristics. As shown, the beams present a variety of types of FRP as prestressing and shear reinforcement (aramid, glass, carbon, parafil), shear span ratios (a/d ranging from 1.5 to 6), prestressing stress levels (σ_{cp}/f_c ranging from about 2% to 20%) and amounts of transverse reinforcement (ρ_{fv} ranging from 0 to 1.5%).

The shear strength of the beams the database has been estimated using the model presented in Section 2. The shear-bond failure mode has been considered only for the nine beam tests by Kueres et al. (2020), since this was the only study providing bond strength data for the FRP bars and in which shear-bond failures were actually observed in beam tests. In addition to the shear failure modes associated to the proposed model, potential shear failures in flexurally uncracked regions have been considered following the equations of Eurocode 2 (European Committee for Standardization 1992).

Table 2 presents the results of the analytical predictions, including the predicted shear strength (V_{pred}) and failure mode, as well as the experimental-to-analytical strength ratios (V_{exp}/V_{pred}). Figure 5 compares the experimental and analytical strengths, and presents statistics of the V_{exp}/V_{pred} ratios. The average value of V_{exp}/V_{pred} is 1.08 and its coefficient of variation (C.V.) is 23%. Hence, the proposed model provides an overall good match with the experimental results. The level of accuracy of the model is similar to that obtained with the original CCCM formulation for steel reinforced and prestressed concrete presented in Cladera et al. (2016), which provided an average of 1.17 and a C.V. of 19%.

Regarding the shear-bond failure mode, specimens LV-1-1, LV-1-2, LV-2-1, LV-2-2 and LV-4 of Kueres et al. (2020) exhibited this type of failure during testing. This type of failure was correctly predicted for the first four specimens with an average value of the strength ratio of 1.03, as depicted from Table 2. The bond failure observed in the fifth specimen (LV-4) was correctly identified analytically, but the strength prediction is very close to the experimental value.

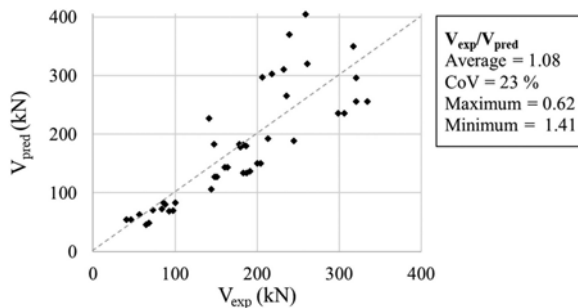


Figure 5. Experimental vs. predicted shear strengths.

4 CONCLUSIONS

A mechanically-based theoretical model to predict the shear strength of prestressed concrete beams with FRP reinforcement has been proposed. The model is an extension of the Compression Chord Capacity Model (CCCM) formulation, which has been modified to account for the brittle nature of FRP transverse reinforcement and potential bond loss of prestressing reinforcement. The accuracy of the model has been verified using a database of 43 shear tests from the literature. The analytical strength estimations are in good agreement with experimental data,

Table 2. Shear test database and analytical predictions.

Study	Test ID	Reinforcement					Analytical predictions		
		Prestressing	Shear	a/d	σ_{cp}/f_c (%)	ρ_{fw} (%)	V_{pred} (kN)	Failure mode*	V_{exp}/V_{pred}
Park & Naaman	C1	CFRP	-	2.4	6.5	0.00	68.8	CC	1.35
	C2	CFRP	-	2.4	6.2	0.00	70.1	CC	1.39
Whitehead & Ibell	3	AFRP	-	2.6	8.1	0.00	54.3	CC	0.75
	14	AFRP	-	2.6	8.1	0.00	54.3	CC	0.86
	15	AFRP	-	2.6	12.2	0.00	63.2	CC	0.89
	17	AFRP	-	2.6	17.5	0.00	71.1	CC	1.03
	19	AFRP	-	2.6	19.4	0.00	72.6	CC	1.15
	20	AFRP	Parafil	2.6	19.4	0.08	83.5	CC	1.03
	22	AFRP	Parafil	2.6	19.4	0.05	79.9	CC	1.10
	27	AFRP	Parafil	2.6	19.4	0.08	83.5	CC	1.20
Nabipay & Svecova	NS1-1.5	CFRP	-	1.5	6.8	0.00	255.8	U	1.25
	NS2-1.5	CFRP	-	1.5	6.8	0.00	255.8	U	1.31
	NS1-2.5	CFRP	-	2.5	6.5	0.00	133.9	CC	1.40
	NS2-2.5	CFRP	-	2.5	6.5	0.00	133.9	CC	1.37
	NS1-3.5	CFRP	-	3.6	6.9	0.00	127.4	CC	1.18
	NS2-3.5	CFRP	-	3.6	6.9	0.00	127.4	CC	1.16
	S1-1.5	CFRP	GFRP	1.5	5.7	0.21	296.2	CC	1.08
	S1-2.5	CFRP	GFRP	2.5	6.5	0.21	150.2	CC	1.36
	S2-2.5	CFRP	GFRP	2.5	6.5	0.21	150.2	CC	1.33
	S1-3.5	CFRP	GFRP	3.6	6.9	0.21	143.3	CC	1.14
	S2-3.5	CFRP	GFRP	3.6	6.9	0.21	143.3	CC	1.12
	NS1-U	CFRP	-	1.7	6.5	0.00	235.5	U	1.27
	NS2-U	CFRP	-	1.7	6.5	0.00	235.5	U	1.30
Grace et al.	C100-C6-3	CFRP	CFRP	3.0	7.5	1.00	320.0	CC	0.82
	C100-C6-4	CFRP	CFRP	4.0	7.5	1.00	310.2	CC	0.75
	C100-C6-5	CFRP	CFRP	5.0	7.5	1.00	303.1	CC	0.72
	C100-C6-6	CFRP	CFRP	6.0	7.5	1.00	297.4	CC	0.69
	C100-C4-3	CFRP	CFRP	3.0	7.5	1.50	369.7	DC	0.65
	C100-C8-3	CFRP	CFRP	3.0	7.5	0.75	265.2	CC	0.89
	C072-C4-3	CFRP	CFRP	3.0	5.4	1.50	404.1	DC	0.64
	C132-C4-3	CFRP	CFRP	3.0	9.9	1.50	349.3	DC	0.91
	C132-00-3	CFRP	-	3.0	9.9	0.00	106.2	CC	1.36
	LV-1-1**	CFRP	CFRP	2.5	2.4	0.19	137.4	B	1.39
Kueres et al.	LV-1-2**	CFRP	CFRP	2.5	2.1	0.19	182.0	B	1.01
	LV-2-1**	CFRP	CFRP	3.5	2.1	0.19	192.4	B	1.11
	LV-2-2**	CFRP	CFRP	3.5	2.1	0.19	227.4	B	0.62
	LV-3	CFRP	CFRP	3.5	4.6	0.19	178.2	CC	1.01
	LV-4**	CFRP	CFRP	3.0	5.5	0.19	182.9	CC	0.97
	LV-5	CFRP	CFRP	3.5	6.0	0.19	182.8	CC	0.81
	LV-6	CFRP	CFRP	3.0	5.2	0.19	180.0	CC	1.04
	LV-7	CFRP	CFRP	2.5	5.3	0.19	188.5	CC	1.30
Preinstorfer et al.	PT3.0S40	CFRP	CFRP	3.9	2.2	0.23	48.2	CC	1.41
	PT4.0S40	CFRP	CFRP	5.2	2.2	0.23	45.9	CC	1.41

* Predicted failure modes: failure of compression chord (CC), shear-bond (B), diagonal compression (DC), and shear failure in uncracked regions (U).

** Test specimens exhibiting shear-bond failures

providing an average experimental-to-predicted strength ratio of 1.08 and a coefficient of variation of 23%. The model has been also shown to identify shear-bond failures in four of the five cases in which this type of failure was reported experimentally. With the appropriate safety factors, the proposed shear strength formulation can be, therefore, employed to efficiently design and assess for shear resistance FRP-prestressed concrete elements.

ACKNOWLEDGEMENTS

The study presented in this paper was developed in the scope of research projects RTI2018-097314-B-C21 and PID2021-123701OB-C21 funded by the Spanish Ministry of Science and Innovation and the European Regional Development Funds (ERDF).

REFERENCES

- ACI 440 American concrete Institute, 2004. ACI 440.4R-04. Prestressing concrete structures with FRP tendons.
- Astuhiko Machida, C.T.U.S., 1997. Recommendations for design and construction for concrete structures using continuous fibre reinforcing materials, Japanese Society of Civil Engineers (JSCE) Concrete Engineering Series.
- Canadian Standards Association (CSA), 2012. Design and Construction of Building structures with Fibre-Reinforced Polymer, CAN/CSA S806-12., Canadian Standards Association.
- Cladera, A., Marí, A.R., Bairán, J.M.J.M., Ribas, C., Oller, E., Duarte, N., 2016. The compression chord capacity model for the shear design and assessment of reinforced and prestressed concrete beams. *Struct. Concr.* 17, 1017–1032. <https://doi.org/10.1002/suco.201500214>
- European Committee for Standardization, 1992. Eurocode 2: Design of concrete structures. Brussels, Belgium.
- Grace, N.F., Rout, S.K., Ushijima, K., Bebawy, M., 2015. Performance of Carbon-Fiber-Reinforced Polymer Stirrups in Prestressed-Decked Bulb T-Beams. *J. Compos. Constr.* 19. [https://doi.org/10.1061/\(asce\)cc.1943-5614.0000524](https://doi.org/10.1061/(asce)cc.1943-5614.0000524)
- Japan Society of Civil Engineers, 1997. Recommendations for design and construction of concrete structures using continuous fiber reinforcing materials., Concrete E. ed. Japan.
- Kueres, S., Will, N., Hegger, J., 2020. Shear strength of prestressed FRP reinforced concrete beams with shear reinforcement. *Eng. Struct.* 206. <https://doi.org/10.1016/j.engstruct.2019.110088>
- Kupfer, H.B., Gerstle, K.H., 1973. Behavior of concrete under biaxial stresses. *J. Eng. Mech. Div.* 99, 853–866.
- Küres, S., 2019. Analysis and Design of Concrete Beams with Pre-tensioned CFRP Reinforcement. Dr. Diss. RWTH Aachen.
- Marí, A., Bairán, J.M., Cladera, A., Oller, E., 2015. Shear design and assessment of reinforced and prestressed concrete beams based on a mechanical model. *J. Struct. Eng.* In Review.
- Marí, A., Bairán, J.M., Cladera, A., Oller, E., Ribas, C., 2014. Shear-flexural strength mechanical model for the design and assessment of reinforced concrete beams. *Struct. Infrastruct. Eng.* DOI: 10.10. <https://doi.org/10.1080/15732479.2014.964735>
- Nabipay, P., Svecova, D., 2014. Shear Behavior of CFRP Prestressed Concrete T-Beams. *J. Compos. Constr.* 18. [https://doi.org/10.1061/\(asce\)cc.1943-5614.0000450](https://doi.org/10.1061/(asce)cc.1943-5614.0000450)
- Oller, E., Marí, A., Bairán, J.M.J.M., Cladera, A., 2015. Shear design of reinforced concrete beams with FRP longitudinal and transverse reinforcement. *Compos. Part B Eng.* 74, 104–122. <https://doi.org/10.1016/j.compositesb.2014.12.031>
- Park, S.Y., Naaman, A.E., 1999. Shear behavior of concrete beams prestressed with FRP tendons. *PCI J.* 44, 74–85. <https://doi.org/10.15554/pcij.01011999.74.85>
- Preinstorfer, P., Huber, P., Huber, T., Kromoser, B., Kollegger, J., 2021. Experimental investigation and analytical modelling of shear strength of thin walled textile-reinforced UHPC beams. *Eng. Struct.* 231. <https://doi.org/10.1016/j.engstruct.2020.111735>
- Whitehead, P.A., Ibell, T.J., 2005. Novel shear reinforcement for fiber-reinforced polymer-reinforced and prestressed concrete. *ACI Struct. J.* 102, 286–294. <https://doi.org/10.14359/14280>

Life-cycle cost of CFRP and steel prestressed concrete elements

J.M. Bairán, J. Murcia-Delso, N. Duarte, E. Oller & A. Mari

*Department of Civil and Environmental Engineering, Universitat Politècnica de Catalunya
(UPC - BarcelonaTech), Barcelona, Spain*

ABSTRACT: Carbon steel reinforcement is vulnerable to corrosion, degrading the structure with time, and has large economic implications for aging infrastructures. CFRP is an alternative in reinforced and prestressed concrete, not prone to corrosion. However, its cost is considerably larger than steel, and its mechanical properties enforce different design criteria. Therefore, it is not evident when CFRP is a convenient solution. In this paper, benefits of CFRP reinforcement are investigated in LCC context. An archetype prestressed-concrete bridge is designed with the two types of reinforcement. Two environment scenarios are analyzed, representative of current and increased chloride concentration in coastal regions. The costs investigated include routine inspections, major repairs and users' affectation. Although requiring less maintenance cost, the design with CFRP has a higher LCC than the steel-reinforced alternative, in the current chloride scenario close to the coast. However, in scenarios of larger chloride exposure, the CFRP solution may be more competitive.

1 INTRODUCTION

Carbon steel reinforced concrete elements may suffer corrosion when located in aggressive environments. As the share of built infrastructures in most countries ages, the economic and social implications of corroded structures have become evident. It has been estimated that worldwide cost of corrosion is in the range of 2.5 trillion dollars per year. According to Pacheco et al (2018), the national budget for maintenance and rehabilitation in many countries has begun to exceed that for new constructions.

In order to mitigate this durability problem, crack limitations, minimum concrete class and cover are required, which frequently may control the design of some elements. Nevertheless, durability requirements have evolved in the last decades, so many existing structures do not comply current standards. Moreover, corrosion has also been observed in some relatively recently built structures.

An alternative approach consists of replacing traditional carbon steel reinforcement with non-corrosive reinforcement, such as stainless-steel reinforcement or fiber reinforced polymers (FRP) reinforcements, either as non-prestressed or prestressed reinforcements. Nevertheless, the mechanical behavior of FRP reinforcement differs greatly from traditional one, being the most relevant characteristics the lower stiffness and brittle failure mode, when compared with carbon-based steel. Therefore, different design strategies are needed. Moreover, the current cost of these alternative reinforcements significantly exceeds that of carbon steel, which has prevented a more extended use of them.

FRP prestressing tendons are typically produced with one of four basic fibers: aramid, carbon, basalt, and glass. Among them, the carbon FRP (CFRP) shows higher strength and elastic modulus than the rest, which suggests possible advantages in terms of stiffness and stress increment at failure.

In order to provide detailed insight of the actual benefits of using CFRP as alternative prestressing reinforcement, an analysis comprising the life cycle cost (LCC) of the structure is carried out in this study. The analysis will take into consideration the cost and durability dimensions of the problem. An archetype prestressed concrete bridge located in a coastal environment will be considered as case study.

Two alternative design solutions will be developed and compared, one with conventional carbon steel and another using CFRP as active and passive reinforcement tendons. Different

corrosion-related requirements will be adjusted to each case, in order to seize the advantages of each reinforcement material. In particular, concrete cover, and allowable crack width will be adjusted as appropriate, while designed for a nominal service life of 100 years. The life-cycle cost of the structure will be computed, considering initial costs and typical maintenance operations during the nominal life. A comparative analysis will be carried out in terms of the LCC in two different environmental scenarios.

2 ARCHETYPE STRUCTURE

A 20 m span bridge deck, consisting of prestressed concrete girders is taken as an archetype structure for this study. This type of bridge is one of the most extended solutions in most countries; hence, it is considered as representative for a big number of situations. Figure 1 shows the cross-section of the deck, showing the general dimensions and the number of girders and general data of the concrete girder. The girder will be prestressed with pre-tensioned strands. It is assumed that the complete bridge has 3 identical simply supported spans of 20 m, with identical deck configuration.

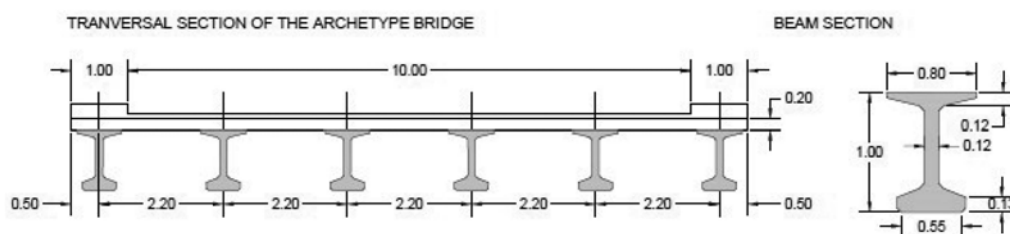


Figure 1. Bridge deck cross-section and concrete girder cross-section general data.

The structure is considered to be located in a coastal environment, at less than 5 km from the Mediterranean coast of Spain. The permanent loads acting on the structure are its self-weight, additional dead load of 3 kN/m^2 , accounting for pavement, rails, and sidewalks. The variable loads considered in the design are a load of 4 kN/m^2 , distributed in the worst position, and a moving vehicle load of 600 kN.

Two alternative designs were carried out; namely, one using carbon steel (CS) tendons and another with CFRP tendons. Passive reinforcements are also made of CS and CFRP, respectively. The minimum cover for the CS prestressed structure was selected as 35 mm, based on Spanish specifications (EHE-08) for this type of environment. This cover must be guaranteed in construction; hence, a bigger specified cover of 40 mm is used, which includes the construction tolerance. The latter is used for the design of the reinforcement, was 40 mm. In addition, the prestressing is designed to guarantee no-decompression under the frequent load combination.

As CFRP tendons are not affected by corrosion, cover and maximum crack width are not controlled by durability requirements. However, concrete cover affects the bond performance of the strands. Therefore, a concrete cover of 10 mm was considered in design, according to the Eurocode 2 draft of version of 2022 (CEN, 2022). The maximum crack width considered in design was 0.4 mm under frequent load combination, defined for aesthetic reasons. Table 1 summarizes the material properties considered in both designs.

FRP reinforcement exhibits linear elastic stress-strain behavior up to failure, with smaller elastic modulus than steel. Limited element ductility of the element can be achieved only through the concrete response, when failure is controlled by concrete crushing rather than reinforcement tension, i.e. over-reinforced design. The smaller elastic modulus is potentially beneficial for reduction of prestress losses, moreover typical relaxation loss of pretension force is also smaller. Particularly, in the case of CFRP, relaxation may be less than 50% of that of steel tendons, ACI 440 (2011), Oller et al (2022), Rossini (2019).

Although FRP is not affected by corrosion degradation, different phenomena degrade its mechanical capacity in the long-term. On one hand, creep-rupture is the tensile fracture of the

Table 1. Material properties considered in design.

Parameter	Steel	CFRP
Strand area (mm ²)	140	140
Wedge penetration (mm)	5	5
Characteristic strength: f_{pk} (MPa)	1860	2137
Elastic Modulus: E (GPa)	190	126

material subjected to sustained high stresses. Typical residual strength at long-term ranges between 30% and 80% of the short-term strength, with smaller values for glass fibers, intermediate values for aramid fibers, and larger sustained resistance in the case of carbon fibers (CFRP). This phenomenon limits the maximum permanent load of the FRP which, in turn, will require lower pretension ratios of the material strength compared with steel. The larger resistance to sustained loads of the CFRP suggests it as more adequate for prestressing applications.

On the other hand, strength is also degraded under temperature produced by solar radiation and aging. In general, guidelines and codes provide reduction factors for the strength and allowable sustained load to consider in design, e.g. ACI-440 (2011), Model Code 2010 (fib, 2013), Eurocode 2 (CEN, 2022). However, it should be noticed that some differences still exist between them when implementing the strength reduction factors and the design safety factors. In this study, the design of the CFRP bridge was carried out following the informative annexes of the latest available draft Eurocode 2 (CEN, 2022).

Two alternative designs were carried out considering steel and CFRP reinforcements, considering ultimate limit state (ULS) of normal and tangential forces. The service limit states (SLS) were considered, including different crack limitations for steel and CFRP reinforcement alternatives, as described above. In both cases, the provided longitudinal reinforcement was controlled by ULS conditions rather than SLS.

Table 2. Comparison of designs with alternative reinforcements.

	Steel	CFRP
Number of strands	18	29
Passive long. reinforcement	4Ø2	-
Transversal reinforcement	1Ø10 stirrups/140 mm	1Ø15 stirrups/300 mm
Cost per girder	5,000 €	13,000 €
Normalized cost to reference girder	1	2.6

Table 2 summarizes the main differences of the two designs, as well as the estimated cost per girder. It is noticed that the CFRP alternative exceeds the cost of the steel girder by a factor of 2.6. This result is consistent with similar costs analyzed in other studies, such as Balafas and Burgoyne (2003). In the following, all costs will be presented normalized to the cost of the steel reinforced alternative.

3 LIFE CYCLE COST

Life cycle cost (LCC) considers the costs related to the construction (CC), inspections (CI), maintenance repairs (CM), and failure cost (CD) during the design life span of the structure, as described in Equation (1). CC is considered to occur at initiation of the service life, which is taken as reference. The remaining costs occur at different time instants during the analyzed time. Therefore, they are adjusted the present value (PV), by multiplying the cost expended in time t by the factor $PV(t)$ defined in Equation (2). It is considered that the decommission cost at the end of life is the same for the two alternative designs. Hence, it has not been included in Equation (1), as the goal of the analysis is comparing the economical differences between them.

$$LCC(t) = CC + CI + CM + CD \quad (1)$$

$$PV(t) = (1 + s)^{-t} \quad (2)$$

In Equation (2), s is the discount rate of money and t is the time, in years, where the cost takes place. The discount rate accounts for the opportunity cost and inflation rate. The choice of the discount rate s depends on the expected economical conditions, capital risk of the facility owner or investor. In previously LCC analyzes conducted on medium length bridge structures s has ranged between 3% in Grace et al (2012), while Hasan et al (2019) used a discount rate of 2%. In this study, the discount rate is taken as the average of these values, $s=2.5\%$.

Inspection costs (CI) accounts for routine inspections to assess the condition of the structure. The associated costs include the displacement of inspection engineers, minor operations. The cost of each inspection is estimated as $0.005CC$, similarly to the adopted value in Grace et al (2012). The previous costs are associated to direct agency expenditure. However, maintenance operations generate additional costs to the users of the infrastructure due to the affectation of the service, which have not always been estimated in previous studies. The present study will consider the cost of the infrastructure users (UC) during maintenance, inspections and repair works.

The users' cost is estimated using the equations proposed in Ehlen (1999). This cost consists of three contributions; namely, the increment of drivers' delay (DD) cost (Equation 3), vehicle operation (VO) cost (Equation 4), and accident increment (AI) cost (Equation 5) during the affectation of the road.

$$DD = \left(\frac{L}{S_a} - \frac{L}{S_n} \right) \times ADT \times N \times w \quad (3)$$

$$VO = \left(\frac{L}{S_a} - \frac{L}{S_n} \right) \times ADT \times N \times r \quad (4)$$

$$AI = L \times ADT \times (A_a - A_n) \times c_a \quad (5)$$

Table 3. Parameters for estimating users costs during inspections and major repairs.

Parameter	Symbol	Units	Inspection	Major repair
Length affected road	L	km	2	5
Average daily traffic	ADT	cars/day	30000	30000
Duration of works	N	days	1	90
Normal speed	S_n	km/h	120	120
Speed during works	S_a	km/h	80	40
Normal accident rate	A_n	1/(veh*km)	1.50E-06	1.50E-06
Accident rate during works	A_a	1/(veh*km)	2.00E-06	2.00E-06
Drivers hourly time value	w	€/h	10	10
Vehicle hourly time cost	r	€/h	8	8
Cost per accident	c_a	€	100000	100000
User cost	UC	€	7500	4725000
Normalized user cost per girder*	UC	CC	0.042	26.25

*considering 18 girders in the bridge

In Equation (3) through (5), L is the road length affected by maintenance works. S_n and S_a are the traffic speed at normal situation and affected by the works, respectively. ADT is the average traffic rate, in vehicles per day. N is the number of days during the affection. A_n and A_a are accidents rate of the road in normal situation and during the affectations, in terms of accidents per number of vehicles in the road and km. w is the drivers' hourly value, r is the vehicle hourly cost, c_a is the cost per accident. The values considered for estimating UC are summarized in Table 3, for routine inspections and major repairs.

The total inspection cost is computed as indicated in Equation (6), where c_i is the cost of a routine individual inspection (0.005CC) in time t_i , and UC is the user cost. Routine inspections are planned at a frequency of 5 years.

Maintenance cost (CM) are computed according to Equation (7), based on the formula used in Hasan et al (2019), where the users' cost has been added. In Equation (7), t_m is the time when a major repair is made, associated to chloride induced corrosion deterioration detected during routine inspections. This repair may consist on the activities associated with the removal of cover, reinforcement protection, and restitution of concrete cover, or the substitution of a heavily deteriorated girder, as well as the auxiliary means needed for the works. The relative cost of a unit major repair (c_r) is estimated as 5CC. UC is the users' cost during a major repair, as shown in Table 3. $P_{sf}(t_m)$ is the probability of the durability limit state failure in time t_m .

The cost of ultimate limit state failure is computed according to Equation (8). The term c_d in Equation (8) includes the cost of bridge replacement, casualties and injuries cost, functional disruption, and environmental, social, cultural and historical cost. It is assumed that $c_d=10CC$, like in Hasan et al (2019). $P_{uf}(t)$ is the probability of failure of the ultimate limit state in time t . Differently from the inspection and maintenance costs, which are expended only during inspections and maintenance, the probable CD cost during each year is computed in the LCC.

$$C_I(t) = \sum_{t_i} PV(t_i)(c_i + UC) \quad (6)$$

$$C_M(t) = \sum_{t_m} PV(t_m)(c_r + UC)P_{sf}(t_m) \quad (7)$$

$$C_D(t) = \sum_t PV(t) c_d P_{uf}(t) \quad (8)$$

4 ANALYSIS SCENARIOS

As described in the previous section, LCC includes the initial construction costs and the maintenance costs associated to regular inspections, planned every 5 years, and major repairs. Major repairs are considered to be triggered by damage already detected during the regular inspections, e.g. steel depassivation, surface cracks, etc. In order to determine the time when a major repair will be carried out, degradation of the nominal reliability to durability limit state (DLS) is simulated.

As depicted in Figure 2, the nominal reliability is considered to be constant until the critical chloride concentration reaches the reinforcement layer. For prestressed steel reinforcement, the critical chloride concentration is taken as 0.3% of the weight of cement, based on EHE-08 (2008). This occurs in the initiation time (t_i), which can be computed from Equation (9), where K_{cl} is the chloride penetration coefficient of the concrete, and d is the reinforcement cover. After this moment, the steel process starts at a corrosion velocity (v_{cor}) that depends on the environmental conditions and chloride concentration. To estimate the rate of DLS reliability, it is considered that the initial reliability is the nominal code annual value (3.0) and decays to a minimum (1.0) when the corrosion produces a pit of 0.01 mm. The ULS reliability is assumed to decay at the same average rate.

$$t_i = \left(\frac{d}{K_{cl}} \right)^2 \quad (9)$$

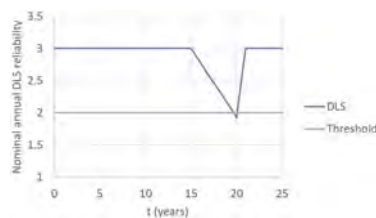


Figure 2. Degradation of annual reliability to DLS and threshold triggering major repairs.

In the years in which regular inspections are made, the DLS reliability is compared with a threshold value and, if detected to be lower than the threshold, a major repair is computed that year. It is assumed that, after each major repair, the durability reliability is completely reestablished, and the process starts again. Notice that, with this maintenance strategy, it is possible that the threshold is crossed in between inspections, but will not be detected until the next inspection. The amount of damage and, consequently, probability of ULS failure increase between inspections.

In the described maintenance protocol, major repairs and probabilities of failure depend on the concentration of chloride in the environment that causes corrosion. In this study, two different scenarios are investigated, summarized in Table 4. Scenario 1 corresponds to the surface chloride concentration of 0.14% of the weight of concrete, as considered for this design exposure class in EHE-08 (2008). This value is of similar to the one reported in Val and Stewart (2003) for atmospheric chlorides at 1 km from the coast. This scenario is considered representative of the current environments. Nevertheless, chloride concentration in air may increase in the future, due to increase of sea level and wind speeds produced by climate change. Therefore, a second scenario is also investigated with a more severe surface chloride concentration of 0.25%. Table 4 also summarized the corrosion velocity considered for each scenario, and the corrosion initiation and propagation times.

Table 4. Chloride exposure scenarios.

Scenario	Cs (% concrete)	v_{cor} ($\mu\text{m}/\text{year}$)	t_i (years)	t_p (years)
1	0.14	20	15	8.5
2	0.25	25	7.7	6.8

Based on the previous scenarios, the DLS reliability degradation are plotted in Figures 3a and 3b, for scenarios 1 and 2, respectively. As CFRP is not affected by chloride corrosion, a minor degradation rate is considered for this reinforcement, as shown in Figure 3c, which is the same for both scenarios. The figure also shows the threshold crossing events for all cases, which trigger a major repair event. Notice the first threshold crossing in scenario 2 occurs 5 years earlier than in scenario 1. Similarly, 4 threshold crossings take place in scenario 1, compared to 6 in scenario 2. No threshold crossing occurs in the CFRP design alternative.

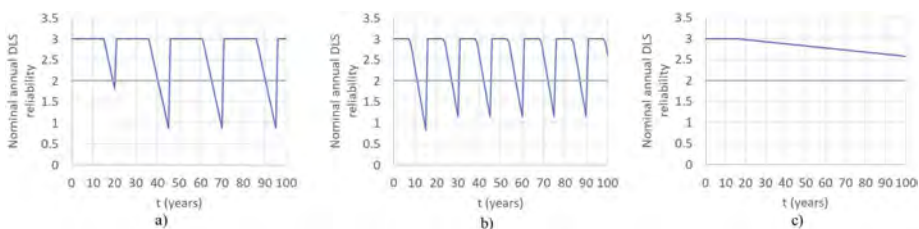


Figure 3. Degradation of nominal DLS annual reliability and threshold triggering major repair. a) Design with steel tendons in scenario 1, b) Design with steel tendons in scenario 2, c) Design with CFRP tendons.

Figure 4 shows the maintenance calendar for each designed structure. The routine inspections, scheduled at a frequency of 5 years, are applied to all three alternatives during the whole service life. Major repairs only take place in designs with steel tendons, as described above.

5 RESULTS

Figure 5 compares the LCC of the steel and CFRP alternative designs under scenario 1 (Figures 5a and 5c) and scenario 2 (Figures 5b and 5d). Curves in the upper row (Figures 5a and 5b) include the users' costs (UC), while this cost was excluded in the bottom row (Figures 5c and 5d) for comparison purpose. All costs are normalized to the CC of the steel tendons alternative.

Although CFRP has an initial cost of 2.6CC, its LCC shows a moderate increment in time, as no major repair was considered. The maximum LCC of CFRP after 100 years is estimated

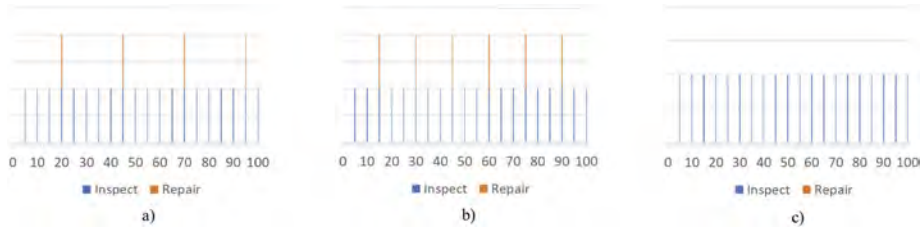


Figure 4. Maintenance calendar showing inspections, and major repairs. a) Design with steel tendons in scenario 1, b) Design with steel tendons in scenario 2, c) Design with CFRP tendons.

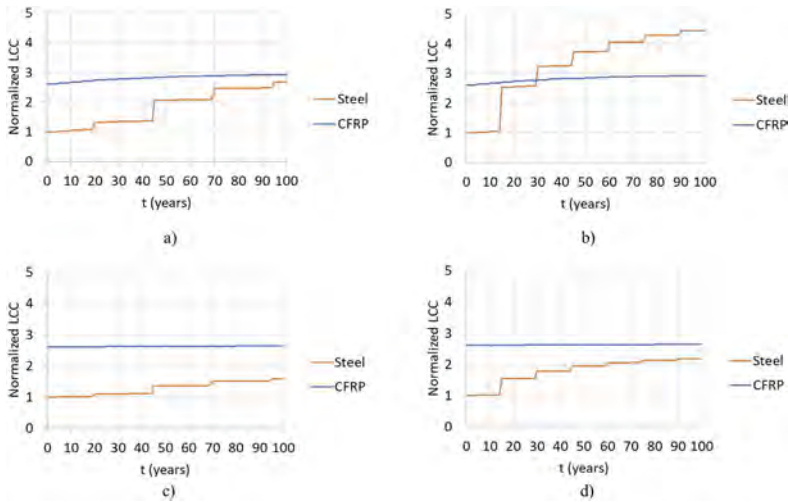


Figure 5. Compared LCC for designs with steel and CFRP tendons. a) scenario 1 including UC, b) scenario 2 including UC, c) scenario 1 without UC, d) scenario 2 without UC.

Table 5. LCC and payback time for each scenario.

Scenario	Users cost	LCC steel (CC)	LCC CFRP (CC)	Payback time(years)
1	included	2.68	2.93	>100
2	included	4.44	2.93	29
1	not included	1.58	2.64	>100
2	not included	2.18	2.64	>100

as 2.93 CC. On the other hand, LCC of steel tendons alternative steel increases up to 2.68 in scenario 1, and 4.44 in scenario 2, when the UC are accounted for. Comparing the top and bottom rows, it is evidenced that the UC contributes with 40% to 50% of the total LCC.

Table 5 compares the computed LCC for the different designs, in the two scenarios. The table also shows the payback time of CFRP alternative, considered as the time needed to recover the initially larger investment of the CFRP reinforcement. Notice, that in the scenario 1, the LCC of the steel alternative does not exceed that of CFRP in scenario 1 during the analyzed time. Therefore, the payback time is reported as larger than 100 years. As the payback time is larger than the period of interest, it is concluded that the steel alternative should be preferred in this scenario.

On the other hand, scenario 2 represents a more aggressive environment, which triggers more major repair works. Even more relevant is the earlier need for major repairs in scenario 2, which implies a larger PV of these works. Therefore, the payback time in scenario 2 occurs on year 29. Conversely, if UC are not accounted for, no payback time is found within the period of analysis.

6 CONCLUSIONS

The LCC of a medium-span prestressed concrete bridge girder was analyzed in a coastal environment. Two alternative designs were investigated, one with carbon steel tendons and passive reinforcement, representative of the majority of current applications. The second alternative used CFRP tendons and transverse reinforcement. In addition to the construction cost, the life cycle costs of inspections, major repairs, users cost, and ultimate failure were valued. The maintenance strategy consisted of routine inspections, expected in the maintenance plan, throughout the life span. Major repair was considered triggered by a degradation threshold. Two environmental scenarios were simulated, representative of surface chloride concentration in current codes (scenario 1), and a potential increment due to climate change (scenario 2). After this analysis, the following main conclusions can be drawn.

The current cost of CFRP reinforcement makes its initial construction cost in the order of 2.6 times the construction cost of the girder with steel tendons. Due to this initial cost, a payback time is not reached in the scenario 1 during the design service life of 100 years. Scenario 2, with the higher chloride surface concentration, showed a payback time within of 29 years, when the cost of the affectation to the users is valued. Although this value lies within the service life of the structure, it might be large from a financial point of view of road managers. An improved design of the concrete steel structure could show a better performance in the LCC, at the expense of a moderate increment of the CC.

The cost of the affectation to the users during maintenance operations has relevant share of the total LCC, particularly, during the major repairs. Neglecting these costs will underestimate the real cost of the maintenance. In this case, no payback time is found in neither of the 2 scenarios analyzed.

ACKNOWLEDGEMENTS

This study was developed in the scope of research projects PID2021-123701OB-C21, funded by MCIN/ AEI/10.13039/501100011033 and European Regional Development Funds (ERDF) “A way to make Europe”, and TED2021-130272B-C21 funded by MCIN/ AEI/ 10.13039/501100011033 “European Union NextGenerationEU/PRTR”.

REFERENCES

- ACI 440.4R-04, 2011, “*Prestressing concrete structures with FRP tendons (Reapproved 2011)*”, American Concrete Institute.
- Balafas, I., Burgoyne, C.J., 2003, “Optimal cost design for beams prestressed with FRP tendons”, *FRPRCS-6*, K. H. Tang (Ed.), Singapore, July, 1391–1400.
- CEN, 2022, “*Eurocode 2: Design of concrete structures — Part 1-1: General rules — Rules for buildings, bridges and civil engineering structures*”, FprEN 1992-1-1 (code draft).
- EHE-08, 2008, “*Instrucción de hormigón estructural*”, Ministerio de Fomento, Spain
- Ehlen, M., 1999, “Life-cycle cost of fibre-reinforced-polymer bridge decks”, *ASCE-J. of Materials in Civil Eng.*, 11 (3): 224–230.
- FIB, 2013, “*fib Model Code for Concrete Structures 2010*”, Féd. Int. du Béton, Ernst & Sohn.
- Grace, N.F., Jensen, E.A., Eamon, C.D., Shi, X., 2012, “Life-Cycle Cost analysis of carbon fiber-reinforced polymer reinforced concrete bridges”, *ACI Structural Journal*, Vol. 109, No 5, 697–704.
- Hasan, Md. A., Yan, K., Lim, S., Akiyama, M., Frangopol, D., 2019, “LCC-based identification of geographical locations suitable for using stainless steel rebars in reinforced concrete bridges”, *Struct. and Infras. Eng.*, DOI: <https://doi.org/10.1080/15732479.2019.1703758>.
- Oller, E., Torres, L, de Diego, A., 2022, “Embedded fibre reinforced polymer (FRP) reinforcement in concrete structures according to the new version of Eurocode 2”, *Hormigón y Acero*, doi: <https://doi.org/10.33586/hya.2022.3098>.
- Pacheco-Torgal F, Melchers RE, Shi X, De Belie N, Van Tittelboom K, Sáez A., 2018, “Eco-efficient Repair and Rehabilitation of Concrete Infrastructures”. *Eco-Efficient Repair Rehabil Concr Infrastructures*. 1–757. <https://doi.org/10.1016/c2016-0-04100-1>.
- Rossini, M., 2019, “*FRP reinforcement for prestressed concrete applications*”, Ph.D. Dissertation, University of Miami.

Numerical analysis of short-term performance of CFRP new composite anchorage

S.Y. Sun

Department of Bridge Engineering, College of Highways, Chang'an University, Xi'an, China

ABSTRACT: The transverse and interlaminar shear strength of carbon fiber reinforced composites (CFRP) is smaller than its tensile strength, and the traditional clip-type anchorages used to anchor steel cables will exert a large occlusal force on the tendons. As a result, the CFRP tendon fails prematurely and cannot fully exert its high axial strength. The composite anchorage avoids the large stress concentration generated by the mechanical clamping anchorage at the anchorage port, and also avoids the bond-slip damage that is prone to occur in the bond-type anchorage, so that the high-strength characteristics of CFRP tendons can be fully utilized. A finite element model of a new type of composite anchorage was constructed, the failure mode of the anchorage, the ultimate load of the tendons, and the slip deformation were explored, and the stress-strain curve and the load-slip curve were obtained. The length of the steel sleeve, the inclination angle of the clip, Influence of parameters such as preload on the pull-out test results of the composite anchorage. The finite element results show that the anchoring efficiency increases with the increase of the bond length, and the anchoring efficiency increases with the increase of the inclination angle of the clip. Increasing the pre-tightening force helps to enhance the anchoring efficiency.

1 INTRODUCTION

Cable-stayed Bridges are used in rivers because of their beautiful appearance, convenient construction and strong crossing ability. The increase of the span of cable-stayed Bridges leads to the increase of the requirements on the length and diameter of cable-stayed Bridges. Because the cable-stayed cables in the state of high stress will receive fatigue vibration and electrochemical corrosion, the service life of cable-stayed Bridges will be limited and the wide application of cable-stayed Bridges will be affected.

Carbon Fiber Reinforced Polymer has the advantages of high strength, high elastic modulus, corrosion resistance and fatigue resistance. (Wang, 2005) Replacing steel cables in cable-stayed bridges can greatly reduce the maintenance cost during the design reference period, and because its specific strength is higher than that of high-strength steel, it can greatly improve the bearing efficiency and span capacity of cable-stayed bridge, which is conducive to the full use of cable-stayed bridges.

Although CFRP has high axial tensile strength, the strength and modulus perpendicular to the fiber direction are much lower than that of the fiber direction. The traditional clip anchorage used to anchor steel cables will produce a large bite force, resulting in the shear failure of tendons at the anchorage port cannot give full play to its advantages. Therefore, a safe and reliable anchorage system is the key to determine whether CFRP reinforcement can be used in cable-stayed bridges. If we want to apply CFRP tendons to bridge engineering better, we need to develop small size, simple anchoring technology, safe and reliable anchorage.

2 DEVELOPMENT OF ANCHORAGE AT THE PRESENT STAGE

According to different anchoring principles, CFRP anchorage can be divided into three types: mechanical clamping anchorage, bonding anchorage and mechanical clamping-bonding composite anchorage.

Mechanical clamping anchorage mainly relies on the friction force and bite force between the clip or cone plug and CFRP tendons to achieve anchoring. Since the transverse shear strength of CFRP tendons is low, the tendons are easy to be sheared at the stress concentration of the anchorage port. Measures should be taken to protect the tendons from being sheared.

Nanni, Sayed And Mahmoud et al. improved the traditional clip anchorages from the aspects of improving the friction between the clips and CFRP tendons and reducing the shear force of the clips on CFRP tendons. However, their reliability is generally not ideal. The surface form of CFRP tendons is required to be high and the versatility is not strong. (Nanni 1996, Sayed-Ahmed 1998, Taha 1998, Taha 2003)

Campbell et al. designed a wedge clip-type anchorage, used finite element method to simulate the stress distribution of tendons in the anchoring area, and tested the static load performance of the anchorage through tests. (Campbell, 2000)

Bonding anchorages mainly transmits the shear force through the bonding force and friction force on the interface, which can prevent excessive stress concentration. The anchorage reliability is high, and the fatigue performance is better than that of mechanical clamping anchorage, but the anchorage length is long.

Meier et al. designed a CFRP anchorage with variable stiffness bonding medium to make the shear stress distribution on the contact surface of bonding medium more uniform than that of single stiffness bonding medium. (Meier, 1996)

Mei Kuihua et al. respectively conducted a static performance test study on the bonding type anchorage system with 6, 11 and 16 CFRP tendons, and applied it to the first domestic CFRP cable-stayed bridge. (Mei, 2005)

Zhang and Fang et al. designed 9 and 12 CFRP tendons bonding type anchorage system using reactive powder concrete as bonding medium, and applied it in two pairs of CFRP slings of Aizhai Bridge. (Zhang 2013, Fang 2015)

The composite anchorage can be connected in series or parallel with the mechanical clamping anchorage and the bonding anchorage to give full play to the advantages of the mechanical clamping anchorage and the bonding anchorage, but there are relatively few relevant studies.

Mei Kuihua proposed a new CFRP tendons composite anchorage, which is made of aluminum casing as the perfusion vessel inside, uses epoxy resin to bond multiple tendons, and exerts pre-extrusion pressure on the adhesive part outside in the way of mechanical clamping, and good anchoring efficiency is obtained. (Mei, 2021)

To solve the above problems, this paper developed a new type of mechanical grip-bond composite anchoring tool with small size and excellent anchoring performance by optimizing the inner wall Angle and anchoring length of the anchoring tool. Its essence is still the bonding anchorage, which provides extrusion pressure for mechanical clamping to improve the bond strength of the anchorage. Through static load test, the anchoring efficiency coefficient and load-slip performance of the anchorage were studied, as well as the influence of inner wall inclination angle, bonding length and other parameters on the anchoring performance of the anchorage. which proves that the new anchorage has good anchoring performance.

3 ANCHORAGE TEST DESIGN

3.1 Anchorage design

The anchorage is composed of steel sleeve, clip, aluminum casing pipe, colloid, tendons and bolt. The bonding medium of the bonding part is wrapped by aluminum casing pipe, which can effectively transfer the pre-tightening force generated by the clip to the bonding medium,

so as to obtain better anchoring effect. The steel sleeve with external constraints is also shaped like an inner cone to better adapt to the shape of the bonding area.

An inclination angle difference of 0.1 degree is set between the inner wall and the outer wall of the steel sleeve. Due to the existence of the inclination difference, there is a gap between the clip and the steel sleeve near the loading end, which can effectively avoid stress concentration.

3.2 Anchorage test process

Push the anchorage assembled by each part to achieve pretightening at both ends. Push the anchorage in place at one time and the thrust force is 130kN.

Before the formal tensioning, the anchorage was pre-tensioned three times, and the pre-tensioned load was 40% of the theoretical breaking force of the cable.

According to the theoretical ultimate tensile strength of CFRP tendons provided by the manufacturer of 78.68kN, the theoretical ultimate tensile strength of cable anchorage is calculated to be 400kN. The cable anchorage system shall be loaded at a constant speed of 0.1F_{ptk}, (40kN) at the loading grade of 0.5F_{ptk} (200.5kN) for 1 hour, and at other load levels for 5 minutes. If no tendon slips or tension occurs when the anchorage system is stretched to 1.0F_{ptk} (400kN), the load shall be maintained for 1h.

The specific experimental loading time-load curve is shown in the figure.

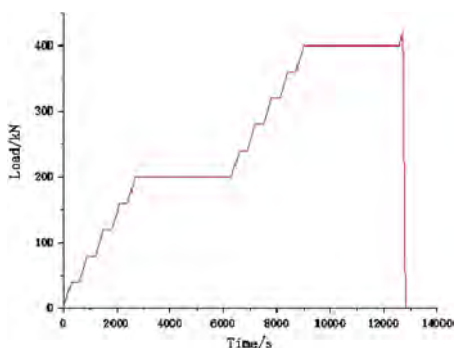


Figure 1. Static load test time load curve.

This model will be developed on the basis of the above experimental scheme.

4 FINITE ELEMENT MODEL

4.1 Material data

4.1.1 Assembly of anchorage

The material parameters required in the experimental model are shown in the following table

Table 1. Mechanical properties of epoxy resin.

Modulus of elasticity / GPa	Poisson's ratio	Tensile strength / MPa	Shear strength / MPa	Compressive strength / MPa
2.61	0.25	40.5	24.3	73.6

4.2 Original model design drawing

The design drawing uses the steel sleeve with a length of 200mm and the clip with a length of 250mm. A composite anchorage with an inner wall inclination angle of 3.9° is designed, that is,

Table 2. Mechanical properties of steel barrel, aluminium tube and CFRP tendon.

Physical Parameters material	Modulus of elasticity /GPa	Poisson's ratio	Ultimate tensile strength /MPa	Ultimate elongation /%
Steel sleeve	210	0.31	600	-
Aluminium casing pipe	71	0.31	90	-
CFRP tendons	147	-	2300	1.44

the inner wall inclination angle of the steel sleeve is 3.9° , the outer inclination angle of the clip is 4° , the inner inclination angle is 3° , and the aluminium casing pipe inclination angle is 3° .

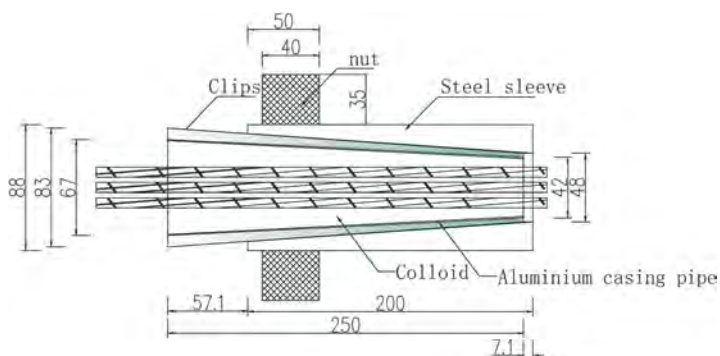


Figure 2. Original anchorage design drawing.

4.3 Establishment of finite element model

4.3.1 Basic model

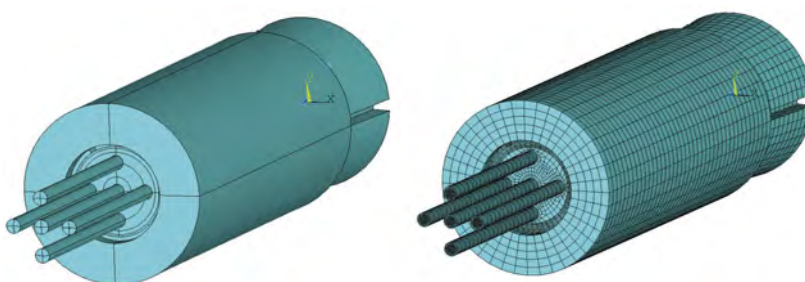


Figure 3. Basic model modeling diagram and Grid division diagram.

Each component of anchorage is simulated by solid65 unit, with 136806 units. The surface-to-surface contact element is used to simulate the interaction between the components of the cable anchorage system. Conta173 and Target170 were used for the contact surface and the target surface respectively. There are 23,784 contact elements in total. The friction coefficient between the steel sleeve and the clip is 0.2; The friction coefficient between the clip and the aluminum casing pipe is 0.2, referring to the friction coefficient between steel and aluminum. The contact algorithm adopts the hybrid method combining Lagrange multiplier method and penalty function method, and the contact surface behavior adopts the non-separation (allow sliding) mode. The external load is applied to the end of the tendons in the form of surface load, and the steel sleeve is treated by consolidation at the free end to simulate the constraint conditions of the anchorage.

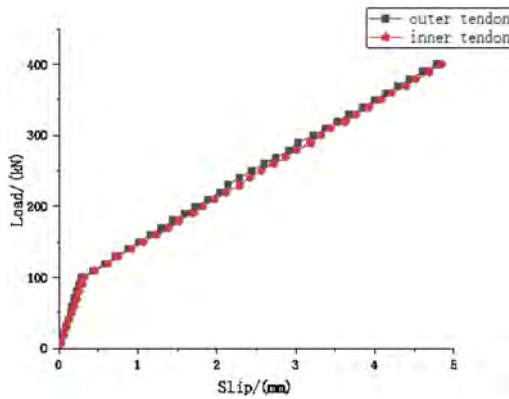


Figure 4. Original anchorage load-slip curve.

The curve development process of finite element calculation is that at the initial stage of loading, the slip of tendon increases slowly with the increase of load. When the load reaches 100kN, the slip begins to increase significantly. The maximum slip of the inner tendon and the outer tendon of the anchorage is 4.8mm and 4.7mm. The slip amount of the inner tendon is slightly larger than that of the outer tendon, which indicates that the layout of the inner and outer layers of the tendon has a certain influence on the axial force distribution of the tendon.

4.4 Variable parameter analysis

4.4.1 Changing the bond length

In this section, the influence of the bond length of anchorage on the anchorage capacity is investigated.

The anchorage length of the anchorage was increased by increasing the size of all members by 30mm. The load-slip curve is shown in the figure.

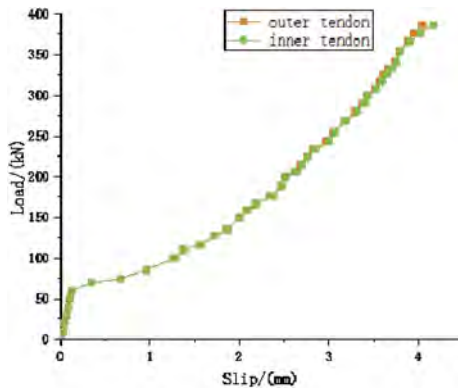


Figure 5. Load-slip curve of anchorage after increasing bonding length.

When the ultimate load is reached, the maximum slip of the inner and outer tendon is 4.1mm, which is about 0.5mm less than the original test result, and the slip of the whole loading process is smaller than that of the original design anchorage. Compared with other models, the slip in the second half of the load changes significantly slower, which indicates that the increase of bonding length mainly plays an important role in the later stage of loading, reducing the slip of the tendon relative to the colloid. It can be inferred that: firstly, the increase of bonding length can increase the contact area between the components of the anchorage, increase the friction force, and reduce the relative slip between the components;

Secondly, the increase of bonding length leads to the increase of the contact area between the tendons and the colloid, thus increasing the bonding force between them, and finally reduces the slip of tendon when loading.

4.4.2 Changing the inclination angle of anchorage

In this section, the influence on the anchorage capacity of the anchorage is investigated by reducing the inclination angle of each component inside the anchorage by 0.5° .

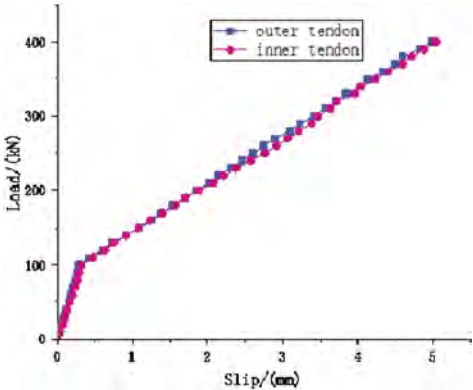


Figure 6. Load-slip curve of anchorage after change of inclination angle.

By comparing the figure with the figure, it can be found that reducing the internal inclination angle of the anchorage by 0.5° has no effect on the time when the relative slip of the tendon occurs. The only difference is that after the internal inclination angle is reduced, the maximum slip of the tendon when reaching the ultimate load increases by 0.2 mm. On the whole, it can be inferred that the overall reduction of the inclination angle of each component in the anchorage has no obvious impact on the anchorage performance of the anchorage.

4.4.3 Changing the jacking force

The influence of preload on anchoring effect of five-tendons anchorage was investigated by changing the preload.

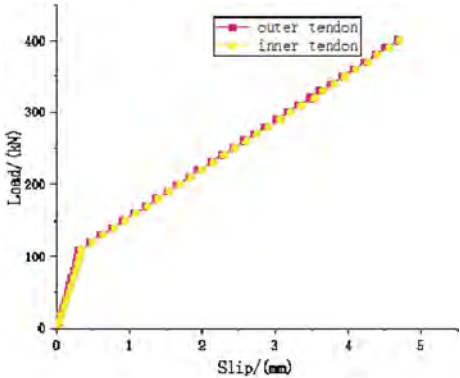


Figure 7. Load-slip curve of anchorage after changing jacking force.

The preload value of the original anchorage was 130kN, and the preload was changed to 145kN by variable parameter analysis, and the load-slip curve of the free end of the inner and outer tendon under different preload was plotted in the figure. First, it can be seen that the change of preload does not make a big difference in the load-slip distribution of the inner and outer tendon. However, when the preload is 130kN, the external load of the tendon is 100kN,

and when the preload is 145kN, the external load corresponding to the obvious slip of the tendon is 110kN respectively.

To sum up, it can be analyzed that: (1) the change of preload will make the load slip of the tendon in the inner and outer layers of the anchorage change at the same time, and the change degree of the inner and outer layers is the same, without obvious difference; (2) Within a certain range, the increase of the preload will make the relative slip of the tendon occur later, mainly because the increase of the preload makes the internal parts of the anchorage more tightly squeezed, and the colloid is subjected to greater extrusion pressure, thus producing greater bonding force and friction force on the tendon; (3) Within a certain range, the increase of the preload will reduce the maximum slip of the tendon. According to the finite element simulation results, when the preloading force reaches 145kN, compared with 130kN, the weakening effect on the tendon slip is small, only decreasing by 0.09mm.

4.4.4 Changing colloidal elastic modulus

For the colloid that plays an important role in anchoring tendons, its main physical properties are elastic modulus, tensile strength, shear strength, compressive strength, friction coefficient and so on. Keeping other parameters of the colloid unchanged, the influence of the change of the physical properties of the colloid on the anchoring efficiency of the anchorage device is investigated by changing its elastic modulus. The elastic modulus of the original model colloid is 2.61Gpa, and the colloidal elastic modulus of anchorages was changed to 2.2Gpa in the finite element simulation, respectively. The relative load-slip curve of the free end of the tendon was shown in the figure.

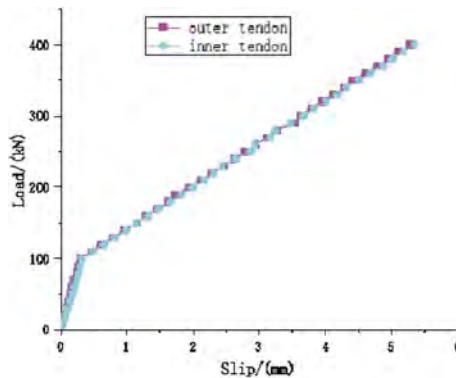


Figure 8. Load-slip curve of anchorage after changing colloidal elastic modulus.

As can be seen from the figure, the change of colloidal elastic modulus has little influence on the inflection point of significant slip of the tendon, and the simulated anchorage has obvious slip of the tendon when the external load reaches 100kN. When the elastic modulus of the model is 2.2Gpa, the slip of the tendon reaches the ultimate load is 0.4mm larger than that of the original model. This shows that within a certain range, when other parameters remain unchanged, the larger the elastic modulus of the colloidal, the better the anchoring performance of the anchorage, mainly because under the same stress conditions, the larger the elastic modulus of the colloidal, the greater the deformation, thus the extrusion pressure and bonding force on the tendon will also increase.

5 CONCLUSION

The finite element model was established according to the size and material parameters of the anchorage, and the load-slip curve of the anchorage under different parameters was compared

by changing one of the parameters of the model for analysis and calculation, and then the influence of different parameters on the anchoring efficiency of the anchorage was deduced.

The conclusions are as follows:

- (1) To a certain extent, the increase of bonding length will reduce the slip of tendon and enhance the anchoring performance.
- (2) On the basis of the original design parameters, changing the internal inclination angle of the anchorage has little effect on the anchoring efficiency of the anchorage, and the inclination angle of the anchorage designed for the static load test does not need to be optimized.
- (3) Increasing preload and colloid elastic modulus has limited effect on improving anchorage performance, so it is unnecessary to greatly increase the cost of anchorage for improving the limited anchorage performance of current anchorage.

REFERENCES

- Campbell, T. I., Shrive, N. G., Soudki, K. A., Al-Mayah, A., Keatley, J. P., & Reda, M. M. (2000). Design and evaluation of a wedge-type anchor for fibre reinforced polymer tendons. *Canadian Journal of Civil Engineering*, 27(5), 985–992.
- Fang, Z., Zhang, K., & Tu, B. (2013). Experimental investigation of a bond-type anchorage system for multiple FRP tendons. *Engineering Structures*, 57, 364–373.
- MEI Kui-hua, LU Zhi-tao, ZHANG Ji-wen, ZANG Hua (College of Civil Engineering, Southeast University, Nanjing 210096, China). Study of Static Load Tests of CFRP Stay Cable Anchors[J]. *Bridge Construction*, 2005(4): 20–23. (in Chinese)
- MEI Kui-hua; SUN Ya-min; SUN Chen-ran; SUN Sheng-jiang; REN Xiang; School of Highway, Chang'an University; School of Architecture and Civil Engineering, Xi'an University of Science and Technology; North China Municipal Engineering Design and Research Institute Co.Ltd.; Short-term Performance of a Novel Mechanical-bond Composite Anchorage with CFRP Tendons[J]. *China Journal of Highway and Transport*, 2021, 34(1): 66–78. (in Chinese)
- Meier, U., & Farshad, M. (1996). Connecting high-performance carbon-fiber-reinforced polymer cables of suspension and cable-stayed bridges through the use of gradient materials. *Journal of Computer-Aided Materials Design*, 3(1), 379–384.
- Nanni, A., Bakis, C. E., O'Neil, E. F., & Dixon, T. O. (1996). Performance of FRP tendon-anchor systems for prestressed concrete structures. *PCI journal*, 41(1), 34–43.
- Sayed-Ahmed, E. Y., & Shrive, N. G. (1998). A new steel anchorage system for post-tensioning applications using carbon fibre reinforced plastic tendons. *Canadian Journal of Civil Engineering*, 25(1), 113–127.
- Taha, M. M. R., & Shrive, N. G. (2003). New concrete anchors for carbon fiber-reinforced polymer post-tensioning tendons—Part 1: State-of-the-art review/design. *Structural Journal*, 100(1), 86–95.
- Taha, M. M. R., & Shrive, N. G. (2003). New concrete anchors for carbon fiber-reinforced polymer post-tensioning tendons—Part 2: Development/experimental investigation. *Structural Journal*, 100(1), 96–104.
- WANG Sheng-yi (Major Bridge Reconnaissance and Design Institute of China Railway Engineering Corporation, Wuhan 430050, China). The application and future of carbon fiber reinforced polymer in bridge structure[J]. *Journal of Chongqing Jiaotong University*, 2005(1): 30–32, 41. (in Chinese)
- Zhang, K., Fang, Z., Nanni, A., Hu, J., & Chen, G. (2015). Experimental study of a large-scale ground anchor system with FRP tendon and RPC grout medium. *Journal of Composites for Construction*, 19(4), 04014073.

Preliminary assessment on the effects of longitudinal cracks on carbonation-induced corrosion

N. Russo, M. Gastaldi & F. Lollini

Department of Chemistry, Materials and Chemical Engineering “Giulio Natta”, Politecnico di Milano, Milan, Italy

L. Schiavi & A. Strini

Construction Technologies Institute, National Research Council of Italy (ITC-CNR), San Giuliano Milanese, Milan, Italy

ABSTRACT: Currently available models for reinforced concrete (RC) durability still lack the inclusion of the effects of cracks, which are inevitable in concrete structures, and literature on the effects of cracks on carbonation-induced corrosion is scarce, especially in case of cracks longitudinal to the reinforcement. This paper presents some preliminary experimental results on the effects of longitudinal micro-cracks on carbonation-induced corrosion, initiation and propagation phases. Experimental tests were performed to evaluate the penetration of carbonation, under accelerated conditions, in cracked and uncracked concrete made with different cement types and *w/c* ratios. Corrosion propagation was monitored, through electrochemical techniques, in longitudinally cracked and uncracked RC specimens subjected either to natural or accelerated carbonation. Results showed a more marked effect of the micro-crack on carbonation penetration in more impervious concretes, while the presence of the micro-crack did not seem to significantly affect corrosion propagation, except when developing to rebar depth.

1 INTRODUCTION

Durability models, based on reliable modelling of the service life of reinforced concrete (RC) structures, are typically performed as a function of the initiation and propagation of corrosion of steel reinforcement, and are of fundamental importance to meet the sustainability targets in the construction field (Bertolini et al. 2013). However, even the most accredited models present some limitations that still need to be addressed to, such as the inclusion of the effects of cracks, which are inevitable in concrete and may alter the corrosive process. The limited knowledge concerning the effects of cracks on durability performances, especially in the case of carbonation-induced corrosion, contributed to slow their improvement at this regard.

Considering the penetration of carbonation in concrete, initially cracks lead to a general increase in the penetration rate of gaseous CO₂ from the environment. Subsequently, as carbonation proceeds, the precipitation of calcium carbonate in the form of calcite, vaterite and aragonite, that occupy a volume about 3 to 20% higher, leads to a partial closure of small cracks with time, as a form of carbonation-induced autogenous healing (Liu et al. 2021). Studies on carbonation penetration in unreinforced specimens and under accelerated carbonation showed that even micro-cracks (width at the exposed surface lower than 100 µm), could significantly affect the resistance to carbonation penetration. In Alahmad et al. (2009), a significant penetration of carbonation perpendicularly to crack walls was reported, similar to uncracked conditions for cracks wider than 60 µm, with a progressive decrease for cracks about 40 µm wide, and negligible for crack narrower than 9 µm. In Bogas et al. (2019), a method was proposed to retrieve the carbonation coefficient inside the crack, founding a carbonation coefficient 3.7 times higher in the crack with respect to uncracked concrete for a 100 µm wide artificial crack (obtained through metallic plates at fresh state), while in specimen with load-induced crack about 150 µm wide the increase resulted of

about 2.7 times. In Carević & Ignjatović (2019), some simulations were performed after carbonation depth measurements under accelerated conditions. It was estimated, according to *fib* Model Code 2010, that in the case of 300 μm wide crack, under natural carbonation, the service life of the structure would have been reduced of about three times with respect to uncracked conditions, assuming depassivation of steel as ultimate limit state.

Considering carbonation-induced corrosion in reinforced concrete, the presence of a crack can alter both the corrosion initiation and propagation processes. In fact, when a crack develops to rebar depth, an alteration in the protective alkaline environment normally provided by sound concrete may occur, and corrosion may preferentially take place where crack tip reaches the steel reinforcement (as observed for chloride-induced corrosion in Leporace-Guimil et al.). Moreover, once corrosion started, corrosion rate could further be increased by the generation of a small anode to large cathode ratio (ACI Committee 201, 2016). Literature on this topic is more limited in the case of cracks in the longitudinal direction of the reinforcement with respect to the transversal direction, which may form in bidimensional elements, or due to shrinkage, or plastic settlement of concrete. Longitudinal cracks may influence the corrosion process to a higher extent, since aggressive species (carbonation, moisture, oxygen, ...) can more easily reach a wider area of embedded steel surface (Shaikh 2018). To conclude, the subject is not only complex due to the number of variables affecting durability parameters, but also to the different experimental procedures and materials used in different studies, which make it difficult to derive unambiguous conclusions.

This paper presents some preliminary experimental results on the effects of cracks on carbonation-induced corrosion initiation and propagation. Experimental tests were performed to evaluate the penetration of accelerated carbonation in cracked and uncracked unreinforced specimens, considering different cement types and *w/c* ratios, and cracked through a specifically developed loading procedure. Corrosion propagation was monitored in cracked and uncracked concrete specimens subjected either to natural or to accelerated carbonation. In this case, concrete was obtained with Portland-limestone cement and *w/c* of 0.45, reinforced with carbon steel bars, and cracked using the same procedure to obtain a longitudinal micro-crack. Electrochemical techniques were used to detect corrosion initiation in specimens subjected to natural carbonation (exposed to outdoor unsheltered environment), and to monitor corrosion propagation in specimens previously subjected to accelerated carbonation and then exposed to outdoor unsheltered environment, considering a different orientation for the cracked surface.

2 MATERIALS AND METHODS

2.1 Specimens layout

Unreinforced specimens were realized considering three different cement types, *i.e.* an ordinary Portland (OPC, type CEM I 42,5R according to EN 197-1), a Portland-Limestone (PLC, type CEM II/A-LL 42,5R), and a Pozzolanic cement (PC, type CEM IV/A(V) 42,5R-SR), and two *w/c* ratios, *i.e.* 0.45 and 0.55. Reinforced specimens were made only with PLC cement type and *w/c* of 0.45. The mixes with 0.45 *w/c* ratio were obtained considering 422 kg/m^3 of cement, 190 kg/m^3 of water and 1731 kg/m^3 of aggregates, while those with *w/c* ratio equal to 0.55 were obtained with 422 kg/m^3 of cement, 232 kg/m^3 of water and 1619 kg/m^3 of aggregates. All the aggregates were crushed calcareous type, subdivided into 5 grain size fractions, with maximum diameter of 9 mm. An acrylic-based superplasticizer was also added to the mixes with 0.45 of *w/c* ratio, to reach, at least, a S3 class of consistency. As reinforcement, carbon steel bars with 16 mm diameters were employed, subject to sandblasting and degreasing with acetone prior casting. Moreover, to avoid side effects, the two ends of each rebar were masked with a styrene-butadiene-modified cement mortar and epoxy, leaving a total length of 80 mm exposed to the concrete.

A total amount of 6 unreinforced specimens per each cement type and *w/c* ratio were realized, out of which 2 in uncracked and 4 in cracked configuration, while a total amount of 16 reinforced specimens were realized, out of which 4 in sound (S), 9 in cracked (C) and 3 in heavily cracked (HC) configuration. All the specimens were characterized by prismatic geometry, with dimensions 120×90×50 mm, as reported in Figure 1. In cracked configuration, specimens presented

a longitudinal notch, about 3 mm depth, to promote the formation of the crack during the cracking procedure. In reinforced configuration, specimens were equipped with one carbon steel rebar (concrete cover thickness of 15 mm), an activated titanium wire (reference electrode) and a titanium wire (counter-electrode) for electrochemical measurements. Both unreinforced and reinforced cracked specimens were subjected to a specifically developed cracking procedure, within 24 hours after casting (thus to have a lower concrete mechanical resistance and a less brittle behaviour). The method was a sort of three-point bending procedure to induce a longitudinal micro-crack in correspondence of the notch. Specimens were encased in a steel confinement system and placed in a universal testing machine with the notch facing downwards, and interposing three stripes of synthetic elastomer membrane, 1.2 mm thick. Two were placed along the downward corners of the specimen, as the supports, and the other in central position on the upward face, as the loading pin. A displacement-controlled load was then applied, equal to 0.5 mm/min in the vertical direction. In unreinforced configuration, the load was applied until an overload level 45-55% higher than that corresponding to the first appearance of the crack was reached. Cracks were measured at the end of exposure to carbonation with the same procedure as in Russo et al. 2020, and resulted 30-160 μm wide and 30-40 mm deep. In reinforced configuration, the load was applied until the simultaneous appearance of the crack on both sides of the specimen, at least one of which was up to the rebar. To the 3 more heavily cracked specimens a further overload of 10 % was applied. For further details on the procedure and on the obtained cracks see past publications (Russo et al. 2020, Russo et al., in press). After the cracking procedure specimens were kept, together with the uncracked ones, in a curing chamber at a temperature of 20 °C and relative humidity higher than 90%, until the starting of tests.

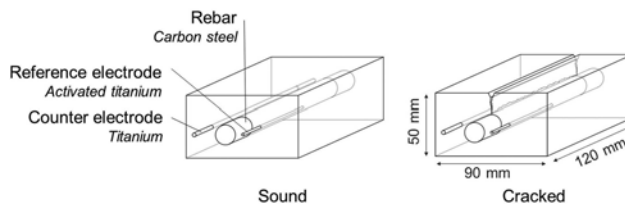


Figure 1. Schematic representation of sound and cracked concrete specimens in reinforced configuration.

2.2 Resistance to penetration of carbonation

Specimens were moist cured for 28 days and subsequently were pre-conditioned and prepared for accelerated carbonation test according to EN 12390-12. All the surfaces of each specimen were then sealed with epoxy, except for the cast surface to be exposed to carbonation. Accelerated carbonation was performed in a chamber with 3% of CO_2 concentration, 60% of relative humidity and 20 °C of temperature for 30 and 70 days of exposure. At each exposure time, one portion of the specimen was split and phenolphthalein was sprayed, in order to highlight the carbonation profile. The split surface of the remaining part of the specimen was sealed again to be exposed for the other exposure time. Carbonation depth measurements were measured with a calliper, and were taken in correspondence of the central point and on three other points on each side, spaced 10 mm each (7 points in total). In cracked configuration the central measurement, *i.e.* in correspondence of the crack, was taken in correspondence of the maximum penetration depth, excluding the notch. The accelerated carbonation coefficient, K_{AC} , was derived according to the formula:

$$x = K_{AC} \cdot \sqrt{t} \quad (1)$$

where x = average carbonation depth; t = time. At each exposure time, in sound configuration a single coefficient was evaluated (K_s), considering the average penetration depth. In cracked configuration two coefficients were evaluated, one in correspondence of the crack (K_{cr}), considering the maximum penetration depth, and the other in the uncracked part of the specimen (K_{uncr}), considering measurements points at ± 20 and ± 30 mm from the central crack.

2.3 Carbonation-induced corrosion monitoring

Reinforced specimens for the monitoring of corrosion were moist-cured for 7 days. After curing, three cracked specimens were exposed to outdoor unsheltered conditions, one with the surface containing the crack oriented horizontally, one vertically and one heavily cracked horizontally. Specimens were periodically monitored, thorough electrochemical measurements, to detect corrosion initiation and monitor corrosion propagation. The other reinforced specimens in uncracked and cracked configurations were exposed to accelerated carbonation to induce corrosion initiation, in the carbonation chamber with 3% of CO₂ concentration, 60% of relative humidity and 20 °C of temperature. Specimens were periodically taken out of the carbonation chamber to electrochemically assess whether corrosion was initiated. After corrosion initiation was detected, specimens were exposed to external unsheltered conditions, considering either horizontal orientation or vertical orientation of the crack (as in a floor or a vertical element, respectively).

As electrochemical measurements, the half-cell potential (E_{corr}) was measured versus a saturated calomel electrode (SCE), placing the electrode on the specimen surface in correspondence of the central part of the rebar, while corrosion current density (i_{corr}) was measured through linear polarization resistance measurement (R_p) according to the equation:

$$i_{\text{corr}} = \frac{B}{R_p \cdot A} \quad (2)$$

where A = surface of rebar exposed to concrete; B = assumed equal to 26 mV.

3 RESULTS AND DISCUSSION

3.1 Effects of micro-cracks on penetration of carbonation

Figure 2 reports the results obtained in terms of K_{AC} , for the different exposure times and for the different concrete types, where histograms represent average values and error bars represent maximum and minimum values. In the Figure, the different mixes are identified with a label recalling the cement type (OPC for Ordinary Portland, PLC for Portland-limestone and PC for Pozzolanic cement type) followed by the w/c ratio. Considering sound and uncracked configurations, a quite good reproducibility of results was obtained in replicate specimens, and, moreover, for each concrete type K_{AC} was very similar for the two configurations. Similar results were also obtained considering the same mix at different exposure times. This result was expected, since carbonation in concrete is generally believed to be not affected by an ageing factor, unlike chloride penetration. To discuss the effect of cement type and w/c ratio, a single value of K_{AC} can be therefore considered, by averaging the values at both the exposure times in sound and uncracked conditions (Table 1).

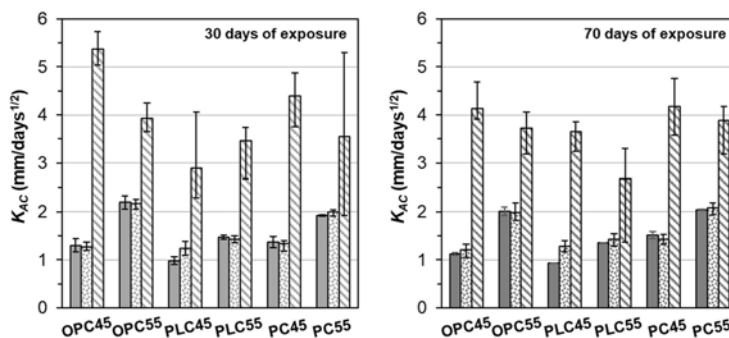


Figure 2. Average accelerated carbonation coefficient (KAC) and variability in sound (K_s, solid), uncracked (K_{uncr}, dotted) and cracked (K_{cr}, hatched) configurations, for different concrete types, after 30 (left) and 70 (right) days of exposure.

Concretes made with w/c equal to 0.45 showed similar K_{AC} in sound and uncracked conditions, except PLC45, for which the sound value unexpectedly resulted lower than $1 \text{ mm/days}^{1/2}$. If for this cement type the value in uncracked condition is considered more accurate, the carbonation coefficient for different cement types resulted quite similar, between 1.2 and $1.4 \text{ mm/days}^{1/2}$. As expected, higher K_{AC} were found for concretes with w/c of 0.55, since these concretes were characterized by higher permeability, which is considered to be one of the main factors affecting the diffusion of carbon dioxide in concrete (Bertolini et al. 2013). K_{AC} for these concretes resulted included between 1.2 and $2 \text{ mm/days}^{1/2}$, showing a percentage increment that depended on the cement type, *i.e.* about 40% for PC, 30% for OPC, and 15% for PLC.

Table 1. Average K_{AC} evaluated considering both the exposure times.

	OPC45	OPC55	PLC45	PLC55	PC45	PC55
$K_s \text{ (mm/days}^{1/2}\text{)}$	1.21	2.10	0.96	1.42	1.44	1.98
$K_{uncr} \text{ (mm/days}^{1/2}\text{)}$	1.24	2.07	1.26	1.43	1.38	2.03

Considering the effect of micro-cracks, these always led to a significant increase in the carbonation depth and therefore in the carbonation coefficient, and in the scatter of data among replicate specimens and for the same concrete type at different exposure duration (hatched histograms and error bars in Figure 2). It is worth noting, however, that this high scatter is also related to the fact that results at different exposure times were obtained on different specimens, characterized by different crack parameters, as well as replicate specimens for the same exposure duration may have been characterized by variable crack widths and depths. Moreover, the adopted cracking procedure did not prove to guarantee replicable cracks widths and depths (Russo et al. 2020). For this reason, the results at different exposure times were not averaged to find a single K_{AC} . To discuss the effects of the micro-crack on the carbonation coefficient, Figure 3 shows the ratio between K_{AC} in micro-cracked and uncracked condition (K_{cr}/K_{uncr}), as a function of K_{uncr} .

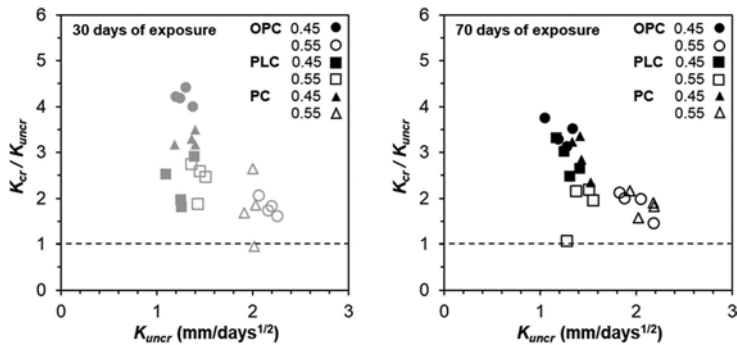


Figure 3. Increase in accelerated carbonation coefficient in the crack with respect to uncracked conditions (K_{cr}/K_{uncr}) as a function of accelerated carbonation coefficient in uncracked conditions, for different concrete types and after 30 (left) and 70 (right) days of exposure.

As can be noticed in Figure 3 an increase in the carbonation coefficient in the micro-crack always occurred, at both the exposure times. Moreover, an increasing trend in the ratio K_{cr}/K_{uncr} could be detected, for decreasing values of K_{uncr} (less permeable concretes). This effect was more pronounced for concretes with w/c of 0.45 (filled symbols), showing K_{cr}/K_{uncr} between 2 and 4.5, considering both the exposure times, and less pronounced for concretes with w/c of 0.55 (empty symbols), being K_{cr}/K_{uncr} mostly between 1 and 2.5. Similar results were obtained by the writing Authors with regard to chloride penetration resistance (Russo et al. 2020, Russo et al. 2022), confirming that a more marked effect of the micro-crack on concrete durability may occur for more impervious concretes. However, the presence of micro-cracks may not be of high concern for

concretes characterized by the w/c ratios typically used for structures subject to carbonation-induced corrosion, which according to EN 206 are 0.50 for exposure class XC4 and 0.55 for XC3.

3.2 Effects of micro-cracks on corrosion initiation and propagation

Figure 4 shows the electrochemical monitoring of corrosion potential (E_{corr}) and corrosion current density (i_{corr}), for cracked and highly cracked specimens exposed to outdoor unsheltered conditions. In particular, one cracked specimen was exposed with the crack in horizontal direction (CH), another one in vertical (CV), while one highly cracked with horizontal direction (HCH). The Figure reports also the outdoor climatic conditions, *i.e.* the daily cumulative rain and the daily average temperature (dark and light grey lines respectively). It can be noticed that over almost two years of exposure temperature fluctuated between 0°C and 30°C, while rain was in general quite scarce, with only 56 days with more than 5 mm of cumulative rain recorded. During the first half of exposure period (up to about 200 days of exposure), and especially in correspondence of the more wet days, HCH specimen already showed significantly lower values of E_{corr} (−200 ÷ −250 mV vs SCE) associated to i_{corr} values around 2 mA/m². It is reasonable to assume that in this specimen the crack developed to rebar depth, by analogy with some specimens realized and cracked with the same procedure but exposed to chlorides (Russo et al., in press), which may have led to corrosion initiation within the first 200 days of exposure. Subsequently, however, during the second half of the exposure period, E_{corr} was on average increased, and i_{corr} remained at values around 1 mA/m² or even lower. This may be associated to a drier climate during this period, or, eventually, to a partial or total closure of the crack due to self-healing and re-passivation of steel rebar. Further monitoring as well as destructive tests are needed to further investigate this aspect.

No significant difference in electrochemical behaviour was instead detected between the two cracked specimens with differently oriented cracked surface (CH and CV), whose values of i_{corr} always remained around 1 mA/m² or even lower, suggesting rebar passivity. For these two specimens it is reasonable to assume that the crack (and carbonation) did not reach rebar depth or, at least, did not involve a sufficiently wide area of steel to detect corrosion initiation with linear polarization method.

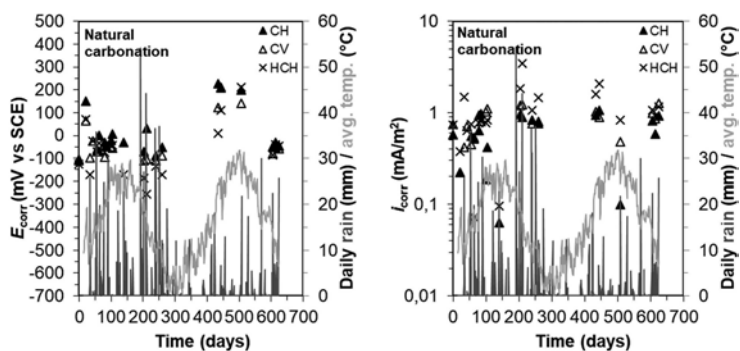


Figure 4. Trend in time of corrosion potential (left) and corrosion current density (right) for reinforced cracked (C) and highly cracked (HC) specimens subjected to natural carbonation with horizontal (H) or vertical (V) orientation.

Figure 5 shows the electrochemical monitoring for sound (S), cracked (C) and highly cracked (HC) specimens subjected to accelerated carbonation to induce corrosion initiation and external outdoor exposure to monitor natural corrosion propagation, with different crack orientation. In the Figure, the hatched area highlights the period in which specimens were in the carbonation chamber, the solid blue and grey areas highlight the measurements that were taken after 4 days of exposure to partial immersion and after one week in the curing chamber ($T=20^{\circ}\text{C}$, $\text{RH}>90\%$), respectively. These measurements were performed to verify, at two different humidity

contents, the corrosion initiation. Subsequently, the dark and light grey lines report the trend of the daily cumulative rain and the daily average temperature during external outdoor exposure.

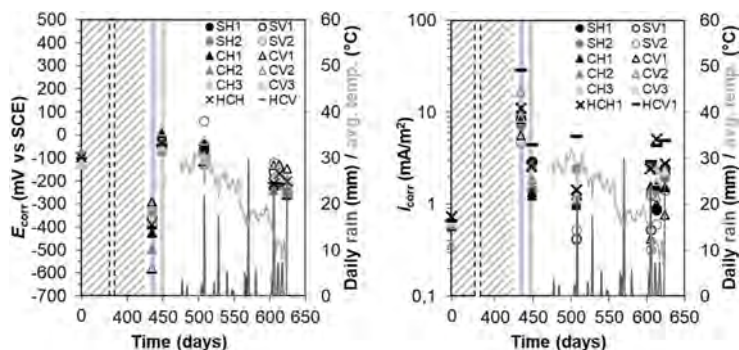


Figure 5. Trend in time of corrosion potential (left) and corrosion current density (right) for reinforced sound (S), cracked (C) and highly cracked (HC) specimens subjected to accelerated carbonation and natural corrosion propagation at outdoor exposure with horizontal (H) or vertical (V) orientation.

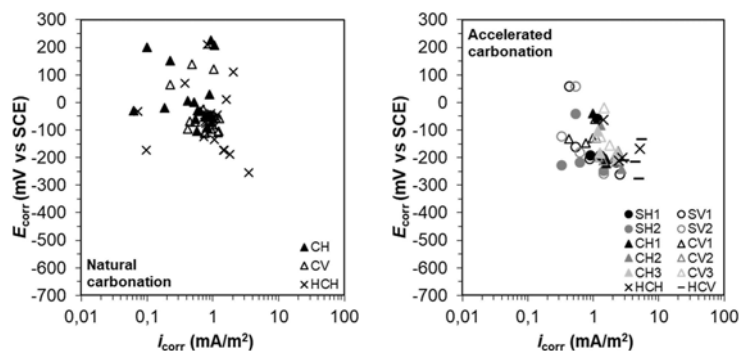


Figure 6. Corrosion potential as a function of corrosion current density for specimens subjected to natural (left) and accelerated (right) carbonation, in sound (S), cracked (C) and highly cracked (HC) configurations, with horizontal (H) or vertical (V) orientation.

The lowest E_{corr} values ($-300 \div -600$ mV vs SCE), together with the highest i_{corr} values (up to 9 mA/m² for sound, S, 17 mA/m² for cracked, C, and 29 mA/m² for highly cracked concrete, HC), were detected as soon after the end of exposure to the carbonation chamber, at partial immersion conditions, confirming that carbonation arrived at rebar depth causing corrosion initiation in all the configurations. At curing chamber conditions, a neat increase of E_{corr} was detected ($0 \div -100$ mV vs SCE), while i_{corr} decreased of roughly one order of magnitude ($1 \div 5$ mA/m²), due to a lower moisture content in concrete and therefore higher concrete electrical resistivity. Specimens were then moved at external conditions during summer and fall, characterized by mild temperatures ($15 \div 30^{\circ}\text{C}$) and very low cumulative rain. Due to the prolonged drought, the values of E_{corr} and i_{corr} remained stable, at values close to the curing chamber conditions, without any particular difference between the cracked (C) and sound (S) conditions and vertical or horizontal orientation, unless for the two sound specimens exposed with vertical orientation, that showed particularly low i_{corr} (0.5 mA/m²). The latest measurements were performed during winter, characterized by a higher amount of precipitations, but no particular difference in values of E_{corr} and i_{corr} were detected, even though i_{corr} seems to slightly increase in time. Again, specimens characterized by vertical orientation (hollow symbols) seemed on average to be characterized by lower values of i_{corr} , while highly cracked specimens by higher i_{corr} , independently from crack orientation.

The same conclusions can be drawn if considering E_{corr} as a function of i_{corr} (Figure 6), where all the measurements during corrosion monitoring are reported for specimens subjected to natural carbonation, while only measurements during corrosion propagation at external exposure are reported for specimens previously subjected to accelerated carbonation. These results may imply that if a crack develops to rebar depth, not only corrosion initiation time may be reduced (excluding possible self-healing effects, not proved to the writing time), but also the corrosion propagation stage, due to a higher corrosion rate. On the other hand, comparable propagation of corrosion may be assumed in carbonated concrete if the crack does not develop to rebar depth, due to comparable corrosion rate values.

4 CONCLUSIONS

This study reports some preliminary results on the effects of cracks on carbonation-induced corrosion. Penetration of carbonation was tested under accelerated exposure conditions in cracked and uncracked unreinforced specimens, while corrosion propagation was monitored in cracked and uncracked concrete specimens subjected either to natural or to accelerated carbonation, considering different orientations of the cracked surface. The adopted cracking procedure was kept constant, to induce micro-cracks in direction longitudinal to the specimen (and the rebar). Carbonation penetration was evaluated through a colorimetric technique while corrosion was monitored through electrochemical techniques to measure corrosion potential and current density.

Results showed that for cracks 30-160 μm wide and 30-40 mm deep, a more marked effect of the crack on carbonation penetration may occur in more impervious concretes, leading to an increase in the carbonation coefficient up to 4 times. The presence of a crack developing down to rebar depth led corrosion initiation within the first 200 days of exposure, and to higher corrosion rates during corrosion propagation. In specimens where crack was supposed not to develop to rebar depth, no particular effect of the presence of the crack, nor of its orientation, was detected.

REFERENCES

- ACI Committee 201 2016. *ACI 201.2R-16 Guide to Durable Concrete*. American Concrete Institute.
- Alahmad, S., Toumi, A., Verdier J. & François, R. 2009. Effect of crack opening on carbon dioxide penetration in cracked mortar samples. *Materials and Structures* 42(5): 559–566.
- Bertolini, L., Elsener, B., Pedferri, P. Redaelli E. & Polder, R.B. 2013. *Corrosion of Steel in Concrete: Prevention, Diagnosis, Repair, Second Edition*. Weinheim: Wiley-VCH.
- Bogas, J.A., Carriço A. & Pontes, J. 2019. Influence of cracking on the capillary absorption and carbonation of structural lightweight aggregate concrete. *Cement and Concrete Composites* 104, 103382.
- Carević, V. & Ignjatović, I. 2019. Influence of loading cracks on the carbonation resistance of RC elements. *Construction and Building Materials* 227, 116583.
- Leporace-Guimil, B., Russo, N., Lollini, F. & Conforti, A. 2023. Morphological and mechanical characterization of reinforcement in cracked elements exposed to chloride-induced corrosion. *Construction and Building Materials* 364, 129822.
- Liu, Z., Van den Heede P. & De Belie, N. 2021. Effect of the mechanical load on the carbonation of concrete: A review of the underlying mechanisms, test methods, and results. *Materials* 14(16), 4407.
- Shaikh, F. 2018. Effect of Cracking on Corrosion of Steel in Concrete. *International Journal of Concrete Structures and Materials* 12(1), 3.
- Russo, N., Gastaldi, M., Marras, P., Schiavi, L., Strini, A., & Lollini, F. 2020. Effects of load-induced micro-cracks on chloride penetration resistance in different types of concrete. *Materials and Structures* 53(6): 1–14.
- Russo, N., Gastaldi, M., Schiavi, L., Strini, A., & Lollini, F. 2022. Chloride penetration resistance in sound and micro-cracked concretes through different experimental techniques. *Construction and Building Materials* 343, 128098.
- Russo, N., Gastaldi, M., Schiavi, L., Strini, A., & Lollini, F. 2023. Effects of cracks on chloride-induced corrosion initiation and propagation of carbon and stainless steel rebar. *Structural Concrete* 24(1):156–169.

Numerical evaluation on electrical resistivity of hardened cement paste using 3D pore model based on X-ray micro-CT images

K. Kawai

Ehime University, Ehime, Japan

T. Nishida

Shizuoka Institute of Science and Technology, Shizuoka, Japan

ABSTRACT: Corrosion resistance against chloride attack and carbonation is essentially associated with electrical resistivity of cover concrete. This study explored numerical simulation on the evaluation of the resistivity of porous materials by FEM analysis. First, 3D model comprised of hardened cement paste and pores fully saturated with pore solution was modelled based on X-ray images taking into consideration the porosity analyzed by mercury intrusion porosimetry. And current flows via ionic conduction through the pores in hardened cement paste are simulated under steady-state condition. And then, the electrical resistivity is evaluated taking into consideration the cell constant in the cubic geometry of 3D model which is of cross section 200 μm each. Based on the results, electrical resistivity is found to be significantly influenced by the presence of connected pores in the hardened cement paste.

1 INTRODUCTION

1.1 Background

The resistance against corrosion is of great importance with regards to durability of reinforced concrete structures (e.g., Kawai et al. 2019). Especially, the resistance against chloride attack is essentially associated with electrical resistivity of cover concrete, which indicates the pore structure. In practice, Wenner method has been widely used for assessing the resistance against the chloride ions in concrete structures as shown in Figure 1. However, the resistivity measured by the method on the actual concrete structure is largely influenced by the water content, the geometry of concrete member, and presence of steel bars. Thus, the measured value would be considered as an indicator for apparent resistivity which should be modified by appropriate cell constant (Morris et al.1996, Minagawa et al. 2022).

On the other hand, the materials property of concrete resistivity is usually measured by the method using cylindrical specimens which are fully saturated (Whiting 1981&1992, AASHTO 2011). The potential difference between the electrodes located at outer sides is measured when constant current is injected between electrodes located at inner sides. And the electrical resistivity (ER) is calculated taking into consideration the cell constant which is $2\pi a$ for most of cases. The cell constant is obtained theoretically; however, it should be modified depending on testing conditions. For example, ionic conduction is essentially limited in cylindrical shape of the specimens. In order to evaluate ER as the materials property of existing concrete structures which possibly have moisture distribution in depth, it is extremely difficult to specify the cell constant depending on many variables as mentioned above. In this study, small samples in 2 mm size obtained from cored concrete are focused on assessing electrical properties associated with pore structure of hardened cement paste. This study utilized X-ray micro-CT images

to model 3D pore structure, which could be a new approach for assessing the mass transport in porous media such as concrete in determining the resistance against ingress of corrosive substances such as chloride ions. This approach is advantageous in assessing the electrical resistance in concrete under dry environment in which the resistivity is not experimentally assessed by the standard method.

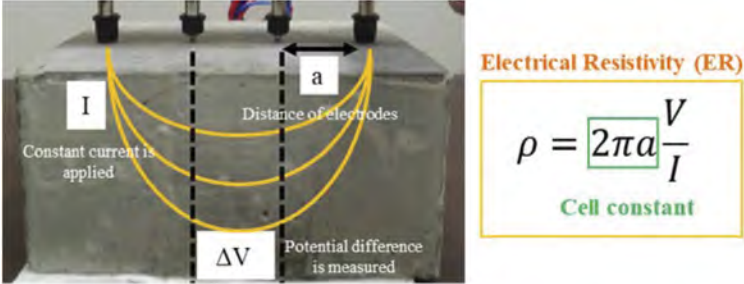


Figure 1. Histogram of grayscale pixel values and modeling of 3D pore structure.

1.2 Objective of this study

Based on the background mentioned above, this study explored the numerical evaluation on the electrical resistivity of hardened cement paste based on X-ray micro-CT images. Especially, the current flows caused by ionic conduction through connected pores are simulated in porous cement matrix. And then, this study compares the results of numerical simulation with those of experimental results measured by conventional Wenner methods.

2 METHODOLOGY

2.1 Materials and specimens

Concrete cylindrical specimens with a diameter of 100 mm and height of 200 mm were made with a water to cement ratio of 0.65. Ordinary Portland cement with a specific gravity of 3.16 g/cm³ was used. Table 1 shows mix proportion of concrete mixture. The specimens were cured under room condition controlled at 20°C until the age of 28 days. The small samples comprised of hardened cement paste in size of 2 mm for X-ray CT images were obtained from the specimens.

Table 1. Mix proportion of concrete mixture.

Unit weight (kg/m ³)				(g/m ³)	
W	C	S	G	SP	AE
165	254	913	954	2538	1.015

2.2 Testing methods

The Wenner method was carried out using four probe method comprised of four stainless electrodes located 50 mm apart. Before the specimens were tested, the specimens were immersed in water tank and fully saturated under vacuum conditions. The results of electrical resistivity were converted to material property taking into consideration modified cell constant depending on the geometry of specimens. And then, the samples were tested by mercury intrusion porosimetry. Porosity and pore volumes with respect to pore size diameter were measured in this study. And porosity of the concrete specimens was also tested by Archimedes method.

2.3 3D pore model based on X-CT images

First, the X-ray micro-CT images were analyzed by image analysis software Simpleware. The size of image is comprised of 1.9 μm in this study. The pore models consist of voxels with scalar/vector values such as absorption rate. Darker color indicates air-filled pores, and in contrast lighter color indicates hardened cement paste with finer aggregate in solid. The 3D voxel models should be divided into two regions including air-filled pores and cement paste in solid by threshold value of pixel value as shown in Figure 2. The dividing line could be determined taking into consideration of porosity measured by mercury intrusion porosimetry and Archimedes method. The latter indicate the porosity with regards to water permeable porosity in the hardened cement paste.

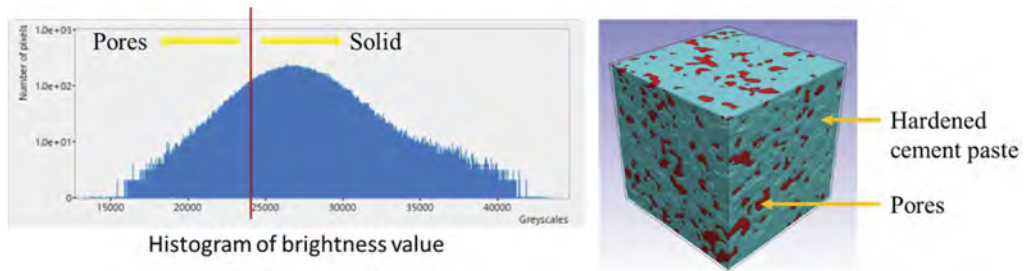


Figure 2. Histogram of grayscale pixel values and modeling of 3D pore structure.

2.4 Numerical simulation

The 3D pore model constructed based on X-CT images as explained in Section 2.3 was further discretized into finite element models using tetrahedral mesh for numerical analysis. The numerical simulation was performed using COMSOL ver. 5.6. When Ohm's law is satisfied and current density is not dependent on time i.e., steady state, and the current density and electric field vector satisfy the following equations:

$$\nabla \cdot J = 0 \quad (1)$$

$$J = \sigma E \quad (2)$$

$$E = -\nabla V \quad (3)$$

where J = current density vector (A/m^2); σ = electro-conductivity (S/m); E = electric field vector (V/m), and V = potentials (V).

As shown in Figure 3, potential difference ΔV is added to the X direction. And the surface integral of current density observed at each plane on the X direction is calculated, which leads to average current I flowing through the porous media. For boundary conditions in the insulation plane, Neumann condition $n \cdot J = 0$ (n : normal vector perpendicular to the plane) is set. Based on the results simulated under steady state, resistivity R can be obtained by the potential V and current I which is known as Ohm's law. In general, the resistivity is proportional to length of the object and inversely proportional to area of the object. The electrical resistivity in terms of volume resistivity without the influence of the geometry can be obtained taking into consideration appropriate cell constant as following equation:

$$\rho = \frac{RA}{L} = \frac{\Delta V A}{I L} \quad (4)$$

where A = area of the object (m^2) and L = length of the object (m).

The calculation is performed in the X, Y, and Z directions in order to confirm the isotropic consistency of the results. the electro-conductivity in the solid and liquid phases is specified as

summarized in Table 2. It should be noted that the electro-conductivity in the liquid phase is largely dependent on the ion concentration and mobility in the pore solution, which meets the requirement of electrical neutrality. The current flows via ion conduction in hardened concrete which is assumed to be fully saturated in the simulation.

Table 2. Electro-conductivity of solid and liquid phases.

Electro-conductivity	S/m
Solid phase (hardened cement paste)	1.0×10^{-12}
Liquid phase (air-filled pores)	5.23

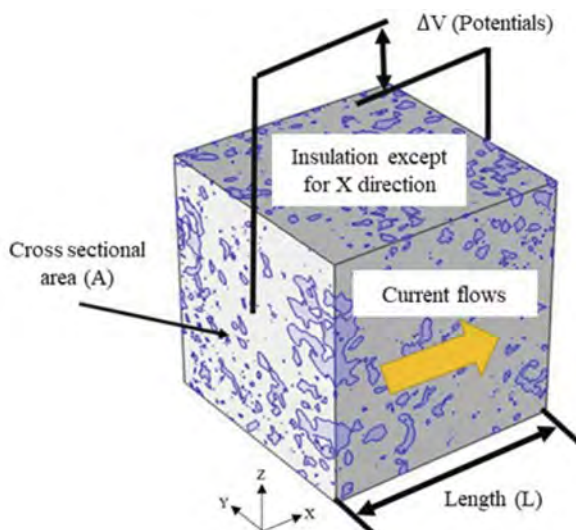


Figure 3. 3D pore model for numerical simulation.

3 RESULTS AND DISCUSSION

3.1 Experimental results of electrical resistivity

Electrical resistivity was measured at the age of 91 days in this study. The values should be converted to volume resistivity without the influence of geometry as mentioned previously. The result was $30.2 \Omega \cdot m$ on average in the case of concrete specimen tested in this study. In addition, mortar specimen was made to measure the resistivity without coarse aggregate, which was $15.7 \Omega \cdot m$ in this study. The difference with regards to the electrical resistance between concrete and mortar is explained by the fact that the aggregate is an electrical insulator in the hardened cementitious materials.

3.2 Porosity and 3D pore models

3D pore model of hardened cement paste is constructed by image analysis using X-ray micro-CT images in this study. The porosity was measured by Archimedes method in the cases of concrete specimens in addition to mercury intrusion porosimetry in the case of small sample obtained from the concrete specimen. Figure 3 shows the porosity measured by the methods,

as can be seen, the porosity 18.51% of hardened cement paste analyzed by mercury intrusion porosimetry ranged between those of concrete and mortar specimens. By setting the porosity of 3D pore model based on the counts of voxels pertaining to each phase of voxel, and the 3D pore models comprising solid and liquid phases are clearly divided. Although the pores especially capillary pores in concrete could range from 3 nm to 30 μm and the gel pores are further smaller than 3 nm, the smaller pores could be recognized as either solid phase or pore phase. The 3D pore model is mostly comprised of larger capillary pores, which could determine the electrical properties by ion conduction in pore solution through connected pores.

As shown in Figure 4, the brightness in determining 3D pore models in cubic shape with a dimension of 200 μm ranged from about 13300 to 13700, which was extracted from 8 locations of original voxel models with a dimension of 2 mm. It should be noted that the locations are mutually exclusive in order to confirm the variations of dividing lines for each phase. As mentioned in Section 2.3, 3D pore models are comprised of two phases such as solid phase and pore phase. Figure 5 shows the regions of pore phase comprising connected as well as isolated pores. As shown in the figure, the pore phase consists of connected pores with 80 to 90% in the total volume of pores.

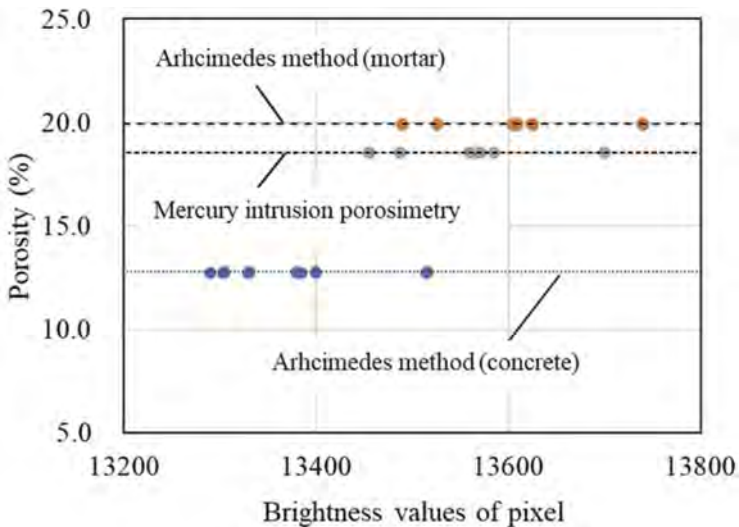


Figure 4. Porosity and variations of threshold value in dividing solid and liquid phases.

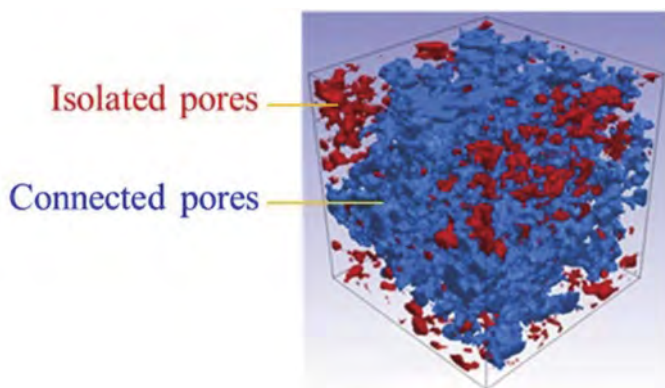


Figure 5. Connected and isolated pores in pore phase.

3.3 FEM analysis on resistivity of porous media

3D pore/voxel model is used for FEM analysis in this study. The FE model comprising tetrahedral mesh was made in this analysis and the number of elements is over 2 million as shown in Figure 6. The mesh size is essentially dependent on the resolution of voxel model made using X-ray CT images. First, a potential difference i.e. 1V is applied between two sides in X, Y, or Z direction as explained in Section 2.4. And then, potential distribution through pores is calculated and is found to be varied depending on the presence of connected pores as shown in Figure 6. It should be noted that the calculation is carried out for total pores (TP) and only connected pores (CP) extracted as mentioned in Section 3.2 to examine the presence of connected pores in pore models.

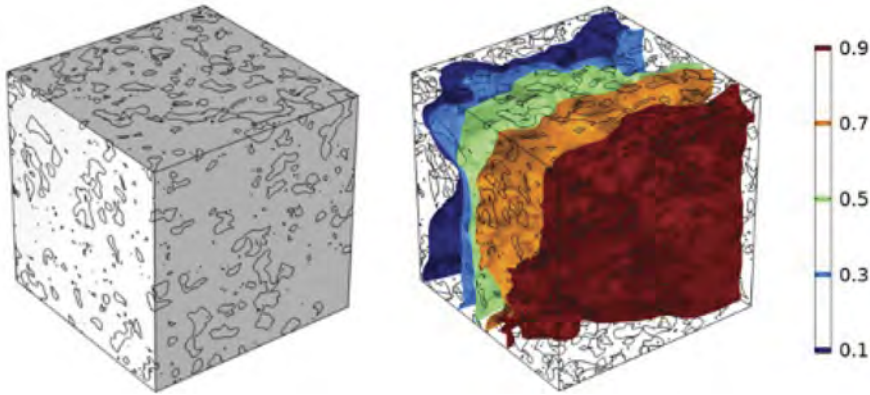


Figure 6. FE model and potential distribution in steady-state.

3.4 Effect of connected pores on electrical resistivity

Figure 7 shows the results of electrical resistivity calculated based on eq. (4). It should be noted that the calculation is made on X, Y, and Z directions to confirm the isotropic property of hardened cement paste. The results are observed to be comparable among the electrical resistivity calculated for X, Y, and Z directions. Based on the results obtained by FEM analysis, the electrical resistivity is $11.71 \Omega\cdot\text{m}$ on average. This is smaller compared to those of mortar specimen ($15.7 \Omega\cdot\text{m}$) and concrete specimen ($30.2 \Omega\cdot\text{m}$) measured by experiments. Although the influence of aggregates present in mortar and concrete could be illustrated by the experimental results which is an insulator to inhibit current flow, the results of FEM analysis are clearly smaller compared to those with the presence of aggregates. This can be explained by the fact that the pore models are mainly comprised of hardened cement paste which led to underestimate the influence of aggregates with respect to the electrical property of concrete. The results seem to suggest that the electrical resistivity could be estimated based on the results of numerical analysis taking into consideration the influence of aggregates as an insulator in concrete or mortar. It should be noted that the electro-conductivity of interfacial transition zone (ITZ) is higher compared to that of cement paste, which should be explored in future research.

In addition, the comparison in the cases of models with total pores (TP) and connected pores (CP) is examined to investigate the effect of connected pores on the electro-conductivity in total pore model. As can be seen in Figure 7, the electro-conductivity is largely dependent on the presence of connected pores since the variation is marginal between two models analyzed especially in the case of PERM-1. As can be seen in Figure 8, the electrical conductivity in the case of results with connected pores is greater by 20 to 30% at most, thus suggesting that the electro-conductivity is largely influenced by the presence of connected pores in which ion movement takes place via ion conduction. In contrast, the presence of isolated pores which are connected each other would have lesser influence on the ion conduction through the pore structure formed in cementitious mixtures.

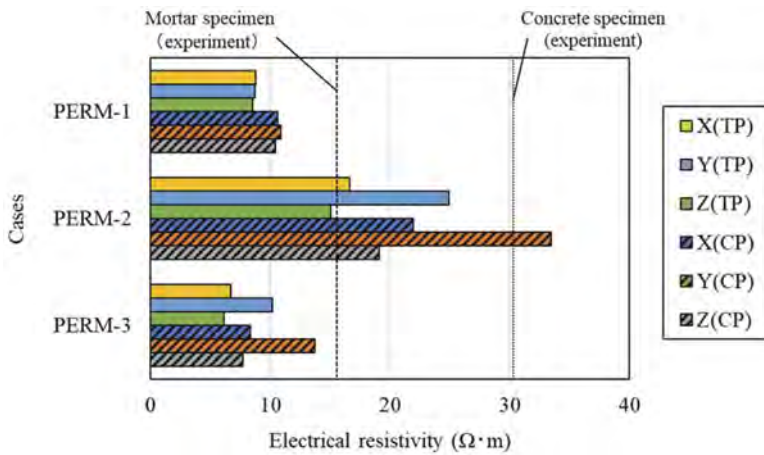


Figure 7. FE model and potential distribution in steady-state.

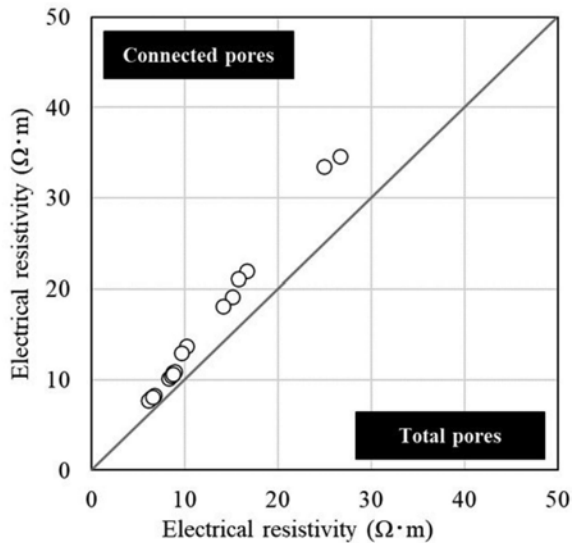


Figure 8. Comparison between ER obtained by TP models and CP models.

4 CONCLUSIONS

This study explored numerical simulation on the evaluation of the resistivity of porous materials by FEM analysis. First, 3D model comprised of hardened cement paste and pores fully saturated with pore solution was modelled based on X-ray micro-CT images with a resolution 1.9 μm . And current flows via ionic conduction through the pores in hardened cement paste are simulated under steady-state condition. It should be noted that 3D pore models are comprised of total pores and only connected pores. And then, the electrical resistivity is evaluated taking into consideration the cell constant in the cubic geometry of 3D model which is of cross section 200 μm each. Based on the results, electrical resistivity is found to be significantly influenced by the presence of connected pores in the hardened cement paste. This study paved the way in evaluating electrical resistivity in existing concrete structure by 3D models analyzed by X-ray micro-CT images.

ACKNOWLEDGEMENT

Financial support by JSPS KAKENHI Grant No. 19H02216 is gratefully acknowledged.

REFERENCES

- Kawaai, K. and Nishida, T. 2019. Corrosion resistance of steel bars in mortar mixtures mixed with organic matter, microbial or other. *Cement and Concrete Research* 124: 105822.
- Minagawa, H., Nakamura, E., Kawaai, K., Miyazato, S., Kato, Y., and Yamaguchi, T. 2022. Reliability of Non-Steady-State Electrophoretic Migration Test. *ACI Materials Journal* 119(3): 223–233.
- Morris, W., Moreno, E.I. and Sagüés A.A. 1996. Practical Evaluation of Resistivity of Concrete in Test Cylinder Using a Wenner Array Probe. *Cement and Concrete Research* 26(12): 1779–1787.
- Standard Method of Test for Surface Resistivity Indication of Concrete's Ability to Resist Chloride Ion Penetration. 2011. *AASHTO* TP 95–11.
- Whiting, D. and Mitchell, T.M. 1992. History of the Rapid Chloride Permeability Test. *Transportation Research Record* 1335: 55–62.
- Whiting, D. 1981. Rapid Determination of the Chloride Permeability of Concrete. *FHWA/RD-81/119*, FHWA, U.S. Department of Transportation.

Coupled deterioration by freeze-thaw and chloride salt on mill-cut steel fiber reinforced concrete

S. Liu & Y. Liu

College of Civil Engineering, Tongji University, Shanghai, China

Y. Li

Shanghai Municipal Engineering Design Institute (Group) Co., Ltd., Shanghai, China

L. Fan

CCCC JUNPU Architecture Technology (Shanghai) Co., Ltd., Shanghai, China

Z. Yang

Shanghai Harex Steel Fiber Technology Co., Ltd., Shanghai, China

ABSTRACT: In order to provide basis for service life of steel fiber reinforced concrete engineered for pavements in frigid region. Long-term freeze-thaw cycles were carried out on mill-cut steel fiber reinforced concrete (MFSRC) in 3.5% NaCl solution, taking into account the fiber volume fraction and cycle index under the coupled deterioration mechanisms of freeze-thaw and chloride penetration. The effect of fiber volumes (0.6%, 1% and 1.4% volume content of concrete) was quantitatively analyzed. The performance degradation of MFSRC was evaluated by surface scaling, mass loss, internal damage, relative dynamic elastic modulus and residual compressive and splitting tensile behaviors. The results show that MSFRC are able to withstand 100 freeze-thaw cycles without significantly surface scaling or degradation in mechanical properties. The internal damage degree of MSFRC sample in 200 saline freeze-thaw cycles is within the acceptable range. When the steel fiber content is increased to 1%, the deterioration of concrete is considerably reduced in the same cycle.

1 INTRODUCTION

Degradation of concrete structures caused by the environmental erosion is regarded as an important durability problem. The use of concrete materials in chilly coastal and seasonal frozen areas is challenging, as concrete structures need to withstand harsh environmental conditions during service (Kuosa et al., 2014). Periodic freeze-thaw changes produce additional internal stress, resulting in cracking, spalling and other deterioration behaviors of concrete (Mayercsik et al., 2016). Moreover, concrete suffers the most severe freeze-thaw damage when the medium is a salt solution with concentration of about 3.5% by weight (Marchand et al., 1999). Both deicing salt and seawater contain a large amount of sodium chloride, which also induce corrosion in reinforcing materials such as steel bars and fibers (Tran et al., 2015). Hence, the ability to withstand chloride erosion and freeze-thaw cycle damage is an important index to improve the durability of concrete.

The effective control of cracks is essential for the service life of structure. The unique morphological characteristics of mill-cut steel fiber enable it to give full play to cracking resistance ability in concrete, inhibit the crack development caused by temperature and expansion stress and effectively delay the penetration rate of chloride ions into the structure (Zeng et al., 2020). Additionally, the addition of steel fiber plays the role of air entraining agent, which enhance the internal gas content of concrete and alleviates the internal stress caused by freeze-thaw cycle (Sun et al., 1999). However, corrosion effect of salt solution on steel fiber may affect

durability of steel fiber concrete (Alsaif et al., 2019). For the prospect of better applying mill-cut steel fiber reinforced concrete (MSFRC) in practical engineering, it is necessary to verify its freeze-thaw resistance in chloride ion medium.

This study aims to investigate the effect of freeze-thaw damage on the performance of MSFRC under accelerated conditions in 3.5% NaCl solution. The level of frost damage was quantified by the matrix spalling, mass loss and the dynamic elastic modulus, which represented external and internal damage degrees respectively. The residual mechanical properties of MSFRC including compressive strength and splitting tensile strength was assessed after being subjected to hundreds of freeze-thaw cycles in NaCl solution. The influence of fiber content on the durability and mechanical properties of MSFRC was also explored, which can be used when analyzing the frost-damaged concrete structures of corresponding materials and may shed some light on the service-life prediction model.

2 EXPERIMENTAL PROGRAMME

2.1 Materials

The cementitious materials consists of 42.5 ordinary Portland cement, with fly ash and slag powder as substitute for 15% cement respectively. Polycarboxylate polymer plasticizer with water reducing rate of 25% was used to enhance the workability of concrete. Natural river-sand with an average fineness modulus of 2.35 was used as fine aggregate. Granite gravel with particle size of 5-25mm was employed as coarse aggregate.

Mill-cut steel fiber (MSF) was mixed into the mixture as reinforced material. The morphological characteristics of steel fiber are illustrated in Figure 1 and Table 1. The mill-cut steel fiber was produced by high-speed milling of the steel ingot with a cylindrical milling cutter. These fibers have rough inner surface and smooth outer surface, with radial distortion of about 20°, and crescent shaped cross section.



Figure 1. Morphologies characteristics and cross-section of mill-cut steel fiber.

Table 1. Physical properties of steel fiber.

Fiber Type	Cross-section	Length, l/mm	Diameter, d/mm	Aspect ratio, l/d	Tensile strength (MPa)
Mill-cut steel fiber	Crescent	32	0.91	35	897

2.2 Concrete mix designs and casting procedures

To explore the influence of mill-cut steel fibers contents of MSFRC under salt freeze-thaw condition, three different mixes were prepared in this study as illustrated in Table 2. Considering the toughening effect and dispersibility, the amount of steel fibers added in MSFRC mixtures were 50 kg/m³, 80 kg/m³ and 110 kg/m³. The mix ID contains letter and number, denoting the type and volume of steel fibers respectively.

The production of MSFRC mixture started with dry components such as cementitious materials and aggregate altogether into the single-shaft mixer and mixing for 2-3 min. Half of the

mixture of superplasticizer and water was then introduced to the mixer, continue stirring for about 5 min to make it adequately reacting. After that, added steel fiber and kept stirring for 3 min until the fibers were dispersed homogeneously. Finally, mixing was continued until the mixture completely uniform, during which the remaining plasticizer` solution was gradually added. Concrete was cast in molds and vibrated on a shaking table for 1min. The specimens were demolded after curing with plastic covering for 48h. Subsequently, all specimens were placed in a curing room with humidity of $92\pm 2\%$ and temperature of $23\pm 1\text{ }^{\circ}\text{C}$ for 28 days.

For measuring the properties of MSFRC after freeze-thaw cycles, cube, prism and beam specimens were cast. Cube specimens with the dimension of $100\text{ mm} \times 100\text{ mm} \times 100\text{ mm}$ were cast for split tensile testing. Prism specimens with the dimension of $100\text{ mm} \times 100\text{ mm} \times 300\text{ mm}$ were used for compressive testing. The beam specimens of $100\text{ mm} \times 100\text{ mm} \times 400\text{ mm}$ dimensions were employed to test resonant frequency at every freeze-thaw period. Meanwhile, surface scaling, mass loss and dynamic modulus of elasticity were measured for each specimen to assess the variation of specimens during freeze-thaw process.

Table 2. Mix proportions of the designed specimens.

No.	Mix proportion (kg/m ³)							
	Cement	Aggregate	Fly ash	Slag	Sand	Water	SP	Fiber
MF0.6	380	1040	85	85	610	149	4.4	50
MF1	380	1040	85	85	610	149	4.4	80
MF1.4	380	1040	85	85	610	149	4.4	110

2.3 Test set-up

2.3.1 Freeze thaw testing

The freeze-thaw resistance of the cube, prism and beam specimens of MSFRC was carried as per GB/T 50082-2009 by rapid freezing and thawing method. The specimens were placed in rubber containers with fully immersing in 3.5% NaCl solution. The containers were then placed into a rapid freezing and thawing machine which could apply continuous freeze-thaw cycles with temperature ranging from $-18\pm 2^{\circ}\text{C}$ to $5\pm 2^{\circ}\text{C}$. Each cycle of freeze-thaw process was completed within 2-4h. The temperature was controlled through the thermocouple embedded in the central specimen.

The damage of concrete caused by freeze-thaw cycles was assessed on several aspects. Through the visual examination of appearance to evaluate the matrix spalling and rusting condition of steel fibers. To quantify the spalling condition of specimen, the mass loss was determined at each freeze-thaw stage. Forced resonance method according to ASTM C215 was employed to obtain the transverse frequency to assess the internal damage. The test set-up is shown in Figure 2, the concrete beam was forced to vibrate by a driver transducer fitted at the middle of specimen, and collect data by the pick up transducer fixed near the edge of specimen. The transducers were pressed on the concrete surface, and petroleum jelly was used as the coupling medium to dispel the air between the surfaces. The dynamic modulus of elasticity of specimens can be determined by Equation (1):

$$E_d = 9.464 \cdot 10^{-4} \cdot ML^3 T f^2 / a^4 \quad (1)$$

where E_d is the dynamic modulus of elasticity (MPa); M is the mass of specimen (kg); f is the transverse fundamental frequency of specimen (Hz); T is the correction factor, $T=1.4$ for a beam specimen; L is the length of specimen (mm); a is the width of square section (mm);

2.3.2 Mechanical properties

The cube specimens were used in splitting tensile test assembly as per GB/T 50081-2019 at a loading rate of 0.05 MPa/s. For compressive strength testing, prism specimens were tested under uniaxial compressive loading at a displacement rate of 0.05mm/min with the help of servo hydraulic testing machine of 1000 kN capacity. Beam specimens were used for freeze-thaw nondestructive testing.

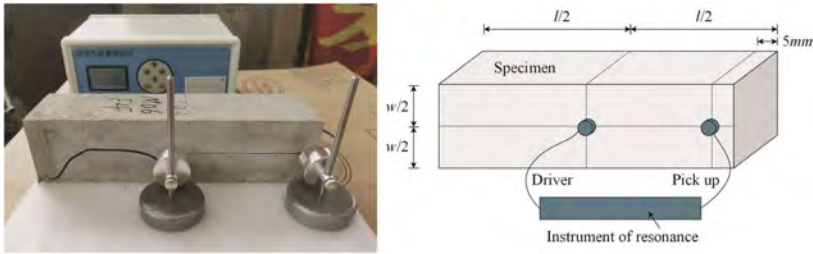


Figure 2. Equipment and schematic view of dynamic elastic modulus testing.

3 RESULTS AND DISCUSSION

3.1 Surface scaling and degradation characteristic

Figure 3 shows the appearance of the cube and prism specimens suffered from freeze-thaw cycles in chloride environment. From diagram it is cleared that hole forming and matrix peeling are the main features of appearance destruction during salt-frost damage. As the number of cycles is increased, surface cementitious layer peels off under the internal stress caused by freeze-thaw cycles, along with the exposure of coarse aggregate and steel fibers at the later stage of freeze-thaw cycles. ASTM C672/C672M determines the visual rating of the concrete surface exposed to freeze-thaw cycles depending on the degree of scaling, as show in Table 3. The cementitious matrix is starting to peel off at 25 cycles of freeze-thaw. After 50 cycles, some corroded steel fibers can be observed on the surface, and the surface layer of M0.6 specimens is totally peeled off. At 75 cycles, M0.6 specimens reaches visual rating 3 with some coarse aggregate visible. Subsequently, after 100 cycles, the exposure degree of coarse aggregate of M0.6 specimens is further aggravated, the concrete is rated as 5 and nearly failed. Meanwhile, the M1 and M1.4 specimens just reach rating 3 at 100 cycles, and then further degenerate to rating 4 at 150 cycles. The surface damage and matrix peeling off during the freeze-thaw cycles is slightly lower when the mill-cut fiber content is 1%. This is a consequence of the appropriate amount of steel fibers can resist the expansion stress caused by the conversion from free water to ice, and relieves the damage degree of matrix peeling off. However, the steel fiber exposed to chloride after the surface mortar stripping is tent to rust, resulting in failure of fiber bridging and spalling together with the matrix. Therefore, excessive fiber content will cause further damage.

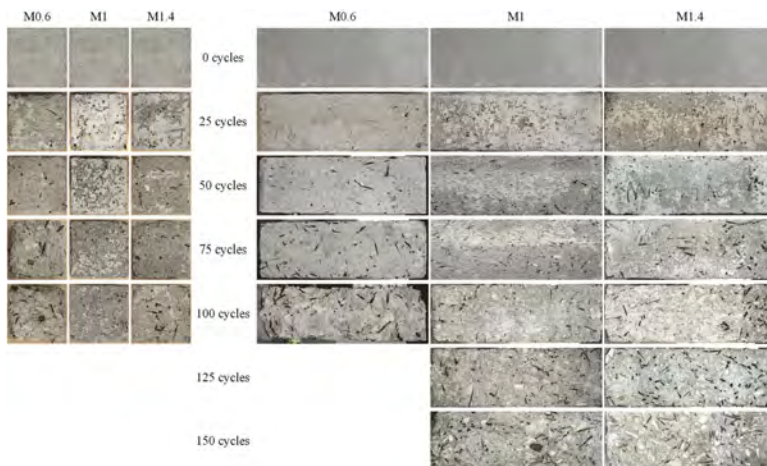


Figure 3. Appearance of specimens before and after freeze-thaw cycles.

3.2 Mass loss after freeze-thaw cycles

The mass loss of specimens was determined after every 25 freeze-thaw cycles. At each specified cycle, each specimen was brushed to remove loose parts and weighed to the nearest 0.1g

Table 3. Visual rating of the surface according to ASTM C672/672M.

Rating	Condition of surface
0	no scaling
1	very slight scaling (3mm depth, max, no coarse aggregate visible)
2	slight to moderate scaling
3	moderate scaling (some coarse aggregate visible)
4	moderate to severe scaling
5	severe scaling (coarse aggregate visible over entire surface)

during the thawing phase. Comparing with the mass before corrosion, the percentage of mass loss after n cycles was calculated according to Equation (2):

$$\Delta W_n = \frac{W_0 - W_n}{W_0} \cdot 100 \quad (2)$$

where ΔW_n is the mass loss rate of specimens after n cycles (%); W_n is the mass measured after n cycles (g); and W_0 is the initial mass of specimens after curing and before testing (g).

The mass loss of specimens of different size versus the number of freeze-thaw cycles in chloride environment is shown in Figure 4 and Table 4. Considering the mass loss and that of per unit area, it is evident that the size effect doesn't play a key role in the freeze-thaw damage of MSFRC. Despite the damage area of small-size specimens under the same freeze-thaw conditions is relatively large, the specimens are not further deteriorated due to the reinforcement of steel fibers. Throughout the test, M0.6 specimens exhibit maximum mass loss, while M1 and M1.4 shows lower mass loss behavior. The M0.6 specimens display a sudden increase at 75 freeze-thaw cycles, indicating a severe damage of specimen after 75 cycles. The mass loss per unit area occurred in M1 and M1.4 specimens is less than 1.5 kg/m^2 after 125 cycles of salt-freezing, and the mass loss rate is less than 5% within 200 cycles, which indicates that the excellent salt-freezing resistance of the two groups according to the failure standard specified by GB/T 50082-2009. The M1 specimens display the lowest rate of mass loss especially after 100 cycles, which is attributed to the presence steel fiber. The interface adhesion between steel fiber and matrix restricts the peeling of mortar.

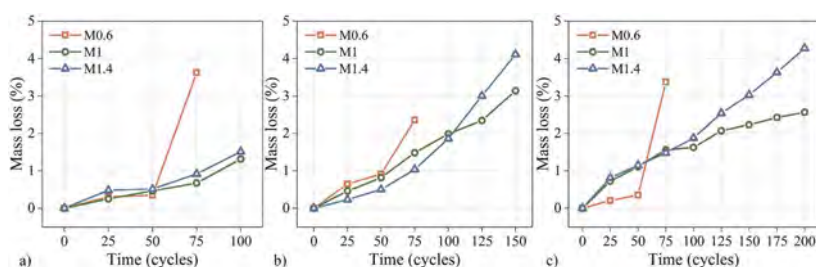


Figure 4. Mass loss due to freeze-thaw cycles. a) MSFRC cubes; b) MSFRC prisms; c) MSFRC beams.

3.3 Dynamic modulus of elasticity

The dynamic modulus of elasticity (DME) of beam specimens with different steel fiber content before and after freeze-thaw cycles are calculated from transverse fundamental frequency using the Equation (1) in section 2.3.1, as shown in Figure 5. Due to the high stress and strain measurement conditions, the DME of non-freezing specimens is above 40000 MPa, which is higher than the static elastic modulus measured under normal conditions. As can be seen from the figure, the initial DME of M1 specimens with 1% fiber content is higher than that of other two groups. During the freeze-thaw cycles, M1 and M1.4 specimens exhibit higher DME, while a sudden drop in DME occurs in M0.6 group when the freeze-thaw cycles reach around 100, indicating that the increase of mill-cut steel fiber content is contribute to improve the frost resistance of concrete. In addition, different from the variation trend of mass loss, the DME of M1

Table 4. Mass loss per unit area for all tested mixes.

Mix	Specimens	Mass loss after n cycles (kg/m ²)							
		25	50	75	100	125	150	175	200
M0.6	cube	0.12	0.14	1.43	5.49				
	prism	0.34	0.48	1.24	3.05				
	beam	0.11	0.19	1.83	4.89				
M1	cube	0.10	0.19	0.27	0.53				
	prism	0.24	0.44	0.79	1.06	1.25	1.67		
	beam	0.39	0.60	0.85	0.88	1.12	1.21	1.31	1.39
M1.4	cube	0.19	0.21	0.37	0.62				
	prism	0.12	0.27	0.55	0.99	1.59	2.18		
	beam	0.45	0.64	0.82	1.04	1.40	1.67	2.01	2.36

specimens increases slightly during 125-150 cycles. This is a likely consequence of the intrusion of salt solution into the matrix, the pulse wave passes directly through the solution in the pores without being blocked by the crack interface. Meanwhile, the steel fiber in the matrix also plays a conductive role, so that the wave velocity presents a rising trend and the DME increases.

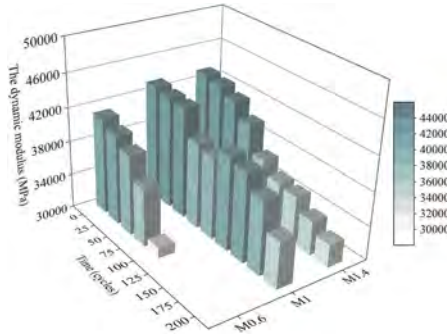


Figure 5. Dynamic modulus of elasticity of MSFRC after freeze-thaw cycles.

3.4 Relative dynamic modulus of elasticity

In this section, the variation of DME after saline freeze-thaw cycles was used to evaluate the internal damage of concrete. As stipulated in ASTM C666, the relative dynamic modulus of elasticity (RDME) after n cycles was calculated by Equation (3):

$$P_n = \frac{f_n^2}{f_0^2} \cdot 100 \quad (3)$$

where P_n is the relative dynamic modulus of elasticity after n cycles of freeing and thawing (%); f_0 is the fundamental transverse frequency at 0 cycles (Hz); f_n is the fundamental transverse frequency after n cycles (Hz).

Figure 6 shows the RDME of the concrete beam specimens as a function of the number of freeze-thaw cycles applied. As a key index reflecting the freezing resistance of concrete, when the RDME drops to the threshold value of 80% defined by GB/T 50082-2009 and RILEM 2004, the specimen can be considered to have reached the freeze-thaw limit. In general, the RDME decreases with the number of freeze-thaw cycles increases. The M1 and M1.4 specimens survived 200 freeze-thaw cycles and their RDME are above 80%, showing good durability. At 100 cycles, M0.6 and M1.4 specimens have a prominent decline stage which represents relatively obvious matrix damage. In particular, the RDME of M0.6 specimens drops below 80% after 100 cycles, indicating that the specimens have failed. Whereas, similar to the DME, M1 specimen shows a special rising stage after 100 cycles. This is mainly due to the invasion of chloride solution, which generate crystalline substances such as Friedel's salt to fill the internal pores and cracks and increase the bonding effect between fiber and matrix.

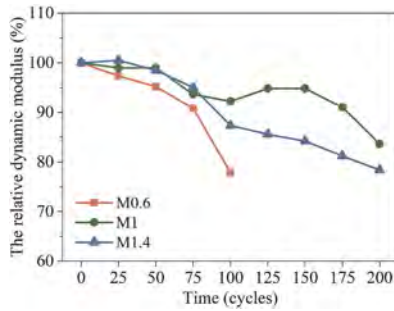


Figure 6. Relative dynamic modulus of elasticity during freeze-thaw cycles.

3.5 Compressive strength

The compressive behavior of the specimens after freeze-thaw cycles are summarized in Figure 7. As can be seen from the figure, with the content of steel fibers increases from 0.6% to 1%, the compressive strength of specimen is raised to 56.9 MPa. However, no further increase in compressive strength is observed when the content reaches 1.4%. Previous studies have also shown that excessive steel fiber content tends to cause uneven fiber dispersion, which leads to the decline of compressive strength (Hasan-Nattaj and Nematzadeh, 2017). As the freeze-thaw cycle proceeds, the compressive strength of M0.6 and M1.4 specimens decreases gradually. Whereas after 75 cycles, M0.6 and M1.4 specimens suffers significant strength loss during 75-100 cycles, while M1 enters a special plateau with strength loss rate remains below 30% until 150 cycles, which is similar to the change trend of RDME. This indicates that the 75th freeze-thaw cycle is the critical point of freeze-thaw damage of MSFRC specimens. According to the previous appearance damage analysis, the external matrix begins to peel off after 75 cycles, lacking or excessive fiber content would aggravate this damage. Meanwhile, too many fibers will cause additional internal initial defects, which weakens the durability and compressive strength of specimens. In conclusion, the content of steel fiber has an obvious effect on the compressive strength of concrete after saline freeze-thaw cycles. The content of mill-cut steel fiber is recommended to be controlled at 1%, which is conducive to improving the frost resistance and compressive strength of concrete, so that the specimen can maintain good durability after 150 cycles.

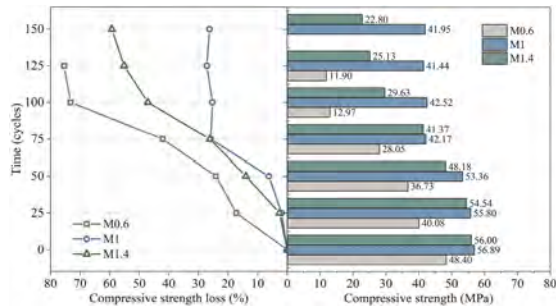


Figure 7. Compressive strength of MSFRC before and after freeze-thaw cycles.

3.6 Splitting tensile strength

Figure 8 shows the split tensile strength of MSFRC specimens under different freeze-thaw cycles. It shows that the splitting tensile strength increases by 11% and 20% respectively, when the fiber content is 1% and 1.4%, compared with M0.6 specimens. The splitting tensile strength loss rate of M0.6 specimen reaches 30% when the freeze-thaw cycle is only 25 times, and the strength deteriorates rapidly after 50 cycles, with the loss rate exceeding 60%. It might be due to the low fiber content has no inhibiting effect on the spalling of the matrix under the freeze-thaw cycle, resulting in serious damage of the small-volume specimen and early entry into the failure stage. In the case of M1 and M1.4 specimens, the splitting tensile strength sustains above 5 MPa during 100 freeze-

thaw cycles, and the strength loss rate is less than 20%, indicating that the material still have good mechanical properties. The results show that the saline freeze-thaw cycle has slight effect on the steel fiber inside the specimen, and the fibers can still play the bridging role and improve the tensile properties of the matrix after the cumulative damage of multiple cycles. The strength loss rate of splitting tensile strength is less as compared to that of compressive strength of MSFRC at their respective freeze-thaw cycles, the presence of fibers has a more obvious effect on the improvement of tensile performance. When the fiber content reaches 1%-4%, MSFRC can be considered to still have good splitting tensile strength after 100 freeze-thaw cycles.

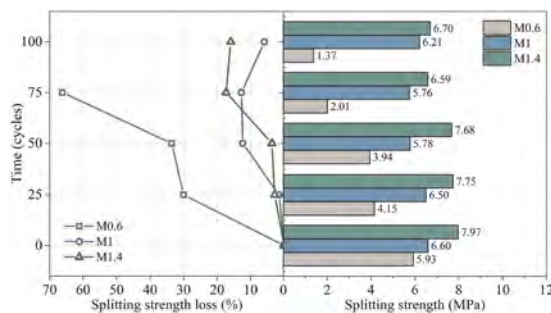


Figure 8. Splitting tensile strength of MSFRC before and after freeze-thaw cycles.

4 CONCLUSIONS

This study assessed the saline freeze-thaw performance of mill-cut steel fiber reinforced concretes (MSFRC). Based on experimental results, some conclusions are as follow:

- 1) The inclusion of mill-cut steel fiber mitigates the negative effects of freeze-thaw, MSFRC with fiber content between 1% and 1.4% can tolerate more freeze-thaw cycles without severe damage. The mass loss rate of specimens is less than 5% after 200 cycles, which is acceptable according to the GB/T 50082-2009.
- 2) Dynamic elastic modulus reflects the changing trend of compressive strength. Within a reasonable steel fiber content range (1-1.4%), the relative dynamic elastic modulus maintains above the critical value (80%) for internal damage during 200 cycles.
- 3) Mill-cut steel fiber is effective to enhance the tensile behavior of concrete, up to 11% and 20% with the increase of fiber content. The presence of steel fibers significantly reduces the loss rate of splitting tensile strength due to the saline freeze-thaw, compared to that in compressive strength.

REFERENCES

- Alsaif A, Bernal S A, Guadagnini M, et al. 2019. Freeze-thaw resistance of steel fibre reinforced rubberised concrete. *Construction and Building Materials* 195, 450–458.
- Hasan-Nattaj F, Nematzadeh M. 2017. The effect of forta-ferro and steel fibers on mechanical properties of high-strength concrete with and without silica fume and nano-silica. *Construction and Building Materials* 137, 557–572.
- Kuosa H, Ferreira R M, Holt E, et al. 2014. Effect of coupled deterioration by freeze-thaw, carbonation and chlorides on concrete service life. *Cement and Concrete Composites* 47, 32–40.
- Mayercsik N P, Vandamme M, Kurtis K E. 2016. Assessing the efficiency of entrained air voids for freeze-thaw durability through modeling. *Cement and Concrete research* 88, 43–59.
- Marchand J, Pigeon M, Bager D, et al. 1999. Influence of chloride solution concentration on deicer salt scaling deterioration of concrete. *Materials Journal* 96(4), 429–435.
- Sun W, Zhang Y M, Yan H D, et al. 1999. Damage and damage resistance of high strength concrete under the action of load and freeze-thaw cycles. *Cement and Concrete Research* 29(9), 1519–1523.
- Tran N T, Pyo S, Kim D J. 2015. Corrosion resistance of strain-hardening steel-fiber-reinforced cementitious composites. *Cement and Concrete Composites* 63, 17–29.
- Zeng W, Ding Y, Zhang Y, et al. 2020. Effect of steel fiber on the crack permeability evolution and crack surface topography of concrete subjected to freeze-thaw damage. *Cement and Concrete Research* 138, 106230.

Construction of hydrogen pipeline utilizing communication pipeline and experimental study on its utilization

T. Ishikawa & K. Itasaka

NIPPON Telegraph and Telephone Corporation, Tsukuba-city, Ibaraki, Japan

ABSTRACT: In this report, we report on hydrogen transportation using a communications infrastructure to achieve a decarbonized society. Due to a reduction in communication cable diameter, the space in the conduit to accommodate the cables has increased. To make effective use of this space, efforts are being made to transport hydrogen by using a double pipeline system. At present, the transportation of hydrogen is mainly carried out by tanker trucks, and further reduction of transportation costs and CO₂ emissions are required in the future. As a solution, transporting by pipeline utilizing existing transmission lines is demonstrated. Hydrogen transportation by pipeline requires airtight transportation, because it is assumed that the gas is supplied under high pressure. Therefore, in the verification, a flexible stainless steel tube will be constructed in an existing communication tube and used as a pipeline for hydrogen transportation.

1 BACKGROUND AND PURPOSE

The 2050 Carbon Neutral Declaration announced by the Japanese government set a goal of achieving a decarbonized society and net-zero greenhouse gas emissions by 2050, and NTT is also considering expanding its efforts to achieve carbon neutrality to society as part of its efforts to achieve the Declaration. As one effort to achieve a decarbonized society, a verification was conducted on a hydrogen transportation initiative using existing communication pipes.

At present, delivery of hydrogen by tanker truck is the mainstream transportation method in Japan, but further reduction of transportation costs and carbon dioxide (CO₂) emission are required in the future. As a solution, we aimed to demonstrate a transportation method by pipeline using a previously-constructed 75-mm communication pipe.

Communication cables have changed from metal- to optical-based ones, and as their diameters have become smaller, the space in communication pipes to accommodate the cables has increased, so we are focusing on that space (Figure 1).

To make effective use of this available space, we aim to design a double pipeline system that enables hydrogen to be transported in a pipeline installed in the empty space. We also aim to conduct various technical demonstrations.

Since transporting hydrogen by pipeline is assumed to be carried at a high pressure, the airtightness of the hydrogen pipeline must be ensured. Generally, hydrogen is said to be highly permeable, and we decided to use a stainless steel tube with less hydrogen permeation.

In this demonstration, the existing communication pipe was constructed using flexible stainless steel pipe, which was assumed to enable it to flexibly deal with both straight and curved cables. Hydrogen is pumped into the pipeline to confirm its workability and operability as a hydrogen pipeline, and to confirm whether transporting hydrogen using a double piping system is possible (Figure 2).

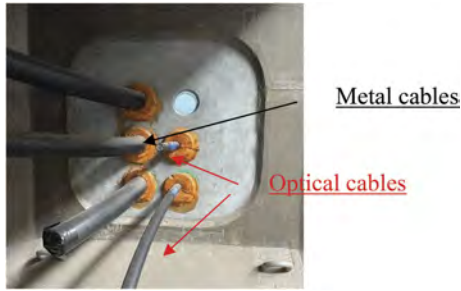


Figure 1. The space in communication pipes to accommodate the cables.

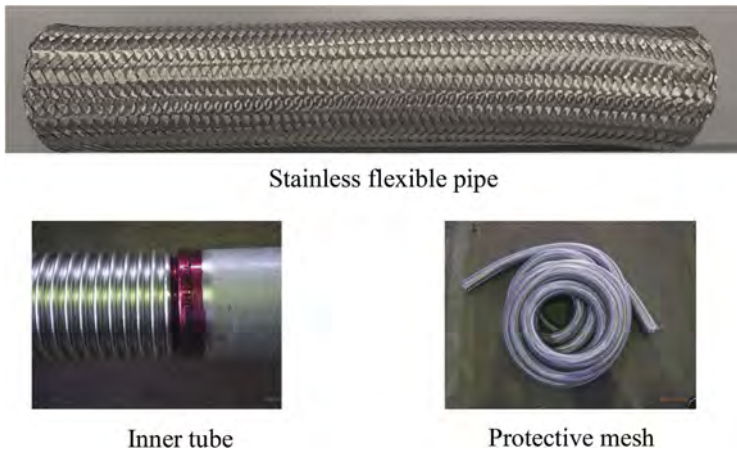


Figure 2. Stainless flexible pipe.

The construction of the double pipeline system can effectively utilize the preexisting pipeline and can maximize the use of existing facilities by eliminating the need for road excavation to resolve any impact of life cycle cost. (Figure 3)

Generally, communication pipes are classified as metal and vinyl pipes. In this demonstration, vinyl conduits were used for the communication pipes as it was assumed that the surface friction force was lower than that of metal.

The constructed pipeline houses a flexible stainless steel tube in an existing vinyl pipe, which is towed through the pipe by a winch from a nearby manhole.



Figure 3. Double piping system.

Since some friction with the pipeline will occur, in this demonstration, the pipe will be towed in a section of up to 150 m to determine its feasibility.

In addition, friction between the vinyl pipe and flexible stainless steel pipe is expected. Therefore, both the communication and flexible stainless pipes are checked for damage by laboratory tests.

The content of the report is as follows:

- 1: Examine whether construction of a double pipeline system is possible that accommodates flexible stainless steel pipelines in communication pipes
- 2: Determine if it is possible to transport hydrogen after construction
- 3: Determine if metal pipe and flexible stainless steel pipe are affected by friction during construction

2 VALIDATION (1)

The verification was carried out to determine whether a double pipeline system could be constructed in which a flexible stainless steel pipeline was housed in the communication pipe.

During construction, plastic elongation is expected to occur when the flexible pipe stainless steel is pulled. In addition, construction with a winch is assumed to not be possible due to plastic deformation, and this will also be confirmed.

As a result of towing the flexible stainless steel tube at a speed of 3 m per minute as shown in Figure 4, the following points were confirmed: construction was possible without any problems with tension, horizontal and vertical bend sections could be constructed without any problems, and the stainless steel flexible tube was stretched because it was pulled during construction but shrank when the winch was removed; this effect would be negligible in future construction.



Figure 4. Construction.

3 VERIFICATION (2): HYDROGEN TRANSPORT VERIFICATION

An airtight check was conducted to ensure that no gas leakage occurred in the system constructed in the verification (1). For confirmation, nitrogen gas with no risk of explosion was pumped to a constructed double piping system, and pressure drop measurements were performed on the supplying and receiving sides under the conditions shown in Table 1. The test pressure was held for 120 minutes, after which a foaming agent was used to detect any leaks or pressure drops.

The airtightness with nitrogen confirmed the possibility of transporting hydrogen using a hydrogen pipe. The pressure during transportation was at 0.95 Mpa. We also determined whether hydrogen was leaking by installing a hydrogen sensor.

Table 1. Pressure drop measurements result.

Normal pressure (MPa)	Test pressure (MPa)	Measurement time (minutes)	Results	Judgment
0.95	1.05	120	No leakage	OK

We confirmed that the stainless steel flexible tube was stretched during hydrogen transportation. In particular, since the extended force is concentrated at a fixed point, problems such as the elongation and meandering of the flexible stainless steel tube between the fixed position in a manhole and the duct opening were confirmed (Figure 5).

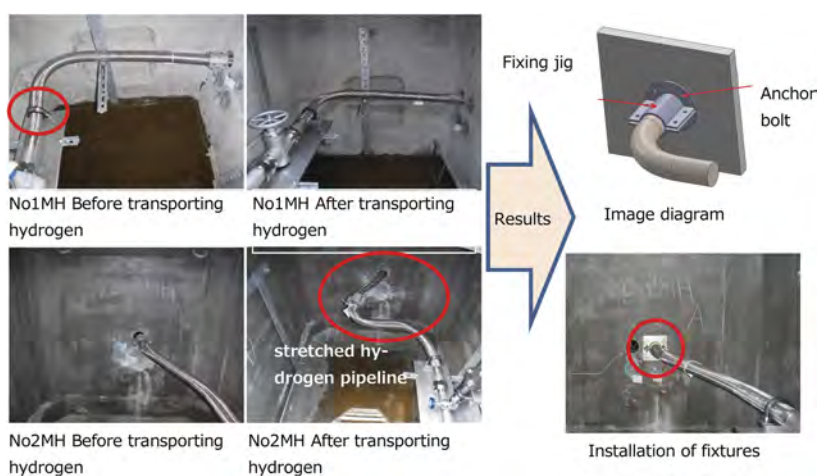


Figure 5. Result.

In response to these problem, we confirmed that the stainless steel flexible pipe extends 5 mm/m at a pressure of 0.95 Mpa when checking how long the pipe extends during hydrogen transportation. Depending on where the extension force is applied, the stainless steel flexible pipe was at risk of buckling, so countermeasures were considered.

We confirmed that the extension of the flexible pipe into the manhole could be suppressed by fixing the pipe at the connection between the manhole and pipeline. When hydrogen was transported at a pressure of 0.95 MPa as in the previous experiment, the elongation of the stainless steel flexible tube was suppressed by the fixation effect.

From this result, it is assumed that since elongation occurs when hydrogen is transported using flexible stainless steel tubes, it is necessary to first fix them in manholes, and any damage to them must be suppressed by countermeasures.

4 VERIFICATION (3): EFFECT OF FLEXIBLE STAINLESS STEEL PIPE INSTALLED IN A METAL COMMUNICATION PIPE

As a number of communication pipes are made of metal, the stainless steel flexible pipe may be damaged due to contact with rust or the like in the metal pipe when towed through it by

a winch. This test confirmed any scratches or breakages when the stainless steel flexible pipe was laid using metal tubing intentionally constructed with rust.

The conditions for the test are as follows. A rusted metal communication pipe (5 m) was prepared, in which a flexible stainless steel tube cut to 30 cm is reciprocated. On the basis of the number of reciprocations, the distance of the flexible stainless steel pipe laid in the metal pipe is calculated. The flexible stainless steel tube is then visually checked for scratches at each distance. The distances verified were between 250 and 2,500 m.

Conclusion:

When the stainless steel flexible tube was pulled for a length equivalent to 2,500 m, a slight scratch occurred on its surface. However, it had no effect when hydrogen was passed it, indicating that the metal tube did not affect the flexible stainless steel tube. (Figure 6)

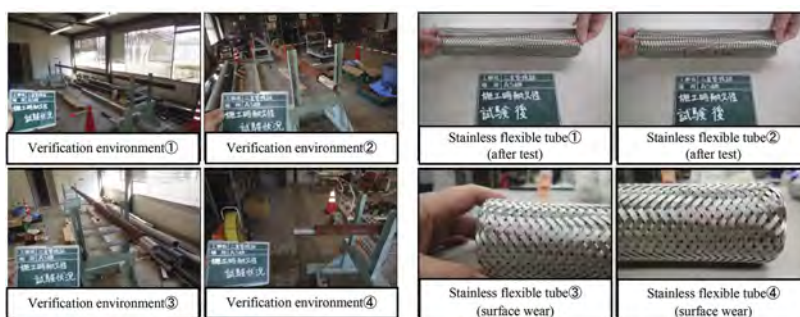


Figure. 6. Result.

5 CONCLUSIONS

We verified whether a hydrogen transportation system could be constructed by utilizing the empty space in existing communication pipes.

- The purpose of this study was to confirm the possibility of constructing a stainless steel flexible conduit for communication pipes in a research facility in Tsukuba City using a double conduit system. It was confirmed that stainless steel flexible tubes can be constructed without any effects even if horizontal or vertical bend sections are present.
- When pumping hydrogen through the constructed system, it was found that the stainless steel flexible tube extends in the manhole space. Therefore, it was confirmed that it was possible to suppress the elongation by taking measures such as fixing it in a manhole.
- A verification was carried out to see if a flexible stainless steel pipe could be laid on a rusted metal communication pipe. It was confirmed that the effect was minor even when towing the pipe over 2500 m.

On the basis of the aforementioned points, the construction of hydrogen facilities that contribute to the reduction of life cycle costs and carbon dioxide generated in construction, is possible by utilizing existing systems, resources, and limiting construction by excavation.

REFERENCES

Katano, Y., Nishizaki, K. and Iwamatsu, J.: Corrosive Environment of Underground Pipes and Prediction of Corrosion, Corrosion Engineering, Vol. 37, pp. 205–211, 1988]

Modelling the thermal response of firestop sealant exposed to standard fire

Z. Ye, A.K. Abu, C.M. Fleischmann & R.P. Dhakal

University of Canterbury, Christchurch, New Zealand

ABSTRACT: Firestopping systems are non-structural passive fire protection elements which are used to seal service penetrations through fire-rated assemblies. They are designed to restrict fire spread for durations of exposure following the standard fire test. Depending on the material used, different firestopping configurations can behave very differently even when exposed to the same heating environment. However, current understanding of fire performance of firestopping systems is based on standard fire testing, without a full appreciation of thermal behavior of the firestopping material (called firestop). As an initial assessment to identify thermophysical properties for firestop materials, this sensitivity study investigates how variations of temperature-dependent thermal property inputs affects the results of the numerical analysis in comparison to test data. The close comparison between the experimental results and numerical prediction highlights the extreme importance of gathering the right fundamental properties for fire behavior modelling.

1 INTRODUCTION

In modern fire safety engineering design, the concept of compartmentation plays a significant role. As a general design principle, a building is considered as composed of multiple fire-protected zones, in which each zone is capable of containing a fire for a reasonable duration (Soja, 2022). Thus fire-resistive barriers, which are used to separate fire compartments, are required to maintain their integrity during their service life in order to prevent flame and smoke passage during fire events. However, in real applications non-structural services, such as piping and electrical communication systems, are run from one part of the building to another; these systems sometimes need to go through fire-rated walls and floors. The existence of these penetrating building components could undermine the physical integrity of original fire separation. To cope with this problem and ensure the overall effectiveness of fire compartmentation, firestops have been well-applied to protect penetrations in fire separations. These firestops are designed to firmly seal installation gaps between penetrations and fire barriers. In theory, they do not fail earlier than the main body of the protected fire-rated assemblies during real fires (The Ministry of Business Innovation and Employment, 2020). Various fire-stop solutions are available in today's market to respond to the demand for different characteristics of protected penetrations (e.g. size of cable bundles, plastic pipe versus metallic pipe, etc.) and fire-rated wall/floor assemblies (e.g. dimensions of apertures, drywall versus concrete wall, etc.). For example, firestop wrap and collar are frequently used for filling the gaps caused by the melting of plastic pipes under heat (Sędłak et al., 2017) while high thermal conductive metal penetrations rather use porous firestop mastic or high-density board systems to retard the heat transfer at contact faces (Soja, 2022). The holistic fire separation assembly is called as a firestopping system. For cases where fire-rated substrate are completely penetrated by service installation (as illustrated in Figure 1) they are known as through-penetration fire-stopping systems (ASTM International, 2017).

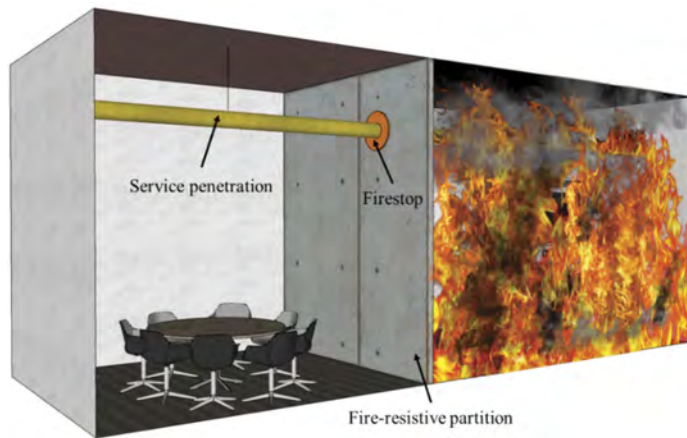


Figure 1. Three main components of a typical through-penetration firestopping system.

Firestopping systems are classified as passive fire protection (PFP) systems which are usually not designed with any load-bearing capacity. Similar to most other PFP systems, their fire performance is rated by a period of time that the systems survive under exposure to a conventional standard fire. The tested performance is standardized as a Fire Resistance Rating (FRR) usually in multiples of 30 minutes. The assessment criteria considers integrity (E) and insulation (I), which examine the capability to block flame propagation through the medium and restrict a rapid temperature rise on the non-fire-exposed side of the medium (International Organization for Standardization, 1999; European Committee for Standardization, 2009; Standards Australia, 2014). Additional criteria such as air leakage (L) and water rating (W) may also be required in certain regions (International Code Council, 2021). Nevertheless, the traditional standard furnace tests never consider performance deterioration nor effects of consequences during service life. For instance, significant seismic damage has been recorded on firestopping systems in recent earthquakes (Baker et al., 2012; Federal Emergency Management Agency (FEMA), 2012). Considering that not all buildings are likely to be fully inspected after every seismic event, especially if only minor and medium earthquakes occur, seismic-induced openings around service penetrations could act as potential paths which channel fire and smoke between adjacent compartments. Namely, the fire protection systems would be left vulnerable and may fail earlier than expected in a future potential large fire. As observed above, this fire safety issue is particularly important for seismically active countries, such as United States, Japan, New Zealand and so on. However, the effective performance of earthquake-damaged firestopping systems has not yet been studied.

During initial investigations of the residual functionality of general firestopping systems in the aftermath of earthquakes, the authors realized that there is a significant lack of knowledge, including the transient thermal behavior of firestop materials at elevated temperatures. This is because the fire engineering design industry focuses on systems that meet a minimum fire resistance rating to the standard fire, which never occurs in a real building fire, to meet standardized design requirements. As such, there is no understanding of the reactions involved and heat transfer mechanisms of various firestop materials in fires. On the other hand, the lack of property information of common firestops also increases the difficulty to simulate the associated thermal behavior through numerical modeling. As a result, it becomes a challenge to predict the actual performance of firestopping systems when exposed to both standard and non-standard fire conditions.

As a credible numerical benchmark model does not yet exist for any firestopping system, largely rooted in the deficiency of fundamental material properties, this paper aims to utilize thermal property inputs to develop a preliminary finite element (FE) heat transfer model for a commonly used firestop acrylic sealant. The model is built based on a standard fire test (Warrington Fire Research Consultancy, 1996). Among all related material parameters, conductivity (k), specific heat capacity (c_p) and density (ρ) are the most important ones that govern the temperature

rise within solids (Wickström, 2016). Information is provided by the product manufacturer on the change in density with temperature. As such the research mainly probes into the impacts of pseudo thermal conductivity (k) and specific heat (c_p) inputs on the accuracy of surface temperature estimates. The thermal response of the firestop solution was modelled in comparison to well-established material models of timber, gypsum board and intumescent paint. The thermal properties of these three materials have been relatively better understood in contrast. A comparison of corresponding numerical results based on different thermal property models is also drawn in this paper.

2 FINITE ELEMENT MODELING

2.1 Description of the simulated fire test

The numerical model presented in this paper was developed based on a standard fire test conducted by Warrington Fire Research Consultancy (1996). The tested assembly consisted of two identical lightweight autoclaved aerated concrete (AAC) substrates, which had dimensions of 0.15×0.15×0.95 m. A rockwool insulation and a non-intumescent firestop acrylic sealant were applied to fill a 30 mm wide gap between the substrates. There was no penetrating element included in the test to avoid any ill-defined thermal interactions. The overall structure of the tested system can be seen in Figure 2a. During the experiment, the rockwool insulation was fully exposed to the hot gases and flame, while the firestop sealant sat behind the rockwool layer. It did not receive any direct heat flux from the furnace. The test strictly followed the normative assessment requirements stipulated in BS 476-20:1987 (British Standards Institution, 1987). The test started at room temperature of 18 °C. The monitored furnace temperature throughout the four-hour test is plotted in Figure 3.

A corresponding three-dimensional thermal model was analyzed by using the finite element solver ABAQUS/Standard (Dassault Systèmes, 2020). In the present model, all solids were discretized into eight-node linear heat transfer bricks (DC3D8) for an uncoupled heat transfer analysis. A fine mesh size of 0.005 m was assigned on each side and it showed an overall good quality of results.

By following the instructions for modelling a standard fire scenario suggested in the standard BS EN 1991-1-2 (European Committee for Standardization, 2002), a convective heat transfer coefficient (h_c) of 25 W/m²K with a emissivity factor (ε) of 0.8 was assigned at the fire-exposed boundary, which is labelled and shaded in Figure 2a. These two parameters help model the incident convective (\dot{q}''_{conv}) and radiative heat flows (\dot{q}''_{rad}) produced by the furnace respectively, and they are assumed to be applied uniformly across all heating boundaries. Overall, the net heat flux ($\dot{q}''_{\text{total,fire}}$) received on the fire-exposed surfaces can be then represented as following equation:

$$\dot{q}''_{\text{total,fire}} = \dot{q}''_{\text{conv}} + \dot{q}''_{\text{rad}} = h_c(T_g - T_s) + 5.67 \times 10^{-8} \Phi \varepsilon \left[(T_g + 273)^4 - (T_s + 273)^4 \right] \quad (1)$$

where Φ represents the view factor, with a default value of one for surface radiation. T_g and T_s stand for the transient furnace temperature (i.e. Figure 3) and surface temperature of element respectively in degree Celsius. The value of T_s at each time step was estimated by solving the related heat balance equations using ABAQUS (Dassault Systèmes, 2006; Nithiarasu, Lewis & Seetharamu, 2016). The convective heat transfer coefficient was set to 9 W/m²K to account for combined heat loss through both convection and radiation on the unexposed surface (ambient side) of the AAC slabs. The other boundaries of the AAC slab were all assumed to be adiabatic.

Besides, a uniform thermal conductance of 3 W/m²K was defined at all contact surfaces in accordance with a battery of sensitivity analysis. This is because the value of thermal conductance is highly variable to the conditions at the contact surfaces (e.g. pressure and gap distance between solids (Dassault Systèmes Simulia Corp, 2011)). However, it is unable to know the exact surface conditions based on the limited information in the original test report. From this, the authors conducted a separate sensitivity analysis and tried to input different thermal

conductance values, like $10^6 \text{ W/m}^2\text{K}$ (an idealized condition which assumes there is no temperature gradient and two contact surfaces achieve the same temperature at the interface), $100 \text{ W/m}^2\text{K}$, $10 \text{ W/m}^2\text{K}$, $5 \text{ W/m}^2\text{K}$, $4 \text{ W/m}^2\text{K}$, $3 \text{ W/m}^2\text{K}$ as well as $1 \text{ W/m}^2\text{K}$, in order to see the difference between the corresponding temperature estimates. Through comparing with the thermocouple data obtained from the original test, it was found that a better agreement could be generated when define the thermal conductance to be $3 \text{ W/m}^2\text{K}$.

Above all, the selections of appropriate material property inputs always play a critical role in simulating the elements behavior. As a result, the authenticity of the overall model also relies on this factor. For numerical heat transfer analysis, the essential property inputs are conductivity (k), specific heat capacity (c_p) and density (ρ). In the current model, the thermal properties of AAC slab and rockwool insulation can employ the material data from the previous research (Hakmi et al., 1993; Benichou et al., 2001; Ghazi Wakili et al., 2015). Nevertheless, the fundamental properties of common firestop acrylic sealants are uncertain. To conquer the problem, this study attempted to use fictitious property values to model the thermal behavior of the tested firestop sealant. The creation of the ‘artificial’ properties is grounded on the test observations, as interpreted below. The reliability of the overall model is justified through comparisons of the simulated temperatures on the unexposed surface of the firestop acrylic sealant to corresponding measured thermocouple data (as indicated in Figure 2b) during the actual test.

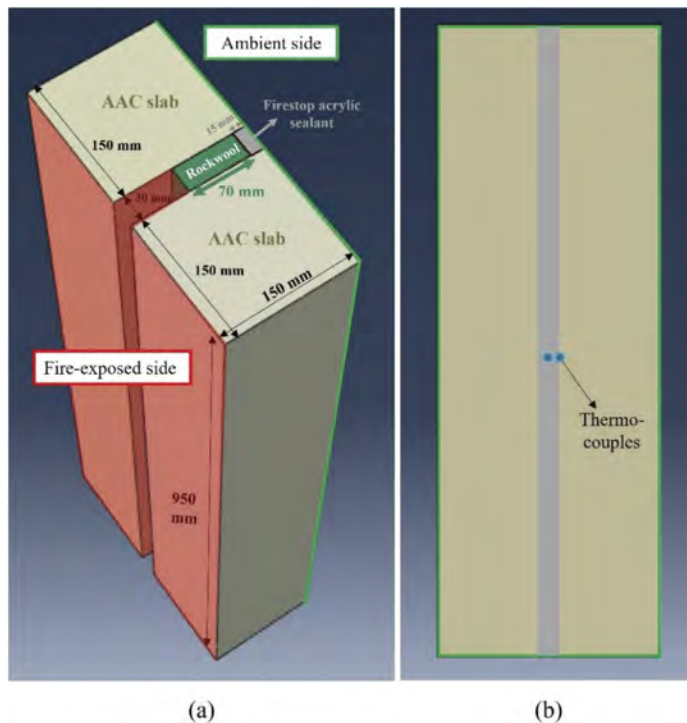


Figure 2. Configuration of tested firestopping specimen: (a) overall dimensions; (b) Thermocouple measurements on non-fire side.

2.2 Thermophysical property inputs for firestop acrylic sealant

In the original test report, visible charring was noticed on the unexposed surface of the firestop acrylic sealant at 146 minutes after the experiment began. This phenomenon was considered as a basis for drawing reference from the temperature-dependent thermal properties of other common charring materials, like timber, gypsum board and organic intumescent polymers.

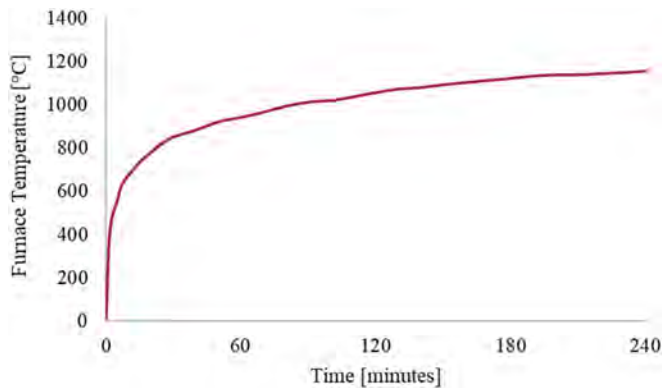


Figure 3. Recorded furnace temperature during the test.

A parametric analysis was therefore conducted to select representative values to adopt. These were developed from variations of combinations of thermal property inputs (i.e. k and c_p). The property combinations were:

- Case 1: Constant thermal conductivity ($k=0.179$ W/mK) and specific heat ($c_p = 1500$ J/kg °C) values for general acrylic materials at ambient condition (Plastic Service Centers, 2021). It is assumed that both properties are completely insensitive to changes of temperature. This case is depicted by the solid black lines in Figure 4.
- Case 2: Apply temperature-dependent thermophysical property ratios following timber properties, as given in Eurocode 5 (European Committee for Standardization, 2004) to the ambient values of general acrylic materials given in Case 1. The modified thermal property results are plotted as per long dash lines in Figure 4.
- Case 3: Employ the same method in Case 2, but use the thermophysical property growth ratios of gypsum board instead (Wang et al., 2012). These modified property profiles are drawn in dash-dot lines in the same plots below.
- Case 4: The last scenario was built based on the thermal property growth patterns of intumescent coatings. The variation of thermal conductivity under high temperatures references a validated effective conductivity model for a solvent-borne acrylic intumescent paint (Nørgaard et al., 2016). The suggested analytical model considered a combined heat transfer effect inside both virgin material and carbonaceous char layer at different temperatures ranges, while the evolution of specific heat employed experimental measurements of a disparate intumescent material as collected by Tabeling (2014). These parameters were represented by the dot lines in the same figure.

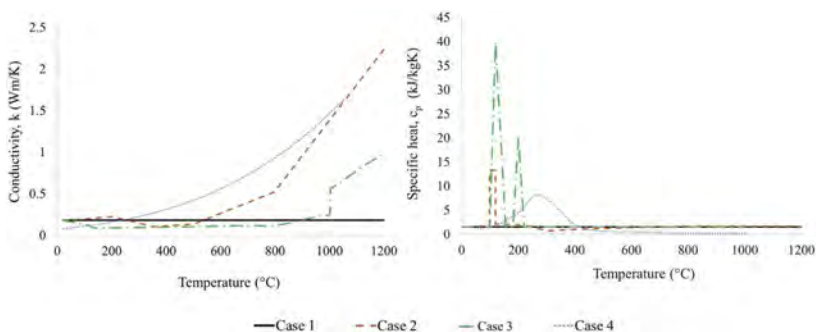


Figure 4. Difference between four different combinations of thermal property inputs.

3 RESULTS AND DISCUSSION

The experimental thermocouple measurements and their corresponding numerical results are plotted in Figure 5. The numerical estimates show a close agreement to the experimental data only within the first 90 minutes. Among the four numerical cases, Case 2 displayed a better consistency to the test results in comparison to the other cases. It can well predict the temperature at center of the sealant until about 130 minutes. But meanwhile, the results at the interface between the sealant and concrete substrate were noticeably overestimated. In contrast, the third model (i.e. Case 3) presented more accurate temperature estimates at this interface up to 180 minutes. However, the temperature outputs at the center of the fire-stop material were consistently underestimated since around 70 minutes. This discrepancy could be due to a significant increase of specific heat in gypsum at about 100 °C (see Figure 4b).

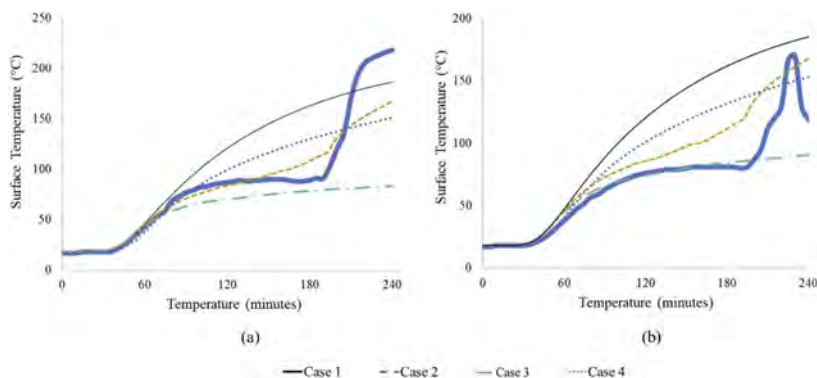


Figure 5. Comparison between temperature measurements and simulation results of surface on non-fire side: (a) at center of sealant; (b) at interface between sealant and AAC substrate.

The results show that none of these models can predict the surface temperature history of the firestop acrylic sealant throughout the four-hour exposure. This could be due to uncertainty around the chemical mixtures of actual firestop sealant product and their sensitivity to changing temperatures. Thermal-induced reactions, such as dehydration, change of internal pore structures, charring and even ignition, can therefore occur at very different times (Mouritz & Gibson, 2007). As a result, the overall heat transfer mechanism is difficult to model accurately without specialized experimental support to determine the temperature-dependent thermophysical properties, e.g. use differential scanning calorimeter (DSC) technique to extract the effective specific heat capacities at elevated temperatures (Daw, 2008).

Moreover, the appropriateness of the experimental data may need some confirmation by additional test data. For instance, the apparent soar of the sealant temperature beyond 100 °C may be as a result of thermal response of the rockwool insulation on the fire-exposed end. Leppänen & Malaska (2019) found that smoldering combustion of mineral wool insulation can contribute to an increase of temperature around 115 to 165 °C. Nonetheless, this hypothesis needs further assessment to confirm its validity.

Based on the above discussion, the authors would like to underline the considerable need to gather the right fundamental properties of frequently used firestop materials. It is only by obtaining the correct thermal properties, a reliable benchmark numerical model is likely able to be generated. On that basis, further research to analyze the heat transfer interactions between different firestopping components as well as comprehend variations in response of identical fire-stop products under distinct fire regimes can then be possibly investigated in the future.

4 CONCLUSIONS

Based on a concern of modelling the behavior of firestopping materials with unknown thermal features, this paper has presented four different sensitivity analyses to simulate the fire response of a typical firestop acrylic sealant with fictitious thermal property inputs. A finite element model was built based on a real standard fire test conducted in 1996. The development of the ‘fictitious’ conductivity and specific heat capacity results were based on the similar attributes between the acrylic sealant and known materials. The materials were charring materials, including timber, gypsum board and intumescent paint. However, none of the cases showed a consistent good agreement to the test data for the entire duration of fire exposure. Thus, in order to realistically model the thermal response and ensure fire safety even under non-standard fire conditions, the authors suggest the acquisition of large pools of experimental properties data of firestops for further development of future numerical models.

REFERENCES

- ASTM International. 2017. *ASTM E814-13a: Standard Test Method for Fire Tests of Penetration Fire-stop Systems*. West Conshohocken: ASTM International. Available: <https://www.astm.org/Standards/E814.htm>.
- Baker, G.B., Collier, P.C.R., Abu, A.K. & Houston, B. 2012. Post-earthquake structural design for fire-a New Zealand perspective.
- Benichou, N., Sultan, M., Maccallum, C. & Hum, J. 2001. Thermal Properties of Wood, Gypsum and Insulation at Elevated Temperatures. Internal Report. (January, 1).
- British Standards Institution. 1987. Available: <https://shop.bsigroup.com/ProductDetail?pid=00000000030296644> [2021, August 16].
- Dassault Systèmes. 2006. ABAQUS User’s & Theory Manuals–Release 6.6-2.11.1 Uncoupled heat transfer analysis. In *ABAQUS Theory Manual*. Providence RI (USA).
- Dassault Systèmes. 2020. ABAQUS 2020 (Version 6.20). Available: <https://www.3ds.com/products-services/simulia/products/abaqus/>.
- Dassault Systèmes Simulia Corp. 2011. *ABAQUS/Standard User’s Manual, Version 6.11*. Available: <http://130.149.89.49:2080/v6.11/books/usb/default.htm?startat=pt09ch35s01alm62.html>.
- Daw, J.E. 2008. *Measurement of specific heat capacity using differential scanning calorimeter*. Idaho National Lab. (INL), Idaho Falls, ID (United States).
- European Committee for Standardization. 2002. *BS EN 1991-1-2:2002: Eurocode 1: Actions on structures - Part 1-2: General actions - Actions on structures exposed to fire*. DOI: ICS 91.010.30; 93.040.
- European Committee for Standardization. 2004. *BS EN 1995-1-2:2004: Eurocode 5: Design of timber structures - General - Structural fire design*.
- European Committee for Standardization. 2009. *BS EN 1366-3:2009 Fire resistance tests for service installations. Penetration seals*. London: CEN.
- Federal Emergency Management Agency (FEMA). 2012. *FEMA E-74: Reducing the Risks of Nonstructural Earthquake Damage – A Practical Guide*. Available: <http://www.fema.gov/earthquake-publications/fema-e-74-reducing-risks-nonstructural-earthquake-damage>.
- Ghazi Wakili, K., Hugi, E., Karvonen, L., Schnewlin, P. & Winnefeld, F. 2015. Thermal behaviour of autoclaved aerated concrete exposed to fire. *Cement and Concrete Composites*. 62. DOI: 10.1016/j.cemconcomp.2015.04.018.
- Hakmi, M., M, D., R, H. & Wang, H.B. 1993. Numerical Temperature Analysis of Hygroscopic Panels Exposed to Fire. *International Journal of Numerical Methods in Thermal Problems*. Vol. VIII:1624–1635.
- International Code Council. 2021. International Building Code 2021 (IBC 2021) - Chapter 7: Fire and Smoke Protection Features. Available: https://codes.iccsafe.org/content/IBC2021P1/chapter-7-fire-and-smoke-protection-features#IBC2021P1_Ch07_Sec714.
- International Organization for Standardization. 1999. *ISO 834-1:1999 Fire-resistance tests - Elements of building construction - Part 1: General requirements*.
- Leppänen, P. & Malaska, M. 2019. Experimental study on the smouldering combustion of mineral wool insulation in chimney penetrations. *Fire technology*. 55(6):2171–2194.
- Mouritz, A.P. & Gibson, A.G. 2007. *Fire properties of polymer composite materials*. V. 143. Springer Science & Business Media.
- Nithiarasu, P., Lewis, R.W. & Seetharamu, K.N. 2016. *Fundamentals of the finite element method for heat and mass transfer*. John Wiley & Sons.

- Nørgaard, K.P., Dam-Johansen, K., Kiil, S. & Català, P. 2016. Engineering model for intumescent coating behavior in a pilot-scale gas-fired furnace. *AICHE Journal*. 62(11):3947–3962.
- Plastic Service Centers. 2021. *Overview of materials for Acrylic, General Purpose*. Available: <https://www.matweb.com/search/DataSheet.aspx?MatGUID=3cb08da2a0054447a3790015b7214d07> [2021, September 04].
- Sędlak, B., Sulik, P., Izydorczyk, D. & Łukomski, M. 2017. Fire-stop Wraps and Collars with Intumescent Materials-Performance Comparison. In *Procedia Engineering*, V. 172. Elsevier Ltd. 961–968. DOI: 10.1016/j.proeng.2017.02.113.
- Soja, E. 2022. *Guide to Passive Fire Protection in Buildings (2nd Edition)*. Wellington. Available: https://www.branz.co.nz/cms_show_download.php?id=bf5b5be7855d2df681dde2e948750d10a918bc8c.
- Standards Australia. 2014. *AS 1530.4-2014: Methods for fire tests on building materials, components and structures - Part 4: Fire-resistance test of elements of construction*. Sydney.
- Tabeling, F. 2014. High temperature behaviour of intumescent coating on steel constructions. *German: "Zum Hochtemperaturverhalten dämmschichtbildender Brandschutzsysteme im Stahlbau"*. Hannover, Leibniz Universitaet Hannover, Institute for steel construction, *Phd-Thesis*.
- The Ministry of Business Innovation and Employment. 2020. *C/AS2: Acceptable Solution for Buildings other than Risk Group SH - For New Zealand Building Code Clauses C1-C6 Protection from Fire (Amendment 2)*. New Zealand: NewZealand Government. Available: <https://www.building.govt.nz/assets/Uploads/building-code-compliance/c-protection-from-fire/asvm/cas2-protection-from-fire-1st-edition-2019.pdf>.
- Wang, Y., Burgess, I., Wald, F. & Gillie, M. 2012. *Performance-Based Fire Engineering of Structures*. CRC Press. Available: <https://books.google.com/books?id=zgnNBQAAQBAJ>.
- Warrington Fire Research Consultancy. 1996. *Hilti CP606 Flexible Firestop Sealant Submission Folder*. Available: <https://docplayer.net/10775228-Hilti-cp606-flexible-firestop-sealant-submission-folder.html> [2021, July 30].
- Wickström, U. 2016. *Temperature calculation in fire safety engineering*. Springer.

Dynamic chain reaction analysis of a cable-stayed bridge by sudden loss of stays considering cable corrosion

Y. Aoki, H. Tsunoda, T. Akiyama & H. Gotou
Akita university, Akita-city, Japan

S. Nakamura
Tokai university, Hiratsuka-city, Japan

ABSTRACT: Regarding design of cable-stayed bridges, cable breakage must be considered as one of the significant events. Therefore, sudden loss of cables is normally considered when a new bridge is designed or built. On the other hand, aging of bridges is getting considerable in recent world. Especially some bridges built during 80s and 90s showed some unexpected damages such as corrosion of cables. Therefore, cable breakage of these old bridges also must be considered. In this study, hypothetical cable-stayed bridge is designed to investigate the possible chain reaction considering and not considering cable corrosion. Also, a new analysis method of chain reaction, which can include the dynamic response, is suggested.

1 INTRODUCTION

In suspension type of bridges, loss of cable should be considered in the design phase. Several research have been proposed and couple of effective numerical methods were introduced (Aoki, et al., 2012; Wolff & Starossek, 2009), regarding to the loss of cable by using dynamic response. However, since previous studies have been conducted on bridges at the time of design phase, cable corrosion or and other factors caused due to aging have not been considered. In recent years, corrosion and deterioration of cables in suspension and cable-stayed bridges, which were built mainly in the 1980s and 1990s, have been recognized as significant issues. The most recent example of the tragic event was collapsed of the Nanfangao Bridge in northeastern Taiwan in October 2019. During the large trunk drove on the bridge, one cable in the center of the span ruptured due to corrosion, and other cables ruptured one after another, like an opened-up zippers (so called as zipper type collapse as well), that caused the arch ribs to collapse and the entire bridge to collapse. This tragedy warned the world that cable corrosion would lead the structures to significant damage. Regarding this accident, some researches were carried out to investigate the situation (Nakamura & Miyachi, 2021).

In this study, a new method is proposed to analyze the chain reaction of the entire bridge subjected to sudden loss of cable with and without cable corrosion. Specifically, this proposed method attempts to dynamic analysis using FEM to investigate whether the possible progressive analysis would simulate rupture of a particular cable or not.

2 BRIDGE MODEL

2.1 *Bridge design concept*

In this study, hypothetic steel cable-stayed bridge model was designed to investigate the chain reaction of this type of bridge. While the concrete superstructure is more commonly used than

steel superstructure, this research focus on aging cable-stayed bridges that are mostly made of steel. The model is shown in Figure 1. This bridge model is assumed as a road bridge, where the main span length as 300 m and total length is 540 m (see in Figure 1(a)). The steel box girder with two vehicle lanes shown in Figure 1(b) is adopted in this research, where the width is 22 m and the web height is 3.0 m. Cables are connected at the center of the deck as it is shown in Figure 1(a), since a single stay cable arrangement is adopted in this study. The displacement at both ends of the main girder are restrained vertically but not horizontally. The tower is A-shaped consisting of three members as shown in Figure 1(c) and the cross section of members is rectangular with several ribs to avoid buckling as shown Figure 1(d). The displacement at the bottom of the oblique members of the tower are restrained in all directions including rotation. For the cables, parallel wire strand (known as PWS) is used (see in Figure 1(e)). The cable consists of steel wires, and it is assumed that the tensile strength is 1,570 MPa. The cable location and the name of cables (such as C1) for the bridge model is shown in Figure 1(a). The cable are connected to the deck mostly at 20 m intervals, while at 10 m intervals at the both ends and outer sides of the towers.

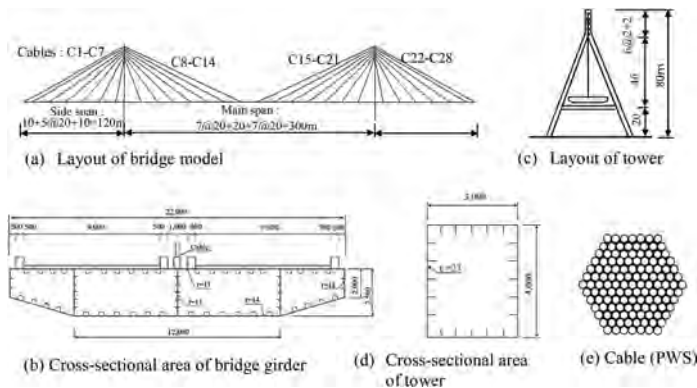


Figure 1. Bridge configuration.

2.2 Dimensions and material properties of numerical bridge model

For the numerical analysis, beam elements are used for all the components (see in Figure 2 (a)). The cross section of the bridge deck is shown in Figure 2(b). The size of deck is same as those of design, while the U-ribs and horizontal stiffeners are abbreviated to reduce the amount of calculation load. In order to avoid the local bending deformations of plates caused by abbreviation of ribs and stiffeners, the thickness of composed plates of deck and tower are increased from 11 mm to 12 mm for upper flange and webs, 14 mm to 16 mm for lower flange and 23 mm to 25 mm for the tower cross section, respectively.

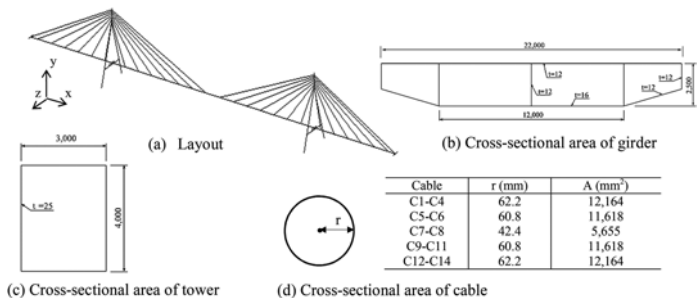


Figure 2. Numerical model.

The PWS cables are modeled by cylinder solids, where the radius of the cables r have variations depending on the position of each, cables, shown in Figure 2(d).

The stress-strain relations of the materials are shown in Figure 3. The stress-strain relation of the steel plates used for main girder and tower, whose steel grade is SM400, is bi-linear with Young’s modulus of 200 GPa, Poisson’s ratio of 0.3, yield stress of 235MPa, and other properties as shown in Figure 3(a). The stress-strain relation of the cables is tri-linear with Young’s modulus of 195 GPa, Poisson’s ratio of 0.3 and other properties as shown in Figure 3(b).

This model calculation is performed by the commercial FEM software Marc Mentat 2021.4.

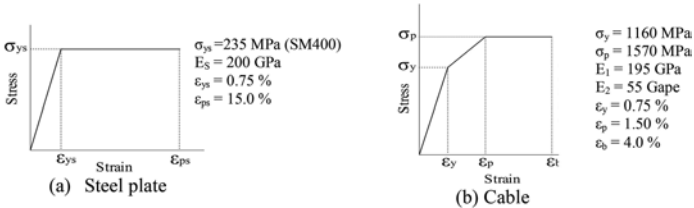


Figure 3. Stress-strain relations of materials.

2.3 Design load and verification of safety of structural members

In this study, design load is decided in accordance with ‘Japanese Road Bridge Specification’ (Japan Road Association, 2014), which is shown in Figure 4.

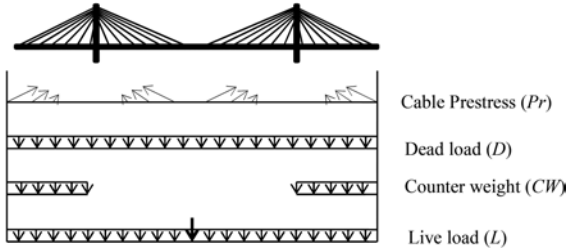


Figure 4. Design loads.

Cable prestress (Pr) is applied for each cable to create the pre-camber. The dead load (D) consists of the steel girder weight (69.7 kN/m), curbs and guardrails (24.5 kN/m), and asphalt (28.4 kN/m). A counter wights (CW , 60 kN/m) are loaded at the side spans to suppress the uplift at the end supports and decrease the bending moments of the girder and the towers. The design live load (L) is assumed the ‘B live load’ which consist of the concentrated load (p_1) represented as heavy vehicle and distributed load (p_2) represented the traffic by normal cars. The load p_1 of 10 kN/m² is applied to a length of 10 m and a width of 5.5 m at the center of the span. The other area of this 10 m span length x 5.5 m width the p_1 is applied as half of 10 kN/m². The distributed load p_2 of 3.5 kN/m² is applied to a width of 5.5 m and half of it for the other part along the entire bridge.

Sectional forces due to design load ($Pr + D + CW + L$) is obtained by numerical analysis and summarized in Table 1. According to this table all the verification value are less than 1.0, which show the assumed member are safe and the bridge model is within the allowable stress range.

3 ANALYTICAL METHODS

3.1 Cable corrosion

In this study, cables are considered as corroded and the assumption of cable corrosion in numerical analysis is explained in this section.

Table 1. Sectional force and stress of critical members.

Model-300		N	M	σ_n	σ_b	γ
Girder	Tower	-31	-59	-45	-89	0.95
	Center	2.8	79	0.2	118	0.85
Tower	Base	-28	19	-82	45	0.93
	Anchor	6.1	0	505	0	0.80
Cable	Center	6.4	0	532	0	0.85

※N :Axial force (MN), M : Bending moment (MN.m), σ_n Axial stress (MPa), σ_b : Bending stress (MPa), γ : Verification value

During corrosion is progressing, corrosion pits would be deepened, and cracks would be occurred, which would lower the ductility and decrease the cable strength. According to Nakamura and Suzumura (2013), the average elongation of the healthy steel wires used for bridge cable is over 4.0%, however the elongation will be decreased to less than half due to corrosion.

On the other hand, Mitamura et al (1992) tested PWS with/without corrosion, which research is only one experimental work of real cable. They reported that the elongation of PWS would be dropped by almost $\frac{1}{4}$ of healthy and yield stress is also decreased by about half according to their experimental work. Also, the corrosion of cable leads to not only reduction of elongation but also reduction of effective cross-sectional area (Nakamura & Suzumura, 2013).

Regarding to these previous researches, the constitutive law of corroded cables is assumed. The Stress-strain relation of healthy cable and corroded cable are presented in Figure 5. The yield stress is reduced by 60% of healthy cable and breakage strain is decreased by 80%, namely 628 MPa for tensile stress and 0.8% for breakage strain. This condition is quite harsh since the main objective of this research is considering the effect of cable corrosion.

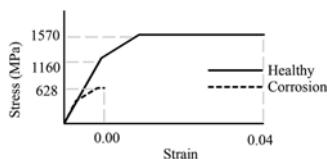


Figure 5. Assumed constitutive laws of cable.

3.2 Numerical method of chain reaction due to loss of cable(s)

A new chain reaction analysis is suggested and introduced in this study. The chain reaction of entire bridge will be occurred due to loss of cable(s). The methodology used in this study is explained in this section. For this analysis, transient (time-history) analysis of the bridges is carried out using Newmark-beta method.

Step 1: In this method, the bridge model having all cables is called as *initial model* shown in Figure 6(a). At first, as shown in Figure 6(b), the combination of design load ($Pr + D + CW + L$) is gradually applied on the bridge model. By doing so, the bridge model is allowed to reach equilibrium state which is basically equivalent to the result of static analysis. After this analysis, time history of tensile force of C1 is taken and plotted shown in Figure 6(c).

Step 2: At this step, a subject cable (C1 or C 14) element is removed from the bridge model (called *cable loss model*) shown in Figure 6(d). For this breakage model, the combination design load is applied, which is same as step1 (see in Figure 6(e)).

In this method, after the bridge model reached the equilibrium state, the cable loss is simulated by the reducing force, which means cable tensile force shown in Figure 6(f) is down to zero over a time step of $\Delta t=0.01$ sec at analytical time of 250 sec. The removal timing against the analysis time is arbitrary. In this research, first 200 sec is used for loading time, 200 sec to 250 sec is for steady state, and cable C1 is lost its tensile force at 250 sec and dynamic transient analysis is carried out during and after removed cable. The time history load shown in Figure 6

(f) is used as applied load on the point of cable connected with the deck and the tower. The applied load has to be applied opposite sign since the time history load is the internal axial force of the removed cable.

Dynamic response of the vertical deflection at the mid-span and tensile force of cable C2 (next to the removal cable) are plotted in Figure 6(g) and (h), respectively. As it can be seen, the tensile force of C2 is decreased to zero at around 255 sec. According to the constitutive laws of cable, shown in Figure 6(i), the corroded cables would be lost their ability to carry tensile stress when they reached to breakage strain. By setting of constitutive law shown in Figure 6(j) to all the cables, cable loss can be calculated such method automatically.

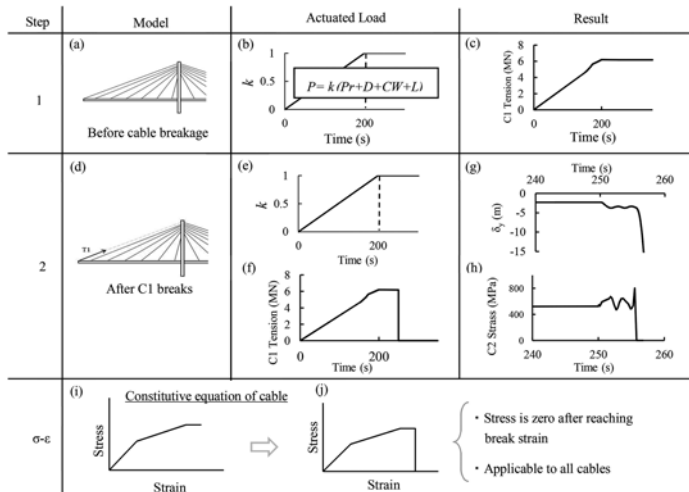


Figure 6. Chain reaction method.

4 RESULTS AND DISCUSSION

In this section, the results of chain reaction are presented. There are three scenarios considered in this research and shown in Table 2.

Table 2. Scenarios considered.

Name	Loss of cable	Corrosion	2 nd yield stress (MPa)	Breakage strain
Scenairo-1	C1	-	1570	0.04
Scenairo-2	C1	○	628	0.008
Scenario-3	C14	○	628	0.008

4.1 Loss of cable C1

Scenario-1

In Figure 7, Deformation diagram of entire bridge at critical timing with sudden loss of C1 is shown. As it is shown in Table 2, all cables are not corroded in this scenario. At 0 sec-ond of analysis time, the bridge was not applied any load. At 250 sec, C1 element is re-moved from the model and maximum deflection at mid-span is obtained at 253sec (see in Figure 7 stage I). The model was fluctuated vertically, and maximum deflection was about 1.77m downwards. At stage II in Figure 7, the model was converged. When all cables are not corroded, single cable loss does note leads to entire bridge collapses. Moreover, all the component of this bridge model was still under yield stress, therefore, the redundancy of this model was also demonstrated.

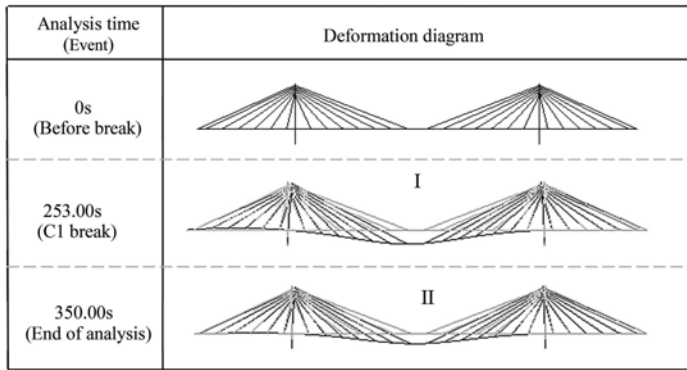


Figure 7. Deformation diagram of entire bridge at critical timing for scenario-1 (scale factor 10).

Scenario-2

In this scenario, the bridge is considered aging and all cables are assumed as corroded.

In Figure 8, deformation diagram of critical timing are shown. At 0 sec, there is no load applied and design load will be applied gradually till 200 sec. At Stage I, the analysis time is at 250 sec, C1 cable element is taken from the bridge model instantly and transient analysis is continued. At Stage II, (time as 251.01 sec), cable C2 and C3 reached to the second yield stress as 628 MPa and lost their elasticity. In Stage III, the deflection is getting significant since cable C4 and C5 are also reached to yield stress and lost their elasticity. Just before the Stage IV in timing of 256 sec, C2 and C3 cables finally reached to breakage strain and eliminated from the bridge model automatically. By this phenomenon, the plastic-hinge is occurred around C5 cable, and the entire bridge is collapsed.

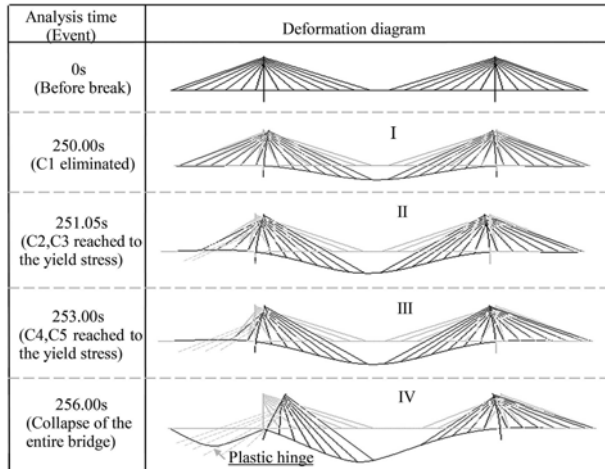


Figure 8. Chain reaction process for loss of cable C1 (scale factor 10).

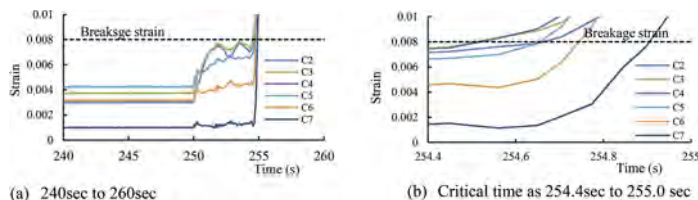


Figure 9. Time history of cable total strain (C2 to C7).

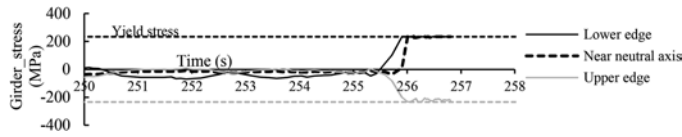


Figure 10. Time-history of stress at the C5 cable anchorage zone (the location plastic hinge was occurred).

In Figure 9, time-history of cable total strain for (a) timing between 240sec to 260sec (before C1 removal till the bridge collapse) and (b) timing between 254.4 to 255.0 (at the cables exceeded the breakage strain) are shown. Cable C2 to C5 reached to the yield stress at 251.1sec and started to increase the strain with fluctuation and reached at the breakage stress almost all together see in Figure 9(b).

The time-history of stress at the critical location, where is around C5 cable anchorage zone is shown in Figure 10. As it can be seen in Figure 10(a), deck around C5 became plastic hinge, which means upper, lower edge and even neutral axis are yielded, just after cables are ruptured at 255 sec.

4.2 Loss of cable C14

Scenario-3: In scenario-3, cable C14 which is connected at the center of main span is eliminated at 250sec in analysis time. The deformation diagram of the entire bridge at critical times are shown in Figure 11. As it was seen in scenario-2, the same trend is detected. After removing cable C14, cable C13 and C12 reached to the second yield stress as 628 MPa at 251.18 sec which is seen in Figure 11 stage II. At 254.58 sec, three cables, named C13, C12 and C11, reached to the breakage strain as 0.008, and these cables are eliminated from the structure automatically (see in stage II in Figure 11). After that, the other cables connected to the left side of main span (named C 10, C9 and C8) are also reached to the breakage strain and removed from the bridge model. According to losing 7 cables, the entire bridge model was collapsed having with plastic hinge seen around the C12 anchorage zone.

In Figure 12,(a) the time-history of cable strain during 240 sec to 260 sec, and (b) time-history of cable strains focused during 254.0 to 255.0 sec are shown. According to Figure 12 (a), all the cables reached to breakage strain almost simultaneously. It can be seen more details in Figure 12(b) that C 11 to C 13 are exceeded the breakage strain during 0.2 sec and the other three cables exceeded the value by 0.1sec delaying respectively.

The time history of stress around the C12 is shown in Figure 13. According to this graph, the stress is fluctuated after removing C14 cable and suddenly reached to the yield stress at the

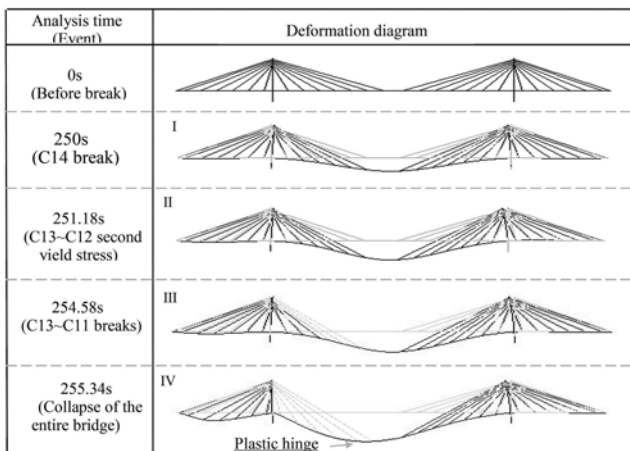


Figure 11. Chain reaction process for loss of cable C14 (scale factor 10).

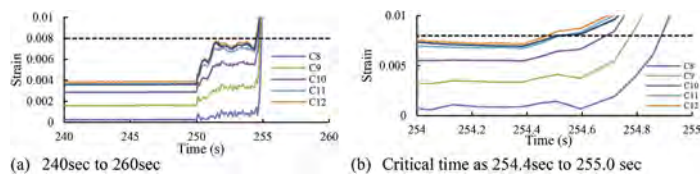


Figure 12. Time history of cable total strain (C8 to C13).

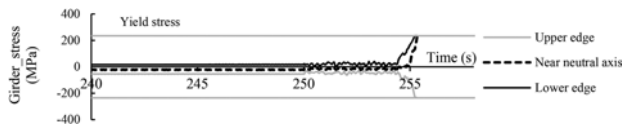


Figure 13. Time-history of stress at the C12 cable anchorage zone (the location plastic hinge was occurred).

bottom of deck and top of the deck at the same time. Moreover, the stress around the neutral axis exceeded to the tensile stress.

5 CONCLUSIONS

In this research, a new chain reaction method by dynamic transient analysis is introduced and considered. As it can be concluded that

- Chain reaction of cable-stayed bridge could be conducted by this introduced method.
- The cable corrosion could be presented by using introduced constitutive laws.
- Chain reaction can be occurred by the rupture of cable connected at the anchorage zone and assumed all the cables were connected.
- Also, the chain reaction was happened when the first ruptured cable was the one connected at the center of the girder, even all the cables were assumed as corroded.
- However, the chain reaction was not occurred when the cable is not corroded.

For the further research, these factors should be considered;

- Confirm the constitutive law assumed in this research by experimental work.
- Calculate the impact from the force created by ruptured cable instantly.
- Confirm the most significant cable related with the loading patterns.

Since the assumption of PWS corrosion in this study is only related to one reference, therefore, it should be updated. It is important to know the actual material characteristics of corroded PWS for the future bridge maintenance.

REFERENCES

- Aoki, Y., Valipour, H., Samali, B. & Saleh, A., 2012. A study on potential progressive collapse response of cable-stayed bridges. *Advanced in Structural Engineering*, 16(4), pp. 387–398.
- Association, J. R., 2014. *Specification for road bridge, I. Common Part II. Steel Bridge Part*. Tokyo: Maruzen.
- Mitamura, T., Nakai, H., Watanabe, E. & Sugii, K., 1992. Recent topics of bridge cables and future prospects. *Proceeding of Japanese Society of Civil Engineers*, 444(VI-16), pp. 97–106.
- Nakamura, S. & Miyachi, K., 2021. Ultimate Strength and Chain-Reaction Failure of Hangers in Tied-Arch Bridges. *Structural Engineering International, IABSE*, pp. 136–146.
- Nakamura, S. & Suzumura, K., 2013. Experimental study on fatigue strength of corroded Bridge Wires. *Journal of Bridge Engineering*, 18(3), pp. 200–209.
- Wolff, M. & Starossek, U., 2009. Cable loss and progressive collapse in cable-stayed bridges. *Bridge structure*, 5(1), pp. 17–28.

Revisiting shape/size effect formulation of EUROCODE 2 for structural concrete members

Sh. Abdo, R. Wan-Wendner & R. Caspeele

Department of Structural Engineering and Building Materials, Gent University, Ghent, Belgium

S.C. Seetharam & Q.T. Phung

Belgian Nuclear Research Centre (SCK CEN), Mol, Belgium

ABSTRACT: The mechanism of concrete shrinkage is mainly controlled by the relative humidity (RH) gradient in its pore-structure. The change in the RH in the long term is mainly controlled by moisture diffusivity and saturation degree, which are affected by many internal and/or external factors. In this paper, the impact of size and shape of the concrete member on the RH gradient and hence the shrinkage behaviour of the member, is explored. Generally, there are many engineering 1D models for time-dependent deformation that can predict the size/shape effect on concrete shrinkage using a parameter called the notional size (h_0) defined by the ratio between the total area of the member's cross-section to the perimeter of the surface that is in contact with the outer environment. A key contribution of this paper is re-examination of the capability of Eurocode 2 to capture shape and size effects that has so far not been accounted for. This is achieved via computationally intensive 3D numerical analysis of different shapes and sizes of concrete members. For the numerical analysis, a Hygro-Thermo-Chemical (HTC) model with elasticity is used, which essentially incorporates heat diffusion, moisture diffusion, hydration reaction and shrinkage. 3D simulations of different shapes and sizes of concrete structural members suggest that the notional size parameter in its present form may be insufficient and does not capture the shape effect, leading to a proposal of shape factors.

1 INTRODUCTION

Much research work has been done since time-dependent deformations, creep and shrinkage, of concrete were discovered early last century. However, creep and shrinkage phenomena of cement-based concrete are still far from being fully understood and modelled (Bažant et al., 2001). This is attributable to the complexity of the phenomena and the nonlinear interaction between internal and external factors affecting time-dependent deformations. Examples of external factors are gradients in the relative humidity and temperature, different shapes and dimensions. Examples of internal factors are concrete the concrete composition and curing procedures (ACI 209R 2008). The complexity of this phenomenon leads to inaccurate predictions of the long-term behaviour of concrete. This may lead to a loss in the functionality of concrete structural members, especially, shrinkage of pre-stressed concrete structures, which can have a significant impact on the prestressing forces in the long term (Gan et al., 2019; Li et al., 2019; Raphael et al., 2012).

There are different types of time-dependent deformations of unloaded-specimens (shrinkage), such as autogenous shrinkage, drying shrinkage and carbonation shrinkage. In this study, the main concern is concrete drying shrinkage and the impact of size/shape of the member on it. The mechanism of drying shrinkage is mainly controlled by the relative

humidity gradient within the concrete pore-structure. This change in the RH in the long term is mainly controlled by the moisture diffusivity and capacity (Bažant et al., 2015; Bažant and Najjar, 1972; Rahimi-Aghdam et al., 2019).

Generally, there are many engineering 1D-prediction-models for time-dependent deformation that can reflect the size/shape effect on concrete shrinkage using a parameter called the notional size such as the Eurocode model included in prEN1992-1-1, the CEB-FIB model (fib 2010), the ACI model (ACI 209R 2008) and the B3 model (Bažant and Baweja, 1995) and B4 model (RILEM, 2015). The notional size is the ratio between the total area of the member's cross-section to the perimeter of the surface that is in contact with the outer environment. In this study, this notional size parameter of the prEN1992-1-1 (designated Eurocode 2 in the remaining of this paper) is revisited using numerical analysis of different shapes and sizes of concrete members. For the numerical analysis a Hygro-Thermo-Chemical (HTC) model with elasticity is used, which essentially incorporates heat diffusion, moisture diffusion, hydration reaction and shrinkage (Di Luzio and Cusatis, 2009a, 2009b). Many investigations and attempts were done to modify the notional size of different codes and to add a shape factor parameter to it (Bažant et al., 1976; Dönmez and Bažant, 2016; Hubler et al., 2015; TC-242-MDC, 2015; Wendner et al., 2015a, 2015b), however the performance of Eurocode 2 in this regard has not been addressed in the studies. Thus, in this study, 3D simulations of different shapes/sizes of concrete structural members are considered to modify the notional size parameter in the Eurocode 2 and to add a shape correction factor to it.

2 PREDICTION OF LONGITUDINAL STRAINS OF A CONCRETE MEMBER DUE TO DRYING SHRINKAGE IN EUROCODE

In the upcoming 2nd generation of Eurocode 2, an averaged cross-section approach is followed for predicting the time-dependent deformation of the member. The total shrinkage is the summation of autogenous shrinkage and drying shrinkage. The drying shrinkage strain can be expressed as follows:

$$\varepsilon_{cd}(t - t_s) = \varepsilon_{cdsfm} \cdot \beta_{RH} \cdot \beta_{ds}(t, t_s) \cdot \alpha_{NDP,d} \quad (1)$$

$$\beta_{ds}(t, t_s) = \left[\frac{(t - t_s)}{(t - t_s) + 0.035 \cdot h_0^2} \right]^{0.5} \quad (2)$$

Where ε_{cdsfm} is the notional drying shrinkage coefficient, β_{RH} is a coefficient to consider the RH effect, $\beta_{ds}(t, t_s)$ is a function that describes the development of drying shrinkage strains with time, t_s is the age of concrete (days) when drying starts, and $\alpha_{NDP,d}$ is considered. As for Equation (2), t is the age of concrete at the considered moment (days). h_0 is the notional size of the cross-section which can be calculated as follows: $h_0 = 2 \cdot A_c / u$ where A_c is the cross-sectional area of the member (mm²), and u is the perimeter of the cross-section that is exposed to the drying environment (mm).

3 NUMERICAL ANALYSIS OF DRYING SHRINKAGE USING HTC MODEL

The HTC model can model the spatial and temporal field of relative humidity RH, temperature T and the overall hydration reaction degree over the structural element. Based on this model, the T and RH can be computed using the enthalpy balance equation and the moisture mass balance equation, respectively (Abdellatef et al., 2019).

The RH of the pore structure is governed by the combination of Fick's law of diffusion and the sorption isotherms of water (Dönmez and Bažant, 2016) as follows:

$$\frac{\partial RH}{\partial t} = \nabla [D(RH, T) \cdot \nabla RH] \quad (3)$$

$$D(RH, T) = \exp\left(\frac{E_{ad}}{R \cdot T_0} - \frac{E_{ad}}{R \cdot T}\right) \cdot D_1 \cdot \left[1 + \left(\frac{D_1}{D_0} - 1\right) \cdot (1 - RH)^n\right]^{-1} \quad (4)$$

where RH is the pore relative humidity (%), t is the time (days), $D(RH)$ is the moisture diffusivity, D_1 and D_0 are the maximum and minimum moisture diffusion coefficient (kg/mm h) at saturation and fully dried state, n is an exponent that governs the transition between D_1 and D_0 , T_0 is the room temperature and $\frac{E_{ad}}{R} \approx 2700K$.

The temperature of the pore structure is governed by the combination of Fourier's law and the enthalpy balance equation as follows:

$$\rho \cdot c_t \cdot \frac{\partial T}{\partial t} = -\nabla \cdot \mathbf{q} + \dot{Q}_c \quad (5)$$

where ρ is concrete density, c_t is specific heat capacity of concrete, q is the heat flux, \dot{Q}_c is the rate of heat generation due to cement hydration, silica fume polymerisation and pozzolanic reactions.

The time-dependent deformation of the unloaded-specimens as a result of the drying process is mainly linked to the diffusion process of concrete or the related change of the RH distribution in the pore network. The free local shrinkage strain rate $\dot{\epsilon}_f$ can be assumed to be proportional to the local rate of RH change (Abdellatef et al., 2019):

$$\dot{\epsilon}_f = \alpha_h \cdot \dot{RH} \quad (6)$$

where α_h represents the hygral shrinkage coefficient.

This 3D numerical work considers concrete members with different cross-section types and sizes as shown in Table 3. The mechanical boundary conditions of this 3D model ensure consistency with the hypothesis of Navier-Bernoulli, which is demonstrated in Figure 1. To this end rigid plates are attached onto both end faces with statically determinate boundary conditions. In addition, it should be noted that creep has been ignored in this instance as a first approximation. In fact, creep plays an important role at high drying shrinkage stresses, which is usual for thinner cross sections.

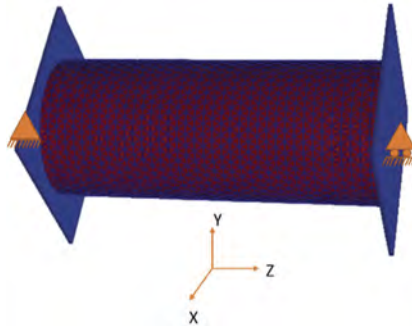


Figure 1. Conceptual model used in the analysis.

4 EUROCODE MODIFICATION PROCEDURE

In this section, the methodology for the modification of $\beta_{ds}(t, t_s)$ is presented. Firstly, numerical analyses of drying shrinkage of real experiments are carried out based on published

experimental data (Bryant and Vadhanavikkit, 1987) for the purpose of validating the Lattice Discrete Particle Model (LDPM). LDPM is a discrete model that represents heterogeneity of concrete by introducing coarse aggregate particles to the mortar. Thus, LDPM is capable of simulating the mechanical interaction between the randomly placed particles and the cement mortar (Cusatis et al., 2011b, 2011a). The input parameters that are used here are based on (Abdellatef et al., 2019) as shown in Table 1. After successful validation by the experiments (see Figure 2), numerical simulations for different shapes and sizes are performed, as shown in Table 2. The specimen sizes and shapes are chosen such that a range of real structural conditions and not only laboratory specimens are covered. The length of all specimens is assumed to be 500 mm. As the functional dependence of drying shrinkage on the shape and size of the cross-section is considered uncertain, the horizontal scaling parameter of the Eurocode time function is replaced by a variable ψ to be determined inversely, resulting in an analytical surrogate model with $\beta_{ds}(t, t_s) = \left[\frac{(t-t_s)}{(t-t_s)+\psi} \right]^{0.5}$. Then, using the least square method, the optimum values of ψ are determined for each cross-section shape and size by fitting the results of the 3D numerical simulations.

Table 1. HTC input parameters.

	Parameter (Units)	Value
Rate of hydration	A_{c1} (h^{-1})	42.55×10^7
	A_{c2}	375×10^{-4}
	η_c	9.3
Heat specific capacity	C_t (kJ/kg°C)	1.1
Thermal conductivity	λ_t (W/m°C)	2.3
Moisture permeability	D_0 (kg/mm h)	0.036×10^{-9}
	D_1 (kg/mm h)	6.5×10^{-7}
Sorption/desorption isotherm	n	6.5
	g_1	1.75
	g_2	0.025
Shrinkage coefficient	α_h	1.4×10^{-3}
Thermal coefficient	A_t	10×10^{-6}
Compressive strength	F_c' (MPa)	50.1

Table 2. Considered shapes and sizes and their corresponding notional size.

Shape (symbol)	Dim. (mm)	h_o (mm)
Circle (D)	D=150, 200, 400	75, 100, 200
Rectangle ($Rec L W$)	Length(L):width(W) $L:W=1$	75, 100, 200
	$W=150,200,400$	
	$L:W=2$	100, 133.3,
	$W=150,200,400$	266.6
	$L:W=3$	112.5, 150,
	$W=150,200,400$	300
	$L:W=4$	120,160,320
	$W=150,200,400$	

Table 3. Prism sizes for autogenous and drying shrinkage of Bryant experiment.

	Dimensions
Autogenous shrinkage	150mm × 150mm × 600mm
Drying shrinkage 100	100mm × 100mm × 400mm
Drying shrinkage 150	150mm × 150mm × 600mm
Drying shrinkage 200	200mm × 200mm × 800mm
Drying shrinkage 300	300mm × 300mm × 1200mm

4.1 Validation of the numerical approach (Bryant experiment)

Bryant conducted a series of shrinkage experiments under sealed and drying conditions (RH=60%, T=20 °C) for different prism sizes as shown in Table 3. The prisms were cured for 9 days, then exposed to the outer environment. The constituents of the cement were as follows, 1985 kg/m³ of crushed basalt, 390 kg/m³ of ordinary Portland cement (CEM I) and a water-to-cement ratio of 0.47 by weight (Bryant and Vadhanavikkit, 1987). Figure (2) shows good correspondence between the numerical simulations and Bryant's experimental results, thus giving confidence in the use of the numerical model for further examining the shape effect.

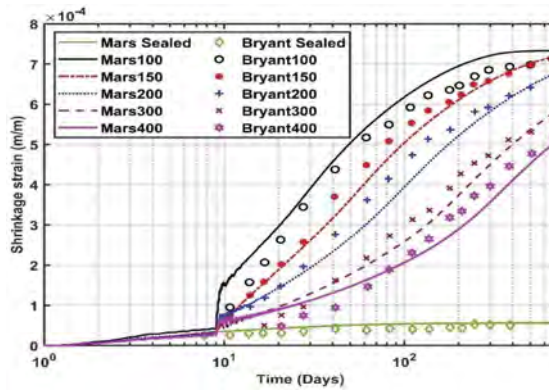


Figure 2. Experimental and numerically simulated shrinkage strain (Bryant and Vadhanavikkit, 1987).

4.2 Predictive numerical simulation for different shapes and sizes

A series of numerical simulations were considered for different shapes and sizes as shown in Table 2 using the same calibrated parameters of Bryant's experiments. All simulations are performed on samples cured for 28 days and then either exposed to drying conditions (RH=75%, $T=20^{\circ}\text{C}$) or completely sealed to capture the autogenous shrinkage. Figure 3 shows the evolution of total shrinkage strains obtained from the numerical analysis for different shapes and sizes.

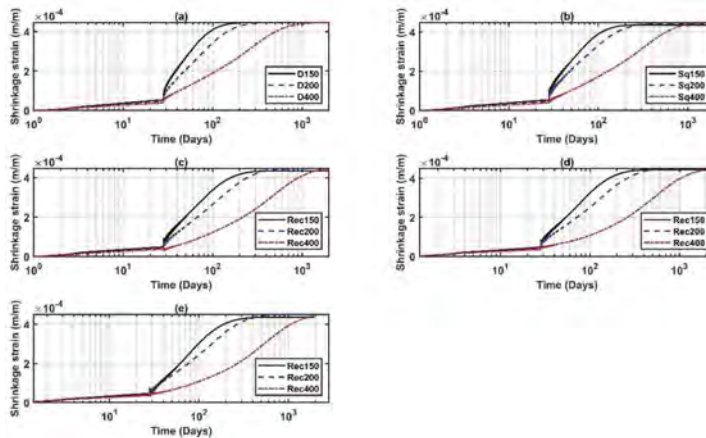


Figure 3. Total shrinkage development for different cross-sections and sizes: (a) Circle, (b) Square, (c) Rectangle with aspect ratio 1:2, (d) Rectangle with aspect ratio 1:3, (e) Rectangle with aspect ratio 1:4.

Figure 3 shows that the evolution of total shrinkage depends not only on notional size but also on the shape of the cross-section. Each subplot represents geometrically similar cross-sections of different size. This is elaborated further in Figure 4, which shows the drying shrinkage development for 2 different shapes predicted by the numerical analysis in comparison to the Eurocode 2 prediction which is shape-independent. The 2 shapes possess the same notional size ($h_0=200$ mm). Eurocode 2 fails to capture the difference in shapes, as shown in Figure 4. Hence, it is recommended to introduce a shape parameter to Eurocode 2.

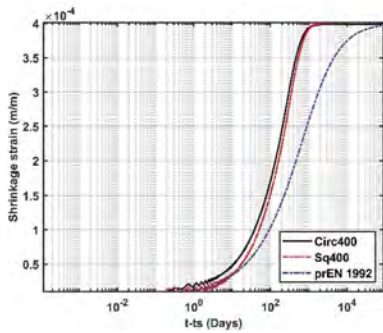


Figure 4. Shape effect on shrinkage behaviour of members with $h_0=200$ mm.

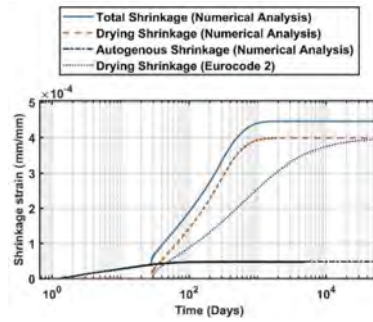


Figure 5. Total shrinkage, autogenous shrinkage and drying shrinkage of a cylinder with 400 mm diameter and 500 mm height.

4.3 Determination of shape factor

The simulations for sealed conditions are considered to capture autogenous shrinkage. Hence, the predicted autogenous shrinkage strains are subtracted from the total shrinkage strains. Consecutively, the drying shrinkage can be extracted as shown in Figure 5. The figure shows the autogenous shrinkage, total shrinkage and the estimated drying shrinkage from the numerical analysis and Eurocode 2 of a cylinder with 400 mm diameter under sealed and drying conditions (RH=75%). Additionally, the figure also shows that Eurocode underestimates the drying shrinkage rate. Using the least-square-method, a ψ value with the least error for each simulation is calibrated.

Figure 6 shows a relationship between ψ and h_0 for each shape/size. From this figure, a shape factor S_f can be derived as shown in Table 4 so that ψ can be expressed as follows: $\psi = 0.0021 \cdot S_f \cdot h_0^2$.

Table 4. Proposed shape factor for different shapes.

Shape	Shape Factor (S_f)
<i>Rectangle</i>	1
<i>Circle</i>	1.33
<i>Square</i>	1.62

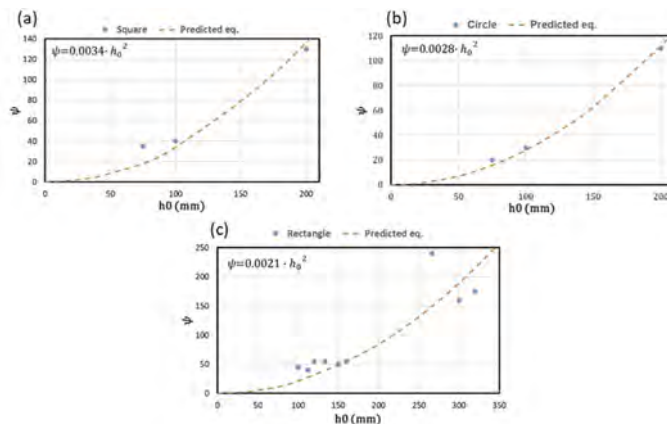


Figure 6. ψ of each shapes/sizes and their corresponding h_0 : (a) Square (b) Circle (c) Rectangle.

5 CONCLUSIONS

In this paper, the impact of size/shape of the concrete member on the relative humidity distribution and in turn the drying shrinkage behaviour has been investigated numerically by a 3D hygro-thermo-chemical analysis and compared to predictions according to the upcoming 2nd generation Eurocode 2. This work concludes the following:

- 1- The used multi-physics framework model succeeds in simulating experiments on concrete prisms with different sizes.
- 2- Virtual tests of different shapes and sizes can be simulated using the multi-physics numerical framework.
- 3- The shape of the cross-section has a noteworthy influence on the development of drying shrinkage, which is not covered by Eurocode 2.
- 4- An approach is presented that allows the development of shape and size-effect correction terms based on elastic 3D multi-physics simulations, which can later be extended to consider damage, creep and reinforcement.

REFERENCES

- Abdellatif, M., Boumakis, I., Wan-Wendner, R., Alnaggar, M., 2019. Lattice Discrete Particle Modeling of concrete coupled creep and shrinkage behavior: A comprehensive calibration and validation study. *Constr. Build. Mater.* 211, 629–645. <https://doi.org/10.1016/j.conbuildmat.2019.03.176>
- ACI Committee 209, 2005. Report on Factors Affecting Shrinkage and Creep of Hardened Concrete.
- Bazant, Z.P., Baweja, S., 1995. Creep and Shrinkage Prediction Model for Analysis and Design of Concrete Structures.
- Bazant, Z.P., Donmez, A., Masoero, E., Aghdam, S.R., 2015. Interaction of Concrete Creep, Shrinkage and Swelling with Water, Hydration and Damage: Nano-Macro-Chemo. *ASCE, Am. Soc. Civ. Eng.* 13, 1576–1580.
- Bazant, Z.P., Najjar, L.J., 1972. Nonlinear water diffusion in non-saturated concrete. *Mater. Struct.* 5.
- Bazant, Z.P., Osman, E., Thonguthai, W., 2001. Prediction of concrete creep and shrinkage: Past, present and future. *Mater. Struct. Constr.* 203, 27–38. <https://doi.org/10.1007/BF02473774>
- Bazant, Z.P., Osman, E., Thonguthai, W., 1976. Practical formulation of shrinkage and creep of concrete.
- Bryant, A.H., Vadhanavikkitt, C., 1987. Creep, Shrinkage-Size, and Age at Loading Effects. *ACI Mater. J.* 84, 117–123.
- Cusatis, G., Mencarelli, A., Pelessone, D., Baylot, J., 2011a. Lattice Discrete Particle Model (LDPM) for failure behavior of concrete. II: Calibration and validation. *Cem. Concr. Compos.* 33, 891–905. <https://doi.org/10.1016/j.cemconcomp.2011.02.010>
- Cusatis, G., Pelessone, D., Mencarelli, A., 2011b. Lattice Discrete Particle Model (LDPM) for failure behavior of concrete I: Theory. *Cem. Concr. Compos.* 33, 881–890. <https://doi.org/10.1016/j.cemconcomp.2011.02.011>
- Di Luzio, G., Cusatis, G., 2009a. Hygro-thermo-chemical modeling of high-performance concrete. II: Numerical implementation, calibration, and validation. *Cem. Concr. Compos.* 31, 309–324. <https://doi.org/10.1016/j.cemconcomp.2009.02.016>
- Di Luzio, G., Cusatis, G., 2009b. Hygro-thermo-chemical modeling of high performance concrete I: Theory. *Cem. Concr. Compos.* 31, 301–308. <https://doi.org/10.1016/j.cemconcomp.2009.02.015>
- Dönmez, A., Bazant, Z.P., 2016. Shape factors for concrete shrinkage and drying creep in model B4 refined by nonlinear diffusion analysis. *Mater. Struct. Constr.* 49, 4779–4784. <https://doi.org/10.1617/s11527-016-0824-6>
- Gan, B.Z., Chiew, S.P., Lu, Y., Fung, T.C., 2019. The effect of prestressing force on natural frequencies of concrete beams – A numerical validation of existing experiments by modelling shrinkage crack closure. *J. Sound Vib.* 455, 20–31. <https://doi.org/10.1016/j.jsv.2019.04.030>
- Hubler, M.H., Wendner, R., Bazant, Z.P., 2015. Statistical justification of Model B4 for drying and autogenous shrinkage of concrete and comparisons to other models. *Mater. Struct. Constr.* 48, 797–814. <https://doi.org/10.1617/s11527-014-0516-z>
- Kassimali, A., 2014. *Structural Analysis*, 5th ed. Cengage Learning, Stamford, USA.

- Li, S., Yang, Y., Pu, Q., Yang, D., Sun, B., Li, X., 2019. Three-dimensional nonlinear creep and shrinkage effects of a long-span prestressed concrete box girder bridge. *Struct. Concr.* 20, 638–649. <https://doi.org/10.1002/suco.201800148>
- Rahimi-Aghdam, S., Rasoolinejad, M., Bažant, Z.P., 2019. Moisture Diffusion in Unsaturated Self-Desiccating Concrete with Humidity-Dependent Permeability and Nonlinear Sorption Isotherm. *J. Eng. Mech.* 145, 1–14. [https://doi.org/10.1061/\(asce\)em.1943-7889.0001591](https://doi.org/10.1061/(asce)em.1943-7889.0001591)
- Raphael, W., Faddoul, R., Geara, F., Chateauneuf, A., 2012. Improvements to the Eurocode 2 shrinkage model for concrete using a large experimental database. *Struct. Concr.* 13, 174–181. <https://doi.org/10.1002/suco.201100029>
- RILEM, 2015. RILEM draft recommendation: TC-242-MDC multi-decade creep and shrinkage of concrete: material model and structural analysis*: Model B4 for creep, drying shrinkage and autogenous shrinkage of normal and high-strength concretes with multi-decade applicabili. *Mater. Struct. Constr.* 48, 753–770. <https://doi.org/10.1617/s11527-014-0485-2>
- TC-242-MDC, R., 2015. RILEM draft recommendation: TC-242-MDC multi-decade creep and shrinkage of concrete: material model and structural analysis*: Model B4 for creep, drying shrinkage and autogenous shrinkage of normal and high-strength concretes with multi-decade applicabili. *Mater. Struct. Constr.* 48, 753–770. <https://doi.org/10.1617/s11527-014-0485-2>
- Wendner, R., Hubler, M.H., Bažant, Z.P., 2015a. Statistical justification of model B4 for multi-decade concrete creep using laboratory and bridge databases and comparisons to other models. *Mater. Struct. Constr.* 48, 815–833. <https://doi.org/10.1617/s11527-014-0486-1>
- Wendner, R., Hubler, M.H., Bažant, Z.P., 2015b. Optimization method, choice of form and uncertainty quantification of Model B4 using laboratory and multi-decade bridge databases. *Mater. Struct. Constr.* 48, 771–796. <https://doi.org/10.1617/s11527-014-0515-0>

Guided tour of the pathological manifestations found at Rossio's historical train station

C. Carvalho & N. Bento

Infraestruturas de Portugal, Lisboa, Portugal

A. Silva

CERIS, Instituto Superior Técnico, Lisboa, Portugal

ABSTRACT: The present study is a guided tour of the pathological manifestations found at Rossio's historical train station, located in the centre of Lisbon, Portugal. Built in the late 19th century, this station is classified as a Monument of National Public Interest, being one of the most visited stations in the country. In this paper, the characterisation of the existing building is presented, based on visual inspection. The most common types of anomalies were identified, as well as some proposed rehabilitation techniques. Some of the most relevant restraints are the fact that the building is classified, its location in Lisbon's downtown and, finally, the lack of information about existing infrastructures, structures, and water courses. The conclusions drawn intend to raise awareness to the importance of regular and adequate maintenance among the industry actors and minimize the development of anomalies and their causes, at the design and application stages.

1 INTRODUCTION

In this study, a guided visit is made to the pathological manifestations found in a Lisbon's historic train station, classified as a Monument of National Public Interest (Figure 1a and 1b). This station was built in the late 19th century, being one of the most visited stations in the country, with approximately 14.5 million annual passengers in 2019 (according to data from the management entity). The station has undergone several interventions over the years, including the installation of electric lighting in 1894, the electrification of the railway in the 1950s and the connection to Restauradores Metro Station in the 1990s.

Since the last general renovation in 2006, the station has been subjected to a natural process of degradation, with the appearance of several anomalies, from the wear of the station's equipment to infrastructural anomalies. Despite some actions of local maintenance that took place over the years, a general rehabilitation is needed, to guarantee the safety of its users and workers, as well as to protect and maintain this national historic building.

In this paper, the characterization of the existing building is presented, based on the visual inspection. The most common types of anomalies were identified, as well as some proposed rehabilitation techniques.

1.1 *Main restraints*

Since the Rossio train station is a historic building with heritage value, some restrictions were found to its rehabilitation. Moreover, the station is in Lisbon's downtown, which implies some access barriers and some caution with the surrounding structures and infrastructures. There is also a lack of information about the existing infrastructures, structures, and water courses around the train station.



Figure 1. Site location and conditioning (a - source: adapted from Google Maps); main façade (b).

2 CHARACTERISATION OF THE BUILDING: EXISTING ANOMALIES

The buildings' deterioration process occurs as soon as they are put into use. Deterioration is a gradual phenomenon associated with physical, chemical, and mechanical degradation agents and with the natural ageing process (Silva et al. 2016a). In this chapter, the characterization of the train station is presented, by identifying the most common types of anomalies identified.

2.1 Exterior

The exterior façade of the station was refurbished in 2019, restoring all the natural stone claddings. These claddings raise the value of buildings while representing the first layer of protection against weather-related agents (de Brito et al. 2020). However, the existing obsolete pest bird's deterrents were not replaced. Due to the constant exposure to weather conditions, and absence of maintenance actions, the actual system is composed of deformed stainless-steel spikes and a deactivated low voltage bird scarer (Figure 2a and b). The deterioration of these systems results in the permanence of pigeons and seagulls on exterior façades and roof. Also, the skylights are devoid of any system that prevents landing and permanence of birds, which leads to being permanently dirty with bird droppings, aiding a negative visual impact for the station (Figure 2c) as well as promoting the corrosion and degradation of the building.

Birds can affect monuments in many ways, causing a lot of alterations: aesthetic, physical, mechanical, chemical, or biological. One of the degradation factors that has more incidence in monuments is bird nesting and the accumulation of bird droppings. Besides the aesthetic effect, bird droppings deteriorate stone substrate and, if not removed periodically, can obstruct the drains, which increases the presence of humidity. The growth of plant roots that germinate on the nests can also cause damage, as well as nests can create stability problems both in structural elements and in ornamental elements. Both can promote the disintegration of stone ornaments, and hence the risk of them falling on people passing by.

Finally, bird control is important not only for the protection of buildings, but also for preserving public health and prevention of spread of diseases (Rodríguez 2022; Spennemann, 2017, 2018).



Figure 2. Existing bird deterrent system (a, b); skylight with permanence of seagulls (c).



Figure 3. Roof handrails (a); brise-soleil and polycarbonates (b, c); paths and stairs (d).

Regarding the roof, part of the existing paths structures must be rehabilitated. Also, there are paths that are dangerous to go through, not having an adequate structure, which does not allow the maintenance plan to be carried out as planned. In addition to that, the glass fibre reinforced polyester handrail structure is severely degraded due to the exposure to weather and UV radiation. The fiberglass is already on the surface, preventing the use of the handrail since it causes irritation when in contact with the human skin (Figure 3a), putting the maintenance workers at risk of falling.

Moreover, the waterproofing capacity of the roof is compromised, with water penetrating inside. Also, the level of luminosity is low, since the translucent polycarbonate elements are dirty with high presence of lichens (Figure 3b and c), as well as the paths and stairs (Figure 3d).

Finally, the paint from iron doors and windows is peeling, resulting in spots of rust and corrosion in the welds of elements connections, which promote the loss of resistance of these materials. Regarding the wooden windows, the paint is also peeling, and the dried wood is cracking, which promotes its rotting as well as infiltrations in the interior of the monument, increasing the risk of deterioration.

2.2 Interior

The interior of the Station has three base levels: ground floor; first floor; and second floor (Figure 4). Some common anomalies to all spaces are the general peeling of paint of ceilings and walls, as well as cracking and leak/infiltration stains. Regarding the Station's illumination, most lights need cleaning, as their level of luminosity is low. The spaces were divided in the categories described in detail in the next sections.

2.2.1 Ticketing atrium

The ticketing atrium presents accumulated dirt on the existing skylights and degradation of its rubbers and silicones, which allows rainwater to enter the atrium, also promoting eventual falls of the station's users and workers due to slippery floors (Figure 4, green area).

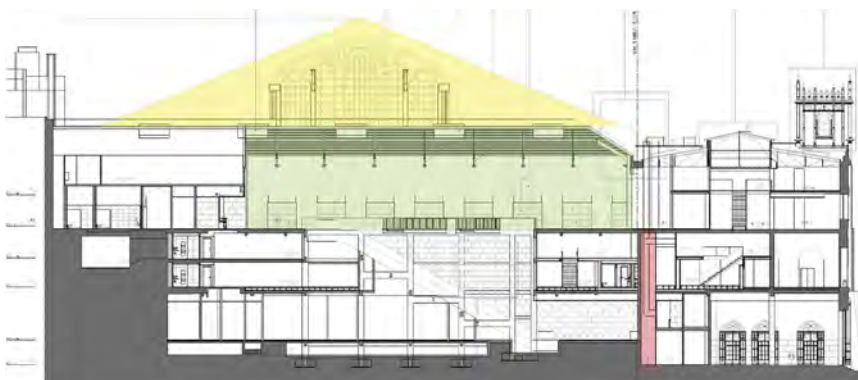


Figure 4. Transversal cut of the station.



Figure 5. Rossio's station platforms (a,b).

2.2.2 Platforms

Regarding the platforms zone (Figure 5a and b), the wall stones present infiltration stains (Figure 6a and b), jeopardising the integrity of the historic tile panel. There is an exterior wall above the north tile panel that shows signs of water entrance, as well as plant growth. The north tile panels present several anomalies, namely the presence of humidity, which promotes paint cracking and blistering due to saturation of the wall (Figure 7a), as well as the growth of salts (Figure 7b), and the opening of joints and support breakdown (Figure 7c). Also, some tiles present glaze loss, dirt, cracking in the ceramic tiles' glazed layer and microcracks. In some of the tiles it was possible to observe surface water run-off.

Regarding the roof, since its waterproofing capacity (Figure 4, yellow area) is compromised, water penetrates inside, resulting in corrosion of the metallic structure, including pillars.

Moreover, the stained-glass window presents dirt, also some glasses are broken or cracked, allowing the rain to enter the building. The false ceiling, as well as the stainless-steel surrounding pillars and wall present punctual spot rust and corrosion.

Regarding the pavements of the platforms, both granite (Figure 6c) and “calçada portuguesa” (Figure 6d) are used. The traditional “calçada portuguesa”, is an artistic typical Portuguese pavement mainly made with white and black limestone or basalt (da Silva et al. 2022). However, an adequate soil compaction is crucial for the efficiency and safety of the pavement's use (DGEG 2009). The pavement shows lack of polishing, as well as punctual lack of material. Also, the pavement shows clear signs of wear and present signs of differential settlements, which increases the risk of tripping of the station's users and workers.

Regarding the tunnel entry, the roof shows infiltrations, which allows water to flow through the tunnel wall, deteriorating the stone claddings.

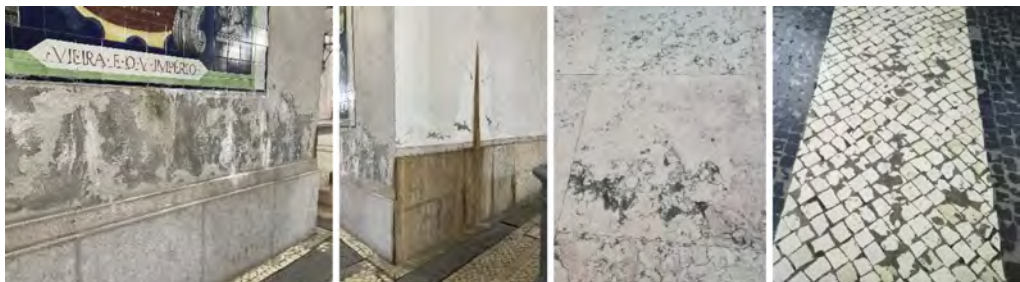


Figure 6. Interior infiltrations (a, b); worn out pavements (c, d).

2.2.3 Gallery

Regarding the gallery behind the store (Figure 4, red area), it is possible to observe rising damp and efflorescence (Figures 8a and b), due to humidity by capillarity. These anomalies promote salubrity problems since mould can cause respiratory problems. The constant presence of water, and the absence of a functional drainage system, promotes the mechanical degradation



Figure 7. Anomalies on the historic tiles (a, b, c).



Figure 8. Gallery (a), rising damp and efflorescence (b) and orange-coloured run-off (c).

of the existing structures. Finally, the water run-off is orange coloured (Figure 8c), which could indicate the corrosion of the existing steel reinforcement bars.

3 PROPOSED REHABILITATION TECHNIQUES

Repairing an anomaly should always begin with eliminating its cause. If not possible, an attempt must be made to avoid the growth of the anomaly and consequent degradation of the element. The purpose of periodic maintenance is to identify the anomalies and degradation condition of buildings and their components, correcting the anomalies and causes, while preventing, or mitigating the occurrence of new anomalies (Carvalho et al. 2018). The maintenance activities allow maintaining the building's performance in adequate levels over its service life. Although there are different definitions in the literature, these interventions can be programmed or not. Generally, maintenance policies can be of many types, preventive, proactive, condition-based, prescriptive, curative or improvement repair techniques (Ferreira et al. 2022).

In this chapter some rehabilitation techniques are proposed, separated by the zones defined in the previous chapter.

3.1 Exterior: Pest birds deterrents

As referred, the exterior façade, composed by stone claddings, was renovated in 2019, therefore it does not need immediate rehabilitation. However, regular maintenance should take place, since it is a relevant factor for the performance and durability of the cladding. Simple planned maintenance works, such as cleaning and inspecting the façade are useful to avoid expensive late repairs (Snethlage 2014; Amaral et al. 2015).

Since Rossio’s station is located near the river, allied to the fact that it’s an extremely touristic place, with unlimited food supply for the birds, both pigeons and seagulls affect the building and its surrounding area. The mentioned animals have great reproductive potential; therefore, the actions must aim to achieve a lasting effect (Rodríguez 2022).

In order to avoid the permanence of the birds on the exterior façade, skylights and ticket hall, the following bird deterrent devices were proposed:

- Roof/skylights: spring-tensioned netting system (Figure 9a);
- Ticket offices hall: spring-tensioned wire; bird netting system; bird gel (Figure 9b);
- Exterior façade: stainless steel spikes and low voltage bird scarer (Figure 10).

According to Spennemann et al. 2018, “the highest-ranking deterrents were bird netting and bird spikes, but they were only considered moderately effective. The costs of installation and maintenance, as well the ease of installation, were all deemed significantly less important than the physical impact, the aesthetic sympathy and the effectiveness of a deterrent method.”

The spring-tensioned wire and netting system are designed to create an unstable landing area, thus avoiding the permanence of birds.



Figure 9. Proposed bird deterrent solutions: ticket offices hall (a); skylights (b).



Figure 10. Proposed new roof paths (a,b,c) and gallery drainage solution (d).

3.2 Exterior/Roof: Safe accessibility

Regarding the roof, to assure the conditions to safely carry out a planned maintenance program, new paths should be executed (Figures 10a, b and c). Also, a new paint-based coating should be applied on the degraded handrail structure, to safeguard the safety of those who use it.

In order to control the existing infiltrations, a full review of the roof should take place, with treatment of infiltration areas, replacement of silicones, rubbers and fasteners. This will avoid future deterioration of the interior metallic structure, as well as eventual falls of the station users and workers due to slippery floors.

Regarding the interior part of the roof, a cleaning of the metallic structure, including pillars, and an evaluation of the existing corrosion points with proper treatment is proposed, in order to safeguard its bearing load capacity.

At last, to increase the luminosity of the station, the translucent polycarbonate elements should be cleaned and restored, with an adequate anti-fungus solution. This will allow to take fully advantage of the solar natural light, being an environment-friendly solution and avoiding extra energy costs.

3.3 *Interior of the station*

To eliminate stains and paint peeling, a general painting of the ceilings and walls of the Station is proposed. Regarding the Station's illumination, all lights will be substituted by LED lamps, to increase the efficiency and become more environment friendly. Moreover, as part of the maintenance plan, all light structures should be cleaned periodically, to maintain the highest luminosity possible.

3.3.1 *Ticketing atrium*

A full inspection and rehabilitation of the existing skylights will take place, as well as a full replacement of all its rubbers and silicones, in order to cease the infiltration of water in the station's atrium, and thus preventing eventual falls of the station users and workers due to slippery floors (Figure 9a).

3.3.2 *Platforms*

Regarding the platforms zone, the exterior wall above the north tile panel will be fully waterproofed, to avoid future infiltrations and thus protecting the historic tiles. Moreover, the stained-glass window will be repaired and broken or cracked glasses will be replaced. The false ceiling, as well as the stainless-steel surrounding pillars and wall will be cleaned, and the punctual spot rust and corrosion will be treated.

Considering the anomalies present in the historic tiles, these need an urgent intervention, in order to safeguard the tile patrimony. Therefore, a specific intervention plan will be developed and carried out by entities specialized in conservation and restoration, equipped with specialized human resources and adequate means.

Regarding the worn and uneven pavements of the platforms, these will be polished, considering an adequate slip resistance of the material. A monitoring plan will be developed, in order to understand if more invasive measures should take place in the near future, such as the total replacement of the pavements with the execution of a new substrate.

Finally, regarding the tunnel entry, the roof will be repaired, in order to cease the infiltrations, and thus eliminating the presence of water into the tunnel wall.

3.3.3 *Gallery*

Regarding the gallery, an insulation and drainage solution will be designed, to ensure the drainage of the groundwater streams that flow from the existing anchored wall, and then accumulate in the gallery behind the train station's assistance/service spaces (Figure 10d). Further studies will be needed in to order to obtain the actual conditions of the existing anchors.

4 CONCLUSIONS

Several difficulties were found during the research, mainly the lack of information about some of the existing structures, infrastructures and water courses. This paper contributes to the dissemination of knowledge on the maintenance of train stations infrastructures, as the presented information may be used to improve and increase the effectiveness of maintenance plans. As future developments, a system that classifies the causes associated with anomalies should be created, as well as a system of classification of the diagnosis methods associated with the characterization of anomalies and causes should be designed. Finally, based on the system, a proper maintenance program should be developed for the station.

ACKNOWLEDGMENTS

The authors are grateful to *Infraestruturas de Portugal*, the site owner, for its permission to the presentation of this paper. Ana Silva also acknowledges the support of CERIS Research Centre and FCT through the individual project CEECIND/01337/2017.

REFERENCES

- Amaral P.M., Fernandes J.C., Pires V., Rosa L.G. 2015 Ornamental stones. In: Gonçalves MC, Margarido F (eds) *Materials for construction and civil engineering: science, processing, and design*. Springer, Cham, Switzerland
- Carvalho, C., de Brito, J., Flores-Colen I., Pereira, C. 2018 *Inspection, diagnosis, and rehabilitation system for vinyl and linoleum floorings in health infrastructures*. *J Perform Constr Facil* 32 (6): 04018078.
- da Silva, C.M., Pereira, S. 2022. *Walking on Geodiversity: the Artistic Stone-Paved Sidewalks of Lisbon (Portugal) and Their Heritage Value*. *Geoheritage* 14, 98
- de Brito, J., Pereira, C., Silvestre, J. & Flores-Colen, I. 2020. *Expert Knowledge-based Inspection Systems: Inspection, Diagnosis, and Repair of the Building Envelope*. Lisbon: Springer.
- Direção Geral de Energia e Geologia 2009. *The Portuguese Pavements Handbook*.
- Rodríguez, E.R. 2022. Birds Effects on Heritage Buildings. *Environmental Analysis & Ecology Studies* (000732) 10 (2): 1119–1126.
- Siegesmund S., Snethlage, R. 2014. *Stone in architecture, Properties, durability*. Springer, Heidelberg, Germany
- Silva, A., de Brito, J., Gaspar, P.L. 2016. *Methodologies for service life prediction of buildings. With a focus on façade claddings*. Springer, Switzerland
- Ferreira C., Silva A., de Brito J., Flores-Colen I. 2022. *Maintainability of Building Envelope Elements. Optimizing Predictive Condition-Based Maintenance Decisions*. Springer Series in Reliability Engineering, Springer Nature, Switzerland. <https://doi.org/10.1007/978-3-031-14767-8>.
- Spennemann, D., Pike, M. & Watson M. 2017. Effects of acid pigeon excreta on building conservation. *International Journal of Building Pathology and Adaptation*. 35 (1): 2–15.
- Spennemann, D., Pike, M. & Watson M. 2018. Bird impacts on heritage buildings: Australian practitioners' perspectives and experiences. *Journal of Cultural Heritage Management and Sustainable Development*. 8 (1): 62–75.

Non-destructive evaluation for voids under airport pavement concrete in-situ

T. Nishida

Shizuoka Institute of Science and Technology, Shizuoka, Japan

F. Izu

Port and Airport Research Institute, Kanagawa, Japan

Y. Kobayashi

Nihon University, Tokyo, Japan

M. Aizawa

C-Tech, Kanagawa, Japan

K. Kawaai

Ehime University, Ehime, Japan

ABSTRACT: When water enters the bottom of the concrete slab of an airport pavement through the joints, aircraft loads can cause granulated grout material particles to erupt from the joints and create voids at the bottom of the concrete slab. The ejected granulated grout causes equipment damage due to suction into the engine. In addition, loss of support and pavement failure can severely affect aircraft navigation, therefore early detection is critical. Therefore, in this study, voids were fabricated in a specimen simulating airport pavement concrete, and various nondestructive investigations were conducted. As a result, it was found that defects could be properly detected by using electromagnetic radar and ultrasonic tomography. Based on the above results, an investigation was conducted at an actual airport pavement to verify the results.

1 INTRODUCTION

When prestressed concrete pavement (referred to as PC pavement) is used for airport pavement, a grout layer is generally injected between the roadbed and the PC pavement to eliminate the unevenness between them. when water penetrates the bottom surface through the joints of PC pavement, the grout material is granulated by the aircraft load and spurts out from the joints of the PC pavement. The granulated grout material is then ejected out of the joints, creating a void at the bottom of the PC pavement (Tanaka et al. 2008) as shown in Figure 1. The grout ejected from the joints can be sucked into aircraft engines, etc., and may have a serious impact on the running of the aircraft. Therefore, it is necessary to identify the areas where grouting has occurred or is likely to occur at an early stage.

In this paper, the possibility of detecting these voids by nondestructive testing was experimentally investigated using a specimen simulating airport PC pavement concrete. Based on the above results, an investigation was conducted at an actual airport to verify the results.



Figure 1. Ejection of granulated grout at airport PC pavement.

2 INVESTIGATION USING SIMURATED SPECIMENS

2.1 *Outline of specimens*

The specimens were prepared based on the design drawings of actual airport PC pavements. The water cement ratio was set to 0.34 in consideration of the mix ratio of prestressed concrete. The specimen is reinforced concrete, 300 mm thick, and its shape and dimensions are shown in Figures 2. During concrete placement, styrene foam was partially placed at thicknesses of 5 mm, 10 mm, 20 mm, 30 mm, and 50 mm as a simulated void (referred to as the “simulated void”). The location of the simulated void was 250 mm from the top of the specimen, considering that the actual thickness of the airport PC pavement is 250 mm. For specimen (1), after repeated nondestructive investigation of the void, the Styrofoam was removed from the red frame (50 mm thick) shown in Figure 2, and saturated sand and soil were re-laid to assume granulated grout (see Figure 3, refer to as “simulated granulated grout”). The non-destructive investigation method considered for this simulated granulated grout was chosen considering the results of the aforementioned investigation using Styrofoam.

2.2 *Types and methods of nondestructive investigation methods*

The nondestructive inspection methods were the rebound hammer method, impact echo method (Sansalone & Streett 1997), electromagnetic radar method (Maeda et al. 2015), and ultrasonic tomography method (ACS Website 2022). The rebound hammer method was conducted in accordance with Japan Industrial standards (JIS A 1155 2012). The impact echo method was conducted in accordance with the iTECS method (i-TECHS website 2022). The electromagnetic radar method and ultrasonic tomography were performed using commercially available equipment. The locations of the simulated voids were searched using various nondestructive investigation methods to detect the void locations and evaluate their accuracy. Figure 4 shows an example of the measured positions.

2.3 *Results and discussions*

Table 1 shows the detection results of voids by various nondestructive inspection methods. Figure 5 shows an example of the measurement results of electromagnetic radar and Figure 6 shows an example of the measurement results of ultrasonic tomography.

(1) Rebound hammer method

Voids with an area of approximately 1 m² (1000 x 1000 mm) or a thickness of 30 mm or more tend to have a rebound force 10 to 20 points lower than the area without voids, and it is generally possible to detect voids with a large area or thickness, but not with a small or thin void. The results are shown in Table 1.

(2) Impact echo method

When the void area was about 1 m², a void with a thickness of 5 mm could be detected. However, when the area was small and the thickness was thin, it was difficult to detect it.

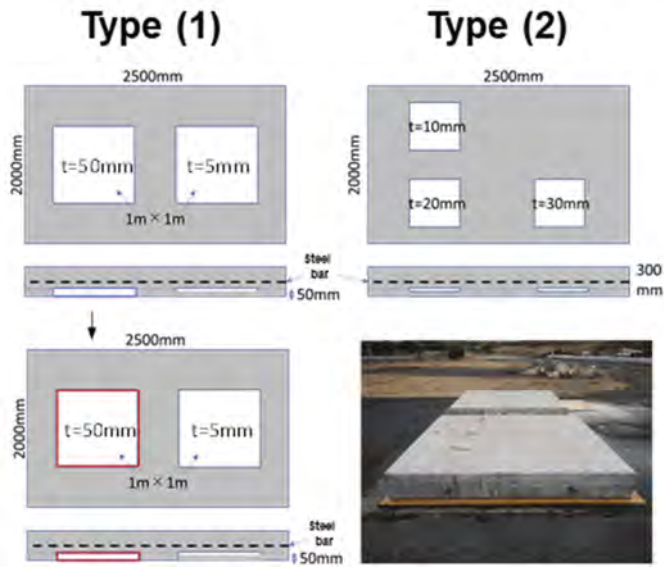
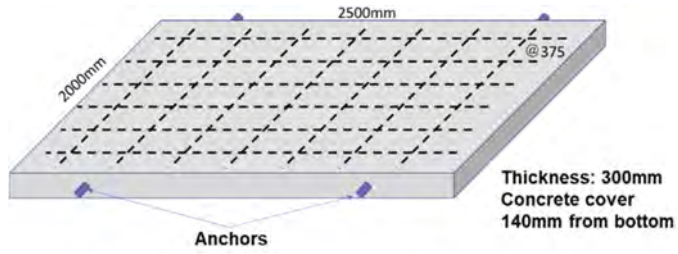


Figure 2. Outline of specimen.



Figure 3. Simulated granulated grout.

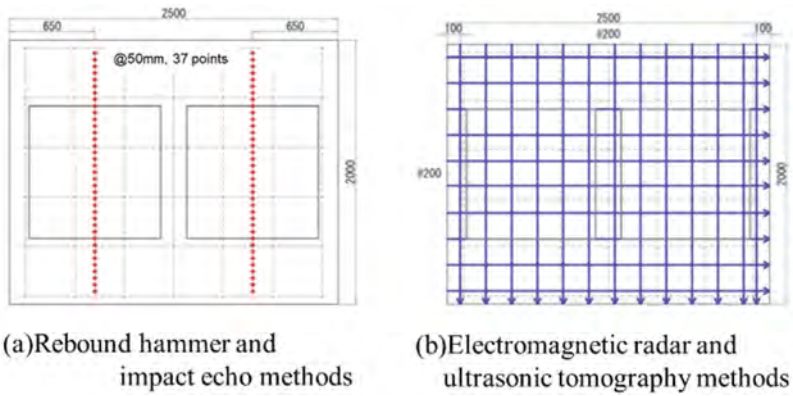


Figure 4. Outline of measurement points.

Table 1. Availability of void detection.

Non-destructive tests	Availability of void detection				
	1000×1000		500×500		
	(area mm)				
	50	5	10	20	30
	(thickness mm)				
Rebound hammer	○	○	×	×	○
Impact echo	○	○	×	×	○
Electromagnetic					
400MHz	○	×	×	×	×
600MHz	○	×	×	○	○
900MHz	○	×	○	○	○
1600MHz	○	○	○	○	○
2000MHz	○	×	○	○	○
2700MHz	○	×	×	○	○
Ultrasonic tomography	○	○	○	○	○

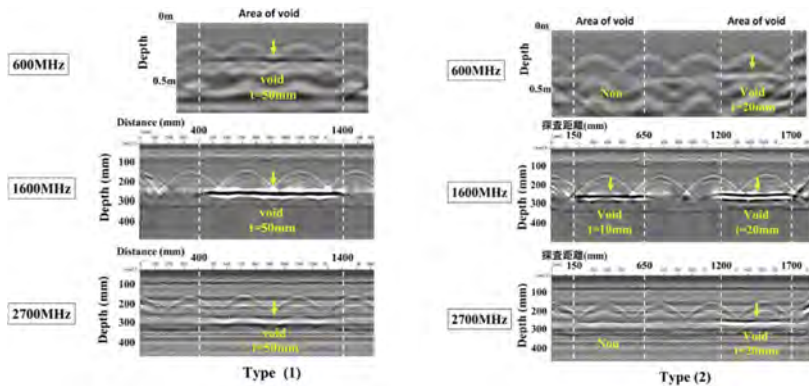


Figure 5. Results of electromagnetic radar.

(3) Electromagnetic wave radar method

In the electromagnetic wave radar method, the thickness of voids varies depending on the antenna frequency; Radar using 1600 MHz electromagnetic waves was able to detect all simulated voids, but radar using 2000 MHz electromagnetic waves was unable to detect small voids due to attenuation of the electromagnetic waves.

(4) Ultrasonic tomography

All voids were detectable in the 3D images, but the smaller the void thickness, the smaller the red and yellow areas with stronger ultrasonic reflections tended to be.

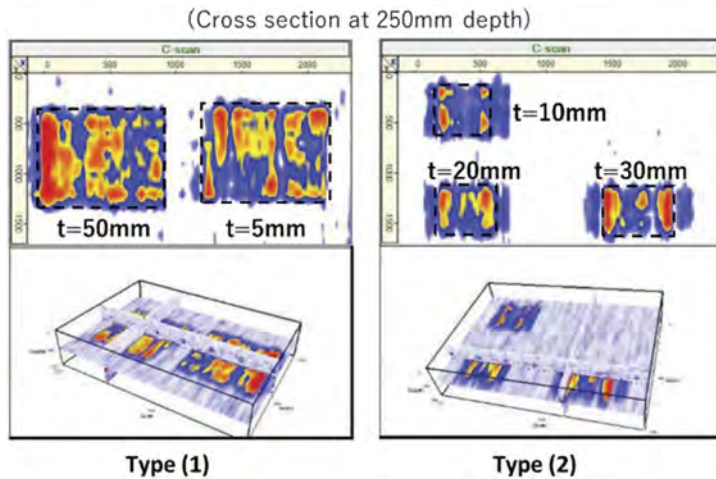


Figure 6. Results of ultrasonic tomography.

The accuracy of void detection in various nondestructive testing methods was determined as follows.

- (1) Rebound hammer method
The ratio of the rebound force at the void location divided into three ranges (30-40, 40-50, 50-60), with 30-40 being the rebound force.
- (2) Impact Seismic Method
Ratio of the length of void detection to the length of the void installation against the length of the void installation.
- (3) Electromagnetic Radar Method
Ratio of the length of void detection to the length of void installation against the length of void installation.
- (4) Ultrasonic tomography method
Ratio of the area of void detection to the area of void installation against the area of void installation.

Figure 7 shows the average detection accuracy of the simulated void locations for each NDT method. The NDT methods with average void detection accuracies exceeding 50% were the electromagnetic radar method and the ultrasonic tomography method. Among the investigated items used in this study, the 1600 MHz electromagnetic radar was found to be the most accurate in detecting voids 250 mm deep placed in specimen.

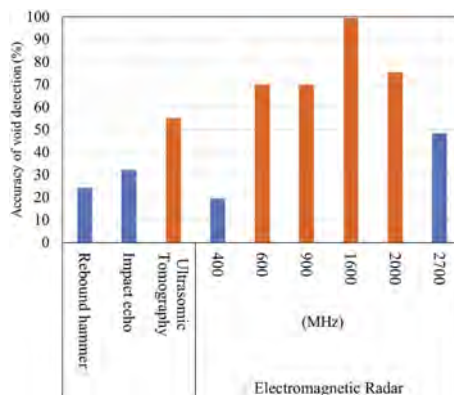


Figure 7. Accuracy of void detection.

The electromagnetic wave radar method and ultrasonic tomography, both of which have high accuracy of void detection, were employed as nondestructive investigation methods for the simulated granulated grouted area.

Two frequency bands, 600 MHz and 1600 MHz, were used for the electromagnetic radar. After about one week of curing, the specimens were turned over again with the defects on the underside of the specimens.

The results of the electromagnetic radar and the ultrasonic tomography at the location of the defect were shown in Figure 8 and 9.

(1) Electromagnetic wave radar method

Both 600 MHz and 1600 MHz electromagnetic wave radar were capable of detecting defects, and the location of defects was clear in the 1600 MHz image.

The detection range of the contour of the simulated granular grout tended to be slightly smaller than that of the void.

(2) Ultrasonic tomography method

The ultrasonic tomography method was also able to detect the simulated grout.

The 3D image of the simulated grout did not differ significantly from the void detection image and was almost the same.

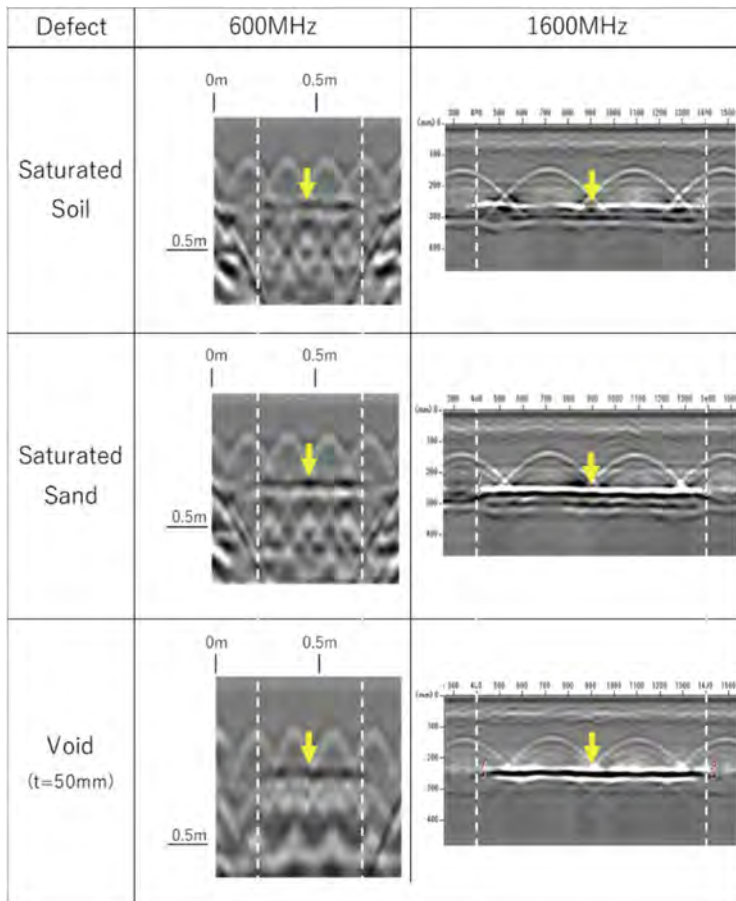


Figure 8. Detection of simulated granulated grout by electromagnetic radar.

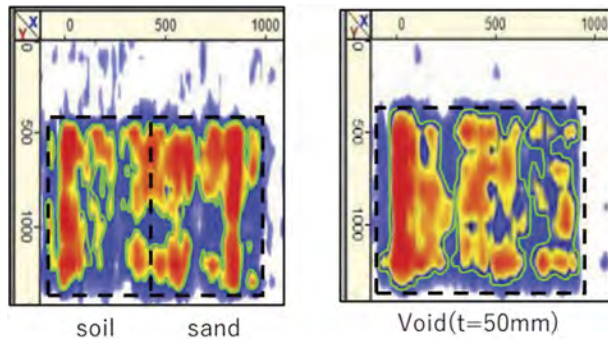


Figure 9. Detection of simulated granulated grout by ultrasonic tomography.

3 IN-SITU INVESTIGATIONS

Following the results of the study using the specimens, verification was conducted on an actual airport pavement. Electromagnetic radar and ultrasonic tomography methods were applied as nondestructive testing methods as shown in Figure 10.

The actual airport is the one operated in Japan, and the white granular grout jet was observed as shown in Figure 1.

Figure 11 shows the results of electromagnetic radar measurements. Note that there were some points where it was difficult to distinguish voids due to the influence of moisture. The results indicate that some of the measured points have signals that appear to be voids.

Figure 12 shows the results of ultrasonic tomography. The ultrasonic tomography results showed signals that were probably due to reflections from the steel and the bottom surface, so it was not possible to detect voids in the lower part of the PC plate, which was the subject of this study.

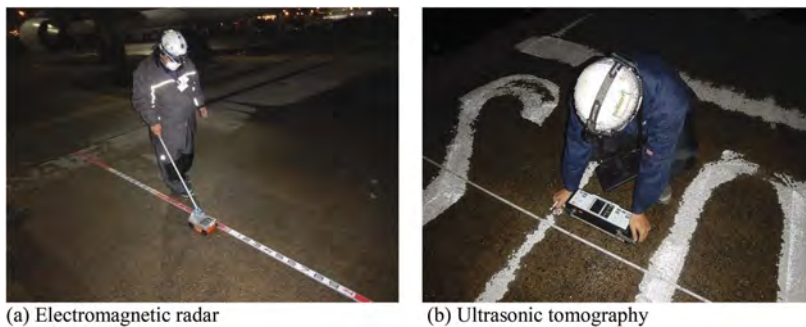


Figure 10. Measurement at actual airport.

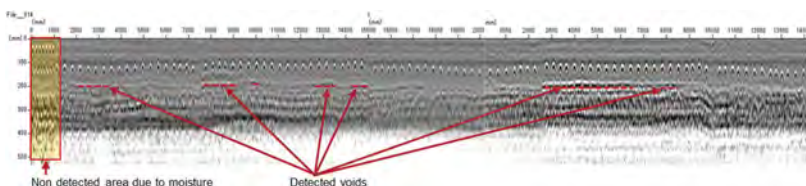


Figure 11. Results of electromagnetic radar in actual airport PC pavement.

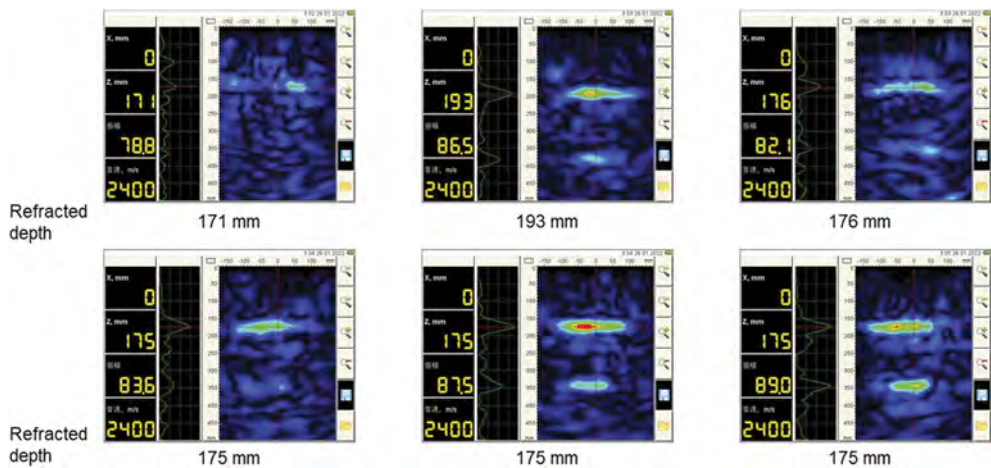


Figure 12. Results of ultrasonic radar in actual airport PC pavement.

4 CONCLUSIONS

The results obtained in present paper are as follows;

- 1) The detection accuracy of the electromagnetic radar method and the ultrasonic tomography method was high and suitable for nondestructive inspection of simulated specimen.
- 2) The electromagnetic radar method was able to detect defects in simulated specimen more accurately than any other methods used in this study at the frequency of 1600 MHz.
- 3) Ultrasonic tomography was able to roughly determine the location and size of defects from the three-dimensional images.

These results suggest that the electromagnetic radar and ultrasonic tomography methods are effective in detecting defects in the lower part of concrete slabs of airport pavements.

A future challenge is that the antenna frequency suitable for defect detection may vary depending on the measurement environment and conditions, and a device is needed for each frequency used. Therefore, it would be desirable to verify electromagnetic radar measurements of concrete on airport pavements using devices with broadband antenna frequencies or devices that can change frequencies.

REFERENCES

- Acoustic Control Systems: <https://acs-international.com/product/a1040-mira/>, 2022.
- JIS A 1155: Method of measuring the resilience of concrete, 2012.
- i-TECHS Association: <https://www.itecs.or.jp/>, 2022.
- Maeda Y., Masahiro Yamada, Masayuki Yasuda, Jun-ichi Yanagida, Manabu Sumi: Study on Visualization Technique of Unfilled Concrete Section by Electromagnetic Radar Method, Proceedings of Symposium on Non-Destructive Testing of Concrete Structures, Vol.5, pp.159–164, 2015.
- Sansalone M. J., W. B. Streett: Impact Echo – Nondestructive Evaluation of Concrete and Masonry, Bullbrier Press, Ithaca, N.Y., 1997.
- Tanaka H., S. Tsunoda, T. Ikeda, and A. Ito: Design of PRC floor slabs for airport taxiways, Proceedings of the 63rd Annual Meeting of JSCE, pp. 295–296, 2008.

How to better exploit the use of LCA analysis for Ultra High Performance Concrete (UHPC) through a constitutive law which integrates chloride and sulfate attack

D. di Summa

Ghent University, Ghent, Belgium
Politecnico di Milano, Milan, Italy

F. Soave, M. Davolio, S.M.J. Al-Obaidi & L. Ferrara

Politecnico di Milano, Milan, Italy

N. De Belie

Ghent University, Ghent, Belgium

ABSTRACT: Structural applications of advanced cementitious materials such as Ultra High Performance Concrete (UHPC) have been already assessed in harsh exposure conditions with presence of chlorides or sulfates. Nevertheless, the limited availability of design standards has not favoured so far a widespread use of these materials. Moreover, previous studies employed a constitutive model only partially representative of the real behavior of such materials when exposed to aggressive conditions. Therefore, this work, employing a “scenario dependent” constitutive law, estimates the serviceability limit state in correspondence of which it is needed to carry out the maintenance activities and investigates, through the Life Cycle Assessment (LCA) methodology, the ecological and economic profile of a UHPC water basin structure subjected to chloride and sulfate attack. The CML impact assessment method has been employed for the specific purpose to compare such structure to one made with ordinary reinforced concrete (ORC) using as system boundary the A1-B7 stages indicated in EN 15804.

1 INTRODUCTION

The construction sector, due to its social and economic impacts in the modern society (e.g. 9% of the gross domestic product of European Union and 18 million of people employed), requires a particular attention to be paid to its overall sustainability (Ortiz et al, 2009) (Oloke et al., 2022). The latter should encompass, from a holistic point of view, environmental, economic and social aspects. This challenge may represent an opportunity for the involved supply chain that has to be, then, rethought within a more sustainable framework starting from the extraction of the single constituent raw materials until the dismantling/recycling of the final product or structure. This means that also the design process of structures/infrastructures has to be based on a Life Cycle Assessment (LCA) approach to predict the future environmental and economic performances of a specific solution in comparison to another. Thus, the designers must be helped to also account the needs of the final users (long durability, reduced maintenance costs, adequate environmental performances) within the intended Service Life (SL). This is also in line with the path outlined by the European Commission action plan adopted in 2020 to favour a transition from linear towards circular production and consumption models. The latter represent a driving force to turn, what has been so far considered as a waste product,

into a secondary raw material and keep (even if modified) its value in the economy as long as possible (European Commission, 2020). These concepts can then be transferred to the design of concrete structures employing a methodology such as the Durability Assessment Based Design (DAD) especially for advanced cementitious based materials such as the Ultra High Performance Concrete (UHPC) accounting for, “a priori”, the interaction of the material with the surrounding environment (Kannikachalam et al., 2022) (di Summa et al., 2022) (Al-Obaidi et al., 2021) (Al-Obaidi et al.2022). This approach can overcome the limitations of the current standards that simply provide prescriptions, such as minimum cement content and maximum water to cement ratio, aimed at implicitly guaranteeing a target service life without considering the evolution of the behavior of the material over time, within the life span of the structure and as a function of its service scenario. In this framework, this work presents as case study a water basin structure aimed to contain geothermal water, characterized by the presence of sulphate and chloride ions. Different degradation phenomena have been taken into consideration, including sulphate attack, leaching and chloride penetration. Then, LCA and Life Cycle Cost (LCC) analysis have been carried out to investigate the potential sustainability of such construction technology in comparison to an ordinary reinforced concrete based solution.

2 DESCRIPTION OF THE CASE STUDY AND DEGRADATION MECHANISMS

2.1 Description of the case study

The analysis has been carried out assessing the case study of a basin aimed at containing the geothermal water coming from the condensation of the vapor extracted from the soil and cooled in a cooling tower and designed for a target service life of 50 years. The structure is 18 m long and 5 m wide, with a height of the compartment walls varying from 3 m up to 4.87 m, depending on the boundary morphological conditions since the structure itself is designed to be partially underground. Two different structural solutions are compared, characterized by two different design philosophies due to the different performance of the employed construction material. In the first scenario, the basin is built with ordinary reinforced concrete (ORC), including steel bars while the second design uses UHPC. They are hereinafter referred as ORC_basin and UHPC_basin, respectively. The mix designs for both cases are reported in Table 1. Figure 1 details the cross section of the vertical elements of both solutions. As it is possible to observe, the structural performance of UHPC (such as its compressive and tensile strength that can reach values around 150 MPa and 10 MPa respectively, much higher than the one of ORC) allowed to shift from the 0.4 m thickness of the ORC_basin to the 0.05 m thick UHPC_basin walls designed as supported by ORC buttresses. Similarly to other works (di Summa et al., 2022) (Kannikachalam et al., 2022) while the first implies the use of reinforcement bars (details shown in Figure 1), the second one has been designed as UHPC slabs supported by 2 m spaced reinforced ORC buttresses, without any reinforcement bars in the slabs. The latter was possible

Table 1. Mix design for ORC_basin and UHPC_basin.

Constituents [kg/m ³]	ORC	UHPC
CEM I 42.5 R	350	-
CEM 52.5 R	-	600
Slag	500	-
Water	207	200
Aggregate 7/12	600	-
Aggregate 4/7	300	-
Sand (0-2 mm)	950	982
Limestone filler	60	-
Superplasticizer	-	33
Steel fibers	-	120
Crystalline admixture	-	4.8

employing, within the model code 2010 (Fédération internationale du béton, 2012), the mechanical properties of UHPC identified in (Lo Monte and Ferrara, 2020) and (Davolio et al., 2022).

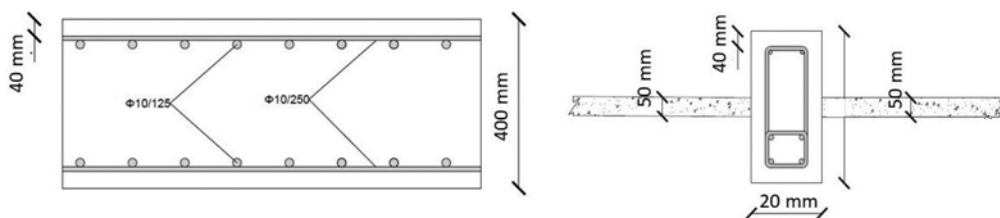


Figure 1. Cross section of ORC_basin (left) and UHPC_basin (right).

2.2 Sulphate attack

The sulphates penetrate into the concrete matrix reacting with the hydration products and causing expansion phenomena which have been here accounted according to the study by Jian et al. (Jian et al., 2018). The latter assessed the behavior of 54 mix designs defining in total three macro groups characterized by different expansion kinetics due to the chemical composition of the cement. Due to its mix design, the ORC_basin belongs to the group characterized by an expansion (EXP) as reported in Equation 1 while the UHPC_basin follows Equation 2, where C_3A is the C_3A cement content expressed in percentage (7.6% for the case of this study), T the time and w/c the water to cement ratio. In both cases, for this type of damage, the ultimate limit state has been defined by the attainment of an expansion ratio equal to 0.5% which is calculated to be reached, for the case of ORC_basin after 38 years and which is even not reached at 100 years for the UHPC_basin as detailed in Figure 2.

$$EXP = 0.0293 \left(\frac{W}{C} * T \right) + 0.000975 (C_3A) * T + 0.0216 \quad (1)$$

$$EXP = 0.0157 \left(\frac{W}{C} * T \right) + 0.0305 \quad (2)$$

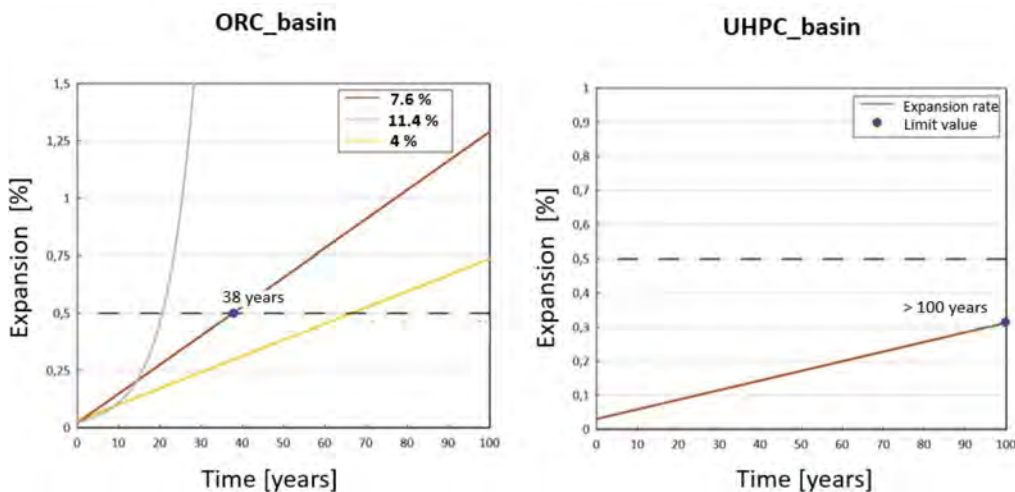


Figure 2. Expansion within a timeframe of 100 years. The graphs referring to the ORC_basin also contain the behaviour that the material would have had in the case of a C_3A content: 7.6%, 11.4 % and 4%.

2.3 Leaching phenomena

The $\text{Ca}(\text{OH})_2$ leaching phenomena are mainly dictated by the permeability of the material itself and by the pressure of the water against the structure, with a consequent reduction of the cross section corresponding to the depth of the leached zone. Therefore, the process has been assessed according to Fagerlund (Fagerlund, 2021) according to Equation 3 where X corresponds to the depth of the leached area, t is the time, while a and k_e are the leaching coefficients considered as equal to $0.1385 \text{ mm/day}^{0.5}$ and 0 mm/day for ORC_basin and $0.0072 \text{ mm/day}^{0.5}$ and 0.006 mm/day for UHPC_basin respectively as in (Fagerlund, 2021).

$$X_{crit} = a\sqrt{t} + k_e * t \quad (3)$$

Therefore, to identify the serviceability limit state for the case of this degradation mechanism, the time when the acting bending moment (M_{Ed}) is equal to the resistant bending moment (M_{Rd}) has been calculated according to the section which is reduced with time for each wall of the ORC_basin. It has been then estimated that for one of the walls of that structure, M_{Rd} and M_{Ed} are equal at 27 years. The same calculation has been performed for UHPC_basin where the limit is observed to be reached only after 58 years. In this regard it must be specified that M_{Ed} was calculated employing a cantilever scheme for ORC_basin while a plate analysis was adopted for UHPC_basin. Figure 3 reports the results above described.

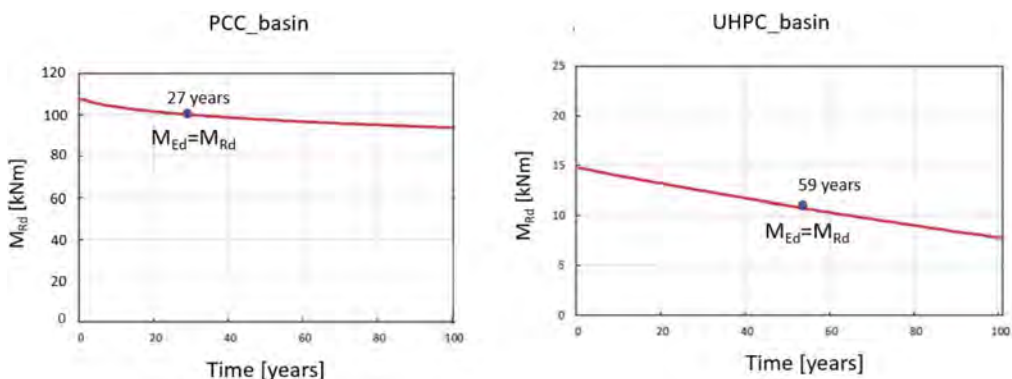


Figure 3. Variation of M_{Rd} according to the leaching phenomena for both ORC_basin and UHPC_basin within a timeframe of 100 years.

2.4 Chloride penetration and steel corrosion

The chloride penetration has been estimated employing the second Fick's law. With regard to ORC_basin both the initiation and propagation times have been estimated as in di Summa et al. (di Summa et al., 2022) and Van Belleghem (2018) obtaining a value lower than 6 months for the initiation. Then, considering for the propagation a localized damage such as a hemispherical pit, the serviceability limit state is assumed to be reached at the moment when 20% of the cross section is lost which is calculated to occur after 3 years for at least one of the walls of ORC_basin. This is in line with previous studies which demonstrated how 20% degree of corrosion can cause significant reduction in terms of strength capacity (Noh et al., 2018) (di Summa et al., 2022) (Bossio et al., 2017). With regard to UHPC_basin, other works already assessed case studies similar to the one here presented (di Summa et al., 2022) (Kannikachalam et al., 2022) but still employing a constitutive law not perfectly representative of the behaviour of the material when exposed to a chloride environment. Such studies considered the cross section, for the sake of simplicity, as progressively reduced along time accordingly to the chlorides penetration and supposed the steel fibers immediately corroded. In this respect, this study takes advantage

of more recent studies (Davolio et al, 2022) (Al-Obaidi et al., 2022) where for the cross sectional equilibrium, the contribution of the region in tension affected by chlorides penetration follows a constitutive law as function of the crack opening and as function of time based on the experimental results and their extrapolation along time. This constitutive law has been obtained in (Davolio et al., 2021) who employed UHPC specimens characterized by the same mix design as the one here employed, and tested them in four point bending and direct tension after having subjected them to simultaneously acting sustained loads and exposure to either XA (acid) or XS (chloride) environment. Employing the constitutive law coming from both the aforesaid experimental campaign M_{Rd} always reaches the value of M_{Ed} after more than 100 years. Figure 4 better explains where the new constitutive law was employed also detailing M_{Rd} of UHP_basin within the time.

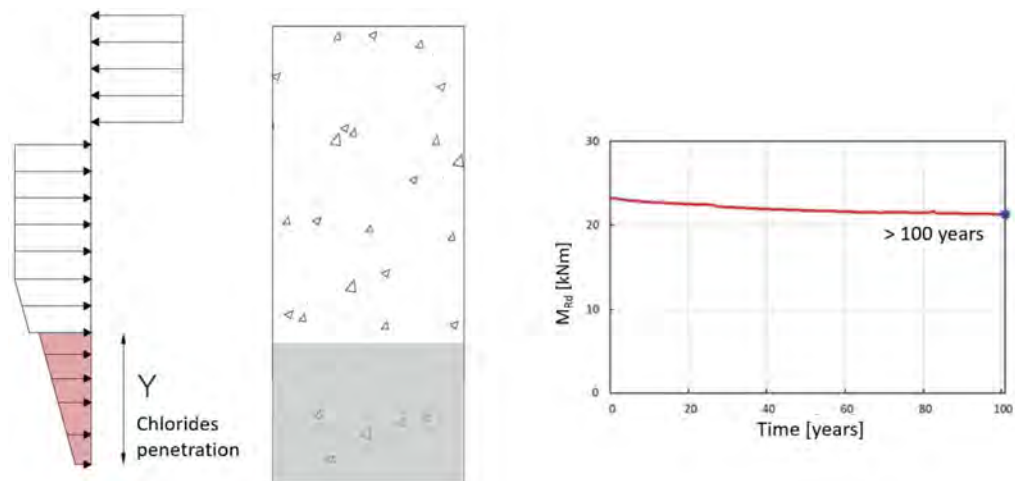


Figure 4. Representation of a generic UHPC cross section with the identification, in red, of the area affected by chlorides in which the new constitutive law can be used to better describe the behavior of the material (left) and M_{Rd} over time for UHPC basin (right).

3 LIFE CYCLE ASSESSMENT AND LIFE CYCLE COST

3.1 The system boundary of the analysis

The LCA analysis has been carried out hypothesizing a cradle to grave system boundary in which the basin is considered as demolished at the end of its service life and treated as a waste material except for the steel scraps which are always considered as recycled according to the European regulations. The maintenance activity hypothesized for the ORC elements consisted in the removal of the damaged concrete cover and reinforcement bars, followed by the replacement of the latter and the realization of a new concrete layer after having applied a primer to favor its adhesion to the substrate. According to what has been stated in 2.2, 2.3 and 2.4, the most severe damage is represented by chloride attack, reason why one maintenance activity every 3 years has been considered for ORC_basin and for the ORC buttresses of UHPC_basin. No further repairing activities were calculated to be needed for UHPC_basin. The 10 CML IA impact method has been employed with the scope to describe all the implications at a global, regional and local scale. The LCC has been further developed according to the construction rates reported in (Regione Toscana, 2022) and (Regione Lombardia, 2022) referring to the Tuscany area, where the basin is supposed to be located. Moreover, a discount rate for the activities that have to be carried out in the future has been accounted for according to Caruso et al. (Caruso et al, 2020) and di Summa et al. (di Summa, 2022).

3.2 LCA and LCC outcomes

The environmental analysis demonstrated a consistent reduction for all of the ten impact indicators when the UHPC_basin is compared to the ORC_basin with advantages of around 80% as for the case of the terrestrial ecotoxicity and 70% as for the case of eutrophication, marine aquatic ecotoxicity, fresh water aquatic ecotoxicity and human toxicity. In general, it is possible to observe that cement and steel have the highest influence, reason why the impacts related to ORC_basin are so high, due to the raw materials needed to restore the functionality of the structure through the maintenance activities. More specifically, the greatest influence is represented by the steel for 6 out of 10 impact indicators of ORC_basin. On the opposite, UHPC_basin, due to the reduced amount of steel ($1.24 \cdot 10^4 \text{ kg}$ in comparison to $3.39 \cdot 10^4 \text{ kg}$ for ORC_basin) registers a higher influence of cement. With regard to the cost analysis, it has been calculated that the maintenance activities affect the overall costs of ORC_basin by about 39% while the overall difference between the two compared solutions is assessed at around of 37%. Figure 5 summarizes these results.

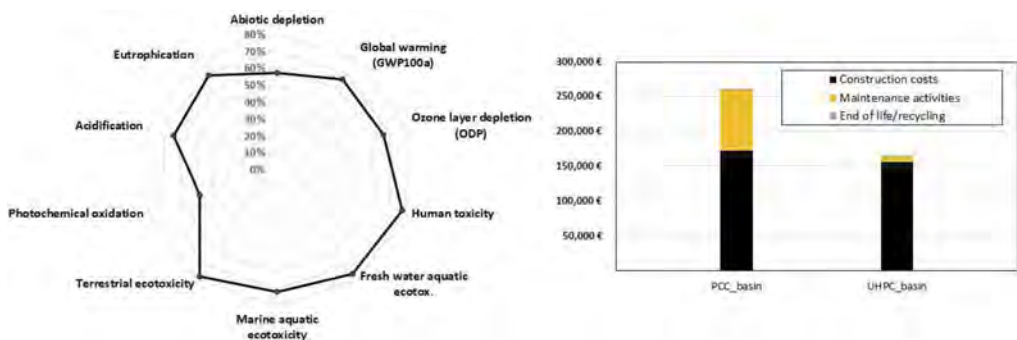


Figure 5. Percentage reduction of impacts of UHPC_basin compared to ORC_basin (left) and total costs within the SL (right).

4 CONCLUSIONS

This work has presented and assessed the implications of a design methodology aimed at including the use of advanced cementitious based materials with a structural design based on the durability of the material and on the life cycle implications, regarded as a pillar concept that should drive the construction sector within the near future. Differently from other recent works, the current study has analyzed not only the chloride penetration phenomena, but also the sulphate attack and the leaching degradation, due to the service scenario of the selected case study, consisting of a basin containing geothermal water. This approach, more structured than a prescription-based one which is normally employed whenever the current standards are simply followed, allowed to figure out the benefits of UHPC in comparison to a traditional solution, based on ordinary reinforced concrete, due to the total absence of maintenance activities for the first. In this regard, the Life Cycle Cost analysis has highlighted a relevant influence of the repairing activities whose reiteration for the ORC elements not only generates an increase of the total expenses but also the need to use more raw materials such as cement and steel whose environmental consequences are well known. Thus, this investigation represents a milestone to support and corroborate the efficacy of advanced cementitious materials even with the absence of the traditional reinforcement steel bars whenever aggressive structural service scenarios have to be met. These improvements are often disregarded in the current design and construction practice due to the false idea that a comparison between ordinary materials and innovative ones has to be based on a cubic meter scale, not taking advantage of durability and structural performance of the materials. This is also due to the absence of appropriate

durability-based design approaches together with the further need to employ tailored, time- and scenario-dependent constitutive laws, which would require additional care in the design phase. In view of this, the DAD, together with LCA and LCC can be a driving force to shape differently the evolution of the construction sector.

ACKNOWLEDGEMENTS



This project has received funding from the European Union's Horizon 2020 research and innovation programme under the Marie Skłodowska-Curie grant agreement No 860006.

REFERENCES

- Al-Obaidi, S., Bamonte, P., Luchini, M., Mazzantini, I. and Ferrara, L.: "Durability-based design of structures made with UHP/UHDC in extremely aggressive scenarios: application to a geothermal water basin case study", *MDPI Infrastructures*, 5(11), November 2020, pp. 1–44, <http://dx.doi.org/10.3390/infrastructures5110102>.
- Al Obaidi, S., Bamonte, P., Animato, F., Lo Monte, F., Mazzantini, I., Luchini, M., Scalari, S. and Ferrara, L.: "Innovative Design Concept of Cooling Water Tanks/Basins in Geothermal Power Plants using Ultra High Performance Fiber Reinforced Concrete with Enhanced Durability", *MDPI Sustainability*, 13(17), 2021, pp., 1–26, <https://doi.org/10.3390/su13179826>
- Al-Obaidi, S., Davolio, M., Lo Monte, F., Costanzi, F., Luchini, M. Bamonte, P. and Ferrara, L.: "Structural validation of geothermal water basins constructed with durability enhanced ultra high performance fiber reinforced concrete (Ultra High Durability Concrete)", *Case Studies in Construction Materials*, Volume 17 December 2022 Article number e01202, <https://doi.org/10.1016/j.cscm.2022.e01202>
- Bossio, A., Lignola, G. P., Fabbrocino, F., et al. "Nondestructive assessment of corrosion of reinforcing bars through surface concrete cracks," *Structural Concrete*, V. 18, No. 1, 2017, pp. 104–17.
- Caruso, M.C., Pascale, C., Camacho, E., Scalari, S., Animato, F., Alonso, M.C., Gimenez, M., Ferrara, L., 2020. Life cycle assessment on the use of ultra high performance fibre reinforced concretes with enhanced durability for structures in extremely aggressive environments: Case study analyses, *RILEM Bookseries*. https://doi.org/10.1007/978-3-030-43332-1_24
- Davolio, M.; Al-Obaidi, S.; Altomare, M. Y.; Lo Monte, F.; Ferrara, L. A methodology to assess the evolution of mechanical performance of UHPC as affected by autogenous healing under sustained loadings and aggressive exposure conditions. *Cement and Concrete Composites*. (Submitted), 2022.
- di Summa, D., Parpanesi, M., Ferrara, L., et al. "Life Cycle Assessment (LCA) and Life Cycle Cost (LCC) analysis as crucial part of a holistic approach to the design of structures with advanced cement based materials." 76th RILEM Annual Week and International Conference on Regeneration and Conservation of Structures (ICRCS 2022), Kyoto, Japan, 2022.
- di Summa, D., Tenório Filho, J. R., Snoeck, D., et al. "Environmental and economic sustainability of crack mitigation in reinforced concrete with SuperAbsorbent polymers (SAPs)," *Journal of Cleaner Production*, V. 358, 2022.
- European Commission. "Communication from the commission to the European parliament, the council, the european economic and social committee.," 2020, COMMUNICATION FROM THE COMMISSION TO THE EUROPEAN p.
- F. du béton and J.C. Walraven. "Model Code 2010: Volume 1. Bulletin (fib Fédération internationale du béton).International Federation for Structural Concrete (fib).," 2012.
- G. Fagerlund, Leaching of concrete : the leaching process : extrapolation of deterioration : effect on the structural stability, vol. 3091. Division of Building Materials, LTH, Lund University, 2000
- Jian, X., Monteiro, P., and Kurtis, K. "Predicting the Expansion of Concrete Exposed to Sulfate Attack with a Regression Model Based on a Performance Classification," 2018.
- Kannikachalam, N.P., di Summa, D., Borg, R.P., Cuenca, E., Parpanesi, M., De Belie, N., and Ferrara, L. Assessment of sustainability and self-healing performances of Recycled Ultra-High Performance Concrete (R-UHPC). *ACI Materials Journal* (accepted).
- Lo Monte, F., and Ferrara, L. "Tensile behaviour identification in Ultra-High Performance Fibre Reinforced Cementitious Composites: indirect tension tests and back analysis of flexural test results," *Materials and Structures*, V. 53, No. 6, 2020, p. 145
- Noh, H. M., Idris, N., Noor, N., et al. "Structural Effects of Reinforced Concrete Beam Due to Corrosion," V. 01024, 2018, pp. 1–9.

- Oloke, O. C., Sholanke, A. B., Akindele, N. A., et al. "A Short Review of the Concept and Principles of Supply Chain Management in Building Construction Industry," IOP Conference Series: Earth and Environmental Science, V. 1054, No. 1, 2022, p. 012050.
- Ortiz, O., Castells, F., and Sonnemann, G. "Sustainability in the construction industry: A review of recent developments based on LCA," Construction and Building Materials, V. 23, No. 1, 2009, pp. 28–39.
- Regione Lombardia, «Prezzario regionale delle opere pubbliche». <https://www.regione.lombardia.it/wps/portal/istituzionale/HP/DettaglioServizio/servizi-e-informazioni/Enti-e-Operatori/Autonomie-locali/Acquisti-e-contratti-pubblici/Osservatorio-regionale-contratti-pubblici/prezzario-opere-pubbliche/prezzario-opere-pubbliche> (accessed on november, 7th 2022).
- Regione Toscana, «Regione Toscana Prezzario», <https://prezzariollpp.regione.toscana.it/2022-1/siena> (accessed on november, 7th 2022).
- Van Belleghem, B. "Effect of Capsule-Based Self-Healing on Chloride Induced Corrosion of Reinforced Concrete." PhD Thesis. Ghent University, Belgium, 2018.

Durability of residential construction in a marine environment

I.N. Robertson

University of Hawaii at Manoa, Honolulu, Hawaii, USA

ABSTRACT: Single and multi-family housing in the United States of America typically consists of timber or cold-formed steel (CFS) framed structures on reinforced concrete foundations with a design life of 40-50 years. Often these houses outlive that period but require considerable maintenance and repair to extend much beyond the design life. This is particularly true for coastal communities exposed to high humidity, airborne salts and termites. Building on 30 years of experience in durability research and design of residential structures in Hawaii, this paper presents some of the best practices for enhancing durability, building performance, reducing maintenance and repair costs, and significantly increasing the life expectancy of residential construction. With a relatively low premium on the initial capital investment, these measures greatly reduce the life-cycle costs and carbon footprint of residential construction in harsh coastal environments.

1 INTRODUCTION

Single and multi-family housing constitutes most of the buildings stock in the USA and many countries worldwide. In the USA, most of this construction is based on timber framing with timber or cement board products as exterior cladding. These buildings are typically supported by slab-on-grade foundations, and less commonly on elevated post-and-pier or cripple wall systems where the first level is a structural floor over a crawlspace or basement. The life expectancy of these buildings is typically assumed to be 40 to 50 years, though they are often utilized for up to 100 years with consistent maintenance.

The annualized life cycle cost of a constructed facility is a function of the initial cost, the maintenance cost and the demolition and disposal cost, divided by the useful life of the facility. One effective way to reduce the annualized life cycle cost of residential construction is to extend the useful life of the building beyond 50 years, while limiting the amount of maintenance required each year.

The life expectancy and anticipated maintenance costs of a building will depend on the building location. For example, in relatively arid environments it is not unusual for timber framed buildings to survive far beyond their design life. On the other hand, coastal environments are particularly harsh on built infrastructure because of the increased humidity and potential for chloride deposition on the building leading to corrosion of metal components. Tropical areas in the southern US states are also exposed to termites that can rapidly consume timber framing if the building is not regularly treated, or other termite control measures implemented. Because of this threat to timber framed homes, many communities in tropical environments are turning to cold-formed steel (CFS) framing to replace timber framing. In the US state of Hawaii, over 50 percent of new residential single- and low-rise multi-family housing is now constructed of CFS instead of timber.

This paper focuses on measures to increase the longevity of residential buildings in Hawaii and provides recommendations for both the concrete and framing elements used in residential construction. Reference is made to two research projects, one relating to the performance of cold-formed steel framing members and connectors in a marine environment, and the other relating to mitigation of reinforcing bar corrosion in concrete foundations and other structural members.

2 CORROSION OF GALVANIZED FASTENERS USED IN COLD-FORMED STEEL FRAMING

This research program investigated the potential for corrosion of galvanized fasteners used in cold-formed steel framing by exposing test samples to a variety of environmental conditions frequently found in Hawaii and elsewhere. The results of this research will aid in the protection of galvanized fasteners and associated framing in various exposure conditions.

Five field enclosures were constructed on the island of Oahu at coastal locations on both windward and leeward shores, and in the interior of the island (Figure 1). Each field enclosure represented various aspects of typical cold-formed steel construction and was equipped with a complete weather station. The full report contains greater detail regarding atmospheric conditions at the field enclosure sites, screwed connection test results, and provides complete photographic documentation of the progression of corrosion at various locations in all field enclosures. A full copy of the final report is available from the Steel Framing Alliance.

Standard cold-formed steel connections with galvanized screws were placed in various locations within each of the field enclosures as a controlled study of the performance of galvanized fasteners in typical CFS framing construction (Figure 2). Identical screwed test connections were subjected to a cyclic salt spray routine in a corrosion chamber to induce accelerated corrosion (Figure 3).

Based on the results of this study, recommendations were made for the protection of cold-formed steel framing and fasteners in coastal environments.



Figure 1. Corrosion field sites on the Island of Oahu (left) and typical field enclosure at location 4 (right).

2.1 Summary of field test observations

After 20 months of field exposure, the interior enclosure at location 5 and the coastal enclosure at location 4 (on the leeward side of the island) showed only minor signs of corrosion of framing fasteners in the fully exposed crawl space. No corrosion was noted in the exposed floor joists, vented attic or enclosed wall framing. After the same exposure, the coastal enclosure at location 3 (on the leeward side of the island) exhibited similar behavior, with the addition of the initiation of corrosion of fasteners and cut ends of CFS framing in the vented attic.

In contrast, fully exposed CFS members and fasteners in the crawl space of the coastal enclosure at location 1 (on the windward side of the island) showed initiation of corrosion after as little as 5 months exposure. This corrosion proceeded rapidly so that by 28 months, the exposed floor joists and supporting posts and cripple wall have experienced severe corrosion. Areas of the floor joists that were enclosed by plywood sheathing show very little signs of corrosion except where exterior air has leaked into the enclosed space through unsealed edge joints.

After 28 months, fasteners in the vented attic at the enclosure at location 1 experienced significant corrosion. The CFS roof framing members were tarnished with some cut end

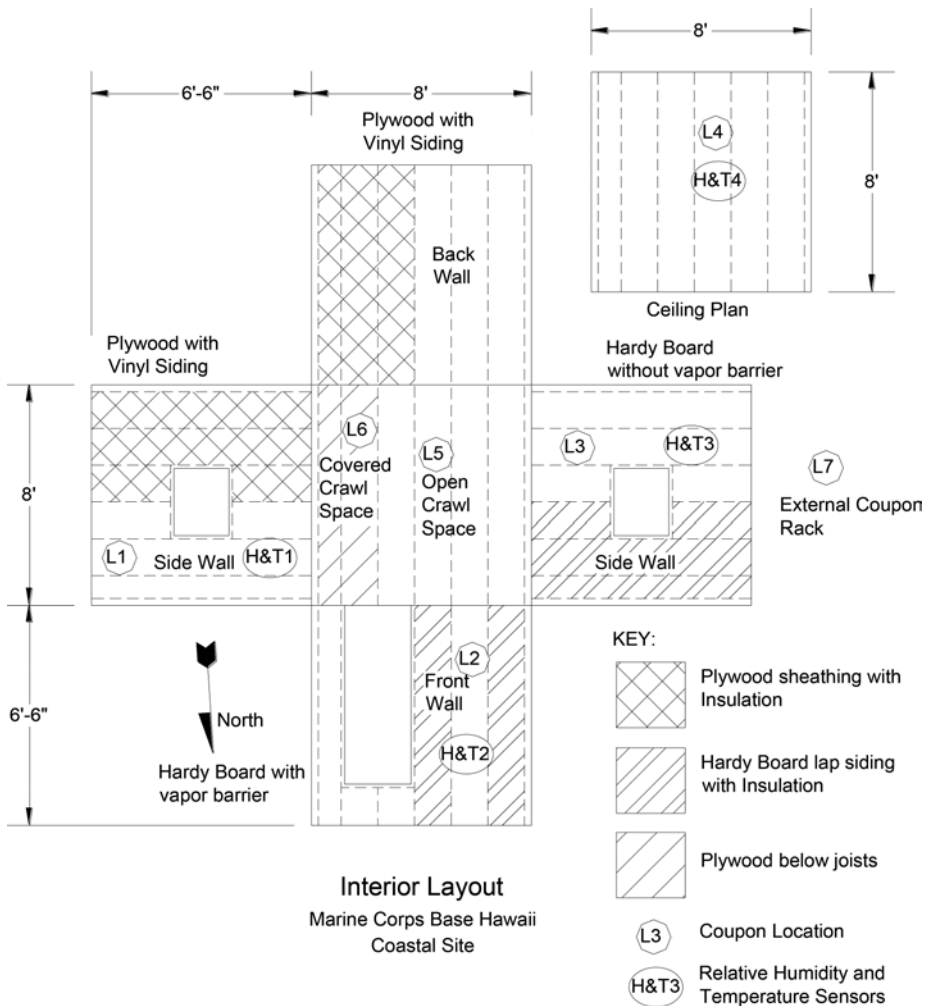


Figure 2. Typical wall layout to study corrosion within walls, floor and ceiling with different exterior coverings.

corrosion. Similar corrosion was noted in the wall with lap siding and no vapor barrier, while the walls with lap siding and vapor barrier, or plywood sheathing, only showed signs of corrosion at the top plate that was exposed to air in the vented attic.

The inland enclosure at location 2 exhibited corrosion levels significantly less than the coastal site at location 1, but more severe than any of the enclosures at locations 3, 4 and 5. The additional distance from the coastline, and the intervening vegetation appear to have provided significant protection for this enclosure.

2.2 Recommendations for improved durability of cold formed steel framing and fasteners

The following recommendations are based on the results observed in this study.

Guidelines for protection of CFS framing and fasteners from atmospheric corrosion induced by air-borne chlorides are presented for the following three exposure categories:

- Category A: Extreme exposure.
- Category B: Moderate exposure.
- Category C: Mild exposure.



Figure 3. Salt spray corrosion chamber with screwed connections (left) and typical connection specimen test (right).

Each building location should be assigned to one of these exposure categories based on geographical location, surrounding features and meteorological records. Table 1 gives suggestions for this assignment:

Table 1. Exposure category assignment.

Distance from shoreline (m)	Site characteristics			
	Onshore wind		Offshore wind	
	Unshielded	Shielded	Unshielded	Shielded
$L \leq 200$	A	A	A	B
$200 \leq L \leq 500$	A	B	B	B
$500 \leq L \leq 1000$	B	B	C	C
$L \geq 1000$	C	C	C	C

Distance from shoreline is the straight-line distance measured perpendicular to the coast.

Onshore and *offshore* wind refers to the predominant wind direction for the building location. If winds are variable or unknown, *onshore* wind should be assumed.

Shielded refers to the presence of vegetation and/or structures, at least as tall as the proposed building, located between the coast and the proposed site. Sites that do not satisfy these conditions are considered to be *Unshielded*. Shielded conditions are afforded by medium to dense vegetation covering at least 25 meters of the straight line distance from the coast. Shielded conditions are also afforded by two or more rows of housing between the proposed site and the coast. A single barrier, such as a wall, fence, or hedge, should not be considered to provide shielded conditions. A small hill or rise with no vegetation should not be considered to provide shielded conditions.

2.2.1 Category A design recommendations

The following recommendations are made for CFS framing in category A exposure conditions:

- No CFS members or fasteners should be exposed to ambient atmospheric conditions. This includes both sheltered and non-sheltered exposure.
- Exposure to atmospheric conditions during construction should be limited. If such exposure is expected to exceed 2 months, protective measures should be taken to prevent chloride accumulation on the CFS members.

- No CFS framing should be exposed in sheltered locations such as crawl spaces or the interior of garages, carports and other unfinished spaces. Plywood sheathing or gypsum board, with sealed joints, is effective for protection of CFS in these locations.
- Protection of CFS framing and fasteners in interior walls and floor systems can be provided by gypsum board coverings on both sides of the wall cavity, and as a ceiling below elevated floor framing. The drywall joints should be taped and all openings sealed. The top of the wall should be sealed from any vented attic space above.
- Attic spaces require particular attention because of the need for venting to prevent moisture accumulation and potential mold development. However, venting in exposure category A conditions permits the ingress of air-borne chlorides. Two options are proposed for these conditions:
 - the attic space can be designed as a sealed environment with insulation placed directly under the roof sheathing (a.k.a. cathedral ceiling), and the area underneath designed as a conditioned space.
 - attic venting, particularly on the coastal elevation, can be kept to the minimum permitted by the applicable building code, while extra protection can be provided for the framing members and fasteners in the attic space through increased galvanizing thickness and/or the addition of zinc rich coatings after fabrication.

Neither of these options was evaluated in this study.

Similar but less restrictive recommendations were provided for Category B and C exposure.

3 PERFORMANCE OF CORROSION INHIBITING ADMIXTURES IN A MARINE ENVIRONMENT

Single- and multi-family homes are generally supported by concrete foundations or slab-on-grade. These foundations are typically reinforced with steel reinforcing bars. When subjected to coastal or marine environments, chlorides will penetrate the concrete and initiate corrosion of the reinforcing steel, leading to concrete spalling and high maintenance costs, or reduction in the useable life of the buildings.

A multi-year study was performed to study the efficacy of corrosion inhibiting admixtures used in reinforced concrete specimens. Accelerated laboratory corrosion testing was performed on 660 concrete specimens and a field study exposed 25 concrete panels to a marine environment in Honolulu Harbor, Oahu, Hawaii (Figure 4) (Robertson and Newton, 2019). Seven different corrosion inhibiting admixtures and two pozzolans were used to compare their effectiveness at preventing or delaying onset of corrosion. This study was funded by the Hawaii Dept. of Transportation, Harbors Division, to evaluate commercially available corrosion inhibiting admixtures when used in concretes made with basalt aggregates common to Hawaii and other Pacific Islands.

The corrosion-inhibiting admixtures included in this project were Darex Corrosion Inhibitor (DCI), Rheocrete CNI, Rheocrete 222+, FerroGard 901, Xypex Admix C-2000, Latex-modifier, Kryton KIM, and the pozzolans were fly ash and silica fume.

After approximately 8 years exposure in a marine environment, the panels were removed and returned to the laboratory for dissection. The mass loss of the test layer of reinforcing steel with 38 mm clear concrete cover to the top surface of the panel, was recorded for each specimen (Figure 5).

Based on the results of both the laboratory and field studies the following conclusions were drawn:

- The control mixture with water/cement ratio of 0.35 showed improved corrosion protection compared with the control mixtures with 0.40 water/cement ratio.
- Mixtures with DCI or Rheocrete CNI at doses of 20 liters per cubic meter showed superior corrosion inhibiting performance compared with the corresponding control specimens. The same admixtures at doses of 10 liters per cubic meter had less satisfactory performance in both laboratory and field specimens.

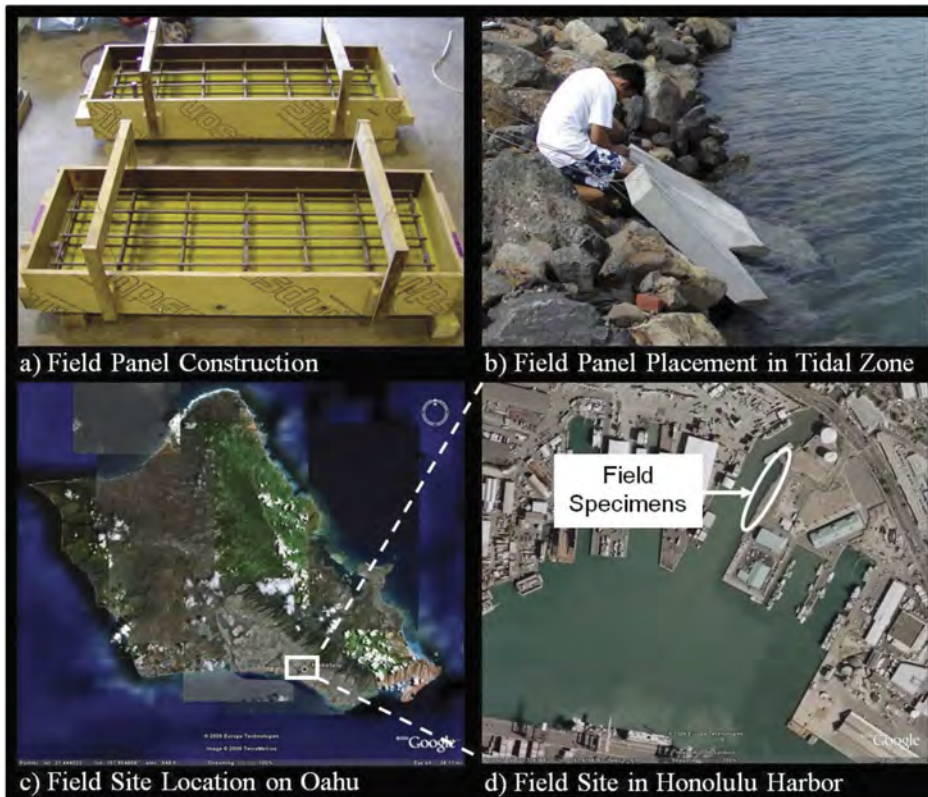


Figure 4. Fabrication and location of Phase III field corrosion panels in a marine environment.

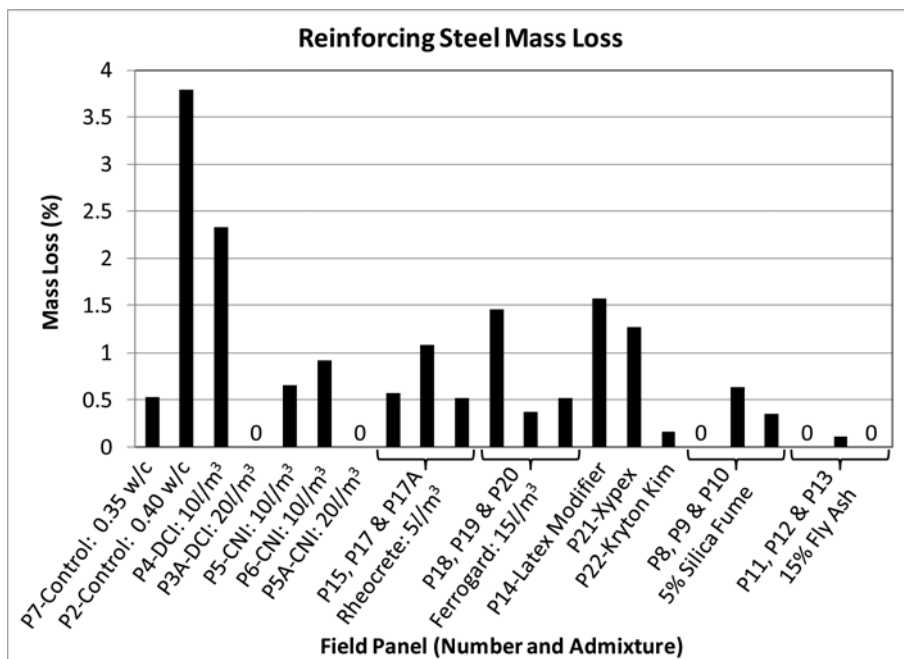


Figure 5. Mass loss due to corrosion of test layer of reinforcing steel.

- Mixtures with 15 percent replacement of cement with Fly Ash or Silica Fume showed superior corrosion inhibiting performance compared with the corresponding control specimens.
- Concrete mixtures using Rheocrete 222+, FerroGard 901, Xypex Admix C-2000 or Latex-modifier showed mixed results.
- Kryton KIM performed well in a field panel, but was not included in the laboratory study.
- A recommended concrete mixture for use in marine environments in Hawaii would have a 0.35 w/c ratio with either DCI or CNI at 20 //m³ and either Fly Ash at 15% cement replacement or Silica Fume at 5% cement replacement. Although this combination was not tested in this study, it is believed that the admixture attributes will complement each other when combined in a concrete mixture.

4 GOLD STANDARD FOR RESIDENTIAL CONSTRUCTION IN A TROPICAL MARINE ENVIRONMENT

Based on the two research projects described above, and decades of inspections of residential buildings exposed to a tropical marine environment, the following measures are recommended to significantly extend the useable life expectancy of residential construction.

4.1 *Framing material*

Both timber framing and cold formed steel framing can provide extended life expectancy if they are protected from termites for the former and corrosion for the latter. Regular tenting of timber framed structures in tropical environments is required to control both ground and aerial termites. Sealed wall and floor cavities and careful venting of attic spaces is required to protect CFS framing from exposure to airborne chlorides.

4.2 *Foundation concrete*

The ACI 318-19 standard (American Concrete Institute, 2019) requires that concrete used in marine and coastal environments exposed to “sea spray” utilize concrete with a water-to-cementitious material ratio of 0.4 or less. This essentially ensures a relatively dense concrete with high compressive strengths. The addition of Fly Ash with 15% more replacement of cement will significantly reduce the concrete permeability and enhance the protection offered to the reinforcing steel. Ensuring 50 mm or greater clear cover to the reinforcing steel will also improve performance. The use of stainless steel bars, particularly when located close to exterior exposed surfaces, will greatly reduce the likelihood of corrosion. Ultimately, replacing the reinforcing steel with bars made of non-corrosive materials such as glass fiber reinforced polymer (GFRP) bars, Aramid FRP (AFRP), basalt FRP (BFRP), or carbon FRP (CFRP) bars will remove the threat of corrosion entirely, though structural members subject to deflection may not perform adequately with these FRP materials because of their relatively low modulus of elasticity compared with steel bars.

4.3 *Concrete placement*

During placement of the concrete in residential foundations and slab-on-grade construction, there is a tendency to overlook the need for consolidation and adequate curing. Poor consolidation of the concrete can provide easy access for chlorides and other corrosive products to the embedded steel components. Lack of adequate curing of concrete can result in shrinkage cracking which again provides entry points for corrosive chemicals. It is therefore essential that concrete be properly consolidated and cured to ensure the required concrete strength, density and low permeability are achieved.

4.4 Exterior CFS wall framing

Cold formed steel used in exterior walls in coastal environments must be well protected from airborne chlorides. This can be achieved by paying close attention to the installation of exterior vapor barriers and the use of holddowns located inside the wall cavity, with stainless steel anchors embedded in the concrete slab (Figure 6, left). A common area of exposure of the CFS is the wall bottom track which is exposed to the concrete slab below and potential air entering between the exterior cladding and the side of the concrete slab. Installation of a protective wrap around the bottom and sides of the track significantly reduce the potential for this source of corrosion (Figure 6, right).



Figure 6. CFS framing in exterior wall cavity with interior holddown (left) and bottom track protective wrap (right).

5 CONCLUSIONS

This paper presents the results of two corrosion studies studying the performance of cold formed steel framing and reinforced concrete to coastal marine environments in Hawaii. The following conclusions are drawn based on these studies and field inspections on numerous residential structures:

- Care must be taken with the concrete mix design, concrete placement, and protection of the reinforcing steel to ensure adequate life expectancy of the foundations with limited maintenance and repair.
- Cold formed steel framing elements, holddowns and fasteners in the exterior walls require particular design and installation attention to reduce the potential for corrosion. Any exposure of these materials to air borne chlorides will lead to rapid corrosion and ultimately loss of structural function.

REFERENCES

Robertson, I.N. and Newton, C., 2019. *Improving Concrete Durability through use of Corrosion Inhibitors*, ACI Materials Journal, V. 116, Issue 5, pp. 149–160.
Steel Framing Alliance, 1201 15th Street, N.W., Washington, DC; www.steel framingalliance.com

Predicting the military load class from bridge data with a multilayer perceptron

M. Haslbeck, J. Flotzinger & Th. Braml
University of the Bundeswehr, Munich, Germany

ABSTRACT: Assessing the load bearing capacity of civilian bridges is a challenging task for routine reassessment jobs, especially in the military context. In order to ensure mobility of troops, the load bearing capacity of bridges needs to be assessed to make the safe crossing of military vehicles possible at home and abroad. For this reason, rapid assessment methods have been developed that allow for classification of civilian bridges after a quick visual reconnaissance. In the absence of verifiable calculations or drawings, the applied methods need to be based on geometrical data that is suspected to be correlated to the military load class of a structure. Current approaches are based on simplified assumptions such as correlations between dead loads and live loads or consist of simplified calculations assuming conservative material properties. In order to improve the current classification method, a Machine Learning (ML)-based methodology is given that classifies slab to a particular military load class without human intervention using a correlation between measured geometrical data and classification result. It is concluded that the usage of ML models is very promising for rough classifications of bridges with unknown military load class (MLC). However, the available training data is insufficient to train reliable models and an expanded amount of training data will be needed for deployment as a software package in the armed forces.

1 INTRODUCTION

1.1 *Importance of bridge assessment*

The assessment of the load bearing capacity of existing bridges is a challenging task when no verifiable calculations or as-built drawings are available. The development of methodologies to assess the maximum bearable traffic load is thus of special interest when the rapid assessment of the bridge geometry is the only source of information. For military bridge assessment, this is the case when convoys have to be guided through unknown terrains or when supply routes have to be planned. Use cases such as these have already been encountered in stabilization missions or similar military operations. (Haslbeck, Hertle & Braml, 2021; Haslbeck, Vallée & Braml, 2021).

Based on those experiences, bridge assessment codes have been developed independently by several nations to ensure a safe crossing of military vehicles over civilian bridges. The approach of most of these methods is to derive the maximum allowable Military Load Class (MLC) of a bridge from geometric parameters of the main structural parts. In order to enable soldiers to classify a bridge in the field, the tablet-based application BRASSCO-NG has been developed by the University of the Bundeswehr that allows for a rapid assessment on site.

For the application of BRASSCO-NG and the user interface please refer to (Haslbeck, Hertle & Braml, 2021; Haslbeck, Vallée & Braml, 2021).

1.2 *Introduction to military load classes and STANAG2021*

As the main output of the presented methodology using machine learning (ML) is the attribution of a military load class (MLC) to a specific bridge in the field, the system of matching vehicle MLC and bridge MLC needs to be discussed briefly.

The framework of STANG2021 (NATO) describes a system of hypothetical vessels that shall reflect the true loading of military vehicles. Due to the different nature of the load distribution, each class comprises a load model for wheeled and for tracked vehicles. Due to reasons of brevity, the reader is referred to (Geissler, 2014) for further information on the MLC system and the attributed load models.

The system of load models describes the shape and the weight of the assumed vehicles both for structural analysis and the classification of the carrier to a certain MLC. Using the load scheme, each bridge can be sorted into a MLC class using the maximum bearable bending moment and shear force. Interpolation between different load classes is permitted, so intermediate MLCs are allowed. As the load bearing capacity for one-way and two-way traffic, the allowable load class is commonly split into a one-lane and a two-lane MLC.

As verifiable calculations are in many cases not available, the attribution of a MLC to a specific bridge often requires the assumption of a correlation between certain observable properties of a structure to its MLC class.

1.3 *Current approach*

Reconnaissance of civilian bridges is based on the recording of geometrical data using folding rules or laser distance meters. From this data, a correlation function is applied that exploits the assumed correlation of dead load and the ultimate load from military vehicles expressed by the capacity to resist a certain unit bending moment. This method for regression relies very much on engineering experience. The correlation function for the ratio of moment from dead load and moment from live load has been calibrated by a large number of verifiable calculations for bridges of different span length and construction types. However, the assumed relation might be improved by a more sophisticated regression using machine learning techniques.

1.4 *Potential of machine learning for bridge assessment and scope of this contribution*

In order to implement a regression for the maximum MLC depending on a set of geometrical input parameters, Artificial Intelligence (AI) can help to go beyond engineering experience and to find correlations that are not visible at first sight.

Using a limited data set available from a NATO database, the potential of machine learning techniques is revealed in this contribution using the example of slab bridges.

After a brief review on the theoretical background of the applied machine learning technique, the required input for the graphical user interface of BRASSCO-NG is depicted. Subsequent to the description of the implementation, several worked examples are given in order to present the results and to discuss the pros and cons of this new approach to military bridge assessment.

2 RELATED WORK

2.1 *Machine learning*

Neural Networks (NNs) are able to solve very complex problems more accurately than other algorithms in the field of machine learning, e.g. linear regression, decision tree (Wu et al., 2008) or random forest (Ho, 1995). The regression of tabular data can be a complex task, for the solution of which the NNs can be particularly suitable. The architecture of Neural Networks is inspired by biological neurons, in the ML context also called nodes. The special feature of NNs compared to other algorithms in the ML domain, is the contained weighted information in nodes forwarded to neighboring neurons. These weights (synapses) are trainable, whereby a transmitted signal can be amplified or attenuated (Goodfellow et al., 2018).

Figure 1 shows the sequence of the forward process that is carried out during inference of tabular data from a bridge. The model that will be used in this work is a multilayer perceptron (MLP), a neural network consisting of linear layers. Each input parameter is fed into the NN. Subsequently, the inputs are multiplied by weights. After having summarized all weighted

inputs of one node, and biases were added, the activation function is applied. The aforementioned operations and the application of the activation function will be executed for all nodes in the hidden layer. For the nodes in the output layer, no activation is applied in order to obtain the result of the regression describing the military loading class.

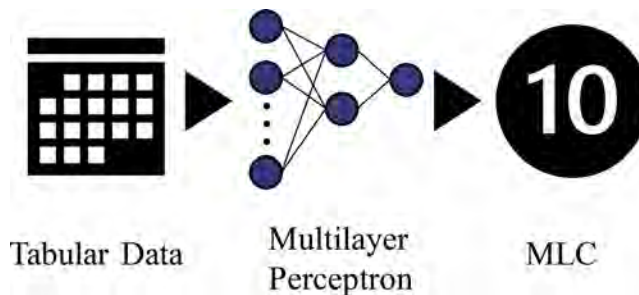


Figure 1. Feed-forward process of the MLP calculating MLC from tabular data.

2.2 Machine learning models for load-carrying capacity

Truong et al. (Truong et al., 2022) have analyzed the applicability of ML models for the estimation of the load-carrying capacity of semi-rigid connected steel structures. They evolved a dataset using the advanced analysis based on beam-column and zero-length elements. The model's input layer consists of member cross-sections and parameters of the high-order non-linear functions characterizing the semi-rigid connection behaviors. They evaluated multiple ML methods: linear regression models, support vector machines, tree-based ensemble algorithms and models from the field of deep learning. The most performant model for solving the problem of depicting the load-carrying capacities of semi-rigid connected steel frames is XGBoost (Chen & Guestrin, 2016).

3 METHODOLOGY

3.1 General

The collection and preparation of data for later evaluation by AI represents a crucial step in the process chain of developing a military AI. The reliability of the trained model depends crucially on the data provided. For the model to be trained within the project, the collection of design drawings with associated MLC classification provided by the Military Engineering Centre of Excellence (MILENG-COE) will be used. In particular, the use of intermediate MLCs representing not only the load models depicted in STANAG 2021 (NATO) but also values representing interpolation between them, could find use in the training process. The geometric dimensions were taken manually from the design drawings.

The modeling of the neural network requires knowledge of the problem and the algorithms to be used as well as insight into the existing dataset. Especially the complexity of the regression model depends on the available data and the correlations. In the context of the investigations, a linear neural network is used, whose theoretical background is discussed in Section 3.2. For the training of the NN and the test of the regression, a MATLAB script has been used where the input is read directly from the NATO database provisioned for the testing of MLC classification methods.

3.2 Multilayer perceptron

The operating principle of the neural network is explained in the following. The geometry information stored in the input variables is summed up in the neurons after the multiplication

by their weighting factors to represent the importance of the information. To this, the bias b is added, which is trained as a parameter.

The nodes in the hidden layer are activated by the sigmoid function according to Equation 1.

$$y = \frac{1}{1 + e^{-\left(-\sum_j c_j x_j - b\right)}} \quad (1)$$

$$y = f(c_1 x_1 + c_2 x_2 + \dots + c_n x_n + b) = f\left(\sum_j^n c_j x_j + b\right) \quad (2)$$

The multilayer perceptron includes one hidden layer with three nodes. The activation function in the hidden layer is the sigmoid function. During one training step all samples are fed into the network. Thus, the batch size corresponds to the number of data points in the training split. The default value of the learning rate of 0.001 is chosen. In total the training process is repeated for 100 epochs.

Table 1. Hyperparameters and architectural parameters of the network.

Parameters	Value
Hidden layers	1
Nodes in hidden layer	3
Activation function	Sigmoid
Batch size	37
Learning rate	$1e^{-3}$
Train epochs	100

4 IMPLEMENTATION OF A NEURONAL NETWORK FOR SLAB BRIDGES

4.1 Engineering background

For the purpose of this paper, the automatic evaluation of slab bridges shall be used as they are common on side roads with few heavy traffic to span over small and medium gaps.

The cross section of a slab bridge is formed by the slab itself and two cantilever arms at both outer faces. Figure 2 shows (a) a slab bridge as it has been found in the KFOR mission in Kosovo and (b) the schematic representation of the cross section with its major parts.

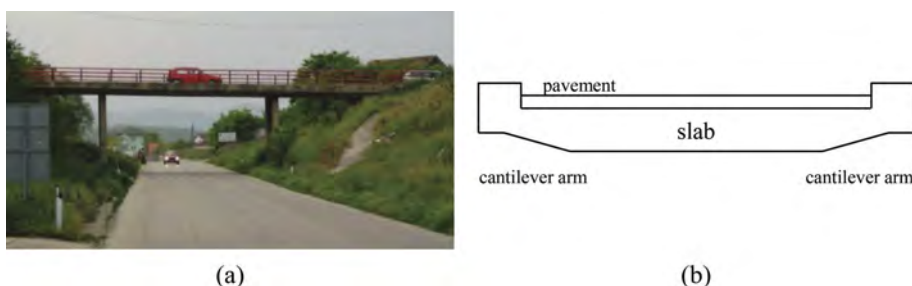


Figure 2. (a) slab bridge in the regional road network in Kosovo from (KFOR) and (b) illustration of the cross section and its parts.

4.2 Input values and dataset

In order to exploit the assumed correlation of maximum load bearing capacity of a bridge and its physical dimensions, data from the cross section and the civil engineering system in

longitudinal direction are part of the input into the BRASSCO-NG code. Figure 3 shows the GUI of the software package and the required dimensions. Especially challenging for the determination of the input was the need to choose a representation that corresponds to the various construction types for slab bridges in different regions. It should be noticed that the evaluation is based on a symmetrical cross section as the load bearing capacity is evaluated for the most unfavorable position of load, so only the weaker half of the superstructure's cross section is shown in the GUI. For the evaluations of this paper, only the height of the slab and the span length has been used as input because these values appear to be the most influential.

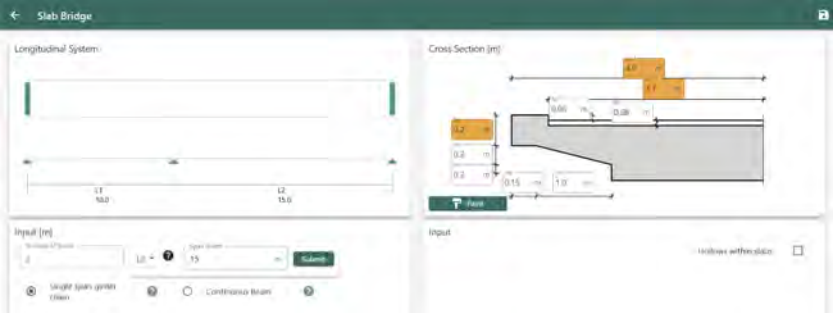


Figure 3. GUI of BRASSCO-NG for slab bridges with the required input L_1 , L_2 , ..., h_e , h_v , h_s , w_e , w_v , h_c , t_p , $w/2$, $w_r/2$.

In order to achieve the best possible result from the training of the neuronal network, a set of data has been chosen that represents a large spectrum of bridges. Figure 4 shows a histogram of the set of MLC for single lane crossing of wheeled vehicles in the training data of size 37.

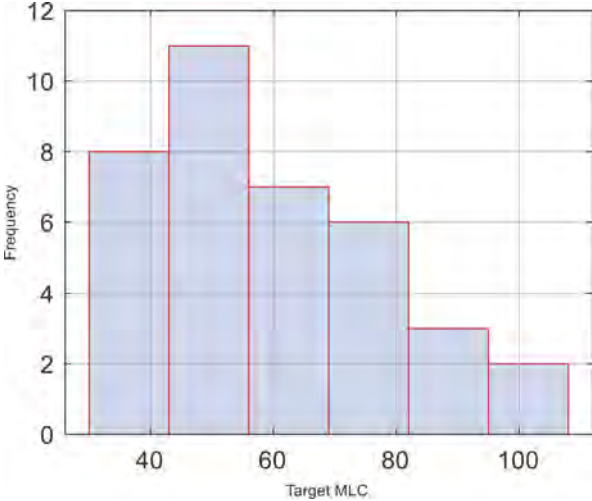


Figure 4. Histogram of the target MLC for the classification of slab bridges for single lane traffic of wheeled vehicles.

The bridges' heights range from 3.7 to 25 meters while the widths and spans range from 0.20 to 0.80 and 4 to 17 meters (Table 2). Generally, the variety in geometries indicates a strong heterogeneity of the underlying data.

Table 3 shows the sample distribution over the data splits. In total the dataset includes information of 40 bridges. The size of the dataset can be considered as small compared to others,

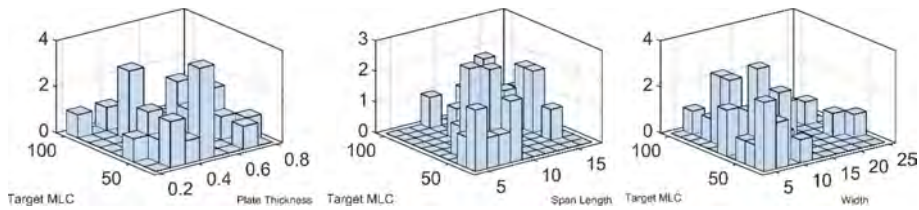


Figure 5. Histograms for the input parameters.

Table 2. Minimum, median and maximum for the input parameters of slab bridges, dimensions in in [m].

Parameter	Min	Median	Max
Height	3.7	7.4	25
Width	0.20	0.44	0.80
Span	4	8.8	17

such as the ones named in chapter 2.1. Therefore, the data was split in into two packages, the training and validation split. The validation split also represents the test data. Usually, datasets consist of a training, validation and test split. The three samples included in the test package approximately describe the whole range of bridges in the dataset regarding the MLC.

Table 3. Train and validation splits for the MILENG plate dataset.

Split	Count
Train	37
Validation/Test	3
Total	40

4.3 Results and discussion

In order to show the applicability and the advantages of machine learning techniques to the subject of military bridge classification, the results of the process of training are presented and discussed.

Figure 6 shows the progress of the loss during training. It can be stated that the loss continually decreases without significant variability and the patterns in the training data are well recognized by the network.

Regarding the differences between predictions and targets in Figure 7 an acceptable performance is observed. Only six predictions differ more than 10 MLC from the target. Most prognosticated samples have a difference, compared to the target, of less than five MLC.

The neuronal network was tested using three examples of bridges that were not part of the training data. To show the applicability, the test set of bridges was chosen such that the lower, medium and higher range of the MLC spectrum is covered. The target values for the three examples can be given by MLC 55, 95 and 20. Table 4 gives the design values, the result from the approach currently implemented in BRASSCO-NG and the result gained from the regression done by machine learning. The results of this small control sample indicate that the application of neuronal networks might be a significant advance for the classification of civil bridges. Even though the classification result does not show perfect agreement to the target values of the structural analysis, the results fit better than the currently implemented approach using the bending moment from dead load or the linear fit of the parameters to the target

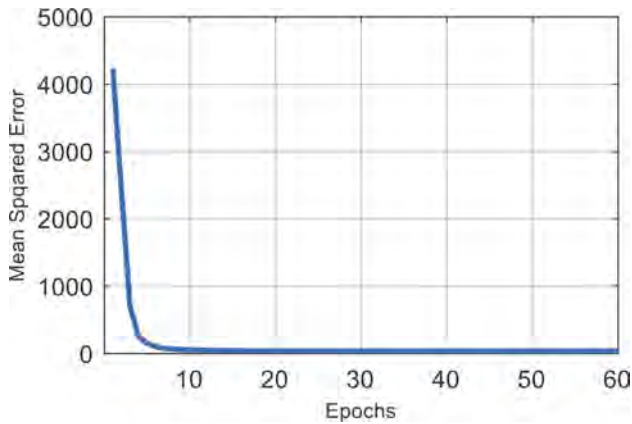


Figure 6. Loss during the training process for slab bridges.

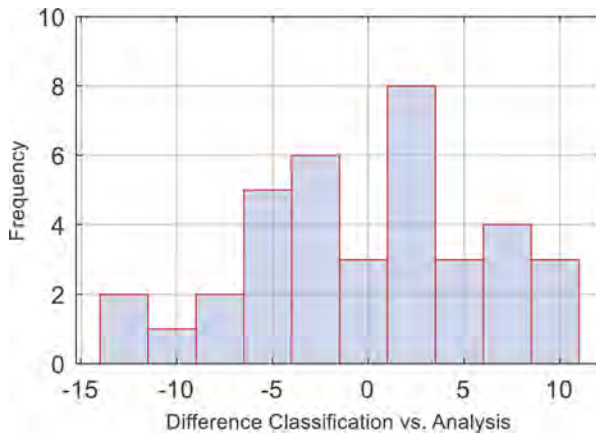


Figure 7. Differences between predictions and targets for slab bridges.

values. However, a larger sample set and a wider range of MLCs is required to improve the regression. This is especially true for the lower part of the MLC spectrum (test sample #3).

Table 4. Comparison of the results for slab bridges (single lane, wheeled vehicles).

Test Bridge no.	Structural analysis (target)	Current approach	ML-approach	Linear regression
#1	55	100	76	86
#2	95	150	81	140
#3	20	80	50	47

5 CONCLUSIONS

In this contribution, a new approach for the classification of civil bridges for military purposes is presented utilizing Machine Learning techniques instead of state-of-the-art engineering approaches. The results show that the methodology is superior both to the current method and a simple least squares regression that was performed for reasons of comparison. It can be reasoned that the application of the presented approach is very promising. However, the data set used for training is not yet sufficient for application in the field and needs further

enlargement. What is more, an analysis of sensitivities for the applied input as well as the amplification of the studied input parameters may give further insights into the correlation of certain features and the load bearing capacity. Supplementary to the measurable geometrical dimensions, the inclusion of the material strength, the percentage of reinforcement or the design load model are very promising for further investigations. Further improvement may also be made when other Machine Learning methods are applied and compared to the implemented linear neuronal network, e.g. decision tree, support vector machines or random forest.

REFERENCES

- Boston Dataset* (1996) [Online]. Verfügbar unter <https://www.cs.toronto.edu/~dave/data/boston/boston-Detail.html> (Abgerufen am 20 Dezember 2022).
- Chen, T. & Guestrin, C. (2016) *XGBoost* [Online]. Verfügbar unter <https://arxiv.org/pdf/1603.02754>.
- Geissler, K. (2014) *Handbuch Brückenbau: Entwurf, Konstruktion, Berechnung, Bewertung und Ertüchtigung* [Online]. Berlin, Germany, Ernst & Sohn. Verfügbar unter <https://onlinelibrary.wiley.com/doi/book/10.1002/9783433603437>.
- Goodfellow, I., Bengio, Y. & Courville, A. (2018) *Deep Learning: Das umfassende Handbuch: Grundlagen, aktuelle Verfahren und Algorithmen, neue Forschungsansätze* [Online], Frechen, mitp. Verfügbar unter <https://ebookcentral.proquest.com/lib/kxp/detail.action?docID=5598176>.
- Haslbeck, M., Hertle, T. & Braml, T. (2021) „Application of mobile devices for the rapid assessment of masonry arch bridges – worked example and benchmarking“, *IABSE Congress, Ghent 2021: Structural Engineering for Future Societal Needs*. Ghent, Belgium, 2/22/2021-2/24/2021, International Association for Bridge and Structural Engineering (IABSE) Zurich, Switzerland, S. 793–800.
- Haslbeck, M., Vallée, H. & Braml, T. (2021) „Elaboration of a rapid assessment method for masonry arches“, *IABSE Congress, Ghent 2021: Structural Engineering for Future Societal Needs*. Ghent, Belgium, 2/22/2021-2/24/2021, International Association for Bridge and Structural Engineering (IABSE) Zurich, Switzerland, S. 783–792.
- Ho, T. K. (1995) „Random decision forests“, *Proceedings of the Third International Conference on Document Analysis and Recognition*: August 14-16, 1995, Montréal, Canada. Montreal, Que., Canada, 14-16 Aug. 1995. LosAlamos, Calif., IEEE Computer Soc. Press, S. 278–282.
- Leung, S. S., Lau, J. T., Xu, Y. Y., Tse, L. Y., Huen, K. F., Wong, G. W., Law, W. Y., Yeung, V. T., Yeung, W. K. & Leung, N. K. (1996) „Secular changes in standing height, sitting height and sexual maturation of Chinese—the Hong Kong Growth Study, 1993“, *Annals of human biology*, Vol. 23, No. 4, S. 297–306.
- NATO: *Military load classification of bridges, ferries, rafts and vehicles*.
- SOCR: Heights and Weights Dataset* (2017) [Online]. Verfügbar unter http://wiki.stat.ucla.edu/socr/index.php/SOCR_Data_Dinov_020108_HeightsWeights (Abgerufen am 20 Dezember 2022).
- Truong, V.-H., Pham, H.-A., Huynh Van, T. & Tangaramvong, S. (2022) „Evaluation of machine learning models for load-carrying capacity assessment of semi-rigid steel structures“, *Engineering Structures*, Vol. 273, S. 115001.
- Wu, X., Kumar, V., Ross Quinlan, J., Ghosh, J., Yang, Q., Motoda, H., McLachlan, G. J., Ng, A., Liu, B., Yu, P. S., Zhou, Z.-H., Steinbach, M., Hand, D. J. & Steinberg, D. (2008) „Top 10 algorithms in data mining“, *Knowledge and Information Systems*, Vol. 14, No. 1, S. 1–37.

Elaboration of a truncated probability function for the Young's modulus of concrete

M. Haslbeck & Th. Braml

University of the Bundeswehr Munich, Bavaria, Germany

ABSTRACT: The necessity of recalculating existing engineering structures has inspired a bunch of methods to ensure reliability. Among them is probabilistic modelling of material properties for the probabilistic structural analysis or methods of Bayesian System Identification that allow for the verification of the model parameters in a finite element calculation. Both methods rely on probability distribution functions to describe scatter in the behavior of an engineering structure. Of special interest in this field are concrete structures as they show a great variance in the material characteristics. Using a Monte-Carlo-Simulation, an approximate lower bound for the truncation of the probability function for compressive strength is given, based on the regulations of conformity testing that were in effect at the time of construction. The introduced methodology is elaborated using examples from different periods of quality management. The lower bound provided by the methodology avoids excessively low values of compressive strength in the probability distribution as they exist in boundless functions. The results of this simulation are afterwards transferred to the concrete's Young's modulus, so that the truncated probability function can be used as a prior in a Bayesian system identification framework.

1 MOTIVATION AND SCOPE

1.1 *Motivation*

The evaluation of failure probabilities and uncertainty quantification for the purpose of statistical modelling for engineering structures by means of uncertainty propagation, variance-based sensitivity analysis and Bayesian updating very much rely on (prior) assumptions, i.e. probability distribution functions to describe uncertainty.

The introduction of additional knowledge, e.g. from quality testing can help to lower uncertainty attributed to parameters in probabilistic calculations.

1.2 *Research question*

As numerical simulations often require the restriction of possible parameter values to a feasible parameter space and as advanced statistical assessment necessitates the introduction of all available knowledge for the assignment of a distribution function to uncertainty in general, this contribution deals with the elaboration of a lower bound for the compressive strength and Young's modulus of concrete from (historic) regulations on quality management.

The presented contribution is an extension and further development of the author's suggestions in (Haslbeck & Braml, 2021) in order to extend the application to other quality standards, to compare the results and to show how the conclusions can be transferred to stiffness parameters.

2 CONFORMITY TESTING AND REGULATIONS

The assessment of conformity is a central element of the concept of quality control in most design standards. Most testing procedures rely on a random sample of at least three specimens from a selected number of charges for concrete and a decision rule on the conformity that has been elaborated based on statistical considerations. In most cases, several criteria have to be considered.

The intention of the regulation is to control the quality of the produced concrete by accepting or rejecting the hypothesis of conformity for a certain concrete strength class and sorting out those charges that do not pass the quality check and are thus of inferior quality. Hence, conformity testing serves as a means of filtering out those lots of concrete below a certain limit value and should thus be considered in the statistical models of strength and stiffness parameters.

As it is the case for every statistical testing procedure, each single criterion for acceptance or rejection has an operational characteristic curve that shows the probability of rejection for every possible realization of any parameter of the distribution function. Due to the limited number of specimens tested, the operational characteristic curve does not show a perfect slope at the intended limit value, but reveals some inaccuracy in the sharpness of separation (DAfStb, 2003). In order to give a sharp boundary for the truncation of the probability distribution function, this contribution assumes an idealized operational characteristic curve of the testing procedure.

As most tests are based on a multi-criterion decision rule, the evaluation can no longer be done analytically, but the assumption shall be based on a numerical experiment using a Monte-Carlo-Simulation. In accordance with the regulations, it is assumed that those structures that do not meet the requirements are demolished or checked by more sophisticated methods of quality assessment. This assumption is consistent with the idea of quality testing and has already been applied by previous work, e.g. in (Loch, 2014; Schnell et al., 2010).

3 RATIONALE OF THE SIMULATION AND ALGORITHMIC IMPLEMENTATION

The general rationale of the procedure originally proposed in (Haslbeck & Braml, 2021) and extended in this contribution is to determine a lower bound of the concrete strength distribution function based on the notion that those samples not passing the test on conformity are considered to be those of lowest quality.

The Monte-Carlo-Simulation is initiated by drawing a number of N samples (f_{c1}, f_{c2}, f_{c2}), where each f_{ci} is a realization of the probability distribution function of the compressive strength of concrete described in section 5.

In a loop, the different criteria to accept or reject the hypothesis of conformity is applied to each sample (f_{c1}, f_{c2}, f_{c2}) sequentially. If a sample does not pass, the counter for rejected samples, called 'num_reject' is increased by 1, otherwise it remains unchanged.

As the operational characteristic curve is assumed to be ideal in its sharpness of separation, those samples sorted out are assumed to be those of inferior quality. In consequence, the ratio between the number of rejected samples after the total number of iterations N is the quantile applied for the truncation of the parent distribution before conformity testing has been carried out.

The transfer of the results to stiffness values can scientifically be reasoned when assuming a monotonic relation between strength and stiffness properties, e.g. Young's modulus. The correlation of these properties is discussed further in section 6.

The algorithmic implementation of the procedure has been carried out using MATLAB. As the number of rejected samples is stored in 'num_reject', the ratio of deficient samples can be expressed by num_{reject}/N . As soon as an appropriate convergence is reached, this proportion shall be seen as the quantile where the original distribution function of concrete strength from section 5 can be cut off at its tail. Figure 1 shows a flowchart of the algorithm which has been implemented in the template.

The idea of this simulation is rather universal and needs only slight adaptation for the implementation of other standards than those described briefly in section 4.

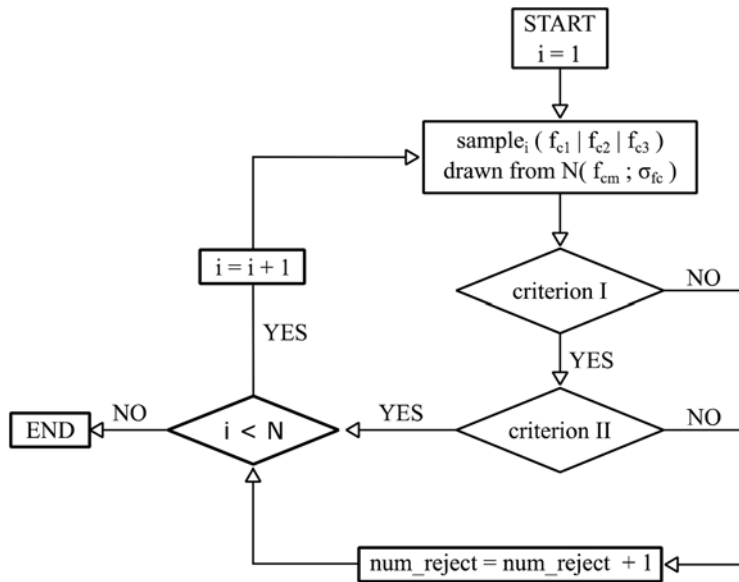


Figure 1. Flowchart of the proposed numerical computation.

4 REGULATIONS

The core of the proposed approach is the numerical replication of the instruction on conformity testing according to the respective applicable standard. The respective regulations for the examined standards are given in the subsequent sections.

DIN 1045:1959-11 (in effect 1959 – 1972) applies the following rules for concrete of strength class B300:

- Three test cubes of edge length 200 mm are tested on their strength after 28 days → (cube compressive strength)
- Criteria I: The mean of the compressive strength values, $mean(f_{c1}, f_{c2}, f_{c3})$ is to meet the compressive strength of the strength class W_{28} , here: $300 \text{ kpl/cm}^2 = 30 \text{ MPa}$
- Criteria II: The minimum of the strength values, i.e. $\min(f_{c1}, f_{c2}, f_{c3})$ must not be less than 85 % of the compressive strength of the strength class W_{28} , here: $0.85 \cdot 300 \text{ kpl/cm}^2 = 255 \text{ kpl/cm}^2 = 25,5 \text{ MPa}$

The implemented regulations in DIN 1045:1972-01 (in effect: 1972 – 1978) for a Bn450 (concrete group B II) can be summarized as follows:

- Three test cubes of edge length 200 mm are tested on their compressive strength after 28 days → f_{c1}, f_{c2}, f_{c3} (cube compressive strength)
- Criteria I: The mean of the compressive strength values $mean(f_{c1}, f_{c2}, f_{c3})$ is to meet the serial strength of the strength class β_{wS} , here: $500 \text{ kpl/cm}^2 = 50 \text{ MPa}$
- Criteria II: The minimum of the strength values, i.e. $\min(f_{c1}, f_{c2}, f_{c3})$ is to meet the nominal strength β_{wN} (5%-fractile), here: $450 \text{ kpl/cm}^2 = 45 \text{ MPa}$

5 COMMON PROBABILISTIC MODEL OF CONCRETE STRENGTH

5.1 General remarks

Scientific studies on the assumable statistical parameters of the concrete compressive strength are plenty and can be found, e.g. in (Hansen, 2004; Murdock, 1953; Six, 2003). However, there are still significant differences in the proposed statistical parameters.

A short literature study on the measures of location and dispersion is given in the following subsections that serves to justify the choice made for the examples of this paper. However, the given values are meant as input for the simulations from section 7 and should be reconsidered for each specific use-case of the presented procedure.

5.2 Type of distribution function

A common assumption for the type of distribution function is a Gaussian one following e.g. the description in (Östlund, 1991; Rüsç, 1969). The assumption of an unbounded normal distribution also reflects best practice in quality testing applications (DAfStb, 2003) and is thus adapted in this paper.

5.3 Standard deviation

The aspired or commonly achieved standard deviation has a major influence on the design of concrete mixtures and vice versa (Rüsç, 1969).

Investigations on the coefficient of variation (abbreviated: COV) for concrete with strength classes according to DIN 1045:1959-11 indicate that a variation coefficient of 5 % has only been reached in rare cases of optimal conditions at site, so coefficients of 15 to 20, up to 25 % are proposed (Graf, 1950). For a B300, standard deviations of 4.5 MPa to 6.0 MPa (COV \approx 0.12 to 0.16) should be assumed for the cube compressive strength.

For DIN 1045:1972-01, (Blaut, 1968) proposes a standard deviation of 5.5 MPa in combination with a normal distribution where the denomination of the strength class can be interpreted as a 5% quantile.

The synopsis of the literature review for the different periods of standardization and the state of the art in concrete production over the last 70 years results in a standard deviation of $\sigma \approx 5$ MPa. This seems appropriate for each of the examined standards. Differing geometry of the reference specimen shall be neglected due to the high range of suggested values from literature.

5.4 Expected value

The assumption of the mean value of compressive strength is a major part of modeling as the targeted compressive strength is very influential in computing the ratio of samples that do not meet the requirements. Of special interest in this field is the allowance to the minimum value when designing the mixture to minimize the number of rejected samples. Therefore, a review on the dimensioning aids of the different time periods was conducted, but could not give consistent advice on an adequate allowance.

For DIN 1045:1959-11 advice is given in (Blaut, 1968). The reference recommends a value of 1.645σ for the allowance to the normative value. This results in an expected value of $1.645 \cdot 300 \text{ kp/cm}^2 = 382.2 \text{ kp/cm}^2 \approx 38.2 \text{ MPa}$ for the considered B300. In comparison, the author reports a value of 340 – 350 kp/cm^2 from experience which corresponds approximately to this value.

For concrete produced after the introduction of DIN 1045:1972-01, the minimum value of β_{wS} should be seen as the 5 %-quantile for a normally distributed probability function and reflects the upcoming statistical quality control at that time. This assumption is consistent with the recommendations of (Blaut, 1968) and exceeds the minimum value of $50 \text{ kp/cm}^2 = 5 \text{ MPa}$ reported in (Rapp, 1971; Walz, 1972). For the example of a Bn450, the assumed value is $\mu = 1.645 \cdot \sigma + \beta_{wS} = 1.645 \cdot 50 \text{ kp/cm}^2 + 450 \text{ kp/cm}^2 = 532.25 \text{ kp/cm}^2 = 53.2 \text{ MPa}$.

6 DISTRIBUTION FUNCTION OF YOUNG'S MODULUS FOR CONCRETE

6.1 Type of distribution function

In most of the studied reference books, the type of distribution function is given as a normal distribution. In contrast to this, it is in a minor number of studies given as a log-normal

distribution function, e.g. in (Six, 2003), or as a Student-t-distribution, e.g. (JCSS, 2001). For this contribution, the probability function is assumed to follow a Gaussian distribution for all the examples of section 1.2.

6.2 Coefficient of variation

Because of the many different strength classes in different standards worldwide and the intermediate values between the strength classes, the scatter in the elastic stiffness is commonly expressed by its coefficient of variation v_E . Table 1 gives a short summary of values taken from different textbooks.

Table 1. Summary of COVs from different references.

Reference	Coefficient of Variation
Six2003(Six, 2003)	0.15
(Rüsch, 1969)	0.12
(Östlund, 1991)	0.10

6.3 Expected value

The assumption on the mean value for the different classes is made according to the current state of the art, i.e. the expression from Eurocode 2 (DIN EN 1992:2004) according to equation (1). For those regulations that are based on cubes of 200 mm edge length, the values need to be converted.

Therefore, a factor of 0.8 is applied, which is approximately the value used in the current standard of Eurocode 2. The mean value of concrete compressive strength for the different standards and the assumed values of Young's modulus are summarized in Table 2.

$$E_{cm} = 22,000 \cdot \left(\frac{f_{cm}}{10}\right)^{0.3} \quad (1)$$

Table 2. Assumed values for the mean of the probability function of elastic stiffness before incorporating information from conformity testing.

Concrete Strength Class	Mean Value of Concrete Strength	Expected Value of E_{cm} after 28 days
B300	$f_{cm} = 38.2 \text{ MPa} \cdot 0.8 = 30,6 \text{ MPa}$	$E_{cm} = 30765 \text{ MPa}$
Bn450	$f_{cm} = 53.2 \text{ MPa} \cdot 0.8 = 42,6 \text{ MPa}$	$E_{cm} = 33977 \text{ MPa}$

6.4 Transferability of the results to the elastic stiffness

Even though the strong connection between the concrete compressive strength has become obvious in section 6.3, the transferability of the simulated quantile needs further justification.

The rationale for the direct adoption of the simulated ratio to the quantile of the lower bound of elastic stiffness is that the monotonic relation between these two properties legitimates the simplified assumption that those charges sorted out for the reason of their low strength are exactly those that have lowest stiffness properties. Scatter in the simultaneous growth of strength and stiffness should be comprised in a larger coefficient of variation of Young's modulus compared to the compressive strength.

6.5 Post hardening

All the standards reviewed in this contribution apply in a strict sense to concrete properties as they are 28 days after production. As the process of hardening is not yet finished at that point

of time, effects of post hardening can be incorporated in the assumed probability function. Experimental studies on the long-time development of the elastic stiffness after 50 or even 100 years are very rare. For the purpose of this contribution, the results presented in (Walz, 1977) were evaluated which leads to an increase of about 15 % in stiffness after 50 years. This time period shall be assumed for the examined standards. In consequence, it is proposed to multiply the expected value of the probability function by 1.15. The scatter that lies in the process of post hardening should be respected by an increase in the coefficient of variation for the distribution function of the Young's modulus described in section 6.2.

For the simulations in this contribution, a value of $\nu_E = 0.20$ is applied that respects the large spectrum of processing, incorporates different qualities of production facilities and comprises uneven post-hardening.

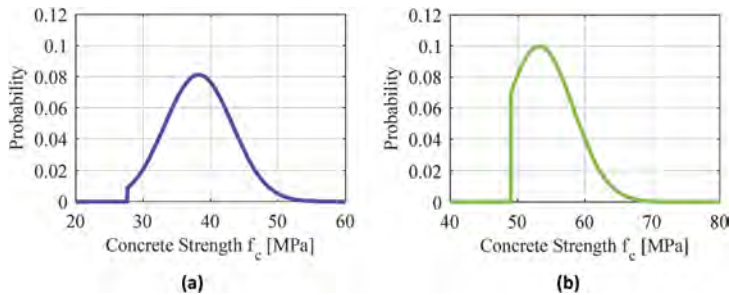


Figure 2. Truncated Probability distribution function for (a) B300 and (b) Bn450 and (c) C20/25.

7 RESULTS

7.1 Concrete compressive strength

The results of the procedure described in section 3 are given in Figure 3 using the examples presented in section 4 and a number of 10^5 simulation runs. For the B300 tested according to the procedure described in DIN 1045:1959-11, a ratio of 0.017 of the tested samples were rejected which corresponds to a lower bound of 27.7 MPa (cube compressive strength). The evaluations result in a decrease in standard deviation after truncation of 5 %.

A stricter rule for rejection seems to be described in DIN 1045:1972-01, where an amount of approximately 21 % of the samples failed. The corresponding limit value for the cube strength was computed as 49.0 MPa. Using the truncation, the standard deviation can be lowered by 24 %.

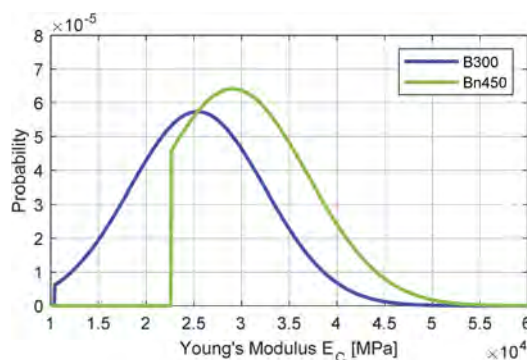


Figure 3. Simulation results for the truncated probability density function elastic stiffness taking post-hardening into account.

7.2 Elastic stiffness

As one of the objectives of this contribution is to transfer the results to stiffness properties, the results of the simulation were used to truncate also the probability distribution for the Young's modulus. Figure 3 shows the result for the two examples. The transfer of the lower bound was done using the quantile of rejected samples and a slightly higher coefficient of variation of $v_E = 0.20$. The expected value of the initial distribution function, i.e. before truncation, was calculated according to equation (1). Post hardening has been taken into account using an increase in the expectation of 15 % and a slightly higher coefficient of variation compared to the experimental studies or theoretical derivations presented in section 6.2. The simulated lower bounds also show that the computed bounds are very promising in terms of computational issues caused by very unequal values in the stiffness matrix when used for the numerical simulation. In most cases, the assumption of a quantile less than the calculated one may be sufficient to ensure numerical stability.

Table 3. (Initially) Expected Value of Young's Modulus after 50 years for the three examined examples.

Concrete Strength Class	(Initially) Expected Value of Young's modulus after 50 years
B300	$E_{cm} = 35379 \text{ MPa}$
Bn450	$E_{cm} = 39073 \text{ MPa}$

8 CONCLUSIONS

Most modern recalculations of existing structures are based on statistical evaluations of certain properties describing a structure's behavior. Therefore, a reduction of uncertainty in the input to such evaluation is of tremendous help.

In order to better describe the uncertainty of a parameter, a procedure is proposed that includes additional information from quality control of concrete to the process of statistical model building by deriving a lower bound for the assumable concrete strength. The developed template is universally applicable for different classes of concrete compressive strength and standards for quality testing.

Additionally, the derived quantile was used to transfer the gained results to elastic stiffness of concrete which is of special interest for the statistical modeling of structures in numerical calculations, e.g., in a finite element analysis.

REFERENCES

- Blaut, H. (1968) *Statistische Verfahren für die Gütesicherung von Beton*, Wiesbaden, Berlin, Bauverl.
- DAfStb (2003) *Heft 526 - Erläuterungen zu den Normen DIN EN 206-1, DIN 1045-2, DIN 1045-3, DIN 10045-4 und DIN 4226*, Berlin, Beuth Verlag GmbH.
- Graf, O. (1950) *Die Eigenschaften des Betons: Versuchsergebnisse und Erfahrungen zur Herstellung und Beurteilung des Betons*, Berlin, Heidelberg, Springer Verlag.
- Hansen, M. (2004) *Zur Auswirkung von Überwachungsmaßnahmen auf die Zuverlässigkeit von Betonbauteilen*, Stuttgart, Fraunhofer IRB Verlag.
- Haslbeck, M. & Braml, T. (2021) „Estimating Concrete Strength Properties for Existing Structures using Historic Quality Regulations for a Monte-Carlo-Simulation“, in *Fédération internationale du béton (Hg.) Proceedings of the 18th fib Symposium: New Trends for Eco-Efficiency and Performance*.
- JCSS (2001) *JCSS: Probabilistic Model Code* [Online]. Verfügbar unter <https://www.jcss-lc.org/jcss-probabilistic-model-code/> (Abgerufen am 6 Januar 2023).
- Loch, M. (2014) *Beitrag zur Bestimmung von charakteristischen Werkstofffestigkeiten in Bestandtragwerken aus Stahlbeton*, Dissertation, Kaiserslautern, Technische Universität Kaiserslautern.
- Murdock, L. J. (1953) „The control of concrete quality“, *Proceedings of the Institution of Civil Engineers*, Vol. 2, No. 4, S. 426–453.

- Östlund (1991) *Reliability of concrete structures: Final report of Permanent Commission I; [contribution à la 28. session plénière du C.E.B., Vienne, Septembre 1991, Lausanne, Comité Euro-International du Béton.*
- Rapp, G. (1971) *Zielsichere und wirtschaftliche Beton-Mischungen mit Beton-Rezepten*, Bauverlag.
- Rüsch, H. (1969) „Die Streuung der Eigenschaften von Schwerbeton“, *IABSE reports of the working commissions*, No. 3, S. 63–73.
- Schnell, J., Loch, M. & Zhang, N. (2010) „Umrechnung der Druckfestigkeit von zwischen 1943 und 1972 hergestellten Betonen auf charakteristische Werte“, *Bauingenieur: die richtungsweisende Zeitschrift im Bauingenieurwesen: offizielle Zeitschrift der VDI-Gesellschaft Bautechnik*, Vol. 85, No. 12, S. 513–518.
- Six, M. (2003) *Sicherheitskonzept für nichtlineare Traglastverfahren im Betonbau* (Zugl.: Darmstadt, Techn. Univ., Diss., 2002), Berlin, Beuth.
- Walz, K. (1972) *Herstellung von Beton nach DIN 1045: Betontechnolog. Arbeitsunterlagen*, 2. Aufl., Düsseldorf, Beton-Verlag.
- Walz, K. (1977) „Festigkeitsentwicklung von Betonen bis zum Alter von 30 und 50 Jahren“.

The impact of surface aspect ratio on the embodied energy, embodied carbon, and embodied water of a building structure

M.K. Dixit

Texas A&M University, College Station, TX, USA

P. Pradeep Kumar

Texas A&M Transportation Institute, Bryan, TX, USA

ABSTRACT: Nearly 48% of the yearly global energy supply is consumed by buildings during their construction and operation in the form of embodied and operating energy, which is responsible for nearly 40% of global carbon emissions. Building materials used for the superstructure, substructure, envelope, and interiors of a building contribute to over 90 percent of the embodied energy. Concrete and structural steels are two major materials used in bulk quantities in the construction industry, which can adversely impact the environmental sustainability of buildings. Concrete alone is responsible for 5-9 percent of the global carbon emissions. The ratio of horizontal to vertical surface area of the building known as the surface aspect ratio is an important parameter for the sustainability of a building because it affects its structural design and the quantities of materials such as steel and concrete. In this study, we analyzed how aspect ratio of a building impacts its structural design and material use in the foundation, framing, and slab of the building, and how it eventually affects the embodied energy (EE), embodied carbon emission (EC), and embodied water (EW). Five different building configurations of a generic reinforced concrete building with 12, 9, 6, 3, and 1 floor/s are modeled, and input-output based hybrid (IOH) models are used to determine the total EE, EC, and EW requirements for concrete and steel for different surface aspect ratios. The results show that for a 12-story building, there is *ca.* 34% increase in EE and EC and *ca.* 27% increase in EW as compared to a 1-story building. These results signify the importance of selecting horizontal vs. vertical building configurations in urban areas to potentially help reduce the environmental footprint of the building construction sector.

1 INTRODUCTION

Nearly half of global energy supply can be spent in buildings' construction and operation alone, which may attribute to up to 40% of global carbon emissions (Baum, 2007; Dixit, 2017). The building sector also consumes extensive amounts of fresh water (Stephan and Crawford, 2014). Looking at the intensifying construction activities and radical weather events causing water scarcity around the globe, shrinking the water footprint of buildings is essential for long-terms environmental sustainability of the building sector (Stephan and Crawford, 2014; Dixit, Kumar and Haghghi, 2022). These extensive energy, carbon and water footprints of the building sector are becoming a big concern (Stephan and Crawford, 2014; Rasmussen *et al.*, 2018; Hong *et al.*, 2019; Dixit, Kumar and Haghghi, 2022). Most of the energy and water impacts come from building operation activities, whereas a sizable portion from embodied impacts due to buildings' construction activities (Stephan and Crawford, 2014; Dixit, Kumar and Haghghi, 2022). The embodied impacts include embodied energy (EE), embodied carbon (EC), and embodied water (EW) (Stephan and Crawford, 2014; Rasmussen *et al.*, 2018; Hong *et al.*, 2019; Dixit, Kumar and Haghghi, 2022). The amounts of

energy and water used directly in construction activities and indirectly by using materials is termed EE and EW, respectively (Stephan and Crawford, 2014; Rasmussen *et al.*, 2018; Hong *et al.*, 2019; Dixit, Kumar and Haghghi, 2022). The EE and EC, therefore, have a direct and an indirect component (Stephan and Crawford, 2014; Rasmussen *et al.*, 2018; Dixit, Kumar and Haghghi, 2022). Because energy sources consumed as EE also incur water use in their generation, extraction, refinement, and delivery, there is a third EW component called the energy related embodied water (EREW), which must also be added to the total EW use of a building (Hong *et al.*, 2019; Dixit, Kumar and Haghghi, 2022). The resulting carbon emission due to the use of EE is termed EC (Rasmussen *et al.*, 2018).

Most EE, EC, and EW impacts stem from the use of construction materials such as steel, concrete, brick, aluminum, and glass, which are highly energy and water intensive (Stephan and Crawford, 2014; Dixit, 2017; Rasmussen *et al.*, 2018). Steel and concrete are two materials that are installed in bulk in buildings' structural systems and can greatly influence the environmental sustainability of buildings (Dixit and Pradeep Kumar, 2022). Concrete, specially is more concerning due to its share of 5-9% in the total global carbon emissions (Benghida, 2017; Cramer, 2019; Di Filippo, Karpman and DeShazo, 2019). Most of these emissions (74%-81%) comes from the production of Portland cement, whereas just 13%-20% from coarse aggregates (Minunno *et al.*, 2021). Likewise, astounding 2 tons of carbon dioxide is released by the production of one ton of steel (Pradeep Kumar *et al.*, 2021). The energy, carbon emission, and water footprints of reinforced concrete structures can be reduced by either lowering the energy, carbon, and water footprints of the production of cement and steel or shrinking the bulk use of concrete in building structure (Benghida, 2017; Monteiro, Miller and Horvath, 2017; Wangler *et al.*, 2019). One of the aspects that may affect the amount of concrete put into a building is the aspect ratio of the building (Beghini and Sarkisian, 2014; Pradeep Kumar *et al.*, 2021). In other words, a building designed for the same floor area can be constructed horizontally and vertically. The big question is which of these configurations may consume more reinforced concrete, answer to which would potentially help urban planners, developers, and policymakers create future city plans and developments that, through design, can help reduce environmental impacts. This paper presents an analysis of how a building's aspect ratio may influence the concrete use and eventually the amount of embodied energy (EE), embodied carbon (EC), and embodied water (EW).

2 SUSTAINABILITY OF REINFORCED CONCRETE

Portland cement and steel are the two most embodied energy (EE), embodied carbon (EC), and embodied water (EW) intensive materials in reinforced concrete structures (Benghida, 2017; Pradeep Kumar *et al.*, 2021). Concrete alone can consume 1 GJ/ton, 35 kgC/ton, and 290 liter/m³ of EE, EC, and EW, respectively (Hammond and Jones, 2008). On average, steel and cement production can incur up to 24.4 GJ/ton, 482kgC/ton, 2.6 kiloliter/ton and 4.6 GJ/ton, 222 kgC/ton, 1.0 kiloliter/ton of EE, EC, and EW usage, respectively (Hammond and Jones, 2008). In fact, steel is found to have the largest EW footprint among common construction materials (Crawford and Treloar, 2005; Choudhuri, 2015; Bardhan and Choudhuri, 2016; Dixit, Kumar and Haghghi, 2022). Key techniques to shrink the energy, carbon, and water impacts of cement mainly strive to reduce or replace the use of Portland cement (Benghida, 2017; Javadabadi *et al.*, 2019). This can be done by either adding materials such as clay and lime that may require lesser processing or replacing cement with pozzolanic materials like natural pozzolans, silica fumes, fly ash, and granulated blast furnace slag (GBFS), which may help shrink the CO₂ emissions by 13%-15% (Naik, 2008; Benghida, 2017; Monteiro, Miller and Horvath, 2017; Javadabadi *et al.*, 2019). Other types of concrete such as fiber-reinforced concrete (FRC) can not only reduce the usage of steel but also time (37% less) and cost (12% less) yielding more savings in carbon emissions (de la Fuente *et al.*, 2019). Other materials such as calcined clay and geo- or inorganic polymers are also added by some studies to replace cement in reinforced concrete (Monteiro, Miller and Horvath, 2017). Recycling is another approach to lower the energy, carbon, and water footprints of reinforced concrete, especially by using recycled concrete aggregates (RCA)

(Javadabadi *et al.*, 2019). Design optimization can also be used to develop mixes that reduce the quantity and improve the quality of concrete in terms of higher durability and strength (Monteiro, Miller and Horvath, 2017; Javadabadi *et al.*, 2019). The size and shape of aggregates as well as packing factor of concrete mix designs can be explored to improve the concrete quality (Monteiro, Miller and Horvath, 2017; Javadabadi *et al.*, 2019). Construction automation technologies such as additive and subtractive construction (e.g., large-scale 3D printing) can be other approaches to reduce the use of concrete (Dixit, 2019). One of the key design parameters that may influence a building's structural design is the aspect ratio of the building (Waldron *et al.*, 2013; Beghini and Sarkisian, 2014; Quaglia *et al.*, 2014; Shadram and Mukkavaara, 2019). The aspect ratio can be defined as a ratio of a building's height to its width or depth (Benghida, 2017). Studies have discussed and analyzed how aspect ratio may impact a building's structural design eventually affecting the use of structural concrete and steel, which apparently has embodied impact implications (Waldron *et al.*, 2013). The aspect ratio of buildings, therefore, can influence their energy and environmental sustainability (Waldron *et al.*, 2013).

3 METHODOLOGY

The primary objective of this study is to evaluate the impact of surface aspect ratio on the total embodied energy, carbon, and water of a building structure. The key objectives are as follows:

3.1 Objectives

- 1) Compute a building's total concrete and steel quantity takeoff based on structural analysis for each defined surface aspect ratio.
- 2) Determine the total embodied energy (EE), carbon (EC), and water (EW) using an input-output based hybrid (IOH) method for each defined surface aspect ratio.
- 3) Compare the results of EE, EC, and EW to understand the impact of surface aspect ratio on these three environmental indicators of the building structure.

3.2 Surface aspect ratio and material takeoff

In this study, aspect ratio is defined as surface aspect ratio (AR_s) which is the ratio of the total horizontal surface area and the total vertical surface area of a building structure. To study the impact of surface aspect ratio, a structural load analysis is conducted on a 12-story commercial building. The surface aspect ratio is varied by changing the total height of the building i.e., by reducing the number of floors while keeping the floor area the same. For this study, a total of five different cases with 12, 9, 6, 3, and 1 floor/s are considered to investigate the impact of AR_s . However, to ensure consistency among the cases being compared, the buildings' total floor area of 10,600 m² is kept constant for all the cases considered. Therefore, the horizontal dimensions are varied to accommodate for the reduction in the height and thereby, the AR_s is varied. Thus, the AR_s increases with decrease in the numbers of floors, i.e., for the buildings with 12, 9, 6, 3, and 1 floor/s the AR_s is obtained to be 0.14, 0.21, 0.37, 0.99, and 4.19, respectively.

The floor plans distinguished by surface aspect ratio are analyzed using ETABS v18 and Rapid Interactive Structural Analysis (RISA) Foundation for evaluating the superstructure and sub-structure, respectively. The structural model is prepared using beam and column assignment for the horizontal and vertical members subjected to standard ASCE7 (ASCE7-16, 2016) loading. The self-weight of the 9-inch-thick exterior wall is applied as a uniformly distributed load along the wall periphery. 104 pounds per linear foot (plf) dead load is assigned to the walls assuming a normal partition stud wall with half inch-thick gypsum board on each side for a wall/floor height of 13 ft. as per ASCE7. The live load is assumed to be 100 pounds per square foot (psf) for the floor and 20 psf for roof in accordance with ASCE7. This analysis does not consider variation in the wind directions and parameters. The structure is analyzed using the standard beam and columns available in the software list for optimal structural design.

The material properties of the elements are assumed as 4 kips per square inch (ksi) for concrete and 60 ksi for rebar steel. RISA Foundation is used for designing the substructure. The base reactions that are computed from the superstructure serve as the input parameters of dead and live load on the foundation. The amounts of concrete and steel used is obtained from the quantity take-offs and are plotted against the surface aspect ratio for several alternatives with differing number of floors and surface aspect ratio. More details of the model, loading and assumptions may be found in Dixit and Pradeep Kumar (Dixit and Pradeep Kumar, 2022).

3.3 *Input output-based model*

The raw *Use* and *Make* tables from the latest United States (US) benchmark input-output (IO) accounts were utilized to develop two input-output-based hybrid (IOH) model. One model is developed for embodied energy (EE) calculation, whereas the other for embodied water (EW). The *Use* table indicates the consumption of different commodities for producing a unit of the output of an industry, whereas the *Make* table the production of commodities by an industry sector. The *Use* and *Make* data are converted into *Use* and *Make* coefficients that are then used to quantify the direct requirements matrix, which listed the direct input of commodities needed to generate a unit of a commodity's output. *Leontief's Inverse* matrix is used to generate the total requirements matrix that showed the total commodity inputs required to produce a unit output of a commodity (Pradeep Kumar, Venkatraj and Dixit, 2022). To compute EE and EW intensities of commodities without using energy and water prices, data of energy and water use by each industry sector was gathered and integrated into the *Use* table in physical units.

3.4 *Computation of Embodied energy (EE) and carbon (EC)*

Energy use data from United States Census Bureau (USCB), United States Department of Agriculture (USDA), and United States Department of Energy (USDOE) is collected for each industry and integrated into the *Use* table. Primary energy factors are then sourced from Dixit et al. (Dixit, Culp and Fernandez-Solis, 2014) and used to convert the energy values into primary energy units. The total EE intensities for concrete and steel (MBtu/\$) commodities are converted into energy per unit weight (MJ/kg) of the respective materials based on their unit weight prices. Using the density of these materials the energy per unit weight is converted into energy per unit volume (MJ/ft³), which is then used to calculate the total EE.

Embodied carbon refers to the total carbon emissions and is directly related to the EE. The coefficients of carbon dioxide emission (kgCO₂e/MBtu) for each energy source are obtained from the United States Energy Information Administration (USEIA) and used to compute the energy source specific carbon emissions per unit volume (kgCO₂e/ft³). These values for both concrete and steel are used to determine the total EC for these two materials.

3.5 *Computation of Embodied water (EW)*

Total water used by all industry sectors of the United States economy that produce different commodities was gathered from USCB and United States Geological Survey (USGS). The collected water use data in physical unit was inserted into the *Use* table. The calculated direct and total requirement matrices now provide EW intensities of a given commodity in gallon/\$. Detailed procedure to determine the embodied water is given in Dixit et al. (Dixit, Kumar and Haghghi, 2022). Unlike EE, EW not only includes direct and indirect embodied water components but also the water used by the energy sources that contribute to the EE, which must be counted as energy related EW (EREW). The EREW of the two materials is determined using the energy source-specific EE for each energy source, a water factor is determined and multiplied with the source specific EE to calculate total EREW. To avoid double counting, EREW is separated from the indirect water component. The total embodied water requirement (Gal./\$) is converted into water per unit weight (Gal./kg) for both concrete and steel based on their respective unit weight prices. Like EE, the density of the materials is used to determine the water per unit volume (Gal./ft³), which is used to calculate the total embodied water (EW).

4 RESULTS

Figure 1 presents the total quantities of concrete and steel used in a building structure with different surface aspect ratio. The figure shows that the total quantity of materials is inversely proportional to the surface aspect ratio of the building. As the number of floors reduces from 12 to 1 i.e., as the surface aspect ratio increases from 0.14 (12 floors) to 4.19 (1 floor), the quantity of concrete decreases by *ca.* 17,000 ft³, whereas the quantity of steel by *ca.* 400 ft³. This reduction in the total structural material usage generated proportional EE, EC, and EW savings.

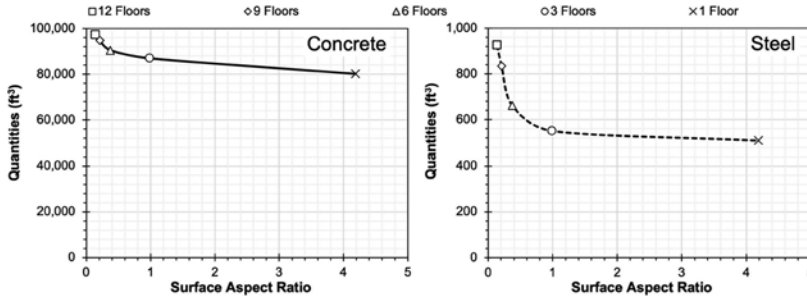


Figure 1. Variation in quantity of the two materials for different surface aspect ratio values.

The EE of both concrete and steel decreases with an increase in the surface aspect ratio. In other words, the EE increases with increase in the number of floors. It is important to note that the contribution of the EE of steel decreases with the increase in the surface aspect ratio. Contribution of steel decreases from 28% for AR_s of 0.14 to 21% for AR_s of 4.19.

Figure 2(A) shows the total embodied carbon of buildings with different surface aspect ratios. The plot shows that the EC due to concrete and steel decreases with increase in the surface aspect ratio. Therefore, with the increase in the number of floors the embodied carbon increases and thus, adversely affects the environment. Like the EE, the contribution of the EC of steel decreases with the increase in the surface aspect ratio. Contribution of steel decreases from 27% for AR_s of 0.14 to 20% for AR_s of 4.19. Figure 2(B) also presents the total embodied water of buildings with different surface aspect ratios. Like the EE and EC, the EW of both the materials decreases with increase in the surface aspect ratio. Although, like EE and EC, the contribution of the EW of steel decreases with the increase in the surface aspect ratio, the variation is relatively lower as compared to EE and EC. The contribution of EW of steel decreases from 14% for AR_s of 0.14 to 10% for AR_s of 4.19.

Figure 3 presents a comparison of the results with respect to a one-story building structure. Figure 3(A) shows the variation in the contribution of material quantities for the different surface aspect ratio cases in comparison with the one-story building with a surface aspect ratio of 4.19. The variation in the quantity of steel for 12, 9, 6, and 3 floors is *ca.* 82%, 64%, 30% and 8%, respectively, while the variation in concrete is *ca.* 21%, 18%, 13% and 9%, respectively. This indicates that the

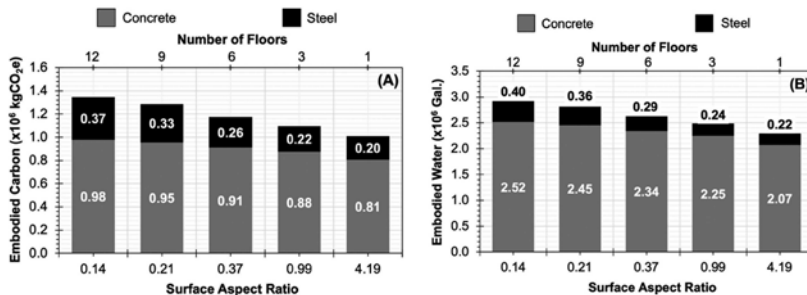


Figure 2. Total embodied carbon and water of buildings with different surface aspect ratio values.

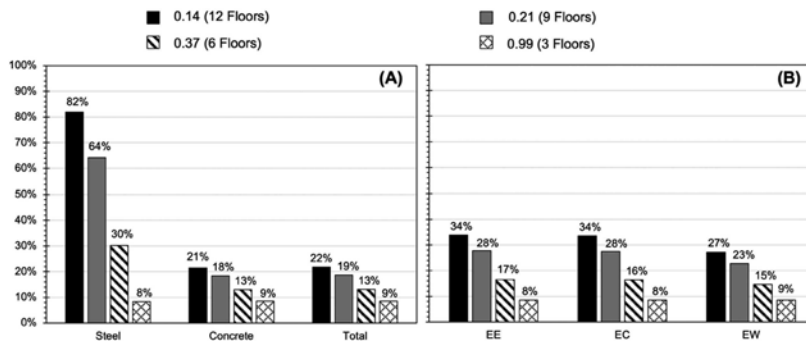


Figure 3. Contribution of (A). steel, concrete, and total quantity of materials, (B). embodied energy, carbon, and water of buildings with different surface aspect ratios with respect to a one-story building.

quantity of steel significantly reduces with the decrease in the number of floors while the decrease in the quantity of concrete is slight. One of the reasons for this could be that the size of the floor slab/s is kept constant for all surface aspect ratio cases since reducing the size of the slab may cause vibration issues that may adversely affect the serviceability of the building structure.

Figure 3(B) shows the variation in the total EE, EC, and EW for the different surface aspect ratio cases in comparison with the one-story building with a surface aspect ratio of 4.19. Results show that the variation in EE and EC for 12, 9, 6, and 3 floors is *ca.* 34%, 28%, 17% and 8%, respectively, while the variation in EW is *ca.* 27%, 23%, 15% and 9%, respectively. The variation is similar for EE and EC since they are related by a constant carbon emission coefficient. However, the difference in the variations between EE and EW increases with decrease in the surface aspect ratio. Since the embodied energy, carbon, and water for each material are directly calculated using the material quantities, the variation in the contribution of EE, EC, and EW of steel and concrete individually is similar to Figure 3(A).

5 DISCUSSION

Results show a reduction in the total quantities of concrete and steel required as the surface aspect ratio of the structure increases i.e., with the reduction in the number of floors. This may be attributed to the fact that the total load on the footings/foundation of a taller building structure is higher as compared to a short building thereby requiring larger size footings that use more concrete and steel. Furthermore, the size of the beams and columns of a tall building increases from the topmost to the bottommost floor. Therefore, the total quantity of concrete and steel required by the structural components of a taller structure is more than that of its shorter counterparts.

The total embodied energy, carbon, and water decrease with an increase in the surface aspect ratio. This is directly related to the total quantity of each material and the contribution of the materials to the total. The contribution of embodied energy, carbon, and water due to steel decrease with increasing surface aspect ratio, i.e., as the number of floors goes up, EE, EC, and EW increase due to the increased use of steel for taller structures attributed to a higher load transferred to the structural components. Reducing the number of floors from 12 to one decreases the share of EE, EC, and EW from 28% to 21%, 27% to 20% and 14% to 10%, respectively. It is important to highlight that the steel contributes to *ca.* 20% to 28% of the building's total EE and EC while it contributes to only 10% to 14% of the buildings total EW, i.e., the contribution of concrete is 86% to 90% of the total EW of a building. This clearly shows that concrete relatively consumes more water than steel as compared to its energy consumption. However, it may be due to the lower volume of steel installed in the structure as compared to concrete. The trade-off between the material level contribution of EE and EW highlights the importance of evaluating the EW in addition to EE since a reduction in EE may not indicate the same reduction in EW.

The results suggest that there is *ca.* 34% increase in EE and EC and *ca.* 27% increase in EW for a 12-story building structure as compared to a 1-story building structure. Evidently, EE

and EW are independent indicators that must be evaluated separately to ensure judicious use of not just energy resources but also water. The variation in material quantities impact the EE, EC, and EW. With an increase in surface aspect ratio, a significant reduction in the usage of steel is seen as compared to concrete, which in turn reduces EE, EC, and EW. Furthermore, the total EE, EC, and EW requirements per unit volume of both steel and concrete vary considerably and thus impact the total EE, EC, and EW differently. The EE and EC requirements per unit volume of steel is *ca.* 40 times that of concrete while the EW requirement per unit volume of steel is only *ca.* 17 times that of concrete. This variation is highly sensitive to the uncertainties associated with the unit weight price of each material. Although the unit volume requirements are huge for steel as compared to concrete, the quantity of steel is typically 2 orders of magnitude lower than concrete. Thus, the variation in total material quantity is often similar to that of concrete as shown in Figure 3(A). The results may indicate that, at the structural level, the horizontal construction may help save materials as well as EE, EC, and EW. However, EE, EC, and EW of a building are also impacted by other building systems such as the building envelope, interiors, and mechanical, electrical, and plumbing (MEP) systems, which may influence these findings. For instance, as compared to vertical structure, a horizontal structure has much larger roof area that may not just influence EE, EC, and EW but also the operational energy used in heating, cooling, and lighting the interior spaces. More detailed study covering all building systems may be needed to understand the effect of an aspect ratio on the use of building materials and embodied and operational impacts.

6 CONCLUSIONS

This paper analyzed the impact of a design parameter, surface aspect ratio, on EE, EC, and EW of a building structure. The results show a decrease in the environmental impacts with an increase in the surface aspect ratio. In other words, horizontal construction seems to favor environmental impacts as compared to vertical construction at the structure level. By increasing the surface aspect ratio, the reduction in EE and EC is observed to be slightly different from that of EW. This highlights the importance of analyzing EE as well as EW to ensure a sustainable built environment. Although the results suggest the use of buildings with higher surface aspect ratio for environmental sustainability, the main aim of the study is to highlight the impact of a design parameter such as surface aspect ratio on the EE, EC, and EW of a building. Therefore, results may be skewed to account for only material level variability which may be misleading from a community level analysis where use of buildings with higher surface aspect ratio may adversely impact the environment if other factors such as flash flood, urban heat island effect, and ground permeability are considered. Nevertheless, studying horizontal vs. vertical construction has profound policy- and planning-level implications for redesigning existing and creating new urban areas to reduce the environmental impacts of built environments.

REFERENCES

- ASCE7-16 (2016) 'ASCE Minimum Design Loads and Associated Criteria for Buildings and Other Structures.', in *American Society of Civil Engineers*. American Society of Civil Engineers.
- Bardhan, S. and Choudhuri, I. R. (2016) 'Studies on virtual water content of urban buildings in India.', *Indian Journal of Science and Technology*, 9(6). doi: 10.17485/ijst/2016/v9i6/87671.
- Baum, M. (2007) *Green Building Research Funding: An Assessment of Current Activity in the United States*. Washington D. C.
- Beghini, A. and Sarkisian, M. (2014) 'Geometry Optimization in Structural Design', *Proceedings of SEAOC 2014 83rd Annual Convention*, pp. 279–290.
- Benghida, D. (2017) 'Concrete as a Sustainable Construction Material', *Key Engineering Materials*, 744, pp. 196–200. doi: 10.4028/www.scientific.net/KEM.744.196.
- Choudhuri, I. R. (2015) 'Assessment of Embodied Water of Construction: Case Study of a Four Star Rated Hotel in New Delhi, India.', *International Journal of Emerging Engineering Research and Technology*, 3(8), pp. 195–199.

- Cramer, N. J. (2019) 'Mitigating Carbon Dioxide Emissions in the Cement Industry Through Carbon Capture and Storage', *The cement industry*, 3.
- Crawford, R. H. and Treloar, G. J. (2005) 'An assessment of the energy and water embodied in commercial building construction.', in *4th Australian Life Cycle Assessment Conference*. Sydney, Australia, pp. 1–10. Available at: <https://www.researchgate.net/publication/242296069>.
- Dixit, M. K. (2017) 'Life cycle embodied energy analysis of residential buildings: A review of literature to investigate embodied energy parameters', *Renewable and Sustainable Energy Reviews*, 79(May), pp. 390–413. doi: 10.1016/j.rser.2017.05.051.
- Dixit, M. K. (2019) '3-D Printing in Building Construction: A Literature Review of Opportunities and Challenges of Reducing Life Cycle Energy and Carbon of Buildings', *IOP Conference Series: Earth and Environmental Science*, 290(1). doi: 10.1088/1755-1315/290/1/012012.
- Dixit, M. K., Culp, C. H. and Fernandez-Solis, J. L. (2014) 'Calculating primary energy and carbon emission factors for the United States energy sectors', *RSC Advances*, 4(97), pp. 54200–54216. doi: 10.1039/c4ra08989h.
- Dixit, M. K., Kumar, P. P. and Haghghi, O. (2022) 'Embodied water analysis of higher education buildings using an input-output-based hybrid method.', *Journal of Cleaner Production*, 365, p. 132866.
- Dixit, M. K. and Pradeep Kumar, P. (2022) 'Analyzing the Impact of the Aspect Ratio of a Building on Concrete Use in Its Structure', *Acta Polytechnica CTU Proceedings*, 33, pp. 133–139. doi: 10.14311/APP.2022.33.0133.
- Di Filippo, J., Karpman, J. and DeShazo, J. R. (2019) 'The impacts of policies to reduce CO 2 emissions within the concrete supply chain', *Cement and Concrete Composites*, 101(June 2017), pp. 67–82. doi: 10.1016/j.cemconcomp.2018.08.003.
- Hammond, G. P. and Jones, C. I. (2008) 'Embodied energy and carbon in construction materials', (May), pp. 87–98. doi: 10.1680/ener.2008.161.2.87.
- Hong, J. *et al.* (2019) 'Water-energy nexus and its efficiency in China's construction industry: Evidence from province-level data.', *Sustainable Cities and Society*, 48. doi: 10.1016/j.scs.2019.101557.
- Javadabadi, M. T. *et al.* (2019) 'Sustainable Concrete: A Review', *International Journal of Structural and Civil Engineering Research*, 8(2), pp. 126–132. doi: 10.18178/ijscer.8.2.126-132.
- de la Fuente, A. *et al.* (2019) 'Sustainability of Column-Supported RC Slabs: Fiber Reinforcement as an Alternative', *Journal of Construction Engineering and Management*, 145(7), p. 04019042. doi: 10.1061/(asce)co.1943-7862.0001667.
- Minunno, R. *et al.* (2021) 'Investigating the embodied energy and carbon of buildings: A systematic literature review and meta-analysis of life cycle assessments', *Renewable and Sustainable Energy Reviews*, 143(March), p. 110935. doi: 10.1016/j.rser.2021.110935.
- Monteiro, P. J. M., Miller, S. A. and Horvath, A. (2017) 'Towards sustainable concrete', *Nature Materials*, 16(7), pp. 698–699. doi: 10.1038/nmat4930.
- Naik, T. R. (2008) 'Sustainability of Concrete Construction', *Practice Periodical on Structural Design and Construction*, 13(2), pp. 98–103. doi: 10.1061/(asce)1084-0680(2008)13:2(98).
- Pradeep Kumar, P. *et al.* (2021) 'Punching above its weight: life cycle energy accounting and environmental assessment of vanadium microalloying in reinforcement bar steel', *Environmental Science: Processes & Impacts*, 23(2), pp. 275–290. doi: 10.1039/d0em00424c.
- Pradeep Kumar, P., Venkatraj, V. and Dixit, M. K. (2022) 'Evaluating the temporal representativeness of embodied energy data : A case study of higher education buildings', *Energy & Buildings*, 254, p. 111596. doi: 10.1016/j.enbuild.2021.111596.
- Quaglia, C. P. *et al.* (2014) 'Balancing energy efficiency and structural performance through multi-objective shape optimization: Case study of a rapidly deployable origami-inspired shelter', *Energy and Buildings*, 82, pp. 733–745. doi: 10.1016/j.enbuild.2014.07.063.
- Rasmussen, F. N. *et al.* (2018) 'Analysing methodological choices in calculations of embodied energy and GHG emissions from buildings', *Energy and Buildings*, 158, pp. 1487–1498. doi: 10.1016/j.enbuild.2017.11.013.
- Shadram, F. and Mukkavaara, J. (2019) 'Exploring the effects of several energy efficiency measures on the embodied/operational energy trade-off: A case study of swedish residential buildings', *Energy and Buildings*, 183, pp. 283–296. doi: 10.1016/j.enbuild.2018.11.026.
- Stephan, A. and Crawford, R. H. (2014) 'A comprehensive life cycle water analysis framework for residential buildings', *Building Research and Information*, 42(6), pp. 685–695. doi: 10.1080/09613218.2014.921764.
- Waldron, D. *et al.* (2013) 'Embodied energy and operational energy: Case studies comparing different urban layouts', *Proceedings of BS 2013: 13th Conference of the International Building Performance Simulation Association*, pp. 1264–1271.
- Wangler, T. *et al.* (2019) 'Digital Concrete: A Review', *Cement and Concrete Research*, 123(May). doi: 10.1016/j.cemconres.2019.105780.

Performance assessment of existing prestressed concrete bridges utilizing distributed optical fiber sensors

H. Burger, T. Tepho & O. Fischer

Technical University of Munich, Munich, Germany

N. Schramm

Büchting + Streit AG, Munich, Germany

ABSTRACT: Many existing prestressed concrete bridges are currently in a poor structural condition with calculative deficits concerning the load bearing. To extend their service life, structural health monitoring could be an effective method. In addition to the permanent surveillance of damage, structural performance could be monitored. Through distributed fiber optical sensing technology, the change of strain along a defined sensor length is measured. Especially local unexpected crack formation can be detected as it can occur on prestressed bridges due to the fracture of single wires in a tendon. On two prestressed highway slab bridges, fiber optical sensors were applied as a part of a major infrastructural monitoring project. An evaluation of the data was made with the help of calibration tests in the laboratory and in in-situ load tests. Furthermore, the influence of temperature on measurements and the accuracy of the measurement system were analyzed.

1 INTRODUCTION

The utilization of distributed fiber optical sensors (DFOS) for structural monitoring has increased in the last few years. There are different sensing technologies and various application methods of DFOS. Recent technical developments make measuring and application easier and more efficient. An overview is given in the research conducted by Bado & Casas (2021). To choose the right measurement system, technical and economic aspects have to be considered. Its choice depends on the needed and expected measurement data. The structural performance of an existing prestressed concrete bridge has to be evaluated by considering its expected behavior. Often, the evaluation of a concrete structure is based on the detection of cracks. The exact location of a crack is often not known in advance, especially in prestressed structures where the potential damage of tendons can lead to cracks or high strain in unexpected locations. Brittle fractures of the prestressing steel can occur due to stress-corrosion cracking, which depends on the corrosive environment, the tensile stress and the steel properties.

With the help of fiber optic technology, it is possible to record the strain distribution along a defined sensor length. Approved measurement systems based on Rayleigh backscattering are limited to obtain data on a sensor length of 50 m with a spatial accuracy down to 0.63 mm (Luna 2020) and allow the detection of small changes in crack width. However, even if a general measurement accuracy and uncertainty is specified, the recording of reliable data is not guaranteed. Depending on various factors such as sensor selection, sensor application, measurement settings, load effects etc., measurement results may deviate from the true value. To avoid discrepancies in a monitoring project, a redundant measurement system should be used and the values of the gathered data should be verified. An evaluation of the data must be done critically and should consider already known results.

As part of a major long-term monitoring project of two existing prestressed concrete bridges DFOS are used to detect cracks and strain changes due to tendon failure. Since the beginning of the monitoring at the end of 2021, various calibration tests were carried out in the laboratory and on the bridges themselves. These generated data under known boundary conditions are used to successfully evaluate the monitoring data. The experience gained over time in the monitoring project simplifies the collection, analysis and interpretation of the data, thus facilitating the application of structural monitoring. In addition to detecting cracks, the detection of the global structural behavior of bridges is possible with DFOS.

Furthermore, the application of DFOS for monitoring generally has to be non-destructive or minimally invasive. These properties cannot be at the expense of the measurement results. Parts that are sensitive to maintenance, such as plug connections or termination of the DFOS, must remain reachable and accessible after installation. Besides that, durability of the components plays a very important role regarding long-term monitoring, which influences the type of the DFOS and its application.

2 APPLICATION OF DISTRIBUTED FIBER OPTIC SENSORS

DFOS are specially sheathed optical fibers. Their design varies according to application type and manufacturer. They can be inserted into concrete while concreting, consequently being bonded to the surface or applied into a milled groove. It is also possible to bond such sensors on the reinforcing bars and in case of post-tensioning concrete structures, DFOS can be inserted in the duct before grouting (Fischer et al. 2019).

For existing structures, sensors are applied superficially or into a groove milled into the structure. In the latter case, the sensor is completely embedded in the adhesive. Consequently, the sensor is better protected from external influences and it is easier to establish a complete bond between the sensor and the measured object. Figure 1 shows a detail of this application method.

The different layers, from the host material (concrete) to the optical fiber, have a significant influence on the measured data. For example, when the host material is subject to mechanical stress, constant strain transfer between the individual layers is not guaranteed. Especially at a very high strain, a slip occurs, which can be locally observed in cracks (Bassil et al. 2020). Furthermore, temperature loads not only cause strain in the concrete component, but also have an influence on the sensor and its sheaths. Therefore, the expected strain change of a structure at different temperatures does not always correspond to the measured one. Due to these influences, it is necessary to perform different calibrations for every sensor application. Hence, the influence of mechanical and thermal stress must be quantified to interpret the measurement data (see Chapter 3).

In addition to the type of application, the correct sensor position must be determined to assess a structural performance and detect signs of tendon fractures. Consequently, the structural behavior must be known in advance and the geometry of the existing bridge identified as precisely as possible. Prestressed cross sections are usually completely under compressive stress in the serviceability limit state (SLS) and the bending moment from the prestressing counteracts the external loads. Fractures of the prestressing steel can occur in older existing bridges due to stress-corrosion cracking, which cause strain changes. The location of these fractures is normally unknown. When one or multiple tendons fail, tensile stress up to cracking in a cross-section can occur. Cracks clearly stand out in the measurements and thus serve as the measurement target. Furthermore, the strain change due to a prestressing steel fracture does not change linearly over the cross-section height (König et al. 1996). Therefore, a crack in the concrete may occur at the level of the tendon. If the steel fracture minimizes the counteracting normal stresses in a section with a high bending moment, the concrete instead cracks at the top or bottom of the cross-section. For this reason, it is often useful to use more than one DFOS per tendon layout.

The position of a sensor on longitudinally prestressed bridges depends on the bridge's cross section. Figure 2 gives possible locations for DFOS in three different cross-section types. At the bottom of the cross-section, where tension due to positive moment appears, an application of the sensors at relevant locations is usually possible without any problems. In the area of negative bending moments (in general the support area), tension, cracks and thus locally high strain are expected on the top side. However, it is usually not possible to apply to the upper surface of the concrete. A possible solution is to open the road and install the sensors on the top side. In the case of T-beams and box girders, sensors can alternatively be attached to the web or at the bottom of the roadway slab. Regarding the web, the position over the height can vary along the span.

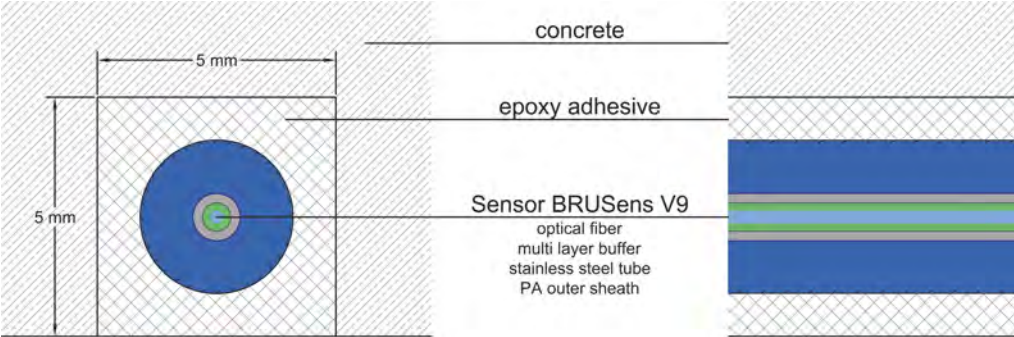


Figure 1. Detail of a BRUSens V9 sensor embedded in a groove; cross-section (left) and longitudinal section (right).

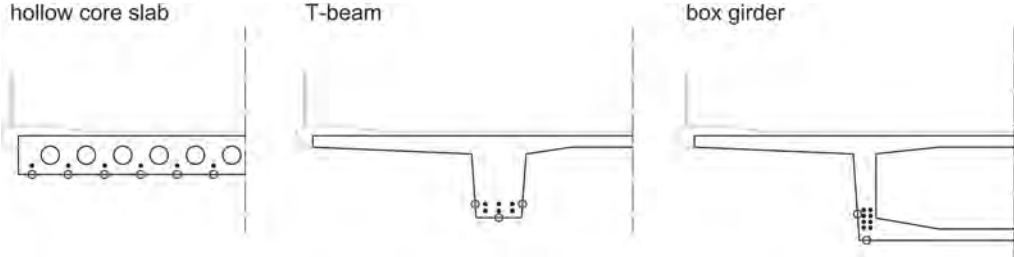


Figure 2. Possible location of the DFOS (blue circles) w. r. t. positive bending moments for various cross-sections of prestressed concrete bridges (tendons shown as black circles).

Once the DFOS have been applied, the exact location of the sensor on the bridge has to be identified. The beginning and end of the sensors are recorded by the measurement system, but noticeable locations, such as the end of bonding, existing imperfections in the concrete or the adhesive matrix, etc. cannot be clearly assigned to the sensor position without prior referencing. Artificially generated local temperature effects can be used to allocate the sensor coordinates in the global coordinate system of the structure. If the sensor is no longer accessible after installation but is still visible, a scale should be applied in the longitudinal direction. This simplifies the detection of cracks at a later stage.

3 CALIBRATION OF THE MEASUREMENT TECHNOLOGY

Fiber optical measurement systems based on Rayleigh backscattering use an active tunable laser and a spatially resolving reflectometer. The emitted light beam is coupled into a reference arm with a fixed path length and into the sensor fiber using a Mach-Zehnder

interferometer. Backscattered light from the sensor fiber is superimposed with the light component from the reference arm. From the interference between reference and measurement signal, a local frequency shift can be derived. This frequency shift is proportional to the strain or temperature change. A relative strain or temperature change can be calculated from these results in consecutive spatial windows along the fiber. (Fischer et al. 2019)

Separate recording of strain change and temperature change on the same bonded sensor is not possible. When DFOS are installed, they have to be specified as strain or temperature sensors. Therefore, Luna (2014) suggests reference values for the calibration constants to convert the frequency shift into strain or temperature change. These conversion factors vary depending on the material properties of the fiber core and the sensor type.

Various tests have to be carried out to ensure the reliability of the calibration constants and the measured strain or temperature change. Known boundaries can be created in a laboratory. These allow researchers to investigate the influence of mechanical and temperature induced loads separately. As an example, the calibration tests carried out in a monitoring project and their results are shown for the sensor application type according to Figure 1.

Before measuring, the distance between centerpoints of consecutive spatial windows along the fiber has to be selected as a general setting. This distance influences the measurement uncertainty of the sensing technology (Luna 2020). Depending on the DFOS type and its strain transfer through the sheaths, the width of the spatial windows has to be chosen. For an application as shown in Chapter 2 and to obtain data with a minimum of general uncertainty, a spatial window of 2.6 mm is chosen for the calibration tests. Additionally, information was gathered on the probation and performance of the application method during the test execution.

3.1 *Strain measurement under mechanical load*

The expected strain at the concrete surface in SLS can be estimated on the basis of the material behavior and mechanical laws. The following considerations apply only to normal strength concrete up to class C50/60 and assume a material behavior according to Eurocode 2 based on average values. Furthermore, influences from prestressing, creep and shrinkage have already been concluded. This represents the case of sensor application on existing bridges. Compressive strain for a cracked section is reasonable up to approximately $-1160 \mu\text{m/m}$ (-1.160 ‰) under only bending moment loading and considering the safety concept according to Eurocode 0. Since 40 % to 60 % of the total load is already present as a dead load before sensor application, a maximum of $-660 \mu\text{m/m}$ (-0.660 ‰) compressive strain is expected from live load in a cracked section.

Tensile strain in concrete without prestressing can increase linearly only up to $100 \mu\text{m/m}$ (0.100 ‰) on average, calculated from the tensile strength divided by the Young's modulus. After exceeding the tensile strength, cracks occur. On prestressed concrete bridges, higher tensile strain from live loads is possible before cracking due to the present compressive stresses, because of prestressing. The compressive stresses are limited at approximately 40 % of the average compressive strength. At the most favorable stress distribution, the tensile strain at the non-cracked cross-section reaches a maximum of $365 \mu\text{m/m}$ (0.365 ‰).

If a crack occurs and crosses the sensor, the maximum strain is only limited by the sensor sheath. BRUSens V9 sensors measure the strain up to $10,000 \mu\text{m/m}$ (10 ‰) according to the manufacturer. In reinforced concrete, however, cracks are measured with their crack width. A crack is present only when the crack edge is completely displaced. This corresponds to a crack width of 0.1 mm (Röhling & Meichsner 2018). According to Eurocode 2, calculated crack widths are limited to 0.2 mm, 0.3 mm or 0.4 mm (Eurocode 2). For prestressed structures, cracks of this size must be detected. The values shown above do not consider extreme events, such as an overload.

The measurement results must be reliable for the mean strain from compression, tension and crack widths. This was investigated in calibration tests using independent reference

measurement technology as strain gauges and displacement transducers. The following calibration tests were carried out under a constant temperature:

- 4-point bending test on prestressed precast hollow core slab
- Crack formation on the tensile test of a concrete bar
- Compression and bending tests on concrete beams

In these various tests, the accuracy specified by the manufacturer was achieved for tensile and compressive strain in comparison to strain gauges on the concrete surface. Luna (2020) gives a system accuracy of 30 $\mu\text{m}/\text{m}$ (0.030 ‰) using the manufacturers' sensors compared to NIST-traceable extensometer measurements. Figure 3 shows the results of the 4-point bending test on a prestressed precast hollow core slab. The diagram shows the strain of strain gauges and the DFOS shortly before first cracking. Furthermore, the measurement of the crack formation is illustrated in this figure, which was only detected by DFOS. When first crack formation was initiated, no significant strain change was recorded by the gauges. Even though data from DFOS show indications for probable microcracks, it is not possible to definitively predict macrocracks in a certain location.

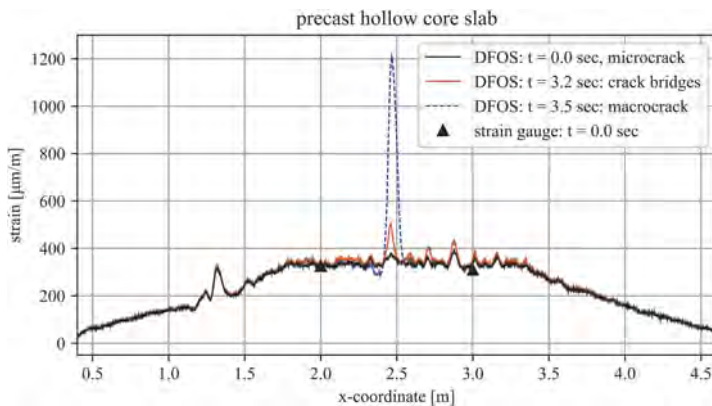


Figure 3. Crack formation on a prestressed hollow core slab.

As shown in Figure 3, a crack generates a strain peak. Nevertheless, it is necessary to ensure that a crack is present at the respective peak. Disruptions in the adhesive or in the concrete can manifest themselves in such strain peaks. In a tensile test of a concrete bar, the crack formation was investigated and the crack width compared with a displacement transducer. It was found that in an opened crack, the crack width change can theoretically be traced down to 0.001 mm by integrating over a peak. In contrast, with conventional techniques, such as a steel ruler, it is possible to record ideally changes of 0.05 mm or with a magnified graticule down to 0.01 mm. (Fischer et al. 2022)

In the case of cyclical loads, a problem occurred. When cracks between 0 and 0.5 mm were repeatedly opened and closed, the crack width change could no longer be reliably recorded by the DFOS. A peak was still displayed, but the crack width measured with DFOS did not match the referenced measurement of the displacement transducer. This might be the cause of a slip.

3.2 Influence of temperature on strain measurement

Since the sensors on the bridge are exposed to the weather, additional tests were carried out on the influence of temperature on the measured data. Uncracked concrete beams and cracked concrete bars were loaded with temperatures ranging from -35°C to $+23^{\circ}\text{C}$. The DFOS were

also embedded into a groove as shown in Figure 1. Mechanical loads were minimized by placing the test samples vertically. Selected results on the cracked concrete bar test are given in Figure 4. At high temperature differences of more than 20 Kelvin, the strain scatters in a range of $\pm 50 \mu\text{m/m}$ ($\pm 0.050 \%$).

The mean value of the recorded strain along the DFOS deviates considerably from the expected values. The coefficient of thermal expansion of concrete is between 8 and $12 \times 10^{-6}/\text{K}$. The value measured in the test is between 15 and $19 \times 10^{-6}/\text{K}$. This result corresponds with the thermal expansion coefficient of the inner stainless steel tube of the BRUSens V9 sensor. According to the manufacturer Solifos AG, the average value is $16 \times 10^{-6}/\text{K}$. For this reason, it can be assumed that the temperature-induced loads cause strain changes in the sheath of the DFOS. This influence must be considered when evaluating measurement data on a supporting structure.

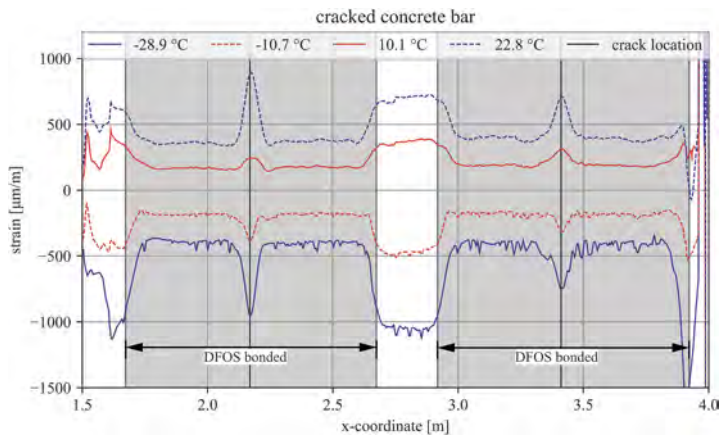


Figure 4. Results of the DFOS on the cracked concrete bar at different temperatures without mechanical loading.

4 RESULTS OF IN-SITU MEASUREMENTS

Due to the results obtained in the calibration tests (see Chapter 3), a differentiation is made between results from long-term and short-term measurements on bridges. In the case of short-term measurements, it is assumed that the temperature remains approximately constant over the measurement period. At two existing prestressed bridges, measurement data was collected on several days for more than one year. These three-span slab bridges are part of the feeder to the German highway network. DFOS were bonded to the bottom of the bridge cross-section as shown in Figure 2 on the left. Sensors were applied along several tendon axes in each span. This results in a total length of 60.5 m of bonded sensor per axis. Their function is to detect cracks or strain changes resulting from possible wire fractures as a part of a major monitoring project.

Short-term measurements for two to ten minutes are carried out at intervals of four months and as a control measurement after an alarm from acoustic emission sensors. Between the individual short-term measurements, referencing is performed and long-term strain changes are recorded. In order to calibrate the monitoring system and to assess the structural behavior, static load tests on the bridges were carried out.

4.1 Static load tests and short-term measurements

The structural performance of the bridges was investigated during two static load tests. In order to analyze the impact of the seasonal effects on short-term measurements, the two tests

were carried out on two different days at an interval of six months. Two 40-ton trucks were used as proof loads. One truck stopped at defined locations on a closed traffic lane. The second truck made simultaneous passes in the flow of traffic in the lane next to it.

Between the two single tests, no significant impacts on the short-term data were observed. In Figure 5, the results of one load test are given. The strain on two different time steps are plotted in this diagram:

- Stop of one truck in the center field on the closed lane (total load ~400 kN)
- Stop of one truck in the center field on the closed lane and passing of the second truck on the lane next to it (total load ~800 kN)

The measured strain is quite low because of the slab load-bearing effect. Tensile strain reaches a mean high of 20 $\mu\text{m/m}$ (0.020 ‰). This strain correlates with parallel recorded strain gauge measurements. During the tests, strain peaks with a maximum prominence of 40 $\mu\text{m/m}$ (0.040 ‰) appear. In the location of most peaks, irregularities were found in the bonding or concrete surface.

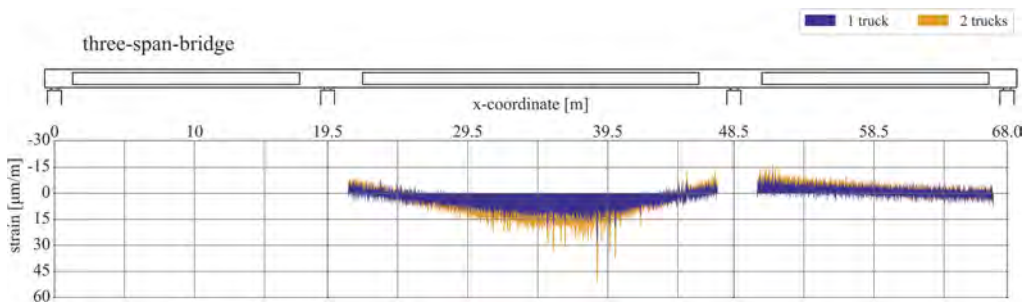


Figure 5. Measurement results on a prestressed hollow core slab bridge obtained from static load tests with two 40-ton trucks (longitudinal section top).

4.2 Long-term measurements

The measurement data (including a temperature change) shows much higher peaks than those due to the test load. At a uniform heating of approximately 8 Kelvin, the prominence of peaks reaches up to 200 $\mu\text{m/m}$ (0.200 ‰). In laboratory tests, such peaks were indicators for cracks. These locations were visually inspected. In the case of the highest peaks, offsets were detected in the concrete surface. This offset causes a local deflection of the sensor's position. Thus, a linear strain transfer between the concrete and optical fiber is not possible at this point, which leads to the above-mentioned results.

Along the remaining area the same influence of temperature was observed as in the laboratory tests. Figure 6 shows the raw data of a measurement at a uniform heating temperature of approximately $\Delta T_N = 7.7$ K and a vertical temperature difference of $\Delta T_{M,heat} = 5.0$ K (warmer on top). If the strain peaks are neglected, a scatter in the range of ± 20 $\mu\text{m/m}$ (± 0.020 ‰) is observed. The diagram in Figure 6 shows the calculated ideal strain on a simple structural model due to the specified temperature load. The corrected data corresponds to the raw data with an offset correction of $-\Delta T_N \times 8 \times 10^{-6}/\text{K}$. The linear trend of both curves essentially coincides.

It is necessary to determine the temperature load of the structure to calculate the right correction factor. This determination is very difficult, as the bridge surface temperature can vary by ± 1.5 K at the same time in different locations. Furthermore, the concrete temperature on the section's top can only be approximated because of traffic on the road. This temperature approximation also includes a time-delayed heat transfer, which depends on various material parameters.

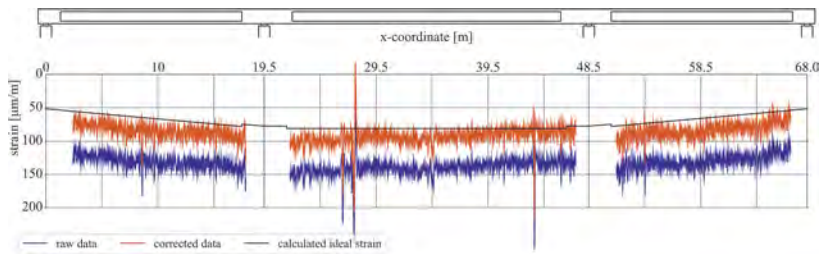


Figure 6. Measurement results on a prestressed hollow core slab bridge from temperature-induced loads: uniform heating $\Delta T_N = \sim 7.7$ K, $\Delta T_{M,heat} = \sim 5.0$ K (top warmer than bottom; longitudinal section top).

5 CONCLUSION

The application of quasi continuous fiber optic sensing technology based on Rayleigh backscattering achieves useful results in the monitoring of existing prestressed bridges. The application has to be evaluated and planned individually for each structure, considering the advantages and disadvantages of the technology. DFOS record strain along the sensor length. Cracks or superficial damages can be monitored, in addition to the assessment of the structural performance. A major advantage of DFOS is the detection of strain changes that cannot be detected visually and aren't known in advance, such as those that occur due to prestressing steel fractures.

There are many different DFOS types on the market as well as different application types. The measurement data varies significantly for different sensors and application types. For this reason, calibration tests must be carried out for each configuration in order to determine the measured data under mechanical and temperature induced load.

At the Chair of Concrete and Masonry Structures at TUM fiber optic strain measurements are used for a various experimental research. Furthermore, it is currently being investigated which further applications are possible in the monitoring of real structures. Considerations are made about automated evaluation and permanent long-term monitoring. The aim is to incorporate the data obtained into a realistic computational assessment of the existing structure.

REFERENCES

- Bado, M.F. & Casas, J.R. 2021. A Review of Recent Distributed Optical Fiber Sensors Applications for Civil Engineering Structural Health Monitoring. In *Sensors* 2021, 21, 1818. Basel, Switzerland. <https://doi.org/10.3390/s21051818>
- Bassil, A., Chapeleau, X., Leduc, D. & Abraham, O. 2020. Concrete Crack Monitoring Using a Novel Strain Transfer Model for Distributed Fiber Optics Sensors. *Sensors*, 20, 2220. Basel, Switzerland. <https://doi.org/10.3390/s20082220>
- Eurocode 2. Design of concrete structures – Part 1-1: General rules and rules for buildings; German version EN 1992-1-1:2004 + AC:2010.
- Fischer, O., Schramm, N., Burger, H. & Tepho, T. 2022. Wirklichkeitsnahe Beurteilung des Brückenbestands mit innovativer Sensorik. SpRK-Monitoring der Kreuzhofbrücken München. In *Innsbrucker Bautage 2022*. Innsbruck: Studia Universitätsverlag Innsbruck.
- Fischer, O., Thoma, S. & Crepez, S. 2019. Distributed fiber optic sensing for crack detection in concrete structures. In *Civil Engineering Design*, 1: 97–105. <https://doi.org/10.1002/cend.201900008>
- König, G., Viet Tue, N., Bauer T. & Pommerening, D. 1996. DAFStb Heft 419 Schadensablauf bei Korrosion der Spannbewehrung. Berlin: Beuth Verlag GmbH.
- Luna, Inc. 2020. Optical Distributed Sensor Interrogator Model ODiSI 6: User's Guide ODiSI 6 Software. <https://lunainc.com/sites/default/files/assets/files/resource-1-brary/ODiSI%206100%20User%20Guide.pdf>
- Luna, Inc. 2014. Distributed Fiber Optic Sensing: Temperature Coefficient for Polyimide Coated Low Bend Loss Fiber, in the 10°C - 80°C Range. https://lunainc.com/sites/default/files/assets/files/resource-library/LT_TD_EN-FY1405_TempCoeff_10to80.pdf
- Röhling, S. & Meichsner, H. 2018. Rissbildungen im Stahlbetonbau. Ursachen - Auswirkungen - Maßnahmen. Stuttgart: Fraunhofer IRB Verlag.

Life-cycle assessment of crack repair systems for fire-damaged concrete

R.M. Galano, R.S. Chan & J.M. Ongpeng
De La Salle University, Manila, Philippines

ABSTRACT: Despite its durability, exposing concrete to excessive changes in temperature causes it to crack. To seal these cracks, repair systems, which can be categorized as active repair and passive self-repairing systems, can be applied. In this study, the potential environmental benefits of passive repair systems were evaluated by comparing traditional mortar filled concrete against two types of self-healing concrete (SHC), namely SHC with *Bacillus subtilis* and SHC with superabsorbent polymers and superplasticizer. Life cycle assessment (LCA) revealed that cement production has the highest contribution across all repair systems, accounting for 62.1% to 81.1% of the overall impact. The polymer based SHC is the most damaging, especially in terms of resource consumption, while the mortar filled concrete has the lowest impact among the three. The bacteria based SHC performs better than mortar filling in categories like terrestrial, marine, and freshwater ecotoxicity. However, active repair is generally better for thicker concrete components.

1 INTRODUCTION

1.1 *Background of the study*

Concrete is one of the most widely used building materials in the world. In fact, the global consumption of concrete is twice as much as the consumption of all other building materials combined (Gagg, 2014). Concrete is used in a wide variety of infrastructure projects such as buildings, bridges, and dams. Its popularity in the construction industry is mainly due to its strength as it is one of the most durable construction materials (Van den Heede et al., 2018). However, concrete has a few limitations. For example, it is susceptible to cracking due to various factors such as tensile forces, shrinkage and creep effects, and temperature (Leonhardt, 1988). Consequently, concrete is a poor conductor of heat. When it is exposed to high temperatures like during a fire, its properties deteriorate (Georgali & Tsakiridis, 2005). Some significant examples are the decrease in compressive strength, spalling and cracking of concrete, the progressive deterioration of the hardened cement paste, and the destruction of the bond between the cement and the aggregates.

1.2 *Significance of the study*

Fire incidence in the Philippines is relatively high, especially during the dry season. These incidents are continuously rising with the first few months of 2022 already experiencing a 13% increase (Caliwan, 2022). Managing the damage caused by fires to concrete is a must as most structures in the country are made from reinforced concrete. In particular, cracks in the concrete must be sealed to hinder structural issues like the accelerated corrosion of embedded steel reinforcement. Hence, it is necessary to compare concrete crack repair systems. However, one area that is often overlooked when comparing these repair systems is their environmental impact.

2 MATERIALS AND METHODS

2.1 Crack repair systems

Table 1 shows the composition and mix design of three concrete repair systems. The conventional method of using mortar filler is compared to two types of SHC. The bacteria based SHC contains *Bacillus subtilis* (*B. subtilis*) with calcium chloride serving as the nutrient source. This spore-forming bacteria induces calcite precipitation which can seal cracks and pores up to 0.5 mm in width (Nikhil et al., 2020). The bacteria is obtained by cultivating cells in an agar culture plate containing distilled water, sodium chloride, yeast, glucose, and peptone from fish protein. On the other hand, the polymer based concrete incorporates superplasticizer and superabsorbent polymers (SAP) at 2.2% and 1.0% of cement by weight respectively. The expansion of SAP when exposed to moisture allows this SHC to seal cracks up to 0.2824 mm in width (Sidiq et al., 2020).

Table 1. Description of concrete crack repair systems.

Repair System	Sealable Crack Width (mm)	Item	Quantity (kg/cum.)	Reference
Concrete w/ Mortar Filler	-	Concrete		Maneeth et al. (2018)
		Cement	426	
		Sand	665	
		Aggregates	1131	
		Water	192	
		Mortar		
Self-Healing Concrete w/ <i>B. subtilis</i>	0.50	Concrete		Ashwin et al. (2019)
		Cement	437.77	
		Sand	778	
		Aggregates	947.79	
		Water	197	
		Bacteria Culture		Ramagiri et al. (2021)
		Peptone	15x10 ⁻³	
		Water	1.0	
		Sodium Chloride	6x10 ⁻³	
		Yeast	3x10 ⁻³	
		Glucose	1x10 ⁻³	
		Calcium Chloride	45x10 ⁻³	
Self-Healing Concrete w/ SAP & Superplasticizer	0.2824	Concrete		Sidiq et al. (2020)
		Cement	415	
		Sand	757	
		Aggregates (7mm)	1004	
		Water	224	
		SAP		Heede et al. (2018)
		Acrylic Acid	3.24	
		Sodium Hydroxide	1.94	
		Ammonium Persulfate	0.02	
		Water	7.26	
Superplasticizer	9.12			

2.2 Life cycle assessment

The objectives of this study are to (1) compare the environmental impacts of three concrete crack repair systems, namely (a) SHC with *B. subtilis*, (b) SHC with SAP and superplasticizer, and (c) ordinary Portland cement (OPC) concrete with mortar filler; (2) assess the suitability of using

SHC for the slabs and walls of a classroom in terms of carbon dioxide emission. To achieve these, the slabs and walls of a classroom in De La Salle University – Manila were used as the functional unit. A case study was conducted in order to quantify the amount of concrete and mortar filler required to construct and repair the damaged classroom. The columns and beams were not considered because the exposed surface is small relative to their volume; hence, the benefits of SHC are less significant. The cradle-to-gate system boundary was applied which covers raw material extraction and production of each type of concrete.

2.3 Structure of microcracks

Cracks can propagate in varying ways depending on the forces applied to the concrete. To conduct LCA on a theoretically damaged classroom, the study of Georgali and Tsakirdis (2005) on the microstructure of fire-damaged concrete was used. By analyzing concrete specimens from an actual fire-damaged building, the researchers showed how crack density varies with depth. The datapoints from this study can then be used to create a function

$$\rho = 34.207x^{-0.1581} \tag{1}$$

where ρ = crack density in meters per square meter; and x = depth of crack in meters
 However, information regarding the crack width and how it varies with depth was lacking. Since cracks typically taper with depth, this study assumes that the crack contracts linearly thereby forming a V shape (Figure 1). Hence, the relationship between crack width and depth is attained

$$w = w_0 - \frac{w_0}{x_0}x \tag{2}$$

where w = crack width; w_0 = crack width at concrete surface; x = depth of crack; and x_0 = total depth of crack. In this study, two values were used for the crack width at surface (w_0), namely 0.2824 mm and 0.50 mm corresponding to the maximum sealable crack widths of the polymer based and bacteria based SHC respectively. Normal strength concrete heated at 600°C, the typical temperature during real case fires, tends to develop cracks ranging from 0.28 mm to 0.94 mm in width (Poon et al., 2001). Therefore, the chosen SHC are capable of repairing some fire-damaged concrete. On the other hand, a total depth (x_0) of 49.6 mm was used as Xu et al. (2020) has found that the damage zone of microcracks in SHC reaches this depth.

In line with these assumptions, the total volume of cracks can be obtained by integrating the product of crack width and crack density with respect to depth.

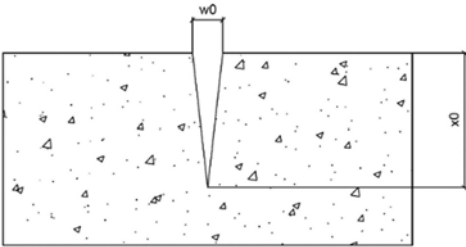


Figure 1. Cross section of crack.

$$dV = w \rho dx \tag{3}$$

By substituting Equations 1 and 2 to make width and density a function of depth, the equation for volume can be obtained

$$V = 40.631 w_0 x^{0.8419} - 18.572 \frac{w_0}{x_0} x^{1.8419} \quad (4)$$

where V = volume in cubic meters per square meter. When depth (x) is equated to total depth (x₀), the resulting volume represents the volume of mortar required to seal 1 sqm. of damaged concrete.

2.4 Methodology

A 53.14 sqm. (5.4 m x 9.8 m) classroom served as the theoretically fire-damaged classroom. The wall thickness was kept constant at 100mm as these are non-load bearing. However, slab thicknesses of 100 mm, 125 mm and 150 mm were used as this can change based on design loads. This was done to establish the thickness of the slab at which SHC would be more sustainable than regular concrete. Overall, LCA was conducted on six cases corresponding to two crack widths and three slab thicknesses. The volume of concrete needed to construct the classroom varies between 19.138 m³, 21.795 m³, and 24.452 m³ while the mass of mortar needed to fill the cracks varies between 191.504 kg and 339.065 kg. The latter was calculated using Equation 4 and based on a dry density of 2014 kg/m³ (Thamboo, Bandara & Jayarathne, 2018).

3 RESULTS AND DISCUSSION

3.1 Impact assessment

The process networks of the three concrete crack repair systems are shown in Figures 2 to 4. It was found from the three networks that concrete, specifically cement, mainly contributes to the overall environmental impact of each of the crack repair systems. The production of cement accounts for 79.3%, 62.1% and 81.1% of the overall impact of the regular concrete, bacteria based SHC, and polymer based SHC respectively. On the other hand, the contributions of mortar filler and *B. subtilis* individually account for only less than 1% of the impact of their respective product systems. Relatively higher contribution of both SAP and superplasticizer was observed as these two individually account for 9.87% and 12.4%, respectively. Hence, if the impact of the concrete crack repair systems is to be reduced, the proportion of the cement should be reduced. Although the process networks shown only represent case 1, similar results were obtained for other cases since only the volume of concrete changes with varying slab thickness and not the composition of the product itself. Nonetheless, the contribution of mortar filler varied slightly based on the crack width used.

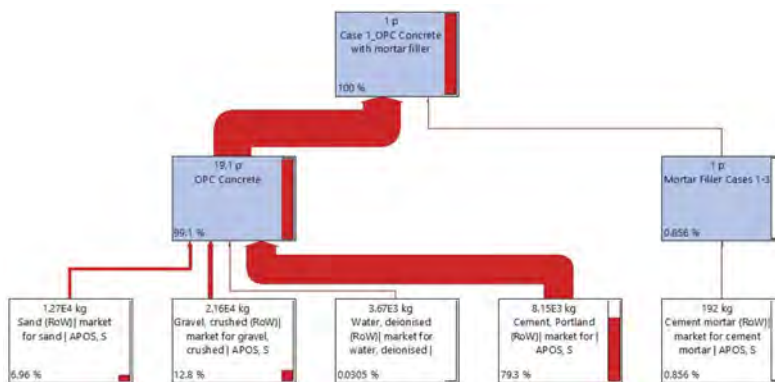


Figure 2. Process network for concrete with mortar filler.

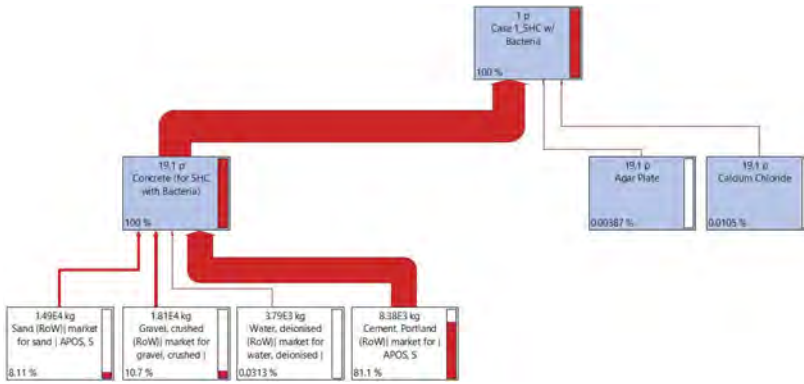


Figure 3. Process network for SHC with *B. subtilis*.

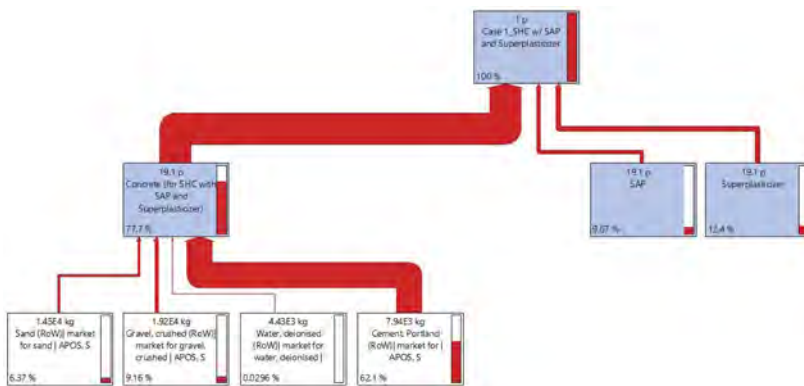


Figure 4. Process network for SHC with SAP and superplasticizer.

Figure 5 shows the damage assessment of cases 1 to 3 in terms of human health, ecosystem, and resources. The impact of the mortar filled concrete and SHC with *B. subtilis* are almost equal in case 1. However, the difference between the two increases with slab thickness due to the constant amount of mortar filler needed in contrast to the increasing amount of bacteria additive needed with increasing slab thickness. Moreover, the SHC with SAP and superplasticizer is consistently the most damaging out of the three. Despite this, the difference between the percent damage of the polymer based concrete and the other two systems do not exceed 5% in terms of human health and ecosystems damage. For damage to resources however, the difference was around 20%. Hence, the addition of SAP and superplasticizer causes a significant increase in damage to resources. Specifically, the polymer based SHC performed worse in terms of fossil resource scarcity and water use. The latter can be attributed to the need for more water in concrete with SAP due to the tendency of SAP to absorb water from the concrete mix which reduces its workability (Poornima et al., 2020). Overall, mortar filling was found to consistently cause the least damage to human health, ecosystems, and resources considering all slab thicknesses.

The same damage assessment was conducted for cases 4 to 6 as shown in Figure 6. Considering human health and ecosystems categories, the mortar filled concrete was found to cause less damage than the bacteria based concrete. Although the difference is only less than 1% in most cases, this difference increases minimally with the slab thickness. When the resources category is analyzed however, the bacteria-based concrete initially causes less damage than the mortar filled concrete. As slab thickness increases however, the two values converge. This implies that regular concrete is less impactful when thick slabs are to be constructed. Overall, the conventional method of mortar filling is generally more sustainable than the bacteria-

based concrete even though the crack width is increased to 0.500mm. Nonetheless, the findings from Figures 5 and 6 have shown that SHC can be more sustainable than mortar filled concrete if SHC capable of sealing larger cracks is used.

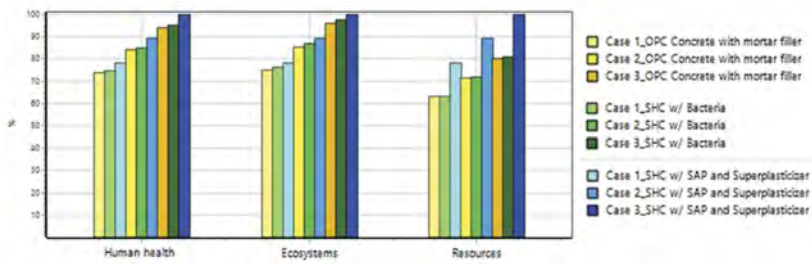


Figure 5. Damage assessment of crack repair systems with 0.2824 mm crack width.

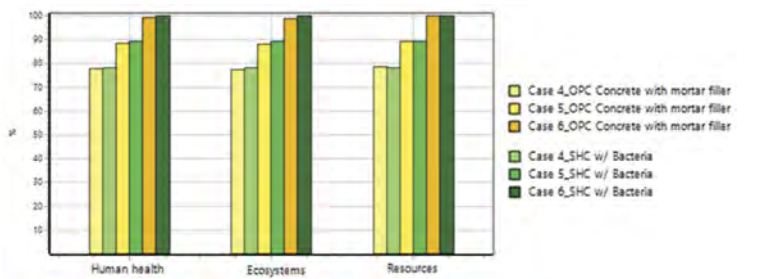


Figure 6. Damage assessment of crack repair systems with 0.50 mm crack width.

3.2 Carbon dioxide emissions

Cement production accounts for roughly 7% of the world’s GHG emission (Busch et al., 2022). As such, reducing the carbon dioxide emission of concrete production is a relevant problem in the construction industry. In this study, airborne emissions of carbon dioxide from land transformation and biogenic sources were analyzed and are shown in Table 2. The carbon dioxide emission of each repair system were then plotted against the slab thickness in Figures 7 and 8. Based on the three datapoints originating from the three slab thicknesses used, linear regression was applied to show the trend and to identify the range of slab thickness where each type of repair systems performs best. SHC with SAP and superplasticizer, SHC with *B. subtilis*, and mortar filled concrete were represented by the blue, green, and orange trendline respectively.

Table 2. The carbon dioxide emissions of concrete crack repair systems.

Crack Repair System	CO ₂ (kg)					
	1	2	3	4	5	6
OPC Concrete with Mortar Filler	134.43	153.18	170.82	136.46	155.21	172.96
SHC with <i>B. subtilis</i>	134.49	153.25	172.02	134.49	153.25	172.02
SHC with SAP and Superplasticizer	147.74	167.53	188.33	-	-	-

Figure 7 shows the trend given a crack width of 0.2824 mm. The blue trendline reveals that SHC with SAP and superplasticizer has the highest carbon dioxide emission. Given that both the slope and intercept of SHC with SAP and superplasticizer are higher than the conventional mortar filled concrete, it can be concluded that the latter will always emit less carbon dioxide regardless of slab thickness. This is further supported by the fact that the highest sealable crack width for the polymer based SHC was already considered. As for SHC with *B. subtilis*, it was

found that the green and orange trendline intersect at a slab thickness of 105.57 mm. Given the larger slope of the green trendline, the figure shows that SHC with *B. subtilis* emits less carbon dioxide for slab thicknesses below 105.57 mm while mortar filled concrete is more ideal for higher slab thicknesses. Nonetheless, a thickness less than 100 mm would be a better estimate since Table 2 has shown that the OPC concrete with mortar filler still emits slightly less carbon dioxide at 100 mm (case 1). This inconsistency is caused by residuals in the trendline.

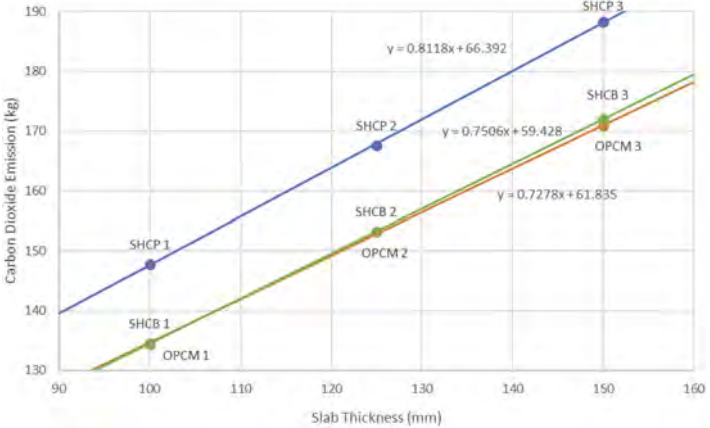


Figure 7. Carbon dioxide emission versus slab thickness with 0.2824 mm crack width.

Figure 8 shows the trend given a crack width of 0.50 mm. In this figure, only SHC with *B. subtilis* and OPC concrete with mortar filler were compared as the crack width is beyond the capability of the polymer based SHC. It can be seen that SHC with *B. subtilis* now emits less carbon dioxide within the considered range of slab thickness. This is due to the fact that a larger crack volume is used which necessitates a higher amount of mortar filler. Equating the orange and green trendlines shows that they intersect at a slab thickness of 203.83 mm. Therefore, it can be concluded that mortar filled concrete always emits less carbon dioxide if the slab thickness is above 203.83 mm given that the maximum sealable crack width of the bacteria based SHC was already considered. On the other hand, SHC with *B. subtilis* is preferred for slab thicknesses below 203.83 mm; however, this is a conservative estimate and would decrease depending on the considered crack width which must be less than or equal to its maximum sealable width of 0.50 mm.

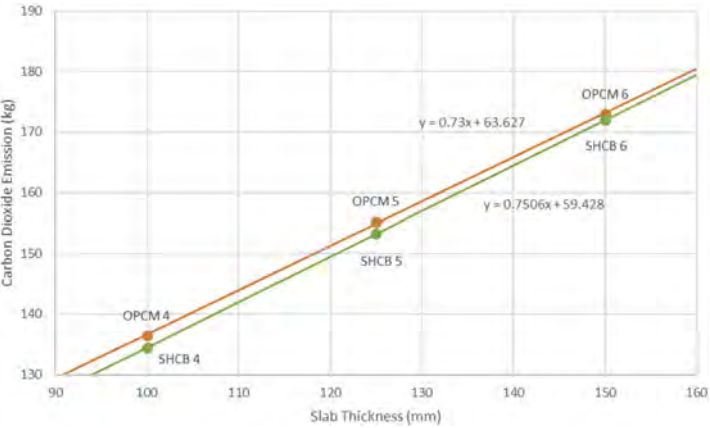


Figure 8. Carbon dioxide emission versus slab thickness at 0.50 mm crack width.

Moreover, the aforementioned slab thicknesses where bacteria based SHC outperforms conventional mortar filled concrete would vary based on the sealable width of the concrete mix used.

4 CONCLUSIONS

The results have shown that for all crack repair systems, cement has the highest environmental impact among the inventory inputs. Moreover, the damage assessment yielded consistent results wherein the mortar filled concrete was the least damaging across almost all impact categories regardless of slab thickness and crack width. In terms of carbon dioxide emissions however, mortar filled concrete is less sustainable than SHC with *B. subtilis* when a slab thinner than 203.83 mm is to be constructed. In contrast, there is no clear environmental benefit of using the polymer based SHC as the SAP and superplasticizer contribute greatly to the environmental impact and the sealable crack width is too small to justify the use of additives instead of mortar filler.

REFERENCES

- Ashwji, L., Nikhil, T., Shanthappa, B., Prakash, M. & Gopinath, S. 2019. A study on strength, workability and fire resistance properties of bacteria induced concrete. *International Journal of Civil Engineering*, 6 (9): 12–15.
- Ashwin, H., Abhirami, V., Anzil, A., Jerry, J. & Joseph, A. 2019. Mechanical and durability characteristics of bacterial concrete. *Proceedings of National Conference on Structural Engineering and Construction Management 2019*: 819–829
- Busch, P., Kendall, A., Murphy, C. & Miller, S. 2022. Literature review on policies to mitigate GHG emissions for cement and concrete. *Resources, Conservation & Recycling*. 182
- Caliwan, C. L. 2022. *Fire incidents up by almost 13% in first 2 months of 2022*. Philippine News Agency.
- Gagg, C. R. 2014. Cement and concrete as an engineering material: An historic appraisal and case study analysis. *Engineering Failure Analysis*, 40: 114–140.
- Georgali, B., & Tsakiridis, P. E. 2005. Microstructure of fire-damaged concrete. A case study. *Cement and Concrete Composites*, 27(2): 255–259.
- Heede, P., Mignon, A., Habert, G. & Belie, N. 2018. Cradle-to-gate life cycle assessment of self-healing engineered cementitious composite with in-house developed (semi-)synthetic superabsorbent polymers. *Cement and Concrete Composites*, 94: 166–180.
- Leonhardt, F. 1988. Cracks and crack control in concrete structures. *PCI Journal*, 33(4): 124–145.
- Maneeth, P., Brijbhushan, S. & Siddharth, B. 2018. Optimum usage of hybrid fibers and their impact on few mechanical properties on M30 grade of concrete. *National Conference on Smart and Sustainable Construction*. Karnataka, India.
- Nikhil, T. R., Shanthappa, B. C., Gopinath, S. M., Chaithra, D. & Prakash, M. R. 2020. A review paper on fire resistance properties of bacteria induced concrete. *International Journal of Innovative Science and Research Technology*. 5(4): 750–756.
- Poon, C., Azhar, S., Anson, M. & Wong, Y. 2001. Strength and durability recovery of fire-damaged concrete after post-fire-curing. *Cement and Concrete Research*, 31: 1307–1318.
- Poornima, V., Venkatasubramani, R., Sreevidya, V., Vignesh, V. & Adithan, K. 2020. Study on SAP with different absorption capacities and its effects on Self Curing HPC.
- Ramagiri, K., Chintha, R., Bandlamudi, R., Maeijer, P. & Kar, A. 2021. Cradle-to-Gate Life Cycle and Economic Assessment of Sustainable Concrete Mixes—Alkali-Activated Concrete (AAC) and Bacterial Concrete (BC). *Infrastructures*, 6(104).
- Sidiq, A., Gravina, R., Setunge, S. & Giustozzi, F. 2020. The effectiveness of Super Absorbent polymers and superplasticizer in self-healing of cementitious materials. *Construction and Building Materials*.
- Thamboo, J., Bandara, A. & Jayarathne, R. 2018. Fresh and hardened properties of various cement and cement-lime masonry mortars. *10th International Masonry Conference*. Milan, Italy.
- Van den Heede, P., Mignon, A., Habert, G., & De Belie, N. 2018. Cradle-to-gate life cycle assessment of self-healing engineered cementitious composite with in-house developed (semi-)synthetic superabsorbent polymers. *Cement and Concrete Composites*, 94: 166–180.
- Xu, J., Peng, C., Wan, L., Wu, Q. & She, W. 2020. Effect of Crack Self-Healing on Concrete Diffusivity: Mesoscale Dynamics Simulation Study. *Journal of Materials in Civil Engineering*, 32(6).

Rehabilitation of underground garages – defining a cost function for use in the decision-making process

J.M. Lozano Valcarcel, C. Gehlen & T. Kränkel

Technical University of Munich, TUM School of Engineering and Design, Department of Materials Engineering, Chair of Materials Science and Testing; Centre for Building Materials, Munich, Germany

A. Schiessl-Pecka

Engineering Consultancy Schiessl Gehlen Sodeikat GmbH, Munich, Germany

J.D. Cassiani & S. Kessler

Helmut-Schmidt-University/ University of the Federal Armed Forces Hamburg, Chair of Engineering Materials and Building Preservation, Hamburg, Germany

ABSTRACT: Performance-based design concepts are a key tool to ensure the durability of reinforced concrete structures. Their application relies on the definition of limit states, for which defined limit state functions represent the probability of exceeding a particular condition. Such limit state functions are available for depassivation (initiation of reinforcement corrosion) in case of concrete carbonation and/or chloride-induced corrosion. Moreover, not only the knowledge about the exceedance of a certain limit state is of interest, but also the related consequences such as the costs for the subsequent repairs. This contribution analyses the inspection reports and the tendering documents of well-documented rehabilitations of parking garages. The focus was set on chloride-induced corrosion since it is the main cause of the rehabilitations. The analysis focused on the following aspects: the estimation of the reliability index value that led to the rehabilitation, the rehabilitation method used, and finally an indicative estimation of the incurred costs. The results unveil that for both conventional and cathodic protection rehabilitations, the reliability index had similar ranges for columns. Furthermore, in one meticulous project, a clear relationship between the estimated reliability index and the incurred costs was observed. However, this finding was less evident in other projects, for which a step cost function was more suitable.

1 INTRODUCTION

1.1 Background

Recently, great focus has been set on developing performance-based design concepts for durability assessment of concrete structures. For example, engineering models for the initiation phase have been developed for carbonation and chloride-induced corrosion (DURACRETE 2000, Gehlen 2000). Three basic principles constitute the base of these concepts: the use of validated material laws (or models); the adequate quantification of both the material resistance and the acting environmental loads or stresses; and finally, a safety concept on a probabilistic basis. This safety concept sets a maximum allowed probability of occurrence of a selected, undesired limit state.

In Germany, the German Committee for Reinforced Concrete (DAfStb) provided in (DAfStb 2008, Gehlen *et al.* 2008) the concepts for the application of this performance-based approach. Here, models for both, carbonation and chloride exposure classes (XC and XS/XD respectively), are given for the initiation phase, i.e., depassivation of the steel reinforcement.

Depending on the exposure class, a maximum allowed probability of reaching the depassivation of the reinforcement is suggested at either 10 or 30%, or in terms of the reliability index $\beta = 1.5$ or $\beta = 0.5$, respectively (DAfStb 2008). These values were set initially based on common targets for

serviceability limit states based on qualitative considerations of economic aspects. Similar to a cost-benefit analysis, the risk associated with the exceedance of these values during the structure service life and the costs of minimizing the risk during the design and construction phase were considered (DAfStb 2008). The present work focuses on the quantification of the risk associated with the exceedance of these limit values. In other words, the costs of the structural rehabilitation that result from the exceedance of the defined limit values.

1.2 Motivation and scope

Recent studies have shown, that in certain cases with a high chloride exposure (e.g. XD3) and an unfavorable material selection (low chloride penetration resistance), structures may not reach the targeted 50 years of service life, even if they have been built in accordance with the standards (fib Bulletin 76 2015). Cases observed in praxis provide evidence supporting this statement (Kessler 2020, Kessler & Gehlen 2020, Lozano Valcarcel *et al.* 2022), thus highlighting the advantage of the use of performance-based approaches for assessing the durability of reinforced concrete structures. By applying this approach, not only the need for (unexpected) premature and costly repairs can be avoided, but also the total costs for the construction and operation of a structure may be optimized. This may also lead to a more efficient and sustainable use of construction materials.

Motivated by this, this contribution analyses a set of rehabilitations of underground garage structures carried out in southern Germany. (Lozano Valcarcel *et al.* 2022) provides a first attempt at estimating the reliability index at which these structures had been rehabilitated. Therein, the difficulties of comparing the resulting costs on a global (building) level for this kind of structure have been discussed. In the present work, the focus is set on the analysis at the structural element level for the repair of column bases (exposure class XD3) for six selected projects. The aim is to study both the values of the reliability index that lead to corrective actions (rehabilitation alternatives) and the resulting incurred costs.

2 METHODOLOGY

Figure 1 shows the general framework of the present work. The inspection reports were analyzed for acquiring relevant information necessary to estimate the reliability index at the time of inspection i.e., just before the rehabilitation. The tender documents were analyzed for information regarding the type of intervention (action taken) and the resulting costs. The objective is to generate pairs consisting of reliability indices and resulting costs to study the relationship between them. The hypothesis was that the resulting costs increase with decreasing reliability index. The analysis focuses on the (structural) element level for column bases (further referred to only as “columns”).

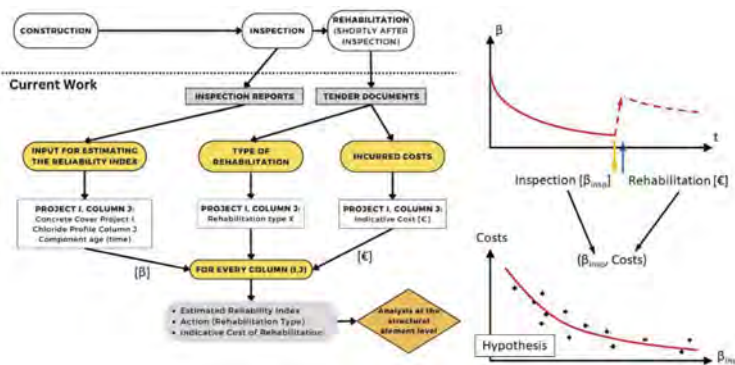


Figure 1. General framework of the present work (left) and initial hypothesis (right).

2.1 Selected model and available information

A modified version of the Duracrete Model based on Fick’s second law of diffusion (DURACRETE 2000, Gehlen 2000) is used to calculate the reliability index. Here, the limit state

function for depassivation is evaluated employing a critical chloride content at the level of the steel reinforcement, as shown in Equation 1:

$$LSE = C_{crit} - C_{S,\Delta x} \cdot \left[\operatorname{erfc} \left(\frac{d_c - \Delta x}{2 \cdot \sqrt{D_{app}(t) \cdot t}} \right) \right] \quad (1)$$

Where C_{crit} = critical, chloride content required to initiate corrosion (depassivation); $C_{S,\Delta x}$ = the substitute surface chloride content; $\operatorname{erfc}()$ = complementary error function; d_c = concrete cover; Δx = depth of the convection zone; $D_{app}(t)$ = apparent chloride diffusion coefficient of concrete (as a function of time); t = time of exposure (Gehlen 2000, fib Bulletin 76 2015).

The inspection reports constituted the information base to quantify the relevant model parameters. A consulting company based in Munich, Germany carried out the inspections. The inspected garages were rehabilitated shortly after the inspections. The reports include normally a visual inspection at points of interest, i.e., corrosion hotspots, the sampling of depth-staggered drill-dust samples, and the determination of the concrete cover, among others. From these measurements, the chloride profiles and the measurements of the concrete cover are highly relevant. Additional information about the type of binder and other parameters regarding the concrete mix was unfortunately not available, since usually, the project owners do not document this kind of information. Therefore, the information available was insufficient to estimate the reliability index following methods found in the literature (Gehlen 2000, Kapteina 2011, Rahimi 2016).

For this reason, the unknown model variables (the substitute surface chloride content and apparent chloride diffusion coefficient) had to be quantified. To achieve this, a Metropolis-Hastings (MET-HAS) algorithm was implemented to estimate these variables using the reported chloride profiles. Since the initial chloride content of the concrete elements was unknown, it was assumed as zero based on (fib Bulletin 76 2015). Values for the other variables were taken from the literature or the reported measurements, as in the case of the concrete cover.

2.2 Estimation of the unknown model variables

Due to limitations in the available information, the distributions of the substitute surface chloride content and the apparent diffusion coefficient (main unknown variables) were estimated using a MET-HAS algorithm. The algorithm was first proposed by (Hastings 1970) based on (Metropolis *et al.* 1953). A detailed description can be found in (Robert & Casella 1999). The reported chloride profiles constituted the base for the analysis. Each of the profiles included usually three points in depths from 0-10, 10-30, and 30-50 mm, which is common practice in Germany. The point near the surface is usually not used for mathematical regressions since it is located in the so-called convection zone, and thus, its behavior deviates from Fick's second law of diffusion (Gehlen 2000). Therefore, only two points were left to estimate the two selected variables for each of the analyzed columns. To overcome this limitation, the algorithm implementation required additional assumptions. The subtrahend of Equation 1 is used as the regression equation, since it describes the diffusion process of chloride into the concrete, as shown in Equation 2:

$$C(x, t) = C_{S,\Delta x} \cdot \left[\operatorname{erfc} \left(\frac{x - \Delta x}{2 \cdot \sqrt{D_{app} \cdot t}} \right) \right] \quad (2)$$

Where $C(x, t)$ = chloride content at depth x and time t ; x = depth measured from the concrete surface; D_{app} = apparent chloride diffusion coefficient of concrete (at the time of the inspection); all other variables as described in Equation 1.

Based on Equation 2, the MET-HAS algorithm was used to estimate the distributions of $C_{S,\Delta x}$ and D_{app} which best fit the observed data. Since the analysis focuses on the structural element level, each column is analyzed individually. For the implementation, a 2-dimension joint normal distribution was used as the proposal distribution for $C_{S,\Delta x}$ and D_{app} . The variance of the proposal distribution was set as a diagonal matrix and calculated in every step of the Markov-Chain using a fixed coefficient of variation. The selected likelihood function

bases on the sum of the squares error (Smith 2014), assuming that the error residuals are homoscedastic and follow a zero-centered normal distribution. Equation 3 shows the used likelihood function (Smith 2014):

$$L(C_{S,\Delta x}, D_{app}|X, \sigma) = \frac{1}{(2 \cdot \pi \cdot \sigma^2)^{n/2}} e^{-\frac{SSE}{2 \cdot \sigma^2}} \quad (3)$$

Where σ = standard deviation of the Gaussian error; n = number of observations (chloride analysis) per chloride profile; SSE = Sum of Square Error, calculated by Equation 4:

$$SSE = \sum_{i=1}^n [C(x, t|C_{S,\Delta x}, D_{app}) - C_{meas}(x, t)]^2 \quad (4)$$

With n = number of observations (chloride analysis) per chloride profile; $C(x, t|C_{S,\Delta x}, D_{app})$ = calculated chloride content with the current Markov Chain values for $C_{S,\Delta x}$ and D_{app} ; $C_{meas}(x, t)$ = measured chloride content reported in the inspection reports.

Because most profiles had only two viable points for the regression (likelihood based on the sum of least squares), the standard deviation of the Gaussian error could not be properly quantified and, therefore, had to be assumed. The assumption was based on the fit of a profile with four viable points and was set constant for the analysis of all the chloride profiles. The authors are aware that this assumption may not hold valid in all cases but consider that the approach is sufficient for the analysis in the present work. Finally, the posterior distribution for the unknown model variables $C_{S,\Delta x}$ and D_{app} is estimated for each of the analyzed profiles. The left side of Figure 2 shows the estimated posterior distribution of the target variables for the profile with four viable points for regression. The right side of Figure 2 shows the estimated 95% credible interval (ETI: Equally Tailed Interval) of the chloride content for this same profile.

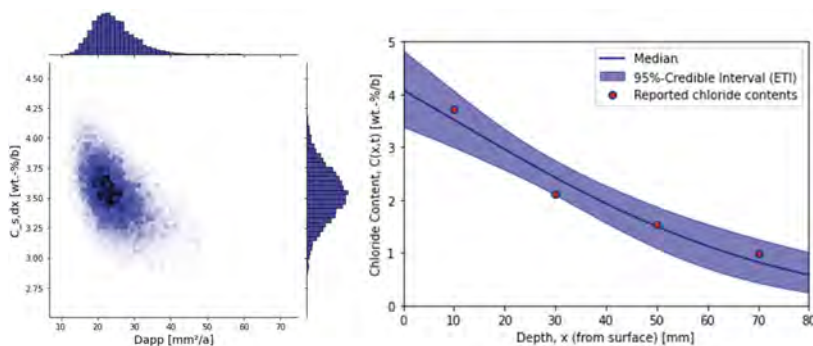


Figure 2. Estimated posterior distribution of the target model variables (left) and resulting 95%-Credible interval of the chloride content as function of the depth from the surface (right).

2.3 Calculation of the reliability index

After the estimation of the two main unknown model variables, the next step is the estimation of the reliability index. To do so, the limit state equation for depassivation (Eq. 1) is evaluated using Monte Carlo Simulations sampling from the posterior space generated with the MET-HAS algorithm. For the other model variables, literature reference values are used. Table 1 shows the variables and their corresponding distributions used to estimate the reliability index for each column.

The reliability index is calculated for each of the columns individually. For a limited number of columns, several chloride profiles were available. Since the chloride exposure varied significantly, only the most critical chloride profile (with the highest chloride content at the reinforcement) was considered. The quantification of the concrete cover (d_c) was not possible at the element level, since in most cases the information was not documented element-wise. Therefore, the parameters of the distribution for the concrete cover of the columns of each project (garage) had to be

calculated globally. It was assumed, that the concrete cover followed the same distribution for all columns of the same project. This assumption may not necessarily hold valid in all cases.

Table 1. Model variables used for calculating the reliability index.

Variable	Unit	Distribution	Parameters				Reference
			Mean	Std. Dev.	a*	b*	
C_{crit}	[wt.-%/b]	Beta	0.60	0.15	0.20	2.0	(Gehlen 2000)
$C_{S,\Delta x}$	[wt.-%/b]	Sampled from MET-HAS space					
d_c	[mm]	Normal	**	**	0	-	(Gehlen 2000)
Δx	[mm]	Deterministic	10				(Rahimi 2016)
D_{app}	[mm ² /a]	Sampled from MET-HAS space					

*a and b are the lower and higher limits (constraints)

**Parameters estimated for each parking garage based on the reported concrete cover measurements

2.4 Rehabilitation alternatives

The following actions or rehabilitation alternatives were found in the tendering documents:

- Conventional: the chloride-contaminated concrete is partially demolished and recast with a repair material. Method 7.2 in (*DIN EN 1504-9:2008-11*, DIBt 2020).
- Cathodic Protection: a cathodic protection system is usually installed without the need of invasive concrete demolitions. This method is referred to as method 10, i. e., 10.1 in (*DIN EN 1504-9:2008-11*, DIBt 2020).
- No (substantial) Intervention: refers to the columns, which were neither repaired using the other two methods. Here, only a surface protection system or coating was applied. Since a similar coating was also applied to columns repaired under the other categories, this method can be seen not as a corrective measure, but rather as a protective measure. Therefore, one could consider this alternative as the zero-alternative: no intervention.

3 RESULTS AND DISCUSSION

3.1 Actions taken at different levels of reliability

Figure 3 shows the estimated reliability indices and the actions taken for the 89 analyzed columns from six different projects. From these, 44 columns were repaired using the conventional method; 29 were repaired using a cathodic protection system; and 16 did not undergo any substantial intervention. The following aspects of Figure 3 are analyzed: the ranges for the “no intervention” category, and the ranges of the conventional and cathodic protection.

To begin with, Figure 3 reveals that columns without rehabilitation (no substantial intervention) presented high values of the reliability index (> 1.5), agreeing with the values recommended by (DAfStb 2008). Nonetheless, a few columns rehabilitated with the other two methods fall also into this range of reliability index. In the case of cathodic protection, an explanation for this can be that cathodic protection systems are usually installed on all the elements of the garage. Hence, it acts not only as a corrective measure for columns with high chloride concentrations but also as a preventive measure for those with little or no exposure so far. On the other hand, marginal repairs could explain the high value of the reliability index on some conventional interventions. Marginal repairs refer to the intervention of a non-critical (or not-so-critical) column, due to the low individual costs in comparison to the total costs. Another explanation is the avoidance of potential future damage in the element, thus avoiding another intervention of the facility and all related consequences (additional costs, partial closure, etc.).

Cathodic protection systems are usually carried out when no substantial damage, like high loss of reinforcement cross section, cracking, or spalling of the concrete cover is present. Conventional rehabilitations can be carried out when substantial damage is present or not. In the case of chloride-induced corrosion, the damage phase takes place rather quickly after the reinforcement is depassivated (fib Bulletin 76 2015). Therefore, it can be expected that the estimated reliabilities for

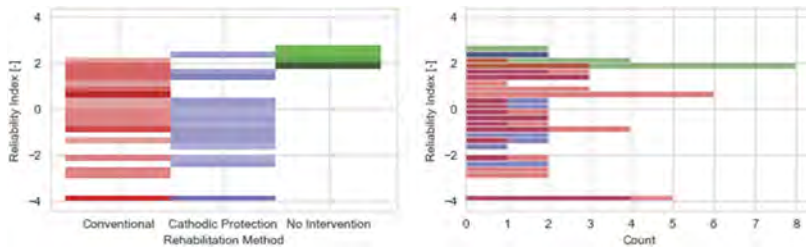


Figure 3. Histograms of the estimated reliability index by rehabilitation method executed for the analyzed repaired columns.

cathodic protection are higher than for conventional interventions. However, no significant difference in the ranges of the estimated reliabilities for cathodic protection and the conventional intervention was found (see Figure 3). This suggests that depassivation as a limit state may not be a proper criterion to define ranges, for which these two alternatives should be executed within the decision-making process. Other limit states in the damage phase (cracking or spalling) may be more suitable for defining target values of the reliability index for these two repair alternatives.

3.2 Cost function in terms of the reliability index

In underground garage rehabilitations, several elements are usually addressed simultaneously. For instance, some columns may need to be repaired due to chloride-induced corrosion, but also other elements like wall segments, the drive-in ramp, and areas near joints or even slabs. The need for repair is very individual for each garage and depends on how it was built, its current condition state and user frequency. Moreover, the rehabilitation works may be used simultaneously for refurbishment or upgrading purposes. Therefore, identifying the relevant cost positions is subject to certain difficulties. Some cost positions are very specific for a certain element, like the depth of the intervention, but others like the site equipment or logistic positions are not. For this reason, the focus is set on two main cost-driving positions that are usually well documented in the analyzed projects: concrete demolition and retrofitting. Both of these positions depend naturally on the depth of the intervention and can be expressed in terms of the intervened area (unit prices).

For one very detailed project rehabilitated with conventional methods, enough information was available to quantify the unit cost of the repair in terms of these two cost positions: demolition of the contaminated concrete and retrofitting of the structural elements. Other cost positions were unfortunately not so well documented and could not be allocated element-wise. Therefore, the reported costs for these two activities were used to build a function in terms of the repaired depth.

In five out of the six analyzed projects, columns were repaired using the conventional rehabilitation method. Figure 4 shows the costs of the concrete (partial) demolition and concrete retrofitting in terms of the repaired depth for one well-documented project. In Figure 4, the y-axis is left without values on purpose due to the approximations taken, which allow only for a qualitative analysis. Figure 4 shows that with increasing depth of the repair, the costs for demolition and retrofitting increase.

Figure 5 presents the calculated reliability indices together with the corresponding indicative costs. The left side of Figure 5 shows the indicative costs of the repair against the estimated reliability index for project C. In this particular case, a clear relationship between the repair costs and the estimated reliability index is found. The lower the reliability index values are, the higher the cost of the repair is. In project C, the depth of the intervention was determined for each of the columns individually and therefore detailed information about the inspection was available at the structural element level. Nonetheless, to achieve this level of detail, expensive inspections are required, such as numerous chloride content analyses and individual concrete cover measurements. The right side of Figure 5 shows a different case. Here, the relationship between the costs and the reliability index for the other four projects takes the shape of a step function: after a certain threshold is surpassed, the decision to repair a column is taken. However, the depth of the repair is left equal, or quite similar, for all repaired columns within a project and thus the unit costs are the same (or similar). This is often the case in column rehabilitations in parking garages.

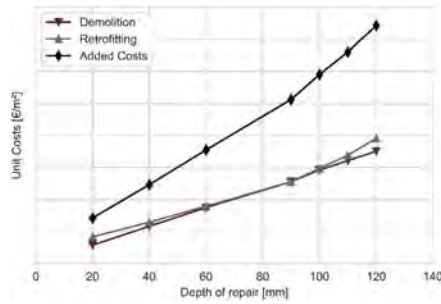


Figure 4. Indicative cost function for demolition and retrofitting of concrete in terms of the repaired depth.

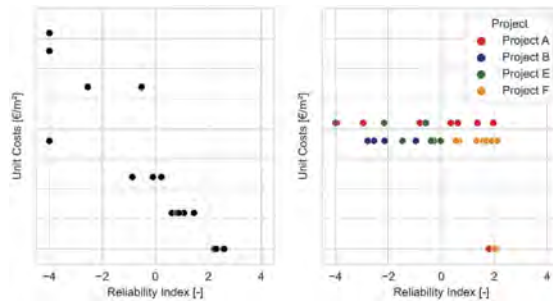


Figure 5. Indicative costs in terms of the estimated reliability index (left: Project C, right: all other Projects).

4 CONCLUSIONS

The inspection reports commissioned for the condition assessment and planning of the subsequent rehabilitation of underground garage structures were analyzed. Based on the available information, the reliability index with depassivation as the limit state was estimated for each of the columns of the garages at the time of inspection (shortly before the rehabilitation). The estimated values of the reliability index were analyzed given the type of repair executed. No significant differences were found in the ranges of the reliability index value for which conventional rehabilitations and the installation of cathodic protection systems were carried out. This result suggests that selecting depassivation as the limit state may not be adequate to define target values for the reliability index in which one of these alternatives should be carried out or not. Nonetheless, a threshold that leads to the decision of “repair” (conventional and cathodic protection) or “not repair” (no substantial intervention) was found to be more evident (around 1.5). Nonetheless, the authors consider that the results of the present work should be considered qualitatively for the time being since only a limited number of projects were analyzed and the reliability indices were calculated using limited data and approximate methods.

Furthermore, an indicative cost function was defined considering two activities that were well documented for each of the structural elements analyzed, in the case of the projects repaired using the conventional method. This cost function was expressed in terms of the depth of the repair, using costs for the (partial) demolition of the concrete and the retrofitting of the columns. As expected, the function showed increasing costs with increasing intervention depth. For a project with a very detailed level of information, a clear relationship between the repair costs and the reliability index was found. This relationship was, in contrast, not so evident for the other analyzed projects, for which a threshold or stepwise function was observed. This outcome suggests that if the reliability index of each column were to be determined, the expected costs would theoretically increase with decreasing reliability index. Nonetheless, this requires very detailed and thus expensive inspections, which are not usually done in practice. It seems that in practical applications a more pragmatic approach is followed, in which a certain threshold is defined for which the columns are either

repaired or not, while the depth of the repair is left constant for all repaired columns. These practical considerations complicate the derivation of a cost function in terms of the reliability index.

Interesting research questions remain open. For instance: what would have been the optimum time of intervention to minimize the repair costs? Which measures during the design and construction phase could have been taken, in avoidance of the need for a costly rehabilitation?

FUNDING NOTE AND ACKNOWLEDGMENT

The IGF project no. 21828 N of the Research Association of the German Concrete and Precast Industry was funded by the German Federal Ministry of Economic Affairs and Climate Action (BMWK) through the German Federation of Industrial Research Associations (AiF) within the framework of the program for the promotion of joint industrial research and development (IGF) on the basis of a resolution of the German Bundestag. The authors gratefully acknowledge the financial support. Furthermore, the authors would like to thank the German Committee for Reinforced Concrete (DAfStb) for the valuable exchange of experiences and ideas in numerous discussions and the Engineering Consultancy Schiessl-Gehlen-Sodeikat for providing us with the documented rehabilitation reports.

REFERENCES

- DAfStb 2008. Positionspapier des DAfStb zur Umsetzung des Konzepts von leistungsbezogenen Entwurfsverfahren unter Berücksichtigung von DIN EN 206-1, Anhang J. *Beton- und Stahlbetonbau*, 103 (12), 837–839.
- DIBt 2020. *Instandhaltung von Betonbauwerken (TR Instandhaltung)*. Technische Regel (Technical Rule). *DIN EN 1504-9: 2008:11 Products and systems for the protection and repair of concrete structures – Definitions, requirements, quality control and evaluation of conformity - Part 9: General principles for the use of products and systems; German version EN 1504-9:2008*. Berlin: Beuth Verlag GmbH.
- DURACRETE 2000. *Brite EuRam III: DuraCrete - Probabilistic Performance based Duability Design of Concrete Structures, Statistical Quantification of the Variables in the Limit State Functions, Contract BRPR-CT95-1032, Project BE95-1347, Document BE95-1347/R9, January 2000*.
- fib Bulletin 76 2015. *fib Bulletin 76. Benchmarking of deemed-to-satisfy provisions in standards: Durability of reinforced concrete structures exposed to chlorides; state-of-the-art report*. Lausanne, Switzerland: Fédération internationale du béton.
- Gehlen, C. 2000. *Probabilistische Lebensdauerbemessung von Stahlbetonbauwerken: Zuverlässigkeitsbetrachtungen zur wirksamen Vermeidung von Bewehrungskorrosion*. Zugl.: Aachen, Techn. Hochschule, Diss., 2001. Berlin: Beuth.
- Gehlen, C., Schiessl, P. & Schiessl-Pecka, A. 2008. Hintergrundinformationen zum Positionspapier des DAfStb zur Umsetzung des Konzepts von leistungsbezogenen Entwurfsverfahren unter Berücksichtigung von DIN EN 206-1, Anhang J, für dauerhaftigkeitsrelevante Problemstellungen. *Beton- und Stahlbetonbau*, 103 (12), 840–851.
- Hastings, W.K. 1970. Monte Carlo sampling methods using Markov chains and their applications. *Biometrika*, 57 (1), 97–109.
- Kapteina, G. 2011. *Modell zur Beschreibung des Eindringens von Chlorid in Beton von Verkehrsbauwerken*. Dissertation. Technical University of Munich.
- Kessler, S. 2020. Probabilistic corrosion condition assessment of a tunnel structure. *Structural Concrete*, 21 (4), 1345–1355.
- Kessler, S. & Gehlen, C. 2020. *Untersuchungen zum Einfluss von Modellparametern auf die Lebensdauerprognose für Brückenbauwerke*. The influence of model parameters on the service life prediction of reinforced bridge structures. Bremen: Fachverlag NW in der Carl Ed. Schünemann KG.
- Lozano Valcarcel, J.M. et al. 2022. Instandsetzung von Tiefgaragen – Wann und warum? *Beton- und Stahlbetonbau*, 117 (12), 946–955.
- Metropolis, N. et al. 1953. Equation of State Calculations by Fast Computing Machines. *The Journal of Chemical Physics*, 21 (6), 1087–1092.
- Rahimi, A. 2016. *Semiprobabilistisches Nachweiskonzept zur Dauerhaftigkeitsbemessung und -bewertung von Stahlbetonbauteilen unter Chlorideinwirkung*. Dissertation. Technical University of Munich.
- Robert, C.P. & Casella, G. (eds) 1999. *Monte Carlo Statistical Methods*. New York, NY: Springer.
- Schiessl, P. et al. 2006. *fib Bulletin 34. Model Code for Service Life Design*. Fédération internationale du béton.
- Smith, R.C. 2014. *Uncertainty quantification: Theory, implementation, and applications*. Philadelphia: Society for Industrial and Applied Mathematics (siam).

The potential for direct reuse of precast concrete slabs in buildings with “wet” joints

P.S. Halding & K. Negendahl

Technical University of Denmark, Kgs. Lyngby, Denmark

ABSTRACT: Today, many buildings are built with precast concrete slabs each year, and as per tradition, these slabs are joined by pouring in-situ mortar in the joints between the slab elements. This is typically done to ensure the structural performance when the entire level of a building needs to perform as one rigid body. However, the consequence of the mortar-joints is that future dismantling is difficult as it requires extensive and costly use of diamond saws. Therefore, disassembly and direct reuse of concrete slab elements are rarely seen. Instead, the concrete is often crushed and used for, e.g., road filling. The global focus on reducing carbon dioxide from cement production and challenges with limited natural resources means that the production of new concrete must be reduced in the future. Direct reuse of concrete elements is essential to this transformation. More recently, methods have been employed to apply “dry” mechanical joints (e.g., steel brackets) specifically to enable a simpler disassembling process after end lifetime of buildings. Several challenges exist for the dry connections, such as more complex elements, labour-demanding assembly, higher cost, and problems with local damages, fire protection and robustness in service. Despite the trend in development and research activities in dry connection joints, the opportunity of modifying the simple, traditional “wet” mortar joints to create Design for Disassembly (DfD) has only been superficially investigated. The article unfolds the potential of a new type of wet concrete joints with a review of the challenges and limitations. The proposed solution to achieve DfD for wet connections is to reduce the mortar strength and stiffness and disassemble by pulling with a crane.

1 INTRODUCTION

Concrete elements from precast buildings are rarely reused. In developed countries, concrete buildings are crushed after the end of life to be used as a substitute for gravel in road filling or, on rare occasions, as aggregates in new concrete. But the direct reuse of entire concrete elements is almost nonexistent even though there is a global potential for enormous savings in the emission of CO₂ by doing so. Eberhardt et al. (2018) showed that 80% of the CO₂ is saved when an entire precast concrete building is reused once.

Worldwide, the construction industry accounts for 38% of the emission of CO₂ (UN, 2020), whereas cement production alone is 5 to 8 % (Figueira, 2021). As the main contributor of carbon emission from concrete, cement accounts for about 0.9 kgCO₂e per kg cement, depending on the specific cement factory (Hertz and Halding, 2021).

Furthermore, the resources to produce concrete are already scarce in many areas worldwide. Continuing the current production trend will accelerate the problems related to climate change and loss of biodiversity (UN, 2019).

To lower the consumption of cement for concrete structures, researchers investigate solutions such as “Green concrete” with less cement, minimal structures with less volume of concrete, and structural elements with combinations of different grades of concrete. However, considering the direct reuse of precast concrete elements is relevant in combination with any other technological gain in concrete buildings if the required forces can be transferred via the joints during the service of the building.

In this article, the emphasis is on the direct reuse of concrete slabs. They are often made with a relatively higher compressive strength (more cement) and constitute a large percentage of the overall volume of a concrete element building. The building industry is often considered to be conservative. Therefore, the scope is to investigate solutions within the current practice regarding erection methods – this means creating “design for disassembly” solutions with cast joints (“wet” joints) between slabs and adjacent elements. The proposed solutions are at a conceptual level. An example of a typical pouring of mortar/concrete over the reinforcement in joints between precast concrete slabs is seen in Figure 1.



Figure 1. Ordinary pouring of joints in a precast concrete building.

1.1 Existing DfD-solutions

The primary research in DfD revolves around mechanical “dry” joints that can typically be disassembled by loosening some bolts or similar steel connectors. Examples of proposed mechanical connections for DfD of precast concrete buildings are presented by, e.g., Kang et al. (2013), Witzany et al. (2015), Aninthaneni et al. (2017), Xiao et al. (2017), Aninthaneni et al. (2018), Ma et al. (2019) and Balineni et al. (2020). All the above research has in common that the DfD solutions rely on alterations of the concrete elements and hence require new processes at the factory and building site.

The only “wet” joint DfD-solutions available in the literature and online are based on cutting with a diamond saw around the slabs’ perimeter. Such methods are cumbersome and expensive, which is why it is not already done in practice.

2 BUILDING DFD-REQUIREMENTS AND LIMITATIONS

To investigate DfD-solutions for “wet” joints, limitations for the type of precast concrete buildings and a location have been chosen as an example. The case study building is positioned in Denmark, with low seismic activity and dominating wind load conditions.

Horizontal load from the wind on the façade is transferred to the stabilizing walls via the slabs and into the foundation. The magnitude of the transferred force to each wall is directly related to the wind pressure and the geometry of the building (the façade area, the position and sizes of the stabilizing walls, etc.). The wind load must be transferred via the joints between the slabs and the stabilizing walls. Hence, a conservative design approach is to dimension the structural system with the largest possible transfer of force in the connections, meaning the following two considerations are taken:

1. Apply the largest wind load on each floor (extra-large storey heights and a very long building).
2. Have the fewest possible stabilizing walls and use only short walls (increasing the shear stress in the joints).

2.1 Case study

2.1.1 Transfer of maximum shear force to stabilizing walls in service

A case study of a “conservative” building is made to show a critical case of load transfer from slabs to walls during use. Figure 2 shows a model of the structural system.

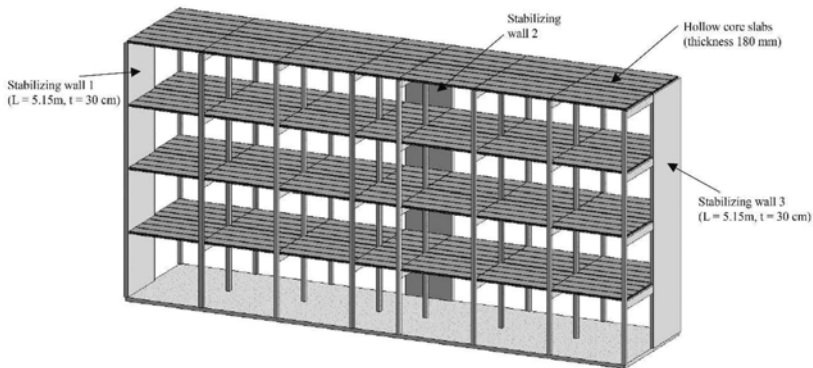


Figure 2. 3D view of the structural system of a precast concrete building with a maximum storey height of 5 m.

The building has a storey height of a maximum of 5 m, a façade length of 41.7 m, and only two transversely positioned stabilizing walls of 5.15 m in length positioned in each gable (stabilizing walls 1 and 3). This setup is more critical regarding the magnitude of transferred shear into the stabilizing walls compared to a similar building with less storey height, smaller façade length, more stabilizing walls, or with longer stabilizing walls.

Requirements for robustness (CEN, 2004) of the structural system means that reinforcement is positioned along the edges of the building and - when applying hollow core slabs - also to some extent in the joints between the slabs. Pure cement-based mortar is usually used in these reinforced joints along the perimeter of each slab, and the compressive cylinder strength is often above 40 MPa.

The slabs' size depends on the building's applied vertical loads for the case building. A maximum design load of 6 kN/m^2 is chosen, including safety factors, self-weight of slabs, services etc. It corresponds roughly to the expected imposed loads for an apartment. 180 mm hollow core slabs (HCS) are used to resist loads and deformations sufficiently, and a cross-section of the slabs and beams of the building is shown in Figure 3, including the pre-tensioning strand positions (red dots) and sizes.

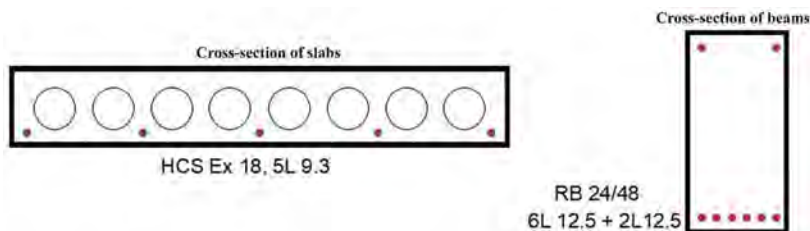


Figure 3. Cross-section of HSCs and rectangular beams in the building designed to resist the applied vertical loads, and self-weights.

According to the Eurocodes (CEN 2005), the wind load can be found as maximum positive and negative pressure on different building surface areas. When distributing the wind load on the façades as a line load on the floors, the force becomes 3.33 kN/m (except for the roof and

ground floor). Since the case building façade is 41.7 m long, the total load from the wind on each floor is $3.33 \text{ kN/m} \cdot 41.7 \text{ m} = 138.9 \text{ kN}$.

This force is evenly distributed to the two transverse stabilizing walls at the gables, and each wall will receive 69.4 kN in each storey. It is now possible to investigate the occurring stresses in the local area with the mortar joint between slabs and stabilizing walls to determine the minimum requirement for the strength of the mortar.

2.1.2 Local investigation of the required mortar strength

FE-models were created to investigate the maximum occurring stresses in the mortar between slabs and stabilizing walls coming from the dominant wind load in combination with self-weight and imposed load.

Autodesk Robot Structural Analysis was used to model the geometry of the structural system of the entire building (see Figure 4 left). The material stiffnesses were given as input to the different members. This was to verify the assumption that the critical wind load would be evenly distributed to the two transversely positioned stabilizing walls. It was again assumed and modelled that the columns did not participate in resisting the wind load. The model also provided the maximum shear stress's location over the stabilising wall's length, which was utilized in a local investigation of the mortar joint between slab and wall.

The program ABAQUS was used to model the local (0.6 m x 0.3 m x 0.3 m) detail where the slab transfers the wind load via the mortar to the stabilizing wall. In Figure 4 (right), the simple ABAQUS model is seen. The right part of the figure shows an example of the distribution of the stresses in the mortar when the relevant load was applied to the local detail. The slab was only supported vertically by the stabilising wall, and all critical combinations of shear, bending moment and normal force from the slab were modelled to be transferred through the mortar.

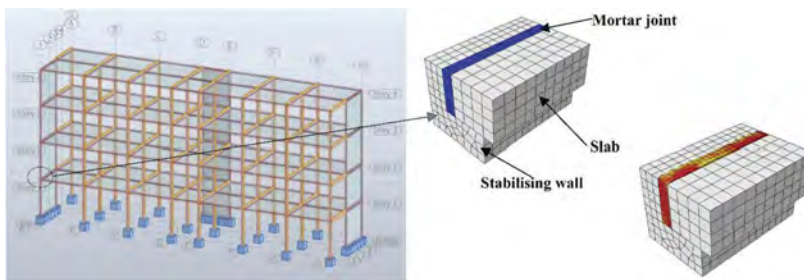


Figure 4. FE-model setup of global and local investigation to find the maximum stress in the mortar based on dominant wind load.

In the local FE-model, the stabilizing wall was fixed at the bottom.

To study the distribution of the stresses in the mortar and to find the largest stress, the model showed the numerically largest 1st and 3rd principal stresses in the mortar part of the assembly.

Based on this approach, the minimum required compressive design strength of the mortar could be determined directly when comparing different mortars with various strengths and stiffnesses, see Table 1. In all cases, the Poisson's ratio was 0.2, and the safety factor when calculating the design strength was 1.45.

Table 1. Mortar properties and maximum stress.

Compressive strength (char.)	Young's modulus	Tensile strength (char.)	Applied max stress	Compressive design strength
8 MPa	25.3 GPa	0.8 MPa	11.0 MPa	5.5 MPa
10 MPa	26.3 GPa	1.0 MPa	11.3 MPa	6.9 MPa
12 MPa	27.0 GPa	1.2 MPa	11.5 MPa	8.3 MPa
16 MPa	29.0 GPa	1.6 MPa	11.9 MPa	11.0 MPa

The small change in the maximum stresses was due to the small deviations in the stiffness. The goal was to determine the required mortar design strength to resist the maximum stress from the applied wind load. The setup from Figure 4 is very conservative since there will also be a contribution to the shear transfer in the surface between slab and wall, which has not been accounted for here. But with this conservative approach, the minimum limit for the strength of the mortar can be determined from Figure 5, where the “mortar design strength to max stress ratio” is plotted against the “mortar design strength”. The linear trendline crosses the ratio = 1 for a design strength of approximately 12 MPa, which corresponds to a characteristic strength of 17.5 MPa.

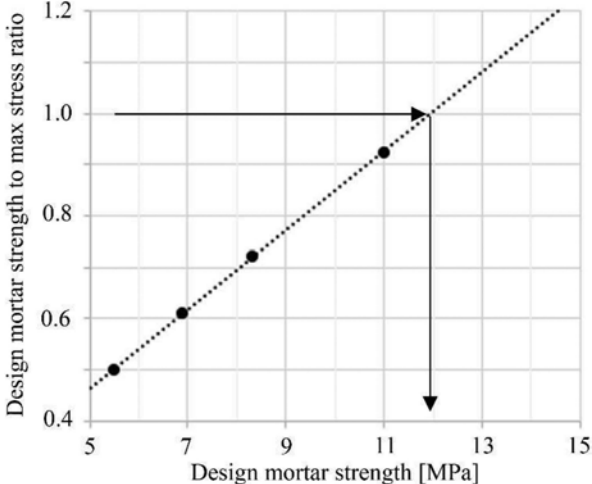


Figure 5. Mortar strength to max stress ratio with the minimum mortar strength limit location at 12 MPa.

If the slabs were higher, the maximum stress is expected to become smaller (if the mortar joint height follows the slab’s height).

The 17.5 MPa compressive strength of the mortar is less than half of what is ordinarily used for precast concrete buildings, and it enables the opportunity for DfD of slabs.

2.1.3 Design for disassembly of slabs with “wet” (poured) joints

The simplest method to remove whole slabs from precast buildings after end-of-life would be to pull out the elements one by one with a crane. The requirement for such method would be:

1. The slab can resist the pulling-out loading scenario and is free to move without significantly deforming adjacent building parts.
2. The crane has the capacity to pull with the required force in a controlled and safe way.
3. The lifting chains and the anchors embedded in the decks have sufficient capacity.
4. There is access to lifting anchors on the surface of the slabs.
5. The joints are weak and will crack along the slab’s edge when pulled up.

To ensure that the slab for disassembly is free to be moved up, one side of the slab must always be free. The edge beam on the side of the first slab to be lifted must be removed first.

Now, one side edge of the slab is exposed, and the longitudinal reinforcement (if present) must also be cut by a diamond saw in the joints in the two opposite corners of the free edge (Figure 6).

The lifting process can be initiated, and if the mortar in the three attached sides is weak enough, it will start cracking around the slab periphery.

Suppose the lift is performed with ordinary lifting chains. In that case, it can be conservatively chosen to use chains with an inclination of 45 degrees vertical and four lifting anchors positioned 300 mm from the ends of the slab and 150 mm from each side of the slab.

The shear resistance can be calculated in the interface and inside each of the materials (concrete and mortar). Along the smooth surfaces of the slab, the interface will be dimensioning for the shear resistance when pulling the slab up. At the ends of the slab, where the holes are located, the shear force must overcome the shear resistance of the mortar in the location of the holes.

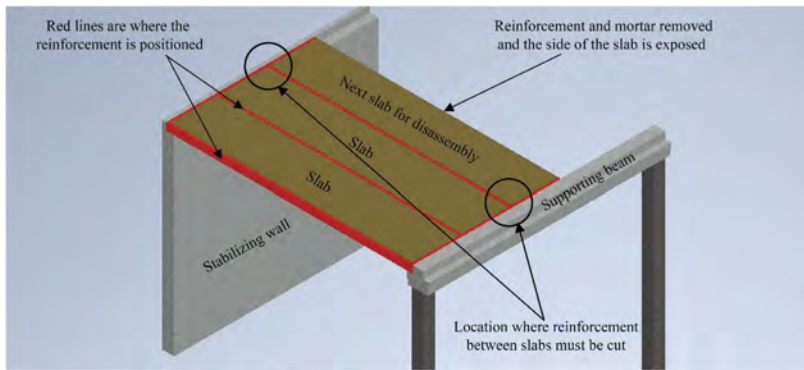


Figure 6. Disassembly setup with the location of reinforcement in mortar joints.

The shear resistance in the interface can be found by e.g., Eurocode 2 (CEN, 2004), and the calculation procedure is not shown here. For further information, the authors can be contacted. In the calculation of the shear resistance, it is assumed that there is no normal force in any of the joints (no wind during disassembly).

In the case building, the slabs have a 6.3 m span, a width of 1.2 m, and a height of 180 mm. Calculating the shear resistance and lifting force from the three sides with mortar joints of 12 MPa compressive strength (found earlier), the result becomes:

- Total shear resistance from holes at the ends of the HCS: 61.5 kN
- Total shear resistance from the remaining part of ends of the HCS: 44.9 kN
- Total shear resistance from the longitudinal joint of the HCS: 166.7 kN
- Self-weight of HCS to be lifted: 19.2 kN
- Total lifting force to overcome shear resistance and self-weight: 292.3 kN

The total load is possible to lift by a mobile crane. A solution for lifting is shown in Figure 7.

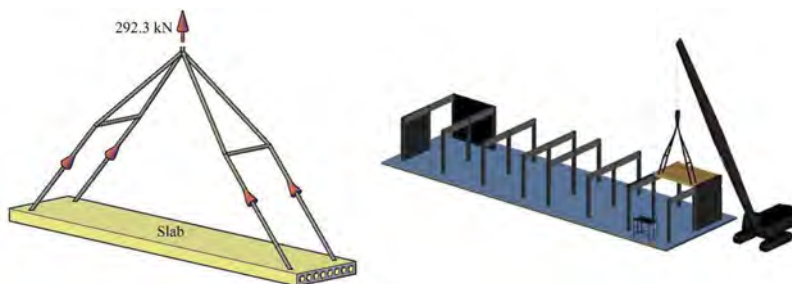


Figure 7. Disassembly setup with crane lift.

If no lifting anchors are available, it may be necessary to lift by applying another method, for instance, special lifting straps around the slabs. When this method is applied, the slabs and surrounding elements should always be checked for sufficient resistance to the disassembly load.

2.1.4 Carbon footprint comparison

Considering only the structural system of the case building, the direct saving of CO₂ by direct reuse of the slabs can be calculated. The concrete of the slabs accounts for 72% of the consumption of concrete in the building, and the concrete grade is higher (55 MPa) than for the columns and stabilizing walls (35 MPa). If we consider only the CO₂-emission from the materials manufacturing, the slabs account for 76.5% of the total emission of the system.

Of course, the dismantling and other processes require emission of CO₂ as well, so a more precise calculation is required when such numbers are available. Still, there is a saving of about ¾ of the emission available by directly reusing the slabs in a new similar building in the future.

3 DISCUSSION AND PROSPECTS

The erection method of the building will remain the same as for an ordinary precast concrete building, with the only difference being the application of a weaker mortar in the joints between the elements. The 12 MPa compressive strength mortar could be created from either a pure cement-based recipe or a combined lime- and cement mortar. Note that the hardening of the mortar is not complete after 28 days (ordinary design assumption). This means that the mortar is slightly stronger than anticipated at the end-of-life of the building if this is not accounted for.

Most of the shear resistance comes from the longitudinal side of the slabs. Therefore, it could be a future investigation to develop a method to “pre-crack” the joints along the longitudinal side to reduce the required lifting force. This could especially be interesting for larger slabs with a bigger self-weight and longer sides. The potential of such a solution could be to develop a disassembly method for slabs from existing precast concrete buildings with stronger joint mortars. This would fast forward the CO₂-saving so that society will benefit immediately.

Another promising future development of the DfD method could be creating a “hybrid” DfD-building with a combination of dry mechanical and wet joints. By doing so, it is possible to achieve the benefits of both methods in combination and create a simpler and more inexpensive way to assemble and disassemble.

The disassembly method also requires a check of the capacity of the slabs for the pulling-out load scenario. It may be necessary to put in slightly more pre-tensioning steel in some new slabs to avoid problems with cracking during disassembly.

To verify the proposed DfD-method, full-scale tests will have to be performed. Especially the sequence of the crane pulling regarding the safety of the workers on the building site and the possible concentration of stresses in the slabs or neighbouring elements are issues that need to be proved in the lab.

Many other aspects are important before we can begin to have large numbers of direct reused concrete slabs, e.g.:

- Documentation of the carrying capacity of the slabs and the remaining component life.
- Check chemicals to ensure contamination is not transferred to new buildings via slabs.
- Where to store the elements before they are reused in a new project.
- Evaluation of the economic consequences.
- Regulations that require reuse at an element level to lower future emissions of CO₂.
- All precast concrete buildings should be designed with a solution for both the erection and disassembly methods.

4 CONCLUSIONS

A new method for Design for Disassembly (DfD) of slabs in precast concrete buildings is proposed. The method relies on the mortar in the poured joints being optimized to have the minimum required strength and stiffness to transfer the required force from the load on the building during service. With the much lower mortar strength, the building can more easily be disassembled after the end of life so that the slab elements can be directly used in a new building without being harmed and without the costly and slow process of cutting all edges with a diamond saw.

The outlined method relies on an ordinary crane to pull out the slabs one at a time. The low strength of the mortar means that the mortar is the weak point in the joined structure, and cracks and later separation failure will occur in the joints. The elements should always have one free side to ensure that the slabs are not interlocked during the crane pull. Therefore, the method relies on removing reinforcement or edge beams along the side of the building before dismantling the first slab. Furthermore, the longitudinal reinforcement in the joints between slabs must be cut locally by using a small diamond saw to ensure a restraint-free removal process. With such a setup, the only resistance towards the crane pull is the shear capacity of the interface between the slab and the mortar.

A conservative case building with a critical loading scenario is presented to show the method. An FE model of the local detail between slab and wall provides a minimum mortar compressive strength of 12 MPa. This strength is determined to be sufficient to transfer the wind load.

Subsequently, the required crane pulling force is found by calculating the shear resistance around the three sides of the slab with a mortar joint. The total required pulling force is 292 kN, which is manageable for a normal mobile crane.

The case building clearly shows that the method is a promising step towards an easier process for disassembling concrete decks in future precast concrete buildings to create CO₂ savings (up to ¾ for future buildings from slabs alone). Nevertheless, several obstacles must be overcome to apply such a method in practice. For instance, full-scale laboratory tests are necessary to prove the concept and to show that the method is safe for the workers on the building site.

ACKNOWLEDGEMENTS

The authors wish to thank the M.Sc. students at DTU Construct who were involved in the case study. The investigations are part of a project funded by the “Ingeniør Kaptajn Aage Nielsen” family fund.

REFERENCES

- Aninthaneni, P. K., Dhakal, R. P., Marshall, J., & Bothara, J. 2017. Seismic Performance of Beam-Column Sub-Assemblies of a Demountable Precast Concrete Frame Building. *In 16th World Conference on Earthquake*. 242.
- Aninthaneni, P. K., Dhakal, R. P., Marshall, J., & Bothara, J. 2018. Nonlinear Cyclic Behaviour of Precast Concrete Frame Sub-Assemblies With “Dry” End Plate Connection. *Structures*, 14. Pp. 124–136. doi.org/10.1016/j.istruc.2018.03.003.
- Balineni, H., Jagarapu, D. C. K., & Eluru, A. 2020. Analysis of dry and wet connections in precast beam-column joint using ABAQUS software. *In proc. Materials Today*, 33. Pp. 287–295. doi.org/10.1016/j.matpr.2020.04.073.
- CEN, European standard, 2004. Eurocode 2: Design of concrete structures – Part 1-1: General rules and rules for buildings.
- CEN, European standard, 2005. Eurocode 1: Actions on structures – Part 1-4: General actions – wind actions.
- Eberhardt, L. C. M., Birgisdottir, H. & Birkved, M. 2019. Potential in circular economy in sustainable buildings. *In Iop Conference Series: Materials Science and Engineering*. 471(9): 092051.
- Figueira, D., Ashour, A., Yildirim, G., Aldemir, A. & Sahmaran M. 2021. Demountable connections of reinforced concrete structures: Review and future developments. *Structures* 34. pp. 3028–39. doi.org/10.1016/j.istruc.2021.09.053.
- Hertz, K. D., & Halding, P. S. 2022. Sustainable light concrete structures. *Springer Tracts in Civil Engineering*, 1st Ed.
- Kang, T. H.-K., & Lee, D. J. 2013. Special precast beam-column connection using pure dry cast method. *In Advances in Structural Engineering and Mechanics*. Pp. 1779–1788.
- Ma, W., Li, Y., Ding, K., Cheng, B., Liu, J., Hao, J., & Tam, V. W. Y. 2019. Mechanical properties of new dry-type beam-column bolt connection joint. *Sustainability*, 11(12). 3348. doi.org/10.3390/su10023348.
- UN, IRP, 2019. Global Resources Outlook 2019, Natural resources for the future we want. ISBN: 978-92-807-3741-7.
- UN, 2020. Global status report for buildings and construction; Towards a zero-emissions, efficient and resilient buildings and construction sector. www.globalabc.org.
- Witzany, J., Zigler, R., Cejka, T., & Polak, A. 2015. A demountable precast reinforced concrete building system of multistory buildings. *In Isek 2015-8th International Structural Engineering and Construction Conference: Implementing Innovative Ideas in Structural Engineering and Project Management*. pp. 219–24.
- Xiao, J., Ding, T., & Zhang, Q. 2017. Structural behavior of a new moment-resisting DfD concrete connection. *Engineering Structures*, 132, pp. 1–13. doi.org/10.1016/j.engstruct.2016.11.019.

Life-cycle assessment of concrete hollow blocks and autoclaved aerated concrete blocks

J.M. Ongpeng & M.V. Umali

De La Salle University, Manila, Philippines

ABSTRACT: The global shortage of natural resources and its effects on the environment are both adversely affected by the construction industry. Environmental criteria must be considered when it comes to selecting sustainable building materials. In this paper, two models for interior wall systems were investigated, the use of conventional concrete hollow block (CHB) and the alternative autoclaved aerated concrete block (AACB). A life cycle assessment (LCA) considering a school building in the Philippines with a cradle-to-gate boundary and a functional unit of 10.5m² was performed to compare the environmental impacts of these walls. In the endpoint categories, the use of AACB resulted a decrease in human health, ecosystems, and resources while in the midpoint categories, the use of AACB walls resulted a decrease in CO₂ emission, fine particulate matter formation, and human carcinogenic toxicity. It is therefore concluded that AACB interior wall systems have substantial potential to reduce the environmental burden caused by the building construction.

1 INTRODUCTION

In comparison to other industries, the construction sector consumes 60% of the world's raw materials (Broun & Menzies, 2011) and is the largest user of materials by weight in the US (Ferrández-García et al., 2016). It has significant effects on the use of energy, production of solid waste, pollution, and greenhouse gas emissions (Broun & Menzies, 2011; Condeixa et al., 2015; Mateus et al., 2013). Additionally, as people's knowledge of environmental issues rises, sustainable construction practices receive increasing attention (Buyle et al., 2013). It is important to use appropriate building design and technology, as well as acceptable construction materials while creating effective buildings. Wasted materials and handiwork result from poor management decisions, suppliers' unreliable performance, and incorrect selection of material parameters (Ferrández-García et al., 2016). As the sustainability concept has grown in construction, there is a popularity of using locally available materials, which establishes the need for more sustainable solutions for construction materials.

A partition wall is a crucial building element that divides a building's interior space into rooms or regions to facilitate better space usage (Broun & Menzies, 2011). Stability to self-weight, eccentric vertical loads, out-of-plane horizontal loads, visual, acoustic, thermal, and water resistance are the key functional criteria for partition walls (Vasconcelos et al., 2013). These interior walls have an impact on the environment depending on the material used, its thermal qualities, and how it is constructed and maintained.

Blocks have been widely employed as a popular option in structures and are one of the essential materials for walls and partitions. Because they dissipate less heat and need fewer resources to produce voids, hollow or solid blocks are more common in developing nations (Wu et al., 2015). Blocks are selected because they can improve aesthetics and lower costs by reducing the number of cut units needed on-site. Grades of partition blocks are determined by the structural and functional performances of the partition and the degree of care the partition is likely to receive (*Build SG - BCA*, n.d.).

The life cycle assessment (LCA) of recycled materials can help in material selection. For the environmental assessment of items covered by the International Organization for Standardization (ISO) 14000 standard series, specifically ISO 14040, LCA methodologies are frequently used (*ISO*

14040:2006, 2014). It plays an important role in the evaluation of environmental impact to enable the selection of environmentally suitable materials (Cabeza et al., 2014). Using all phases of a product's life cycle, the LCA is a scientific methodology that enables the identification and quantification of inputs and outputs linked to a product in accordance with its primary function (Agarski et al., 2016; Frenette et al., 2010). The comparison of various building materials, their embodied energy, CO₂ footprint, and the comparison of material performance within construction are all topics covered by LCA research (Agarski et al., 2016; Frenette et al., 2010). The environmental impact of materials can be reduced by selecting more environmentally acceptable materials, particularly if the sources are sustainably managed or the products have renewable sources.

In this LCA study, the two selected models for interior wall systems (IWS) will be investigated and compared as shown in Figure 1. The first one is the traditionally built non-load-bearing concrete hollow blocks (CHB) with dimensions of 0.40 m (length) by 0.20 m (height) by 0.10 m (thick), three (3) cores jointed and built with 12.5mm of cement mortar and 16mm of cement plaster on both faces (Fajardo, 2000). The second one is the alternative autoclaved aerated concrete blocks (AACB) with dimensions of 0.60 m (length) by 0.20 m (height) by 0.10 m (thick) jointed and built with 5.0mm of adhesive mortar.



Figure 1. Concrete Hollow Blocks (CHB) and Aerated Autoclaved Concrete Blocks (AACB).

2 MATERIALS AND METHOD

2.1 Building interior wall system

The structure considered in this study is a 2-storey school building in Bulacan State University (BulSU) located in City of Malolos, Bulacan, Philippines. The building made up of reinforced concrete has a total area of 355 m² as shown in Figure 2. The elevation and section of CHB and AACB wall systems are shown in Figures 3 and 4 respectively. The building was constructed in accordance with the 2015 National Structural Code of the Philippines (NSCP, 2015).

In the first model, as shown in Figure 3, blocks of CHB wall were laid in the running bond method. The reinforcing steel bar used is 10mm in diameter. As illustrated, the vertical bars are installed at every 600mm on the center and the horizontal bars are installed at every 3 layers of CHB. Mortar beds of 12.50mm thick and 16mm thick cement plastered at both faces of CHB were applied. In the second model shown in Figure 4, blocks of AACB wall were also laid in the running bond method. As illustrated, the vertical bars are installed at every 2 units of the blocks of the first row. Horizontal bars are installed on the side at every 3 layers of AACB. The 10mm diameter dowels used for both vertical and horizontal have a length of 200mm where the 50mm length of rebar was drilled in the concrete while the remaining 150mm length was exposed. An adhesive mortar 5.0mm thick was patched in between the blocks and no cement plaster was required since both faces of the block were already smooth and ready to receive paint.

To ensure a direct comparison, the equal compressive strength of the mortar in both walls has been considered. It is assumed that installation procedures will not vary in significant ways. The secondary sources of data are utilized as shown in Table 1.

2.2 Life Cycle Assessment (LCA)

LCA studies should consist of four separate phases: goal and scope definition, life cycle inventory, life cycle impact assessment, and interpretation. This document is organized in accordance with these recommendations. SimaPro 9.3.0.3 software was used to conduct an LCA (Pré, 2014). The definition of the goal and scope establishes the parameters and limits of the study, while LCIA

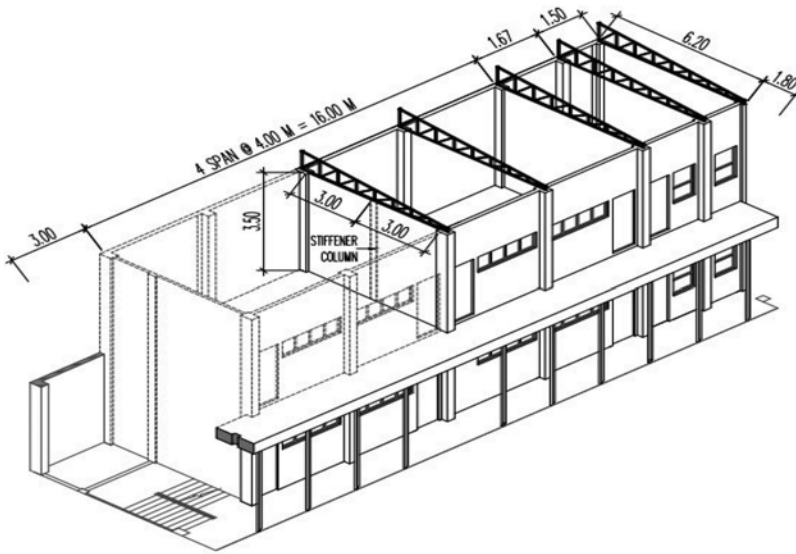


Figure 2. Structural plan of the building.

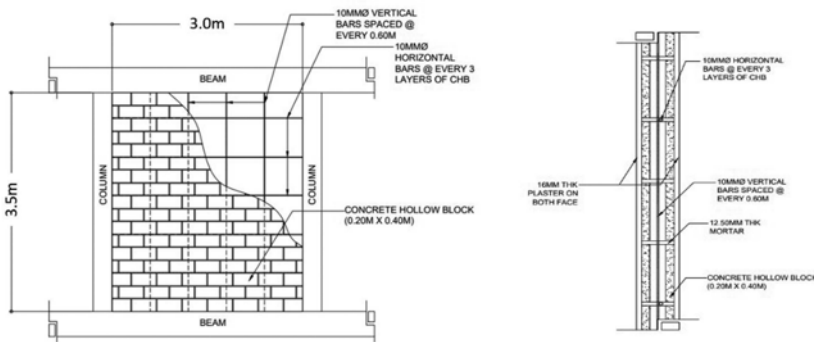


Figure 3. Elevation and section of CHB wall system.

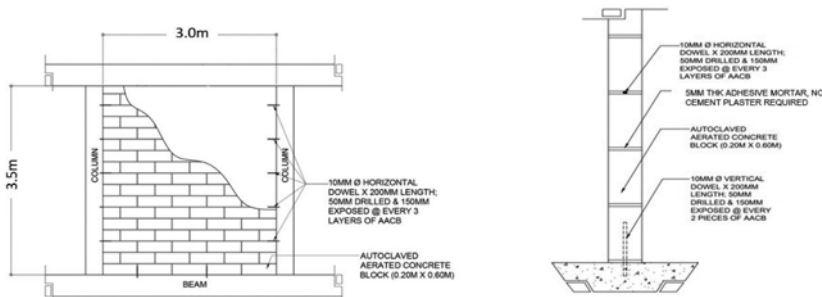


Figure 4. Elevation and section of AACB wall system.

measures the impacts in terms of damage categories and the interpretation is present throughout all phases and influences the choice of data (*ISO 14040:2006*, 2014b). LCI provides information about the input and output of processes. Cost analysis was also added to the LCA.

Table 1. Data for interior wall system based on secondary sources.

Model of Wall System	Compressive Strength	Composition	Design Mix (kg/m ³)	Reference
Concrete Hollow Blocks	3-5 N/mm ²	Cement	415.84	(Dolores et al., 2020)
		Sand	1610.56	
		Water	207.92	
Autoclaved Aerated Concrete Blocks	3-5 N/mm ²	Cement	384	(Kumar et al., 2021; Sethy, 2018)
		Sand	298.67	
		Lime	50.371	
		Aluminum Powder (600 kg/m ³)	0.13%	
		Water	296.3	

The main aim of this study is to conduct a comparative LCA study on the environmental impacts of two models of interior wall systems, CHB and AACB. The aim is also to come to conclusions and make recommendations that will help in the decision-making process for choosing the most cost-effective and environmentally friendly building material for internal partition walls.

The functional unit is defined as the measure applied in evaluating the performance of systems or products (ISO 14040, 2006). In this study, a functional unit considered is a 10.50 m² (3.0mW x 3.5mH) interior wall represented in Figures 3 & 4 with a thickness of 0.10 m for the single-layer walls, excluding paint. The area is calculated by multiplying the width by the height of the wall.

The system boundaries are represented in Figure 5. The performance of IWS is primarily examined in this research from the viewpoint of cradle-to-gate boundaries. The pre-construction phase took into account the extraction of raw materials and the production of essential products, while the construction phase evaluated the preparation and installation processes. It was also considered how the products would get from the location of material extraction to the project site and its corresponding transportation distances. The effects of each of these processes on the environment are evaluated. The use phase has been excluded from this study.

The LCA methodology mandates the establishment of a life cycle inventory for the specific product or process after defining the purpose and scope. Comprehensive tracking of all flows into and out of the product system, including those of raw materials, energy by type, water, and emissions of a given substance into the air, water, and land, constitutes a life cycle inventory. A bill of materials was also created and converted into the functional unit described in this study. SimaPro version 9.3.0.3 is used to execute each approach with varied material needs for evaluation and interpretation (Ortiz et al., 2010). Data consistency was maintained using the Ecoinvent 3 library and the ReCiPe 2016 Endpoint H/World 2010 H/A endpoint method. The LCA software integrates the supplied data with data obtained from the background database to get an accurate picture of the effects of a specific product. Characterization results for each midpoint category are analyzed as the obligatory level of impact assessment.

3 RESULTS AND DISCUSSION

3.1 Life Cycle Inventory (LCI)

Table 2 summarizes the material quantities required for each of the IWS. These material quantities are used as input to SimaPro.

In the life cycle inventory for CHB and AACB, the input data for the Ecoinvent 3 library's materials and processes are based on Rest-of-the-World (RoW) or global (GLO) geographic locations. The GLO dataset refers to cover the average global production, but the RoW dataset reflects the world minus all local geographies for which a process is recorded in the database (Ecoinvent, 2021). The typical GLO dataset selections include tap water, diesel, heat, and electricity. For portland cement, sand, rebars, adhesive, blocks, and transportation, the RoW dataset was selected. The midpoint categories with the most impact are shown as output in the inventory.

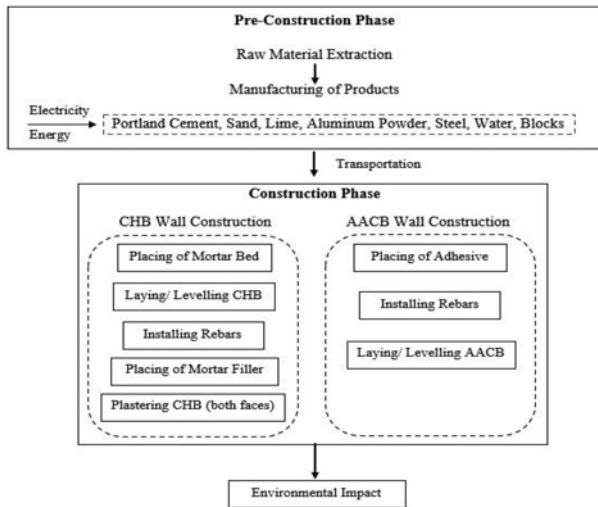


Figure 5. System boundary used in the study.

Table 2. Summary of the bill of materials for each IWS, per functional unit 10.5m² area.

Interior Wall System	100 mm Blocks	Portland Cement*	Sand*	Adhesive*	Rebars	Water
CHB	1056	380	1539		23.61	114
AACB	630			63	2	19

All quantities are expressed in kilograms. *The background color denotes non-included materials.

The three categories that have the greatest impact are (1) human carcinogenic toxicity (measured in kg 1.4 DCB released eq), (2) particulate matter generation (measured in kg PM_{2.5} eq), and (3) global warming potential (measured in kg CO₂ eq). Human carcinogenic toxicity is noted to risk an increase in cancer and non-cancer disease incidence (Huijbregts et al., 2016). Air pollution that results in primary and secondary aerosols in the atmosphere and can have a significant detrimental effect on human health, ranging from respiratory complaints to hospital admissions and mortality, is accounted for by particle matter formation (Lelieveld et al., 2015). The rise in temperature known as “global warming” ultimately harms ecosystems and people’s health.

3.2 Process network

The process network illustrates the materials used in the assembly or the flow of any process. As shown in Figure 5, using SimaPro to analyze the process network in CHB, portland cement production contributes the highest impact with about 42.1%. The next contributor is concrete block production with about 28.4% then followed by reinforcing steel with about 22.4%. The impacts of the other materials such as sand and water including the transportation process, electricity, diesel, and heat are negligible compared to the major environmental contributors.

As illustrated in Figure 6, AACB production contributes the highest impact with about 63.6%. The next contributor is the adhesive mortar with about 31.5% then followed by reinforcing steel with about 3.06%. The reduced impact of cement as compared to the CHB wall is due to the application of adhesive as a replacement for the cement mortar.

3.3 LCA comparison

As shown in Figure 7, the midpoint categories are first evaluated to identify which are considered problem-oriented categories (Bautista et al., 2022). The results demonstrate that AACB has the least impact in almost all the midpoint categories except for the ionizing radiation and mineral resource scarcity wherein AACB has more impact than CHB. Ionizing radiation in human health disperses the radionuclide throughout the environment and exposure to the radiation will damage

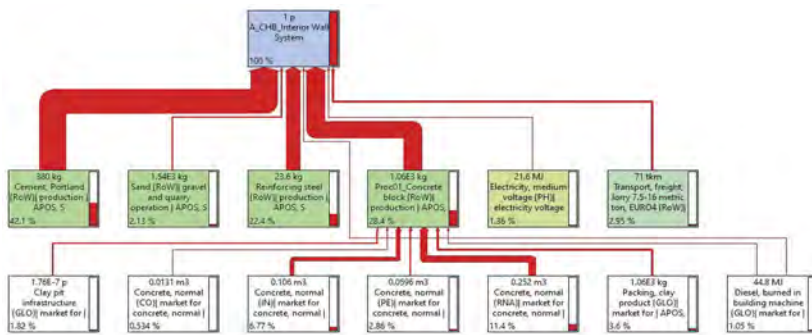


Figure 6. CHB wall process network.

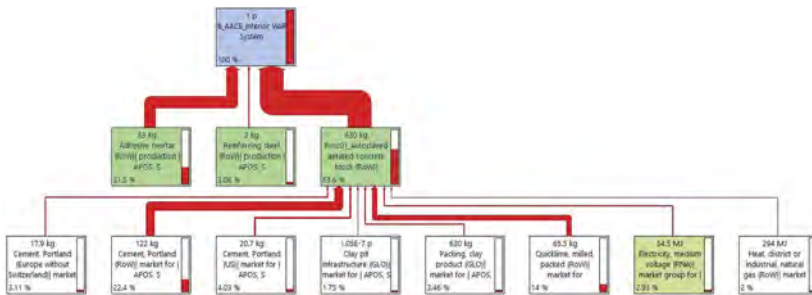


Figure 7. AACB wall process network.

DNA-molecules of a person which can lead to a certain illness (Huijbregts et al., 2016). A higher impact in this category is primarily due to the materials such as lime and aluminum powder added to the block and the higher power generation stage in the curing process of AACB. Meanwhile, the categories which obtained the most variation of CHB vs. AACB are human carcinogenic toxicity and water consumption. AACB uses a lesser amount during block production and installation. After the midpoint categories, the comparative endpoint categories or damage-oriented parameters are evaluated by investigating the impacts on human health, ecosystem, and resource availability as shown in Figure 8 with tabular results in Table 3. LCA results show that

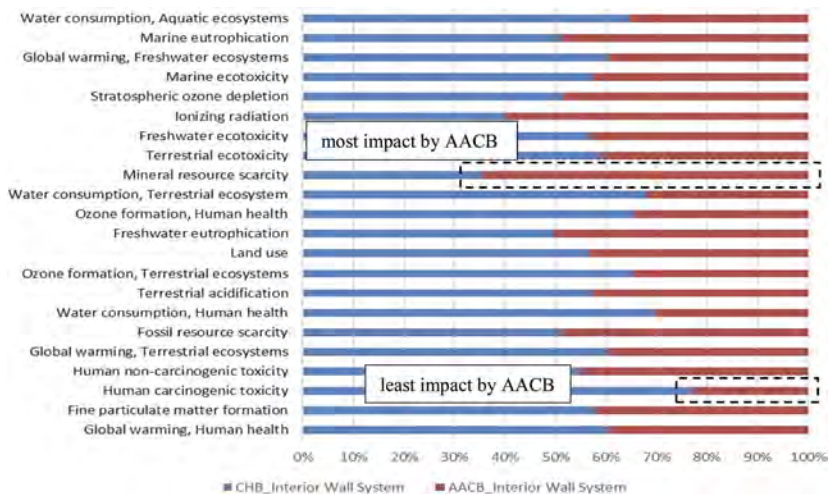


Figure 8. Comparison of impact assessment characterization for CHB and AACB.

the method with the least impact on the endpoint categories is AACB. This means that the installation of an interior wall system using CHB yields a higher impact compared to AACB. As was mentioned, out of all the components taken into consideration, cement is the biggest contributor. AACB wall is considered as the model with the least environmental impact.

The analysis of the results revealed that the cost per square meter of the CHB wall (₱ 966.00) was lower than the AACB wall (₱ 1,462.00). AACB leads to faster and easier installation thus showing lower labor cost but the results depict that CHB cost has reduced by 34% and therefore conclude more advantageous in terms of the total cost in wall construction.

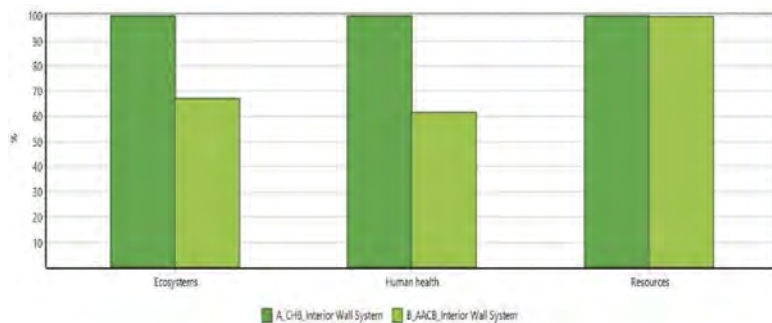


Figure 9. Comparative endpoint LCA results for concrete and autoclaved blocks.

Table 3. Tabular impact assessment comparison of endpoint categories for two models.

Damage Category	Units	CHB Wall	AACB Wall
Human Health	DALY	0.00112	0.000693
Ecosystems	species.yr	2.3E-6	1.54E-6
Resources	USD2013	22.8	22.7

4 CONCLUSIONS

Results of the LCA process network show that cement production has a greater environmental impact than the production of adhesive, steel, sand, and other energy sources like electricity, fuel, and freight transportation, aside from the production of the blocks themselves.

In the endpoint categories, the use of AACB in the interior wall of a building resulted in a 38% decrease (DALY units) in human health, 33% decrease (species.yr units) in ecosystems, and 0.61% decrease in resources. Regarding the midpoint categories, the study also confirms that CO₂ emission, fine particulate matter formation, and human carcinogenic toxicity are the environmental impact categories with the highest impact. Installing of AACB interior wall resulted in a 35% decrease in kg CO₂ eq, a 40% decrease in kg PM 2.5 eq, and 63% in kg 1.4-DCB emitted to urban air eq. It is therefore concluded that AACB walls have a lesser environmental impact between the two models. In terms of cost, it validates that the use of CHB interior walls in the construction of a building is more advantageous than the use of AACB. But in terms of its lightweight property, durability, fire resistance, fast installation, and most especially environmental impact, AACB is still beneficial in the overall design and construction of the building.

Both systems have areas that might be strengthened in terms of production, transport, and installation. The CHB supply chain's construction features must be adjusted to reduce environmental impacts across its lifecycle, particularly in terms of human health, ecosystems, and resources, while the output of by-products in the AACB must be enhanced. In the course of future work, it is recommended to further investigate the process or material production improvements as they can be the source of environmental impact mitigation. The use of recyclable materials in material development can also be explored to reduce costs and negative impacts.

REFERENCES

- Agarski, B., Budak, I., Vukelic, D., & Hodolic, J. 2016. Fuzzy multi-criteria-based impact category weighting in life cycle assessment. *Journal of Cleaner Production*, 112, 3256–3266. <https://doi.org/10.1016/j.jclepro.2015.09.077>
- Association of Structural Engineers of the Philippines (ASEP). 2015. *National Structural Code of the Philippines*; Association of Structural Engineers of the Philippines (ASEP); Quezon City, Philippines
- Bautista, B. E., Ongpeng, J. M. C., & Razon, L. F. 2022. LCA of Mortar with Calcined Clay and Limestone Filler in RC Column Retrofit. *Sustainability (Switzerland)*, 14(3). <https://doi.org/10.3390/su14031175>
- Broun, R., & Menzies, G. F. 2011. Life cycle energy and environmental analysis of partition wall systems in the UK. *Procedia Engineering*, 21, 864–873. <https://doi.org/10.1016/j.proeng.2011.11.2088>
- Buildability series publications*. Building & Construction Authority. (n.d.). Retrieved November 21, 2022, from https://www.bca.gov.sg/publications/BuildabilitySeries/buildability_series.html
- Buyle, M., Braet, J., & Audenaert, A. 2013. Life cycle assessment in the construction sector: A review. *Renewable and Sustainable Energy Reviews*, 26, 379–388. <https://doi.org/10.1016/j.rser.2013.05.001>
- Cabeza, L. F., Rincón, L., Vilariño, V., Pérez, G., & Castell, A. 2014. Life cycle assessment (LCA) and life cycle energy analysis (LCEA) of buildings and the building sector: A review. *Renewable and Sustainable Energy Reviews*, 29, 394–416. <https://doi.org/10.1016/j.rser.2013.08.037>
- Condeixa, K., Qualharini, E., Boer, D., & Haddad, A. 2015. An inquiry into the life cycle of systems of inner walls: Comparison of masonry and drywall. *Sustainability (Switzerland)*, 7(6), 7904–7925. <https://doi.org/10.3390/su7067904>
- Dolores, A. J. S., Lasco, J. D. D., Bertiz, T. M., & Lamar, K. M. 2020. Compressive strength and bulk density of concrete hollow blocks (CHB) infused with low-density polyethylene (LDPE) pellets. *Civil Engineering Journal (Iran)*, 6(10), 1932–1943. <https://doi.org/10.28991/cej-2020-03091593>
- Ecoinvent. 2021. *Online Access - ecoinvent*. Ecoinvent - Ecoin-vent. <https://ecoinvent.org/the-ecoinvent-database/online-access/>
- Fajardo Jr., M. 2000. *Simplified Construction Estimate* (3rd edition). 5138 Merchandising.
- Ferrández-García, A., Ibáñez-Forés, V., & Bovea, M. D. 2016. Eco-efficiency analysis of the life cycle of interior partition walls: A comparison of alternative solutions. *Journal of Cleaner Production*, 112(1), 649–665. <https://doi.org/10.1016/j.jclepro.2015.07.136>
- Frenette, C. D., Bulle, C., Beaugregard, R., Salenikovitch, A., & Derome, D. 2010. Using life cycle assessment to derive an environmental index for light-frame wood wall assemblies. *Building and Environment*, 45(10), 2111–2122. <https://doi.org/10.1016/j.buildenv.2010.03.009>
- Huijbregts, M., Steinmann, Z. J. N., Elshout, P. M. F. M., Stam, G., Verones, F., Vieira, M. D. M., Zijp, M., & van Zelm, R. 2016. ReCiPe 2016. *National Institute for Public Health and the Environment*, 194. <https://www.rivm.nl/bibliotheek/rapporten/2016-0104.pdf>
- ISO 14040:2006. 2014, August 12. ISO. <https://www.iso.org/standard/37456.html>ISO.
- ISO 14040. 2006. *Environmental Management: Life Cycle Assessment: Principles and Framework*. Geneva: ISO
- Kumar, R., Thakur, A., & Tiwary, A. K. 2021. A Comparative Study on Conventional Clay Bricks and Autoclaved Aerated Concrete Blocks. *IOP Conference Series: Earth and Environmental Science*, 889(1), 1–13. <https://doi.org/10.1088/1755-1315/889/1/012061>
- Lelieveld, J., Evans, J. S., Fnais, M., Giannadaki, D., & Pozzer, A. 2015. The contribution of outdoor air pollution sources to premature mortality on a global scale. *Nature*, 525(7569), 367–371. <https://doi.org/10.1038/nature15371>
- Mateus, R., Neiva, S., Bragança, L., Mendonça, P., & Macieira, M. 2013. Sustainability assessment of an innovative lightweight building technology for partition walls - Comparison with conventional technologies. *Building and Environment*, 67, 147–159. <https://doi.org/10.1016/j.buildenv.2013.05.012>
- Ortiz, O., Castells, F., & Sonnemann, G. 2010. Operational Energy in the life cycle of residential dwellings: The experience of Spain and Colombia. *Applied Energy*, 87(2), 673–680. <https://doi.org/10.1016/j.apenergy.2009.08.002>
- Pré. 2014. *Simapro Database Manual*. 3–48. <http://www.pre-sustainability.com/download/DatabaseManualMethods.pdf>
- Sethy, K. 2018. Aerated Concrete: A Revolutionary Construction Material. *International Journal of Engineering Technology Science and Research*, 5(988–993), 988–993.
- Vasconcelos, G., Lourenço, P. B., Mendonça, P., Camões, A., Mateus, R., Bragança, L., Brito, A. G., & Poletti, E. 2013. Proposal of an innovative solution for partition walls: Mechanical, thermal and acoustic validation. *Construction and Building Materials*, 48, 961–979. <https://doi.org/10.1016/j.conbuildmat.2013.07.079>
- Wu, J., Bai, G. L., Zhao, H. Y., & Li, X. 2015. Mechanical and thermal tests of an innovative environment-friendly hollow block as self-insulation wall materials. *Construction and Building Materials*, 93, 342–349. <https://doi.org/10.1016/j.conbuildmat.2015.06.003>

Temperature effect on static and quasi-static bridge measurements

K. Dakhili, T. Kebig, M. Schäfer & M. Maas

University of Luxembourg, Luxembourg, Luxembourg

M. Bender

Trier University of Applied Sciences, Trier, Germany

A. Zürbes

Bingen Technical University of Applied Sciences, Bingen, Germany

ABSTRACT: The performance of bridge damage assessment based on model updating approaches relies on correctly identifying the structural responses in the undamaged state. However, environmental uncertainties, such as temperature changes, influence structural responses in the same order of magnitude as damages. Therefore, a prestressed concrete bridge beam is studied in this paper. Temperature influences on static experiments in 2 test periods are minimized with physical temperature compensation technique. Displacement fluctuations decrease at least 60% after temperature compensation, making the summer and winter measurements comparable. Next, temperature-compensated Influence Lines (ILs), static flexibility and stiffness matrices are obtained. Comparing the results reveal the importance of performing measurements only on cloudy days. This paper contributes to differentiating between temperature effects and damages, which is crucial for a successful damage assessment.

1 INTRODUCTION

Bridges play a crucial role in connecting transport networks. Bridge safety and integrity are a fundamental concern of Structural Health Monitoring (SHM) as failures result in excessive losses. SHM should not merely rely on numerical models since the results differ from the measurements due to environmental and operational uncertainties (Dakhili et al. 2022; Ozer & Feng 2020).

Damage assessment can be achieved by tracking the stiffness matrix changes. In practice, flexibility is calculated first based on experimental data, and the stiffness matrix is obtained by calculating the inverse of the flexibility matrix. Despite numerous studies on dynamic flexibility matrix (Catbas et al. 2008; Schommer et al. 2017; Zhang & Moon 2012), the static flexibility matrix should be further investigated.

Among the environmental factors, temperature changes are a dominant component in bridge responses. Daily and seasonal temperature changes influence dynamic (Cross et al. 2013; Hu et al. 2018; Nandan & Singh 2014) and static measurements (Kromanis et al. 2016; Kulprapha & Warnitchai 2012; Nguyen et al. 2016) in the same manner as damages. Therefore, it is important to minimize temperature influence to distinguish damages from environmental uncertainties.

(Kulprapha & Warnitchai 2012) developed an analytical model of a small-scale prestressed concrete bridge to study nonlinear temperature distributions. Although the measured and predicted deflections and strains matched well for the scaled-down bridge, any mistakes in predicting thermal responses lead to unsuccessful damage identification (Xu et al. 2019).

(Nguyen et al. 2016) proposed a physical temperature compensation method to reduce the effect of temperature variations on the Deflection Lines (DLs). The proposed method was later combined with Principal Component Analysis (PCA), and the two-step temperature compensation technique

was utilized to compensate for the temperature effects from experimentally acquired natural frequencies of two different bridges (Nguyen et al. 2020).

As mentioned, the effect of temperature changes on the static flexibility and stiffness matrix should be further investigated. This paper studies the structural responses of a prestressed concrete bridge beam under outdoor conditions. The displacements and temperatures at different points are measured. Static and quasi-static experiments are performed using a trolley that moves along the beam. The static flexibility and stiffness matrices are calculated with temperature-compensated data. The reference static structural matrices in the undamaged state can be later implemented in damage assessment techniques based on model updating approaches.

2 EXPERIMENTAL SETUP

The experimental setup and the Finite Element (FE) model are described in this section.

2.1 The investigated beam

The prestressed concrete bridge connecting Mersch – Luxembourg was demolished in 2016, and a $24.9 \times 1.45 \times 2.10$ m (L×W×H) T-beam was transported to the University of Luxembourg. The beam was prestressed with 8 steel tendons in the longitudinal direction. An asphalt layer with a thickness of about 0.07m is still on the bridge beam. The beam is simply supported similar to the original setup. Figure 1 shows the investigated beam.



Figure 1. The prestressed bridge beam under study.

Seven displacement sensors (SV_i) measure the vertical displacements at different locations, while SH8 measures the horizontal displacements at the movable bearing. Additionally, temperature sensors (T1 – T4) record the concrete temperatures. Sensors T5 and T6 measure the asphalt and ambient temperatures, respectively.

The static and quasi-static experiments are performed with the help of a trolley that can move along the bridge. The trolley weighs about 8.8t, and it has an approximate speed of 1m/min. The schematic diagram of the beam, the sensor, and the trolley positions is shown in Figure 2.

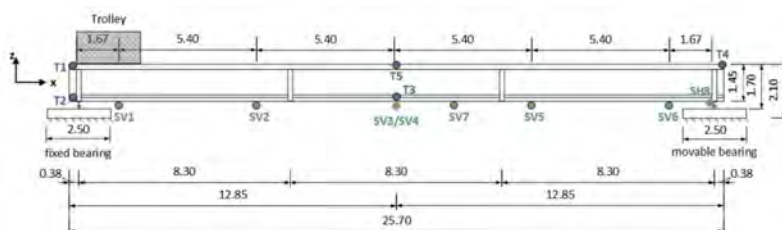


Figure 2. The schematic diagram of the beam.

2.2 The numerical model

The Finite Element (FE) model is created with Ansys Parametric Design Language (APDL). A linear model with mapped mesh is used to reduce computational costs. The trolley is modeled as 2 cuboids each with a different density to stimulate the weight distribution. Table 1 provides a summary of the material properties. Figure 3 demonstrates the FE model.

Table 1. Material properties of the FE model.

Material	Young's modulus [MPa]	Poisson's ratio	Density [kg/m ³]
Concrete	30e3	0.16	2500
Prestressed steel	205e3	0.3	7850
Asphalt	2e3	0.4	2350
Trolley	210e3	0.3	2440 – 5244

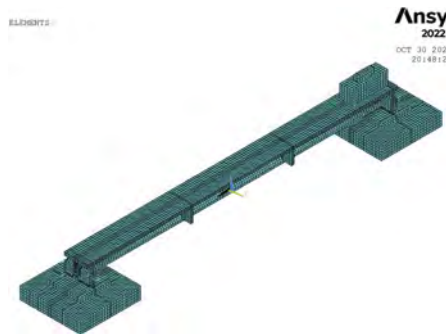


Figure 3. The FE model with the trolley over the fixed bearing.

3 METHODOLOGY

The flexibility and stiffness derivation together with the physical temperature compensation method is briefly explained.

3.1 Flexibility and stiffness matrix

A flexibility component is defined as the deflection at point i when the unit force is applied to point j . The static flexibility matrix is formulated as below (Thorby 2008):

$$\{x\} = [F]\{f\} \quad (1)$$

where $\{x\}$ = displacement vector, $[F]$ = flexibility matrix, and $\{f\}$ = force vector.

The Influence Lines (ILs) are measured during quasi-static tests. To do so, the trolley starts moving from the fixed bearing to SV1. It stops over SV1 for a few minutes, then it moves to SV2. This process is repeated to measure the ILs when the trolley is above SV3, SV5, and SV6. The flexibility matrix can be easily determined as each IL corresponds to one column of this matrix. Nevertheless, damage localization with $[F]$ is only indirectly feasible (Schommer et al. 2017). Thus, the inverse of the flexibility, i.e. the stiffness matrix should be obtained ($[K] = [F]^{-1}$). Local decrease in stiffness can be directly associated with damage location.

3.2 Physical temperature compensation

Static and quasi-static experiments are performed in two periods. The temperature data and the temperature difference between the upper and lower part of the beam, ΔT is plotted in Figure 4. The temperatures vary differently during the winter and summer. Hence, the measurements in two different seasons cannot be compared unless the temperature effects are compensated.

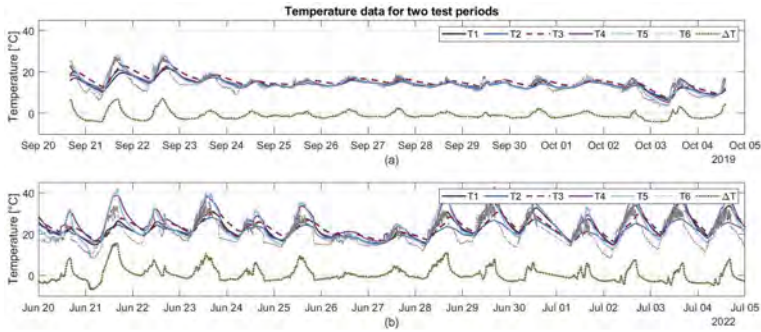


Figure 4. Temperature measurement ($\Delta T = T_5 - T_3$) a) winter b) summer.

Vertical deflection in the middle of the beam (SV3) and horizontal displacement at the movable bearing (SH8) are observed during one (un)loading state. These movements occur due to temperature changes. Figure 5 indicates that SV3 and SH8 are correlated with the temperature at the bottom of the beam (T3), and the temperature difference between the top (T5) and bottom of the beam. Since the linear relation between the SH8 and T3 is pronounced, this information is used to obtain the regression line slopes required for temperature compensation. The average regression line slopes are utilized to map the displacement data from the measured T3 temperature to $T_{ref} = 16^\circ\text{C}$ (Nguyen et al. 2016).

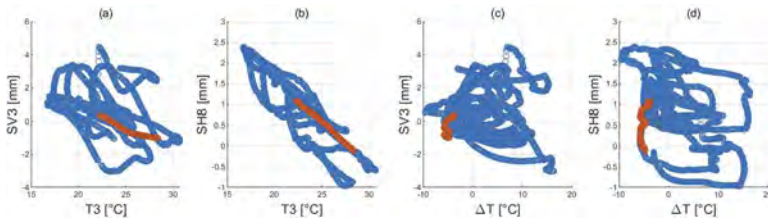


Figure 5. Displacement and temperature scatter plots – unloading state 20.06.2022 – 28.06.2022.

In this study, physical temperature compensation is only performed for the periods after the peak temperature of the day, when T1, T2, and T4 temperatures are almost equal according to Figure 4. For instance, one of the selected data segments is highlighted in Figure 5. As can be seen, for these data series there is no considerable between the displacements and the temperature difference of the top and bottom of the beam (ΔT).

The performance of this method highly depends on correct data selection, and it must be carefully handled to ensure successful damage detection. For instance, if the displacement information at the hottest time of the day is selected, the slope of the regression lines increases. This results in an increase of the scatter in the temperature-compensated displacements. In that case, the physical temperature compensation technique cannot fully reduce the temperature effects.

4 RESULTS

The FE model is verified with the experimental results by comparing deflections when the trolley is over the fixed bearing. As Table 2 indicates, the FE model is validated with the experimental results. Nevertheless, this validation is achievable only after temperature compensation.

4.1 Loading/Unloading states

Figure 6 depicts raw and temperature-compensated SV3 values. Loaded and unloaded states correspond to the trolley in the middle of the beam and the trolley over the fixed bearing, respectively. The results confirm that without considering the temperature effects, one might

Table 2. Comparison of simulated and measured deflections – trolley over fixed bearing.

Sensors	SV1	SV2	SV3	SV5	SV6
Simulation	0.82	3.13	4.18	3.13	0.82
Measurement	0.84	3.14	4.14	3.22	0.87
Error	2.3%	0.3%	1.0%	2.8%	5.7%

associate the increase in the displacements in summer with damage. However, the temperature-compensated values confirm that the bridge beam is still in the healthy state during these two periods. Table 3 presents a summary of the results.

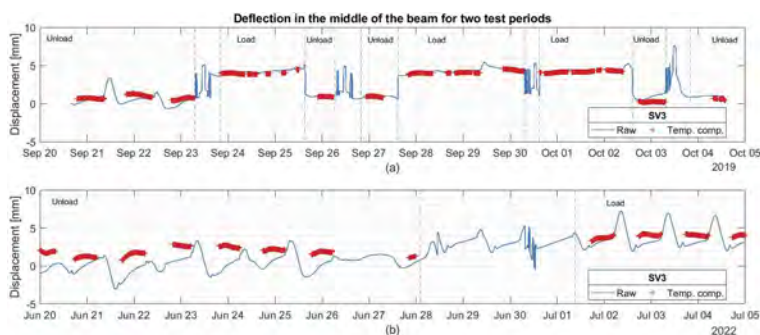


Figure 6. Raw and temperature compensated SV3 values a) winter b) summer.

Table 3. Summary of temperature compensation effect on static data.

	Winter		Summer	
	Loaded state	Unloaded state	Loaded state	Unloaded state
Raw SV3 [mm]	3.63 – 5.47	-0.66 – 3.37	1.89 – 7.21	-3.03 – 3.37
Temp. comp. SV3 [mm]	3.86 – 4.61	0.14 – 1.28	3.28 – 4.27	0.70 – 2.86
Range Decrease (%)	59.2	71.7	81.4	66.2

4.2 Quasi-static experiments

Flexibility is calculated based on the Influence Lines (ILs). Several experiments are performed in the winter and summer. As an example, Figure 7 illustrates the raw and temperature-compensated ILs measured with SV3 for two tests. Although the results are only shown for SV3, temperature compensation is performed on every sensor data. In order to better explain the results, the asphalt temperature at the top (T5) and the concrete temperature at the bottom of the beam (T3) are plotted in Figure 8.

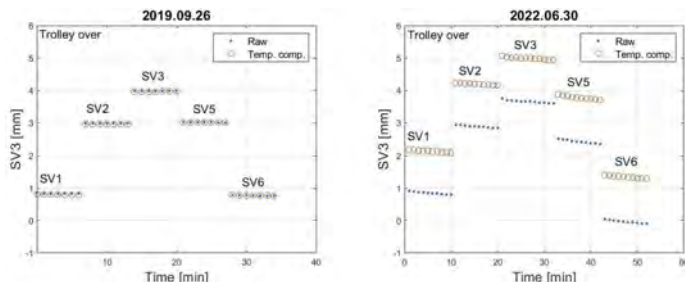


Figure 7. Raw and temperature-compensated IL measured with SV3 at different trolley positions.

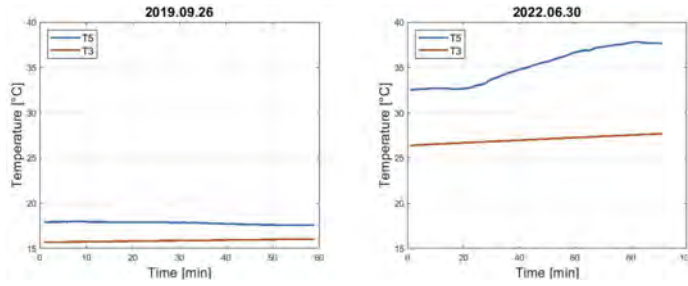


Figure 8. T5 and T3 during the quasi-static tests.

As stated, the reference temperature is chosen to be $T_{ref} = 16^{\circ}\text{C}$. Figure 8 indicates that when the difference between T3 and T_{ref} is bigger, the effect of temperature compensation becomes more apparent. The temperatures are closer to T_{ref} during the winter, and they are more consistent. In contrast, being considerably higher than T_{ref} , the temperatures change sharply in the summer. Therefore, not only temperature compensation is recommended, but also experiments should be performed on cloudy days when there is no or little solar radiation to avoid considerable nonhomogeneous temperature distributions over the bridge beam.

4.3 Flexibility and stiffness matrix

The beam deflection due to its weight is subtracted from the Influence Lines (ILs) in the previous section. Then, the results are divided by the trolley weight, 8.8t to calculate the flexibility matrix. As explained, the stiffness matrix is obtained by calculating the inverse of the flexibility. Figures 9 and 10 show the temperature-compensated flexibility and stiffness matrices for the tests in the previous section.

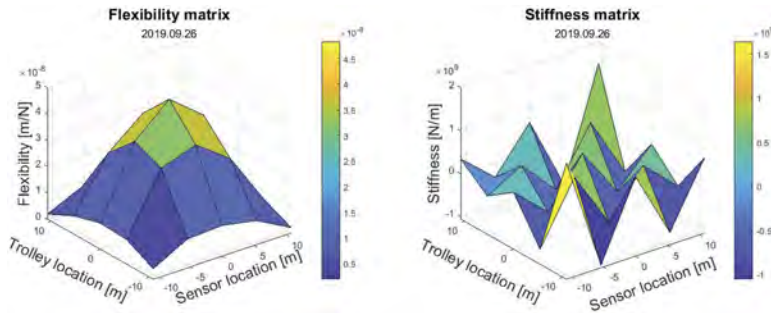


Figure 9. An example of the flexibility and stiffness matrix for a test in winter.

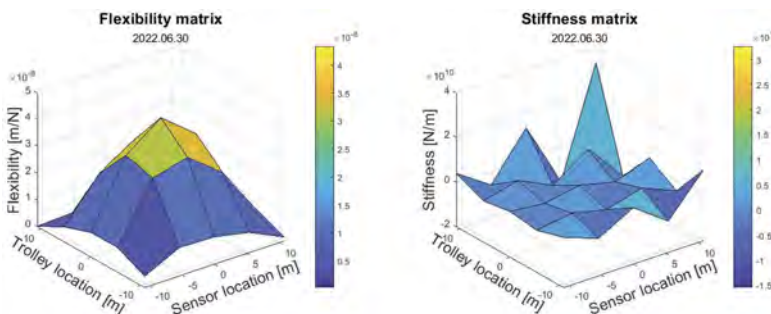


Figure 10. An example of the flexibility and stiffness matrix for a test in summer.

Although there is a similarity between the flexibility matrices in winter and summer, the difference between the stiffness matrices in these two seasons is noticeable. In order to better analyze the results, the diagonal arrays of these matrices are compared in Figure 11.

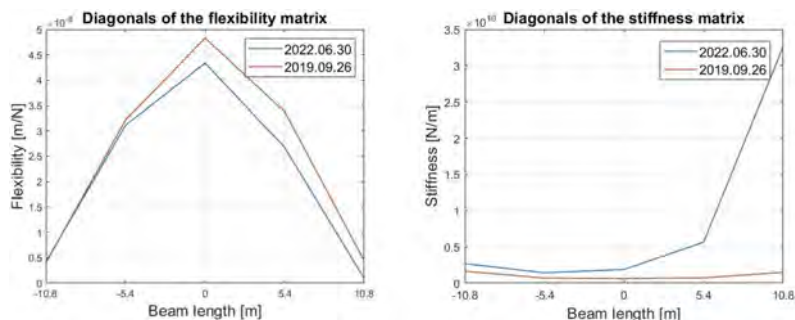


Figure 11. Comparison of diagonal arrays of the flexibility and stiffness matrices.

According to Figure 11, although flexibility matrices in summer and winter may be comparable with a difference of about 10%, the difference between the diagonal arrays of the stiffness matrices cannot be neglected. Therefore, it is suggested to either perform the 2-step temperature compensation proposed by (Nguyen et al. 2016) or to perform measurements only on cloudy days with minimum solar radiations.

5 CONCLUSIONS

Establishing an accurate model to represent the undamaged state is critical to guarantee a successful damage assessment. This paper demonstrated that daily and seasonal temperature change influences may be mistaken for damage. Therefore, this study aimed to minimize temperature effects with a physical temperature compensation method.

Firstly, the horizontal movement of the bridge beam was shown to be strongly correlated with the concrete temperature in the middle of the beam. The displacements for loaded (trolley in the middle) and unloaded (trolley over the fixed bearing) states were temperature compensated. The results showed that although temperatures are considerably different in summer and winter, physical temperature compensation could reduce the fluctuations for the selected segments.

Secondly, the temperature compensation of the Influence Lines (ILs) was investigated. This information was required to calculate the static flexibility matrix. Being more consistent, the temperatures were closer to the reference temperature in winter, while the temperatures changed sharply during the tests conducted in summer. Thus, it is suggested to implement a 2-step temperature compensation or perform measurements only on cloudy days.

Finally, flexibility and stiffness matrices in summer and winter were compared with two tests as examples. In practice, the flexibility matrix is calculated based on the ILs, which is a straightforward procedure. However, tracking the changes in the stiffness matrix by comparing the undamaged and damaged states provides information about the damage location. Therefore, the stiffness matrix should be obtained by calculating the inverse of the flexibility.

The results showed that although the diagonal arrays of the flexibility matrices vary by roughly 10% in the summer and winter, the stiffness matrix arrays are not comparable. Thus, it was confirmed again that the cloudy days with minimum solar radiation should be selected as test days.

REFERENCES

- Catbas, F. N., Gul, M., & Burkett, J. L. 2008. Damage assessment using flexibility and flexibility-based curvature for structural health monitoring. *Smart Materials and Structures*, 17(1). <http://dx.doi.org/10.1088/0964-1726/17/01/015024>

- Cross, E. J., Koo, K. Y., Brownjohn, J. M. W., & Worden, K. 2013. Long-term monitoring and data analysis of the Tamar Bridge. *Mechanical Systems and Signal Processing*, 35(1–2), 16–34. <http://dx.doi.org/10.1016/j.ymsp.2012.08.026>
- Dakhili, K., Kebig, T., & Maas, S. 2022. Effects of various outdoor conditions on Structural Health Monitoring (SHM) of bridges using data from Luxembourg. 7. *VDI-Fachtagung Baudynamik*, 209–220. <https://doi.org/10.51202/9783181023792-209>
- Hu, W. H., Tang, D. H., Teng, J., Said, S., & Rohrmann, R. G. 2018. Structural health monitoring of a prestressed concrete bridge based on statistical pattern recognition of continuous dynamic measurements over 14 years. *Sensors*, 18(12). <http://dx.doi.org/10.3390/S18124117>
- Kromanis, R., Kripakaran, P., & Harvey, B. 2016. Long-term structural health monitoring of the Cled-dau bridge: Evaluation of quasi-static temperature effects on bearing movements. *Structure and Infrastructure Engineering*, 12(10), 1342–1355. <http://dx.doi.org/10.1080/15732479.2015.1117113>
- Kulprapha, N., & Warnitchai, P. 2012. Structural health monitoring of continuous prestressed concrete bridges using ambient thermal responses. *Engineering Structures*, 40, 20–38. <http://dx.doi.org/10.1016/j.engstruct.2012.02.001>
- Nandan, H., & Singh, M. P. 2014. Effects of thermal environment on structural frequencies: Part I - A simulation study. *Engineering Structures*, 81, 480–490. <http://dx.doi.org/10.1016/j.engstruct.2014.06.046>
- Nguyen, V. H., Kebig, T., Golinval, J. C., & Maas, S. 2020. Reduction of temperature effects for bridge health monitoring. *Proceedings of the International Conference on Structural Dynamic, EURO DYN, 1*, 1195–1204. <http://dx.doi.org/10.47964/1120.9096.19343>
- Nguyen, V. H., Schommer, S., Maas, S., & Zürbes, A. 2016. Static load testing with temperature compensation for structural health monitoring of bridges. *Engineering Structures*, 127, 700–718. <http://dx.doi.org/10.1016/j.engstruct.2016.09.018>
- Ozer, E., & Feng, M. Q. 2020. Structural health monitoring. *Start-Up Creation*, 345–367. <http://dx.doi.org/10.1016/B978-0-12-819946-6.00013-8>
- Schommer, S., Mahowald, J., Nguyen, V. H., Waldmann, D., Maas, S., Zürbes, A., & Roeck, G. De. 2017. Health monitoring based on dynamic flexibility matrix: Theoretical models versus in-situ tests. *Engineering*, 09(02), 37–67. <http://dx.doi.org/10.4236/eng.2017.92004>
- Thorby, D. 2008. *Structural Dynamics and Vibration in Practice An Engineering Handbook* (D. Thorby (ed.); 1st ed.). Butterworth-Heinemann. <http://dx.doi.org/10.1016/B978-0-7506-8002-8.00014-6>
- Xu, X., Huang, Q., Ren, Y., Zhao, D.-Y., Yang, J., & Zhang, D.-Y. 2019. Modeling and Separation of Thermal Effects from Cable-Stayed Bridge Response. *Journal of Bridge Engineering*, 24(5), 1–16. [http://dx.doi.org/10.1061/\(asce\)be.1943-5592.0001387](http://dx.doi.org/10.1061/(asce)be.1943-5592.0001387)
- Zhang, J., & Moon, F. L. 2012. A new impact testing method for efficient structural flexibility identification. *Smart Materials and Structures*, 21(5). <http://dx.doi.org/10.1088/0964-1726/21/5/055016>

Robot-BIM integration for underground canals life-cycle management

H. Pourhosseini, F. Zahedi & J. Majrouhi Sardroud
Central Tehran Branch, Islamic Azad University, Tehran, Iran

ABSTRACT: Today, global warming causes unpredictable climate changes and issues, such as torrential rains, that leads professionals to anticipate future needs to control sudden floods. In this regard, to reduce the impacts of these consequences, and secure residents, a perfect surface water collection system is crucial. In this paper, the application of building information modeling (BIM) in the entire life cycle of underground surface water collection canals has been reviewed. Then a new-emerged robotic innovation is presented that exploits various technologies to monitor and evaluate channel health in the presence of flammable gasses and moisture. And finally, an integration framework is presented. Based on field verifications, it has anticipated that employing this technology will provide a trustworthy platform for predictive maintenance throughout the whole life-cycle of the underground channels. Meanwhile, during the pre-construction phase, BIM and other technologies integration assist the engineering teams in striding toward the best design output.

1 INTRODUCTION

Underground utility infrastructures create a complex system that needs a comprehensive understanding and reliable tools to manage it throughout the life cycle. Any error during infrastructure engineering, construction, and operation will lead to critical consequences, which could influence urban areas (Chong *et al.*, 2016). Infrastructure management has been facilitated by exploiting recent technological advancements, such as BIM (Hijazi and Omar, 2017). For instance, BIM benefits are five times more than conventional approaches, such as employing CAD-based applications (Kumar *et al.*, 2017). Also, applying BIM to infrastructure management allows operation teams to identify the exact location of underground facilities over a shorter period (Wang *et al.*, 2019). Infrastructure BIM (I-BIM) has developed more in Asia and America compared with other regions. One of the advantages of employing I-BIM in the design stage is that it provides an intelligent model which enables designers to maintain automatic changing interoperability. In contrast, conventional CAD models require controlling the impacts of a change on other dimensions. Stakeholders would also manage and review the 3D virtual model of the built environment, and the model allows them to make-do decisions (Vignali *et al.*, 2021). An intelligent mobile robot has been invented to facilitate periodic infrastructure health monitoring, making well-grounded decisions, exploring any defect in the infrastructure, and reporting it through various technologies.

2 BIM CONTRIBUTION TO INFRASTRUCTURE

The crucial value of BIM lies in generating information iteratively and producing a persistent flow of updated information to project participants (Vignali *et al.*, 2021). To enhance the data gathering accuracy, researchers and practitioners turned to exploit automatic processes. Employing robots

allows teams to access real-time data to compensate for a lag between construction or maintenance and models (Alonso *et al.*, 2019; Lu *et al.*, 2019; Lundeen *et al.*, 2019).

BIM provides several benefits to the construction industry. BIM could improve pre-construction activities in designing, programming, estimation, and planning, and helps engineering teams to design efficiently with fewer conflicts and lower time. Also, BIM enables teams to make required redesigns and reviews employing a 3D virtual model and explore any clashes (Anumba *et al.*, 2010; Azhar, 2011; Barlish *et al.*, 2012; Latiffi *et al.*, 2013; Shou *et al.*, 2015). Meantime, it prepares cost and time estimation to enable project managers to make pragmatic decisions (Anumba *et al.*, 2010; Azhar, 2011; Latiffi *et al.*, 2013; Shou *et al.*, 2015; BorjeGhale *et al.*, 2016; Sardroud, Ghaleh, *et al.*, 2020; Sardroud, Mehranpour, *et al.*, 2020). On the other hand, the 3D model could provide not only an accurate quantity survey but also a practical schedule for anticipating and planning the resource flow throughout the construction phase (Anumba *et al.*, 2010; Latiffi *et al.*, 2013; Shou *et al.*, 2015; BorjeGhale *et al.*, 2016; Sardroud, Ghaleh, *et al.*, 2020). Before starting construction, BIM assists teams in deciding on the site usage and occupation for building, facilities, and mobilization. During the construction phase, the seamless flow of information enhances and facilitates communication between stakeholders. Due to BIM applicability for as-built construction, shop drawings will be practical with less material loss, rework, and waste. Cash flow is accurately controlled, and risks are dramatically reduced. Project managers, on the other hand, will trace material flow and could monitor the site's commutes and material flow (Anumba *et al.*, 2010; Barlish *et al.*, 2012; Bennett *et al.*, 2013; Latiffi *et al.*, 2013; Shou *et al.*, 2015; BorjeGhale *et al.*, 2016; Sardroud, Ghaleh, *et al.*, 2020). BIM could pursue any component and its life cycle to provide continuous operation. In case of crisis, operation teams could react abruptly and efficiently (Anumba *et al.*, 2010; Latiffi *et al.*, 2013; Shou *et al.*, 2015; Kameli *et al.*, 2021).

Infrastructure BIM (I-BIM) concentrates on horizontal construction to monitor and predict infrastructure construction and operation precisely (Vignali *et al.*, 2021), which is neglected in building construction. Fanning *et al.* juxtaposed two similar bridge construction projects and deduced that applying I-BIM lessens construction costs by 5 to 9% (Fanning *et al.*, 2015), but the critical aspect to consider is the level of detail defined in the model to exploit the full potential of I-BIM. (Kim *et al.*, 2014) showed in tunnels, a high level of detail is required. Considering the time and cost involved in I-BIM models, stakeholders could identify upcoming conflicts to assess the construction procedure, measure the schedule alteration impacts, observe project progression at any stage visually, and prevent teams' interference. On the other hand, any model modification will result in a real-time error-free automated bill of quantity, time, and cost update, as well as the plans and sections' automatic update (D'Amico *et al.*, 2020). Expanding the I-BIM application requires the addition of two more dimensions; 6D, for instance, represents the application of geographical information of the construction site and components, and 7D applies to facility management to associates throughout the whole infrastructure life-cycle (Samimpay and Saghatforoush, 2020). On the other hand, construction 4.0 is an integration of different emerged technologies such as the Internet of Things (IoT), Simulating (BIM), Augmented and Virtual Reality (AR/VR), Robotics and Automation, and 3D printing (Turner *et al.*, 2020) (Figure 1).



Figure 1. Construction 4.0 components.

In the proposed robotic system, to detect and locate defects accurately, several technologies are integrated with the robot (e.g., geographical information system (GIS), augmented reality (AR), and sensors.)

3 I-BIM'S LOD

For ease of assessment, a Norwegian standard project phase identification, called “Next Step,” selected in Figure 2, and the LoD (Level of Details) could have developed in each phase with the aim of the BIM efficient application proposed (Knotten *et al.*, 2016).



Figure 2. Life-cycle phases using the Next Step method.

The level of graphic details defined in a 3D BIM-based software has divided into five steps. LOD 100 is a conceptual volumetric model of the built environment used for quantity survey and cost estimation (Coates, 2013) and is usually utilized for feasibility study, pre-planning, or rough cost estimation (Latiffi *et al.*, 2015). At LOD 200, the model has mobilized with approximate geometry, including accurate values, size, shape, and position (Coates, 2013; Latiffi *et al.*, 2015). LOD 300 provides accurate geometry suitable for conventional construction drawings (Coates, 2013), which results in cost and time-precise estimation with more accurate quantity, shape, size, and location and will reflect employer requests. Also, the required performance defined by the owner could be considered in the model (Latiffi *et al.*, 2015). LOD 400 is suitable for construction and installation, which is usually related to shop drawings (Coates, 2013). And LOD 500 consists of construction as-built drawings suitable for operation and maintenance (Coates, 2013), which is the most accurate digital model of the building (Digital twin) (Latiffi *et al.*, 2015). Figure 3 presents the graphical LOD of each defined step.



Figure 3. Steps' graphical LOD.

4 ROBOTICS

The first step is examining common approaches used globally. It is necessary because operators must have up-to-date information to control and manage structures and devices, including underground and open channels. The data should then be processed, and the best strategies and methods adopted to manage it. Three approaches have generally been proposed for gathering information from any facility presented in Table 1 below.

According to Table 1, Industry 4.0 technologies contribute to imagining a machine that can enter the channel instead of personnel; and they can be controlled by an expert or programmed

Table 1. Methods of collecting data from each structure.

Methods	Description	Problems	Result
Visual inspection	An expert personally enters the site and inspects the equipment, facilities, and structure.	Lack of oxygen, the presence of flammable gases, insects and vermin, and the difficulty of carrying the device inside and other dangers for humans	Lack of adequate conditions to have enough concentration to identify and fix anomalies, and also the unsuitable situation for a human visit.
Field impression	An expert or a representative of this person enters the channel and takes photos and videos.	Same problems as visual inspection.	An unsuitable situation for a human to visit.
Automatic system	A series of surveillance cameras are placed inside the canal to monitor the canal.	Cannot be done due to environmental conditions, the number of required cameras, and high maintenance costs.	Using other 4 th generation of the industrial revolutions.

to perform the mission automatically. According to the data taken by the device, specialists can design strategies to repair and preserve the canal without going into the channel and being in this predicament. In addition, experts can use the device as often as they need and whenever they want to update information in the fastest, safest, and most efficient way possible.

This study focuses on using Industry 4.0 technologies to efficiently collect data and maintain underground water channels. The proposed method involves creating a machine that alerts the operator of maintenance needs in the canal and takes action. While drones equipped with lasers and cameras are suitable for monitoring open canals, it is difficult to use them for underground canals due to the risk of explosion from the drone's sparks. Therefore, a different device that can capture the canal path and relay information to the operator without producing sparks is necessary.

A prototype has been developed to test for defective areas within water canals while addressing safety and cost concerns. It is a scaled-down version of the life-size robot, designed to ensure safety in the presence of gas. System requirements include non-explosiveness, waterproofing, obstacle bypass, video and image capturing, remote control, maneuverability, pressure, height, and temperature measurement.

5 PROPOSED FRAMEWORK

To prevent soil and groundwater pollution caused by sewage leakage in underground storm-water canals, detecting defects early is crucial. A proposed integration framework between BIM and a newly invented robot, as shown in Figure 4, enables the exchange of information for a deeper understanding and necessary actions. The framework supports technology integration throughout the canal's life cycle. In the pre-construction phase, engineering teams create a detailed 3D virtual model using BIM software like AutoCAD 3D.

Then they could upload layouts, plans, and cross sections into I-BIM for a comprehensive 3D smart model with automatic updating capability. Adding cost and time features allows teams to employ a 5D I-BIM; enables stakeholders to make any desired changes and explore its effects on the final deliverables and related time and cost. Therefore, making do-decisions will be facilitated during engineering.

GIS technology applied to I-BIM allows for real-time tracking of resources during construction, controlling conflicts and interference. A robot using 7D I-BIM measures construction quality and reports errors with location and images. 7D I-BIM also supports sustainable maintenance through periodic inspections. Integrated with the 3D model, GIS identifies locations, and IoT assesses defect characteristics, while AR aids decision-making with a realistic defect representation.

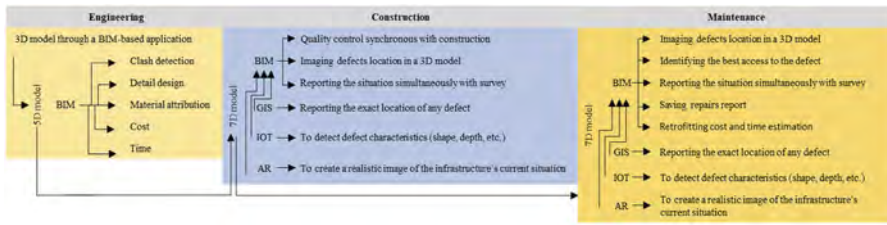


Figure 4. Proposed BIM-Robotics framework.

6 FINDINGS AND DISCUSSION

The research identified the need for canal harvesting devices in buried canals. The first phase gathered information on management methods and device requirements, including the need for non-sparking, non-explosive devices in the presence of combustible gases and waterproofing due to moisture in the canals.

For monitoring buried water canals, the device needs to be waterproof, spark-free, and obstacle-friendly, with video recording and remote control. It should move on a 20-degree incline, monitor pressure, height, and temperature, detect anomalies, and alert the operator.

The aim was to use point cloud scanners to measure a tunnel's dimensions and compare them to a 3D model to detect any inconsistencies. However, since the scanners were costly and not readily available, alternative solutions were explored. The necessary equipment was obtained by researching available tools. The robot's controller was programmed using Python software, allowing for remote operation and monitoring via a mobile phone's web browser. The robot's internal components were identified and connected before being modeled in Solid software and 3D printed. Figure 5 illustrates a sample modeled in Solid software, and Figure 6 depicts the robot's final appearance.

To test the robot's functionality, a prototype duct was created using Sketch-Up software and five 20 cm diameter tubes, and four 45- and 90-degree elbows. Artificial anomalies were added to the floor and ceiling using sand, stone, and wood to challenge the robot. The results showed that the robot was able to move effectively through the obstacles and identify anomalies, demonstrating acceptable performance.

This study employed Industry 4.0 technologies for continuous monitoring and control of water channels, which can improve their maintenance. The robot developed in the study was tested and found to be able to easily navigate obstacles in gas and moisture-filled environments and detect anomalies using sensors and cameras. The study concludes that the use of Industry 4.0 technologies in water channel maintenance can help prevent sediment accumulation and disturbances, which can cause blockages and failures in the channel. By detecting and addressing these issues early, the costs and damages associated with flooding and other dangers can be minimized. The robots developed can also be used to efficiently create as-built drawings of the channels. Overall, the study suggests that Industry 4.0 technologies can improve the speed and efficiency of information retrieval compared to traditional methods.

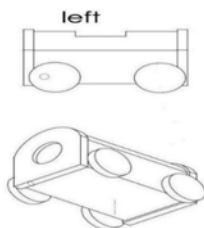


Figure 5. The modeled robot in solid software.



Figure 6. Final view.

A proposed framework is intended to guide the robot's application through the pre-, post-, and construction stages and facilitate communication and information exchange among stakeholders throughout the life cycle of an underground infrastructure. The integration of innovative robots, automation, and other technologies could ensure the continuous real-time monitoring of canals, which is crucial for public safety. The framework aims to create a reliable information platform for teams to explore the current state of the built environment and to provide accurate time and cost estimates during the engineering phase. During construction, the framework allows teams to control construction quality, detect defects in real-time, and inform construction teams for corrections and repairs. Additionally, the technology could accelerate the as-built drawing process. During maintenance, the study assists operators in finding defects in the canal, their location, and characteristics, and transferring the information to an I-BIM-based virtual model.

7 CONCLUSIONS

This research proposed a robot to monitor and maintain buried canals. The robot provides online real-time about the current state of canals, including any structural defect through measuring defects and obstruction on the channels by measuring any change in diameter. Hopefully, through its performance, during operation, teams can detect any defect in the early stages of happening and take preventive action to predict future problems, such as blocking the canal due to sediments or disruption of operation due to destruction or leakage. Also, toward nD I-BIM, a framework is proposed to work closely with the robot. The framework aims to create a seamless flow of information and a reliable platform to notify maintenance teams to take any required action to avoid crucial problems. Meantime, it could provide reliable reports through augmented reality in a 3D virtual environment that can show the exact location and dimension of the damage.

Although this research concentrated on the operation phase, it could be extended into the engineering and construction phases, when teams could exploit its advantages. The proposed hardware can monitor and measure quality during construction. AR feature will transfer a high-resolution picture of the defect and any error with the exact location, characteristics, and an augmented defect image. And before construction, teams could fully understand the project deliverables by creating a realistic model with a walking-through ability. Overall, it is expected that the proposed technology aims projects teams toward the following achievements:

- Exporting a reliable time and cost estimation and scheduling ability
- Quality control measures during construction
- Construction progression control
- As-built drawing
- Defect detection
- Maintenance monitoring
- Environmental issues management

To perform this research, due to restrictions, researchers could not provide the required technologies for Big Data. Therefore, the authors suggest developing the proposed robot by using Big Data to collect cloud point data for analysis.

REFERENCES

- Alonso, R., Borrás, M., Koppelaar, R. H. E. M., Lodigiani, A., Loscos, E. and Yöntem, E. (2019) 'SPHERE: BIM Digital Twin Platform', Multidisciplinary Digital Publishing Institute Proceedings, 20(1), p. 9. doi: 10.3390/proceedings2019020009.
- Anumba, C. J., Dubler, C. R., Goodman, S., Kasprzak, C., Kreider, R., Messner, J., Saluja, C. and Zikic, N. (2010) BIM Project Execution Planning Guide. Computer Integrated Construction Research Program, The Pennsylvania State University.

- Azhar, S. (2011) 'Building Information Modeling (BIM): Trends, Benefits, Risks, and Challenges for the AEC Industry', *Australasian Journal of Construction Economics and Building*, 11(3), pp. 241–252. doi: 10.5130/ajceb.v12i4.3032.
- Barlish, K. and Sullivan, K. (2012) 'How to measure the benefits of BIM- A case study approach', *Automation in Construction*, 24, pp. 149–159. doi: 10.1016/j.autcon.2012.02.008.
- Bennett, L. and Mahdjoubi, L. (2013) 'Construction health and safety, BIM and cloud technology Proper integration can drive benefits for all stakeholders', in 2013 IEEE International Conference on Cloud Computing Technology and Science, pp. 215–218. doi: 10.1109/CloudCom.2013.128.
- BorjeGhale, R. M. and Majrouhi Sardroud, J. (2016) 'Approaching Industrialization of Buildings and Integrated Construction Using Building Information Modeling', in *Procedia Engineering*, pp. 534–541. doi: 10.1016/j.proeng.2016.11.655.
- Chong, H. Y., Lopez, R., Wang, J., Wang, X. and Zhao, Z. (2016) 'Comparative Analysis on the Adoption and Use of BIM in Road Infrastructure Projects', *Journal of Management in Engineering*, 32(6), p. 05016021. doi: 10.1061/(ASCE)ME.1943-5479.0000460.
- Coates, S. P. (2013) *Bim Implementation Strategy Framework for Small Architectural Practices*. The University of Salford.
- D'Amico, F., D'Ascanio, L., Falco, M. C. De, Ferrante, C., Presta, D. and Tosti, F. (2020) 'BIM for Infrastructure: An Efficient Process to Achieve 4D and 5D Digital Dimensions', *European Transport/ Trasporti Europei*, 77.
- Fanning, B., Clevenger, C. M., Ozbek, M. E. and Mahmoud, H. (2015) 'Implementing BIM on Infrastructure: Comparison of Two Bridge Construction Projects', *Practice Periodical on Structural Design and Construction*, 20(4), p. 04014044. doi: 10.1061/(asce)sc.1943-5576.0000239.
- Hijazi, A. A. and Omar, H. A. (2017) 'Level Of Detail Specifications, Standard S And File-Format Challenges In Infrastructure', *WIT Transactions on the Built Environment*, 169, pp. 143–154. doi: 10.2495/WIT170141.
- Kameli, M., Hosseinalipour, M., Majrouhi Sardroud, J., Ahmed, S. M. and Behravan, M. (2021) 'Improving maintenance performance by developing an IFC BIM/RFID- based computer system', *Journal of Ambient Intelligence and Humanized Computing*. Springer Berlin Heidelberg, 12(2), pp. 3055–3074. doi: 10.1007/s12652-020-02464-3.
- Kim, J., Ji, S., Jeong, T. and Seo, J. (2014) 'A Feasibility Study to Adopt BIM-based Infrastructure Management System', *Journal of the Korean Society of Civil Engineers*, 34(1), pp. 285–292.
- Knotten, V., Hosseini, A., Klakegg, O. J. and Jonny, O. (2016) "Next step": a new systematic approach to plan and execute AEC projects', in *Proceedings of the CIB World Building Congress*. Available at: https://ntnuopen.ntnu.no/ntnu-xmlui/bitstream/handle/11250/2486003/Vegard_Knotten.pdf?sequence=5#page=158.
- Kumar, B., Cai, H. and Hastak, M. (2017) 'An Assessment of Benefits of Using BIM on an Infrastructure Project', in *International Conference on Sustainable Infrastructure*, pp. 88–95.
- Latiffi, A. A., Mohd, S., Kasim, N. and Fathi, M. S. (2013) 'Building Information Modeling (BIM) Application in Malaysian Construction Industry', *International Journal of Construction Engineering and Management*, 2(4A), pp. 1–6. doi: 10.5923/s.ijcem.201309.01.
- Latiffi, A. A., Brahim, J., Mohd, S. and Fathi, M. S. (2015) 'Building Information Modeling (BIM): Exploring Level of Development (LOD) in Construction Projects', *Applied Mechanics and Materials*, 773, pp. 933–937. doi: 10.4028/www.scientific.net/amm.773-774.933.
- Lu, Q., Xie, X., Heaton, J., Parlikad, A. K. and Schooling, J. (2019) 'From BIM towards Digital Twin: Strategy and Future Development for Smart Asset Management', in *International Workshop on Service Orientation in Holonic and Multi-Agent Manufacturing*. Springer, Cham, pp. 392–404.
- Lundeen, K. M., Kamat, V. R., Menassa, C. C. and McGee, W. (2019) 'Autonomous motion planning and task execution in geometrically adaptive robotized construction work', *Automation in Construction*, 100, pp. 24–45. doi: <https://doi.org/10.1016/j.autcon.2018.12.020>.
- Samimpay, R. and Saghatforoush, E. (2020) 'Benefits of Implementing Building Information Modeling (BIM) in Infrastructure Projects', *Journal of Engineering, Project, and Production Management*, 10 (2), pp. 123–140. doi: 10.2478/jeppm-2020-0015.
- Sardroud, J. M., Ghaleh, R. M. B. and Kameli, M. (2020) 'An investigation on Building Information Modelling Role in Industrialization of Building', in the *Creative Construction e-Conference*. Budapest, Hungary, pp. 650–660.
- Sardroud, J. M., Mehranpour, H. and Arzanloo, A. (2020) 'An Investigation into the Integration of Building Information Modeling with Pre-Construction Industry in the Developed Countries and Iran', in the *Creative Construction e-Conference 2020*. Budapest University of Technology and Economics, pp.2–10. doi: <https://doi.org/10.3311/CCC2020-011>.

- Shou, W., Wang, J., Wang, X. and Chong, H. Y. (2015) 'A Comparative Review of Building Information Modelling Implementation in Building and Infrastructure Industries', *Journal of Archives of Computational Methods in Engineering*, 22(2), pp. 291–308. doi: 10.1007/s11831-014-9125-9.
- Turner, C. J., Oyekan, J., Stergioulas, L. and Griffin, D. (2020) 'Utilizing Industry 4.0 on the Construction Site: Challenges and Opportunities', *IEEE Transactions on Industrial Informatics*, 17(2), pp. 746–756. doi: 10.1109/TII.2020.3002197.
- Vignali, V., Acerra, E. M., Lantieri, C., Vincenzo, F. Di, Piacentini, G. and Pancaldi, S. (2021) 'Building Information Modelling (BIM) Application for an Existing Road Infrastructure', *Automation in Construction*. Elsevier B.V., 128, p. 103752. doi: 10.1016/j.autcon.2021.103752.
- Wang, M., Deng, Y., Won, J. and Cheng, J. C. P. (2019) 'An Integrated Underground Utility Management and Decision Support Based on BIM and GIS', *Automation in Construction*. Elsevier, 107, p. 102931. doi: 10.1016/j.autcon.2019.102931.

Life-cycle cost analysis of possible solutions for converting existing single-family house into nZEB

C. Marincu & D. Dan

Department of Civil Engineering and Building Services, Politehnica University Timisoara, Timisoara, Romania

ABSTRACT: The obligation of the nZEB building standard has become a certainty of almost two years for all new buildings in Romania. This is even more relevant in the current context of the energy price crisis, as more and more building owners become aware of the importance of energy efficiency and the use of renewable energy systems. Thus, in this paper possible solutions for converting an existing single-family building into a nearly zero-energy building are analyzed and presented. The building has been designed and executed in such a way as to have an energy performance above the minimum required according to the technical regulations in force at the time of design. The current energy performance of the building has been evaluated both theoretically using a dedicated calculation program and based on energy bills for one year period. Based on the current energy performance, a series of solutions have been proposed to increase the energy performance up to the nZEB level. Analyses in terms of energy consumption and life-cycle cost were performed to identify the cost optimal solution that leads to the nZEB upgrade.

1 INTRODUCTION

1.1 *General information*

The building sector, due to its major share in total energy consumption and CO₂ emissions at a global level, plays a key role in the long-term strategy of greenhouse gasses reduction assumed by the European Union (EU). Improving energy efficiency in buildings represents a mandatory action towards the carbon-neutrality goal by 2050 (European Commission, 2019). A major step in improving the energy performance of buildings in the EU was the adoption of Directive 2002/91/EC (The European Parliament, Directive 2002/91/EC, 2002) which introduced energy certification of buildings, minimum energy requirements for new buildings and the promotion of energy renovation of existing ones. In the interest of clarity, the EPBD was recast in 2010 (The European Parliament, Directive 2010/31/EU, 2010), with the main purpose of strengthening the energy performance improvement of buildings in the EU. The latter introduced the nearly zero-energy building (nZEB) concept as the mandatory standard of energy performance for new public and private buildings after 2018 and 2020. In Romania, up until recently, the investment in energy conservation measures have been seen as a burden for most building owners and investors, due to the higher initial costs. However, in the context of significant increase and instability of energy prices, ways of reducing the energy consumption costs of buildings in the operational phase has become a common preoccupation amongst building owners/users and investors. Thus, the life-cycle costs approach has become more and more relevant rather than choosing options with lowest initial investments. This is a tendency that is not limited to the new buildings or in the case of major rehabilitation interventions, becoming interesting also for buildings that are relatively new, built in the past 10 years, when the nZEB standard was not yet mandatory. This paper explores the possibilities of increasing the energy performance of a typical Romanian single-family house up to the NZEB standard. These possibilities are analyzed in terms of both energy use and life-cycle cost.

1.2 Nearly zero-energy building definition in Romania and reference values for residential

As of 2021, all new buildings must be nZEB, in Romania as well as in all the Member States of the EU. EPBD recast does not give a uniform approach for implementing nZEBs, allowing the Member States to develop definitions that reflect the national, regional, or local conditions, including a numerical indicator of primary energy use expressed in kWh/m² per year (The European Parliament, Directive 2010/31/EU, 2010). In Romania, nZEB is defined as a building with a very high energy performance, where the energy requirement to ensure the comfort conditions and energy performance is almost equal to zero or is very low and is covered in proportion of at least 30% with energy from renewable sources, including energy from renewable sources produced on site or nearby, within a radius of 30 km from the GPS coordinates of the building (Romanian Law No. 372/2006, republished). If the renewable energy share has a fixed value, independently on the building category and climatic zone, the level of energy performance that must be achieved in Romanian nZEB's is given through maximum admissible specific total primary energy consumption and CO₂ equivalent emissions, differentiated on building category and climate zone, presented in Table 1 (Mc001, 2022).

Table 1. Maximum values of total primary energy consumption and of equivalent CO₂ emissions for NZEB single-family buildings.

Climatic zone	Specific total primary energy [kWh/m ² ,year]	CO ₂ equivalent emissions [kg/m ² ,year]
I	120,1	14,7
II	127,9	16,0
III	133,3	17,1
IV	140,6	18,5
V	147,9	19,9

2 METHODOLOGY

2.1 nZEB characterization: Primary energy, CO₂ emissions and renewable energy share

The methodology applied in the present paper includes energy and life-cycle cost assessment of a relatively new building for which energy performance solutions are proposed to reduce the energy related costs of the building and to achieve the nZEB standard as it is defined in Romania. In order to compare the energies from different energy vectors, it is necessary to convert the final energy consumed into primary energy. Primary energy can be renewable primary energy and non-renewable primary energy. The total primary energy of a building includes both. As explained in the previous chapter, in Romania, one of the indicators for nZEB is the amount of specific total primary energy, which includes typical uses of the building for heating, domestic hot water, cooling, ventilation, lighting and auxiliary energy (measured in kWh/year or kWh/m².year in the case of specific primary energy). More precisely, the energy performance will be quantified in terms of specific total primary energy consumption, CO₂ emissions and renewable energy share as these are the main indicators in defining nZEB's in Romania. The conversion of final energy of a building to primary energy is made by means of primary energy factors, which indicate the amount of primary energy used to provide a unit of end use energy. These conversion factors are usually different for each country in the EU, reflecting national particularities. For the transformation of the final energy into primary energy, the conversion factors proposed by the Romanian Methodology for calculating the energy performance of buildings (Mc001, 2022) were used. The formula for primary energy calculation is presented in Equation 1 below:

$$E_P = \sum_i (Q_{f,x,i} \cdot f_{Ptot,i}) - \sum_i (Q_{ex,i} \cdot f_{Ptot,ex,i}) [kWh/year] \quad (1)$$

where $Q_{f,i}$ = final energy consumption of type i, in kWh/year; $f_{P_{tot},i}$ = primary energy conversion factor for energy type i, values given at national level, presented in Table 2; $Q_{ex,i}$ = final energy of type i, produced at the building level and exported, in kWh/year; $f_{P_{tot},ex,i}$ = primary energy conversion factor for energy type i, produced at the building level and exported, values given at national level, presented in Table 2.

The specific primary energy is obtained by dividing the total primary energy consumption to the useful floor area.

Table 2. Primary energy and CO₂ equivalent emissions conversion factors to be used in Romania.

Energy source	Primary energy conversion factor			CO ₂ emissions conversion factors
	Non-renewable $f_{P_{ren}}$	Renewable $f_{P_{ren}}$	Total $f_{P_{tot}}$	
Natural gas	1,17	0,00	0,00	0,202
Thermal energy produced with solar panels	0,00	1,00	1,00	0,000
Environmental thermal energy	0,00	1,00	1,00	0,000
Electrical energy from the national grid	2,00	0,50	2,50	0,107
Electrical energy produced on-site or nearby and consumed directly by the building	0,00	1,00	1,00	0,00
Electrical energy produced on-site or nearby and exported to the national grid	2,00	0,50	2,50	0,202

The renewable energy share is to be determined as the ratio between renewable primary energy consumed by the building based on total primary energy consumption. The calculation of CO₂ emissions is carried out considering the conversion coefficients in Table 2 (Mc001, 2022).

2.2 Life cycle cost analysis

The life cycle cost analysis is based on the global cost calculation procedure in the European Standard 15459-1 (EN 15459-1, 2017). The global cost calculation includes the following types of costs, described as well in Equation 2: initial investment, sum of annual costs, residual value and disposal costs (if the case). The calculation can also be extended by adding the cost value for CO₂ emissions in the sense of the monetary quantification of the damage caused to the environment by CO₂ emissions released into the atmosphere. The different types of costs (initial investment costs, replacement costs, annual costs, and energy costs), as well as the final (residual) value are converted into present value global cost applying the appropriate discount factor.

$$CG = CO_{INIT} + \sum_j \left[\sum_{i=1}^{TC} (CO_{a(i)}(j)) * (1 + RAT_{xx(i)}(j)) + CO_{CO2(i)}(j) * D_{f(i)} + CO_{fm(TLS)}(j) \right] - VAL_{fm(TC)}(j) \quad (2)$$

where CG = global cost; CO_{INIT} = initial investment cost; $CO_{a(i)}(j)$ = annual costs in year i for component or service j; $RAT_{xx(i)}(j)$ = price increase rate in year i for component or service j; $CO_{CO2(i)}(j)$ = Cost for CO₂ emissions in year i for component or service j; $CO_{fm(TLS)}(j)$ = disposal costs; $VAL_{fm(TC)}(j)$ = residual value for component j.

3 CASE STUDY

3.1 Selected building description

The building chosen as the case study is a typical single-family house, located in Timisoara and built in 2017. The building has been designed and executed in such a way as to have an energy

performance above the minimum required according to the technical regulations in force at the time of design. Even though the building was constructed before the mandatory nZEB regulation was in force, the owner decided to use a higher level of thermal insulation than the minimum necessary for closing elements and highly energy performant windows (triple glazing windows). The architectural and geometrical description of the building can be seen in Figure 1.

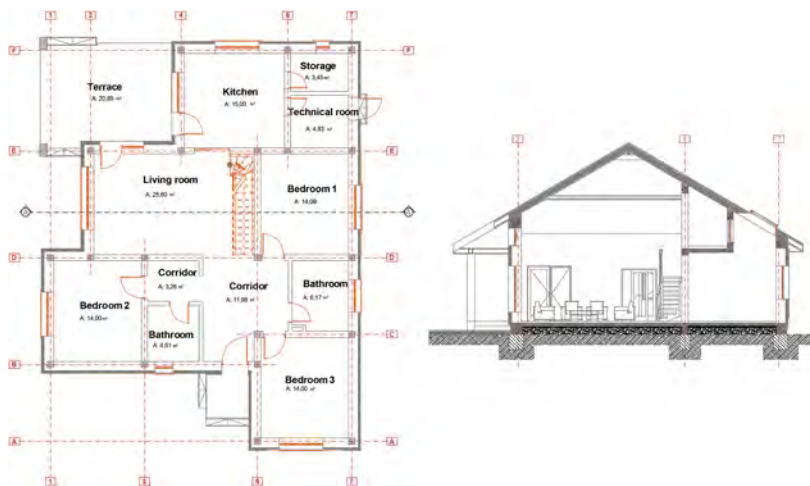


Figure 1. Architectural description of the case study building.

The height capacity of the building includes the ground floor where the main spaces of the house are and an attic which contains a guest's room, an office, and a bathroom. The total heated floor area is approximately 204,16 m², while the interior heated volume is about 584,14 m³. The building hosts a family of 4 persons. The building has a typical structural system for new single-family houses in Romania, consisting in confined masonry walls with reinforced concrete small columns and belts. The floor is made of reinforced concrete, while the pitched roof is made of wood covered with tiles. The foundation system is made of continuous reinforced concrete foundations under the structural walls. The external walls of the house are realized with masonry made clay bricks with hollows (380 mm) and thermal insulation of stone wool (150 mm). The ground floor is thermally insulated with extruded polystyrene (100 mm) placed under the reinforced concrete plate. The sloped roof (slope angle 30°C) is insulated with two layers, one of stone wool (200 mm) and one of mineral wool with aluminum vapor barrier (100 mm). The windows are triple glazing with low-E coating and PVC frame. The heating system of the building is composed by a radiant floor supplemented by radiators installed only in bathrooms. The heating radiant floor and the steel sheet radiators are supplied with heat agent (water) produced by the gas heating system located in the technical room. The domestic hot water is produced by the same gas heating system through a thermal boiler installed in the technical room. The domestic hot water production circuit is auto connected with priority to the hot water produced for heating. Cooling is only provided locally in the living room and bedroom 2 using a common air-conditioning unit and the building occupants claim this is enough to ensure comfortable indoor environment during the summer. The artificial lighting is made using LED lighting fixtures. The quality of indoor air is maintained through controlled natural ventilation (windows opening twice a day).

3.2 Energy assessment

The energy consumption of the existing buildings was firstly assessed using the electricity and natural gas invoices for a one-year period. In Table 3 are presented the total annual values for energy consumption for each type of energy carrier.

Table 3. Energy consumption of the building derived from one year period of energy invoices.

Energy source	Total annual energy consumption [kWh]	Total specific annual energy consumption [kWh/m ² .year]
Natural Gas (heating and DHW)	21524,14	105,43
Electricity (lighting, cooling, household appliances)	2860,36	14,01

Since the electricity and natural gas consumption retrieved from the invoices is not divided separately into consumption categories (heating, domestic hot water, cooling, lighting), the decision was taken to perform as well an energy consumption calculation following the monthly method described by the Romanian Methodology for Calculation the Energy Performance of Buildings (ref). A simplified calculation model was developed based on the input data summarized in Table 4. The energy consumption calculations are further presented in Table 5. It can be observed a relatively small difference between the calculated values and the ones derived from energy invoices.

Table 4. Input data related to building envelope and ventilation.

Characteristic	Description
Useful floor area	240,16 m ²
Thermal transfer characteristics	Element
	U-value [W/(m ² K)]
	Area [m ²]
	exterior walls
	0,218
	154,60
	ground floor
	0,294
	127,01
	roof
	0,136
	168,78
	windows
	0,800
	33
Condensing gas boiler (for heating and domestic hot water)	useful power 8.4 – 24.6kW, efficiency 91.5%,
Natural ventilation air change rate n _a	0,5 h ⁻¹
Artificial lighting	LED lighting fixtures
	Total installed power 503,5 W
Interior temperature during the heating season	Actual temperature preferred by the users 23° C
Climate data	Building located in climatic zone II of Romania. Values provided in national regulations were used.

Table 5. Calculated energy consumption of the case study building.

Energy source	Heating [kWh]	Cooling [kWh]	DHW [kWh]	Lighting [kWh]	Specific total energy consumption [kWh/m ² .year]
Natural Gas	15981,90	0,00	6465,75	0,00	109,95
Electricity	0,00	775,5	0,00	1876,23	12,99

3.3 Solutions to increase energy performance

In the existing configuration, the building does not have any renewable energy system that could cover the energy demand of the building. To comply with the nZEB criteria as it is defined in Romania, several solutions for increasing the energy performance of the building were investigated. The focus was on solutions that could be easily implemented in the existing building without any major construction works. Thus, the proposed solutions consist in photovoltaic panels systems of different capacities for on-site electricity production and solar collectors for domestic hot water and are briefly presented in Table 6. The proposed number

of PV panels and solar collectors consider the available surface on the pitched roof on each orientation. The total primary energy is calculated using the formula presented in the methodology chapter, considering all the energy flows of the building, including solar thermal, electricity from photovoltaic panels, but also the excess energy that is delivered to the grid. The same principle is applied for calculating the CO₂ equivalent emissions. The renewable energy share is determined based on total primary energy consumption. The estimated energy performance indicators are listed in Table 7 and plotted in the graph in Figure 2 for each of the investigated scenarios.

Table 6. Description of energy efficiency solutions.

Individual solutions	Description	Estimated annual electrical energy production [kWh]	Estimated annual thermal energy production [kWh]
S1	8 kW on grid PV system 20 monocrystalline PV panels integrated on the roof (angle 30°C, East)	7737	0,00
S2	6.4 kW on grid PV system 16 monocrystalline PV panels integrated on the roof (angle 30°C, West)	6159	0,00
S3	3.2 kW on grid PV system 8 monocrystalline PV panels integrated on the roof (angle 30°C, South)	3800	0,00
S4	Solar collectors system for DHW 3 flat plane solar collectors integrated on the roof (angle 30°C, South)	0,00	3078
Packages of solutions			
P1	S1+S4	7737	3078
P2	S2+S4	6159	3078

Table 7. Estimated energy performance indicators for the investigated scenarios.

Case scenario	Total specific primary energy consumption [kWh/(m ² year)]	Renewable energy share [%]	Specific CO ₂ equivalent emissions [kgCO ₂ /(m ² year)]
Existing building (EB)	161,1	4%	29,46
S1	79,4	16%	19,32
S2	98,6	13%	21,39
S3	127,4	10%	24,47
S4	158,4	14%	25,63
P1	76,6	38%	15,49
P2	95,9	30%	17,56

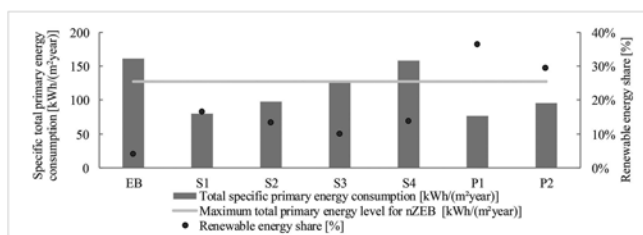


Figure 2. Energy performance indicators for the investigated scenarios.

3.4 Life cycle cost analysis and payback period

The global cost calculations were performed for a period of analysis of 30 years and using a discount rate of 3%. The initial investment includes only the costs related to the proposed energy efficiency scenarios were considered. The annual maintenance costs were established as percentages of the initial investment of each component that requires maintenance (EN 15459-1, 2017). Considering the information available on the National Authority for Regulations in Energy field (2022), the price of natural gas was set to 0,061 €/kWh (including acquisition, transport, distribution, taxes and VAT) and an average price of electricity of 0,371 €/kWh was used, including taxes and VAT. The electricity exported to the grid was accounted with a price of 0,122 €/kWh. The payback assumed to be achieved in the year in which the discounted global cost of a scenario becomes less than the discounted global cost of the existing building. The global cost calculation results are presented in Table 8. As it can be noticed, the highest global cost is achieved by the existing building scenario followed by S4 which includes the implementation of 3 flat plane solar collectors integrated on the roof of building. The lowest global cost is achieved in case of scenario P1, which includes 20 monocrystalline PV panels integrated on the roof (angle 30°C, orientation East) and 3 flat plane solar collectors integrated on the roof of building. The payback period has similar values for scenarios S1, S2, S3, P1 and P2 and a significantly higher value for scenario S4.

Table 8. Global cost calculation results and payback period.

Scenario	Initial investment [€]	Global cost [€]	Payback period [years]
EB	0	72.921,86	0
S1	9800	42.414,40	5
S2	7800	44.045,92	4
S3	5500	47.963,33	4
S4	3000	72.145,51	16
P1	12800	41.638,05	6
P2	10800	43.269,56	5

3.5 Results and discussions

The graph in Figure 3 shows the investigated scenarios in terms of specific total primary energy consumption and specific global cost. The specific global cost and specific primary energy consumption have very close values for scenario P1 compared to S1 and for scenario P2 compared to S2. The least effective scenario is S4, which leads to a specific global cost and primary energy consumption very close to the one of the existing building. Moreover, this scenario does not comply with any of the energy performance indicators for single-family NZEB's in Romania.

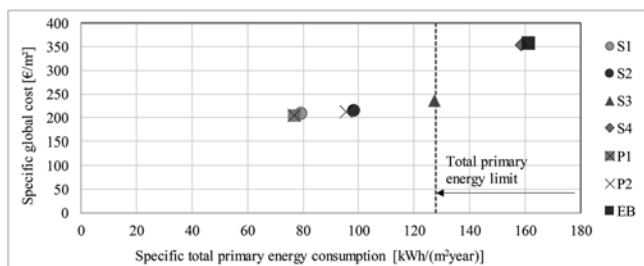


Figure 3. Specific global cost and total primary energy consumption graph.

The degree of compliance with the nZEB criteria is presented in Table 9 for all the investigated scenarios. As it can be noticed, scenario P1 complies with all the 3 criteria.

The most difficult criteria to achieve is the one related to the CO₂ emissions limitation and the one related to the renewable energy share. The specific primary energy consumption criteria was

Table 9. nZEB criteria verification.

Case scenario	Criteria 1 – renewable energy share	Criteria 2 – specific total primary energy consumption	Criteria 3 – specific CO ₂ equivalent emissions
EB	✗	✗	✗
S1	✗	✓	✗
S2	✗	✓	✗
S3	✗	✓	✗
S4	✗	✗	✗
P1	✓	✓	✓
P2	✓	✓	✗

achieved for all scenarios except S4. However, it is worth mentioning that the low values of primary energy consumption are largely due to the quantification of the electrical energy produced in excess and delivered to the grid by subtracting it from the total value of primary energy.

4 CONCLUSIONS

This paper explored the possibilities of increasing the energy performance of a typical Romanian single-family house up to the nZEB standard. The proposed solutions considered the options that can be implemented easily, without causing discomfort to the occupants or additional works inside the building. Several scenarios were analyzed in terms of both energy use and life-cycle cost. Among the investigated scenarios, the one including 20 monocrystalline PV panels integrated on the roof (angle 30°C, orientation East) and 3 flat plane solar collectors led to compliance with all the criteria of the nZEB building as defined by the technical regulations in Romania. Moreover, the same scenario proved to be cost optimal as well because it leads to the lowest global cost on the considered period of analysis. The payback period this scenario is of approximately 6 years, compared to the existing building. The results of this study emphasize the fact that in a single-family house where that major consumption comes from natural gas, to achieve the nZEB standard, it is not enough to just implement a system of PV but also a solution that reduces the natural gas energy consumption.

ACKNOWLEDGMENT

This work was supported by a grant of the Ministry of Research, Innovation and Digitization, CCCDI - UEFISCDI, project number PN-III-P2-2.1-PED-2021-4137, within PNCDI III - CT 714PED/2022.

REFERENCES

- European Commission. 2019. Communication from the commission to the European Parliament, the European Council, the council, the European economic and social committee and the committee of the regions, The European Green Deal.
- EN 15459-1. 2017. Energy performance of buildings. Economic evaluation procedure for energy systems in buildings Calculation procedures.
- National Authority for Regulations in Energy field. 2022. <https://www.anre.ro/ro/info-consumatori/comparator-de-tarife>
- Romanian Parliament. 2020. Law No. 372 regarding the energy performance of buildings, republished.
- Romanian Methodology Mc001. 2022. Methodology for calculating the energy performance of buildings, Indicative Mc001/2006: Methodology revision and application examples.
- The European Parliament. 2010. Directive 2010/31/EU of the European Parliament and of the Council of 19 May 2010 on the energy performance of the buildings.
- The European Parliament. 2002. Directive 2002/91/EC of the European Parliament and of the Council of 16 December 2002 on the energy performance of building, 2010

End-of-life rule checking for transport infrastructure: The case of navigation locks

K.E. Bektas & I.E. Ozer
TNO, Delft, The Netherlands

ABSTRACT: Determining the end-of-life of infrastructures is an important decision in the Netherlands, where the large stock of assets currently reaches their design life. The Dutch Road Authority has set up a research program to address this on a national level. Currently, there are various documents describing the rules of aging. Yet information specifications are not defined. This forces the experts to focus on technical aging only and consider structures that are aged/too expensive to maintain in later stages. Since the scoping and budget assignment is based on the earlier prognosis, the process becomes suboptimal. There is a need for a holistic approach to identify ageing rules for the assessment of different object types. This paper presents an information model for navigation locks as a first step of such approach. It declares information needed to check rules automatically via case studies and proposes utilization of a technology as a future step.

1 INTRODUCTION

Public asset managers, particularly in the infrastructure domain, are challenged with renewing the large number of infrastructure due to physical ageing. Only in the Netherlands, there are 85,000 bridges and viaducts, 83,000 culverts, 2,400 km of quays and 7,800 pumping stations (Bleijenberg, 2021). A substantial amount of structures will reach the end of their service life in the coming decades given their design life time of 80 to 100 years (Klanker et al, 2016). For resources to be allocated on time, a long term prognosis of future renovation and replacement needs is required. In this context, the Dutch Road Authority (RWS) has set up a research program called Replacement and Renovation (V&R) to address the aging of infrastructures on a national and portfolio level. The first step of this program refers to an intake decision, where the ‘candidates’ are selected based on their end of service life and the budget prognosis is determined. This selection is important, since the objects in V&R are financed nationally and not by regular maintenance budgets of the regions at RWS. There are various documents established by different public entities for the selection process. They describe theoretic conditions categorized under technical, functional, and economic end-of-life (e.g. I&M (2013), VONK (2012)). There are also studies performed by RWS where the aging of structures is approached from a life cycle perspective and a metric (Economic End of Life Indicator -ELI) is established by Bakker et al (2016).

Currently, there are fundamental challenges in analyzing objects on portfolio level. Between various organizations, differences are observed in how they identify the theoretic end of life rules that are used as a eligibility to the V&R Program. Although these rules are explicitly defined and categorized as the technical, functional, and economic end-of-life in official documents, the rules are high-level, human-interpreted, do overlap and reside in various forms of documentation. Information specifications per rule are not always well defined and interrelations of shared issues are not set yet. This forces the experts to focus solely on technical ageing that they are the most familiar and exclude the other rules while assessing the end-of-life of an object. Another challenge is the large amount of available data that are collected by RWS and

also by the regional asset managers. The data from these two sources does not always match, has complex structures and takes cumbersome effort for the V&R expert to obtain a relevant dataset. This is challenging to do per object type and even more difficult to do on a large number of objects. In relation with the two challenges above, a categorization of objects is often done based on common issues and extrapolations: Objects that are prone to similar technical problems are grouped in relation with their theoretic life time and included in the intake. This was done based on characteristics rather than actual condition data of the objects.

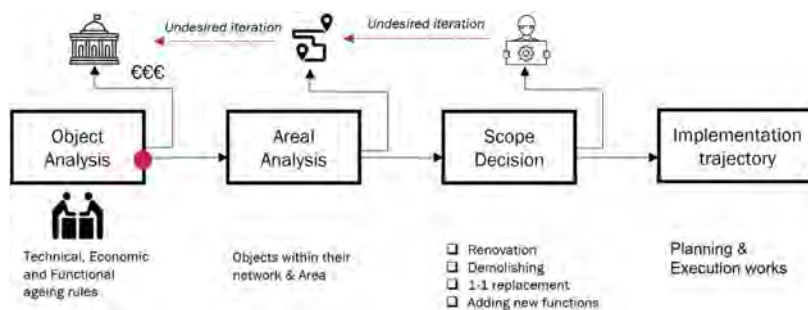


Figure 1. The V&R process and the intake decision moment as Step 1 (Bektas, 2021).

Considering this situation, the ultimate aim of this research is to develop an integral end-of-life model as an automated rule checking system that supports the V&R experts with more objective and accurate analysis leading to improved scope definition. This research proposes to (1) objectify aging rules under functional, economic and technical ageing, (2) specify information and data use per object type and (3) enable automatic checking of those rules which can optimize the intake decision making. This would lead to a more accurate scope and budget definitions and ease communications between involved parties.

Automated rule checking has been identified as a potential to provide significant value to the AEC (Architecture, Engineering and Construction) industry from both regulatory and industry perspectives. It is used to translate rules based on human language to computer interpretable rules, so that the object's compliance against the rules can be determined (e.g. building regulations compliance, safety regulation compliances). In this field, the key scholars are Eastman et al (2009), Solihin (2015), Solihin & Eastman (2015), Pauwels et al (2011); Pauwels et al (2017); Pauwels & Zhang (2015), Nawari (2012), Song et al (2018); Song et al (2020). The four stages of Eastman et al (2009) are: 1) Rule interpretation, 2) Model preparation, 3) Rule execution, 4) Rule reporting and visualization. This approach has been widely used in the building design domain particularly for objectifying human-language rules as building regulations, quality assurances and mostly on BIM (Building Information Model) data. Yet there is little evidences on the use of this approach for infrastructure domain, particularly on the aging of structures. Through such an approach, available technical information that is scattered across design documentation, inspections and planning are acquired, interpreted, and translated to the end-user. In that way, scattered data aims to be translated to decision information. This can provide a great insight into the identification of issues for the portfolio level of objects in an faster and explainable way.

In this paper, the focus is given on navigation locks and a multi-case study method is used. Four cases were selected as examples of navigation locks in the Netherlands, namely the complexes of Delden, Hengelo, Eefde and Volkerak. In Section 2, critical design characteristics that can have an influence on defining the end-of-life of these locks are listed. Later, the changed conditions over time (i.e. common issues) are identified and discussed under different aging categories. The ultimate result from the case studies become the main component of an automated rule checking system: Information Model for Locks that is presented in Section 3. This corresponds to the Stage 1 of Eastman et al (2009). Based on this, a proposed approach is selected for model preparation (Stage 2 of Eastman et al (2009)). This information model can be seen as

a kernel of the programming activities that will be conducted in the future to build the final rule checking engine that is explained in Section 4. Conclusions are given in Section 5.

2 CASE STUDY: END-OF-LIFE RULES FOR NAVIGATION LOCKS

2.1 *General information on the navigation locks*

The main purpose of a navigation lock is to overcome the water level differences between two water stretches for shipping, while maintaining the difference in water level. They are also used for water management purposes, e.g. to discharge a predefined amount of water within a certain period of time. A lock consists of a lock chamber, closed by different types of closing elements (e.g. gates) which are located in the lock heads. Below and adjacent to the structure, cut-off walls are usually used to prevent seepage and/or piping. Raising or lowering the water level in the chamber can be achieved by letting in/out the water through the gates or a by-pass pipe. Considering the operational aspects of a lock for shipping purposes, three main design requirements are defined. Firstly, lock dimensions must be sufficient enough to allow the normative ships to pass in the considered waterway. Secondly, the lock capacity (i.e. number of ships passing within a certain time interval) must be sufficient considering the present and future requirements (e.g. traffic intensity). Lastly, the time losses during a passage must be kept at a minimum (Molenaar & Voorendt, 2020).

In order to define the end-of-life aging rules, four navigation locks are analyzed, namely the complexes of Delden, Hengelo, Eefde and Volkerak. They are part of the main water network. A rich set of data is collected from inspection reports, FMECA analysis, 6-yearly inspection data, planning and measurement data as well as integral reports. The integral reports of the four locks, such as Arcadis (2012a; 2012b; 2014a; 2014b), become governing documents to identify potential V&R issues under aging rules. In the following sections, the critical design characteristics that can have an influence on defining the end-of-life are identified and also changed conditions over time are listed in Table 1. The differences and categorization became a conversation starter with the asset manager who decides whether large interventions are required and thus the objects become eligible to enter to the V&R Program of the RWS.

2.1.1 *Case Delden*

The Delden complex consists of a lock (1933), a pumping station, a fixed bridge over the lower head, several buildings, an emergency power plant and a channel leading to the pumping station. Due to the increase in shipping, ship sizes have reached its maximum value for this lock (CEMT class IV and limited Va) which minimizes the space between ships and chamber walls and the gate. This causes a higher risk of collision damage. The scaling up of the shipping class also means that there is an increase in engine power and the development of concentrated propeller jets creates a higher load on the bottom protection. This leads to damage on the bottom protection in the chamber and around the lock. Due to climate change, large flows have to be discharged more often. The composition of shiploads has changed significantly since construction, with an increase in the number of ships with dangerous cargo. This has possible consequences for safety on the lock itself, but also on the external environment safety around the complex.

2.1.2 *Case Hengelo*

The complex Hengelo also consists of a lock (1936), a pumping station, a fixed bridge over the lower head, a railway bridge and a channel leading to the pumping station. Similar to Delden complex, there is a higher risk of collision damage due to increase in shipping class. The consequences of a collision is expected to be greater due to the increased ship size. Large flows have to be discharged more often. Damage on the bottom protection in the chamber and around the lock is expected due to the increase in engine power which creates concentrated propeller jets.

2.1.3 *Case Eefde*

The complex Eefde consists of a lock (1933), a front lock (1952), pumping stations, drainage systems and various waiting locations and berths. Increase in ship size and engine power is

also a common issue for this lock. Due to heavier and larger ships, there is a restriction with regard to vertical clearance of the lifting doors. Changed safety factors for the loads and materials are more unfavorable than was considered during the design. As a result of the increased capacity of the drainage systems and pumping stations, greater flow velocities occur which affects the safety of shipping traffic. Due to heavier loads and modified standards, the assessment of fatigue is less favorable than at the time of design.

2.1.4 Case Volkerak

The Volkerak complex is the busiest and largest inland navigation lock complex in Europe. It consists of three adjacent locks (Locks 1 to 3) for commercial vessels and a yacht lock for recreational vessels. There are two bascule bridges across Lock 1, which allow an unlimited vertical clearance. Increase in ship size and engine power is also a common issue for this lock. Studies are currently being conducted to speed up the shedding process by increasing the lifting speed of the leveling gates. This can cause greater loads on the ships in the chamber and on the bottom protections. Arcadis (2014b) concludes that the loads on the ships are already too high and that the lifting speed must be reduced rather than increased. In the recent years, the number of ships has increased sharply. Despite the expansion of the third chamber ten years after the construction, it is expected that a fourth chamber is needed to keep waiting times within the accepted value.

Table 1. Critical characteristics of the complexes of Delden, Hengelo, Eefde and Volkerak.

Characteristics	Delden	Hengelo	Eefde	Volkerak (Lock 1)
Dimensions	Passage height: 6.20 m	Passage height: 5.30 m	Passage height: 6m	Passage height: unlimited
	Chamber length: 128 m	Chamber length: 119.7 m	Chamber length: 140 m	Chamber length: 308.9 m
	Chamber width: 12 m	Chamber width: 12 m	Chamber width: 12 m	Chamber width: 24.1 m
CEMT class	Suitable for class IV & limited suitable for class Va	Suitable for class IV & limited suitable for class Va	Suitable for class Va with draft limitation of 2.80 m	Suitable for class VIb
Built year	1933	1936	1933	1957-1977
National monument	Yes	Yes	Yes	No
Diff. in water level	6 m	9 m	6 m	
Function of the canal	Main waterway (Vw2)	Main waterway (Vw2)	Main waterway (Vw2)	Main waterway (Vw2)
Material of the chamber walls	Steel sheet piles	Concrete	Concrete	
Max discharge capacity	34.5 m ³ /s	-	100 m ³ /s	
Type of the gates/doors	Lifting gates	Upper head: lifting gates Lower head: two roller gates with lev- elling slides	Lifting gates	Electro- mechanically driven steel pointed gates
Vertical clearance	Limited	Limited	Limited	Unlimited
A flood defense?	No	No		
No. of ship per year	8400	1400	5650	
Average lock time	30 mins	30 mins	> 30 mins	

2.2 Identifying the aging rules

In order to define the object-specific aging rules, a database is constructed which includes the important key parameters of the locks that are investigated above. As a next step, a list of issues related to locks are analyzed to check whether there is a major problem regarding their structural safety or function. If the issues that cannot be solved by a regular maintenance and require a large intervention, they are then identified as a potential V&R issue. Later, the object-specific aging rules for locks are developed based on the theoretical aging rules that are found in the literature. These identified issues are then linked to the specific aging types by considering the rules that are given in Table 3. Lastly, the findings are enriched by inspection reports, external data and interviews with V&R experts. Some examples are given in Table 2.

One of the identified technical aging issue for a lock chamber is the corrosion of the sheet piles. If the chambers are made of steel sheet piles, major corrosion can lead to a thickness reduction of the walls. In this case, the stability and strength of the walls may not be ensured. Therefore, this issue is indicated as a technical end-of-life for a lock chamber wall. Another example of a technical aging issue is the critical components of the lock, such as gates, being obsolete. In this case, the lock cannot function properly until the related parts are changed. Since in this case the replacement is not possible, the gates reaches their technical end-of-life. Another common issue that is observed in all case studies is the CEMT classes being no longer suitable due to the increased ship size and relatively low gate heights (i.e. limited vertical clearance). This is an accurate example of the lock being reached to its functional end-of-life. When these issues are checked with the theoretical aging rules, they define more specific starting point of departures for V&R experts to analyze aging conditions for navigation locks. Table 3 presents this synthesis.

3 INFORMATION MODEL FOR NAVIGATION LOCKS

The information model synthesizes and declares all the parameters that are necessary to compute and check ageing rules. The scope of this information model is the rules defined in Table 1. Table 2 illustrates the main concepts modelled for navigation locks and end of life rules. The model has four realms. The first realm is *Network and Corridor Information*. Here the data concerning functional requirements number of ships passing, useful shipping dimensions, waiting time, width/length/depth of canal, maximum allowed ship classes as well as asset management district can be exemplified. The second realm is *Physical Decomposition Information*. The data here deals with specific objects forming the lock complexes, peak water discharge capacity, water level differences, lifting speed, chamber details, gate types and dimensions, network details and material of components. The decomposition is arranged based on the NEN 2667-4 standard. The third realm is *Condition of Navigation Locks*. Any red flags as aging rules use this information linked to the physical decomposition. It contains degradation mechanisms, damage assignment. The main source of the data is inspection results here. The fourth realm is *Risks and Measures for Navigation Locks*. The risk associated to the condition findings and planned measures are detailed here. Thus the information model contains data concerning functional requirements, decomposition, technical condition and cost of maintenance. It then becomes possible to use relevant data for selected functional, technical and economic ageing rules.

4 FOLLOW-UP TOOLING

The ultimate result of the case studies become the main component of an automated rule checking system: Information Model for Locks. This corresponds to the Stage 1 of Eastman (2009). Based on that a proposed approach is selected for model preparation (Stage 2 of Eastman (2009)). The information model is a kernel of the programming activities conducted in future to build the rule checking engine (to be presented in future as Stage 3 and 4). There are different approaches to build a rule checking model such as procedural or declarative programming. The follow-up of this project will follow declarative programming based on the benefits listed by Pauwels et al. (2011). The approach will particularly focus on a semantic model that declares domain concepts and properties to be able to control the data for rule checking. Semantic knowledge models aim to capture domain knowledge and can make it available for non-domain decision makers. The information model will be (automatically) translated to a semantic model by the help of open

Table 2. Critical V&R issues related to the locks that are assessed and linked to the specific aging type.

Aging Reason	Issue	Cause of the issue	Limit statement	V&R Measure	Mng. object (NEN 2767-4 lev.1)	Component (NEN 2767-4 lev.2)		Element (NEN 2767-4 lev.3)	Function	V&R Rules
						Chamber	Wall			
Technical	Reduction of thickness	Corrosion	x% of the wall thickness	Replacement of Sheet pile walls of the chamber.	Lock	Chamber	Wall		Shipping and water level management	[T1]
Functional	Increased load on the bottom protection	Scaling up the shipping class	x% increase in the average engine power	Replacement or Adding Bottom Construction.	Lock	Chamber	Bottom		Shipping	[F1]
Technical	Pits at the bottom construction	Erosion, Sedimentation, even Subsidence	x% material loss due to pits.x° inclination angle of the pits	Replacement or Adding Bottom Construction.	Lock	Chamber	Bottom		Shipping	[T1]
Functional	High risk of collision with a greater damage	Increase in ship size	Max dimensions for the relevant shipping class	Widening, deepening the chamber.	Lock	Chamber	Chamber dimensions		Shipping	[F1]
Functional	Larger flows have to be discharged more often	Climate change	Discharge capacity of the pump(s) + gate	Renovate whole pumping station/ Upgrade pumps.	Pumping station	Pump	Capacity		Water level management	[F1]
Functional	Collision with a greater risk	Increase in number of ships with dangerous cargo	Length of ships in relation to length of chamber /waiting area	Widening, deepening or renewing the chamber.	Lock	Chamber, Waiting Area	Chamber dimensions, Waiting Area dimensions		Shipping	[F1]
Technical	Cracks (with or without leakage)	Fatigue	Size of the cracks (mm)	If obsolete, replacement of gate (whole system).	Lock	Lock Head	Doors		Shipping & water level management	[T2]
Technical/Functional	High truss forces from the translation waves	Relatively high lifting speed of the top door during locking process	x% increase in the forces	-	Lock	Lock Head/ Gate	Doors		Shipping & water level management	-
Technical	Obsolescence of a critical component	(varies)	Special door types not produced anymore	Custom-made or replacement of the whole gate system.	Lock	Gate	Doors		Shipping	[T2]

Table 3. The overview of the theoretical and object-specific aging rules.

Theoretical aging rules	Object-specific aging rules (via the cases)
<p>Technical end-of-life</p> <p>[T1]When a structure has serious structural defects</p> <p>[T2]When a (critical) component is obsolete.</p>	<p>When the lock chamber is made by steel sheet piles, and there is a corrosion-led thickness reduction, and structural risk is registered</p> <p>When the lock doors of their chamber are not produced anymore (thus obsolete) and not in-stock.</p>
<p>Functional end-of-life</p> <p>[F1]When an asset no longer fulfils its designed function due to changing environment, requirements, demand.</p> <p>[F2] When there are new functions needed from the asset itself or the location where the asset is.</p>	<p>When the total discharge capacity of the pump(s) + gate is no anymore sufficient to handle peaks (m³/s), as larger flows need to be discharged</p> <p>When a lock (waiting area + chamber + lock-head) is limited to allow bigger ship sizes (CEMT classes Va vs V). And/or When the movable bridge is lifted bridge that has insufficient clear height.</p>
<p>Economic end-of-life</p> <p>[E1]When ELI indicator of Bakker et al (2016) comes closer to 1.</p> <p>[E2] When an asset is too expensive to maintain.</p>	<p>When EELI is > e.g. 0.8</p>

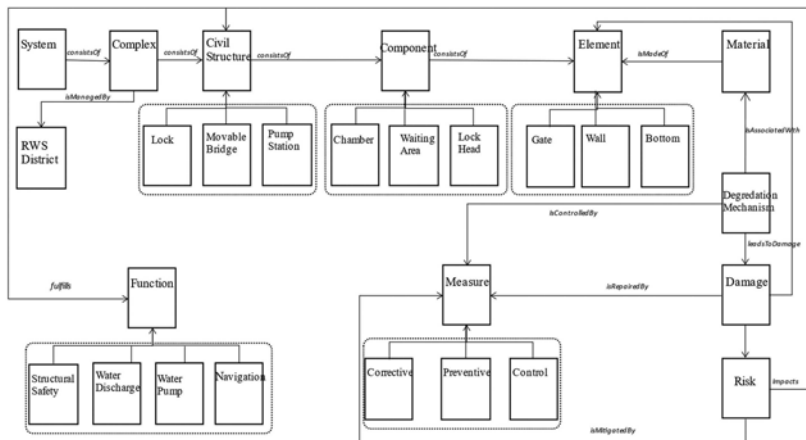


Figure 2. The top-model of the information model (simplified version excluding data properties and cardinality constraints).

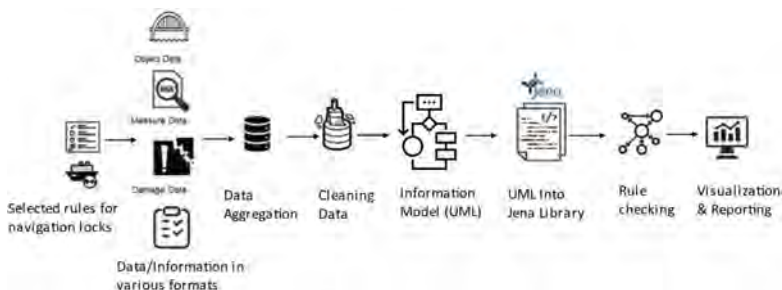


Figure 3. The proposed pipeline for the tooling process.

frameworks (i.e. Kehllo for Java). When the real life objects are defined according to these models, knowledge graphs are generated and inferencing and rule checking is done via the graphs. The open source tooling based on Apache Jena is foreseen as a follow-up since it is a free and open source Java framework composed of different APIs interacting together to process RDF

data and build Semantic Web and Linked Data applications. Figure 3 illustrates the main development steps for the tooling.

5 CONCLUSIONS

The end-of-life model with a rule driven approach aims to assist V&R experts and regional asset managers with clear, explainable, and justifiable assessments for the V&R intake. The information model is a kernel data model that clarifies links between data and concepts from network to component level. It is an outcome of in-depth case analysis in order to understand typical representative problems for each object type. Available yet scattered data and information (across RWS systems and accessible openly) has been utilized. The information model binds relevant data from an object perspective, i.e. decomposition, condition, planning, functional data with a holistic view. The model can also be used as a data acquisition template for a large number of navigation locks as a minimum-set of information and can provide a common agreement between third parties and RWS. In the future, the proposed model will systematically identify how characteristics of certain components contribute to the network performance of objects and how network characteristics influence the object performance. By this, a large number of objects (thousands) can be scanned quickly and efficiently in future for a more comprehensive prognosis.

REFERENCES

- Arcadis (2012a) *Integrale rapportage Delden RINK 2011 - Cluster 2*.the Netherlands.
- Arcadis (2012b) *Integrale rapportage Hengelo RINK 2011 - Cluster 2*.the Netherlands.
- Arcadis (2014a) *RINK 2012/2013 Cluster 2, Sluiscomplex Eefde Integrale Rapportage*.the Netherlands.
- Arcadis (2014b) *RINK 2012/2013 Cluster 2, Volkerakcomplex Integrale Rapportage*.the Netherlands.
- Bakker, J., Roebers, J. H. & Knoops, J. (2016) Economic end of life indicator (EELI), *Life-Cycle of Engineering Systems*. the Netherlands: CRC Press.
- Bektas, K. E. (2021) End-of-life rule checking for the intake decision-making of the Dutch replacement and renovation program for the transport infrastructure, *The Eastman Symposium Scientific Presentation, Digital Building Laboratory (DBL) of Georgia Tech*.
- Bleijenberg, A. N. (2021) *Instandhouding civiele infrastructuur Proeve van landelijk prognoserapport vervanging en renovatie*, Delft, the Netherlands.
- Eastman, C., Lee, J., Jeong, Y. & Lee, J. (2009) Automatic rule-based checking of building designs. *Automation in construction*, 1;18(8):1011–33.
- I&M (2013) *Beslisnota, Procesmatige Spelregels Programma Vervanging en Renovatie*.
- Klanker, G., Klatter, L. & Bakker, J. (2016) Issue approach for medium term renovation and replacement planning, *Maintenance, Monitoring, Safety, Risk and Resilience of Bridges and Bridge Networks*. the Netherlands: CRC Press.
- Molenaar, W. & Voorendt, M. (2020) *Hydraulic Structures, General Lecture Notes*. the Netherlands: TU Delft.
- Nawari, N. (2012) The challenge of computerizing building codes in a BIM environment, *In International Conference on Computing in Civil Engineering*, 285–292.
- Pauwels, P., Deursen, D. V., Verstraeten, R., Roo, J. D., Meyer, R. D., Walle, R. V. D. & Campenhout, J. V. (2011). A semantic rule checking environment for building performance checking. *Automation in construction*, 1;20(5):506–18.
- Pauwels, P., Farias, T. M. D., Zhang, C., Roxin, A., Beetz, J., Roo, J. D. & Nicolle, C. (2017) A performance benchmark over semantic rule checking approaches in construction industry. *Adv. Eng. Informatics*, 33, 68–88.
- Pauwels, P. & Zhang, S. (2015) Semantic rule-checking for regulation compliance checking: An overview of strategies and approaches, *In 32rd international CIB W78 conference*.
- Solihin, W. (2015) *A simplified BIM data representation using a relational database schema for an efficient rule checking system and its associated rule checking language*.
- Solihin, W. & Eastman, C. (2015) A knowledge representation approach to capturing BIM based rule checking requirements using conceptual graph, *In CIB W78 Conference Proceedings*. 370–402.
- Song, J., Kim, J. & Lee, J. K. (2018) NLP and deep learning-based analysis of building regulations to support automated rule checking system, *In ISARC Proceedings of the International Symposium on Automation and Robotics in Construction*. IAARC Publications, 1–7.
- Song, J., Lee, J. K., Choi, J. & Kim, I. (2020) Deep learning-based extraction of predicate-argument structure (PAS) in building design rule sentences. *Journal of Computational Design and Engineering*, 7(5), 563–576.
- VONK (2012) *Technical Committee: Einde levensduur natte kunstwerken notitie*.

Environmental and economic assessment of service life extending repairs for a concrete silo

N. Renne & A. Audenaert

Energy and Materials in Infrastructure and Buildings (EMIB), University of Antwerp, Antwerp, Belgium

M. Buyle

Energy and Materials in Infrastructure and Buildings (EMIB), University of Antwerp, Antwerp, Belgium

Unit Sustainable Materials Management, Flemish Institute for Technological Research (VITO), Mol, Belgium

B. Craeye

Energy and Materials in Infrastructure and Buildings (EMIB), University of Antwerp, Antwerp, Belgium

Durable Building in Team (DuBiT), Department of Industrial Sciences & Technology, Odisee University College, Aalst, Belgium

ABSTRACT: In order to illustrate the relevance of sustainable concrete maintenance and repair, a case study of a concrete silo situated in an industrial area with corrosion damage is selected. The environmental and economic impact is determined through life cycle assessment (LCA) and life cycle cost analysis (LCCA) for six concrete repairs: (i) conventional repair, (ii) conventional repair with surface protection, (iii) galvanic cathodic protection with zinc foil, (iv) galvanic cathodic protection with zinc gauze, (v) impressed current cathodic protection with titanium gauze and (vi) impressed current cathodic protection with a conductive coating. Moreover, three different indented service life extensions are evaluated: 20, 40 and 50 years. In general, a repair with impressed current cathodic protection is indicated as the most sustainable for this case study. However, for other service life extensions (e.g. 15, 30 or 45 years) certain techniques could perform better regarding the environmental or economic impact.

1 INTRODUCTION

In the 1960s and 70s, the construction industry experienced a peak in the construction of reinforced concrete (RC) structures. Due to this fact, there is now and in the near future a high need for repair, because an increasing number of structures will or did already surpass their initial estimated technical life span. This is demonstrated by frequently occurring news articles of failing structures, sometimes even with deadly accidents (Vrt, 2022, Baker et al., 2021, Fumagalli, 2021).

More than 65% of the occurring damage at RC structures is related to reinforcement corrosion (Jones et al., 1997). This damage is caused by carbonation of the surrounding cementitious matrix, chloride ingress or a combination of the two. Corrosion affects the durability and safety of RC structures by (i) cracking and spalling of the concrete cover caused by the expansion of corrosion products around the reinforcement, and (ii) cross-section reduction of the rebars leading to a reduced bearing capacity of the element. Because the covering concrete layer is the main protective mechanism against the ingress of water, O₂, CO₂ and other aggressive compounds, accelerated deterioration of the RC structure will happen when this layer is damaged. In order to prevent and repair damage at RC structures, multiple interventions can be conducted with varying labor intensities and effects. This becomes even more important because climate change effects are expected to substantially impact corrosion acceleration and therefor the degradation of RC structures in the future (Pacheco-Torgal, 2018).

Instead of demolishing deteriorated concrete structures, their service life can still be extended by repair interventions. This is in most cases more environmentally and economically friendly than demolishing and rebuilding as their residual value is preserved (Renne et al., 2022). With the European transition towards a circular economy and the sustainable development goals in mind, it is

important to also consider the environmental impact along with the technical requirements and life cycle cost over the entire life cycle. The construction industry can even be considered one of the key actors in the global stage of sustainability (Maxineasa and Taranu, 2018). In order to fulfill this need, the quantitative assessment methods, life cycle assessment (LCA) and life cycle cost analysis (LCCA), can be used to determine, respectively, the environmental and economic impact of different strategies. In this manner, an optimization of the performance of products, processes and services over a life cycle perspective is possible.

A case study of a concrete silo situated in a Belgian industrial area and damaged due to reinforcement corrosion, selected for this study, illustrates the relevance of sustainable concrete interventions. A combination of carbonation and chloride ingress caused the damage. Moreover, six frequently used repair techniques for RC structures are analyzed: (i) conventional repair (CR), (ii) conventional repair with surface protection (CR-SP) and four electrochemical treatments to stop the corrosion process: (iii) galvanic cathodic protection with zinc foil (GCP-F), (iv) galvanic cathodic protection with zinc gauze (GCP-G), (v) impressed current cathodic protection with titanium gauze (ICCP-G) and (vi) impressed current cathodic protection with a conductive coating (ICCP-C). The service life extension of these interventions is estimated by the engineering office Sanacon which did an investigation about the state of the structure. They also provided reports with data (e.g. description case, quantities, prices, etc.) necessary to perform the LCA and LCCA. In this paper, three functional units (FU) are considered by assuming three service life extensions of 20, 40 and 50 years.

The amount of research about concrete repair and maintenance decision-making through LCCA and particularly LCA is rather limited (Renne et al., 2022). Additionally, the results of different cases are challenging to compare as they are strongly case-dependent. There is only one study comparing multiple repair strategies through LCA and LCCA of the ones that are considered in this paper (Wittcox et al., 2022). The study evaluates five interventions for revamping reinforced concrete balconies. For a service life extension of 20 and 40 years, ICCP is economical the most beneficial followed by CR and GCP. However, regarding the environmental impact, the order is the other way around. Only for 40 years, CR is less bad than GCP. In addition, two studies are found considering only the economic cost for more than one repair strategy selected in this paper. (Polder et al., 2016) report cathodic protection (CP) as less costly than CR for a service life extension of 35 years of a bridge. For an extension of 35 to 100 years, the order remains the same. However, these two repairs are the worst options of the five considered solutions. Secondly, for RC columns and a service life extension of 20 to 75 years CP with conductive coating should be less beneficial than CP with titanium mesh (Binder, 2013). Moreover, studies conducting only a LCA for the selected repairs were not found. So, the quantitative sustainability assessment of concrete repair is still in its infancy, which is a clear knowledge gap given its societal importance.

Therefore, this paper has the goal of estimating the environmental and economic impact of six repair technologies for a corrosion damaged RC silo, given that the deterioration diagnosis and damage assessment are already done adequately on beforehand. In this manner, the knowledge gap about the environmental and economic impact of RC repair strategies will be tackled. It can be determined which method is preferred above the other ones. This can be useful for repair selection in practice considering the necessary transition towards a sustainable economy.

2 RESEARCH METHODS

For this study a concrete silo situated in an industrial area in Belgium was selected, containing a silo 'block' with 23 round silos and a rectangular silo 'tower' attached to it. The silo was built in 1968 and has a height of approximately 35.3 m for the block and 47.1 m for the tower. The silo block has 11 cylinders on the outside with a diameter of 7.2 m, and are attached to each other in the middle with a concrete wall of ± 1.8 m wide. Furthermore, they are horizontally and vertically reinforced with ribbed rebars of respectively 14 and 10 mm with a spacing of 200 and 300 mm. Secondly, the beam shaped silo tower has a length of 18.2 m and a width of 6.6 m. Furthermore, the tower is reinforced horizontally and vertically with non-ribbed rebars of 10 mm with a spacing of 250 mm. An investigation was done by a Belgian engineering office which reported a really bad and dangerous condition of the construction. More particular, based on the carbonation depth and chloride content a residual life span of zero was

estimated for the silo block and on average 66 years for the silo tower. However, for some parts of the tower also a residual life span of zero was calculated. Based on this data, it can be concluded that a repair intervention is highly needed to achieve a safe state and a service life extension for the structure. A visualization of the particular silo can be seen in Figure 1. The total area of reinforced concrete subjected to the outside environment is 6690 m², containing approximately 50.4 tons of steel rebars. This data and other quantities and prices for further study are based on the reports of the engineering office.

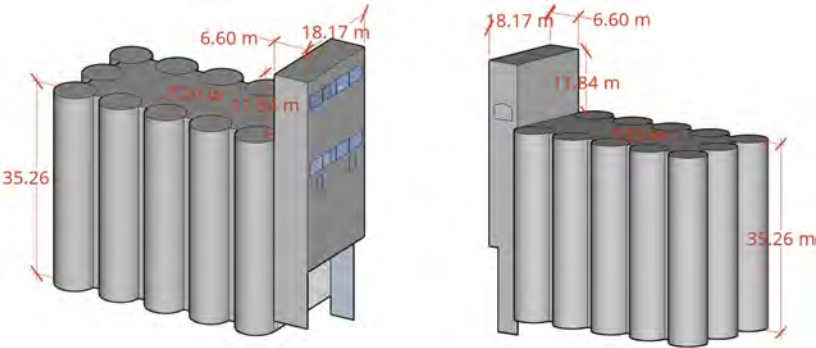


Figure 1. 3D-model of case study silo.

For the analysis six repair methods are considered: CR, CR-SP, GCP-F, GCP-G, ICCP-G and ICCP-C for three functional units (FU 1, FU 2 and FU3). The multiple FU's are necessary due to the consideration of different intended service life extensions (i.e. 20, 40 and 50 y.). Therefore, the FU can be described as “the service life extension of a reinforced concrete silo, as specified in this paper, to an excellent condition for an additional lifetime extension of 20, 40 and 50 years”.

The potential of the repair methods to extend the service life is based on the experience of the engineering office which conducted the investigation of the structure. In addition, the included activities of the interventions with associated quantities are based on data provided by the same company. A schematical overview of the life cycle of each repair strategy is shown in Figure 2. Every time an intervention is needed, it is shown in the figure. In addition, the volume of concrete (in %) that is removed at each intervention and during maintenance is shown below the bar of each repair. It is assumed that the corrosion process has not yet corroded the reinforcing steel rebars to a degree in which the bearing capacity is no longer guaranteed.

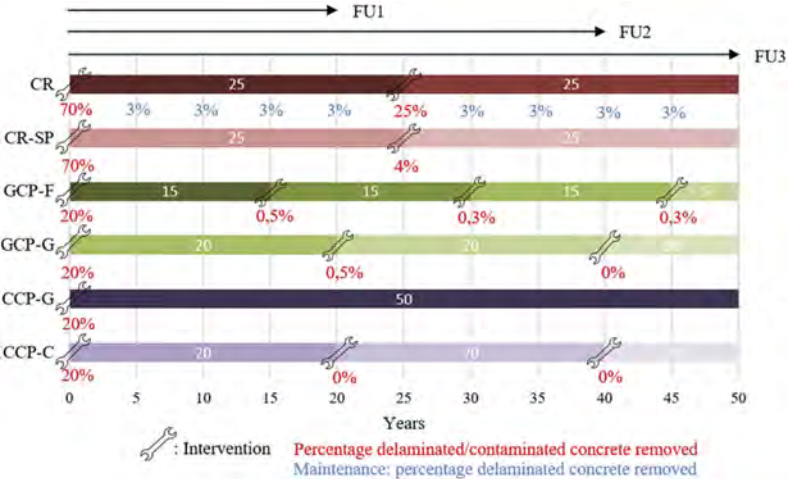


Figure 2. Schematical overview life cycle repair methods for 2 FU's.

Moreover, a description of the included activities and the maintenance strategy of the different repairs, considered in both the LCA and LCCA, are shown in Table 1. The number of interventions shown in Figure 2 corresponds with the number displayed in the table.

Table 1. Overview activities of repair methods for each intervention during the life cycle.

Description activity	CR			CR-SP		GCP-F			GCP-G			ICCP-G		ICCP-C	
	1	2	M*	1	2	1	2	3	4	1	2	3	1	2	3
Removing delaminated concrete	x	x	x	x	x	x	x	x	x	x	x	x			x
Removing contaminated concrete	x	x		x											
Cleaning and protecting accessible rebars	x	x	x	x		x				x			x		x
Repair mortar	x	x	x	x	x	x	x	x	x	x	x	x	x		x
Galvanic anodes on edges repaired zones	x	x		x											
Cleaning and levelling concrete surface				x	x	x	x	x	x				x		x
Conductive glue & zinc foil					x		x	x	x						
Zinc gauze										x	x				
Zinc mortar										x	x	x			
Titanium Gauze													x		
Shotcrete													x		
Primer anode															x
Conductive coating															x
Primary anode															x
Coating				x	x	x	x	x	x						x
Reference electrodes					x					x			x		x
Electricity use													x		x
Yearly control measurements					x		x	x	x	x	x	x	x		x

*M: Maintenance

2.1 Life cycle assessment

For the environmental evaluation of the different repair strategies, a LCA is conducted. In this LCA study, the changes to environmentally relevant flows are described as a response to possible decisions by using the consequential modeling approach. The two most important aspects here are the identification of marginal suppliers and the substitution of dependent co-products (Weidema et al., 2013). Moreover, the study includes the entire life of each repair scenario by following a cradle-to-cradle approach. This means that the following life cycle phases are taken into account: demolishing of the damaged or contaminated parts of the existing structure, reconstruction according to the procedure of the different repair strategies (see previous section), the operation phase and the end-of-life of each intervention. For the end-of-life, the recycling potential or system expansion approach is followed (Weidema et al., 2013). In addition, the impact of production is geographically delimited to Europe, while transportation to the construction site is approached in a Belgian context.

The ecoinvent database v3.8 was used to model background processes, applying the default principle of marginal supplier identification of ecoinvent. For materials or processes for which no ecoinvent records were available, an approximation is made based on expert judgements and literature values. For the impact assessment, the ReCiPe 2016 v1.07 method was used. It implements both midpoint (problem-oriented) and endpoint (damage-oriented) categories and uses a set of weighting factors to calculate a single score impact. However, only the single score is presented in this manuscript because a detailed analysis of the midpoints is beyond the scope. Full details of these midpoints can be found in the supplementary information. In the discussion section will still varying midpoint results compared with the endpoint results be highlighted.

2.2 Life cycle cost analysis

For the economic evaluation of the different repair strategies, a LCCA is performed. The processes considered in the previous assessment (i.e. LCA) are also considered here. The prices of these actions are based on data from the available reports provided by the particular engineering office. The Net Present Value (NPV) for the defined FU's is calculated according to Equation 1 (Jawad and Ozbay, 2006). In this manner, costs and revenues at different stages in time are compared, which is called discounting. It emphasizes the importance of present cash flows rather than future ones due to inflation and earning power (Moins et al., 2020).

$$NPV = I_0 + \sum_{i=1}^N \frac{CF_i}{(1+d)^i} \quad (1)$$

where I_0 = Initial investment; N = study period; i = year; CF_i = cashflow in year i ; d = real discount rate

The real discount rate can be calculated with Equation 2 (Jawad and Ozbay, 2006). In this study, d_n and r_{inf} are assumed to be 6.0 % and 2.0 % respectively to get a discount rate of 3.92 %, which is a reasonable value (Galle, 2016).

$$d = \frac{d_n - r_{inf}}{1 + r_{inf}} \quad (2)$$

where d = real discount rate; d_n = nominal discount rate; r_{inf} = inflation rate

3 RESULTS AND DISCUSSION

In this section, the results of both assessment methods are shown. First, the results from the LCA are discussed after which the LCCA results are discussed in turn. Subsequently, both groups of results are compared with each other.

3.1 Life cycle assessment

In Figure 3, the cumulative impact of the different scenarios is shown on a timeline which shows when an impact occurs as a result of an intervention. In general, ICCP is found to be the most environmentally friendly option. Certainly for FU1 and FU2, both ICCP alternatives (i.e. coating and titanium gauze) are the best out of six. ICCP-C has the lowest impact of 9.5 kPt closely followed by ICCP-G with an impact of 11.2 kPt for FU1. The other techniques have an impact of 1.7 to 3.3 times higher compared to this first strategy. The high impact of GCP-F is due to the need for zinc foil renewal already after 15 years. Secondly, for FU2, the impact of ICCP-C goes beyond this of ICCP-G to a total of 17.6 kPt compared to 12.1 kPt for ICCP-G. Furthermore, the difference between the repair with the lowest impact and the other techniques becomes just bigger with values which are 1.9 to 3.9 times higher. Lastly, for a service life extension of 50 years, ICCP-G remains the best option to pick with an impact of 12.5 kPt. However, ICCP-C becomes the third option with a value of 25.2 kPt closely followed by CR-SP with 26.2 kPt. The second most beneficial option is CR with an impact of 23.4 kPt. The GCP options have no good results, mainly due to the need for intensive intervention during the assumed service life extension. The impact of ICCP-G increases over the years slightly because only one repair intervention is needed. The increasing impact is due to the use of electricity by the system.

This study takes both endpoints and midpoints into account by the ReCiPe method. Similar trends are found for the midpoint indicators compared with the single score results. However, for several midpoints (e.g. global warming, ionizing radiation, fine particulate matter formation, ozone formation, terrestrial acidification, marine eutrophication, human carcinogenic toxicity, land use, mineral resource scarcity, water consumption) varying outcomes are achieved. Only the single score is presented in this manuscript because a detailed analysis of the midpoints is beyond the scope. Detailed information about the midpoints can be found in the supplementary materials.

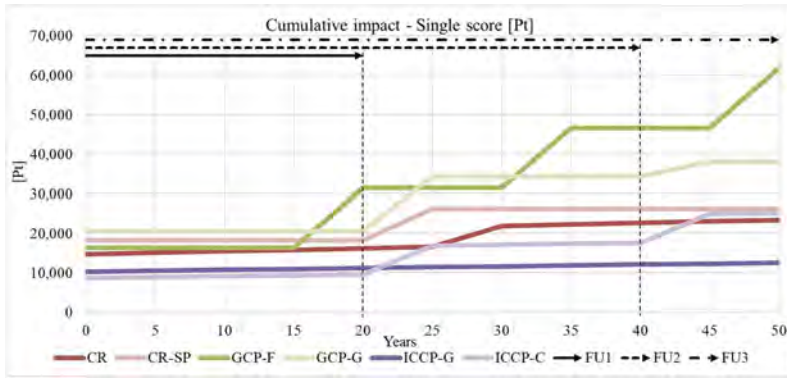


Figure 3. Cumulative environmental impact (single score) for FU1, FU2 and FU3.

3.2 Life cycle cost analysis

The discounted cumulative cost during the life cycles of the six repair strategies is determined by calculating the NPV of each cost at every year and adding this to the total cost of previous years. For the different FUs, varying results are obtained, which can be seen in Figure 4. ICCP-C is found to have the lowest cost of m€ 2.20 for a service life extension of 20 years. The other strategies are quite more expensive for this FU with a cost of m€ 2.57 for GCP-F until m€ 3.35 for CR-SP. GCP-F is the second-best alternative, however, for a service life extension until 15 years, it is the cheapest option. In addition, this is also the case for an extension of 25 to 30 years. When FU2 is considered, ICCP-C remains the most beneficial option with a cost of m€ 2.64. The order of the other repairs is still the same, only ICCP-G became less expensive than GCP-F. They have respectively a cost of m€ 2.90 and m€ 2.93 for FU2. Moreover, GCP-G, CR-SP and CR have an economic cost really close to each other but on average 36 % higher than this of ICCP-C. Lastly, the same trends can be seen for FU3, only GCP-G became the worst option (m€ 3.76) instead of CR-SP and CR at FU1 and FU2 respectively. Besides, a change is present in the difference between ICCP-G and ICCP-C and GCP-F. More particular, the cost of ICCP-G and ICCP-C converted to each other resulting in a value of respectively m€ 2.91 and m€ 2.84. Furthermore, the difference between GCP-F and ICCP-G knows an increase to 7.5 % instead of 1.1 % at FU2. Therefore, for a service life extension of 50 years ICCP and more specifically ICCP-C is economically speaking the most beneficial option.

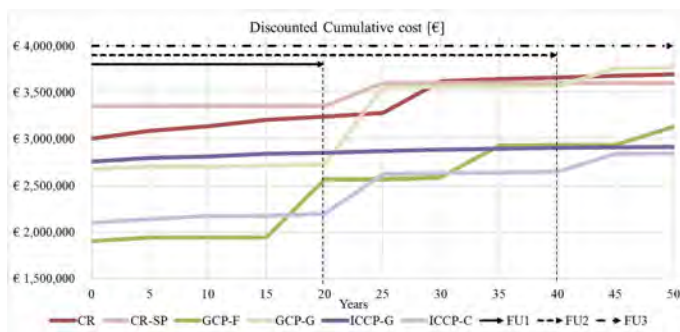


Figure 4. Discounted cumulative economic impact (NPV) for FU1, FU2 and FU3.

3.3 Comparison LCA vs. LCCA

The total environmental and economic life cycle cost for FU1, FU2 and FU3 are combined in Figure 5. In this manner, it can be seen if a strategy scores the best for both criteria or where certain repairs score better or worse than the others. A pareto front is not drawn due to the rather limited number of results to do this adequately. For FU1, it can be seen that ICCP-C scores the

best for both criteria. Therefore, this strategy should be conducted for an intended service life extension of 20 years. Regarding the other repairs, the results show that some score well for the economic cost (e.g. GCP-F) and others for the environmental impact (e.g. ICCP-G). Secondly, there is no consensus regarding the two criteria for FU2. Namely, ICCP-C has still the lowest economic cost but ICCP-G has the lowest environmental impact. However, the other four repairs don't score better than these two, so a good selection can still be made. Finally, the ICCP strategies are again the most sustainable for FU3. Only CR scores a little bit better (7.5 %) than ICCP-C for the environmental impact. In addition, regarding the LCCA, ICCP-C has a 2.5 % lower cost than ICCP-G. Overall, it can be concluded that ICCP is mostly the most suitable option.

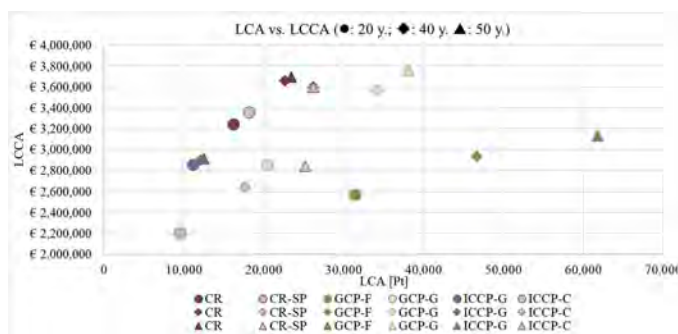


Figure 5. LCA vs. LCCA for FU1, FU2 and FU3.

4 CONCLUSIONS

In order to improve the sustainability of existing reinforced concrete structures over their life cycle, a key factor is to reduce the environmental and economic impact of repair and maintenance interventions. These impacts can be determined by the quantitative assessment tools named LCA and LCCA by which a mutual comparison between the strategies can be done and sustainable decisions can be made. In this paper, a corrosion damaged concrete silo of 6690 m² exposed concrete surface situated in a Belgian industrial area is selected as case study. Six different frequently used repair strategies for addressing corrosion damage are evaluated through a life cycle assessment (LCA) and life cycle cost analysis (LCCA): (i) conventional repair (CR), (ii) conventional repair with surface protection (CR-SP), (iii) galvanic cathodic protection with zinc foil (GCP-F), (iv) galvanic cathodic protection with zinc gauze (GCP-G), (v) impressed current cathodic protection with titanium gauze (ICCP-G) and (vi) impressed current cathodic protection with a conductive coating (ICCP-C). So, the environmental and economic impact of these life extending repair actions with corresponding activities are evaluated over the entire life cycle of the concrete silo. This is done for three different intended service life extensions: 20, 40 and 50 years.

For a service life extension of 20 years, ICCP-C is the preferable option on the environmental and economic level. Furthermore, it is still economical the best option for a service life extension of 40 years. However, ICCP-G scores here better at the LCA. Thirdly, ICCP-G is found to have almost the lowest impact for both criteria at a service life extension of 50 years. Only, the economic cost of ICCP-C is 2.5 % lower. Therefore, the electro-chemical ICCP treatments are in general good options to conduct for this case study. This can be explained by the low initial cost/impact for ICCP-C and the low need for interventions after the first repair for ICCP-G.

Economically, the same trend was seen for FU1 and FU2 by (Wittcox et al., 2022) who reported ICCP as the most beneficial option for a service life extension of 20 to 40 years for balconies. Nevertheless, CR and GCP were environmentally speaking more sustainable than ICCP. For a bridge, (Polder et al., 2016) report CP in general as less costly than CR for a service life extension of 35 years. This is in line with the results of this study. Although, for an extension of 35 to 100 years these repairs should be the least beneficial of the five considered repairs. Moreover, CP with conductive coating should be more expensive than CP with titanium mesh for a service life extension of

20 to 75 years for RC columns according to (Binder, 2013). In contrast, the opposite result is seen in this case study. The comparison with other research shows the case-dependency of LCA and LCCA studies and the fact that results and conclusions cannot be generalized.

Finally, ICCP can still not be specified as the most sustainable option for every situation. When for example another service life extension is intended, other techniques can score better like GCP-F economically for an extension of 15 years. Therefore, we also want to highlight the importance of the assumed potential of the repairs to extend the service life as it can have a big impact on the results. Here, these values are determined based on expert judgement of the engineering office Sanacon. However, further research is needed about the service life extension of repairs by which the highest effect on the life cycle impact/cost is expected. Secondly, for some activities and products general prices and proxy LCA records are used. A more in-depth analysis of the necessary activities and materials with corresponding impacts and costs could improve the results.

ACKNOWLEDGMENTS

We thank the engineering office Sanacon for providing data and the Research Foundation Flanders (FWO-Vlaanderen) for supporting Matthias Buyle with a post-doctoral fellowship (Postdoctoral Fellow - junior; 1207520N).

REFERENCES

- Baker, M., Singhvi, A. & Mazzei, P. 2021. Engineer Warned of ‘Major Structural Damage’ at Florida Condo Complex. *The New York Times*. <https://www.nytimes.com/2021/06/26/us/miami-building-collapse-investigation.html>.
- Binder, F. 2013. Life cycle costs of selected concrete repair methods demonstrated on chloride contaminated columns. *11th International Probabilistic Workshop, Brno*. Beton-und Stahlbetonbau.
- Fumagalli, M. 2021. The corrosion of the Morandi Bridge: the story of a predictable collapse. *ipcm*. <https://www.ipcm.it/en/article/corrosion-morandi-bridge-the-story-of-a-predictable-collapse.aspx>.
- Galle, W. 2016. Scenario based life cycle costing: an Enhanced Method for Evaluating the Financial Feasibility of Transformable Building. *Doctoral thesis Vrije Universiteit Brussels*: 418.
- Jawad, D. & Ozbay, K. 2006. The discount rate in life cycle cost analysis of transportation projects. *85th Annual Meeting of the Transportation Research Board, Washington DC, 22-26 January 2006*.
- Jones, A. E. K., Marsh, B. K., Clark, L. A., Seymour, B. P. a. M. & Long, A. M. 1997. Development of a holistic approach to ensure Cement, the durability of new concrete construction. *British Cement Association (Report C/21)*: 81.
- Maxineasa, S. G. & Taranu, N. 2018. 24-Life cycle analysis of strengthening concrete beams with FRP. In Pacheco-Torgal, F., Melchers, R. E., Shi, X., De Belie, N., Van Tittelboom, K. & Sáez, A. (Eds.) *Eco-efficient Repair and Rehabilitation of Concrete Infrastructures*: 673–721. Woodhead Publishing.
- Moins, B., France, C., Van Den Bergh, W. & Audenaert, A. 2020. Implementing life cycle cost analysis in road engineering: A critical review on methodological framework choices. *Renewable and Sustainable Energy Reviews* 133: 17.
- Pacheco-Torgal, F. 2018. 1-Introduction. In Pacheco-Torgal, F., Melchers, R. E., Shi, X., De Belie, N., Van Tittelboom, K. & Sáez, A. (Eds.) *Eco-Efficient Repair and Rehabilitation of Concrete Infrastructures*: 1–12. Woodhead Publishing.
- Polder, R., Pan, Y., Courage, W. & Peelen, W. H. 2016. Preliminary study of life cycle cost of preventive measures and repair options for corrosion in concrete infrastructure corrosion in concrete infrastructure. *Heron* 61 (1): 13.
- Renne, N., Kara De Maeijer, P., Craeye, B., Buyle, M. & Audenaert, A. 2022. Sustainable Assessment of Concrete Repairs through Life Cycle Assessment (LCA) and Life Cycle Cost Analysis (LCCA). *Infrastructures* 7 (10): 32.
- Vrt. 2022. Antwerp municipal theatre to be demolished. *Vrt.be*. <https://www.vrt.be/vrtnws/en/2022/05/16/antwerp-municipal-theater-to-be-demolished/>.
- Weidema, B. P., Bauer, C., Hischer, R., Mutel, C., Nemecek, T., Reinhard, J., Vadenbo, C. & Wernet, G. 2013. Overview and methodology: Data quality guidelines for the ecoinvent database version. *Swiss Centre for Life Cycle Inventories (Ecoinvent Report)* 3: 170.
- Wittocx, L., Buyle, M., Audenaert, A., Seuntjens, O., Renne, N. & Craeye, B. 2022. Revamping corrosion damaged reinforced concrete balconies: Life cycle assessment and life cycle cost of life-extending repair methods. *Journal of Building Engineering* 52: 24.

Foundation for risk-based asset management for storm surge barriers

Y. Kharoubi, M. van den Boomen & M.J.C.M. Hertogh

Faculty of Civil Engineering and Geosciences, Delft University of Technology, Delft, The Netherlands

J. van den Bogaard

Rijkswaterstaat Ministry of Infrastructure and the Environment, Utrecht, The Netherlands

ABSTRACT: Due to climate change, the risk of flooding is increasing with potentially severe consequences on highly populated and economically developed coastal zones. Storm surge barriers protect against such events with the critical task of closing during extreme weather conditions to prohibit the propagation of water. This highlights the importance of maintaining the high reliability of these structures and the challenge to reach this goal for rarely operated and unique infrastructures. To deal with this challenge, the study creates a foundation to set an asset management approach for storm surge barriers or assets with similar characteristics. This is done by studying the case of The Netherlands with the aim to [1] describe the asset management approach, [2] identify key features of the approach, [3] investigate the connection between these features and the characteristics of the barriers, and [4] conclude the influence of the characteristics on the establishment of an asset management approach.

1 INTRODUCTION

The climate is changing with increasing global sea levels, surface temperatures, and precipitation among others. Despite the efforts to reduce emissions and global warming, the effects of climate change will continue to have an influence. The risk of flooding is unavoidable and measures to deal with it are crucial. Hard (infrastructures) and soft (nature-based) protective measures against sea level rise will support the continuity of coastal cities (Pörtner et al. 2022). However, the soft measures are not sufficient to reduce 2100 risks. Hard flood protection measures such as Storm Surge Barriers (SSBs) are required (Du et al. 2020).

SSBs are crucial for flood management especially in responding to climate change effects and complying with strict safety requirements (Jonkman et al. 2013). They are flood defences that are operated during extreme events to avoid catastrophic consequences. This requires high reliability of SSBs during extreme and rare events (Jordan et al. 2019). However, climate change challenges operation and maintenance (O&M) and imposes increasing expenses to sustain the current safety levels of protection measures (Pörtner et al. 2022). High sea level rise scenarios diminish the flood safety provided by SSBs and lead to more frequent closures of SSBs. Furthermore, SSBs deteriorate faster when design water levels are surpassed (Haasnoot et al. 2020). Therefore, O&M of SSBs are intrinsically challenged with strict requirements and are additionally confronted with climate change complications.

To preserve the safety levels provided by these structures, maintenance is performed based on intensive work and planning in systematic asset management (AM) approach (Jordan et al. 2019). AM supports organisations to perform O&M with limited budgets and under strict requirements in risky and uncertain conditions (Almeida et al. 2022). However, organisations face challenges such as ageing assets, changing operating conditions, limited resources, and loss of knowledge. AM tries to deal with these challenges through structured decision-making and balanced performance, risk, and resources (Shah et al. 2017). Despite its importance, the needed effort for AM is underrated, knowledge sharing among countries is disrupted, and research on the maintenance of flood defences in relation to their performance is limited

(Jordan et al. 2019). The latter can be supported with information on AM from other assets since AM as an approach is similar in many ways. However, it differs between assets due to the influence of special characteristics of an asset (Herder & Wijnia 2012). Furthermore, standards like the ISO 5500x cover AM requirements but do not cover “how” to fulfil the requirements and provide limited guidance for infrastructure assets. Models from practice can provide a better perspective while fulfilling the ISO requirements (Wijnia & Croon 2015). This is especially important for SSBs since they are relatively new structures, with the first SSB completed in 1958 (Mooyaart & Jonkman 2017), and the importance and complications of their AM is increasing. Therefore, the research aims to create the foundation for setting an AM approach for SSBs or similar assets by studying AM for SSBs from practice and analysing the approach relative to the characteristics of SSBs. This leads to the research question: How do the characteristics of SSBs influence the formation of the AM approach?

2 RESEARCH METHOD

In this paper, the AM for SSBs is investigated with a focus on the influence of SSBs’ characteristics on the AM approach. This is done based on literature and case study research. The characteristics of SSBs are derived from literature based on the following iterative process: articles were analysed such that different sections were associated with specific characteristics, the latter were compiled to reach more general characteristics with supporting content, then characteristics with limited evidence were further researched. For the study of the AM approach, the case of The Netherlands was investigated from papers addressing the AM approach, guidelines describing the approach, four interviews with experts who were involved in the development of the AM approach, and supporting documentation from the organisation managing the SSBs. The different sources supported the development of the overview of the AM approach such that general concepts were clarified from papers, detailed topics of the AM approach were explained from guidelines, and connections between topics into processes were concluded based on interviews and documentation from the organisation. Moreover, the data from the different sources were analysed by coding and categorising to identify the key features of the AM approach to reveal the core ideas based on which the overall approach is formed. These key features were then analysed relative to SSBs characteristics based on associations identified from the interviews with experts. Hereafter, the research question is answered and the influence of characteristics on shaping the AM approach is clarified.

3 STORM SURGE BARRIERS AND THEIR CHARACTERISTICS

This section introduces SSBs with clarification of characteristics (in italics) which in turn reveal general and unique properties of SSBs, their functionality, and their history.

A SSB is a *system within a system*. It is part of the flood defence system with the role of controlling water passage, reducing the flood risk, shortening the coastline without closing an estuary (Jonkman et al. 2013), and reducing the disruption of the landscape and environment (Walraven et al. 2022). Under normal conditions, SSBs remain open. They close to protect against flooding in case of storm surges. For SSBs to perform these functions, they consist of sub-systems (structural, mechanical, electrical, software). These sub-systems are studied to assess the sole failure of the SSB system (Mooyaart & Jonkman 2017) which is used for the overall assessment of the flood defence system.

Being part of a national flood defence system, SSBs are *public infrastructures* that are built and operated with national budgets to fulfil national safety requirements. In the USA, the United States Army Corps of Engineers (USACE) built and operated SSBs with different safety levels ranging between 100 and 500-year event (Morang 2016). In The Netherlands, the law specifies the acceptable failure probabilities for sections of the flood defence system with a range of 1:100 to 1:10⁶ (Jonkman et al. 2018). These safety levels are reached with *high investment costs* such as the Maeslant barrier with initial costs of \$940 million and O&M

expenses reaching \$17 million annually (Mendelsohn et al. 2022). Being public and expensive, SSBs are subject to *political processes* and *long-lead times until their construction*. Political reasons, such as funding processes, public support, assessments, and permits, contribute to long-lead times. The lead time for SSBs mentioned in Hill's study spanned between 14 and 37 years with construction time ranging between 8 and 10 years (Hill 2012).

These public structures protect against extreme flood events, thus SSBs are considered *critical infrastructures* as in The Netherlands (NCTV 2017) and the USA (CISA n.d). Critical infrastructures are systems or assets that are vital to a nation because any disturbance in their service can influence national security, economy, health, and safety (Alcaraz & Zeadally 2015). For the case of SSB, the loss in their service leads to flooding from extreme weather events, which in turn results in massive consequences. Such drastic events might occur because SSBs protect high-value economic and urban areas (Aerts 2018) in low-lying coastal zones with increasing populations and growing economies (Jonkman et al. 2013). Besides their primary role, SSBs are *multi-functional* with an impact on the economy, society, and ecology. SSBs reduce the risk of failure and costs of strengthening defences behind them (Nogueira & Walraven 2018) and enable less strict standards in the hinterland which then reduces disruption of the landscape and environment (Walraven et al. 2022). Moreover, SSBs allow navigation to resume especially for port cities and contribute to the economic development of delta regions (Meyer & Nijhuis 2013) SSBs' impact on ecology can be considered by allowing tidal and saltwater exchange (Mooyaart & Jonkman 2017). With these different functions, an *integrated approach* is required to account for the multiple functions of SSBs and their influences (Jonkman et al. 2013). In port cities such as Rotterdam and New Orleans, protection against flooding interacts with urban growth, economic development, and environmental issues (Meyer & Nijhuis 2013).

In practise, an integrated approach leads to *unique* structures that request innovative designs. SSBs are considered prototypes with a unique combination of the physical environment, requirements, and design (Walraven et al. 2022). The location of SSBs in estuaries and deltas with soft soils requires innovations in the design and construction of complicated foundations (Mooyaart & Jonkman 2017). Besides the geological complexity, being in water bodies in socio-economically important regions complicates the design and construction of SSBs. Innovations in science and technology were necessary to reach the design in the USA and The Netherlands (Meyer & Nijhuis 2013). After the challenges in design and construction, a *long life awaits SSBs*. They are designed for long periods such as the Eastern Scheldt barriers with 200 years of lifetime with consideration of 50 cm sea level rise (McRobie et al. 2005). Such design assumptions of the long-life structures might become incompatible as more knowledge is gained. For example, scenarios with accelerated sea level rise (beyond design assumptions) are probable (Haasnoot et al. 2020).

During this long life, SSBs' *operation is limited and dependent* on external conditions and intended use. The closure of SSBs is based on constant water level thresholds or constant annual exceedance probability that is used to update the triggering water level for closure with sea level rise (Chen et al. 2020). Generally, SSBs are designed for irregular storm surges whose occurrences are rare. Most of the barriers in the USA have not yet been operated at or near their peak design height (Morang 2016). In The Netherlands, the frequency of closure ranges from 1 every 10 years to a few times (1-8) a year (Nogueira & Walraven 2018). This dependency on the operation and the long life of SSBs lead to *dynamic operation*. For example, SSBs have to close more frequently and with longer closure duration due to sea-level rise that leads to more recurring water level exceedances (Chen et al. 2020).

4 ASSET MANAGEMENT FOR STORM SURGE BARRIERS: CASE OF THE NETHERLANDS

To investigate the AM for SSBs, the case of The Netherlands is studied based on data collected and analysed from various sources. The low-lying land has a long history of flood protection, strict safety standards, and frequent assessments. To comply with regulations, the so-called "ProBO: Probabilistic Operations and Maintenance" (now known as "Risk-based operations and maintenance") was set and followed by Rijkswaterstaat (Jorissen et al. 2016). ProBO enables demonstrating the fulfilment of performance requirements, provides constant

control of the system's performance level, sets O&M processes based on risks that affect performance, and triggers improvement. This is achieved with the different parts of ProBO shown in Figure 1 and elaborated in the following sections.

ProBO covers three main aspects technical, organisational, and contracting. Technical aspects focus on analyses to describe the system, assess risks, and determine performance levels. Organisational aspects cover operations, maintenance, and control and supporting processes. And contracting aspects focus on performance in relation to external parties performing maintenance activities. To sustain and optimise performance levels, the Deming cycle with Plan-Do-Check-Act phases is set as a framework (Bogaard & Akkeren 2011). Accordingly, ProBO is explained by distinguishing between the preparation of the three aspects of the PDCA cycle and the execution of the PDCA cycle.

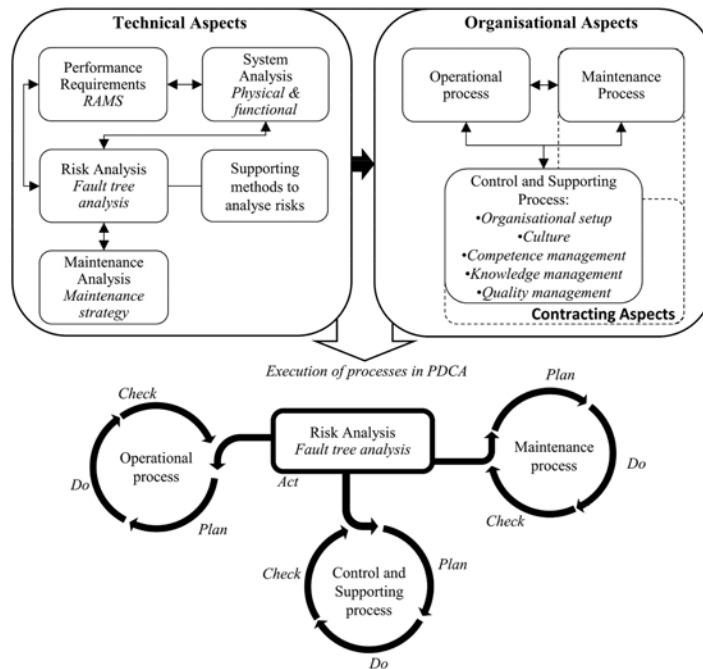


Figure 1. Illustration of ProBO – AM approach for SSBs.

4.1 Preparation

4.1.1 Technical aspect

The starting point of ProBO is the technical aspects. First, the performance requirements are derived from legislations and policies and translated in terms of quantitative reliability and availability requirements and other qualitative requirements of RAMS (Reliability, Availability, Maintainability, Safety). Afterward, the system is analysed and decomposed into physical and functional breakdown structures. A System Breakdown Structure (SBS) based on design information is performed and functions of elements and components and their interrelations to operate as a whole are determined and quantified in relation to performance requirements. These analyses are used for the risk analysis to reveal the risks that influence performance levels and guide towards actions that deal with these risks. Various methods are used and developed to support the risk analysis as shown in Figure 1. The results of the latter support the development of the fault tree that leads to quantifying the unreliability or unavailability and comparing them with requirements. The comparison leads to an iterative process as shown in Figure 1 with the double arrows. The iterative process aims to eventually meet performance requirements and

optimise when possible. Based on the risk analysis, the O&M is studied to sustain performance at acceptable levels and minimise lifecycle costs. The maintenance analysis looks into maintenance strategies using the concept of Reliability Centred Maintenance (RCM) and is based on information from the risk analysis. The aim is to select suitable maintenance to reduce the likelihood of a failure or its consequences. Then, maintenance and inspection activities are determined. The results of the maintenance analysis can be prioritised from a risk perspective such that components contributing most to the performance levels are given more attention in improving maintenance. Furthermore, the analysis can optimise the maintenance and minimise lifecycle costs as long as performance requirements are met (Bogaard & Akkeren 2011).

4.1.2 *Organisational aspects*

The results of the technical aspects are used to set up the organisational aspects of ProBO: operational, maintenance, and control and supporting processes. The operational process focuses on operating the system while ensuring functionality in accordance with performance requirements. So, operational scenarios, activities, procedures, instructions, preconditions, and resources are determined while considering performance requirements, human errors, and repair work during operations. Similarly, preparations for the maintenance process are performed based on the maintenance analysis previously described. The maintenance activities are derived from the analysis and described with the necessary procedures. These procedures are described while considering ways to facilitate repairs and reduce human errors and common cause failures. For both processes, the organisational setup, culture, and knowledge management are clarified with the help of the control and supporting process. Tasks, processes, responsibilities, and roles are linked to the activities to be performed in the O&M processes. The roles are specified in RASCI-method (Responsible, Accountable, Supportive, Consulted, and Informed) to clarify the distribution of roles and the communication between them. Furthermore, knowledge levels, competencies, and skills for the different positions within the department are identified along with development plans and training. To preserve the knowledge, ProBO includes Human Resource Management (HRM) plan. This plan clarifies the distribution of knowledge within the organisation and with external parties. The different features of control and supporting process are clarified in Figure 1 (Bogaard & Akkeren 2011).

4.1.3 *Contracting*

Since external parties are involved in the regular and major maintenance activities, contracting becomes an essential part that requires analysis and preparation in line with the objectives of ProBO. Accordingly, the decision to outsource and the degree of outsourcing are analysed by considering different stages of the PDCA of the maintenance process in relation to failure probabilities. Furthermore, the decision to outsource considers criteria in line with the objectives of ProBO such as: the organisation remains in control and meets performance requirements, risks are small or manageable, and the market situation permits outsourcing. To decide on the degree of outsourcing, the following are evaluated: integration of regular and major maintenance, combining disciplines, and responsibilities of the contractor. In the case of outsourcing, plans and processes are arranged to prepare contractors for applying ProBO. Furthermore, contracts clarify various points (such as contracted activities, performance requirements of the outsourced activities, maintenance mode, procedures, training levels, and documentation requirements) to ensure performance levels are met. In addition, the organisation has to prepare itself with the competencies and necessary knowledge to be able to control the processes and activities of the contractor (Bogaard & Akkeren 2011). Based on the above description, the contracting aspect can be seen in the maintenance process and control and supporting process.

4.2 *Execution of PDCA*

After the preparations are complete, continuous PDCA cycles are performed to preserve performance levels as required. The PDCA cycle is divided such that plan-do-check phases are applied to each of the three processes: operations, maintenance, control and support. Then, the information from the check phases of the processes is combined in a single act phase that evaluates the risk analysis to assess actual performance and compare it with the requirements.

The PDCA cycle starts with creating explicit plans for the processes by covering activities, methods for execution, organisation, and contracting. O&M activities covered in the previous analyses are scheduled and clustered to account for periods during which maintenance cannot be performed. The different details of the organisational and contracting aspects are planned such as work procedures to be followed are clarified, the tasks to be executed are set and allocated, staff training is scheduled, requirements for contracts are defined, and the quality system is set. Then, the plans are executed in the Do stage. The O&M activities are performed while complying with preparations done earlier. It is necessary to follow procedures in order to validate the risk analysis and demonstrate performance. During the do stage, the work is tracked with documentation on deviations, quality, and time. Furthermore, records are kept on actual data on processes, activities, detected anomalies, operational problems, and impractical work procedures among others. These records have to be linked to corresponding activities for assessments and future improvements. In the check phase, the processes are monitored and assessed based on collected data. For technical aspects, the data is used to identify trends and deviations in technical conditions and assumptions used in the risk analysis. For organisational and contracting aspects, the checks include: the quality of performed work of internal and external parties, deviations in the process and schedule, workability of procedures, and training level to further reduce errors. To support the act phase, the check phase also evaluates plans, the impact of proposed improvements, and unexpected behaviours. Accordingly, the check phase leads to a further understanding of all aspects, follow-up actions for improvements, and up-to-date data to be used in the risk analysis. At that time, the act phase proceeds to update the risk analysis and determine actual performance levels that are then compared to requirements. In case the requirements are not met, performance killers are identified and analyses are performed to suggest actions that improve performance to acceptable levels. The analyses look into the data and proposals from the Check phase in relation to performance, organisational maturity, and working methods. When the requirements are met, the influence of the follow-up actions is evaluated, changes to preconditions are analysed, improvement proposals are generated and approved, and clarifications on updates to plans are submitted. At the end of this phase, the input for the following PCDA cycles is set in a report including the new performance levels and follow-up actions. Finally, the plan stage restarts with information from the act stage (Bogaard & Akkeren 2011).

5 ANALYSIS AND DISCUSSION

By analysing the AM approach for SSBs followed in The Netherlands with coding collected data and categorising, the key features of the AM approach are identified as follows:

- Holistic Approach: Covers and connects technical, organisational, and contracting aspects via a risk analysis with the aim to meet performance requirements
- Comprehensive approach: Detailed preparation (analyses, procedures, instructions, process descriptions) and guidance for execution
- Strict approach: Requires following procedures and preparations to validate the risk analysis
- Risk-based: Risk analysis is the core based on which all three processes (Operation, Maintenance, Control and support) are set to manage risks that influence performance
- Quantitative approach: Provides evidence of compliance with performance requirements by assessing reliability and availability performance levels
- Execution that provides constant control: Constant control of the system's performance with regular assessment and checks with PDCA-based execution
- Continuous improvement: Continuous improvement at different levels (PDCA cycles, development plans and training for personnel, quality control, and audits)
- Connection between risks and people: Internal and external parties connected to risks by covering human errors, knowledge, competencies, and culture in relation to risks in the control and supporting process and linking the contracting aspect to the risk analysis

The key features noted above emerged during the development of ProBO which was initially designed for the Maeslant barrier to demonstrate the reliability of the barrier. Various requirements,

challenges, and drivers shaped ProBO into how it is now. The fact that the barrier is a public and critical infrastructure with strict safety requirements triggered the quantitative approach to demonstrate and control performance levels and improve maintenance to reach acceptable performance levels. A comprehensive, quantitative, and risk-based approach was needed to deal with the barrier's limited operation that hinders the direct understanding of performance. The limited operation challenged the maintenance of the components with information from suppliers that were assessed as insufficient due to operating conditions different from prescribed. This required an analysis (in this case fault tree) that is detailed to a level that can guide activities and support the calculation of performance from inspection and testing information. The fault tree analysis was inspired by [1] the design and construction phases that used this analysis to prove the requirements are met and [2] the nuclear power plants that have similar safety demands. This shows the influence of having strict requirements and being a critical infrastructure with safety-related regulations on the choice of approach. Furthermore, being a system within a system is another characteristic that had a role in choosing a quantitative and risk-based approach. The barrier protects the dike ring in the hinterland and supports the dikes in meeting their requirements, so the reliability of the barrier during O&M is needed to calculate the dike's probability to hold a certain water level.

As ProBO developed with more analyses, it became a holistic approach covering more than just maintenance. Initially, the design for operating the Maeslant barrier was fully automated to avoid human failure risks. However, human interaction was introduced to correct technical failures and improve the performance of the barrier. With the addition of human interaction, procedures, instructions, and training were added to reduce failure rates due to human errors. This is especially important for the closure of the barrier where the team follows strict procedures and instructions for certain failures or incidents that are analysed and detailed in the fault tree. Furthermore, human resource management was introduced to prepare the teams with the necessary knowledge and skills. Knowledge is managed since SSBs have a long life and are unique, so the learning possibilities from other similar assets are limited and it is necessary to learn from the specific asset.

Since the approach covers various details, its application is not unified for all SSBs. The details of the comprehensive approach are directly influenced by the uniqueness of SSBs, their multi-functionality, and their frequency of operation. For instance, the location and design of the SSB influence the O&M in different ways such as frequency, level of flexibility, and difficulty. Similarly, the multiple functions of SSBs (such as the discharge of rivers and navigation) influence the maintenance planning and the operation frequency controls the amount of asset information used in the analysis. Multi-functionality is also related to the risk-based and quantitative features of ProBO since they enable studying the influence on safety from other functions and demands of stakeholders. Safety remains the primary function of SSBs and other demands are considered after attaining the required safety levels with the risk analysis. Furthermore, the results of the risk analysis can be used to provide evidence of the performance level and the request for certain budgets for improvement from the government. Since the maintenance relies on budgets granted by the government, political processes can impact the ability to continuously improve and be in control of performance.

6 CONCLUSIONS

The current research investigated the unique characteristics of SSBs and how these shaped the AM approach for SSBs in the Netherlands. The derived characteristics provided background information on SSBs and helped in realising the challenges or requirements that certain characteristics create for the AM approach. This was further analysed in the case study that showed the development and implementation of an AM approach in practice. The results showed that certain characteristics of SSBs (such as limited operation and strict requirements) have a clear and direct connection to key features of the AM approach which has matured over time. Therefore, the study connects general characteristics, that apply to SSBs and other assets, to key features of an AM approach that can be considered for the AM of SSBs and assets with similar characteristics. Furthermore, future considerations for AM as noted by experts include [1] benefiting from advances in maintenance and data management, [2] starting

early with innovations and solutions for maintenance complications due to climate change, and [3] considering O&M in the design phase since the design might over-complicate the situation. These results are preliminary, and this case is part of a wider study on AM for SSBs.

REFERENCES

- Aerts, J. C. 2018. A review of cost estimates for flood adaptation. *Water*, 10, 1646.
- Alcaraz, C. & Zeadally, S. 2015. Critical infrastructure protection: Requirements and challenges for the 21st century. *International journal of critical infrastructure protection*, 8, 53–66.
- Almeida, N., Trindade, M., Komljenovic, D. & Finger, M. 2022. A conceptual construct on value for infrastructure asset management. *Utilities Policy*, 75, 101354.
- Bogaard, J. V. D. & Akkeren, K. V. 2011. Leidraad risicogestuurd beheer en onderhoud conform de ProBO werkwijze. IN RIJKSWATERSTAAT (Ed. The Netherlands).
- Chen, Z., Orton, P. & Wahl, T. 2020. Storm Surge Barrier Protection in an Era of Accelerating Sea-Level Rise: Quantifying Closure Frequency, Duration and Trapped River Flooding. *Journal of Marine Science and Engineering*, 8, 725.
- Cisa, C. a. I. S. A. n.d.. Dams Sector.
- Du, S., Scussolini, P., Ward, P. J., Zhang, M., Wen, J., Wang, L., Koks, E., Diaz-Loaiza, A., Gao, J. & Ke, Q. 2020. Hard or soft flood adaptation? Advantages of a hybrid strategy for Shanghai. *Global Environmental Change*, 61, 102037.
- Haasnoot, M., Kwadijk, J., Van Alphen, J., Le Bars, D., Van Den Hurk, B., Diermanse, F., Van Der Spek, A., Essink, G. O., Delsman, J. & Mens, M. 2020. Adaptation to uncertain sea-level rise; how uncertainty in Antarctic mass-loss impacts the coastal adaptation strategy of the Netherlands. *Environmental Research Letters*, 15, 034007.
- Herder, P. & Wijnia, Y. 2012. A systems view on infrastructure asset management. *Asset Management*. Springer.
- Hill, D. 2012. The lessons of Katrina, learned and unlearned. *Journal of Coastal Research*, 28, 324–331.
- Jonkman, S. N., Hillen, M. M., Nicholls, R. J., Kanning, W. & Van Ledden, M. 2013. Costs of adapting coastal defences to sea-level rise—new estimates and their implications. *Journal of Coastal Research*, 29, 1212–1226.
- Jonkman, S. N., Voortman, H. G., Klerk, W. J. & Van Vuren, S. 2018. Developments in the management of flood defences and hydraulic infrastructure in the Netherlands. *Structure and Infrastructure Engineering*, 14, 895–910.
- Jordan, P., Manojlovic, N. & Fröhle, P. 2019. Maintenance of Flood Protection Infrastructure in the North Sea Region—An Analysis of Existing Maintenance Strategies. *Coastal Structures 2019*, 654–662.
- Jorissen, R., Kraaij, E. & Tromp, E. 2016. Dutch flood protection policy and measures based on risk assessment. *E3S Web of Conferences*. EDP Sciences.
- Mcrobie, A., Spencer, T. & Gerritsen, H. 2005. The big flood: North Sea storm surge. *Philosophical Transactions of the Royal Society A: Mathematical, Physical and Engineering Sciences*, 363, 1263–1270.
- Mendelsohn, R., Fairbank, A. & Rajaoberison, A. 2022. The Economics of Storm Gates. *Coastal Management*, 1–14.
- Meyer, H. & Nijhuis, S. 2013. Delta urbanism: planning and design in urbanized deltas—comparing the Dutch delta with the Mississippi River delta. *Journal of Urbanism: International Research on Place-making and Urban Sustainability*, 6, 160–191.
- Mooyaart, L. & Jonkman, S. N. 2017. Overview and design considerations of storm surge barriers. *Journal of Waterway, Port, Coastal, and Ocean Engineering*, 143, 06017001.
- Morang, A. 2016. Hurricane barriers in New England and New Jersey: History and status after five decades. *Journal of Coastal Research*, 32, 181–205.
- Nctv 2017. Weerbare vitale infrastructuur. IN VEILIGHEID, N. C. T. E. (Ed. Den Haag, the Netherlands).
- Nogueira, H. I. S. & Walraven, M. 2018. Overview storm surge barriers. Rijkswaterstaat, Deltares, I-Storm.
- Pörtner, H.-O., Roberts, D. C., Poloczanska, E. S., Mintonbeck, K., Tignor, M., Alegria, A., Craig, M., Langsdorf, S., Löschke, S., Möller, V. & Okem, A. 2022. IPCC, 2022: Summary for Policymakers. *Climate Change*.
- Shah, R., Mcmann, O. & Borthwick, F. 2017. Challenges and prospects of applying asset management principles to highway maintenance: A case study of the UK. *Transportation Research Part A: Policy and Practice*, 97, 231–243.
- Walraven, M., Vrolijk, K. & Kothuis, B. B. 2022. Design, maintain and operate movable storm surge barriers for flood risk reduction. *Coastal Flood Risk Reduction*. Elsevier.
- Wijnia, Y. & Croon, J. D. 2015. The asset management process reference model for infrastructures. *9th WCEAM Research Papers*. Springer.

Lessons learned from past earthquakes for horizontally curved bridges

E. Namlı

Emay International Engineering & Consultancy Inc., İstanbul, Turkey

T. Öztürk

Prof. Dr., İstanbul Technical University, İstanbul, Turkey

ABSTRACT: Transportation has an important and wide impact on the economy, social and cultural structure of countries. Highways and railways are part of the transportation system network where bridges and viaducts are the most critical structures of this system. Therefore, bridge damages not only result in direct losses, but also have social and economic impacts. Seismic behavior of bridges in curved alignment plane contain additional potential damages due to their complex geometries, although similar damages were observed for curved and straight bridges as examined in past earthquakes. In this study, the damages observed in horizontally curved bridges in the past earthquakes were investigated and the lessons to be learned according to the results obtained from past earthquakes on the curved bridges were examined.

1 INTRODUCTION

Transportation systems from past to present and the bridges that are a part of them have been one of the most important factors determining the level of civilization of the country as well as providing the transportation network in the countries. Damages in bridges after major earthquake ground movements not only affected transportation but also indirectly affected social-economic conditions of countries according to damage level. Therefore, it is of great importance to determine the seismic behavior of bridges and to design them according to that criteria. By examining the damage types occurred in the past earthquakes, a number of studies have been carried out in order to develop bridge designs in this aspect.

With the increasing population, the coincidence of urban and suburban roads has led to the need for different intersection solutions. Therefore, the use of horizontally curved bridges have become widespread for their aesthetic and economic advantages which exhibit geometric compatibility. On the other hand, due to their geometric irregularities, curved bridges are more sensitive to earthquake ground movements than straight bridges. Although similar damages were observed for both bridge types, more complex and destructive damage types were encountered due to the geometry of the curved bridges. For this reason, many studies have been carried out in order to understand the seismic behavior of horizontally curved bridges and to take necessary measures in the designs to be made.

Particularly as a result of the heavy damages in the bridges after the 1971 San Fernando earthquake, the behavior of these bridges under the influence of large ground movements became more remarkable. In the following years, the 1989 Loma prieta earthquake, the 1992 Petrolia Earthquake, the 1994 Northridge earthquake, the 2008 Wenchuan earthquakes brought more attention to the importance of the damage to the bridge in many horizontal curve alignments. The main damage types in bridges are; unseating of the superstructure, column shear collapse, foundation collapse, bearing collapse and insufficient column bending capacity. In this study, the damages observed in the bridges after the major earthquakes were mentioned and information was given about the determination of the seismic behavior of the horizontally curved bridges.

2 OBSERVED CURVED BRIDGE DAMAGES AND REASONS DURING PAST EARTHQUAKES

Transportation has an important and wide impact on the economy, social and cultural structure of the countries. Highways and railways are part of the transportation system network and bridges and viaducts are the most critical structures of this system. Therefore, bridge damages not only result in direct losses, but also social and economic impacts. Direct costs are defined as the state of post-earthquake functionality of the bridge, while repairing the bridge will restore its past function [1]. Indirect losses include the closure of traffic lanes, the decrease in traffic volume, or the complete closure of the bridge after damages in bridges and viaducts due to the earthquake ground motion. If the bridge is severely damaged, this road can be completely closed and if the process is long, it can have significant effects on the regional economy.

Some of the damage types that cause bridge closure are; unseating of the superstructure, column shear collapse, foundation collapse, bearing collapse and insufficient column bending capacity.

Seismic behaviour of bridges in the curve alignment includes additional potential damages, although similar damages were observed when the straight bridges and curved bridges were examined in the past earthquakes.

2.1 1971 San Fernando earthquake

2.1.1 1971 San Fernando earthquake features

San Fernando earthquake occurred at the northern part of the metropolitan Los Angeles which had a huge population of 8 million. The magnitude of the shock was 6.6 and it was generated by thrust faulting. San Fernando valley was thrusting under the Gabriel mountains and this earthquake rearrange these pressures. The relative motion across the fault plane was generated by the rock above moving upward along the fault and the rock beneath moving downward along the fault that was reverse thrust faulting.

2.1.2 1971 San Fernando earthquake bridge damages

According to the reports released after the earthquake 450 homes, 60 apartment buildings, 400 commercial buildings had severe damage; 600 homes, 200 apartment buildings and 450 commercial buildings had significant damage; and some 20000 structures had minor damage. Also 42 bridges had appreciable damage and 5 of the bridges had collapsed.

The major damage had occurred at the Golden State Freeway (Interstate 5)-Antelope Valley Freeway (California SR14 Interchange) Interchange. South Connector Overcrossing along this interchange, which was a curved nine-span reinforced concrete highway bridge with diaphragm abutment collapsed [3]. The bridge was completed at the time of San Fernando Earthquake. The bridge superstructure was divided into 5 separate segments by using 4 expansion joints. There were three tie bars used at each expansion joints in order to prevent the longitudinal deflection of the superstructure because of the creep and temperature effects (Figure 1).

According to the damage survey reports, as a result of the strong amplitude vibrations during earthquake the deck separation at expansion joint 2 initiated in the longitudinal direction. Therefore, it lead the tie bars at the expansion joints to be yielded and failed.

The failure of the restrainers caused the span four to fall of from its support because of unseating of the hinge locations the superstructure between expansion joints 1 and 2 (span 3 and 4) and the column 4 collapsed as seen in Figure 2.

The southbound SR14/I-5 Separation and Overhead structure was a 10-span curved concrete box-girder bridge with seat-type abutment and single column bent. The structure was constructed in five segments with four intermediate expansion joints. It was under construction at the time of the 1971 San Fernando earthquake. The damage of the superstructure occurred as a result of the settlement of the false work.

Golden State (I-5) and foothill freeway interchange (Interstate 210) interchange consisted many overcrossings and bridges.

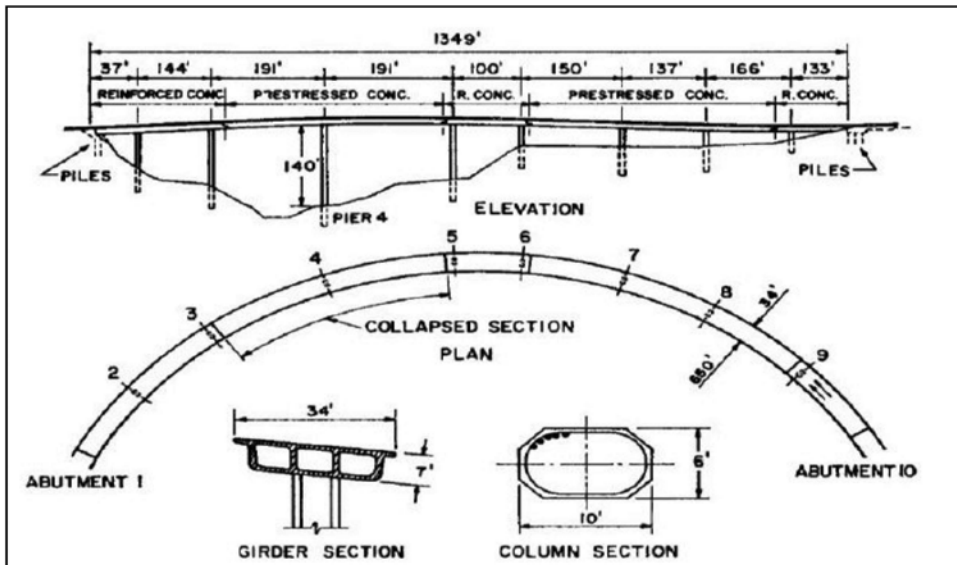


Figure 1. The structural system of the SR14/I-5 South Connector Overcrossing (Tseng, Penzien 1975).



Figure 2. The collapsed sections of South Connector Overpassing after the San Fernando Earthquake (Shirazi 2015).

At the time of the earthquake many structures were completed but not open to traffic. Many collapses and failures occurred in the interchange.

2.1.3 Lessons learned from 1971 San Fernando earthquake

The main structural elements damaged after San Fernando Earthquake are can be listed as follows; Expansion joints, Columns, Column caps, Abutment walls & wing walls.

The bridges damaged or collapsed during the earthquake had commonly in span hinges with gaps and tie bars. Because of inadequate seat width of the deck at the expansion joints during the strong ground motion the displacement of the deck followed by falling of the spans. The reasons of the column damages were; inadequate ties both in size and spacing. For column caps

they were mainly poor of reinforcement for tying column bents to the deck/superstructure. Confinement reinforcements should be increased to prevent that type of the damage. In addition, column foundations had inadequate anchorage of main reinforcement bars that had caused the foundation failures. Also, behind the abutment the backfill should be improved in order to prevent the settlement during the shock. Thus, Abutment walls & wing walls need to be strengthened to better engage forces transmitted through backfill earth pressures

2.2 1994 Northridge earthquake

2.2.1 1994 northridge earthquake features

The Northridge earthquake M_w 6.7 occurred on January 17, 1994, beneath the San Fernando Valley. The mainshock hypocenter was at 19 km depth in the lower crust and it had a thrust faulting focal mechanism. After the mainshock, eight aftershocks of magnitude $M \geq 5.0$ and 48 aftershocks of magnitude $4 \leq M \leq 5$ occurred which form a diffuse spatial distribution around the mainshock rupture plane. The fault mechanism and the location of the Northridge Earthquake can be seen in Figure 3 [8]. San Fernando 1971 and 1994 Northridge Earthquakes differ mainly in the dip direction of the faults and the depth of faulting. The 1971 north-north-east trend of left-lateral faulting (Chatsworth trend) was not activated in 1994.

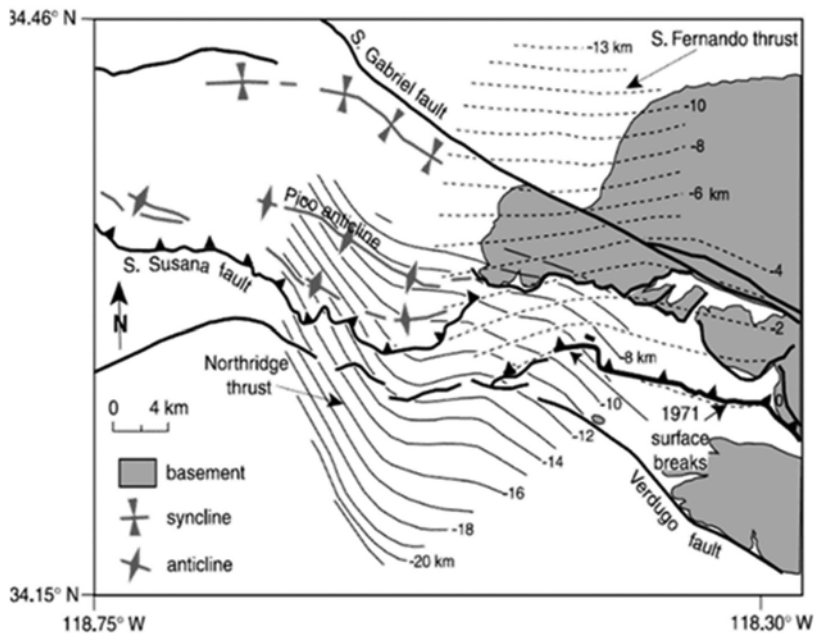


Figure 3. Map view of interpretation of fault planes (Carena, Suppe 2002).

2.2.2 1994 northridge bridge damages

During Northridge earthquake in 1994 ($M_w = 6.7$), seven major highway bridges collapsed and 157 bridges suffered from heavy damages [5]. Two out of collapsed bridges were horizontally curved in plane.

These curved bridges were the parts of Golden State Freeway (Interstate 5)-Antelope Valley Freeway (California SR14 Interchange) Interchange, called Southbound Separation and Overhead Ramp and North Connector Overcrossing Ramp (Figure 4).

These bridges had been designed before 1971 but constructed after 1971 after San Fernando Earthquake. Southbound Separation and Overhead bridge was a 10-span curved concrete box-girder bridge with seat-type abutment and single column bent. The structure was composed of five

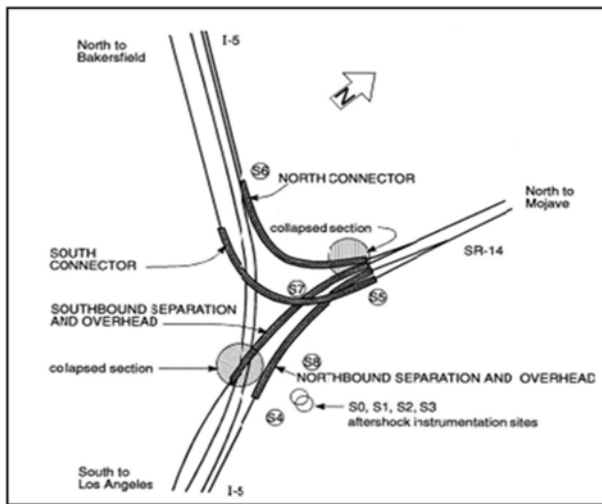


Figure 4. Plan view of SR14/I-5 Interchange and the observed damaged and collapsed regions of the bridges after earthquake (Shirazi 2015)

segments with four in-span expansion joints. Since the structure was under construction during 1971 San Fernando earthquake the damages were mostly settlement of the false work (Figure 5).

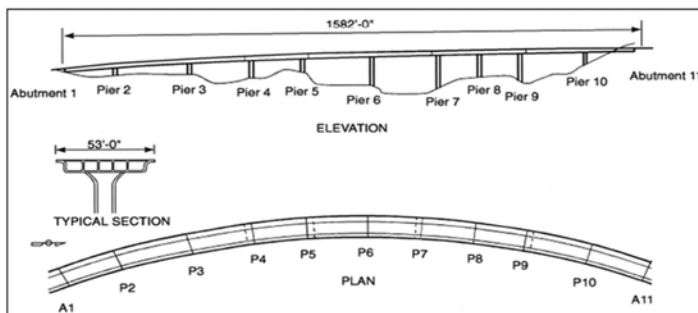


Figure 5. Plan and elevation view of southbound separation and overhead bridge (Moehle, Buckle 1994).

In the Northridge Earthquake the Pier 2 with a short and stiff column had failed and crushing of this pier followed with the collapse of the spans 1, 2 and 3 because of seat loss of the hinges. Pier 3 had also failed due to the collapse of the spans.

The other bridge collapsed during the Northridge earthquake was the North Connector Overcrossing. The structure had a curved concrete box-girder deck with 10 spans, seat-type abutment, and single column bent.

The bridge was composed of of five segments with four in-span hinges. In the Northridge earthquake, similar collapse mechanism had been observed like the Southbound Separation and Overhead bridge. Pier 2 was shorter and stiffer than the adjacent piers.

The collapse of the frame between abutment 1 and pier 3 had been initiated by the failure of Pier 2 because of its short height and consequently large stiffness. After the failure of Pier 2, the simply supported span between abutment 1 and the first hinge collapsed.

2.2.3 Lessons learned from 1994 northridge earthquake

The main structural elements damaged after Northridge are; Expansion joints, Columns, Column caps, superstructure. The bridges damaged or collapsed during the earthquake had commonly in span hinges with gaps and tie bars.

Because of inadequate seat width of the deck at the expansion joints during the strong ground motion the displacement of the deck followed by falling of the spans. The shorter but stiffer columns relatively to the adjacent pier columns generally failed and it was followed by other collapses. Columns inadequate ties both in size and spacing. For column caps they were mainly poor of reinforcement for tying column bents to the deck/superstructure. Confinement reinforcements should be increased to prevent that type of the damage.

2.3 2008 Wenchuan earthquake

2.3.1 2008 Wenchuan earthquake features

The Wenchuan earthquake with a magnitude of 8.0 according to CEA occurred in Sichuan Province, China on May 12, 2008. The earthquake killed 69,227 people and 17,923 people were still missing by October 8, 2008. The hypocenter of the earthquake was close to In Yinxiu Town. almost all buildings were destroyed and about 7,700 people, nearly 80% of the residents, were dead or missing.

The rupture of the Longmen Shan Fault induced the Wenchuan earthquake. Large scale thrusting of the Tibetan Plateau towards the east of the rigid block of Sichuan Basin resulted in the NE-SE dip-slip reverse fault. The fault zone extended from Yingxiu Town, Wenchuan County, to Mianzhu City, Beichuan County, and to Qingchuan County. The epicenter was located at Yingxiu Town. Extensive damage occurred in nearly 300 km long and 50 km wide regions along the fault.

2.3.2 2008 Wenchuan earthquake bridge damages

During the 2008 Wenchuan, many highway bridges damages were observed and reported China earthquake. The curved bridges, especially with high pier columns, exhibited complex dynamic behavior when they were subjected to vertical and horizontal ground motions simultaneously.

The reasons of this problem was defined as because of the mass eccentricity. It might have caused more complex behavior by generating additional bending moments and torsional effect. Baihua Bridge was one off the bridges that suffered from damage during the Wenchuan Earthquake. The bridge was an 18-span reinforced structure composed of straight and curved segments (Figure 6). The spans of the curved segment were supported by tall two-column bent and lateral beam that provided the lateral restraint between the columns. There were five intermediate expansion joints at the bents and two exterior joints at two seat-type abutments. At both ends of each segment, the bridge superstructure rested on the bent cap beam, while the intermediate piers did not have a cap beam.

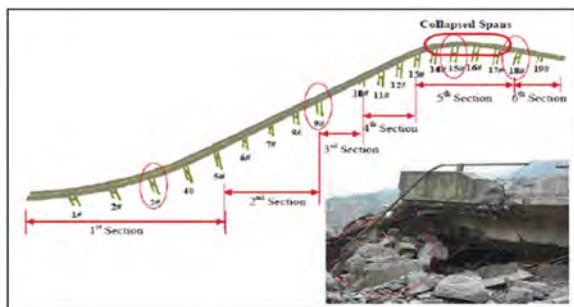


Figure 6. Schematic of Baihua Bridge before the earthquake and column shear and flexural failure at bent (Moehle 1994).

During the earthquake, the four span continuous curved section had been collapsed completely. The first failure mechanism was stated that, as a consequence of transverse displacement of the bridge, lateral beam-column connections failed because of inadequate lateral confinement. Since the capacity at the connection of the column and lateral beam decreased in larger

drift the bridge collapsed. The dislocation of the girders from the seat in the longitudinal direction because of insufficient seat length and connection failure of the rubber pads supported the girders could be the other possible failure mechanism of the bridge. It is also stated that the curved alignment of the bridge could cause the complicated behaviour as seen in Figure 7.



Figure 7. Possible failure mechanism of Baihua Bridge and collapse of the bent 5 (Kawashima, Takahashi, Ge., Wu, Zhang 2009).

The other bridge damaged during Wenchuan Earthquake was the structures in the Huilan Interchange which consisted of a viaduct and four ramps. The ramps had circular reinforced concrete columns with low transverse volumetric ratio where some of them were fixed at their top to the box-girder and the others were connected to the superstructure via rubber bearings. During Wenchuan earthquake, flexural-shear failure in the circumferential direction of the short columns in the ramp bridge, including crushing of the concrete core, buckling of the longitudinal reinforcements, and rupturing of the transverse hoops, occurred at the top of the pier. The column failure led to fracture at the bottom of the box-girder. The low confinement of the column might be one of the major causes of damage to the columns, which were fixed at the top. The large uplift of the deck at the abutment resulted in damage to the rubber bearings under the box-girder and separation of the abutment and box-girder.

2.3.3 Lessons learned from 2008 Wenchuan earthquake

The main structural elements damaged after Wenchuan Earthquake the Northridge are can be listed as follows; Columns, Cap beams, Curved box girder superstructure. The dislocation of the girders from the seat in the longitudinal direction because of insufficient seat length and connection failure of the rubber pads supported the girders caused collapse of the bridges. In addition, the capacity at the connection of the column and lateral beam decreased in larger drift because of insufficient confinement.

3 CONCLUSIONS

In this study, the damages observed in horizontally curved bridges in the past earthquakes were investigated and the lessons to be learned according to the results obtained from past earthquakes on the curved bridges will be examined and summarized. In the scope of this study the destructive earthquakes; 1971 San Fernando, 1994 Northridge and 2008 Wenchuan were studied based on the damages and collapses occurred at the horizontally curved bridges. The major damage types that cause bridge closure are; unseating of the superstructure, column shear collapse, foundation collapse, bearing collapse and insufficient column bending capacity.

Researches have shown that although the similar damages had been observed for straight and curved bridges, the curved ones should be investigated precisely as they have potential risk because of the geometrical irregularities. The seismic response of the curved bridges should be studied regarding the earthquake direction effect. For seismic design of horizontally bridges performing time history analyses can be more beneficial instead of response spectrum analyses. Besides, in-span expansion joints on the superstructure of the curved bridges and the shorter but stiffer columns relatively to the adjacent pier columns should be avoided. The flexural and shear capacity of the piers should be investigated properly. Consequently, the seismic response of the curved bridges should be investigated in consideration of the lessons taken from past earthquakes and these effects should be taken into consideration at both design and construction stages of the horizontally curved bridges.

REFERENCES

- Mackie, K. & Stojadinović, B. (2005), "Fragility Basis for California Highway Overpass Bridge Seismic Decision Making", Berkeley: Pacific Earthquake Engineering Research Center, University of California, Berkeley.
- Paul C. Jenning (June,1971) "Engineering Features of the San Fernando Earthquake of February 9, 1971", EERL 71-02, Pasadena California.
- Tseng, W. & Penzien, J. (1975), "Seismic Response of Long Multiple-Span Highway Bridges", Earthquake Engineering and Structural Dynamics, Volume 4, p. 25–48.
- Reihaneh Sarraf Shirazi (2015), "Seismic Response and Analytical Fragility Functions for Curved Concrete Box-Girder Bridges", University of Nevada, Reno.
- Moehle, J. P. (1994), "Preliminary report on the seismological and engineering aspects of the January 17, 1994 Northridge earthquake", Earthquake Engineering Research Center, University of California, Berkeley.
- Buckle, I. (1994), "The Northridge, California Earthquake of January 17, 1994: Performance of Highway Bridges", National Center for Earthquake Engineering Research, MCEER, Buffalo.
- Kevin J. Thompson (March 2007), "Major Earthquakes in California and the Development of Seismic Safety in Bridge Design", Caltrans: California Department of Transportation, California.
- Carena S., Suppe J. (April 2002) "Three-Dimensional Imaging of Active Structures Using Earthquake Aftershocks: The Northridge Thrust California", Journal of Structural Geology, 24: 887–904.
- Hauksson E. & Jones L. & M., Hutton K. (10 July 1995), "1994 Northridge Earthquake Sequence in California: Seismological and Tectonic Aspects", JGR Solid Earth- Papers on Seismology.
- Kawashima, K., Takahashi, Y., Ge, H., Wu, Z., & Zhang, J. (2009), "Reconnaissance Report on Damage of Bridges in 2008 Wenchuan, China, Earthquake", Journal of Earthquake Engineering, 13:7, 965–996.
- Densmore, A.L., Ellis, M.A., Li, Y., Zhou, R., Hancock, G.S. & Richardson N. (2007), "Active tectonics of the Beichuan and Pengguan faults at the eastern margin of Tibetan Plateau, Tectonics, Vol. 26, TC4005.
- Lekkas, E.L. (2008), "Wenchuan earthquake, Sichuan, China-geotechnical regime and damage Macro-distribution, Proc. 14th WCEE, Paper No. S31-015, Beijing, China.
- Li Qiao & Zhao Shichun (editors)(2008), "Analysis of seismic damage of engineering structures in Wenchuan earthquake", Southwest Jiatong University, China.
- Qiang, H. et al. (2009), "Seismic damage of highway bridges during the 2008 Wenchuan earthquake", Earthquake Engineering And Engineering Vibration, 8(2), p. 263–273.
- Yen, P. et al. (2011), "China Earthquake Reconnaissance Report: Performance of Transportation Structures During the May 12, 2008, M7.9 Wenchuan Earthquake", McLean: U.S. Dept. of Transportation, Federal Highway Administration, Research, Development, and Technology, Turner-Fairbank Highway Research Center.
- Sun, Z. et al. (2012), "Lessons Learned from the Damaged Huilan Interchange in the 2008 Wenchuan Earthquake", ASCE, Journal of Bridge Engineering, 17(1), p. 15–24.

Using the USGS database to study parameter uncertainty when assessing pier scour using the HEC-18 framework

G. Gavriel, M. Pregnolato & P.J. Vardanega
University of Bristol, Bristol, UK

ABSTRACT: Bridges are important lifelines linking communities and their collapse due to flood events can result in severe social and economic impacts for communities. Estimation of maximum bridge scour depth is important for determining effective mitigation and adaptation procedures. HEC-18 is a well-established methodology to calculate scour depth. However, it is also often reported to yield conservative estimates of maximum scour depth in various publications. This paper presents a simple sensitivity study to assess the key inputs that affect the computation of maximum scour depth using the HEC-18 framework. The parameter ranges used in this analysis are sourced from an openly accessible database from the United States Geological Survey (USGS). In this study, HEC-18 is assessed against field measurements. The primary aim of this research is to study the impact of each key input parameter on HEC-18 estimates of maximum scour depth estimates.

1 INTRODUCTION

1.1 Background

Scour is the removal of material from the riverbed due to hydraulic actions. Bridges become unstable due to the presence of scour holes near the piers. This paper focuses on bridge pier scour, which is a type of local scour (see Maddison 2012 for a review of scour types). Improved understanding of bridge scour processes can assist with further development of probabilistic assessments (e.g. Maroni et al. 2022), and can also aid specification of scour monitoring systems (see Prendergast & Gavin 2014, Vardanega et al. 2021 for recent reviews of scour monitoring technologies). In this paper field data from the United States Geological Survey (USGS) scour database (Benedict & Caldwell 2014a, b, USGS 2004), hereafter referred to as the ‘USGS database’, are used along with the equations of HEC-18 to carry out a one-at-a-time sensitivity study to rank the effect of key parameters on computed maximum scour. The USGS database has been used in Gavriel et al. (2023) to examine the effect of different data sub-sets on the levels of conservatism from estimations of maximum scour depth using HEC-18 while this paper focusses on input parameter sensitivity.

The HEC-18 framework (e.g. FHWA 1993, Richardson & Davis 1995, Richardson & Davis 2001, Arneson et al. 2012) (along with other scour prediction frameworks) comprises a series of equations developed using laboratory flume tests (e.g. Richardson & Davis 1995, Richardson & Davis 2001, Zevenbergen 2010, Arneson et al. 2012, Briaud 2015a, b, Qi et al. 2016). Maximum scour depth of bridge piers is characterized by the following equation as given from Arneson et al. (2012):

$$\frac{y_s}{y_1} = 2.0K_1K_2K_3\left(\frac{a}{y_1}\right)^{0.65} F_r^{0.43} \quad (1)$$

the terms in Eq. 1 are defined in Table 1. An additional constant, named K_4 , was part of the HEC-18 equation in the previous version of HEC-18 (Richardson & Davis 2001). K_4 is used to correct for armouring of the piers caused by bed material. K_4 has been removed from the latest version of the framework (Arneson et al. 2012), it is therefore not included in Eq.1 and in this work. Further updates to the framework after the release of Arneson et al. (2012) are discussed in Shan et al. (2016) but these have not be incorporated into the analyses presented in this paper.

Many studies showed that HEC-18 framework gives conservative predictions when used to estimate field scour (Richardson & Davis 1995, Mueller & Wagner 2002, Zevenbergen 2010, Qi et al. 2016, Gavriel et al. 2022). Pizarro & Tubaldi (2019) compared the HEC-18 equations from Richardson & Davis (2001) to four other scour prediction methods using numerical data and concluded that all the studied methods produce conservative results. Yan (2013) and Rathod & Manakar (2020) also investigated the reliability of the HEC-18 equations compared to other scour methodologies concluding that the reliability of HEC-18 is predominately related to the model uncertainty. Figure 1 shows the results of the comparison between 19 flume test results from Kiraga et al. (2020) with estimated values from the HEC-18 equation for maximum bridge pier scour depth. In Figure 1, 14 out of the 19 scour depths are overestimated compared to the results from the flume tests.

Table 1. Definition of HEC-18 parameters (Arneson et al. 2012).

Parameter	Units	Notation	Definition
Pier Width	m	a	Width of the pier in the direction of flow
Pier Length	m	L	Length of the pier
Flow Depth	m	y_1	Flow depth directly upstream from the pier
Approach Velocity	m/s	V_1	Average flow velocity directly
Attack Angle	°	ϑ	Approach angle of the water in relation to the pier during a flood event
Scour Depth	m	y_s	Maximum depth of scour hole below the riverbed
Pier nose geometry correction factor	-	K_1	Correction factor based on the pier nose geometry
Bed condition correction factor	-	K_2	Correction factor based on the angle of attack of flow
Attack angle correction factor	-	K_3	Correction factor based on the bed conditions
Froude Number	-	F_r	Froude number

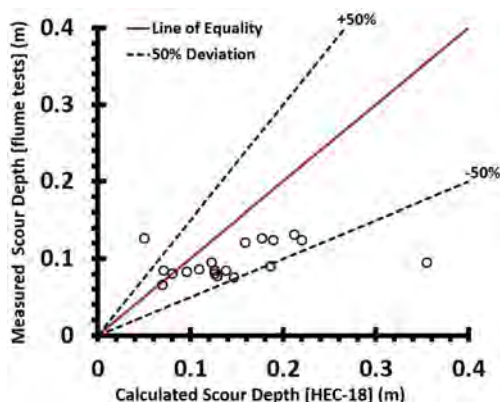


Figure 1. Comparison of scour depth measured in 19 flume tests by Kiraga et al. (2020) compared with the scour depth calculated using the HEC-18 framework (data from Kiraga et al. (2020)).

The full series of equations for the HEC-18 framework and detailed analysis on how to calculate scour depth can be found in Arneson et al. (2012). To calculate scour depth, the method

considers *bed material characteristics* (K_3), *flow characteristics* (V_1, y_1, ϑ), *fluid properties* (Fr_1) and the *geometry of the pier* (L, a) (Richardson & Davis 2001, Arneson et al. 2012). HEC-18 considers a round shaped pier as the base case scenario and thus K_1 corrects for the pier shape in the case it is either square (10% higher scour depth) or sharp (10% lower scour depth) (Richardson & Davis 2001, Arneson et al. 2012). K_2 corrects for the case where ϑ takes a value which is not zero (Richardson & Davis 2001, Arneson et al. 2012). K_3 takes the value of 1.1 except in the scenario of dunes which are higher than 3000 mm, where scour depth is considered to be 30% larger when compared to dunes which are less than 3000 mm high (Richardson & Davis 2001, Arneson et al. 2012). For more information on dune height, see Section 7.1 in Arneson et al. (2012). Out of the 936 datapoints, no value is higher than 1.1 for K_3 (Richardson & Davis 2001, Arneson et al. 2012). To rank the key parameters (from Table 1) that affect the HEC-18 computation and hence potentially contribute uncertainty in the results, a simple one-at-a-time sensitivity study was carried out using the HEC-18 equations and the USGS database.

1.2 Study aims

This research analyses the HEC-18 framework against 936 field datapoints to investigate its validity using real field data. The study aims to: (1) illustrate the conservatism of the HEC-18 approach by comparing maximum scour depth predictions to those from the USGS database and (2) perform an sensitivity analysis of the key HEC-18 parameters by using field data from the USGS database.

2 METHODOLOGY

2.1 USGS database

The USGS database includes data from 936 bridge piers from 31 out of the 50 states in the USA. The measurements of V_1, y_1 and ϑ are all taken during high flows. L and a were collected in times of low flow (Norman 1975, Jarrett & Boyle 1986, Butch 1991, Southard 1992, Mueller et al. 1994, Wilson 1995, Atkins & Hedgecock 1996, Hayes 1996, Hodgkins & Lombard 2002, Holnbeck 2011). For further details of the measurement of the scour depth hydraulic properties, soil properties and other information on HEC-18, the reader is directed to Benedict & Caldwell (2014a, b) and USGS (2004). Figure 2 shows that about 90% of the data is overestimated, confirming the results of past research (cf. Zevenbergen 2010, Arneson et al. 2012, Qi et al. 2016) that the method over-estimates the scour depth assessment.

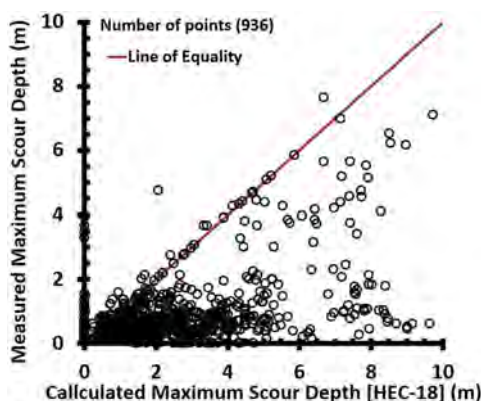


Figure 2. Measured maximum scour depth against calculated maximum scour depth using HEC-18 using 936 datapoints from USGS database; 839 out of 936 points over-estimated (data from the USGS database).

2.2 Parameter distributions

Figure 3 shows the distributions of the parameters given in Table 1 from analysis of the USGS database used in this study. a , V_I , y_I and ϑ were compared against their frequencies to reveal approximately normal distributions (from a visual inspection of Figure 3). The histograms for a , y_I and V_I in Figure 3 reveal a distribution which can be approximated as normal. For the aforementioned inputs, there is a higher concentration of data near the mean and less data around one standard deviation above and below the mean. The assumption that ϑ is normally distributed is less reasonable and another distribution may potentially fit the data better. Analysis of the distribution of the parameters and the best-fit probability density functions will be undertaken in future work to refine the results presented in the present paper.

The data distribution for L is shown in Figure 3 but it should be noted that since 311 out of the 936 field datapoints were unavailable the unknown L inputs were calculated based on the 625 defined L values. 11.7 is the average of the L/a ratio of the defined a inputs therefore $L = 11.7a$. Also, K_1 , K_2 and K_3 input parameters are determined from primary data from the USGS database therefore their distributions are not shown on Figure 3. K_1 , K_2 and K_3 are studied in the following sensitivity study for completeness, however, any conclusions regarding their relative influence on the calculations should be made with caution.

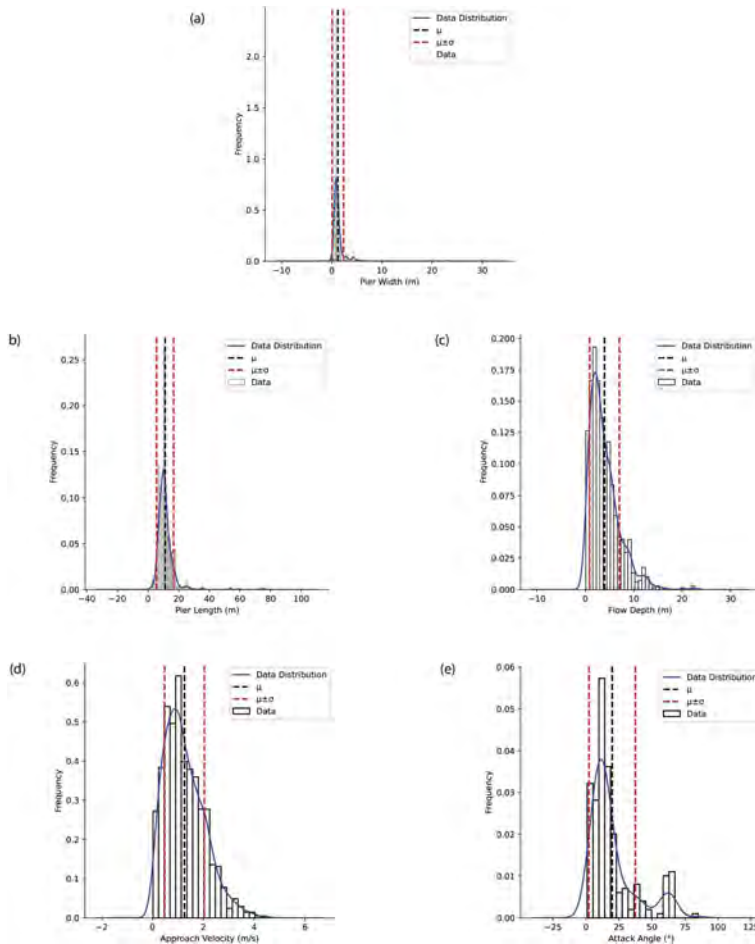


Figure 3. Histograms showing the distribution of the input data against the normal distribution; σ = standard deviation; μ = mean; (a) a ; (b) L ; (c) y_I ; (d) V_I ; (e) ϑ (data from the USGS database).

2.3 Sensitivity analysis

The following analysis assesses the impact each input parameter has on the pier scour estimation using the HEC-18 framework. For this analysis, the mean (μ), minimum, maximum and standard deviation (σ) were calculated for each input based on the 936 data from the USGS database (Table 2) (see Figure 3). Then, two base case scenarios are defined. For Base Case scenario 1 (BC1), all inputs are equal to their mean except ϑ which is equal to zero (this represents the case of zero bridge skew angle which occurs for about 80% of the records in the database). BC1 gives a value of scour depth equal to 2.04m. For Base Case scenario 2 (BC2), all inputs are equal to their mean. BC2 gives a scour depth value equal to 5.04m. Then, one input from each base case scenario is substituted on each iteration with the calculated minimum, maximum, $\mu \pm \sigma$ or $\mu \pm 0.5\sigma$. Each time an input changes, the result calculated from HEC-18 is recorded (Table 3). Table 3 shows all the scour depths calculated from substituting one input parameter at a time. To assess what impact each input has on the scour depth estimation, for each input a ratio of the computed answer against the base case scour depth is calculated. The difference between the maximum ratio and the minimum ratio for each input is shown by Table 3 as ‘maximum difference’. The difference in ratio between ‘ $\mu \pm 0.5\sigma$ ’ is also calculated. The difference in ratio is shown as ‘ $\pm 0.5\sigma$ difference’ in Table 3. The equation for calculating the spread for each iteration is shown by Eq. 2. Eq. 3 shows the calculation performed to determine the maximum difference between the iterations for each input parameter. A similar procedure was performed to calculate the ‘ $\pm 0.5\sigma$ difference’. Eqs.2 and 3 are as follows:

$$\gamma_s = \frac{y_c}{y_{bc}} \times 100 \quad (2)$$

where, γ_s = spread, y_c = calculated scour depth, y_{bc} = calculated scour depth from the base case scenario,

$$\gamma_{s(\Delta)} = \gamma_{s(max)} - \gamma_{s(min)} \quad (3)$$

where, $\gamma_{s(D)}$ = maximum difference in variation between calculated γ_s values for the input parameter considered, $\gamma_{s(max)}$ = maximum value from the calculated γ_s values for the input parameter considered, $\gamma_{s(min)}$ = minimum value from the calculated γ_s values for the input parameter considered.

The larger is the γ_s the higher the input factor influences the projected scour depth. The $\mu \pm 0.5\sigma$ is also calculated, in addition to $\mu \pm \sigma$ to test whether the rank changes when the inputs change. Values equal to zero have been eliminated from the computations for V_I and y_I because zero values give an error when scour is estimated (due to division by zero). Additionally, 81% of the USGS database consists of attack angles taken as zero. To better assess ϑ , two different base cases were considered to run the analysis as mentioned earlier. The parameter rank order changes for each base case scenario. For BC1, for which ϑ is considered to be zero, the rank remains unchanged for ‘maximum difference’ and ‘ $\mu \pm 0.5$ difference’. From BC1, a is ranked first indicating that it has the greatest impact on the scour depth estimation for HEC-18. V_I has the second highest difference, followed by y_I . For ‘ $\mu \pm 0.5\sigma$ difference’, V_I appears to be the most influential followed by ϑ .

For BC2 however, the rank changes between ‘maximum difference’ and ‘ $\mu \pm 0.5\sigma$ difference’. For ‘ $\mu \pm 0.5\sigma$ difference’ the results agree with Rathod & Manekar (2020) which found that ϑ is the most influential factor whereas the y_I was found to be the least influential. The rank for ‘maximum difference’ does not agree with Rathod & Manekar (2020). The inconsistency between the findings of this research paper and Rathod & Manekar (2020) may be because Rathod & Manekar (2020) performed a sensitivity analysis based on 19 laboratory based flume tests and random values produced from Monte Carlo analysis, whereas this research paper uses field data from the USGS database. In the instance of BC2, for which the attack angle is the mean of all

the non-zero θ angles, the difference is not the same for the ‘maximum difference’ and the ‘ $\mu \pm 0.5\sigma$ difference’. For the case of ‘maximum difference’, a appears to have the most impact on the scour depth estimation followed by V_I . K_I is listed as the least influential factor. Likewise, in the case of ‘ $\pm 0.5\sigma$ difference’, θ is again the most influential followed by a .

3 DISCUSSION

The difference in the ranking between the two base case scenarios shows that when θ takes a value which is not zero, θ impacts the scour depth estimation. In the case for which θ is zero, a is highly influential on the final scour depth, although its influence reduces when θ takes a value which is not zero. V_I has a high impact on the scour depth estimation, no matter the value of the attack angle. y_I appears to be of medium importance, since its rank ranges between places 3 to 5 (see Table 4).

Table 2. Parameter ranges from the USGS database.

Parameter*	μ	min.	max.	σ	$\mu+\sigma$	$\mu+0.5\sigma$	$\mu-\sigma$	$\mu-0.5\sigma$	c_v (%)
a (m)	1.23	0.29	22.86	1.14	2.37	1.80	0.09	0.66	93
L (m)	11.15	2.44	74.88	5.49	16.65	13.90	5.66	8.40	49
y_I (m)**	3.96	0.10	22.52	3.07	7.03	5.49	0.89	2.42	78
V_I (m/s)**	1.26	0.02	4.48	0.78	2.04	1.65	0.48	0.87	62
θ (°)**	19.91	1.00	85.00	17.55	37.46	28.69	2.36	12.14	88
K_I	1.00	0.90	1.10	0.06	1.06	1.03	0.93	0.96	6

*units given in brackets, if parameter is dimensionless no unit is shown. ** y_I calculations exclude values equal to zero (6 cases), V_I calculations exclude values equal to zero (13 cases) since $V_I = 0$ results in $y_s = 0$ which is unreasonable, θ calculations exclude values equal to zero (712 cases); c_v = Coefficient of Variation = σ/μ . $K_3 = 1.1$ for all cases considered in this paper.

Table 3. Results for trialed combinations for which the pier scour depth is calculated using HEC-18 by varying one parameter at a time; μ = mean; σ = standard deviation [K_I calculations not shown for brevity].

Parameter	a (m)		L (m)		y_I (m)		V_I (m/s)		θ (°)	
	BC1*	BC2**	BC1	BC2	BC1	BC2	BC1	BC2	BC1	BC2
μ	2.04	5.04	2.04	5.04	2.04	5.04	2.04	5.04	2.04	5.04
Min	0.80	2.27	2.04	2.79	1.24	3.06	0.35	0.87	-	2.25
Max	13.62	14.54	2.04	5.83	2.58	6.38	3.52	8.71	-	8.57
$\mu + \sigma$	3.13	5.73	2.04	5.83	2.21	5.45	2.51	6.21	-	6.57
$\mu + 0.5\sigma$	2.61	5.39	2.04	5.64	2.13	5.27	2.29	5.66	-	5.97
$\mu - \sigma$	0.38	1.08	2.04	3.71	1.67	4.12	1.35	3.33	-	2.51
$\mu - 0.5\sigma$	1.36	3.90	2.04	4.40	1.91	4.72	1.74	4.30	-	3.92
$\gamma_s(\Delta)$ [Eqs. 2 & 3]	648	266	0	60	66	66	155	155	-	125
$\gamma_s(\Delta)$ [Eqs. 2 & 3] for $\pm 0.5\sigma$	30	30	0	25	11	11	27	27	-	41

*Base Case 1 (BC1): μ of each input parameter from the USGS database except θ which equals to zero (accounts for 81% of the database for which $\theta = 0$). **Base Case 2 (BC2): μ of each input parameter from the USGS database.

Table 4. Ranking of the parameters showing the level of influence on estimation of pier scour depth using HEC-18 to calculate it for four different cases.

	$\pm \sigma$		$\pm 0.5\sigma$	
	Rank (BC1)	Rank (BC2)	Rank (BC1)	Rank (BC2)
a (m)	1	1	1	2
L (m)	5	5	5	4
y_I (m)	3	4	3	5
V_I (m/s)	2	2	2	3
θ (°)	-	3	-	1
K_I	4	6	4	6

4 CONCLUSIONS

This paper used 936 datapoints from the USGS database, to carry out a one-at-a-time sensitivity study for the HEC-18 framework. The analysis showed that the influence of the inputs change depending on whether the angle of attack takes a non-zero value. For BC1 the attack angle is zero; in this case, pier width is the most influential followed by the flow velocity. For BC2 the attack angle is a non-zero value and the attack angle and the pier width are highly influential. A more detailed analysis should consider additional distributions (other than the normal distribution) to better determine the most influential factor(s) affecting maximum scour depth predictions using the HEC-18 framework.

5 DATA AVAILABILITY

This study has not generated new experimental data.

REFERENCES

- Arneson, L.A., Zevenbergen, L.W., Lagasse, P.F. & Clopper, P.E. 2012. *Evaluating Scour at Bridges Fifth Edition, Hydraulic Engineering Circular No. 18*, U.S. Department of Transportation, Federal Highway Administration, Publication no. FHWA-HIF-12-003. Available from: < <https://www.fhwa.dot.gov/engineering/hydraulics/pubs/hif12003.pdf> > [01/03/2023].
- Atkins, J.B. & Hedgecock T.S. 1996. Scour at Selected Bridge Sites in Alabama, 1991-94, U.S. Geological Survey, *Water Resources Investigation Report 96-4137*. <https://doi.org/10.3133/wri964137>
- Benedict, S.T. & Caldwell, A.W. 2014a. A Pier-scour Database: 2,427 Field and Laboratory Measurements of Pier Scour. US Geological Survey, Reston, VA, USA, *Data Series 845*. <https://doi.org/10.3133/ds845>
- Benedict, S.T. & Caldwell, A.W. 2014b. The 2014 USGS Pier Scour Database (PSDb – 2014). US Geological Survey, Reston, VA, USA, Version 1.0. Available from: < <https://pubs.usgs.gov/ds/0845/> > [01/03/2023].
- Briaud, J.L. 2015b. Scour Depth at Bridges: Method Including Soil Properties. II: Time Rate of Scour Prediction. *Journal of Geotechnical and Geoenvironmental Engineering* 141 (2):[04014105].
- Briaud, J-L. 2015a. Scour Depth at bridges: Method Including Soil Properties. I: Maximum Scour Depth Prediction. *Journal of Geotechnical and Geoenvironmental Engineering* 141 (2):[04014104].
- Butch, G.K. 1991. Measurement of Bridge Scour at Selected Sites in New York, Excluding Long Island. U.S. Geological Survey, *Water-Resources Investigations Report 91-4083*. <https://doi.org/10.3133/wri914083>
- FHWA (Federal Highway Administration) 1993. Evaluating Scour at Bridges, Edition 2. *Publication no. IP-90-017*. Available from: < <https://www.fhwa.dot.gov/engineering/hydraulics/pubs/hec/hec18ed2.pdf> > [01/03/2023].
- Gavriel, G., Vardanega, P.J. & Pregonolato, M. 2022. Preliminary comparison of scour depth estimation methods. In: *Bridge Safety, Maintenance, Management, Life-Cycle, Resilience and Sustainability: Proceedings of the Eleventh International Conference on Bridge Maintenance, Safety and Management (IABMAS 2022)*, Barcelona, Spain, July 11-15, 2022 (Casas, J.R., Frangopol, D.M. & Turmo, J. (eds.)), CRC Press/Balkema Taylor & Francis Group, London, UK, 2107–2113.

- Gavriel, G., Vardanega, P.J. & Pregnotato, M. 2023. Comparison of maximum scour estimations using the HEC-18 method with field data from the USGS database. *under review*.
- Hayes, D.C. 1996. Scour at Bridge Sites in Delaware, Maryland, and Virginia. U.S. Geological Survey, *Water-Resources Investigations Report 96-4089*. <https://doi.org/10.3133/wri964089>
- Hodgkins, G. & Lombard, P. 2002. Observed and Predicted Pier Scour in Maine. *Water-Resources Investigations Report 02-4229*, US Geological Survey. Available from: < <https://me.water.usgs.gov/reports/wrir02-4229.pdf> >[01/03/2023].
- Holnbeck, S.R. 2011. Investigation of Pier Scour in Coarse-Bed Streams in Montana, 2001 through 2007, U.S. Geological Survey, *Scientific Investigation Report 2011-5107*. Available from: < <https://pubs.usgs.gov/sir/2011/5107/sir2011-5107.pdf> >[01/03/2023].
- Jarrett, R.D. & Boyle, J.M. 1986. Pilot Study for Collection of Bridge-scour Data, U.S. Geological Survey, *Water-Resources Investigation Report 86-4030*. <https://doi.org/10.3133/wri864030>
- Kiraga, M., Urbański, J. & Bajkowski, S. 2020. Adaptation of Selected Formulas for Local Scour Maximum Depth at Bridge Piers Region in Laboratory Conditions. *Water* 12 (10):[2663].
- Maddison, B. 2012. Scour failure of bridges. *Proceedings of the Institution of Civil Engineers – Forensic Engineering* 165(1): 39–52.
- Maroni, A., Tubaldi, E., McDonald, H. & Zonta D. 2022. A monitoring-based classification system for risk management of bridge scour. *Proceedings of the Institution of Civil Engineers – Smart Infrastructure and Construction* 175(2): 92–102.
- Mueller D.S., Miller R.L. & Wilson J.T. 1994. Historical and Potential Scour Around Bridge Pier and Abutments of Selected Steam Crossings in Indiana, U.S. Geological Survey, *Water-Resources Investigations Report 93-4066*. <https://doi.org/10.3133/wri934066>
- Mueller, D.S. & Wagner, C.R. 2002. Analysis of Pier Scour Predictions and Real Time Field Measurements. In: *First International Conference on Scour of Foundations, ICSF-1 Texas A&M University, College Station, Texas, USA* November 17-20, 2002 (Chen, H-C. & Briaud, J-L (eds.)). Texas Transportation Institute, Publications Dept. 257–271.
- Norman, V.W. 1975. Scour at Selected Bridge Sites in Alaska, U.S. Geological Survey, *Water-Resources Investigation* 32-75. <https://doi.org/10.3133/wri7532>
- Pizarro, A. & Tubaldi, E. 2019. Quantification of Modelling Uncertainties in Bridge Scour Risk Assessment under Multiple Flood Events. *Geosciences* 9 (10):[445].
- Prendergast, L.J. & Gavin, K. 2014. A review of bridge scour monitoring techniques. *Journal of Rock Mechanics and Geotechnical Engineering* 6(2): 138–149.
- Qi, M., Li, J. & Chen, Q. 2016. Comparison of existing equations for local scour at bridge piers: parameter influence and validation, *Natural Hazards* 82(3): 2089–2105.
- Rathod, P. & Manekar, V. L. 2020. Parameter uncertainty in HEC-RAS 1D CSU scour model. *Current Science* 118(8): 1227–1234.
- Richardson, E.V. & Davis, S.R. 1995. Evaluating Scour at Bridges Third Edition. Hydraulic Engineering Circular Number 18, *Publication no. FHWA-IP-90-017*. Available from: < <https://www.fhwa.dot.gov/engineering/hydraulics/pubs/hec/hec18si.pdf> > [01/03/2023].
- Richardson, E.V. & Davis, S.R. 2001. Evaluating Scour at Bridges Fourth Edition. Hydraulic Engineering Circular Number 18, *Publication no. FHWA-NHI-01-001*, Available from: < <https://www.fhwa.dot.gov/engineering/hydraulics/pubs/hec/hec18.pdf> > [01/03/2023].
- Shan, H., Kilgore, R., Shen, J. & Kerenyi, K. (2016). Updating HEC-18 Pier Scour Equations for Non-cohesive Soils, U.S. Department of Transportation, *FHWA-HRT-16-045*. Available from: < <https://rosap.ntl.bts.gov/view/dot/35713> > [01/03/2023]
- Southard, R.E. 1992. Scour around bridge piers on streams in Arkansas, U.S. Geological Survey, *Water-Resources Investigations Report 92-4126*. <https://doi.org/10.3133/wri924126>
- USGS (U.S. Geological Survey) 2004. National Bridge Scour Database. U.S. Geological Survey, Available from < <https://water.usgs.gov/osw/techniques/bs/BSDMS/> >[01/03/2023]
- Vardanega, P.J., Gavriel, G. & Pregnotato, M. 2021. Assessing the suitability of bridge-scour-monitoring devices. *Proceedings of the Institution of Civil Engineers - Forensic Engineering* 174(4): 105–117.
- Wilson, K.V. 1995. Scour at Selected Bridge Sites in Mississippi. U.S. Geological Survey, *Water-Resources Investigation Report 94-4241*. <https://doi.org/10.3133/wri944241>
- Yan, J. 2013. Reliability Analysis of the HEC-18 Scour Equation and AASHTO Deep Foundation Design Codes. *M.Eng. (Civil) thesis*, The City College of New York of the City University of New York, New York, NY.
- Zevenbergen, L.W. 2010. Comparison of the HEC-18, Melville, and Sheppard Pier Scour Equations. In: Burns, S.E. et al. (eds.), *Proceedings 5th International Conference on Scour and Erosion (ICSE-5)* November 7-10, San Francisco, USA: 1074–1081, Reston, VA, American Society of Civil Engineers.

Time-variant reliability analysis of corroded steel girder

Y. Wang, W. Wang & C.Q. Li
RMIT University, Melbourne, Victoria, Australia

W. Yang
The University of Melbourne, Melbourne, Victoria, Australia

ABSTRACT: Due to the long-term environmental exposure, steel bridge is threatened by loading capacity degradation caused by corrosion. Service life prediction is essential for steel bridges using time-variant reliability methods. This paper attempts to present a reliability-based methodology for the serviceability assessment of a steel girder subjected to corrosion. A corrosion growth model is adopted in this paper to evaluate the reliability of a corroded steel girder over time. A stochastic model of load effects is developed, and the first passage probability with a developed analytical solution is employed. To facilitate the practical application of the proposed methodology, a case study is presented. The method presented in this paper can serve as a rational tool for developing rehabilitation or maintenance strategies for steel bridges

1 INTRODUCTION

Corrosion-induced deterioration of steel almost certainly decreases the structural integrity. Many researchers (e.g., Li & Yang 2021, Wasim et al. 2020, Wang et al. 2018, Fernandez et al. 2015) indicated that corrosion not only reduces the cross-sections of structural components but also decreases the material properties. Accordingly, massive costs of repair and life disruption are induced. For example, the corrosion-induced annual losses in the building sector were approximately \$22.6 billion in the United States (Koch et al. 2001). Therefore, it is necessary to develop a cost-effective assessment method for corroded steel structures with an understanding the corrosion mechanism.

Corrosion on the steel surface is initialized by being exposed to oxygen and moisture and the corrosion growth can be accumulated by chloride chemicals (Gong & Frangopol 2020). For atmospheric corrosion, the progress is a combination of Oxygen reduction reaction and hydrogen evolution reaction (Revie 2008):



In Equation (2), H_2 can be stored in the micro-voids of steel to produce pressure, inducing the grain cracks that cause mechanical deterioration.

Field studies suggested that corrosion growth on steel is a random phenomenon, showing considerable variability (Gong & Frangopol 2020, Czarnecki & Nowak 2008). It is related to many factors such as environmental chloride level, moisture, and protection level. The deterministic approaches to predict the capacity of corroded steel structural components may not

be practical enough due to the random nature of corrosion growth and the inherent uncertainties of materials. As such, it is rational to probabilistically assess the service life and structural integrity of steel structures based on time-variant reliability theory.

This paper intends to present a time-variant reliability method for predicting the failure probability of corroded steel girder. The time-variant variables, such as the corrosion growth, are considered in the reliability analysis. A stochastic model of the load effect is developed. A worked example is presented to illustrate the proposed method. The significance of the proposed method in this paper is that it can predict failure time and be used for developing a time-dependent maintenance strategy.

2 TIME-VARIANT RELIABILITY

A failure criterion needs to be established to predict the probability of structural failure over its lifetime. In reliability theory, the failure criterion is expressed as follows (Melchers 1999):

$$G(t) = L(t) - R(t) \quad (3)$$

where $G(t)$ is the limit state function at time t , $L(t)$ is the load effect on the structures at time t , $R(t)$ is the acceptable limit (resistance) at time t .

The probability of failure can be determined as follows:

$$p_f(t) = P[G(t) \geq 0] = P[L(t) \geq R(t)] \quad (4)$$

where $P[\cdot]$ denotes the probability of an event. Equation (4) represents a typical upcrossing problem, as shown in Figure 1.

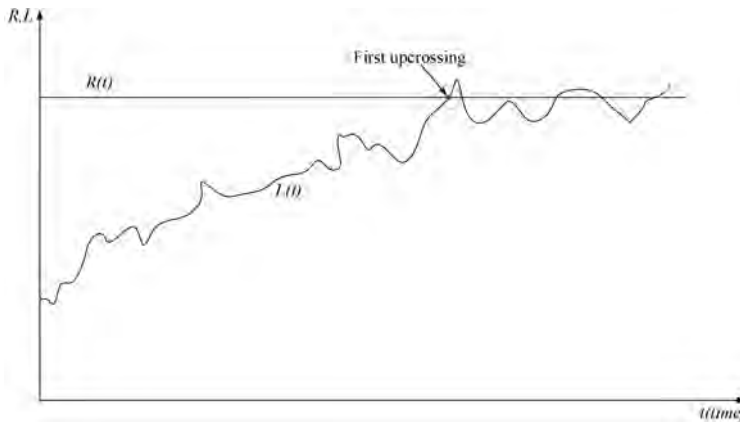


Figure 1. A schematic illustration of the first upcrossing.

The probability of upcrossing can be determined by the first passage probability as follows (Melchers 1999):

$$p_f(t) = 1 - [1 - p_f(t = 0)] \exp\left(-\int_0^t v dt\right) \quad (5)$$

where p_f denotes the probability of failure, and v denotes the mean upcrossing rate, which can be evaluated from the well-known Rice formula (Rice 1944) as follows:

$$v = v_R^+ = \int_{\dot{R}}^{\infty} (\dot{L} - \dot{R}) f_{L\dot{L}}(R, \dot{L}) d\dot{L} \quad (6)$$

where v_R^+ is the upcrossing rate of the load effect process $L(t)$ relative to the threshold $R(t)$, \dot{R} is the slope of $R(t)$ with respect to time, \dot{L} is the time derivative process of $L(t)$, $f_{L\dot{L}}$ is the joint probability density function for $L(t)$ and \dot{L} .

Li & Melchers (1993) derived an analytical solution to Equation (6) for non-stationary Gaussian process, which is expressed as follows:

$$v_R^+ = \frac{\sigma_{\dot{L}|L}}{\sigma_L} \phi\left(\frac{R - \mu_L}{\sigma_L}\right) \left[\phi\left(\frac{\dot{R} - \mu_{\dot{L}|L}}{\sigma_{\dot{L}|L}}\right) - \left(\frac{\dot{R} - \mu_{\dot{L}|L}}{\sigma_{\dot{L}|L}}\right) \Phi\left(-\frac{\dot{R} - \mu_{\dot{L}|L}}{\sigma_{\dot{L}|L}}\right) \right] \quad (7)$$

where μ and σ are the mean and standard deviation of random variables represented by subscripts L and \dot{L} , “|” denotes the condition, ϕ and Φ indicate the standard normal probability density function and cumulative distribution function, respectively.

For a given Gaussian stochastic process with a mean function $\mu_L(t)$ and auto-covariance function $C_{LL}(t_i, t_j)$, all terms in Equation (7) can be obtained as follows:

$$\mu_{\dot{L}|L} = E[\dot{L}|L = R] = \mu_{\dot{L}} + \rho_L \frac{\sigma_{\dot{L}}}{\sigma_L} (R - \mu_L) \quad (8)$$

$$\sigma_{\dot{L}|L} = [\sigma_{\dot{L}}^2 (1 - \rho_L^2)]^{\frac{1}{2}} \quad (9)$$

With

$$\mu_{\dot{L}} = \frac{d\mu_L(t)}{dt} \quad (10)$$

$$\sigma_{\dot{L}} = \left[\frac{\partial^2 C_{LL}(t_i, t_j)}{\partial t_i \partial t_j} \Big|_{i=j} \right]^{1/2} \quad (11)$$

$$\rho_L = \frac{C_{L\dot{L}}(t_i, t_j)}{[C_{LL}(t_i, t_j) \cdot C_{\dot{L}\dot{L}}(t_i, t_j)]^{1/2}} \quad (12)$$

$$C_{L\dot{L}}(t_i, t_j) = \frac{\partial C_{LL}(t_i, t_j)}{\partial t_j} \quad (13)$$

In time-variant reliability, it is justifiable to model the load effect $L(t)$ as a stochastic process. A generic model of stochastic process of the load effect $L(t)$ can be expressed as follows (Li & Melchers 2005):

$$L(t) = L_l(t) \cdot \zeta_L \quad (14)$$

Where $L_l(t)$ is a pure time function of load effect, ζ_L is a random variable accounting for all variability of basic random variables with unity mean, i.e., $E(\zeta_L) = 1$ and constant coefficient of variation (CoV).

The mean and auto-covariance function of $L(t)$ can be determined as follows (Li & Melchers 2005):

$$\mu_L(t) = E[L(t)] = L_l(t) \cdot E[\zeta_L] = L_l(t) \quad (15)$$

$$C_{LL}(t_i, t_j) = (CoV)^2 \rho_L L_l(t_i) L_l(t_j) \quad (16)$$

where $\mu_L(t)$ is the mean of load effect at time t , $C_{LL}(t_i, t_j)$ is the auto-covariance function of load effect between two points in time t_i and t_j , ρ_L is the auto-correlation coefficient for $L(t)$ between two points in time t_i and t_j .

As there are many random variables involved in the load effect, its mean and standard deviation function can be numerically obtained by using the Monte Carlo simulation (MCS) method. Since the load effect $L(t)$ is a function of many variables, such as the corrosion damage size, pipe geometry and loading, it is reasonable to be assumed as non-stationary Gaussian processes based on the central limit theorem.

3 WORKED EXAMPLE

To illustrate the application of the method, an example is adapted from Nie et al. (2020). In this case study, a simple supported H-steel girder ($150\text{mm} \times 150\text{mm} \times 8\text{mm} \times 8\text{mm}$) is selected, as shown in Figure 2.

The limit state function of the corroded steel girder can be established based on the maximum stiffness and bearing capacity as follows (Nie et al. 2020):

$$G(t) = \gamma_x W_x(t) f_y(t) - M_D - M_l \quad (17)$$

where γ_x is the plastic coefficient and $\gamma_x = 1.05$ for H-steel, $W_x(t)$ is the section modulus at time t , $f_y(t)$ is the nominal yield strength and it is assumed to be 287 MPa, M_D is the bending moment caused by the dead loads, M_l is the bending moment caused by live loads.

In Equation (17), the section modulus $W_x(t)$ can be calculated as follows:

$$W_x(t) = \frac{I_x(t)}{\frac{H}{2} - h(t)} \quad (18)$$

where $h(t)$ is the corrosion depth which can be expressed as a power-law model as follows:

$$h(t) = at^b \quad (19)$$

where $a=70.6$ and $b=0.789$ are the empirical fitted coefficients obtained from Kayser (1988).

$I_x(t)$ is the inertial moment of corroded steel girder that can be expressed as follows:

$$I_x(t) = \frac{(t_w - 2h(t))(H + 2h(t) - 2t_f)^3}{12} + \frac{2(B - 2h(t))(t_f - 2h(t))(H - t_f)^2}{4} + \frac{(B - 2h(t))(t_f - 2h(t))^3}{12} \quad (20)$$

where t_w is the web thickness and t_f is the flange thickness. The distribution types, mean and variation coefficient of the essential parameters are shown in Table 1.

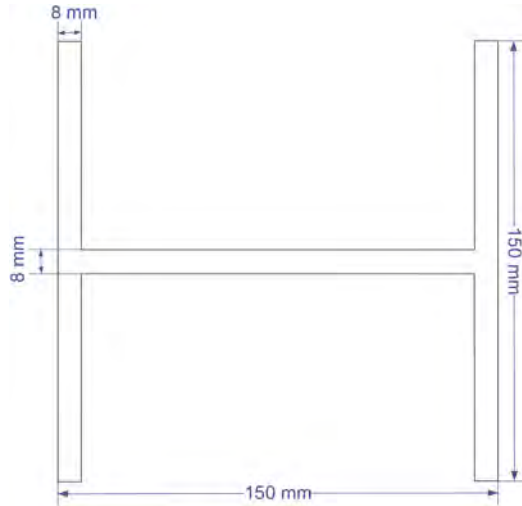


Figure 2. Cross-section of the girder.

Table 1. Essential parameters in the example girder.

Parameters	Distribution	Mean	Variation coefficient
Dead load $D \left(\frac{kN}{m} \right)$	Normal distribution	6.80	0.07
Live load $l \left(\frac{kN}{m} \right)$	Gumbel distribution	0.88	0.23
Section width $B \text{ (mm)}$	Normal distribution	150	0.03
Section height $H \text{ (mm)}$	Normal distribution	150	0.03
Flange thickness $t_f \text{ (mm)}$	Normal distribution	8	0.03
Web thickness $t_w \text{ (mm)}$	Normal distribution	8	0.03

4 RESULTS

The load effect is calculated by Equations (14), (15) and (16). The mean of function and standard deviation can be calculated as a function of time using Monte Carlo simulation (MCS) together with the proposed model of corrosion depth. The up-crossing rate can be obtained

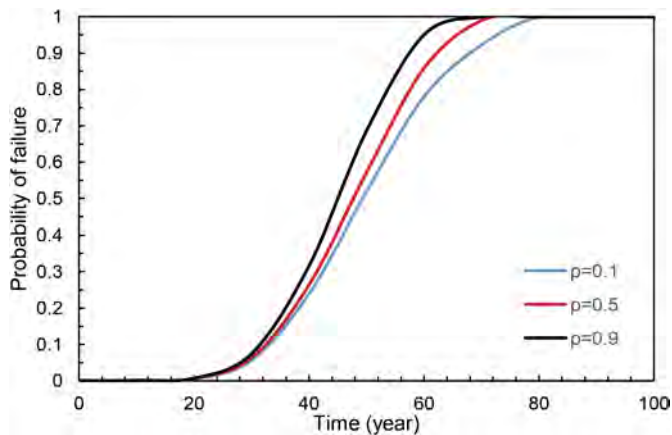


Figure 3. Probability of girder failure.

from Equation (7) for a given auto-correlation coefficient, and the probability of failure can be calculated by Equation (5).

The calculation results of the probability of failure with different autocorrelation coefficients are shown in Figure 3. The probability of girder failure increases with the exposure time due to the growth of corrosion depth. Moreover, the auto-correlation coefficients affect the girder failure significantly since the girder failure depends on many factors. These factors, such as girder geometries, loads, and corrosion depth, are interrelated at different time points in service life. As a result, the load effect is correlated in the time domain. The considerable difference in the probability of failure under different justifies the necessity of using a time-variant reliability method based on the concept of first passage probability theory. However, there is a lack of time-history statistical data for estimating the autocorrelation coefficient.

5 CONCLUSIONS

In this study, the time-dependent failure probability of steel girder was quantified. First passage probability theory was employed. A case study was provided to illustrate the proposed method. From the results of the worked example, it has been found that the probability of failure is related to the auto-correlation coefficients. Statistical data obtained from site-specific measurements and laboratory tests are recommended to establish the correlation among the parameters. The proposed method can be used for developing rehabilitation strategies for existing steel structures.

REFERENCES

- Czarnecki, A.A. & Nowak, A.S. 2008. Time-variant reliability profiles for steel girder bridges. *Structural Safety* 30(1): 49–64.
- Fernandez, I., Bairán, J.M. & Mari, A.R. 2015. Corrosion effects on the mechanical properties of reinforcing steel bars: Fatigue and σ - ϵ behavior. *Construction and Building Materials* 101: 772–783.
- Gong, C. & Frangopol, D.M. 2020. Reliability of steel girder bridges with dependent corrosion growth. *Engineering Structures* 224: 111125.
- Kayser J.R. 1988. *The effects of corrosion on the reliability of steel girder bridges*. PhD Thesis, University of Michigan, Ann Arbor, MI, USA
- Koch, G. H., Brongers, M. P., Thompson, N. G., Virmani, Y. P., & Payer, J. H. 2001. *Corrosion costs and preventive strategies in the United States*. Washington, DC: FHWA, 979.
- Li, C.Q. & Melchers, R.E. 1993. Outcrossings from convex polyhedrons for non-stationary Gaussian processes. *Journal of engineering mechanics* 119(11): 2354–2361.
- Li, C.Q. & Melchers, R.E. 2005. Time-dependent reliability analysis of corrosion-induced concrete cracking. *ACI Structural Journal* 102(4): 543.
- Li, C.Q. & Yang, W. 2021. *Steel Corrosion and Degradation of its Mechanical Properties*. London: CRC Press/Taylor & Francis Group.
- Melchers, R.E. 1999. *Structural reliability analysis and prediction* (2nd edition). Chichester: John Wiley & Sons.
- Nie, B., Xu, S. & Wang, Y. 2020. Time-dependent reliability analysis of corroded steel girder. *KSCE Journal of Civil Engineering* 24(1): 255–265.
- Revie R.W. 2008. *Corrosion and corrosion control: an introduction to corrosion science and engineering*. Chichester: John Wiley & Sons.
- Rice, S.O. 1944. Mathematical analysis of random noise. *The bell system technical journal* 23(3): 282–332.
- Wang, W., Li, C-Q., Robert, D. & Zhou, A. 2018. Experimental investigation on corrosion effect on mechanical properties of buried cast iron pipes. *Journal of Materials in Civil Engineering* 30(8): 04018197.
- Wasim, M., Li, C-Q., Robert, D. & Mahmoodian, M. 2020. Fracture toughness degradation of cast iron due to corrosive mediums. *International Journal of Pressure Vessels and Piping* 186: 104151.

Quantification of the effect of corrosion on the compressive membrane action in restrained hollow core slabs

T. Thienpont, W. De Corte, R. Van Coile & R. Caspeepe

Department of Structural Engineering and Building Materials, Ghent University, Ghent, Belgium

ABSTRACT: Precast concrete hollow core slabs are often designed with a limited concrete cover considering the high quality control for prefabricated members. However, experiments on prestressed concrete members have illustrated that corrosion can lead to a substantial reduction in the load carrying capacity, which can eventually lead to a structural failure. Although the design of hollow core slabs typically assumes simply supported boundary conditions, the support conditions of these units in real structures are often restrained, especially in the central part of a large hollow core slab floor. In case of restrained end supports, compressive membrane action can be activated, which can considerably enhance the load-carrying capacity. This can delay or even prevent a progressive collapse, increase the structural reliability and consequently increase the robustness of the structure. This paper presents a numerical study on the positive effect of axial and rotational restraints and the formation of compressive membrane action in case of corroded prestressed hollow core slabs in relation to its ability to prevent a structural collapse in case of severe corrosion.

1 INTRODUCTION

Nowadays, prestressed concrete hollow core (HC) slabs are widely used for structural flooring, due to their economic design, highly automated production process and ease of installation. Due to their reduced self-weight they allow for longer spans up to 20 m, and shallower construction depths. Like all concrete members, HC slabs are vulnerable to corrosion, especially since traditionally they are designed with a limited concrete cover, considering the high quality control for prefabricated members. Experiments on corroded prestressed concrete members have illustrated that high degrees of corrosion can lead to a substantial reduction in the load carrying capacity (Vereecken et al., 2021). In some cases corrosion can also lead to a change in the failure mode, passing from a ductile to a brittle failure (Belletti et al., 2020). In case of severe corrosion, the capacity of prestressed members can be so severely reduced that it can cause the collapse of the structure under live loading (Nagi & Whiting, 1992).

In principle, HC slabs are designed to be simply supported. In practice however, HC slabs are assembled to form extensive floors, by filling the joints between the members or through the addition of a topping layer (Walraven & Mercx, 1983). Therefore, the support conditions of HC units are often restrained rather than simply supported, especially in the central part of a large HC slab floor. In case of restrained end supports, compressive membrane action (CMA), also referred to as compressive arching action, can be activated, which can considerably enhance the load-carrying capacity. This increased resistance to the applied loads originates from the vertical component of the compressive arching forces in the member (Wang, 2002), as illustrated in Figure 1.

The formation of CMA in HC slab floors can delay or even prevent a progressive collapse, increase the structural reliability and consequently increase the robustness of the structure (Thienpont et al., 2022a). This contribution studies the positive effect of axial and rotational restraints, and the formation of compressive membrane action in case of corroded prestressed HC slabs in relation to its ability to prevent a structural collapse in case of severe corrosion. To

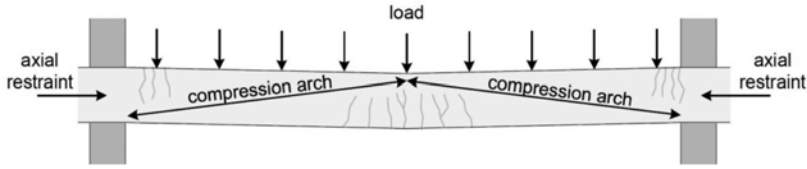


Figure 1. Principle of compressive membrane action (Thienpont et al., 2022b).

this end, a detailed finite element model is developed in Abaqus. Load displacement simulations are performed to study the cracking patterns, displacements and failure loads. Subsequently, a parametric study is conducted to investigate the combined influence of a corrosion degree and a degree of restraint on the ultimate carrying capacity and failure mode of prestressed HC slabs.

2 NUMERICAL MODEL

To study the effect of axial and rotational restraint on structural behavior of prestressed concrete HC slabs with corroded reinforcement strands, numerical evaluations are performed using the Abaqus finite element analysis software (Dassault Systemes, 2014). Herein, a previously validated numerical model by the authors (Thienpont et al., 2022a) is extended to take into account the reduction in material properties of the prestressing strands if subjected to corrosion. In the following, the applied material models for corroded prestressing steel and concrete are briefly discussed. Subsequently, an overview of the modelling assumptions is provided.

2.1 Material model for corroded prestressing steel

Besides a reduction in cross-sectional area of the prestressing strands, corrosion also strongly affects the mechanical properties and stress-strain curve of prestressing steel (Lu et al., 2016, Belletti et al, 2020). Previous studies have identified that corrosion of prestressing strands typically results in a reduced elastic modulus and ultimate strength, as well as a reduction in the ultimate strain, and loss of the yielding plateau and strain hardening region if the corrosion degree is larger than a critical value (Vereecken et al., 2021).

To model the degradation of the prestressing steel due to corrosion both a reduction on strands area and reduced mechanical properties are considered. To account for the latter, an adapted stress-strain curve for the corroded prestressing steel is needed. Various models, which take into account the effect of corrosion on the stress-strain curve of prestressing steel, have been proposed (Wang et al., 2017, Tu et al., 2019, Jeon et al., 2019, Franceschini et al, 2022). In this contribution, the model by Lu et al. (2016) is used. The latter is a damage model based on a series of tests on prestressing strands subjected to chloride attack, in which the mechanical properties are dependent on the corrosion level $C(t)$. The proposed reduction factors for the elastic modulus k_E , ultimate strength k_f and ultimate strain k_{ε_u} are presented in Eq. (1), Eq. (2) and Eq. (3), respectively.

$$k_E = \frac{E'_s}{E_s} = 1 - 1.8 \cdot f(C) \quad (1)$$

$$k_f = \frac{f'_u}{f_u} = 1 - 2.8 \cdot f(C) \quad (2)$$

$$k_{\varepsilon_u} = \frac{\varepsilon'_u}{\varepsilon_u} = 0.1 + 0.9 \cdot e^{(-20 \cdot f(C))} \quad (3)$$

Herein, E_s is the elastic modulus, f_u is the ultimate strength and ε_u the ultimate strain, all of the virgin strand. Similarly, E'_s , f'_u and ε'_u are respectively the elastic modulus, the ultimate

strength and the ultimate strain of the corroded strand. The factor $f(C) = C(t)$ is the degree of corrosion at time t , and is defined in Eq. (4).

$$C(t) = \frac{A - A'}{A} \quad (4)$$

Herein, A is the uncorroded cross sectional area of the prestressing strand and A' is the corroded area at time t . The constitutive model is characterized by Eq. 5.

$$\sigma(\varepsilon) = \begin{cases} E'_s \cdot \varepsilon, & \varepsilon \leq \varepsilon'_y \\ 0.85 \cdot f'_u + \frac{0.15 f'_u}{\varepsilon'_u - \varepsilon'_y} (\varepsilon - \varepsilon'_y), & \varepsilon'_y \leq \varepsilon \leq \varepsilon'_u \end{cases} \quad (5)$$

Herein $\varepsilon'_y = 0.85 f'_u / E'_s$ is the yield strain of the corroded strand. Note that the model takes into account that the hardening plateau disappears for corrosion degrees larger than 8%, i.e. in these cases the stress-strain curve only contains the elastic branch. The stress-strain curves for various corrosion degrees are illustrated in Figure 2.

The above model by Lu et al. has been applied by Belletti et al. (2020) to model naturally corroded prestressed beams, with a good approximation of the ultimate displacement and the ultimate load obtained from experiments.

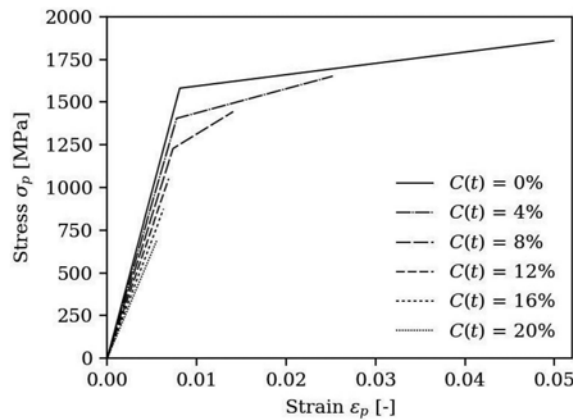


Figure 2. Constitutive model of corroded prestressing strand (based on Lu et al., 2016).

2.2 Material model for concrete

The excessive loading of concrete members usually involves crushing of concrete and/or severe cracking. Therefore, a non-linear concrete material model is used to simulate this behavior correctly. The compressive stress-strain relation of concrete is based on the analytical expressions provided in EN 1992-1-2 (CEN, 2004), as shown in Figure 3.a. The tensile behaviour is modelled based on *fib* Model Code 2010 (fib, 2012), as shown in Figure 3b and c. Herein, in the uncracked state, linear elastic behaviour is assumed up until the ultimate tensile stress is reached. Thereafter, a multilinear softening curve is applied. The area under this curve is related to the tensile fracture energy, which is calculated based on the recommendations in *fib* Model Code 2010.

2.3 Numerical modelling assumptions

In the numerical evaluations, the concrete is discretized using 8-noded hexahedral (brick) elements (C3D8) with an average size of 25 mm. For the prestressing steel, 2-noded linear truss elements (T3D2) are used. Assuming perfect bond, the prestressing strands are embedded within the concrete element, using the embedded constraint option in Abaqus.

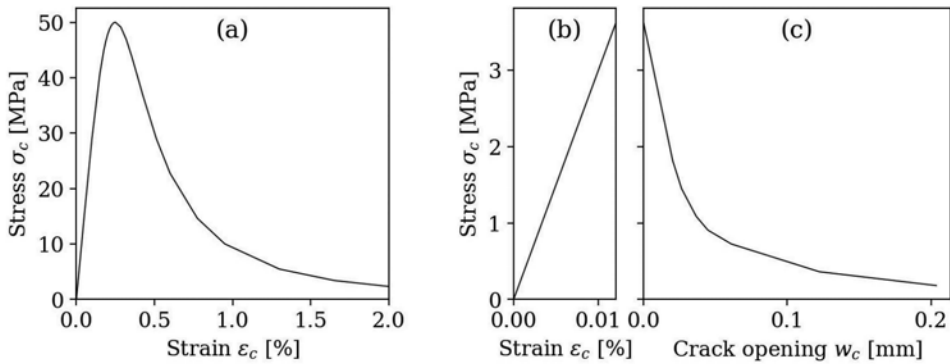


Figure 3. Constitutive model for concrete with compressive strength $f_c = 50$ MPa: (a) stress-strain diagram concrete in uniaxial compression; (b) stress-strain diagram for uncracked concrete in uniaxial tension; (c) stress vs. crack opening relation for concrete in uniaxial tension.

Figure 4 shows a schematic overview of the boundary conditions of the numerical model. To evaluate the structural behavior of restrained HC slabs with corroded prestressing reinforcement, a four-point bending setup is employed. To simulate the influence of a stiff surrounding structure, the outward displacements and the rotations of the slab ends are partially restrained by a set of axial springs with stiffness K (in kN/mm) and a set of rotational springs with stiffness R (in kNmm/rad). It is assumed that the axial springs act on the section ends at the mid-depth of the slab, as shown Figure 4. A recent study by Zhu et al. (2021) has found a non-negligible influence of the eccentricity on the CMA capacity in reinforced concrete slabs. In a more elaborate analysis, other values of the eccentricity could therefore be considered as well, but this is considered outside the scope of the current contribution.

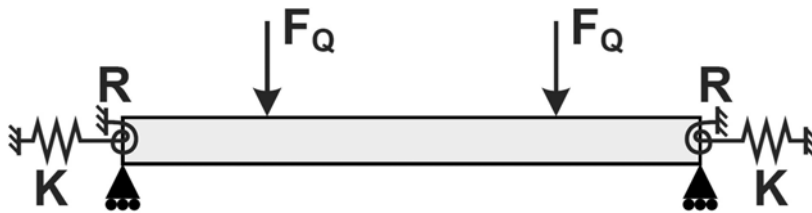


Figure 4. Schematic overview of numerical restrained four-point bending model.

3 SIMULATING THE EFFECT OF CORROSION ON CMA IN HOLLOW CORE SLABS

In the following a numerical parameter study is performed, in which the ultimate capacity and failure mode of precast HC slabs with corroded prestressing strands are investigated for a wide range of axial and rotational stiffnesses of the surrounding structure. Two HC slab sections with heights 320 mm and 500 mm are evaluated, which will be referred to as HC320 and HC500, respectively. The section geometries and corresponding reinforcement arrangements of the slabs are depicted in Figure 5.

In the figures below, the ultimate capacity of the studied sections is evaluated for various degrees of axial and rotational restraint. Herein, the degree of restraint is expressed in terms of a relative axial restraint stiffness k and a relative rotational restraint stiffness r , as defined in Eq. (6) and Eq. (7), respectively:

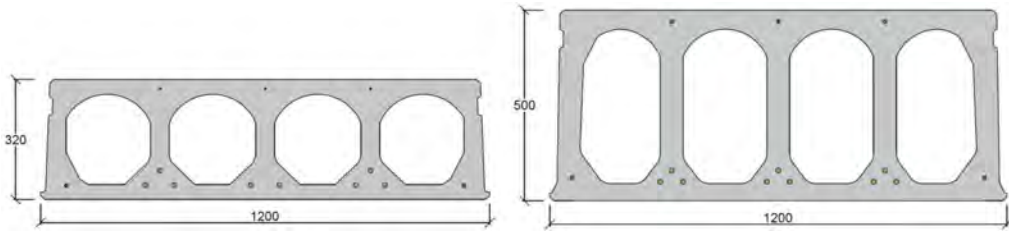


Figure 5. HC slab sections used in parameter study: (left) HC320; (right) HC500 (dimension in mm).

$$k = \frac{K}{K_{HC}} = \frac{K}{\left(\frac{E_c A}{L}\right)} \quad (6)$$

$$r = \frac{R}{R_{HC}} = \frac{R}{\left(\frac{E_c I}{L}\right)} \quad (7)$$

Where K and R are respectively the axial and rotational spring stiffness used in the numerical model, K_{HC} and R_{HC} are respectively the axial stiffness and rotational stiffness of the HC slab, E_c is the Young's modulus of concrete, A is the effective cross-section of the HC slab, L is the span of the HC slab and I is the cross-sectional moment of inertia of the HC slab.

3.1 Results HC320

Figure 6.a illustrates the effect of corroded prestressing steel on the load-displacement behaviour of prestressed concrete HC slabs, for a simply supported HC320 section, with a span length of 8 m. The curves clearly indicate that an increased degree of corrosion leads to a reduction in the load-carrying capacity. Additionally, the deflection at which the failure occurs also decreases with increased corrosion degree. This reduced deflection at failure can be attributed to the reduced ductility of the corroded steel. For HC320 slabs with a corrosion degree higher than 8%, the ductility of the steel is reduced to such extent that the slab tends to fail almost immediately after the formation of the first bending cracks. The figure also indicates that the degree of corrosion does not affect the mode of failure for this type of HC slab in case of unrestrained support conditions.

Figure 6.b depicts a similar set of load-displacement curves, but for a highly restrained HC320 section ($k = r = 1$). From the graph it is clear that the restrained boundary conditions result in a significant additional capacity, which can be attributed to the formation of CMA. For the cases where the degree of corrosion is below 8%, this additional capacity greatly counteracts the loss in capacity resulting from the degraded steel strands. Nonetheless, for higher corrosion degrees, no significant CMA can develop, and the slab fails in bending shortly after the formation of the first bending cracks. Unlike the unrestrained case, the results also indicate that the mode of failure of the studied HC slab changes depending on the degree of corrosion. The less corroded HC slabs tend to fail due to shear, whereas the highly corroded slabs fail in bending.

The above results are summarized in Figure 7, in which the ultimate capacities and failure modes from analyses for three degrees of restraint are considered, and compared to the results from a simply supported slab. For all considered degrees of restraint, the ultimate capacity tends to reduce when the degree of corrosion increases. Furthermore, all curves show a similar significant reduction in capacity when the degree of corrosion exceeds 8%. This drop can be directly related to the constitutive model for corroded prestressing steel, as discussed in Section 2.1. According to this model, the hardening plateau completely disappears when the corrosion degree exceeds 8%, and the stress-strain curve only contains the elastic branch.

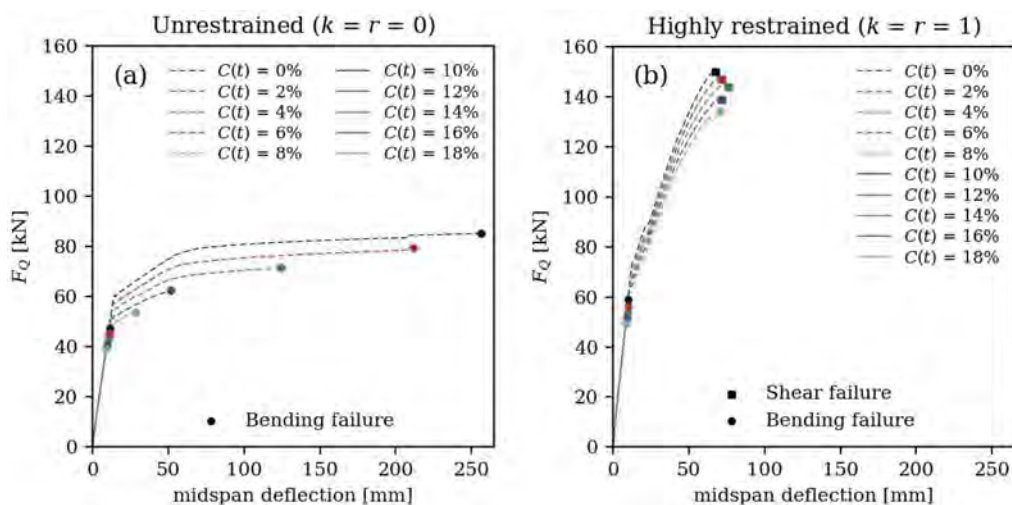


Figure 6. Effect of the level of corrosion on the load-displacement behaviour and mode of failure of restrained HC320 slabs with 8 m span length: (a) unrestrained ($k = r = 0$); (b) highly restrained ($k = r = 1$).

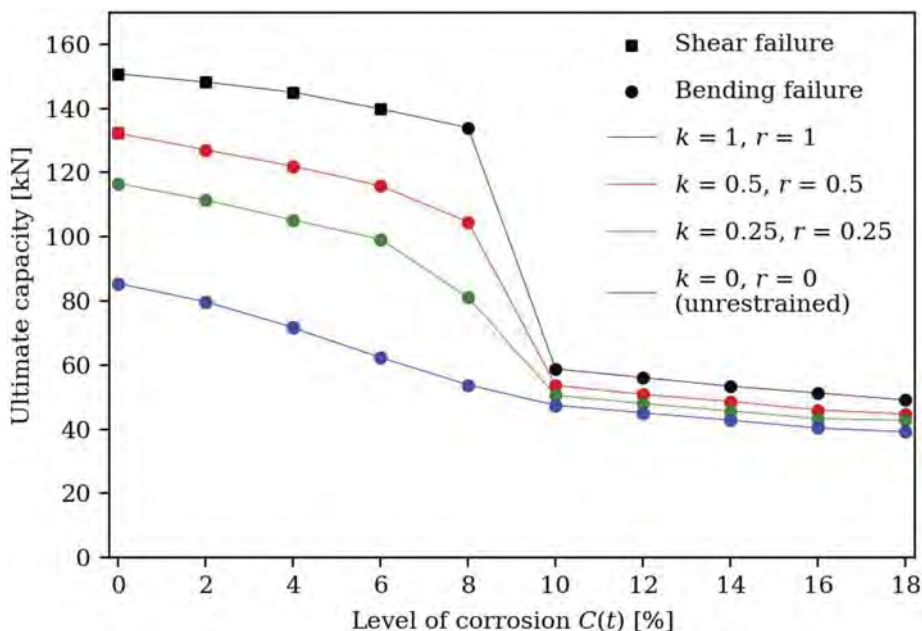


Figure 7. Effect of the level of corrosion on the ultimate load-carrying capacity and mode of failure of axially and rotationally restrained HC320 slabs with 8 m span length ($L/h = 25$).

3.2 Results HC500

The results from a similar set of analyses, performed on a taller HC500 section with a 12.5 m span length, are depicted in Figure 8. Overall, the graph indicates a similar effect of corrosion on the capacity of the HC slab members, both in the simply supported and restrained cases. When the degree of corrosion is below 6%, the additional capacity originating from the formation of CMA is able to counteract the reduced capacity resulting from the corroded prestressing strands. It is noted, that unlike the HC320 type slabs, the highly restrained HC500 members tend to fail due to crushing of the top flange, rather than due to a shear failure.

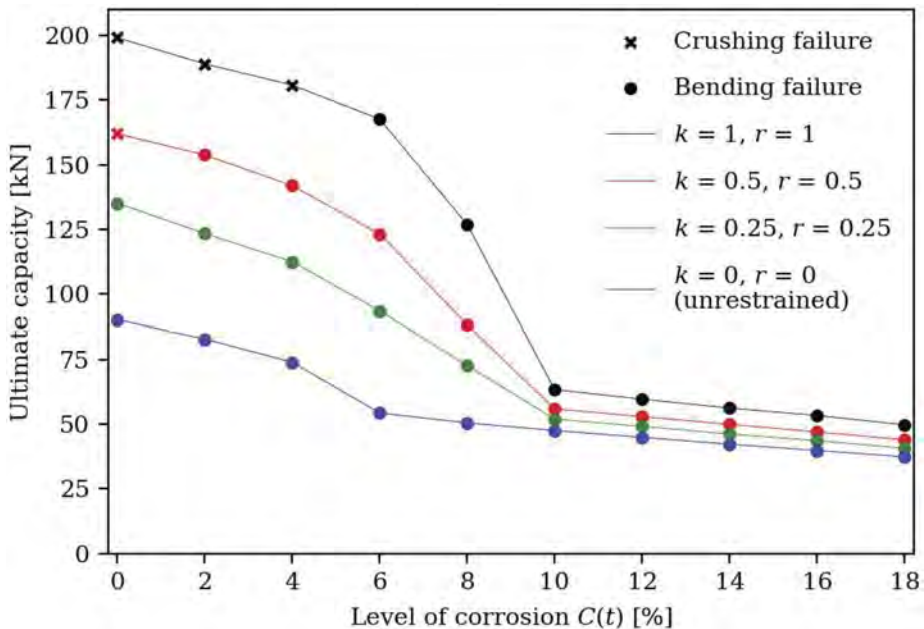


Figure 8. Effect of the level of corrosion on the ultimate load-carrying capacity and mode of failure of axially and rotationally restrained HC500 slabs with 12.5 m span length ($L/h = 25$).

4 CONCLUSIONS

In the present study, the effect of corrosion on the load bearing capacity and failure mode of axially and rotationally restrained concrete hollow core (HC) slabs is studied numerically. As a general conclusion, it is observed that the reserve capacity that can be achieved through the activation of compressive membrane action is in many cases larger than the loss in capacity resulting from corrosion in the prestressing strands. In case of severe corrosion however ($C(t) > 8\%$), the failure strain of the prestressing strands is reduced to such an extent that no compressive membrane action can develop to counteract the loss in load-carrying capacity caused by the corrosion. The presented results indicate that a mechanism like compressive membrane action may activate a certain level of reserve capacity in concrete structures which have suffered considerable damage associated with the effects of ageing and deterioration processes.

ACKNOWLEDGEMENTS

The authors wish to thank the Research Foundation of Flanders (FWO) for the financial support on the research project (Grant number 11F5520N) “Performance-based analysis and design for enhancing the safety of prestressed concrete hollow-core slabs in case of fire and unforeseen events”. The computational resources (Stevin Supercomputer Infrastructure) and services used in this work were provided by the VSC (Flemish Supercomputer Center), funded by Ghent University, FWO and the Flemish Government – department EWI.

REFERENCES

Belletti, B, Vecchi, F, Bandini, C, Andrade, C & Montero, JS. 2020. Numerical evaluation of the corrosion effects in prestressed concrete beams without shear reinforcement. *Structural Concrete*. 21: 1794–1809. <https://doi.org/10.1002/suco.201900283>

- CEN. 2004. EN 1992-1-1. Eurocode 2: Design of concrete structures - Part 1-1: General rules and rules for buildings. Brussels.
- Dassault Systemes. 2014. Abaqus 6.14: Abaqus/CAE User's Guide 2014.
- Franceschini, L, Belletti, B, Tondolo, F & Sanchez Montero, J. 2022. A simplified stress-strain relationship for the mechanical behavior of corroded prestressing strands: The SCPS-model. *Structural Concrete*. <https://doi.org/10.1002/suco.202200170>
- fib. 2012. fib Model Code 2010, Final draft – Volume 1. Fédération internationale du béton (fib).
- Lu ZH, Li F & Zhao YG. 2016. An investigation of degradation of mechanical behaviour of prestressing strands subjected to chloride attacking. *International conference on durability of concrete structures, ICDCS 2016*; 57–65. <https://doi.org/10.5703/1288284316111>
- Nagi, W & Whiting, D. 1992. Corrosion of prestressed reinforcing steel in concrete bridges: State of the art. *ACI-SP* 151–2
- Thienpont, T, De Corte, W, Van Coile, R & Caspeele, R. 2022a. Compressive membrane action in axially restrained hollow core slabs: Experimental investigation. *Structural Concrete*. 23: 3007–3020. <https://doi.org/10.1002/suco.202100684>
- Thienpont, T, Caspeele, R, Van Coile, R & De Corte, W, 2022b. Failure modes of hollow core slabs taking into account compressive membrane action, *Proceedings of the 6th fib international congress 2022*: 1840–1849.
- Tu B, Dong Y & Fang Z. 2019. Time-dependent reliability and redundancy of corroded prestressed concrete bridges at material, component, and system levels. *Journal of Bridge Engineering*. 24 (9). [https://doi.org/10.1061/\(ASCE\)BE.1943-5592.0001461](https://doi.org/10.1061/(ASCE)BE.1943-5592.0001461)
- Vereecken, E, Botte, W, Lombaert, G & Caspeele, R. 2021. Assessment of corroded prestressed and post-tensioned concrete structures: A review. *Structural Concrete*. 22: 2556–2580. <https://doi.org/10.1002/suco.202100050>
- Walraven, JC & Merx WPM. 1983. The bearing capacity of prestressed hollow core slabs. *Heron* 28(3).
- Wang, YC. 2002. Steel and composite structures: behaviour and design for fire safety. CRC Press.
- Zhu YJ, Zhou M, Zhu JM, Nie X. 2021. Analytical models for load capacities of variable thickness reinforced concrete slabs considering compressive membrane action and boundary effects. *Engineering Structures*. 246:113067. <https://doi.org/10.1016/j.engstruct.2021.113067>.

Bayesian pre-estimation of bridge life-cycle costs

T. Vagdatli & K. Petroutsatou

Department of Civil Engineering, Aristotle University of Thessaloniki, Thessaloniki, Greece

P. Panetsos & Z. Barmpa

Egnatia Odos S.A., Thessaloniki, Greece

N. Fragkakis

University of West Attica, Athens, Greece

ABSTRACT: Motorway bridges constitute one of the most crucial parts of transportation networks, with proper life-cycle cost (LCC) estimation being of paramount importance for cost-efficient projects. This paper introduces a probabilistic framework for concrete bridge LCC estimation based on dynamic Bayesian Network (DBN) modelling that stakeholders can consult in projects' preliminary stages for proper decision-making. Firstly, probability distributions of material quantities and construction costs for the superstructure and foundation are estimated. Subsequently, the maintenance costs of deck expansion joints are illustratively presented, as they are considered vulnerable bridge elements with frequent repairs. The proposed DBN contains continuous and time-dependent variables thoroughly registered over multiple time stages. The DBN is formulated using actual records of 60 concrete bridges' construction, inspections, condition and maintenance from the Egnatia Odos motorway in Greece. The presented approach is an effective tool for bridge management enhancement owing to stochastic dynamic interdependencies among parameters and continuous information updating.

1 INTRODUCTION

Bridges are considered a vital asset in transportation networks as communication channels that foster public prosperity. Although bridges constitute only a small percentage of a highway's length, their construction costs account for a substantial portion of the highway's total construction cost (Antoniou et al., 2018). Furthermore, a considerable proportion of their total cost is incurred after their construction (Ammar et al., 2013). Hence, robust models that can reliably predict LCCs in the preliminary stages of such projects seem to be of paramount importance.

Due to the crucial aspect of uncertainty associated with various design, deterioration and maintenance parameters of bridge structures, LCC analysis based on stochastic parameter modelling can improve the effectiveness of final decisions when conducting feasibility studies. The extant literature has focused almost exclusively on deterministic methods for construction cost estimation (Fragkakis et al., 2011, Lambropoulos et al., 2010) and LCCs analyses (Zhou et al., 2020) of concrete bridges. The existing probabilistic analyses are either restricted to the LCC of the bridge's single components, especially on decks (Shen et al., 2021), or individual cost categories, such as maintenance or repair costs (Gui et al., 2021).

The scope of this study is to introduce a dynamic perspective of a generalized probabilistic approach for pre-estimating construction and maintenance costs of concrete bridges and enlightening the stochastic relationships among modifying factors for providing reliable information to decision-makers during the life-cycle of bridge projects towards more adaptable asset management. Bayesian networks (BNs) are suggested for facilitating economically

sustainable asset management since they are acknowledged as one of the most effective modelling frameworks in the field of probabilistic knowledge representation and reasoning (Bertone et al., 2018), especially for engineering risk analysis (Luque & Straub, 2016).

2 PROPOSED DYNAMIC BAYESIAN NETWORK MODEL

A BN represents a set of stochastic variables and the causal probabilistic relationship among them using a Direct Acyclic Graph (DAG). For modelling the stochastic and dynamic behavior of the system in a sequence of time slices, BN was extended to a DBN by introducing temporal dependencies among its parameters. The proposed BN structure consists of 2 modules, the “Construction phase” and “Operational phase” modules, which altogether include 12 variables, both discrete and continuous, related to the construction, inspection, condition and maintenance actions of bridge components. Uncertainty is expressed through probability distributions attributed to random variables.

The first module refers the BN corresponding to the beginning of the project ($t = 0$) and its structure is different from the other stages. Material quantities and expected construction costs of the superstructure and foundation for specific construction methods were estimated. The second module investigates the maintenance costs specifically for the deck expansion joints since they constitute one of the most frequently maintained bridge components and their deterioration may affect components of pivotal importance such as superstructure (Lee Kelly et al., 2019). This module includes the time slices of the operational life of the bridge ($t = 1, 2, \dots, T$) and here is restricted to ten years since this is the life-cycle of the examined expansion joints. However, owing to the flexibility of BNs to readjust their parameters without any particular computational cost, both the number of time slices can be modified and additional sub-models can be added for representing features of different bridge components such as bearings, substructure etc.

2.1 A continuous variable bayesian network for construction costs ($t=0$)

The “Construction phase” BN module investigates the factors related to the construction of the superstructure spans consisting of cast-in-situ box girders and the construction of the socket foundation. The final sample includes complete actual data from 47 superstructure spans consisting of cast-in-situ box girders and 26 sockets used for the foundation of piers.

Regarding the socket foundation, previous statistical analysis (Fragkakis et al., 2011) indicated that among other explanatory variables, the length of the deck, “Lsup”, has significant impact on its material quantities. Likewise, for the cast-in-situ construction method of superstructure, the adjusted length of span, “Ladj”, was chosen to be used as explanatory variable (Lambropoulos et al., 2010). The concrete volume (Vc), the reinforcing steel weight (Bs), and the prestressing steel weight (Bp) represent the three dependent variables. All the parameters were modelled as oval nodes as they constitute random variables (Figure 1). Using Bayesian inference (Eq. (1)), the final product was the development of posterior distributions for the material quantities of Vc, Bs, and Bp and their corresponding costs.

$$p(y) = \int p(\theta)p(y|\theta)d\theta \quad (1)$$

where $p(\theta)$: the prior distribution, $p(y|\theta)$: the likelihood function and $p(y)$: the posterior distribution.

BNs do not necessarily imply influence by Bayesian statistics (Murphy, 1998), but it is common to utilise frequentist methods to estimate the probability distributions parameters (Horný & Lin, 2018). In this specific case, where the parameters of the DAG are continuous, the “maximum likelihood estimation” method (Paniego, 2019) (Eq. (2)) was used for establishing the parameters of the marginal probabilities for the parent nodes. The conditional distributions of child nodes were computed via Bayesian inference using multiple regression analysis as functional

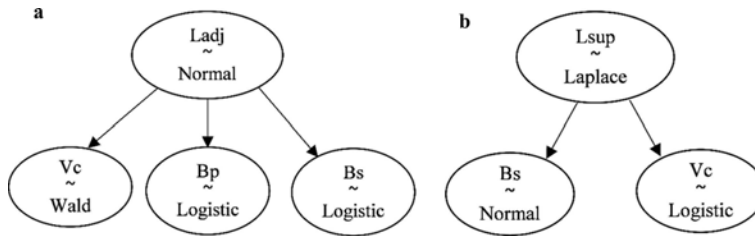


Figure 1. DAGs of parent & child nodes for (a) cast in situ box girders and (b) socket foundation.

linkage forms among parent and child nodes. Specifically, the used regression equations were derived from previous studies of Fragkakis et.al. (Fragkakis et al., 2011, Lambropoulos et al., 2010) since they concerned our study parameters. The Kolmogorov-Smirnov and Anderson-Darling goodness of fit tests were used to validate the compatibility of the dataset fitting to certain theoretical probability distributions.

$$L(X_1, \dots, X_n, \theta) = f(X_1, \theta) f(X_2, \theta) \dots f(X_n, \theta) \quad (2)$$

Consecutively, for conducting Bayesian inference of construction quantities, the Python computer programming language was used, specifically the PyMC3 package specialized in Bayesian computation and analysis. The No-U-Turn (NUTS) sampling algorithm, a highly computationally efficient Markov Chain Monte Carlo (MCMC) method, was implemented for model fitting since it allows the sampling from models with continuous parameters (Salvatiere et al., 2016). Sixteen MCMC chains in a total of 5000 iterations were generated. Once the posterior distributions of material quantities (Vc, Bs & Bp) have been determined, the total expected construction costs can be determined by multiplying the obtained probabilities with unit prices of the published detailed price lists of the relative works.

2.2 A dynamic bayesian network for LCCs of deck expansion joints ($t=1,2, \dots, T$)

The “Operational phase” module comprises a DBN consisting of discrete variables associated with risk-based maintenance of deck expansion joints. For running the simulation model, the process was assumed to: a) follow the first-order of the Markov model, namely the state variables at time “t” depends only on the state variable at time (t-1) and other variables at time “t”, and b) be stationary, i.e., the structure and parameters of the model do not change over

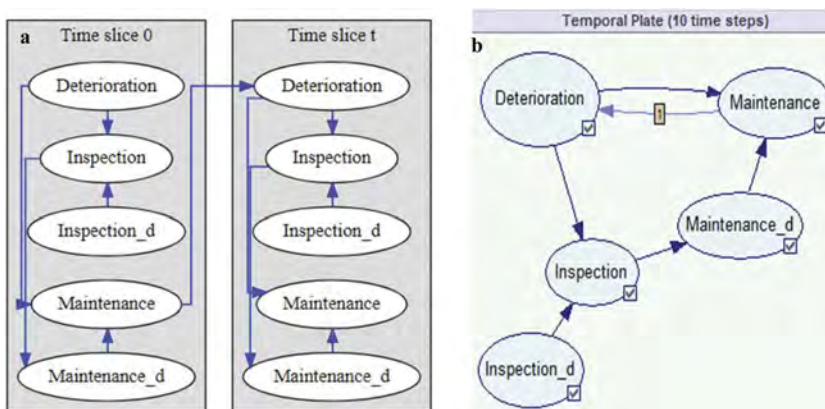


Figure 2. (a) The 2-TBN for “Operational phase” module & (b) temporal plate of the DBN in the GeNIe software.

time. In this case, the DBN can compactly be represented as 2-time-slice Bayesian network (2-TBN) (Koller & Friedman, 2009) (Figure 2a).

Figure 2b indicates the general form of the proposed DBN which was created in GeNIe (v2.1) software (Genie, 2016). The full specification of the DBN's nodes can be found in Table 1. Since the DBN was built as a homogeneous model, the transition probabilities matrixes remained constant over the examined time slices. The nodes included in the model concern deterioration before and after any given maintenance treatment, inspection occurrence, inspection outcome and maintenance actions. Indicatively, the decay types of I_t node range from cracking in injected asphalt mastic joint (state 8) to transition mortar breakage (state 7), joint failure (state 5) and elastomeric part failure (state 3). All maintenance treatments (e.g.: crack repairs, injected asphalt mastic joint repair, elastomeric part/anchor system replacement) corresponding to the decay types of I_t node assume 100% maintenance efficiency, i.e., the expansion joint is returned to its initial state (state 9).

It is noted that this module can be operated using different records derived from transportation agencies. Moreover, different condition-based or time-based maintenance strategies can be conducted using the proposed module for their direct comparison and optimal decision-making. For illustrative purposes, all the conditional probability tables of the nodes were fitted using actual records of 50 joints from the Egnatia Odos S.A. using the percentage prediction method. Also, in the presented numerical case, the captured maintenance strategy combines both minor and major treatments on examined joints of the Egnatia Odos network.

Table 1. Full description of DBN's nodes.

PARENT NODES			
Node name	Number of states	Conditional probability table structure & size	Description of states
Deterioration ($D_{t=0}$)	9	$P(D_o) \rightarrow n_D \times 1$: [1,0,0,0,0,0,0,0,0]	$D_{t=0} = \{9-1\}$: initial condition states using the FHWA scale
Inspection_d ($I_{d,t}$)	2	$P(I_{d,t}) \rightarrow n_{Id} \times 1$: [0,1]	$I_{d,t} = 0$: "No inspection" $I_{d,t} = 1$: "Inspection"
CHILD NODES			
Inspection (I_t)	8	$P(I_t D_t, I_{d,t}) \rightarrow n_I \times n_D \times 2$	$I_t = 0 = 0$: "No deterioration detection" $I_t = 0 = \{1-6\}$: Seven possible decay types $I_t = 7$: "No inspection" made
Maintenance ($M_{d,t}$)	2	$P(M_{d,t} I_t) \rightarrow n_M \times n_I$	$M_{d,t} = 0$: "No maintenance" $M_t = 1$: "Maintenance"
Maintenance (M_t)	9	$P(M_t D_t, M_{d,t}) \rightarrow n_D \times n_D \times 2$	$M_{d,t} = \{9-1\}$: Transition matrix of the adopted maintenance policy for each condition state
Deterioration ($D_{t>0}$)	9	$P(D_{t>0} D_{m,t-1}) \rightarrow n_D \times n_D \times 2$	$D_{t>0} = \{9-1\}$: Deterioration transition matrix under the adopted maintenance policy

Finally, the expected maintenance costs of a given expansion joint were calculated using the Eq. (3).

$$E[C_{M(t)}] = \sum_{s=1}^S P_{M,s} * c_{M,s} \quad (3)$$

Where S is the total number of independent condition states of the expansion joints, s is the condition state, $P_{M,s}$ is the probability that condition state s will occur at a given time t , $C_{M,s}$ is the unit cost associated with maintenance strategy at condition state s .

3 RESULTS & DISCUSSION

The implementation of the Bayesian analysis for the continuous variables of the “Construction phase” module yielded posterior distributions (Figures 3-5) together with their statistics results (Table 2 & Table 3) for the examined material qualities. The model checking incorporated two components, the convergence diagnostic and the goodness of fit test. The Gelman-Rubin convergence diagnostic R-hat was found < 1.1 (Table 2 & Table 3), namely the MCMC chains were concluded to be converged. Also, the stationary trace plots and divergence zero rate indicated the sample’s convergence. The goodness of fit was verified visually using appropriate PyMC3 functions.

As it becomes apparent, the bulk of the exported posterior distributions does not follow a normal distribution but rather Logistic, Laplace and Inverse Gauss distributions. This confirms that normality assumptions are not the case in real-world situations. Especially in infrastructure projects, uncertainties are inherent as the information tends to change frequently with the project’s progress. Various fruitful outcomes for decision-makers can be exported from the proposed probabilistic analysis. For instance, if the user intends to predict the V_c material quantities of the superstructure span with a risk of 20%, namely their occurrence range with 80% probability, these quantities would be between 236.771 m³ and 1,200 m³ per span. Furthermore, in light of new data, users can extract even more customized results via Bayesian updating.

Users could estimate probabilistic cost ranges considering the above material quantities ranges and appropriate unit values. A special case of cost ranges has been demonstrated in this study using unit prices from Greece’s detailed road price lists and 2017 as reference year (Table 2 & Table 3).

Table 2. Descriptive statistics of posterior distributions for the stochastic variables for the construction method of cast-in-situ for the bridge’s superstructure (using the summary() function of PyMC3).

Random Variables	Distribution type	Parameters (mean; sd)	Lower limit HPD _{97%}	Upper limit HPD _{97%}	Gelman-Rubin convergence test (R-hat)
$Ladj$ (m)	Normal	(35.13 m; 10.08)	16.126 m	53.565 m	1.00
V_c (m ³ /span)	InvGauss (Wald)	(349.98 m ³ ; 245.802)	63.226 m ³	767.911 m ³	1.00
C_{Vc} (€/span)	InvGauss (Wald)	(73,495.8 €; 51,618.42)	13,277.46 €	161,261.31€	1.00
B_s (Kg/span)	Logistic	(41,718.33 Kg; 14,145.39)	14,783.05Kg	68,372.07Kg	1.00
C_{Bs} (€/span)	Logistic	(41,718.33 €; 14,145.39)	14,783.05 €	68,372.07 €	1.00
B_P (Kg/span)	Logistic	(14,302.26 Kg; 6,730.641)	1,597.84 Kg	26,366.46Kg	1.00
C_{Bp} (€/span)	Logistic	(94,394.916 €; 44,422.23)	10,545.744€	174,018.64€	1.00

The result of the DBN simulation for the “Operational phase” module can be seen in Figure 6a. It is evident that the maintenance strategy followed by Egnatia Odos S.A. does not let the expansion joints fall below critical deterioration states since there are no joints reached the 1 and 2 states, guaranteeing the safe operation of the bridge. Moreover, only a percentage of the total joints returned to their initial state every year since budget constraints do not allow perfect preventive maintenance. Besides, this is the mainly common way of dealing with the maintenance treatments of infrastructure assets in practice. Owing to the homogeneous transition matrix used during the life-cycle of the expansion joints, a roughly steady line was formed from the fourth year onwards without extraordinary line peaks reflecting alternative maintenance strategies.

Subsequently, the obtained probabilities were multiplied by specific actual Greek maintenance unit costs to obtain the unit expected costs during the given lifetime span (Figure 6b). There was no significant increment in the maintenance costs for the considered states from the third year onwards, as the probability of each state remained approximately the same. Each user can consider the total number of damaged joints and their corresponding meters for calculating the total expected budget that should be committed for joints repair.

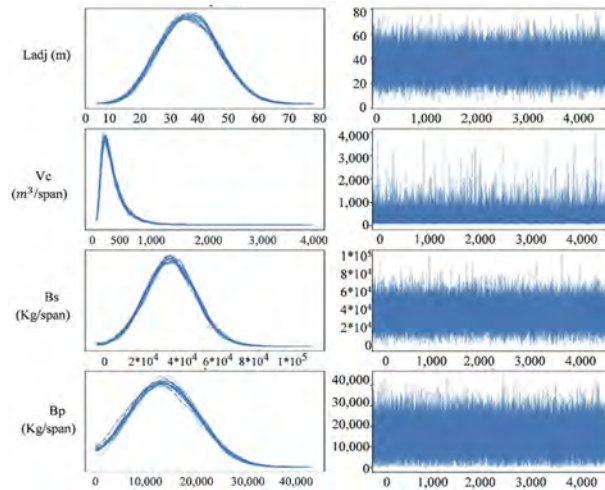


Figure 3. Posterior distributions and trace plots of the continuous random variables for the sub-model “Cast-in-situ” construction method of the superstructure.

Table 3. Descriptive statistics of posterior distributions for the stochastic variables of bridge’s socket foundation (using the summary() function of PyMC3).

Random Variables	Distribution type	Parameters (mean; sd)	Lower limit HPD _{97%}	Upper limit HPD _{97%}	Gelman-Rubin convergence test (R-hat)
L_{sup} (m)	Laplace	(94.823 m; 37.30)	21.212 m	165.255 m	1.001
V_c ($m^3/socket$)	Logistic	(972.218 m^3 ; 371.183)	236.771 m^3	1,658.726 m^3	1.001
C_{V_c} ($€/socket$)	Logistic	(82,444.086€; 31,476.318)	20,078.18 €	140,659.96€	1.008
B_s ($Kg/socket$)	Normal	(58,797.777 Kg; 30.736,16)	14,373.07Kg	109,399 Kg	1.001
C_{B_s} ($€/socket$)	Normal	(58,797.777 €; 30.736,16)	14,373.07 €	109,399 €	1.006

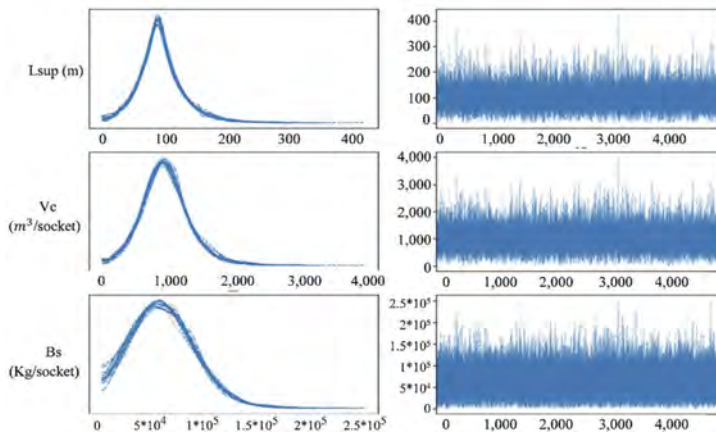


Figure 4. Posterior distributions and trace plots of the continuous variables for the sub-model of socket foundation.

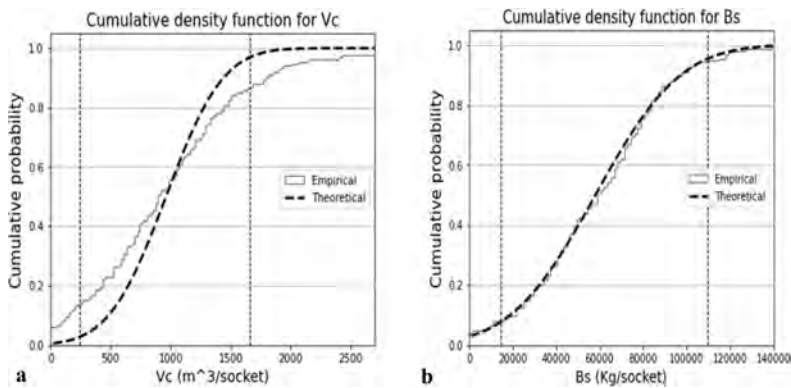


Figure 5. Cumulative distributions for material quantities of (a) V_c & (b) B_s for socket foundation.

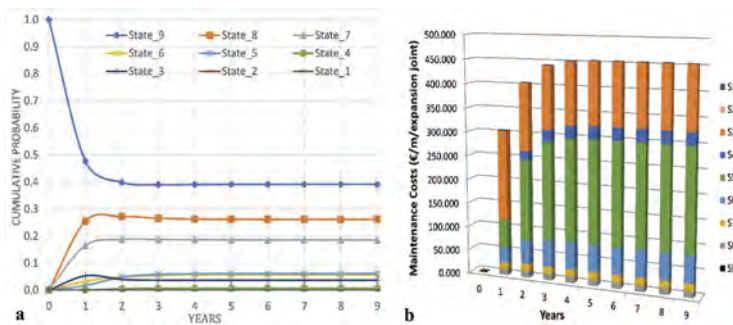


Figure 6. (a) The output of the DBN model for the nine probabilistic deterioration curves; (b) Expected maintenance costs (£/m/expansion joint) per state using expected cost model.

4 CONCLUSIONS

Cost estimation is a crucial management step facilitating optimal investment decisions and overrun avoidance during an asset’s life-cycle. For supporting decision-making under uncertainty during the early stages of a project, the proposed “Construction phase” module has two purposes for its users (either public authorities or a project manager); the prediction of the occurrence probability of a specific cost value and the derivation of the cost ranges based on their risk tolerance. Hence, the user can decide on the sustainable implementation of a project by referring to the fluctuation of its expenses using the probabilistic results within confidence intervals. Regarding the “Operational phase” module, although the exported results were affected by the monetary distribution of the available resources over the years, a change in the economic conditions or maintenance strategies implemented by each user may modify the management policy, which can be incorporated into the presented model owing to the adaptable environment of DBNs. Therefore, it can be readily used in practice for promoting viable alternative strategies. The Bayesian updating approach can be used in the current models in light of new data of uncertain parameters for supporting adaptive management. The proposed model is towards developing a comprehensive validated DBN that can be used by engineering practitioners and project managers for robust LCC analysis.

ACKNOWLEDGEMENTS

The implementation of the doctoral thesis of Vagdatli Theodora was co-financed by Greece and the European Union (European Social Fund-ESF) through the Operational Programme «Human Resources Development, Education and Lifelong Learning» in the context of the

Act “Enhancing Human Resources Research Potential by undertaking a Doctoral Research”
Sub-action 2: IKY Scholarship Programme for PhD candidates in the Greek Universities.



REFERENCES

- Ammar, M., Zayed, T., & Moselhi, O. 2013. Fuzzy-Based Life-Cycle Cost Model for Decision Making under Subjectivity. *Journal of Construction Engineering and Management* 139(5): 556–563. [https://doi.org/10.1061/\(ASCE\)CO.1943-7862.0000576](https://doi.org/10.1061/(ASCE)CO.1943-7862.0000576).
- Antoniou, F., Konstantinidis, D., Aretoulis, G., & Xenidis, Y. 2018. Preliminary construction cost estimates for motorway underpass bridges. *International Journal of Construction Management* 18(4): 321–330. <https://doi.org/10.1080/15623599.2017.1358076>.
- Bertone, E., Sahin, O., Stewart, R. A., Zou, P. X. W., Alam, M., Hampson, K., & Blair, E. 2018. Role of financial mechanisms for accelerating the rate of water and energy efficiency retrofits in Australian public buildings: Hybrid Bayesian Network and System Dynamics modelling approach. *Applied Energy* 210: 409–419. <https://doi.org/10.1016/j.apenergy.2017.08.054>.
- Fragkakis, N., Lambropoulos, S., & Tsiambaos, G. 2011. Parametric Model for Conceptual Cost Estimation of Concrete Bridge Foundations. *Journal of Infrastructure Systems* 17(2): 66–74. [https://doi.org/10.1061/\(asce\)is.1943-555x.0000044](https://doi.org/10.1061/(asce)is.1943-555x.0000044).
- Genie. (2016). GeNIe Modeler Manual. In *Genie*.
- Gui, C., Zhang, J., Lei, J., Hou, Y., Zhang, Y., & Qian, Z. 2021. A comprehensive evaluation algorithm for project-level bridge maintenance decision-making. *Journal of Cleaner Production* 289. <https://doi.org/10.1016/j.jclepro.2020.125713>.
- Horný, M., & Lin, M. 2018. Bayesian networks. *Handbook of Machine Learning*.
- Juszczak, M. 2019. Early Cost Estimates of Bridge Structures Aided by Artificial Neural Networks. In *VIII International Scientific Siberian Transport Forum; 8th International Scientific Siberian Transport Forum, Novosibirsk, 22-27 May 2019*. Cham. doi: 10.1007/978-3-030-37919-3_2.
- Koller, D., & Friedman, N. 2009. *Probabilistic Graphical Model Principles and Techniques*. Massachusetts: The MIT Press.
- Lambropoulos, S., Pantouvakis, J.-P., & Fragkakis, N. 2010. A cost estimate method for bridge superstructures using regression analysis and bootstrap. *Organization, Technology & Management in Construction: An International Journal* 2(2): 182–190.
- Lee Kelly, A., Atadero, R. A., & Mahmoud, H. N. 2019. Life Cycle Cost Analysis of Deteriorated Bridge Expansion Joints. *Practice Periodical on Structural Design and Construction* 24(1). [https://doi.org/10.1061/\(asce\)sc.1943-5576.0000407](https://doi.org/10.1061/(asce)sc.1943-5576.0000407).
- Luque, J., & Straub, D. 2016. Reliability analysis and updating of deteriorating systems with dynamic Bayesian networks. *Structural Safety* 62: 34–46. <https://doi.org/10.1016/j.strusafe.2016.03.004>.
- Murphy, K. 1998. *A Brief Introduction to Graphical Models and Bayesian Networks*.
- Paniego, S. 2019. *Visualization and interpretation in large Bayesian networks* [Universidad Politecnica de Madrid].
- Salvatier, J., Wiecki, TV., & Fonnesbeck, C. 2016. Probabilistic programming in Python using PyMC3. *PeerJ Computer Science* 2: e55. <https://doi.org/10.7717/peerj-cs.55>.
- Shen, L., Soliman, M., & Ahmed, S. A. 2021. A probabilistic framework for life-cycle cost analysis of bridge decks constructed with different reinforcement alternatives. *Engineering Structures* 245. <https://doi.org/10.1016/j.engstruct.2021.112879>.
- Zhou, Z., Alcalá, J., & Yepes, V. 2020. Environmental, Economic and Social Impact Assessment: Study of Bridges in China's Five Major Economic Regions. *International Journal of Environmental Research and Public Health* 18(1): 122. <https://doi.org/10.3390/ijerph18010122>.

A service value predictive system of componentized infrastructure assets

K. Petrousatou, T. Vagdatli & M. Voutsis

Department of Civil Engineering, Aristotle University of Thessaloniki, Thessaloniki, Greece

P. Panetsos & Z. Barmpa

Egnatia Odos S.A., Thessaloniki, Greece

ABSTRACT: Prevention is an imperative necessity in all systems, whether natural or artificial ones for their proper functionality and life span's extension. Infrastructure assets are preeminently multi-components systems with existing dependencies between their components. The extant literature approaches generally the issue of maintenance models in multi-component systems without referring to specific items or deals mainly with systems of machinery and equipment. This research aims to conceptualize the necessary steps for determining the remaining economic status of infrastructure assets by calculating their "Service Value" via a probabilistic dynamic integrated predictive system and implement appropriate maintenance plans that can prohibit false life-cycle cost estimation. The model will be introduced on road bridges as ones of the most critical and difficult to analyze structures in road infrastructure systems. The proposed framework guarantees the financial sustainability of the project, its uninterrupted operation and unplanned traffic delays reduction, thus preventing adverse productivity, mobility and economic impacts.

1 INTRODUCTION

Prevention is arguably an imperative necessity in all systems, whether natural (human, environmental, etc.) or artificial ones (construction, equipment, etc.), for their (stable) proper functionality and life span's extension. This is the challenge of asset management which is properly recognized by the owners. Albeit, an efficient and sustainable approach is missing and within this context the tools and practices used are oversimplified by concentrating in single specific parts of the whole system. Infrastructure assets are preeminently multi-components systems with existing dependencies between their components. The incorporation of the componentization approach (the separate investigation of individual components that constitute integral elements of the asset system) seems to be of paramount importance in multi-component systems for the correct assessment of an asset's value as a whole since there are dependencies among individual components uncaptured in current evaluation methods (Leviäkangas et al., 2019). The extant literature approaches generally the issue of maintenance models in multi-component systems with reference to specific items without consider how each individual item reacts within the holistic system where it belongs. One possible reason might be the fact of the paucity of available data. Furthermore, the asset management is usually owned and managed by public institutions or concessionaires companies in addition the required data refers to sensitive economic issues where authorities or companies are unwilling to share let alone to publicize (Petrousatou et al., 2012). Moreover, the assessment of the condition of an infrastructure and the calculation of the investment needed for its maintenance and operation determine the life-cycle cost of the asset (Petrousatou et al., 2021). Thus, the objective of this research is to determine the remaining economic status of infrastructure assets by calculating their "Service

Value” (SV) via a dynamic integrated predictive system and to implement appropriate maintenance and/or replacement plans that can prohibit false estimation of life-cycle cost. This guarantees not only the financial sustainability of the asset but also the continuous and uninterrupted operation of the infrastructure, the operation of the neighboring settlements, the reduction of the unplanned delays and traffic disruptions and thus preventing any adverse impacts on productivity, mobility and economy in general.

Furthermore, saving resources are considered to be of high significance. The aim is to achieve cost efficiency in infrastructure development by the implementation of appropriate tools for the value of money, in addition when the available resources are limited (Marinelli et al., 2018). The challenge is the shift toward a life-cycle oriented construction cost analysis in order to reduce life-cycle costs of infrastructure assets (Biondini & Frangopol, 2018). This research aims to handle the inherent uncertainties during the whole life-cycle of infrastructure assets in line with construction analysis. A probabilistic framework based on dynamic Bayesian Network (DBN) modelling is introduced for adaptive management in different time stages of an infrastructure project and consulting stakeholders for proper decision-making. The definition of SV will be performed by the method of the “future economic benefits” expected of the asset, as adopted by the OECD (OECD, 2013). It is highlighted that in this method the asset incorporates all the economic benefits it will pay off in the future, as an accumulated wealth stock consumed throughout its service life. This is identical to the approach established by Certified Public Accountants of Australia (CPA), that the “future economic benefits” are equivalent to service potential (CPA, 2013).

The valuation of assets SV via the “future economic benefits” approach reflects the reality of their financial position and business ability, as opposed to the current accounting valuation which adopts the linear depreciation method used primarily for tax purposes and may provide the asset owners with a misleading view in terms of the essential actions to be taken for assets’ management. This thoroughly significant fact is highlighted by the theoretical pioneering research of (Leviäkangas et al., 2019), which refers to a road asset, and points out that the cumulative divergence of the two aforementioned approaches is about 11% only in the first 10 years of the road’s service life by ending up in 200% in approximately 30 years. The purpose of this research is to present a conceptual model for the “future economic benefits” of an asset as a correct asset management accounting that can prohibit over and under estimation of investments and repair debt.

This approach through a dynamic integrated predictive system guarantees the proper functionality and operation of the asset and prohibit false estimation of life-cycle cost. Moreover, the continuous and uninterrupted operation of the infrastructure, the operation of the neighboring settlements, the reduction of the unplanned delays and traffic disruptions and thus preventing any adverse impacts on productivity, mobility and economy in general are safeguarded. The conceptual model will be introduced on road bridges as ones of the most critical and difficult to analyze components in road infrastructure systems.

2 BIBLIOMETRIC ANALYSIS

A bibliometric analysis was performed over the last two decades via the VOS-Viewer software for extracting useful outcomes of maintenance models in multi-components systems, as can be seen in Figure 1 (Chen et al., 2018). The peer-reviewed articles’ searching was performed by the Web of Science (WoS) Core Collection and Scopus bibliographic databases, which are two of the most widely accepted and well-recognized databases for high-quality bibliometric analysis (Shukla, A.K et al., 2019). The two-level structure of keywords and Boolean operators used for data mining among the fields of titles, abstracts and authors keywords into the WoS and Scopus are presented in Table 1.

Our analysis identified researches that either approach generally the issue of systems maintenance with many interdependent components without referring to specific items (Nguyen et al., 2015), (Vu et al., 2014), (Zhang et al., 2015), (Olde et al., 2017) or deal mainly with systems of machinery (Liang et al., 2017), equipment (Iung et al., 2016), (Lee & Pan, 2017) vehicles (Bouvard et al., 2011) etc. The methods applied in the literature are limited to finding optimized maintenance solutions for interdependent system components. In contrary, this

Table 1. Literature search syntax used in WoS and Scopus databases.

WoS: "TS" field
Scopus: "TITLE-ABS-KEY" field
"service value" OR "economic evaluation" OR "multi component system" OR "accounting" OR "BCA*" OR "component*" OR "bridge" OR "asset management"
AND
road OR highway OR freeway OR transport* infrastructure OR transport* investment* OR infrastructure project*OR maintenace

research proposal will investigate the interdependencies of the bridges individual components and expand on the calculation of their SV according to the dynamics of their interactions to orient a more holistic approach to asset management.

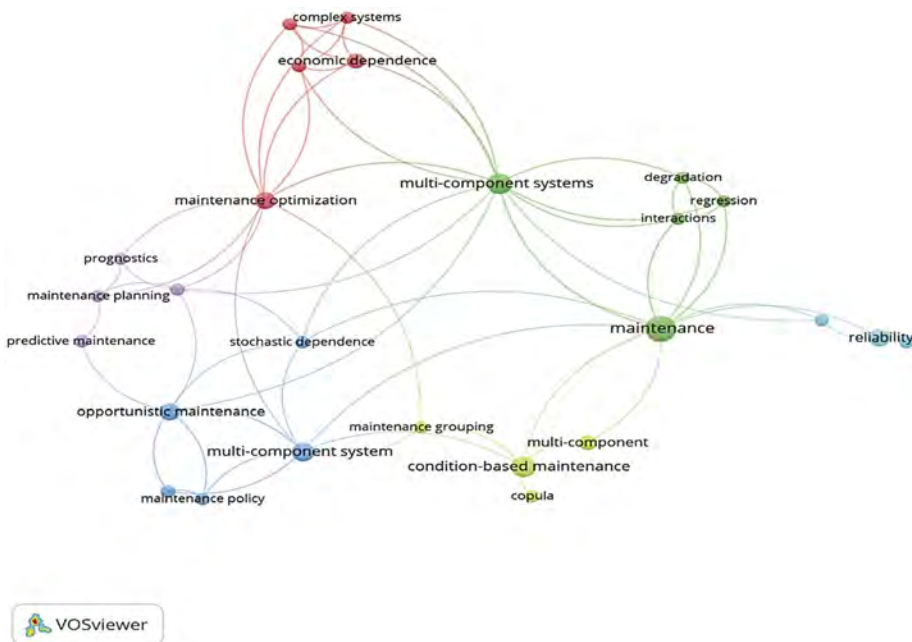


Figure 1. VOS-Viewer for searching maintenance models in multi-component systems.

This new “componentization approach” of infrastructure systems will be performed within a probabilistic framework, by estimating the variables within certain limits, based on experience and available historical data. According to this, the decision-makers will take into account the inherent uncertainties of bridges structures and they will be capable of predicting realistically bridges’ performance capacity in probabilistic terms (Frangopol, 2002), (Sirvio, 2017). Hence, the results will move within safe confidence limits giving more secure predictions. In this way, inadequate and non-optimal solutions derived from purely deterministic models, which does not include the inherent volatility of examined systems, will be avoided (Dhawan, 2005).

A dynamic Bayesian-based approach is a suitable tool that could incorporate the above issues for the reliability assessment of multi-component systems since they deal with interactions between the components of a system or time dependencies (Bensi et al., 2013). Moreover, Bayesian networks provide the merit of updating the probabilistic model in light of new information, hence improving the prediction of the system’s economic performance and reducing the uncertainty of the results (Ramírez & Utne, 2015).

3 CONCEPTUAL MODEL – METHODOLOGY AND IMPLEMENTATION

Bridges are the most neural parts of infrastructure projects not only because they contribute to the preservation of the network's consistency and continuity, offering precious time and cost savings, but also owing to their cost, difficulty in construction and the increased security they have to provide against natural deterioration and seismic hazard (Saeed et al., 2017) (Frangopol & Bocchini, 2012). Any cause that may induce restrictions, disruptions or hazards to their use should be avoided, as it is almost impossible to find alternatives-routes. It is therefore very crucial to acknowledge the bridges health status for the implementation of rational management strategies that maintain their performance at satisfactory levels of operation and safety throughout their service life. Supporter in this venture is the asset management which enables its owners to develop strategies to align their resources with the level of SV throughout the asset's life. Therefore, this process preserves the aforementioned parameters of functionality and safety, dealing timely with durability and reliability issues and keeping assets performance within acceptable levels throughout their life cycle (Frangopol et al., 2017). This knowledge gives an additional benefit because it requires assets' owners to ensure of allocating the required financial resources by avoiding prioritizing the short-term optimal solution. This latter approach hides the real picture resulting in higher future costs (Qiao et al., 2015). The bridge's SV reflects its condition and determines its future performance. The SV of the bridges proposed in this study is calculated using the "future economic benefits" method (OECD, 2013), which applies the annual rate of return generated by the assets and is essentially the same philosophy as the "Present Value" method. The proposed conceptual method will be implemented as a brand-new proposal since its application to infrastructure projects has not been found to exist via a thorough review of international academic articles conducted (Section 2).

The economic valuation of bridge assets will be accomplished by calculating the SV of bridges through a dynamic predictive system as shown in Figure 2. The proposed model will be fed with data from 1.200 bridges belonging to the main and vertical axes located along Egnatia Motorway that crosses North Greece from West to East borders, 640km of the main axe. Real data will be provided by the Inspection and Management Dept. of Egnatia Odos company responsible for the construction and operation of the motorway, based on systematic/frequent inspections and condition evaluations from the last 15 years. For the majority of the bridges, their inspection records start from the time of the first investment (the time of their construction completion and of their setting in service); for some of these bridges (10 % of the population), constructed in 80's or 90's, their deterioration records help to have a better understanding of the environmental/climate impact and of the life-cycle performance of the bridge components and of the whole structures. Various components of these bridges are considered, on the basis of their structural and functional representativeness; beams, slabs and box girders for the bridge superstructures, single or multi columns and walls for the substructures and bearings or monolithic for the connection between their two basic structural parts. Records of over-weighted oversized vehicles and traffic flows are also available to consider the traffic load impact to the deterioration of the proposed bridge network. Componentization based on different initial investment classes, governed by the three basic types of construction method, balanced cantilevering, incremental launching and pre-casting is also possible as it can be based on available as built cost records. Finally, routine, heavy maintenance and inspection cost records will be also available, of the last 15 years of bridge management. Egnatia Motorway is not only one of the biggest road bridge networks, belonging to Trans European Network (TEN), but it is also built with high, uniform and modern standards, and thus represents a typical European road bridge condition.

3.1 *Service value method*

As stated in subchapter 3, OECD (2013) guidelines recommends that an asset should be depreciated via the deduction of its consumed value from stock. The rate of return of unconsumed stock determines the value to be consumed. According Leviakangas et al. (2019), the formula to be used for the accumulated net benefits is shown in Equation 1 below:

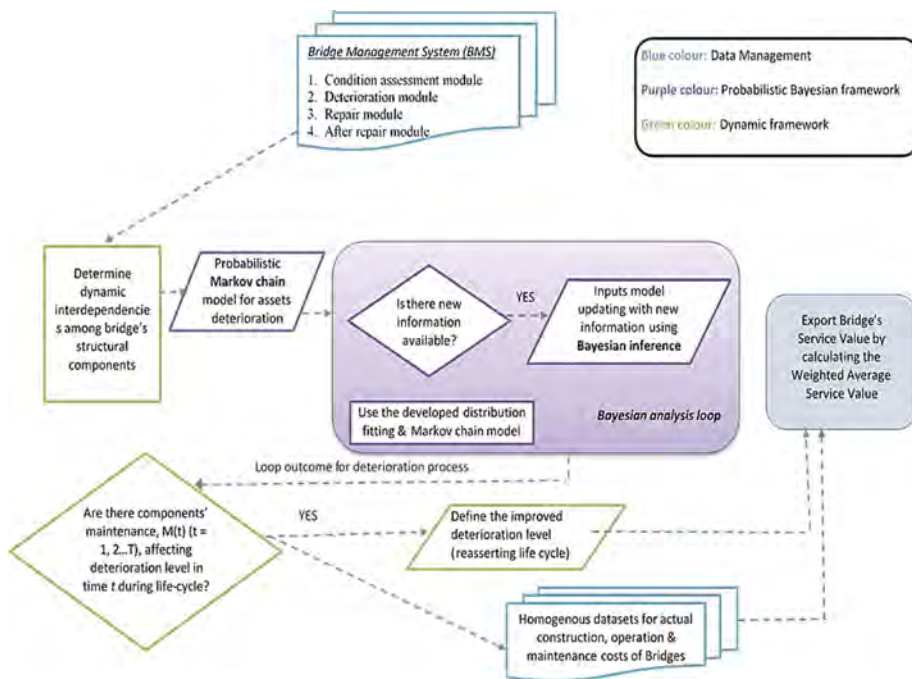


Figure 2. Proposed conceptual model.

$$B_n = (1 + i)^n - I_0 - I_n, \quad n = 0, 1, 2, \dots, t \quad (1)$$

where B_n is the accumulated stock in year n , i is the time value estimated by the asset managers and t is the SV of the asset or the component without any maintenance in its entire life. I_0 is the initial construction cost and I_n represents the improvements or additional investments made to the asset. The SV is given in percentage (%) presented in the Equation 2 below:

$$SV = \frac{(1 + i)^t - (1 + i)^n}{(1 + i)^t - I_0 - I_n} \times 100\% \quad (2)$$

If the return rate i is high then the asset's future benefits are higher, this results to different SV with different decline curves. Moreover, when repairs, renewals and maintenance in general take place for example in time t' , the expected service life of the asset is prolonged from t to k . Equation 3 incorporates these interventions as follows:

$$SV = \begin{cases} \frac{(1+i)^t - (1+i)^n}{(1+i)^t - I_0} \times 100\%, & m \text{ runs from } t' \text{ to } t + k. \\ \frac{(1+i)^{t+k} - (1+i)^m}{(1+i)^t - I_0 - I_{t'}} \times 100\%, & \end{cases} \quad (3)$$

3.2 Bridge componentization system

According the manual of structural and operation evaluation of bridge sufficiency of Egnatia Odos SA (2018), the structural components of a road bridge are: i. substructure, ii. bearings, iii. superstructure, iv. wearing surface, v. transmission embankment, as depicted in Figure 3. This is a system dynamic framework, the deterioration of one component affects the system structure

based on the evaluation system of the company that is similar to the American Valuation System PONTIS and the National Bridge Inventory (NBI). The sufficient rate (SR) used by the company (in line with the Federal Highway Administration (F.H.W.A.)) is based on the periodic visual inspections and structural instrumental measurements on field. According the company's data, the construction cost distribution of a bridge according the construction method is given in Figure 4.

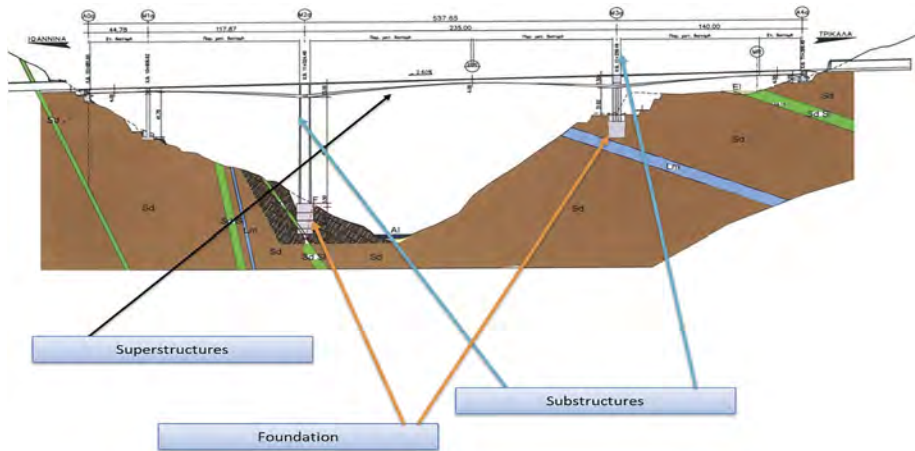


Figure 3. Bridge's structural components.

Based on actual costs from the company's archives, the investment needed to construct a road bridge can be divided between components (accessories, superstructure, substructure, foundation) according the construction method used (incremental launching, balanced cantilever, precast prestressed beams, traditional scaffolding, travelling formwork). The weighted average service value (WASV) for the entire system of a road bridge takes the form given by Leviakangas et al. (2019) in Equation 4:

$$WASV = \sum_{j=1}^4 I_j \frac{(1+i)^{t_j} - (1+i)^n}{(1+i)^n - I_o} \times 100\% \quad (4)$$

where $WASV$ is in year n ; I_j is the relative share of component j of the total construction cost of bridge, expressed as percentage; $j = 1, 2, 3, 4$ the components (accessories, superstructure, substructure, foundation); I_o is the initial construction cost; when a component j is replaced or renewed for a second life cycle, t_j is changed to $2t_j$ and so forth (Figures 4–5).

3.3 Service value and accounting indexes for road bridges

The best asset management strategy is the one that maximizes SV always in relation with the investment (i.e. initial construction cost, repairs, renewals etc.), the last signifies the cumulative investment (CI) providing the value for money (VfM). The best strategy if the one that helps the curve of the ratio $WASV/CI$ to follow a smooth decline over the life-cycle of the asset.

Most accounting systems use the straight-line depreciation method. This method has a major risk that of over or under-depreciation if the real deterioration does not follow the depreciation line. This situation after 30 years (usually for bridges the life-cycle ranges between 50-70 years) can reach a high cumulative difference.

ID	Insp_Date	Bed Protection	SR	Maint_Date	Maint_Action	Units	Price per unit	Total_Cost
1	3/6/2011	5	82.91					
2	30/5/2012	5	81.91	8/8/2012	Joint Repair (m)	22.4	1,500.00 €	33,600.00 €
3	7/3/2013	5	83.91					
4	18/1/2014	5	83.91					
5	12/5/2015	5	83.91					
6	16/3/2016	5	83.91					
7	7/2/2017	5	58.91	5/6/2017	Joint Repair (m)	7.4	1,500.00 €	11,100.00 €
8	15/6/2018	5	58.91					
9	30/5/2019	5	58.91					
10	23/7/2020	5	58.91	5/10/2020	Joint Repair (m)	15.7	1,500.00 €	23,550.00 €
11	5/2/2021	5	58.91					

Figure 4. Bridges' construction costs of maintenance.



Figure 5. Bridge SR after repairs over its life-cycle.

4 CONCLUSIONS

By searching the extant literature, it was evident that there is a limited research regarding the dynamic interdependencies among an asset, in our case, the road bridge. This is a very important issue when comes to operation and maintenance of such structures. The componentization helps to reveal bridge's dynamic interdependencies and thus better estimate its life-cycle as a system and extending its service life. This entirely new approach of bridge's valuation in contrary with the accounting straight line depreciation method reveals that an asset such a road bridge might be seriously underestimated during its life-cycle, if system's structural interdependencies are not taken into consideration. Furthermore, managerial decision-making must be made by unbiased assessments of asset value something that could drive to overestimate its repair debt. The last one coupled with the "Grand Challenge" of reducing life-cycle costs of civil infrastructure projects by 50% by 2025 makes this venture even more noteworthy (Biondini & Frangopol, 2018).

REFERENCES

Bensi, M., Kiureghian, A. Der, Straub, D., 2013. Efficient Bayesian network modeling of systems. *Reliab. Eng. Syst. Saf.* 112: 200–213. <https://doi.org/10.1016/j.res.2012.11.017>

Biondini, F. & Frangopol, D.M., 2018. Life-Cycle Performance of Civil Structure and Infrastructure Systems: Survey, *J. Struct. Eng.* 144(1).

Bouvard, K., Artus, S., Bérenguer, C., Cocquempot, V., 2011. Condition-based dynamic maintenance operations planning & grouping. *Application to commercial heavy vehicles, Reliability Engineering and System Safety* 601–610. <https://doi.org/10.1016/j.res.2010.11.009>.

- Chen, Q., García de Soto, B., Adey, B.T., 2018. Construction automation: Research areas, industry concerns and suggestions for advancement. *Autom. Constr.* 94: 22–38. <https://doi.org/10.1016/j.autcon.2018.05.028>
- CPA (Certified Public Accountants of Australia), 2013. *Valuation and depreciation. A guide for the not-for-profit and public sector under accrual based accounting standards*. Melbourne.
- Dhawan, R., 2005. Usefulness of Probabilistic System Dynamics in Dynamic Decision Making. *International Conference of the System Dynamics Society*. Boston.
- Frangopol, D.M., 2002. Reliability Deterioration and Lifetime Maintenance Cost Optimization. *1st International ASRANet Colloquium on Integrating Structural Reliability Analysis with Advanced Structural Analysis*. Glasgow.
- Frangopol, D.M. & Bocchini, P., 2012. Bridge network performance, maintenance and optimisation under uncertainty: Accomplishments and challenges. *Struct. Infrastruct. Eng.* <https://doi.org/10.1080/15732479.2011.563089>.
- Frangopol, D.M., Dong, Y. & Sabatino, S., 2017. Bridge life-cycle performance and cost: analysis, prediction, optimisation and decision-making. *Struct. Infrastruct. Eng.* 13: 1239–1257. <https://doi.org/10.1080/15732479.2016.1267772>.
- Lung, B., Do, P., Levrat, E. & Voisin, A., 2016. Opportunistic maintenance based on multi-dependent components of manufacturing system. *CIRP Ann. - Manuf. Technol.* 65: 401–404. <https://doi.org/10.1016/j.cirp.2016.04.063>.
- Lee, D., Pan, R., 2017. Predictive maintenance of complex system with multi-level reliability structure. *Int. J. Prod. Res.* 55: 4785–4801. <https://doi.org/10.1080/00207543.2017.1299947>
- Leviäkangas, P., Pargar, F., Sirvio, K., Khabbaz Beheshti, B. & Love, P.E.D., 2019. Service Value and Componentized Accounting of Infrastructure Assets. *J. Infrastruct. Syst.* 25: 1–12. [https://doi.org/10.1061/\(ASCE\)IS.1943-555X.0000497](https://doi.org/10.1061/(ASCE)IS.1943-555X.0000497).
- Liang, Z., Parlikad, A.K., Srinivasan, R., Rasmekomen, N., 2017. On fault propagation in deterioration of multi-component systems. *Reliab. Eng. Syst. Saf.* <https://doi.org/10.1016/j.res.2017.01.025>.
- Marinelli, M., Petrousatou, K., Fragkakis, N. & Lambropoulos, S., 2018. Rethinking new public infrastructure value for money in recession times: the Greek case. *Int. J. Constr. Manag.* 18: 331–342. <https://doi.org/10.1080/15623599.2017.1358131>
- Nguyen, K.A., Do, P. & Grall, A., 2015. Multi-level predictive maintenance for multi-component systems. *Reliab. Eng. Syst. Saf.* <https://doi.org/10.1016/j.res.2015.07.017>
- OECD, 2013. *Understanding the Value of Transport Infrastructure Guidelines for macro-level measurement of spending and assets*.
- Olde Keizer, M.C.A., Flapper, S.D.P., Teunter, R.H., 2017. Condition-based maintenance policies for systems with multiple dependent components: A review. *Eur. J. Oper. Res.* <https://doi.org/10.1016/j.ejor.2017.02.044>.
- Petrousatou, K., Maravas, A., & Saramourtsis, A., 2021. A life cycle model for estimating road tunnel cost. *Tunnelling and Underground Space Technology*, 111, <https://doi.org/10.1016/j.tust.2021.103858>.
- Petrousatou, K., Georgopoulos, E., Lambropoulos, S. & Pantouvakis J.P., 2012. Early Cost Estimating of Road Tunnels Construction Using Neural Networks. *Journal of Construction Engineering and Management*, ASCE, 138(6): 679–687
- Qiao, Y., Dawson, A.R., Parry, T. & Flintsch, G.W., 2015. Evaluating the effects of climate change on road maintenance intervention strategies and Life-Cycle Costs. *Transp. Res. Part D Transp. Environ.* <https://doi.org/10.1016/j.trd.2015.09.019>.
- Ramírez, P.A.P., Utne, I.B., 2015. Use of dynamic Bayesian networks for life extension assessment of ageing systems. *Reliab. Eng. Syst. Saf.* <https://doi.org/10.1016/j.res.2014.09.002>
- Saeed, T.U., Moomen, M., Ahmed, A., Murillo-Hoyos, J., Volovski, M., Labi, S., 2017. Performance Evaluation and Life Prediction of Highway Concrete Bridge Superstructure across Design Types. *J. Perform. Constr. Facil.* 31. [https://doi.org/https://doi.org/10.1061/\(ASCE\)CF.1943-5509.0001051](https://doi.org/https://doi.org/10.1061/(ASCE)CF.1943-5509.0001051).
- Sirvio, K., 2017. *Advances in predictive maintenance planning of roads by empirical models*. Aalto University.
- Shukla, A.K.; Janmajaya, M.; Abraham, A.; Muhuri, P.K., 2019. Engineering Applications of Artificial Intelligence: A Bibliometric Analysis of 30 Years (1988–2018). *Eng. Appl. Artif. Intell.* 85: 517–532, doi:10.1016/j.engappai.2019.06.010.
- Vu, H.C., Do, P., Barros, A., Bérenguer, C., 2014. Maintenance grouping strategy for multi-component systems with dynamic contexts. *Reliab. Eng. Syst. Saf.* 132: 233–249. <https://doi.org/10.1016/j.res.2014.08.002>.
- Zhang, Z., Wu, S., Li, B., Lee, S., 2015. (n, N) type maintenance policy for multi-component systems with failure interactions. *Int. J. Syst. Sci.* 46: 1051–1064. <https://doi.org/10.1080/00207721.2013.807386>.

Powder wastes from concrete recycling as a sustainable source of calcium carbonate mineral admixture

K.M. Masunaga & T. Iyoda

Shibaura Institute of Technology, Koto, Tokyo, Japan

ABSTRACT: Carbonation technology applied to cement-based materials from concrete recycling has been investigated as a promising approach to achieve carbon neutrality and to reintroduce these wastes into concrete's life cycle. In this research, carbon uptake potential of powder wastes from concrete recycling (PWCR) was evaluated. Samples were obtained from recycled concrete aggregate production – Recycled Concrete Aggregate Powder (RCAP), and from dewatered wash-out of returned fresh concrete – Concrete Slurry Waste (CSW). PWCR were used as mineral admixture replacing the sand, and it was observed that RCAP was naturally a fine powder with high CaCO_3 content, resulting in good mortar performance. In contrast, the coarse powder and with low CaCO_3 content CSW reduced mortar's performance. But with accelerated carbonation, carbonated CSW (CCSW) showed satisfactory performance when used in mortar. Therefore, there is high a potential to explore PWCR as a sustainable source of CaCO_3 to be reused as a mineral admixture.

1 INTRODUCTION

Concrete has been an essential material for the development of human society, and inevitably up to 10% of the ready-mix concrete returns to the industry (Xuan et al. 2018). Also, with the increasing deterioration of existing constructions, demolition and reconstruction sometimes is the most practical alternative, given the difficulties and costs of maintaining in use and safely recovering a deteriorated structure, and this generates large amounts of hardened concrete debris. Therefore, it is important to implement concrete recycling effectively to save the consumption of natural resources and to allow a circular and sustainable concrete industry economy (Lu et al. 2018, Ho et al. 2021).

Recycled concrete aggregates have already been reused, after being extracted from the demolished concrete, through a crushing process. A fine powder is produced as a final residue, which has been used as backfill and soil stabilization material, but it has not been incorporated into the life cycle of concrete. Also, from the returned fresh concrete, the aggregates can be separated from the fresh cement paste, through a washing process, and reused. But the solid agglomerated powder that remains, after decanting and filtering the slurry, usually is discarded.

These powder wastes from concrete recycling (PWCR) are composed of cement and aggregates particles, so usually they are not contaminated with other substances and are a high content calcium material. As cement-based materials can spontaneously uptake CO_2 from the air through the carbonation phenomenon, accelerated carbonation of PWCR may produce a material similar to ground limestone powder (calcium carbonate) to be reincorporated into the life cycle of concrete. That is the reason why combining carbonation and concrete recycling can be considered as a Carbon Capture, Utilization and Storage (CCUS) technology, and it has been investigated as one of the most feasible and valuable approaches to neutralize CO_2 emissions in the cement and concrete industry (WBCSD & IEA 2009). In this research, the viability of using PWCR as a source to obtain calcium carbonate mineral admixture was evaluated. Also, accelerated carbonation technology applied to PWCR was investigated as a technique to standardize these materials,

through analyses of the powder's chemical composition and the mechanical performance of mortars produced with non-carbonated and carbonated PWCR.

2 MATERIALS AND METHODS

2.1 Powder Wastes from Concrete Recycling (PWCR)

Two types of PWCR were evaluated: the by-product of recycled concrete aggregate production (Recycled Concrete Aggregate Powder – RCAP) and the dewatered slurry from returned fresh concrete (Concrete Slurry Waste – CSW). Material characterization was done by X-ray diffraction (XRD) and thermogravimetric analysis (TGA). The XRD patterns were obtained using a Bruker AXS D2 PHASER equipped with the LYNXEYE detector. The measurement range was 5° to 60° 2θ with a step-size of approximately 0.025° per second. TGA (Netzsch) was conducted on approximately 50 mg of manually ground samples in open vessel heated continuously in temperature range from 25°C to 1000°C , at a heating rate of $20^{\circ}\text{C}/\text{min}$, in a nitrogen atmosphere, with a flow rate of 150 ml/min.

2.2 Accelerated carbonation methods applied to the PWCR

For solid-air carbonation, the water content of the samples, water-solid ratio (w/s), was varied in mass by adding distilled water. The samples were placed at an accelerated carbonation chamber of 5% CO_2 concentration, 60% of relative humidity (RH), 20°C temperature for 7 days.

For aqueous carbonation, solutions containing samples at a concentration of 25g/l were prepared with potable water containing CO_2 dissolved in it, using a commercial carbonated water maker (Aqueous A) and with distilled water and a gas flow CO_2 concentration of 100% (Aqueous B) and of 5% (Aqueous C), blown into the liquid using a gas washing bottle (scrubbing bottle) with glass filter. In all methods, the solution was stirred at atmospheric pressure using a magnetic stirrer. After the solutions' pH dropped from 12.5 to approximately 8.3, indicating the change in the alkalinity, each mixture was filtered using a paper filter, which retains $7\mu\text{m}$ size particles, and the solid material was dried at 40°C to remove the free water.

2.3 Mortar tests using PWCR

For mortar mix design, Ordinary Portland Cement (OPC) and OPC with 50% ground granulated blast furnace slag (GGBFS) replacement were used as binder. The water/cement ratio (W/C) was set at 0.55 and the sand/cement ratio (S/C) at 3:1. The PWCR types used were RCAP, CSW and the CSW carbonated using solid-air method with w/s >0.50, identified as carbonated-CSW (CCSW). More powder information is presented in section 4. They were added as a sand replacement at 15% content. Also, pure limestone powder (LSP), with specific surface of $6,800\text{ cm}^2/\text{g}$ and average particle diameter of $3.26\mu\text{m}$ and D90 of $20\mu\text{m}$, was used as powder addition (Table 1).

Table 1. Mortar mix design.

Identification	Cement type	Powder addition	Slump flow
1 N	OPC	None	Control
2 B	OPC+GGBFS (50%)	None	Control
3 N-LSP	OPC	Limestone powder (LSP)	+ 39%
4 B-LSP	OPC+GGBFS (50%)	Limestone powder (LSP)	+ 38%
5 N-RCAP	OPC	Recycled concrete aggregate powder (RCAP)	+ 63%
6 B-RCAP	OPC+GGBFS (50%)	Recycled concrete aggregate powder (RCAP)	+ 63%
7 N-CSW	OPC	Concrete slurry waste (CSW)	+ 17%
8 B-CSW	OPC+GGBFS (50%)	Concrete slurry waste (CSW)	+ 9%
9 N-CCSW	OPC	Carbonated concrete slurry waste (CCSW)	+ 15%
10 B-CCSW	OPC+GGBFS (50%)	Carbonated concrete slurry waste (CCSW)	+ 25%

* Slump flow was controlled using polycarboxylic acid ether based high-range water reducer admixture.

2.3.1 Compressive strength test

The test was performed with cylindrical mortar specimens 50 mm diameter and 100 mm height cured in water.

2.3.2 Archimedes porosity test

Specimens were saturated with water in a vacuum chamber and the saturated and submerged masses were measured. After being kept in a chamber at 40°C and 40% RH until mass stabilization, the dry mass was obtained to calculate the porosity using the Archimedes principle.

2.3.3 Evaporation test

After finishing the 28 days curing period, mass variation due to the water evaporation was recorded continuously for mortar specimens 40x40x160 mm. Evaporation condition was 20°C temperature and RH of 60%.

2.3.4 Accelerated carbonation test

After 28 days of water curing, 40x40x160 mm specimens were dried at a 20°C and 60% RH environment for more 28 days and the 2 faces sealed specimens were carbonated in an accelerated carbonation chamber (20°C, 60% RH, CO₂ concentration of 5%). The carbonation depths were measured (in mm) using a phenolphthalein solution sprayed on a freshly split mortar surface. Average values were plotted as function of the square root of the exposure time *t* (in days) to determine the accelerated carbonation coefficient *K* (in mm/ $\sqrt{\text{days}}$).

3 RESULTS AND DISCUSSION

3.1 Material characterization

Figure 1 shows the XRD results of RCAP and CSW before and after being carbonated using solid-air and aqueous carbonation methods. For RCAP, there was a high peak of CaCO₃ and SiO₂, for both non-carbonated and carbonated samples, suggesting that previous natural carbonation occurred during concrete lifecycle and/or during the recycled concrete aggregate production. For CSW before carbonation, it was possible to find a high peak for Ca(OH)₂, but after the solid-air carbonation with w/s 0.50 and aqueous carbonation, the peak changed to CaCO₃. Especially for aqueous methods, the intensity peak for calcite was stronger, making clear the effectiveness of this method for CSW.

From TG-DTA, Ca(OH)₂ and CaCO₃ contents in the samples were quantified (Figure 2). RCAP showed no content of Ca(OH)₂, and high content of CaCO₃ even before carbonation (28%). And after 7 days of solid-air carbonation, changing w/s ratio from 0 to 1.00, or aqueous carbonation, in all samples there was a maximum increase of 4.6% in CaCO₃ content. Differently, for CSW as w/s ratio increased, solid-air carbonation progressed more than in lower water content samples and it was possible to verify complete change of Ca(OH)₂ to CaCO₃, specially for high water content samples.

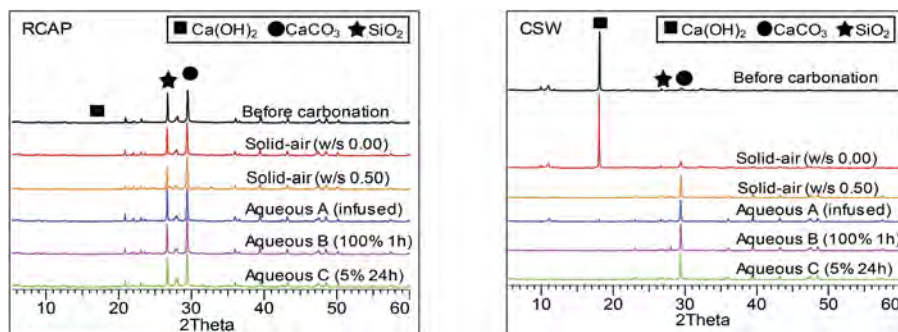


Figure 1. XRD pattern of RCAP and CSW carbonated using different methods.

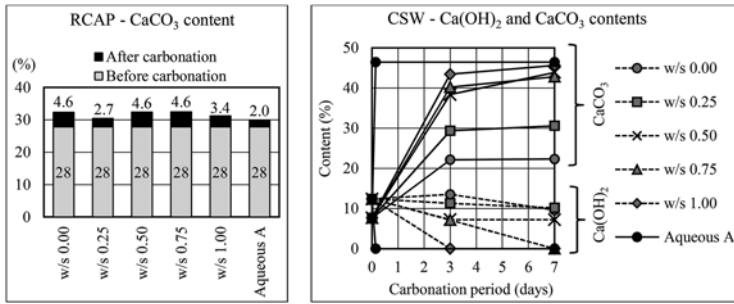


Figure 2. Ca(OH)_2 and CaCO_3 contents of RCAP and CSW carbonated using different methods.

3.2 CO_2 uptake determination

CO_2 uptake was determined as the amount of CO_2 absorbed by the powder during the accelerated carbonation and fixed in the solid phase as CaCO_3 . This was calculated from the mass loss due to CaCO_3 decomposition of the carbonated and non-carbonated samples after TGA (Xuan et al. 2016, Kaliyavaradhan et al. 2020). As shown in Table 2, CO_2 uptake of CSW for the solid-air method increased as the w/s ratio increased. The maximum value was obtained for the aqueous method and was 22.14%, which means that 1 kilogram of the CSW analyzed can absorb approximately 221.4g of CO_2 in optimum conditions. For RCAP, CO_2 uptake varied between 1% to 2% and there was no correlation with the amount of water in the sample. Ho et al. (2021) reported that smaller particles size, less aggregate contamination, and thus a higher content of effective Ca ions, favored carbonation reaction under atmospheric pressure and low CO_2 concentration. Oppositely, the presence of fines from crushed aggregates, which are usually composed of silicate and limestone, decrease the percentage of effective Ca ions slightly and are essentially inert in relation to the carbonation process, reducing the CO_2 uptake. This explains RCAP low CO_2 uptake and CSW high CO_2 uptake, especially for samples with water availability.

Table 2. CO_2 uptake of PWCR samples carbonated using different methods.

Carbonation method		RCAP	CSW
Solid-air	w/s 0.00	1.47	7.23
	w/s 0.25	1.02	12.54
	w/s 0.50	1.49	20.27
	w/s 0.75	2.01	20.96
	w/s 1.00	1.09	21.74
Aqueous	A	1.36	22.14

3.3 Mortar performance

3.3.1 Compressive strength test results

The axial compressive strength test results are presented in Figure 3. It was estimated that the highest resistances were obtained for LSP mixes (with pure limestone powder), but the use of LSP resulted in only early age resistance gain compared to the control mixes N and B and did not affect the final mechanical resistance. About the PWCR addition, mortars with RCAP resulted in high axial compressive strength values. The use of CSW resulted in significantly different strengths for non-carbonated (CSW) and carbonated (CCSW) powder. Carbonation of the CSW improved the mechanical performance of the mortars with this mineral admixture. It was expected to have a slightly increase in early age with the use of non-carbonated CSW, attributed to the high content of hydration products and the seeding effect of C-S-H, which it is said to provide nucleation sites for the growth of hydration products, accelerating the early hydration period and increasing the early strength, but the current results showed a different pattern than observed in the literature (Lu et al. 2018).

3.3.2 Accelerated carbonation test results

The relationships between porosity and carbonation coefficient K and evaporation ratio and the coefficient K are shown in Figure 4 for OPC mortars and OPC+GGBFS mortars.

For OPC mortars, a good correlation could be established between porosity and coefficient K, but for OPC+GGBFS mortars, the differences in carbonation resistance for the mixes could not be explained only by the mortar's porosity. This is an indication that porosity of mortars with GGBFS replacement may have a complex porosity network, which cannot be evaluated considering only the total porosity amount. But when the evaporation ratio was correlated with the coefficient K, a good correlation could be found, both for OPC and OPC+GGBFS binders. For both binders, reduced water evaporation ratio resulted in improvement of the carbonation resistance. This shows that the water available inside the pores is a crucial factor that affects the progress of carbonation. About the effect of powders addition, RCAP addition improved carbonation resistance both for OPC and OPC+GGBFS mortars. On the other hand, the worst performance was obtained for CSW addition.

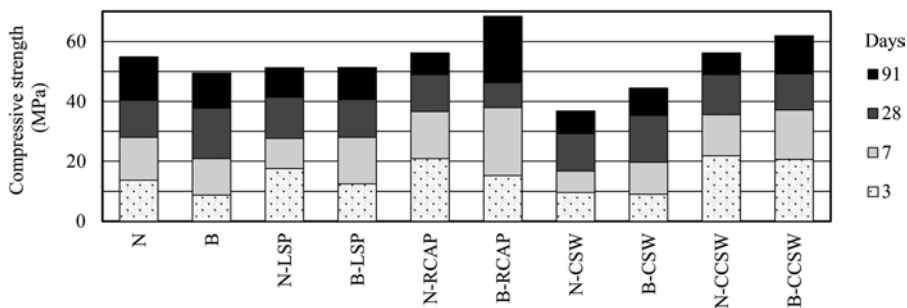


Figure 3. Mortar's compressive strength.

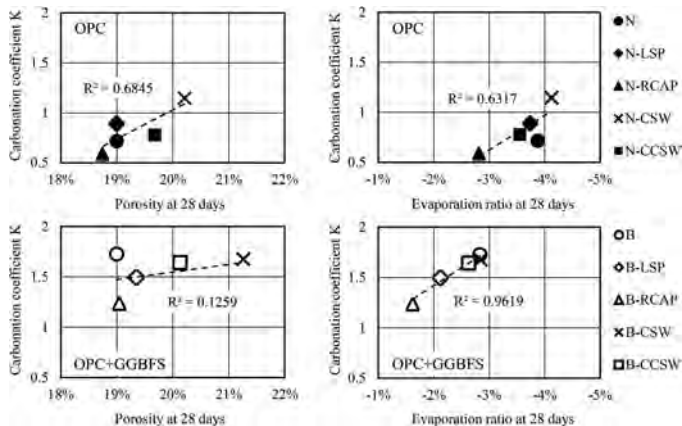


Figure 4. Relationship between porosity and carbonation coefficient K and evaporation ratio and carbonation coefficient K of mortars.

4 DISCUSSION

4.1 Effect of particle size and $CaCO_3$ content of PWCR

Limestone powder is a widely available and low-cost material. Its action combined with cement-based materials has been reported to be complex and dependent on several factors, such as particle size, dosage, polymorph of limestone, cement composition and supplementary cementitious materials (Wang et al. 2018). As shown in session 3.1, PWCR are composed of

hardened cement paste, which can be rich in calcium from $\text{Ca}(\text{OH})_2$ and C-S-H, and of fine aggregate particles, which may have CaCO_3 or SiO_2 in their composition. Therefore, they can be naturally or artificially a source to produce recycled limestone powder.

The effect of using PWCR in the mortar tests seems to be related to the particle size of the powders and the CaCO_3 content. As shown in Figure 5, RCAP is obtained after having undergone a crushing and grinding process, which naturally results in a fine powder. Oppositely, in CSW powder, hexagonal CH crystals and needle like ettringite are present from the ongoing hydration, which agglomerates the particles and results in a coarse powder without a proper treatment, such as drying and grinding. This difference in the particle size was not treated with the solid-air accelerated carbonation of CSW, showing to be one factor that influenced mortar's performance.

Another factor affecting mortar mixes performance was the CaCO_3 content. Cement producers add some percentage of calcium carbonate in industrialized cements, but many studies reported that there is an ideal amount of CaCO_3 to maximize performance of hardened cementitious materials, and that this can be higher than the tolerances regulated by current cement standards. Regarding the potential of reusing PWCR, it has been reported that precipitated CaCO_3 from carbonation of brines rich in Ca ions can potentially provide benefits to cement hydration (mineralogical changes), workability, strength and durability, when replacing cement at 10% mass content (McDonald et al. 2019). Also, carbonated hardened cement paste powder replacing 10% to 20% of cement increased strength up to 90 days in Lu et al. (2018) investigation. This is explained in literature, firstly, by the presence of calcite, that even in low weight percentages is sufficient to lead to formation of the calcium aluminates hemicarboxylate and monocarboxylate, thus to a stabilization of ettringite. And these chemical reactions can result in lower porosity and higher compressive strength. In the experimental tests results, the positive results obtained for the mixes with CaCO_3 from PWCR, especially when combined with GGBFS seems to be related to the extra amount of alumina from this supplementary cementitious material, that affected reactivity of CaCO_3 . The second reason in literature explaining the positive influence of CaCO_3 from PWCR is the combination of additional nucleation and growth sites for hydration products lead to a chemical activation of the hydration of cement (Lothenbach et al. 2008). And finally, even with the use of high levels of calcite, most of them can still act as a filler, filling pores and micro-cracks, and this also explains the strength increase with the use of carbonated powders containing CaCO_3 (Liu et al. 2021). However, for a higher (30%) substitution of cement, there would be less hydration products, causing performance to decrease (Lu et al. 2018).

In this experimental study, PWCR replaced sand, so the filler effect was already expected. Coincidentally, the percentage of CaCO_3 in the powder wastes RCAP and CCSW, was similar and around 40% (Table 3), which resulted in the mortar mixes containing around 4.5% CaCO_3 solid material content, except for the percentage content inside the OPC (Figure 6). This content resulted in satisfactory performance for the mortars evaluated. But for LSP addition, which is a 99% CaCO_3 , there was no increase in performance, even it was the finest powder.

Additionally, there are reports about carbonation of cement-based materials producing not only CaCO_3 , but also (alumina)-silica gel and that it can quickly react with CH and result in the formation of more C-S-H (Zajac et al. 2020). Lawrence et al. (2003) also reported that short-term degree of hydration in mortar containing chemically inert quartz powders for a wide range of fineness (between 180 and 2000 m^2/kg) and cement replacement rates (up to 75%) was always higher than the reference mortar. This experimental study focused only on the CaCO_3 and did not focus on the influence of the supposed inert SiO_2 , nor the amorphous phase of the non-carbonated and carbonated powder wastes. Therefore, these components may also have a positive effect on the hardened cementitious material, especially if treated properly to an adequate particle size, maybe nanoscale particles (Li et al. 2015).

Table 3. $\text{Ca}(\text{OH})_2$ and CaCO_3 content in PWCR.

Content	LSP	RCAP	CSW	CCSW
$\text{Ca}(\text{OH})_2$	0%	2%	10%	2%
CaCO_3	99 %	36 %	7%	44%

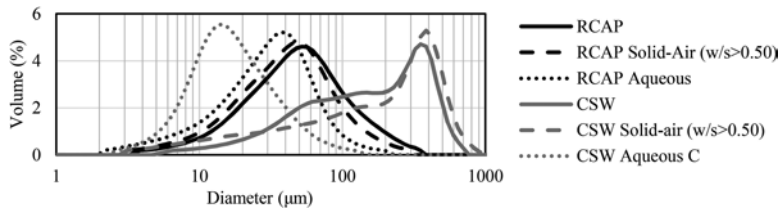


Figure 5. Particle size distribution of PWCR.

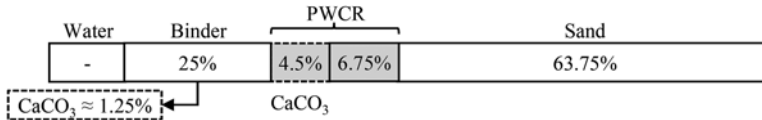


Figure 6. CaCO_3 content in mortars with RCAP and CCSW addition.

4.2 Carbonation applied to CSW for use as a value-added material

From session 3.3, the best mortar performance was obtained for B-RCAP mix, because of the combined filler effect for being a fine powder and hydration acceleration for containing CaCO_3 . However, setting other parameters for mortar mixes evaluation, as shown in Table 4, B-CCSW also showed a satisfactory mortar performance, adding the positive aspect of CO_2 uptake, compared to the mix B-RCAP. In this research, the carbonation technology applied to CSW, was the solid-air carbonation method, resulting in effective CaCO_3 formation, but without significant changes in the particle size distribution (PSD). As shown in Figure 5, the aqueous carbonation method can not only precipitate CaCO_3 , but finer CaCO_3 , not requiring grinding or other energy demanding processes. Therefore, it is expected to achieve even better performance for OPC+GGBFS mortars produced using CCSW carbonated with aqueous methods, transforming it into a value-added material and contributing holistically to the reduction in CO_2 emission, the CO_2 uptake and the concrete recycling.

Table 4. Evaluation of mixes' performance.

Mix design	Parameters			
	CO_2 emission reduction	CO_2 uptake	Concrete recycling	Mortar Performance
1 N	-	-	-	-
2 B	○	-	-	-
3 N-LSP	-	-	-	-
4 B-LSP	○	-	-	-
5 N-RCAP	-	-	○	○
6 B-RCAP	○	-	○	●
7 N-CSW	-	-	○	x
8 B-CSW	○	-	○	x
9 N-CCSW	-	○	○	○
10 B-CCSW	○	○	○	○

* Legend for the symbols:

- Extremely positive contribution
- Positive contribution
- Neutral contribution
- x Negative contribution

5 CONCLUSIONS

- Carbonation of PWCR: CSW showed high content of hydration products and it was a coarse powder. Both solid-air and aqueous carbonation changed the chemical

composition of CSW, transforming a still hydrating material to a chemically stable CaCO_3 . In the solid-air method, increasing the w/s improved the CO_2 uptake, but also stimulated the hydration of anhydrous cement from CSW, making it an even coarser powder. Therefore, it is necessary to have a grinding process (energy) to obtain fine powder material. But the aqueous method showed high efficiency for CO_2 uptake and also precipitated finer CaCO_3 , changing the particle size distribution. Differently, RCAP was naturally a fine powder, with high content of CaCO_3 and SiO_2 , from the crushing and grinding processes and/or previous natural carbonation, and its accelerated carbonation did not change the chemical composition nor the particle size distribution.

- Effect of PWCR in the mortar's performance: Compressive strength and carbonation resistance was improved with the addition of RCAP and CCSW, resulting in better performance than the control mixes. This indicates that there is an unexplored potential to reuse PWCR as a mineral admixture for mortar or concrete. This improvement showed to be related to the CaCO_3 content, which in RCAP and the carbonated CCSW samples was around 40%, resulting in approximately 5% CaCO_3 content of total solid material, and it was obtained regardless of the particle size of the powder, as RCAP was a fine and CCSW was a coarse powder. PWCR addition showed better performance combined with blended cement (OPC+GGBFS). This suggests that the mortar performance was influenced not only by an inert filler effect but also by a chemical effect (changes in hydration) caused by the CaCO_3 from the PWCR.

Therefore PWCR, both CSW and RCAP, can be a source of CaCO_3 . Also, the accelerated carbonation technology showed to be an adequate and valuable method to transform CSW to a value-added material and to promote its re-utilization, incorporating into the life cycle of concrete and leading to a circular and sustainable concrete industry economy.

REFERENCES

- Ho, H.J., Iizuka, A., Shibata, E. 2021. Chemical recycling and use of various types of concrete waste: A review, *Journal of Cleaner Production* 284: 124785.
- Kaliyavaradhan, S.K., Ling, T.C., Mo, K.H. 2020. CO_2 sequestration of fresh concrete slurry waste: Optimization of CO_2 uptake and feasible use as a potential cement binder, *Journal of CO_2 Utilization* 42: 101330.
- Lawrence, P., Cyr, M., Ringot, E. 2003. Mineral admixtures in mortars: Effect of inert materials on short-term hydration, *Cement and Concrete Research* 33(12): 1939–1947.
- Li, W., Huang, Z., Cao, F., Sun, Z., Shah, S.P. 2015. Effects of nano-silica and nano-limestone on flowability and mechanical properties of ultra-high-performance concrete matrix, *Construction and Building Materials* 95: 366–374.
- Liu, B., Qin, J., Shi, J., Jiang, J., Wu, X., He, Z. 2021. New perspectives on utilization of CO_2 sequestration technologies in cement-based materials, *Construction and Building Materials* 272: 121660.
- Lothenbach, B., Le Saout, G., Gallucci, E., Scrivener, K. 2008. Influence of limestone on the hydration of Portland cements, *Cement and Concrete Research* 38(6): 848–860.
- Lu, B., Shi, C., Zhang, J., Wang, J. 2018. Effects of carbonated hardened cement paste powder on hydration and microstructure of Portland cement, *Construction and Building Materials* 186: 699–708.
- McDonald, L., Glasser, F.P., Imbabi, M.S. 2019. A New, Carbon-Negative Precipitated Calcium Carbonate Admixture (PCC-A) for Low Carbon Portland Cements. *Materials* 12(4): 554.
- Wang, D., Shi, C., Farzadnia, N., Shi, Z., Jia, H. 2018. A review on effects of limestone powder on the properties of concrete, *Construction and Building Materials* 192:153–166.
- WBCSD, IEA 2009. Cement Technology Roadmap: carbon emissions reductions up to 2050. Technology Roadmaps: Cement. IEA Technology Roadmaps. OECD.
- Xuan, D., Zhan, B., Poon, C.S., Zheng, W. 2016. Carbon dioxide sequestration of concrete slurry waste and its valorization in construction products, *Construction and Building Materials* 113: 664–672.
- Xuan, D., Poon, C.S., Zheng, W. 2018. Management and sustainable utilization of processing wastes from ready-mixed concrete plants in construction: A review, *Resources, Conservation and Recycling* 136: 238–247.
- Zajac, M., Skibsted, J., Skocek, J., Durdzinski, P., Bullerjahn, F., Haha, M.B. 2020. Phase assemblage and microstructure of cement paste subjected to enforced, wet carbonation, *Cement and Concrete Research* 130: 105990.

Travel time gains VS time constancy - An irresolvable contradiction?

M. Hoffmann

Institute of Transportation, TU Wien, Vienna, Austria

Hoffmann - Consult, Vienna, Austria

ABSTRACT: Systematic analyses of market developments and transport trends are the basis for the evaluation of investments in transport infrastructure in common approval procedures. Traditional cost benefit analysis (CBA) considers time savings between connected locations as a key benefit of the expansion of transport infrastructure. With reference to almost constant time expenditures for mobility, some researchers argue that there are no relevant time savings and thus no real benefits. As the literature analysis and empirical data show, both the time savings between locations after expansion and approximately constant time expenditures for mobility in the transport system over the long term can be observed. Resolving this issue is therefore the key for consistent economic analysis of transport infrastructure investments. Using a location-theoretic model and empirical data, the paper shows that expansion projects reduce transportation costs, increase efficiency, and largely translate the time savings into accessibility benefits. The centralized production and division of labor is then the basis for economies of scale efficiency gains with diminishing marginal utility. As the resulting environmental impacts and resource consumption are not adequately reflected in standard economic theory, the development in transport is largely unsustainable yielding high external costs. A possible solution would thus be to contrast the efficiency gains in the market with the life cycle costs and external costs of these investments.

1 INTRODUCTION

1.1 *Impacts and comparison of projects*

The origins of such an economic evaluation of projects can be found in the development of welfare economics at the end of the 19th century. The first regular systematic comparisons of benefits and costs of public infrastructure projects are known from the U.S between 1930 and 1940. The pressure for more efficiency led to a subsequent standardization and increasing use of cost-benefit analysis (CBA) from 1950 to 1970. Between 1970 and 1980, the concept of life-cycle cost analysis (LCCA) considering all costs and benefits was established. The concept of “whole life cycle costing” (WLCC), developed in the period from 1990 to 2000 takes the stochastic nature of input parameters, possible risks and external effects into account. As life cycle cost analysis requires extensive data and knowledge, it has rarely used in decision practice.

Investigating transport investment projects and alternatives with a cost-benefit analysis (CBA) is a well-established practice in transport planning since decades. The main methods in CBA are Impact Analysis (IA), Utility Analysis (UA), Cost Effectiveness Analysis (CEA), Benefit-Cost Analysis (BCA). The IA is a pure comparison of the pros and cons without overall decision criteria as a first starting point. The UA allows an evaluation according to weighted criteria and is well suited for topics that are difficult to quantify. The CEA contrasts the quantitative costs with a qualitative benefit i.e. how much benefit can be achieved per cost unit. The BCA compares quantified costs and benefits in a limited time frame. Depending on the selected method and parameters the results may vary significantly.

Since no infrastructure project takes place in a vacuum, the decision is usually based on a comparison of existing transport networks without further investment (Option #0) and alternative courses of action (Option #1 to #n) in a given time frame (Figure 1). For any project assessment, the system delimitation regarding function, space, and time has to be assessed. In terms of investment costs considering initial investments or the entire life cycle is a crucial difference. Assessing benefits is critical if only revenues or greater economic effects such as time savings, traffic safety, etc. during service life are taken into account. Since the majority of the costs are incurred in the initial phase, and the benefits are mostly generated later during service life with increasing capacity utilization, the selected interest rate is also crucial as later benefits and costs are depreciated.

From a cost perspective, emissions and impacts on the environment occur primarily during construction and deconstruction, and to a lesser extent during rehabilitation. In the operating phase, there are generally negative effects as a result of traffic emissions which can have a negative impact on the economy. However, as environmental quality is not adequately represented in standard economic theory, mainly negative aspects of transport infrastructure are largely underestimated in decision making. The concepts to incorporate environmental costs range from inadequate (e.g. “willingness to pay”) to promising (e.g. “costs to repair/replace”). As there is still no functioning market for environmental quality in capitalist societies these aspects are underrepresented in economic decisions explaining the low sustainability in the sector (Hoffmann 2019).

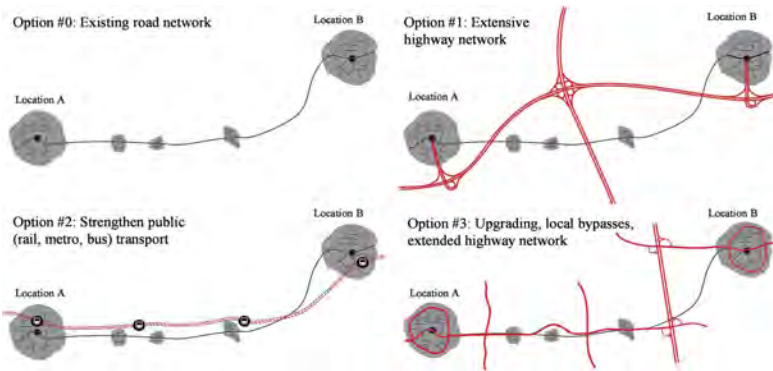


Figure 1. Development and comparison of transport infrastructure projects and alternatives.

1.2 Travel time gains from A to B

In individual choice on traffic mode and route selection as well as in aggregated Cost Benefit Analysis (CBA) the travel time between locations is a key factor. In a typical Benefit-Cost Analysis (BCA) the monetized time savings between locations account for 70 to 80 percent of benefits. The remaining benefits are mainly related to reduced accident rates and lower emissions from fewer traffic jams. The main advantage of using monetized time savings is the possibility to predict and observe increased average speed and reduced average travel time on existing and new routes on the short run. Figure 2 provides an overview on the relevant literature on this topic.

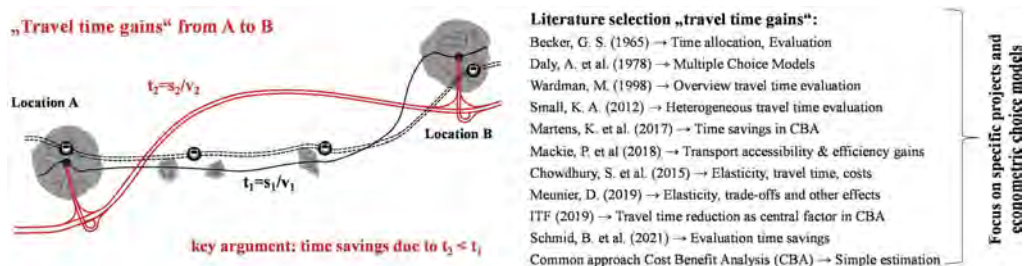


Figure 2. Travel time gains from A to B due to infrastructure improvements with selected literature.

1.3 Time constancy in transport systems

With the CBA becoming more popular in the last five decades the critique regarding the methods, the system delimitation, and the parameters has been mounting. As Flyvbjerg et al. (2003) and others have shown there is ample evidence on deliberate systematic decreasing of costs and increasing of benefits to improve success in the approval process. With the focus on time savings as a key factor there is substantiated critique both regarding the methods and results. The literature survey consistently shows that the total travel time in the entire transport system has remained largely constant over decades (Figure 3). This holds true for regions all over the world despite huge differences both in population, regional development, economic growth and transport investments. According to the CBA that would mean that there are no benefits from time savings. Furthermore, building roads to fight congestion is mostly a temporary solution. Despite observed accessibility gains there are saturation effects on medium to long-term and the improved transport network is becoming congested again. The data consistently shows that increasing transport speed and efficiency leads to longer transport distances and higher transport volumes with overall negative environmental effects. As there is a clear relation between transport network length and efficiency to economic growth, investing in transport infrastructure is not a zero-sum game. In summary, the argument of a lack of benefits due to approximately constant time expenditures in the system is therefore just as untenable as the focus on local time gains of individual projects.

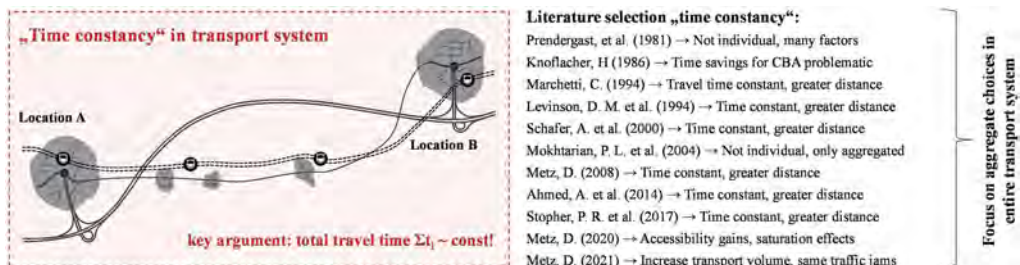


Figure 3. Time constancy in systems regardless of infrastructure improvements with selected literature.

2 AN EMPIRICAL LOOK AT THE WORLD

2.1 Motorization, highway length, and transport

Transportation infrastructure represent an essential social and economic resource. They structure the use of space and enable access to and exchange of people and goods between locations having a significant influence on economic development. The motorization rate increases with economic growth slowing down for a GDP/Capita of \$20,000 to \$50,000 (Figure 4). Apart from saturation effects the quality of public transport in agglomerations is the main explanatory factor. The network length of paved roads increases with the level of wealth, reaching about 4 m/C. on average at about \$10,000 and about 9 m/C. at \$50,000. A highway network emerges only above a certain level of development and wealth at a GDP/C. of \$3,000 to \$5,000 growing also slightly degressive with increases in wealth. In contrast, passenger and freight transport performance grows almost linearly with increasing levels of prosperity and is on average 12,000 pkm/C. and 5,500 tkm/C. per year for a GDP/C. of \$50,000. The large deviations at the same level of wealth are mainly related to territorial, spatial and other structural factors that are not considered here.

2.2 Energy consumption, emissions, investments, and travel time

Technological and economic development are major explanatory factors in relation to the increase in life expectancy, the reduction in birth rates and the development of energy

consumption. As shown in Figure 5 the energy consumption increases degressively with increasing wealth whereas the total CO₂ – emissions per Capita increase at first until a GDP/Capita of roughly \$10,000 and stagnates thereafter. This effect is related to the ability to afford cleaner technologies despite higher energy consumption. However, this currently does not hold true for the mobility sector as both the mobility and the emissions exhibit a degressive increase with increasing wealth.

As positive economic developments generate taxes and funds for further investments, there is a clear relation between economic welfare and investments in transport infrastructure. The wide range of data shows that a comparable level of prosperity does not necessarily require a large high-level transportation network. The degressive growth of the prosperity level with increasing network length, can be seen in the meta-analysis from the literature (e.g. Melo et al. 2013) confirming the decreasing marginal utility for consecutive periods. As the negative environmental impacts are largely not accounted for in the classical economic view it can be assumed that the benefits of additional highways in developed societies will be very limited in most cases.

As previously shown the time savings due to improved (road) transport infrastructure can be directly experienced and measured before and after the implementation of projects. Therefore, this aspect is very well known both at the level of planners and the general population. Revisiting and extending the data on travel time budget proves that the total time spent in traffic largely remains the same regardless of the level of welfare or the spending's on transport infrastructure (Figure 5). With both empirical observations being more or less true, the common models are clearly failing to account for previous and actual developments. Thus, there is a need for a conclusive unifying theory as a basis for an efficient and sustainable transport planning of the future.

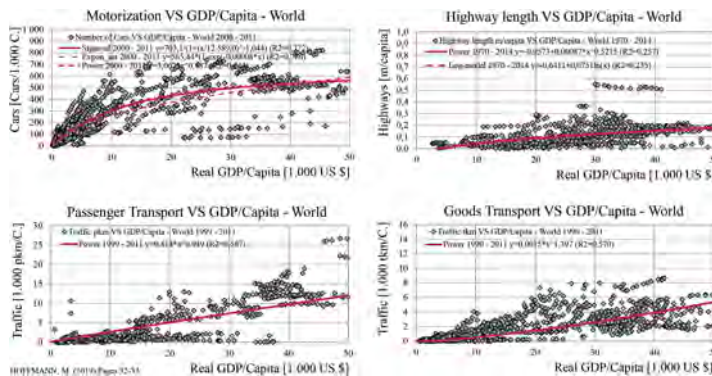


Figure 4. Motorization, highway length, passenger & goods transport VS real GDP/Capita in the world.

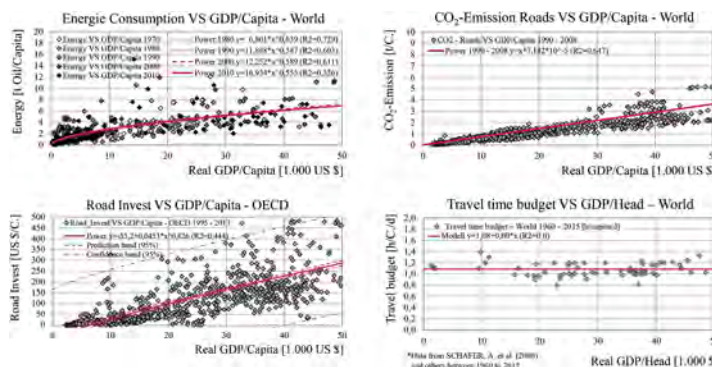


Figure 5. Energy consumption, emissions, investments, and travel time VS real GDP/Capita in the world.

3 SOLVING THE CONTRADICTION

3.1 *A new theoretical framework*

As current approaches are of limited value in solving these contradictions, there is a need for a theoretical framework providing a consistent explanation. This framework must be applicable both for developing and developed countries providing consistent explanation for past and predicted developments. As a framework accounting for all possible factors is beyond the scope, only the main factors shall be addressed here. A largely extended analysis and a vast array of empiric data on these issues can be found in the literature (Gruebler et al. 1991, Rodrigue et al. 2013, Hoffmann 2019).

The theoretical framework in Figure 6 provides an analysis of the impact of transport infrastructure on market equilibrium, consumer prices, regions, and population in three steps. Starting from two central locations each producing a comparable product (“A” \approx “B”) at defined unit costs, the costs for supplying the market will increase with the distance to the production location (costs for transport, wear and tear, loss, etc.). Price levels in this initial state before expansion of the transport network may differ due to differences in conditions at the locations (wage levels, materials, etc.). High transport costs will therefore have a prohibitive effect on the import of the particular product for similar products, thus staking out the primary catchment area of the market. Transport distances beyond the limit of equivalent product prices will accordingly be uneconomical and therefore the exception.

For the second step the transport network between the two locations is significantly expanded increasing transport capacity with decreasing travel time and transport costs as a short-term effect. As the transport costs of the connected locations are reduced equally, the geometric analysis directly shows that the location with lower unit costs in production is favored (expansion of catchment area). In the case of perfect competition and infrastructure equipment, the costs of expansion and any consequential costs for the environment and third parties are offset by the savings from lower prices (consumer return), and the use of additional opportunities of available services. In the case of imperfect markets and neglect of environmental impacts as external costs, there will be an over-provision of transport infrastructure and correspondingly unsustainable developments.

The third step includes the medium to long term reaction of the market participants to the new opportunities created by the expansion of the transport infrastructure. The combination of growth in the catchment area of central locations and further expansion of the transport infrastructure allows more economical central production of the product at location “A” due to falling unit costs for large quantities (economies of scale). This immediately increases consumer returns at both locations due to cheaper products, but leads to the abandonment of production at location “B”. As a consequence, additional jobs and opportunities are created at location “A”, which are lost at “B”. If these losses cannot be compensated by competitive or non-substitutable other products or opportunities, there will be a further migration of population, production, and services from “B” to “A” as an increasingly dominant central location.

An increase in transport costs by internalizing external costs of the transport infrastructure leads to a parallel shift of the cost function for all market participants in the case of one-time access costs (vignette). Mileage-based costs make products from central production locations more expensive and thus have the opposite effect as an expansion of transport networks. The life-cycle costs of transport infrastructure are therefore always paid for indirectly via taxes (with or without taking external effects into account) or directly as a user charge. However, this does not mean that the expansion of transport infrastructure is a zero-sum game. On the contrary, it is the expansion of the transport infrastructure that allows for a division of labor in production and efficiency gains.

As with any production function, there is a decreasing marginal benefit as shown in several meta-studies (e.g. Melo et al. 2013). Extrapolating the economic benefits from past projects generally leads to an overestimation of the benefit/cost ratio, since the benefit decreases degressively and the costs of higher-ranking transport infrastructures increase progressively, especially at central locations. Furthermore, the expansion of transport infrastructure has the effect of redistributing benefits and costs with a shift to high-ranking locations and low-cost production sites (globalization) and is accompanied in the medium to long term by emptying

peripheral areas and strengthening of agglomerations (polarization). Along developed routes, transport prices become less important with products and price levels converging on the global market (homogeneity).

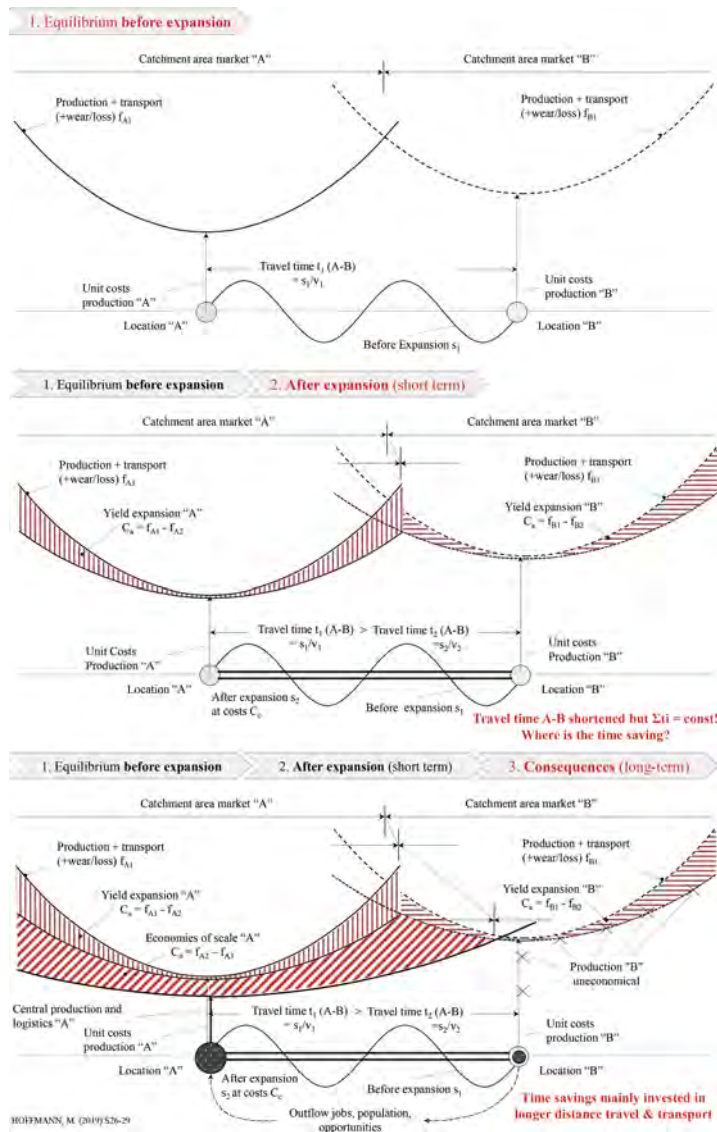


Figure 6. Impact of transport infrastructure on market equilibrium, consumer prices, regions, and population.

4 CONCLUSIONS

The development of regions, population and their economy are closely linked to their transport infrastructure enabling access to resources, products, and markets. The volume of the transport market can be seen as a function of population, economic power, production, and market shares in relation to surrounding locations. If the economic power and population in regions grow, the demand for goods, services and the possibilities increase and the transport market together with the demand for infrastructure rise accordingly. With transport infrastructures

demanding high initial investments and ongoing reinvestments, they constitute a long-term commitment of limited resources. Since decades it is therefore a well-established practice to investigate transport planning strategies and projects with different types of economic analysis.

Traditional cost benefit analysis considers local time savings and avoidance of traffic jams on project level as key benefit of transport infrastructure investments. As these investments have been mostly temporary solutions and the travel time budget in the transport system has remained largely constant critics argue that there are no relevant time savings. Using a location-theoretic model and empirical data, the paper shows that expansion projects reduce transportation costs, increase efficiency, and largely translate the local time savings into accessibility benefits. The centralized production and division of labor is then the basis for economies of scale efficiency gains with diminishing marginal utility. With environmental impacts and resource consumption not being adequately reflected in decision making, the development in transport was and is largely unsustainable yielding high external costs.

Econometric input-output analysis based on elasticities are also a classic method to assess the benefits of transport infrastructure investments on the economy. With diminishing marginal returns towards an economic saturation level looking to past benefits when there was no developed transport network is grossly misleading. Furthermore, the average benefits of projects bundles cannot distinguish between efficient and meaningless specific projects. In addition, the negative effects are systematically underestimated in this type of analysis as there are no functioning markets and limited awareness for environmental quality. Thus, even using revealed and stated preference approaches for accounting of environmental effects largely underrate these costs.

The provided theoretical framework in this paper explains both the short and long-term effects and interactions of transport infrastructure investments on market equilibrium, consumer prices, regions, and population. Furthermore, it explains why high-level transport infrastructure does not benefit all connected locations equally driving competition in extended markets. In this regard transport infrastructure investments are drivers of globalization increasing urbanization in agglomerations and depopulation in peripheral regions. Although this development is largely unsustainable, a radical turnaround with unilateral pricing of external costs has severe repercussions due to increasing consumer prices and loss of competitiveness. As a general strategy, a multilateral shift on a transnational level to a sustainable, efficient, multi-modal transportation system minimizing externalities would be optimal. With diminishing marginal returns and the majority of the environmental impact in the construction phase, an efficient operation and maintenance is key. Finally, with an intact environment as a key future resource countries prioritizing sustainable modes of transport and efficient investments will have a competitive edge on the long run.

REFERENCES

- Ahmed, A., & Stopher, P. 2014. Seventy Minutes Plus or Minus 10-a Review of Travel Time Budget Studies; *Transport Reviews* 34 (5): 607–625. <https://doi.org/10.1080/01441647.2014.946460>.
- Chowdhury, S. & Ceder, A. & Schwalger, B. 2015. The effects of travel time and cost savings on commuters' decision to travel on public transport routes involving transfers; *Journal of Transport Geography* Volume 43, February 2015, Pages 151–159; <https://doi.org/10.1016/j.jtrangeo.2015.01.009>.
- Daly, A. & Zachary, S. & Hensher, D. & Dalvi, Q. 1978. Improved multiple-choice models; in *Identifying and Measuring the Determinants of Mode Choice*.
- Flyvbjerg, B. & Bruzelius, N. & Rothengatter, W. 2003. MegaProjects and Risk: An Anatomy of Ambition; in *International Journal of Public Sector Management* 17(3); DOI: 10.1108/09513550410530199.
- Gruebler, A. & Nakicenovic, N. 1991. Long Waves, Technology Diffusion, and Substitution; *International Institute for Applied Systems Analysis Laxenburg; Reprinted from Review XIV(2): Spring 1991*, pp. 313–342.
- Hoffmann, M. 2019 *Lebenszykluskosten der Straßeninfrastruktur Optimierung von Investitionsstrategien und technischen Maßnahmen, Bau- und Betriebsweisen für Straßenanlagen in ihrem Lebenszyklus*; ISBN 978-3-901912-36-8, Habilitationsschrift (Monographie) an der TU Vienna – Institut für Verkehrswissenschaften; Wien; 560 S.

- ITF. 2019. What is the Value of Saving Travel Time?, ITF Roundtable Reports, No. 176, OECD, Paris.
- Knoflachner, H. 1986. Kann man Straßenbauten mit Zeiteinsparungen begründen?, *Internationales Verkehrswesen*, 38, 454–457.
- Levinson, D. M., & Kumar, A. 1994. The rational locator: Why travel times have remained stable. *Journal of the American Planning Association*, 60(3), 319–332. <https://doi.org/10.1080/01944369408975590>.
- Mackie, P. & Batley, R. & Worsley, T. 2018. Valuing transport investments based on travel time savings—a response to David Metz; *Case Studies on Transport Policy Volume 6, Issue 4, December 2018*, Pages 638–641; <https://doi.org/10.1016/j.cstp.2018.08.002>.
- Marchetti, C. 1994. Anthropological invariants in travel behavior. *Technological Forecasting and Social Change*, 47, 75–88.
- Martens, K. & Di Ciommo, F. 2017. Travel time savings, accessibility gains and equity effects in cost–benefit analysis, *Transport Reviews*, <https://doi.org/10.1080/01441647.2016.1276642>.
- Melo, P. C. & Graham, D. J. & Brage-Ardao, R. 2013. The productivity of transport infrastructure investment: A meta-analysis of empirical evidence; *Regional Science and Urban Economics Volume 43, Issue 5, September 2013*, Pages 695–706; <https://doi.org/10.1016/j.regsciurbeco.2013.05.002>.
- Metz, D. 2008. The myth of travel time saving. *Transport Reviews*, 28, 321–336. <https://doi.org/10.1080/01441640701642348>.
- Metz, D. 2020. Time constraints and travel behavior; *Transportation Planning and Technology*, <https://doi.org/10.1080/03081060.2020.1851445>.
- Metz, D. 2021. Economic benefits of road widening: Discrepancy between outturn and forecast; *Transportation Research Part A: Policy and Practice Volume 147, May 2021*, Pages 312–319; <https://doi.org/10.1016/j.tra.2021.03.023>.
- Meunier, D. 2019. Mobility Practices, Value of Time and Transport Appraisal, *International Transport Forum Discussion Papers, No. 2019/12*, OECD Publishing, Paris.
- Mokhtarian, P.L. & Chen, C. 2004. TTB or not TTB, that is the question: a review and analysis of the empirical literature on travel time (and money) budgets, *Transportation Research Part A: Policy and Practice*, Vol. 38, Issues 9–10, Pages 643–675, ISSN 0965-8564, doi.org/10.1016/j.tra.2003.12.004.
- Nadiri, M. I. & Mamuneas, T. P. 1996. Contribution of highway capital to industry and national productivity growth; FHWA Report; USA.
- Prendergast, L. S., & Williams, R. D. 1981. Individual travel time budgets. *Transportation Research A: General*, 15, 39–46. [https://doi.org/10.1016/0191-2607\(83\)90014-6](https://doi.org/10.1016/0191-2607(83)90014-6).
- Rodrigue, J.P. & Comtois, C. & Slack, B. 2013. *The Geography of Transport Systems*, 3rd Edition ISBN: 978-0-203-37118-3 Routledge, NY.
- Schafer, A. & Victor, D. G. 2000. The future mobility of the world population; *Transportation Research Part A* 34 (2000) 171–205; [https://dx.doi.org/10.1016/S0965-8564\(98\)00071-8](https://dx.doi.org/10.1016/S0965-8564(98)00071-8).
- Schmid, B. & Molloy, J. & Peer, S. & Jokubauskaite, S. & Aschauer, F. & Hössinger, R. & Gerike, R. & Jara-Diaz, S. R. & Axhausen, K. W. 2021. The value of travel time savings and the value of leisure in Zurich: Estimation, decomposition and policy implications; *Transportation Research Part A* 150 (2021) S186–215; <https://doi.org/10.1016/j.tra.2021.06.015>.
- Small, K. A. 2012. Valuation of travel time; *Economics of Transportation Volume 1, Issues 1–2, December 2012*, Pages 2–14; <https://doi.org/10.1016/j.ecotra.2012.09.002>.
- Stopher, P.R., Ahmed, A. & Liu, W. 2017. Travel time budgets: new evidence from multi-year, multi-day data. *Transportation* 44, 1069–1082. <https://doi.org/10.1007/s11116-016-9694-6>.
- Wardmann, M. 1998 The Value of Travel Time: A Review of British Evidence; *Journal of Transport Economics and Policy* Vol. 32, No. 3 (Sep., 1998), pp. 285–316 (32 pages); <https://www.jstor.org/stable/20053775>.

Reliable estimation of investment and life-cycle costs from road projects to single road assets

M. Hoffmann

Institute of Transportation, TU Wien, Vienna, Austria
Hoffmann - Consult, Vienna, Austria

V. Donev

Institute of Transportation, TU Wien, Vienna, Austria

ABSTRACT: The estimation of investment costs of road projects is a key task at every stage of planning and implementation. From the initial project idea to detailed planning and legal approval, the costs of transport infrastructures play a decisive role for investors, authorities, and the public. Although each project is different and some deviations between estimation and actual costs are to be expected, there is ample evidence from the literature on systematic underestimation and the main reasons for this effect. Beyond investment costs, reliable estimations of life cycle costs from single assets and projects up to entire road networks are of an increasing importance to determine budgeting needs, preserve asset value, and define contracts between stakeholders. In all cases, systematic methods and a large database on road projects and individual measures are needed to provide a sufficient basis for cost estimations and validation. This paper tries to fill this gap by providing unit costs both at the project and asset level for construction and rehabilitation measures with adjusted prices for the year 2022. Thereby, the cost estimates are based on extensive research and collected cost data from projects on regional roads and highways in Austria over the last two decades. In addition, the paper presents calibrated standardized live cycle costs for key road assets together with life cycle cost factors providing the means to estimate life cycle costs based on construction costs alone. Finally, the adjustment of prices for different regions and years of construction are highlighted, allowing for a validation of individual project appraisals.

1 INTRODUCTION

1.1 *Construction costs and construction prices*

The provision of transport infrastructure requires high initial investments as well as ongoing reinvestment with a long-term commitment of funds due to extensive service lives of these assets. Therefore, the estimation of investment costs of these projects is a key task at every stage of planning and implementation. From the initial project idea to detailed planning and legal approval, the costs of transport infrastructures play a decisive role for investors, authorities, and the public. Despite their importance in many cases, the provided information is based on rather rough estimations instead of a thorough statistical analysis. Furthermore, the information on the price basis, the reference year or which items are included or not included in the calculation are rather vague. In many cases it is therefore difficult to distinguish between price inflation, price increases due to unforeseen circumstances or regulatory requirements, and deliberate deception about actual costs.

Apart from individual circumstances of projects, it is important to understand the principal connection between costs factors and the development of construction costs and prices. According to EUROSTAT, the output prices of contractors depend on the development of the factor prices (e.g. material, labour, energy), the productivity, and a profit margin. The total costs for the client include additional costs (e.g. VAT, planner fee) and an additional profit. Apart from cost factors, there will be a final selling price on the market depending on

the supply and demand. These final prices represent what was actually paid and what shall be analysed further in this paper (Figure 1).

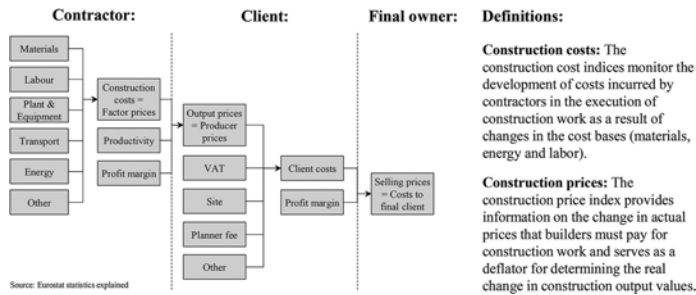


Figure 1. Input factors and difference between construction costs and prices explained.

1.2 Regional cost factors and price indices

Although every transport construction project is different, there are systematic similarities that have to be accounted for. In general, the prices for similar goods as well as construction works may differ both between regions and reference years due to differences and changes in the input factors as well as the market situation. Therefore, the national and international statistic bodies provide a systematic analysis on cost and price changes over time. The provided construction cost indices describe the monthly, quarterly, or yearly change of costs incurred by contractors based on the comparison of a weighted average of the prices of a basket of goods and services. The construction price indices describe the change of final market prices that builders must pay on a similar basket. Moreover, the construction costs and prices between different regions or countries can also be described in a similar way based on a representative basket. In this regard, Figure 2 provides the basis for the comparison of baskets as well as an example for adjusting projects costs for different years. In the second example project prices from one region are converted to those of another region based on purchasing power parities for civil works in Europe. As a rule for cost estimations and price comparisons, it should be mandatory to always provide information on the year and the region as well as adjusting for purchasing power and price changes over time. Furthermore, additional information on the project specifics and the sources of the price estimates should be provided to allow validation and updating.

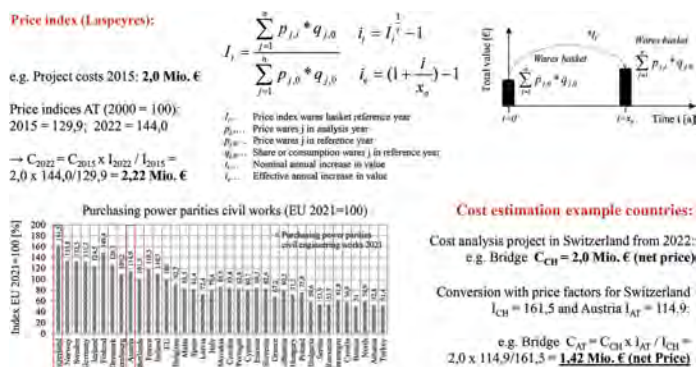


Figure 2. Price index from annual baskets of goods and purchasing power parities (PPP) with examples.

1.3 Development of construction costs and prices in Austria

Depending on the market situation, prices for goods and services may change over a comparative period. A general increase in prices in a sector is referred to as inflation, while falling prices are

referred to as deflation. The consumer price index indicates how the prices of weighted representative goods and services of private household's change compared with a reference year. The consumer price index is therefore an important benchmark for wage negotiations and overall market development. The cost and price indices also play an important role in life cycle cost analysis. They are the basis for the adjustment and comparison of project costs from different years of construction for a reference year as well as a prerequisite for the determination of future costs and prices. In addition, prices in contracts can be negotiated as fixed or as variable prices from a given base year and adjusted accordingly with these indices. According to the data from Statistics AUSTRIA, the consumer price index increased in average with +2,2% per year. The year 2022 was truly exceptional, as the consumer prices increased by +8,6%. The construction prices for civil engineering works, road works and bridges increased in average with +1,85%, +1,87%, and +1,55% per year in the analysis period. In contrast, the construction costs for roads and bridges increased in average by +3,66% and +3,49% per year. Comparing construction cost and price increases reveals a systematic annual gap of 1,79% and 1,94%.

Figure 3 shows an analysis of the development of construction costs and construction prices for roads and bridges from 1990 to 2022 with a simple forecast to 2030 based on linear regression. This systematic gap means that by doing nothing the profit margin of the civil construction sector in Austria would decrease by the same amount every year. However, as this is not an uncommon situation, there are a few ways out of this dilemma. The first possibility is to be more innovative and efficient, increasing the productivity every year. A second way would be to shrink market supply by reducing the number of companies and employees in the sector or by finding a cheaper work force. A third way are cartelization and price-fixing to ensure survival on a difficult market. A fourth possibility is reducing the quality of materials and civil works resulting in reduced functional quality, safety, and service life on the medium to long run. There is sufficient evidence in the construction sector showing the exploration of each of these possibilities with a varying degree of success. Beyond these systematic considerations, the price indices are used in this paper to adjust the provided unit prices to 2022 (Hoffmann 2019).

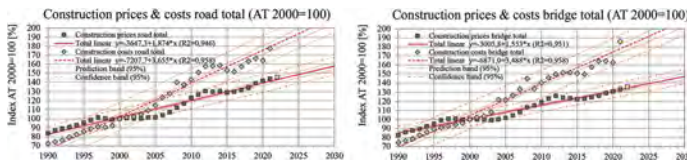


Figure 3. Construction cost and price indices development for road and bridge works in Austria.

2 ROAD CONSTRUCTION PRICES

2.1 Unit prices of highways and regional roads

The road construction costs are all final unit prices for the year 2022 per square meter or lane kilometer including 20% VAT. These unit prices include the entire range of construction works from pavements and civil structures in an unspecified amount (Figure 4). The construction prices of highways amount to an average of 1.522 €/m² and a median of 1.146 €/m² ($n=26$) resulting in an average of 9,0 Mio. €/lane.km and a median of 6,79 Mio. €/lane.km. The rehabilitation costs cover mainly small to medium size projects with average costs of 289 €/m² and a median of 226 €/m² ($n=32$) leading to 1,65 Mio. €/lane.km in average and a median of 1,41 Mio. €/lane.km. The adjusted unit prices for regional roads are significantly lower mainly due to lower share of civil structures (e.g. bridges and tunnels), lower traffic volumes, as well as lower legal requirements. The average unit prices for constructing regional roads amount to 713 €/m² and a median of 569 €/m² ($n=90$) resulting in an average of 2,82 Mio. €/lane.km and a median of 2,12 Mio. €/lane.km. As regional roads are comparatively older, the average costs of 205 €/m² with a median of 169 €/m² ($n=80$) translating into 0,71 Mio. €/lane.km in average and a median of 0,56 Mio. €/lane.km cover the entire range from

small repairs to replacement. The distribution of the unit prices can be approximated by a normal or other distributions, with unit prices being right skewed with the mean being larger than the median due to a few projects with exceptionally high unit prices.

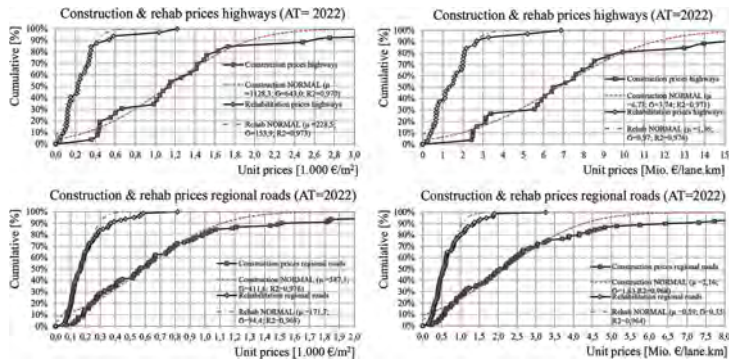


Figure 4. Unit prices highways and regional roads in Austria (prices 2022).

2.2 Unit prices bridges and tunnels

The analyzed unit prices for bridges and tunnels cover both projects on regional roads and highways of various size, materials and construction techniques in Austria. A deeper analysis on the contribution factors to the unit prices is feasible but beyond the scope of this paper. The unit prices of rehabilitation measures can be clustered depending on initial condition, type of M&R, and impact duration in small, medium and large measures (Hoffmann 2017, 2019, Hoffmann & Kammersberger 2012). As shown in Figure 5, the mean unit prices for road bridges in 2022 are 2.150 €/m² with a median of 1.896 €/m² ($n=125$) resulting in an average of 10,31 Mio. €/lane.km and a median of 9,00 Mio. €/lane.km. Very short bridges exhibit significantly higher average unit prices due to the foundation works being distributed over a limited bridge area. Bridges with a large span usually result in higher unit prices due to sophisticated statics and construction. The rehabilitation prices of bridges amount to 872 €/m² with a median of 717 €/m² ($n=230$) resulting in an average of 4,11 Mio. €/lane.km (median 3,59 Mio. €/lane.km).

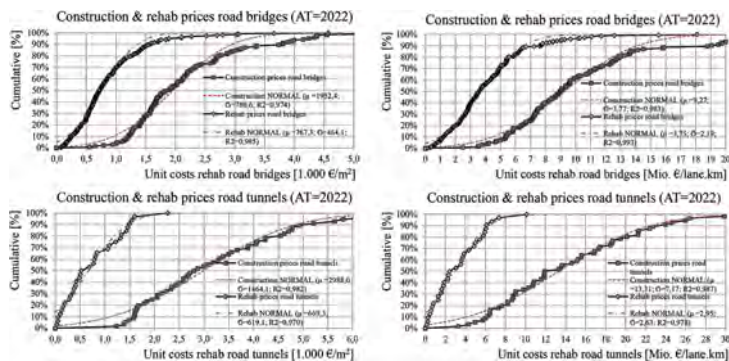


Figure 5. Unit prices bridge and tunnels construction and rehabilitation in Austria (prices 2022).

The mean unit prices for road tunnels are 3.229 €/m² with a median of 2.839 €/m² ($n=56$) resulting in 14,21 Mio. €/lane.km and a median of 12,62 Mio. €/lane.km. For rehabilitation, the mean unit prices are 753 €/m² with a median of 605 €/m² ($n=32$) resulting in 3,28 Mio. €/lane.km (median 2,73 Mio. €/lane.km). In contrast to road bridges covering the full range from small to large measures, the tunnel data on rehabilitation consist mainly of small to

medium rehab due to a rather young asset stock in Austria. With extensive distress type and M&R measures on asset element level already available, the price database on road assets can be extended even further.

2.3 Unit prices pavement works

In this paper, the unit price analysis of asphalt pavement works covers structural measures which result in a sustained substantial improvement of the pavement condition and a corresponding extension of service life. The analyzed measures cover full-depth asphalt replacement including improvements in the unbound layers as well as partial-depth asphalt replacement (surface and binder layer). Furthermore, surface layer replacement and surface treatments/micro-surfacing are covered. The unit prices are analyzed both based on their cost distribution per square meter as well as the economies of scale unit costs and the total paved area. Together with service lives these economy of scale costs functions is the key to an advanced pavement management with optimal treatment selection, timing, and work-zone length (Donev & Hoffmann 2020, Hoffmann 2019). Typical full-depth asphalt replacements exhibit mean unit prices of 84 €/m² or 0,29 Mio. €/lane.km ($n=95$) with typical asphalt layer thickness from 12 to 18 cm. Treatments with surface & binder replacement show unit prices of 39 €/m² or 0,13 Mio. €/lane.km ($n=166$) and typical asphalt layer thickness of 9 to 12 cm. The replacement of surface layers with a thickness of 3 to 5 cm has mean unit prices of 23 €/m² or 0,074 Mio. €/lane.km ($n=138$). Surface treatments have a typical layer thickness of 1 cm exhibiting mean unit prices of 7 €/m² or 0,023 Mio. €/lane.km ($n=40$). The analysis in Figure 6 shows consistently declining unit costs with increased work-zone length or pavement area as the fixed costs are distributed and a higher efficiency is achieved.

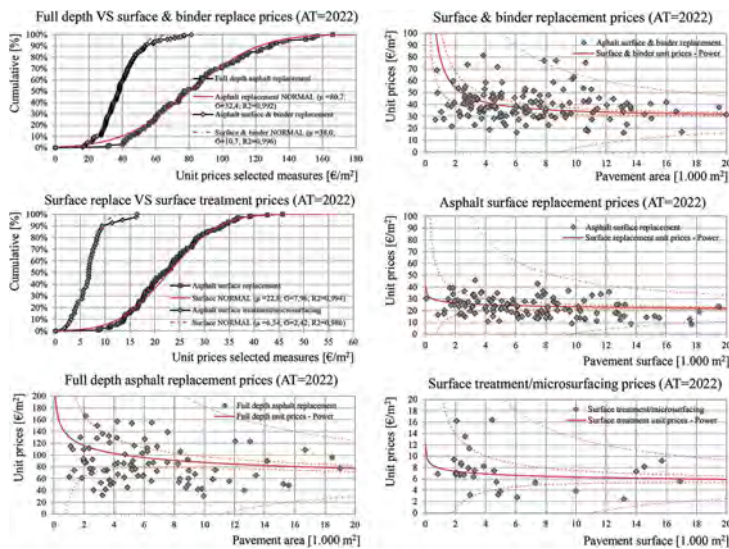


Figure 6. Unit prices pavement measures from full depth to surface treatment (prices 2022).

3 STANDARDIZED LIFE CYCLE COSTS

3.1 Standardized deterministic life cycle

In the fields of transport infrastructure cost-benefit analysis with aggregated condition grades and cost-benefit criteria are employed in Pavement Management (PMS) and Bridge Management Systems (BMS). Since 1970 these approaches have been extended towards considering economic

impacts from “cradle to grave” with deterministic life cycle cost analysis (LCCA). Starting between 1990 to 2000 extensive research has been conducted into the integration of user and environmental aspects in decision making. Due to the stochastic nature of material parameters and loading a quantitative assessment of structural condition, reliability and risk are the main focus in current research on life cycle costing of transport infrastructure (Dhillon 2010, Hoffmann 2019).

With the focus on generalized investment and life cycle costs in this paper the stochastic nature of both construction costs and service lives will not be addressed here. Instead, the emphasis will be on a standardized framework for calculating deterministic life cycle costs of selected road assets based on an extensive costs database. Deterministic continuous models describe a functional relationship between determined input parameters x_i and precise outcomes y_i based on a deterministic function $f(x_i)$ without any variation. In such models, a hypothetical exact relationship between input parameters and outcomes without uncertainty or unknowns is assumed. Thus, a predicted cost or condition performance will always be the same for all assets or asset elements, resulting in identical service lives. In order to account for deviations in asset costs or performance, these deterministic models are commonly aligned (calibrated) to the actual development.

The presented standardized framework for a deterministic life cycle cost analysis in Figure 7 provides the necessary terms, parameters, and formulas to calculate total costs, present value, annual costs, condition performance, and residual asset value. The example shows a comparison of a simple replacement cycle with a rehabilitation prior to failure. In this case, the rehabilitation option yields lower annual costs being the economic solution. The condition performance in the framework is modelled using a power function. The residual asset value is calculated based on the remaining service life of the assets. In the example, the comparison of the investment alternatives shows that there are no sunk costs if assets are still needed and a rehabilitation is efficient. The results of such standardized deterministic life cycles can be used in early planning stages, cost estimations, and asset valuation as well as a validation of M&R recommendations. Furthermore, such standardized deterministic LCC can be extended to full stochastic LCC both at the project and the network level e.g. with a Monte Carlo Simulation (MCS).

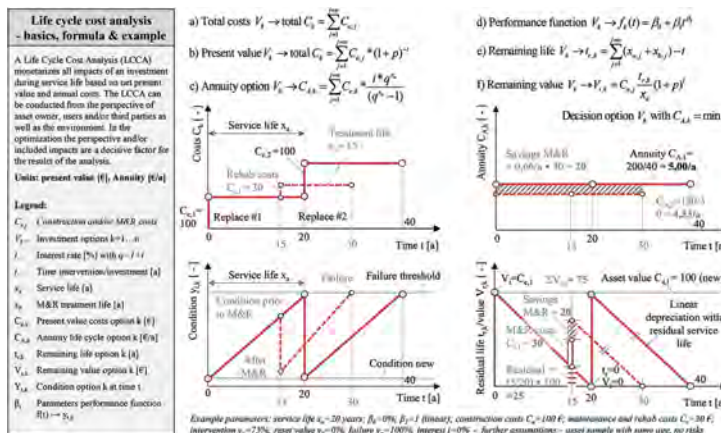


Figure 7. Standardized deterministic LCC with total costs, annual costs, condition, and residual value.

3.2 Standardized deterministic LCC for pavement, bridges & tunnels

The standardized deterministic life cycle costs for pavements, bridges and tunnels build on previous research (Hoffmann 2017, 2019, Hoffmann & Kammersberger 2012) with a largely extended database on costs of road projects from 2022. The standardized pavement life cycle covers planning, construction, crack sealing, surface replacement and a surface & binder replacement as well as operation and administration costs for 60 years (Figure 8). The

resulting pavement life cycle costs on this basis amount to 190-200 €/m², a present value of 120-125 €/m² and average annual costs between 5-6 €/m². For a typical regional road with 7,5 m width this translates into total costs of 1,5 Mio. €/km, a PV of 0,9 Mio. €/km and annual costs of 40 k€/km.

The standardized life cycle costs for road bridges and road tunnels are calculated based on median construction prices, as the costs distributions are skewed due to a few projects with very high unit prices. In the case of bridges, land use, planning, construction as well as small, medium and large-scale rehabilitation until deconstruction are considered in an 80-year cycle. The total costs including operation and administration amount to 4.800-4.900 €/m², a PV of 2.700-2.800 €/m² and annual costs of 110-120 €/m². The total bridge costs for a typical width of 10 m are thus roughly between 47,5-50,0 Mio. €, a PV of 26-28 Mio. € and annual costs of 1,1 to 1,2 Mio. €/km.

The standardized life cycle costs for road tunnels include land use, planning, construction as well as small, medium and large-scale rehabilitation together with decommission in a 90-year cycle. The total costs including operation and administration amount to 7.500-7.700 €/m², a PV of 4.100-4.300 €/m² and annual costs of 160-180 €/m². The total tunnel costs for a typical width of 10 m can be estimated with 75-77 Mio. €, a PV of 41-43 Mio. € and annual costs of 1,6 to 1,8 Mio. €/km. Although the presented standardized life cycle costs of pavements bridges and tunnels consider construction costs on highway level as well, the provided estimates mainly address the regional road network. For highways the provided life cycle costs would be at least 10-20% higher mainly due to the safety and environmental standards as well as significantly higher operation and administration costs.

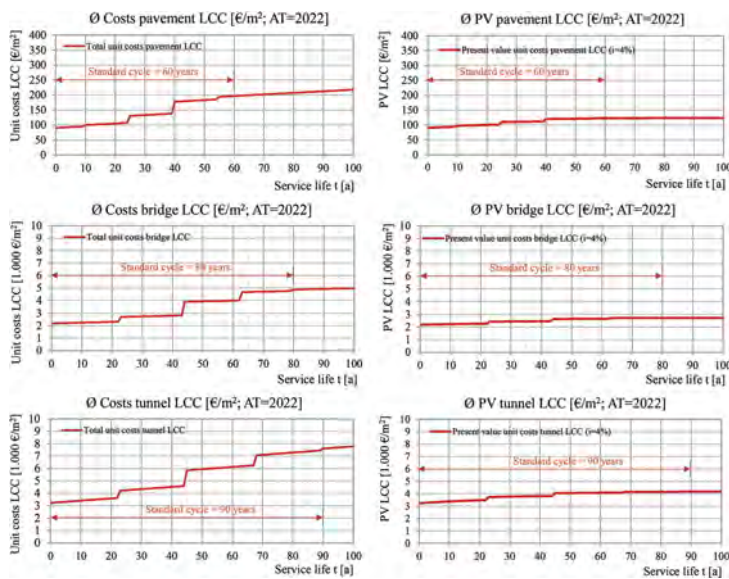


Figure 8. Standardized life cycle costs road pavements, bridges & tunnels in Austria (prices 2022).

4 CONCLUSIONS

The estimation of investment costs of road projects is a key task at every stage of planning and implementation. From the initial project idea to detailed planning and legal approval, the costs of transport infrastructures play a decisive role for investors, authorities, and the public. Despite their importance in many cases the provided information is based on rather rough estimation instead of a thorough statistical analysis. The presented research aims to close this

gap providing the basis for a reliable estimation of investment costs from road projects to single assets. Furthermore, calculating LCC from single assets and projects up to entire networks is of increasing importance to determine budget needs, preserve asset value, and define contracts between stakeholders. In all cases, systematic methods and a large database on road projects and specific measures with unit prices and impact duration are needed to provide a sufficient basis for estimation and validation.

Apart from individual circumstances of projects it is important to understand the principal connection between costs factors and the development of construction costs and prices. Adjusted prices for different regions and years of construction are a crucial precondition for any cost estimation and validation. Based on extensive research and projects on regional roads and highways in Austria over the last two decades, the paper provides unit construction and rehabilitation prices for highways and regional roads for the reference year 2022. Furthermore, the unit prices on asset level for construction and rehabilitation works on road bridges and road tunnels are given. The analyzed pavement measures cover surface treatments, surface layer replacement as well as partial-depth and full-depth asphalt replacement with local improvements in the unbound layers.

Beyond construction prices, the paper shows a framework for calibrated standardized deterministic life cycle costs. The provided terms, parameters, and formulas allow a simple calculation of total costs, present value, annual costs, condition performance, and residual asset value. Drawing on previous research and an updated database on construction and M&R measure unit prices from 2022, the paper provides standardized life cycles for pavements, bridges and tunnels in Austria. The provided total costs, present value and annual costs are a sound basis for the validation of project cost estimates, asset valuation and investment decisions. As standardized distress catalogues and M&R measures for all main road assets have already been developed, the next step will be the extension and implementation in an asset management software.

ACKNOWLEDGEMENT

The presented research on cost estimation and life cycle costs of road assets was not funded by others sources or third parties and is largely based on the methods and database from previous research. As a basis for several national guidelines on cost estimation and cost-benefit analysis the price database was largely extended in 2022 thanks to data from regional road administrations of Carinthia, Styria, Upper and Lower Austria as well as the highway operator ASFINAG. Without these valuable contributions the provided results would not have been possible.

REFERENCES

- Dhillon, B.S. 2010. *Life cycle costing for engineers*. Boca Raton: CRC Press Taylor & Francis Group.
- Donev, V. & Hoffmann, M. 2020. Optimization of pavement maintenance and rehabilitation activities, timing and work zones for short survey sections and multiple distress types. *International Journal of Pavement Engineering* 21(5): 583–607. <https://doi.org/10.1080/10298436.2018.1502433>.
- Hoffmann, M. 2017. *Holistic asset management and life cycle costs of road tunnels*. In J. Bakker, D. M. Frangopol & K. van Breugel (eds), *Life-Cycle of Engineering Systems: Emphasis on Sustainable Civil Infrastructure*. London: Taylor & Francis Group.
- Hoffmann, M. 2019. *Lebenszykluskosten der Straßeninfrastruktur Optimierung von Investitionsstrategien und technischen Maßnahmen, Bau- und Betriebsweisen für Straßenanlagen in ihrem Lebenszyklus* [Life cycle costs of road infrastructure]. ISBN 978-3-901912-36-8. Habilitation. Vienna: TU Wien.
- Hoffmann, M. & Kammersberger, A. 2012. *Asset management and life cycle cost optimization for bridges on network, asset and element level*. In A. Strauss, D. Frangopol & K. Bergmeister (eds), *Life-Cycle and Sustainability of Civil Infrastructure Systems*. London: Taylor and Francis Group.

Legal governance for BIM – rights management and lawful data use

B. Weber

Institute for Information Systems, Hof University, Hof, Germany

M. Achenbach

Office for Structural Safety, LGA, KdöR, Hof, Germany

ABSTRACT: The use of BIM-modeling (BIM) within the building life cycle depends on different (specialist) models as well as a detailed as-built-model. The legally compliant transfer of data and models is decisive for the vision of a consistent use of BIM. Past legal research has mainly dealt with the question of copy and IP rights in contracts. The new EU legal framework of data law is now a game changer as codified legal rules for data use are on their way. The paper will reflect these requirements and link them to the relevant ISO norms. The paper will show how legal governance of BIM-models can be designed by a consistent model rights management which is linked to the technical delivery of information and present guidelines for a legally compliant transfer of BIM-models and data, promoting the trustworthy sharing of data and models within the building life cycle.

1 OBSTACLES FOR COMPLIANT DATA USE IN CONSTRUCTION LIFE CYCLE

1.1 *Legal uncertainty as inhibiting factor of model exchange*

Sharing data and the exchange of BIM-models as “shared digital representation of a built asset to facilitate design, construction and operation processes to form a reliable basis for decisions” (DIN EN ISO 19650, hereinafter: ISO 19650) is often declined by participants of the building process referring to legal uncertainties. Changing paper-based or pdf-based (planning) to BIM, questions as the authentication of participants and the integrity of documents as well as the description of BIM-model rights within the construction life cycle arise. Moreover, sharing data including BIM-models in a common data environment (CDE) must be designed according to new EU Law. “CDE” is defined by ISO 19650 as agreed source of information for any given project or asset for collecting, managing and disseminating information through a managed process, whereas the term “data space” is used in a wider sense as market for data, data products and services (European Commission 2020).

1.2 *Different special models in the construction life cycle require open rights management*

The use of BIM within the complete building life cycle depends on different (specialist) models, i.e. planning models, structural engineer models and technical building equipment models as well as a detailed and correct as-built-model (Borrmann et al. 2021). There exist two general approaches to organize the rights management according to copy right and design law. In theory, a BIM-model could be created and then enriched by information of subsequent adaptations. Legal consequence would be installing one rights holder of one holistic model seeking to achieve all license rights for his legal entity. Any new model, i.e. of the structural engineer subsequently to the architect, would be legally based on the original model and then seen as a mere adaptation or transformation of the original model requiring consent of the original model author and/or holder of the right to exploitation.

A different approach prefers the use of linked models (Beetz et al. 2021; Scherer et al. 2014). From the legal perspective, linked models are easier to handle although rights of exploitation must be spread over different legal entities. Different models implicit the existence of different authors as rights holders and require therefore a rights management while transferring the BIM-model. If the use of BIM-models is limited to one contractual relationship within the planning period, i.e. between an architect and the builder or the general contractor, participants in the building period will not get all sufficient rights to use the model. In any case, there won't be a rights transfer to the period of use or reuse of a building as builder and operator of the building will often differ. Consequently, the transfer of rights must be agreed for contractual as well as subsequent purposes which go beyond the legal entities of contracting partners.

1.3 *Gap between delivery of models, technical and legal information*

Codified law and contractual agreements create legal obligations which are often not integrated into the technical processes. This creates harmful effects on the one hand as liability for contract breaches may arise. On the other hand, value-adding activities as sharing data or models are not undertaken due to the unclear legal situation although data sharing rights had been conceived. The separation of technical and legal information creates a serious obstacle to the use of a BIM-model during the construction life cycle. As long as the legal information is only stored in the frame of the contractual relationship of the initial participants, it is not very likely that the legal information will be transferred from planning to construction and then to operation requiring each a separate contract with the subsequent participant of the construction process. The separation of legal and technical information will also impede the use of the legal information for the "Digital Building Pass" and for possible conversion of buildings and therefore decline the sustainability of construction life cycles. The use and documentation of rights will only be successful if the legal information is handed over with the technical information within the complete life cycle, e.g. by annotated IFC-files. Three hypotheses are presented in this paper:

- (1) Legal uncertainty can be solved by a standardized Data Governance Model and rights management.
- (2) Data Governance and rights management should be developed from a legal-entity based to an open data ecosystem-oriented perspective.
- (3) The fulfilment of legal Data Governance and rights management can only be secured if legal data are transferred parallel or inclusive to technical data and models.

The paper will show how legal uncertainties can be resolved by a structured rights management as well as sharing data based on a legally compliant Data Governance model respecting the new EU legal framework. It will also demonstrate that data spaces within the complete construction life cycle depend on an open rights management enabling data sharing outside the limits of a contractual relationship. In Section 2 a brief description of the legal and interdisciplinary research method is given. The governing legal framework is analyzed in Section 3. Proposals are made in Section 4 to include the legal information into the general information delivery within construction projects. Finally, the results are summarized in Section 5. The paper does not deal with questions of liability apart from the rights management.

2 METHODOLOGICAL APPROACH

2.1 *Legal doctrine and interdisciplinary approach*

"Legal doctrine means the description and explanation of legal groundings and solution schemes for the law applicable. It seeks to explain the law by analyzing code regulation, jurisprudence and legal sciences based on a system of sentences as definitions and principles. In contrast to natural or technical sciences, normative criteria can be described and discussed but not verified as true or false." (Weber & Achenbach 2023). Legal research as normative science seeks to explain and justify ratio of value decisions and hierarchies (Möllers 2020). New technologies must be searched and interpreted in the light of existing or upcoming legislation. The method of legal doctrine was applied in this paper in the context of new technologies sharing data and models, i.e. BIM, as well as a new legislative framework of EU law regulating the use and sharing of data.

The interdisciplinary approach means applying methods of different disciplines aiming not only to set up multidisciplinary perspectives but to integrate them in order to resolve complex problems and create a better understanding of them (Repko et al. 2021; Roberts 2017). The research of technical norms and standards is mainly technical. Models and structures represent knowledge which can be transformed to information, e.g. by norms and standards. The combination of the technical models with the perspective of the legal doctrine aiming to integrate legal requirements into the technical process can create an interdisciplinary research approach (Weber & Achenbach 2023). In this way the structured compliance approach as transforming material law into technical processes creates an interdisciplinary method itself (Weber 2020).

According to the method described above, the codifications of IP rights, especially copyrights, have been analyzed including their traditional implementations in bi- or trilateral contracts. Secondly, the upcoming EU legal framework of data law, i.a. the Data Governance Act (DGA), has been considered with focus on the legal requirements of sharing data in data economies and of transferring BIM-models accordingly. In a third step, the existing bundle of technical and organizational standards related to information management in the construction sector has been researched as they state practical and technical sharing of data and delivery of information in a CDE as well as the question of handling BIM-models.

2.2 *Further development of data governance and rights model*

Whereas data governance is part of research in different disciplines since years (see Mahanti 2021 with a literature overview), legal data governance is an upcoming research field as the codification is just on its way (see below in section 3.2.). Some authors still deny the necessity of a general data law widening the existing data protection law (Kühling 2021). Based on a structured compliance approach, Weber has developed a data governance and rights model which implements the legal and ethical requirements in a holistic way aiming to include all legal disciplines, i.e. data law, data protection law, IT-law, competition law, antidiscrimination law as well as sustainability and ethics (Weber & Gernert 2022). This model was already linked to the postulate of “data sovereignty” within the construction process (Weber & Achenbach 2023) and was widened to the transfer of data and models in a CDE by the current research.

3 ANALYSIS OF LEGAL FRAMEWORK AND RELATED RESEARCH

3.1 *Intellectual property rights and contractual implementation*

xPast legal research and practice about BIM have dealt with the question of Intellectual Property (IP) and copy rights as well as their implementation in contractual provisions because a codified legal framework of data use and data rights was missing (Bellenger & Blandin 2019; BIM4INFRA 2020; Eschenbruch 2019; Klemm-Albert 2018; Richard 2020; Wessendorf 2019). It is no surprise that the indication of the missing or rudimentary codified legal framework for BIM in the field of construction law comes from French and partially German literature (Richard 2020; Weber & Achenbach 2023) as both countries are mainly governed by codified law in contrast to the Common Law governed countries as US and UK which are mainly based on case law. Whereas the legal work in the construction domain concentrates more on technical standards and norms below the level of codification, the field of general data law is still enlarging tremendously since the last wave started with the General Data Protection Regulation (GDPR) in 2018, followed by the DGA in 2022 and the draft of Data Act in 2022. The handling of BIM-models has therefore to be widened from the mere contractual to a holistic perspective of codified data law and technical standards.

3.2 *EU legal framework for data governance*

3.2.1 *Definition of data governance*

Data governance in general can be defined as a system of policies, rules, standards, processes, practices and structures, roles and responsibilities, controls, and decision rights to oversee the

management of data. It should not be confused with the technical management of data. Legal data governance is currently not defined by law. On 30 May 2022 the EU has adopted the so called “Data Governance Act - DGA” which will be applicable by 24 September 2023 for new and by 24 September 2025 for existing data intermediators (European Parliament & Council 2022). As the DGA does not provide a definition, legal data governance was defined by Weber (Weber & Achenbach 2023; Weber & Gernert 2022) as the legally compliant handling of data as part of the corporate governance or process compliance. A legally compliance data governance model therefore includes six dimensions of legal model check: (1) the compliant use of data, (2) data protection, (3) data quality, (4) data security as well as the (5) observance of competition law, IP rights, trade secrets (and other relevant law) and (6) the ethical, sustainable and non-discriminatory use of data including transparency and explainability of data use and methods. As the paper focusses on the legally compliant use and transfer of BIM-models with the construction life cycle, the aspects of data governance are described as follows: lawful data use which means sharing the BIM-data legally in a CDE and building up data infrastructures according to the DGA and a rights management handling the rights of the participants legally according to their contribution and role in data spaces within the complete life cycle of a building.

3.2.2 *Legal provisions of DGA for handling BIM*

Data Governance and compliance have been addressed as important aspects of digitalization of the construction sector (Weber-Lewerenz 2022). Data Governance for BIM was discussed even before the DGA was enacted (Alreshidi et al. 2018). The requirements of the DGA for BIM has been treated by the authors regarding data sovereignty within the construction process (Weber & Achenbach 2023). At first, the DGA regulates the exchange of data aiming to promote data sharing of sovereign data owners while separating data intermediation and the use of data (Art. 12 DGA). Data intermediation services are those which establish commercial relationships for the purposes of data sharing between an undetermined number of data subjects and data holders on the one hand and data users on the other. There are two important exemptions to the application of the DGA. The obligations of data intermediates do not apply to data services of aggregation, enrichment or transformation aiming to add substantial value to them and license the use of the resulting data to data users, without establishing a commercial relationship between (an undefined number of) data holders and data users. Secondly, the DGA is not applicable to closed contractual relationships (Art. 2 par. 11c DGA). This includes services which are exclusively offered to one data holder in order to enable the use of “his” data and services that are used by multiple legal persons, but in a closed group. Consequently, supplier or customer relationships and collaborations established by contract do not have to fulfill the provision of separation of services and data. Applying DGA to CDE and BIM, the relevant question is the open structure of the data sharing. BIM is enrolled in four variations (Borrmann et al. 2021) as described in Figure 1.

From the legal perspective the level of data exchange is decisive: “Little closed BIM” as an insular solution has the legal consequence that no data sharing with other legal entities is to be agreed upon, and the DGA is not applicable. “Little open BIM” can be within the scope of the DGA if the specialist model and data are shared multilaterally. “Big closed BIM” is excluded from the provisions of DGA if it is limited to a certain construction project with mutual but closed legal relationships. This leaves the main field of application of DGA in BIM for “Big open BIM” with the establishment of a CDE in open structures.

3.3 *Technical norms and standards referring to BIM*

Standardization organizations have set up certain norms regarding information management in the construction sector including BIM. ISO 19650 seeks to support the collaboration of stakeholders in the building life cycle. Rights management of data and IP rights are only linked to the contract management. Legal data governance is currently not included in the exchange information requirements. Nevertheless, information shall be stored in a suitable knowledge store for the use in future projects. This creates the obstacles described above for the open use of data beyond the current project. The DIN EN ISO 16739 (DIN EN ISO 16739-1) introduces the IFC classes for data sharing in the construction and facility management industries as

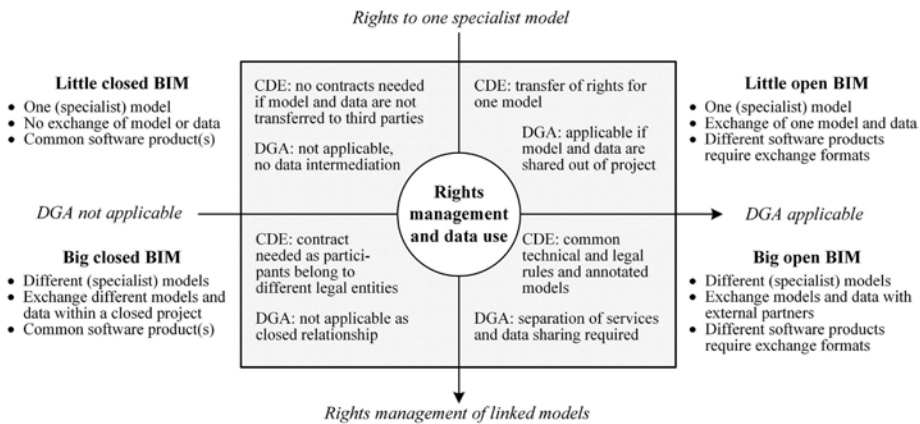


Figure 1. Rights management and application of DGA for different variations of BIM.

an open standard using XML for the data schema. The readability of XML as a text-based format bears the potential of transferring legal information in metadata. An automated rights management should therefore be compliant to IFC-based data sharing according to ISO 16739. Draft of ISO 17549-1 (DIN EN 17549-1) contains rules for BIM-modelling regarding the information structure to exchange data templates and data sheets for construction projects. Data exchange can take place including attributes as geometry, technical specifications, official requirements and economic aspects. Object association enables to associate sources of information such as documents, approvals or constraints to object definitions. Document association means to associate documents to objects indicating external files. Documents could even be referenced to their entirety, e.g. data sheets or product brochures. This means that document association would also work for associating legal materials, e.g. license sheets. The draft states that typical document meta data such as issue date, editor etc. could be covered by association whereas the document content would remain with the external files. This could reduce the volume of data exchange.

4 IMPLEMENTING LAWFUL DATA USE AND RIGHTS MANAGEMENT INTO INFORMATION DELIVERY AND LINKED MODELS WITH BIM

4.1 Compliant use of data

4.1.1 Data sharing and/or data intermediation according to DGA

The DGA applies to data spaces or infrastructures irrespective of the question if a platform or any virtual data environment is created. The DGA provides that data intermediaries are not entitled to offer data and services in one technical infrastructure by the same legal entity. The DGA therefore applies to the creation and transfer of BIM-models within a CDE, as BIM includes the design of a BIM-model as a service and the transfer and sharing of the respective data. There exist two possibilities to organize a construction project in a CDE compliant to DGA:

- (1) Operating the CDE in a closed project environment including all participants bound by contracts or
- (2) Separating the role of sharing data to an undefined number of participants (data hub) from offering services as designing a BIM-model (service hub).

Services as designing an architecture model or structural planning must then be provided by the stakeholders directly or via a platform being a separate legal entity from the data intermediary (service hub). BIM-models as result of planning services could be stored in decentralized information containers (Schmid & Blandini, 2021). The technical implementation has already been described according to ISO 19650 (Hagedorn et al. 2022). Separation of data and model can be handled via information referencing to an external information source (model referencing information) (Klemt-Albert & Bahlau 2017).

Figure 2 shows that CDE as “Big open BIM” can also be established compliant to DGA by a centralized data sharing while separating data and services in two hubs. If no separate service hub will be created, planner and other BIM service provider must offer their services decentralized, sharing only the data representing the models created as results of their services by the data hub, not the services themselves (Weber et al. 2023). A platform as data hub could support the stakeholders in acquiring data as asset-information and other resources. Essential prerequisite of the data hub is neutrality which creates trust and acceptance of the data holder and data user. Data cooperatives or adequate corporate structures could serve as trustworthy data intermediators.

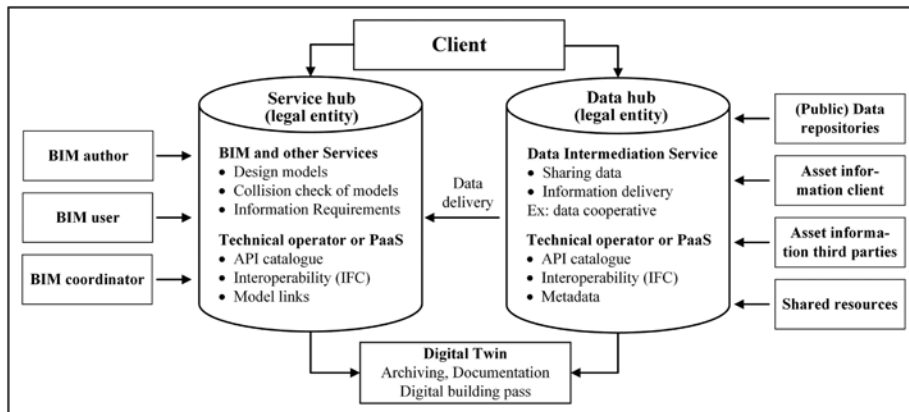


Figure 2. CDE separating services and data intermediation compliant to DGA; (PaaS: platform as a service).

4.1.2 Collision check of models as service

According to the provisions of DGA the check of model conflicts by the BIM-coordinator in open BIM is difficult to handle. On the one hand, the BIM-coordinator merges data from different sources and models which could create a role of intermediation. On the other hand, the BIM-coordinator himself offers the service of coordination and clash detection. Again, only data should be shared via the data hub while communicating the modification requirements of a model which are versioning, result of collision check etc. If practice shows that separation of data exchange and clash detection service will not work, the BIM-coordinator must fall back into the closed structure of a construction project. In both cases, the BIM-coordinator is not entitled to share data out of the project. Otherwise, he takes the risk to slide into the role of a data intermediary being forced to refrain from his services of coordination and model check.

4.1.3 Attribution of files exchanging data

Data sharing via decentralized, federated information container aiming to share data and BIM-models requires common standards in a CDE (BuildingSMART 2022). Challenges in decentralizing the data storage are a persistent, transparent storage management where data are up-to-date and findable by common formats and attributes. As shown above, technical standards, (open) data formats and common standards for the description of meta data as type of file, indexing and description of rights as comments in properties or attributes are suitable for legal information and should be agreed upon in the information exchange requirements. The exchange of IFC-files show that different attribution fields complicate the data exchange. If one field is marked as optional and the other participant rejects optional fields, data exchange won't work or at least not mutually (Borrmann & Koch 2021). Therefore, legal information should be linked to data drops obligatorily.

4.1.4 Legal authentication by qualified electronic signatures BIM- and XML-files

Personal signatures have the function of authentication of the author, integrity of the document and content proof. The signature must be tightly linked to the document. Paper-based documents can be annotated by handwriting and fulfil the said requirements. The legal requirement of authentication of BIM-authors or other annotating persons can be fulfilled by a qualified electronic

signature (QES), Art. 25 par. 2 (eIDAS 2014). The QES is based on an asymmetric encryption including a public and a private key. The certificate must be issued by an accredited certification provider. Signing a BIM-File by QES, i.e. an IFC-file, would meet the legal form. If a BIM-model should be annotated, i.e. by building permission authorities or for a structural safety check, the annotation of the original IFC-file would be saved to an XML-file which again have to fulfil the legal requirements which is to say a QES to be documented, i.e. signature element. Message integrity as non-alteration of parts of the content after signing and authentication as proof of possession are guaranteed. The trustworthiness of the certificate can be checked by the receiver (IBM 2022).

4.2 Rights management: Intellectual property rights and business secrets

The most preferable solution of BIM-rights management would be the integration of a standardized data and rights management scheme for metadata in relevant ISO norms. Limitation of data rights including business secrets and time limits could then be commented and serve for the rights management based on a standardized rights-and-role-concept. Until a common standard will enter into force, the rights management must be imposed by contract aiming legal certainty, preferably also via standardized contract templates which reflects the metadata descriptions.

5 CONCLUSIONS

The use of BIM for the description of the whole life cycle is based on the idea that models are enriched with information and can be passed over to subsequent steps. This requires a solid legal framework to share data. Data governance and rights management will only be legally compliant and to handle in practice within the complete construction life cycle, if data sharing and transfer of BIM-models include the technical and legal information shared. Standardized description of specialist models and typical data and rights management by standard contract clauses are a first step. Aiming the use and re-use of legal data in the whole building life cycle, legal data governance and legal information have to be included in the exchange information requirements to reach practicability. Technical data must be attributed at least with a legally binding description of (1) model or data task (2) quality, (3) author and (4) license information. Relevant information must be presented to the model user.

Further interdisciplinary discussions will focus on the practicability of implementing the legal information into the meta data attribution scheme, i.e. the relevant field of IFC-attribute, preferably not an optional but mandatory field of data exchange, as well as into link-models, i.e. into the index file or the creation of legal information containers.

ACKNOWLEDGMENTS

This research work was enabled by the support of the German Federal Ministry of Economic Affairs and Climate Action to the funding of the GAIA-X project “intelligent Empowerment of COstruction industry - iECO”.

REFERENCES

- Alreshidi, E. & Mourshed, M. & Rezgui, Y. 2018. Requirements for cloud-based BIM governance solutions to facilitate team collaboration in construction projects. *Requirements Engineering* 23 (1): 1–31.
- Beetz, J. & Pauwels, P. & McGlenn, K. & Tormä, S. Linked Data im Bauwesen. In A. Borrmann & M. König & C. Koch & J. Beetz (eds) 2021. *BIM-modeling, Technologische Grundlagen und industrielle Praxis*: 223–241. Wiesbaden: Springer Vieweg.
- Bellenger, A.-M. & Blandin, A. 2019. *Le BIM sous l'angle du droit*, Paris: Eyrolles.
- BIM4INFRA 2020. Umsetzung des Stufenplans Digitales Bauen. *Rechtsgutachten 1: Klärung von Rechtsfragen*. <https://bim4infra.de/downloads>.
- Borrmann, A. & Koch, C. Software-Interoperabilität im Bauwesen – Hintergrund und Motivation. In A. Borrmann & M. König & C. Koch & J. Beetz (eds) 2021. *BIM-modeling, Technologische Grundlagen und industrielle Praxis*: 89–94. Wiesbaden: Springer Vieweg.

- Borrmann, A. & König, M. & Koch, C. & Beetz, J. Die BIM Methode im Überblick. In A. Borrmann & M. König & C. Koch & J. Beetz (eds) 2021. *BIM-modeling, Technologische Grundlagen und industrielle Praxis*: 1–28. Wiesbaden: Springer Vieweg.
- BuildingSMART 2022. *Standards und Standardisierung*. <https://www.buildingsmart.de/bim-knowhow/standards-standardisierung>.
- Council 2022. *Proposal for a Regulation (...) on artificial intelligence – prep for Coreper*, 3.11.2022, <https://artificialintelligenceact.eu/wp-content/uploads/2022/11/AIA-CZ-Draft-for-Coreper-3-Nov-22.pdf>. Brussels.
- DIN EN 17549-1:2022-07 - Draft. *BIM-modelling (BIM) - Information structure based on EN ISO 16739-1:2018 to exchange data templates and data sheets for construction objects - Part 1: Data templates and configured construction objects*. Berlin: Beuth.
- eiDAS 2014. Regulation (EU) No 910/2014 of 23 July 2014, on electronic identification and trust services for electronic transaction in the internal market, OJEU L 257/73-114.
- Eschenbruch, K. 2019. Die Vertragsabwicklung mit BIM. In K. Eschenbruch & S. Leupertz (eds), *BIM und Recht*: 8–104. Cologne: Wolters Kluwer.
- European Commission 2020. *A European strategy for data*, COM (2020) 66 final, 19.2.2020; https://ec.europa.eu/info/sites/default/files/communication-european-strategy-data-19feb2020_en.pdf.
- European Parliament & Council 2022. *Regulation on European data governance (Data Governance Act)*, 2018/1724, 30 May 2022, OJ, 3.6.2022, L 152/1-44.
- Hagedorn, P. & Block, M. & Zentgraf, S. & Sigalov K. & König M. 2022. Toolchains for Interoperable BIM Workflows in a Web-Based Integration Platform. *Applied Sciences* 12 (12): 5959.
- IBM 2022. xml signature. <https://www.ibm.com/docs/en/was-nd/8.5.5?topic=authentication-xml-digital-signature>.
- ISO 16739-1:2018. *Industry Foundation Classes (IFC) for data sharing in the construction and facility management industries - Part 1: Data schema*.
- ISO 19650-1:2018 and -2:2018. *Organization and digitization of information about buildings and civil engineering works, including BIM-modelling (BIM) - Information management using BIM-modelling- Part 1: Concepts and principles, part 2: Delivery phase of the assets*.
- Jernigan, F. E. 2008. *BIG BIM – Little BIM: The practical approach to BIM-modeling: Integrated practice done the right way!* Salisbury: 4 Site Press.
- Klemt-Albert, K. & Bahlau, S. 2017. Das BIM-Modell als Single Source of Truth. *Bauwirtschaft* 2: 74–79.
- Klemt-Albert, K. & Ritter, N. & Hartung, R. 2018. Rechtliche Rahmenbedingungen für die Implementierung von BIM. *Bautechnik* 95: 207–214.
- Kühling, J. 2021. Der datenschutzrechtliche Rahmen für Datentreuhänder. *Zeitschrift für Digitalisierung und Recht* 1: 1–26.
- Mahanti, R. (ed.) 2021. *Data Governance and Compliance: Evolving to Our Current High Stakes Environment*. Singapore: Springer Singapore.
- Möllers, T.M.J. (ed.) 2021. *Juristische Methodenlehre*. München: C.H. Beck.
- Repko, A. F. & Szostak, R. 2021. *Interdisciplinary Research: Process and Theory*. USA: SAGE Publ. Inc.
- Richard, D. 2020. *Le droit du BIM (BIM-modeling)*. Paris: LexisNexis.
- Roberts, P. 2017. Interdisciplinary in Legal Research. In M. McConville & W. Hong Chui (eds), *Research Methods for Law*: 90–133. Edinburgh: Edinburgh University Press.
- Scherer, R. J. & Schapke, S.-E. 2014. Multimodellbasierte Zusammenarbeit in Bauprojekten, in: R. J. Scherer & S.-E Schapke, *Informationssysteme im Bauwesen* 1: 3–38.
- Schmid, F. & Blandini, L. 2021. Werkzeuge für die digitale Transformation des Hochbaus. Ein Bericht aus dem Projekt DigitalTWIN. *Stahlbau* 90 5: 356–367.
- Weber, B.; Achenbach, M. 2023: Data sovereignty within the construction process, in: Hjelseth, E., Sujan, S. F. & Scherer, R. (eds.): *Work and eBusiness in Architecture, Engineering and Construction: ECPPM 2022*, CRC Press 2023.
- Weber, B. & Achenbach, M. & Niederländer, A. 2023: Rechtskonformes Datenteilen im Bauprozess – Anforderungen des Data Governance Act in Common Data Environments, *Bauingenieur*, 3/2023, accept. for publication.
- Weber, B. & Gernert, R. 2022. Data Governance – Datenteilung in Ökosystemen rechtskonform gestalten. In M. Rohde & M. Bürger & K. Peneva & J. Mock (eds), *Datenwirtschaft und Datentechnologie*. Wiesbaden: Springer Vieweg.
- Weber, B. 2020. Daten- und Rechtemanagement in agilen Strukturen – Integration der rechtlichen Anforderungen durch kollaboratives Arbeiten, *ITRB* 4: 89–92.
- Weber-Lewerenz, B. 2022. Unternehmerische Compliance im digitalen Transformationsprozess – Teil 2, *Risk, Fraud & Compliance* 2: 63–68.
- Wessendorf, N. 2019. Datenhoheit, Datenschutz, Vertraulichkeiten und Urheberrecht. In K. Eschenbruch & S. Leupertz (eds), *BIM und Recht*: 293–295. Cologne: Wolters Kluwer.

Advanced life-cycle assessment of reinforced concrete bridges using digital twin concept

J. Rymeš, J. Červenka, M. Herzfeldt & R. Pukl
Červenka Consulting s.r.o., Prague, Czech Republic

ABSTRACT: This paper proposes a concept for enhancing the maintenance of aging reinforced concrete bridges using online bridge monitoring system coupled with advanced non-linear numerical modelling. Based on the on-site measurement data, a calibrated non-linear numerical model is developed and then further used for the simulation of the degradation mechanisms, such as chloride-induced reinforcement corrosion. This allows assessing the reduced structural load-bearing capacity and thus predict the rate of structural degradation. An example pilot study is presented showing the development and application of the digital twin for a two-span reinforced concrete bridge. The obtained numerical data are discussed and evaluated within the framework of the valid *fib* Model Code standard.

1 INTRODUCTION

In light of the ongoing climate change, the requirements for better environmental sustainability in the concrete industry becoming more and more urgent. It is estimated that the ecological footprint of the cement clinker production is up to 7 % of the total man-made CO₂ (Barcelo et al., 2014). Furthermore, as the World is still recovering from the COVID-19 pandemic, the global economy stagnates, and many contractors face a supply shortage of construction materials. Therefore, there is a demand for a long service life of the existing civil structures.

On the other hand, the long-term degradation acting on reinforced concrete bridges may compromise the serviceability and even safety of the civil infrastructure. One of the means how to face this issue is the development of computational models capable of estimating the impacts of long-term degradation on structural performance.

In this study, we present a pilot application example of a coupled system used for online bridge monitoring and subsequent advanced non-linear finite element (FE) simulation. Then, models for chloride ingress and reinforcement corrosion are incorporated into the FE static analysis, which allows for estimating the response of the structure affected by a chloride attack. By varying the duration of the degradation, the structural load-bearing capacity can be assessed at several stages of the structure's service life. Finally, the reduction of the design structural resistance in time is evaluated based on the method implemented in the *fib* 2010 model code for the safety assessment by nonlinear analysis.

This paper extended the previous study (Červenka and Rymeš, 2023) by implementing the reinforcement bond properties into the model and modifying the loading protocol used for the numerical simulation.

2 ON-SITE DATA ACQUISITION

2.1 *Vogelsang bridge*

The on-site data were measured on a two-span section of the Vogelsang Bridge located in Esslingen am Neckar, Germany. The monitored part represents a reinforced concrete bridge with spans of 13.8 m and 13.2 m. The girder has a constant height of 0.6 m.

The bridge is loaded by the traffic loads and subjected to deterioration mechanisms from the external environment, mainly carbonation of the concrete cover and the chloride attack due to the use of the de-icing salts for road maintenance in the winter period. Both these mechanisms gradually reduce the pH concentration in the concrete and may eventually lead to reinforcement corrosion and thus reduce the mechanical performance of the structure.

2.2 Bridge monitoring

The bridge monitoring was conducted within the framework of the European cyberBridge research project (www.cyberbridge.eu). The data acquisition took 61 days from January until March 2019. The iBWIM (Bridge-Weigh-In-Motion) system was provided by Petschacher, ZT-GmbH, and consists of strain gauges installed on the underside of the bridge deck coupled with a laser rangefinder for detecting the passing traffic. Coupling the structural monitoring sensors with traffic detection allows for obtaining the data needed for structural assessment as well as daily traffic data.

The sensitivity of the system is suitable for monitoring traffic with a gross weight above 3.5 t. Before the data acquisition, the monitoring system was calibrated by trucks of known weight. Further information about the bridge monitoring can be found for instance in reference (Červenka and Rymeš, 2023), including examples of the obtained data. These on-site data were further used to calibrate the numerical model.

3 NUMERICAL SIMULATION

3.1 Non-linear numerical modelling

A non-linear FE model for structural analysis of the bridge was developed using the ATENA software (Červenka, Jendele and Červenka, 2022). The software allows realistic simulation of the material behaviour, including concrete cracking in tension or crushing in compression according to the material model developed by Červenka et al. (Červenka, Červenka and Eligehausen, 1998) and Červenka and Papanikolaou (Červenka and Papanikolaou, 2008). In this model, the softening after tensile cracking is evaluated based on the amount of dissipated fracture energy using the smeared crack approach with a crack band while the plasticity approach is used for the simulation of concrete crushing in compression. Reinforcement can be implemented either as smeared or discrete while its material response follows a multilinear stress-strain diagram allowing simulation of reinforcement yielding or even rupture.

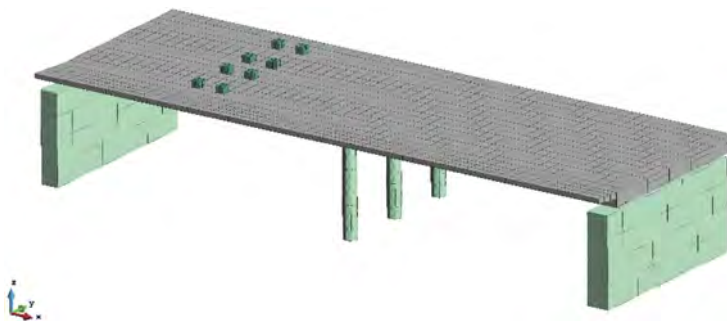


Figure 1. Finite element model of the Vogelsang Bridge.

These advanced numerical techniques can be applied in the development of a digital twin of the bridge. This concept is used in many engineering fields to simulate the behaviour of a real product. A suitable tool for covering the structural performance aspects of the digital

twin is the application of the non-linear FE method. Such an approach allows for the simulation of crack propagation in the model thus providing a realistic structural response. In this context, a non-linear FE model capable of simulation of long-term deterioration mechanisms represents an important step towards utilising the digital twin concept in the field of structural engineering and aging management.

The FE model of the Vogelsang Bridge is shown in Figure 1. The model was calibrated using the on-site measured data, mainly the information about the weights of the truck and the strain it induces when crossing. Further information can be found in reference (Červenka and Rymeš, 2023).

3.2 Chloride ingress and reinforcement corrosion

In the case of reinforced concrete bridges, one of the main degradation mechanisms reducing the structural performance is the use of de-icing salts for route maintenance during the winter season. The chloride ions presented in the salts gradually penetrate the concrete microstructure towards the steel reinforcement, which leads to a decrease in the pH level. Eventually, as the alkalinity of the concrete decreases, the corrosion protective function of the concrete cover is lost, and the reinforcement corrosion is initiated leading to the reduction of its cross-section. In the ATENA software, this mechanism is simulated with a chloride ingress model coupled with a reinforcement corrosion model.

The chloride transport through the concrete porous system is a combined diffusion/binding process as the transported ions are absorbed into the C-S-H gel or precipitate as new compounds within the concrete microstructure (Taylor, 1997). In engineering practice, this is commonly modelled using the diffusion equation with a time-dependent diffusion coefficient. Additionally, when cracks occur in the concrete cover as a result of mechanical loads, chloride transport is accelerated. In the case of the structural calculations, as the chloride transport is limited to the regions below the surfaces subjected to the chloride attack, the chloride penetration can be simulated as a 1D diffusion process. Such an implementation reduces the time needed for the solution of the diffusion problem, which reduces the overall computational time.

During the calculation, chloride concentration at the depth of the reinforcement is checked and once it exceeds a critical level, the reinforcement corrosion is initiated. Its rate depends on the chloride concentration, temperature conditions, and the duration of the corrosion process. Since the corrosion products are larger in volume than the uncorroded steel, the pressure builds up in the concrete cover, and eventually spalling of the cover occurs. In the corrosion model, this is considered by evaluating the corrosion depth against the tensile strength of the concrete and once the spalling occurs, it is assumed that the corrosion process continues at the rate controlled by conditions of the external environment.

The long-term chloride attack is simulated in multiple steps during this calculation. At each step, the degree of corrosion is calculated and then used to reduce the cross-section area of the reinforcement elements in the model. Based on this, a new static equilibrium is found and the crack width is updated. In the next solution step, the updated crack width is used to accelerate the chloride diffusion process.

The implemented models are mainly based on the research of Liu and Weyers (Liu and Weyers, 1998) and the recommendations published in the DuraCrete report (The European Union–Brite EuRam III, 2000). Further details about the simulation of the chloride penetration and the reinforcement corrosion and how it is implemented into the static FE calculation can be found in the reference (Hájková *et al.*, 2016), including validation of the approach.

3.3 Reinforcement bond

In the case of FE simulations of reinforced concrete structures, either smeared or discrete reinforcement modelling is generally used. In the case of the smeared reinforcement, the cross-

section area of the reinforcement is assumed to be smeared over the entire thickness of the concrete solid element thus effectively increasing the element's tangent modulus. Compared to the smeared modelling, discrete reinforcement modelling introduces additional one-dimensional finite elements in the model, which correspond to the actual reinforcement placement in the structure. During the analysis run, the strain continuity between the solid concrete elements and the 1D reinforcement links is assumed during the assembling of the stiffness matrix; however, in a real concrete sample, a slip between the concrete and reinforcement may occur.

For sufficiently fine meshes, the strain discontinuity between the concrete and reinforcement can be simulated as cracking of the elements surrounding the discrete reinforcement elements. It has been shown that this approach can reproduce the crack patterns and the crack width obtained in laboratory experiments if fine elements of the size of several centimeters are used (Cervenka *et al.*, 2022). However, in the case of typical engineering applications, the mesh size is often one or two orders higher. Such course meshes cannot adequately capture the localization process of the fine microcracking around the steel reinforcement bars. Therefore, to capture the bond-slip in engineering simulation, an additional degree of freedom is added to represent the slip between the steel. The bond strength-slip law then enters the simulation as a non-linear material constitutive law, which needs to be met during the iterative solution.

The bond strength-slip material law used in this study was based on the fib MC 2010 standard (International Federation for Structural Concrete, 2013). Furthermore, as the goal of the numerical simulation is to assess structural degradation due to reinforcement corrosion, the relationship between the reinforcement corrosion and relative bond strength by Bhargava *et al.* (Bhargava *et al.*, 2007) was used and is plotted in Figure 2.

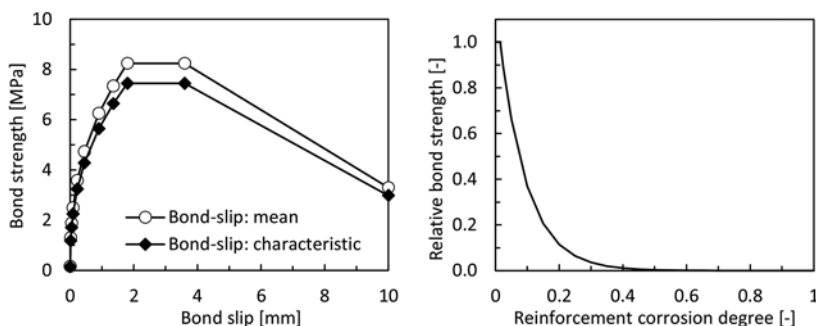


Figure 2. (left) Reinforcement bond strength-slip function for the calculation with mean and characteristic material properties and (right) relative function for reducing the bond strength as a function of reinforcement corrosion (Bhargava *et al.*, 2007).

3.4 Analysis workflow

In the case of non-linear analyses, the structural response under a given load combination cannot be assessed as a simple superposition of the given load action as in the case of linear calculation. As the load induces irreversible material response mainly in a form of tensile concrete cracking, each sequence of load applications induces a unique structural response. Therefore, the application of load in a non-linear numerical model should respect the load sequence of the real structure. Furthermore, as the mechanical crack width influences the rate of chloride ingress, the load level also affects the rate of degradation when exposed to the chloride attack.

In this study, the investigated load combination at the ultimate limit state (ULS) includes the permanent load actions (i.e., the dead loads) and the variable load actions (i.e., the distributed and concentrated traffic loads). For the durability study, the following sequence of load intervals was used to simulate the service life structural history:

- 1) Design dead loads: self-weight and other dead loads,
- 2) Design live loads: concentrated and distributed traffic loads,
- 3) Unloading design live loads from 2),
- 4) Simulation of the chloride degradation,
- 5) Overloading with design live loads.

The application of the ULS design loads in intervals 1) and 2) should simulate a critical overloading situation, which may occur during the structure's service life. In the non-linear model, such an event results in crack development. On the other hand, the long-term degradation mechanism act on the structure at lower loads than the USL design load level thus the application of the chloride attack at the ULS load level may overestimate the real situation. Therefore, the model was unloaded to the design dead load level, which resulted in a partial reduction of the previously localized cracks. Subsequently, the chloride attack with a duration of 25, 50, 75, 100, 125, and 150 years was simulated. Finally, the live loads were again gradually applied until reaching the peak load.

3.5 Safety framework

The results from the non-linear calculations were evaluated based on the *fib* MC 2010 standard (International Federation for Structural Concrete, 2013), which permits the application of non-linear simulations for structural assessment. It is worth mentioning that a similar approach is about to be introduced into the new generation of Eurocodes.

Generally, the safety method can be divided into three categories: full probabilistic, global resistance, and partial factor methods. In this study, the ECoV method, which belongs to the global resistance category, is applied. The general design requirement specifies that the design structural resistance (R_d) should be greater than the effects of the design loads (E_d). Therefore:

$$E_d < R_d. \quad (1)$$

The underlying assumption of the ECoV method is that the structural resistance follows the log-normal distribution, which can be described by the mean (R_m) and characteristic (R_k) structural resistances. These values can be obtained by two analysis runs, one using the mean and one using the characteristic parameters for the applied material models. Then, the coefficient of variation (V_R) of the structural resistance can be calculated as:

$$V_R = \frac{1}{1.65} \ln \left(\frac{R_m}{R_k} \right). \quad (2)$$

The global resistance factor (γ_R) is calculated as:

$$\gamma_R = \exp(\alpha_R \beta V_R), \quad (3)$$

where $\alpha_R = 0.8$ and $\beta = 3.8$ are the sensitivity factor and reliability index, respectively.

Finally, the design structural resistance according to the ECoV method gives:

$$R_{d,ECov} = \frac{R_m}{\gamma_R \gamma_{Rd}}, \quad (4)$$

where γ_{Rd} is the uncertainty of the numerical model. In the case of the ATENA software, $\gamma_{Rd} = 1.16$ for all failure modes (Červenka, Červenka and Kadlec, 2018).

4 RESULTS

A typical outcome of the durability analysis is shown in Figure 3 using the model with mean material characteristics and a 150-year-long chloride attack. The crack patterns in concrete are shown for several stages of the calculation. First, when the ULS design load is applied, maximum cracks of approximately 0.3 mm open in the mid-span and above the center piers of the bridge. Upon unloading to the design dead load level, these cracks partly close, and their width is mostly below 0.1 mm. At this stage, the chloride penetration and subsequent reinforcement corrosion are simulated on the top and bottom surfaces of the bridge deck. As a result, the reinforcement cross-section area reduces, the cracks grow, and the mid-span deflection increases. Finally, after 150 years of chloride-induced degradation, cracks of approximately 0.3 mm are predicted in the mid-spans of the decks as well as above the center piers at the design dead load level. As the load level is increased, the reinforcement yielding soon occurs, which results in rapid crack growth. At the peak load, cracks exceeding 3.5 mm are predicted by the model.

Similarly, in Figure 4, the development of the stresses in the discrete reinforcement elements is plotted during the calculation. It can be observed how the reinforcement stress increases as a result of the reinforcement corrosion.

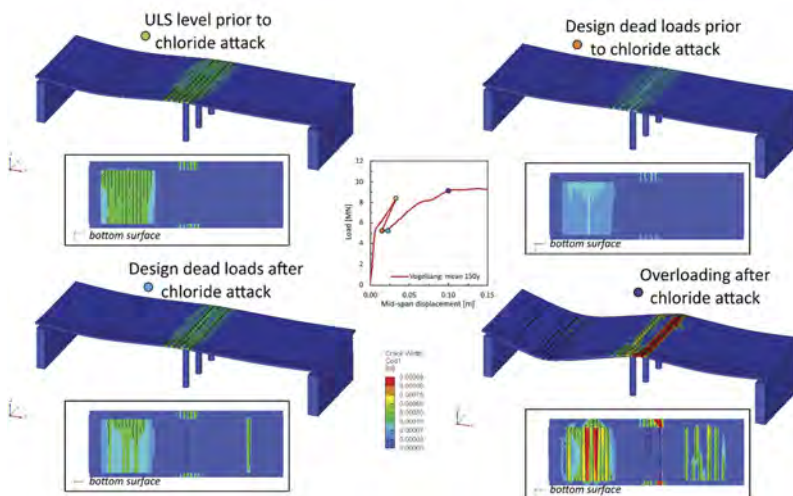


Figure 3. Distribution of the crack width in the concrete at various stages of the calculation for the model with mean material properties and 150-year-long chloride attack (deformation magnified 15x, only cracks larger than 0.1 mm are emphasized).

The structural response for each analysis run can be represented in a form of a load-displacement (L-D) diagram as shown in Figure 5 (left), where examples of curves for models with mean material properties are plotted. As described previously, the load is first increased to the ULS design load level to simulate a critical loading scenario; however, the chloride-induced reinforcement corrosion is simulated at a lower load level. This is exhibited by the increase of the deformation at constant load on the L-D diagram. While for the model of a 50-years-long chloride attack, the degradation is rarely visible, for longer degradation periods, it can be seen how the mid-span deflection increases because of reinforcement corrosion, and subsequently, both stiffness and maximum load-bearing capacity are reduced during overloading simulation.

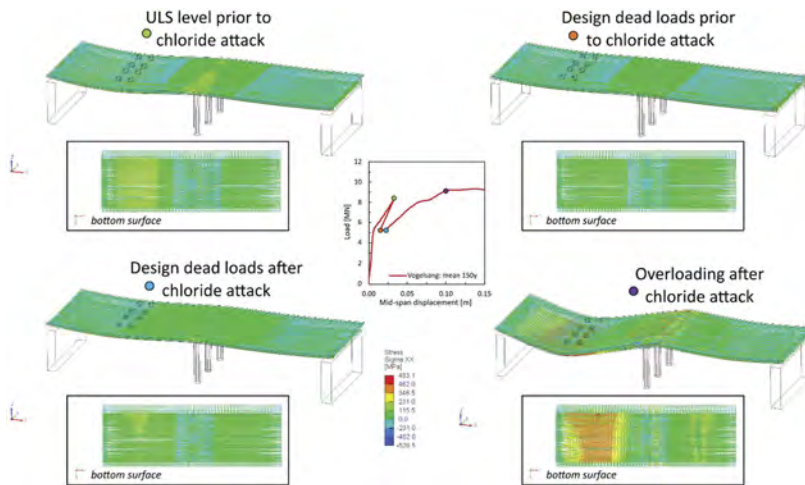


Figure 4. Stresses in the reinforcement at various stages of the calculation for the model with mean material properties and 150-year-long chloride attack (deformation magnified 15x).

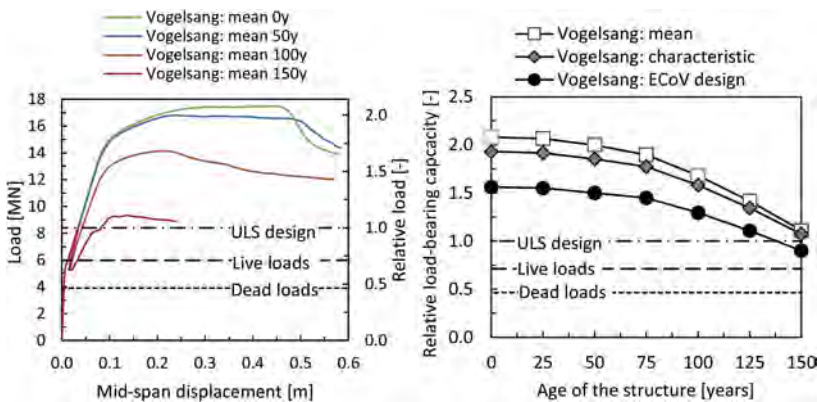


Figure 5. (left) Typical load-displacement diagrams for the calculation with mean material parameters for bridge unaffected by the chloride attack and for chloride attack of 50, 100, and 150 years and (right) reduction of the structural load-bearing capacity in time.

To deduce the design structural resistance, the analysis is conducted with mean and characteristic material properties for each duration of the chloride attack. Then, based on the maximum load from both analysis runs, the design load-bearing capacity is calculated using the ECoV method (see section 3.5) for the given age of the structure. From the plot in Figure 5 (right), it can be observed that the design load-bearing capacity exceeds the ULS design load level until the age of the structure of 125 years.

5 CONCLUSIONS

This study presents a comprehensive approach to the assessment of the long-term structural performance of reinforced concrete bridges. In the first step, a bridge monitoring system is used for the data acquisition from the existing reinforced concrete bridge. Subsequently, this data is used to develop a finite element model of the structure, which can be used for

structural assessment. Furthermore, advanced chloride diffusion model was used to simulate the structure degradation due to the use of de-icing agents. This model takes into account the degradation of reinforcement cross-sectional area and also its bond parameters due to corrosion. The presented approach can predict the reduction of the structural performance in time. The obtained results are evaluated according to the *fib* MC 2010 standard to obtain the design load-bearing capacity of the bridge.

ACKNOWLEDGEMENTS

The financial support provided by the Czech Technological Agency under the project CK03000023 “Digital twin for increased reliability and sustainability of concrete bridges” is greatly acknowledged.

REFERENCES

- Bhargava, K. *et al.* (2007) ‘Corrosion-induced bond strength degradation in reinforced concrete-Analytical and empirical models’, *Nuclear Engineering and Design*, 237(11), pp. 1140–1157. doi: 10.1016/j.nucengdes.2007.01.010.
- Červenka, J., Červenka, V. and Eligehausen, R. (1998) ‘Fracture-plastic material model for concrete, application to analysis of powder actuated anchors’, in *Proceedings FRAMCOS (3)*, pp.1107–1116.
- Červenka, J. and Papanikolaou, V. K. (2008) ‘Three dimensional combined fracture–plastic material model for concrete’, *International Journal of Plasticity*, 24(12), pp. 2192–2220. doi: 10.1016/J.IJPLAS.2008.01.004.
- Červenka, J. and Rymeš, J. (2023) ‘Digital Twin for Modelling Structural Durability’, in Rossi, P. and Tailhan, J.-L. (eds) *Numerical Modeling Strategies for Sustainable Concrete Structures. SSCS 2022. RILEM Bookseries*. Cham: Springer International Publishing, pp. 79–89. doi: 10.1007/978-3-031-07746-3_8.
- Cervenka, V. *et al.* (2022) ‘Simulation of the crack width in reinforced concrete beams based on concrete fracture’, *Theoretical and Applied Fracture Mechanics*, 121(June), p. 103428. doi: 10.1016/j.tafmec.2022.103428.
- Červenka, V., Červenka, J. and Kadlec, L. (2018) ‘Model uncertainties in numerical simulations of reinforced concrete structures’, *Structural Concrete*, 19(6), pp. 2004–2016. doi: 10.1002/suco.201700287.
- Červenka, V., Jendele, L. and Červenka, J. (2022) *ATENA Program Documentation: Part I Theory*. Prague.
- Hájková, K. *et al.* (2016) ‘Reinforcement corrosion in concrete due to carbonation and chloride ingress up and beyond induction period’, *ECCOMAS Congress 2016 - Proceedings of the 7th European Congress on Computational Methods in Applied Sciences and Engineering*, 2 (June),pp. 2460–2470. doi: 10.7712/100016.1974.11003.
- International Federation for Structural Concrete (2013) *fib Model Code for Concrete Structures 2010*.
- Liu, T. and Weyers, R. W. (1998) ‘Modeling the Dynamic Corrosion Process in Chloride Contaminated Concrete Structures’, *Cement and Concrete Research*, 28(3), pp. 365–379. doi:10.1016/S0008-8846(98)00259-2.
- Taylor, H. F. W. (1997) ‘Cement chemistry’, *Cement chemistry*. doi: 10.1680/cc.25929.
- The European Union–Brite EuRam III (2000) *Probabilistic performance based durability design of concrete structures: Final technical report of Duracrete project*.

Sustainable reuse of public real estate assets meeting structural, conservation and territorial needs

G. Concu, D.R. Fiorino & E. Pilia

Department of Civil and Environmental Engineering and Architecture, University of Cagliari, Italy

ABSTRACT: Currently, the recovery of existing buildings assumes a fundamental role, especially the restoration and reuse of the large state-owned properties characterised by significant cultural values, but often underutilised or even abandoned. This wide patrimony can instead represent an opportunity to satisfy the still existing needs of settlements, infrastructures, and services, without further consumption of land. The paper analyses the problem of integrating the conservation-architectural-social criteria for defining new uses of state-owned buildings with the need to meet structural requirements and performance according to current Italian technical standards for construction. A methodological protocol is proposed, based on the definition of sets of indicators, aimed at quantifying the degree of sustainability of new use design hypothesis according to the impact in terms of demand for structural performance upgrading compared with the overall sustainability of the intervention. The methodology application to the case study of a military building is presented and discussed.

1 INTRODUCTION

Approximately 70% of the Italian building heritage, by age, techniques, and construction materials, is approaching the end of its life cycle, and this exposes it to the risks of seismic and hydrogeological vulnerability, to degradation, to energy inefficiency. At the same time, the current European policies of urban regeneration push towards the effective zeroing of land consumption and the sustainability of any building and urban transformation that affects the building heritage (National Council of the Green Economy 2017).

In this context, the recovery of the built heritage assumes a fundamental role and place itself rightfully among the actions promoting sustainable development. In fact, the advantages associated with the reuse of existing buildings involves environmental, economic, and socio-cultural issues. The environmental advantages relate to i) the protection of the built heritage from degradation, ii) the waste reduction, iii) the energy conservation, iv) the reduction of urban decay. The economic advantages relate to i) the reduction of management costs, ii) the boost to the use of local resources, iii) new investment opportunities. The socio-cultural advantages relate to i) the positive impact in terms of job opportunities and income, ii) the promotion and preservation of historical memory, iii) the protection of the historical-cultural identity of places.

In this framework, special relevance assumes the restoration and reuse of large state-owned properties, which in Italy appear to be largely for military use (Fiorino 2021), characterised by cultural values, but often underutilised or even abandoned and which can instead represent an opportunity to satisfy the still existing needs of settlements, infrastructures, and services, without further consumption of land. The issue of the disposal and reuse of historic state-owned assets is very topical and pushes on the one hand to highlight the general institutional stalemate that has led to the abandonment of many assets of great historical value, and on the other to build sustainable reuse scenarios, capable of guaranteeing their conservation and, at the same time, of responding to the pressing needs of containing public spending and identifying new containers of services for the community.

The choice of the reuse scenario, or adaptive reuse, of the asset is a very delicate issue, which involves both cultural, social, and territorial aspects as well as technical, technological, and economic aspects. Morandotti (2012) effectively focuses on the fact that the sustainable refurbishment of the building heritage should be based on an integrated approach that takes into consideration i) the evaluation of the functional compatibility between the reuse and the building, in terms of both the compatibility between the facilities located in the building and the needs of the current users, and the need for regulatory, operating and system adaptation; ii) the prospect of optimizing the building's performance in relation to its material consistency, residual structural capacity, and state of conservation, but with a view to increasing its energy efficiency; iii) the long-term sustainability of the refurbishment, in the sense of minimizing future interventions, through a monitoring strategy aimed at the planned conservation/maintenance of the building. Besana et al. (2018) highlight the concept of resilience, which in case of the historical built heritage means tolerable transformation that an existing building can undergo without the resulting impacts generating undesirable effects. This means that the building can adapt to accommodate the transformations deriving from reuses maintaining its identity, distinguishability, functionality suitable for new uses and respectful of the historical values of the asset.

Several studies propose methodologies to support the built heritage reuse decision-making, analysing the factors affecting adaptive reuse decision-making and developing general models for adaptive reuse strategies for heritage buildings (Aigiwi et al. 2019, Alhojaly et al. 2022, Bertolin & Loli 2018, Della Spina 2021, Mısırlısoy & Günçe 2016, Ribera et al. 2020, Śladowski et al. 2021). However, to the best of the author's knowledge, the literature is lacking with respect to the specific theme of the influence of the residual structural capacity of the building, and the extent of the structural intervention necessary to meet the reuse needs, on the choice of the reuse scenario.

The present paper aims to bring a contribution to this theme by proposing a qualitative methodology to support the decision-making process in which the impact of the structural intervention on the reuse scenario of the asset is made explicit. The methodology, which is divided into a series of steps, is substantially based on the comparative and integrated analysis of i) the structural performance required by the reuse scenario, ii) the residual structural capacity of the asset, iii) the definition of the category of structural intervention necessary to fulfil the reuse scenario demand. The methodology application to the case study of a military building is presented and discussed.

The research illustrated in this paper is part of a larger project, SOS Labs - Research-action laboratories for urban sustainability - funded by the Italian Ministry of Ecological Transition, aimed at supporting the development of the Sardinian SRSvS (National Strategy for Sustainable Development). The research was carried out thanks to a special agreement between the Italian Ministry of Defence and the University of Cagliari.

2 THE METHODOLOGY

The proposed methodology is based on the concept that the choice of possible strategies for the reuse of the asset should necessarily deal with the structural scheme of the building and with the material with which it was built. Therefore, an essential action is the verification of structural compatibility between the current state of the building and the requirements necessary for the reuse scenario, in terms of structural configuration and load conditions. The outline of the methodology is illustrated in Figure 1, which presents a flow chart whose steps are detailed below.

2.1 *Step 1. Identification of reuse scenarios*

The identification of the possible reuse scenarios of the asset derives from the confluence of various factors, among which, i) the possible need to assign to the asset a specific function already identified a priori, ii) needs deriving from the system of relationships that rest on the territory in which the asset is inserted, iii) willingness to satisfy demand of a social nature, iv) previous successful experiences of regeneration of abandoned assets, v) options arising from discussions with stakeholders. This last factor is fundamental to guarantee the correct inclusion of the new function of the asset in the socio-economic-territorial fabric.

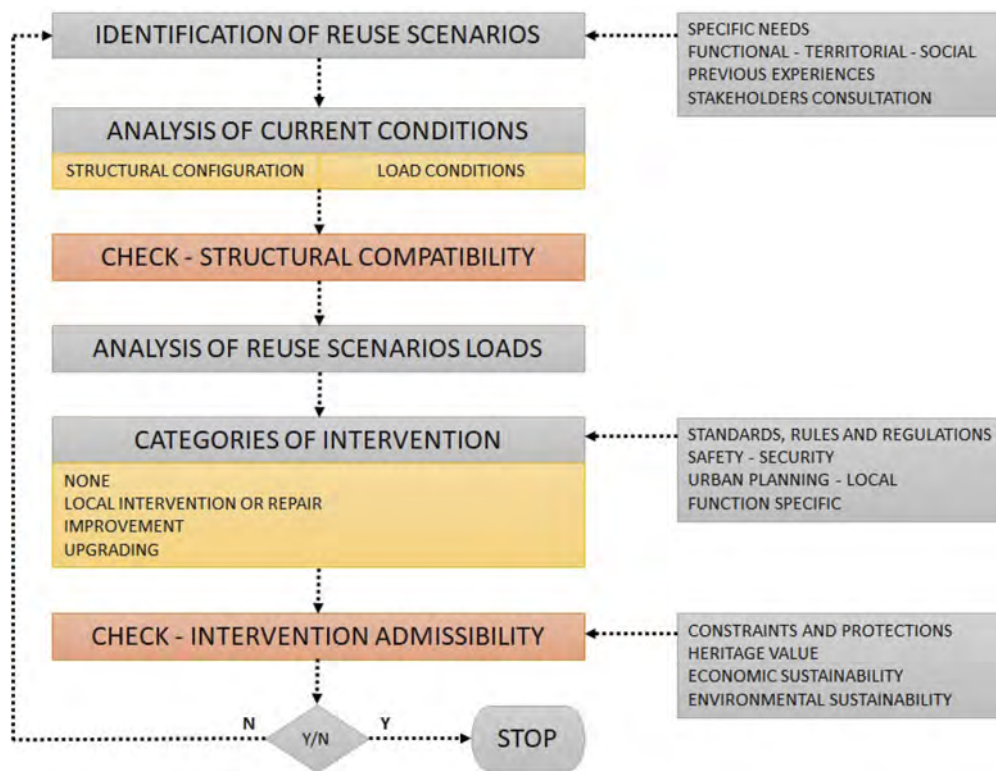


Figure 1. Methodology outline. Step-by-step process.

2.2 Step 2. Analysis of current conditions

The analysis of the actual conservation condition of the asset should lead to recognising and evaluating the residual capacity of the building in terms of quality of materials, static scheme, loads and load-bearing capacity, and global behaviour, for better orientating the strategies of any interventions. This also to comply with the needs of restoration and conservation, i.e., to preserve the existing historical materials, stratigraphies, structures (foundations, load-bearing walls, arches and vaults, horizontal elements, chains), minimising the interventions to replace the historical constructive elements and materials with new ones.

2.3 Step 3. Check of structural compatibility

The check of structural compatibility between the current conditions of the asset and the performance request linked to the reuse scenario has the purpose of avoiding important alterations of the overall structural behaviour of the building, which could affect the original distribution of loads requiring significant structural interventions. Making the most of the static characteristics of the existing structural system allows minimizing the invasiveness of the intervention, and consequently the impact on the identity of the asset itself and, last but not least, the maintenance costs over time.

The decisive aspect in the check of structural compatibility is linked to the entity of the overloads, or imposed loads, which include the loads linked to buildings intended use, and the seismic action, with respect to which the existing buildings, especially the historic ones, can be lacking. Technical regulations, such as the Italian NTC (Technical Standards for Constructions 2018), provide indications for the assessment of the loads, and therefore of the actions, acting on buildings according to their type and intended use.

2.4 Step 4. Categories of intervention

Depending on the outcome of the structural compatibility check, the type of structural intervention to be carried out on the asset is by and large defined to satisfy the performance requirement linked to the reuse scenario.

It should be noted that the type of intervention may also be influenced by other factors linked to other standards, rules, and regulations, such as urban planning and local ones, those relating to safety requirements (fire prevention), those specific to the new function of the property (space, systems, facilities), etc.

According to Italian NTC, the following three categories of intervention are identified.

- Local interventions or repair. Interventions involving individual structural elements and which, in any case, do not reduce the pre-existing safety conditions.
- Improvement interventions. Interventions aimed at increasing the pre-existing structural safety, without necessarily reaching the safety levels established for new buildings.
- Upgrading interventions. Interventions aimed at increasing the pre-existing structural safety, achieving the safety levels set for new buildings.

In the case of assets of cultural interest, upgrading interventions are to be considered, in general, not compatible with conservation needs, since to achieve upgrading it is almost always necessary alter the material and significantly modify the structural behaviour of the building. Therefore, improvements interventions and local interventions or repair are considered acceptable for these assets. Some factors useful for discriminating the improvement intervention from the upgrading one are the following:

- increase in foundation loads less than 10% compared to the original loads,
- modification of the position of the stiffness barycentre, for each floor, by an amount less than 10% of the dimension of the building measured perpendicular to the direction of application of the seismic action,
- modification of the position of the mass barycentre, for each floor, by an amount less than 5% of the dimension of the building measured perpendicular to the direction of application of the seismic action.

2.5 Step 5. Check of intervention admissibility/sustainability

The last step of the methodology involves checking the eligibility of the intervention (upgrading, improvement, repair) to be carried out on the asset. The extent and outcomes of the intervention should in fact be assessed in terms of i) compatibility with the heritage value of the asset, and therefore with any constraints and protections that concern it, ii) economic sustainability, iii) environmental sustainability. The positive outcome of this check implies the admissibility of the intervention, while the negative outcome requires rethinking the specific reuse scenario.

As stated in GBC (GBC Historic Building® HandBook 2017), the need to recover and improve assets of cultural significance focuses on safeguarding the structural behaviour and historical material. Regardless of the assets in which strategic or relevant functions are performed, it can be accepted that the intended use of a building, in general, can be chosen based on the response of the consolidated and restored structures to the overload. In this way, forced upgrading that distort the behaviour of historical structures could be avoided.

3 CASE STUDY. THE CARLO EDERLE BARRACKS

The proposed methodology was tested on the case study of the Carlo Ederle Barracks.

The Carlo Ederle Barracks is a military complex, located in Cagliari (Italy) in the so-called S. Elia promontory, named after the Major of artillery, Gold Medal for Military Valour, Carlo Ederle, who fell heroically on the Piave in 1917. The area, owned by the State Property Administration since 1860, moved from civil to military state property in 1925. It is a complex of buildings built on the initiative of the Ministry of the Interior and to be used as a correctional home for minors, then completed and partly adapted as a military district headquarters. Historically, the first Department encamped in the Barracks was the 13th Engineering Battalion of the Savoy Division, which was followed over time by further and various departments, up to hosting, starting from 1993, the Military District of Cagliari.

Currently, the Barracks is closed into a trapezoidal perimeter wall long about 633 m that encloses an area of 23380 m² and consist of 16 buildings used for different military uses. In particular, the entire area can be divided into two distinct sub-areas, one rectangular and one triangular, separated by the driveway entrance on the north side. The rectangular area, based on the difference in elevation, can be divided into three zones, zone 1 including buildings A, B and C with a difference in height of -3 m compared to zone 2, including buildings E, D, Q which in turn has a difference in height of -3 m compared to zone 3, including buildings G, F, P, H, I, L, M, N, O (Figures 2 and 3).



Figure 2. The Carlo Ederle Barracks. Aerial view.



Figure 3. The Carlo Ederle Barracks. Location of buildings and construction evolution.

The Barracks reuse scenarios were defined based on a review of successful regeneration experiences of abandoned buildings and preliminary interviews with stakeholders, as well as on a preliminary recognition of the current state of conservation of the asset. Considering this, the adaptive reuse of the military site considers four possible scenarios: i) hotel complex, ii) residential and social housing, iii) creative hub, and iv) community cooperatives.

Table 1. The Carlo Ederle Barracks. Main information.

Location	S. Elia Promontory - Cagliari
Chronology of the construction	1860 1926 1945
Current use	Barracks
Surface	23317 m ² (7694 m ² indoor 15623m ² outdoor)
Restriction measures	Military state property Restriction of cultural interest
Protected areas in which the asset is inserted	S. Elia Promontory – Cagliari Environmental restriction
Availability/Accessibility	Available and accessible only to employees of the barracks. Extraordinary openings for cultural events. Seasonal public connections only.
Agreements	Protocol agreement between Italian Ministry of Defense and Local Administration for the coordination of military activities in the Region of Sardinia

The state of conservation of the asset was detected through an investigation protocol consisting of indirect and direct analyses. The indirect analyses, aimed at the reconstruction of the historical and architectural evolution of the complex, as well as the identification of its cultural values, were carried out through the critical-interpretative and cross-reference study of the historical documentary and iconographic sources found. This historical-critical analysis was aimed not only at acquiring all the documentation relating to the building history of the asset, but also to that of its past restorations, allowing for a broader understanding of the state of conservation considering previous interventions. The direct analyses consisted of the experimental investigation on the asset through geometric, architectural, and structural surveys, analysis of materials and techniques and state of conservation, aimed at understanding the architectural, material, structural and chronological components of the buildings. All the information were collected within a framework based on the so-called Raumbuch methodology, in which all the constructive elements are represented in details and assessed both in terms of consistency and cultural value.

The overloads relevant to each of the reuse scenarios were extracted from Italian NTC Tab. 3.1.II - Overload values for the different categories of use of buildings.

The comparison between the current structural condition of the Barracks and the structural performance required by the reuse scenarios led to the by and large identification of the type of intervention necessary for each of the buildings making up the complex.

Finally, the compatibility of the interventions with the need to protect the heritage value of the asset was assessed, aiming at quantifying the degree of sustainability of the proposed reuse scenarios. Since now no assessments have been made regarding the environmental and economic sustainability of the interventions.

4 RESULTS

As an example of the analysis process carried out on each building of the military complex, the results relating to the building identified as block 4 (Figure 4) are reported below.

Table 2 shows the overloads associated with possible reuse scenarios and previous use. Table 2 refers to the intended use categories indicated in Italian NTC Tab. 3.1.II - Overload values for the different categories of use of buildings.

The integrated analysis of the performance required by the reuse scenarios, including the fulfilment of standards, rules, and regulations other than NTC as mentioned in 2.4, and the current static conditions of the building led to the by and large identification of the type of intervention to be carried out on the building according to the reuse scenario. The result is shown in Table 3.

The outcome of the integrated analysis shows how the level of intervention is different according to the building reuse scenario. It can be noted that one of the scenarios would require an upgrading intervention, involving substantial changes in the overall structural behaviour of the building.



Figure 4. The Carlo Ederle Barracks. Building's labelling.

Table 2. Overloads according to the reuse scenario (Italian NTC Tab. 3.1.II - Overload values for the different categories of use of buildings).

Overload* (KN/m ²)	Use Scenario				
	Previous Offices (B1)**	Scenario 1 Hotel Complex (C2)	Scenario 2 Housing (A)	Scenario 3 Creative Hub (C3)	Scenario 4 Community Coop (D1)
q _k	2	4	2	5	4
Q _k	2	4	2	5	4
H _k	1	2	1	3	2

*q_k = uniformly distributed vertical loads; Q_k = concentrated vertical loads; H_k = linear horizontal loads
 **B1 = internal offices; C2 = fixed seating areas; A = residential areas; C3 = Areas susceptible to crowding;
 D1 = shops.

Table 3. Categories of intervention according to the reuse scenarios (Italian NTC Tab. 3.1.II - Overload values for the different categories of use of buildings).

Intervention	Scenario 1 Hotel Complex	Scenario 2 Housing	Scenario 3 Creative Hub	Scenario 4 Community Coop
Local/Repair Improvement	X	X		X
Upgrading			X	

The illustrated procedure was applied to all the buildings of the Barracks, leading to a framework of general interventions which constitutes a fundamental tool for the decision-making process relating to the choice of final reuse scenario.

The framework of the interventions to be carried out on each building should obviously be evaluated as a whole and should be included in the set of useful indicators for evaluating the sustainability of the intervention itself and of the reuse scenarios.

5 CONCLUSIONS

The present paper presents a methodology to support the choice of the reuse scenario of large state-owned assets focused on the impact of the structural intervention that the asset should

undergo to satisfy the demand for structural capacity connected to the reuse scenario. The key element of the methodology is the check of structural compatibility between the current conditions of the asset and the performance demand of the reuse scenario, whose main factor is given by the entity of the overloads, imposed by the specific standards, depending on the intended use. The methodology was applied to the case study of a military complex, the Carlo Ederle Barracks in Cagliari (Italy).

The results support the concept that the structural capacity of the asset should be considered a key indicator for the choice of the reuse scenario. The methodology could become an important tool to support the public administration in the recovery and reuse strategies of state-owned real estate assets.

REFERENCES

- Aigwi, I.E., Egbelakin, T., Ingham, J., Phipps, R., Rotimi, J. & Filippova, O. 2019. A performance-based framework to prioritise underutilised historical buildings for adaptive reuse interventions in New Zealand, *Sustainable Cities and Society*, 48, 101547, <https://doi.org/10.1016/j.scs.2019.101547>.
- Alhojaly, R.A., Alawad, A.A. & Ghabra, N.A. 2022. A Proposed Model of Assessing the Adaptive Reuse of Heritage Buildings in Historic Jeddah. *Buildings*, 12, 406. <https://doi.org/10.3390/buildings12040406>
- Bertolin, C. & Loli, A. 2018. Sustainable interventions in historic buildings: A developing decision making tool, *Journal of Cultural Heritage*, Volume 34, 291–302, <https://doi.org/10.1016/j.culher.2018.08.010>.
- Besana, D., Greco, A., & Morandotti, M. 2018. Resilience and sustainability for the reuse of cultural heritage/Resilienza e sostenibilità per il riuso del patrimonio costruito. *Technè*, (15), 184–193.
- Della Spina, L. 2021. Cultural Heritage: A Hybrid Framework for Ranking Adaptive Reuse Strategies. *Buildings*, 11, 132. <https://doi.org/10.3390/buildings11030132>
- Fiorino, D.R. 2021. *Sinergie. Percorsi interistituzionali per la riqualificazione delle aree militari*, Cagliari, Unicapress.
- GBC Historic Building® HandBook For the restoration and sustainable refurbishment of historic buildings. Edition 2016 - Revision May 2017.
- Mısırlısoy, D. & Günçe, K. 2016. Adaptive reuse strategies for heritage buildings: A holistic approach, *Sustainable Cities and Society*, 26, 91–98, <https://doi.org/10.1016/j.scs.2016.05.017>.
- Morandotti, M. 2012. Contenuto vs. contenitore? Criteri predittivi di impatto e soglie di resilienza nella prospettiva del recupero sostenibile. *IN_BO. Ricerche e progetti per il territorio, la città e l'architettura*, 3(5), 161–178.
- National Council of the Green Economy (Consiglio Nazionale della Green Economy) 2017 - Verso l'attuazione del Manifesto della Green Economy per l'architettura e l'urbanistica. https://www.statigenerali.org/wp-content/uploads/2017/11/ssge_2017_documento_gdl_architettura_urbanistica.pdf
- Ribera, F., Nesticò, A., Cucco, P. & Maselli, G. 2020. A multicriteria approach to identify the Highest and Best Use for historical buildings, *Journal of Cultural Heritage*, 41, 166–177, <https://doi.org/10.1016/j.culher.2019.06.004>.
- Śladowski, G., Szewczyk, B., Barnaś, K., Kania, O. & Barnaś, J. 2021. The Boyen Fortress: structural analysis of selecting complementary forms of use for a proposed adaptive reuse project. *Heritage Sciences* 9, 76. <https://doi.org/10.1186/s40494-021-00550-z>
- Technical Standards for Constructions (Norme Tecniche per le Costruzioni). D.M. 17.01.2018, Italian Ministry of Infrastructures and Transportation, 2018.

Evaluation of low-velocity impact damage in metal/composite layered structure

Stephanie TerMaath & Benjamin Ingling
University of Tennessee, Knoxville, TN, USA

John Noland & Daniel Hart
Naval Surface Warfare Center Carderock Division, Bethesda, MD, USA

ABSTRACT: Internal damage caused by low velocity impact loading, such as hail, tool drops, and daily use, is a concern when evaluating the lifecycle of composite overlays used to repair or reinforce metallic structure. To investigate internal damage relative to external visible damage, inform inspection/maintenance, and provide validation data for future computational modeling, five configurations of composite/metal structure were experimentally tested by impact at two energy levels to cause low velocity impact damage. Plates were fabricated with an E-glass/epoxy or a carbon fiber/epoxy composite co-cured to an Aluminum 5456 substrate. In addition to collecting test data such as force/displacement and impact conditions, computerized tomography imaging was performed on the impacted plates to analyze the internal damage in 3D. Primary findings illustrate that both applied impact energies damaged all configurations and that the internal damage was more substantial than indicated by external (visible) damage.

1 INTRODUCTION

Repair and reinforcement solutions using composite overlays of complex shape effectively restore damage tolerance and load-carrying capacity of damaged metallic structure (Figure 1a), as proven through widespread applications encompassing aircraft, ships, offshore platforms, infrastructure, and vehicles (Baker et al., 2003, Zhao and Zhang, 2007, Hollaway, 2003, Bakis et al., 2002, Grabovac, 2005). While composite overlays provide significant benefits over traditional repairs and single material designs, for example (Noury et al., 2002, Weitzenböck, 2012), a continuing concern is the internal damage accumulated throughout the structure's lifetime caused by low velocity impact loading, such as hail, tool drops, and daily use (Figure 1b).

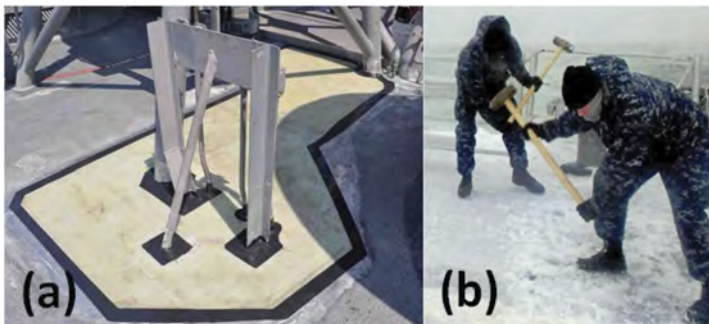


Figure 1. (a) Composite overlay installed on a ship deck and (b) Low velocity impact on a ship deck (Photos courtesy of the US Navy).

The impacting object may rebound, partially penetrate, or completely penetrate (Belingardi and Vadori, 2002). Permanent damage caused by partial or complete penetration will be visible and thus readily identified for additional evaluation or repair during inspection. However, a rebound event, common with low velocity impacts, can result in visually undetectable internal damage that is significant enough to reduce the structural stiffness and load carrying capability (Katunin et al., 2020). Strength reduction from matrix and fiber damage hampers the overlay's effectiveness in transferring and carrying loads from the metal. And, delaminations can significantly reduce the load-carrying capacity by reducing load transfer across the layers, acting as a stress concentration with the potential for subsequent growth, and increasing susceptibility to buckling (De Freitas and Reis, 1998). Given the lack of non-destructive evaluation (NDE) techniques to reliably identify delamination in the composite and disbond at a bi-material joint (Roland et al., 2004, Floros et al., 2015, Katunin et al., 2020), it is imperative to correlate impact conditions such as size, velocity, and visible external damage to internal damage (Baker and Jones, 1988) to inform inspection intervals and evaluation techniques to predict subsequent damage propagation and determine maintenance schedules.

1.1 *Impact damage overview*

As an impactor strikes, its kinetic energy is initially transferred to the plate as elastic strain energy (Lopes et al., 2009). When the ultimate material strength is reached at a location within the plate, elastic strain energy dissipates through permanent damage, such as delamination, disbond, matrix cracking, fiber breaks, and plastic deformation. As the impactor's velocity reaches zero, all of its kinetic energy has either been transformed to elastic strain energy or dissipated through damage. If elastic strain energy remains, the impactor and plate deformations reverse and accelerate in the opposite direction, transforming this strain energy back into kinetic energy and causing the impactor to rebound. The plate then continues to vibrate, dissipating more energy.

While the resulting damage in composites and metals individually from impact loading has been widely studied, investigations on the effect of low-velocity impact on the bi-material interface between a composite overlay and metal base have not been as widely published, especially for the thick metal structure common in infrastructure and marine applications. Impact studies on Fiber Metal Laminates (FMLs) and ceramic/metal structure dominate the literature. While similar in terms of layering metal and composites, FMLs tend to be significantly thinner (metal layers on the order of 0.5 mm or less) as are the other plates investigated for the primary application of aircraft (Akimoto et al., 2000a, Akimoto et al., 2000b). This thinner structure tends to result in visible damage, such as cracking and petaling, from a penetrator impact instead of the non-visible damage associated with the much thicker patched structure investigated herein (Lee et al., 2018, Bieniaś and Jakubczak, 2017, Carrillo et al., 2019, Sadighi et al., 2012, Sharma and Velmurugan, 2022). And, ceramic is typically adhesively joined to metal as ballistic protective armor, and therefore, the ceramic layer is intended to sustain destructive damage to absorb the impact energy thus protecting the metal layer underneath (Lee and Yoo, 2001, Goncalves et al., 2004).

In the current study, the composite is co-cured to the metal resulting in an adhesive layer comprised of the resin used to fabricate the composite. As delaminations in composites tend to occur between plies of differing orientations due to interlaminar shear stresses (Evcı and Gulgeç, 2012, Lopes et al., 2009), disbonds similarly occur in such interfaces due to the differing impact behaviors and stiffnesses of the joined materials (Soutis et al., 1999).

1.2 *Objectives*

This research was performed to achieve 3 objectives:

1. Correlate internal damage to visible external damage to inform inspection and maintenance of composite overlays;
2. Compare the effects of varying materials, configurations, and impact energy on structural performance to inform composite overlay design; and,
3. Provide validation data for future computational modeling of impact events and the prediction of damage propagation after impact.

2 MATERIALS AND METHODS

A summary of the panel configurations and testing information is provided as follows, and additional details are available in the test report (Hart et al., 2016). This paper expands on the initial test program by investigating internal damage using computed tomography (CT).

2.1 *Materials and composite overlay configurations*

Composite overlays were co-cured to 6.35 mm 5456 aluminum substrate to fabricate 406.4 mm square test panels (Table 1). Five composite overlay configurations were investigated (Tables 2–4), and four test panels were fabricated for each configuration. All overlays consisted of an open plain weave (PW) fabric (Hexcel 7500) at the metal/composite interface, followed by a symmetric schedule, and a tight satin weave (SW) fabric (Hexcel 7781) as the final cover ply. The 7500 PW fabric has a warp-to-fill fiber ratio of 16:14, while the 7781 SW has a fiber ratio of 57:54. The higher fiber count of the 8 harness SW results in a tighter weave with approximately the same aerial weight. Overlay stiffness was calculated using Classical Laminate Theory, and overlays were designed to provide varying levels of theoretical stress intensity reduction for semi-infinite cracks in the aluminum using Rose’s model. The same toughened resin epoxy system (Pro-Set M1002 with 237 hardener) with a mix ratio of 100 parts resin to 28 parts hardener by volume was used for all panels and required an elevated temperature post-cure.

Table 1. Specimen fabrication process.

-
- Abrasion of the aluminum surface with nominal 60 grit sandpaper
 - Scrub with commercially available metal cleaner
 - Apply coupling agent
 - Hand lay-up to apply resin to metal and lamina
 - Consolidate by vacuum bag at 10 in-Hg until initial cure
 - Post-cure for a minimum of 8 hours at 60° C
-

Table 2. Fabrics used in composite overlay fabrication.

Symbol	Materials	Architecture	Density (g/m ²)
7500	ØHexcel 7500-F81 E-Glass	0/90 1:1 PW	325
7781	ØHexcel 7781-F81 E-Glass	0/90 8 harness SW	300
E-BX	ØVectorply E-BX 1200 E-Glass	±45 biaxial stitch	410
E-LT	ØVectorply E-LT 1800 E-Glass	0/90 stitch	610
E-LR	ØVectorply E-LR 1708 E-Glass	Unidirectional*	610
C-BX	ØVectorply C-BX 1800 Carbon	±45 stitch	580
C-LT	ØVectorply C-LT 1800 Carbon	0/90 stitch	630
C-LA	ØVectorply C-LA 1812 Carbon	Unidirectional*	610

* Unidirectional on a chopped mat base

2.2 *Impact testing*

Experimental testing was performed at the US Naval Academy using an Instron Dynatup model 9250HV spring-assisted drop tower. The impactor was a 50.8 mm diameter steel cylinder with a 9.652 mm face depth and a 2322.58 mm² maximum impact area. The lab temperature was 70°F with an approximate RH of 80% per the environmental condition of Room Temperature Dry, the ambient temperature of a temperature-controlled lab with the as-manufactured moisture content. To simulate an object falling from 3.048 m, two impact energies (406.7 J and 813.5J) were tested using a constant impact velocity of 7.62 m/s. Each panel configuration was tested at both target impact energies with two panels of a single configuration tested at each energy. Panels were 406.4 mm square with a 355.6 mm square unsupported region. Samples were clamped in place using a bolted frame with the bolt pattern outside of the 16-inch specimen perimeter. Specimens were centered in the frame and the bolt pattern was evenly torqued enough to not cause laminate

Table 3. Overlay configurations.

Configuration/Abbreviation	Laminate Schedule
8-Ply Baseline E-Glass (8PlyQuasiGlass)	PW/([45/-45]/[0/90]/[45/-45])s/SW (7500/E-BX/E-LT/E-BX/E-BX/E-LT/E-BX/7781)
10-Ply Directional E-Glass (10PlyQuasiGlassUni)	PW/([mat/0]/[45/-45]/[mat/0]/[45/-45])s/SW (7500/E-LR/E-BX/E-LR/E-BX/E-BX/E-LR/E-BX/ E-LR/7781)
10-Ply Directional E-Glass/Carbon (10PlyGlassCarbonUni)	PW/([mat/0]/[45/-45]/[mat/0]/[45/-45])s/SW (7500/C-LA/E-BX/C-LA/E-BX/E-BX/C-LA/E-BX/ C-LA/7781)
6-Ply Quasi-isotropic Carbon (6PlyQuasiCarbon)	PW/([0/90]/[45/-45])s/SW (7500/C-LT/C-BX/C-BX/C-LT/7781)
6-Ply Directional Carbon (6PlyCarbonUni)	PW/([mat/0]/[45/-45])s/SW (7500/C-LA/C-BX/C-BX/C-LA/7781)

Table 4. Overlay properties.

Configuration	Thickness (mm)	E_x (MPa)	E_y (MPa)	G_{xy} (MPa)	ν_{xy}	ν_{yx}
8PlyQuasiGlass	4.1	12169	12169	4324	0.27	0.27
10PlyQuasiGlassUni	5.7	18616	9349	4377	0.32	0.16
10PlyGlassCarbonUni	6.5	45340	7619	4049	0.33	0.06
6PlyQuasiCarbon	4.4	28213	28213	9501	0.28	0.28
6PlyCarbonUni	4.4	37859	12604	9708	0.59	0.20

damage but to secure the panel. Impact velocity was determined by the control computer. Mass of the impact sled was adjusted to obtain the desired impact velocity, and a plywood and foam sandwich panel was used as a catch block to prevent secondary impacts.

2.3 Imaging

The CT method involves the use of x-ray beams rotating around the object being scanned. As the x-ray beams pass through the object, special detectors capture the remnants of the beam and digitize an image. CT is different from X-ray, because the CT scans in a circle around the object instead of from one vantage point, allowing for a 3D view of the scanned object. Thus, viewing the composite overlay is possible, because for portions of the scan the aluminum isn't exposed to the x-ray beam and doesn't distort the image due to its higher density (Garcea et al., 2018, Gao et al., 2021). Alternatively, a strong enough wave of particles is needed to penetrate the lighter density of the composite and the higher density of the aluminum. If the wave isn't sufficient to penetrate the aluminum, then beam hardening occurs and the aluminum in the image turns white, distorting the rest of the image. All specimens were scanned to evaluate internal damage.

3 RESULTS AND DISCUSSION

Force/displacement curves (Figures 2 and 3) and imaging data (Figure 4 and Table 5) are provided for all but two of the impacted panels. The carriage weights were loose during the testing of panels, 8PlyQuasiGlass-1A and 10PlyQuasiGlassUni-1A, causing noisy and erroneous data; therefore, these results are not included in the comparisons and discussion.

3.1 Overview of test data

As seen in Figures 2 and 3, all 6 and 8 layer panels exhibited similar force/displacement curves at both impact energies. The 10 ply panels all have smaller displacements but higher forces than the 6 and 8 layer panels, although, the total energy absorbed is not significantly different statistically. At the lower energy, the 10 Ply Directional E-glass panel had higher maximum and total displacements than both 10 Ply Directional E-glass/Carbon panels, while they

exhibited larger forces throughout the test. At the higher impact energy, the trend is the same except that the 10 Ply Directional E-glass/Carbon panel (2B) has a total displacement equal to that of the largest total displacement of the 10 Ply Directional E-glass panels (2B).

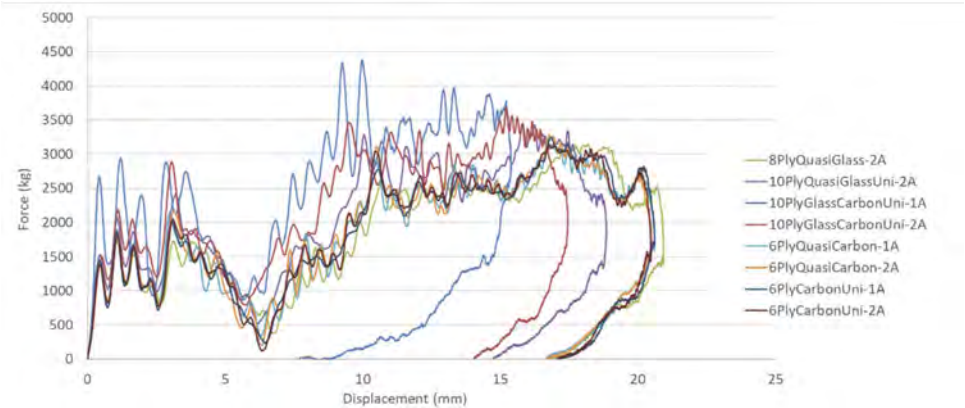


Figure 2. Force/Displacement curve of impacts at a target energy of 406.7 J.

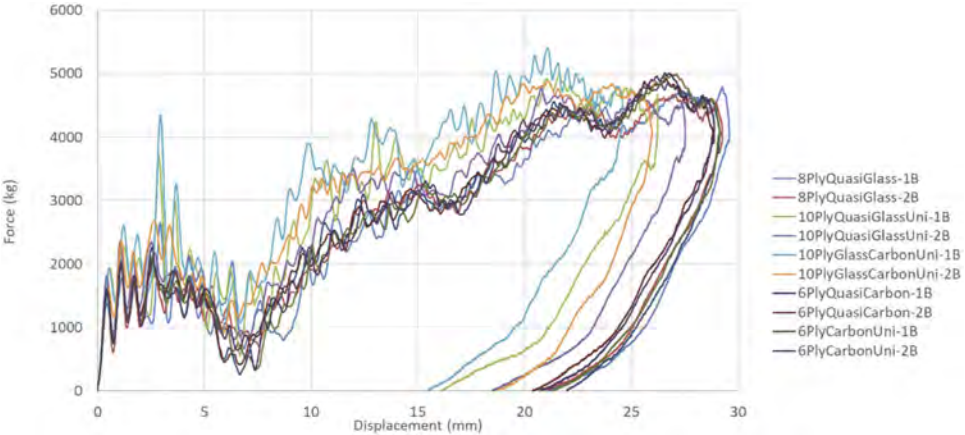


Figure 3. Force/Displacement curve of impacts at a target energy of 813.5 J.

3.2 External and internal damage comparison

For consistent comparison across panels, all damage was measured along a vertical line perpendicular to the top of the panels and passing through the center of the impact strike location (Figure 4). This view orientation had the smallest length scale between image slices allowing for higher resolution in identifying maximum damage. External composite damage was characterized by visible damage areas centered around the impactor strike location (Figure 5). At the lower impact energy, visible external composite damage was less than the impact diameter for all panels except for the 6 Ply QuasiCarbon panels. At the higher impact energy, the 6 Ply panels in general had larger visible damage areas.

The depth of the composite indentation ranged from 0 for all 10 Ply panels at the lower impact energy up to 7.9 mm for the 8 Ply E-glass panel (2B) at the higher impact energy. While small, impact locations are visible on the composite side and could be identified during an inspection as locations for internal evaluation. On the Al side, plastic deformation manifested as a smooth slope from the edge of the panels to the location of maximum deformation

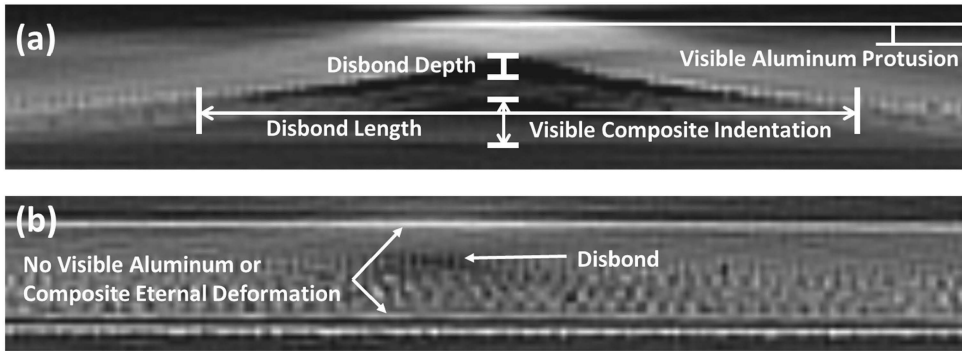


Figure 4. Through the thickness CT images showing the measurements for disbands, visible composite indentation, and visible aluminum plastic deformation. (a) The representative image of the 6 and 8 ply overlays (specimen 6 Ply QuasiCarbon 2A) exhibits a large disbond with damage growing into the composite. Evidence of fiber breaking and matrix cracking is visible. External composite indentation and aluminum plastic deformation is observable on the physical panels. (b) 10 ply overlay behavior (for representative specimen 10 Ply QuasiCarbon 1A) shows a much smaller internal disbond and no visible aluminum or composite deformation externally.

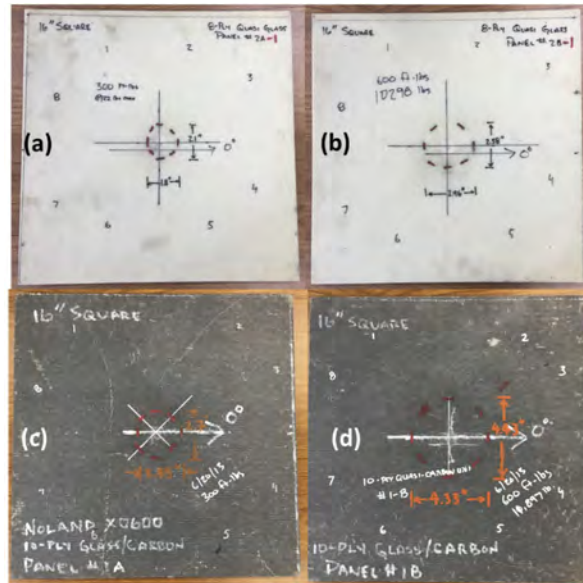


Figure 5. Comparison of external damage on the composite side of representative 8 Ply E-glass Panels (a,b) with 10 Ply E-glass/Carbon Panels at both energy levels (low-left, high-right).

directly under the impact location. Given the relatively small deformations, ranging from 0 to 8.3 mm, and the resulting low grade of the slope across the panel, identifying areas for internal evaluation would be challenging when inspecting the AI side.

Internal damage was identified in the CT images as two forms. All 6 and 8 ply panels at both impact energies, exhibited the damage shown in Figure 4a characterized by a disbond between the composite and Al which extended through the composite with continued growth as delamination between composite layers. Additional damage in the form of fiber breaks and matrix cracking was also identified in the images. At the lower impact energy, the 10 Ply panels contained internal damage that was distinct from the other configurations (Figure 4b). Given that there was no visible external deformation for these panels and a small region of visible surface damage, this internal damage would be difficult to locate during an inspection.

Table 5. Summary of data collected from testing and CT image measurements.

Panel Designation	Energy (J)	t (mm)	Visible External Damage			Internal Disbond	
			Comp Depth (mm)	Comp Length (mm)	AI Depth (mm)	Length (mm)	Depth (mm)
8PlyQuasiGlass-2A	365	10.6	3.8	20.8	3.0	23.9	1.5
10PlyQuasiGlassUni-2A	367	12.3	0.0	20.8	0.0	47.7	0.8
10PlyGlassCarbonUni-1A	335	13.8	0.0	22.9	0.0	48.1	1.6
10PlyGlassCarbonUni-2A	372	13.1	0.0	38.5	0.0	64.6	0.8
6PlyQuasiCarbon-1A	367	10.0	3.6	82.5	3.1	72.5	2.2
6PlyQuasiCarbon-2A	367	10.0	5.4	86.3	6.5	97.5	3.0
6PlyCarbonUni-1A	370	10.0	2.2	39.2	3.1	77.7	2.9
6PlyCarbonUni-2A	369	10.0	3.8	32.3	3.1	73.9	2.3
8PlyQuasiGlass-1B	708	10.3	5.3	80.9	7.1	92.2	3.0
8PlyQuasiGlass-2B	701	10.6	7.9	80.0	8.3	93.9	3.0
10PlyQuasiGlassUni-1B	670	12.7	2.4	55.5	4.7	62.5	2.4
10PlyQuasiGlassUni-2B	691	12.2	3.0	69.8	6.4	102.4	3.7
10PlyGlassCarbonUni-1B	677	13.9	2.3	63.8	4.7	92.8	3.7
10PlyGlassCarbonUni-2B	725	13.1	2.3	74.3	6.2	109.8	3.9
6PlyQuasiCarbon-1B	724	10.1	3.0	100.5	3.4	111.8	3.0
6PlyQuasiCarbon-2B	691	9.9	4.7	91.8	6.7	102.1	3.2
6PlyCarbonUni-1B	702	10.2	7.0	92.0	6.8	117.6	3.1
6PlyCarbonUni-2B	697	10.1	6.8	87.0	7.3	102.8	3.0

While initially relatively smaller, this damage forms a stress concentration which could propagate under service loads. At the higher impact energy, the 10 Ply panels did show visible damage. The 6 Ply panels on average had larger disbond lengths, followed by the 8 Ply and 10 Ply panels respectively, while the disbond depths were slightly higher on average for the 10 Ply panels. The depth and length of this internal disbond damage depended on panel configuration and impact energy. For the 6 and 10 Ply configurations, doubling the impact energy caused an approximate average increase in disbond length of 1.5 while disbond depth increased moderately. The 8 Ply panels, however, demonstrated a nearly 4 time increase in disbond length with double the average disbond depth than the 8 Ply panel impacted at the lower energy level (though it should be noted there was only one valid specimen).

4 CONCLUSIONS

The primary finding from this investigation is that low velocity impact can result in significant internal damage with minimal externally visible damage. This non-visible damage state can be detrimental to the structural reliability of composite overlays to adequately transfer loads from the metal substrate, especially given that the damage state is of the form of disbond and delamination. Future work in computational modeling of the impact event using the obtained images for validation will enable a comprehensive investigation of composite materials and configurations to optimize overlay design. Moreover, analysis and computational simulation of damage propagation based on models of the existing internal damage using the 3D data collected through this research will inform inspection by quantifying the size of damage area that degrades performance and the rate of damage propagation under service loads. This information can then be used to schedule inspection intervals to identify and repair damage before it causes structural degradation.

REFERENCES

- Akimoto, H., Toda, M., Miyashita, J., Shonaike, G., Hara, S., Murakami, A., Hogg, P. & Ahmandinia, A. 2000a. Impact performance of macrocomposite laminates-2. Effect of adhesive layers. *Journal of Reinforced Plastics and Composites*, 19, 1268–1292.
- Akimoto, H., Toda, M., Miyashita, J., Shonaike, G., Murakami, A., Hogg, P. & Ahmadnia, A. 2000b. Impact performance of macrocomposite laminates-1. Evaluation of energy absorbed in non-penetration impact test. *Journal of Reinforced Plastics and Composites*, 19, 1363–1378.
- Baker, A. & Jones, R. 1988. *Bonded Repair of Aircraft Structures*, Springer.
- Baker, A. A., Rose, L. F. & Jones, R. 2003. *Advances in the bonded composite repair of metallic aircraft structure*, Elsevier.
- Bakis, C., Bank, L. C., Brown, V., Cosenza, E., Davalos, J., Lesko, J., Machida, A., Rizkalla, S. & Triantafyllou, T. 2002. Fiber-reinforced polymer composites for construction-state-of-the-art review. *Journal of Composites for Construction*, 6, 73–87.
- Belingardi, G. & Vadori, R. 2002. Low velocity impact tests of laminate glass-fiber-epoxy matrix composite material plates. *International Journal of Impact Engineering*, 27, 213–229.
- Bieniaś, J. & Jakubczak, P. 2017. Impact damage growth in carbon fibre aluminium laminates. *Composite Structures*, 172, 147–154.
- Carrillo, J., Gonzalez-Canche, N., Flores-Johnson, E. & Cortes, P. 2019. Low velocity impact response of fibre metal laminates based on aramid fibre reinforced polypropylene. *Comp Structures*, 220, 708–716.
- De Freitas, M. & Reis, L. 1998. Failure mechanisms on composite specimens subjected to compression after impact. *Composite Structures*, 42, 365–373.
- Evcı, C. & Gulgec, M. 2012. An experimental investigation on the impact response of composite materials. *International Journal of Impact Engineering*, 43, 40–51.
- Floros, I., Tserpes, K. & Löbel, T. 2015. Mode-I, mode-II and mixed-mode I+ II fracture behavior of composite bonded joints: Experimental characterization and numerical simulation. *Composites Part B: Engineering*, 78, 459–468.
- Gao, Y., Hu, W., Xin, S. & Sun, L. 2021. A review of applications of CT imaging on fiber reinforced composites. *Journal of Composite Materials*, 56, 133–164.
- Garcea, S. C., Wang, Y. & Withers, P. J. 2018. X-ray computed tomography of polymer composites. *Composites Science and Technology*, 156, 305–319.
- Goncalves, D., De Melo, F., Klein, A. N. & Al-Qureshi, H. A. 2004. Analysis and investigation of ballistic impact on ceramic/metal composite armour. *International Journal of Machine Tools and Manufacture*, 44, 307–316.
- Grabovac, I. 2005. *Composite reinforcement for naval ships: concept design, analysis and demonstration*. RMIT University.
- Hart, D., Udinski, E. & Noland, J. 2016. CG task force composite patch material testing. *West Bethesda, MD: NSWCCD-65-TR-2015/15, Naval Surface Warfare Center Carderock Division*.
- Hollaway, L. 2003. The evolution of and the way forward for advanced polymer composites in the civil infrastructure. *Construction and Building Materials*, 17, 365–378.
- Katunin, A., Wronkiewicz-Katunin, A. & Dragan, K. 2020. Impact Damage Evaluation in Composite Structures Based on Fusion of Results of Ultrasonic Testing and X-ray Computed Tomography. *Sensors*, 20.
- Lee, D.-W., Park, B.-J., Park, S.-Y., Choi, C.-H. & Song, J.-I. 2018. Fabrication of high-stiffness fiber-metal laminates and study of their behavior under low-velocity impact loadings. *Composite Structures*, 189, 61–69.
- Lee, M. & Yoo, Y. 2001. Analysis of ceramic/metal armour systems. *International Journal of Impact Engineering*, 25, 819–829.
- Lopes, C. S., Seresta, O., Coquet, Y., Gürdal, Z., Camanho, P. P. & Thuis, B. 2009. Low-velocity impact damage on dispersed stacking sequence laminates. Part I: Experiments. *Composites Science and Technology*, 69, 926–936.
- Noury, P., Hayman, B., McGeorge, D. & Weitzenböck, J. 2002. Lightweight construction for advanced shipbuilding-recent development. *Proceedings of the 37th WEGEMT Summer School*, 11-15.11.
- Roland, F., Manzon, L., Kujala, P., Brede, M. & Weitzenböck, J. 2004. Advanced joining techniques in European shipbuilding. *Journal of ship production*, 20, 200–210.
- Sadighi, M., Alderliesten, R. & Benedictus, R. 2012. Impact resistance of fiber-metal laminates: A review. *International Journal of Impact Engineering*, 49, 77–90.
- Sharma, A. P. & Velmurugan, R. 2022. Damage and energy absorption characteristics of glass fiber reinforced titanium laminates to low-velocity impact. *Mechanics of Advanced Materials and Structures*, 29, 6242–6265.
- Soutis, C., Duan, D. M. & Goutas, P. 1999. Compressive behaviour of CFRP laminates repaired with adhesively bonded external patches. *Composite Structures*, 45, 289–301.
- Weitzenböck, J. R. 2012. *Adhesives in marine engineering*, Elsevier.
- Zhao, X.-L. & Zhang, L. 2007. State-of-the-art review on FRP strengthened steel structures. *Engineering Structures*, 29, 1808–1823.

Development of high durable precast PC deck with ultra-high-strength fiber-reinforced concrete layer

H. Hayashi & Y. Yasukawa

East Nippon Expressway Company Limited, Tokyo, Japan

N. Oba & K. Sasaki

Obayashi Corporation, Tokyo, Japan

ABSTRACT: In the renewal of old road bridges, precast decks are used to make construction time shorter and quality better. A waterproof layer is applied at the top surface of the deck to avoid the intrusion of water accelerating concrete deterioration. However, waterproofing is one of the causes of construction time delays because waterproof work must be conducted under dry conditions. From this reason, we have been hoping to develop a precast deck to omit waterproofing at the site. To satisfy this hope, we have just developed a high durable PC deck with waterproof performance by ultra-high-strength fiber reinforced concrete (UFC) on the top surface of the deck. On this report, we are going to state the feature of this new deck and the experiments conducted to confirm the waterproof performance required for 100 years of road track service.

1 INTRODUCTION

The East Nippon Expressway Company Limited (hereinafter referred to as NEXCO EAST) has been conducting large-scale renewal work of bridges and tunnels as part of an expressway renewal project since 2015. The purpose of this work is to maintain the safe and comfortable highway network to contribute social and economic activities from 100years. In case of bridge work, we replace deteriorated RC decks of existing bridges with more durable deck, that is prestressed concrete decks as standard. And as a construction, it is desirable to maximally shorten working days because traffic restrictions, such as a decrease in the number of lanes over a long period have a large impact on traffic. Precast decks are widely adopted to minimize the impact of traffic restrictions during construction and to shorten the process.

Deck replacement work is conducted to avoid busy traffic seasons, such as year-end and New Year holidays, long holidays, and summer vacations. Currently, Japan is experiencing a rainy season and snow and ice season. Deck waterproofing, which cannot be installed in rainy weather, hinders the shortening of traffic restrictions. Therefore, if the types of work affected by weather that cannot be controlled by human power during on-site construction can be eliminated, it is expected to contribute significantly to process control.

In this study, we focused on ultra-high-strength fiber-reinforced concrete (UFC), which is high-strength, dense, and excellent in waterproofing, and attempted to develop a precast PC deck with a UFC layer for waterproofing (hereinafter referred to as UFC PC DECK).

2 UFC PC DECK

2.1 Outline of UFC PC DECK

Figure 1 shows an outline of the UFC PC DECK. It is a precast deck with UFC layer on lower based concrete. To prevent cracks from occurring under the designed load during service, a deck thickness of 220 mm and a UFC thickness of 20–50 mm (that changes according to tensile stress), and this UFC layer is used as a waterproof.

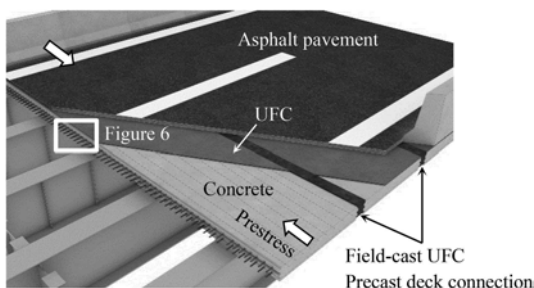


Figure 1. Outline UFC PC DECK.

Contrary to the method of overlaying the UFC on the top surface of hardened deck concrete, the UFC is poured by layering before the lower based the concrete hardens. This method can reduce the binding force acting on UFCs with large self-contractions. In addition, the UFC layer and concrete could be attached more strongly. And furthermore, prestresses can be introduced in the lower based concrete as well as in the UFC layer.

The minimum thickness of the UFC was set to 20 mm, considering the viscosity of the material at the time of fabrication, crack suppression after curing, and variations in construction thickness. Decks are manufactured at the factory and joined onsite. By adopting the UFC for deck connections, the entire bridge surface can be covered with the UFC for waterproofing.

2.2 UFC used for the precast PC deck and deck connection

The mix proportions of the UFC used in this method are listed in Table 1. The premixed powder includes cement, silicate filler, fine aggregate, water, and special superplasticizers. High-strength steel fibers with strengths greater than 2 GPa are used to form the UFC. The shape of the fiber is straight, and its length and diameter are 13 and 0.16 mm, respectively. The volume fraction of the fibers is 2.0%. This UFC have a compressive strength of 180 MPa and tensile strength of 8.8 MPa by standard curing (both characteristic values).

Table 1. Mix proportions of UFC used for the precast PC deck and deck connection.

Unit content (kg/m ³)				Steel fiber (kg/m ³)
Water	Premixed powder	Sand	Superplasticizer	
230	1830	350	32	157

3 WATERPROOFNESS OF UFC LAYER

3.1 Required performance of the waterproof layer

The required performance of the waterproofing layer of the UFC PC DECK must be equal to or higher than the current waterproof layer material in the technical standards of

expressways. The design service life is set to 100 years, which is the same as the design service period of the bridge.

Hydraulic conductivity is used as an index for the evaluation of waterproof performance. As waterproof performance is required for the deck, the upper limit value of the hydraulic conductivity is set assuming the water pressure and action time acting on the deck during the service period.

The time required for the moving vehicle to pass in the wet state is determined as the cumulative time for the water pressure to act on the deck. The number of times the vehicle passed is assumed using data measured on actual expressways, and the number of days when the upper surface of the deck is in a wet state is assumed using meteorological data.

The load by the tires is calculated with a ground pressure of 0.5 MPa assuming a large vehicle, and the relationship between the depth of water penetration into the waterproof layer and hydraulic conductivity is calculated during the 100 years of service. The calculation results are listed in Table 2.

The hydraulic conductivity required for the UFC layer is determined to be 1.0×10^{-13} m/s or less with a certain margin for the calculated value of the water penetration depth, that is not to reach the lower base concrete, in the design life at the minimum thickness of the UFC layer of 20 mm.

Table 2. Hydraulic conductivity requirement of waterproof layer.

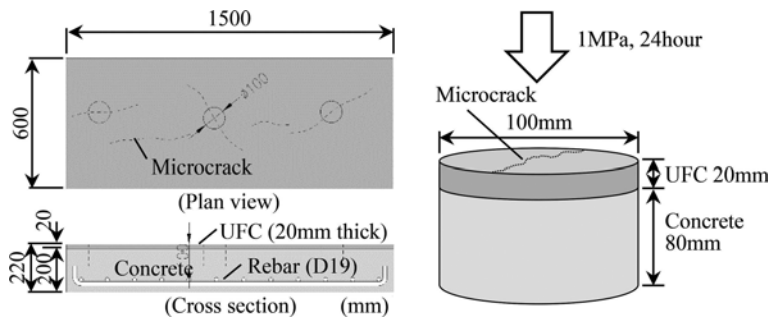
hydraulic conductivity (m/s)	water penetration depth (mm)
1.0×10^{-11}	49.3
1.0×10^{-12}	15.6
1.0×10^{-13}	4.9
1.0×10^{-14}	1.6
1.0×10^{-15}	0.5

3.2 Performance confirmation test (water permeability test)

Using a specimen simulating the UFC PC DECK, the hydraulic conductivity was confirmed via a hydraulic permeability test. Figures 2 and 3 show the outline of the specimen. The UFC was placed on the upper 20 mm layer of the UFC PC CECK with a thickness of 220 mm. The lower based concrete is high-early-strength with a design standard strength of 50 MPa, assuming an actual structure. In addition, we intentionally have induced microscopic cracks (hereafter referred to as microcracks) on the surface of the UFC layer that cannot be observed by close visual observation. Hydraulic conductivity was measured by collecting test specimens with a diameter of 100 mm and height of 100 mm from the site where the microcrack occurred. In the water permeability test, water was infiltrated into the test piece with a water pressure of 1 MPa and pressurization time of 24 h using the input method. After completion of pressurization, the specimen was split along a microcrack to measure the penetration depth, and hydraulic conductivity was determined from the penetration depth of the split surface. The maximum hydraulic conductivity obtained by the test was 1.78×10^{-14} m/s, and it was confirmed that both were less than 1.0×10^{-13} m/s.

Furthermore, we confirmed the waterproofing performance after applying tensile fatigue and freeze-thaw loads to the UFC layer. Using a specimen that was intentionally induced microcracks, a specimen of $100 \times 100 \times 400$ mm was drawn from the location where the microcrack occurred.

In the tensile fatigue test, the tensile stress at the design load of the deck is simulated, and the bending tensile tension was applied such that a tensile stress of 4 MPa acted on the outermost edge of the UFC layer, and tensile tension was applied for two million cycles at a stress amplitude of 0–4 MPa. In the freeze-thaw test, freeze-thaw action was performed for 300 cycles. The hydraulic conductivity was measured in the same manner as described above, and it was confirmed that the maximum was 1.48×10^{-14} m/s, and that both were 1.0×10^{-13} m/s or less.



Figures 2 & 3. Layered concrete for making microcracks; Specimen of water permeability test.

4 STRUCTURAL INTEGRITY OF UFC PC DECK

4.1 Outline

Because UFC PC DECK is overlaid before the lower based concrete hardens, it is essential to ensure the adhesion between these dissimilar materials. And furthermore, other important adhering points are the asphalt pavement - UFC and UFC - concrete. At the deck connection, there is a joint between the UFC of the connection and UFC layer of the precast deck. In addition, the adhesion between the UFCs is important.

4.2 Asphalt pavement - UFC adhesion performance

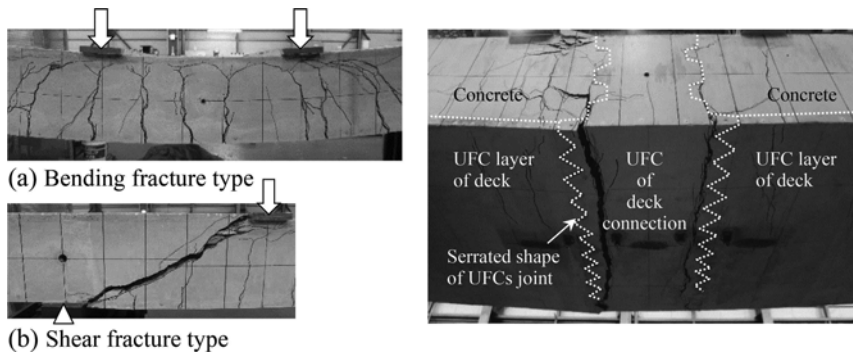
According to the condition of temperature and load, the performance of pavement, that is adhesion and shear, is changing. So, each test ruled as NEXCO's technical standards has been done. The result of tensile adhesion tests and shear adhesion tests under each test condition were satisfied required level.

4.3 UFC - concrete adhesion performance

The adhesion between the UFC and concrete was confirmed by tensile adhesion tests, shear adhesion tests, and bending loading tests of the beam specimens. In the bending loading test, the adhesion between the UFC and concrete at the time of fracture was confirmed using bending fracture type and shear fracture type specimens. The beam height was 220 mm and UFC was 20 mm, assuming the thickness of the deck, and the shear span was 1000 mm for the bending fracture type and 500 mm for the shear fracture type. The bending fracture is shown in Figure 4a. In the bending fracture specimen, the tensile rebar yielded as in a general concrete beam, the UFC was finally crushed, and the load was reduced. The shear fracture situation is shown in Figure 4b. In the shear fracture specimen, after the tensile rebar yielded, the oblique crack extended and eventually penetrated the UFC layer, thereby reducing the load. None of the specimens exhibited any phenomenon in which the UFC layer peeled off until the maximum bearing capacity was reached. Thus, it was confirmed that adhesion could be secured even if the UFC was layered on fresh concrete.

4.4 UFC - UFC adhesion performance

The adhesion performance between the UFCs was confirmed by fabricating test specimens with vertical joints between UFCs and measuring the tensile strength of the joint surface using a uniaxial tensile test. The average tensile strength was 6.8 MPa, which was lower than the crack initiation strength of the UFC, 8.0 MPa. Therefore, the tensile stress acting on the joint must be lower than the tensile strength of the joint.



Figures 4 & 5. Cracks of the bending test; Cracks of the bending test at UFCs joints.

Additionally, a bending loading test of the beam test specimen at the joint was conducted. The UFC joints were serrated, as shown in Figure 6. The UFC layer was loaded such that the joint was tensile in nature. The crack did not expand at the UFC joint but was destroyed at the deck connection UFC (Figure 5). Although the tensile strength of the UFC joint surface was lower than the crack initiation strength, it was confirmed that the tensile performance was equal to or better than that of the UFC base part by adopting a serrated shape of the joint part.

5 CONNECTION OF UFC PC DECK

UFC PC DECKS are joined using the same UFC as the decks (Sasaki 2021). The upper layer had a serrated shape, as shown in Figure 6. As mentioned above, because the tensile performance of the joint between UFCs is lower than the crack initiation strength, the stress acting by giving the joint surface an angle is reduced, and this is not a weak point. As shown in Figure 7, the interface between the UFCs was resisted by tension and shear, and the joints did not fail.

6 FATIGUE DURABILITY OF UFC PC DECK

6.1 Outline

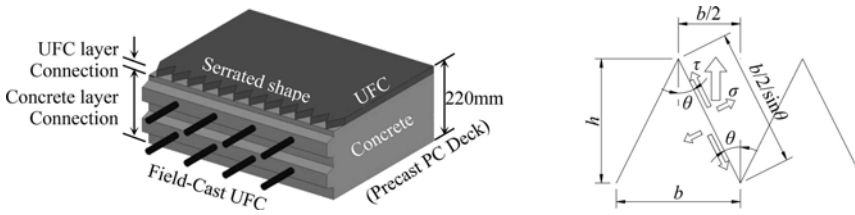
As we mentioned before, we have had several tests to confirm the required performances, however, it is necessary to have tests similar to the utmost to real state for adopting this new UFC PC DECK on site. So, we have conducted a wheel load running test using UFC PC DECK specimen that simulated a full-scale.

6.2 Specimen

An outline of the specimen used in the wheel-load running test is shown in Figure 8. The plane dimension is 4,500 mm in the longitudinal direction and 2,800 mm in the perpendicular direction. The thickness of the deck is 220 mm, and the upper UFC layer is 20 mm. The deck span is 2,500 mm. A hanch thickness of 50 mm is provided at the fulcrum, and the total thickness is 270 mm. The UFC on the upper layer of the specimen is poured after the lower layer of concrete is poured and hardened, as in other specimen production. After concrete hardening, using PC steel bars arranged as shown in Figure 8, prestress was introduced in the direction perpendicular to the bridge axis using the post-tension method. The prestress amount introduced was 312 kN per PC steel rod, to ensure that the stress degree of concrete was 5.0 MPa.

6.3 Loading method

The wheel load running tester is a crank type, and loading range is 1,500 mm front and rear from the center of the tester, with a total length of 3,000 mm. The loading rate was 30 times/min.



Figures 6 & 7. Deck connection of UFC PC DECKS; Stress at serrated shape joint.

Iron wheels with a width of 500 mm were used. The loading conditions are shown in Figure 8, and the test status is shown in Figure 9.

The loading conditions are as follows: Step 1 under drying conditions and Step 2 under immersion conditions, both of which had a load of 100,000 cycles of 250 kN. A load of 100,000 cycles of 250 kN corresponded to the simulated fatigue load in designed period of 100 years. After completion of Step 1, Step 2 is performed with the surface filled with water. The water is filled a space 10 mm × 3,800 mm × 2,000mm. And red colored water is used to make it easier to observe leakage.

The static loads are loaded at times 1, 1000, 10,000, 40,000, 80,000, and 100,000 for both steps. For each static load, the deflection of the deck was measured and cracks were observed.

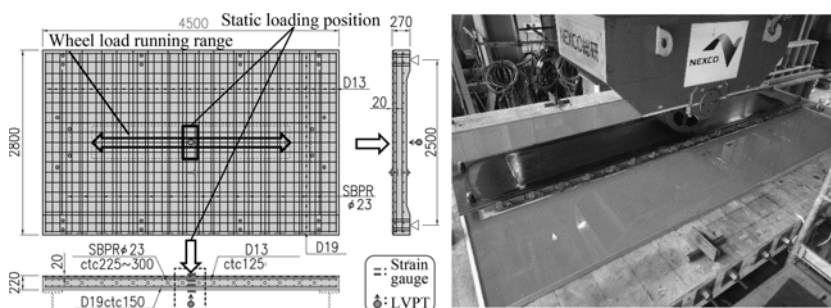
6.4 Test results

6.4.1 Cracks and deflection on the lower surface of the specimen

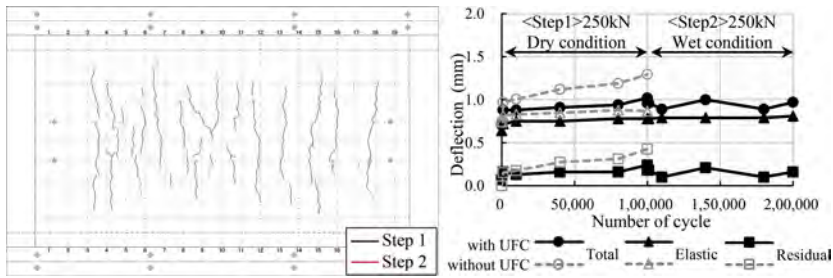
Figure 10 shows the occurrence of cracking on the lower surface of the specimen after the test is completed. No remarkable crack extension was observed from Steps 1 to 2. Figure 11 shows the change in deflection over time immediately below the loading point. The figure shows the transition of the residual deflection, elastic deflection, and total deflection at the center of the specimen. The figure also shows the test results for an existing PC deck specimen without a UFC layer, under the same test conditions. The PC deck without the UFC layer showed a gradual increase in total deflection owing to the increase in residual deflection in Step 1, while the UFC with deck showed stable fatigue properties without a large increase in residual deflection. From this result, we have confirmed the remarkable effect of the UFC layer from the point of load carrying capacity.

6.4.2 Cracks on the upper surface of the specimen and water penetration

Figure 12 shows the cracking situation on the upper surface of the deck after the test, and Figure 13 shows an example of the cut surface. Cracks are primarily microcracks that are intentionally generated during specimen preparation. Visual observation of the cut surface revealed no water penetration of the underlying concrete through the UFC layer to the lower based concrete.



Figures 8 & 9. Wheel load running test.



Figures 10 & 11. Cracks of lower surface; Deflection-cycle relationship.

6.4.3 Hydraulic conductivity of cracked areas

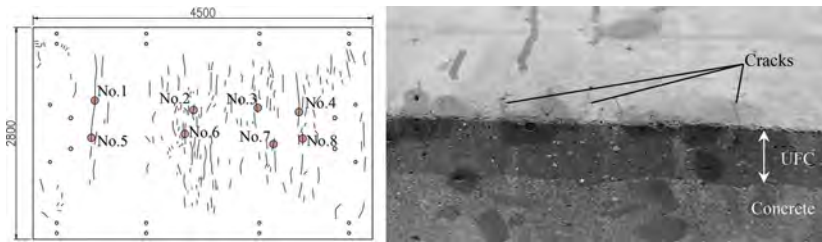
Collecting the specimens collected from the positions shown in Figure 12, a hydraulic permeability test was performed on six specimens. The maximum hydraulic conductivity obtained by the test was 1.92×10^{-14} m/s, and it was confirmed that both were less than 1.0×10^{-13} m/s.

6.4.4 UFC - concrete adhesion performance

The cut surface was visually checked to determine whether the adhesion of the UFC and concrete was secured. As shown in Figure 13, no peeling was observed at the interface between the UFC and concrete on the cut surface after the test.

7 MANUFACTURE OF UFC PC DECK

The UFC PC DECK is manufactured in a factory that manufactures conventional precast PC decks. For UFC PC DECK, the adhesion between the concrete and UFC is important, and it is necessary to layer the UFC layer before the lower based concrete hardens. Therefore, we start pouring the UFC layer approximately 30 min after the casting of the lower based concrete, and strictly manage the time to ensure that the UFC layering work has been completed within 2 h after casting the lower based concrete (Figure 14). The surface of the underlying



Figures 12 & 13. Cracks of upper surface; Status of deck cross section after the test.



Figure 14. Powering of UFC on fresh concrete.

concrete is roughened to achieve better adhesion to the UFC. After a certain period, the surface of the UFC is smoothed with a steel trowel, covered with a curing mat, and flooded, and the entire deck is steam-cured. After steam curing is completed, it is confirmed that the concrete has reached the specified strength, and prestressing is introduced to the deck. Subsequently, they are cured in water for 7 days.

8 LIFE CYCLE COST

By the adoption of UFC PC DECKs on bridges with a length of 277 m and width of 10 m, the construction cost has increased by 154 million JPY compared to conventional precast PC decks due to the high cost of UFC materials. However, in the case of conventional technology, it is estimated that deck waterproofing work needs to be updated three times in 100 years, and that the initial deck waterproofing work is 26 million JPY, and the waterproofing work at the time of renewal is 43 million JPY per time. When the life cycle cost of the design service life of 100 years is calculated, it is almost equivalent to this technology and conventional technology (Table 3). In addition, the traffic restriction period for one pavement renewal is 25 days because deck waterproofing work is required with conventional technology, however, with this technology it is shortened to 5 days (Table 4).

Table 3. Direct effects of UFC PC DECKs (life cycle costs).

	(A) With UFC layer	(B) Conventional technology	(A-B)
	million JPY	million JPY	million JPY
100 years LCC (a+b)	154	169	- 15
(a) Construction cost (incremental)	154	26	+ 128
(b) Maintenance cost:	0	143	- 143
Delay cost due to bad weather	0	17	- 17

Table 4. Indirect effects of UFC PC DECKs (traffic restriction period).

	(A) With UFC layer	(B) Conventional technology	(A-B)
	days	days	days
Traffic regulation period through 100 years (a+b)	51	121	- 70
(a) Regulation period for deck renewal	34	37	- 3
(b) Regulation period for pavement renewal	17	84	- 67
Additional period due to bad weather	0	25	- 25

9 CONCLUSIONS

By developing the new technology of UFC PC DECK, it is possible to realize a precast deck with high durability and waterproof function for the entire bridge surface. In addition, because deck waterproofing is not required, it is possible to shorten the traffic restriction period and avoid the risk of process delays owing to unseasonable weather. In the future, to make effective use of this technology, we aim to standardize the deck replacement business in NEXCO EAST.

REFERENCES

- Sasaki, K. 2021. Experimental study on precast deck connection using ultra-high-performance concrete. In Yokota & Frangopol (eds), *Bridge Maintenance, Safety, Management, Life-Cycle Sustainability, and Innovations*: 2469–2476. London: Taylor & Francis Group.

Development of digital rules for optimal auto-routing design of pipe

S.-E. Park, S.-W. Choi & E.-B. Lee

Pohang University of Science and Technology (POSTECH), Pohang, Gyeongsangbuk-do, Korea

ABSTRACT: Due to the recent retirement of engineering personnel, the number of piping engineers is rapidly decreasing. They are not actively responding to frequent design change requests from the owner. This study aims to develop digital rules for auto-mating pipe routing design. To this end, the piping design rules of EPC plants, codes and standards for piping design, and owner's requirements were collected. A total of 8 stages of piping design rule taxonomy were established to categorize the piping design rules. The collected piping design rules were analyzed by experts, and a digital code of account for system recognition was established based on the classified rule taxonomy. Finally, the code of account for pipe route design was converted into a digital rule. The digital rule developed in this study can be used as a database for efficient information management as well as pipe route design.

1 INTRODUCTION

As the plant industry is intensive with high added value, it is a convergence with the characteristics of manufacturing and service industries simultaneously. It contributes greatly to the advancement of the industrial structure. The domestic plant industry has seen rapid growth as a new export power source, with overseas orders soaring more than 50% annually since 2003. However, many parts of the core design sector and equipment supply depend on developed countries. As profitability deteriorates due to low-priced orders, various improvement efforts are being made simultaneously to overcome this. Among them, piping design occupies the most prominent portion of all plant project design tasks, and many related tasks need to be considered during design. The result of route selection has a significant influence on subsequent work. In addition, most of the estimated amount is not only determined by the quantity calculated during the pipe design but also is one of the most burdensome industries due to the complex design conditions.

Due to the recent aging and retirement of engineering personnel, the number of experienced piping, electrical, and instrumentation engineers is rapidly decreasing, and they are not actively responding to frequent design change requests from the owners. In addition, as the plant becomes more extensive and complex, the type and amount of piping increase. Furthermore, the design of the piping route is not automated yet, so the designer's capabilities significantly affect the design quality. Therefore, there is a need for a plan to increase work efficiency in the entire design process for piping design engineers by presenting an optimal route by automating the piping route design in the initial design stage. The need for piping auto-routing systems is increasing by applying artificial intelligence (AI) technology. This study aims to develop a digital rule for pipe design that can be recognized by machines necessary for developing AI-based piping auto-routing technology. To this end, pipe design rules of Engineering, Procurement, and Construction (EPC) plants, codes & standards for pipe design, and owner's requirements were collected. Subject matter experts (SMEs) analyzed the collected design regulations for pipe design. It was digitally categorized based on the analyzed piping design rules. A piping design rule taxonomy for digital categorization was established according to the Work Breakdown Structure (WBS). Finally, a digital rule for system recognition was developed by making

code for each pipe design rule so that computers could recognize it. The scope of the study was limited to pipe routing design among the engineering fields of EPC plant projects, and the study was conducted on the codes & standards and owner's requirements for piping design.

2 LITERATURE REVIEW

Previous studies were reviewed by classifying the contents to be performed in this study into two categories. The first is a prior study on the piping process, and the second is a study on the code classification system. The authors reviewed the approaches of similar studies and analyzed limitations through this.

2.1 *Piping design automation*

Yan and Ubald (2012) implemented a system that derives assembly sequence information automatically by algorithmizing constraints in a pipe installation plan. However, there is a limitation that auto-routing cannot be performed in the initial design stage, considering only the constraints. Nguyen et al. (2016) developed an improved Dijkstra algorithm that exports the shortest route with minimal bending and elbow in piping design. However, this study has a limitation: optimal route design is impossible considering only the shortest route. Shin et al. (2020) studied the automation of piping route design in a ship's engine room using reinforcement learning in the initial design stage. Nevertheless, there is a limitation that unlearned routes cannot be designed due to the failure to consider the design conditions applied to the actual industry and the AI model that selects routes based on learned information. Min et al. (2020) proposed a Jump Point Search (JPS)-based pipe automatic routing algorithm to find the optimal pipe route. However, this study has a limitation: nodes in the preference area should be allocated as temporary targets to optimize the route.

2.2 *Code of account in engineering*

Lee and Kang (1994) attempted to develop a standardized information classification system of construction that can be applied to construction management techniques. To this end, a construction division system was developed that was classified into three stages: facility element, structure element, and construction element. Kang and Kwak (2001) developed and proposed an integrated standard of specification classification code centered on the quantitative calculation standard code system. However, there is a limitation that code composition is impossible if there are specific items that cannot be classified based on quantitative calculation. Wang et al. (2010) developed a classification system for electric construction industries. Moreover, an effective management method using an integrated management system was presented through the computerization of the specifications of the electric work used. However, this study has a limitation in that it takes much time to build a DB, and it is difficult to respond quickly to new technologies or new construction methods by organizing different types of specifications for each public institution into a unified format. Moon and Han (2014) added work management units and expanded the site classification in developing the river sector work classification system based on the construction information classification system. Lee et al. (2015) identified the problems with the existing piping material code classification system. They derived an improvement structure of the piping material code classification system through a hierarchical classification structure. However, this study had limitations in that it was challenging to distinguish material specifications through codes due to the increased number of code digits up to 20 digits.

This study established a digital category and taxonomy of piping design rules in consideration of the approaches and limitations of previous studies. The authors classify more detailed piping design rules to overcome the limitations of previous studies and levels 0 to 7, a total of eight stages. This study aims to overcome the limitations of previous studies and develop digital rules according to the code of account for pipe design that the system can recognize for rule-based piping auto-routing.

3 RESEARCH OVERVIEW

This study aims to develop digital rules for pipe design that can be recognized by the system during auto-routing. To this end, in addition to the design rule and piping installation manual, codes & standards and owner's requirements were collected. A digital category structure for system recognition was defined for the collected piping design rules. A piping design rule taxonomy for onshore plants was established according to the WBS. Based on the rule taxonomy, the pipe design specification of codes & standards, ITB, and other pipe design rules were discussed with pipe design SMEs to analyze pipe design rules and classify them. Based on the design rules analyzed above, a code of account for pipe route design was established for efficient design rule classification and the establishment of a digital category structure for system recognition. The code classification system for pipe path design consisted of four categories: main category, sub-category, sub-sub category, and others. The attribute classification was subdivided into seven levels, and the code consisted of 11 digits. Digitally coding rules developed digital rules and owner's requirements are analyzed according to the classified code system. Each rule was composed of a total of 11 digits systems with a classification symbol indicating the classification status of each type. Details of this are described in Chapter 4. This study was conducted in 5 steps, as shown in Figure 1, and the details of each step are as follows.

- Step 1: Collection of rules related to piping design among codes & standards and owner's requirements for piping design
- Step 2: Development of digital categories and taxonomy of piping design rules
- Step 3: Analysis of piping design rules
- Step 4: Establishment a code of account for piping auto-routing
- Step 5: Development of digital rules for piping auto-routing

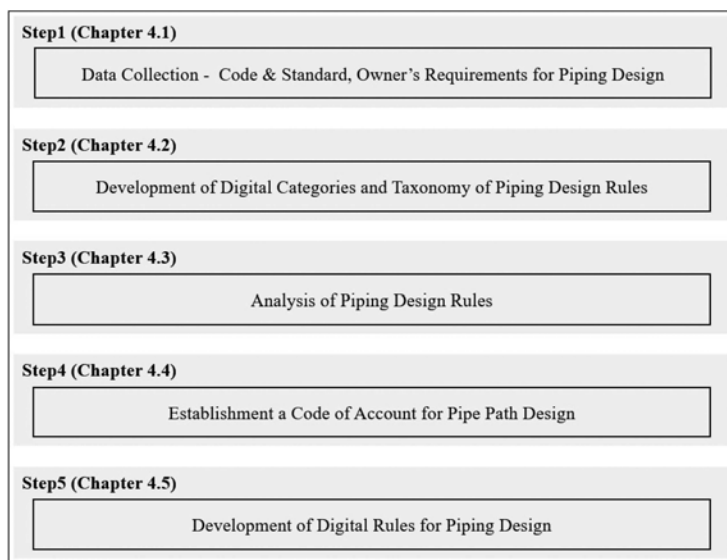


Figure 1. Research process.

4 MODELLING AND IMPLEMENTATION

4.1 Data collection

EPC plant design reflects various design regulations and requirements, including design rules and guidelines, piping installation manual, and classification, as well as international codes & standards such as API, ASME, and owner's requirements. Therefore, in this study, piping design rules applied to EPC plant projects were collected through large EPC companies carrying out EPC plant projects.

4.1.1 Collection of codes & standards for piping auto-routing

The design regulations of the plant project are prepared with international codes & standards as well as the basic data provided by the owner (Kim et al., 2018). This is used as primary data for the basic and detailed design stages, and standardizes details such as engineering design work and manufacturing inspection to reduce repetitive time and cost and enable standard design. In addition, the ultimate goal of codes & standards is to enable mutual compatibility when the same standard is applied.

The major codes & standards used in the piping system of plant projects are the American Petroleum Institute (API), American Society of Mechanical Engineers (ASME), and American Society for Testing and Materials (ASTM), which are American standard codes. In addition, there are European Standards (EN), Norwegian Standards (NORSOK), and Canadian Welding Beuro (CWB). Depending on the type and location of the project, the standards used are different.

Korean EPC companies' plant projects carried out overseas followed the US standard codes API, ASME, and ASTM. Some projects used European Standard (EN) and Japan Industrial Standards (JIS) were used. Recently, it has been a trend that follows group standard codes such as API, ASME, and ASTM. This study collected piping-related codes among ASME Standard (ASME, 2021).

4.1.2 Collection of owner's requirements for piping auto-routing

Since the ultimate purpose of an EPC plant project is to provide results that meet the owner's needs, the owner's requirements must be reflected in design rules and, codes & standards. However, in the initial design stage, it is difficult to format in the form of information that can be reflected in the design, such as the large variability of the owner's requirements and the lack of specific information provision. Such a situation reduces the reliability of the project's direction and goals, causes a delay in decision-making and reversal of work, and results in deterioration of design quality. Therefore, this study collected Invitations to Bid (ITB) and Scope of Work (SoW) of 20 EPC plants to identify the owner's requirements. Table 1 below lists a part of the collected ITB and SoW.

Table 1. Collected owner's requirements data list.

Owner's Requirements	
No.	Projects name
T1	Norway_Aasta Hansteen_FPSO_SoW
T2	Nigeria_Gbaran Ubie IOGP_CPF&New Manifolds_EPC_SoW
T3	Saudi_Onshore plant_SoW
T4	Lotte Versalis Elastomers_LVSR_EPC_SoW
T5	Texas_Trailblazer Energy_FEED Report
T6	Chevron Lummus Global_Saudi_Engineering Design Package
T7	Taeon_thermal power plant_SteamTurbine_Tech Spec
T8	India_Hindustan Petroleum_Flue Gas Scrubbing Unit_EPCM_SoW

4.2 Development of digital categories and taxonomy of piping design rules

Based on the collected codes & standards and owner's requirements, a digital category structure for system recognition of piping design rules was defined. A rule taxonomy of piping design for EPC plants was established for digital categorization. Taxonomy originated from the Greek word taxis+nomos (law or science), also known as containment hierarchies, as a classification of tree structures for a set of objects (Choi and Lee, 2022).

To this end, the hierarchical structure of the EPC plant project was first analyzed. EPC plant projects are divided into engineering, production, and construction, and engineering disciplines are subdivided into the process, civil and structure, mechanical, piping, and electrical. Among them, piping is primarily classified into Material, Installation, and Stress analysis & supports, and piping installation can be divided into layout modeling and piping routing. This study further subdivided pipe routing for accurate pipe design rule analysis. In the case of pipe routing, it was separated into Above Ground piping (AG piping), a line passing over the ground, and

Under Ground piping (UG piping), a line buried under the ground, depending on the location of the pipeline. In addition, it was further divided into Rough and Detailed in consideration of the possibility of developing a system that automatically optimizes the piping route when designing pipes in the future. Rough refers to a design rule for quick routing, including control and PSV valves, to check the results, adjust the layout, and adjust the equipment position and P/R Dimension. Detailed refers to routing, including all components of P&ID.

Rule taxonomy was established based on the hierarchical structure of the EPC plant project. To this end, this study adopted the WBS system. WBS is a system that visually classifies a classification system into multiple layers based on dependencies and has the advantage of being able to classify complex project ranges and visualize the results linked to projects and dependencies. Therefore, this study classified digital rules for pipe design according to the WBS system, and classified them into a total of eight stages from level 0 to 7 for more detailed pipe design rule classification.

- Level 0: EPC Plant Project
- Level 1: Engineering, Procurement, Construction
- Level 2: Process, Civil and Structure, Piping, Electrical,
- Level 3: Piping Materials, Piping Installation, Piping Stress Analysis & Supports
- Level 4: Plant Layout Modeling, Pipe Routing
- Level 5: AG Piping, UG Piping
- Level 6: Rough, Detail
- Level 7: General, Local, Global

4.3 Analysis of piping design rules

Rule analysis was performed on the pipe design specifications and other pipe design rules of the collected owner's requirements (ITB). EPC plant pipe design experts classified pipe design rules based on the previously established pipe design taxonomy.

Most of the rules are common to the project, and not only do the original sentences and source data for each rule are not accumulated, but there are many rules for ordinary design

Table 2. Analysis of design rules according to the classification of pipe path design rules.

L1	L2	L3	Rule Description
Pipe Routing	Piping	General	Piping shall be routed to ensure the shortest practical length.
			Piping, break flanges and valves at grade shall not be located above manholes or drain trenches, nor supported from grade above buried lines and cables.
			Special considerations shall be given to lines with two-phase flow particularly with regard to the supporting systems.
Piperacks	Piping	General	Adequate space shall be provided to support instrument cable racking and electrical lighting conduits from the piperack structure.
			For units requiring overhead installation of electrical power, space for electrical cable racking shall also be included.
			Piperacks shall include for 20% unoccupied space for each level of piperack for the addition of future lines.
Offsite Piping	Piping	General	All piping shall be located on pipe tracks at grade and supported on concrete sleepers.
			Individual pipes can be supported from concrete piers.
			Consideration shall be given to the size of headers and the size of supporting steel and the thickness of any insulation.

experiences. Therefore, in this study, in addition to the collected codes & standards and ordering requirements, about 2,000 of know-how accumulated from design experience when carrying out projects (about 20) were classified and organized into 400 design issues. The following figure is a part of the Excel data sheet for pipe rule analysis and is the result of detailed design regulations for each level.

4.4 Establishment of a code of account for pipe route design

Based on the analyzed design rules, a code of account for pipe route design was established for design rule classification and rule analysis. The design codes can be used as databases for procurements, construction, estimation, cost control, and design, and are essential for providing the shape of 3D modeling of pipes. It is crucial to design them with the value of information use and future scalability. The design code classification systems should be carefully reviewed in consideration of automation and efficiency before coding.

In this study, based on the functions and types of codes reviewed in Chapter 2 and the analysis and classification of design rules performed in Chapter 3, a piping code system was established to develop a digital category structure for system recognition. The code classification system for pipe route design consists of four categories: main category, sub-category, sub-sub category, and others, and the attribute classification was subdivided into seven levels. A category is structured so that rule properties can be specified as it descends to the lower classification structure, as shown below (Figure 2).

- Main category: Layout/Routing Classification, Applied Location, Applied Method
- Sub-category: Applied Range, Item Classification
- Sub-sub category: Item Detailed Classification
- Others: Rule Description

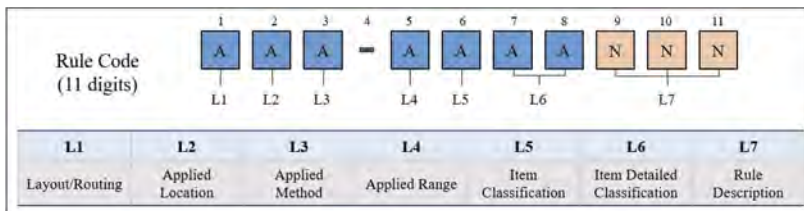


Figure 2. The classification of a rule code system for piping design.

The number of code digits consisted of 11 digits. The design rule code consisted of letters, numbers, arbitrary symbols, or a combination of them assigned to item properties for information processing according to the order of the already defined classification system.

4.5 Development of digital rules for piping auto-routing

For efficient data processing during auto-routing, data coding that the system can recognize is required. It is challenging to maintain data consistency and causes a decrease in efficiency if the data code used in the actual model is not clearly defined. Therefore, in this study, the digitally coded rules and owner's requirements analyzed according to the code system classified above were named digital rules.

Each rule is assigned a classification symbol indicating the classification status of each type to form a digital rule in a total of 11 digits, and each rule has an independent rule code. The set of digital rules becomes the basis for generating the rule table's attributes; eventually, the rule table consists of a set of rule attributes and parameters. This rule table is a criterion for selecting an appropriate design rule according to the design situation condition during auto-routing. Design rules for general and local issues of AG piping and UG piping among pipe routing are coded and displayed as digital rules. Figure 3 below displays a part of the digital rule table for onshore plants.

L1		L2		L3		L4		L5		L6		L7		Code		
Code	Name	Code	Name	Code	Name	Code	Name	Code	Name	Code	Name	Rule Description				
R	Pipe Routing	A	AG Piping	R	Rough	G	General	B	Base	BS	Basic	The lowest point of all flanges or insulation on pipe running in trenches shall be minimum 150 mm from the bottom of trench.		RUD-BGTR080		
												Process piping shall not be buried.		RUD-BGTR030		
												Where individual pipes at grade are required to cross a road, they shall be buried and pass under the road with a minimum cover height of 1200mm.		RUR-GBSD040		
												Changes in direction shall be accomplished by flat turning.		RAD-BPPR170		
												Regulating, throttling or control valves shall be accessible for hand operation.		RAD-GBBS370		
												A suction line to a centrifugal pump with side or end entry shall be installed with an eccentric reducer (top flat) adjacent to the pump nozzle or nozzle size valve.		RAD-LPCN070		
								P	Pump	CN	Pump Centrifugal	All overhead suction lines shall drain toward the pump without vapour pockets.		RAD-LPCN010		
												The reducer shall be located 2D apart from pump suction nozzle.		RAD-LPCN080		
												CO	Tower	Adequate space shall be allowed between adjacent lines and between lines and the vessel shell to allow the installation of pipe supports and insulation.		RAD-GBSD010
														The back of pipe to vessel shell distance shall normally be 450mm for non-insulated lines and 550mm for insulated lines.		RAD-GBBS420
												VS	Vertical Vessel	Piping for vertical vessels should be located radially around the vessel on the pipe rack side, or should align with adjacent equipment.		RAD-LVCO050
														Piping of size NPS 1 1/2 and less shall not be run in piperacks. (I.e. min pipe rack line size NPS 2).		RAD-BPPR110
B	Global	P	Piping Way	PR	Pipe Rack	If pipe racks intersect, establish different elevations for lines running north-south versus east-west.		LSS-SPPR041								

Figure 3. An example of a digital rule table.

5 CONCLUSION AND FUTURE WORKS

5.1 Conclusions and contributions

This study developed a digital rule for pipe design that machines can recognize for automating pipe routing design. To this end, design rules and guidelines, piping installation manuals, and classification rules, as well as international codes & standards and owner's requirements, were analyzed. In addition, a rule taxonomy according to the WBS system was established. Based on the established rule taxonomy, about 2,000 design issues, including know-how accumulated from experience, were collected, classified, and organized into about 400 issues by a discussion with piping design experts. Based on the analyzed design rules, a code of account for pipe route design was established for efficient design rule classification and analysis. A digital rule was developed according to the established code system.

Digital rules developed through this study can be used not only as primary data to check consistency and inconsistencies between various documents such as design regulations, installation manuals, and advanced rules but also for developing systems for pipe route design. In addition, it can be used to develop training datasets for AI models, such as rule-set classification algorithms and automatic route placement learning algorithms based on digital rules for classified piping design. The developed digital rules can be applied as a database for procurements, construction, estimation, and cost control. The code classification system can be widely used in the design stage, such as generating commodity codes, establishing piping material specifications, and creating piping 3D specifications. In addition, it can be combined with the latest AI technology to develop a piping auto-routing design system. This not only makes it possible to shorten the design period drastically but also gives an advantage to bidding competitiveness by confirming the pipe design quickly during project bidding and responding quickly to the owner's requirements. It is expected that the design errors and quality degradation caused by the lack of experienced engineers in most Korean companies can be supported by automatic designing by computers, which also contributes to improving the firm's competitiveness and management efficiency.

5.2 Limitations and future works

The limitations of this study and the discussions on further research are as follows. First, most of the pipe design rules are common to the project and not only accumulate source data for each rule, but there are many rules for everyday design experience; therefore, the support from pipe design experts is essential for rule analysis. Also, there is a limitation in that it takes time to build an initial code classification system. Second, since the number of code digits is limited to 11, there is a problem in that the number of digits cannot be expanded according to the user's convenience. This problem can eventually cause user randomness when new rules or additional elements are required. Research on adding code digits for new rules is required in the future.

Finally, the authors plan to develop training data for AI models, such as a rule set classification algorithms based on the digital rules of piping route design developed in this study. Additional research is needed on developing 3D model-based piping optimal route automatic placement technology. In addition, developing a system that automatically optimizes the piping route of an engineering plant by applying AI technology is also required.

REFERENCES

- ASME, <https://www.asme.org/codes-standards>, (accessed on January 5, 2023)
- Choi, S.W. & Lee, E.B. 2022. Contractor's Risk Analysis of Engineering Procurement and Construction (EPC) Contracts Using Ontological Semantic Model and Bi-Long Short-Term Memory (LSTM) Technology. *Sustainability*, 14, 6938.
- Kang, L.S. & Kwak, J.M. 2001. Integrated Code Classification System for Work Sections in Standard Method of Measurement and Construction Standard Specifications. *Journal of The Korean Institute of Construction Engineering and Management*, 2: 80–91.
- Kim, M.H., Lee, E.B. & Choi, H.S. 2018. Detail Engineering Completion Rating Index System (DECRIIS) for Optimal Initiation of Construction Works to Improve Contractors' Schedule-Cost Performance for Offshore Oil and Gas EPC Projects. *Sustainability*, 10, 2469.
- Kim, H. & Lee, G.H. 2020. A Development of Offshore plant Piping Process Monitoring System Based on 3D CAD Model. *Journal of the Korea Academia Industrial Cooperation Society*, 21: 58–65.
- Lee, B.H. & Kang, L.S. 1994. Project Informations Classification System for Civil Works. *Journal of the Society of Civil Engineers of Korea*, 14: 897–905.
- Lee, J.P., Moon, Y.J. & Lee, J.H. 2015. Improvement of the Code Classification Structure in Piping Material Management for Petrochemical Plant Projects. *Plant Journal*, 11: 39–49.
- Min, J.G., Ruy, W.S. & Park, C.S. 2020. Faster pipe auto-routing using improved jump point search. *International Journal of Naval Architecture and Ocean Engineering*, 12: 596–604.
- Moon, J.S. & Han, C.H. 2014. Extension of the "Standardization of information Classification in the Construction Industry" Elements Classification for River Construction. *Journal of the Korea Academia-Industrial cooperation Society*: 410–411.
- Nguyen, H., Kim, D.J. & Gao, J. 2016. 3D piping route design including branch and elbow using improvements for Dijkstra's algorithm. *2016 International Conference on Artificial Intelligence: Technologies and Applications*. Atlantis Press.
- PIPING GUIDE, <https://www.pipingguide.net/2010/08>, (accessed on October 25, 2022)
- Shin, D.S., Park, B.C., Lim, C.O., Oh, S.J., Kim, G.Y. & Shin, S.C. 2020. Pipe Routing using Reinforcement Learning on Initial Design Stage. *Journal of the Society of Naval Architects of Korea*, 57: 191–197.
- Wang, Y.P., Ahn, J.H., Han, H.J., Kim, W.H. & Hyun, S.Y. 2010. An Integrated Management System of Electrical Construction Specification Using Work-Section Classification System. *Journal of The Korean Institute of Electrical Engineers*: 352–354.
- Yan, W. & Ubald, N. 2012. Automatic generation of assembly sequence for the planning of outfitting processes in shipbuilding. *Journal of Ship Production and Design*, 28: 49–59

Structural response of corroded concrete columns with different rebar confinements under cyclic compressive loading

H.O. Aminulai, N.S. Ferguson & M.M. Kashani
University of Southampton, Southampton UK

ABSTRACT: The new codes have recently introduced seismic detailing for new structures, but there are still older reinforced concrete structures without proper ductile detailing for earthquake resistance. These structures are further impacted by the corrosion of their embedded rebars which further reduces the strength and ductility under loading. This paper presents summary of the results of an experimental investigation performed on short RC columns, with different confinement configurations subject to varying degrees of corrosion, to investigate the structural responses to cyclic loading. The experiment was conducted on 20 short RC columns (square and circular) with two levels of confinements and steel reinforcement corrosion loss ranging from 0% to to ~30% subjected to cyclic compressive load. The test results show that corrosion and rebar confinements significantly impact the structural responses of corroded columns.

1 INTRODUCTION

Reinforced concrete (RC) columns are commonly used to construct civil engineering structures. They are affected by factors such as dry and wet cycles, freeze-thaw cycles, ageing of the materials, and the corrosion of reinforcement steel (Chen et al., 2022, Luo et al., 2020). Among all these factors, steel corrosion has been the most devastating, with chloride-induced corrosion the most severe, leading to catastrophic failure and collapse of structures (Ma et al., 2022). The corrosion of reinforcements in RC members significantly degrades their structural performance leading to structures with reduced load-carrying capacity, ductility and structural safety (Biswas et al., 2020). Furthermore, corrosion significantly reduces the confinement effectiveness of transverse bars and the buckling resistance of longitudinal bars in RC columns, especially structures in severely corrosive environments and subjected to seismic loading (Luo et al., 2020).

Numerous old RC and steel bridges in the marine environment and cold regions (using deicing salt) are suffering from steel corrosion resulting in the durability degradation of RC bridges (Akiyama et al., 2011, Ou et al., 2013, Kashani et al., 2019, Ni Choine et al., 2016). In addition, these bridges are designed with the old codes without proper confinement detailing and seismic resistance, making them vulnerable to collapse under seismic excitation.

While several studies have been dedicated to investigating the structural vulnerability of corrosion-damaged RC members, there is paucity in the literature on the influence of corrosion damage, confinement levels and cross-sectional shape on the seismic behaviour of ageing RC bridge columns/piers. Several numerical and analytical models have been used to investigate the effect of corrosion and transverse reinforcement confinements on RC members' seismic response and failure (Kashani et al., 2016a, Kashani et al., 2016b, Kashani et al., 2018, Su et al., 2015). However, these works have mostly not been validated with experimental tests. Therefore, there is a need for experimental investigation of the seismic response of corroded RC columns to corrosion damage and inadequate confinements under cyclic compressive loading.

Cyclic experiments are a major method to provide insight into the seismic performance of the structural component. However, although it is recognised that the corrosion-induced

damage on coastal bridge piers significantly affects the safety of the structures during the long-term service period, the damage mechanism and the mechanical behaviour are still seldom understood. This paper investigates the effect of corrosion and confinement on the cyclic performance of ageing low-strength concrete RC columns.

2 EXPERIMENTAL CAMPAIGN

2.1 Specimen preparation and material characterisation

Twenty RC columns (ten squares and ten circulars) with five targeted corrosion mass losses (0%, 5%, 10%, 20% and 30%) and two confinement ratios, high ($L/D=5$) and low ($L/D=13$), were used and labelled as shown in Table 1. All the columns have the same length (600mm), with the square columns having 125×125 mm cross-section incorporating 4 $\Phi 10$ mm longitudinal bars, while the circular columns are 125mm diameter with 5 $\Phi 10$ mm longitudinal bars. The columns are confined with $\Phi 6$ mm stirrups in the middle 400mm zone, while the 100mm ends have the stirrups at 25mm spacings. Furthermore, the 100mm ends were strengthened with epoxy-coated GFRP to prevent localised damage at the top and bottom ends of the columns and ensure that the failure occurs at the 400mm middle zone.

Table 1. Experimental test matrix.

Circular columns			Square columns		
Specimen label	Confinement level	Targeted corrosion (%)	Specimen label	Confinement level	Targeted corrosion (%)
C5A0	5	0	S5A0	5	0
C5A5	5	5	S5A5	5	5
C5A10	5	10	S5A10	5	10
C5A20	5	20	S5A20	5	20
C5A30	5	30	S5A30	5	30
C13A0	13	0	S13A0	13	0
C13A5	13	5	S13A5	13	5
C13A10	13	10	S13A10	13	10
C13A20	13	20	S13A20	13	20
C13A30	13	30	S13A30	13	30

The concrete was designed as low-strength concrete representing ageing columns with an expected mean compressive strength of 20MPa. Concrete samples with the same configuration as the square and circular columns were collected during the casting to determine the actual strength of the concrete. The test was done with the servo-hydraulic 630kN Instron Schenk machine at the Testing and Structures Research Laboratory (TSRL), University of Southampton. The average compressive strengths of the concrete are 13.8MPa and 12.6Mpa for the square and circular columns, respectively.

2.2 Accelerated corrosion procedure

The electrochemical method was applied to the corrosion process to hasten corrosion process in the laboratory. This method has been shown to have similar results as natural corrosion (Hou et al., 2019, Mak et al., 2019, Yuan et al., 2007).

The rebars were joined together and connected to the anode, while the stainless steel sheet was linked with the cathode of the direct current (DC) power supply. The power supply was adjusted to supply a constant current of 2Amp for the corrosion of the rebars in the columns submerged in 10% sodium chloride solution (Figure 1(a-b)). Faraday's 2nd law of electrolysis (Equation 1) was used to estimate the expected corrosion mass loss by calculating the duration to achieve such mass loss (Kashani et al., 2013a). The actual mass loss, γ , is estimated at the

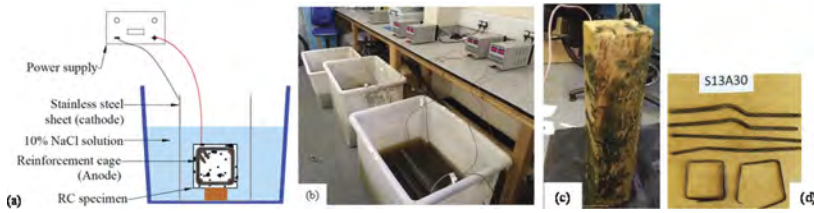


Figure 1. Accelerated corrosion procedure; (a) Schematic setup drawing, (b) laboratory setup (c) corroded columns after completion of corrosion and (d) corroded rebars after cleaning.

end of testing by weighing the rebars after removing and cleaning the rust (Figure 1(c-d)) and concrete from the surface (Equation 2). Equation 2 gives an average corrosion loss (mass loss) along the length of the rebar.

$$m_l = \frac{MIT}{ZF} \quad (1)$$

$$\gamma = \frac{m_0 - m}{m_0} \times 100 \quad (2)$$

where m_l = estimated mass loss (g), M = molar mass of the iron (56g/mol), Z = ionic charge for iron ($Z=2$), F = Faraday's constant (96500 C/mol), I = applied current (Ampere, A), T = estimated time to achieve the desired corrosion (s), m_0 = mass per unit length of the uncorroded rebar, and m = mass per unit length after cleaning.

2.3 Cyclic loading protocol and instrumentation

The RC columns were tested under axial compressive cyclic loading. The loading protocol was set to have 20 cycles with ten different mean strains, each strain peak repeating twice, as shown in Figure 2. The mean strain was estimated from the displacement values of a similar experimental test done on corroded RC under monotonic loading. The first five lower strain peaks were applied at 0.1mm/sec loading rate while the remaining peaks were at 0.15mm/sec. The cyclic loading protocol was set up using the Instron Wavemetrics software.

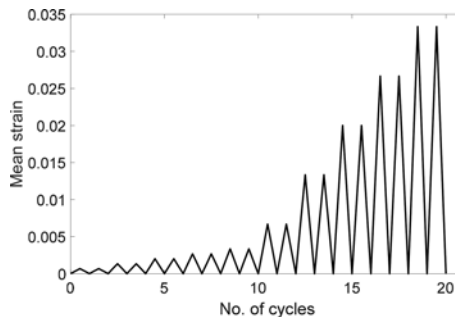


Figure 2. Cyclic compressive loading protocol.

3 EXPERIMENTAL SETUP

The RC columns were tested under axial cyclic compressive load using displacement control with a lower loading rate for the first ten cycles. After that, the remaining cycles were at a slightly higher rate. Also, the test is conducted under complete axial cyclic compression loading, with each loading cycle repeated twice without going into the tension zone. The setup of the experiment is shown in Figure 3(a). The displacement at the middle 400mm zone of the RC columns is

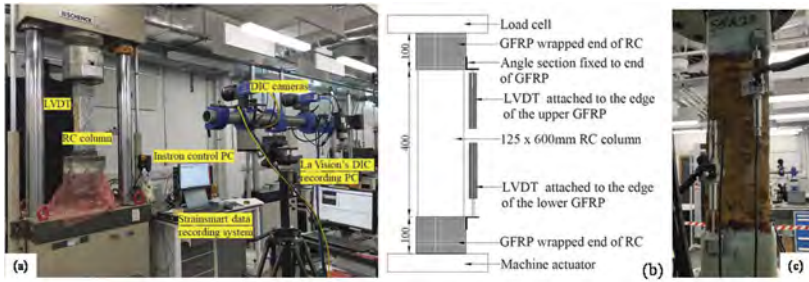


Figure 3. Experimental test setup (a) laboratory setup; (b) schematic of the LVDT connection; (c) Image of the LVDT connections to the RC samples.

measured with the Linear Variable Differential Transformers (LVDTs) fixed to the edge of the Glass fibre-reinforced polymers (GFRP) strengthened ends (Figures 3(b) and 3(c)). This ensures that the LVDTs measure the axial deformations in the differently confined 400mm section of the columns, which are recorded via a data acquisition unit (Strainsmart 8000).

4 EXPERIMENTAL RESULTS

4.1 Calculation of corrosion and mass loss ratio

The actual mass losses resulting from the accelerated corrosion process estimated from Equation 2 are presented in Figure 4. The results showed that the transverse bars had more severe corrosion than the longitudinal bars under the same constant current and duration (Li et al., 2022) in all the columns.

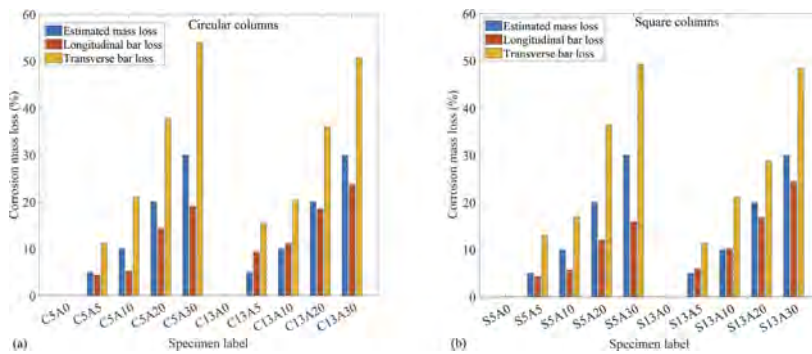


Figure 4. Accelerated corrosion mass loss for the RC columns (a) circular and (b) square.

This mass loss results from the closeness of the transverse bars to the surface of the concrete, leading to a higher concentration of chloride ions and an early start of corrosion (Gu et al., 2020). Furthermore, the diameter of the longitudinal rebar (10mm) was greater than that of the stirrups (6mm). In this regard, the mass loss ratio of transverse stirrups with smaller diameters was higher than that of the longitudinal rebar, according to Faraday's second law of electrolysis (Kashani, 2017).

4.2 Axial cyclic testing of the RC columns

The stress-strain responses of the RC columns to the applied axial cyclic compressive load are presented in Figure 5(a-h). The observed cyclic responses of the RC columns are similar at the elastic range until yield and afterwards becomes nonlinear beyond the peak stress due to the corrosion and confinements of the rebars. The hysteretic curve of the corroded columns within each

confinement's configuration was compared with the non-corroded ones. It showed a gradual decrease in the strength, stiffness and ductility of the columns as the corrosion increased. Consequently, columns with very close mass loss have their maximum strengths relative to each other, especially at low corrosion between 5% and 10% (Figure 5(a, c, e and g)). For example, the strength loss between the highly confined circular columns (Figure 5(a-b)) was reduced by 13%, 22%, 26%, and 37% for the 5%, 10%, 20% and 30% estimated mass loss, respectively. This trend is also observed in the lowly confined ($L/D=13$) columns having between 10% to 48% reduction (Figure 5(c-d)).

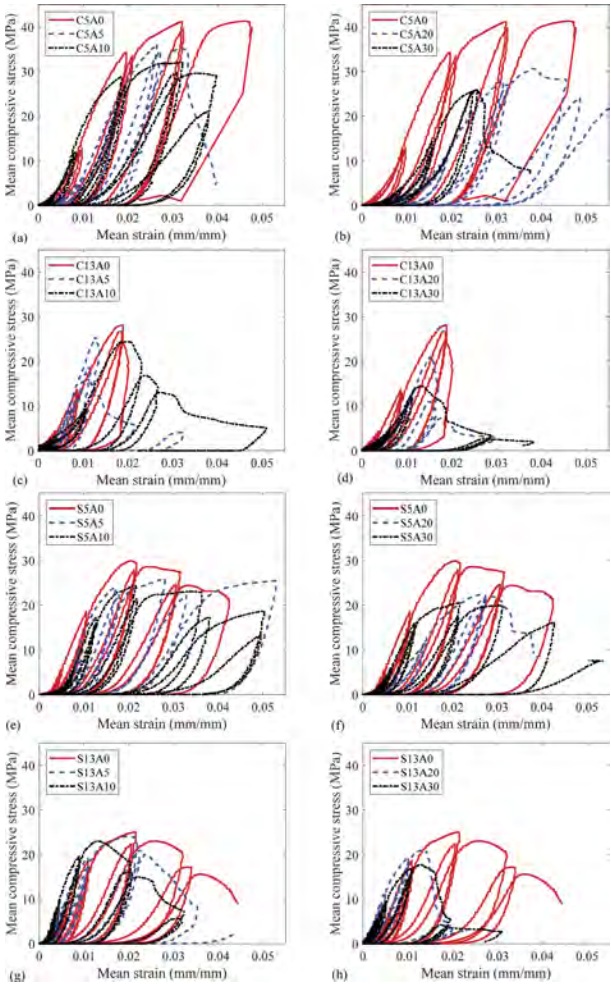


Figure 5. Axial cyclic stress-strain response of the RC columns; circular ($L/D = 5$ (a-b) and $L/D = 13$ (c-d)) and square ($L/D = 5$ (e-f) and $L/D = 13$ (g-h)).

4.3 Impact of corrosion on energy dissipation capacity

The plots of the normalised accumulated hysteretic energy dissipated by the RC columns against the number of cycles are presented in Figure 6(a-d). The graphs showed similar behaviour for all the columns, with very low energy dissipated at the smaller loading cycles (low strain loading rates) and a steep increase in the energy dissipated after the 10th cycle. The steep increase in the dissipated energy is more significant at high corrosion and low confinement in both the circular and square columns.

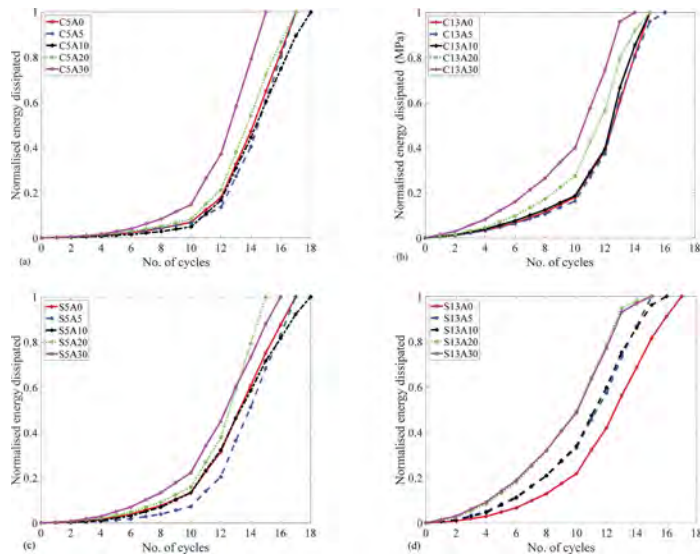


Figure 6. Normalised dissipated energy of the RC columns; circular ((a) $L/D = 5$, (b) $L/D = 13$); square ((c) $L/D = 5$, and (d) $L/D = 13$).

4.4 Impact of corrosion on buckling of vertical reinforcement

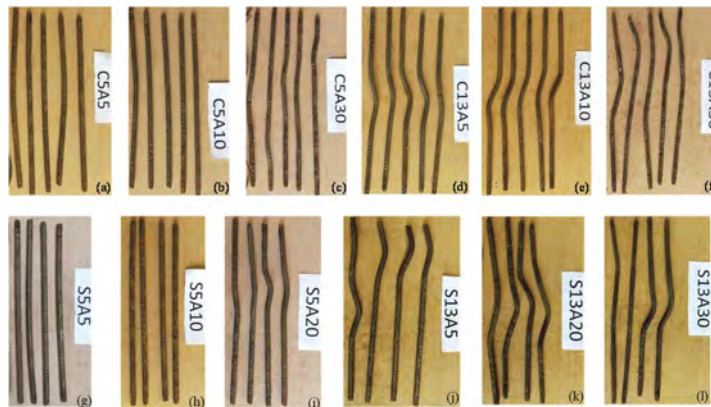


Figure 7. Observed buckling failure of the longitudinal reinforcement in the RC columns. Circular; $L/D = 5$ (a-c), and $L/D = 13$ (d-f), square; $L/D = 5$ (g-i), and $L/D = 13$ (d-f).

The corrosion and confinement of rebars affect the buckling behaviour of the longitudinal bars. This buckling is more pronounced in bars with pitting corrosion, resulting in a localised reduction of the cross-section area along the corroded bar (Kashani et al., 2013a). As a result, the bars in the highly confined circular columns had less buckling at low corrosion (Figure 7(a-b)). Conversely, the buckling of the rebars in the highly confined columns is more pronounced at high corrosion (Figure 7(d)), where the effect of pitting corrosion is prevalent (Kashani et al., 2013b, Kashani, 2017). Furthermore, the buckling of the rebars in the lowly confined columns is more severe even at low corrosion levels from the combination of corrosion and inadequate confinement of the column (Figure 7(d-f)). Similar behaviour is observed in the buckling response of the square columns (high confined Figure 7(g-i) and low confined (Figure 7(j-l)).

5 CONCLUSIONS

Twenty RC column specimens with five different reinforcement corrosion levels and two confinement configurations were tested under axial cyclic compressive load. Moreover, the relationship between the seismic behaviour, such as rebar corrosion loss ratio, ultimate strength, normalised dissipated energy, and inelastic buckling of rebar, was investigated. The following conclusions can be drawn from this study.

Transverse reinforcement showed much higher vulnerability to chloride-induced deterioration in the RC columns than the respective longitudinal reinforcement. Consequently, the ultimate failure of the columns reduced as corrosion damage increased and confinement effectiveness was diminished. Well-confined specimens showed a lesser loss in strength and deformability after corrosion than under-confined specimens.

Corrosion of transverse confining steel affects the strength and deformability of confined concrete. The effectiveness of confinement reinforcements in confining the core concrete reduces as the corrosion increases. Higher corrosion levels and low confinement lead to more severe degradation of the seismic behaviour of RC columns. The highly corroded columns, where the corrosion loss ratio is 20–30%, have reduced seismic response: poor hysteretic response, stiffness degradation, steep descending branch in the envelope curve, and energy dissipation reduction. It can be concluded that the design of new confined concrete elements should consider the possible/anticipated loss due to corrosion during the structure's life to enable a safe ductile response, which is crucial in earthquake-prone regions.

REFERENCES

- Akiyama, M., Frangopol, D. M. & Matsuzaki, H. 2011. Life-cycle reliability of RC bridge piers under seismic and airborne chloride hazards. *Earthquake Engineering & Structural Dynamics*, 40, 1671–1687.
- Biswas, R. K., Iwanami, M., Chijiwa, N. & Uno, K. 2020. Effect of non-uniform rebar corrosion on structural performance of RC structures: A numerical and experimental investigation. *Construction and Building Materials*, 230, 116908.
- Chen, J., Wang, Z., Xu, A. & Zhou, J. 2022. Compressive Behavior of Corroded RC Columns Strengthened With Ultra-High Performance Jacket. *Frontiers in Materials*, 9, 1–14.
- Gu, X.-L., Dong, Z., Yuan, Q. & Zhang, W.-P. 2020. Corrosion of Stirrups under Different Relative Humidity Conditions in Concrete Exposed to Chloride Environment. *Journal of Materials in Civil Engineering*, 32, 04019329.
- Hou, L., Zhou, B., Guo, S., Aslani, F. & Chen, D. 2019. Corrosion behavior and flexural performance of reinforced concrete/ultrahigh toughness cementitious composite (RC/UHTCC) beams under sustained loading and shrinkage cracking. *Construction and Building Materials*, 198, 278–287.
- Kashani, M. M. 2017. Size Effect on Inelastic Buckling Behavior of Accelerated Pitted Corroded Bars in Porous Media. *Journal of Materials in Civil Engineering*, 29, 04017022.
- Kashani, M. M., Crewe, A. J. & Alexander, N. A. 2013a. Nonlinear cyclic response of corrosion-damaged reinforcing bars with the effect of buckling. *Construction and Building Materials*, 41, 388–400.
- Kashani, M. M., Crewe, A. J. & Alexander, N. A. 2013b. Nonlinear stress–strain behaviour of corrosion-damaged reinforcing bars including inelastic buckling. *Engineering Structures*, 48, 417–429.
- Kashani, M. M., Lowes, L. N., Crewe, A. J. & Alexander, N. A. 2016a. Computational Modelling Strategies for Nonlinear Response Prediction of Corroded Circular RC Bridge Piers. *Advances in Materials Science and Engineering*, 2016, 2738265.
- Kashani, M. M., Lowes, L. N., Crewe, A. J. & Alexander, N. A. 2016b. Nonlinear fibre element modelling of RC bridge piers considering inelastic buckling of reinforcement. *Engineering Structures*, 116, 163–177.
- Kashani, M. M., Maddocks, J. & Dizaj, E. A. 2019. Residual Capacity of Corroded Reinforced Concrete Bridge Components: State-of-the-Art Review. *Journal of Bridge Engineering*, 24, 1–16.
- Kashani, M. M., Salami, M. R., Goda, K. & Alexander, N. A. 2018. Non-linear flexural behaviour of RC columns including bar buckling and fatigue degradation. *Magazine of Concrete Research*, 70, 231–247.
- Li, Q., Dong, Z., He, Q., Fu, C. & Jin, X. 2022. Effects of Reinforcement Corrosion and Sustained Load on Mechanical Behavior of Reinforced Concrete Columns. *Materials (Basel)*, 15.

- Luo, X., Cheng, J., Xiang, P. & Long, H. 2020. Seismic behavior of corroded reinforced concrete column joints under low-cyclic repeated loading. *Archives of Civil and Mechanical Engineering*, 20, 40.
- Ma, J., Yu, L., Li, B. & Yu, B. 2022. Stress-strain model for confined concrete in rectangular columns with corroded transverse reinforcement. *Engineering Structures*, 267, 1–14.
- Mak, M. W. T., Desnerck, P. & Lees, J. M. 2019. Corrosion-induced cracking and bond strength in reinforced concrete. *Construction and Building Materials*, 208, 228–241.
- Ni Choine, M., Kashani, M. M., Lowes, L. N., O'connor, A., Crewe, A. J., Alexander, N. A. & Padgett, J. E. 2016. Nonlinear dynamic analysis and seismic fragility assessment of a corrosion damaged integral bridge. *International Journal of Structural Integrity*, 7.
- Ou, Y.-C., Fan, H.-D. & Nguyen, N. D. 2013. Long-term seismic performance of reinforced concrete bridges under steel reinforcement corrosion due to chloride attack. *Earthquake Engineering & Structural Dynamics*, 42, 2113–2127.
- Su, J., Wang, J., Bai, Z., Wang, W. & Zhao, D. 2015. Influence of reinforcement buckling on the seismic performance of reinforced concrete columns. *Engineering Structures*, 103, 174–188.
- Yuan, Y., Ji, Y. & Shah, S. P. 2007. Comparison of two accelerated corrosion techniques for concrete structures. *ACI Structural Journal*, 104, 344–347.

Structural behaviour of axially loaded corroded low-strength RC columns with different confinement ratios

H.O. Aminulai, N.S. Ferguson & M.M. Kashani

University of Southampton, Southampton, UK

ABSTRACT: Many ageing structures in earthquake-prone regions are vulnerable to failure by seismic actions resulting from poor detailing, environmental degradation and quality of materials used. Insufficient column confinement and corrosion of the embedded rebars have been identified as some of the problems with structures in such environments leading to severe damage during earthquakes. This paper presents summary of the result of an experimental investigation on low-strength reinforced concrete (RC) columns with different confinement levels and varying degrees of corrosion. The experiment was done on 20 short RC columns (10 squares and 10 circulars) with two confinements ratios and steel corrosion loss (0% to 30%) subjected to monotonic axial load. The result showed that the axial load carrying capacity and ductility of corroded RC columns reduced with increased in the corrosion mass loss ratios.

1 INTRODUCTION

Over time, the ageing in reinforced concrete (RC) structures results in the degradation of the engineering properties of structures by limiting the capacity and resistance to failure (Karapetrou et al., 2017, Yang et al., 2016). This failure is more pronounced in RC structures in aggressive and marine environments located in seismic regions subject to corrosion effects and poor quality of materials used in construction. Corrosion of reinforcement in concrete is one of the most common and dangerous environmental deteriorations affecting the structural performance of ageing structures in chloride-laden and high seismic environments (Kashani et al., 2015a, Vu et al., 2017). Furthermore, it significantly reduces the diameter (Du et al., 2005), strength (Vu and Bing, 2018) and axial load-bearing capacity of reinforcing bars in corroded RC structures (Shen et al., 2021), which further results in the reduction in the concrete core confinement leading to the degradation in ductility and the long-term performance of the RC structure (Ma et al., 2022, Fang, 2020). Chloride-induced corrosion significantly degrades RC structures, resulting in substantial economic loss worldwide (Altoubat et al., 2016). For example, the United States of America reported needing about \$125 billion to repair ageing and existing bridges (American Society of Civil Engineers (ASCE), 2021). In comparison, the United Kingdom estimated the cost of corrosion damages to highway bridges in Wales and England (approximately 10% of the total bridges in the United Kingdom) at £1 billion per year (Wallbank, 1989).

Ageing RC columns/piers generally fail through the buckling of the vertical reinforcement bars together with the crushing of core confined concrete and the fracture of the longitudinal bars (Kashani et al., 2019), resulting from inadequate confining transverse reinforcements. This confinement reinforcement provides the compressed concrete with higher flexibility and stability, which helps to prevent collapse during vibrations (Mander et al., 1988). Thus, the higher the level of confining stress in the concrete, the more its ductility and strength gain (Zeng, 2017).

Several numerical and analytical models have been developed to investigate the effect of confinement on the axial load capacity and stress-strain behaviour of RC columns (Zeng, 2017, Saatcioglu and Razvi, 1992, Mander et al., 1988, Liang et al., 2015, Hoshikuma et al., 1997). However, these models are primarily on plain normal and high-strength RC columns without considering the effect of corrosion. These models have been incorporated into design guidelines for new RC bridge columns/piers. However, many inadequately confined old bridge columns with low concrete strength are still in the seismic regions. Therefore, their response to the combined effects of degradation and axial load needs to be investigated.

The stress-strain responses of non-corroded RC columns have been extensively investigated numerically (Andisheh et al., 2021). Still, there are very few experimental investigations of the effects of corrosion on the stress-strain behaviour of confined concrete columns. This research presents the results of an experiment on ageing low-strength circular and square RC columns subject to reinforcement corrosion, confinement ratios and axial load. Twenty low-strength RC columns were designed and grouped into five targeted corrosion losses (i.e., 0%, 5%, 10%, 20% and 30%) with two confinement ratios ($L/D = 5$ and $L/D = 13$) under monotonic axial load. The different degrees of reinforcement corrosion was obtained by accelerated corrosion technique using the electrochemical process. In addition, the effect of reinforcement corrosion and confinement ratios on the load-deformation responses of the RC columns was analysed.

2 METHODOLOGY

2.1 Specimen details and material properties

A total of twenty RC columns (ten squares and ten circulars) were designed, as shown in Figure 1, with two confinement levels and five targeted corrosion losses. The square columns are $125 \times 125 \times 600\text{mm}$, incorporating 4 No. 10mm diameter longitudinal bars, while the circular samples (125mm diameter $\times 600\text{mm}$ long) have 5 No. 10mm longitudinal bars. The columns were designed with two different confinement ratios in the middle 400mm zone, while the 100mm ends have transverse bars spaced at 25mm (Figures 1a and 1b). Furthermore, the 100mm ends are wrapped with epoxy-coated GFRP to prevent localised damage at the top and bottom ends of the columns and ensure that the failure occurs at the RC columns' middle zone. All the rebars in the columns were connected with tie wires to ensure that the transverse and longitudinal bars corrode simultaneously during the corrosion process.

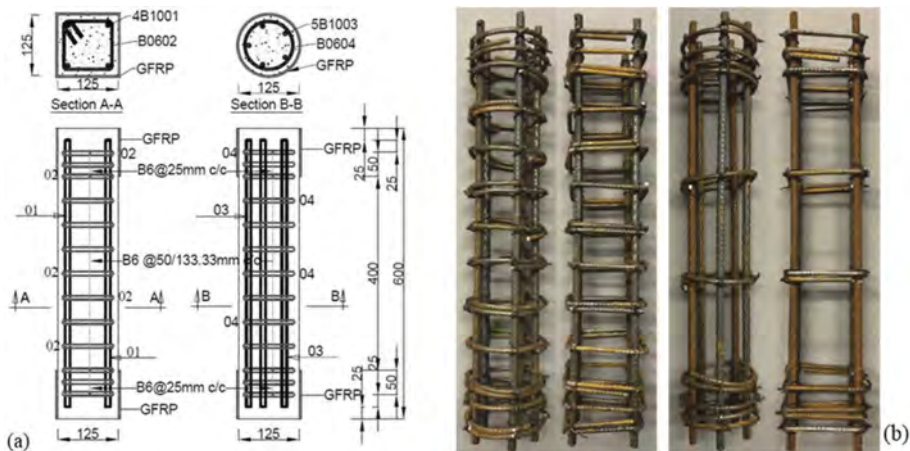


Figure 1. Specimen details; (a) schematic drawing and (b) Reinforcement layouts (cages) of the high and low confinement (circular and square columns).

The concrete was designed as low-strength concrete representing a non-code conforming column with an expected mean compressive strength of 20MPa and a nominal cover of 10mm. Compressive strength tests were done on concrete samples collected during the casting of the columns at the Testing and Structures Research Laboratory (TSRL), University of Southampton, using the servo-hydraulic 630kN Instron Schenk machine. The columns were tested using the displacement control at a constant loading rate of 1mm/min until failure. The samples used for this test were not the conventional cube/cylinder samples but with the same configurations as the reinforced ones. The compressive strength of the concrete is estimated to be 12.1MPa.

2.2 Accelerated corrosion procedure

The natural corrosion process usually takes a more extended period which could be several years or decades (Kashani et al., 2019). As such, the electrochemical process known as the accelerated corrosion method is often adopted in the laboratory to simulate the corrosion process. The RC samples' corrosion was done by passing a constant current of 2A through the reinforcing bars connected to the anode of the DC power supplies while also connecting the stainless steel plate to the cathode. Then, the connected specimen is placed in a salt bath with 10% sodium chloride (NaCl) by water weight to simulate the corrosive environment (Figure 2 (a and b)).

This process is used to get an estimated corrosion mass loss by calculating the duration expected to achieve the desired mass loss using Faraday's 2nd law of electrolysis (Equation 1) (Kashani et al., 2013b). Conversely, the actual mass loss is estimated at the end of testing by weighing the rebars after removing and cleaning the rust and concrete from the surface (Equation 2). Equation 2 gives an average corrosion loss (mass loss) along the length of the rebar.

$$\Delta m = \frac{MIT}{ZF} \quad (1)$$

$$\gamma = \frac{m_0 - m}{m} \times 100 \quad (2)$$

where Δm = mass loss (g), M = molar mass of iron (56g/mol), Z = ionic charge for iron, F = Faraday's constant (96500 C/mol), I = applied current (A), T = time to achieve corrosion (s), m_0 = mass per unit length of original rebar, and m = mass per unit length of the corroded rebar.

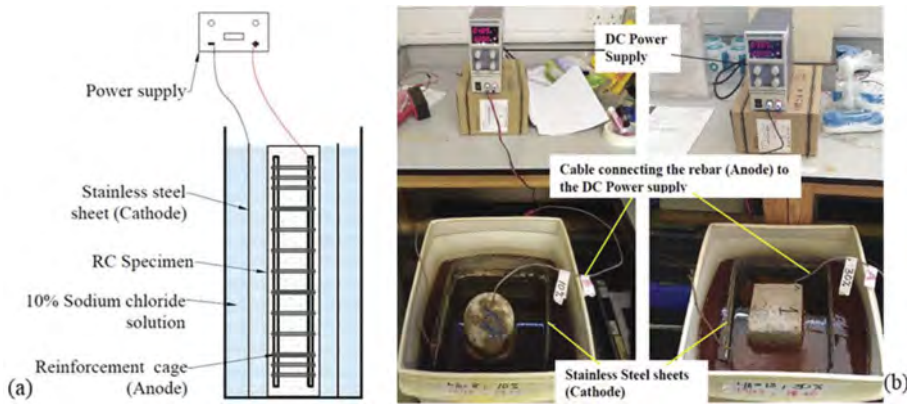


Figure 2. Accelerated corrosion procedure; (a) Schematic setup drawing, (b) laboratory setup.

3 EXPERIMENTAL SETUP

This experiment studies the response of low-strength RC columns to axial compressive loading using the servo-hydraulic 630kN capacity Instron Schenck machine having a 250mm travel at the Testing and Structures Research Laboratory (TSRL) of the University of Southampton. The test is conducted at a constant loading rate of 1mm/min using the displacement control settings in the Instron software. The laboratory setup of the experiment is shown in Figure 3(a). The displacement at the middle section of the column is measured with two Linear Variable Differential Transformers (LVDT) fixed to the edge of the GFRP strengthened end Figure 3(b-c).

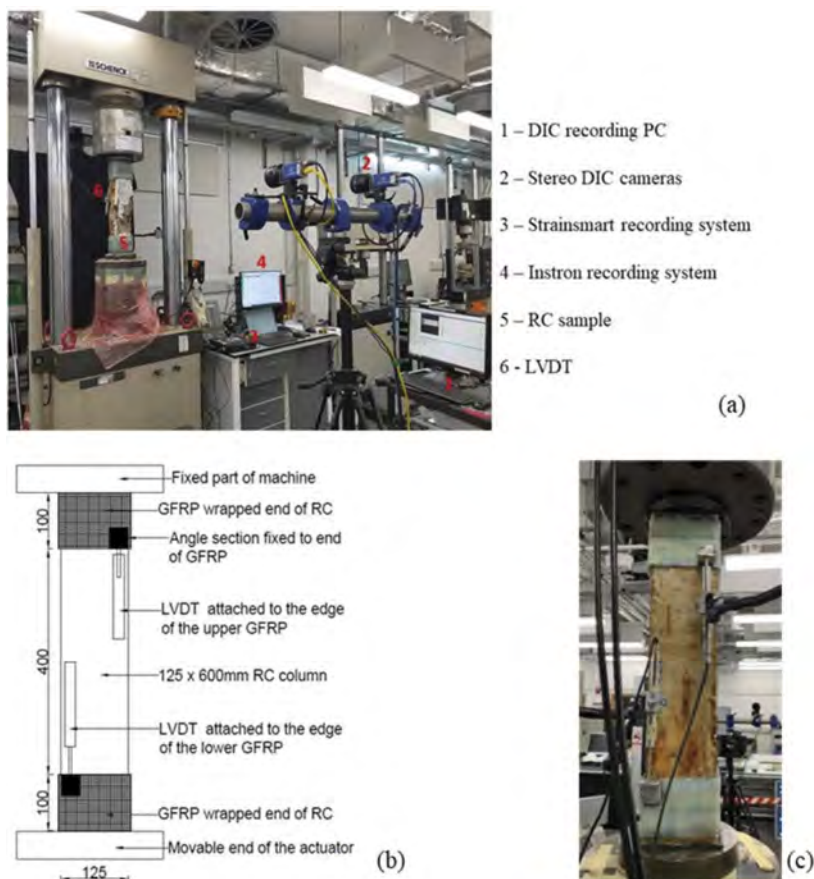


Figure 3. Experimental test setup (a) laboratory setup; (b) schematic of the LVDT connection; (c) Image of the LVDT connections to the RC samples.

4 EXPERIMENTAL RESULTS

4.1 Calculation of corrosion and mass loss ratio

The mass loss results are illustrated in Table 1 for the circular and square columns. The results indicate that the transverse stirrups had more severe corrosion than the longitudinal bar under the same constant current and duration (Li et al., 2022). This results from the closeness of the transverse bars to the surface of the concrete, leading to a possibly higher concentration of chloride ions and an early start of corrosion (Gu et al., 2020). Furthermore, the diameter of the longitudinal rebar (10mm) was greater than that of the stirrups (6mm). In this regard, the mass loss ratio of transverse stirrups with smaller diameters was higher than that of the longitudinal rebar, according to Faraday's second law of electrolysis (Kashani et al., 2013b).

4.2 Axial stress-strain response of RC columns

The stress-strain responses of the circular and square columns to the applied axial compressive load are presented in Figures 4 (a-b) and 4 (c-d). The stress-strain response plotted was from the LVDTs data, which captures the deformation of the sample at the 400mm middle section. The compressive response of the columns is similar at the elastic range until yield and afterwards reduces beyond the peak load due to corrosion and confinements of the rebars (Dong et al., 2018).

Table 1. Corrosion properties of the RC columns.

Circular columns				Square columns			
Specimen label	Estimated mass loss (Eq. 1) (%)	Measured mass loss of longitudinal bars (Eq. 2) (%)	Measured mass loss of transverse bars (Eq. 2) (%)	Specimen label	Estimated mass loss (Eq. 1) (%)	Measured mass loss of longitudinal bars (Eq. 2) (%)	Measured mass loss of transverse bars (Eq. 2) (%)
C5B0	0	0	0	S5B0	0	0	0
C5B5	5	4.1	8.8	S5B5	5	3.4	10.9
C5B10	10	7.3	21.2	S5B10	10	6.8	17.1
C5B20	20	10.8	29.4	S5B20	20	13.8	37.0
C5B30	30	20.6	39.8	S5B30	30	18.4	46.3
C13B0	0	0	0	S13B0	0	0	0
C13B5	5	6.0	12.7	S13B5	5	6.2	11.8
C13B10	10	12.5	30.1	S13B10	10	8.8	17.4
C13B20	20	16.1	37.2	S13B20	20	10.7	25.3
C13B30	30	27.6	45.9	S13B30	30	20.2	30.3

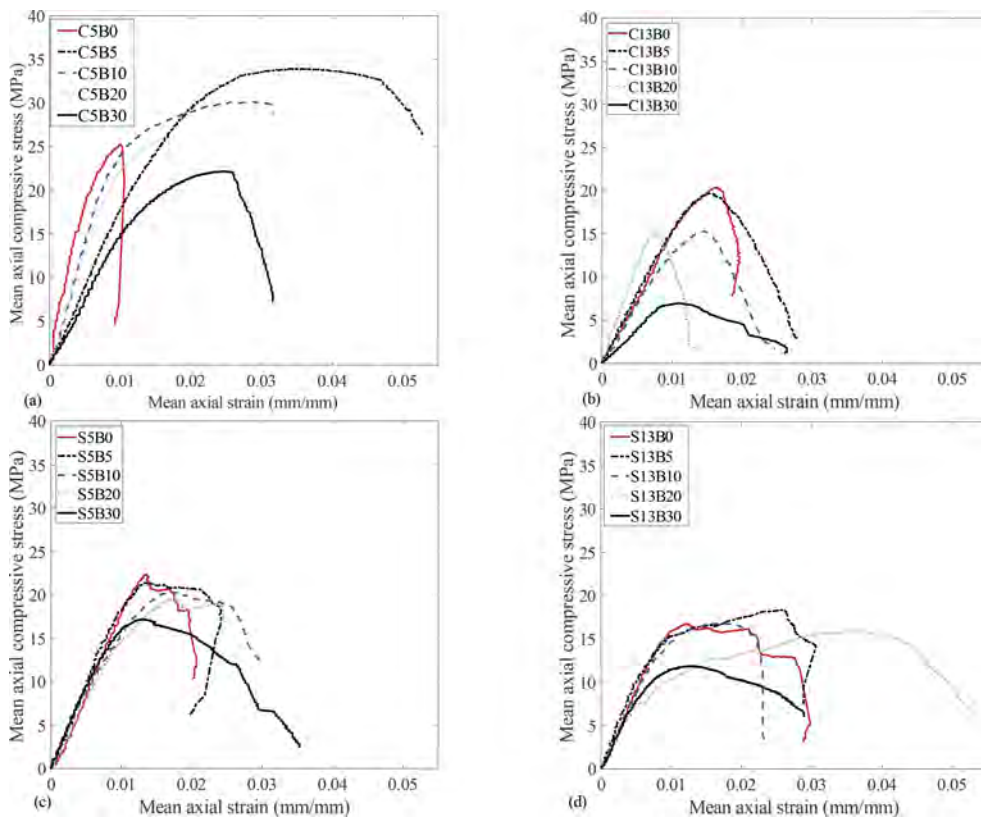


Figure 4. Axial compressive stress-strain responses of RC columns (a) circular $L/D = 5$, (b) circular $L/D = 13$, (c) square $L/D = 5$, and (d) square $L/D = 13$.

The axial load-carrying capacities of the columns generally decrease with an increase in the corrosion level within each confinement configuration of columns, except in some cases where the control sample (0% corrosion) recorded low capacity due to the premature failure of the strengthening GFRP at the top/bottom of the column. The failure of the GFRP at the

top/bottom of the column leads to stress concentration and premature failure of the columns. It is observed that the circular columns generally have better axial load-carrying capacities and axial strain than the square columns (Liang et al., 2015, Dizaj and Kashani, 2020). This results from the effectiveness of the transverse ties in the circular column, which has more significant confinement effectiveness coefficients than the square columns (Liang et al., 2015)

4.3 Impact of corrosion on the strength of confined RC column

The strength loss resulting from the corrosion and confinement ratios of the RC columns is determined by normalising the ultimate strength of the corroded columns to the ultimate strength of the uncorroded. The normalised strength loss of the differently confined RC columns is plotted relative to the percentage of corrosion mass loss. Linear trend lines are fitted to the test data to estimate the strength reduction due to corrosion and confinement ratios. The R-square values obtained from the trendlines are 0.95 and 0.90 for the circular columns with high and low confinement ratios, respectively, while the variation for the square columns is 0.99 and 0.96 for similarly confined columns (Figure 5). The ultimate strength of the confined corroded RC columns is reduced with an increase in the confinement degree and corrosion mass loss. For example, the high-confined circular columns (Figure 5(a)) have a strength reduction range of 4.7%, 14%, 26% and 36.7% for the 4.1%, 7.3%, 10.8% and 20.6% corrosion mass loss, respectively. Also, the high-confined square columns (Figure 5(b)) have a strength reduction range of 5.1%, 10.6%, 19.6% and 29.6% for the 3.4%, 6.8%, 13.8% and 18.4% corrosion mass loss, respectively. A similar trend is observed in the low-confined columns, with the strength reduction increasing with an increase in the corrosion mass losses in the circular and square columns.

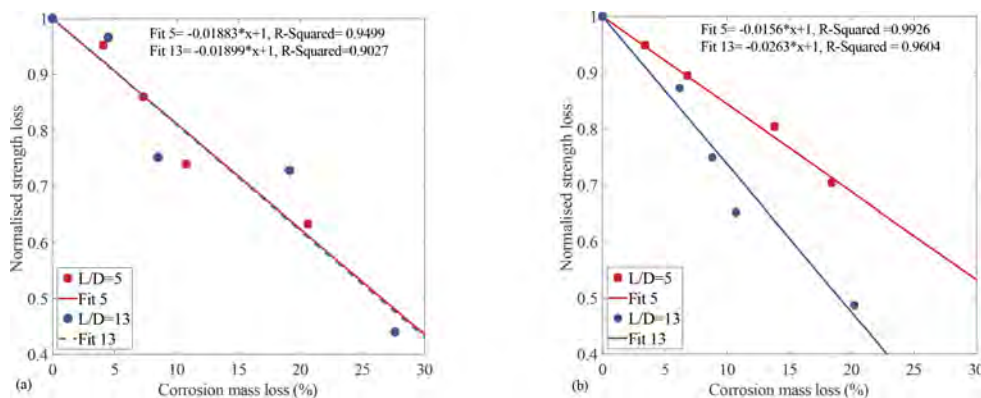


Figure 5. Strength variation of the confined RC columns with corrosion (a) circular and (b) square.

4.4 Impact of corrosion on inelastic buckling behaviour of vertical reinforcement

Corrosion generally reduces the cross-sectional areas of bars available to sustain the applied load (Kashani, 2017). This reduction becomes more severe in bars with pitting corrosion, resulting in localised reduction in the cross-sectional areas of the bars, causing rebar fracture and localised buckling. Longitudinal bars in columns with $L/D = 5$ confinement had less buckling failure, especially at lower corrosion than bars from the $L/D = 13$ configurations. The buckling from the columns with $L/D = 5$ rebars at higher corrosion levels results from the unsymmetrical cross-sections arising from the pitting corrosion causing imperfections in the bar and leading to additional bending moment and local stresses at the pitted sections (Kashani et al., 2013b, Kashani et al., 2013a). Meanwhile, the buckling from the columns with $L/D = 13$ results from the combination of pitting corrosion and inadequate confinement provisions leading to premature yielding and squashing of the weakest section even at lower corrosion degrees (Kashani et al., 2015b).

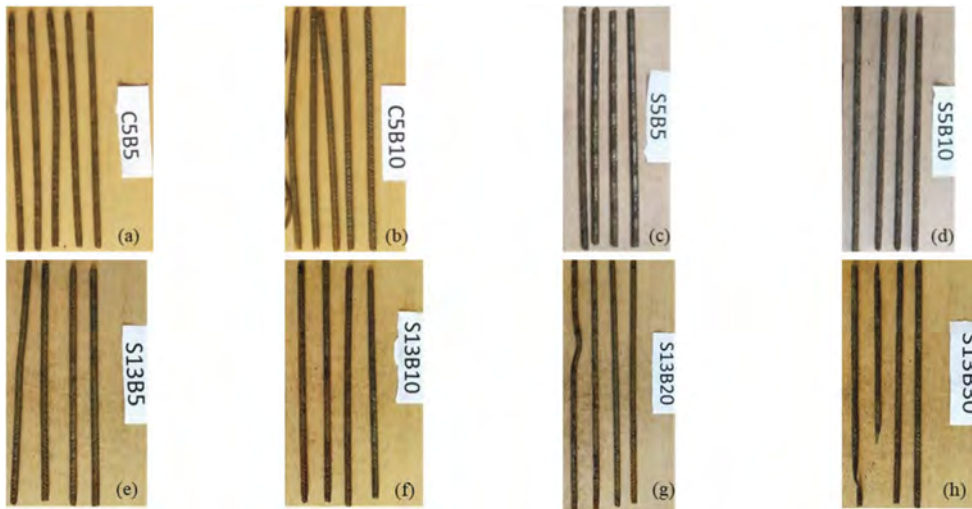


Figure 6. Observed buckling failure of the longitudinal reinforcement after testing; $L/D = 5$ (a-d) and $L/D = 13$ (e-h).

5 CONCLUSIONS

The effects of corrosion on the axial load capacity of differently confined RC columns have been studied experimentally. The primary conclusions drawn from the analysis of the experimental data are as follows.

Corrosion of reinforcements severely reduces the load-carrying capacity and stiffness of RC columns. Therefore, local buckling is more severe for specimens with high corrosion rates and buckling always occur in the sections with more rust products. This is evidence that the local buckling of the rebar is strongly related to its corrosion condition. Furthermore, the inelastic buckling mechanism of bars is affected by non-uniform pitting corrosion. The observed buckling modes showed that the buckling mechanism of corroded bars is a function of the mass loss due to corrosion and the distribution of pits along the bar length. Hence, the bars with more corrosion mass loss experienced more buckling and fracture than columns at low corrosion losses.

Confinement also significantly impacts corroded rebars' stress-strain response and buckling, as the high-confined columns have higher load-carrying capacities than the low-confined ones. Also, highly confined columns at low corrosion have less buckling than columns with the same confinement at high corrosion. Meanwhile, low-confined columns fail due to inadequate confinement and corrosion, even at low corrosion levels.

REFERENCES

- Altoubat, S., Maalej, M. & Shaikh, F. U. A. 2016. Laboratory Simulation of Corrosion Damage in Reinforced Concrete. *International Journal of Concrete Structures and Materials*, 10, 383–391.
- American Society Of Civil Engineers (ASCE) 2021. 2021 Report Card for America's Infrastructure.
- Andisheh, K., Scott, A. & Palermo, A. 2021. Effects of Corrosion on Stress-Strain Behavior of Confined Concrete. *Journal of Structural Engineering*, 147, 04021087.
- Dizaj, E. A. & Kashani, M. M. 2020. Numerical investigation of the influence of cross-sectional shape and corrosion damage on failure mechanisms of RC bridge piers under earthquake loading. *Bulletin of Earthquake Engineering*, 18, 4939–4961.
- Dong, H.-L., Wang, D., Wang, Z. & Sun, Y. 2018. Axial compressive behavior of square concrete columns reinforced with innovative closed-type winding GFRP stirrups. *Composite Structures*, 192, 115–125.

- Du, Y. G., Clark, L. A. & Chan, A. H. C. 2005. Residual capacity of corroded reinforcing bars. *Magazine of Concrete Research*, 57, 135–147.
- Fang, S. 2020. Axial Compressive Performance of Corroded Concrete Columns Strengthened by Alkali-Activated Slag Ferrocement Jackets. *Frontiers in Materials*, 7, 1–12.
- Gu, X.-L., Dong, Z., Yuan, Q. & Zhang, W.-P. 2020. Corrosion of Stirrups under Different Relative Humidity Conditions in Concrete Exposed to Chloride Environment. *Journal of Materials in Civil Engineering*, 32, 04019329.
- Hoshikuma, J., Kawashima, K., Nagaya, K. & Taylor, A. W. 1997. Stress-Strain Model for Confined Reinforced Concrete in Bridge Piers. *Journal of Structural Engineering*, 123, 624–633.
- Karapetrou, S. T., Fotopoulou, S. D. & Pitolakisa, K. D. 2017. Seismic Vulnerability of RC Buildings under the Effect of Aging. *Procedia Environmental Sciences*, 38, 461–468.
- Kashani, M. M. 2017. Size Effect on Inelastic Buckling Behavior of Accelerated Pitted Corroded Bars in Porous Media. *Journal of Materials in Civil Engineering*, 29, 04017022.
- Kashani, M. M., Alagheband, P., Khan, R. & Davis, S. 2015a. Impact of corrosion on low-cycle fatigue degradation of reinforcing bars with the effect of inelastic buckling. *International Journal of Fatigue*, 77, 174–185.
- Kashani, M. M., Crewe, A. J. & Alexander, N. A. 2013a. Nonlinear cyclic response of corrosion-damaged reinforcing bars with the effect of buckling. *Construction and Building Materials*, 41, 388–400.
- Kashani, M. M., Crewe, A. J. & Alexander, N. A. 2013b. Nonlinear stress–strain behaviour of corrosion-damaged reinforcing bars including inelastic buckling. *Engineering Structures*, 48, 417–429.
- Kashani, M. M., Lowes, L. N., Crewe, A. J. & Alexander, N. A. 2015b. Phenomenological hysteretic model for corroded reinforcing bars including inelastic buckling and low-cycle fatigue degradation. *Computers & Structures*, 156, 58–71.
- Kashani, M. M., Maddocks, J. & Dizaj, E. A. 2019. Residual Capacity of Corroded Reinforced Concrete Bridge Components: State-of-the-Art Review. *Journal of Bridge Engineering*, 24, 1–16.
- Li, Q., Dong, Z., He, Q., Fu, C. & Jin, X. 2022. Effects of Reinforcement Corrosion and Sustained Load on Mechanical Behavior of Reinforced Concrete Columns. *Materials (Basel)*, 15.
- Liang, X., Beck, R. & Sritharan, S. 2015. Understanding the Confined Concrete Behavior on the Response of Hollow Bridge Columns. Department of Civil Construction and Environmental Engineering. Iowa State University.
- Ma, J., Yu, L., Li, B. & Yu, B. 2022. Stress–strain model for confined concrete in rectangular columns with corroded transverse reinforcement. *Engineering Structures*, 267, 1–14.
- Mander, J. B., Priestley, M. J. N. & Park, R. 1988. Theoretical stress-strain model for confined concrete. *Journal of Structural Engineering*, 114, 1804–1826.
- Saatcioglu, M. & Razvi, S. R. 1992. Strength and Ductility of Confined Concrete. *Journal of Structural Engineering*, 118, 1590–1607.
- Shen, D., Li, M., Liu, C., Kang, J., Li, C. & Yang, J. 2021. Seismic performance of corroded reinforced concrete beam-column joints repaired with BFRP sheets. *Construction and Building Materials*, 307, 124731.
- Vu, N. S. & Bing, L. 2018. Seismic Performance Assessment of Corroded Reinforced Concrete Short Columns. *Journal of Structural Engineering*, 144, 1–12.
- Vu, N. S., Yu, B. & Li, B. 2017. Stress-strain model for confined concrete with corroded transverse reinforcement. *Engineering Structures*, 151, 472–487.
- Wallbank, E. J. The Performance of Concrete in Bridges: a Survey of 200 Highway Bridges. 1989.
- Yang, S.-Y., Song, X.-B., Jia, H.-X., Chen, X. & Liu, X.-L. 2016. Experimental research on hysteretic behaviors of corroded reinforced concrete columns with different maximum amounts of corrosion of rebar. *Construction and Building Materials*, 121, 319–327.
- Zeng, X. 2017. Finite Element Analysis of Square RC Columns Confined by Different Configurations of Transverse Reinforcement. *The Open Civil Engineering Journal*, 11, 292–302.

Impact of as-recorded mainshock-aftershock excitations on seismic fragility of corrosion-damaged RC frames

Ebrahim Afsar Dizaj

Department of Civil Engineering, Azarbaijan Shahid Madani University, Tabriz, Iran

Mohammad Reza Salami

School of Engineering and the Built Environment, Birmingham City University, UK

Mohammad Mehdi Kashani

Faculty of Engineering and Physical Sciences, University of Southampton, Southampton, UK

ABSTRACT: The experience from the past seismic events shows that the accumulated damage induced by the previous earthquakes increases the vulnerability of Reinforced Concrete (RC) structures. Moreover, RC structures constructed in aggressive environments such as those located in the coastal area suffer from the ageing and degradation phenomena. Therefore, the concurrent influence of successive seismic hazards and corrosion-induced degradation might result in undesired seismic failure of these RC structures. From this perspective, this paper investigates the seismic performance of RC frames affected by chloride-induced corrosion of reinforcements subject to as-recorded (real) mainshock-aftershock excitations. To this end, a prototype RC frame is analysed under real mainshock-aftershock ground motions at different times since corrosion initiation. First, a suite of mainshock-aftershock records is selected from a unique database using the Conditional Mean Spectrum (CMS) methodology. Then, an advanced numerical model capable of tracking the low-cycle fatigue degradation and inelastic buckling of reinforcements is used to simulate the nonlinear dynamic behaviour of the studied frames with different levels of corrosion. Finally, the seismic performance and fragility of the considered structures are evaluated using the outputs of nonlinear static and incremental dynamic analyses. The results show that the vulnerability of corroded reinforced concrete frames is significantly increased under successive earthquake events. Moreover, the results of this paper show that the probability of failure of corrosion-damaged RC frames depends crucially on the magnitude of the aftershocks.

1 INTRODUCTION

The past decade witnessed several disastrous sequential earthquakes globally (Jeon et al. 2015, Raghunandan et al. 2015, Salami et al. 2019). The experience of past earthquakes shows that civil engineering structures are more vulnerable under multiple earthquake events than a single excitation. The consequence of such earthquake chains is significant damage/collapse of RC structures (Manafpour & Moghaddam 2019). Consequently, investigating the seismic performance of RC structures subject to mainshock-aftershock sequences has received considerable attention during the last decades. The outcome of these studies shows that the accumulated damage during the mainshock (MS) event significantly affects the probability of failure of structures under the second event, i.e., aftershock (AS) (Goda & Taylor 2012, Iervolino et al. 2020, Hosseinpour & Abdelnaby 2017, Salami et al. 2021).

RC structures are generally exposed to multiple stressors in their lifetime. Among the several degradation mechanisms, the chloride-induced corrosion of reinforcements has been classified as

one of the leading causes of the premature collapse of several RC structures/infrastructures (Afsar Dizaj & Kashani 2020, Afsar Dizaj et al. 2021, Cui et al. 2019, Panchireddi & Ghosh 2019). Several researchers have investigated the adverse influence of corrosion-induced damage on the structural performance of RC structures (Apostolopoulos & Papadakis 2008, Du et al. 2005a,b). Moreover, the seismic performance of such structures has been extensively investigated. The outcome of these studies confirms the poor seismic performance of corroded RC structures compared to their pristine status (Alipour et al. 2011, Kashani et al. 2019, Afsar Dizaj & Kashani 2022a).

The accumulated damage in the first seismic event, coupled with the increased corrosion-induced damage, can exacerbate the seismic performance of RC structures located in high seismicity regions. However, the literature review shows a significant scarcity in investigating the vulnerability of corroded RC structures subject to mainshock-aftershock excitations. To this end, this study aims to study the nonlinear dynamic behaviour and fragility of corroded RC frames subject to real (as-recorded) mainshock-aftershock ground motions. In the following sections, the details of the study are presented.

2 PROTOTYPE RC FRAME

2.1 Structural details

Figure 1 shows the geometry and structural details of the prototype RC frame considered here to study the combined effects of earthquake sequences and corrosion-induced degradation on the seismic fragility of RC structures. The frame is located in California, US, with harsh environmental conditions. It is designed according to the requirements of ACI 318–02 (2002) and ASCE 7–02 (2002). In Figure 1, H and B denote the depth and width of components; ρ_l is the vertical reinforcement ratio; ρ_v is the volumetric ratio of transverse reinforcements; S_h is the spacing of hoops; and ρ_{top} and ρ_{bot} are longitudinal reinforcement ratio at the top and bottom of beam section, respectively. Further information on design assumptions and details of this frame is available in (Afsar Dizaj et al. 2022).

Different corrosion statuses, including (i) pristine, (ii) slightly corroded and (iii) highly corroded conditions, are considered to investigate the influence of corrosion degree on the structural performance of the considered RC frame. The material and geometrical properties of the frame are updated using the mass loss ratio of rebars (ψ) in any of the corrosion statuses mentioned above. This parameter can be calculated using Equation 1 (Afsar Dizaj 2022):

$$\psi = 1 - \left(\frac{XD - 1.05 \times (1 - W/C)^{-1.64} \times t^{0.71}}{XD} \right)^2 \quad (1)$$

where X is cover thickness, D is the diameter of main bars; W/C is the water-to-cement ratio, and t is the time from corrosion initiation. In order to induce the hypothetical corrosion degrees mentioned above, t is assumed to be 0, 10, and 100 years for pristine, slightly corroded and highly corroded conditions, respectively. Further details can be found in (Afsar Dizaj 2022).

2.2 Numerical model

In this study, the advanced nonlinear finite element model developed in (Afsar Dizaj et al. 2018a, b) is employed to simulate the nonlinear behaviour of the case-study RC frame. Figure 2 shows the numerical model of the hypothetical RC frame. This model can simulate the inelastic buckling behaviour and low-cycle fatigue degradation of reinforcements. As Figure 2 shows, columns and beam are divided into several fibre sections in their entire length in this model. Moreover, each component is modelled using three force-based elements: a zero-length section element to simulate the slippage of reinforcement at connection adjacent, a force-based element with three integration points and another element with five

integration points. The details of this modelling technique are presented in the systematic modelling guidelines provided in (Afsar Dizaj & Kashani 2022b).

The material properties used in numerical modelling are tabulated in Table 1.

Table 1. Steel and concrete material properties.

Notation	Description	Value	Unit
f_y	yield strength of main bars	420	MPa
f_u	ultimate strength of main bars	620	MPa
f_{yh}	yield strength of hoops	300	MPa
E_s	modulus of elasticity of steel	210	GPa
f_c	compressive strength of concrete	35	MPa
ϵ_u	ultimate strain of main bars	0.18	-
ϵ_s	strain at maximum stress of hoops	0.15	-

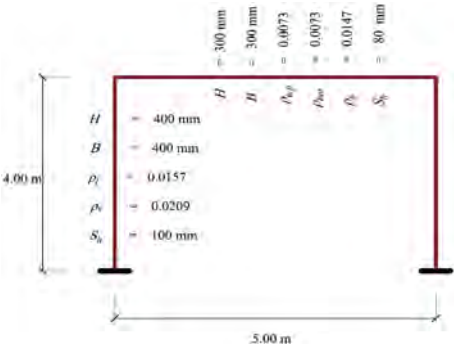


Figure 1. Structural details of the prototype RC frame.



Figure 2. Finite element model of the prototype RC.

3 PUSHOVER ANALYSIS

In order to quantify the time-dependent damage limit states, nonlinear pushover analysis is carried out on the considered RC frames with different hypothetical corrosion statuses. Before conducting the pushover analysis, the material and geometrical properties of the frame are modified to incorporate corrosion-induced degradation. Moreover, the bases of the columns are assumed to be fully fixed. The P-delta effects are also included in the analyses.

Figure 3 shows the time-dependent pushover analysis results for each considered time from corrosion initiation. Results show that as the corrosion level increases, the ductility and lateral load capacity of the frame significantly decrease. The onset of bar yielding, cover concrete spalling, core concrete crushing, and bar fracture are mapped on each capacity curve. The results indicate that each of these damage limit states reaches in lower drift ratios for higher corrosion degrees. For instance, while the core cover spalling occurs at approximately 0.021 drift ratio for the slightly corroded frame, it took place at the vicinity of 0.015 drift ratio for the highly corroded frame. These time-dependent damage limit states are used in this study to develop time-dependent fragility curves.

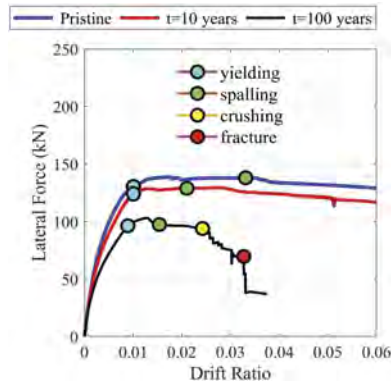


Figure 3. Time-dependent pushover analysis results.

4 MAINSHOCK-AFTERSHOCK GROUND MOTION SELECTION

The selection of aftershocks is a critical step toward conducting incremental dynamic and fragility analysis of structures. The review of previous studies shows that improper selection of mainshock-aftershock ground motions can significantly bias the expected seismic performance of RC structures (Goda 2015). Several researchers have welcomed using as-recorded MSAS ground motion records in recent years (Goda & Taylor 2012, Goda 2015). Similarly, in this study, as-recorded (real) MSAS record sequences are selected to conduct vulnerability analysis of studied RC frames with varied corrosion levels.

Here, conditional mean spectrum (CMS) methodology is used to select a sufficient number of MSAS sequences. To this end, the spectral acceleration at the first fundamental period of the frame is considered as the intensity measure (IM). Moreover, the local seismicity level and soil class of the site are taken into account. Further details about the MSAS ground motion selection are presented in (Afsar Dizaj et al. 2022). In total, forty-eight MSAS ground motion records are selected to be utilised in IDAs. Figure 4 shows the disaggregation data and spectral acceleration response of selected ground motions. The summary of the selected as-recorded MS-AS ground motion sequences is available in Afsar Dizaj et al. (2022).

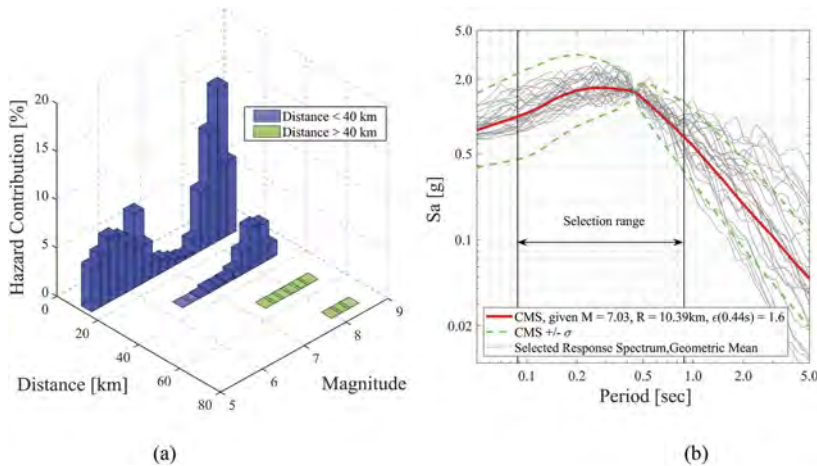


Figure 4. Selected ground motions: (a) disaggregation data, and (b) selected MSAS sequences.

5 RESULTS AND DISCUSSION

5.1 IDA results

Using the selected MSAS ground motion records, IDA is conducted on studied RC frames. First, the MS acceleration histories with scaled-up intensities in $Sa(T_1)$ were applied to the frames, and the structural response in terms of maximum lateral drift was recorded. Then, a 60 seconds rest time was inserted between the MS and AS records, and the assembled MSAS sequence was used as input to conduct MSAS IDAs.

Figure 5 compares the IDA results under MS event with MSAS excitation. This figure shows that for a drift ratio less than 0.025, the median MSAS IDA curves are approximately the same as MS IDA curves. However, for higher drift ratios, for a specific intensity of earthquake record, the frame experiences greater drift ratios under MSAS sequence rather than a single MS record (Figure 5a). As Figure 5b shows, a likewise trend can be seen for $t=10$ years. However, as Figure 5c shows, the median IDA response of severely corroded frame under MSAS sequence is approximately the same as that of MS. Such a trend in median IDA outputs can be attributed to premature material failure in higher corrosion levels. Consequently, the frame fails under the MS event before the upcoming event (i.e., AS) occurs. The results obtained in the shake table experiment of severely corrosion-damaged RC columns (Ge et al. 2020) confirm the results obtained in this study.

5.2 Fragility curves

In this section, the failure probability of examined frames under MS and MSAS records is investigated. To this end, the following fragility function is used:

$$P[EDP \geq DS | IM = x] = 1 - \Phi \left(\frac{\ln(DS) - \ln(\mu)}{\beta} \right) \quad (2)$$

where $P[.]$ is the probability that the engineering demand parameter (EDP) exceeds a damage state (DS) provided that the intensity of the earthquake equals x . Here, the EDP is assumed to be the peak drift ratio. On the right side of Equation 2, $\Phi(.)$ is the lognormal distribution function with the logarithmic mean, and standard deviation of $\ln(\mu)$ and β , respectively, which can be obtained using Equations 3-4:

$$\ln(\mu) = \frac{\sum_{i=1}^n \ln(EDP_i)}{n} \quad (3)$$

$$\beta = \sqrt{\frac{\sum_{i=1}^n (\ln(EDP_i) - \ln(\mu))^2}{n - 1}} \quad (4)$$

In Equations 3-4, n is the number of records, and EDP_i is the peak drift ratio associated with a given value of IM for the i_{th} record.

Figure 6 shows the MS and MSAS fragility curves for all frames. Figure 6 shows that the probability of exceeding the collapse threshold under MSAS records is somewhat greater for a given IM than MS records. This indicates that the studied RC frames with varied corrosion levels are slightly more vulnerable under MSAS ground motions sequences than MS records. Therefore, it can be concluded from the results that, as observed in IDA results (Figure 5), the real MSAS records have a negligible impact on the nonlinear dynamic behaviour and fragility of corroded RC frames.

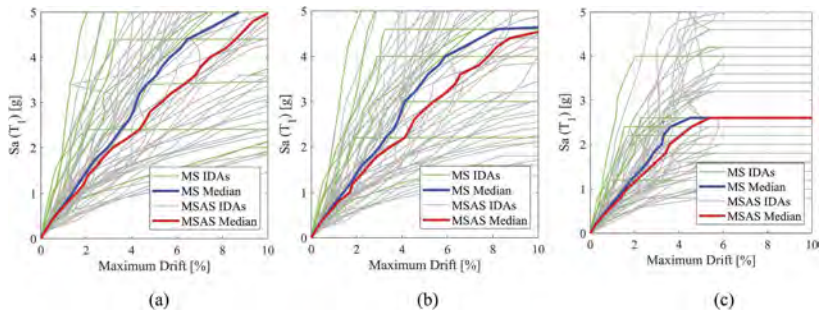


Figure 5. IDA results: (a) pristine frame, (b) $t = 10$ years and (c) $t = 100$ years.

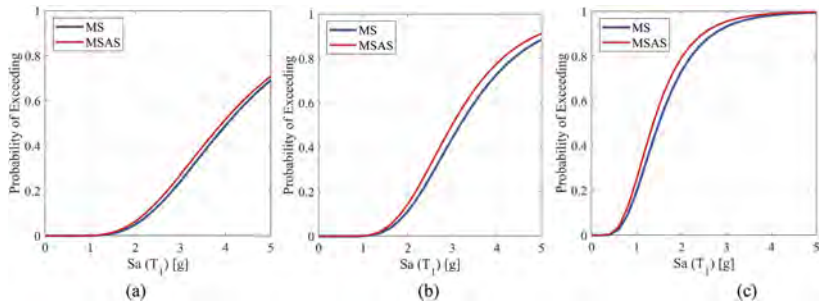


Figure 6. Fragility curves: (a) pristine frame, (b) $t = 10$ years and (c) $t = 100$ years.

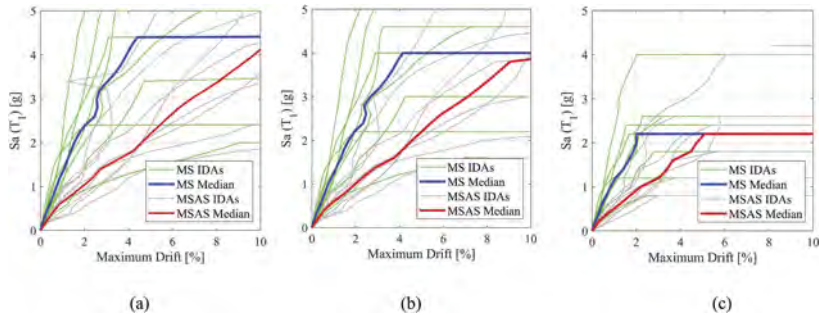


Figure 7. IDA results for records with higher AS/MS PGA ratio: (a) pristine frame, (b) $t = 10$ years and (c) $t = 100$ years.

5.3 Impact of aftershock intensity

The results presented in the previous section indicated that the MSAS records slightly increase the failure probability of RC frames, regardless of aftershock magnitude. In this section, the influence of aftershock to mainshock intensity ratio on nonlinear dynamic behaviour and fragility of studied RC frames is investigated. To this end, from the entire 48 selected MSAS sequences, those with aftershock PGA to mainshock PGA greater than or equal to unity are selected. There are eight ground motion records with this property. In Figure 7, presents the median IDA results of the frames under these eight records. As Figure 7 shows, under the stronger aftershock records, all the frames experience significantly higher drift ratios in all the frames. This implies that the response of a RC frame under MSAS sequence crucially depends on the intensity of the aftershock records.

Figure 8 shows the failure fragility curves under the selected MSAS sequence records with higher PGA of aftershocks to their MS. As this figure shows, the collapse probability of the pristine frame and the slightly corroded frame is not remarkably affected by the PGA ratio of

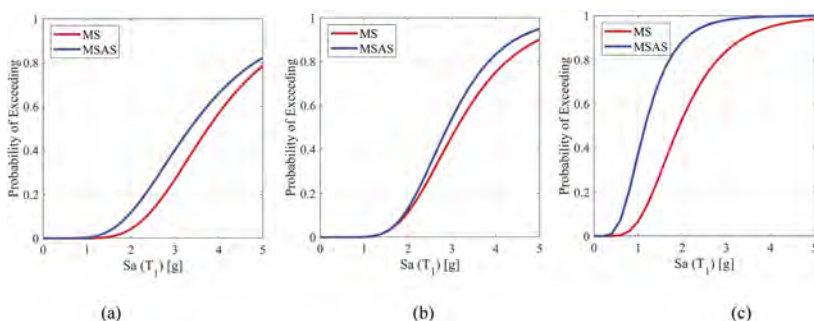


Figure 8. Fragility curves for records with higher AS/MS PGA ratio: (a) pristine frame, (b) $t=10$ years and (c) $t=100$ years.

aftershock to the mainshock. However, as shown in Figure 8c, the highly corrosion-damaged frame is much more fragile under the MSAS sequence than MS records. This infers that the PGA ratio of aftershock to mainshock is a critical factor in the fragility analysis of corrosion-damaged RC frames.

6 CONCLUSIONS

In this study, the seismic performance of corrosion-damaged RC frames under MSAS sequences is investigated. To this end, an advanced modelling methodology was employed to accurately simulate the nonlinear behaviour of RC frames with varied corrosion levels, including an uncorroded frame, a slightly corroded frame and a highly corroded frame. First, nonlinear pushover analysis is carried out on the studied RC frames to quantify the time-dependent seismic damage limit states. Subsequently, IDAs conducted using a suite of 48 as-recorded mainshock-aftershock ground motion records. Finally, the fragility curves were developed using the IDA outputs for the frames under MS records and MSAS sequences.

Overall, the results show that using the real mainshock-aftershock sequences, the failure probability of corrosion-damaged frames slightly increases with respect to MS events. Notably, for the highly corroded frame, the results show that in most cases, the structure fails under the MS record before the subsequent event (i.e., aftershock) comes up. This is due to the brittle failure mode of extremely corroded RC frame due to premature failure of confinements.

Moreover, results show that the PGA ratio of aftershock to mainshock plays a critical role in the vulnerability assessment of corroded RC frames. This conclusion is drawn based on eight MSAS records with higher PGA of aftershock records, where the results showed a significantly higher failure probability of structure under MSAS records.

REFERENCES

- ACI. 2002. Building code requirements for structural concrete. ACI 318-02, *American Concrete Institute*, Farmington Hills.
- Afsar Dizaj, E. 2022. Modelling Strategy Impact on Structural Assessment of Deteriorated Concrete Bridge Columns. *Proceedings of the Institution of Civil Engineers-Bridge Engineering* 175 (4): 246–262. <https://doi.org/10.1680/jbren.21.00003>.
- Afsar Dizaj, E. & Kashani, M.M. 2020. Numerical investigation of the influence of cross-sectional shape and corrosion damage on failure mechanisms of RC bridge piers under earthquake loading. *Bulletin of Earthquake Engineering* 18: 4939–4961. <https://doi.org/10.1007/s10518-020-00883-3>.
- Afsar Dizaj, E. & Kashani, M.M. 2022a. Influence of ground motion type on nonlinear seismic behaviour and fragility of corrosion-damaged reinforced concrete bridge piers. *Bulletin of Earthquake Engineering* 20: 1489–1518. <https://doi.org/10.1007/s10518-021-01297-5>.
- Afsar Dizaj, E. & Kashani, M.M. 2022b. Nonlinear Structural Performance and Seismic Fragility of Corroded Reinforced Concrete Structures: Modelling Guidelines. *European Journal of Environmental and Civil Engineering* 26(11): 5374–5403. <https://doi.org/10.1080/19648189.2021.1896582>.

- Afsar Dizaj, E., Madandoust, R., Kashani, M. M. 2018a. Exploring The Impact of Chloride-Induced Corrosion on Seismic Damage Limit States and Residual Capacity of Reinforced Concrete Structures. *Structure and Infrastructure Engineering* 14(6): 714–729. <http://dx.doi.org/10.1080/15732479.2017.1359631>.
- Afsar Dizaj, E., Madandoust, R., Kashani, M.M. 2018b. Probabilistic seismic vulnerability analysis of corroded reinforced concrete frames including spatial variability of pitting corrosion. *Soil Dynamics and Earthquake Engineering* 114: 97–112. <https://doi.org/10.1016/j.soildyn.2018.07.013>.
- Afsar Dizaj E, Padgett J.E., Kashani, M.M. 2021. A Markov Chain-Based Model for Structural Vulnerability Assessment of Corrosion-Damaged Reinforced Concrete Bridges. *Philosophical Transactions of The Royal Society A Mathematical Physical and Engineering Sciences* 379 (2203). <https://doi.org/10.1098/rsta.2020.0290>.
- Afsar Dizaj, E., Salami M.R., Kashani, M.M. 2022. Seismic Vulnerability Assessment of Ageing Reinforced Concrete Structures under Real Mainshock-Aftershock Ground Motions. *Structure and Infrastructure Engineering* 18(12): 1674–1690. <https://doi.org/10.1080/15732479.2021.1919148>.
- Alipour, A., Shafei, B., Shinozuka, M. 2011. Performance evaluation of deteriorating highway bridges located in high seismic areas. *Journal of Bridge Engineering* 6: 597–611. [https://doi.org/10.1061/\(ASCE\)BE.1943-5592.0000197](https://doi.org/10.1061/(ASCE)BE.1943-5592.0000197).
- Apostolopoulos, C.A., Papadakis, V.G. 2008. Consequences of steel corrosion on the ductility properties of reinforcement bar. *Construction and Building Materials* 22(12): 2316–2324. <https://doi.org/10.1016/j.conbuildmat.2007.10.006>.
- ASCE-7. 2002. Minimum design loads for buildings and other structures. Structural Engineering Institute.
- Cui, Z., Alipour, A., Shafei, B. 2019. Structural performance of deteriorating reinforced concrete columns under multiple earthquake events. *Engineering Structures* 191: 460–468. <https://doi.org/10.1016/j.engstruct.2019.04.073>.
- Du, Y.G., Clark, L.A., Chan, A.H.C. 2005a. Residual capacity of corroded reinforcing bars. *Magazine of Concrete Research* 57(3): 135–147. <https://doi.org/10.1680/mac.2005.57.3.135>.
- Du, Y.G., Clark, L.A., Chan, A.H.C. 2005b. Effect of corrosion on ductility of reinforcing bars. *Magazine of Concrete Research* 57(7): 407–419. <https://doi.org/10.1680/mac.2005.57.7.407>.
- Ge, X., Dietz, M.S., Alexander, N.A., Kashani, M.M. 2020. Nonlinear dynamic behaviour of severely corroded reinforced concrete columns: shaking table study. *Bulletin of Earthquake Engineering* 18: 1417–1443. <https://doi.org/10.1007/s10518-019-00749-3>.
- Goda, K., Taylor, C.A. 2012. Effects of aftershocks on peak ductility demand due to strong ground motion records from shallow crustal earthquakes. *Earthquake Engineering and Structural Dynamics* 41 (15): 2311–30. <https://doi.org/10.1002/eqe.2188>.
- Goda, K. 2015. Record selection for aftershock incremental dynamic analysis. *Earthquake Engineering and Structural Dynamic* 44(7): 1157–1162. <https://doi.org/10.1002/eqe.2513>.
- Hosseinpour, F. & Abdelnaby, A. E. 2017. Effect of different aspects of multiple earthquakes on the nonlinear behavior of RC structures. *Soil Dynamics and Earthquake Engineering* 92: 706–725. <https://doi.org/10.1016/j.soildyn.2016.11.006>.
- Iervolino, I., Chioccarelli, E., Suzuki, A. 2020. Seismic damage accumulation in multiple mainshock–aftershock sequences. *Earthquake Engineering and Structural Dynamics* 49(10): 1007–1027. <https://doi.org/10.1002/eqe.3275>.
- Kashani, M. M., Maddocks, J., & Afsar Dizaj, E. 2019. Residual capacity of corroded reinforced concrete bridge components: A state-of-the-art review. *Journal of Bridge Engineering* 24(7): 03119001. [https://doi.org/10.1061/\(ASCE\)BE.1943-5592.0001429](https://doi.org/10.1061/(ASCE)BE.1943-5592.0001429).
- Manafpour, A.R. & Moghaddam, P.K. 2019. Performance capacity of damaged RC SDOF systems under multiple far- and near-field earthquakes. *Soil Dynamics and Earthquake Engineering* 116: 164–173. <https://doi.org/10.1016/j.soildyn.2018.09.045>.
- Panchireddi, B., Ghosh, J. 2019. Cumulative vulnerability assessment of highway bridges considering corrosion deterioration and repeated earthquake events. *Bulletin of Earthquake Engineering* 17: 1603–1638. <https://doi.org/10.1007/s10518-018-0509-3>.
- Raghunandan, M., Liel, A.B., Luco, N. 2015. Aftershock collapse vulnerability assessment of reinforced concrete frame structures. *Earthquake Engineering and Structural Dynamics* 44: 419–439. <https://doi.org/10.1002/eqe.2478>.
- Salami M.R, Afsar Dizaj E, Kashani M.M. 2019. The behavior of Rectangular and Circular Reinforced Concrete Columns under Biaxial Multiple Excitation. *Computer Modeling in Engineering & Sciences* 120 (3): 677–691. <https://doi.org/10.32604/cmescs.2019.05666>.
- Salami M.R., Afsar Dizaj E., Kashani, M.M. 2021. Fragility analysis of rectangular and circular reinforced concrete columns under bidirectional multiple excitations. *Engineering Structures*, 233, 111887. <https://doi.org/10.1016/j.engstruct.2021.111887>

Seismic fragility analysis of nonuniformly corroded irregular RC bridges

Ebrahim Afsar Dizaj

Department of Civil Engineering, Azarbaijan Shahid Madani University, Tabriz, Iran

Mohammad Reza Salami

School of Engineering and the Built Environment, Birmingham City University, UK

Mohammad Mehdi Kashani

Faculty of Engineering and Physical Sciences, University of Southampton, Southampton, UK

ABSTRACT: Reinforced Concrete (RC) bridges in over crossings are typically constructed with unequal-height piers. The resulting substructure irregularity triggers an unbalanced seismic behaviour of these bridges, which increases their seismic vulnerability. The seismic irregularity of such bridge structures might be further intensified if the piers of varying heights expose to unsymmetrical chloride-induced corrosion damage. To accurately evaluate the seismic vulnerability of corroded irregular RC bridges, this paper studies the seismic fragility of a benchmark multi-span irregular RC bridge with five different corrosion damage scenarios, including unsymmetrical corrosion of piers. Toward this objective, first, monotonic nonlinear pushover analysis is used to quantify the time-dependent seismic capacity limit states by employing an advanced three-dimensional nonlinear finite element model. Then, Incremental Dynamic Analysis (IDA) and seismic fragility analysis are carried out to investigate the nonlinear dynamic behaviour and vulnerability of selected corroded bridges. The results show that, depending on the corrosion scenario, the distribution of seismic ductility demands can be varied in unequal-height bents, which can change the critical bent within a bridge system. Furthermore, results indicate that severe unsymmetrical corrosion damage can cause a synchronised failure of unequal-height piers.

1 INTRODUCTION

Bridges supported on piers of unequal heights are commonly the only construction choice in over-crossings (Kappos et al. 2002, Guirguis and Mehanny 2012). The substructure irregularity of such bridges triggers unbalanced distribution of seismic ductility demand among the piers of varying heights. Some design codes provide recommendations to ensure the regular seismic behaviour of multi-span RC bridges (AASHTO 2011, Caltrans 2013). Moreover, several methodologies have been proposed in the literature to mitigate the unbalanced distribution of seismic demand in irregular multi-span RC bridges (Priestley 2007, Xiang and Li 2020, Ishak and Mehanny 2017, Jara et al. 2013).

The seismic behaviour analysis of irregular RC bridges has been widely studied in the literature (Soleimani et al. 2017, Soltanieh et al. 2019, Hu & Guo 2020, Saiidi et al. 2012, Camacho et al. 2022). Gomez-Soberon et al. (2019) evaluated the seismic behaviour of highway bridges with different irregularity conditions. Their results showed that the adjacent piers of unequal heights considerably affect the vulnerability of concrete bridges. Sensitivity analyses on RC bridges with various irregularity conditions conducted by Soleimani et al. (2017) indicated

that earthquake intensity level, pier height, pier diameter, longitudinal reinforcement ratio, concrete compressive strength, and span length are the most important parameters determining the seismic performance of RC bridges with the irregular layout. Hu and Guo (2020) evaluated the seismic response of high-speed railway bridge-track systems with unequal-height pier configurations. The results showed that increasing the height difference of adjacent bridge piers intensifies the seismic displacement responses of the shear alveolar, moveable bearings, and sliding layer. Jara et al. (2015) found that hard soil ground motion records cause moderate damage in bridge columns, whereas soft soil records trigger considerable damage in columns.

Over the past few years, corrosion damage and ageing of RC bridges have become a challenging problem among structural engineers and bridge owners (ASCE 2021, Ghosh & Sood 2016, Afsar Dizaj& Kashani 2022, Afsar Dizaj et al. 2021). A survey conducted by Department for Transport and Highways England estimated that corrosion damage to concrete bridges costs about £1 billion/per year in England and Wales (Comptroller and Auditor General 2014, Broomfield 2007). Previous studies on seismic fragility assessment of corroded concrete bridges commonly supposed a uniform corrosion scenario, where the average time-dependent corrosion level of piers is assumed to be the same (Choe et al., 2009, Zhang et al. 2019). However, constructing bridges over highways, rivers, railways, and valleys leads to various corrosion scenarios in bridge piers. Therefore, the seismic behaviour of concrete bridges with substructure irregularity can be significantly affected if they are located in chloride-laden environments.

The nonuniform chloride-induced corrosion of piers can exacerbate the unbalanced seismic demand and affect the transverse seismic behaviour of irregular bridges. Moreover, it can change the pattern of demand distribution, affect the damage mechanisms, and alter the failure sequence of bents of varying heights. This paper aims to investigate the seismic performance and fragility of irregular nonuniformly corroded bridges.

2 BRIDGE DETAILS AND NUMERICAL MODELLING

2.1 Geometry and details

In this study, the details of a two-span RC bridge tested in the shake table facility of the University of Nevada are considered here to study the combined effects of corrosion damage and substructure irregularity on the seismic fragility of RC bridges (Johnson et al. 2008). Figure 1 shows the geometry and structural details of this prototype irregular benchmark RC bridge. As shown in Figure 2, the total bridge length is 2050.0 cm, and the span length is 914.0 cm; the clear height of the piers from the top of the foundation is 182.9 cm, 243.8 cm and 152.4 cm for bent 1, bent 2 and bent 3, respectively. Six 9.1 tons, two 10.8 tons, and two 2.3 tons of super-imposed weights are placed on the superstructure. Moreover, the diameter of all columns is 30.5 cm; the longitudinal reinforcement ratio is approximately $\rho_l = 1.56\%$, and the spiral reinforcement ratio is $\rho_s = 0.9\%$. Further details on the structural details and material properties of this bridge specimen can be found in (Johnson et al. 2008).

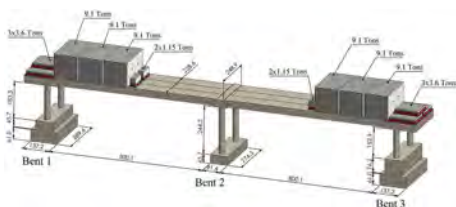


Figure 1. Geometry of the benchmark bridge.



Figure 2. Three-dimensional finite element model of benchmark RC bridge.

2.2 Finite element model

In this study, the advanced nonlinear finite element modelling technique developed by Afsar Dizaj and Kashani (2022) is extended to simulate the nonlinear structural response of the benchmark RC bridge. The adequacy of this model in simulating seismic response of bridge piers under biaxial loading was demonstrated by Salami et al. (2019). Figure 2 shows the three-dimensional numerical model of the considered reference RC bridge. This model can simulate the inelastic buckling behaviour and low-cycle fatigue degradation of reinforcements. As Figure 2 shows, bridge piers and deck beams are divided into several fibre sections in their entire length in this model. Moreover, each component is modelled using five force-based elements: two zero-length section elements at the top and bottom to simulate the slippage of reinforcement at connection adjacents, two force-based elements with three integration points at the top and bottom and an intermediate element with five integration points. Further details about the developed model and numerical validation are available in Afsar Dizaj et al. (2022, 2023).

2.3 Corrosion damage scenarios

To investigate the influence of corrosion damage on the seismic fragility of the benchmark irregular concrete bridge, three corrosion statuses of piers, including (i) pristine, (ii) slightly corroded and (iii) highly corroded conditions, are considered. The material and geometrical properties of the corroded hypothetical bridge piers are updated using the mass loss ratio of rebars (ψ) in any of the corrosion statuses mentioned above. This parameter can be calculated using Equation 1 (Afsar Dizaj 2022):

$$\psi(t) = \left(\frac{d_b d_c - 1.05(1 - W/C)^{-1.64} t^{0.71}}{d_b d_c} \right)^2 \quad (1)$$

where d_c is cover thickness, d_b is the diameter of main bars; W/C is the water-to-cement ratio, and t is the time from corrosion initiation.

In this study, five different corrosion scenarios are considered. Scenario 1 is the benchmark bridge specimen tested by Johnson et al. (2008) where all the piers are considered pristine (uncorroded). In scenario 2, all the piers are assumed to be slightly uniformly corroded. For this scenario, it is assumed $t=5$ years; therefore, from Eq. (5), the mass loss ratio of spiral and longitudinal reinforcement is obtained as 15.8% and 5.5%, respectively. For scenario 3, it is assumed $t=5$ years; therefore, for this condition, the mass loss ratio of spiral and longitudinal reinforcement is calculated to be 50% and 18.9%, respectively. Therefore, in this scenario, all piers are severely corroded uniformly.

In addition to the uniform corrosion damage scenarios (scenarios 2 and 3), two non-uniform corrosion statuses are considered where the corrosion levels of different piers are assumed to be spatially variable. To this end, in scenario 4, the piers of bent 2 are taken to be severely corroded, and the others are slightly corroded. Finally, in scenario 5, while the piers of bent 1 and bent 2 are slightly corroded, the piers of bent 3 are assumed to be severely corroded.

3 CAPACITY LIMIT STATES

Nonlinear pushover analysis is carried out on the three bents of hypothetical bridge layouts with different corrosion levels to quantify the time-dependent capacity limit states. To this end, the material and geometrical properties of the frame are modified to incorporate corrosion-induced degradation. Moreover, the bases of the columns are assumed to be fully fixed, and the P-delta effects are also included in the analyses.

Figure 3 compares the capacity curves of bents with different corrosion percentages. The capacity limit states associated with bar yielding, cover concrete spalling, and core concrete crushing are mapped on each curve. Moreover, the onset of core concrete crushing is considered the onset of the collapse as it takes place just before a significant drop in capacity curves. As Figure 3 shows, the ductility and capacity of each bent significantly decrease as the corrosion level increases. Remarkably, the severely corroded bents experience a sudden drop in their post-peak response, showing a considerable decrease in their ductility. The capacity limit states quantified in this section are used in Section 4.3 to develop seismic fragility curves.

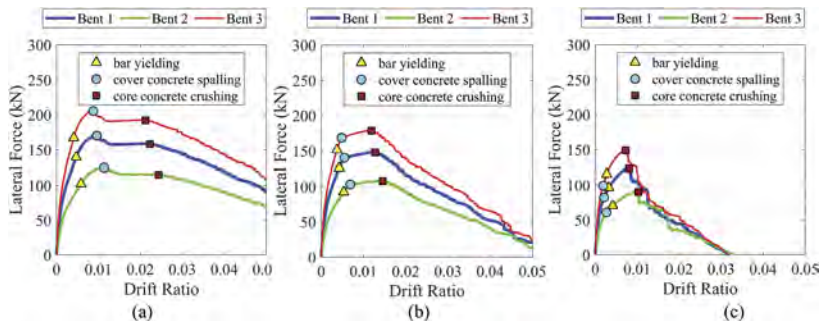


Figure 3. Capacity curves and capacity limit states: (a) uncorroded bents; (b) slightly corroded bents, and (c) severely corroded bents.

4 INCREMENTAL DYNAMIC ANALYSIS (IDA)

4.1 Selected ground motions

To carry out incremental dynamic analyses, 32 individual earthquake records are selected from the far-field ground motion records available in FEMA P695 (2009). Detailed information on the characteristics of selected ground motion records is provided in Afsar Dizaj et al. (2022, 2023). It should be noted that the primary transverse vibration mode of the reference bridge specimen is its second mode; therefore, selected ground motion records were scaled up by 0.1g steps (from 0 to 2.2g) in terms of $S_a(T_2, 5\%)$ and used as input for incremental dynamic analyses.

4.2 IDA results

Figure 4 compares the median IDA curves of each bent to investigate the nonlinear behaviour and failure mechanism of the hypothetical bridge layouts. Figure 4 shows that median IDA response of all bents becomes a plateau at approximately $S_a(T_2, 5\%) = 1.2g$. However, results show that for a given $S_a(T_2, 5\%)$, bent 1 experiences higher drift ratios. For example, while $S_a(T_2, 5\%) = 1g$ corresponds to approximately 0.039 peak drift ratio in piers of bent 1, for the same median intensity measure of ground motion records, bent 2 and bent 3 tolerate about 0.019 and 0.022 maximum drift ratios, respectively. This shows that 1 in scenario 1, bent 1 is more vulnerable than the other two bents. However, as Figure 4(c) shows, the median IDA response of all bents in the severely uniformly corroded bridge (i.e., scenario 3) is approximately identical. This can be due to the insufficient confinement in the piers of this bridge specimen as a result of the premature fracture of severely corroded spirals.

Figure 4(b) indicates that the slight uniform corrosion of piers causes a 25% reduction in the associated intensity level with the plateau response of bents. However, like the uncorroded bridge (scenario 1), bent 1 sustains higher displacement demands. This infers that the failure sequence of bents has not experienced a significant change compared to scenario 1. Figure 4(c)

show that the considerable reduction in the capacity of bents due to the severe uniform corrosion of piers results in near-synchronised flexural failure of all piers. Therefore, it can be inferred from the results presented in Figure 4(c) that all the bents fail almost simultaneously for the RC bridge supported on severely uniformly corroded piers. This can be attributed to the premature fracture of extremely corroded spirals, where the core concrete is almost unconfined.

Figure 4(d) shows that the onset of failure of columns of bent 2 (taller columns) coincides with that of columns of bent 3 (shorter columns). This implies that the higher ductility demand attracted by the stiffer piers of bent 3, is regulated significantly by the greater corrosion percentage of bent 2. Consequently, the columns of these two bents with different stiffnesses are collapsed at approximately the same intensity of input ground motions. Finally, Figure 5(e) shows that the nonuniform corrosion of piers in scenario 5 has resulted in the near-synchronised collapse of bent 1 and bent 3 at approximately $Sa(T_2, 5\%)=0.6g$.

4.3 Seismic fragility curves

In this section, the failure probability of studied RC bridges is investigated. To this end, the following fragility function is used:

$$P[MDR \geq CLS \mid IM = y] = 1 - \Phi \left(\frac{\ln(CLS) - \ln(\mu)}{\beta} \right) \quad (2)$$

where $P[.]$ is the probability that the maximum drift ratio (MDR) exceeds a capacity limit state (CLS), given that the intensity measure (IM) equals y . Moreover, $\Phi(.)$ is the lognormal distribution function with the logarithmic mean, and standard deviation of $\ln(\mu)$ and β , respectively, which can be obtained using Equations 3-4:

$$\ln(\mu) = \frac{\sum_{i=1}^n \ln(MDR_i)}{n} \quad (3)$$

$$\beta = \sqrt{\frac{\sum_{i=1}^n (\ln(MDR_i) - \ln(\mu))^2}{n - 1}} \quad (4)$$

In Equations (3-4), n is the number of records, and MDR_i is the maximum drift ratio associated with a given value of IM for the i_{th} record. It is noteworthy that the MDR associated with concrete crushing (as shown in Figure 5) of piers is assumed as the collapse capacity limit state in Equation. (2).

Figure 5(a) shows that in scenario 1, the probability of failure of bent 1 is higher than in other bents. For instance, for $IM=1.2g$, while the failure probability of bent 1 is approximately 94%, it is around 62% and 71% for bent 2 and bent 3, respectively. Likewise, in Figure 5(b), the same trend can be seen with a slightly higher probability of collapse due to the uniform corrosion of piers. However, Figure 5(c) indicates that in scenario 3, the fragility curves of bent 2 and bent 3 are almost in line with that of bent 1. Especially for higher IMs (i.e., higher than $IM=0.6g$), the probability of collapse of all bents is approximately the same. This implies the near-synchronised brittle failure of bents, which is consistent with the conclusion of the IDA results presented in Figure 4(c).

Figure 5(d) compares the failure probability of bents in the nonuniformly corroded bridge scenario 4. As this figure shows, due to the higher degree of corrosion in the intermediate piers, the fragility curves of bent 3 and bent 2 are similar. This implies the synchronised failure of these two bents just after the failure of bent 1. Finally, Figure 5(e) shows that the fragility curve of bent 3 is on top of others.

This indicates that, in this scenario, the collapse probability of shorter columns is higher than others. Therefore, it can be concluded that various corrosion scenarios can result in diverse seismic behaviour and failure sequences of multi-span RC bridges with unequal-height piers.

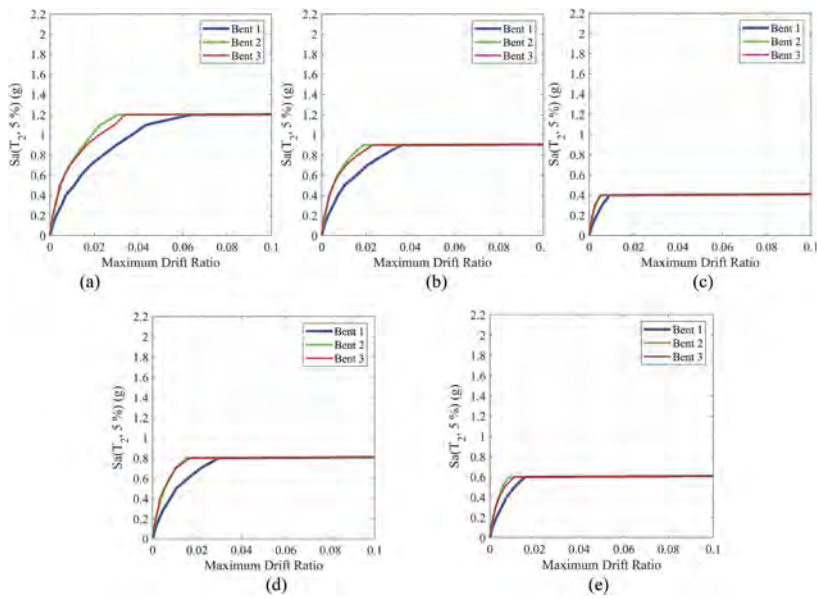


Figure 4. Median incremental dynamic analysis results: (a) scenario 1; (b) scenario 2; (c) scenario 3; (d) scenario 4, and; (e) scenario 5.

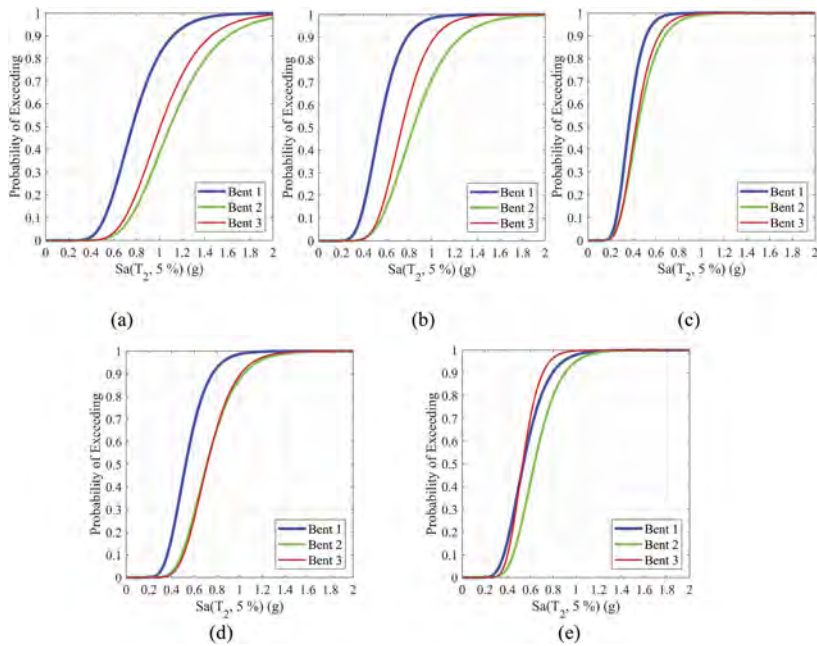


Figure 5. Collapse fragility curves of bents: (a) scenario 1; (b) scenario 2; (c) scenario 3; (d) scenario 4, and; (e) scenario 5.

5 CONCLUSIONS

This study evaluated the seismic performance and vulnerability of corrosion-damaged multi-span RC bridges with substructure irregularity. To this end, an advanced three-dimensional modelling methodology was employed to simulate the nonlinear behaviour of multi-span

irregular RC bridges accurately. The developed numerical model was then successfully verified against the large-scale shake table test results of an irregular two-span concrete bridge. Five hypothetical corrosion damage scenarios were considered, including uniform and nonuniform corrosion scenarios of piers. The failure modes and nonlinear dynamic behaviour of studied bridges with varied corrosion scenarios were assessed using nonlinear pushover and incremental dynamic analyses. Finally, the time-dependent fragility curves were developed using the IDA outputs for the frames under the selected ground motion suite.

The obtained results indicated that the unbalanced seismic demand distribution due to the substructure irregularity of the uncorroded bridge (scenario 1) causes the earlier failure of medium-height piers. This causes the higher vulnerability of bent 1 in this bridge specimen. The slight symmetrical corrosion level (around 5.5% in terms of rebar mass loss, $t=5$ years) of the bridge columns (Scenario 2) causes an approximately 25%, 35%, and 20% reduction in median failure IM of bent 1, bent 2, and bent 3, respectively. However, it does not affect the failure sequence of bents, where bent 1 tolerates higher seismic ductility demands than other bents. Moreover, results showed that the severe uniform corrosion of bridge piers (scenario 3) results in near-synchronised flexural failure of bents. This can be attributed to insufficient confinement in severely corroded bridge piers, resulting in brittle failure. The other important finding of the current study was that, depending on the corrosion damage scenario of piers, the nonuniform corrosion of bridge piers in an irregular RC bridge could regulate or exacerbate the unbalanced seismic ductility demand distribution across piers of unequal heights. For example, results showed that, in scenario 4, the adjusted seismic demand on severely corroded bent 2 results in the near-simultaneous collapse of taller and shorter piers.

REFERENCES

- AASHTO. 2011. AASHTO Guide Specifications for LRFD Seismic Bridge Design. Washington: American Association of State Highway and Transportation Officials.
- Afsar Dizaj, E. 2022. Modelling Strategy Impact on Structural Assessment of Deteriorated Concrete Bridge Columns. *Proceedings of the Institution of Civil Engineers-Bridge Engineering* 175 (4): 246–262. <https://doi.org/10.1680/jbren.21.00003>.
- Afsar Dizaj, E. & Kashani, M.M. 2022. Nonlinear Structural Performance and Seismic Fragility of Corroded Reinforced Concrete Structures: Modelling Guidelines. *European Journal of Environmental and Civil Engineering* 26(11): 5374–5403. <https://doi.org/10.1080/19648189.2021.1896582>.
- Afsar Dizaj, E. & Kashani, M.M. 2022. Influence of ground motion type on nonlinear seismic behaviour and fragility of corrosion-damaged reinforced concrete bridge piers. *Bulletin of Earthquake Engineering* 20: 1489–1518. <https://doi.org/10.1007/s10518-021-01297-5>.
- Afsar Dizaj E, Padgett J.E., Kashani, M.M. 2021. A Markov Chain-Based Model for Structural Vulnerability Assessment of Corrosion-Damaged Reinforced Concrete Bridges. *Philosophical Transactions of The Royal Society A Mathematical Physical and Engineering Sciences* 379 (2203). <https://doi.org/10.1098/rsta.2020.0290>.
- Afsar Dizaj, E., Salami, M.R., Kashani, M.M. 2022. Nonlinear dynamic behaviour and seismic fragility analysis of irregular multi-span RC bridges. *Structures* 44: 1730–1750. <https://doi.org/10.1016/j.istruc.2022.08.112>.
- Afsar Dizaj, E., Salami, M.R., Kashani, M.M. 2023. Seismic vulnerability analysis of irregular multi-span concrete bridges with different corrosion damage scenarios. *Soil Dynamics and Earthquake Engineering* 107678. <https://doi.org/10.1016/j.soildyn.2022.107678>.
- American Society of Civil Engineers. 2021. Report card for America's infrastructure. <http://www.infrastructurereportcard.org>.
- Broomfield, J.P. 2007. Corrosion of Steel in Concrete, Understanding, investigation and repair. Taylor & Francis, London.
- Caltrans. 2013. Caltrans Seismic Design Criteria-Version 1.7. Sacramento, California: California Department of Transportation.
- Camacho, V.T., Lopes, M., Oliveira, C.S. 2022. Multivariate analysis of regular and irregular RC bridges and characterization of earthquake behaviour according to stiffness-based indexes. *Bulletin of Earthquake Engineering*, 20: 415–448. <https://doi.org/10.1007/s10518-021-01223-9>.

- Choe, D.E., Gardoni, P., Rosowsky, D., Haukaas, T. 2009. Seismic fragility estimates for reinforced concrete bridges subject to corrosion. *Structural Safety* 31(4): 275–83. <https://doi.org/10.1016/j.strusafe.2008.10.001>.
- Comptroller and Auditor General, Maintaining Strategic Infrastructure: Roads, HC 169, Department for Transport and Highways Agency, London, 6 June 2014.
- FEMA P695. 2009. Quantification of building seismic performance factors. Federal Emergency Management Agency, Washington, DC.
- Ghosh, J., & Sood, P. 2016. Consideration of time-evolving capacity distributions and improved degradation models for seismic fragility assessment of aging highway bridges. *Reliability Engineering & System Safety* 154: 197–218. <https://doi.org/10.1016/j.res.2016.06.001>.
- Gómez-Soberón, M.C., Pérez E., Salas, D., León-Escobedo, D.D. 2019. Seismic vulnerability through drift assessment for bridges with geometrical irregularities. *European Journal of Environmental and Civil Engineering*. <https://doi.org/10.1080/19648189.2019.1686428>.
- Guirguis, J.E.B., Mehanny, S.S.F. 2012. Evaluating code criteria for regular seismic behavior of continuous concrete box girder bridges with unequal height piers. *Journal of Bridge Engineering* 18(6):486–498. DOI: 10.1061/(ASCE)BE.1943-5592.0000383.
- Hu, Y. & Guo W. 2020. Seismic response of high-speed railway bridge-track system considering unequal-height pier configurations. *Soil Dynamics and Earthquake Engineering* 137: 106250. <https://doi.org/10.1016/j.soildyn.2020.106250>.
- Ishac, M.G., Mehanny, S.S.F. 2017. Do mixed pier-to-deck connections alleviate irregularity of seismic response of bridges with unequal height piers? *Bulletin of Earthquake Engineering*, 15(1): 97–121. <https://doi.org/10.1007/s10518-016-9958-8>.
- Jara, J.M., Villanueva, D., Jara, M., Olmos, B.A. 2013. Isolation parameters for improving the seismic performance of irregular bridges. *Bulletin of Earthquake Engineering*, 11: 663–686. <https://doi.org/10.1007/s10518-012-9398-z>.
- Jara, J.M., Reynoso, J.R., Olmos, B.A., Jara, M. 2015. Expected seismic performance of irregular medium-span simply supported bridges on soft and hard soils. *Engineering Structures* 98:174–185. <https://doi.org/10.1016/j.engstruct.2015.04.032>.
- Johnson, N., Ranf, R.T., Saiidi, M.S., Sanders, D., and Eberhard, M. 2008. Seismic testing of a two-span reinforced concrete bridge. *Journal of Bridge Engineering* 13(2): 173–182. [https://doi.org/10.1061/\(ASCE\)1084-0702\(2008\)13:2\(173\)](https://doi.org/10.1061/(ASCE)1084-0702(2008)13:2(173)).
- Kappos, A.J., Manolis, G.D., Moschonas, I.F. 2002. Seismic assessment and design of R/C bridges with irregular configuration, including SSI effects. *Engineering Structures* 24(10): 1337–1348. [https://doi.org/10.1016/S0141-0296\(02\)00068-8](https://doi.org/10.1016/S0141-0296(02)00068-8).
- Priestley, M. J. N. 2007. The need for displacement-based design and analysis. Advanced earthquake engineering analysis, Vol. 494, *CISM International Center for Mechanical Sciences*, Springer, Vienna, Austria, 121–132.
- Saiidi, M.S., Vosooghi, A., Nelson, R.B. 2012. Shake-table studies of a four-span reinforced concrete bridge. *Journal of Structural Engineering* 139(8): 1352–1361. [https://doi.org/10.1061/\(ASCE\)ST.1943-541X.0000790](https://doi.org/10.1061/(ASCE)ST.1943-541X.0000790).
- Salami M.R, Afsar Dizaj E, Kashani M.M. 2019. The behavior of Rectangular and Circular Reinforced Concrete Columns under Biaxial Multiple Excitation. *ComSputer Modeling in Engineering & Sciences* 120 (3): 677–691. <https://doi.org/10.32604/cmescs.2019.05666>.
- Soleimani, F., Vidakovic, B., DesRoches, R., Padgett, J. 2017. Identification of the significant uncertain parameters in the seismic response of irregular bridges. *Engineering Structures* 141: 356–372. <http://dx.doi.org/10.1016/j.engstruct.2017.03.017>.
- Soltanieh, S., Memarpour, M.M., Kilanehei, F. 2019. Performance assessment of bridge-soil-foundation system with irregular configuration considering ground motion directionality effects. *Soil Dynamics and Earthquake Engineering* 118: 19–34. <https://doi.org/10.1016/j.soildyn.2018.11.006>.
- Xiang N. & Li J. 2020. Utilizing yielding steel dampers to mitigate transverse seismic irregularity of a multi-span continuous bridge with unequal height piers. *Engineering Structures* 110056, <https://doi.org/10.1016/j.engstruct.2019.110056>.
- Zhang, Y., DesRoches, R., Tien, I. 2019. Impact of corrosion on risk assessment of shear-critical and short lap-spliced bridges. *Engineering Structures*, 189: 260–271. <https://doi.org/10.1016/j.engstruct.2019.03.050>.

Study on the applicability of repairing rubber bearing covers by resurface vulcanization in the field

A. Matsumoto & R. Takahara

Nippon Expressway Research Institute Company Limited, Tokyo, Japan

T. Imai & W. Abe

Rubber Bearing Association, Tokyo, Japan

ABSTRACT: In Japan, where earthquakes occur frequently, rubber bearings are used in many road bridges because of their effectiveness in improving the seismic resistance of bridges. NEXCO (Nippon Expressway Company) has adopted the use of rubber bearings as a standard. The rubber bearings have a 10 mm cover rubber on the side surface to protect them from the environment (ultraviolet rays, ozone, etc.). But cracking due to ozone deterioration have been reported in the cover rubber manufactured according to standards prior to 2000. In recent years, ozone cracking has been observed not only in cold regions in Japan, but also throughout the country. Repair methods for ozone cracks include covering the surface of rubber bearings with tape or paint-based repair materials. However, such repair methods have problems, such as floating or peeling of the repair material. In this paper, the applicability of a new and effective repair method, in which vulcanization (reconstruction) of the cover rubber performed in the field, is examined.

1 INTRODUCTION

As one of the main structural components of a bridge, bearings have an important function in ensuring the safety of the entire bridge. This function must be maintained over the long term. And proper maintenance is vital to continuously maintain the function of the bearings.

Bearings are broadly classified into two types, rubber bearings and steel bearings, depending on the materials used. Since the Hyogo-ken Nanbu Earthquake, a major earthquake that struck Japan in 1995, rubber bearings have been used in many road bridges because of their effectiveness in improving the earthquake resistance of bridges.

The sides of the rubber bearings are covered with a rubber coating of about 10 mm (Figure 1) to protect the rubber bearing body from the environment (ultraviolet rays, salt, humidity, heat, ozone, etc.). In recent years, however, there have been reports of cracking of rubber bearings in service due to ozone deterioration. Natural rubber used for rubber bearings has an unsaturated structure called a double bond in its molecular structure. These double bonds are highly reactive with ozone. Ozone degradation is a phenomenon in which ozone molecules act on the double bonds of the rubber surface and break the molecular chains. Under tensile strain, this phenomenon develops into a crack, which is called an ozone crack. Initially, ozone cracking was observed only in cold climates. And have been taken against this problem, such as improving the formulation of weathering protectants. However, in recent years, ozone cracking has been observed not only in cold regions in Japan but also throughout the country. To deal with ozone cracks, repair work using tape or paint-based repair materials to cover the rubber bearing surface and prevent ozone from entering the bearing has been promoted. But these repair materials have problems, such as peeling and floating. This paper reports on a study on the applicability of a new repair method, the in-situ vulcanization of the cover rubber.

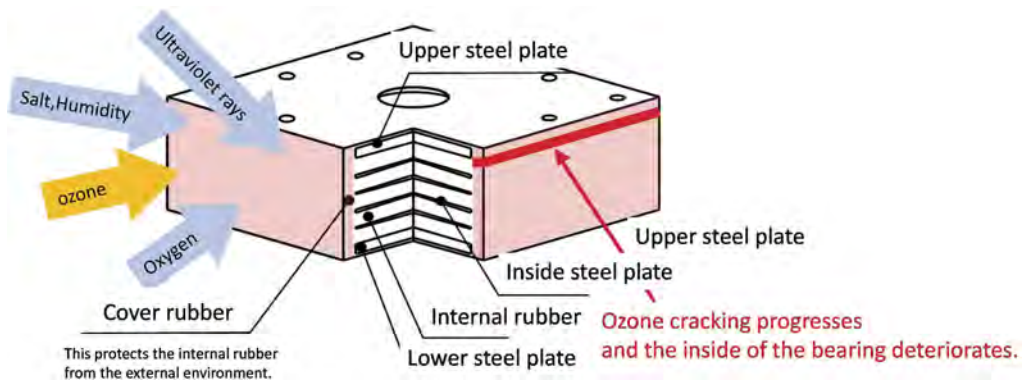


Figure 1. Covered rubber of rubber bearing.

2 STUDY ON THE APPLICABILITY OF REPAIR BY RE-VULCANIZATION IN THE FIELD

2.1 Repair by re-vulcanization

In the manufacturing process of rubber bearings, reinforcement, compounding materials, etc. are added to raw rubber and kneaded together. Next, the compounded rubber is laminated with adhesive-treated steel sheets, etc. and formed. Finally, the molded product is pressurized and heated to cross-link the rubber molecules to complete the process. Repair by re-vulcanization is a method of repairing existing rubber bearings by applying pressure and heat to the molded rubber to form chemical bonds between the rubber molecular chains, a reaction called vulcanization.

In this study, the applicability of on-site repair by vulcanization was examined.

2.2 Shear deformation performance test using 420mm size specimen

2.2.1 Examination overview

Because rubber materials harden by heat, the effect of heat applied during the vulcanization repair process on the shear deformation performance of the rubber bearing was checked. The test specimens are shown in Figure 2. The main material is natural rubber. The specimens are 420 mm in the bridge axis direction \times 420 mm perpendicular to the bridge axis, and 138mm in height, with 6 layers of 9 mm thick rubber, and 10 mm of cover rubber. Their shear modulus of elasticity is 1.2. Three test specimens with the same dimensions and configuration were made.

- (1) Rubber bearing in its as-made condition (hereinafter referred to as “no processing”)
- (2) Rubber bearing with simulated cracks (hereinafter referred to as “with simulated cracks”)
- (3) Rubber bearings with simulated cracks repaired by vulcanization (hereinafter referred to as “simulated crack repaired”)

Shear deformation performance tests were conducted on the above three types of bearings.

Ozone cracks tend to occur perpendicular to the direction of force action, and often occur near the upper and lower steel plates in the plane perpendicular to the bridge axis. Therefore, simulated cracks were placed at four locations, two at the top and two at the bottom, on the plane perpendicular to the bridge axis. The depth of the cracks was 15 mm to confirm whether or not 10 mm of cover rubber could be vulcanized.

2.2.2 Processing of test pieces

The flow for fabrication of the specimen is shown in Figure 3. First, a simulated crack was placed and a fixture was attached to hold the specimen under shear deformation of 70% (37.8 mm for this specimen). Although it is desirable to repair rubber bearings with the rubber body in an upright position as much as possible, the actual work is expected to be performed

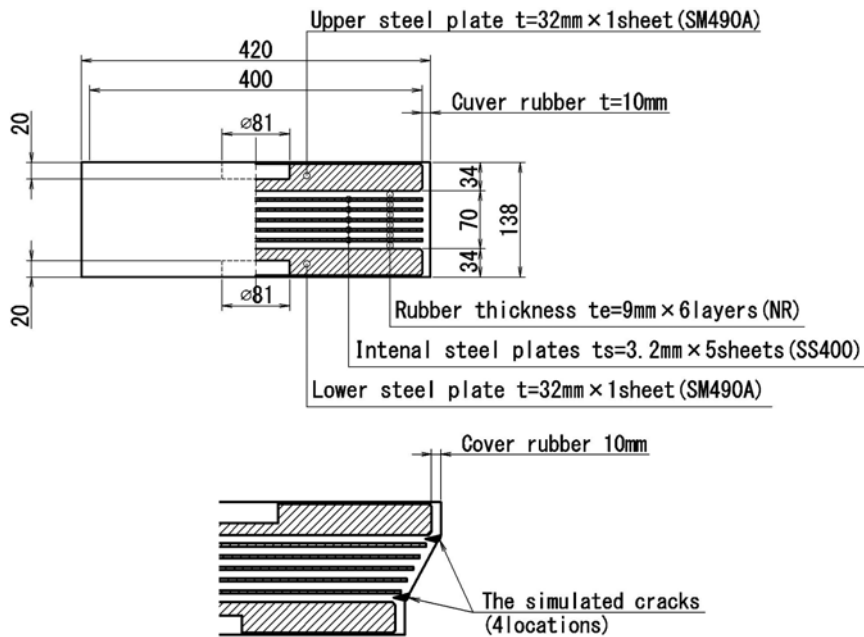


Figure 2. Cross-sectional view of the test specimens.

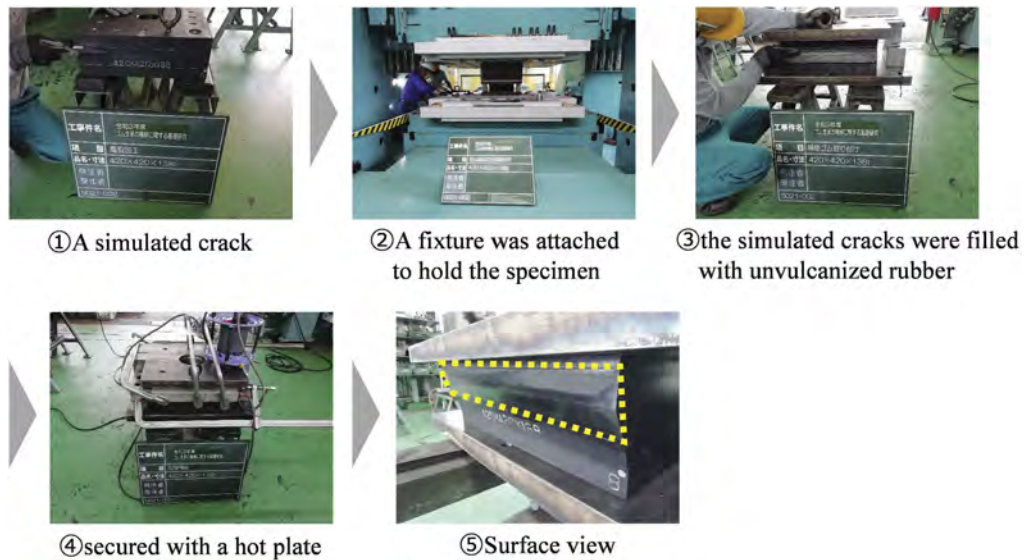


Figure 3. The flow for fabrication.

in a deformed state. In the present study, the rubber bearing was deformed by 70% of the allowable shear strain at any given time, and the vulcanization repair was performed while the bearing was fixed with a fixture.

Next, the simulated cracks were filled with unvulcanized rubber and secured with a hot plate. The heat plate was held at 110°C for 30 minutes until the surface temperature reached 110°C, and then held at 110°C for 90 minutes. The vulcanization temperature was set not to exceed 140°C -150°C, as vulcanization is generally performed at 140°C -150°C when producing the main body of the rubber bearing.

2.2.3 Test conditions

The test conditions are shown in Table 1. A biaxial load testing machine was used for the tests, and the test conditions were based on the bearing manual. Test D was terminated when the shear strain exceeded 330% to 340% to prevent damage to the testing machine.

2.2.4 Results

The results of Tests A, B, and C are shown in Figure 4. Each figure shows horizontal displacement (mm) on the horizontal axis and horizontal force (kN) on the vertical axis. The history curves for each test show almost the same history trend. The results of each test indicate that the difference in shear stiffness is about 1%-2%, which is considered to be within the range of variation of each product. This confirms that there is no influence of hardening due to the heat of the vulcanization process. In Test D, each specimen was subjected to shear deformation of 330% or more, but they did not fracture, and the test was terminated.

The surface of the specimens could be visually confirmed to be vulcanized, but the condition of the interior was not visible. Therefore, in order to confirm whether vulcanization had progressed to the inside, the specimen was cut after the test was completed and the inside condition was observed. The condition after cutting is shown in Figure 5. Some parts of the vulcanized rubber were found to be not vulcanized on the body side. Vulcanization is controlled by temperature and time, but once again, the heating temperature and time control were found to be the issues.

Table 1. Shear deformation performance test condition.

Test name	Test A	Test B	Test C	Test D
Temperature	23±2°C			
Share strain	175%	250%	300%	Break off
Vertical load	Equivalent to surface pressure 6.0N/mm ²			
Number of horizontal excitation	5	6	2	monotonic load

2.3 Shear fatigue test using 920mm size specimen

2.3.1 Examination overview

Rubber bearings are subjected to repeated shear deformation due to expansion and contraction of the girder caused by temperature variation. Therefore, shear fatigue tests were conducted to confirm whether or not the vulcanized rubber bearing dropped, protruded, or peeled off under repeated shearing.

The test specimen is shown in Figure 6. The dimensions of the specimen for shear fatigue tests were close to the 1,000 mm square, used in the NEXCO test method 418, to confirm whether repair by vulcanization is possible even if the dimensions of the rubber bearing enlarge. The main material of the specimens was natural rubber. The specimen was 920 mm in the direction of the bridge axis x 920 mm perpendicular to the bridge axis, and 296mm in height, with 6 layers of 22 mm thick rubber, 10 mm of cover rubber. The specimen had a shear modulus of elasticity of 1.2.

As with the 420 mm square specimen, simulated cracks with a depth of 10 mm were made in four locations, two on each side perpendicular to the bridge axis. The specimens were then subjected to shear deformation of 70% (92.4 mm for this specimen) and the simulated cracks were repaired by vulcanization.

2.3.2 Test conditions

The test conditions are shown in Table 2. The test conditions were set with reference to the bearing manual.

2.3.3 Results

The appearance of the specimen after the fatigue loading test is shown in Figure 7. No abnormalities such as dropout, protrusion, or peeling of the re-vulcanized area were observed.

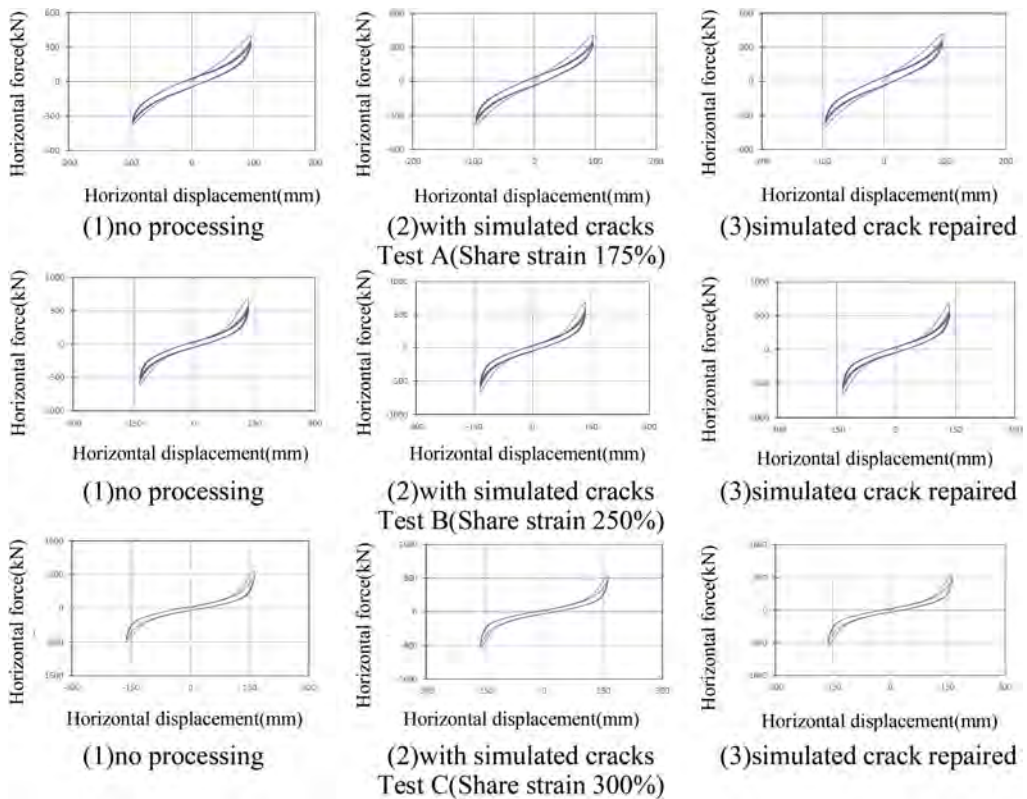


Figure 4. History curve for each test.

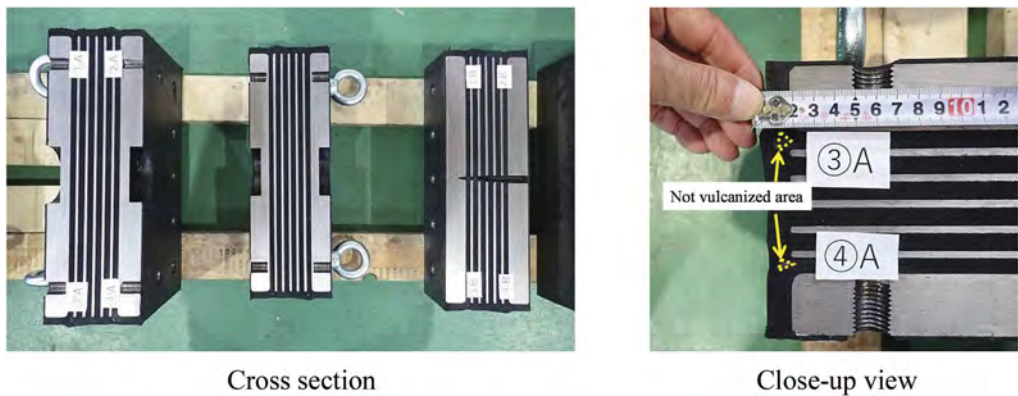


Figure 5. The condition after cutting.

The cut specimen is shown in Figure 8. Though no deformation was observed at the vulcanized area (Left side of Figure 8), cracks were seen (Right side of Figure 8). But the cracks did not reach the main body rubber and were contained within the area (10 mm) of the vulcanized cover rubber.

2.3.4 Confirmation of changes in physical properties in vicinity of re-vulcanization repair area

The effect of heat applied during the vulcanization process on the vicinity of the vulcanized area was confirmed. Specimens were cut out and tested for elongation at break and tensile

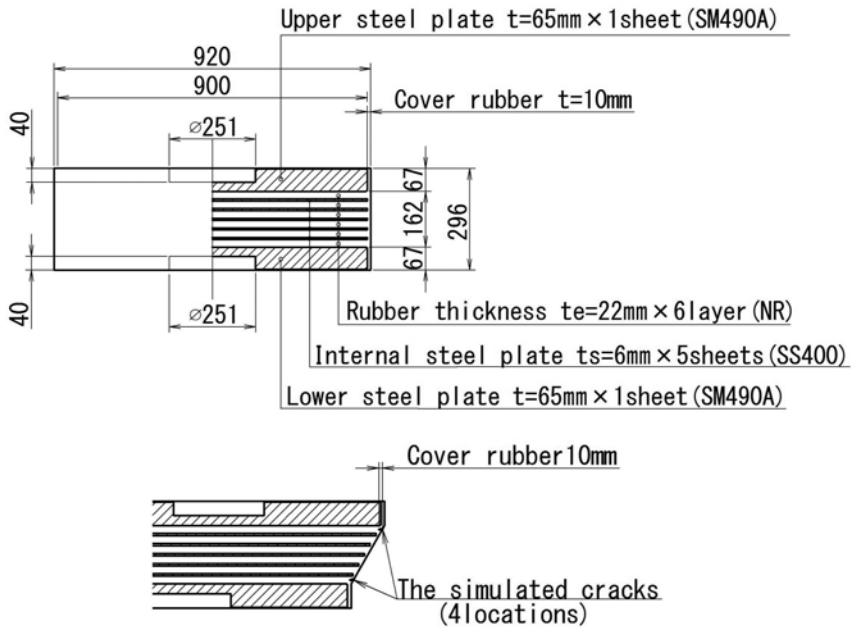


Figure 6. Cross-sectional view of the test specimens.

Table 2. Shear deformation fatigue test condition.

Temperature	23±2°C
Share strain	70%
Vertical load	Equivalent to surface pressure 6.0N/mm ²
Number of horizontal excitation	5,000 times

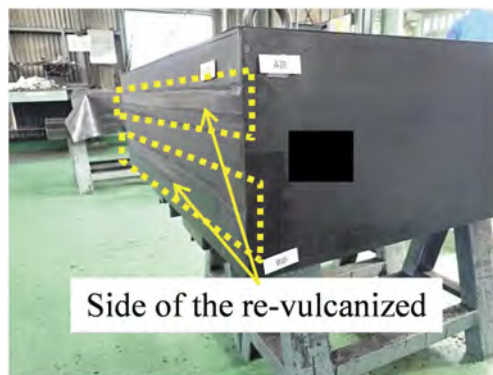


Figure 7. The appearance of the specimen after the fatigue loading test.

strength, which are basic properties of rubber materials. The locations where the test specimens were cut out are shown in Figure 9. Test specimens (dumbbell No. 3 specimens) were cut from the first layer (N①, S②) and the second layer (N③, S④) of the body rubber that had undergone the resurface vulcanization repair. The test results are shown in Table 3. The elongation at break and tensile strength were above the specified values, even in the vicinity of the vulcanized area. This indicates that heat hardening did not occur during vulcanization. No significant difference in the test results was observed between the first layer near the vulcanized area and the second layer away from the vulcanized area.

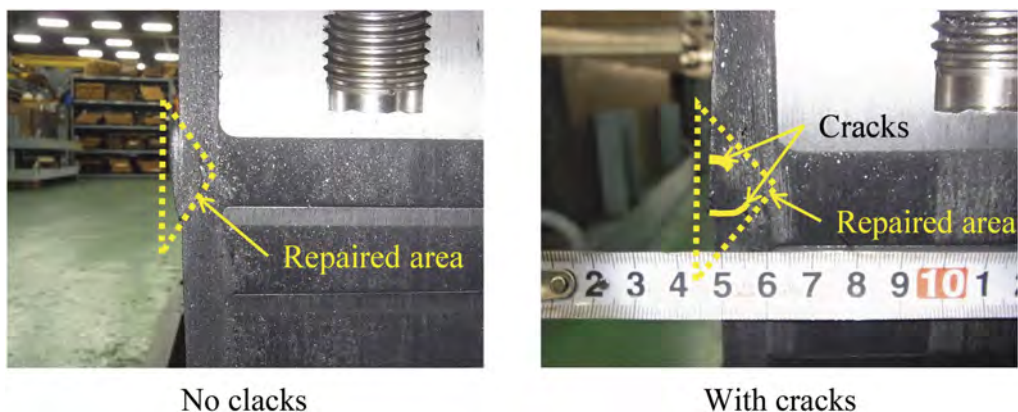


Figure 8. Cut surface.

3 CONCLUSIONS

In this study, various experiments were conducted to confirm the applicability of in-situ vulcanization as a new repair method for rubber bearings. The main results at present are as follows:

- (1) It was confirmed that shear deformation performance was not affected by the heat of vulcanization under the temperature and time set in these tests.
- (2) It was confirmed that the vulcanized portion did not drop out, protrude, or delaminate due to repeated shear deformation.

Going forward, we will continue to study the standardization of the construction procedure and quality control method for the vulcanization repair method. Eventually, we plan to develop draft technical standards that include a flow chart for selecting repair methods for covered rubber



Figure 9. Cutting surface of 920mm.

Table 3. Specimen results.

Test items	Standard value	Initial value (Sheet)	1st layer		2nd layer		
			N①	S②	N③	S④	
Elongation at break	%	450over	550	480	500	490	480
Rate of change			1.00	0.873	0.909	0.891	0.873
Tensile strain	N/mm ²	15over	28.3	26.5	27.3	28.1	28.3
Rate of change			1.00	0.936	0.965	0.993	1.00

bearings. This repair method eliminates the need to replace the rubber bearing if only the rubber coating is cracked. This is expected to reduce the construction cost required for the replacement, enabling effective repair at a lower cost, leading to a reduction in maintenance and management.

REFERENCES

- East, Central, West Nippon Expressway Company. 2016. *Design Guidelines Vol.2 Bridge Construction Edition*. Japan: East, Central, West Nippon Expressway Company.
- Editorial Committee for the Report on the Hanshin-Awaji Earthquake Disaster. 1997. *Report on the Hanshin-Awaji Earthquake Disaster, Investigation of causes of damage to Civil Engineering Structures, Concrete Structures, Steel Structures*. Japan: Japan society of civil engineers.
- Itoh, Y., Yazawa, A., Satoh, K., Haosheng, G., Kutsuna, Y. & Yamamoto, Y. 2005. Study on environmental deterioration of rubber material for bridge bearings. *Proceedings of Japan Society of Civil Engineers* No. 794: 253–266.
- Itoh, Y., Satoh, K., Haosheng, G. & Yamamoto, T. 2005. Study on the long-term deterioration of natural rubber of bridge bearings. *Proceedings of Japan Society of Civil Engineers* No.801: 185–196.
- Itoh, Y. 2009. Prediction of aging characteristics in natural rubber bearings used in bridge. *Journal of Bridge Engineering* Vol.14 No.2: 122–128.
- Japan Road Association. 2017. *Specifications for highway bridges*. Japan: Japan Road Association
- Japan Road Association. 2018. *Manual of highway bridge bearing*. Japan: Japan Road Association
- Kawashima, K. 1988. Development and future scope of seismic utilization of structures –A Reviews. *Journal of Japan Society of Civil Engineers*. Vol.398: 1–10
- Ohtake, Y. 2009. *Degradation and life prediction of polymeric materials*. Japan: S&T Publishing Inc.
- Public Works Research Center. 2011. *Manual for seismic Isolation and seismic response control design methods for road bridges (Draft)*. Tokyo: Public Works Research Center.

Application of BIM in design review processes for buildings

M. Achenbach & P. Rivas
LGA KdöR, Nürnberg, Germany

B. Weber
Hof University, Hof, Germany

ABSTRACT: The design review process – as part of the building permit – is mandatory for numerous construction projects in Germany. The paper-based review process is currently state of the art due to the obligation of documentation by law with legally binding signatures, e.g. for the construction process.

The application of BIM in the construction industry is increasing. Though the process of model sharing is specified in EN ISO 19650-4, the integration of the design review process has not been examined using BIM yet. In the review process, it is necessary to check structural analysis and other documents, too. Hence, the process of design review using various documents shall be linked to the steps proposed in ISO 19650-4.

The authors recommend a BIM-based digitalized design review process based on ISO 19650-4. It is shown how the template for the review process can be adjusted to legal requirements for digital proceedings and can be used for the complete life cycle of a building better than the paper-based documentation.

1 INTRODUCTION

The life cycle of a building can be characterised by different stages and perspectives. Regarding sustainable transformation, the stages production, construction process, use and end-of-life are identified (DIN EN 15978 2011). But it must be remembered that buildings are also part of the built environment. Therefore, buildings are embedded in building regulations in order to ensure that public interests, e.g. structural or fire safety, are considered. The process and life cycle of buildings from the view of building authorities are displayed in Figure 1, using the IDEF0 notation (IDEF – Integrated DEFINition Methods (IDEF) 2022). It can be shown that approved construction drawings are a necessary input for the execution on site. The complete documentation, containing as-built drawings and accompanying documents, e.g. the structural analysis and the check of fire safety, is needed for commissioning and the stages to follow. The life cycle shown in Figure 1 can be run in many cycles in case of refurbishment, e.g. by a change of usage from an office to a residential building. The life cycle can also be finished by demolition, following the permit of demolition issued by building authorities.

The review process of the structural analysis, the check of the fire safety and the corresponding drawings are mandatory for most public buildings in Germany (MBO 2020). This review process is part of the building permit: executing members and parts of the building as well as the commissioning of the building require legally a successful review process. The aim of the review process is proving compliance with building codes, i.e. that structural and fire safety are fulfilled by the proposed design according to legal codes and technical standards. Therefore, approved drawings and approved corresponding documents, i.e. documentation of the structural analysis

and check of the fire resistance, are part of the life cycle of a building. In fact, refurbishment and predictions on the service life of existing buildings require the documentation of the complete construction process including permits and other relevant conditions. If no documentation is available, expensive and time-consuming measurements on site and the determination of material properties are necessary.

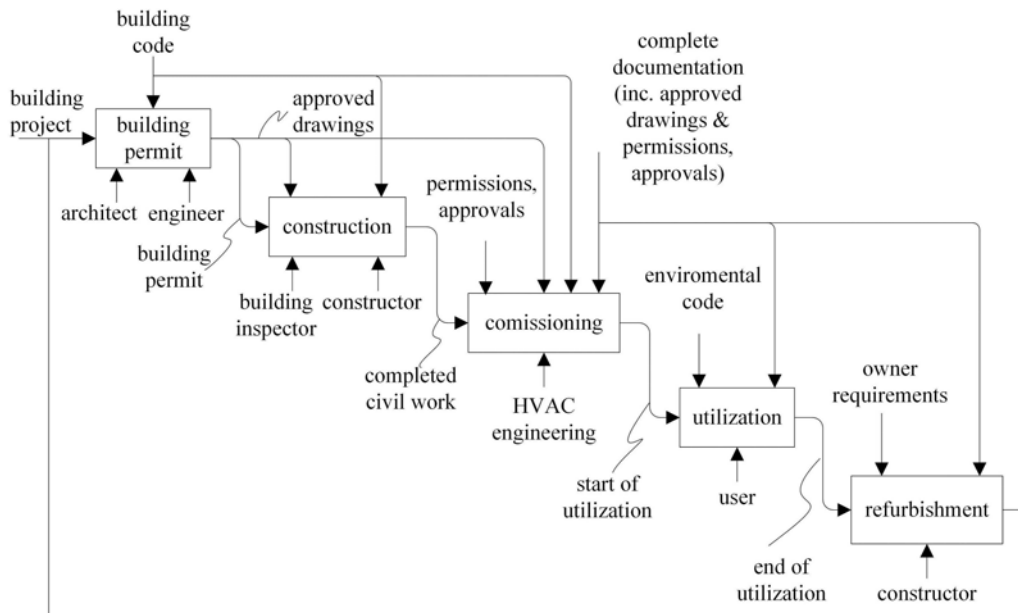


Figure 1. Life cycle of building according to IDEF0 – view of building authorities (HVAC: heating, ventilation, air conditioning).

Whereas the application of the BIM method in design, construction and operation of buildings is widely accepted (Borrmann *et al.* 2021), the application of BIM for the process of building permission in Germany is limited to research projects (König *et al.* 2022). It has to be noted, that the process of design review is part of the building permit: if BIM is not applied for the building permit, the field of application in design review is very limited accordingly. Hence, the use of BIM for the design review process in Germany is currently limited to the exchange of models to generate structural models suitable for commercial design software (Oltmanns *et al.* 2019).

On the other hand, the application of BIM for federal buildings and highways in Germany is stimulated by the government (Bundesministerium des Inneren, für Bau und Heimat and Bundesministerium der Verteidigung 2021, Bundesministerium für Verkehr und digitale Infrastruktur and Bundesministerium der Verteidigung 2021). Therefore, there is a need to integrate the process of design review in the BIM methodology as prerequisite for the application of BIM in the complete building permit process.

The state of the art of the design review process and the concepts for sharing data using BIM is given in Section 2. A proposal for a BIM-based digitalized design review process is developed in Section 3. The proposal is worked out according to the German building code template (MBO 2020), but can be easily transferred to other countries or other review processes.

2 APPLIED METHODS AND STATE OF THE ART

The process of building permission, design review, execution and commissioning is described in the German federal building code template (MBO 2020), which is adapted in each of the 16 federal states to state building law. The necessary documents and corresponding formats are detailed in the federal template for the required building documentation template

(MBauVorIV 2020) which stipulates the use of documents in the electronic PDF format as standard format. As the dynamics of change in the federal states varies widely from establishing the electronic form as standard in Lower Saxony (NBauVorIVVO 2021) including optional data formats as IFC, to adhering to the paper-based form as standard with experimentation clauses, e.g. in Bavaria (DBauV 2021) in autumn 2022, only a part of building authorities allowed the use of PDF instead of paper not yet including BIM. Others still insist in practice on a paper-based building permit process. The corresponding process of design review (M-PPVO 2012) is illustrated in Figure 2 using the BPMN 2.0 notation (ISO/IEC 19510 2013), which allows to visualize the process and the exchange of documents and messages.

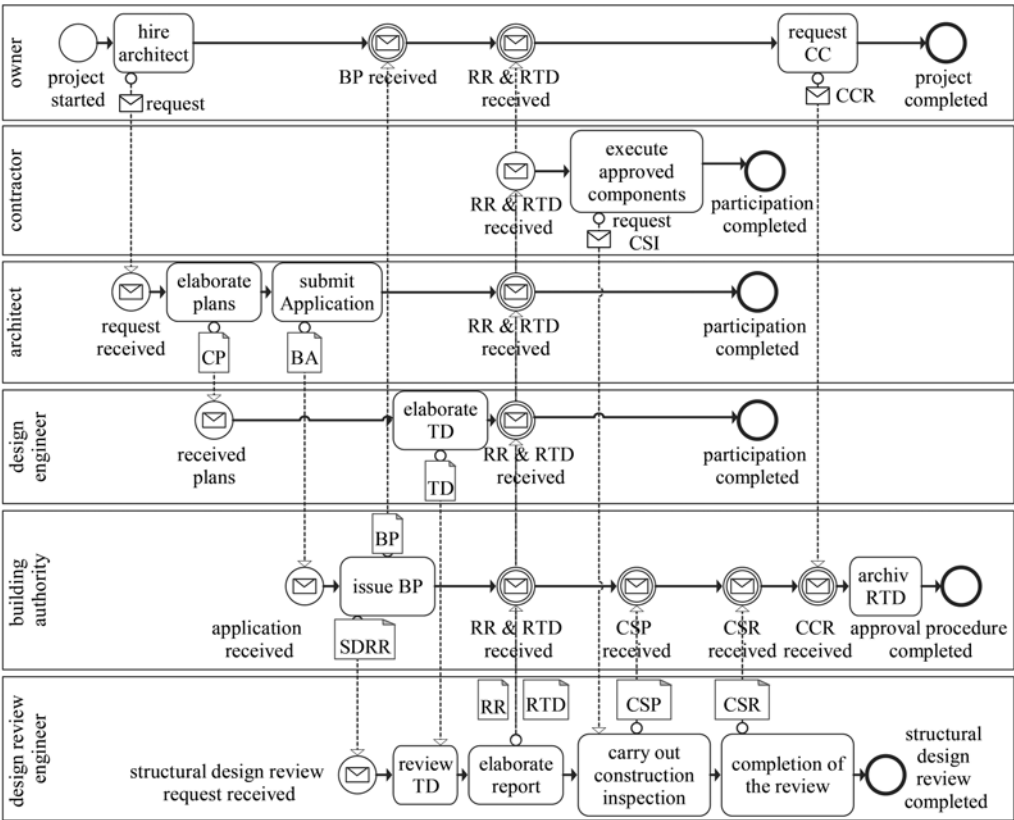


Figure 2. Paper-based design review process, abbreviations given in Table 1.

Table 1. Abbreviations for the paper-based design review process.

BP	building permit
BA	building application
CCR	certificate of occupancy requirement
CP	construction plans
CSI	construction supervision inspection
CSP	construction supervision protocol
CSR	construction supervision report
RTD	reviewed technical documentation
RR	revision report
SDRR	structural design review requirement
TD	technical documentation (structural analysis and drawings)

The well-established paper-based design review process using additional, signed copies of the original revised and signed documents allows a paper-based documentation of the building. The reviewed documents shall be signed by legally binding signatures in handwriting to identify and authenticate the reviewing engineer. In case of a replacement of paper by PDF, which can be seen as first step towards the digitalization of the review process, qualified electronic signatures (QES) representing the person or qualified electronic seals representing the organization shall replace legally binding manual signatures. The transition from paper to PDF becomes more and more accepted by design engineers and design review engineers, but needs agreement by local building authorities, as described above. Legally, the substitution of hand-written signatures by QES is compliant to EU regulation of electronic identification (eIDAS 2014).

The application of BIM in the construction industry is increasing and many fields of application are established (Borrmann *et al.* 2021). The benefits of BIM for the owner, namely collaboration between involved parties and a comprehensive documentation, cover the whole life cycle of a building. The EU leaves the application of BIM for public work contracts to the discretion of the member states (Art. 22 par. 4 Directive 2014/24/EU and Art. 40 par. 4 Directive 2014/25/EU). The EU member states have imposed different national legislations (Bidaut & Hassine 2021). Whereas France leaves the decision to the public authority in the respective procurement procedure, if BIM is seen as “necessary (Art. R.2132-10 Code de la commande publique 2022), Germany, for example, is restricting the choice of the authorities (§ 12 par. 2 VgV) for the application of BIM for public work contracts stepwise. BIM becomes mandatory during the next years for federal infrastructure planning starting with federal traffic road construction, widening to rail- and waterways and finally to building construction related to the contract volume (Bundestag 2022; BMI 2021). In order to allow the collaboration, the use of a common data environment (CDE) (DIN EN ISO 19650-1 2019) is stipulated. The process of information exchange using a CDE is described in DIN EN ISO 19650-4 (2021) and displayed in Figure 3 in the BPMN notation (ISO/IEC 19510 2013).

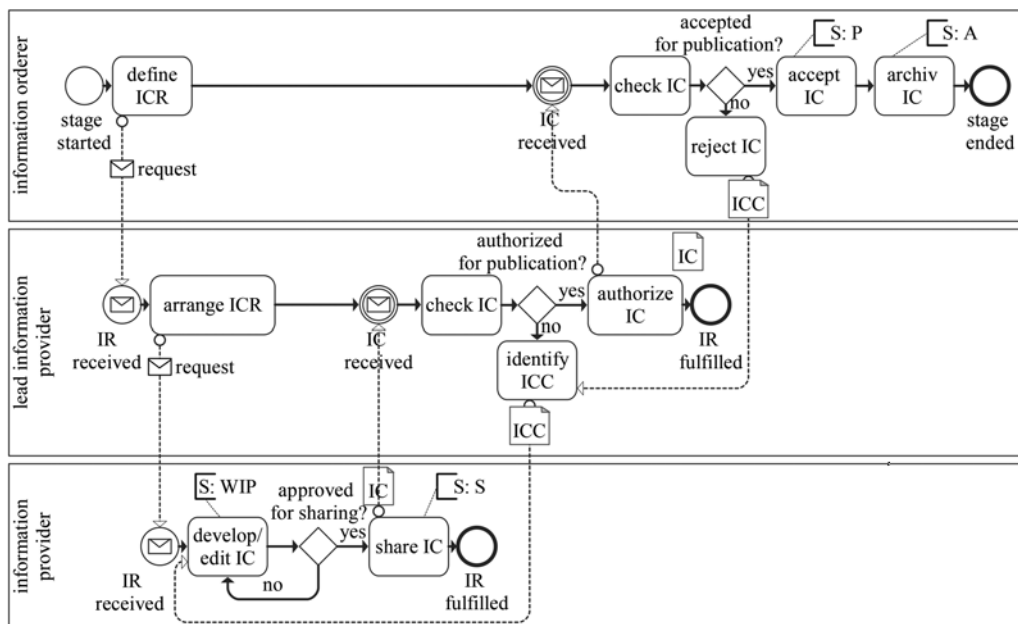


Figure 3. Information exchange according to DIN EN ISO 19650-4, abbreviations given in Table 2.

An information container is described as a set of information, e.g. a folder containing several files or a BIM model including meta data. Information is interpreted as readable representation of data, in which the reader can be human or a machine. The information orderer starts the

Table 2. Abbreviations for the information exchange acc. to DIN EN ISO 19650-4.

IC	information container
ICC	information container correction
ICR	information container requirement
IR	information required
S:A	status: archived
S:P	status: published
S:S	status: shared
S:WP	status: work in progress

process of information exchange by a request for information. The request is passed over to the lead information provider, which passes it over to the decisive information provider. The provider processes the request and prepares the needed information. This information is shared to the lead provider at first and then passed on to the orderer of the requested information. The information orderer has to confirm that the provided information fulfills the request (DIN EN ISO 19650-4 2021). After approval, the requested information is also available for general use in subsequent phases. If the stage of work is finished, the retrieved information can be archived.

It is obvious, that the process of information exchange can be transferred to the process of design review. In the following section, the considered roles are specified and the status is adjusted to the needs of the review process. In addition, the options for each stage and the possibility to publish must be adapted in compliance to the legal framework in the design review process.

3 PROPOSAL FOR A BIM-BASED DIGITALIZED DESIGN REVIEW PROCESS

The process of design review can be transferred from a paper-based version to a BIM-based process. Models of the building are necessary to carry out the structural analysis. The structural analysis is a requirement for the design of structural members and the corresponding drawings for the execution on site. Technical documents, i.e. structural analysis and drawings, can be reviewed and approved with comments or amendments and it is possible to sign them by legally binding signatures as QES, which are mandatory in the design review process according to building regulations. Technical models, like a BIM-model of the building, can be reviewed and comments can be submitted within the review process, e.g. using the BIM Collaboration Format ((BCF) 2022). If the comments are given in a separate file, it is possible to seal and encrypt these files for a safe transfer and authentication. The problem of integrating legally binding signatures in BIM models is under development (Siebenhütter 2020) and not yet common in commercial applications. Therefore, the review process must be split in a review process for documents and one for models, because signatures and the treatment of annotations differ. The review process for documents is displayed in Figure 4 and for BIM models in Figure 5.

The responsible structural engineer submits the technical documentation, e.g. structural analysis and drawings, to the design review department for review, as shown in Figure 4. The review is carried out by a co-worker or the design review engineer itself. If the technical documentation is incomplete, the review process cannot start and a revised version of the documentation must be submitted. After the review of the documents is done, the status of the document can change to “shared” and the structural engineer can view the annotations. The submitted technical documentations are collected and published together with the report to other interested parties. Note, that the design review engineer attributes the status “published”. According to German building regulations, the design review engineer has to assign the revised documents to the report (M-PPVO 2012). This is done by stamping and signing all reviewed documents. This step allows to use documents, e.g. drawings, without report, because it is proved, that the review process is completed. In a digitalized review process, electronic signatures are used to replace manual signatures. For the design review engineer, QES are necessary to replace legally binding manual signatures. For the co-worker, other forms of authentication and authorization as an advanced electronic signature may be sufficient.

For drawings on site, it is common practice to revise the drawings by the structural engineer according to the comments by the design review. It depends on the type of review process, if these revised drawings must be re-submitted for a final review to check, if the comments have been addressed. The proposed process in Figure 4 can be repeated in many cycles until the last set of documents is submitted. The technical documentation can be archived if the complete review process is finished.

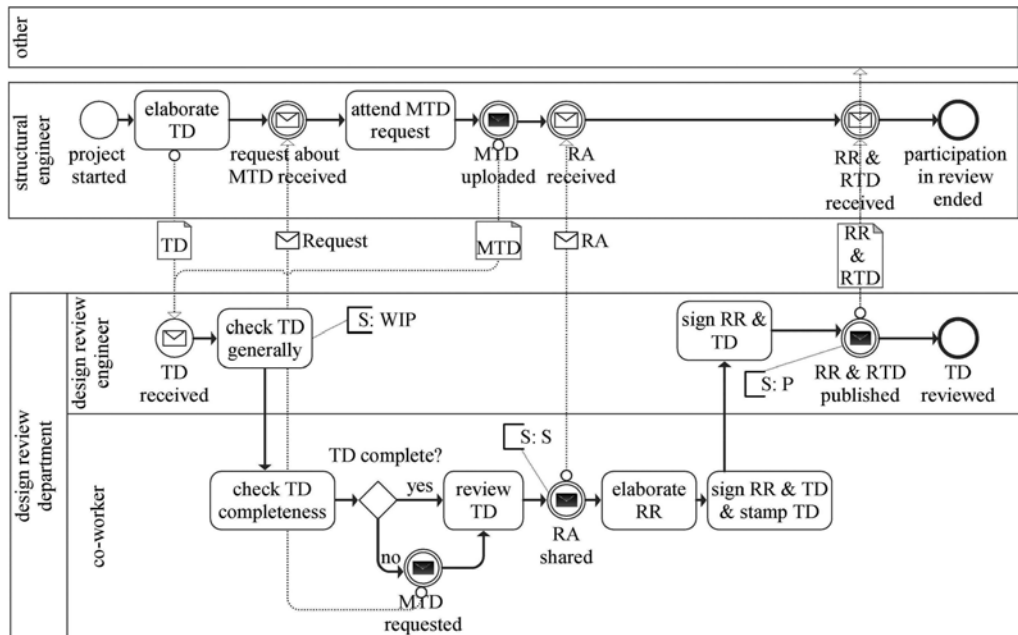


Figure 4. BIM-based design review process for documents, abbreviations given in Tables 2 and 3.

Table 3. Abbreviations for the BIM-based design review process for documents.

MTD	missing technical documentation
RA	review annotations
RR	review report
RTD	reviewed technical documentation
TD	technical documentation (structural analysis and drawings)

The review process of the technical model is initiated by the start of the workflow in the CDE as indicated in Figure 5. First steps are the checks by the design review engineer and the co-worker in order to check if the model is complete, i.e. if all necessary parts for review are involved and if the required level of detail is given. In case of an incomplete submission, an updated model must be provided to start with the review. If the model or the considered parts are complete and have the required level of detail, the status changes to “work in progress”. Annotations can be shared within the review process, e.g. by BCF (BIM Collaboration Format (BCF) 2022). After the review is finished by the co-worker, the report is prepared. The legally binding signed report lists the submitted BIM model including the date, file name and a unique identifier. Also, it is mentioned if there are annotations to the model. These annotations are contained in the BCF file, which is published together with the model. Integrity and content proof can be achieved by encrypting the BCF file. The report is uploaded and the design review engineer sets the status “published” at the same time.

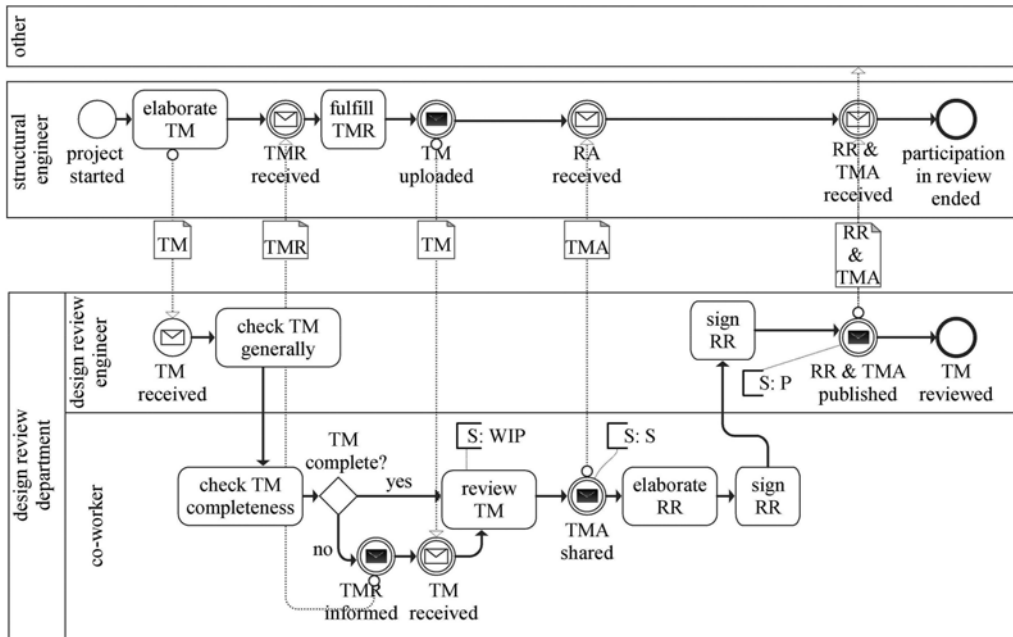


Figure 5. BIM-based design review process for models, abbreviations given in Tables 2 and 4.

Table 4. Abbreviations for the BIM-based design review process for models.

CTM	corrected technical model
RA	review annotations
RR	review report
RTM	reviewed technical model
TM	technical model
TMA	technical model annotations
TMR	technical model requirements

It must be pointed out, that the process of design review in Germany is well regulated by building authorities (M-PPVO 2012, MBauVorIV 2020, MBO 2020). This gives legal certainty for the review process, but causes special requirements regarding documentation and authentication. In case of PDF documents, these requirements can be transferred easily. Annotations can be embedded in the PDF and can be signed using QES. All reviewed documents can be listed in the reports. For BIM models, the legally compliant transfer of annotations binding all participants is object of current research. The reviewed BIM model is listed together with separate BCF file containing annotations in the review report and can be used for following stages of the life cycle as indicated in Figure 1.

4 CONCLUSIONS

The design review process for buildings can be fully integrated in a BIM workflow using a CDE. This allows to use the benefits of BIM: collaboration between the involved participants and a full documentation, which can be handed over to following stages of the life cycle of the building. The paper-based process can be transformed to a digitalized process with the same level of security. Legally binding manual signatures can be replaced by qualified electronic signatures signing electronic documents, which allows the authentication of the design review engineer. The legally binding electronic signature of BIM-models is still object of current research. A suitable rights and roles concept in a CDE can substitute the corresponding roles in a paper-based process. The status of the revised documents and BIM-models can be announced in a CDE using the proposed status of DIN

EN ISO 19650-4 (2021). At least, two different workflows are necessary for a document-based process and for a process handling BIM models. Whereas documents can be annotated, revisions of BIM-models require a modified model and a BCF-file transferring the comments. Summing up, the design review process can take part in the consistent use and sharing of data in the complete building life cycle making available its results and certificates to use and reuse of buildings.

ACKNOWLEDGEMENTS

This research work was enabled by the support of the German Federal Ministry of Economic Affairs and Climate Action to the funding of the GAIA-X project “intelligent Empowerment of CONstruction industry - iECO”.

REFERENCES

- Bidault, L., Hassine, C. 2021: Guide d'une operation de construction publique en BIM, Éditions du Moniteur, Antony.
- BIM Collaboration Format (BCF) [online], 2022. *buildingSMART Technical*. Available from: <https://technical.buildingsmart.org/standards/bcf/> [Accessed 10 Nov 2022].
- Borrmann, A., König, M., Koch, C., and Beetz, J., eds., 2021. *Building Information Modeling: Technologische Grundlagen und industrielle Praxis*. 2., aktualisierte Auflage. Wiesbaden [Heidelberg]: Springer Vieweg.
- Bundestag 2022. Eckpunkte “Digitalisierung vorantreiben - Planung und Genehmigung beschleunigen”, Drs. 20/2715, 7 July 2022
- BMI 2021. Bundesministerium des Inneren, für Bau und Heimat and Bundesministerium der Verteidigung, eds., 2021. Masterplan BIM für Bundesbauten - Erläuterungsbericht.
- BMI 2021. Bundesministerium für Verkehr und digitale Infrastruktur and Bundesministerium der Verteidigung, eds., 2021. Masterplan BIM Bundesfernstraßen.
- Code de la commande publique, 2022. last modification 21 October 2022.
- DBauV 2021. Digitale Bauantragsverordnung, 2 February 2021, GVBl., p. 26.
- DIN EN 15978, 2011. *Nachhaltigkeit von Bauwerken – Bewertung der umweltbezogenen Qualität von Gebäuden – Berechnungsmethode*.
- DIN EN ISO 19650-1, 2019. *Organisation und Digitalisierung von Informationen zu Bauwerken und Ingenieurleistungen, einschließlich Bauwerksinformationsmodellierung (BIM) - Informationsmanagement mit BIM - Teil 1: Begriffe und Grundsätze (ISO 19650-1:2018); Deutsche Fassung EN ISO 19650-1:2018*.
- DIN EN ISO 19650-4, 2021. *Organisation und Digitalisierung von Informationen zu Bauwerken und Ingenieurleistungen, einschließlich Bauwerksinformationsmodellierung (BIM) - Informationsmanagement mit BIM - Teil 4: Informationsaustausch (ISO/DIS 19650-4:2021); Deutsche und Englische Fassung prEN ISO 19650-4:2021*.
- Directive 2014/24/EU of 26 February 2014 on public procurement, OJEU L 94/65-143.
- Directive 2014/25/EU of 26 February 2014 on procurement by entities operating in the water, energy, transport and postal services sector, OJEU L 94/243-331.
- eIDAS 2014. Regulation (EU) No 910/2014 of 23 July 2014 on electronic identification and trust services for electronic transactions in the internal market, OJEU L 257/73-114.
- IDEF – Integrated DEFINition Methods (IDEF) [online], 2022. Available from: <https://www.idef.com/> [Accessed 27 Oct 2022].
- ISO/IEC 19510, 2013. *Information technology - Object Management Group: Business Process Model and Notation*.
- König, M., Vonthron, A., Drahtler, T., Drahtler, M., and Hoffmann, N., 2022. *Bericht zur ersten BIM-basierten Baugenehmigung in Nordrhein-Westfalen*. Bochum, Dortmund: Ruhr Universität Bochum.
- MBauVorIV, 2020. *Musterbauvorlagenverordnung (MBauVorIV), Fassung Februar 2007, Änderung 25. 09.2020*.
- MBO, 2020. *Musterbauordnung (MBO), Fassung November 2002, Änderung 25. 09.2020*.
- M-PPVO, 2012. *Muster-Verordnung über die Prüflingenieur und Prüfsachverständigen nach §85 Abs. 2 MBO (M-PPVAO), Fassung Dezember 2012*.
- NBauVorIVO 2021, Niedersächsische Bauvorlagenverordnung, 23 November 2021, Nds. GVBl. 2021, 760, No 21072.
- Oltmanns, H.-G., Oltmanns, H., and Dirks, A., 2019. BIM-Modelle und die Bearbeitung durch Prüflingenieur: Modellbasiertes Prüfen – gesamtheitliches Denken und neue Beurteilungskriterien. *Bautechnik*, 96 (3), 250–258.
- Siebenhütter, K., 2020. *Entwicklung einer Methode zum Festhalten des Standes von geprüften Bauwerksmodellen*. Technische Universität München, Masterthesis.

A basic study on the evaluation of the protective effect of silane-based impregnation on mortar using electrochemical impedance spectroscopy

S. Nagaoka, K. Nakayama & M. Iwanami
Tokyo Institute of Technology, Tokyo, Japan

ABSTRACT: In this study, we investigated the electrical properties of silane-based impregnated mortar to quantitatively evaluate the effect of silane-based impregnation on the mitigation of chloride ions penetration. Electrical resistivity and frequency characteristics were measured using electrochemical impedance spectroscopy on mortar specimens simulating the incomplete modification effect and deterioration of the silane-based impregnating. The diffusion coefficients of chloride ions were also determined by chloride migration tests. As a result, we found a correlation between the electrical resistivity and the effective diffusion coefficient of chloride ions. Using the frequency response of impedance, the electrical resistivity of the silane-impregnated layer and that of the unimpregnated mortar could be extracted in a single measurement. These results showed the possibility of quantitatively evaluating the effect of silane-based impregnation on the mitigation of chloride ions penetration from the electrical properties of silane-impregnated mortars.

1 INTRODUCTION

Silane-based impregnations are widely used to modify the surface of concrete structures to improve their durability. These surface treatment agents are mainly composed of silicone molecules such as silane and siloxane, which have water-repellent properties (Vries et al. 1997). After being applied to the concrete surface, silanes penetrate several millimeters to several centimeters into the concrete to provide a water-repellent effect. This effect prevents water and deterioration factors from penetrating into the concrete, thereby mitigating the deterioration of the structure caused by salt damage, frost damage, and ASR. In addition, silanes have many advantages, such as being relatively easy and inexpensive to apply and not altering the appearance of the concrete, allowing direct visual inspection of the concrete surface even after the application. Previous studies on silane have shown that in some cases the protective effect lasted for more than 20 years (Christodoulou et al. 2013). On the other hand, it has been pointed out that depending on the application conditions and environment, the performance and durability may be deteriorated relatively quickly. Quantitative and nondestructive evaluation of the protective effect and durability of the effect by silanes is important for structural maintenance.

This study fundamentally investigated a method to evaluate the chloride ion penetration of mortar specimens modified by silane-based impregnation by electrical properties. It is known that electrical properties are correlated with the diffusion coefficient of chloride ions in non-surface treated concrete (Meilun et al. 1999, Minagawa et al. 2010). However, few studies have been conducted on surface-treated concrete with silanes. Therefore, we simulated inadequate modification of the mortar specimens by the application method of the silane and accelerated deterioration after the application of the silane. The electrical resistivity and impedance of each specimen were measured. The water contact angle test, penetration depth test, and migration test were conducted as indices for evaluating the protective effect of silane. From the relationship between these test results and electrical properties, an evaluation of the protective effect of silane by electrical properties was investigated.

2 MATERIALS AND METHODS

2.1 Materials and specimens preparation

This study conducted tests on cylindrical mortar specimens of $\Phi 100 \times 50$ mm. The mortar was mixed with a water-cement ratio of 50% and a cement-fine aggregate ratio of 1:3 by volume. Ordinary Portland cement with a density of 3.16 g/cm^3 , crushed sand with a surface dry density of 2.62 g/m^3 and water absorption of 1.30 % were used as cement and fine aggregate. The specimens were demolded 24 hours after casting and cured in water until 12 days of age. The specimens were then cured in the air at 20°C in a room until 21 days of age. On the 21st day of age, a silane was applied to one side of the specimens, and they were cured in a room at 20°C until 28 days of age.

The flow of this experiment is shown in Figure 1. In addition, application and deterioration acceleration conditions are listed in Table 1. Two specimens were prepared for each condition. Silane-siloxane silicone with a concentration of 80 % was used as the silane-based impregnation. Normal condition in Table 1 indicates that 0.2 kg/m^2 silane was applied to specimens with a surface moisture content of 6 %. For Dilute, 0.2 kg/m^2 of silane diluted 5-fold with water was applied. These specimens were used to evaluate the protective effect of silane with a low amount of active ingredient. Masking specimens were covered with 6 mm wide aluminum tape on a portion of the coated surface, as shown in Figure 2. These specimens were used to investigate the effect of the incomplete application on the electrical properties. Silane was applied over the seal, and the tape was removed after curing. Wet specimens were immersed in water for 1 hour, and silane was applied when the surface moisture content was 10%. Dry specimens were dried in an automatic oven at 50°C for 6 hours before silane was applied. Since the penetration depth of silane depends on the surface moisture content of the applied surface, the effect of silane penetration depth on electrical properties was investigated in these specimens. Alkali specimens were immersed in a saturated calcium hydroxide solution with sodium hydroxide at $\text{pH} = 13$ for 7 days, starting 7 days after the silane application under normal conditions. These specimens were used to investigate the effect of reduced water repellency due to strong alkali on the electrical properties.

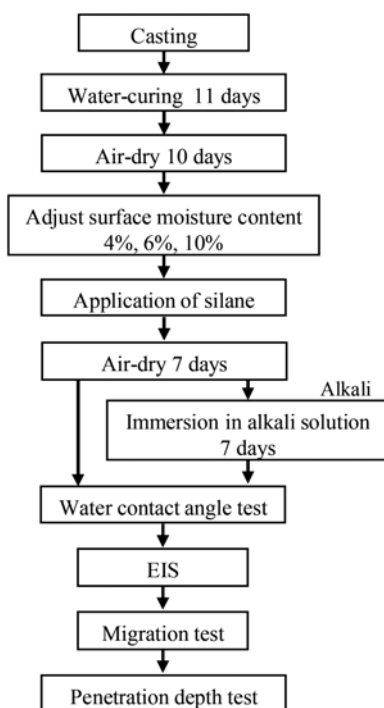


Figure 1. The flow of this study.

Table 1. Parameters in this study.

Name of specimens	Application conditions	Deterioration accelerating conditions
Blank	Non-application	-
Sound	Normal condition	-
Alkali	Normal condition	Immersion in alkaline aqueous solution after application.
Dilute	A silane-based impregnation diluted five times with water was applied.	-
Masking	Applied to 6mm wide masked specimens.	-
Wet	Applied to specimens with a wet surface.	-
Dry	Applied to specimens with a dry surface.	-



Figure 2. The masking specimen.

2.2 Electrochemical Impedance Spectroscopy

Electrochemical Impedance Spectroscopy (EIS) is one of the effective measurement methods to evaluate the pore structure of concrete. It is a method to evaluate the electrical properties of an object to be measured using impedance, which is the ratio of current to voltage in an AC circuit. To evaluate the electrical properties of concrete, an equivalent circuit of concrete is used for analysis. Figure 3 shows a simplified equivalent circuit of concrete. The equivalent circuit of concrete consists of solution resistance (R_0), concrete resistance (R_c), and capacitance (C). The impedance of this equivalent circuit, represented as a complex number, is shown in Equation (1).

$$Z = R_0 + \frac{R_c}{1 + j\omega R_c C} \quad (1)$$

Where $j = \sqrt{-1}$ and ω is frequency of AC current (Hz).

From this equation, the Nyquist diagram in Figure 4 is plotted, from which the values of the solution resistance and concrete resistance can be determined.

Figure 5 shows the condition of measurement. A stainless-steel electrode of 85 mm in diameter and 6 mm thick was brought into contact with the specimen via a gel electrolyte mixture of NaCl, carboxymethyl cellulose, and water in the ratio of 3:3:94, and measurements were made using

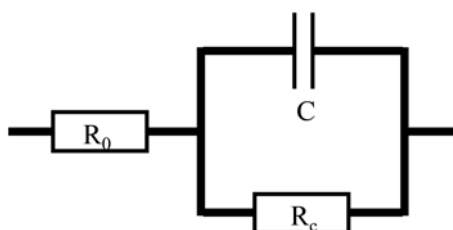


Figure 3. Equivalent circuit of a simplified model of concrete.

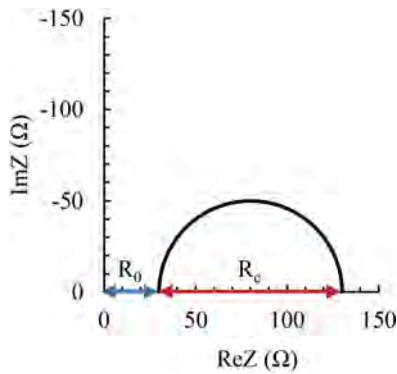


Figure 4. Nyquist diagram ($R_b=30\Omega$, $R_c=100\Omega$).

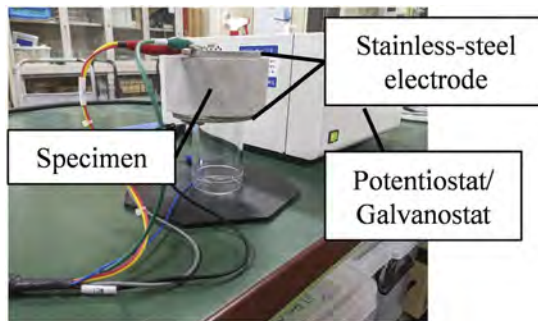


Figure 5. Condition of EIS.

a Potentiostat. In this measurement, the potential difference was 100 mV, and the impedance was measured at five frequencies, each order of magnitude, within the range of 500 mHz to 500 kHz. The concrete resistance was identified from the Nyquist plot to calculate the electrical resistivity.

2.3 Water contact angle test

To evaluate the water-repellent performance of silane, the water contact angle was calculated by photographing using a digital microscope. If the water contact angle is 90° or greater, the silane is deemed to have water-repellent performance.

2.4 Penetration depth test

To observe the depth of silane penetration, the specimen was split in two. Water was sprayed on the split surface, the length of the water-repellent layer was measured at four points equally divided into five sections, and the average value was determined as the depth of silane penetration. For Masking, the area directly under the aluminum tape was also observed.

2.5 Migration test

A migration test was conducted following JSCE-G 571-2003 by applying a DC with a potential difference of 15 V with the silane-applied surface on the cathode side to obtain the effective diffusion coefficient of chloride ions.

3 RESULTS AND DISCUSSION

3.1 Electrical resistivity

Figure 6 shows the electrical resistivity of each specimen on the seventh day after the silane application. In this figure, the average electrical resistivity of the two specimens is plotted.

Comparing Blank and Sound, the electrical resistivity of Sound was about twice that of Blank. This is because the surface of the specimens was modified by silane, which is thought to result in higher electrical resistivity. The silane-impregnated area (water-repellent layer) has a lower water content due to the water-repellent effect. The electrical resistivity of the silane-impregnated mortar was high because the electrical resistivity of the hardened cement is high when the water content is low. In addition, the electrical resistivity of the silane-impregnated mortar specimens was compared. Alkali and Masking showed lower electrical resistivity than Sound. In contrast, the electrical resistivity of Dry was significantly higher. It is believed that the electrical resistivity was increased because the specimens were strongly affected by drying.

3.2 Penetration depth

The results of the penetration depth test are shown in Figure 6. Only Dry had a significantly greater penetration depth, while other specimens had similar penetration depths. This result is consistent with previous studies showing that the lower the surface moisture, the greater the silane penetration depth (Hosoda et al. 2010). In Masking, no silane penetration was observed in the area covered by the aluminum tape (Figure 7), which is thought to be responsible for the low electrical resistivity of Masking.

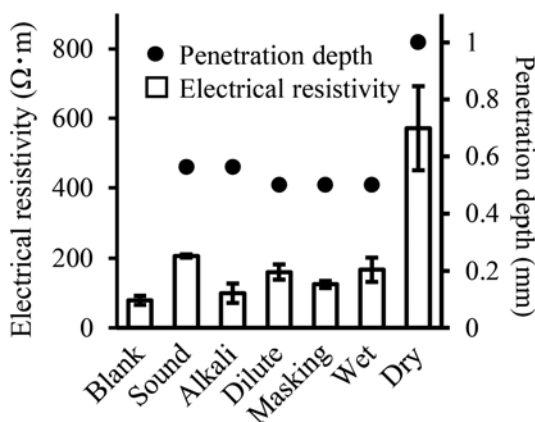


Figure 6. Electrical resistivity and penetration depth of silane-based impregnation.

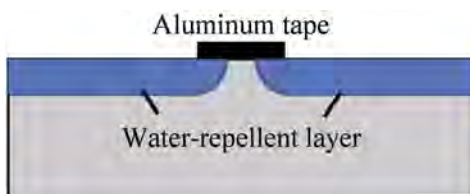


Figure 7. Water-repellent layer of Masking.

3.3 Water contact angle

The water contact angle test results showed that Alkali and Dilute had low water repellency (Figure 8). The water contact angle of the other specimens was greater than 90 degrees, like Sound, indicating that they were water-repellent. Alkali had a water contact angle of more than 90 degrees before immersion in the strong alkaline solution. However, after immersion, the water repellency decreased. Therefore, it is thought that the decrease in water repellency was caused by the alkali solution. However, the water contact angle of Dilute exceeded 80 degrees, indicating that it was more water-repellent than Alkali. These results suggest that the low electrical resistivity of Alkali was due to its low water repellency. The water repellency of Dilute was higher than Alkali, suggesting that the water repellency did not affect the electrical resistivity of Dilute.



Figure 8. Water contact angle of Sound, Alkali, and Dilute.

3.4 Effective diffusion coefficient

Figure 9 shows the results of the migration test. The effective diffusion coefficient of Sound was about half of Blank. Minor differences in effective diffusion coefficients were observed between the silane-impregnated specimens. Therefore, it is thought that the effect of incomplete modification of silane on the effective diffusion coefficient was small.

Next, the relationship between the effective diffusion coefficient and electrical resistivity was investigated. The results are shown in Figure 10. In this figure, the results for Dry, which had a higher electrical resistivity due to water content, are not plotted to investigate the influence of the protective effect of silane on the electrical resistivity. For this result, an approximate curve was obtained using the power of the electrical resistivity as an explanatory variable (Minagawa et al. 2010). The coefficient of determination of this approximate line shows that there is a correlation between the effective diffusion coefficient and electrical resistivity even in silane-treated mortar. These results indicate the possibility of evaluating the protective effect of silane by electrical properties.

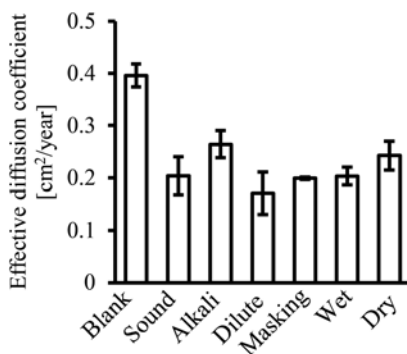


Figure 9. Results of the migration test.

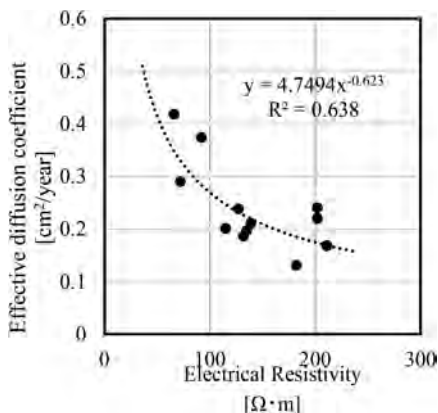


Figure 10. Relationship between electrical resistivity and effective diffusion coefficient.

3.5 EIS

The EIS results for Blank and Sound are plotted on the Nyquist diagram (Figure 11). Blank plots a single semicircle, whereas Sound plot an irregular semicircle. This distorted semicircle can be thought of as a plot of two partially overlapping semicircles. From this plot, the equivalent circuit of Sound can be assumed to be the circuit shown in Figure 12. CPE (Constant Phase Element) is an element used in fitting to the distorted semicircle and represents the electrical capacitance affected by material inhomogeneity. Then, by fitting the EIS data for Sound using the equivalent circuit in Figure 12, an electrical resistance of 587Ω for R_{c1} and 1108Ω for R_{c2} can be obtained. The EIS data for Blank were fitted using the equivalent circuit in Figure 3, and the electrical resistance R_c was calculated to be 764Ω . Since R_{c1} and R_c are close in value, it is assumed that the electrical resistance of the part of the specimen non-modified with silane is R_{c1} , and that of the part modified with silane is R_{c2} . Figure 13 shows the fitting results for each specimen. In each specimen, R_{c1} is close to R_c . Focusing on R_{c2} , which is the electrical resistance of the modified part, it is assumed that the electrical resistance of the poorly modified specimen is lower than that of Sound due to the effect of the modified state. In addition, the electrical resistance R_{c2} of Dry was significantly higher, but the effective diffusion coefficient was not smaller than that of the other specimens. This high electrical resistance was not due to the protective effect, but to the greater depth of silane penetration and lower water content in the modified part. These results indicate that the electrical resistance of the modified area is strongly affected by the low water content at the time of silane application.

The migration test results do not provide an accurate evaluation because of the difference in principle from the actual diffusion of chloride ions. In particular, it is difficult to accurately evaluate the diffusion of chloride ions by the migration test because the penetration of chloride ions is mitigated in concrete treated with silane due to its water-repellent effect. Therefore, in future studies, we plan to conduct accelerated permeation tests based on principles similar to those of actual chloride ion permeation. In such tests, the diffusion of chloride ions is mitigated by the modified part, and thus only the protective effect of the modified part should be focused on. In future studies, we plan to investigate the evaluation of the effect of silane on

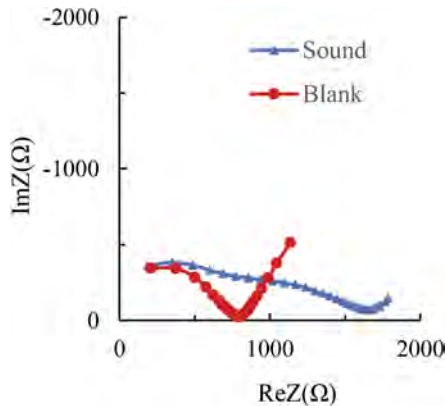


Figure 11. Nyquist diagram of Sound and Blank.

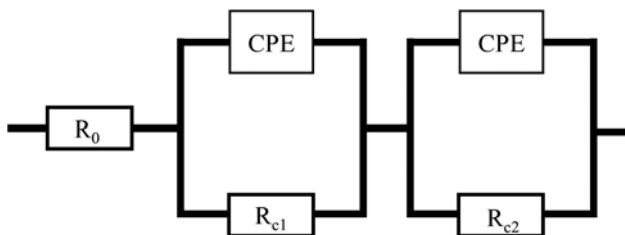


Figure 12. Equivalent circuit of silane-modified mortar.

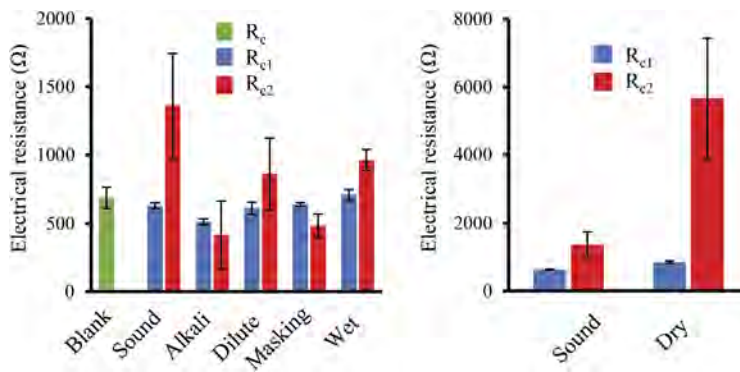


Figure 13. Electrical resistance R_c , R_{e1} , and R_{e2} obtained by the analysis.

the reduction of chloride ion penetration by silane by using the electrical properties of the modified part. Since it was found in this study that the electrical resistance of the modified part by silane can be determined, a more accurate evaluation will be possible.

4 CONCLUSIONS

To establish a method for evaluating the protective effect of silane-based impregnation, evaluation by electrical properties was attempted. The following tests were conducted on mortar specimens to simulate the deterioration of the protective effect due to silane application conditions and post-application environmental conditions. 1) electrochemical impedance spectroscopy (EIS), 2) water contact angle test, 3) penetration depth test, and 4) migration test.

The following findings were obtained from this study.

1. In the silane-impregnated mortar, the approximate curve using the power of electrical resistivity as an explanatory variable revealed a correlation between electrical resistivity and effective diffusion coefficients of chloride ions. This indicates the possibility of evaluating the protective effect of silane by electrical properties.
2. From the Nyquist plot obtained by the EIS, an equivalent circuit for the silane-impregnated specimen was proposed. Using this equivalent circuit, the electrical resistances of the silane-modified and non-modified layers were obtained. By obtaining the electrical resistance of the silane-modified part, the possibility of a more accurate evaluation of the protective effect of silane was indicated.

REFERENCES

- Christodoulou, C., Goodier, C. I., Austin, S. A., Webb, J. and Glass, G. K. 2013. Long-term performance of surface impregnation of reinforced concrete structures with silane. *Construction and Building Materials* 48: 708–716.
- Hosoda, A., Matsuda, Y. and Kobayashi, K. 2010. Optimum Surface Protection System with Silane Type Water Repellents. *Journal of Advanced Concrete Technology* 8: 291–302.
- Minagawa, H., Hisada, M., Ehara, A., Saito, Y., Ichikawa, M. and Inoue, H. 2010. Fundamental study on relationship between electric resistivity and chloride ion diffusivity of concrete. *Proceedings of JSCE* 66 (1): 119–131 (in Japanese).
- Shi, M., Chen, Z. and Sun, J. 1999. Determination of chloride diffusivity in concrete by AC impedance spectroscopy. *Cement and Concrete Research* 29: 1111–1115
- Vries, J. & Polder, R.B. 1997. Hydrophobic treatment of concrete. *Construction and Building Materials* 11(4): 259–265.

Life-cycle of existing asphalt to build new highway foundation pavements: Environmental procedures according to new Italian standards, geotechnical and durability performance assessments, construction methods

M. Biasioli, F.T. Isfahani, D. Giometti & C. Beltrami

Lombardi Ingegneria s.r.l., Milan, Italy

G. Piovano, F. Vergano & M. Marino

Co.Ge.Fa. SpA, Torino, Italy

ABSTRACT: An innovative design and construction procedure has been implemented for the life cycle assessment of geo materials in highway pavement renovation. In most cases old asphalt material after demolition is considered a “waste” material and therefore it is not allowed the recycle directly as construction material. In this case a specific study has been carried out developing different items: implement an environmental testing and administration procedure in order to obtain the positive approval by local Italian authority on the “end of waste” legislation (according to the new Italian law D. 69/18); develop a large prequalifying testing procedure by sampling existing asphalt material and studying in laboratory all the mechanical and chemical transformations and performances, also by the study of cement mix add; implement a construction field procedure that makes the demolition of an existing asphalt pavement possible and locally provides a mechanical and chemical transformation in order to give new life to the material as sub foundation layer of a new highway pavement. The result of the process was successful and could show an innovative prospective in the life cycle use of asphalt and geotechnical materials in existing highway renewal process.

1 ENVIRONMENTAL MANAGEMENT OF ASPHALT DERIVED FROM GRINDING OPERATIONS

1.1 *Recent changes on environmental Italian legislation concerning management of wastes from asphalt grinding operations*

Asphalt from grinding operations is typically manages, across EU, as waste, with EWC (European Waste Code – EER in Italian) 17 03 02.

In 2018, a major change in legislation was approved by implement an environmental testing and administration procedure in order to obtain the positive approval by local Italian authority on the “end of waste” legislation (according to the new Italian law D. 69/18).

The abovementioned law (D. 69/18), named “*Regolamento di disciplina della cessazione della qualifica di rifiuto (End of waste) di conglomerato bituminoso*” introduced criteria and management specifications to be fulfilled in order to consider asphalt (strictly deriving from grinding operations) as an End of Waste material (i.e. no longer a waste) and reuse it for construction operations.

In particular, according to Ministerial Decree 69/2018 the grinded asphalt (“fresato d’asfalto” in Italian) ends to be classified as a waste if it fulfills the following criteria:

- a) will be reused for the specific operations listed in part a) of Annex 1 to the decree;
- b) it is compliant to the standards listed in UNI norms EN 13108-8 (serie 1-7) or EN 13242 in relation with the specific scope;

c) it is compliant to the specific of part b) of Annex 1 to the decree.

In a few words, if the grinded asphalt fulfills both environmental and geomechanical parameters, it can be de-classified from “waste” to “non-waste”, in order of ad immediate reuse in construction operations.

The Decree was originally conceived by the Legislator to be mainly applied to production plants that typically verify the asphalt they are receiving (from grinding operations) and, if this latter results in compliance with criteria of the decree 69/2018, re-use it in new production activities.

However, in the case described in the current article (maintenance interventions on the Italian A4 highway), the new Decree was successfully applied On Site, to a construction lot of maintenance and enlargement operations, resulting as a consequence in:

- a massive reuse of what would have been otherwise considered as a waste;
- a drastic reduction in external supply of construction material;
- an overall major increase of sustainability and circular re-use of the construction Site.

1.2 Field application of the End-of Waste concept

In the case study described Co.Ge.Fa. contractor, with the technical support of Lombardi Engineering staff has applied the Decree 69/18 to an enlarging and renewing intervention on the A4 highway Turin-Milan.

The works included the grinding of about 44 000 m³ (about 88 000 t) of old asphalt. According to the design of the works, this material had to be considered as a waste and transferred off-site for disposal to Authorized plants.

The choice of the Contractor, instead, was to propose to the Local Authorities and to the Client, the adoption of the Decree 69/18 directly on the construction Site and, once fulfilled the criteria, consider the grinded asphalt as an “End of Waste” and re-use it in the same construction activity.

This was done applying, after obtaining Environmental Authorization from the Municipality of Milan, a sampling and analytical protocol according to the UNI norm 10802:2013 on the existing asphalt before its removal. The protocol was applied on a regular sampling grid through taking a composite sample resulting from 5 sub-samples from each grid. Then, comparing geomechanical and environmental results from the samples taken, once verified their compliance with what described in Annex 1 to the Decree 69/18, the material resulting from grinding operation could be already considered as a non-waste and therefore either immediately re-used on site (with cement treatment) or transferred to the deposit areas of the construction works to be reused in other lots of the intervention.



Figure 1. On site activities.

The activities were carried out during the period 2021-2022. At the end of 2022, an overall amount of 55 890 t of asphalt managed as End-of-Waste (i.e. compliant with the requirement of Decree 69/18) was reused in the same construction Site as material for new embankments and foundation pavement.

2 MATERIAL ASSESSMENT

The usage of stabilization agent is aiming to restore the properties or recover the cold recycled mixtures performance. Various type of stabilization agent could be used in the recycling technology such as lime, fly ash and cement [F. Xiao et al., 2018]. In this study cement has been used as the stabilization agent.

In order to obtain the required performance in terms of compressive strength and indirect tensile strength prescribed by the client, a tentative procedure has been employed to adjust the ingredient of the final mixture. There are several parameters playing a role in the strength performance of the cement stabilized recycled asphalt: bitumen type and pH, cement content and type, moisture content, granulometric distribution of the aggregates, etc.

Bitumen emulsion has been utilized to fabricate the existing asphalt pavement in this study. In the emulsification process, bitumen and water are put through a high shear mill with an emulsifier chemical and eventually the bitumen is dispersed in the water and an oil-in-water condition form. The emulsifier dominates the charge of the bitumen emulsion. Since the surface of bitumen droplets are charged, the interface between the bitumen emulsion and aggregate is enhanced when the aggregate particles are oppositely charged. When emulsified bitumen is mixed with aggregate, the bitumen tends to separate from the water and adhere surround the surface of the aggregate particles. Moreover, the mineral source and moisture of aggregate have a significant influence on the emulsion breaking. In this process, the bitumen emulsion places a role of lubrication agent, and the breaking is required to occur before compaction procedure.

The bitumen emulsion is classified as anionic and cationic. The anionic type possesses high(alkali) pH and the cationic possesses low(acidic) pH.

The compatibility between type of bitumen and aggregate is an important factor in their adhesion. Anionic bitumen emulsion has excellent adhesion with acidic aggregate. On the contrary, the cationic bitumen emulsion has good adhesion with alkaline aggregate. Therefore, type of bitumen emulsion shall be determined so that the type of cement and aggregate, to be added to the final cement-stabilized cold recycled asphalt mixture, could be selected in compliance with the bitumen type.

By reference to Table 3, the bitumen type of the grind asphalt is anionic as the pH is alkaline. For anionic bitumen emulsion, a cement type containing high lime content is recommended because adhesion between the anionic bitumen and alkaline solids (aggregates/cement) is favorable. Therefore, based on Table 1 of EN 197, "Portland-limestone cement" is recommended for this study. Cement content should also be adjusted, and the range is normally between 3%-5% [Mollenhauer et al. 2016].

Normally a portion of virgin aggregates are needed to meet the required performance for the cement-stabilized cold recycled asphalt mixture. In order to improve strength performance, fine aggregates with the size $<0.063\text{mm}$ are essential. Therefore, it is necessary to investigate the granulometric curve of the grinded asphalt and the portion of fine aggregates $<0.063\text{mm}$ should be adjusted so that the best strength performance could be achieved. The recommended value for the fines $<0.063\text{mm}$ is 4%-10%.

The moisture content of the final cement -stabilized cold recycled asphalt mix is another factor which leads to enhancement of the strength performance. The optimum moisture content should be tentatively investigated in conjunction between the initial moisture content of grinded asphalt and cement content. The range of moisture content of the final cement-stabilized cold recycled asphalt is in the range of 3%-10%.

The following tests are planned to investigate tentatively the optimum value of the above-mentioned parameters, which result in the best strength performance of the finale mixture. The performance requirements for each specific test in the following is complaint with Supplemento al Bollettino Ufficiale della Regione Toscana n. 22 del 31.5.2006.

3 GEOTECHNICAL TESTS

3.1 *Qualification tests*

Laboratory tests were performed on samples withdrawn from a highway stretch where the on-site grinding had been carried out. Tests were articulated in two phases:

Phase 1: preliminary tests to assess that samples fit technical specification and literature requirements.

The stratigraphy of the existing highway pavement was first determined on two 150 mm diameter and 50mm high bituminous concrete cores.

Two samples were contextually withdrawn from the grain-size reduced bituminous concrete, first sample after a single run of *pulvimixer*, second sample after two runs. The following tests were performed on these two samples:

- grain-size analysis on the milled asphalt and on the aggregates after extracting bitumen;
- determination of moisture content;
- determination of bituminous binder content;
- determination of the quantity of impurities in recovered bituminous concrete;
- petrographic test on aggregates and measure of pH of bitumen emulsions (to identify the type of bitumen in the existing pavement and assess suitability to treatment with Portland cement).

Phase 2: tests on samples defined by means of phase 1 tests, added with Portland 32.5 III/B-LL cement (4% in weight) to verify resistances properties.

Second phase was aimed to evaluate properties of a cement-bound material made with on-site grinded material added with 5% sand and 4% Portland 32.5 II/B-LL cement. Based on the experimentally determined properties, suitability of the cement-bound material to form the pavement foundation was evaluated, according to the quoted “Technical specifications”.

Samples were obtained by two runs of *pulvimixer* and the following tests were carried out:

- determination of void index;
- uniaxial compression strength;
- indirect traction tests (so called “Brazilian test”).

Three mixes were prepared with water content respectively 3%, 5% and 7%, after 180 cycles of gyratory compactor at 20°C. On such mixes, uniaxial compression strength and indirect traction tests (together with void index and mass density) were carried out after 7 days ageing, on three samples/each test.

It was thus determined an optimum water content of 5%.

Uniaxial compression and indirect traction tests were then repeated after 3 and 7 days on bituminous concrete added with 5% sand (see below) and 4% Portland CEM II/BLL 32.5, and then compacted with 5% water content.

3.1.1 Requirements

The following tables resume the grain size and resistance requirements provided by the “Technical specifications for work control and realization – Cement bound granular material” issued by the Client.

Table 1. Grain size requirements.

UNI Sieves	Minimum passing fraction [%]	Maximum passing fraction [%]
31.5	100	100
20	80	100
16	66	87
8	41	61
4	24	39
2	18	30
0.5	9	19
0.063	5	10

Table 2. Resistance requirements of the mix, prepared by gyratory compactor.

Property	Reference code	Unit measure	Requirements	
			3 days	7 days
Indirect traction resistance at 25°C	UNI EN 13286-42	MPa	0.30÷0.50	0.32÷0.60
Uniaxial compression strength at 25°C	UNI EN 13286-41	MPa	1.40÷3.60	2.50÷5.50

3.1.2 Test results

Main results of phase 1 tests are summarized hereafter.

Table 3. Phase 1 main results.

Bitumen content	<5%
Impurities	none
Water content	2.50%
pH	8.1
suitability to treatment with Portland cement	suitable

Grain size distribution fulfilled requirements in Table 1 except for the fine sand percentage which was slightly below the lower limit; fine sand was added in the measure of 5% in weight. Main results of phase 2 tests are summarized hereafter.

Table 4. Phase 2 main results.

Uniaxial compression strength UCS	[MPa]	3gg ageing			7gg ageing		
		3.11	2.94	3.4	3.91	3.74	4.19
Average UCS	[MPa]	3.15			3.95		
Mass density after compaction	[t/m ³]	2.176	2.163	2.181	2.175	2.182	2.178
Dry mass density	[t/m ³]	2.072	2.060	2.077	2.071	2.078	2.074
Void index	[%]	13.4	13.9	13.2	13.4	13.2	13.3
Indirect traction strength ITS	[MPa]	0.42	0.44	0.43	0.51	0.55	0.53
Average ITS	[MPa]	0.43			0.53		
Mass density after compaction	[t/m ³]	2.244	2.246	2.240	2.206	2.204	2.130
Dry mass density	[t/m ³]	2.137	2.139	2.133	2.1	2.099	2.208
Void index	[%]	10.7	10.6	10.9	12.2	12.3	11.9

All results fulfill technical specification requirements.

3.2 Control tests

After the treatment, some in situ and laboratory tests were performed on samples withdrawn from material treated following the described procedure.

In situ tests:

- n. 2 plate load test after 15h from compaction + n. 2 plate load tests after 3 days from compaction;
- n. 4 Light Weight Deflectometer tests after 15h from compaction

3.2.1 Laboratory tests

- grain size analysis;
- determination of maximum mass density;
- determination of apparent unit weight;
- n. 3 uniaxial compression tests at 3, 7, 14 days after compaction;
- n. 3 indirect traction resistance (Brazilian) tests at 3, 7, 14 days after compaction.

During the trial pit operations, moreover, the water content of the treated material was determined to check the achievement of the goal value of 5% (see above).

3.2.2 Requirements

The reference technical specifications for cement-bound mix require the following.

- Minimum results of LWD:
 $M_{LWD} = 60 \text{ MPa}$ 4 h after compaction
 $M_{LWD} = 200 \text{ MPa}$ 24h after compaction
- In situ density:
 $\geq 94\%$ of laboratory compacted samples (180 rounds in gyratory compactor), in 100% of measures.
- Plate load modulus M_d , at first load in load interval 150÷250 kPa and 12÷24h after compaction:
 $M_d \geq 150 \text{ MPa}$.

Moreover, same prescriptions on grain size distribution and resistance, as seen about pre-qualification tests, apply.

3.2.3 Results

Main results of control tests are summarized hereafter.

3.2.3.1 Plate load tests

Tests were carried out in two separated points on the surface of treated material and gave the following values of modulus in the load interval 150÷250 kPa.

15h after compaction:

point 1: $M_d = 214.3 \text{ MPa} > 150 \text{ MPa} = M_d$ minimum design requirement

point 2: $M_d = 176.5 \text{ MPa} > 150 \text{ MPa} = M_d$ minimum design requirement

72h after compaction:

point 1: $M_d = 214.3 \text{ MPa} > 150 \text{ MPa} = M_d$ minimum design requirement

point 2: $M_d = 157.9 \text{ MPa} > 150 \text{ MPa} = M_d$ minimum design requirement

3.2.3.2 LWD Light Weight Deflectometer

Tests were carried out in same points as plate load tests:

point 1: $M_{LWD 1.1} = 187.5 \text{ MPa}$
 $M_{LWD 1.2} = 189.1 \text{ MPa}$

point 2: $M_{LWD 2.1} = 218.5 \text{ MPa}$
 $M_{LWD 2.2} = 177.2 \text{ MPa}$

Obtained moduli are:

- satisfying requirement at 24h in one case (LWD 2.1)
- within 89÷95% interval of requirement at 24h in all other cases

When considering that tests were carried out at 15h after compaction, it can be concluded that obtained values are fulfilling the technical specification requirements.

3.2.3.3 Laboratory test resistance

Table 5. Strength test results on treated material.

		ageing		
		3 days	7 days	14 days
Uniaxial compression strength UCS	[MPa]	3.59	3.98	4.30
Indirect traction strength ITS	[MPa]	0.41	0.55	0.54

It can be observed that results lie within the reference intervals (and in the upper half of the intervals themselves) according to the design technical specifications at both 3 days and 7 days ageing.

3.2.3.4 In situ density

Two determinations gave respectively 95.9% and 99.3% of reference mass density, i.e. of average dry density of samples compacted by gyratory compactor for resistance tests, which is 2179 g/cm³. Both values fulfill the design requirement ($\geq 94\%$).

Moreover, the residual void index in 6 determinations lies within the interval:

$$e_{\text{res}} = 8.5 \div 10.4 \%$$

$$(e_{\text{res}} = 9.1 \div 9.6\% \text{ in 4 tests out of 6}).$$

Such values are lower than those obtained in laboratory during prequalification tests, which mean a better compaction.

3.2.3.5 Grain size distribution

Grain size analyses confirmed the absence of particles with $D > 31.5\text{mm}$, as required by the design technical specifications.

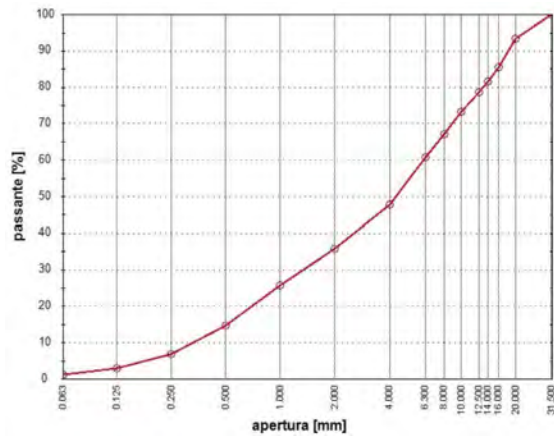


Figure 2. Grain size analysis on the treated material (grinded + sand + cement).



Figure 3. On site activities.

4 CONCLUSIONS

Because of the extension of the construction in large cities and industrial area and the closure of more and more natural quarries materials induce the road and the geotechnical engineering to improve the technology and the optimal material to build for embankment or pavements by recycled materials. The innovative procedure that has been presented could build a new highway pavement using the old asphalt with a new role: foundation strata.

The results showed that the grinded asphalt aggregate could be recycled as the aggregate for construction of a new road base, by adding 4% of a limestone cement. The fine sand by weight percentage of the 5% was added and moisture content of the mixture was adjusted to 5% as the optimum value. The performance requirements such as compressive strength and indirect tensile strength were measured based on the prescriptions of the highway manager and [6]. The results showed that the compressive strength and indirect tensile strength of 7 days curing was in the range of 2.5-5.5 MPa, 0.32-0.6 MPa, respectively.

It is concluded that recycled asphalt aggregates as demolition waste containing 5% bitumen residue could be reused by following a tentative and planned laboratory tests prior to the execution of road construction. The cold cement-stabilized recycled asphalt mixture was successfully used as a base for the new road in the same construction site.

This type of road “circular performance” we hope would be implemented in future works in the asphalt and road engineering, implemented in technical standards. Providing and innovative step head in the “life cycle” of materials, according to the best practices of circular economy.

ACKNOWLEDGEMENTS

The authors would like to acknowledge Peletta Luigi Srl for the specific construction know-how provided and the original machine work implemented for this construction and material cycle process. In addition, the authors would like to acknowledge for the technical support of Ing. Salvatore Buscemi and for laboratory and in situ tests Studio Sperimentale Stradale srl. and in particular Ing. Paolo Ferrari. Finally, the authors would like to acknowledge the final client highway manager SATAP S.p.A. and construction supervision SINA S.p.A. for their support for this innovative project in road engineering.

REFERENCES

- EWC (European Waste Code – EER in Italian) 17 03 02: Construction and demolition wastes (including excavated soil from contaminated sites).
- F. Xiao et al., *Construction and Building Materials* 180 (2018) 579–604.
- K. Mollenhauer, D. Simnofske, J. Valentin, Z. Čížková, J. Suda, F. Batista, C. McNally, 6th Eurasphalt & Eurobitume Congress, 1-3 June 2016, Prague, Czech Republic.
- Supplemento al Bollettino Ufficiale della Regione Toscana n. 22 del 31.5.2006, “CAPITOLATO SPECIALE D’APPALTO TIPO A CARATTERE PRESTAZIONALE PER L’UTILIZZO DI MATERIALI INERTI RICICLATI DA COSTRUZIONE E DEMOLIZIONE”.
- UNI EN 13108-8:2016, “Miscele bituminose - Specifiche del materiale - Parte 8: Conglomerato bituminoso di recupero”.
- UNI EN 13242:2008, “Aggregati per materiali non legati e legati con leganti idraulici per l’impiego in opere di ingegneria civile e nella costruzione di strade”.

Infrastructure asset management and the role of structural health monitoring

A. AlBanwan, A. AlFoudari & R. AlBehbehani

Kuwait Institute for Scientific Research, Kuwait City, Kuwait

ABSTRACT: Although modern-day infrastructure is designed to ensure structures operate safely in harsh environments under various loading conditions, deterioration and damage can occur during their operational life. Consequently, the protection, maintenance, and repair of infrastructure assets are crucial. Achieving optimal asset management is challenging, as the lifecycle costs of these activities must be minimized while ensuring infrastructure performance and reliability related to the asset's condition, serviceability, safety, and capacity are adequately addressed. Structural Health Monitoring (SHM) is a modern technology that can address these challenges. It is used to assess structural performance, detect damage, and monitor structure conditions, enabling data collection to support asset management analysis and evaluation. However, SHM does not provide actionable information to support asset management decision-making. This paper reviews current infrastructure asset management practices and identifies literature gaps. We examine SHM's role in asset management and identify areas where it can have the most impact.

1 INTRODUCTION

Infrastructure is defined as the essential facilities and systems that help societies operate, such as but not limited to buildings, roads, and bridges. Through the design phase of any infrastructure project, there is an intended and specified lifespan where the structure will continue to operate safely. However, due to environmental and operational effects, structures tend to degrade and fail before the end of their design lifespan. Given how crucial it is to maintain a country's economy and standard of living, the structural health of its infrastructure requires ongoing care. This calls for constant inspection, monitoring, and repair against damage, which is defined by Li & Hao (2016) and Farrar & Worden (2006) as the emergence of changes in a structure's material and geometric properties, boundary conditions, and connectivity of the system, that impacts its current or future performance, but has not yet interfered with the user's ability to utilize the system, which is known as failure.

Currently, asset management methods rely heavily on visually inspecting structures for signs of damage, which is challenging because inspections are inherently subjective and qualitative (Phares et al. 2007). Therefore, the need for strategies that can help evaluate bridge damage, condition, and performance and ultimately resolve these issues is imperative. Structural health monitoring systems can collect reliable data and provide continuous real-time information regarding bridge condition and performance to assist asset managers in making informed decisions (Omenzetter et al. 2011). However, in order to achieve the potential benefits of SHM and use it in a cost-effective manner, an understanding of the underlying drivers of asset management and its current shortcomings is necessary.

The general literature on SHM and asset management is extensive. However, there are very few studies that link them together. In this paper, we briefly examine the traditional approach to developing decision tools for asset management and discuss the value of using SHM to support asset management decision-making. The research question is addressed through a comprehensive literature review of recent advances in structural health monitoring in the emerging bridge asset management discipline. The discussion focuses primarily on bridges but is intended to apply to a wide range of infrastructure projects.

2 ASSET MANAGEMENT OVERVIEW

Asset management is a recognized process used to ensure that an asset, such as a bridge, operates in a way that enhances the asset's life, optimizes maintenance and management costs, and meets present and long-term needs (Kim et al. 2010).

2.1 *Asset management process*

There are various models that describe the asset management process, and asset managers are encouraged to assess what works best for them depending on their assets' nature and context (The Institute of Asset Management 2022). The UN Handbook on Managing Infrastructure Assets provides an asset management framework that identifies what needs to be in place for an asset management system (Figure 1). To implement asset management, bridge managers should define service levels, performance measures, and targets. Furthermore, data should be collected to identify issues, and decisions must be made to adapt solutions to meet the changing risk profiles of a network. Additionally, bridge managers must ensure that strategic goals are met and that the network is maintained in a manner that meets the needs of all end-users (Bush et al. 2012).

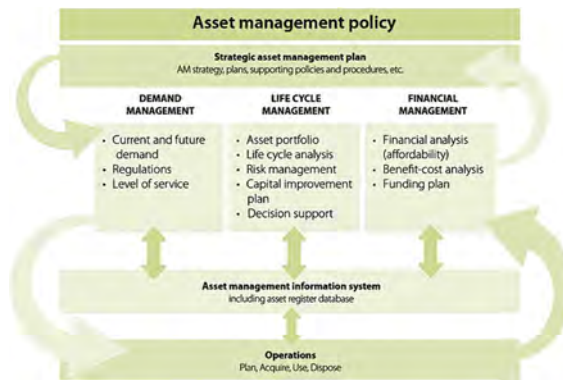


Figure 1. Asset Management Framework (From Managing Infrastructure Assets for Sustainable Development, by United Nations, © 2021 United Nations. Reprinted with permission of the United Nations).

The International Infrastructure Management Manual (IIMM) developed an internationally recognized asset management process that links level of service, performance measures, data collection, decision-making, and implementation (Hughson et al. 2006). The manual promotes two levels of asset management: core and advanced. The primary goal of core asset management is to understand the asset and its requirements. In contrast, advanced asset management involves understanding the relationship between performance, funding requirements, as well as the risks associated with failing to meet service-level agreements (Bush et al. 2012).

According to audits undertaken by the US Government Accountability Office USGAO (2008) and The New Zealand Office of the Auditor General NZOAG (2010), data gaps exist in existing asset management practices that have hindered the development of advanced asset management practices. Many bridge managers still follow the more traditional data collection approach, where decision-making is based purely on scheduled visual inspections and basic performance assessments. A move away from this perspective and toward a strategic decision-making system will significantly improve asset management outcomes by providing better information to strategic decision-makers (Bush et al. 2012).

2.2 *Asset management decision-making*

Effective asset management decision-making is critical in order to maximize the value realized over the lifetime of an organization's assets (The Institute of Asset Management 2015). Decisions made at each stage of an asset's lifecycle will impact subsequent stages. The choice of asset

acquired will impact its performance, risk, and maintenance requirements during its operational life, as well as the methods and costs of its decommissioning. Furthermore, how an asset is operated and maintained determines the length of its useful life and the costs and complications associated with its end-of-life. Therefore, asset management decisions must balance competing priorities, such as asset performance vs. asset maintenance, capital expenditures vs. operating expenses, and short-term benefits vs. long-term sustainability (The Institute of Asset Management 2015).

2.3 *Data collection practices*

Three approaches are available to help bridge managers understand how an asset is functioning. This includes visual inspection (VI), non-destructive evaluation (NDE), and structural health monitoring (SHM). A review of bridge asset management practices found little evidence of the full integration of all three systems (Bush et al. 2012). Furthermore, visual inspections have significant drawbacks, such as high outcome variability, lack of repeatability, and low accuracy, as data is based primarily on inspectors' judgment (Phares et al. 2007). Therefore, for an advanced asset management approach to be successful, the data and the data collection practices must be updated. This can be achieved by integrating NDE and SHM into the data collection processes (Omenzetter et al. 2015).

3 STRUCTURAL HEALTH MONITORING OVERVIEW

SHM is commonly defined as the procedure of obtaining and evaluating data acquired from the installation of sensors to assess the structural health of a structure (Güemes et al. 2020). It puts in place a strategy for locating and repairing damage in infrastructure and plays a valuable role in the management and maintenance of structures (Farrar & Worden 2007). For instance, condition-based maintenance (CBM) is an approach that prevents severe damage to structures by actively monitoring asset conditions to perform maintenance only when it is needed (Phares 2018).

3.1 *SHM technologies*

Technologies for structural health monitoring can be classified into two categories: Local techniques, in which damage detection is limited to the area directly under the sensor, as well as global techniques, in which damage detection is possible anywhere in the structure via an adequately distributed network of sensors (Güemes et al. 2020). The type of data measured determines the type of sensor that is used for damage detection. Hassani et al. (2021) present various sensor types that can be used to monitor various mechanical properties of a component.

3.2 *SHM primary goals*

According to Li & Hao (2016), SHM is intended to achieve the following six primary goals: I) validation of design assumptions and assessment of structural performance; II) early identification of potential damages to ensure structural and operational safety; III) provision of real-time information for safety assessment following disasters and extreme events; IV) assessment of structural conditions, load-carrying capacities, and prediction of remaining service life; V) provision of a decision tool for optimal inspection, rehabilitation, and maintenance planning; and VI) collection of massive amounts of in-situ data for cutting-edge research to improve design specifications and guidelines. These applications make SHM a valuable resource for bridge asset managers as the collection of reliable data is essential for ensuring that bridges continuously perform at the required level, and SHM can supplement this by developing advanced knowledge about bridge condition and performance.

3.3 *SHM limitations*

SHM has been the subject of many global studies due to its dual goal of preventing catastrophic failure and empowering infrastructure owners with quantitative data for designing a reliable and cost-effective asset management plan (Li & Hao 2016). While SHM has the potential to

improve asset management, it has only been able to make limited development from research to application due to its relatively high installation and operation costs (Phares 2018). A key aspect of transitioning SHM into an economically feasible asset management strategy is the ability to quantify the tangible benefits of the system to justify capital costs (Lynch et al. 2016).

4 ROLE OF SHM FROM AN ASSET MANAGEMENT PERSPECTIVE

Asset management offers significant potential for integrating SHM systems, especially ones designed considering operations and maintenance performance metrics. The information generated by the SHM system may be integrated with an owner’s asset management platform to facilitate the issuance of work orders and provide better situational awareness for the bridge management personnel (Dubbs 2018). SHM could also be used to update deterioration forecasts in real-time, enabling owners to have a realistic and accurate representation of their bridge condition. The main challenge, however, lies in the ability of SHM systems to report actionable information that can be utilized for decision-making (Wong 2001) (Dubbs 2018) (Heldt et al. 2019).

Wong (2001) presents that SHM, alone, is of little value other than a latent technical accomplishment, as it is an integral part of a value chain (that focuses on “understanding” the risk) and argues that the information generated by SHM should be used to assist the owner in making financial decisions (thereby “managing” the risk). To achieve this and fully transition SHM into a commercially viable asset management strategy, Heldt et al. (2019) emphasize the need for decision-mapping before scoping and implementing SHM. This includes understanding what decisions SHM is trying to inform, what the likely outcomes are, how the data will be used, what the value proposition of SHM is, and how it can be targeted to support decision-making at all levels.

4.1 Frameworks for the integration of SHM into bridge asset management

The process of identifying the place of SHM in the emerging bridge asset management discipline has been under development by a few authors. A data collection and monitoring strategy for asset management of road bridges has been developed by Bush et al. (2011). Bridges in a network are classified into one of three data collection categories: core, intermediate, or advanced. The classification considers the risk profile and the criticality of each bridge in the network, and a simple scoring scheme is proposed. Depending on a bridge’s level of criticality and risk, its data collection regime shifts from core to intermediate to advanced, as illustrated in Figure 2.

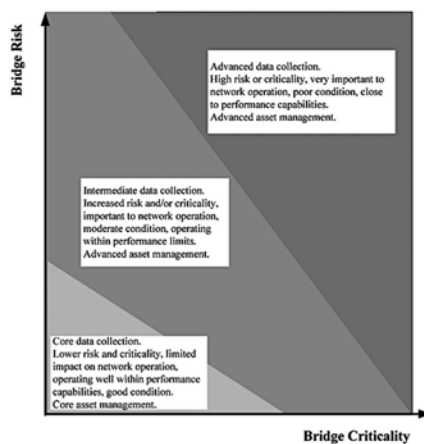


Figure 2. Risk and criticality-based bridge classification for data collection (Bush et al. 2011).

Correspondingly, the bridge is moved towards higher levels of data collection that involve collecting more detailed and reliable data, as presented in Table 1. High-level data collection

regimes require proactive and planned integration of SHM systems for asset management. By providing some degree of flexibility in the data collection regime, the bridge asset manager can tailor the strategy following local network requirements, risk tolerance, and budget, thereby ensuring cost-effective strategy implementation. For example, increasing the number of bridges assigned to intermediate and advanced regimes will require additional resources as more comprehensive data will be collected for those bridges. Alternatively, keeping more bridges in the core regime will be more economical since data collection techniques will be limited.

Table 1. Risk and criticality-based bridge data collection strategy (Bush et al. 2012, © 2012 NZ Transport Agency. Amended with permission from Waka Kotahi NZ Transport Agency).

Data collection regime	Bridge risk-criticality	Risk assessment reporting	Inspection frequency	Data collection techniques
core	low	overall bridge risk	visual inspections every 3-6 years	limited, usually reactive SHM
intermediate	intermediate	individual element risk	visual inspections every 2-3 years	some, reactive and proactive SHM
advanced	high	individual structural component risk	visual inspections every 1-2 years	extensive, mostly proactive SHM

Omenzetter et al. (2011) propose a similar philosophy for integrating SHM into broader data collection and asset management by focusing on the risk that failures of individual bridges can pose to the overall functionality of the transportation system. The recommendation is that detailed and real-time data on the condition of all bridges is not necessary, but only for those bridges whose failure is likely to have more significant consequences on the network operation. In other words, only bridges with higher risk should receive priority for enhanced data collection using SHM.

4.2 Successful cases of SHM integration with asset management

A few authors have shown that the integration of SHM into bridge asset management has proved successful.

Figueiredo et al. (2011) developed an approach to integrate SHM into a bridge asset management system to analyze engineering and economic factors and to assist authorities in determining how and when to make decisions regarding the maintenance, repair, and rehabilitation of structures. This approach was validated on standard data sets from a real-world bridge. It was concluded that bridge safety, repair, and maintenance were successfully achieved with visual inspections accompanied by results from long-term monitoring.

Ni & Wong (2012) designed and implemented an integrated SHM and maintenance management system for 21 sea-crossing viaduct bridges on the Hong Kong Link Road. In this system, the structural degradation of the bridge was monitored through SHM and assessed evolutionarily to facilitate CBM. The inspection and monitoring results were linked to an updatable rating system based on criticality and vulnerability, as in the work of Bush et al. (2011). This linkage enabled decision-makers to utilize SHM data directly to prioritize and make bridge inspections and maintenance decisions. This provided solutions for minimizing and eliminating unnecessary repairs, preventing catastrophic bridge failures, and reducing the negative impact of maintenance on the profitability of the in-service bridges under study.

More recently, Phares (2018) developed a bridge asset management system utilizing real-time performance and condition data to prioritize bridge repairs and maintenance in a similar fashion to Ni & Wong (2012). By combining the continuous real-time bridge condition data collected by SHM with bridge inventory data, a CBM framework facilitated by SHM was developed. Through implementing this framework on Iowa's Sugar Creek Bridge, Phares (2018) determined that the potential extension in the service life of the bridge and the expected savings in maintenance, repair, and monitoring costs make SHM economically justifiable.

Dubbs (2018) presents a case study that demonstrates how an in-service SHM system has been integrated into a bridge agency's asset management software platform. The integration

of SHM into asset management provided valuable, actionable information on five discrete areas, as shown in Figure 3. This includes maintenance work orders, operations, public safety, structural safety, and security. This suggests that the integration of SHM can inform decisions regarding the structural performance of the structure, as well as maintenance and operations, thus paving the way to the realization of an advanced asset management system.



Figure 3. Potential Uses of SHM-Asset Management Integration (Dubbs 2018, © 2018 ASCE. Reprinted with permission from ASCE).

5 RESULTS AND DISCUSSION

5.1 Key challenges

Based on the literature review, it appears that the key challenges of infrastructure asset management are characterized by the need for advanced knowledge about the condition and performance of the concerned asset, in addition to the need for reliable data for planning to ensure that assets continue to perform at the expected level well into the future. Moreover, when it comes to utilizing SHM systems in asset management, the main obstacle faced is the challenge of effectively transforming the complex and often noisy data generated by SHM into actionable information to support the decision processes inherent in asset management.

5.2 Key findings

From the literature that has been reviewed, we can summarize our findings on how to achieve the best practice use of SHM as an asset management tool as follows:

5.2.1 Appropriate application of SHM

Since SHM is not meant to replace visual bridge inspection, it is best used after a visual inspection has deemed a bridge to be structurally inadequate in order to objectively determine the actual state of the bridge. As highlighted by Bush et al. (2011), SHM is not required for every structure but for structures that, when correctly assessed, have a high potential of resulting in considerable cost savings for the owner. Whether SHM is appropriately applied depends on the significance of the network being monitored, specifically whether the bridge network is critical or part of a group of routine bridges. Since both these situations involve diverse bridge management choices, the SHM requirements specified for each will be considerably different from one another.

5.2.2 Shift from core asset management to advanced asset management

NZOAG (2010) and Bush et al. (2012) suggest that bridge asset managers must transition to an advanced asset management approach and improve the connection between operating

processes and strategic outcomes by applying SHM. Since not all bridges on a given network share similar conditions, demands, and importance, not all bridge managers will require an advanced asset management approach. Whereas some critical bridges will require a more advanced asset management approach, more basic asset management approaches will be sufficient for other simpler bridges. In order to achieve advanced asset management, managers need to increase the amount of data collected and the precision of data for the most critical bridge routes. To achieve this, Omenzetter et al. (2015) propose better integration between VI, NDE, and SHM, as well as a data collection model that accounts for broader performance requirements for bridges.

5.2.3 Risk and criticality

Bush et al. (2011) emphasize the importance of considering risk and criticality as factors in the data collection strategy in bridge asset management. To do so, rather than collecting data as if all bridges are the same, we need to adopt a more systematic, individualized approach for managing bridge assets and gathering relevant data. It is necessary to integrate SHM data into asset management in a planned and proactive manner as bridge risk and criticality increase. Accordingly, a simple asset management approach must be adopted for lower-risk and criticality bridges, and an advanced asset management approach for higher-risk and criticality bridges.

5.2.4 Shift from Time-Based Maintenance (TBM) to Condition-Based Maintenance (CBM)

Implementing an asset management framework that includes SHM can improve the maintenance strategy of a bridge by shifting from the current time-based approach (whereby maintenance is performed according to a planned schedule) to the modern CBM approach (whereby asset conditions are actively monitored to perform maintenance only when it is needed). This enhances the execution of inspection and maintenance activities of bridges and substantially decreases the inspection and maintenance costs (Ni & Wong 2012). Phares et al. (2018) list the advantages of SHM-CBM integration for asset management decision-making as follows:

- I. Continuous and near real-time SHM data to support maintenance decisions
- II. Improved collection of a variety of quantitative data
- III. Reduced uncertainty about structural performance
- IV. Elimination or reduction of over-maintenance and deterioration caused by insufficient information about the actual condition of a bridge

6 CONCLUSIONS

In this paper, the literature was thoroughly reviewed to determine the role of SHM in the asset management of bridges. The current trends in bridge asset management were summarized, the value proposition for using SHM was explored, and the key factors for successfully integrating SHM and asset management were outlined. Through a detailed review, the authors observed that the reliability and efficiency of both asset management and SHM systems could be improved when these two systems are properly integrated. Additionally, the authors have discussed the importance of SHM in asset management, not only as an asset management tool but as a means to achieve advanced asset management. Through an examination of different frameworks and strategies, this paper presents key conclusions from various authors in a collective manner to assist future asset managers in realizing SHM's role in the asset management practice. As a final note, we have identified three areas for future research. First, a comprehensive set of performance and maintenance metrics that provide real value to bridge asset managers must be established. Second, a bridge asset management system that utilizes data to determine bridges' performance and maintenance requirements must be developed. This system must include strategies for optimizing the management of bridge assets. By developing these metrics and bridge decision-making tools, SHM can maximize the value of data collected and, in turn, allow the data to directly contribute to asset management decision-making. Finally, to achieve the potential benefits of SHM and use it cost-effectively, a deeper understanding of management aspects such as the cost-benefit ratio is necessary, as well as its impact on the type of issues to be monitored and the probability of detection.

ACKNOWLEDGEMENT

The authors wish to acknowledge the generous financial support from the Kuwait Foundation for the Advancement of Science (KFAS) to present this paper at the conference under the research capacity building/scientific missions program.

REFERENCES

- Bush, S., McCarten, P., Omenzetter, P. & Henning, T. 2011. A risk and criticality-based data collection and monitoring strategy for asset management of road bridges. *8th Austroads Bridge Conference Sydney, Australia*: 3–16.
- Bush, S., Omenzetter, P., Henning, T. & McCarten, P. 2012. Data collection and monitoring strategies for asset management of New Zealand road bridges. *NZ Transport Agency research report (475)*: 157.
- Dubbs, N.C. 2018. Expanding the Case for Structural Health Monitoring: A Focus on Its Role in Maintenance and Operations and Asset Management Systems Structures Congress 2018. Philadelphia PA: American Society of Civil Engineers.
- Farrar, C. R. & Worden, K. 2007. An introduction to structural health monitoring. *Philosophical Transactions of the Royal Society A: Mathematical, Physical and Engineering Sciences*, 365(1851): 303–315.
- Figueiredo, E., Radu, L., Park, G. & Farrar, C. 2011. Integration of SHM into Bridge Management Systems: Case Study-Z24 Bridge. *8th International Workshop on Structural Health Monitoring – CA, United States 2011* : 725–732.
- Güemes, A., Fernandez-Lopez, A., Pozo, A. R. & Sierra-Pérez, J. 2020. Structural health monitoring for advanced composite structures: a review. *Journal of Composites Science*, 4 (1):13/01 – 13/15.
- Hassani, S., Mousavi, M., & Gandomi, A. H. (2021). Structural health monitoring in composite structures: a comprehensive review. *Sensors*, 22 (1):153/1 – 153/45.
- Heldt, T., Lake, N., Ngo, H., Seskis, J. & Eskew, E. 2019. Bridge Management-Using Structural Health Monitoring. 9th Australian Small Bridges Conference 2019.
- Hughson, G., Roberts, L., Smith, R., McIlveen, J., Kettle, D., Murray, S., Busch, W., Hollier, R., Urquhart, T., Bryne, R. & Muir, S. 2006. *International infrastructure management manual*. Wellington: National Asset Management Steering (NAMS) Group.
- Kim, J.R., Chae, M.J., Park, J.W., Lee, G. & Cho, M.Y. 2010. Review of wireless sensors for road and bridge asset management. Banff, Alberta: American Society of Civil Engineers.
- Li, J. & Hao, H. 2016. A review of recent research advances on structural health monitoring in Western Australia. *Structural Monitoring and Maintenance*, 3(1): 33–49.
- Lynch, J., Farrar, C. & Micheals, J. 2016. Structural Health Monitoring: Technological Advances to Practical Implementations. *Proceedings of the IEEE* 104(8): 1508–1512.
- New Zealand Office of the Auditor General (NZOAG). 2010. *NZ Transport Agency: information and planning for maintaining and renewing the state highway network*. Wellington: New Zealand Office of the Auditor General.
- Ni, Y.Q. & Wong, K.Y. 2012. Integrating Bridge Structural Health Monitoring and Condition-Based Maintenance. *Management Civil Structural Health Monitoring Workshop (CSHM-4) – Lecture 06*.
- Omenzetter, P., Bush, S., Henning, T. & McCarten, P. 2011. Risk based bridge data collection and asset management and the role of structural health monitoring *Proceedings of Spie Digital library (7983)*: 79830K-1.
- Omenzetter, P., McCarten, P. & Bush, S. 2015. Guidelines for data collection and monitoring for asset management of New Zealand road bridges. *Roading Infrastructure Management Support, Wellington*.
- Phares, B.M., Graybeal, B.A., Rolander, D.D., Moore, M.E. & Washer, G.A. 2007. Reliability and accuracy of routine inspection of highway bridges. *Transportation Research Record: Journal of the Transportation Research Board* 1749: 82–92.
- Phares, B. 2018. Integration of Structural Health Monitoring (SHM) into Multilayer Statewide Bridge Maintenance and Management Practices – SHM-Facilitated Condition Based Maintenance (SHM-CBM) Prioritization System. Midwest Transportation Center.
- The Institute of Asset Management. 2015. *Asset Management – An Anatomy*. United Kingdom: IAM.
- The Institute of Asset Management. 2022. *The Pathway to Excellence in Asset Management: IAM Maturity Scale & Guidance*. United Kingdom: IAM.
- United Nations. 2021. *Managing Infrastructure Assets for Sustainable Development: A Handbook for Local and National Governments*. New York: United Nations.
- US Government Accountability Office (USGAO). 2008. Highway bridge program: clearer goals and performance measures needed for a more focused and sustainable program. Washington DC: US Government Accountability Office.
- Wong, F. & Yao, J. 2001. Health Monitoring and Structural Reliability as a Value Chain. *Computer-Aided Civil and Infrastructure Engineering* 16: 71–78.

Inclusion of Stochastic Petri-net models on a risk-based tool for the maintenance of road drainage systems

L.G. Rodrigues & L.C. Neves

The University of Nottingham, Nottingham, UK

J. Wallis, R. Brook & K. Morosiuk

XAIS Asset Management Ltd, Doncaster, UK

ABSTRACT: Maintenance of road drainage systems requires efficient use of public funding and resources. Current periodic gully pot cleansings can be improved through risk-based decision-making tools that use inspection and historical data. This paper proposes a framework to define gully cleansing regimes making use of stochastic Petri nets and Machine Learning. The stochastic Petri net model is used to predict gullies' sediment level ranges over time based on historical data. Machine learning techniques are used to classify gullies and overcome data absence. The probabilistic distributions used to predict sediment levels are also utilized to derive the probability of reaching a limit state given an assigned cleansing frequency. The framework enables a risk-based analysis to optimize maintenance costs. The results show that the stochastic Petri net model is suitable for representing sediment level condition states and the risk-based tool is useful for maintenance decision-making.

1 INTRODUCTION

Infrastructure networks are vital for the economy and society. Under the Highways Act 1980, Highway Authorities are responsible for maintaining the highway and drainage systems in a safe and functional condition. Gullies are important for preventing solid materials from flowing into the sewerage system and causing blockages. An inadequate cleansing regime can lead to flooding of the carriageway and subsequent damage to the highway surface or sub-structure, shortening its lifespan. Moreover, inadequate maintenance can also increase hazards for motorists and pedestrians, especially during wet and freezing conditions. Local Highway Authorities (LHA) have been forced to manage their assets effectively due to austerity and take risk-based approaches according to UK Department for Transport (2016). Some LHAs have reinforced their cleansing programs with subsequent reactive maintenance measures to deal with faults or blockages. However, current cyclical cleansing approaches involve cleaning road gullies on a planned and regular basis, irrespective of the need for cleaning that specific item. Austerity has led to a reduction in gully cleansings to cover cyclical activities, resulting in a substantial increase in emergency cleanses due to intense rainfall, which is predicted to increase due to climate change. Emergency cleansings disrupt the cyclical cleansing program and are more expensive than a planned route. Therefore, the current methods of assessing cleansing operations and planning on-site works need to be re-evaluated to optimize available resources and ensure effective maintenance of the drainage systems.

This paper proposes a framework for defining gully cleansing regimes using Machine Learning and stochastic Petri nets. The approach includes probabilistic functions to model transitions between consecutive gully conditions, allowing the definition of cumulative distribution functions for different limit states that can be used in a risk analysis. A case study of East Sussex County Council (ESCC), one of the largest Highways Authorities in the United Kingdom, is provided to demonstrate the framework's application.

2 METHOD

The framework is based on historical data collected during the cyclical cleansing programme defined by ESCC, which includes information about the sediment level and time interval between consecutive interventions. Using these data, the monthly sediment level rising rate is calculated, and gullies are classified as slow, medium, or fast deteriorating, based on historical values of sediment accumulation. The Classification learner, available in Matlab Machine Learning Toolbox, is used to train a model that generates predictions of gully classification based on environmental variables, gully stock properties, and other road section variables. The resulting model is employed when historical cleansing data is poor or unavailable. A stochastic Petri net formalism is used to model the condition of gullies over time. This approach includes the definition of consecutive condition states and timed transitions, between states, that represent the time that a gully lasts in the prior condition before moving to the next. Timed transitions are represented by probabilistic distributions with parameters estimated using the maximum likelihood method. This aims to obtain the best set of parameters that fit the condition score data obtained through in-situ measurements. The probability of reaching distinct limit state levels is derived based on the probabilistic functions used to model the transition times between states. The framework comprises a risk analysis to provide a decision tool for gully cleansing regimes that considers different road maintenance hierarchies and flood risk zones.

3 CASE STUDY: EAST SUSSEX COUNTY COUNCIL

The ESCC road network has six different categories of roads based on classifications proposed by the UK Department for Transport (2016). The road hierarchy is structured as Strategic Route (2), Main Distributor (3a), Secondary Distributor (3b), Link Road (4a), Local Access Road (4b), and Minor Road (5). Strategic Route includes trunk and principal ‘A’ class roads with limited pedestrian crossings and parking restrictions. Main Distributor routes link urban centres to the strategic network with limited frontage access and parking restrictions. Secondary Distributor includes ‘B’ and ‘C’ roads with frontage access and unrestricted on-street parking. Link Road hierarchy includes interconnecting residential or industrial roads with 20 or 30-mph speed limits and uncontrolled parking. The Local Access Road hierarchy includes roads serving limited properties carrying only access traffic, and the Minor Road hierarchy includes roads serving very few properties. These road classifications help to determine gully cleansing frequencies and risk management strategies in the maintenance of road drainage systems. The Drainage Management System (DMS) used by ESCC helps identify the location of surface water runoff assets in various road hierarchies. The historical data available at the DMS comprises around 849k complete cleansings since 2008, where the sediment levels are recorded. Table 1 shows the distribution of gullies in different road hierarchies and the number of assets in different zones of the flood risk maps. The framework proposed does not distinguish between road gullies and kerb inlets. If the asset has a sediment pot, it will be treated as a road gully pot.

Table 1. Distribution of gullies per Road Hierarchy and Flood Risk Level.

Road Hierarchy	Flood Risk Level				Total
	High	Medium	Low	Very Low	
Strategic Route (2)	1583	831	1593	2007	6014
Main Distributor (3a)	1613	1012	1942	3521	8088
Secondary Distributor (3b)	2899	1788	3935	7117	15739
Link Road (4a)	2433	1739	3460	4059	11690
Local Access Road (4b)	12991	8824	16553	1605	54419
Minor Road (5)	24	13	23	41	101

4 CLASSIFIER LEARNER FOR GULLIES

The proposed decision-making tool classifies gullies into three categories based on their mean monthly sediment level rising rate (SLRR): slow, medium, and fast. This rate is calculated for each gully based on consecutive inspections recorded in the DMS. Slow gullies have a mean SLRR below the 16th percentile, while fast gullies have a mean SLRR above the 84th percentile. Medium gullies have mean SLRR between the 16th and 84th percentiles. To ensure statistical significance, only gullies with more than 4 consecutive inspections are considered. The complete gully stock has an average SLRR of 4.95% per month and a standard deviation of 1.87% per month. The SLRR values are assumed to follow a normal distribution. However, insufficient data exist for some gullies in the stock to accurately classify them and determine a cleansing regime. To address this, a Machine Learning model is trained on a labelled dataset to identify the relationship between input features (such as environmental variables, gully stock properties, and other road section variables) and their corresponding SLRR classes. The objective is to enable the model to learn a general pattern that can predict the SLRR class of gullies based on input features.

4.1 Features and output variable

ESCC flood event location data is used to tag gullies located less than 100m from a flood spot as “near a flood spot.” The Environment Agency’s flood risk maps are also used to identify potential hazards related to the gully stock. The XAIS Asset Management Ltd system (XA) provides information on the longitudinal gradient of road sections, used to identify sag points where floating debris accumulates. Gullies within 100m of a sag point are tagged as “near a sag point.” The classification learning app in Matlab considers variables such as road hierarchy, gritting routes, zone type, and the average time between cleansings recorded in the ESCC database. Table 2 summarizes the variables considered in the classification learning app.

Table 2. Variables used to classify gullies.

Variables	Values					Type	
	High	Medium	Low	Very Low			
Flood Risk						Categorical	
Road Hierarchy	2	3a	3b	4a	4b	5	Categorical
Gritting Route	Yes	No	-	-	-	-	Categorical
Zone Type	Urban	Rural	-	-	-	-	Categorical
Near Flood Spot	Yes	No	-	-	-	-	Categorical
Near Sag Point	Yes	No	-	-	-	-	Categorical
Avg. Time Between Cleansings	ranges from 4.9 months to 27.1 months						Numerical
Gully Deteriorating Class	Slow	Medium	Fast				Categorical

4.2 Gullies regime classification

The Fine Tree model is used to predict the gullies’ cleansing regime. It is a Decision Tree model that uses Gini’s diversity index as the split criterion with a maximum of 100 splits. The model is validated using holdout validation, where the training and test sets are partitioned into 75% and 25%, respectively. The feature importance scores are sorted using the Maximum Relevance – Minimum Redundancy MRMR algorithm (Zhao, Anand, and Wang 2019) and the Confusion Matrix obtained through the Matlab Classifier Learner is shown in Figure 1.

The model achieved an 81.6% validation accuracy, with normal and fast gullies correctly classified 82.1% and 85.4% of the time, respectively. Slow gullies were correctly classified in 75.4% of cases. The False Discovery Rate (FDR) values are evaluated to determine if the model provides distant predictions. None of the gullies predicted as fast were classified as slow. Moreover, only 0.1% of the gullies predicted as slow were classified as fast. According to the MRMR algorithm, the most influential feature in classifying gullies is the average time between cleansings, meaning that the SLRR is greater with a shorter time between cleansings.

Other factors include the flood risk zone, location on a gritting route, and whether the gully is in a rural or urban area. The model suggests that the road hierarchy and proximity to a flood spot or sag point have minimal impact on the results. The Fine Tree model exported from Matlab was employed to classify the gullies with insufficient cleansing data, and the resulting predictions were merged with the previous classifications based on historical cleansing data. Most gullies (49957) were classified as having a medium SLRR, while 10280 gullies were classified as fast, and 35815 gullies were classified as slow.

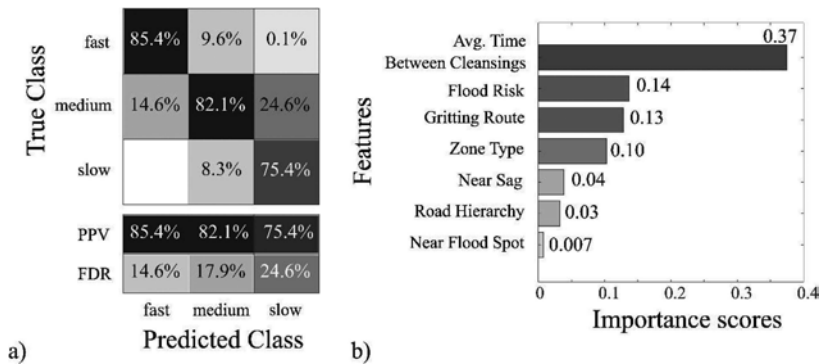


Figure 1. Confusion Matrix and Feature Importance scores using the MRMR algorithm.

5 CONDITION PROJECTION CURVES BASED ON STOCHASTIC PETRI NETS

A Petri net formalism is used to predict the condition of gullies. The method is based on Dugan et al. (1984), which walked on the road paved by Petri (1962), which developed the original concept. The Petri net considered herein has four components: Places, Transitions, Arcs, and Tokens. In this case, 5 places are associated with distinct sediment level ranges, as presented in Figure 2. The state of a gully is represented by the location of the token, while transitions model the time that a token lasts in the previous place. An arc transports Tokens and connects a place with a transition, or vice-versa. This formalism has been successfully applied to model the deterioration of assets based on qualitative condition scores (Andrews 2013; Yianni et al. 2017), which is the case of sediment level at gully pots since surveyors usually define the sediment level as a percentage of the pot height through a visual inspection. Compared to alternative methodologies used to model discrete conditions states (e.g. Markov Chains), Stochastic Petri Nets (STP) allow for the use of a range of distributions to model transition times, the use of the same model for different classes of structure, by assigning colours to tokens, and the ability to integrate advanced modelling features, like the effect of maintenance and inspection actions.

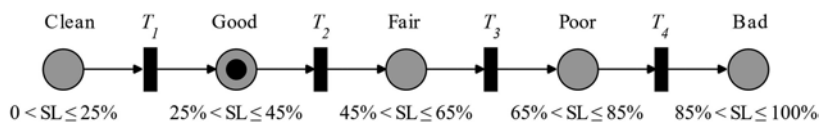


Figure 2. Petri net scheme of a gully with a sediment level between 25% and 45% of the underlying pot.

The term stochastic is used to classify the Petri net given that timed transitions are represented as random variables. A similar approach was applied to predict the degradation of ceramic claddings (Ferreira et al. 2020) where the transition times were modelled with five probabilistic distributions (Exponential, Weibull, Log-Normal, Gumbel and Normal distribution), which provides higher versatility when compared to other competitor models such as Markov based models. In the present work, exponential distributions are used to model transitions with parameters obtained through the maximum likelihood method (Kalbfleisch &

Lawless 1985). The likelihood is defined as the predicted probability of occurrence of the observed transitions:

$$L = \prod_{i=1}^n \prod_{j=1}^k p_{ij} \quad (1)$$

where i is the condition in the initial instant; j is the condition in the final instant; n is the number of elements of the historical database; k is the number of intervals between inspections; and p_{ij} is the probability of transition from condition level i to condition level j . The log-likelihood is commonly used to improve optimization algorithms' robustness in the estimation of the probability function parameters. The log-likelihood is given by:

$$\log L = \sum_{i=1}^n \sum_{j=1}^k \log p_{ij} \quad (2)$$

The probability of occurrence of the observed transitions, p_{ij} , is estimated by Monte Carlo simulation. The Latin Hypercube Sampling (LHS) (Olsson and Sandberg 2002) was used in this work to generate a set of transition times (simulations), in which each realization corresponds to four timed transitions that are assumed as random variables following the exponential distribution. The parameters that define each timed transition of the Stochastic Petri Net can be obtained through numerical optimization methods, where the objective is to maximize the likelihood function given by equation (2). The constrained optimization by linear approximation (COBYLA) created by Powell (1994) is used in this work and is suitable for constrained problems where the derivative of the objective function is not known. Figure 3 summarizes the steps required to reach the parameters of the exponential distributions used to represent each transition. For each gully classification (slow, medium, and fast) one must upload the historical condition data available. Each entry of the historical condition data corresponds to consecutive measurements of silt level at a gully pot at two spaced times. The number of simulations (n_{sim}) is equal to 1000, while each timed transition is initialized with a mean value of 1 month.

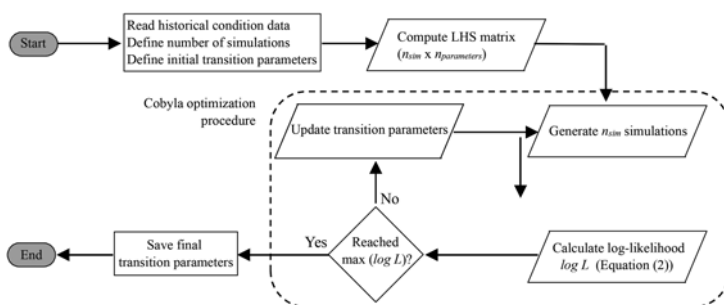


Figure 3. Optimization procedure used to determine timed transition parameters.

Table 3 shows the optimal parameters obtained for the timed transition exponential distribution functions. The Latin Hypercube sampling can be further used to present condition projection curves based on the optimal parameters.

Table 3. Optimal parameters obtained for timed transitions.

Classification	Mean Value (months)				$- \log L$
	T_1	T_2	T_3	T_4	
Slow	17.4	6.2	21.2	10.6	119561
Medium	7.8	3.8	12.5	7.9	850293
Fast	5.8	1.4	7.3	5.6	280196

6 RISK-BASED ANALYSIS FOR CLEANSING REGIME DEFINITION

During the design phase, the spacing of road gullies is determined based on rainfall intensity, which is dependent on the depth of rainfall in millimetres falling at a site for 2 minutes with an average return period of 5 years. For sites located in the ESCC, the value ranges from 3.0mm to 4.0mm. Thus, this analysis considers rainfall with an average return period of 5 years and predefined limit states for different road hierarchies. In other words, the study aims to evaluate whether the gullies meet their respective performance levels during a storm event with a 5-year return period. The probability of compliance (P_c) of one gully can be determined by the equation below:

$$P_c = 1 - \sum_{i=0}^{n_{intervals}} F_d(i \cdot t) \cdot P_{EXP}(\Delta t), \text{ with } n_{intervals} = T_c/\Delta t \quad (3)$$

where T_c is the time between cleansings, Δt is the time step considered to calculate the probability, F_d is a limit state cumulative probability function that depends on gully classification, as well as on its assigned performance level, and $P_{EXP}(\Delta t)$ is the probability of the rainfall being exceeded at least once during Δt . It is worth noting that the sum presented in equation (3) represents the probability of failure, which considers the cumulative probability function given that $P_{EXP}(\Delta t)$ is considered constant for any time interval. The latter can be obtained through the equation below:

$$P_{EXP} = 1 - e^{-\frac{\Delta t}{5.12}}, \text{ with } \Delta t = 0.1 \text{ month} \quad (4)$$

6.1 Limit states cumulative probability curves

Three limit states (LS) are defined for levels of sediment accumulation in the gully pot, which are associated with different performance levels: trapping efficiency, hydraulic efficiency, and outlet blockage. Trapping efficiency (or sediment retaining efficiency) is compromised when sediment levels range from 45% to 65% of the pot height, while hydraulic efficiency (ability to pass flow without becoming surcharged) is affected when sediment levels are between 65% and 85%. A gully is considered blocked when sediment levels exceed 85% of the pot height.

The present work exploits the exponential distributions with parameters presented in Table 3, obtained through the stochastic Petri net formalism resulting in empirical cumulative distribution functions (ECDF) for each limit state. A limit state can be defined as $LS = \{D \geq d\}$, such that sediment level (D) exceeds a specific height of the pot (d). Alternatively, these curves represent the conditional distribution function $F_d(x)$ of the capacity of a gully to remain uncleaned until reaching an undesirable limit state. The following equation represents the conditional distribution function $F_d(x)$, which can be consulted in Khetwal, Pei, and Gutierrez (2021):

$$F_d(x) = P[D \geq d | X = x] \quad (5)$$

where D is an uncertain limit state, d is a threshold of D , X is the uncertain time between cleansings, x is a particular value of X , and $F_d(x)$ represents a cumulative probability function for damage state d evaluated at x . Figure 4 presents the cumulative probability functions for the three limit states considered, as well as their respective 95% confidence intervals, which were estimated by using Greenwood's formula available in Matlab Statistic and Machine Learning Toolbox. Figure 4 also shows the lognormal cumulative probability functions that were fitted using the maximum likelihood method. Lognormal CDFs are adequate for the present analysis given that time cannot assume negative values. In addition, lognormal CDF are widely used to represent the probability of reaching a particular limit state or damage level as a function of an intensity measure, especially based on empirical data, as well as numerical model results (Nguyen and Lallemand 2022). The same principle is adopted here, however, the limit state data is obtained through LHS sampling method that uses the parameters available in Table 3.

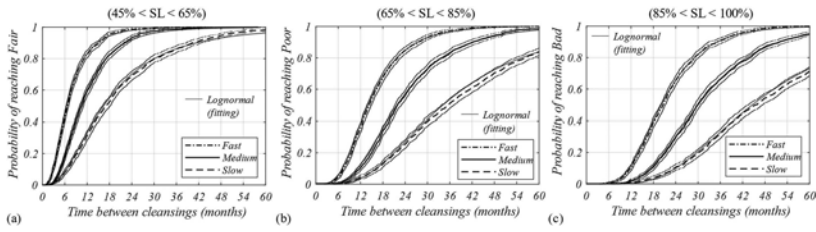


Figure 4. Cumulative probability functions for distinct limit states.

6.2 Application of risk-based analysis for the definition of cleansings programmes

The gullies located in roads with hierarchies from (2) to (4a) must have hydraulic efficiency and trapping efficiency when the 5-year return period rainfall occurs. Consequently, the cumulative probability functions considered for those gullies refer to the Fair condition. For the gullies located on local access roads and minor roads, the objective is to guarantee hydraulic efficiency, which corresponds to the limit state Poor. The analysis presented here will compare three cleansing regimes: current; Proposal 1, improved efficiency for (2) and (3a) roads; and Proposal 2, reduced blocked outlet times. Table 4 presents their correspondent cleansings and percentage of compliances. Proposal 1 allows a reduction of 21.3% in the number of visits while reducing 6.7% the prediction of compliances. This approach can free up one weekday to perform inspections and carry out other maintenance measures. Proposal 2 results in a similar number of cleansings but reduces blocked gullies on principal roads by almost 50%, along with the time that these gullies remain full. From the cumulative probability curves corresponding to the Bad condition, one can obtain the blocked outlet times. Figure 5 provides valuable information for defining inspection strategies and planning reactive measures. Principal roads require less urgent cleaning, while roads serving limited properties are more prone to require exceptional maintenance. On the other hand, released working hours from cyclical cleansings can be used for inspections to mitigate the risk of blocked gullies.

Table 4. Total number of visits for distinct cleansing programmes (horizon of 36 months).

Road Hierarchy	Current	Proposal 1	Proposal 2
Strategic Route (2)	13112	19977	24217
Main Distributor (3a)	22246	29496	29496
Secondary Distributor (3b)	36930	28187	42278
Link Road (4a)	28909	20849	30848
Local Access Road (4b)	99604	59629	71522
Minor Road (5)	237	101	101
Total number of visits	201038	158239	198462
Percentage of compliances	(84.8%)	(79.1%)	(85.8%)

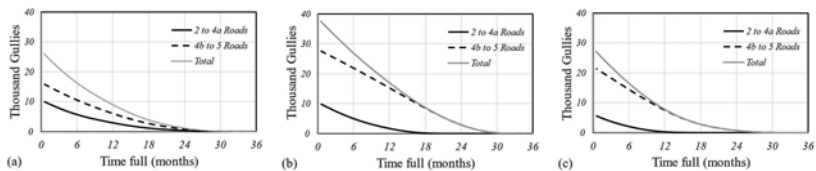


Figure 5. The blocked outlet times: (a) Current programme; (b) Proposal 1; (c) Proposal 2.

7 CONCLUSIONS

The present contribution provides a framework for the definition of gully cleansing regimes. A real case study is presented that corresponds to the definition of the cleansing regimes of East Sussex Highways, which is one of the largest Highways Authorities in the United Kingdom.

The framework utilizes Machine Learning to classify gullies based on their monthly sediment level rising rate, with key features including the average time between cleansings, flood risk zone, location at a gritting route, and zone type (urban or rural). Future improvements may involve adding data on nearby trees and hedges, as well as the gully pot depth, which affects sediment accumulation (Post et al. 2016). Stochastic Petri-nets are employed to model transition times between gully condition scores (sediment levels). Exponential distributions were used to model the timed transitions. The results demonstrate that gullies' segregation into different classes results in reduced computational effort and lower uncertainty for each class, which facilitates effective maintenance planning and decision-making for road authorities. Cumulative probability functions were derived for different service levels using simulation techniques and the Latin Hypercube Sampling. A risk analysis was conducted considering a 5-year return period rainfall and predefined service levels. The framework was tested in three scenarios, aiming to reduce the time gullies spend blocked and improve hydraulic efficiencies on principal roads, and can be widely applicable. To account for uncertainties in cleansing operations, future developments should include transitions that capture the duration that a gully remains uncleaned before being emptied.

ACKNOWLEDGEMENTS

This work had the financial support of the UK Research and Innovation through the Knowledge Transfer Partnership (KTP) programme. The authors would like to acknowledge the contribution and encouragement of East Sussex Highways. The authors would also like to express their gratitude to Lee Garrett, Barry Roughley, Peter Turland, and Daniel Palmer for the knowledge shared.

REFERENCES

- Andrews, John. 2013. "A Modelling Approach to Railway Track Asset Management." *Proceedings of the Institution of Mechanical Engineers, Part F: Journal of Rail and Rapid Transit* 227 (1): 56–73.
- Dugan, J B, K S Trivedi, R M Geist, and V F Nicola. 1984. "Extended Stochastic Petri Nets: Applications and Analysis."
- Ferreira, Cláudia, Luís Canhoto Neves, Ana Silva, and Jorge de Brito. 2020. "Stochastic Maintenance Models for Ceramic Claddings." *Structure and Infrastructure Engineering* 16 (2): 247–65. <https://doi.org/10.1080/15732479.2019.1652657>.
- Kalbfleisch, J D, and J F Lawless. 1985. "The Analysis of Panel Data under a Markov Assumption." *Journal of the American Statistical Association* 80 (392): 863–71. <https://doi.org/10.1080/01621459.1985.10478195>.
- Khetwal, Sandeep Singh, Shiling Pei, and Marte Gutierrez. 2021. "Stochastic Event Simulation Model for Quantitative Prediction of Road Tunnel Downtime." *Tunnelling and Underground Space Technology* 116 (October). <https://doi.org/10.1016/j.tust.2021.104092>.
- Nguyen, Michele, and David Lallemand. 2022. "Order Matters: The Benefits of Ordinal Fragility Curves for Damage and Loss Estimation." *Risk Analysis* 42 (5): 1136–48. <https://doi.org/10.1111/risa.13815>.
- Olsson, Anders M J, and Göran E Sandberg. 2002. "Latin Hypercube Sampling for Stochastic Finite Element Analysis." *Journal of Engineering Mechanics* 128 (1): 121–25.
- Petri, Carl A. 1962. "Kommunikation Mit Automaten." Darmstadt, Germany: Technische Universität Darmstadt.
- Post, J A B, I W M Pothof, J Dirksen, E J Baars, J G Langeveld, and FHLR Clemens. 2016. "Monitoring and Statistical Modelling of Sedimentation in Gully Pots." *Water Research* 88: 245–56.
- Powell, M J D. 1994. "A Direct Search Optimization Method That Models the Objective and Constraint Functions by Linear Interpolation." In *Advances in Optimization and Numerical Analysis*, edited by Susana Gomez and Jean-Pierre Hennart, 51–67. Dordrecht: Springer Netherlands. https://doi.org/10.1007/978-94-015-8330-5_4.
- UK Department for Transport. 2016. "Well-Managed Highway Infrastructure: A Code of Practice." <https://www.gov.uk/government/publications/well-managed-highways-infrastructure-code>.
- Yianni, Panayioti C., Dovile Rama, Luis C. Neves, John D. Andrews, and David Castro. 2017. "A Petri-Net-Based Modelling Approach to Railway Bridge Asset Management." *Structure and Infrastructure Engineering* 13 (2): 287–97. <https://doi.org/10.1080/15732479.2016.1157826>.
- Zhao, Zhenyu, Radhika Anand, and Mallory Wang. 2019. "Maximum Relevance and Minimum Redundancy Feature Selection Methods for a Marketing Machine Learning Platform." In *2019 IEEE International Conference on Data Science and Advanced Analytics (DSAA)*, 442–52. <https://doi.org/10.1109/DSAA.2019.00059>.

Rehabilitation, strengthening and life-cycle assessment of an historical water channel Cavour masonry bridge crossing Cervo River after an extreme flood erosion at foundation pier causing massive settlement and large structural damages

C. Beltrami, M. Capalbo, G. Giacalone, M. Vittone, G. Comaita, I. Vangelisti, F.T. Isfahani, F. Damiani, R. Salomone, L. Casti, J. Salvioni & D. Cagliani
Lombardi Engineering S.r.l., Milan, Italy

F. Burlone & M. Fossati
Associazione Irrigazione Est Sesia, Novara, Italy

M.F. Carera
Impresa Luigi Notari S.p.A., Milan, Italy

ABSTRACT: A seven span masonry bridge water channel (> 150-year-old) crossing river Cervo, as a part of “Cavour water line”, has been struck by a flood during an extreme rain event. The intermediate pier P2 has suffered a massive settlement of the foundation ($\Delta Z > 0.5$ m), with displacement and rotation components, so to induce a large damage to the masonry arched spans (near collapse) and the masonry upper water channel. A full life-cycle design approach was developed addressing historical structures studies, topographic survey, material and structural testing and laboratory campaign, detailed structure inspection, B.I.M. models, provisional structures, durability assessment, strengthening strategies, structural monitoring, bridge testing, water-proofing, seismic risk assessment, residual service life assessment. The result of many studies makes possible to increase the service life of the bridge, saving a critical water infrastructure that for more than 150 years has played a central role for the economy in northern Italy.

1 INTRODUCTION

Cavour canal bridge, which crosses the Cervo torrent in the Municipality of Formigliana (VerCELLI, Italy), has been subject to an extreme flood event of 2nd – 3rd of October 2020 and for this reason it has suffered an important damage that almost lead to the collapse of the structure. The main damage is shown by the partial collapse of pier P2. This pile is positioned in the wet bed of the Torrente Cervo together with pile P1 (Figure 1).

As shown in the satellite images of previous years, pier P3 is at the edge of the wet riverbed, while piers P4-P5-P6 are located in a part of the riverbed on the left bank characterized by a sedimentary deposit covered with vegetation (including shrubs). The following studies were developed for the damaged bridge: detailed inspection of the bridge, survey and structural monitoring, structure project and durability assessment, global seismic structural verification of the bridge, as-built BIM project, service life (residual) assessment.

2 BRIDGE HISTORICAL DATA AND PRELIMINARY DAMAGE ASSESSMENT

2.1 *Structural geometry properties of the old bridge*

The canal bridge was built between 1863 and 1866 and is of the multiple arch type in masonry and stone. The static scheme is composed of 7 continuous spans of approximately 18 m in length, with 6 intermediate piers and two end abutments.

The piers have an overall height of 4.1m and are characterized by an elongated rectangular solid blade section (L=24.2m wide) in masonry, at the ends there is a semi-circular rostrum covered in stone. The foot of the piers consists of a plinth covered in stone 4m wide, the shaft

of the pier is made of masonry with a height of 2.5m and a thickness with a truncated cone which varies from 3.2m at the base to 2.9m at the top. At the top of the pier there is a trapezoidal masonry element 0.82m high on which the base of the arches is located.

The pier foundation is of the indirect type, with a massive ribbon-like plinth $h=1.9\text{m}$ high and $b=4.5\text{m}$ wide supported by a group of wooden piles (for a total of about 42 piles). Due to the peculiarity of the canal bridge, the structure of the deck is characterized by two overlapping and collaborating parts, the arches (A) and the super-structure of the canal (B) (see Figure 2).



Figure 1. Pile numbering highlighting the P2 pile in which the failure was detected, upstream and downstream damages.

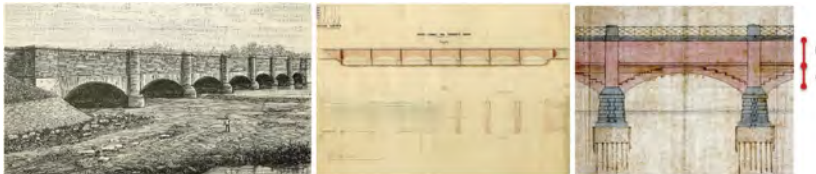


Figure 2. Bridge on torrent Cervo after construction around 1863, drawings of the original bridge project.

The arches are of the segmental arch type ($\alpha=40^\circ$, $2\alpha\leq 120^\circ$), with a clear span of 15 m and a deflection of about 2.66 m. The thickness of the arch is equal to 1.0m in the impost section and 0.7m in the key section. The “external” arch has the arrangement of the front of the bricks of the “thickness” type. The “external” arch is characterized by a stepped extrados. The “external” arch is surmounted in elevation by a “head wall” 1.5m thick which rises with a variable height from min 0.25m in key to max 2.9m in stack axis, the top of this wall is edged externally by a horizontal shutter $h=0.15\text{m}$ protruding from two bricks. This upper level coincides with the bottom level of the channel, note how this external marking had in the past the purpose of distinguishing the substructures of the arch from the wall elevations of the banks of the channel in order to understand the position of any potential water infiltrations.

The “internal” arch is hypothesized to have been built as frequently in “thickness”. The “internal” arch is on the top filled with light material with a maximum height of 0.41m in correspondence with the pier axis and a minimum of 0.1m in correspondence with the key section.

It should be noted that in these types of segmental arches ($\alpha=40^\circ$, $2\alpha\leq 120^\circ$) the horizontal line (Figure 3) passing through A and A' must always be between the two horizontal lines for points C and D. This constraint derives from one of the stability conditions of the arches, for which they need to contain in its thickness at least one thrust line (J.F. Hater, Heyman J.). The volume above the masonry thickness of the “internal” arch is characterized by fillings in lightened material. In particular, in the pier axis there is a particular elliptical lightening brick-element (elliptical internal cavity 3.5m x 1.4m). The superstructure of the canal consists of a massive “bank wall”, which stands out from the “external” arch, 1.5m thick and 3.5m constant in height, which performs the function of lateral bank. The bottom slab of the channel, for waterproofing purposes (G. Curioni), is made of a lower layer of greasy concrete 0.1m thick and a bed of bricks 0.15m thick.

In correspondence of the pier axis, the elevation made up of the “head wall” and the “bank wall” is locally reinforced by a semicircular protruding masonry stiffener with a diameter of 1.68m. The cross section of the channel is about 3.5m in height and 20.7m in width. At the time of the collapse, the water level of the canal was about 2.5m height.

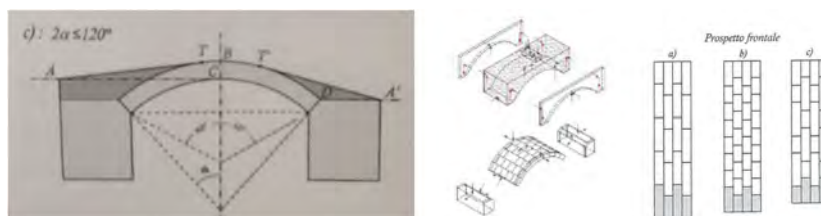


Figure 3. Geometry of structural stability of the arch type and 3D view of the constitutive elements of a bridge arch and the mutual forces exchanged between the elements.

2.2 Masonry mechanical properties of the old bridge

Information has been found in the literature regarding the resistance of the masonry of the original construction of this bridge. In particular G. Curioni (G. Curioni, 1864-1884) reports the essential data to define the strength of the masonry: the tests ordered by the Civil Engineering Inspector on the bricks used for the construction of the Cavour canal (1863-1866) are reported. Regarding the strength of the mortars produced at the end of the 19th century, the same source (G. Curioni, 1864-1884) collected data on compressive strength, the density of mortars and cements and tensile strength.

According to the historical data the compressive strength of the bridge bricks was between 100 and 150 kg/cm², the compressive strength of the bridge masonry mortar was found between 70 and 140 kg/cm². As far as the “bank wall” is concerned, the literature (G. Curioni, 1864-1884) suggests to guarantee the hydraulic seal “... it is better to make them with good materials and with excellent hydraulic mortar; and the joints of the internal walls must be carefully grouted, or covered with a general plaster of good cement.”

2.3 Preliminary damage assessment of the old bridge

Just after the damage event, it was possible to make some observations regarding the general state of conservation of the bridge and a possible interpretation of the instability that occurred following the flood on 2nd-3rd October 2020. It could be observed that some extended superficial areas of the masonry of the bridge, both on the intrados of the arches and on the “head walls” and at the base of the “bank walls”, exhibit whitish spots which can be seen against the red-brown color of the masonry. These surface defects in the masonry would appear to be “efflorescence”, or infiltrations of water coming from the canal which has passed through the capillarity of the masonry bringing sulphates, carbonates or nitrates into solution. When the water reached the external surface of the masonry it evaporated, depositing the salt crystals on the surface.

The actual conservation/consistency of the base layer of the canal itself, originally envisaged in concrete and masonry, cannot be seen from the photos inside the canal. It is probable that this finish has eroded over time due to the flow of water and reduced in thickness (H bank wall 3.5m).

Pier P2 showed a subsidence of foundational origin on the upstream side (approx. 40cm) and downstream side (approx. 5cm), having occurred in river flood conditions with high material transport. It was presumed that the foundation had undergone erosion due to undermining of the basis. From the photos, the subsidence was accentuated at the upstream end of the pier, thus highlighting that the erosion phenomenon occurred in the point most subject to the hydrodynamic thrust of the river. The kinematics of the differential settlement between the upstream and downstream spurs highlights the occurred rotation of the pier/foundation along the longitudinal axis of the bridge. This configuration would in theory be congruent with two possible scenarios: either following shear damage to the pier (in an intermediate section) or with an overall rigid rotation of the pier. In this last case the average vertical settlement of the pile would be

22.5cm. This aspect can be ascertained by inspecting the masonry face of the P2 pile shaft. In both cases, the settlement resulted in a horizontal crack in the “head wall”, symmetrical with respect to the axis of pier P2 or on span P1-P2 and P2-P3, at the same height on both sides or at the top at approximately 2- 4 courses of bricks below the protruding horizontal shutter which is placed at the bottom level of the canal. The horizontal lesion on the upstream side is much more significant and denotes the lack of a portion of masonry at the kidneys of the “external” arch and the “head wall”. The following Figure 4 illustrate the instability scenario visible at both ends of pier P2.



Figure 4. Horizontal crack in the “head wall” downstream (a), and wide horizontal crack in the “head wall” and missing portion of the masonry at the kidneys of the “external” arch and the “head wall” upstream (b).

It was also observed that in the upstream elevation the lack of masonry at the kidneys of the “external” arch was probably motivated by the activation of a kinematic system linked to two concomitant unfavorable factors: the collapse of pier P2 has generated a geometry variation in the arc, this has favored the kinematic mechanisms of the arch in which it is envisaged to open a joint on the extrados, the detachment from the superstructure of the channel at pier P2 has in fact determined a change in the vertical load bearing mechanism, which is now asymmetrical on the “external” arch, which is in fact subject to the load only in the half span towards pier P1 and P3.

The sum of the two effects was unfavorable for the “external” arch, which therefore activated a kinematic mechanism with two hinges close to the kidneys. The “internal” arch behaved more favorably as it suffered the effects of only the yielding but not that of the asymmetry of the vertical load, given the distribution of the water pressures of the channel which are always uniform along the span. From the internal photos of the channel in correspondence of the bottom slab near the P2 pier, a differential settlement was detected with evident openings, such as to have captured the water inside the bridge. This flow involved the inside of the elliptical lightening present above the pier, between arch P1-P2 and P2-P3, which therefore probably resulted in being flooded (cavity) and eroded (lightening material). However, this configuration was statically balanced and this is evident from the serviceability of the channel, which remained operational for about 24 hours after the instability occurred. It was therefore necessary to define the failure mechanism that was occurred: the subsidence caused on the downstream, with length about 5m, a single horizontal crack in the “head wall”. The subsidence caused a horizontal crack of about 40cm on the upstream side in the “head wall” and loss of the portion of masonry relating to the “external” arch. It can be observed that the order of magnitude of the settlement (40cm) is equal to the thickness of the backfill on the pier axis (41cm), this produces a very critical effect on the arch because the absence of two straight lines A and A’ (see Figure 3) falling between points C and D inevitably produces the loss of the funicular of the loads. In essence, the pronounced yielding activated a direct traction in the section of the “external” arch causing a partial collapse for a stretch of about 2-3m at the kidneys, or with a kinematic mechanism that opened an arch lesion on the intrados. The width of the “external” arch that collapsed could be estimated (CNR-DT 213/2015) at about 2.9m ($b = d + 2 \times s = 1.5m + 2 \times 0.7m = 2.9m$), not more different by 1.5m that is the footprint of the load bearing wall at the top (head and bank). The subsidence caused a difference in height on the bottom of the channel, causing a local failure of the waterproof bottom layer.

Considering the failure mechanisms that have occurred and the current condition of equilibrium of the structure, the exploitation of the following currently active resistant mechanism was assumed. The “external” wall and the “bank” wall constitute a very rigid element which, given the “loss” of support on pier P2, constitutes a structural element with a high wall which develops on a double span (from P1 to P3, i.e. span $L=32m$). The effective span could be intermediate, about 25m taking into account the arc effect on pier P1 and P3. The “external” arch is partially interrupted in

correspondence with the ceded pier, however highlighting how the remaining intact stretch is joined to the “head” wall.

3 DETAILED BRIDGE INSPECTION

With reference to the recent “*Guidelines for risk classification and management, safety assessment, and monitoring of existing bridges*” (CSLP 04.17.2020) following the instability, a detailed inspection of the bridge has been carried out. This inspection had the purpose of acquiring information useful for deepening knowledge of the phenomena of deterioration and the structural condition of the work, since exceptional events such as floods have occurred and have affected the stability of the work. The detailed inspection has been developed in direct contact with the structures, and have been completed by non-destructive tests. The inspection has been carried out by certified bridge inspectors and the results of the structural inspection have been implemented in a B.I.M. model specifically set for inspection data, that could be useful to compute statistical frequency of different type of masonry structure defects.

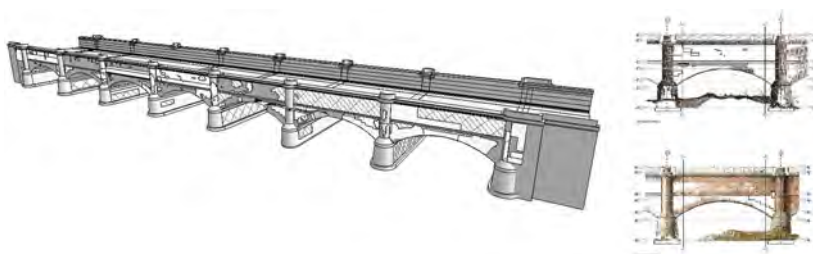


Figure 5. B.I.M. for the detailed bridge inspection.

4 SURVEY, INVESTIGATIONS AND STRUCTURAL MONITORING

In order to implement the structural assessment of the bridge the following studied have been developed: geometric survey of the bridge, with the aim of reconstructing the current geometry of the bridge with high precision and acquiring the photographic map of the surface; structural investigation plan on the masonry, with the aim of acquiring an adequate level of knowledge on the mechanical characteristics of the masonry; structural monitoring plan, with the aim of acquiring kinematic information of the spans of the bridge in the current configuration, during the works and the reconstruction phases, up to the final operational phase.

A series of non-destructive and destructive tests had to be carried out on masonry bridge structure. These types of tests are used to obtain indications on the physical-mechanical characteristics of the materials and their state of degradation. These types of investigations have been carried out, where possible, in as many points as possible and on all the structural elements. The objective of the structural investigation plan was to obtain the following characteristics of the materials from tests in situ or in the laboratory: physical parameters of bricks and mortar (specific gravity and porosity), mechanical parameters of brick, mortar and stone (compressive strength), mechanical parameters of the masonry (compressive strength, shear strength, elastic modulus), stress and deformation state of the masonry, chemical parameters of bricks and mortar, characterization of surface degradations.

For the bridge project of rehabilitation, it was implemented a structural health monitoring system, which periodically allows the measurement of the displacements in three directions S_x - S_y - S_z of a series of significant points of the bridge in the spans subject to instability and neighboring as well as monitor the opening of cracks /main fissures. The information provided by the monitoring could be used with the following purposes: verify the trend of the global and local displacements of the structure over time in order to intercept any premonitory signal of a worsening of the deformations/damage/cracking regime; verify the stability conditions of the bridge during the safety and subsequent restoration phases; verify the final testing phases.

5 STRUCTURE REFURBISHMENT AND DURABILITY ASSESSMENT

The bridge structural project has been developed considering different steps: a first intervention will concern the safety works, to secure the bridge during the construction period (by the use of external metal structures, contrasts, wooden structures); a second intervention for the definitive restoration and reinforcement works of the structure/spans pertaining to pier P2; implementation of a real case load testing of the bridge span object of restauration works; after the dismantling of all provisional works, additional arches strengthening where finally developed.

The overall safety of the bridge was implemented through a series of interventions aimed at ensuring the local and global stability of the bridge in the affected area. In particular, since these are main vaulted masonry elements, such as arches, and wall elements, such as walls, the provisional works for safety are arranged in order to prevent any type of kinematics: for walls overturning and/or buckling, for arches loss of shape and/or detachment of ashlars.

The design for the safety of the bridge were belting with steel ropes for the walls of the elevations, with the possibility of complete winding of the cross section of the span according to a sequence of closed ropes placed at 1-1.5m center distances. This solution was expected to transversely counteract the base and the top of the bank walls inside the channel, by means of steel truss beams. In addition for both the “external” and “internal” arches: the insertion of steel ribs.

Based on the analysis of the state of stress of the structure in pre- and post-instability conditions, it was highlighted that the stress rates in the masonry were still within acceptable limits. However, the increase in the traction regime was the most critical element and the commissioning works have the purpose to mitigate the risk of activation of new potential local or global collapses.



Figure 6. Bridge safety works: belting with steel ropes and internal channel steel truss beams, internal steel ribs similar shape to the wooden type of the original arches construction period.

Thanks to the implementation of the safety measures, it was therefore possible to proceed with a reconstruction and consolidation of the bridge with the following main works:

- Consolidation of the bearing ground of the foundations, for pier P2 and then P1-P3. This intervention was also extended to all the remaining foundations in order to avoid the repetition of future similar potential settlements.
- A new connection between pier P2 and the “head wall”, by means of castings with light-weight concrete and clogging of the crack pattern. In order to pursue a monolithic nature with the existing structure, all the massive reconstruction castings of masonry volumes was provided for the creation of preventive grouting with reinforcing bars, suitably arranged on the sound portions of the masonry.
- Jetting, with ultra-light weight concrete, and reconstruction of the bottom of the channel above the “internal” arches, after checking and repairing the filler/backfill layers on the extrados of the arches. New waterproofing of the horizontal and vertical surface of the channel.
- Application of FRCM strengthening at the lower bound of the arches, to increase bending moment capacity ad the end of construction works.



Figure 7. Bridge strengthening: arches renew by cast in situ of lightweight concrete, FRCM intrados of arches, load test on the strengthened spans of the channel with water intake.

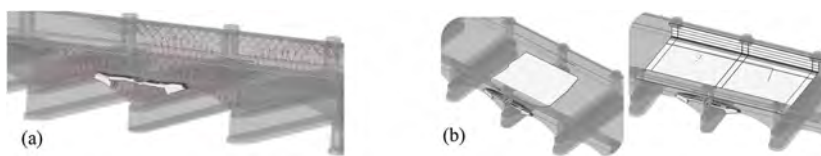


Figure 8. Bridge strengthening and renew by net of carbon bars drilled inside the masonry walls, sealing and stitching with stainless steel bars of main arch cracks (a), ultra-light weight concrete to fill and stabilize the deck slab, new waterproofing (b).

The numerical analyses carried out on global arches (internal and external), in the P1-P2-P3 spans, made it possible to evaluate the collapse modes of the same both in terms of kinematics adhering to the current conditions of instability and in terms of the value of the vertical displacement that the pier P2 can bear before inducing the collapse of the arches, i.e. the ultimate failure of the system.

The result of the collapse calculation allowed to characterize the ductility value of the vertical displacement of the pile in 1.27, a number which denotes limited plastic reserves of the structure. Considering the asymmetrical conditions of the settlement, caused by the rotation of the pile, the potential of activation of transverse collapse mechanisms was also investigated. However, this study, although approximated since it does not take into account large displacements, has shown that the activation of this mechanism was always secondary with respect to a longitudinal mechanism, therefore it would not be critical for the system (unless large displacements occur). In conclusion, having clarified the modalities of current instability and the possible modalities of progression of the mechanism up to the global collapse, it was estimated (by energy approach) the work that was necessary to be done by the reaction of the pile P2 to produce a global collapse with reference to a vertical translational kinematics. The admissible limit of the average incremental vertical settlements (therefore in the bridge axis) of the P2 pile foundation was estimated, taking into account the variability factor assumed for the materials (30%) and a safety factor (min 1.5): $\Delta Z = 4.0\text{cm} \times 0.7/1.5 = 1.8\text{cm}$

By the arch strengthening, mainly due to cracks bridging and FRCM intrados, the critical average vertical displacement was increased by almost 28%: $\Delta Z = 5.0 \text{ cm} \times 0.7/1.5 = 2.3 \text{ cm}$

All the new construction materials used for the project were subject to a detailed “durability” assessment with the objective to minimize the interaction with the old bridge structure (mainly because of the high level of humidity of the masonry due to the near river and upper channel), starting from an environmental and existing material tested performance and physical/chemical properties characterization.

6 SERVICE LIFE RESIDUAL ASSESSMENT

The service life of structures intended for civil use is influenced by the surrounding environment and consequently by various degradation phenomena which lead to a decrease in structural capacity over time. Considering the specific case of the Cavour canal bridge, through empirical observation in the field and bibliographic research relating to degradation phenomena that affect masonry structures, the following have been identified as the main degradation phenomena: degradation linked to Freeze-Thaw cycles; degradation linked to efflorescence phenomena.

Once the degradation processes and their influence on the structural capacity were characterized, it was important to evaluate the evolution of structural reliability over time and the achievement of limit levels of reliability for which the structure no longer satisfies certain requirements. The Monte Carlo simulation was used to consider and integrate the uncertainties related to the characteristic parameters of the materials, specifically the compressive strength of the masonry f_c . In the specifics of this analysis, the number of Monte Carlo simulations performed was 10^7 .

Limit states related to the operating stresses and limit states related to the ultimate flexural capacity were analyzed for the main structural elements of the bridge Cavour. In each of the cases the structure has shown good structural reliability up to the exceeding of the reliability limits proposed by various codes. In particular, the thicknesses available in the critical sections of the masonry seem to exhibit conditions of maintenance of performance in relation to the phenomena of degradation minimal for several hundred years. Therefore, it was clear that the future critical conditions of the structure will probably not depend on environmental phenomena that have been

examined. It was therefore recommended to: carry out periodic inspections of the structure, to monitor the trend of the main structural deterioration, the geotechnical conditions of the abutments, the state of integrity of the canal waterproofing; maintain constant knowledge of the hydraulic conditions of the river (Cervo turrent) in terms of geometry of the seabed, i.e. conditions of hydraulic risk with respect to all spans and related foundations; check for any damage following seismic events or extreme climatic events. It was important to highlight that the forecasts in terms of time values do not represent deterministic forecasts but are connected to a probability of exceeding the limit state and depend on multiple factors, such as the time interval considered for the analysis (in this case equal to 100 years) and the value chosen for the reliability limit.

7 CONCLUSIONS

Advanced studies and works were developed with the scope to save and quickly put in service by renew and strengthen a large damage occurred to the 150y old masonry bridge. The bridge showed an expected “robustness” structural behavior, making possible the doubling of the span of the deck masonry channel by foundation collapse in pier P2. A deep historical review of the bridge, the detailed inspection, a large material testing investigation could develop a project to put in safety the damaged structure with advanced materials thanks to the durability assessment. The service life (residual) assessment could show the importance in this massive masonry bridge of hydraulic river behavior and the exposure to extreme natural events as the most important risk exposure. The large use of BIM methodology in inspection mapping and as-built design could provide to the infrastructure owner the best opportunity to take future maintenance strategy.

ACKNOWLEDGEMENTS

The authors would like to acknowledge the value collaboration with contractor Luigi Notari SpA (Milan) and the construction field director Ing. Paolo Pancini, the geotechnical designers Ing. Achille Balossi and Ing. Elena Rovetto, the collaboration with materials suppliers by Mapei, Laterlite and Ruredil, the structural health monitoring by Field/Sisgeo and the testing (in situ and labs) of materials/3D laserscan by TecnoIn. The authors would also like to acknowledge the technical support of Ing. Francesco Arecco and the collaboration with University of Pavia Prof. Andrea Penna for advanced FRCM testing on construction site and laboratory.

REFERENCES

- Camilla Torre, *Ponti in Muratura*, dizionario storico-tecnologico, 2003
CNR-DT 213/2015 - Istruzioni per la Valutazione della Sicurezza Strutturale di Ponti Stradali in Muratura
Drysdale et Al, “*Masonry Structures: Behaviour and Design*”, 1994.
Eurocode 6. Progettazione delle strutture di muratura.
Fagerlund, G. “*The critical degree of saturation method of assessing the freeze/thaw resistance of concrete*”, Materials and Structures, pp. 217–230, 1977.
fib Task Group 5.1, Bulletin No. 22: Monitoring and Safety Evaluation of Existing Concrete Structures: State-of-art Report, 2003.
Giovanni Curioni, *L'arte di fabbricare, ossia Corso completo di istituzioni teorico-pratiche per gli Ingegneri, per Periti in Costruzione e per Periti Misuratori* – Costruzioni Civili, Stradali ed Idrauliche, 1864–1884
Heyman J., *Il saggio di Coulomb sulla statica*, 1999
International Organization for Standardization (ISO) “*General Principles on Reliability for Structures*” 2015.
Probabilistic model code, Joint Committee on Structural Safety, 2007.
Vademecum STOP – Schede tecniche delle opere provvisorie per la messa in sicurezza post-sisma da parte dei vigili del fuoco. Ministero dell'Interno – Corpo Nazionale dei Vigili del Fuoco. Nucleo Coordinamento Opere Provvisorie. Aprile 2010.
Vicente N. Moreira et al., “*Reliability-based assessment of existing masonry arch railway bridges*”, Construction and Building Materials, vol. 115, p. 544–554, 2016.
Vilma Ducman et Al., “*Frost resistance of clay roofing tiles: Case study*”, Ceramics International, vol. 37, p. 85–91, 2011.
Zuhua Zhanga et Al., “*Efflorescence and sub-efflorescence induced microstructural and mechanical evolution in fly ash-based geopolymers*” Cement and Concrete Composites, vol. 92, p. 165–177, 2018.
Xiao Yao et Al., “*Compressive strength development and shrinkage of alkali-activated fly ash–slag blends associated with efflorescence*”, Materials and Structures, vol. 49, p. 2907–2918, 2016.

High performance computing methods for concrete surface damage identification and prevision in service highways tunnel concrete linings

I. Vangelisti & C. Beltrami

Lombardi Ingegneria S.r.l., Milan, Italy

G. Rozza

SISSA, Mathematics Area, mathLab, Italy

ABSTRACT: visual inspection of highways bridges, viaducts and tunnels has nowadays a crucial role in infrastructures life-cycle management. In this paper two visual inspection numerical support methods are discussed. Both methods aim to reduce direct and indirect costs of visual inspection and to automate the inspection procedure. This is possible thanks laser scanner images of the tunnel, which are quickly acquired with remarkable decrease of money investment and with no need for *in loco* presence of engineers and then used as input for the calculations. The former method is based on Dynamic Modal Decomposition and it uses laser scanner acquisition to predict damage evolution. The latter one is based on a convolutional neural network and it aims to evaluate damage gravity according to a predefined severity scale. Both methods have been tested on Italian highways tunnels images.

1 INTRODUCTION

In order to guarantee the full functionality and safety of highway tunnels, it is necessary to carry out accurate inspections at regular intervals of time, so that to the highways manager is able to identify the structures degradations and provide for their rapid repair. The inspection process is costly and time-consuming; it requires partial or total closure of the analyzed asset, which may have a detrimental impact on the traffic flow, resulting in an increase of car accidents rate. So, it may be of interest to develop tools that make it possible to promptly and automatically identify which are the tunnels characterized by the highest risk level, in order to optimize inspections and maintenance, giving priority to these assets which present the most important safety issues.

In this context, methods capable of predicting the temporal evolution of the various defects present in a gallery can play a fundamental role. Among them, techniques such as Dynamic Mode Decomposition (DMD) and its variants are particularly promising, given their qualitative and quantitative predictive capabilities and the few necessary basic inputs.

The first aim of this paper is to carry out a preliminary study on the applicability of the DMD method to the problem under investigation; this may clarify the type of input data to be used and any problems encountered in their gathering, identify the necessary preprocessing operations and build one prototype pipeline that can be used as a starting point for more detailed future studies. The preliminary procedure is hereby applicated to three tunnels of various Italian Highways.

In the context of inspections and maintenance optimization and prioritization, it may be of interest to study and develop evaluation tools which can automatically highlight the tunnel lining critical areas. Appropriate neural networks may allow a quickly and accurately estimation of these areas, starting from a few inputs. Thus, the second objective of this paper to study prototype neural networks application to speed up and to automate the inspection process, highlighting potential limitations and fallacies of the proposed method.

2 DYNAMIC MODE DECOMPOSITION PREDICTION AND RECONSTRUCTION

2.1 *Mathematical framework*

The DMD is one of the most recent and universally applicable mathematical models and has made it possible to obtain very satisfactory results in various fields. The base idea of the DMD consists in considering a series of observations of a system at regular intervals that can be used to assemble a linear operator which approximates the time evolution between two successive observations; the modal analysis of the operator can then be used to obtain predictions of the future state of the system, or more generally, to reconstruct the state at a given instant.

To evaluate the effectiveness of the DMD method applied to the problem under investigation, various examples for the tunnels at disposal will be considered, are chosen with the aim of exploring different and complementary scenarios. The analysis was performed using the PyDMD package developed by Demo et al. (2018).

2.2 *Application of DMD*

Input data for DMD method are images derived from laser scansion of the tunnel lining. For tunnel T1 are available eight scans from 2006 to 2017 and for T2 five scans from 2012 to 2015.

The critical analysis of laser scanner images highlights many issues:

- Due to the maintenance procedures provided by the highways manager on selected lining portions, many defects may not show a general worsening year after year;
- Due to different environmental conditions or to different laser scanner used for the images acquisition, the same lining portion may be characterized by different color shades year from year. This may affect the input process of the neural network;
- For the same reasons, the same lining area or segment may be characterized by different dimensions in different scans.

The reported issues imply a partial loss of data preprocessing automation, given that only a manual selection can underline which are the not affected lining portions that can be used as input.

Four scenarios are hereby reported. The first one deals with DMD application to T1 tunnel without any preprocessing. DMD is here used with a dual purpose: reconstruction of the system state in 2009 and prediction of its state in 2011. Figure 1 shows the obtained results.

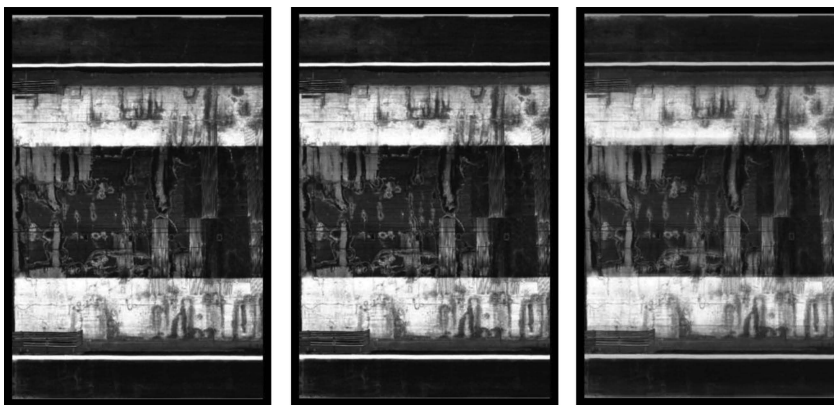


Figure 1. Lining scan: original (left), DMD reconstruction (center) in 2009 and DMD prevision for 2011.

The reported results show how DMD can replicate the state system in 2009 with high accuracy, while the obtained images are lacking in accuracy and focus for 2011. This is caused by the lining variation in dimensions and colors in the scans year from year.

In the second scenario DMD is applied with a focus on a defect located in tunnel T1 which is present in all the scan between 2006 and 2017 and which does not show a significant evolution

in the reference period. The defect shows, however, oscillation of the color shade, color brightness and relative position in the scan. These issues can cause blurring in DMD predictions and hence it is necessary to apply preprocessing techniques, which consist in i) manually isolating the region containing the defect under investigation ii) rescaling it to a reference size iii) and standardizing its brightness via standard techniques (i.e. histogram equalization).

Figure 2 shows DMD predictions after preprocessing.

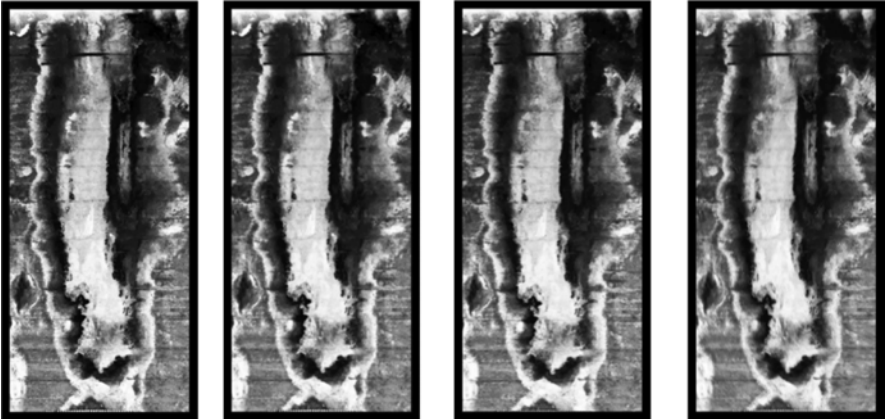


Figure 2. DMD prediction for the defect under investigation: one year (left), two years (center) and three years (right).

Thanks to preprocessing, the obtained images are clearer and sharper than those shown in Figure 1. DMD prediction, besides, do not show a significant variation year from year, according to the input data. The general prediction stability can also be highlighted with reference to the modal dynamics detected by DMD, which are shown in Figure 3. Only an almost constant mode (blue line) contributes to the long-term prediction, while the contribution of the other modes tends to quickly to zero.

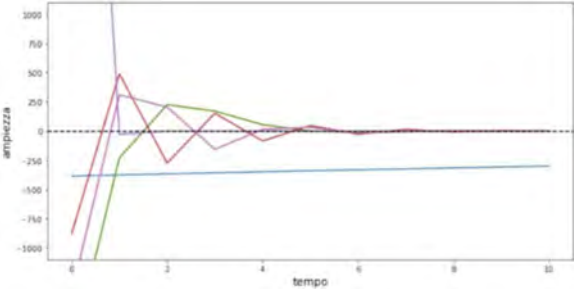


Figure 3. DMD images detected dynamics.

Let's now focus our attention on a significant worsening trend defect, detected in tunnel T2 and reported in five scans. Again, preprocessing is applied in order to limit the detrimental effects described before. Since the area of the defect is very limited, the image resolution will consequently be low; it is therefore not possible to evaluate the sharpness of the reconstructions (Figure 4) or of the predictions (Figure 5), but only verify that they evolve in time. It is interesting to note how in Figure 5 the DMD predictions actually change year from year, differently from what obtained in the second scenario; this evolution is also confirmed by the dynamics graph in Figure 6, where, in addition to the usual constant mode (in blue), other modes, which present a periodic dynamic, can be underline, although this dynamic is probably only partially correct (as shown by the inexact reconstruction of the year 2015 in Figure 4) given the limited number of scans.

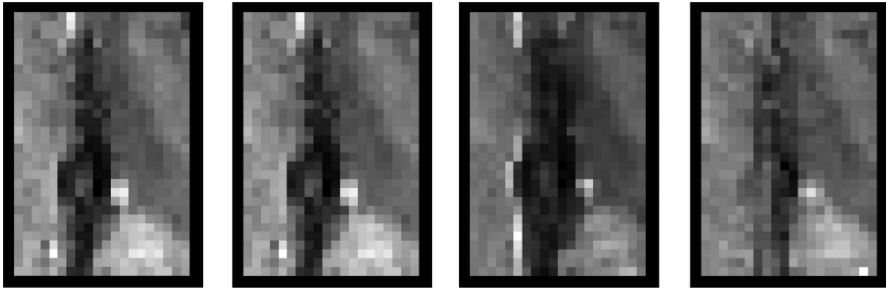


Figure 4. Defect in tunnel T2: 2014 original and DMD reconstructed (left) and 2015 original and DMD reconstructed (right).

This third scenario therefore confirms the potential applicability of the DMD method to determine the temporal evolution of defects in tunnels, once the appropriate preprocessing interventions have been performed (when necessary), even if to reach a high likelihood of the predictions, a sufficiently high number of observations is required.

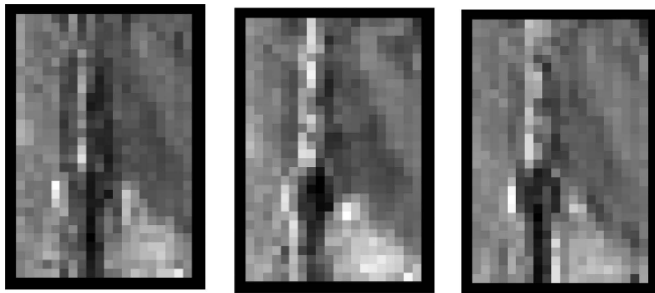


Figure 5. Tunnel T2 defect prediction: one year (left), two years (center) and three years (right).

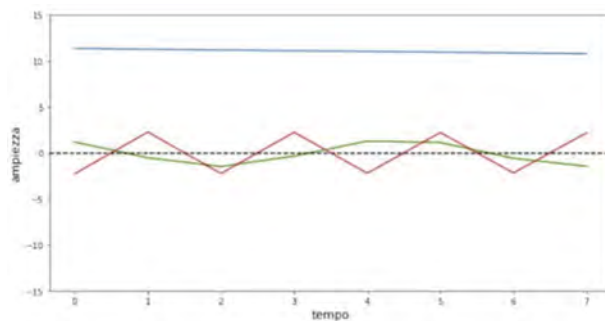


Figure 6. DMD images detected dynamics.

3 TOWARDS MULTI-LEVEL NEURAL NETWORK DEGRADATION IDENTIFICATION AND CLASSIFICATION

3.1 *Neural network I: Detecting lining element*

3.1.1 *Training and neural network structure*

Images derived from the scans of five tunnels, named as T4, T5, T6, T7 and T8 have been used in the neural network I training; the first four tunnels have been used for the training while the last tunnel has been used for a training quality check.

The neural network architecture is known as UNet, based on a ResNet-50 type structure. The U-Net architecture is divided in two parts: initially the input images pass through a series of so-called convolutional layers (basically a ResNet-50), that reduce their dimensions allowing, at the same time, to capture the most important characteristics for the segmentation problem; subsequently, a series of transposed convolutional layers brings back the input images to to their original size, keeping intact the information about the detected features. Therefore, the output of a U-Net will simply be the same input laser scan, accompanied by additional information useful to identify the type of defect to which a given pixel belongs. The network, implemented in Python3 through the fastai library (fastai library, Howard & Gugger (2020)) based on PyTorch (Paszke et al. (2019)) was trained for a period of twenty epochs (i.e. twenty iterations on all the data), using a learning rate parameter varying from 10^{-6} to 10^{-5} depending on the depth of the layer. As said before, at the end of the training process, the T8 scans were used to evaluate the quality of the obtained results.

3.1.2 Results

Examples extracted from the training are shown in Figure 7.

Training results are quite satisfying. Though a limited database was involved in the process, the neural network I was able to identify with a good definition the jet fans and at a sufficient level deterioration and water ingresses. Increasing the input database would consequently improve the network's prediction capability.

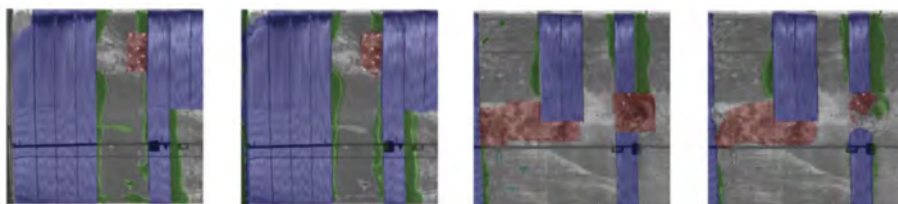


Figure 7. Original and neural network reconstructed images of concrete lining extracted from the training process.

3.2 Neural network II: Classifying the degradation severity

3.2.1 Training and neural network structure

A second neural network is hereby introduced with the aim of classifying the deterioration level starting from an images database. Two degradations categories are introduced: NU class, which involves 2, 2E and 3 level according to IQOA classification, and U class, which involves high risk level defects as 3U and S.

Thus, the presented procedure goal is to identify the lining degradation with a first neural network (semantic segmentation) that uses the laser scans and *classify* their severity with a second neural network that uses degradation images gathered during previous visual inspections.

3065 images from four tunnels, named as T9, T10, T11 and T12 have been used by the neural network II, 2465 during the training phase and 600 for a quality check. All the images, randomly divided for the two goals, have been scaled to the same size. These images are characterized by many critical aspects:

- the IQOA class is usually spray-marked on the lining surface and its presence in the images could negatively affect the functioning of the neural network, since it could not learn anything useful about the characteristics of the defect itself but would make its predictions by simply reading the class in the image. This problem could be solved by considering black/white images rather than color ones; an equally satisfying solution consists in transforming the images from the RGB colour representation to HBS or HLS and selecting only the B or L channel;
- defects of the same class of severity can be reconducted to different categories, such as alterations of fractures; conversely, defects of the same category can have different class of severity. Both issues affect classification process and can be solved with an appropriate cataloguing of the images, not only based on the severity but also to the type of defect.

The architecture of the neural network II is known as ResNet-152: by passing the images through a series of 152 convolutional layers, which reduce their size while highlighting their main features, this network learns to recognize the most important details for classification in a photograph, and based on these elements provides a prediction of the severity of defects. Four ResNet networks have been considered, with the aim of covering all the cases of interest: color images with U/NU classification, b/w images U/NU classification, color images with fine IQOA classification (2, 2E, 3, 3U and S) and finally b/w images with fine IQOA classification.

The same training process was performed for all the cases, again through the fastai library (fastai library, Howard & Gugger (2020), Paszke et al. (2019)) and required a period of eighty epochs (i.e. eighty iterations on the entire dataset), divided in four phases of twenty epochs each:

- In the first phase, the network is initialized with parameters obtained through a pre-training on the ImageNet dataset; during the twenty epochs of training, performed with learning rate equal to 3×10^{-4} , only the parameters of the last layer of the are changed, while those of all the previous layers are kept the same. This procedure, known as transfer learning, is usually used to reduce the training time, as it makes it possible to start from a set of parameters that are already able to recognize basic structures in the images and which only need to be adapted to the problem under investigation. In addition, during this first phase, the height and width of the images are halved, and they will therefore be 288×384 in size;
- In the second phase, known as fine-tuning, the parameters of all the layers are modified, but using a lower learning rate that varies from 3×10^{-6} to 3×10^{-5} depending on the depth of the layer, providing as input images of size 288×384 ;
- The third phase is identical to the first, but the size of the images corresponds to the original one (576×768) and the initialization parameters are those obtained at the end of the second phase;
- The fourth phase is identical to the second, except for using images of size 576×768 .

Changing the images size during training is a technique known as *progressive resizing*, and it helps to speed up learning due to the smaller data size and it induces the network to detect defect features that are not scale invariant. The simultaneous use of *transfer learning* and *progressive resizing* has produced better results for many Artificial Intelligence application and has now become a standard procedure. Finally, the so-called *data augmentation* technique was also applied: this means that during training, transformations were randomly applied to the photographs (rotations, enlargements, changes in brightness and contrast) to make sure that the network predictions are less sensitive to such variations, which are not decisive for classification purposes.

3.2.2 Results

U/NU classification is firstly considered. Starting from a database of 45% NU defects and 55% U defects, ResNet-152 networks are able to reach 93% of correct previsions for color images and 82% for b/w images. Figure 8 shows the confusion matrixes for this first classification.

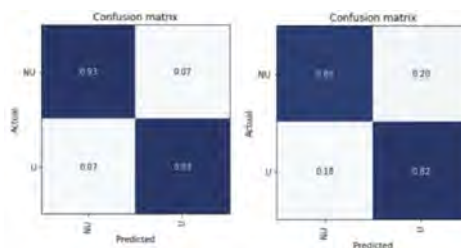


Figure 8. U/NU classification results.

According to these results, it could be easily observed that the neural network gives better results when working on color rather than on b/w images but obtaining such high correct prediction rate may raise some suspicions, given the goal complexity, according to the aforementioned possibility that the network only reads the writing included in the images. With the aim of validating the procedure, it is therefore crucial to use methods, such as the so-called *heatmap*

technique which allow to highlight what the network learnt and on which elements it based its prediction. An example of heatmap application is reported in Figure 9. It is clearly shown that the network trained on color images focused mainly on these regions spray-marked, while the one trained on b/w images, focused mainly on the regions where the defect is present.

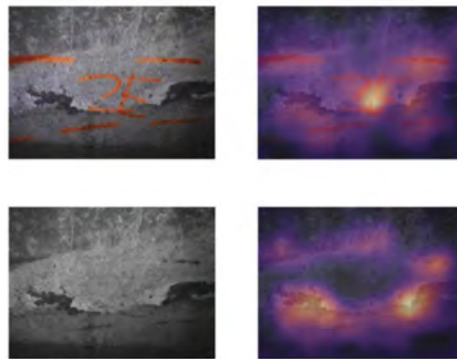


Figure 9. Heatmap for U/NU classification: color images (top) and b/w ones (bottom).

Thus, it is possible to conclude that the high correct prediction rate obtained by working on color images is simply correlated to the spray inscriptions detected by the network in the images; the network learnt to correlate the spray inscription to the degradation severity. On the other hand, working on b/w photographs provides more reasonable and reliable results since the network is less influenced by the spray writing.

As shown by the confusion matrixes in Figure 10, the network is able to reach an unrealistic 92% correct prediction rate using color images and a 69 % correct prediction rate is instead obtained by working on b/w images. Figure 11 provides for the related heatmap.

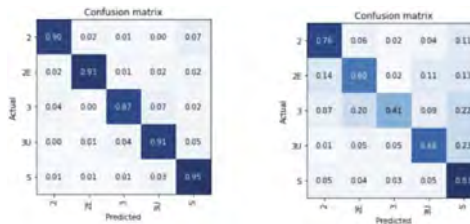


Figure 10. Confusion matrixes for fine IQOA classification.

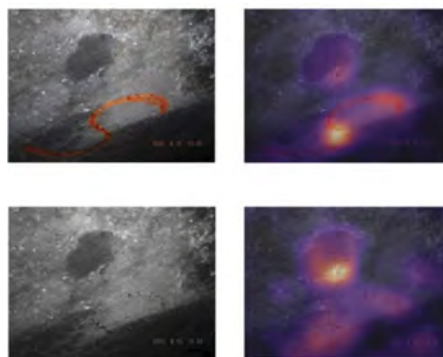


Figure 11. Heatmap for fine IQOA classification: color images (top) and b/w ones (bottom).

4 CONCLUSIONS

In this paper, two high performance computing methods possible application for highways tunnel concrete lining damage identification, classification and prediction have been studied. DMD can be helpful in degradation evolution prediction, which is a crucial goal for the prioritization of maintenance and rehabilitation interventions. Starting from regular time-spaced observations of a system, DMD assembles the linear operator which approximates the system evolution between two successive observations. Then, by the modal analysis of this operator, it can develop prediction on the future states of the system. DMD have been applied on a set of laser scans derived from different Italian highways tunnels. It has been shown that, with a proper pre-processing of the scans, DMD is able to reconstruct and predict the lining defect evolution, even if, in order to reach a high likelihood of the predictions, a large number of observations is required.

In the second part of the paper, a system of two neural networks has been analyzed. It can help the highway manager to obtain detailed information about the lining defects, without visual inspections, but simply by the proper utilization of laser scan and defects images, with a considerable time and money saving. The first neural network detects the lining elements while the second network classifies the defects severity.

Finally, by the application of DMD and neural networks methods, starting from laser scan images and defects images gathered during the previous inspections, so with no need for further visual inspections on the highway's tunnels, it is possible to obtain satisfactory information about the lining defects severity and evolution. This process allows to obtain strategic information for the management and prioritization of maintenance and rehabilitation, with a considerable money and time saving compared with the classical visual inspection-based processes.

ACKNOWLEDGEMENTS

The authors would like to acknowledge the technical support of SISSA mathLab and the team of Dr. Antonio Sciarappa (and the valuable work of his PhD thesis) and researchers Prof. Giovanni Stabile, Dr. Nicola Demo, Dr. Marco Tezzele. The authors would also like to acknowledge the technical support of Eng. Francesco Arecco.

REFERENCES

- CETU – Centre d'Etudes des tunnels, 2015. Livre 2: guide catalogue désordres.
- Demo, N. et al., 2018. PyDMD: Python dynamic mode decomposition. *Journal of open source software*, 3(22), 530.
- Fastai library, <https://docs.fast.ai/>.
- Howard, J. & Gugger, S., 2020. Deep learning for coders with fastai and PyTorch: AI applications without a PhD. 1st edition, O'Really Media Inc.
- Howard, J. & Gugger, S., 2020. Fastai: a layered API for deep learning. *Information* 2020, 11(2), 108.
- Ministero delle infrastrutture e mobilità sostenibili, 2022. Italian guidelines for risk management and classification, safety assessment and monitoring of existing highways tunnels.
- Paszke, A. et al., 2019. An imperative style, high-performance deep learning library. In Wallach, H. et al., eds. *Advances in natural information processing systems* 32. Curran associates, Inc., pp 8024-8035.
- Sciarappa, A. et al, 2020. Life cycle – Tunnels: advanced numerical studies for lining defects prediction in highways tunnels. Lombardi group and SISSA MathLab. *Final report of the research project*.

Experimental study on quantification of carbon dioxide adsorption by different cement types and mix proportions

Takeshi Iyoda & Erika Ishikawa
Shibaura Institute of Technology, Tokyo, Japan

Yosaku Ikeo
Takenaka Corp., Chiba, Japan

ABSTRACT: Efforts are underway in concrete to build a carbon dioxide-free society. The degree of CO₂ adsorption and fixation by hardened cement, concrete depend on the type of cement and water-binder ratio of the hardened cement. In this study, we analyzed various types of hardened cement by TG-DTA to determine the amount of CO₂ adsorbed and examined the possibility of quantifying the amount of CO₂ adsorbed by weight increase as a simple method. As a result, it was shown that the amount of adsorption differs depending on the type of cement, that water is necessary for CO₂ adsorption mechanism, and that the amount of adsorption can be determined simply by the weight change.

1 INTRODUCTION

The global effort to move away from carbon dioxide has a significant impact on the concrete industry. The manufacture of cement, one of the raw materials for concrete, emits enormous amounts of carbon dioxide, which must be curbed. Therefore, in addition to cement production using energy-saving technologies as much as possible, technologies to use large quantities of alternative cement materials with low carbon dioxide emissions are being developed worldwide. On the other hand, concrete has long been known to undergo carbonation and is said to absorb carbon dioxide during service. This is believed to lead to a decrease in the small amount of carbon dioxide in the atmosphere. For carbon dioxide to be adsorbed and immobilized as calcium carbonate, a large amount of calcium is required in the concrete. On the other hand, a factor that increases the depth of carbonation is thought to be the use of cement with more admixture or a higher water-cement ratio to penetrate carbon dioxide deeper into the concrete. Furthermore, it has been pointed out that the presence of water is important for the carbonation phenomenon.

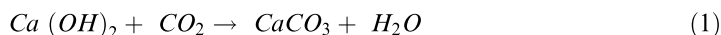
Therefore, the purpose of this study was to compile data that would contribute to the quantification of the amount of carbon dioxide fixed by carbonation of hardened cement. Specifically, we quantified the amount of calcium carbonate produced when environmental conditions and water content were varied in order to sort out the effects of water content in the reaction field. Furthermore, the amount of calcium carbonate produced was determined by changing the total amount of calcium by varying various cement types and water-cement ratios. In addition, the amount of calcium carbonate produced was investigated by adjusting the pores so that carbon dioxide gas could enter deep into the specimens. Furthermore, we attempted to quantify the amount of calcium carbonate produced by changing the weight of the sample so that the ratio of calcium carbonate produced could be easily measured.

2 OVERVIEW OF EXPERIMENTS

2.1 Changes in hydrates and voids due to carbonation

Carbonation of cement hydrates results in carbonation of the hydrates as shown in the chemical equation below. In this process, it is considered that the increase in volume due to the binding of carbon dioxide and the dissipation of the water produced occur simultaneously.

As indicated in the literature, it is also pointed out that carbonation of calcium hydroxide may result in densification of pores due to the formation of calcite, while carbonation of CSH may result in coarsening or opening of pores with the collapse of CSH as well as the formation of vaterite. Especially in cements containing a large amount of blast furnace slag powder, the change in porosity is known to be significant, suggesting that it also affects the progression of carbonation depth.



2.2 Preparation for the test

To organize how much carbon dioxide is adsorbed and immobilized by various types of hardened cement, it can be imagined that there are influencing factors such as the test environment (temperature and humidity, carbonation gas concentration), carbonation period, carbonation in air (dry) and in water (wet) as test conditions, as shown in Figure 1. Also, the type of cement (calcium content), water-cement ratio, and specimen size (shape) can be considered as influencing factors in the mixing conditions of the hardened specimens. We quantified the amount of carbon dioxide fixation by using samples with these factors.

In preparing the specimens, the powders used were ordinary Portland cement (Density 3.16 g/cm³) and blast furnace slag fine powder (Density 2.91 g/cm³). Three types of cement were prepared: OPC, B50 (50% replacement of blast furnace slag fine powder), and B70 (70% replacement of blast furnace slag fine powder), with a water binder ratio of 0.5.

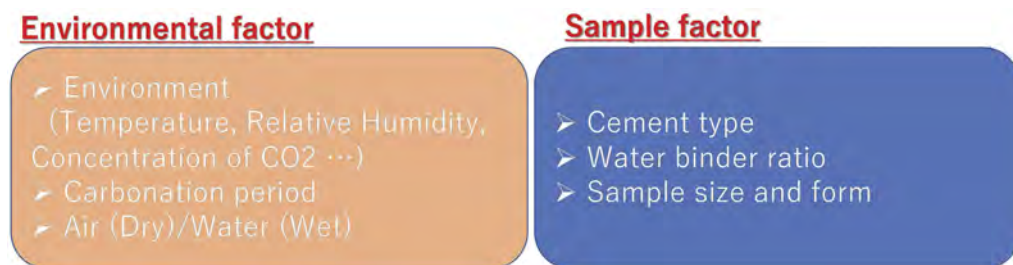


Figure 1. Influencing factor for absorption of Carbon dioxide.

For the determination of carbon dioxide adsorption, (1) the amount of calcium carbonate and calcium hydroxide were determined using TG-DTA, and (2) the amount of carbon dioxide adsorption by weight increase was determined. Because it was considered that the measurement of weight change would be difficult if affected by moisture absorption or moisture transpiration before and after carbonation, the samples were stored in a humidity-controlled environment using a desiccator so that the temperature and humidity were the same as those in the carbonated environment, as shown in Figure 2.

After 7 days of sealing and curing, the prepared specimens were placed in a humidity-controlled environment (20°C, 60% R.H.) for 21 days until there was no change in mass after the specimens were shaped. The specimens were then accelerated carbonated in a carbonation environment (20°C, 60% R.H., 5% carbon dioxide concentration) for 7, 14, 21, and 28 days, and the changes were measured by the methods described in TG-DTA and weight change.

(1) Determination of calcium hydroxide and calcium carbonate by TG-DTA

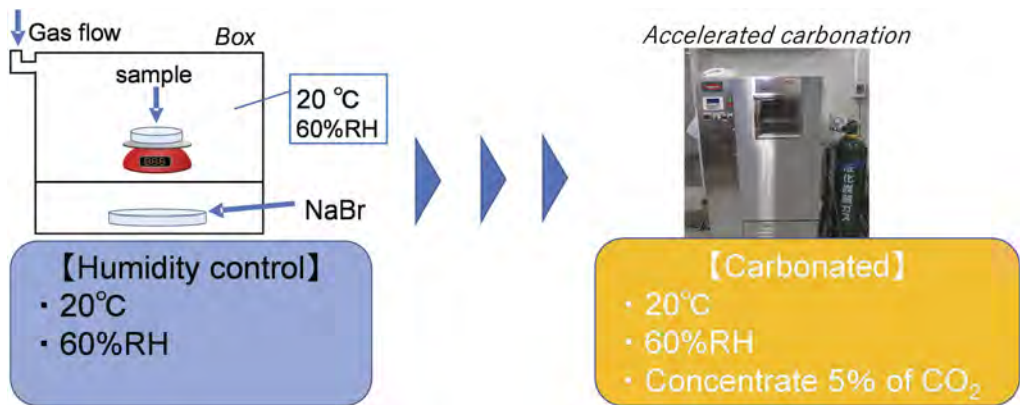


Figure 2. Weight change for determining the CO₂ absorption by easily methods.

The temperature range was 20 to 1000°C, and the rate of temperature increase was 10°C / min. The amount of dehydration of calcium hydroxide (CH) and calcium carbonate (CaCO₃) was estimated from the inflection point of the DTA curve and calculated from the decrease in weight change with endothermic peak. Tests were conducted under a nitrogen gas environment to eliminate the effects of oxidation and carbonation during the measurement.

(2) Determination of absorb carbon dioxide easily by Weight change

To quantify the amount of carbon dioxide adsorbed, the mass change was measured using an electronic balance capable of measuring down to 0.1 mg. After measuring the mass of the specimens after humidity conditioning was completed, mass measurements were taken for each carbonation material age, and the amount of carbon dioxide adsorbed was calculated from their differences.

3 RESULTS OF CARBON DIOXIDE ABSORPTION

3.1 Effects of cement type, carbonation period, and specimen shape

(1) Outline

The specific surface area of the specimen was examined for possible effects of the surface in contact with carbon dioxide and the voids in the hardened sample. As a sample, a fixed amount of cement paste was poured into a 38 x 40 x 2 mm zippered plastic bag, and the bag was sealed and cured for 7 days. After that, as shown in Figure 3, a “hardened” specimen and a “powder” specimen were prepared by grinding the specimen to less than 150 μm using a grinding mill.

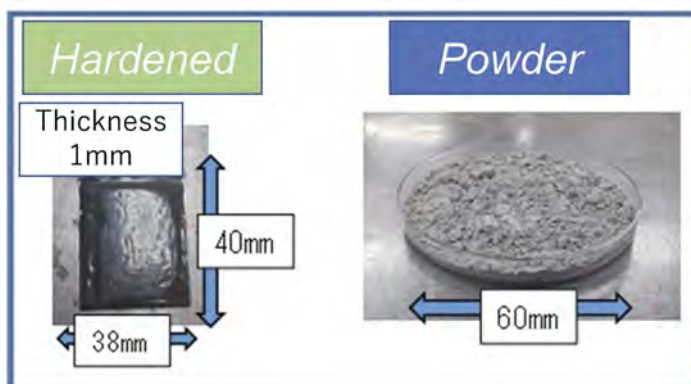


Figure 3. Sample size and form.

(2) Results

Figure 4 shows the percentage of CaCO_3 content in the samples calculated by TG. The results are organized by different cement and specimen geometries. In addition, the total CaCO_3 content derived from CH were separated. Based on the amount of CH calculated from the sample prior to carbonation, the difference between the amount of CH remaining during each carbonation period was calculated as the lost CH turned into CaCO_3 . It was also assumed that the total amount of CaCO_3 minus the amount of CH-derived CaCO_3 was produced by the carbonation of CSH and aluminate hydrates.

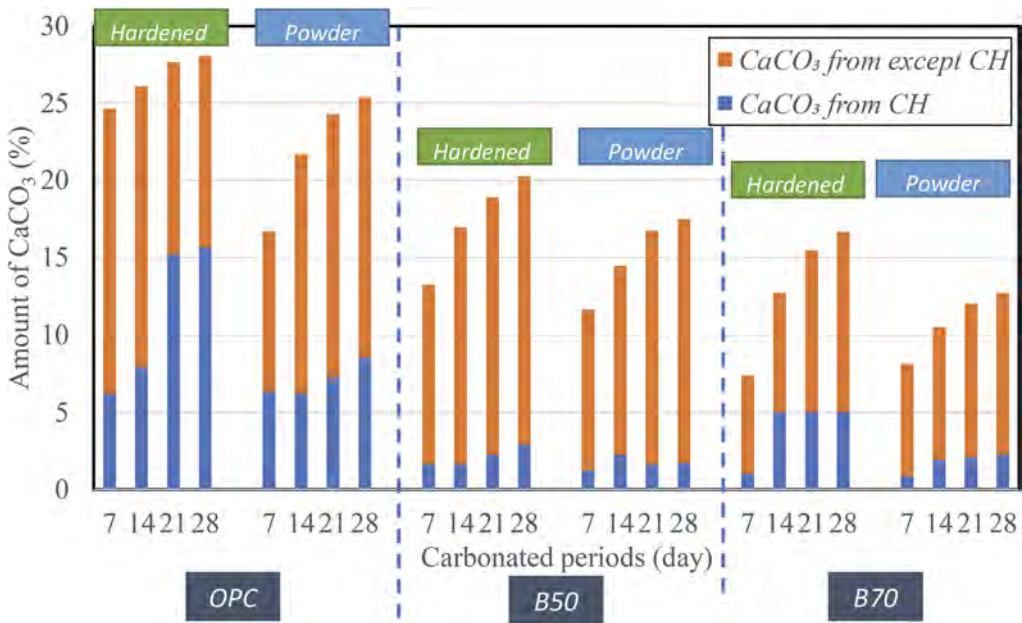


Figure 4. Amount of CaCO_3 by different cement type and sample forms.

From these results, the first comparison of cement types shows that OPC produces the most CaCO_3 , followed by B50 and B70. This means that the amount of CO_2 absorption decreases as more blast furnace slag fine powder is substituted. In addition, the effect of each carbonation period shows that the amount of CaCO_3 gradually increases, but the increase in adsorption after 14 days is not large. The subsequent examination of the specimen forms shows that for all cement types, the “hardened” specimens have a higher amount of CaCO_3 than the “powder” specimens. Initially, it was assumed that more CO_2 adsorption would occur in the powder with a larger specific surface area, but the results were different. In addition, when the origin of CaCO_3 production was compared, the amount of CH-derived CaCO_3 production was estimated to be lower when “powder” was used. Naturally, it is understandable that the addition of blast furnace slag fine powder to the cement type reduces the amount of CH, and therefore the amount is reduced, but the following study should be conducted to determine the reason for the smaller amount of “powder”.

3.2 Moisture content during carbonation

(1) Outline

The results verified in 3.1 showed that the “powder” with a larger specific surface area produced less CaCO_3 than the “hardened” specimen. Considering that the reaction of carbonation takes place through moisture, we thought that this might be because the powder almost lost its liquid phase, whereas the “hardened” could create a liquid phase even at 60% RH in the microporosity. In other words, we think that it may be extremely difficult for CH to become CaCO_3 if the moisture content of the sample is low. Therefore, we decided to test the “powder” and

humidity-controlled samples by adding water to the samples prior to carbonation. The Figure 5 shows the amount of water added to the samples. A fixed amount of water was added to the powdered sample to create an excess of water before accelerated carbonation was performed.



Figure 5. Moisture contents during carbonation.

(2) Results

Figure 6 shows the amount of CaCO_3 after carbonation for samples with 0, 30, 50, and 70% moisture addition. The amount of CaCO_3 derived from CH and from other sources as same as Figure 4, respectively. Even though the cement types are different, the amount of CaCO_3 is higher for those with more water added. The amount of CaCO_3 derived from CH also increased significantly. On the other hand, the amount of CaCO_3 derived from other sources did not increase that much. In addition, the carbonation periods were 3, 5, and 7 days, and although the amount of CaCO_3 gradually increased, no significant changes were observed. This indicates that the larger the moisture content in the sample, the more carbonation of CH is likely to occur, indicating that the presence of moisture is important. It is also clear that the carbonation of powder does not progress most rapidly at 60% RH.

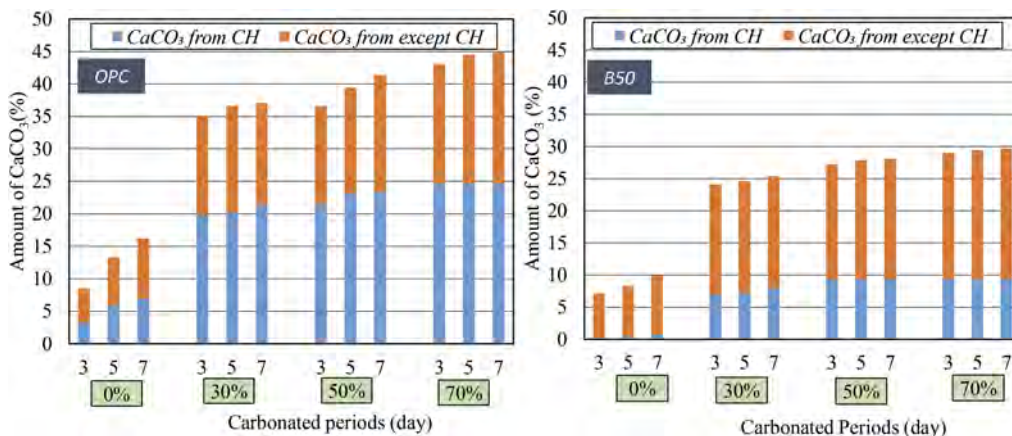


Figure 6. Amount of CaCO_3 by different of water contents.

3.3 Effect of cement type and water binder ratio

(1) Outline

To consider that the amount of CO_2 adsorption by carbonation depends on CaO , the effects of cement type and water binder ratio were varied. OPC and GGBFS cements were used, with replacement ratios of 30, 50, and 70%. Cement pastes were prepared by changing the water-binder ratio to 0.3, 0.5, and 0.7, respectively. The prepared samples were the same as those used in 3.1 and were ground before conditioning. Water was added to 70% of the sample mass just before carbonation to clarify the CO_2 adsorption potential of the hardened product, since water content has a significant effect as obtained in 3.2. The accelerated carbonation conditions were the same as in 3.1, and the number of days of carbonation was measured at 3 and 7 days. The items measured were TG-DTA and mass measurement.

(2) Results

Figure 7 shows the amount of CaCO_3 produced at each cement and water binder ratio, separated into those from CH and those from other sources. Although there was some variation in the data for each cement, it was observed that the cement with a low water-binder ratio of 0.3 tended to adsorb more CO_2 and produce more CaCO_3 . On the other hand, when looking at CH-derived CaCO_3 , the higher water-binder ratio produces more CaCO_3 . This is thought to be because of water content.

Figure 8 further shows the relationship between the amount of CaO and the amount of CaCO_3 produced. The higher the amount of CaO in the cement paste, the more CaCO_3 is produced, and the more CO_2 is adsorbed.

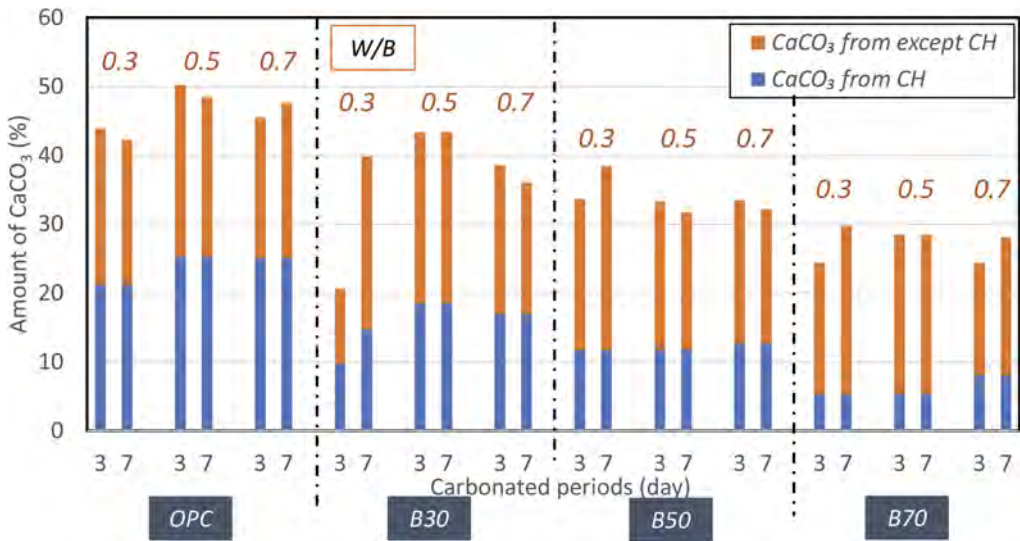


Figure 7. Amount of CaCO_3 by different water binder ratio.

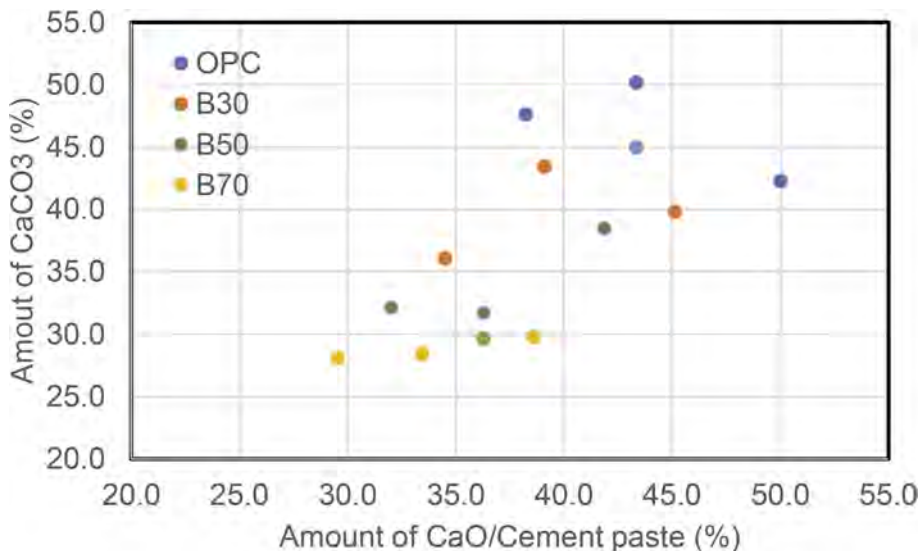


Figure 8. Relationship between the Amount of CaO and CaCO_3 .

3.4 Relationship between weight change and the amount of CO₂ capture

Figure 9 shows the relationship between the measured weight change and the amount of CO₂ adsorption determined from TG. All results are included for cement type, carbonated periods, specimen shape, and moisture adjustment performed in 3.1,3.2 and 3.3. There is generally a positive correlation between the rate of weight change and the amount of CO₂ adsorption, and that a proportional relationship is also nominated. The higher the replacement ratio of blast furnace slag, the smaller the weight change and CO₂ adsorption, and the larger the weight change and CO₂ adsorption are for OPC alone. The effect of the addition of moisture is greater in the case of the sample with additional moisture. This indicates that the CO₂ adsorption amount of cement paste can be estimated by determining the weight change before and after carbonation, although the accuracy needs to be examined in the future.

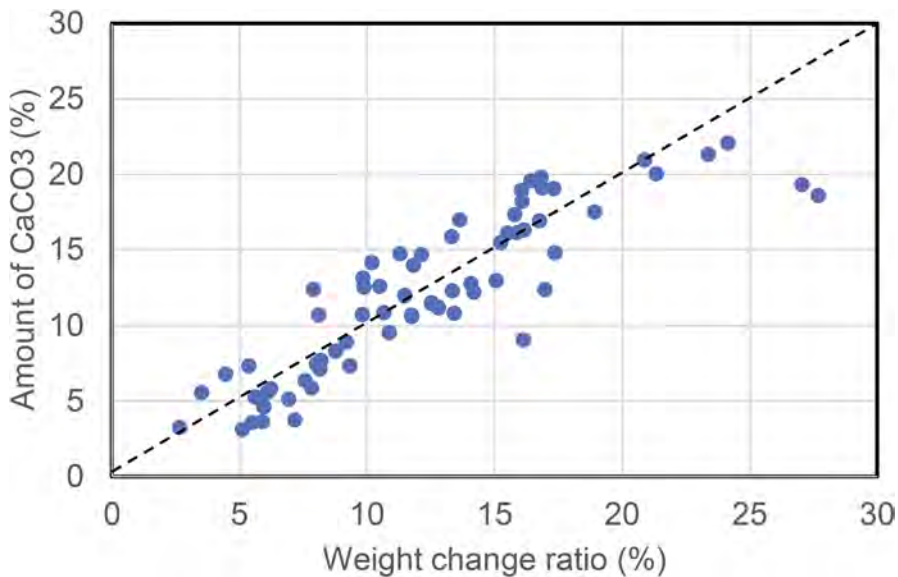


Figure 9. Relationship between the weight change and CO₂ absorption ratio.

4 CONCLUSIONS

The results obtained from this study are summarized as follows.

- (1) The CO₂ adsorption potentials of different cement types tended to be highly dependent on the calcium content of the cement.
- (2) In carbonation, carbonation reaction proceeds at 60%RH in hardened cements because water can be retained in the capillary pores, but in powders, carbonation of CH is less likely to proceed because of the lack of water retention.
- (3) It is possible to estimate the amount of CO₂ adsorbed from the weight change of a cement paste sample under humidity-controlled conditions and a sample after carbonation.

In the future, we will investigate the relationship in the water-binder ratio and aim to quantify the amount of CO₂ adsorption by weight change in mortar and concrete blocks containing aggregate.

ACKNOWLEDGMENT

This paper is based on results of “Development of Materials, Manufacturing Methods and Quality Control System on Innovative Carbon Negative Concrete”, JPNP21014, commissioned

by the New Energy and Industrial Technology Development Organization (NEDO). Experiments were conducted by students in Iyoda Laboratory. We would like to express our gratitude.

REFERENCES

- Seishi G. & Junya N. & Takeshi I. 2019. Carbonation kinetics -What is the difference in kinetics between accelerated condition and natural condition-, *Cement Science and Concrete Technology*, Vol. 73, pp.38–43
- Takeshi I.& Junya N. & Seishi G. 2018. A discussion on the mechanism of carbonation -The difference conditions between natural and accelerated-, *Cement Science and Concrete Technology*, Vol. 72, pp.225–232
- Takeshi I. & Erika H. 2017. Effect for environments factors such as supplying water by carbonation mechanism on real concrete structures, *Concrete Research and Technology*, Vol. 28, pp.113–122
- Karen M. M. & Takeshi I. 2022. CO₂ uptake of concrete recycled fines carbonated using solid-air and aqueous carbonation, *The 16th southeast Asian technical university consortium symposium*

Value of information for a rational experimental and testing budget applied to a regional old Italian bridges database

I. Vangelisti & C. Beltrami

Lombardi Ingegneria S.r.l., Milan, Italy

ABSTRACT: Experimental investigations and testing have a strategic rule in maintenance of civil structures. They allow to improve knowledge about security level, performance and maintenance of structural system. They require to be applied within a rational approach, in order to operate according to the “optimal scenario”, that is the scenario which let to gather the maximum level of useful information with the minimum money investment. The problem of allocate the optimal number of tests to each structure is here approached with the method of Value of Information, applied to an Italian regional bridge database in an ideal working scenario. It will be shown how VoI could represent a useful support to understand if testing can bring to significant information about structural maintenance, and to estimate which is the optimal number of test repetitions.

1 INTRODUCTION

In this paper an ideal scenario in which the public manager of a road network needs to decide whether to provide maintenance for a sample of bridges is proposed. In order to better orient the decisions, and limit the significative uncertainties which affect the decision, the manager requires to execute many structural tests (carbonation test, steel reinforcement tensile strength test and georadar) four times on the assets. For economic reasons, it is necessary to evaluate what could be the optimal number of each test. “Optimal” means “the minimum number of test repetition which allows to gather the maximum amount of significant information”. This is a common professional scenario, characterized by a limited amount of resources which must be spread on a certain number of operations. This “optimal” number of each test is estimated using the Value of Information, which could be assumed as a rational criterion to solve the problem. In the initial part of the elaboration, a first scenario in which the network manager requires four repetitions of each test for each structural element of each bridge (piers, pier caps, beams, decks and abutments) is presented. Ninety-nine bridges extracted from the Valle d’Aosta regional bridge database will be considered. We want to answer the following question “Is it possible to decrease the number of tests requested by the manager without losing a significant amount of the maintenance information?” In the second part of the paper, the procedure is studied and developed, modelling a complete probabilistic approach, required to face the remarkable uncertainties which characterize the working scenario. Finally, we come up with the optimal number of each typology of test, for each structural element and for each bridge.

2 BRIDGES DATABASE FEATURES

The bridge database is composed of ninety-nine bridges included in the system of State Roads in the Italian region “Valle d’Aosta”. Since very few information were initially available, it was necessary to introduce many hypotheses: i) the construction year of each bridge was assumed the same of the that of the roads (from 1928 to 1956), ii) each bridge is modelled as a simple-supported reinforced concrete beam structure, iii) beam transversal spacing is 2 m, and each carriageway is 10.5 m wide and iv) the amount of each structural element was estimated according to the span number of each bridge, which was originally known.

Figure 1 summarizes length and span number for each bridge.

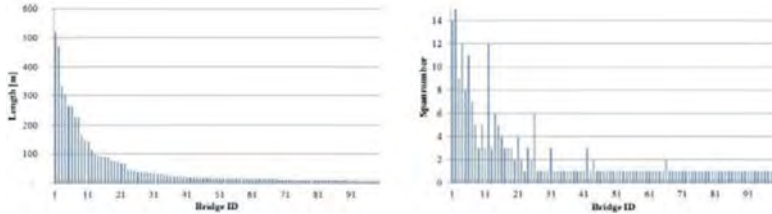


Figure 1. Bridges length and span number.

3 GENERAL REVIEW OF VOI FOR PERFECT AND IMPERFECT TESTS

The Value of Information is a decision-making method that takes its origin from economical applications (Howard 1966, Miller 1975) and it has been successfully applied to civil engineering scenarios. According to Leander & Karoumi (2018), it is defined as the difference between the amount that would be spent basing test campaign planning on the structural information available in the initial scenario and the one which would be spent after the rationalization, providing only for the optimal number of tests. It allows to estimate the utility of the tests: a VoI equal or minus than zero indicates that no useful information could be obtained from its execution. It also represents the maximum amount that the rational manager should be willing to pay for the test. Finally, it quantifies the economical values of the gathered information. VoI is here applied following the procedure proposed by Pozzi & Der Kiureghian (2011) and used by Zonta et al. (2013).

3.1 *Vol of a perfect test and imperfect test*

According to Pozzi & Der Kiureghian (2011), we assume that a bridge extracted from the database can only be in one of two discrete, mutually exclusive and collectively exhaustive states: Damaged state (D), which means unsafe structural behavior or Undamaged state (U), which means a safe structural behavior. The public manager can't know which is the state of the bridge; he can simply estimate the probability of being in both D and U, $P(D)$ and $P(U)$ according to his technical experience. The possible choices are do nothing (N), with a null cost if the bridge is U but with a social and economic cost C_r if it is D, or develop a rehabilitation plan (R), with C_m cost regardless of the state of the bridge. Assuming a general minimum costs target, the decisional criterion will suggest proceeding with rehabilitation if the estimated cost C_m will be less than the quantity $C_r \cdot P(D)$. According to this criterion, the cost C_0 of the base scenario will be:

$$C_0 = \min(C_m, P(D) \cdot C_r) \quad (1)$$

We now introduce the possibility to perform a perfect test on the bridge, which allows to know which is the bridge state with no uncertainty. This is obviously just an ideal scenario. Thus, the public manager will know if the bridge is U or D and will proceed with rehabilitation only if the test will show damage on the bridge. The cost C_1 of the final scenario is:

$$C_1 = C_m \cdot P(D) \quad (2)$$

According to Leander & Karoumi (2018), Pozzi & Der Kiureghian (2011) & Zonta et al. (2013), the VoI of the perfect test is:

$$VoI_{perfect\ test} = C_0 - C_1 = \min(C_m \cdot P(U), (C_r - C_m) \cdot P(D)) \quad (3)$$

from which the cost C_1 of the test will eventually be subtracted.

An imperfect test is characterized by uncertainty and it can give false positive or false negative results. Let's consider a test able to investigate if the bridge is damaged with an alarm (A)

or undamaged with silence (S). As reported by Pozzi & Der Kiureghian (2011), it is necessary to define the probability of false positive $P(A|U)$ and the probability of false negative $P(S|D)$. Using the Total Probability Theorem, the probabilities of having an alarm $P(A)$ and a silence $P(S)$ can be easily calculated:

$$P(A) = P(A|D) \cdot P(D) + P(A|U) \cdot P(U) \quad P(S) = P(S|D) \cdot P(D) + P(S|U) \cdot P(U) \quad (4)$$

where $P(A|D) = 1 - P(S|D)$ and $P(S|U) = 1 - P(A|U)$.

Moreover, using Bayes' Theorem, probability of damage can be updated:

$$P(D|A) = P(A|D) \cdot P(D) / P(A) \quad P(D|S) = P(S|D) \cdot P(D) / P(S) \quad (5)$$

It is now possible to evaluate the expected costs when the test gives alarm or silence, using the same general minimum costs target explained at 3.2:

$$C_{2,A} = \min(C_m, P(D|A) \cdot C_r) \quad C_{2,S} = \min(C_m, P(D|S) \cdot C_r) \quad (6)$$

Finally, we can calculate the expected cost after a structural test execution and the VoI:

$$C_2 = C_{2,A} \cdot P(A) + C_{2,S} \cdot P(S) \quad VoI = C_0 - C_2 \quad (7)$$

from which the cost C_1 of the performed imperfect test will eventually be subtracted.

In this paper we only focus on the VoI for imperfect test, since it enables to obtain a more realistic simulation. VoI will be calculated for each bridge, for each test performed on each of the considered structural element.

4 MATHEMATICAL PROCEDURE

4.1 Definition of C_r , C_m and C_t

As explained at 3.2, C_r represents the total amount that the manager is forced to pay when a bridge collapses. It includes direct and indirect costs resulting from the collapse (construction of a new bridge, social and economic costs). For the sake of simplicity, it is assumed equal to the current value of the bridge, increased by 10% for a proper evaluation of indirect costs. According to these assumptions, C_r is estimated equal to 1250 €/m². Figure 2 shows the value for each bridge.

Since we want to focus on the test performed on each structural element, it is necessary to define C_r resulting from the collapse of the single structural element. Let's introduce a general criterion for the evaluation of the C_r of the i th structural element:

$$C_{r,i} = K_{tot} \cdot \alpha_i / n_i \quad (8)$$

where K_{tot} is the bridge current value, α_i considers the value of the portion of bridge lost due to the i th element collapse and n_i is related to the number of elements collapsed. Proposed values for α_i and n_i are reported in Table 1. C_m is the rehabilitation cost that the manager may decide to perform according to the decisional criterion (1). It is estimated, similarly to (8), as

$$C_{m,i} = K_{tot} \cdot \alpha_i / n_i \quad (9)$$

where K_{tot} as above, α_i is the rate cost for the rehabilitation of the i th element/cost of bridge total rehabilitation and n_i is the total number of i th elements; values for α_i and n_i are shown in Table 1.

C_t is the cost of the execution of a structural test, derived from average market prices in Italy. It must be defined for each structural test, on each structural element from one to four times.

4.2 Tests and limit states

As shown in 3.2 and 3.3, the evaluation of VoI requires the estimation of the probability of damage $P(D)$ of the bridge under consideration. The probability $P(D)$ is then estimated with reference to specific limit states, which are not to be considered as limit state for design, but simply as limit conditions against which calculate $P(D)$, with a full probabilistic approach.

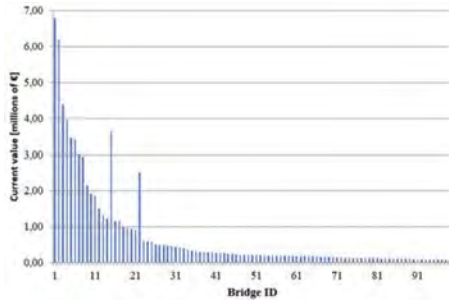


Figure 2. Current value in millions of € for each bridge.

Table 1. Proposed values for the evaluation of the cost $C_{r,i}$ (top) and $C_{m,i}$ (bottom).

	Piers	Pier caps	Beams	Decks	Abutments
$\alpha_i (C_r)$	1	1	0,5 o 1	0,5 o 1	1
$\alpha_i (C_m)$	0.10	0.05	0.20	0,10	0,10
n_i	$n_{span}/2$	$n_{span}/2$	n_{span}	n_{span}	$n_{span} / n_{abutments}$

4.2.1 Limit state for concrete carbonation test

Carbonation spread in concrete can be described by Fick's first diffusion law:

$$x_c = A \cdot t^n \quad (10)$$

where x_c [mm] is concrete cover degraded by carbonation, A [mm/years^{0.5}] is the carbonation coefficient, t is the elapsed time since the triggered of carbonation and n is equal to 0.5, suggested by technical literature. For our scenario i) A is a normal random variable, with mean and standard deviation assumed according to Recanati (2011). Mean values will be lower for beams and decks because they expose a lower surface to carbon dioxide, ii) t is equal to the bridge age as it is assumed that carbonation trigger goes back to its construction. Since A is a random variable, x_c is a random variable too. The limit state can be defined with reference to the reinforcement corrosion: when carbonation layer reaches the steel bars, their corrosion begins; when corrosion have destroyed more than 66% of the single steel bar in the maximum positive bending moment section, the bridge becomes damaged. Hence, it requires two equations, the first of which is:

$$g_1 = x_{real} - x_c \quad (11)$$

where x_{real} is the cover thickness of the structural element and the probability of failure is $P(g_1 < 0)$.

Is it possible to model x_{real} as discrete random variable since it varies from bridge to bridge. (11) is a necessary but not sufficient condition to go beyond the limit state. Only when $g_1 < 0$, we introduce an analytical model for uniform steel corrosion, according to Val et al., 1998:

$$d(t) = i_{corr} \cdot t_{corr} \quad (12)$$

where $d(t)$ is corrosion depth [μm], i_{corr} is the corrosion annual rate [μm/yr] and t is time of exposure to the chemical agent [yr]. i_{corr} is assumed equal to 70 μm/yr as suggest by Pedferri, (2004) and it is modeled as a random variable with mean 70 μm/yr and standard deviation 5.34 as reported by Leander & Karoumi (2018). Assuming a safety factor equal to 1.5 for bridges design, corrosion damages the bridge if it destroys more than 66% of a steel bar or the 43% of its diameter. We can finally define the second equation of limit state as

$$g_2 = 0.43 \cdot d_0 - d(t) \quad (13)$$

where d_0 is the original diameter of the bar, modeled as a random variable according to a predetermined discrete distribution via a MCS. 10,000 simulations of (11) and 10,000 simulations of (13) when resulted $g_1 < 0$ have been performed. The probability of damage $P(D)$ for the i th bridge and for the j th element with reference to the carbonation limit state is then calculated taking into account the total number of simulations in which $g_1 < 0$ and $g_2 < 0$.

4.2.2 Limit state for steel reinforcement tensile strength test

A limit state can be formulated considering the actual and the measured yield stress of the steel. When the latter is more than 5% less than the former, the limit state is overlapped. 10,000 simulations have been performed according to the following steps: i) two steel grades, FeB44k and FeB32k, were assigned to the bridges with the same frequency ii) each grade was modeled using a normal distribution according to Verderame, et al. (2001) iii) via a MCS 10,000 samples of yield stresses have been extracted, assuming a failure when the difference between the actual and the measured values is more than 5% only by default.

4.2.3 Limit state for georadar test

With reference to i , reinforcement bars spacing, and Φ , reinforcement bars diameter, we assume that the failure occurs when, at the same time, bars spacing is more than 50% of the design spacing and bars diameter is less than 80% of the design one. The probability of failure $P(D)$ is equal to the probability of the union of the two event $P(\Phi \cup i)$, where $P(\Phi)$ is the probability of having a failure on the diameter of the bars and $P(i)$ is the probability of having a failure on the spacing. 10'000 simulations have been performed to estimate $P(D)$ according to the following steps: i) the mean value of Φ is 26 mm for piers, piers cap and abutments and 16 mm for beams and decks ii) the mean value of i is 0 iii) since is unlikely to observe diameter greater than design diameter or spacing lower than the design one, the two random variables have been modelled using skewed normal distribution iv) in each simulations, a value of Φ and i have been sampled and compared to the introduced thresholds v) $P(D)$ has been estimate taking into account the number of simulations in which thresholds have been overlapped.

4.3 False positive and false negative probabilities framework

As said at 3.3, a proper evaluation method of probabilities of false positive and false negative when tests are performed many times (type I and II errors) is required. According to Pozzi & Der Kiureghian (2011), $P(A|U)$ and $P(S|D)$ must be lower than 0.5 in order not to have a pathological test. Two methods are hereby introduced: the first one based on Bernoulli trials and the second one based on a qualitative approach. Type I and II errors are the only "degree of freedom" of the proposed procedure, since the costs shown in the past chapters are forced by economical features.

4.3.1 Bernoulli trials

The multiple execution of the structural tests can be considered as Bernoulli trials because i) the test results in only two possible outcomes (D and U) ii) type I and II probabilities are the same for each repetition iii) observations are independent from each other. Among three test samples, the probability of false positive can be defined as the probability of having two or more A when the bridge is U. There are four possible combinations for this outcome 1) AAA 2) AAS 3) ASA 4) SAA. Hence, $P(A|U)$ for three repetitions of the test, according to iii, can be calculated as $P(1)+\dots+P(4)$. For our purpose, $P(2)$, $P(3)$ and $P(4)$ are totally equal to each other since the false positive is obtained regardless of the order of the single repetitions. Thus

$$P_{fp} = P(1) + \dots + P(4) = P(A|U)^3 + (3|1) \cdot (1 - P(A|U)) \cdot P(A|U)^2 \quad (14)$$

If the number of samples is four, there will be many *pathological* combinations with two A outcomes followed by two S outcomes, that could equally be interpreted as false positive or false negative. Hence, we suppose that for 50% they are classified as false positive and for 50% are classified as false negative. Finally, we can estimate the probabilities of type I and II errors for multiple repetitions assuming the ones for the single repetition (0.20 for carbonation test, 0.15 for tensile strength test and 0.30 for georadar).

4.3.2 Qualitative approach

Type I and II probabilities have also been studied using a qualitative approach, with the aim of investigating the mathematical process stability. Starting from the general principle according to which these probabilities must decrease as the number of repetitions increases, we propose four different functions, linear, hyperbolic, parabolic and exponential rates, calibrated thanks to multiple successive iterations, considering the lack of similar data in technical literature.

5 RESULTS AND DECISIONAL CRITERION

The main results of the proposed procedure are hereby presented. For the sake of simplicity, VoI has been calculated for each bridge, for each test just for one structural element of each type.

Figure 3 shows VoI trend from one to four repetitions of carbonation test executed on a reference pier for each of the functions introduced in 4.3.2.

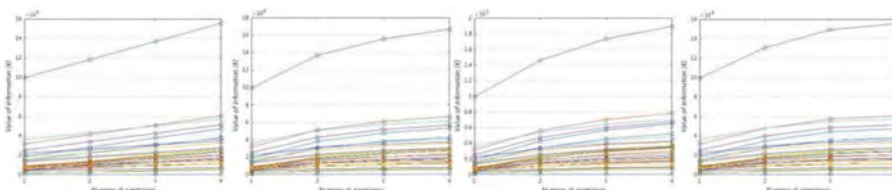


Figure 3. VoI plot for multiple carbonation test repetitions on a pier, using linear (1), hyperbolic (2), exponential (3) and parabolic (4) type I and II functions.

Since the test is applied on a pier, single span bridges are not included in the graphs. It is evident that i) VoI trend does not depend on the functions used to modelled type I and II occurrence probabilities and it anyway is inversely correlated to them ii) VoI increases as the number of repetitions grows up. In fact, a test becomes accurate and accurate when it is performed many and many times, with an ideal infinite VoI when it is executed infinite times (but with an ideal very high cost). For this reason, VoI can't be taken as decisional criterion, since, in this case, the manager would always plan the execution of the maximum number of tests as possible iii) the curve upon all the others represents a single pier 3-roadways bridge (ID 22), for which, at the same time, the current value is particularly high and the consequences of the collapse of the piers are dramatic (loss of the structure). With the aim of preventing the collapse of the pier and consequently of the entire structure, it is strategic for the manager to investigate and to gather information about the pier, and it is attested by the very high VoI. Similarly, curves located in the upper part of the graphs, correspond to bridges for which rate current value/n of piers is quite elevate.

Figure 4 reports VoI trend for tensile strength test applied on the reference deck obtained with Bernoulli trials formulation. All the features previously pointed out are still valid. VoI trend is inversely correlated to the one of type I and II occurrence probabilities, it swiftly increases from two to three repetitions as the probability of false positive and negative decreases in the same step and it is substantially constant from one to two and from three to four repetitions. Moreover, VoI variation is steeper and steeper as the current value of the bridge is higher and higher because it is generally economically worth to gather information for the bridges whose economic collapse consequences are remarkable.

In order to develop a decisional criterion, it is necessary to involve costs of the tests in the decisional process, for example by assuming the rate VoI/test cost as a decisional criterion. Nevertheless, this would again lead to increasing quantities as the number of repetitions grows up. For this reason, a more reliable criterion would be to link the VoI variation recorded when the number of test increases of one to the cost required to execute this specific number of tests. Thus, a new dimensionless ratio called $\Delta = \Delta \text{VoI} / \text{test cost}$ is defined. Δ generally decreases as the number of tests repetitions increase. This is an expected outcome since, after a number of test executions, the information not detected by the previous tests that could be gathered with another execution, becomes increasingly limited, facing, on the other hand, an increase in test cost.

Figure 5a shows Δ trend for carbonation test performed on a reference pier with a linear variation of false positive and negative probabilities. As expected, Δ decreases as the number of test repetitions increases. With a single execution of carbonation test, it is possible to obtain a maximum benefit of about 200 (again the top curve is related to bridge 22). Performing two tests will instead lead to a significantly more limited benefit.

Figure 5b reports Δ trend for carbonation test performed on a reference beam with an exponential variation of false positive and negative probabilities. The trend is significantly different

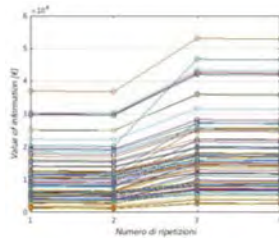


Figure 4. VoI for tensile strength test repetitions on a deck, using Bernoulli trials formulation.

from the previous one. Two remarkable tendencies can be underlined in the chart: the former presents its maximum for one repetition of the test, and it is related to “low” current value bridges, for which could not be convenient to allocate huge tests budget because of the limited (just in mathematical meaning) consequences of their collapse (limited VoI); the latter presents its maximum for two repetitions and it corresponds to “high” current value bridges, for which, on the other hand, it could be worth to plan extensive structural test campaigns (high VoI).

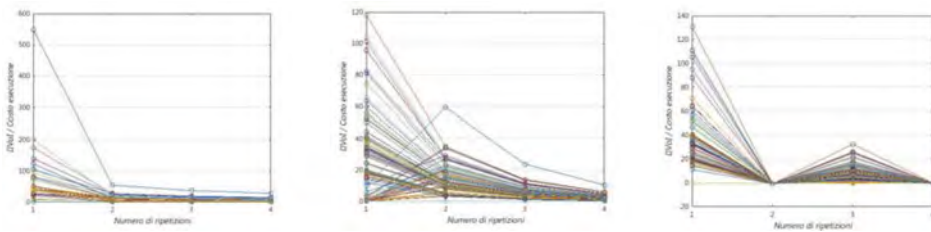


Figure 5a. (left) Δ for carbonation test on a pier and linear variation of false positive and negative, (center, 5b). Δ for carbonation test on a beam and an exponential variation of false positive and negative (right 5c) Δ for georadar on pier and Bernoulli for false positive and negative (right, 5c).

Figure 5c shows Δ for georadar performed on a reference beam using Bernoulli trials. Maximum Δ is obtained for one repetition, while Δ is null for two repetitions since the probabilities of false positive and negative according to binomial distribution are the same for one and two executions. It is possible to observe how Δ is higher for those structural elements like piers (ref. Figures 5a vs 5b) whose collapse will cause a greater damage of the bridge.

According to the decisional criterion, the optimal number of tests, associated with the maximum Δ , can now be estimated. Figure 6 reports the optimal number of steel tensile strength test on beams when the functions for false positive and false negative are used (ref 4.2.3). The bars show that the process outcomes are substantially the same regardless of the false positive and negative functions, that confirms the method stability. Again, the maximum number of repetitions occurs for those bridges whose current value is considerable high. The optimal number of tests is null for particularly recent bridges, for which the method expects good structural conditions.

An economic comparison between the starting and the optimal scenario is finally shown. In the starting scenario, the manager required to perform four tests of each category on each structural element of each bridge. According to the costs introduced at 4.1, a total of 1,284 million of € is required. The rational decisional criterion introduced in this paper, with reference to the studied qualitative functions for false positive and negative, requires the amounts reported in Table 2. For the sake of simplicity, the optimal number of tests calculated for a reference element is then taken as optimal number for all the elements of this type of this bridge.

Again, the stability of the method is proved since the expected costs variation about 16%.

The mean money saving between initial and rational scenarios is 554553.3 €, corresponding to the 43% of the total initial cost.

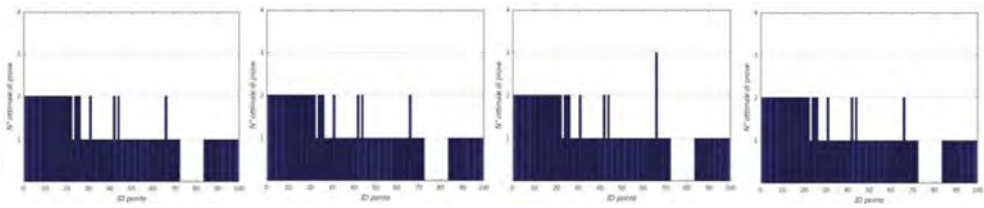


Figure 6. Optimal number of carbonation tests on beams for linear, hyperbolic, parabolic and exponential false positive and negative variation trends.

Table 2. Expected costs for the rational scenario.

False positive/negative function	Linear	Hyperbolic	Parabolic	Exponential
Total cost of the campaign [€]	745360	701802	789247	683198

6 CONCLUSIONS

In this paper a rational criterion based on VoI for the optimization of an experimental and testing campaign on a regional bridge database has been developed with a full probabilistic approach. Carbonation test, steel tensile strength test and georadar are asked to be performed by the manager on each structural element (abutments, piers, piers caps, beams and decks) four times. The aim of the paper was to study if it would be possible to reduce, in a rational way, the number of tests without a significant loss of information. For each test, a limit state has been introduced, according to which probabilities of failure required by the calculation of VoI of an imperfect test proposed by Pozzi & Der Kiureghian (2011), have been estimated. Probabilities of false positive and negative of the imperfect tests have been modelled both via binomial distribution (Bernoulli trials) and via a qualitative approach (linear, hyperbolic, parabolic and exponential functions).

Then, VoI has been computed for each test and for each element. The decisional criterion was based on the ratio “increase of VoI when another test is performed/cost of these tests”. According to the criterion the optimal number of tests has been estimated for each bridge, for each test and for each element. It has been shown as this rational criterion could allow to obtain a mean money saving of 43% of the budget estimated for the execution of four repetitions of each test.

REFERENCES

- Howard, R.A., 1965. Information value theory. *IEEE transactions on system science and cybernetics*.
- Leander, J. & Karoumi R., 2018. The value of monitoring the service life prediction of a critical steel bridge. *Life-cycle analysis and assessment in civil engineering: towards an integrated approach*.
- Leander, J. et al., 2018. A decision support framework for fatigue assessment of steel bridges. *Engineering failure analysis*.
- Miller, A.C., 1975. The value of sequential information. *Management science* 22(1):1–11.
- Pedefferri, P., 2004. *La corrosione delle armature nel calcestruzzo*. Milan Polytechnic.
- Pozzi, M. & Der Kiureghian A., 2011. Assessing the value on information for long-term structural health monitoring. *Health monitoring of structural and biological systems*.
- Recanati, M., 2011. *Parametri sperimentali per il progetto della vita di servizio di strutture in calcestruzzo armato*. Master of science thesis.
- Val, D.V. et al., 1998. Effect of reinforcement corrosion on reliability of highway bridges. *Engineering structures*, Vol.20, No.11, pages 1010–1019.
- Verderame, G.M. et al., 2011. *Le caratteristiche meccaniche degli acciai impiegati nelle strutture in calcestruzzo armato realizzate dal 1950 al 1980. XXVI AICAP national congress, 19-21/05/2011*.
- Zonta, D. et al., 2013. Value of information impact of monitoring on decision-making. *Structural control and health monitoring*.

Multi-risk analysis methodology for evaluating climate change impacts at different scales

F.V. De Maio, R. Valsecchi, S. Osmani, C. Solari & P. Basso
RINA Consulting SpA, Genova, Italy

ABSTRACT: The Intergovernmental Panel on Climate Change (IPCC) report on Climate Change 2021 is a “code red for humanity”. It is thus essential to work on a climate resilient society. The purpose of the paper is to present the New Enabling Visions and tools for End-useRs and stakeholders thanks to a common MOdeling fRamework towards a climatE neutral and resilient society (NEVERMORE) project. The NEVERMORE project focuses on the modelling theory to take a significant step forward to overcome the current silo approach in favour of an integrated assessment one for evaluating impacts, risks and interactions of climate change across sectors. The activity will include the analysis and modelling of extreme events in their compound attributes (magnitude, frequency, timing). For each type of extreme events identified in each case study region, the Expected Annual Loss (EAL) is provided as the relation between the probability of damage occurrence and the loss expressed.

1 INTRODUCTION

When assessing the risk posed by a certain hazard the first parameter to be qualified is its frequency of occurrence. The definition is deeply related to the relevant historical data for a given geographic reference. The definition of exposure calls into play the time and spatial correlation as some areas might be more prone to a certain hazard rather than others. Along with the determination of possible threats and relevant frequencies, the vulnerability of the asset shall be determined as well using a structural and logistics assessment. The impact could be evaluated for different assets as well as for different kinds of targets. The NEVERMORE approach integrates information from physical modelling of impacts and risk analysis methodologies and aligns them across different scales via case studies that represent various socio-ecological EU contexts.

2 HAZARD ASSESSMENT

In the proposed methodologies the Hazard is considered through the definition of the relation between the frequency of occurrence and the relative Intensity Measure (IM) of a certain hazard. The Hazards considered by this methodology are strictly related to Natural events.

Table 1. Hazards intensity measures.

Hazard	Earthquake	Wind	Flood	Wildfire	Landslide	Rockfall	Avalanche
IM	acceleration	velocity	water height	fire intensity	flow height	diameter	pressure
Unit	[g]	[m/s]	[m]	[-]	[m]	[m]	[Pa]

For the Hazard data collection, it will be possible to consider the following sources: Literature Databases, National Codes, Websites Databases, and Thematic maps on hazard distribution

produced at the national level. In the following, the hazard assessing procedure is explained. The Hazards considered are approached in different ways: Direct hazards, such as Earthquake and Wind; Indirect hazards, such as Flood, Wildfire, Landslide, Rockfall, and Avalanche. The main difference, as can be seen in the following, is related to the fact that some of them lead to a hazardous event in case of some triggering causes. One important example is the Landslide hazard that can be triggered by two direct events, the earthquake, and the rain. While the earthquake and wind are directly related to a ground shake and windy event.

2.1 State of the art on hazard curve definition

The base for the development of a multi-hazard framework for the risk assessment must be set according to a strong base. In so doing the most solid framework for the risk assessment of natural hazards is of course related to the earthquake risk assessment. Since it is one of the most relevant and most studied natural phenomena that affect negatively the infrastructure, it is also wider implement inside the Nation and International codes.

The intensity measure is usually given for 4 different percentages of exceedance in 50 years, which are commonly 2%, 10%, 50%, and 68%, common in earthquake engineering. The hazard is often expressed in terms of exceedance probability, rather than in terms of exceedance rate (number of events per unit of time). The exceedance probability is the probability that a certain intensity will occur at least once in a given period. The two can be related using a concept called a Poisson process, which is a stochastic process which counts the number of events and the number of times in which they occur. The relationship is explained in the following formula:

$$MAF = -\ln(1 - p)/t \tag{1}$$

Where MAF is the mean annual frequency, P is the percentage of exceedance, and t is the time. So, The Mean Annual Frequency (MAF) can be computed by the given percentage of exceedance, usually with t = 50 years. For each site is possible to define the hazard curve by fitting the 4 points.

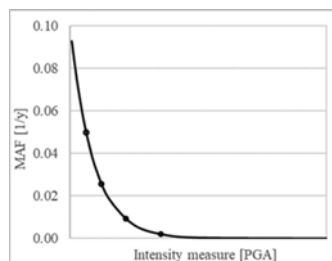


Figure 1. Typical hazard curves for direct hazard.

2.2 Implementation on hazard curve definition

Here it can be highlighted, that there are two main obstacles to the definition of a homogenized procedure to assess the hazard. First, besides the case of having the whole vector of 4 exceedance and 4 intensities, it is very common to find less detailed information, such as unique intensity measures or a list of historical data from literature Database. Thus, in the case of having a limited number of IMs with the associated frequency/probability of occurrence. In this case, the few data available can be used to build up the hazard curve. This procedure can be performed through some different procedures able to give back the relationship between the frequency and intensity measure. Secondly, different natural event means different physical phenomena. These differences are mainly related to the physics of the natural elements involved; the relation triggering phenomena vs occurring events; last but not least the possible influence of the human footprint.

Before starting with the description of the hazard homogenization framework, here are described the procedure for the evaluation of the so-called indirect hazard. The Flood Hazard can be

triggered by the rainfall phenomena and the change in a generic stream flow. Starting from this definition, the inputs used in the computation are related to the average flow discharge and its variance in a certain period, that per each stream; their combination results in the definition of 4 percentage of exceedance. After that, the combination of the 4 discharges and the digital terrain model gives back water heights in the nearby asset. From these parameters is possible to draw a flood hazard curve, by an exponential fitting, in accordance to National Research Council (2015).

The Wildfire Hazard is the most complex to assess, mainly due to the different aspects that should be considered in the fire assessment. Besides that, three different aspects must be considered as input for this evaluation, as described by Scott et al. (2013): the relation between the driving wind and how the fire growth; the historical data; the relation between soil moisture and the type of vegetation. The combination of these aspects results in a wildfire hazard curve.

The Landslide/Rockfall (Soil) Hazard can be triggered mainly by different events, excessive rainfall and earthquake. Besides that, the information needed for the assessment of the hazard is of course the 4-point curve of the earthquake hazard and the rainfall event. The acceleration and the rainfall height can be easily implemented in the evaluation of the factor of safety of an inclined slope. So, the combination of them, the digital terrain model (slope evaluation), and the geological model (soil/rock physical characteristics) result in the intensity measure (flow height/block diameter), as described by Klar et al. This procedure is performed with a Monte Carlo iteration, which led to the definition of a set of Occurrence vs. Intensity values used to build the final hazard curve.

Avalanche Hazard is a complex phenomenon since its occurrence is mainly related to both human and terrain morphology, as described by Ciolli & Zatelli (2000). The approach used here is quite like the landslide case since the snow is considered a granular material, such as the soil. Besides that, three different aspects must be considered as input for this evaluation: the Boolean function related to slope triggering condition; the historical data on occurrence; the probability density function (PDF) of the avalanche pressure. The combination of all these aspects gives back the avalanche hazard curve.

This framework can assess the regional scale, by considering information in a raster format, i.e. thematical maps. In this way, all the assets that relay in a certain region can be assessed together. A schematic representation, for wildfire, of this evaluation is shown below.

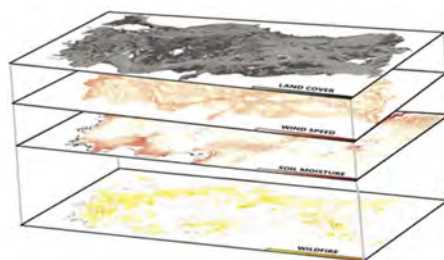


Figure 2. Schematic representation of the evaluation of an indirect hazard.

2.3 Hazard harmonization

A fundamental step in the definition of this methodology consists of the harmonization of the different procedures of hazard assessment. The harmonization procedure consists of several steps, not always needed for all the hazard categories. The common procedure can be described as the selection of the Input data, MAF evaluation through the Poisson process, and evaluation of the hazard curve by fitting the results.

The input data elaboration is located between the Input Data and MAF evaluation phases. This step must be implemented in two cases. First, the data given must be elaborated to pass from single values to the 4 values needed for the relation with the probability of exceedance. Secondly, the raw input data has a period time of observation different from the selected one. This can be performed by fitting a new probability of exceedance for the different values of the time.

After the MAF evaluation is usually defined the direct hazard. This step should be defined as an intermediate one, for those hazards that are defined as indirect. Since this value represents the assessment of its triggering factor and not the hazard itself.

Therefore, for the indirect hazards, the local morphology must be considered. This step allows computing how the trigger can lead to the hazard occurrence. Must be evaluated the threshold above which the direct hazard triggers the indirect one. These steps are listed in a tabular form per hazard, to give a more understandable idea of the concept of hazard harmonization.

Table 2. Hazard harmonization scheme.

	DIRECT HAZARDS			INDIRECT HAZARDS		
	Earthquake	Wind	Flood	Soil	Avalanche	Wildfire
Input	4 IM[g] vs. P in 50y	IM_{avg} [m/s] vs. P in 15y to 50y	IM_{avg} [m ³ /s] + σ_{IM} in 15y to 50y	4 IM [g][mm/h] vs. P in 50y	-	IM_{avg} [m/s] vs. P in 15y. to 50y
Period Harm.	-	-	-	-	-	-
Form Harm.	-	4 IM vs. P	4 IM vs. P	-	-	4 IM vs. P
MAF eval.	Poisson	Poisson	Poisson	Poisson	-	Poisson
Trigger Local morph.	-	-	Q [m ³ /s] Stream section $A_{sec} \rightarrow h_w$	g[m/s ²]/h[mm] Slope info FS = f(g;h)	- Historical data + Slope + PDF	v [m/s] Historical data + Moisture
Results	MAF vs g [m/s ²]	MAF vs v [m/s]	MAF vs H _w [m]	MAF vs H[m]	MAF vs P[kPa]	MAF vs FII[-]

3 VULNERABILITY DEFINITION

Vulnerability is a measure of asset damage/failure due to a hazardous event. As an alternative, it could be also defined as the target's inability to deter and withstand the specific disaster. The assessment can be defined considering three different factors: Geographical location; Hazard response; Target hardness. The vulnerability assessment is made by an exhaustive Database generated through the knowledge from literature, internal resources or by directly inputting the fragility curves parameters, in case of ad hoc developed fragility curves.

The definition of the vulnerability for an Asset is inhere defined according to a set of 4 fragility curves. They are set following the main studies performed in the field of risk assessment, i.e. the Federal Emergency Management Agency (FEMA). The 4 curves are defined following the 4 damage states level defined to represent the most important damage scenarios, following the Hazus Manual subdivision of damage levels. The 4 levels are used in this analysis to reach a desirable level of simplicity, without losing the minimum level of accuracy required.

The first damage state (DS1) is associated with slight damage defined as flexural or shear-type hairline cracks in some beams and columns near joints or within joints. The second one (DS2) is associated with moderate damage, corresponding to the exhibition of hairline cracks on most beams and columns; for ductile frames, some of the elements have reached yield capacity, showing larger flexural cracks and spalling, while for nonductile frames may exhibit larger shear cracks and spalling. The third one (DS3) is associated with extensive damage, corresponding to the reaching of the ultimate capacity of some elements; for ductile frames, large flexural cracks, spalled concrete and buckled reinforcement occur, while for the nonductile elements may experience shear or bond failures at reinforcement splices, or broken ties or buckled reinforcement in columns, leading to a partial collapse. The last one (DS4) is associated to complete damage, which corresponds to the structure collapse or the imminent danger of brittle failure of nonductile elements or loss of frame stability.

For the selection of the appropriate Fragility curve, many parameters are considered, such as the principal construction material, construction typology, year of construction, the type of the code

during the design phase, dimensions (e.g. footprint, ground floors, n° of stories etc.). A specific database can be built with standardized unitary values to overcome the potential lack of information. So, starting from the main characteristics of the asset, the fragility function can be defined.

4 IMPACT

The Impact is defined as the presence of people, livelihoods, species or ecosystems, environmental functions, services, resources, infrastructure, or economic, social, or cultural assets in places and settings that could be adversely affected by a hazard. Therefore, it can be seen as the scale of the consequences of a hazard, Basso et al. The impact is normally quantified in the determination of damages and losses caused to stakeholders, the environment and human life. In this study case, the analysis of the impact is based on the analysis of three different categories, according to Sousa et al.: impacts on People (fatalities/injuries); impacts on the Physical System/Infrastructure (damages on the structures); impacts on Service continuity (interruptions/downtime).

The evaluation of each component is provided in economic terms; in such a way that the combination of them provides a unique impact value following the work done by Basso et al.

4.1 Impact on people

The analysis of the impact on the people (IP_{DSi}) is based on the evaluation of the number of fatalities and injuries due to the occurrence of a certain hazard. The methodology used is based on the definition of three categories: Death, Slightly injured, and Severely injured. The evaluation is provided according to the relation carried out by Cimellaro et al., the percentage of death and injured people is related to the damage state that occurred after the hazardous event.

Table 3. Normalized human losses ratios for different damage states defined by Cimellaro et al.

	U.M.	DS1	DS2	DS3	DS4
Death _{DSi}	%	0.000	0.000	0.0015	12.500
Injury _{DSi}	%	0.000	0.030	0.1005	22.500

The number of deaths can be obtained by multiplying the death loss ratio shown above by the number of people inside the hospital, considering also a reduction coefficient δ_t that considers the effect of the asset preparedness on the people evacuation.

Furthermore, thanks to the Syner-G deliverable a further distinction could be made on the injury. They are divided into slightly and severely injured through the severity injured ratio that is typically set equal to 1/3. The total number of severe injuries can be assessed by multiplying of injury loss ratio shown above with the severity coefficient explained before, also considering a reduction through δ_p is the percentage of people evacuated within the due time. This value is also called Hospital Treatment Demand (HTD), since it must consider that some severe injury needs rapid surgical treatment, due to the threats. To do that the reduction of the treatment capacity must be assessed as the Hospital Treatment Capacity (HTC). This parameter can be assessed by multiplying the number of surgical operations that can be performed in a day with the service reduction, also considering a reduction through δ_{int} is the coefficient that considers the goodness of internal coordination among facilities and departments.

In the end, the economic loss (IP_{DSi}) can be evaluated by considering the direct death due to the event (computed by people inside the hospital), and the indirect death determined as the severely injured people that cannot have access to the surgical treatment (If $HTD > HTC$). Therefore, the number of human life losses can be multiplied by the mean value of human life.

$$IP_{DSi} = [D_{DSi} + (HTD - HTC)_{DSi}] \cdot V_L \quad (2)$$

In which D_{DSi} is the number of direct death, $[(HTD-HTC)]_{DSi}$ represent the number of indirect death, and V_L has expressed the value of life. It must be pointed out that HTD must

be reduced by considering the number of patients that can be relocated during an emergency among different hospitals, also considering a contribution of δ_{E2} which represents the coefficient related to hospital redistribution capacity during an emergency.

4.2 Impact on physical system

The impact on the physical system (ID_{DSi}) can be defined as the impact cost due to the direct damage experienced by the facility. The economic loss can be ease defined as the multiplication between two parameters: the damage value of each damage state according to the definition of Kappos et al.; the reconstruction cost expected to take back the asset to full operation.

4.3 Impact on service continuity

The impact on service continuity (IR_{DSi}) can be related to the effects of the reduction of the service due to damage. The evaluation is based on the information on the average recovery time and service reduction per each damage state, according to the relation carried out by Cimellaro et al.

The additional time that people need to get access to healthcare facilities is the base of the economic loss evaluation. As can be seen in the following formula the recovery is considered a linear function, which considers three main components:

$$IR_{DSi} = (t_{r,DSi} \cdot S_{DSi} \cdot NP) (t \cdot V_t) \delta_{rec} \quad (3)$$

Where: in the first parenthesis is shown the evaluation of the total number of people, by considering the people per day (NP), the percentage of them which are affected by the downtime (S_{DSi}), and the time of service reduction per each DS ($t_{r,DSi}$); in the second one is shown the cost per person, evaluated by taking into account additional time for accessing other healthcare facilities (t) and the value of the time per each person (V_t); at least is considered also the effect of δ_{rec} which represent the efficiency of the recovery. It must be pointed out that NP must be reduced by considering the availability of mobile healthcare posts (δ_{E1}); and of course, the number of patients that can be endorsed in it.

5 RESILIENCE

The term resilience means the ability to prepare for and adapt to changing conditions and withstand and recover rapidly from disruptions, it includes the ability to withstand and recover from occurring threats or incidents. Inside this framework, the resilience evaluation is based on the assessment of the preparation, planning capacity, internal, and external resourcefulness following what was done by Basso et al. In this methodology resilience is defined to affect the impact analysis. So, the resilience coefficients are defined to be considered into the impact analysis.

5.1 Influence on impact on people

As already described in the previous chapters, some resilience indicators influence the evaluation of the impact. In this section, the theory behind their use is described.

The evaluation of the casualties should consider the capacity of the people to evacuate in the best way. Usually, this capacity can be related to the existence or not of emergency plans, its quality, and the training frequency. In the work done by Li et al., the evacuation efficiency is assessed firstly through an exit attraction capacity factor and by a people evacuation behaviour/coordination factor. The parameter varies linearly between $\delta_t = 0.15/1.00$ from best to worst.

Another aspect of preparedness is considered, the community preparedness. This resilience coefficient is very important to fit the real number of people heated by a hazardous event. It is known from the literature that exists a relationship between warning time and people evacuated from a certain area. The two boundaries find in literature, Jonkman 2007, can be associated with one of the community experiences, namely less than 10 years and more than the 100 years.

An important aspect to consider is internal resourcefulness. The coefficient δ_{int} considers the goodness of the internal coordination among facilities and departments. It is related to the

factors that describe the organizational and the human component during emergencies, according to Syner-G. The parameter is $\delta_{int} = 0.57/1.00$, for the case of good/lack of coordination.

At last, it should be considered is external resourcefulness, especially related to the health care system efficiency, at the interhospital level. The coefficient, in this case, can be related to hospital redistribution capacity during an emergency. Therefore, the value of δ_{E2} is defined initially as a Boolean function (0/1) if the answers are all equal, while 0.5 if they are opposite.

5.2 Influence on impact on service continuity

As already described in the previous chapters, some resilience indicators influence the evaluation of the impact. In this section, the theory behind their use is described.

During the aftermath of the event, an important role is played by recovery efficiency. The recovery coefficient is set to consider the change in recovery performance. This variation is related to internal resourcefulness and preparedness, according to Cimellaro et al. The recovery of economic loss is related to the unserved goods/services in a certain period. Therefore, the coefficient is simply evaluated as the reciprocal of the area under the recovery functions. The parameter varies linearly between $\delta_{rec} = 0.19/0.50$ from best to worst.

An important aspect that should be considered is external resourcefulness, especially related to the institution efficiency. The coefficient, in this case, can be related to the accessibility to the eventual mobile healthcare post, which can ensure a certain level of treatment capacity despite the service reduction due to the damage experienced. Therefore, the value of δ_{E1} is defined initially as a Boolean function (0/1) if the answers are all equal, while 0.5 if they are opposite.

6 EXPECTED ANNUAL LOSS

The first step in the evaluation of the Expected Annual Loss (EAL) consists of the combination of the hazard and vulnerability. The results of this combination are representing the probability of damage occurrence of the impact. The Damage probability per each damage state (P_D) can be computed as the convolution integral between the Hazard curve, if available, and the fragility curves of the limit state DS. The last step of this study consists of the definition of the EAL, which is used in this methodology as the quantification of the risk level. This final value considers all the different components of the risk assessment theory, such as the probability of damage occurrence and the total impact. The EAL, can be built using the total impact and the damage.

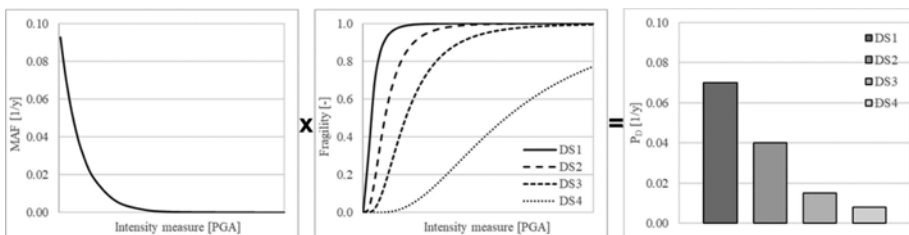


Figure 3. Damage probability per each DS.

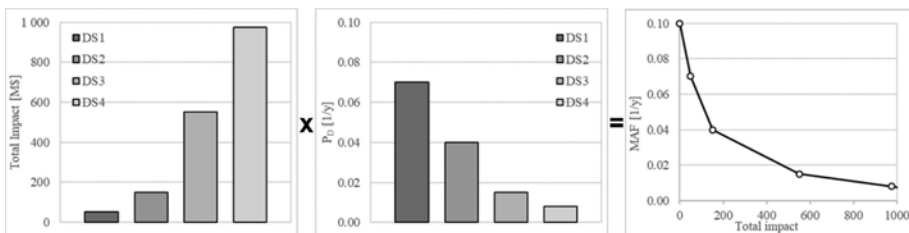


Figure 4. EAL evaluation.

Finally, the area under the EAL curve is computed. Therefore, the EAL is the final measure of the risk per a certain asset, subjected to a generic hazard.

7 CONCLUSIONS

In this methodology, the Expected Annual Loss (EAL) is used as the quantification of the risk level. This final value considers all the different component of the risk assessment theory, such as the probability of damage occurrence (Hazard and Vulnerability) and the total impact (Impact and Resilience). This framework is developed considering a wide range of different hazards within the NEVERMORE project. The way in which they are computed is based on the concept of hazard harmonization. This procedure permits the users to compare and sum the different risk values since the weight of the different hazards is directly calibrated in the harmonization procedure as already shown in the very beginning.

The impact is normally quantified as the consequence of damages and losses caused to stakeholders, the environment and human life. The analysis of the impact is consequently based on the definition of the impacts on People, on the Physical System/Infrastructure, and Service continuity. The consideration of all these different aspects of the impact leads to a real representation of the current value of the critical infrastructure sectors.

The already mentioned criticality level should be defined uniquely. In so doing each level, labelled DS1, DS2, DS3, and DS4, always represent the same damage state, per each asset analyzed. In this way, this methodology can be easily extended to another infrastructure category.

The losses are evaluated as a function of time as can be appreciated in the impact analysis. This is mainly related to the concept of damage and service which can be recovered in a certain time, called recovery time. The way in which the impact is assessed allows considering the resilience as a coefficient able to affect the recovery function. The result is a scalar value calculated as the area under the loss curve, that should be used to compare the risk among the different assets.

REFERENCES

- Basso, P., Osmani, S., Scolari, M. & Valsecchi, R. 2021. A seismic risk assessment framework for loss estimation of critical infrastructure–hospitals case. *8th International Conference on Computational Methods in Structural Dynamics and Earthquake Engineering*, Vol 1, 2643–2658.
- Cimellaro, G.P., Reinhorn, A.M. & Bruneau, M. 2010. Seismic resilience of a hospital system. *Structure and Infrastructure Engineering*, Vol.6, 127–144.
- Ciulli, M. & Zatelli P. 2000. Avalanche risk management using GRASS GIS. *1st Italian GRASS users meeting proceedings, Geomatics Workbooks*, Vol 1.
- FEMA 2013. Hazus-MH2.1 - Multihazard Loss Estimation Methodology - Earthquake - Technical Manual.
- Jonkman N. 2007. Loss of life estimation in flood risk assessment; theory and applications. *Delft University – Civil Engineering department*.
- National Research Council. 2015. Tying flood insurance to flood risk for low-lying structures in the floodplain. National Academies Press.
- Kappos, A.J., Panagopoulos, G., Panagiotopoulos, C. & Penelis G. 2006. A hybrid method for the vulnerability assessment of R/C and URM buildings. *Bulletin of Earthquake Engineering*, 4:391–413.
- Klar, A., Aharonov E., Kalderon-Asael, B. & Katz O. 2011. Analytical and observational relations between landslide volume and surface area. *Journal of geophysical research*, Vol. 116.
- Li, S., Zhai, C. & Xie, L. 2015. Occupant evacuation and casualty estimation in a building under earthquake using cellular automata. *Physica A: Statistical Mechanics and its Applications*, 424, 152–167.
- Scott, J.H., Thompson, M.P. & Calkin, D.E., 2013. An analytical framework for quantifying wildland fire risk and fuel treatment benefit. *General Technical Report 315, US Department of Agriculture*.
- Sousa, M.L. & Tsonis, G. 2019. Recommendation for a National Risk Assessment for Disaster Risk Management in EU - Approaches for identifying, analysing and evaluating risk. *JRC Science for policy report*. Version 0. Cap.9, 56–67.
- Syner-G 2012. D6.7 Application and validation study to a hospital facility (Italy). *Systemic Seismic Vulnerability and Risk Analysis for Buildings, Lifeline Networks and Infrastructures Safety Gain*.

Evaluation of the safety factor in masonry buildings as acceleration varies: A quick approach

E. Garavaglia

Department of Civil and Environmental Engineering, Politecnico di Milano, Milan, Italy

ABSTRACT: The topic addressed in this paper is the search for a quick method of evaluating the seismic behaviour of masonry buildings that can be easily extended to portions of historical buildings. The proposed method is the extension to the probabilistic field of the evaluation of safety factors already present in the literature. The method applied to the proposed case study shows how the fragility curves describing the variation of the safety factors with the variation of the expected accelerations could be a useful support tool in the planning of safeguard interventions and how they are able to show, in probabilistic terms, the possible impact of seismic improvement interventions on the expected structural response.

1 INTRODUCTION

The assessment of the seismic behaviour of existing buildings undamaged by the earthquake is an important topic for the classification and subsequent safety of the historic buildings in the entire Italian territory.

The procedure that leads to the large-scale seismic performance assessment of masonry buildings must necessarily be a simple and reliable procedure. It is assumed that it should provide elements in support of a possible assessment starting from data that can be easily found in the municipal archives without necessarily requiring visits and surveys on site (which are, however, not always possible).

Approaches that address the issue of studying the seismic vulnerability and the propensity to damage of the existing buildings have been developed over the last few years by the Italian scientific community, but often the post-earthquake assessment is the starting point (Rosti, Rota & Penna 2009; Zuccaro, Perelli, De Gregorio & Cacace 2021). The models proposed are often very refined models that require an in-depth knowledge of the building and professionals qualified in the use of the calculation processes and important processing times (Saloustros, Pelà, Roca & Portal 2015).

The purpose of this research is to find a procedure to estimate the global seismic performance of existing buildings not yet damaged by an earthquake, which is reliable and easily extendable to the assessment of an entire urban area. The procedure can be useful for public administrations as a tool on which to base maintenance planning.

The approach proposed here is a probabilistic extension, of the method proposed by Borri, De Maria & Casaglia (2014) and Borri, Corradi, Castori & De Maria (2015) relating to three types of simplified verification: simplified gravity verification, simplified global horizontal loading verification and simplified local mechanism verification. The results of the three simplified checks are compared with the safety levels required by the Italian NTC2018 (NTC Italian Building Code 2018) standards for the limit state of safeguarding human life (SLV) referred to the site in question, the building type considered and the intended use class. These results are expressed in terms of conventional safety factors.

To extend this procedure to the field of probabilistic prediction in Angielu, Cardani & Garavaglia (2022) the construction of fragility curves which could describe the variation of the global safety factor, SF_G , was studied, as the expected accelerations vary in a certain seismic zone.

In this paper the method is also extended to the prediction of the variation of the local safety factor, SF_L ; this evaluation requires somewhat more detailed information than that

required by the evaluation of SF_G . The method is applied here on a case study on which the information allowed the evaluation of both factors. The SF_G evaluation was performed for the initial situation of the building; the SF_L evaluation was performed both for the initial situation of the building (pre-seismic improvement) and for the current situation (post-seismic improvement). The two probabilistic assessments were then compared.

2 THE DAMAGE PARAMETER SF

The expeditious assessment of the residual capacities of a building located in a seismic risk area requires the use of a parameter that is sufficiently reliable and quantifiable on the basis of data available from shared databases. A parameter that has these characteristics is the safety factor, SF, proposed by in Borri, De Maria & Casaglia (2014). The safety factor is a parameter capable of describing the performance of the structure when subjected to a certain acceleration. This performance is the measure of the loss in safety of the structure after the event, loss quantified through appropriate parameters.

In Borri, De Maria & Casaglia (2014) two types of safety parameters are distinguished: the global parameter, SF_G , which describes the performance of the entire building and the local parameter, SF_L , which describes the possible collapse mechanism that can locally affect some points of the building.

The global parameter SF_G can be obtained from the geometry of the structure, and from the empirical evaluation of the masonry quality, data easily available from existing databases (Cadastrale, municipal archive, vulnerability cards, etc.) The local parameter, SF_L , requires, instead, a little more detailed knowledge of the structure; in fact, its evaluation requires the estimate of the analysis of the loads and the definition of the framework of the decks (more details in section 4).

The parameters SF_G and SF_L are deterministic and associated with a specific building. In Angjeliu, Cardani & Garavaglia (2022), such approach was the basis of the study for a probabilistic application that also showed the possibility of extending the method to the evaluation of the safety of the different types of masonry buildings as the expected acceleration values varied.

3 FRAGILITY CURVES

The method consists in the construction of curves that allow a probabilistic prediction of the occurrence of a certain phenomenon when a certain condition varies, such as the probability of reaching a certain damage threshold when the level of acceleration recorded varies, as in Garavaglia et al., (2008, 2021), but also in Singhal & Kiremidjian (1996), Flora, Perrone and Cardone (2020) or Sandoli, Lignola & Calderoni (2021). The safety factors SF_G and SF_L proposed in Borri, De Maria & Casaglia (2014) are able to describe this behaviour, so they can be assumed as damage indices to be studied from a probabilistic point of view.

The construction of the curves starts from the modelling, with an appropriate probability density function (p.d.f.) of the values of the selected variable, here generally called SF, present in a certain range of the ground acceleration a^* . Therefore, in the cases studied, the fragility curve defines the probability for a system to reach the loss of a certain value of SF at a defined acceleration \bar{a} . Once the damage threshold \overline{sf} is defined, the probability of this threshold being reached at instant a^* is described by the area to the left, below the p.d.f. (dashed area).

On the opposite, the probability of exceeding this threshold is described by the area below the p.d.f. to the right in the solid area (Figure 1a).

By constructing the probability density function for the chosen random variable for each of the chosen intervals, or acceleration values, it is easy to see how it is possible to construct the fragility curve linked to the experimental evidence or, better called, the experimental fragility curve $F_{\bar{a}}(a^*)$ (Figure 1.b).

The area above the threshold \overline{sf} is calculated using the survival function reported in (1):

$$\mathfrak{S}_{sf}(SF, a^*) = \Pr\{sf > SF\} = 1 - F_{sf}(SF, a^*) \quad (1)$$

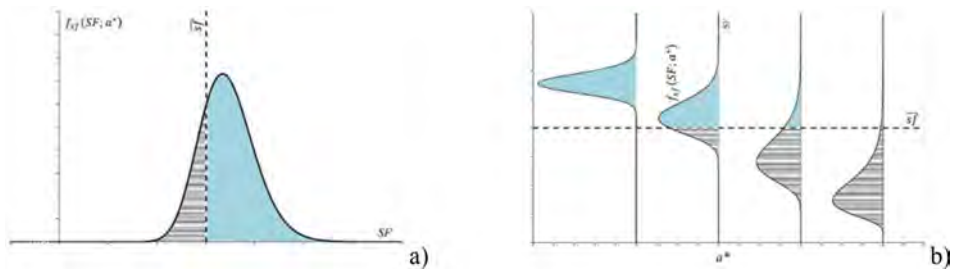


Figure 1. Probability of reaching and exceeding threshold \bar{sf} : (a) qualitative p.d.f. for a given value of a^* ; (b) p.d.f. built for different values of a^* .

where $F_{sf}(SF, a^*)$ is the cumulative distribution of sf at each acceleration a^* and describes the probability that the variable sf reaches values greater than a certain value SF , in this case $SF=sf$.

The area below the threshold \bar{sf} is given by the cumulative distribution $F_{sf}(SF, a^*) = \Pr\{sf \leq SF\}$, which describes the probability that sf can assume values not exceeding SF , in this case $SF=\bar{sf}$. The investigated variable SF shown in Figure 1a will be modelled using a Log-Normal distribution, while the experimental fragility curves will be created using the Cumulative distribution function, $F_{sf}(SF, a^*)$ and considering the dashed areas in Figure 1b.

4 THE CASE STUDY

The case study chosen for the application of the proposed method is a rural building which shows the structural typology typical of rural areas in Lombardy.

Cascina Cuccagna (Figure 2 and Figure 3) is located in Milan. The Milan area is classified as a seismic area, more precisely with a medium-low seismicity, but given that the typology is typical of the whole region, the behaviour the farmstead has been studied for a series of accelerations (PGA) foreseen for a medium-high area seismicity. Such areas are still present on the Lombard territory (eg: Salò area and Lake Garda).

As often happens, the construction of historic buildings evolves over the centuries and this induces points of vulnerability in the structures that may become real weaknesses in the event of seismic action. In a project funded by the Cariplo Foundation and conducted by ACCC (Associazione Consorzio Cantiere Cuccagna), Politecnico di Milano and Hydea (PRE.CU.R.S.OR project), the diagnostic and structural analysis of the farmstead showed points of static weakness and structural vulnerability that required both interventions of static reinforcement and of seismic improvement.



Figure 2. Cascina Cuccagna: aerial view.

4.1 The overall behaviour of the building.

As already explained, since the typological characteristics of Cascina Cuccagna are recurrent in Lombardy the evaluation of the factors SF_G and SF_L (Borri, De Maria & Casaglia 2014), is performed here for the acceleration interval (a_g) $0.15g < a_g \leq 0.25g$, typical of the Italian seismic



Figure 3. Cascina Cuccagna: a) first floor; b) ground floor. The shadow areas are involved in seismic and static improvement.

zone 2. The design spectrum was constructed for this area and the characteristic acceleration parameters (PGA) were obtained as well as the spectral amplification factor, F_0 , (Table 1).

Table 1. Seismic parameters Italian seismic zone 2 Garda Lake.

Years	PGA	F_0
30	0.042	2.551
50	0.057	2.483
475	0.158	2.483
975	0.206	2.485
2475	0.283	2.466

On the basis of some parameters, all or in part, easily available from existing databases (the number of floors above ground and their height, the covered surface, the presence in the plant of resistant walls in the x and y direction, their length and thickness, the possible characteristics of the masonry and its specific weight, the presence or absence of cracks and a plausible analysis of the loads) it is possible to measure the loss of the global safety factor as the values of accelerations imposed vary and construct the consequent curves of fragility.

The application of the method proposed in Borri, De Maria & Casaglia (2014) made it possible to quantify the experimental parameter SF_G (assumed here as random variable) as the different accelerations imposed varied in a certain interval. Such values were then normalised to the maximum value ($1-SF_{Gmax}$) obtained and a probabilistic modelling was performed on them. The purpose of this modelling was to obtain a fragility curve which, as the acceleration set varied, could describe the probability of recording a loss value ($1-SF_G$) as a percentage of the maximum expected sever value ($1-SF_{Gmax}$). Figure 4a shows the curve of fragility for the building studied relative to a value of $(1-SF_{Gmax})=58\%$.

The experimental data were then modelled with a Gamma-type probabilistic curve.

Figure 4 shows that the structural typology examined responds quite well to the accelerations expected for the seismic zone 3 ($0.05g < a_g \leq 0.15g$), that is the seismic zone to which it belongs. In fact, the probable loss of performance in the $0.05g-0.15g$ interval (typical of seismic zone 3) is to be considered between 0 and 32% of $(1-SF_{Gmax})$, while for the $0.15g-0.25g$ interval (typical of seismic zone 2) the loss of performance is certainly more consistent and it is between 32% and 94% of $(1-SF_{Gmax})$.

4.2 Fragility curves for different levels of performance loss SFG

Following the approach presented in Section 3, a further investigation to be carried out is the assessment of the loss of performance for different percentage thresholds. In this way it is

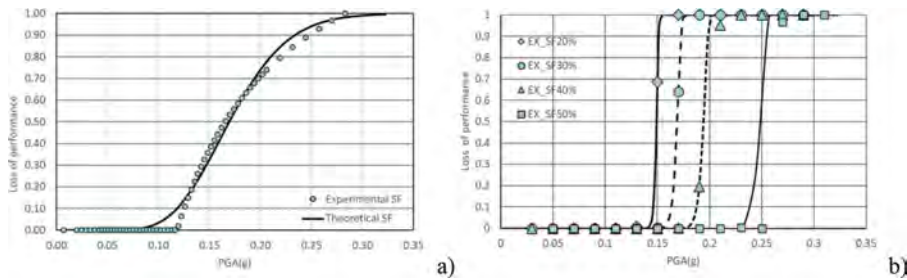


Figure 4. A) Fragility curve of the probability of reaching a value $SF \leq \overline{sf}$ ($\overline{sf} = 58\%$); b) Experimental (dots) and theoretical (lines) fragility curves describing the probability of losing for different levels of SF as acceleration varies.

possible to read the probability of reaching or exceeding a certain level of loss as the acceleration varies. In this case the experimental data are evaluated in absolute value and not normalised to the $SF_{G_{max}}$ value.

The experimental data were modelled with a Weibull-like probability function. The choice of the function is related to the behaviour of the event studied: the probability of reaching the level of maximum loss of performance increases as the acceleration value increases; such a phenomenon requires a probabilistic modelling with distributions having an increasing immediate risk function, Weibull and Gamma distributions respond well to this need. In the specific case it is believed that the Weibull distribution, with a hazard rate tending to infinity for increasing values of a_g , is the most correct distribution to describe the behaviour of the parameter $(1 - SF_G)$ as a_g varies.

For the case study of Cascina Cuccagna in Milan, Figure 4b shows the fragility curves for different loss thresholds.

Figure 4b shows the good overall behaviour of the structural typology of the farmstead. In fact, performance losses exceeding 50% are not detectable and losses of 50% seem to be predictable for accelerations around 0.20g-0.25g.

4.3 A specific vulnerability of Cascina Cuccagna

A building can show local vulnerabilities that can change the level of performance as the acceleration set varies. However, the knowledge of these vulnerabilities requires more in-depth investigations and the data necessary for it cannot be obtained from public documents, as is instead possible for the verification of overall behaviour.

In the proposed case study, during the development of the PRE.CU.R.SOR project, the survey and diagnostics carried out on the building made it possible to have sufficient elements to further investigate the local behaviour of a part of the building (Garavaglia, Anzani, Maroldi & Vanerio, 2020).

The documents collected showed a very marked flexural deformation in an inter-floor slab and the lack of clamping of the slab-perimeter walls (Figure 5). Failure to clamp the slab made the perimeter walls, subjected to the thrust of the roof, vulnerable to overturning. The evaluation of the local safety factor for the deteriorated situation, called “pre-improvement”, will then be proposed on this portion of the building.

The seismic improvement required the replacement of the main beam and the deteriorated elements of the strongly inflected floor, the stiffness of the floor was improved with the introduction of two layers of crossed boards and the masonry-floor clamping was obtained by means of inclined drills (Figure 6). The static improvement was carried out with the introduction of line break devices for the flexural improvement of the floor beams.

After the execution of work, a new evaluation of the local safety factor SF_L was carried out for the situation that we can call “post-improvement”.

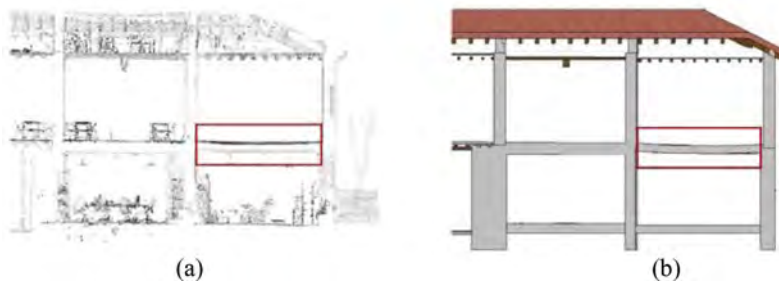


Figure 5. Survey of flexural anomaly in a floor beam (a) laser scanner survey (b) section redrawing.

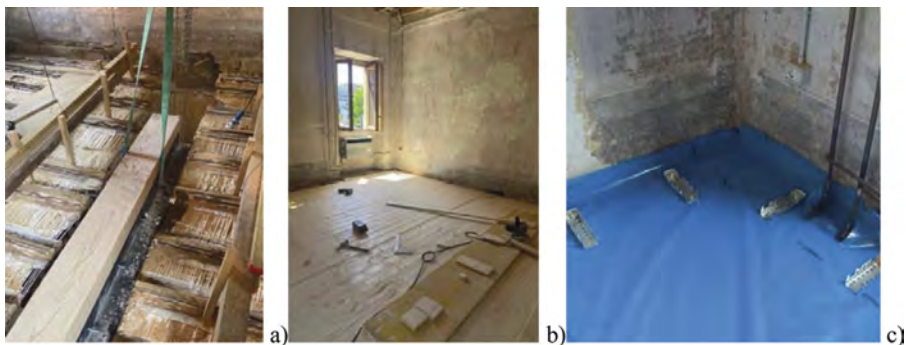


Figure 6. Room 33 seismic improvement actions (a) main beam replacement; (b) cross deck placement; (c) floor-wall connections with inclined drills.

4.4 The local behavior and the parameter SFL

The PRE.CU.R.SOR. project on *Cascina Cuccagna* has made it possible to have a significant and diagnostic documentation useful to formulate some hypotheses on the local behaviour of the walls and floors in the areas with the highest specific vulnerability.

Still applying the method proposed by Borri, De Maria & Casaglia (2014) for local mechanisms and considering the overturning mechanism, the database of local safety factors ($1-SF_L$) was built and the curves of fragility for the local behaviour of masonry portions were evaluated in the area subjected to static and seismic improvement. Local behaviour was assessed both in the original pre-improvement situation and in the post-improvement situation. The results are shown in the follow.

In Figure 7a it can be seen how the static improvement made to the floor of rooms 2 (ground floor) and 31 (first floor) has induced an improvement in local performance. In fact, for an acceleration of 0.15g (upper limit value and inferior respectively for the seismic zones 3 and 2 considered here) the expected loss of performance goes from 0.89 to 0.77 di ($1-SF_{Lmax}=78\%$), which is certainly still high, but the loss of performance analysed is a loss almost on the verge of collapse.

Figure 7b shows the fragility curves of the walls of rooms 5 (ground floor) e 33 (first floor) subjected to seismic improvement of the floor. In this case, the loss of performance recorded for the accelerations analysed is around 67% of the initial performance ($1-SF_{Lmax}=67\%$). The figure shows how the seismic improvement has induced a more evident performance improvement; the expected loss of performance for an acceleration of 0.15g goes from 0.8 to 0.56 ($1-SF_{Lmax}=67\%$), showing how important it is to ensure a good clamping between vertical and horizontal elements.

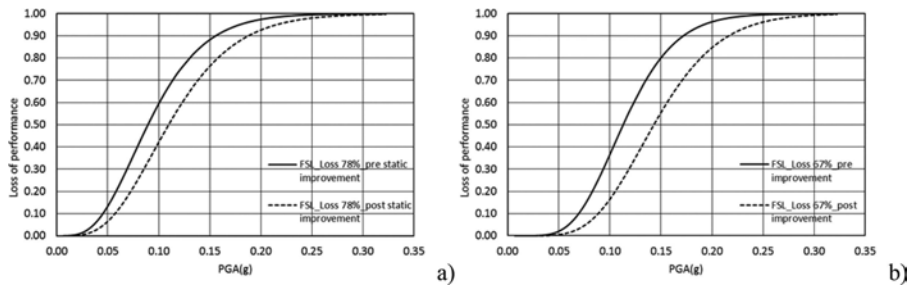


Figure 7. (a) Room 2-ground floor and 31-first floor (Figure 3 shadow area); fragility curve for pre and post static improvement; (b) Room 5-ground floor and 33-first floor (Figure 3 shadow area); fragility curves for pre - e post - seismic improvement.

4.5 Curves of fragility for different levels of performance loss SFL for rooms 5 and 33

Following the approach presented in Section 3, the fragility curves for different levels of performance loss were constructed for the rooms subjected to seismic improvement.

Figure 8 shows the results obtained for the initial situation (pre-seismic improvement) (Figure 8a) and for the current situation (post-seismic improvement) (Figure 8b).

From the two figures compared, it is possible to observe how the probability of exceeding the thresholds is translated on the acceleration axis of quantities varying from 0.019g for the curve relating to the loss of performance of 20% to 0.037g for the curve relating to the loss of performance of 50%.

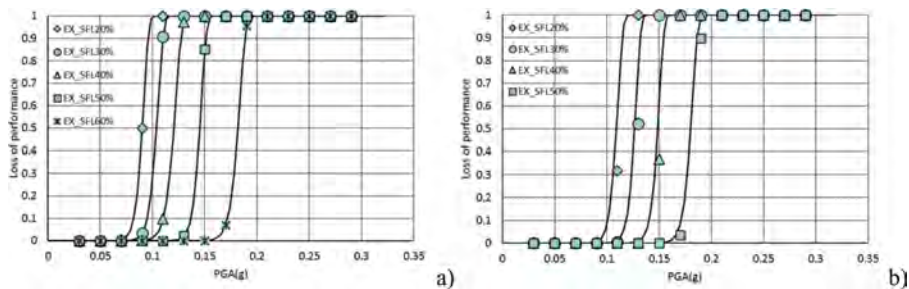


Figure 8. Fragility curves for different SF_L thresholds for rooms 5 and 33: (a) pre-seismic improvement; (b) post-seismic improvement.

Also from this analysis it is highlighted how the seismic improvement introduces an improvement of the local performances for all the investigated thresholds.

Considering that the examined structure is located in seismic zone 3, we can deduce that there have been implementation measures in the structure; the worst forecast seems to foresee a loss of local performance of no more than 40%.

5 CONCLUSIONS

The method proposed in this paper shows how the probabilistic evaluation of the global seismic performance of a historic masonry building can be carried out quickly, also on the basis of data already in the possession of public bodies, and how it can offer a first outline of priority interventions. The picture will certainly not be exhaustive, it would be important to investigate the local seismic performance as well, but these investigations require a more detailed information campaign.

The case study presented allowed us to investigate the variations of both the global and the local safety factor. The results obtained show that the improvement in the behaviour of the building obtained with local seismic improvements is difficult to detect from the analysis on the variation of the global safety factor. However, the general method can already suggest to a public body or the municipality on which buildings it would be useful to plan more detailed diagnostics.

If it were also possible to undertake an investigation on the variation of local seismic factors, this analysis would be able to predict the impact of some structural choices on the future behaviour of the building, in terms of less loss of local safety.

ACKNOWLEDGMENTS

The following research is funded by the CARIPLO Foundation, Milan, Italy, in the context of the 2017 Art and Culture-Cultural Heritage at Risk Calls, Thanks to the ACCC, Hydea s.p.a. and Lares s.r.l. for the collaboration undertaken in this project. Thanks also to the RELUIS Group and in particular to Professor Giuliana Cardani with whom I started developing this approach.

REFERENCES

- Angjeliu, G.; Cardani, G. & Garavaglia, E. 2022. Seismic Vulnerability Assessment of Historic Masonry Buildings through Fragility Curves Approach, in *Proc of 15th World Cong. on Comput. Mech. (WCCM-XV) and 8th Asian Pacific Cong. on Comput. Mech. (APCOM-VIII)*, Yokohama, Japan, July 31 to August 5, 2022, *Structural Mechanics, Dynamics and Engineering*, Seiichi Koshizuka editor, The Congress Chair, The University of Tokyo, Japan: 1-12.
- Borri, A., De Maria, A. & Casaglia, S. 2014. The EAL-M method for the seismic classification of the existing masonry buildings: A comparison between different methods and preliminary evaluations of other typologies, *Progett. Sismica*, 5: 11–29.
- Borri, A.; Corradi, M.; Castori, G. & De Maria, A. 2015, A method for the analysis and classification of historic masonry. *Bull. Earthq. Eng.* 13: 2647–2665.
- Flora, A.; Perrone, G. & Cardone, D. 2020 Evaluating Collapse Fragility Curves for Existing Buildings Retrofitted Using Seismic Isolation, *Appl. Sci.* 10 (8) 2844: 1–12.
- Garavaglia E.; Pavani R. & Sgambi L. 2021. The Use of Fragility Curves in the Life-Cycle Assessment of Deteriorating Bridge Structures, *Computation*, 9(25): 1–17.
- Garavaglia, E.; Anzani, A.; Binda, L. & Cardani, G., 2008. Fragility curve probabilistic model applied to durability and long term mechanical damage of masonry, *Materials and structures*, 41(4): 733–749.
- Garavaglia, E.; Anzani, A.; Maroldi, F. & Vanerio F. 2020. Non-Invasive Identification of Vulnerability Elements in Existing Buildings and Their Visualization in the BIM Model for Better Project Management: The Case Study of Cuccagna Farmhouse. This article belongs to the Special Issue Nondestructive Testing (NDT), Lacidonia G. Editor, *Appl. Sci.* 10(6): 1–24,
- NTC2018, Italian Building Code, adopted with DM 18/01/2018, 2018.
- Rosti, A.; Rota, M. & Penna, A. 2018. Damage classification and derivation of damage probability matrices from L'Aquila (2009) post-earthquake survey data, *Bull. Earthq. Eng.*, 16(9): 3687–3720.
- Saloustros, S.; Pelà, L.; Roca, P. & Portal J. 2015. Numerical analysis of structural damage in the church of the Poblet Monastery, *Eng. Failure Analysis*, 48: 41–61,
- Sandoli A.; Lignola, G.P., Calderoni B. & Prota 2021. A. Fragility curves for Italian URM buildings based on a hybrid method, *Bul. of Earthq. Eng.* 19(12): 4979–5013.
- Singha, I A. & Kiremidjian, A.S. 1996. Method for probabilistic evaluation of seismic structural damage, *J.I of Structural Eng.* 122(12): 1459–1467.
- Zuccaro, G.; Perelli, F.L.; De Gregorio, D. & Cacace F., 2021. Empirical vulnerability curves for Italian masonry buildings: evolution of vulnerability model from the DPM to curves as a function of acceleration, *Bull. Earthq. Eng.*, 19(8): 3077–3097.

Attack of aggressive carbon dioxide on hardened Portland and blast furnace slag cement paste

F. Wagemann & F. Schmidt-Döhl

Institute of Materials, Physics and Chemistry of Buildings, Hamburg University of Technology, Hamburg, Germany

A. Rahimi

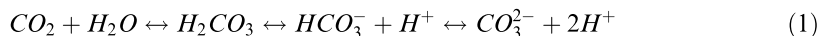
Federal Waterways Engineering and Research Institute, Karlsruhe, Germany

ABSTRACT: Natural groundwater and soil can contain substances which are aggressive to concrete and cement-based structures. Especially aggressive carbon dioxide occurs frequently. Chemical attack by aggressive carbon dioxide occurs in several phases in commercial cements used in foundation engineering. After a period of carbonation a leading front where calcium hydroxide is dissolved, depending on the availability in the binder matrix, is generated. As the attack progresses, the calcium carbonate formed is dissolved, leaving a layer rich in amorphous silicon dioxide, which has lower mechanical strength. This can result in problems in the long-term load-bearing behavior of more sensitive components with smaller dimensions and under tensile stress, in particular ground anchors and micro piles, which are manufactured using cement suspensions in the subsoil. This study evaluates the mechanisms induced by aggressive carbon dioxide in CEM III/A and CEM III/B compared with CEM I paste. Cement paste specimen with water-cement ratios of 0.4 and 0.5 stored in about 90 mg/l (exposure class XA2) aggressive CO_2 for 3, 6 and 12 months are investigated. The methods include X-Ray fluorescence analysis as well as polarized light microscopy on thin sections. The depth of impact is measured and evaluated in terms of durability of geotechnical elements.

1 INTRODUCTION

1.1 Sources and determination of aggressive carbon dioxide

Carbonic acid is a common part of natural groundwater. Carbon dioxide is required for its formation. Sources of carbon dioxide in subsoils and groundwater are decomposition processes of organic materials or current or recent volcanic activity in the geologic past (Terzaghi 1949; White 1957). The carbonic acid reacts to different species depending on the temperature and pH value of the water. Those species are carbonic acid H_2CO_3 , hydrogen carbonate HCO_3^- and carbonate CO_3^{2-} as shown in Equation (1).



The carbonate equilibrium describes the temperature-dependent equilibrium of carbonate dissolved in the water and the amount of carbonic acid. In case of an excess of free carbon dioxide, the water is calcite aggressive. When carbon dioxide is depleted, precipitation of calcium carbonate occurs. Figure 1 visualizes the carbonate equilibrium according to Tillmans & Heublein (1912) for a temperature of 10 °C, which corresponds to the mean value of the groundwater temperature of the isothermal zone in Germany (Hölting & Coldewey 2013). There is no free CO_2 at equilibrium. A hypothetical groundwater sample is depicted with pairs of values that lie above the equilibrium curve. Thus, this groundwater is calcite aggressive

(lime dissolving). However, only a fraction of the free CO_2 is calcite aggressive, which can be calculated by the translation to the equilibrium curve (see Figure 1). The slope of the straight line is $-1/2$ from the stoichiometric relationship that when 1 mole of calcium carbonate is dissolved, 1 mole of carbonic acid and 2 moles of hydrogen carbonate go into solution. The point of intersection with the carbonate equilibrium curve gives the corresponding y-axis intercept and thus the content of calcite aggressive CO_2 . It's worth mentioning that this amount is difficult to determine. It can be specified by the marble test for water stability or calculated from the total concentration of all species of a groundwater sample.

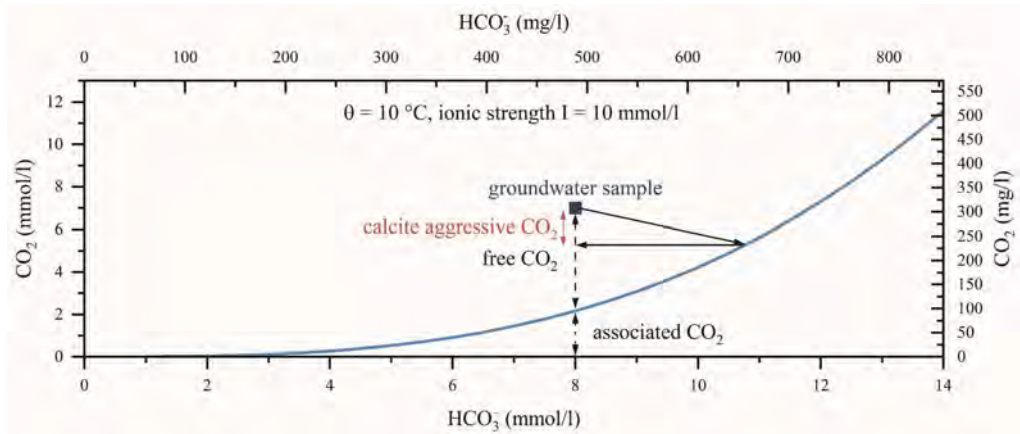


Figure 1. Visualization of the carbonate equilibrium with definition of the terms associated, free and calcite aggressive CO_2 ; calculation of the Tillman equation.

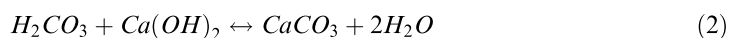
The degree of chemical attack on concrete structures is defined in EN 206-1 (DIN EN 206-1:2001-07) and in Germany additionally in conjunction with DIN 1045-2:2008-08. Table 1 shows the concentrations of aggressive carbon dioxide and the linked classification of aggressiveness XA from the German standards.

Table 1. Limiting values for the assessment of the rate of attack and description of aggressiveness for aggressive carbon dioxide in natural groundwater according to DIN EN 206-1:2001-07.

Exposure class	XA1	XA2	XA3
Action	weakly corrosive	moderately corrosive	strongly corrosive
$CO_{2,aggressive}$ (mg/l)	≥ 15 to ≤ 40	> 40 to ≤ 100	> 100 until saturation

1.2 Mechanism of chemical attack by aggressive carbon dioxide

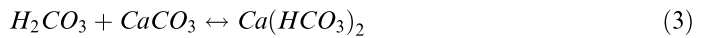
Aggressive carbon dioxide in groundwater damages cement paste through reactions with calcium-containing hydrate phases. The attack proceeds in several stages. Groundwater containing aggressive carbon dioxide enters the pore volume of cement-based elements and lowers the pH value. As a result, calcium hydroxide is getting unstable and dissolves in the pore space. It reacts with the present carbonate ion CO_3^{2-} under precipitation of calcium carbonate as shown in Equation 2.



Depending on the pH value, temperature and supersaturation calcium carbonate can occur in three polymorphs: calcite, aragonite and vaterite (Stepkowska et al. 2003). This new phase formation is associated with an increase in volume, which reduces the pore space (Pham & Prince 2014). Other hydration products like C-S-H and ettringite in the binder matrix also carbonate under the effect of carbon dioxide (Borges et al. 2010; Grounds et al. 1988). Unreacted

clinker may react with CO_2 to form calcium carbonate (Rochelle & Milodowski 2013). The formation of a carbonation front is associated with an ahead area in which the portlandite content gradually decreases (Samarakoon et al. 2022).

With further ingress of carbonic acid, the calcium carbonate is converted into easily soluble calcium hydrogen carbonate as shown in Equation 3.



The dissolved calcium hydrogen carbonate is transported through the pore space out of the binder matrix. An amorphous silicon dioxide gel with high content of aluminium and iron remains as the end product of the attack (Locher et al. 1984). The amorphous gel layer is rich in water and characterised by low mechanical strength and high porosity (Koelliker 1985).

1.3 State of research on the durability of cement-based geotechnical elements

In the past, numerous laboratory studies have been carried out on the attack of lime-dissolving carbonic acid. The experimental programs differed in the boundary conditions and the sample composition, as concretes were frequently tested. Depth of material loss of after 20 years immersion in a solution with 100 mg CO_2/l was 6 mm for Portland cement and 4 mm for blast furnace slag cement with a water-cement ratio of 0.5 (Locher et al. 1984). The observations of lower material loss and the resulting corrosion depth during previous experiments led to assessment that blast furnace slag cement is beneficial regarding the resistance to aggressive carbon dioxide (Nebel et al. 2022). This is controversial though it is well known that blast furnace slag cements have a lower resistance to carbonation (exposed to the air) due to the reduced amount of portlandite (Borges et al. 2010). Nevertheless, in foundation engineering, blast furnace slag cements are preferred in order to increase the resistance of the construction material to aggressive carbon dioxide (Schäfer et al. 2007).

Portland cement paste (w/c = 0.45) had a corrosion depth, i. e. mechanically instable layer, of 1 mm after 1 year storage in aggressive carbon dioxide with 90 mg/l (Hof et al. 2004). A few laboratory tests investigated the effect of aggressive carbon dioxide on the pull-out resistance of ground anchors (Manns 1997; Hof 2004; Triantafyllidis & Schreiner 2008). After 12 months a reduction of the anchorage force of about 20 % to 75 % was observed for varying concentrations up to 100 mg CO_2/l . Due to these results and the associated uncertainties for the use of ground anchors in the presence of aggressive carbon dioxide in groundwater on construction sites, a research project was initiated at the Federal Waterways Engineering and Research Institute in Germany (BAW) to investigate the aspects action, load-bearing capacity of geotechnical elements and resistance of the building materials.

The subject of this paper are cement paste samples which were stored in water containing aggressive CO_2 connected to a large-scale experiment described in (Herten & Heidenreich 2022).

2 INVESTIGATION METHODS AND EXPERIMENTAL PROGRAMME

2.1 Materials and sample overview

The resistance of cement paste to the aggressive carbon dioxide is investigated in this study for three different cement types: CEM I 42.5 R (CEM I), CEM III/A 52.5 L-SR/HO (CEM III/A) and CEM III/B 42.5 N-LH/SR (CEM III/B). The water-cement ratios of the neat cement suspension were 0.4 and 0.5. The mixing, casting and curing was done according to DIN EN 196-1:2016-11. In order to increase the number of samples, the prisms with the dimensions of $40 \times 40 \times 160 \text{ mm}^3$ were produced and cut in half. The chemical and mineralogical composition of the used cements are given in Tables 2 and 3, respectively.

Porosity characteristics derived from mercury intrusion porosimetry (MIP) tests are shown in Table 4. The tests were performed with a Micromeritics Pore Sizer 9420 mercury porosimeter with corresponding software Auto Pore IV 9500. The pressure range was 0.005 - 400 MPa with corresponding intrudable pore radii between 151.4 μm and 1.9 nm. The sample were cured under tap water for at least 56 days and subsequently oven-dried at 70 °C until mass constancy was achieved. The compressive strength was determined according to DIN EN 196-1:2016-11.

Table 2. Chemical composition of the used cements determined with X-ray fluorescent analysis applying the NIST 1881a standard.

Cement type	Chemical composition								
	Wt.-%	CaO	SiO ₂	Al ₂ O ₃	Fe ₂ O ₃	MgO	Na ₂ O	K ₂ O	SO ₃
CEM I	63.7	20.0	5.7	2.5	1.7	0.26	0.8	3.0	2.1
CEM III/A	51.2	26.1	8.5	1.9	4.9	< 0.1	0.8	4.0	2.1
CEM III/B	46.7	29.1	10.0	1.1	6.0	0.3	0.6	3.6	1.5

Table 3. Mineralogical composition of the used cements.

Cement type	Mineralogical composition					
	Wt.-%	C ₃ S	C ₂ S	C ₃ A	C ₄ AF	C ₂ F
CEM I	54.2	17.8	10.1	7.5	0	0
CEM III/A	n.d.	n.d.	n.d.	n.d.	n.d.	55.0
CEM III/B	n.d.	n.d.	n.d.	n.d.	n.d.	69.2

Table 4. Porosity measured by mercury intrusion porosimetry (sample age: 56 days); compressive strength.

Cement type	w/c	Median pore radius	Intrudable porosity	Compressive strength
		µm	Vol.-%	N/mm ²
CEM I	0.4	0.0516	24.7	56.90
CEM I	0.5	0.0448	28.4	48.54
CEM III/A	0.4	0.0248	21.5	50.58
CEM III/A	0.5	0.0210	27.8	40.42
CEM III/B	0.4	0.0140	25.6	55.43
CEM III/B	0.5	0.0143	33.4	45.85

2.2 Exposure conditions

The cement paste samples were stored in tap water until the exposure began. Due to distortions caused by the Corona pandemic, storage was delayed so that the sample age was about 1 year instead of 56 days planned. The cement paste samples were marked with identity tags on cable ties and carefully stored in a stainless-steel tank on grids. The solution had a mean concentration of aggressive carbon dioxide of 89 ± 14 mg/l and a temperature of 14.5 ± 3.2 °C. The tanks were uniformly flown through with the attacking medium by an inlet device at a speed of 5.5 l/h.

2.3 Change in weight

The change in weight $m_{i,t}$ at time t in relation to the initial weight $m_{i,0}$ at the beginning of storage is a simple test method that provides an initial, straightforward assessment of the resistance of the cement paste samples. After 3-, 6- and 12-months storage in free solution, two samples were carefully taken out from each cement paste series. Adhering water was removed by dripping. The prisms were weighed to the accuracy of 0.1 g. The samples were then packed airtight in plastic boxes for further examination. The change in weight Δm was determined by Equation 4 and is given as the mean value of both samples. Reference storage in tap water was used to validate the weight change.

$$\Delta m = \frac{1}{n} \sum_{i=1}^n \frac{m_{i,0} - m_{i,t}}{m_{i,0}} \quad (4)$$

2.4 X-ray fluorescence analysis

X-ray fluorescence analysis (XRF) is used to determine the elemental composition of a material. During the measurement, the material is irradiated with X-rays and electron transitions are triggered in the near-nuclear region. The energised atoms emit an element-specific X-ray fluorescence radiation. The qualitative element composition is determined with the help of the respective wavelength. The intensity of the fluorescence radiation provides information on the quantitative elemental composition. (Schmidt-Döhl 2013)

The investigations were conducted with the XGT 7200 V by Horiba. This is an energy dispersive device for local μ -XRF with a resolution of up to 10 μm . To determine the depth of influence qualitative measurements were conducted. The measurements were carried out on sections of two samples per series at each time of removal from exposure. The variation of the composition of relevant elements over the depth of a sample enables statements about the degradation process. Due to the attack mechanism of aggressive carbon dioxide, mainly the element calcium was used for evaluation. Iron, aluminium and silicon served as plausibility checks. For this purpose, mappings were created over areas of min. $4 \times 4 \text{ mm}^2$. This measuring field size was determined from preliminary tests, as it was optimal in terms of resolution and measuring time and at the same time representative for the entire sample. For statistical validation, 4 measurements were carried out per sample series. The measurements were performed with an energising voltage of 50 kV, an amperage of 1.0 mA and a minimum number of accumulations of 3 with the 10 μm capillary.

2.5 Polarized light microscopy on thin section

Polarized light microscopy permits optical examination of samples down to a resolution in the micrometre scale. Both the microstructure of the specimen and the phase composition can be examined with linearly polarized light or with crossed polarizing filter (crossed polars) (Schmidt-Döhl 2013). A representative section of a sample series was selected for each time point of removal from exposure.

2.6 Definition of the term depth of impact

The term damage or corrosion depth is not generally defined for cementitious building materials under chemical attack. The *fib* Model Code 2010 (International Federation for Structural Concrete 2013) contains a model for describing the degradation of concrete by acids. This attack with decalcification results in a corrosion depth relative to the original surface which is comprised of the removal depth and the depth of the corroded material.

In principle, damage due to chemical attack includes a chemical and subsequent mechanical change in the properties of the material. Depending on the component or structure a relevant depth of impact can be defined. For several geotechnical elements the friction at the surface of the component is essential for the load-bearing capacity and the stability of the system. The attack of aggressive carbon dioxide in groundwaters results in different types of layers over the depth of the cross-section. A distinction is drawn between an amorphous layer, a carbonated layer and a layer in which portlandite is depleted. While the hardness as a benchmark for the mechanical strength of the carbonated layer of a Portland cement paste increases by about 100 % the mechanical strength of the amorphous silica layer is reduced to 39 % of the microhardness of unaltered cement paste (Kutchko et al. 2007). With regard to the durability of cement-based geotechnical elements exposed to aggressive carbon dioxide, in this study the amorphous layer with reduced mechanical strength is defined as depth of damage. However, the thickness of the preceding chemically altered layers are also reported, as they are indicators of the development of the attack and mark the depth of impact.

3 RESULTS

3.1 Change in weight

The change in weight for 3 different exposure duration is given in Figure 2. The results indicate that with increasing exposure duration, the effect of lower porosity becomes negligible

due to the lower w/c ratio. The cement type CEM III/A shows the lowest weight loss as a result of the decalcification by aggressive carbon dioxide. The attack causes a comparable loss of mass in CEM III/B and CEM I hardened cement paste specimens.

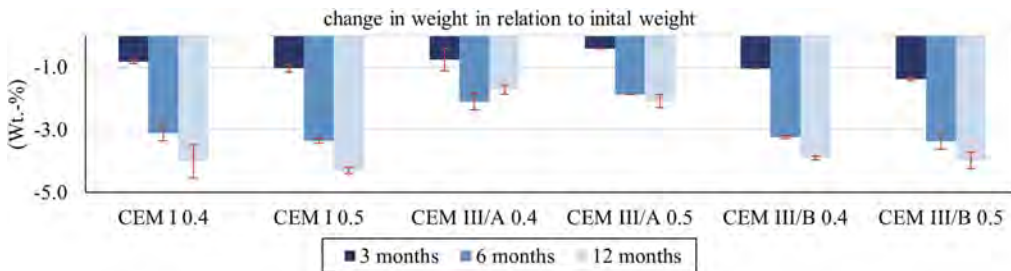


Figure 2. Change in weight of cement paste samples in relation to initial weight for different exposure duration in aggressive carbon dioxide.

3.2 Determination of depth of impact by XRF and polarized light microscopy

Figure 3 shows the determination of different layers due to the attack by aggressive carbon dioxide. The amorphous layer is recognisable in the XRF images by only a few Ca-counts. The calcium intensity increases in the carbonated layer. The preceding layer with portlandite depletion is often better visualised by using image processing tools, e.g. by segmentation with ImageJ. The carbonated layer and the decrease in calcium concentration overlap with increasing duration of attack. The thin section microscopy gives further insights of the attack. The amorphous layer was stabilized with epoxy resin before thin section preparation. In cross polarized light the porosity of the amorphous layer is significantly distinguishable by the blue impregnating resin. Relicts of clinker and small amounts of calcite are found in this layer. Unreacted slag grains are also found for the CEM III/A and CEM III/B samples.

The carbonated layer is characterized by pale high-order interference colours in cross-polarized light. Calcite is extremely birefringent. Portlandite is high birefringent in cross-polarized light and stands out against the almost isotropic binder matrix. (Ingham 2013) Portlandite depletion is evident in the increase in isotropic character of the cement paste.

In Figure 4 the measured layer thicknesses of the investigated samples are plotted. The thickness of the individual layers increases with increasing exposure duration. The lower clinker content of CEM III/A and CEM III/B cement types and the small amount of portlandite available for carbonation result in smaller carbonated, low portlandite layers and a larger amorphous layer than in the CEM I samples. Thicknesses measured by XRF and thin section microscopy usually show good correlation. The determination of the carbonated layer is more difficult to assess for the blast furnace slag cements. Figure 4 also shows good agreement between the two test methods with regard to the

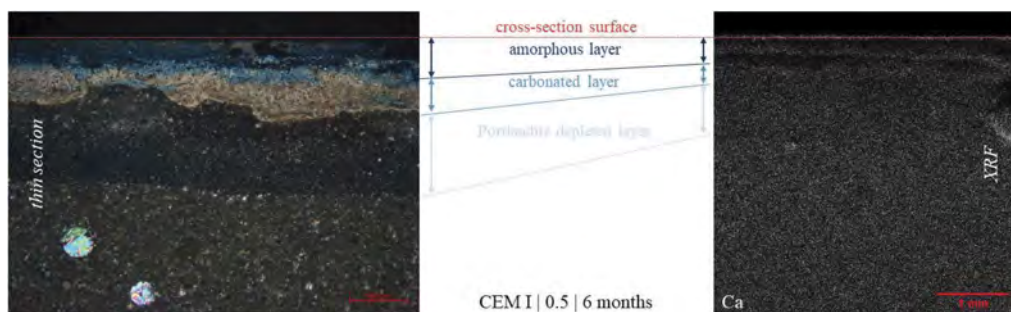


Figure 3. Exemplary determination of different layers as a result of the attack of aggressive CO_2 ; left: thin section with crossed polars (scale bar corresponds to 500 μm); right: elemental distribution of Calcium by XRF (scale bar corresponds to 1 mm).

layer thicknesses for CEM I and CEM III/A specimens. Due to a major delay in the preparation of thin sections, the 12-month samples were previously measured only by XRF. The development of the layer thicknesses indicates a trend according to the square root of time law, which has been described by other authors for attack by aggressive carbon dioxide (Grube & Rechenberg 1987).

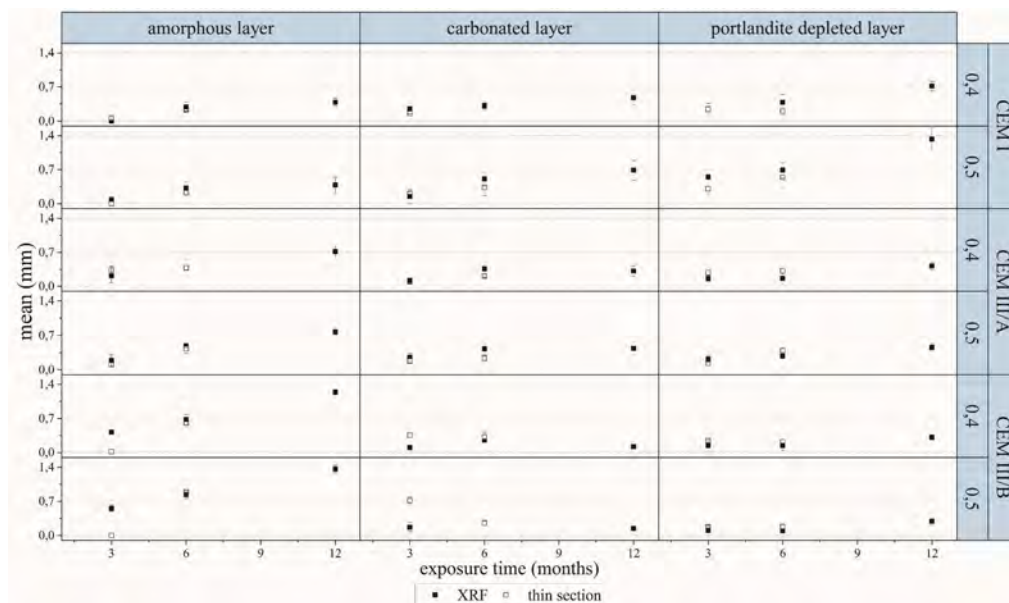


Figure 4. Thickness of layers under aggressive carbon dioxide exposure. Filled symbols: mean values of XRF method, blank symbols: mean values of thin section microscopy.

4 CONCLUSIONS

Three different cement types were investigated regarding their resistance against aggressive carbon dioxide. Though formulations containing slag are described beneficial in literature the results in this paper cannot confirm this. The results of the weight change during exposure time show hardly any difference between CEM I and CEM III/B specimens. The CEM III/A samples, however, show lower mass losses in comparison. The effect of a lower w/c ratio is less pronounced with increasing duration of exposure. The depth of impact was determined by means of XRF and thin section microscopy. The attack by aggressive carbon dioxide leads to the formation of three different layers in the corroded binder matrix: an amorphous, a carbonated and a portlandite depleted layer. Regarding the decrease in mechanical strength in the amorphous layer, its thickness becomes relevant for durability of geotechnical structures and their load-bearing capacity.

Due to their lower calcium hydroxide content, the buffer capacity of the CEM III/A and CEM III/B samples is limited. This results in the formation of a thicker amorphous and a thinner carbonated layer than with the Portland cement samples. The thickness of all layer types and thus the total depth of the chemically modified binder matrix is deeper for all cement types with higher w/c ratio. The change in weight of the samples correlates with the depth of impact. However, the distribution of the layer thicknesses and especially the formation of the mechanically less stable amorphous layer cannot be deduced from it.

For lower concentrations of aggressive carbon dioxide in groundwater in the range of XA1, Portland cement formulations seem to be favourable at least for a short service life as the investigations carried out lasted a maximum of 1 year. In this service life period CEM III/A cements can also be considered favourable. For statements about durability in the long-term further investigations are advisable. The mechanical characteristic of the amorphous layer is of major importance for the transfer of forces of geotechnical elements. The unhydrated clinker and slag grains can have a beneficial effect.

REFERENCES

- Borges, P. H., Costa, J. O., Milestone, N. B., Lynsdale, C. J. & Streatfield, R. E. 2010. Carbonation of CH and C–S–H in composite cement pastes containing high amounts of BFS. *Cement and Concrete Research* 40(2): 284–292.
- DIN 1045-2 2008-08. *Tragwerke aus Beton, Stahlbeton und Spannbeton – Teil 2: Beton – Festlegung, Eigenschaften, Herstellung und Konformität – Anwendungsregeln zu DIN EN 206-1*. Berlin: Beuth.
- DIN EN 196-1 2016-11. *Prüfverfahren für Zement – Teil 1: Bestimmung der Festigkeit; Deutsche Fassung EN 196-1:2016*. Berlin: Beuth.
- DIN EN 206-1 2001-07. *Beton Teil 1: Festlegung, Eigenschaften, Herstellung und Konformität*. Berlin: Beuth.
- Grounds, T., G Midgley, H. & V Novell, D. 1988. Carbonation of ettringite by atmospheric carbon dioxide. *Thermochemica Acta* 135: 347–352.
- Grube, H. & Rechenberg, W. 1987. Betonabtrag durch chemisch angreifende saure Wässer. Teil 1. *Beton* 37(11): 446–451.
- Herten, M. & Heidenreich, F. 2022. Kalklösende Kohlensäure im Grundwasser und die Konsequenzen. In: Bundesanstalt für Wasserbau (ed.) *Projekte in der Geotechnik an Bundeswasserstraßen*. Karlsruhe: 17–22.
- Hof, C. 2004. *Über das Verpressankertragverhalten unter kalklösendem Kohlensäureangriff*. Dissertation. Ruhr-Universität Bochum.
- Hof, C., Triantafyllidis, T. & Schmidt-Döhl, F. 2004. Über die Abnahme der Tragfähigkeit von Verpressankern unter Angriff von kalklösender Kohlensäure. *Bautechnik* 81(5): 357–363.
- Hölting, B. & Coldewey, W. G. 2013. *Hydrogeologie. Einführung in die Allgemeine und Angewandte Hydrogeologie*. 8. Auflage Heidelberg: Spektrum Akademischer Verlag.
- Ingham, J. P. 2013. *Geomaterials under the microscope. A colour guide; building stone, roofing slate, aggregate, concrete, mortar, plaster, bricks, ceramics and bituminous mixtures*. London: Manson Publishing.
- International Federation for Structural Concrete 2013. *fib Model Code for Concrete Structures 2010*. Weinheim, Germany: Wiley-VCH.
- Koelliker, E. 1985. Method for microscopic observation of corrosion layers on concrete and mortar. *Cement and Concrete Research* 15(5): 909–913.
- Kutchko, B. G., Strazisar, B. R., Dzombak, D. A., Lowry, G. V. & Thaulow, N. 2007. Degradation of well cement by CO₂ under geologic sequestration conditions. *Environmental science & technology* 41(13): 4787–4792.
- Locher, F. W., Rechenberg, W. & Sprung, S. 1984. Beton nach 20-jähriger Einwirkung von kalklösender Kohlensäure. *Beton* 34(5): 193–198.
- Manns, W. 1997. Long-term influence of aggressive carbonic acid upon the bearing capacity of ground anchors. *Otto-Graf-Journal* 8: 63–74.
- Nebel, H. S., Ramler, D. & Matschei, T. 2022. Dauerhaftigkeitsnachweis chemisch beanspruchter Betone: Angriff durch kalklösende Kohlensäure. *Beton* 72(6): 208–211.
- Pham, S. T. & Prince, W. 2014. Effects of Carbonation on the Microstructure of Cement Materials: Influence of Measuring Methods and of Types of Cement. *International Journal of Concrete Structures and Materials* 8(4): 327–333.
- Rochelle, C. A. & Milodowski, A. E. 2013. Carbonation of borehole seals: Comparing evidence from short-term laboratory experiments and long-term natural analogues. *Applied Geochemistry* 30: 161–177.
- Samarakoon, M. H., Ranjith, P. G. & Wanniarachchi, W. 2022. Properties of well cement following carbonated brine exposure under HTHP conditions: A comparative study of alkali-activated and class G cements. *Cement and Concrete Composites* 126: 104342.
- Schäfer, R., Höfer, U. & Triantafyllidis, T. 2007. Herstellung von Verpresspfählen zur Auftriebssicherung unter dem Einfluß kalklösender Kohlensäure. *Bautechnik* 84(1): 8–14.
- Schmidt-Döhl, F. 2013. *Materialprüfung im Bauwesen*. Stuttgart: Fraunhofer IRB Verlag.
- Stepkowska, E. T., Pérez-Rodríguez, J. L., Sayagués, M. J. & Martínez-Blanes, J. M. 2003. Calcite, vaterite and aragonite forming on cement hydration from liquid and gaseous phase. *Journal of Thermal Analysis and Calorimetry* 73(1): 247–269.
- Terzaghi, R. D. 1949. Concrete deterioration due to carbonic acid. *Journal of the Boston Society of Civil Engineers* 36(2): 136–152.
- Tillmans, J. & Heublein, O. 1912. Über die kohlen-sauren Kalk angreifende Kohlensäure der natürlichen Wässer. *Gesundheits-Ingenieur* 35: 669–677.
- Triantafyllidis, T. & Schreiner, V. 2008. *Tragverhalten von Verpressankern unter kalklösender CO₂-Belastung. Nachfolgeprojekt*. Stuttgart: Fraunhofer IRB Verlag. (Bauforschung T; 3167).
- White, D. E. 1957. Thermal waters of volcanic origin. *Geological Society of America Bulletin* 68(12): 1637–1658.

Big data in construction project management: The Colombian northeast case

S. Zabala-Vargas, M. Jiménez-Barrera & L. Vargas-Sánchez
Corporación Universitaria Minuto de Dios-UNIMINUTO, Bogotá, Colombia

M. Jaimes-Quintanilla
Fundación Universitaria Internacional de la Rioja-UNIR, Bogotá, Colombia

ABSTRACT: In recent years, the information associated with project management in organizations has grown exponentially. Delays, cost overruns, risk management problems in projects are recurrent situations. In this sense, the literature review shows that emerging technologies such as Big-Data and Data-Science have become very important for decision making. The present research is developed in the northeastern region of Colombia - South America. The proposal allowed to evaluate, with qualitative research, the state of incorporation of emerging technologies in companies of the construction sector. This was done through the focus group technique with 20 construction companies selected at convenience. A literature review was also carried out. Among the main results are: Low knowledge and appropriation of the companies of the sector on related technologies, interest in incorporating strategies that allow generating greater value to the productive chain and the intention of initiating R&D&I processes in the field of knowledge.

1 INTRODUCTION

The construction industry is one of the sectors with the greatest impact on Colombia's economy. According to the National Administrative Department of Statistics - DANE, this line of the economy in the year 2022 (third quarter of the year) contributed about 14% of the country's Gross Domestic Product; employing more than 1,700,000 people throughout the national territory (Departamento Administrativo Nacional de Estadística - DANE, 2022). Now, it is indicated in Project Management Institute (2017) that project management has multiple challenges, such as: communication problems, scope affectation, failure to meet objectives, inadequate risk management, among others. The high volume of information, and its mismanagement, especially in highly complex projects, becomes a problem and a loss of value for the project (Saltz, 2015).

These challenges in project information management, especially in the handling of large volumes of data and the strategies to make sense of them, have been addressed with emerging concepts/tools such as: A-) Big-Data, understood as the handling of large volumes of data (capture, management, storage and analysis) in order to generate relevant information and consolidate data interoperability (Chang and Grady, 2019; Gupta and Rani, 2019), B-) Data Analytics (also called Data Science), oriented to decision making from the extraction of information from large volumes of data, determining patterns and trends (Haider, 2015; Kelleher and Tierney, 2018) and C-) Artificial Intelligence (IA), as the strategy based on algorithms that allows machines (from a broad understanding of that definition) to perform processes, make decisions and in general emulate the human brain (Boden, 2017; Rouhiainen, 2018). In Colombia, some strategies have been proposed for the modernization of the construction sector, among them the National BIM Strategy 2020-2026 (Gobierno Nacional de Colombia, 2020); focusing on the use of the

Building Information Modeling (BIM) methodology as a construction management system. It is in this type of bets where the present research has enough importance and commitment, since it seeks to generate an integral model that allows the construction sector to strengthen its competitiveness. There are several references in other countries that are of interest for the research (Huang et al., 2021; Wu and AbouRizk, 2023; Zhang et al., 2017).

However, the concept of Big Data is a relatively recent idea. Cites Gupta and Rani (2019), that the concept of Big Data defines an “avalanche” of data generated from current processes, and that it has become a new scientific paradigm; understood in a broad view in data science. The most important processes associated with Big-Data are: knowledge extraction from data, knowledge discovery, information gathering, data archeology, pattern processing and exploration in data analysis; having applications in a large panorama of industries and economic sectors (Varian, 2014). From a technological point of view, the processing of this information is performed from the use of specialized software, which is considered a new generation of tools and architectures designed to extract, in the most economical and efficient way possible, relevant information from large volumes of data. This is sought to be done in the shortest possible time and with the greatest contribution to the organization (International Data Corporation, 2017).

It is at this point where these technologies connect with project management and administration. A literature review has been proposed with the following characteristics: Bibliographic index: SCOPUS; Search equation: (((“project management” OR “project administration”) AND (“big data” OR “data science”)); Revision period: 2014 – 2022 and Type of documents: Scientific articles, conference communications, literature reviews, books and book chapters.

This review shows a total of 534 records associated with the subject. In 2014 (12), in 2017 (40), in 2021 (121) and in 2023 (73). Further details are presented in the results section. In the following lines some important aspects resulting from this review are presented. Ruchi and Srinath (2018) highlight that Big Data and Machine learning (another important concept), is developed in organizations in multiple factors: product analysis, customer identification, market strategy definition, risk management and project management. In this case, they propose a framework for the analysis and processing of information associated with schedule management, project cost, risk analysis, project resources, among others. The use of these technologies allows optimizing project management by having the information processed and analyzed for decision making. The work presented by Saltz (2015) emphasizes the importance of reviewing methodologies, frameworks and tools to incorporate Big Data to the effective management of teams, as a strategy to enhance the development and monitoring of projects. This research considers that the development of technological tools, operations research and business intelligence are fields where it is possible to define the use of Big Data with an important impact.

On the other hand, Xiao et al. (2020) propose the integration between BIM technology and Big Data to optimize the way of managing business data, resulting in the improvement of the project life cycle and generating an implementation path with higher quality and efficiency. Zhu, et al (2022), presents complementary arguments of the importance of the use of intelligent technologies, such as Big-Data, for the optimization of project management in the construction area. The high levels of fragmentation, their complexity, the high turnover of the actors involved in construction management, the complex and, in many cases, hostile environments; are major challenges that hinder the proper management of projects in the construction area. It is also in this case that the proposal of Wu & AbouRizk (2023), suggests a novel route for the transformation of project management in a reliable and timely manner.

Conceptually, there are two central themes for research: Big-Data and Data Science. The concept of Big-Data has been developing for a little more than a decade. There are several meanings for this idea, according in many cases to the preceding theoretical perspective, to the conceptual and methodological application of the same, and in some cases to the associated technology. This concept refers to the set of data whose size is beyond the capacity of typical software tools for database management; oriented to capture, store, manage and analyze relevant information for decision making. The primary characteristics are high levels of: Volume (size), Velocity, variability, veracity, validity and value of information (Gupta & Rani, 2018). From this perspective, two additional concepts are presented to understand the purpose of this research: Big Data Engineering (BDE) and Big Data Analytics. The first refers to the development of the scalable technological infrastructure necessary for the capture, collection, storage and efficient

preparation of data. This proposal modifies the traditional paradigm that uses relational databases, and proposes flexible, decentralized, and highly dynamic strategies to achieve efficient information management (NIST, 2015). Now, Big Data Analytics, refers to all processes that require the use of large databases to discover and obtain meaningful knowledge for decision making.

Depending on the type of industry, the type of data analysis, the knowledge objective, Big Data Analytics requires specific and diverse skills, generating the concept of Data Science (Haider, 2015). The central objective of Data Science is to foster efficient decision making based on the extraction of information from large volumes of data. Among the elements that make up this activity are principles, context definitions, algorithms and processes to extract the not-so-obvious information from data. It seeks to establish patterns that facilitate decision making. Determining marketing trends, verifying and tracking scope, identifying segmentation and characteristics of a project's stakeholders, establishing strategies to manage risks and classifying communications are key aspects of project management that can be supported by Data Science (Kelleher & Tierney, 2018). It is important to point out that although the design and construction of architectural and civil works are consecutive and separate phases, there is an important relationship between them. Besides being mutually dependent. The constructions suffer constant modifications in the design that are informed in the execution, as well as bidirectional processes until the product is delivered to satisfaction (completion of the project). In the construction analysis phase, designers must consider all the particularities of the construction process, which is usually a type of knowledge that resides with highly experienced architects. Many researchers have proposed to "take advantage" of Big Data and Data Science, to develop knowledge in constructive design and generate rules that facilitate the development of projects (Freischlad, Schnellenbach-held, & Pullmann, 2006).

However, data collected after construction, i.e. while the building or structure is in operation, are little used in design (or redesign). Occupancy evaluation, bioclimatic characteristics, commissioning review, among others, allow to verify subsystems and make adjustment decisions. It is important then to consider comprehensive evaluations of buildings, understood as projects under development, to determine proposals for performance improvement, feedback to designers-architects, document successes and failures; and generally, increase the body of knowledge for future projects (Loyola, 2019). It is in this context and with the problems previously described, this paper presents the first results of a research whose main objective: To establish a methodological route for the incorporation of emerging technologies (Big Data and Data Science) in the management of construction projects and civil works in Colombia; in order to optimize project management and facilitate decision making. Particularly a mixed research route was selected. In this work the qualitative results are presented.

For the methodology, the focus group technique was used, applied to 20 companies of the construction sector of Northeastern Colombia. The main category was the determination of the level of appropriation of new technologies (Big-Data and Data Science) in the sector. The data were processed with the support of the Atlas.ti tool. As a result of the research, two aspects are found: 1- Low level of appropriation of emerging technologies (Big-Data and Data-Science) in the management of construction projects in Northeastern Colombia, 2- Broad interest of the sector (companies to which the focus group was applied) to appropriate new technologies, and 3- Set of guidelines and initial recommendations of the research team from the review of the state of the art of the subject. Finally, the present work has a novel factor in reviewing the incorporation of Big-Data and Data-Science in project management in the construction sector, and its articulation with BIM.

2 METHODOLOGY

The paradigm selected for the research is mixed. For the present document, the qualitative part is related to the qualitative part. A categorical analysis was developed based on the maturity level of appropriation of emerging technologies in companies of the construction sector. The focus group was the tool used (Krueger and Casey, 2014). The design did not include a control group.

2.1 *Participants*

The sample used was made up of 20 companies in the construction sector in the northeastern region of Colombia. Two focus groups were formed, each of 10 companies. There was representation from project management or the technical area. The selected companies are part of the database of the Colombian Chamber of Construction-Camacol.

2.2 *Procedure*

The research had five stages. The first step was the design of the instrument (questions) to be applied in the focus group. The questions were created from the references (Saltz, 2015; Wu and AbouRizk, 2023; Zhang et al., 2017).

The second step was the review of the scientific literature in Scopus. The main contributions specific to the topic of interest were extracted. The article quality assessment proposed by (Petticrew and Roberts, 2006), adapted by articles (Zabala-Vargas et al., 2020), was applied. The third step was the application of the interview protocol in the focus groups. This interview is presented in the Materials and Instruments section. The number of members per focus group did not exceed 12 (10) (Baumgartner et al., 2005). A single session was conducted for each focus group, lasting approximately 45 minutes. Each focus group had a moderator and an assistant. Atlas.ti was used to analyze data. The fourth step was the qualitative analysis of the data, adapting the best possible practices (Baumgartner et al., 2005; Krueger and Casey, 2014; Onwuegbuzie et al., 2011).

A deductive analysis was used. The initial category was the level of maturity in technology appropriation in companies in the construction sector. To ensure the validity of the qualitative analysis and avoid rater bias, a second rater was involved in the process. Inter-rater reliability was evaluated by comparison for the different categories, and a value (Cohen's Kappa coefficient) of 0.81 was found. Differences were resolved through dialogue and adjustments were made to the analysis. The last step was to generate an initial set of recommendations and guidelines for companies in the sector, mainly on tools and strategies that can be used as an initial phase of implementation of emerging technologies.

2.3 *Categories*

Three categories of analysis have been considered in this proposal: 1-) Maturity level of appropriation of emerging technologies (N_M), 2-) Relevance of the use of technology (I_U_TIC) and 3-) Interest in investing in emerging technologies for project management (INV). The three categories focus directly on organizations in the construction sector.

2.4 *Instruments and materials.*

For data collection, the focus group technique was implemented. The focus group was selected due to the possibility of fostering a brainstorming and discussion environment among the representatives of the constructors (Krueger and Casey, 2014). The specific Keyword in context-KWIC technique proposed by (Glaser, 1992) was considered. The source of the analysis was the verbatim transcription of each participant's contribution and each session was videotaped. An analysis of the emerging categories was conducted, also considering the opinion of both those who support the use of technology in project management and those who consider themselves dissenters (focus group members who disagree with the group in general). A set of nine questions was used: 5 for category 1 (N_M), 3 for category 2 (I_U_TIC) and 1 for category 3 (INV). The questions are presented in Table 1, being a semi-structured interview adapted for the focus group.

A second instrument allows tabulation of the main fields associated with the articles obtained from the literature review in Scopus. These fields are: Authors, Title, Year, Affiliations, Abstract, Methodology and Main results.

The quality of the articles was checked using 11 quality criteria extracted from Petticrew and Roberts (2006). Each criterion was evaluated on three scales: 1) 0, not defined, 2) 0.5, presented but not clearly, and 3) 1, presented clearly. To be included in the systematic review, the articles had to have a score of at least 6.5 for all 11 criteria, at least half of the maximum number of points possible.

Table 1. Focus group questions by category.

ID	Category	Question
N_M_1	Maturity level of appropriation of emerging technologies (N_M)	Does the organization have installed technological capabilities (hardware and software) for project management?
N_M_2		Is there clarity in the processes to develop projects with technological incorporation in the organization?
N_M_3		Does the organization have information systems for project management? If yes, which ones?
N_M_4		Does the organization identify the concepts of Big-Data and Data Science?
N_M_5		Does the organization incorporate Big-Data and Data Science concepts in project management?
I_U_TIC_1	Relevance of the use of technology (I_U_TIC)	Does the organization consider the use of technology important in the development of its processes?
I_U_TIC_2		Do the contractors of your organization use technological tools for the management of different projects and services?
I_U_TIC_3		Does technological development play an important role within the organization?
INV_1	Interest in investing in emerging technologies for project management (INV)	Is the organization interested in investing in technologies that facilitate the management of information for decision-making in project management?
INV_2		Within the annual budget planning, is there a specific item for the company's technological development?
INV_3		Is the organization interested in participating in Research-Development-Innovation processes?

3 RESULTS AND ANALYSIS

3.1 *Bibliometric analysis*

This section presents the main aspects of the bibliometric analysis performed. Figure 1 shows the number of documents per year. There is a total of 534 publications in the period 2014-2022. There is evidence of a significant increase in the last 4 years. The maximum production peak was in the year 2021. In relation to the authors with the highest level of publication, it is J. S. Saltz, from Syracuse University, who has the highest number of records in the area of knowledge. The top 6 authors, with the number of papers produced in the review window, are: Saltz, J.S (17), Shamshurin, I (8), Miller, G.J (6), Tamura, Y. (6), Yamada, S (5) and Earley, S. (4).

In the dynamics of publication by country, the Top 5 are: China (181), United States (77), Germany (30), United Kingdom (26) and Australia (20). In terms of papers by affiliation, there are: Syracuse University (18), Beijing Jiaotong University (7), Tottori University (6), Wuhan University of Technology (6), Tsinghua University (6) and Managing Consultant Maxmetrics (5).

3.2 *Categorical analysis*

For the categorical analysis, the initial categories with which the focus group instrument was created are taken as a reference. These categories are: Maturity level of appropriation of emerging technologies (N_M), Relevance of the use of technology (I_U_TIC) and Interest in investing in emerging technologies for project management (INV). The two focus groups and the subsequent analysis of the information in Atlas.ti generated the map of categories shown in Figure 2.

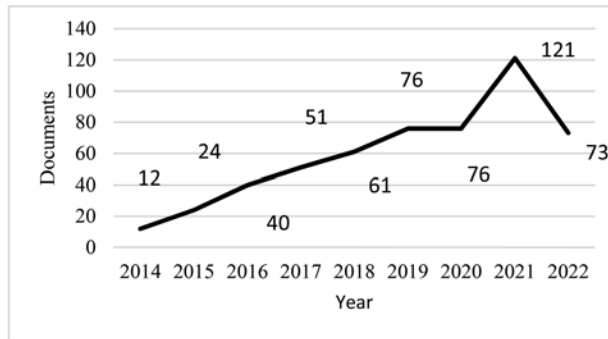


Figure 1. Documents vs Year (Scopus 2023).

The category with the highest density is the Maturity level of appropriation of emerging technologies (N_M). One of the first emerging categories is Infrastructure, which is made up of both software components (information systems and licenses for other applications) and hardware devices. In this last category, the importance for organizations to have servers, clustered computing equipment and devices to ensure information security is detected. Another of the initial categories (Relevance of the use of I_U_ICT technology) also appears in the focus group analysis, focusing on the existence of established processes for the incorporation of technology (which are not always found in organizations in an explicit and standardized way) and the low level of appropriation, associated with low knowledge, of the technologies that are the focus of this research (Big-Data and Data Science). It should be noted that in this case the organizations state that they are aware of the topic, but do not have a detailed level of knowledge or appropriation, at least identified, in the organization. The other key aspect is associated with the interest in investing in emerging technologies for project management (INV), of which there are two important aspects. The first is that the organizations, in general, declare broad interest in investing in technology; even considering the recognition of these in all their management. In turn, it is stated that there is annual budget planning for these investments. The other emerging category is the low or medium interest in Research, Development and Innovation processes, which is mainly associated to not clearly knowing the benefits that projects in this line can generate. In this last aspect, some organizations state that they are aware of the existence of tax benefits if they invest in research, development and innovation projects.

3.3 Summary of guidelines and recommendations

This paper briefly presents some recommendations or guidelines that can be adopted by companies in the construction sector, integrated to the development of the BIM strategy in Colombia (Gobierno Nacional de Colombia, 2020); with projection to the year 2026. In the first instance, it is key to recognize that in the world, as cited by Saltz (2015), a single methodology for the incorporation of Big-Data and Data-Science in project management is still under discussion. Therefore, it is very important to generate specific versions for each country that adapt these technologies to the context and market dynamics of the work performed. To carry out this methodology requires a pro-fund identification of the dynamics of the sector and a more effective relationship between academia, the IT industry and the construction sector itself.

Another important strategy arises from the identification of agile project management methodologies, which articulated with Big-Data and Data-Science, allow effective solutions. In this sense, it is important to define a Big-Data orientation for project or product life cycle management. As proposed by Zhang et al. (2017), a strategy mediated by: 1-) Registration and data collection; from the incorporation of sensors, embedded devices, among others; 2-) Storage and processing of information; from the integration of distributed computing using Big-Data and databases (structured, semi-structured and unstructured), 3-) Development of

data mining models; for clustering, association, classification and prediction processes; and finally 4-) the integration of Big-Data and Data-Science throughout the project life cycle. From the hardware point of view, integrate server technology (own or in the cloud), as well as IT security solutions to protect the data and finally the organizational knowledge.

The integration of specific software for the integration of BIM methodology with the management of large volumes of data is also fundamental in the incorporation process. Another important recommendation for the construction sector is the planning, execution and follow-up of training and recognition processes for the project team in the basic concepts of Big-Data and Data Science, as well as in the specific training of the technological infrastructure (hardware, software and data networks) required for the incorporation of these emerging technologies. Finally, a strategy to determine the lessons learned from the technological incorporation, which allows iterative optimization of the projects that are being developed; optimizing both the design phase and the construction phase.

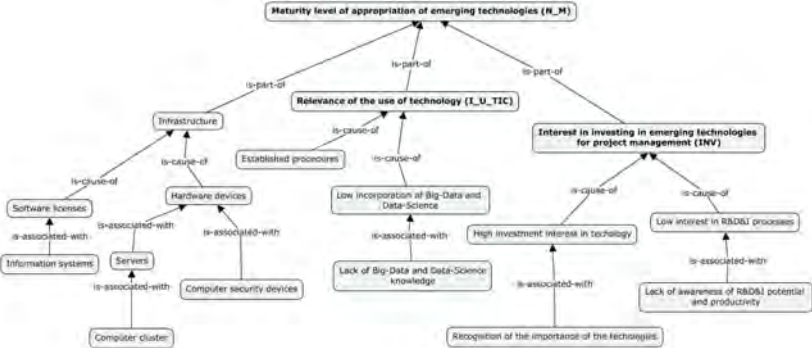


Figure 2. Map of categories resulting from the focus group.

4 DISCUSSION AND CONCLUSIONS

The development of this research shows that the construction sector in Northeastern Colombia still has a long way to go in the incorporation of emerging technologies, such as Big-Data and Data-Science. One of the important aspects is to determine its own methodologies, adapted from state-of-the-art knowledge, for the incorporation of strategies that optimize the project life cycle. These methodologies, as cited by Saltz (2015), are constantly developing and evolving. Having a specific framework for the incorporation of emerging technologies (Big-Data, Data-Science, among others) is also fundamental. These frameworks articulate so many methodological processes, incorporation of tools and technological infrastructure, development of models for data cleaning and analysis, and the application of related technologies in the project life cycle. This, in a very consistent way, with what was proposed by (Zhang et al., 2017).

On the other hand, determining new strategies for construction project management (CPM), also point to issues of project regulation and supervision. In agreement with Huang et al. (2021), many researches have focused on the construction phase, resorting to digital tools or methods; but other phases of the project life cycle do not present the same incorporation and development. In this sense, it is important not only for the case study of this paper, but in general for the construction sector; to continue strengthening the incorporation of frameworks, methodologies and models; based on Big-Data and Data-Science in the construction sector. Finally, as Wu and AbouRizk (2023) indicate, there are many fragmentation phenomena along the value chain of construction projects, high complexity and uncertainty, transience of the parties involved and hostile environments. All this generates that the data obtained in construction projects remain noisy, fragmented and very heterogeneous; generating barriers for its use. It is for this reason that it is worthwhile to continue researching on the subject and generating strategies for decision-making in projects, based on reliable real-time data.

REFERENCES

- Baumgartner, T.A., Strong, C.H. & Hensley, L.D. 2005. *Conducting and reading research in health and human performance*, 4th ed. McGraw-Hill, New York.
- Boden, M.A. 2017. *Inteligencia artificial*. Turner.
- Chang, W. & Grady, N. 2019. *NIST Big Data Interoperability Framework: Volume 1, Definitions*. <https://doi.org/10.6028/NIST.SP.1500-1r2>.
- Departamento Administrativo Nacional de Estadística – DANE. 2022. Indicadores Económicos Alrededor de la Construcción (IEAC). Bogotá.
- Gobierno Nacional de Colombia, 2020. Estrategia Nacional BIM 2020-2026. Bogotá.
- Gupta, D. & Rani, R. 2019. A study of big data evolution and research challenges. *Journal of Information Science* 45, 322–340. <https://doi.org/10.1177/0165551518789880>.
- Haider, M. 2015. *Getting started with data science: Making sense of data with analytics*. IBM Press.
- Huang, Y., Shi, Q., Zuo, J., Pena-Mora, F. & Chen, J. 2021. Research status and challenges of data-driven construction project management in the big data context. *Advances in Civil Engineering* 2021, 1–19.
- Kelleher, J.D. & Tierney, B. 2018. *Data science*. MIT Press.
- Krueger, R.A. & Casey, M.A. 2014. *Focus groups: A practical guide for applied research*, 5th ed. Sage publications, Los Angeles.
- Onwuegbuzie, A., Dickinson, W., Leech, N. & Zoran, A. 2011. Un marco cualitativo para la recolección y análisis de datos en la investigación basada en grupos focales. *Paradigmas* 3, 127–157.
- Petticrew, M. & Roberts, H. 2006. *Systematic Reviews in the Social Sciences: A Practical Guide*. Wiley-Blackwell.
- Project Management Institute. 2017. *Guía de los Fundamentos Para la Dirección de Proyectos (Guía del Pmbok)*, 6th ed.
- Rouhiainen, L. 2018. *Inteligencia artificial*. Madrid: Alienta Editorial.
- Ruchi, S. & Srinath, P. 2018. Big Data Platform for Enterprise project management digitization using Machine learning. *Presented at the 2018 Second International Conference on Electronics, Communication and Aerospace Technology (ICECA)*, IEEE, pp. 1479–1484.
- Saltz, J.S. 2015. The need for new processes, methodologies and tools to support big data teams and improve big data project effectiveness. *Presented at the 2015 IEEE International Conference on Big Data (Big Data)*, IEEE, pp. 2066–2071.
- Varian, H.R. 2014. Big data: New tricks for econometrics. *Journal of Economic Perspectives* 28, 3–28.
- Wu, L. & AbouRizk, S. 2023. Towards construction's digital future: A roadmap for enhancing data value. *Presented at the Canadian Society of Civil Engineering Annual Conference, Springer*, pp. 225–238.
- Xiao, X., Liu, J. & Ren, L. 2020. Study on Construction Engineering Management Based on BIM from the Perspective of Big Data. *Presented at the 2020 International Conference on Computer Information and Big Data Applications (CIBDA)*, IEEE, pp. 111–115.
- Zabala-Vargas, S., Ardila-Segovia, D., García-Mora, L. & de Benito, B. 2020. Aprendizaje Basado en Juegos (GBL) aplicado a la Enseñanza de la Matemática en Educación Superior: Una revisión Sistemática de Literatura. *Formacion Universitaria* 13, 13–26. <https://doi.org/10.4067/S0718-50062020000100013>.
- Zhang, Y., Ren, S., Liu, Y., Sakao, T. & Huisingsh, D. 2017. A framework for Big Data driven product lifecycle management. *Journal of Cleaner Production* 159, 229–240.
- Zhu, H., Hwang, B.-G., Ngo, J. & Tan, J.P.S. 2022. Applications of Smart Technologies in Construction Project Management. *Journal of Construction Engineering and Management* 148, 04022010–04022010.

Numerical analysis of prestressed sleepers affected by expansive mechanisms

R.P. Randi & L.M. Trautwein

State University of Campinas, Campinas, São Paulo, Brazil

D.J.M. Mariata

Methodist University of Angola, Luanda, Luanda, Angola

L.F.M. Sanchez

University of Ottawa, Ottawa, Canada

A.C. Santos

Federal University of Uberlândia, Uberlândia, Minas Gerais, Uberlândia, Brazil

ABSTRACT: This paper assesses the effects of expansion mechanisms in prestressed concrete sleepers. A consequence of these mechanisms in concrete is the decrease in some mechanical properties such as compressive strength, tensile strength and Young's modulus. Using the software ATENA 3D, based on the Finite Element Method, four geometrically identical sleepers were simulated with different expansion level rates. The values of the reduction of the mechanical properties were obtained through experimental tests results. From the results of the numerical analysis it was possible to correlate the maximum displacement, the states of stress-strain and the crack pattern with the loss of mechanical properties. It was observed that the shoulder region of prestressed sleepers tends to be more susceptible to the appearance of cracks, a phenomenon caused mainly as a consequence of the sleepers manufacturing process by prestressing, causing loss of bond in the regions close to the edge of the sleepers.

1 INTRODUCTION

Expansive Reactions in concrete are due to chemical processes and causes cracks and deterioration of the material during its service life cycle. According to Hasparyk & Kuperman (2021) these reactions depend on the type of causative agent, the materials involved, the dimension of the structural element and the environment exposition. These expansive mechanisms may be caused by the Alkali-Aggregate Reaction (AAR), the Sulfate Attack or both combined.

A specific case of Sulfate Attack is the Delayed Ettringite Formation (DEF). This mechanism occurs due to the high heat of hydration as a result of exothermic reactions of cement, leading to high temperatures on concrete at early ages; or thermal curing of the concrete at high temperatures. (Hasparyk & Kuperman, 2021)

Several authors have published researches correlating expansive reactions to the loss of mechanical properties of concrete. Among these authors, Nixon & Bollinghaus (1985), Hoobs (1988), Larive (1997), Marzouk & Langdon (2003), Smaoui et al. (2004), Sanchez et al. (2017) and Gorga (2018), showed that the expansive mechanisms, in fact, directly affects the compressive strength, the tensile strength and the Young's modulus of concrete.

Prestressed concrete sleepers are generally manufactured using the techniques of prestressing reinforcement and thermal curing of concrete. These techniques are essential for increasing the speed of production of these structural elements. One of the objectives of using thermal curing

in the manufacture of precast concrete elements is to increase the rate of Portland cement hydration reactions and, consequently, obtain a gain in compressive strength at early ages. The gain of compressive strength at the early ages allows the application of stress in the reinforcement, which are anchored by adhesion between steel and concrete.

Figure 1 presents the behavior of the prestressed reinforcement anchored by adherence, where l_{bp} is the anchorage length, $\varnothing 0$ is the diameter of the reinforcement without prestressing loads, $\varnothing 1$ is the diameter of the reinforcement with prestressing load and σ_{P0} is the value of the initial prestressed stress. It is possible to observe a length at the end face in which the prestressing level is not complete, decreasing the stiffness of the element in this region, leading to the appearance of cracks.

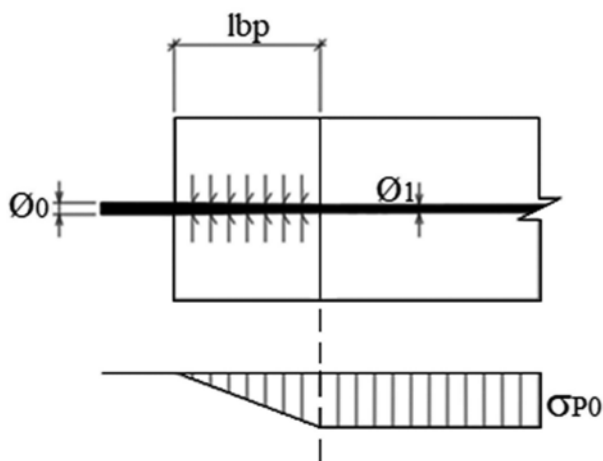


Figure 1. Adherence between steel and concrete in prestressed elements. Adapted from Pfeil (1984).

Figure 2 presents the distribution of mapped cracks on the shoulder of a prestressed concrete sleeper. The appearance of these mapped cracks may be explained by two phenomena occurring simultaneously: the occurrence of expansive mechanisms of concrete and the loss of the adherence between steel and concrete in these region, as discussed before.



Figure 2. Crack pattern in the shoulder of a prestressed concrete sleeper.

2 METHODOLOGY

Four prestressed concrete sleepers were numerically simulated, through non-linear analysis, in the software ATENA 3D, 5.9.1 version, based on the Finite Element Method. The concrete sleepers were geometrically identical, but with mechanical properties of concrete that vary with the level of expansion by 0.00%, 0.05%, 0.12% and 0.30%.

2.1 Numerical simulations

The constitutive model *CC3DNonLinearCementitious2* was implemented to simulate the concrete. According to Cervenka & Papanikolaou (2008), this material model is based in a Fracture-Plastic Constitutive Model, which allows the simulation of the behavior of the concrete associated to plastification when submitted to compressive stresses and fracture when submitted to tensile stresses. For the reinforcement steel material (wires), the discrete model *ReinforcementEC2* was implemented, presenting a Uniaxial Stress State based on the Hooke's Law and a Plastic Model based on the Von Mises Criteria. The sleeper's supports and the load application region were simulated with a set of steel plates and natural rubber. For the steel plates material it was implemented an Isotropic Model, *CC3DBiLinearSteelVonMises*, being the stress-strain relation bilinear with a yielding patamar and Von Mises Criteria. The natural rubber material was simulated through the *CC3DElastIsotropic Model*, being the stress-strain relation linear for compressive and tensile. More details about the constitutive models of materials are described in Cervenka et al. (2021).

The numerical models were submitted to the Negative Bending Moment test in the center of the sleeper based on AREMA (2020), being this test one of the prescriptions for the approval of sleepers. The test consists of applying a load in the center of the overturned sleeper with the intention to simulate the behavior of the sleeper in service, which has a centralized negative bending moment due to the elastic support of the sleeper (ballast). However, as the objective of this paper is to assess the crack pattern in the shoulder region, the analyzed models were loaded only up to the load of the opening of the first centralized crack with a width of 0.10 mm in order to prevent that these cracks which form the failure plane of the sleeper has any influence on the formation of cracks in the shoulders.

Totally, 102 load steps were applied to the models. The two first steps are related to the applying of prestress in the wires, consisting of the imposition of an initial strain in each wire, representing an initial prestressing force of 15.00 kN. The other 100 load steps are related to the application of the load to open the first crack, being applied to the upper steel plate of the models. Each load step represents 2.50 kN or totally 5.73 MPa applied in the steel plate area.

The boundary conditions (constraints) were imposed in three distinct points, restraining the translation of the model: on the bottom faces of the support plates (axis x, y and z) and on the top of the loading plate (axis x). Finally, a structured mesh of finite elements with average dimensions of 50.00 mm was applied.

Figure 3 presents the sleepers geometry, the dispose of the thirteen steel wires in the transversal section and the numerical model. The bottom of the sleepers has 291.00 mm. The top of the sleepers has 206.00 mm and 190.00 mm, in the center section and in the rail seat section, respectively.

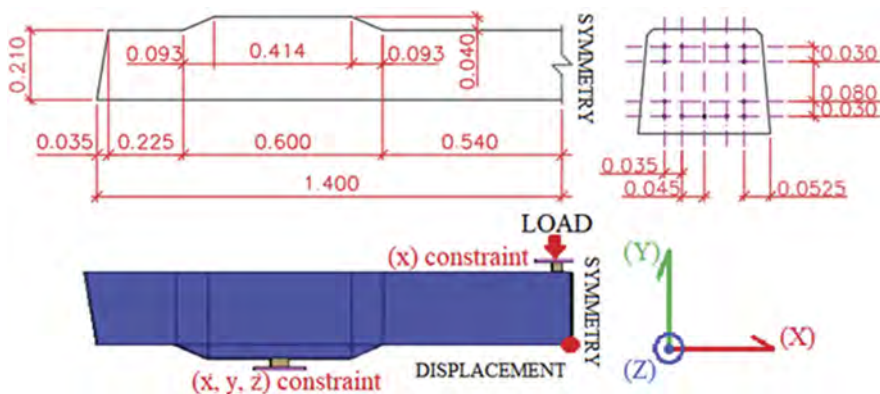


Figure 3. Sleepers' geometry, wires dispose in the transverse section and numerical model, measurements in meters.

2.2 Mechanical properties of the materials

The proposed nomenclature for the four sleeper models is formed by the suffix PCS (Prestressed Concrete Sleeper) followed by 0.00, 0.05, 0.12 and 0.30, which represents the expansion level of each sleeper, being respectively, PCS0.00, PCS0.05, PCS0.12 e PCS0.30.

PCS0.00 model is the base for the other three models. This model was simulated with a compressive strength of 42.00 MPa and with the other mechanical properties calculated by the CEB-FIP Model Code 2010. The compressive strength, the tensile strength and the Young's modulus of the PCS0.05, PCS0.12 and PCS0.30 models were reduced according to the study by Sanchez et al. (2017) and will be presented below.

The thirteen prestressed wires has 6.00 mm diameter and are of the low relaxation steel bar type, notched, with a strength class of 1560/1750 MPa and a Young's modulus of 205 GPa, according to ASTM A421 (2021) and ASTM A881 (2017).

The supports are constituted of a set of SHORE A 50 hardness natural rubber strips with dimensions 50.80 x 25.40 x 190.00 mm in the supports and 25.40 x 12.70 x 291.00 mm in the load application point (length x thickness x width). The supports are complemented by steel plates with a yield strength of 550 MPa and Young's modulus of 205 MPa, with dimensions 150.00 x 12.70 x 291.00 mm (length x thickness x width).

Sanchez et al. (2017) performed a multi-level analysis on concrete specimens (100 mm x 200 mm) of compressive strengths of 25, 35 and 45 MPa with different types of reactive and non-reactive aggregates and twenty different types of concrete trace. Microscopic tests (SDT and DRI) and destructive mechanical tests (compressive strength, the tensile strength and the Young's modulus) were carried out in order to relate the changes in the mechanical properties of the material with the level of expansion.

Among the many traces tested by the authors, Tx + Hp 45 was chosen to implement to the numerical models. This trace is composed by High-purity fine-grained limestone from Newfoundland in Canada and Polymictic sand (granitic, mixed volcanic, quartzite, chert, quartz) from El Paso in the United States. Table 1 presents the mechanical properties loss in each expansion level studied in this research.

Table 1. Mechanical properties loss for different expansion levels according to Sanchez et al. (2017).

Exp. Level (%)	Days	Compressive Strength (%)	Tensile Strength (MPa)	Tensile Strength (%)	Young's modulus (MPa)	Young's modulus (%)	Fracture Energy* (MN/m)
0.00	28	00.0	42.00	00.0	2.54	00.0	34688.7
0.05	19	11.5	37.16	57.9	1.07	30.1	24230.8
0.12	33	12.2	36.86	60.3	1.01	28.4	24822.6
0.30	99	21.9	32.81	59.5	1.03	50.6	17118.5

*Fracture Energy according to CEB-FIP Model Code 2010.

3 RESULTS

The results related to the Load *versus* Displacement curves, tensile strength, opening of the first cracks and the stresses in the directions of the x and z axis will be presented. All these results will be presented for the first crack opening load at 0.10 mm.

3.1 Load versus Displacement curves, tensile strength and opening of the first cracks

Table 2 presents the values of the first crack opening load (0.10 mm) and the vertical displacements in the center section of the models (Figure 3).

According to the Table 2 the PCS0.05, PCS0.12 and PCS0.30 models reached the first crack of 0.10 mm with load at 4.07%, 3.78% and 5.73% lower when compared to the model PCS0.00. Regarding to the displacements, the models with expansion showed increases of 20.25% (PCS0.05 and PCS0.12) and 38.05% (PCS0.30) in relation to the model without expansion.

Table 2. First crack opening load and vertical displacement for the four models.

	PCS0.00	PCS0.05	PCS0.12	PCS0.30
Load (kN)	88.00	84.42	84.67	82.96
Displacement (mm)	1.63	1.96	1.96	2.25

Figure 4 presents the Load *versus* Displacement curves of the numerical models PCS0.00, PCS0.05, PCS0.12 and PCS0.30 and the graphs of Figure 5 show the relations between loss of mechanical properties *versus* load and displacement.

Analyzing the Load *versus* Displacement curves, the difference in stiffness in the models can be noted; an expected result since the models PCS0.05, PCS0.12 and PCS0.30 presents a decrease in the Young's modulus as a consequence of the expansive mechanisms.

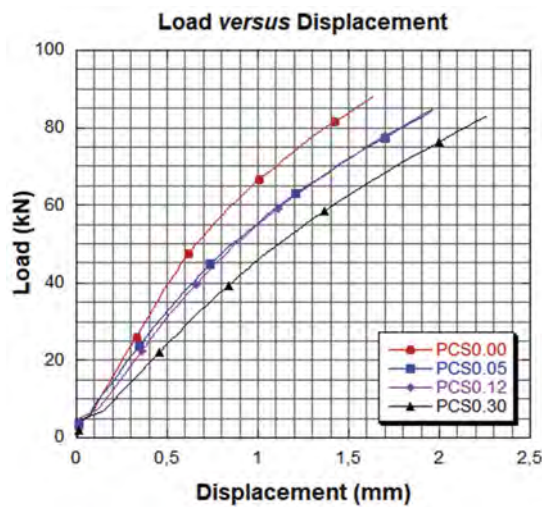


Figure 4. Load *versus* Displacement curves of the four numerical models.

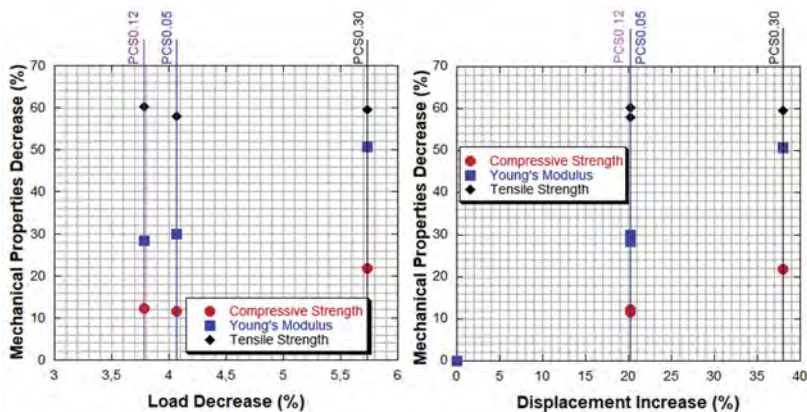


Figure 5. Mechanical properties *versus* load decrease and displacement increase.

Through the graphs shown in Figure 5, a greater influence of the Young's modulus on the behavior of models with expansion can be noted in relation to the model without expansion. This is observed by the greater variation in displacements than in crack opening load which would be affected by the tensile strength. This phenomenon can be explained by the fact that the sleeper is prestressed, delaying the opening of the cracks, even for lower tensile strengths.

Figure 6 presents the lateral and top faces of the center of the four numerically simulated sleepers in the load step of the opening of the first crack. The tension range presented on the side of each sleeper show the maximum value as the tensile strength of each model.

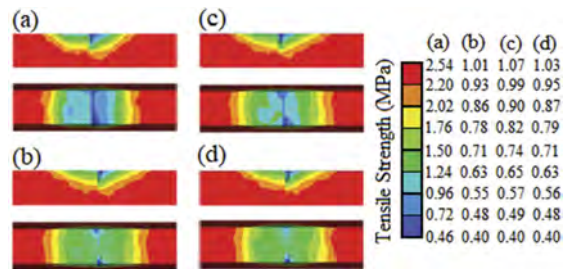


Figure 6. Distribution of tensile strength and cracks. (a) PCS0.00, (b) PCS0.05, (c) PCS0.12 e PCS0.30.

This behavior was already expected, since sleepers in prestressed concrete present the same behavior as prestressed beams, in which the first cracks appear centralized in the maximum moment section, whether in sections of positive or negative bending moments. Analyzing Figure 6, it is possible to note the decrease of the tensile strength in centralized regions of the sleeper, caused by the degradation of the material due to bending, leading to the opening of cracks. An important observation in the models presented in Figure 6 is the non-reduction of tensile strength in the decentralized sections, including shoulder region. This indicates that for the first crack opening load step there is no evidence of cracking in these regions.

Finally, Figure 7 presents the crack pattern of the four models, with crack range varying from zero to 0.10 mm. It is important to highlight that in the regions of the shoulders there was no cracks (already verified by the tensile strength in Figure 6), with the cracks concentrating in the central section of the sleepers. It is noteworthy that the first cracks appeared in the centralized region of the sleepers for the four sleepers, phenomenon also observed by Bastos (1999) and Neiva et al. (2020).

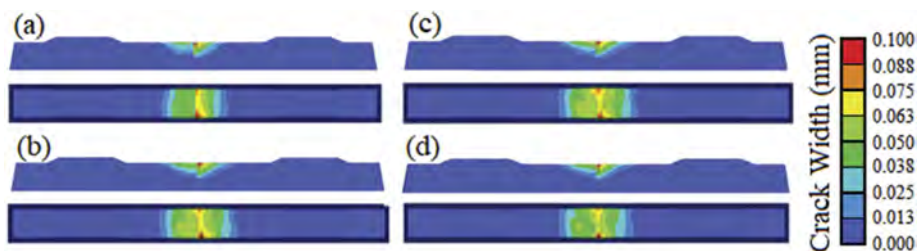


Figure 7. Crack pattern in models (a) PCS0.00, (b) PCS0.05, (c) PCS0.12 e PCS0.30.

3.2 Stresses in the directions of the x and z axis

Aiming to assess the possibility of the appearance of crack in the shoulders of the sleepers (Figure 2), the stresses in the directions of these cracks (axis x and z) were analyzed. Figure 8 present the stresses in x and z at the opening of the first crack with 0.10 mm, limited by the

tensile strength of each of the four models. Stresses in the x and z directions lead to cracks in the orthogonal directions to the axis, that is, y and x, respectively.

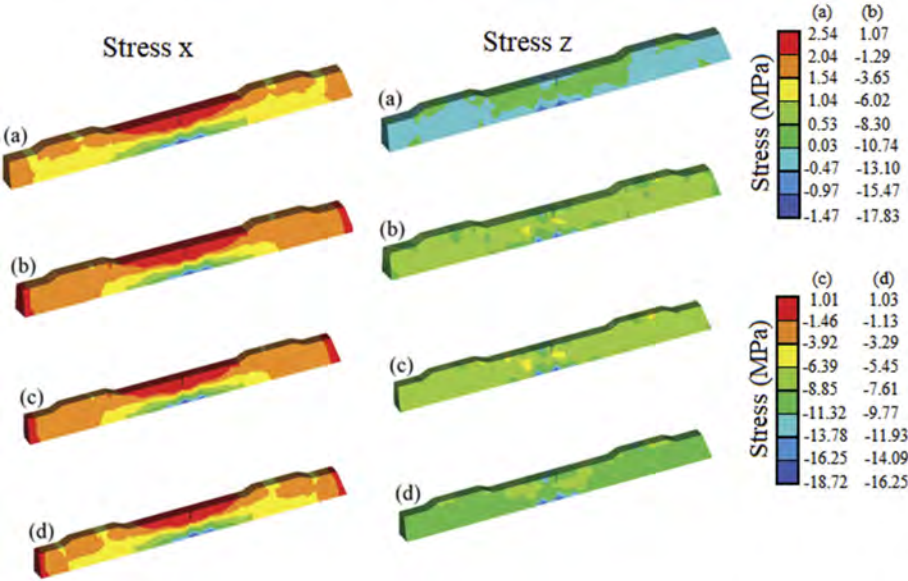


Figure 8. Stresses in the x and z directions of models (a) PCS0.00, (b) PCS0.05, (c) PCS0.12 e PCS0.30.

Observing Figure 8, it can be noticed that for the models with expansion mechanisms (PCS0.05, PCS0.12 e PCS0.30), the ends of the sleepers are on the eminence of crack opening on the front, side and upper faces (region in red, x axis), since the tensile strength was reached. It can be highlighted, as an important observation, that these regions may have been weakened by the degradation of the concrete resulting from the manufacturing process by prestressing and also by the loss of adhesion at the ends, applying an initial stress to the concrete in the first stages of the simulation.

In the case of stresses in the z axis direction, there are few observations regarding these results, since the predominant stresses are still compressive as a result of the prestressing applied to the models. As there are no loads applied in this direction, the stresses in the z axis direction are due to the state of stress to which the concrete is subjected and even for the models with lower tensile strengths, there are few possibilities of opening cracks in this direction.

4 CONCLUSIONS

In general, the numerically simulated sleepers showed expected results for the type of analysis performed, that is, they did not show major changes in structural behavior for changes made in mechanical properties.

The Load *versus* Displacement curves showed similar behavior, being influenced by the decrease in the Young's modulus of each model. As a consequence, the models with expansive mechanisms (PCS0.05, PCS0.12 e PCS0.30) presented lower stiffness when compared to the intact model (PCS0.00), greater vertical displacements and lower loads of first crack opening.

An important observation is the greater influence of the modulus of elasticity in relation to the mechanical properties of compressive and tensile strength. This fact is evidenced by the greater discrepancy between the displacements when comparing the crack opening loads, being 20.25%, 20.25%, 38.05% and 4.07%, 3.78% and 5.73% for models PCS0.05, PCS0.12

and PCS0 .30, respectively. It should be noted that the crack opening loads do not show great differences due to the fact that the sleeper is prestressed.

Regarding the opening of cracks, the models showed proximity in the results. The first cracks tend to appear in the section with the highest bending moment, that is, the central section of the sleeper. This behavior is observed in experimental tests of both sleepers and prestressed beams.

Finally, the stresses in the x axis direction show that the shoulders of sleepers with lower mechanical properties tend to present stresses closer to the tensile strength, being regions more susceptible to the opening of cracks. It can be stated that if the test were carried out at higher loads, cracks would be observed in the shoulder regions of the sleepers, presenting behavior similar to Figure 2. As for the stresses in the z axis direction, the results show that there is no tendency to opening of cracks, it is concluded that analyzes are necessary at the chemical level of the materials used or the implementation of constitutive models that simulate the degradation of concrete due to expansive mechanisms.

REFERENCES

- American Railway Engineering and Maintenance Association. 2020. *Manual for Railway Engineering. AREMA*. Volume 1 and 2, 2020.
- ASTM Standard A421. 2021. *Standard Specification for Stress-Relieved Steel Wire for Prestressed Concrete*. ASTM International, West Conshohocken, PA, 2021.
- ASTM Standard A881. 2017. *Standard Specification for Steel Wire, Indented, Low-Relaxation for Prestressed Concrete*. ASTM International, West Conshohocken, PA, 2017.
- Bastos, P.S.S. 1999. *Análise experimental de dormentes de concreto protendido reforçados com fibras de aço*. Ph. D thesis, Engineering School of São Carlos, University of São Paulo, São Carlos, São Paulo, Brazil, 1999.
- Cervenka, V. & Papanikolaou, V. K. 2008. *Three dimensional combined fracture-plastic material model for concrete*. International Journal of Plasticity, v. 12, n. 4, p. 2192–2220, 2008.
- Cervenka, V.; Jandele, L. & Cervenka, J. 2021. *ATENA program documentation, Part I: Theory*. Prague, Republic Czech: Cervenka Consulting, 2021.
- Comite Euro-Internacional Du Béton. 2010. *Model Code 2010 – First Complete Draft*. Lausanne, Switzerland, 2010.
- Gorga, R.V. 2018. *Engineering-based FE approach to appraise slender structures affected by Alkali-Aggregate Reaction (AAR)*. M.Sc. dissertation, Department of Civil Engineering, University of Ottawa, Ottawa, Ontario, Canada, 2018.
- Hasparyk, N.P.; Kuperman, S.C. 2021. *Reações expansivas deletérias no concreto*. Concrete & Buildings (ISSN 1809-7197), edition 102, Apr-Jun, 2021. DOI: dx.doi.org/10.4322/1809-7197.2021.102.0001.
- Hobbs, D.W. 1988. *Alkali-silica Reaction in Concrete*. London: Thomas Telford, 1988.
- Larive, C. 1997. *Apport combinés de l'expérimentation et de la modélisation à la compréhension de l'alcali-réaction et ses effets mécaniques*. Ph.D. thesis, Éc. Natl. Ponts Chaussées, Paris, France, 1997.
- Marzouk, H. & Langdon, S. 2003. *The effect of alkali-aggregate reactivity on the mechanical properties of high and normal strength concrete*. Cement Conc. Compos., v. 25, n. 4-5, p. 549–556, Jun 2003.
- Nixon, P.J & Bollinghaus, R. 1985. *The effect of alkali aggregate reaction on the tensile strength of concrete*. Durability. Building. Materials., v. 2, p. 243–248, 1985.
- Pfeil, W. 1984. *Prestressed Concrete – Introduction*, 2^o edition, Technical Books and Science. Brazil, 1984.
- Sanchez, L.F.M.; Fournier, B.; Jolin, M.; Mitchell, D. & Bastien, J. 2017. *Overall assessment of Alkali-Aggregate Reaction (AAR) in concretes presenting different strengths and incorporating a wide range of reactive aggregate types and natures*. Cement Concr. Res., v. 93, p. 17–31, 2017.
- Silva, R.; Silva, W.V.; Farias, J.Y.; Santos, M.A.A. & Neiva, L.O. 2020. *Experimental and Numerical Analyses of the Failure of Prestressed Concrete Railway Sleepers*. MDPI Journal - Materials 2020, v. 13, p. 1704, 2020. Doi:10.3390/ma13071704
- Smaoui, M.; Bérubé, A; Fournier, B.; Bissonnette, B. & Durand, B. 2004. *Evaluation of the expansion attained to date by concrete affected by ASR – Part I: experimental study*. Can. J. Civ. Eng., v. 31, n. 5, p. 826–845, 2004.

The probabilistic fatigue life of plain concrete under low-frequency stress reversal loading

E.C. Ferreira, P. Sotoudeh, G. Fiorillo & D. Svecova

University of Manitoba, Winnipeg, MB, Canada

ABSTRACT: There is an inherent error in selecting concrete strength for establishing maximum fatigue loads for a new experiment, due to the large variability in experimental results of compressive and split cylinder tests. Procedure presented in an earlier research was used to determine concrete strengths values with safety levels ranging between 90% to 99%. Similar process based on determining safety level is implemented in this work to determine fatigue life of concrete cylinders. Most research on fatigue of plain concrete focuses on frequencies above 1 Hz. The effects of stress reversal combined with low-frequency loading are explored in this experimental program. The program focuses on establishing the fatigue life of plain concrete cylinders subjected to cyclic tensile-compressive stresses at 0.1 Hz frequency. Concrete cylinders with 36 MPa compressive strength were studied under three high tensile stress levels, reversed fatigue loading, and a constant stress range of 11 MPa at 0.1 Hz.

1 INTRODUCTION

Infrastructures sustain different loading conditions during their lifetime. One particular loading condition that structures are prone to is fatigue loading. Fatigue is the accumulation of damage in a material due to repetitive loads, leading to cracks or complete fractures after numerous repetitions (ASTM International, 1996). It was first observed in train axles in the late 1800s and has been studied since. Concrete, among other materials, has observed its fair share of fatigue investigations by numerous researchers exploring the subject since the early 1900s (Kachkouch et al., 2022). The consensus among researchers is that there exists a large scatter in the number of cycles to failure, which is referred to as the fatigue life of concrete (Cornelissen, 1984; Tepfers, 1982; Thun et al., 2007; van Leeuwen & Siemes, 1979).

There are standard procedures to follow for the characteristic investigation of materials. However, standard procedures often disregard the fact that specimens of materials might differ in character while originating from the same batch, which is particularly true for concrete, which is heterogeneous by nature. This can be remedied by increasing the number of tested specimens and using of statistical approach rather than the use of a limited number of specimens or trivial average values of features. Therefore, the need for a statistical approach in combination with an experiment, rather than a purely experimental approach, is urged. A number of researchers addressed the challenge in different manners. For example, Khademi et al. (Khademi et al., 2015) utilized multiple linear regression and artificial neural networks to predict the compressive strength of concrete for different concrete mixtures. Although not the main focus of their study, it is interesting to know that their experimental data comprised of 2 specimens per mixture for a total amount of 90 specimens, and they used the average compressive strength value of each 2 specimens for every particular concrete mixture. This was an attempt to obtain more accurate results. To investigate the influence of the optimum number of samples for fatigue tests, Paskova and Meyer (Paskova & Meyer, 1994) ran fatigue tests on 20 cubic concrete specimens. After a statistical evaluation of their data, they

concluded that at least 5 samples and at least 3 different stress ranges are required to reach a trustworthy result on the fatigue life estimation of concrete. In another study, Nieto et al. (Nieto et al., 2006) proposed a technique to approximate the S-N curve of concrete using the fatigue results of 10 concrete specimens. They concluded that their proposed approximation method substantially reduces the amount of data required to make a prediction on S-N curves.

In designing a fatigue experiment, if the concrete strength is determined using only a limited number of tests, the inherent variability in concrete strength must be considered when selecting strength to determine stresses to be applied during the fatigue tests. If the selected strength value is too small, the specimens will experience larger fatigue life compared to those with higher strength. This is potentially the reason why many researchers agree that there is an inherent variability in the predicted fatigue life of concrete. If the strength is determined with higher accuracy, the variability may be reduced. Another approach for estimating fatigue life consists in fitting a probability distribution to a limited number of fatigue test results. If the number of specimens is limited, the distribution error may be so significant that the predictions are either over- or under-estimated. To investigate the importance of the number of specimens for the probabilistic analysis of fatigue life, Ortega et al. (Ortega et al., 2018) proposed a method to estimate the compressive fatigue life of plain concrete that accounts for the error's dispersion, and the number of tests performed. This method introduced probabilistic design curves that can be adjusted, based on a maximum tolerable error referred to as safety level.

In this study, the Ortega's method is adjusted to the case of stress-reversal fatigue analysis and the statistical approach is extended to cover characterization tests of concrete as well. To this end, a combination of experimental tests and statistical analysis was interchangeably implemented that would show the influence of sample size in either characterization tests or experimental fatigue analysis.

2 PROCEDURE AND RESULTS

Statistical analysis was used in this study to improve the efficacy of selecting concrete strength values for fatigue strength testing. First, concrete tensile and compressive strength tests were performed, and basic parameters of their statistical distributions were obtained. Then, using the aforementioned results, Ortega's approach was applied to determine the strength for the fatigue tests. In the third step, the strength values acquired in step two were used to design and perform experiments on concrete specimens under stress reversal. Finally, using these results, design curves were calibrated to estimate fatigue life and probability of failure. These steps are discussed in detail in the following sections.

3 EXPERIMENTAL PROGRAM

The total number of cylindrical specimens prepared and used for this study was 71. The cylinders are 8-in high with 4-in diameter. In order to obtain compressive strength, 23 specimens were tested in compression, while 12 specimens were tested in splitting tension to obtain tensile strength. The resulting mean compressive and tensile strengths were 36 MPa and 3 MPa, respectively. The COV of those two tests were 11.4% and 11%, respectively. For the fatigue tests, three maximum stress levels, 0.90, 0.85, and 0.80 of the tensile strength, were selected. To consider the effect of stress reversal, the stress range was kept constant at 11 MPa. Only a limited number of split tensile specimens was available in this program. Therefore, by selecting the mean value of tensile strength would overestimate the concrete strength under fatigue. In the case of compressive strength, the number of specimens was sufficient. The specific value of the stress range was obtained from an ongoing research program on an existing dam in Manitoba, Canada, that endures such stress range in a yearly cycle. A sine loading function with a frequency of 0.1 Hz was selected to test the specimens under low frequency, which is the lowest achievable frequency

with the testing equipment. A total of 36 fatigue tests were performed, 14 at the stress level of 0.90, 12 at the stress level of 0.85, and 10 at the stress level of 0.80.

4 STATISTICAL ANALYSIS

It is widely accepted that the fatigue life of concrete follows either a Lognormal or Weibull distribution (ASTM International, 2010). The larger the number of data samples from a population, the better the fit. Ortega et al. established a relationship between distribution fit error and sample size, suggesting that the appropriate sample size lies between 15 and 20 specimens (Ortega et al., 2018). Inspired by their work, the method proposed in this study is first employed to determine concrete strength value to calculate the load corresponding to each stress level and to implement conservative estimates of fatigue life of specimens subjected to stress reversal fatigue tests.

A 2-parameter Weibull distribution was fitted to each set of values obtained from compressive and splitting tensile concrete strength tests. The resulting distribution is referred to as the reference distribution. Then, 25,000 realizations were randomly sampled from the reference distribution, maintaining the same size as the original data, or 23 data points. That means that in the case of compressive strength samples, each realization contained 23 values randomly sampled from the reference distribution of compressive strength data. A 2-parameter Weibull distribution was then fitted to each randomly sampled dataset. The plot of the resulting 25,000 Weibull distributions is referred to as the scatter band, the region where any random sample of that size is likely to fall. Consequently, the bandwidth at a probability level represents the maximum variability from the reference distribution.

The observed error e_o is the relative difference between the reference distribution and each curve in the scatter band at any probability level. The error is assumed to be normally distributed with mean and standard deviation estimated from the 25,000 generated realizations. The observed error was calculated for all 25,000 curves at each of the 1000 probability levels, from 0 to 0.999 in 0.001 increments. In the distribution of the observed error, the safety level, SL, is defined as the probability that a specific error, e_p , will not be exceeded, and this value is the maximum error. Thus, for the safety level SL, the maximum error e_p is determined at each probability level as the inverse of the cumulative normal distribution function of the observed error e_o at that level.

A design curve is a correction of the reference distribution for a predetermined safety level SL. A design curve for the safety level SL is obtained by correcting the reference distribution at each probability level, according to Equation 1 below.

$$[N]_{DC} = [N]_{RD} \times \left[\frac{1}{1 + e_p} \right] \quad (1)$$

where DC and RD are indexes that refer to the design curve and reference distribution, respectively, N is the concrete strength, and e_p is the maximum error calculated at that probability level.

For each design curve, the deviation from the reference distribution is evaluated at the 5th, 50th, and 95th percentiles. The design curve for concrete strength is optional if the average deviation at those three percentiles is lower than 5%. On the other hand, a design curve for concrete strength is recommended if the average deviation is greater than 5%.

5 CONCRETE STRENGTH TESTS

Using the aforementioned method, 23 compressive strength and 12 splitting tensile strength tests were analyzed. Therefore, sample sizes of 23 and 12 were used for producing the 25,000 random realizations from the compressive and tensile reference distributions, respectively. All

reference distributions, scatter bands, and design curves were analyzed using the commercial software MATLAB vR2022a. The reference distributions were obtained using the “wblfit” built in function, and a MATLAB code was written to obtain the scatter bands and design curves according to the process described in the previous section.

The resulting scatter bands are plotted in Figure 1 for compressive strength and Figure 2 for tensile strength data. In those plots, the vertical axis is the cumulative distribution function (cdf), and the horizontal axis is the concrete strength. In both plots, the bandwidth is larger at lower probability levels indicating larger strength variability at those levels. As the probability of failure increases, the variability decreases, reaching its minimum just over 0.6 in Figure 1, and over 0.7, in Figure 2.

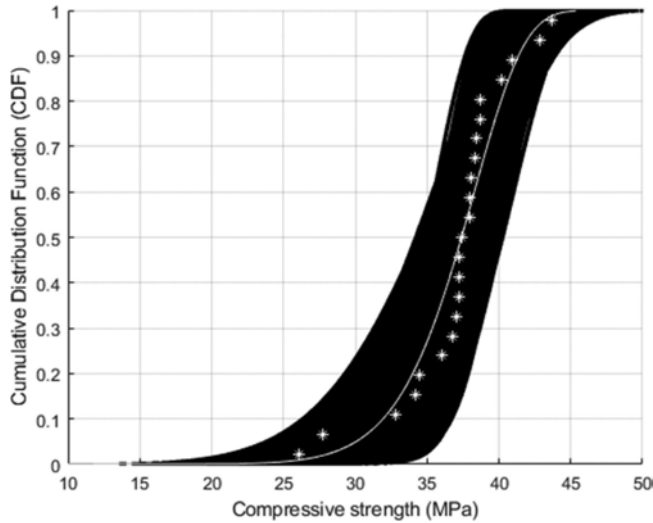


Figure 1. Compressive strength scatter band.

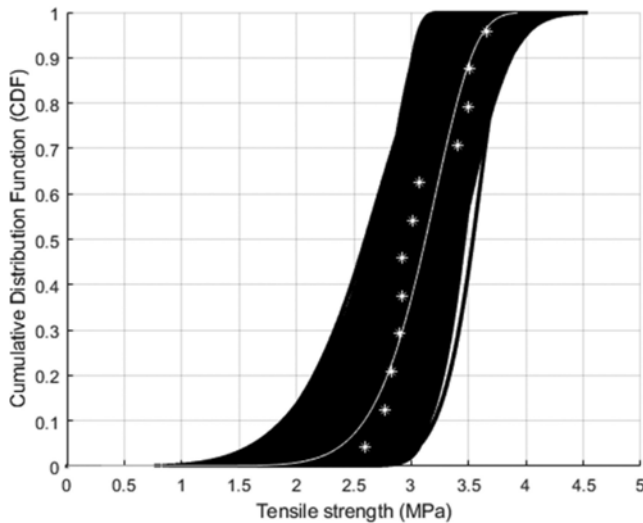


Figure 2. Tensile strength scatter band.

The scatter band limits and bandwidth for the 5th, 50th, and 95th percentiles, along with the corresponding values of the reference distributions, were calculated. Additionally, the ratio of bandwidth to reference distribution for each of the percentiles, referred to as the Normalized range of dispersion, was determined. The normalized range of dispersion in the compressive strength reduces from 40% at the 5th percentile to 16% at the 95th percentile. A higher dispersion is observed in the tensile strength, where the same percentiles show a reduction from 60% to 26%, respectively. The 12 data points in the tensile strength dataset size was much smaller than the 23 in the compressive strength dataset. The more significant variability observed in the tensile strength compared to the compressive strength is related to the smaller number of specimens tested in that case. In both cases, the same trend of reducing the variance with increasing probability level was observed, which agrees with the scatter band plots.

The design curves for concrete compressive and tensile strengths are shown in Figure 3 and Figure 4, respectively. In both figures, the vertical axis represents the cumulative distribution function (cdf), whereas the horizontal axis represents the concrete strength. Design curves in both figures are calculated for three safety levels, namely, 90%, 95%, and 99%. Both plots show the same behavior. The distance between the reference distribution and the design curves is more prominent at lower probabilities of failure and gets less significant as the probability increases. Although the observed behavior is the same in both plots, the magnitude is not. The difference between reference distribution and design curves is more prominent in the tensile tests in Figure 4 than it is for the compressive tests in Figure 3. Table 1 depicts the 5th, 50th, and 95th percentiles of concrete compressive and tensile strength for the reference distribution and the design curves at 90%, 95%, and 99% safety levels.

Table 1. Distribution of concrete strength (MPa).

Percentiles	Compressive strength				Tensile strength			
	Reference distribution	Safety levels			Reference distribution	Safety levels		
		90%	95%	99%		90%	95%	99%
5th	30.1	28.0	27.5	26.7	2.9	2.7	2.6	2.6
50th	37.4	36.4	36.2	35.7	3.1	3.0	3.0	2.9
95th	42.3	41.4	41.1	40.6	3.3	3.2	3.2	3.1

For compressive strength, as shown in Table 1, the design curve for the 99% safety level gives an 11.3%, 4.5%, and 4.0% deviation at the 5th, 50th, and 95th percentiles, respectively. The deviation is reduced for higher percentile failure probabilities and for this set of specimens, is relatively low. For the 50th percentile value, the strength changes from 37 MPa for the reference distribution to around 36 MPa for the design curves. Therefore, the use of a design curve at this level of probability of failure is not necessary. However, if the 5th percentile or lower percentile values were being considered, the conservatism of the process would be increased. Thus, the compressive strength selected for the fatigue experiment was 36 MPa, the average of the 50th percentile values for all three design curves, which coincidentally corresponds to the average of the 23 compressive strength test results.

Table 1 also shows the 5th, 50th, and 95th percentiles of the tensile strength of concrete from the reference distribution and three design curves. The design curve for the 99% safety level gives a 10.4%, 7.3, and 5.9% deviation at the 5th, 50th, and 95th percentiles, respectively. The deviation is again reduced for higher percentile failure probabilities but, for this set of specimens, is significant enough to be disregarded. For the 50th percentile value, the strength changes from 3.1 MPa for the reference distribution to 2.8 MPa for the design curves. Therefore, the use of a design curve at this level of probability of failure is necessary. Thus, the tensile strength selected for the fatigue experiment was 2.8 MPa. That value is the mean of the design curve at the 99% safety level.

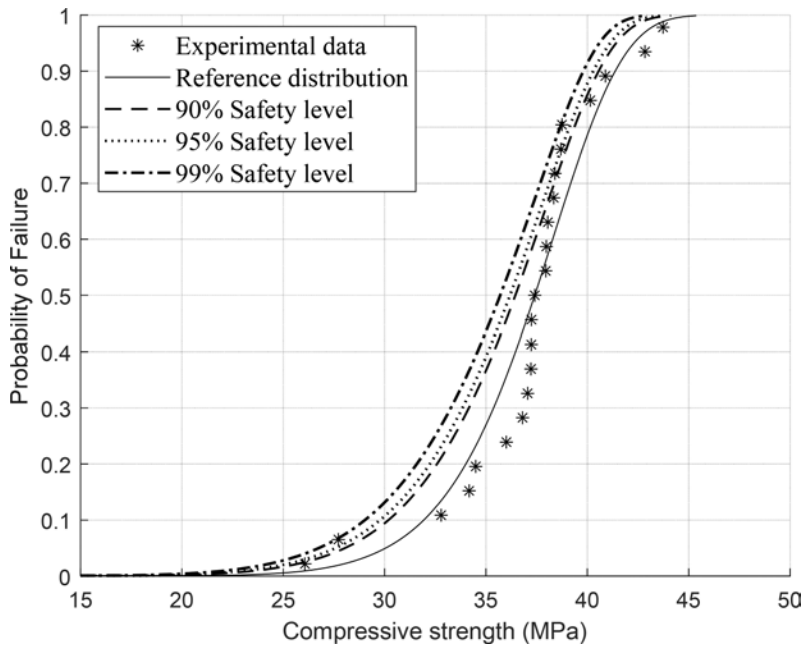


Figure 3. Concrete compressive strength design curves.

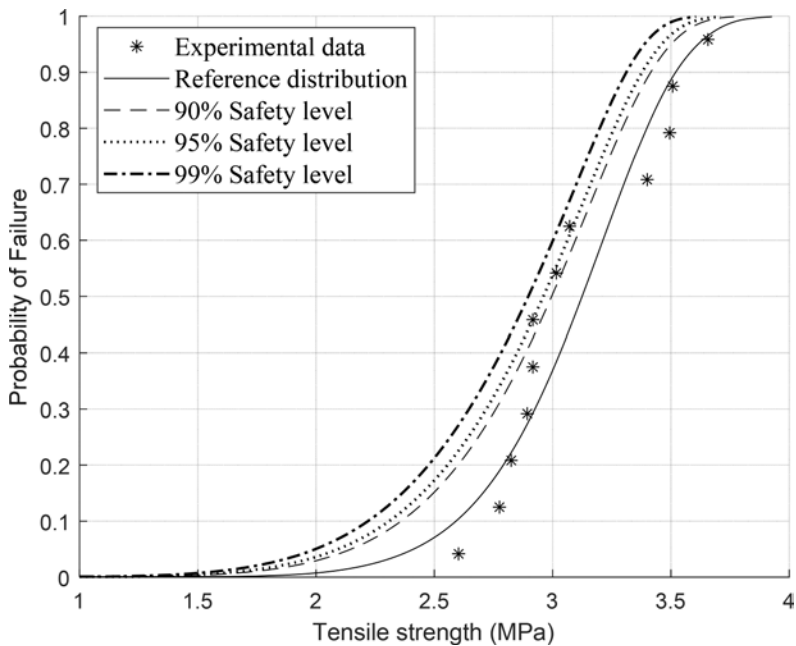


Figure 4. Concrete tensile strength: design curves.

6 STRESS REVERSAL FATIGUE TESTS

The method described in the previous section can be used for fatigue tests with one slight change in the correction of the reference distribution, replacing Equation 1 with Equation 2, below. The only difference between the two is the representation of the number of cycles to

failure in a fatigue experiment, which must be presented in a log scale. Therefore, $\text{Log}(N)$ in Equation 2 represents the logarithm of the number of cycles to failure.

$$[\log(N)]_{DC} = [\log(N)]_{RD} \times \left[\frac{1}{1 + e_p} \right] \tag{2}$$

The proposed statistical analysis was carried out on fatigue test results under stress reversal and constant stress range for 3 maximum stress levels. The same safety levels used for concrete strength were used for obtaining the design curves for the fatigue tests. The sample size for the 25,000 random samples in each case was: 14 at the stress level of 0.90, 12 at the stress level of 0.85, and 8 at the stress level of 0.80. For all cases, MATLAB was used to determine the reference distributions, scatter bands, and design curves. The mean of the reference distribution and design curves are summarized in Table 2.

Table 2. Estimated number of cycles to failure.

	Stress levels*		
	0.80	0.85	0.90
Reference distribution	4868	957	762
90% Safety level	1852	468	398
95% Safety level	1471	394	340
99% Safety level	992	293	258

*Tensile stress levels

Table 2 shows a significant reduction in the predicted mean fatigue life when moving from the reference distribution to the design curves in all three cases. However, the magnitude of the reduction, predicted mean fatigue life at the reference distribution minus the design curve for the 99% safety level, is correlated to the number of tests performed in each case. At 0.80 stress level, there were only 8 specimens tested, and the predicted mean fatigue life reduction was 79.6%. At 0.85 stress level, with 12 specimens tested, the reduction was 69.4%. Lastly, at 0.90 stress level, the predicted mean fatigue life reduction was 66.1%, where 14 specimens were tested.

7 CONCLUSION

This study presented a method that accounts for the distribution fitting error when a low number of tests is available to determine the concrete strength for fatigue experiments and the analysis of fatigue test results. The method benefits from employing design curves rather than mean values from experimental results. These curves can be obtained based on predetermined safety levels. The method was applied to five datasets, including compressive and tensile strength tests and fatigue tests at three stress levels. Out of the five datasets, only one, compressive strength, had more than 15 specimens and was the only one to show no significant deviation between design curves and data means. The remaining datasets, on the other hand, showed a deviation between design curves and reference distributions, and as the number of data points reduced, the deviation increased. There was also a higher deviation from the reference curves at levels of failure below 50%. These results show that when dealing with determining concrete strength or estimating the fatigue life of concrete under stress reversal, it is advised to use design curves instead of mean values of test results when the number of tests at hand is lower than a certain limit. The fatigue life of concrete was significantly reduced when the stress level was increased from 0.8 to 0.9. For all three stress levels, the deviation from reference distribution to safety level curves increased with decreasing the number of specimens in the data set. This should be considered when designing the data set size of a fatigue experiment.

ACKNOWLEDGEMENT

The authors would like to acknowledge financial support from Manitoba Hydro and NSERC.

REFERENCES

- ASTM International. 1996. ASTM International E1823-20b - Standard Terminology Relating to Fatigue and Fracture Testing. *ASTM International*, Reapproved 2020: 1–25.
- ASTM International. 2010. ASTM International E739-10 - Statistical Analysis of Linear or Linearized Stress-Life. *ASTM International*, Reapproved 2015: 1–7
- Cornelissen, H. A. W. (1984). Constant-amplitude tests on plain concrete in uniaxial tension and tension-compression. *Delft University of Technology, Stevin Laboratory (Report 5-84-1)*: 1–78.
- Kachkouch, F. Z., Noberto, C. C., de Albuquerque Lima Babadopulos, L. F., Melo, A. R. S., Machado, A. M. L., Sebaibi, N., Boukhelf, F., & el Mendili, Y. 2022. Fatigue behavior of concrete: A literature review on the main relevant parameters. *Construction and Building Materials*, 338, 127510.
- Khademi, F., Akbari, M., & Mohammadmehdi Jamal, S. 2015. Prediction of Compressive Strength of Concrete by Data-Driven Models. *I-Manager's Journal on Civil Engineering*, 5(2): 15–23.
- Nieto, A. J., Chicharro, J. M., & Pintado, P. 2006. An approximated methodology for fatigue tests and fatigue monitoring of concrete specimens. *International Journal of Fatigue*, 28(8): 835–842.
- Ortega, J. J., Ruiz, G., Yu, R. C., Afanador-garcía, N., Tarifa, M., Poveda, E., Zhang, X., & Evangelista, F. 2018. Number of tests and corresponding error in concrete fatigue. *International Journal of Fatigue*, 116(June): 210–219.
- Paskova, T., & Meyer, C. 1994. Optimum number of specimens for low-cycle fatigue tests of concrete. *Journal of Structural Engineering*, 120: 2242–2247.
- Tepfers, R. (1982). Fatigue of Plain Concrete Subjected to Stress Reversals. *ACI Symposium Publication*, 75: 195–215.
- Thun, H., Ohlson, U., & Ekilgren, L. (2007). Tensile Fatigue Capacity of Concrete. *Nordic Concrete Research*, 36(1–2): 48–64.
- van Leeuwen, J., Siemes, A. J. M. (1979). *Miner's Rule with Respect to Plain Concrete*. Delft. Stevin-Laboratory of the Department of Civil Engineering of the Delft University of Technology.

Influence of different coarse aggregate types on porosity and various properties in concrete

N. Matsuda & T. Iyoda

Shibaura Institute of Technology, Tokyo, Japan

ABSTRACT: Greater utilization of recycled aggregate concrete is desirable to realize a sustainable society. To achieve sustainable, it is necessary to clarify the factors that reduce the strength and mass transfer resistance of low-quality recycled aggregate concrete and to develop technologies to improve these factors. In this study, the porosity in the concrete and its effect on each property were identified using a variety of coarse aggregates in order to identify the porosity in recycled aggregate concrete that leads to a reduction in strength and mass transfer resistance. The results show that low-quality recycled aggregate concrete has reduced strength and mass transfer resistance due to increased porosity in the new mortar and at the interface between the aggregate and the new cement paste. A C-S-H type accelerator agent was used as a solution to this problem. Strength and mass transfer resistance of low-quality recycled aggregate concrete were improved by the use of a C-S-H type accelerator.

1 INTRODUCTION

In recent years, concrete waste has been increasing in Japan due to demolition and renewal of aging concrete structures. Figure 1 shows the projected future generation of concrete waste in Tokyo. Concrete waste will continue to increase and is projected to be approximately 1.5 times greater in 2050 than in 2022. Concrete waste is reused as aggregate for roads. However, as road construction in Japan is expected to decrease in the future, new ways of using concrete waste are needed. On the other hand, the use of natural aggregates in concrete needs to be curbed in order to reduce the environmental impact. Against this background, we believe that concrete waste should be recycled as aggregate for concrete and used as recycled aggregate concrete. To promote the use of recycled aggregate concrete, it is necessary to use low-quality recycled aggregate, which can be produced with less energy and cost than the energy and cost-intensive production of high-quality recycled aggregate. However, low-quality recycled aggregate concrete is not widely used because its strength and mass transfer resistance are lower than those of normal concrete. Therefore, it is necessary to clarify the factors that reduce the strength and mass transfer resistance of low-quality recycled aggregate concrete and to develop technologies to improve these factors. So, we thought that the strength and mass transfer resistance of concrete are related to the porosity in the concrete. In this study, the porosity of concrete made with various aggregates was compared with that of low-quality recycled aggregate concrete in order to identify the porosity that leads to reduced strength and mass transfer resistance of low-quality recycled aggregate concrete. The porosity in the concrete was classified as porosity in the aggregate, porosity in the new mortar, and porosity at the interface between the aggregate and the new cement paste. Then, we investigated the use of C-S-H type accelerator as a technique to improve the porosity in the concrete.

2 COARSE AGGREGATE AND CONCRETE OVERVIEW

2.1 *Type and characteristics of coarse aggregate*

The study used the following coarse aggregates to determine the factors that reduce the strength and mass transfer resistance of low-quality recycled aggregate concrete. Table 1 shows the characteristics

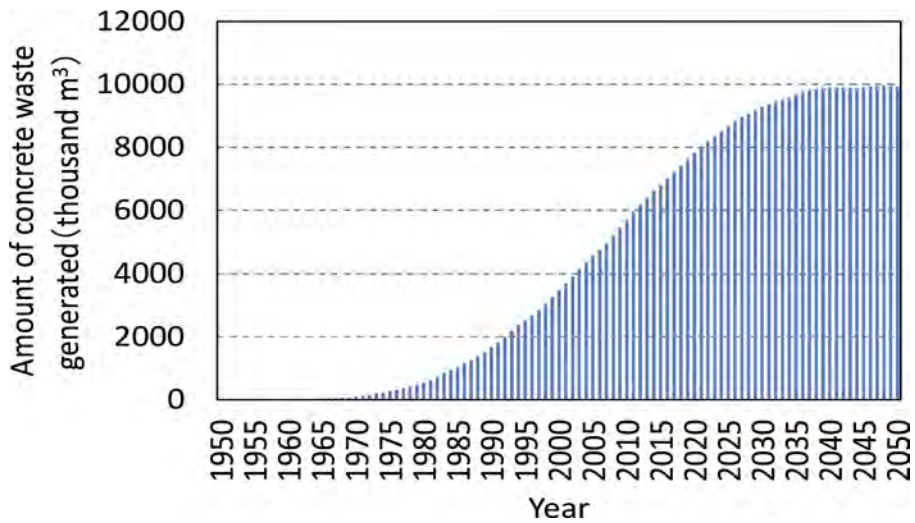






Figure 1. The projected generation of concrete waste in Tokyo.

of the coarse aggregates used. Hard sandstone was used because it has lower water absorption than low-quality recycled aggregate. Limestone was used because it has a lower water absorption rate than low-quality recycled aggregate and its main constituent is calcium carbonate. Recycled aggregate was low-quality recycled aggregate. The concrete waste used in this recycled coarse aggregate was constructed in 1966. The cement type of this concrete waste was ordinary Portland cement, and the compressive strength of the concrete was expected to be approximately 22.5 N/mm² based on the JASS 5. Artificial lightweight aggregate was used because it has a very high water absorption rate compared to low-quality recycled aggregate. RLG and LWG are assumed to have high porosity in the aggregate due to high water absorption. We believed that there is a relationship between aggregate porosity and strength, so we conducted a crush value test. The crush value test is specified in JIS A 5023. However, the load was changed from 100kN to 200kN to obtain clear results. Crushed samples passing through a 2.5mm mesh sieve were also measured. The crushing values were larger in the order of HSG < LSG < RLG < LWG. The results indicate that LWG is vulnerable due to the high porosity in the aggregate. The results indicate that LWG is more fragile than RLG due to higher porosity in the aggregate. On the other hand, it has been reported that moisture in artificial lightweight aggregates affects the internal curing effect of concrete. Therefore, we conducted a moisture loss test of RLG and LWG. This method of moisture loss testing was conducted using a drying oven to check for changes in aggregate mass. The temperature and humidity in the drying oven were 20°C and 40-50%, respectively. Since air was circulating inside the drying oven, the specimens were placed in a wire mesh basket and the surrounding area was sealed to prevent sample errors. In addition, covers were installed to prevent wind from blowing directly onto the upper and lower surfaces of the wire mesh cage. The sample was approximately 500 g, and the saturated condition was used as the base point. The moisture loss rate is calculated using Equation 1. The moisture loss rate is expressed as a percentage of the amount of moisture loss relative to the total water in the unit fine aggregate volume. Figure 2 shows the change in moisture loss rate over time. RLG increased moisture loss up to 24 hours, with 30% of the moisture in the aggregate lost at 24 hours. LWG was slower in moisture loss, and 10% of the moisture in the aggregate was lost in 24 hours. From these results, it can be inferred that LWG has a slow moisture loss from the aggregate and provides an internal curing effect in the concrete.

$$\text{moisture loss rate}(\text{vol}\%) = \frac{(\text{saturated mass} - \text{mass of each hour})}{(\text{saturated mass} - \text{oven dry mass})} / \text{unit volume} \quad (1)$$

Table 1. The characteristics of the coarse aggregate.

Type	Hard sandstone	Limestone	Low-quality Recycle aggregate	Artificial lightweight aggregate
Symbol	HSG	LSG	RLG	LWG
Appearance				
Oven dry density (g/cm^3)	2.64	2.69	2.31	1.33
Water absorption (%)	0.69	0.53	6.58	27.00
Crushing value (%)	4.1	9.7	14.0	22.9

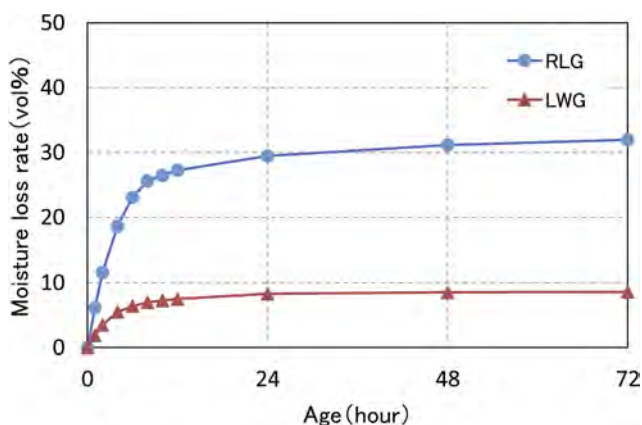


Figure 2. Moisture loss rate.

2.2 Mix proportion of concrete

Table 2 shows the mix proportions. Ordinary Portland cement(OPC) (density: $3.15 \text{ g}/\text{cm}^3$) and blast furnace slag cement type B(BB)(density: $3.04 \text{ g}/\text{cm}^3$) were used as cement. The reason for using blast furnace slag cement was the thought that the effect on porosity in concrete depends on the type of cement. The fine aggregate consisted of crushed sand (saturated density: $2.64 \text{ g}/\text{cm}^3$) and sand (mountain sand) (saturated density: $2.58 \text{ g}/\text{cm}^3$) in a 7:3 ratio by volume. AE water reducer was used as an admixture. The amount of admixture added was set to achieve a slump of $12 \pm 2.5 \text{ cm}$ and an air of $4.5 \pm 1.5\%$.

3 OUTLINE OF EXPERIMENT

3.1 Compressive strength test

Three specimens of $\phi 100 \times 200 \text{ mm}$ were prepared for each case, and after curing in water for 28 days, a compressive strength was tested in accordance with JIS A 1108.

Table 2. The mix proportions.

Symbol	Aggregate	Cement	W/C (%)	s/a (%)	Air (%)	Unit Weight (kg/m ³)			
						W	C	S	G
NHSG	HSG								937
NLSG	LSG	OPC							951
NRLG	RLG							853	866
NLWG	LWG								595
BHSG	HSG		50.0	48.0	4.5	170	340		931
BLSG	LSG	BB							945
BRLG	RLG							847	861
BLWG	LWG								592

3.2 Air permeability test

Cylindrical specimens of $\phi 100 \times 200$ mm size were used for the test, cured in water at 20°C for 28 days, and cut into cylindrical specimens of $\phi 100 \times 50$ mm in size. The specimens were dried in a drying room at 40°C until the mass was constant. After that, air was allowed to permeate through at a pressure of 0.1 MPa, and the amount of air permeation was measured using water displacement method using cylinder, and permeability coefficient was calculated.

3.3 Porosity test

Cylindrical specimens of $\phi 100 \times 200$ mm size were used for the test, cured in water at 20°C for 28 days, and cut into cylindrical specimens of $\phi 100 \times 50$ mm in size. After that, it was the specimens were dried at 40 °C in a drying oven until the weight loss became constant and measured the mass in an absolutely dry state. The porosity was calculated by the Archimedes method using these values.

4 RESULTS AND DISCUSSION

4.1 Compressive strength test

Figure 3 shows the compressive strength. The mix proportions using OPC resulted in the lowest compressive strength of the RLG. This result was 67% of the compressive strength of HSG. On the other hand, LWG resulted in higher compressive strength than RLG. The BB mix proportions resulted in the lowest compressive strength of the RLG. This result was 82% of the compressive strength of HSG. LWG also showed greater water absorption and crushing values than RLG, but there was no relationship between these results and compressive strength.

4.2 Air permeability test

Figure 4 shows the results of the air permeability test. The permeability coefficient of RLG was large than that of HSG. Comparing OPC and BB results, the overall air permeability of BB was greater. In particular, LWG resulted in a very large air permeability when BB was used. The reason for this may be that the type of porosity affecting the air permeability coefficient is different between OPC and BB cement. These results indicate that the compressive strength and air permeability coefficient of low-quality recycled aggregate concrete are significantly lower than those of ordinary concrete. This is thought to be due to the effect of porosity in the concrete.

4.3 Effect of porosity in concrete on compressive strength and air permeability coefficient

Figure 5 shows the relationship between porosity and compressive strength in concrete. LWG had the largest porosity in the concrete, but the compressive strength results were higher than RLG. This trend was also true for BB. The reason for the increased porosity of concrete with

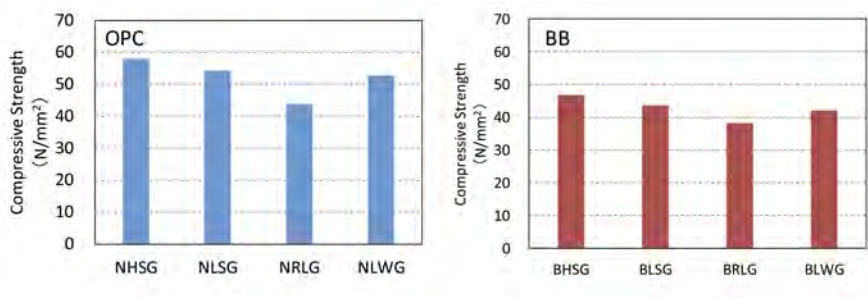


Figure 3. Compressive strength.

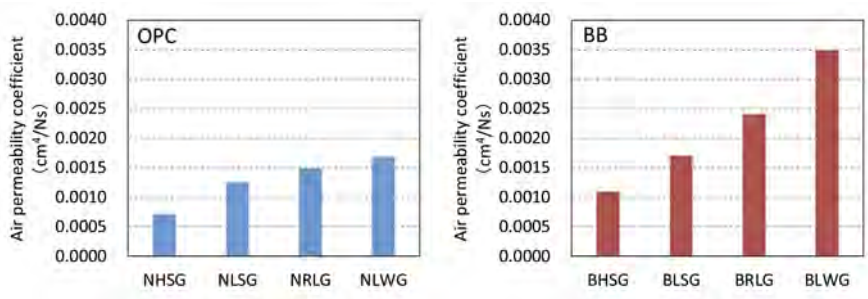


Figure 4. Air permeability coefficient.

LWG may be the high porosity in the aggregate. Therefore, the weak spots in the concrete can be considered to be the interface porosity between the new mortar or aggregate and the new paste, rather than the porosity of the aggregate. Figure 6 shows the relationship between the porosity and air permeability coefficient of concrete. The air permeability coefficient of the OPC mix proportions with the increase in the porosity in the concrete. RLG has an increased porosity and larger permeability in the concrete than HSG, suggesting that mass transfer resistance is reduced. On the other hand, the slope of the equation calculated by the method of least squares based on the relationship between the porosity and permeability in concrete is different for OPC and BB. Based on these results, we believe that the type of porosity depended on is different between OPC and BB. Therefore, we classified the porosity in concrete into aggregate porosity and other porosities and investigated the effect of porosity on the compressive strength and mass transfer resistance of low-quality recycled aggregate concrete.

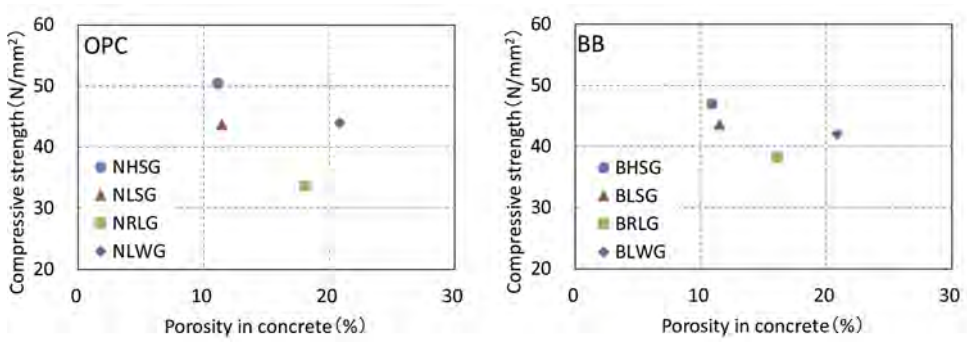


Figure 5. The relationship between porosity and compressive strength in concrete.

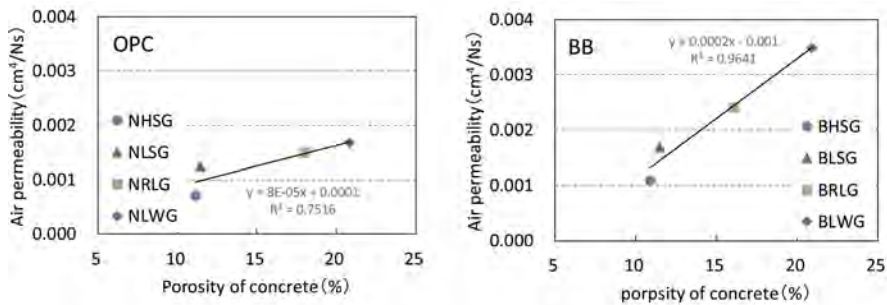


Figure 6. The relationship between porosity and air permeability coefficient in concrete.

5 CLASSIFICATION OF POROSITY IN CONCRETE

5.1 Method for classifying porosity in concrete

The porosity in concrete was classified into aggregate porosity and other porosity, and the factors that reduce the compressive strength and mass transfer resistance of low-quality recycled aggregate concrete were examined. Therefore, the porosity in concrete was classified into aggregate porosity, new mortar porosity, and interface porosity between the aggregate and the new cement paste (aggregate interface). Aggregate porosity was calculated by multiplying the water absorption of coarse aggregate by the absolute volume of coarse aggregate. The porosity of the new mortar was calculated by the Archimedes method, and the porosity in the new mortar was multiplied by the absolute volume of the new mortar. The porosity at the interface between the aggregate and the new cement paste was defined as the porosity in the concrete minus the porosity in the aggregate and in the new mortar.

5.2 Porosity in classified concrete

Figure 7 shows the results of the classification of porosity in concrete. LWG has the largest increase in porosity in the concrete. However, the majority of the porosity in the aggregate. RLG shows an increase in porosity at the new mortar and aggregate interface. This trend is more pronounced for OPC than for BB. Therefore, low-quality recycled aggregate concrete exhibits reduced compressive strength and mass transfer resistance due to increased porosity at the interface between the new mortar and aggregate. On the other hand, the LWG also has less porosity at the new mortar and aggregate interface than the RLG. We believe the reason for this is the internal curing effect of the artificial lightweight aggregate. The high-water absorption of the artificial lightweight aggregate may have promoted hydration of the interface between the new mortar or aggregate and the paste through an internal curing effect. However, we believe that low-quality recycled aggregate has different moisture behavior in the aggregate than artificial lightweight aggregate. The reason for this is that, since low-quality recycled aggregate has no internal curing effect, we believe that moisture movement from the aggregate increased the porosity of the new mortar and the interface between the aggregate and the new cement paste. However, BB showed a slight increase in porosity in the new mortar of the LWG. This is thought to be an increase in large capillary pores, given the results of the air permeability coefficient. These results suggest that the effects of moisture and moisture movement in aggregates may differ between OPC and BB.

6 TECHNOLOGY TO IMPROVE POROSITY IN CONCRETE

The C-S-H type accelerator was used to improve the porosity in the new mortar and the interface porosity between the aggregate and the new cement paste in low-quality recycled

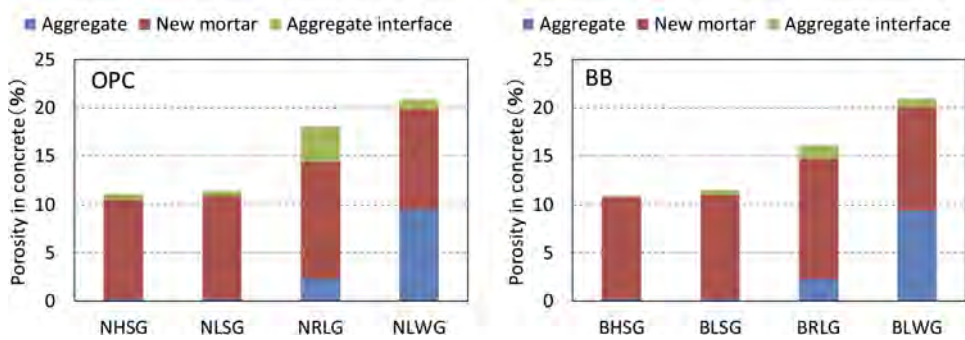


Figure 7. The classification of porosity in concrete.

aggregate concrete. C-S-H type accelerator are new admixtures containing CSH nanoparticles. In previous studies, it has been reported that C-S-H nanoparticles improve compressive strength and mass transfer resistance by densifying the porosity at the new mortar and aggregate interface. Therefore, we used the C-S-H type accelerators in the mix proportions of BB shown in Table 2. The reason for using C-S-H type accelerator in BB is that previous studies have reported that the reaction of blast furnace slag is accelerated by the addition of C-S-H type accelerator. Based on the above, we believe that the C-S-H type accelerator can improve the strength and mass transfer resistance of low-quality recycled aggregate concrete.

Figure 8 shows test results for compressive strength and air permeability test of concrete with C-S-H type accelerator. Compressive strength and permeability of LSG and RLG were improved by the use of C-S-H type accelerator. This is due to the improved porosity of the new mortar and aggregate interface. This image is shown in Figure 9. HSG and LWG have fewer porosity in the concrete, making it difficult for C-S-H nanoparticles to penetrate into the porosity. LSG has fewer porosity in the concrete, but the aggregate features calcium carbonate, which promotes the effect of the C-S-H type accelerator. On the other hand, RLG increases the porosity at the new mortar aggregate interface, which makes it easier for CSH nanoparticles to penetrate into the porosity. We believe that the compressive strength and air permeability coefficient were improved by the C-S-H nanoparticles densifying the porosity. The reason for using C-S-H type accelerator in BB is that previous studies have reported that the reaction of blast furnace slag is accelerated by the addition of C-S-H type accelerator. Based on the above, we believe that the C-S-H type accelerator can improve the strength and mass transfer resistance of low-quality recycled aggregate concrete.

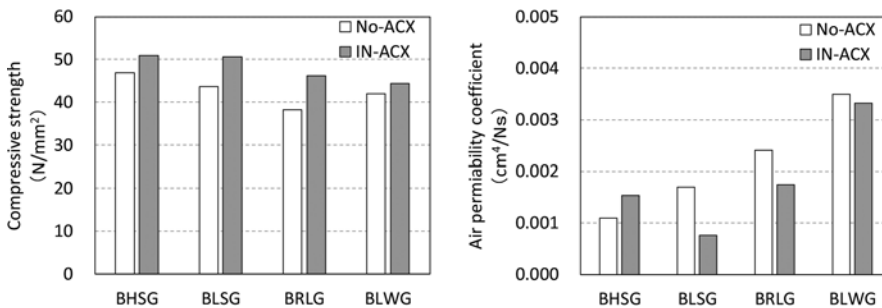


Figure 8. Test results of concrete with C-S-H type accelerator.

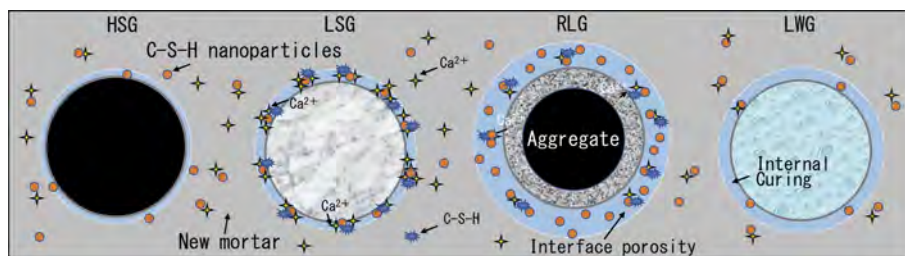


Figure 9. Image of porosity improvement by C-S-H type accelerator.

7 CONCLUSION

- 1) Compressive strength and mass transfer resistance of low-quality recycled aggregate concrete were lower than those of normal concrete.
- 2) The low quality recycled aggregate concrete had increased porosity at the new mortar and aggregate interface. This would have resulted in a decrease in compressive strength and mass transfer resistance.
- 3) The compressive strength and permeability of concrete made with limestone aggregate and low-quality recycled aggregate were improved by using the C-S-H type accelerator.

In the future, we will study the moisture behavior of low-quality recycled aggregate. In addition, we would like to investigate carbonation technology as a method to control moisture movement from the aggregate.

REFERENCES

- Japanese Architectural Standard Specification, JASS5 Reinforced Concrete Work, 1965.
- Japanese Industrial Standard, JIS A 5023(Recycled aggregate concrete-Class L) regulation E.
- Ninomura K, Ishida T, Physical property changes of mortar specimens with low water to binder ratio focusing on moisture transport and equilibrium, Proceedings of the Japan Concrete Institute, Vol.37, No.1, pp 505–510, 2015.
- Imoto H, Hanafusa K, Koizumi S, Sugiyama T, Effect of C-S-H type accelerator on the strength development of slag cement concrete, Proceedings of the Japan Concrete Institute, Vol.37, No.1, pp 175–180, 2015.

Visual inspection of bridges and tunnels in Italy: By experience made with different owners and methods to a new proposal for a better and more efficient inspection procedures

R. Salomone, F. Damiani, M. Vittone, M. Scarsi Napolitano, I. Vangelisti, G. Giacalone, A. Bombace, M. Brescia, M. Rabbia & C. Beltrami
Lombardi Ingegneria S.r.l., Milan, Italy

ABSTRACT: In this paper principal aspects of recent years experience of visual inspection of thousands of road and highways bridges and tunnels are critically presented. Inspection activities have been carried out on bridges, viaducts, tunnels, overpasses and underpasses of different structural typologies (prestressed concrete beam, composite steel-concrete deck, cast-in-place concrete, ecc), along Italian highways and State highways. These activities allowed to pursue awareness regarding operators safety's importance, developing deep consciousness respect to proper site organization and alternative safety-enhancing procedures. Moreover, a comparison between different inspection checklist and procedures developed by the highways management company is analyzed as current Italian practice and a new proposal for a better and more efficient inspection procedures. Besides, possible application of UAS and AI as supporting tools for visual inspections are pointed out.

1 INTRODUCTION

Nowadays, visual inspections on infrastructures represent a crucial activity for the identification of structures' condition states, safety evaluation and proper allocation of economic resources. This work provides a critical review of inspection methodologies and their development over the years, deeply analyzing Italian background in terms of both structural context and national regulations. A brief overview of international methodologies and procedures is also outlined. Moreover, site organization and safety issues are critically discussed, highlighting national regulations' lack of a proper approach to the above-mentioned matter.

However, inspection of road infrastructure represents only the starting point of the management process, which is based on life cycle of structures and aims to determine structural performance, conduct surveillance activities, and implement maintenance interventions evaluating its effectiveness over time.

Therefore, in this paper, importance of monitoring and supporting technologies is also discussed, focusing on their connection with the visual inspection and their potential impact on work quality and future developments.

1.1 *Italian infrastructure background*

The first Italian highways were built starting from the 1920s, but the considerable growth of the highways network took place in the second post-war period, until the 1970s, when the highway development boom brought to an end. At that time, Italy was, for highways overall length, the third nation in the world beyond United States and Germany.

The great growth that Italian highways network, together with the German and French ones, experienced until the 1970s suffered a strong slowdown in its development already in 1980, remaining in fact unchanged from 1980 to present. Therefore, most of the Italian infrastructural heritage is reaching the end of their service life, exhibiting more than 50 years of lifetime (Beltrami & et al., 2021).

Furthermore, the worsening of environmental and climatic conditions as well as the constant increase in transport exploitation certainly had a negative influence on the current infrastructures' conditions (Beltrami C., 2020). Therefore, inspection procedures, monitoring activities, and maintenance interventions are essential to ensure adequate long-term structural performance and avoid unpleasant consequences.

2 INSPECTIONS METHODOLOGIES

In the following chapter, a general overview of infrastructures' inspection procedures is presented. Starting from first developed instructions on structural surveillance, this work outlines methodologies evolution path that led to modern inspection and safety evaluation procedures. In addition, some brief references regarding other countries methodologies are also provided.

2.1 Past methodologies

In Italy, first guidelines regarding infrastructure safety through in-situ inspections and deficiencies evaluation came with the (Circolare n° 6736/61, 1967). The *Circolare 67* claimed the need of periodical safety and stability checks (charged to the road owners) and pointed out the importance of surveillance and maintenance due to relevant problems such as: age, influence of further interventions and increase of traffic intensity.

Frequency of inspections was set to a minimum of once every three months. Activities were based on visual examination of structural surfaces and development of a brief report for each work. The three main categories of inspection were:

- *daily inspection* of the general infrastructure conditions, whose aim was notifying the competent offices of any anomalies or new occurrences
- *scheduled inspection* for the pertinent structures with also possible tests and essays
- *extraordinary inspection* "... whenever, some symptom or fact gives rise to the conviction that something is not normal"

Further instructions came with the (Circolare n°34233, 1991) which focused on the document collection for existing works and introduced main characteristics that structural ancillary parts (such as joints, flooring, etc.) must have. During those years, manuals of inspections were generally developed by the companies in charge of activities, which tended to keep them confidential and to continue updating them in-house.

Another important step in the development of inspections methodologies was the introduction of a *Management Plan*, which provides and schedules both the control and maintenance activities of a structure, in order to maintain its functionality, quality characteristics, efficiency and economic value over time.

Management Plan was first requested in (Legge Merloni, 1994) and then more detailed in its contents with the presidential decree (D.P.R n. 207, 2010). Maintenance activities include all administrative and practical operations intended to increase the useful system's life. Planning of maintenance activities is strictly linked with inspections course.

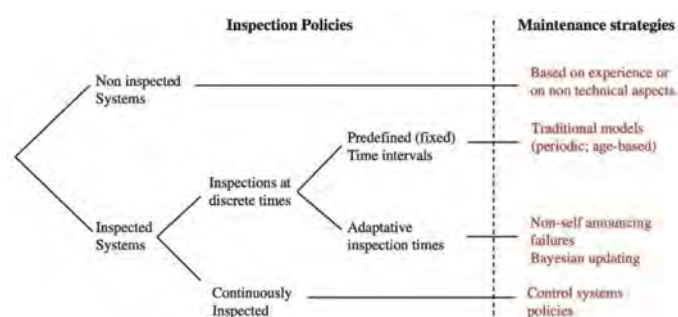


Figure 1. Relationship between inspection and maintenance policies (M. Sanchez-Silva, 2016).

For infrastructures, where often is not possible to continuously observe their conditions, pre-planned inspections aimed at determining system status at a given moment play a fundamental role and are an integral part of maintenance strategy. Figure 1 illustrates a tree structure that describes the relationship between inspection and maintenance policies and how they are deeply linked.

2.2 New procedures

In the last years in Italy, inspection methodologies have still been based on instructions from (Ministero dei Lavori Pubblici, 1967) and (Ministero dei Lavori Pubblici, 1991), but they also depended on the owner’s operating manuals and on structural typologies.

Regarding inspections frequencies, the main division between basic (every three months) and advanced (once a year) inspections have always been kept, but structure’s characteristics and conditions leading to those mentioned cases were often different from one owner to another.

IQOA CLASSIFICATION cracks / alterations		IQOA CLASSIFICATION water associated deficiencies	
1	Good conditions	1	Only moisture spots
2	Superficial deficiencies	2	Relevant water presence, possible degradation long-term evolution
2E	Evolving superficial deficiencies	2E	Relevant water presence, strenghten surveillance and take actions
3	Deep degradation with intervention need	3	Users safety
3U	Deep degradation with urgent intervention need		
5	Users safety		

Figure 2. IQOA civil (left) and water associated (right) deficiencies classification.

For tunnels, the main reference has been the CETU Guidelines (Centre D’Etudes des Tunnels, 2015). Starting from that, and with the aid of Inspection Guides (Inspection guide, 2015) the inspection activity was mainly based on the observation and description of deficiencies and deteriorations. The goal was to identify the defect, to classify it with a specific codification (CETU), to detect it within a metric reference and to give it a weight in terms of severity/dangerousness. The latter was accomplished through an alphanumeric code based on the IQOA assessment method, which also regulates interventions’ planning over time.

In some cases, those tunnels inspections have been carried out as “*Point Zero Inspection*”, whose purpose was to evaluate “*ex novo*” the structure state of consistency, defining lining thickness, reinforcement presence, location of possible voids, presence and position of superficial deficiencies and mechanical characterization of structural materials.

Dealing with bridges is instead a more heterogeneous scenario, due to the presence of many different structural typologies, in terms of both materials and static scheme. This leads to a wider range of possible deteriorations and, inherently, to a different reporting method. For each defect, generally reported data are its extension, severity, location, codification and element information.

Those modern procedures have been applied during last years, until the recent implementation of new guidelines for risk classification and management, safety assessment and monitoring.

2.2.1 UAS and supporting technologies

Historically infrastructure inspections are conducted by employing special and costly vehicles. Cranes, by-bridges, buckets mounts are all necessary to document any issues, simultaneously with roads closure and consequent traffic delays. Use of supporting technologies represents a powerful tool which can provide several advantages for the inspection activity:

- improve the efficiency of visual inspections for complex infrastructures with relevant extension and difficult accessibility
- improve the operator’ safety during the inspections
- minimize usage of traditional special site vehicles
- reduce working site’s realization and related times
- inferior inconveniences to traffic and road users
- development of 3D models and automatic structural defects detection

The Unmanned Aerial System (UAS) plays a role as a substitute of the human operator leading to a not only more efficient, safe, and detailed inspection but also less time consuming.

Despite all these advantages, actual methodologies in Italy do not include specific procedures neither recommendation about the use of UAS and UAV in visual inspections.

2.2.2 LLGG 2022 – Tunnels and bridges

Nowadays, Italy is dealing with a crucial step in the new era of infrastructures inspections and maintenance. The new *Guidelines LLGG 2022* (Linee Guida, 2022) introduce an innovative approach for the evaluation of tunnels and bridges risk and safety. This new method is based on a multi-level approach, in which the inspection activity represents what is named Level 1. The Level 0 represents instead the initial structures census and main characteristics acquisition. The core process lies in Level 2, developed for the definition and attribution of an “Attention Class”, which leads to the safety evaluation of the structure (Level 3 to 5) and to the planning of successive inspections, interventions, and monitoring plans.

Regarding inspection methodologies, main differences with past approaches is related to the different codifications for deficiencies and their severity, as well as the need of new parameters acquisition. There is indeed some information regarding road platform, mechanical systems and road signage that must be acquired in order to better determine the correct Attention Class.

The visual inspections are aimed at verifying the reliability of the data collected in Level 0, collecting further information about actual geometry, structural characteristics, surrounding environment, and assessing the structures’ conservation degree through evaluation of main degradation phenomena in specific reporting sheets, fill out in terms of intensity and extension.

Differentiated defect sheets are provided for each type of element and construction material (for bridges) or for each uniform segment (for tunnels).

Collected information on the sheets are then used to determine the *defectiveness level*, one of the main parameters acting in Level 2 classification method, based on factors of risk, vulnerability and exposure as shown in Figure 3.



Figure 3. Flow chart for attention class determination.

2.3 Other countries overview

Outside of Italy, international procedures generally have comparable approaches in terms of both inspection typologies and activities’ frequency.

In the United States of America, Federal Highway Administration encourage usage of codes and instructions in (FHWA, 1995). Maximum interval between normal inspections is set as 2 years while special non-scheduled inspections are required after unusual events. Similar example is given by (Bridge Inspection Manual, 2017), introduced in 2017 by The Department of Transportation of NY State. It outlines several types of inspection such as general, in-depth and special, whose frequency is on an annual base, and often depends on rare conditions and occurrences.

In Western Australia, according to (Australia, Main Roads Western, 2013), routine visual inspections are carried out on an annual cycle and are responsibility of the bridge owner. Where the condition of some components is not clear during the routine visual inspection, a further detailed inspection is planned.

On the same wavelength, other countries such as France (CISR, 2008) or Germany (DIN 1076, 2013) settled infrastructure inspection on annual bases and with different detailing levels, while monthly inspections are hardly ever required by authority and regulations.

Regarding the use of UAVs during inspections, specific methodologies are widely spread all over the world. Cutting edge country is France, where the IMGC (Ingénierie de la Maintenance du Génie Civil) proposed a new type of procedures for visual inspection and, in particular, recommendation for indirect observation tools, such as UAV or UAS. They defined different detail steps for different inspection levels.

3 SITE ORGANIZATION AND SAFETY ISSUES

In this chapter most relevant aspects about site organization for infrastructures' inspection are developed together with some issues related with safety on the work site, defined according to D.lgs 81/08 (D.Lgs n.81, 2008). These two aspects strongly depend on the required type of inspection, as presented in the previous chapter.

In general, all the activities must be carried out prior execution of all necessary measures for the protection and indication of the construction site equipment and operators standing in the working area, as indicated in the “New Traffic Laws” (Nuovo Codice della Strada, 1992). The latter lacks any prescription about how to proceed in case of infrastructures' inspection, which are never mentioned among all possible activities on the road area. The only developed example of guidelines is the “Road operator safety guidelines” (Linee guida ASPI, 2016), which regulate operators' behavior in order to reach an acceptable level of safety during inspections.

Due to this legislative deficiency, according to the road section along which the inspected infrastructure is located, agreement between the designed inspectors and infrastructure managers must be defined in order to organize a suitable and safe working site area.

For the basic *by-foot* inspections, the site is organized allowing the operator to proceed with a mean of protection behind him, walking inside the so-called “inspection area”, delimited with the installation of appropriate road-protective signage consisting of aligned traffic cones. This procedure has the aim to ensure operator safety against dangers coming from vehicular traffic. The operators advance in the inspection together with the delimited inspection area.

In *close-up* inspections, which involve usage of special site vehicles (i.e. by-bridge, elevating platform) the road section is partially or completely closed to traffic in order to allow their positioning and safety. At least one lane must be closed to the vehicular traffic to ensure a suitable working safety range. This has the aim of limiting the oscillation of the working machine caused by the passage of heavy vehicles and to avoid the accidental fall of material. Otherwise, it will be mandatory to proceed with the complete closure to vehicular traffic in order to guarantee safety's conditions. In both cases, definition of a working site area has a relevant impact on the vehicular traffic, especially for highway infrastructures, so that suitable advice to the road users must be provided, showing warning messages on the “variable message boards”. An example of site working areas in the case of a three lanes tunnel inspection is reported in Figure 4.



Figure 4. Example of delimited working site area for 3 lanes tunnel inspections.

It is important to underline how these safety issues together with the definition of a suitable working area have a key role in the development of infrastructures' inspection.

Differently from traditional inspection method, the development of new supporting technologies, such as UAV and UAS guarantees a significant improvement in the operator' safety together with an even better efficiency during the inspection itself.

Considering a case study of a 60 span PSC viaduct in central Italy, the use of UAVs, compared to traditional tools, allowed to reduce inspection's duration from 8 hours of traffic closure to zero (1.5 hours of flight without interaction with traffic).

4 NEW PROPOSAL AND FUTURE DEVELOPMENTS

In this chapter new proposals and possible future developments for infrastructures' inspection procedures are described in order to improve efficiency and safety with respect to traditional ones.

4.1 UAS and AI supporting tools

Within the infrastructures' inspection field, the use of supporting technologies such as UAV and UAS represents a powerful development tool. UAV systems allow to systematically collect pictures of the entire work in complete safety. The data is then combined (using the principles of photogrammetry) to build a 3D model to provide a complete and measurable overview of the structure, where engineers could pinpoint issues and highlight critical areas (Figure 5).

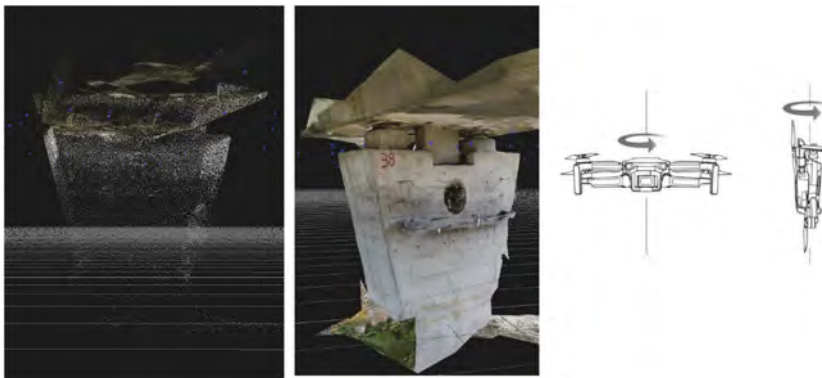


Figure 5. Example of a 3D bridge pile model reconstruction (by Unmanned Aerial Vehicle, UAV).

The interoperability of generated 3D models with BIM (Building Information Model) software creates an historical record of the infrastructure where each, new or existing, issue could be checked during time.

In conjunction with the acquisition realized with UAV, computer vision techniques offer promising non-contact solutions to improve infrastructure assessment. As described in (Spencer Jr, Vedhus, & Yasutaka, 2019), the most important goal of this system is to automatically convert image or video data into actionable information, identifying structural components, characterizing local and global visible damages, and detecting changes from a reference image.

All these supporting technologies represent useful and powerful tool able to improve the quality and above all the applicability of the results, differently from the traditional methods which requires more effort to make them ready for structural applications. Moreover, modern inspection's methods produce a great amount of data hard to handle with only operators' capacities. They require indeed usage of supporting systems able to quickly elaborate and store them, or even better, usage of artificial intelligence (AI) tools whose role inside the infrastructures' inspection and monitoring field is under continuous study.

Preliminary research has been carried out (Ciclo di Vita - Gallerie, 2020) about advanced numerical models as supporting tools for tunnels life-cycle assessment based on:

- Dynamic Mode Decomposition (DMD) algorithms to predict defects evolution
- definition of risk assessment indices and possibility of artificial Neural Networks usage to automate and accelerate the diagnostic procedure

4.1.1 Monitoring

In the field of structural assessment, usage of a monitoring system represents a great support for visual inspection procedures, considering also the highly increased demands in terms of traffic loads with respect to original ones. In particular, monitoring activities are generally devoted to only specific cases such as strategic infrastructures, severely damaged ones or with problems of difficult accessibility.

The modern and mostly developed structural monitoring technology is represented by the SHM (Structural Health Monitoring) which allows the detection and identification of damage that may occur in tunnel or bridges due to aging, materials' degradation, actions exceeding design values as well as natural or anthropic exceptional events, according to what prescribed in (Guidelines for structural health monitoring, 2016). Two different types of monitoring system can be applied:

- *static monitoring*: used to control structural parameters, such as cracks opening, which vary slowly during a significant observation period (chosen to catch their trend)
- *dynamic monitoring*: able to detect undergoing mechanical vibrations of infrastructures when subjected to variable actions (such as wind or vehicular traffic) over time.

In general, SMH systems are made up of four relevant components:

- sensors: instruments able to “read” structural data
- data transmission unit
- processing unit
- post-processing and interface software for read and work with monitored data

Wireless sensor chains are mostly used for infrastructures, able to transmit continuous data to a remote unit, covering also wide range distances, in the order of kilometers.

An interesting and powerful alternative in monitoring sensors is represented by the dynamic monitoring cameras I-SHM (Intelligent Structural Health Monitoring). I-SHM technology is based on usage of one or more machine vision cameras and passive measurement reflectors to be installed at the infrastructure’s location. The system allows to measure structural parameters such as deformations and displacements based on processing very high-resolution images and can perform measurements with high frequencies and at great distances, suitable for tunnel or bridges.

4.2 *Improvable aspects*

On the base of experience during recent years, considering the new *LLGG procedures* and their first on-field application, some aspects have been deeply analyzed and could be improved and optimized in order to simplify and enhance inspectors’ job, both during and after in-situ activities.

Regarding tunnels inspection, actual deficiencies detection and their in-plan localization, as well as their statistical extrapolation and information analysis, represent a crucial aspect of the entire evaluation process. In place of many paper sheets and long transcription processes, usage of tablet within a developed informatic tool/software capable of simplify deficiencies representation and data acquisition could potentially enhance quality of work results and, above all, led to a less time-consuming procedure.

Another important improvement could come from the availability of relevant information regarding as-built documentation and survey outcomes (both structural and geotechnical). Those data can be indeed directly compared with the results coming from carried out inspections and surveys during infrastructure’s life, evaluating potential deficiencies’ evolution and subsistence of design conditions.

Significant considerations could derive from those mentioned aspects, in terms of inspections and maintenance’s influence on structure’s residual life. The probability of failure determined at designed stage is susceptible of changes due to external agents related to the structure diagnostic framework. Therefore, actual likelihood of collapse would be higher than starting one, and it can be evaluated through a *Bayesian* approach, as better discussed in (M. Sanchez-Silva, 2016).

The subjectivity of infrastructures’ traditional inspections related to the operator’s point of view and the large amount of information and data hard to process and manage, represent a major problem of the current inspection procedure system. Therefore, an improvement can be achieved with usage of supporting tools able to automate the diagnostic procedure and to detect deficiencies evolution, such as Neural Networks. This procedure is still at a starting point of development, but the idea to be followed in the near future is to merge together inspection procedures with infrastructure life cycle assessment, coming up with a whole new asset governed by numerical algorithms capable of manage the entire inspection and monitoring framework and post-process all produced data.

5 CONCLUSIONS

The paper has been devoted to discuss the Italian infrastructures’ inspection procedures development over the years, with a brief overview of also international strategies. From this general overview it is possible to appreciate the strict link between inspection methodologies and infrastructures’ development and maintenance.

In the next future, practical application of new *LLGG 2022* would represent a key step for inspection methodologies evolution. For instance, the development of specific procedures and their connection with information from past inspections and surveys represent an important matter. Moreover, a national standard regarding usage of UAS as inspection supporting tools will be hopefully developed in the future, following other countries leading way.

Then, importance of other aspects regarding inspection process such as construction site organization, safety issues and artificial supporting tools, is highlighted through the aid of past experiences. Crucial issue is the use of UAS as inspection and maintenance tool, particularly for strategic or problematic structures. For those cases, consequent benefits are costs' reduction, safety enhance, faster procedures and better-quality results.

However, optimal strategy in terms of costs and benefits is generally given by a trade-off mechanism between implementation of a suitable monitoring system and execution of in-situ maintenance activities.

Finally, studies regarding usage of AI are ongoing and they are necessary to be able in the future to manage a great amount of data and to achieve an automatized diagnostic procedure. Primary aim is definition of a new global asset, accounting for all infrastructure-related aspects, starting from initial design stage, as-built information, past inspections and surveys, ending in modern maintenance and monitoring procedures linked with life-cycle assessment concept.

REFERENCES

- Australia, Main Roads Western. (2013, may 6). Routine Visual Bridge Inspection Guidelines (Level 1 Inspections) for Bridges.
- Beltrami, C. (2020). La manutenzione delle infrastrutture e il ciclo di vita di ponti e gallerie. "passaggi sicuri - Ponti, Gallerie e infrastrutture" *L'Ufficio Tecnico*, aprile 2020, Maggioli Editore.
- Beltrami, C., & et al. (2021). Bridge visual inspections: Experience of local authorities and the case study of the Corso Grosseto viaduct. *Bridge Maintenance, Safety, Management, Life-Cycle Sustainability and Innovations*. CRC Press.
- Bundesministerium für Verkehr, Bau und Stadtentwicklung. (2013). DIN 1076. *Bauwerksprüfung nach: Bedeutung, Organisation, Kosten*.
- Centre D'Etudes des Tunnels. (2015). *Linee Guida CETU*.
- Comité Interministériel de la Sécurité Routière. (2008, février 13). CISR. *L'insécurité routière n'est pas une fatalité*.
- D.Lgs n.81. (2008, aprile 9). *Attuazione dell'articolo 1 della legge 3 agosto 2007, n.123, in materia di tutela della salute e della sicurezza nei luoghi di lavoro*.
- D.P.R n. 207. (2010, ottobre 5). *Regolamento di esecuzione ed attuazione del decreto legislativo 12 aprile 2006, n. 163 (n° 207)*.
- Department of Transportation, NY State. (2017). *Bridge Inspection Manual*.
- Guidelines for structural health monitoring. (2016). 11634, *UNI/TR*.
- Ingénierie de Maintenance du Génie Civil. (2022). Recommandations pour les inspections télévisuelles.
- Inspection guide. (2015). *Road tunnel civil engineering Book 2: Catalogue of deteriorations*.
- Inspection guide. (2015). *Road tunnel civil engineering Book 1: from disorder to analysis, from analysis to rating*.
- Legge Merloni. (1994, febbraio 11). *Legge quadro in materia di lavori pubblici (n° 109)*.
- Linee guida ASPI. (2016, gennaio 15). *Linee guida per la sicurezza dell'operatore su strada*.
- M. Sanchez-Silva, G.-A. K. (2016). Reliability and Life-Cycle Analysis of Deteriorating Systems.
- MathLab, Lombardi Group & SISSA. (2020). Ciclo di Vita - Gallerie. *Studi numerici avanzati per la previsione dell'evoluzione dei difetti superficiali in gallerie autostradali*.
- Ministero dei Lavori Pubblici. (1967, Luglio 19). *Circolare n° 6736161*.
- Ministero dei Lavori Pubblici. (1991, Febbraio 25). *Circolare n°34233*.
- Ministero delle Infrastrutture e della Mobilità Sostenibili. (2022). Linee Guida. *Linee guida per la classificazione e gestione del rischio, la valutazione della sicurezza ed il monitoraggio dei ponti esistenti*.
- Ministero delle Infrastrutture e della Mobilità Sostenibili. (2022). Linee Guida. *Linee guida per la classificazione e gestione del rischio, la valutazione della sicurezza ed il monitoraggio delle gallerie esistenti*.
- Nuovo Codice della Strada. (1992). art. 176 D.Lgs. 30. 4.92n.285.
- Spencer Jr, B., Vedhus, H., & Yasutaka, N. (2019). Advances in computer vision-based civil infrastructure inspection and monitoring. *Engineering* 5.2, 199–222.
- U.S Department of Transportation. (1995, december). FHWA. *Recording and Coding Guide for the Structure Inventory and Appraisal of the Nation's Bridges*.

Inspection of highway retaining walls and geotechnical sites, state of the art in Italy and possible proposals for improving procedures and effectiveness

M. Scarsi Napolitano, D. Bonassi, R. Morè & C. Beltrami
Lombardi Engineering S.r.l., Milan, Italy

ABSTRACT: In this paper principal results of recent years' experience of inspection of hundreds of highways retaining walls and geotechnical sites are critically presented. Inspection activities have been carried out on different geotechnical works, along Italian highways. These activities allowed to build an accurate damage database whose main features and statistics are discussed below. Then, a comparison between different inspection checklist and procedures developed by the highways management company is analyzed as current Italian practice and a new proposal for a better and more efficient inspection procedures. Besides, possible application of UAS and AI as supporting tools for visual inspections are pointed out.

1 INTRODUCTION

Due to its geographical conformation, the Italian territory presents a great landscapes variety, from coast to hills, from plains to mountains. However, the mountain and hill areas cover the largest portion in terms of surfaces of the national territory. Related to the capillarity reached by the national highway system, consequently, the long sections of the network are set up in areas with irregular morphologies and, by their nature, therefore subject, above all, to a high degree of hydrogeological and seismic hazard.

In the following the geotechnical inspection activity carried out between 2021 and 2022 and regarding the state of art of the geotechnical aspects of the Italian highway network will be presented.

The Italian highway network is almost 6000 km long and counts about 705 tunnels and 1626 between bridges and viaducts. The first Italian highway dates to 1924 with the “Autostrada dei Laghi” from Milan to Varese, the second highway in the world only after the “Long Island Motor Parkway” in the New York state (USA).

Globally in recent years there has been growing attention towards the infrastructures to determine structural performance of the engineering works, through the implementation of visual inspections and maintenance surveillance; particularly, in Italy where the infrastructural network often dating back to the post-war period hence infrastructures are now of a considerable age.

After the economic boom, took place between 1958 and 1963, the construction activities of the time meant an important booster for the local economy. From now on and for the following decades, however, the aspects of aging and durability of building materials have been neglected. These, added to the fact that there was often a bad habit of building “on savings”, inevitably means that today these infrastructures present in several cases a state of degradation, that can even compromise the stability and functionality of the infrastructure itself, leading to collapse as recent news has reminded us.

Only in recent decades the importance of visual inspection, surveillance, and subsequently maintenance activities are beginning to be understood.

Above all, these activities allow the prevention of tragedies, and have a positive return from an economic point of view.

The periodic inspection activity allows to evaluate how an infrastructure, or a site, evolves over time. This evaluation returns an overview of the various points of interest. Moreover, the systematical inspection repeated over the years and the comparison of both the results of the inspections and both of several similar situations, it is possible to maintain, before the failure happens, giving tragic outcomes.

1.1 *Inspection procedure*

In Italy, according to the management procedure established by the highway managing authority, the asset of interest can be divided into geotechnical asset (i.e. road embankment, trench, natural slopes, rockfall barriers, and drapery mesh) and retaining walls.

The purpose of the asset of interest inspection is to identify anomalies already manifest or potential related to the asset.

The inspection procedure involves checking and examining previous inspections reports, after that, it provides for a purely visual type of inspection. In fact, the monitoring of asset of interest is primarily based on “visual” observation of places. The visual examination of the instability of the highway site and of the infrastructure together with the observation of the evidence present in slopes and in land near the highway site, in fact, allow a first evaluation of deformation processes and instability phenomena that may be present.

This first summary identification of the in-progress phenomena allows us to define the most appropriate corrective measures/actions to be activated (monitoring and/or maintenance interventions) and the possible need to resort to a qualified specialist technical support. The asset of interest hereinafter will be reported as “site”.

In the case of site already equipped with instrumental monitoring systems, before the visual inspection, the available monitoring data must be retrieved and examined. During the inspection, the state of conservation of the installed system must be evaluated. Based on evidence found on site and the results of previous inspections, the need to install, to update or to restore the monitoring system is evaluated.

Each asset of interest, must be fully inspected starting from highway platform to the foot of the embankment/fence, if it is an embankment highway, or up to the guard ditch at the top/fence, if you are inspecting a trench and for its entire extension in case of support or garrison work, both in the sense longitudinal and transversal and in height, including complementary structures such as ditches, gutters, channels, rockfall barriers, etc.

For each site, the anomalies must be described according to the inspection form, established by the managing authority. For the geomorphological and/or structural anomalies must be described the typology and the geometric position. To the inspection form will have to be added: *i*) photographic report of the main anomalies observed on site; *ii*) sketch in case of retaining wall with indication of anomalies (i.e. position, extension typology and photograph number); *iii*) recognition of the extent of the damage with respect to the overall state of the structure and summary evaluation of the extent of the single damage also in combination with other anomalies and indication of the potential evolution of the phenomena.

Currently, given the increased use of Unmanned Aerial Vehicles (UAV) in many activities, the employ of UAV has also been introduced for site inspection, especially for the inspections of particularly steep site (i.e. rockfall barriers or drapery mesh) and for geotechnical asset difficult to reach. For these sites (Figures 1-2) the employment of UAV allows for faster and safer inspection, with respect to a traditional one. UAV system allows to systematically collect site photos and if structural defects have been identified, suggesting a more thorough inspection, for example through specialized personnel such as rock climbers, the method and the timing of insights must be shared with the managing authority.

The last part of the inspection process is a synthetic evaluation of the preservation state of the site. This evaluation is based on all the observation done on site, the presence/absence of anomalies, their extensions, their typology, their proximity to the highway, and on the base of inspector experience. The evaluation, hence, is based on a semi-qualitative method that

may slightly change from inspector to inspector. The possible evaluation of the site, according to the maintenance procedure, are: *i*) absence of anomalies; *ii*) anomalies to monitor, *iii*) plan a restore, and *iv*) urgent restore. Neglecting the absence of anomalies whose meaning is already explained by the name; anomalies to monitor is the evaluation given to that site which present anomalies which in their state, observed during inspection, do not represent a safety problem, but which must be controlled so that they do not become one. Plan to restore is the evaluation given to that site which show anomalies that in brief time could lead to a safety problem, and urgent restore is the evaluation given to that site which show serious anomalies that already represent an incipient safety risk.

For geotechnical asset in general, is established an annual frequency of inspection. For the retaining walls, the rockfall barriers and drapery mesh on the rocky slopes, the inspection frequency is every four years. If significant anomalies are found or the monitoring inspection highlights the presence of a rapid evolution of degradation, as well as proposing (request) specialized investigations from the managing authority, the area will become a “geotechnical asset” to be inspected with annual frequency.



Figure 1. Particularly step geotechnical asset difficult to reach and close to the highway.



Figure 2. An example of geotechnical asset difficult to reach, in this case the inspection concerns the slope below the highway, that in this particular case is the riverbed.

2 INSPECTIONS RESULTS

During the period of activity, 905 inspections have been carried out. Among these, 480 have been regarded retaining walls and 425 geotechnical assets.

While retaining wall include a specific category of concrete structures and reinforced lands, geotechnical assets include various types of situations, among these we can find mountain slopes subject to geomorphological or hydrogeological instability phenomena, rockfall barriers or drapery nets, structures for the prevention and mitigation of hydrogeological risk such as weirs or selector weirs, embankments and highway trenches or areas with a high rate of erosion such as the bed of rivers on which the foundations of bridges are set.

The following tables and figures summarize the defects found during the inspections for retaining walls (Table 1, Figure 3) and geotechnical sites (Table 2, Figure 4), their frequency and degree of severity:

Table 1. Distribution of defects among retaining walls.

Retaining walls	
Defect type	%
No anomaly	6.2
Presence of lesions/cracks	27.3
Presence of deterioration of the facade	10.8
Presence of moisture stains/efflorescence	30
Armor in sight	13
Abnormal injuries /openings on joints	8.5
Rotations/dislocations	3.8
Vegetation between joints	9.3

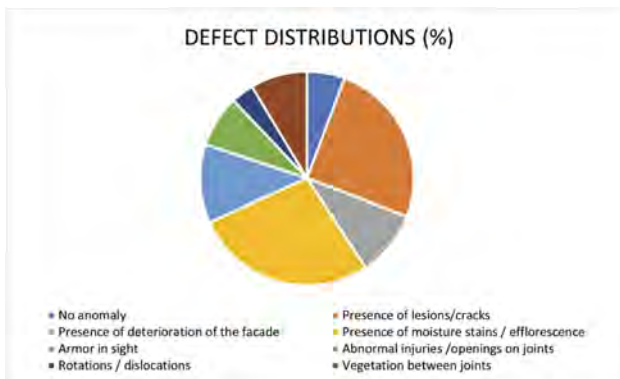


Figure 3. The cake diagram shows the distribution (%) of each type of defect found in the retaining walls inspected.

3 HIGHWAY GEOTECHNICAL INSPECTION ABROAD

For a long time, in Italy, the geotechnical asset management have been underestimated and only in the last decades start to improve a geotechnical asset management program.

Only in recent years Italian highways authorities started a geotechnical asset inspection program, and in several case a common line, for the inspection criteria, was not followed by the different managing authorities. At the same time, many other countries worldwide started with national highway asset management program long time ago. For example, one of the most advanced countries is USA, where are already developed national asset management programs, even focus on geotechnical asset management.

Table 2. Distribution (%) of defects with evaluation of gravity among geotechnical sites.

Geotechnical sites	Absence of anomalies	Anomalies to monitor	Recovery to schedule	Urgent restoration
Widespread landslides	0	4	0.2	0
Drainage duct obstruction	0	0.2	0	0
Pavement injury	0	7.3	0	0
Diffuse erosion	0	10.4	0.2	0.2
Channelled erosion	0	3.76	0.2	0
Detachment niches	0	1.18	0.2	0
Wall injury/work in reinforced concrete	0	5.65	1	0.2
Deteriorated conteniment net	0	1.65	0	0
Dected subsidence/quay	0	4.7	0.2	0
Animal burrows in the embankment	0	0.2	0.2	0
Lanslide	0	5.4	0.5	0
No anomaly	19	0	0	0

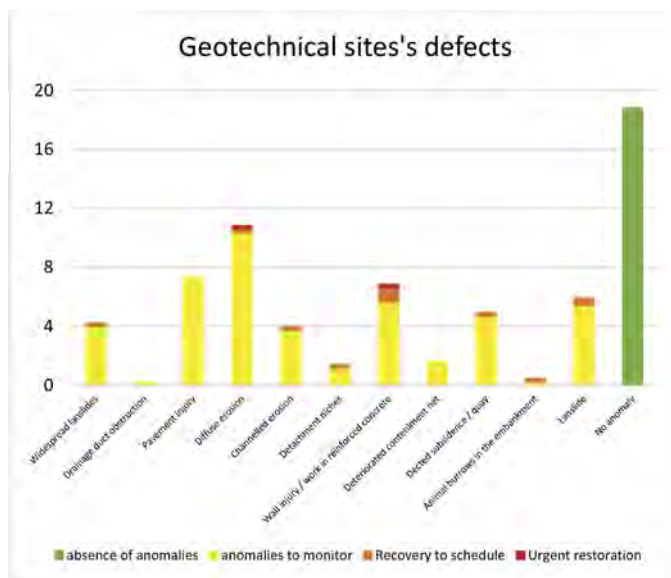


Figure 4. The histogram shows the distribution of defects found in the geotechnical sites and the gravity of each.

3.1 USA perspective

Since 2012 with the 112th United States Congress US enacted a law for founding a reform of surface transportation called Moving Ahead for Progress in the 21st century act (MP-21). This reform changes the policy and the programmatic framework for investment for growth and development of the surface transportation infrastructure. With MP-21 the investment has been driven through a base-performance program.

Starting from that moment in USA have been developed a TAM program (AASHTO, 2011 e AASHTO, 2016) (Transport Asset Management), where was included lately GAM (Geotechnical Asset Management).

With the NCHRP Project 24-46 “Development of an implementation manual for geotechnical asset management for transportation agencies” have been collected all information, case study, to develop a Volume 1 of NCHRP Research report 903, giving a background for implementing and correct application of the GAM method.

The transportation agencies can implement a GAM program focusing on a risk-based method where all existing asset defined as: *i*) embankment; *ii*) slopes; *iii*) retaining walls; *iv*) subgrades following the principles of: *i*) do minimum; *ii*) maintain; *iii*) rehabilitate; *iv*) reconstruct; and *v*) restore. In this way it is possible to prioritize the treatment based on risk and driving the investment correctly.

The prioritize process can develop following the items: *i*) inventory and assessment; *ii*) risk management; *iii*) risk prioritization; *iv*) investment prioritization; and *v*) candidate treatment.

Same approach has been used for the implementation of GAM in Networks Rail system and England Highway in UK (Power, 2012 and Network Rail, 2017).

4 BRIEF COMPARISON AND FUTURE PERSPECTIVE

Geotechnical inspection recently has been improved in Italy, embracing the state-of-the-art method, following the path of many other countries, and focusing on semi-quantitative risk-based approach.

The preliminary application of GAM gives a successful inventory of all geotechnical assets in Italian highway network, and his own condition.

Actually ranking the risk is purely a subjective of the inspector, for this reason a further improvement of the GAM could be to introduce a risk analysis method as reported on the volume 2 of NCHRP Research report 903, where the precision of the risk analysis has been improved using two-dimensional graphic including the likelihood and consequence of two axis, or use a 3D matrix (Anderson, 2016), where the three axis of the cube report: *i*) the class of asset; *ii*) risk source;- and *iii*) the performance goals.

Other parameters to include in the ranking of the risk is the proximity to the highway (HD41/03) and the timeframe.

The experience acquired during this period could be used to update the inspection manuals issued by Italian highway authorities.

4.1 Future perspective

The achieved experience in geotechnical inspections, lead us to massively employ UAV for reaching far geotechnical asset (i.e. example rocky slope, or torrents). UAV allows to obtain fine details for single structure inspected, to obtain a better overview of the area of interest, and to repeat the same inspection over years. In particular, the UAV employment allow to reach the inspection target with a substantial saving of time and a significant increase in safety. Moreover, the inspection data has been collected in a GIS-like portal, called AGE. This GIS-like portal is also a database to report the inspection results carried out over the years.

This first technological approach demonstrates how the most advanced technology in survey and remote sensing can give huge benefit in terms of inspection efficiency and its quality. The NCHRP synthesis 582 (National Academies of Science, Engineering, and Medicine, 2022) confirm that the state of practice of the inspection use web-GIS, like AGE, GPS/GNSS positioning system, UAV, areal/terrestrial photogrammetry dominating the inspection procedure and becomes the common practice in the last years.

The challenge for the next future inspection practice will be to push over the limit of use advanced technology, like standardize the employment of photogrammetry, LIDAR, laser scanning, and thermal camera. These technologies will permit to have exactly position of structures and a precise 2D/3D model, improving the registration of the failures and its time-related evolution.

Employing UAV could upgrade geotechnical asset inspections. UAV systems allow to systematically collect pictures in complete safety. The collected data are combined (using the

principles of photogrammetry) to build a 3D model to provide a complete and measurable overview of the site. The interoperability of 3D models, generated at each periodic inspection, with BIM (Building Information Model) software creates an historical record of the infrastructure where each, new or existing, issue could be checked during time.

Furthermore, an implementation of e-ticketing system will permit to have in real-time data of failure and reduce the time gap of action for the stage of maintenance, rehabilitation, reconstruction; simultaneously the development of these kinds of systems increases dramatically the type of data registered and its amounts.

5 CONCLUSION

Geotechnical asset inspection has been started recently, implementing a GAM method for the asset management by the Italian highway authorities.

Due to the early-stage implementation of GAM many improvements must be develop, like a more precise definition of the risk management using the latest methods issued in scientific literature.

The latest technologies can be used as a booster for improving the quality of the data collection and its own management, even more speeding up the field inspections and increase the safety of the inspectors.

REFERENCES

- AASHTO. 2011. AASHTO Transportation Asset Management Guide: A Focus on Implementation. American Association of Highway and Transportation Officials, Washington, D.C.
- AASHTO. 2016. AASHTO Guide for Enterprise Risk Management. American Association of Highway and Transportation Officials, Washington, D.C.
- Anderson, S. A. 2016. "Communicating Multiobjective Risk: A New Geotechnical Need for Transportation." Transportation Research Record: Journal of the Transportation Research Board, No. 2580, Transportation Research Board, Washington, D.C., pp. 80–88. DOI: 10.3141/2580-10
- A Summary of Highway Provisions - MAP-21 - Moving Ahead for Progress in the 21st Century | Federal Highway Administration. <https://www.fhwa.dot.gov/map21/summaryinfo.cfm>.
- Gate, B., Park, B. V., & Midlands, W. 2011. B90 8AE.
- Highways Agency (2003) Maintenance of Highway Geotechnical Assets. HD41/03HM Treasury (2010) Spending Review 2010
- National Academies of Sciences, Engineering, and Medicine. 2022. *Highway Infrastructure Inspection Practices for the Digital Age*. Washington, DC: The National Academies Press. <https://doi.org/10.17226/26592>.
- Network Rail. 2017. Earthworks Asset Policy (March 2017). Network Rail Infrastructure Limited.
- Power, C., D. Patterson, D. Rudrum, D. Wright. 2012. "Geotechnical Asset Management for the UK Highways Agency," In: T. A. Radford (ed.), *Earthworks in Europe*. Geological Society of London, London, UK. Doi: 10.1144/EGSP26.
- Stanley D.A. 2011. Asset Management in a World of Dirt: Emergence of an Undereveloped Sector of Transportation Asset Management. National Academies of Sciences, Engineering, and Medicine (U.S.). Transportation Research Board.
- Thompson PD. 2016. Geotechnical Asset Management Plan: Technical Report. Juneau: Alaska Department of Transportation and Public Facilities.
- Vessely, M. 2019. Geotechnical asset management for transportation agencies: volume 1: research overview; volume 2: implementation manual. Transportation Research Board.

Using shape optimization and principal stress line based stiffness improvement of thin-shell structure and reduce construction costs

Y.X. Sun, Y.Y. Yang & L.J. Leu

Department of Civil Engineering, National Taiwan University, Taipei, R.O.C

K. Yamamoto

Faculty of Engineering, System and Information, University of Tsukuba, Ibaraki, Japan

ABSTRACT: There is a gradual rise in movements for the realization of a circular economy and the resolution of environmental issues by presenting modern architectural form that proposes new materials, constructions, and lifestyles that reduce the environmental cost. In modern architecture, thin-shell structures are widely used especially on roofs of buildings, such as the roof of Kresge Auditorium at Massachusetts Institute of Technology (MIT), because it is easy to make architectural forms look beautiful.

To uses less material to obtain the aesthetic and high stiffness roof, designing structural optimization is an easy way to reduce construction costs and improve the service life of structures. This study uses the non-uniform rational B-spline (NURBS) method and finite element method as free-form surface technology to build thin-shell structures to improve stiffness of these structures. After obtaining the optimal thin-shell structure, add the principal stress line to improve the stiffness of this thin-shell structure in the same volume. Use the principal stress lines of different layers in the flat plate to create the stiffening beams under the thin-shell structure, which adds to the stiffness of the thin-shell structure.

Applying these techniques to solve real shell structure optimization problems will be practical optimal designs. Consequently, this technique allows engineers and architects to design aesthetic shape structures with high stiffness and low cost.

1 INTRODUCTION

The design of modern architectural structures is typically streamlined or aesthetically based, where modernistic and innovative structural systems are widely implemented, introducing non-conventional beam-column-based buildings all over the world. Most roof of modernistic structures are used thin-shell structures with free-form surface designs and are gaining popularity. However, the balance between structural stiffness and aesthetics is rather tricky for these designs. In order to enhance the structural stiffness of the thin-shell, construction material used would increase dramatically and would not meet the requirement of circular economy. This study aims to investigate the volume optimization of construction materials while maintaining both their appearance and excellent structural mechanics behavior.

In the past, thin-shell structures may adopt various free-form surface designs, where most of them controlled their structural geometry through certain geometric parameters. Commonly seen design construction approaches are the Bézier curve (Bézier, 1968), uniform B-spline, and non-uniform rational B-spline (NURBS) (Versprille, 1975). Kegl & Brank (2006) opted for the Bezier curve with design optimization to construct their curved surface and implemented their method on truss structures. Espath *et al.* (2011) combined NURBS and optimization theory to optimize the design of flat plates with different shapes, using both linear and non-linear optimization algorithms to produce two different optimal design outcomes.

For design optimization of thin-shell structures, Tomàs & Matri (2010) opted a famous thin-shell structure in Spain, i.e., Universal Oceanographic Park as the initial structural model of their design optimization workflow. Whereas Kanta (2015) took a stadium-based design approach, investigating their structural mechanical behaviors with an emphasis on the linear and non-linear buckling evaluation of thin-shell structures. Marino *et al.* (2016) used the auditorium of the Massachusetts Institute of Technology (MIT) as an example, where they implemented Bézier curves in spherical coordinate system to simulate similar geometric shapes. An optimized geometric model was generated through shape optimization in their study. Veenendaal *et al.* (2017) designed the thin-shell roof of Nest Hilo in Switzerland from its initial structural design phase towards the final construction of the actual thin-shell roof. They considered various influencing factor towards the design of thin-shell structure, including various loading conditions, buckling evaluation, structural strength assessment, structural thickness, and so on. By performing design optimization with the inclusion of these factors, structural design with the best stiffness performance was selected for the building.

Apart from the implementation of free-form surfaces in thin-shell structures, Michell (1904) was amongst the earliest to study optimal mesh-based structural mechanics prior to the development of principal stress line related applications. Well-known analytical solutions of truss structures were derived, in which Michell-cantilever is the most widely known optimized structure. Rozvany (1998) further consolidated and verified that analytical solution, concluding that specific truss structure has the best structural stiffness performance for cases of light materials. This finding has in turn confirmed the tight relationship between the principal stress line and Michell-cantilever.

Halpert (2013) is one of the studies that implemented principal stress line in the stiffening of flat-slab structure. The study uses in-house principal stress line generation tool to investigate the slab structure designed by Italian structural designer Pier Luigi Nervi, confirming that the real slab system with high stiffness possess a high fitting degree to the principal stress line layout. This finding has proven the practical feasibility of principal stress line in actual engineering applications. In order to reinforce the structural stiffness of thin-shell structures, this study adopted stiffening girder for structural strengthening with principal stress line layout, which can enhance the structural stiffness of thin-shell structures effectively.

In this study, we aim to present a design concept with themes of environmental protection and circular economy, alongside aesthetic presentation. This study explores a methodology to construct a free-formed surface thin-shell structure, under a fixed volume of material, integrating the optimization theory and principal stress line in the design consideration. The outcomes of this methodology could potentially enhance the structural stiffness of the thin-shell structure while maintaining its aesthetics.

2 STRUCTURAL OPTIMIZATION

Structural optimization design can be categorized into three types based on processing approaches, namely sizing optimization, shape optimization, and topology optimization. The design workflows for these three approaches are mostly similar, from initial model definition and finite element analysis to reaching convergence in optimization process. Their key differences lie within the design parameter (variable) and the implemented algorithm. This study mainly adopted the structural optimization approach based on shape optimization in conjunction with dimension optimization, in order to optimize the design of thin-shell structures.

2.1 Shape optimization

Shape optimization achieves the best solution for its objection function by changing the geometric shape of target structure, until it reaches the minimum structural compliance. Shape optimization has been used in various structural systems. For instance, simply by changing the node coordinates of truss structure, the truss system can achieve higher structural stiffness under identical loading mode.

As aesthetic demand arises in modern engineering, many smooth streamlined parametric curves (surfaces) are developed. There are various ways to construct their geometric models. Commonly seen methods are cubic spline, Bézier curve, B-splines, non-uniform rational B-spline (NURBS), and so forth. Amongst these, NURBS has higher flexibility and accuracy in dealing with analytical functions and establishing shapes of geometric models, not to mention its faster computation speed and numerical stability.

2.2 Non-uniform rational B-spline

Non-uniform rational B-spline (NURBS) is proposed by Versprille (1975), where NURBS surface is defined as follows,

$$\mathbf{S}(u, v) = \frac{\sum_{i=0}^n \sum_{j=0}^m N_{i,p}(u) N_{j,q}(v) w_{ij} \mathbf{P}_{ij}}{\sum_{i=0}^n \sum_{j=0}^m N_{i,p}(u) N_{j,q}(v) w_{ij}}, \quad 0 \leq u, v \leq 1 \quad (1)$$

$$N_{i,p}(u) = \frac{u - u_i}{u_{i+p} - u_i} N_{i,p-1}(u) + \frac{u_{i+p+1} - u}{u_{i+p+1} - u_{i+1}} N_{i+1,p-1}(u) \quad (2)$$

$$N_{i,0} = \begin{cases} 1 & u_i \leq u < u_{i+1} \\ 0 & \text{otherwise} \end{cases}$$

where P_i is a given set of control points, i is number of control points, $N_{i,p}$ is the basis function dependent on the node vector \mathbf{U} , w_i is the weighting, p is the curve polynomial order, n is the control point amount, $m+1$ is the node amount.

The main difference between NURBS and B-spline is the inclusion of the weighting w_i . While NURBS possesses the advantages of B-spline, it forms a more accurate and smoother curve (surface) when dealing with complex geometry, reducing the formation of angular edges. This approach allows the construction of a smoother and irregular free-form surface with localized effect.

2.3 Structural compliance

In order to generate optimized outcomes, this study adopted the compliance factor derivation method from Xie *et al.* (1993), the coordinate node of variable element e is first assumed, giving a structural stiffness variation of

$$\mathbf{K}' - \mathbf{K} = -\mathbf{K}^e \quad (3)$$

where \mathbf{K} is the structural stiffness prior to changing the coordinate of e , whereas \mathbf{K}' is the new structural stiffness. Their difference is then the stiffness \mathbf{K}^e . The change in displacement can be expressed in stiffness and external force by

$$\begin{aligned} \Delta \mathbf{u} = \mathbf{u}' - \mathbf{u} &= (\mathbf{K}')^{-1} \mathbf{F} - \mathbf{K}^{-1} \mathbf{F} = [(\mathbf{K} - \mathbf{K}^e)^{-1} - \mathbf{K}^{-1}] \mathbf{F} \\ &= \mathbf{K}^{-1} [\mathbf{K} - (\mathbf{K} - \mathbf{K}^e)] (\mathbf{K} - \mathbf{K}^e)^{-1} \mathbf{F} = \mathbf{K}^{-1} \mathbf{K}^e (\mathbf{K}')^{-1} \mathbf{F} \end{aligned} \quad (4)$$

in which \mathbf{u} and \mathbf{u}' are the displacement amount prior and after the element coordinate change, respectively, $\Delta \mathbf{u}$ is the change in displacement, and \mathbf{F} is the external force. \mathbf{F} is assumed to be invariant to the change in coordinate e , a rearrangement would give

$$\Delta \mathbf{u} = \mathbf{K}^{-1} \mathbf{K}^e \mathbf{u}' \quad (5)$$

Assuming the change in displacement prior and after the element coordinate variation is infinitesimal, $\Delta \mathbf{u}$ can be expressed as

$$\Delta \mathbf{u} = \mathbf{K}^{-1} \mathbf{K}^e \mathbf{u}' \cong \mathbf{K}^{-1} \mathbf{K}^e \mathbf{u} \quad (6)$$

This gives us the structural compliance variation ΔC due to the element coordinate variation,

$$\begin{aligned}\Delta C &= C' - C \\ &= \mathbf{F}^T \mathbf{u}' - \mathbf{F}^T \mathbf{u} = \mathbf{F}^T (\mathbf{u}' - \mathbf{u}) = \mathbf{F}^T \Delta \mathbf{u}\end{aligned}\quad (7)$$

By substituting $\Delta \mathbf{u}$, we get

$$\Delta C = \mathbf{F}^T \mathbf{K}^{-1} \mathbf{k}^e \mathbf{u} = \mathbf{u}^T \mathbf{k}^e \mathbf{u} = C_e \quad (8)$$

where C_e is the structural compliance after the change in e element coordinate, which is inherent twice the element strain energy of the element e . Through derivations above, the structural compliance formula is now

$$C = \mathbf{F}^T \Delta \mathbf{u} = 2U, \quad C \propto \frac{1}{\mathbf{K}} \quad (9)$$

From the equation above, we can observe that structural compliance is twice the strain energy and is inversely proportional to the stiffness. It means the structural compliance C is larger, the stiffness is smaller, and vice versa, as shown in Figure 1.

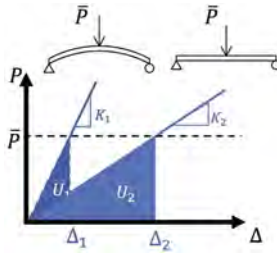


Figure 1. Strain energy figure.

2.4 Free-form surface and shape optimization

To validate the proposed methodology in this study, an initial shape of a square flat plate with 10 m length at all sides is created. The modeled shape had Young's modulus of 30 GPa, Poisson's ratio of 0.3, density of 2500 kg/m³, flat plate thickness of 30 cm, and supports at four, where its structural schematic is as shown in Figure 2.

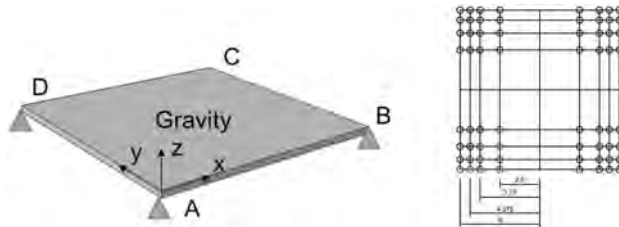
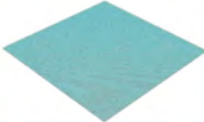
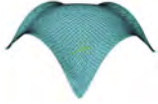


Figure 2. Flat plate model and control point and comparison diagram.

64 control points were allocated on this flat plate model, where their positions were layout continuously at the midpoints of side lengths.

Compared to the original flat plate, Table 1 shows a S4R5 element, the structural compliance decreased from 19189 N-m to 131N-m at the same volume, lead to the objective function of the optimized surface CV to be 0.007 times the initial structure. This means that the stiffness per unit volume has increased by 146 times.

Table 1. Flat plate shape and optimal shape.

Element type	S4R5	
	Flat plate	optimal shape
Shape		
C(N.m)	19189	131
V(m ³)	30	
CV (N.m ⁴)	575691	3930
(times)	(1)	(146)

3 PRINCIPAL STRESS LINE

This study implemented thin-shell structure with principal stress line approach to design a stiffening girder, in order to enhance the stiffness of the thin-shell. Finite element analysis is used to discretize series of principal stress vector fields, as the iterative source for numerical integration. The first step to obtaining the principal stress line is through the eigenvalue analysis of the element. Since shell element is a flat plate stress element, its stress magnitude and direction can be calculated through post-processing.

3.1 Principal stress line algorithm

According to the definition of Cauchy stress tensor, which is a second-order tensor,

$$\mathbf{T}^{(n)} = \mathbf{n}\boldsymbol{\sigma} \text{ or } T_i^{(n)} = \sigma_{ij}n_j \quad (10)$$

$$\boldsymbol{\sigma} = \begin{bmatrix} \sigma_{xx} & \tau_{xy} \\ \tau_{xy} & \sigma_{yy} \end{bmatrix} \quad (11)$$

where \mathbf{n} is the unit vector of an imaginary surface, $\mathbf{T}^{(n)}$ is the stress tensor passing through the imaginary surface, and σ_{ij} is the stress state at any specific points. By projecting Cauchy stress tensor onto a planar surface, it can be formulated as

$$\mathbf{T}^{(n)} = \boldsymbol{\sigma}\mathbf{n} = \lambda\mathbf{n} \text{ or } T_i^{(n)} = \sigma_{ij}n_j = \lambda n_i \quad (12)$$

The stress state of any arbitrary point can be determined through eigenvalue analysis, which gives the corresponding principal stress magnitude and direction. λ is the eigenvalue and the principal stress of the specific point, \mathbf{n} is the eigenvector and the direction of the principal stress. Since eigenvalues are in pairs, by sorting the eigenvalue in decreasing order, the maximum and the minimum magnitudes and directions of principal stresses are determined as σ_1, n_1 and σ_2, n_2 , respectively.

After determining the principal stress vector field at arbitrary point, the next step is to construct the principal stress line tangential to the principal stress direction. The streamline of the principal stress (displacement field) reveals the original streamline trajectory and generate a corresponding streamline field, as demonstrated in Figure 3.

3.2 Curved surface of the principal stress line based stiffened member

Building on the example in Section 2.4, principal stress line analysis is performed on the flat plate model, by separate analyses on upper, middle, and lower layers. This study first applied dimensional optimization on the stiffened model, involving design parameters of thickness t_s , width b and depth h . Considering the actual building mode, the three layers of principal stress line is designed to be stiffened at the bottom of the flat plate model, as shown in Table 2. It can be

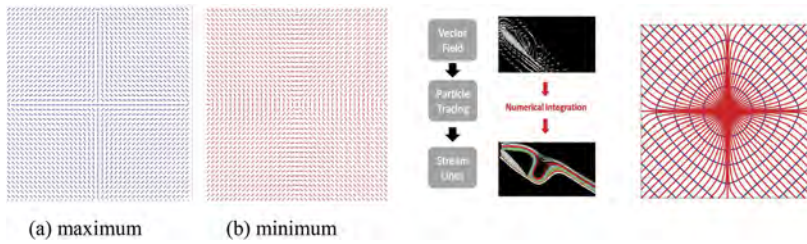


Figure 3. Principal stress direction, stream line sketch diagram (Chien, 2019) and principal stress line.

observed that the stiffening performance using the principal stress line of middle layer was the best amongst the three, with an increment of 1.8 times. Table 3 shows the analysis result where the stiffness enhancement using shape optimization had the most significant improvement.

3.3 Summary

This section introduced the background of principal stress line, through the application case of the stiffened girder in Section 2.4 which included both shape optimization and principal stress line distribution. The stiffness was evaluated between the flat plate model and the optimized curved surface model. From Table 2 and Table 3, when principal stress line at the middle layer is used to stiffen internal layers, the flat plate model with both shape optimization and stiffening can achieve stiffness enhancement of around 238 times, under similar volume condition. In other words, with similar material amount as the original flat plate model, the improved design possesses significantly better structural stiffness, validating that the principal stress line stiffening approach proposed in this study is beneficial towards the enhancement of structural stiffness.

Table 2. Stiffening analysis with different principal stress line.


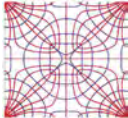
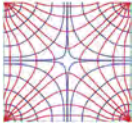
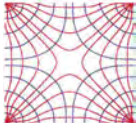
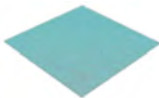
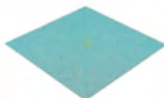


	shape optimization	principal stress line lower layer	principal stress line mid layer	principal stress line upper layer
				
C (N.m)	114	94	61	75
V(m ³)	34			
CV (N.m ⁴)	3955	3274	2121	2612
(times)	(1.00)	(1.21)	(1.86)	(1.51)

Table 3. Compare with original flat plate, optimal shape and shape with stiffening.

	flat plate	flat plate with stiffening	shape optimization	shape optimization with stiffening
				
C (N.m)	19190	4398	131	81
V(m ³)	30			
CV (N.m ⁴)	575,692	131,946	3,930	2,417
(times)	(1.00)	(4.36)	(143.94)	(238.18)

4 CASE DESIGN

In order to validate the practical feasibility of the proposed approach, this study simulated it in a case design based on the Kresge Auditorium at Massachusetts Institute of Technology (MIT). The case design needs to account for the structural strength, structural displacement, structural loading and its loading combination. Therefore, the best way to present the structural optimization of thin-shell structures is by expressing this in maximizing the stiffness per unit volume (i.e. minimizing the product of structural compliance and volume), and setting the design criteria as constraints.

4.1 Kresge Auditorium, MIT

Kresge Auditorium is constructed from one-eighth of a sphere, where its official geometrical dimensions are 15.24 m in height and 34.50m in span. However, only these two data is not enough to modeled, so this study also referred to the third paragraph of the literature reviews in Marino *et al.* (2016), where the radius of auditorium, a triangular side length, midpoint height and midpoint height of the triangular side is 34.3m, 48.5m, 14.5m and 8.1m, respectively. These dimensional data may have slight discrepancies in decimal points, they are sufficient in outlining the initial shape design for this study, and is quite accurate even when compared to the photograph of the real building, as shown in Figure 4.



Figure 4. Kresge Auditorium initial design and real building figure.

4.2 Case study analysis





The geometrical projection of the structure is an equilateral triangle, and the analysis outcomes are shown in Table 4. There has large significant variation between the optimized shape and the original structure, which highly improved the stiffness per unit volume. With shape optimization and fixed volume conditions, buckling limit is used as the constraint condition in the analysis. The stiffness enhancement using shape optimization was around 7 times, then using the principal stress line further increased this up to 50%. For joint optimization using both shape optimization and principal stress line, there were stiffness enhancement up to 10 times under similar material volume.

5 CONCLUSION

With the rise of environmental awareness, the reduction and reuse of construction materials have come into attention for engineers. This study performed a design optimization on thin-shell structure using similar material volume. Stiffness enhancement with principal stress line is implemented on thin-shell structure, which significantly increased its structural stiffness.

There are two parts to this study, namely the free-form surface and the principal stress line-based stiffening girder. The free-form surface was investigated using NURBS design, where the

Table 4. Comparison table for Kresge Auditorium.

	initial shape	initial shape with stiffening	optimal shape	optimal shape with stiffening
Shape				
t_s (cm)	50	16	50	17
V(m ³)	564			
CV(N·m ⁴)	237,242,310	145,898,691	33,740,768	23,964,751
(times)	(1.00)	(1.63)	(7.03)	(9.90)

best shape was generated using CV as the objective function, which is the product of structural compliance and material volume. Under similar material volume, the stiffness of the shape-optimized model is 146 times the original flat plate model. As for the principal stress line based stiffened girder analysis, the principal stress lines of upper, middle, lower layers for the internal of the flat plate model were evaluated in stiffness analysis. The overall stiffness enhancement of the principal stress line-based structure can reach 1.5 times the shape-optimized thin shell structure, proving its effectiveness under similar material conditions.

In order to validate the practical feasibility of the proposed approach, this study performed a case study on Kresge Auditorium at MIT. The stiffness enhancement of the thin-shell roof structure after shape optimization is 7 times, whereas the inclusion of principal stress line analysis can further improve the original stiffness up to 10 times, under similar material volume. These results have proven that the proposed methodology is effective in improving structural stiffness of thin-shell structures, through shape optimization and principal stress line approach, with similar material condition and volume. Through these optimization workflows, the overall aesthetic appearance of the thin-shell structures can be maintained while reducing the usage of construction materials.

REFERENCES

- Bézier, P. E. 1968. How Renault uses numerical control for car body design and tooling (No. 680010). *SAE Technical Paper*.
- Chien, M.S. 2019 Application of Principal Stress Lines on Structural Optimization Design. *Master's thesis, National Taiwan University*. Airiti Library.
- Espath, L. F. R., Linn, R. V., & Awruch, A. M. 2011. Shape optimization of shell structures based on NURBS description using automatic differentiation. *International Journal for Numerical Methods in Engineering*, 88(7), 613–636.
- Kegl, M., & Brank, B. 2006. Shape optimization of truss-stiffened shell structures with variable thickness. *Computer methods in applied mechanics and engineering*, 195(19-22), 2611–2634.
- Marino, E., Salvatori, L., Orlando, M., & Borri, C. 2016. Two shape parametrizations for structural optimization of triangular shells. *Computers & Structures*, 166, 1–10.
- Michell, A. G. M. 1904. LVIII. The limits of economy of material in frame-structures. *The London, Edinburgh, and Dublin Philosophical Magazine and Journal of Science*, 8(47), 589–597.
- Tomás, A., & Martí, P. 2010 Shape and size optimization of concrete shells. *Engineering Structures*, 32(6), 1650–1658.
- Rozvany, G. I. N. 1998 Exact analytical solutions for some popular benchmark problems in topology optimization. *Structural Optimization*, 15(1), 42–48
- Veenendaal, D., Bakker, J., & Block, P. 2017 Structural design of the flexibly formed, mesh-reinforced concrete sandwich shell roof of NEST Hilo. *Journal of the International Association for Shell and Spatial Structures*, 58(1), 23–38.
- Versprille, K. J. 1975 *Computer-aided design applications of the rational b-spline approximation form*. Syracuse University, New York.
- Xie, Y. M., & Steven, G. P. 1993 A simple evolutionary procedure for structural optimization. *Computers & structures*, 49(5), 885–896

Numerical verification of vehicle-bridge interaction system identification using a 3D models

E. Mudahemuka, S. Ryota & K. Yamamoto

University of Tsukuba, Tsukuba, Japan

ABSTRACT: Bridges are not built to last forever, and the cost to replace them is very high. To extend their service life and ensures that they continue their normal function without abrupt failure, preventive maintenance is required. Current practice of uniformly inspecting all bridges in inventory is ineffective and inefficient. For decades, estimating natural frequency and other modal parameters from vehicle vibration has been investigated. These parameters require information about the intact bridge, which is challenging to obtain. This study proposes a method to estimate system parameters of both vehicle and bridge systems, from vehicle acceleration and position data. In this study, the vehicle is modeled as a 3-D rigid body connected by springs and dashpot and the bridge system as a Kirchhoff-Love plate. Vehicle system (body mass, suspension stiffness and damping, unsprung masses and unsprung stiffness) parameters and bridge system (Rayleigh damping coefficients, and flexural rigidity) parameters are estimated.

1 INTRODUCTION

Bridges play an essential role in the transport and mobility of people and goods across the globe. The aging problem threatens these critical infrastructures on which our lives depend. In developed countries, where the bridge transport system is predominant, most of their bridges have been in service for 40 years or more. As reported in the 2021 ASCE infrastructure report card, 42% of all USA bridges were at least 50 years old in 2021, with 7.5% reported as structurally inefficient (ASCE, 2021). The biggest issue is that replacing a bridge is expensive, and governments and private bridge owners prefer repairing or preventive maintenance options.

Preventive maintenance is done after conducting a bridge health condition assessment. This is done by estimating the health condition, locating the defective section of a given bridge infrastructure, and then carrying out repair works accordingly (Malekjafarian, McGetrick and Obrien, 2015). The bridge visual checking technic plays an essential role in bridge health condition assessment and maintenance decision-making. However, its results are variable, tedious, highly dependent on the inspectors' experience, and sometimes require closing the road/bridge section. In addition, it is only possible to find a defect if it is not visible to the surface.

The analysis of the bridge's dynamic response under vehicular load started in the 90s (Olsson, 1991), (Yang, Yau and Hsu, 1997). With the development of sensing technology, the bridge's dynamic response analysis is put to another level by analyzing the data captured by sensors. This technique is realized either using bridge vibration data or vehicle vibration data. The former uses sensors mounted on a bridge in different locations, which might present installation and monitoring challenges depending on the type and location of the bridge. The latter uses sensors mounted on a moving vehicle on its body, suspension, and tire assembly, known as the "drive-by monitoring method," and it provides a way to monitor many bridges simultaneously effectively. This method was investigated for the first time by (Yang, Lin and Yau, 2004). In their method, the vehicle is modeled as a sprung mass and the bridge as a simply supported beam. Through the analysis of vehicle acceleration response by FFT (Fast Fourier Transform), they confirm that four main frequencies dominate the vehicle response: vehicle frequency, vehicle drive frequency $2\pi v/L$, and two shifted bridge's first natural frequency $f_b \pm \pi v/L$.

An experimental verification (Yang and Lin, 2005) by scanning the fundamental frequency of the bridge using a two-wheeled cart mounted on a light truck confirms the extraction of the first bridge's natural frequency from the acceleration spectrum of the cart moving at 40 km/h. The same verification has been carried out using EMD (Empirical Mode Decomposition) technique and identifying up to the seventh bridge vibration mode (Yang and Chang, 2009). These experimental verifications have recommended that natural bridge frequency be extracted using multiple passes for a heavier vehicle moving below 40km/h. The feasibility becomes much higher if prior knowledge of test vehicle properties and their calibration is available.

Extracting natural frequency from vehicle acceleration response is challenging due to the dominance of vehicle frequencies in the spectrum caused by the road surface profile. Identifying bridge frequency requires prior knowledge of frequencies and modal shapes of the intact structure. Simplified models used in previous studies do not fully capture the vehicle and bridge representation. The issue with optimization cost encountered while using methods like particle swarm optimization, and genetic algorithm (Zhao, Nagayama and Xue, 2019), is worked on by adopting the (NM) Nelder-Mead algorithm. The NM algorithm is a more suitable optimization method as it does not require a differentiable objective function and is easy to implement.

This paper proposes a method for estimating the vehicle and bridge's mechanical parameters from the vehicle's acceleration data and its position as an alternative to natural frequency estimation. The VBI (Vehicle-Bridge Interaction) mechanical system parameters and the road profile are estimated. Those parameters are continuously updated via the NM algorithm until the road profile at the front and rear axle are equal or approximately equal. The HC (Half Car) model is extended to FC (Full Car) model, and the Kirchhoff-Love theory is used to model the bridge system. Implementing this approach can help optimize maintenance schedules and allocate resources more effectively, ultimately improving the safety and longevity of bridges.

2 VEHICLE-BRIDGE INTERACTION SYSTEM MODEL

2.1 Vehicle system model

This study uses an eight-degree-of-freedom vehicle model that takes into account both pitching and rolling effects. The model includes translation, rotational motion (pitching and rolling), vertical tire motion, and rigid body equilibrium conditions, as represented in the following mathematical expressions (Jazar, 2008). The expression for the translation equation of motion of the vehicle body is given as:

$$m_s \ddot{w}_{sG} = - \left\{ \sum_{i=1}^n k_{si}(w_{si} - w_{ui}) + c_{si}(\dot{w}_{si} - \dot{w}_{ui}) \right\} \quad (1)$$

Where n indicates the number of tires considered and w_{sG} is given by the following expression.

$$w_{sG} = \frac{d_2 l_2 w_{s1} + d_1 l_2 w_{s2} + d_2 l_1 w_{s3} + d_1 l_1 w_{s4}}{(d_1 + d_2)(l_1 + l_2)} \quad (2)$$

Where w_{si} and w_{ui} represent the vertical displacement of the i th sprung mass and the i th un-sprung mass respectively, l_1 , l_2 , d_1 and d_2 represent the distance from the gravity point to the position of the left tires, to the position of the right tires, to the position of the front tire, and the position of the rear tires, respectively. The following expression gives the rolling motion expression:

$$I_x \ddot{\theta}_x = \sum_{i=1}^n a d_j \{ k_{si}(w_{si} - w_{ui}) + c_{si}(\dot{w}_{si} - \dot{w}_{ui}) \} \quad \begin{cases} a = -1, j = 1, & \text{for } i \text{ odd} \\ a = 1, j = 2, & \text{for } i \text{ even} \end{cases} \quad (3)$$

$$I_x = d_1 d_2 m_s \quad (4)$$

Where I_x is the vehicle body's inertia moment in the y -direction and θ_x is the pitch angle of the vehicle body in the x -direction.

The expression for pitching motion follows the same patterns as the expression for rolling motion and it is given below:

$$I_y \ddot{\theta}_y = \sum_{i=1}^4 a l_j \{ k_{si}(w_{si} - w_{ui}) + c_{si}(\dot{w}_{si} - \dot{w}_{ui}) \} \quad \begin{cases} a = -1, j = 1, & \text{for } i \leq 2 \\ a = 1, j = 2, & \text{for } 2 < i \end{cases} \quad (5)$$

$$I_y = l_1 l_2 m_s \quad (6)$$

Where I_y is the vehicle body's inertia moment in the x -direction and θ_y is the pitch angle of the vehicle body in the y -direction. In the same manner, the equation of motion of wheels is described.

$$m_{ui} \ddot{w}_{ui} = k_{si}(w_{si} - w_{ui}) + c_{si}(\dot{w}_{si} - \dot{w}_{ui}) - k_{ui}(w_{ui} - u_i) \quad (7)$$

In addition to the translation, rolling, and pitching equation of motion, the rigid body equilibrium conditions are considered, which helps to avoid the singular matrices.

$$\theta_x = \frac{d_1(w_{s1} - w_{s3}) + d_2(w_{s2} - w_{s4})}{(d_1 + d_2)(l_1 + l_2)} \quad \theta_y = \frac{l_2(w_{s1} - w_{s2}) + l_1(w_{s3} - w_{s4})}{(d_1 + d_2)(l_1 + l_2)} \quad (8)$$

Solving the above equalities and performing first and second derivatives with time, we can get the following three expressions for the vehicle model stability.

$$(w_{s1} - w_{s2} - w_{s3} + w_{s4}) + (\dot{w}_{s1} - \dot{w}_{s2} - \dot{w}_{s3} + \dot{w}_{s4}) + (\ddot{w}_{s1} - \ddot{w}_{s2} - \ddot{w}_{s3} + \ddot{w}_{s4}) = 0 \quad (9)$$

The above expressions are summarized into a matrix form as a general representation of the vehicle equation of motion.

$$\mathbf{M}_v \ddot{\mathbf{w}}_v(t) + \mathbf{C}_v \dot{\mathbf{w}}_v(t) + \mathbf{K}_v \mathbf{w}_v(t) = \mathbf{F}_v \mathbf{u}(t) \quad (10)$$

Where,

$$\mathbf{K}_u = \begin{bmatrix} 0 & 0 & 0 & 0 & k_{u1} & 0 & 0 & 0 \\ 0 & 0 & 0 & 0 & 0 & k_{u2} & 0 & 0 \\ 0 & 0 & 0 & 0 & 0 & 0 & k_{u3} & 0 \\ 0 & 0 & 0 & 0 & 0 & 0 & 0 & k_{u4} \end{bmatrix}^T \quad \mathbf{F}_v = \mathbf{K}_u \mathbf{u}$$

$$\mathbf{w}_v = [w_{s1}, w_{s2}, w_{s3}, w_{s4}, w_{u1}, w_{u2}, w_{u3}, w_{u4}]^T \quad \mathbf{u} = [u_1, u_2, u_3, u_4]^T$$

2.2 Bridge system model

A simply supported 3-dimensional Kirchhoff-Love plate with length, L , width b , elastic modulus E , and material density ρ is used whose general dynamic equation is given in equation 11.

$$\rho h \ddot{y}(x, y, t) + D \left[\frac{\partial^2}{\partial x^2} \frac{\partial^2 y(x, y, t)}{\partial x^2} + 2 \frac{\partial^4 y(x, y, t)}{\partial x^2 \partial y^2} + \frac{\partial^2}{\partial y^2} \frac{\partial^2 y(x, y, t)}{\partial y^2} \right] = \mathbf{P}(t) \quad (11)$$

$$D = \frac{Eh^3}{12(1 - \nu^2)} \quad (12)$$

$$\mathbf{P}(t) = \sum_{i=1}^n \delta(y - x_k) P_i \begin{cases} k = 1, & \text{for } i \text{ is odd} \\ k = 2, & \text{for } i \text{ is even} \end{cases} \quad (13)$$

Where $\mathbf{P} = [p_1, p_2, \dots, p_n]^T$ is the contact force vector and h is the thickness of the plate respectively. The matrix form of the Kirchhoff-Love plate response to a moving time-varying contact force from the vehicle is given by the following general expression Eq.14.

$$\mathbf{M}_b \ddot{\mathbf{w}}_b + \mathbf{K}_b \mathbf{w}_b = \mathbf{F}_b \quad (14)$$

Where the matrices \mathbf{M}_b , \mathbf{K}_b , and force vector \mathbf{F}_b are given by solving the following integral expressions. Substituting the approximate solution $w_b = \mathbf{w}_b \cdot \mathbf{N}$ and $\omega = \boldsymbol{\omega}$ into Eq.14

$$\mathbf{M}_b = \int_0^L \rho h \mathbf{N} \mathbf{N}^T dx \quad \mathbf{K}_b = \int_V \mathbf{B} \mathbf{D} \mathbf{B}^T |J| dV \quad (15)$$

$$\mathbf{B} = \left\{ \frac{\partial^2 \mathbf{N}}{\partial x^2} \quad \frac{\partial^2 \mathbf{N}}{\partial y^2} \quad \frac{\partial^2 \mathbf{N}}{\partial x \partial y} \right\} \quad \mathbf{D} = \begin{bmatrix} D & \nu D & 0 \\ \nu D & D & 0 \\ 0 & 0 & \frac{(1-\nu)}{2} D \end{bmatrix} \quad (16)$$

$$\mathbf{F}_b = \sum_{i=1}^4 N(x_i) \mathbf{P}_i = [N(x_1) \quad N(x_2) \quad N(x_3) \quad N(x_4)] [P_1 \quad P_2 \quad P_3 \quad P_4]^T \quad (17)$$

Where N is the Hermite shape function, J is the Jacobian matrix. For numerical stability, the Rayleigh damping matrix is added to the bridge equation of motion and is given by the following expression.

$$\mathbf{C}_b = \alpha_c \mathbf{M}_b + \beta_c \mathbf{K}_b \quad (18)$$

Where α_c and β_c are mass and stiffness proportion coefficients for the Rayleigh damping matrix whose values are given in Table 2. For the details on how to calculate the derivative components of the stiffness \mathbf{K}_b , and mass \mathbf{M}_b matrices the reader should refer to (Ferreira, 2009).

$$P_i = -m_{si}(g + \ddot{w}_{si}) - m_{ui}(g + \ddot{w}_{ui}) \quad (19)$$

3 PROPOSED METHOD

This paper proposes a method to simultaneously estimate vehicle and bridge system parameters and road profiles from vehicle acceleration data and position. First, the vehicle model is extended to a 3-dimensional model, and the bridge is extended to the Kirchhoff-Love model. Vehicle acceleration is used as measured data. It is obtained by solving the VBI equation of motion, which requires the knowledge of VBI system parameters in this paper set with reference to (Keenahan, Ren and OBrien, 2020) and are given in Table 1 and Table 2. The vehicle is excited by the input profile $\mathbf{u}(t)$ whose value is composed of road unevenness $\mathbf{r}(t)$ referred here as road profile on one hand and the bridge vibration $\hat{\mathbf{y}}(t)$. The whole process is depicted in diagram of Figure 1.

$$\mathbf{u}(t) = \mathbf{r}(t) + \hat{\mathbf{y}}(t) \quad (20)$$

The vehicle acceleration can be used to calculate the input profile and road profile from equations 10 and 20, respectively. The objective function is formulated to minimize the error between the road profile under the front and rear axles, which is optimized using the NM algorithm described in section 5.1.

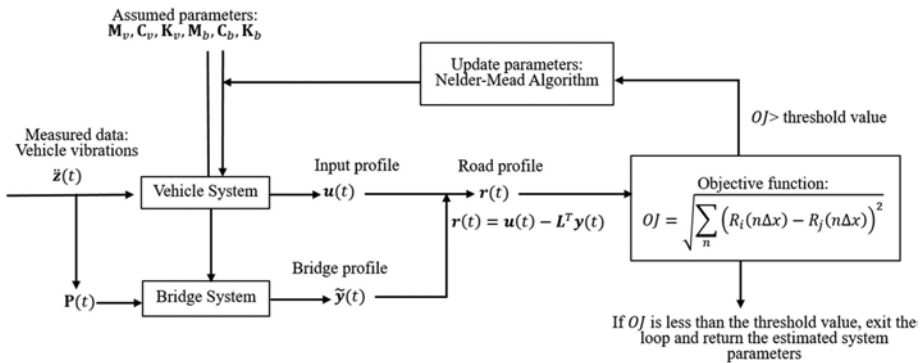


Figure 1. Process of the proposed method.

4 NUMERICAL EXPERIMENT

4.1 Input parameters

The profile over the entire road surface is not continuously the same, so it is assumed that the right and left track profiles are different in this experiment. The profile for both the right and left tracks are given in the following Figure 2. A 21tonnes full-car model with natural frequencies of 0.159Hz, 1.353Hz, 1.815Hz, 2.181Hz, 8.306Hz, 8.318Hz, 9.953Hz, and 9.989Hz, and

a 20 m long and 4m wide Kirchhoff-Love plate with natural frequencies of 0.428Hz, 1.388Hz, 2.239Hz, 2.896Hz, 4.560Hz, 4.956Hz, etc. are used. The VBI system parameters are given in Table 1 and Table 2.

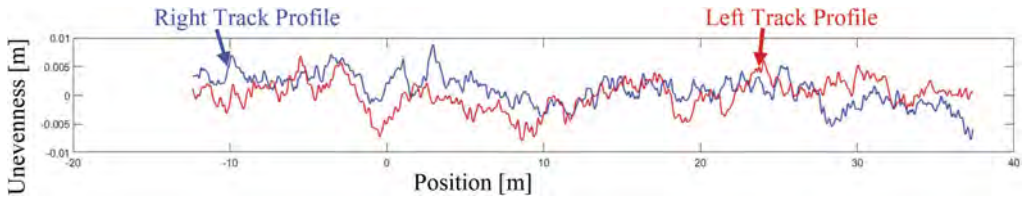


Figure 2. Randomly generated road profile for the right and left track.

Table 1. Vehicle system parameters.

Vehicle body and suspension parameters								
m_s [kg]	C_{s1} [Nsm ⁻¹]	C_{s2} [Nsm ⁻¹]	C_{s3} [Nsm ⁻¹]	C_{s4} [Nsm ⁻¹]	k_{s1} [Nm]	k_{s2} [Nm]	k_{s3} [Nm]	k_{s4} [Nm]
16620	11720	16620	11720	16620	381764	1053990	381764	1053990
Unsprung mass and tire characteristic								
m_{u1} [kg]	m_{u2} [Nsm ⁻¹]	m_{u3} [Nsm ⁻¹]	m_{u4} [Nsm ⁻¹]	k_{u1} [Nsm ⁻¹]	k_{u2} [Nm]	k_{u3} [Nm]	k_{u4} [Nm]	
790	1223	790	1223	1763507	3694467	1763507	3694467	
Vehicle body dimensions								
d_1 [m]	d_2 [m]	l [m]			r [m]			
2.375	2.375	1.200			1.200			

Table 2. Bridge system parameters.

ρb [kgm ⁻²]	E [Nm ³]	L_x [m]	L_y [m]	α	γ
2.4×10^3	50.0×10^9	2.0×10^1	0.4×10^1	$2.7 \times 10^\circ$	2.4×10^{-5}

4.2 Numerical experiment results

This section presents the results of a numerical experiment. First, the vehicle system is excited by an input profile that is purely a road profile, before the vehicle enters the bridge section. The input profile is updated to include the effects of the bridge response to the vehicle's vibration until the vehicle leaves the bridge section Eq.1. The vehicle acceleration response from the numerical experiment is used as measured data in the VBISI (vehicle-bridge interaction system identification).

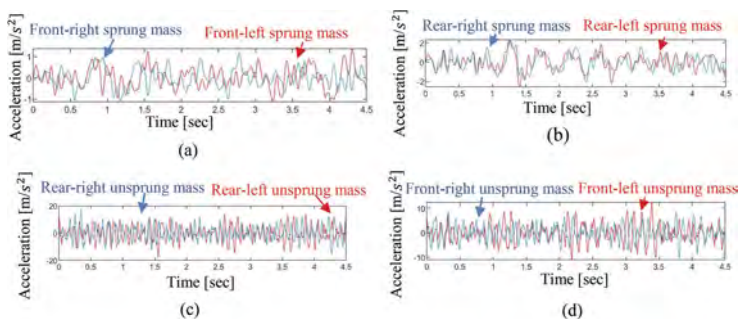


Figure 3. Measured vibration data (a) Front sprung mass (b) Rear sprung mass (c) Rear unsprung mass (d) Front unsprung mass.

5 VBI SYSTEM IDENTIFICATION METHOD

5.1 Overview of the Nelder-Mead algorithm

The Nelder-Mead (NM) algorithm finds the optimal value of an objective function in n dimensions using a simplex of $n+1$ vertices, say $\{ \mathbf{X}_1, \mathbf{X}_2, \mathbf{X}_3, \dots, \mathbf{X}_{n+1} \}$. The algorithm classifies the vertices as best, intermediate, worst, and second worst, and uses four operations (reflection, contraction, expansion, and shrink) to generate a new set of vertices by replacing the worst vertex on each iteration.

First, the worst function value is reflected through the centroid of the remaining.

$$\mathbf{X}_r = \mathbf{X}_c + \alpha(\mathbf{X}_c - \mathbf{X}_w) \quad (21)$$

Where α is the reflection coefficient whose value is greater than 0. If the reflected vertex is better than the best vertex so far, the reflected vertex is expanded.

$$\mathbf{X}_e = \mathbf{X}_c + \gamma(\mathbf{X}_r - \mathbf{X}_c) \quad (22)$$

Where γ is the expansion coefficient whose value is $\gamma > \alpha$. It can happen that the reflected vertex is not better than the second-worst vertex, in this case, the contraction step is performed.

$$\mathbf{X}_{cont} = \mathbf{X}_c + \rho(\mathbf{X}_r - \mathbf{X}_c) \quad (23)$$

With ρ being the contraction coefficient whose value is $0 < \rho \leq 0.5$. Note that coefficient ρ can be positive in case of external contraction when $f_r < f(x_{n+1})$ and negative in the case of internal expansion when $f_r > f(x_{n+1})$. If the fitness of the contracted vertex is better than the fitness of the worst vertex i.e. $f(x_{cont}) \geq f(x_{n+1})$ then the worst vertex is replaced by the contracted vertex if it is not the case, the shrinking step is performed where all vertices except the best recorded are replaced with new values.

$$\mathbf{X}_s = \mathbf{X}_1 + \sigma(\mathbf{X}_i - \mathbf{X}_1), \quad i = 2, \dots, n+1 \quad (24)$$

With σ being the shrinking coefficient whose value is $0 < \sigma \leq 0.5$. A more detailed explanation of Nelder-Mead can be found in (Nelder and Mead, 1965) and (Singer and Nelder, 2009) as explained in the original work of the original author where the above equations are referenced.

With X_r reflected vertex, X_c centroid vertex, X_w worst vertex, X_e extended vertex, and X_{cont} contracted vertex.

5.2 System parameters identification process

The vehicle and bridge system parameters are unknown, and they need to be estimated. The NM algorithm requires an initial guess of input parameters. It is possible to give a rough initial estimate of the VBI system parameters within a given range. The following table gives the range over which the initial random system parameters are chosen.

Table 3. VBI system parameters' initial range.

$C_{sis}, k_{sis}, k_{uis}, m_{uis}, \rho b, a_1, a_2$	d_i, l	D
0.8-1.2 times true values	0.1-0.9 times true values	0.8-1.2 times true values

Vehicle dimension parameters are assumed to be known since they can be measured accurately. The randomly initialized system parameters are substituted into the equation of motions to calculate input profile $\mathbf{u}(t)$ and bridge vibration response $\mathbf{y}(t)$. The objective function minimizes the error between the road profiles under the front and the rear axle.

$$\mathcal{R} = \sqrt{\frac{\sum_n (\mathbf{R}_1(n\Delta x) - \mathbf{R}_2(n\Delta x))^2}{n(\mathbf{R}_1)}} + \sqrt{\frac{\sum_n (\mathbf{R}_3(n\Delta x) - \mathbf{R}_4(n\Delta x))^2}{n(\mathbf{R}_3)}} \quad (25)$$

Where $n(\mathbf{R}_i)$ denotes the length of vector \mathbf{R} , the \mathbf{R}_i value is an estimate of the road profile under each i th tire.

6 RESULTS AND DISCUSSION

6.1 System parameters estimation

In this paper, both vehicle and bridge system parameters, as well as bridge profile, are simultaneously estimated. The results are limited to a non-damaged bridge case and vehicle data without noise.

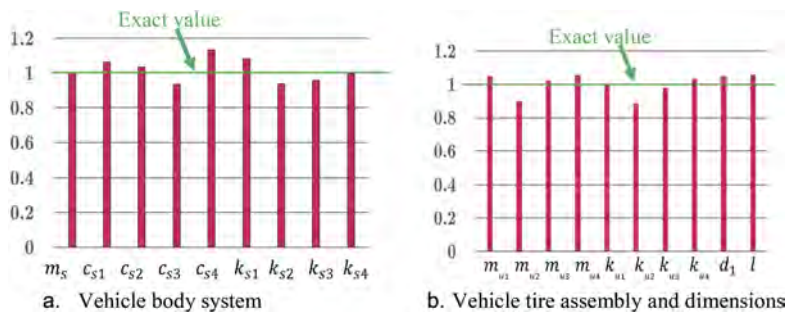


Figure 4. Estimated vehicle system parameters.

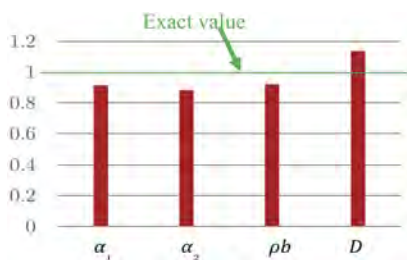


Figure 5. Estimated Bridge System Parameters.

Figure 6 shows the estimated road profile. The observation shows an estimation error observable especially on the rear axle. The previous research shows that this error is likely due to the position of the observation point to the gravity point. Even though the errors are present, the vehicle inputs can be estimated.

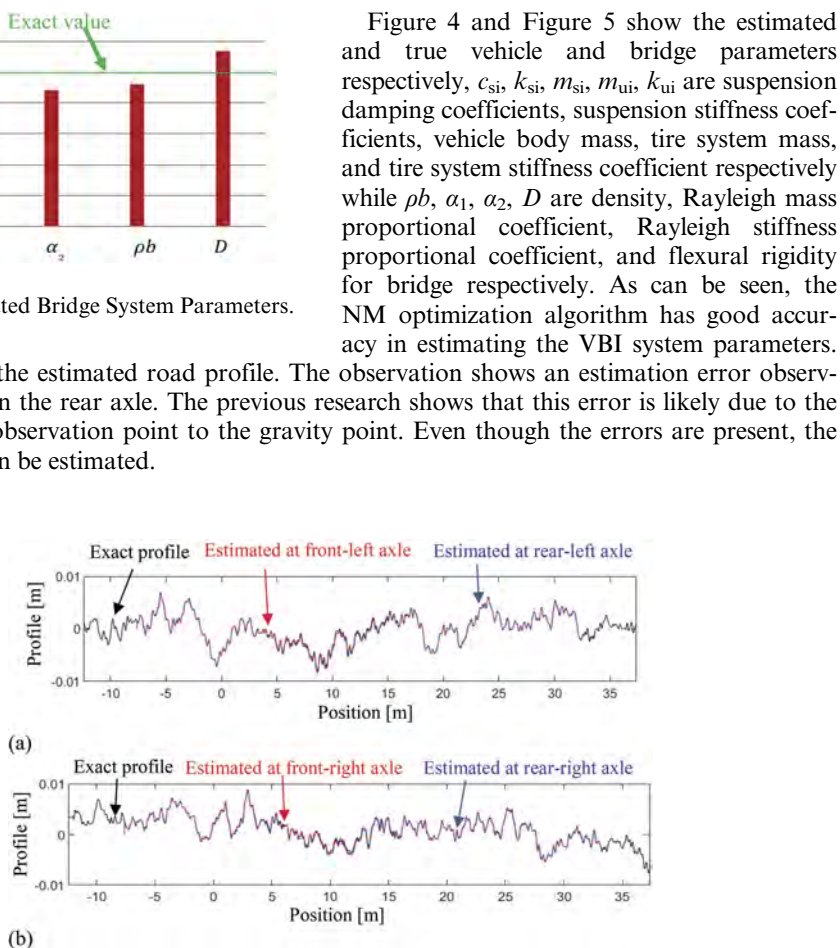


Figure 6. Road profile (a) left track (b) right track.

The estimation error in this study is small but the estimate has not improved much compared to the range of initialized parameters. The results are comparable to previous research, but some considerations are different. The study achieved comparatively accurate results compared to (Keenahan, Ren and OBrien, 2020) but comparatively low accuracy compared to (Zhao, Nagayama and Xue, 2019) due to the difference in the number of parameters estimated and the VBI model adopted.

7 CONCLUSION

In this paper, the applicability of the NM algorithm to Drive-by monitoring is investigated by estimating VBI system mechanical parameters and road profile. A 3-dimensional vehicle bridge interaction model is developed to simulate the 3-D VBI system model response. The numerical results of the model are obtained. The identification of VBI system parameters is performed using the NM algorithm by optimizing the error between the profile under the front axle and the profile under the rear axle. The results obtained by applying this algorithm are compared to the results obtained by (Zhao, Nagayama and Xue, 2019) and the results obtained by (Keenahan, Ren and OBrien, 2020), and they are found to be numerically accurate.

The accuracy of the estimated system parameters depends on the initial guess, and a poor guess can lead to longer processing times and less accurate results. The Nelder-Mead algorithm performs better than the PSO in estimating VBI system parameters, and future work includes experimental validation and extending the methodology to multiple vehicles, bridges, and runs.

FUNDING

This study is supported by MEXT/JSPS KAKENHI Grant Number JP19H02220.

REFERENCES

- ASCE (2021) 'Structurally Deficient Bridges | Bridge Infrastructure | ASCE's 2021 Infrastructure Report Card', pp. 18–25. Available at: <https://infrastructurereportcard.org/cat-item/bridges/>.
- Ferreira, A.J.M. (2009) *MATLAB codes for finite element analysis: Solids and structures, Solid Mechanics and its Applications*.
- Jazar, R.N. (2008) *Vehicle dynamics: Theory and applications, Vehicle Dynamics: Theory and Applications*. doi:10.1007/978-0-387-74244-1.
- Keenahan, J., Ren, Y. and OBrien, E.J. (2020) 'Determination of road profile using multiple passing vehicle measurements', *Structure and Infrastructure Engineering*, 16(9), pp. 1262–1275. doi:10.1080/15732479.2019.1703757.
- Malekjafarian, A., McGetrick, P.J. and OBrien, E.J. (2015) 'A review of indirect bridge monitoring using passing vehicles', *Shock and Vibration*, 2015(1). doi:10.1155/2015/286139.
- Nelder, J.A. and Mead, R. (1965) 'A Simplex Method for Function Minimization', *The Computer Journal*, 7(4), pp. 308–313. doi:10.1093/comjnl/7.4.308.
- Olsson, M. (1991) 'On the fundamental moving load problem', *Journal of Sound and Vibration*, 145(2), pp. 299–307. doi:10.1016/0022-460X(91)90593-9.
- Singer, S. and Nelder, J. (2009) 'Nelder-Mead algorithm', *Scholarpedia*, 4(7), p. 2928. doi:10.4249/scholarpedia.2928.
- Yang, Y. Bin, Yau, J.D. and Hsu, L.C. (1997) 'Vibration of simple beams due to trains moving at high speeds', *Engineering Structures*, 19(11), pp. 936–944. doi:10.1016/s0141-0296(97)00001-1.
- Yang, Y.B. and Chang, K.C. (2009) 'Extraction of bridge frequencies from the dynamic response of a passing vehicle enhanced by the EMD technique', *Journal of Sound and Vibration*, 322(4–5), pp. 718–739. doi:10.1016/j.jsv.2008.11.028.
- Yang, Y.B. and Lin, C.W. (2005) 'Vehicle-bridge interaction dynamics and potential applications', *Journal of Sound and Vibration*, 284(1–2), pp. 205–226. doi:10.1016/j.jsv.2004.06.032.
- Yang, Y.B., Lin, C.W. and Yau, J.D. (2004) 'Extracting bridge frequencies from the dynamic response of a passing vehicle', *Journal of Sound and Vibration*, 272(3–5), pp. 471–493. doi:10.1016/S0022-460X(03)00378-X.
- Zhao, B., Nagayama, T. and Xue, K. (2019) 'Road profile estimation, and its numerical and experimental validation, by smartphone measurement of the dynamic responses of an ordinary vehicle', *Journal of Sound and Vibration*, 457, pp. 92–117. doi:10.1016/j.jsv.2019.05.015.

Parametric study of the vehicle-bridge interaction system identification method

R. Shin

University of Tsukuba, Tsukuba, Ibaraki, Japan

Y. Okada & K. Yamamoto

University of Tsukuba, Tsukuba, Ibaraki, Japan

Center for Artificial Intelligence Research, Tsukuba, Ibaraki, Japan

ABSTRACT: Bridges have been instrumental in facilitating efficient transportation. However, bridges are prone to deterioration due to daily use and natural disasters. If left unattended, this deterioration can lead to structural damage. Monitoring is crucial because structural damage can have significant economic consequences and even be life-threatening. Therefore, we are focusing on bridge monitoring using vehicle vibration. This study clarifies the characteristics of vehicles that are effective for identifying the vehicle-bridge interaction system. This study clarified that the proposed method is affected by the damping of the vehicle and the frequency ratio between the vehicle and the bridge. The results are consistent with previous studies that have demonstrated the reduced accuracy of bridge modal parameter estimation from vehicle vibration. It is practical to design the vehicle frequency to be lower than that of the bridge when estimating the bridge's features. This paper shows that the characteristics of vehicles that are advantageous for vehicle response analysis clarified in previous studies are also important in the proposed method and show the usefulness of bridge maintenance management methods using vehicles. In the future, we will verify the feasibility of the proposed method in cases where different types of bridges and colors of noise are present.

1 INTRODUCTION

Road infrastructure is essential for efficient mobility and transportation. In particular, bridges are built to facilitate the crossing of rivers and valleys. Therefore, bridges have a significant impact on traffic. However, damage can occur due to fatigue caused by daily use and corrosion. Damage to bridges has a significant economic impact and can sometimes be fatal. Therefore, monitoring is vital to prevent structural damage to bridges. Skilled engineers support the monitoring of bridges. However, inspections of intact bridges are often wasteful. In addition, human error cannot be prevented, and there is a risk of missing damage to bridges. Bridge monitoring using sensing has therefore been proposed. Bridge inspections can be made more effective by screening bridges with a high probability of damage in advance and prioritizing inspections by skilled engineers. In addition, it is possible to conduct a practical evaluation based on the data.

Two main types of research focus on vibration as a bridge-sensing method. One is direct bridge monitoring. Direct bridge monitoring can reveal sudden structural damage to bridges caused by accidents or disasters in almost real-time. However, direct bridge monitoring is expensive because each must be equipped with multiple sensors. On the other hand, drive-by monitoring (Yang et al., 2004) has been proposed as an indirect bridge monitoring method. Drive-by monitoring is economically inexpensive because only the vehicle needs to be equipped with sensors. Drive-by monitoring is particularly effective for small and multi-span bridges in rural areas because it can easily monitor inaccessible bridges.

Drive-by monitoring uses vehicle-bridge interaction (VBI), which occurs when a vehicle travels over a bridge. One advantage of this monitoring method is that it can be used on small

and medium-span bridges. Small and medium-span bridges are rarely the target of direct bridge monitoring. In general, bridges are built individually according to construction conditions, and few bridges are the same. However, building a separate simulation model for each bridge is not realistic. Therefore, a simple mechanical model is required that can be used for a wide variety of bridges. However, it is susceptible to short VBI time, the roughness of the road surface, and environmental factors (Malekjafarian et al. 2015). Therefore, the accuracy of drive-by monitoring is generally low. Consequently, it is necessary to improve the accuracy by integrating multiple data (Malekjafarian et al. 2022).

The authors propose the VBI system identification (VBISI) method as a drive-by monitoring method that enables integrated data analysis (Yamamoto et al. 2022). The parameters estimated by the VBISI method are physical quantities based on the equations of motion and thus can use values calculated by other methods. Xue et al. (2020) use road unevenness estimated for a single vehicle to estimate vehicle mechanical parameters. Using a Kalman filter, they can estimate road surface roughness with high accuracy, even under high noise conditions. The VBISI method combines method that proposed by Xue et al. (2020) with numerical simulation of bridges to enable the estimation of mechanical parameters of bridges as well. Keenehan et al. (2020) use road unevenness estimated for multiple vehicles to estimate vehicle mechanical parameters. Most drive-by monitoring methods proposed so far focus on numerous runs of the same vehicle. However, the method proposed by Keenehan et al. (2020) allows the integrated analysis of data measured by various vehicles in the same scheme.

Since the VBISI method was proposed by Yamamoto et al. (2022), its applicability has been investigated through numerical simulations (Yamamoto et al. 2021) and field tests (Shin et al. 2023). However, these papers focus on a single bridge and do not examine the relevance of the VBISI method in multiple situations. Therefore, in this study, the applicability of the VBISI method is clarified by numerical simulations for the realization of bridge screening by drive-by monitoring. Therefore, we conducted a parametric study to show that the VBISI method is applicable to multiple bridges.

2 METHODOLOGY

This section describes the mathematical representation of VBISI. The vehicle and bridge system is shown in Figure 1. The vehicle is modeled as an RBSM (rigid-body-spring model). The bridge is based on the Euler-Bernoulli theorem. The vehicle system takes the input profile as input and outputs the vehicle vibration. The input profile is the sum of the bridge profile and road profile. A profile represents the vibration at the position of the front and rear axles. On the other hand, the bridge system takes contact force as input and outputs bridge vibration. Contact force is calculated from vehicle vibration. Therefore, the vehicle and the bridge system correspond to the input and the output, respectively (Yamamoto et al. 2021).

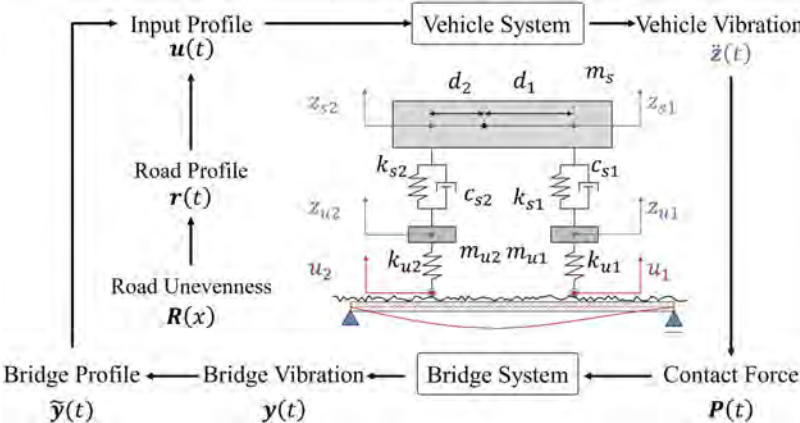


Figure 1. Conceptual diagram of VBI system.

2.1 Vehicle model

The vehicle is equipped with acceleration sensors on the vehicle body and axle. Since the acceleration sensors are installed on the front and rear wheels, there are four sensors. Body vibration and axle vibration are z_{si} and z_{ui} , respectively. The input profile is u_i . Let m_s and m_{ui} be the vehicle's body weight and tire weight, respectively. Suspension stiffness/damping and tire stiffness are k_{si} , c_{si} , and k_{ui} . The distance between the axle and the vehicle's center of gravity is d_i . The subscript i corresponds to the axle, with 1 being the front wheels and 2 being the rear wheels.

$$\mathbf{z}(t) = \{z_{s1}(t) \ z_{s2}(t) \ z_{u1}(t) \ z_{u2}(t)\}^T \quad (1)$$

$$\mathbf{M}_v = \begin{bmatrix} \frac{d_2 m_s}{d_1 + d_2} & \frac{d_1 m_s}{d_1 + d_2} & & \\ \frac{m_s d_1 d_2}{d_1 + d_2} & -\frac{m_s d_1 d_2}{d_1 + d_2} & & \\ & & m_{u1} & \\ & & & m_{u2} \end{bmatrix} \quad (2)$$

$$\mathbf{C}_v = \begin{bmatrix} c_{s1} & c_{s2} & -c_{s1} & -c_{s2} \\ d_1 c_{s1} & -d_2 c_{s2} & -d_1 c_{s1} & d_2 c_{s2} \\ -c_{s1} & 0 & c_{s1} & 0 \\ 0 & -c_{s2} & 0 & c_{s2} \end{bmatrix} \quad (3)$$

$$\mathbf{K}_v = \begin{bmatrix} k_{s1} & k_{s2} & -k_{s1} & -k_{s2} \\ d_1 k_{s1} & -d_2 k_{s2} & -d_1 k_{s1} & d_2 k_{s2} \\ -k_{s1} & 0 & k_{s1} + k_{u1} & 0 \\ 0 & -k_{s2} & 0 & k_{s2} + k_{u2} \end{bmatrix} \quad (4)$$

$$\mathbf{F}_v(t) = \{0 \ 0 \ k_{u1}u_1(t) \ k_{u2}u_2(t)\}^T \quad (5)$$

$$\mathbf{M}_v \ddot{\mathbf{z}}(t) + \mathbf{C}_v \dot{\mathbf{z}}(t) + \mathbf{K}_v \mathbf{z}(t) = \mathbf{F}_v \quad (6)$$

\mathbf{M}_v , \mathbf{C}_v and \mathbf{K}_v are the mass, damping and stiffness matrices of the vehicle (Yamamoto et al. 2021).

2.2 Bridge model

The bending stiffness and the bridge weight per unit length are $EI(x)$, $\rho A(x)$. The equations of motion of the bridge system are expressed as follows

$$\rho A(x) \ddot{y}(x, t) + \frac{\partial^2}{\partial x^2} EI(x) \left(\frac{\partial^2}{\partial x^2} y(x, t) \right) = p(x, t) \quad (7)$$

where $y(x, t)$ denotes the deflection, x represents the position. $p(x, t)$ denotes the external force distribution. $(\ddot{\ })$ denotes the second-order derivative in the time domain. The finite element method creates a global structural matrix and external force vector.

$$\mathbf{M}_b \ddot{\mathbf{y}}(t) + \mathbf{K}_b \mathbf{y}(t) = \mathbf{F}(t) \quad (8)$$

Given the Rayleigh damping,

$$\mathbf{C}_b = b_0 \mathbf{M}_b + b_1 \mathbf{K}_b. \quad (9)$$

$$b_0 = \zeta_b \frac{2\omega_{b1}\omega_{b2}}{\omega_{b1} + \omega_{b2}} \quad (10)$$

$$b_1 = \zeta_b \frac{2}{\omega_{b1} + \omega_{b2}} \quad (11)$$

\mathbf{M}_b , \mathbf{C}_b and \mathbf{K}_b are the mass, damping and stiffness matrices of the bridge. ζ_b represents the damping ratio of the bridge. ω_{b1} and ω_{b2} were obtained by eigenvalue decomposition (Yamamoto et al. 2021).

2.3 Vehicle-bridge interaction

The input profile, which is the input to the vehicle system, is expressed as follows

$$\mathbf{u}(t) = \mathbf{r}(t) + \tilde{\mathbf{y}}(t) \quad (12)$$

The input profile is the sum of the bridge profile and the road profile. bridge profile represents the bridge vibration at the moving point. bridge profile is calculated from the bridge vibration at the fixed point using the finite element method.

$$\tilde{\mathbf{y}}(t) = \mathbf{L}^T(t)\mathbf{y}(t) \quad (13)$$

$$\mathbf{L}(t) = [\mathbf{N}(x_1(t)) \quad \mathbf{N}(x_2(t))] \quad (14)$$

The road profile represents the road surface roughness at the moving point.

$$r_i(t) = \mathbf{R}(x_i(t)) \quad (15)$$

The contact force, an input to the bridge system, is calculated from the vehicle vibration and vehicle dynamics parameters (Yamamoto et al. 2021).

$$\mathbf{F}(t) = \mathbf{L}(t)[V_1(t) \quad V_2(t)] \quad (16)$$

$$V_1(t) = -\frac{d_2 m_s}{d_1 + d_2}(g + \ddot{z}_{s1}) - m_{u1}(g + \ddot{z}_{u1}) \quad (17)$$

$$V_2(t) = -\frac{d_1 m_s}{d_1 + d_2}(g + \ddot{z}_{s2}) - m_{u2}(g + \ddot{z}_{u2}) \quad (18)$$

2.4 Object function

In this study, the VBISI method is used to identify the dynamic parameters of the following VBI systems.

$$\mathbf{X} = [d_1, c_{s1}, c_{s2}, k_{s1}, k_{s2}, m_{u1}, m_{u2}, k_{u1}, k_{u2}, \rho A, EI_1, EI_2, EI_3, EI_4, EI_5, EI_6, EI_7, \zeta_b] \quad (19)$$

The input profile is inversely estimated from the measured vehicle vibration using a Kalman filter (Kalman 1965). A dynamic simulation calculates the bridge profile using the contact force as input. The road profile is obtained by subtracting the bridge profile from the input profile. The road profile and vehicle position information are used to estimate the road surface roughness at each axle. Assuming the vehicle moves straight ahead, the estimated road profile should be the same for the front and rear wheels. However, if the dynamic parameters are incorrect, the road surface roughness will not match. Therefore, the objective function is the sum of squares of the road surface roughness of the front and rear wheels. Search for a combination of parameters that minimizes the objective function using optimization techniques. In this study, the Neldermead (Nelder & Mead 1965, Gao & Han, 2012) method is used as the optimization method.

$$J(\mathbf{X}) = \sum |R_1(x) - R_2(x)|^2 \quad (20)$$

3 PARAMETRIC STUDY

Vehicle-bridge interaction occurs when a vehicle travels over a bridge. According to Yang et al. (2004), the following four vibration frequency are included in the vehicle vibration due to VBI.

- ① the vehicle frequency [w_v]
- ② driving frequency of the moving vehicle [$2\pi v/L$]
- ③ shifted frequencies of the bridge [$w_b \pm \pi v/L$]

In this study, a parametric study is conducted to investigate the feasibility of the VBISI method. Five influencing factors are considered, considering the main vibration frequencies in the vehicle.

3.1 Numerical model

Numerical simulations are carried out using the vehicle and bridge models depicted in Figure 1.

A sub-structuring method is utilized to reproduce vehicle vibration by separating the vehicle model from the bridge model. The displacement vibrations of both the vehicle and bridge are obtained through numerical integration of acceleration vibrations using the Newmark- β method (Average constant acceleration). The axial distance of the vehicle is set to 4 [m], with the distance from the center of gravity to the axle being 2 [m]. The unit mass of the bridge was assumed to be 4400 [kg/m]. The bridge length is set to 30 [m], with a 10 [m] road surface provided before and after the bridge. The time increments are set to 1.0×10^{-3} [s]. The parameters used in the numerical simulations are summarized in Table 1. Important values are bolded to make it easier to distinguish them from other cases. It is assumed that the vehicle vibration includes measurement noise. The magnitude of the added noise is estimated from the actual measured acceleration waveform (Shin et al. 2023). The bridge stiffnesses estimated for each case are summarized in Figure 3. f_b and f_v are the natural frequencies of the damped free vibration, respectively.

Table 1. Parameters used in the base case and the other 13 cases.

case	Road Level	m_s [kg]	m_{ui} [kg]	k_{si} [N/m]	c_{si} [kg/s]	k_{ui} [N/m]	f_v [Hz]	f_b [Hz]	v [m/s]	ζ_b	EI [Nm ³]
Base	A	8000	500	3,595,000	85,000	35,950,000	2.77	3.37	10	0.03	1.56×10^{11}
1	B	8000	500	3,595,000	85,000	35,950,000	2.77	3.37	10	0.03	1.56×10^{11}
2	C	8000	500	3,595,000	85,000	35,950,000	2.77	3.37	10	0.03	1.56×10^{11}
3	A	8000	500	5,325,000	120,000	53,250,000	3.37	3.37	10	0.03	1.56×10^{11}
4	A	8000	500	14,380,000	140,000	143,800,000	5.49	3.37	10	0.03	1.56×10^{11}
5	A	8000	500	3,595,000	85,000	35,950,000	2.77	3.37	15	0.03	1.56×10^{11}
6	A	8000	500	3,595,000	85,000	35,950,000	2.77	3.37	20	0.03	1.56×10^{11}
7	A	8000	500	3,595,000	85,000	35,950,000	2.77	3.37	* ₁	0.03	1.56×10^{11}
8	A	8000	500	3,595,000	85,000	35,950,000	2.77	3.37	* ₂	0.03	1.56×10^{11}
9	A	8000	500	3,595,000	85,000	35,950,000	2.77	3.37	* ₃	0.03	1.56×10^{11}
10	A	8000	500	3,595,000	55,000	35,950,000	2.76	3.37	10	0.03	1.56×10^{11}
11	A	8000	500	3,595,000	115,000	35,950,000	2.78	3.37	10	0.03	1.56×10^{11}
12	A	8000	500	3,595,000	85,000	35,950,000	2.77	3.37	10	0.01	1.56×10^{11}
13	A	8000	500	3,595,000	85,000	35,950,000	2.77	3.37	10	0.05	1.56×10^{11}

*₁: The vehicle accelerates towards the bridge center (from 9 to 11 [m/s]) and decelerates thereafter (from 11 to 9 [m/s]).

*₂: The vehicle continues to accelerate (from 8 to 12 [m/s]).

*₃: The vehicle continues to decelerate (from 12 to 8 [m/s]).

3.2 Base case

The base model was analyzed using the VBISI method as a preliminary study for the Parametric study. Table 2 summarizes the estimated parameters. All dynamic parameters were normalized to the correct values. The base statistics were generated based on 25 runs. The estimated values converge around the correct values. Figure 2 shows the estimated road surface irregularities. The estimated road unevenness for the front and rear wheels is close to the correct value.

Table 2. Estimated dynamic parameters.

	m_{s1}	m_{s2}	c_{s1}	c_{s2}	k_{s1}	k_{s2}	m_{u1}	m_{u2}	k_{u1}	k_{u2}
mean	0.98	1.02	0.99	1.02	0.99	1.00	1.02	0.98	1.00	1.04
std	0.05	0.05	0.06	0.06	0.07	0.06	0.07	0.06	0.06	0.06
	EI_1	EI_2	EI_3	EI_4	EI_5	EI_6	EI_7	ρA	ζ_b	
mean	0.98	1.02	1.00	1.02	1.02	0.99	1.04	1.02	1.03	
std	0.06	0.08	0.10	0.08	0.08	0.07	0.08	0.08	0.06	

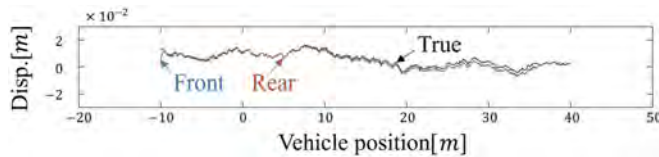


Figure 2. Estimated element stiffness.

3.3 Effect of road surface roughness

When a vehicle travels on a rough road surface, the vehicle is excited by the bridge's vibration and the road's unevenness. As a result, roughness-related frequencies appear in the vehicle vibration, which may make the identification of bridge vibration difficult (Yang & He 2022). Therefore, this study examined the effect of different road surface roughnesses on the estimation accuracy of the VBISI method. The power spectral density function introduced in ISO 8608 (ISO 2016). was employed to simulate road surface roughness. In Case 1, road rank B was considered, and in Case 2, road rank C was evaluated.

The results show that the VBISI method is largely insensitive to Road roughness.

3.4 Effect of vehicle frequency

For the successful extraction of bridge frequencies from vehicle vibration, the vehicle/bridge acceleration amplitude ratio should be less than 3. It is also pointed out that i) initial vehicle/bridge acceleration amplitude, ii) vehicle speed and iii) bridge/vehicle frequency ratios are essential for the vehicle/bridge acceleration amplitude ratio (Yang & Chang 2009). Yang & Chang (2009) pointed out that bridge/vehicle frequency ratio are unimportant in estimating natural bridge frequencies because they cannot be controlled. However, the discussion of bridge and vehicle frequencies is essential to discuss what type of vehicle should be used for the VBISI method. Therefore, Case 3 was set up so that the bridge/vehicle frequency ratios are almost equal to 1. In Case 4, the bridge/vehicle frequency ratios were set to be smaller than 1.

As a result, the estimation accuracy decreased in Case 3. In addition, Case 4 demonstrated a noteworthy decline in accuracy. This implies that the VBISI method may be more effective when the bridge-to-vehicle frequency ratio is more significant than one. The natural frequency of a typical vehicle is lower than the first natural frequency of a bridge.

3.5 Effect of vehicle speed

High vehicle velocities can augment the vibration of higher-order modes on bridges. However, vehicle velocity increases and the vehicle's vibration become more contaminated by road surface roughness. Additionally, the duration of the measurement of vehicle vibration decreases, and the performance of frequency domain decomposition deteriorates (Kim et al. 2011). Therefore, in Case 5, the vehicle speed was set to 15 [m/s], and in Case 6, the vehicle speed was set to 20 [m/s]. In practical applications, it is challenging to maintain a constant vehicle speed. In Case 7, the vehicle accelerates towards the center of the bridge (from 9 to 11 [m/s]) and decelerates after that (from 11 to 9 [m/s]). In Case 8, the vehicle continues accelerating (from 8 to 12 [m/s]). In Case 9, the vehicle decelerates (from 12 to 8 [m/s]).

The findings imply that the accuracy of the VBISI method is not easily compromised by vehicle speed. This method may be suitable for use with trucks and buses in service if the bridge is adequately stimulated by the vehicles.

3.6 Effect of vehicle damping

Vehicle damping may influence the VBISI method due to its transmission of vibrations to the vehicle body. For a typical passenger vehicle, the suspension's damping ratio is frequently designed within the range of 0.2 to 0.4 for a comfortable ride (Calvo et al. 2005). Therefore, in this study, the vehicle's damping ratio in Case 10 was set to 0.2. In Case 11, the vehicle damping ratio was set to 0.4.

The findings reveal no alteration in the accuracy of the bridge stiffness estimate in Case 10. However, Case 11 showed a slight decrease in accuracy. Yang et al. (2022) observed that vehicle damping affects mode shape estimation, albeit limited. While the VBISI method is not a direct mode shape estimation technique, it is considered somewhat relevant.

3.7 Effect of bridge damping

Bridge damping ratios are generally minimal, ranging from 0.01 to 0.05 (He & Yang 2021). As the VBI system considers both steady-state and transient vibration, the duration of transient vibration is influenced by the bridge damping ratio. The smaller the bridge damping ratio, the longer the duration of transient vibration (Paz & Kim 2012). As the transient vibration dissipates, the excitation of the bridge to the measurement vehicle stabilizes, and the estimated pavement irregularity converges with the original road unevenness (He & Yang 2021). Therefore, the bridge damping ratio was set to 0.01 in Case 12 and 0.05 in Case 13.

The results show that the VBISI method is largely insensitive to bridge damping.

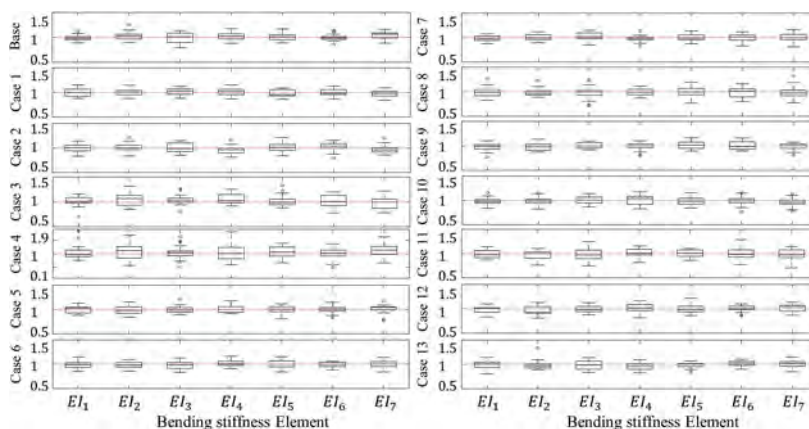


Figure 3. Estimated element stiffness.

4 CONCLUSIONS

A parametric study was conducted to assess the suitability of the VBISI method. The study focused on parameters that affect the primary vehicle vibration frequencies, specifically the roughness of the road surface, the vehicle's frequency, speed, damping ratio, and the damping ratio of the bridge. The findings suggest that the VBISI method is not sensitive to road surface roughness.

An important point revealed in this study is that the accuracy of bridge stiffness estimation is significantly degraded when the vehicle frequency is greater than the bridge frequency. Heavy vehicles, which tend to have lower frequencies, are suitable for use with the VBISI method. The accuracy is not compromised by typical vehicle speeds and is also insensitive to changes in vehicle speed. If the vehicle's damping ratio is high, the accuracy of the VBISI method is somewhat reduced. As the vehicle damping ratio diminishes the accuracy of mode

shape estimation, it is believed that this effect reduces the accuracy of the bridge stiffness estimate. The damping ratio of the bridge has a negligible impact on the VBISI method.

One constraint of this research is that only 13 cases were examined for each study subject. Each parameter should be scrutinized more thoroughly. This is because the VBISI method involves an optimization process, and accuracy verification for certain cases requires time. Consequently, implementing a technique that can expeditiously search for the optimal solution is necessary.

As a subject of investigation, it is necessary to examine the case in which the characteristics of the bridge are altered. In this study, we examined a bridge with constant stiffness throughout. In reality, there are bridges with variable stiffness, such as arch and truss bridges. Therefore, a model with different bridge structures and boundary conditions is utilized. Furthermore, only measurement noise is considered environmental noise. In the VBI research, it is noted that environmental noise is a factor that diminishes accuracy. If the noise satisfies whiteness, the Kalman filter can mitigate the impact. However, it has not yet been investigated for colored noise, such as traffic vibration. Given that the linear Kalman filter assumes white noise, it is anticipated that accuracy will be compromised with colored noise.

REFERENCES

- Calvo, J., Diaz, V. & Roman, J. 2005. Establishing inspection criteria to verify the dynamic behaviour of the vehicle suspension system by a platform vibrating test bench. *International Journal of Vehicle Design*. 38, 290–306.
- Gao, F. & Han, L. 2012. Implementing the Nelder-Mead simplex algorithm with adaptive parameters. *Computational Optimization and Applications*, 51(1), 259–277.
- He, Y., & Yang, J.P. 2021. Using Kalman filter to estimate the pavement profile of a bridge from a passing vehicle considering their interaction. *Acta Mechanica*, 232(11), 4347–4362.
- Malekjafarian, A., McGetrick, P.J. & O'Brien, E.J. 2015. A review of indirect bridge monitoring using passing vehicles. *Shock and vibration*, 286139.
- Malekjafarian, A., Corbally, R. & Gong, W. 2022. A review of mobile sensing of bridges using moving vehicles: Progress to date, challenges and future trends. *Structure* 44: 1466–1489.
- Nelder, J.A., & Mead, R. 1965. A simplex method for function minimization. *The computer journal*, 7(4), 308–313.
- Keenahan, J., Ren, Y. & O'Brien, E.J. 2020. Determination of road profile using multiple passing vehicle measurements. *Structure and Infrastructure Engineering*, 16(9), 1262–1275.
- Paz, M. & Kim, Y.H. 2012. *Structural Dynamics: Theory and Computation*, 6th edn. Springer Science & Business Media, New York.
- Shin, R., Okada, Y. & Yamamoto, K. 2023. Discussion on a Vehicle–Bridge Interaction System Identification in a Field Test. *Sensors*, 23(1), 539.
- Kalman, R.E. 1960. A new approach to linear filtering and prediction problems. *Journal of Basic Engineering*, 82, 35–45.
- Kim, C.W., Isemoto, R., Toshinami, T., Kawatani, M., McGetrick, P. & O'Brien, E. J. 2011. Experimental investigation of drive-by bridge inspection. In *5th International Conference on Structural Health Monitoring of Intelligent Infrastructure (SHMII-5)*, Cancun, Mexico, 11-15 December, Instituto de Ingeniería, UNAM.
- ISO. 8608: Mechanical Vibration–Road Surface Profiles–Reporting of Measured Data; ISO: London, UK, 2016.
- Xue, K., Nagayama, T. & Zhao, B. 2020. Road profile estimation and half-car model identification through the automated processing of smartphone data. *Mechanical Systems and Signal Processing*. 142, 106722.
- Yamamoto, K., Fujiwara, S., Tsukada, K., Shin, R. & Okada, Y. Numerical Studies on Bridge Inspection using Data obtained from sensors on vehicle. In *Proceedings of the 13th IWSHM, Stanford*, 7–9 December 2021, CA, USA.
- Yamamoto, K., Murakami, K., Shin, R. & Okada, Y. 2022. Application of Particle Swarm Optimization method to On-going Monitoring for estimating vehicle-bridge interaction system. *arXiv preprint: 2201.08014*.
- Yang, Y.B., Lin, C.W. & Yau, J.D. 2004. Extracting bridge frequencies from the dynamic response of a passing vehicle. *Journal of Sound and Vibration* 272(3-5): 471–493.
- Yang, Y. B. & Chang, K. C. 2009. Extracting the bridge frequencies indirectly from a passing vehicle: Parametric study. *Engineering Structures*, 31(10), 2448–2459.
- Yang, Y.B., Xu, H., Wang, Z.L., & Shi, K. 2022. Using vehicle–bridge contact spectra and residue to scan bridge's modal properties with vehicle frequencies and road roughness eliminated. *Structural Control and Health Monitoring*, e2968.
- Yang, Y.B. & He, Y. 2022. Damage detection of plate-type bridges using uniform translational response generated by single-axle moving vehicle. *Engineering Structures*, 266, 114530.

Influence of various admixture materials on pore structure and mass transfer characteristics

R. Yahiro & T. Iyoda

Shibaura Institute of Technology, Tokyo, Japan

ABSTRACT: Durability is important for the life cycle of reinforced concrete structures. Pore structure and mass transfer characteristics are related. Understanding the pore structure is necessary but difficult. It has been shown that gas and liquid have different mass transfer characteristics, and we thought that this difference could be express the pore structure. In this study, air permeability tests, Water penetration rate coefficient test, and porosity measurements were conducted. Various admixtures were used because the porosity is different depending on the admixture. As a result, it's clear that the mass transfer characteristics are different depending on the admixtures and amount of its content. Silica fume and blast furnace slag fine powder in high proportion showed high mass transfer resistance, and the water penetration rate coefficient was about 1/2 that of N. The difference between the air permeability and water penetration rate coefficients indicates the possibility of expressing the complexity of pores.

1 INTRODUCTION

Durability is important for the life cycle of reinforced concrete structures. Carbonation and salt damage, which are representative of the deterioration of reinforced concrete structures, cause steel corrosion and cracks in concrete. Since steel corrosion is progressed by the supply of water and oxygen, it is very important to understand the mass transfer characteristics in concrete. In Japan, steel corrosion by water penetration was added to the durability verification in the revision of the Standard Specification for Concrete Design, and a Water penetration rate coefficient test was devised in 2017. deterioration factors such as carbon dioxide, chloride ions, water, and oxygen penetrate the concrete using the pores as movement pathways. Therefore, it is often considered that pore structure and mass transfer properties are very closely related and are often discussed together with durability. Therefore, it is necessary to understand the pore structure of hardened cement in order to understand the mass transfer characteristics. In recent years, the use of various admixtures and chemical admixtures has been focusing in order to improve durability and reduce the effects on the environmental. It is known that the use of admixture materials changes the pore structure. However, it is difficult to accurately determine the pores in concrete because there are pores of different sizes and different shapes, each of which is complexly connected to the others. Thus, we considered inferring the pore structure of hardened cement when various admixtures are used, by using mass transfer characteristics and porosity. In this study, we tested hardened cement used the admixtures such as ground granulated blast-furnace slag, fly ash, silica fume, and C-S-H hardening accelerator agent. Air permeability tests, moisture penetration tests, and porosity measurements were conducted to sort out the pore structure and mass transfer characteristics formed using admixture materials. The combination of these tests was also investigated to understand the pore composition.

2 OUTLINE OF EXPERIMENT

2.1 Materials and mass ratio of cement and admixtures of mortar

In this study, mortar specimens were used to eliminate the influence of coarse aggregate. Also various admixtures were used and specimens were tested with different curing times in order to vary the diameter and distribution of pores. Ordinary Portland cement (OPC, Density 3.16 g/cm³, Blaine 3080 cm²/g) was used as cement, and blast furnace slag fine powder (BFS, Density 2.91 g/cm³, Blaine 4190 cm²/g), fly ash type II (FA, Density 2.33 g/cm³, Blaine 4460 cm²/g), and silica fume (SF, Density 0.27 g/cm³, Blaine 18.5 m²/g) were used as admixtures for the mortar. In case of using BFS, anhydrous gypsum was added to the BFS in an amount equivalent to 2% SO₃. Admixtures was replaced by mass ratio to cement. A C-S-H hardening accelerator (ACX) was used as a chemical admixture, which is thought to contribute to pore densification. Table-1 shows the mass ratio of cement and admixtures of mortar. The water-binder ratio was 50% and the binder: fine aggregate mass ratio was kept constant at 1:3.

Table 1. Mass ratio of cement and admixtures of mortar.

		Mass ratio (%)		
Admixtures	W/B (%)	OPC	Admixtures	ACX (W×%)
N	-	100	0	
B20		80	20	
B50	BFS	50	50	
B85		15	85	-
FA30	FA	70	30	
SF30	SF	70	30	
ACX	ACX	100	0	10

2.2 Porosity test

The specimen used in the water penetration test was crushed and a 25 mm square specimen was taken out. The samples were saturated with water by a vacuum desiccator. After measuring the saturated weight and the weight in water, the samples were left to dry at 40°C, RH 30% until their weights became constant, and the weight in a dry state was then measured. Porosity was calculated by Archimedes method.

2.3 Water penetration rate coefficient test

This test was conducted in accordance with JSCE-G 582-2018. Figure 1 shows an illustration of the test. Cylindrical specimens of $\phi 50 \times 100$ mm were made, and after curing, they were placed in the chamber at 40°C and RH30% until their mass became constant. After the specimens were removed from the chamber and the temperature was lowered to room temperature. The sides were sealed with aluminum tape and two sides were open. The mass of the specimen was measured, and 10mm from the bottom of the specimen was immersed in water and removed after 5, 24, and 48 hours. After the mass was measured again, the specimen was split

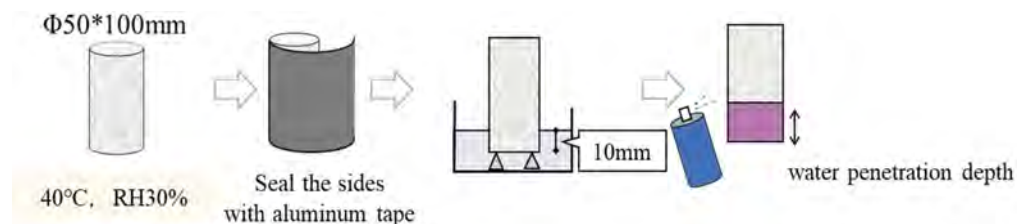


Figure 1. Outline of water penetration rate coefficient test.

open and sprayed with a moisture sensing agent. The range of coloration was defined as the water penetration depth, and the slope of the water penetration depth relative to the square root of the soaking time was calculated as the water penetration rate coefficient.

2.4 Air permeability test

The test was carried out using the output method with a disk-shaped specimen of $\phi 100 \times 20$ mm. In the pre-treatment, the specimens that finished the curing period were dried. The specimens were placed in an environment of 40°C , 30% RH and dried until the weight became constant. Air was injected at 0.1 MPa, and after confirming that the air flow had become constant, the permeability was measured using a graduated cylinder by water displacement method (Figure 2). The air permeability coefficient was calculated using the Darcy rule using the following equation (1).

$$K = \frac{2LP_2}{(P_1^2 - P_2^2)} \cdot \frac{Q}{A} \quad (1)$$

where K: Air permeability coefficient ($\text{cm}^4/\text{N} \cdot \text{s}$), L: Specimen thickness (cm), P_1 : Loading pressure (N/mm^2), P_2 : Outflow side pressure (N/cm^2), Q: Amount of air permeability (cm^3/s), A: permeable area (cm^2)

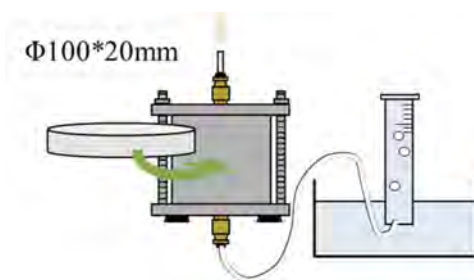


Figure 2. Outline of air permeability test.

3 RESULTS OF TESTS

3.1 Porosity

Figure 3 shows the results of porosity calculated by Archimedes' method for each mix proportion. The porosity showed a decreasing trend as the curing period was extended. This may be because of the hydration reaction of the cement, or the reaction caused by the admixture material. It was also clarified that even with the same number of curing days, the porosity was different depending on the type of admixture and the replacement ratio. The porosity is largest in B85, suggesting that the hydration reaction may not be sufficiently complete.

3.2 Water penetration characteristics

Figure 4 shows a specimen that had been cured for 28 days and was sprayed with a water sensing agent on the split surface of the specimen after 48 hours of immersion. It was confirmed that the use of admixture materials suppressed water penetration. B50 and SF30 showed smaller depths of water penetration than N, and SF30 showed higher resistance to water penetration, less than 1/2 that of N. On the other hand, the water penetration characteristics were different depending on the admixture and its amount of content. Especially, it was observed that the higher the BFS replacement ratio, such as B85, the more water was penetration at the sides of the cylindrical specimen and the greater the water penetration depth compared to the

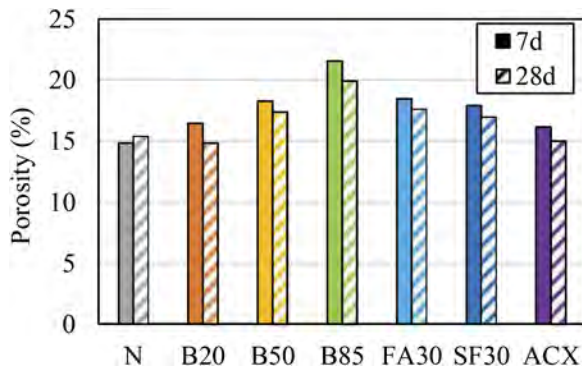


Figure 3. Results of porosity test.

center of the specimen. This was reported in previous studies to be caused by changes in the pore composition affected by drying in the case of high BFS replacement. This result may have been obtained in B85 because drying was performed as a pretreatment. While the effect of drying was small for N, however, B85 was greatly affected by drying before the test was conducted, and the water penetration behavior was different between the center and the sides of the specimen. Therefore, it is clear that the water penetration behavior is different depending on the mixed material and its content.

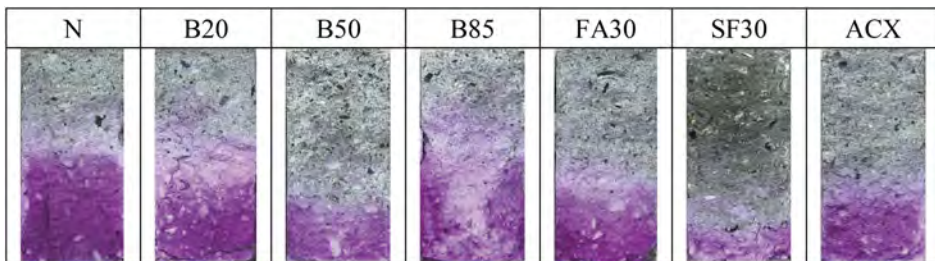


Figure 4. Results of water penetration characteristics.

3.3 Air permeability coefficient

Figure 5 shows the air permeability of each mix proportions calculated from the results of the pressure air permeability test. As a general trend, the permeability decreased as the number of curing days increased. FA30 shows a significant decrease at 28 days of curing compared to 7 days of curing. It is considered that this is because of the densification of the pores due to the long-term occurrence of the pozzolanic reaction of FA in addition to the hydration reaction of cement. In addition, regardless of the number of curing days, B85 and FA30 showed significantly higher values of permeability than the other mix proportions. On the other hand, B20, B50, SF30, and ACX showed similar or slightly smaller values than N. Thus, it can be seen that the use of admixtures improves the mass transfer resistance.

4 DISCUSSION AS EXPRESSION OF PORE COMPOSITION BY MASS TRANSFER TEST

4.1 Relationship between water penetration rate coefficient and air permeability coefficient

Figure 6 shows the relationship between the water penetration rate coefficient and the air permeability. No correlation was observed between them. This may be because the water penetration rate coefficient test and the air permeability test are affected by different factors. Group

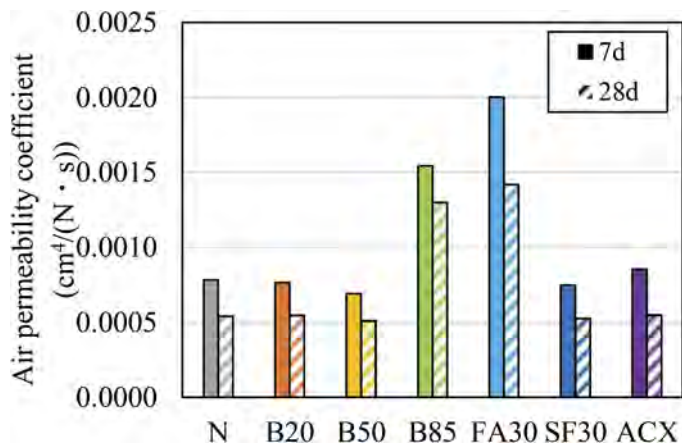


Figure 5. Results of air permeability coefficient.

A and Group B in Table 2 show some mix proportions with similar porosity. The relationship between the water penetration rate coefficient and the air permeability coefficient in these mix proportions shows that some hardened materials with the same porosity show similar values in group A but group B shows different values. In other words, even hardened materials that have the same porosity, but they are expected to show different trends depending on the pore composition, the material used in the mass transfer test, and the driving force of the test.

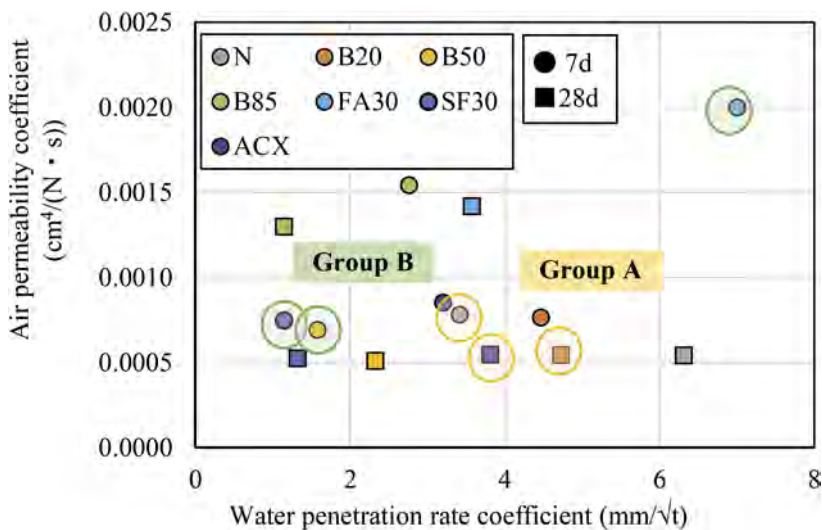


Figure 6. Relationship between water penetration rate coefficient and air permeability coefficient.

4.2 Relationship between porosity and mass transfer tests

Figure 7 shows the relationship between porosity and air permeability coefficient, and Figure 8 shows the relationship between porosity and water penetration rate coefficient. Figure 7 shows a positive correlation between porosity and permeability coefficient, with a decrease in permeability coefficient with decreasing porosity. On the other hand, Figure 8 shows a slightly negative correlation between porosity and water penetration rate coefficient. This relationship was different from that of the water penetration rate coefficient.

This result suggests that both of the water penetration rate coefficient test and the air permeability test evaluated the mass transfer in the hardened cement in the same way, but the results were affected by different factors, which may have caused the differences in the air

Table 2. The mix proportions with similar porosity.

Group	Mix proportion	Curing days	Porosity(%)	Marks
A	N	7	14.81	●
	B20	28	14.84	■
	ACX	28	15.00	■
B	SF30	7	17.89	●
	B50	7	18.26	●
	FA30	7	18.43	●

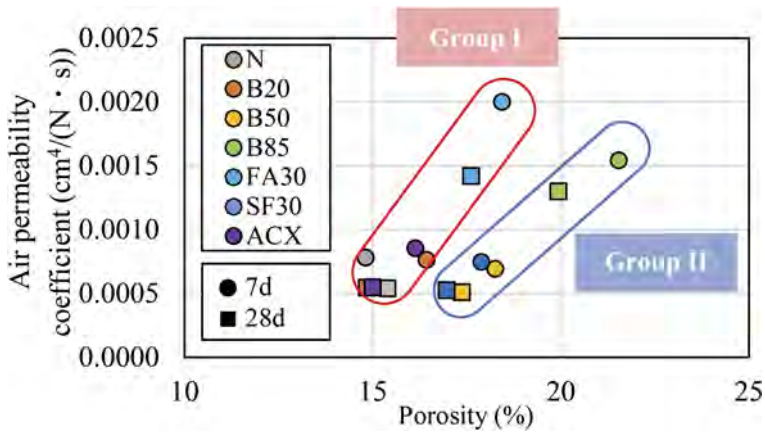


Figure 7. Relationship between porosity and air permeability coefficient.

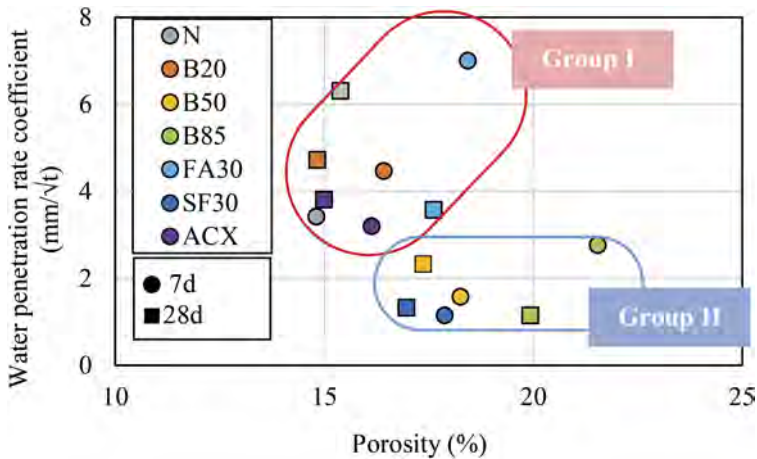


Figure 8. Relationship between porosity and water penetration rate coefficient.

permeability test, a correlation was observed between them, suggesting that the pore volume in the hardened cement affects the air permeability. However, a different trend was observed in the water penetration rate coefficient test, which suggests that other factors besides pore volume, such as the complexity of the pore composition, may have an effect on water penetration. In Figure 7 and Figure 8, the two groups shown in Table3 are N, ACX, FA30, and B20 (Group I) and B50, B85, and SF30 (Group II).

In Group I, it can be seen that both the water penetration rate coefficient and air permeability coefficient decrease with decreasing porosity. On the other hand, in Group II, the air permeability

Table 3. Groupings in Figures 7 and 8.

group	Mix proportion	Color of the mark
I	N	○ □
	ACX	● ■
	FA30	○ □
	B20	○ □
II	B50	○ □
	B85	○ □
	SF30	● ■

coefficient decreases with decreasing porosity as in Group I. However, the water permeability rate coefficient does not change so much with decreasing porosity. From these results, it was considered that B50, B85, and SF30, which were classified as Group II, had complex porosity. The complexity of the porosity composition may have affected the water permeability rate coefficient, resulting in a smaller water penetration rate coefficient, even with a large porosity. In addition, even if the porosity is the same, the air permeability coefficient of Group II shows a slightly smaller value than that of Group I. The relationship between porosity and air permeability coefficient also suggests that Group II has a complex pore composition. Therefore, it is suggested that the complexity of the pore composition can be expressed by combining the results of the water penetration rate coefficient test with the porosity and air permeability coefficient.

5 CONCLUSION

- (1) The mass transfer characteristics and porosity showed different trends depending on the admixture material and its content. In particular, the mix proportion with a high replacement of blast furnace slag fine powder showed large water penetration at the side of specimen and that is significantly different from that of other mix proportion.
- (2) It was found that even hardened cements having similar porosity showed different tendency in several mass tests depending on the test method transfer such as air and water.
- (3) The water penetration rate coefficient may be affected by the complexity of the pore composition, suggesting that the complexity of the pore composition may be expressed by evaluating the combination of the air permeability coefficient and porosity.
- (4) Since the size and diameter of each pore in this study were not measured, in the future a mercury intrusion porosimeter will be used to measure the porosity in detail.
- (5) Only gas pressure injection and water permeation have been conducted, so we hope to understand the pore structure more clearly by conducting mass transfer tests using different materials and driving power.

REFERENCES

- Japan Society of Civil Engineers, Standard Specifications for Concrete Structures “Design”, 2017
- Shiraishi, M. and Iyoda, T., Influence of Differences in Pore Characteristics Formed by Various Hydrates on Mass Transfer Properties, Proceedings of the Japan Concrete Institute, Vol.44, No.1, pp.184–189, 2022
- Koga, H., Katahira, H. and Nakamura, E., Challenges and Expected Efforts to Extend the Service Life of Concrete Structures Expected Initiatives, Concrete journal, Vol.57, No.5, pp. 313–317, 2019
- Iyoda, T., Mizuno, H. and Sugiyama, T.: Investigation of the mechanism on progress for strength and air permeability of concrete using C-S-H hardening accelerator, Cement Science and Concrete Technology, Vol.72, No.1, pp. 204–210, 2018
- Shibuya, A. and Iyoda, T.: Study on pore structure of mortar based on mass transfer test, Proceedings of the Japan Concrete Institute, Vol.43, No.1, pp. 335–340, 2021
- Mizuno, H., Iyoda, T., Influence of pore structure change of carbonated ground granulated blast furnace slag cement hardened body on water permeability, Proceedings of the Japan Concrete Institute, Vol. 41, No. 1, pp. 665–670, 2019
- M. Anwar, Dina A. Emarah, Pore structure of concrete containing ternary cementitious blends, Results in Materials, Vol.1, p. 100019, 2019

Research on the anti-sliding performance of cable clamps in an irregular elliptical suspen-dome structure

H.J. Wang

CITIC General Institute of Architectural Design and Research Co., Ltd, Wuhan, China
College of Civil Engineering of Tongji University, Shanghai, China

X.D. Ren

College of Civil Engineering of Tongji University, Shanghai, China

S.W. Xiao & L. Li

CITIC General Institute of Architectural Design and Research Co., Ltd, Wuhan, China

B. Luo

College of Civil Engineering of Southeast University, Nanjing, China

ABSTRACT: The anti-sliding performance of the cable clamp is significant to the safety of the suspend-dome structure, the anti-sliding test was designed and the results showed that the anti-sliding bearing capacity of the cable clamp is greater than double the internal force difference between the two ends of the cable clamp under the most unfavorable working conditions of the design, and the FEM analysis of the cable clamp showed that the error between the anti-sliding bearing capacity of simulation and the test value is within 10%, indicating that the length and structure of the designed cable clamp met the design requirements.

1 INSTRUCTIONS

The suspend-dome structure has become the preferred structural form for the roof of the gymnasium because of its light structure, clear force transmission route, simple node structure and convenient construction. The anti-sliding performance of the cable clamp has a great influence on the mechanical performance of the suspend-dome structure. The lack of anti-sliding capacity of the cable clamp will lead to the slip of the cable, even change the stress state and structural form of the cable net structure, which may result in the instability and collapse of the structure.

In view of the force analysis of the anti-sliding performance of the cable clamp, a series of studies have also been carried out by relevant scholars. Luo *et al.* 2012. Proposed the concept of slip force density to describe the anti-sliding performance of such nodes through experiments and simulations of chord-supported dome cable clamp joints, and found that ribbing in the nodal groove can effectively improve the anti-sliding ability of the joint. Tian.2015. and Li *et al.* 2017. Found that cable tension and radial creep after compression were the main causes of bolt preload loss by experimentally analyzing the cable clamp slip process, and on this basis, the influence of bolt pretension, friction coefficient and other factors on the anti-sliding performance of the cable clamp was analyzed by finite element means. Ali *et al.* 2019. Combined the linear complementarity method in finite element analysis and dynamic relaxation method to study the mechanical behavior of the tension structure system that generated slip, which provided ideas for the analysis and calculation of similar structures. Ruan *et al.* 2019. Revealed the anti-sliding mechanism of cable clamps by presenting a theoretical model considering the effects of long-term creep and cable tension, and carried out the anti-sliding tests to verify the theoretical model. Wang *et al.* 2022. Further found that the bolt preload, the cable tension, the sequence of screwing bolts and stretching the cable and the diameter of the bolt would affect the anti-slip performance of the cable clamp by changing the normal pressure of the cable-clamp interface.

Considering the diversity of cable clamp joints in the actual engineering suspend-dome roof structure, the combination of component test and finite element simulation is still a reliable research method when conducting anti-sliding research on such components. This paper aims to study whether the cable clamp at the abrupt change of cable line type meets its required anti-slip force through experiments and finite element analysis, and provide data and method basis for subsequent research.

1.1 Engineering background

Located in Chibi City, Hubei Province, China, the Chibi Sports Center project has a total land area of about 543 acres, including a 15,000-person stadium and a 5,000-person gymnasium and a national fitness park. The main structure of the sports center is a concrete frame structure, and the roof is a suspend-dome structure (outer field) and single-layer grid shell and local tension string beam structure (infield). The model of the roof of the gymnasium is shown in Figure 1 and the ring cable and radial cable are all made of GALFAN plated steel strand clues.

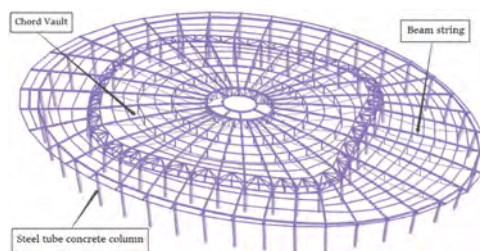


Figure 1. Axonometric drawing of the stadium roof model.

Due to the different architectural functions of the gymnasium, the infield roof is divided into a suspend-dome part and a string beam part, which causes the roof of the suspend-dome part to be extremely irregular. The regular chord branch dome structure will show overall downward deflection under the action of vertical load and live load, and the roof dome structure of this project due to its irregularity, resulting in deformation under vertical load presents a special phenomenon of local downward flexural and local upturning. This phenomenon was mainly caused by the irregularity of the roof, and there was a sudden change in the internal force of the ring cable at the junction of the radial and circumferential directions. The maximum internal force difference between the two ends of the cable clamp reached 92kN and 196kN respectively under the combination of the most unfavorable load conditions, so it is necessary to verify the anti-sliding capacity of which by tests and FEM analysis.

2 INTRODUCTION OF THE EXPERIMENT

The main purpose of the test is to measure the anti-sliding capacity of the cable clamp. Compared with the specimen used in the sports center, the test specimen was simplified: the cable-way in the test specimen is straight rather than arc-shaped.

The test specimen is two D70 central ring cables and D110 outer ring cables, the test cables are all GALFAN plated steel strand clues, the diameter is 70mm and 110mm respectively and the corresponding test cable clamps are configured, the test cable clamps are G20Mn5QT steel casting cable clamps, the specific material properties are shown in the "Cast Steel Joint Application Technical Regulations" (CECS235:2008), the structure and specifications of the test cables are consistent with the engineering cables. Before the test, the cable clamp is preloaded with high-strength bolts before the cable tensioning. The specific specifications of the cable body are shown in Table 1, and the detailed drawings of the dimensions of the corresponding cable clamps are shown in Figure 2 and Figure 3.

Table 1. Test cable specification sheet.

Structural parameters				
specimen	material	diameter /mm	Effective cross-sectional area /mm ²	Minimum breaking force /kN
D70	1670 grade high vanadium	70	2840	4310
D110	Coated steel strands	110	7020	10560

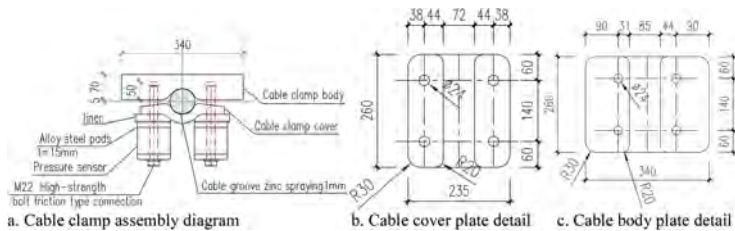


Figure 2. Detailed view of the D70 test cable clamp.

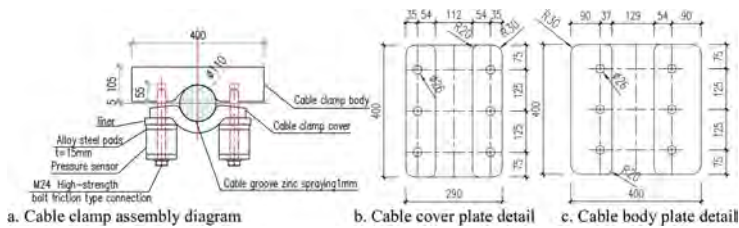


Figure 3. Detailed view of the D110 test cable clamp.

3 EXPERIMENTAL RESULTS

According to the measured data, the tightening force attenuation curve of each high-strength bolt after the initial tightening with time is shown in Figure 4. The average initial tightening force, final tightening force and relaxation rate of the bolts on each cable clamp calculated by the tightening force curve was shown in Table 2. The test shown that the tightening force attenuation rate of the high-strength bolt is basically about 38%.

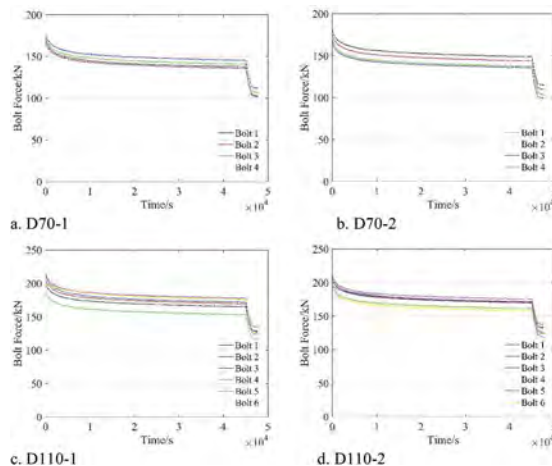


Figure 4. Attenuation curve of the bolt force.

Table 2. Bolt force on each cable clamp.

Specimen	Average initial force /kN	Average final force /kN	Average decay rate
D70-1	173.13	106.75	38.34%
D70-2	172.40	105.37	38.88%
D110-1	204.43	125.39	38.66%
D110-2	202.49	125.28	38.13%

Figure 5 shows the sliding curve between the cable and cable clamp which was calculated according to the measurement index. The anti-sliding test results are shown in Table 3, where the anti-sliding friction coefficient was calculated according to Equation (1). The friction coefficients of cable clamps are all greater than 0.15 specified in Specification for Design of Highway Suspension Bridges (JTG/TD65-05-2015).

$$\mu = \frac{F}{m \sum P_e} \quad (1)$$

In Equation (1), μ represents the friction coefficient of cable clamp; F is anti-sliding bearing capacity of cable clamp; m represents the number of friction surfaces between the cable clamp and the cable, which is 2.0, $\sum P_e$ represents the sum of the tightening forces of all bolts when the cable clamp slips (also the effective tightening forces of bolts). The anti-sliding bearing capacity of D70 and D110 cables is taken as the minimum of the two groups of data, which are 220kN and 520kN respectively. Under the combination of the maximum load conditions, the maximum internal force difference between the two ends of the cable clamp is 92kN and 196kN respectively. The anti-sliding safety factor of the cable clamp is 2.4 and 2.7 respectively, both greater than 2.0 which shown that the anti-sliding ability of the cable clamp meets the design requirements.

Table 3. Results of cable clamp anti-sliding test.

specimen	Effective bolt force /kN	Anti-sliding capacity /kN	Composite friction factor	Average comprehensive friction coefficient
D70-1	427.00	235.00	0.27	0.26
D70-2	421.48	220.00	0.26	
D110-1	752.34	560.00	0.37	0.35
D110-2	751.68	520.00	0.34	

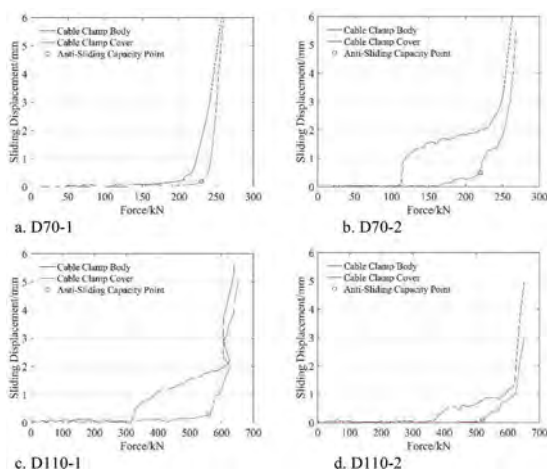


Figure 5. Thrust - slip curve of cable clamps.

4 NUMERICAL SIMULATION

In order to verify the anti-sliding test results, the finite element analysis software ABAQUS was used to simulate the cable clamp test process, and the test results were compared with the finite element analysis results to verify the rationality of parameters setting of the nonlinear finite element model, which could be used as the basis for the further analysis of the applied engineering specimens.

4.1 Model

The high-strength bolts connecting the cable clamp were simplified in FEM model, the gasket and thread details of the bolt connection pair were omitted, and the cable twisted by multiple steel wires was simplified into a uniform solid cylinder of equal diameter. Appropriate material properties and cell types was chosen to assign to the model components, and the face-to-face contacting was defined. Finally, the finite element model is solved under reasonable boundary and loading constraints.

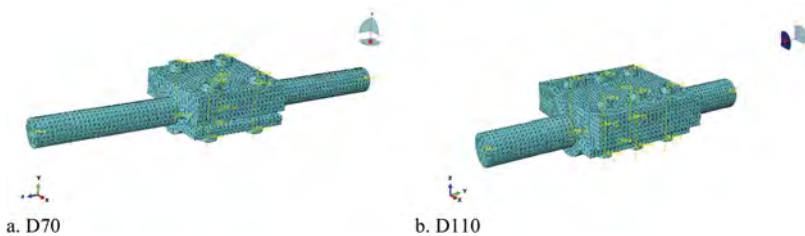


Figure 6. FEM models of cable clamp.

4.2 Material

To simplify the calculation, the stress-strain curves of various materials in the model are modeled by bilinear hardening model, the elastic modulus of the strengthening stage is αE , the coefficient α is 3%, and the strength of the material wouldn't increase after reaching the ultimate tensile strength. The D70 and D110 ring cables are made of steel wire twisting, and the sections were simplified to attain the deformation consistency of the two cables, the axial and the radial elastic modulus of the cable reduced according to Equation (2). The parameters are shown in Table 4.

$$E_e = \frac{EA_e}{A} \quad (2)$$

In Equation (2), E_e represents the radial and transverse equivalent elastic modulus of cable body; E is elastic modulus of cable, which is $2.06 \times 10^5 \text{MPa}$, $1.60 \times 10^5 \text{MPa}$; A_e is equivalent cross section area of the cable; A represents the nominal section area of cable, which is also the section area of cable in the FEM.

Table 4. Material parameters of each part in the FEM.

Part Name	Material	f_y/MPa	Axial modulus of elasticity E/GPa	Radial modulus of elasticity E_r/GPa	Poisson's ratio
Cable clamp plate	G20Mn5	385	206	160	0.3
High-strength bolt	20MnTiB	640	206	160	0.3
D70 Cable	Zinc-coated wire	1670	152.10	118.13	0.3
D110 Cable	Zinc-coated wire	1670	152.25	118.25	0.3

4.3 Assembly and mesh

Every part of the model was established and assembled respectively according to the test conditions. Considering that some parts in the model were irregular in shape and various parts were segmented to different degrees in the modeling and assembly process, all parts were automatically meshed through tetrahedral elements. In terms of the element selection, considering the large number of contact surfaces in the model, a modified second-order tetrahedral solid element (C3D10M) is selected, which is designed to be applied to complex contact simulation problems. The mesh partition is shown in Figure 6. The contacting surfaces of the model includes bolts and the cable clamps as well as the cable and the cable clamps. Considering that the main function of bolts is tightening the cable clamps, the vertical contact surface between screw and cable clamps was set smooth, and the horizontal contact surface was set bound and restrained. Coulomb friction was used for the contact surface between the cable and the cable clamps, and the friction coefficient was the average friction coefficient obtained by the test. Finally, the axial temperature expansion coefficient is set in the material part of the bolt to apply the bolt preload.

4.4 Boundary condition

The pre-tightening force of bolts was applied by the virtual temperature method according to the Specification for Design of Highway Suspension Bridges (JTJ/TD65-05-2015). In order to prevent the calculation from not converging due to small rigid displacement of the structure, displacement loads are applied to the top and bottom of the bolts. Firstly, all the degrees of freedom at both ends of the cable were fixed, and then the axial degrees of freedom at one end of the cable were released for the hierarchical tension of the cable after the contact between all the components is complete. In addition to the constraint on the end face of the cable, the coupling of the top and bottom surfaces of the cable clamps and the top and bottom surfaces of the bolt was also carried out through the reference points to apply the load and control the degree of freedom of the component surface in the process.

4.5 Numerical analysis results

The sliding curves of D70 and D110 cable clamps got by the FEM analysis are shown in Figure 7, and the anti-sliding bearing capacity is compared in Table 5. It can be seen that: the error of the calculated anti-sliding bearing capacity of D70 cable clamp is within $\pm 5\%$, and that of D110 cable clamp is within $\pm 10\%$. Compared with the test, the thrust force of the model remains basically unchanged after the slip occurs. The reason is that the body and the cover of the cable clamps remained horizontal during the loading process and slid at the same time.

Figure 8 shows the variation curve of tightening force of high-strength bolts in the two types of cable clamps along with the tension of the cable during the test process. The tightening force attenuation of high-strength bolts showed two stages: before the tension of the cable, the tensile force of bolts decays with the stress adjustment between the cable clamp and the cable. During the tension of the cable, the bolt tightening force decreases linearly with the extension of the cable. Based on the simulation results, the tightening force relaxation rate of high-strength bolts of D70 cable clamp during the process is 31.16%, and that of D110 cable clamp high-strength bolt is 31.49%, which is less than the test value, because the isotropic materials used in the FEM was simplified on the basis of the actual material, and the radial elastic modulus of the model is larger than the actual modulus. Therefore, the tightening force relaxation rate of the high-strength bolt was less at the stress adjustment stage of the cable clamp, which led to a final less relaxation rate.

Table 5. Comparison of the anti-sliding bearing capacity.

Specimen	Capacity of test/kN	Capacity of the FEM /kN	Error
D70-1	235.00	226.54	-3.60%
D70-2	220.00	226.54	2.97%
D110-1	560.00	517.10	-7.66%
D110-2	520.00	517.10	-0.56%

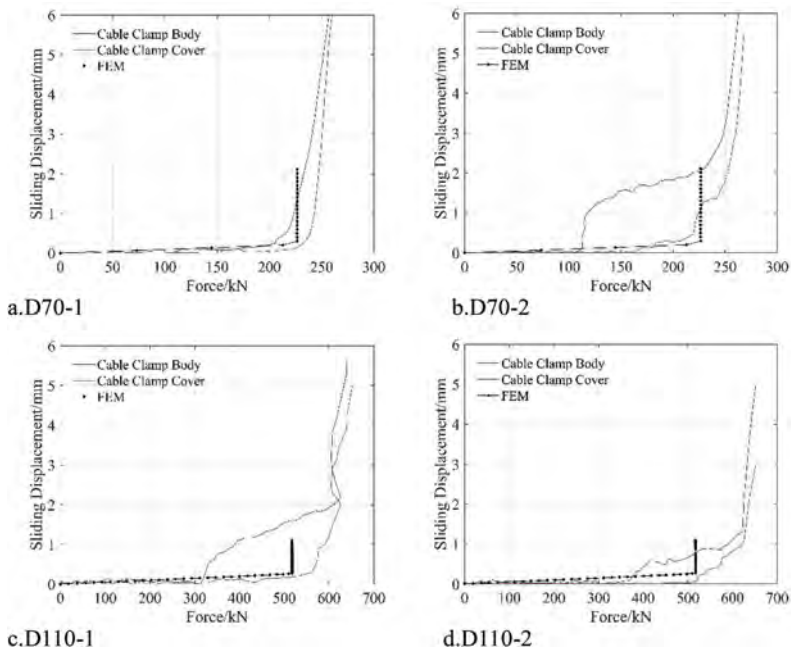


Figure 7. Comparison of simulation and anti-sliding test.

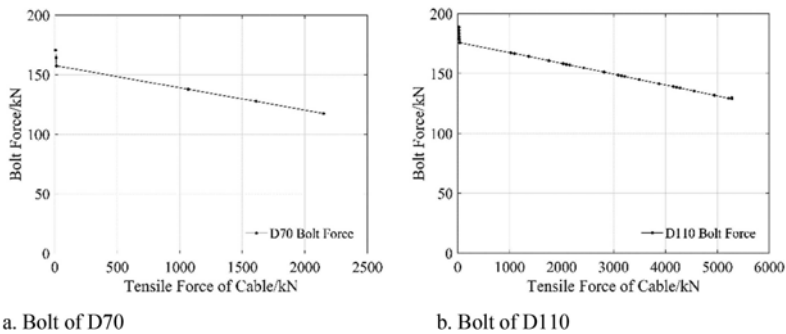


Figure 8. High-strength bolt fastening force-cable tension curve.

5 CONCLUSION

In this study, the anti-sliding tests and the FEM analysis of two kinds of cable clamps were designed and carried out, the observations and conclusions of the study were summarized as follows:

- (1) The test results showed that the cable clamps D70 and D110 at the position of the unbalanced maximum force had the anti-slip bearing capacity of 220 kN and 520 kN respectively. The maximum internal force difference between the two ends of the cable clamp is 92kN and 196kN, and the anti-sliding safety factor of the cable clamp is 2.4 and 2.7 respectively, indicating that the anti-sliding ability of the cable clamp meet the design requirements and has a certain degree of safety.
- (2) The results of the FEM analysis and anti-sliding tests were compared, which showed that the error between the test and the finite element analysis of anti-sliding bearing capacity of cable clamps is within 8.0%. The decline of bolts tightening force in the FEM and the tests

were basically consistent with each other, and the former is about 7% less. The comparison results indicated that the numerical simulation is basically consistent with the test results, and these two methods confirmed each other, which can ensure the anti-sliding ability of the cable clamps and the safety of the main structure of the project.

- (3) In order to facilitate the test, the cable clamps in the test and FEM were simplified, resulting that there were some differences in the stress state between the cable clamps of the test (also the FEM) and the actual project. In the further research, the arc-shaped cable clamps can be tested and simulated to get the corresponding relationship between the anti-slip bearing capacity of the arc-shaped cable clamp and the straight cable clamp of the same length, which is convenient for engineering design.

REFERENCES

- Luo YF, Wang F, Ni JG, Xu LX. 2012. Experimental research on the slipping performance of cable-strut joints. *Journal of Chongqing University*, 35(04):65–71. in Chinese.
- Tian W. 2015. Research on the Anti-sliding Performance of Galfan Cable Clips. Southeast University. in Chinese.
- Li JF. 2017. Analysis and Experimental Research on Anti-sliding Performance of Cable Clamp with Full Lock Coil Strand in High Stress State. Southeast University. in Chinese.
- Nizar Bel Hadj Ali et al. 2019. On static analysis of tensile structures with sliding cables: the frictional sliding case. *Engineering with Computers*, 37(prepublish): 1–14.
- Ruan YJ, Luo B, Ding MM, Huang LF, Guo ZX. 2019. Theoretical and experimental study on the anti-sliding performance of casting steel cable clamps. *Adv Civil Eng* 2019; 1438754.
- Wang ZQ et al. 2022. Anti-slip performance of cast steel cable clamps for prestressed cables. *Structures*, 46pp. 353-368.
- CECS235:2008[S]. Technical specification for application of connections of structural steel casting. Beijing: China Planning Press; 2008. in Chinese.
- JTG/TD65-05-2015 [S]. Specifications for Design of Highway Suspension Bridge. Beijing: People's Communications Publishing House Co., LTD; 2015. in Chinese.

Lessons learned from highway tunnels inspection, analysis, assessment and refurbishment works

A. Damiani, E. Crippa & M. Rabbia
Lombardi Ingegneria s.r.l., Milan, Italy

ABSTRACT: Civil engineering infrastructures in Italy were intensively developed since the 1960s and now-adays most of existing tunnels is affected by aging and deterioration processes. To face this challenge, the main Italian motorway agency has adopted a sound approach for the assessment of more than 350 km of tunnels and for the definition of specific interventions, conceived for the defects detected during inspections. It is important to emphasize that the fact-finding phase is fundamental to identify the best solution to repair the defects. This paper illustrates the effectiveness of the adopted methodology aimed at identifying defects, considering their nature, location, extension and origins, based on visual inspections and instrumental diagnostic methods. Great efforts have been devoted to defining and developing proper interventions in order to solve critical situations, reduce impacts of deterioration, prevent the evolution of defects and fulfill functionality and safety requirements. Several repair techniques and rehabilitation schemes are presented in this paper.

1 INTRODUCTION

Starting from 2020, there has been an intensification of inspection activities in existing tunnels in Italy. The performance of the inspection of tunnels and of structural elements in general, although already envisaged by current legislation, however, was mostly delegated to the single Concessionaire who acted by adopting his own criteria and analysis, according to the law interpretation; in recent years it can be said that inspections has begun to be addressed systematically according to shared procedures and methods defined by Decrees or Standards that had the merit of better focusing and framing this activity.

In the context of this situation, it should be noted that in recent years in Italy there have unfortunately been some important collapses of structures belonging to both national roads and motorways, which in some cases have caused victims. This chain of events, if there were still any need, has led to the awareness of how much the national heritage of galleries, among other things very heterogeneous and extensive if compared to the situation in other European countries, is characterized by an average age in many cases higher than 50 years, usually considered for this type of construction. Furthermore, this figure is often accompanied by a less than optimal state of conservation exacerbated by the fact that the older tunnels do not present waterproofing systems.

This article aims at providing an examination of the activities connected to the inspections of the motorway tunnels in which Lombardi Ingegneria has taken part in the last 3 years; the main objective is to create the so-called “Zero Point” of the state of conservation of the tunnels, in order to define any interventions to make the structure safe, dictating the various priorities for action.

2 THE HIGHWAY TUNNELS INSPECTION IN ITALY

2.1 *Reference legislation*

The inspection of motorway tunnels in Italy in particular, as well as for other types of structures, is envisaged in the National Decree no. 6736-61-A1 of 19 July 1967, which foresees periodic checks as regards stability conditions of the various structures and the state of conservation in order to maintain constant efficiency. The Decree defines the characteristics of the inspection (thorough technical checks or minor inspections) and their frequency (annual or quarterly). It represents the first attempt aimed at introducing and making systematic the controls on structures and their connected elements (including foundations, slopes, etc. . .). The Decree also establishes the minimum frequency of inspections, starting with in-depth inspections to be performed at least once a year, up to not in-depth inspections to be scheduled at least quarterly. For several decades, this regulatory reference represented the only one to provide the minimum guidelines for the surveillance of road infrastructure.

In recent years, however, other Decrees and Guidelines has been issued focusing on the supervision of tunnels and related activities, as briefly summarized below. The Manual issued by Ministry of Transportation on 05/26/2020, identifies and clarifies the key points of the visual inspection, in particular, with regard to the so-called “Point Zero” inspection. The Supplementary Decree issued on 07/07/2020, has introduced the possibility of investigating the condition of the tunnel linings using methods other than direct vision, provided that the methods and technologies used prove effective.

Furthermore, the Decree no. 152 of 04/09/2021, provides guidelines for the preparation of the “surveillance plan” for tunnels that have already been inspected. This plan must take into account the results of the inspections and the interventions carried out. Lastly, the new ministerial guidelines for existing road and motorway tunnels were approved, in August 2022. These guidelines are a tool for classifying existing tunnels according to “attention classes”, on the basis of which investigations, inspections, monitoring activities and interventions can be planned. Their purpose is in fact to ensure homogeneity of risk classification and in the management, assessment and monitoring of existing tunnels along the road and motorway network.

3 INVESTIGATING THE LINING CONDITION

Lombardi Ingegneria was commissioned to carry out detailed inspections of the final lining of all the tunnels of one of the main motorway concessionaires operating in Italy.

The main objective of the activity is to create the so-called “Point Zero” of the state of conservation of the tunnels, in order to define interventions, dictating the different priorities for action.

Following the Client’s request to propose a new inspection method compared to what had been done so far, the adoption of the inspection manual approved by the “Center d’Etude des Tunnels” (CETU) in 2005, already applied in Italy for the Mont Blanc tunnel section, was proposed. The manual represents a consolidated reference because it has been used for years abroad and complies with the requirements of the Italian Standards n. 6736/61 of 19.7.1967 and n. 34233 of 25.02.1991.

The proposed system considers the deterioration related to both the structure and the presence of water and is based on two documents published in the last revision in 2015, which constitute the Guidelines (Book 1: from disorder to analysis, from analysis to rating and Book 2: Catalogue of deteriorations).

The CETU guidelines propose a catalogue of 47 defects, divided into 12 types. All defects found during an inspection are traced back to these types and are classified according to their nature (structural or water presence) and their severity, in accordance with the “IQA” scheme, “Image qualité des ouvrages d’art”, which, as defined in the name, provides an insight into the health of the structure. With reference to the civil part, the IQOA Classification takes into consideration cracking defects, damage and alteration in general, identifying them with

an alphanumeric code that describes the severity/dangerousness, in relation to which the rehabilitation can be planned over time, as far as the safety of users is concerned. The same approach is followed for water-related defects.

The activity mainly concerned the tunnels built between 1930 and 1979, characterized by the absence of waterproofing behind the final lining. The aims are:

- to define the inspection methods for the tunnels and the classification of their defects;
- to define the types of intervention for the most frequent maintenance work;
- to analyze the results of the georadar surveys, in order to obtain the thickness of the concrete, the presence of voids behind the lining, the presence of rebars and defects; these results will form the database, together with the design and construction documentation available in the client's archives;
- to carry out inspection after dismantling of the corrugated sheets present in the crowning and on the walls, thorough visual inspection of the lining, carrying out instrumental and diagnostic investigations deemed necessary (georadar and video endoscopies; tests on concrete samples; flat jacks testing; ultrasonic tomography; doorstopper tests. . .) and coordinating the execution of the surface demolition of unstable concrete;
- to define the types of rehabilitation works for the defects detected.

The working methodology is composed in detail of the following phases:

- general knowledge phase: retrieval and analysis of available historical documentation (executive project, as-built, results of previous inspections);
- instrumental diagnostic phase, georadar execution; Phase I: 3 or 5 longitudinal profiles depending on the section of the tunnel (2-lane or 3-lane respectively) and Phase II: in-depth analysis with localized georadar profiles on the basis of the results of visual and sound inspections (with hammer percussion), on the first phase georadar, direct checks and calibrations with video endoscopies and concrete sampling (n° 3 samples every 50m);
- inspection phase with visual and sound inspection (with hammer percussion), detection of defects (with relative definition of the class/grade) and detection of any deterioration of previous refurbishment;
- intervention phase with definition of the typological interventions to be implemented and definition of any areas to be monitored.



Figure 1. Inspection of the tunnel lining with MEWP.

The first essential step of the activity is to fully know the consistency of the existing tunnel. It is therefore essential to proceed first with the recovery of all available historical documentation. This may consist of design documentations and final accounting of the original works, including reports and drawings, as well as projects and accounting of rehabilitation carried out during the tunnel's operating life. To this documentation it is useful to add, if available, the historical archive of inspections carried out to date, which, containing the identification of defects, represents an important indication of the evolution that they have undergone over time.

All the information collected during this phase must then be verified in terms of truthfulness and completeness during the subsequent inspection phase and must finally form a specific set up by the Italian Ministry of Transport.

The inspection of “Point Zero”, as previously mentioned, is detailed with reference to the final lining (walls, crown) and includes: a) visual and auditory inspection of critical areas of the surface of the lining, with particular attention to areas that show alterations or cracks that could cause concrete surface detach; b) identification of cracks on the lining with vertical, horizontal, diagonal direction, with indication of their width; c) traces of salts, encrustations or deposits; d) identification of efflorescence; e) identification of water leaks; f) detection of surface detachments and their dimensions; g) detection of the presence of cortical voids and their dimensions; h) detection of visible local reinforcement; etc.

At the end of the inspection, the tunnel is open to traffic, except in case of defects that compromise the safety of users, classified with the letter “S” in accordance with the CETU Guidelines. If there is an “S” defect, a technical design team will determine the type of temporary intervention to be implemented so that the tunnel opened to traffic as soon as possible, compatibly with the rehabilitation measures to be implemented.

This is followed by a “back office”, during which the investigation will be reproduced in a graphic document and in a report, in order to present, as accurately as possible, the state of the structure at the time of the inspection. All data is then collected in tabular form, so as to constitute a “database” that summarizes the state of conservation of each tunnel and that will represent the knowledge base for future inspections and maintenance.

4 REFURBISHMENT WORKS

The activity involved more than 90 tunnels. The maintenance work are identified according to the type of defect to be worked on. The range of maintenance work can vary from simple steel mesh fixed with dowels to the tunnel lining to contain the detachment of the concrete aggregates to bolting. Maintenance works are also foreseen in the presence of water infiltrations inside the tunnel, for the treatment of cracks in the thickness of the final concrete lining and for the filling of cavities. For particularly severe conditions, in the presence of diffuse and open cracks, with pushing masses and where the bolts did not guarantee adequate performance in the geomechanical context, under-arch interventions with ribs and shotcrete were foreseen. Where, on the other hand, the concrete of the lining was particularly poor, in terms of mechanical characteristics, and with unsuitable residual thicknesses, the refurbishment of the lining was carried out by using self-supporting prefabricated formworks integrated in the new lining, after controlled demolition of the existing one. All maintenance works are subjected to a validation process by the Politecnico di Torino, identified as external reviewers.

An examination of the main types of maintenance works is given in the following paragraphs. For their execution, a discriminating factor to be taken into account is the possibility of carrying out the works in the absence or in the presence of traffic; this aspect is very delicate due to the considerable impact that any type of intervention to be carried out may have on vehicular traffic, especially if inside a tunnel.

The execution of the maintenance works in the absence of traffic represents the most desirable solution as it allows the workers to have no particular constraints on site operations, for example, the possibility of using the “jumbo” for the installation of bolts otherwise not be possible with vehicular traffic. On the other hand, the closure of one carriageway leads to traffic being diverted onto the opposite carriageway, with inevitable traffic delays and queues of vehicles. Depending on the section of motorway affected by the works, the closure times were in any case a constraint that the workers had to take into account. Given the wide variety of types of defects found, it is necessary to define the appropriate type of maintenance works for the resolution of each defect. Clearly these are the culmination of the entire activity. Furthermore, in order to make the intervention more targeted and effective, the root causes of the defect itself should be identified. In fact, the defect can also be classified according to the dominant cause that generated it with reference to fundamental influencing factors (defects) such as: Site and Construction. As regards the

Site, the causes of defects are: water action, environment (freeze-thaw, water chemistry, etc). Regarding the Construction factors, these are: design, execution and material. Site-related defects are those that affect an element or part of the structure and that occur gradually or rapidly, denoting a change. Construction defects, on the other hand, are the result of faulty workmanship.

The following table shows the main investigation techniques for achieving the above goals.

Table 1. Instrumental diagnostic methods and their aims.

AIMS		LASER SCANNER	GEORADAR	VIDEO- ENDOSCOPY	CONCRETE SAMPLING	PULL-OUT	FLAT-JACKS SIMPLE	SEISMIC TOMOGRAPHY
Geometrical and constructional characteristics of the lining	a) <i>Geometry</i>	X		X				
	b) <i>Lining thickness</i>			X	X			
	c) <i>Presence of reinforcement and evaluation of the concrete cover</i>			X				
	d) <i>Presence and position of steel supporting beams (single and/or double)</i>			X				
	e) <i>Cracks</i>	X						
Criticality in the lining	f) <i>Water and humidity zones</i>	X						
	g)			X	X			
	h)			X				X
	i)			X	X			X
	j)			X	X			
	Determine/verify the concrete mechanical characteristics of the full thickness of the lining					X		
Determine/verify the mechanical characteristics of the concrete in the surface part of the lining for the verification of the superstructure foundations (plants, protective nets, etc.)						X		
Define the stress state of the lining and possibly monitor critical situations							X	
Verify the state of consistency of the lining covered by protective nets			X	X		X		

4.1 *Shallow interventions*

4.1.1 *Steel and FRP nets*

This solution is typically applied on surface deteriorations up to 5 cm of thickness, on concrete lining, with or without waterproofing, and can also be applied in presence of cracks. After any preliminary scarification of the surface, light protective nets (e.g. welded stainless steel mesh ϕ 1.6 mm, 12.7x12.7 mm) are applied with overlapping heavy protective nets (e.g. welded stainless steel mesh ϕ 5 mm, 50x50 mm). These nets are fixed to the tunnel intrados by means of steel dowels. The steel mesh can be replaced by fiberglass mesh.

4.1.2 *Treatment of shallow cavities*

It is applied on deteriorations in the absence of water on concrete coverings, with/without waterproofing, both in rock and soils. The work involves the preliminary removal of any unstable portions, followed by restoration of the thickness with high-strength gunite reinforced with electrowelded mesh. After the final smoothing, protective stainless-steel mesh is laid. The joint between the gunite and the existing cladding is made by laying steel dowels. In presence of water, radial drains must be provided in order to set up a water collection system. These drains, made of PVC pipes, must have a blind section and a windowed section in order to intercept the water at the top of the tunnel without the risk of dispersing it inside any discontinuity in the thickness of the concrete.

4.1.3 Replacement of reinforcement bars

In case of deterioration of the reinforcement and concrete up to 20 cm depth and in the absence of water, with/without waterproofing, with prior scarification of the concrete, the interventions can be provided where the reinforcement is in good condition and only superficially rusted, removal of the superficial rust layer from the iron and application of protective products based on two-component anti-corrosive cement mortar and in areas where the reinforcement is intensely degraded, the steel bars must be replaced. The degraded concrete area will be replaced with reinforced gunite. The final phase involves the application of stainless-steel mesh and anchors. As an alternative to stainless steel mesh, a panel system composed of layers of high-strength GFRB grid may be used.

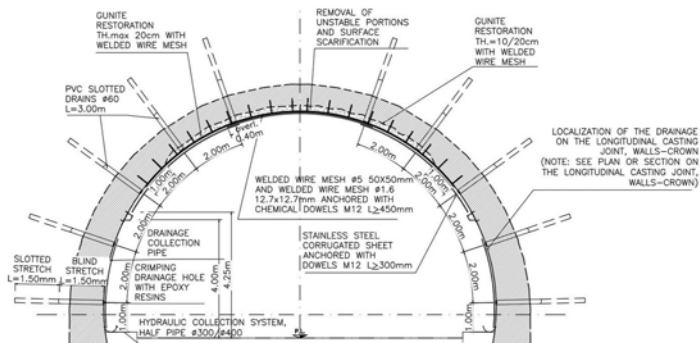


Figure 2. Example of treatment of shallow cavities.

4.1.4 Leakage collection

The collection of diffuse or concentrated water from the concrete lining, in the absence of surface deterioration, can be achieved by the installation of stainless steel corrugated sheets. The plates are fixed to the tunnel intrados by means of steel dowels. They are typically interrupted at the footings and convey water to drainage gutters. The drains normally consist of micro-slotted PVC pipes covered with non-woven fabric; the drains have both a blind and a windowed cross section in order to intercept the water at the tunnel top without the risk of dispersing it within the discontinuities in the thickness of the concrete.

4.2 Deep interventions

4.2.1 Interventions in presence of deep detachments (20-40 cm)

The intervention is applied in the presence of deep detachments (between 20-40 cm) in the absence of water, on concrete linings, without waterproofing, and in rock masses. Initially, the potentially unstable portions are removed, and the surface regularized; then connectors are installed and anchored into the lining. The missing thickness is then restored with high-strength gunite, reinforced with electrowelded mesh. A stainless-steel mesh will then be applied, joined to the lining by means of self-drilling radial bolts. The bolting operation thus makes it possible to ensure complete cooperation between the existing lining and the supplementary casting. If, during the drilling of the radial bolting, significant water leaks are found, the intervention must include the installation of the corrugated sheets described above.

4.2.2 Treatment of cavities at the ground-lining interface

In presence of significant voids within the linings (min. residual thickness > 30 cm) due to lack of filling during casting and possible deep cavities in absence of diffuse or concentrated water, the following intervention can be envisaged. Initially, the unstable portions are removed, followed by radial bolting with Swellex type bolts, length to be defined according to the geometry of the cavity at the contour, arranged with mesh according to the specific case. In the presence of a cavity at the boundary, a pumping phase will be carried out with material such as cemented expanded clay, until the cavity above is completely filled. A final bolting mesh will be created executing self-drilling bolts and drilling radial drains made in order to intercept the

water at the top of the tunnel. Finally, stainless steel corrugated sheets will be laid on the peripheral sections where the drains are located.

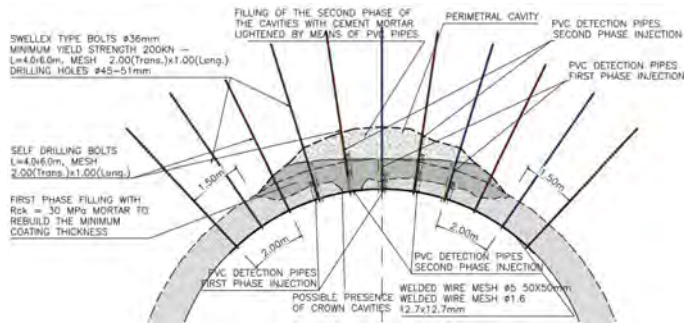


Figure 3. Example of treatment of cavities at the ground-lining interface.

4.2.3 Structural arches at the intrados

This consists of protection in the presence of open and persistent cracks on concrete linings, including those associated with significant stress level, both in rock and soft soil, in the presence of diffuse or concentrated water. The specifications, such as the type of profile, the spacing and the construction details will have to be defined on a case-by-case basis during the design of the intervention, according to the context found in the tunnel. The intervention, in general, is made of positioning of the steel supporting beams and execution of the redirective profile. The absence of interference between the dimensions of the new intervention and the space-proofing must first be verified by means of detailed topographical surveys along the stretch concerned.

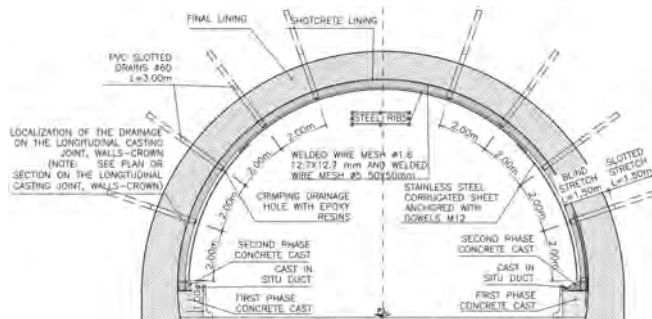


Figure 4. Structural arches at the intrados.

4.2.4 Lining demolition and reconstruction

The intervention consists in the demolition, in sections, and reconstruction of the arch of the lining or of the entire lining. The intervention, in relation to the geological, geomechanical and hydrogeological conditions, requires a preliminary phase of consolidation of the cavity, carried out from inside the tunnel. Once the consolidation phase has been completed, demolition must proceed according to precise design geometries, which will have to be detailed on a case-by-case basis in relation to the number of lanes, geological boundaries conditions and defects in the concrete. If local instability is found during horizontal cutting operations, work must be stopped and all safety procedures implemented. Once the milling phase has been completed, it may be necessary to even out the surface with a layer of shotcrete before laying the waterproofing. This is followed by the laying of the reinforcements, the precast elements (or the formwork) and the concrete casting.



Figure 5. Examples of lining reconstruction.

4.3 Rehabilitation works in presence of traffic

In order to carry out the reconstruction or the repair of the lining in presence of traffic and at the same time reduce the inconvenience of a long closure of the tunnel, a reinforced concrete protection shield is used in some cases, to keep the tunnel in operation. The shield allows the normal flow of motorway traffic from the construction site in conditions of maximum safety, separating and protecting it from falling material during the various phases of execution. The reinforced concrete protective shield has the purposes to support for the passage of construction site vehicles over the shield, to protect for the vehicles on the road during repair work, to delimit the roadway and to guarantee the workers safety in the personnel paths adjacent to the roadway.

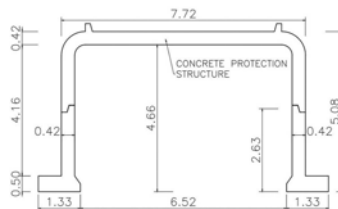


Figure 6. Concrete protection shield layout.

5 CONCLUSIONS

The tunnel assessment experience described in this paper was a national novelty in terms of inspections. Over the months, it has undergone refinements in the procedures for carrying out inspections, also in definition the types of intervention to be adopted on the various types of defects. Other improvements will emerge in the future, e.g. with reference to the adoption of tablets during the inspection phase, connected to the cloud and with pre-loaded information already available, lightening the amount of work related to the extrapolation of statistical data (types, dimensions, location, etc. . .). This will also allow a better understand the evolution of defects over time and the identification of the need for the refurbishment of the tunnels.

Other improvements already underway concern the use of Artificial Intelligence for defect recognition and evaluation over time. Lombardi Ingegneria, already in 2020, started specific research and studies with some leading University Centres for its application in road infrastructure.

REFERENCES

- Damiani, A. & Crippa, E. 2022. Chapter 7: Tunnel Refurbishment - *SIG Handbook on Tunnels and Underground Works. – Vol. 2 “Construction – Methods, Equipment, Tools and Materials”*
- Selleri, A. 2021. Autostrade per l’Italia “To start from zero point” – *Strade&Autostrade, Infrastructures and road network*

Deterministic and probabilistic damage calculation of offshore wind turbines considering the low-frequency fatigue dynamics

N. Sadeghi, P. D'Antuono, K. Robbelein, N. Noppe, W. Weijtjens & C. Devriendt
Offshore Wind Infrastructure-lab (OWI-lab) | Vrije Universiteit Brussel (VUB), Brussels, Belgium

ABSTRACT: With the ultimate goal of extending the lifetime of offshore wind turbines, applying monitoring data to develop fatigue damage calculations is of great interest. However, uncertainty in recorded loads and potential underestimation must be considered. This study analyzed the interface loads of a wind turbine in the North Sea using three years of strain and SCADA (Supervisory Control And Data Acquisition) data to predict lifetimes deterministically and probabilistically. The deterministic method calculated short-term damages through Rainflow cycle-counting and Palmgren-Miner rule. While the first probabilistic method additionally used bootstrapping to obtain confidence intervals, the second, binned short-term damages in wind speed groups. As the chronological order of load cycles is lost by constructing datasets from bootstrapping or binning, to account for the effect of Low-Frequency Fatigue Dynamics (LFFD), an amplifier factor from (Sadeghi et al., 2022) was applied to the total damage. Finally, the deterministic/probabilistic methods with/without LFFD impact were compared.

1 INTRODUCTION

Offshore wind turbines are fatigue-driven assets that are aging and beginning to reach their design lifetime. To make decisions regarding a future lifetime extension of the turbine and its foundation, a precise assessment of fatigue damage and lifetime is desired for each wind turbine. During design, each wind turbine's fatigue is calculated using numerical simulations. (Ziegler & Muskulus, 2016) and (Bouty et al., 2017), for instance, examined these simulation-based fatigue assessments for OWT substructures. However, the outcomes of these simulations are subject to uncertainty due to the limited number of simulations conducted and the modeling errors. Therefore, there may be a significant discrepancy between the conservative design assumptions and the actual performance of that turbine, allowing us to extend the lifetime (Byrne et al., 2015) (Ziegler, et al., 2019).

The new recommendation (DNVGL-RP-C203, 2019) advises using measured data when available since it is an essential complement to simulation-based assessments, diminishes numerical simulation uncertainty, and provides a more accurate damage calculation that is turbine-specific. In the current data-based practices, the Rainflow cycle counting (ASTM, 2017) and the Palmgren-Miner rule (Palmgren, 1924) (Miner, 1945) are utilized to estimate the damage. However, applying the data-based approach also has inherent uncertainties (Zwick & Muskulus, 2015) (Hafele et al., 2018). Therefore, the long-term extrapolated damages can vary depending on different assumptions that we make (e.g., uncertainty in the recorded loads or the limited measurements).

Recently, several researchers tried to use different sampling techniques, such as Monte Carlo (Hübler et al., 2019) or bootstrapping (Hübler et al., 2018) to consider the uncertainty of damage calculations caused by insufficient data. Using probabilistic methodologies, we can consider some uncertainties in our data-based evaluation and provide a Confidence Interval for the lifetime we ultimately compute. (Petrovska et al., 2020) and (Marsh, 2016) estimated the uncertainty of the extrapolation by bootstrapping, a statistical resampling method. In this study, sample-based bootstrapping with replacements is also introduced to the current

measurement-based process to augment the limited recorded damages and decrease the results' degree of uncertainty.

In a higher step, binning the data can also improve the lifetime estimation. For extrapolation in time, (Hübler & Rolfes, 2022) compared different approaches and concluded that binning extrapolation has the lowest percentage errors of predicted damage values compared to actual damage values among all extrapolation methods. It also showed that using environmental and operational conditions (EOCs), i.e., SCADA (Supervisory Control And Data Acquisition) data, is beneficial compared to a deterministic extrapolation based on pure strain data. Some researchers focused on the correlations of the uncertainty of the fatigue damage calculation with EOCs by applying binning (Petrovska et al., 2020) (Marsh, 2016), and usually, bootstrapping is used to calculate the uncertainty. Some possible parameters for binning the damages are wind speed, turbulence intensity, wind direction, or wave height (Hübler et al., 2018) (Noppe et al., 2020) (Pacheco et al., 2022). According to (Hübler et al., 2018), if the recorded damages are divided up into wind speed bins for their data type, the most accurate lifespan estimates are feasible. Therefore, in this study, we solely concentrate on wind speed binning as a starting point. The probability of occurrence of each bin can be either from the turbine's recorded wind speeds (Mai et al., 2019) or the theoretical or design wind speed distributions.

The binning method is founded on the concept that varying environmental and operational circumstances are the primary cause of variances in fatigue damage. Therefore, it is not required to have lifelong recorded fatigue damage. It is sufficient to be aware of the EOCs over a lifetime after the relationship between EOCs and fatigue damage has been established. The probability of EOCs is typically known for the turbine's life, which is the basis for fatigue design. Moreover, they can be easily validated, even in the absence of fatigue data, as relevant parameters are included in the SCADA data, e.g., wind speed. Therefore, the main problem is determining how fatigue damage and EOCs relate. Techniques like statistical analysis or machine learning (Santos et al., 2022) (Dimitrov & Natarajan, 2019) can be used to determine this correlation (Hübler & Rolfes, 2022). Binning is the simplest choice that can consider this correlation. Based on (Hübler et al., 2018), for each wind speed bin, the occurrence probability should be based on data rather than design or theoretical documents. Based on (Hübler & Rolfes, 2022), since the enhancements of grouping data into operational cases are not significant, it is adequate for many purposes to omit clustering the data based on operating circumstances. In this study, we followed the approach applied by (Noppe et al., 2020) to consider the uncertainties of our extrapolation, based on bootstrapping and binning on wind speeds from as-measured distribution.

On the other hand, another point that should be considered is the full effect of loads. The short recorded strain measurements in ten-minute windows cannot capture all physical processes occurring at very low frequencies, which may have periods of several days, e.g., the slow variation of windspeed over several days. These incomplete cycles are represented as so-called residual or half-cycles. As the half-cycles do not fully reflect the total size of a sizeable slow-varying cycle, the use of half-cycles does result in non-conservative life estimates. Concatenating the segmented time series in the time window of interest, e.g., joining 52596 10-minute measurements into a single dataset of one year before cycle-counting, is the most obvious way to address this problem. But this choice requires much calculation time, memory, and preferably uninterrupted measurements. To resolve, (Pacheco et al., 2022) considered 24-h long strain time series and found an 11% increase in damage compared to when they used 10-min long strain windows. (Marsh et al., 2016) proposed a technique that considerably saves calculation time without sacrificing accuracy in the final result, and we implemented it in our recent work (Sadeghi et al., 2022). But this method requires the cycle-counted histograms to remain chronologically stored. However, during binning or bootstrapping, this chronological order of stress cycles (cycle count histograms) is lost, so this technique cannot be used in this work to resolve the low-frequency cycles. Therefore, we followed the outcomes of our earlier research to account for the Low-Frequency Fatigue Dynamics (LFFD) effect (Sadeghi et al., 2022) by applying an amplifier factor to the final calculated damage without the need to restart our analysis from the histograms.

This work aims to add more confidence to our analysis, for which we should consider the uncertainties and the full effect of loads. We study the common (deterministic) method's confidence level to predict the lifetime and check the refinements to that by applying binning. We

select different data window sizes to verify if the methods give trustable results from short measurement durations. The LFFD factor would be applied in each method to observe the effect of low-frequency cycles.

2 MEASUREMENT SETUP

OWI-lab received a dataset with three years' worth of data, including the strain and SCADA 10-min subsets from an offshore wind turbine (<5MW installed on a monopile) located in the North Sea. The turbine is equipped with six strain gauges at the tower-transition piece interface. These sensors are utilized to determine bending moments in the fore-aft (FA) and side-side (SS) directions using the nacelle orientation of the turbine from the SCADA data (The mean yaw angle and mean wind speed are among the SCADA parameters provided). (Sadeghi et al., 2022) explains how sensors' strain measurements are converted to the FA and SS bending moments.

For each 10-min interval, the accumulated short-term damage was calculated based on the classical approach using rainflow counting and Miner's rule, as given by (1), where D is the accumulated fatigue damage, n_i is the occurred number of cycles, and N_i is the number of cycles to failure, given for every stress range by the chosen S-N curve.

$$D = \sum_{i=1}^k \frac{n_i}{N_i} \leq 1 \tag{1}$$

Therefore, a dataset of about 157000 (3 years) 10-min FA bending moments is used in this study to compare different methods. The same approach can be applied to any other parameter (e.g., SS bending moment or heading strain).

3 LONG-TERM DAMAGE METHODOLOGIES

Short-term (10 min) damages must be calculated in the first step to analyze the damage extrapolation in time. As the short-term damage calculation is a relatively standardized procedure and is not the focus of this work, it is not explained in detail. A thorough explanation of the standard short-term damage calculation procedure is given by (Hübler et al., 2018). We

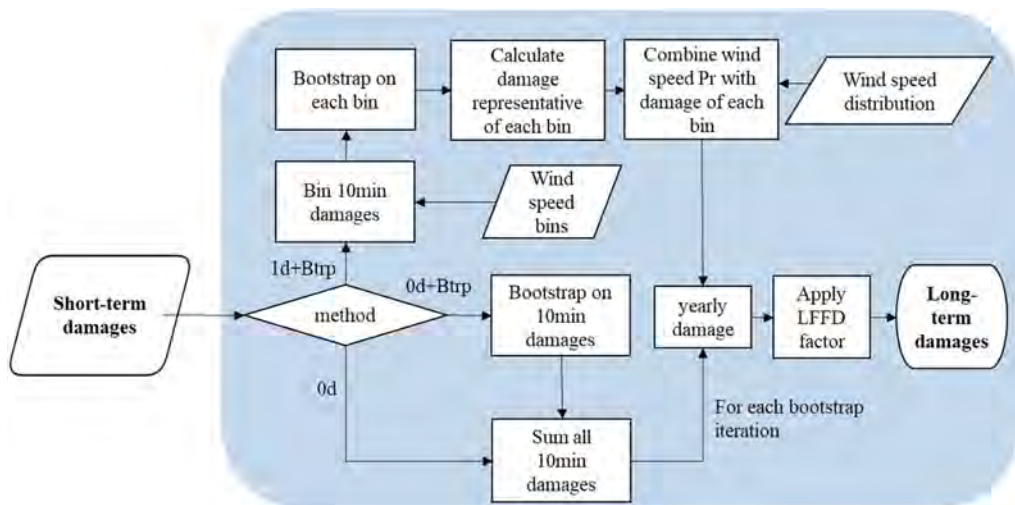


Figure 1. Flowchart of the long-term damage calculation methodologies.

could have several options to reach the yearly damages from these short-term damages. All short-term damages could be used as one pool (as done for 0d) or can be sorted into one or more environmental and operational conditions (EOCs) bins (xd). The number and type of considered EOCs and the sizes of the bins can differ.

In the following flowchart of Figure 1, three different methods to reach long-term damage are mentioned. Among these methods, 0d is deterministic, and the other two methods (0d+Btrp and 1d+Btrp) are probabilistic. In the following subsections, each method is explained in detail.

3.1 *Deterministic approach (0d)*

In this method, we directly sum the short-term damages of three years and apply a data completeness factor to compensate for the missing short-term damages (calculated based on the number of missing points of the three years). From this sum, the average yearly damage is obtained without considering the uncertainties of the limited damages or the EOCs.

3.2 *Probabilistic approaches*

To consider the uncertainties of the limited recorded damages, by using the bootstrapping sampling method, we have two options: bootstrapping on the damage pool (0d+Btrp) or the binned damages (1d+Btrp). In these methods, we apply proper factors to reach the equivalent annual damage. These factors will be explained for each method in the following subsections.

In statistics, bootstrapping (Efron, 1992) is frequently used to estimate an unknown distribution based on limited known samples. In the context of wind energy, bootstrapping was already applied, for example, in the presence of limited wind data (Gass et al., 2011). The general concept of bootstrapping relies on random sampling with replacement, i.e., the same measurement can be picked more than once. For this study, bootstrapping is used to estimate the unknown empirical damage distribution in the collected damage data, and the resampling is repeated multiple times to give an estimate of the damage distribution. In the following, the two probabilistic approaches are explained.

3.2.1 *Bootstrapping method without binning (0d+Btrp)*

In this method, we randomly select with replacement (a datapoint can be selected more than once) a sample with the sample size of the measurement length (the number of recorded damages in that window) from the 10min damage pool. The size of the damage pool is selected as one year and three years to find the effect of increasing the data size on the lifetime uncertainty. The methods are named '0d+Btrp 1y', and '0d+Btrp 3y', respectively. For Bootstrapping, the resample size should be similar to the sample size. Otherwise, the distribution that the Bootstrapping gives for the sample mean, is not the true distribution. So, for example, for '0d+Btrp 1y' method, the bootstrap resample size is less than the number of 10min intervals in a year, since there is data gap in the measurement. We sum all the selected damages in the bootstrap sample. To convert the '0d+Btrp 1y' sum to a 'complete' yearly damage, we use the data completeness factor of the first year, while for '0d+Btrp 3y', we follow the same factor as the (0d) approach. This process is repeated 10000 times to reach an acceptable spread in the final calculated annual damages. Then for each yearly damage, we extrapolate in time to find the lifetime. The lifetime is calculated by linear extrapolation, which is the inverse of the annual damage.

3.2.2 *Binning and bootstrapping method (1d+Btrp)*

For this method, binning is used to consider the environmental uncertainties, and bootstrapping is applied to each bin to estimate the unknown empirical damage distribution by only using the available damage values. For this study, we only focused on the wind speed because, as explained by (Hübler et al., 2018), if the damage data is divided into wind speed bins, the most accurate lifetime estimates for the current data are made possible. The bin size is selected as two m/s to comply with the design. The binning and bootstrapping procedure results in damage scatter in each bin. This spread will be reduced to one value based on the chosen metric. The choice of the statistical damage parameter is quite essential. E.g., for each bin, the

mean value of all bootstrapped damage values can be calculated. However, a high percentile (e.g., the 90th) can be used to be more conservative. The mean (as advised in (Hübler et al., 2018)) values are selected for this study. The bootstrap resampling size for each bin equals the number of measurements in that bin. Then from each bootstrap iteration, we choose the mean damage of the resampled bin.

Bins for which the specific combination of EOCs might not occur during the monitoring campaign (empty bins), especially bins of higher dimension, need to be filled with well-considered values. For instance, each empty bin can be filled with the maximum value found in the neighboring bins. Because we had a relatively long measurement, we had no empty bins, although some bins with high speeds had few numbers of data points (around 3-4). So for this work, we did not apply a bin-filling method. In case it is needed, (Hübler et al., 2018) and (Pacheco et al., 2022) compared different ways of bin filling. The filling might be data-driven or based on design documents, according to the availability of the necessary information (Noppe et al., 2020).

Finally, each bin has a certain occurrence probability ($Pr(j)$). $Pr(j)$ can either be determined using measurement data (e.g., several years of SCADA data) or given in design documents or theoretical relations. On the one hand, probabilities given in theoretical documents are typically based on long-term data (20 years and more), making them more reliable. On the other hand, even if a site-specific OWT design is conducted, the EOC's distributions are typically not derived for the particular site of the considered turbine, which might lead to biased results. In this work, we use the three-year measured wind speed distributions. The measured distributions can be either the as-measured probabilities or the fitted distribution to the as-measured wind speeds. We used the as-measured histograms. Then with Equation 2, we can apply the wind speed probability of occurrence to the damage of bins ($D(j)$). This analysis repeats this procedure 10000 times for every bin, resulting in 10000 values for the estimated yearly damage.

$$yearly\ damage = \sum_{j=0}^{bin\ number} Pr(j) \times D(j), \quad (2)$$

where $Pr(j)$ is the probability of occurrence of bin j , and $D(j)$ is the representative year-size damage of bin j . Year-size damage means if we consider the average value of each bin, we multiply it by 52596 (number of 10-min damages in a year) to have the damage in a yearly order of magnitude and not in the 10-min scale.

Applying the LFFD factor and the damage linear extrapolation in time are the last steps shared between all the previously mentioned methods. We used the LFFD factor of 1.09 for FA considering the SN curve of 'DNV-D-W' with the slope of $m=3$ and in free corrosion condition. This factor was obtained by accumulating three years of FA damage with and without considering the LFFD effect (Sadeghi et al., 2022). The predicted lifetime L (in years) is the inverse of the yearly damage ($L = 1/yearly\ damage$). The resulting distributions from the bootstrapping can then be plotted for each method, giving a histogram of the resulting extrapolated lifetime's mean.

4 CASE STUDY

We applied different methods to our measurements, starting from the standard deterministic approach to the binning process to increase our confidence in the predicted lifetime. As mentioned in the previous section, in the 1d binning method, the short-term damages are spread in each wind speed bin. Figure 2 shows boxplots of the FA binned damages before bootstrapping and the mean of each bin (blue markers). For confidentiality, binned damages (pink dots) are normalized to the maximum 10min damage. By comparing the average and the 75p (the top end of boxplots), we see that although the 75p damage is more conservative for the middle bins, there is no significant difference between the average and 75p values for the lowest and highest bins. As the mean and median do not align, the spread in each bin is not gaussian. Based on the central limit theorem, regardless of the distribution of damages in each bin, after enough bootstrap iterations, the distribution of the mean of each bin would be

gaussian and enables having the desired statistics. Therefore to have the confidence intervals of the selected parameter (mean), for this study, we achieve the distribution of the mean in each bin by performing bootstrapping. This plot shows that despite the spread in the bins, there is a clear relationship between wind speed and damage. So, grouping damages into wind speed bins should at least consider part of the EC uncertainties.

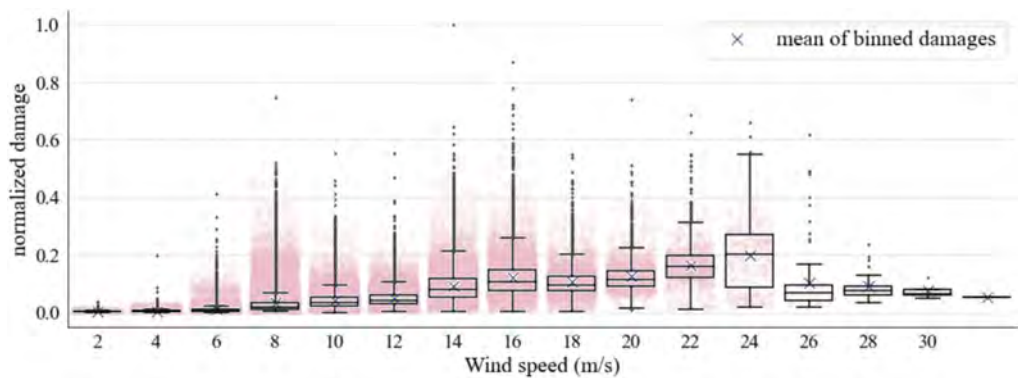


Figure 2. Boxplots show normalized FA damages from a three-year damage pool before bootstrapping on each bin. Blue markers are the average of each bin.

Figure 3 shows the result of the first method (deterministic, 0d, after LFFD) (in black) as the reference. We considered the three-year deterministic lifetime as “reality” because that is the closest available value to reality. The results from all processes are normalized to the lifetime from 0d after LFFD. The deterministic lifetimes of the 0d approach before and after applying the LFFD factor are compared with the distribution of the lifetimes’ mean from 10000 iterations of bootstrapping for each probabilistic method.

The red vertical line indicates the lifetime from 0d before LFFD. The LFFD effect decreases the deterministically predicted lifetime by 8%, which is still quite limited because of the choice of the SN curve (Sadeghi et al., 2022). The two blue histograms show the 0d approaches with bootstrapping after LFFD. From right to left, the data size was increased from one year to three years. It shows that increasing the data size changes the average value of 0d+btrp methods by 15%. So, if we only had one year of available measurement, we would predict a lifetime that its distribution does not even include the deterministic value. The problem with the 0d approach with a limited dataset is that we do not have control over the conditions seen during that period and, thus, the conditions used to extrapolate. The fact that the predicted lifetime decreased by adding more data is somehow a coincidence, as the third year had harsh EOCs, but if the order of the first and third years was reversed, then the result would increase with the more data we added. Although 0d+bootstrapping gives probabilistic insights, it does not provide the desired precision in case of limited data.

The close result of 0d and 0d+3y bootstrapping shows that bootstrapping does not change the final result if the damage pool is similar to the deterministic pool. It gives the 95% confidence interval of the deterministic mean, which means we are 95% sure that the average life would be in the range (0.995-1.005), 0.5% off the deterministic lifetime. We used binning to address the issue of the 0d method regarding the limited data. So, in such cases, using longer available SCADA data will yield a better lifetime prediction. The green histograms show the 1d method from one and three-year damage pools. The comparison of ‘0d+Btrp 1y’ and ‘1d 1y’ shows that binning improves the results by almost 7% (closer to the deterministic value) because in the 1d approach, we also consider wind speed distribution. Although the error of the lifetime prediction based on the limited measurement is better when we use binning, we still have a significant error (The “1d 1y” method is around 7% far from the 0d from three years), which means that the binning should be improved to consider other EOC uncertainties as well.

Regarding the distributions, the 0d+Btrp histograms are wider than the 1d results. The reason is that 1d binning also considers the uncertainty of the wind speed, so the result is less scattered due to the omitted uncertainty from wind speed. In both 0d and 1d methods, when we increase the damage pool size from one year to three years, the distributions become narrower because by increasing the measurement data, we decrease the uncertainty from the limited measurement, and therefore, we have less spread in the distribution.

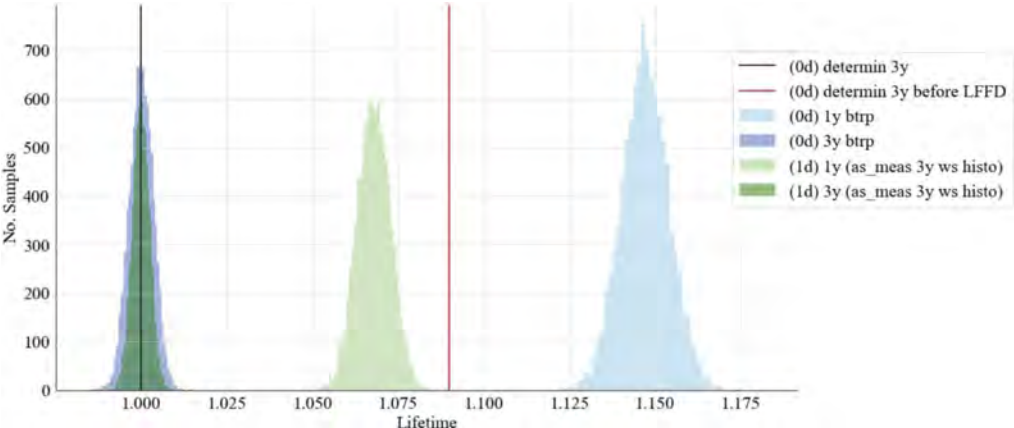


Figure 3. Histograms of the means of 10000 (bootstrap iterations) lifetimes for each probabilistic method with LFFD + deterministic (0d) value (before and after LFFD).

5 CONCLUSIONS AND FUTURE WORK

In this contribution, we used different deterministic and probabilistic approaches to compare their long-term extrapolation to a lifetime and their corresponding uncertainty. In the deterministic method (0d), we summed the damages. In the probabilistic approaches, we used bootstrapping (0d+btrp) or binning and bootstrapping (1d). Comparing the results of 0d from three years of data without and with bootstrapping shows the distribution of the 0d mean lifetime. By selecting different data sizes (1 and 3 years) for the 0d+btrp method, we showed that increasing the data size affects the results of this method, which is not desirable, as one year of data should be enough to have a reliable long-term prediction (Hübler & Rolfes, 2022). 1d binning using the wind speed bins results in a better extrapolation in case of limited measurements, compared to bootstrapping without binning, and in general, 1d gives a narrower bound compared with 0d+Btrp. The improvement is that 1d binning also considers the wind speed’s uncertainty. When we increase the damage pool size in either the 0d or 1d methods from one year to three years, the distributions in both cases become narrower because the increased measurement data reduces the uncertainty resulting from the limited measurement, which results in a smaller spread in the distribution. Although 1d binning seems a better method than 0d+Btrp, it still can be improved.

Comparing the deterministic lifetimes before and after applying the LFFD factor, a difference of 8% of the lifetime was observed for the under-study turbine, under the corrosion-free condition (SN curve with m=3), and for a critical weld.

All turbine operational cases (producing, non-operating, and events) were considered together in one group for this work. So in future studies, to obtain the full effect of EOCs, in addition to wind speed, other environmental and operational conditions will be used as binning dimensions. A series of statistical criteria will be introduced to determine the required minimum number of data points in each bin and evaluate the binning quality and the binned data. We only considered FA damages to compare the methodologies, but we can use the damages in the critical heading for a realistic lifetime calculation.

ACKNOWLEDGMENTS

This research is conducted within the project MAXWind, funded by the Belgian Energy Transition Fund (ETF).

REFERENCES

- ASTM International. 2017. Standard Practices for Cycle Counting in Fatigue Analysis, vol. 85.
- Bouty, C. et al. 2017. Lifetime extension for large offshore wind farms: Is it enough to reassess fatigue for selected design positions?. *Energy Procedia* 137: 523–530.
- Byrne, B. W. et al. 2015. New design methods for large diameter piles under lateral loading for offshore wind applications. *Offshore Geotech* 705–710.
- Dimitrov, N. & Natarajan, A. 2019. From SCADA to lifetime assessment and performance optimization: how to use models and machine learning to extract useful insights from limited data. *Journal of Physics: Conference Series* 1222(1): 12–32.
- DNVGL-RP-C203. 2019. Fatigue design of offshore steel structures', Recommended Practice.
- Efron, B. 1992. Bootstrap methods: another look at the jackknife. *Breakthroughs in statistics*. Springer: 569–593.
- Gass, V. et al. 2011. Assessing the effect of wind power uncertainty on profitability. *Energies* 15(6): 2677–2683.
- Hafele, J. et al. 2018. A comprehensive fatigue load set reduction study for offshore wind turbines with jacket substructures. *Energies* 118: 99–112.
- Hübler, C. et al. 2018. Reliability analysis of fatigue damage extrapolations of wind turbines using offshore strain measurements. *Physics. Conference Series* 1037: 32–35.
- Hübler, C. et al. 2019. Validation of Improved Sampling Concepts for Offshore Wind Turbine Fatigue Design. *Energies* 12(4): 603.
- Hübler, C. & Rolfes, R. 2022. Probabilistic Temporal Extrapolation of Fatigue Damage of Offshore Wind Turbine Substructures Based on Strain Measurements. *Wind Energy Science*: 1–29.
- Mai, Q. A. et al. 2019. Prediction of remaining fatigue life of welded joints in wind turbine support structures considering strain measurement and a joint distribution of oceanographic data. *Marine Structures* 66: 307–322.
- Marsh, G. 2016. Fatigue load monitoring of offshore wind turbine support structures. Thesis.
- Marsh, G. et al., 2016. Review and application of Rainflow residue processing techniques for accurate fatigue damage estimation. *International Journal of Fatigue* 82: 757–765.
- Miner, M. A. 1945. Cumulative damage. *Fatigue journal of applied mechanics* 12(3): 159–164.
- Noppe, N. et al. 2020. Validated extrapolation of measured damage within an offshore wind farm using instrumented fleet leaders. *TORQUE*.
- Pacheco, J. et al. 2022. Fatigue Assessment of Wind Turbine Towers: Review of Processing Strategies with Illustrative Case Study. *Energies* 15(13): 4782.
- Palmgren, A. 1924. Die lebensdauer von kugellagern. *Zeitschrift Vereines Duetscher Ingenieure* 68(4): 339.
- Petrovska, E. et al. 2020. Application of Structural Monitoring Data for Fatigue Life Predictions of Monopile-Supported Offshore Wind Turbines. *International Conference on Offshore Mechanics and Arctic Engineering* 84416.
- Sadeghi, N. et al. 2022. Fatigue damage calculation of offshore wind turbines' longterm data considering the low-frequency fatigue dynamics. *TORQUE*.
- Santos, F. et al. 2022. Data-driven farm-wide fatigue estimation on jacket-foundation OWTs for multiple SHM setups. *Wind Energy Science* 7(1): 299–321.
- Ziegler, L. & Muskulus, M. 2016a. Fatigue reassessment for lifetime extension of offshore wind monopile substructures. *Physics. Conference Series* 753: 092010.
- Ziegler, L. & Muskulus, M. 2016b. Lifetime extension of offshore wind monopiles: Assessment process and relevance of fatigue crack inspection. 12th EAWE PhD Seminar, DTU Lyngby, Denmark.
- Ziegler, L. et al. 2019. Structural monitoring for lifetime extension of offshore wind monopiles: Verification of strain-based load extrapolation algorithm. *Marine structures* 66: 154–163.
- Zwick, D. & Muskulus, M. 2015. The simulation error caused by input loading variability in offshore wind turbine structural analysis. *Wind Energy* 18(8): 1421–1432.

Developing a cost-control and project-planning based implementation of circular construction in temporary works: A framework of core supportive technologies

F. Tizzani

Department of Architecture, National University of Singapore, Singapore
Leighton Contractors (Asia) Limited – Singapore Branch, Singapore

P. Herthogs

Singapore-ETH Centre, Future Cities Lab Global Programme, CREATE campus, Singapore

R. Stouffs

Department of Architecture, National University of Singapore, Singapore
Singapore-ETH Centre, Future Cities Lab Global Programme, CREATE campus, Singapore

ABSTRACT: Construction is often solely associated with the Permanent Works (PW) that need to be constructed, leaving behind all those activities that are necessary to support the construction of PW. These activities fall into the definition of Temporary Works (TW), representing a significant part of any construction project, sometimes 50% or more of the construction's cost. Because of its significant impact on the construction process, we think that TW could be a particularly valuable use case to study the implementation of Circular Construction (CC) approaches related to designing and reusing materials and components in the TW process. Reuse practices may already take place on many construction sites, but currently, there are no standard or Circular-Economy-centric approaches. As a first exploration of the suitability of TW as a starting point to implement CC approaches, this paper introduces a high-level framework defining a system of three core tasks and technologies central to enabling Temporary Works' Circular-ity: data collection standards, data capturing methods, and a digital TW trading platform.

1 INTRODUCTION

1.1 *Scarcity of materials in the construction sector*

The construction industry is the largest consumer of raw materials, with civil construction responsible for 60% of the raw materials extracted from our planet (Zabalza Bribián et al., 2011). In the next decades, the demand for natural resources will increasingly rise due to the expected population growth, leading to increasing resource extraction and waste production. Therefore the main challenge in future will be to deal with the upcoming waste, as well as the supply of sufficient land, material and natural resources. To tackle this upcoming global problem, a growing consensus among policymakers, industry stakeholders, and researchers from academia is promoting Circular Construction (CC) approaches to maximise reuse and recycling rates and consequently minimise the consumption of raw materials and decrease the production of waste and its impact on the environment. CC aims to establish a resource-efficient economy where materials and higher-level construction products can be reused so that what previously would have become waste is now a valuable resource to start the next production cycle (Kovacic et al., 2020) and maintain their value in the economy as long as possible (eur, 2015). Most of the CC research in the built environment focuses on recycling and reusing building materials; as a result, assessment tools to support circular buildings and material flow analyses typically focus on a long life-cycle of 50 years or more (Khasreen et al., 2009).

1.2 A focus on shorter life-cycle systems

As the industry increasingly focuses on applying CC principles, one should remember that the construction industry is concerned with more than just the final assets it delivers but also with the construction processes and methodologies applied during the construction phase, including Temporary Works (TW) built to support these processes. There is a need to validate CC approaches in the built environment on a shorter life-cycle ecosystem. Because the “mini-system” of TW has a shorter life-cycle, and is typically governed by fewer stakeholders and decision-makers, we argue that it would be easier to apply and monitor recycling/reusing practices, assessment tools and material flow analyses, which in turn could result in clear insights with tangible results to enable further progress and refinement on their more extended applications.

2 BACKGROUND

2.1 Working with temporary works

Given any construction site, the core focus for a construction operation team is to plan, manage and execute all necessary activities to enable and support the construction of Permanent Works (PW). These activities represent a significant part of any construction project, sometimes 50% or more of the construction’s cost (Hewlett et al., 2014). Although the terminology used to define such activities varies across the world, in many countries, especially where there is a significant application of British standards, these are defined as TW. On every construction project, contractors deal with the safe implementation of TW design to enable the construction of PW. There are many definitions of TW, with differing emphases; this paper follows the definition of the BS 5975: 2019 (bsi, 2019), which defines TW as “*all those activities that provide an engineered solution that is used to support or protect either an existing structure or the permanent works during construction or to support an item of plant or equipment, or the vertical sides or side-slopes of an excavation during construction operations on site or to provide access. It is used to control stability, strength deflection, fatigue, geotechnical effects and hydraulic effect within defined limits*”.



Figure 1. This flowchart of Leighton Asia’s procedure for the design and control of temporary works illustrates how TW processes are structured in large construction firms.

TW structures are designed to support the construction of the PW in their temporary state. Examples are scaffolds, working platforms, falseworks and excavation-lateral-supports (ELS). Every construction project, to a greater or lesser degree, will involve the need for TW, which are usually removed during or at the end of construction. The main reasons why TW is a critical part of any construction site and a necessity to deliver PW are:

- Safety provided to the workforce involved in construction;
- Support provided to structural members to achieve adequate strength while under construction;
- Access provided to areas where construction is ongoing and direct access is not possible or unsafe.

TW can impact construction projects in many ways. However, just as successful TW can enhance project outcomes, inadequate, poorly planned or poorly executed TW can have significant negative consequences. Hence, many organisations have developed and implemented “Design and Control of TW” procedures, often following the principles promulgated by the Temporary Works forum (TWf), one of the most important associations in the industry based in the UK. These procedures are maintained to standardise and monitor the safe implementation of the TW activities on site and usually describe the processes to design, manage, control, erect, maintain and dismantle TW. The primary aim of these processes is to ensure that TW

are implemented to allow the construction of the PW safely, economically, and efficiently considering all constraints and risks intrinsic to the construction site. Construction organisations develop and apply these procedures with different levels of sophistication, but they follow the same general principles as illustrated in Figure 1.

The nature of TW results in several characteristics that arguably make these types of construction works an interesting case study and application domain for studying and implementing CC approaches:

- Short lifespan: TW have a relatively short lifespan, typically ranging from a few weeks to a few years. This means that they go through a complete life cycle in a much shorter period of time than PW, making them an ideal “mini cycle” to study and test CC approaches in a short period of time;
- Single handler: it is considered common practice for PW designers not to consider TW in their design/submission, and it is the industry practice to leave this entire activity to the contractors, which makes them the only handler of the whole TW life-cycle;
- Modular and compatible: some TW are designed in a modular fashion and can be easily disassembled and reassembled in different configurations. This makes them more versatile and suitable for reuse in different projects;
- Changes in ownership: some commonly used types of TW (e.g. scaffolding) can change ownership multiple times during their lifespan, as they are often rented or leased rather than purchased outright. This means that they may be used by multiple parties over their lifespan, which can affect their potential for reuse and the feasibility of implementing circularity approaches.

We argue these properties make TW an interesting ground to study and test circularity approaches, at the end of “a package Life Cycle” some TW can be disassembled and reused on other packages/projects, giving researchers the possibility to verify and test CC approaches more easily, which could help to set the direction for a more comprehensive implementation of CC throughout the life-cycle of PW.

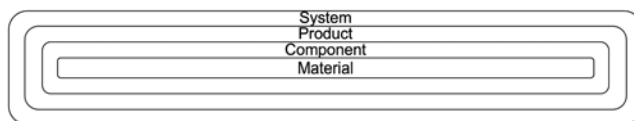


Figure 2. This BAMB diagram identifies the four building composition levels and their hierarchy levels covered in materials passport (Matthias Heinrich, 2019).

2.2 *Introducing the concept of materials passport*

Materials Passports (MP) are one of the critical tools to support the implementation of CC approaches (Eichstädt, 1982), bringing benefits (Luscuere, 2017) to the industry such as:

- Maintain a database to identify materials that can be reused;
- Provide relevant data for impact assessments; and
- Monitor the material’s change in value over time.

In the built environment sector, an MP is a qualitative and quantitative documentation of the materials composition of a building or an asset, displaying materials embedded in buildings as well as showing their recycling potential and environmental impact, providing accurate information for reuse and recovery (Debacker and Manshoven, 2016). Most of the work on MPs in the Built Environment focuses on their development at the building level, as exemplified by the work of the European project “Buildings As Material Banks” (BAMB). Within BAMB, an MP is defined as “a digital set of data describing defined characteristics of materials and components in products and systems that give them value for present use, recovery, and reuse”. BAMB describes relevant MP data categories such as physical, chemical, and production data to be collected for different composition levels as in Figure 2 (Mulhall et al., 2017):

- A System refers to a product in its complex form, including a product that constitutes multiple components and parts from different manufacturers;
- A Product represents an item that is manufactured and sold, and it generally constitutes a commercial name, a serial number and a producer ID;
- A Component is one of the parts that make a product (raw materials such as timber, clay and stone are also considered at this level); and
- A Material includes the chemical properties that make up a component.

3 METHODOLOGY

3.1 *The aim of the framework*

The proposed framework aims to facilitate and support the analysis of a standardised dataset collected among a large number of TW packages scattered around one or multiple construction sites, to identify the material becoming available and inform the Designer for consideration in his design. It is essential to have a standard to capture the data homogeneously so that data collected by different people on different packages and possibly on different construction sites can be analysed together and compared.

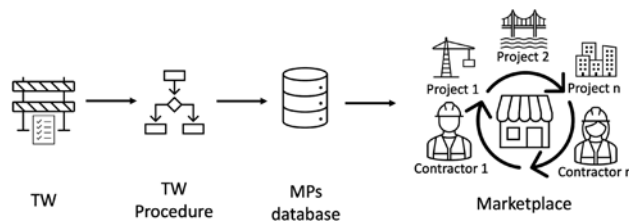


Figure 3. Schematic of the proposed high-level framework and the key actions to enable temporary works' circularity.

3.2 *Enabling circularity in temporary works: A framework and key innovations*

As a first step, this paper proposes a high-level framework mapping key innovations required to enable Temporary Works' Circularity, consisting of three key actions and three key technologies. The three key actions, showcased in Figure 3 are:

1. Identify key TW component properties and the potential applicability of MP to track information, such as the type and quantity of materials used, their sourcing and manufacturing processes, history and current status/location.
2. Develop a collecting and reporting system, possibly through an existing process. For instance the temporary works procedure could include a step for identifying and tracking the materials used in the temporary works, and for recording this information in the MP.
3. Establish a TW reuse network of stakeholders who are interested in using these components. This can include construction companies, suppliers, and other organisations that have a need for TW components. By establishing this network, one could create a marketplace for the trade of TW components, which could help to reduce waste and extend the life cycle of these components.

Three core technologies that can benefit the implementation of this framework are:

1. A Digital Twin to create virtual models of temporary works to store data, enhance design performances and increase collaboration across projects.
2. Asset and Data management to track the life-cycle of temporary works, including information about their design, construction, and use, and identify opportunities for reuse.
3. Integration of distributed ledger technologies (e.g. Blockchain) or other technologies to improve transparency and traceability in the supply chain by introducing trust between different parties that need to rely on the history, certifications and quality assurance of the materials.

3.3 *How to use the framework and the necessity for a temporary works materials passport*

Current practices focus on material information at the building scale with little attention to the micro-scale, like in our case with TW design packages. This requires integrating information from the construction project systems and at the site level. The value of an MP increases when it is created and updated during the asset's Life Cycle. Therefore, this paper proposes a direction to extrapolate MP data from current industry, practices and procedures set to automate the updating process in the background. Under these considerations, a Temporary Works Materials Passport (TWMP) to support TW Circularity should:

- Describe TW using composition levels;
- Collect properties in parallel with the TW procedure; and
- Associate properties and TW steps to create a historical log.

In construction, as a general framework for planning and organizing tasks and resources, there are four “Ws” consistently asked before every activity commences: “Who does What, When and Where?”. Following this principle, the critical information that needs to be collected to temporarily and economically quantify TW are:

- The actors that generate and consume data across the TW Life Cycle (Who);
- The material information, including the certificates, the lab tests, the quantities, their cost, and the history of the usage of each structural element, including the aggressiveness of the environment of erection: corrosive, marine, tunnel, adverse chemical, etc. (What);
- The planned time of erection and dismantling (When);
- The planned location of the erection (Where).

The information listed above can be considered part of the TWMP. Linking the data of the TWMP to a project timeline would allow for a contract-based trading platform that informs TW designers on what is available, when and where and influence their design based on resource availability. In the beginning, this platform can be substituted by simple access to the TWMP as a starting point and developed into a more visual environment to enhance clarity and usability. A blockchain trading module can also be developed based on the TWMP data and the unique identification of each component.

4 CASE STUDY FROM THE INDUSTRY

The first author of this paper is an employee of Leighton Asia, an international contractor in the construction, civil engineering and offshore oil and gas sectors headquartered in Hong Kong and part of the CIMIC Group. The following review of Leighton Asia Temporary Works procedure is based on the author's first-hand experience on the topic and the training material available at the company level, of which a few copies exist in the public domain thanks to webinars and sessions organised with the Construction Industry Council Hong Kong (Sein, 2022). In Leighton Asia, the design and control of TW is a high-level framework (Figure 1) that specifies a series of steps that need to be followed to ensure TW are appropriately managed and controlled; these are:

- Planning and risk allocation;
- Designing and checking;
- Procuring and constructing;
- Verifying as-built and safe removal; and
- All steps are running while considering and managing changes to the design.

The core objective of this procedure is to provide a framework to ensure TW are appropriately managed and controlled. Although this procedure may look quite simple to implement, divergence arise during the TW life-cycle due to day-to-day construction activities or due to the dynamic nature of TW involving multiple stakeholders, staff turnover, competing concurrent site activities, resource demands, and ever-changing constraints over time often add unforeseen complexity to what should otherwise be a straightforward process.

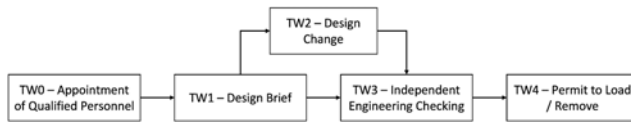


Figure 4. This flowchart identifies a specific temporary works form for each stage of Leighton Asia’s procedure for the design and control of temporary works.

4.1 *The design and control of temporary works procedure*

This high-level procedure (Figure 1) develops in a series of forms, as outlined in Figure 4, to be filled and signed to certify the completion of a particular step.

4.1.1 *The TW0 Form and the appointment of qualified person*

The first step of the procedure is planning and risk allocation, initiated with the “Appointment of Qualified Persons”, which records the nomination and appointment by the Project Director of persons with commensurate qualifications and competency to take responsibility for their respective roles under the TW procedure. Subsequently, the planning of TW activities can start. The correct planning of the TW design and activities generates a Temporary Works Master Schedule (TWMS) that collects these essential records:

- The TW Design Package Number;
- The TW Design Package Description;
- The Risk Categories associated with each package;
- The allocation of all Stakeholders based on the TW0;
- The required approval date with adequate provision for design, approval, procurement and construction; and
- The Estimated Date of dismantling.

[Relation to the framework]: The difficulty of this step is to envisage and foresee the complete set of TW designs required to enable the construction of the PW. The redaction of the TWMS is particularly critical because it becomes the baseline that would trigger the Responsible Site Person (RSP) to initiate the next step.

4.1.2 *The TW1 Form and the design brief*

The second stage of the TW procedure is the design and checking based on the design brief initiated by the RSP and issued to the Temporary Works Coordinator (TWC), which reviews the design request and coordinates with a Temporary Works Designer (TWD) the design process. During this process, the TW1 Form collects information into two categories: technical and commercial. The technical part is filled by the TWD and collects information ranging from:

- The TW Design Brief Number;
- The TW Design Package Number;
- The TW Design Documentation;
- The Loading Criteria;
- The Survey information regarding the area of erection;
- The Material Requirements; and
- The TW Installation and the Removal Methodologies.

[Relation to the framework]: It is at this stage when it would be useful to have a TW database of available material of reuse to match the requirements outlined in the TW1 Form.

The commercial part is filled by the quantity surveyor assigned to the design package and identifies:

- The Estimated quantities of the design materials;
- The Estimated cost of the design;
- The Estimated cost of the construction;
- The Procurement Reference;
- The Comparison against the budget of the works;

- The cost code reference for the material; and
- The estimated construction date (to complete the procurement on time).

4.1.3 The TW3 Form and the independent checking

Once the design review has been completed and approved (after multiple rounds of proposals for discussion with the extended project team), the selected design option is ready to be issued of endorsement to the Independent Checking Engineer (ICE) prior to construction. A TW3 Form is created and issued to the ICE for review and endorsement. The TW3 Form is generally solely related to a design check and does not carry any particular or relevant information other than the approval date and signature. Once endorsed, the TW package will move to the site for construction.

[Relation to the framework]: This is when actual planned materials need to be measured and checked for availability in the reusable TW market database.

4.1.4 The TW4 Form and the permit to load and remove

When the construction is completed, an inspection is to be carried out to verify the compliance of the site construction with the approved design and a new TW4 Form is generated by the RSP for the TWC to inspect the works and issue the approved “Permit to Load” which allows the RSP to load the TW and start the construction of the PW. Similarly, when the construction of the PW is completed, the TW are ready to be dismantled, and a new TW4 Form needs to be raised by the RSP to verify that the TW structures take no more loads and can be removed. The TWC carries out another inspection, and a “Permit to Remove” is issued to the RSP to start the safe removal and dismantling of the TW.

[Relation to the framework]: At this stage, the MP needs to classify the current condition of the material and verify that it was never overstressed during its use. If it was, this must be recorded into the MP to clearly mark it as not suitable for further use.

Both TW4 Forms carry valuable information like:

- The location of the inspections;
- The TWC checking remarks;
- The ICE checking remarks; and
- The dates of each inspection, including any remark regarding the deviation of the initially assumed loads and the effects of the actual loads on the structures.

[Relation to the framework]: These are historical insights that can help evaluate and assess a particular component or element of the TW structure before being reused.

4.1.5 The TW2 Form and the managing of the changes

Whenever a design change occurs during the process just described, a TW2 Form needs to be raised by the RSP to initiate a TW design change. The TWC reviews it and issue it to the TWD to update the design. Once the design update is completed, the TW2 Form needs to be reviewed and approved by the TWC, the RSP and the ICE, similarly to what happened with the original TW1 Form. The TW2 Form also outlines the design changes in quantities, including all the commercial changes identified by the quantity surveyor, the new estimated construction date and the approval date of the new design.

Composition Level	System				System				Product	Component	Material	System	Material												
	What	Who	When	Where	When	What				Where	When	What													
4Ws																									
TW Proprieties	Design Package Number	Design Package Description	Risk Categories	Stakeholder Allocation	Approval Dates	Estimated Date of Dismantle	Survey Data	Estimated Construction Date	Design Package Number	Design Brief Number	Design Documentation	Loading Criteria	Estimated Cost of Design	Procurement Ref. Number	Comparison vs. budget	Estimated Cost of Construction	Removal Method Statement	Installation Method Statement	Material Cost codes	Estimated Quantities	Material Requirements	Actual Location	Inspection Dates	TWC Checking Remarks	ICE Checking Remarks
TW Forms	TWMS				TW1/TW2										TW4										

Figure 5. Mapping table that links together TW proprieties (Section 4.1) against the BAMB composition levels (Section 2.2), the construction 4 Ws (Section 3.3) and the TW procedure Forms (Section 4.1).

[Relation to the framework]: The issuing of a TW2 should, in fact, refresh and update all TW properties stored in the MP to capture the latest changes.

5 CONCLUSIONS

The main contribution of this paper is to identify Temporary Works as a miniature Life Cycle system to experiment and validate the application of Circular Construction approaches and to enable circularity at the construction site scale. It identifies the requirements for a specific TWMP, designed around the data collected while applying the Design and Control of Temporary Works procedure. The TWMP could even replace the TW Forms and become the central repository for storing the TW procedure data. Mapping (Figure 5) TW properties to generate a TWMP can significantly improve the construction industry by providing a comprehensive and accurate record of all materials used in the TW process and to track the life cycle of all materials used in the project. The proposed TWMP can be implemented on many construction sites with an existing TW procedure, enhancing the application of CC and potentially creating a new material/component market between construction sites that can reduce waste and generate savings for the main contractors.

ACKNOWLEDGEMENT

Part of this research was conducted at the Future Cities Lab Global at Singapore-ETH Centre. Future Cities Lab Global is supported and funded by the National Research Foundation, Prime Minister's Office, Singapore, under its Campus for Research Excellence and Technological Enterprise (CREATE) programme and ETH Zurich (ETHZ), with additional contributions from the National University of Singapore (NUS), Nanyang Technological University (NTU), Singapore and the Singapore University of Technology and Design (SUTD).

REFERENCES

- Eur, (2015). Closing the loop - An EU action plan for the Circular Economy. Technical report, European Commission.
- Bsi, (2019). Code of practice for temporary works procedures and the permissible stress design of falsework. bs 5975: 2019. Technical report, British Standard Institute.
- Debacker, W. & S. Manshoven (2016, November). D1 Synthesis report on State-of-the-art: Key barriers and opportunities for Materials Passports and Reversible Building Design in the current system. Technical report, Buildings As Material Bank.
- Eichstädt, J. (1982, January). Rationalised factory modernisation. *Batiment International, Building Research and Practice* 10(3), 176–176.
- Hewlett, B., R. Hare-Winton, & A. Barnes (2014). Clients' guide to temporary works. Technical report, Temporary Works forum.
- Khasreen, M., P. F. Banfill, & G. Menzies (2009, September). Life-Cycle Assessment and the Environmental Impact of Buildings: A Review. *Sustainability* 1(3), 674–701.
- Kovacic, I., M. Honic, & M. Sreckovic (2020, November). Digital Platform for Circular Economy in AEC Industry. *Engineering Project Organization Journal* 9(1).
- Luscuere, L. M. (2017, February). Materials Passports: Optimising value recovery from materials. *Proceedings of the Institution of Civil Engineers - Waste and Resource Management* 170(1), 25–28.
- Matthias Heinrich, W. L. (2019). Material passports - best practice: Innovative solutions for a transition to a circular economy in the built environment. Technical report, Technische Universität München, in association with BAMB.
- Mulhall, D., K. Hansen, L. Luscuere, R. Zanatta, R. Willems, J. Bostrom, & L. Elfstrom (2017). Framework for Materials Passports for the web. Technical report, Buildings As Material Bank.
- Sein, D. (2022, September). Leighton design and control of temporary works.
- Zabalza Bribián, I., A. Valero Capilla, & A. Aranda Usón (2011, May). Life cycle assessment of building materials: Comparative analysis of energy and environmental impacts and evaluation of the eco-efficiency improvement potential. *Building and Environment* 46(5), 1133–1140.

Life-cycle assessment of buried water-transmission concrete mains

H. Yáñez-Godoy & S.M. Elachachi

Institut de Mécanique et d'Ingénierie (I2M), Université de Bordeaux, Talence, France

ABSTRACT: The progressive decline in performance of aged pipes is not always evident in practice, particularly for buried water-transmission mains. A geomechanical approach can provide interesting elements to assess and/or predict their integrity. Simplified Winkler-type models can effectively represent the complexity of soil-pipe interaction. The spatial variability of the soil is necessary to understand how this variability can be used to study the structural behaviour of the buried pipe. The numerical modelling of the soil-pipe system adopted in this study combines different strategies and steps in order to speed up and optimise the computation in an uncertain context that involves the execution of several simulations. The quantification of criticality indicators, in a context of asset management, allows to evaluate the performance of a pipe, according to a reliability approach, with respect to limit states defined in the framework of inspection, maintenance or renewal strategies of the pipelines.

1 INTRODUCTION

The renewal of drinking water buried pipes is necessary because of their “natural” and/or anthropogenic ageing, which leads to a progressive decrease in their performance level. Monitoring, during the implementation of the worksite as well as during the operation of new portions of a linear to be renewed, is an important issue in order to constitute an experimental record of the work. Indeed, this is a way of acquiring a better knowledge of the mechanical behaviour and mechanisms of the soil-pipe system. The acquisition of data through the instrumentation of the renewed pipes brings on the one hand, information which is not contained in the data bases or exploitation and on the other hand, allows to validate and to qualify the mechanical/numerical models adopted to study the short- and long-term behaviour of the pipe.

Reinforced concrete pipes consist of a steel cylinder positioned between two layers of concrete (Figure 1). The concrete not only acts as a passive layer on the steel cylinder core but also serves as a bending reinforcement. The outer concrete cover is reinforced with steel wire coils. These pipes are also known in France as Bonna pipes and are designed and manufactured according to the recommendations of French standards (Afnor 1995).

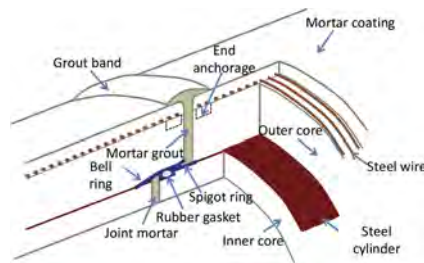


Figure 1. Diagram of a Bonna type pipe.

2 METHODOLOGY FOR LIFE-CYCLE ANALYSIS OF A BURIED PIPELINE

The proposed methodology for buried drinking water pipes aims at optimizing resources for maintenance (Yáñez-Godoy et al. 2017). It is about implementing an efficient risk management during the whole life cycle of the network which leads to associate diagnosis, prognosis and decision making concerning the desired performance (the structural integrity of the pipes, the need to ensure the continuity of the service, etc.). This methodology is based on:

- The acquisition of interesting parameters (e.g. embedded defects generated during pipe laying; long-term defects as corrosion of wires, steel joints or steel cylinder) that are relevant for aging and degradation assessment of concrete pipes
- The use of some of the identified parameters in the previous item as input to geomechanical models to study the behaviour of concrete pipes
- The use of other pipe degradation monitoring parameters (e.g. detection of broken wires; condition of joints) to validate the numerical models and readjust them to improve their predictive function
- The integration of geomechanical models, used in a probabilistic context, in an inspection and maintenance optimization approach

The first three items mentioned above imply a precise follow-up during the installation of the pipes as well as a long-term monitoring of the degradation mechanisms of the pipe materials. These points are outside the scope of this study. The last item (geomechanical models) can be considered in a geomechanical approach and is explained in the following section.

3 GEOMECHANICAL APPROACH

3.1 *Input data*

For the modelling of the geomechanical behaviour of Bonna pipes, it is necessary to build a numerical model which represents the pipe laid in a heterogeneous medium. The input data required for this model include:

- The geometric characteristics of the pipe section: most of these data are the easiest to obtain as there are generic documents from the supplier
- The mechanical characteristics of the pipe section: if the data are not available, the assumptions that can be made will be the most appropriate ones based on the characteristics of typical materials such as steel and concrete
- The geomechanical properties of the surrounding soil: the uncertainties of these data are more easily identified and their treatment is more efficient when geotechnical data are available; pressuremeter tests should be considered for example to determine the Young's modulus of the soil
- The spatial structure of the soil: data from instrumented sites (Yáñez-Godoy et al. 2019) makes it possible to simulate a random field to model the spatial variability of the soil along the axis of the pipe; this random field would make it possible to deduce the response of the structure under certain loading conditions and to observe its sensitivity to differential settling
- The vehicle loading: this data has some sensitivity due to its variability
- The temporal variability of the properties of the soil-pipe system: on the one hand, access to information from databases (e.g. <http://www.ad.es.eaufrance.fr>) that record the monitoring of groundwater management for a specific area and for several years seems very relevant in order to assess possible seasonal stresses on the pipe; on the other hand, non-destructive testing techniques (e.g. geophysical measurements with geological radar), would allow the study of natural seasonal fluctuations of the site (soil moisture) and look at their effect on the mechanical behaviour of the structure; this point is outside the scope of this study

3.2 *Geomechanical model*

In order to ensure a safer design of a new pipe or to assess the residual life of an existing buried pipe, a reliable assessment of the soil stresses applied on the pipe due to soil and pipe

movement is required. The design of longitudinal pipes in the literature is approached by models which consider pipes as articulated elastic beams laying on an elastic continuum (Yu et al. 2013). These models are grouped in two categories: the local continuous medium models (the soil is represented by a linear or non-linear medium with a mechanical behaviour described by stress-strain relationships) or the global simplified models (the local behaviour of soil is replaced by a simplified mechanical model; the most used common model to represent soil-structure interaction is the unidimensional Winkler model). The rigid or flexible pipes are vulnerable due to generated stresses due to soil displacements. Some studies addressing the influence of settlements on the behaviour of pipes and particularly on the behaviour of joints exist (Buco et al. 2008). The rigidity of joints depends on the used technology and their geometry (flexible joints, welded joints). In order to represent the non-linear and non-homogeneous soil characteristics, spatial variability and uncertainties have to be taken into account.

The pipeline model used in this study consists of a set of pipe segments. Each pipe segment of finite length is decomposed into a number of beams connected to each other by nodes. At the ends of segments, a pair of two independent nodes is used to represent the joints. Each beam element is subjected to a uniformly distributed loading, q , and rests on a soil modeled, according to the Winkler model, by a set of independent springs with a coefficient of subgrade reaction or soil reaction coefficient, k_s , in order to take into account the soil-structure interaction. This model is described by a uniaxial distribution of the form:

$$p(x) = k_s \cdot w(x) \quad (1)$$

with $p(x)$ the pressure applied to the abscissa x , $w(x)$ the displacement in the direction transverse to the abscissa x . The soil reaction coefficient, k_s is not a measurable physical quantity and depends on the properties of the pipe, in addition to those of the soil it is supposed to represent. The determination of its value has been the subject of many studies and several semi-empirical relationships have been proposed (Elachachi et al. 2004). These formulas involve geometric and mechanical characteristics of the pipes as well as mechanical properties of the soil, including the soil modulus, E_s and the soil Poisson's ratio, ν_s . The values derived from these models are not only quite different but also result in values that are widely dispersed. Here, k_s is related to the mean soil modulus, E_s by Vesic model (Vesic 1961):

$$k_s = \frac{0.65}{d} \sqrt[12]{\frac{E_s d^4}{E_p I_p}} \cdot \frac{E_s}{1 - \nu^2} \quad (2)$$

with E_p the modulus of elasticity of the pipe, I_p the moment of inertia of the pipe, ν the soil Poisson coefficient and d the diameter of the pipe.

The pipe sections and the soil are considered to have a linear behaviour. The main limitation of this longitudinal model is that it is unable to take into account the effects in the cross-section, such as the effect of the internal hydraulic pressure and the effect of the lateral soil, hence the interest in thinking about the coupling of longitudinal and transverse effects, which we have translated into a hybrid model with a transverse model of the pipe cross-section, called 2.5D model.

3.2.1 2.5D hybrid model

The model used to represent the studied soil-pipe system was based on 1D (Euler-Bernoulli beam model) and 2D (plane stress model) models. The 1D model allows to obtain the settlement profile of the pipe, as well as the stresses coming from the bending effects. The 2D model allows the evaluation of the various circumferential stresses developing in the cross-section of the pipe, taking into account the transverse effects of the soil and the effect of the internal pressure. The combination of the two models has been named "2.5D hybrid model" (Darwich 2019) as a coupling is taken into account. Placing the pipeline in a frame of reference where the x-axis is the axis passing through the left and right ends of the pipe, the y-axis is the vertical axis, and the z-axis is the longitudinal axis of the pipe (Figure 2), the assumptions made for this 2.5D modelling result in the combination of two stress systems, based on different assumptions in the state of planar stresses. In the 1D model, the stresses in the cross-section, σ_{xx} , σ_{yy} , and σ_{xy} are assumed to

be zero and the axial stress σ_{zz} can vary longitudinally. Whereas in the 2D model, non-zero stresses σ_{rr} , $\sigma_{\theta\theta}$, and $\sigma_{r\theta}$ are sought to be calculated, with the axial stress σ_{zz} assumed to be constant along the pipe. Three points in the thickness of the pipe cross-section are considered at four critical locations: left and right ends and top (crown) and bottom (invert) ends. As the left and right ends are symmetrical, only one end is retained. The combination of stresses for the proposed 2.5D model is based on the following assumption:

$$\sigma_{2.5D} = \sigma_{1D} + \sigma_{2D} \quad (3)$$

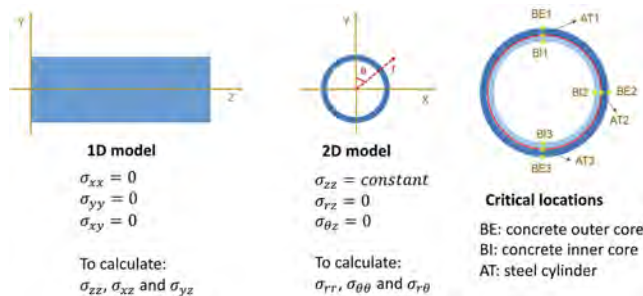


Figure 2. Assumptions for stresses in 1D and 2D models and critical locations in the pipe cross-section.

3.2.2 Uncertainties and random variability of soil properties

The variability and/or uncertainty related to soil characteristics and therefore to the soil response coefficient comes from: the soil which is in fact a material with spatial heterogeneity resulting from its deposition and aggregation process; the inaccuracy of measurements; the model's uncertainty. The soil modulus, E_s , is assumed to characterize the spatial randomness of the soil as it is a geomechanical property which is indirectly dependent on soil density and soil moisture. A cross section of a pipe is shown in Figure 3 where the interaction with the soil is done by springs of stiffness k_{sh} for springs not belonging to the support arc of angle α of the pipe and of stiffness k_{sb} for springs belonging to it. k_{sb} parameter is associated with the pipe laying bed supposed to be compacted. This modelling allows to take into account the different horizontal and vertical loads on the pipeline, q_h and q_v respectively, but also the reaction of the laying bed. It should be noted that the vertical loads are mainly due to the weight of the soil and surface overloads due to road traffic or to overlying buildings and structures.

The role of longitudinal variability can be studied by considering random fields (Vanmarcke 1977). Random fields let to model the spatial variability characteristics of k_s through some parameters as the mean value m_{k_s} , the variance $\sigma_{k_s}^2$ and the correlation length l_c . This last parameter is linked to autocorrelation function, $\rho(\tau)$, where τ indicates the distance between two points and describes the spatial structure of the correlation of soil properties. Both parameters, l_c and E_s are important factors for understanding the spatial behaviour of the soil-pipe system (Elachachi et al. 2012, Onyejekwe et al. 2016).

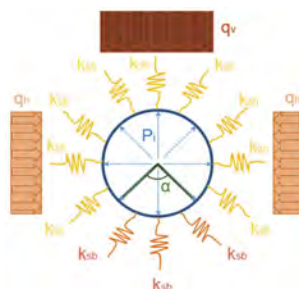


Figure 3. 2D model representing soil-pipe interaction and applied loads, q_b and q_v and internal hydraulic pressure P_i .

3.2.3 Criticality indicators or performance criteria

Three main potential failure modes for a buried pipe are identified: an excessive displacement of the pipe; an excessively high stress on the pipe, thus compromising the structural integrity of the pipe; and an excessively high joint opening (which could compromise the tightness of the pipes and result in a drop in pressure, unserved users, etc). These failure modes are linked through three different criticality indicators, I_{cri} ($i = 1,2,3$), which will help to understand which phenomenon or potential event has the highest occurrence. Indeed, the models developed are used in a probabilistic context and allow the formation of a set of performance criteria that are defined from the definition of limit states. The criticality indicators help to optimize pipeline renewal strategies, e.g., through a proactive approach, by identifying alert thresholds, etc. The probabilistic approach makes it possible to identify the areas that are likely to deteriorate in a pipe and to forecast the evolution of the indicators in the long term.

For each of the failure modes, two reliability indices β will be calculated for two distinct limit states:

- The serviceability limit state (SLS), the exceeding of which compromises normal service conditions (induces minor effects)
- The ultimate limit state (ULS), corresponding to the state which, if reached, could lead to damaging consequences at the level of a portion of the pipe or in its totality.

The expression for the reliability index β is given by:

$$\beta = \frac{\ln\left\{\frac{R}{S} \left[\frac{(1 + COV_S^2)}{(1 + COV_R^2)} \right]^{1/2}\right\}}{\left\{ \ln\left[(1 + COV_S^2)(1 + COV_R^2) \right] \right\}^{1/2}} \quad (4)$$

with R the value of the acceptable stress, S the mean maximum stress, COV_R the coefficient of variation of the acceptable stress (here taken to be zero, as R is supposed to be deterministic) and COV_S the coefficient of variation of the maximum stress, assuming that both R and S follow a lognormal distribution. The values of β for the ULS and SLS can be specified by the user according to the standards or the desired performance levels. For example, Eurocode 0 (Afnor 1990) recommends a value of 1.5 for the SLS, which corresponds to a probability of failure of 6.7×10^{-2} , and a value of 3.8 for the ULS, which corresponds to a probability of failure of 7×10^{-5} .

For buried pipes, 3 levels of performance or criticality indicators, I_{cri} , can be considered:

- Safe pipe: no intervention by the manager is necessary; all calculated β values are higher than the value indicated as acceptable, that is to say $I_{cri} = 0$
- Pipe to be inspected: the manager must carry out a follow-up in terms of inspection for the pipe studied; there is at least one computed β value (not several) that is lower than the value indicated as acceptable, that is to say $I_{cri} = 1$
- Pipe to be maintained or renewed: there is a high probability that a failure of the pipe would have occurred; maintenance or renewal is then necessary because several calculated β values are lower than the value indicated as acceptable, that is to say $I_{cri} = 2$

4 CASE STUDY

The case study presented in this section concerns the renewal of a Bonna type pipe of 1100 mm inner diameter in an urban municipality. The pipeline consists of 15 individual segments, each 6 m long, for a total length of 90 m. The pipe is laid at a mean depth of 2 m in a sandy clay soil. The laying quality is assumed to be good. The pipe operating pressure is 6 bar. The static load due to road traffic is considered to be 67 kN/m^2 (mean value). In order to arrange the large amount of input data and outputs, the following sections present the organization process.

4.1 IT tool for decision-support

The computer tool developed in Matlab is an autonomous set of scripts allowing to execute, through a graphic interface, a geomechanical computation (in an uncertain context) of

a buried pipe. It allows, according to parameters given by the user such as the geometrical, mechanical or geotechnical characteristics, to obtain as output of a probabilistic computation:

- The values of maximal displacements, stresses and joint opening angles
- Then, by post-processing, quantify and display on a window, criticality indicators that will indicate to the user the global state of the pipe and thus know, thanks to the model, where the pipe is in terms of structural integrity and tightness (these are the two monitored performances)

4.2 Data acquisition from available databases

The characteristics of the concrete pipe, the geomechanical properties and the loads and boundary conditions are shown in Table 1.

Table 1. Characteristics of the soil-pipe system.

Geometrical characteristics	Mechanical characteristics
Inner diameter: 1100 mm	Young's modulus of concrete: 30 GPa
Number of pipe segments: 15	Young's modulus of steel: 210 GPa
Pipeline length: 90 m	Diameter of steel wire: 10 mm
Thickness: 88 mm	Number of steel wires per meter: 25
Burial depth: 2 m	
Type of joint gasket: welded	
Geomechanical properties	
Type of soil: sandy clay	
Volume weight of the backfill: 20 kN/m ³	
Soil modulus: 125 MPa	
Poisson coefficient: 0.4	
Modulus of subgrade reaction: 58.78 MN/m ³ (calculated by Vesic model)	
Quality of the pipe laying bed: good	
Loads and boundary conditions	
Internal pipe pressure: 6 bar	
Intensity of rolling surface loads: 67 kN/m ²	
Ratio of horizontal to vertical stresses in the pipe (this parameter depends on both the quality of the pipe laying bed and the type of soil): 1	
Threshold values for the limit states	
Circumferential pipe stresses: SLS: 5 MPa; ULS: 8 MPa	
Pipe displacement: SLS: 30 mm; ULS: 60 mm	
Pipe joint opening: SLS: 0.01°; ULS: 0.02°	

4.3 Data acquisition by instrumentation of a pipe: Correlation length of soil modulus

The experimental acquisition of quantities of interest such as the correlation length, l_c , of soil properties was presented in (Yáñez-Godoy et al. 2019). Results in (Yáñez-Godoy et al. 2017) showed that for horizontal l_c values between 6 and 18 m, the increase in the probability of failure of the pipeline (i.e., the reliability index decreases) is greater than for smaller values. A forthcoming study by the authors suggests that the horizontal l_c of the soil below the pipeline could have a more important effect on the structural integrity of the pipe. The spatial variability below the pipeline was assumed to correspond to the soil modulus parameter, E_s , in the model.

From these studies we know that for the correlation length of E_s a mean value of 6 m is a good choice for assessing the effects of spatial variability. A coefficient of variation, COV, of the order of 0.5 (relationship between the standard deviation and the mean value of E_s) is taken into account, it will define the variability of this parameter. Although naturally the variability of E_s can be very large, in the case of non-linear soil behaviour problems, very high values of COV (higher than 0.5) tend to a numerical non-convergence of the result.

4.4 Tool outputs: Geomechanical responses of the pipe

The values of the calculated stresses, displacements and joint openings are shown in Figure 4. For all N simulations ($N = 1 \times 10^4$), the mean and standard deviation of the maximum values of the three relevant outputs and the 5% and 95% fractiles of the maximum displacements and pipe joint openings are calculated (top of Figure 4a). It is possible to display for each of the simulations performed (here, simulation number 7 at the bottom of Figure 4a) the spatial variability of the modulus of subgrade reaction in parallel with the displacement of the pipe. In particular, Figure 4b shows the cumulative distribution function of the circumferential stress at the point BE1 of the pipe where the mean maximum value occurs.

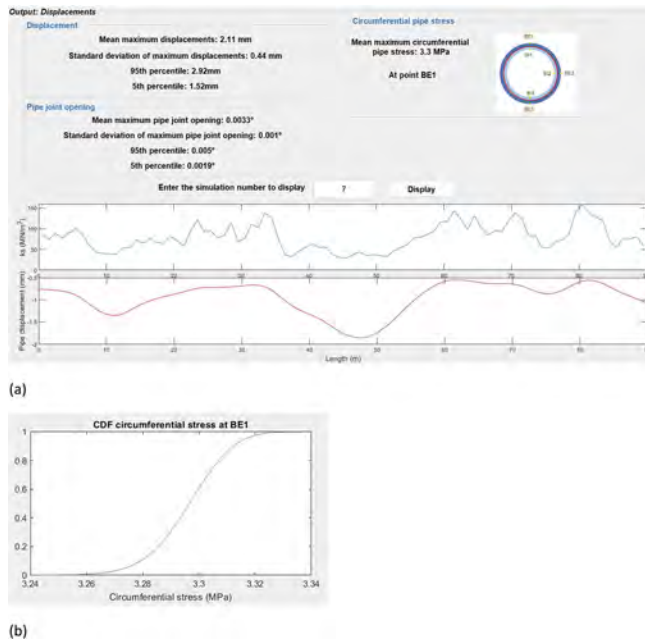


Figure 4. (a) Values of the calculated stresses, displacements and joint openings; (b) Cumulative distribution function of the mean maximum circumferential stress at the point BE1 of the pipe.

4.5 Tool outputs: Criticality indicators of the pipe

In the IT tool, three criticality indicators are present. They are calculated by the method described in 3.2.3 and allow a quick understanding of whether or not an intervention should be considered



Figure 5. Criticality indicators of the pipe.

on the studied pipeline. Figure 5, shows that the three indicators are green, which means that for the three main failure modes, the study has not revealed any particular risk.

5 CONCLUSIONS

This study presented the different steps of a geomechanical approach to allow a drinking water network manager, thanks to an IT tool, to evaluate its performance with regard to the different performance criteria. These steps aim to optimise the resources allocated to asset management through an effective life cycle risk management process. The experimental campaigns provide access to key elements for the understanding of the soil-pipe behaviour. Indeed, these elements provide a good knowledge of aspects that are not sufficiently known, such as soil variability, on real sites with pipelines in operation. The coupling of the geomechanical approach with durability aspects, which take into account degradation kinetics, is feasible and constitutes a very complete analysis tool. This IT tool can provide experts with decision elements for better safety calibration in soil-pipe interaction problems where soil variability is an influential parameter.

ACKNOWLEDGMENTS

The authors would like to thank Syndicat des eaux d'Ile de France (SEDIF) for its involvement in this project. Created in 1923, SEDIF is a public utility that is responsible for supplying drinking water to subscriber towns and municipalities in the Greater Paris area. SEDIF is the leading public drinking water utility in France and is one of the largest in Europe. Producing 765000 m³ of water every day, SEDIF delivered 254 billion liters to users in 2019 through a network of pipes stretching 8767 km. The authors also thank G. Darwich and A. Darolles for their contributions to the development of the IT tool.

REFERENCES

- Afnor 1990. NF EN 1990 Eurocodes structuraux - Bases de calcul des structures - Annexe nationale à la NF EN 1990:2003. Afnor (ed).
- Afnor 1995. NF EN 639 Prescriptions communes pour tuyaux pression en béton y compris joints et pièces spéciales. Afnor (ed).
- Buco, J., Emeriault, F., Kastner, R. 2008. 3D Numerical Analyses of the Soil Variability Impact on Longitudinal Behaviour of Buried Pipes. In: *Proc. 12th Int. Conf. of Int. Assoc. for Comp. Meth. & Adv. in Geomech. (IACMAG)*, Goa, 1-6 October 2008.
- Darwich, G. 2019. *Modélisation du comportement géo-mécanique d'une conduite de transfert et évaluation de sa performance en contexte incertain*. Génie mécanique. Université de Bordeaux.
- Elachachi, S.M., Breyse, D., Houy, L. 2004. Longitudinal variability of soils and structural response of sewer networks. *Comput. and Geotech.* 31: 625–641.
- Elachachi, S. M., Breyse, D. & Denis, A. 2012. The effects of soil spatial variability on the reliability of rigid buried pipes. *Comput. and Geotech.* 43: 61–71.
- Onyejekwe, S., Kang, X. & Ge, L. 2016. Evaluation of the scale of fluctuation of geotechnical parameters by autocorrelation function and semivariogram function. *Eng. Geol.* 214: 43–49.
- Vanmarcke, E. H. 1977. Probabilistic Modeling of Soil Profiles. *J. Geotech. Eng. Div.* 103(11): 1227–1246.
- Vesic, A.S. 1961. Beams on elastic subgrade and Winkler's Hypothesis. In *Proc. of the 5th int. conf. soil mech. found. engng., Paris 1961*.
- Yáñez-Godoy, H., Elachachi, S.M. & Darwich, G. 2017. Geomechanical behaviour of large diameter pressure water pipelines in unidimensional heterogeneous soils. In C. Bucher, B.R. Ellingwood, D. M. Frangopol (eds.), *Saf., Reliab., Risk, Resil., & Sustain. of Struct. & Infrastruct.; Proc. 12th Int. Conf. on Struct. Saf. & Reliab. (ICOSSAR2017)*, Vienna 6-17 August 2017. TU-Verlag Vienna.
- Yáñez-Godoy, H., Elachachi, S.M., Chesneau, O. & Feliars, C. 2019. Identification of key determinants of geo-mechanical behavior of an instrumented buried pipe. In *Proc. 13th Int. Conf. on Appl. of Stat. & Probab. in Civ. Eng., ICASP13, Seoul, 26-30 May 2019*. College of Engineering/Engineering Practice School, Dept. of Civil & Environmental Engineering.
- Yu, J., Zhang, C., Huang, M. 2013. Soil-pipe interaction due to tunnelling: Assessment of Winkler modulus for underground pipelines. *Comput. and Geotech.* 50: 17–28.

Shear strength investigation of carbon fiber reinforced polymer strips-wrapped concrete beams with regression analysis and experiments

P. Fan, H.F. He & S.S. Cheng

Research Institute of Highway Ministry of Transport, Beijing, China

S.S. Guo & C. Liu

Tongji University, Shanghai, China

ABSTRACT: With the increase of the service time of concrete structure, the bearing capacity of the structure will decrease to a certain extent. In order to ensure that the structure meets the needs of serviceability state, the structure needs to be reinforced and transformed to improve the bearing capacity. In this paper, the method of carbon fiber reinforced polymer strips-wrapped concrete beams is used to strengthen the concrete beam, and the calculation method of the shear bearing capacity is studied and analyzed. However, the shear behavior of reinforced concrete beams (RC) is complex. To analyze the shear capacity of RC beams strengthened with carbon fiber reinforced polymer (CFRP) strips, the main factors affecting the shear performance are summarized and analyzed based on existing literature firstly. Then, the calculation formula of shear capacity of CFRP is determined by regression analysis of test data and is verified with model tests. Finally, the applicability of the calculation model proposed by author is analyzed and compared with previous shear models. The results show that: (1) the main factors affecting the shear performance include the effective height of CFRP strips, the spacing of CFRP strips, the width and thickness of CFRP strips, the axial compressive strength of concrete, the inclination angle of crack of reinforced concrete beams and CFRP strips; (2) the shear capacity of RC beams strengthened with CFRP with previous calculation models are conservative, and the maximum error is 29.47%; (3) The calculation results of the model proposed by author are consistent with the test results of side obliquely pasted CFRP, and the error is 6.21%. But there is a large error with the test results of U-shaped pasted CFRP strips.

1 INTRODUCTION

The shear behavior of reinforced concrete beams remains a significant subject of research. The shear theories still need modification with regard to reinforced concrete members. It is important to note that shear failure of concrete structures is exceedingly hazardous because it is rarely expected and usually occurs explosively. Therefore, improving the properties of concrete has become imperative. The use of Fiber-Reinforced Polymer (FRP) to enhance the shear behavior by strengthening, repairing, and rehabilitating RC elements has significantly increased. Fiber reinforced polymer has the advantages of light weight, high strength, corrosion resistance and fatigue resistance. It has been gradually used in civil engineering structures since the 1980s. Currently, fiber reinforced polymer has become a mainstream composite material in bridge reinforcement. Carbon fiber reinforcement technology is convenient and efficient and has broad development prospects in the field of structural reinforcement (Dittrich et al., 2014, Kim and Harries, 2011, El-Saikaly and Chaallal, 2015). Research (Li and Gu, 2012, Zhang et al., 2010) shows that FRP reinforcement can not only improve the flexural

capacity of the bridge, but also effectively improve the shear capacity. It plays a significant role in improving the stiffness of the structure, reducing the deflection, and delaying the emergence and development of cracks. For reinforced concrete beams strengthened with FRP, the shear capacity gradually improves with the increase of the effective height of CFRP and the decrease of the spacing. Daniel Baggio(Baggio et al., 2014) et al. conducted the research on the method of improving the shear capacity of concrete beams with FRP. They pointed out that fiber reinforced polymer composites can significantly improve the shear capacity of reinforced concrete beams through the change of FRP type and anchorage mode. Moreover, the anchoring method will not change the failure mode, but only improve the shear capacity of reinforced concrete beams. Based on the shear tests of concrete beams strengthened with CFRP, scholars put forward the calculation methods of shear capacity through the research and analysis of the shear mechanism of concrete beams. J. F. Chen, J.G. Teng(Chen and Teng, 2003a, Chen and Teng, 2003b) put forward the calculation theory of shear capacity of reinforced concrete beams strengthened with CFRP. They analyzed the factors affecting the shear strengthening effects of CFRP combined with the failure mode of concrete beams - peeling failure or tensile failure. A. Bukhari(Bukhari et al., 2010) gave the calculation formula of shear capacity of reinforced concrete beams in the form of power function based on a large number of test results of reinforced concrete beams with small shear span-depth ratio. During the process, they considered the relationship between effective strain and ultimate strain of CFRP and adopted the method of regression analysis.

At present, the reinforcement technology with carbon fiber sheets is relatively mature in the world. There are several codes for fiber composite reinforcement and prestressed carbon fiber-reinforced polymer plate reinforcement. Many experiments have been conducted to analyze the shear capacity of reinforced concrete beams strengthened with CFRP. However, the test results are discrete due to the complexity of the shear behavior of concrete beams. Many experiments will greatly increase the cost, which is more troublesome and uneconomical.

The regression analysis method based on previous test results can become easier to give the prediction on the shear capacity of reinforced concrete beams strengthened with CFRP compared with the experiments. In the paper, the shear calculation model of CFRP is determined with the regression analysis of test data in the existing literature. Then, the theoretical model is verified by experiment. Finally, the accuracy of the calculation method is compared and analyzed.

2 EXISTING CALCULATION METHODS OF SHEAR CAPACITY OF CONCRETE BEAMS REINFORCED WITH CFRP

Scholars in the world have carried out a large number of researches on the shear reinforcement effects of concrete beam bridges with FRP. Through theoretical derivation, numerical analysis and regression analysis, some calculation methods of the shear capacity of reinforced concrete beams strengthened with FRP have been obtained. Here, a part of calculation methods have been collected and sorted out through literature research.

(1) Triantafilou 1998(Triantafillou, 1998)

$$V_f = \frac{0.9}{\gamma_f} \rho_f E_f b_w \varepsilon_{fe} d (1 + \cot \alpha) \sin \alpha \quad (1)$$

(2) Triantafilou and Antonopoulos 2000(Yost et al., 2001)

$$V_f = \frac{2 w_f t_f E_f \varepsilon_{fe} d_f}{s_f} \quad (2)$$

(3) Matthys and Triantafillou 2001(Matthys and Triantafillou, 2001)

$$V_f = \frac{2 w_f t_f E_f \varepsilon_{fe} d_f}{s_f} \quad (3)$$

(4) Pellegrino and Modena 2002(Pellegrino and Modena, 2002)

$$V_f = (A_f / s_f) 0.9 d f_{fe} (1 + \cot \beta) \sin \beta = \rho_f b_w 0.9 d R f_{fu} (\sin \beta + \cos \beta) \quad (4)$$

(5) Khalifa and Nanni 2002(Khalifa and Nanni, 2002)

The calculation model adopts the correction coefficient “R” to reduce the effective strain of FRP, and the calculation model is as follows:

$$V_f = \frac{A_f f_{fe} (\sin \beta + \cos \beta) d_f}{s_f} \quad (5)$$

(6) Taljsten 2003(Taljsten, 2003)

$$V_f = 2 t_f \varepsilon_f E_f 0.9 d (\cot \alpha + \cot \beta) \sin^2 \beta \cos^2 \beta \quad (6)$$

(7) Chen and Teng 2003(Chen and Teng, 2003b)

$$V_f = 2 f_{fe} t_f w_f \frac{h_{fe} (\cot \theta + \cot \alpha) \sin \alpha}{s_f} \quad (7)$$

(8) Wang Suyan et al. 2007(Suyan and Yingwu, 2007)

Wang Suyan et al. obtained the calculation expression of equivalent effective strain through regression analysis of the test data and put forward corresponding calculation model considering the influence of the ultimate strain of FRP, the non-uniformity of strain distribution along the crack, the inclination angle of crack and other factors.

$$V_f = \rho_f E_f \varepsilon_{f,ee} b d (1 + 0.835 \cot \alpha) \sin \alpha \quad (8)$$

$$\varepsilon_{f,ee} = 0.005229 (\rho_f E_f^{1.23})^{-0.6152} \quad (9)$$

(9) Mofidi and chaallal2011(Mofidi and Chaallal, 2011)

$$V_f = \frac{2 t_f \varepsilon_{fe} E_f w_f (\cot \theta + \cot \alpha) \sin \alpha \alpha_f}{s_f} = \rho_f E_f \varepsilon_{fe} b d_f (\cot \theta + \cot \alpha) \sin \alpha \quad (10)$$

$$\varepsilon_{fe} = \frac{\beta_c \beta_L \beta_w \tau_{eff} L_e}{t_f E_f} = 0.31 \beta_c \beta_L \beta_w \sqrt{\frac{f'_c}{t_f E_f}} \leq \varepsilon_{uf} \quad (11)$$

(10) Bukhari et al. 2013 (Bukhari et al., 2013)

Based on the test results of reinforced concrete beams with small shear span-depth ratio, the proposed calculation model is as follows:

$$V_{Rd,f} = 0.9 \rho_f b_w \varepsilon_{fe} E_f d (\cot \theta + \cot \alpha) \sin \alpha \quad (12)$$

$$\varepsilon_{fe} = \varepsilon_{fu} [0.0812 (\rho_f E_f)^{-0.9434}] \quad (13)$$

3 CALCULATION METHOD OF SHEAR CAPACITY OF REINFORCED CONCRETE BEAMS STRENGTHENED WITH CFRP

Regression analysis is the basic method of prediction. It is a statistical analysis method to determine the interdependence between two or more variables. A functional equation approximately expressing the quantitative relationship between variables is established by analyzing the relationship between dependent variables and independent variables. The regression equation is used to predict the numerical change of dependent variables. A reasonable calculation

formula of shear capacity of concrete beams strengthened with FRP is obtained through regression analysis based on the research results in the previous literature. During the process, the existing calculation methods of the shear capacity in the literature are referred. The main factors considered during the regression analysis include the effective height of CFRP strips, the spacing of CFRP strips, the width and thickness of CFRP strips, the axial compressive strength of concrete, the inclination angle of crack of reinforced concrete beams and CFRP strips.

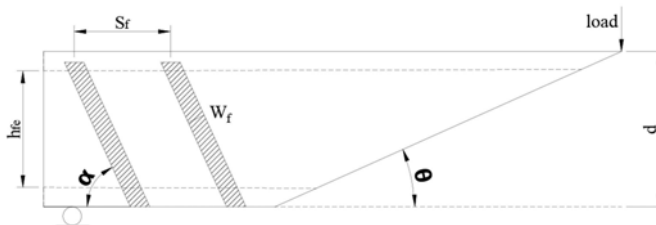


Figure 1. Calculation model.

In Figure 1: w_f is the width of CFRP strips; s_f is the distance of two adjacent CFRP strips; θ is the angle between oblique cracks and the longitudinal axis of the beam; α is the angle between the CFRP strips and the longitudinal axis of the test beams; d is the depth of the test beam; h_{fe} is the effective height of CFRP strips; b_w is the width of the cross section; n is the number of layers of CFRP strips; t_f is the thickness of CFRP strips; E_f is the elastic modulus of CFRP strips; f_{fu} is the ultimate tensile stress of CFRP strips; ε_{fu} is the ultimate tensile strain of CFRP strips; ε_{fe} represents the effective strain of CFRP strips; f_c is the axial compressive strength of concrete; $f_{cu,k}$ is the cube compressive strength of concrete; f_{ck} is the prismatic compressive strength of concrete; f_t is the tensile strength of concrete. Where, A_f represents the area of CFRP strips, ρ_f is the distribution rate.

(1) Theoretical calculation method

Different relationships between the ultimate tensile strain and effective tensile strain of carbon fiber cloths are given based on the consideration of the compressive strength of concrete. The theoretical formulas are listed, and the unknown parameters are determined by regression analysis using the existing test data. The derivation of the theoretical formulas is as follows.

$$V_f = 2 \varepsilon_{fe} E_{fe} t_f w_f \frac{h_{fe} (\cot \theta + \cot \alpha) \sin \alpha}{s_f} \quad (14)$$

$$\varepsilon_{fe} = \varepsilon_{fu} [\alpha_1 (\rho_f E_f)^{-\alpha_2}] f_c^{\alpha_3} \quad (15)$$

Among them, α_1 , α_2 and α_3 is unknown.

Through regression analysis, the theoretical formula is obtained.

$$V_f = 2 \varepsilon_{fe} E_{fe} t_f w_f \frac{h_{fe} (\cot \theta + \cot \alpha) \sin \alpha}{s_f} \quad (16)$$

$$\varepsilon_{fe} = \varepsilon_{fu} [1.4378 (\rho_f E_f)^{-0.6301}] f_c^{0.6382} \quad (17)$$

4 EXPERIMENTS

(1) Experimental design

The rectangular concrete beams with the length, height and width of 3600 mm, 500 mm, and 200 mm with simply supported ends were manufactured and tested. The strength grade of

concrete was C40. The longitudinal tensile reinforcement adopted HRB400 steel, the compressive steel reinforcement and stirrup adopted HPB300 steel. The longitudinal tensile and compressive reinforcing bars with nominal diameters of 25 mm, 12mm were used in the specimens. Besides, the transverse reinforcements were made of two stirrups (8 mm in diameter) and the spacing between stirrups was 200mm. A reinforced stirrup was added at the beam end, 50mm away from the beam end. The reinforcing details of the test beam are shown in Figure 2.

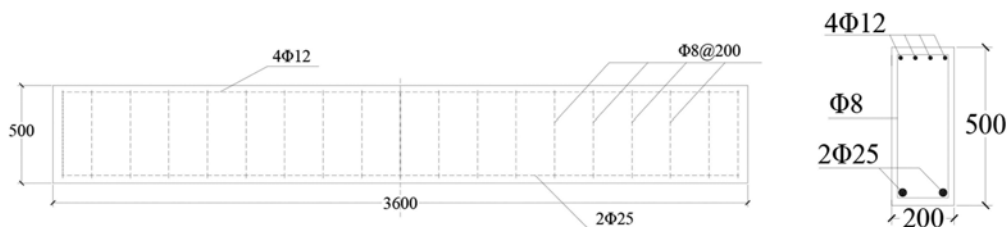


Figure 2. Sectional diagram of reinforced concrete beam.

(2) Reinforcement

① Reinforcement type

In this test, the oblique and U-shaped bonded carbon fiber sheets were used to strengthen concrete beams to verify the theoretical model of shear capacity of reinforced concrete beams strengthened with carbon fiber sheets. The reinforcement methods are shown in Figure 3.

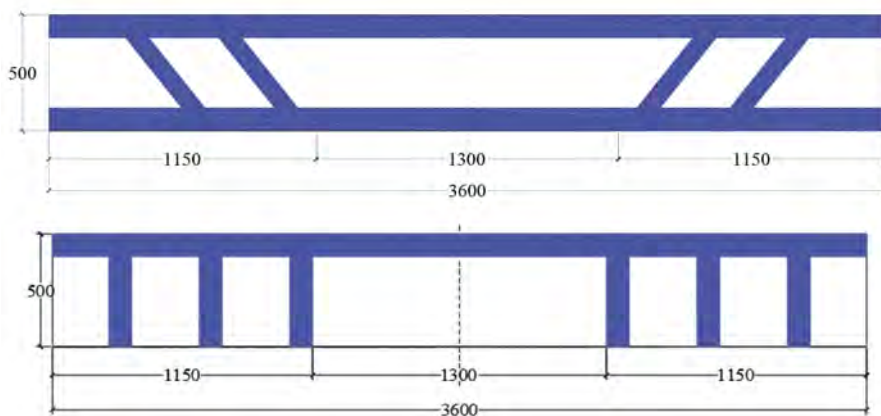


Figure 3. Obliquely and U-shaped pasted carbon fiber cloths.

② Loading test

In the experiment, each beam was simply supported and loaded monotonically at four-points to failure. 4000kN hydraulic testing machine was used during the loading. By distributing steel beam, two synchronous and equivalent concentrated forces were symmetrically applied on the test beams, and the concentrated forces were transmitted to the test beams through rubber bearing.

(3) Materials

① Concrete

The beams were made of normal concrete, and the strength grade of concrete was C40. Nine cubes whose dimensions of $150 \times 150 \times 150 \text{ mm}^3$ were poured on site. After 28 days of curing under the same conditions, material properties of concrete cubes were measured in the laboratory. The test results were as follows: the cube compressive strength is 41.1MPa, the axial compressive strength is 31.24MPa, and the axial tensile strength is 3.05MPa.

② Reinforcement

The longitudinal reinforcement used in the tests was HRB400, and the stirrup was HPB300. The material properties are shown in Table 1.

Table 1. Material properties of reinforcement (unit: MPa).

Reinforcement model	Reinforcement grade	Yield strength (MPa)	Ultimate tensile strength (MPa)
B25	HRB400	440	615
A12	HPB300	–	520
A8	HPB300	–	565

(4) Test results

① The test beam strengthened with obliquely pasted carbon fiber strips

The test beam was strengthened by obliquely pasted carbon fiber strips. It was difficult to observe the initial cracks in the middle span and bending shear section because of the application of longitudinal strips. When the test beam was loaded to 60kN, cracks began to appear in the mid span; When the load increased to 180kN, oblique cracks in the shear zone began to appear; After 220kN, the inclined cracks in the shear zone became wider obviously; When the load reached 410kN, the width of inclined cracks reached 0.45mm. Finally, the carbon fiber strips of the test beam were torn. The ultimate load was 530kN, as shown in Figure 4.



Figure 4. Experimental phenomena of concrete beams strengthened with obliquely bonded carbon fiber strips.

② The test beam strengthened with U-type pasted carbon fiber strips

When the test beam strengthened with U-shaped carbon fiber strips was loaded to 60kN, the cracks in the mid span first appeared; loaded to 120kN, oblique cracks in the shear zone began to appear; When the load reached 190kN, the inclined cracks in the bending shear zone became wider obviously; When the load was up to 280kN, the width of inclined cracks reached 0.4mm. Finally, the carbon fiber strips in the test beam showed peeling failure, as shown in Figure 5.



Figure 5. Experimental phenomena of concrete beams strengthened with U-shaped bonded carbon fiber strips.

5 COMPARATIVE ANALYSIS OF SHEAR CAPACITY OF REINFORCED CONCRETE BEAMS STRENGTHENED WITH CARBON FIBER STRIPS

The calculation method of shear capacity of reinforced concrete beams strengthened with CFRP was determined by regression analysis method in the paper. Combined with the existing calculation methods of shear capacity of concrete beams strengthened with CFRP, the shear capacity of the test beams was calculated and compared. The calculation results are shown in Table 2.

Table 2. Summary of calculation results of shear capacity of concrete beams strengthened with obliquely pasted carbon fiber strips.

Serial number	Calculation model	Theoretical value(A) (kN)	Test value(A) (kN)	Error(A) (%)	Theoretical value(B) (kN)	Test value(B) (kN)	Error(B) (%)
1	Triantafillou 1998	214.77	265	18.96	210.63	255	17.40
2	Triantafillou and Antonopoulos2000	244.81	265	7.62	233.86	255	8.29
3	Matthys and Triantafillou 2001	208.09	265	21.48	208.09	255	18.40
4	Pellegrino and Modena 2002 (Crack width)	186.91	265	29.47	186.91	255	26.70
5	Pellegrino and Modena 2002 (Effective stress model)	225.82	265	14.78	221.22	255	13.25
6	Khalifa and Nanni2002	226.07	265	14.69	221.46	255	13.15
7	Taljsten 2003	279.63	265	-5.52	206.78	255	18.91
8	Chen and Teng 2003	342.06	265	-29.08	281.10	255	-10.23
9	Wang Suyan et al. 2007	246.17	265	7.11	232.77	255	8.72
10	Mofidi and Chaallal2011	281.10	265	-6.08	281.10	255	-10.23
11	Bukhari et al.2013	266.38	265	-0.52	230.05	255	9.78
12	Regression analysis(author)	248.54	265	6.21	215.45	255	15.51

Where, A: shear capacity of concrete beams strengthened with obliquely pasted carbon fiber strips; B: shear bearing capacity of concrete beams strengthened with U-shaped pasted carbon fiber strips

It can be seen from Table 2 that the calculation results of previous calculation models are quite different from the experimental values, and most theoretical calculation results are conservative compared with the experimental values. For the test beam strengthened with obliquely pasted CFRP, the error of theoretical model proposed by author is 6.21%, and the calculation accuracy is higher. However, for the test beam strengthened with U-shaped pasted CFRP, the theoretical model given in this paper has an error of 15.51%, which is rather conservative. Therefore, the theoretical calculation model determined by regression analysis is properly used to calculate the shear capacity of concrete beams strengthened by obliquely pasted carbon fiber cloths. The accuracy of theoretical calculation method for U-shaped reinforcement still needs to be improved.

6 CONCLUSIONS

CFRP is a widely used material in civil engineering. The calculation method of shear capacity of RC beams strengthened with CFRP should be studied more clearly to promote its application. In the paper, regression analysis method is used to calculate the shear capacity of reinforced concrete beams strengthened with CFRP. At the same time, model tests are used to verify the prediction results. The study indicates that:

- (1) Carbon fiber cloths can significantly improve the shear capacity of reinforced concrete beams, and limit or even prevent the development of cracks efficiently;
- (2) Based on the existing test data, the theoretical calculation results determined by regression analysis of the shear capacity of concrete beams strengthened by obliquely pasted CFRP strips have smaller errors compared with the test results, and the error is 6.21%. The calculation method can be used in actual projects. However, the difference of theoretical results and test values is relatively large for RC beams strengthened with U-shaped pasted CFRP;
- (3) The calculation results of the existing theoretical models for the shear capacity of reinforced concrete beams strengthened with carbon fiber cloths are conservative, and the maximum error is 29.47%. Based on experimental data obtained through literature, the theoretical model by regress analysis is proposed in the paper. The theoretical calculation results of the shear capacity of reinforced concrete beams strengthened with obliquely pasted CFRP are more consistent with the experimental results, which can significantly improve the efficiency of CFRP.

REFERENCES

- Baggio, D., Soudki, K. & Noel, M. 2014. Strengthening of shear critical RC beams with various FRP systems. *Construction and Building Materials*, 66, 634–644.
- Bukhari, I. A., Vollum, R., Ahmad, S. & Sagaseta, J. 2013. Shear Strengthening of Short Span Reinforced Concrete Beams with CFRP Sheets. *Arabian Journal for Science and Engineering*, 38, 523–536.
- Bukhari, I. A., Vollum, R. L., Ahmad, S. & Sagaseta, J. 2010. Shear strengthening of reinforced concrete beams with CFRP. *Magazine of Concrete Research*, 62, 65–77.
- Chen, J. F. & Teng, J. G. 2003a. Shear capacity of fiber-reinforced polymer-strengthened reinforced concrete beams: Fiber reinforced polymer rupture. *Journal of Structural Engineering*, 129, 615–625.
- Chen, J. F. & Teng, J. G. 2003b. Shear capacity of FRP-strengthened RC beams: FRP debonding. *Construction and Building Materials*, 17, 27–41.
- Dittrich, B., Wartig, K. A., Mulhaupt, R. & Schartel, B. 2014. Flame-Retardancy Properties of Intumescent Ammonium Poly(Phosphate) and Mineral Filler Magnesium Hydroxide in Combination with Graphene. *Polymers*, 6, 2875–2895.
- El-saikaly, G. & Chaallal, O. 2015. Cyclic performance of reinforced concrete T-beams strengthened in shear with fiber-reinforced polymer composites: Sheets versus laminates. *Journal of Reinforced Plastics and Composites*, 34, 1040–1058.
- Khalifa, A. & Nanni, A. 2002. Rehabilitation of rectangular simply supported RC beams with shear deficiencies using CFRP composites. *Construction and Building Materials*, 16, 135–146.
- Kim, Y. J. & Harries, K. A. 2011. Fatigue behavior of damaged steel beams repaired with CFRP strips. *Engineering Structures*, 33, 1491–1502.
- Li, X. & Gu, X. 2012. Bending bearing capacity of low strength reinforced concrete beams strengthened with carbon fiber composite sheets. *China Civil Engineering Journal*, 45, 23–29.
- Matthys, S. & Triantafillou, T. 2001. Shear and torsion strengthening with externally bonded FRP reinforcement. *Composites in Construction: A Reality*.
- Mofidi, A. & Chaallal, O. 2011. Shear Strengthening of RC Beams with EB FRP: Influencing Factors and Conceptual Debonding Model. *Journal of Composites for Construction*, 15, 62–74.
- Pellegrino, C. & Modena, C. 2002. Fiber reinforced polymer shear strengthening of reinforced concrete beams with transverse steel reinforcement. *Journal of Composites for Construction*, 6, 104–111.
- Suyan, W. & Yingwu, Z. 2007. New Concept in Shear Strength Prediction of RC Beam Bonded With FRP. *Industrial Construction*, 269–276.
- Taljsten, B. 2003. Strengthening concrete beams for shear with CFRP sheets. *Construction and Building Materials*, 17, 15–26.
- Triantafillou, T. C. 1998. Shear strengthening of reinforced concrete beams using epoxy-bonded FRP composites. *Aci Structural Journal*, 95, 107–115.
- Yost, J. R., Goodspeed, C. H. & Schmeckpeper, E. R. 2001. Flexural performance of concrete beams reinforced with FRP grids. *Journal of Composites for Construction*, 5, 18–25.
- Zhang, W., Wang, X. & Gu, X. 2010. Flexural behavior of corroded reinforced concrete beams strengthened with carbon fiber composite sheets. *China Civil Engineering Journal*, 43, 34–41.

Multi-criteria assessment of reinforced limestone powder concrete slabs and columns

A. Radović

Faculty of Technical Sciences, University of Priština in Kosovska Mitrovica, Kosovska Mitrovica, Serbia

H. Hafez

École Polytechnique Fédérale de Lausanne, Construction Materials Laboratory, Lausanne, Switzerland

N. Tošić

Civil and Environmental Engineering Department, Universitat Politècnica de Catalunya, Barcelona, Spain

S. Marinković

Faculty of Civil Engineering, University of Belgrade, Belgrade, Serbia

A. De la Fuente

Civil and Environmental Engineering Department, Universitat Politècnica de Catalunya, Barcelona, Spain

ABSTRACT: Given the established incentive to produce more sustainable concrete, the application of alternative and environmentally preferential materials, such as limestone (LS) powder, as partial cement (OPC) replacement, can make a significant global contribution toward sustainability. This paper presents the sustainability aspect of this green concrete through its potential application in reinforced concrete slabs and columns. For that purpose, 26 experimentally verified, concrete mixtures with and without LS powder were evaluated using the multi-criteria decision analysis framework ECO_2 . The conducted analyses show the significant potential and competitiveness of concrete with reduced cement and high LS powder content and their potential application in all types of reinforced concrete structures. In the case of slabs, the best ECO_2 score was obtained for concrete containing LS powder. In the second case, due to the nature of the structural performance requirements in columns, approximately equal sustainability potential of OPC and LS concretes was observed.

1 INTRODUCTION

Decarbonization of the construction sector could play an essential role in achieving a carbon neutral future. In the whole sector, the concrete industry is recognized as the largest emitter of CO_2 , principally because of the cement production phase (Working group UNEP-SBCI, 2015). It is estimated that about 90% of greenhouse gas in concrete are attributable to ordinary Portland cement (OPC), (Marinković et al., 2010). Moreover, 7–8% of total anthropogenic CO_2 emissions are a consequence of cement production with a tendency to grow up to 10% by 2030 (Miller et al., 2016). With this in mind, the application of locally available and environmentally preferential supplementary cementitious materials (SCMs), such as limestone (LS) powder, to partially replace OPC can make a significant global contribution toward sustainability.

Although numerous tests of the physical and mechanical properties of concrete have been successfully conducted in which more than 50% of cement has been replaced by LS powder, the average LS powder content in cement is only 6–7% globally (Working group UNEP-SBCI, 2015). These results show that adequate mechanical (Chen et al., 2014; Proske et al.,

2014), durability (Palm et al., 2016), as well rheological properties (Kwan et al., 2015; Rezvani et al., 2019) and workability (Proske et al., 2014) were achieved, even at high percentages (50%) of cement replacement. This makes LS concrete an attractive and potentially more sustainable alternative, which is crucial for its wide practical structural application.

Unfortunately, previous investigations were not followed by the appropriate economic and environmental assessments, and these are still missing. However, some studies in which the global warming potential (GWP) of LS concrete is analyzed were found (Celik et al., 2015). These studies show a potential reduction in GWP by up to 50% (Palm et al., 2016; Proske et al., 2014). The percentage of GWP reduction is usually closely related to cement reduction.

To fill the knowledge gap, the paper provides a holistic assessment of the suitability of structural application of concrete with a high LS powder content, by combining the environmental, economic, and structural performances. This could be a significant contribution to the research community as well as the construction sector. For that purpose, a multi-criteria decision analysis (MCDA) methodology is required. Evaluations of alternatives and determination of the optimal choice were done by using the MCDA framework ECO₂ method. The ECO₂ combines ECOlogical and ECONomic assessment (Hafez et al., 2021). Finally, the structural performances are taken into account by the appropriate adoption of functional units (FU).

2 MATERIALS AND METHODS

2.1 Materials

To ensure the structural applications, all concretes must meet certain conditions and the set criteria. The most important conditions include satisfactory workability, appropriate compressive strength as well as durability, i.e. service life. Besides that, as the main goal of this paper is the sustainability assessment of structural concrete with a high LS powder content, only concretes with partial replacement of cement by LS powder ($\geq 15\%$) including their control OPC concretes were considered. All selected conditions and criteria are listed in Table 1.

Table 1. Conditions and the set criteria that concrete must fulfill.

Criteria	Condition	Targets
1. Mix compositions	cement replacement	$\geq 15\%$
2. Workability*	slump/flow class	S2 ($\geq 50\text{mm}$)/F2 ($\geq 350\text{mm}$)
3. Compressive strength**	class	C20/25 ÷ C45-55
4. Durability/service life**	exposure class XC3	50 years

*(EN 12350-2, 2010; EN 12350-5, 2010); **(EN 1992-1-1, 2015).

The listed criteria were used during the literature search which was conducted in relevant databases such as Science Direct and Scopus. After applying the first criterion, over 150 tested concrete mixtures were selected from 10 studies (Radović et al., 2022). Finally, it was determined that 26 concrete mixtures, including 4 of our own, fulfill all the prescribed criteria. Nine mixes were control (OPC only) and 17 mixes included different ranges of partial

Table 2. Number of concrete mixtures in terms of cement content.

Number of mixtures	Cement content [kg/m^3]			
	>300	250–300	200–250	<200
Total	22	20	21	23
Selected	9	9	5	3

replacement by LS powder (nine with 15% LS, five with a 25–30% replacement range, and three mixtures in which 45–55% of cement is replaced by LS powder). For further analyses, mixes were grouped according to the total amount of cement (per m³), as follows: >300 kg (G1); 250–300 kg (G2); 200–250 kg (G3); <200 kg (G4) as shown in Table 2.

The composition of the selected concrete mixtures is shown in the database compiled by (Radović et al., 2022), which is available online. Mixtures have the following designations: XX-Y%-Z, where X is the symbol for the country of origin of the study, Y represents the percentage of cement replacement and Z is the mass per unit volume of the CEM I component in the concrete mix.

2.2 Applying the ECO₂ framework

2.2.1 LCA: Scope, Alternatives, and Scenarios definition

The first step of the ECO₂ analysis involves defining the scope of the LCA study, the scenarios, and the alternatives. A possible Cradle-to-Grave scope includes three main phases: “Production”, “Use” and “End-of-Life”. End-of-life phase activities such as the demolition, landfilling, or recycling of concrete into aggregates are omitted due to high future uncertainties. Similarly, in a lack of a reliable model to predict the CO₂ uptake of LS powder concrete, it was decided to exclude the “Use” phase too. The concrete production, transportation, and casting phases are the same for all alternatives and these were neglected, without affecting the comparisons. Finally, in this study, the Cradle-to-Gate scope which includes only the production and transportation of concrete mix constituents to the concrete batching plant was accepted, Figure 1.

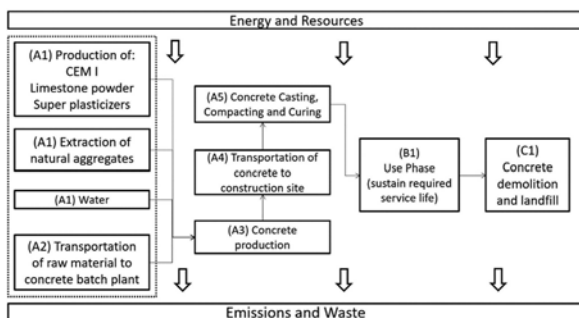


Figure 1. LCA boundary and the scope (Radović et al., 2022).

The alternatives under comparison in LCA are all the concrete mixes that passed the criteria specified in Table 1, and these are listed in the online database (Radović et al., 2022).

To perform a comprehensive analysis and include a sufficient number of parameters, two possible scenarios which include two types of structural elements were formed. In the first, the horizontal elements loaded in bending and shear, such as slabs, were analyzed. The second one included typical vertical elements - columns, dominated by the axial load.

2.2.2 LCA: Functional unit calculations

The functional unit (FU) is responsible for the quantification of the environmental and economic impact indicators. To allow proper evaluation and comparison of alternatives, FU has to include strength, durability, as well as serviceability (Marinković et al., 2021). Hence, the volume of concrete per 1 m² of the surface area of an RC slab and 1 m³ of the height of an RC column, required for the same strength, service life, and serviceability, was adopted for the FU.

For each scenario of structural element and loading, the minimum concrete cover that fulfills the required service life of 50 years was calculated. Concrete elements inside buildings with moderate humidity (exposure class XC3) were chosen. In the absence of a model for assessing the

durability of concrete with a high LS powder content, the proposal given in the draft of the new version of Eurocode 2 (prEN 1992-1-1, 2021) was used. Based on the measured carbonation depth, the carbonation rate $k_{(i)}$ is determined in accordance with (EN 12390-10, 2018) and compared to exposure resistance classes XRC, (CEN/TC 250/SC 2/WG 1/TG 10, 2021). Finally, the value of XRC was converted to a minimum concrete cover (Radović et al., 2022), by reading corresponding values from the table given in (CEN/TC 250/SC 2/WG 1/TG 10, 2021).

In the next step, the FU was corrected for strength and serviceability. A reduced amount of cement paste generally leads to reduced shrinkage and creep of LS concrete (Kwan et al., 2015; Rezvani et al., 2019), so similar serviceability (slab deflections, column displacement) was assumed for all alternatives in both scenarios. Therefore, there is no need for serviceability adjustment of the FU, only for strength.

In the case of the RC slab, scenario 1, the compressive strength of concrete has little influence on the load-bearing capacity, so it is neglected. This property is only indirectly (through carbonation resistance) included in FU, by the size of the concrete cover (c_{nom}). Assuming the same amount of reinforcement in the slabs, their flexural strength depends only on the effective depth d . Thus, the influence of reinforcement is the same for all alternatives and is also excluded from further analysis. Finally, in scenario 1, RC slabs with $d = 200$ mm, were adopted.

In scenario 2, RC columns on the ground floor of a 10-story building with the estimated ultimate axial load of $N_{Ed} = 4,000$ kN were analyzed. The design axial strength of column N_{Rd} can be expressed as:

$$N_{Rd} = N_{Ed} = A_c \cdot f_{cd} + A_s \cdot \sigma_s \quad (1)$$

where A_c = cross-sectional area of concrete; σ_s = compressive stress in the reinforcement.

The influence of reinforcement amount (A_s) on the resistance of the cross-section, since the same (minimum) area resulted the same in all alternatives, was neglected in the analysis. The required cross-sectional area can be determined from Equation 1, and thus the FU for each alternative in scenario 2.

Calculated FUs for all alternatives in both scenarios are available in the database (Radović et al., 2022).

2.2.3 LCA: Inventory data and impact assessment

Collecting the necessary inventory data is the last step before the impact assessment. It implies sourcing data on the energy and emissions associated with all materials and activities. Because of the dispersion of the experimental data sources and to increase the reliability of the assessments, a combining of databases such as Ecoinvent and data from previously published papers (Chen et al., 2010; Habert et al., 2012; Kurda et al., 2019; Tošić et al., 2015) was done by averaging the values.

The environmental impact was shown through six mid-point indicators: Global Warming Potential (GWP), Acidification Potential (AP), Eutrophication Potential (EP), Abiotic Depletion Potential (ADPE), Photochemical ozone creation potential (POCP), and Cumulative Energy Demand (CED).

The economic impact is encompassed through the market price, which includes all constituent materials and transportation costs.

The inventory database of the average values for each ingredient and the selected indicators is available online as well, (Radović et al., 2022).

For all alternatives, impacts per unit volume are calculated by multiplying the inventory of producing and transporting impacts of each constituent by its quantity. Variations in concrete performances across the different mixtures are taken into account by multiplying the total impact per unit volume and the functional unit of each alternative. Finally, all indicators are then normalized, according to Equation 2:

$$GWP_n = \frac{1.1 \cdot \max(GWP_i) - (GWP_i)}{1.1 \cdot \max(GWP_i) - 0.9 \cdot \min(GWP_i)} \quad (2)$$

In this way, the maximum values of indicators were enlarged and the minimum ones were diminished by 10% (Josa et al., 2021). Therefore, the alternative with the lowest impact gets a maximum value (< 1) and the one with the highest impact has a minimum value (> 0).

2.2.4 ECO_2 score calculations

Averaging all normalized environmental impact indicators, a single environmental impact indicator V is obtained. Finally, by weighting the normalized single environmental score V and the normalized market price X for each alternative, the ECO_2 score is calculated, Equation 3:

$$ECO_{2,i} = V_i \cdot W_1 + X_i \cdot W_2 \quad (3)$$

In this study, for each scenario and alternative, ECO_2 scores were calculated for 3 weight distributions, namely: the equal weights distribution ($W_1 = W_2$), the environmental advantage distribution ($W_1 = 2W_2$), and the economic advantage distribution ($W_2 = 2W_1$).

3 RESULTS AND DISCUSSION

The calculated sustainability (ECO_2) scores, for each alternative, regarding the cement content (for scenario 1) and concrete compressive strength (for scenario 2) are shown in Figure 2.

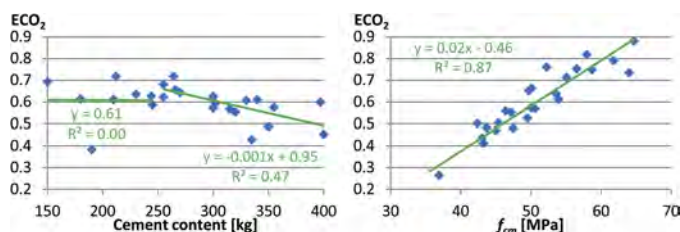


Figure 2. ECO_2 scores vs. cement content for scenario 1 (a) and compressive strength for scenario 2 (b).

Comparing ECO_2 scores and cement content (scenario 1), there are no reliably determined relations, but the trendlines appear to follow a bilinear relationship, with practically no dependence of the ECO_2 score on the cement content up to 250 kg and a somewhat inverse linear relationship afterwards ($R^2 = 0.0; 0.47$).

The main reason for this is the increased content of quite expensive plasticizers in some low-cement mixtures (< 250 kg), which impairs economic and consequently sustainability scores. Therefore, the sustainability benefit brought by lower cement content is not always guaranteed.

In scenario 2, a good positive correlation ($R^2 = 0.87$) between ECO_2 scores and compressive strength is clear. Due to the different structural performance requirements for vertical (versus horizontal) elements, this property is the most important. Every 10 MPa increase in compressive strength is followed by an average increase in the ECO_2 score of approximately 0.2, indicating its importance.

Figure 3 presents the calculated ECO_2 scores for the three best alternatives (with the highest ECO_2 scores) from each G1–G4 group in both scenarios. It seems that higher variations are observed in groups with lower cement content (particularly G4). In scenario 1, groups G1 and G2 showed the smallest score value variation of 0.02–0.06. The group G3 had slightly more (0.09), but G4 had the largest variation within the top three alternatives in each group, as much as 0.31. In scenario 2, the results of the top three alternatives within the groups are additionally influenced by the concrete compressive strength, so the variations are greater. Here, one should bear in mind the different numbers of mixtures in each group (only 3 mixtures in G3).

ECO_2 scores with a different distribution of weight coefficients (equal importance, the environmental advantage 2:1, and the economic advantage 1:2) for the best three concrete mixtures in both scenarios are shown in Figure 4.

For scenario 1, all these mixtures contain LS: IT-15%-212 (G3); CH-15%-264 (G2); RS-55%-150 (G4). As can be seen, groups G3 (200–250 kg), G2 (250–300 kg), and G4 (<200 kg) participate with one mixture each, i.e. there is no OPC (G1) concrete. The differences in ECO_2 scores between these mixtures are small enough (0.03), that none can be declared the best. In other words, all three should be considered potentially optimal solutions. Almost the same values of the ECO_2 scores (0.69–0.72) of the three best alternatives in this scenario, together with a high difference (0.22–0.26) in individual (environmental and economic) scores make alternatives sensitive to changing weight coefficients. This is especially pronounced for the mixtures which have a large deviation of the economic and environment scores, such as RS-55%-150 (0.56–0.83) and CH-15%-264 (0.61–0.82). Thus, in the case of environmental advantage, RS-55%-150 became the mixture with the highest score and CH-15%-264 with the lowest ones and vice versa, when criteria weights are changed in favor of the economy.

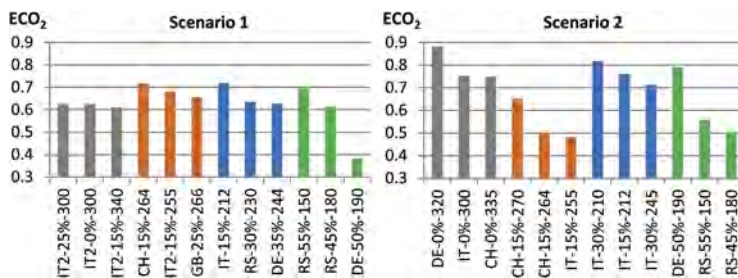


Figure 3. ECO_2 scores for the best three alternatives from each group: a) Scenario 1; b) Scenario 2.

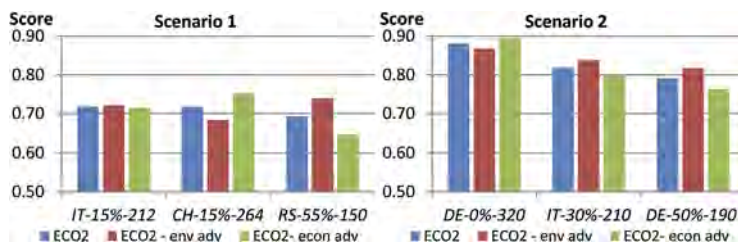


Figure 4. ECO_2 scores for the best three mixtures with different weight distributions: a) Scenario 1; b) Scenario 2.

The results obtained for scenario 2 showed a different order of alternatives. The three concrete mixtures with the highest ECO_2 score were: DE-0%-320 (G1), IT-30%-210 (G3), and DE-50%-190 (G4). One of the top three mixtures is from the G1 (>300 kg) group and two others contain LS (G3 and G4). The differences between the first and third mixture in the ECO_2 scores are about 0.09, three times higher than in the previous scenario. Due to the best economic (0.92) and good environmental (0.84) score, mixture DE-0%-320 with the ECO_2 score of 0.88 in scenario 2, followed by IT-30%-210 with a score of 0.82 represent potentially the most sustainable choice. Smaller differences between the environmental (0.04) and cost (0.21) criteria in scenario 2 make alternatives almost insensitive regardless of the value of the weights (the order of alternatives is unchanged).

4 SENSITIVITY ANALYSIS

The impact of critical variables (variation of concrete cover depth, costs of OPC, LS powder and superplasticizer, as indicated in Figure 4) on the sustainability scores was tested by sensitivity

analysis, Figure 5. The results showed that there is no effect of the tested variables on the ranking of best alternatives in scenario 2 (only a change in relative differences), but it has in scenario 1. This is due to negligible differences between the overall ECO_2 scores of the alternatives in scenario 1, as well as the large differences in individual indicator scores within certain alternatives. Accordingly, the variation in the input data does not cause excessive changes in the final sustainability scores, but relatively small changes are sufficient to affect the ranking.

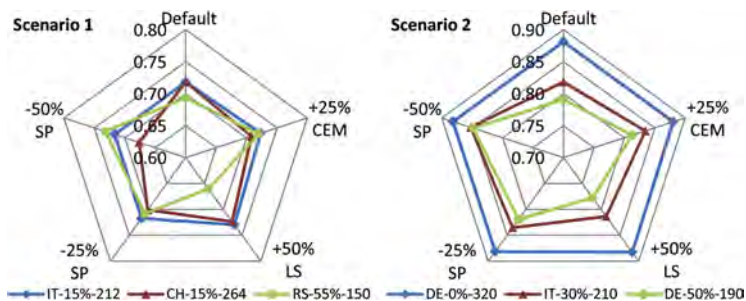


Figure 5. ECO_2 scores regarding sensitivity analysis for the best 3 mixtures: a) Scenario 1; b) Scenario 2.

5 CONCLUSIONS

In this paper, a multi-criteria analysis framework ECO_2 was used to assess the sustainability potential of reinforced LS powder and comparable OPC concrete slabs and columns. For this purpose, 26 experimentally verified concrete mixtures were evaluated through economic, environmental, as well as performance-based criteria. Mixtures were grouped according to the amount of cement in four groups: >300 kg (G1); 250–300 kg (G2); 200–250 kg (G3); <200 kg (G4).

Based on the conducted research, the following conclusions can be drawn:

- Concrete compressive strength has an indirect effect (through the concrete cover depth) on FU for flexural elements (slabs), while it is crucial for axially loaded elements (columns). When it comes to columns, increasing the concrete compressive strength by every 10 MPa brings a high average increase in ECO_2 scores of about 0.2.
- In the case of RC slabs (scenario 1), the best five mixtures with almost equal ECO_2 scores (0.67-0.72) represent potentially optimal solutions. All these mixtures belong to LS concretes: CH-15%-264, IT-15%-255, GB-25%-266 (G2); IT-15%-212 (G3); RS-55%-150 (G4).
- In the case of RC columns (scenario 2), there are only two potentially optimal solutions: DE-0%-320 (G1), and IT-30%-210 (G3). Due to the higher compressive strength of OPC concrete, and its decisive influence, an equal presence of LS and OPC concretes was observed.
- Large deviations between environmental and economic scores within some mixtures in scenario 1, coupled with the close overall scores, make these sensitive to eventual changes in input parameters or weights.
- At the same time, the results showed that the inputs or weights changes have influence only in relative differences of alternatives in scenario 2; therefore, the order is unchanged.

The results of this study depend on numerous assumptions and should not be generalized when interpreting conclusions until further research is conducted with a large number of alternatives and a wider range of input parameters.

FUNDING

This work was supported by The Ministry for Education, Science and Technology, Republic of Serbia [grant number TR36017].

REFERENCES

- Celik, K., Meral, C., Petek Gursel, A., Mehta, P.K., Horvath, A., Monteiro, P.J.M., 2015. Mechanical properties, durability, and life-cycle assessment of self-consolidating concrete mixtures made with blended portland cements containing fly ash and limestone powder. *Cem. Concr. Compos.* 56, 59–72. <https://doi.org/10.1016/j.cemconcomp.2014.11.003>
- CEN/TC 250/SC 2/WG 1/TG 10, 2021. Background Document for prEN1992-1-1:2020 D7 clause 6 - Durability. Eur. Comm. Stand. Brussels.
- Chen, C., Habert, G., Bouzidi, Y., Jullien, A., Ventura, A., 2010. LCA allocation procedure used as an incitative method for waste recycling: An application to mineral additions in concrete. *Resour. Conserv. Recycl.* 54, 1231–1240. <https://doi.org/10.1016/j.resconrec.2010.04.001>
- Chen, J.J., Kwan, A.K.H., Jiang, Y., 2014. Adding limestone fines as cement paste replacement to reduce water permeability and sorptivity of concrete. *Constr. Build. Mater.* 56, 87–93. <https://doi.org/10.1016/j.conbuildmat.2014.01.066>
- EN 12350–2, 2010. Testing fresh concrete – Part 2: Slump test. Eur. Comm. Stand. Brussels.
- EN 12350–5, 2010. Testing fresh concrete – Part 5: Flow test. Eur. Comm. Stand. Brussels.
- EN 12390–10, 2018. Testing hardened concrete - Part 10: Determination of the carbonation resistance of concrete at atmospheric levels of carbon dioxide. Eur. Comm. Stand. Brussels.
- EN 1992-1-1, 2015. Eurocode 2: Design of concrete structures - Part 1-1, General rules and rules for buildings. Eur. Comm. Stand. Brussels.
- Habert, G., Arribe, D., Dehove, T., Espinasse, L., Roy, R. Le, 2012. Reducing environmental impact by increasing the strength of concrete: Quantification of the improvement to concrete bridges. *J. Clean. Prod.* 35, 250–262. <https://doi.org/10.1016/j.jclepro.2012.05.028>
- Hafez, H., Kurda, R., Al-Ayish, N., Garcia-Segura, T., Cheung, W.M., Nagaratnam, B., 2021. A whole life cycle performance-based ECONomic and ECOlogical assessment framework (ECO2) for concrete sustainability. *J. Clean. Prod.* 292. <https://doi.org/10.1016/j.jclepro.2021.126060>
- Josa, I., Tošić, N., Marinković, S., De La Fuente, A., Aguado, A., 2021. Sustainability-oriented multi-criteria analysis of different continuous flight auger piles. *Sustain.* 13, 1–16. <https://doi.org/10.3390/su13147552>
- Kurda, R., de Brito, J., Silvestre, J.D., 2019. CONCRET_{Top} - A multi-criteria decision method for concrete optimization. *Environ. Impact Assess. Rev.* 74, 73–85. <https://doi.org/10.1016/j.eiar.2018.10.006>
- Kwan, A.K.H., Chen, J.J., Jiang, Y., 2015. Adding limestone fines as cement paste replacement to reduce shrinkage of concrete. *Mag. Concr. Res.* 65, 942–950. <https://doi.org/10.1680/mac.13.00028>
- Marinković, S., Carević, V., Dragaš, J., 2021. The role of service life in Life Cycle Assessment of concrete structures. *J. Clean. Prod.* 290. <https://doi.org/10.1016/j.jclepro.2020.125610>
- Marinković, S., Radonjanin, V., Malešev, M., Ignjatović, I., 2010. Comparative environmental assessment of natural and recycled aggregate concrete. *Waste Manag.* 30, 2255–2264. <https://doi.org/10.1016/j.wasman.2010.04.012>
- Miller, S.A., Horvath, A., Monteiro, P.J.M., 2016. Readily implementable techniques can cut annual CO₂ emissions from the production of concrete by over 20%. *Environ. Res. Lett.* 11. <https://doi.org/10.1088/1748-9326/11/7/074029>
- Palm, S., Proske, T., Rezvani, M., Hainer, S., Müller, C., Graubner, C.A., 2016. Cements with a high limestone content - Mechanical properties, durability and ecological characteristics of the concrete. *Constr. Build. Mater.* 119, 308–318. <https://doi.org/10.1016/j.conbuildmat.2016.05.009>
- prEN 1992-1-1, 2021. Eurocode 2: Design of concrete structures - Part 1-1: General rules - Rules for buildings, bridges and civil engineering structures. Eur. Comm. Stand. Brussels.
- Proske, T., Hainer, S., Rezvani, M., Graubner, C.-A.A., 2014. Eco-friendly concretes with reduced water and cement content – Mix design principles and application in practice. *Constr. Build. Mater.* 67, 413–421. <https://doi.org/10.1016/j.conbuildmat.2013.12.066>
- Radović, A., Hafez, H., Tošić, N., Marinković, S., de la Fuente, A., 2022. ECO2 framework assessment of limestone powder concrete slabs and columns. *J. Build. Eng.* 57, 104928. <https://doi.org/10.1016/j.jobe.2022.104928>
- Rezvani, M., Proske, T., Graubner, C.A., 2019. Modelling the drying shrinkage of concrete made with limestone-rich cements. *Cem. Concr. Res.* 115, 160–175. <https://doi.org/10.1016/j.cemconres.2018.09.003>
- Tošić, N., Marinković, S., Dašić, T., Stanić, M., 2015. Multicriteria optimization of natural and recycled aggregate concrete for structural use. *J. Clean. Prod.* 87, 766–776. <https://doi.org/10.1016/j.jclepro.2014.10.070>
- Working group UNEP-SBCI, 2015. Eco-efficient cements: Potential economically viable solutions for a low-CO₂ cement-based materials industry. United Nations Environ. Progr. - Sustain. Build. Clim. Initiat. 1–64.

Development of life-cycle inventory for timber products to support the circular economy in construction

S. Ge, P.J. McGetrick, C. O’Ceallaigh & A.M. Harte

Timber Engineering Research Group, Ryan Institute, University of Galway, Galway, Ireland

ABSTRACT: The supply of raw materials from Irish forests is forecasted to double between 2017-2035, creating opportunities to increase the output of timber products for construction. Furthermore, residential building construction in Ireland needs to achieve an average annual rate of completion of up 35,000 within the next decade to meet housing demands and population growth. A significant challenge for sustainable construction globally is materials with high embodied carbon, like steel and concrete, remain the primary structural material choices. Although the potential increase in carbon emissions from future construction can be minimised through substitution using timber products, full lifecycle assessment and comparison of such structural solutions to quantify the climate mitigation benefits can be limited by a lack of detailed lifecycle data. Therefore, this paper summarises the development of a national reference database for this lifecycle information and presents a quantification of the lifecycle impacts of Irish timber solutions for sustainable construction.

1 INTRODUCTION

The latest assessment report launched by the IPCC showed we are currently at 1.5 times the greenhouse gas (GHG) concentrations compared with the 1850 level (IPCC, 2014). In Ireland, the total GHG emissions (excluding LULUCF) in 2021 were 61.53 Mt CO₂ eq (EPA, 2022), with agriculture, transport, and energy industries being the first three influential sectors, accounting for 71.9%; still, the contribution of the building sector is not clearly stated in this report. A recent study outlined that the Irish built environment is responsible for 37% of Irish GHG emissions in a standard year (i.e., 2018), containing operational (23%) and embodied carbon (14%) (IGBC, 2022). To mitigate the pressure of climate change, Ireland has committed to reducing GHG emissions to half of the 2018 level by 2030 and reaching net zero by 2050. In the total emissions reduction, the building sector is allocated to a challenging 44-56% burden within executive measures, such as retrofitting houses and introducing renewable energy heating systems for both existing and new dwellings (Government of Ireland, 2021). Moreover, similar to global trends, the Central Statistics Office (CSO) reported that Ireland’s population is forecasted to increase to between 5.6 and 6.7 million by 2051, bringing more housing demand simultaneously. The National Development Plan 2021-2023 predicts that 600,000 new homes will be required by 2040, meaning roughly 33,000 new residential buildings are needed each year. Considering the rising housing demand and the significant load the building industry takes to mitigate GHG emissions, timber is an excellent structural material option for building construction.

Unlike traditional building materials like concrete and steel, timber is a low embodied carbon material; its use in place of concrete and steel can considerably reduce the embodied carbon emissions in building projects. Operational carbon emissions (OCE) and embodied carbon emissions (ECE) are two leading indicators to assess a building’s atmospheric impact. OCE indicates the emissions caused by energy consumption during the building’s use stage, while ECE is mainly related to the emissions from materials and other stages like construction,

transportation, deconstruction, etc. Many studies have substantiated the excellent performance of timber in decreasing carbon emissions. Skullestad et al. (2016) studied timber and reinforced concrete structures under different building heights, finding that the former caused 34-84% less climate change impact than the latter. Assuming natural gas heating is replaced by the incineration of recovery wood residues, the climate change impact saving by timber structures can be increased to 220% approximately (Skullestad et al., 2016). Laurent et al. (2018) studied an existing arena in North America that integrated glued laminated timber beams with steel. They found that the hybrid structure reduced the total emissions by 83 tonnes of CO₂ eq compared to the whole steel structure. Moreover, Murphy et al. (2015) localised LCA research on Irish timber products in seven manufacturing scenarios. They found that GHG emissions can be further reduced by integrating combined heat and power (CHP) plants with sawmills, as CHP plants can transform the co-products during production (e.g., sawdust) into energy and feed it back for production (Murphy et al. 2015).

Considering the great potential of wood in GHG emissions reduction, this paper focuses on timber construction products and subsequent contexts are organised as follows: Section 2 analyses the Irish timber products and gives some reasons for low timber frame application in Ireland. Section 3 introduces the lifecycle assessment (LCA) and compares Irish and international LCA practices in timber construction. Section 4 presents a general lifecycle inventory (LCI) model for Irish timber products. After a simple application of EPD, Section 5 discusses several controversial points in timber's lifecycle assessment.

2 IRISH TIMBER PRODUCTS ANALYSIS

Timber products used in Ireland can be broadly classified into structural and non-structural use. Sawn timber and wood-based panels (WBP) are the most representative products in the former category, and the latter includes wood used for energy generation, paper production, horticulture, etc. Sawn timber indicates products made from large diameter logs, which can provide excellent performance for structural use. WBP commonly refers to the panels comprising compressed layers of wood, typically combined through adhesives or fasteners. Based on the wood size used in panels, this paper divides WBP into four levels, shown in Figure 1. The smallest wood size level is the fibre level, of which medium-density fibreboard (MDF) is a typical representative. Strand level products include oriented strand board (OSB), laminated strand lumber (LSL) and parallel strand lumber (PSL); PSL organises wood strands in parallel - OSB and LSL are layered in perpendicular directions. At the veneer level, normal plywood laminates wood sheets with adhesives in a direction where the grain of adjacent layers is perpendicular to each other. In laminated veneer lumber (LVL), the grain of all layers is oriented in the same direction; laminated veneer board (LVB) organises internal layers in a grain-parallel way, with outer layers perpendicular to the inner direction. The last level is the semi-manufactured level, meaning the wood used in these products has already been processed. Cross-laminated timber (CLT) and glue-laminated timber (GluLam) are both manufactured by gluing layers of sawn lumber together, but the grain in adjacent CLT layers is cross-oriented and GluLam layers are in parallel. Unlike CLT and GluLam, dowel laminated timber (DLT) and nail laminated timber (NLT) use wood dowels and metal nails, respectively, to fasten multiple boards to make larger panels.

Ireland is export-oriented in the forest products sector, and over 80% of WBP is exported overseas, where the UK, Germany, and Benelux countries are the primary markets. However, the application rate of timber frames in Ireland is much lower than in many other European countries. The Timber Frame Housing Report 2002 estimated that timber frame housing accounted for up to 15% of the total output in 2001 and 2002 (Government of Ireland, 2002). The Irish Timber Frame Manufacturers Association (ITFMA) also pointed out that about 30% of new dwellings are timber frame (IFFPA, 2016), and as of 2022, this figure could be as high as 50% for low rise residential buildings. However, these figures are far lower than Finland's at 80%, Scotland's at 83%, and Sweden's at 90% (Kitekuzman et al., 2017). In addition, annual wood-flow reports by COFORD from 2010 to 2018 show that the average proportion of timber products used in construction is 26%. However, Ireland's total roundwood harvest (including

firewood) keeps increasing from 2.9 million cubic meters in 2010 to 3.7 million cubic meters in 2018 and is forecasted to double to 7.9 million cubic meters in 2035 (IFFPA, 2016). In summary, there is significant potential to increase the use of Irish wood for construction applications.

The reasons for Ireland’s low timber frame application rate can be boiled down to two points. First, Ireland has the lowest forest area (%of land area) in EU countries, excluding Malta and the Netherlands. Although Ireland has extended its forest area from 6.7% in 1990 to 11.4% in 2020, it is still lower than the average value (i.e., 34.1% in 2020) of EU countries (The World Bank Group, 2020). Secondly, there is no significant culture of building with wood in Ireland, and there are many misconceptions about how timber frame construction will behave in Ireland’s climate. Finally, there is a lack of lifecycle assessment data on Irish timber products which would give the general public and building specifiers confidence when specifying environmentally sustainable solutions such as wood for buildings. Addressing this final point is the focus of the paper, and the next section will specifically analyse the gaps between Irish and international LCA practices in timber construction.

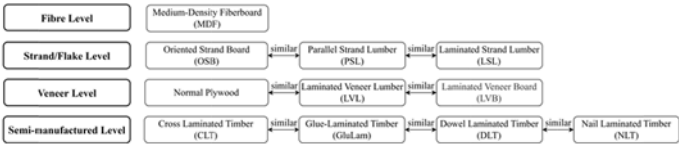


Figure 1. Classification of the wood-based panel (WBP).

3 COMPARISON OF LCA PRACTICES IN TIMBER CONSTRUCTION

Lifecycle assessment (LCA) in the construction industry indicates the environmental impact estimation of building projects within a defined system boundary. A typical LCA starts with the goal and scope definition, then followed by inventory analysis and impact assessment, and ends with specific interpretations (ISO 14040:2006). For particular projects, LCA is flexible in the research object and system boundary definition. The studied target can be the whole building or a single product, and the system boundary can be cradle-to-gate, cradle-to-grave, and cradle-to-cradle. I.S. EN 15978:2011 defines the system boundary for the building’s lifecycle assessment, composed of four stages: (i) the product stage, (ii) the construction stage, (iii) the use stage, and (iv) the end-of-life stage (Figure 2). The cradle-to-gate system refers to the first stage (i.e., A1-A3), and the cradle-to-grave system indicates the whole building life (i.e., A1-C4). After considering materials recovery and reuse within the boundary, it can be called the cradle-to-cradle system or circular economy (i.e., A1-D). If categorised by the type of carbon emissions, B6 and B7 phases are related to OCE, and ECE happens in the rest phases, of which A1-A3 contribute the most. This paper focuses on the embodied sector of Irish and international LCA practices for four timber products frequently used in construction: sawn timber, OSB, MDF, and CLT.

3.1 Overview of Irish and international LCA practices

Environmental product declarations (EPDs) provide a universal approach to comparing and evaluating the environmental performances of a product. The international EPD system is now the oldest operational EPD programme in the world and the reference of many national programmes. In March 2018, the Irish Green Building Council (IGBC) activated a localised EPD programme, EPD Ireland, enabling Irish manufacturers to develop EPDs for their products. However, there are no mandatory regulations or laws for their use in Ireland, which limits their use. By contrast, MPG (Milieu Prestatie Berekening) is already in force in the Netherlands for every environmental permit concerning all new-built residential and office buildings over 100 m², whether public or private. The MPG combines all environmental indicators into the shadow cost of materials applied in the building with the unit of Euro per square meter GFA (gross floor area) per year. France also issued a decree (No. 2021-1104) in

July 2021 on energy and environmental performance requirements for all new buildings, including residential, office, and primary or secondary educational buildings. The climate impact indicators include two categories, one for materials and site impact (similar to OCE) and another for energy consumption (similar to ECE).

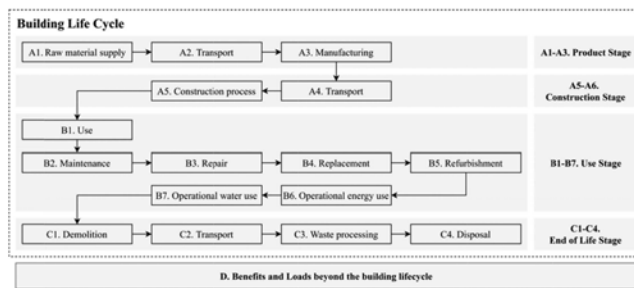


Figure 2. System boundary definition.

In addition to the absence of mandatory regulations, Ireland falls behind many nations in the amount of declared EPDs, particularly for wooden products. Several EPD websites were searched using the following keywords: timber, lumber, wood, CLT, MDF, and OSB. At the time of writing, the EPDs published by EPD Ireland have just exceeded 80 EPDs, with about 11 linked to wood products. In comparison, the IBU of Germany has collected 1734 published EPDs, of which 50 EPDs are related to wood products. The INIES of France contains approximately 150 EPDs about wood products of 6977 environmental data in total. The following section discusses the differences between the EPDs of selected timber products between Ireland and other countries.

3.2 EPD comparison

The comparison examines five EPDs from different countries (including Ireland) for four timber products, as outlined in Table 1. All selected EPDs comply with ISO 14025 and I.S. EN 15804, so they are comparable with each other. The UK or European level is chosen as a reference where an EPD from Ireland is unavailable, and only three EPDs are collected and compared for OSB.

Tables 1 and 2 highlight that Ireland only has EPDs for MDF and OSB. The International EPD System is the most frequently used programme among the 18 studied EPDs, e.g. EPD Turkey and EPD Australasia are aligned as regional members of this system. Following the global standard, the IBU of Germany is the second programme with high adoption, covering all four products. Although EPD Ireland is independent of the International EPD System, IGBC has joined the Eco Platform, an organisation of European EPD programme operators, ensuring that all the EPDs published by EPD Ireland can be visible across Europe.

Furthermore, differences can be found in some specific EPD items between Irish and international LCA practices. First, nearly 80% of the studied EPDs select 1 m³ as the declared unit, and some use 1 m² with a defined thickness for WBPs, while Ireland uses 1 tonne to calculate the environmental impact of MDF and OSB. Second, I.S. EN 15804 was revised in July 2019 (i.e., I.S. EN 15804+A2), increasing the required indicators to nineteen from eleven. In the latest version, the global warming potential (GWP) is divided into three sub-indicators: GWP-F, GWP-B, and GWP-Luluc, accounting for GWP related to fossil fuels, biogenic carbon and land use and land use change, respectively. In Table 1, nearly half of EPDs contain all three categories, and some only include the total GWP value due to their early issue time. The EPDs published by EPD Ireland have not incorporated the GWP-Luluc.

Finally, I.S. EN 15804+A2 states that modules A1-A3, C1-C4, and D must be declared in all construction products unless the conditions to exclude modules C1-C4 and D are met. The declared modules of EPDs are shown in Table 2, where 50% of them cover all the required

stages, and 80% incorporate environmental impacts from the wood waste treatment (i.e., modules C3-C4) and corresponding benefits and burdens beyond the building life (i.e., module D). However, the EPD for MDF from MEDITE omits the D stage, and the EPD for OSB from SMARTPLY only declares the A1-A3 stages. Therefore, Ireland still has a long way to go compared with other countries in LCA practices for timber products.

Table 1. EPDs used in comparison.

Category	Declared unit	EPD owner	Validity	Scope	Programme
Sawn timber	1 m ³ kiln dried planed or machined sawn timber used as structural timber ¹	Wood for Good	10/04/17-09/04/22	UK	BRE
	1 m ³ sawn kiln-dried softwood	Wood Solutions	14/02/22-14/02/27	Australia	EPD Australasia
	1 m ³ kiln dried, rough sawn and planed EGGER timber	Fritz EGGER GmbH	29/07/21-09/05/26	Germany	IBU
	1 m ³ Swedish sawn dried timber of spruce or pine	Swedish Wood	22/01/21-22/01/26	Sweden	International EPD System
	1 m ³ radiata pine sawn board	Baskegur	07/10/19-03/10/23	International ²	International EPD System
MDF	1 t MEDITE clear MDF	MEDITE	12/03/21-12/03/26	Ireland	EPD Ireland
	1 m ² uncoated MDF, 200mm thick	Daiken New Zealand Ltd	25/01/19-25/01/24	New Zealand	EPD Australasia
	1 m ³ EGGER MDF, uncoated	Fritz EGGER GmbH	10/05/21-09/05/23	Germany	IBU
	1 m ³ raw MDF	Financier Maderera S.A.	12/04/22-12/04/27	Spain	International EPD System
	1 m ³ MDF	Kastamonu Entegre Agac Sanayi ve Ticaret A.S.	10/02/21-09/02/26	International ³	EPD Turkey
OSB	1 t SMARTPLY OSB3	SMARTPLY	11/11/19-11/11/24	Ireland	EPD Ireland
	1 m ³ EGGER OSB	Fritz EGGER GmbH	03/09/18-02/09/23	Germany & Romania	IBU
	1 m ³ Norbord OSB	Norbord Europe Ltd	31/01/20-30/01/25	International ⁴	International EPD System
CLT	1 m ² of coated Rock Mineral Wool CLT, 100 mm thick ⁵	Knauf Insulation Sprl	10/12/21-10/12/26	Europe	International EPD System
	1 m ³ CLT, packaged	Red Stag Wood Solutions	08/02/22-08/02/27	New Zealand	EPD Australasia
	1 m ³ of Binderholz CLT BBS	Binderholz Bausysteme GmbH	20/03/19-19/03/24	Austria & Germany	IBU
	1 m ³ CLT	Stora Enso	10/02/21-11/02/26	Austria & Sweden	International EPD System
	1 m ³ Crosslam Kuhmo CLT	CrossLam	12/04/21-28/01/26	Finland	RTS

1 Take the UK level as the reference for Irish sawn timber.

2 The EPD data is from four companies, representing 65% of the sawn wood in the Basque Country.

3 The assumptions of the C and D modules are referred to as the global.

4 The OSB is manufactured by two factories in Inverness (UK) and Genk (Belgium) and supplied globally.

5 Take the European level as the reference for Irish CLT.

Table 2. LCA modules declared in EPDs.

Category	Indicators ¹ (GWP-)	A1-3	A4	A5	B1-7	C1	C2	C3	C4	D
Sawn timber	T	X	X	X		X	X	X	X	X
	F/B/T	X						X	X	X
	F/B/Luluc/T	X				X*	X	X	X*	X
	F/B/Luluc/T	X				X	X	X	X*	X
	T	X								
MDF	F/B/T	X	X				X	X	X	
	F/B/T	X						X	X	X
	F/B/Luluc/T	X				X*	X	X	X*	X
	F/B/Luluc/T	X				X*	X	X	X	X
	F/B/Luluc/T	X				X	X	X*	X	X
OSB	F/B/T	X								
	T	X						X		X
	T	X	X							
CLT	F/B/Luluc/T	X	X	X	X*	X*	X	X*	X	X
	F/B/T	X						X	X	X
	T	X		X			X	X		X
	F/B/Luluc/T	X	X	X	X*	X	X	X	X	X
	F/B/Luluc/T	X	X	X		X*	X	X	X	X

1 GWP-F: GWP fossil fuels, GWP-B: GWP biogenic, GWP-Luluc: GWP land use and land use change, GWP-T: GWP total. * No environmental impact in the stage, although it is declared.

4 THE LIFECYCLE INVENTORY FOR IRISH TIMBER PRODUCTS

In terms of the gaps identified during the comparison, this sector develops a general lifecycle inventory (LCI) for lifecycle analysis of Irish timber products. Before the LCI analysis, the studied system boundary needs to be defined; modules A1-A3, C1-C4, and D are mandatory stages (I.S. EN 15804+A2). In addition, as the contribution of GWP-Luluc in different stages for the eight EPDs is less than 1%, this indicator is excluded from the following discussion.

4.1 Modules A1-A3

Modules A1-A3 refer to the production stage, from the raw materials supply to the packaging of finished products, also called the cradle-to-gate system. For timber products, this stage should include all steps from tree seeding to the completed products leaving the factory. During the production phase, the sources of GHG emissions and removals are from three sectors: (i) energy consumption, (ii) materials, and (iii) waste treatment.

Energy consumption to produce timber products must consider electricity and thermal energy, as almost all the manufacturing of timber products requires the drying process to reduce the moisture content. In 2020, the energy input to Ireland's electricity generation was still dominated by natural gas (i.e., 52%), although the contribution of renewable energy has increased to 42% from 6% in 2005. Thanks to the greener energy mix, the CO₂ intensity of Ireland's electricity grid has decreased to 296 g CO₂/kWh in 2020 from 636 g CO₂/kWh in 2005 (SEAI, 2020). As for emissions from thermal energy, it depends on how much carbon is stored in the wood waste used as biomass fuel. Thus, factory-specific data needs to be recorded during the manufacturing process.

Different from conventional construction materials, such as concrete and steel, timber contributes carbon removals due to CO₂ sequestration during its growth. The stored, or biogenic, carbon relates to the GWP-B indicator. I.S. EN 16449 provides a formula to calculate CO₂ from the biogenic carbon in wood, and all studied EPDs comply with this method.

$$P_{CO_2} = \frac{44}{12} \times cf \times \frac{\rho_w \times V_w}{1 + \frac{w}{100}} \quad (1)$$

where 44/12 indicates 1 kg biogenic carbon equals 44/12 kg CO₂; cf = carbon fraction of woody biomass (default value is 0.5); ω = moisture content of the product (%); ρ_ω = density of woody biomass of the product at that moisture content (kg/m³); V_ω = volume of the wood material in the product at that moisture content (m³).

Other materials required in timber products, such as glue for the lamination of wood boards, should also be considered. The EPD owner should ask for the original data from material suppliers to calculate corresponding GHG emissions if the materials are not produced in the same factory. Finally, the processing up to the end-of-waste state should be included for all wastes in this stage, like wood and packaging materials.

4.2 Modules C1-C4 & D

Modules C1-C4 (i.e., end-of-life stage) start from building dismantling to transportation of wastes and end with waste treatments. As module D needs to declare the benefits and burdens related to waste treatments, it is also discussed in this sector. Furthermore, modules C1-C2 are excluded because the product market might be worldwide, and four end-of-life scenarios are listed below.

Table 3. GHG emissions in four end-of-life scenarios for wood material.

Scenarios	C3	C4	D
Reuse	BR	ND	Benefits of avoiding producing the same amount of new products
Recycling	BR + emissions from processing wood waste to a ready-for-recycling state	ND	Benefits of avoiding producing the same amount of new materials
Incineration	BR	ND	Energy recovery
Landfill	ND	ND	ND

BR: biogenic carbon release. ND: not declared.

In all studied EPDs that cover modules C3 and C4, 33% use mix scenarios for the wood waste treatment and 26% calculate the ECE separately in different scenario assumptions. Only one scenario is taken into account for the remainder, with 5 EPDs considering incineration and 1 EPD considering landfill. As shown in Table 3, each scenario can get corresponding benefits declared in module D except for landfill. However, the landfill gas generated from degrading organic carbon in the wood waste can also be combusted for energy recovery, and EPD Australasia has already applied this. In terms of Ireland, the EPD for MEDITE MDF defines a 50/50 allocation for incineration and landfill. However, research showed that about 96% of the wood waste in Ireland is used as biomass fuel; only 4% goes to landfill (Cristescu et al., 2020). The differences between product EPDs and the national market highlight that as much data as possible should be collected and analysed for precise end-of-life scenario allocations.

In addition to applying reasonable end-of-life assumptions, other data should be considered. For example, most EPDs assume wood properties will not change during usage, but the density and moisture content in the wood waste should be remeasured for a more accurate biogenic carbon estimation. Moreover, it still requires data related to energy consumption in waste processing and facility efficiency in energy recovery for GHG emissions calculation.

4.3 A simple EPD application in Ireland

An EPD application on a typical Irish timber frame house with 2 storeys (Table 4) reveals more issues waiting to be solved. It can be seen that modules A4-A5 and C1-C2, omitted in the LCI analysis, contribute 40% of the total GWP when applying the EPD owned by Wood for Good. These components are too significant to be excluded. Moreover, the EPDs of EGGER and Swedish Wood both assume 100% incineration at the end-of-life, but the figures vary significantly (i.e., -4941 and -1415 kg CO₂ eq, respectively) for adopting different incineration efficiency and energy types for recovery.

Table 4. Application of EPD for Irish sawn timber (12.2 m³).

EPD owner	GWP-T (kg CO ₂ eq)								
	A1-A3	A4	A5	C1	C2	C3	C4	D	Total
Wood for Good	-8686	95	506	155	90	9455	112	-3062	-1336
Wood Solutions	-9321	-	-	-	-	0	706	-3	-8618
Fritz EGGER GmbH	-8491	-	-	0	18	9833	0	-4941	-3581
Swedish Wood	-9077	-	-	3	81	9443	0	-1415	-965
Baskegur	-8320	-	-	-	-	-	-	-	-8320

5 CONCLUSION

Based on the EPDs reviewed in this paper, modules A1-A3, C3-C4, and D are expected to be included in the LCA for Irish timber products. Considering that the UK is the primary market for Irish timber, modules A4-A5 and C1-C2 should also be added according to typical transit modes and construction styles in the UK. To build a precise Irish LCI for timber products, further research will be oriented towards (i) obtaining more specific details on Irish wood products to make suitable assumptions in filling the gaps in required modules and (ii) determining a realistic end-of-life scenario for Irish wood waste.

REFERENCES

- Cristescu, C. et al. 2020. Design for deconstruction and reuse of timber structures-state of the art review.
- EPA. 2022. *Ireland's provisional greenhouse gas emissions (1990 – 2021)*. Wexford: Environmental Protection Agency.
- Government of Ireland. 2002. *Timber frame housing report 2002*. Dublin: The Department of Environment, Local Government and Heritage.
- Government of Ireland. 2021. *Climate action plan 2021*. Dublin: Department of Environment, Climate and Communications.
- Government of Ireland. 2021. *National development plan 2021-2030*. Dublin: Department of Public Expenditure and Reform.
- IFFPA. 2016. *An overview of the Irish forestry and forest products sector 2016*. Dublin: Irish Forestry and Forest Products Association.
- IGBC. 2022. *Whole life carbon in construction and the built environment in Ireland (the fourth draft)*. Dublin: The Irish Green Building Council.
- IPCC. 2015. *Climate change 2014: synthesis report*. Cambridgeshire: Cambridge University Press.
- I.S. EN 15804. Sustainability of construction works - Environmental product declarations - Core rules for the product category of construction products.
- I.S. EN 15978:2011. *Sustainability of construction works - Assessment of environmental performance of buildings - Calculation method*.
- I.S. EN 16449:2014. *Wood and wood-based products - Calculation of the biogenic carbon content of wood and conversion to carbon dioxide*.
- ISO 14025:2006. *Environmental labels and declarations — Type III environmental declarations — Principles and procedures*.
- ISO 14040:2006. *Environmental management — Life cycle assessment — Principles and framework*.
- Kitek Kuzman, M., Lähtinen, K., Sandberg, D. 2017. Initiatives Supporting Timber Constructions in Finland, Slovenia and Sweden. *Forest Sector Innovations for a Greener Future*. Vancouver, BC. 12-16 June.
- Laurent, A.-B., Van Der Meer, Y., Villeneuve, C. 2018. Comparative Life Cycle Carbon Footprint of a Non-Residential Steel and Wooden Building Structures. *Current Trends in Forest Research*.
- Murphy F., Devlin G., Mc Donnell K. 2015. Greenhouse gas and energy based life cycle analysis of products from the Irish wood processing industry. *Journal of Cleaner Production* 92: 134–141.
- SEAI. 2020. *Electricity statistics in Ireland*. Viewed in November 2022. <https://www.seai.ie/data-and-insights/seai-statistics/key-statistics/electricity/>
- Skullestad, J.L., Bohne, R., Lohne, J. 2016. High-rise Timber Buildings as a Climate Change Mitigation Measure – A Comparative LCA of Structural System Alternatives. *Energy Procedia* 96: 112–123.
- The World Bank Group. 2020. Forest area (% of land area) in Ireland. Viewed in November 2022. <Forest area (% of land area) - Ireland | Data (worldbank.org)>

Life-cycle assessment and sensitivity analysis of a clayey sediment-based geopolymer concrete

L. Monteiro, H. Yáñez-Godoy, J. Saliba & N. Saiyouri

Institut de Mécanique et d'Ingénierie (I2M), Université de Bordeaux, Talence, France

ABSTRACT: This article evaluates, through a life cycle assessment (LCA), the environmental impacts of a sediment-based geopolymer mortar mixed with alkaline reagents. The obtained results were compared to the use of classic Ordinary Portland Cement (OPC) for treating dredged sediment with similar compressive strength. Dredging methods as well as transport were taken into account in addition to the mix-design and fabrication methods. In order to quantify the sensibility of the chosen hypothesis, a sensitivity analysis was also conducted to make the methodology more robust. Throughout the analysis, it could be concluded that the use of alkaline reagent reduces the impact on climate change but does not lead to better impact results than OPC for all other categories considered. Therefore, the use of alternative local precursors is not sufficient and market potential of geopolymer mortars will depend on an alternative to the alkaline reagents currently used for geopolymerization.

1 INTRODUCTION

In 1978, the French chemist Davidovits (2005) coined the term geopolymer to describe a class of aluminosilicate inorganic materials obtained by reaction between a precursor, aluminosilicate material, and alkaline reagents. Considered as mineral binders due to their properties similar to OPC, geopolymers represent a potential replacement for cement. For this reason, their low carbon impact is an important leitmotif in the studies published to date. Davidovits (2013) estimates that the manufacturing process of geopolymers requires 9 times less energy than the production of Portland cement and emits 8 to 10 times less greenhouse gases. Indeed, the materials used for geopolymerization do not require a calcination process, contrary to clinker production. In the most favourable case, when the manufacture of the precursors is not taken into account, it achieves an 80% reduction in CO₂ emissions compared to Portland cement. These results, although similar to other studies (Robayo-Salazar et al., 2018; Salas et al., 2018), are highly dependent on the assumptions made in LCA. In the literature, CO₂ emission reduction values ranging from 9% to 80% are observed. The factors responsible for these variations are: the variability of the precursors used, the different transport distances considered, the high alkali content, whether or not the solid fraction of the silicate is taken into account, and the requirement for high-temperature processing. Despite diverging results, there is a general consensus towards the same conclusion: geopolymer production produces less CO₂ than cement production.

One of the strategies identified as essential to the competitiveness of geopolymers on the market, is the use of local resources that allow to decrease the costs related to the manufacture of materials and their transport. Among the identifiable local resources, dredged sediments are a source of interest due to their adequate mineralogical composition and their significant quantity. Annually in Bordeaux, 9 million m³ of sediments are dredged. Several studies have successfully evaluated the potential of dredged sediments for use in geopolymer matrices (Ferone et al., 2013; Komnitsas, 2016; Lirer, 2017). Using sodium silicate (Na₂SiO₃), Ferone et al. (2013) obtain a value of 3.44 MPa at 28 days for a mortar with calcined sediments. Similarly, Mograhbi et al.

(2018) obtained at the age of 28 days 0.2 MPa for untreated sediments from the Grand Port Maritime of Dunkerque. However, despite the technical viability, to the authors' knowledge, there is no study on the LCA of such process. Furthermore, existing studies on the ecological impact of geopolymer applications focus on the impact regarding climate change, but the true environmental profile of these materials goes far beyond that and will define the true limits for the development of this technology in a sustainable construction industry.

Through a LCA, this paper fills a knowledge gap by presenting the impacts of the full LCA of a geopolymer mortar formulated from untreated dredged sediments taking into account the activities associated with the extraction of raw materials, transport and the manufacture of 1 m³ of mortar. In addition, in order to minimise the uncertainties associated with the assumptions and choices made in the study, a Monte-Carlo sensitivity analysis was performed. Three different scenarios were considered for two different mortars based on untreated dredged sediments: a reference cement-based mortar and a geopolymer-based mortar. The impact of mortars was evaluated based on four environmental indicators: climate change, acidification, eutrophication and water pollution.

2 SCOPE DEFINITION AND METHODOLOGY

2.1 *Goal, scope definition and life cycle assessment*

The objective of this study is to compare the ecological performance of two different treatments to formulate a mortar from untreated dredged sediments from the Garonne. The functional unit retained in this study is the production of 1 m³ of mortar with cement or alkaline reagents with equivalent mechanical resistance. It was decided in this study to focus on the early parts of the life cycle with a “cradle to gate” approach. The boundaries of the system are therefore the extraction and production of materials, the dredging and processing of sediments in addition to the transport and manufacturing energy required to produce 1 m³ of mortar. Other processes related to on-site implementation, sustainability, end-of-life and recycling were not considered in this study. Sensitivity analyses were performed to take into account market developments in geopolymerization and circumstantial changes in transport distances of activators.

The scenarios of the different mortars were established according to ISO 14 040 and ISO 14 044 and were modelled in SimaPro using the EcoInvent 3.2 database. The calculations were then carried out according to the NF EN 15804+A1/CN (2014) and CML-IA method (2016).

2.2 *Mix design*

The geopolymerized mortars were obtained from untreated dredged sediments from the Garonne River as a precursor. The sediments are used at a water content of 30% to limit the additional external water input and to facilitate the treatment by eliminating additional operations such as screening and crushing. The production of geopolymerized mortar from dredged sediments is based on the alkaline activation of 70% sediment with 30% activator by mass. The activator mixture is a combination of a 4M solution of NaOH and Na₂SiO₃ with an optimum weight ratio of SiO₂/Na₂O solution of 1.2. Sodium hydroxide (NaOH) was used in the form of pellets (99% purity) which were dissolved in a ready-to-use silicate solution (Na₂SiO₃) supplied by Xatico. The choice of these activators is motivated by their classical use in most studies, allowing the results obtained to be compared with those known in the literature. A first formulation of geopolymer-based sediments (GBS) was established using this methodology. The reference formulation with OPC is a mixture of 80% sediment and 20% conventional Portland cement. The formulations and mechanical strengths of the two solutions are detailed in Table 1. The volume and the water/solid ratio are kept constant at 1 m³ and 0.40 respectively.

2.3 *Life cycle assessment*

The data for cement and alkaline reagents (NaOH, Na₂SiO₃) are taken from the EcoInvent database. The data for OPC in EcoInvent corresponds to the production of cement consisting

Table 1. Mix design and compressive strength of the studied mortars.

Mix	Mix proportions for 1m ³				Mechanical Strength [MPa]
	Sediment	OPC	NaOH	Na ₂ SiO ₃	
OPC	1319.00	172.70	-	-	1.67
GBS	1138.18	-	14.43	153.10	4.78

of 0.9 kg of clinker for one kg of cement. The molarity of the NaOH solution was taken into account according to the mass of pellet added. For sodium silicate (Na₂SiO₃), only the solid fraction of the silicate is considered in this study. There is no dredging process for sediments on EcoInvent so the impact of dredging was modelled as follows:

- Moving the dredger in the estuary to the dredging area in Pauillac, Gironde (*transport, freight, inland waterways, barge*)
- Hydraulic suction dredging operation (*sand quarry operation, sediment extraction from river bed*)
- Dumping of sediments with shovels and skips (*excavation, hydraulic digger + transport, freight, lorry 3.5-7.5 metric ton*)
- Natural dewatering of the sediments in landfills (*process-specific burdens, inert material landfill*).

For transport, it is assumed that the concrete production plant is located in Bassens next to the Port of Bordeaux, while the dredging of the sediments is located in the Pauillac area upstream of the estuary. The material suppliers were chosen as close as possible to the concrete production plant. The distance assumptions are presented in Table 2.

Table 2. Transport inventory.

Materials/Process	Supplier	Distance from supplier	Mode
Portland cement	Lafarge (France-Bassens)	1.4km	Road
NaOH	Sigma Aldrich (Germany)	1146km	Road
Na ₂ SiO ₃	Xatico (Spain – Saint Gugat del Vallès)	638km	Road
Sediment	-	-	-
Round trip	-	75km	Estuary
Unloading platform	-	0.2km	Road
Landfill deposit	-	48.8km	Road

3 RESULTS AND DISCUSSIONS

3.1 Global impacts

Table 3 presents the calculated impact values for each category related to the production of 1m³ of the formulations compared in this study. Figure 1 shows the comparison of the values in relative terms for each impact category. Considering the Climate Change impact, which represents the CO₂ emissions emitted per 1 kg of mortar produced, a clear decrease is observed for geopolymerized solutions. OPC emits 227.54 kg.CO₂.eq against 180.1 kg.CO₂.eq for GBS. The use of a geopolymer binder relative to the use of OPC, allows a reduction of carbon emissions by 21%. Although the GBS shows a lower performance for the climate change category than OPC, results shows that geopolymer treatment has a higher environmental score regarding the other impact categories such as Acidification (A), Eutrophication (E) and Water Pollution (WP) which increases by 47%, 68% and 56% respectively. Thus, this questions the ecological benefit of using alkaline reagent in order to develop the mechanical strength. The use of local sources of materials has been identified as one of the major keys to reduce the environmental impact of geopolymer (Turner & Collins, 2013) yet, despite the use of local and

alternative precursors such as dredged sediments, high impact in A, E and WP were observed. Alkaline reagents are often targeted when questioning the environmental potential of geopolymer. Indeed, sodium silicate (Na_2SiO_3) process, through the electrolysis, is responsible for the high value in those categories. The reduction of environmental scores for geopolymers will require the search for new, more environmentally friendly activators which are often identified as the major source of contribution.

Table 3. Results for each impact category.

Impact category	Unit	OPC	GBS
Acidification (A)	kg. SO_2 .eq.	0.57	1.06
Eutrophication (E)	kg. PO_4 .eq.	0.14	0.44
Water Pollution (WP)	m^3	2.39	5.50
Climate Change (CC)	kg. CO_2 .eq.	227.53	180.06

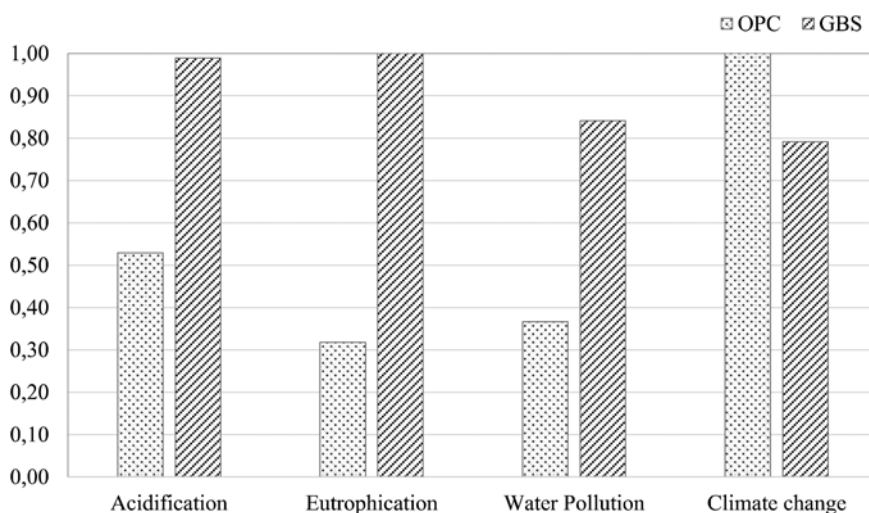


Figure 1. Global impacts of each mortar calculated with the EN 15-806 and CML-IA.

3.2 Sensitivity analysis

3.2.1 Deterministic model

In order to test the robustness of the results and their sensitivity to the chosen initial hypotheses, a deterministic sensitivity analysis was carried out. The objective is to define the limit values of the study in order to be able to study the sensitivity of the results related to the input parameters. Among the hypotheses defined in the study, the transport distances and the extraction of the sediments are considered. As Davidovits (2013) pointed out, it is difficult to compare the cement industry, implemented in France for several years now with hundred cement factories which implies an easy proximity supply in France, with the importation of alkaline reagent. For the sake of comparison and in anticipation of market forces, the new impacts of geopolymer mortars should be calculated assuming nearby suppliers. Concerning sediments, it can be assumed that, as sediments are considered as waste and because their extraction is linked to port activities, the consideration of this process can be neglected in the sensitivity analysis. Table 4 shows the results for OPC and GBS impact categories when transport distances for GBS are considered similar as cement and when sediment extraction is not taken into account for both mixtures.

Table 4. Results for each impact categories after sensibility analysis.

Impact category	Unit	OPC	GBS
Acidification (A)	kg.SO ₂ .eq.	0.43	0.88
Eutrophication (E)	kg.PO ₄ .eq.	0.13	0.38
Water Pollution (WP)	m ³	0.45	3.94
Climate Change (CC)	kg.CO ₂ .eq.	202.35	138.95

The reduction of transport distances and the non-inclusion of sediment extraction lead to an environmental gain for every impact category. Transport and sediment extraction are identified as key parameters in this first analysis. A study including uncertainties for these parameters is carried out to analyse their impact in the following section.

3.2.2 Stochastic model

In order to observe the sensitivity of the emissions for the different impact categories in Table 3, three scenarios, y_{sci} , are considered. Each scenario is defined by Equation 1 below:

$$y_{sci} = \sum_1^k F_j \cdot X_j \quad (1)$$

where F_j is the emission factor (defined in EcoInvent 3.2 database) for each input parameter X_j , that are stated for OPC mortar as follows:

- X_{OPC1} : amount of cement (kg)
- X_{OPC2} : amount of electricity (kWh)
- X_{OPC3} : amount of excavation (m³)
- X_{OPC4} : amount of landfill of inert material (kg)
- X_{OPC5} : amount of sediment extraction (kg)
- X_{OPC6} : transport, freight, inland waterways, barge (t.km)
- X_{OPC7} : transport, freight, lorry 16-32 metric ton (t.km)
- X_{OPC8} : transport, freight, lorry 3.5-7.5 metric ton (t.km)

and for GBS mortar:

- X_{GBS1} : amount of electricity (kWh)
- X_{GBS2} : amount of excavation (m³)
- X_{GBS3} : amount of landfill of inert material (kg)
- X_{GBS4} : amount of sediment extraction (kg)
- X_{GBS5} : amount of NaOH (kg)
- X_{GBS6} : amount of Na₂ SiO₃ (kg)
- X_{GBS7} : transport, freight, inland waterways, barge (t.km)
- X_{GBS8} : transport, freight, lorry 16-32 metric ton (t.km)
- X_{GBS9} : transport, freight, lorry 3.5-7.5 metric ton (t.km)

The three scenarios, y_{sci} , that have been identified are listed below:

- y_{sc1} : this scenario is considered the baseline scenario with all the input parameter X_i where current distance from raw material suppliers for activators (Table 2) are taken into account
- y_{sc2} : this scenario is similar to y_{sc1} for OPC mortar but for GBS mortar we consider a market of raw material suppliers located in the region, the impact of transport (X_{GBS8}) being therefore minimal
- y_{sc3} : this scenario considers that the extraction of sediments is a necessary action for the maintenance of the waterways and is therefore not a source of emission allocated to the production of mortars from the dredged sediments (X_{OPC5} and X_{OPC6} , for OPC mortar, and X_{GBS4} and X_{GBS7} , for GBS mortar, are not considered in Equation 1).

For the following input parameters, X_i , an uncertainty range was identified which allowed us to define them as random variables: X_{OPC5} , X_{OPC6} , X_{OPC7} , X_{GBS4} , X_{GBS7} and X_{GBS8} . Indeed, using the Monte-Carlo method, we perform a sensitivity analysis to measure their impact on the calculation of different scenarios defined above. Having identified three values characterizing the uncertainty: a minimum, a most likely and a maximum value, as shown in Table 5, we have modeled these variables with Beta probability distributions. For example, Figure 2 shows the probability distributions for the variables X_{OPC5} and X_{OPC6} by considering a coefficient of variation (ratio between standard deviation and mean value), $COV = 10\%$. The interval values correspond, for transport (t.km), to the minimum and maximum distances that lorry must travel to transport the materials. For X_{OPC5} and X_{GBS4} , the minimum corresponds to the non-consideration of sediments in the analysis, the most likely interval represents the minimum to be dredged for $1m^3$ of the defined formulation and the maximum value corresponds to the total quantity of sediment dredged per operation.

Table 5. Uncertain input parameters with their value intervals.

Random variable	Value intervals		
	Minimum	Most likely	Maximum
X_{OPC5} (kg)	0.00	1319.00	4350.00
X_{OPC6} (t.km)	0.00	98.93	172.60
X_{OPC7} (t.km)	0.12	64.69	83.97
X_{GBS4} (kg)	0.00	1138.18	4350.00
X_{GBS7} (t.km)	0.00	85.36	149.01
X_{GBS8}^* (t.km)	55.79	169.76	225.79

*For y_{sc2} this variable is not random but deterministic with the minimum value

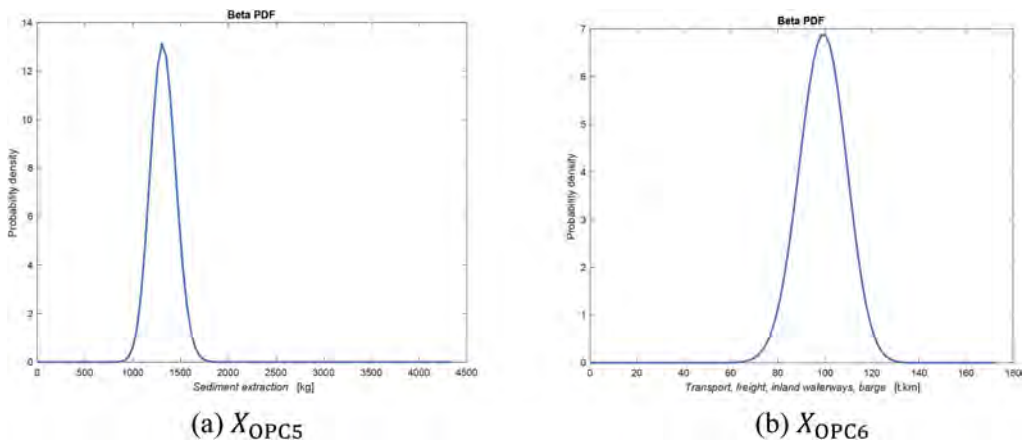


Figure 2. Beta probability distributions for the variables X_{OPC5} and X_{OPC6} , $COV = 10\%$.

3.2.3 Results of sensitivity analysis

1000 Monte Carlo simulations were performed to assess the sensitivity of each scenario, using the model in Equation 1, for each mortar and for the different impact categories. An uncertainty of $\pm 5\%$ was assumed for the emission factor, F_i . A uniform probability distribution was used to model this uncertainty. Table 6 ($COV = 10\%$) and Table 7 ($COV = 30\%$), present the overall results obtained, where μ and σ are the mean and standard deviation values respectively, and the values in square brackets is the 95% confidence interval.

Table 6. Results of the sensitivity analysis for each impact category, $COV = 10\%$.

Impact category	OPC			GBS		
	y_{sc1}	y_{sc2}	y_{sc3}	y_{sc1}	y_{sc2}	y_{sc3}
Acidific. [kg.SO ₂ .eq]	$\mu = 0.569$ $\sigma = 0.014$ [0.544; 0.593]	$\mu = 0.570$ $\sigma = 0.014$ [0.545; 0.593]	$\mu = 0.511$ $\sigma = 0.013$ [0.490; 0.534]	$\mu = 1.064$ $\sigma = 0.026$ [1.016; 1.108]	$\mu = 1.001$ $\sigma = 0.024$ [0.960; 1.039]	$\mu = 1.015$ $\sigma = 0.026$ [0.969; 1.060]
Eutrophic. [kg.PO ₄ .eq]	$\mu = 0.139$ $\sigma = 0.003$ [0.132; 0.145]	$\mu = 0.139$ $\sigma = 0.003$ [0.132; 0.144]	$\mu = 0.119$ $\sigma = 0.003$ [0.114; 0.124]	$\mu = 0.436$ $\sigma = 0.009$ [0.420; 0.453]	$\mu = 0.420$ $\sigma = 0.009$ [0.405; 0.436]	$\mu = 0.419$ $\sigma = 0.009$ [0.404; 0.435]
Wat. Pollut. [m ³]	$\mu = 2.397$ $\sigma = 0.204$ [2.026; 2.823]	$\mu = 2.391$ $\sigma = 0.193$ [2.014; 2.779]	$\mu = 0.506$ $\sigma = 0.013$ [0.482; 0.527]	$\mu = 5.581$ $\sigma = 0.192$ [5.224; 5.970]	$\mu = 5.524$ $\sigma = 0.188$ [5.171; 5.901]	$\mu = 3.957$ $\sigma = 0.092$ [3.795; 4.109]
Clim. Chan. [kg.CO ₂ .eq]	$\mu = 227.3$ $\sigma = 5.839$ [217.5; 237.1]	$\mu = 227.5$ $\sigma = 6.103$ [217.1; 237.7]	$\mu = 219.4$ $\sigma = 6.085$ [209.4; 229.4]	$\mu = 180.1$ $\sigma = 4.676$ [171.0; 188.7]	$\mu = 160.5$ $\sigma = 3.635$ [154.3; 166.8]	$\mu = 173.4$ $\sigma = 4.681$ [163.9; 182.1]

Table 7. Results of the sensitivity analysis for each impact category, $COV = 30\%$.

Impact category	OPC			GBS		
	y_{sc1}	y_{sc2}	y_{sc3}	y_{sc1}	y_{sc2}	y_{sc3}
Acidific. [kg.SO ₂ .eq]	$\mu = 0.569$ $\sigma = 0.020$ [0.526; 0.606]	$\mu = 0.568$ $\sigma = 0.021$ [0.523; 0.607]	$\mu = 0.514$ $\sigma = 0.017$ [0.478; 0.541]	$\mu = 1.064$ $\sigma = 0.040$ [0.980; 1.132]	$\mu = 0.999$ $\sigma = 0.026$ [0.954; 1.047]	$\mu = 1.016$ $\sigma = 0.037$ [0.940; 1.081]
Eutrophic. [kg.PO ₄ .eq]	$\mu = 0.139$ $\sigma = 0.006$ [0.128; 0.149]	$\mu = 0.139$ $\sigma = 0.006$ [0.127; 0.149]	$\mu = 0.119$ $\sigma = 0.004$ [0.110; 0.125]	$\mu = 0.436$ $\sigma = 0.012$ [0.413; 0.458]	$\mu = 0.420$ $\sigma = 0.010$ [0.403; 0.438]	$\mu = 0.419$ $\sigma = 0.012$ [0.396; 0.439]
Wat. Pollut. [m ³]	$\mu = 2.407$ $\sigma = 0.586$ [1.361; 3.633]	$\mu = 2.385$ $\sigma = 0.576$ [1.380; 3.609]	$\mu = 0.504$ $\sigma = 0.016$ [0.470; 0.532]	$\mu = 5.587$ $\sigma = 0.500$ [4.735; 6.604]	$\mu = 5.517$ $\sigma = 0.484$ [4.631; 6.518]	$\mu = 3.957$ $\sigma = 0.093$ [3.801; 4.126]
Clim. Chan. [kg.CO ₂ .eq]	$\mu = 227.4$ $\sigma = 6.971$ [213.5; 240.1]	$\mu = 227.5$ $\sigma = 6.968$ [213.4; 239.6]	$\mu = 219.8$ $\sigma = 6.800$ [206.4; 231.4]	$\mu = 179.8$ $\sigma = 9.754$ [159.6; 194.5]	$\mu = 160.8$ $\sigma = 3.899$ [153.8; 167.7]	$\mu = 173.2$ $\sigma = 9.451$ [153.2; 187.4]

3.2.4 Discussion

With regard to the above sensitivity analysis, the obtained results shows that a strong dependence exist between the final impact category score and the subjective choice of input parameters. Furthermore, results found for both sensitivity analyses are similar to the one calculated with a deterministic approach even more when the coefficient of variation is set to 30%. It can be estimated that for OPC, Climate change is the less sensitive category with a variation range of -11% to 6% from the referring value of 227.535 kg.CO₂.eq, followed by Acidification that can vary from -16% to 7% compared to an initial value of 0.569 kg.SO₂.eq. Eutrophication present similar range value as a variation of -21% to 8% has been observed. However a relevant variation from -80% to 52% is observed for the Water Pollution impact. As for GBS, results shows that Eutrophication is characterized by low variation (-9% to 5%) followed by Acidification (-12% to 6%) and Climate Change (-15% to 8%). Water Pollution for GBS also presents the highest variations ranging from -31% to 19% from the referring value of 5.500 m³. Despite the variations observed in the final life cycle analysis results, conclusions remain the same. In all three of the scenarios, GBS presents a lower impact in Climate Change and higher impact on Acidification, Eutrophication and Water Pollution.

4 CONCLUSION

Throughout this study, life cycle analysis score of a geopolymer-based sediments mortar has been compared with an OPC-based sediments mortar. In accordance with the results obtained for the climate change impact category, this article argues that geopolymer can be a better option for reducing CO₂ emissions in comparison with the traditional use of OPC. However, the highest score for this article argues that geopolymer can be a better option for reducing CO₂ emissions in comparison with the traditional use of OPC the Acidification, Eutrophication and Water Pollution impact categories were observed for GBS due to the use of alkaline reagent. In order to analyze the sensibility of the results toward the chosen scenarios, a sensitivity analysis was performed on the input parameters. High range of variation were observed for Water Pollution when transport and sediment extraction were taken into account however conclusion toward the environmental score of GBS compared to OPC remains unchanged.

If climate change scores could make geopolymers viable competitors to cement, it is appropriate, in perspective, to study the use of alternative alkaline reagent in order to improve the environmental scores of geopolymerized mortars from dredged sediments.

ACKNOWLEDGMENTS

This work is carried out within the framework of the ValoSed project financed by the Nouvelle Aquitaine region and the FNTP. Acknowledgments: Nouvelle Aquitaine Region, FNTP, Grand Port Maritime de Bordeaux, SIBA, Grand Port Maritime de Bayonne, Grand Port Maritime de la Rochelle, Eiffage, NGE, Spie Batignolles and Solétanche Bachy.

REFERENCES

- CML, Department of Industrial Ecology CML-IA Characterisation Factors. Available online: <https://www.universiteitleiden.nl/en/research/research-output/science/cml-ia-characterisation-factors>
- NF EN 15804+A1, Contribution des ouvrages de construction au développement durable - Déclarations environnementales sur les produits - Règles régissant les catégories de produits de construction.
- Davidovits, J., 2005. Geopolymers: Inorganic polymeric new materials. *J. Therm. Anal. Calorim.* 37, 1633–1656. <https://doi.org/10.1007/bf01912193>
- Davidovits, J. Geopolymer cement a review. *Inst. Géopolimère 2013*, 21, 1–11, St. Quentin, France. Available online: <http://www.geopolymer.org>
- Ferone, C., Colangelo, F., Cioffi, R., Montagnaro, F., Santoro, L., 2013. Use of reservoir clay sediments as raw materials for geopolymer binders. *Adv. Appl. Ceram.* 112, 184. <https://doi.org/10.1179/1743676112Y.0000000064>
- Komnitsas, K., 2016. Co-valorization of marine sediments and construction & demolition wastes through alkali activation. *J. Environ. Chem. Eng.* 4, 4661–4669. <https://doi.org/10.1016/j.jece.2016.11.003>
- Lirer, S., 2017. Mechanical and chemical properties of composite materials made of dredged sediments in a fly-ash based geopolymer. *J. Environ. Manage.* 7.
- Moghrabi, I., 2018. Modélisation du comportement mécanique des sédiments traités et étude d'une nouvelle voie de leur valorisation par des géopolymères (These de doctorat). Nantes.
- Robayo-Salazar, R., Mejía-Arcila, J., Mejía de Gutiérrez, R., Martínez, E., 2018. Life cycle assessment (LCA) of an alkali-activated binary concrete based on natural volcanic pozzolan: A comparative analysis to OPC concrete. *Constr. Build. Mater.* 176, 103–111. <https://doi.org/10.1016/j.conbuildmat.2018.05.017>
- Salas, D.A., Ramirez, A.D., Ulloa, N., Baykara, H., Boero, A.J., 2018. Life cycle assessment of geopolymer concrete. *Constr. Build. Mater.* 190, 170–177. <https://doi.org/10.1016/j.conbuildmat.2018.09.123>
- Turner, L.K., Collins, F.G., 2013. Carbon dioxide equivalent (CO₂-e) emissions: A comparison between geopolymer and OPC cement concrete. *Constr. Build. Mater.* 43, 125–130. <https://doi.org/10.1016/j.conbuildmat.2013.01.023>

Research on calculation method of creep and shrinkage effects of steel-concrete-Ultra-High-Performance Concrete (UHPC) composite bridge considering construction process

X.G. Ma, D.W. Zhang, H.W. Ling & H.J. Shen

Shanghai Pudong Architectural Design & Research Institute Co., Ltd, Shanghai, China

S.S. Guo & C. Liu

Tongji University, Shanghai, China

ABSTRACT: Creep and shrinkage effects of concrete plays an important role in the design of composite bridge. In the past, many analysis on the creep and shrinkage effects of concrete and other materials has been carried out based on experiments, and a general theoretical calculation method has been formed, which makes the calculation of creep and shrinkage effects in the design of concrete bridges and steel-concrete composite bridges more accurate. However, it is only used in concrete bridges and ordinary steel-concrete composite bridges currently. For steel-concrete-UHPC composite bridges, no calculation and analysis has been carried out yet. The steel-concrete-UHPC composite bridge involves the creep and shrinkage effects of concrete and UHPC, and the influence of age and external load simultaneously needs to be considered. The performance of steel-concrete-UHPC composite bridges under the creep and shrinkage effects of concrete and UHPC is different from that of ordinary concrete bridges and steel-concrete composite bridges. In this paper, based on the previous theoretical calculation methods of creep and shrinkage effects of concrete and UHPC, the equivalent cooling method and metal creep theory are used to simulate the creep and shrinkage effects of concrete and UHPC for steel-concrete-UHPC composite bridges. Then, the stress and deformation of steel-concrete-UHPC composite bridges under the creep and shrinkage effects are analyzed and studied with calculation results, which provides a reference for subsequent calculation and analysis of the creep and shrinkage performance of composite bridges.

1 ENGINEERING BACKGROUND

The bridge is a three-span continuous steel-concrete composite girder bridge. The span is $40+60+40=140\text{m}$, and the width is 16.5m . The layout of the bridge deck is: 0.5m (anti-collision guardrail) $+7.5\text{m}$ (motor vehicle lane) $+0.5\text{m}$ (central separation pier) $+7.5\text{m}$ (motor vehicle lane) $+0.5\text{m}$ (anti-collision guardrail). Bridge deck pavement is made with 2mm waterproof layer and 100mm asphalt mix.

Bridge deck is a composite bridge deck, in which the inner thickness is 270mm , the thickness of the root of the cantilever slab is 370mm . The thickness of bottom steel plate is 8mm . Steel plate and concrete are connected with T-type steel ribs and studs. The cross section is shown as follows.

2 RESEARCH SIGNIFICANCE

Due to the difference of the properties of steel and concrete in steel-concrete composite bridges, the shrinkage and creep of concrete will have a significant impact on the force

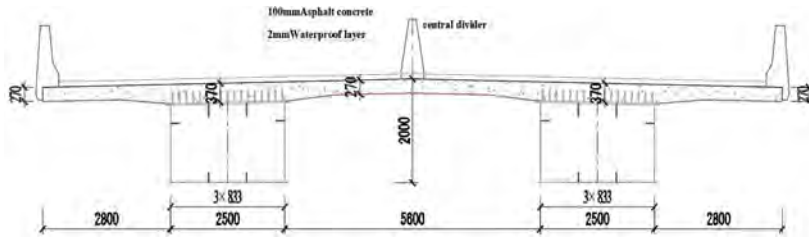


Figure 1. Cross section of main bridge.

distribution of entire structure. In previous studies, scholars have calculated and analyzed this effect. However, the structure proposed in this paper involves three materials—steel, normal concrete and UHPC, and the concrete and UHPC are constructed in batches. There are certain differences in the shrinkage and creep properties of the two types of materials, which should be considered in the design. This paper conducts calculation analysis and research on the shrinkage and creep effects of composite bridge under the influence of concrete and UHPC and provides a reference for bridge design.

3 CALCULATION METHOD

The shrinkage and creep effects of concrete and UHPC are relatively complex, mainly affected by the construction age, humidity and size effects. The shrinkage effect is similar to the temperature effect, and the cooling method is used for analysis here given the provisions of the specification.

3.1 Concrete shrinkage

Concrete shrinkage coefficient is determined according to Specifications for Design of Highway Reinforced Concrete and Prestressed Concrete Bridges and Culverts (JTG-3362-2018). The calculation method is shown as follows.

$$\varepsilon_{cs}(t, t_s) = \varepsilon_{cs0} \cdot \beta_s(t - t_s) \quad (1)$$

$$\varepsilon_{cs0} = \varepsilon_s(f_{cm}) \cdot \beta_{RH} \quad (2)$$

$$\varepsilon_s(f_{cm}) = [160 + 10\beta_{sc}(9 - f_{cm}/f_{cm0})] \cdot 10^{-6} \quad (3)$$

$$\beta_{RH} = 1.55 \left[1 - (RH/RH_0)^3 \right] \quad (4)$$

$$\beta_s(t - t_s) = \left[\frac{(t - t_s)/t_1}{350(h/h_0)^2 + (t - t_s)/t_1} \right]^{0.5} \quad (5)$$

Where:

t - Calculation age of concrete (d);

t_s -Concrete age at the beginning of shrinkage can be assumed to be 3~7d;

$\varepsilon_{cs}(t, t_s)$ - the contraction strain corresponding to considered concrete age (t);

ε_{cs0} - nominal shrinkage factor;

β - coefficient of shrinkage over time;

f_{cm} - Average cylindrical compressive strength (MPa) of concrete at the age of 28 days,

$f_{cm} = 0.8 f_{cu,k} + 8\text{MPa}$;

$f_{cu,k}$ -concrete cube compressive strength standard value (MPa) with a guaranteed rate of 95%;

β_{RH} - The coefficient related to the annual average relative humidity, applicable to $40\% \leq RH < 99\%$;

RH -Environmental average relative humidity (%);

β_{sc} - The coefficient depends on the type of cement; for normal Portland cement or rapid hardening cement, $\beta_{sc} = 5.0$;

h -Theoretical thickness of the member (mm), $h = 2A/u$, A is the cross-sectional area of the member, u is the perimeter of the component in contact with the atmosphere;

$RH = 100\%$; $h_0 = 100mm$; $t = 1d$; $f_{cm0} = 10MPa$.

In addition, the nominal shrinkage coefficient of concrete ϵ_{cs0} can be determined according to annual average relative humidity (%) of the environment. The relation between nominal shrinkage factor and Environmental annual average relative humidity RH (%) is shown in Table 1.

Table 1. The relation between nominal shrinkage factor and Environmental annual average relative humidity RH (%).

Environmental annual average relative humidity RH (%)	[40,70)	[70,99)
ϵ_{cs0}	$0.529 \cdot 10^{-3}$	$0.310 \cdot 10^{-3}$

3.2 UHPC shrinkage

The shrinkage coefficient of UHPC is determined according to the specification for the application of Ultra High-Performance Concrete for highway bridges and culverts (the draft for comments).

In this project, UHPC is cured at normal temperature. For standard cured UHPC, the shrinkage strain can be calculated according to the following formula:

$$\epsilon_{cs}(t) = \epsilon_{cs,0} \cdot e^{\frac{c}{\sqrt{t+d}}} \quad (6)$$

Where:

$\epsilon_{cs}(t)$ - the shrinkage strain at the considered age t ;

$\epsilon_{cs,0}$ - nominal ultimate shrinkage strain ($700\mu\epsilon$);

t - UHPC age(d);

c, d - fitting coefficient, for low shrinkage cement, $c = -2.48$, $d = -0.86$.

Shrinkage curve of UHPC with time is shown in the Figure 2.

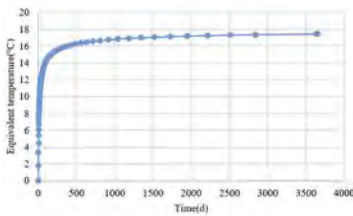


Figure 2. Shrinkage curve of UHPC with time.

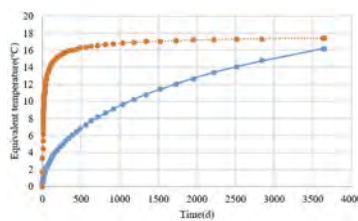


Figure 3. Comparison of shrinkage curve of UHPC and concrete with time.

The calculation here is based on the shrinkage and creep of the material within 10 years. There are certain differences in the shrinkage process of UHPC and normal concrete, as shown in Figure 3. UHPC shrinks faster in the early stage and slower in the later stage, while normal concrete shrinks more gently. The feature results in the difference of shrinkage effects compared with that of steel concrete composite bridges.

Among them, the shrinkage curve of UHPC is a dotted line, and the shrinkage curve of normal concrete is a solid line.

3.3 Creep effect of concrete

The calculation method of creep effect of concrete is considered with reference to the specification, and the calculation method is as follows.

$$\phi(t, t_0) = \phi_0 \cdot \beta_c(t - t_0) \quad (7)$$

$$\phi_0 = \phi_{RH} \cdot \beta(f_{cm}) \cdot \beta(t_0) \quad (8)$$

$$\phi_{RH} = 1 + \frac{1 - RH/RH_0}{0.46(h/h_0)} \quad (9)$$

$$\beta(f_{cm}) = \frac{5.3}{(f_{cm}/f_{cm0})^{0.5}} \quad (10)$$

$$\beta(t_0) = \frac{1}{0.1(t_0/t_1)^{0.2}} \quad (11)$$

$$\beta_c(t - t_0) = \left[\frac{t-t_0}{\beta_H + \frac{t-t_0}{t_1}} \right]^{0.3} \quad (12)$$

$$\beta_H = 150 \left[1 + \left(1.2 \frac{RH}{RH_0} \right)^{18} \right] \frac{h}{h_0} \quad (13)$$

Where:

t_0 - concrete age at loading (d);

t - concrete age (d) at the moment of consideration;

$\phi(t, t_0)$ - concrete creep coefficient considering the age (t);

ϕ_0 - nominal creep coefficient;

β_c - development coefficient of creep with time after loading.

In the formula, f_{cm} , f_{cm0} , RH , RH_0 , h , h_0 , t_1 is the same as other formulas.

3.4 UHPC creep effect

As a new type of material, UHPC has relatively complex components, and the research on durability is still incomplete. Here, the provisions in the current specifications are used for calculation and analysis. The code stipulates that when the compressive stress borne by UHPC is less than 0.4 times the UHPC compressive strength, UHPC manifested as the linear creep, and the creep coefficient can be calculated according to the following formula:

$$\phi(t, t_0) = \phi_0(t_\infty, t_0) \frac{(t - t_0)^a}{(t - t_0)^a + b} \quad (14)$$

Where, $\phi(t, t_0)$ - UHPC creep coefficient considering the age (t);

$\phi_0(t_\infty, t_0)$ - ultimate UHPC creep coefficient at the loading age;

t - UHPC age(d);

t_0 - UHPC age when firstly loaded (d);

a, b - Fitting coefficient, the value can be taken from the table below.

Table 2. Ultimate creep coefficient and coefficient a, b of UHPC.

Loading age $t_0(d)$	Conservation system	Ultimate Creep coefficient $\phi t_0(t_\infty, t_0)$	Coefficient a	Coefficient b
4	standard maintenance	1.2	0.6	3.2
7	standard maintenance	1.0	0.6	4.5
28	standard maintenance	0.8	0.6	10
	90°C steam curing for 2 days or 80°C steam curing for 3 days	0.2	0.6	10

4 CONSTRUCTION PROCESS

There are many construction methods to choose for bridge construction. Since the overpass bridge is located in the urban area, the impact on the surrounding area should be minimized. This bridge adopts the formwork of steel structure for bridge deck construction, which can reduce the impact on the surrounding environment and improve performance of the overall structure in the meanwhile.

After comprehensive consideration, the construction process of the bridge is as follows:

- (1) The steel structure is carried out on the bracket first, and the bracket is removed after the splicing is completed;
- (2) For the concrete pouring of the bridge deck, the steel structure that has been processed bears the concrete self-weight load (shrinkage of the concrete starts to be considered at the time);
- (3) UHPC is poured 1 to 4 days after concrete pouring. At this time, the self-weight of UHPC is borne by the steel-concrete composite section (UHPC shrinkage and concrete creep starts to be considered), forming an overall structure and bearing the second-phase load.

5 COMPUTATIONAL ANALYSIS

According to the bridge construction method, the bridge adopts the staged construction method. And there is a problem of structural system conversion during the construction process. The initial load of the steel structure is borne by the lower bracket. After the construction of the steel structure is completed, the bracket is removed and the concrete is poured. The self-weight of the concrete is borne by the steel structure; similarly, when concrete reaches a certain strength to pour UHPC, the self-weight of UHPC is borne by composite beams formed of steel and concrete.

The realization of general construction process is relatively easy to realize in special bridge software, such as Midas, Bridge Doctor, etc., but it is difficult to realize in 3D general software such as Ansys and Abaqus. The Ansys software provides the function of unit life and death, that is, during the construction process of this stage, the components of the next stage are passivated and activated in the next stage. Through this function, the staged construction of the bridge can be realized.

Shell181 element is used to simulate the steel beam, and the solid185 element is used to simulate concrete and UHPC. Nodes are connected. Reinforcement bars and internal stiffeners are connected to concrete and UHPC units by coupling elements. Constraints are used to constrain the lower nodes of the steel main girder according to the constraints of the three-span continuous beam.

5.1 Shrinkage calculation method

Since concrete shrinkage has nothing to do with structural stress, the calculation of concrete shrinkage is relatively simple, and it is realized by cooling in Ansys. The basic condition for the calculation of concrete bridges is an average humidity of 70%.

5.2 Creep calculation method

Using the metal creep function in ANSYS, the concrete creep calculation is realized by specifying the creep strain increment in the unit time interval. Creep is a rate-dependent material non-linearity, that is, the characteristic of continuous deformation of materials under constant load. Conversely, if the displacement is fixed, the reaction force or stress will decrease with time.

Creep can be divided into three stages. In the initial creep stage, the strain rate decreases with time, and this stage generally occurs in a relatively short period. In the second creep stage, there is a constant strain rate, so the strain develops at a constant rate, and in the third creep stage, the strain rate increases rapidly until the material fails. Implicit and explicit integration methods are used to analyze creep analysis in ANSYS, both of which can be applied to static and transient analysis. The implicit creep analysis method is more powerful, faster, and more accurate, and it is generally recommended to use the implicit creep analysis. It can handle temperature-dependent creep constants and simultaneously simulate creep and isotropic hardening plasticity models. The calculation and analysis in this paper adopt the implicit integral method for calculation and analysis of creep effects.

6 CALCULATION RESULT ANALYSIS

Ansys is used to calculate and analyze the shrinkage and creep effects of composite bridges. Considering the shrinkage and creep effects of construction stages and different materials, the calculation is carried out according to the age of 10 years. The calculation results are shown below.

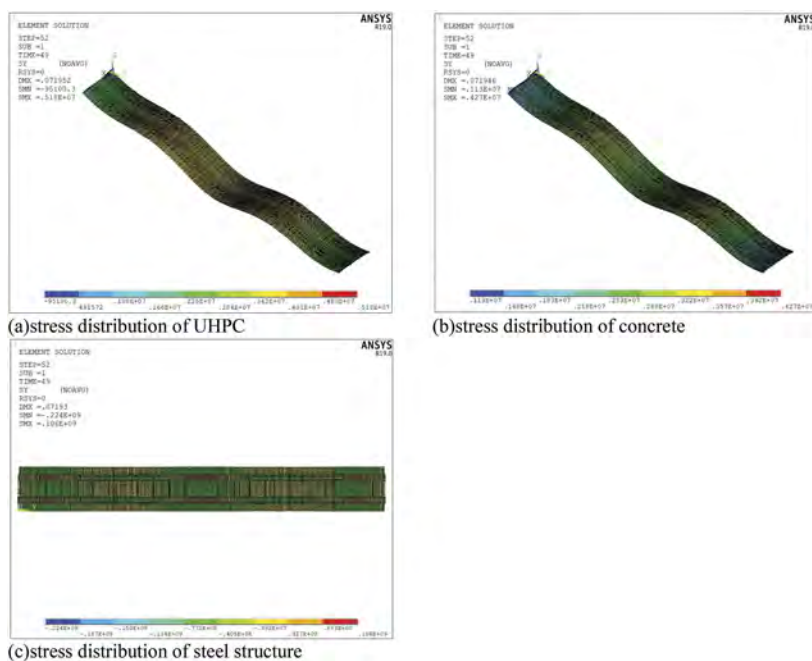


Figure 4. Stress distribution along bridge direction of composite bridge.

For three-span continuous girder bridges, the bridge deck over the support along the bridge direction is under tension and is easy to crack, so force control should be carried out; the stress at the root of the cantilever slabs is mainly considered in the transverse bridge direction, and it is clarified that under the applied load. The stress of specific key parts under the action of shrinkage, creep and construction self-weight is shown in the Table 3.

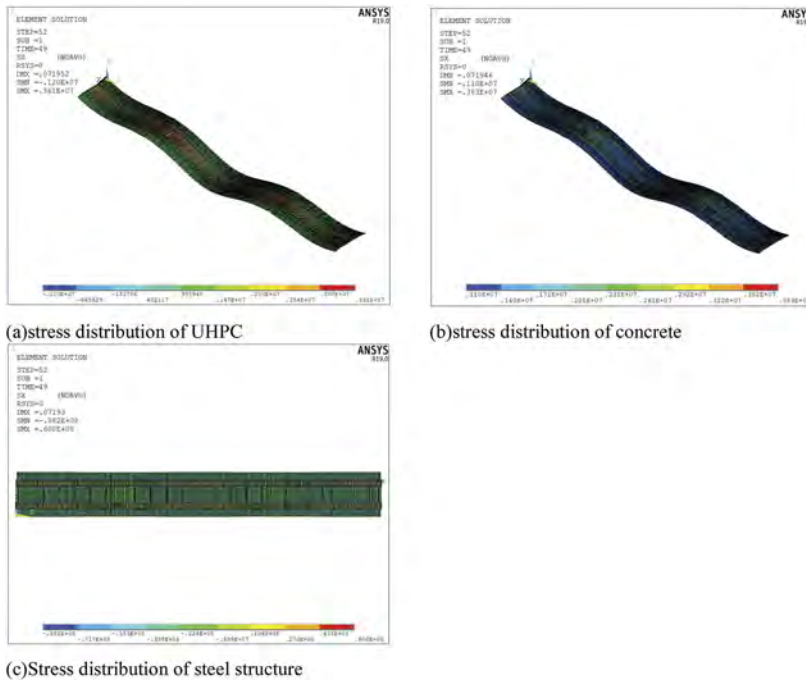


Figure 5. Stress distribution in transverse bridge direction of composite bridge.

Table 3. The stress of critical position.

Serial number	Location	Direction	Stress (MPa)
1	UHPC of negative bending moment area over the support	along the bridge	4.01
2	Concrete of negative moment zone over the support	along the bridge	3.57
3	Steel plate of negative moment zone over the support	along the bridge	13.2
4	UHPC at the root of the cantilever slabs	cross bridge direction	1.39
5	Concrete at the root of the cantilever slabs	cross bridge direction	1.33
6	Steel plate at the root of the cantilever slabs	cross bridge direction	-48.4

7 CONCLUSION

Shrinkage and creep effect is an extremely complex effect, which is affected by various factors in the environment. This paper combines the existing calculation methods and applies the finite element calculation method to calculate the shrinkage and creep effect of steel-concrete-UHPC composite bridge deck based on the provisions on the shrinkage and creep effects of materials in the latest codes. It can be seen that,

- (1) The shrinkage and creep are long-term effects, and the shrinkage of UHPC develops more rapidly in the early stage. So, the construction process should be considered in the calculation analysis;

- (2) By comparing the calculation results, it can be seen that the shrinkage and creep effects of concrete and UHPC have more influence in the negative bending moment area over the bearing along the bridge than on the transverse effect of the composite bridge. But for the lower steel plate, the creep and shrinkage effects have a higher influence on the bottom plate in transverse directions.
- (3) The shrinkage and creep effect has an adverse effect on the force in the negative moment zone of the bridge. In order to make full use of the excellent performance of UHPC, part of the effect of shrinkage and creep can be eliminated by high temperature steam curing, thereby improving the performance.

REFERENCES

- Wang Longfei. 2021. Comprehensive Simulation on Shrinkage and Creep Effects of Concrete in Bridges during Time-varying Process. *Journal of Highway and Transportation Research and Development*, 38 (02),54–61. (in Chinese)
- Degtyarev, Vitaliy V. 2016. “Finite Element Modeling of Concrete Shrinkage in Composite Deck Slabs”. *CCFSS Proceedings of International Specialty Conference on Cold-Formed Steel Structures (1971-2018)*. 2.<https://scholarsmine.mst.edu/isccss/23iccfss/session9/2>
- Ministry of Transport of the People’s Republic of China. 2018. *Specifications for Design of Highway Reinforced Concrete and Prestressed Concrete Bridges and Culverts (JTG 3362-2018)* Beijing: China Communication Press. (in Chinese)
- Ministry of Transport of the People’s Republic of China. Specification for application of Ultra high-performance concrete for highway bridges and culverts (draft) (in Chinese)

Interactive visualization of uncertain embodied GHG emissions for design decision support in early stages using open BIM

K. Forth & A. Borrmann

Technical University of Munich, Munich, Germany

A. Hollberg

Chalmers University of Technology, Gothenburg, Sweden

ABSTRACT: To meet the European climate goals in the building sector, a holistic calculation and optimization of embodied greenhouse gas (GHG) emissions using the method of life cycle assessment (LCA) in early design stages are necessary. Hence, this paper presents a comprehensive and transparent design-decision-making approach for reducing embodied GHG emissions in early design stages by interactive, model-based visualizations of uncertain results. The proposed approach is based on a previously developed Natural Language Processing (NLP) based methodology of matching elements of a Building Information Model (BIM) to those of an LCA database. With the help of a prototypical implementation and a case study, the uncertainties of the derived LCA results are visualized using different levels of transparencies. This paper shows that open BIM models and the proposed 3D color coding support the hotspot analysis in combination with box plot diagrams for visualizing uncertain GWP results for decision-making in early design stages.

1 INTRODUCTION & MOTIVATION

In order to reach the international climate goals, the AEC sector with its impact of 40% of the global Greenhouse gas (GHG) has a significant impact (UN 2021). Currently, the embodied GHG emissions, meaning those from material extraction, manufacturing of construction products, etc., are responsible for up to 12% of the GHG emissions (EU Commission 2022a). Life cycle assessment (LCA) has been an established method to evaluate these embodied GHG emissions in the design phase of new buildings. Several national and international frameworks are currently including LCA in their assessments for comparing sustainability of building designs, for example LEVEL(s), which is also used for ensuring current EU Taxonomy classification system (EU Commission 2022b).

In a market survey with 161 participants from Germany, Schumacher et al. (2022) identified significant potential of using Building Information Models (BIM) for a loss-free data-exchange, as well for understandable and user-friendly communication of LCA results. This also means that in future, non-LCA-experts should be able to understand LCA results and make design decisions based on these results.

Nevertheless, most of the existing tools and methods in the field of BIM-based LCA focus either on closed BIM approaches, developed for architects, designers or BIM modellers, or require a high level of LCA expertise to conduct and interpret LCA results. Building owners or clients, who are usually making design decisions, often have not the required expertise in LCA and are increasingly using open BIM models. Therefore, in this paper we propose an interactive and comprehensive approach of visualizing uncertain embodied GHG emissions for design decision making by non-LCA-experts using open BIM models in early design stages.

2 BACKGROUND & RELATED WORKS

Several related publications were investigated with regards to variant selection and visualization. Wiberg et al. (2019a) presented in their publication a chronology of the development of a visual, dynamic and integrated approach of LCA of building. Regarding the dynamic aspect, they identified several approaches of integration using Visual Programming Language, such as Dynamo and Revit or Rhino and Grasshopper. Furthermore, they classified other approaches of parametric approaches as well as dashboards using Revit models or district models, where generally only the models were shown, but not used to highlight or visualize results. As a next step, they propose a visualization approach using Virtual Reality for improved stakeholder participation (Wiberg et al. 2019b). For this, they used Revit models to color the models with the LCA results and used the VR to interact with the model, which was concluded as a “good platform for communicating and visualising complex data [...] not only for researchers but also for the general public” (Wiberg et al. 2019b).

The recent review of Hollberg et al. (2021) regarding visualizing LCA results describes current practice and presents a systematic overview of different strategies and potentials. The methodology using BIM models to visualize LCA has shown great potential for synergies (Röck et al. 2018a, b, Mousa et al. 2016). In these approaches, color coding was mainly used to visualize final LCA results in authoring tools. In another visual method for detailed analysis of LCA results by Kiss and Szalay (2019), this model-based color coding was used to highlight certain aspects of the results in combination with a sunburst diagram. For implementation, Kiss & Szalay used Rhino and Grasshopper.

Miyamoto et al. (2022) proposed an approach for integrating LCA and LCC results as a basis for design decision-making. Although they did not use BIM models, they discussed the growing importance of integrating a spreadsheet approach with BIM workflows, however focusing on architects and not other stakeholders. Hollberg et al. put target users in the focus of their user-centric LCA tool development for early planning stages (Hollberg et al. 2022). Different stakeholders such as architects, sustainability engineers and consultants as well as real-estate developers were involved in the process. However, only fixed results were visualized, and no active interaction with the model was envisioned. Also, uncertainties and different levels of development have not been considered. To visualize these aspects, Abualdenien & Borrmann (2020) present several approaches of visualizing geometric and semantic uncertainties of building elements in early design stages. As one main conclusion of several approaches, “the combination of color value and transparency for quantifying the reliability of the semantics resulted in relatively high intuitiveness and acceptance” (Abualdenien & Borrmann 2020).

Furthermore, Ströbele (2022) introduced an approach of fuzzy life cycle assessments (fLCA) considering vaguenesses by distribution curves instead of single results. Schneider-Marín et al. (2022) established an EarlyData knowledge database for deciding material choices in a design stage, where no detailed information about specific materials is available. In this methodology, the semantic uncertainty is also visualized by assessing “a vast number of possible material combinations at once” using boxplot diagrams that visualize the ranges of the Global Warming Potential (GWP) (Schneider-Marín et al. 2022).

Petrova et al. (2019) propose a methodology for decision support for sustainable design based on knowledge discovery in disparate building data. They are using different matching mechanisms between project data repositories and Common Data Environments (CDE), such as data mining, direct semantic queries and geometric feature matching. The direct semantic queries are based on different ontologies, such as Building Topology Ontology (BOT) (Rasmussen et al. 2017) or product specific ontologies.

In summary, the discussed publications show the relevance of using BIM models to visualize LCA results and describe first approaches. However, an integration in an open BIM workflow was not investigated and also the interactive exploration of the results was not presented. This documents the gap existing regarding an interactive, design-decision tool for non-LCA-experts based on open BIM methodology in early design stages. The main focus of this publication is how to visualize uncertainties of the rough model semantics and vague results in a comprehensive way.

3 INTERACTIVE VISUALIZATION OF UNCERTAIN LCA RESULTS USING BIM

3.1 General workflow

As shown in Figure 1, the general methodology consists of the LCA knowledge database and four main steps. Overall, the methodology bases on a LCA knowledge database (LKdb), which consists of conventional elements and all information for calculating a holistic LCA, such as layer-specific replacement rates, LCI datasets using Ökobaudat, missing End-of-Life scenarios, etc. Details about the LKdb can be found in (Forth et al. 2021, 2022).

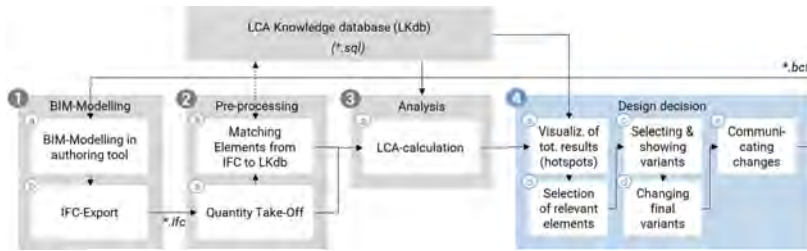


Figure 1. General workflow for visualizing uncertain embodied GHG emissions for design decision support in early design phases using open BIM.

The first step of the general method comprises the creation of the BIM model in an authoring software (step 1.a) and the subsequent IFC model export, which is performed by the BIM modeler (step 1.b). The next step consists of deriving the quantity take-off and element matching. The quantity take-off parses all geometric and semantic information of the IFC model for the calculation of the LCA, including base quantities, such as area, amount, layer thicknesses or length, as well as density, materials and the name of the element, its GUIDs and classification (step 2.a). The expressions of the materials and element are used in the next step for the matching of the IFC elements to the LKdb (step 2.b). This step has been previously introduced and validated (Forth et al. 2022, 2023). This matching is based on an existing NLP network, and compares cosine similarities of the element and material expressions in the IFC model and all elements and material categories and material options of the corresponding classification group in the LKdb. The most similar element of the LKdb is being matched to each IFC element.

After completing the element matching step, all missing information about LCA datasets, life spans or missing layers are filled by the datasets of the matched LKdb element. Afterwards, the results of the LCA are calculated taking into account the uncertainty of the element matching (step 3.a). Depending on the level of matching (see Section 3.3), a range of material options for each element's layer is taken into account and leads to a range of LCA results for each element and the whole building.

In this paper, the focus is on the concept for the final step of the general methodology, the design decision process (step 4.a-e).

3.2 Design decision support concept

The goal of the proposed workflow is to support non-LCA-experts in the decision making of construction-element and material-related variants. For supporting the decision maker in the early design stages, several hierarchical visualization goals are proposed, based on Hollberg et al. (2021). To identify hotspots for the design optimization, the 3D color code is recommended as an intuitive visualization type, which can be implemented using open BIM models (Figure 2). For comparing different design options, box plot diagrams are the only type which also include uncertainties in its visualization. Additionally, the selection boxes of each element variant or material option can be also color coded, normalised to benchmarks. As LCA benchmarks on element level are still missing according to the German classification systems used in this approach, the colors are normalised relatively to all potential design alternatives within one classification group. Once

benchmarks will be available also on the third level of cost groups according to DIN 276, the colors can be normalised according to these benchmarks.

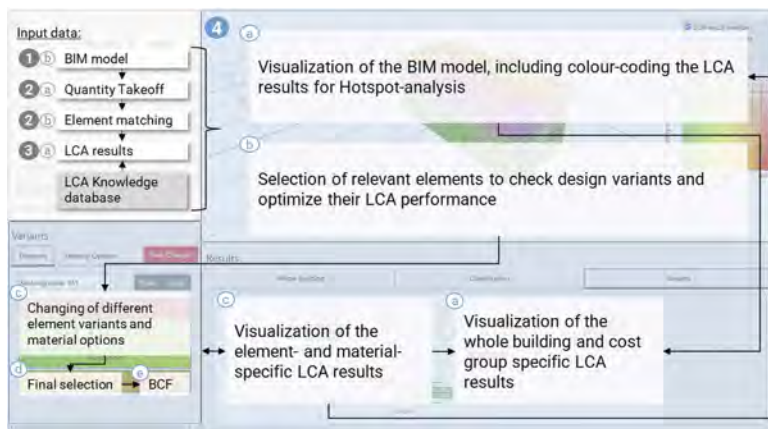


Figure 2. Concept of frontend visualization and interaction workflow for LCA-optimized design decision making.

This design decision process is based on the previous calculation and matching results including its uncertainties and is generally divided into five steps, as shown in Figure 2. First, the LCA results are visualized using a model viewer and conventional criterion-specific charts (4.a). When summing up the LCA results for each cost group and the whole building, Boxplot diagrams are suitable to visualize the ranges of possible results (bottom right). Furthermore, the element-specific results will be color coded on the BIM viewer to highlight the performance hotspots (top right). As a next step (4.b), the worst performing elements can be selected in the model viewer for design optimization (top left).

In the following step (4.c), variant results are visualized for the element selected in the model viewer, and different element variants of the same classification group can be selected (bottom left). Variants are derived on element and on material level according to the existing alternatives of each classification group in the LKdb. For every element in the BIM model, the LCA results of all design variants are previously calculated (step 3.a), independently of the matched element (bottom middle). In the last two steps, the final changes of variants are saved (4.d), and communicated back to the BIM modeler using the BIM Collaboration Format (BCF) as an open BIM standard (4.e).

3.3 Visualization of matching-related uncertainties

There are important features which are taken into account, based on the previous findings. On the one hand, the cosine similarity of the matching performance is an indicator for the degree of similarity the matching is based on. On the other hand, there are different cases how the elements are matched from the IFC model to the LKdb, as described in the following list.

IFC elements are matched to:

1. default element of the classification group in the LKdb (worst case)
2. most similar element expression, as there are no materials available
3. most similar element expression, as the material matching performs worse
4. element with the most similar material category
5. element with the most similar material option

These different cases lead to different levels of reliability of the resulting LCA results. Therefore, this information needs to be considered when visualizing the semantic-related uncertainties.

As previously mentioned, Abualdenien et al. already concluded that the combination of color value and transparency of an element is highly intuitive and accepted for visualizing the

reliability of semantics (Abualdenien & Borrmann 2020). Therefore, the transparency value for each element t_e is derived by the following equation:

$$t_e = \frac{\sum_{l=1}^m c_e * \cos(\theta)_{e,l}}{m} \quad (1)$$

where l = layer number; m = maximum layer number; c_e = matching case of each element; and $\cos(\theta)_{e,l}$ = cosine similarity of each element's layer (according to (Forth et al. 2022)). The values of the above mentioned five matching cases for each element c_e are distributed as followed: case 1 = 20%; case 2 = 40%; case 3 = 60%; case 4 = 80%; and case 5 = 100%.

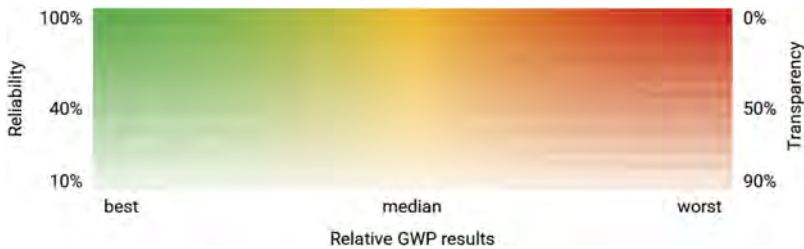


Figure 3. Color coding scheme for visualizing relative & uncertain GWP results.

To combine both information of semantic-related uncertainties and the relative performance of GWP results in the hot spot analysis, a color scheme matrix is established in Figure 3. On the x -axis, the relative GWP results according to the normalisation in each classification group is plotted. Generally, the legend of the relative colours ranges from green, representing the best performing variant, to red for the worst performing variant.

On the y -axis, the transparency value for each element t_e is visualized derived by equation 1. For the selection boxes of the element variants and material options, the same color range is used using 0% as transparency.

For the visualisation of the pre-calculated GWP results (according to (Forth et al. 2022)) on whole building and classification group level, box plot benchmarks of a study of 50 buildings by the German Sustainable Building Council (DGNB) are used to compare the correlating box plot GWP results (Braune et al. 2021).

4 CASE STUDY & IMPLEMENTATION

4.1 Case study project

To validate the approach using a prototypical implementation, an IFC model of a real-world office building with 1950 m² is used as a case study. The matching results and the LCA results have been previously validated (Forth et al. 2023). As the project is located in Germany, the classification follows the standard of German cost groups according to DIN 276 (DIN276 2018). The German database Ökobaudat was used as the materials and elements are named in German language (BBSR 2021). For the element matching the best performing NLP network BERT is used, as previously evaluated in (Forth et al. 2022). The case study model consists of 307 individual elements, which are from 16 different object types. The total surface area of all elements sums up to ca. 5824 m².

4.2 Prototypical implementation

The prototypical implementation is based on conventional web development tools using HTML, JavaScript and CSS. The web-ifc-viewer library of IFC.JS (Gonzalez Viegas 2022) is used as model viewer, which is a state-of-the-art the open-source toolkit based on JavaScript library three.js for 3D scenes in web browsers (Mrdoob 2022). For the hotspot analysis, every element surface is colored according to its performance relative to the classification group and the mentioned color scheme of Section 3.3.

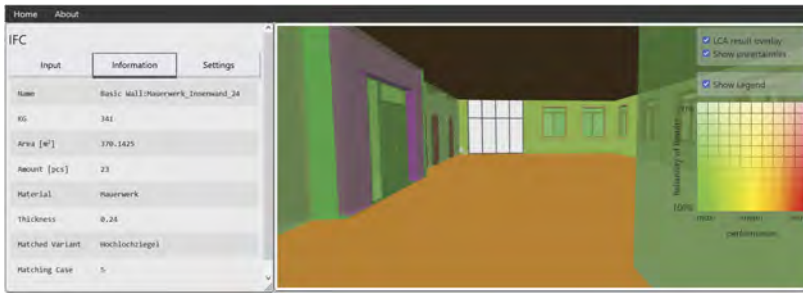


Figure 4. Prototypical implementation of the hot spot analysis using the case study (step 4.a-b).

Figure 4 illustrates the first part of the prototypical implementation using the case study. On the left side, all relevant quantities and semantical information of the selected element are shown (step 1-3), such as classification group (KG), element name, amount of elements of this object type, material name, layer thicknesses, the matched element variant and the matching case. On the right side, the 3D color coded hot spot analysis is applied on the uploaded IFC model using the color scheme and transparency values for showing the matching-related uncertainties (step 4.a). In the following step 4.b, one highlighted element with bad performance is selected to check design variants and optimize its GWP performance.

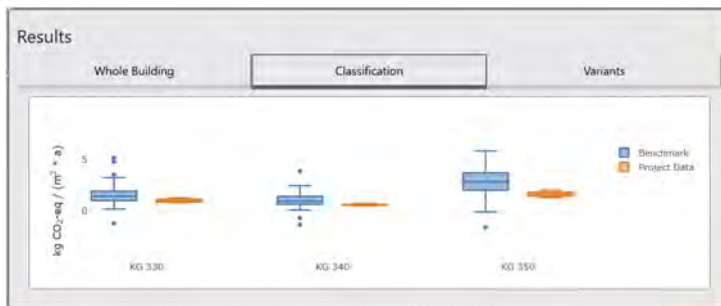


Figure 5. Prototypical implementation of the result on classification group level for comparing to benchmarks (step 4.a).

Figure 5 visualizes the GWP results in [kg CO₂-eq./ (m²*a)] of each classification group compared to the DGNB benchmark results ranges (step 4.a). For comparing the GWP results to the DGNB benchmarks, the results are normalized using the net floor area and the reference study period of 50 years. As the DGNB benchmarks include 50 different case studies, the resulting range is wider than the ones of the case study. Nevertheless, a general performance trend of the designed model can be identified intuitively for non-LCA-experts.

In the next step 4.c according to the proposed visualization approach, different element variants (Figure 6) and material options (Figure 7) are visualized. On the left sides, the name of each element variant or material option is color-coded according to its normalized GWP range compared to the other selectable alternatives. On the right side of Figure 6, the box plot diagrams of all element variants are shown. As every material option is connected to one pre-calculated LCA result, it is visualized as a differently colored dot mapped on top the box plot diagram of the selected element variant (Figure 7).



Figure 6. Prototypical implementation of the element variant comparison comparing variants of cost group 342 Non-load-bearing interior walls (step 4.c).

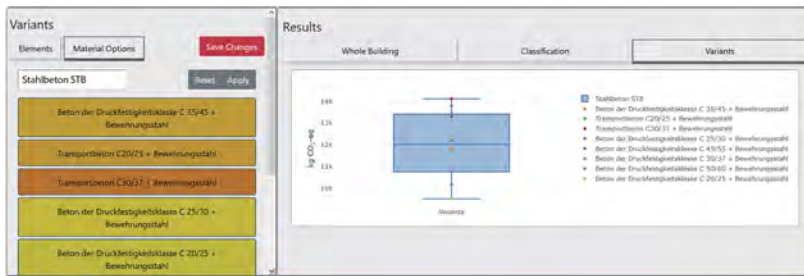


Figure 7. Prototypical implementation of the material option comparison of reinforced concrete (step 4.c).

5 CONCLUSIONS

This paper proposes a comprehensive and transparent approach for design decision making in early design stages in order to optimize embodied GHG emissions of new buildings. With the help of open BIM models and its 3D color coding for the hotspot analysis in combination with box plot diagrams for visualizing uncertain GWP results, an interactive process for non-LCA-experts is introduced.

Based on a previously validated method of NLP-based similarity assessment, this publication uses the results of the automatic element matching, where those elements of the IFC model are matched to the most similar ones in an LCA knowledge databases. The level of element matching and similarity analysis are taken into account for visualizing the uncertainty and reliability of the derived LCA results. Due to missing benchmarks on a level of elements and classification groups, the results are normalized based on the relative performance in each classification group and implemented for the 3D color coding as well as for the element variant and material option selection.

In the future, the proposed methodology will be evaluated by user testing and online surveys. Test users will be asked to assess different features in terms of intuitiveness, acceptance and applicability. The test users will be non-LCA-experts with different professional backgrounds.

To finalize the implementation of the proposed methodology, all relevant information of the Quantity Take-Off, Element Matching and LCA calculation will be stored and archived. Furthermore, the last step of the proposed methodology will be implemented using the BIM Collaboration Format (BCF) based on a server solution in order to communicate the feedback of the decision making back to the BIM modeller using authoring software. Thereby, an approach of archiving the design decision including the LCA results and further project information, such as the results of the element matching, needs to be considered.

The proposed methods is a first approach of supporting design decision making in early stages using BIM models and different visualizations, considering uncertainties of LCA results. In a next step, this prototype will be evaluated by non-LCA-experts from practice.

REFERENCES

- Abualdenien, J. & Borrmann, A. 2020. Vagueness visualization in building models across different design stages. *Advanced Engineering Informatics* 45: 101107
- BBSR 2021. ÖKOBAUDAT <https://www.oekobaudat.de/>
- Braune, A., Ekhvaia, L. & Quante, K. 2021. Benchmarks for greenhouse gas emission from building construction: Results of a study with 50 buildings.
- DIN 276 DIN 276:2018-12 2018. Kosten im Bauwesen. (Beuth Verlag GmbH)
- European Commission 2022. Buildings and construction. https://single-market-economy.ec.europa.eu/industry/sustainability/buildings-and-construction_en
- European Commission & Directorate-General for Environment 2022. The Level(s) Calculation and Assessment Tool (CAT).
- Forth, K., Abualdenien, J., Borrmann, A., Fellermann, S. & Schunicht, C. 2021. Design optimization approach comparing multicriterial variants using BIM in early design stages. *Proceedings Of 38th International Symposium On Automation And Robotics In Construction (ISARC 2021)*: 235–242.
- Forth, K., Abualdenien, J. & Borrmann, A. 2022. NLP-based semantic model healing for calculating embodied carbon in early building design stages. *Proc. Of European Conference On Product And Process Modeling 2022*.
- Forth, K., Abualdenien, J. & Borrmann, A. 2023. Calculation of embodied GHG emissions in early building design stages using BIM and NLP-based semantic model healing. *Energy and Buildings*: 112837.
- Gonzalez Viegas, A. 2022. IFCjs/web-ifc-viewer: Graphics engine and toolkit for client applications. <https://github.com/IFCjs/web-ifc-viewerreadme>
- Hollberg, A., Kiss, B., Röck, M., Soust-Verdaguer, B., Wiberg, A., Lasvaux, S., Galimshina, A. & Habert, G. 2021. Review of visualising LCA results in the design process of buildings. *Building And Environment* 190: 107530.
- Hollberg, A., Tjäder, M., Ingelhart, G. & Wallbaum, H. 2022. A Framework for User Centric LCA Tool Development for Early Planning Stages of Buildings. *Frontiers In Built Environment* 8.
- Kiss, B. & Szalay, Z. 2019. A Visual Method for Detailed Analysis of Building Life Cycle Assessment Results. *Applied Mechanics And Materials* 887: 319–326.
- Miyamoto, A., Allacker, K. & Troyer, F. 2022. Visual tool for sustainable buildings: A design approach with various data visualisation techniques. *Journal Of Building Engineering* 56: 104741.
- Mousa, M., Luo, X. & McCabe, B. 2016. Utilizing BIM and Carbon Estimating Methods for Meaningful Data Representation. *Procedia Engineering* 145: 1242–1249.
- Mrdoob 2022. three.js: JavaScript 3D Library. <https://github.com/mrdoob/three.js/>
- Petrova, E., Pauwels, P., Svidt, K. & Jensen, R. 2019. Towards data-driven sustainable design: decision support based on knowledge discovery in disparate building data. *Architectural Engineering And Design Management* 15: 334–356.
- Rasmussen, M. H., Pauwels, P., Hviid, C. A. & Karlshoj, J. 2017. Proposing a central AEC ontology that allows for domain specific extensions. *Proceedings Of The Joint Conference On Computing In Construction (JC3)* 1: 237–244.
- Röck, M., Hollberg, A., Habert, G. & Passer, A. 2018a. LCA and BIM: Integrated Assessment and Visualization of Building Elements' Embodied Impacts for Design Guidance in Early Stages. *Procedia CIRP* 69: 218–223.
- Röck, M., Hollberg, A., Habert, G. & Passer, A. 2018b. LCA and BIM: Visualization of environmental potentials in building construction at early design stages. *Building And Environment* 140: 153–161.
- Schneider-Marín, P., Stocker, T., Abele, O., Margesin, M., Staudt, J., Abualdenien, J. & Lang, W. 2022. Early-Data knowledge base for material decisions in building design. *Advanced Engineering Informatics* 54: 101769.
- Schumacher, R., Theien, S., Höper, J., Drzymalla, J., Lambertz, M., Hollberg, A., Forth, K., Schneider-Marín, P., Wimmer, R., Bahlau, S. & Meins-Becker, A. 2022. Analysis of current practice and future potentials of LCA in a BIM-based design process in Germany. *E3S Web Of Conferences* 349, 10th International Conference On Life Cycle Management (LCM 2021).
- Ströbele, B. 2022. Ermittlung von Umweltwirkungen im Lebenszyklus von Gebäuden innerhalb der Planungsphase auf der Grundlage von unscharfen Daten.
- United Nations Environment Programme 2021. Global Status Report for Buildings and Construction: Towards a zero-emissions, efficient and resilient buildings and construction sector.
- Wiberg, A., Wiik, M., Auklend, H., Sl, M., Tuncer, Z., Manni, M., Ceci, G. & Hofmeister, T. 2019b. Life cycle assessment for Zero Emission Buildings – A chronology of the development of a visual, dynamic and integrated approach. *IOP Conference Series: Earth And Environmental Science* 352: 012054.
- Wiberg, A., Lvhaug, S., Mathisen, M., Tschoerner, B., Resch, E., Erdt, M. & Prasolova-Frland, E. 2019a. Visualisation of KPIs in zero emission neighbourhoods for improved stakeholder participation using Virtual Reality. *IOP Conference Series: Earth And Environmental Science* 323: 012074.

Port facilities asset management: Coping with aging infrastructure and constrained budgets on the long term

H. Voogt

Port of Rotterdam, Rotterdam, Zuid-Holland, The Netherlands

ABSTRACT: With the aging port infrastructure around the world, it is crucial to understand the current condition state of these structures and adopt cost effective and sustainable strategies to repair and maintain these assets. Over the past decade, considerable work was conducted on the mechanisms responsible for the deterioration of structures exposed to harsh environments and how to report condition and performance. Recently, a new generation of deterioration models and risk based management approaches combined with state-of-the-art geographical and sensor data technology have seen the day and are used to assist port owners and engineers in optimizing the use of funds in keeping their ports as safe and competitive as possible. This presentation covers the asset management approach and its underlying principals in one of the world's largest port to build a long term asset planning that is able to visualize the consequences of constraints in available budget.

1 INTRODUCTION

The Port of Rotterdam is after being the world's largest port for many years in terms of handled goods, still the major port in Europe. On a yearly bases the Port handles a total of approximately 470 million tons of goods. Only 27 percent of this amount is filled in by in a total of 14,5 million TEU's, the major part is dominated by liquid and dry bulk. Furthermore the Port of Rotterdam accommodates ships up to a water depth of 75 feet (24 meters) and is visited by approximately 30.000 sea-going vessels and 120.000 inland ships per year. As the Port of Rotterdam is a landlord port, the asset management department is responsible for a wide set of assets, amongst others over 50 miles of waterfront structures (quay walls and jetties) with a total replacement value estimated at \$2 billion USD. More than two-third of these quay walls are exposed to varying salinity seawater which causes degradation in the form of corrosion for the substructures constructed of steel sheet piling or steel combi walls (combination of tubular piles and sheet piles) and chloride ingress followed by rebar corrosion of the concrete elements. Almost 50 % is older than the design lifetime but still in good condition, even though the Port of Rotterdam is facing these challenging conditions.

With the typical service life of their waterfront structures around 50 years and the port in constant expansion, the Port of Rotterdam needed to implement a rigorous approach and protocols to efficiently track required annual maintenance as well as forecast the short- and long-term costs of keeping their structures in service for their tenants.

Upon completion of the first phase of implementation, the Port of Rotterdam's resulting system accurately provides current condition state, simulates various maintenance strategies on the basis of the inspection results so that the most efficient and cost-effective inspection regime and maintenance scenario for the structures in question can be selected and applied, provides insight on the consequences – such as reduction in remaining service life or availability of the structure – of postponing specific maintenance measurements, and determines the consequences of different alternative maintenance measures.

The approach considers the possible risks and causes that endanger the structures (or parts of it) relating to availability, structural safety, sustainability and aesthetics and it ranks the risks associated with retaining the desired functionality, then presents the financial consequences of postponing required maintenance for budgetary or economic reasons.

Based on the predictive deterioration models and risks, a multi-criteria approach, called business value is used to prioritize the maintenance tasks to be carried out. Required maintenance tasks are ranked based on – commercial importance, availability requirements, and end of contract date.

This prioritization approach of maintenance tasks, based on a multi-criteria analysis, ensures that expenditure and maintenance are performed on the structures that are most economically important to the Port of Rotterdam Authority and where the safety risks are the highest. Not for the next year, but also long term over a period of 30-50 years.

2 DETERIORATION OF WATERFRONT INFRASTRUCTURE ASSETS

The maritime assets of ports add enormous value to the business of the port and are a facilitator of added value to several regions and countries, but due to the function these structures serve and the maritime environment, these assets are relatively costly to construct and maintain. When not looked properly after, the harsh conditions of the maritime environment will cause major deteriorations of the assets. But not only the circumstances can cause problems with the structural integrity of the assets. Also the management strategies or the company policy can make things worse than needed. Here is a list of some examples:

- Deferred maintenance costs: is often seen in organizations where the budgets are cut due to several reasons. Despite the saying that the most expensive maintenance is deferred maintenance, this strategy is not completely banned.
- Inadequate capital allocation: is often seen in organizations where there are constraints on the available budget for asset management, which leads to not being able to do the full set of maintenance measurements
- Run-to-failure repair & maintenance programs: is sometimes called the fire fighter approach and is often seen in organizations that do not have achieved a certain maturity level in order to be able to implement preventive maintenance plans.
- Inspections based on random observations: is often seen in organizations where there is no insight in where the vulnerable structures are that are under high risk of deterioration. A risk based approach can help identify these structures.

All these forementioned examples will lead to a loss of competitive edge and productivity or even worse safety and security concerns for the port and need full attention of not only the asset management staff. A well-performing asset management system for waterfront infrastructure is very important.

3 CHALLENGES OF THE ASSET MANAGER

For Port Authorities, waterfront assets like quay walls, wharves and jetties are the pivot of their business cases. The Port's income will depend on whether the asset is capable of performing adequately during the lease period of the tenant. Of course, when there is no availability for the tenant to load and unload goods, he will certainly not pay the lease fee for the use of these assets. In the short term, this will mean a loss of profit for the port, but in the long term, it will mean that there will be a decrease in cash flow and no potential opportunities for future developments or rebuilds. Finally, as a landlord port, disrupting the business of the tenant with unexpected big repairs or with notifications that part of these assets no longer meet the agreed program of requirements in terms of load or safety, is the most unwanted situation.

Apart from the need to accommodate the tenant in a proper way, there are more challenges for the asset manager. The more intensive use of the assets due the growing amount of calls of

ships because they are handled more efficiently, will have an effect on the condition of the quay walls and jetties. Not to mention the ever increasing size of the vessels, in a very short period for instance container vessels have grown from 8.000 TEU to a nowadays standard of 22-24.000 TEU, while the assets are still the same and have a design based on the a program of requirements that describes the mooring of 8.000 TEU ships. Compared with the standard design lifetime of a waterfront asset, which is typically 50 years, there is a huge mismatch in keeping up with the speed of growth. The ships are far bigger than calculated in the design. This means that the program of requirements and thus the quay wall or jetty is stretched to the maximum.

On top of that the internal organization of the Port Authority also rises some challenges for the asset manager, first he will have to explain (sometimes justify) to the board the needed budget in order to prevent the budget from being cut. The board might have some questions about the budget, such as: “what will happen if next year’s budget is not granted, or if it has to be cut in half?” Or, the wish of the financial director to level out the peaks in the long-term budget for the coming years. These are tricky questions because typical deterioration of assets usually takes much longer than just one year, so the answer will often be that next year will be fine, but nevertheless the problems are “postponed” to the upcoming years. An insight on the effect on the long term asset planning is needed to come to the right decision. Secondly there is the commercial desire to extend the tenant’s contract for a longer period preferably with a commitment of the asset manager that major investments are not needed to extend the useful lifetime of the assets involved. Thus, the “end of contract” becomes an important date.

Within the organization therefore, asset management, including an understanding of the life-cycle position of their broad portfolio of assets and a risk-based approach to the allocation of the capital resources, becomes a strategic imperative for every port in the world.

Therefore the asset management within a organization must have a minimum level of maturity. In the beginning all asset management will be reactive, with projects based on the available budget, that itself is based on the budget of last year and less reduction of risk by the invested budget. The aim is to be proactive instead of reactive where budgets are based on future needs, high risk assets are replaced before the moment they fail and the focus is on a high benefit to cost ratio. As the maturity level grows, the attitude will shift from “cost focus” to “value focus”. Consequently, costs will go down, and value and performance will increase.

4 STEPSTONES IN ASSET MANAGEMENT

In order to reach a higher level of maturity in asset management and so being able to be proactive and focus on value and performance there is a roadmap with 7 stepstones available that can be followed.

1. Document the assets owned and managed, Ask yourself: “How many assets do I have to take care of?” and subsequently “Are all dimensions known, and /or are drawings and specs available?” These are very simple questions, but not always so easy to answer. It takes time and effort to sort this out, but it is a necessary first step.
2. Understand the current condition of the asset in respect to the useful lifetime. Once you have an overview of all the assets, the next step is to inspect the current condition of every single asset. The way that this is done, depends on the structure and the material and can vary from a simple visual inspection to an extended life time inspections with a subsequent predicting model.
3. Understand what budget is needed to catch up, keep up and move forward. With the result of the previous step, it is now possible to examine whether the condition of an asset is meeting the required standard or needs extra attention. The required actions can then be identified and followed by a maintenance plan and a needed budget for the coming years.
4. Understand what endangers the functionality: risk analysis. You do not want to spend your available budget on assets of which the functionality is not at risk. To obtain this insight a in-depth risk analysis needs to be done. The basic question in the risk analysis is:

“What phenomena can endanger the asset’s functionality?” “What are the effects and what is the probability of occurrence. Once these risks are known and identified, preventive maintenance measures can be listed to mitigate these risks. If maintenance measures are not executed, then this will inevitably lead to the risks to occur. Several proven methods are available for risk analysis, so use one that fits your assets the most.

5. Understand the business value, the business value is a multi-criteria calculated figure that represents how much an asset contributes to the goals of the organization. In other words, in the case of an port authority, a frequently used quay walls need more attention and higher prioritization than a quay wall that is rarely used.
6. Establish the level of service for an asset and calculate the cost of service Not all the assets need the same level of service, for instance highly visible assets will often have a higher level of service. Or some tenants have based on their SLA agreed a higher level of service than others. This will lead to an extra effort in asset management and thus to extra needed budget that must be calculated and incorporated in the (long term) financial asset planning.
7. Prioritize the needed budget based on risk and business value: required maintenance tasks are ranked by the business value: a quality mark which is made up of various factors – commercial importance, availability requirement and end of contract term. By using this quality marking system in conjunction with the level of risk to be covered, it’s possible to create a prioritized list of all maintenance measures, a high quality mark combined with a top-ranked risk gives a maintenance action the highest priority. A low quality mark with a bottom-ranked risk gives it the lowest priority.

5 DEVELOPING AND USING AN EXPERT SYSTEM

Port of Rotterdam has been investing in a tool that is able to support the asset manager in doing the tasks as explained in the seven stepstones above. Most organizations and also Port of Rotterdam will have a triangular shaped IT backbone in place that comprises of an ERP system (Port of Rotterdam uses SAP), a document management system like Sharepoint or an equally qualified system and a geographic information system (GIS). When it comes to documenting all the assets, the functionalities of these IT systems will be sufficient to create a register and breakdown structure of all the assets, store the drawings and other documents and produce a map with the exact location of your assets.

To support the other stepstones you will need expert systems that do a specific task and that get their master data from the forementioned main IT systems. Port of Rotterdam developed an asset management tool that compares the results of deterioration models with the “end of contract” date to identify if and when the functionalities of the structure are endangered and uses the risk analysis and business value of a quay wall to clarify its maintenance priorities. A screenshot is presented in Figure 1. It provides the asset owner and asset manager with a LTAP (long term asset planning) tool to efficiently manage a portfolio of quay walls or other maritime civil engineering structures. Different scenarios can be evaluated, in the case of underspending risks of loss of functionality will arise over the years, in the case of overspending budget is spent too early. In current times with constraints on the budget, this will help to find the optimum scenario.

6 PREDICTIVE ASSET MANAGEMENT: REMAINING USEFUL LIFETIME

The typical service life for the port and maritime structures is approximately 50-75 years. A large proportion of these assets in the Port of Rotterdam will be nearing the end of their service life in the coming decades. In order to effectively and efficiently manage these assets, it is critical to have a system in place to track the yearly required maintenance as well as forecast the short and long-term costs of keeping these structures in service.



Figure 1. Screenshot of the landing page of Port of Rotterdam's expert system.

A quay wall's remaining lifetime and system integrity is mainly determined by the quality of the substructure and the superstructure. Other components of a quay wall are most of the time replaceable and do not influence the strength of the structure. When the quay wall's integrity is in danger, it's often due to two aspects: namely accelerated low water corrosion occurring at the substructure or concrete deterioration in the superstructure.

More than two-thirds of the quay walls in Port of Rotterdam are deteriorating from accelerated low water corrosion because the substructure is made of steel sheet piling or steel combi walls (combination of tubular piles and sheet piles). The concrete top structures are also degrading due to the chloride ingress from the salt water and carbonization due to CO₂ in the air.

Port of Rotterdam drew up and validated a steel deterioration model based on corrosion rates that is capable of predicting the safety factor on both the strength of the structure and soil retention over the remaining lifetime of a quay wall, and if needed, to present the ultimate moment to start maintenance. a similar method is being used to predict the aging of concrete. Both models need input from field inspections. In the case of the steel substructure this done by doing ultrasonic thickness measurements or check the effectiveness of the cathodic protection system. For the concrete model prediction cores are drilled from the quay wall and tested in the laboratory. These results in combination with GPR measurements on the concrete cover and HCP measurement to locate initiated corrosion of the rebar are input for the model to calculate the remaining useful life. Figure 2 shows a screenshot of the outcome of the life-time calculations.

With the aid of its highly advanced deterioration models, the expert system can predict when the lower safety limit for a quay wall will be reached, how the inspection regime must then be detailed and what maintenance measures must be done in order to meet the asset owner's required functionalities (such as availability for use, or asset lifetime).

7 THE EFFECT OF MAINTENANCE STRATEGIES ON THE LIFETIME

The model is capable of simulating various maintenance strategies, So it gives insight on the effect of the applied strategy. The strategy can consist of several measures with an in between

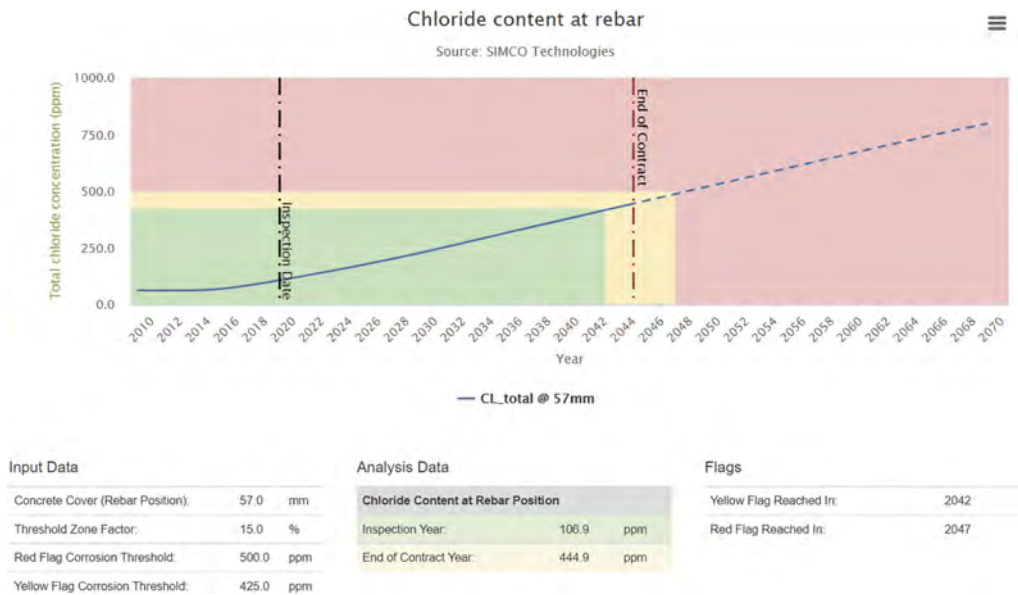


Figure 2. Screenshot of the progress of chloride content at rebar over time.

period of several years. So the most efficient and cost-effective maintenance scenario for the quay wall in question can be selected and applied.

It will also provide insight into the consequences – such as a reduction in the remaining service life or availability of the structure – of postponing specific maintenance measures or the effects of a do nothing scenario.

The results of these simulations, what maintenance measures in what year are used in the Port of Rotterdam’s expert system to draw up the LTAP (Long Term Asset Planning). Putting all assets in the planning and combining this with the regular O & M costs of the assets, will give insight in the needed budget over the coming years and can be used to make the most optimized financial investment plan.

8 RISC MANAGEMENT IN MAINTENANCE STRATEGIES

One of the best methods to make the most out of the constraint budgets, is to apply risk management on the activities.

Not all risks that endanger the functionality of the quay wall (or parts of it) will lead to a highly unwanted situation. The risk figure is calculated by multiplying the probability of failure by the consequence of failure. The consequence of failure (CoF) of (the part of) an asset can be calculated by ranking the effects on the business in terms of financial, image, safety, availability etc, by using the redundancy and by using the measures taken to reduce the CoF. The CoF can be seen as a more or less constant figure that will not change radically over time, when an asset fails these are the consequences. On the other hand the probability of failure (PoF) will change over time in a more or less same speed as the deterioration. If the condition of an asset goes down, the PoF will grow. With that in mind, the assets that have a low CoF will in case of failure have acceptable consequences and thus will have a different maintenance strategy (run to failure) than an asset with a high and unacceptable CoF, where an intensive monitoring can be the preferred maintenance strategy. So even in the case of constrained budget, there is still a way to make choices that do not affect the business in an unacceptable way and lead to more damage for the company than needed.

9 LONG TERM ASSET PLANNING

Once the asset manager finalizes prioritizing the required maintenance on each structure, the sum of the individual identified maintenance actions, whether they are CAPEX or OPEX, over a period time will give a long term asset planning for that asset. The Long Term Asset Planning will provide the asset manager on overview of the needed budget over the next 50 years. This will give the financial department the possibility to make a financial planning and if needed the effects of peak shaving can be made visible and the plan can be adjusted.

Compiling work packages for multiple structures containing similar tasks means these packages can then be procured under one contract in order to reduce installation time and cut costs. The prioritization of maintenance tasks, based on a multi-criteria analysis, ensures that expenditure and maintenance is performed on those structures that are the most economically important to the Port of Rotterdam Authority – and where the safety risks are highest.

If necessary, when maintenance work is postponed to the next calendar year, (for example, due to budgetary constraints), the system will then translate the consequences of this directly into the maintenance budget for subsequent years. In effect, it translates the risks of not performing a certain maintenance task into a higher priority for the coming years.

10 CONCLUSIONS

The Port of Rotterdam succeeded in developing an asset management tool based on a simple but effective method that can help the asset manager to make the right decision in regards to the (constrained) maintenance budget. Not only based on lifetime prediction of the most vulnerable parts, but also on business value of the asset and the risks involved.

It will allow the Port of Rotterdam to predict the degradation of quay walls, whether they are built of concrete, steel or a combination of both. It will also provide a good indication about when preventive maintenance should be done, the costs that are involved and the safety of the structure for its tenants. When Port of Rotterdam faces the need to constrain the available budget to whatever reason, the consequences of different scenarios in terms of budget, condition and risk can be calculated and the optimum scenario for the given situation can be chosen.

The method that was developed in the Port of Rotterdam is based on a simple stepstone method that is applicable in any other port in the world. Whereas Port of Rotterdam has put extensive effort in developing state of the art degradation models, the use of more simple methods can also lead to acceptable results to give insights in the different scenarios.

REFERENCES

Jongbloed, B. P. 2019. From Inspection to Prediction of Corrosion-Induced Degradation of Quay. Walls in Port of Rotterdam. Rotterdam, The Netherlands: Port of Rotterdam Authority.

Modeling and characterization strategy as a basis for improved prediction of concrete fatigue degradation in wind power plants

A. Baktheer, M. Aguilar, H. Becks, M. Classen, J. Hegger & R. Chudoba
Institute of Structural Concrete, RWTH Aachen University, Aachen, Germany

ABSTRACT: The fatigue behavior of concrete has been usually investigated experimentally for loading scenarios with constant amplitudes. However, in reality, concrete components and structures such as wind turbine towers are subjected to loading scenarios with variable amplitudes. Current design rules insufficiently capture the effect of amplitude changes and loading sequence within load scenarios on the fatigue behavior of concrete and can lead to both uncertain and uneconomic design. A purely experimental investigation of the sequence effects in cyclic loading of concrete is not feasible due to the large number of possible combinations of experimental parameters. In this paper, the concept of a combined numerical-experimental methodology is presented with the aim to develop an engineering model that will deliver more realistic predictions of the fatigue life of concrete towers, thus increasing the reliability and economic viability of wind turbines. A microplane fatigue model recently developed by the authors is used to study and analyze the fatigue behavior of concrete covering a wide range of applications, accounting for any kind of loading scenario. The paper presents recent advances in modeling and characterization of fatigue behavior of concrete, considering the effect of loading sequence and provides an outlook of the prospective methodology for deriving design rules for fatigue life prediction in wind power plants.

1 INTRODUCTION

A realistic prediction of the fatigue life of concrete under high-cycle loading scenarios with variable amplitudes is of utmost importance for a reliable and economically efficient design of structural infrastructure for energy supply such as wind power plants. In modern high-performance RC structures, the compressive fatigue of concrete gains crucial importance due to the high material utilization (Schmidt, Schneider, and Marx 2019). This is especially important for prestressed slender structures, such as the concrete towers of wind turbines, where cyclic loading leads to stress fluctuations around considerably high permanent compressive stresses. The fatigue behavior of concrete has been mainly studied experimentally under constant amplitudes in the last decades, e.g. (Kim and Kim 1996; Schneider, Humme, Marx, and Lohaus 2018). Based on these studies, the fatigue life of concrete is typically characterized by the Wöhler/S-N curves (fib Model Code 2010). However, in reality, concrete members and structures are subjected to complex loading scenarios with variable amplitudes such as the stochastic wind actions in the onshore and offshore wind power plants (Lenschow 1980).

Since the experimentally determined Wöhler curves characterize only uniform fatigue loading, more refined methods are needed to evaluate fatigue damage due to fatigue loading with variable amplitude. In current design codes, e.g. (fib Model Code 2010; EN-1992-2 2005), the widely used Palmgren-Miner P-M (Palmgren 1924; Miner et al. 1945) rule is considered. This rule assumes that the cumulative fatigue life for a loading scenario consisting of n loading ranges is estimated by linear interpolation of the fatigue life for each loading range individually. The fatigue failure is assumed when

$$\eta = \sum_{i=1}^n \frac{N_i}{N_i^f} = 1, \quad (1)$$

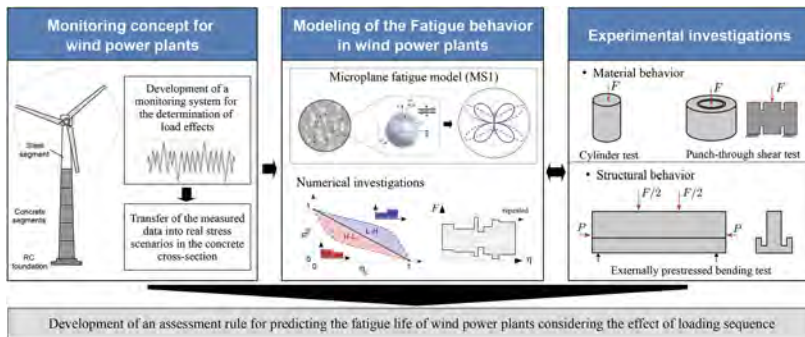


Figure 1. Summary of the planned methodology for characterizing the fatigue loading sequence effect in wind power plants.

where N_i^f is the number of cycles to failure achieved under a constant amplitude loading corresponding to the level i and N_i is the number of applied cycles at the load level i during a multi-level loading scenario. Although this hypothesis is widely used, experimental evidence is so far lacking. On the contrary, the few available published experimental results show that the P-M rule can lead to a very unsafe lifetime prediction (Holmen 1979; Baktheer and Chudoba 2021). Therefore, it is necessary to derive engineering models that allow a more realistic prediction of concrete fatigue lifetime in wind power plants.

A purely experimental investigation of the sequence effects during cyclic loading of concrete is not feasible due to the large number of possible combinations of loading parameters. Within a joint research project named (WinConFat-Structure) funded by the German Federal Ministry of Economic Affairs and Climate Action (BMWi), the main goal is to characterize the concrete fatigue behavior in wind power plants considering the effects of loading sequence as a basis for an improved engineering model.

For a more realistic prediction of the fatigue life of concrete, the support of advanced numerical and theoretical models that describe the fatigue damage process in a thermodynamically consistent way is urgently needed. A physically based microplane fatigue model MS1 developed recently by the authors (Baktheer, Aguilar, and Chudoba 2021) will be used for an efficient simulation of the fatigue damage development in the critical concrete cross-sections and zones of wind power plants over the entire lifetime in combination with the development of a monitoring system to determine load effects and load sequences in wind power plants. The modeling approach will be calibrated and validated with recently developed experimental setups at both the material and structural levels (Becks and Classen 2021; Becks, Baktheer, Marx, Classen, Hegger, and Chudoba 2022) as shown in Figure 1.

The overall view of the research project is summarized in Figure 1. The current paper highlights the main concept of the research project (WinConFat-Structure) with the intended combined numerical-experimental methodology for characterizing the effect of loading sequence on the fatigue lifetime of concrete, and presents recent advances in modeling and characterizing the fatigue behavior of concrete considering the effects of the loading sequence.

2 MODELING OF CONCRETE FATIGUE RESPONSE

2.1 Microplane fatigue model MS1

A recently developed microplane material model for concrete fatigue MS1 (Baktheer, Aguilar, and Chudoba 2021), that introduces the cumulative shear fatigue hypothesis (Baktheer and Chudoba 2018; Chudoba, Vořechovský, Aguilar, and Baktheer 2022) at the microplane level, will be used in the combined numerical-experimental methodology for characterizing the concrete fatigue behavior considering the effect of loading sequence (Aguilar, Baktheer, and Chudoba 2021). By linking fatigue damage evolution to a cumulative measure of inelastic shear

strain, the triaxial stress redistribution within the concrete material structure in response to subcritical fatigue loading can be captured (Figure 2). The model was formulated within the microplane framework using the kinematic constraint to project the macroscopic strain tensor to the microplanes and the principle of virtual work and energy equivalence to obtain the macroscopic stress tensor.

In the following sections, examples of fatigue simulation of concrete using the described model are presented, showing the ability of the model to capture the main phenomena of concrete fatigue.

2.2 Fatigue under uniaxial compression

To study the feasibility of the model to simulate the concrete fatigue behavior, simulations of a single material point behavior are considered in this section. Assuming that the dissipative effects governing the compressive fatigue behavior of concrete within a cylindrical specimen are uniform within its volume, the state evolution of the specimen can be idealized as uniform uniaxial stress and strain over its fatigue life.

A recently performed experimental program on cylinder specimens with a compressive strength of 60 MPa under uniaxial compression including several loading scenarios is used to identify the model parameters. The calibration of the model was achieved by simultaneously considering the monotonic scenario and the fatigue loading scenarios with several upper load levels. The experimentally obtained curves for monotonic and fatigue loading and the simulated curves reproduced by the calibrated model are depicted in Figures 3a-c. To study the applicability of the calibrated model to any loading scenario, its predictions for a pre-peak cyclic loading with step-wise increasing upper load level are compared with the obtained experimental results as shown in Figures 3d-f.

The model shows the ability to simulate the monotonic and fatigue behavior of concrete under compression with a consistent set of material parameters. Furthermore, the numerically predicted fatigue creep curve for the step-wise loading scenario in Figure 3f shows a realistic prediction, indicating a promising capability of the model to simulate the concrete behavior under more complex loading scenarios.

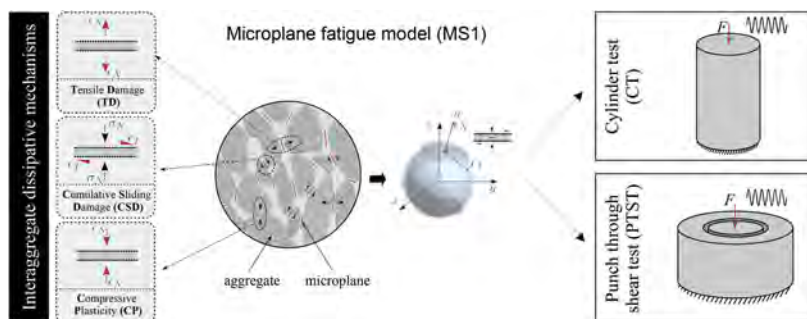


Figure 2. Interaggregate dissipative mechanisms included in the developed microplane fatigue model MS1 and illustration of the microstructure containing a system of dissipative microplanes that are integrated within 3D hemisphere idealization.

2.3 Fatigue under combined shear-compression loading

The developed thermodynamic-based microplane model MS1 described in Sec. 2.1, hypothesized that fatigue evolution in the concrete material structure can be realistically modeled by defining a cumulative measure of inelastic shear strain as the fatigue driving mechanism. The standard method of fatigue characterization using cylinder specimens induces shear only as a secondary effect within the volume of the specimen. To validate the hypothesis, experimental methods with dominant shear strain appear more appropriate. A recently developed Punch-

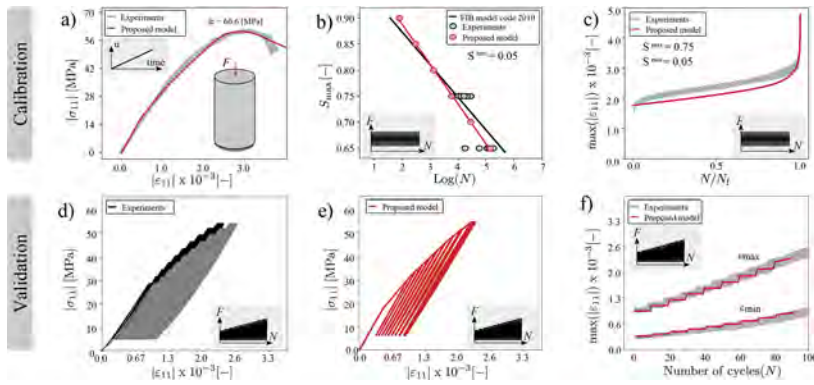


Figure 3. Cylinder test simulation under compression with the developed microplane model MS1 with calibration-validation procedure based on performed tests: a) stress-strain response under monotonic loading; b) Wöhler curve representing fatigue life; c) fatigue creep curve at the upper load level; d, e) stress-strain response under pre-peak cyclic loading; f) corresponding fatigue creep curves.

Through Shear Test (PTST) setup (Becks and Classen 2021) induce shear-dominated strain within the volume of the specimen (Figure 4a) with controllable level of compressive stresses (Becks, Aguilar, Chudoba and Classen 2022).

To provide an example of using the developed MS1 model within a finite element discretization to simulate the response of the PTST, an elemental study is shown in Figure 4. As shown in Figure 4a, an axisymmetric idealization is used in this example, to allow efficient cycle-by-cycle simulation of the PTST fatigue behavior, which nevertheless realistically represents the governing principles of fatigue propagation. The dimensions of the model are 50 mm height and 100 mm diameter. The center of the notch is located 26 mm from the axis of symmetry, has a width of 4 mm, and a depth of 10 mm. To examine the ability of the model to reproduce the shear fatigue response in combination with lateral confinement, a study with subcritical shear upper load level of 70 kN, lower level of 20 kN, and a lateral confinement of 7.5 MPa is shown in Figure 4b. The example shows a low cycle fatigue response with fatigue failure after 39 load cycles. The obtained load-displacement curve demonstrates the ability of the model to reproduce plausible cyclic behavior with a realistic shape of hysteretic loops.

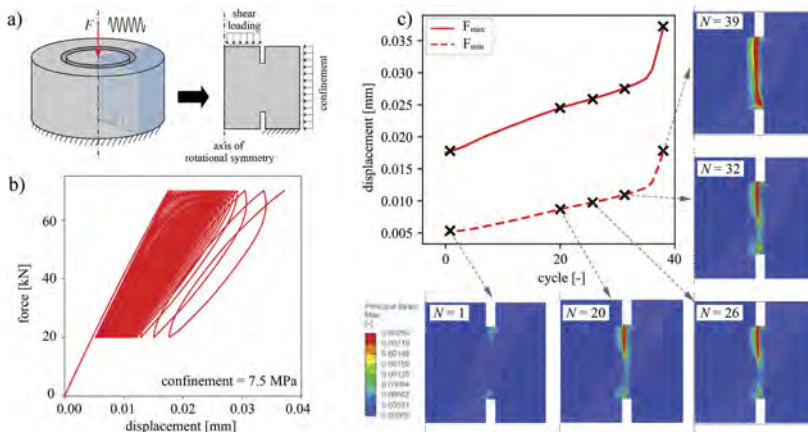


Figure 4. Elementary example of fatigue simulation of the PTST a) test setup with axisymmetric idealization used in the numerical simulation; b) force-displacement curve for cyclic shear loading with a range of 70 kN for the upper level and 20 kN for the lower level; c) corresponding fatigue creep curves at the upper and lower load level with the contour plots of the development of the principal strain during fatigue life.

Furthermore, the corresponding fatigue creep curves, i.e. the displacement increase at the upper and lower load levels during fatigue life are shown in Figure 4c. The obtained response reveals the typical shape of fatigue creep curves observed usually during fatigue experiments. The crack propagation during cyclic loading is visualized in Figure 4c, where the contours of the maximum principal strain are plotted for selected load cycles during the fatigue life.

The formulation of the model in the framework of thermodynamics allows isolating the energy release due to the individual mechanisms such as plastic deformation, plastic strain hardening effects, and damage evolution. This feature of the model can be used for objective characterization of stress redistribution effects within the material structure under fatigue loading with any complex loading scenario. Further detailed analysis of the energy dissipation during fatigue life is documented in (Aguilar, Baktheer, and Chudoba 2022).

3 EFFECT OF LOADING SEQUENCE

One of the most complex phenomena in characterizing the fatigue behavior of concrete is the effect of loading sequence on the fatigue life due to the inevitably large scatter and high cost of fatigue testing. This effect is of great relevance for any structure subjected to fatigue loading due to the nature of repeated loading in the reality. Without studying the effects of load sequencing and variable amplitudes, safety factors can be set uneconomically large or dangerously low. Due to the complexity of characterizing this effect, only little experimental research has been reported in the literature on this topic.

Recently, comprehensive studies of the concrete fatigue behavior under several uniaxial compression loading scenarios that include pre-peak and post-peak cyclic loading, low and high cycle fatigue, as well as the effect of loading sequences with variable amplitudes have been performed by the authors (Baktheer and Chudoba 2021). The results presented in Figure 5a-c show the effect of load sequence on the compressive fatigue behavior of concrete with considerable scatter of the obtained fatigue life for both High-Low (H-L) and Low-High (L-H) loading scenarios. These studies confirmed earlier observations (Holmen 1979) that the Palmgren-Miner (P-M) rule is not able to capture the load sequence effect correctly, revealing the existing deficit in the current design codes (EN-1992-2 2005). The obtained results allowed an energetic interpretation of the fatigue loading sequence effect. Assuming that energy is dissipated uniformly within the volume of the cylindrical test specimen during subcritical compressive cyclic loading the superposition of energy dissipation profiles along the lifetime measured for constant amplitudes becomes possible and can explain the experimentally observed misfit with respect to the P-M rule. The situation is sketched using energy dissipation profiles due to damage for two levels of loading in Figures 5d, e.

The recently developed PTST that allows for a simultaneous control of shear and compressive stresses can be used to systematically isolate the influence of the degree of confinement on the fatigue life of concrete under subcritical fatigue shear loading. Comprehensive experimental studies on the monotonic and fatigue behavior of concrete using the PTST test setup with radial notches (Figure 6a) have been recently performed by the authors (Becks, Aguilar, Chudoba and Classen 2022). The influence of different degrees of confinement on monotonic and fatigue behavior is depicted in Figure 6a, b. As can be seen from the experimental results, the number of cycles to failure remains nearly uniform for the studied confinement load levels (Figure 6c). Interestingly enough, the scatter of the results tends to decrease with an increasing level of confinement. This configuration offers a promising opportunity to characterize the effects of loading sequence, which are typically difficult to observe in classical experimental setups, such as cylinder tests and three-point bending tests, due to the large scatter of results as documented by (Tepfers, Friden, and Georgsson 1977; Baktheer, Becks 2021), hence only few studies focusing on the load sequence are available in the literature.

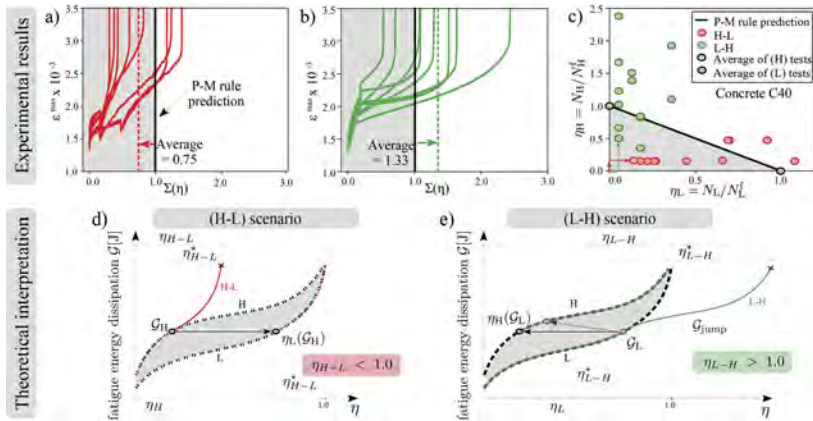


Figure 5. Experimentally observed effect of the loading sequence on concrete fatigue behavior under uniaxial compression: a, b) fatigue creep curves for (H–L) and (L–H) loading scenario, respectively; c) comparison with the predicted fatigue life using the P–M rule; d, e) theoretical interpretation based on superposition of energy dissipation profiles for (H–L) and (L–H) scenarios, respectively.

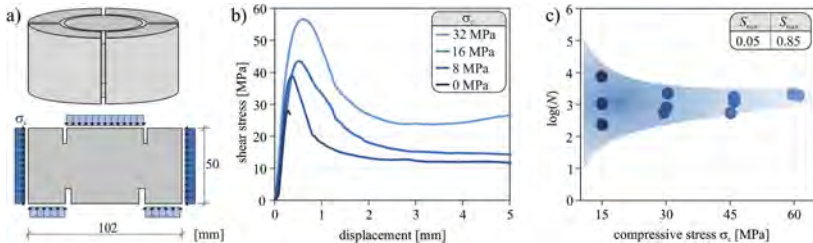


Figure 6. A) PTST setup with controllable lateral confinement; b) monotonic behavior at several levels of lateral confinement; c) fatigue life at several levels of lateral confinement.

4 CONCLUSIONS

The developed fatigue model MS1 shows promising results both at the level of a single material point and in the finite element simulation of the fatigue behavior of concrete. The model will be validated at the material level using PTST and at the structural level using prestressed bending tests that allow studying the propagation of compressive fatigue that is expected in reality. The development of a monitoring system to determine the loading effects and the transformation of the measured data into real stresses in the critical cross sections will be used to refine the space of loading parameters relevant in wind power plants. Based on this data, the validated model can be used for further investigations of the fatigue behavior of concrete under a wide range of complex loading scenarios, which in the long run can lead to the derivation of improved engineering rules for predicting the fatigue life of wind power plants that consider the effect of loading sequence.

ACKNOWLEDGMENT

The authors gratefully acknowledge the support for this research by the German Federal Ministry of Economic Affairs and Climate Action (BMWi), in the framework of the joint project (WinConFat-Structure), Project No: 03EE3060C.

REFERENCES

- Aguilar, M., Baktheer, A. & Chudoba, R. 2021. Numerical Investigation of Load Sequence Effect and Energy Dissipation in Concrete Due to Compressive Fatigue loading Using the New Microplane Fatigue Model MS1. *COMPLAS 2021*; Barcelona, Spain. doi:10.23967/complas.2021.053.
- Aguilar, M., Baktheer, A. & Chudoba, R. 2022. On the energy dissipation in confined concrete subjected to shear cyclic loading. *Proceedings in Applied Mathematics and Mechanics*.
- Baktheer, A., Aguilar, M. & Chudoba, R. 2021. Microplane fatigue model MS1 for plain concrete under compression with damage evolution driven by cumulative inelastic shear strain. *International Journal of Plasticity*, 143, 102950. doi: 10.1016/j.ijplas.2021.102950.
- Baktheer, A., & Becks, H. 2021. Fracture mechanics based interpretation of the load sequence effect in the flexural fatigue behavior of concrete using digital image correlation. *Construction and Building Materials*, 307, 124817. doi: 10.1016/j.conbuildmat.2021.124817.
- Baktheer, A. & Chudoba, R. 2018. Pressure-sensitive bond fatigue model with damage evolution driven by cumulative slip: Thermodynamic formulation and applications to steel- and FRP-concrete bond. *International Journal of Fatigue*, 113, 277–289. doi:10.1016/j.ijfatigue.2018.04.020.
- Baktheer, A. & Chudoba, R. 2021. Experimental and theoretical evidence for the load sequence effect in the compressive fatigue behavior of concrete. *Materials and Structures*, 54(2),1–23. doi: 10.1617/s11527-021-01667-0.
- Becks, H., Aguilar, M., Chudoba, R. & Classen, M. 2022. Characterization of high-strength concrete under monotonic and fatigue mode II loading with actively controlled level of lateral compression. *Materials and Structures*. doi: 10.1617/s11527-022-02087-4.
- Becks, H., Baktheer, A., Marx, S., Classen, M., Hegger, J. & Chudoba, R. 2022. Monitoring concept for the propagation of compressive fatigue in externally prestressed concrete beams using digital image correlation and fiber optic sensors. *Fatigue & Fracture of Engineering Materials & Structures*, 2022. doi: 10.1111/ffe.13881.
- Becks, H. & Classen, M. 2021. Mode II Behavior of High-Strength Concrete under Monotonic, Cyclic and Fatigue Loading. *Materials* 14.24 (2021): 7675. doi: 10.3390/ma14247675.
- Chudoba, R., Vořechovský, M., Aguilar, M. & Baktheer, A. 2022. Coupled sliding–decohesion–compression model for a consistent description of monotonic and fatigue behavior of material interfaces. *Computer Methods in Applied Mechanics and Engineering*, 398, 115259. doi:10.1016/j.cma.2022.115259.
- EN-1992-2. 2005. Eurocode 2: Design of concrete structures, Part 2: Concrete bridges - Design and detailing rules. European Committee for Standardisation.
- fib Model Code 2010. International Federation for Structural Concrete. doi:10.1002/9783433604090.
- Holmen, J. O. 1979. Fatigue by Constant and Variable Amplitude Loading. Institutt for Betonkonstruksjoner, Bulletin No. 79-1, Trondheim.
- Kim J.-K. & Kim Y.-Y. 1996. Experimental study of the fatigue behavior of high strength concrete. *Cement and Concrete Research*, 26, 1513–1523. doi:10.1016/0008-8846(96)00151-2.
- Lenschow, R. 1980. Long term random dynamic loading of concrete structures. *Matériaux et Construction*, 13, 274–278. doi: 10.1007/BF02474050.
- Miner, MA. 1945. Cumulative fatigue damage. *Journal of applied mechanics*, 12, A159–A164.
- Palmgren, A. 1924. Die Lebensdauer von Kugellagern (Durability of ball bearings). *Zeitschrift des Vereines Deutscher Ingenieure (ZVDI)*, 14, 339–341.
- Schmidt, B., Schneider, S. & Marx, S. 2019. Concrete fatigue-safety and development potential of current design concepts. *BAUTECHNIK*, 96, 329–337.
- Schneider, S., Hümme, J., Marx, S. & Lohaus, L. 2018. Untersuchungen zum Einfluss der Probekörpergröße auf den Ermüdungswiderstand von hochfestem Beton. *Beton- und Stahlbetonbau*, 113, 58–67. doi: 10.1002/best.201700051.
- Tepfers, R., Fridén, C. & Georgsson, L. 1977. *Magazine of Concrete Research*, 29, 123–130. doi: 10.1680/mac.1977.29.100.123.

Sustainability concept of design of concrete bridges based on LCA

B. Vlasatá

Faculty of Humanities, Charles University, Prague, Czech Republic
University Centre for Energy Efficient Buildings, Czech Technical University in Prague, Bustehrad, Czech Republic

J. Pešta

University Centre for Energy Efficient Buildings, Czech Technical University in Prague, Bustehrad, Czech Republic

C. Fiala, P. Hájek & M. Novotná

Faculty of Civil Engineering, Prague, Czech Technical University in Prague, Czech Republic
University Centre for Energy Efficient Buildings, Czech Technical University in Prague, Bustehrad, Czech Republic

ABSTRACT: Sustainability should become a basic concept for efficient/high quality design and operation of any structure through entire life cycle. Concrete is gradually becoming a building material with a high potential for such new technical solutions that meet new requirements, leading to the necessary reduction of environmental impacts and consequent improvement of social and economic conditions. The specific type of structures are bridges, where traditionally dominant requirements are efficiency of structural performance connected with cost efficiency, and due to a visual exposure to their architectural form and aesthetics. However, environmental quality is not usually considered. The need for an environmental assessment of different alternatives is becoming increasingly important due to the need to reduce environmental impacts, especially the carbon footprint. Environmental assessment could be done using existing standard methodologies of LCA in line with the concept of implementation of sustainability principles of concrete structures in the new fib ModelCode 2020. The paper presents a LCA case study focusing on concrete footbridge over the Labe river in Čelákovice, Czech Republic. One alternative is traditional design, and the second two represent advanced design using precast elements from UHPC. The detailed LCA analysis performed compares all three alternatives from an environmental impact point of view.

1 INTRODUCTION

The new fib ModelCode 2020 (MC2020) not only addresses traditional safety and serviceability requirements, but sustainability is seen as an overriding fundamental requirement responding to broader issues such as social responsibility, environmental quality, and economic efficiency. An intention and principal goal of MC2020 is to raise awareness of all participants and stakeholders in the process of design, construction, and operation of concrete structures regarding a wide range of sustainability criteria – social aspects, environmental aspects, and economic aspects. This should be considered within the entire life cycle of a structure (Hájek et al., 2011). An environmental assessment must be performed on complex systems (e.g., considering the whole life cycle of the entire structure) where LCA could show how particular materials could contribute in a positive or negative way to the environmental sustainability of the entire system (Asadollahfardi et al., 2021, Berndt, 2015, Blankendaal et al., 2014, Hájek, 2017, Hájek, 2013) or even considering the possible use in the following life cycle as a recycled product (Marinkovic et al., 2010, Pavlu et al., 2019).

The specific type of structures are bridges, where traditionally dominant requirements are the efficiency of structural performance connected with cost efficiency and due to a visual exposure

of their architectural form and aesthetics. However, environmental quality is not usually considered. The need for environmental assessment of different alternatives is becoming more and more important due to the need for the reduction of environmental impacts, especially of carbon footprint (Lupisek et al., 2021). The environmental assessment could be performed using existing LCA standard methodologies, which is standardised by ISO 14040 (ISO, 2006a) and ISO 14044 (ISO, 2006b). Life Cycle Assessment (LCA) is a technique to evaluate the benefits or impacts of a product or process on the environment (Laiblova et al., 2019, Pesta et al., 2020, Zenisek et al., 2020). Specific requirements for conducting an LCA study on construction products are described in EN 15 804 +A2 (CEN, 2020). According to these standards, an LCA study of construction products consists of the following phases: Goal and scope, Life Cycle Inventory (LCI), Life Cycle Impact Assessment (LCIA), and Interpretation.

The goal and scope of the study mainly consist of describing the aim of the study and the system boundary considered (Guinee, 2001). The second phase of LCA is the LCI, which involves summarising all elementary flows between the environment and the product system. That covers the consumption of raw materials, the generation of waste & emissions, and energy flow as well. LCIA is used to find the magnitude of environmental impact under different impact categories (Pesta et al., 2020). In the last part of the LCA study, the results obtained are interpreted.

The presented LCA study focused on the comparison of three variants of the bridge, which use different types of concrete and steel structures. Concrete is a composite silicate material with great potential for new technical solutions that meet new requirements. There is a challenge and expectation that the use of new types of composite silicate materials in advanced technologies could lead to the necessary reduction of environmental impacts. The goal of the presented case study is to show and discuss in detail how new advanced technology approaches could mitigate potential environmental impacts and therefore contribute to the Sustainable Development Goals (SDGs) set by the UN in 2015 as an action plan up to 2030.

2 METHODOLOGY

2.1 Footbridge

The footbridge is located in Čelákovice in the Czech Republic. It enables the crossing of the Labe river for pedestrians, cyclists, and emergency vehicles. In the tender documents, a cable-stayed footbridge with a composite superstructure consisting of two longitudinal steel side beams, steel cross beams, and a concrete slab was designed (variants V1, V2 in Figure 1). The composite slab was designed from precast concrete elements of C110/130 with steel fibre reinforcement, the elements were supported on the bottom flange of the side beams and cross beams. The contractor proposed an alternative solution of a segmental bridge deck made entirely of concrete C130/150 (for LCA analysis C110/130 only was considered) with steel fibre reinforcement (Figure 2) and the arrangement of spans 43+156+43 m.

Steel pylons with a total height of 37 m are fixed on the foundation blocks on in-situ cast piles. Stays are arranged in two planes, the lower adjustable anchorages are located on the side of the deck. The deck is supported by fully locked cable stays with galvanisation corrosion protection. The abutments on both banks of the river are massive reinforced concrete blocks in piles that form a counterweight to the uplift reactions of the superstructure. The walkable surface of the deck is covered with a sprayed waterproofing of 5mm thickness. The steel railings are 1.3 m high.

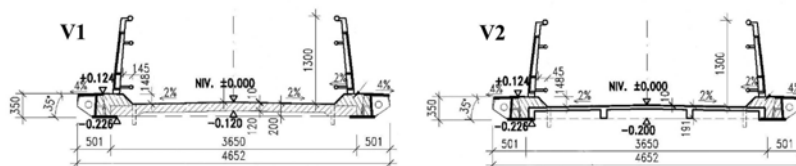


Figure 1. Variants V1 and V2 of the footbridge deck (Kalny, 2018).

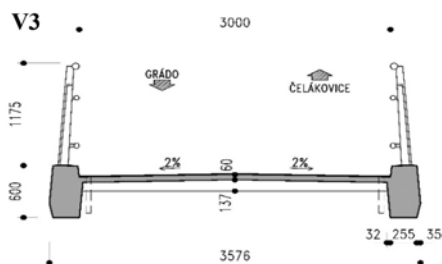


Figure 2. Cross-section (Variant V3 UHPC segments) (Kalny, 2018).

2.2 Description of variants

During the conceptual study phase, 3 conceptual variants of cross section were thoroughly analysed and later evaluated from the point of view of environmental aspects. The cross-sections of variants of the footbridge deck are in Figure 1, those were not built. The cross-section of the footbridge deck that was built is in Figure 2. In variants V1 and V2 the footbridge deck is designed from longitudinal steel side beams, steel cross beams and precast concrete panels (their material consumption is described in Table 1). Variant V1 used precast panels from concrete C45/55, the variant V2 used panels from UHPC.

Table 1. Balance of input data of assessment variants.

Construction phase				
Balance of input data of assessed variants	unit	V1 Steel+ C45/55	V2 Steel+UHPC	V2 Segment UHPC deck
Cement CEM I 42,5 R	t	87.5	75.5	117.8
Sand I Gravel	t	147.4	138	210.4
Crushed gravel	t	208.2	61.2	61.9
Microsilica	t	0	7.2	13.2
Slag	t	0	5.8	10.6
Steel fibres/steel microfibres	t	0	11.52	21.1
Superplasticizer	t	0.91	2.81	4.91
Water	t	34.6	20.5	22.8
Reinforcing bars	t	29.6	12.7	22.3
Construction steel	t	203.2	203.2	156.2
Prestressing steel	t	56.1	48	48
Freight traffic – long-distance	tkm	133 321	133 601	141 783
Freight traffic - local	tkm	4 515	3 062	3 488
Utilization phase				
Cement I CEM 42,5 R	t	15.8	5	1.6
Sand I Gravel	t	32.5	10.3	3.2
Crushed gravel	t	38.6	12.2	3.8
Superplasticizer	t	0.18	0.06	0.02
Water	t	6.1	1.9	0.6
Reinforcing bars	t	2.96	1.27	2.23
Freight traffic – long-distance	tkm	5 990	2 019	1 323
Freight traffic - local	tkm	3 543	1 124	349
End-of-life phase				
Demolition of RC structures	t	767.6	586.3	592.3
Freight traffic – long-distance	tkm	0	0	0
Freight traffic - local	tkm	23 028	17 589	17 769

2.3 Environmental assessment

In accordance with the ISO 14040 (ISO, 2006a) and ISO 14044 (ISO, 2006b), the LCA study of the Čelákovice footbridge consists of four steps: Goal and scope definition, LCI, LCIA, and interpretation of results. A study of the LCA of each footbridge variant, which consists of different proportions and different types of steel and concrete components, was carried out to evaluate environmental impacts. The goal of the present study is to compare the environmental consequences of each proportion and sort of steel and concrete structure. The scope of the study is to design a footbridge variant with UHPC segment usage and to compare the influence of using different proportions and types of structures on the overall environmental impact. The considered system boundary in the scope called cradle to grave includes extraction, processing, and transportation of raw materials to the plant, manufacturing of construction elements, and construction, usage and demolition of the footbridge. The functional unit considered was the Čelákovice footbridge. The inventarization data was conducted in SimaPro software (Herrmann and Moltesen, 2015), which was also used for the creation of product system models. Specific data were used to model the proportion of materials in each variant (see Table 1) and environmental data related to processes were modelled using generic modules described in Table 2, which were obtained from the Ecoinvent 3.9 database (Frischknecht et al., 2005).

Table 2. Product system processes and the corresponding Ecoinvent module (Frischknecht et al., 2005).

Product processes	Ecoinvent modules
Cement CEM I 42,5 R	Portland (Europe without Switzerland) market for Cut-off, S
Sand I Gravel	Sand (RoW) market for sand Cut-off, S
Crushed gravel	Gravel, crushed (RoW) market for gravel, crushed Cut-off, S
Microsilica	Activated silica (GLO) market for Cut-off, S
Slag	Supplementary cementitious materials (RER) basic oxygen furnace secondary metallurgy slag, for recovery to generic market for supplementary cementitious materials Cut-off, S
Steel fibres	Reinforcing steel (GLO) market for Cut-off, S
Superplasticizer	Plasticiser, for concrete, based on sulfonated melamine formaldehyde (GLO) market for Cut-off, S It is used for mixing the materials for the preparation of mortar
Water	Water, unspecified natural origin, CZ
Reinforcing bars	Reinforcing steel (GLO) market for Cut-off, S
Construction steel	Steel, unalloyed (GLO) market for Cut-off, S
Prestressing steel	Hot rolling, steel (GLO) market for Cut-off, S
Freight traffic (long-distance and (local)	Transport, freight, lorry 16-32 metric ton, euro6 (RER) market for transport, freight, lorry 16-32 metric ton, EURO6 Cut-off, S
Demolition of RC structures	Waste concrete (Europe without Switzerland) market for waste concrete Cut-off, S/Scrap steel (Europe without Switzerland) market for scrap steel Cut-off, S

In the LCIA phase, the impact on the environment due to the consumed energy, fuel and emissions was characterised using the EF 3.0 method (Sala et al., 2022) provided in SimaPro software. The assumptions and limitations considered in the study are as follows.

- Steel element production was defined to be 14 km from the construction site.
- Production of monolithic concrete and prefabricated elements was defined as 8 km from the site. The recycling centre for concrete waste was assumed to be 30 km from the construction site.
- In the utilization phase, it was assumed to repair the surface of ordinary concrete (10% of the surface) two times.
- The concrete in waste was assumed to be recycled, and so no process was considered for waste disposal. The life cycle of the footbridge was assumed to be 100 years.
- Normalization and weighting of the obtained results were performed according to EF 3.0 method available in SimaPro software.

3 RESULTS AND DISCUSSION

The results of the environmental assessment of the design of the Čelákovice footbridge are presented in Table 3. Characterization was performed according to the EF 3.0 method.

Table 3. Results of indicators according to the EF 3.0 characterization method.

Impact category	Abbreviations	Unit	V1	V2	V3
Climate change (GWP)	GWP-total	kg CO ₂ eq	5.86E+05	5.61E+05	6.22E+05
Ozone depletion	ODP	kg CFC ₁₁ eq	3.27E-02	3.16E-02	4.22E-02
Ionising radiation	IRP	kBq U-235 eq	2.07E+04	1.94E+04	2.56E+04
Photochemical ozone formation	POCP	kg NMVOC eq	2.42E+03	2.34E+03	2.49E+03
Particulate matter	PM	disease inc.	3.54E-02	3.51E-02	3.67E-02
Human toxicity, non-cancer	HTP-nc	CTUh	1.01E-02	9.84E-03	1.02E-02
Human toxicity, cancer	HTP-c	CTUh	2.80E-03	2.69E-03	2.61E-03
Acidification	ADP	mol H+ eq	2.10E+03	2.13E+03	2.58E+03
Eutrophication, freshwater	EP-fw.	kg P eq	2.15E+02	2.11E+02	2.18E+02
Eutrophication, marine	EP-mar.	kg N eq	5.29E+02	5.09E+02	5.67E+02
Eutrophication, terrestrial	EP-ter.	mol N eq	5.44E+03	5.27E+03	5.93E+03
Ecotoxicity, freshwater	ETP-fw.	CTUe	1.18E+07	1.19E+07	1.28E+07
Land use	SQP	Pt	2.48E+06	2.41E+06	2.57E+06
Water use	WDP	m ³ depriv.	1.22E+05	1.21E+05	1.78E+05
Resource use, fossils	ADP-fos.	MJ	5.44E+06	5.33E+06	6.63E+06
Resource use, minerals and metals	ADP-min.	kg Sb eq	1.03E+00	1.46E+00	2.78E+00
Climate change - Fossil	GWP-fos.	kg CO ₂ eq	5.85E+05	5.60E+05	6.21E+05
Climate change - Biogenic	GWP-bio.	kg CO ₂ eq	3.34E+02	3.57E+02	5.22E+02
Climate change - LULUC	GWP-luluc	kg CO ₂ eq	2.00E+02	1.95E+02	2.52E+02
Human toxicity, non-cancer – organics	HTP-nc.-o.	CTUh	1.64E-04	1.67E-04	2.13E-04
Human toxicity, non-cancer – inorganics	HTP-nc.-i.	CTUh	6.65E-03	6.48E-03	5.87E-03
Human toxicity, non-cancer – metals	HTP-nc.-m.	CTUh	3.33E-03	3.25E-03	4.17E-03
Human toxicity, cancer – organics	HTP-c.-o.	CTUh	1.82E-03	1.77E-03	1.60E-03
Human toxicity, cancer – inorganics	HTP-c.-i.	CTUh	0.00E+00	0.00E+00	5.35E-15
Human toxicity, cancer – metals	HTP-c.-m.	CTUh	9.86E-04	9.15E-04	1.02E-03
Ecotoxicity, freshwater – organics	EP-fw.-o.	CTUe	1.25E+05	1.19E+05	1.43E+05
Ecotoxicity, freshwater – inorganics	EP-fw.-i.	CTUe	7.82E+05	8.94E+05	1.18E+06
Ecotoxicity, freshwater - metals	EP-fw.-m.	CTUe	1.09E+07	1.08E+07	1.14E+07

*LULUC – Land Use and Land Use Change

To analyse and compare results in different impact categories, the normalized and weighted results of the three design variants of the bridge in Čelákovice were considered. Results show that the difference among impact categories for all three bridge variants is not significant. However, it can be concluded that the second bridge variant performs the best in most of the impact categories. The sum of normalized and weighted results for each variant is shown in Figure 3.

The following graphs show the results for each of the footbridge options. In Figure 4., results for the first variant are shown. In the first footbridge variant, the production process of construction steel has the largest share in all impact categories. The second largest share in most of the impact categories is represented by the production process of reinforcing steel.

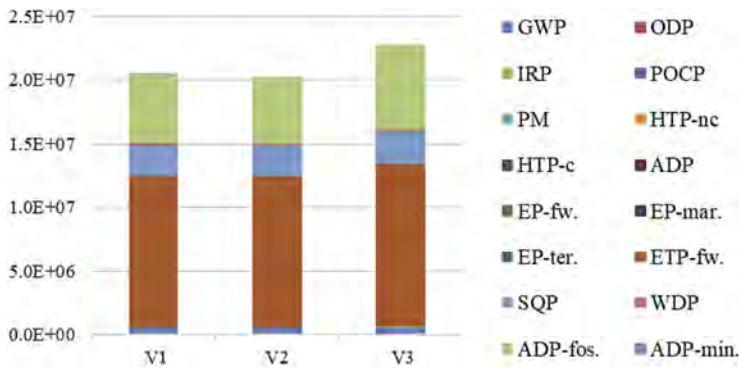


Figure 3. Normalized and weighted results (according to the EF 3.0 method).

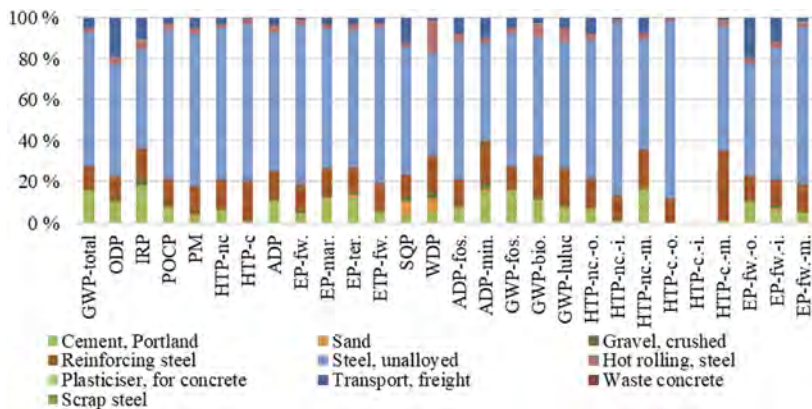


Figure 4. Relative contribution of processes in each category, V1 (according to the EF 3.0 method).

In Figure 5, the results for the second variant are shown. In this footbridge variant, the production process of construction steel has again the largest share in all impact categories. The second largest share in most of the impact categories is represented by the steel production process, but with a smaller share in the total result of each impact category. In contrast, the share of the cement production process is higher than in the previous variant.

In the third variant of the bridge, the impact of the production processes of structural steel and reinforcing steel remains significant. However, the plasticiser share is also important in this variant. In Figure 6, the relative contributions of processes for the third variant are shown.

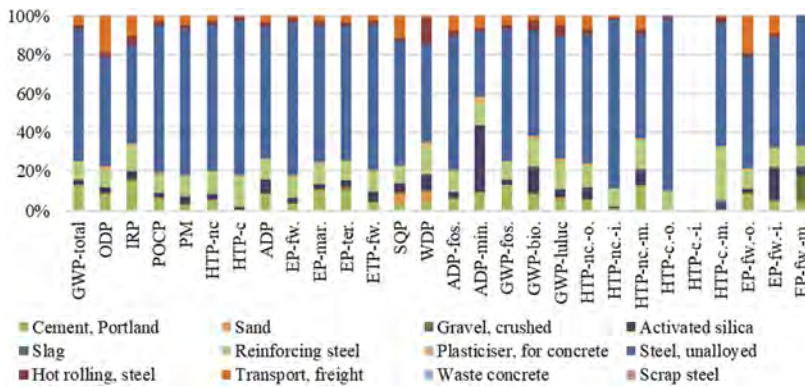


Figure 5. Relative contribution of processes in each category, V2 (according to the EF 3.0 method).

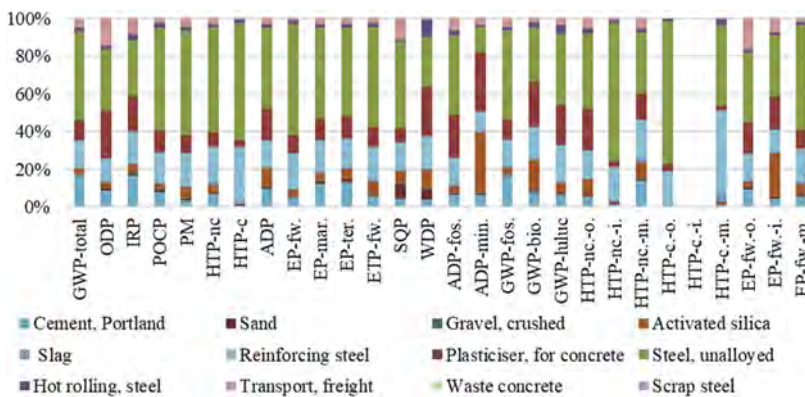


Figure 6. Relative contribution of processes in each category, V3 (according to the EF 3.0 method).

4 CONCLUSIONS

The perspective of sustainability should be implemented in the high-quality design and operation of any structure. Therefore, the new fib ModelCode 2020 covers even environmental assessment aiming to reduce the potential impacts of a designed concrete structure. To propose the possible use of environmental assessment in the design phase, the LCA case study was performed comparing three variants of the footbridge. Based on the LCA case study, the following conclusion can be drawn:

- The second variant has the lowest environmental impact, while the third variant has the highest overall impact.
- The result of the freshwater ETP represent main contribution to the overall impact.
- The LCA study provides detailed insight into potential environmental impacts of processes in life cycle of a concrete structure and can be used to optimized a proposed design.

Unfortunately, the final decision of the developer is usually not based only on the environmental performance of the considered structures. Therefore, the sustainability assessment in ModelCode 2020 should cover also environmental perspectives and provide robust support to assess different variant of concrete structures.

ACKNOWLEDGEMENT

This work was supported by the Grant Agency of the Czech Technical University in Prague, grant No. SGS21/094/OHK1/2T/11 project—Application of alternative materials in textile concrete and their evaluation at room temperature and at elevated temperature.

REFERENCES

- Asadollahfardi, G., Katebi, A., Taherian, P. & Panahandeh, A. 2021. Environmental life cycle assessment of concrete with different mixed designs. *International Journal of Construction Management*, 21, 665–676.
- Berndt, M. L. 2015. Influence of concrete mix design on CO₂ emissions for large wind turbine foundations. *Renewable Energy*, 83, 608–614.
- Blankendaal, T., Schuur, P. & Voordijk, H. 2014. Reducing the environmental impact of concrete and asphalt: a scenario approach. *Journal of Cleaner Production*, 66, 27–36.
- CEN 2020. Sustainability of construction works – Environmental product declarations – Core rules for the product category of construction products (EN 15804 A2).
- Frischknecht, R., Jungbluth, N., Althaus, H. J., Doka, G., Dones, R., Heck, T., Hellweg, S., Hischier, R., Nemecek, T., Rebitzer, G. & Spielmann, M. 2005. The ecoinvent database: Overview and methodological framework. *International Journal of Life Cycle Assessment*, 10, 3–9.
- Guinee, J. 2001. Handbook on life cycle assessment - Operational guide to the ISO standards. *International Journal of Life Cycle Assessment*, 6, 255–255.
- Hájek, P., Fiala, C. & Kynčlová, M. 2011. Life cycle assessments of concrete structures – a step towards environmental savings. *Structural Concrete*, 12, 13–22.
- Hájek, P. 2013. *Integrated life cycle assessment of concrete structures*.
- Hájek, P. 2017. Concrete Structures for Sustainability in a Changing World. *Procedia Engineering*, 171, 207–214.
- Herrmann, I. T. & Moltesen, A. 2015. Does it matter which Life Cycle Assessment (LCA) tool you choose? - a comparative assessment of SimaPro and GaBi. *Journal of Cleaner Production*, 86, 163–169.
- ISO 2006a. Environmental management - Life Cycle Assessment - Principles and Framework (ISO 14040:2006).
- ISO 2006b. Environmental management - Life Cycle Assessment - Requirements and guidelines (ISO 14044:2006).
- Kalny, M. 2018. Innovations and Value Engineering Contribute to Sustainable Structures. *ACI Symposium Publication*, 326.
- Laiblova, L., Pesta, J., Kumar, A., Hajek, P., Fiala, C., Vlach, T. & Koci, V. 2019. Environmental Impact of Textile Reinforced Concrete Facades Compared to Conventional Solutions-LCA Case Study. *Materials (Basel, Switzerland)*, 12.
- Lupisek, A., Trubacik, T. & Holub, P. 2021. Czech Building Stock: Renovation Wave Scenarios and Potential for CO₂ Savings until 2050. *Energies*, 14, 2455.
- Marinkovic, S., Radonjanin, V., Malesev, M. & Ignjatovic, I. 2010. Comparative environmental assessment of natural and recycled aggregate concrete. *Waste Management*, 30, 2255–2264.
- Pavlu, T., Koci, V. & Hajek, P. 2019. Environmental Assessment of Two Use Cycles of Recycled Aggregate Concrete. *Sustainability*, 11.
- Pesta, J., Pavlu, T., Fortova, K. & Koci, V. 2020. Sustainable Masonry Made from Recycled Aggregates: LCA Case Study. *Sustainability*, 12.
- Sala, S., Biganzoli, F., Mengual, E. S. & Saouter, E. 2022. Toxicity impacts in the environmental footprint method: calculation principles. *International Journal of Life Cycle Assessment*, 27, 587–602.
- Zenisek, M., Pesta, J., Tipka, M., Koci, V. & Hajek, P. 2020. Optimization of RC Structures in Terms of Cost and Environmental Impact-Case Study. *Sustainability*, 12, 8532.

Fundamental experiments for monitoring water leakage of underground structures using plastic optical fibers

Haihua Zhang, Zhibin Liu, Xianfeng Ma & Jiangu Qian

Department of Geotechnical Engineering, College of Civil Engineering, Tongji University, Shanghai, China

Shinichi Akutagawa

Department of Civil Engineering, School of Engineering, Kobe University, Kobe, Japan

ABSTRACT: In coastal metropolises, strict regulations regarding the exploitation and utilization of groundwater have resulted in a continuous rise in groundwater levels over the past few decades. As a result, underground concrete structures are now at a higher risk of water leakage than ever before. To detect water leakage in underground structures as early as possible, this paper introduces a plastic optical fiber (POF) sensor. This sensor has a prism tip formed by two bonded parallel POFs, which enables it to detect water in real time. When the sensor comes into contact with water, the returning visible light changes due to the reflection and refraction at the prism interface. Fundamental experiments were conducted to verify the feasibility of the POF sensor. The results showed that the POF sensor is effective in detecting water in real time by measuring light intensity. Furthermore, the change of light intensity over time allowed for the observation of the water penetration process in hardened mortar specimens, enabling the estimation of the permeability of the mortar at a definite quantity. Finally, future work is discussed briefly.

1 INTRODUCTION

Groundwater is a crucial resource for human living, industrial production and agricultural irrigation. However, excessive exploitation of groundwater has led to a significant drop in groundwater levels in urban areas, causing environmental problems, such as ground subsidence and fissure. To mitigate these issues, many cities have implemented strict groundwater regulations and active water recharge methods during underground structure construction. These measures have had a positive effect, as seen in Tokyo, Osaka, and Shanghai, where groundwater levels stopped dropping after the implementation of groundwater regulations (see Figure 1). However, these measures have also led to new problems in geotechnical engineering, such as sand liquefaction, ground heaving, and building floating. Furthermore, as the groundwater level rises, water leakage in underground concrete structures becomes more difficult to manage, impacting the maintenance and durability of such structures.

Water typically leaks from tinny cracks in concrete or between the joints of new and old concrete. Leaking water can seep into poorly waterproofed underground concrete, causing cracks to form. Over time, this can lead to the corrosion of steel bars in concrete, weakening overall underground structure. To detection of water leakage early, several nondestructive inspection (NDI) technologies have been developed. However, the application of these technologies is often limited to important underground structures, as specialized equipment is required. By the time when water is found on the surface of structure, it may already be too late. Therefore, it is essential to detect underground water leakage using simple methods as early as possible, given the continuous rise of groundwater.

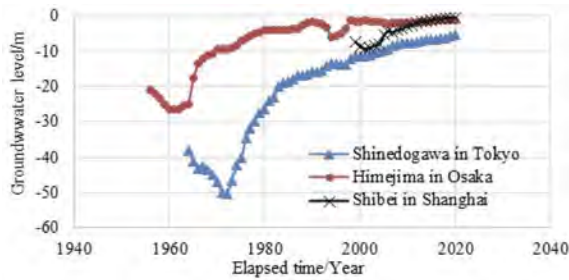


Figure 1. Groundwater level change over time in typical coastal big cities.

This paper proposes a new method for investigating water leakage in underground concrete structures using POF sensors. A fundamental experiment was conducted to verify the feasibility of this method, and the results demonstrate that it is possible to detect water leakage in concrete structures at an early stage. Future work is discussed finally.

2 METHODOLOGY

The proposed POF sensor is capable of detecting water through the reflection of visible light from a prism structure, utilizing a 1 mm diameter POF as the media of light transmission. A right triangle prism is formed directly at one end where two parallel bare optical fibers are bonded together, as shown in Figure 2. In air, when the light from the first fiber hits the sloped interface, internal reflection occurs rather than dispersion. Some of the light is reflected into the second fiber, passing through the boundary of the two fibers. The light is then reflected again at the sloped surface of the second fiber, which can be seen directly at the end of the second fiber. When the POF sensor is placed in water, the light is dispersed instead of reflected at the two sloped surfaces. Consequently, the light from the end of the second fiber becomes weak.

To measure the emitted light intensity, a light state sensing system (LS^3) was produced, which includes a light source, a data logger and a computer (see Figure 3). The light intensity is presented in a 12-bit RGB system, with a maximum value of 7093. The measured data can be recorded and analyzed using a notebook computer.

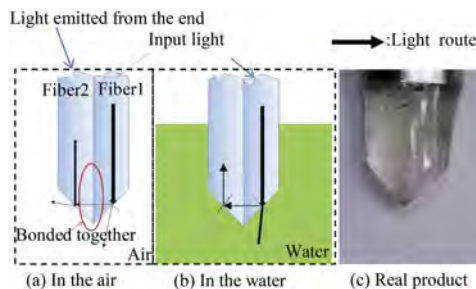


Figure 2. Structure of sensor and light refraction/reflection.

The POF sensor was tested to find the difference between the water and air (see Figure 4 (a)). Two POF sensors were set up in the water completely at different heights. Then, the water in the beaker was heated at the bottom so that the water level declined gradually due to evaporation. As shown in Figure 4(b), both sensors experienced a sudden change of light intensity when the sensing planes of these sensors were exposed to the air from the water. Hence, it is seen that the POF sensor could distinguish the air and water clearly by the change of returning light intensity.

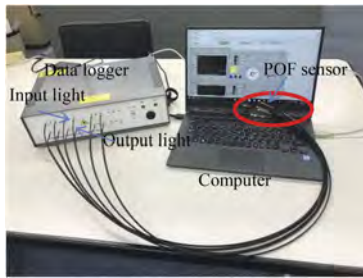


Figure 3. Light state sensing system (LS³).

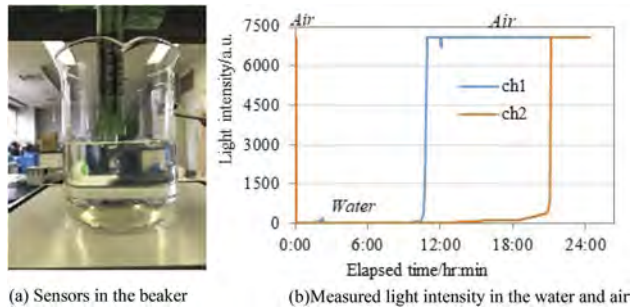


Figure 4. Water lowering test with POF sensors.

3 EXPERIMENTAL SETUP AND TESTING PROCEDURE

To evaluate the performance of POF sensors when detecting water leakage of hardened mortar specimens, the fundamental experiment was conducted. Four similar specimens were prepared and tested by immersing them half in water. The mixture proportions of fresh mortar are presented in Table 1. As shown in Figure 5, two POF sensors are set up in each specimen, with their tips located 5mm from the bottom of the specimen.

The experiment was carried out on Mar. 24th, 2020, 3 months after the placement of mortar. It is thought that most of the mortar hardening had been completed. The data record started before the four specimens were immersed half in the water. In about two days, the water was added so that the specimens were almost submerged completely in the water. Then on Mar. 27th, the specimens were taken out of the water and dried naturally in the room, as shown in Figure 6. The experiment lasted for about 10 days and ended on April 4th, 2020.

Table 1. Mortar mix proportions.

W/C(%)	Volume (8L)			
	Water(kg)	Cement(kg)	Sand(kg)	Air Entrainment (kg)
50.0	1.99	4.13	10.69	36.34

4 MONITORING RESULTS AND ANALYSIS

The experiment started at 11:30 on Mar. 24th. The monitoring data is shown in Figures 7–9. There are two groups among them. One is the group of ch1-6, the other is the group of ch7 and ch8. From the experiment in Section 2, we know that the POF sensor could detect the water as soon as the water arrived at the tip of the sensor. Firstly, it is found in Figure 7 that the measured light intensities began to change at intervals between 11:40 and 12:30. The light intensity of ch7 was the first to change and decreased sharply, which indicates there existed

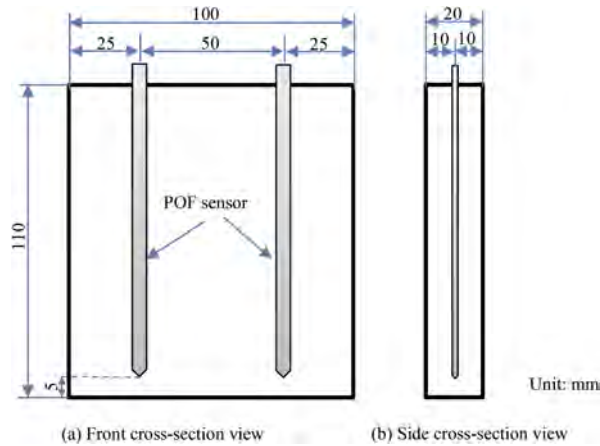


Figure 5. POF sensors setup in the mortar specimen.

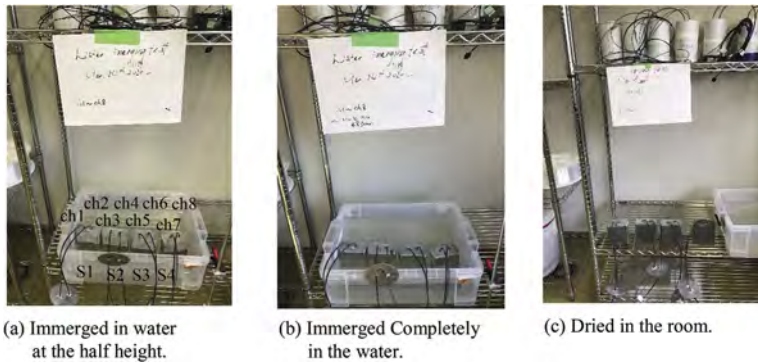


Figure 6. Water leakage test of mortar specimen.

some cracks or holes in the bottom of specimen S4 so that the water penetrated these spaces quickly (see Figure 7(b)). Secondly, the light intensity of ch2 decreased at a considerable gradient from 11:53. Thirdly, the light intensities of the other channels decreased gradually when they took action on the arrival of water. It should be noted that the initial light intensities of the 8 channels were measured under the condition of their corresponding incident light.

As shown in Figure 8, the light intensities of all the channels were tending to be stable at 9:36 on Mar. 26th. In order to make sure whether the water had penetrated the specimen to where the POF sensors were located, the water was added to immerse the specimens completely at 14:39 on Mar. 26th. There seemed to be no obvious effect on the light intensity change. Moreover, the light intensities of the 8 channels became stable on Mar. 27th. Therefore, the water immersing test ended in the afternoon. In this experiment, the coefficient of mortar permeability shall be calculated simply as follows:

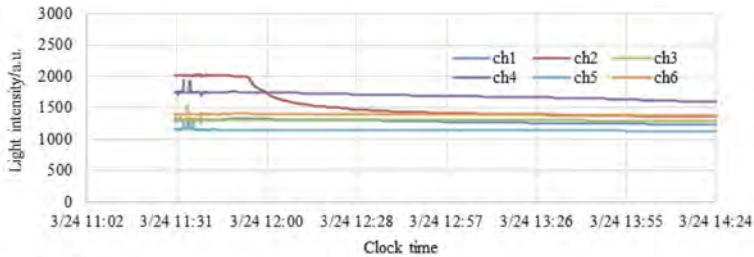
$$k = \frac{L}{T} \quad (1)$$

where k is the coefficient of cement mortar permeability (cm/sec); L is the water penetration distance ($L=0.5\text{cm}$); and T is the time in seconds over which the L is measured.

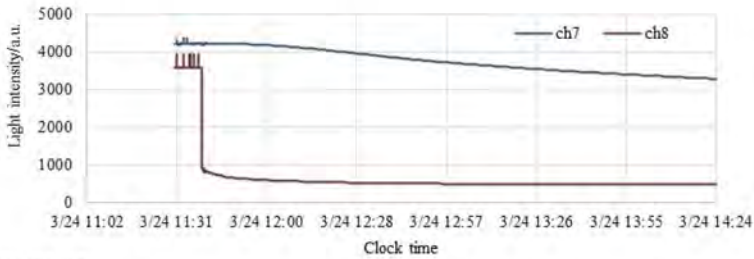
Table 2 shows the permeability coefficient k measured by POF sensors. It can be seen that the coefficient of mortar permeability is in the order of 10^{-4} . The permeability coefficient k of Specimen S4 is about 2-3 times larger than that of the other 3 specimens.

Table 2. Coefficient k of mortar permeability.

Specimens	S1			S2			S3			S4		
Channels	ch1	ch2	ch3	ch4	ch5	ch6	ch7	ch8	ch1	ch2	ch3	ch4
k ($\times 10^{-4}$ cm/s)	2.17	3.57	1.40	2.58	2.02	1.69	5.10	8.06				

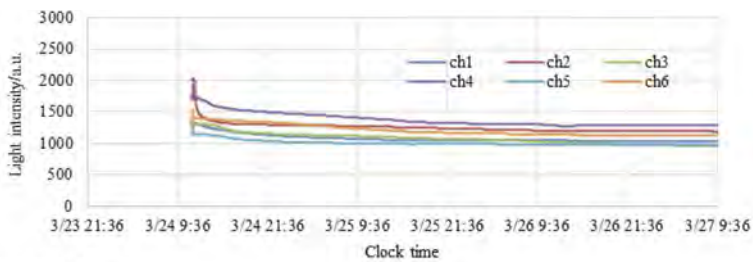


(a) ch1-ch6

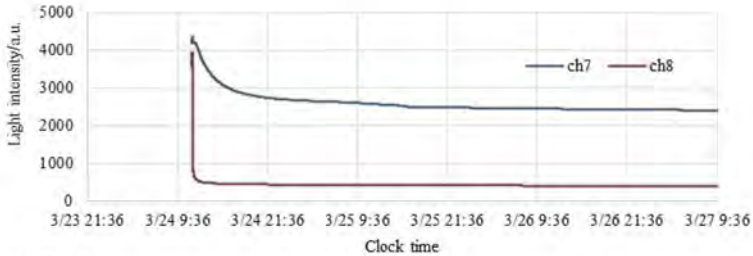


(b) ch7-ch8

Figure 7. Light intensity change over time (from 11:30 to 14:24 on Mar. 24, 2020).



(a) ch1-ch6



(b) ch7-ch8

Figure 8. Light intensity change over time (from 11:30 on Mar. 24 to 9:36 on Mar. 27, 2020).

As long as the light intensities kept stable in the mortar permeability test, the 4 specimens were taken out of the water and dried naturally in the room. Figure 9 shows the light intensity change from Mar. 24, 2020 at 11:30 to April 3, 2020 at 0:00. As shown in Figure 9, there was some disturbance in the light intensities when the specimens were taken out of the water at 10:10 on Mar. 27th. But it is thought the trends of the light intensities would not be affected.

It is found that the light intensity (ch1-6) increased gradually with a gentle but steady gradient (see Figure 9(a)). On the other hand, the light intensities of ch7 and 8 increased dramatically till Mar. 30th and then developed slowly during the drying test (see Figure 9(b)).

Based on the previous study (Zhang et al. 2022), the light intensity would have a steep variation when the POF sensor meets the water, if there is a void around the tip of sensor (see Figure 10). Therefore, it is strongly believed that there were some non-negligible voids around the tips of the two POF sensors in Specimen S4.

It can be seen that the reduction process of water could also be monitored in detail according to the change in light intensity during the drying test. The void around the tip of POF sensor in the mortar would affect the development of light intensity.

The light intensities of ch1-8 measured at the end of the drying test were larger than their initial values in the permeability test. The existence of water at the interface between the POF sensor and the mortar might have some effect on light refraction and reflection. Further study should be taken to investigate the reason.

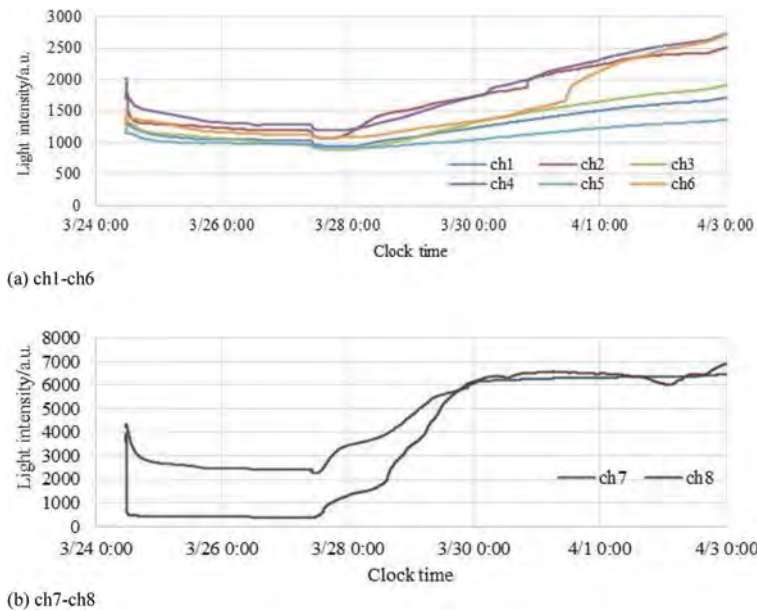


Figure 9. Light intensity change over time (from 11:30 on Mar. 24 to 0:00 on April 3, 2020).

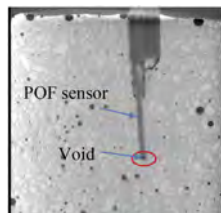


Figure 10. Void around the tip of POF sensor (X-ray Photo).

5 DISCUSSIONS

The placement and installation of POF sensors are critical to ensure accurate and effective detection of water leakage. Ideally, sensors should be installed in areas with a high probability of water leakage during the concrete placement phase of new constructions. For existing underground structures, the sensors can be installed by drilling a hole in the concrete and ensuring that the waterproofing work is adequately performed. The sensor should make contact with the concrete, as even small voids can negatively impact the accuracy of the measurement. While water leakage can still be detected in the presence of a void, critical information such as the rate of water penetration may not be accurately captured.

Future work should focus on studying the influence of water on the interface between the POF sensor and concrete or mortar to better understand the observed changes in light intensity. Additionally, developing a compact monitoring device to visualize the detection of water leakage by on-site light emitting would be a useful and effective way to detect water leakage of underground structures during their life cycles. Overall, the proposed POF sensor offers a promising solution for detecting and monitoring water leakage in underground structures, which can lead to improved durability and reduced maintenance costs.

6 CONCLUSIONS

In conclusion, the proposed POF sensor has shown great potential for detecting water leakage in underground structures at an early stage. The experiments conducted in this study have demonstrated that the POF sensor can accurately distinguish between water and air, detect the arrival of water in hardened mortar specimens, and monitor the development of water penetration over time. The information obtained from the POF sensor can provide valuable insight into the permeability of the mortar and the effectiveness of protective layers, allowing for early detection and remediation of water leakage issues.

ACKNOWLEDGMENTS

The work was financially supported by Kumagai Gumi Company in Japan, the Fundamental Research Funds for the Central Universities (No. 22120220151) in China, and the National Natural Science Foundation of China (Grant No. 52178345).

REFERENCES

- Akutagawa, S., Nishio, A., Matsumoto, Y., Takahashi, A. & Machijima, Y. 2014: A new method for reading local deformation of granular material by using light, *Proc. of 48th US Rock Mechanics/Geomechanics Symposium, American Rock Mechanics Association*: 1–6.
- Akutagawa, S., Machijima, Y. & Katayama, T. 2015. A new method for interpreting changes in arbitrary engineering quantities by using optic fiber, *Proc. of 9th International Symposium on Field Measurements in Geomechanics*: 439–451.
- Akutagawa, S. & Machijima, Y. 2015. A new optical fiber sensor for reading RGB intensities of light returning from an observation point in geo-materials, *Proc. of 49th US Rock Mechanics/Geomechanics Symposium, American Rock Mechanics Association*: 1–7.
- Akutagawa, S., Machijima, Y., Sato, T. & Takahashi, A. 2017: Experimental characterization of movement of water and air in granular material by using optic fiber sensor with an emphasis on refractive index of light, *Proc. of 51st US Rock Mechanics/Geomechanics Symposium, American Rock Mechanics Association*: 1–8.
- Akutagawa, S. & Tanaka, Y. 2018. Experimental observation of hardening process of engineering materials by optic fiber sensor, *Proc. of 52nd US Rock Mechanics/Geomechanics Symposium, American Rock Mechanics Association*: 1–6.
- Han, L., Chen, J., Li, H., Liu, G., Leng, B., Ahmed, A. & Zhang, Z. 2022. Multispectral water leakage detection based on a one-stage anchor-free modality fusion network for metro tunnels, *Automation in Construction* 140 104345: 1–15.

- Inaba, T., Nagaya, J., Kasugai, M., Oshima, A., Isono, E., Kitada, N. & Tanimoto, H. 2019. Long-term variation of groundwater level and ground settlement in Osaka area, Kansai Geo-Symposium 2019, *Japan Geotechnical Society*: 187–192.
- Karashima, N., Uenohara, I., Kida, K., Kokubun, K., Ogawa, K. & Ohzawa, K. 2021. Land Subsidence due to Groundwater Withdrawal, 2020. *Annual Report C.E.S.T.C.*, TMG: 43–60.
- Luo, Y., Ye, S., Wu, J., Jiao, X. & Wang, H. 2015. Characterization of land subsidence during recovery of groundwater levels in Shanghai, *Geological Journal of China Universities* 21(2): 243–254.
- Li, L., Chen, H., Huang, Y., Xu, G. & Zhang, P. 2022. A new small leakage detection method based on capacitance array sensor for underground oil tank, *Process Safety and Environmental Protection* 159: 616–624.
- Zhang, H., Ogata, A., Tezuka, H., Kanamori, S., Shimizu, S., An, L. & Akutagawa, S. 2022. Monitoring of the hardening of concrete/mortar using plastic optical fiber sensors: fundamental experiment and data interpretation, *Journal of Japan Society of Civil Engineers (JSCE)* 10(1): 206–218.

Effects of structural rehabilitation on modal parameters of the Marlo Bridge

B. Siedziako, T.S. Nord & A. Fenerci

Department of Ocean Operations and Civil Engineering, Norwegian University of Science and Technology, Ålesund, Norway

ABSTRACT: This paper examines the effects of structural rehabilitation on the modal parameters of the Marlo Bridge, which suffered damage to one of its pillars. Natural frequencies, mode shapes and damping ratios have been identified using time series of accelerations recorded at the site prior to and after the repair. In addition, complementary studies using the corresponding finite element model have been performed. It is shown that modal analysis can be a useful tool that gains insight into changes in structural behavior due to damage. The finite element model was able to accurately capture the dynamic behavior of the Marlo Bridge in its repaired state; however, the mode shapes obtained and the natural frequencies in the damaged state did not correspond well with those identified using measurement data and were found challenging to be reproduced.

1 INTRODUCTION

The Norwegian Consulting Engineers' Association estimated in 2021 that rail and road maintenance costs exceed 2 billion NOK (RIF - Rådgivende Ingeniørers Forening, 2021). A significant portion of these infrastructure maintenance costs relates to transport infrastructure that is owned by the county municipalities, and they are gradually increasing as a result of the deteriorating infrastructure combined with a risk of more common extreme loading events. Currently the state evaluation of bridges in Norway is based on visual inspections or non-destructive field and laboratory testing (Statens Vegvesen, 2019). Inspection results are then stored in BRUTUS – a database for Norwegian bridges and ferry docks that is used to prioritize maintenance works.

However, inspections are prone to errors, delays or postponements and often lack consistency as well as simple objectivity, when assessing the scale of damage. Therefore, the structural health monitoring (SHM) framework has become a very active field of research in recent years, as it has the potential to eliminate the above-mentioned issues and aid decision-makers in distributing resources more efficiently. Still, as real damage is rare, in order to examine the consequences due to its presence and validate different SHM frameworks, re-searchers have relied on numerical simulations (Ghiasi et al., 2022; Johnson et al., 2004) or laboratory tests on representative models (Malekzadeh et al., 2015; Teng et al., 2022). As pointed out in several studies, however, the research concerning SHM should be focused on tests of real structures to further develop the possibilities of employing SHM on bridges (An et al., 2019; Moughty & Casas, 2017). A great example in line with that recommendation is the Hell Bridge test arena (Svendsen, 2021), where one of the 35m spans of a railway bridge has been moved to new foundations on land to serve researchers validating different SHM strategies, and where different types of damage have been introduced onto the real structure (Svendsen et al., 2020). Another possibility for investigating changes in structural behavior in real case scenarios can be accessed during rehabilitation and upgrading projects (Costa et al., 2013) or bridge failures by conducting measurements prior to and after the repair.

Following this philosophy, we present in this paper the results from a modal analysis performed on a real structure that suffered serious damage. In this study we aim to investigate the effect of rehabilitation on the modal parameters of the Marlo Bridge in Norway, which underwent repairs during the winter of 2021/2022. The repair works included the replacement of a bridge pillar, sealing cracks with sprayed concrete, and painting the main steel beams.

2 CASE STUDY – MARLO BRIDGE

2.1 Bridge description

The Marlo Bridge shown in Figure 1 is used as a case study in this paper. The bridge is located on the FV2646 road in Skjåk in Norway. It was opened to traffic in 1959 and it is expected to be in service for 37 more years. However, in recent years, maintaining this piece of infrastructure has been troublesome for the county. The bridge had to be closed in 2018 due to damage to one of the pillars and in 2019 it was a subject of maintenance works aiming to improve the foundation under the middle pillar. Recently, the bridge was severely damaged by ice actions in 2021 and was rehabilitated in early 2022.

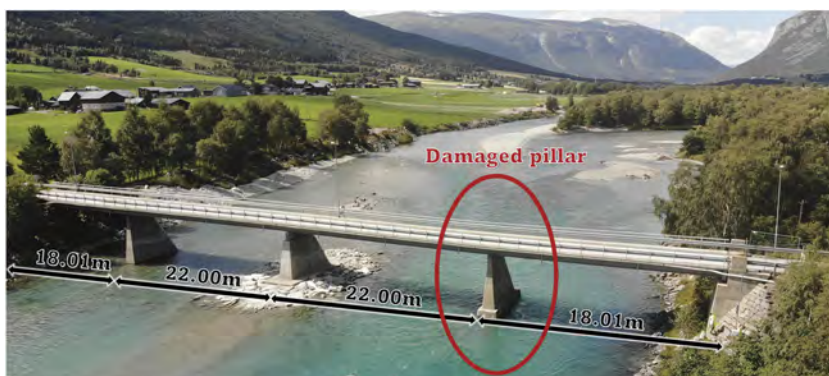


Figure 1. Picture of the Marlo Bridge – photography taken from Brutus (Statens Vegvesen, 2022). Red circle indicates the pillar that was damaged.

2.2 Damage description

Figure 2 shows the scope of the damage to the Marlo Bridge as of November 2021 before repairs. Although not certain, the most likely explanation for this damage is ice thermal expansion between the pillar and end support. It can be seen that pillar displacements caused by ice forces (Figure 2d) introduced stresses that led to bursting of the concrete at the support (Figure 2a). As a result of that, the bridge superstructure lost its two original support points, sank several centimeters, and rested instead on one of the concrete crossbeams that were originally not designed to serve that purpose. Figures 2c) and e) show clearly that there is large gap between the original bearings and the concrete pillar. The deflections caused by changes in boundary conditions at the Marlo Bridge were clearly visible when at the site (Figure 2b).

Although the damage on the Marlo Bridge can be considered to be very serious, forcing bridge closure, and are easily detectable by anyone present on the bridge without the need for any sensors, it was uncertain whether the state of the damage could be equally easy to identify utilizing data from measurements conducted at the site. This is because, as long as the concrete crossbeam supported the bridge deck in a similar manner to the original bearings and no significant cracks that could lead to the reduction of the stiffness of the bridge deck were present, the bridge remained almost unchanged from a structural perspective.

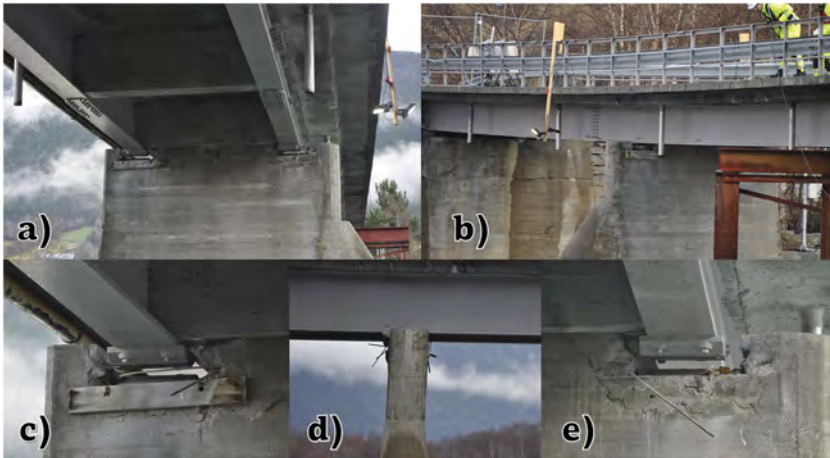


Figure 2. Overview of damage on Marlo Bridge – pictures taken in November 2021. Figures a), c) and e) show bursts in concrete at the support, d) – tilt of the damaged pilar, b) – forced deflection.

3 EXPERIMENTAL VIBRATION ANALYSIS

3.1 Instrumentation

The acquisition system used in this study was designed to provide flexibility when it comes to sensor placement and the possibility of fast deployment. It consists of 20 wireless G-Link-200 3-axis accelerometers with waterproof enclosure from Parker LORD MicroStrain and WSDA-2000 gateways that can communicate with a laptop via Ethernet or USB cable. The accelerometers' range and sampling frequency were set to $\pm 2g$ and 128 Hz respectively, resulting in noise density equal to $25 \mu g/\sqrt{Hz}$ as defined by the supplier (Parker Hannifin MicroStrain Sensing, 2020). The sensors were attached to the superstructure magnetically using small steel plates that were first glued to the bridge deck. These steel plates were left at the site after the tests were conducted to ensure that accelerometers will be mounted in the same positions in the second round of measurements. The location of the installed sensors and naming convention is shown in Figure 3.

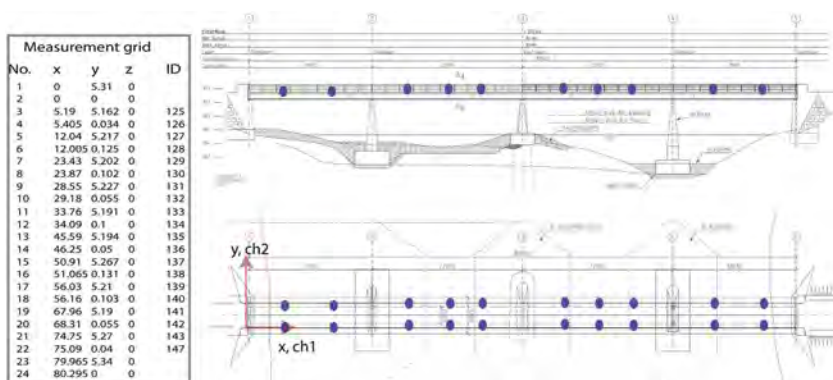


Figure 3. Sensor placement at the Marlo Bridge. The sensors were placed at exactly the same spots after bridge rehabilitation.

3.2 Vibration excitation

On-site measurements were taken both before (November 2021) and after (May 2022) the repair process in order to investigate the effects of the structural rehabilitation on the modal

parameters. Several excitation methods were used to produce time series (Figure 4). In the repaired state natural traffic was used, while in the damaged state, vibrations were forced by running along the bridge and jumping or hitting with a hammer as the bridge was closed to traffic. Although the hammering was able to induce larger accelerations, it produced data that performed poorly in the modal analysis. Therefore, the data gathered from running along was used in this study. In addition, some level of vibrations induced by the river hitting the pillars is also present in the signal.

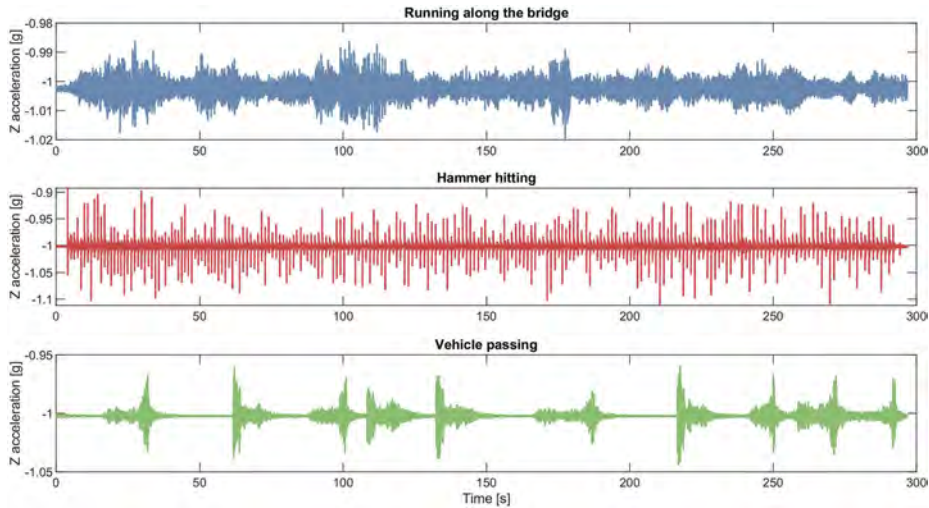


Figure 4. Time-series of vertical accelerations for sensor 142 recorded using different excitation methods.

3.3 Results from modal analysis

Modal analysis was performed with the use of the covariance-driven stochastic subspace identification algorithm (Döhler & Mevel, 2013; Reynders et al., 2008). The number of block-rows was set to 100 and the number of blocks for the covariance of the subspace matrix was set to 20. The data was high-pass filtered with a cut-off frequency of 0.5 Hz prior to the identification process. Figures 5 and 6 present the modes that were manually selected from the stabilization diagrams from the repaired and damaged states respectively.

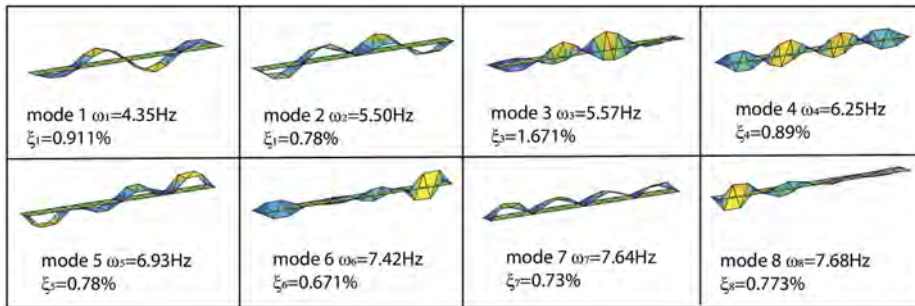


Figure 5. First 8 vibration modes of Marlo Bridge – repaired state.

It can be seen that there are significant differences between the modes identified in the damaged and repaired states. In the repaired state, torsional and bending modes are clearly

distinguishable, while in the damaged state, they tend to blend together. Another distinction is the presence of a first mode in the damaged state at 2.57 Hz, which is significantly lower frequency than for the first mode in the repaired state, at 4.35 Hz. The modes in the repaired state tend to be symmetric or antisymmetric, which is expected from a symmetrical structure such as Marlo Bridge. This remark can be taken as a sign of a successful repair as it indicates that the damaged span and pillar have been restored to their original state. On the contrary, the vibration modes identified in the damaged state do not manifest the same property. It should also be mentioned that in the repaired state there were fewer closely-spaced in frequency, leaving a less chaotic stabilization diagram.

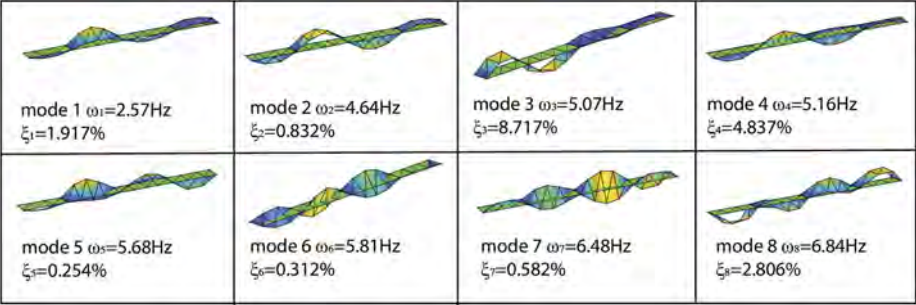


Figure 6. First 8 vibration modes of Marlo Bridge – damaged state.

4 FINITE ELEMENT MODEL

4.1 Model preparation

Complementary to the experimental studies, numerical simulations by means of finite element method were performed in order to investigate whether the results from field measurements can be reproduced. A finite element model of the Marlo Bridge is displayed in Figure 7. The model was created based on the existing drawings (see Figure 8 for cross-sectional dimensions) and it consists of DIMEL80 main longitudinal beams, concrete 300x760 mm cross-beams and a concrete bridge deck with a thickness of a maximum 20 cm. The beams were modelled using quad-trilateral finite membrane-strain shell elements with reduced integration (S4R), while the bridge deck was modelled using 8-node linear brick 3D elements with reduced integration (C3D8R) in Abaqus.

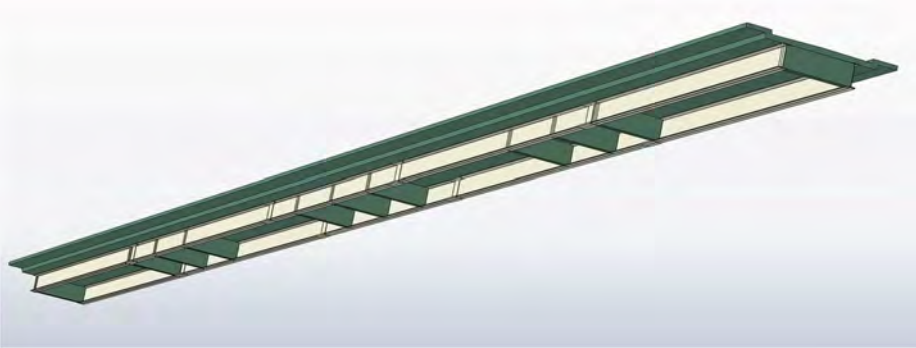


Figure 7. A finite element model of Marlo Bridge in Abaqus.

The upper flanges of the steel beams are connected to the bottom surface of the bridge deck using tie constraints such that there is no relative motion between them. The bridge is

supported in the vertical, longitudinal, and transverse directions at the locations of the pillars and abutments. The mesh was generated using a 80 mm seed size for the solid elements assigned to the bridge deck and 200 mm seed size for the shell elements assigned to steel beams.

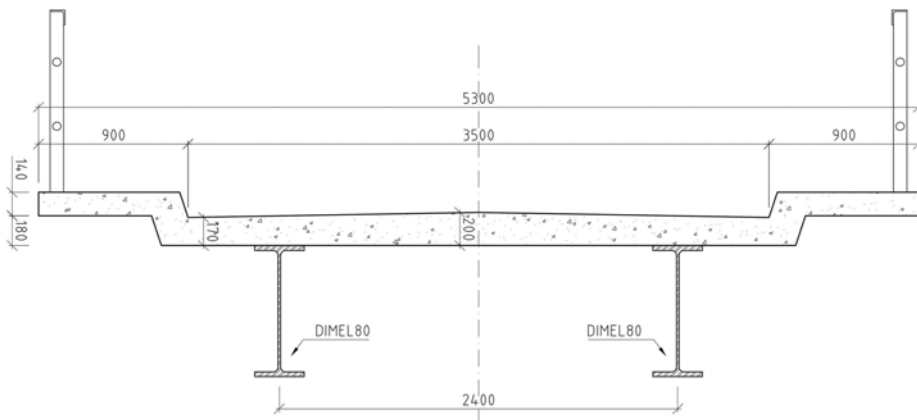


Figure 8. Cross-sectional dimensions used to model the Marlo Bridge in Abaqus.

The Young's modulus of $E=210$ GPa, Poisson ratio $\nu=0.3$ and density $\gamma=7850$ kg/m³ were assigned to the steel beams, while for the concrete elements those properties were set to $E=21$ GPa, $\nu=0.2$ and $\gamma=2500$ kg/m³. As the type of concrete used on the Marlo Bridge is unknown, the value of the Young's modulus in the model was selected based on results from parametric studies, where the objective was to minimize the weighted error between the natural frequencies obtained from both system identification and Abaqus. MAC values were not considered due to the limited number of sensors. Weights were assigned linearly between 1.0 and 0.0 for, respectively, the first and eighth modes.

4.2 Results

Figure 9 shows the mode shapes obtained from Abaqus model of the Marlo Bridge in the re-paired state. The values of the natural frequencies and mode shapes correspond very well to those obtained using measurement data and presented in Figure 5. The order of modes 6 and 7 has been flipped and the 8th mode was not properly reproduced when using the finite element model, but, overall, it can be argued that the numerical model presented in this study is a good representation of the Marlo Bridge. It is believed that by applying more advanced finite element updating techniques such as the sensitivity method (Mottershead et al., 2011) and taking into account the stiffness provided by the pillars, would enhance the similarity between the results from the numerical simulations and system identification.

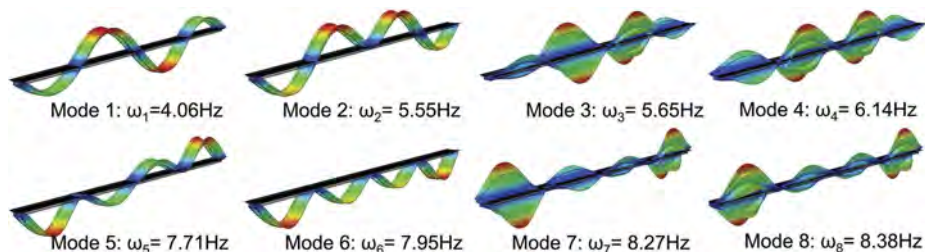


Figure 9. Mode shapes from Abaqus – repaired state.

When it comes to the damaged state, it should be emphasized that damage modelling is not a trivial task and there are many factors that influence a bridge's dynamic behavior that can-not be verified in this case, such as the precise support conditions or the presence of the axial forces due to forced displacements on the pillar. Therefore, in this study, only a simplified approach to simulate the damage state on the Marlo Bridge was attempted. It was assumed that the damage consisted of forced displacements: 120 mm in the vertical direction and 50 mm in the transverse direction, moving the support conditions from the bearings to the bottom of the concrete crossbeam, and a 50% reduction in the Young's modulus of the bridge deck due to cracking (Norsk Standard, 2005) on the two spans in contact with the damaged pillar. To simulate that, a new step was created in Abaqus where displacements were forced, and then modal analysis was performed on the deformed model with the new support conditions. The results from this analysis are displayed in Figure 10.

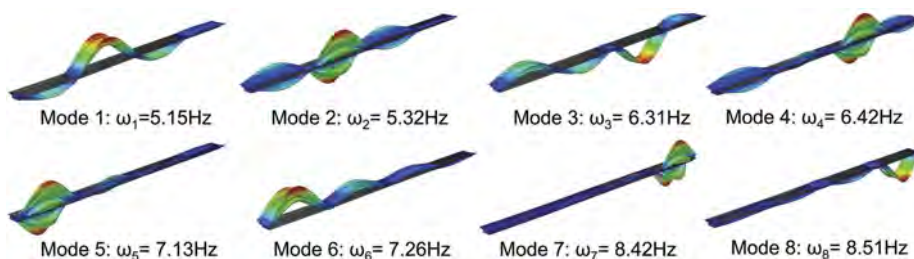


Figure 10. Mode shapes from Abaqus – damaged state.

This time, there were few similarities between the results obtained based on the measurement data (Figure 6) and the finite element model (Figure 10). The torsional and vertical modes were well separated in Figure 10, which was not the case for the modes based on measurements. The finite element model did not capture the low frequency mode of 2.57 Hz that appeared only in the damaged state, and further attempts to model this mode lies beyond the scope of this paper.

5 CONCLUSIONS

In this study, we examined the effects of structural rehabilitation on the modal parameters of the Marlo Bridge, which had suffered damage to one of its pillars. The natural frequencies, mode shapes and damping ratio were identified using acceleration measurements taken at the site prior to and after the repair. In addition, complementary numerical studies were performed in order to investigate whether the results could be reproduced in Abaqus software using the corresponding finite element bridge model.

Based on the presented results, it can be concluded that modal analysis can be a useful tool that gains insight into changes in structural behavior due to damage. It has been shown that the differences in the dynamic behavior of the Marlo Bridge due to the presence of damage can be distinguished using information about the mode shapes and natural frequencies in the repaired and damaged states. In the repaired state, many of the mode shapes obtained are symmetric or antisymmetric, which implies that the repair was successful, as only one of the bridge pillars suffered from the damage.

Studies using a finite element model of the Marlo Bridge have shown that, with a simple tuning of the concrete stiffness, it was possible to obtain the mode shapes and values of the natural frequencies that correspond closely to those identified using measurements. Knowing that concrete stiffness can be related to its strength, the measurements taken at the site can be further used as a non-destructive testing method for strength assessment of the concrete used at the Marlo Bridge.

Finally, an unsophisticated attempt to model the scope of the damage to the Marlo Bridge in the finite element software was deemed unsuccessful. The damage was simulated by forcing displacements on the pillar, changing the support conditions and reducing the concrete stiffness due to cracking. Nevertheless, the mode shapes and natural frequencies obtained from Abaqus did not correspond well to those identified using measurements. This study shows that proper modelling of a damaged structure is a complex process and often the full scope of the damage is difficult to evaluate. To obtain more accurate results, further work is needed.

ACKNOWLEDGEMENTS

The study was conducted with support from the Research Council of Norway through the Norwegian Regional Research fund in Møre og Romsdal county (SHMBru project 331578). This research was conducted with financial support from the Møre og Romsdal fylke. The authors gratefully acknowledge this support from Møre og Romsdal County during planning and execution of instrumentation and measurements.

REFERENCES

- An, Y., Chatzi, E., Sim, S. H., Laflamme, S., Blachowski, B., & Ou, J. 2019. Recent progress and future trends on damage identification methods for bridge structures. *Structural Control and Health Monitoring* 26(10): 1–30.
- Costa, B. J. A., Magalhães, F., Cunha, Á., & Figueiras, J. 2013. Rehabilitation assessment of a centenary steel bridge based on modal analysis. *Engineering Structures* 56: 260–272.
- Döhler, M., & Mevel, L. 2013. Efficient multi-order uncertainty computation for stochastic subspace identification. *Mechanical Systems and Signal Processing* 38(2): 346–366.
- Ghiasi, A., Ng, C. T., & Sheikh, A. H. 2022. Damage detection of in-service steel railway bridges using a fine k-nearest neighbor machine learning classifier. *Structures* 45: 1920–1935.
- Johnson, E. A., Lam, H. F., Katafygiotis, L. S., & Beck, J. L. 2004. Phase I IASC-ASCE Structural Health Monitoring Benchmark Problem Using Simulated Data. *Journal of Engineering Mechanics* 130(1): 3–15.
- Malekzadeh, M., Atia, G., & Catbas, F. N. 2015. Performance-based structural health monitoring through an innovative hybrid data interpretation framework. *Journal of Civil Structural Health Monitoring* 5(3): 287–305.
- Mottershead, J. E., Link, M., & Friswell, M. I. 2011. The sensitivity method in finite element model updating: A tutorial. *Mechanical Systems and Signal Processing* 25(7): 2275–2296.
- Moughy, J. J., & Casas, J. R. 2017. A state of the art review of modal-based damage detection in bridges: Development, challenges, and solutions. *Applied Sciences* 7(5).
- Norsk Standard. 2005. *NS-EN 1998-3:2005+NA:2013, Eurocode 8: Design of structures for earthquake resistance – Part 3: Assessment and retrofitting of buildings*.
- Parker Hannifin MicroStrain Sensing. 2020. MicroStrain Sensing Product Datasheet, 3DM-CV5-IMU.
- Reynders, E., Pintelon, R., & De Roeck, G. 2008. Uncertainty bounds on modal parameters obtained from stochastic subspace identification. *Mechanical Systems and Signal Processing* 22(4): 948–969.
- RIF - Rådgivende Ingeniørers Forening. 2021. State of the nation.
- Statens Vegvesen. 2022. Brutus - management system for bridges, ferry quays and other load-bearing structures in Norway.
- Statens Vegvesen. 2019. Håndbok V441 Bruinspeksjon.
- Svendsen, B. T. 2021. Numerical and experimental and structural health. Doctoral thesis. Norwegian University of Science and Technology.
- Svendsen, B. T., Frøseth, G. T., & Rönnquist, A. 2020. Damage Detection Applied to a Full-Scale Steel Bridge Using Temporal Moments. *Shock and Vibration* 2020(10): 1–16
- Teng, S., Chen, X., Chen, G., Cheng, L., & Bassir, D. 2022. Structural damage detection based on convolutional neural networks and population of bridges. *Measurement: Journal of the International Measurement Confederation* 202: 111747.

Simulation of chloride ingress into aging surface-coated concrete

C. Yoshii & F. Biondini

Politecnico di Milano, Milan, Italy

M. Iwanami & K. Nakayama

Tokyo Institute of Technology, Tokyo, Japan

ABSTRACT: This paper presents a calibration of prediction model for chloride ingress into surface-treated reinforced concrete (RC) structures. Since the research on long-term durability of the coating materials is still limited, the coating degradation model about chloride resistivity is investigated and established from experimental results with accelerated deterioration tests and chloride migration tests (CMT). On the other hand, the results of AgNO₃ spray tests for surface-coated concrete specimens exposed to CMT show that chloride ions would penetrate mainly from the defective areas such as cracks and delamination in surfaces. Therefore, two different deterioration models are proposed for the coating system: averaged time-variant diffusivity and increase of local defects in coated surface. The deterioration models are implemented into diffusion analysis based on cellular automata and applied to a coated RC cross-section to investigate the residual lifetime associated with corrosion initiation of steel reinforcement.

1 INTRODUCTION

Surface coating is one of the main means to prevent chloride ingress into reinforced concrete (RC) structures in coastal environment and subsequent corrosion of steel rebars. Many researchers have reported effectiveness of coating materials against chloride penetration by investigating chloride diffusion coefficients (Buenfeld & Zhang 1998, Almusallam et al. 2003, Pan et al. 2017). Investigation on the durability has contributed to improvement on life-cycle management for surface-treated RC structures. Effects of thermal and moisture variations on coating permeability has been evaluated by Almusallam et al. (2002). In addition, the time-variant diffusivity of coated concrete specimens has been investigated with immersion tests by Moradillo et al. (2012). However, the knowledge of time-variant property of coating diffusivity is still limited to accurately predict the lifetime of surface-treated RC structures exposed to salinity of marine environment.

This paper investigates the property of chloride resistivity change of surface coating materials with chloride migration tests (CMT). An AgNO₃ spray test is also conducted to confirm the chloride path in the surface-coated concrete during CMT. The results inform two different assumptions on deterioration process of coatings on structural surface: disperse micro-damage and local defects occurrence such as cracks and delamination. In the case study of simulation of chloride ingress into a RC cross-section, the effects of these assumptions are investigated using different coating deterioration models.

2 CHLORIDE DIFFUSIVITY

2.1 Accelerated deterioration test

The experimental study with the accelerated deterioration test and CMT was conducted to investigate the long-term chloride resistivity of surface-coated concrete (Yoshii & Iwanami 2022).

The plain concrete and surface-treated concrete specimens of $\phi 100 \times 50$ mm were prepared with the same size formworks (Figure 1a). The substrate concrete had a 0.50 water/cement ratio, and 0.45 sand/aggregate ratio with the maximum aggregate size of 20 mm. Following to the casting, the concrete surface facing the casted panel were painted with four layers of

epoxy-made coating: primer, putty, middle and top coating (Figure 1b). The total thickness of the coating system was assumed as 1.0 mm.

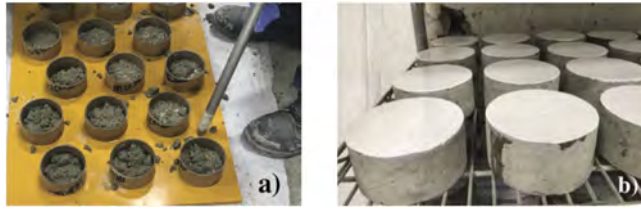


Figure 1. (a) Casted and (b) surface-treated concrete specimens.

The test protocol shown in Figure 2a was applied for the accelerated deterioration with cyclic condition used to damage the specimens with reference to the study on coating durability by Almusallam et al (2002) and the standard of JIS-A6909-2021 (2021). The cycle of 70 ° with RH 80% and -10 ° with RH 20% was repeated each day.

CMT is one of the most useful means to estimate the chloride diffusivity of concrete specimens. This method is useful to measure high chloride resistivity of surface-treated concrete by accelerating the chloride ion migration with induced electric potential difference. Figure 2b represents a used diffusion cell following the standard of JSCE-G571-2003 (2003). During CMT, the coated surface was exposed to NaCl solution, and 60 V was induced to promote chloride ion penetration while 15 V was applied for the substrate specimen.

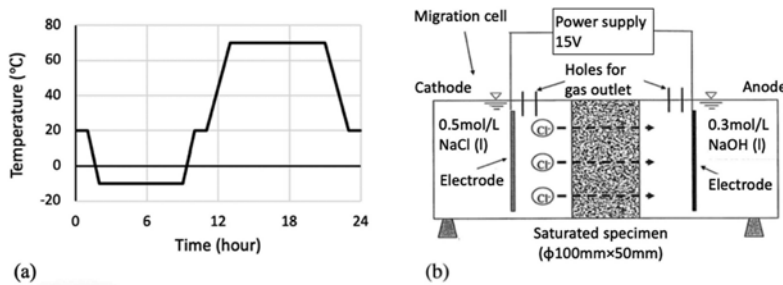


Figure 2. Experimental setup: (a) condition of the cyclic test and (b) chloride diffusion cell (adapted from JSCE-G571-2003).

Measuring chloride flux J_{cl} in the anode cell during the test, the effective diffusion coefficient D^e , the index of chloride resistivity, can be calculated as follows (JSCE-G571-2003):

$$D^e = \alpha J_{cl} \frac{L}{\Delta V} = \alpha \frac{L}{\Delta V} \cdot \frac{V^H \Delta c_{cl}^H}{A \Delta t} \left(\alpha = \frac{RT}{|Z_{cl}|FC_{cl}} \right) \quad (1)$$

where ΔV = electric potential difference between specimen surfaces; L , A = thickness and cross-section area of specimen; V^H = volume of anode solution; $\Delta c_{cl}^H / \Delta t$ = slope of chloride ion concentration change in the anode cell during the steady state; R = gas constant; T = absolute temperature (= 293.2 K); Z_{cl} = a charge of chloride ion (= 1 C), F = Faraday constant; and C_{cl} = measured chloride concentration in the cathode side.

From CMT for the specimens exposed to the accelerated deterioration test for the different duration, the change of the effective diffusion coefficient was obtained as shown in Figure 3, where D_{su}^e and D_c^e refer to the substrate and coated concrete specimens, respectively. The cyclic number t_n is equivalent to the total days under the deteriorative condition.

While the chloride diffusivity of the substrate concrete increased gradually by 220 cycles and then decreased to the initial value, that of the surface-coated concrete increased continuously. In addition, it can be seen the deterioration rate increased gradually.

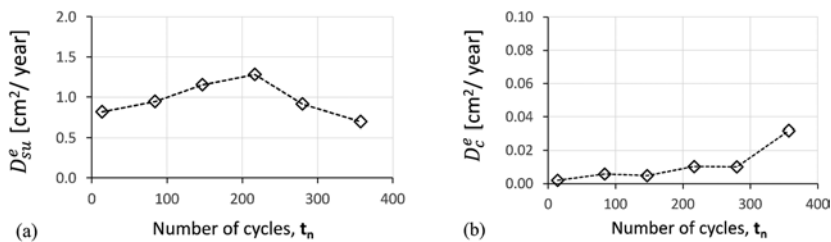


Figure 3. Change of chloride diffusivity: (a) substrate concrete, D_{su}^e and (b) surface-coated specimens, D_c^e .

The ratio of chloride resistivity between substrate and surface-treated specimens, D_{su}^e/D_c^e , will be used to develop the simulation of chloride ingress into the aging surface-coated concrete structure. To obtain the diffusivity change corresponding to the real time scale based on the experimental results, it is assumed that each cycle of the deterioration test deserves one week exposure under natural environment and the coating lifetime is 20 years (i.e., $D_{su}^e = D_c^e$ at $t = 20$ years). Figure 4 represents the experimental data of the ratio, D_{su}^e/D_c^e , complemented with the assumed lifetime of $D_{su}^e/D_c^e(t = 20 \text{ years}) = 1$. As a result of a nonlinear regression, the following exponential approximation has been obtained for the time-variant diffusivity ratio with correlation $R^2 = 0.882$:

$$\frac{D_{su}^e}{D_c^e} = 400 \times \exp(-0.299t) \quad (2)$$

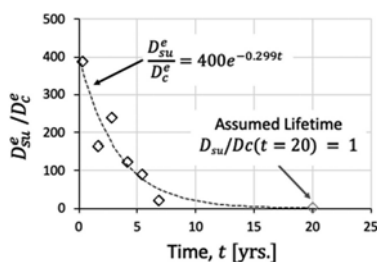


Figure 4. Estimate of the change of diffusivity ratio, D_{su}^e/D_c^e .

2.2 AgNO₃ spray test

The AgNO₃ spray test was carried out to confirm the chloride ion path during CMT, which can be distinguished from the difference in colors derived from AgCl (white) and Ag₂O (brown) products (Otsuki et al. 1993). First, the coated specimens exposed to CMT were cut using a dry cutter along the direction of chloride ion penetration. After wetting the cut surface with water to promote the chemical reaction, AgNO₃ solution with 0.1 mol/L was sprayed. The chloride ion path was observed in pictures of reacted surface taken about one hour after the spray.

The test was conducted for three types of the surface-treated specimens to clarify the property of the chloride ion path during CMT. The specimens had different features of surficial defects as follows: (i) pinhole, (ii) small cracks, and (iii) no visible defects. Figures 5, 6 and 7 show the reacted surface of the specimens exposed to the deterioration test and CMT after the AgNO₃ spray.

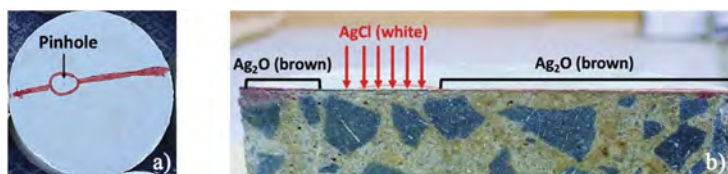


Figure 5. Specimen with a pinhole: (a) before cutting and (b) after AgNO₃ spray.

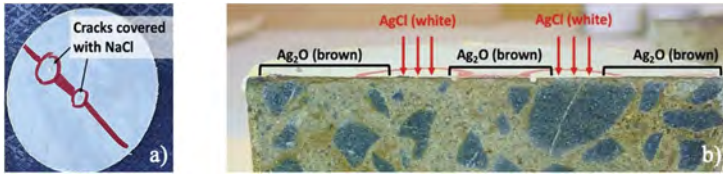


Figure 6. Specimen with small cracks: (a) before cutting and (b) after AgNO₃ spray.

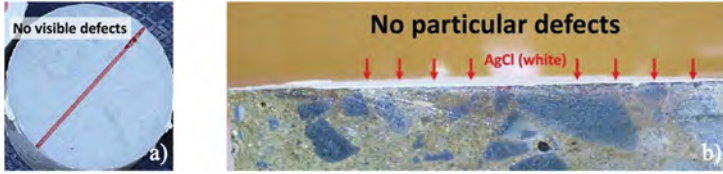


Figure 7. Specimen with no visible defects: (a) before cutting and (b) after AgNO₃ spray.

In the case of a pinhole (Figure 5) the white product of AgCl was found at the part around the pinhole depicted with red arrows while the brown product of Ag₂O was found under the undamaged part of coating. Similarly, the distribution of AgCl and Ag₂O was also confirmed in the specimen with small cracks near the border between cracked and undamaged part (Figure 6). This result indicates that the chloride ion penetrated mainly from the defective part during CMT where the chloride diffusivity must be much higher compared to the undamaged parts. However, as for the specimen with no visible defects, the chloride ion seemed to pass through the coated surface entirely because the white product of AgCl can be confirmed under the coating (Figure 7). This might be because there was no local severe damage in this coated surface.

In summary, chloride ions should move into the concrete from the defective area during CMT in the specimen with a pinhole or small cracks. On the other hand, the ions penetrated equally from the whole surface of the specimen with no visible damage.

3 COATING DIFFUSIVITY

Based on the results of AgNO₃ spray test, two types of coating degradation process have been considered: gradual loss of impermeability of coating layers due to micro-damage; occurrence of visible defects such as cracks, pinholes, and delamination (with the order of 1.0-10 mm). Different models should be considered for deterioration processes. The mean time-variant chloride diffusivity of the coating system $D(t)$ would be effective to represent the disperse micro-damage on coating capacity while the increase of local defects in coated surface, $A_{dam}(t)$ would be suitable when assuming the occurrence of the visible defects. In the following, each time-variant function is introduced based on the results of CMT.

3.1 Averaged time-variant diffusivity

The assumption of the continuity condition of chloride flux during CMT is used to obtain the mean chloride resistivity of the surface coating system (Buenfeld & Zhang 1998):

$$J_{cl} = D_c^e \frac{\Delta V_o}{\alpha L_c} = D_{st}^e \frac{\Delta V_o - \Delta V_i}{\alpha L_{st}} = D_{su}^e \frac{\Delta V_i}{\alpha L_{su}} \quad (3)$$

where D_c^e , D_{st}^e and D_{su}^e = diffusion coefficient of the coated specimen, surface treatment, and substrate concrete respectively; L_c , L_{st} and L_{su} = thickness of each; and ΔV_o and ΔV_i = electric potential difference induced by the power supply and difference between two sides of the substrate, respectively.

Based on Figure 3b, which includes the diffusivity of both the substrate and coating parts, it is necessary to calculate the actual diffusivity of coating part. Considering the equilibrium of the specimen's thickness, Equation (3) can yield:

$$\begin{cases} L_c = L_{st} + L_{su} \\ \frac{L_c}{D_c^e} = \frac{L_{st}}{D_{st}^e} + \frac{L_{su}}{D_{su}^e} \end{cases} \quad (4)$$

Considering that $L_{st} \ll L_{su}$ in CMT, the following equation is obtained:

$$\frac{D_{st}^e}{D_{su}^e} = \frac{L_{st}}{L_c} \left(\frac{D_{su}^e}{D_c^e} - 1 \right)^{-1} \quad (5)$$

where the ratio of the chloride diffusivity between the substrate and surface-coated concrete, D_{su}^e/D_c^e , is approximated as Equation (2) based on the experimental results and the designed lifetime of the coating for 20 years, and $L_{st} = 50$ mm and $L_c = 1.0$ mm are substituted based on the experimental condition.

3.2 Change of defective areas

The time-variant defective area $A_{dam}(t)$ is an alternative approach to represent the deterioration of coating materials. This considers the increase of the delaminated area in coated surface. Assuming the diffusivity of surface treatment remaining extremely low, and the chloride ions pass through the specimen only from the defective areas during CMT, the relationship between the concrete diffusivity D_{su}^e and chloride flux J_{cl} is established as follows:

$$D_{su}^e = \alpha J_{cl} \frac{L}{\Delta V} = \alpha \frac{L}{\Delta V} \cdot \frac{V^{II}}{A_{dam}} \frac{\Delta c_{cl}^{II}}{\Delta t} \left(\alpha = \frac{RT}{|Z_{cl}|FC_{cl}} \right) \quad (6)$$

Comparing with Equation (1), the ratio between the time-variant defective area A_{dam} and the cross-sectional area of specimens A can be represented as that of the effective diffusion coefficient between the surface-treated specimen and substrate. Thus, the time-variant function of the defective ratio A_{dam}/A results in the inverse of the time-variant diffusivity ratio:

$$\frac{A_{dam}}{A} = \frac{D_c^e}{D_{su}^e} \quad (7)$$

When applying this deterioration model into the diffusion analysis, there is spatial uncertainty in occurrence of defects in surfaces. Monte Carlo simulation is hence applied for the analysis with the assumption of the local defects occurrence to obtain the statistical results.

4 CHLORIDE INGRESS INTO SURFACE-COATED RC CROSS-SECTION

As a case study, the RC pier cross-section of a cable-stayed bridge investigated in Biondini et al. (2006) is considered. The chloride ingress into the surface-coated RC cross-section is investigated using cellular automata (Biondini et al. 2004). This application shows the effect of the coating deterioration in the prediction of corrosion initiation time of steel rebars.

4.1 Cellular automata

The cellular automata method based on Fick's Second Law is adopted for diffusion analysis. The governing equation can be represented as follows by considering the inflow and outflow of chloride ions among divided cells (Biondini et al. 2004):

$$C_i^{n+1} = \phi_0 C_i^n + \sum_j^d \left(\phi_j^- C_{i-1,j}^n + \phi_j^+ C_{i+1,j}^n \right) \quad (d = 1, 2, 3) \quad (8)$$

where C_i^n = concentration in the cell i at time t_n ; ϕ_0 , ϕ_j^- and ϕ_j^+ = evolutionary coefficients related to the chloride diffusivity; and d = dimensions. i.e. 1D, 2D, or 3D.

The homogeneous condition is applied for simplification and the relationship among evolutionary coefficients yields as follows based on the mass conservation law:

$$\phi_j^- = \phi_j^+ = \frac{\Delta t}{\Delta x^2} D, \quad \phi_0 = 1 - 2d \frac{\Delta t}{\Delta x^2} D \quad (9)$$

where D = diffusivity; Δx and Δt = size of each cell and time increment, respectively.

As for the boundary conditions of the interface between the coating and concrete, the following relationship proposed by Crank (1974) is applied as an expanded form for 2D diffusion:

$$C_s^{n+1} = C_s^n + \frac{2\Delta t}{c_s + \Delta x} \left\{ \frac{D_{su}}{\Delta x} (C_{s+1}^n - C_s^n) - \frac{D_{st}}{c_s} (C_s^n - C_{s-1}^n) \right\} \quad (10)$$

where C_s^n , C_{s-1}^n , and C_{s+1}^n = concentration at time t_n in the cells at the interface s , in coating $s - 1$, and in concrete $s + 1$; c_s = total thickness of the coating system.

4.2 Structural model

The RC cross-section model shown in Figure 8 is used for the simulation of chloride ingress (Biondini et al. 2006). The simulation assumes the chloride penetration with constant concentration C_0 from external surface. Table 1 provides the information on the parameters related to the diffusion and structural properties.

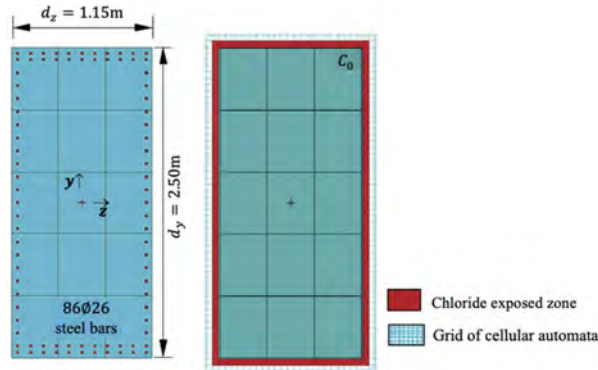


Figure 8. RC cross-section: model and grid of the cellular automaton (adapted from Biondini et al. 2006).

Table 1. Parameters for diffusion analysis in coated RC pier.

Size of cell	Δx [m]	0.025	Section width	d_y [m]	1.15
Time increment	Δt [year]	0.010	Section height	d_z [m]	2.50
Concrete diffusivity	D_{su} [m ² /s]	1.0×10^{-11}	Cover thickness	c [m]	0.075
Chloride content on surface	C_0 [kg/m ³]	13.0	Coating thickness	c_s [m]	0.0010
			Bar spacing	s [m]	0.10

Two surface-treated RC pier models adopting different assumption of the coating diffusivity change are considered: (A) the averaged time-variant diffusivity; (B) the increase of local defects in coated surface represented by Equations (5) and (7), respectively. The goal is to investigate the effect of each deterioration process on the lifetime of surface-treated RC members and structures.

4.3 Comparison between uncoated and coated RC cross-section

Figure 9 shows the chloride concentration $C(t)$ over a 50-year lifetime at the depth of the outer layer of 66 reinforcing steel bars ($c = 7.5$ cm) for the uncoated RC cross-section as well

as for the two cases with coatings. Chloride threshold regarding corrosion initiation of the rebars is defined as $C_{cr} = 2.0 \text{ kg/m}^3$.

The coated cases reach the threshold value much later than the uncoated one due to high chloride resistivity of coating. On the other hand, the critical time T_{cr} when $C(t)$ reaches C_{cr} , is different between the two coated cases. Chloride concentration increases rapidly around defective areas in case (B), which leads to earlier corrosion initiation compared to case (A) where chloride ions diffuse homogeneously along the coated surface (Figure 10). Thus, the simulation assuming coating capacity change based on increase of local defects leads to safer evaluation of the structural lifetime compared to that using the averaged diffusivity.

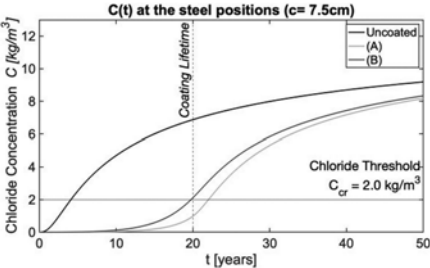


Figure 9. Chloride concentration at the depth of the outer layer of 66 reinforcing steel bars ($c = 7.5 \text{ cm}$).

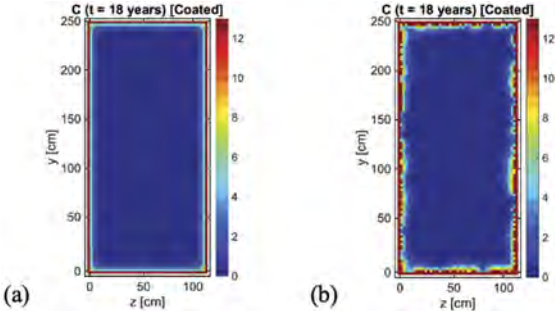


Figure 10. Concentration maps ($t = 18 \text{ years}$): (a) averaged diffusivity and (b) defective area change.

4.4 Effect of mesh size

It is worth noting that in case (B), the mesh size of cellular automata may influence the size and distribution of the defects in surfaces under the structural aging process. Figure 11 compares case (A) and case (B) with mesh size of 25, 12.5, and 5 mm in terms of average chloride concentration (Figure 11a) and dispersion around mean of the corrosion initiation time (Figure 11b) for the outer layer of 66 steel bars as obtained from Monte Carlo simulation with 1000 repetitions.

The results show that the chloride content increases as the size of each cell becomes smaller. However, the corresponding decrease of the corrosion initiation time is less remarkable. This is because smaller defects spread widely from early aging stage in the case with small meshes based on Equation (7). These results show that the determination of the defects size in coated structures is important to predict the actual corrosion initiation time.

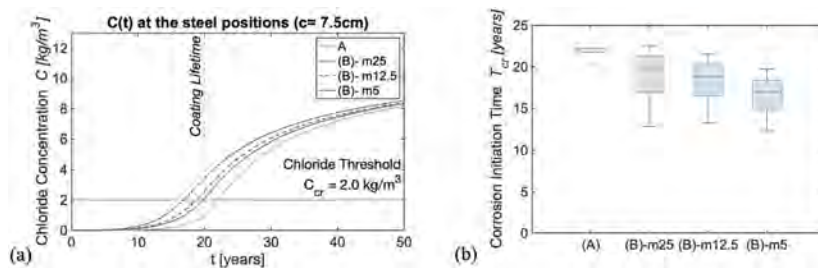


Figure 11. Effect of mesh size: (a) chloride concentration and (b) corrosion initiation time.

5 CONCLUSIONS

This study has presented an approach to predict the time-variant coating diffusivity into the chloride diffusion analysis for surface-treated RC structures based on the results of CMT and the AgNO₃ spray test. The exponential decay of the coating capacity has been estimated from the experiments with the cyclic deterioration test and CMT. Then, two deterioration models of the coating diffusivity have been established: averaged time-variant diffusivity and occurrence of local defects in coated surface. Simulation of chloride ingress into a coated RC cross-section has shown that the model assuming the local defects occurrence predicts earlier corrosion initiation compared to the averaged coating capacity loss. To improve the lifetime prediction of the coated structures, it is expected to investigate the dominance of each deterioration process in real phenomenon and determine defect sizes in coated surface of existing structures.

REFERENCES

- Almusallam, A., Khan, F.M. & Maslehuddin, M. 2002. Performance of concrete coatings under varying exposure conditions. *Materials and Structures* 35: 487–494.
- Almusallam, A.A., Khan, F.M., Dulaijan, S.U. & Al-Amoudi, O.S.B. 2003. Effectiveness of surface coatings in improving concrete durability. *Cement and Concrete Composites* 25(4): 473–481.
- Biondini, F., Bontempi, F., Frangopol, D.M. & Malerba P.G. 2004. Cellular automata approach to durability analysis of concrete structures in aggressive environments. *ASCE Journal of Structural Engineering* 130(11): 1724–1737.
- Biondini, F., Frangopol, D.M. & Malerba P.G. 2006. Time-variant structural performance of the Certosa cable-stayed bridge. *Structural Engineering International* 16: 235–244.
- Buenfeld, N. R. & Zhang, J.Z. 1998. Chloride diffusion through surface-treated mortar specimens. *Cement and Concrete Research* 28(5): 665–674.
- Crank, J. 1975. *The mathematics of diffusion*. London: Oxford University Press.
- JIS-A6909-2021. Coating materials for textured finishes of buildings. *Japanese Standard Association*.
- JSCE-G571-2003. Test method for the effective diffusion coefficient of chloride ion in concrete by migration. *JSCE Standards*.
- Moradillo, M. K., Shekarchi, M. & Hoseini, M. 2012. Time-dependent performance of concrete surface coatings in tidal zone of marine environment. *Construction and Building Materials* 30: 198–205.
- Otsuki, N., Nagataki, S. & Nakashita, K. 1993. Evaluation of AgNO₃ solution spray method for measurement of chloride penetration into hardener cementitious matrix materials. *Construction and Building Materials* 7(4): 195–201
- Pan, X., Shi, Z., Shi, C., Ling, T.C. & Li, N. 2017. A review on surface treatment for concrete - Part2: Performance. *Construction and Building Materials* 133: 81–90
- Yoshii, C. & Iwanami, M. 2022. Improvement on deterioration prediction about surface coating for RC structures against chloride penetration. *76th RILEM annual week 2022; International conference on regeneration and conservation of structures, Kyoto, 7-9 September 2022*.

Embedded fibre optical strain monitoring of a bio-composite bridge

M. Weil, Y. Bel-Hadj, W. Weijtjens & C. Devriendt

Offshore Wind Infrastructure-lab (OWI-lab)/Vrije Universiteit Brussel (VUB), Brussels, Belgium

Y.-A. Janssens & E. Voet

Com&Sens, Eke, Belgium

ABSTRACT: Three pedestrian and bicycle bridges made from a fully recyclable bio-composite material are developed in the context of the Interreg NWE Smart Circular Bridge (SCB) project. These bridges incorporate Structural Health Monitoring (SHM) technology to assess their structural integrity and provide data for future designs. The SHM setup includes strain, vibration and environmental sensors. This paper focuses on the 90 strain and temperature sensors in the first circular bridge. The data shows a strong temperature dependency of the strain, which is addressed using a temperature compensation strategy. Traditional polynomial temperature compensation is compared to a strategy using the Savitsky-Golay filter, the latter removes almost all temperature variability in the data. The strain sensors are also used to capture the bridge dynamics, accurately tracking the first vertical mode, using DBSCAN for automated tracking. The large number of sensors allows for the tracking of the mode shape for potential damage detection.

1 INTRODUCTION

Climate protection and circular economy are increasingly important in the construction industry, leading to the development of three pedestrian and bicycle bridges in Germany and the Netherlands as Smart Circular Bridges (SCB) using an innovative, fully recyclable bio-composite material. The SCB project is part of the shift towards natural and sustainable materials in the updated EU's action plans towards a sustainable bio-economy for Europe (European Commission and Directorate-General for Research and Innovation, 2018). These bridges also incorporate Structural Health Monitoring (SHM) technology to assess their structural integrity and provide data for future designs with the novel material. The SHM system includes Fibre Bragg Gratings (FBG) strain sensors, accelerometers and environmental sensors. This generates early warnings before critical levels of material degradation occur. Additionally, the SCBs enable the acquisition of new insights into the use of bio-composites in the construction industry, promoting the use of more sustainable resources.

Previous research details the vibration monitoring of the Almere SCB through both design validation and automated Operational Modal Analysis using the 3 installed accelerometers (Weil et al., 2022). This paper focuses on the use of embedded FBG strain gauges installed by our partners at Com&Sens in the first circular bridge in Almere, the Netherlands. Early results show strong temperature variability in the collected strain data. This is accounted for by installing additional temperature sensors inside the structure of the bridge. However, given effects such as solar radiation, shadow (e.g. from the handrail) and the material properties (high thermal insulation and unknown thermal property), the temperature compensation is challenging. To resolve this, a novel temperature compensation strategy using a Savitsky-Golay (SavGol) filter (Savitzky and Golay, 1964) is developed, to remove the polynomial temperature trend in every strain sensor.

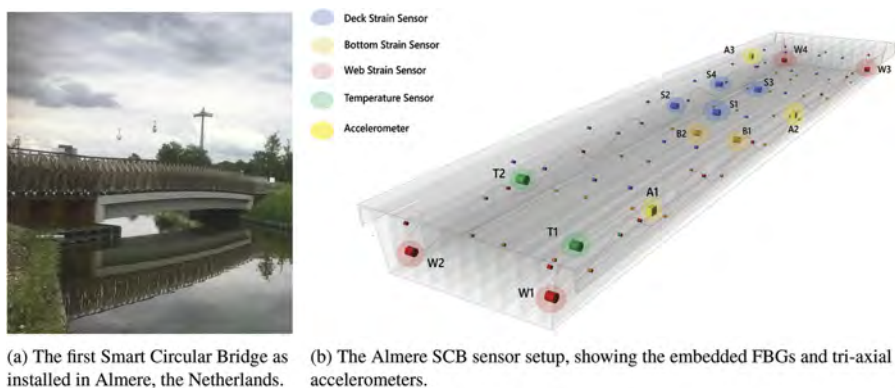


Figure 1. The Almere SCB.

Alongside the static properties, the dynamic response of the bridge available in the strain sensors is explored. It is shown that the first vertical mode can be tracked through an Operational Modal Analysis (OMA) (Devriendt et al., 2014) when the bridge sees some activity. The Linear Square Complex Frequency Estimator (LSCF) algorithm is used to detect the different modes (Magalhães and Cunha, 2011). The tracking of detected modes is done using the Density-based clustering of applications with noise (DBSCAN) algorithm (Ester et al., 1996). Because of the dense network of fibre optical sensors a lot of spatial information is contained, and in this paper, we explore the feasibility to detect and track the strain mode shapes.

2 THE ALMERE SMART CIRCULAR BRIDGE

The Smart Circular Bridge innovates both through the use of novel sustainable materials and through the use of an embedded monitoring system, making the bridge circular, safe and smart. This section will go over the first bridge installed in Almere as shown in Figure 1a and detail the installed monitoring technology shown in Figure 1b.

2.1 *Bio-composite material*

The Smart Circular Bridge in Almere is the first bridge in the world to be built from 100% natural flax fibres reinforced with 25% bio-resin (Huijgen, 2022). The material selection and bridge design were based on bending and tensile tests conducted by the project partners at the TU Eindhoven and KU Leuven to determine the material's strength and stiffness under different conditions. Following this, the 15-meter-long bridge was built at FibreCore using a vacuum-infusion method combined with internal foam shapes and external moulds. During construction, strain sensors were embedded inside the bridge and accelerometers were installed on the surface. After construction, the bridge was installed at the Floriade expo in Almere and the SHM system was connected. Data has been gathered since the 4th of April 2022 and is available on a public dashboard at <https://dashboard.smartcircularbridge.eu>.

2.2 *Embedded FBGs*

The Smart Circular Bridge has a monitoring system that includes strain, dynamic, and environmental sensors. The strain sensors are Fiber Bragg Grating (FBG) sensors, which were integrated into the bridge's structure during construction. There are 82 FBG strain sensors and 8 FBG temperature sensors on the bridge.

The dynamic sensors are tri-axial, high-resolution industrial micro-electromechanical systems (MEMS) accelerometers, which are glued to the side of the bridge at three locations. The accelerometers are used to capture vibrations and continuously track modal parameters

through automated Operational Modal Analysis (OMA) (Devriendt et al., 2014). A weather station is used to monitor the wind, air temperature, and relative humidity to normalize changes and assess the effect of the changing environment on the material.

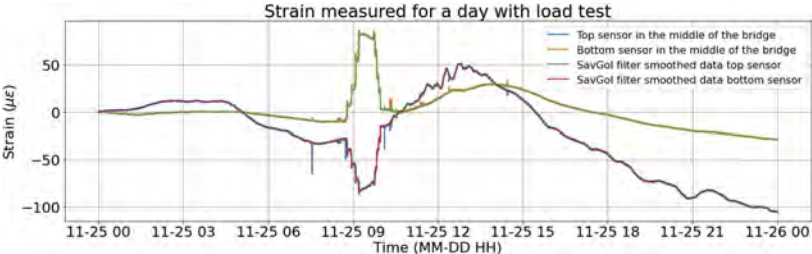


Figure 2. One-day strain measurements and results of the SavGol filter for the 25th of November, during which a static load test using a 4-ton load is performed. The temperature variability of the strain data highlights the importance of a good temperature compensation strategy.

A previous research details how the accelerometers are used for controlled and field tests to extract modal parameters (Weil et al., 2022). On the other hand, the strain sensors are primarily used for material monitoring during construction, creep measurement, event analysis and novelty detection.

3 TEMPERATURE EFFECTS

FBG sensors are often used for strain monitoring in SHM systems due to their small physical size, lightweight and ability to be multiplexed. Additionally, FBGs can easily be embedded in a composite structure. This allows the placement of many sensor points, capturing highly spatial information about the structure. However, one issue arising when using FBG sensors is their temperature sensitivity. This can be especially problematic in a bio-composite bridge, as the material is thermally isolated, leading to slow heating and cooling of the bridge. This combined with the shadow cast by the handrails creates very local and complicated heating effects on the structure. On top of this, the thermal expansion coefficient of this material is much more complex than traditional materials such as steel and concrete, leading to complicated temperature effects (Heinen, 2022).

Furthermore, the temperature variability can hide significant events occurring on the bridge as 10°C of temperature variation can lead to an increase of more than 10µε, greatly exceeding the effects of any structural load. To demonstrate, Figure 2 shows the measured strain in 1 top and 1 bottom sensor for an entire day, during which a static load test was conducted on the bridge. The test consisted of placing and then removing 4 cubic metres of water one by one on the bridge from 8.40 am until 10.00 am. This 4-ton load results in approximately 80µε, which doesn't exceed the daily temperature variability for a day in November by far and is even dwarfed by the strain variability of more than 300µε in the top sensor due to temperature observed on a warm summer day as illustrated by the top sensor measurement in Figure 4. If we want to correctly detect the effect of a single person on the bridge, it is clear that temperature compensation is required.

3.1 Traditional regression based temperature compensation

FBG strain sensor manufacturers outline different strategies to deal with high-temperature variability in the strain data (HBK, 2021). The common practice is to install a separate temperature compensation sensor next to each FBG sensor and remove temperature effects based on the thermal expansion coefficient of the material α combined with the thermal expansion coefficient of the fibre. However, this increases the cost and complexity of the monitoring system, basically requiring an equal amount of temperature sensors as strain sensors. To balance costs in this project, for example, only 8 temperature FBG sensors are placed for 82 strain sensors. This means the relationship between the temperature and strain sensor needs to be learned. Additionally,

contrarily to steel, the bio-composite has a temperature-dependent thermal expansion coefficient $\alpha(T)$, making the relationship between temperature and strain more complex.

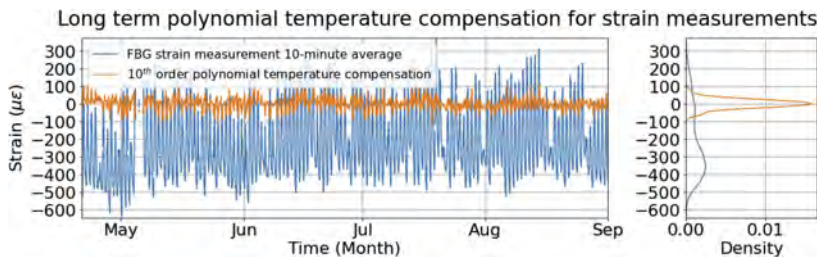


Figure 3. Polynomial temperature compensation for a single sensor located close to a temperature sensor in the Almere SCB. The temperature variability is reduced from $900\mu\epsilon$ to $200\mu\epsilon$.

One potential solution to this issue is to use machine learning algorithms to compensate for the temperature effects on the FBG sensors. A temperature compensation scheme using a multiple linear regression algorithm for a bio-composite bridge is given in (Heinen, 2022). The results show a prediction error below 5% but in absolute values, this is approximately $50\mu\epsilon$ or equivalent to a static load of 2 tons on the middle strain sensors.

Polynomial regression for the strain sensors closest to a given temperature sensor is tried on the SCB, and the long-term results are shown in Figure 3. This reduces the spread of the thermal effects from $900\mu\epsilon$ to $200\mu\epsilon$. A reduction of the temperature effects is observed, but even the remaining variability can hide significant events occurring on the bridge. Additionally, this could only work for the 8 sensors close to a temperature sensor. It is clear that an alternative solution is necessary to remove the temperature effects from the strain data and isolate the strain caused by the different events occurring on the bridge.

3.2 Savitsky-Golay filter for temperature compensation

In this research an alternative approach for temperature compensation is explored, using a Savitsky-Golay (SavGol) filter to follow the polynomial trend of all the temperature effects (Savitzky and Golay, 1964).

The SavGol filter is a digital filter that is commonly used for data smoothing and denoising. The SavGol filter works by fitting a set of polynomial coefficients to a window of data points by the method of linear least squares. The polynomial degree p and the size of the window n can be adjusted to control the amount of smoothing and the degree of differentiation. The window is then moved in the same way as for a moving average. The equation for the SavGol filter can be written as shown in Equation 1.

$$y(i) = \sum_{k=0}^n A_k(p) * x(i + k - m) \quad (1)$$

Here, $y(i)$ is the filtered value at point i , $x(i)$ is the original data at point i and m is the centre of the window. $A_k(p)$ are the coefficients of the polynomial derived by fitting a polynomial of degree p through a linear least squares method to the data for every window n . By adjusting the values p , n and m , the SavGol filter can be tailored to the specific needs of the data being processed.

In the context of this research, the SavGol filter is not used as a denoising filter, but rather to remove the polynomial temperature trend that is present in the strain measurements. This temperature trend is caused by changes in ambient temperature and can mask the strain changes caused by events of interest, such as a pedestrian crossing the bridge. Because the temperature effects show slow and smooth strain variations when compared to the events, the SavGol filter with an appropriate window size is able to remove the temperature trend and reveal the strain on the bridge caused solely by the events. This allows for more accurate

analysis of the event strain data and a better understanding of the behavior of the bridge under different loading conditions.

The results of applying the filter with a second order polynomial and window length of 1800 samples or 36 seconds are shown in Figure 4. In this Figure, the strain measurements and SavGol smoothed data of one top and one bottom sensor for an entire day are shown. The SavGol filter can adequately track the complex temperature trend generated in the strain sensors, enabling the removal of the trend. By removing the filtered data from the original data, the strain resulting from the events remains as shown by the pink and brown lines in Figure 4 and again in Figure 5. The temperature compensated data has a 0 strain rest state and a deviation from 0 when an event occurs. The top sensor is loaded in compression and has negative strain, whilst the bottom sensor is loaded in tension and has a positive strain. After temperature compensation, it is thus possible to use threshold-based event detection (Sadeghi et al., 2023) and labelling based on measured strain values. Additionally, it is easy to extract statistics for the different events like maximum, amount of peaks, etc. Enabling an event classification and event anomaly detection in a future study.

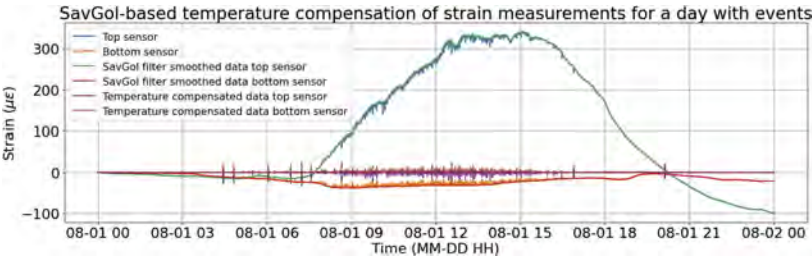


Figure 4. Strain data for a top (blue) and bottom (orange) sensor in the middle of the bridge on a - summer day. The SavGol filter is applied on both sensors (green and red) and the filtered signal is subtracted from the original data, isolating the strain generated by the events (purple and brown).

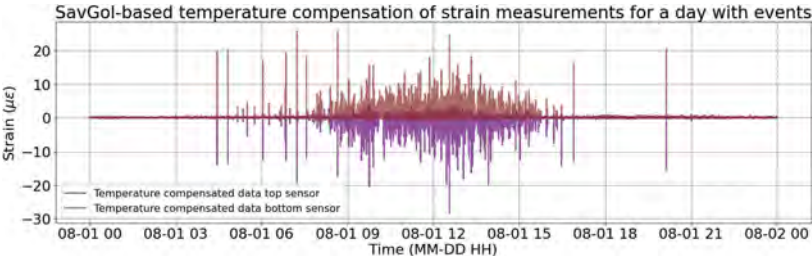


Figure 5. SavGol-based temperature compensated strain data for a top (purple) and bottom (brown) sensor on a warm summer day.

4 EMBEDDED FBG OPERATIONAL MODAL ANALYSIS

The modal analysis of the structure is conducted in previous research using the three accelerometers (Weil et al., 2022). Here, the modal frequencies and damping ratios are identified first through a controlled test at the construction site consisting of an Experimental Modal Analysis (EMA), and later during a field test comprising an Operational Modal Analysis (OMA). The first vertical mode, which has the highest energy for this type of structure, is identified at around 6.9Hz and shows a strong temperature dependency.

However, as only 3 accelerometers are permanently installed, the spatial resolution of the mode shape is limited. Higher resolution mode shapes were extracted from an EMA using a roving hammer experiment. But when trying to infer damage from changes in the mode

shapes (Anastasopoulos et al., 2021, 2022), then this would require reproducing a roving hammer experiment or installing more accelerometers. In contrast, the FBG sensors, which offer a high spatial resolution, open an opportunity to obtain continuous monitoring of detailed mode shapes.

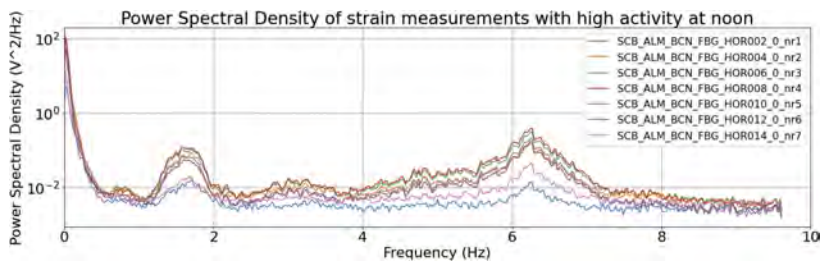


Figure 6. PSD for 1 hour strain measurements with high activity on the bridge at Noon. Stepping frequency at 1.7Hz and first vertical frequency at 6.3Hz clearly stand out.

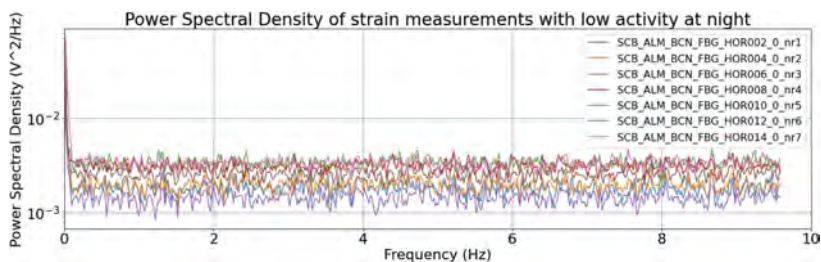


Figure 7. PSD for 1 hour strain measurements with no activity on the bridge at night. No frequencies stand out when the bridge isn't excited.

4.1 DBSCAN automated OMA tracking

If the strain sensors can capture the structure's dynamics, it is possible to track the mode shape thanks to the many strain measuring locations. With a sampling frequency of 50Hz for the FBG strain sensors, it is expected that the first vertical frequency at 6.9 Hz can be detected. This is confirmed in the Power Spectral Density (PSD) computed for the data gathered by the Bottom-Center-North (BCN) sensor line during 1 hour with a lot of activity on the bridge. In the PSD shown in Figure 6, two frequencies clearly stand out; the stepping frequency at around 1.7 Hz and the first vertical modal frequency at around 6.3 Hz. This is significantly lower than the 6.9Hz capture during the previous OMA. This is due to the temperature dependency of the first vertical mode, which tends to be lower during warmer days. Unfortunately, no dynamics are captured by the strain measurements when there is no activity on the bridge, as shown in the PSD at Figure 7 for a 1 hour measurement during the night.

The PSDs illustrate that the strain sensors can capture dynamic properties of the bridge when the bridge experiences a lot of activity, and that it should be possible to track the first vertical mode for these time periods. The modes are calculated for one month on the BCN strain line. Because there are 6 sensor locations on this strain line, it is possible to capture the vertical mode shape. The modes are calculated using the Linear Square Complex Frequency Estimator (LSCF) algorithm on 10 minutes of data with a model order of 32 and window length of 30 (Devriendt et al., 2014; Magalhães and Cunha, 2011). During this month, the bridge had a lot of activity during the day time but very little to none at night. This is clearly shown by the gaps in the extracted modes displayed in Figure 8. This figure shows that

multiple modes are detected in the 2-7 Hz range. An automated tracking method using Density-based clustering of applications with noise (DBSCAN) (Ester et al., 1996) is used to track the different modes and separate the first vertical mode. The DBSCAN is implemented because it can accurately separate cluster modes using the modal frequency, damping ratio, size in the LSCF algorithm and the time difference. Additionally, it labels many points as noise with a *label* = -1. Currently, the DBSCAN hyper-parameters ϵ and *minPts* are optimized manually. An automated tuning for this tracking algorithm is part of future research.

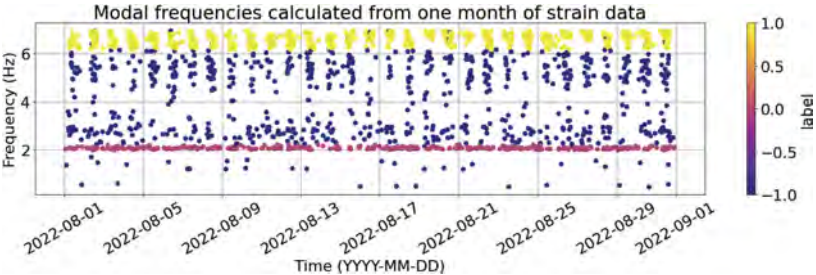


Figure 8. Modal frequencies calculated using the LSCF algorithm for the entire month of August 2022. The tracking and labelling of the calculated modes is then done using the DBSCAN algorithm. The different tracked modes are represented by different colours.

4.2 First vertical mode shape

The mode shape for the mode tracked above 6Hz (*label* = 1 or yellow in Figure 8) is plotted for all modal parameter estimations in Figure 9. This extracted shape confirms that the mode at 6.3 Hz is the first vertical mode. These preliminary results show the feasibility to obtain a mode shape estimate from FBGs inside the bridge. However, simultaneously shows a significant amount of scatter that still needs to be resolved in order to apply the damage detection methods (Anastasopoulos et al., 2021).

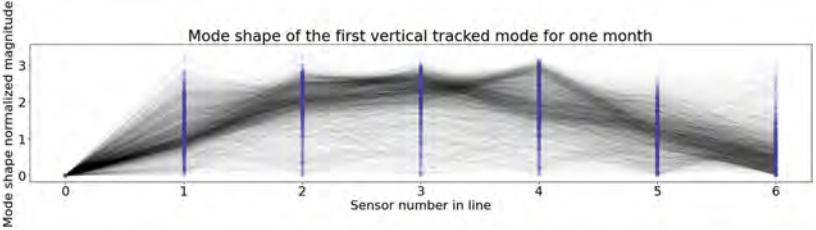


Figure 9. Early results for the mode shape of the tracked first vertical mode in the 6-6.5Hz range. This mode shape confirms that the mode is indeed the first vertical mode.

5 CONCLUSIONS

One of the key achievements of the research presented is the use of the SavGol filter for temperature compensation. This is effective in removing practically all temperature effects on the strain measurements and isolating the event strains. This is not possible using a more traditional approach involving polynomial regression and a nearby temperature sensor. A second achievement of the research is the ability to accurately track the first vertical mode using strain measurements only. This is made possible by the observation of dynamic behavior in the strain sensors through a PSD. However, the dynamic response only appears when the bridge sees high activity. The LSCF algorithm is used to calculate the modal frequency, damping ratio and mode shape for an entire month. The calculated modes are later tracked using

the DBSCAN algorithm that isolates the first vertical mode in the 6-6.5Hz range. Finally, the use of many sensor locations allows for the determination of the mode shape, which is plotted and confirms that this is indeed the first vertical mode. This provides a more complete understanding of the structural behavior of the bio-composite bridge. These achievements demonstrate the potential of the embedded FBG strain gauges and the temperature compensation techniques developed in this study for use in the structural health monitoring of bio-composite materials and structures. The methods developed in this research will be applied to the two other Smart Circular Bridges currently under construction and other types of structures. This exercise will be done to validate the findings of this study and to explore the potential of these techniques for use in other applications.

ACKNOWLEDGEMENTS

This research is being conducted within the Bio-Economy Strategy of the European Union and is supported by the Interreg North-West Europe Programme under the “Smart Circular Bridge for a circular built environment” project title.

REFERENCES

- Anastasopoulos, D., G. De Roeck, and E. P. Reynders (2021). One-year operational modal analysis of a steel bridge from high-resolution macrostrain monitoring: Influence of temperature vs. retrofitting. *Mechanical Systems and Signal Processing* 161, 107951.
- Anastasopoulos, D., E. P. Reynders, S. François, G. De Roeck, G. Van Lysebetten, P. Van Itterbeeck, and N. Huybrechts (2022). Vibration-based monitoring of an frp footbridge with embedded fiber-bragg gratings: Influence of temperature vs. damage. *Composite Structures* 287, 115295.
- Devriendt, C., F. Magalhães, W. Weijtjens, G. De Sitter, Cunha, and P. Guillaume (2014, November). Structural health monitoring of offshore wind turbines using automated operational modal analysis. *Structural Health Monitoring* 13(6), 644–659.
- Ester, M., H.-P. Kriegel, J. Sander, and X. Xu (1996). A density-based algorithm for discovering clusters in large spatial databases with noise. In *Proceedings of the Second International Conference on Knowledge Discovery and Data Mining, KDD'96*, pp. 226–231. AAAI Press.
- European Commission and Directorate-General for Research and Innovation (2018). A sustainable bioeconomy for europe: strengthening the connection between economy, society and the environment: updated bioeconomy strategy.
- HBK (2021). Measuring with strain gauges: How to prevent unwanted temperature effects on your measurement result. <https://www.hbm.com/en/6725/article-temperature-compensation-of-strain-gauges/>. Accessed: 2022-01-02.
- Heinen, D. (2022). Predicting thermal response of the bio-based bridge in ritsumasyl, using temperature distributions and a regression model.
- Huijgen, A. (2022). Le premier pont en lin du monde inauguré aux pays-bas. Accessed: 2022- 12-21.
- Magalhães, F. and A. Cunha (2011, 07). Explaining operational modal analysis with data from an arch bridge. *Mechanical Systems and Signal Processing* 25, 1431–1450.
- Sadeghi, N., M. Weil, N. Noppe, W. Weijtjens, and C. Devriendt (2023). Fatigue analysis on four months of data on a steel railway bridge: Event detection and train features’ effect on fatigue damage. In P. Rizzo and A. Milazzo (Eds.), *European Workshop on Structural Health Monitoring*, Cham, pp. 669–679. Springer International Publishing.
- Savitzky, A. and M. J. E. Golay (1964). Smoothing and differentiation of data by simplified least squares procedures. *Analytical Chemistry* 36(8), 1627–1639.
- Weil, M., Y. Bel-Hadj, A. Fernandes, W. Weijtjens, and C. Devriendt (2022). Experimental and operational modal analysis of a bio-composite pedestrian bridge. In *ISMA Conference*.

Dissipative steel and steel-concrete composite beam-to-column joints

G. Skarmoutsos & U. Kuhlmann

Institute of Structural Design, University of Stuttgart, Stuttgart, Germany

ABSTRACT: The present paper deals with the behaviour of bolted steel and steel-concrete beam-to-column joints with endplate connections under seismic loading.

While partial-strength all-steel joints have been part of recent scientific works, the behaviour of the common composite joints for seismic loading remains unclear. Currently, in the engineering practice construction criteria according to (CEN EN 1998-1, 2004) are applied taking care that the contribution of the concrete slab is neglected, thus the joint is designed as an all-steel one.

In a recently completed experimental campaign 3 all-steel and 9 steel-concrete composite joints with 5 parameters varied were tested under seismic loading. Joints of common configuration were chosen and slightly modified by applying on them the basic seismic design principles.

Based on the experimental results composite joints can be an important and universal source of energy dissipation. They can find application in different structural systems and areas of various seismicity levels.

1 INTRODUCTION

Often in low to medium seismicity areas partial-strength beam-to-column joints according to (CEN EN 1993-1-8, 2005) and (CEN EN 1994-1-1, 2009) are used. In the current (CEN EN 1998-1, 2004) the possibility to use partial-strength joints is given provided that experimental results are available. The absence of experimental data and of a specific design process, though, do not allow for the broad use of partial-strength composite joints.

The present paper presents the objectives, methodologies and concepts followed for investigating the double-sided all-steel and steel-concrete composite joints experimentally as part of (Hoffmeister, et al., in prep.). It also provides a first insight in the results of the recently completed experimental campaign.

2 DESIGN OF SPECIMENS

2.1 *Literature on partial-strength all-steel and steel-concrete composite joints - selected parameters with an influence on the joint mechanical behaviour*

(Kuhlmann, et al., 2009), (Kuhlmann, et al., 2017) & (Rölle, 2013) investigated bolted partial-strength beam-to-column endplate connections in view of optimising their robust response to extreme events, such as the loss of a column. Among other parameters, the thickness of the endplate t_{ep} and the distance e_4 of T-stub bolt series, see Figure 2, have been experimentally and numerically investigated and their influence on the joint mechanical properties proven. An overview of the design methodologies for ductile joint response when designing for robustness is given in (Demonceau, et al., 2021). The 2 parameters, t_{ep} and e_4 , were selected also for the work presented herein and in this case the values were chosen for optimal seismic behaviour.

In (Landolfo, et al., 2017) partial-strength all-steel joints were investigated and a design process developed, which among others covers aspects such as the detailing of welds as well as the size of bolts. Those recommendations and also the concept concerning the hierarchy of strength of the different connection parts for partial-strength joints have been followed herein.

Regarding the influence of the slab on the steel part of the connection, (CEN EN 1998-1, 2004) foresees that composite joints can be designed as all-steel ones provided that in a radius equal to $2 \cdot b_{eff}$ around the column, the concrete is fully disconnected from the steel beams. Similarly, (ANSI/AISC 358-16, 2016) foresees for composite joints that no shear connectors within 1,5 times the beam depth from the face of the connected column flange are placed. The aforementioned clauses take care to mechanically disconnect the concrete slab from the steel profile in the area of the joint. Nevertheless, the continuity of the slab in combination with its high stiffness should not be neglected, since it can lead to a restriction of the (i) connection rotation and (ii) flexural deformation of the beam. Therefore, the position of the 1st shear stud was chosen as parameter.

In addition, the reinforcement ratio of the slab ρ was selected as parameter.

Generally, for seismic design symmetrical configurations are preferred. Due to the presence of the concrete slab composite joints of typical configuration are by nature unsymmetrical, so at least the steel part of the connection is usually designed as a symmetrical one. On the other hand, in very low seismicity areas where no seismic design is performed, often joint configurations with 3 bolt rows are used. It has been goal of the experimental campaign to also investigate joints as applied in the practice. Therefore, aside from the 8 composite specimens with 4 bolt rows, also 1 composite specimen with 3 bolt rows was tested. Necessary modifications, compared to the ones for non-seismic design, were realised, such as the stiffening of the column and strengthening of the welds.

2.2 Design process for the specimens

Two structural typologies were investigated (i) all-steel joints of industrial buildings, HEB 300 columns and HEA 240 beams, and (ii) composite joints of office buildings, HEA 300 columns and IPE 300 composite beams. For the optimisation of the energy dissipation the appropriate combination of moment capacity M , rotational stiffness S and rotation capacity θ is required. With the help of the component model and of a FEM model two limit cases were considered for the dimensioning of the specimens:

- 1st limit case: $M_{max}, S_{max}, \theta_{min} \rightarrow$ probably min ductility and max energy dissipation
- 2nd limit case: $M_{min}, S_{min}, \theta_{max} \rightarrow$ probably max ductility and min energy dissipation

2.3 Selected parameter values

In a FEM parametric study, not presented herein, it has been observed that for the given beam and column sections, $t_{ep} = 15$ mm serves as a lower boundary for partial-strength joints designed to be dissipative, whereas for $t_{ep} = 25$ mm yielding takes place mainly at the beams and not the endplates. The latter case is not fully in line with the concept of partial-strength joints but can be favourable for the joint seismic behaviour. The selected parameter values have been $t_{ep} = [15, 20]$ mm. For $t_{ep} = 20$ mm, aside from plastification of the endplate, also significant yielding of the beam was observed, which resulted for high deformations in a plastic hinge in the beam. The thickness of the endplate is considered as the parameter governing the response of the steel connection.

Two values for e_4 have been selected as (i) the minimum possible distance, $e_4 = 100$ mm, and (ii) the maximum one for sufficient energy dissipation, $e_4 = [130, 150]$ mm, for industrial and office buildings configurations, respectively.

For the parameter $l_{shear\ stud}$ the first value selected is $l_{shear\ stud} = 1,5 \cdot h_{beam} = 450$ mm, according to the (ANSI/AISC 358-16, 2016), and the second value is the minimum distance, $l_{shear\ stud} = 190$ mm from the face of the column or $l_{shear\ stud} = 120$ mm from the end of the concrete slab for $\varnothing 22/100$ mm shear studs. Additionally, a gap of 70 mm was foreseen between the concrete slab and the face of the column.

Regarding reinforcement ratio of concrete slab ρ two representative values were chosen. The conventions for the naming of the specimens are given in Table 1.

Table 1. Conventions – name of specimens.

Column profile	Steel or Composite	Beam profile	Steel or Composite	t_{ep}	e_4	$l_{shear\ stud}$	ρ
HEA 300-HA30	S/C	IPE 300-I30	S/C	(mm)	(mm)	(mm)	(%)

3 TEST SETUP AND TEST INSTRUMENTATION

3.1 Test instrumentation

In total 64 measuring channels per test were available, of which 16 for transducers and inclinometers and 48 for strain gauges.

The arrangement of all measurement equipment, strain gauges, inclinometers and cable transducers, as well as the boundary conditions are given in Figure 1. A photo of the test setup and of a typical composite joint specimen configuration is given in Figure 3.

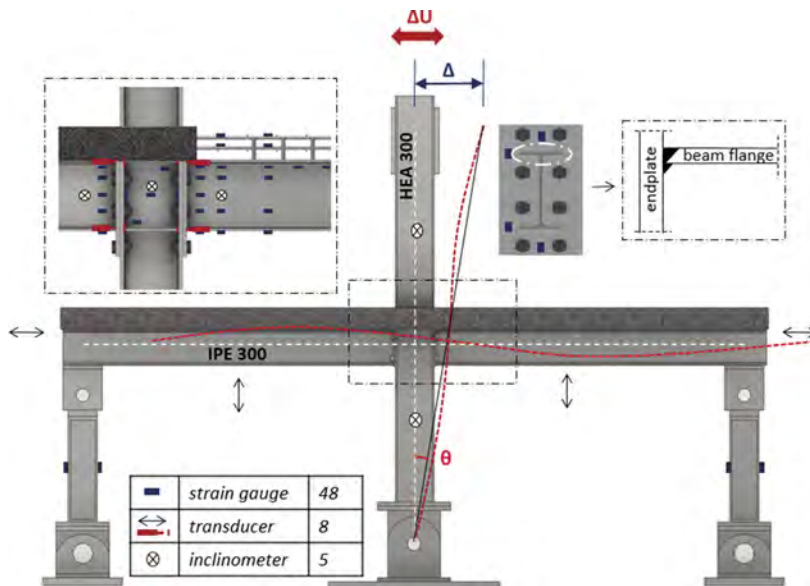


Figure 1. Measurement equipment, boundary conditions and type of beam-to-endplate welds.

3.2 Loading protocol

The ANSI/AISC 341-16 loading protocol for the prequalification of beam-to-column connections was used with slight modifications. More specifically, for all tests of (Hoffmeister, et al., in prep.) 2 additional load steps at 25 mrad and 35 mrad with 2 cycles each were added.

4 EXPERIMENTAL RESULTS

4.1 Influence of the varied parameters on the mechanical properties of the joints

4.1.1 All-steel joints

It is worth mentioning that for the investigated partial-strength joints the increase of moment capacity M and rotational stiffness S through the variation of a parameter is usually accompanied by a decrease or by no reduction of the rotation capacity S . For the specimen

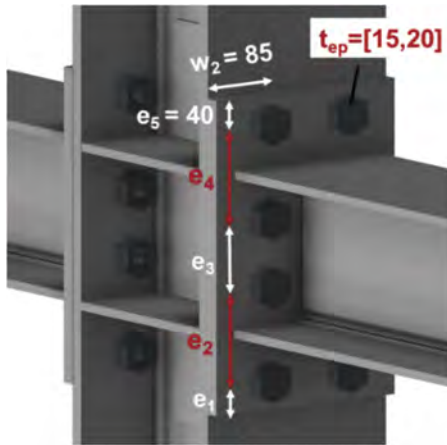


Figure 2. Typical steel connection configuration.



Figure 3. Typical configuration of steel-concrete composite specimen, here K-HA30V-I30V-15-100-450-p1.

K-HB30S-HA24S-20-100, the minimum value of $e_4 = 100 \text{ mm}$ leads to an increase of M and S but also of the rotation capacity θ compared to the specimen K-HB30S-HA24S-20-130. Here θ increases due to the activation of a more favourable failure mode for specimen K-HB30S-HA24S-20-100, formation of a plastic hinge in the beam after plastification of the endplate 4a.

Table 2. Influence of the varied parameters on M , S and θ .

	$e_4 \downarrow$	$e_4 \uparrow$	$t_{ep} \downarrow$	$t_{ep} \uparrow$
S	\uparrow	\downarrow	\downarrow	\uparrow
M	\uparrow	\downarrow	\downarrow	\uparrow
θ (mrad)	\uparrow	\downarrow	n.a.	n.a.

4.1.2 Composite joints

The influence of the varied parameters e_4 , t_{ep} , $l_{sh. stud}$, ρ and number of bolt rows for the endplate connection on the joint moment capacity M , rotational stiffness S and rotation capacity θ is given in Table 3.

Table 3. Influence of the varied parameters on M , S and θ .

	$e_4 \downarrow$	$e_4 \uparrow$	$t_{ep} \downarrow$	$t_{ep} \uparrow$	$l_{sh. stud} \downarrow$	$l_{sh. stud} \uparrow$	$\rho \downarrow$	$\rho \uparrow$	3 bolt rows	4 bolt rows
S	\uparrow	\downarrow	\downarrow	\uparrow	\uparrow	\downarrow	(-)	(-)	\downarrow	\uparrow
M	\uparrow	\downarrow	\downarrow	\uparrow	\uparrow	\downarrow	(-)	(-)	\downarrow	\uparrow
θ (mrad)	\downarrow	\uparrow	\uparrow	\downarrow	(-)	(-)	(-)	(-)	\uparrow	\downarrow

As expected lower values of e_4 lead to an increase of M and S and to a decrease of θ . The latter, however, is 45 mrad and in such way sufficient for seismic loading conditions, so that lower values of e_4 can be characterised as favourable for the joint seismic behaviour. In a similar way, thicker endplates result in higher moment capacity M and rotational stiffness S accompanied with lower values of rotation capacity θ , compared to thinner endplates.

No difference on the rotation capacity θ is observed, when construction measures for the disengagement of the concrete slab adopted. There is observed though, an increase of the stiffness S and moment capacity M if no construction measures taken, see Table 3. The higher stiffness, thanks to the enhanced composite action, is also observed through a more intensive cracking pattern on the concrete slab, see Figure 7b. Consequently, the seismic response of partial-strength composite joints significantly differs from the one of all-steel joints, whether the slab is locally disconnected from the beam, in a length of $1,5 \cdot h_{beam}$, or not. The high stiffness of the

composite beam restricts the deformation of the endplate, see Figure 8, and also leads to a reduced flexural deflection of the beam. It is noteworthy that only one steel profile size, IPE 300, has been tested. Stronger steel profiles might lead to a different joint behaviour.

The composite joint with unsymmetrical steel connection, 3 bolt rows, has, as expected, significantly lower moment capacity and stiffness for positive moments, 50% lower M . But for negative moments an increase of M and S is observed. The latter proves aside from the system response of two-sided joints that the concrete slab had not been fully activated. The failure took place for all specimens at the welds, in the heat affected area of the beam flange in tension.

4.2 Failure mode & experimentally derived M - θ curves

4.2.1 All-steel joints

All-steel joints presented a very ductile response up to (70-110) mrad. Such high rotations are not necessarily of benefit for seismic design and can be attributed mainly to the small beam profile size which led to a significant in plane flexural deformation of the beam. The latter resulted in a delayed activation of the connection, see Figure 5.

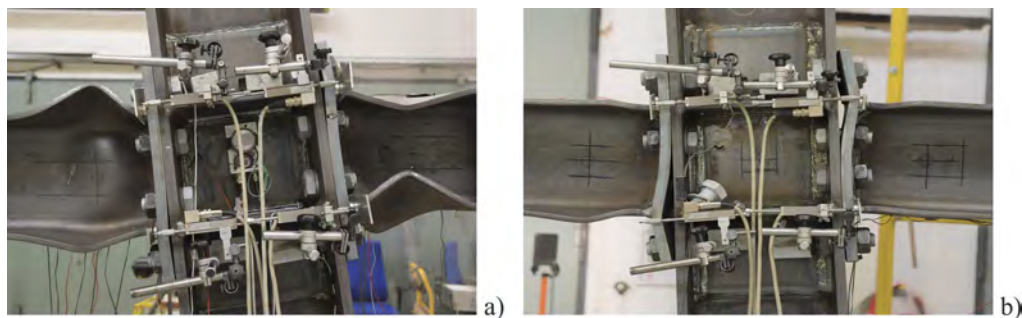


Figure 4. (a) Joint deformation at a rotation of 100 mrad for K-HB30S-HA24S-20-100 and (b) bolt failure after significant endplate plastic deformation at a rotation of 100 mrad for K-HB30S-HA24S-20-130.

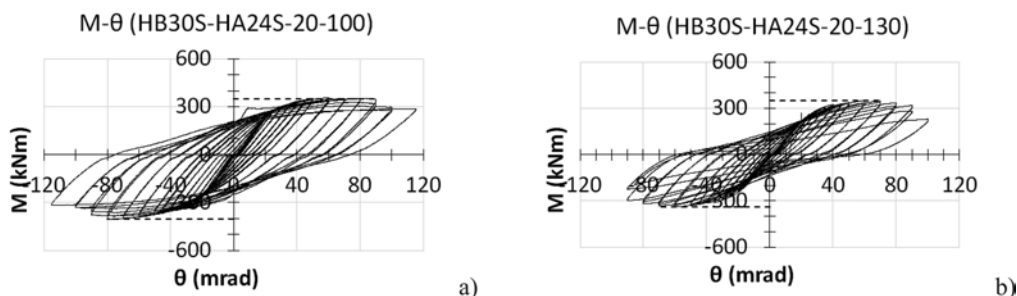


Figure 5. M - θ curve ($M_{\text{connection}}$) for all-steel joint (a) K-HB30S-HA24S-20-100 vs. (b) K-HB30S-HA24S-20-130. Lower values of e_4 enhance the dissipative behaviour of the joint. See Figure 4 for failure mode.

The use of higher steel profile sections may activate earlier the connections. The important observation on the 2 experiments presented is that through the variation of the two most important geometrical parameters, t_{ep} and e_4 , different failure modes were activated, see Figure 4. The all-steel joints will be further optimised through FEM analyses regarding size of steel profiles.

4.2.2 Composite joints

For all composite joints a crack formed at the beam flange in the area of welds connecting the steel profile to the endplate and quickly developed till failure. Starting from a rotation of 40

mm small cracks of around 0,1 mm appeared, see Figure 6a. At the following load step, here 45 mrad, the crack further develops and forms a clear crack of more than 2 cm, see Figure 6b. At that point a clear reduction of the moment capacity of the concerned connection can be observed, while the complete failure of the specimen comes the latest in the next load step, with the rotation capacity of the composite joints tested lying between 45 mrad and 60 mrad. Additionally, concrete crushing in the area of the connection, see Figure 7a, was observed for some specimens, while the crack pattern of the slab is given in Figure 7b.

Should the damaged specimens be further tested at higher load levels, the crack formed in the beam flanges further develops and extends also to the beam web until the crack grows throughout the entire height of the steel beam. At that point the load carrying capacity of the concrete slab is preserved with no serious damages.

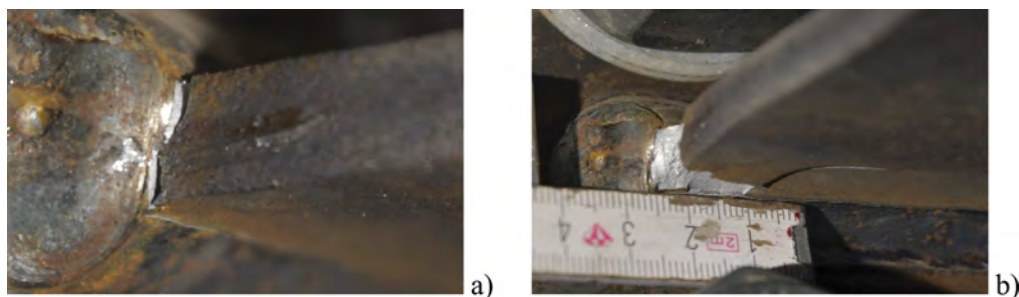


Figure 6. (a) Crack initiation at a rotation of 40 mrad – weld at lower beam flange to endplate (b) crack propagation at a rotation of 45 mrad.

It should be noted that total joint rotations of more than 45 mrad are not necessary, with (CEN EN 1998-1, 2004) foreseeing for partial-strength joints a minimum plastic rotation capacity

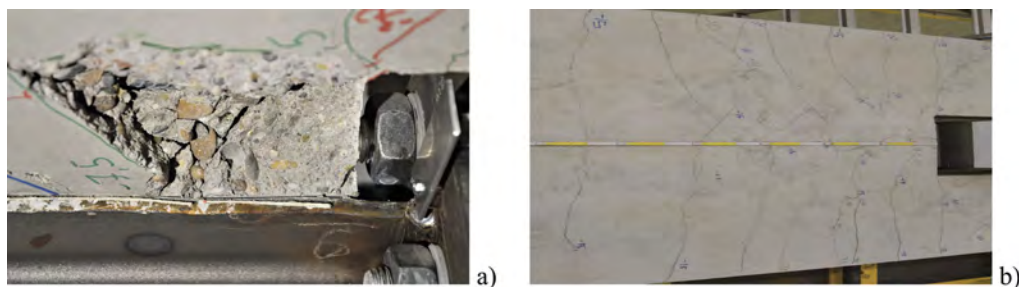


Figure 7. (a) Concrete crushing in the area of connection at a rotation of 45 mrad (b) crack pattern of the concrete slab at a rotation of 45 mrad.



Figure 8. HA30C-I30C-20-100-170-p2: no significant deformation of the endplate at a rotation of 45 mrad, yet good dissipative behaviour thanks to the contribution of endplate, beam and concrete slab.

of 15 mrad and 25 mrad for areas of low and medium seismicity, respectively. Thus, the joints conform to the minimum rotation capacity requirements of (CEN EN 1998-1, 2004).

In Figure 9a the M- θ curve of the composite joint till failure, 45 mrad, while in Figure 9b the part of the M- θ curve of the equivalent all-steel joint up to 45 mrad (test stopped at 110 mrad) is shown, so that direct comparison is easier. It can be observed that the area of hysteretic loops for the composite joint till 45 mrad is larger than the one of all-steel joint. In such way the composite joints demonstrate an enhanced dissipative behaviour compared to the all-steel ones.

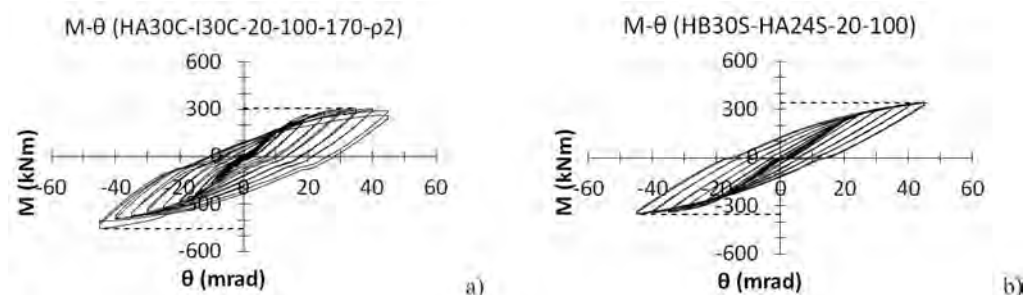


Figure 9. M- θ curve (a) composite vs. (b) all-steel joint (M- θ curve plotted up to only 45 mrad for easier comparison with the composite joint).

5 CONCLUSIONS

Based on the experimental results following conclusions can be drawn:

- Partial-strength all-steel and steel-concrete composite joints can be designed as dissipative ones. Necessary modifications compared to the non-seismic design are the strengthening of the columns and of the welds. Also, the parameters influencing the joint mechanical characteristics should be selected in view of optimal seismic behaviour and not of simply largest ductility. In fact, low values of t_{ep} and very high values of e_4 would eliminate the dissipative behaviour. The activation of the beam additionally to the endplate is of advantage.
- The seismic behaviour of composite joints significantly differs from the one of all-steel joints, also if care is taken to mechanically disconnect the slab from the steel beam in a length equal to $1,5 \cdot h_{beam}$, see (ANSI/AISC 358-16, 2016). Despite the fact that the deformations in the endplates are small due to the high stiffness of the concrete slab, the seismic behaviour of composite joints is overall better than all-steel ones. The optimisation of the concrete slab strength with reference to the one of steel beam and steel connection can further enhance the seismic behaviour, here e.g. a higher steel profile size.
- Composite joints with a symmetrical steel connection part, 4 bolt rows, present a better dissipative behaviour than asymmetrical ones, 3 bolt rows. The potential of asymmetrical connections depends also on the extent up to which the joints will enter the area of positive moments for the seismic load combination in a real structure. Therefore, also pushover static analyses for some representative structural typologies will be performed.
- It has been observed on the experiments that connections with thinner endplates failed due to bolt failure at an earlier load stage compared to connections with thicker endplates. The connections were identical except of the endplate thickness, the bolts being M30 in all cases. More specifically, the specimen HB30S-HA24S-15-100 failed due to bolt failure at 70 mrad, while the specimens HB30S-HA24S-20-100 & HB30S-HA24S-20-130 failed the earliest at 100 mrad. For T-stub connections having a failure mode 2 the deformation of the bolt induced by the endplate can lead to premature failure of the bolts. Therefore, in (Skarmoutsos, in prep.) a deformation approach for the design of (i) ductile and (ii) ductile-dissipative beam-to-column connections with a failure mode 2 will be followed.

- A joint of low stiffness may develop plastic deformations only at very large rotation angles, which would have probably already caused global stability problems. Partial-strength joints present a dissipative behaviour for a limited value range of their geometrical parameters. The number of tests needed on partial-strength joints before these can be implemented in structures can be significantly reduced through the use of refined FEM models. A methodology for the design of partial-strength joints as dissipative ones will be developed (Skarmoutsos, in prep.), using validated FEM models and the experimental results. To achieve a dissipative behaviour the appropriate combination of joint (i) stiffness, (ii) strength and (iii) energy dissipation capacity is needed.

ACKNOWLEDGEMENTS

The experimental campaign presented herein is part of the research project (Hoffmeister, et al., in prep.) and financed through the Research Association for Steel Application (FOSTA), the German Federation of Industrial Research Associations (AiF) and the German Federal Ministry of Economic Affairs and Climate Action. The joint project is carried out at the Institute of Structural Design of the University of Stuttgart and at the Centre for Wind and Earthquake Engineering of RWTH-Aachen University. The presented tests were performed at the Materials Testing Institute of University of Stuttgart.

REFERENCES

- ANSI/AISC 358-16, 2016. *Prequalified Connections for Special and Intermediate Steel Moment Frames for Seismic Applications*. Chicago, Illinois: American Institute for Steel Construction.
- CEN EN 1993-1-8, 2005. *Eurocode 3: Design of steel structures-Part 1-8: Design of joints*. Brussels: European Committee for Standardization.
- CEN EN 1994-1-1, 2009. *Eurocode 4: Design of composite steel and concrete structures*. Brussels: European Committee for Standardization.
- CEN EN 1998-1, 2004. *Eurocode 8: Design of structures for earthquake resistance*. Brussels: European Committee for Standardization.
- Demonceau, J. F., Golea, T., Jaspert, J. P., Elghazouli, A., Khalil, Z., Santiago, A., Santos, A. F., Simoes da Silva, L., Kuhlmann, U., Skarmoutsos, G., Baldassino, N., Zandonini, R., Bernardi, M., Zordan, M., Dinu, F., Marginean, I., Jakab, D., Dubina, D., Wertz, F., Weynand, K., Obiala, R., Candeias, M., Charlier, M. and Anwaar, O., 2021. *Design recommendations against progressive collapse in steel and steel-concrete buildings*, Brussels, Belgium: ECCS - European Convention for Constructional Steelwork.
- Hoffmeister, B., Balaskas, G., Don, R., Vulcu, C., Kuhlmann, U. and Skarmoutsos, G., in prep. (*IGF no. 21383 N11/FOSTA-P-1481*) *Entwicklung von standartisierten Stützen-Riegel-Anschlüssen für Stahl- und Verbundkonstruktionen in deutschen Erdbebengebieten*, s.l.: s.n.
- Kuhlmann, U., Hoffmann, N., Jaspert, J. P., Demonceau, J. F., Zandonini, R., Baldassino, N., Hoffmeister, B., Colomer, C., Korndörfer, C., Hanus, F., Charlier, M., Hjiat, M. and Guezouli, S., 2017. *Robust impact design of steel and composite building structures (ROBUSTIMPACT)*, Grant Agreement RFSR-CT-2012-00029, Brussels: European Commission.
- Kuhlmann, U., Rölle, L., Jaspert, J. P., Demonceau, J. F., Vassart, O., Weynand, K., Ziller, C., Busse, E., Lendering, M., Zandonini, R. and Baldassino, N., 2009. *Robust structures by joint ductility, Final report of the project RFSR-CT-2004-00046*, Brussels: European Commission.
- Landolfo, R., D' Aniello, M., Costanzo, S., Tartaglia, R., Stratan, A., Dubina, D., Vulcu, C., Maris, C., Zub, C., Da Silva, L., Rebelo, C., Augusto, H., Shahbazian, A., Gentili, F., Jaspert, J.P., Demonceau, J.F., Van Hoang, L., Elghazouli, A., Tsitos, A., Vassart, O., Nunez, E. M., Dehan, V. and Hamreza, C., 2017. *European pre-QUALified steel JOINTS (EQUALJOINTS): Final Report of the project RFSR-CT-2013-00021*, Brussels: European Commission.
- Rölle, L., 2013. *Das Trag- und Verformungsverhalten geschraubter Stahl- und Verbundknoten bei vollplastischer Bemessung und in außergewöhnlichen Bemessungssituationen*. Stuttgart: Dissertation - Institute of Structural Design, University of Stuttgart.
- Skarmoutsos, G., in prep. *Dissipative all-steel and steel-concrete composite joints*. Dissertation: Institute of Structural Design, University of Stuttgart.

Seismic and energetic renovation of existing masonry buildings by innovative FRLM composite materials

D. Pugliese, V. Alecci, S. Galassi, A.M. Marra & M. De Stefano
University of Florence, Florence, Italy

ABSTRACT: The energy and seismic requalification of the existing building heritage is a crucial topic, usually investigated by separate approaches and procedures. In this context, the designed technologies must reflect on solutions that can be applied in redevelopment interventions from the perspective of Life Cycle Thinking. Moreover, the choice of a specific solution in the construction sector must face the rise of mechanical and energy performance levels according to the market requests, as well as the demands of a regulatory landscape increasingly focused on the principles of sustainability and LCA-based environmental impact of the entire building process.

In this framework, this research aims to design, test and implement innovative strengthening systems made of bio-composite mortar mixtures in which a high-strength fiber is embedded, covering an integrated assessment of new composite materials to reduce the seismic vulnerability of historic masonry buildings while complying with energy saving, sustainable development, and reduction of greenhouse gases emissions.

After an initial literature review outlining the progress in innovative techniques for the integrated structural and energy retrofit of existing masonry buildings, the study focuses on the applications of fibre-reinforced lime matrices (FRLM) as thermal plasters, analyzing their mechanical properties and thermo-hygrometric behaviour.

Next, a selection of thermal plasters to be used as a matrix of the innovative composite material was carried out; then, the mechanical properties were investigated through compressive and bending tests. The mortar with better mechanical properties was used to assemble composite specimens to be tested under a direct tensile test. Dynamic thermohygrometric simulations by WUFI® Pro and EnergyPlus and numerical FEM simulations using the Abaqus software were performed to check structural and thermal contributions when applied on typically arranged masonry panels of existing buildings.

The objective is to demonstrate how it is possible to provide solutions that can encourage ecological and environmental sensitivities of processes and products and define approaches for future projects to achieve sustainable targets positively.

1 INTRODUCTION

Most European masonry buildings are made in the absence of anti-seismic standards and thermal insulation requirements and do not pay attention to either structural safety or energy performance. The conservation and valorization of this heritage require a multidisciplinary approach, capable of reducing structural vulnerability by upgrading the energy performance while respecting environmental sustainability principles, from a Life Cycle Thinking perspective.

In the current literature, several methods exist to improve the thermal performance of masonry buildings (Litti et al., 2015) and for the seismic vulnerability assessment (Karantoni et al., 2012) but operate in a disjoint way.

In addition, only a few research projects are available on an integrated approach to evaluate new methods of structural and energetic requalification of existing masonry buildings (Giresini, Casapulla, et al., 2021; Giresini, Stochino, et al., 2021): a comparison between thermal performance and seismic capacity of different interventions on masonry structures, in terms of economic (e/m^2) and ecological ($kgCO_2/m^2$) costs is proposed in (Mistretta et al., 2019).

The reinforcement of masonry structures is one of the most important applications for FRLM (Fiber Reinforced Lime Matrix) composite materials. The reinforcement, defined by a fibrous base, guarantees an improvement of the mechanical characteristics, while the matrix allows the application of the reinforcement to the structural system, sometimes improving the thermo-hygrometric performance also. The challenge in introducing technological solutions as innovative composite materials compatible with the organism to preserve (Battisti et al., 2018), able to increase mechanical resistance, improving the inertia and thermal transmittance, without burdening the structures, is the aim to create sustainable strategies to improve the existing masonry heritage building subjected to energy losses and earthquake loading.

This paper aims to develop one or more innovative FRLM composite materials made by a balanced bi-axial mesh of basalt fiber and thermal plasters based on natural hydraulic lime mortar. Thermal plasters are mortars for masonry that show excellent insulating characteristics (UNI EN 998-1, 2016) and can be produced using lightweight aggregates of natural origin or recycled or recyclable materials, as a starting point to reduce the environmental impact of the construction sector. The concept of environmental impact is to be understood by observing the “From Cradle to Cradle” approach, following the Life Cycle Assessment (LCA) method, to study the influence that the production process has on factors related to climate change (Napolano et al., 2015).

Starting from these premises, first, a comparative analysis of eleven thermal plasters was made to identify the one with the best performance from a mechanical, thermo-hygrometric, and environmental perspective.

The thermohygrometric properties of the thermal plasters were evaluated through dynamic simulations with the WUFI® Pro software, while the mechanical properties were investigated through three-point bending and compression tests. The thermal plaster with the best properties was assembled with basalt fibers and tested at the laboratory under direct tension tests.

Finally, Finite element analyses with Abaqus software were performed to estimate the composite’s mechanical contributions and failure mechanism.

2 ANALYSIS OF THE INORGANIC MATRICES FOR THE FRLM COMPOSITES

After a detailed study of the state of the art through an original analysis of the products present in the literature and the international market, the first part of the research work involved the identification of lime-based thermal plasters with mechanical and energetic characteristics for the rehabilitation of existing masonry buildings.

The requirements imposed on the properties of the thermal plasters were identified concerning the following parameters: 1) compressive strength σ [N/mm^2]; 2) thermal conductivity λ [W/mK]; 3) density [kg/m^3]; 4) natural aggregates; 5) recycled or recyclable aggregates.















Table 1. lists the composition of 11 selected thermal plasters declared by manufacturers on data sheets. The symbols next to the codes (Int.01- Int.11) indicate the type of compound, in particular:

- ✓ indicates that the thermal plaster is characterized by a $\sigma \simeq 1,50 N/mm^2$ and $\lambda \simeq 0,10 W/mK$;
- 🌿 indicates that the thermal plaster is made of natural materials;
- ♻️ indicates that the thermal plaster is made of recycled or recyclable materials.

3 HYGROTHERMAL PERFORMANCES OF THE SELECTED MATRICES

With the purpose to investigate the one-dimensional transient hygrothermal behaviour of multilayer building components, thermodynamic simulations were performed using the

Table 1. Composition of Int.01- Int. 11 matrices.

Thermal Plaster	Compressive strength σ [N/mm ²]	Thermal Conductivity λ [W/mK]	Density [kg/m ³]	Binder
Int.01 ✓ 	> 3.0	0.077	380	Natural Hydraulic Lime (NHL) 3.5
Int.02 ✓  	0.4 to 2.5	0.075	380	Natural Hydraulic Lime (NHL) 3.5
Int.03 ✓ 	3.5 to 7.5	0.046	395	Natural Hydraulic Lime (NHL) 5
Int.04 ✓ 	≥ 2.0	0.086	385	Natural Lime
Int.05 ✓  	2.0	0.064	365	Natural Hydraulic Lime (NHL) 3.5
Int.06 ✓ 	2.0	0.048	380	Natural Hydraulic Lime (NHL) 3.5
Int.07 ✓  	1.5	0.104	400	Slaked Lime
Int.08 ✓ 	0.4 to 2.5	0.0757	390	Natural Hydraulic Lime (NHL) 3.5
Int.09 ✓ 	0.4 to 2.5	0.067	≤ 400	Natural Hydraulic Lime (NHL)
Int.10 ✓ 	0.4 to 2.5	0.137	1300	Natural Hydraulic Lime (NHL)
Int.11 ✓ 	0.4 to 2.5	0.057	400	Natural Hydraulic Lime (NHL) 5

WUFI ® Pro 6.5.2 software (Wärme- Und Feuchttransport Instationär Heat and Moisture Transiency) according to UNI EN standard (UNIEN15026, 2008).

The climatic reference conditions of Florence were considered with a simulation time of ten years.

Three specific technical solutions for masonry buildings were considered for the simulation, selected from the list provided by UNI/ TR standard (UNI/TR11552, 2014) in particular:

- Mas.1: one-and-a-half brick masonry, with a thickness of 380 mm;
- Mas.2: stone masonry, with a thickness of 500 mm;
- Mas.3: sack masonry with weakly bonded filling, with a thickness of 480 mm.

In the field of seismic and energy requalification of the historical heritage, the 11 selected thermal plasters were applied on both sides of the wall considering 60 mm thick on the exterior and 40 mm thick on the interior. to investigate the hydrothermal behaviour of the different scenarios varying the thermal plasters adopted to replace the traditional plaster.

For all the investigated solutions, the simulations show that the water content inside the wall [kg/m³] increases over the ten years: initially, the structure is not yet in dynamic equilibrium with the environment; once this equilibrium has been reached, the variations of the water content inside the wall depends on seasonal variations.

As regards the water content inside the internal plaster layer [kg/m³], the products with the lowest annual average value are Int.01 and Int.06. Furthermore, the results obtained from the simulations carried out with Int.06 showed no water accumulation within any of the three analyzed construction types.

Figure 1. reports each configuration's thermal transmittance values [W/m²K] of the three building envelope solutions Mas.1, Mas.2, and Mas.3 for the climate of Florence.

4 EXPERIMENTAL INVESTIGATION OF THE MECHANICAL PROPERTIES

The experimental campaign was carried out at the Laboratory of Materials and Structures of the University of Florence, which involved:

- bending tests for three points and uniaxial compression tests of the 11 selected thermal plasters;
- direct tensile test on basalt textile;
- direct tensile test on the FRLM composite constituted by the structural reinforcing textile embedded in the better thermal plaster from the structural and thermodynamic point of view.

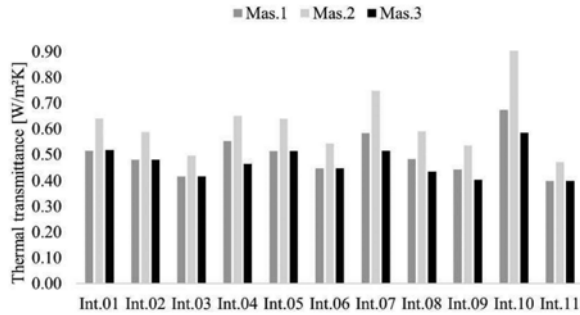


Figure 1. Comparison between the thermal transmittance values of the different configurations.

4.1 Mechanical properties of the thermal plasters

Three mortar specimens 40·40·160 mm³ in size for each type of thermal plaster (Int.01-Int.11) were obtained using special standardized metal moulds and tested, after curing for 28 days in a controlled temperature room, under three-point bending tests, according to UNI standards (UNIEN1015, 2019). Then, axial compression tests on the two stumps obtained after the failure of each specimen due to the bending test were performed.

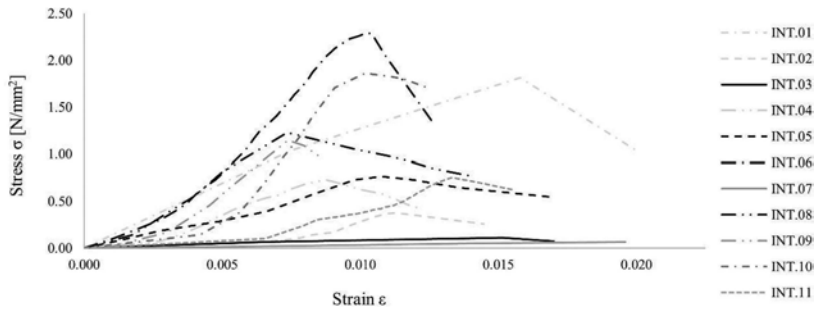


Figure 2a. a) Compressive stress-strain curves of Int.01-Int.11.

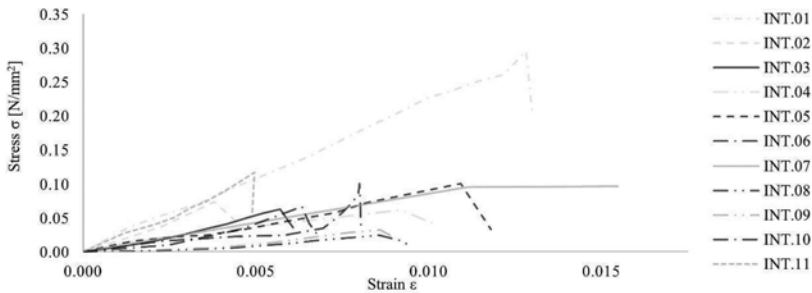


Figure 2b. b) Flexural stress-strain curves of Int.01-Int.11.

The tests were carried out under displacement control, using an universal hydraulic machine with a 600 kN hydraulic actuator. Results of the three-point bending test and compression test were summarized in Table 2 in terms of compressive strength (f_c), compressive elastic modulus (E_c), and flexural strength (f_b). Elastic modulus was calculated and evaluated between 30% and 60% of the maximum load (Alecci et al., 2019; Simões et al., 2015; Valluzzi et al., 2005) in the first linear branch of the stress-strain curves.

Compressive and flexural stress-strain curves of the texted thermal plaster specimens are plotted in Figures 2a) and 2b).

The results obtained from the experimental campaign concerning the four resistance categories of plaster mortar reported in the technical standards for the design, execution, and testing of masonry buildings (UNIEN998-1, 2016) identified the thermal plasters tested as belonging to category CS I ($0.4 \div 2.5 \text{ N/mm}^2$), with an average compressive strength of 1.13 N/mm^2 . For the flexural and compressive strengths, respectively, the values are in the ranges of 0.02 N/mm^2 and 0.30 N/mm^2 for flexural and 0.11 N/mm^2 and 2.49 N/mm^2 for compressive strength. Accordingly, the flexural and uniaxial compression tests show that the thermal mortar with the best compressive strength is INT.06, with a value of compressive strength equivalent to 2.46 N/mm^2 . It can be noted that thermal plasters INT.06, INT.01, and INT.10 showed the highest value of compressive strength, flexural strength, and Young's modulus, respectively.

Table 2. Mechanical properties of Int.01- Int.11 matrices (laboratory results).

Thermal Plaster	Compressive strength f_c [N/mm^2]	Compressive Young's modulus [N/mm^2]	Flexural strength [N/mm^2]
Int.01	2.41	138.7	0.30
Int.02	0.38	75.9	0.07
Int.03	0.46	10.7	0.06
Int.04	0.73	132.0	0.06
Int.05	0.89	63.7	0.10
Int.06	2.49	292.5	0.27
Int.07	0.11	3.2	0.10
Int.08	1.23	222.2	0.02
Int.09	1.15	211.3	0.03
Int.10	1.86	385.1	0.07
Int.11	0.76	77.30	0.12

4.2 Mechanical properties of the basalt textile

The textile used for the reinforcement of the new FRLM composite is a balanced bi-axial mesh made of special basalt fiber and stainless-steel micro threads.

Direct uniaxial tensile tests investigated the mechanical properties of the basalt textile, performed under controlled displacement by an universal testing machine equipped with a 600 kN load cell (Barducci et al., 2020). The load was applied with a rate of 0.25 mm/min . The tests were carried out according to the ASTM Standard (ASTMD3039/D3039M17, 2017).

Specifically, four basalt textile specimens consisting of one (1BT), two (2BT), three (3BT), and four (4BT) longitudinal multifilaments were prepared and tested.

The tensile strength f_{tf} was obtained as shown in Equation 1:

$$f_{tf} = F_{\max} / A_f \quad (1)$$

where F_{\max} is the maximum load value, $A_f = n \cdot b_f \cdot t_f$ represents the equivalent cross-sectional area of the fiber, n is the number of longitudinal fiber bundles of the specimen, b_f is the pitch between the bundles of fibers, and t_f is the equivalent thickness.

Young tensile modulus E_{tf} was evaluated in the first linear branch of the stress-strain curve.

Table 3. Mechanical properties of basalt textile.

Specimen	Tensile strength f_{tf} [N/mm^2]	Tensile Young's modulus E_{tf} [N/mm^2]	Ultimate strain ϵ_{tf}
BT	865	60487	0.017

4.3 Mechanical properties of the composite material

Basalt textile was embedded in the matrix Int.06, and six coupons labelled INT06_1-6, 500·65·10 mm³ in size, after curing for 28 days at room temperature, were tested under direct tension. Two steel plates bolted with a pressure controlled by a torque wrench were used (Figure 3). The tests were performed in displacement control, with a 0.2 mm/min rate, using an universal machine with a 600 kN load cell.

The local displacements were captured using a proper extensometer 50 mm axial gauge length positioned in the middle of each specimen (Figure 4.).

Figure 5 shows the direct tensile stress and strain response curves obtain in a direct tensile test. As visible, the tested coupons showed similar mechanical behaviour for INT06_1 and INT06_4, and for INT06_3 and INT06_5 where after reaching maximum stress, the curves show a constant descending trend. When the peak load was reached, the failure of a multifilament of the basalt textile occurred.

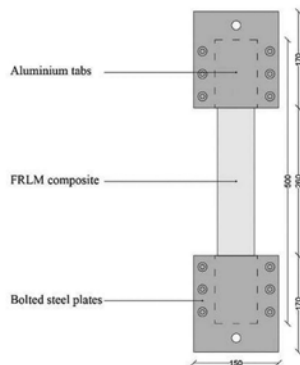


Figure 3. FRLM direct tensile test set-up (dimension in mm).

Figure 4. Tensile test on INT06_1.

The increase of the existing cracks characterized the post-peak softening branch, and the formation of new cracks and specimens highlighted large displacements without a high increase in applied load.

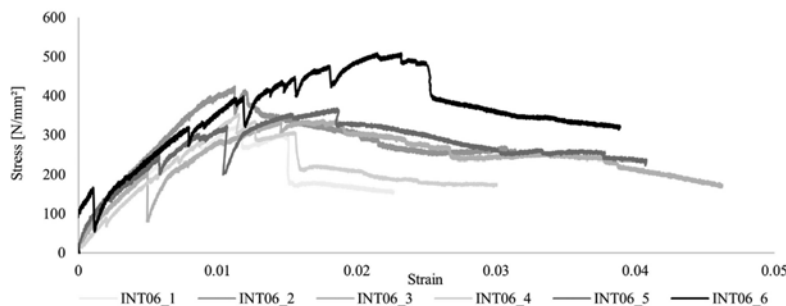


Figure 5. Stress-strain curves of the six samples INT06_1 to INT06_6.

In terms of maximum load F_{max} , tensile strength f_r , Young's modulus E , and maximum deformation ϵ_r , the results are reported in Table 4.

5 FINITE ELEMENT MODELLING

Numerical analyses were carried out using Abaqus CAE software to simulate the behaviour of a non-reinforced (NRM) and a reinforced (RM) masonry wall subjected to a diagonal

Table 4. Mechanical properties of the composite material.

Coupon	F_{\max} [N]	f_r [N/mm ²]	E [N/mm ²]	ϵ_t
INT06_1	681	327	36310	0.01
INT06_2	881	424	66577	0.01
INT06_3	704	338	34718	0.02
INT06_4	735	353	44960	0.01
INT06_5	764	367	48250	0.02
INT06_6	1059	509	52920	0.02
Average value	804	386	47289	0.015

compression test, conducted according to ASTM standards (ASTME519-07, 2010). Three parts characterize the NRM model, i.e., a brick masonry panel 1200·1200·120 mm³ in size and two steel plates fixed at the two corners of the diagonal coinciding with the load direction (Figure 6a). The steel plate on the top distributes the load on a larger surface, avoiding the concentration of compression stresses; horizontal and vertical translational constraints are located at the base of the bottom plate. Regarding the RM, model, the FRLM composite was applied at each side (with a thickness of 15 mm) of the masonry panel by considering an isotropic linear elastic behaviour (Figure 6b).



Figure 6. a) Mesh configuration of the NRM model b) Mesh configuration of the RM model.

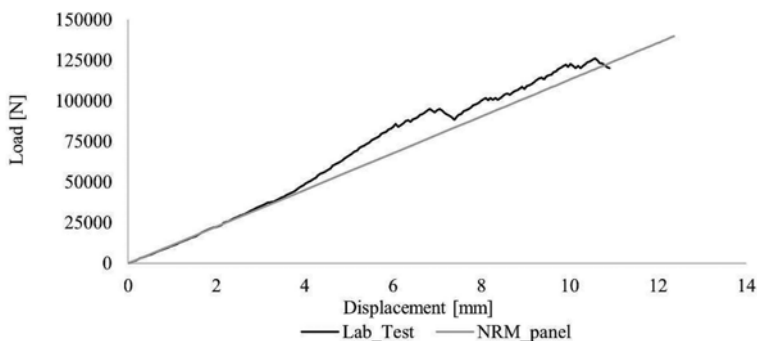


Figure 7. Comparison of the experimental and numerical results.

The steel plates were modelled with a linear elastic isotropic material, characterized by Young's modulus equal to 210000 N/mm² and a Poisson ratio of 0.30.

A first analysis was carried out for the NRM model, characterized by a linear elastic behaviour with Young's modulus and Poisson ratio defined to match the results of the experimental shear tests conducted previously by the Authors (Alecci, Fagone, Rotunno, & De Stefano, 2013).

Figure 7 compares the numerical and the experimental results in load-displacement evaluated at the top of the tested brick masonry panel.

Once the linear elastic analysis had been carried out, the masonry panel was studied with a nonlinear behaviour (NL_NRM), using the “concrete damage plasticity” (CDP) model implemented in Abaqus CAE, adequately calibrated according to experimental tests conducted by the authors (Alecci, De Stefano, Luciano, Marra, & Stipo, 2020). Regarding the analyses on the nonlinear FEM, they are not reported since they are still in progress.

6 CONCLUSIONS

Through a theoretical-experimental analysis, based on data in the literature and materials on the market, it was found that the identification of thermal plasters compatible with the masonry substrate to be reinforced, and characterized by good mechanical as well as thermal properties, is a crucial step for the design of innovative composite materials to be used for the energy and structural upgrading of the historic building, in compliance with the instances of compatibility, sustainability, and reversibility (Romano et al., 2021).

The results reported in this paper show that Int.01, Int.06, and Int.10 mortars have good mechanical behaviour in terms of compressive strength, flexural strength, and Young's modulus values.

Regarding the energetic performance, it was observed that the walls with the lowest thermal transmittance were those retrofitted with Int.06, applied on both sides to both sides of the wall.

Finally, the INT.06 product represents the ideal matrix from both points of view and can be considered a good solution to regenerate the thermohygrometric performances of the historical envelopes, without changing their mechanical and aesthetic features.

The next step of the research will involve the seismic retrofit of masonry panels strengthened with such a composite by a nonlinear FEM analysis while enlarging the list of thermal plaster mixtures evaluated as potential matrices of the FRLM composites.

REFERENCES

- Alecci, V. et al., 2020. Numerical Investigation on the Use of Flat-Jack Test for Detecting Masonry Deformability. *Journal of Testing and Evaluation*.
- Alecci, V., Fagone, M., Rotunno, T. & De Stefano, M., 2013. Shear strength of brick masonry walls assembled with different types of mortar. *Construction and Building Materials*, Volume 40, pp. 1038–1045.
- Alecci, V. et al., 2019. Estimating elastic modulus of tuff and brick masonry: A comparison between on-site and laboratory tests. *Construction and Building Materials*, Volume 204, pp. 828–838.
- ASTMD3039/D3039M17, 2017. Standard Test Method for Tensile Properties of Polymer Matrix Composite Materials, (West Conshohocken, PA: ASTM International).
- ASTME519-07, 2010. Standard Test Method for Diagonal Tension (Shear) in Masonry. Assemblages.
- Barducci, S. et al., 2020. Experimental and Analytical Investigations on Bond Behavior of Basalt-FRCM Systems. *Journal of Composites for Construction*, Volume 24.
- Giresini, L., Paone, S. & Sassu, M., 2020. Integrated Cost-Analysis Approach for Seismic and Thermal Improvement of Masonry Building Façades. *Buildings*.
- Romano, R. et al., 2021. Innovative and eco-compatible materials for the regeneration of the historical buildings located in the med area. *CEES 2021*, pp. 1–8.
- Simões, A., Bento, R., Gago, A. & Lopes, M., 2016. Mechanical Characterization of Masonry Walls With Flat-Jack Tests. *Experimental Techniques*, 40(3), pp. 1163–1178.
- Triantafyllou, T. C., Karlos, K., Kefalou, K. & Argyropoulou, E., 2017. An innovative structural and energy retrofitting system for URM walls using textile reinforced mortars combined with thermal insulation: Mechanical and fire behavior. *Construction and Building Materials*.
- UNI/TR11552, 2014. *Opaque envelope components of buildings - Thermo-physical parameters*.
- UNIEN1015, 2019. *Test methods for masonry mortars. Part 11: Determination of flexural and compressive strength of hardened mortar*.
- UNIEN15026, 2008. *Hygrothermal performance of building components and building elements - Assessment of moisture transfer by numerical simulation*.
- UNIEN998-1, 2016. *Specification for mortar for masonry - Part 1: Rendering and plastering mortar*.
- Valluzzi, M. R., Binda, L. & Modena, C., 2005. Mechanical behaviour of historic masonry structures strengthened by bed joints structural repointing. *Construction and Building Materials*, 19(1), pp. 63–73.

Development of a method for resource-efficient structural maintenance of reinforced concrete buildings based on digital BIM models

J.-I. Jäkel, L. Kloesgen, T. Koenig & K. Klemm-Albert

Institute for Construction Management, Digital Engineering and Robotics in Construction (ICoM), RWTH Aachen University, Aachen, Germany

H. Morgenstern & M. Raupach

Institute for Building Materials Research (ibac), RWTH Aachen University, Aachen, Germany

ABSTRACT: In the Federal Republic of Germany, around 70% of all construction work in the area of building construction is carried out on existing buildings. This large amount emphasises the need to consider the lifecycle-oriented maintenance management of buildings. Using digital methods and technologies, the existing, mostly manual processes can be optimized and automated. In addition, there is a need to integrate sustainability aspects into the decision-making process for maintenance tasks. In this technical article, a holistic method for resource-efficient building maintenance is developed by using the Building-Information-Modeling (BIM) method in combination with the integration of sustainability aspects. Thereby, methods of laser scanning are combined with the BIM method, digital maintenance and AR technology, resulting in a partially automated and interoperable workflow. In the first step, the status quo of digital maintenance at reinforced concrete structures is analyzed in a literature review. The following step is to define the process-related and data-technical fundamentals. Based on this, data acquisition is carried out using laser scanning methods and modern diagnostic procedures as well as partially automated data processing to create a refined BIM model. A digital model with integrated diagnostic data is developed from the recorded data and a comparison of different maintenance scenarios is carried out using intelligent algorithms in the context of costs, time and CO₂ emissions. For further transparent use of the digital as-built model in operational maintenance management, the model is embedded in an augmented reality environment and a common data environment. The process steps are validated using a real demonstrator at the end. The result of the article shows a partially automated process chain and decision support for resource-efficient maintenance management of reinforced concrete structures.

1 INTRODUCTION

To fight climate change, Germany decided along with the European council to pass laws aiming to reduce greenhouse gas emissions and energy expenditure, while increasing energy efficiency (*Bundes-Klimaschutzgesetz (KSG)*, Bundesministerium für Justiz, 2021). To become a climate neutral society, a reduction of 53 million tons CO₂-equivalent is required within the building sector, as it is one of Germany's main emission sources (Deutsche Energie-Agentur, 2021b). In practice, this means an emission-reduction of 65% in the year 2030 as compared to 1990 (*Bundes-Klimaschutzgesetz (KSG)*, Bundesministerium für Justiz, 2021; United Nations, 1997). Consequently, new building projects prioritize energy efficiency and the integration of renewable energies and sustainable material which necessitate digitalization and automatization of all construction processes (Hofstadler and Motzko, 2021). Thereby, energy efficiency and sustainability can be maximized, while minimizing costs and worktime (Hofstadler and Motzko, 2021; Schäfer et al., 2022). While optimizing new buildings is an active area of research, digitalization of construction processes in existing buildings has been largely avoided; probably as preexisting data of these buildings is lacking (Mellado et al., 2020). However, advancements in this area are crucial for two main reasons. Firstly, 99% of German buildings were built before 2010, contributing to 35% of

Germany's energy use (Bundesministerium für Wirtschaft und Energie, 2014; Deutsche Energie-Agentur, 2021a). Hence, around 70% of all construction work in the area of building construction is carried out on already existing buildings (Bundesinstitut für Bau-, Stadt- und Raumforschung, 2021). In addition, many processes from construction sites are still carried out manually by engineers and construction workers and there is a low degree of automation and digitization (McKinsey Global Institute, 2017). Secondly, refurbishments are costly and often carry higher risks than a new building project (Mellado et al., 2020). Digitalization can be used to incentivize refurbishments, as it enables automatization of more construction processes, thus reducing costs and risks (Mellado et al., 2020). Both facts evidently reinforce the need to consider a lifecycle-oriented maintenance management of buildings, while optimizing and automating manual processes using digital methods and technology. To address this problem and encourage further research, this article presents a holistic method for resource-efficient building maintenance that uses the digital method Building Information Modeling (BIM) while integrating sustainability aspects.

2 METHODOLOGY

The scientific article is structured in three sections - (i) literature review, (ii) concept elaboration, and (iii) proof-of-concept validation. In the first section, the status quo is reviewed and related research work is presented. The literature is searched using scientific databases (Scopus, Web of Science, Google Scholar). In the second part, the concept of the method for resource-efficient maintenance is elaborated. In this context, the procedure of the method is presented in a process model, the individual process steps are explained in more detail and the technologies used are specifically described. The data acquisition uses laser scanning technologies for the building geometry and methods of and low and non-destructive testing for the diagnostic data. The further processing of the data into an object-oriented and semantically enriched digital BIM model focuses on the openBIM approach using open data exchange formats. In the further progress of the method, the BIM model serves as the central database for the following sustainability analysis and the linking with immersive technologies. The validation of the method concept is subsequently conducted in the third part using a proof-of-concept on a real demonstrator. This demonstrates the basic feasibility of the concept. At the end of the article, the elaborated results are discussed, limitations are pointed out and an outlook on future research activities is given.

3 RELATED WORKS

In line with governmental goals to tackle climate change, approaches have been developed to address the reduction of greenhouse gas emissions and resource demand. Recently, Life-Cycle-Assessment (LCA), an inter-period approach, has received increasing attention. It uses a digitalized methodology to record and use all building data throughout planning, construction and use. One of the most common methods is BIM, a software that includes, among others, all workflows, cost- and time data, in one open-source, 3D-Model for all stakeholders (Görsch et al., 2021). (Naneva et al., 2020) shows that on the one hand, BIM has potential to reduce the effort of LCA. On the other hand, a glimpse into today's economy demonstrates that companies are not using BIM appropriately or the integration is implemented too late in the decision-making process (Morgens-tern and Raupach, 2022b; Naneva et al., 2020). Therefore, the authors are developing an integrated BIM-LCA approach using an already existing cost estimation technique that aims to implement LCA continuously through the life cycle of the building. They demonstrate that combining LCA with BIM simplifies the use and implementation of this methodology, an incentive for interested companies. Moreover, it supports the decision-making process in all life-cycle phases (Naneva et al., 2020). Furthermore, (Wastiels and Decuypere, 2019) present different strategies in relation to the BIM-LCA integration. In their first approach, a BIM-based bill of quantities, which includes all building material data, is imported to the LCA software, in which the bill of quantity is linked to predefined profiles and then analyzed in the software itself. In contrast, the authors introduce another possibility where the LCA profiles are inserted into a BIM environment as a first step. This yields the advantage that BIM objectives can be linked with LCA data, and the planning

process can be supported by a real-time data transfer. There are other sustainable methods that link material passports to the BIM model as a basic requirement for a circular economy with differences mainly in the data transfer. These material passports are material information regarding for example the greenhouse-gas emissions and circular potential and are provided by in huge data bases (Bartels et al., 2022). One approach is to export all material data from the BIM-model into a software tool that supports the user with information regarding the recyclability, costs or possible reuse of the materials (Theißen et al., 2022). In other approaches users are directly provided with a data set of material passports that can be implemented in BIM. Consequently, used materials can be linked to the data banks in the planning process before allowing data transfer between BIM and the software. As a result, the software generates a review regarding the circular potential of the project (Atik et al., 2020; Atta et al., 2021; Honic et al., 2019). Considering all the above, it is prominent that digital and sustainable construction processes receive increasing attention with many projects working on the topic of circular economy. Nevertheless, most of them focus on the implementation of new construction sites while disregarding possible applications in existing building and redevelopment projects. Therefore, the project ReBaDI introduces an implementation of BIM in a refurbishment process including automated supportive renovation suggestions based on further attributes of the materials, as their CO₂-equivalent and costs per unit. The method of ReBaDI is a further development in the area of resource-efficient building maintenance based on the precious research of Morgenstern and Raupach (Morgenstern and Raupach, 2022a).

4 DEVELOPMENT OF THE CONCEPT

The method is designed for resource-efficient and sustainable maintenance of building structures using digital methods and techniques. In this case, the focus is on building structures of reinforced concrete. Laser scanning, BIM, intelligent algorithms and AR technologies are linked along the entire process chain. For a better understanding of the method, the individual process steps were transferred into a BPMN process model (Figure 1). The method is divided into four process phases - surveying/laser scanning, building diagnostics, BIM analysis and AR data visualization. The first process phase is the laser scanning of the building structure and the semiautomated transformation of the scan data into a digital BIM-model. At the beginning the responsible engineer needs to select the preferred laser scan methods. After scanning and quality check of the acquired data, the digital model of the building structure is semi-automatically generated. In the second phase of the process, the building diagnosis is carried out to record further data sets on the structural condition and the state of the structure. Depending on the intended objective, different non-destructive or low-destructive testing methods need to be selected. After the selection of the methods, relevant parameters (e.g. concrete cover, chloride ingress, etc.) are determined. After completion and control of the data, it is stored on an additional diagnostic database, linked to the Common Data Environment (CDE). In the third process phase (BIM-analysis), the BIM model is semantically enriched with the relevant diagnostic data in the first sub-step and the recorded data is evaluated automatically. From the analyzed diagnostic data, the necessary maintenance measures for the improvement of the building structure can be derived. Furthermore, the diagnostic data can be visualized directly in the digital model. In the further progress of the phase, the digital model will act as the main database for the sustainability assessment of the resulted maintenance operations. For this purpose, the BIM model is enriched with additional sustainability parameters (e.g. CO₂-factor and transport emission for the material, etc.) and linked to a database with further sustainability parameters of individual materials. For the sustainability assessment, an algorithm based on formalized expert knowledge is used in this context, acting as a decision support system. Based on the data from the BIM model and the sustainability parameters from the database, the algorithm compares different materials and methods for the maintenance of the building structure.

The result of the consideration shows different proposals with ecological and economic priorities. This serves as a decision support for the maintenance planning. In this way, the most optimal solution for the condition optimization of the building structure can be selected. To ensure that at the end of the process chain all relevant data for the further life cycle are always

stored and managed transparently and consistently, the digital model and all diagnostic and sustainability data are transferred to a CDE. In this way, all project participants can view and use the data. The data is provided by means of open data exchange formats. For example, the digital model in IFC format, adhering to the openBIM approach. For optimized display and availability on the construction site of the digital building model including diagnostic data, the data can also be transferred to an augmented reality system after analysis (process phase 5). For this purpose, they are transferred and processed via an interface in a software/engine for augmented realities. As a result, the data can be used directly on the construction site via a terminal device (e.g. cell phone, tablet, AR glasses) and the BIM model and diagnostic data can be displayed. The use of AR and the possibility of using the data on demand in a visualized form improves the awareness of the existing condition of the building structure and at the same time offers the possibility to make internal components visible. In addition, existing problems can be detected directly on site and predictive action can be taken.

5 PROOF-OF-CONCEPT

After the method concept has been presented in detail in the previous chapter, its validation is conducted in the form of a proof-of-concept on a physical demonstrator in the next section. The demonstrator is a room of an office building of reinforced concrete structure. The validation considers the individual process phases of the method and is divided into three sub-steps - data acquisition, data processing and data provision.

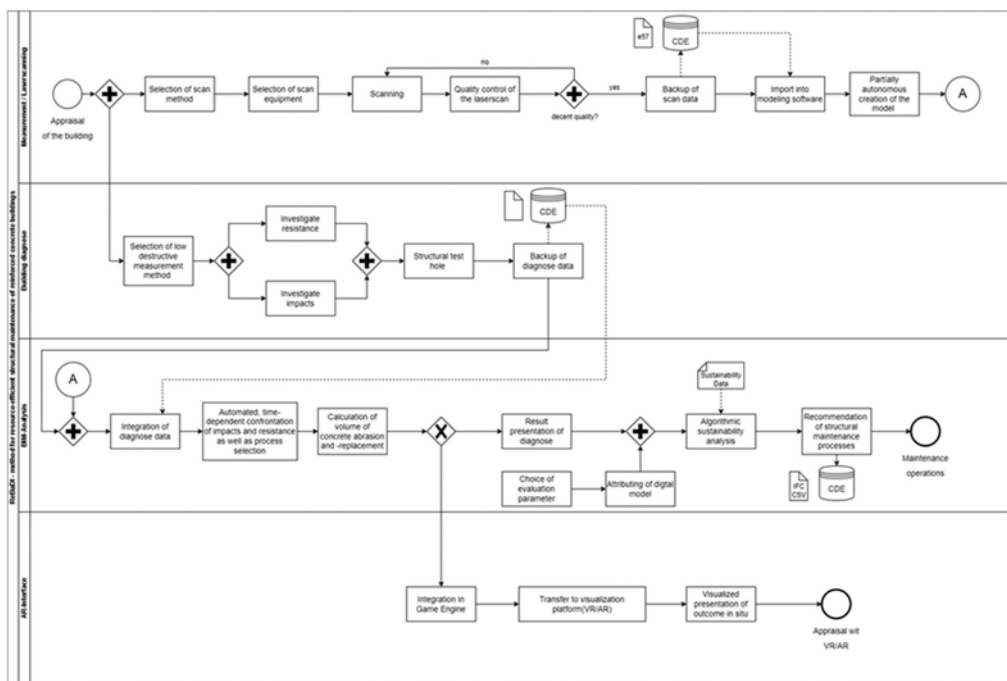


Figure 1. ReBaDI process model.

The first step of validation is the data acquisition. On the one hand, the structure of the building is recorded by laser scanning, and on the other hand, the diagnostic data is recorded using a rebar detector. Geometric data of the existing structure was collected using a terrestrial laser scanner (Trimble X7). 3D-scans of the corridor and the adjacent rooms are also required in order to determine the wall's thickness. During the scanning process, each scan is automatically registered in Trimble's authoring software (s. Figure 2).

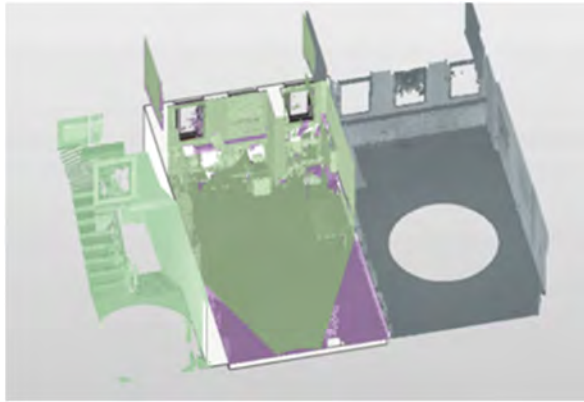


Figure 2. Laser Scan of the demonstrator.

The fully registered point cloud is stored as an open data exchange format e57 in a CDE and can be utilized for post-modeling to an “as-is model”. The gathering of data from building components is the next stage in building diagnostics. For this, non-destructive and low-destructive measuring techniques are required. The positions of the rebars in the wall were determined through an areal scan with a grid size of 25 cm, leading to 30 (8 horizontal + 22 vertical) line scans. As a result, several measuring points were available for each rebar, so that not only the concrete cover could be determined for several points of a rebar, but also the orientation of the reinforcement could be derived. The measurement was calibrated and validated through a probe opening, gathering information about the exact concrete cover at that spot as well as the diameter of the rebars for both layers (front and rear). After the scan and diagnostic data have been successfully recorded using the real demonstrator, they were processed further in the following sub-process (data processing). The scan data were transferred into an authoring software system (Autodesk Revit) and the as-is BIM-model was created. The procedure was partially automated using the Faro Add-in “As-built” for the used authoring system Autodesk Revit. The result is a model as a reinforced concrete room which can be enriched with further semantic information. For the handling of the data series from the rebar detector and its further processing, an additional algorithm was developed. With the use of the algorithm, all lines of the rebar detection were automatically viewed and compared. In the process, measurement errors such as slippage of the displacement transducers or inaccuracies of starting points were identified and corrected. As a result, line scans orthogonal to the bars containing the points where a rebar was crossed over are transformed into lines describing the actual position and orientation of the rebars. From this transformed data, reinforcement elements were then automatically generated as digital representations, so that the actual position of the reinforcement was implemented in the model, see Figure 3.

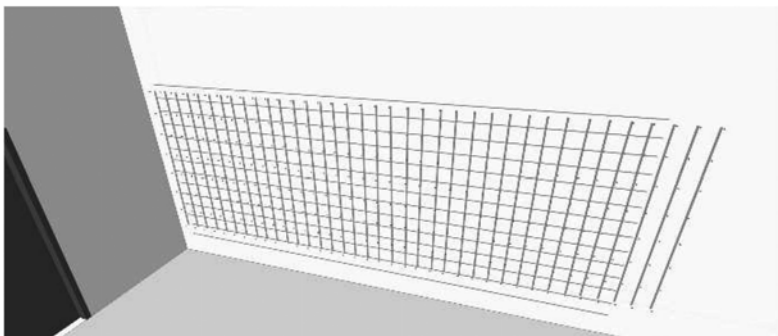


Figure 3. Digital representation of the reinforcement in the BIM-model.

For an integrated and partially automated sustainability assessment to compare maintenance operations, an additional algorithm was developed. Therefore, the open-source visual programming tool Dynamo has been used to enable an interface between the BIM model and an external database. As a minimal example, this study used an Excel spreadsheet to store all relevant material parameters rather than an entire database system. In order to be able to store the ecological and economic parameters and the results of the sustainability study directly in the model, additional common parameters were integrated. The algorithm was developed for an automated sustainability evaluation of accruing maintenance operations. In the context of the article, two scenarios are considered for the analysis as validation. One scenario considers the comparison of maintenance measures in terms of environmental sustainability with regard to CO₂-emissions. The other scenario focuses on economic sustainability by comparing the costs incurred. As parameters for each maintenance scenario, the CO₂ emissions (in kg), the material name and the associated refurbishment costs (in €) are created. The building component and accompanying face that are intended to be renovated must be chosen to employ the Dynamo script. The algorithm then calculates all scenarios and automatically extracts the data from the database. The script then analyzes the data and returns two scenarios: one with the lowest costs and another with the lowest CO₂-emissions. It then enriches these economic and ecological factors in the BIM model so that decision-makers can take them into account.

The last step of the validation is the provision of the processed data. Two different types of data provision are considered in this context. The first form is data integration and representation using AR technology, and the second is the use of a CDE as a unified single-source-of-truth. After the BIM model has been created and semantized, the method can be used to provide the data via augmented reality in addition to the sustainability analysis. As part of the validation, the BIM model of the room structure, including diagnostic data, was loaded into the Visual Live game engine (s. Figure 4).



Figure 4. Representation of the BIM-model in an augmented reality.

Through this interface, the BIM model can be used and displayed directly on site via app. For an optimal representation of the data, a uniform coordinate system between the real asset and digital model was defined after the data transfer. This results in an exact overlap of the digital image in the physical space and the data can be displayed directly without any deviations. Figure 4 shows an excerpt of the interface. Here, the exact reinforcement location and the remaining concrete cover (colored dots in the image) are displayed as digital objects on the real wall in augmented reality. With this step, hidden components, e.g. in these prototypes the

reinforcement position and properties of the wall that are not visible to the eye, can be visualized and made available to the engineer on site. This enables important properties of the building structure to be made comprehensible and efficient for maintenance management. For the permanent, consistent and transparent storage and management of data throughout the operational phase, the BIM model is transferred in IFC format and all relevant data in a CDE. This serves as a single source of truth in the operational phase of the building structure. By using the CDE, the data can be viewed and used by all relevant project participants.

6 DISCUSSION

The basic feasibility of the developed procedure is demonstrated by validation on a real demonstrator. In the context of the validation, each phase depicted in the process model is conducted and implemented in practice. By combining digital technologies, such as laser scanning, digital building models, algorithms and augmented reality, maintenance management can be further digitized and existing processes automated. As a result, the building structure and its condition can be accurately captured and represented in a digital and semantically refined BIM model and serve as a consistent database for further actions and analysis. In addition, by linking the digital model with further sustainability data, necessary maintenance measures can be evaluated so that the most sustainable variant in terms of the life cycle is always selected. Furthermore, the digital image can make all hidden conditions in the structure visible and available directly on the construction site via an AR interface.

Although this work enabled an efficient and automated workflow to identify economic and sustainable solutions, there are limitations to this method. First of all, it should be noted that the project focuses only on four different materials and strategies, preventing a more sophisticated evaluation of several materials. Furthermore, the evaluation process is based on material attributes, but to reduce the complexity of the project and enable an easy comparison between the different strategies, the focus is set on the costs and CO₂-emissions of the materials. Lastly, only one wall of one project room was considered, reducing the complexity of the algorithm.

Considering these aspects, further research is needed in order to enable evaluations of multiple building components of multiple rooms and creating a general method for a sustainable redevelopment process. The aforementioned restrictions highlight how the workflow can be enhanced or totally automated. An Excel table with four different materials was used as the bare minimum sample in this study. A bigger data collection can be considered by integrating a material data base or material passport data into the Dynamo script. Additionally, more scenarios with higher complexity can be examined in complement to the original two. Another issue that has to be addressed is that the Dynamo script is now used twice - once for scenario analysis and once for building diagnostics - and is only partially automated. By allowing only one tool to evaluate all incoming parameters, these several scripts can be consolidated into one to increase the workflow's level of automation. The level of automation in this situation can also be increased that the algorithm fully identifies the components which require correction and initiates the relevant analysis. This would enable more efficient evaluation and analysis of bigger construction structures or even transfer the application to other areas such as bridges.

7 CONCLUSION

This article presents a partially automated procedure for a resource-efficient and digital maintenance management of reinforced concrete structures. A process chain was developed to describe the procedure and the individual phases were presented specifically. For validation, the method was applied to a real demonstrator and the results discussed in the article. By using the method, existing structures and conditions of the building can be recorded and represented in a digital BIM model. Furthermore, necessary maintenance measures can be identified and analyzed under consideration of sustainability aspects. In addition, the approach enables the provision and use of the data in a CDE as well as via augmented reality directly in the real environment of the building.

ACKNOWLEDGEMENT

This research (Project ReBaDI, 10.08.18.3-22.31) is supported by the Federal Institute Research on Building, Urban Affairs and Spatial Development in the Federal Office for Building and Regional Planning in the funding program ZukunftBau.

REFERENCES

- Atik, S., Domenech Aparisi, T. and Raslan, R. (2020) 'Investigating the effectiveness and robustness of performing the BIM-based cradle-to-cradle LCA at early-design stages: a case study in the UK', *Building Simulation and Optimization* [Online]. Available at <https://discovery.ucl.ac.uk/id/eprint/10112217>.
- Atta, I., Bakhoum, E. and Marzouk, M. (2021) 'Digitizing material passport for sustainable construction projects using BIM', *Journal of Building Engineering*, Volume 43.
- Bartels, N., Höper, J., Theißen, S. and Wimmer, R. (2022) *Anwendung der BIM-Methode im nachhaltigen Bauen: Status quo von Einsatzmöglichkeiten in der Praxis* [Online], Springer Vieweg. Available at <https://doi.org/10.1007/978-3-658-36502-8> (Accessed 11 November 2022).
- Bundesinstitut für Bau-, Stadt- und Raumforschung (2021) *Strukturdaten zur Produktion und Beschäftigung im Baugewerbe: Berechnungen für das Jahr 2020* [Online], Berlin, Bundesinstitut für Bau-, Stadt- und Raumforschung. Available at https://www.bbsr.bund.de/BBSR/DE/veroeffentlichungen/bbsr-online/2021/bbsr-online-32-2021-dl.pdf?__blob=publicationFile&v=3.
- Bundesministerium für Justiz (2021) *Bundes-Klimaschutzgesetz (KSG)*.
- Bundesministerium für Wirtschaft und Energie (2014) *Sanierungsbedarf im Gebäudebestand* [Online], Berlin, Bundesministerium für Wirtschaft und Energie. Available at https://www.bmwk.de/Redaktion/DE/Publikationen/Energie/sanierungsbedarf-im-gebäudebestand.pdf?__blob=publicationFile&v=3 (Accessed 28 October 2022).
- Deutsche Energie-Agentur (2021a) *Fokusthemen zum Klimaschutz im Gebäudebereich* [Online]. Available at https://www.dena.de/fileadmin/dena/Publikationen/PDFs/2021/dena-GEBAEUDEREPORT_2021_Fokusthemen_zum_Klimaschutz_im_Gebaeudebereich.pdf (Accessed 18 November 2022).
- Deutsche Energie-Agentur (2021b) *Leitstudie Aufbruch Klimaneutralität* [Online]. Available at https://www.dena.de/fileadmin/dena/Publikationen/PDFs/2021/Abschlussbericht_dena-Leitstudie_Aufbruch_Klimaneutralitaet.pdf (Accessed 28 October 2022).
- Görsch, C., Schönbach, R., Klemt-Albert, K. and Löhnert, G. (2021) 'Prozessbasierte Analyse zur Integration von Nachhaltigkeitsaspekten in die Methode Building Information Modeling (BIM)/Abstract Process Based Analysis of Sustainability Issues for Integration into Building Information Modeling (BIM)', *Bauingenieur*, vol. 96, no. 03, pp. 60–69.
- Hofstadler, C. and Motzko, C. (2021) *Agile Digitalisierung im Baubetrieb* [Online], Springer Vieweg. Available at <https://doi.org/10.1007/978-3-658-34107-7>.
- Honic, M., Kovacic, I. and Rechberger, H. (2019) 'Concept for a BIM-based Material Passport for buildings', *IOP Conference Series: Earth and Environmental Science*, Volume 225.
- McKinsey Global Institute (2017) *Reinventing Construction through a Productivity Revolution* [Online]. Available at <https://www.mckinsey.com/business-functions/operations/our-insights/reinventing-construction-through-a-productivity-revolution>.
- Mellado, F., Wong, P. F., Amano, K., Johnson, C. and Lou, E. C. W. (2020) 'Digitisation of existing buildings to support building assessment schemes: viability of automated sustainability-led design scan-to-BIM process', *Architectural Engineering and Design Management*, vol. 16, no. 2, pp. 84–99.
- Morgenstern, H. and Raupach, M. (2022a) 'BIM-centred building diagnoses as a decision support tool for maintenance and repair', *e-Journal of Nondestructive Testing*, vol. 27, no. 9.
- Morgenstern, H. and Raupach, M. (2022b) 'Quantified point clouds and enriched BIM-Models for digitalised maintenance planning', *MATEC Web of Conferences*, vol. 364.
- Naneva, A., Bonanomi, M., Hollberg, A., Habert, G. and Hall, D. (2020) 'Integrated BIM-Based LCA for the Entire Building Process Using an Existing Structure for Cost Estimation in the Swiss Context', *Sustainability*, vol. 12, no. 9, pp. 1–17 [Online]. DOI: 10.3390/su12093748 (Accessed 31 October 2022).
- Schäfer, S. F., Gorke, N. T., Cevirgen, C., Park, Y.-B. and Nyhuis, P. (2022) 'Elemente der „Fabrik der Zukunft“', *Zeitschrift für wirtschaftlichen Fabrikbetrieb*, vol. 117, 1-2, pp. 20–24.
- Theißen, S., Pelzer, B., Höper, J., Drzymalla, J., Claudius, F., Bergmann, P. and Meins-Becker, A. (2022) 'Open BIM-based LCA of HVAC and circularity assessment using the Madaster platform'.
- United Nations (1997) 'Kyoto Protocol to the United Nations Framework Convention on Climate Change' [Online]. Available at https://unfccc.int/kyoto_protocol.
- Wastiels, L. and Decuyper, R. (2019) 'Identification and comparison of LCA-BIM integration strategies', *IOP Conference Series: Earth and Environmental Science*, vol. 323, no. 1, p. 12101.

Cost-optimization based generalized target reliabilities for reinforced concrete slab exposed to fire

F. Put, R.K. Chaudhary, A. Lucherini, B. Merci & R. Van Coile
Ghent University, Ghent, Belgium

ABSTRACT: Risk-based design of structures can be based on lifetime cost-optimization, which involves balancing the future costs with the benefits of safety investments. However, such calculations are impractical for most individual projects due to complexity and computational challenges. In normal design conditions, the explicit cost-benefit assessment has been replaced by precalculated maximum levels of failure probability (i.e., target reliability levels). For fire design, these targets have not been defined. In this study, target reliabilities for fire design are specified by generalizing optimum reliabilities obtained through lifetime cost-optimization. First, the influence of the appropriate parameters on the optimum reliability level is investigated. This is followed by the evaluation of target reliabilities considering the variability in parameters influencing lifetime cost for common types of structures.

1 INTRODUCTION

Structural fire design is traditionally presumed to be adequate when prescriptive design requirements are satisfied. These requirements reflect experience of the profession obtained over time, following disasters that indicated the need for new prescriptive guidance (Spinardi et al., 2017). As a result, prescriptive guidance focuses on common and pre-existing buildings, while new and modern structures are not covered. Moreover, technological advancement and the development of innovative structural materials and design solutions render prescriptive design guidance inapplicable (Spinardi et al., 2017). For such structures, a performance-based design (PBD), which ensures that structures meet predefined objectives, is more suitable (Van Coile et al., 2019b).

Designing a structure according to a PBD approach involves dealing with the uncertainties of the structural system (Van Coile et al., 2019a). In this respect, a probabilistic or risk-based structural design can be used where uncertainties are explicitly quantified. Generally, such probabilistic structural design should meet the ‘As Low As Reasonably Practicable’ (ALARP) criterion (Van Coile et al., 2019b), which requires a lifetime cost-minimization and involves balancing the future costs of a safety investment with its benefits (BSI, 2019). Nevertheless, such evaluations are often complicated and computationally challenging, making them impractical for application to most individual projects. This issue is not inherent to the fire design conditions, but also occurs in normal design conditions, for which design guidance proposes target reliabilities, e.g., (JSCC, 2001). These target reliabilities are predefined maximum (target) levels of failure probability and act as a substitute for the explicit cost-benefit (risk) assessment in normal design conditions.

For fire design, no generally accepted target reliabilities have been defined. The Natural Fire Safety Concept proposes to divide the normal design maximum failure probability by the fire frequency (Cajot et al., 2002). As pointed out in earlier work (Van Coile et al., 2017), these targets for normal design conditions cannot be readily transposed for structural design under fire, although the cost-optimization approach used to derive them stays relevant (Fischer, 2014). Previous work on the development of optimum reliability levels for structural fire design using such cost-optimization approach focused on the influence of the fire exposure (fire load density and opening factor) on the optimum reliability levels using a protected steel column as reference case (Chaudhary et al., 2022).

This study further elaborates on the methodology used in the latter work (Chaudhary et al., 2022), investigating the influence of the economic parameters on the optimum reliability levels through application of the lifetime cost-optimization approach. In addition, optimum reliability levels are determined for common types of structures. These optimum reliability levels can be considered as suggested values for specifying a target reliability index. The example of the reinforced concrete slab subjected to bending and exposed to natural fire from the bottom is revisited (Van Coile et al., 2014) and the axis distance is varied to obtain the optimum reliability level.

2 COST-OPTIMIZATION METHODOLOGY

The cost-optimization approach used in this study has been previously derived and a more detailed description can be found in previous work (Chaudhary et al., 2022).

The process of lifetime cost-optimization is generally achieved by maximization of the lifetime utility, which can be defined as the difference between the benefit of the structure's existence and the lifetime cost. As the expected benefit can be assumed independent of the safety investments, the maximization of lifetime utility reduces to a minimization of lifetime cost (Rackwitz, 2000).

The lifetime cost (K) can be split into three contributions, as indicated in Equation 1:

$$K = C + A + D \quad (1)$$

where C is the total cost of the structure, A refers to the obsolescence cost and D represents the cost of structural failure. The total cost of the structure, C , can be further divided into the cost of the structure, C_0 , and the added cost of the safety measure, C_1 , while for an infinite time horizon, the present net value obsolescence cost, A , can be rewritten in terms of the total cost of the structure according to Equation 2:

$$A = C \frac{\omega}{\gamma} = (C_0 + C_1) \frac{\omega}{\gamma} \quad (2)$$

where ω is the obsolescence rate and γ the continuous discount rate.

The cost of structural failure comprises direct and indirect costs related to structural failure such as reconstruction, business interruption, costs of injuries and fatalities, environmental costs etc. Although these costs generally depend on case-specific parameters, the cost of structural failure is often simplified to a factor of the initial construction cost, ξC_0 (Steenbergen et al., 2015). The structural failure cost for adverse events such as fire is assessed as the present net value of the (annual) expected structural failure cost over the entire lifetime of the structure (Steenbergen et al., 2015; Van Coile et al., 2019a). Equation 3 evaluates this present net value of the future annual expected failure costs over the lifetime of the structure (infinite time horizon):

$$D = \frac{\lambda P_f(p)}{\gamma} \xi C_0 \quad (3)$$

where λ is the annual probability of fire event occurrence and $P_f(p)$ is the structural failure probability considering a fire event, with p the design parameter being optimized. Substituting Equations 2 and 3 in Equation 1 and considering that the total cost of the structure can be rewritten as a sum of the cost of the structure and the added cost of the safety measure, the lifetime cost-minimization becomes:

$$\min_p \left[C_0(1 + \varepsilon(p)) \left(1 + \frac{\omega}{\gamma} \right) + \frac{\lambda P_f(p)}{\gamma} \xi C_0 \right] \quad (4)$$

where $\varepsilon(p) = C_1/C_0$ is the investment cost factor for the design.

As C_0 is constant and therefore does not take part in the minimization process, the final expression for the lifetime cost-minimization results in Equation 5.

$$\min_p \left[\varepsilon(p) \left(1 + \frac{\omega}{\gamma} \right) + \frac{\lambda P_f(p)}{\gamma} \xi \right] \quad (5)$$

It should be noted that Equation 5 is strictly speaking valid only when the investment in structural fire safety does not affect other performance metrics for the structure, such as its failure probability with respect to other accidental events. These effects are not considered here, and the fire design optimization is done in isolation. In the following, a constant value for the design value of the resistance in normal design conditions is maintained.

3 CASE STUDY: REINFORCED CONCRETE SLAB

As case study to investigate the influence of the economic parameters on the optimum reliability level and to derive optimum reliability levels for common types of structures, the reinforced concrete slab presented in (Van Coile et al., 2014) is adopted. The additional fire protection is the result of an increase in axis distance of the rebars (i.e., distance between the axis of a rebar and the fire exposed concrete surface), whilst maintaining the same ambient bending capacity (i.e., increasing the reinforcement area to compensate for the loss of lever arm). The sections below will discuss the slab details as well as the investment and failure costs.

3.1 Case study details

The considered slab is a simply supported one-way solid concrete slab with a fixed width and height of respectively 1 m and 0.2 m. Before cost-optimization, the slab is reinforced with Ø10 mm rebars with a 10 cm spacing. The initial axis distance is 20 mm and the resulting design value of the bending capacity in normal design conditions is 58.55 kNm. The slab is purely loaded in bending. The characteristic value of the bending moments induced by both the permanent load and imposed loads on the slab are calculated as 22.12 kNm (load ratio $\chi = 0.5$), considering full utilization in normal design conditions and combination factor ψ_0 equal to 0.7 (e.g., residential and office areas). The probabilistic models for the basic variables can be found in Table 1.

Table 1. Stochastic parameters for material properties (Qureshi et al., 2020), fire loading (CEN, 2002), mechanical loading and model uncertainties (Jovanović et al., 2021) for the analyzed concrete slab.

Stochastic variables	Distribution	Mean	COV*
Slab height, d	Normal	0.2 m	0.025
20°C concrete compressive strength, $f_{c,20}$	Lognormal	42.9 MPa	0.15
Yield strength reduction factor, $k_{fy(\theta)}$ with $f_{y,20}=581.4$ MPa	Logistic	Temperature-dependent	Temperature-dependent
Fire load density, q_f	Gumbel	Nominal value (500 – 1500 MJ/m ²)	0.3
Opening factor, O	Deterministic	0.04	
Permanent load, M_G	Normal	22.12 kNm	0.1
Imposed load, M_Q	Gamma	0.2×22.12 kNm	0.95
Resistance estimation, K_R	Lognormal	1.1	0.11
Load estimation, K_E	Lognormal	1	0.1

* Coefficient Of Variation

3.2 Cost components

The investment cost of additional fire protection, C_1 , results from the increase in reinforcement area to maintain the same ambient design bending capacity when the axis distance of the rebars is increased. The cost of steel is obtained from (Gordian, 2022) and amounts to \$2.89/kg and includes material, labor and overhead. Similarly, the initial cost of the compartment, C_0 is determined to be \$1500/m² (Table 2). Figure 1a visualizes how the investment cost increases with increasing axis distances and how this investment cost relates to the investment cost factor, $\varepsilon(p)$.

The estimated failure cost over the lifetime of the structure requires computation of the failure probability of the structural system. Failure of a system is associated with the limit state equation (denoted Z), $Z = R - E$, taking negative values, indicating that the load effect, E , exceeds the resistance effect, R . Hence, for a slab subjected to bending solely, the failure probability can be written as the probability that the induced bending moment exceeds the resisting moment of the slab, as in Equation 6:

$$P_f = P[K_R M_R - K_E M_E < 0] \quad (6)$$

where M_R is the bending resistance of the slab, M_E is the induced bending moment, K_R is the model uncertainty for the resistance effect and K_E is the model uncertainty for the load effect.

The slab is exposed from the bottom to Eurocode parametric fire curves (CEN, 2002). The fire load density is varied between 500 and 1500 MJ/m² (roughly the range from office to library), while the opening factor is kept constant at 0.04 m^{1/2} to represent a critical case with prolonged and moderate fire exposure instead of short and intense exposure. The probabilistic analysis for failure during these different fire exposures is discussed in detail elsewhere (Chaudhary et al., 2021). Figure 1b presents how the cost of the slab and failure probability for different fire load densities vary with the reinforcement axis distance to the exposed surface.

Table 2. Default values for economic parameters.

Variable	Default value	Reference
Cost of the structure C_0	1,500 USD/m ² *	(Gordian, 2022)
Steel cost	2.89 USD/kg	(Gordian, 2022)
Obsolescence rate ω	0.022 [1/year]	(Bokhari and Geltner, 2018)
Discount rate γ	0.03 [1/year]	(Fischer, 2014)
Probability of fire occurrence λ	0.151×10^{-2} (office)	(Manes and Rush, 2019)
Relative cost of structural failure ξ	4	Representative value

* Realistic estimation based on single-family dwelling and commercial office data in Table 3.

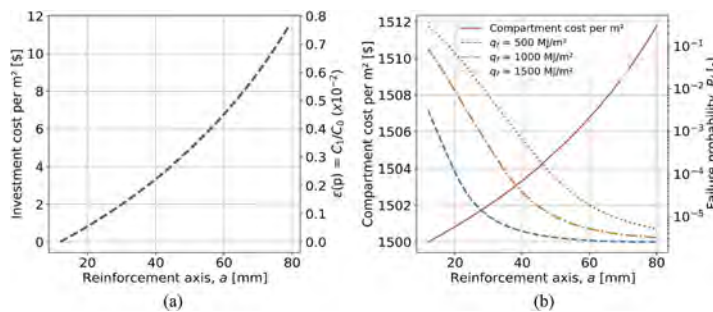


Figure 1. Influence of the reinforcement axis distance on (a) the investment cost C_1 per m² and investment cost factor $\varepsilon(p)$ and (b) the compartment cost C_0 per m² and the failure probability for different fire load densities. The cost of steel is set to \$2.89/kg and the reference cost of the compartment is \$1500/m².

The quantification of the relative cost of structural failure, ξ , in Table 2 is challenging because it depends on the extent of damage, which varies widely. The damage resulting from the failure of a slab exposed to fire, for example, can be limited to the compartment itself and its contents, but could also induce progressive collapse of an entire building. In the first scenario, the relative cost of structural failure would be several times (e.g., 2 or 3, considering the entire compartment would be lost, i.e., $\xi=1$, together with its contents (FEMA, 2015) the structural cost of the compartment, C_0 , while in the second scenario, the damage can be orders of magnitude larger than C_0 .

In order to find a representative relative cost of structural failure, the probability of different scenarios should be considered. In most cases, the damage due to failure of a slab will be limited to the compartment for which the slab fails. The probability of progressive collapse after failure of a slab is significantly lower. Consequently, a representative value for ζ is assumed to be primarily dominated by damage limited to the compartment for which the slab fails, with a slight adjustment to a higher value to account for low-probability scenarios with large consequences. Therefore, the reference value for the relative cost of structural failure is set to 4, which is in line with the values obtained for reference cases in Table 3. For comparison purposes, a value of 6.9 is listed for office buildings in earthquake scenarios (Kanda and Shah, 1997).

3.3 Optimum reliability and sensitivity analysis

The lifetime cost-minimization expression in Equation 5 is a function of multiple economic parameters (i.e., $\varepsilon(p)$, ω , γ , λ and ζ). In the sections below, these parameters are split into two groups, i.e., factors influencing the investment cost and factors influencing the failure cost. The discount rate, γ , influences both investment and failure costs and will be discussed separately.

The result of the lifetime cost-minimization is an optimum value for the axis distance of the rebars from the exposed surface of the slab. From this optimum axis distance, an optimum value for the failure probability can be determined. This optimum failure probability can be converted into an optimum reliability level as follows:

$$\beta = -\Phi^{-1}(P_f) \tag{7}$$

where β is the reliability level and Φ is the standard normal cumulative density function.

The investment cost is affected by the investment cost factor, $\varepsilon(p)$, and the obsolescence rate, ω . The obsolescence rate is constant and can readily be varied. A sensitivity study of the investment cost will be achieved by altering the cost of steel with a multiplicative factor (the ‘steel cost increase factor’). Note that this cost of steel will typically have only a very limited effect on the initial cost of the compartment, C_0 (see Figure 1b). Therefore, C_0 will be treated as constant. The resulting influence of variations in steel cost and obsolescence rate can be found in Figures 2a and 2b respectively.

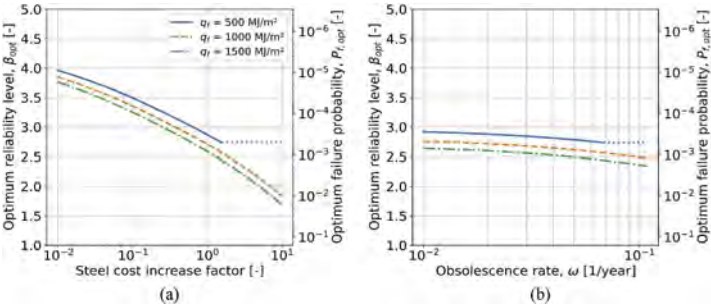


Figure 2. Influence of (a) increase in steel cost and (b) obsolescence rate on the optimum reliability level. Horizontal dotted lines mark cases with optimum axis distance outside the treated range 12 mm to 80 mm.

Both an increase in obsolescence rate and steel cost will lead to an increase in lifetime cost (Equation 5). As a result, the optimum axis distance for the rebars will be lower, which will result in a higher optimum failure probability and thus lower optimum reliability level. This behavior is also exhibited in Figures 2a and 2b. Furthermore, it can be observed that the influence of the obsolescence rate is limited compared to the influence of the steel cost.

The present net value of the structural failure cost over the lifetime of the structure depends inter alia on the consequences of failure, indicated by the relative cost of structural failure, ζ , and the annual probability of fire occurrence, λ . An increase of one of these parameters (or both) will cause an increase in lifetime cost. Further, Equation 5 indicates that ζ and λ are simply multiplying factors for the cost of structural failure. Therefore, variations in one parameter can be directly translated into an equivalent change in the other parameter, resulting in the same expected annual failure cost and thus leading to the same optimum reliability level.

Figure 3a visualizes the influence of the multiplication of the relative cost of structural failure, ζ , and the probability of fire occurrence, λ , on the optimum reliability levels. When the consequences of failure or probability of fire occurrence are low, a small value for the optimum reliability level is obtained. In these cases, it is not economic to strongly invest in additional safety as the expected cost of structural failure is low. Therefore, the optimum axis distance will be low, resulting in a higher failure probability and a lower optimum reliability level.

The discount rate, γ , influences both the investment cost and failure cost. Figure 3b demonstrates how the optimum value for the reliability level varies with the discount rate. In general, the influence of the discount rate on the optimum reliability level is limited compared to the steel cost and the factors influencing the failure cost.

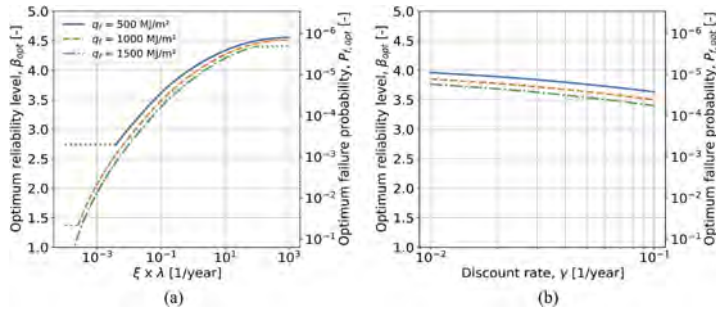


Figure 3. Effect of (a) relative cost of structural failure ζ and probability of fire occurrence λ and (b) discount rate on the optimum reliability level. For (a), the dotted horizontal lines indicate cases for which the optimum axis distance is outside the optimization range.

4 OPTIMUM RELIABILITY LEVELS FOR COMMON TYPES OF STRUCTURES

A majority of the parameters used in the cost-minimization in Equation 5 are case-dependent. The relative cost of structural failure, for example, will be higher if the contents of the building are more valuable. Also, the probability of fire occurrence will differ. To guide the specification of target reliability levels, the optimum reliability level for 3 common types of structures will be determined: a single-family dwelling; a governmental office; and a commercial office. The natural fire exposure is represented by the Eurocode parametric fire curve with fire load densities according to Annex E of EN 1991-1-2:2002 and the opening factor equal to $0.04 \text{ m}^{1/2}$. The values of the fire load density are specified in Table 3.

Table 3. Realistic estimations of economic parameters for common types of structures.

Type of structure	Average structure cost (Gordian, 2022)	Fire probability λ (Manes and Rush, 2019)	Fire load density q_f (CEN, 2002)	Relative cost of structural failure ζ *
Single-family dwelling	1,305.5 USD/m ²	0.00151	780 MJ/m ²	2.6
Governmental office	3,903 USD/m ²	0.002	420 MJ/m ²	3.25
Commercial office	1,674.43 USD/m ²	0.00423	420 MJ/m ²	3.25

* Sum of content loss factor (FEMA, 2015) and indirect loss factor (Ramachandran and Hall Jr, 2002).

The relative cost of structural failure is highly dependent on the extent of failure. As a simply supported slab and compartment fire are considered, the cost of the structure and investment cost are for a single compartment only, while the extent of failure can reach beyond the compartment

boundaries. In the most severe cases, the failure of the slab can result in progressive collapse of the entire structure. The values of ζ provided in Table 3 are reference values, but can differ significantly from case to case. They consist of a content loss factor, including the loss of property and content, and an indirect loss factor, considering, e.g., cost of injuries and deaths, business interruption etc. An overview of how the optimum reliability level changes as a function of ζ for the types of structure in Table 3, can be found in Figure 4. Based on the reference values for ζ in Table 3, optimum reliabilities are derived. For a single-family dwelling, governmental office and commercial office, the optimum reliability indices are 2.59, 3.19 and 3.16 respectively.

In order to verify whether the calculated optimum reliabilities can be considered generally applicable for these types of buildings and can thus be recommended as target reliabilities, a sensitivity analysis is performed for the relative cost of structural failure, ζ . The influence of variations in fire probability, cost of the structure and relative cost of structural failure are the same (meaning that a doubling of the fire probability has the same effect as a doubling of the relative failure cost). Therefore, of these parameters only the relative cost of structural failure, ζ , is considered below. The obsolescence rate and discount rate are not considered as the previous results have already indicated the insensitivity of the optimum reliability level for variations in these parameters.

The results, provided in Table 4, indicate that the obtained target reliability levels are relatively insensitive to changes in the relative cost of structural failure. These results suggest that a target reliability index of approximately 3.2 could be recommended for non-residential buildings (governmental office, commercial office), while for residential buildings a lower target reliability index of 2.6 could be recommended on cost-optimization grounds.

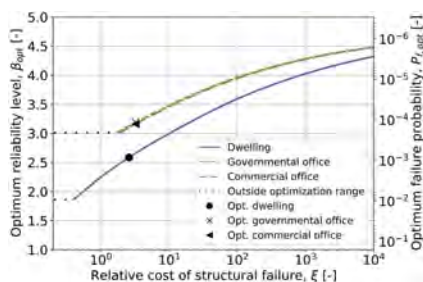


Figure 4. Target reliabilities for different buildings types as function of the expected relative cost of structural failure ($\omega = 0.022$; $\gamma = 0.03$). Lines for governmental and commercial offices approximately coincide.

Table 4. Sensitivity analysis for calculated target reliabilities based on a 10% increase of ζ .

Type of structure	Percentage change optimum reliability level
Single-family dwelling	1.20%
Governmental office	0.82%
Commercial office	0.81%

5 CONCLUSIONS

The influence of economic parameters on the optimum reliability level in fire has been determined using an explicit cost-benefit analysis. This analysis was based on the reference case of a reinforced concrete slab exposed to natural fire. It was found that the cost of additional fire protection, the probability of fire occurrence and the relative cost of structural failure have a significant influence on the optimum reliability level, whereas the influence of the obsolescence rate and discount rate are limited.

Based on reference values for the economic parameters, the optimum reliability level has been determined for common types of structures. First, the optimum reliability index was presented as a function of the relative cost of structural failure, because the extent of damage due to structural failure significantly influences this optimum reliability index. Based on reference values for these

relative costs of structural failure, the target reliability indices have been determined to be 2.59, 3.19 and 3.16 for a single-family dwelling, governmental office and commercial office respectively. The results of the sensitivity analysis indicate that these values are insensitive to changes in input parameters. Except for situations where the expected consequences are significantly higher than normally expected from structural failure due to fire exposure, these values can be considered as a basis for defining target reliabilities for structural fire engineering. Thus, a target reliability index of 3.2 is put forward for the structural fire design of non-residential buildings (office), while a target reliability index of 2.6 is put forward for residential buildings. These target reliabilities were derived from a case study of a simply supported reinforced concrete slab. Further case studies are recommended before adoption in guidance documents.

ACKNOWLEDGEMENTS

The authors thank the Research Foundation of Flanders (FWO) for the financial support on the research grant number 1137123N “Characterization of the thermal exposure and material properties of concrete during the fire decay phase for performance-based structural fire engineering”.

REFERENCES

- Bokhari, S., Geltner, D., 2018. Characteristics of Depreciation in Commercial and Multifamily Property: An Investment Perspective. *Real Estate Economics* 46, 745–782.
- BSI, 2019. PD 7974-7. Application of fire safety engineering principles to the design of building: Probabilistic risk assessment. British Standards Institution, London, UK.
- CEN, 2002. EN 1991-1-2: Eurocode 1: Actions on structures - Part 1-2: general actions - Actions on structures exposed to fire. European Committee for Standardization, Brussels, Belgium.
- Chaudhary, R.K. et al., 2021. Potential of Surrogate Modelling for Probabilistic Fire Analysis of Structures. *Fire Technol* 57, 3151–3177. <https://doi.org/10.1007/s10694-021-01126-w>
- Chaudhary, R.K. et al., 2022. Cost-optimization based target reliability for fire design of insulated steel columns. *Acta Polytech CTU Proc* 36, 59–65. <https://doi.org/10.14311/app.2022.36.0059>
- Cajot, L. et al., 2002. Natural fire safety concept : valorisation project : final report. European Commission, Directorate-General for Research and Innovation.
- Federal Emergency Management Agency (FEMA), 2015. Earthquake loss estimation methodology, Hazus-MH 2.1: Advanced engineering building module (AEBM) - technical and user’s manual. Gordian, 2022. RSMMeans Data [WWW Document].
- Jovanović, B. et al., 2021. Review of Current Practice in Probabilistic Structural Fire Engineering: Permanent and Live Load Modelling. *Fire Technol*. <https://doi.org/10.1007/s10694-020-01005-w>
- JSCC, 2001. Probabilistic Model Code: Part 1 - Basis of Design. Joint Committee on Structural Safety.
- Fischer, K. 2014. ‘Societal decision-making for optimal fire safety’, PhD thesis, ETH Zürich, Zürich, Switzerland, <https://doi.org/10.3929/ethz-a-010164481>.
- Kanda, J., Shah, H., 1997. Engineering role in failure cost evaluation for buildings. *Struct. Saf.* 19, 79–90.
- Manes, M., Rush, D., 2019. A Critical Evaluation of BS PD 7974-7 Structural Fire Response Data Based on USA Fire Statistics. *Fire Technol* 55, 1243–1293. <https://doi.org/10.1007/s10694-018-0775-2>
- Qureshi, R. et al., 2020. Probabilistic Models for Temperature-Dependent Strength of Steel and Concrete. *Journal of Structural Engineering* 146, 1–18. [https://doi.org/10.1061/\(asce\)st.1943-541x.0002621](https://doi.org/10.1061/(asce)st.1943-541x.0002621)
- Rackwitz, R., 2000. Optimization - the basis of code-making and reliability verification. *Struct. Saf.* 27–60.
- Ramachandran, G., Hall Jr, J.R., 2002. SFPE Handbook of Fire Protection Engineering, Measuring Fire Consequences in Economic Terms.
- Spinardi, G., Bisby, L., Torero, J., 2017. A Review of Sociological Issues in Fire Safety Regulation. *Fire Technol* 53, 1011–1037. <https://doi.org/10.1007/s10694-016-0615-1>
- Steenbergen, R.D.J.M. et al., 2015. Economic and human safety reliability levels for existing structures, in: *Structural Concrete*. Wiley-Blackwell, pp.323–332. <https://doi.org/10.1002/suco.201500022>
- Van Coile, R., Caspeele, R., Taerwe, L., 2014. Lifetime Cost Optimization for the Structural Fire Resistance of Concrete Slabs. *Fire Technol* 50, 1201–1227. <https://doi.org/10.1007/s10694-013-0350-9>
- Van Coile, R. et al., 2017. The meaning of Beta: Background and applicability of the target reliability index for normal conditions to structural fire engineering, in: *Procedia Engineering*. Elsevier Ltd, pp. 528–536.
- Van Coile, R., Gernay, T., Hopkin, D., Khorasani, N.E., 2019a. Resilience targets for structural fire design: An exploratory study. 17th International Probabilistic Workshop.
- Van Coile, R. et al., 2019b. The Need for Hierarchies of Acceptance Criteria for Probabilistic Risk Assessments in Fire Engineering. *Fire Technol* 55, 1111–1146. <https://doi.org/10.1007/s10694-018-0746-7>

Sensitivity of the seismic response to the modelling variables defining constitutive models of reinforced concrete frames

G. Karaki

Department of Engineering Design and Mathematics, University of the West England Bristol, UK

ABSTRACT: Probabilistic performance-based methods are well integrated into earthquake engineering applications. Therefore, the seismic response uncertainty and its sources must be adequately characterized for a more reliable seismic assessment. The paper examines the sensitivity of the RC frames response to the variables defining the constitutive models and their uncertainties. Floor displacements, floor accelerations, and section curvature were used in the sensitivity analysis, and the effect of the input variables defining the nonlinear material behavior on seismic response was investigated. The approach's algorithm was applied to a reinforced concrete moment-resisting frame. It was found that the variables defining the constitutive models; compressive strength of concrete, yield strength of steel, ratio of confined concrete strength to unconfined strength, variable that influences the shape of transition steel material curve, and modulus of elasticity of steel had a significant influence when considering inelastic behavior. This pattern was more evident for the curvature.

1 INTRODUCTION

The probabilistic performance methods have been intensively integrated into earthquake engineering applications. Many publications document probabilistic performance methodologies and their implementation for a broad representation of structural types and configurations, e.g. fib 2012, Ghosh et al. 2017, Karaki 2018, and Li et al. 2019, among others. Furthermore, the influence of the uncertainty of the input variables on the seismic response has also been investigated, and adequate characterization of output uncertainty to assess the reliability of the seismic response and design has been performed (e.g. Saha et al. 2016). Therefore, it is of essential importance to identify the main variables that contribute the most to the uncertainty of the seismic response. Sensitivity analysis is used to quantify the effects of inputs uncertainty on the output of interest. Many studies addressed the application of sensitivity analysis in earthquake engineering. However, the focus is given to the ones that included the uncertainty of material properties in their examination. Lee and Mosalam (2005) performed a sensitivity analysis and studied the uncertainty of global structural response, i.e., peak roof acceleration and displacement and maximum inter-story drift ratio, and local structural responses, i.e., curvature demand at critical sections. The material properties considered in this study were compressive strength of concrete, yield strength of steel, and moduli of elasticity E_c and E_s of concrete and steel, respectively. Kim and Han (2013) investigated design variables' influence on the seismic response of staggered wall structures. They used tornado diagrams and first-order second-moment method to determine the sensitivity and reliability measures. The yield strength of steel and ultimate strength of concrete were the considered variables defining the material behavior. Furthermore, the fragility curves to assess the seismic risk and loss estimation have been used as an objective function for the uncertainty and sensitivity analysis. For example, Padgett and DesRoches (2007) examined the sensitivity of seismic response and fragility to input variables uncertainty. They reported that preliminary screening of modeling variables might achieve savings in the simulation and computational effort in

fragility estimation. Other studies considered loss and risk functions as their objective function for the uncertainty and sensitivity analysis, e.g., Gokkaya et al. (2016) quantified the modeling uncertainty of ductile and non-ductile reinforced concrete buildings using Monte Carlo simulations. The influence of the uncertainty of the variables was evaluated for fragility functions, mean annual rates for drift limits and collapse, and the values of drift demands. The inclusion of the modeling uncertainty (input variables uncertainty) increased the mean annual frequency of collapse and drift ratios, affecting the buildings' seismic performance assessment. Celarec and Dolšek (2013) studied the impact of modeling uncertainties on seismic performance assessment of reinforced concrete frame buildings. The authors concluded that explicit consideration of epistemic uncertainties in the assessment of structural performance could lead to more accurate results and a more reliable assessment of seismic risk.

Only a few uncertainty and sensitivity studies have considered the nonlinear material properties in their analysis. For example, Celarec et al. (2012) studied the sensitivity of the seismic response to uncertain variables of masonry-infilled reinforced concrete frames; among the considered variables were the concrete and steel strengths, the infill material properties, and the plastic hinge properties. Heo & Kunnath (2009) examined the sensitivity of the seismic response to constitutive models used in the nonlinear analysis of reinforced concrete frame systems. Barbato et al. (2014) investigated the uncertainty of the seismic response due to the variability of input variables defining the material nonlinearity of steel and concrete.

In this study, a methodology to perform a sensitivity analysis to measure the effect of input variables defining nonlinear material behaviour on the maximum temporal responses was developed. In this examination, we aim to investigate the effect of the variables defining constitutive models on the uncertainty of seismic responses. The methodology allows essential screening of the input variables in a time-efficient manner. The output of the screening process may justify more experimental work or simplifications in the models used in the assessment or design frameworks.

2 METHODS

2.1 Sensitivity analysis

There are many methods to conduct sensitivity analysis; one way to categorize them is local and global methods. Local sensitivity analysis also known as one-at-time (OTA) is performed by keeping all input variables fixed and varying one input variable and examining the effect of this variation on the output. Global sensitivity analysis (GSA) examines the variation of all input variables on the output (all-at-a-time). GSA uses a probabilistic framework, therefore, it is often a computationally expensive method. A group of GSA methods, the so-called Morris screening method, can be described as an enhanced OTA method. The screening method mainly ranks input variables by their importance in descending order using only a relatively small number of model evaluations. Morris screening was used in this study.

2.2 Morris screening method

Screening methods, also known as elementary effects methods, belong to the One-at-Time (OAT) design class. These methods are attractive as they are computationally inexpensive and ideal for models with many input variables. Morris method overcomes the shortcomings of a typical local sensitivity method, running multiple OTA for the variable to explore all possible variations covering its feasible range. The average response of these multiple OTA is a measure of the sensitivity index (Saltelli et al. 2008). Therefore, screening methods can be considered as examples of global sensitivity analysis. In this study, we adapted the elementary effects method to perform the sensitivity analysis. The main algorithm of the method was retrieved from Morris (1991).

The input variable $X = (X_1, X_2, \dots, X_k)$ is any selected value in p-level Ω with a transformed point $X + e_i \Delta$, in which p is number of selected levels, Ω is the possible space of the input

variables, and Δ is the relative distance in the coordinate X_i . The elementary effect of the i^{th} input variable is defined as

$$EE_i = \frac{Y(X_1, X_2, \dots, X_i + \Delta, \dots, X_k) - Y(X_1, X_2, \dots, X_k)}{\Delta} \quad (1)$$

The distribution of elementary effects associated with the i^{th} input variables is obtained by randomly sampling \mathbf{X} from Ω and is denoted F_i , i.e., $EE_i \rightarrow F_i$.

Morris (1991) proposed two sensitivity measures; the mean value (μ) of F_i , which captures the overall influence of the i^{th} variable and the standard deviation (σ) of F_i , which estimates the nonlinear effects between the variables (Saltelli et al., 2008).

However, in the case of more complex models, Campolongo et al. (2007) proposed using the corrected average μ^* , which considers the absolute EE_i in the calculations of μ^* . Such a modification prevents the canceling of variable influence if opposite signs exist in EE_i values.

$$EE_i^* = \left| \frac{Y(X_1, X_2, \dots, X_i + \Delta, \dots, X_k) - Y(X_1, X_2, \dots, X_k)}{\Delta} \right| \quad (2)$$

To estimate these sensitivity measures μ^* and σ , the elementary effects method consists of sampling a number r of elementary effects. Therefore, the implementation algorithm for the sampling procedure of elementary effects method consists of creating r trajectories of $(k+1)$ points from the input space.

The randomized sampling matrix \mathbf{B}^* is built as follows:

$$\mathbf{B}^* = \left(\mathbf{J}_{\{k+1,1\}} \mathbf{P}^* + \left(\frac{\Delta}{2} \right) [(2\mathbf{B} - \mathbf{J}_{\{k+1,1\}}) \mathbf{D}^* + \mathbf{J}_{\{k+1,k\}}] \right) \mathbf{M}^* \quad (3)$$

in which \mathbf{B} is a $(k+1) \cdot k$ matrix with elements that are 0s and 1s such that for every column two rows of \mathbf{B} differ in only one element (a convenient choice is a strictly lower triangular matrix of 1s), $\mathbf{J}_{\{k+1,1\}}$ is a $(k+1) \cdot k$ matrix of 1s, \mathbf{D}^* is a k diagonal matrix with elements either +1 or -1 with equal probability and \mathbf{M}^* is a $(k \cdot k)$ random permutation matrix in which each column contains one element equal to 1 and all others equal to 0 and no two columns have 1s in the same position (Saltelli et al., 2008). Simulations are required to calculate screening measures $r \cdot (k+1)$. An important point when implementing the elementary effects method is the value of Δ . It must always represent a sampling step in the range of $[0, 1]$. In the case of non-uniform distribution and different scales of input variables, Δ should represent the variation in the quantiles for the variables, and the inverse of the cumulative distribution function is used to retrieve the values of the variables from their distribution functions.

2.3 Implementation process

MATLAB code (MATLAB, 2014a) is responsible for generating random samples of input variables, creating and exporting the ground motion records following a seismic hazard level to OpenSees, processing the output of analysis from OpenSees, and determining the sensitivity measures defined in the earlier sections. The numerical model in OpenSees includes the definition of the structure's geometry, nonlinear constitutive models, the structure's elements and their connectivity, boundary constraints, and analysis variables and types. The computational cost of the proposed sensitivity algorithm is the time required to run $m \cdot (r \cdot (k+1))$, in which m is the number of examined ground motion records, r is the number of sample trajectories, and k is the number of input variables. The implementation of the methodology is computationally efficient as r and k are taken below 50; this gives the approach a competitive advantage over other methods.

3 CONSTITUTIVE MODELLING

3.1 Constitutive modeling of concrete

The stress–strain curve of concrete in compression, confined or unconfined, starts with an ascending curve up to the maximum compressive strength followed by a descending line up to the residual strength, as displayed in Figure 1. The equation defining the ascending curve of the stress–strain curve was proposed by Sargin (Sargin, 1971):

$$\frac{f'_c}{f'_{co}} = \frac{A\varepsilon_c/\varepsilon_{co} + (D - 1)(\varepsilon_c/\varepsilon_{co})^2}{1.0 + (A - 2)(\varepsilon_c/\varepsilon_{co}) + D(\varepsilon_c/\varepsilon_{co})^2} \quad (4)$$

in which f'_c and ε_c are the strength and corresponding strain of the concrete, respectively, and f'_{co} and ε_{co} are the corresponding unconfined maximum strength and corresponding strain, respectively. Factors A and D depend on materials used to produce the concrete. For the purpose of this study, a similar form of the stress–strain curve was used for both unconfined and confined concrete. The constitutive model is available in OpenSees.

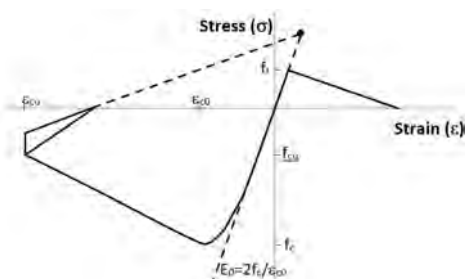


Figure 1. The constitutive model of concrete.

Confined models for concrete: the effect of confining reinforcement is generally modelled as a strength enhancement using a magnifying factor to f_{co} . A widely used model for predicting the strength of confined concrete was proposed by (Mander et al. 1988) and is expressed by the following equation:

$$\frac{f'_{cc}}{f'_{co}} = 2.254 \sqrt{1 + 7.94 \frac{f_L}{f'_{co}}} - 2 \frac{f_L}{f'_{co}} - 1.254 \quad (5)$$

in which f_L is the effective lateral confining pressure. The model of strength enhancement has been considered to account for the confined concrete in this study.

3.2 Constitutive modelling of steel

There are a limited number of models for the constitutive laws of the reinforcing bars; the one used in this investigation is a smoothed bilinear model with isotropic hardening, referred to as Steel02 in OpenSees (Figure 2). The model exhibits linear behaviour with an initial elastic modulus E_s up to yield stress f_y , followed by a strain hardening branch with a slope of $b \cdot E_s$. The transition curve between the curves branches asymptotes is governed by the parameter R_0 , which represents the Bauschinger effect (Menegotto and Pinto 1973).

3.3 Probabilistic models for material properties

The probabilistic models used in the sensitivity analysis are presented which some are adopted from the literature and others are assumed due to the lack of statistical studies. Table 1

documents the variables that define the probabilistic model of the material input variables. A correlation was assumed between the compressive strength (f_c) and the modulus of elasticity (E_c). The assumed correlation coefficient was 0.8 (Lee and Mosalam 2005). The modal damping ratio (ζ) of the frame system is taken as a random variable with a nominal value of 5% and COV of 40% (Lee and Mosalam 2005).

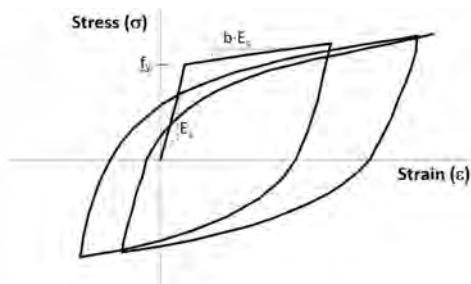


Figure 2. The constitutive model of steel.

4 NUMERICAL ANALYSIS & RESULTS

The developed algorithm was applied for a reinforced concrete frame system. The frame is a three-story three-bay frame with a column height of four meters and a beam span of seven meters. The frame's geometry and its reinforcement details are presented in Figure 3. The frame was taken from a building designed following the capacity design requirements following the seismic design regulations of the 90's, which was moderately new. The construction in that period lacked strict quality assurance protocols regarding building material testing. Therefore, uncertainty in the material behaviour is expected for such buildings, especially its nonlinear behaviour, and this uncertainty needs to be assessed and quantified.

Table 1. Variables defining the probabilistic model of input variables of constitutive models.

Variable	Probabilistic Model Description	Reference
Compressive strength (f_c)	Concrete grade C25 $F_{co} = \exp(m'' + tvs''(1+1/n'')^{0.5})$	JCSS
Modulus of elasticity (E_c)	Write the equation for the distribution	JCSS
Ratio of confined to unconfined concrete (k_{cf})	Normal Distribution, mean=1.3 COV=0.19	—
Ratio of residual to ultimate maximum stress (k_{res})	Normal Distribution, mean=0.2 COV=0.2	—
Concrete Ultimate strain (ϵ_{ult})	Lognormal Distribution, mean =0.37% COV=0.21	Baji 2014
Yield strength (f_y)	Normal Distribution, mean=420MPa COV=0.05	Nowak and Szerszen 2003
Modulus of elasticity (E_s)	Normal Distribution, mean=202GPa COV=0.04	Wisniewski 2012
(R_0) variable that influences the shape of transition curve	Normal Distribution, mean=15, COV=0.20	—
Strain hardening ratio (b)	Normal Distribution, mean= 0.15 COV=20%	—

The numerical model of the frame system, a two-dimensional idealization, was developed using the modelling capabilities of the software OpenSees. The frame's beams and columns were modeled using Force-Based Beam-Column Element with fibers representing concrete cover, concrete core, and reinforcement layers. The beam-column element has two transitional and

one rotational degree-of-freedom at the end nodes, and it has five monitoring cross-sections with fiber element discretization. As described above, Concrete02 (linear tension softening) was used for concrete and Steel02 (Menegotto-Pinto model with isotropic strain hardening) was used for reinforcing bars. The mass of the building was modelled using lumped masses at the nodes; the source of the nodal masses was the total dead load. The Newmark b-method was used as the time integrator with typical coefficients $\gamma=0.50$ and $\beta=0.25$. The time integration algorithm of nonlinear time history analysis (NLTH) uses a time step of half the time discretization of the generated ground motions. Furthermore, the solution algorithm of NLTH uses a modified Newton–Raphson solution algorithm that updates the stiffness matrix at the beginning of each time step. Newton with line search algorithm and Boyden algorithms were used in failing convergence in the given order. The sensitivity analysis examined the effect of input variables on the dynamic response considering two seismic hazard levels following ASCE 7-16; BSE-1E seismic event (50% exceedance in 50 years) and BSE-2N (10% exceedance in 50 years).

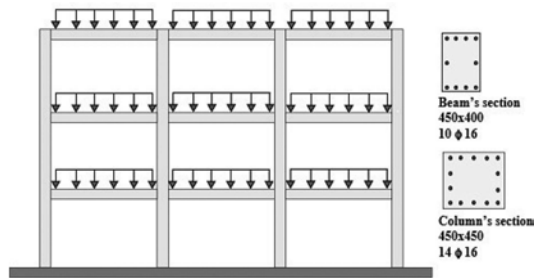


Figure 3. The details of the reinforced concrete frame used in the numerical simulation.

For the sensitivity analysis, the samples of the input variables were created taking $p=6$, $\Delta = 0.167$ and $r=50$. The elementary effects EE_i of the examined variables were determined for the maximum values of temporal responses. The examined input variables were: the compressive strength of concrete (f_c), the modulus of elasticity for concrete (E_c), ratio of confined to unconfined concrete (k_{cf}), ratio of residual to ultimate maximum stress for concrete (k_{res}), ultimate strain at concrete crushing (ϵ_{ult}), yield strength of steel (f_y), modulus of elasticity for steel (E_s), (R_0) variable that influences the shape of transition curve and takes into account the Bauschinger effect during first loading, the strain hardening ratio (b), and damping ratio (ζ). The EE_i 's were calculated r times, and the corrected average value (μ^*) for EE_i was calculated to rank the variable's influence on the examined output. The symbol μ is used instead of μ^* for convenience in discussing the results.

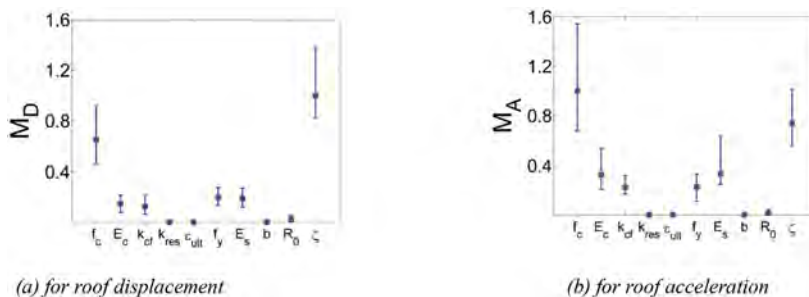


Figure 4. Screening measures considering the global responses considering for BSE-1E events.

The same procedure was repeated $m=25$ times for different sets of random ground motion records to assess the confidence of the identified rank for the input variables. The sensitivity measures were normalized to compare the results of the different responses. Furthermore, to check the consistency of the ranking of the input variables when considering different sets of

ground motion records, the sensitivity measures (μ) were calculated $m=25$ times. The median (M) of the (m) sensitivity measure (μ) was calculated and used for the final ranking of the variable's influence on the response maximum value.

The median values (M) of μ and their upper and lower values considering global responses; roof displacement and acceleration, are shown in Figure 4 and Figure 5. For the BSE-1E event, variables are classified into three groups based on their influence on the global response, high influence; f_c , ζ , intermediate influence; E_s , k_{cf} , f_y , E_c , and low influence; R_0 , b , k_{res} , ϵ_{ult} . Furthermore, the variation of sensitivity measures indicates that the ranking of the input variables of strong influence was more sensitive to record-to-record variability. For the BSE-2N event, variables were of three groups in their influence on the response, strong influence; ζ , f_c , R_0 , f_y , E_s , intermediate influence; k_{cf} , E_c , and low influence; b , k_{res} , ϵ_{ult} .

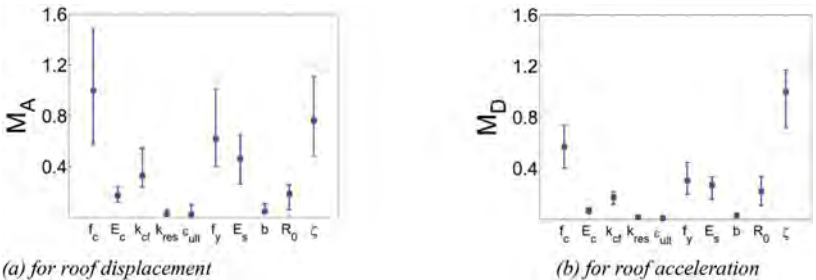


Figure 5. Screening measures considering the global responses considering for BSE-2N.

The median (M) values of sensitivity measure (μ) and their upper and lower values for the input variables considering the local response, curvature, are shown in Figure 6. For the BSE-1E event, variables groups of influence on the response were: strong influence; f_c , ζ , and intermediate influence; E_s , k_{cf} , f_y , E_c . This finding is even clearer for the seismic event BSE-2N as the variables f_c , ζ , R_0 , f_y , k_{cf} are of high ranks of influence on the response. The impact of constitutive model and its uncertainties is higher on local responses when compared with the global ones.

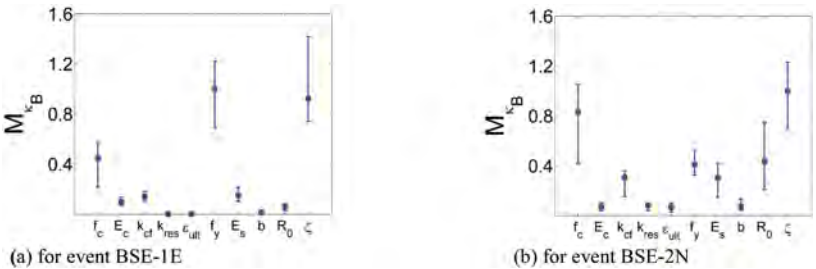


Figure 6. Screening measures considering the local responses.

5 CONCLUSIONS

The elementary effects method was adapted to rank the influence of the input variables, especially the variables that define the nonlinear constitutive models of concrete and steel. The elementary effects were determined for the maximum structural responses local and global. The method's algorithm was applied to a reinforced concrete moment-resisting frame considering two seismic events; the responses examined were the structure's displacement, acceleration, and curvature of the frame's section. It was found that the variables defining the constitutive models, f_y , E_s , f_c , R_0 and k_{cf} were significantly influential when considering stronger seismic events as inelastic behavior is expected. The input variables defining the material nonlinearities that indicate hysteresis damping has an impact as the viscous damping on the maximum response.

REFERENCES

- Baji, H. 2014. The effect of uncertainty in material properties and model error on the reliability of strength and ductility of reinforced concrete members. Master's thesis. The University of Queensland, Australia.
- Barbato, M. Zona, A. & Joel, P.C. 2014. Probabilistic nonlinear response analysis of steel-concrete composite beams. *Journal of Structural Engineering*, 140(1): 04013034.
- Campolongo, F. Cariboni, J. & Saltelli, A. 2007. An effective screening design for sensitivity analysis of large models. *Environ Model Soft*, 22, 1509–1518.
- Celarec, D. & Dolšek, M. 2013. The impact of modelling uncertainties on the seismic performance assessment of reinforced concrete frame building. *Engineering Structures*, 52, 340–354.
- Celarec, D. Ricci, P. & Dolšek, M. 2012. The sensitivity of seismic response parameters to the uncertain modelling variables of masonry-infilled reinforced concrete frames. *Engineering Structures*, 35, 165–177.
- Ghosh, S. & Chakraborty, S. 2021. Seismic fragility analysis in the probabilistic performance-based earthquake engineering framework: an overview. *International Journal of Advances in Engineering and Sciences and Applied Mathematics*, 13, 122–135.
- Gokkaya, B. U. Baker, J. W. & Deierlein G. G. 2016. Quantifying the impact of modeling uncertainties on the seismic drift demands and collapse risk of buildings with implications on seismic design checks. *Earthquake Engineering & Structural Dynamics*, 45, 1661–1683.
- Heo, Y. & Kunath, SK. 2009. Sensitivity to Constitutive Modeling in Fiber-Based Discretization of Reinforced Concrete Members for Performance-Based Seismic Evaluation. *Advances in Structural Engineering*, 12(1),37–51.
- Karaki, G. 2018. Implications of performance-based seismic design of nonstructural building components on life cycle cost of buildings. Analysis and Assessment in Civil Engineering: Towards an Integrated Vision: Proceedings of 6th International Symposium on Life-Cycle Civil Engineering (IALCCE 2018) Ghent University, Ghent, Belgium.
- Kim, J. & Han, S. 2013. Sensitivity analysis for seismic response of reinforced concrete staggered wall structures. *Magazine of Concrete Research*, 65(22),1348–1359.
- Lee, T. H. & Mosalam, K. 2005. Seismic demand sensitivity of reinforced concrete shear-wall building using FOSM method. *Earthquake Engineering and Structural Dynamics*, 34, 1719–1736.
- Mander, J.B. Priestley, M.J.N. & Park, R. 1988. Theoretical stress-strain model for confined concrete. *Journal of Structural Engineering ASCE*, 114(8), 1804–826.
- MATLAB. version R2014a. The MathWorks Inc., Natick, Massachusetts, 2014.
- MckKenna, F. Fenves, G.L., Scott, M.H. & Jeremic, B. 2014. Open system for earthquake engineering simulation. Pacific Earthquake Engineering Research Center, Berkeley, CA, 2014.
- Menegotto, M. & Pinto, P. 1973. Method of Analysis of Cyclically Loaded RC Plane Frames Including Changes in Geometry and Non-Elastic Behavior of Elements Under Normal Force and Bending, Preliminary Report, IABSE, Zurich, No.13:15–22.
- Morris, M. D. 1991. Fractional sampling plan for preliminary computational experiments. *Technometrics*, 33(2),161–174.
- Padgett, J. E. & DesRoches, R. 2007. Sensitivity of seismic response and fragility to parameter uncertainty. *Journal of Structural Engineering*, 133, 1710–1718.
- Saha, SK. & Matsagar, V., Chakraborty S. 2016. Uncertainty quantification and seismic fragility of base-isolated liquid storage tanks using response surface models. *Probabilistic Engineering Mechanics*, 43, 20–35.
- Saltelli, A. Ratto, M. Andres, T. Campolongo, F. Cariboni, J. Gatelli, D. Saisana, M. & Tarantola, S. 2018. *Global sensitivity analysis: the primer*. John Wiley.
- Sargin, M. 1971. Stress-Strain Relationship for Concrete and the Analysis of Structural Concrete Sections, PhD Dissertation, University of Waterloo, Canada.

Effect of concrete age on the reliability of existing reinforced concrete columns

L.C.R. Castro

ISQ, Belo Horizonte, Brazil

S.M.C. Diniz

Federal University of Minas Gerais, Belo Horizonte, Brazil

ABSTRACT: Condition assessment of existing reinforced concrete (RC) structures has been a major issue. Nevertheless, analysis of existing structures requires a distinct approach as compared to design of new ones, with particular emphasis on the selection of the target reliability index. When comparing reliability levels of new RC structures and existing ones, it must be considered that the analysis corresponds to two different times. In the design of new structures, there is an unaccounted extra safety margin due to concrete strength gain with age. The research presented herein evaluates the reliability of existing RC columns based on the same time reference. To this end, an equivalent 28-day concrete strength is obtained from the one associated to the existing structure. Probabilities of failure are computed by Monte Carlo simulation and the effects of different parameters are investigated. The results indicate that the effect of concrete gain with age should not be overlooked.

1 INTRODUCTION

Concrete is the most used construction material in the world; its production and utilization are responsible to 5 – 10 % of the global production of CO₂. Moreover, concrete production and utilization involve large resources consumption and waste generation. As such, life-cycle extension of existing RC structures and infrastructures is a major issue, and, consequently, adequate tools for condition assessment of existing RC structures are needed.

Different reports and initiatives (e.g. ACI 562; ASCE 2021) have corroborated the need for extension of the life cycle of structures and infrastructures. For instance, according to the 2021 ASCE Report Card for America’s Infrastructure (ASCE 2021), in 2021, 7.5 % of the US bridge inventory were rated “*structurally deficient*” (46,154 out of 617,000); 42% of all bridges are at least 50 years old. It is estimated that 178 million trips are taken across these structurally deficient bridges every day.

One of the key tasks in the decision making process over strengthening/ retrofitting or demolishing an existing structure or infrastructure is its condition assessment and checking against expected performance rules, usually established in technical codes (Badimuena & Diniz 2018).

From the perspective of the treatment of uncertainties, the problem of performance evaluation of existing RC structures and infrastructures is quite distinct from design of new ones (Melchers 2001). Design codes for new structures deal with uncertainties related to design and construction process; on the other hand, there is a change in the nature of such uncertainties, from inherent to epistemic, for a number of the variables involved in the performance of the existing RC structure.

Design of new reinforced concrete (RC) structures/ components is based on semi-probabilistic approaches. An important concept in the semi-probabilistic design format is the target reliability index, β_T , used in the calibration of a given design code (Diniz 2008). In the assessment of existing structures, there is no consensus on the target reliability index to be used. However, different

aspects - economic, social and sustainability - point to the need to accept lower reliability indexes than those taken as reference for new structures (Diamantidis *et al.* 2012).

In the development of procedures for the condition assessment of existing RC structures, it is important to define the target reliability index to be used in this context. This is a complex issue and very different understandings exist on this topic. For instance, Steenbergen *et al.* (2015) point out that the requirements for the same target reliability for existing and new structures is uneconomical. Similarly, ISO 13822 (ISO 2010) suggests that lower target reliability levels for existing structures may be used if they can be justified on the basis of socio-economic criteria. On the other hand, Wang & Ellingwood (2015), in the context of bridge engineering, state that rehabilitated bridges should have comparable reliability to new bridges.

There is still another issue related to the reliability of existing RC structures that has not received proper attention. When comparing reliability levels of new RC structures and existing ones, it must be taken into account that the analysis corresponds to two different times. Along the life cycle of the structure, concrete is affected by two different phenomena: (i) strength gain with age, and (ii) strength loss due to sustained loads (Diniz 2005; Diniz & Frangopol 2003). In the design of new structures, there is an unaccounted extra safety margin due to concrete strength gain with age. Therefore, a rational comparison between the safety levels associated to new and existing RC structures shall be based on the same time reference.

In this research, reliability levels associated with short, axially-loaded, existing RC columns are evaluated. The scope of the research presented in Badimuena & Diniz (2018) is enlarged by including the effect of concrete age on the concrete compressive strength used in the analysis. The influence of different parameters (number of cores, concrete compressive strength and attendant coefficient of variation, strength gain with age, dead-to-live-load ratio, and longitudinal reinforcement ratio) on the resulting reliability levels is discussed.

2 DETAILS OF THE SELECTED COLUMNS

The selected columns have been defined and analyzed according to the requirements of ACI 562 (2016) for minimum reinforcement and minimum cross-sectional dimensions. They correspond to square cross-sections (30 x 30 cm²) and three mean concrete compressive strengths ($f_{cm} = 15, 30,$ and 50 MPa), defining column series P1, P2, and P3, respectively.

It was assumed that the information on the concrete strength comes from extracted cores; the number of samples, n , taken as 3 and 8. The former value is the minimum number of cores recommended by ACI 562. The coefficient of variation (COV) of concrete (cores strength) is assumed as 5, 10, and 15 %. As a reference, 10 % is the value of the COV that has been used in the calibration of ACI 318, i.e. in the design of new structures.

With respect to the concrete strength gain with age, as related to the 28-day strength, three different assumptions were made: (i) no gain, meaning that this effect would be disregarded; (ii) 30% increase; and (iii) 18.5% increase (designated as I, II, and III, respectively). The values of 30% and 18.5% increase in concrete compressive strengths are suggested by Mehta and Monteiro (2006) when comparing 5-yr to 28-day strengths.

Three longitudinal steel ratios ($\rho_l = 1, 2,$ and 4 %) are considered. The characteristic steel yield strength is taken as 500 MPa for all columns. Details of the selected columns are presented in Table 1. In each column series, three dead-to-live-load ratios are assumed: 0.5, 1.0, and 2.0 resulting in 486 axially-loaded RC columns.

3 STRUCTURAL RELIABILITY BASICS

The basic problem of structural reliability may be cast as a supply versus demand problem, i.e. to ascertain that the supply (e.g. column capacity), X , is larger than the demand (e.g. load effects), Y , throughout a reference period (e.g. the newly defined service life of the existing structure), represented by ($X > Y$). Considering the uncertainties associated to these variables, this assurance is possible only in terms of the probability $P(X > Y)$, thus providing a metric of the reliability of the structural component (Ang & Tang 1984).

Table 1. Summary of the selected columns.

Series	COV (%)	n	ρ_I (%)	r	Type	
P1, P2, P3 $f_{cm} = 15, 30, 50$ MPa	5	3	1	0.5, 1, 2	I, II, III	
			2	0.5, 1, 2	I, II, III	
			4	0.5, 1, 2	I, II, III	
		8	1	0.5, 1, 2	I, II, III	
			2	0.5, 1, 2	I, II, III	
			4	0.5, 1, 2	I, II, III	
		10	3	1	0.5, 1, 2	I, II, III
				2	0.5, 1, 2	I, II, III
				4	0.5, 1, 2	I, II, III
	8		1	0.5, 1, 2	I, II, III	
			2	0.5, 1, 2	I, II, III	
			4	0.5, 1, 2	I, II, III	
	15	3	1	0.5, 1, 2	I, II, III	
			2	0.5, 1, 2	I, II, III	
			4	0.5, 1, 2	I, II, III	
8		1	0.5, 1, 2	I, II, III		
		2	0.5, 1, 2	I, II, III		
		4	0.5, 1, 2	I, II, III		

The supply-demand problem may be formulated in terms of the margin of safety, $M = X - Y$. Since X and Y are random variables, M is also a random variable with probability density function, $f_M(m)$. Failure is associated to the condition ($M < 0$); if the probability distribution of M is known, the corresponding probability of failure, P_f , may be computed by:

$$P_F = \int_{-\infty}^0 f_M(m) dm = F_M(0) \tag{1}$$

where $F_M(\cdot)$ is the cumulative distribution function of the variable M . Graphically, this probability is represented by the area below zero under the curve $f_M(m)$.

For statistically independent random variables X and Y , represented by Normal distributions, i.e., $N(\mu_X, \sigma_X)$ and $N(\mu_Y, \sigma_Y)$, respectively, the margin of safety M is also a Normal random variable, $N(\mu_M, \sigma_M)$. The notation $N(\mu, \sigma)$ represents a Normal variable with mean μ and standard deviation σ . In this case, the probability of failure is given by:

$$P_F = F_M(0) = \Phi\left(\frac{-\mu_M}{\sigma_M}\right) = 1 - \Phi\left(\frac{\mu_M}{\sigma_M}\right) = \Phi(-\beta) \tag{2}$$

where Φ is the standard Normal cumulative distribution function, and the probability of non-failure, P_S , is:

$$P_S = 1 - P_F = \Phi\left(\frac{\mu_M}{\sigma_M}\right) = \Phi(\beta) \tag{3}$$

From Eq. (3) it is seen that reliability is a function of the ratio μ_M/σ_M , which is the margin of safety expressed in units of σ_M and is known as “reliability index” and denoted by β . In this specific case (linear performance function and Normal variables), the reliability index can be computed based solely on the information on the means and the standard deviations of the basic variables pertaining to the problem (Ghosn *et al.* 2016). For nonlinear performance functions and/or non-Normal variables, other methods such as FORM or Monte Carlo simulation shall be used (Ang & Tang 1984).

4 PERFORMANCE FUNCTION

The ultimate limit state function for short, axially-loaded RC columns is given by:

$$M = [\alpha_c F_c (A_g - A_s) + F_y A_s] E_M - (G + Q) \quad (4)$$

In the above equation, M is the margin of safety, and the random variables F_c is the 28-day equivalent concrete compressive strength, A_g is the area of the gross cross-section, F_y is the steel yield strength, G and Q are the dead and live loads acting on the column, respectively, and E_M is the model error associated to the estimation of column resistance. The area of longitudinal steel, A_s , is taken as deterministic; the deterministic parameter α_c is taken as a function of the concrete grade. It should be noted that, according to the goals of the research reported herein, the random variable F_c incorporates the effects of the concrete strength gain with age and the action of sustained loads on concrete compressive strengths. This topic will be discussed in the following section.

5 STATISTICS OF THE BASIC VARIABLES

The statistics of the basic variables, to be used in the Monte Carlo simulation procedure for the safety assessment of existing RC columns, are discussed in this section. As a full-probabilistic approach, Monte Carlo simulation requires the complete description of all random variables in the attendant performance function, Eq. (4).

The procedure used in the definition of the statistics of the load effects (mean dead load, μ_G , and mean live load, μ_Q) is summarized in Badimuena and Diniz (2018). For each selected column, design loads, S_d , from which the statistics of the acting loads may be derived, are obtained by assuming $S_d = R_d$, i.e. design loads are equal to design column resistance (Diniz & Frangopol 1997).

In the calculation of the design column resistance, R_d , according to ACI 362 (2016), the value of the equivalent specified compressive strength, f'_{ceq} , is required. The equivalent specified compressive strength is given by:

$$f'_{ceq} = 0.9f_{cm} \left[1 - 1.28 \sqrt{\frac{(k_c V)^2}{n} + 0.0015} \right] \quad (5)$$

where f_{cm} is the mean resistance of cores (after adjustments for size effects and humidity), V is the coefficient of variation of the cores strength, n is the number of cores used in the estimation of f_{cm} , and k_c is a modification factor for the coefficient of variation of the cores strength that depends on the number of cores (assumed as $n = 3$ and 8 in this study).

For each column, based on the corresponding design loads, S_d , the assumed load ratio r ($r = \mu_G/\mu_Q$), and the information presented in Galambos *et al.* (1982) for the dead load, G , and the live load, Q , then the complete statistics (mean, COV, and type of distribution) of G and Q are defined. In this study, the following values are assumed for the ratio r : 0.5, 1.0, and 2.0.

Regarding the statistics of the variables related to column resistance, special attention was given to those associated to the *in situ* concrete compressive strength. A discussion on the statistics to be used in the description of the *in situ* concrete compressive strength as given by concrete cores extracted from the existing RC structure is presented in Castro & Diniz (2020).

A summary of the statistics of the basic variables related to the corresponding performance function (Eq. 4) is displayed in Table 2.

In this paper, the effect of the concrete strength gain with age in the reliability of existing RC structure is sought. As such, the same time reference is used, given by the 28-day strength. To this end, after obtaining the concrete strength information for the existing structure, as given by the extracted concrete cores, the equivalent 28-day strength is calculated by dividing the strength obtained from cores by a factor $(1 + i/100)$, where i is the strength gain in percentage. It is assumed that the full potential for the concrete strength development has been achieved.

As such, an important issue is the value of the strength gain to be considered in the analysis. In this study, three different considerations are made: (a) neglecting the effect of the strength

gain, (b) assuming a 30 % increase, and (c) assuming an 18.5 % increase. For the same concrete strength obtained from extracted cores, a higher strength gain translates into a smaller equivalent 28-day compressive strength. Additionally, an existing RC structure has also been affected by the action of sustained loads. In order to account for this effect, the strength obtained from the extracted cores is further divided by a factor, k_{sl} , given by (Diniz & Frangopol 2003):

$$k_{sl} = 1 - 0.2 \left(\frac{r}{r + I} \right) \quad (6)$$

where r is the ratio mean dead load, μ_G , to mean live load, μ_Q .

Table 2. Statistics of the basic variables.

Mean	Coefficient of Variation (%)	Type of distribution	Reference
Concrete Compressive Strength $f_{cm} = 15, 30, 50$ MPa	5, 10, 15	Lognormal	Assumed
Longitudinal Steel $f_{ym} = 572.5$ MPa	10	Lognormal	Assumed
Cross-Section Geometry B=30 cm H= 30 cm	1.93 1.93	Normal Normal	JCSS (2001)
Model Error 1.0	11	Normal	Diniz & Frangopol (1997)
Dead Load μ_G	10	Normal	Galambos <i>et al.</i> (1982)
Live Load μ_Q	25	Gumbel	Galambos <i>et al.</i> (1982)

6 RELIABILITY RESULTS

The reliability assessment was performed for the 486 existing RC columns described in Table 1. Loads acting on the column have been obtained from the assumption $S_d = R_d$, where R_d is taken as the column resistance according to ACI 562 (ACI 2016). Monte Carlo Simulation was used in the reliability analysis of each existing RC column with respect to the ultimate limit state. Probabilities of failure (and corresponding reliability indexes) were computed for each column at a given scenario (V_c , n , and concrete strength gain with age). Considering the large volume of data that resulted from these analyses, only reliability indexes are presented in Tables 3 and 4 (corresponding probabilities of failure are given by Eq. (2)).

Tables 3 and 4 display reliability indexes for the scenario $n = 3$ which represents the minimum number of cores allowed by ACI 562, and an upper bound for the probabilities of failure in each case. It is seen that V_c has a great influence on the corresponding reliability index. For instance, the results shown in the first line of Table 3, representing an existing RC column with $f_{cm} = 15$ MPa, $\rho_l = 1\%$ $r = 0.5$, $n = 3$, and neglecting the effect of the strength gain, the reliability indexes are 3.57, 3.26, and 2.98, for V_c equal to 5, 10, and 15 %, respectively. All other factors remaining the same, the values displayed in Table 3 (neglecting concrete strength gain) represent upper bounds for the reliability indexes.

For the sake of brevity the results corresponding to 18.5 % strength gain are not shown here, they are found in Castro (2019). From the results obtained, it was found that the higher the concrete gain, the smaller the equivalent reliability index. This fact is easily understood; for the same strength measured by extracted cores, the higher the strength gain the smaller the equivalent 28-day strength and, consequently, the smaller the equivalent reliability index.

In this paper, the assessment of the reliability levels of existing RC columns is based on the same time reference as used in the design of new ones. To this end, an equivalent 28-day concrete strength is obtained from the one associated to the existing structure according to the methodology described in Section 5. The number of cores, assumed here as 3 or 8 cores, has a positive impact on the safety levels as the sample size increases. For instance, for $n = 3$, $f_{cm} = 15$ MPa, $\rho_l = 1\%$, $r = 0.5$, and neglecting concrete strength gain, reliability indexes are 3.57, 3.26, and 2.98, corresponding to $V_c = 5, 10$, and 15% , respectively. For $n = 8$ and all other conditions remaining the same, reliability indexes are 3.59, 3.44, and 3.28, corresponding to $V_c = 5, 10$, and 15% , respectively. Accordingly, the discussion presented herein will be based on results related to $n = 3$.

It is noted that the higher the coefficient of variation, the higher the impact of the number of cores on the resulting reliability index. While this impact is minimum in the case of smaller values of V_c , the differences are more significant for higher values of V_c . In the previous example, an increment in the number of cores from 3 to 8 translates into an increase of about 0.02 in the reliability index for $V_c = 5\%$; conversely, this increase is about 0.30 in the case of $V_c = 15\%$.

Tables 3 and 4 display reliability indexes for the scenarios “neglecting strength gain” and “30% strength increase”, respectively. It is seen that the coefficient of variation associated to the concrete strengths has a significant impact in all the considered scenarios. For instance, for $n = 3$, $f_{cm} = 15$ MPa, $\rho_l = 1\%$, $r = 0.5$, and neglecting concrete strength gain, reliability indexes are 3.57, 3.26, and 2.98 for $V_c = 5, 10$, and 15% , respectively; for “30% strength increase” the reliability indexes are 3.32, 3.05, and 2.79 for $V_c = 5, 10$, and 15% , respectively. The condition “neglecting strength gain” represents usual assumptions in reliability analyses. The reliability indexes in Table 3 are in the range 3.51 – 3.99, 3.23 – 3.62, and 2.87 – 3.34, for $V_c = 5, 10$, and 15% , respectively.

Table 3. Reliability index, $n = 3$, neglecting the effect of the concrete strength gain.

Series	ρ_l (%)	r	β		
			5 %	10 %	15 %
1	1	0.5	3.57	3.26	2.98
1	1	1.0	3.66	3.28	2.95
1	1	2.0	3.67	3.23	2.87
1	2	0.5	3.55	3.34	3.14
1	2	1.0	3.65	3.39	3.15
1	2	2.0	3.70	3.38	3.09
1	4	0.5	3.51	3.39	3.27
1	4	1.0	3.62	3.46	3.32
1	4	2.0	3.68	3.49	3.31
2	1	0.5	3.67	3.39	3.10
2	1	1.0	3.79	3.43	3.09
2	1	2.0	3.87	3.42	3.02
2	2	0.5	3.65	3.42	3.19
2	2	1.0	3.77	3.47	3.20
2	2	2.0	3.83	3.48	3.15
2	4	0.5	3.61	3.44	3.28
2	4	1.0	3.72	3.53	3.32
2	4	2.0	3.81	3.55	3.30
3	1	0.5	3.76	3.49	3.21
3	1	1.0	3.87	3.55	3.22
3	1	2.0	3.99	3.57	3.17
3	2	0.5	3.74	3.49	3.26
3	2	1.0	3.85	3.56	3.28
3	2	2.0	3.95	3.59	3.24
3	4	0.5	3.68	3.49	3.30
3	4	1.0	3.80	3.58	3.34
3	4	2.0	3.90	3.62	3.34

Table 4. Reliability index, $n = 3$, 30 % strength increase.

Series	ρ_l (%)	r	β		
			5 %	10 %	15 %
1	1	0.5	3.32	3.05	2.79
1	1	1.0	3.37	3.03	2.74
1	1	2.0	3.36	2.97	2.64
1	2	0.5	3.30	3.12	2.94
1	2	1.0	3.36	3.14	2.93
1	2	2.0	3.36	3.09	2.85
1	4	0.5	3.30	3.20	3.10
1	4	1.0	3.37	3.25	3.13
1	4	2.0	3.39	3.24	3.09
2	1	0.5	3.39	3.12	2.85
2	1	1.0	3.46	3.13	2.81
2	1	2.0	3.47	3.07	2.72
2	2	0.5	3.33	3.11	2.91
2	2	1.0	3.39	3.13	2.88
2	2	2.0	3.40	3.08	2.80
2	4	0.5	3.29	3.15	3.01
2	4	1.0	3.36	3.19	3.02
2	4	2.0	3.38	3.17	2.96
3	1	0.5	3.44	3.18	2.92
3	1	1.0	3.51	3.20	2.90
3	1	2.0	3.55	3.17	2.82
3	2	0.5	3.35	3.13	2.91
3	2	1.0	3.42	3.16	2.90
3	2	2.0	3.44	3.12	2.81
3	4	0.5	3.29	3.13	2.96
3	4	1.0	3.35	3.16	2.96
3	4	2.0	3.37	3.12	2.90

Considering that in this study the analyzed columns follow ACI 562, in this research, β_T will be taken as 3.5 as suggested in ACI 440 (2017). From the values displayed in Table 3, it is seen that β_T is met in all columns corresponding to $V_c = 5\%$. The target is also met in columns corresponding to $V_c = 10\%$, exception made for the combination of low concrete compressive strengths ($f_{cm} = 15$ MPa) and small amount of longitudinal steel ratio ($\rho_l = 1\%$). The target is not met in columns corresponding to $V_c = 15\%$. The scenario “30 % strength increase” (Table 4) represents concretes made with usual cements, thus providing an upper bound on the probabilities of failure of existing RC columns (and lower bounds on the corresponding reliability indexes). The reliability indexes displayed in Table 4 are in the range 3.29 – 3.55, 2.97 – 3.25, and 2.64 – 3.13, for $V_c = 5, 10$, and 15 %, respectively. This corresponds to a drop of 0.22, 0.26, and 0.23 in the minimum β values from the “neglecting strength gain” condition to the “30 % strength increase” one, for $V_c = 5, 10$, and 15 %, respectively. In this scenario, β_T is not met in almost all cases, even for $V_c = 5\%$. Considering, for instance the reliability index decrease from 3.51 (“neglecting strength gain”) to 3.29 (“30 % strength increase”), this translates in terms of probabilities of failure in an increase from 2.24×10^{-4} to 5.01×10^{-4} , i.e. more than doubling the probability of failure.

7 CONCLUSIONS

The results obtained point out to the need to address the effect of the concrete strength gain with age on the safety of existing RC columns. All other parameters remaining the same, the larger the strength gain, the smaller the corresponding 28-day equivalent reliability index. By neglecting this effect, an overestimation of the reliability index is obtained. In other words,

this reduced 28-day equivalent reliability index reflects the reliability of the existing column that will not be able to offer a hidden safety margin in its extended service life. The results also indicate that the number of cores and coefficient of variation of the cores' strength have an important effect on the existing column reliability. Reliability indexes below target values ($\beta_t = 3.5$) were found for the combination of minimum number of extracted cores ($n = 3$) and higher values of V_c (15 %), even in cases when concrete strength gains are neglected. The decrease in the reliability index is roughly 0.2-0.4 when the strength gain effect is considered and $V_c = 5$ %; nevertheless, the associated probability of failure may be twice or six times higher. This may be particularly important in the case of life cycle costs where probabilities of failure should explicitly be taken into account.

REFERENCES

- American Concrete Institute. 2016. *ACI 562: Code Requirements for Evaluation, Repair, and Rehabilitation of Concrete Buildings*. Farmington Hills.
- American Concrete Institute. 2017. *Guide for the design and construction of externally bonded FRP systems for strengthening concrete structures (ACI 440.2R)*, Farmington Hills.
- American Society of Civil Engineers. 2021. *ASCE 2021 Report Card for America's Infrastructure*, <https://infrastructurereportcard.org/cat-item/bridges-infrastructure/>
- Ang, A.H-S. & Tang, W.H. 1984. *Probability Concepts in Engineering Planning and Design – Decision, Risk, and Reliability*, Vol. II.
- Badimuena, B.L. & Diniz, S.M.C. 2018. Code development for existing structures: influence of concrete strength statistics, *Maintenance, Safety, Risk, Management and Life-Cycle Performance of Bridges*, CRC Press.
- Castro, L.C.R. 2019. *Confiabilidade Estrutural de Pilares Existentes de Concreto Armado: Influência da Perda de Armadura de Aço e da Idade do Concreto* (in Portuguese), M.Sc. Thesis, Federal University of Minas Gerais, Brazil.
- Castro, L.C.R. & Diniz, S.M.C. 2020. The joint effect of *in situ* concrete compressive strength and cross-sectional reduction of longitudinal steel on the reliability of existing RC columns, *10th International Conference on Bridge Maintenance, Safety, and Management (IABMAS 2020)*.
- Diamantidis, D., Holický, M., Sýkora, M., Marková, J., Vrouwenvelder, T., Tanner, P., Arteaga, A., Lara, C., Croce, P., Toprak, S., Senel, S.M., Inel, M. 2012. *Innovative methods for the assessment of existing structures*. Prague: Czech Technical University in Prague, 148 p.
- Diniz, S.M.C. 2005. Effect of concrete age specification on the reliability of HSC columns. *Proceedings of the 9th International Conference on Structural Safety and Reliability*, ICOSSAR'05, Rome, Italy, June 19-23, 2005, Millpress.
- Diniz, S.M.C. 2008. Structural Reliability: Rational Tools for Design Code Development. *Crossing Borders: 2008 Structures Congress*. Reston, EUA, ASCE.
- Diniz, S.M.C. & Frangopol, D.M. 1997. Reliability Bases for High-Strength Concrete Columns, *Journal of Structural Engineering*, 123 (10), ASCE.
- Diniz, S.M.C. & Frangopol, D.M. 2003. Safety evaluation of slender high-strength concrete columns under sustained loads. *Computers and Structures*. 81, 1475–1486.
- Galambos, T., Ellingwood, B., MacGregor, J., Cornell, A. 1982. Probability based load criteria: assessment of current design practice. *Journal of Structural Division*, ASCE, pp.959–977.
- Ghosn, M., Frangopol, D.M., McAllister, T.P., Shah, M., Diniz, S.M.C., Ellingwood, B.R., Manuel, L., Biondini, F., Catbas, N., Strauss, A., and Zhao, X.L. (2016). Reliability-Based Performance Indicators for Structural Members, *Journal of Structural Engineering*, ASCE, 142(9).
- International Organization for Standardization. 2010. *Basis for Design of Structures – Assessment of Existing Structures* ISO 13822:2010.
- Joint Committee on Structural Safety (2001). Probabilistic Model Code, JCSS <<http://www.jcss.ethz.ch/>>.
- Mehta, P. & Monteiro, P.J. 2006. *Concrete: Microstructure, Properties and Materials*. 3rd ed., New York, McGraw Hill.
- Melchers, R.E. 2001. Assessment of Existing Structures – Approaches and Research Needs, *Journal of Structural Engineering*, ASCE, 127(4).
- Steenbergen, R.D.J.M., Sýkora, M., Diamantidis, D., Holický, M., Vrouwenvelder, T. 2015. Economic and human safety reliability levels for existing structures. *Structural Concrete*, 323–332.
- Wang, N. & Ellingwood, B.R. 2015. Limit state design criteria for FRP strengthening of RC bridge components. *Structural Safety*, Elsevier.

A microservice for evaluating resilience of water distribution network

X.Y. Yu, Y.N. Xu & F. Liu

State Key Laboratory of Disaster Reduction in Civil Engineering, Tongji University, China
Key Laboratory of Geotechnical and Underground Engineering (Tongji University), Ministry of Education, Shanghai, China

X.N. Zhou

Department of Civil and Environmental Engineering, Rice University, Houston, TX, USA

ABSTRACT: Infrastructure Smart Service System (iS3) is an open source and dataflow-integrated platform that promotes the data sharing in the life-cycle civil engineer. As the application layer of iS3, this paper constructed a microservice for evaluating lifecycle resilience of water distribution network (WDN). The implementation of the microservice includes two main steps: (1) encapsulate the resilience assessment module WARA into a microservice based on Django framework; and (2) deploy the microservice on iS3 platform by calling a WebAPI. An application of the microservice was demonstrated through a WDN in a seismically active region. The results were calculated in the microservice and then returned to the iS3 platform. The iS3-based resilience assessment microservice for WDN may serve as a handy yet scientific tool to evaluate the disaster resistance capability of WDN over its life cycle, and provide a reproducible template for other smart infrastructure application in the field of life-cycle civil engineering.

1 INTRODUCTION

The traditional infrastructure governance mode (i.e., “smokestack” mode) in the field of life-cycle civil engineering often suffers from “isolated” data and low efficiency of urban management, and has been no longer suitable for the development of future cities (Lv et al., 2020). With the rapid development of information technology (e.g., the Internet of Things, big data and artificial intelligence), intelligent management of infrastructure injects new thought to the innovation of urban infrastructure development mode and brings the tangible development benefits for urban residents (Gharaibeh et al., 2017). However, a truly open source and dataflow-integrated platform have not been well developed (Gharaibeh et al., 2017) to considerably exploit the value of the shared-data. The current research particularly focuses on a certain stage of the information flow chain and develops mutually independent systems, such as smart Internet of Things system (Jin et al., 2014, Lv et al., 2020, Talari et al., 2017), and smart analysis system (Tang et al., 2017, Ullah et al., 2020). To make up this deficiency, infrastructure Smart Service System (iS3) was developed by Tongji University (Zhu et al., 2018) from the perspective of information flow to serve infrastructure objects such as tunnels (Zhen et al., 2021, Chen et al., 2020), metro stations (Chen et al., 2020), roads, bridges, pipe corridors (Yang, 2018), and foundation pits. In some sense, iS3 is essentially an “operating system” and a shared data warehouse. As an application of iS3 platform, this paper developed a microservice by building a Django-based WebAPI for evaluating lifecycle resilience of WDN, where the resilience of the entire WDN could be attained in the microservice and then

will be returned to the iS3 platform by calling the WebAPI. The innovations of this paper are twofold: (1) to improve the efficiency of engineering data analysis in the field of life-cycle civil engineering by structuring the data and storing them in the data layer of iS3; and (2) to make an attempt to the smart WDN application and provide a reproducible template for other smart infrastructure application in the field of life-cycle civil engineering based on iS3.

2 THE BASIC OF IS3

iS3 is an integrated decision-making service system for the data collection, processing, expression, analysis and integrated decision services of the life-cycle data of infrastructure. Meanwhile, equipped with a microservice architecture and rich data and graphical interface (Zhu et al., 2018), iS3 could enable a microservice to be deployed on iS3 platform in a pluggable way (Li et al., 2020). The core functions of iS3 include 2D/3D graphics, GIS maps, databases, project object management, and project life-cycle data management (Zhu et al., 2017). The system framework of iS3 can be divided into five layers: base layer, data layer, service layer, application layer and user layer, as shown in Figure 1. The base layer is the hardware equipment set of the system. The data layer is to provide the service layer with the required computing and storage resources. The service layer is a logical layer that provides data access and analysis service interface for the application layer, which unifies the way of data access and the calling way of the underlying hardware devices, and ensures the security of data. The application layer is a user-oriented client program that provides users with friendly access to the system. At present, iS3 has developed four types of applications, namely iS3 Desktop, iS3 Web, iS3 Mobile and iS3 Cloud, to meet different user requirements. The iS3 project is now hosted on github at <https://github.com/iS3-Project>.

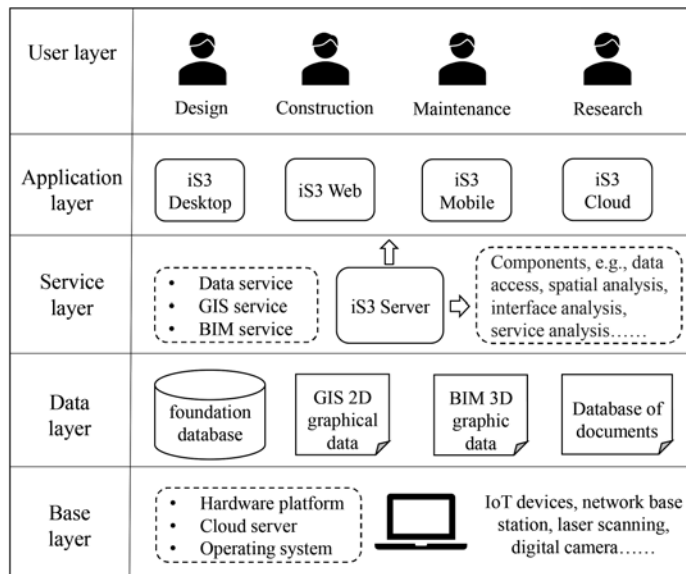


Figure 1. The architecture of iS3 platform (Zhu et al., 2018).

3 IMPLEMENTATION

3.1 Lifecycle resilience evaluation for WDN

The life-cycle resilience evaluation for WDN in this paper is based on the model WARA of Zhou et al. (2019), the workflow of which is shown in Figure 2. As shown in Figure 2, the life-

cycle resilience of a WDN is evaluated considering internal deterioration and external perturbation in a predefined exposure time period at different hazard scenario:

$$h_i = [(d_1, t_1), (d_2, t_2), (d_3, t_3) \dots \dots (d_k, t_k)] \tag{1}$$

where h_i is the i^{th} hazard scenario, and d_k is the hazard intensity measure at time $t_k = k\Delta t$.

At each time step t_k , a six-step analysis is conducted for resilience calculation, which includes (1) random hazard scenario generating, (2) component survival assessment considering the simultaneous effect of deterioration and perturbation, (3) system response analysis through hydraulic simulation to gain the system functionality, (4) recovery analysis, (5) functionality trajectory obtaining, and (6) resilience of that scenario quantifying. By dividing the life cycle of the WDN into different time t_k and repeating the above six-step analysis at each time t_k , the life-cycle resilience of WDN would be obtained. Details about the model are available in the reference (Zhou et al., 2019).

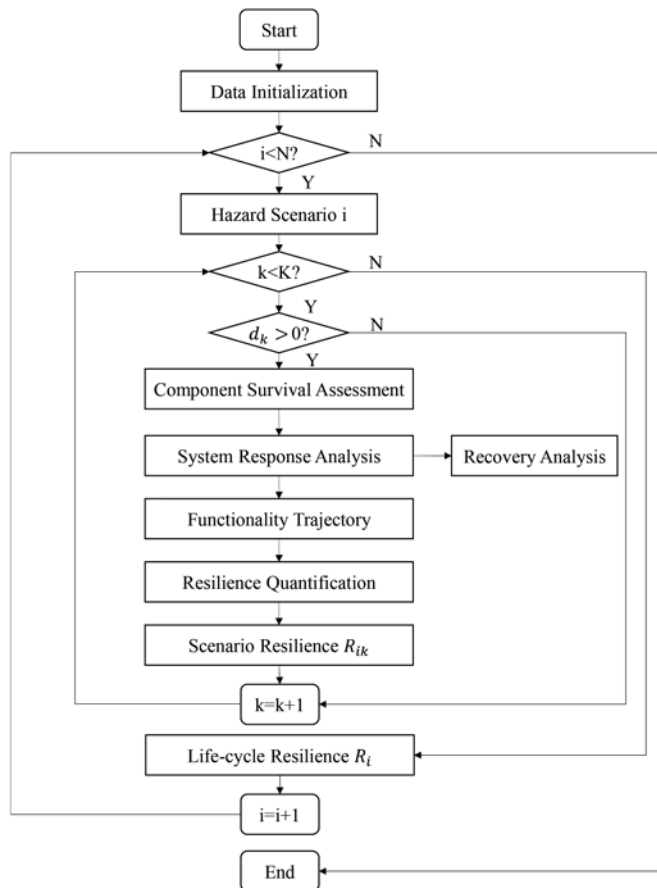


Figure 2. Workflow of WARA (Zhou et al., 2020).

3.2 Microservice development

Compared with stand-alone programs, microservices have the advantages of flexible updating and reusing. Thus, this study encapsulated WARA into a microservice by building a Django-based WebAPI (Django-Software-Foundation, 2022). The workflow of encapsulating WARA is shown in Figure 3. We firstly built a python-based virtual environment to avoid the contradiction caused by different application services required by different versions of dependent libraries. Secondly, we structured the data of WDN based on the data standard of iS3 and

uploaded the structured data into the data layer of iS3 platform through the data interface of iS3. The structured data are shown in Table 1.

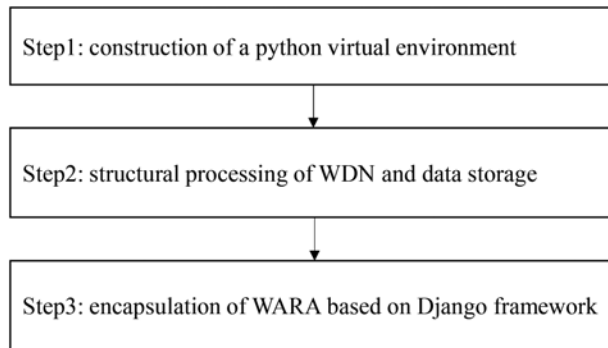


Figure 3. The workflow of encapsulating WARA.

Table 1. Pipe network components and properties.

Element	Attribute
demand nodes	ID, coordinates, altitude, initial water demand
pipe	ID, start node, end node, length, diameter, roughness, age, material, status
tank	ID, altitude, initial water level, the highest water level, the lowest water level, diameter, coordinates
reservoir	ID, initial water head, coordinates
pump	ID, start node, end node, type, pump speed setting
valve	ID, start node, end node, diameter, type

Finally, we encapsulated the WARA module based on the MTV response pattern of Django framework (see Figure 4). The purpose of template is to essentially control the display of content and accept user input, where the HTML code is usually placed to render the data. We mainly encapsulated python code of WARA in view and model modules. The project framework is shown in Figure 5. As shown in Figure 5, the setup file is the internal parameter file of the whole website, which sets all the basic parameters of the website running, including the database instance name, WebAPI name, template name and other basic content. The URL file identifies the locations where all websites invoke resources. To maintain independence and portability, the WARA module is placed in WebAPI, which is a sub-application that runs on the web site. The HTML template is used to send front-end files to the browser so that the client can receive content from the server graphically. Model file is the classes that interact with the database. View control file contains a series of functions, which calls the corresponding view function and sends it to the front end to change the content of the front end after receiving the response from the client. The URL file contains the location of all resources in the WebAPI, which can be directly invoked in the URL file at the website level. The script file is a script file that calls all the libraries in the python internal environment for specific project instance operations, and can be used to try to call functions inside the file. The Manage.py file is a website-level control file that enables operations such as starting servers and setting ports.

3.3 *Microservice deployment on iS3*

iS3 is a platform with a microservice architecture (Li et al., 2020), which provides various interfaces (e.g., data and visualization interface) for microservice to invoke and present the

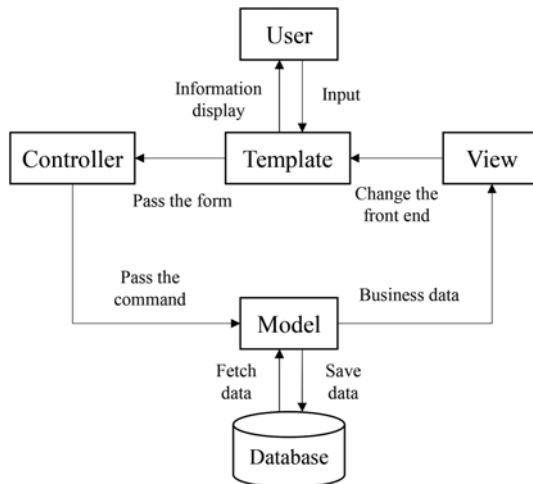


Figure 4. MTV response pattern diagram.

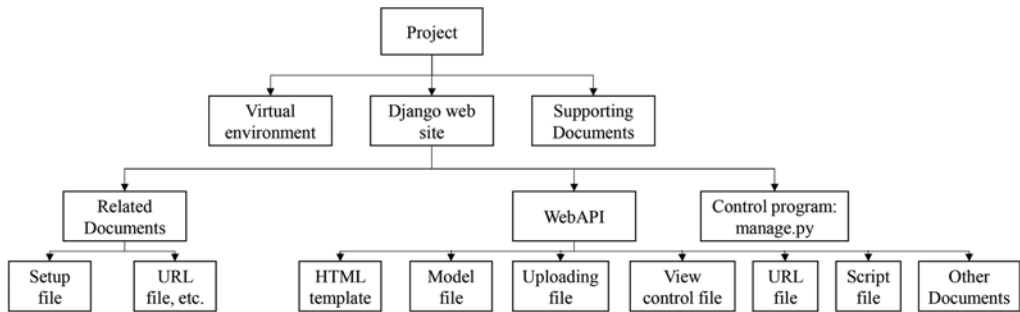


Figure 5. Project frame drawing.

calculation results at visualization center by calling the WebAPI of the microservice. Figure 6 shows the deployment of the microservice on iS3 platform.

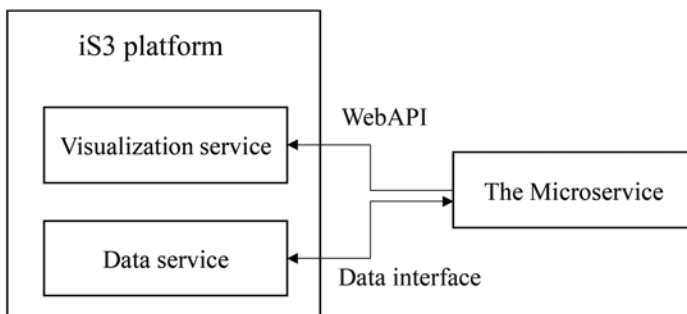


Figure 6. Deployment of the microservice module on iS3 platform.

4 APPLICATION

4.1 Description of the WDN application

A hypothetical Water District exposed to an earthquake disaster was studied to examine the capability of the microservice. The water network is composed of 2 reservoirs, 3 tanks, 2

pumps, 92 demanding nodes, and 117 pipes, and the basic hydraulic data is accessible from the Water Distribution System Operational Toolkit Website (<http://www.uky.edu/WDST/index.html>). Due to the information about the pipes that constitute the WDN and the earthquake disaster is unavailable, some assumptions were made, details of which can be referred in literature (Zhou et al., 2019). Besides, it was assumed that the entire WDN was in good condition before the earthquake, and only the aging impact on the system performance was considered before the simulation of earthquake perturbation.

4.2 Result and future work

A total of two earthquake levels ($PGV = 6.6$ and $PGV = 7.0$) were considered. A total of 1000 Monte Carlo simulations were conducted to simulate various possible earthquake damage states. The visualization of the basic data and damage scenario were presented on iS3 platform

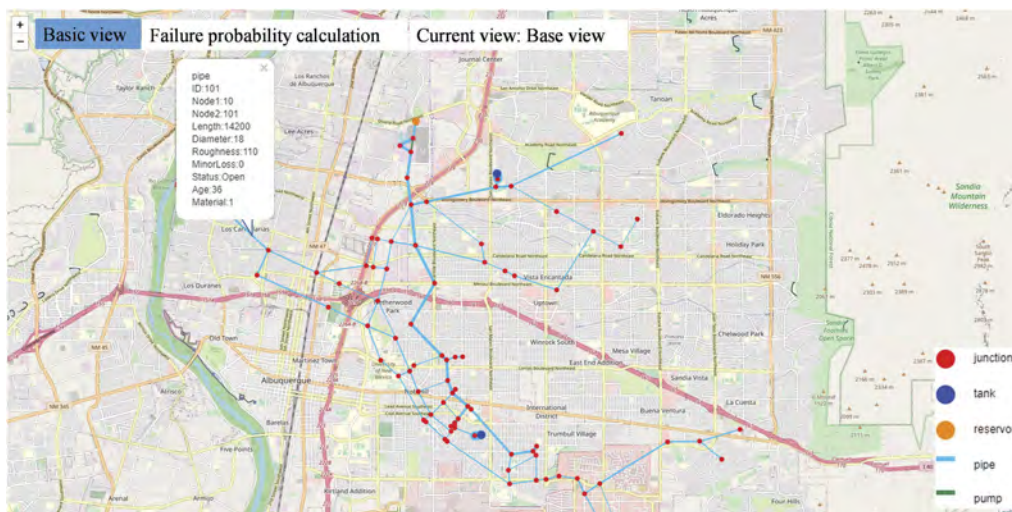


Figure 7. Visualization of the basic information of WDN on iS3 platform.

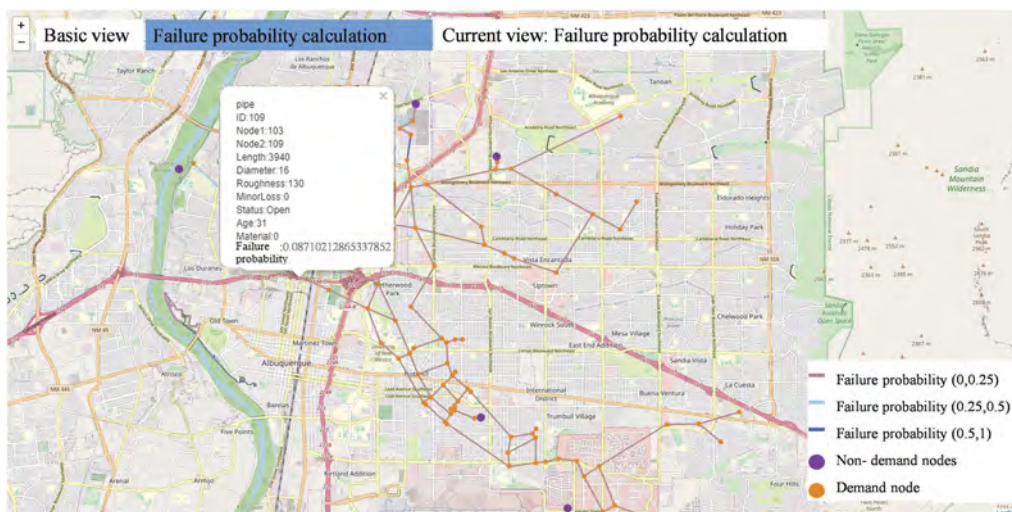


Figure 8. Visualization of pipeline failure probability on iS3 platform.

(see Figure 7-8). Figure 7 shows the interactive interface for users to obtain the basic information of the WDN application when they click the pipe or the node, and Figure 8 presents the interactive results of failure probability of pipelines returned from the microservice.

The statistical results of the lifecycle resilience of the WDN at the given magnitude of earthquake were obtained in the form of pictures (see Figure 9), which were calculated in the microservice and returned to the back end of iS3 platform by calling the WebAPI. It can be seen from the analysis results in Figure 9 that with the increase of pipe age, the resilience of the WDN presents an obvious downward trend. Meanwhile, the higher the earthquake magnitude, the lower the resilience of the WDN will be.

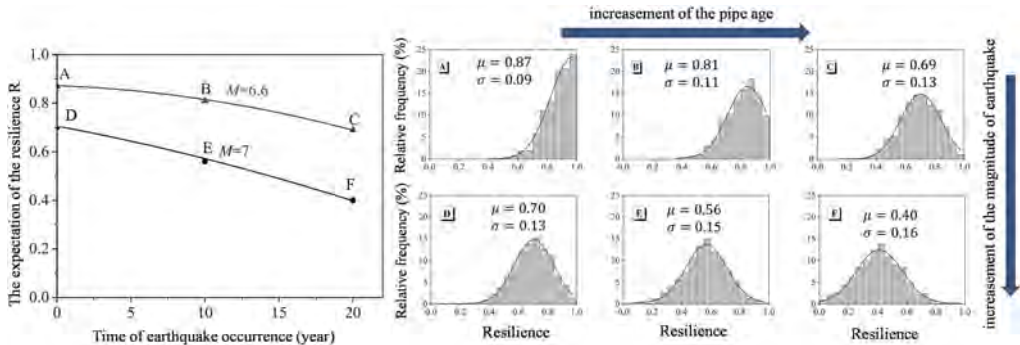


Figure 9. (a)The expectation of the resilience R at given magnitude of earthquake M_0 and year t_0 . (b) The frequency distribution of the resilience R at given M_0 and t_0 of points in (a).

It is noteworthy that the date and key parameters of the simulation are pre-defined. In the future, we plan to expand the function that users can interactively input the basic parameters and obtain the predicted analysis results presenting on iS3 platform, as shown in Figure 10.

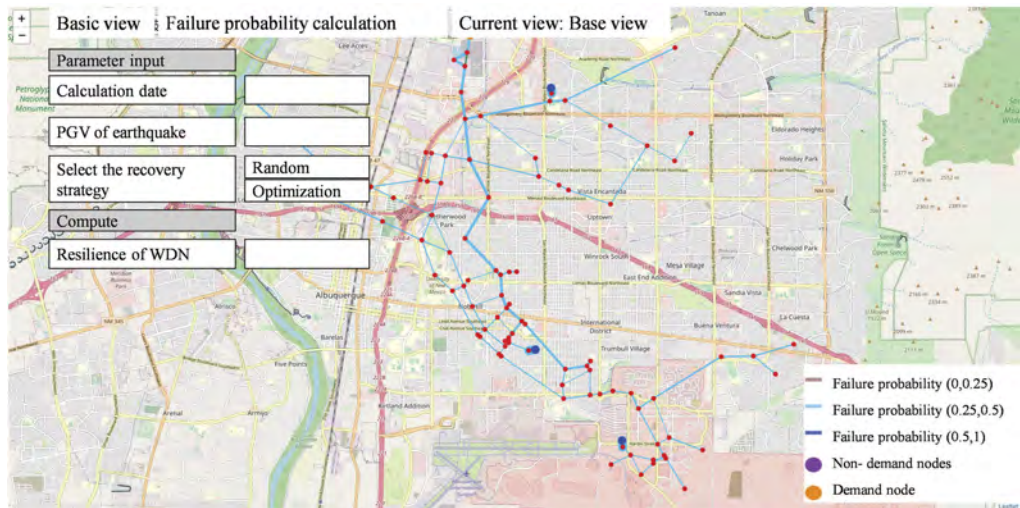


Figure 10. The future work we plan to realize.

5 CONCLUSIONS

This paper developed a microservice for evaluating lifecycle resilience of WDN considering both the internal degradation and external perturbation over its lifecycle under the framework

of Django based on the iS3 platform. Especially, this paper structured the data of WDN and stored them in the data layer of iS3 platform, which greatly improves the efficiency of life-cycle engineering data analysis. Meanwhile, the advantage of the flexible updating and easy sharing of microservice greatly benefits the iteration and development of smart WDN application. The iS3-based resilience assessment microservice for WDN provides a handy yet scientific tool to evaluate the disaster resistance capability of WDN over its life cycle. As the application layer of iS3 platform, this paper could also be a template for developing other smart infrastructure applications. In the future, we would consider further improving the accuracy of resilience evaluation module and expanding the interactive display function on the iS3 platform.

ACKNOWLEDGEMENT

This study is supported by the Ministry of Science and Technology of China (with grant No. SLDRCE19-B-15), and National Key R&D Program of China (with grant No. 2020YFB2103300-3).

REFERENCES

- Chen, Z. Y., Zhu, H. H., Li, X. J., Liu, R. M. & Du, J. Y. 2020. Tunnel in situ stress measurement by hydraulic fracturing based on the iS3 platform. *IOP Conference Series: Earth and Environmental Science* 570(5): 052069.
- Django-Software-Foundation. 2022. Django: the web framework for perfectionists with deadlines.
- Gharaibeh, A., Salahuddin, M. A., Hussini, S. J., Khreishah, A., Khalil, I., Guizani, M. & Al-Fuqaha, A. 2017. Smart Cities: A Survey on Data Management, Security, and Enabling Technologies. *Ieee Communications Surveys and Tutorials*, 19, 2456–2501.
- Jin, J., Gubbi, J., Marusic, S. & Palaniswami, M. 2014. An Information Framework for Creating a Smart City Through Internet of Things. *Ieee Internet of Things Journal* 1(2): 112–121.
- Li, P. N., Shi, L., Liu, J. & Li, X. J. 2020. Complex Geological Modeling and Numerical and Digital Integration Based on iS3. *Journal of Chongqing Jiaotong University (Natural Science)* 39 (3): 142–148. (in Chinese).
- Lv, Z. H., Hu, B. & Lv, H. B. 2020. Infrastructure Monitoring and Operation for Smart Cities Based on IoT System. *Ieee Transactions on Industrial Informatics* 16(3): 1957–1962.
- Talari, S., Shafie-khan, M., Siano, P., Loia, V., Tommasetti, A. & Catalao, J. P. S. 2017. A Review of Smart Cities Based on the Internet of Things Concept. *Energies* 10(4): 1–23.
- Tang, B., Chen, Z., Hefferman, G., Pei, S. Y., Wei, T., He, H. B. & Yang, Q. 2017. Incorporating Intelligence in Fog Computing for Big Data Analysis in Smart Cities. *Ieee Transactions on Industrial Informatics* 13(5): 2140–2150.
- Ullah, Z., Al-Turjman, F., Mostarda, L. & Gagliardi, R. 2020. Applications of Artificial Intelligence and Machine learning in smart cities. *Computer Communications* 154: 313–323.
- Yang, D. 2018. Application of intelligent management system of integrated pipeline corridor construction based on iS3. *Water Resources Planning and Design* 2:151–154. (in Chinese).
- Zhen, L., Ni, W. Q., Liu, F. & Xu, W. Y. 2021. Informationized management system of pip jacking construction based on iS3 platform and its application. *Modern Tunnelling Technology* 58 (S1): 411–415. (in Chinese).
- Zhou, X. N., Liu, F., Ye, Y. X. & Yu, X. Y. 2019. A Python-Driven Application for Evaluating Lifecycle Resilience of Water Distribution Network. *3rd International Conference on Information Technology in Geo-Engineering (ICITG)*. Guimaraes, PORTUGAL, Springer International Publishing Ag.
- Zhu, H. H., Li, X. J. & Lin, X. D. 2018. Infrastructure Smart Service System (iS3) and its application. *China Civil Engineering Journal* 51(1): 1–12. (in Chinese).
- Zhu, H. H., Wu, W., Li, X. J., Chen, J. Q. & Huang, X. B. 2017. High-precision Acquisition, analysis and service of rock tunnel information based on iS3 platform. *Chinese Journal of Rock Mechanics and Engineering* 36(10): 2350–2364. (in Chinese).

Project management and life-cycle cost evaluation using infrastructure-building information modeling techniques: A railway infrastructure design case study

M. Pasetto & G. Giacomello

Department of Civil, Environmental and Architectural Engineering, University of Padua, Padua, Italy

ABSTRACT: Building Information Modeling has reached a certain level of maturity in the field of vertical constructions, but it is still in an initial phase in the field of horizontal ones as transport infrastructures. This is due to the lack of a proper format for data interchange, capable of representing all the peculiarities of such constructions, like the wide extension of the model over a surface and its very heterogeneous components. In recent years, this gap has been partially bridged with the development of the Industry Foundation Classes (IFC) format for different categories of transport infrastructures, as also for the railway infrastructure sector. The goal of this work is to assess the maturity of the available tools and the difficulties concerning the project management of transport infrastructures using Building Information Modeling software in the design phase with special attention to interoperability of the data. The authors focused their attention on the identification of a new railway layout in Italy (Padua - Chioggia connection), through the implementation of an information flow between different software tools to test the information exchange and the export of data in the IFC 4x3 standard format. Starting from the definition of the territorial constraints, the geometric parameters, the unit costs and the railway service of the project, a set of design alternatives was generated. Through the railway line life-cycle cost and a decision-making analysis, the optimal solution was identified among the various track layouts. The several issues related to different software packages demonstrate that the information exchange for horizontal constructions is still far from reaching a good degree of maturity, especially regarding the lack of a univocal transfer of information. To spread the Building Information Modeling methodology as a standard for infrastructure design, it is required to overcome these technical obstacles to get a collaborative work process.

1 INTRODUCTION

Transport infrastructures are important elements for all human activities because they contribute to the social and economic development of the inhabited areas. A transport infrastructure during its life cycle follows a path that starts from its conception, passes through the design, its construction and continues during operation and maintenance up to the end of its useful life. Within this process, the actors involved in the different phases are many: from the designer to the construction company, from the work owner to the maintenance company. Often this process and this multitude of actors involved do not allow an adequate information exchange.

The Building Information Modeling (BIM) method allows the works life cycle process to be more efficient and sustainable, not so much for the digital representation potential, but above all for the possibility of transmitting information from one phase to the next without any loss or distortion. The BIM is a consolidated technique used to design, build, manage and monitor different vertical or punctual works, such as buildings and bridges (Deng et al. 2022, Alwisly et al. 2019). Recently, this method was successfully applied to various engineering works, such as old buildings monitoring, archaeological findings study (Skrzypczak et al. 2022, Biancardo et al. 2020) and horizontal structures, such as roads, railways and airport, i.e. transport infrastructures (Bosurgi et al. 2022, Vignali et al. 2022, Matejova & Sestáková 2021, D'Amico et al. 2020). BIM also helps the

check of a work during its life through the information storage and distribution using a sensors network (Lenart et al. 2021). BIM allows for economic and time savings (better investment planning, cost reduction, design errors identification, etc.), leading to the correct definition of the costs and the schedule of the works in the design phase (Biancardo et al. 2023; Cantisani et al. 2022, Santos et al. 2019). The information exchange allows for other possible evaluations in the work design phase that can maximize the design efforts, such as energy performance, operational management (maintenance of the work throughout the life cycle) and risks/accidents prevention (Yakhou et al. 2023, Deng et al. 2022, Rezaei et al. 2019).

The digitization of processes and the exchange of information allow to optimize and streamline all the steps necessary for the construction phase of a work and therefore it is possible to industrialize and make the construction sector more productive thanks to new technologies and the integration of data (physical, commercial, environmental, etc.). This allows to align all the subjects who participate in the life cycle of the construction and optimize each phase.

Unfortunately, the level of maturity of the BIM methodology for transport infrastructures is still in an initial phase: the software for transport infrastructures have not yet implemented methods for importing and exporting the model according to all the standards and, above all, the standard is still being implemented. The buildingSMART international (bSi) organization and researchers are carrying out a complex harmonization and standardization of the different parts/components of a transport infrastructure (Häußler et al., 2021). The Industry Foundation Classes (IFC) format for the information exchange of the BIM model was standardized according to the ISO 16739 standard for vertical constructions. During the last years, the IFC standard was expand and made it usable also to develop BIM models of horizontal structures. Recently the lack of entities that would represent the components of the infrastructure in the IFC language for the linear/horizontal structures was overpassed: the layout entities and the specific geometrical railway aspects (e.g., cant and transition curves) are introduced realizing the file interoperability.

Although the use of BIM in transport infrastructure projects is still limited, in Italy the implementation of BIM for public works contracts and design competitions has been provided for by some laws, introducing the use of methods and tools electronic gradually. Some specifications provide for a particular section regarding the presentation of projects developed through BIM and the Italian railway organization published a masterplan for the BIM implementation (Italferr SpA 2019). It is therefore important to improve the IFC standard and the related data model to have the most appropriate tool possible. Some shortcomings have recently been corrected in the extension project IfcRail of bSi, validating the new standard for railways. In Italy, recently, the guidelines have been also released for the application of the IFC language for bridges and viaducts, while for roads have recently been published. However, a study in 2021 demonstrated the limited use of the BIM in railways and the insufficient knowledge of the technical standards and the BIM tools for infrastructures (Minnucci & Alfieri 2021).

With this work the authors evaluate how the issues currently influence the use of BIM in the field of transport infrastructures. Among these, the main one is constituted by the technical limitations concerning the flow of information, mainly due to the lack of interoperability between the different software tools and the modeling of the infrastructure components. These technical limitations can be solved by developing software with better functionality. It is important to highlight that the elements constituting the railway infrastructure have significant differences in scale between them, varying from centimeters to kilometers, and therefore their modeling could represent a problem. By defining specific BIM uses, it is possible to define the granularity of the information necessary for a specific purpose (preliminary design, maintenance plan, etc.).

The authors focused the work on a technical-economic feasibility of the new railway line between Padua and Chioggia in Veneto Region, to identify the best railway layout and giving valuable help to decision makers. This railway line is important both for passenger and freight traffic because would connect local touristic beach resorts and seaport of Chioggia with the city and dry port of Padua (Pasetto & Giacomello, 2023). The authors evaluated five possible railway layouts using the results from a software (named Software 1), assessing the costs of the projects to manage the railway line for the useful life. Using Multi-Criteria Analysis (MCA) and Analytic Hierarchy Process (AHP), the authors defined the best railway layout, designing all parts of this layout through a second software (named Software 2) and evaluating the BIM techniques issues.

2 METHODS AND TOOLS

2.1 *Methods: Life-cycle cost and multicriteria analyses*

The design of transport infrastructures in Italy is regulated by state laws since generally are public works. The main design steps are technical-economic feasibility design, final and executive ones. In this study, BIM methodologies were applied to the project management of a new railway line, from the identification of the railway line layout to the assessment of the life-cycle cost (LCC) of the designed line. The authors carry out the project of a railway line at a preliminary level (technical-economic feasibility), through the definition of several layouts, the subsequent evaluation of the best option and the preliminary design of this layout.

LCC analysis is most effective when it is conducted in the initial phases (i.e., planning and design phases) of a construction project. Cost planning in the design phase and monitoring in the construction phase are very important management activities that can determine the success of a construction project. The LCC evaluation (Santos et al. 2019, Lee et al. 2020, Shin & Cho 2015) involves all the phases in the life of the transport infrastructure. The total cost is defined as the LCC of the transport infrastructure, and it is divided into the planning and design cost (expenses for planning, field survey, design activities, etc.), construction cost (contracts, site management, inspection, support, etc.), management cost (personnel, control and signaling systems, surveillance, etc.) and maintenance cost (check and control operations, personnel, vehicles, etc.).

Although the increased focus on the economic performances of construction projects, there have few studies in the literature focused on the application of the BIM approach with the evaluation of the LCC for transport infrastructure. Moreover, the LCC analysis required a large volume of data and information. For these reasons, in this work the analysis was limited to a small number of design alternatives and a roughly evaluation of the costs was performed. In this study the LCC is conducted excluding the costs not directly affected by the selection of de-sign alternatives (i.e., construction, service and maintenance costs of the stations and the stops; purchase, service and maintenance costs of the trains, etc.). The LCC is calculated per alternative by adding up the costs according to the type of alternative. In addition, the LCC analysis depends on the software used to calculate it. Although, each software used the same data and information given by the authors at the initial design step, the information exchange between software depends on the file format.

The MCA is used to evaluate the best solution from a range of possibilities, also in the case of a railway line (Yücel & Taşabat 2019, Camargo Pérez et al. 2015). In complex decision-making problems, where the wide choice between alternative solutions is not related to a single goal, this type of analysis allows to compare and order the possible solutions based on data relating to the objectives set. It is therefore a method to support the decision maker to carry out a given project.

The process is carried out with the AHP method by structuring criteria and elements in a hierarchical form and comparing the elements to each other in pairs. With this comparison, the preference (i.e., the judgment) of an alternative over the other is expressed for each criterion, up to an overall weight for each alternative that represents the synthesis of the analysis. The alternative with the greatest weight (referring to the established criteria) is the best. The goodness of the analysis is verified by means of the sensitivity analysis to check the results stability (Saaty 1987).

2.2 *Tools: Software and information exchange*

There are several software which already integrate the BIM methodology, design railway lay-outs and export or import IFC files. Since this type of language is constantly evolving, software often must update itself. bSi established the ways to evaluate the interoperability of software assessing of the Model View Definition (MVD). This is the definition of a subset of the IFC schema that must be implemented in software to meet the data exchange requirements of a defined process or activity, described in the Information Delivery Manual (IDM). In this work, two different software were used to evaluate the status of the current information exchange by inserting the model produced by one software into another one.

The Software 1 allows engineers in the construction of the alignment from the starting point to the ending one and transport infrastructure alternatives analysis to create the most efficient layout. This software includes tools for the infrastructures planning. In this paper, the optimal railway

layout of the case study was evaluated with the Software 1 (see Section 3). Starting from the definition of the constraints of the study area (inhabited areas, existing infrastructures, rivers, and Venice Lagoon), and the stations (i.e., the fixed points of the route), the Software 1 has drawn the axis of various layouts (Figure 1a). Having set the size and the cost per unit of length of the infrastructure for the different section types (embankments, trenches, bridges, etc.), the costs of the various layouts were inserted into the LCC analysis. Identifying the best solution from the result of the MCA, the railway layout was designed with the Software 2. This is a traditional railway design software implementing BIM functions allowing to produce, edit, share and analyze railway information models. Starting from a three-dimensional Digital Terrain Model (DTM) and implementing data and the information from the Software 1, the Software 2 specifically defines the planimetric and the altimetric layouts, the cross sections and other parts of the project of the railway line (Figure 1b).

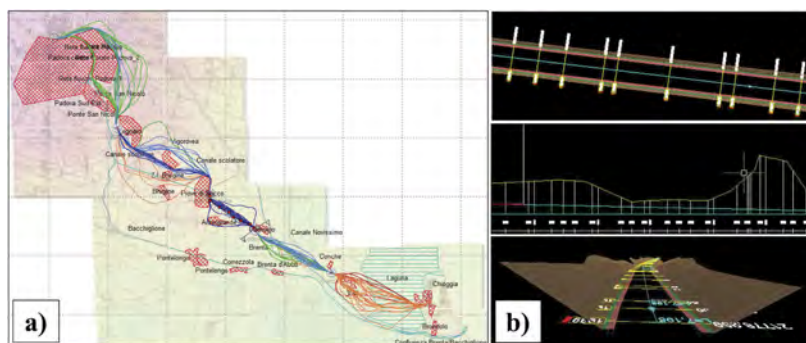


Figure 1. a) Example of the alternative railway layouts drawn with the Software 1 between Padua and Chioggia; b) Project drawings of the railway layout with the Software 2.

3 THE ITALIAN RAILWAY CASE STUDY

3.1 *Railway line design data and railway timetable evaluation*

The case study concerns the project of a new railway line between Padua and Chioggia. Padua is an important economic and historical city and a railway junction located in center of the Veneto Region. Chioggia is a city located on the sea, geographically placed in the southern part of the Venice lagoon, with many beach resorts which attract about 2 million tourists per year (both local inhabitants and foreign tourists). Chioggia is part of the Venice seaport through the North Adriatic Sea Port Authority, and it is one of the main fishing seaports of Italy. The construction of the new railway line could be a great opportunity for the territory due to the improvement both the regional public transport (passenger flow increase) and the rail intermodal freight transport (expected increase in the capacity of the port terminals of Chioggia).

Setting design criteria and territorial constraints, the authors defined several planimetric railway layouts between the stations of Padua and Chioggia using the Software 1. It was therefore decided to design a single-track railway line, managing the intersection of the trains in the stations. Some layouts designed with the Software 1 are unfeasible due to the economic boundaries. Then, the authors selected only the five layouts listed in the Table 1.

All the layouts start from the existing railway station of Padua, pass through railway station of Piove di Sacco and arrive to the existing railway station of Chioggia. The layouts n. 1, 2 and 5 pass also through the existing railway station of the dry port of Padua (“dry port PD”, i.e., a logistic terminal inland), while the layouts n. 3 and 4 pass through the eastern suburbs of Padua (“east suburbs PD”). Moreover, the layouts n. 2, 4 and 5 use the existing railway stretch between Piove di Sacco and Pontelongo stations, passing through the existing railway stop of Pontelongo. This is currently part of the Adria-Mestre railway line. Only the layout n. 5 does not cross the Venice lagoon with a bridge (Table 1).

Table 1. Summary of five railway layouts selected from the Software 1.

Layout number	dry port PD/ east suburbs PD	Use of existing railway stretch between Piove di Sacco and Pontelongo	Venice Lagoon bridge
1	dry port PD	NO	YES
2	dry port PD	YES	YES
3	east suburbs PD	NO	YES
4	east suburbs PD	YES	YES
5	dry port PD	YES	NO

The authors estimated the travel time necessary from Padua to Chioggia stations and evaluated the number of trains that can transit in one hour in both directions per layout. To design the rail service, the authors considered both tourist and local movements. Traffic data from re-cent years show systematic mobility with a flow of around 2000 people per day per direction (Padua and Chioggia). About 270,000 tourists (100,000 are from Veneto region) arrive in Chioggia every year. Since about 70% of tourist arrivals are concentrated in summer (between June and September), there could be about 1500 people per day, which, added to the previous one, would lead to an average daily flow in the summer months of about 3500 people per day. If 30% of the users may prefer to travel with the train, the daily movements would be around 1000 (people/day). By referring to the most recent trains with four-car composition with a capacity of about 500 seats, the minimum number of trains to satisfy the travel demand should be about two.

Similarly to previous study (Pasetto et al. 2017), the authors hypothesized some data to evaluate the rail service: distance travelled between every stop/station, travel time of these di-stances, stopping times at the single stops/stations (4 minutes in the stations with more than one track, to allow trains coming from opposite directions to pass, and 2 minutes in the other stops), average speed.

The travel time between Padua and Chioggia results as being 67 minutes. In 1 hour, two pairs of trains can transit in opposite directions, with a minimum time separation of about 30 minutes (Figure 2a). It was hypothesized that the transport service could be scheduled following the passengers peak-hours, placing most of the trips during the morning, the noon and the evening.

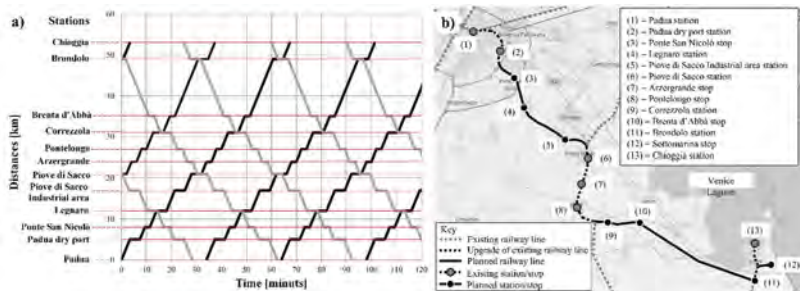


Figure 2. a) The best option for the railway layout between Padua and Chioggia (Pasetto & Giacomello, 2023); b) Example of timetable for the railway layout n. 5.

3.2 Life-cycle cost assessment

The LCC analysis was carried out according to the design alternatives. The construction costs of the different railway layouts were calculated using the Software 1. The authors used an Excel spreadsheet to integer the data obtained from the Software 1 to complete the LCC analysis with the service and maintenance costs, supposing that the railway line has a useful life of 50 years.

The data obtained from Software 1 are readily compatible with the Excel Software. The data have been extracted automatically using the BIM methodologies (IFC/XML) and have been entered manually in the Excel spreadsheet. In the Table 2 were depicted the costs of the construction phase, meanwhile in the Table 3 were displayed the costs of the operation and maintenance phases. To calculate the construction costs, it was used the length of the railway lay-out not already built, while to calculate the service and maintenance costs it was used the total length of

the railway layout. The unitary costs come from the price list of the Italian railway infrastructure manager (Rete Ferroviaria Italiana SpA 2022).

Table 2. Construction costs of the railway layout alternatives.

	Total length of railway layout *	Embankment/ Trench costs	Bridges cost	Infrastrucuture cost	Signaling system cost	Total cost
N.	[km]	[millions of Euros]				
1	45.0 (37.5)	0.89 €	143.20 €	356.25 €	9.00 €	509.34 €
2	51.0 (36.5)	1.06 €	160.40 €	346.75 €	10.20 €	518.41 €
3	52.0 (47.5)	0.75 €	158.00 €	451.25 €	10.40 €	620.40 €
4	53.0 (41.5)	0.76 €	160.40 €	394.25 €	10.60 €	566.01 €
5	53.0 (36.5)	0.75 €	16.00 €	346.75 €	10.60 €	374.10 €

* Length of the railway layout to be built is indicated between brackets.

Table 3. Service and maintenance costs of the railway layout alternatives.

	Total length of bridges*	Bridges cost	Infrastrucuture cost	Signaling system cost	Total cost
N.	[km]	[millions of Euros]			
1	3.6	0.86 €	67.50 €	0.09 €	68.45 €
2	4.2	1.02 €	76.50 €	0.10 €	77.62 €
3	4.0	0.95 €	78.00 €	0.10 €	79.05 €
4	4.2	1.02 €	79.50 €	0.11 €	80.62 €
5	0.9	0.21 €	79.50 €	0.11 €	79.82 €

* The length of railway bridges includes the existing ones.

Table 4. Criteria and weights of the MCA/AHP analysis.

Criteria	Railway layout alternatives				
	1	2	3	4	5
Layout total cost	0.16	0.20	0.17	0.22	0.25
Environmental impact	0.17	0.19	0.17	0.19	0.28
Project complexity	0.22	0.22	0.18	0.18	0.20
Transport efficiency	0.22	0.22	0.17	0.17	0.22
Total weight of the alternative	0.19	0.21	0.18	0.19	0.24

Summarizing the results, the cost in millions of Euros for each railway layout is: 1) 577.79 €, 2) 596.03 €, 3) 699.45 €, 4) 646.63 € and 5) 453.92 €. The layout n. 5 is the cheapest and the n. 3 is the most expensive. These results are used to select the best layout (see section n. 3.3).

3.3 Selection of the best layout

The authors perform the selection of the best layout using MCA and AHP methods based on technical and economic data of the five layouts described. In the Table 4 the criteria and the weights of the MCA/AHP are displayed.

The criteria used in the MCA/AHP are project complexity and transport efficiency (data from the railway timetable evaluation, see section n. 3.1), total cost of the layout (data from the LCC analysis, see section n. 3.2) and environmental impact. Using the AHP method, the authors subdivided the criteria “environmental impact” and “transport efficiency” in 6 and 3 sub-criteria, respectively. The sub-criteria for “environmental impact” are production of waste materials, materials to be taken to the construction site, work footprint on the territory, transit on the Venice Lagoon, bridges visual impact on the landscape, and layout length in areas subjected to constraints. The sub-criteria for “transport efficiency” are layout travel time, number of locations served, and passage through the dry port of Padua.

As result from the MCA/AHP methods, the best railway layout is the n. 5 (Figure 2b).

Table 5. Cut and fill volumes calculation in the two software.

	Software 1	Software 2
	[m ³]	
Cut (trenches)	448,000.00	797,704.00
Fill (embankments)	562,000.00	250,610.00

3.4 Design and exchange information issues

During the design phase with the Software 1 and during the information exchange between the two software, some problems were found. The first concerned the difficulty to import into the Software 1 the information regarding the DTM (the file format was not compatible with Software 1). Another problem arose when, having found a compatible format, the file was loaded by the Software 1, generating a file with dimensions that could not be managed by the computer. The issue was solved by making use of an image editing software. Moreover, the data for the LCC analysis were extracted from the Software 1 in a partial way due to the impossibility to transfer data from the proprietary file format to the IFC/XML file format.

Additional problems were encountered in the transition from the two software. By exporting the file from Software 1 using landXML file format, the DTM was not transferred to Software 2. To overcome this problem, another DTM (using another file format) was imported into Software 2, which led to a different representation of the ground from that used in the Software 1. This aspect led to a different calculation of the cut and fill volumes in the two software (Table 5). The lines drawn by Software 1 to define the planimetry and the longitudinal profile, once imported into the Software 2, were read as generic lines because the information was not correctly transferred from one software to the other one. For the same reason, the LCC performed on the data from the Software 2 change respect to the analysis done with the data from the Software 1.

Finally, the last issue refers to the design regulations. In Italy, the national railway infrastructure manager has specific standard for the infrastructure design. Software 1 does not contain this regulation, while software 2 contains it and can design the railway layout complying with this standard. Therefore, transferring the information from Software 1 to Software 2, the layout is not correctly designed according to the Italian rules.

These aspects jeopardize the correct information exchange flow through different software respect to that indicated by the BIM methodologies.

4 CONCLUSIONS

For a fully integration and exploitation to BIM full potential, a reorganization of the design process within the construction sector is necessary. The development of a collaborative approach between the various actors involved in the process and a push towards digitization are required to encourage the adoption of BIM by both professionals involved in the design and public bodies.

This study is an example of the issues encountered in the transport infrastructures design with BIM methodologies. The way to reach a full interoperability in the data/information transfer between different software is still long: the software and the IFC language are not still adequately developed for such works and the collaborative design between different expert in this fields is not possible yet. Currently the information exchange is difficult, and the information are not written into a file format that use the standards promoted by bSi. Furthermore, software often requests data with file extensions that are not always available.

Although the IFC language and the software change very quickly, the transport infrastructure design is far from a fast and effective exchange of information that allow to a full project management, that include the LCC analysis and the definition of the railway timetable.

As proved, currently the management of the project is fragmented, and the various actors involved are unable to exchange information in a suitable way.

REFERENCES

- Alwisy, A., Hamdan, S.B., Barkokebas, B., Bouferguene, A. & Al-Hussein, M. 2019. A BIM-based automation of design and drafting for manufacturing of wood panels for modular residential buildings. *International Journal of Construction Management* 19(3): 187–205.
- Biancardo, S.A., Gesualdi, M., Savastano, D., Intignano, M., Henke, I. & Pagliara, F. In press. An innovative framework for integrating Cost-Benefit Analysis (CBA) within Building Information Modeling (BIM). *Socio-Economic Planning Sciences* 85: 101495
- Biancardo, S. A., Russo, F., Veropalumbo, R., Vorobjovas, V. & Dell'Acqua, G., 2020. Modeling roman pavements using heritage-BIM: A case study in Pompeii. *Baltic Journal of Road and Bridge Engineering* 15(3): 34–46.
- Bosurgi, G., Pellegrino, O. & Sollazzo, G. 2022. Pavement condition information modelling in an I-BIM environment. *International Journal of Pavement Engineering* 23(13): 4803–4818.
- Camargo Pérez, J., Carrillo, M.H. & Montoya-Torres, J.R. 2015. Multi-criteria approaches for urban passenger transport systems: a literature review. *Annals of Operations Research* 226: 69–87.
- Cantisani, G., Panesso, J., Del Serrone, G., Di Mascio, P., Gentile, G., Loprencipe, G. & Moretti, L. 2022. Re-design of a road node with 7D BIM: geometrical, environmental and microsimulation approaches to implement a benefit-cost analysis between alternatives. *Automation in Construction* 135: 104133.
- D'Amico, F., Calvi, A., Schiattarella, E., Di Prete, M. & Veraldi, V. 2020. BIM And GIS Data Integration: A Novel Approach Of Technical/Environmental Decision-Making Process In Transport Infrastructure Design. *Transportation Research Procedia* 45: 803–810.
- Deng, L., Lai, S., Ma, J., Lei, L., Zhong, M., Liao, L. & Zhou, Z. 2022. Visualization and monitoring information management of bridge structure health and safety early warning based on BIM. *Journal of Asian Architecture and Building Engineering* 21(2): 427–438.
- Häubler, M., Esser, S. & Borrmann, A. 2021. Code compliance checking of railway designs by integrating BIM, BPMN and DMN. *Automation in Construction* 121: 103427.
- Italferr SpA. 2019. Innovating to design the future. Rome: Italferr.
- Matejova, A. & Sestáková, J. 2021. The Experiences with utilization of BIM in railway infrastructure in Slovak Republic and Czech Republic. *Transportation Research Procedia* 55:1139–1146.
- Minnucci, G. & Alfieri, E. 2021. openBIM for Rail: stato del BIM nel settore ferroviario in Italia, Roma: iBIMi - buildingSMART Italy.
- Lee, J., Yang, H., Lim, J., Hong, T., Kim, J. & Jeong, K. 2020. BIM-based preliminary estimation method considering the life cycle cost for decision-making in the early design phase. *Journal of Asian Architecture and Building Engineering* 19(4): 384–399.
- Lenart, S., Janjic, V., Jovanovic, U. & Vezocnik, R. 2021. Real-time monitoring and analyses of sensory data integrated into the BIM platform. In Stjepan L. (ed.), *Road and Rail Infrastructure VI; Proc. 6th Intern. Conf. on Road and Rail Infrastructure, Zagreb, 20-21 May 2021*. Zagreb: University of Zagreb.
- Pasetto, M. & Giacomello, G. 2023. Technical-economic assessments on the feasibility of new infrastructures serving seaport and dry port of Venice. *Transportation Research Procedia* 69: 839–846.
- Pasetto, M., Giacomello, G., Pasquini, E. & Baliello, A. 2017. Feasibility and preliminary design of a new railway line in the Dolomiti area of Veneto region. In Wegman F., Dell'Acqua G. (ed.), *Transport Infrastructure and Systems; Proc. AIIT intern. congr., Rome, 10–12 April 2017, Leiden: CRC Press/Balkema*.
- Rete Ferroviaria Italiana SpA. 2022. Tariffa dei Prezzi RFI. Rome: Rete Ferroviaria Italiana SpA
- Rezaei, F., Bulle, C. & Lesage, P. 2019. Integrating building information modeling and life cycle assessment in the early and detailed building design stages. *Building and Environment* 153: 158–167.
- Saaty, R.W. 1987. The analytic hierarchy process - What it is and how it is used. *Mathematical Modelling* 9(3-5):161–176.
- Santos, R., Aguiar Costa, A., Silvestre, J.D. & Pyl, L. 2019. Integration of LCA and LCC analysis within a BIM-based environment. *Automation in Construction* 10:127–149.
- Shin, Y.-S. & Cho, K. 2015. BIM Application to Select Appropriate Design Alternative with Consideration of LCA and LCCA. *Mathematical Problems in Engineering* 2015, 281640:1–14.
- Skrzypczak, I., Oleniacz, G., Leśniak, A., Zima, K., Mrówczyńska, M. & Kazak, J. K., 2022. Scan-to-BIM method in construction: assessment of the 3D buildings model accuracy in terms inventory measurements. *Building Research & Information* 50(8): 859–880.
- Vignali, V., Acerra, E. M., Lantieri, C., Di Vincenzo, F., Piacentini, G. & Pancaldi, S. 2021. Building information modelling (BIM) application for an existing road infrastructure. *Automation in Construction* 128: 1–10.
- Yakhou, N., Thompson, P., Siddiqui, A., Abualdenien, J. & Ronchi, E. 2023. The integration of building information modelling and fire evacuation models. *Journal of Building Engineering* 63: 105557.
- Yücel, N. & Taşabat, S.E. 2019. The Selection of Railway System Projects with Multi Criteria Decision Making Methods: A Case Study for Istanbul. *Procedia Computer Science* 158: 382–393.

A non-Gaussian algorithm to simulate the earthquake motion phase difference

Tadanobu Sato

Emeritus Professor, Kyoto University, Kyoto, Japan

Research Associate, Kobe-Gakuin University, Kobe, Japan

ABSTRACT: The purpose of this paper is to develop a method to simulate the earthquake motion phase for simulating a design response compatible earthquake acceleration time history. A method is developed to calculate the earthquake motion phase as a function of the circular frequency without the unwrap procedure. Then the earthquake motion phase is decomposed into a linear delay and fluctuation parts. The fluctuation part of phase is named the phase throughout of this paper. First, a mean phase gradient is defined by dividing the phase difference with its circular frequency interval. The probability density characteristics of the mean phase gradient is discussed, and it is found that the mean phase gradient is obeyed the Levy-flight distribution. A new stochastic process is developed and named the fractional Levy-flight process to simulate the mean phase gradient.

1 INTRODUCTION

The classic seismic intensity method has been used for long time, but it was created to consider the flexibility of structure system in the seismic design method, which is the response spectrum (Housner, 1941). Since many observed acceleration time histories have demanded high level design response spectra (Douglas, 2002), the yield strength demand spectrum (YSDS) (Iemura & Mikami, 2001) has become a common tool for designing large scale civil infrastructures. The designed structures, however, must be checked their seismic performance through the dynamic analyses. The design response spectrum compatible acceleration time history (DRSCATH) becomes very common for an input motion to the structural system to evaluate the seismic performance of designed structural systems (Tsai, 1972).

Because the time history of DRSCATH is strongly affected by the assigned Fourier phase spectrum (Shrihande & Gupta, 1996) we propose a method to extract the probability density function of the mean phase gradient from an observed acceleration time history at the design site and to simulate many sample Fourier phase spectra that can be used to simulate Fourier phase spectrum at the design site. The phase is decomposed into the linear delay and fluctuation parts. First, the phase difference of the fluctuation part is divided by the circular frequency interval, This is named the mean phase gradient, then develop a method to simulate non-Gaussian process for the mean phase gradient. It is discussed a possibility to express the mean phase gradient by a Levy-flight probability density function (Nolan, 2015). Then the mean phase gradient is expressed by a new stochastic process, namely, the fractional Levy-

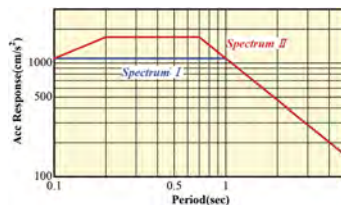


Figure 1. The design response spectrum used in this analysis. (red line).

flight motion, by which a stochastically rigorous sample earthquake motion phase can be simulated. This is made possible by using the Levy-flight noise process and the kernel with the fractional characteristic (Sato, 2017).

2 USED DESIGN RESPONSE SPECTRUM AND CONVERGENCE

The used design response spectrum is shown in Figure 1 by spectrum II (red line), which is defined in the code to design railway facilities in Japan. This design response spectrum is expressed by $S_E(T)$, in which T is the natural period of the structural system. To simulate DRSCATH we must assign the fixed Fourier phase $\phi_a(\omega)$ and the initial Fourier amplitude $A_0(\omega)$, which is modified as $A_l(\omega)$ at the iterative calculation step l . The acceleration time history at the step l is expressed by $x_l(t)$, which is obtained by using the Fourier inverse transform of $A_l(\omega)e^{i\phi_a(\omega)}$, of which elastic response spectrum is expressed by $S_l(T)$. The matching rate in the iteration is evaluated by the following equations.

$$E_l(T) = \left| \frac{S_E(T) - S_l(T)}{S_E(T)} \right| \quad (1)$$

$$e_l = \sqrt{\frac{1}{T_L} \int_{T_s}^{T_e} (E_l(T))^2 dT} \quad (2)$$

The $E_l(T)$ at each natural period T is integrated as expressed by Eq.2, in which $T_L = T_e - T_s$, T_s and T_e are the natural periods of a single degree of freedom system to evaluate the matching rate of $E_l(T)$. To estimate $x_l(t)$, the modification of the initial Fourier amplitude $A_0(\omega)$ is needed. Let $l = 1, 2, \dots, \infty$ be the repetition number and the Fourier amplitude $A_l(\omega)$ at the l step, then $x_l(t)$ is obtained by the Fourier inverse transform of $A_l(\omega)e^{i\phi_a(\omega)}$. At the l step, $A_{l+1}(\omega) = (S_E(T)/S_l(T))A_l(\omega)$ is assumed to be effective under the assumption of $T = 2\pi/\omega$.

The initial Fourier amplitude is chosen to be the Fourier amplitude $A_a(\omega)$, which is calculated from the same acceleration time history to obtain the phase $\phi_a(\omega)$, because the causality condition must be satisfied at the initial stage as a minimum requirement.

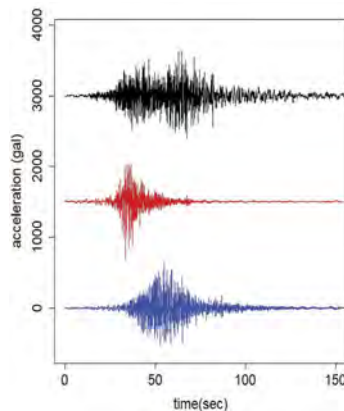


Figure 2. The DRCATHs calculated by using the fixed Fourier phase $\phi_a(\omega)$ and the initial Fourier amplitude $A_a(\omega)$ that are obtained from the recorded observed at Kushiro(black line), Kobe(red line) and Kameoka(blue line) Observatories.

For six different acceleration time histories observed at Kushiro, Suttsu, Nemuro, Amagasaki, Kobe and Miyagi observatories, the relationship between e_l and the repetition number l is obtained. All e_l go down until e_l reaches to certain % around $l=27$ and then fluctuate around

e_1 = certain % as the repetition number l increases. Therefore, $l = 27$ is fixed to calculate the DRSCATH for assigned $\phi_a(\omega)$.

As examples Figure 2 shows three DRSCAHs that are obtained by using three different observed acceleration time histories recorded at Kushiro (black line), Kobe (red line) and Kameoka (blue line) observatories, from which the initial Fourier amplitudes and fixed phases are obtained. From this figure, it is concluded that the time histories of DRSCATHs are strongly affected by the assigned Fourier phase spectrum.

3 MODELING PHASE SUECTRUM

3.1 Phase computation

To avoid a trouble-some unwrap procedure of argument phase, the increment of arctangent phase is calculated (Sato, 2017) by

$$d\phi(\omega) = \frac{d\Im(\omega)\Re(\omega) - \Im(\omega)d\Re(\omega)}{\Re^2(\omega) + \Im^2(\omega)} \quad (3)$$

$$\phi(\omega) = -\omega t_0 + \psi(\omega) \quad (4)$$

in which $\Re(\omega)$ and $\Im(\omega)$ are the real and imaginably parts of the Fourier transform of observed acceleration time history. By integrating $d\phi(\omega)$ with respect to (wrt) the circular frequency ω , the phase $\phi(\omega)$ is obtained as a function of ω . $\phi(\omega)$ is decomposed into a linear delay part $-\omega t_0$ and the fluctuation part $\psi(\omega)$ as expressed by Eq.4.

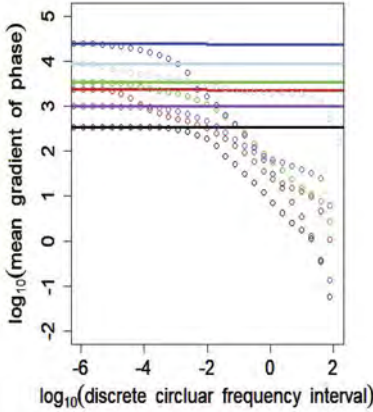


Figure 3. Change of the variance of mean phase gradient $\Delta\psi/\Delta\omega$ for the circular frequency interval $\Delta\omega$. The variance of the mean phase gradient approaches to a constant value when $\Delta\omega$ approaches zero. The color differences of open circles are the difference of observed records.

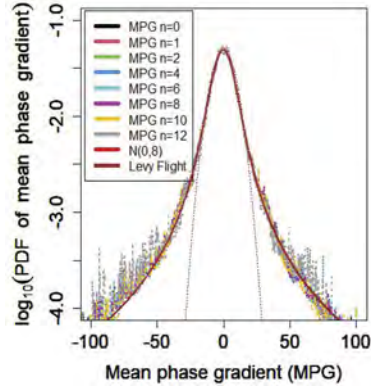


Figure 4. The probability density functions (PDFs) of the mean phase gradient for Kushiro record with different circular frequency intervals $\Delta\omega$, which are defined by $(n = 0, 1, 2, 4, 6, 8, 10, 12)$. All PDFs coincide each other and its theoretical PDF is defined by Levy-flight distribution function with parameters of $\alpha = 1.5$ and $\gamma = 5.9$.

All numerical analyses are discretized. We, therefore, use a small circular frequency interval of $d_0\omega = 100\pi/2^{25}$ rad and the circular frequency is a discretized as $\omega_l = l \cdot d_0\omega$, then the small discretized phase difference is obtained by $d\psi_l = \psi(\omega_l) - \psi(\omega_l - d_0\omega)$. Moreover, the larger circular frequency interval is calculated by $\Delta\omega = k \cdot d_0\omega = 2^n d_0\omega$. The difference of fluctuation part of phase for this large circular frequency interval is calculated by Eq.5.

$$\Delta\psi_i = \sum_{l=0}^{k-1} d\psi_{k(i-1)+l} \quad (5)$$

$$X_i = \left\{ \frac{\Delta\psi_i}{\Delta\omega} \right\} \quad (6)$$

where $(i = 1, 2, \dots, M)$, M is a total number of discrete points to calculate the phase difference for a large circular frequency interval $\Delta\omega = 2^n d_0\omega$, which is defined by changing n values.

Since the value of the phase difference depends on the circular frequency interval $\Delta\omega$, a stochastic valuable is defined by Eq.6. This value is a mean gradient of fluctuation part of phase, which is called, hereafter, the mean phase gradient. Figure 3 shows the change of the variance of X_j wrt the circular frequency interval. It is concluded that the variance of X_j approaches a constant value as approaches zero without depending on the observed records. Because the mean phase gradient approximates the grope delay time, the grope delay time can be used as the stochastic value to evaluate phase. Figure 4 shows the probability density function (PDF) of $\{X_j\}$ for several $\Delta\omega = 2^n d_0\omega$ values, in which n values are controlled the values of $\Delta\omega$ Even if n values were changed as $(n = 0, 1, 2, 4, 6, 8, 10, 12)$, all cases are coincided each other. This means that the mean phase gradient has the fractal characteristic (Falconer, 2003). The brown line in Figure 4 is the symmetric Levy-flight probability density function $s(\alpha, \gamma, X_j)$ with the characteristic index $\alpha = 15$ and the scale parameter $\gamma = 5.9$. Then the PDF of $\{X_j\}$ is expressed by

$$p(X_j) = s(\alpha, \gamma, X) \quad (7)$$

The red dotted line is the normal probability density function $N(0,8)$, which means that the PDF of $\{X_j\}$ is non-Gaussian.

3.2 Definition of the Levy-flight noise process

Based on the previous study (Sato, 2017) of the stochastic process, of which PDF is defined by Eq. 7, it needs that a simple noise process obeying the Levy-flight distribution similar to the Brownian noise (Karatzas & Shreve, 1991), which has used as the fundamental stochastic process to develop the modern stochastic theory. This process is called the Levy-flight noise process, $dy(\omega)$, and defined as follows:

$$dy(\omega) = (d\omega)^{1/\alpha} \gamma_L Z(\omega) \quad (8)$$

in which α and γ_L the parameters to define the Levy-flight noise process, $Z(\omega)$ is a random number at ω generated from the standard Levy-flight distribution function $S(\alpha, 1, Z)$ based on the independent and identically distributed (iid) assumption. To make clear the stochastic characteristics of this noise process, we consider the following discretized process $\{d_0 y_i\}$ with the small circular frequency interval $d_0\omega = 100\pi/2^{25}$ rad:

$$d_0 y_i = (d_0\omega)^{1/\alpha} \gamma_L Z_i \quad Z_i \sim S(\alpha, 1, Z) \quad (9)$$

in which the lower suffix means the value at the discretized circular frequency ω_i . Moreover, we consider a new Levy-flight noise process Δy_j with a large circular frequency interval $\Delta\omega = k \cdot d_0\omega = 2^n d_0\omega$ that is realized by summing up k numbers of $d_0 y_i$ as follows:

$$\Delta y_i = \sum_{l=1}^k d_0 y_{k(i-1)+l} = (d_0\omega)^{1/\alpha} \gamma_L \sum_{l=1}^k Z_{k(i-1)+l} \quad (10)$$

Because Δy_i is a sum of random numbers generated from the standard Levy-flight distribution under the iid assumption we can use the generalized central limit theorem (Mantegna & Stanley, 2004), which gives the relationship $k(d_0\omega)\gamma_L^\alpha = \Delta\omega\gamma_L^\alpha$ to get the following relation for Δy_i :

$$\Delta y_i = (\Delta\omega)^{1/\alpha} \gamma_L Z_i \quad (11)$$

in which Z_i is an iid generated random number from $S(\alpha, 1, Z)$. Because the formulas expressed by Eqs 8 and 11 are almost the same. This means that Δy_i is independent to the value of $\Delta\omega$, therefore, the Levy-flight noise process has the fractal nature. Moreover, the process $y(\omega)$ is a continuous but un-differentiable wrt the circular frequency ω due to the facts that Δy_i approaches zero and $\Delta y_i/\Delta\omega$ diverges infinite as $\Delta\omega$ approaches zero.

Here a simple procedure is introduced to simulate a stochastic process obeying Eq.7. Without losing generality we can write $\Delta\psi = \psi - \psi_0$ and $\Delta\omega = \omega - \omega_0$ as well as $\psi_0 \equiv 0$ and $\omega_0 \equiv 0$. Then Eq. 7 is rewritten as follows:

$$\psi/\omega^{1/\alpha} \sim S(\alpha, \gamma, Y) \quad (12)$$

To simulate the stochastic process ψ obeying Eq.12, we need almost the same algorithm to simulate the fractional Brownian motion process (Karatzas & Shreve, 1991).

3.3 Fractional Levy-flight process

The essential problem to simulate phase difference is that the phase is an asymmetric function wrt the circular frequency. This condition requires the following constrain:

$$\phi(\omega) = \phi(-\omega) \quad (13)$$

This means that the fluctuation part of phase $\psi(\omega)$ defined in Eq.4 and its difference have the same characteristic. The circular frequency domain defining the phase is $[0, \infty]$ and then its value in $[-\infty, 0]$ can be defined automatically by using Eq.13. Therefore, the phase cannot be simulated by only applying the simple fractional Levy-flight process defined by the similarity of the fractional Brownian motion (Sato, 2017). We discuss this point in this session.

To develop a phase process satisfying the constrain given by Eq.13, the phase process at the circular frequency ω is assumed to be composed of two functions, one is a function $\psi_1(\omega)$ expressing the contribution from the zero circular frequency, and the other is the function $\psi_2(\omega)$ expressing the contribution from the infinite circular frequency as follows:

$$\psi(\omega) = \psi_1(\omega) + \psi_2(\omega) \quad (14)$$

Here we assume that those two functions are expressed by the following Lebesgue-Stieltjes integral using the Levy-flight noise process $dy(\tau)$ defined in Eq.8 as follows:

$$\psi_1(\omega) = \eta \int_0^\omega K_1(\omega - \tau) dy(\tau), \quad \psi_2(\omega) = \eta \int_\omega^\infty K_2(\tau - \omega) dy(\tau) \quad (15)$$

in which η is the coefficient that controls the equality of Eq.15, the integral kernels of $K_1(\omega - \tau)$ and $K_2(\tau - \omega)$ as well as β are defined by

$$K_1(\omega - \tau) = (\omega - \tau)^\beta, \quad K_2(\tau - \omega) = (\tau - \omega)^\beta \quad (16)$$

$$\beta = 1 - 1/\alpha \quad (17)$$

To make clear the stochastic characteristic of phase difference, it is discretized by using the circular frequency interval $\Delta\omega$ but to do so it is necessary to take care of the direction calculating the phase difference. If we considered a case taking the backward difference for the function $\psi_1(\omega)$ it was given by ${}_b\Delta\psi_1(\omega) = \psi_1(\omega) - \psi_1(\omega - \Delta\omega)$ but for the function $\psi_2(\omega)$ it should be ${}_b\Delta\psi_2(\omega) = \psi_2(\omega) - \psi_2(\omega + \Delta\omega)$, because the origin of both functions are at the circular frequency of ω . Then the backward difference of $\psi(\omega)$ is expressed by the sum of ${}_b\Delta\psi_1(\omega)$ and ${}_b\Delta\psi_2(\omega)$ as follows:

$${}_b\Delta\psi(\omega) = \{ \psi_1(\omega) - \psi_1(\omega - \Delta\omega) \} + \{ \psi_2(\omega) - \psi_2(\omega + \Delta\omega) \} \quad (18)$$

The terms appeared in the first parentheses $\{ \}$ of the right side of Eq.18 are expressed by

$$\psi_1(\omega) = \eta \int_0^\omega K_1(\omega - \tau) dy(\tau), \quad \psi_1(\omega - \Delta\omega) = \eta \int_0^{\omega - \Delta\omega} K_1(\omega - \Delta\omega - \tau) dy(\tau)$$

For $\psi_2(\omega)$ and $\psi_2(\omega + \Delta\omega)$, similar formulas are obtained. The discrete formula of this first parentheses of Eq.18 with the circular frequency interval $\Delta\omega$ is, therefore, given by

$${}_b\Delta\psi_i = (\Delta\omega)\eta\gamma_L \left\{ \sum_{l=0}^{i-1} {}_bP_{il}Z_l + 0 \cdot Z_i + \sum_{l=i+1}^{\infty} {}_bF_{il}Z_l \right\} \quad (19)$$

in which γ_L is an undefined parameter of the Levy-flight noise process appeared in Eqs.8 and 11. The procedure to define this value is given later. ${}_bP_{jl}$ and ${}_bF_{jl}$ are defined by

$${}_bP_{il} = (i - l)^\beta - (i - 1 - l)^\beta, \quad {}_bF_{il} = (l - i)^\beta - (l - i - 1)^\beta \quad (20)$$

On the other hand the forward difference of $d\psi_1(\omega)$ and $d\psi_2(\omega)$ are expressed by ${}_f\Delta\psi_1(\omega) = \psi_1(\omega + \Delta\omega) - \psi_1(\omega)$ and ${}_f\Delta\psi_2(\omega) = \psi_2(\omega - \Delta\omega) - \psi_2(\omega)$. Then the discretized forward difference of $\psi(\omega)$ is given by the sum of these two expressions as follows:

$${}_f\Delta\psi_i = (\Delta\omega)\eta\gamma_L \left\{ \sum_{l=0}^{i-1} {}_fP_{il}Z_l + 2 \cdot Z_i + \sum_{l=i+1}^{\infty} {}_fF_{il}Z_l \right\} \quad (21)$$

${}_fP_{jl}$ and ${}_fF_{jl}$ are defined by

$${}_fP_{il} = (i + 1 - l)^\beta - (i - l)^\beta, \quad {}_fF_{il} = (l - i + 1)^\beta - (l - i)^\beta \quad (22)$$

Taking mean of backward and forward differences, the phase difference can be defined by

$$\Delta\psi_i = \frac{1}{2} \{ {}_b\Delta\psi_i + {}_f\Delta\psi_i \} = (\Delta\omega)\gamma_L \sum_{l=0}^{\infty} W_{il}Z_l \quad (23)$$

in which W_{jl} is given by

$$W_{il} = \begin{cases} \frac{1}{2} ({}_bP_{il} + {}_fP_{il}) & l \leq i - 1 \\ 1 & i = l \\ \frac{1}{2} ({}_bF_{il} + {}_fF_{il}) & i + 1 \leq l \end{cases} \quad (24)$$

Separating the weight W_{il} into the $l \leq i - 1$ part and the $i + 1 \leq l$ part, and rewriting them as P_{il} and F_{il} , the following formulas are obtained:

$$P_{il} = \left((i + 1 - l)^\beta - (i - 1 - l)^\beta \right) / 2 \quad (25)$$

$$F_{il} = \left((l + 1 - i)^\beta - (l - 1 - i)^\beta \right) / 2 \quad (26)$$

To simplify the formula of $\Delta\psi_i$, a new weighting sequence $\{a_m\}$ is defined by using an integer number $m = |i - l|$, which is increased from 1 to infinite.

$$a_m = \frac{1}{2} \left\{ (m + 1)^\beta - (m - 1)^\beta \right\} \quad (27)$$

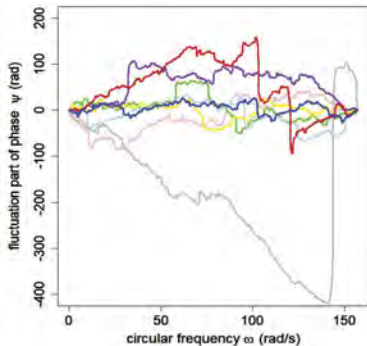


Figure 5. The simulated sample fluctuation part of phases. The parameters defining PDF of the fluctuation part of phase is defined in Eq.7.

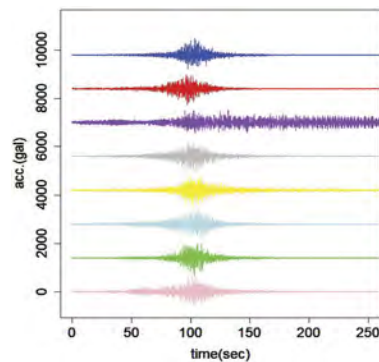


Figure 6. Eight different design response spectrum compatible acceleration time histories (DRSCATHs).

Eq.23 can be rewritten by using $\{a_m\}$ as follows:

$$X = \gamma_L \left(\sum_{m=1}^L a_m Z_{i-m} + Z_i + \sum_{m=1}^L a_m Z_{i+m} \right) \quad (28)$$

in which γ_L is defined in Eq.8. Because $\{Z_i\}$ is the iid random numbers generated from $s(\alpha, \gamma = 1, Z)$, the value of γ_L is obtained by using the generalized central limit theorem (Mantegna & Stanley, 2004) as follows:

$$\gamma_L = \frac{\gamma}{A}, A = \left(2 \sum_{m=1}^L a_m^\alpha + 1 \right)^{1/\alpha} \quad (29)$$

Based on the algorithm introduced here we can simulate earthquake motion phases. If $\{X_i\}$ is simulated, $\{\Delta\psi_i\}$ is obtained by multiplying $\Delta\omega$ to $\{X_i\}$. Figure 5 shows the simulated eight fluctuation part of phases, which are obtained by using eight different initial random number to generate iid random number series $\{Z_i\}$.

Then calculating the cumulative sum of $\{\Delta\psi_i\}$, $\{\psi_i\}$ is obtained. Substituting $\{\psi_i\}$ into Eq.4, in which $t_0 = 98s$ is assigned, from which $\{\phi_i\}$ is obtained. Using eight different series of $\{\phi_i\}$, DRSCATHs can be simulated, which are shown in Figure 6. The eight-time histories with different colors are obtained, which are correspond to the colors in Figure 5.

3.4 Autocorrelation coefficient of mean phase gradient

The autocorrelation coefficient of the mean phase gradient is shown in Figure 7 by the light-blue zigzag line, which is obtained by using acceleration time history recorded at Kushiro observatory. The theoretical autocorrelation function $R(k)$ is obtained by

$$R(k) = E[X_i X_{i+k}] \quad (30)$$

from which the theoretical autocorrelation coefficient $\rho(k)$ is defined by

$$\rho(k) = R(k)/R(0), k = 0, 1, \dots, \infty \quad (31)$$

X_i is obtained (Sato, 2017) and automatically and X_{i+k} is defined by

$$X_i = c \left\{ \sum_{l=1}^L a_l Z_{i-l} + a_0 Z_i + \sum_{l=1}^L a_l Z_{i+l} \right\} \quad (32)$$

$$X_{i+k} = c \left\{ \sum_{l=1}^L a_l Z_{i+k-l} + Z_{i+k} + \sum_{l=1}^L a_l Z_{i+k+l} \right\} \quad (33)$$

The blue squares in Figure 7 are the theoretically obtained autocorrelation coefficients for $k = 0, 2^2, 2^4, 2^{10}, 2^{18}, 2^{23}, 2^{24}$ under the following assumption for any number of k .

$$E[Z_j Z_l] = \begin{cases} 0 & j \neq l \\ \sigma_c^2 & j = l = k + i \end{cases} \text{ for arbitrary } i$$

4 YIELD SEISMIC COEFFICIENT DEMAND SUECTRUM

The yield strength demand spectrum is commonly used for designing economical structures, but we propose a new concept, which is named the yield seismic coefficient k_h demand spectrum (YSCDS) defined by dividing yield strength with the structural weight.

Table 1. Summary of yield seismic coefficient of Kushiro record case at different natural period (the first line) and ductility responses for different record cases (below the second lines).

T	0.5	0.7	1.80
k_h	0.4606	0.2867	1481
Kushiro ph.	4	4	4
Kobe ph.	4.320	5.484	4.189
Kameoka ph.	4.263	4.848	2.670

4.1 Definition of YSCDS and their uncertainty

Figure 8 shows the relationship between T and k_h relation keeping a constant response ductility μ value such as $\mu = 4$, which is named the yield seismic coefficient demand spectrum (YSCDS). There is no effect of Fourier phase on the linear response of structural system because the input acceleration time history is the DRSCATH. However, the case for nonlinear response of the structural system. The yield strength P_y , in other word, the yield seismic coefficient k_h , fluctuate strongly as shown in Figure 8. For examples, corresponding to the colored lines, it is possible to read that $k_h = 0.4606, 0.4838, 0.4880$ at $T = 0.5s$, $k_h = 0.2867, 0.4718, 0.329$ at $T = 0.7s$ and $k_h = 0.1481, 0.1561, 0.1039$ at $T = 1.8s$, respectively.

Assuming that the YSCDS for Kushiro (black line) in Figure 8 is the YSCDS for design purpose. The first line in Table 1 gives k_h at $T = 0.5, 0.7$ and $1.8s$ for Kushiro DRSCATH, of course $\mu = 4$ as given in the second line in Table 1. Below the third line, we show the ductility responses of structures designed by using the seismic coefficient in the first line. These ductility responses are obtained for structures inputting the different DRSCATHs (Kobe and Kameoka), which are shown in Figure 2. To make clear uncertainty of response ductility, it is assumed that the Kushiro YSCDS is the design YSCDS, and the structures are designed at the natural period of $T = 0.5, 0.7$ and $1.8s$. The yield seismic coefficients at these natural periods are given in the first line of Table 1 as $k_h = 0.4606, 0.2867$ and 0.1481 , respectively. Simulating 1000 of DRSCATHs at Kushiro site, we calculate the probability density function of ductility responses. Figure 9 shows the PDF of ductility responses at the natural period of $T = 0.5, 0.7$ and $1.8s$.

The brown, blue and red lines corresponding to the natural period of $T = 0.5, 0.7$ and $1.8s$, respectively. The gray vertical line is for $\mu = 4$. From this figure it is concluded that the uncertainty of ductility responses is the largest at $T = 1.8s$.

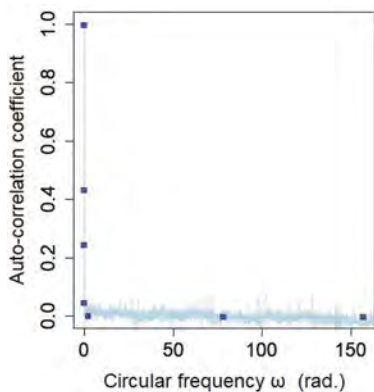


Figure 7. The autocorrelation coefficient of the mean phase gradient of Kushiro record (zigzag light blue line) and theoretically derived one at the designated circular frequency (blue squares).

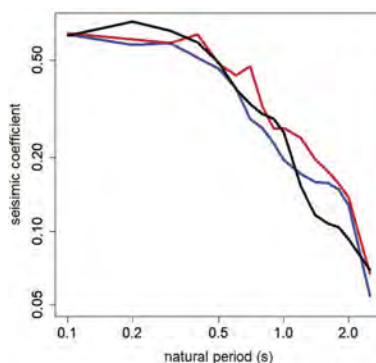


Figure 8. Yield seismic coefficient demand spectrum obtained by using DRSCATHs shown in Figure 2. Each color corresponds to the recorded acceleration time history, from which the fixed Fourier phase $\phi_d(\omega)$ and the initial Fourier amplitude $A_d(\omega)$ are obtained.

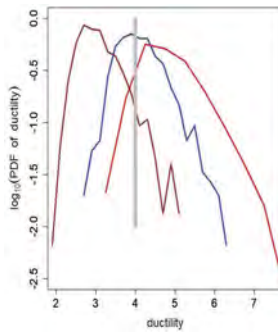


Figure 9. The probability density function (PDF) of ductility response at the natural period of 0.5, 0.7 and 1.8s. Simulating 1000 DRSCATHs at Kushiro site and calculate ductility responses. The distribution of these ductility responses is plotted as the PDF. The brown, blue, red lines are corresponding to each natural period.

5 CONCLUSIONS

It has been discussed that the effect of earthquake motion phase uncertainty on the nonlinear response of the structural system. The main research results are summarized as follows: The discussion was placed on the convergence of the response spectrum calculated from the design response spectrum compatible acceleration time history (DRSCATH) to the target design response spectrum. The DRSCATH was strongly affected by the assigned phase. A method to calculate the phase as a function of the circular frequency was introduced. A method to identify the stochastic characteristic, especially, the probability density function of the mean phase gradient was introduced. The method to simulate earthquake motion phase was introduced. A method to evaluate the phase uncertainty was discussed based on the nonlinear response of structural system. For that purpose, the Clough type constitutive relation of the structural system was used. The uncertainty of ductility responses of nonlinear systems was discussed mainly.

ACKNOWLEDGEMENT

This research was funded by Grant-in-Aid Scientific Research, JSPS (#21K04242) and the author would like to acknowledge Japan Meteorological Agency and National Research for Earth and Disaster Resilience to provide valuable observed earthquake motion records.

REFERENCES

- Douglas, J. 2002. Earthquake ground motion estimation using strong-motion records: A review of equations for estimation of peak ground acceleration and response spectral ordinates, *Earth-Science Reviews*, **61**(1–2): 43–104.
- Falconer, K. 2003. *Fractal Geometry; Mathematical Foundation and Application*, 2nd ed. John Wiley & Sons, Ltd, The Atrium, Southern Gate, Chichester.
- Housner, G. 1941. Beginning of calculation of response spectrum, Ph.D of Caltech, 1941.
- Iemura, H. & Mikami, T. 2001. Demand spectra of yielding strength and ductility factor for required seismic performance objectives, *Journal of JSCE*(in Japanese), No.689/I-57, pp. 333–342.
- Karatzas, I. & Shreve, S. 1991. *Brownian Motion and Stochastic Calculus*, Springer-Verlag, New York.
- Mantegna, N. R. & Stanley H. E. 2004. *An Introduction to Econophysics Correlations and Complexity in Finance*, Cambridge University Press, New York.
- Nolan J. P. 2015, *Stable Distribution: Models for Heavy Tailed Data*, (<http://academic2.american.edu/~jpnolan/stable/chap1.pdf>), Browsing November 13.
- Sato, T. 2017. Stochastic process of earthquake motion phase and its inherent features-Modeling of group delay time with indefinable variance-Proceeding of JSCE (Structural and Earthquake Engineering) (in Japanese), Vol.73, No.2, 344–362.
- Shrihande, M. & Gupta, V.K. 1996. On generating ensemble of design spectrum-compatible accelerograms *European Earth. Eng.*, Vol.10, pp. 49–56.
- Tsai, N.C. 1972. Spectrum-compatible motion for design purpose, *Journal of Engineering Division*, ASCE, Vol.98, No.2, pp. 345–356.

Health monitoring of long-span bridges using deep learning driven by sensor measured and numerical response data

Z. Xue, W. Sebastian & D. D'Ayala
University College London, London, UK

ABSTRACT: Both the vibration and quasi-static load responses of cable-stayed bridges affect their long-term behaviours (eg in fatigue) and so their structural integrity. The associated modal behaviours and (owing to their statically indeterminate nature) the static response are strongly influenced by the spatial stiffness profiles of the bridges. Translation into loads and response of data from a comprehensive network of multi-sensors, shows huge potential to drive a deep learning (DL) approach which can identify these spatial stiffness profiles, and so can reveal any spatial stiffness perturbations arising from any damage states. The role of sensor-verified FE analysis is discussed in providing a means to assess likely damage states for training the DL approach to enable the early defect detection. A significant impact of data quality and sample size on the DL method is discussed in the paper. This paper compares generation of data sets, establishment of learning frameworks, and performance of each DL application. A review of existing literature in the wider field of SHM is also provided, to strengthen the case for this novel approach.

1 INTRODUCTION

With the continuous construction of long-span bridges, bridge damage caused by dynamic problems becomes an increasingly important consideration. Accidents caused by dynamic load, such as seismic load, wind load and passing vehicle load are common during bridges' service period. The Viadotto Polcevera bridge in Italy collapsed during a rainstorm on 14 August 2018, lead to forty-three people deaths. The Silver bridge crossed Ohio River in U.S. collapsed under the weight of rush-hour traffic on 15 December 1967, resulting in the deaths of forty-six people. Damage detection technology is crucial to preventing these serious bridge accidents.

Over the years, with the rapidly development of computer-based technologies, structural damage detection methods have evolved from the traditional visual inspection to the modal parameter identification (Salawu et al. 1997), (Pandey et al. 1991), (Sampaio et al. 2003) to the CNN-based image recognition method (Sandeep Sony et al.). To this end, due to its low cost and high accuracy, vibration-based deep learning is increasingly popular in recent years (Avci et al. 2021).

In the structural health monitoring of large civil structures, the application of deep learning method driven by monitoring data of sensor networks in damage identification has also attracted great attention of researchers. Deep learning networks were presented that they have better performance than shallow learning (like support vector machine) while processing data mining under noise effects (Lin et al. 2018). Another review is provided of the application of deep learning in SHM, including the vibration method and visual processing method (Azimi et al. 2020). Meanwhile, new technologies are being introduced that are aimed at identifying SHM damage, such as sensors and UAVs. The damage detection methods of bridge structures based on big data and artificial intelligence methods in recent years are summarized (Sun et al. 2020).

A review of the papers that have been published most frequently during the past decade is presented in this paper. The purpose of this review is to provide an overview of bridge SHM, and DL techniques (Convolutional neural network methods are mainly focused on in this paper) in defect detection, summarize the most recent research developments, and discuss future directions. Following is a description of the paper's structure. In section 'Bridge structural

health monitoring’, This paper discusses first the types and locations of potential defects in long-span bridges, then it introduces the sensor networks in SHM systems. In section ‘Vibration-based defect detection’, it mainly focuses on structural defect detection method using DL method driven by time series vibration data. The generation of damage data sets is the core content of deep learning damage detection. In this section, the methods for generating damage data sets are divided into three categories, including vibration testing, numerical simulation, and the combination of vibration testing and numerical models. The performance of deep learning models in different applications is discussed respectively. Section ‘Summary and prospects’ discusses the limits, challenges, and future trends of structural defect detection using DL method.

2 BRIDGE STRUCTURAL HEALTH MONITORING

2.1 Defect of long-span bridge structures

Cable stayed bridges are the most widely used long-span bridges in the world. a cable-stayed bridge is mainly composed of the main girder, pylons and stay cables. Figure 1 shows the axial force paths in a cable-stayed bridge. The main girder is generally a composite steel-concrete structure, the pylons are mostly concrete structures, and the stay cables are made of high-strength materials.



Figure 1. Force paths of cable-stayed bridges.

As to the cables, continual exposure to environmental factors will cause corrosion of steel, which will result in cracks or even fractures in the cable. As a result, it can seriously degrade the stress state of the cable-stayed bridge. Furthermore, the stiffness of the cable is low, making it easy for external loads to cause vibration. Vibrations of this intensity will accelerate the abrasion of the anti-corrosion coating on the cable and aggravate the corrosion of the cable. Vibrations will also accelerate the development of original defects. Stay-cables and its anchoring details are the most common positions for defects (Pulkkinen et al. 2015).

The main girder of long-span cable-stayed bridge is usually composed of steel-concrete. Contact with soil and water will also cause corrosion of the main girder exposed to the air. Furthermore, vehicle overloads and traffic accidents may damage the structure locally, causing cracks and peeling of the main girder surface. In addition, the changes in cable force and the deflection deformation of the pylons will also cause the structural damage of the main girder.

The pylons of the cable-stayed bridge are usually composed of concrete. Common defects of the pylon include deflection deformation, fatigue crack and shear crack. Natural load like wind and unbalanced tension between cables can cause pylons to deflect. In the anchorage area of the cable, frequent changes in cable force and temperature can lead to fatigue cracking of the concrete. The shear crack usually caused by bridge state changes. The shear crack was discovered on the Viadotto Polcevera bridge collapsed in 2017 (Sandberg et al. 2010).

According to above, the stay cable is the most susceptible to damage in a long-span cable-stayed bridge, followed by the main girder and the pylons. It is corrosion and fatigue cracking that cause the majority of damage to structures. To study fatigue damage on long-span bridges, a 1:4 suspension bridge model was developed in 2019 (Zeng et al. 2019), the model includes the main cable, anchorage zone, hanger, and box girder. Fatigue experiments were applied to the model. The high-strength steel wires of the hangers were gradually evolving into a fatigued state after 2 million loading cycles, and some of them broke after 2.4 million loading cycles. The hanger wire lost transfer force ability after 2.8 million loading as a result. This shows that the early fatigue damage in the cable will gradually accumulate over time and eventually lead to structural failure.

According to an analysis of the fatigue damage in the bridge by establishing the finite element model of Tsing Ma bridge (Chan et al.2015). The FE model was updated by comparing the modal characteristics identification results based on measured data (using SHM system on

the Tsing Ma bridge) and FE model results. It is found that the stress spectra in the elements were reduced when considering fatigue damage effects.

The defects of long-span cable-stayed bridges have strong randomness, which brings challenges to the damage detection and maintenance of bridges (Sandberg et al. 2010). A sea crossing cable-stayed bridge was detected that the shortest cable near the pylon was overstress. In 2004, fatigue cracks were detected in new cables after the first round of maintenance and a small amount of cable replacement in 1999. The condition of only a small number of cables is monitored by an acoustic monitoring system, which is not capable of accurately assessing the health of the remainder. In order to ensure safety, all remaining cables were replaced as part of the project.

In conclusion, it can be observed that a method of accurately detecting damages to key parts of a cable-stayed bridge is extremely important for ensuring the safety of the bridge.

2.2 Long-span bridge sensor networks

The interest in structural health monitoring (SHM) has grown in order to objectively manage civil infrastructure systems. Use of a long-term SHM can enable determination of structural property changes over a long period of time, by either continuous monitoring or by intermittent live load tests. The health of a bridge is monitored by the use of sensors that measure external loads, dynamic responses, etc. For instance, strain gauges were used to infer the biaxial response to live loads in a bridge with reduced transverse distribution capability (Sebastian et al. 2018).

Over the past few decades, a large number of newly built long-span bridges have been equipped with rich sensor networks for real-time monitoring of environmental response and response signals on bridges. It provides a valuable and large database for the condition description of bridges.

Table 1 lists several SHM sensor networks installed on the bridges opened in recent decades. The rich sensor network provides a barge bank of sensor data that enables quantification of both the loads and the associated responses, both traffic and environmental loads can be assessed.

Table 1. SHM sensor networks of long-span bridges.

Long-span bridge	Open year	Length of main span	Number of sensors	SHM sensor networks*										
				Acc	Str	Dis	Tem	Cor	DWIM	GPS	Ane	Til	Bar	
Sutong cable-stayed bridge	2008	1088 m	1000	☑	☑	☑	☑	☑			☑			
Stonecutters Bridge	2009	1018 m	1505	☑	☑	☑	☑	☑	☑	☑	☑	☑		☑
Queensferry Crossing Bridge	2017	2*650 m	2280	☑	☑	☑	☑	☑	☑	☑	☑	☑	☑	☑
Ting Kau Bridge	1998	475 m	238	☑	☑	☑	☑			☑	☑			
Kap Shui Mun Bridge	1997	430 m	272	☑	☑	☑	☑				☑		☑	
Jindo cable-stayed bridge	1984	334 m	113	☑	☑		☑						☑	
Charles W. Cullen Bridge	2012	289 m	144	☑	☑	☑							☑	☑

* Accelerometer (Acc), Strain gauge (Str), Displacement transducer (Dis), Temperature and humidity sensor (Tem), Corrosion system (Cor), Dynamic Weigh-in-Motion system (DWIM), GPS, Anemometer (Ane), Tiltmeter (Til), Barometer (Bar)

3 VIBRATION-BASED DEFECT DETECTION

3.1 Deep learning-based defect detection method

Structural health monitoring (SHM) is a promising technique, it can identify the presence, severity and location of any damaged areas by analysis of recorded signals in various forms.

Convolutional neural network (CNN), as an important branch of deep learning, can be used to automatically discover various features in large raw datasets by backpropagation algorithm, it can reduce both research time and expert knowledge of physical problems.

With rapid advances in deep learning technology, the structural health monitoring community has witnessed a prominent growth in deep learning-based condition assessment techniques of structural systems. Deep learning has ushered in many breakthroughs in vision-based detection via convolutional neural networks (CNNs), but the vibration-based structural damage detection by CNN remains being refined. Thus, a fast and accurate structural damage detection system using one dimensional (1D) CNNs was presented in recent years. One major advantage is that a real-time and low-cost hardware implementation is feasible due to the simple and compact configuration of 1D CNNs. Figure 2 illustrates the flow chart of a typical CNN model training process.

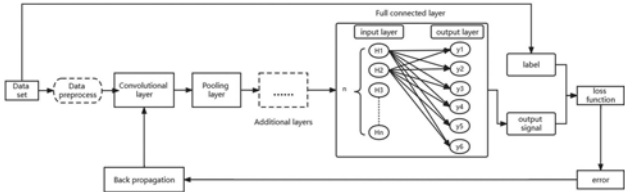


Figure 2. A CNN training flow chart.

Convolutional layers extract features, pooling layer reduces the dimension of the data, and a full connection layer classifies the input signal, then compares it to a preset label to determine the loss function. Trained models with a lower loss function have a higher classification accuracy.

Next, according to different methods of generating damage data sets, the structural damage detection based on CNN method will be introduced in three categories: vibration test, numerical simulation, and using numerical simulation together with vibration test. The content includes the characteristics of each study, the unique CNN model stratification, the existing shortcomings, etc.

3.2 Vibration test

CNN training requests a damage dataset with a large capacity. Only if the damage can be easily added to the structure, a large number of damage data can be collected through vibration tests at low cost. Using loosened bolts is a repairable method to applying damage in steel structures (Osama et al. 2017). Damage at the steel frame can be simulated by loosening the bolts at joints. A modal shaker excited the structure, and acceleration signals were collected at the joints.

Figure 3 shows an effective way to increase the capacity of the dataset by slicing the signal with overlay. To that end, in their follow-up research (Onur et al. 2018), the acceleration sensors in the experiment was replaced by wireless sensors with a computationally low cost. On this basis, they represented a 1D-CNN-based damage detection method with only two experiments (Osama et al. 2018): test on undamaged structure and test on fully damaged structure. This method can enable judgement as to whether the structure is damaged under the condition of limited damage data.

Adding extra mass blocks is another way to applying repairable damage to real structures. A three-span reinforced continuous beam bridge was established using the finite element method (He et al. 2020). As part of this study, the damage was simulated by loading extra block masses (20kg and 40kg, respectively) where it is expected to occur (close to the mid span). Experiments conducted on the beam at both a laboratory scale and in a numerical model show that this method accurately predicts damage along its middle span.

A similar method to obtain the damage data of a steel girder bridge (Zhang et al. 2019). According to the results, the proposed CNN model is sensitive to tiny local mass changes at 8 different positions of the in-lab steel beam structure. It can greatly detect the tiny mass changes.

At the end of this section, Table 2 summarizes the CNN-based defect detection approaches that generate damage data sets through vibration tests, including the applied excitations, the various types of damage, the dataset capacity, and the performance of the defect detection.

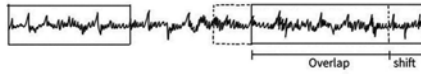


Figure 3. Data augmentation method.

Table 2. Review of CNN-based defect detection methods, datasets collected by vibration tests.

Ref	Test structure	Type of damage	Data generation	Dataset capacity	Performance
(Osama et al. 2017)	A 4.2m length steel grandstand simulator	Loosen the bolts at beam-to-girder connections	Random shaker excitation	12288 acceleration samples	Damage identification and damage localization
(Onur et al. 2018)	A 4.2m length steel grandstand simulator	Loosen the bolts at beam-to-girder connections	Random shaker excitation	5280 acceleration samples	Damage identification and damage localization
(Osama et al. 2018)	A 3.6m height four-story steel benchmark frame	Loosen the bolts and remove the brave members	Random shaker excitation	8988 acceleration samples	Damage quantification
(He et al. 2020)	A 9.8m length girder bridge	Adding additional mass blocks	Random shaker excitation	800 acceleration samples	Damage localization and quantification
(Zhang et al. 2019)	A 2.09m steel beam (S1), a 6.45m girder bridge (S2) and a 27.3m long girder bridge (S3)	Adding additional mass blocks	Random shaker excitation (S1 and S2), white noise excitation (S3)	14465 acceleration samples (S1), 8595 samples (S2), 4800 acceleration samples (S3)	Damage localization and quantification

3.3 Numerical simulation

For structures in service, it is often difficult to obtain the data set under damage state, which brings difficulties to the training of deep learning model. In this case, numerical models provide damage simulation and data generation efficiently. As to a rectangular section beam with 40 beam elements, damage cases can be easily simulated by reducing the local stiffness of beam elements (Guo et al. 2020). In total of 1.5×10^6 samples were generated for training and 5×10^4 samples for validation. This method is robust to data loss and noise interference, and the damage location and damage degree can be well detected.

It should be noted that the actual structure of the application often has errors with the model used in training. Therefore, the randomness of structural parameters should be taken into account when establishing the finite element model (Yulin et al. 2021). With the enhancement of noise, the accuracy of the model considering the randomness of structural parameters in training is significantly higher than that of the model without randomness.

The damage was also simulated by reducing the stiffnesses of the beam elements in a three-span continuous concrete beam (Yang et al. 2021). As stiffness and flexibility are reciprocal, when a structure is damaged, the local stiffness will decrease and the local flexibility will increase. This article briefly introduces the application of CNN method in prestressed concrete structures.

Due to the difficulty in extracting damage-sensitive and noise-resistant features from the response of structures, structural damage detection remains a challenging problem. It has an excellent performance of the deep learning method in detecting damage under the influence of

noise in the data set (Lin et al. 2017). In this basis, to gain a physical understanding of how the network works, hidden layers were visualized in the network.

As the main weighing component of long-span bridge, the health of the cables largely determines the health state of the bridge. The Fourier amplitude spectra (FAS) of acceleration responses are used without extensive pre-processing for modal identification directly from the raw measurement data (Duan et al. 2019) (Chen et al. 2021). According to their results, the current CNN has been shown to be robust under a variety of observational noise levels and wind speeds.

At the end of this section, Table 3 summarizes the CNN-based defect detection approaches that generate damage data sets through numerical simulations.

Table 3. Review of CNN-based defect detection methods, datasets generated by numerical simulations.

Ref	Test structure	Type of damage	Data generation	Dataset capacity	Performance
(Guo et al. 2020)	A numerical model of Euler-Bernoulli beam	Reduce the stiffness of local beam elements	Gaussian white noise excitation	1.5*10 ⁶ mode shape samples	Damage localization and quantification
(Yulin et al. 2021)	A 2m length simply supported concrete FE beam model	Reduce the stiffness of local beam elements	Random hammer excitation	20000 acceleration samples	Damage localization and quantification
(Yang et al. 2021)	A 55m length continuous beam bridge	Reduce the stiffness of local beam elements	No excitation, analyzed by ANSYS	Flexibility diagonal curvature as samples	Damage localization and quantification
(Lin et al. 2017)	A 10m length simply supported beam	Reduce the stiffness of local beam elements	Random white noise excitations	6885 acceleration samples	Damage localization and quantification
(Duan et al. 2019) (Chen et al. 2021)	A 2-D FE model of a 140m length tied-arch bridge	Decrease the cross-sectional area	Wind force excitations	28950 Fourier amplitude spectra samples	Damage localization and quantification

3.4 Combination of numerical simulations and vibration tests

It is easy and efficient to acquire damage data when a numerical model is established. A major problem is the failure to match the numerical model to the original structure, which may lead to a reduction in data quality. Hence, using the data from actual structural experiments used to update a numerical model, it is available to efficiently enhance the fidelity of the numerical model, then to accurately simulate a wide range of damage data (Franchini et al. 2022).

The updated numerical model can be used to generate recurrence graph for CNN training (He et al. 2020). However, the proposed method is an image recognition method in essence. The vibration signal is converted into a recursive graph, and then the damage is detected by image recognition. This will lead to complex computation for large structures.

In order to ensure the fidelity of the dataset generated by Finite element (FE) models, it's necessary to consider various uncertainties, including modeling errors, measurement errors, and environmental noises based on FE model and real intact state (Zohreh et al. 2020).

In order to ensure the fidelity of damage dataset generated by numerical models, it is also necessary to compare the modal parameters of actual structure and numerical model under damage conditions (Hakim et al. 2015). The damage in the experiment can be achieved by introducing a slot in turn obtained by grinding from the different locations of the structure. Meanwhile the damage was simulated by reducing the local stiffness in FE model.

The measured data from the vibration experiment as well as the data generated by the finite element model can both be used as input signals when training the deep learning model, which further guarantees the fidelity of the dataset (Teng et al. 2019). In this study, the data set required for CNN training was generated through the finite element model, and then the training results were verified by the data collected from the laboratory scale structure.

Table 2 summarizes the CNN-based defect detection approaches that generate damage data sets through the combination of numerical simulations and vibration tests.

Table 4. Review of CNN-based defect detection methods, datasets based on numerical simulations & vibration tests.

Ref	Test structure	Type of damage	Data generation	Dataset capacity	Performance
(He et al. 2020)	A 9.8m length girder bridge and a 75m length FE model	Reduce the local stiffness, load additional mass blocks	Random hammer excitation (Exp), noise excitations (FE)	800 recurrence graph samples (Exp), 10000 samples (FE)	Damage localization and quantification from 10 structural states
(Zohreh et al. 2020)	A 2m height jacket structure and its FE model	Remove the diagonal braces	Shaker excitations (Exp), noise excitations (FE)	500 FRFs samples (Exp), 1500 samples (FE)	Damage localization from 5 structural states
(Hakim et al. 2015)	A 3.2m length steel I-beam structure and its solid FE model	Grinding the structure (Exp), remove solid elements (FE)	Random shaker excitations (Exp), modal analysis (FE)	104 sets of mode shape value samples (52 Exp), (52 FE)	Damage localization and quantification from 101 structural states
(Teng et al. 2019)	A 10.62m length steel frame with 381 rods and its FE model	Cut rod section (Exp), reduce the stiffness of the rods (FE)	Hammer excitations (Exp)	17 modal strain energy samples (Exp), 44 samples (FE)	Damage localization from 136 structural states

4 CONCLUSIONS

In this paper, a systematic overview of vibration-based deep learning techniques in structures is provided, several conclusions can be drawn as follows.

Deep learning methods based on CNN have great potential for detecting structural damage to bridges. An important factor in determining the detection accuracy is the quality of the data set formed by the vibration response signal. A large capacity and high-fidelity data set are prerequisites for the successful application of this method in bridge structures.

The combination of vibration test and numerical model is an advanced method. The numerical model can be updated using modal parameter identification with the measured data from real structures. It can greatly improve the fidelity of the generated dataset from numerical models. To this end, the SHM sensor network of the bridge can provide vibration response data sets under different environments and vehicle excitation, which will greatly improve the robustness of the depth learning model to environmental and other impacts when conducting damage identification.

In conclusions, it is a low-cost and efficient way to update the high-fidelity numerical model based on the measured data of its sensor network and generate a large sample size damage dataset to train the deep learning model, which should be a future trend of bridge SHM.

REFERENCES

- Abdeljaber, O., Avci, O., Kiranyaz, S., Gabbouj, M., Inman, D.J. 2017. Real-time vibration-based structural damage detection using one-dimensional convolutional neural networks. *Journal of sound and vibration*. Vol.388: 154–170.
- Abdeljaber, O., Avci, O., Kiranyaz, S., Kiranyaz, M.S., Boashash, B., Sodano, H., Inman, D.J. 2018. 1-D CNNs for structural damage detection: verification on a structural health monitoring benchmark data. *Neurocomputing (Amsterdam)*. Vol.275: 1308–1317.
- Franchini, A., Sebastian, W., D’Ayala, D. 2022. Surrogate-based fragility analysis and probabilistic optimisation of cable-stayed bridges subject to seismic loads. *Engineering Structures*. Volume 256: 113949.
- Avci, O., Abdeljaber, O., Kiranyaz, M.S., Hussein, M., Inman, D.J. 2018. Wireless and real-time structural damage detection: a novel decentralized method for wireless sensor networks. *Journal of sound and vibration*. Vol.424: 158–172.

- Avci, O., Abdeljaber, O., Kiranyaz, M.S., Boashash, B., Sodano, H., Inman, D.J. 2018. Efficiency validation of one dimensional convolutional neural networks for structural damage detection using a SHM benchmark data. 25th International Congress on Sound and Vibration.
- Avci, O., Abdeljaber, O., Kiranyaz, S., Hussein, M., Inman, D.J. 2021. A review of vibration-based damage detection in civil structures: From traditional methods to Machine Learning and Deep Learning applications. *Mechanical systems and signal processing*. Vol.147: 107077.
- Azimi, M., Eslamlou, A.D., Pekcan, G. 2020. Data-driven structural health monitoring and damage detection through deep learning: State-of-the-art review. *Sensors*. Vol.20 (10): 2778.
- Chan, T.H.T., Guo, L., Li, Z.X., Das, P.C., Frangopol, D.M., Nowak, A.S. 2015. Assessment of fatigue damage in the tsing ma bridge under traffic loadings by finite element method. *Current and future trends in bridge design, construction and maintenance 2*.
- Chen, Q.Y., Yun, C.B., Duan, Y.F. 2021. Cable damage identification of tied-arch bridge using convolutional neural network. *The 16th East Asian-Pacific Conference on Structural Engineering and Construction*.
- Duan, Y.F., Chen, Q.Y., Zhang, H.M., Yun, C.B., Wu, S.K., Zhu, Q. 2019. CNN-based damage identification method of tied-arch bridge using spatial-spectral information. *Smart Structures and Systems*. Vol. 23: 507–520.
- Guo, T., Wu, L.P., Wang, C.J., Xu, Z.L. 2020. Damage detection in a novel deep-learning framework: a robust method for feature extraction. *Structural health monitoring*. Vol.19 (2): 424–442.
- Hakim, S.J.S., Abdul, R.H., Ravanfar, S.A. 2015. Fault diagnosis on beam-like structures from modal parameters using artificial neural networks. *Journal of the International Measurement Confederation*. Vol.76: 45–61.
- He, H.X., Zheng, J.C., Liao, L.C., Chen, Y.J. 2020. Damage identification based on convolutional neural network and recurrence graph for beam bridge. *Structural health monitoring*. 147592172091692.
- Lin, Y.Z., Nie, Z.H. 2017. Structural damage detection with automatic feature-extraction through deep learning. *Computer-Aided Civil and Infrastructure Engineering* 32: 1025–1046.
- Lin, Z.B., Pan, H., Wang, X.Y., Li, M.L. 2018. Data-driven structural diagnosis and conditional assessment: from shallow to deep learning. *Sensors and Smart Structures Technologies for Civil, Mechanical, and Aerospace Systems*. 1059814.
- Mousavi, Z., Varahram, S., Ettefagh, M.M., Sadeghi, M.H., Razavi, S.N. 2020. Deep neural networks-based damage detection using vibration signals of finite element model and real intact state: An evaluation via a lab-scale offshore jacket structure. *Structural health monitoring*: 147592172093261.
- Pandey, A.K., Biswas, M., Samman, M.M. 1991. Damage detection from changes in curvature mode shapes. *Journal of sound and vibration*. Vol.145 (2): 321–332.
- Pan, H., Azimi, M., Yan, F., Lin, Z.B. 2018. Time-frequency-based data-driven structural diagnosis and damage detection for cable-stayed bridges. *Journal of bridge engineering*. Vol.23 (6): 4018033.
- Pulkkinen, P., Kiviluoma, R., Parke, G., Disney, P. 2005. Maintenance issues in the design of long-span cable-stayed bridges. *Proceedings of the 5th International Conference on Bridge Management*. 314–320.
- Salawu, O.S. 1997. Detection of structural damage through changes in frequency: a review. *Engineering structures*. Vol.19 (9): 718–723.
- Sampaio, R.P.C., Maia, N.M.M., Silva, J.M.M. 1999. Damage detection using the frequency-response-function curvature method. *Journal of sound and vibration*. Vol.226 (5): 1029–1042.
- Sandberg, J., Hendy, C.R. 2010. Replacement of the stays on a major cable-stayed bridge. *Proceedings of the Institution of Civil Engineers*. *Bridge engineering*, Vol.163 (1): 31–42.
- Sun, L., Shang, Z.Q., Xia, Y., Bhowmick, S., Nagarajaiah, S. 2020. Review of bridge structural health monitoring aided by big data and artificial intelligence: From condition assessment to damage detection. *Journal of structural engineering (New York, N.Y.)*. Vol.146 (5).
- Teng, S., Chen, G.F., Liu, G., Lv, J.B., Cui, F.S. 2019. Modal strain energy-based structural damage detection using convolutional neural networks. *Applied sciences*. Vol.9 (16): 3376.
- Sebastian, W.M., Johnson, M. 2018. Interpretation of sensor data from in situ tests on a transversely bonded fibre-reinforced polymer road bridge. *Structural Health Monitoring*. Vol.18 Issue 4.
- Yang, S.Q., Huang, Y. 2021. Damage identification method of prestressed concrete beam bridge based on convolutional neural network. *Neural computing & applications*. Vol.33 (2): 535–545.
- Zeng, Y., Tan, H.M., Zhong, H.D., Yu, Q. 2019. Fatigue experiment of sectional integrated model of a suspension bridge. *Structures and Buildings*. 172(1): 5–16.
- Zhan, Y.L., Lu, S.J., Xiang, T.Y., Wei, T. 2021. Application of convolutional neural network in random structural damage identification. *Structures (Oxford)*. Vol.29: 570–576.
- Zhang, Y.Q., Miyamori, Y., Mikami, S., Saito, T. 2019. Vibration-based structural state identification by a 1-dimensional convolutional neural network. *Computer-aided civil and infrastructure engineering*. Vol.34 (9): 822–839.

Progressive collapse behavior of RC frames subjected to reinforcement corrosion

L.C. Ding

College of Civil Engineering, Tongji University, Shanghai, China

Y.B. Peng

Shanghai Institute of Disaster Prevention and Relief, Tongji University, Shanghai, China

State Key Laboratory of Disaster Reduction in Civil Engineering, Tongji University, Shanghai, China

J.B. Chen

College of Civil Engineering, Tongji University, Shanghai, China

State Key Laboratory of Disaster Reduction in Civil Engineering, Tongji University, Shanghai, China

ABSTRACT: Ageing reinforced concrete (RC) structures were observed to be much more vulnerable to progressive collapse than newly constructed ones. Deterioration due to severe reinforcement corrosion can significantly affect progressive collapse resistances of the RC structures. Hence, this contribution aims at numerically investigating the progressive collapse behavior of the deteriorated RC frame structures subjected to uniform reinforcement corrosion. Both static and dynamic progressive collapse analyses in relation to a deteriorated RC frame subjected to a middle column removal scenario are carried out. It is observed that both static and dynamic progressive collapse resistances significantly decrease with increasing corrosion level. The reinforcement corrosion is found to be the predominant cause to the deterioration of the progressive collapse resistances, while the effect of concrete deterioration has limited influence. Reinforcement corrosion in the beams in the bays directly above the removed column controls the structural progressive collapse performance, while the reinforcement corrosion in other locations has little influence. The dynamic resistances are found to decrease larger in percentage than the static resistances with increasing corrosion level.

1 INTRODUCTION

Progressive or disproportionate collapse of reinforced concrete (RC) building structures due to accidental loads may cause considerable losses of life and property (Ding et al., 2018, Parisi et al., 2019, Feng et al., 2021, Ding et al., 2021). Considering civil engineering structures are prone to ageing and deterioration processes from aggressive chemical attacks (Feng et al., 2021, Biondini and Vergani, 2014), it is of great importance to not only reduce the risk of progressive collapse for new constructions but also assess the structural robustness or safety of existing buildings (Parisi et al., 2019). RC structures may suffer from carbonation of concrete cover and penetration of chloride ions, which will result in reinforcement corrosion and significantly reduce the performance of the structures. In this context, a life-cycle performance assessment becomes very important (Biondini and Frangopol, 2016). However, at present very limited information is available in literature with respect to its quantification in the context of structural robustness or progressive collapse (Botte et al., 2016, Feng et al., 2021, Yu et al., 2017). Botte *et al.* (2016) numerically investigated the influence of corrosion effects on the tensile membrane behavior of RC slabs subjected to middle support removal scenarios. A significant influence on the ultimate load-bearing capacity of the slabs due to the corrosion was observed, even for a small corrosion level. Yu *et al.* (2017) studied progressive collapse behavior of ageing RC frame structures subjected to middle column removal scenarios. The ageing structures with

severe corrosion were observed to be much more vulnerable to progressive collapse than newly constructed ones. The ultimate deformation capacity was reduced by over 40% after 50 years of corrosion, while the ultimate load-bearing capacity was reduced almost by 20%-30%. Feng *et al.* (2021) numerically studied the time-dependent reliability and redundancy of a RC frame subjected to column removal scenarios. All of these investigations show that corrosion can significantly affect the progressive collapse behavior of RC structures.

In light of the above background, this contribution aims at numerically investigating progressive collapse performance of deteriorated RC frame structures subjected to uniform reinforcement corrosion. Following the introduction of the implemented deterioration models in Section 2, an example RC frame is described in Section 3. Subsequently, the influence of different deterioration models (Section 4), different corrosion locations (Section 5), as well as dynamic effects (Section 6) are investigated. Eventually, conclusions are addressed in Section 7.

2 CORROSION MODELING

The process of corrosion in RC structures includes an initiation phase and a propagation phase (Botte *et al.*, 2016, Yu *et al.*, 2017). The reinforcement in RC structures will become depassivated due to the ingress of chlorides or carbonation in the initiation phase. In the propagation phase the actual cross-sectional area of the reinforcements is reduced and the volume of the bars start to expand due to the accumulation of corrosion products. Currently, only the propagation phase is considered in this contribution, as the duration of the initiation phase and the end of service life determination is not within the objectives of the investigations in this contribution. In general, damage modeling includes the following four aspects (Biondini and Vergani, 2014, Botte *et al.*, 2016, Yu *et al.*, 2017): (1) Reduction of cross-sectional area of the corroded reinforcement; (2) Reduction of mechanical properties of the reinforcement; (3) Deterioration of concrete due to cracking and spalling (expansion of corrosion products); and (4) Reduction of bond behavior between the reinforcing bars and the surrounding concrete. The reduction of bond behavior is not taken into account in the present work and can be the subject of future investigations.

2.1 Effect of corrosion on cross-sectional area of reinforcing steel

The reduction of cross-sectional area of reinforcing bars is one of the most relevant effects of corrosion (Cairns *et al.*, 2005). The corrosion mechanism can relate to uniform corrosion, pitting corrosion, or a mix of both (Biondini and Vergani, 2014). Generally, the carbonation of concrete cover may produce uniform corrosion, while pitting corrosion is mainly developed in the presence of chloride ions (Du *et al.*, 2005). In the following uniform corrosion is considered to investigate the progressive collapse behavior of deteriorated RC frames. However, the analysis could be also extended to take into account pitting corrosion by incorporation of a pitting factor (Biondini and Vergani, 2014).

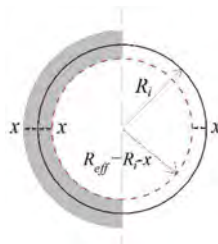


Figure 1. Modeling of cross-section reduction of a corroded bar.

The average loss of cross-sectional area in case of uniform corrosion can be calculated if the corrosion penetration depth x is known, see Figure 1. The original radius of the reinforcing bar is R_i , while the effective radius after corrosion is $R_{eff} = R_i - x$. Consequently, the percentage of cross-sectional area loss α (or corrosion level) can be calculated as follows:

$$\alpha = \frac{\Delta A_s}{A_s} \times 100\% \quad (1)$$

where ΔA_s is the area reduction due to corrosion; and A_s is the original area of the bar.

An empirical model can be adopted to determine the time-dependent corrosion penetration depth x . The corrosion rate i_{corr} is calculated by (Biondini and Frangopol, 2016):

$$i_{\text{corr}}(t) = 0.85 \cdot i_{\text{corr}}(0) \cdot t^{-0.29} \quad (2)$$

$$i_{\text{corr}}(0) = \frac{2.7(1 - w/c)^{-1.64}}{d_c} \quad (3)$$

where $i_{\text{corr}}(t)$ [$\mu\text{A}/\text{cm}^2$] is the corrosion rate at time t [year] since corrosion initiation; $i_{\text{corr}}(0)$ is the corrosion rate at the start of corrosion propagation; w/c is the water cement ratio; and d_c [cm] is the concrete cover. Consequently, the corrosion penetration depth x [mm] can be calculated using Equation (4) as an integral of the corrosion rate:

$$x(t_n) = 0.0116 \int_0^{t_n} i_{\text{corr}}(t) dt \quad (4)$$

where 0.0116 is the unit conversion factor since $1 \mu\text{A}/\text{cm}^2 = 0.0116 \text{ mm/year}$.

2.2 Effect of corrosion on mechanical properties of reinforcing steel

The influence of corrosion on the strength of reinforcement steel, i.e. the yield stress and the ultimate strength, has been studied by many researchers (Almusallam, 2001, Du et al., 2005, Cairns et al., 2005, Zhu and François, 2013). However, contradictory conclusions were drawn. Several investigations (Almusallam, 2001, Botte et al., 2016) indicated that the tensile strength of steel bars was not influenced by the level of reinforcement corrosion when the actual (reduced) area of cross-section was adopted. In this regard, the reduced cross-section area (i.e. actual area of the corroded rebar) can be used to simulate the reduction of the capacity of the corroded rebar, where no reduction of the yield stress and the ultimate strength is considered in the current study.

Almost all experimental studies explicitly showed that corrosion may result in significant reduction of the ductility of reinforcement steel (Botte et al., 2016, Coronelli and Gambarova, 2004). Based on fitting of available experimental data, different mathematical models for the ductility loss have been developed. According to references (Biondini and Vergani, 2014, Feng et al., 2021), the loss of steel ductility is expressed as an exponential reduction model, which is adopted herein, as the following model:

$$\varepsilon_{su,c} = \begin{cases} \varepsilon_{su}, & 0 \leq \alpha < 0.016 \\ 0.1521\alpha^{-0.4583} \varepsilon_{su}, & 0.016 \leq \alpha \leq 1 \end{cases} \quad (5)$$

2.3 Effect of corrosion on concrete properties

With increasing reinforcement corrosion level, considerable internal pressure can be developed due to the formation of corrosion products (i.e. iron oxides) along the surface of reinforcing bars and this may lead to cracking and spalling of the concrete cover. The mechanical properties of both the cover concrete and the core concrete may be affected. Regarding the cover concrete, the effect of cracking and spalling is considered by reducing the compressive strength of the concrete (Coronelli and Gambarova, 2004). The reduced concrete strength f_c^* is expressed as follows:

$$f_c^* = \frac{f_c}{1 + \kappa(\varepsilon_{cr}/\varepsilon_{c1})} \quad (6)$$

where f_c is the concrete peak compressive strength with no reduction; κ is a coefficient related to bar roughness and diameter, where a value of 0.1 has been adopted for medium-diameter ribbed bars (Coronelli and Gambarova, 2004); ε_{c1} is the concrete peak strain; and ε_{cr} is the average tensile strain in the cracked concrete and is calculated by (Coronelli and Gambarova, 2004):

$$\varepsilon_{cr} = n_{\text{bar}}\omega_{cr}/b_0 \quad (7)$$

$$\omega_{cr} = 2\pi(\gamma_{rs} - 1) \cdot x \quad (8)$$

where b_0 is the initial section width; n_{bar} is the number of bars under compression; ω_{cr} is the total crack width for a given corrosion level; γ_{rs} is the ratio of volumetric expansion due to corrosion products (Figure 1), which is set as 2 based on the assumption that all corrosion products accumulate around the corroded bar and are incompressible; and x is the corrosion penetration depth.

In terms of the core concrete, the strength and ductility may decrease as well, since the confinement effect provided by the transverse bars decreases due to the corrosion. When updating the reduced properties of the core concrete, the reduced cross-sectional area of the corroded transverse bar is adopted. The modified Kent-Park model can be adopted to calculate the strength of the core concrete (Feng et al., 2021):

$$K = 1 + \frac{\rho_{st}f_{yt}}{f_c} \quad (9)$$

$$f_{c,cor} = Kf_c \quad (10)$$

$$\varepsilon_{c,cor} = K\varepsilon_{c1} \quad (11)$$

where K is the confinement ratio; ρ_{st} is the volume ratio of corroded transverse reinforcement; f_{yt} is the yield stress of corroded transverse reinforcement; and $\varepsilon_{c,cor}$ is the peak strain corresponding to the strength $f_{c,cor}$ of the confined core concrete.

3 DESCRIPTION AND NUMERICAL MODELING OF A RC FRAME

A 5-story 4-bay RC frame shown in Figure 2a is used to investigate progressive collapse behavior of RC frames subjected to simulated reinforcing corrosion in this work. The height of the first story is 4.5 m, while the height for the other four stories is 3.6 m for each. The dimensions of beams and columns are 250 mm × 500 mm and 500 mm × 500 mm, respectively. Details of reinforcement is also shown in Figure 2a. The columns are labelled as A, B, C, D and E from left to right (Figure 2a). The concrete cover is 30 mm in all elements. The concrete of type C20/25 (CEN, 2004) is used, i.e. the characteristic cylinder compressive strength is $f_{ck} = 20$ MPa, while the mean compressive strength of the concrete is assumed to be $f_{cm} = f_{ck} + 8 = 28$ MPa and the mean tensile strength is $f_{ctm} = 0.3(f_{ck})^{2/3} = 2.2$ MPa (CEN, 2004). The compressive peak strain for the concrete is $\varepsilon_{c1} = 0.0021$. The elastic Young's modulus for the concrete is $E_{ci} = 30.3$ GPa. The aforementioned modified Kent-Park model is used to calculate the confinement effect on core concrete. The characteristic yield stress and tensile strength of reinforcing steel are $f_{yk} = 500$ MPa and $f_{uk} = 575$ MPa (ductility class C), respectively (CEN, 2004). Mean yield stress of the steel is assumed to be $f_{ym} = f_{yk} + 2\sigma_1 = 560$ MPa, where $\sigma_1 = 30$ MPa is the standard deviation (JCSS, 2001). The mean tensile strength is assumed to be $f_{um} = f_{uk} + 2\sigma_2 = 655$ MPa, where $\sigma_2 = 40$ MPa is the standard deviation (JCSS, 2001). The ultimate strain for the reinforcing steel is $\varepsilon_u = 12\%$. The elastic Young's modulus for the reinforcing steel is 205 GPa.

A finite element (FE) model for the RC frame using the software package OpenSees (OpenSees, 2006) is created. Regarding the beam and column components, the force-based fiber beam-column elements with 5 integration points is used. The co-rotational transformation is adopted to consider geometrical nonlinearity. The ConcreteD material and the Steel02 material in OpenSees are adopted for concrete and steel fibers, respectively. More details can be found in relevant references (Feng et al., 2021, OpenSees, 2006). To validate the previously described modeling techniques, a 1/3-scale 3-story 4-bay RC frame (Figure 2b), experimentally tested by Yi *et al.* (2008), subjected to a middle column removal scenario is employed. Figure 2c shows that results between the numerical simulation and the experimental test agree well with each other, which means a good performance of the modeling techniques.

4 INFLUENCE OF MATERIAL DETERIORATION

4.1 Corrosion of reinforcement

In this work, the RC frame subjected to a ground middle column C removal scenario (Figure 3a) is investigated. The mean values with respect to the material mechanical properties in Section 3 are adopted. The FE model is subsequently adopted to perform nonlinear static pushdown analyses. As a first step in the assessment of the influence of corrosion, it is assumed that all the beams and columns are exposed on four sides and all the reinforcements in both the beams and the columns are subjected to uniform corrosion, i.e. deterioration of concrete is not considered and will be investigated in the following section. Note that all the reinforcement is assumed to be subjected to a same corrosion level at a certain moment and no pitting corrosion is considered, i.e. a general influence of the corrosion degradation is investigated rather than localized (spatial variable) degradation phenomena. In the static pushdown analyses, uniformly distributed vertical loads are imposed on the entire structural system. A displacement-controlled analysis is carried out, where the displacement at the top of the removed column C is controlled. The displacement at the control point against the imposed load is recorded, which results in the pushdown curves in Figure 3b.

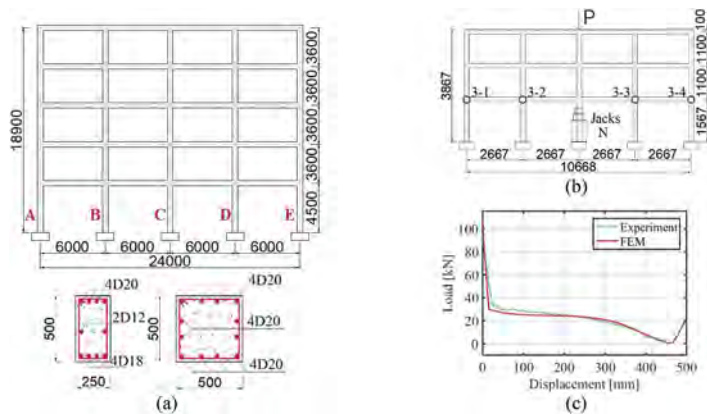


Figure 2. (a) Layout of the RC frame and column and beam cross-sections; (b) 1/3-scale RC frame used for validation; and (c) comparison between test and simulation results. (dimensions in mm).

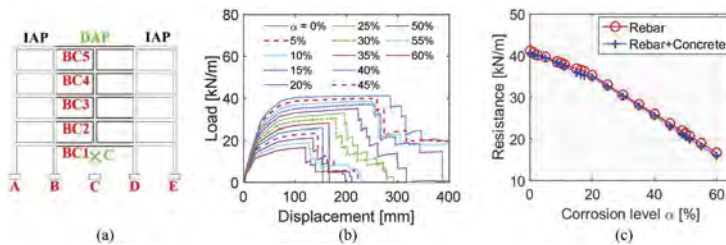


Figure 3. (a) Removal of the ground column C; (b) load-displacement relationships considering different corrosion levels; and (c) resistance vs. corrosion level.

Figure 3b shows the load-displacement (pushdown) curves under different corrosion levels α . It can be observed that both ultimate load-bearing capacities (corresponding to a first local failure) and corresponding displacements decrease with increasing corrosion level. This is as expected because a larger reduction of the reinforcement cross-sectional area is obtained under a higher corrosion level. Moreover, the corroded rebar becomes less ductile with increasing corrosion level. It is worth emphasizing that different failure modes may be observed, considering different

corrosion levels. In general, the first failure (either concrete crushing or reinforcement rupture) in a system is important, as it can be considered as the onset of failure. The progressive collapse analysis beyond the first failure after column removal is outside of the scope of investigations herein. Different failure modes (varying among the beam ends of BC1 – BC5 in Figure 3a) are observed under different corrosion levels. First failure always occurs in the bays directly above the removed column but varies at different beam ends (i.e. beam ends in different floors). The change of the failure modes may result from the load redistribution mechanism, such as the Vier-eendeel action. Code-compliant shear capacity verifications are also included in all the progressive collapse simulations. Shear failure is never observed in these progressive collapse simulations. The ultimate load-bearing capacities obtained from the results in Figure 3b against the corrosion levels are collected and presented in Figure 3c (the curve designated as ‘Rebar’).

4.2 Deterioration of concrete

Based on the models introduced in Section 2.3, the phenomenon of cracking and spalling in the compressed cover concrete is simulated by reducing its compressive strength, while the confinement effect on the core concrete is determined by using the modified Kent-Park model with the properties of the corroded transverse bars. Likewise, the frame subjected to the loss of the column C (Figure 3a) is considered and pushdown analyses are carried out. Results of resistances against corrosion levels are presented in Figure 3c (the curve designated as ‘Rebar + Concrete’). Compared to the response without considering the deterioration of concrete (the curve ‘Rebar’), the same tendency is observed and the results are almost identical. The influence of concrete deterioration on the progressive collapse resistance is very limited, i.e. resulting in only a slight reduction of the load-bearing capacity. This indicates that the reinforcement corrosion is the predominant cause to the deterioration of structural progressive collapse resistance.

5 INFLUENCE OF CORROSION AT DIFFERENT LOCATIONS

When the RC frame is subjected to the loss of column C (Figure 3a), the bays immediately above the removed column can be regarded as the directly affected part (DAP), while the remaining part is the indirectly affected part (IAP). The DAP will be the most affected part in the context of progressive collapse since large deformations are expected to occur there. Considering that corrosion may occur at specific locations in a frame, the generalized influence of having corrosion at different locations is investigated. In order to do so, the same column C loss situation as that in Section 4 is considered and static pushdown analyses considering two additional cases are performed.

The first case is that all the beams from the first to the fifth floors (designated as ‘Beam:12345’) are subjected to reinforcement corrosion. The curve of resistance against corrosion level is presented in Figure 4a. Note that the curve designated as ‘Entire’ corresponds to the situation where the entire system, i.e. the reinforcement in all beams and columns, is subjected to corrosion as investigated in Section 4 (Figure 3c). It is found that the curve ‘Beam: 12345’ is almost identical to the curve ‘Entire’, which means the corrosion effects in the beams completely governs the reduction of structural load-bearing capacity with increasing corrosion level.

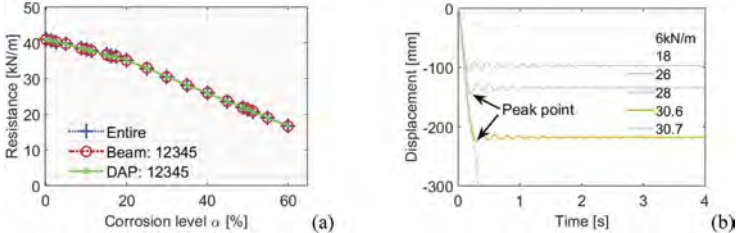


Figure 4. (a) Resistance vs. corrosion level considering corrosion at different locations; and (b) time history displacement responses when $\alpha = 20\%$.

Next, a situation is considered such that only the beams from the first to the fifth floors in the DAP are subjected to reinforcement corrosion (designated as ‘DAP: 12345’). In this case no reinforcement corrosion is considered in the beams in the IAP. Again, the curve ‘DAP: 12345’ is almost identical to the curves ‘Entire’ and ‘Beam: 12345’ (Figure 4a). This indicates that the load-bearing capacity for the RC frame subjected to the reinforcement corrosion is determined by the capacities of the beams in the DAP for the particular case under investigation.

6 INFLUENCE OF DYNAMIC EFFECTS

Incremental dynamic analyses (IDA) (Parisi and Scalvenzi, 2020, Ding et al., 2021) are performed to investigate dynamic progressive collapse behavior of the deteriorated RC frame, through progressively increasing the imposed uniform loads on all beams until collapse. The entire RC frame subjected to reinforcement corrosion (in all beams and columns) is considered. The IDA including a series of nonlinear time history analysis are carried out for the removal of column C (Figure 3a). Rayleigh damping with a damping ratio of 5% is adopted in all dynamic analyses (Parisi and Scalvenzi, 2020). To accurately determine the ultimate load-bearing capacity, a final load increment resolution of 0.1 kN/m is taken. An IDA is executed for each corrosion level. For instance, the time history displacement responses when corrosion level $\alpha = 20\%$ are shown in Figure 4b. The system oscillates around the equilibrium position and the oscillation decays due to damping effect after the sudden column removal. Further, the peak values of the time history displacement responses against the imposed loads are collected to get dynamic capacity (or IDA) curves. The IDA curves for different corrosion levels obtained from the IDA are shown in Figure 5a. It can be seen that the ultimate load-bearing capacities and the ultimate displacements decrease significantly with increasing corrosion levels from 0% to 60%. Note that the static load-displacement (or pushdown) curves are also presented in Figure 5a, as a comparison. The IDA curve is significantly lower than the pushdown curve at the same corrosion level, which means the influence of dynamic effects is significant. The maximum displacements in the IDA curves are almost identical to the displacements corresponding to the ultimate load-bearing capacities (corresponding to the first local failure) in the pushdown curves. Moreover, the failure mode of the dynamic analysis is found to be similar to that in the static analysis at the same corrosion level.

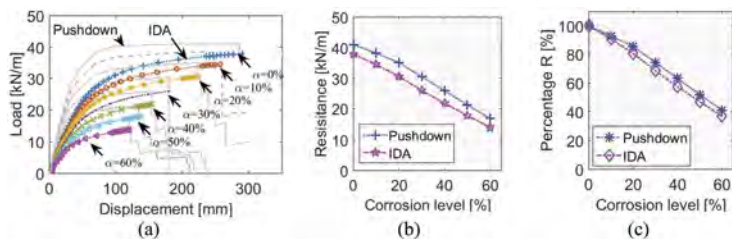


Figure 5. (a) Load - displacement relationship; (b) resistance vs. corrosion level; and (c) percentage of resistance vs. corrosion level.

Subsequently, the dynamic resistances obtained from the IDA are collected to plot the resistance - corrosion level curve, as shown in Figure 5b. As expected, the curve from the IDA is markedly lower than the curve from the static pushdown analysis. Figure 5c further shows the percentages of the dynamic and static resistances (R_d) against corrosion levels, comparing to the corresponding values at $\alpha = 0\%$ (R_0), i.e. R_d/R_0 . It can be seen that the dynamic resistances almost always decrease larger than the static resistances with increasing corrosion levels, resulting in larger dynamic amplification factors. Actually, the influence of the coupling of the corrosion effects and the dynamic effects needs to be further investigated.

7 CONCLUSIONS

In this contribution the progressive collapse behavior of a deteriorated RC frame subjected to a middle column removal scenario has been investigated, particularly with respect to the

influence of reinforcement corrosion, the influence of deterioration of concrete due to the corrosion effect, the influence of different corrosion locations, and the influence of dynamic effects.

Both static and dynamic progressive collapse resistances of the deteriorated RC frame are found to significantly decrease with increasing corrosion level. The reinforcement corrosion is found to be the major cause to the deterioration of the progressive collapse performance with increasing corrosion level, while the effect of concrete deterioration is observed to have limited influence. It is found that the reinforcement corrosion in the beams in the DAP controls the structural performance for the column loss case. The reinforcement corrosion in other locations has little influence. The progressive collapse resistances obtained by dynamic analyses are significantly lower than the static resistances. Moreover, the dynamic resistances are found to decrease slightly larger in percentage than those from static analyses with increasing corrosion level.

It must be emphasized that the obtained results are on the basis of some assumptions, e.g. uniform corrosion is assumed but pitting corrosion may be more realistic in real RC structures and the bond behavior between reinforcing bars and concrete is not taken into account. Nonetheless, the above investigations provide a first stepping stone towards further investigation of progressive collapse in case of degrading concrete structures.

ACKNOWLEDGEMENTS

This research is supported by the National Natural Science Foundation of China (Grant Nos. 51678450 and 51725804) and the China Postdoctoral Science Foundation (Grant No. 2022M722427).

REFERENCES

- Almusallam, A.A. 2001. Effect of degree of corrosion on the properties of reinforcing steel bars. *Construction and Building Materials*, 15, 361–368.
- Biondini, F. & Frangopol, D.M. 2016. Life-cycle performance of deteriorating structural systems under uncertainty: Review. *Journal of Structural Engineering*, 142, F4016001.
- Biondini, F. & Vergani, M. 2014. Deteriorating beam finite element for nonlinear analysis of concrete structures under corrosion. *Structure and Infrastructure Engineering*, 11, 519–532.
- Botte, W., Caspeele, R. & Taerwe, L. 2016. Membrane behavior in RC slabs subjected to simulated reinforcement corrosion. *Engineering Structures*, 123, 45–58.
- Cairns, J., Plizzari, G.A., Du, Y.G., Law, D.W. & Franzoni, C. 2005. Mechanical properties of corrosion-damaged reinforcement. *Aci Materials Journal*, 102, 256–264.
- CEN 2004. *Eurocode 2: Design of concrete structures—Part 1-1: General rules and rules for buildings*, EN 1992-1-1.
- Coronelli, D. & Gambarova, P. 2004. Structural assessment of corroded reinforced concrete beams: Modeling guidelines. *Journal of Structural Engineering*, 130, 1214–1224.
- Ding, L., Botte, W., Van Coile, R. & Caspeele, R. 2018. Robustness-evaluation of a stochastic dynamic system and the instant equivalent extreme-value event. *Beton- und Stahlbetonbau*, 113, 33–37.
- Ding, L., Van Coile, R., Botte, W. & Caspeele, R. 2021. Quantification of model uncertainties of the energy-based method for dynamic column removal scenarios. *Engineering Structures*, 237, 112057.
- Du, Y.G., Clark, L. A. & Chan, A.H.C. 2005. Effect of corrosion on ductility of reinforcing bars. *Magazine of Concrete Research*, 57, 407–419.
- Feng, D.C., Xie, S.C., Li, Y. & Jin, L. 2021. Time-dependent reliability-based redundancy assessment of deteriorated RC structures against progressive collapse considering corrosion effect. *Structural Safety*, 89, 102061.
- JCSS 2001. *Probabilistic model code*, Joint Committee on Structural Safety.
- OpenSees 2006. *Open system for earthquake engineering simulation*, University of California, Berkeley.
- Parisi, F. & Scalvenzi, M. 2020. Progressive collapse assessment of gravity-load designed European RC buildings under multi-column loss scenarios. *Engineering Structures*, 209, 110001.
- Parisi, F., Scalvenzi, M. & Brunesi, E. 2019. Performance limit states for progressive collapse analysis of reinforced concrete framed buildings. *Structural Concrete*, 20, 68–84.
- Yi, W.J., He, Q.F., Xiao, Y. & Kunnath, S.K. 2008. Experimental study on progressive collapse-resistant behavior of reinforced concrete frame structures. *ACI Structural Journal*, 105, 433–439.
- Yu, X.H., Qian, K., Lu, D.G. & Li, B. 2017. Progressive collapse behavior of aging reinforced concrete structures considering corrosion effects. *Journal of Performance of Constructed Facilities*, 31, 04017009.
- Zhu, W. & François, R. 2013. Effect of corrosion pattern on the ductility of tensile reinforcement extracted from a 26-year-old corroded beam. *Advances in Concrete Construction*, 1, 121.

Numerical simulation of non-Fick moisture diffusion of pultruded GFRP bolt connection

Y. Sun, Y. Liu & X. Wang
Tongji University, Shanghai, China

H. Xin
Xi'an Jiaotong University, Xi'an, China

ABSTRACT: With the advantage of easy construction and disassembly, the bolt connection is the most common form of pultruded GFRP profile connections. In coastal areas, long-termed exposure to the combination of high temperature and humidity leads to the degradation of mechanical property of FRP material. The moisture diffusion process plays a significant role in understanding the degradation of pultruded GFRP bolt connection in hygrothermal environments. In this paper, the non-Fick moisture diffusion process in pultruded GFRP bolt connection is numerically simulated. The moisture diffusion parameters were calibrated by gravimetric test of pultruded GFRP coupons. Parametric analysis is conducted to reveal the effect of temperature (40°C, 60°C, 80°C), solution type (fresh water and artificial sea water) and moisture absorption path in single-bolt connection. Besides, the moisture absorption of multi-bolt connection with different arrangements is compared. The results showed that the moisture absorption of specimen exposed to artificial sea water was obviously higher than specimen exposed to fresh water. For structures without damage, the moisture enters the panel mainly from surface; for structures with damage, the moisture from the open-hole plays an important role. The moisture diffusion behavior of specimens under 40°C environment was similar to specimens under 60°C environments. The moisture diffusion of specimen at 80°C was significantly more severe. By comparing multi-bolt connection with different arrangements, it was found that for structures with damage the moisture distribution was more concentrated near the open-hole in parallel bolt distribution than staggered bolt distribution.

1 INTRODUCTION

In the past few decades, fiber reinforced polymers (FRP) have attracted an increasing attention in the field of civil engineering, both in the maintenance of existing structures and the construction of new structures (Bakis et al. 2002; Keller 2001). Since joints are usually the weakest part of load-bearing structures, the short-term and long-term behavior of joints is crucial to achieve expected structure performance. With the advantage of easy construction and disassembly, the bolt connection is the most common form of pultruded GFRP profile connections (Galinska 2020). In coastal areas, long-termed exposure to the combination of high temperature and humidity leads to the degradation of mechanical property of FRP material. The open-hole and discontinuous geometry characteristics can both contribute to the acceleration of degradation of GFRP bolted joints' mechanical properties in hygrothermal environments.

The moisture diffusion process plays a significant role in understanding the degradation of pultruded GFRP bolt connection. In fact, moisture diffusion, stress redistribution and damage evolution constitute a complicated coupled multi-physics process (Ye & Zhang 2022). The effect of moisture diffusion includes: (i) polymer chain relaxation and plasticization of the resin due to bulk volume expansion, which is caused by hydrogen bonds between water molecules (Hu et al. 2020); (ii) fiber/polymer interface decohesion due to capillary transport into the defects at the interface or through microcracks in the bulk matrix (Prolongo 2012).

The previous research showed that the moisture uptakes of a pultruded GFRP plate can be divided into three stages: diffusion-dominated uptake, polymer relaxation-dominated uptake, and composite damage-dominated uptake (Xin et al. 2016). Xin developed a numerical simulation model to investigate the non-Fick moisture uptake behavior of GFRP plates, which corresponds well with the gravimetric test results (Xin et al. 2021a).

The primary objective of this paper is to clarify the moisture diffusion process in pultruded GFRP bolted connection by numerical simulation. The non-Fick moisture diffusion model was adopted in the simulation to consider the coupling effect of diffusion, stress redistribution and damage evolution. Parametric analysis is conducted to reveal the effect of temperature (40°C, 60°C, 80°C), solution type (fresh water and artificial sea water) and moisture absorption path in single-bolt connection. Besides, the moisture absorption of multi-bolt connection with different arrangements is compared.

2 MODELING OF NON-FICK MOISTURE DIFFUSION

2.1 Moisture diffusion theory

The basic solution variable is the normalized concentration, which is defined as follows (Abaqus 2019):

$$\phi = \frac{c}{s} \quad (1)$$

where c is the mass concentration of the diffusing material and s is its solubility in the base material.

Due to the requirement of mass conservation for the diffusing phase, the diffusing problem can be defined as following equation (Abaqus 2019).

$$\int_V \frac{dc}{dt} dV + \int_S \mathbf{n} \cdot \mathbf{J} dS = 0 \quad (2)$$

where V is any volume whose surface is S , \mathbf{n} is the outward normal to S , \mathbf{J} is the flux of concentration of the diffusing phase, and $\mathbf{n} \cdot \mathbf{J}$ is the concentration flux leaving S .

The diffusion is driven by the gradient of a general chemical potential, which is defined by the following relation (Abaqus 2019):

$$\mathbf{J} = -s\mathbf{D} \cdot \left[\frac{\partial \phi}{\partial x} + \kappa_s \frac{\partial}{\partial x} (\ln(\theta - \theta^z)) + \kappa_p \frac{\partial p}{\partial x} \right] \quad (3)$$

where $\mathbf{D}(c, \theta)$ is the diffusivity; $s(\theta)$ is the solubility; $\kappa_s(c, \theta)$ is the ‘‘Soret effect’’ factor, providing diffusion because of temperature gradient; θ is the temperature; θ^z is the value of absolute zero on the temperature scale being used; $\kappa_p(c, \theta)$ is the pressure stress factor, providing diffusion driven by the gradient of equivalent pressure stress.

In previous research (Xin et al. 2016), the moisture diffusion in pultruded GFRP laminate exhibit non-Fick behavior. Time varying boundary conditions are applied to describe this behavior by multi-stage points in the amplitude table. The values of the multi-stage points are determined by calibration of experimental data in the previous publication (Xin et al. 2021b).

2.2 Diffusion parameters

In the previous publication (Xin et al. 2021a), gravimetric tests for thin plates were conducted to calibrate one-dimensional moisture diffusion parameters of pultruded GFRP laminates. The moisture diffusion coefficients of pultruded GFRP laminates are summarized in Table 1. The freshwater refers to distilled water while the artificial seawater was made from artificial sea salt dissolved in distilled water. The concentration of artificial seawater is 3.5%, whose content can be found in (Xin et al. 2016). The solubility of GFRP laminates is assumed to be 1.0. Table 2-4 are the time-varying boundary conditions for specimens aged in both freshwater and artificial seawater environments at different temperatures. The parameters of boundary conditions were calibrated by gravimetric tests under different environments.

Table 1. Moisture diffusion coefficients of pultruded GFRP laminates (units:mm²/s).

temperature	freshwater		artificial seawater	
	D11	D22(D33)	D11	D22(D33)
40°C	1.75×10 ⁻⁶	0.94×10 ⁻⁶	2.04×10 ⁻⁶	1.13×10 ⁻⁶
60°C	2.35×10 ⁻⁶	1.53×10 ⁻⁶	2.50×10 ⁻⁶	2.61×10 ⁻⁶
80°C	3.69×10 ⁻⁶	3.59×10 ⁻⁶	3.38×10 ⁻⁶	6.04×10 ⁻⁶

Table 2. Parameters of time-varying boundary conditions under 40°C environments.

freshwater				artificial seawater			
D ₁₁		D ₂₂		D ₁₁		D ₂₂	
time	amplitude	time	amplitude	time	amplitude	time	amplitude
0.00E+00	0.013	0.00E+00	0.002	0.00E+00	0.003	0.00E+00	0.003
1.50E+06	0.013	1.00E+06	0.002	1.51E+04	0.003	2.50E+05	0.003
3.78E+06	0.017	4.00E+06	0.003	1.92E+05	0.007	1.00E+06	0.004
6.25E+06	0.022	9.00E+06	0.004	1.56E+06	0.012	4.00E+06	0.006
9.00E+06	0.028	1.60E+07	0.005	5.58E+06	0.018	9.00E+06	0.011
1.23E+07	0.032	-	-	1.61E+07	0.026	1.60E+07	0.014
1.80E+07	0.037	-	-	-	-	2.50E+07	0.016

Table 3. Parameters of time-varying boundary conditions under 60°C environments.

freshwater				artificial seawater			
D ₁₁		D ₂₂		D ₁₁		D ₂₂	
time	amplitude	time	amplitude	time	amplitude	time	amplitude
0.00E+00	0.025	0.00E+00	0.002	0.00E+00	0.013	0.00E+00	0.009
1.00E+06	0.025	1.00E+06	0.002	2.50E+05	0.013	1.00E+06	0.009
2.25E+06	0.037	4.00E+06	0.003	1.00E+06	0.017	2.25E+06	0.010
4.00E+06	0.052	9.00E+06	0.004	2.04E+06	0.019	4.00E+06	0.017
6.25E+06	0.093	1.60E+07	0.005	4.00E+06	0.028	5.60E+06	0.019
9.00E+06	0.208	-	-	5.71E+06	0.039	9.00E+06	0.028
9.79E+06	0.417	-	-	7.60E+06	0.132	1.60E+07	0.038
1.17E+07	0.548	-	-	9.70E+06	0.346	2.50E+07	0.044
1.28E+07	0.602	-	-	1.15E+07	0.433	-	-
-	-	-	-	1.50E+07	0.600	-	-

Table 4. Parameters of time-varying boundary conditions under 80°C environments.

freshwater				artificial seawater			
D ₁₁		D ₂₂		D ₁₁		D ₂₂	
time	amplitude	time	amplitude	time	amplitude	time	amplitude
0.00E+00	0.086	0.00E+00	0.040	0.00E+00	0.043	0.00E+00	0.020
1.00E+06	0.086	1.00E+06	0.040	1.00E+06	0.043	1.00E+06	0.020
3.00E+06	0.129	3.00E+06	0.060	3.00E+06	0.065	3.00E+06	0.030
3.40E+06	0.172	3.40E+06	0.080	3.40E+06	0.065	3.40E+06	0.030
6.00E+06	1.719	6.00E+06	0.800	5.70E+06	1.737	5.70E+06	0.800
-	-	-	-	6.00E+06	2.000	6.00E+06	1.600

2.3 Finite element models

As is shown in Figure 1, the diffusion process in single-bolted and multi-bolted FRP joints were simulated using the Abaqus/Mass Diffusion solver. Linear heat transfer brick elements DC3D8 were used with a mesh size of 1mm. D_{11} time-varying boundary conditions were applied to the left edge of panel, which described the non-Fick moisture diffusion along the roving direction. The right edge was a cutting edge, and therefore no boundary conditions were applied. The top surface and two side surfaces were all applied D_{22} time-varying boundary conditions, which described the non-Fick moisture diffusion vertical to the roving direction. No boundary conditions were applied to the bottom surface. In order to consider the effect of absorption path, there are two kinds of models, i.e. for structures without damage and for structures with damage. For structures with damage, the hole wasn't applied to any additional boundary conditions, since in the undamaged situation, the bolt and FRP panel surface are in good contact, which prevents the moisture enters the open-hole. However, for structures with damage, the moisture enters the FRP open-hole due to the loss of bolt pre-load and the cracks near the hole. Therefore, the hole was applied D_{11} time-varying boundary condition.

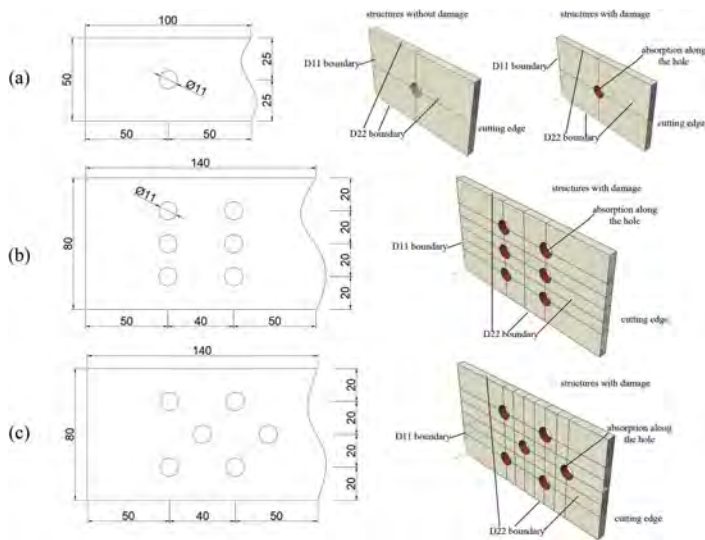


Figure 1. Geometry and schematic diagram of finite element models (units: mm).

3 MOISTURE DIFFUSION SIMULATION OF GFRP SINGLE BOLT CONNECTION

3.1 Effect of temperature

Figures 2-4 show the moisture diffusion process of undamaged single-bolt connection exposed to freshwater at the temperature of 40°C, 60°C and 80°C respectively. With the time increasing, the normalized mass concentration CONC of the whole single-bolt connection specimen gradually increased. The higher the environment temperature, the higher the mass concentration at same diffusion time. The moisture diffusion from the end of the panel was more pronounced than the moisture diffusion from the panel surface. The moisture diffusion behavior of specimens under 40°C environments was similar to specimens under 60°C environments, with the moisture diffusion from the end of the panel dominating the whole diffusion process. The moisture diffusion of specimen at 80°C was significantly more severe, in which the moisture diffusion from the surface of the panel plays an important part.

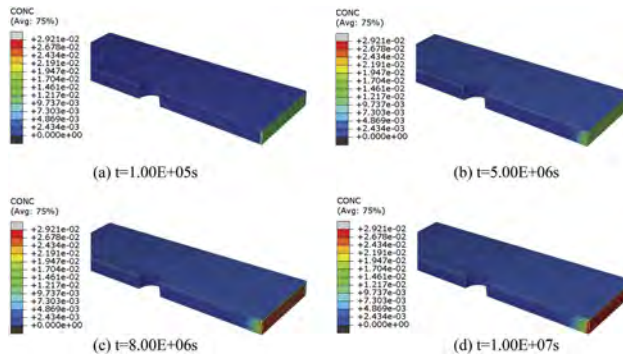


Figure 2. Mass diffusion process of undamaged single-bolt connection exposed to the freshwater at 40°C.

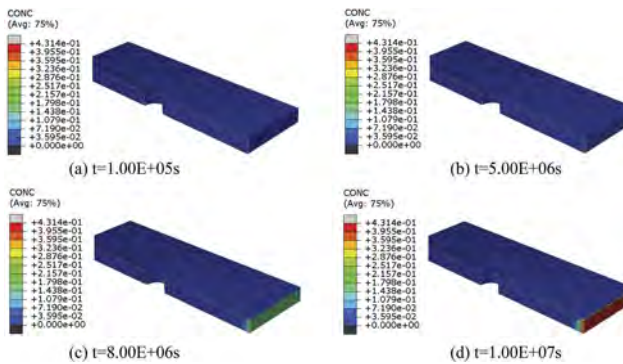


Figure 3. Mass diffusion process of undamaged single-bolt connection exposed to the freshwater at 60°C.

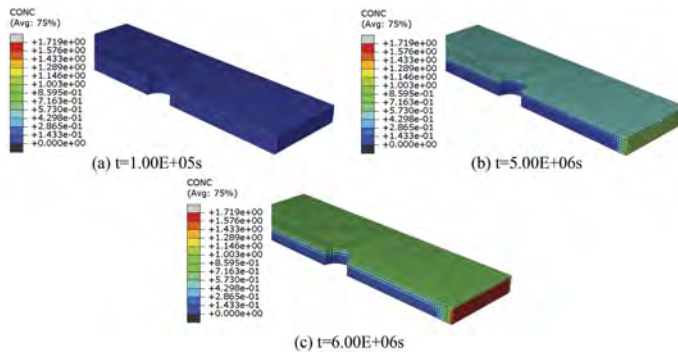


Figure 4. Mass diffusion process of undamaged single-bolt connection exposed to the freshwater at 80°C.

3.2 Effect of solution type

Figure 5 shows the moisture diffusion process of undamaged single-bolt connection exposed to artificial seawater at the temperature of 60°C. Comparing Figure 3 and Figure 5, the mass diffusion process of specimens under artificial seawater was quite same as the diffusion process under freshwater, because the diffusion rate along the roving direction has little difference between the freshwater environment and the artificial seawater environment. Figure 6 shows the mass distribution of mid cutting plane at $t=1.00E+07s$. The maximum CONC along the hole

was 4.13×10^3 ppm for the specimen exposed to freshwater environment while the maximum CONC along the hole was 2.94×10^4 ppm for the specimen exposed to artificial seawater environment. The moisture absorption of specimen exposed to artificial seawater was obviously higher than specimen exposed to freshwater. It was because that the diffusion rate vertical to the roving direction in artificial seawater environment was larger than in the freshwater environment.

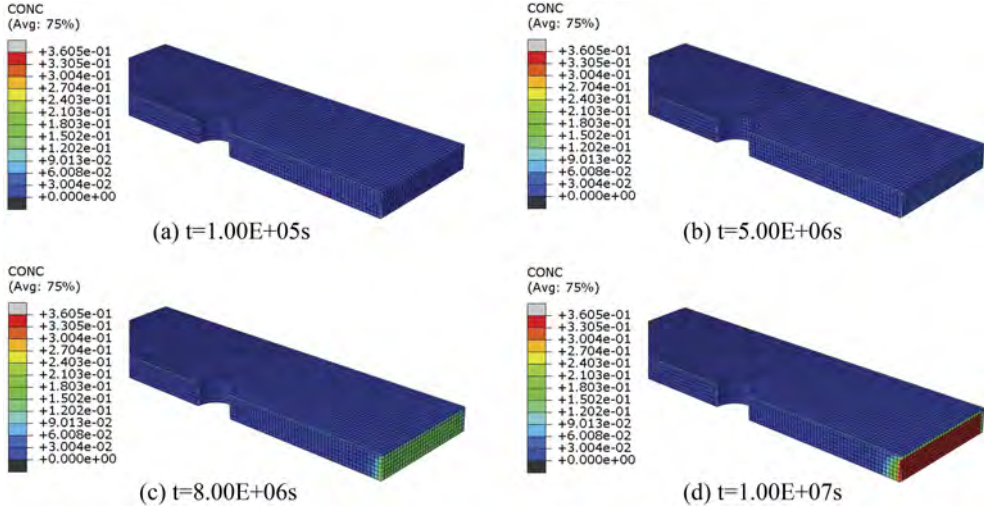


Figure 5. Mass diffusion process of undamaged single-bolt connection exposed to the artificial seawater at 60°C.

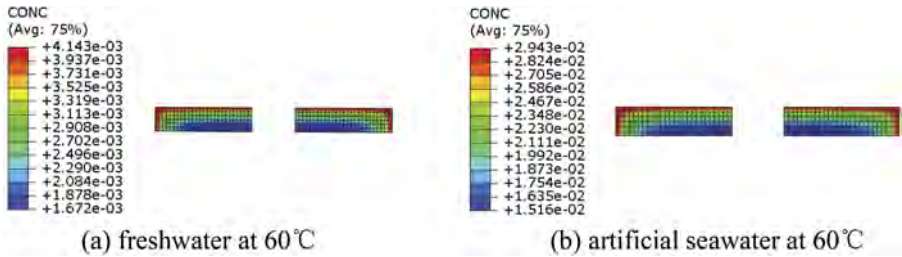


Figure 6. Mass distribution of mid cutting-plane of undamaged single-bolt connection at $t=1.00E+07s$.

3.3 Moisture absorption path

Figure 7 shows the moisture diffusion process of damaged single-bolt connection exposed to freshwater at the temperature of 60°C. Figure 8 shows the moisture distribution of mid cutting-plane of undamaged and damaged single-bolt connection. The maximum CONC along the hole was 4.31×10^5 ppm for the damaged single-bolt connection exposed to the freshwater at 60°C, which is nearly 104 times of the undamaged structures. For structures without damage, the moisture enters the panel mainly from surface; for structures with damage, significant amount of moisture enters the panel from the open-hole. The moisture from the open-hole could be detrimental, since the moisture diffusion is usually coupled with stress concentration and damage evolution in the open-hole areas.

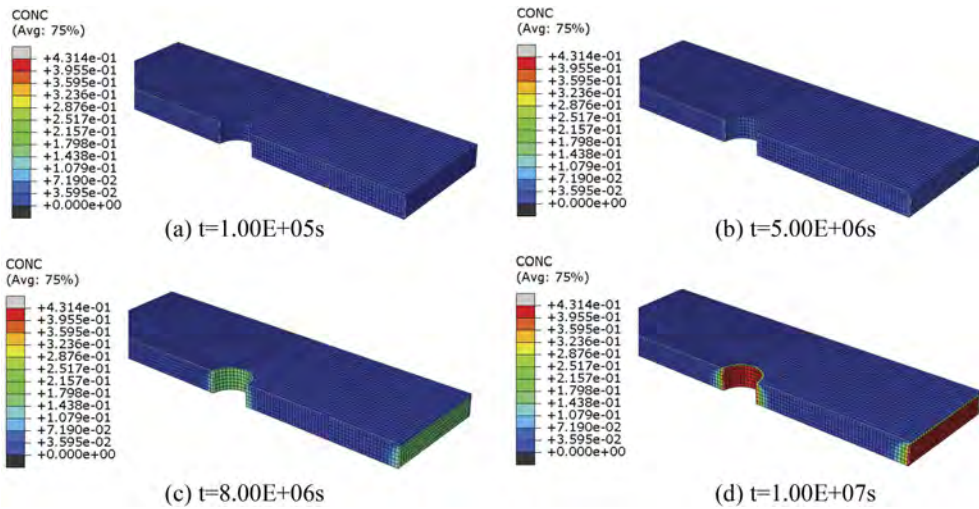


Figure 7. Mass diffusion process of damaged single-bolt connection exposed to the freshwater at 60°C.

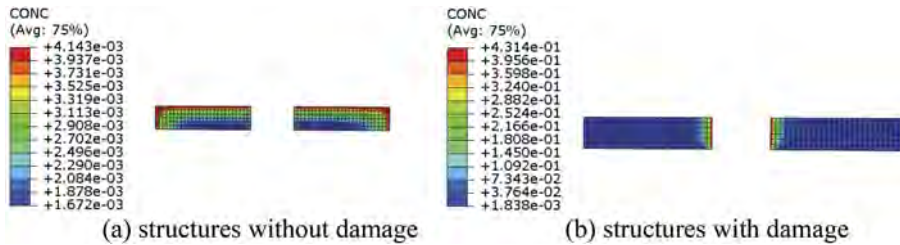


Figure 8. Mass distribution of mid cutting-plane of single-bolt connection exposed to freshwater under 60°C environments at $t=1.00E+07s$.

4 MOISTURE DIFFUSION SIMULATION OF GFRP MULTI BOLT CONNECTION

Figure 9 shows the surface moisture distribution of parallel and staggered bolt distribution exposed to freshwater under 60°C. It was found that the moisture distribution was more concentrated near the open-hole area in parallel bolt distribution than staggered bolt distribution. Compared with parallel bolt distribution, the spacing between bolts was larger in staggered bolt distribution, with the same ratio of e/d and w/d . Therefore, the coupling effect between moisture absorption from adjacent open-holes is weaker. As a result, the moisture distribution was less concentrated near the open-hole area in staggered bolt distribution.

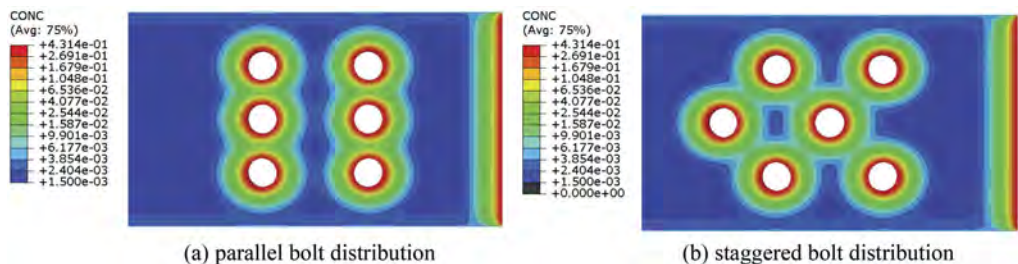


Figure 9. Surface moisture distribution of (a)parallel and (b)staggered bolt distribution exposed to freshwater under 60°C at $t=1.00E+07s$.

5 CONCLUSION

In this paper, the non-Fick diffusion process in pultruded GFRP bolt connections is numerically simulated using time-varying boundary conditions. The moisture diffusion parameters and multi-points value in the amplitude of boundary conditions were calibrated by gravimetric tests. Then, the effects of temperature, solution type and absorption path on single bolt connection and the effect of bolt distribution on multi bolt connection were investigated. The main conclusions are summarized as follows:

- (1) The moisture diffusion behavior of specimens under 40°C environments was similar to specimens under 60°C environments, with the moisture diffusion from the end of the panel dominating the whole diffusion process. The moisture diffusion of specimen at 80°C was significantly more severe, in which the moisture diffusion from the surface of the panel plays an important part.
- (2) The diffusion rate along the roving direction has little difference between the freshwater environment and the artificial seawater environment. However, the diffusion rate vertical to the roving direction in artificial seawater environment was larger than in the freshwater environment.
- (3) Under 60°C freshwater environment, the maximum CONC along the hole was 4.31×10^5 ppm for the damaged single-bolt connection, which is nearly 104 times of the undamaged structures.
- (4) For GFRP multi bolt connections, the moisture distribution was more concentrated near the open-hole in parallel bolt distribution than staggered bolt distribution.

ACKNOWLEDGEMENTS

This research study was funded by National Natural Science Foundation (Grants # 52078362) of People's Republic of China.

REFERENCES

- Bakis CE, Bank LC, Brown VL, Cosenza E, Davalos JF, Lesko JJ, et al. 2002. Fiber-reinforced polymer composites for construction—state-of-the-art review. *Journal of Composites for Construction* 6 (2):73–87.
- Keller T. 2001. Recent all-composite and hybrid fibre-reinforced polymer bridges and buildings. *Progress in Structural Engineering and Materials* 3(2):132–40.
- Galińska A. 2020. Mechanical joining of fibre reinforced polymer composites to metals—a review. part i: bolted joining. *Polymers* 12(10), 2252.
- Ye JY, Zhang LW. 2022. Damage evolution of polymer-matrix multiphase composites under coupled moisture effects. *Computer Methods in Applied Mechanics and Engineering* 388, 114213.
- Hu Y, Ji WM, Zhan LW. 2020. Water-induced damage revolution of the carbon nanotube reinforced poly (methyl methacrylate) composites. *Composites Part A: Applied Science and Manufacturing* 136, 105954.
- Prolongo SG, Gude MR, Urena A. 2012. Water uptake of epoxy composites reinforced with carbon nanofillers. *Composites Part A: Applied Science and Manufacturing* 43(12), 2169–2175.
- Xin HH, Liu YQ, Mosallam A, Zhang YY, Wang CZ. 2016. Moisture diffusion and hygrothermal aging of pultruded glass fiber reinforced polymer laminates in bridge application. *Composites Part B: Engineering*. 100 (Sep):197–207.
- Xin HH, Liu YQ, Mosallam A, Correia J, Zhang YY, He J. 2021a. Numerical simulation of non-fick moisture diffusion of pultruded composite GFRP bridge deck plates. *Journal of Performance of Constructed Facilities* 35(6): 04021079.
- ABAQUS. user's guide.
- Xin, HH, Liu, YQ, Mosallam A, Zhang YY, He J. 2021b. Moisture diffusion in web-flange junctions of pultruded glass fiber reinforced polymeric bridge profiles. *Polymer Composites* 42(12), 6570–6587.

A methodology for the service life estimation of timber structures

D. Marranzini, G. Iovane, L. Cascini, R. Landolfo, M. Nicolella & B. Faggiano

University of Naples Federico II, Naples (NA), Italy

ABSTRACT: Driven by the development of energy saving and environmental sustainability policies, the use of timber as a building material has found wide development during the last decades. An integral part of the design of timber buildings is the evaluation of durability, which strongly affects the material performances and therefore the building service life. In the design process the service life of the building components can be estimated through different methodologies. A deterministic approach is based on the *Factor Method* (ISO 15686). In this regards, the present paper briefly introduce an innovative application of the Factor Method for the prediction of the service life of timber structures. The proposal is based on the use of the *Multi-Criteria Decision-Making (MCDM) methods* as support tool for the determination of the correction factors. The method is applied and validated on a sample of four case studies.

1 INTRODUCTION

Nowadays, timber-based materials such as glued laminated timber and cross laminated timber (CLT) are competitive in the construction world. Especially in the last decade, the use of CLT in residential buildings has also spread in Italy. Thus, new records have been achieved in the field of timber constructions (Svatoš-Ražnjević et al., 2022). This trend is certainly due to a greater knowledge of the potential of timber buildings in terms of thermal, acoustic and structural performances, as well as to the sustainability of wood.

Although timber constructions are a good answer to the demand for sustainable, thermally efficient and resilient buildings, they are susceptible to environmental degradation. Prolonged exposure to the deteriorating agents can cause decay of thermo-hygrometric performance and, in the most severe cases, structural problems, up to the collapse of the structure, undermining the safety of the users. Therefore, design and maintenance require great awareness to this issue.

In such scenario, the methods for the service life design of timber structures fit in. Nowadays several methods for service life prediction of building components are spread in literature. Among them the Factor method (ISO 15686:2011) stands out as simple and effective. Nevertheless, the application to timber structures is limited to specific cases and therefore still under development.

In this paper a combined method based on Factor method (FM) and Multi-Criteria Decision-Making (MCDM) methods is proposed for the evaluation of the service life of timber structures. The method is applied and validated on a sample of four case studies that are located in Southern Italy, allowing for the evaluation of suitability of the proposed methodology.

2 SERVICE LIFE AND DURABILITY CONCEPTS

Since the end of the 1980s, the concept of durability has spread in the building sector. The Construction Products Directive (CPD) (EU, 1988) was the first regulatory reference to introduce the concept of durability and sustainability in the production of building materials. The aim was

to direct the building sector on a new path, based on the limited use of non-renewable resources, as well as the reduction of management and maintenance costs in the building life-time. Subsequently the topic was at the center of the international research. Thus a new regulation (ISO 15686:2011) was published in short time, it providing the know-how about the methodologies for service life planning. Nowadays it is still considered one of the most relevant sources of information in this field. The concept of service life (SL) was developed, it being defined as the actual period of time after manufacturing or installation during which relevant properties of a component meet or exceed minimum acceptable values (Landolfo and Vesikari, 2008).

Afterward, the concept of durability was also brought to the light in the field of structural design. It was understood that a material deterioration process could lead to such a performance decrease that a structure may not be able to respond to service or safety requirements before the design life is over. This is due to the fact that either the actions on the structures or the capacity of the structure are time-dependent variables; furthermore, in absence of an adequate and planned maintenance operation, the resistance tends to decrease over time due to the deterioration process of the material. Within Eurocode 0 (EN 1990:2006) and ISO 13823 (ISO 13823: 2008) general indications for the design of structure service life (SL) were definitely given. The EN 1990 prescribes that degradation can be estimated through calculations, experimental tests or empirical methods. These methods are aimed at estimating the period of time during which a structure or any component is able to achieve the performance requirements defined at the design stage with an adequate degree of reliability (Landolfo and Vesikari, 2008). About the calculation methods, different approaches can be used to assess the SL: prescriptive, deterministic, semi-probabilistic or probabilistic approaches (Trinius and Sjöström, 2005).

3 THE SERVICE LIFE OF TIMBER STRUCTURES

3.1 *Main durability issues*

Durability is a fundamental requirement for a construction. It is influenced by several factors, like physical properties of materials, service condition, design, as well as protection and maintenance measures put in place to prevent degradation of materials and structures.

Timber is particularly susceptible to the deterioration process. The wood decay agents are generally classified into biotic and abiotic (Piazza, 2005). The first category includes insects, fungi, bacteria and marine organisms. Concerning the condition favourable for the biotic attack, the action of most insects is generally influenced by the wood species, whereas the action of fungi and bacteria is strongly influenced by the moisture contents of wood (Viitanen et al., 2010). In this case the environmental thermo-hygrometric conditions and the presence of water determine the risk of degradation. In this regard, different scenarios of degradation are evaluated through the “classes of use” defined by the EN 335 (EN 335:2013). Insects generally produce a reduction of the cross section of a timber member. This can also occur in case of fungi and bacteria attacks, which in addition alterate the chemical composition of the material with consequent deterioration of the mechanical properties of timber (Wood handbook, 2021). Photolysis and chemical degradation processes belong to the abiotic category (Wood handbook, 2021). In the latter case the magnitude of damage caused is typically lower than the biotic one.

Generally, as function of the physical and chemical composition of wood, a different behaviour against degradation is shown by different wood species. A ranking of the most resilient timber species is given by the EN 350 (EN 350:2016) through the “durability classes”. However, in addition to the inherent durability of the timber members, degradation conditions can be mitigated through appropriate design choices, preservative treatments and proper design of construction details (Ayanleye et al., 2022), as well as by the efficient planned maintenance activities.

3.2 *The service life design methods*

Different approaches can be used to evaluate the reliability of timber structures against durability. The standards prescriptive approach consists in instructions and design rules aimed at

preserving the components against typical degradation process. About timber constructions Eurocode 5 (EC5, EN 1995-1-1:2004, section 2.1.3) establishes that durability should be a fundamental design requirement and provides a framework of rules for the design of timber structures exposed to biological degradation (section 4.1). However, these are general and qualitative indications that do not allow an analytical evaluation of the service life (SL).

To this purpose, the factor method (FM; ISO 15686:2011) provides the SL estimation according to a deterministic approach. At the state of the art, the applications of FM to timber structures are limited to the secondary components, as timber claddings (Viitanen et al., 2011; Silva and Prieto, 2021). Further to FM, other calculation methods, based on deterioration models, have been proposed. Among them empirical deterioration models were proposed by Wang et al. (2008) and Leicester et al. (2003) for predicting the depth of fungal attack as a function of the time of exposure, for both in and above-ground decays, by Viitanen et al. (2010) for the prediction of the mass loss due to the brown rot attack as a function of the climate condition. Isaksson et al. (2013) defined a deterioration model based on experimental tests, namely “dose-response function”. Besides, a risk-based method to predict the fungal timber decay has been recently proposed by Gaspari et al. (2021). It is based on a decision trees model, where a risk class can be assigned to the timber component and proper prediction function for decay depth estimation can be selected.

4 THE PROPOSED GLOBAL DURABILITY FACTOR METHOD

The Global Durability Factor Method (GDFM), herein proposed, is based on the combined application of the factor method (FM) and the Multi Criteria Decision Making (MCDM) method.

The FM (ISO 15686:2011) allows to simply estimate the service life (ESL; in years) of a building element by adjusting the value of the reference service life (RSL) through a set of modification factors, *A, B, C, D, E, F, G*, related respectively to quality and design level of components, work execution level or skill level of the installers, indoor and outdoor environments, service conditions, maintenance level (Equation 1):

$$ESL = RSL \cdot A \cdot B \cdot C \cdot D \cdot E \cdot F \cdot G \quad (1)$$

The ESL takes into account the differences from the reference conditions through the modification factors. The RSL is determined on the basis of data gained from experimental tests on components, as well as codes, expert judgments and construction site environment, while the modification factors (A-G) have to be defined by the designers, based on expertise and real service data. The proposal intervenes at this stage, by introducing the MCDM methods (MCDMm) for the determination of the correction factor of the RSL.

MCDMm are tools commonly used in the decision-making process when the decision makers have to choose among different alternatives. Indeed, MCDMm provides the optimum solutions among a set of alternatives available to the decision maker. Nowadays the MCDMm are used in a wide range of fields (Zavadskas et al., 2014). At the state of art several types of MCDMm are spread (Gebre et al., 2021), among them TOPSIS method (Hwang and Yoon, 1981) stands out for the simplicity and efficiency. The latter is already commonly used in building/civil engineering for different scopes, like for quick level vulnerability assessment of the built-up (Faggiano et al., 2011) and for comparative analysis of structural retrofitting systems (Terracciano et al., 2015; Formisano and Mazzolani, 2015). The TOPSIS method is generally based on the preliminary definition of criteria qualifying the alternatives (such as the examined buildings) according to the specific solving problem, and their weight that measures the relative impact on the decisional process (Bagga et al., 2019). Each criteria can be classified as benefit or cost criteria. The final result consists of an index for each alternative, which provides the relative closeness of the alternative to the ideal solutions (positive A^+ and negative A^-). A^+ and A^- are obtained by considering for each criterion the best and the worst performance offered by the examined alternatives. Subsequently the calculation of the Euclidean distances (S_i^+ and S_i^-) of each real alternative from the ideal positive and negative solutions is

carried out. In the end, the relative closeness (RC) index of each alternative to the ideal solutions can be evaluated through the Equation 2:

$$RC = Si^- / (Si^+ + Si^-) \quad (2)$$

Higher the relative closeness, RC index, to the ideal solution is, better is the alternative. Based on this a rank is achieved.

Definitely, in the proposal, the TOPSIS method is applied. The criteria correspond to the FM factors. They are set taking into account the aspects that influence the durability of timber constructions. Hence, for each factor a set of sub-factors is fixed (Table 1). It is relevant to highlight as the sub-factor “E5 – Use class” and “F1 – Shock class” respectively are the most and least influential sub-factors. Therefore every timber case study can be qualified through the FM factors. It is also necessary to introduce and qualify the reference case (C_r) corresponding to ESL = RSL, further to the ideal positive and negative solutions. Through the RC indexes calculated for each case, it is possible to determine a single modification factor, called “Global Durability Index” (I_{GD}), according to Equation 3, which is a function of all the subfactors:

$$I_{GD} = RC_i / RC_{Cr}; \quad I_{GD} = f(A \cdot B \cdot C \cdot D \cdot E \cdot F \cdot G) \quad (3)$$

Evidently for C_r it is $I_{GD}=1.00$.

Therefore the ESL is calculated as it follows (Equation 4):

$$ESL = RSL \cdot I_{GD} \quad (4)$$

It is apparent that higher is the I_{GD} , higher is the ESL of the structure. It means that in a set of structures, the one with the highest I_{GD} is the less vulnerable to the deterioration process. In Table 1 the numbers corresponding to the order of importance assumed for the subfactors are reported.

Table 1. List of durability factors and sub-factors (ISO 15686:2011).

Factor	Sub-Factor (criterion)	
A Quality of components	A1 Type of timber product	10
	A2 Presence of sapwood	5
	A3 State of conservation	9
	A4 Wood species	3
	A5 Quality of storage system at the building site	18
	A6 Quality of transport system (from industry to building site)	22
	A7 Presence of quality management system of industry (ISO 9001)	20
	A8 Presence of Declaration of Performance (DoP) (CPR 305/2011)	19
B Design level of a component or assembly installation	A9 Quality of wood seasoning	4
	B1 Quality of construction details (as designed)	14
C Work execution level or skill level of the installers	B2 Type of protective treatment	7
	C1 Quality of construction details (as built)	15
D Indoor environment	C2 Quality of protection system during the construction steps	21
	D1 Amount of environmental humidity	11
E Outdoor environment	D2 Water condensation risk	12
	E1 Climate zone	6
	E2 Average annual precipitation	13
	E3 Service class (NTC 18)	2
	E4 Average annual solar irradiance	16
F In-use condition	E5 Use class (EN 335)	1
	F1 Impact class	23
G Maintenance level	G1 Inspectability conditions	17
	G2 Quality of maintenance	8

5 APPLICATION OF THE GDFM TO THE CASE STUDIES

The method is applied and validated on four simple case studies located in different municipalities of the Southern Italy. They are selected for the sake of representativeness of recurrent timber types of constructions and structural types, as well as different environmental exposure and age of construction (Recorded Lifetime: RLT). The proposed method is applied to specific members of the case studies, as shown in Figure 1 (a, b, c, d). The survey has allowed to identify the characteristics and the state of conservation (Faggiano et al., 2022). Although the state of preservation of the investigated structures is not critical, they show different degradation types:

case a) It is placed outdoor, part of the member has fine cracks due to direct exposure to UV radiation and contact with rainwater;

case b) The roofing structure is placed outdoor; some parts are directly exposed to UV radiation and rainwater, showing discoloration, while columns show also fine cracks;

case c) The intermediate floor is placed inside a residential building; the beams show the evidence of insect attack (*Cerambycidae*), due to the presence of sapwood; however, the decay is confined to a thin layer of the cross-section.

case d) The structure is placed at the roof level; struts and ties show degradation by insect attack (*Cerambycidae* and *Anobium*), mainly due to the presence of sapwood in the members.

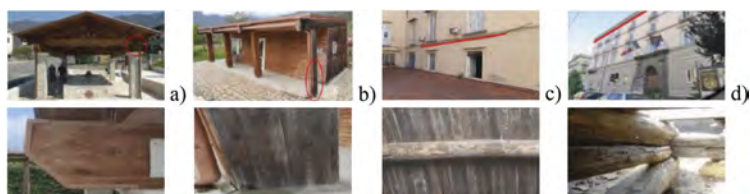


Figure 1. Case studies (specific component): roofing structure a) primary beam; b) column; residential building c) primary beam of the intermediate floor; d) struts and ties of the roof.

The global durability factor (I_{GD}) and the ESL, calculated for each case studies, are shown in Table 2. In absence of experimental tests and considering the design life prescribed by the Italian building Code (D.M. 17/01/2018) for ordinary buildings, a RSL equal to 50 years is assumed for all. The longest ESL is determined for case studies “c” and “d” (52 and 59 years respectively), probably because they are placed in indoor environment, although case studies “a” and “b” are made of “new timber”, but they are outdoor. Nevertheless, the ESL values obtained for cases c) and d) are far from the recorded lifetime (RLT), since they were built more than 150 years ago and they are still in service. At the same time for cases a) and b) a ESL equal to 50 years has been found. Hence, they should still keep in service for a lifetime respectively equal to 44 and 39 years.

Table 2. The results of GFM application to the case studies (a, b, c, d).

Case study	RSL	RC	I_{GD}	ESL	RLT
	years			years	years
a)	50	0.49	1.00	50	6
b)	50	0.49	1.00	50	11
c)	50	0.52	1.05	52	150
d)	50	0.59	1.19	59	200
C_r	50	0.49	1.00	50	-
A^+	-	1.00	1.74	-	-
A^-	-	0.00	0.76	-	-

6 CONCLUSIVE REMARKS

The design of timber structures taking into account the durability issues is a very topical subject, since deterioration is one of the most recurrent cause that leads to a reduction of serviceability or safety performances during the structures service life. In this context the methods for predicting the service life, as the factor method (FM), fit in.

A new method, namely Global Durability Factor Method (GDFM), based on the application of FM combined with TOPSIS method is proposed for estimating the service life (ESL) of timber structures, by determining the modification factors. Thus, the aspects influencing the durability of timber structures are evaluated and proposed as factor and sub-factors, they being ordered according to the impact on durability. In the end the “Global Durability Index, I_{GD} ” is calculated, as a single parameter accounting for all the durability factors. The GDFM is applied on simple case studies, proving the feasibility and the effectiveness.

Future work will aim at the validation of the methodology on a larger sample of timber structures with heterogeneous characteristics and service conditions.

REFERENCES

- Ayanleye, S., Udele, K., Nasir, V., Zhang, X., Militz, H., 2022. Durability and protection of mass timber structures: A review. *J. Build. Eng.* 46: 103731.
- Bagga, P., Joshi, A., Hans, R., 2019. QoS based Web Service Selection and Multi-Criteria Decision Making Methods. *Int. J. Interact. Multimed. Artif. Intell.* 5: 113.
- CPR 305:2011. Construction Products Regulation: Regulation (EU) N. 305/2011 of the European parliament and of the council of 9 March 2011 laying down harmonized conditions and repealing Council Directive 89/106/EEC.
- EN 335:2013. Durability of wood and wood-based products – Use classes: definitions, application to solid wood and wood-based products. Brussels: European Standard.
- EN 350:2016. Durability of wood and wood-based products – Testing and classification of the durability to biological agents of wood and wood-based materials. Brussels: European Standard.
- EU: 1988. Council Directive of 21 December 1988 on the approximation of laws, regulations and administrative provisions of the Member States relating to construction products. Brussels: European Union.
- Faggiano, B., Formisano, A., De Gregorio, D., De Lucia, T., Mazzolani, F.M., 2011. A quick level methodology for the volcanic vulnerability assessment of buildings. *Applied Mechanics and Materials.* 82: 639–644.
- Faggiano, B., Nicoletta, M., Iovane, G., Marranzini, D. 2022. A survey form for the structural health assessment of timber constructions. In: *The 6th International Conference on Structural Health Assessment of Timber Structures SHATIS22*. Prague, Czech Republic, 7–9 September 2022.
- Formisano, A., & Mazzolani, F.M., 2015. On the selection by MCDM methods of the optimal system for seismic retrofitting and vertical addition of existing buildings. *Comput. Struct.* 159: 1–13.
- Gaspari, A., Giongo, I., Piazza, M., 2021. A risk-based approach for timber building decay prediction. *Procedia Struct. Integr.* 37: 811–819.
- Gebre, S.L., Cattrysse, D., Alemayehu, E., Van Orshoven, J., 2021. Multi-criteria decision-making methods to address rural land allocation problems: A systematic review. *Int. Soil Water Conserv. Res.* 9: 490–501.
- Hwang, C. L., & Yoon, K., 1981. Methods for multiple attribute decision making. *Multiple Attribute Decision Making. Lecture Notes in Economics and Mathematical Systems.* 186: 58–191.
- Isaksson, T., Brischke, C., Thelandersson, S., 2013. Development of decay performance models for outdoor timber structures. *Mater. Struct. Constr.* 46: 1209–1225.
- ISO 15686-1:2011. Buildings and constructed assets - Service life planning - Part 1: General principles and framework. International Organization for Standardization, Geneva, Switzerland.
- ISO 13823:2008. General Principles on the Design of Structures for Durability International Organization for Standardization, Geneva, Switzerland.
- ISO 9001:2015. Quality management systems – Requirements. International Organization for Standardization, Geneva, Switzerland.
- Landolfo, R., & Vesikari, E., 2008. State of the art report on service life design methods. In Proc. of *COST C25 Dresden Seminar on “Sustainability of Constructions”*. Dresden: Luis Bragança editor. 4.11–4.22.

- Leicester, R.H., Wang, C.H., Ngyen, M.N., Thornton, J.D., Johnson, G., Gardner, D., Foliente, G.C., MacKenzie, C., 2003. An engineering model for the decay in timber in ground contact. Document No IRGWP 03-20260. International Research Group on Wood Protection, Stockholm.
- Piazza, M., Modena, R., Tomasi, R., 2005. Strutture in legno. Materiale, calcolo e progetto secondo le nuove normative europee. Hoepli Editore.
- Silva, A., & Prieto, A.J., 2021. Modelling the service life of timber claddings using the factor method. *J. Build. Eng.* 37: 102137.
- Svatoš-Ražnjević, H., Orozco, L., Menges, A., 2022. Advanced Timber Construction Industry: A Review of 350 Multi-Storey Timber Projects from 2000–2021. *Buildings*. 12: 404.
- Terracciano, G., Di Lorenzo, G., Formisano, A., Landolfo, R., 2015. Cold-formed thin-walled steel structures as vertical addition and energetic retrofitting systems of existing masonry buildings. *European Journal of Environmental and Civil Engineering*, 19(7): 850–866.
- Trinius, W., & Sjöström, C., 2005. Service life planning and performance requirements. *Building research & information*. 33(2): 173–181.
- Viitanen, H., Toratti, T., Makkonen, L., Peuhkuri, R., Ojanen, T., Ruokolainen, L., Räisänen, J., 2010. Towards modelling of decay risk of wooden materials. *Eur. J. Wood Wood Prod.* 68: 303–313.
- Viitanen, H., Toratti, T., Makkonen, L., 2011. Development of Service Life Model for Wooden Structures. *Int. Conference Durab. Build. Mater. Components*. 1–8.
- Wang, C.H., Leicester, R., Nguyen, M., 2008. Decay Above-Ground USP2007/04, 1–109.
- Wood handbook, 2021. wood as an engineering material. General Technical Report FPL-GTR-282. Madison, WI: U.S. Dept. Agriculture, Forest Service, Forest Products Laboratory. 543.
- Zavadskas, E.K., Turskis, Z., Kildiene, S., 2014. State of art surveys of overviews on MCDM/MADM methods. *Technol. Econ. Dev. Econ.* 20: 165–179.

Multi-scale structural integrity assessment of a series of identical components in cultural-heritage structures: The case of the Clifton suspension bridge

R. De Risi, T. Moody, E. Voyagaki, S. Gunner, M. Pregnotato, N. Grilli & C. Taylor
University of Bristol, Bristol, UK

ABSTRACT: Cultural-heritage structures may be characterised by structural elements that are geometrically identical for cosmetic or functional reasons but can be subjected to a significant variable stress distribution because they are located in different positions on the structural system. This can lead to a variety of damage and failure phenomena that will probably occur asynchronously. Damage occurrence triggers discussions among the stakeholders and decision-makers. For heritage structures, repair and restoration actions are costly and constrained by laws regulating grade-listed systems. Therefore, it becomes imperative to understand if such actions are necessary and to identify the most suitable intervention. The research question is: how can future maintenance costs be minimised while preserving the historical value of legacy structures? The answer lies in the reduction of uncertainties using a multi-scale approach that combines: (a) multi-scale knowledge of the material nature and fabrication, (b) multi-scale empirical evidence on material mechanical properties, (c) detailed geometrical description of the system, and (d) multi-scale numerical models. The challenge is finding the optimal trade-off between maintenance and historical value. Such a multi-scale framework is applied to the parapet stanchions of the Clifton Suspension Bridge in Bristol, UK. Stanchions are vertical cast-iron structural elements providing: (a) lateral support to parapets and anti-climb barriers and (b) partial support to the maintenance under-deck gantry. There are 162 identical parapet stanchions on the bridge. These structural elements may suffer heavy damage due to wear and tear. The damage consists of cracking in zones of stress concentration. This damage is unrepairable, and stanchions must be replaced when cracks appear. Their substitution is operated by the Clifton Suspension Bridge Trust (CSBT), which is particularly interested in science and technology for conservation and awareness. By applying the proposed multi-scale assessment framework, we provided essential insights into the structural integrity of such elements that are fundamental for informed decision-making.

1 INTRODUCTION

Many components of the built environment present a degree of repetitiveness in terms of structural and non-structural elements. This feature is even more distinct in cultural-heritage structures, where the repetitiveness of geometrically identical elements is due to functional or cosmetic reasons. Figure 1a shows four typical structural, non-structural and hybrid elements that can be found in cultural-heritage structures: mullioned windows, balustrades, stone columns, canopies and shelters. These elements are generally placed in a precise order according to specific patterns that may be locally interrupted only in some discontinuity areas of the system fabric. Such a spatial variability leads to a variable stress distribution induced by the spatial variability of vertical loadings (e.g. self-weight, live load), horizontal loadings (e.g. wind, earthquake, crowd push), distortion (e.g. thermal distortion), settlements, and ageing phenomena (e.g. protected vs unprotected areas against atmospheric agents). These different stress distributions and ageing phenomena may lead to the asynchronous onset of defects and damages that have multiple consequences (e.g. structural integrity) and raise several questions. First, a symmetric system with a pattern of identical structurally damaged elements will behave globally asymmetrically, changing the stress distribution in the whole structure. Second, the residual life of damaged components must be adequately assessed so that, when damage is identified after an inspection, maintenance and restoration of

damaged and undamaged elements can be planned well in advance. Finally, it is well known that repair and restoration operations for cultural heritage assets are costly and constrained by laws regulating grade-listed systems; therefore, it is essential to achieve solutions from a technical point of view that are compatible with conservation restrictions.

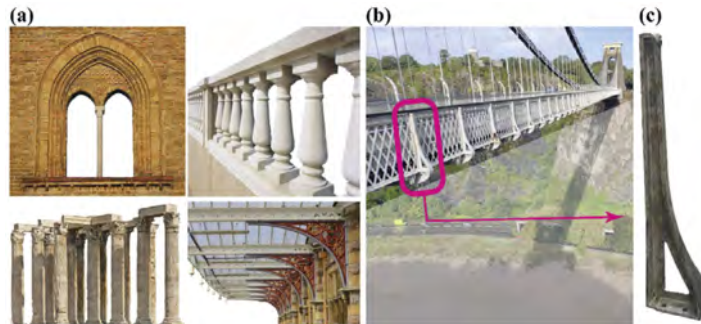


Figure 1. (a) Examples of identical components in cultural-heritage structures. (b) Side view of the Clifton Suspension Bridge. (c) Zoom in on the parapet stanchion.

In other words, the issue, and therefore the challenge, is the trade-off among inspection, damage-tolerance assessment, maintenance costs and the preservation of the historical value of legacy structures. To address such a challenge, uncertainties must be reduced and knowledge improved within a multidisciplinary framework comprising surveying engineering, material science, mechanical testing, non-destructive testing, and analytical and numerical structural modelling. Such a holistic approach requires a multi-scale methodology encompassing both temporal and spatial scales. Multi-scale approaches in the field of cultural heritage are not new (Salonia et al., 2009; Parent et al., 2017; Noardo, 2018; Sileo et al., 2022). The temporal scale is essential because collecting information along the asset lifespan of maintenance, restorations, and replacements allows the development of probabilistic models that can be used to forecast successive damages and consequent interventions. The spatial scale is also critical in the context of conservation and safeguarding because it is oriented to the detailed knowledge of the geometrical features of the asset of interest, including detailed description and representation of damages and imperfections.

In this study, three levels of multi-scale assessment are employed to identify the structural integrity of a component: (i) material, (ii) geometry, and (iii) structural modelling. Regarding the material level, the multi-scale approach spans from studying the material nature and fabrication to identifying the mechanical properties. The geometric multi-scale approach spans from the simple description of the system to advanced laser scanning. Finally, structural modelling can shift from simplistic elastic beams to a complete non-linear continuous finite element model. The more uncertainties decrease, the more sophisticated the assessment can be, i.e. it is possible to evolve from a simple analysis scale, requiring scarce to little data, up to a superior analysis scale, where more advanced information can be retrieved. Such a methodology has been preliminarily applied to the parapet stanchions of the Clifton Suspension Bridge (Figure 1b,c) in Bristol (UK).

1.1 *The parapet stanchions of the Clifton Suspension Bridge (CSB)*

The CSB spans the Avon Gorge in Bristol, UK. The bridge was initially designed by Isambard Kingdom Brunel; it was completed after his death by William Barlow and John Hawkshaw in 1864. A detailed description of the bridge can be found in Macdonald (2008), Pregnolato et al. (2022) and Voyagaki et al. (2022). The bridge is about 215 m long between the centerlines of the piers; however, the suspended part is about 194 m long. It is supported by a wrought iron catenary system connected to saddles on rollers in the towers and then anchored into the rock on each side via inclined shafts. Rods hold up the roadway, which is made of wooden planks. Figure 2a shows a partial cross-section of the bridge. The roadway is about 6.10 m wide between the two longitudinal girders, which are supported by rods at about 2.44 m interspaced along the bridge.

Footways on both sides of the deck, outside the girders, are present. The total deck width between the parapets is about 9.46 m. Figure 2b shows side and top views of the parapet stanchion.

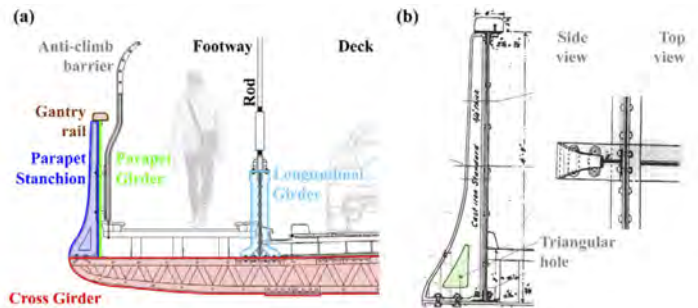


Figure 2. (a) Partial cross-section of the bridge. (b) Side and top views of the parapet stanchion.

The parapet stanchions are $\frac{3}{4}$ " (about 20 mm) thick cast iron cantilever beams with a variable I-shape cross-section. They are about 1450 mm tall and are installed symmetrically on both footways with the same spacing as the suspension rods (i.e. about 2.44 m) for a total of 162 (2×81) elements. Four bolts connect the stanchions to the cross girders (the red component in Figure 2a). Close to the bottom flange, there is a triangular hole (presumably initially realised to reduce the weight of the component) that presents some re-entrant corners with a radius that is not sufficient to reduce the stress concentration. The parapet girder (the white rhombic lattice shown in Figure 1b, and indicated with a green line in Figure 2a) is connected to the stanchions with two bolts, one at the top and one at the bottom. On top of the parapet girder, a timber rail (the brown element shown in Figure 2a) is installed to allow the maintenance gantry to run under the bridge deck. Finally, anti-climb barriers are clamped to the stanchions with four bolts.

1.2 Loadings and observed damage

Parapet stanchions are subjected to several loading conditions. First, the wind pressure acting on the parapet girder and the anti-climb barrier is directly transferred to the stanchions as a horizontal action. Second, the crowd pushing on the barriers is also transformed into a horizontal action on the stanchions. Third, the gantry produces both vertical (self-weight) and horizontal actions on the stanchions. The gantry is subjected to wind and, when in use, can induce crabbing forces on the rail. Wind and crabbing forces act transversally and longitudinally to the bridge axis, respectively. Other stresses generated in the stanchions are due to the global behaviour of the deck; the stanchions create a C-section with the cross girder. In addition, the stanchion is subjected to thermal expansion-contraction cycles and vehicular- and pedestrian-induced vibrations. Figure 3 illustrates the damage typically observed in the stanchions utilising magnetic particle inspection.

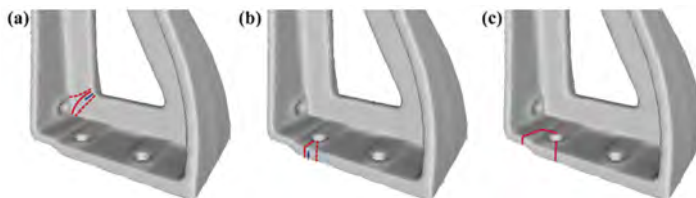


Figure 3. Observed damage in the (a) corner and on the (b, c) bottom flange.

More specifically, Figure 3a shows typical corner cracks evolving in the web of the stanchion. In some cases, the cracks are just partial-thickness (blue line), i.e. they do not extend the full thickness of the flange; in many other cases, the crack extends the entire width of the corner and is characterised as full-thickness (red lines). Figures 3b and c show typical cracks

developed in the base flange of the stanchion. Such cracks can be either full-thickness (red lines) or partial-thickness (blue lines). Also, these can be a single crack (Figure 3b) or double cracks isolating an entire piece of the base flange (Figure 3c). In both cases, cracks are in the region of the holes where the bolts tighten the stanchion to the cross girder.

Since 1993, 21 stanchions have been replaced; a storm damaged a few in 1990, while others were substituted due to crabbing of the gantry. Two more stanchions are planned to be replaced in the near future. There are no historical records of stanchions damaged before 1990. Other defects that can be identified mainly include: (i) casting defects creating blow holes on the surface and (ii) corrosion. The latter can occur only at the bottom of the base flange of the stanchion as it is the only element that is unprotected, i.e. not painted. However, it has been demonstrated by COWI, engineering consultants managing the maintenance of the bridge, that corrosion is not a primary driver of the observed damage, as the stress induced by the oxide expansion does not exceed the material's capacity. All these observations led the Clifton Suspension Bridge Trust (CSBT) to start studying this issue with two questions in mind: (i) what is the main driver of the problem, and (ii) what is the residual life of the parapet stanchion after the onset of the damage? In the following, the envisaged structural integrity assessment provides an initial answer to the first question. Future steps necessary to answer the second question are also identified in the Conclusions. The answers provided in this paper are derived from studying two damaged stanchions that the CSBT provided to the University of Bristol. One of the two stanchions was in the form of chopped pieces used to test welding strategies (Figure 4a).

2 MATERIAL

Multiple techniques and technologies can be exploited to understand a construction material and its properties, from the microstructure level to the adoption of destructive and non-destructive tests (Figures 4b,c). The first step of the multi-scale approach was the microscopy study of a few samples extracted from the S2-p4 piece (Figure 4a), polished with colloidal silica. The microscopy was carried out at multiple magnifications (10 \times , 20 \times , and 50 \times). Figures 5a and b show the results for a magnification of 10 \times before and after etching with Nital 2%. The combination of pearlites and flakes of graphite provides an early indication that this is grey cast iron due to the high percentage of graphite and the nature of flakes distribution. According to the ASTM A247-19 (2019), given the long shape of the flakes in a matrix of ferrite and pearlite, the graphite can be classified as ranging from A to C, most probably type B. Figure 5c shows that the pearlite constitutes the majority of the microstructure which suggests a moderate cooling rate. A higher cooling rate would have produced a higher fraction of cementite with smaller graphite flakes. Using a Matlab-based image-processing tool to highlight the dark colour of graphite, an average content of about 7.5% was identified. This is consistent with the typical range of 6%-10% for grey cast iron.

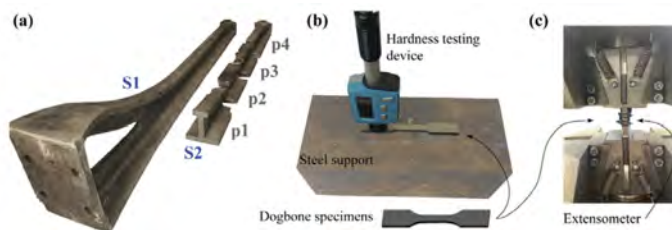


Figure 4. (a) Available stanchions. (b) Non-destructive and (c) destructive tests setup.

A considerable amount of porosity was also observed in the microscopy images. The microstructure shows that the web has a higher porosity content than the flanges. Specifically, using the same Matlab-based tool used for the quantification of the graphite content, a maximum porosity of about 3% and 0.5% is assessed for the web and the flanges, respectively. Also, porosity can be seen without microscopy in elements extracted from the web and the joint between the web and the flange. The porosity was also investigated by looking at the density

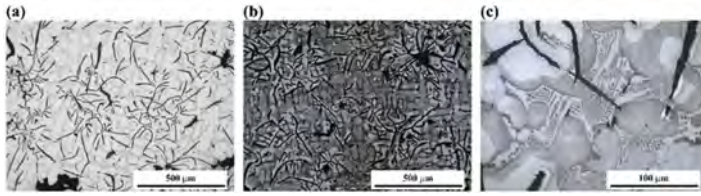


Figure 5. Microscopy at (a) 10× before etching, (b) 10× after etching, (c) 50× after etching.

of the material. To measure the density, the immersion in fluid method (commonly used for geotechnical applications) was employed (BS EN ISO 17892-2, 2014). The experimental data provide an overall density of 7 t/m^3 ; the density of the web is, on average, 1.2% lower than the overall density and 1.4% lower than the flanges density.

Such porosities made it very difficult to cut the material into standardised dog-bone (DB) specimens using Electrical Discharge Machining according to the ASTM E8/E8M – 13a (2013); therefore, a slitting saw was used to cut a total of 40 pieces: 27 DBs from the S2-p1 piece and 13 DBs from the S2-p3 piece (Figure 4a). An additional 8 non-standard chunky prismatic elements have also been obtained from the S2-p4; these non-standard elements have been used to preliminary investigate the tensile strength of the material and to test the non-destructive assessment.

The non-destructive testing consisted of using the Equotip Piccolo 2 device (Figure 4b), a portable metal hardness tester (Proceq, 2016). This is a spring-loaded device that launches an impact body consisting of a metal indenter at a sample. This impact body rebounds, and the velocities before and after the impact are measured through a voltage reading. The ratio of these velocities multiplied by 1000 is known as the Leeb hardness (Leeb 1978). The Equotip device can convert the Leeb hardness to the Brinell (1990), Vickers (Smith and Sandland, 1922), and Rockwell (1914) harnesses using empirical relationships (e.g., ISO 18265, 2013) after defining the material in hand. These hardness tests have been carried out for all specimens subsequently tested to destruction, both standard and non-standard. This verification intends to check if any correlation exists between the destructive and non-destructive tests, i.e. between the yield/tensile strength and the hardness index, similar to Tabor (1951). Tensile tests with a 0.001 mm/min loading rate have been performed to measure the tensile strength of the material (Figure 6).

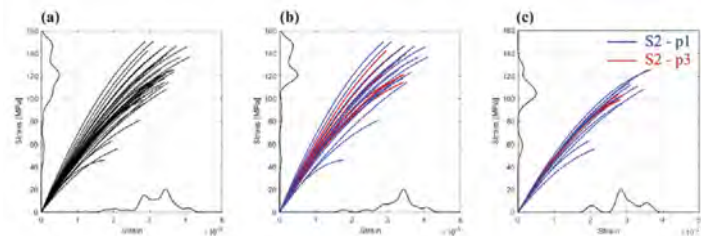


Figure 6. (a) All tensile-test results. (b) Flange tensile-test results. (c) Web tensile-test results.

Figure 6a shows the experimental results for all 40 available standardised DBs specimens. The material exhibits a brittle behaviour; therefore, only the tensile rupture strength can be retrieved (Figure 6a). Also, looking at the non-parametric distributions of both strain and stress reported on the horizontal and vertical axes (with thick black lines), it is possible to observe that the variability is high. Figures 6b and c show the tensile strength of the flange and the web, respectively. The strength values of elements extracted from the flanges are larger than those from the web. Also, it seems that the variability of S2-p1 (blue curves) and S2-p3 (red curves) are comparable. This result may indicate that the geometry does not influence the strength.

Studying only the first 5% of available force and strain data, it is possible to obtain an estimate of the elastic modulus. The value obtained by averaging all the tests is 60 GPa. However, experimental data for the flanges show a 7% higher elastic modulus with respect to the web.

Finally, by comparing the tensile strength and the hardness indexes, interesting observations were made. First, the Leeb hardness index should be preferred to the other. Second, for the non-standardised prismatic elements coming from the S2-p4, it was possible to identify a ratio between hardness index and tensile strength ranging between 2 and 3, which is not far from some literature observations (e.g., Baron and Palatkina, 2016; Kim et al., 2008). On the contrary, very small values are obtained when such correlations are repeated for the standardised specimens. For the latter case, also hardness scale saturation was observed. This result is probably associated with the adopted non-destructive testing protocol and the fact that standardised specimens are tiny and sometimes full of imperfections. Finally, on the basis of the collected information and following the ASTM A48/A48M – 03 (2016), it is possible to conclude that the material at hand can be classified as a class 20 grey cast iron, at best. This new knowledge is very important as, so far, literature values have been used for these elements (DMRB BD21, 2021).

3 GEOMETRY

Survey methodologies play a primary role in the understanding of cultural heritage. Structural and non-structural components in cultural heritage structures can have very sophisticated geometries that may be very difficult to represent with conventional 2D drawings. A simple 2D representation of the parapet stanchion is herein provided in Figure 2b. However, better documentation and representation are recognised as essential to guarantee asset preservation and promotion and educate the broader public towards these ambitions (Noardo, 2018). The demand for 3D models of cultural heritage assets is continuously increasing in the field of conservation. To this aim, laser scanning was carried out using an Artec Eva device, which is ideal for medium-sized objects. The point cloud obtained from the survey has been adequately post-processed in Rhino (McNeel et al., 2020) to obtain a mesh of the system. Figure 7a shows the setup employed to suspend the stanchion for easier survey operations. Figure 7b shows the post-processing of the acquired data with a focus on critical parts such as the top part and the top and bottom views of the bottom flange. These data allow remote measurements of the beam as well as structural modelling.

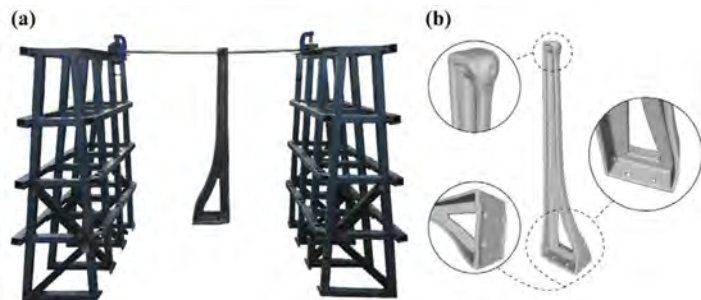


Figure 7. (a) Setup for the laser scanning. (b) Laser-scanning results.

4 STRUCTURAL MODELLING

Multi-scale finite element (FE) modelling in the field of cultural heritage may have multiple interpretations. Some research studies proposed a virtual lab where destructive tests are modelled with FE, materials properties are modified in order to match the experimental results, and eventually, such properties are applied to the larger asset of interest at a larger scale (e.g., Parent et al., 2017). This is also known as the shift from micro-modelling to macro-modelling (Giordano et al., 2021). Another potential interpretation consists of modelling the system of interest with an increasing level of sophistication, initially using beams (Figure 8a), then bi-dimensional elements such as plates and shells (Figure 8b), and eventually 3D continuum elements, such as bricks and tetrahedra (Figure 8c). This research adopted the second interpretation of the multi-scale modelling approach. As FE modelling tool, the OpenSees software was used (McKenna et al., 2011) employing the advanced Graphical User Interface STKO (Petracca et al., 2017).

The first modelling level employs beam elements. This approach may not always be possible; when it is possible, simplifications should be applied. For the case of the stanchion, both prismatic and non-prismatic beams have been used. The most irregular parts connecting the different sections that could have been modelled as beams were modelled as rigid links (Figure 8a). This modelling approach does not allow appropriate studying of the stress concentration in the corners that are the main driver for the damage onset. Therefore, to study such an aspect, either code-based providing stress concentration factors as a function of the geometrical features of the system are used (e.g., Annex H, BS 5400-10, 1999), or a sub-structuring approach can be employed. A substructuring approach consists of more precisely modelling the connection zones with shells or bricks, using the reactions coming from the beam schematisation as loading conditions.

The second modelling level employs shell elements (Figure 8b). This approach requires a manual interpretation of the geometry using CAD tools. Layered shell elements were used in this case. A simple support has been used for the bottom flange. No specific care was paid to the bolted connection, as this was a preliminary analysis. A maximum load of 5 kN was applied to the top of the beam, which corresponds to the wind loading on the under-deck gantry combined with crowd pushing (this is an unusual situation here investigated just for the sake of representation). Elastic modelling was considered. Figure 8b presents the FE analysis results in terms of vertical stress. It is possible to observe a tensile stress concentration in the web corner where the damage is usually experienced.

The last modelling level consists of using solid tetrahedral FE elements. The model and corresponding results are provided in Figure 8c. As for the previous modelling approach, in this case, it is possible to observe a stress concentration in the web corner. As previously, simple support has been used for the bottom flange. No specific care was paid to the bolted connection, as this was a preliminary analysis. As before, for this case, a loading of 5 kN was used, and elastic modelling was used. Computational time increases exponentially with respect to the previous case.

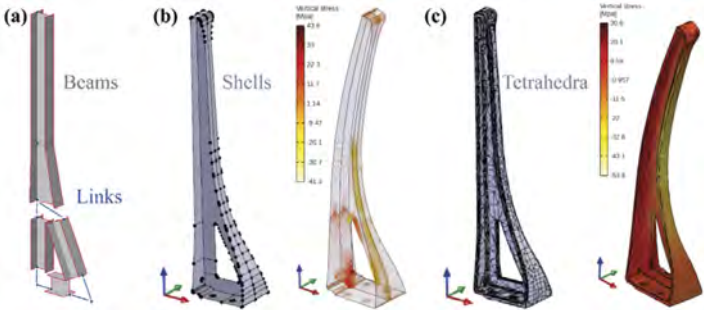


Figure 8. (a) Beam-based, (b) shell-based, and (c) tetrahedra-based FEM modelling.

5 CONCLUSIONS

A multi-scale approach oriented on assessing the structural integrity of the parapet stanchions of the Clifton Suspension Bridge was presented. Three aspects have been investigated: materials, geometry, and structural modelling. New insights were identified into the material properties, and the material porosity is identified as the potential cause of the observed damage. Structural models have been developed after the acquisition of geometry. Next steps to study the residual life of the system after damage include: (1) fatigue tests, (2) additional non-destructive tests, (3) shaking table tests on both damaged and undamaged elements to study the frequency response, and lastly (4) the S1 parapet stanchion will be tested with a cyclic protocol to experimentally investigate how many cycles a damaged stanchion can resist before being ultimately damaged to destruction.

REFERENCES

- ASTM E8/E8M – 13a. (2013). Standard Test Methods for Tension Testing of Metallic Materials.
- ASTM A48/A48M – 03. (2016). Standard Specification for Gray Iron Castings.
- ASTM A247. (2019). Standard Test Method for Evaluating the Microstructure of Graphite in Iron Castings.
- Baron, A. A., & Palatkina, L. V. (2016). Influence of the parameters of the structure of gray cast iron on the hardness and strength of castings. *Izvestiya VolgGTU. Problems of materials science, welding and strength in mechanical engineering*, 15(194),106–109.
- Brinell, J. A. (1900). Ein Verfahren zur Härtebestimmung nebst einigen Anwendungen desselben. *Gießlers Baumaterialienkunde*, 5, 276–280.
- BS EN ISO 17892-2. (2014). Geotechnical investigation and testing - laboratory testing of soil. Determination of bulk density.
- BS 5400-10 (1999). Steel, Concrete and Composite Bridges - Part 10: Code of Practice for Fatigue. Recommends methods for the fatigue assessment of parts of bridges which are subject to repeated fluctuations of stress.
- DMRB BD21 (2021). Design Manual For Roads And Bridges. The Assessment of Highway Bridges and Structures.
- Giordano, N., De Risi, R., Voyagaki, E., Kloukinas, P., Novelli, V., Kafodya, I., . . . & Macdonald, J. (2021). Seismic fragility models for typical non-engineered URM residential buildings in Malawi. In *Structures* (Vol. 32, pp. 2266–2278). Elsevier.
- ISO 18265. (2013). Metallic materials — Conversion of hardness values.
- Kim, Y. J., Shin, H., Park, H., & Lim, J. D. (2008). Investigation into mechanical properties of austempered ductile cast iron (ADI) in accordance with austempering temperature. *Materials Letters*, 62(3),357–360.
- Leeb, D. (1978). New dynamic method for hardness testing of metallic materials. *Rev Metal* 15:123–128
- Macdonald, J. H. G. (2008). Pedestrian-induced vibrations of the Clifton Suspension Bridge, UK. In *Proceedings of the Institution of Civil Engineers-Bridge Engineering* (Vol. 161, No. 2, pp. 69–77). Thomas Telford Ltd.
- McKenna, F. (2011). OpenSees: a framework for earthquake engineering simulation. *Computing in Science & Engineering*, 13(4),58–66.
- McNeel, R., et al. (2020). Rhinoceros 3D, Version 7.0. Robert McNeel & Associates, Seattle, WA.
- Noardo, F. (2018). Architectural heritage semantic 3D documentation in multi-scale standard maps. *Journal of Cultural heritage*, 32, 156–165.
- Parent, T., Domede, N., & Sellier, A. (2017). Multi-scale mechanical behavior of a gothic monument composed of ashlar masonry. Application to the design of a reinforcement technique. *International Journal of Architectural Heritage*, 11(3),399–414.
- Petracca, M., Candeloro, F., & Camata, G. (2017). “STKO user manual”. ASDEA Software Technology, Italy.
- Pregolato, M., Gunner, S. D., Voyagaki, E., Gavriel, G., Carhart, N. J., Macdonald, J. H. G., Tryfonas, T. and Taylor, C. A. (2022). Towards Civil Engineering 4.0: concept, workflow and application of Digital Twins for existing infrastructure. *Automation in Construction* 141: 104421. <https://doi.org/10.1016/j.autcon.2022.104421>
- Proceq, (2016). Operating Instructions: Portable Metal Hardness Tester Piccolink Software Equotip piccolo bambino 2, U.S. Patent No. 8074496.
- Rockwell, H. M., & Rockwell, S. P. (1914). Hardness-tester. US Patent, 1294171–1919.
- Salonia, P., Scolastico, S., Pozzi, A., Marcolongo, A., & Messina, T. L. (2009). Multi-scale cultural heritage survey: Quick digital photogrammetric systems. *Journal of Cultural Heritage*, 10, e59–e64.
- Sileo, M., Gizzi, F. T., Donvito, A., Lasaponara, R., Fiore, F., & Masini, N. (2022). Multi-scale monitoring of rupestrian heritage: methodological approach and application to a case study. *International Journal of Architectural Heritage*, 16(3),469–484.
- Smith, R. L and Sandland, G. E. (1922). An accurate Method of Determining the Hardness of Metals, with Particular Reference to Those of a High Degree of Hardness. *Proc. Inst. Mech. Eng.* 102 pp 623–641.
- Tabor, D. (1951). The hardness and strength of metals. *J. Inst. Metals*, 79, 1.
- Voyagaki, E., De Risi, R., Gunner, S., Pregolato, M., Macdonald, J.H.G., Carhart, N., Gavriel, G., Tryfonas, T., Taylor, C.A. (2022). Towards a Digital Twin Prototype for the Clifton Suspension Bridge (UK). ICOSAR 2021-2022 13th International Conference on Structural Safety and Reliability, Shanghai, China, 13-17 September.

Assessment of energy redistribution of structural collapse under seismic loads using wavelet transforms

Nabeel S.D. Farhan, Jinyu Lu, Wael A. Altabay & Zhishen Wu

International Institute for Urban Systems Engineering (IIUSE), Southeast University, Nanjing, China
Southeast University, Nanjing, China

Ahmed Silik

International Institute for Urban Systems Engineering (IIUSE), Southeast University, Nanjing, China
Nyala University, Nyala, Sudan

Mohammad Noori

California Polytechnic State University, San Luis Obispo, USA
Visiting Professor, University of Leeds, Leeds, UK

ABSTRACT: Damages due to complex loading or under natural disasters may cause progressive collapse (PC) in structures have not received much attention despite the importance of the potentially catastrophic impact of these types of deteriorations. When a structure is exposed to external excitations, an energy flow in the structural components is accumulated and stored depending on the effective stiffness of these components. Any modification in the material properties, connections between components, or structural continuity would modify the effective stiffness, thus leads to the energy distribution variation in structural components. Once a member fails the load supported by the lost member is redistributed to the adjacent structural members. If these members are incapable of withstanding the additional loading, they continue to fail and that gives rise to damage and may result in a PC. The objective of this study is to use continuous wavelet transform (CWT) to study the consequences of the PC distribution trend and the energy redistribution after one of the structural members is lost due to external loading event. An efficient strategy based on various scenarios is developed and used via a robust finite element computational tool to model and simulate the damage in order to capture the structural vibration responses. Nonlinear static and dynamic analyses are used using Abaqus and CWT are used for investigation purposes. The results show proper and effective analysis of the structures having high potential to PC.

1 INTRODUCTION

All buildings types may be exposed to extreme events due to natural hazards. Such events can lead to local damage to the structure, which can cause collapse. This is where the term progressive collapse (PC) comes in and describes the initial local failure spread (ASCE 2016). According to (ASCE/SEI 7-05 2005), the PC is defined as the propagation of initial localized failure from element to element, leading to the entire collapse or a disproportionately large part of a structure. The PC is triggered by abnormal loading that causes localized failure of one or more columns if the building lacks sufficient ductility, continuity, and redundancy. The column loss can be caused by natural disasters such as earthquakes, or accidental actions such as explosions (Mahmoud *et al.* 2018). After failure of the columns, an alternative load path transfers the load to other structural members. Suppose adjacent elements are not designed to withstand the redistributed loads. In that case, failure will occur with a large redistribution of the load until equilibrium is reached, leading to structure failure. The localized collapse can result in casualties and damage disproportionate to the initial failure. The interest in PC is traced back to the partial collapse of the Ronan Point apartment in London in 1968 due to an

accidental gas explosion. This event prompted extensive research on PC and led to developing guidelines for the PC prevention (Tavakoli and Amir 2017).

In recent years, various work have been carried out in this regard. Marjanishvili et al. (Marjanishvili and Agnew 2006) analyzed a 9-story steel moment-resisting frame (SMRF) considering the edge column loss through linear and nonlinear static and dynamic analyses and recommended nonlinear dynamic analysis. Hyun et al. (Kim *et al.* 2009) analyzed 2D- 2-storey and 3-storey SMRF regarding intermediate column loss. The results showed that the dynamic amplification factor could be larger than two as stated by (GSA 2003). Fu (Fu 2009) studied a multi-story steel building's response considering various column removal scenarios using 3-D models. It was concluded that multiple column removal yields different plasticity formations. Tavakoli et al (Tavakoli *et al.* 2012) investigated the SMRFs capability with various damaged columns scenarios under seismic loading based on Iranian seismic codes to resist the PC. It was stated that the buildings in question were able to withstand PC under various scenarios, involving the ground floor columns loss. Tavakoli and Hasani (Tavakoli and Amir 2017) studied the seismic capacity for the PC of SMRF to special moments. The results showed that the probability of PC relies on the floors number and the earthquake characteristics, and the removed column. Shi et al (Shi *et al.* 2017) investigated the effect of composite slabs on the PC resistance of SMRF. It was concluded that the presence of slabs increases the ductility of the structure and its PC resistance. Chuquitaype et al. (Chuquitaype *et al.* 2016) investigated the gravity frames effects in mitigating collapse in SMRF buildings exposed to extreme loads such as earthquake and explosion scenarios.

Despite various studies carried out in recent years, there is still no practical guidance to prevent a structure's collapse due to the localized damage of structural member. Most of the studies reported in the literature are static on sub-assemblages and dealt with resisting mechanisms quantification using the 2D frame. To the best of the authors' knowledge no study has been reported in the investigating the consequences of the PC distribution trend and the energy redistribution to evaluate seismic collapse potentials of a steel frame. This study aims to create a 3-D model and remove a column under earthquake to evaluate the resistance performance based on the energy redistribution. This work novelty is the development of an algorithm based on CWT to evaluate the internal energies redistribution.

2 WAVELET TRANSFORM

Wavelet analysis is a multi-resolution analysis in the time and frequency domain. Due to its potential characteristics can provide valuable information about the damage and analyze the signal's energy distribution at different bands. The idea is to correlate the signal $x(t)$ with a set of known functions and then quantify the similarity between them (Silik *et al.* 2021b).

$$w = \int_{-\infty}^{\infty} x(t) \cdot \psi_n^*(t) dt \quad (1)$$

The scaled and translated version are associated with the adopted mother wavelet $\psi(t)$.

$$\psi_{s,\tau}(t) = \frac{1}{\sqrt{s}} \psi\left(\frac{t-b}{s}\right) \quad (2)$$

2.1 Energy distribution-related features

The total energy is computed by squaring the magnitude of the data and integrating it. In the wavelet domain, the energy distribution is generated by the transform's squaring modulus.

$$SG(a, b) = |W(a, b)|^2 \quad (3)$$

The mean wavelet spectrum is estimated by the integration over the time variable as

$$S_{wt}(a) = \frac{2}{C_g} \left[\frac{1}{T} \int_0^T SG(a, b) db \right] \quad (4)$$

Energy accumulations in the frequency domain are defined by at each frequency band as

$$E(f_i) = \int_{f_1}^{f_i} S_{WT}(f_0/f)df \text{ for } i = 1, 2, \dots, n \quad (5)$$

Similarly, a time analog to the MWS may be defined by

$$s_{WT}(b) = - \int_{f_1}^{f_n} SG(f_0/f, b)df \quad (6)$$

Energy accumulations in the time domain are then appropriately determined by

$$E(b_j) = \int_{b_1}^{b_j} S_{WT}(t)db \text{ for } j = 1, 2, \dots, m \quad (7)$$

A decrease in potential energy ratio is defined as (Noori *et al.* 2018):

$$E = \frac{E_0 - E_f}{E_0} \quad (8)$$

where E_0 and E_f are the potential energies of models at the initial and final states, respectively.

2.2 The cross wavelet transforms

The theoretical distribution of the signal cross-wavelet power with background power spectra P_k^X and P_k^Y is given in Torrence and Compo (1998)

$$D\left(\frac{|W_b^X(S)W_n^{Y*}(S)|}{\sigma_X\sigma_Y} < p\right) = \frac{Z_v(p)}{v} \sqrt{P_k^X P_k^Y}, \quad (9)$$

where $Z_v(p)$ is the confidence level associated with the probability p defined by the square root of the product of two χ^2 distribution (Silik *et al.* 2021a).

For wavelet selection, the Morlet wavelet is a complex function that can be considered as a modulated Gaussian function (Silik *et al.* 2020). It has equal variance in time and frequency and is suited to detect time and frequency localized information (Silik *et al.* 2021a). It is similar to the impulse component, which is indicative of damage in many dynamic signals (Silik *et al.* 2021c). Thus, it was chosen for this research and expressed as

$$\psi(t) = \frac{1}{\sqrt{\pi F_b}} e^{i2\pi F_c t} e^{-\frac{t^2}{F_b}} \quad (10)$$

F_b is a bandwidth factor that controls the wavelet shape, and F_c is a central frequency that define the oscillations number. Mostly, $F_c = 6$ for engineering applications, and trainable parameter F_b is taken as [0.5, 1, 1.5, 2]. It is seen that 1.5 is better for tradeoff between them as shown in Figure 1.

3 FINITE ELEMENT MODEL

3-D finite element model of steel frame is developed using Abaqus version 6.13. The models are initially built using beam elements in Abaqus. The C3D8 element for column and beam and C3D20R for the slab is used to build up the models. Both elements are integrated numerically

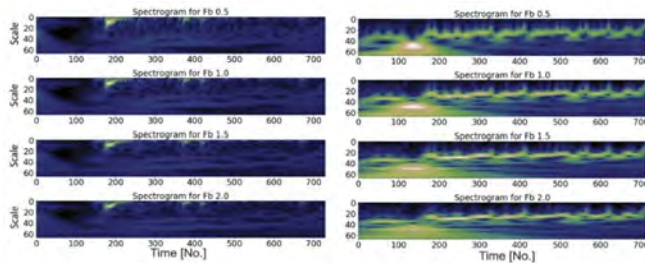


Figure 1. Acceleration of the FE models: (left) undamaged state; (right) damaged state.

over the section, where the material behavior is evaluated independently at each point. The loads considered are dead loads, live loads, and the El-Centro earthquake (EQ). Dead and live loads were 1 and 2.0kN/m², respectively, while the infill effects are not considered. According to GSA, dead loads plus 25% live loads are applied downward to the structure for dynamic analysis purposes. The structure characteristics have been considered so that the study can be generalized for a wide range of two-story short buildings. All members are tied to each other using the tie constraint, equivalent to providing a rigid connection (GSA 2003). In this study, a corner column in the ground floor has been removed under an EQ to investigate the PC potential of the structure. The EQ record was normalized to PGA to exert the severe effects of EQ loads on the structure. The EQ record was applied to the model in the horizontal direction Z. Figure 2 shows the two-bay steel frame model; the beams and columns are connected through their centroid using default rigid connections. All the models have two bays in each direction and two stories. Bay width is 4 m in the long and 2 m in short direction, and each floor height 2m. A reinforced concrete slab with a 130 mm thickness and concrete characteristic strength is 25 MPa. The longitudinal and transverse rebar in the slabs were arranged with 150-mm spacing. The external perimeter frames are designed to withstand the lateral and gravity loads, while the inner frames to withstand only gravity loads. The Isotropic material properties were assigned throughout the structure. Poisson's ratio, young's modulus, ultimate tensile, and minimum steel yield stress are 0.3, 2.06×10^5 N/mm², 460 N/mm², and 355 N/mm², respectively. The steel density is 7850 kg/m³. All column supports were defined as fully fixed in all translational and rotational axes.



Figure 2. Finite element model of the two-bay steel frame structure.

4 STRUCTURE PERFORMANCE UNDER THE COLLAPSE

In this study, the Abaqus was used for creating a model and performing the analysis. Both material and geometric nonlinear behaviors were considered. For investigating seismic collapse potentials of the SMRF, the corner column of analytical models was exposed to seismic excitations of the El-Centro earthquake, which caused a sudden loss of the column. The maximum acceleration of the excitation was scaled to 0.4g for dynamic analysis (GB50011,2010). After the column is removed, the structure goes through various stages and tries to resist the collapse using various mechanisms in order to compensate for the missing vertical components of the building by finding another load path or by redistributing the load to adjacent undamaged structural members, which can prevent further damage from scattering. The damaged propagation is tracked to understand these mechanisms and follow the collapse distribution trend in the model. Figure 3 shows the behavior of the building subjected to El-Centro wave. The relative distortion is shown in term of acceleration and displacement distribution on the model to show the collapse distribution patterns

due to the removal of the corner column and its effects. Before the column removal, there seemed to be no significant damage, while after the column removal damages appear. It is showed that the collapse mainly starts from the top of column removed in the first ceiling and then propagates to the beams connected to the removed column and the corresponding beams of the first and the upper floor. Finally, it is distributed to other structural elements. It is clear that after the damage, the load was redistributed. The adjacent columns carried more loads than before the column was removed. An alternate load path occurred in the steel frame after the sudden removal of a column, and the column removal did not lead to the PC because of the concrete slab's influence. After the column removal, the loads and internal forces are redistributed in the remaining columns and beams. The redistribution occurred in the remaining structure as a result of the concrete slab's action. Based on the analytical results, as shown in the Figure 3, the floor slab action has adequate load paths and redundancy to resist the local collapse spread owing to sudden column removal. This reflects the ability of energy dissipation of the remaining structure after a corner column is removed. Also, it is clear that there is a less spatial effect, and so the model members may dissipate the energy. The distribution of the structure's collapse occurs around the removed column's location, vertically along with the structure height, mainly from the bottom to the top, then horizontally in the floors. It can be concluded that the columns neighboring the failed column are the key ones that affect the redistribution of internal force and should be strengthened. Also, the beams directly connected to the removed column are the most likely elements to cause collapse because the moment in the beams increases when the columns are suddenly removed, and the contact action also provides an additional tensile force in the beams.

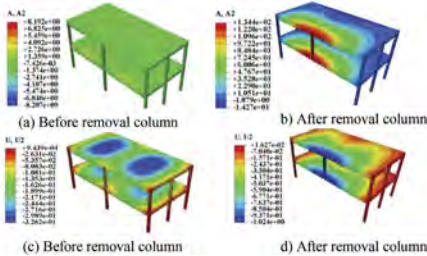


Figure 3. Acceleration and displacement distribution on the finite element model.

5 NUMERICAL ANALYSIS RESULTS AND DISCUSSION

For evaluating the collapse distribution trend, collapse distribution scenarios were investigated based on the nonlinear time history analyses under earthquake records, in such a way that the collapse sequence followed from the element to the other, one after another, until the structural system became unstable. The critical elements and the collapse propagations were predictable in the two-story frame due to the corner column removal in the ground floor. The internal energy redistributions were compared as shown in the Figure 4 to evaluate collapse potentials. The T-F energy distribution from points near the removed column was analyzed using wavelet cross-spectrum, T-F -amplitude representations, and wavelet power spectrum. Figure 4 compares internal force redistribution in terms of the entire energy. The energy change can lead to ambiguous results even if the total energy is different. Generally, at the moment of component failure, internal forces are redistributed in the structure, and damage does not occur yet. Thus, the structure's dynamic effects after loss of vertical components are of greater concern.

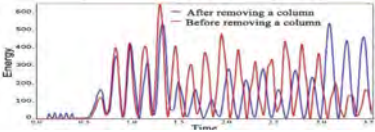


Figure 4. The total energy of the model in both states.

Figure 5 a, b shows the node above the removed column's acceleration representation in the time and in T-F domain before and after damage. In the time-domain after removing the column, the signal shows apparent semi-periodicity after 0.5 seconds reflecting the column's oscillation cyclic nature. The signal periodicity may be due to the combined effect of the beam and the slab motion. Figure 5c, d shows wavelet scalograms for both states, which reveal the signal energy distribution and shows how the signal energy density is distributed with respect to time and frequency. The x-axis represents position along the time, y-axis represents the frequency, and the color scale at each x-y point reflects the increasing power from blue to violet. Finally, it is clear that the removed column forces the signal energy to migrate towards lower frequencies. There are a lot of T-F dynamics contained within 12-13Hz thus, there seem to appear some features are present that are sort of leaking out. For understanding the instantaneous effect on the structural behavior, Tensor Flow implementation of the CWT is conducted and represented as in Figure 6. It can be seen that the coefficients in Figure 6 right under small scale (<45) are huge only at time number 100 and then continue in the time axis, which is precisely the moment that the corner column of the first story is removed. It should also be noted that lack of a continuous line in Figure 5 left corresponds to the fact that frequencies are not constant in time. Figure 7 shows regions in time-frequency space to localize time-frequency energy density where the signals show high power across time for all frequencies. The cross wavelet's high values indicate a vigorous structure response to an input with corresponding scale at a given time instant. This reflects the spread the of local collapse due to sudden column removal. The analyzed signals are aligned, reflecting the T-F energy distribution and localizing the similarities in energy redistribution. Figure 8 shows T-F -amplitude representations. It is shown that there are multiple time-varying frequencies and how rapidly the coefficient magnitude grows. This reflects the signal's spectral content evolution in time due to variations in the signal components' amplitudes and frequencies.

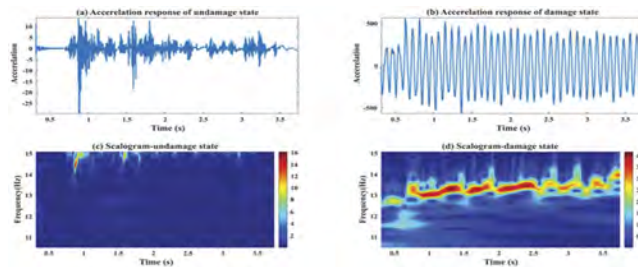


Figure 5. Time history and T-F representations.

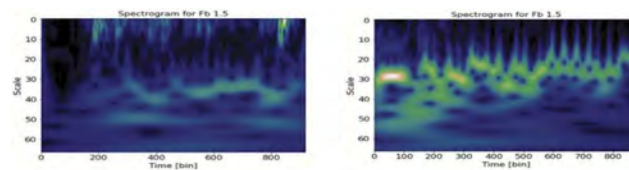


Figure 6. The time-frequency energy distribution (left) undamaged state; (right) damaged state.

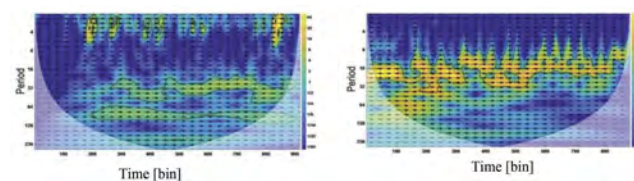


Figure 7. A local time-frequency energy density (left) undamaged state; (right) damaged state.

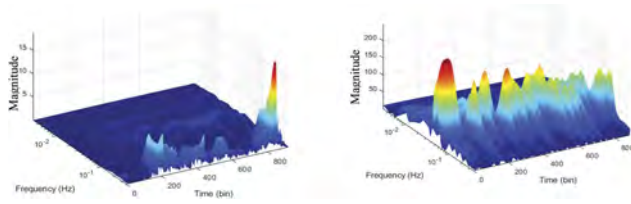


Figure 8. T-F amplitude representations (left) undamaged state; (right) damaged state.

Figure 9 shows wavelet power spectrum (WPS) over time and over scale, which is normalized to equal the analyzed signal variance. The WPS describes how the power of a time signal is distributed with frequency or scale. The power over scale before damage ranges between 0-5, whereas, after the damage, it ranges between 0.1-0.6. Also, power overtime before the damage is between 0-800, whereas after damage range between 0-300. Figure 9c shows how the power is redistributed within the model and reflects the energy distribution over time and the remaining structure's energy dissipation. Since the internal energy acquisition is synchronized, the cross- WPS's content and energy distribution show the global change in the frame energy. At lower scales, information about abrupt changes can be obtained, while at higher scales, information about slowly changing damages can be extracted. To validate the technique effectiveness, short Fourier transform and CWT are used to track the peak of internal energy distribution (IED) and their results is compared. Figure 10 shows the tracking of IED in model of removal column. Its clear that the proposed technique-based CWT show better results than a method based on short Fourier transform.

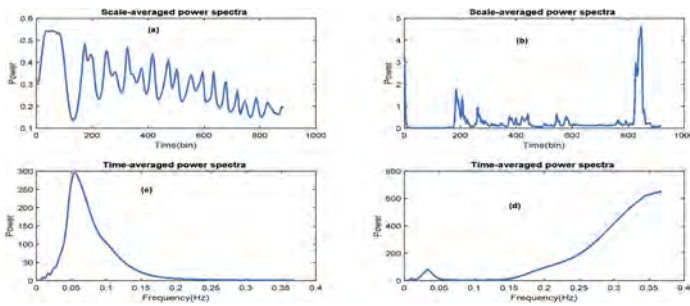


Figure 9. Various wavelet power spectrums (a) after removal column (b) before removal column (c) after removal column (d) before removal column.

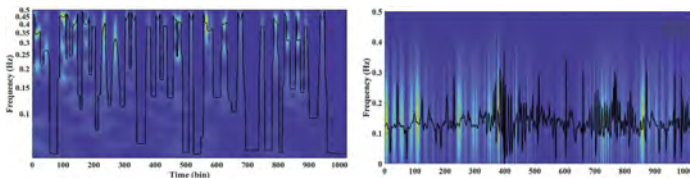


Figure 10. Tracking of the peaks of internal energy distributions (left) based on CWT (right) based on Short Fourier transform.

6 CONCLUSIONS

In this study, a 3-D 2-story steel frame model is developed and investigated using the nonlinear dynamic procedure in Abaqus software to simulate lower steel frame buildings' behavior under a sudden column loss. A two-story conventional frame building was used because, as it is known, many old and traditional buildings around the world are low-rise buildings, and the PC mechanism of such buildings is not considered. The beam and shell elements are used to simulate the

steel frame and concrete slab, respectively, from the Abaqus library. The analysis is conducted under corner column removal scenarios. Observations regarding the PC's behavior were drawn while focusing on energy action values. Continuous Wavelet are adopted to evaluate the distributed damage effect. Based on the analytical results, the following conclusions are drawn. The columns neighboring to the removed column are the key ones that affect the internal force redistribution. The beams connected to the removed column are the most probable elements to be affected, so the moment in the beams increases under sudden column removal. Implementation of CWT makes it possible to get a precise energy redistribution that allows the user to detect the PC's effect on the structure components. Based on the analytical results, it is concluded that cross wavelet analysis is a powerful technique for testing energy linkages between two-time series, and CWT affords multiscale analysis of absorption features due to PC and the spectral continuum that offers an opportunity to capture the relevant information that is manifested at different scales and show how the energy is redistributed and finally show the high potential to PC.

REFERENCES

- ASCE/SEI 7-05. 2005. American Society of Civil Engineers Standard Minimum Design Loads for Buildings and Other Structures.
- ASCE. 2016. ASCE STANDARD Loads for Buildings.
- BSi. 2000. BS 5950-1- Structural use of steelwork in building - Part 1: Code of practice for design - Rolled and welded sections. Part.
- Fu, F. 2009. Progressive collapse analysis of high-rise building with 3-D finite element modeling method. *Journal of Constructional Steel Research*, <https://doi.org/10.1016/j.jcsr.2009.02.001>.
- GSA. 2003. Progressive Collapse Analysis and Design Guidelines. Buildings.
- Kim, H.S., Kim, J. and An, D.W. 2009. Development of integrated system for progressive collapse analysis of building structures considering dynamic effects. *Advances in Engineering Software*, <https://doi.org/10.1016/j.advengsoft.2008.03.011>.
- Mahmoud, Y.M., Hassan, M.M., Mourad, S.A. and Sayed, H.S. 2018. Assessment of progressive collapse of steel structures under seismic loads. *Alexandria Engineering Journal*, 57, 3825–3839, <https://doi.org/10.1016/j.aej.2018.02.004>.
- Málaga-Chuquitaype, C., Elghazouli, A.Y. and Enache, R. 2016. Contribution of secondary frames to the mitigation of collapse in steel buildings subjected to extreme loads. *Structure and Infrastructure Engineering*, <https://doi.org/10.1080/15732479.2014.994534>.
- Marjanishvili, S. and Agnew, E. 2006. Comparison of Various Procedures for Progressive Collapse Analysis. *Journal of Performance of Constructed Facilities*, [https://doi.org/10.1061/\(asce\)0887-3828\(2006\)20:4\(365\)](https://doi.org/10.1061/(asce)0887-3828(2006)20:4(365)).
- Noori, M., Wang, H., Altabay, W.A. and Silik, A.I.H. 2018. A modified wavelet energy rate-based damage identification method for steel bridges. *Scientia Iranica*, 25, 3210–3230, <https://doi.org/10.24200/sci.2018.20736>.
- Shi, F., Wang, L. and Dong, S. 2017. Progressive Collapse Assessment of the Steel Moment-frame with Composite Floor Slabs Based on Membrane Action and Energy Equilibrium. *The Open Construction and Building Technology Journal*, <https://doi.org/10.2174/1874836801711010200>.
- Silik, A., Noori, M., Altabay, W.A., Ghiasi, R. and Wu, Z. 2021a. Comparative analysis of wavelet transform for time-frequency analysis and transient localization in structural health monitoring. *SDHM Structural Durability and Health Monitoring*, <https://doi.org/10.32604/sdhm.2021.012751>.
- Silik, A., Noori, M., Altabay, W.A., Dang, J., Ghiasi, R. and Wu, Z. 2021b. Optimum wavelet selection for nonparametric analysis toward structural health monitoring for processing big data from sensor network: A comparative study. *Structural Health Monitoring*, <https://doi.org/10.1177/14759217211010261>.
- Silik, A., Noori, M., Altabay, W.A. and Ghiasi, R. 2021c. Selecting optimum levels of wavelet multi-resolution analysis for time-varying signals in structural health monitoring. *Structural Control and Health Monitoring*, <https://doi.org/10.1002/stc.2762>.
- Silik, A.I., Noori, M. and Altabay, W.A. 2020. Wavelet-Based Damage-Sensitive Features Extraction. In: *Experimental Vibration Analysis for Civil Structures*, <https://doi.org/10.1201/9781003090564-1>.
- Tavakoli, H.R. and Amir, H. 2017. Effect of earthquake characteristics on seismic progressive collapse potential in steel moment resisting frame. *Earthquake and Structures*, <https://doi.org/10.12989/eas.2017.12.5.529>.
- Tavakoli, H.R., Rashidi Alashti, A. and Abdollahzadeh, G.R. 2012. 3-D Nonlinear Static Progressive Collapse Analysis of Multi-story Steel Braced Buildings. 15th World Conference on Earthquake Engineering (15WCEE).

Application of infrared thermography in civil engineering: Limits and drawbacks

D. Meloni, G. Sechi & G. Concu

Department of Civil and Environmental Engineering and Architecture, University of Cagliari, Italy

ABSTRACT: Infrared thermography (IRT) is an effective diagnostic methodology for existing buildings monitoring, whose efficiency is however affected by the operator's technical knowledge. This paper presents experimental research aimed at evaluating the accuracy of IRT temperature measurements with respect to the incorrect setting of five input parameters required to be set by the operator: emissivity, reflected apparent temperature, ambient temperature, relative humidity, and distance. The goal was to highlight how their accurate evaluation and setting affects the thermographic survey and the post-processing stage. To this end, IRT experimental investigations were carried out on materials characterized by different emissivity and surface roughness, such as concrete, granite and steel. The experimentation outcome has pointed out the factors that most affect the temperature measurement error and allowed to quantify the error on the temperature measurements deriving from the incorrect setting of these parameters during the acquisition phase of the thermogram.

1 INTRODUCTION

Thermal controls represent the set of methods in which appropriate devices for the detection of heat are used to measure the temperature variation in physical components, structures, systems, or processes. Among the thermal control methods, Infrared Thermography (IRT) is a non-destructive investigation technique without physical contact with the inspected element based on the measurement of the electromagnetic energy radiated by the object in the infrared range of the electromagnetic spectrum. Infrared rays are related to heat as they originate from the emission of energy resulting from collisions between the molecules of the body because of their thermal agitation. All bodies having a temperature above absolute zero emit infrared radiations with increasing intensity as the body temperature increases due to the greater thermal energy radiated. Therefore, IRT remotely measures the thermal energy possessed by an object starting from the detection of the intensity of the infrared radiation emitted, allowing to trace back to the object surface temperature. Thanks to the amount of data that can be collected, the ease of inspection and the immediacy of the information, IRT used in the context of existing buildings diagnostics makes it possible to identify:

- thermal bridges,
- defects in thermal insulation,
- non-homogeneity of the walls,
- possible detachment of plasters or coatings,
- presence of humidity, condensation, water infiltrations,
- concealed systems,
- non-visible structural elements.

In addition, it is a supporting tool for:

- energy certification of buildings,
- investigations on historic buildings,
- diagnostics and restoration of decorated surfaces.

The main tool of IRT investigations is the infrared camera or thermal camera, which detects the intensity of the infrared radiation emitted by the body and generates thermal maps or thermograms in chromatic scale representative of the distribution of temperatures in the scenario framed by the thermal camera, in which the hot spots, the cold ones and the heat gradients existing between the various parts of the examined surface are highlighted and quantified. In this way, a representation of the thermal gradients between different areas of the body and a model of the thermal distribution is obtained. However, thermal cameras observe the energy radiated by objects and not their temperature, therefore the temperatures are calculated indirectly by means of algorithms needing the setting of appropriate parameters - emissivity, reflected apparent temperature, ambient temperature, relative humidity, and distance - that the operator provides to the instrument in the phases preceding the measurement.

This paper reports an experimental work aimed at evaluating the accuracy of the temperature measurements, carried out by IRT, with respect to an incorrect setting of these parameters, to highlight how fundamental their accurate evaluation and setting is before running the thermographic survey and afterwards in the post-processing stage. To this end, IRT was carried out on specimens made of different materials, namely concrete, granite and steel, characterized by different physical characteristics.

2 INFRARED THERMOGRAPHY

The thermal camera not only detects the radiation emitted by the object, but also that which originates in the surrounding objects and reflected by the object itself. Both radiations vary according to atmospheric absorption, and the measurement can be strongly influenced by the ambient temperature. For a precise detection of the surface temperature of the object it is therefore necessary to consider these phenomena through appropriate algorithm and parameters that allow to account for the characteristics of the inspected elements and the operative environmental conditions, to correct the disturbance factors of the measurement. These parameters are the following.

- Emissivity ϵ of the object. Emissivity refers to the amount of thermal energy radiated by the object and expresses the ratio between the radiation emitted by the body at a given temperature and that emitted by the black body at the same temperature ($\epsilon=1$); its values are therefore included in the range 0-1. A body with an emissivity close to 0 reflects all the incident energy, while if the emissivity is close to 1 the object has a behavior like the black body, tending to absorb all the incident energy without any reflection. The values included in the range 0-1 are typical of the so-called grey bodies, where part of the incident radiation is absorbed, and part reflected. The emissivity coefficient depends on the material, the surface conditions (roughness), the temperature and the wavelength.
- Reflected apparent temperature T_{rif} . The reflected environmental temperature permits to balance the radiation reflected by the object and that emitted from the atmosphere between the thermal camera sensor and the object itself. It is of fundamental importance to accurately set this value when the emissivity is low, the distance from the element under investigation is very high and its temperature is like that of the environment.
- Distance d between the object and the thermal camera. Setting this distance is important to balance the radiation absorption between the object and the thermal camera due to the transmittance, which decreases as the distance increases. When operating IRT, it is necessary to consider the presence of a medium between the source and the detector, represented in general by the atmosphere, whose gases have thermal properties as well, which need to be considered to avoid excessive attenuation of the radiation emitted by the object.
- Atmospheric temperature T_{atm} . It affects the thermal properties of the environment and the object.
- Relative humidity RH%. Relative humidity affects the transmittance to a certain extent. However, for short distances between object and detector and for standard humidity a default value of 50% can be used without excessive error.

The radiation recorded by the thermal camera is converted into an electronic signal which is then processed by specific software to produce digital images and map the distribution of

surface temperatures through analytical calculations. The thermal camera's own processing algorithm operates based on a mathematical model according to a relationship of the type:

$$T = f(\varepsilon, T_{\text{rif}}, d, T_{\text{atm}}, \text{RH}\%) \quad (1)$$

IRT efficiency is therefore conditioned by the operator's technical knowledge and his ability to recognize and interpret the phenomena taking place around the object at the time of acquisition of the thermograms, as thermal cameras typically require the operator to set the five input parameters previously mentioned. Since the relationship (1) is highly non-linear, to evaluate the specific influence of the input parameters, in this paper the error was studied as a function of each individual parameter. It's worth underlying that the thermograms can be revised afterwards by previously mentioned post-processing codes, but information about real-time environmental conditions is needed and are to be recorded in situ. Another parameter which influences thermograms is surface roughness. In fact, the surface characteristics of the object are decisive for measuring the temperature by means of IRT. Depending on the surface condition, the degree of roughness and the type of coating, the emissivity changes. Smooth, shiny, mirror and/or polished surfaces usually have lower emissivity than matt, textured, rough, broken and/or scratched surfaces. The influence of surface roughness has been also investigated in this paper.

3 MATERIALS AND METHODS

3.1 Materials

IRT has been applied on specimens made of different building materials having different emissivity and with different surface roughness, as specified in Table 1. Specimens are also shown in Figure 1.

Table 1. Specimens' properties.

Material	Size (mm)	Roughness	Emissivity
Concrete	150x150	low	0.95
Concrete	150x150	high	0.95
Granite	120x200	low	0.80
Granite	120x110	high	0.77
Steel	50x80	low	0.35
Galvanized steel	50x80	high	0.27

3.2 Methods

IRT has been carried out using a high-resolution thermal camera SC660 R&D by FLIR Systems (Figure 2a).

Atmospheric temperature T_{atm} and Relative humidity $\text{RH}\%$ have been measured using a thermo-hygrometer MENGSHEN M350 (Figure 2b).

Emissivity ε and Reflected apparent temperature T_{rif} have been determined according to the procedures specified in standard ISO 18434-1:2008 Part 1, Annex A.2 and A.1 respectively.

To avoid interferences, during IRT running the specimens were housed in a structure specially made for shielding the rays reflected from other bodies (Figure 2c).

The Distance d between the specimen and the thermal camera has been set at 1m.

The active IRT has been carried out heating the specimens with two 400 W halogen lamps.

Having completed the preliminary operations and having introduced the input parameters into the thermal camera, the indirect measurement of the temperature has been carried out, acquiring the thermograms relating to the specimen at regular object temperature intervals, and subsequently proceeding to their post processing by means of the supplied software of the thermal camera.

To evaluate the influence on the temperature returned by the thermograms of the error committed in setting the input parameters of the thermal camera, sensitivity analyses have been conducted, consisting in analysing the deviation of the temperature returned by the



Figure 1. Specimen type. Concrete – low roughness (a), Concrete – high roughness (b), Granite – low roughness (c), Granite – high roughness (d), Steel – low roughness (e), Galvanized steel – high roughness (f).



Figure 2. Instrumental set. Thermal camera (a), Thermohygrometer (b), Shielding structure (c).

thermogram with respect to the exact temperature measured with a contact thermometer, by varying a single input parameter at a time. The variation of each input parameter has been established within a range that simulated real operating conditions.

4 RESULTS AND DISCUSSION

4.1 Sensitivity analysis. Emissivity

Figure 3 shows the percentage deviation δT_{IRT} of the temperature returned by the thermogram with respect to the temperature T_{exact} measured with the contact thermometer as a function of the percentage emissivity deviation $\delta \epsilon$ with respect to the correct value ϵ_{exact} for the concrete specimen with low surface roughness. The latter has been determined according to the procedure recalled in ISO 18434-1 Part 1, Annex A.2, at different temperatures. The terms involved in the subsequent diagrams are defined in Equations 1 and 2 as follows:

$$\delta T_{IRT} = \frac{T_{IRT} - T_{exact}}{T_{exact}} \cdot 100 \quad (2)$$

$$\delta \in = \frac{\varepsilon - \varepsilon_{\text{exact}}}{\varepsilon_{\text{exact}}} \cdot 100 \quad (3)$$

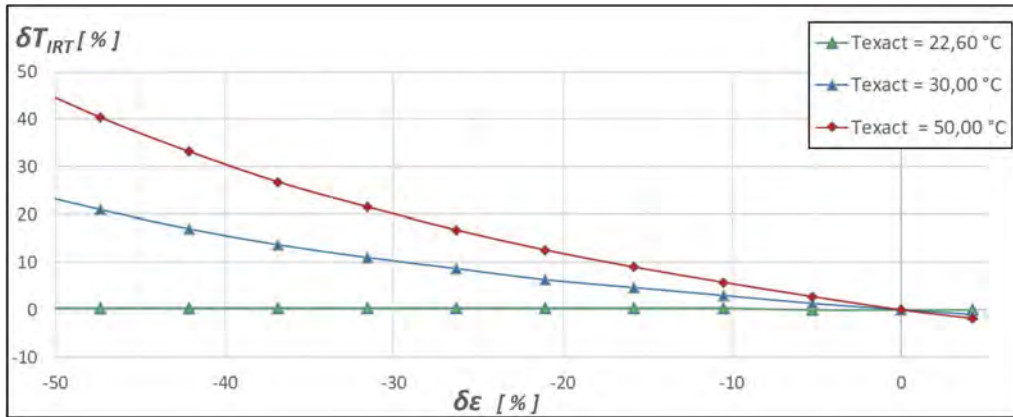


Figure 3. Influence on the temperature T_{IRT} returned by the thermograms of the error $\delta\varepsilon$ committed in setting the emissivity for the concrete specimen with low surface roughness.

With the same parameters meaning defined above, Figure 4 shows the deviation δT_{IRT} of the temperature returned by the thermogram with respect to the temperature T_{exact} as a function of the emissivity variation $\delta\varepsilon$ for the granite specimen with low surface roughness.

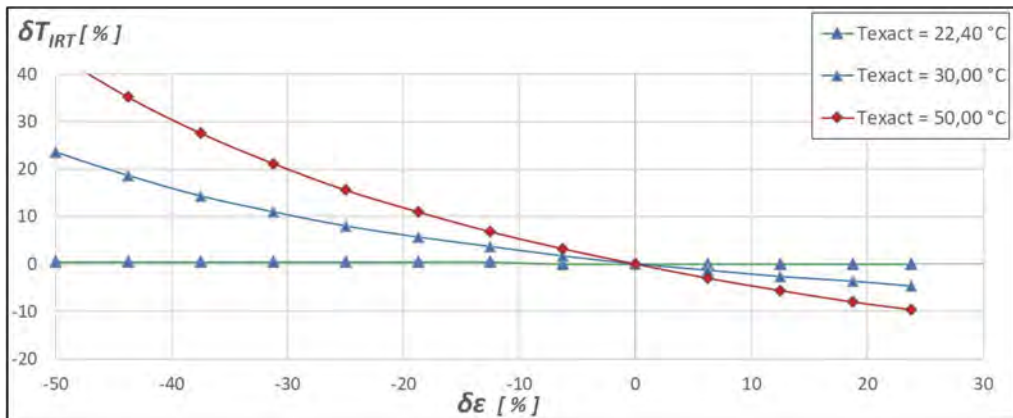


Figure 4. Influence on the temperature T_{IRT} returned by the thermograms of the error $\delta\varepsilon$ committed in setting the emissivity for the granite specimen with low surface roughness.

Figure 5 shows the deviation δT_{IRT} of the temperature returned by the thermogram with respect to the temperature T_{exact} as a function of the emissivity variation $\delta\varepsilon$ for the steel specimen with low surface roughness.

A summary of the errors according to the type of material and surface roughness is shown in Table 2.

4.2 Sensitivity analysis. Reflected temperature

Figure 6 shows the deviation δT_{IRT} of the temperature returned by the thermogram with respect to the temperature T_{exact} measured with a thermometer as a function of the reflected apparent temperature deviation δT_{rif} with respect to the exact value $T_{\text{rif,exact}}$, for the

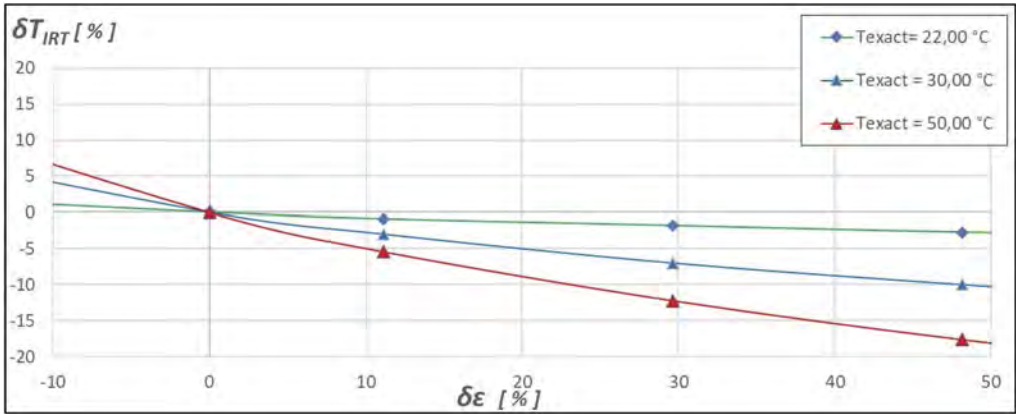


Figure 5. Influence on the temperature T_{IRT} returned by the thermograms of the error $\delta\epsilon$ committed in setting the emissivity for the steel specimen with low surface roughness.

Table 2. Deviation δT_{IRT} with respect to T_{exact} as a function of material and surface roughness.

	Concrete	Granite	Steel
LR*	up to +45%	up to +120%	up to -38%
HR**	up to +140%	up to +110%	up to -42%

*Low Roughness, **High Roughness.

galvanized steel specimen with high surface roughness, defined as follows in Equation 4, the latter being determined according to the procedure recalled in ISO 18434-1 Part 1, Annex A.1, making use of a reflector made of a crumpled aluminium foil:

$$\delta T_{rif} = \frac{T_{rif} - T_{rif,exact}}{T_{rif,exact}} \cdot 100 \quad (4)$$

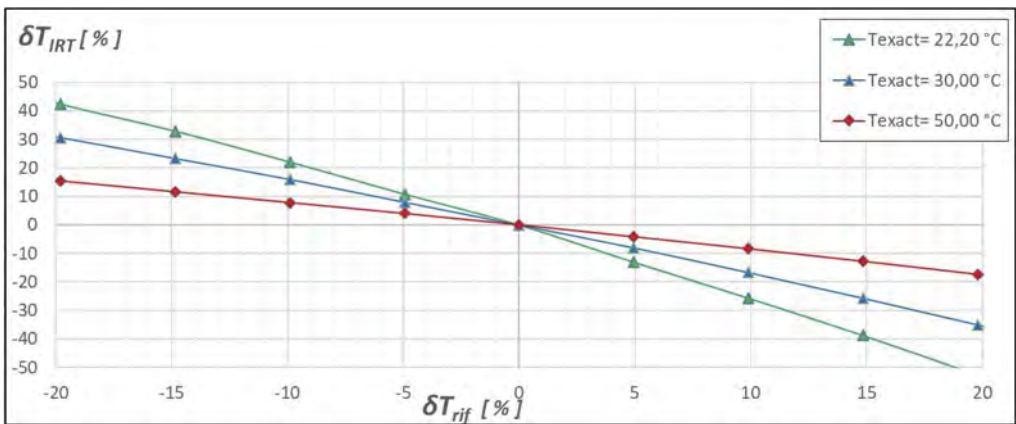


Figure 6. Influence on the temperature T_{IRT} returned by the thermograms of the error δT_{rif} committed in setting the reflected temperature for the steel specimen with high surface roughness.

A summary of the errors according to the type of material and surface roughness is shown in Table 3.

Table 3. Deviation δT_{IRT} with respect to T_{exact} as a function of material and surface roughness.

	Concrete	Granite	Steel
LR*	$\pm 2\%$	$\pm 9\%$	$-80\% + 60\%$
HR**	$\pm 2\%$	$\pm 10\%$	$-110\% + 90\%$

*Low Roughness, **High Roughness.

4.3 Sensitivity analysis. Atmospheric temperature, relative humidity, and distance

Table 4 summarizes the deviation δT_{IRT} of the temperature returned by the thermogram with respect to the temperature T_{exact} measured with a thermometer as a function of the Atmospheric temperature T_{atm} , the Relative humidity RH%, and the Distance d.

Table 4. Deviation δT_{IRT} with respect to T_{exact} as a function of material and surface roughness determined for T_{atm} , RH%, and d variation.

	Concrete		Granite		Steel	
	LR*	HR**	LR*	HR**	LR*	HR**
T_{atm}	0.2%+0.4%	0.3%+0.4%	0.4%+0.4%	0.4%+0.4%	0.9%+0.5%	1%+0.9%
RH%	0.2%+0.3%	0.3%+0.2%	0.3%+0.2%	0.2%+0.3%	0.4%+0.2%	0.3%+0.3%
d	+3%	+3%	+3%	+3%	+3%	+3%

*Low Roughness, **High Roughness.

4.4 Discussion

The results of the tests carried out on materials with different emissivity and surface roughness show that the input parameters that most influence the error of temperature measurement via IRT are the emissivity ϵ of the object and the reflected apparent temperature T_{rif} , while the other parameters, i.e., atmospheric temperature, relative humidity, and distance, have a less significant, even negligible, influence.

The results also highlight that the roughness of the surfaces can significantly affect the correct value of the temperature measurement, especially in the case of concrete and steel, since they affect remarkably the emissivity.

For all materials examined, the incidence of emissivity deviation increases with increasing temperature difference between the object and the environment, while the incidence of reflected temperature increases with decreasing temperature difference.

The influence of the latter error component increases significantly the more the material has a reduced emissivity, and therefore a high reflectivity, such as steel.

The results point out that the incorrect setting of emissivity has a strong impact on the accuracy of the temperature measurement. Since the thermal camera allows the user to set a single emissivity value for each object falling into its focus range at the time of acquisition of the thermogram, it is essential to identify the different emissivity of each framed object. In this regard, it is useful to examine Tables 5, 6 and 7, which report the entity of the possible errors in the case of material with high emissivity such as concrete (Table 5), medium-high emissivity such as granite (Table 6), low emissivity such as steel (Table 7).

Table 5. Error of T_{IRT} measurement as a function of incorrect setting of ϵ for concrete. $T_{atm} = 20^\circ\text{C}$.

$\epsilon = 0.95$ (correct value)		$T_{exact} = 30^\circ\text{C}$	$T_{exact} = 50^\circ\text{C}$
$\epsilon = 0.65$	$\delta\epsilon = 30\%$	$\delta T_{IRT} = 11\%$	$\delta T_{IRT} = 22\%$
$\epsilon = 0.50$	$\delta\epsilon = 48\%$	$\delta T_{IRT} = 21\%$	$\delta T_{IRT} = 40\%$
$\epsilon = 0.30$	$\delta\epsilon = 68\%$	$\delta T_{IRT} = 48\%$	$\delta T_{IRT} = 89\%$

Table 6. Error of T_{IRT} measurement as a function of incorrect setting of ϵ for granite. $T_{atm} = 20^{\circ}C$.

$\epsilon = 0.80$ (correct value)		$T_{exact} = 30^{\circ}C$	$T_{exact} = 50^{\circ}C$
$\epsilon = 0.55$	$\delta\epsilon = 30\%$	$\delta T_{IRT} = 11\%$	$\delta T_{IRT} = 21\%$
$\epsilon = 0.40$	$\delta\epsilon = 50\%$	$\delta T_{IRT} = 24\%$	$\delta T_{IRT} = 45\%$
$\epsilon = 0.30$	$\delta\epsilon = 62\%$	$\delta T_{IRT} = 39\%$	$\delta T_{IRT} = 71\%$

Table 7. Error of T_{IRT} measurement as a function of incorrect setting of ϵ for steel. $T_{atm} = 20^{\circ}C$.

$\epsilon = 0.27$ (correct value)		$T_{exact} = 30^{\circ}C$	$T_{exact} = 50^{\circ}C$
$\epsilon = 0.35$	$\delta\epsilon = 30\%$	$\delta T_{IRT} = 7\%$	$\delta T_{IRT} = 12\%$
$\epsilon = 0.40$	$\delta\epsilon = 48\%$	$\delta T_{IRT} = 10\%$	$\delta T_{IRT} = 18\%$
$\epsilon = 0.95$	$\delta\epsilon = 250\%$	$\delta T_{IRT} = 23\%$	$\delta T_{IRT} = 40\%$

It is interesting to note that if for concrete (Table 5) or granite (Table 6) the emissivity of steel is accidentally set ($\epsilon=0.30$) a temperature measurement error of up to 70% can be made. Similarly, if for steel (Table 7) the emissivity of concrete ($\epsilon=0.95$) is accidentally set, a temperature measurement error of up to 40% can be made. With this respect, it is worth noticing that, even though in post-processing codes it is usually possible to set different values of emissivity or reflected apparent temperature on different areas of thermograms, while carrying out an in-situ survey, the contemporary presence of different materials on the frame can be a critical issue, since the distribution of temperatures and consequent observations can be seriously affected. Therefore, when thermography is employed for in situ investigations aimed at real-time searching for structural anomalies or criticalities, attention need to be paid to a proper setting of the parameters.

5 CONCLUSIONS

This paper analyzed the influence on the temperature measurement via IRT of the incorrect setting of the input parameters that the operator must set in the thermal camera before the test, i.e. the emissivity of the object, the reflected apparent temperature, the atmospheric temperature, the relative humidity and the distance between the camera and the object.

The tests were carried out on samples of building materials with different emissivity and different surface roughness.

The results showed that the most influential parameters on the error are the emissivity and the reflected temperature, and that this influence generally increases as the surface roughness increases.

The operator must therefore be able to set these parameters correctly to avoid significant measurement errors which would distort the results of the IRT test and affect the temperature gradients in the thermograms to an extent that the structural anomalies or damage searched for in civil engineering surveys could be undetectable.

REFERENCES

- Huang Y., Shih, P., Hsu K.-T. & Chiang C.-H. 2020. To identify the defects illustrated on building facades by employing infrared thermography under shadow. *NDT&E International* 111, 102240, <https://doi.org/10.1016/j.ndteint.2020.102240>.
- ISO 18434-1:2008 Condition monitoring and diagnostics of machines — Thermography — Part 1: General procedures
- Ochs, M., Horbach, T., Schulz, A., Koch, R. & Bauer, H.J. 2009. A novel calibration method for an infrared thermography system applied to heat transfer experiments. *Measurement Science and Technology*, 20 075103, doi 10.1088/0957-0233/20/7/075103
- Waldemar, M. & Sebastian, D. *Infrared thermography: errors and uncertainties*, John Wiley & Sons Inc. September (2009)
- Waldemar, M. & Sebastian, D. Simulation analysis of uncertainty of infrared camera measurement and processing path, *Technical University of Czestochowa, Science Direct, Volume 39, October (2006)*

Soundness evaluation of small-scale bridge decks with portable FWD tests

Taichi Sasaki & Atsuya Tsuboi

Graduate School of Arts and Science, Iwate University, Morioka, Japan

Yuma Sugimoto, Haruto Kakeda & Hiroshi Onishi

Faculty of Science and Engineering, Iwate University, Morioka, Japan

ABSTRACT: The number of aging bridges that have been constructed more than 50 years is increasing in Japan. It is necessary to establish an efficient and quantitative bridge inspection method. From this background, we proposed an efficient deck health evaluation method using an impact vibration test with a portable FWD (Falling Weight Deflectometer). The objective of this study is to improve the accuracy of damage detection of slabs by FWD testing with field test and FE analysis. In the field FWD test, we got response acceleration data from several points on deck before and after the slab replacement. By comparing them, we found that the correlation coefficient of response acceleration between the measurement points was related to the soundness of the slab. We also estimated the damage area of the deck by correlating the difference in response acceleration between the measurement points. From the 3D FE (Finite Element) analysis modeling the target bridge, the effect of partial deterioration of the deck slab on the vibration response from field test was simulated.

1 INTRODUCTION

Development inspection methods for bridges is important issue in Japan. Visual inspection is one of the most common inspection methods used for periodic inspections (National Roads and Engineering Division. 2019), but it lacks quantitiveness. Vehicle loading tests (Chiba. 2016) (Kasai. 2015) are often used to confirm the effectiveness of bridge reinforcement and the load-bearing capacity of newly constructed bridges. This inspection method uses many sensors, making quantitative testing possible, but consideration of sensor locations is difficult.

In this study, a quantitative and simple method for evaluating the health of bridge decks was investigated using impact vibration tests with a portable Falling Weight Deflectometer (FWD). Previous studies focused on the natural frequencies of the entire bridge for evaluating the bridge soundness (Haneya. January 2008) (Sasaki. June 2021). On the other hand, the authors aimed to estimate the local damage location in the deck slab which was difficult to do only by identifying the natural frequencies by using response acceleration obtained from the portable FWD test. First, the correlation of the difference in response acceleration between multiple measurement points was investigated, and the results were compared before and after the slab replacement work. Second, a 3D FE model of the target bridge was created, and a dynamic analysis was conducted to reproduce the portable FWD test. From the analysis results, the effect of partial damage to the deck slab on the vibration response was investigated.

2 STUDY OVERVIEW

2.1 Target bridge

The bridge has been in service for more than 40 years since 1974, and various damages were found during a periodic inspection in 2015. The upper structure of this bridge is a steel composite simple H-girder bridge consisting of three main girders and RC (Reinforced Concrete) slabs (slab thickness: 160 mm) with a bridge length of 16.0 m, a width of 8.2 m, and a girder

Table.1. Akayama bridge specification (Unit: mm).

Superstructure	Steel composite, Simple H-beam bridge
Substructure	Reversed T-type abutment
Foundation work	Spread foundation
Deck type	RC deck
Bridge bearing	Steel line bearing
Bridge length	16,000
Span length	15,550
Width	600+7,000+600=8,200
Skew	83°
Design load	TL-14



Figure 1. The exterior appearance of Akayama Bridge.



Figure 2. Portable FWD & accelerometer.

height of 700 mm. The bridge has a slant angle of 83°. Corrosion was found in the girder members, and cracks and damage suspected to be ASR (Alkali Silica Reaction) due to drying shrinkage were found in the deck slabs. Therefore, reinforcement work including slab replacement was performed in 2019. Table 1 and Figure 1 show the specifications and the exterior appearance of the target bridge, respectively.

2.2 Portable FWD test

In this study, shock and vibration tests were conducted using the portable FWD system “FWD-Light” manufactured by Tokyo Measuring Instrument Lab. The tester consists of a weight, a drop mechanism, and a loading board, and is equipped with displacement values transducer and a load cell. The free-fall of the weight applies a constant impact force to the slab, and the load value and displacement can be measured. Since the purpose of this test was to obtain response acceleration, an accelerometer was used near the FWD as an external sensor to measure the vertical response acceleration caused by the impact vibration. The weight of the portable FWD was 25 kg, the drop height was 1 m, and the sampling interval for the acceleration measurement was 0.1 ms. Figure 2 shows the appearance of the portable FWD, and accelerometer used in the test.

3 CONSIDERATION BY RESPONSE ACCELERATION DIFFERENCE

3.1 Outline of examination

In this study, 9 accelerometers were placed on the slab to measure the response acceleration generated by the impact vibration of a portable FWD. The names of the loading points and measurement points are CH1 to CH9 as shown in Figure 3.

Figure 4 shows a schematic chart of the method used to investigate the difference in response acceleration. The impact generated by the portable FWD vibrates each part of the slab and arrives at each measurement point, and the response acceleration is measured by

each accelerometer. In Figure 4, two sections OA and OB, consisting of two accelerometers A and B equidistant from the loading point of the portable FWD and accelerometer O are the sections under consideration. If the stiffness of the slab is the same in the two sections, the same acceleration values are measured at the measurement points A and B. In contrast, if the stiffness is different, the measured values are considered to be different. The same trend can be obtained for the difference between the measured values at accelerometer O and accelerometers A and B, “O-A” and “O-B”. By comparing the difference in response acceleration at the two measurement points, it is possible to estimate slab soundness.

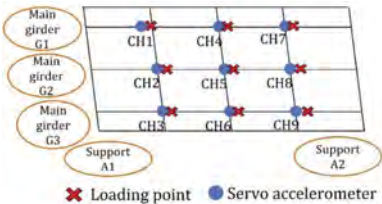


Figure 3. Arrangement of loading points and accelerometers.

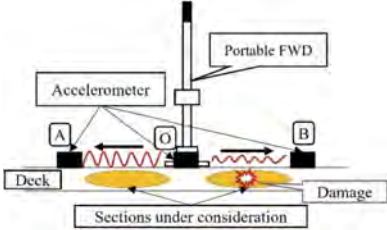


Figure 4. Schematic chart of Acceleration gap.

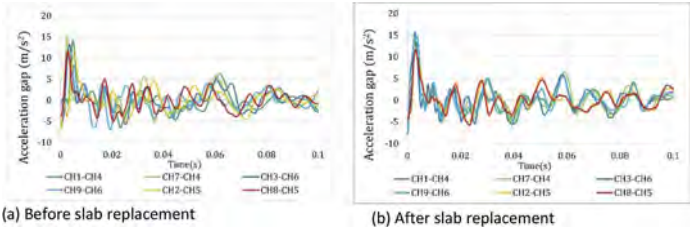


Figure 5. The time variation curve of the acceleration gap (loading at 1/4,3/4 points of span).

In impact vibration tests using portable FWD, the weight falls and bounces multiple times. In this study, to remove the influence of the impact from the second and subsequent bounces, the acceleration data was extracted for 0.5 seconds after the maximum value of acceleration due to the first impact. The effect of noise is reduced by averaging the acceleration at each time (every 0.1 ms). Next, standardization processing described in Equation (1) is performed to suppress variations in the magnitude of the amplitude of the vibration at each measurement point.

$$z_i = (x_i - \bar{x})/s \tag{1}$$

z_i : Standardized data, x_i : Original data(Average acceleration), \bar{x} : Average of original data, s : Standard deviation of original data

The data after the standardization process was used to calculate the time variation of the response acceleration difference between the loading point and the other measurement points.

3.2 Calculation of correlation coefficient of response acceleration difference

As an example, Figure 5 shows the time variation of the acceleration gap between the measurement points in longitudinal direction when striking the 1/4 and 3/4 points of the main girders G1 and G3. In the following text and figures, “CH4-CH1” and “CH4-1” are used to denote “(loading point)- (measurement point where acceleration difference is taken)”. Before the slab replacement, the acceleration difference waveforms are generally more erratic than after the slab replacement, and the agreement between each section is lower. The different vibration response of each section is assumed to be due to the non-uniform stiffness of the slab before the repair

work. On the other hand, after the slab replacement, the acceleration gap waveforms in each section are good agreement because the slab stiffness became uniform after the repair work.

Table 2. Measured correlation coefficient (Section of longitudinal direction).

Section combination	Deck replacement	
	Before	After
(CH1-4) ×(CH7-4)	0.44	0.84
(CH1-4) ×(CH3-6)	0.65	0.68
(CH1-4) ×(CH9-6)	0.19	0.86
(CH7-4) ×(CH3-6)	0.68	0.75
(CH7-4) ×(CH9-6)	0.27	0.77
(CH3-6) ×(CH9-6)	0.17	0.77

Table 3. Measured correlation coefficient (Section of transverse direction).

Section combination	Deck replacement	
	Before	After
(CH1-2) ×(CH7-8)	0.54	0.78
(CH1-2) ×(CH3-2)	0.69	0.76
(CH1-2) ×(CH9-8)	0.06	0.80
(CH7-8) ×(CH3-2)	0.79	0.75
(CH7-8) ×(CH9-8)	0.40	0.87
(CH3-2) ×(CH9-8)	0.32	0.79

Table 4. Measured correlation coefficient (Section of diagonal direction).

Section combination	Deck replacement	
	Before	After
(CH1-5) ×(CH7-5)	0.40	0.84
(CH1-5) ×(CH3-5)	0.52	0.74
(CH1-5) ×(CH9-5)	0.38	0.85
(CH7-5) ×(CH3-5)	0.81	0.77
(CH7-5) ×(CH9-5)	0.29	0.92
(CH3-5) ×(CH9-5)	0.28	0.81

Regardless of whether before or after the slab replacement, the waveforms of the acceleration gap between the section on the outer girder and the section on the middle girder show different shapes. This reason is that the section on the outer girder is strongly affected by torsional vibration when struck on the outer girder, while the section on the middle girder shows bending vibration behavior when struck on the middle girder.

To quantitatively evaluate the degree of agreement between the acceleration differences of the two intervals, the correlation coefficient is first used in this study. The correlation coefficient is calculated by Equation (2).

$$r = s_{xy}/s_x s_y \quad (2)$$

s_{xy} : Covariance of acceleration x & y , s_x : Standard deviation of acceleration x , s_y : Standard deviation of acceleration y

In general, when the absolute value of the correlation coefficient is 0~0.2, there is almost no correlation, 0.2~0.4 indicates a weak correlation, 0.4~0.7 indicates a moderate correlation, and 0.7~1.0 indicates a strong correlation. In this study, the correlation coefficients of the acceleration gap before and after the slab replacement were calculated for three different sections in longitudinal direction, transverse direction, and diagonal direction when loading the 1/4 and 3/4 points of the G1 and G3 main girder supports, respectively.

3.3 Correlation coefficient results and discussion

Tables 2-4 show the correlation coefficients for the combined acceleration differences for the sections along longitudinal direction (CH1-CH4, CH7-CH4, CH3-CH6, CH9-CH6), transverse direction (CH1-CH2, CH7-CH8, CH3-CH2, CH9-CH8), and diagonal direction (CH1-CH5, CH7-CH5, CH3-CH5, CH9-CH5) when loading the 1/4 and 3/4 points of the span on main

girders G1 and G3. The correlation coefficients increased for all combinations after the slab replacement, and all correlations are stronger than 0.7. On the other hand, the correlation coefficients before the slab replacement are lower than those after the slab replacement for all combinations of sections. As shown in red in the table, the correlation coefficients for all combinations including CH9-CH6, CH9-CH8, and CH9-CH5 are particularly low compared to the other combinations.

As mentioned above, the correlation coefficients for the acceleration differences between adjacent measurement points in longitudinal direction, transverse direction, and diagonal direction were determined. For all combinations of sections, the correlation coefficients tended to be higher after the slab replacement than before the replacement. This may be because the stiffness of the slab became uniform throughout the slab after the slab replacement. In the three-directional combinations, the correlation coefficients between CH9-CH6, CH9-CH8, and CH9-CH5, which include the section where CH9 was hit before the slab replacement, tend to be particularly low. This suggests that changes in the relative vibration characteristics of the slab occurred in the vicinity of these sections and CH9 before the slab replacement.

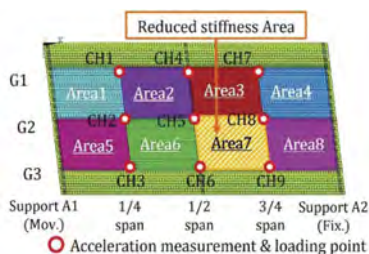


Figure 6. Overview of FE model.

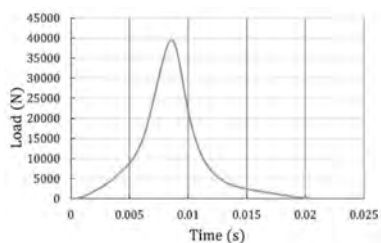


Figure 7. Impact load curve.

Table 5. Material properties of the FE model.

	RC deck	Steel
Young's Modulus (N/mm ²)	31,000	200,000
Poisson's Ratio	0.167	0.300
Unit volume weight (kN/m ³)	24.5	77.0

Table 6. Natural frequency obtained from measured acceleration and FE model.

Vibration mode	Natural Frequency (Hz)	
	After deck replacement (Measured)	FE model (Healthy state)
1st bending	7.94	7.93
1st torsional	8.85	8.86
2nd bending	21.1	20.43
2nd torsional	22.6	22.54

4 DYNAMIC FE ANALYSIS

4.1 Analysis model overview

In this study, a FE model of the target bridge superstructure was created using the 3D FE analysis software ANSYS. The slab, main girder, and transverse girder were created using shell elements. Rigid beam elements are used to connect the upper flanges of the main girders and end transverse girders to the vertical direction of the deck slab. Figure 6 shows a three-dimensional model of the bridge. The model is set up so that the Young's modulus and other properties of the members can be changed for each color range. The Young's modulus of the RC slab was obtained by substituting the design basis strength of the replaced slab, 40 N/mm², into Equation (3).

$$E_c = \left(3.1 + \frac{f'_c - 40}{50} \right) \times 10^4 \quad (3)$$

E_c : Young's modulus (N/mm²), f'_c : Design basis strength of concrete (N/mm²)

Here, $40 \leq f'_c < 70$. Table 5 shows the material properties of the model.

To simulate the boundary conditions of target bridge, a translational spring element that restrains horizontal movement was introduced to the movable bearing. In the following analysis, a spring element with a spring constant of 1.1×10^4 N/mm is applied to the movable bearing. In a previous study, the authors obtained the natural frequencies of the first order and second order bending and torsional vibration modes of the subject bridge before and after the replacement of the deck slab from measured accelerations. Table 6 shows the measured natural frequencies of each vibration mode and the natural frequencies of the first order and second order bending and torsional vibration modes of the FE model.

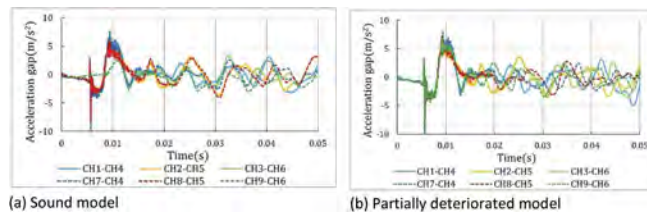


Figure 8. The time variation curve of the acceleration gap obtained from FE analysis (Sections of longitudinal direction).

4.2 Time history response analysis

The impact loads applied to the FE model were the measured loads recorded by the load cell built into the portable FWD in the field test. Figure 7 shows the impact load curves used in the time history response analysis. As in the portable FWD test on the actual bridge, impact loads were applied to the 1/4, 1/2, and 3/4 points of the G1~G3 girders, and a time history response analysis was conducted. The difference in response acceleration in the vertical direction is output at nine measurement points from CH1 to CH9. The response acceleration data is output for 0.5 seconds (5000 data) at a sampling interval of 0.1 ms.

In a study based on the acceleration gap obtained by field measurements, a change in vibration response relative to other parts of the slab was estimated in the vicinity of the area including the sections CH9-CH6, CH9-CH8, and CH9-CH5 before the slab replacement. Therefore, in this analysis, a sound model and a partially deteriorated model were created and analyzed in order to confirm the change in vibration response. The sound model has a uniformly stiffened slab using the material properties shown in Table 5. The partial degradation model has reduced Young's modulus in Area 7, which includes the sections CH9-CH6, CH9-CH8, and CH9-CH5, as shown in Figure 6. The Young's modulus of the slab is reduced from 10% to 50%.

In previous studies (Chiba, December 2021), the authors used 0.5 seconds of data (5,000 data) immediately after the impact to calculate the correlation coefficient. In this study, the authors calculated the correlation coefficient using 0.05 seconds of data (500 data) and compared it with the result calculated using 0.5 seconds of data.

4.3 Analysis results and discussion

Figure 8 shows the time variation of the acceleration difference between the healthy model and the partially deteriorated model (Young's modulus 50%) in longitudinal section when impact loads were applied to CH1, 3, 7, and 9. The waveform of the acceleration gap in the partially deteriorated model (Figure 8(a)) is generally scattered. On the other hand, the waveform of the sound model (Figure 8(b)) shows less variation. These trends are also observed for the transverse sections and the diagonal direction. Figure 8 shows that the sections on the G2 girder (CH2-CH5 and CH8-CH5) behave differently from the sections on the G1 and G3 girders. This is thought to be due to the difference in response behavior caused by torsional vibrations that are strongly excited when a point on the outer girder is struck. This feature tended to be same in field test.

Table 7 shows the correlation coefficients between the sound model and the partially deteriorated model for each combination of three directional sections. This is the result of the

correlation coefficient calculation when the Young's modulus of Area7 is 100%, 90%, 80%, and 50%. In both cases where the data range was 0.5 and 0.05 seconds, the correlation coefficient tended to decrease as the Young's modulus of Area 7 decreased. When the Young's modulus of Area 7 was high, the correlation coefficients tended to be larger than those of other combinations of sections with point symmetry at the center of the slab (CH5) (e.g., (CH1-4)×(CH9-6) and (CH1-2)×(CH9-8)). This is considered to be due to the similar vibration characteristics of the diagonal sections of the bridge, since the bridge is a diagonal bridge and its shape is point symmetrical around the center of the deck (CH5). These two characteristics are common to the three directional sections: longitudinal, transverse, and diagonal direction.

Table 7. Correlation coefficients for each interval calculated from FE analysis results.

	Sampling time							
	0.5 sec.				0.05 sec.			
	Decreasing rate young's modulus							
	100%	90%	80%	50%	100%	90%	80%	50%
Longitudinal direction								
(CH1-4) ×(CH7-4)	0.60	0.56	0.47	0.37	0.73	0.71	0.69	0.62
(CH1-4) ×(CH3-6)	0.62	0.54	0.42	0.49	0.76	0.77	0.77	0.71
(CH1-4) ×(CH9-6)	0.73	0.81	0.68	0.51	0.64	0.95	0.91	0.71
(CH7-4) ×(CH3-6)	0.90	0.86	0.74	0.49	0.96	0.94	0.90	0.71
(CH7-4) ×(CH9-6)	0.46	0.66	0.61	0.54	0.41	0.81	0.81	0.68
(CH3-6) ×(CH9-6)	0.50	0.63	0.62	0.50	0.48	0.85	0.85	0.72
Transverse direction								
(CH1-2) ×(CH7-8)	0.75	0.67	0.61	0.53	0.92	0.92	0.90	0.83
(CH1-2) ×(CH3-2)	0.77	0.66	0.57	0.57	0.93	0.92	0.87	0.85
(CH1-2) ×(CH9-8)	0.94	0.73	0.55	0.36	0.98	0.96	0.89	0.55
(CH7-8) ×(CH3-2)	0.93	0.87	0.79	0.40	0.98	0.97	0.92	0.72
(CH7-8) ×(CH9-8)	0.79	0.80	0.76	0.56	0.94	0.94	0.93	0.78
(CH3-2) ×(CH9-8)	0.76	0.76	0.78	0.47	0.92	0.89	0.83	0.47
Diagonal direction								
(CH1-5) ×(CH7-5)	0.63	0.60	0.42	0.30	0.74	0.70	0.66	0.54
(CH1-5) ×(CH3-5)	0.65	0.60	0.49	0.63	0.75	0.70	0.64	0.71
(CH1-5) ×(CH9-5)	0.85	0.71	0.52	0.36	0.97	0.94	0.85	0.64
(CH7-5) ×(CH3-5)	0.88	0.76	0.57	0.24	0.94	0.88	0.78	0.28
(CH7-5) ×(CH9-5)	0.65	0.73	0.74	0.51	0.78	0.80	0.80	0.59
(CH3-5) ×(CH9-5)	0.62	0.59	0.55	0.34	0.75	0.75	0.73	0.53

In the results for the longitudinal section in Table 7, the decrease in the correlation coefficient is uniform for all combinations, making it difficult to determine which part of the slab is damaged compared to the measured results. In the results for the transverse section in Table 7, when the Young's modulus of Area 7 was reduced to 50%, the correlation coefficient was smaller for the combination including CH9-8 than for the others. In the results for the diagonal section in Table 7, the correlation coefficients were smaller for the combination including CH9-5 on Area 7 when the data range was 0.5 seconds, but the correlation coefficients were also weaker for the section not included in Area 7. However, it was difficult to determine the damaged area because a weak correlation was obtained even in the section not included in Area 7.

One difference between the 0.5 second and 0.05 second data ranges is that the correlation coefficient is not very high when the data range is 0.5 seconds, even if the Young's modulus of Area 7 is high, while the correlation coefficient is generally high for all combinations when the data range is 0.05 seconds. The acceleration difference data for the 0.5-second period includes data affected by damped vibration after the loading, which may have led to the overall decrease in the correlation coefficient due to waveform distortion. On the other hand, the

0.05 second acceleration difference data does not include the effect of damped vibration, so the correlation coefficient is expected to be higher overall.

In the model used in this analysis, the Young's modulus of Area 7, which includes the intervals CH9-CH6, CH9-CH8, and CH9-CH5, was reduced. However, the section CH9-CH6 and CH9-CH8 are located on the boundary of Area 7. Therefore, the decrease in Young's modulus had less effect on the acceleration difference between these sections than expected, which may have made it difficult to determine the damage site. Further study is needed to determine the extent to which Young's modulus should be reduced.

5 CONCLUSION

This study proposed a method for detecting damage locations on slabs using correlation coefficients from response acceleration data obtained from portable FWD tests. The summary of this study are as follows.

- (1) Portable FWD tests were conducted on the target bridge before and after reinforcement work, including slab replacement, and applied a load and measured response accelerations at 1/4, 1/2, and 3/4 points along the three main girder spans. Using the acceleration data, the degree of agreement of the response acceleration differences between the measurement points was compared for each section in longitudinal direction, transverse direction, and diagonal direction using correlation coefficients to detect relative damage areas in the slab. The correlation coefficients tended to be lower for combinations that included certain sections before slab replacement, suggesting that changes in relative vibration characteristics may have occurred in the vicinity of these sections.
- (2) A 3D FE model was created by introducing spring elements into the movable bearings of the target bridge, and a time history response analysis was conducted to reproduce the time history response analysis. The analyses were conducted using a sound model with a uniform Young's modulus for the entire slab and a partially deteriorated model with a reduced Young's modulus for a portion of the slab, and the response acceleration in the vertical direction was obtained. Correlation coefficients were calculated for the difference in acceleration between each measurement point using the obtained response acceleration. The correlation coefficients for each section were found to decrease in accordance with the partial decrease in Young's modulus of the slab.
- (3) In the 3D FE analysis, the range of data used to calculate the correlation coefficient was also examined. 0.5 and 0.05 seconds of data were used to calculate the correlation coefficient. This is thought to be because of the damping vibration of the impact load on the waveform of the response acceleration.

In the future, we would like to conduct a more detailed study on how to estimate the damage areas of slabs from 3D FE analysis, and to investigate an evaluation method using an index different from the correlation coefficient.

REFERENCES

- H. Haneya. January 2008. Diagnosis of the Soundness of Substructure of Railway Bridges by Impact Vibration Test Method: Special Issue on Concrete Technology Supporting Urban Functions. Vol. 46. No.1 National Roads and Engineering Division, Road Bureau, Ministry of Land, Infrastructure, Transport and Tourism. 2019. Bridges periodic inspection guidelines: 2–20
- T. Kasai, S. Iwasaki, H. Onishi, H. Deto, K. Yamamura. 2015. A Study on the Evaluation of the Stiffness of the Kunenbashi-Bridge using Static and Dynamic Loading Tests: Steel Structure annual papers. vol.23
- T. Sasaki, H. Onishi, R. Ishikawa, Y. Kimura. June 2021. A study on the deck replacement on small bridge vibration characteristics using portable FWD test: 10th International Conference on Structural Health Monitoring of Intelligent Infrastructure
- Y. Chiba, H. Onishi, S. Iwasaki, K. Sasaki, H. Deto. 2016. Investigation of Post repair Behavior of Kunenbashi-Bridge Using Static Loading Tests: Steel Structure annual papers. vol. 24
- Y. Chiba, H. Onishi, S. Iwasaki, Y. Kimura, T. Sasaki. December 2021. Estimation of RC slab deterioration by response acceleration measured at multiple points: Reliability Symposium. Vol. 33: 2–10

Rut depth estimation by distortion analysis of images taken by an in-vehicle camera

Wenchao Gao, Kai Xue, Tomonori Nagayama, Boyu Zhao & Di Su
Department of Civil Engineering, The University of Tokyo, Tokyo, Japan

Kai Xue & Boyu Zhao
SmartCity Research Institute, Tokyo, Japan

ABSTRACT: Rut depth is one of the main indices in road maintenance. The current practice to evaluate rut depth is by manual inspection or by an irradiator and a special camera installed on an inspection vehicle. A new method to estimate rut depth by image processing that only needs an in-vehicle camera is presented. Images extracted from video captured by a camera are transformed into top-view images, and then two consecutive images are compared through feature matching techniques to evaluate the image distortion due to rutting. Rut depth information can thus be obtained from 2D camera images. This method is applied to road surfaces and estimation results are compared with true values. The results show that rut depth can be evaluated with good accuracy in this inexpensive and efficient way.

1 INTRODUCTION

Road infrastructure maintenance relates to the safety and comfort level of roads. In Japan, roads are mainly performed from IRI (International Roughness Index), crack ratio, and rut depth. Evaluation of the rut depth, which is the focus of this paper, is by manual inspection or by an irradiator and a special camera installed on an inspection vehicle now as shown in Figure 1. The efficiency of manual measurement is low while the irradiator is expensive, which limits frequent measurements. Thus, an inexpensive and efficient way to measure rut depth is expected. With the evolution of smartphones and the development of algorithms, IRI and crack ratio now can be evaluated using GNSS, IMU (Inertial Measurement Unit), and camera in a smartphone. This inspires us to consider estimating rut depth only using a smartphone in an image-processing way. In this paper, a method of distortion analysis of images taken by an in-vehicle camera via top-view transformation is proposed to estimate rut depth.



Figure 1. Current methods for rut depth measurement.

2 RELATED WORK

2.1 Structure from Motion (SfM)

(Tomasi et al., 1993) published a paper titled “Shape and Motion from Image Streams: a Factorization Method,” which established the foundation for the Structure from Motion (SfM) technique. SfM is a photogrammetric range imaging method that estimates three-dimensional structures from two-dimensional image sequences, potentially combined with local motion signals.

(Imai et al., 2021) attempted to use the SfM software Agisoft Metashape to measure the depth of blocks with asphalt pavement. They found that rut depth could be estimated using 4K 60fps video shot by a camera on a bicycle, with an error of about 40%. Besides, because only images taken from one direction were used and images were acquired through the windshield, point cloud data reconstructed by both 4K and 8K images taken inside the vehicle were curved. Unfortunately, the experiment did not involve actual road surfaces with rutting, but rather asphalt paving slabs with recessed areas. Therefore, the results of the road cross section obtained through SfM were not compared to the true value.

The process of rut depth estimation by SfM can be summarized in Figure 2. Points are matched between every two images, requiring $n(n-1)/2$ matching operations for n input photos. This process can be time-consuming, as it must be completed before the 3D model can be reconstructed.

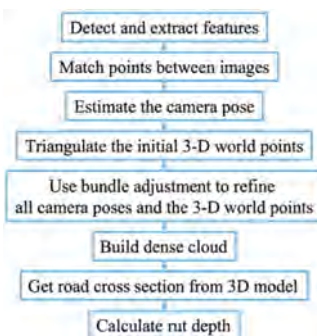


Figure 2. Rut depth estimation by SfM.

2.2 Top-view transformation

(Geda et al., 2022) proposed a vision-based top-view transformation algorithm for road crack ratio evaluation. This method involves capturing video with an in-vehicle smartphone camera, with parameters calibrated using parallel lane lines and circular manholes. The top-view image can be obtained by transforming the camera-view image with the following equations:

$$x' = \frac{f'}{H_{VC}} \cdot \frac{H_C x}{f \sin \theta - y \cos \theta} \quad (1)$$

$$y' = \frac{f'}{H_{VC}} \cdot \left\{ \frac{H_C (f \cos \theta + y \sin \theta)}{\sin \theta - y \cos \theta} - D_{VC} \right\} \quad (2)$$

where x and y are the pixels coordinated from the camera view. x' and y' are the corresponding top-view coordinates after transformation. f and f' are the focal lengths (in pixels) of the in-vehicle camera and virtual camera, respectively.

By assuming the presence of a virtual camera above the road surface, top-view transformation allows for easier analysis of road features.

3 METHODS

To address the challenges of reconstructing road cross sections using images taken from inside a vehicle and the high computation cost of SfM, we propose a method for measuring rut depth that involves two steps using top-view transformation and the basic perspective principle: 1) Obtain the shape of rutting by extracting rut information from the video. The unit of rut depth at this stage is in pixels. 2) Convert the pixel information in step 1 into millimeters to measure rut depth by determining the scale.

3.1 Basic idea

Figure 3(a) and (b) show two images taken by an in-vehicle camera as the vehicle passes a road surface with severe rutting and a shadow cast by a pillar. Figure 3(c) and (d) show the results of applying the top-view transformation to these images. The shadow, which should be straight, is distorted due to the rutting. By applying image binarization, the shape of the shadow can be extracted from the two images, as shown in Figure 3(e). The level of distortion of the shadow in the two images is different because the virtual camera of the top-view transformation is located at different positions relative to the shadow as the vehicle approaches it. This difference in distortion can be used to extract rutting information.

This concept can be extended to a road surface without shadows, i.e., a general road surface. As shown in Figure 4, the road surface can be thought of as a combination of a flat surface and a rutted surface. Since the distance between the flat surface and the virtual camera is smaller than the distance between the rutted surface and the virtual camera, there should be a difference in the y direction for the same area when the viewing angle changes. This means that rutting information can be extracted by matching the same part in images taken from different angles.

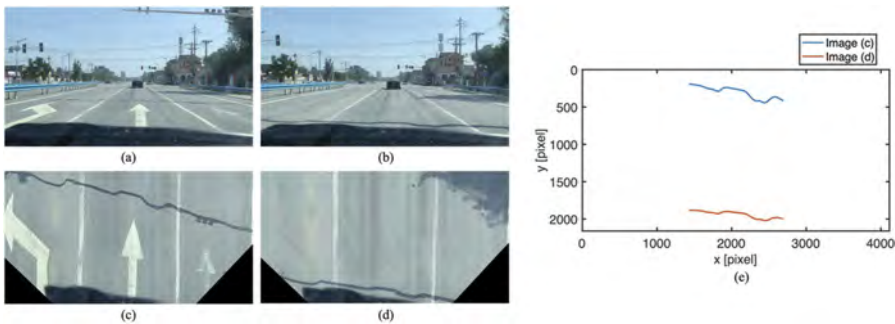


Figure 3. Road surfaces and top-view transformed images.

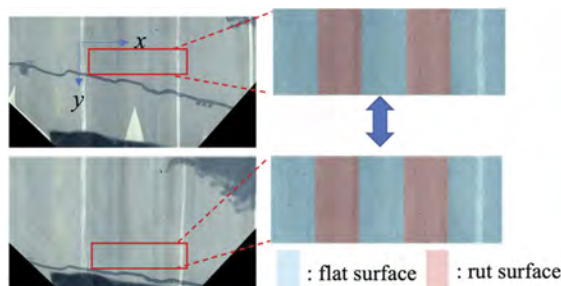


Figure 4. Flat surface and rut surface.

3.2 Matching

However, traditional matching methods may not be suitable in this case. According to Sun et al. (2021), most existing matching methods follow a sequential process of feature detection, feature description, and feature matching. The first step, feature detection, involves identifying salient points, such as corners and edges, as interest points in each image. This may be unsuccessful in extracting enough repeatable interest points between images due to various factors such as poor texture and motion blur. Road surfaces, which are often made of asphalt and concrete, tend to have poor textures. In addition, the two images used for matching are obtained from top-view transformed images, with the upper image (the farther part in the original images) being more blurred than the lower image. This further complicates the matching condition. E.g., as shown in Figure 5, Using the SIFT (Lowe, 2004) matching algorithm, there are no matches found for the right images in this case.

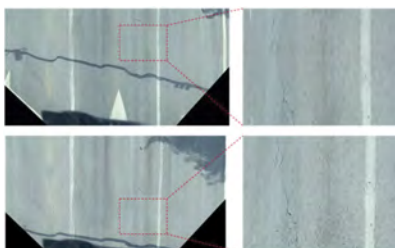


Figure 5. Bad matching condition for detector-based methods.

To address the limitations of traditional matching methods, detector-free local feature matching methods have been explored in the field of computer vision. One such method is LoFTR (Sun et al., 2021), which establishes pixel-wise dense matches at a coarse level and then refines the good matches at a fine level using convolutional neural networks (CNNs). This allows LoFTR to find correspondences on texture-less surfaces, Figure 6 shows the result of applying LoFTR to the road surface in Figure 5.

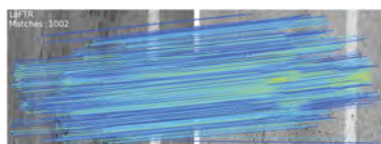


Figure 6. Matching result by LoFTR.

3.3 Rut shape calculation

The shape of the rut is calculated from the matching result, so the number of matches affects the accuracy. To increase the number of matches, we use six 640x480 pixel images with 320x480 pixel overlap for each road cross section being measured, as shown in Figure 7(a). The images are this size because LoFTR was trained with this size. Figure 7(b) shows the integrated matching result for images taken at a 2-meter interval.

To extract the shape of the rut from the matching result, the following data processing steps are followed: 1) Calculate the difference between the y-coordinates of every pair of matches. 2) Average the differences corresponding to the same x-coordinate, assuming that the rut depth for every road cross-section within the 480-pixel length range is the same. This process can be expressed in Equation (3), where x and y are the coordinates of the data point to be used to generate the rut shape, (x_i, y_i) and (x'_i, y'_i) are the coordinates of matches of the 1st and 2nd image respectively, and n_x is the number of x . 3) Interpolate the data to make the road cross

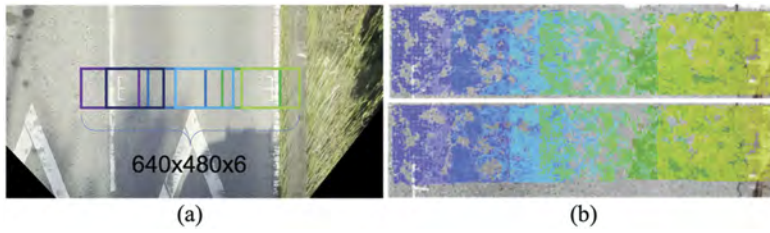


Figure 7. Images with overlap and integrated matching result.

section successive. 4) Calculate the moving average of the data to smooth the road cross-section. 5) Calculate the distance from each data point to the line connecting the leftmost and rightmost data points, to correct for the incline introduced by the top-view transformation, as shown in Equation (4), where p_i is the coordinate of data point i , p_l and p_r are the coordinates of the leftmost and rightmost data point, respectively.

$$y = \frac{1}{n} \sum_{x_i=x} (y'_i - y_i) \quad (3)$$

$$d_i = \frac{\left| \frac{p_r - p_l}{p_i - p_l} \right|}{\|p_r - p_l\|} \quad (4)$$

3.4 Calibration

To convert the rut shape information (expressed in pixels) into rut depth (expressed in millimeters), calibration is required. This can be done using a plate ($910 \times 450 \times 18$ millimeters in this experiment). As shown in Figure 8, the thickness of the plate occupies a different number of pixels in two images taken at a 2-meter interval. This information is used to convert the pixel-by-pixel information into millimeters.

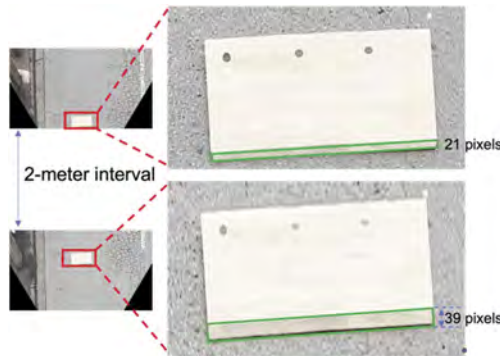


Figure 8. Calibration by the thickness of a plate.

4 EXPERIMENTS

4.1 In-vehicle smartphone setup

The smartphone used in this study is an iPhone 13 Pro, mounted on the vehicle's windshield with the camera facing the road, as shown in Figure 9. The measurement video was recorded at 4K (3840×2160) resolution and 30 frames per second. At the same time, the global navigation satellite system (GNSS) was also recording the vehicle's position once per second. The

vehicle used was a Honda N-BOX, chosen because its short nose allows for a wider view of the closer part of the road from the camera.



Figure 9. In-vehicle smartphone setup.

4.2 Measurement

A 100-meter road in Koshigaya city, Saitama Prefecture, Japan, was measured both manually as the true value and by a smartphone for estimation. The interval between each road cross section was 10 meters, as shown in Figure 10.

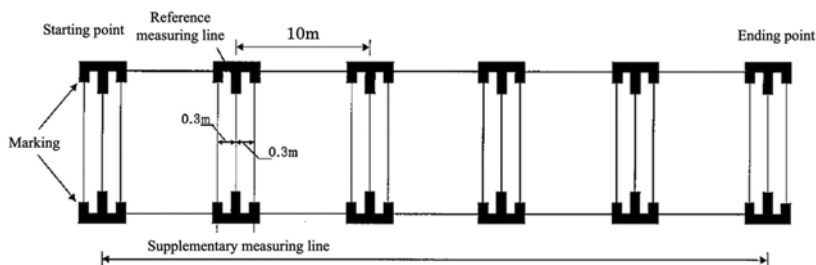


Figure 10. Overview of the measurement target (Nichireki, 2022).

4.3 Results

Figure 11 shows the results of the true value (blue), proposed method (red), and SfM (yellow). Based on the definition shown in Figure 12 (OWP: Outer Wheel Path, IWP: Inner Wheel Path), D_1 and D_2 are calculated as shown in Figure 13. The road cross section calculated by SfM differs significantly from the true value, while the proposed method provides a good fit. The errors in D_1 and D_2 , show that most results of the proposed method are within the criterion of 3mm, while most results of SfM are outside this range.

5 CONCLUSION

This paper presents a novel image-processing-based method for estimating rut depth. The proposed method involves performing top-view transformation and using a detector-free matching method to analyze image distortion caused by rutting. Our experiments demonstrate that the proposed method outperforms SfM in estimating rut depth. We believe that the proposed method offers a promising approach for evaluating rut depth and could potentially be extended to other challenging scenarios, such as evaluating potholes.

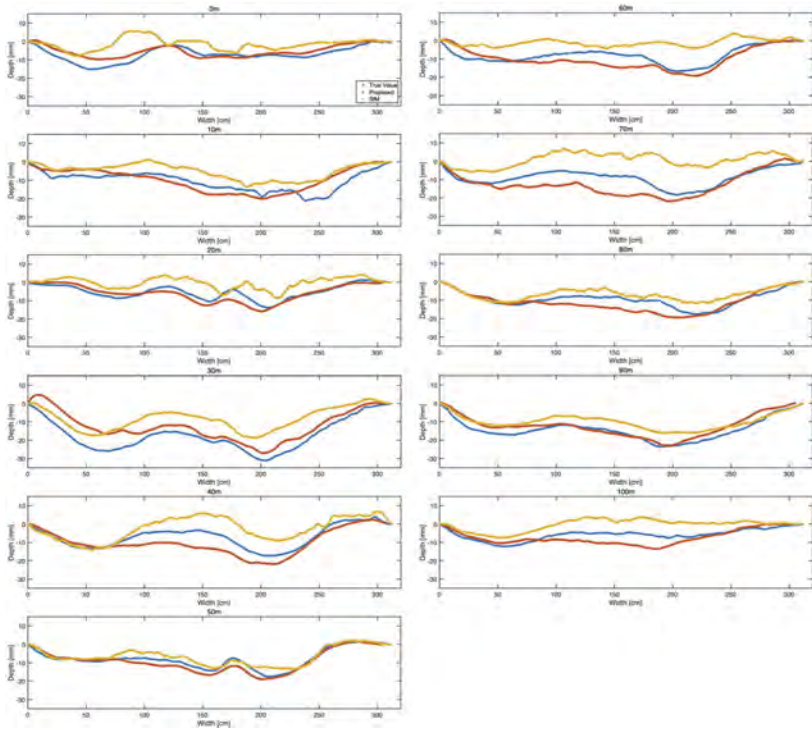


Figure 11. Comparison between true value (blue), proposed method (red) and SfM (yellow).

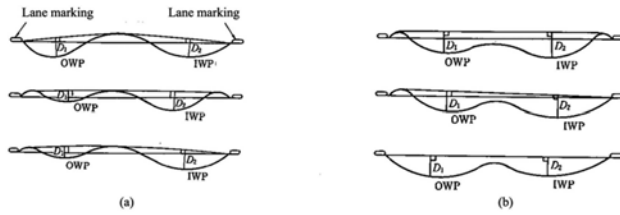


Figure 12. Definition of rut depth (JARA, 2019).

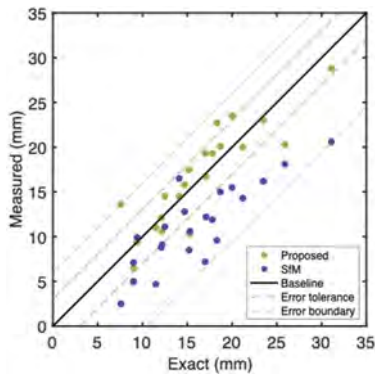


Figure 13. Comparison of D1 and D2.

REFERENCES

- Geda, J.M.G., Xue, K. & Nagayama, T. 2023, “Automatic Top-View Transformation and Image Stitching of In-Vehicle Smartphone Camera for Road Crack Evaluation” in *Experimental Vibration Analysis for Civil Engineering Structures* Springer, pp. 567–579.
- Imai, R. & Nakamura, K. & Tsukada, Y. 2021, “Research on Pavement Inspection Method Using Artificial Intelligence”.
- Japan road association. 2019. Handbook of Pavement Survey and Testing Methods. *Japan road association*.
- Lowe, D.G. 2004, “Distinctive image features from scale-invariant keypoints”, *International journal of computer vision*, vol. 60, no. 2, pp. 91–110.
- MLIT.GO.JP. Available at: <https://www.mlit.go.jp/common/001267619.pdf> (Accessed: December 30, 2022).
- Road Surface Investigation. NICHIREKI CO., LTD. Available at: https://www.nichireki.co.jp/product/consult/consult_list05/consult05_01.html (Accessed: December 30, 2022).
- Structure from motion (2022) Wikipedia. Wikimedia Foundation. Available at: https://en.wikipedia.org/wiki/Structure_from_motion (Accessed: December 30, 2022).
- Sun, J., Shen, Z., Wang, Y., Bao, H. & Zhou, X. 2021, “LoFTR: Detector-free local feature matching with transformers”, *Proceedings of the IEEE/CVF conference on computer vision and pattern recognition*, pp. 8922.
- Tomasi, C. & Kanade, T. 1993, “Shape and motion from image streams: a factorization method.”, *Proceedings of the National Academy of Sciences*, vol. 90, no. 21, pp. 9795–9802.
- Zhao, B. & Nagayama, T. 2017, “IRI estimation by the frequency domain analysis of vehicle dynamic responses”, *Procedia Engineering*, vol. 188, pp. 9–16.

M-integral applied to fatigue life prediction in notched elastic-plastic material

Z.J. Zhang & Q. Li

State Key Laboratory for Strength and Vibration of Mechanical Structures, School of Aerospace, Xi'an Jiaotong University, Xi'an, China

ABSTRACT: In this paper, an innovative fatigue model is investigated based on the concept of *M*-integral in notched elastic-plastic material. The new form of fatigue damage evolution rate (dA_D/dN) and fatigue driving force (ΔM) are introduced. The fatigue experimental evaluations of No. 45 steel with a circular notch have been carried out. The change of the total potential energy (*CTPE*) is introduced to measure the value of *M*-integral. The results demonstrate that dA_D/dN shows an apparent power law relation with ΔM in notched elastic-plastic material. The slope *n* and intercept λ of $\lg(dA_D/dN)$ - $\lg(\Delta M)$ curve has linear correlation with the initial notch radius *R*, but not with applied stress σ . Moreover, the model can clearly describe the two-stage process from the initiation of microcracks to the growth of macrocracks in notched body. It is concluded that the proposed fatigue model can accurately predict the fatigue lifetime of the notched elastic-plastic material.

1 INTRODUCTION

A lot of fatigue failure problems in engineering structures are due to the existence of notches (Wen et al., 2018). During past years, numerous efforts have been made to predict the fatigue limit of a given material or structure in presence of notch. Among those, the methodologies can be classified under two main headings: (i) critical distance or stress based approach and (ii) fracture mechanics based approach. In general, both critical distance and stress based approach can be included in the classical fatigue techniques, which correlate stress or strain at the notch area with the number of cycles to failure, for example, the S-N curve introduced by Wöhler (1871). As for the method based on fracture mechanics, the Paris's law (Paris and Erdogan, 1963; Lesiuk et al., 2018) is the mostly adopted one. However, there is a large scale yielding plastic zone occurred along the notch, thus the total fatigue lifetime consists of crack initiation life accompanying with the formation of plastic zone and crack propagation life. On one hand, it is difficult to evaluate the fatigue lifetime in ductile metals accurately since the lifetime of crack initiation and propagation are mixed together by the critical distance or stress based approach. On the other hand, the Paris's law is hardly used to character the notch at the initial stage of fatigue cycle in the absence of macrocracks (Rice, 1968; Sangid, 2013). Therefore, there is a lack of reliable fatigue model which can predict the lifetime of elastic-plastic material with considering both notch and material elastic-plastic behavior, and is suitable for total stage from crack initiation to propagation. For this reason, it is important to study the damage calibration criterion and establish an appropriate fatigue model to predict the lifetime of notched elastic-plastic material.

In recent years, the theory of configurational forces attracted the attention of many scholars for the investigations of material fracture and failure. Basically, the concept of configurational forces is defined as the driving forces associated with the dissipative mechanisms related to the configuration (e.g., size, shape and location) changes of material points (Maugin, 2011). Eshelby (1951) proposed the concept of energy-momentum tensor in continuum mechanics of solids. After decades of development, several invariant integrals have been proposed to describe the failure behavior of materials. Among them, it is known that the *M*-integral has the apparent physical interpretations which can be explained as the energy release rates due to the self-similar expansion of defects (Chen, 2001a, b; Ma et al., 2001). The *M*-integral is carried out along an arbitrarily chosen closed path enclosing all defects due to its path independence property

(Knowles and Sternberg, 1972), which implies it can be used to describe the failure behavior of materials with complex defects. As a result, it is expected that the concept of M -integral has the potential applicability to predict the failure of notched elastic-plastic materials.

Typically, Hu and Chen (2009) studied the relationship between effective elastic modulus and the M -integral when the coalescence of cracks and other defects occurs. Li et al. (2013) proved that the M -integral is inherently related to the change of total potential energy ($CTPE$) due to the formation of the defects with the addition of the nonlinear elastic strain energy within the area enclosed by the integral contours. A unified failure criterion based on M -integral was proposed (Yu and Li, 2013), in which the Π -parameter was derived to characterize the damage level of materials by the appropriate formulation via the M -integral, the remote load, and the inner variable of the damaged area. Lv et al. (2019) put forward a method of equivalent damage area calibration by M -integral, which can quantify the damage level caused by different types of defects.

In this paper, the M -integral method is introduced to study the fatigue lifetime of notched elastic-plastic material since it has a unique advantage in dealing the complicated failure problems in material space. The new definitions of fatigue damage evolution rate dA_D/dN and fatigue driving force ΔM are presented on the basis of M -integral, where A_D denotes the equivalent damage area of notch, plastic zone and cracks, N is the number of cycles, and ΔM corresponds to the M -integral range per load cycle. Then a unified notch fatigue model is proposed to predict the lifetime of elastic-plastic material. The equivalent damage area characterized by the M -integral in elastic-plastic material is calculated numerically. An experimental method for measuring the M -integral and the notch fatigue damage evolution rate of elastic-plastic materials is proposed. Finally, the apparent power law relation is found between the ΔM and dA_D/dN . The slope n and intercept λ of $\lg(dA_D/dN)-\lg(\Delta M)$ curve has linear correlation with the initial notch radius R , but not with applied stress σ . It is demonstrated that the proposed fatigue model based on M -integral is able to predict the lifetime of the notched elastic-plastic material under cyclic loading.

2 DAMAGE CALIBRATION BASED ON THE M -INTEGRAL

The original formulation of the M -integral is given as follows (Knowles and Sternberg, 1972):

$$M = \oint_C (wx_i n_i - T_k u_{k,i} x_i) ds \quad (i, k = 1, 2) \quad (1)$$

where w denotes the total strain energy density, T_k denotes the traction acting on the outside of a enclosed contour C surrounding whole defects, σ_{ij} and u_k are the components of stress tensor and displacement vector, respectively, and s is the arc length of the contour C .

Generally, the fatigue failure process of notched elastic-plastic material under cyclic loading can be divided into two stages: (i) the stage of the formation and growth of plastic zone accompanying the initiation of microcracks (Stage I) and (ii) the stage of macrocracks propagation and finally sudden fracture (Stage II) (Zerbst et al., 2018), as shown in Figure 1.

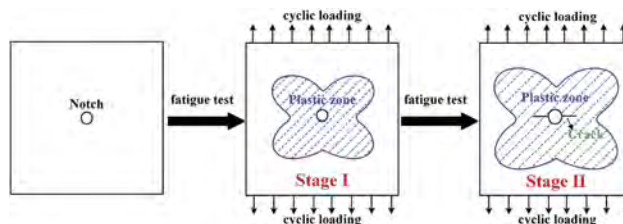


Figure 1. Fatigue process of notched elastic-plastic material.

However, it is difficult to use a unified method to evaluate the overall complex damage level of notched materials. The previous researches demonstrated that M -integral can characterize the influences of loading conditions, material properties and defect morphology on damage

level when the integration path was enclosed curve and all defects were surrounded in calculation of M -integral (Knowles and Sternberg, 1972). In this case, a unified standard defined by the equivalent damage area A_D is proposed with the aid of M -integral. The damage area can be contributed from the inherent defects inside body and plastic zone induced by the remote loading. Herein, it is assumed that the damage area induced by underlying multiple defects in elastic-plastic material is equivalent to the area of an individual circular notch in elastic material when the values of M -integral are equal for both cases. The equivalent damage area A_D in notched elastic-plastic material is depicted in Figure 2. The same M -integral value represents the same damage level, so the damage level caused by complex defects can be quantified by the equivalent elastic circular notch area with the equivalent M -integral under the same load.

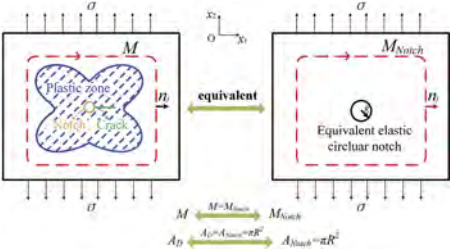


Figure 2. Schematic diagram of the equivalent damage area A_D in notched elastic-plastic material.

In order to facilitate a better understanding of the proposed damage calibration method, numerical implementation (FEM) is performed to calculate A_D in notched elastic-plastic material. The calculation of M -integral only requires the evaluation of contour integrals along a path enclosing all defects. It has been demonstrated that the M -integral is path-independent enclosing the notches in elastic material (Radi, 2011). In present study, the plate with dimensions of 30mm×30mm is simulated, the radius R of the central notch is 2.0mm. The selected material is No. 45 steel, whose elastic modulus and Poisson’s ratio are 195.6GPa and 0.3, respectively. The yield strength is 344.4MPa and a multi-linear elastci-plastic stress-strain curve is input by APDL program in the form of data points for numerical computation. The integration paths are circles surrounding the central notch with radius of 14.0mm.

The evolution of plastic zone (gray segment) in elastic-plastic material with a central notch ($R=0.5$ mm) for increased remote load is presented in Figure 3. As shown in Figure 4, the

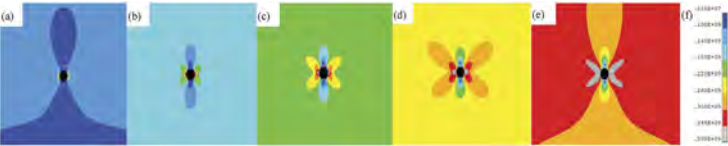


Figure 3. Plastic zone distribution characterized by von-Mises stress in elastic-plastic material for increased remote load when $R=0.5$ mm (gray segment): (a) $\sigma=100$ MPa; (b) $\sigma=150$ MPa; (c) $\sigma=200$ MPa; (d) $\sigma=250$ MPa; (e) $\sigma=300$ MPa; (f) the contour of von-Mises stress (unit: MPa).

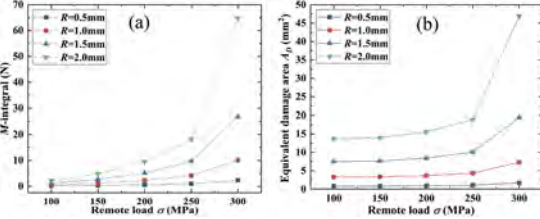


Figure 4. Numerical results of the M -integral and A_D for elastic-plastic specimens with different magnitude of initial notch: (a) the M -integral versus remote load σ ; (b) the A_D versus remote load σ .

M -integral and A_D of the elastic-plastic material both increase with the increase of remote load. This phenomenon is introduced by the enlarged plastic deformation due to the increased load in elastic-plastic materials as presented in Figure 3. In comparison with the pure linear elastic problems, the equivalent damage area A_D shows a typical loading dependence for non-linear elastic-plastic material. The new parameter A_D can effectively characterize the damage level of elastic-plastic notched material. Furthermore, a new fatigue model is proposed in the following sections based on the advantages of M -integral and A_D .

3 FATIGUE MODEL BASED ON M -INTEGRAL AND ITS EXPERIMENTAL IMPLEMENTATION

3.1 Fatigue model via the M -integral

It has been demonstrated that the M -integral is inherently related to $CTPE$ regardless of the detailed damage characterizations (Chen, 2001a, b; Ma et al., 2001), which provides the driving force of defects evolution. Based on this, we define ΔM (the M -integral range per load cycle, that is, the difference between the M -integral corresponding to the maximum load and the minimum load for per load cycle) as the fatigue driving force. According to the A_D , the fatigue damage evolution rate is defined as dA_D/dN (the growth of equivalent damage area per load cycle). Therefore, the notch fatigue model of elastic-plastic material with a central notch is given as

$$dA_D/dN = \lambda(\Delta M)^n \quad (2)$$

where λ and n are material parameters determined by experiments.

3.2 Relationship between M -integral and the Change of the Total Potential Energy ($CTPE$)

In order to measure the value of M -integral effectively and conveniently, an experimental method is described as below.

Recently, Ma et al. (2001) studied the relationship between the M -integral and $CTPE$, which can be expressed as:

$$M = 2CTPE \quad (3)$$

For the specimen with circular notch subjected to remote load, $CTPE$ is as follows:

$$CTPE = \frac{1}{2} \int_{-\pi}^{\pi} [\sigma_{\theta}(\theta)u_{\theta}(\theta) + \sigma_r(\theta)u_r(\theta)]d\theta \quad (4)$$

where $\sigma_{\theta}(\theta)$ is the circumferential stress on the elastic integration path, $u_{\theta}(\theta)$ is the circumferential displacement of the elastic integration path under internal load $\sigma_{\theta}(\theta)$, $\sigma_r(\theta)$ is the radial stress on the elastic integration path, and $u_r(\theta)$ is the radial displacement of the elastic integration path under internal load $\sigma_r(\theta)$. Actually, the stress equivalent relationship of the specimen with circular notch can be decomposed according to the principle of superposition, as shown in Figure 5.

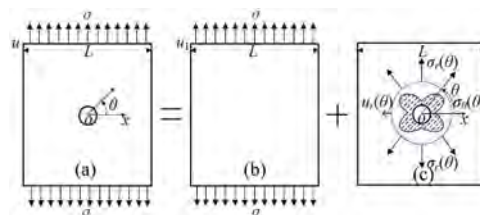


Figure 5. The stress equivalent relationship of the specimen with circular notch according to the principle of superposition. (a) the notched specimen under remote load; (b) the non-defective specimen under remote load; (c) the notched specimen under internal load (blue area: plastic zone; red line: integration path).

It can be proved that the plate with circular notch can be equivalent to the combination of the flawless continuum under the same remote load and the plate with circular notch under the internal load of the same magnitude acting on the elastic integration path (Wang, 2004). Therefore, the total work of the remote load per unit thickness in the notched specimen can be written as

$$\frac{1}{2}\sigma Lu = \frac{1}{2}\sigma Lu_1 + \frac{1}{2}\int_{-\pi}^{\pi} [\sigma_{\theta}(\theta)u_{\theta}(\theta) + \sigma_r(\theta)u_r(\theta)]d\theta \quad (5)$$

where L is the width of the specimen, u is the remote displacement of the notched specimen under remote load, as shown in Figure 5(a), u_1 is the remote displacement of the non-defective specimen under the same remote load, as shown in Figure 5(b). Comparing Eq. (4) and Eq. (5), it can be found that the second term on the right side of Eq. (5) is the $CTPE$. So the $CTPE$ is equal to the difference of external force work between the notched specimen and the non-defective specimen with the same size. Therefore, the M -integral can be obtained as

$$M = 2CTPE = \sigma L(u - u_1) \quad (6)$$

The detailed process to measure $CTPE$ is depicted in Figure 6. Firstly, the load-displacement curve L_0 is obtained by applying monotonic increasing uniaxial load p to the non-defective specimen as shown in Figure 5(b). Secondly, fatigue tests are carried out for the notched specimen as shown in Figure 5(a). The maximum fatigue load is p_{max} , and the minimum fatigue load is p_{min} . Finally, the load-displacement curve L_N after N fatigue cycles of the notched specimen is recorded by a uniaxial tensile test. According to the physical significance of $CTPE$, the area enclosed by the curves L_0 , L_N , $p=p_{max}$ (shaded by blue lines in Figure 6) is $CTPE$. The area enclosed by the curves L_0 , L_N , $p=p_{max}$, $p=p_{min}$ (yellow shadow in Figure 6) is named as $\Delta CTPE$. Therefore, the ΔM of notched specimens after N fatigue cycles can be calculated as:

$$\Delta M = 2\Delta CTPE \quad (7)$$

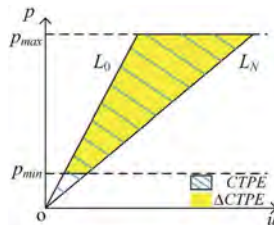


Figure 6. The detailed process to measure the M -integral and ΔM : the graph of $CTPE$ and $\Delta CTPE$.

3.3 Experimental procedure: Material, specimens and equipment

In this section, a series of fatigue tests have been carried out to validate the effectiveness of the proposed notch fatigue model based on the concept of M -integral. The experiments are implemented with No. 45 steel. The mechanical properties of No.45 steel are measured by uniaxial tensile tests, which shows a typical elastic-plastic behavior. In details, the elastic modulus is 195.6GPa while the yield strength is 344.4MPa. Specimens are particularly designed for the fatigue tests. In the center of the specimen, the circular notches with various radius (0.5mm, 1.0mm, 1.5mm, 2.0mm, and 2.5mm) are prefabricated as the initial notch.

MTS-880/25T electro-hydraulic servo universal testing machine is employed in this experiment to provide the cyclic loading. Experiments are performed in the force control mode with the various maximum load (p_{max}) of 22kN, 24kN, 26kN, 28kN, 30kN and 32kN, the loading ratio of 0.1, and a sinusoidal waveform at a frequency of 20Hz. All experiments are carried out at room temperature.

4 RESULTS AND DISCUSSIONS

The relationship between fatigue damage evolution rate and fatigue driving force is discussed for the notch fatigue test of No. 45 steel. This paper conducts experiments for different applied stresses and several hole radii. Each test is repeated twice, and finally a total of 60 groups of fatigue tests have been carried out.

In experiments, through observation of specimens by high-definition camera, it is found that the fatigue process can be divided into two stages: (i) the stage of the formation and growth of plastic zone accompanying the initiation of microcracks (Stage I) and (ii) the stage of macrocracks propagation and finally sudden fracture (Stage II), as shown in Figure 7. From Figure 8, when the crack length reaches 1.0 mm, it indicates that the macrocrack initiates, which is defined as the turning point of Stage I and Stage II. The corresponding number of cycles (N_C) when macrocrack initiates in each specimen is recorded. The first stage accounts for about 90% of the total fatigue life, and the second stage accounts for about 10% of the total fatigue life. In the following paragraphs, the fatigue process of the central notched elastic-plastic material will be described uniformly by the aid of the M -integral and A_D .

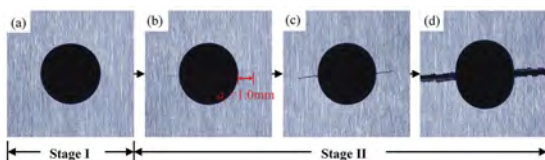


Figure 7. Fatigue process of the central notched elastic-plastic material. (a) the formation and growth of plastic zone; (b) the initiation of macrocrack; (c) the growth of macrocrack; (d) the sudden fracture.

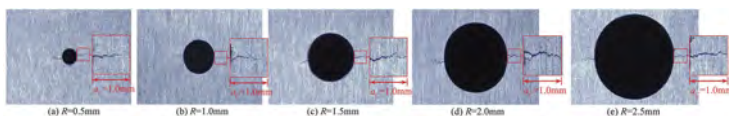


Figure 8. Photos at the macrocrack initiation time.

As discussed in Section 2, the A_D can be calculated after obtaining M -integral experimentally, then the relationship between A_D and N can be given, further we can get the relationship between dA_D/dN and ΔM . The turning point of A_D is written as A_{DC} , when macrocrack initiates from the physical phenomenon. According to the N_C of each specimen, the corresponding A_{DC} is calculated.

The logarithmic operations of dA_D/dN versus ΔM are made and the results are presented in Figure 9. According to the N_C mentioned above, this paper divides the relation between dA_D/dN and ΔM into two stages. The first stage $n < N_C$, that is, when there is no macrocrack (crack length < 1.0 mm); The second stage $n \geq N_C$, that is, after the appearance of macrocrack. We define dA_D/dN corresponding to N_C as $(dA_D/dN)_C$, which is the turning point of damage evolution rate between the first and second stages. It can be seen from that the damage evolution rate dA_D/dN shows a logarithmic linear relationship with ΔM , which has the following three characteristics:

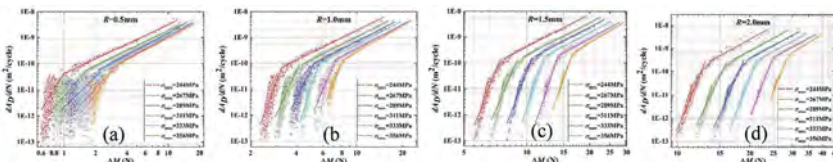


Figure 9. dA_D/dN correlated with ΔM : (a) $R=0.5\text{mm}$; (b) $R=1.0\text{mm}$; (c) $R=1.5\text{mm}$; (d) $R=2.0\text{mm}$.

1) The relationship between dA_D/dN and ΔM is a two-stage logarithmic linear relationship, denoting that there is a unified relation between the fatigue damage evolution rate dA_D/dN and fatigue driving force ΔM for notched elastic-plastic specimens.

2) The intercept λ of $\lg(dA_D/dN)-\lg(\Delta M)$ curve correlated with applied stress σ of elastic-plastic specimens with different magnitude of initial notch is shown in Figure 10(a)(b), and the intercept λ correlated with initial hole radius R is shown in Figure 10(c)(d). It can be found that λ does not change significantly with the increase of σ both in Stage I and Stage II, while λ is linearly related to the initial hole radius R . Therefore, it can be considered that λ is only related to R , but not to σ . The slope n also satisfies this law.

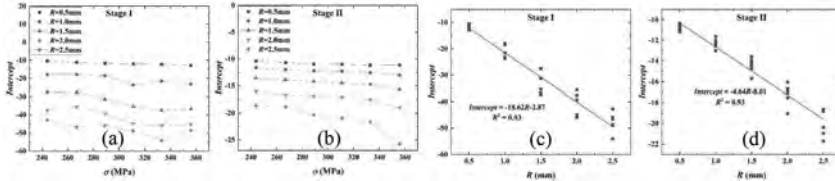


Figure 10. The slope n and intercept λ of $dA_D/dN-\Delta M$ curve correlated with σ and R : (a) $\lambda_1-\sigma$ curve in Stage I; (b) $\lambda_2-\sigma$ curve in Stage II; (c) λ_1-R curve in Stage I; (d) λ_2-R curve in Stage II.

3) The turning points of two fitting lines are not fixed value, but its distribution seems to meet a certain rule. The $(dA_D/dN)_C$ and ΔM corresponding to the initiation of macrocrack of all specimens are plotted in one diagram, as shown in Figure 11. It is found that there is a good logarithmic linear relationship between $(dA_D/dN)_C$ and ΔM . Therefore, we define the turning point from the physical phenomenon, and mathematically show that the turning point satisfies the simple mathematical law, i.e., the logarithmic linear relationship between the $(dA_D/dN)_C$ and ΔM .

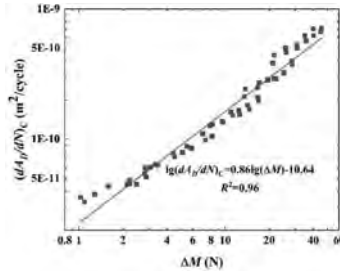


Figure 11. The turning point $(dA_D/dN)_C$ correlated with ΔM of all specimens.

By substituting the fitting formula of n and λ changing with R in Figure 10 into Eq. (2), we can get the fitting formula of $dA_D/dN-\Delta M$, shown as below:

$$\begin{cases} \lg(dA_D/dN) = -18.62R - 2.87 + (10.45R + 2.55) \lg(\Delta M) & (\text{Stage I, } dA_D/dN < (dA_D/dN)_C) \\ \lg(dA_D/dN) = -4.64R - 8.01 + (2.66R + 0.56) \lg(\Delta M) & (\text{Stage II, } dA_D/dN > (dA_D/dN)_C) \end{cases} \quad (8)$$

where $\lg(dA_D/dN)_C = 0.86\lg(\Delta M) - 10.64$.

5 CONCLUSIONS

In present work, an innovative fatigue model is proposed for the notched elastic-plastic material based on the concept of M -integral. The main conclusions are as follows:

1) Two new parameters, the equivalent damage area (A_D) and the M -integral range (ΔM) are introduced to characterize the damage level of notched elastic-plastic material. dA_D/dN is defined to characterize the fatigue damage evolution rate of elastic-plastic material. ΔM is termed as the driving force of fatigue damage evolution.

- 2) The fatigue tests of No. 45 steel with circular notch show that the notch fatigue damage evolution of elastic-plastic material can be divided into two stages from the initiation and aggregation of microcracks to the growth of macrocracks. And $(dA_D/dN)_C$ is the turning point, which has a logarithmic linear correlation with ΔM . At whole stage (Stage I and Stage II), the relationship between dA_D/dN and ΔM keeps logarithmic linear correlation. The slope n and intercept λ of $\lg(dA_D/dN)-\lg(\Delta M)$ curve has linear correlation with the initial notch radius R , but not with applied stress σ .
- 3) The proposed fatigue model of the notched elastic-plastic material is verified and can accurately describe the damage process including the formation of plastic zone, the microcrack initiation and the macrocrack growth. The significance of the research is to put forward a standard which can be applied to evaluate the damage level and predict fatigue lifetime of the notched elastic-plastic material or structure.

ACKNOWLEDGEMENTS

This work was supported by the National Natural Science Foundation of China (Nos.11772245, 12002256), the Fundamental Research Funds for the Central Universities, XJTU in China (xzy022022016), and the Qin Chuangyuan “Scientists + Engineers” Team Construction Project in Shaanxi Province (2022KXJ-085). The author Qun Li gratefully acknowledges the support of K.C.Wong Education Foundation.

REFERENCES

- Chen, Y.H., 2001a. M-integral analysis for two-dimensional solids with strongly interacting cracks, Part I: In an infinite brittle solids. *Int. J. Solids Struct.* 38, 3193–3212.
- Chen, Y.H., 2001b. M-integral analysis for two-dimensional solids with strongly interacting cracks, Part II: In the brittle phase of an infinite metal/ceramic biomaterial. *Int. J. Solids Struct.* 38, 3213–3232.
- Eshelby, J.D., 1951. The force on an elastic singularity. *Philos. Trans. R. Soc. Lond.* 244, 87–112.
- Hu, Y.F., Chen, Y.H., 2009. The M integral description for a brittle plane strip with two holes before and after coalescence. *Acta. Mech.* 76, 109–123.
- Knowles, J.K., Sternberg, E., 1972. On a class of conservation laws in linearized and finite elasticity. *Arch. Ration. Mech. An.* 44, 187–211.
- Lesiuk, G., Szata, M., Rozumek, D., Marciniak, Z., Correia, J., De Jesus, A., 2018. Energy response of S355 and 41Cr4 steel during fatigue crack growth process. *J. Strain. Anal. Eng.* 53, 663–675.
- Li, Q., Hu, Y.F., Chen, Y.H., 2013. On the physical interpretation of the M-integral in nonlinear elastic defect mechanics. *Int. J. Damage Mech.* 22, 602–613.
- Lv, J., Zhu, W., Li, Q., 2019. Damage evaluation for the dispersed microdefects with the aid of M-integral. *Int. J. Damage Mech.* 28, 647–663.
- Ma, L.F., Chen, Y.H., Liu, C.S., 2001. On the relation between the M-integral and the change of the total potential energy in damaged brittle solids. *Acta. Mech.* 150, 79–85.
- Maugin, G.A., 2011. *Configurational forces: thermomechanics, physics, mathematics, and numerics.* CRC Press, Paris.
- Paris, P., Erdogan, F., 1963. A critical analysis of crack propagation laws. *J. Basic. Eng.* 85, 528–533.
- Radi, E., 2011. Path-independent integrals around two circular holes in an infinite plate under biaxial loading conditions. *Int. J. Eng. Sci.* 49, 893–914.
- Rice, J.R., 1968. A path-independent integral and the approximate analysis of strain concentration by notches and cracks. *J. Appl. Mech.* 35, 379–386.
- Sangid, M.D., 2013. The physics of fatigue crack initiation. *Int. J. Fatigue.* 57, 58–72.
- Wang, X., 2004. Elastic T-stress solutions for penny-shaped cracks under tension and bending. *Eng. Fract. Mech.* 71, 2283–2298.
- Wen, Z., Pei, H., Yang, H., Wu, Y.W., Yue, Z.F., 2018. A combined CP theory and TCD for predicting fatigue lifetime in single-crystal superalloy plates with film cooling holes. *Int. J. Fatigue* 111, 243–255.
- Wöhler, A., 1871. Test to determine the forces acting on railway carriage axles and the capacity of resistance of the axles. *Engineering* 11, 199.
- Yu, N.Y., Li, Q., 2013. Failure theory via the concept of material configurational forces associated with the M-integral. *Int. J. Solids Struct.* 50, 4320–4332.
- Zerbst, U., Madia, M., Vormwald, M., Beier, H.T., 2018. Fatigue strength and fracture mechanics - A general perspective. *Eng. Fract. Mech.* 198, 2–23.

Dynamic performance of connection between frame-structure and jacked caisson

X.Z. Lan

Department of Geotechnical Engineering, Tongji University, Shanghai, China

W.F. Wu

Shanghai Tunnel Engineering & Rail Transit Design and Research Institute, Shanghai, China

C. Li

Department of Civil Engineering, Shanghai Jiaotong University, Shanghai, China

Y. Yuan

Department of Geotechnical Engineering, Tongji University, Shanghai, China

ABSTRACT: This paper presents a study on seismic response of a metro station, constructed with cut-cover and jacking method, in Shanghai. As the station structure constructed by the combined structures of jacked caisson and culvert frames on both sides, differences in stiffness would induce unknown seismic effects. Shaking table tests, at geometric scale of 1/20, were carried out to investigate the seismic performance of the station structure, with flexible connection or rigid connection. The test results showed that the flexible connection, pipe-jacking portion at the end of frame portion with the larger mass has larger peak accelerations. Using the rigid connection, the overall circumferential-joint extensions of caisson portion is larger than that of the flexible connection.

1 INTRODUCTION

The urban subway plays an important role in improving travel efficiency. Besides the Daikai Station, many subway stations suffered great damage by Osaka-Kobe Earthquake in 1995 which indicated that dynamic performance of underground structures should be paid particular concern.

Previous research has established that shaking table test is an effective method to study the dynamic characteristics of underground structures. Numerous authors have treated this subject, including Iwatate *et al.* (Iwatate *et al.*, 2000) and Yang *et al.* (Yang *et al.*, 2003).

So far, however, there has been little discussion about dynamic performance of subway station with the connection between frame-structure and jacked caisson. Composite construction

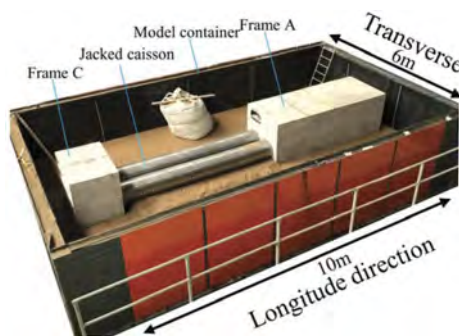


Figure 1. Overview of the model experimental setup.

method subway station with open-cut frame at both ends and underground pipe jacking in the middle has stiffness mutation problem. In this paper, shaking table tests were performed to investigate the influence of joint stiffness of pipe jacking structure and frame structure on the seismic performance of the station. The prototype station of the tests is Jing'an Temple station of Shanghai rail transit line 14.

2 SHAKING TABLE TEST

2.1 Test apparatus and scaling relations

The shaking table tests were studied with the help of the shaking table system at Tongji University. The size of the shaking table is 10m long and 6m wide in plane, which can produce three dimensional motion, namely, transverse, longitudinal and rotational. The maximum permissible acceleration of the shaking table was 1.5g with the maximum proof mass of 140t, where g is the gravitational acceleration. The frequency of the input motion ranged from 0.1 Hz to 50 Hz.

As depicted in Figure 1, the rigid model container used in shaking table tests was installed on the shaking table by high-strength bolts. Fifteen horizontal H-steel layered frames made up main structure of the container. The external dimensions of the container are 10m long, 6m wide and 2m tall with the internal operation space size of 9.5m in length, 5.5m in width, and 2m in height. To mitigate boundary effect, energy absorption material is stuck to the inside of lateral wall.

Taking account of the size and capacity of the shaking tables (combined), an $S_l = 1/20$ geometry scale factor was selected for the experiments. The other scaling relations were derived through combination of the Vaschy-Buckingham Π theorem, dimensional analysis (Funglsang & Ovesen, 1988) and dynamic equilibrium (Fung, 1977). Firstly, based on the hyperbolic model proposed by Konder (Konder, 1963), the nonlinear stress-strain response of soil could be expressed by Equation1:

$$\sigma_1 - \sigma_3 = \frac{\varepsilon}{a - b\varepsilon} \quad (1)$$

where σ_1 and σ_3 are major and third principle stress, respectively; ε is the strain; a and b are constants. Therefore the similarity ratio of strain can be derived as 1. Assuming the soil as a continuous medium, based on Hooke's law and stress-strain relation (Kramer, 1996), the dynamic equilibrium in the x-direction can be written in terms of displacements:

$$\rho \frac{\partial^2 u}{\partial t^2} = (\lambda + G) \frac{\partial \varepsilon}{\partial x} + G \nabla^2 u \quad (2)$$

where λ and G are the Lamé's constants; and ∇^2 is the Laplacian operator; ρ , u and t are density, displacement and time, respectively. Equation 2 indicated the relationships of similitude ratios of density, acceleration, displacement and shear modulus. It could be written as:

$$S_\rho S_a = \frac{S_G}{S_l} \quad (3)$$

where S_ρ , S_a , S_G and S_l are similitude ratios of density, acceleration, shear modulus and geometry, respectively.

In this study, the similitude ratios of density, shear modulus and geometry are basic scale factors, considering the limitation of model container and experimental materials. They are set to $S_l = 1/25$, $S_\rho = 1/2.5$, and $S_G = 1/63.3$, respectively. Table 1 presents the main similitude relations of the synthetic model soil, obtained by applying the Vaschy-Buckingham Π theorem.

2.2 Model soil and model structure

The prototype soil profile is multi-layered. Accurate simulation of prototype soil is quite complicated and does not fall within the scope of this work. Regarding the prototype soil as

Table 1. Scaling relations of model soil to prototype soil.

Physical quantities	Similitude relations	Scale factor
Displacement	S_l	1/25
Density	S_ρ	1/2.5
Shear modulus	S_G	1/63.3
Acceleration	$S_a = S_l^{-1} S_\rho^{-1} S_G$	1/1
Time	$S_t = S_l S_\rho^{1/2} S_G^{-1/2}$	1/5
Frequency	$S_f = S_l^{-1} S_\rho^{-1/2} S_G^{1/2}$	5/1

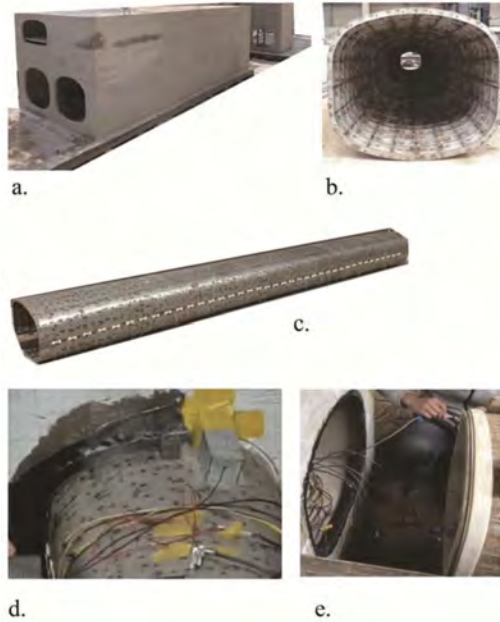


Figure 2. Station structure: (a) overview of frame-structure part; (b) interior view of the pipe jacking structure; (c) overview of the pipe jacking structure; (d) rigid connection in the tests; (e) flexible connection in the tests.

deposit as a single model soil layer, the prototype soil's average density, equivalent shear wave velocity and equivalent shear modulus are available. The model soil should satisfy the similitude relations of Equation 3. Considerable work was undertaken to test the properties of different kinds of synthetic model soil. Key properties of the model soil are summarized as follow: density $\rho = 860 \text{ kg/m}^3$ and maximum shear modulus $G_0 = 4.47 \text{ MPa}$.

The station structure of model consists of frame-structure part and jacked caisson part. Both of the two parts meet the requirement that the relative stiffness of prototype station structure and prototype soil should be the same as the relative stiffness of model structure and model soil:

$$A_s^m = A_s^p S_l^2 S_E / S_f \quad (4)$$

where A_s^m and A_s^p are area of reinforcement for model and prototype sections, respectively; S_l , S_E and S_f are similitude ratios of geometry, elastic modulus and tensile strength.

As depicted in Figure 1, the Frame A part is 3.5m long in longitude direction and the Frame C part is 1.0m long in longitude direction, which are both 1.432m in width and 1.153m in height. As for the pipe jacking structure of the model, it is the combination of steel pipe sections which meet the requirement of relative stiffness. Every steel pipe section is 0.1m long in longitude direction.

As depicted in Figure 2d and e, two kinds of connection methods are adopted in the tests. The rigid connection shaped like flange plate is made up of carbon textile and epoxy resin while foamed rubber is used to fill the gap between frame-structure part and jacked caisson part in flexible connection.

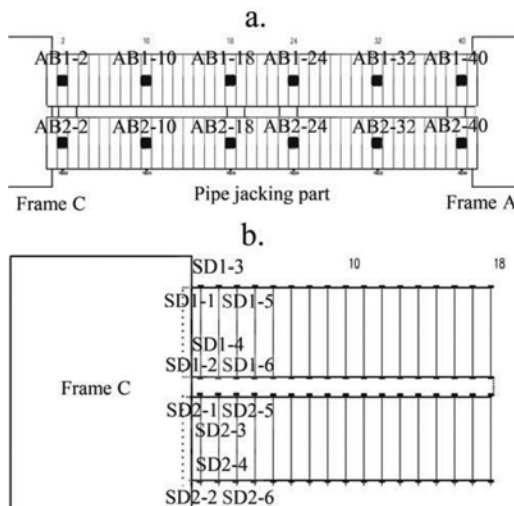


Figure 3. Shaking table model layout: (a) top view of the acceleration sensors in pipe jacking part and (b) top view of the circumferential-joint extensions sensors.

2.3 Instrumentation

Acceleration sensors and strain sensors are used to examine the dynamic response of soil and station structure throughout a series of tests. The sensors consist of three components: acceleration sensors in the soil, acceleration sensors in the station structure and sensors of circumferential-joint extensions.

A series of acceleration sensors are arranged in the soil at equal heights along the burial depth to measure the soil acceleration response. Every pipe in pipe jacking part is made up of 41 steel pipe sections. The pipe section nearest to the frame A is numbered 1 and is numbered in turn to the ring furthest from the Frame A, numbered 41. As depicted in Figure 3a, at the top of the six key sections of the pipe jacking part the pipe ring acceleration points are placed, numbered AB1-2, 10, 18, 24, 32, 40 and AB2-2, 10, 18, 24, 32, 40. The first digit represents the number of the pipe the sensor is on and the second digit represents the number of the pipe section the sensor is on.

Strain gauge based displacement sensor are arranged on both sides of the pipe joints to measure the circumferential-joint extensions, numbered SD1-1, ..., SD1-80 and SD2-1, ..., SD2-80. As depicted in Figure 3b, the first digit represents the number of the pipe in which the sensor is located, the second digit represents the position of the circumferential-joint in which the sensor is located, alternating the numbering on both sides of the tube ring starting from 1.

Table 2. Input motions applied to the models in model scale.

No.	Case ID	Earthquake motion	Amplitude (g)	Excitation direction
1	WN-0.05	White noise	0.05	Longitude (X)
2	SH-0.1X	Artificial wave	0.1	Longitude (X)
3	SH-0.1Y	Artificial wave	0.1	Transverse (Y)

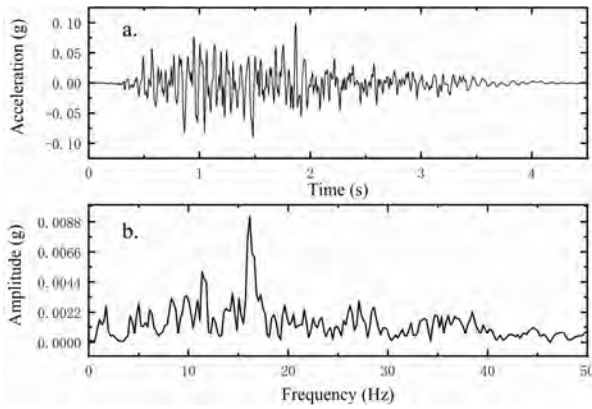


Figure 4. (a) Artificially synthetic earthquake wave and (b) its Fourier spectra (model scale with PGA = 0.1g).

2.4 Input motions

Seismic motions are imposed in both transverse and longitudinal directions. Two kinds of earthquake sequences are employed in shaking table tests as summarized in Table 2. One is the white noise motion, and the other one is the artificially synthetic earthquake waves (representative of the construction site). The artificially synthetic earthquake excitation is illustrated in Figure 4, along with its Fourier spectrum.

3 TEST RESULTS

3.1 Transfer function of the model soil

One-dimensional site response based on the wave method can be used to inversely extrapolate the bedrock response from the surface recorded seismic response, i.e. the transfer function (TF). According to the assumption of a linearly elastic homogeneous site, the transfer function is only related to the site stiffness and damping ratio. The transfer function can therefore be used to verify the validity of the shaker test design. As depicted in Figure 5, the test result and the 1D analytical solution are in good agreement over a wide frequency range. Test result is the transfer function of free field, recorded by acceleration sensor of model ground surface in Case WN-0.05. The 1D analytical solution (Kramer, 1996) is computed by:

$$F(\omega) = 1 / \sqrt{[\cos\left(\frac{\omega H}{v_s}\right)]^2 + \left(\zeta \frac{\omega H}{v_s}\right)^2} \quad (5)$$

where ω is the frequency; H is the depth of model ground; v_s is the shear wave velocity; ζ is the damping ratio which is usually considered as 0.05.

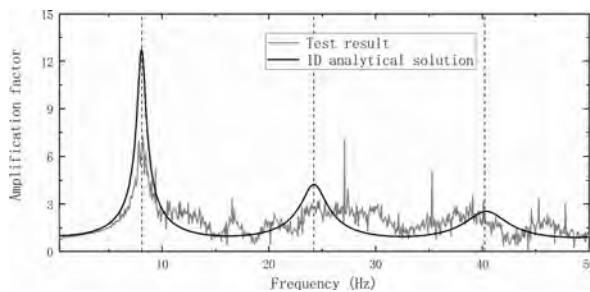


Figure 5. Transfer function of tests results and analytical solution of damped ($\zeta = 0.05$) elastic soil on rigid base.

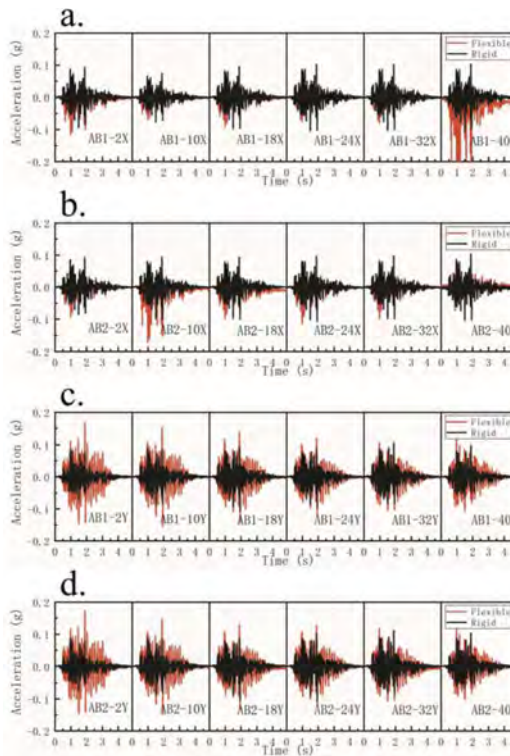


Figure 6. Time history of experimentally measured jacked caisson acceleration for different input motions: (a) acceleration sensors on pipe #1 for artificially synthetic earthquake wave in longitude direction; (b) acceleration sensors on pipe #2 for artificially synthetic earthquake wave in longitude direction; (c) acceleration sensors on pipe #1 for artificially synthetic earthquake wave in transverse direction; (d) acceleration sensors on pipe #2 for artificially synthetic earthquake wave in transverse direction. ‘Flexible’ is for flexible connection and ‘Rigid’ is for rigid connection as previously mentioned, respectively.

3.2 Acceleration of jacked caisson part

The two types of connection with different stiffnesses lead to different dynamic responses of the jacked caisson part. Figure 6 presents the time history of jacked caisson acceleration. With a flexible connection, the peak acceleration of the pipe due to motion input along the longitude direction is essentially at the same level, while the peak acceleration is inconsistent when motion input along the transverse direction. As depicted in Figure 7, the peak acceleration near Frame A is smaller than that near Frame C when motions are input along transverse direction. For artificially synthetic earthquake wave SH-0.1Y, the peak acceleration of sensor AB1-40 is 0.127g while the peak acceleration of sensor AB1-2 is 0.164g. The peak acceleration of sensor AB1-2 is 29% greater compared to that of sensor AB1-40. There is no significant trend in peak acceleration for the station model with rigid connections.

In combination with the above analysis, the motion input along the transverse direction when a flexible connection is used will cause the pipe to produce an uneven distribution of peak acceleration along longitude direction. It may be caused by the uneven quality of the frame at both ends. Inputting motions in transverse direction, the overall peak acceleration of the pipe is greater than that in longitude direction. It suggests that the stiffness of station structure in longitude direction is greater than that in transverse direction. Rigid connection could reduce the peak acceleration of pipe compared to flexible connection, with all other conditions being equal.

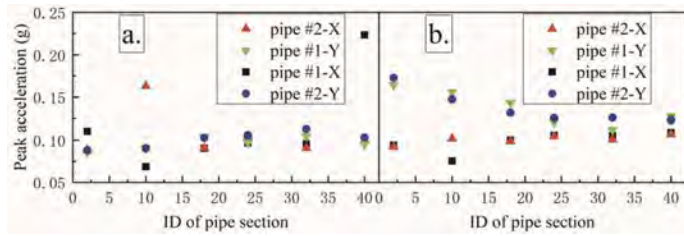


Figure 7. Peak acceleration of key sections in pipes: (a) rigid connection is adopted and (b) flexible connection is adopted.

3.3 Circumferential-joint extension

Figure 8 presents the maximum of circumferential-joint extension in the condition with case ID SH-0.1Y. When using a flexible connection, the overall circumferential-joint extension is generally small, with a maximum value of 0.008 mm. The maximum of peak circumferential-joint extension of all pipe sections increases to 0.172 mm while the overall circumferential-joint extension also increases with the adoption of rigid connection. In the rigid connection test, many mutation points of peak circumferential-joint extension occur in the middle part of pipe. Regardless of whether a flexible or rigid connection is adopted, the peak circumferential-joint extension near the Frame-A end is greater overall than the peak circumferential-joint extension near the Frame-C end.

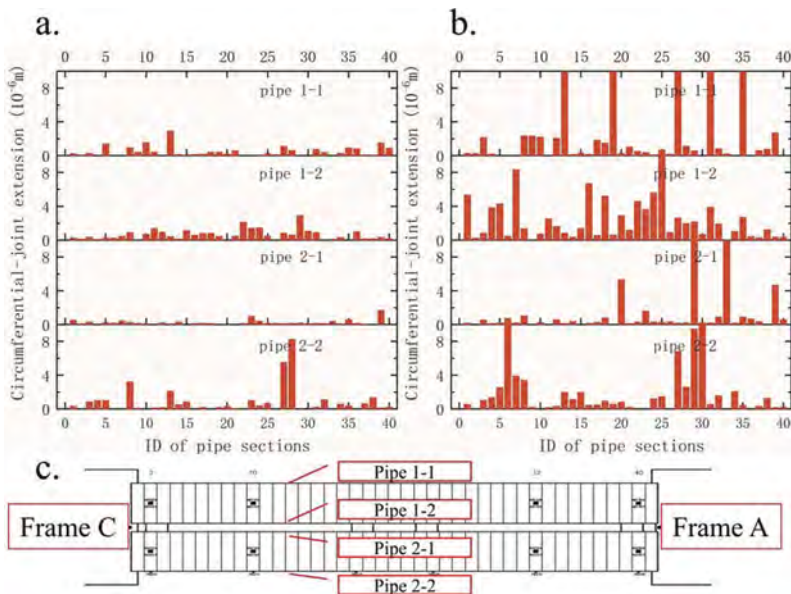


Figure 8. Maximum of circumferential-joint extension: (a) flexible connection is adopted and (b) rigid connection is adopted.

4 CONCLUSIONS

In this study, the behavior of a metro station with combined construction method in soft soil was investigated by performing shaking table tests on a scaled model. From the results of the shaking table tests, the following conclusions were obtained:

- (1) When a flexible connection is adopted, the peak acceleration of the pipes increases when the seismic wave is input in transverse direction compared to when it is input in longitude

direction. With the adoption of flexible connection, when ground vibrations are input in transverse direction, the peak acceleration of pipes is higher at the end with the higher mass due to the different masses of the frame structure at the two ends of the jacked caisson part. With the adoption of rigid connection, The peak acceleration of the pipes is evenly distributed along the longitudinal direction, and the different seismic wave input directions have little effect on the peak acceleration of the pipes.

- (2) With the adoption of flexible connection, the peak circumferential-joint extension is much smaller than that with the adoption of rigid connection. Due to the asymmetrical mass of the frame at both ends, the stiffness of the jacked caisson has a smaller degree of sudden change when using a flexible connection, reducing the maximum of peak circumferential-joint extension. Whether a flexible or rigid connection is used, there is a phenomenon that the maximum of peak circumferential-joint extension is greater on the side with the greater mass of the frame and less on the side with the smaller mass, which is more obvious when a flexible connection is used.

The behavior of a metro station with combined construction method in soft soil was very complicated because of stiffness mutation and different forms of soil-structure interaction. Hence, further improvements in analysis of acceleration and circumferential-joint extension should be attempted in future studies.

REFERENCES

- Iwatate, T., Kobayashi, Y., Kusu, H. & Rin, K. 2000 Investigation and shaking table tests of subway structures of the hyogoken nanbu earthquake. *Proceedings 12th World Conference on Earthquake Engineering*. Auckland, New Zeland.
- Yang, L., Ji, Q., Zheng, Y. & Yang, C. 2003. Shaking table test on metro station structures in soft soil. *Modern Tunnelling Technology* 01: 7–11.
- Fuglsang, L.D. and Ovesen, N.K. 1988. 'The application of the theory of modelling to centrifuge studies', in *Centrifuges in Soil Mechanics*. CRC Press.
- Fung, Y. C. 1993. *A First Course in Continuum Mechanics*. Prentice–Hall.
- Kondner, R.L. 1963. Hyperbolic stress-strain response: Cohesive soils, *J.soil Mech. & Found.div*, 89(1): 115–143.
- Kramer S L. 1996. *Geotechnical earthquake engineering*. Pearson Education India.

Robustness of RC girder bridges: The case of half-joint bridges

P. Martinelli, M. Colombo & M. di Prisco

Department of Civil and Environmental Engineering, Politecnico di Milano, Milan, Italy

ABSTRACT: Considerable research efforts have been made on the progressive collapse resistance of buildings. This effort is much more limited in the case of bridges, where robustness criteria are just as, or even more important than in buildings. Existing studies dealing with the robustness of bridges, although appreciable, often are limited to qualitative considerations that can provide designers with valuable pointers when designing new bridges. It is equally important to assess not only the safety but also the robustness of existing bridges through reliable metrics that can be used in the prioritization of interventions by the managing authority. According to this aim, this paper applies a selected measure of robustness to a particular type of reinforced concrete (RC) girder bridge, namely half-joint bridges. The Annone viaduct, which collapsed in 2016 after the passage of a heavy truck, is used as a case study.

1 INTRODUCTION

In the last decade, considerable research efforts have been made on the evaluation of the progressive collapse resistance – or equivalently in enhancing the structural robustness – of buildings with a particular focus on reinforced concrete frame buildings. Looking at the bridges, this research effort is much more limited and robustness criteria are just as, or even more important than in buildings. Existing studies on the robustness of bridges, although appreciable, are often limited to qualitative considerations that can provide designers with valuable indications for the design of new bridges. The dramatic series of bridge collapses that occurred in Italy in the last years has highlighted the need for urgent treatment of the worldwide infrastructural heritage, which consists mainly of reinforced concrete (RC) and precast concrete structures. In this regard, it is equally important to assess the safety and robustness of existing bridges. The robustness of existing bridges can be assessed through reliable metrics that can be used in the prioritization of interventions by the managing authority. In this context, the paper applies a measure of robustness available in the literature to a particular type of RC girder bridge, namely half-joint bridges. A simple methodology based on the notional removal of critical elements is applied for quantifying the structural robustness. Half-joint bridges represent a not insignificant amount of the Italian (and European) infrastructural stock and they are considered among the most critical infrastructures. The Annone viaduct, an RC half-joint bridge that collapsed in 2016 after the passage of a heavy truck, is used as a case study. The bridge was built in the early 60s in northern Italy and it consisted of a central suspended span and two side spans having a cantilever scheme, for a total length of 56.10 m.

2 BACKGROUND ON ROBUSTNESS INDICATORS

Objective measures of robustness are required to assess safety against progressive collapse, estimate losses, and decide whether a level of robustness is acceptable or not. Furthermore, a quantitative measure of robustness is useful for prioritizing maintenance and repair work on existing structures. Several indicators for measuring robustness are available in the literature,

some of them formulated in deterministic terms, others in probabilistic or risk-based terms. A comprehensive selection of robustness measures proposed in the literature can be found in Adam et al. (2018). To date, there is no unanimous consensus on a univocal measure of robustness. This limits the adoption of robustness indicators on a large scale.

Deterministic measures of robustness are typically based on the consequences of an assumed initial damage in the structure. In particular, such measures quantify the change in structural properties, such as stiffness or strength, having in common one basic idea: the comparison between the intact and the damaged structure. Although there are no specific robustness indicators for bridges, a careful analysis of the metrics available in the literature allows some indicators to be favoured over others based on the type of collapse mechanism (Starossek 2017).

Among the deterministic indicators of robustness that can also be calculated using linear elastic material behaviour, the ‘reserve-based measure’ R_r proposed by Starossek (2017) is considered particularly suitable for the study of half-joint bridges. It is based on the redistribution of forces following the failure of a structural element. This measure of robustness is called a ‘reserve-based measure’ because the redistribution of forces is only possible when the structure has reserves of bearing capacity. Let us consider a beam suspended on rods in the intact initial configuration of Figure 1a. The load applied to the beam induces stresses in the rods. Assume a local failure in the rod j . When the rod j is removed (Figure 1b), the force in the rod k increases by the quantity ΔF_k . The maximum dynamic force in the rod k F_{kj} ($F_{kj} = F_k + \Delta F_{kj}$) can be compared with the bearing capacity of the rod ($F_{k, ult}$). The index R_r can then be expressed as:

$$R_r = 1 - \max_{k,j} \frac{F_k + \Delta F_{kj}}{F_{k,ult}} \quad (1)$$

Positive values of the index R_r indicate robustness as failure does not propagate. Negative values of R_r indicate progressive collapse and lack of robustness. The maximum value of R_r , in this formulation is of the order of $1 - \phi$ where ϕ represents the average resistance safety factor.

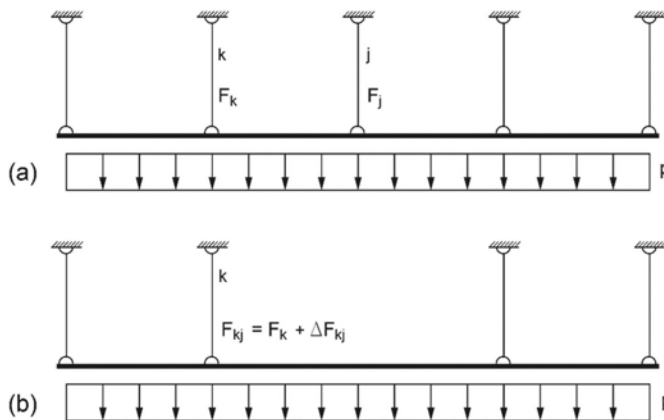


Figure 1. Example of a beam suspended on rods to illustrate the index R_r (adapted from Starossek 2017).

Although the index R_r is referred to by Starossek (2017) as a measure of robustness, it is perhaps mainly connected to structural redundancy since it shows the ability of the system to redistribute loads after damage to a single or a few members. The terms structural robustness, redundancy, and static indeterminacy are often used as synonymous in the literature but they denote different properties of the structural system. The fundamental difference between these terms is addressed in Biondini et al. (2008) where multiple examples are given as well. It has been also demonstrated that the degree of static indeterminacy is not a consistent measure of structural redundancy (Frangopol & Curley 1987; Biondini et al. 2008). Although structural

robustness strongly depends on redundancy and alternative load paths may enhance structural redundancy, the latter does not necessarily lead to increasing structural robustness (Biondini 2009, André 2020). In fact, the redistribution of internal actions on the damaged system may promote the evolution of damage reducing robustness.

3 CASE STUDY DESCRIPTION

3.1 *Geometry*

The bridge case study is the Annone overpass, a precast concrete structure built in the 1960s and collapsed in 2016 due to the shear failure of a half-joint during the passage of a heavy truck. The bridge was located in Annone, a small town in the province of Lecco (northern Italy), and designed as a second category bridge according to Circular 14 February 1962 n.384 (1962). The bridge consisted of a central suspended span (drop-in) and two side spans having a cantilever scheme, for a total length of 56.10 m and a total width of 7.4 m. The two side spans were simply supported on the abutments and on the intermediate walls each having a cantilever of about 2.80 m at the end. The central beams were simply supported on the two lateral beams employing half-joints thus reproducing a statically determinate condition. The span of the central beams was equal to 19.0 m. The geometric details of the bridge are here omitted but can be found in di Prisco et al. (2018, 2023). Five prestressed prefabricated beams (PC beams in the following), with a spacing between their axes of 1.35 m and disposed along the longitudinal bridge direction, supported a continuous cast in situ RC slab. The RC top slab was clamped at the abutments. RC transversal beams – five in the central span and four in the side spans – were cast in situ in the orthogonal direction. A schematic plan view of the central span is shown in Figure 2a together with the nomenclature of the 10 half-joints (R1 – R10), while a vertical section of the bridge is illustrated in Figure 2b.

3.2 *Load configuration*

This section describes the nominal applied loads on the elements of the central span due to their self-weight and live loads according to the NTC 2018 (Infrastructure Ministerial Decree, 2018). For the sake of brevity, bending moments and shear forces at mid-span are omitted and only the load acting on the half-joints is evaluated.

Regarding the central span, the overall self-weight of the bridge, including safety barriers, pavement, curbs, beams, and RC slab, was equal to 1690 kN, a value higher than that assumed by the designer, set to 1521 kN. The dimension of conventional lanes, the load positions, and the amplitudes are described in Figure 3 according to NTC 2018 (Infrastructure Ministerial Decree, 2018). Two load configurations are assumed to maximize the load on supports R1-R5 (symmetrical load with respect to the mid-span can be assumed to maximize the load on supports R6-R10): (i) lane 1 loaded according to the diagram in Figure 3 and (ii) lanes 1 and 2 both loaded according to the diagram in Figure 3. The first load configuration is schematized in Figure 2a as the load area highlighted in green – and half of the light grey area – resulting in a total live load of 1132 kN, a combination of concentrated and distributed loads. The second load configuration is schematized in Figure 2 as the load area highlighted in green, grey, and red, for a total live load of 1693.5 kN.

It should be emphasised that these live loads are significantly higher than those envisaged in the design phase. The bridge was in fact designed following the provisions of Circular 14 February 1962 n.384 (1962) as a bridge of second category. Even assuming that the distance between two subsequent vehicles is equal to zero, the maximum overall live load applied on the central span is equal to 88 t. This load must be increased with a dynamic amplification coefficient that depends on the bridge span and that can be considered equal to 1.284 if the span between the central piers is considered resulting in a maximum live load of 113 t (1109 kN vs 1693.5 kN).

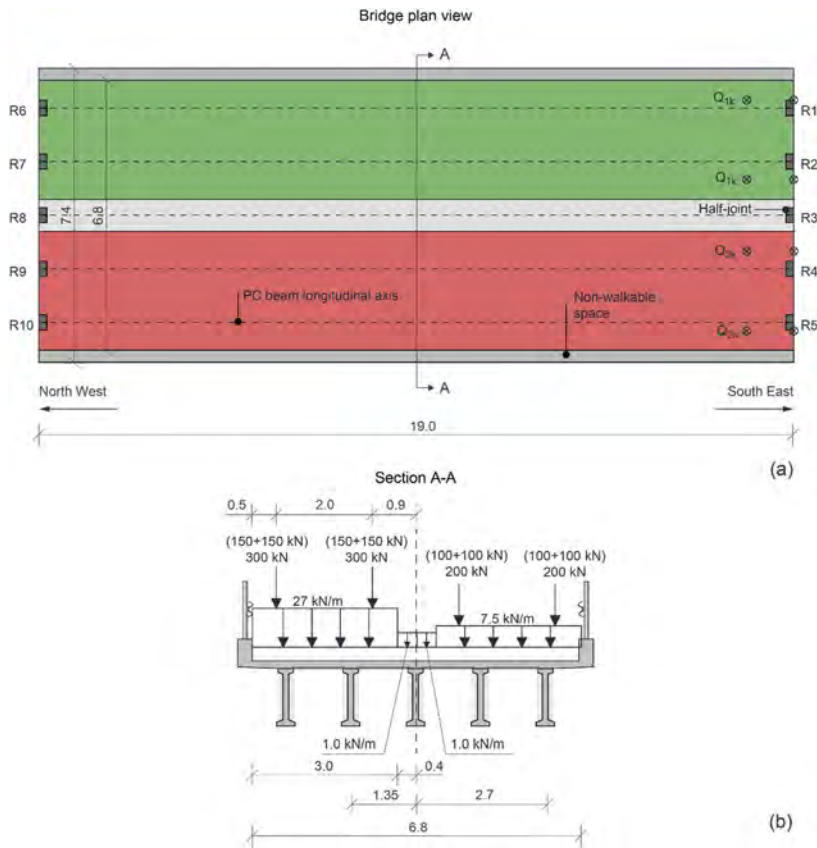


Figure 2. Loads on the central suspended span according to NTC 2018 (Infrastructure Ministerial Decree 2018): (a) plan view and (b) vertical cross-section.

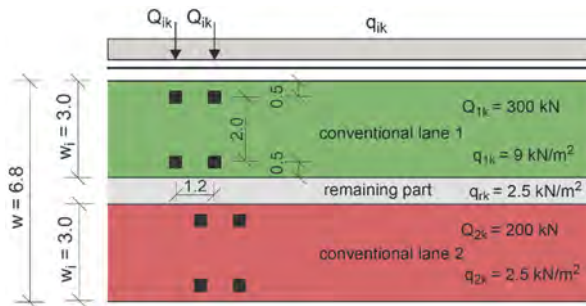


Figure 3. Dimension of conventional lanes and loading scheme according to NTC 2018 (Infrastructure Ministerial Decree 2018).

3.3 Half-joint resistance

Equation (1) involves calculating the ultimate capacity of the half-joints ($F_{k,ult}$), which are considered the critical element of the entire system. The estimation of $F_{k,ult}$ is based on the strut-and-tie models presented in di Prisco et al. (2023) which reproduced the half-joint geometry

and reinforcement details. On this last aspect, an as-built reinforcement situation with nominal bar diameters is assumed. The ultimate load for each half-joint is then estimated at 578.5 kN.

4 FINITE ELEMENT MODELS

The robustness quantification is carried out using linear elastic finite element (FE) models. The basic – intact – model used in this study is the same as that adopted in di Prisco et al. (2023) and named ‘num. 2A’. This FE model is a 3D simplified model in which the side spans are not reproduced. This model is therefore only used to conduct analyses on the bridge central span. The side spans are assimilated to elastic constraints for the central span according to the loading scheme shown in Figure 4a. Such a loading scheme provides a stiffness k equal to 6.06E7 N/m. Values of elastic constants for PC beams, transversal RC beams, and top RC slab are here omitted but are given in di Prisco et al. (2023).

Elastic constraints (translational springs in the Y direction) are applied to the ends of the beams of the central span as shown in Figure 4b. A 3D mesh view of the simplified FE model is shown in Figure 4c. Two types of 3D finite elements are used for different regions of the bridge: the top RC slab is discretized with shell-type elements, while the longitudinal and transversal beams are discretized as linear beam-type elements.

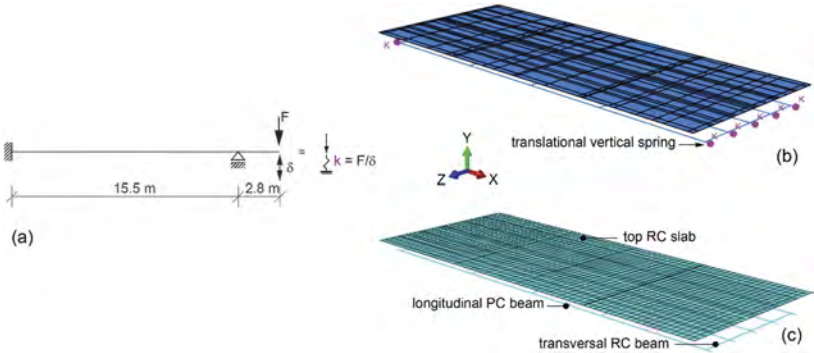


Figure 4. Simplified FE model: (a) lateral span loading scheme used for estimating the stiffness (k) of half-joints (b) details of the boundary conditions and (c) mesh view (adapted from di Prisco et al. 2018).

5 NOTIONAL REMOVAL APPROACH FOR HALF-JOINT BRIDGES

Design from actions resulting from unspecified hazards can be treated with a notional damage scenarios approach. According to the draft version of the *fib* Model Code 2020 document, notional damage scenarios can include (i) notional deterioration scenarios or (ii) notional removal scenarios.

In case (i), the geometrical and/or material properties of one or more structural elements are notionally reduced and the structure is checked for disproportionate consequences.

In case (ii), structural elements are notionally removed and the structure is checked for disproportionate consequences, for example by conducting an alternative load path design. Columns (one or more), panels/walls or nominal wall length (one or more) and any other elements judged vital to the structural performance are among the structural elements that can be notionally removed.

Notional removal scenarios – usually considered to be related to the failure of a connection or structural member due to an unidentified hazard – have been largely applied to evaluate the robustness of buildings (see for example Rodriguez et al. 2021 and Martinelli et al. 2022, among the others). The notional removal scenarios strategy is here applied to the bridge under

study by removing the half-joints, considered to be the most critical elements of the entire bridge (di Prisco et al. 2023). It is worth mentioning that the notional removal scenarios approach herein adopted is more conservative than the notional deterioration scenarios approach.

The scenarios that will be considered include the removal of a single half-joint at a time. Given the symmetry of the loads described in §3.2 with respect to the centreline of the bridge, it will be sufficient to consider the loss of the half-joints R1-R5 (loss of half-joint R1, loss of half-joint R2, etc.).

6 RESULTS AND DISCUSSION

The simplified FE models described in §4 allow the computation of the index R_r (Starossek 2017) with the load configurations described in §3.2. Figure 5 shows the reactions in half-joints R1-R5 in the case of intact situation and for the half-joint loss scenarios described in §5. Figure 5a considers the loads on lane 1, whilst Figure 5b considers the loads on both lanes 1 and 2. As one would logically expect, the reaction in the removed half-joint is nil. The most severe condition occurs when the end half-joint R1 in lane 1 is removed. In this condition, the adjacent half-joint R2 registers the maximum reaction. For both load configurations (Figure 5), another severe load condition compared to the intact condition is the loss of the half-joint R2. When loads are applied on both lanes (Figure 5b), another severe load condition compared to the intact condition is the loss of the other end half-joint R5. The loss of centre half-joints allows a more homogenous redistribution of reactions, making these scenarios less critical than the loss of end half-joints.

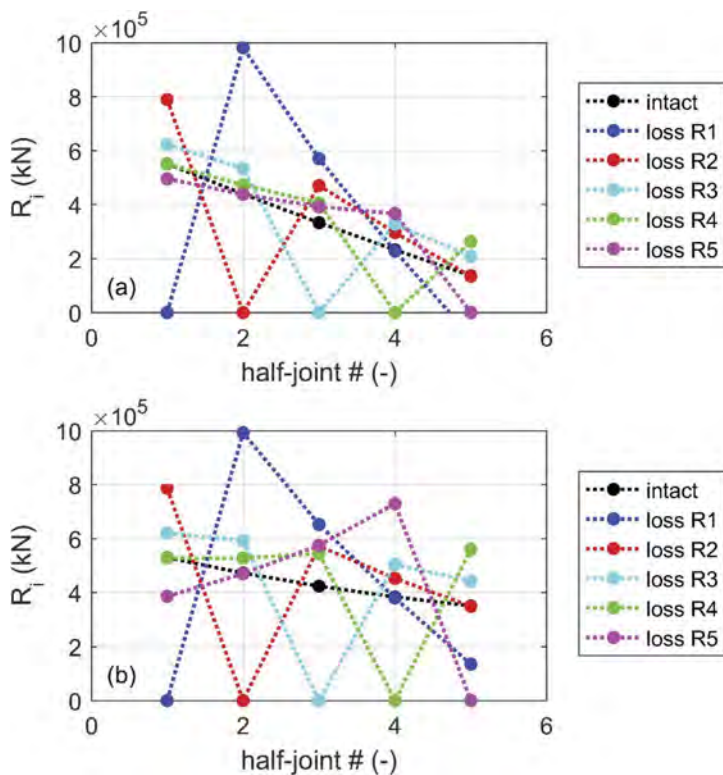


Figure 5. Reactions in half-joints R1-R5 in case of intact situation and for several half-joint loss scenarios: (a) loads on lane 1 and (b) loads on lanes 1 and 2.

Figure 6 shows the index R_r , calculated with Equation (1) for several half-joint loss scenarios. Regarding loads applied on lane 1 only, positive values of R_r are obtained when half-joints R4 or R5 are removed. Looking at the load configuration where loads are applied on both lanes, positive values of R_r are obtained only when half-joint R4 is removed. In both load situations and in agreement with the results of Figure 5, the most unfavourable situation is the loss of the half-joint R1.

While the results in Figure 6 show a lack of robustness for most of the scenarios considered (negative values of R_r), it should be remembered that the unit load multiplier ($\alpha = 1$) applied to the load configurations described in §3.2 is very severe. Concerning the load configuration involving loads on both lanes, the ratio between the live loads calculated according to Circular 14 February 1962 n.384 (1962) – and for which the bridge was designed – and according to NTC 2018 is 0.66. Applying a load multiplier equal to this ratio ($\alpha = 0.66$), Figure 7 compares the values of R_r for loads applied on lanes 1 and 2 and load multipliers $\alpha = 1$ and $\alpha = 0.66$. The two curves show very similar trends but with higher values of R_r for $\alpha = 0.66$. This case shows how the loss of central half-joints R3 or R4 – with positive values of R_r – does not lead to a propagation of failure. The most unfavourable situation is the loss of the end half-joint R1.

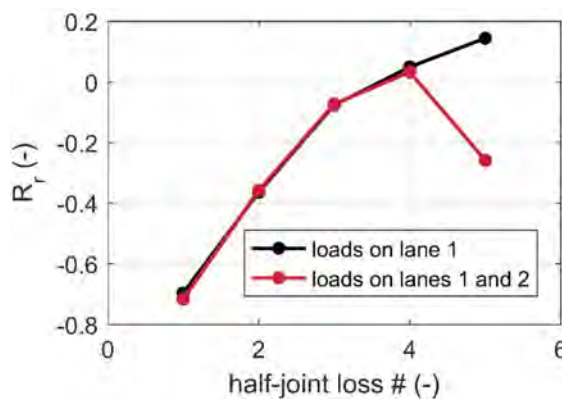


Figure 6. Index R_r (Starossek 2017) for loads applied on lane 1 only and loads applied on lanes 1 and 2.

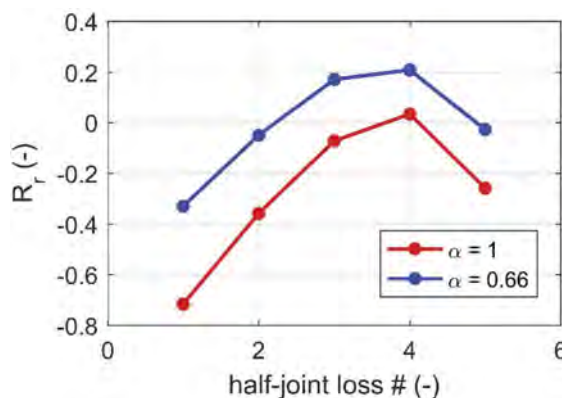


Figure 7. Index R_r (Starossek 2017) for loads applied on lanes 1 and 2 and load multipliers $\alpha = 1$ and $\alpha = 0.66$.

7 CONCLUSIONS

In this paper, a selected measure of robustness – typically adopted for buildings – is applied to a particular type of reinforced concrete (RC) girder bridge, namely half-joint bridges.

A simple methodology based on the notional removal of half-joints – which represent the critical elements for this type of bridge – is applied. The analysis of the structural system under notional removal scenarios is herein executed through linear static analyses where dynamic effects are neglected. The Annone viaduct, an RC half-joint bridge that collapsed in 2016 after the passage of a heavy truck, is used as a case study. Using two of the heaviest load combinations in accordance with the current standard NTC 2018, the following conclusions can be drawn.

The results obtained show greater robustness when central half-joints are removed compared to when end half-joints are removed. In the former case, the loss of a half-joint is followed by a redistribution of actions in the adjacent Gerber saddles that do not propagate the initial damage. Conversely, the loss of an end half-joint results in an absence of robustness for both load configurations considered. This result is in line with the prescriptions adopted for some bridges whereby the transit of exceptional heavy trucks must take place in the centre of the carriageway. This requirement was also foreseen for the Annone bridge, but it was unfortunately disregarded by the heavy truck that then triggered first the rupture of the half-joint R1 and then the collapse of the entire bridge.

ACKNOWLEDGMENTS

This work has been supported by the project “FIRMITAS: multi-hazard assessment, control and retrofit of bridges for enhanced Robustness using sMart IndusTriAlized Solutions” funded by the Italian PRIN project 2020, grant n. 2020P5572N.

REFERENCES

- Adam, J.M., Parisi, F., Sagaseta, J., & Lu, X. 2018. Research and practice on progressive collapse and robustness of building structures in the 21st century. *Engineering Structures* 173: 122–149. <https://doi.org/10.1016/j.engstruct.2018.06.082>.
- André, J. 2020. Structural robustness: A revisit. *Structural Engineering and Mechanics* 76(2): 193–205.
- Biondini, F., Frangopol, D.M. & Restelli, S. 2008. On Structural Robustness, Redundancy and Static Indeterminacy. *ASCE Structures Congress 2008*, Vancouver, B.C., Canada.
- Biondini, F. 2009. A Measure of Lifetime Structural Robustness. *ASCE/SEI Structures Congress 2009*, Austin, TX, USA, April 30-May 2, 2009. In: Proceedings of the Structures Congress 2009, L. Griffis, T. Helwig, M. Waggoner, M. Hoit (Eds.), American Society of Civil Engineers, USA.
- Circular 14 February 1962 n.384. 1962. Norme relative ai carichi per il calcolo dei ponti stradali.
- di Prisco, M., Colombo, M., Martinelli, P., & Coronelli, D. 2018. The technical causes of the collapse of Annone overpass on SS.36. In M. di Prisco & M. Menegotto (Eds.), *Italian Concrete Days 2018* (p. 16).
- di Prisco, M., Colombo, M., & Martinelli, P. 2023 Structural aspects of the collapse of a RC half-joint bridge: the case of the Annone overpass. *Journal of Bridge Engineering*.
- fib Model Code 2020. 2022. Draft Sub Chapter 30.9 (Design for robustness), Fédération Internationale des Bétons, Lausanne.
- Frangopol, D.M. & Curley, J.P. 1987. Effects of Damage and Redundancy on Structural Reliability. *ASCE Journal of Structural Engineering* 113(7): 1533–1549.
- Infrastructure Ministerial Decree. 2018. Norme tecniche per le costruzioni. NTC 2018.
- Martinelli, P., Colombo, M., Ravasini, S., & Belletti, B. 2022. Application of an analytical method for the design for robustness of RC flat slab buildings. *Engineering Structures* 258, 114117. <https://doi.org/10.1016/j.engstruct.2022.114117>.
- Rodríguez, D., Brunesi, E., & Nascimbene, R. 2021. Fragility and sensitivity analysis of steel frames with bolted-angle connections under progressive collapse. *Engineering Structures* 228, 111508, <https://doi.org/10.1016/j.engstruct.2020.111508>.
- Starossek, U. 2017. Measures of robustness and collapse resistance. In *Progressive Collapse of Structures*, Second edition, 129–140. ICE Publishing. <https://doi.org/10.1680/pcos.61682.129>.

Research on imaging technology of concrete bridge bottom apparent disease detection based on machine vision

S.G. Cao, X.Y. Li, Y. Pan, J.L. Fu & H. Tian

College of Civil Engineering, Tongji University, Shanghai, China

Key Laboratory of Road and Bridge Detection and Maintenance Technology of Zhejiang Province, Hangzhou, Zhejiang, China

Zhejiang Provincial Engineering Research Center for Intelligent Operation and Maintenance Technology of Highway Bridge and Tunnel, Hangzhou, Zhejiang, China

ABSTRACT: At present, the inspection of the beam bottom apparent diseases mainly depends on the visual inspection and special inspection carried by the inspection vehicle. Such methods cannot form a standardized and digital data management of the apparent diseases, also it cannot guarantee the personal safety of the inspectors. The imaging principle of optical camera was introduced and a standardized imaging strategy for beam bottom scanning based on optical camera was proposed in this paper. The strategy has been verified on the bridge and can meet the requirements of concrete apparent disease detection in the specification. The results show that two standardized imaging modes, physical fixed focus and dynamic zoom, were proposed. According to the two imaging modes, the relationship between camera operating parameters was analyzed. The standardized imaging mode provides the calculation basis for the design and selection of the beam bottom apparent disease detection equipment. Based on the idea of grid division of beam bottom area, two basic scanning strategies in longitudinal and transverse directions were proposed. The transverse scanning method was recommended for the surface inspection of the bottom of the variable cross-section continuous box girder bridge. The apparent disease detection and imaging technology based on machine vision can facilitate the management of process parameters and the preservation of results, also it can provide reference for the rapid detection of apparent diseases at the bottom of other bridges of the same types.

1 INSTRUCTIONS

At present, the inspection of apparent diseases of concrete continuous box girder bridges mainly depends on the visual inspection and special inspection carried out manually by inspection vehicles. Such methods cannot form standardized and digital data management of apparent diseases, and cannot guarantee the personal safety of patrol inspectors. The whole inspection strategy is time-consuming and laborious, which directly limits the development of cutting-edge technologies such as artificial intelligence and the Internet of Things in bridge management and maintenance technology (He et al. 2017). At the same time, due to the change of continuous beam bridge height and the high difficulty of management and maintenance inspection, the workload of disease detection and management has increased (Xie et al. 2003, Xuan & Shen 2007).

In order to solve the defects of traditional manual visual inspection methods, a feasible method is to use automatic imaging equipment to replace the detection workers to detect the apparent diseases. At present, airborne equipment that has begun to take shape includes unmanned aerial vehicles (Hallermann & Morgenthal 2014), autonomous cruise vehicles (Zhao et al. 2020), robots (Wang et al. 2021), underwater detectors (James 2000), cable climbing robots (Xu et al. 2021), etc. For example, cable climbing robot can replace manual automatic scanning of cable surface diseases. Aerial camera UAV can take pictures of the top of

the high bridge and the bottom of the deep tower from the air, avoiding the risk of artificial aerial work. The airborne equipment used for disease detection attracted more and more attention from researchers at home and abroad.

Based on the needs of rapid detection of continuous beam bridges, the characteristics of the detection scene and the imaging strategy of the airborne visual system for rapid detection of apparent diseases of concrete continuous beam bridges are studied in this paper. The scanning method of bridge bottom disease is proposed based on the camera photography and image mosaic technology. So, in the acquisition of disease photos, the imaging principle of the camera, lens selection, and focus mode are introduced. In terms of image splicing requirements, the longitudinal and transverse scanning modes of bridge bottom diseases are introduced. Finally, a transverse scanning method based on optical camera is proposed. And the site verification is carried out relying on the Hangzhou Jiangdong Bridge.

2 IMAGING PRINCIPLE OF OPTICAL CAMERA

The basic principle of camera imaging is based on the principle of convex lens imaging (see in Figure 1). The convex lens is replaced by a photographic objective, and the optical image of the object is obtained through an array type light sensitive element. The main parameters of the optical camera are as follows:

- (a) Resolution. It refers to the number of pixel points of each image collected by the camera, which corresponds to the number of pixels arranged on the target surface of the light-sensitive chip (i.e. photoelectric sensor, CCD). The commonly mentioned camera pixels (such as 5 million, 8 million, etc.) refer to the resolution.
- (b) light-sensitive chip (CCD) size. The size of each pixel and the resolution determine the size of the CCD target. The size of the CCD target surface includes the size of horizontal width (V) and vertical height (H).
- (c) Field of view(FOV). It refers to the actual viewing angle range corresponding to the image taken by the camera, including horizontal width (V) and vertical height (H).
- (d) Working distance(WD). The distance from the lens to the object is also called object distance.
- (e) Lens focal length(f). Focal length refers to the distance from the main point to the focus after lens optics. The focal length of the lens determines the image size, field angle, depth of field and perspective of the picture.

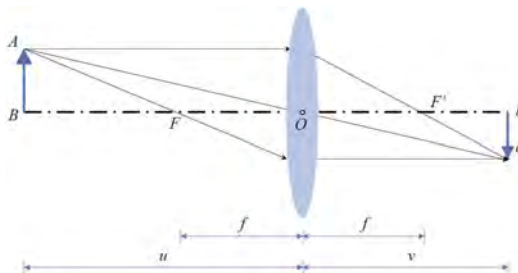


Figure 1. Convex lens imaging principle (AB-object, ab-image, O-optical center, F-object focal length, F'-image focal length, f-focal length, u-object distance, v-image distance).

The physical quantities f , u and v in Figure 1 meet the formula (1):

$$\frac{1}{u} + \frac{1}{v} = \frac{1}{f} \quad (1)$$

For each type of camera and lens, its resolution and CCD target size are determined, and there is a certain recommended working distance range. According to the accuracy required by the target, the above parameters of the camera can be inversely calculated and selected or customized according to the actual product model. Modern cameras are divided into zoom and fixed focus.

Among them, f , u and v of zoom camera are variable, while only u and v of fixed focus camera are variable. However, in the case of actual photography, a clear image can be formed when the formula (1) is not strictly satisfied. At the imaging position before and after the focus, the foreground dispersion circle and the background dispersion circle can be formed according to the light gathering and dispersion. It can be seen that if you want to obtain higher imaging accuracy, the field of vision will inevitably be reduced. In other words, fast detection equipment cannot obtain a large range of objects at a time with high imaging accuracy at a long distance.

3 ANALYSIS OF STANDARDIZED IMAGING STRATEGY OF OPTICAL CAMERA

A major disadvantage of traditional manual detection is that the working parameters of the camera are often unknown when shooting disease images, so it is necessary to record the morphological characteristics of the disease through manual measurement. The advantage of processing disease images based on computer vision is that as long as the relationship between camera image coordinate system and world coordinate system is established through laboratory calibration, the relationship between pixel size and actual physical size can be accurately obtained. Therefore, in order to realize the standardized detection of diseases based on optical sensors and computer vision, it is necessary to carry out overall planning and analysis research from the following aspects:

- (1) Acquisition. According to the characteristics of the disease, the imaging parameters are formulated on the basis of the optical principle to achieve the accuracy required for quantitative evaluation;
- (2) Storage. Standardized storage management for disease images according to the component and location of the disease;
- (3) Processing. Quantitative processing and description of sequential disease images through panoramic splicing or positioning control points;
- (4) Recognition. For quantitative disease images, it use computer vision technology to extract structural disease features, and then identify disease information in unknown images;

The lens of an optical camera can be divided into a fixed focus lens and a zoom lens. For a fixed focus lens, because its focal length is fixed, it is necessary to take an image at a relatively fixed working distance to get a clear picture, and its imaging accuracy is a fixed value. For zoom lens, the focal length can be adjusted within a certain range (i.e., zoom magnification), the working distance can be adjusted within a certain range and the imaging accuracy will change accordingly. Based on this, two standardized imaging modes can be formed:

- a) Physical focusing. Through the method of physical or mechanical constraints, the camera can always shoot with the same attitude (i.e. fixed distance, fixed focus) in the process of shooting at the beam bottom, and then a series of standard images with the same imaging parameters are obtained.
- b) Dynamic zoom. The imaging parameters are not strictly constrained, but the camera attitude parameters are captured and stored for each imaging. In the subsequent image processing, the algorithm is used to analyze, normalize and adjust, and then the standard images are obtained.

4 ANALYSIS OF BEAM BOTTOM SCANNING STRATEGY FOR AIRBORNE EQUIPMENT

4.1 Camera lens selection

The Chinese Code for Maintenance of Highway Bridges and Culverts (JTG 5120-2021) provides the inspection methods and relevant provisions for various diseases, such as cracks, honeycombs, segregation, water seepage, whitening and calcification, concrete damage and exposed reinforcement. The Standard for Evaluation of Technical Conditions of Highway Bridges (JTG/T H21-2011) is the evaluation standard for various diseases of concrete bridge superstructure, such as honeycomb, pitting, peeling, corner loss, cracks. For the description

and measurement requirements of apparent diseases in the above specifications, the imaging accuracy of the visual method is determined to be 0.1mm/px. The actual physical size represented by each pixel in the image is 0.1mm. Based on this imaging accuracy, the camera lens and corresponding working parameters (resolution, pixel size, field of view, working distance, lens focal length) are preliminarily determined according to the above optical camera imaging principle, physical focusing and optical zoom mode.

(1) Physical focus mode

After the fixed focus lens has determined the model of the camera's photosensitive chip, it is necessary to select the corresponding model lens according to the imaging accuracy requirements to adapt the camera for work. At present, the common size of the camera sensor chip is shown in Table 1.

Table 1. Dimensions of conventional photosensitive chip.

Chip type	Length (mm)	Width (mm)	Diagonal (mm)
1/6"	2.3	1.73	2.878
1/4"	3.2	2.4	4
1/3"	4.8	3.6	6
1/2.5"	5.76	4.29	10.18
1/2"	6.4	4.8	8
1/1.8"	7.2	5.3	8.9

According to the parameters in Table 1 and the imaging accuracy requirements of 0.1mm/px, The physical size range of the actual field of view represented by the 4k (3840×2160) resolution image is 384mm×216mm. From this, the relationship between camera lens and working parameters is shown in Table 2. The focal length of lenses in Table 2 is listed in the common focal length models (2mm~100mm). The focal length can also be customized according to requirement. In practical use, within the range of clear imaging, the working distance of the camera is less than or equal to the median value in the table which can meet the accuracy requirements.

Table 2. Relation between lens focal length and camera working distance.

Focal length (mm)	Working distance (mm)					
	1/6"	1/4"	1/3"	1/2.5"	1/2"	1/1.8"
2	249.711	180	120	100.6993	90	81.50943
2.4	299.6532	216	144	120.8392	108	97.81132
2.6	324.6243	234	156	130.9091	117	105.9623
2.8	349.5954	252	168	140.979	126	114.1132
3	374.5665	270	180	151.049	135	122.2642
3.1	387.052	279	186	156.0839	139.5	126.3396
3.6	449.4798	324	216	181.2587	162	146.717
3.9	486.9364	351	234	196.3636	175.5	158.9434
4.2	524.3931	378	252	211.4685	189	171.1698
4.3	536.8786	387	258	216.5035	193.5	175.2453
5	624.2775	450	300	251.7483	225	203.7736
6	749.1329	540	360	302.0979	270	244.5283
8	998.8439	720	480	402.7972	360	326.0377
12	1498.266	1080	720	604.1958	540	489.0566
16	1997.688	1440	960	805.5944	720	652.0755
25	3121.387	2250	1500	1258.741	1125	1018.868
35	4369.942	3150	2100	1762.238	1575	1426.415
50	6242.775	4500	3000	2517.483	2250	2037.736
75	9364.162	6750	4500	3776.224	3375	3056.604
100	12485.55	9000	6000	5034.965	4500	4075.472

(2) Dynamic zoom mode

A typical 4k industrial camera movement is shown in Figure 2. It includes a photosensitive module and an optical zoom module. Its maximum resolution is 3840×2160 , 30 times optical zoom can be achieved, and the focus range is 6.9 mm~207 mm. According to the calibration results, the zoom magnification and the corresponding maximum working distance can be determined when the camera meets the requirements of imaging accuracy.



Figure 2. Industrial camera movement.

4.2 Scanning strategy of the beam bottom

For beam bottom scanning, due to objective hardware conditions, it is impossible to obtain a large range of images at a time with high imaging accuracy over a long distance. Therefore, in the process of taking photos of apparent disease images, it is inevitable to patrol and take photos of the beam bottom area in multiple groups. Therefore, the beam bottom area can be meshed and decomposed, and the coordinate system can be established along the bridge direction and across the bridge direction. The precision of single imaging determines the granularity of grid division. The higher the precision, the smaller the field of view, and the denser grid.

In traditional manual detection, due to the lack of standardization limit in shooting, the captured images often cannot be positioned on the bridge. Pictures and text records are formed for statistical summary when cracks are observed. In practice detection, the inspector can only roughly estimate the segment where the disease is located according to the moving position of the bridge inspection vehicle, and then shoot and describe the location. Therefore, the final retained image data are only sporadic images. Based on the requirements of standardized imaging, image panoramic splicing and disease location, it is necessary to specify the scanning path of equipment at the beam bottom.

For panoramic image mosaic and disease location, the relative coordinates of images are necessary information. In order to organize and calculate the position relationship between images, it is advantageous and necessary to decompose the beam bottom scanning task into several groups of ordered subtasks. As shown in Figure 3, it is a strategy for longitudinal bridge scanning zone division, and Figure 4 is a strategy for transverse bridge scanning zone division.

For the scanning detection work under the longitudinal bridge navigation belt division, the single navigation belt detection area is large. However, the detection personnel need to adjust the position repeatedly on the bridge deck. Also, the occupation of the bridge deck area is large and it takes a long time. In contrast, the scanning detection work under transverse bridge navigation belt division will gradually advance the detection area along the longitudinal bridge direction, and the occupation of the bridge deck area is in the process of dynamic progress.

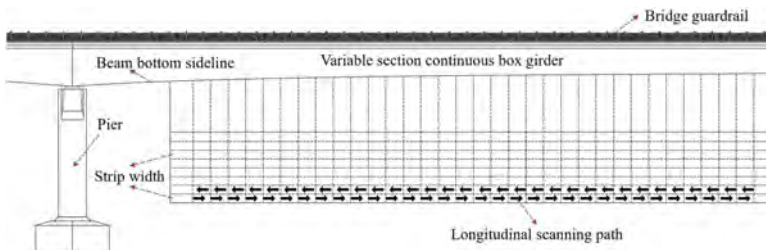


Figure 3. Diagram of longitudinal bridge scanning navigation belt division.

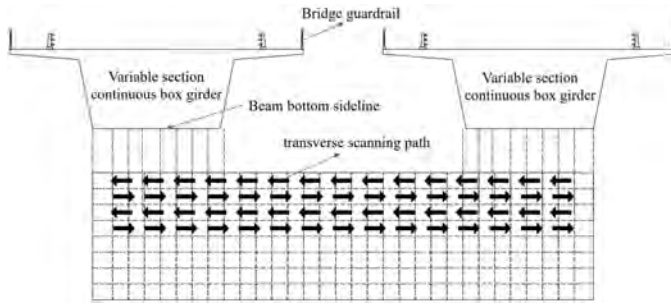


Figure 4. Diagram of transverse bridge scanning navigation belt division.

At the same time, longitudinal scanning and transverse scanning also put forward different requirements for the adaptability of airborne equipment and variable cross-section. As shown in Figure 5, for the scanning detection work under the longitudinal bridge scanning navigation belt division, it needs to go through a significant height change when each navigation belt works. For example, the beam height is 3.5m-5.0m, and the height difference is 1.5m. For the physical focusing imaging mode, the device is required to travel along the beam bottom surface and adapt to the change of beam height through the adjustment of mechanical structure during the travel. For the optical zoom imaging mode, in order to maintain the standardization of image sequences, it is necessary to constantly adjust the magnification of the optical zoom. Otherwise, there will be constant changes in the field of view as shown in Figure 5, which also means constant changes in imaging accuracy.

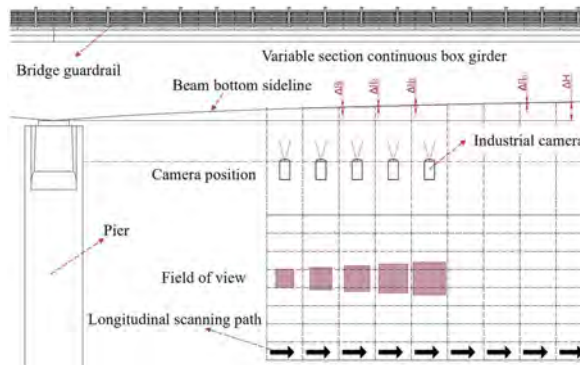


Figure 5. Change of section height in the navigation belt under the longitudinal bridge scanning navigation belt division.

On the other hand, for the scanning detection work under transverse bridge scanning navigation belt division, the beam height change amplitude of each navigation belt detection work is relatively small, mainly from the height difference change within the field of view.

In general, for the variable cross-section beam, the transverse scanning method with high degree of subdivision is conducive to building the standardized imaging conditions of the equipment. At the same time, it can also relatively save the construction space of the bridge deck and it has obvious advantages compared with the longitudinal scanning method. Therefore, the transverse scanning method is recommended for the surface inspection of the bottom of the variable section continuous box girder bridge.

5 CASE STUDY

5.1 Engineering introduction

The Hangzhou Jiangdong Bridge is located in Zhejiang province of China. The bridge with a total length of 3552.66 meters has eight lanes and a single carriageway with a net width of 15.50 m. It is a fully closed and fully overpass expressway. The main bridge structure is a space cable self-anchored suspension bridge, and the approach bridge structure is a prestressed concrete continuous beam bridge. According to the 2016 regular inspection report, the concrete beams of the approach bridge appear to have coating peeling, cracks and other defects. Among them, the largest crack width of the 30th span of non-navigable which connects with the steel box girder is 0.8mm, and cracks of 0.2mm. The number of cracks with a width of 0.2mm or more accounts for 34% of the total number of cracks, which seriously threatens the safety of bridge operation. The management and maintenance department once repaired the surface, and strengthened the side webs outside the box with steel plates. However, it found that there were new longitudinal and transverse cracks on the outer bottom and web of the box in the recent inspection. The pressure of the management and maintenance department is high. So, a convenient and fast detection method is urgently needed to provide technical support for bridge management and maintenance.

5.2 Imaging of beam bottom disease detection

The on-site inspection is divided into three stages:

- (1) Erection of cableway system. The traction cableway is pulled through the beam bottom by unmanned aerial vehicle. The cableway system through the beam bottom is built to carry the beam bottom scanning device.
- (2) Erection of bridge deck walking system. Namely, the bridge deck support, walking device and power supply equipment supporting the cableway system are quickly erected on site;
- (3) Beam bottom scanning. The scanning device at the bottom of the beam is equipped, and the apparent image acquisition task starts after the control terminal is connected.

According to the transverse scanning method in Section 4.2, the transverse scanning navigation belt (as shown in Figure 6) is obtained. It is spliced to form a panoramic image of the beam bottom through image correction (as shown in Figure 7). The Figures 6 and 7 only verify the above process, and describe a small part of beam bottom disease photos. After scanning the apparent diseases at the beam bottom, a panoramic mosaic image which can be subsequently used for disease identification is formed.

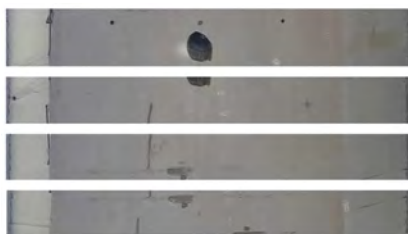


Figure 6. Transverse scanning navigation belt of beam bottom.



Figure 7. Panoramic splicing of beam bottom.

The whole process of panoramic mosaic image based on computer vision is automatically carried out based on artificial intelligence algorithm. The whole process of data acquisition and disease identification is digitalized and automated, and the images are easy to call and storage. The image diseases based on the transverse scanning method are basically consistent with the results of manual inspection. The apparent disease detection and imaging technology based on machine

vision can facilitate the management of process parameters and the preservation of results. The degree of digitalization has obvious advantages over manual detection. It can provide a reference for the rapid detection of the apparent diseases at the bottom of other bridges of the same type.

6 CONCLUSIONS

The imaging principle of optical camera is introduced, and the standardized imaging strategy of optical camera and the scanning strategy of airborne equipment under the beam bottom are studied. Combined with the requirements of concrete apparent disease detection, a transverse scanning imaging strategy for the beam bottom is proposed and verified on the Jiangdong Bridge. The conclusions are as follows:

- (1) Two standardized imaging modes, physical fixed focus and dynamic zoom, are proposed. The corresponding camera working parameter relationship is analyzed and calculated according to the two imaging modes, which provides a calculation basis for the subsequent design and selection of airborne equipment.
- (2) Based on the idea of grid division of beam bottom area, two basic scanning strategies in longitudinal and transverse directions are proposed. The transverse scanning method is recommended for surface inspection of the bottom of the variable section continuous box girder bridge.

ACKNOWLEDGEMENTS

The authors would like to acknowledge the supports of the Key Research and Development Program of Zhejiang Province (2021C01106), the Project of Science and Technology of Department of Transportation, Zhejiang Province (2020048), and the Independent Research and Development Projects of Zhejiang Scientific Research Institute of Transport (Grant No. ZK202204, ZK202301).

REFERENCES

- Hallermann, N. & Morgenthal, G. 2014. Visual inspection strategies for large bridges using Unmanned Aerial Vehicles (UAV). *Proceedings of the 7th International Conference of Bridge Maintenance, Safety and Management, IABMAS 2014*: 661–667.
- He, S.H., Zhao, X.M., Ma, J., et al. 2017. Review of highway bridge inspection and condition assessment. *China Journal of Highway and Transport* 30(11): 63–80.
- James, E. 2000. Robotic system for underwater inspection of bridge piers. *IEEE instrumentation & measurement magazine* 3(3):32–37.
- Wang, Z.P., He, B., Zhou, Y.M., Liu, K. & Zhang, C.H. 2021. Design and implementation of a cable inspection robot for cable-stayed bridges. *Robotica* 39(8): 1417–1433.
- Xie, K.Z., Zeng, Z.X. & Wang, X.Y. 2003. The research of load checkout test technology on bridge. *Journal of Guangxi University(Nature Science Edition)* (S1): 208–211.
- Xu, F.Y., Dai, S.Y., Jiang, Q.S. & Wang, X.S. 2021. Developing a climbing robot for repairing cables of cable-stayed bridges. *Automation in Construction* 129(6):103807.
- Xuan, J.M. & Shen, F.X. 2007. Research and engineering application of bridge inspection and testing techniques. *Bridge Construction* (S1): 158–160.
- Zhao, J., Li, X.L. & Ma, H.F. 2020. The Application of BP neural network algorithm in rapid design of the vertical boom of bridge inspection vehicle. *Journal of Physics Conference Series, 3rd International Conference on Advanced Algorithms and Control Engineering* 1570: 012005.

Semi-probabilistic methods for the assessment of existing concrete structures: An overview

Lorenzo Casti & Franziska Schmidt

Université Gustave Eiffel, Champs-sur-Marne, France

Fabio Biondini & Nisrine Makhoul

Politecnico di Milano, Milano, Italy

ABSTRACT: Life-cycle assessment of the residual performance of existing structures usually involves a wider spectrum of uncertainties compared to a standard approach for designing new structures. The main differences are related to the modification of structural capacity and demand in time, f.i. due to aging and structural deterioration processes. Furthermore, climate change has a significant impact on this evolution. In order to account for these aspects, full probabilistic approaches are often exploited for assessing existing structural systems. However, these methodologies are time-consuming and may require significant knowledge and expertise for numerical implementation. Therefore, the development of semi-probabilistic methodologies for existing structures considering the impact of climate change, including proper validation and calibration for incorporation in design codes and standards, is nowadays of essence. This paper provides an overview of recent accomplishments and available literature regarding semi-probabilistic code formats for the assessment of existing reinforced concrete structures, including insights on how to incorporate climate change effects on these methodologies.

1 INTRODUCTION

The evaluation of the residual performance of structural systems, such as bridges and infra-structural facilities, is currently a key issue since a large stock of existing structures is approaching the end of the design service life (Fabio Biondini & Frangopol 2016, 2018). The exploitation of conservative simplified approaches tailored for design of new structures may lead, in several cases, to expensive and unnecessary repairs due to the intrinsic differences with the assessment of existing systems (JRC 2015). Moreover, although existing constructions may not fulfill actual requirements for new design, in many cases these systems may still have adequate levels of performance for a target service life.

Structural design may be addressed as a decision problem involving uncertainties, in which the structural resistance $R=R(t)$ is required to be larger than the demand $E=E(t)$ over time t . The uncertainties involved in this problem are modified during the lifetime of the system, mainly due to aging and structural deterioration, leading to a decay of the resistance and possible evolution of the demand, related either to changes in loadings or internal stress redistributions. Furthermore, climate change is observed to have an impact on both structural loading (Mishra & Sadhu 2022), e.g. snow load or wind speed, and structural capacity (Nasr et al. 2021), e.g. enhancing deterioration mechanisms such as chloride- and carbonate-induced corrosion. In this context, it is important to properly assess the performance of existing structures considering the long-term evolution of environmental parameters (Retief 2022).

Following the international standards ISO 13822 (2001) and ISO 2394 (2015), the decision process regarding both the design of new structures and assessment of existing systems should be based on probabilistic evaluations which may be carried out at different levels of detail, from risk-informed decision-making to semi-probabilistic design. The latter methodology usually involves the lowest level of detail; nonetheless, it represents an important guidance for engineers to deal with common design situations and uncertainties within a reasonable range

of time and complexity. Several international design standards, e.g. Eurocodes (CEN EN1990 2002), AASHTO (2020) and ASCE 7-22 (2022), exploit the so-called load and resistance factor design (LRFD) format (Ravindra & Galambos 1978) for new structures providing, for a selected parameter a , the reference design values a_d through characteristic values a_k and partial safety factors γ . Reliability requirements are defined in order to determine a_k and γ , usually referring to this procedure as code calibration.

This paper provides an overview of recent accomplishments on the calibration of semi-probabilistic code format focusing on the assessment of existing structures. Firstly, a discussion of different methodologies for calibration is presented. Secondly, the semi-probabilistic code format is addressed based on research studies specifically dealing with the assessment of existing Reinforced Concrete (RC) structures. Finally, an insight into recent code calibration methodologies accounting for climate change effects on structural safety is also presented. The benefits and drawbacks of the methodologies discussed are addressed with emphasis on possible incorporation of long-climate prediction impacts on structural capacity and demand models.

2 BACKGROUND ON SEMI-PROBABILISTIC CODE FORMAT CALIBRATION

Code calibration may be described as the determination of the values of all parameters in a given code format (ISO 2394 2015), and it has been performed following different methodologies, based on past experiences, judgment, fitting, or a combination of these. In a broader sense, the calibration approach may be considered as a decision problem involving risk and uncertainties.

In ISO 2394 (2015), three different decision methodologies are defined for the design and assessment of structures considering different levels of detail. The risk-informed decision represents the highest level of detail (Level 4). In this case, the decision-making process should explicitly consider economic and safety consequences, as well as the modeling of uncertainties, aiming to maximize the expected utility. Although this approach is very powerful and flexible, it is not usually applied in engineering practice due to complexity and time constraints. Furthermore, in the context of code regulation, standardization and replicability are important aspects which may be archived exploiting simplified methodologies. Indeed, a simpler alternative is represented by reliability-based decision (Level 3). This approach relies on the satisfaction of predefined reliability requirements, which can be based on experience or on formal calibration through the Level 4 approach. The requirement may depend on the consequences and the cost of the specific decision implementation, although the consequences are not explicitly treated in the reliability considerations. Similarly, a reliability-based decision problem can be afforded involving simplified uncertainties representation and reliability computation (Level 2). Eventually, the semi-probabilistic approach corresponds to the lowest level of detail (Level 1).

The semi-probabilistic approach relies on the satisfaction of the safety deterministic criterion stating that the design resistance must be larger than the design demand. The design values are generally determined through the multiplication or division of the characteristic values by the partial safety factors, which are calibrated in order to meet the prescribed reliability requirements. This approach is proposed by several national and international design standards, such as the Eurocodes (CEN EN1990 2002), when dealing with common situations in terms of uncertainties and consequences. It should be noted that the described approaches, even if related to a different level of detail, are strongly interconnected; indeed, higher-level methodologies should be compliant and used in order to calibrate the lower levels. The different levels of decision-making strategy are reported in Table 1.

Consistently, semi-probabilistic code format calibration is usually based on reliability considerations where a given level of safety, measured by the reliability index β , should be assured by the definition of the reliability elements of the code, e.g. partial safety factors γ and combination factors ψ . The purpose of calibration of a semi-probabilistic code format, in addition to the formulation of a safe, economically efficient and simple tool for the design of ordinary structures, is to optimally select the parameters of the code by maximizing the benefits for the society. In this context, code calibration for a semi-probabilistic design is usually formulated as an optimization problem, which should be solved in order to retrieve the required reliability-based design factors.

Table 1. Levels of decision methodologies according to ISO 2394 (2015), based on Baravalle & Köhler (2016) and Köhler & Baravalle (2019).

Approach	Applicability	Objective	Norm
Risk-Informed (Level IV)	Exceptional design situations with respect to uncertainties and consequences.	Maximization of the expected utility for the decision maker.	Guidelines, e.g. ISO 2394 (2015).
Reliability-Based (Level III and II)	Unusual design situations with respect to uncertainties.	Fulfillment of reliability requirements.	Probabilistic codes, e.g. JCSS (JCSS 2001).
Semi-Probabilistic (Level I)	Usual design situations with respect to uncertainties and consequences.	Achievement of deterministic design criteria.	Semi-Probabilistic codes, e.g. EN1990 (2002).

Furthermore, appropriate treatment of uncertainties and the consequent selection of probabilistic models is fundamental in the calibration procedure. Indeed, structural engineering models are associated with a certain level of uncertainty, affecting both the structural demand and capacity. The Joint Committee on Structural Safety (JCSS) provides guidelines for the appropriate characterization of uncertainties, categorizing three main sources of uncertainty (intrinsic physic, parameter and model uncertainty), and suggesting the probabilistic models for the basic random variable (JCSS 2001), although the selection should always be tailored to the peculiar case study.

3 REVIEW ON SEMI-PROBABILISTIC CALIBRATION FOR EXISTING STRUCTURES

3.1 *Semi-probabilistic format calibration*

Calibration of the structural standards is currently a critical research issue, especially concerning existing structures. Indeed, for the aforementioned case, the semi-probabilistic format should be able to incorporate the potential updated information on geometry, loadings, materials and the different reliability requirements, in order to avoid non-effective decisions (Diamantidis 2001). Furthermore, the built environment is experiencing a change in environmental conditions which are likely not anymore the ones considered during the design; these climatic changes are reported to not have a negligible impact on both the evolution of structural capacity and demand. For this reason, code calibration of semi-probabilistic design format accounting for the actual evolution of the structural performance in a changing climate is fundamental.

Code calibration has been systematically researched in the past decades, e.g. by Cornell (1969), Ravindra et al. (1978), Thoft-Christensen & Baker (1982), Faber & Sørensen (2003), Madsen et al. (2006) and Ditlevsen & Madsen (2007). Based on this research, a standardization, specifically regarding reliability-based calibration, for semi-probabilistic design code is reported in ISO 2394 (2015). Among others, the selection of a target reliability β_T is a fundamental assumption in reliability-based calibration. In Baravalle & Köhler (2017) and Köhler et al. (2019) a discussion regarding the selection of β_T according to different strategies, addressing the benefit and drawbacks of each methodology, is presented. The definition of target reliability level for existing structures considering economic optimization and the marginal life-saving costs principle is addressed by Sýkora et al. (2017). Furthermore, Baravalle & Köhler (2019) proposed a comprehensive approach to code calibration of the reliability target through all levels of design. This article provides a background regarding the selection of the target reliability defining an extension of existing approaches for code optimization. A framework for reliability-based calibration of the load partial safety factor is proposed by Köhler et al. (2019). In this study, a generic limit state is considered for the calibration of the load safety factors of the Eurocodes. The results indicate that the partial safety factors proposed in the code are higher for permanent loads and lower for live loads. It is also observed that the reliability target assumed in the Eurocodes is higher than the average reliability level implied by the current safety factors.

A risk-based calibration problem is formulated by Köhler & Baravalle (2019), where economic considerations are explicitly considered in the optimization problem through the definition of a minimum expected cost. This is observed to be more consistent with respect to reliability-based optimization for which the definition of a generally accepted reliability target is observed to be hardly achievable.

In the approach proposed by Arrayago et al. (2022), the calibration of reliability indices and partial safety factors is based on First Order Second Moment (FOSM), considering both US and EU frameworks, and eventually compared with the results obtained exploiting First Order Reliability Methods (FORM). The results show that this simplified formulation is sufficiently accurate for the definition of reliability indices and partial safety factors, and it may provide a reference to the specification committees in the calibration process. Nevertheless, it is important to highlight that the comparison between the FOSM and FORM developed in the research involves only steel structures subjected to gravity and wind loads and it is limited to a specific sensitivity factor assumed for the calibration.

3.2 Assessment of existing RC structures

A comparison of semi-probabilistic vs full-probabilistic safety formats for RC structures based on limit states and partial factors of Eurocode 2 (2005) are presented in Biondini et al. (1999). The application of proper probabilistic models to the non linear analysis allows to assess the actual safety level with reference to the computed random distributions of structural response. The results include information about the large scattering of the reliability index, the sensitivity of the structure to the production control of higher level and the capacity of plastic adaptation under the applied load distributions. Semi-probabilistic approaches explicitly addressing the assessment of existing structures can be found in the *fib* Bulletin N°80 (2016). The described methodologies consider the residual service life, information from in situ and laboratory tests, measurements of variable actions, and reduced target reliability levels according to both economical and human safety criteria, focusing on standard RC structures. Specifically, two methodologies devoted to the recalibration of the partial safety factors for existing structures are presented: the design value method (DVM) and the adjusted partial factor method (APFM). The DVM, which has been introduced in the ISO 2394 (2015) and then adopted in the Eurocodes (CEN EN1990 2002), provides formulas for the calibration of partial safety factors of both material resistances and actions, exploiting appropriate probabilistic models derived by from the prior knowledge, test results, and observations related to the existing structure under investigation. The APFM (Caspelle & Taerwe 2012) is a simpler approach that allows to update the partial safety factors defined by Eurocodes for new structures, by means of “adjustment coefficients”.

The application of DVM and APFM has been performed in the past years for different RC structures by several researchers. In Sýkora et al. (2013), the DVM is applied to the pier and the slab of an existing RC bridge subjected to permanent and traffic loading. The results show that the semi-probabilistic format recommended for structural design in current codes may lead to conservative results and non-optimal decisions concerning rehabilitation of existing RC bridges. Caspele et al. (2013) exploited the DVM and APFM for the assessment of an existing RC beam and a short column subjected separately to wind and imposed variable loads, providing a framework for the application of the latter methodology. Gino et al. (2020) use the methodologies proposed in *fib* Bulletin 80 (2016) in order to evaluate the residual safety and performance of an existing prestressed RC bridge. The obtained outcomes are eventually compared with the results obtained based on the Eurocodes (CEN EN1990 2002), showing that recalibration of partial safety factors accounting for updated information may avoid expensive and not useful interventions. Nevertheless, the authors highlighted the absence of a definition for the probabilistic models to update partial safety factors for prestressing and imposed deformations in *fib* Bulletin 80 (2016) and the need of further research on this issue. The DVM and APFM methodologies are applied in Orcesi et al. (2021) for the assessment of two different existing RC bridges. The study illustrates the procedure for the application of the methodologies and provides a discussion regarding the assumption involved in both the approaches. It is evidenced that major simplifications rely on the consideration of

statistical uncertainty associated with the new measurements only in the estimate of characteristic values of basic variables and the assumption of standardized sensitivity factors or types of probabilistic distributions.

An important limitation common for the aforementioned studies regards the detrimental processes affecting RC structures, e.g. corrosion, which are assumed to be negligible. Moreover, no explicit consideration concerning the impact of climate change for the calibration of resistance and demand partial safety factors is addressed. In the context of calibration of partial safety factors for the assessment of existing RC structures subjected to corrosion-induced deterioration, preliminary considerations are undertaken by Tanner et al. (2011). In this paper, the uncertainties related to the resistance models for corrosion-damaged RC beams are estimated, showing how the partial safety factor for resistance should be incremented in the case of existing structures affected by corrosion. Nonetheless, the results obtained are not exploitable for the direct calibration of partial safety factors since more refined modeling should be devoted to characterize the resistance of deteriorating structures. An explicit formulation for the calibration of partial safety factors considering chloride-induced corrosion in RC structures is reported in Holicky et al. (2008). The research compares the partial safety factors obtained accounting and neglecting deterioration for different reliability targets, highlighting how the reliability level over time is strongly influenced by detrimental processes and, consequently, the calibration of partial factors. In this case, the limitation relies on the fact that the obtained results are significantly dependent on the model used. Consequently, more advanced corrosion modeling should be exploited, implementing the impact of climate change on the initiation and propagation phases, as well as more refined load modeling considering different ratio between permanent and variable loading. The calibration of the partial safety factors for the assessment of anchorage capacity in existing RC structures under corrosion is addressed in Blomfors et al. (2019). In this study, the partial safety factors are calibrated for different levels of corrosion, and considering the presence or the absence of stirrups. The obtained results are verified by exploiting Monte Carlo simulation for several design situations. The discussed methodology may, in principle, be extended to the calibration of partial safety factors for existing structures subjected to chloride-induced corrosion or carbonate-induced corrosion. Nevertheless, further research is needed for the quantification of the sensitivity factors in deteriorating structures.

The Technical Specification CEN/TS 17440 (2020) focuses on the assessment of existing structures suggesting the exploitation of the partial safety factors format of the Eurocodes (CEN EN1990 2002) as the initial method for the verification of the structural safety. In Lara et al. (2021), the assessment of an RC beams of an existing industrial building is performed, following the indication of the technical specification CEN/TS 17440 (2020) and applying both the DVM and APFM to compare the results with the outcomes of a full probabilistic analysis. The comparison shows that DVM incorporates the updated information more accurately than APFM. Furthermore, the full probabilistic assessment is reported to be in good agreement with the results obtained from DVM and APFM.

The assessment of existing structures may require the evaluation of the structural capacity at the system level exploiting nonlinear finite elements analyses (NLFEAs). In this context, Pimentel et al. (2014) propose the application of the global resistance safety factor approach into the semi-probabilistic format. The proposed methodology, which is consistent with the guidelines provided in the Swiss Standard for existing structures (SIA 2010; Brühwiler et al. 2012) and CEN EN1992-2 (2005), relies on the application of the partial safety factors to the overall system resistance. The main assumptions deal with the selection of a lognormal probability density function for the resistance and the estimation of the coefficient of variation. It is shown that the global resistance safety factor format may be more accurate than the partial safety factor, even at the member level. Nevertheless, the assumed lognormal distribution is not always adequate for the analysis. A discussion about a semi-probabilistic approach compliant with NLFEAs for the assessment of existing RC structures using different safety formats is presented in Castaldo et al. (2019). Methods for the assessment of uncertainties and estimation of the coefficient of variation of the resistance of RC structures are also presented in Novák et al. (2022).

3.3 *Insight into calibration considering climate change*

Calibration of a semi-probabilistic design format has been usually performed under the assumption of a stationary climate. Nowadays, climate change is extensively reported in the Intergovernmental Panel on Climate Change assessments (IPCC 2022), and its impact on structural demand and resistance is recognized in a large number of studies (Nasr et al. 2021; Mishra & Sadhu 2022). Consequently, design codes should incorporate considerations regarding climate change when calibrating the semi-probabilistic format in order to appropriately estimate structural safety and performance. Recent studies have tried to perform code calibration explicitly considering climate change.

Target structural performances have been investigated in terms of resilience and sustainability under climate change effects and other hazards (ASCE 2018). In Hong et al. (2021), a reliability-based design code calibration is performed in the context of possible implementation in the National Building Code of Canada (NBCC), focusing on the definition of design wind load, design snow load, and companion load factors. In the study, the stationary extremes derived from observed meteorological data and the nonstationary climate change effects are considered. Based on the performed analysis and the results from the climate change modeling results, sets of load scaling factors accounting for climate change effects are calibrated for different regions in Canada. Despite the calibrated load factors for climate change effects are specifically addressed to the Canadian environment and climate change effects may significantly vary from region to region, the proposed calibration procedure for nonstationary extremes is amenable to generalization. An extensive review of available information on climate change to identify methodologies and tools that would help the civil engineering profession to address the impacts of climate change on the life-cycle structural safety of structures and infrastructure facilities is currently ongoing within a SEI/ASCE special project (SEI/ASCE 2022).

In the context of European Standardization, the work proposed in Arnold & Kraus (2022) focused on the calibration of semi-probabilistic code formats considering the evolution of climate. In this research, FORM methodologies are extended to a nonstationary approach incorporating the reliability index and sensitivity factor and exploited for calibration. A practical application is presented involving a simply supported beam subjected to snow action in order to describe the proposed framework. The drawbacks of the work rely on the uncertainties involved in climate projection and on the selection of the time window which may significantly influence the results.

4 CONCLUSIONS

In this paper, recent research advances addressing the assessment of existing RC structures based on a semi-probabilistic approach are discussed. The aim of the study is to provide an overview of the current state-of-the-art for semi-probabilistic format code calibration and application, aiming at future implementation of the climate change impact on these methodologies.

The concepts of decision-making in engineering and calibration are introduced. A review of several studies is proposed concerning:

1. General calibration strategies for the semi-probabilistic code format applicable to different types of structures and analyses.
2. Methodologies for the definition of semi-probabilistic code key elements, as safety factors, for existing RC structures.
3. Calibration of the semi-probabilistic code format considering the impact of climate change on structural safety.

The review highlighted the significant amount of research advances in these fields, but also that further research is needed to appropriately calibrate semi-probabilistic formats for the assessment of existing RC structures subjected to detrimental processes such as corrosion. Moreover, the changes in current and future climate are affecting structural systems, and in general the built environment, influencing both structural capacity and demand. Further developments are needed also along these lines of research in order to provide semi-probabilistic methodologies for the assessment of RC structures subjected to detrimental processes in a changing climate. Eventually, although some studies analyzed the non-stationary

evolution of climate and its impact on environmental actions, more steps for the characterization of uncertainties and the definition of basic assumptions are needed for the consequent calibration of semi-probabilistic design codes.

ACKNOWLEDGMENTS

This project has received funding from the European Union's Horizon 2020 research and innovation programme under the Marie Skłodowska-Curie COFUND grant agreement No 101034248.

REFERENCES

- AASHTO. 2020. *LRFD Bridge Design Specifications*, 5th Ed. with Interims. Washington: American Association of State Highway and Transportation Officials.
- Arnold, R., & Kraus, M. 2022. On the nonstationary identification of climate- influenced loads for the semi-probabilistic approach using measured and projected data. *Cogent Engineering*, 9(1): 2143061.
- Arrayago, I., Zhang, H., & Rasmussen, K. J. R. 2022. Simplified expressions for reliability assessments in code calibration. *Engineering Structures*, 256: 114013.
- ASCE. 2018. *Climate-resilient infrastructure: Adaptive design and risk management*, Committee on adaptation to a changing climate, Manual of Practice 140. Reston: American Society of Civil Engineers.
- ASCE 7-22. 2022. *Minimum design loads and associated criteria for buildings and other structures*. Reston: American Society of Civil Engineers.
- Baravalle, M., & Köhler, J. 2016. Risk and Reliability Based Calibration of Design Codes for Submerged Floating Tunnels. *Procedia Engineering*, 166: 247–254.
- Baravalle, M., & Köhler, J. 2017. A framework for estimating the implicit safety level of existing design codes. In *Proceedings of the 12th International Conference on Structural Safety and Reliability, TU Wien, Vienna, 6-10 August 2017*, Vienna: TU-Verlag.
- Baravalle, M., & Köhler, J. 2019. A risk-based approach for calibration of design codes. *Structural Safety*, 78: 63–75.
- Biondini, F., Bontempi, F., & Toniolo, G. 1999. Comparison of Semi-Probabilistic vs Full-Probabilistic Safety Formats for Concrete Structures. *3rd International Conference on Analytical Models and New Concepts in Mechanics of Concrete Structures, Wroclaw, Poland, 16-19 June 1999*.
- Biondini, Fabio, & Frangopol, D. M. 2016. Life-Cycle Performance of Deteriorating Structural Systems under Uncertainty: Review. *Journal of Structural Engineering*, 142(9): 1–17.
- Biondini, Fabio, & Frangopol, D. M. 2018. Life-Cycle Performance of Civil Structure and Infrastructure Systems: Survey. *Journal of Structural Engineering*, 144(1): 1–7.
- Blomfors, M., Larsson Ivanov, O., Honfi, D., & Engen, M. 2019. Partial safety factors for the anchorage capacity of corroded reinforcement bars in concrete. *Engineering Structures*, 181: 579–588.
- Brühwiler, E., Vogel, T., Lang, T., & Lüchinger, P. 2012. Swiss standards for existing structures. *Structural Engineering International*, 22(2): 275–280.
- Caspeele, R., Sykora, M., Allaix, D. L., & Steenbergen, R. 2013. The Design Value Method and Adjusted Partial Factor Approach for Existing Structures. *Structural Engineering*, 23(4): 386–393.
- Caspeele, R., & Taerwe, L. 2012. Updating partial factors for material properties of existing structures in a Eurocode framework using Bayesian statistics. *Advances in Safety, Reliability and Risk Management (ESREL 2011)*, Troyes, 18-22 Septemeber 2011, London: CRC Press/Balkema.
- Castaldo, P., Gino, D., & Mancini, G. 2019. Safety formats for non-linear finite element analysis of reinforced concrete structures : discussion, comparison and proposals. *Engineering Structures*, 193: 136–153.
- CEN/TS 17440. 2020. *Technical Specification - Assessment and Retrofitting of Existing Structures*. Brussels: European Comitee for Standardization.
- CEN EN1990. 2002. *Eurocode 0: Basis of structural design*. Brussels: European Comitee for Standardization.
- CEN EN1992-2. 2005. *Eurocode 2: Design of concrete structures - Concrete bridges - Design and detailing rules*. Brussels: European Comitee for Standardization.
- Cornell, A. C. 1969. Structural safety specifications based on second-moment reliability analysis. *International Association of Structural and Bridge Engineers (IABSE) Report: On Concepts of Safety of Structures and Methods of Design*, 235–246.
- Diamantidis, D. 2001. *Probabilistic Assessment of Existing Structures*, RILEM Publications.
- Ditlevsen, O., & Madsen, H. O. 2007. *Structural Reliability Methods*. Department of Mechanical Engineering at the Technical University of Denmark, <http://www.od-website.dk/index-2.html/books.htm>.
- Faber, M. H., & Sørensen, J. D. 2003. Reliability Based Code Calibration - The JCSS Approach. *Proceedings of the 9th International Conference on Applications of Statistics and Probability, San Francisco, 6-9 July 2003*, Holland: Millpress.

- fib. 2016. *Bulletin N°80: Partial factor methods for existing concrete structures*. Lausanne: Fédération internationale du béton.
- Gino, D., Castaldo, P., Bertagnoli, G., Giordano, L., & Mancini G. 2020. Partial factor methods for existing structures according to fib Bulletin 80 : Assessment of an existing prestressed concrete bridge. *Structural Concrete*, 21(1): 15–31.
- Holicky, M., Markova, J., & Sykora, M. 2008. Partial factors for assessment of existing reinforced concrete bridges. *Proceedings of the 6th International Probabilistic Workshop, Darmstadt*, 26-27 November 2008, Darmstadt: Dirk Proseke Verlag.
- Hong, H. P., Tang, Q., Yang, S. C., Cui, X. Z., Cannon, A. J., Lounis, Z., & Irwin, P. 2021. Calibration of the design wind load and snow load considering the historical climate statistics and climate change effects. *Structural Safety*, 93: 102135.
- IPCC. 2022. *Climate Change 2022: Impacts, Adaptation and Vulnerability*. Contribution of Working Group II to the Sixth Assessment Report of the IPCC. Cambridge: Cambridge University Press.
- ISO 13822. 2001. *Basis for Design of Structures - Assessment of Existing Structures*. Geneva: International Organization for Standardization.
- ISO 2394. 2015. *General principles on reliability for structures*. Geneva: International Organization for Standardization.
- JCSS. 2001. *Probabilistic model code*. Zurich: Joint Committee on Structural Safety.
- JRC. 2015. *New European technical rules for the assessment and retrofitting of existing structures*. Brussels: CEN/TC250/WG2.
- Köhler, J., & Baravalle, M. 2019. Risk-based decision making and the calibration of structural design codes – prospects and challenges. *Civil Engineering and Environmental Systems*, 36(1): 55–72.
- Köhler, J., Sørensen, J. D., & Baravalle, M. 2019. Calibration of existing semi-probabilistic design codes. *13th International Conference on Applications of Statistics and Probability in Civil Engineering, Seoul*, 26-30 May 2019, Seoul National University.
- Lara, C., Tanner, P., Zanuy, C., & Hingorani, R. 2021. Reliability Verification of Existing RC Structures Using Partial Factors Approaches and Site-Specific Data. *Applied Science*, 11: 1653.
- Madsen, H. O., Krenk, S., & Lind, N. C. 2006. *Methods of structural safety*. New York: Dover Publications.
- Mishra, V., & Sadhu, A. 2022. Towards the effect of climate change in structural loads of urban infrastructure : A review. *Sustainable Cities and Society*, 89: 104352.
- Nasr, A., Björnsson, I., Honfi, D., Larsson Ivanov, O., Johansson, J., & Kjellström, E. 2021. A review of the potential impacts of climate change on the safety and performance of bridges. *Sustainable and Resilient Infrastructure*, 6(3–4): 192–212.
- Novák, L., Červenka, J., Červenka, V., Novák, D., & Sýkora, M. 2022. Comparison of advanced semi-probabilistic methods for design and assessment of concrete structures. *Structural Concrete*.
- Orcesi, A., Boros, V., Kušter Marić, M., Mandić Ivanković, A., Sýkora, M., Caspeele, R., Köhler, J., O'Connor, A., Schmidt, F., Di Bernardo, S., & Makhoul, N. 2021. Bridge Case Studies on the Assignment of Partial Safety Factors for the Assessment of Existing Structures. *18th International Probabilistic Workshop, University of Minho, Guimarães*, 12-14 May 2021, Guimarães: Springer.
- Pimentel, M., Brühwiler, E., & Figueiras, J. 2014. Safety examination of existing concrete structures using the global resistance safety factor concept. *Engineering Structures*, 70: 130–143.
- Ravindra, M. K., Cornell, C. A., & Galambos, T. V. 1978. Wind and Snow Load Factors for Use in LRF. *Journal of the Structural Division*, 104(9): 1443–1457.
- Ravindra, M. K., & Galambos, T. V. 1978. Load and resistance factor design for steel. *Journal of the Structural Division*, 104(9): 1337–1353.
- Retief, J. V. 2022. Assessment of Existing Structures Under Climate Change. *Acta Polytechnica CTU Proceedings*, 36: 6–14.
- SEI/ASCE. 2022. Effects of climate change on the life-cycle performance, safety, reliability, and risk of structures and infrastructure systems. *SEI/ASCE International Workshop*, 22 September 2022, Reston: Structural Engineering Institute, American Society of Civil Engineers.
- SIA. 2010. *SIA 269 – basis for examination and interventions*. Zurich: Swiss Society of Engineers and Architects.
- Sýkora, M., Holicky, M., & Marková, J. 2013. Verification of existing reinforced concrete bridges using the semi-probabilistic approach. *Engineering Structures*, 56: 1419–1426.
- Sýkora, M., Diamantidis, D., Holicky, M. & Jung, K. 2017. Target reliability for existing structures considering economic and societal aspects. *Structure and Infrastructure Engineering*, 13(1): 181–194.
- Tanner, P., Lara, C., & Prieto, M. 2011. Semi-probabilistic models for the assessment of existing concrete structures. *In Proc. ICASPI1, ETH Zurich*, 1-4 August 2011, Leiden: CRC Press/Balkema.
- Thoft-Christensen, P., & Baker, M. J. 1982. *Structural Reliability Theory and Its Applications*, Heidelberg: Springer Berlin.

Digital fatigue test of rib-to-deck welded joint details in orthotropic steel deck

P.Y. Li & C.S. Wang

Department of Bridge Engineering, School of Highway, Chang'an University, Xi'an, China

Y. Li & D.D. He

Bay Area Super Major Bridge Maintenance Technology Center of Guangdong Highway Construction Co., Ltd, Guangzhou, China

ABSTRACT: In order to investigate the fatigue crack propagation properties of rib-to-deck weld joint toe and root details for orthotropic steel decks, the suspension bridge with the 1688 m main span of the Nizhou bridge in Nansha bridge project was selected as the engineering background and the digital fatigue tests of these details were carried out based on extended Finite Element Method (XFEM) and numerical fracture mechanic theory, which could reflect the actual stress characteristic. The welding residual stress field simulation was carried out for the orthotropic steel deck manufacturing process. The residual stress result shows that there is a large residual tensile stress in the welding area of the rib-to-deck toe and root details, and the peak value of the Von-Mises stress at the rib-to-deck joint is close to the yield stress of Q345 steel. A multi-scale whole bridge finite element model was established considering construction condition for the orthotropic steel deck construction process. The fatigue crack propagation could be simulated by XFEM coupling with welding residual stress field, live load and dead load stress field. The results of fatigue crack propagation behavior display that the fatigue crack at the weld root is led by mode I, which could keep in the plane during the crack propagation. And the fatigue crack at the weld toe is mix mode I-II-III crack led by mode I, which cannot keep in the plane during the crack propagation, but slightly deflection.

1 INTRODUCTION

The orthotropic steel decks are widely applied in modern bridge construction due to their excellent mechanical properties, construction convenience and attractive shape. However, the fatigue cracks often appear in the orthotropic steel decks shortly after opening to traffic because of their complex structure, inevitable welding defects during the bridge deck manufacturing process, dead-load stress introduced during the construction process and live load stress during operation process. Hence it is necessary to investigate the orthotropic steel decks fatigue character. The physical fatigue tests based on stress analysis method are widely used in the fatigue problem researches, which has been gotten kinds of research achievement and could display of test phenomena intuitively. With development of finite element theory, digital twin simulation (Yeratapally et al. 2020) is applied in the steel bridge fatigue characteristic research, which could overcome the defects of manpower-consuming and time-consuming for conventional physical fatigue test.

The digital fatigue test based on normal conventional finite element method is often used in bridge researches. Kiss and Dunai (Kiss and Dunai 2002) based on FEM software CRAXIM to achieve cyclic loading and establish two-level stress analysis models. The actual bridge fatigue life assessment was based on the fracture mechanics method. Wang (Wang et al. 2019) established the three-dimensional fracture mechanics model to evaluate the fatigue life of a riveted steel bridge before and after reinforcement, considering the coupling effect of fatigue and corrosion, and the results show that the method could evaluate the fatigue life evaluation of riveted steel bridge.

Calculation consuming will be expensive and the residual welding stress could not be considered because of element remeshing. While extended finite element method (XFEM) (Belytschko and Black 1999; Moës et al. 1999) could solve remeshing problems by introducing the enrichment function into the conventional finite element displacement function. Based on

DOI: 10.1201/9781003323020-476

the extended finite element method, Nagy(Nagy et al. 2015) established a segmental model of orthotropic steel deck, and studied the fatigue crack propagation characteristics and fatigue life of the easily fatigue-sensitive details at the top deck plate. The results show that the load sequence seems to have an important influence on the crack propagation, but does not affect the crack size in the final stage. Wang et al.(Wang et al. 2020) studied steel bridge web gaps and orthotropic steel decks' typical fatigue details' fracture mechanic properties. They took a series of digital fatigue test based on XFEM and digital fracture mechanics, considering welding residual stress. Multi-scale digital fracture mechanic models of the rib-to-diaphragm detail of a cable-stayed bridge were established.

However, large-size cracks are used in the existing research, so it is difficult to reflect the actual situation at the initial crack growth stage. Thus, it cannot completely simulate the whole process of crack propagation. Moreover, the residual stress is calculated using a small-scale FEM model, which is not consistent with the actual welding situation in the factory.

In this paper, the rib-to-deck detail of Nizhou suspension bridge was selected as the engineering background, and the muti-scale digital fatigue test models were established. The welding residual stress was simulated for the factory welding process, and rational boundary conditions in the thermal-stress analysis were put forward. Based on the numerical fracture mechanics theory and extended finite element method (XFEM), different propagation stage fatigue propagation behavior of these two details was revealed. Research results are beneficial in investigating the the fatigue crack propagation mechanism

2 ENGINEERING BACKGROUND AND FINITE ELEMENT MODEL

A suspension bridge with the 1688 m main span of the Nizhou bridge in Nansha bridge project was selected as the engineering background as shown in Figure 1 (a). The height of the main girder is 3,5m, and the width of transverse direction is 49.7m as shown in Figure 1 (b). Q345qD is used in this steel bridge. The thickness of steel deck is 18mm; the longitudinal stiffener ribs adopt closed trapezoidal cross section with the section parameters of 300 mm × 280 mm × 8 mm as shown in Figure 1 (c). This steel box girder is a fully welded structure, and the partial penetration fillet weld joints are used in of rib-to-deck details.

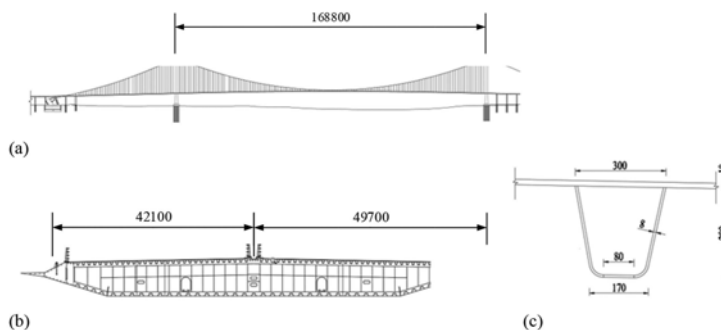


Figure 1. Structural dimensions of steel deck (Unit: mm): (a) bridge elevation; (b) girder cross section; (c) U-rib detail drawing.

In order to consider the dead stress caused by bridge construction process, the muti-scale whole bridge model was established. The tower and girder were established by girder elements, the cables were simulated by truss elements. Shell elements was used to simulate the flat steel box girders sub-model. And local sub-model was established by shell elements which is connected with concerning detail directly. The concerning fatigue detail was established by solid elements as shown in Figure 2. In the rib-to-deck detail model, the deck plate length and width are 600mm × 400mm, and the height of the U-rib is 280mm. And in order to match small-size of fatigue cracks and improve the computational efficiency, the transition grid

method was applied in the meshing process; as shown in Figure 2, the grid size was transitioned from 1mm to 15mm. Considering the fatigue crack size is far smaller than the solid model, the transition grid method is selected in the digital fatigue simulation, and this meshing result will be also used in the welding process simulation.

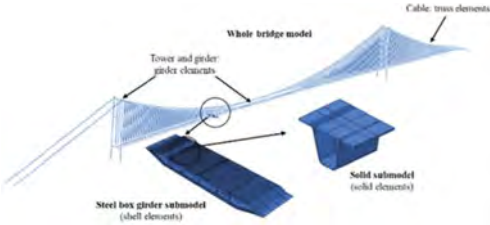


Figure 2. Multi-scale whole bridge element model.

3 WEDLIGN PROCESS SIMULATION

The influence of residual welding stress on fatigue performance at joint details cannot be neglected. Some research results show that there exists large residual stress in rib-to deck details (Wang et al. 2013). Therefore, it is necessary to research the residual welding stress at this typical detail in the orthotropic steel deck. However, small-scale solid models were often used to simulate the residual welding stress in most research, which could partially illustrate the residual stress distribution, but the constraints will be much strong. Hence, whether the boundary conditions are correct determines whether the residual welding stress distribution could be rational.

3.1 Welding simulation finite element model

The sequential coupled thermal analysis method is applied in this paper (effect of only temperature field on stress field). In order to simulate the actual welding process, the segmental steel deck sub model and the welding solid sub-model were established in this paper, as shown in Figure 2.. The dimension of the segmental steel deck model is the same as the actual welding process, which could provide a relatively exact boundary condition for the sub-model as shown in Figure 3.

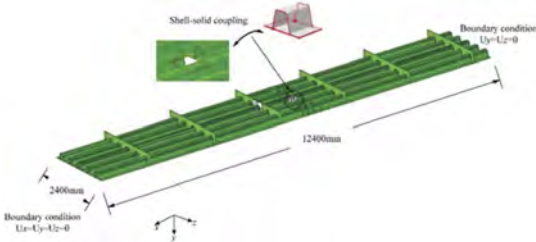


Figure 3. FEM model of welding stress analysis for steel deck.

3.2 Welding analysis methodology

The welding process simulation is divided into two steps by thermal-stress sequential coupling method. In the first step, a thermal analysis model is established to simulate the arc heat transferring to the weld joint. In the second step, residual stress is calculated based the thermal analysis to simulate welding thermal stress.

The initial environmental temperature was set to 20 °C, the absolute zero is - 273.15 °C, and the Stefan-Boltzmann constant is $5.67 \times 10^{-8} \text{ W m}^{-2} \text{ K}^{-4}$. CO2 gas-shielded welding is adopted in rib-to-deck welding. In order to realize the dynamic simulation of temperature filed, double ellipsoidal heat source model(Goldak et al. 1984) was adopted. And Fortran language was used to compile

program to achieve moving heat source loading. The heat source parameters could be inputted like: thermal energy, moving speed, and time. The thermal parameters can be seen at Table 1.

Table 1. Parameters of weld heat source model.

Parameters	Value	Unit
melting width	10	mm
penetration depth	18	mm
Front axle length	3	mm
back axle length	5	mm
coefficient f_f	0,6	
coefficient f_r	1,4	
Welding speed	5	mm/s
Voltage	35	V
Current	350	A

3.3 Residual welding stress analysis

Residual welding stress cloud atlas of rib-to-deck detail after welding process is shown in Figure 4. During the welding process, the stress at melted welds is small, but the stress of the weldments around the weld pool is close to the yield stress of the steel. After welding cooling process, the stress along X-direction and Z-direction of weld joint around the weld pool is close to the yield stress of Q345.

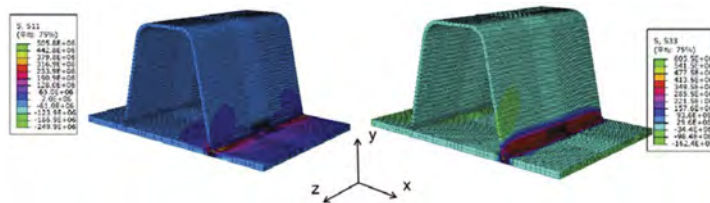


Figure 4. Residual welding stress along X-direction and Z-direction cloud atlas (Unit:Pa).

The local coordinate system is defined for the weld joints. Along the x-direction, the distribution curves of different residual welding stress components are drawn at top, middle and bottom surface of deck, as shown in Figure 5. The longitudinal residual stress σ_z and the transverse residual stress σ_x are both the largest at top surface and the lowest at bottom surface. Although the thickness of deck plate is only 14mm, the stress distribution also shows a significant difference along the deck thickness direction. This means that the closer to the welding heat source, the greater the welding residual stress. And the peak values of σ_z and σ_x both appear at 143mm and 155mm for the bottom surface where the positions are the weld toe position and weld root position,

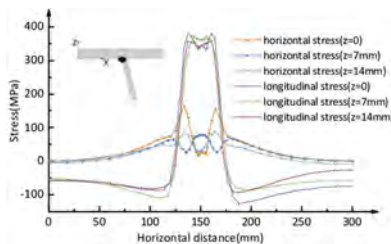


Figure 5. Residual stress distribution of rib-to-deck in half section.

respectively. In the approximate 50mm range near the weld toe and root, longitudinal residual stress σ_z change rapidly, and the peak value of σ_z reaches to the yield stress of Q345. transverse residual stress σ_x is uniformly distributed along the x-direction, and the maximum is 168MPa for the top surface. Therefore, weld root and weld toe of rib-to-deck could be prone to fatigue detail.

4 FATIGUE CRACK PROPAGATION SIMULATION

4.1 Fracture mechanics parameters

Extend finite element method was applied as the calculation tool, and crack dynamic propagation was accomplished based linear elastic fracture mechanics theory. There are three fracture modes of metal, and two or three mix fracture mode are common in real engineering. Therefore, it is necessary to apply fracture criterion considering three fracture mode. Mixed-mode fracture criterion is expressed as(Wu and Reuter Jr 1965):

$$\left(\frac{\Delta K_I}{\Delta K_{th}}\right)^2 + 1.9\left(\frac{\Delta K_{II}}{\Delta K_{th}}\right)^2 + 2.1\left(\frac{\Delta K_{III}}{\Delta K_{th}}\right)^2 = 1.0 \quad (1)$$

where ΔK_I , ΔK_{II} , and ΔK_{III} stand for the SIF ranges of Mode I, II, and III cracks, respectively.

According to the relationship between energy release rate G and stress intensity factor K , mixed-mode fracture criteria can be expressed in the form of energy release rate(Wu and Reuter Jr 1965):

$$\frac{G_I}{G_{th}} + 1.9\frac{G_{II}}{G_{th}} + 2.1\frac{G_{III}}{G_{th}} = 1.0 \quad (2)$$

where G_I , G_{II} , and G_{III} stand for the strain energy release rate of Mode I, II, and III cracks; G_{th} = the threshold of energy release rate. In order to directly use the strain energy release rate calculated by VCCT improving the working rate.

Based on liner elastic fracture mechanics, the Paris formula for the expression of crack propagation is presented in Eq(3)(Paris and Erdogan 1963).

$$\frac{da}{dN} = C \cdot \Delta K^m \quad (3)$$

where C, m refers to material constants; a refers to crack length; N refers to loading cycles; $\Delta K = Y \cdot \Delta \sigma \cdot \sqrt{\pi \cdot a}$; Y refers to the modified factor; $\Delta \sigma$ refers to stress range. According to the BS7910(British Standards Institution 2019), the material constant of the Paris formula in this paper $C=1.28 \times 10^{-12}$ mm \cdot cycle; $m=3.0$.

In the digital fatigue test, the crack propagation rate is calculated by the energy method, which is expressed as follows(Paris and Erdogan 1963):

$$\frac{da}{dN} = c_1 \cdot \Delta G^{c_2} \quad (4)$$

where c_1 and c_2 refer to material constants; ΔG refers to strain energy release rate amplitude. When the crack tip meets $G_{th} < \Delta G$, cracks begin to grow; G_{th} refers to the energy release rate threshold.

The maximum tangential stress criterion(MTS) is applied to determine the fatigue crack propagation direction, the expression is shown as(Erdogan and Sih 1963):

$$\theta = \cos^{-1}\left(\frac{3K_{II}^2 + \sqrt{K_I^4 + 8K_I^2 K_{II}^2}}{K_I^2 + 9K_{II}^2}\right) \quad (5)$$

Where θ is measured with respect to the crack plane.

4.2 Modeling methodology

In order to simulate initial defect introduced by welding process, the initial crack should be inserted in the typical detail at digital fatigue test. Half ellipse shape cracks were adopted in models of other details. Dimension of the half ellipse shape and the quarter ellipse-shaped crack was $a_0/c_0 = 0.5\text{mm}/1.0\text{mm}$ in this paper as shown in Figure 6 (where a_0 is the length of an elliptical semi-short axis and c_0 is the length of the elliptic semi-long axis). To simulate live load caused by fatigue vehicle, fatigue load model III in JTG D64 (Ministry of Transport of the People's Republic of China 2015).

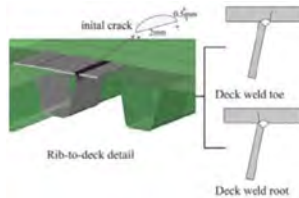


Figure 6. Fatigue crack insertion position.

4.3 Crack propagation analysis of rib-to-deck weld joint detail

Initial cracks size at rib-to-deck weld toe and root were assumed as $a_0/2c_0=0.5\text{mm}/2\text{mm}$. Initial crack plane surface was parallel to the direction of deck thickness. The propagation trend of crack planes in rib-to-deck weld toe is shown in Figure 7. The crack at weld toe propagated along the weld joint and plate thickness direction. The crack size propagated to $a/2c=5\text{mm}/18.5\text{mm}$ after 2.7 million cycle of loadings. Although the long and short axial ratio of semi-elliptical cracks $a/2c$, has been changed during the propagation process, the semi-elliptical shape could be remained basically. The cracks in the propagation process cannot keep in the plane surface, but a slightly deflection as shown in Figure 7. And the crack propagation direction even appeared transverse direction of bridge propagation trend after 2.7 million cyclic loading, which is a phenomenon seriously affecting the safety of bridge use. It was believed that fatigue cracks were mixed-mode cracks with the crack propagation, and the crack plane deflection was caused by the cracks of Mode II and Mode III. Hence, residual welding stress not only make crack grow but also change the propagation direction of the fatigue crack.

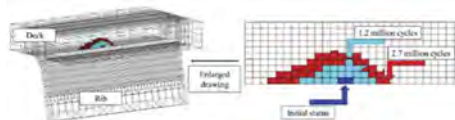


Figure 7. Fatigue crack propagation in the weld toe of deck plate.

In order to judge the fatigue crack mode, the cumulative strain energy release rates of G_I , G_{II} , and G_{III} are calculated as shown in Figure 8. Because Mode II and Mode III were pretty close, the proportional curve of G_{III}/G_I is only drawn to analyze another two Mode cracks' influence, and red dotted line is represented the trend of G_{III}/G_I as shown in Figure 8. At crack propagation initial stage, Mode I was the leading position, and influence of Mode II and Mode III could be ignored. The G_{III}/G_I reached 10% after 1.5 million cycles, and the effect of Mode II and Mode III crack on fatigue crack propagation direction can not be neglected. Between 2.2 million and 2.7 million loading cycles, the proportion of G_{II} and G_{III} increased sharply. At 2.7million cycles, G_{II}/G_I and G_{III}/G_I were about 26.3% and 21.4%. Therefore, the influence of Mode II and III cracks at the crack propagation in the rib weld toe of rib-to-deck detail cannot be ignored during the crack propagation. They will not only affect the fatigue crack propagation rate but also crack propagation direction at this detail.

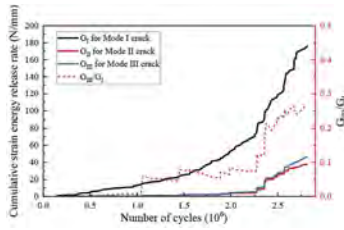


Figure 8. The cumulative strain energy release rate in weld toe of deck plate.

Fatigue crack grown from the deck weld root of rib-to-deck detail is another fatigue mode, also detected in actual bridges. The fatigue propagation behavior differed from the crack initiating from the deck weld toe. Figure 9 illustrates the propagation process of cracks initiating from the deck weld root under a given initial crack condition. The cracks mainly propagated along the long axis of the semi-ellipse cracks. They propagated to the inside of the weld when the propagation trend was along the deck thickness direction. The crack plane was kept in the plane during the propagation process, which indicated that the dominant type of fatigue crack in the weld root of rib-to-deck detail was the I-mode crack. Crack propagation rate and direction was controlled by Mode I crack at this detail.

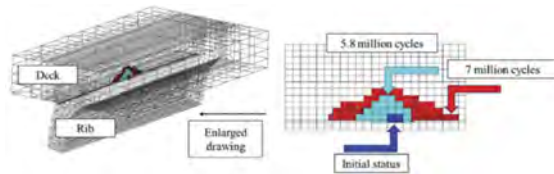


Figure 9. Fatigue crack propagation process in weld root of deck plate.

The cumulative strain energy release rate curve during the crack propagation process is shown in Figure 10. The cumulative strain energy releasing rate G_I of Mode I cracks was dominant during the whole crack propagation process. The increasing rate of these three types strain energy release rate between 0 to 5.8 million cycles was relatively slow. The increase rate G_I of Mode I between 5.8 million to 7 million cycles loading was fast which reached to 102 N/mm at about 2million loading cycles, while the increase rates G_{II} and G_{III} were still slow. G_{II}/G_I and G_{III}/G_I were about 2.4% and 2.7% at the end of 7 million cycles. Hence, the influence of Mode II and III cracks could be ignored during the crack propagation process at this detail.

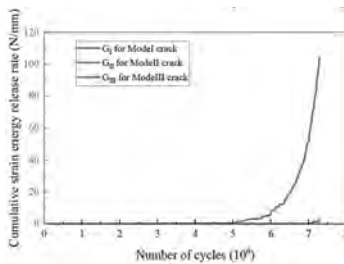


Figure 10. The cumulative strain energy release rate at the rib-to-deck weld root.

5 CONCLUSIONS

Digital fatigue test was selected to simulate the fatigue crack propagation at rib-to-deck detail. In this paper, the multi-scale whole bridge model was established, and properties analysis of fatigue crack propagation properties considering the residual welding stress was set.

1. A rational boundary of residual welding process was put forward. The welding process analysis was shown that there existed large residual stress at rib-to-deck detail. Von-Mises residual stress reached to the mental yield stress of Q345. Hence, the residual stress of rib-to-deck detail could not be neglected.
2. The fatigue crack propagation state and cumulative strain energy release rate analysis result shows that the crack at the weld toe of the rib-to-deck is led by mix mode I-II-III led by mode I, while the influence of mode II and mode III cannot be neglected. And the crack will not keep in plane at the crack propagation due to the existence of mode III.
3. The crack at the weld root of the rib-to-deck was led by mode I, while the influence of mode II and mode III is little. And the crack will keep in plane at the crack propagation. The fatigue crack propagation behavior of these two details are consistent with those obtained by experiments.

ACKNOWLEDGEMENTS

The authors gratefully acknowledge the financial support provided by the Program of National Ten Thousand People Plan Science and Technology Innovation Leading Talents (W03020659), intelligent fatigue monitoring and evaluation of Nansha bridge steel box girder under ultra saturation traffic load and temperature load.

REFERENCES

- Belytschko, T., and T. Black. 1999. Elastic crack growth in finite elements with minimal remeshing. *Int. J. Numer. Meth. Engng.*, 45 (5): 601–620.
- British Standards Institution (Ed.). 2019. Guide to methods for assessing the acceptability of flaws in metallic structures: British standard BS 7910. BSI British standards. London.
- Erdogan, F., and G. C. Sih. 1963. On the crack extension in plates under plane loading and transverse shear. *Journal of Basic Engineering*, 85 (4): 519–525.
- Goldak, J., A. Chakravarti, and M. Bibby. 1984. A new finite element model for welding heat sources. *MTB*, 15 (2): 299–305.
- JTG D64-2015: Specifications for Design of Highway Steel Bridge. Beijing: China Communications Press, 2015. (in Chinese).
- Kiss, K., and L. Dunai. 2002. Fracture mechanics based fatigue analysis of steel bridge decks by two-level cracked models. *Computers & Structures*, 80 (27–30): 2321–2331.
- Moës, N., J. Dolbow, and T. Belytschko. 1999. A finite element method for crack growth without remeshing. *International journal for numerical methods in engineering*, 46 (1): 131–150. Wiley Online Library.
- Nagy, W., P. van Bogaert, and H. de Backer. 2015. LEM Based Fatigue Design for Welded Connections in Orthotropic Steel Bridge Decks. *Procedia Engineering*, 133: 758–769.
- Paris, P., and F. Erdogan. 1963. A Critical Analysis of Crack Propagation Laws. *Journal of Basic Engineering*, 85 (4): 528–533.
- Wang, C. S., B. N. Fu, Q. Zhang, and Y. C. Feng. 2013. Fatigue Test on Full-scale Orthotropic Steel Bridge Deck. *China Journal of Highway and Transport*, 26 (2): 69–76.
- Wang, C. S., Y. Z. Wang, B. Cui, L. Duan, N. X. Ma, and J. Q. Feng. 2020. Numerical simulation of distortion-induced fatigue crack growth using extended finite element method. *Structure and Infrastructure Engineering*, 16 (1): 106–122.
- Wang, C. S., Y. Z. Wang, L. Duan, S. C. Wang, and M. sai Zhai. 2019. Fatigue Performance Evaluation and Cold Reinforcement for Old Steel Bridges. *Structural Engineering International*, 29 (4): 563–569.
- Wu, E. M., and R. C. Reuter Jr. 1965. Crack extension in fiberglass reinforced plastics. *T and M Report, University of Illinois*, 275.
- Yeratapally, S. R., P. E. Leser, J. D. Hochhalter, W. P. Leser, and T. J. Ruggles. 2020. A digital twin feasibility study (Part I): Non-deterministic predictions of fatigue life in aluminum alloy 7075-T651 using a microstructure-based multi-scale model. *Engineering Fracture Mechanics*, 228: 106888.

Nonstructural performance improvements for seismic resilience enhancement of modern code-compliant buildings

M.R. Joo & R. Sinha

Indian Institute of Technology Bombay, Mumbai, India

ABSTRACT: Rapid recovery of functionality after disaster is an important attribute of resilient infrastructure. Modern code-compliant buildings are designed based on life-safety principles and may experience severe damage during earthquakes leading to loss of their use for long periods. Contributors to occupancy and functionality losses should be first identified for enhancing performance and developing resilience-based design guidelines. This study assesses economic, reoccupancy, and functionality losses and subsequent recovery for an archetypical building, considering performance of structural and nonstructural components under a probabilistic performance-based earthquake engineering framework. The study provides deeper understanding of the root causes of functional vulnerability of code-compliant buildings and opportunities to reduce. The contribution of various components to loss of immediate occupancy and functionality is evaluated and implications of various nonstructural improvements on different component-level and building-level resilience metrics are assessed. The study illustrates the necessity of explicit nonstructural design options to enhance seismic resilience of buildings.

1 INTRODUCTION

Recent disasters, including major earthquakes, have demonstrated their potential to set back decades of progress and investment in an instant. Buildings form an important backbone of built infrastructure to support community functioning. Modern buildings are designed following life-safety-based standards using perspective specifications that do not provide an explicit understanding of performance during earthquakes. They have been found to perform better in collapse prevention and life-safety objectives and thus reduce the risk of casualties (Molina Hutt *et al.* 2016, 2022, Du *et al.* 2021, Joo and Sinha 2022, 2023, Joo *et al.* 2022, Terzic and Kolozvari 2022). However, high social expectations (higher performance than code goals, continued functionality after earthquake, etc.) are associated with modern code-conforming and engineered buildings. Experience shows that substantial damage is experienced by various structural and non-structural components which leads to uneconomical repairs, building demolition, occupancy and functionality losses, loss of essential services, long-term societal disruption (Du *et al.* 2021, Joo and Sinha 2023, Joo *et al.* 2022, Terzic and Kolozvari 2022). Such evidences reflect lack of resilience characteristics. The communities take significantly long to recover to pre-earthquake condition, which adds to the indirect seismic losses.

Conventional assessment and design approaches focus on structural performance and loss estimation immediately after an earthquake and do not consider post-event parameters to quantify recovery. The performance is indicated by response parameters, annualized losses, or collapse risk. Performance-based earthquake engineering (PBEE) framework (Moehle and Deierlein 2004, FEMA P-58-1 2018) provides avenues for explicit quantification of performance using various metrics of interest for effective decision making. Several studies (Goulet *et al.* 2007, Molina Hutt *et al.* 2016, del Gobbo *et al.* 2018, Cardone *et al.* 2019, Du *et al.* 2021) employed performance-based approaches to estimate direct and indirect losses. Goulet *et al.* (2007) used PBEE approach to evaluate the seismic response of a low-rise reinforced concrete (RC) structure using collapse risk and economic losses. Cardone *et al.* (2019) assessed the efficacy of various retrofit strategies for RC buildings to reduce expected annual loss. Gobbo *et al.* (2018) evaluated the performance of Eurocode-8 compliant braced RC frame buildings in terms of repair cost.

Rapid recovery is an important attribute of resilience and missing from current code provisions. Functional recovery bridges the gap between design provisions and community resilience (EERI 2019) and thus requires serious consideration for incorporating recovery-based performance objectives in design, assessment, and retrofitting methods for essential facilities. FEMA P-58 (2018) methodology integrates procedures for performance-based design of buildings and enables estimation of direct losses and repair times of various building contents based on their damage levels. While PBEE approach can be extended to quantify recovery and estimate building downtime, a very limited number of studies (Molina Hutt *et al.* 2016, 2022, Du *et al.* 2021, Joo and Sinha 2022, Terzic and Kolozvari 2022) attempted to consider post-earthquake scenario and assess repair or recovery time. Molina Hutt *et al.* (2016) utilized FEMA P-58 approach and evaluated the performance of a tall building using financial losses and downtime as performance metrics and compared different resilience strategies. Du *et al.* (2021) compared seismic performance of RC frame structures with and without structural enhancements using decision variables including repair times. Terzic and Kolozvari (2022) evaluated the functional recovery of a tall building and revealed the need to develop design requirements to improve post-earthquake functional performance of buildings.

Past studies (Du *et al.* 2021, Molina Hutt *et al.* 2022) have focused on improvement of building performance using various structural retrofits. Damage to non-structural systems, essential to a building's operations, can require expensive repairs and lead to unacceptable downtime. Controlling nonstructural damage is essential to maintain post-earthquake occupancy and functionality (Gebelein *et al.* 2017) and only limited number of studies (Molina Hutt *et al.* 2016, Joo and Sinha 2023) have considered nonstructural performance improvements. Therefore, a need exists to quantify the contribution of nonstructural components to occupancy and functionality losses and subsequent recovery. Identifying contributors of occupancy and functionality losses of important buildings forms a basis to understand the post-disaster scenario and opportunities for performance improvement during future events and development of resilience-based design guidelines.

In this study, seismic resilience assessment of an archetypical building, representing state of design and existing construction practices, is conducted to identify components and quantify their contributions to occupancy and functionality losses. Two seismic hazard levels: design basis earthquake (DBE) and maximum considered earthquake (MCE) are considered. The study benchmarks the performance of a midrise RC archetypical commercial office building. It considers component-level damage, building reoccupancy and functionality losses and their subsequent recovery under a probabilistic PBEE framework in line with the requirements of decision-making. The damage probability of each system contributing to occupancy and functionality loss is assessed. The study reveals that high building functionality losses is expected due to a design-level seismic event, which is mainly attributed to extensive damage experienced by various nonstructural building contents. Increasing deformation capacity of various non-structural components is a useful approach for resilience enhancement, as its implementation is comparatively simpler. Therefore, a range of improved non-structural components with high resilience to earthquake damage are explored for improved building performance to minimize the reoccupancy and functionality losses and downtime in expected future events. Their implications on various resilience metrics including economic, reoccupancy, and functionality losses as well as reoccupancy, functional recovery and full recovery time are evaluated. The study illustrates advantages of considering different non-structural design and installation options to build a seismic resilient system for better performance in the wake of future disasters. Contribution of each improved element in reducing the probability of occupancy or functionality loss and the overall effects on building recovery time and recovery trajectories are also presented. The study advocates that performance of non-structural components should be considered by design standards to enhance resilience of buildings and ensure rapid functional recovery. The results provide key indicators of resilience enhancement that enable various stakeholders to contribute to improving building functional performance and recovery.

2 METHODOLOGY

Building-specific resilience assessment was conducted in accordance with the probabilistic PBEE frameworks (FEMA P-58-1 2018, ATC 138-3 2021) for which various steps are outlined

in Figure 1. The details about the selection of archetypical building, structural and non-structural components, ground motion selection, structural modeling and analysis, damage and loss assessment procedure, and functionality loss and subsequent recovery approaches are presented in the subsections below.

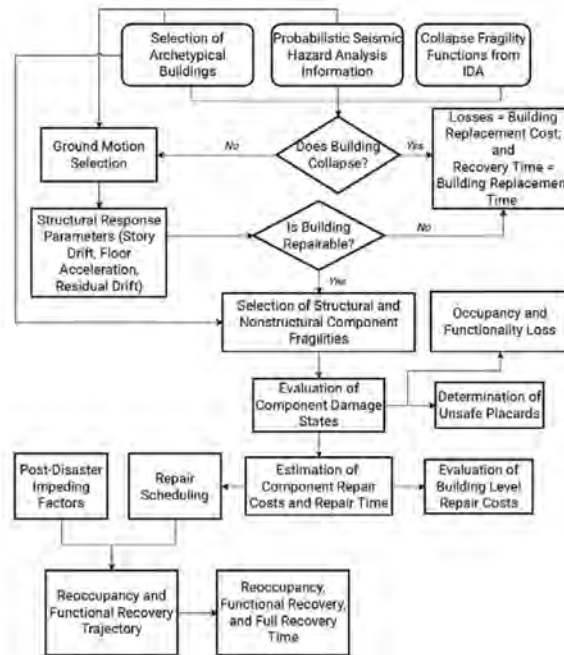


Figure 1. Resilience assessment methodology adopted in the current study.

2.1 Design of archetypical building and selection of components

A special RC moment frame archetypical building (ID-2215), representing a typical commercial building and designed as per Indian standards for New Delhi, India (seismic zone IV), is selected from a suite of archetypes (Badal and Sinha 2019). It represents the state of design and construction scenario for a typical midrise RC structure. The design has given due consideration to existing building stock in the region and can therefore be used to represent the behavior and seismic performance of a class of buildings. The material and geometric characteristics, design load scenarios, member design, and detailing are provided elsewhere (Badal and Sinha 2019). The building is 7 stories high, has 9×3 bays spanning 8.2 m in each direction, typical regular story height of 3.9 m, and first story height of 4.5 m due to foundation depth. The floor area of 1815.48 m^2 is constant across all the levels. The building replacement cost, used for the estimation of direct economic losses in case of collapse or irreparable damage (see Figure 1), was estimated based on the building footprint area. A building replacement time of 910 days (about 2.5 years) was used to represent the recovery time in case of collapse or irreparable damage.

The component fragilities for the RC structural members were obtained from FEMA P-58 fragility database (FEMA P-58-3 2018) based on the closest match of properties with structural design of members. Quantities of structural components were based on architectural and structural design details of the building. Non-structural components were selected based on a review of the inventory of structural and architectural drawings of several real buildings in India, literature survey (del Gobbo *et al.* 2018, Du *et al.* 2021) and recommendations from the normative quantity estimation tool (FEMA P-58-3 2018). The component details, quantities, and dispersion are available in Joo (2022) and other details, including different damage states and corresponding consequence functions, can be referred from the fragility database (FEMA P-58-3 2018).

2.2 Structural analysis and ground motion selection

A two-dimensional structural model employing concentrated plasticity approach and incorporating P-delta effects using *PDelta* nonlinear geometric transformation of the members and a leaning column frame was developed in OpenSees (McKenna *et al.* 2000) to simulate the nonlinear behavior of RC frames under earthquakes. Considering capacity-based shear design for the building, the nonlinearity of beams and columns was modelled using zero-length nonlinear flexural hinges at each end with hysteretic behavior defined using the modified Ibarra-Medina-Krawinkler model (Ibarra *et al.* 2005). The key points and cyclic deterioration parameters for defining backbone curve are derived using semi-empirical relationships (Panagiotakos and Fardis 2001, Haselton *et al.* 2016) and secant stiffness to 40% of yield moment is used as initial stiffness. The effects of longitudinal reinforcement bond-slip behavior, finite beam-column joints, and foundation flexibility are also considered (Joo *et al.* 2022).

Seismic hazard estimation for the selected site in New Delhi, India (28.61°N, 77.21°E) was from a recent probabilistic seismic hazard analysis (Raghukanth 2020). Two intensity levels based on widely used probability of exceedance (POE) - 10% POE in 50 years (DBE) and 2% POE in 50 years (MCE) were selected for the analysis. The site and building-specific conditional mean spectra (Baker 2011) for DBE and MCE intensity levels were developed at analytical fundamental period (T_1) of 2.55 s and used as a target spectra. Twenty pairs of recorded ground motions were selected and scaled at each hazard level to match the arithmetic logarithmic mean of the ground motion suite with the target spectrum. The selection was based on minimum mean squared error between the target spectrum and the scaled ground motion spectrum over the period range of $0.2T_1$ to $2T_1$ (del Gobbo *et al.*, 2018; FEMA P-58-1, 2018). Further details about the selection and scaling parameters are available Joo *et al.* (2022).

2.3 Damage and loss assessment procedure

Damage states and consequent repair costs and repair time of various building components were evaluated in accordance with FEMA P-58 (2018) approach (see Figure 1). Various uncertainties in structural response, damage states, repair cost, impeding time, and repair time are incorporated utilizing 5000 realizations of Monte Carlo simulations. Building collapse fragility functions obtained using incremental dynamic analyses are taken from Badal and Sinha (2022). Component fragility functions from FEMA P-58 fragility database (FEMA P-58-3 2018) are used to relate the response parameters to damage states. The damage results are converted into loss values (repair costs and repair time) using probabilistic consequence functions defined for each component damage state and aggregated for building-level loss estimation (see Figure 1). For each realization, the building is first examined for collapse. If the building does not collapse, it is further evaluated for reparability based on residual drift ratio and building irreparability fragility curve (see Figure 1). For a repairable building, the damage states, and consequences (repair cost, repair time) are evaluated for each component as shown in Figure 1.

2.4 Functionality loss and recovery assessment approach

The damage assessment results are utilized to evaluate the building's occupancy and functionality immediately following an earthquake and until it fully recovers in accordance with the post-earthquake functional recovery framework (Cook *et al.* 2022). The damage states experienced by the components were utilized to assess system-level operational performance, and building-level performance states. The framework used a series of fault trees to correlate component damage to system operation and building function. For a building to be occupiable, the building safety, story access, and user safety of a particular space were verified. The building's functionality was assessed as a function of reoccupancy and user and occupancy-specific functionality requirements.

The repair time obtained from FEMA P-58 analysis is only one contributor of overall downtime (see Figure 1). Various impeding factors delaying the start of repair works, construction constraints, worker allocations, repair priorities and repair optimization are also considered to estimate recovery time (Cook *et al.* 2022). To estimate the time until damaged components are repaired and building function is restored, a building repair schedule

determines repair sequence and work allocation of each building components, instead of only those components affecting function. The entire procedure, including the fault trees to access the functionality of subsystems, repair scheduling algorithm, and impeding factors are available in literature (ATC 138-3 2021, Cook *et al.* 2022). The FEMA P-58 and ATC-138-3 (Beta) methodologies, implemented in SP3 software (SP3 2022) are used in the current study.

3 NON-STRUCTURAL PERFORMANCE IMPROVEMENTS

In this study, resilience assessment of an archetypical building was carried out to understand and identify various vulnerable components and corresponding pathways or strategies for improving component-level as well as overall building resilience. The building (referred to here as baseline model) consists of a bare RC frame as structural system and other typical non-structural components which were assumed to be designed and installed without seismic design considerations, as per typical industry practices in India. Different performance metrics, quantifying scenario losses and recovery times were evaluated and are discussed in subsection 4.1. Various vulnerable non-structural components, contributing significantly to building functionality loss (> 5% realizations at DBE or 10% realizations at MCE) were identified and replaced with improved non-structural components with better seismic performance. The enhanced components can withstand significantly larger deformations or accelerations before reaching a particular damage state which result in less damage to the components for same demand parameters. Major modifications in the building performance model (improved model) and their component fragilities from FEMA P-58 database are listed below:

1. Stairs were assumed to have seismic joints that accommodate drift (C2011.001a).
2. Suspended ceilings with vertical as well as lateral support (C3032.003a-d) were considered.
3. Independent pendant lighting was presumed to be seismically rated (C3034.002).
4. Motor control center was either hard anchored or vibration isolated with seismic snubbers/restraints (D5012.013c).
5. Potable water piping and bracing fragilities of higher (D, E, or F) seismic design category (D2021.013a-b) were considered.
6. Sanitary waste piping and bracing fragilities of higher (D, E, or F) seismic design category (D2031.023a - b) were considered.
7. Heating ventilation and air conditioning (HVAC) fan was either hard anchored or vibration isolated with seismic snubbers/restraints (D3041.103b)
8. HVAC air handling unit was either hard anchored or vibration isolated with seismic snubbers/restraints (D3052.013b).

The improvements in scenario economic, reoccupancy, and functionality losses and subsequent recovery time are detailed in the subsection 4.2.

4 RESULTS AND DISCUSSIONS

4.1 *Baseline model*

Table 1 shows the performance assessment results for the baseline model. The average repair cost ratio, referred to as scenario expected loss (SEL) for DBE and MCE events was 3.5% and 12.4%, respectively, of the building replacement cost. The estimated repair time, in days, based on FEMA P-58 floor-wise parallel and series repair scheduling, respectively, are 6 and 22 at DBE and 21 and 75 at MCE. The archetypical building is immediately reoccupiable after DBE event while taking 102 days after an MCE event. However, functional recovery is achieved only after 174 days and 234 days at DBE and MCE, respectively. The expected (median) time to full recovery to pre-earthquake condition is 207 days and 291 days at DBE and MCE, respectively.

The major contributors to loss of building reoccupancy at DBE level are stairs and interior falling hazards while stairs, red tag, interior falling hazard, and damage to exterior enclosure majorly contribute to occupancy loss at MCE, as shown on the left sides of dashed lines in Figure 2a. Other major components contributing to functionality loss at DBE, in addition to

those resulting in reoccupancy loss include HVAC ventilation, heating, cooling, and exhaust elements, elevators, and sanitary plumbing (see right side of the dashed line, Figure 2a). While, at MCE, the major contributors include HVAC ventilation, heating, cooling, and exhaust elements, elevators, interior space, sanitary plumbing, potable water piping, and electrical equipment (see right side of the dashed line, Figure 2b). The potential of each system to result in building reoccupancy or functionality loss at DBE and MCE can be obtained from the percentage of realizations in which each system affects occupancy, functionality, or both (see Figure 2).

Reoccupancy or functionality of any structure is dynamic and evolves over time due to repairs being carried out in the post-earthquake phase. Figures 3a and 3b, respectively, show the probability of building reoccupancy and functionality over time at DBE and MCE. The reoccupancy and functional recovery trajectories for the baseline model at DBE and MCE are almost parallel (see Figure 3) with different values suggesting that the governing components are same for the two levels but with different damage levels. The governing components for reoccupancy are stairs and for functionality, HVAC elements (see Figure 2). The significant building functionality loss over time reveals a need to focus on recovery-based design philosophies and guidelines and nonstructural performance in design and assessment.

Table 1. Scenario losses, repair time, and recovery time assessment results.

Intensity Level	Model	Scenario Expected Loss (%)	Repair Time (Days)		Median Recovery Time (Days)		
			Parallel	Series	Reoccupancy	Functional Recovery	Full Recovery
10 % in 50 years (DBE)	Baseline	3.5	6	22	0	174	207
	Improved	2.6	5	18	0	0	150
2 % in 50 years (MCE)	Baseline	12.4	21	75	102	234	291
	Improved	10.7	20	69	3	3	261

DBE = Design Basis Earthquake, MCE = Maximum Considered Earthquake

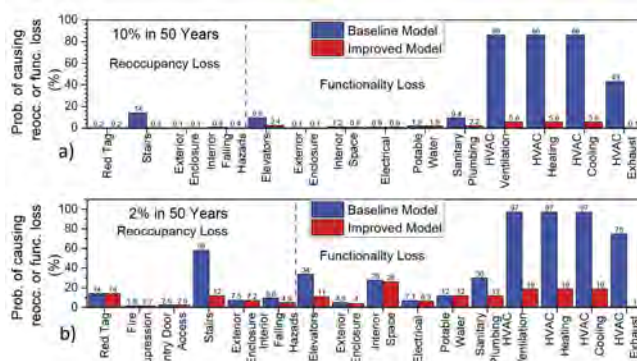


Figure 2. Percentage of realizations for different systems leading to occupancy or functionality loss at (a) DBE (10% in 50 years) and (b) MCE (2% in 50 years).

4.2 Non-structural improvements

The non-structural performance improvements listed in section 3 were undertaken to investigate their potential in reducing scenario economic and functionality losses and downtime. Table 1 presents the loss values and recovery time for the improved model for both scenarios. SEL reduced from 3.5% to 2.6% and 12.4% to 10.7% at DBE and MCE, respectively. Marginal reduction of repair time was also observed. Median building reoccupancy time sharply reduced from 102 days to 3 days at MCE. Functional recovery was also achieved much faster as the median time reduced from 174 days to 0 days at DBE and 234 to 3 days at MCE. The

full recovery time reduced from 207 days to 150 days and 291 days to 261 days at DBE and MCE, respectively. The substantial improvement in reoccupancy and functional recovery implies considerable resilience enhancement with use of enhanced nonstructural components.

The improvement in individual performance (probability of leading to occupancy/functionality loss) at DBE and MCE can be seen in Figure 2. The stairs and HVAC system show significant reduction in probability of occupancy/functionality loss from 14% to 0.5% and 86% to 5.6% at DBE. Similarly, improved stairs, HVAC systems, elevators, sanitary plumbing play a major role to reduce occupancy or functionality losses at MCE (see Figure 2). The percentage of realizations reduced from 58% to 12% for stairs, 34% to 11% for elevators, and 97% to 19% for HVAC components. The improvements for other elements are also shown in Figure 2. Figure 3 shows significant improvement in building reoccupancy and functionality over time after earthquake.

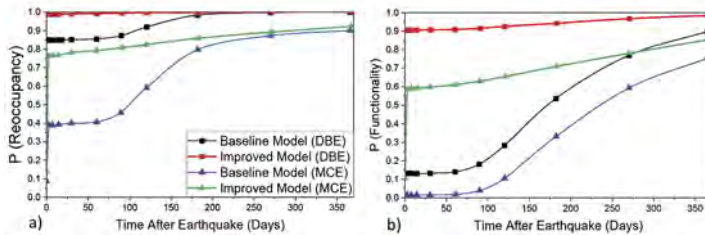


Figure 3. Variation of probability of (a) reoccupancy and (b) functionality, over time in the post-earthquake phase for baseline and improved model.

5 CONCLUSIONS

The study presents resilience assessment of modern code-complaint archetypical building to identify their contributors to reoccupancy and functionality losses and identifies opportunities to improve performance by enhancing capacity of vulnerable nonstructural components. The study considers an archetypical building that was designed, modeled, and analyzed for DBE and MCE scenarios. Damage, functionality loss, and subsequent recovery assessments were conducted in accordance with PBEE approaches. The results identify the various components that lead to functionality loss and the impact of improving their performances. Some of the key conclusions from the study are given below:

- The unacceptably long downtime for code-compliant buildings calls for considering non-structural performance in design approach and emphasizes the need to advance recovery-based design philosophies.
- Damage to conventional stairs is a major contributor of reoccupancy loss at both DBE and MCE scenarios and therefore require improved seismic design considerations.
- HVAC elements are the major contributors to extended functionality loss at DBE as well as at MCE. These elements should either be designed for higher demand parameters or/and buildings should be designed with well-ventilated systems to allow desired functionality without HVAC in the post-disaster phase.
- The use of resilient nonstructural components enables a significant reduction in overall losses and downtime, attributing to major reduction in damage to stairs, HVAC elements, elevators, and other exterior and interior components.
- The reduction of reoccupancy time from 102 days to 3 days at MCE, and functional recovery time from 174 days to 0 days at DBE and from 234 days to 3 days at MCE illustrate the significance of nonstructural improvements in resilience enhancement.

ACKNOWLEDGEMENTS

Authors acknowledge PMRF award to first author for his PhD studies at Indian Institute of Technology Bombay. The authors also thank HBRisk group for free academic access to SP3 software.

REFERENCES

- ATC 138-3, 2021. *Methodology for Assessment of Functional Recovery Time*. Redwood City, California.
- Badal, P.S. and Sinha, R., 2019. Selection of Archetypical Building Configuration for Special Reinforced Concrete Moment-Resisting Frames. *Department of Civil Engineering, Indian Institute of Technology Bombay*. https://www.civil.iitb.ac.in/~rsinha/TechRep_SMRF_Archetype.
- Badal, P.S. and Sinha, R., 2022. A Framework to Incorporate Probabilistic Performance in Force-based Seismic Design of RC Buildings as per Indian Standards. *Journal of Earthquake Engineering*, 26 (3), 1253–1280.
- Baker, J.W., 2011. Conditional Mean Spectrum: Tool for Ground-Motion Selection. *Journal of Structural Engineering*, 137 (3), 322–331.
- Cardone, D., Gesualdi, G., and Perrone, G., 2019. Cost-Benefit Analysis of Alternative Retrofit Strategies for RC Frame Buildings. *Journal of Earthquake Engineering*, 23 (2), 208–241.
- Cook, D.T., Liel, A.B., Haselton, C.B., and Koliou, M., 2022. A framework for operationalizing the assessment of post-earthquake functional recovery of buildings. *Earthquake Spectra*, 38 (3), 1972–2007.
- Du, K., Bai, W., Bai, J., Yan, D., Gong, M., and Sun, J., 2021. Comparative Seismic Performance Assessment of Reinforced Concrete Frame Structures with and without Structural Enhancements Using the FEMA P-58 Methodology. *ASCE-ASME Journal of Risk and Uncertainty in Engineering Systems, Part A: Civil Engineering*, 7 (4), 04021047.
- EERI, 2019. *Functional Recovery: A Conceptual Framework with Policy Options*. Oakland, California.
- FEMA P-58-1, 2018. *Seismic Performance Assessment of Buildings Volume 1-Methodology*. Washington DC.
- FEMA P-58-3, 2018. *Seismic Performance Assessment of Buildings, Volume 3 – Supporting Electronic Materials and Background Documentation*. Washington DC.
- Gebelein, J., Degenkolb, M.B., Burton, H., Cochran, M., Tomasetti, T., McLellan, R., Gumpertz, S., Heger, &, and Porter, K., 2017. Considerations for a Framework of Resilient Structural Design for Earthquakes. *In: SEAOC Convention*. SEAOC Convention.
- del Gobbo, G.M., Williams, M.S., and Blakeborough, A., 2018. Seismic performance assessment of Eurocode 8-compliant concentric braced frame buildings using FEMA P-58. *Engineering Structures*, 155, 192–208.
- Goulet, C.A., Haselton, C.B., Mitrani-Reiser, J., Beck, J.L., Deierlein, G.G., Porter, K.A., and Stewart, J.P., 2007. Evaluation of the seismic performance of a code-conforming reinforced-concrete frame building—from seismic hazard to collapse safety and economic losses. *Earthquake Engineering & Structural Dynamics*, 36 (13), 1973–1997.
- Haselton, C.B., Liel, A.B., Taylor-Lange, S.C., and Deierlein, G.G., 2016. Calibration of Model to Simulate Response of Reinforced Concrete Beam-Columns to Collapse. *ACI Structural Journal*, 113 (6), 1141–1152.
- Ibarra, L.F., Medina, R.A., and Krawinkler, H., 2005. Hysteretic models that incorporate strength and stiffness deterioration. *Earthquake Engineering & Structural Dynamics*, 34 (12), 1489–1511.
- Joo, M.R., 2022. *Performance-Based Seismic Resilience Assessment of Reinforced Concrete Buildings*. Annual Progress Seminar. Department of Civil Engineering, Indian Institute of Technology Bombay.
- Joo, M.R., Badal, P.S., and Sinha, R., 2022. Recovery-Based Seismic Resilience Assessment of IS Code-Conforming RC Buildings. *In: 17th Symposium on Earthquake Engineering, IIT Roorkee, India*.
- Joo, M.R. and Sinha, R., 2022. Adaptive Pathways for Disaster-Resilient Infrastructure – Resilience Assessment as a Fundamental Requirement. *In: Proceedings of DRI Technical Conference*. New Delhi, India: CDRI.
- Joo, M.R. and Sinha, R., 2023. Performance-based Selection of Pathways for Enhancing Built Infrastructure Resilience. *Sustainable and Resilient Infrastructure*, DOI: <https://doi.org/10.1080/23789689.2023.2188347>
- McKenna, F., Fenves, G.L., and Scott, M.H., 2000. Open System for Earthquake Engineering Simulation.
- Moehle, J. and Deierlein, G.G., 2004. A framework methodology for performance-based earthquake engineering. *In: 13th World Conference on Earthquake Engineering*. Vancouver, B.C., Canada
- Molina Hutt, C., Almufti, I., Willford, M., and Deierlein, G., 2016. Seismic Loss and Downtime Assessment of Existing Tall Steel-Framed Buildings and Strategies for Increased Resilience. *Journal of Structural Engineering*, 142 (8), C4015005.
- Molina Hutt, C., Hulsey, A.M., Kakoty, P., Deierlein, G.G., Eksir Monfared, A., Wen-Yi, Y., and Hooper, J.D., 2022. Toward functional recovery performance in the seismic design of modern tall buildings. *Earthquake Spectra*, 38 (1), 283–309.
- Panagiotakos, T.B. and Fardis, M.N., 2001. Deformations of Reinforced Concrete Members at Yielding and Ultimate. *ACI Structural Journal*, 98 (2).
- Raghukanth, S., 2020. Development of probabilistic seismic hazard map of India. *Personal Communication*.
- SP3, 2022. Seismic Performance Prediction Program. Haselton-Baker Research Group
- Terzic, V. and Kolozvari, K., 2022. Probabilistic evaluation of post-earthquake functional recovery for a tall RC core wall building using F-Rec framework. *Engineering Structures*, 253, 113785.

Fatigue performance simulation of UHPFRC composited deck for steel truss girder bridge

C.H. Zhu, L. Duan, C.S. Wang & P.Y. Li

Department of Bridge Engineering, College of Highways, Chang'an University, Xi'an, China

Z. Kang

Xi'an Rail Transit Group Company, Xi'an, China

J. Kang

China Railway Major Bridge Reconnaissance & Design Institute Co., Ltd, Wuhan, China

ABSTRACT: A combined highway and railway steel truss bridge with upper stiffening was taken as an engineering background to explore solution of improving fatigue performance of bridge deck. For highway orthotropic steel deck in upper layer, a layer of ultra-high performance fiber reinforced cementitious composite material (UHPFRC) was composited on deck plate by gluing corrugated steel plate shear connector (CSPC). The stress intensity factor (SIF) amplitude of rib-to-deck detail was analyzed based on linear elastic fracture mechanics. Numerical fracture mechanics results reveal SIF amplitude at the crack tip is lower than the threshold of crack propagation. For railway bridge deck in lower layer, a UHPFRC layer combined with deck plate was proposed. Fatigue stress for rib-to-deck detail under multi-field coupling effect was analyzed. Results show that fatigue stress amplitude was reduced by about 40% compared with steel deck without pavement.

1 INTRODUCTION

Orthotropic steel bridge decks have become the most widely used structures in modern large and medium span steel bridges due to its light weight, high bearing capacity and recyclability, etc. (Wang & Feng 2009, Conner & Fisher 2006, Xiao et al., 2006). However, the fatigue problem of orthotropic steel bridge deck is remarkable due to residual tensile stress, initial imperfection caused by the welding of a large number of connecting welds, long-term traffic load and environmental corrosion. The rib-to-deck detail subjected to high transverse bending moments under wheel load and simultaneously affected by welding method, penetration rate is the most prone to fatigue cracking position in orthotropic steel bridge deck, which reduces durability of pavement (Wang et al., 2017). Fatigue cracks in rib-to-deck detail located on the top of the steel girder are also the most difficult cracks to repair in steel bridge deck. Moreover, the pavement of steel bridge deck is prone to fatigue and durability damage problems such as cracking, rutting, sliding delamination under traffic and environmental loads.

Therefore, the design of new bridges should conform to the concept of higher durability, easy maintenance and long life to adapt to the characteristics of high speed, heavy load, large traffic volume and special environment of modern traffic (Duan et al., 2015). Composite steel bridge deck which improves the cooperative bearing capacity, increases the local stiffness of the steel deck and reduces the stress concentration is a significant method to solve the problem of fatigue cracking of steel bridge deck and the lack of durability for pavement. Duan et al. proposed to replace part of the traditional asphalt concrete pavement with ultra-high

performance fiber reinforced cementitious composite material (UHPFRC) to form UHPFRC composite steel bridge deck (Duan et al., 2020).

UHPFRC has fine strain strengthening characteristics, bending ability and fracture resistance (Brühwiler 2019). Thus, the crack width control ability and fatigue resistance of UHPFRC layer are enhanced, which satisfies the technical requirements of cooperating with the steel bridge deck and improving the stress state of pavement layer. Extensive researches of fatigue performance of UHPFRC composited steel bridge deck have been carried out. Dieng et al. carried out the full-scale tests and finite element analysis to study the application of UHPFRC as the pavement of OSD (Dieng 2013). The results showed that UHPFRC overlay reduce the stain at the weld root of rib-to-deck connection by 60% compared with OSD without pavement. Chen investigated the fatigue behavior of UHPC-orthotropic steel composite deck in hogging bending and evaluated the fatigue strength of cracks in the low portion of rib web and fatigue damage of the short headed studs (Chen 2019). Ma conducted fatigue analysis of UHPFRC composite deck considering the bridging degradation of cracked UHPFRC and the bond stiffness degradation at UHPFRC-steel interface (Ma 2021). Domestic and foreign scholars have carried out a large number of studies on composite layer design. Shear stud is the most common combination design. However, welding studs will cause a large number of welding fatigue details in where fatigue cracking is likely to occur under coupling of residual stress, heavy traffic and initial crack. Cold connection composite design adopted epoxy bonding and cold bonding shear connector avoid fatigue vulnerable welded details, reduce the technical difficulty of replacing the composite layer and become the research focus of long-life composite steel bridge deck in recent years. Wang developed the UHPFRC-steel composite bridge decks with cold-connectors to improve the local stiffness of the steel deck and avoid or reduce the welded shear connector, therefore, increasing the interface stiffness of UHPFRC composite steel decks (Wang et al., 2017). WANG proposed a modified steel strip-UHPFRC composite deck to increase the tensile strength at the bottom of UHPFRC (Wang & Shao 2020). Parametric static test and fatigue test were carried out and S-N curve of the steel strip-UHPC composite members was proposed.

The above literature review shows that improving the fatigue resistance and durability of steel bridge deck is necessary to ensure structural safety. The design method and research of UHPFRC composite steel bridge deck still need further research to provide technical support for the application. A cross-scale digital fatigue analysis model was established to study the fatigue performance of bridge decks of a steel truss bridge under the coupling of vehicle load, dead load, residual stress and initial crack. The thermal-solid coupling numerical model was used to simulate the welding process and calculate the welding residual stress field. For highway steel deck, a composite layer of UHPFRC with adhesive cold bonding corrugated steel plate shear connector was proposed. And the SIF amplitude of rib-to-deck detail was analyzed. For railway bridge deck, fatigue stress amplitude for rib-to-deck detail was analyzed.

2 FINITE ELEMENT MODEL OF BRIDGE STRUCTURE

A combined highway and railway steel truss bridge with upper stiffening in which upper highway and lower railway all laid on orthotropic steel bridge deck integrally connected with chord top plate was taken as the engineering background to investigate the fatigue performance of the UHPFRC combined with cold bonding connectors for composite bridge deck.

The cross section of this ten-span continuous steel truss with a length of 1410m is shown in Figure 1(a). The center distance and height of main truss are 30.5m and 12m, respectively. The height of the upper stiffening chord is 32m. The thickness of the deck is 16mm to 20mm. The geometrical dimension of the longitudinal U rib is 300mm×280mm×8mm with a spacing of 600mm. As shown in Figure 1, the conventional OSD was designed as a 70mm thick asphalt pavement. The UHPFRC overlay was reinforced with steel meshes where 30mm thick of asphalt was applied to protect the UHPFRC layer. In order to provide a great connection between steel plate and UHPFRC, the cold bonding corrugated steel plate was used at the OSD-UHPFRC overlay interface. The material properties of UHPFRC and epoxy resin refer

to previous test study (Duan et al., 2017). The multi-scale continuous steel truss bridge finite element was established as shown in Figure 1(b). The full-scale steel truss bridge was modeled using beam element. A five panel lengths main girder segment all modeled by shell element was established. The solid elements were used for the steel deck segment sub model, rib-to-deck sub model, asphalt layer, UHPFRC layer and cold bonding corrugated steel plate shear connector. The cohesive element was used for epoxy layer.

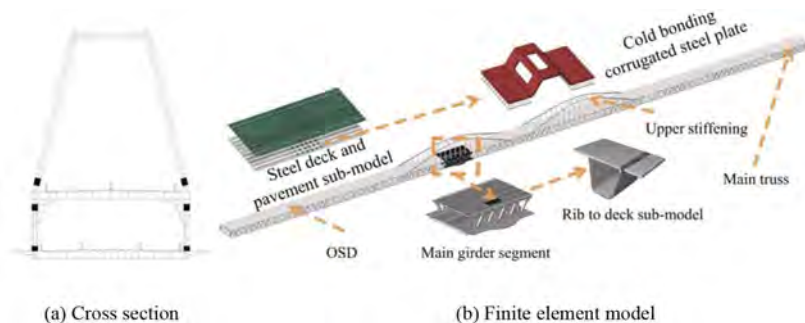


Figure 1. Background and finite element model.

3 NUMERICAL FATIGUE SIMULATION OF UPPER BRIDGE DECK

3.1 Numerical simulation of residual stress

It was found by fatigue stress test that the welded details in the compressive stress zone which indicated that the influence of residual stress on fatigue performance at joint details cannot be neglected. Zhao and Berg estimated and analyzed the welding residual stress of a U-rib stiffened plate. The results showed that residual stress near the weld seam was closed to material yielding stress. Considering the actual welding sequence, material parameters and construction technology of bridge deck, the thermal-stress sequence coupling method was used to simulate the welding residual stress. The solid sub-model as shown in Figure 2 was determined. The horizontal length and longitudinal width of deck are 600mm and 200mm respectively. And the thermo-dynamic parameters refer to previous studies (Zhao & Wu 2012).

Double ellipsoidal heat source model was used to realize the dynamic simulation of temperature filed. Figure 3 shows that the shape of the molten pool and the size of the weld during the welding process are relatively close, indicating that the parameters refer to existing research results.

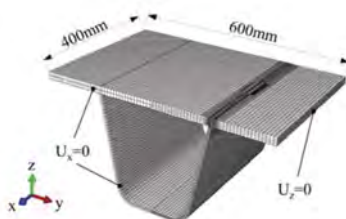


Figure 2. Rib-to-deck sub model.

The Von mises stress after cooling around the weld joint were large and closed to yield stress of steel material. The edges at the top surface, middle section and bottom surface of the deck plate were selected as paths to analyze stress. In Figure 4, the transversal and longitudinal residual stress were plotted at three paths. The transverse stress which was perpendicular propagation direction of cracks initiated at the weld toe and weld root of the deck and had a significant effect on fatigue performance of the fatigue cracks. The transverse and longitudinal

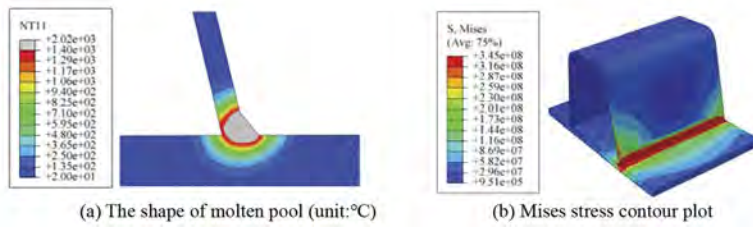


Figure 3. Result of welding numerical simulation.

residual stress values of the deck changed dramatically in the transverse range of about 60mm at weld joint. The maximum of transverse stress was 405MPa and the maximum of longitudinal stress exceeded 350MPa.

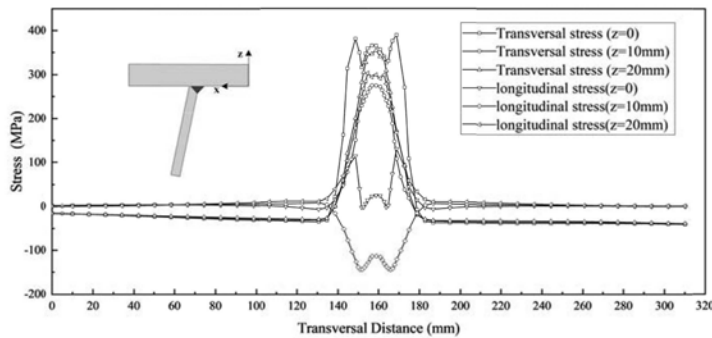


Figure 4. Residual stress distribution of rib-to-deck weld in 1/2 section.

3.2 Fatigue load model

The fatigue load model III of the Chinese specification for the design of highway steel bridges was used as the loading model to analyze the fatigue performance of the composite bridge deck as shown in Figure 5. Load positions changed by applying Fortran programming and axle load was converted to equivalent surface load. Each axel load was 120kN and the contact area of wheel landing was 200mm×600mm so that the single wheel equivalent surface pressure was 0.5MPa. There were eight transversal loading cases named HLC1 to HL6 with 150mm transverse spacing as shown in Figure 6. Longitudinal loading cases TLC1 to TLC250 were adopt. The longitudinal speeds of vehicle were 120mm/s, 60mm/s and 10mm/s. The vehicle velocities were 60mm/s and 10mm/s when the wheel arrived area of 240mm and 120mm away from the crack, respectively.

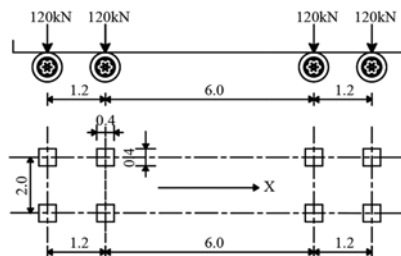


Figure 5. Fatigue load vehicle.

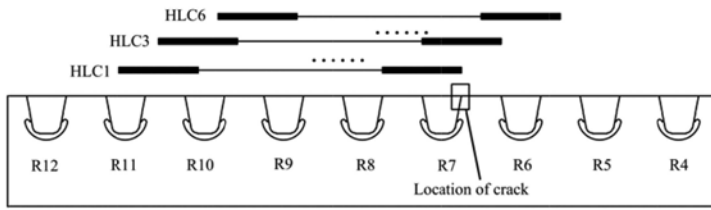


Figure 6. Transverse loading case of a rib-to-deck plate connection between crossbeam.

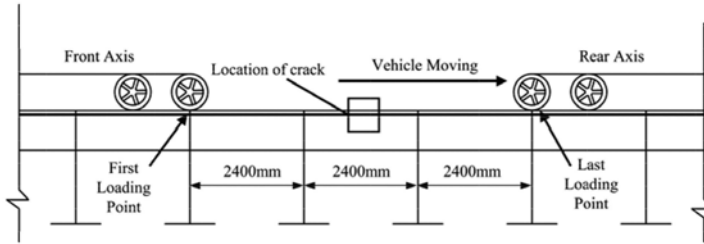


Figure 7. Longitudinal loading case.

3.3 Analysis of stress intensity factor

There are two type typical cracks in rib-to-deck detail, namely fatigue cracks D1 and D2 initiating from the deck-side weld toe and weld root respectively of rib-to-deck welding joint. A half ellipse was used to simulate the initial crack, with a size of $a_0/2c_0=0,5\text{mm}/2\text{mm}$, where a_0 and c_0 were length of major and minor axe respectively. Digital fracture parameter analysis of the two typical fatigue cracks were carried out under coupling effect of dead load stress field, live load stress field and welding residual stress field. Crack would propagate when the magnitude of the stress intensity factor ΔK is greater than the threshold ΔK_{th} . Fatigue crack propagation threshold of $63\text{MPa}\cdot\text{mm}^{1/2}$ in BS7910 was adopted in this paper. Cracks in steel bridge deck are often mixed mode cracks. The mixed mode fatigue crack propagation criterion was shown in Eq 3.1 (Jin & Li 1978). And The equivalent stress intensity factor K_e could be determined by Eq 3.2 (Jin & Li 1978).

$$(K_I + K_{II})^2 + \frac{1}{1 - 2\nu} K_{III}^2 = K_{IC}^2 \quad (3.1)$$

where K_I , K_{II} , and K_{III} are stress intensity factor of crack tip of Mode I, Mode II, and Mode III; ν is Poisson's ratio; and K_{IC} is critical stress intensity factors of modes I crack.

$$K_e = \sqrt{(K_I + K_{II})^2 + \frac{1}{1 - 2\nu} K_{III}^2} \quad (3.2)$$

Figure 8 shows the stress intensity factors of crack D1 versus the locations of the wheel load. It was found that the crack was mixed mode cracks led by mode I. The SIF of the crack modes II and III was 17.9% and 23.6% lower than crack mode I at case LLC-154, which indicated that cracks modes II and III could not neglect. Thus, equivalent SIF K_e must be considered to predict the crack growth at the detail. Figure 8(d) provides the maximum equivalent SIF of the conventional OSD compared with the UHPFRC-steel composite bridge decks. The maximum equivalent SIF ΔK_e at crack tip of crack D1 for the conventional OSD was $84.3\text{MPa}\cdot\text{mm}^{1/2}$, which denoted that ΔK_e was higher than the threshold ΔK_{th} proposed in BS7608. It can be noticed that the crack will propagate under the effect of live loads combined

with the welded residual stresses and dead load. Consequently, the composite bridge deck was applied to arrest the fatigue crack propagation in the typical detail. It was found that adopting the composite bridge decks with cold bonding connectors reduced the maximum equivalent SIF to $36.2\text{MPa}\cdot\text{mm}^{1/2}$. The equivalent stress intensity factors were lower than the recommended ΔK_{th} proposed for this detail. It denoted that adopting the composite bridge decks with cold-connectors could stop the fatigue crack propagation.

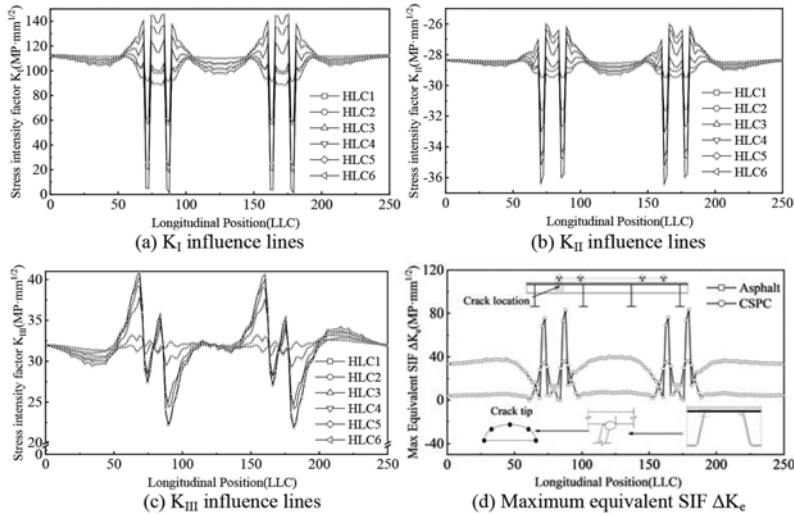


Figure 8. SIF of crack D1 in rib-to-deck detail.

Figure 9 shows the stress intensity factors of crack D2 versus the locations of the wheel load. It was found that the crack mode I was mainly propagated and cracks modes II and III could not neglect. The maximum equivalent SIF ΔK_e was $73.0\text{MPa}\cdot\text{mm}^{1/2}$ for conventional OSD calculated at crack tip of D2, which means that the crack will propagate. Figure 9(d) shows that by adopting the UHPFRC-steel composite bridge decks with CSPC, ΔK_e was $23.8\text{MPa}\cdot\text{mm}^{1/2}$. Compared with ΔK_{th} , it could be found that adopting the composite bridge decks with CSPC could arrest the fatigue crack propagation.

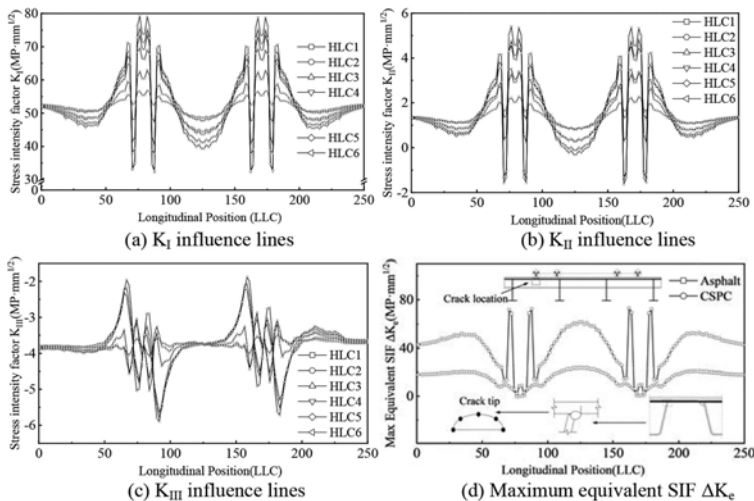


Figure 9. SIF of crack D2 in rib-to-deck detail.

4 NUMERICAL FATIGUE SIMULATION OF LOWER BRIDGE DECK

Urban railway is laid on lower bridge decks. The train is a B-type metro vehicle with a length of 19.52 m, a vehicle distance of 12.6 m, an axial spacing of 2.2 m, and a maximum axle load of 145 kN. The longitudinal speed of train was 150mm/s and there were 148 longitudinal cases realized by Fortran programming. The stress variations at two points D3 and D4 which are located at deck-side weld toe and weld root separately of rib-to-deck welding joint were studied when the steel bridge deck was paved with UHPFRC and without pavement under effects of train load, dead load and welding residual stress.

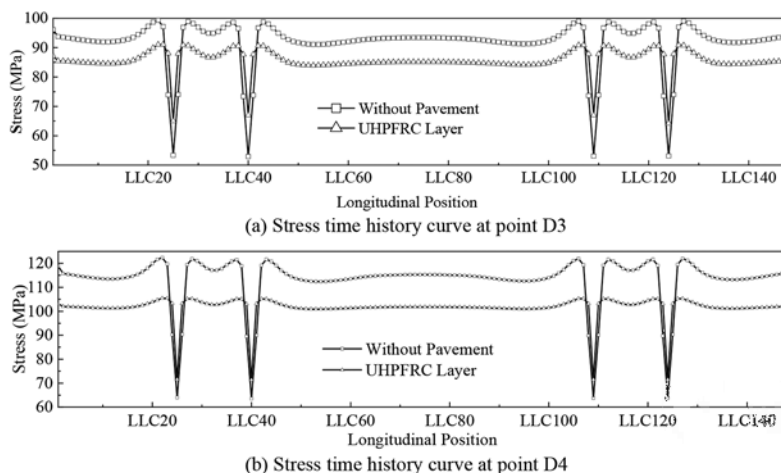


Figure 10. Stress change under train load and residual welding stress.

Figure 10 gives the stress time history curve. The stress at rib-to-deck detail was symmetrically distributed, and the stress peaked when the axle are near the detail. The stress amplitudes at D3 and D4 were 46.4 MPa and 58.8 MPa respectively when the bridge deck had no pavement layer. The stress amplitudes at D3 and D4 were 26.8 MPa and 35.1 MPa respectively when UHPFRC layer was used. It could be seen that the stress amplitudes at D3 and D4 were reduced by about 42.2 % and 40.3 % respectively by using UHPFRC layer compared with no pavement.

5 CONCLUSIONS

Fatigue cracking of orthotropic steel deck and pavement damage are typical engineering problems. UHPFRC layer with cold bonding connector is possible solution for typical engineering problems of fatigue cracking in orthotropic steel deck and pavement durability problem. This paper takes the UHPFRC-steel composite bridge decks with cold bonding connectors as the research object. A cross-scale digital fatigue analysis model was established to study the fatigue performance of UHPFRC composite bridge decks of a steel truss bridge under the coupling of vehicle load, dead load, residual stress and initial crack. The following conclusions can be drawn:

1. The welding process analysis was proved the existence of large residual stress at rib-to-deck detail. Residual stress reached to the mental yield stress, and thus the residual stress of rib-to-deck detail could not be neglected.
2. For highway steel deck, UHPFRC-steel composite bridge decks with cold bonding corrugated steel plate shear connector reduced equivalent SIF amplitudes below the threshold at

crack tip of crack initiating from the deck-side weld toe of rib-to-deck welding joint, so did the crack initiating from the deck-side weld root. It denoted that fatigue crack propagation will be stopped.

3. For railway steel deck, the stress amplitudes in rib-to-deck detail was reduced by about 40% when UHPFRC layer was used.
4. This research was concentrated on the fatigue performance simulation of UHPFRC composited deck for steel truss girder bridge. In the future, experimental tests for the UHPFRC-steel composite bridge decks under the wheel load should be carried out, and in-site monitoring during in-service stage are needed to analyze the performance of the composited deck.

ACKNOWLEDGEMENT

The authors gratefully acknowledge the financial support provided by the National Natural Science Foundation of China (52078044), Scientific Research and Development Project of China Railway Major Bridge Reconnaissance & Design Institute CO., Ltd.

REFERENCES

- Brühwiler, E. 2019. UHPFRC technology to enhance the performance of existing concrete bridges. *Structure and Infrastructure Engineering*: 16(1):1–12.
- Chen, S. et al. 2019. Experimental study on fatigue performance of UHPC-orthotropic steel composite deck. *Thin-Walled Structures*: 142: 1–18.
- Connor, R.J. & Fisher, J.W. 2006. Identifying Effective and Ineffective Retrofits for Distortion Fatigue Cracking in Steel Bridges Using Field Instrumentation. *Journal of Bridge Engineering*: 11(6):745–752.
- Dieng, L. et al. 2013. Use of UHPFRC overlay to reduce stresses in orthotropic steel decks. *Journal of Constructional Steel Research*: 89:30–41.
- Duan, L. & Houankpo, T.O.N. & Wang, C.S. et al. 2015. UHPFRC strengthening method for existing bridges. *IABSE Conference, Geneva 2015: Structural Engineering: Providing Solutions to Global Challenges*: 1179–1186
- Duan, L. & Brühwiler E. & Wang C.S. 2020. Cold stiffening of orthotropic steel decks by a composite UHPFRC layer. *Journal of Constructional Steel Research*: 172 (2020) 106209.
- Duan, L. & Wang C.S. et al. Steel fiber reinforced concrete composited steel bridge deck based on bonded corrugated shear connector:201710621402.7. (in Chinese)
- Jin, J.S. & Li, R.F. 1978. Engineering fracture mechanics. *Journal of Chongqing University (Natural Science)*: 1(4): 79–119. (in Chinese)
- Ma, C.H. et al. 2021. Fatigue analysis of a UHPFRC-OSD composite structure considering crack bridging and interfacial bond stiffness degradations. *Engineering Structures*: 249: 113330.
- Wang, C.S. & Feng, Y.C. 2009. Review of Fatigue Research for Orthotropic Steel Bridge Decks. *Steel Construction*: 24(9): 10–13. (in Chinese)
- Wang, C.S. & Zhai, M.S. & Tang, Y.M., et al. 2017. Numerical fracture mechanical simulation of fatigue crack coupled propagation mechanism for steel bridge deck. *China Journal of Highway and Transport*: 30(3): 82–95. (in Chinese)
- Wang, Y. & Shao X.D. et al. 2020 UHPC-based strengthening technique for significant fatigue cracking steel bridge decks *China Civil Engineering Journal*: 53(11): 92–101, 115. (in Chinese)
- Xiao, Z.G. & Yamada, K. & Inoue, J. 2006. Fatigue Cracks in Longitudinal Ribs of Steel Orthotropic Deck. *International Journal of Fatigue*: 28(4): 409–416.
- Zhao, Q. & Wu, C. 2012. Numerical analysis of welding residual stress of U-rib stiffened plate *Engineering Mechanics*: 29(8): 262–268. (in Chinese)

Redundancy, importance, and robustness analyses for damage scenarios of bridges

S. Sarmiento, J. González-Libreros & G. Sas
Luleå University of Technology, Sweden

I. Björnsson & S. Thöns
Lund University, Sweden

ABSTRACT: Bridges are an important part of the traffic infrastructure, which are subjected to high safety requirements and economic consequences in case of functionality failure. Therefore, it is needed to consider potentially substantial direct and indirect risks during service life, i.e., the need for risk and robustness analyses. Over the last decades, various quantitative performance criteria have been developed but their interrelation and compatibility has hardly been systematically studied. This paper contains a proposal of a novel and complementary formulation of interrelations between reliability- and risk-based robustness, importance, and redundancy indicators. The classification, derivation, and exemplification of the interrelations between these indicators are presented and formulated for two case studies of a pre-stressed concrete bridge considering different hazard scenarios namely overloading and chloride attack. The analyses and applications lead to the identification of interrelations between the reliability based robustness, redundancy and importance indicator indicators and with the risk based robustness indicator.

1 INTRODUCTION

During the services life, bridges are exposed to several environmental conditions that might contribute to their deterioration and therefore the decrease of their safety level. Existing structures were designed under the assumption that the failure of their critical element induces the failure of the overall structural system. This, for some cases, leads to an underestimation of the structural system capacity since the contribution of secondary elements is not considered, ignoring the ability of the structure to redistribute loads (known as redundancy), and the capacity of withstanding additional load despite the failure of one of its elements (known as robustness) (Ghosn et al. 2010).

Through the years, several authors have proposed and further improved, different indicators aimed to quantify the redundancy, robustness, and element importance of existing structures. For example, Frangopol & Curley (1987) who introduced an indicator based on the reliability index, which was later modified by Feng et al. (2020) by incorporating the concept of progressive collapse probabilities. Similarly, Ghosn & Moses (1998) proposed reliability-based redundancy and robustness measures. Indicators expressed in terms of failure probabilities were developed by Rabi et al. (1989), which were later modified by Lind (1995). Later, Baker et al. (2008) introduced a risk-informed robustness measure to account for failure consequences, for which Faber et al. (2017) introduced a probabilistic characterization. Additionally, Praxedes et al. (2022) develop a new risk-based robustness index aimed to account for the full spectrum of risk. Other researchers have expanded the scope of these measures by adding damage progression, optimization, and combinatorial principles, among others (e.g., Biondini et al. 2008, Straub & Kiureghian 2011, Cavaco et al. 2013). Biondini (2009) is an example of a key study on the evaluation of robustness of structural subjected to continuous degradation in which a methodology for life-time assessment of concrete structures is used together with time-variant analysis.

Despite the large number of contributions in this area, there are hardly any studies, which analyze jointly such indicators nor document their interrelations. Therefore, this paper contains a first step towards a classification, derivation, and exemplification of interrelations between reliability- and risk-based robustness, importance, and redundancy indicators. The objective of this proposal is to facilitate the general understanding, and differences between the information that the indicators provide. The quantification of the indicators requires the implementation of reliability, and risk analyses, introduced in Section 2 together with the classification, derivation and illustration of the interrelation of the indicators under study. The exemplification is performed through for two case studies of a pre-stressed concrete bridge which represent two relevant damage scenarios. The description of the example application is presented in Section 4, followed by the analysis of the results and discussion in Section 5. Finally, the conclusions are presented in Section 6.

2 METHODOLOGY

2.1 Reliability and risk analyses of damage scenarios

Initially, the modeling of failure scenarios is performed by considering the critical element(s) of the system, i.e., the elements most probable to fail first due to the identified exposure(s). This paper considers two of the most common sources of damage to multibeam bridges: overloading and chloride attack (see e.g., Ghaffary & Moustafa 2020). These two exposures are studied separately to compare the structural system's element and system behavior. Given the exposure, two different failure scenarios are modeled, namely Scenario 1 (s_1) and Scenario 2 (s_2), for overloading and chloride attack, respectively.

Two system states and one element state are analyzed to determine the robustness of a determined structure. The first system state corresponds to the intact structure which represents the structure under analysis subjected to normal loading, before being exposed to any hazard. The element state corresponds to the analysis of the critical element(s) due to a determined exposure, and the second system state corresponds to the damaged structure which represents the case in which the critical elements have failed and are discarded as a part of the structure.

After obtaining the failure scenarios, the reliability analysis is performed, which aims to quantify the safety level of a determined structure. This safety level is commonly expressed in terms of the reliability index (β) and its associated probability of failure ($P(F)$). The failure event F with random variables resistance R and load S is then defined as:

$$F: g(\mathbf{X}) = R - S \leq 0 \quad (1)$$

$g(\mathbf{X})$ is the limit state function, and \mathbf{X} is the vector of random variables.

In this paper, a metamodel-based reliability analysis is performed to obtain the values of P (F) and β . This methodology is an iterative process that consists of obtaining points from the random space using the Latin Hypercube Design (LHD) to assess the value of $g(\mathbf{X})$ at each point and then, by a Gaussian interpolation, a new limit state function is obtained denominated as $\hat{g}(\mathbf{X})$. With the new limit state function, the Monte Carlo simulation (MCs) is used to calculate $P(F)$, and β . The process described previously is repeated until a convergence criterion is satisfied, and in each iteration is enhanced by using a learning function. More details regarding the implemented methodology can be found in Sarmiento et al. (2022).

The values of $P(F)$ and β are obtained for the different failure scenarios mentioned above, i.e., the intact system, the critical element(s), and the damaged system. Therefore, three different limit state functions are formulated and shown in Equation 2. The limit state function of the intact system $g_{F_S}(\mathbf{X})$ works for both scenarios since it is the case of the structure in normal conditions. $g_{F_l}(\mathbf{X})$ and $g_{F_S|F_l}(\mathbf{X})$ are different for s_1 and s_2 since the critical element(s) might be different for each one, and thus different damaged systems are obtained.

$$F_S: g_{F_S}(\mathbf{X}) = R_S - S \leq 0, F_l: g_{F_l}(\mathbf{X}) = R_l - S \leq 0 \text{ and } F_S | F_l: g_{F_S|F_l}(\mathbf{X}) = R_S(F_l) - S \leq 0 \quad (2)$$

where R_S is the intact system resistance; R_l is the resistance of the critical element l ; and $R_S(F_l)$ is the system resistance given failure F_l of the critical element l .

Finally, a risk analysis is conducted to obtain the risk-based robustness indicator. In structural engineering risk is set up as the product of the probability of failure $P(F)$ and the corresponding failure consequence C_f (see e.g., Faber 2008), which is normally expressed in terms of costs, i.e., a monetary value. The values of risks provide a measure of what probability different ranges of consequences will occur (Faber 2008). Risk can be classified into direct and indirect, which are normally related to the probability of local damage and to the failure of the overall system, respectively (Baker et al. 2008, Faber 2008). Direct (R_{Dir}) and indirect (R_{Ind}) risks can be calculated using Equation (3). Different types of consequences can be considered when performing structural risk analysis, and they can also be classified as direct and indirect consequences, as shown in Equation 3. C_{Dir} is associated with the costs related to the failure of the critical element(s), whereas C_{Ind} is the additional consequences that are not counted as direct (Faber 2008).

$$R_{Dir} = P(F_l) \cdot C_{Dir} \cdots \text{and} \cdots R_{Ind} = P(F_l) \cdot P(F_S|F_l) \cdot C_{Ind} \quad (3)$$

where $P(F_l)$ is the probability of failure of the critical element(s), $P(F_S|F_l)$ is the conditional probability of the system failure F_S due to the critical element F_l , C_{Dir} is direct consequences of failure, and C_{Ind} indirect consequences of failure.

2.2 Redundancy, importance, and robustness analyses

In bridge engineering, importance, redundancy, and robustness are important concepts related to the safety and performance of a bridge system. Various reliability-based, or risk-based indicators relating to redundancy, importance and robustness characteristics can be found in the scientific literature. Importance refers to the significance of a component or element in maintaining the overall structural integrity (e.g., Straub & Kiureghian 2011), meanwhile redundancy is related to the existence of alternative load paths, so that if one element fails, the load is transferred to other elements in the system (e.g., Dusenberry et al. 2022). Furthermore, robustness refers to the ability of the system to maintain its structural integrity without excessive changes in system capacity, reliability, or performance during the occurrence of adverse events (e.g., Starossek & Haberland 2010 and Baker et.al. 2008). Despite the different meanings of the redundancy, importance and robustness indicators, it is observed that there is a common basis in reliability element and system analysis subjected to a damage or element failure scenario.

For an overview, Table 1 contains a denotation, formulation, and a classification of the redundancy, importance and robustness indicators. The denotation is harmonized for consistency with the definition of the indicators. The indicators classification shows that the indicators include (1) either ratios or differences of probabilities and reliabilities or both, differences, and ratios (Table 1).

The robustness contains by sums aggregated direct and indirect risk for hazards, component damage states and system failure states (see e.g., Faber 2008). In this paper a reformulation is introduced with consideration of single hazard, damage, and failure scenarios s and rewrite robustness index as:

$$I_{rob}(s) = \frac{P_{Dir}(s) \cdot C_{Dir}(s)}{P_{Dir}(s) \cdot C_{Dir}(s) + P_{Ind}(s) \cdot C_{Ind}(s)} \quad (4)$$

where $P_{Dir}(s)$ and $C_{Dir}(s)$ are the direct probability and consequences, respectively, related to $R_{Dir}(s)$, and $P_{Ind}(s)$ and $C_{Ind}(s)$ are the indirect probability and consequences, respectively, related to $R_{Ind}(s)$.

If $P_{Dir}(s)$ and $P_{Ind}(s)$ are associated with the probabilities defined in Equation 3 it can be established that:

$$P_{Dir}(s) = P(F_l(s)) \text{ and } P_{Ind}(s) = P(F_l(s)) \cdot P(F_S(s)|F_l(s)) \quad (5)$$

The scenario-wise formulation of Equation 4 facilitates the introduction of a probability ratio $Q_P(s)$ as:

$$Q_P(s) = P_{Ind}(s)/P_{Dir}(s) \quad (6)$$

The robustness index can then be rewritten as:

$$I_{rob}(s) = C_{Dir}(s)/(C_{Dir}(s) + Q_P(s) \cdot C_{Ind}(s)) \quad (7)$$

Replacing Equation 5 into Equation 6, $Q_P(s)$ can be simplified as:

Table 1. Redundancy and robustness index summary and their classification.

Indicator denotation	Formulation	Ratio	Diff.	Rel.-based	Risk-based	Reference
System and component reliability difference	$\Delta\beta_u = \beta_S - \beta_I$		X	X		Ghosn & Moses (1998)
Damaged system and component reliability difference	$\Delta\beta_d = \beta_{F_S F_I} - \beta_I$		X	X		
Component importance ratio	$IR_S = P(F_S)/P(F_I)$	X		X		Rabi et al. (1989)
Damaged system importance ratio	$IR_d = P(F_S F_I)/P(F_S)$	X		X		
Reliability difference ratio	$\beta_r = \beta_S/(\beta_S - \beta_{F_S F_I})$	X	X	X		Frangopol & Curley (1987)
Importance difference ratio	$RI = (P(F_S F_I) - P(F_S))/P(F_S)$	X	X	X		
Single element importance	$SEI = P(F_S F_I) - P(F_S)$		X	X		Straub & Kiureghian (2011)
Direct risk to total risk ratio	$I_{rob} = R_{Dir}/(R_{Dir} + R_{Ind})$	X	X	X	X	Baker et al. (2008)

$$Q_P(s) = \frac{P_{Ind}(s)}{P_{Dir}(s)} = P(F_S(s)|F_I(s)) \quad (8)$$

In this study, complementary formulations of the indicator I_{rob} are derived with the objective of creating an interrelation between the risk-based robustness index and the reliability-based redundancy/robustness indicators. Equations 9-11 show how the re-formulation of Equation 6 can be obtained using IR_d , IR_S , RI , and SEI since they are calculated based on the probabilities of failure. It is considered that the failure of the intact system $P(F_S)$ is independent of the scenario.

$$Q_P(s) = \frac{P(F_S(s)|F_I(s))}{P(F_S)} \cdot \frac{P(F_S)}{P(F_I(s))} \cdot P(F_I(s)) = IR_d(s) \cdot IR_S(s) \cdot P(F_I(s)) \quad (9)$$

If using the indicator RI , $Q_P(s)$ can be re-written as:

$$Q_P(s) = P(F_S) \cdot (RI(s) + 1) = IR_S(s) \cdot (RI(s) + 1) \cdot P(F_I(s)) \quad (10)$$

or in function of SEI :

$$Q_P(s) = SEI(s) + P(F_S) \quad (11)$$

It is also possible to express the reliability-based indicators in function of the factor $Q_P(s)$, by re-arranging Equations 9-11, and for the indicators $\Delta\beta_d$ and β_r as:

$$\Delta\beta_d(s) = -\phi^{-1}(Q_P(s)) - \beta_I(s) \quad \text{and} \quad \beta_r(s) = \beta_S/(\beta_S + \phi^{-1}(Q_P(s))) \quad (12)$$

The expressions above can be illustrated by evaluating the indicators for different $Q_P(s)$ values, which can be obtained by considering the domain $0 \leq I_{rob} \leq 1$, and relevant consequences values. Figure 1 displays an illustration of the indicators, for different values of $Q_P(s)$ considering the values of the consequences ($C_{Dir}(s) = 9.2 \times 10^5$ and $C_{Ind}(s) = 1.8 \times 10^8$) and probabilities ($P(F_I) = 2.28 \times 10^{-6}$ and $P(F_S) = 5.41 \times 10^{-11}$) obtained in Sarmiento et al. (2022).

When the coefficient Q_P , i.e., the probability of system failure given element failure $P(F_S(s)|F_i(s))$, increases, the robustness index I_{rob} decreases linearly. The damaged system and component reliability difference $\Delta\beta_d$ also decreases, but with different inclinations, i.e., partly exponential, and partly linear following the inverse standard normal CDF. The reliability difference ratio β_r behaves similar to $\Delta\beta_d$, but with a smaller amplitude. The SEI , IR_d and RI indicators increase with increasing Q_P values, linearly for low Q_P and exponential for higher Q_P . Both IR_d and RI yield in the same numerical values due to a very small $P(F_S)$. The value of the indicators IR_S and $\Delta\beta_u$ are 2.37×10^{-5} and 2.42×10^8 , respectively, and they remain constant for different Q_P since they are independent of $P(F_S(s)|F_i(s))$.

Structure's failure probabilities are usually very small; therefore, indicators defined by probability ratios tend to be either really small or high (e.g., IR_d and RI) making their interpretation more difficult. When an interrelation between the different robustness and redundancy indicators exists, an easier comparison and interpretation can be obtained. For instance, it is observed that a value of $IR_d = 3.2E+09$ in Figure 1 corresponds to $Q_P \approx 1.75E-01$ and therefore a value of $I_{rob} \approx 0.23$ (or $\beta_d \approx 3.65$) is obtained, which can be interpreted as a low robustness level (value far from $I_{rob}=1.0$).

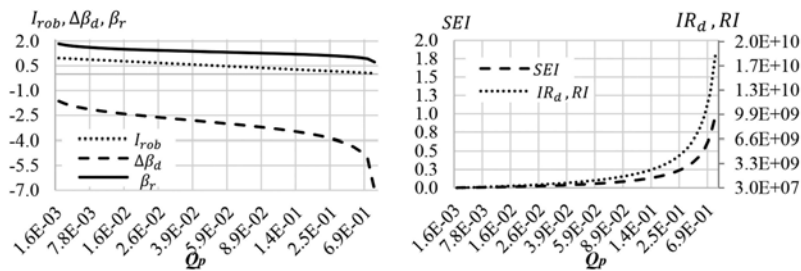


Figure 1. Variation of importance, robustness, and redundancy indicators for different values of q_p , where ir_d and ri have the same numerical values, i.e., follows the same curve.

3 EXEMPLARY REDUNDANCY, IMPORTANCE AND ROBUSTNESS QUANTIFICATION

The classification and derivation of the interrelations between the redundancy, importance, and robustness indicators (Section 3) are formulated and exemplified for two case studies of a pre-stressed concrete bridge considering overloading (s_1) and chloride attack (s_2). The geometry of the structure analyzed is presented in Figure 2. It is considered that the structure under normal conditions is subjected only to traffic loads, which are represented through the design truck HL-93 (AASHTO, 1965). For s_1 the structure is subjected to an unexpected overload located at the weakest point of the bridge superstructure, i.e., the mid-span of the external girder. Therefore, the damaged system considers the failure of one of the external girders by removing this element from the FEM.

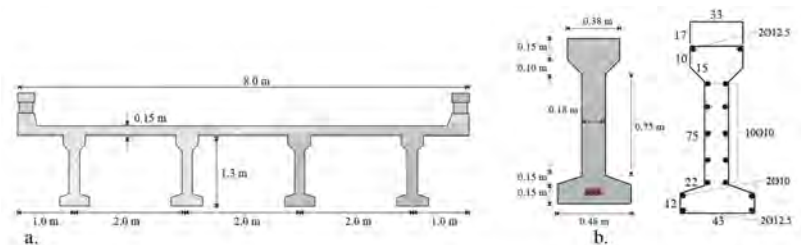


Figure 2. The geometry of a. the transversal section of the superstructure and b. the beam and reinforcement configuration of the section at mid-span.

For s_2 the structure is subjected to chloride ingress through the concrete surfaces, which leads to reinforcement corrosion (pitting corrosion). Given the normal loads of the structure, i.e., the traffic loads, the critical section is the same as s_1 . For the reinforcement in this section, due to the high concentration of stresses, corrosion propagates faster leading to an earlier failure. Therefore, the damage system is represented by removing the two rebars and four prestressing cables from the external girder, since they are located at the same distance to the bottom concrete surface.

The structure capacity is assessed using Nonlinear Finite Element Analysis (NLFEA), and to develop the FE models of both scenarios, the software ATENA Studio v.5.9 is implemented. The capacity of the four tendons and two bars system is obtained analytically, using the expressions in Tu et al. (2019) to obtain its reduced resistance due to the transversal area reduction. The probabilistic parameters for the reliability analysis are listed in Table 2. The probabilistic models are based on standards (CEB-FIP 1993, JCSS 2000) and previous studies (Akgul & Frangopol 2004, Nowak & Collins 2012, Dias-da Costa et al. 2019). Correlation between concrete properties is modelled, and the correlation coefficients were taken from Strauss et al. (2009). The formulations for I_{rob} and $Q_P(s)$ described in Equations 4-5 can be obtained for the case study if considering the $P_{Dir}(s)$ and $P_{Ind}(s)$ as described in Table 3, for both s_1 and s_2 .

Table 2. Random variables and probabilistic parameters.

Scenario 1 and Scenario 2				Scenario 2			
Variable	Distribution	Mean	COV	Variable	Distribution	Mean	COV
f_c (MPa)	Log-normal	38.16	0.18	D (m ² /s)	Normal	$2.5 \cdot 10^{-2}$	0.18
f_t (MPa)	Weibull	2.77	0.18	C_s (%)	Normal	$2.5 \cdot 10^{-2}$	0.18
E_c (MPa)	Log-normal	$3.34 \cdot 10^4$	0.15	C_{cr} (%)	Normal	$4.0 \cdot 10^{-3}$	0.23
G_f (N/m)	Weibull	140.61	0.2	M_R	Log-normal	1.2	0.05
A_{ps} (m ²)	Normal	$4.96 \cdot 10^{-4}$	0.0125	M_A	Log-normal	1.0	0.05
DL (kN)	Normal	15.81	0.1				
P_e (kN)	Normal	429.33	0.05				
P_{ve} (kN)	Gumbel	134.1	0.25				

Table 3. Direct and indirect probabilities for the analyzed scenarios.

	$P_{Dir}(s)$	$P_{Ind}(s)$		$P_{Dir}(s)$	$P_{Ind}(s)$
S_1	$P(F_{beam})$	$P(F_S F_{beam}) P(F_{beam})$	S_2	$P(F_{T,B})$	$P(F_S F_{T,B}) P(F_{T,B})$

f_c is the concrete compressive strength, f_t the concrete tensile strength, E_c the concrete modulus of elasticity, G_f the concrete fracture energy, A_{ps} the prestressing tendons' transversal area, DL the death load (self-weight of the structure), P_e the prestressing effective force, P_{ve} the vehicle load, D the diffusion coefficient of chloride, C_s the surface chloride content, C_{cr} the critical chloride content, M_R the resistance uncertainty factor, and M_A the analysis uncertainty factor.

where F_{beam} represents the failure of the external beam, $F_{T,B}$ the failure of the tendons and bars system, and F_S the failure of the system.

4 RESULTS AND DISCUSSION

The results obtained through the reliability analysis are presented in Table 4, which show that the reliability of the intact system is considerably higher than the reliability of the critical element for both scenarios. The damaged system for s_1 has a higher reliability $\beta_{FS|FI}$ since no material degradation is considered in contrast to s_2 , where, additionally to the failure of tendons and bars on the external beam, also degradation of the remaining reinforcement due to chloride attack is considered.

Figure 3 Shows, by building upon Figure 1, the indicators according to Table 1 for a range of Q_P . The values of Q_P and indicators are highlighted with the vertical line at $Q_P \approx 1.31E-02$ for s_1 , and $Q_P \approx 2.5E-02$ for s_2 . It is worth noticing that the indicators IR_S and $\Delta\beta_d$ are not

illustrated since they remain constant due to their independency on $P(F_s(s)|F(s))$. Table 5 contains the individual values of the indicators.

Table 4. Reliability results.

	β_t	β_S	$\beta_{F_S F_t}$	$P(F_t)$	$P(F_S)$	$P(F_S F_t)$
s_1	5.04	6.46	2.22	2.3×10^{-6}	5.4×10^{-11}	1.3×10^{-2}
s_2	4.02	6.46	1.95	1.8×10^{-5}	5.4×10^{-11}	2.5×10^{-2}

Table 5. Indicators values obtain from a reliability and risk analysis.

	$\Delta\beta_d$	IR_d	I_{rob}	IR_S	RI	SEI	β_r	$\Delta\beta_u$
S_1	-2.8	2.4×10^8	0.8	2.4×10^{-5}	2.4×10^8	1.3×10^{-2}	1.52	1.42
S_2	-2.1	4.6×10^8	0.62	3.0×10^{-6}	4.6×10^8	2.6×10^{-2}	1.43	2.44

All shown indicators are sensitive to a change of Q_P . For increasing values of the damaged system failure probability ($Q_P = P(F_s(s)|F(s))$) the indicators I_{rob} , $\Delta\beta_d$ and β_r experience a linear decrease. This decrease is due to a higher loss on the system's reliability after the failure of the critical element. In contrast, indicators SEI , IR_d and RI increase exponentially, as the importance of the failed element becomes higher with an increasing damaged system failure probability.

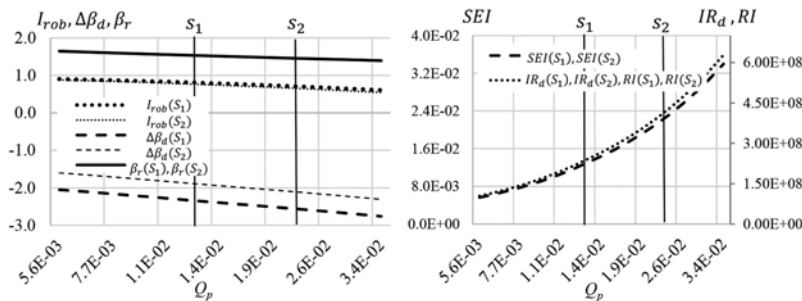


Figure 3. Variation of the indicators in function of the coefficient Q_P .

The indicators β_r , SEI , IR_d and RI coincide for the evaluated Q_P values for both scenarios since the intact system failure probability ($P(F_S)$) is the same. The indicators I_{rob} and $\Delta\beta_d$ have different values for s_1 and s_2 because they depend on the critical element failure probabilities ($P(F_t(s))$), which are different for s_1 and s_2 . The negative $\Delta\beta_d$ values indicate that the system reliability given element failure is lower than the critical element reliability. Thus, lower values of $\Delta\beta_d$ can be interpreted as lower reliability-based robustness levels. In contrast, higher values of IR_d represent higher failure probability after the failure of the critical element, i.e., an increase in reliability-based vulnerability. Lower values of I_{rob} are obtained when the indirect risks, i.e., risks associated with the system's failure, have a bigger influence on the total risks, which represents lower risk-based robustness levels.

The increase on values reflect an increase difference of the system failure probability before (intact) and after (damaged) the element's failure. Thus, higher SEI values represent a higher probabilistic-based importance of the critical element on the system. The indicator RI provides a normalized version of SEI ; therefore, a higher probabilistic-based importance of the element is also reflected through higher RI values. The indicator β_r is higher for lower differences between the system reliability before and after the failure of the element, and therefore higher β_r reflects better reliability-based redundancy levels.

The indicator IR_S is another probabilistic-based measure of the element importance, and its value provides the ratio between the intact system and element's failure probability. Therefore, values closer to one represent equal failure probabilities, thus, lower redundancy levels. A relation between the reliabilities of the intact system and the element is also provided by $\Delta\beta_u$. The indicator gives the difference between both reliabilities in a way that higher $\Delta\beta_u$ values, i.e., higher intact system's reliability in comparison with the element's reliability, represent higher reliability-based redundancy levels.

5 CONCLUSIONS

This paper presents a summary and classification of the available reliability- and risk-related redundancy, importance, and robustness indicators. Also, it contains the development of new complementary formulations of interrelation between the different indicators. A case study of a prestressed concrete bridge is used to exemplify, illustrate, and compare the derived formulations.

Based on the analyses presented it can be concluded that the studied indicators provide different structural performance measures, such as reliability-based robustness and redundancy ($\Delta\beta_d$, IR_d , β_r and $\Delta\beta_u$), importance (SEI , IR_S and RI) and risk-based robustness (I_{rob}). Furthermore, an interrelation of robustness, redundancy and importance indicators can be derived with the introduction of the indirect to direct failure probability ratio Q_p for which the indicators $\Delta\beta_d$, IR_d , β_r , SEI , RI and I_{rob} show to be sensitive. The derived formulations provide a way of translating the values of the reliability-based indicators into the risk-based robustness index I_{rob} . This translation allows an easier comparison and a better understanding for indicators such as IR_d , IR_S and RI . With an example application, the robustness, redundancy and importance indicator calculation and their interrelation are illustrated and the identified interrelations of the reliability based indicators and the risk based robustness indicators are exemplified.

REFERENCES

- Akgül, F. & Frangopol, D. M. 2004. Lifetime performance analysis of existing prestressed concrete bridge superstructures. *Journal of Structural Engineering* 130 (12): 1889–1903.
- AASHTO. 1965. A Policy on Geometric Design of Highways and Streets. *American Association of State Highway Officials, Washington, D.C.*
- Baker, J. W., Schubert, M. & Faber, M. H. 2008. On the assessment of robustness. *Structural safety* 30 (3): 253–267.
- Biondini, F., Frangopol, D. M. & Restelli, S. 2008. On structural robustness, redundancy, and static indeterminacy. *Structures Congress 2008: Crossing Borders*, ASCE, Reston, VA: 1–10.
- Biondini, F. 2009. A measure of lifetime structural robustness. In *Structures congress 2009: Don't mess with structural engineers: Expanding our role*, 30 April – 2 May. Austin, Texas, USA.
- Cavaco, E. S., Casas, J. R., Neves, L. A. C. & Huespe, A. E. 2013. Robustness of corroded reinforced concrete structures. A structural performance approach. *Structure and Infrastructure Engineering* 9(1): 42–58.
- CEB-FIP, M. 1993. Model code for concrete structures. *Comité Euro-International du Béton, Secretariat Permanent*, Case Postale, 88.
- Dias-da Costa, D., Neves, L., Gomes, S., Hadigheh, S. & Fernandes, P. 2019. Time-dependent reliability analyses of prestressed concrete girders strengthened with CFRP laminates. *Engineering Structures* 196: 109–297.
- Dusenberry, D. O. 2022. New SEI/ASCE disproportionate collapse mitigation standard. *J. Struct. Eng.* 148 (4): 04022014.
- Faber, M. H., Ed. 2008. Risk Assessment in Engineering - Principles, System Representation & Risk Criteria, *JCSS Joint Committee on Structural Safety*.
- Faber, M. H., J. Qin, S. Miraglia and S. Thöns. 2017. On the Probabilistic Characterization of Robustness and Resilience. *Procedia Engineering* 198 (Supplement C): 1070–1083.
- Feng, D. C., Xie, S. C., Xu, J. & Qian, K. 2020. Robustness quantification of reinforced concrete structures subjected to progressive collapse via the probability density evolution method. *Engineering Structures* 202: 109877.
- Frangopol, D. M. & Curley, J. P. 1987. Effects of damage and redundancy on structural reliability. *Journal of structural engineering* 113(7): 1533–1549.

- Ghaffary, A. & Moustafa, M. A. 2020. Synthesis of repair materials and methods for reinforced concrete and prestressed bridge girders. *Materials* 13(18): 40–79.
- Ghosn, M. & Moses, F. 1998. NCHRP report 406: redundancy in highway bridge superstructures. *Transportation Research Board, National Research Council*, Washington, DC.
- Ghosn, M., Moses, F., & Frangopol, D. M. 2010. Redundancy and robustness of highway bridge superstructures and substructures. *Structure and Infrastructure Engineering* 6 (1-2): 257–278.
- JCSS. 2000. Guideline for reliability-based assessment of existing structures. *The Joint Committee on Structural Safety*, Denmark.
- Lind, N. C. 1995. A measure of vulnerability and damage tolerance. *Reliability Engineering System Safety* 48(1): 1–6.
- Nowak, A. S. & Collins, K. R. 2012. Reliability of structures. *CRC Press: Boca Raton, FL, USA*.
- Praxedes, C., Yuan, X. X. & He, X. H. C. 2022. A novel robustness index for progressive collapse analysis of structures considering the full risk spectrum of damage evolution. *Structure and Infrastructure Engineering* 18(3): 376–394.
- Rabi, S., Karamchandani, A. & Cornell, C. A. 1989. Study of redundancy of near-ideal parallel structural systems. *5th International Conference on Structural Safety and Reliability, ASCE, New York*: 975–982.
- Sarmiento, S., Gonzalez-Libreros, J. H., Sas, G., Thöns, S., Björnsson, I., & Diaz, R. S. 2022. A risk-based robustness evaluation of a prestressed concrete bridge. *In Bridge Safety, Maintenance, Management, Lifecycle, Resilience and Sustainability*: 2045–2052.
- Starossek, U. & M. Haberland. 2010. Disproportionate collapse: Terminology and procedures. *J. Perform. Constr. Facil* 24 (6): 519–528.
- Straub, D. & Der Kiureghian, A. 2011. Reliability acceptance criteria for deteriorating elements of structural systems. *Journal of Structural Engineering, Trans. ASCE* 137 (12): 1573–1582.
- Strauss, A., Hoffmann, S., Wedner, R. & Bergmeister, K. 2009. Structural assessment and reliability analysis for existing engineering structures, applications for real structures. *Structure and Infrastructure Engineering* 5 (4): 277–286.
- Sørensen, J. D., Rizzuto, E., Narasimhan, H. & Faber, M. H. 2012. Robustness: Theoretical framework. *Structural Engineering International* 22(1): 66–72.
- Tu, B., Dong, Y. & Fang, Z. 2019. Time-Dependent Reliability and Redundancy of Corroded Prestressed Concrete Bridges at Material, Component, and System Levels. *Journal of Bridge Engineering* 24(9):04019085.

Structural behavior of composite truss girder with thicker concrete deck at side span in a cable-stayed bridge

M.Y. Yang & C.S. Wang

Department of Bridge Engineering, College of Highways, Chang'an University, Xi'an, China

Y.Q. Li & Y.C. Feng

CCCC First Highway Consultants, Xi'an, China

ABSTRACT: Composite cable-stayed bridge is more and more widely used, which fills the economic gap between traditional concrete cable-stayed bridge and steel girder cable-stayed bridge. This paper studied the behavior of composite truss girder with thicker concrete, based on a composite truss girder cable-stayed bridge with thicker concrete at side span. The multiple scale models of the whole bridge were established to investigate the distribution of normal stress of concrete and steel truss under dead load and live load. The finite element results showed that the stress of concrete is main compressive stress, and the distribution of stress of cable section concrete is uneven with obvious shear lag phenomenon. The stress of lower chord at the pier's top section is large. As the thickness of concrete increases, the stress distribution becomes more uniform, and the thickness of concrete is recommended to be 40 cm ~ 50 cm.

1 INTRODUCTION

The composite truss girder comprises a steel truss girder, bridge deck, and shear connectors with a strong spanning capacity. The concrete slab is connected through the shear connectors with the upper chord of the truss and the steel cross beam, respectively. The composite truss girder takes full advantages of the tensile properties of steel and the compressive properties of concrete to improve the material utilization and bearing capacity, which has the characteristic of light weight, less steel consumption, and strong spanning ability. The concrete slab in composite truss girder is beneficial to increase the stiffness of the main truss, improve traffic conditions and reduce the engineering cost. Concrete slab not only plays the role of bridge deck, the main truss horizontal and vertical connection, but also assists the main truss in bearing shear force. On the one hand, the concrete slab bears and transmits the bridge deck load, on the other hand, it forms a stable spatial structure with the main truss, which makes the lateral bending stiffness and torsional stiffness of the bridge larger. The composite structure is suitable for bridges with larger spans. The composite girder cable-stayed bridge structure is a kind of cable-stayed bridge structure first proposed by German bridge designer Leonhardt in 1980. It combines the advantages of concrete cable-stayed bridges and steel cable-stayed bridges, and has strong economic advantages.

Many scholars have studied the structural behavior of simple composite girders. Wang et al. (2008) studied the performance of high strength steel and concrete composite girders through numerical simulation, considering parameters of the geometrical dimension of concrete slabs, transverse reinforcement ratio, and material strength. The numerical analysis results showed that the longitudinal slip was affected by material strength, the width of the concrete slab, and transverse reinforcement during the in-elastic stage. Machacek & Cudejko (2009) investigated the longitudinal connection of the steel truss and concrete slab through parametric studies, finding that the greater the concrete slab dimensions, the greater the values of longitudinal shear.

At the whole bridge scale, Li et al. (2013) studied the influence of concrete shrinkage and creep on deformation, internal force, and stress of composite cable-stayed bridges through numerical simulation. The simulated results showed that the shrinkage and creep of concrete cause stress redistribution. Additional tensile stress is produced in the concrete slab, and the main beam undergoes axial compression deformation. Jin et al. (2010) established a finite element model to study the deck response and the stress state of truss joints of truss composite girder cable-stayed bridge under dynamic load, considering the influence of geometric nonlinearity and material nonlinearity.

There are many scholars have studied the shear lag effect in composite girders. Johnson & Lewis (1966) studied the effective width at the limit state of the continuous composite girder under uniform load. Macorini et al. (2006) calculated the effective width of a composite girder under long-term impact using the finite element method, considering the shrinkage and creep of concrete. Pedro & Reis (2010) established the whole bridge model of a composite cable-stayed bridge, and analyzed the mechanical performance at the end of the construction and service stages. Wang et al. (2022) carried out finite element analysis on composite cable-stayed bridges and then calculated the distribution of effective width coefficients of the whole bridge. The results showed that cable spacing and bridge width have a great influence on the effective width. Giaccu et al. (2022) proposed a calculation method for the effective width of the composite girder considering the combined axial force and bending moment through a finite element model of a whole composite cable-stayed bridge.

The mechanical properties of simple system composite structure girder bridges and composite girder cable-stayed bridges with bridge deck thicknesses of 25 cm~30 cm have been further studied. However, there are few studies on the mechanical performance of composite truss girder structures in a cable-stayed bridge with a concrete deck thickness of 40 cm on average. Therefore, it is necessary to carry out some research on it. In this paper, based on a composite truss girder with a thicker concrete deck at the side span in a cable-stayed bridge, the main span is 930 m, a finite element model is established to study the behavior of composite truss girders with a thicker concrete deck.

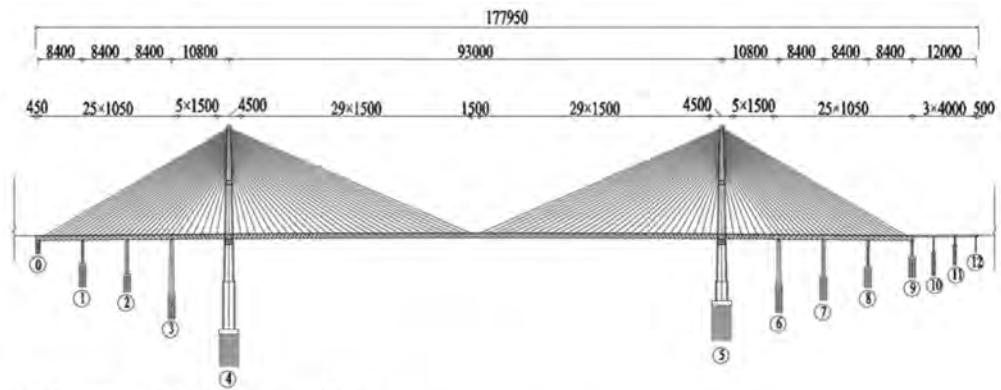
2 NUMERICAL ANALYSIS

2.1 *Bridge description*

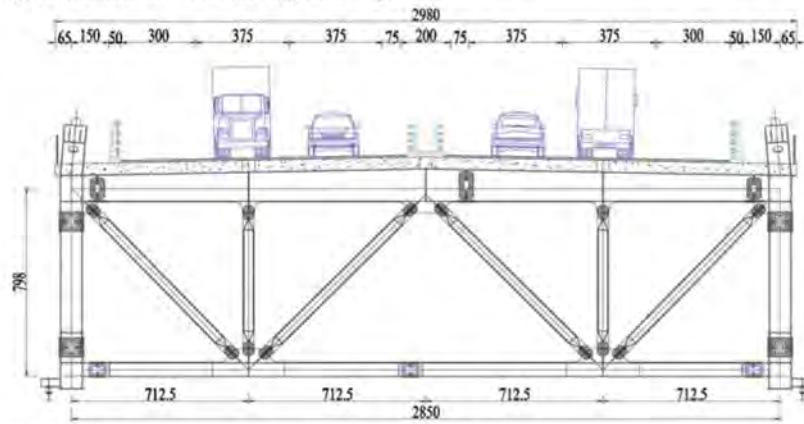
In this paper, the research object is a composite girder cable-stayed bridge with two diamond-type towers and two parallel strand cables, as shown in Figure 1. The full length of this bridge is 1650m. Three auxiliary piers are installed in each side span, so the bridge has nine spans ($3 \times 84 + 108 + 930 + 108 + 3 \times 84 = 1650$ m). The main span girder is a steel composite truss girder with an orthotropic steel deck, while the side span is a steel composite truss girder with a thicker concrete deck. The length of the side span is 360 m, and the total width is 29.8 m. The truss girder comprises N-shaped main truss, transverse truss, secondary crossbeam, a longitudinal girder, and bottom laterals. The standard girder length of the main truss is divided into 7.5 m and 10.5 m. The height of the main truss is 7.98 m, and the thickness of the concrete slab is 46.8 cm. The steel truss girder and the concrete slab are connected through shear connectors. The standard cable distance is 15 m, and the cable distance in the dense cable area of the side span is 10.5 m. Q420 steel is used for the upper and lower chord of the main truss, Q345 steel is used for the rest chords, and C55 concrete is used for the deck of the side span.

2.2 *Finite element model*

The full bridge finite element model was established through Midas Civil to determine the rational completion cable force of the bridge. The results showed that the 3# auxiliary pier is the most unfavorable position where the stress is largest under the dead and live loads. Then, a multiple-scale model was built to study the structural behavior of the composite truss girder with thicker concrete near the 3# auxiliary pier. In the finite element analysis, to improve the



(a) Elevation of the cable-stayed bridge



(b) Standard cross-section of the main girder at side span

Figure 1. The general layout of the cable-stayed bridge (unit: cm).

calculation efficiency, the solid element (C3D8R) with reduced integration was used to simulate the concrete slab, the shell element (S4R) was selected for the main truss girder, and the truss elements (T3D2) was chosen for the reinforcement in the concrete slab as well as the cables. The towers and the rest girders are simulated by the beam element (B31) to improve the calculation efficiency. The elastic modulus of concrete is 3.6×10^4 MPa, and Poisson's ratio is 0.2. The elastic modulus of the steel truss girder is 2.06×10^5 MPa, and Poisson's ratio is 0.3. The finite element model is shown in Figure 2. Ignoring the interface slip between the concrete slab and the steel girder, the "Tie" command simulates the connection between the concrete slab and the steel truss girder without considering the nonlinear effect. To simplify the model, the longitudinal and transverse slopes of the bridge are not considered.

The dead load accounts for a large proportion of the total load in a cable-stayed bridge, and the live load is also one of the bridge load forms which acts on the slab directly. Therefore, it is significant to study the structural behavior of the thicker concrete under dead and live loads. Highway-I lane load was used to calculate the effect of live load. According to the code (China's Ministry of Transportation 2015) provisions on live load, lane load consists of concentrated force and uniform load. Four lanes were considered in this paper. The uniform load of the load is 10.5 kN/m, and the concentrated force is 360 kN. The transverse reduction coefficient of the lane is 0.67, and the longitudinal reduction coefficient is 0.94. The sidewalk was not considered.

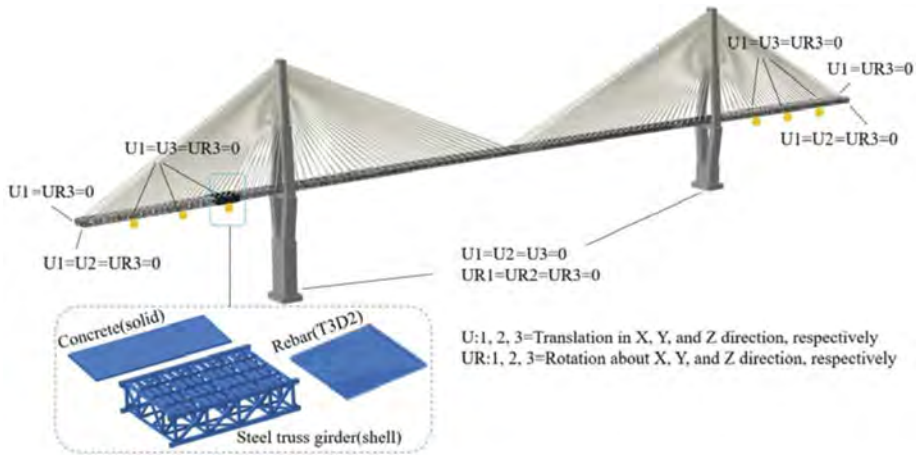


Figure 2. Finite element model.

3 RESULTS ANALYSIS

3.1 Analysis of concrete

The stress of cable section and pier's top section is more complex. So three typical sections are studied. S1 and S3 are the cable sections, while S2 is between the two cables, and S3 section is at the top of 3# auxiliary pier. Because of the large thickness of the concrete deck, it is necessary to select the upper, middle, and lower sections along the thickness direction to analyze the stress distribution along the thickness direction, as shown in Figure 3(a). The distribution of normal stress of concrete slab under dead load and live load is indicated in Figure 4. It can be seen that the distribution of normal stress of concrete is symmetrical along the central axis of the bridge. And the stress level of the concrete section is not large. The normal stress of three sections changes obviously at the position of small stringers. The stress fluctuation in cable anchor sections (S1, S3) is serious, while the stress changes greatly along the thickness direction in the S2 section. Obviously, there exists a significant shear lag effect in the concrete slab. Due to the large negative bending moment at the top of the pier, the compressive stress of the S3 section is smaller than that of the other two sections, and there even exists tensile stress which does not exceed the limitation.

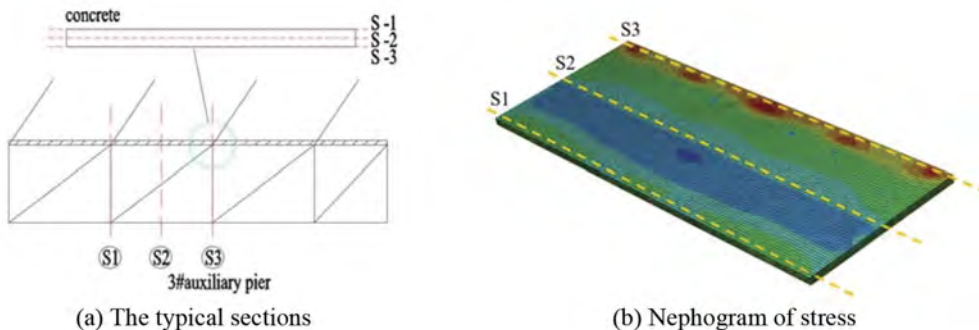


Figure 3. Normal stress nephogram of typical sections.

The concrete thicknesses of 250 mm, 300 mm, 400 mm and 500 mm are selected to study the influence of concrete thickness on stress distribution, and the normal stress of concrete in S3 section is shown in Figure 5. The normal stress of concrete with 250 mm thickness is the largest and the distribution is the most uneven. When the thickness of concrete is 500 mm, the normal stress

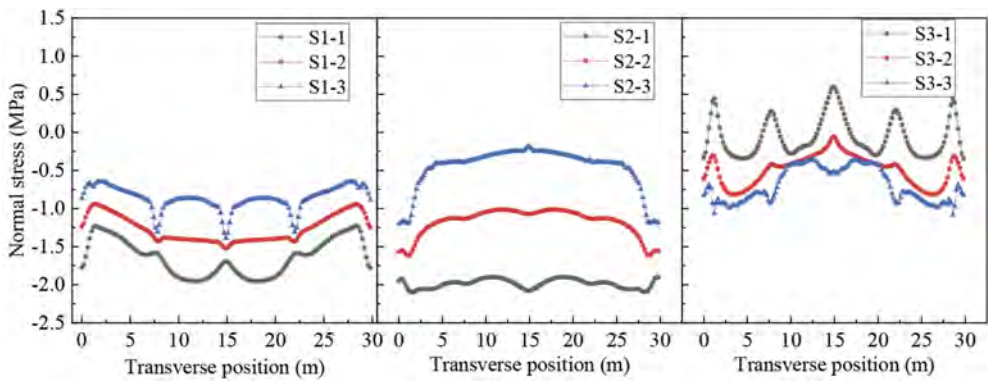


Figure 4. Distribution of normal stress of concrete.

is smaller and the distribution is more uniform. Figure 6 shows the distribution of normal stress on the upper surface and the lower surface of the concrete with different thicknesses at the pier's top section. It can be seen from the figure that with the increase in thickness, the stress distribution of concrete is more uniform and the stress degree of the concrete slab decreases. This is because as the concrete thickness increases, the stiffness of the structure becomes larger. On the one hand, thicker concrete can play a role of pressure, on the other hand, the stress level is lower and the stress distribution is more uniform. Therefore, it is suggested that the concrete thickness can be larger in the design of cable-stayed bridges and 400 mm ~ 500 mm thick is recommended.

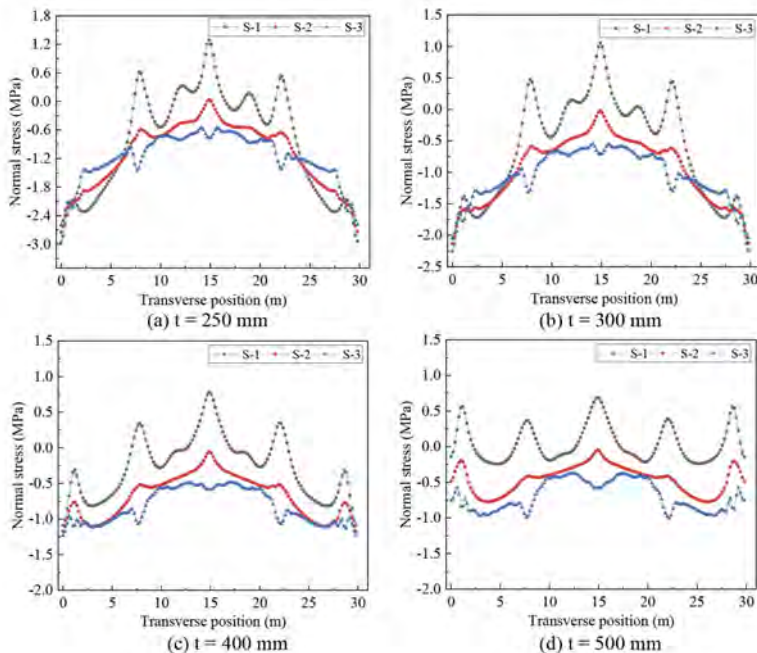


Figure 5. Distribution of normal stress of concrete with different thicknesses.

3.2 Analysis of steel truss girder

The steel truss girder is the essential component that takes most loads of the bridge. The Mises stress of the upper and lower chords of three typical sections under dead load is shown

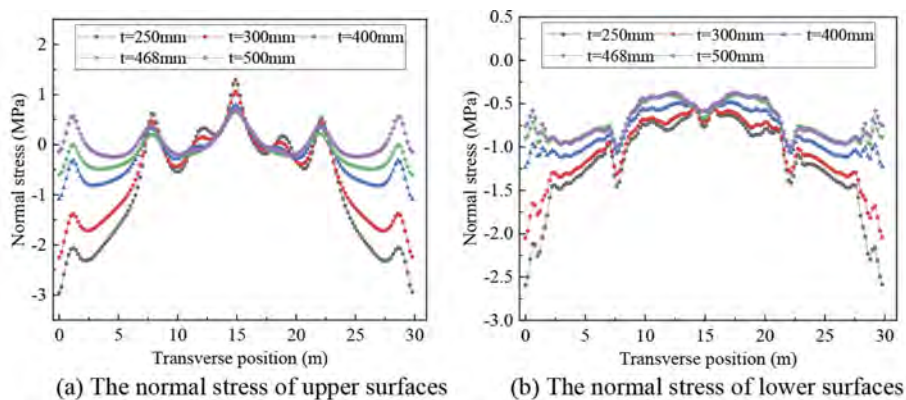


Figure 6. Comparison of normal stress of concrete with different thicknesses.

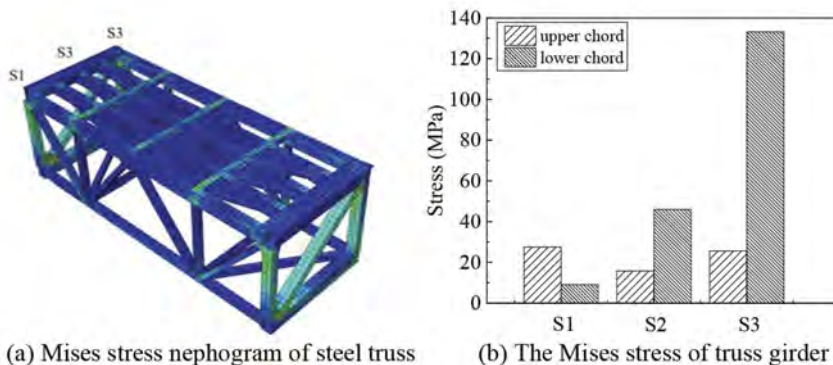


Figure 7. Distribution of Mises stress of truss girder.

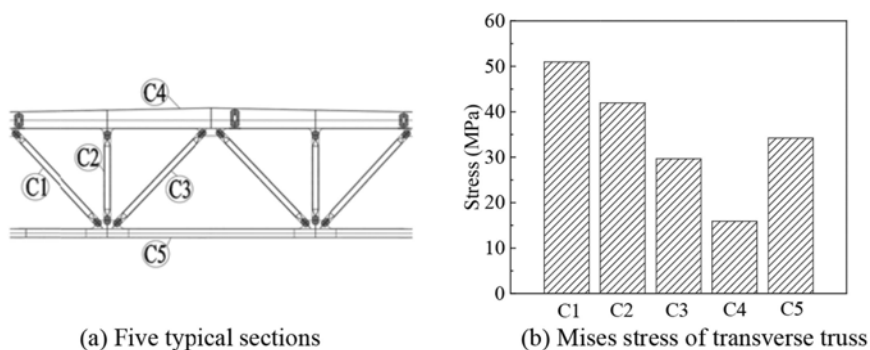


Figure 8. Distribution of Mises stress of transverse truss section.

in Figure 7. It can be seen that the stress of the upper chord at three typical sections is similar, and the stress of cable anchor sections (S1、S3) is slightly greater than that of the non-cable section (S2). In addition, the closer, the lower chord is to the auxiliary pier, the greater the stress is. The stress of the lower chord of S3 located at the top of the auxiliary pier is much larger than the other sections.

The main transverse truss section of the pier's top section is shown in Figure 8(a). Two diagonal belly poles, vertical belly poles, upper chord, and lower chord are numbered C1 ~ C5 respectively. The Mises stress of each member of the transverse truss is shown in Figure 8(b). The stress of diagonal belly poles near the main truss is the largest, and the closer to the central axis of the bridge, the smaller the stress is. The upper chord stress of the transverse truss is smaller than the lower chord stress, only half of the lower chord stress.

4 CONCLUSIONS

The structural behavior of the composite truss girder with the thicker concrete deck at the side span in a cable-stayed bridge was studied in this paper by simulation. The conclusions were summarized as follows:

- (1) In the cable-stayed bridge, the concrete slab is mainly subjected to compressive stress. The small stringers greatly influence the stress distribution in the concrete.
- (2) The shear lag effect in the concrete slab is prominent. The distribution of normal stress of thicker concrete slab along the thickness direction is also non-uniform.
- (3) The normal stress degree of thicker concrete is smaller and more evenly distributed. Considering the side-span ballast and the normal stress distribution, the concrete thickness of 400 mm ~ 500 mm is recommended in this paper.
- (4) The stress of the truss girder at the auxiliary pier is large, especially the lower chord. For the main transverse truss, the stress of diagonal belly poles near the main truss is the largest.

ACKNOWLEDGEMENTS

The authors gratefully acknowledge the financial support provided by the Innovation Capability Support Program of Shaanxi (2019TD-022), the Research on Key Technology of Design of Long-span Composite Truss Girder Cable-stayed Bridges with Super High Towers in Mountainous and Deep Valley Areas — Subject 2: Research on reasonable structure and design method of plate - truss composite girder (Topic 4, Topic 5).

REFERENCES

- Du, X.G. et al. 2010. Dynamic Analysis of Steel Plate-Truss Composite Girder on Long Span Two-layer Cable-stayed Bridge. *Journal of Civil Architectural & Environmental Engineering*.
- Giaccu, G.F. et al. 2022. Numerical simulation and simplified calculation of the effective slab width for composite cable-stayed bridges. *Structures* 39: 512–526.
- Johnson, J.E. & Lewis, A.D.M. 1966. Structural Behavior in a gypsum roof-deck system. *Journal of the Structural Division* 92(2): 283–296.
- JTG D60-2015, *General Code for Design of Highway Bridges and Culverts*. Beijing: People's Communications Press 2015. (in Chinese)
- Li, F.X. et al. 2013. Influence of shrinkage and creep of steel-concrete composite girder cable-stayed bridge. *Journal of Highway Communication Technology* 30(10): 54-60+121. (in Chinese)
- Machacek, J. & Cudejko, M. 2009. Longitudinal shear in composite steel and concrete trusses. *Engineering Structures* 31(6):1313–1320.
- Macorini, L. et al. 2006. Long-term analysis of steel–concrete composite beams: FE modeling for effective width evaluation. *Engineering Structures*. 28(8): 1110–1121.
- Pedro, J.J.O. & Reis, A.J. 2010. Nonlinear analysis of composite steel–concrete cable-stayed bridges. *Engineering Structures* 32(9): 2702–2716.
- Wang, C.S. et al. 2008. Structural Behaviour Analysis of High Strength Steel-concrete Composite Girders. *Journal of Traffic and Transportation Engineering* 8(02): 27–33. (in Chinese)
- Wang, C.S. et al. 2022. Shear lag effect of twin I-shaped composite girders in cable-stayed bridges. *Thin-Walled Structures* 180: 109822.

Assessment of mechanical properties for ancient timber through visual and ND methods

S. Verre, G.F. Cauteruccio, G. Fortunato, A.A. Zappani & L. Ombres

University of Calabria, Arcavacata di Rende (CS), Italy

M. Brunetti & M. Nocetti

National Research Council of Italy (CNR-IBE), Sesto Fiorentino (FI), Italy

N. Ruggieri & M. Togni

University of Florence, Florence, Italy

D. Marranzini, G. Iovane & B. Faggiano

University of Naples Federico II, Naples (NA), Italy

ABSTRACT: The Italian built heritage is characterized by an extensive use of timber as building material, realizing floor and roof structures of palace, churches and buildings. Conservation and restoration are needed for the safeguard of the timber-built heritage. However, given the lack of knowledge about the mechanical capabilities of the ancient structural members, often the blind removal takes place. In this context a research program for the mechanical characterization of ancient timber elements through an experimental campaign is ongoing at the University of Calabria, through a cooperation with the University of Naples Federico II, the University of Florence and the National Research Council. In particular, 18 ancient timber members are studied through the application of innovative survey methods, visual strength grading, non-destructive, destructive and long-term bending tests. In this paper a first part of the experimental work concerning survey, visual strength grading and non-destructive tests on 8 specimen is presented.

1 INTRODUCTION

In Italy most of the built-up consists of masonry buildings that are generally characterized by timber floors and roofs structures. Timber was already used in advanced systems since the Roman times (Stellacci and Rato, 2021). In southern Italy, during the Borbone reign, it even realized the first example of anti-seismic construction technique (Ruggieri, 2022). Furthermore, since the ancient times timber was widely used for medium and large span structures in churches and prestigious buildings (Faggiano et al., 2018). The conservation of the architectural heritage is a policy of protection, recently also raised to a social relaunch of territorial context as the Italian inner areas (Rossitti et al., 2022). At the same time, since Italy is heavily exposed to seismic and hydrogeological risks, conservation also aims at reducing the vulnerability of the built-up. Further to the structural function, also the authenticity, both ideal and material, in a condition of sufficient safety (ICOMOS, 1999; Tampone and Ruggieri, 2016) should be conserved.

Interventions on existing structures need adequate knowledge of material and structure characteristics, as well as of survey and diagnostic techniques. Therefore a preliminary assessment aiming at defining history, geometry and mechanics of timber structures is required (Cruz et al., 2015). In particular ancient timber is usually affected by defects, irregular geometries and degradations that influence the behavior, so that the lack of knowledge often directs the design choices towards the replacement of members, causing economic, cultural and environmental losses.

Inspired by this motivation a research program for the mechanical characterization of ancient timber members is ongoing at the University of Calabria, through a cooperation with the

University of Naples Federico II, the University of Florence and the National Research Council. In particular, the experimental campaign aims at the *in-situ* determination of the mechanical properties of timber members through the application of smart non-destructive technologies. In particular the following methods and techniques are included: visual strength grading, also aided by laser scanner acquisitions, non-destructive tests, like stress waves propagation, vibration and drilling resistance tests, destructive bending tests and long-term bending tests.

The first part of the experimental work regarding the survey, visual strength grading (VSG) and non-destructive test (NDT) on 8 specimens (ID: 2, 7, 9, 10, 11, 13, 17, 18) is herein presented.

2 VSG AND NDT FOR MECHANICAL CHARACTERIZATION OF ANCIENT TIMBER MEMBERS

2.1 *The sample features*

The 18 timber specimens in structural dimensions are part of the rafters extracted from the roof trusses of the XIX century building, the lyceum gymnasium Bernardino Telesio, in the historic center of Cosenza (Italy; Ruggieri and Serra, 2019). The specimens date back approximately to the mid eighteenth century, since after the Cosenza earthquake (1854) the roof was reconstructed. In 2020 the timber trusses were replaced and the 18 rafters were deposited at the “DINCI” Laboratory for tests on materials and structures of the University of Calabria, in Rende (Cosenza).

Rafters have an average 4.00 m length with an approximately square cross section, with an average size of 20 cm. The sample timber species identification was performed through the visual analysis: most of the members (13) are in Corsican Pine (*Pinus nigra* subsp. *laricio* (Poir.) Maire); the others (5) in Chestnut (*Castanea Sativa*). In particular Corsican Pine (PNL) is characterized by resinous and rounded knots having modest dimensions, as well as by differentiated heartwood in the transversal cross section; while Chestnut (CS) is characterized by large and elliptical knots, porous rings and the typical flaming appearance of the grain on the tangential section.



Figure 1. a) Timber trusses extracted from the lyceum gymnasium Bernardino Telesio, Cosenza (Italy); b) Timber rafters stored in the DINCI Laboratory, Rende (CS); c) Survey of two rafters with laser scanner.

2.2 *Sample survey*

Visual inspection and size measurement were carried out, they being fundamental steps in the assessment of historic timber structures. Visual inspection provides information about the overall state of conservation of the structure, as well as the presence of any sign of mechanical damage or decay, whereas size measurement aims at defining geometry and main dimensions of timber members. In general these analyses are performed through on-site observation and traditional survey techniques. However, thanks to the technological progress, innovative survey techniques are spreading. Indeed, laser scanners and photogrammetry have been recently used (Riggio et al., 2015; Nocetti et al., 2021; Abraldes et al., 2022) for the evaluation of wooden elements: from morphological, geometric and mechanical aspects to visual and degradation aspects. Therefore, as part of the experimental campaign, both 3D acquisition methodologies were applied, in order to generate three-dimensional models useful for the mechanical characterization of the study specimen. In particular, the accurate geometry of the specimens was surveyed, allowing the determination of volumes, as well as attention was paid to the restitution of textures useful for carrying out visual classification (VSG) even remotely.

2.3 Visual Strength Grading (VSG)

For the on-site mechanical characterization of timber members the visual strength grading (VSG) approach was firstly applied. It allows to attribute a strength grade to the members according to the visual criteria defined by regulations (Piazza and Riggio, 2008). Grading rules take into account macroscopic features of timber, such as size of knots, slope of grain and presence of shake. In Italy two national standards are available for VSG: UNI 11119 providing procedures for the on-site classification and UNI 11035 used for newly sawn structural timber, although it is used also for ancient timber. According to UNI 11119 three visual grades (I, II, III) can be assigned both to Corsican Pine and Chestnut, whereas according to UNI 11035 three (S1, S2, S3) and only one (S) visual grades can be respectively assigned to Corsican Pine and Chestnut. Both standards provide a strength class, in terms of allowable stresses (UNI 11119) or characteristic values (UNI 11035), as function of the assigned visual grade.

During the experimental campaign 8 rafters were graded according to the aforementioned standards. VSG was performed considering only the macroscopic characteristics located in the middle third of each member, since this part mostly affect the bending behavior of the member. VSG was performed both in laboratory and in-remote, using the high-resolution images acquired with photogrammetry survey (Figure 2). The latter methodology was found to be advantageous as it allowed the research group to share information and work even remotely.

More in detail, the 3D acquisition methodologies applied were phase-difference ToF laser scanner (LS) survey and close-range photogrammetric (P) survey, for which FARO Technologies, Inc. Focus Plus 150 laser scanner and a Fujifilm X-T2 nonmetric camera combined with Fujifilm XF 18-55 f/2.8-4R LM OIS lens were used, respectively.

The laser scanner survey was carried out for all the specimens under daylight ambient light conditions, in two stages: point detection and HDR frame acquisition. Scan registration and point cloud orientation operations were performed using SCENE software by FARO. After the cleanup actions, a point cloud of about 13 million points, with a density of 1.75 points/mm² was obtained for each specimen. The clouds were then processed to obtain meshes in Geomagic Wrap 2021 by 3D Systems, Inc. The cloud was sampled to make the point density homogeneous. The resulting meshes possessed approximately 10 million triangles per specimen.

The close-range photogrammetry was applied in conjunction with Structure from Motion software, only for specimens 16-P, 17-P, which were surveyed individually under daylight ambient light conditions. An average of 420 frames per specimen were taken. Photogrammetric processing was done using Metashape Professional produced by Agisoft LLC. Point clouds of about 45 million points per specimen with a density of 13.1 points/mm² were obtained. Meshes generated have approximately 10 million polygons. The 3D models were textured with high-definition.

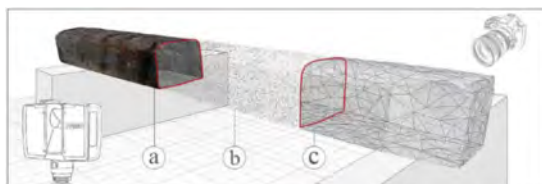


Figure 2. High-definition 3D model obtained by laser scanning and photogrammetry: a) Model textured; b) Point Cloud; c) Model Wireframe.

2.4 Non-Destructive Techniques (NDT)

Non-destructive techniques (NDT) are complementary to VSG. They are frequently used in professional practice and research fields, in order to collect information, principally about the state of conservation and the mechanical properties of timber members. The most common techniques can be grouped in three different categories: probing, acoustic and vibration techniques (Llana et al., 2020). Probing category includes drilling resistance method (Nowak et al., 2015; Faggiano et al., 2011), needle penetration, screw withdrawal and core drilling tests. Acoustic methods are based on the propagation of stress waves through material in order to

estimate the timber member stiffness. Generally, two types of waves are used: sonic stress waves for frequencies within the audible range and ultrasonic stress waves at frequencies above 20 kHz (Dackerman et al., 2014). Vibration methods are based on natural frequency of timber member, which is directly related to the stiffness. Both acoustic and vibration methods are used to estimate the dynamic modulus of elasticity (MOE_{dyn}) from which static modulus of elasticity (MOE) can be derived through linear regression laws (Nocetti et al., 2010; Brunetti et al., 2013).

In this work drilling resistance, acoustic and vibration tests were carried out on the sample (Figure 3). Moisture content (MC) and mass were also measured. For each specimen a single MC measurement was taken on transversal face, through the hygrometer Hydromette CH 17 GANN, with a 60mm electrode length. Drilling resistance test was carried out using the Resi PD 400 Resistograph®. The penetration length and the average resistance to drilling (R_m) are the outputs provided by the device. For each specimen two measurements transversal to the grain were taken at each face, near the specimen end. The R_m measure was evaluated excluding the zones of the chart with no resistance. The device FAKOPP Microsecond timer® was used for acoustic test. It measures the time of flight of an acoustic stress wave induced by a hammer excitation. For each specimen five measurements were carried out using different sensor placement arrangements: one direct measurement (parallel to the grain) and four indirect measurements (one for each specimen face, placing sensors on the face with a same angle orientation (about 60°). During the test the length between sensors was measured in order to obtain the stress wave speed (SWS) through the time of flight (TOF) evaluated by the device. In the end, vibration test was conducted using the VISCAN Portable® Microtec device. It measures the natural frequency of vibration in the longitudinal direction of a timber piece by a laser interferometer exciting the specimen with a hammer (Berti et al., 2015). For each timber rafter one measurement was done in longitudinal direction.



Figure 3. Application of NDTs: a) the drilling resistance (DRM); b) acoustic; c) vibrational methods.

3 RESULTS

3.1 Visual Strength Grading (VSG)

Through visual inspection mechanical cracks were detected at the head of 4 members, probably caused by an excess of compressive stress at the joint between rafters and tie-beams. Other typical aspects of ancient timber noticed are the irregular geometry of the cross section (waned and distortions) along the specimen length, double piths (on 4 specimens), iron stain discoloration on CS members, sign of superficial decay due to insect attacks (*Cerambycidae*, *Hyloterpes bajulus*; *Anobium*, *Anobiidae*), ring shakes at the member ends for most of the specimens. It is worth to notice that for VSG, defects as ring shakes, double piths and insect attacks are not taken into account, they being outside the specimen middle third. Moreover, geometrical irregularities were also not considered, because they would be very penalizing for the specimens, they being a widespread peculiarity of ancient timber structural members of the Mediterranean area.

The main geometric features of the specimens have been extracted from the 3D models generated through LS and P survey (Table 1). Given the irregular geometry of the specimens, the size of the cross section have been referred to a nominal section. Furthermore volume measured with both LS and P survey methods led to similar values, ranging from 132 dm³ to 193 dm³. Textured 3D models obtained from P survey has been used for VSG.

In order to assign a strength grade to the specimens, quantitative evaluations were carried out. For Chestnut specimens 2, 7, 9, large knots are inside the middle third, specimen 10 only shows insect damage also inside the middle third. Thus, three specimens (2, 9, 10) are classified as grade III (UNI 11119), while specimen 7 as grade II. According to UNI 11035 specimen 7 falls into

grade S, while specimens 2, 9,10 are not classifiable as timber structural members, since they show defects above the prescribed limits. Corsican Pine specimens 7, 13, 17 are characterized by a grain slope up to 14%, specimen 18 has knots with diameter larger than 70mm. Thus, according to UNI 11119 three rafters (13, 17, 18) are classified as grade III and specimen 7 as grade II. At the same time specimens 13, 17, 18 are graded as S3 and specimen 7 as S2 according to UNI 11035.

3.2 Non-destructive methods (NDT)

In general, the moisture content (MC) of the specimen is higher than the normal content: the average value of MC is about 14.6% (maximum value is 23% for specimen 7). This is the consequence of unprotected storage of material until it was transported to the laboratory. The density ρ is similar for both wood species, being in average approximately equal to 600kg for CS and 550kg for PNL (maximum value is 723kg/m³ for CS specimen 2). A slight data dispersion is recorded for CS (COV:17%) than PNL (COV:12%). Higher value of density for CS are probably due to the widespread presence of large knots.

In Table 1 the average value of the drilling resistance measures (R_m) are shown. It is apparent that for CS R_m values are higher (R_m :27.0%) than for PNL (R_m :21%). The higher value is for specimen 2 (R_m : 34.1%), it being closely related to the high density of the member. From drill charts it is also apparent that rafters 7, 9 and 18 belonged to very old trees, since they have a large number of rings. The acoustic tests and vibrational tests results are also given in Table 1. It is apparent that for both wood species stress wave speed (SWS) is directly proportional to density. The mean value of SWS is equal to 4,392 m/s for CS and to 4,264m/s for PNL. However, the values are much more dispersed for PNL (COV:17%) than for CS (COV:4%). The dynamic elastic modulus (MOE_{dyn}) calculated has average values equal to 11,600 MPa for CS and 10,500 MPa for PNL. Again, a greater dispersion characterizes PNL (COV:47%) as respect to CS (COV:26%).

With regards to vibrational tests, it is noted that for the whole sample frequencies are quite close and equally distributed, with an average value of 531Hz for CS and 511Hz for PNL. Unlike the acoustic test, for CS sample the average value of MOE_{dyn} is lower than for PNL (10,400 MPa and 11,100MPa, respectively). MOE_{dyn} values obtained from acoustic and vibration techniques vary by a maximum of 10%. Only for the CS specimens 2 and 10 there is a variation ranging from 20% to 25%. Also, in this case for PNL specimens MOE_{dyn} is statistically more dispersed than Chestnut (COV:51% versus 17%). Furthermore, it is worth to notice that for specimen 7 the MOE_{dyn} values are not affected by the high MC values. This is probably due to the good characteristic of the member that has been graded as II and S2 in VSG.

Table 1. Strength grading and non-destructive test results.

Wood Species	Density Kg/m ³		DRM		Acoustic test				Vibrational test			
			R_m		SWS		MOE_{dyn}		Frequency		MOE_{dyn}	
	Av.	Cov	Av.	Cov	Av.	Cov	Av.	Cov	Av.	Cov	Av.	Cov
CS	597	17%	27.0	19%	4.39	4%	11.60	26%	531	6%	10.40	17%
PNL	552	12%	21.0	0%	4.26	17%	10.50	47%	511	13%	11.10	51%

(CS: *Castanea Sativa*, PNL: *Pinus Nigra* subs. *Laricio*, DRM: drilling resistance method, R_m : average drilling resistance, SWS: stress wave speed; Av.: Average, Cov: coefficient of variation)

4 CONCLUSIVE REMARKS

In this paper the first part of a larger experimental campaign is showed. The work involved the application of innovative survey method, visual strength grading and non-destructive test on a sample of ancient timber members. The following conclusive remarks can be drawn:

- Innovative survey methods are effective methods to support the assessment of ancient timber members. Photogrammetry has produced 3D models with extremely precise and accurate geometry (useful for section extraction, volume measurements, etc.) and characterized by high resolution texture, which makes the technique more suitable for carrying out the VSG (useful for measuring knots, slope of the grain, etc.). 3D models, generated from data acquired by laser scanner adopted, resulted in less detailed meshes than photogrammetry, but there were no appreciable differences in volume and section measurements; texture quality proved to be unsuitable for visual analysis (due to the colorimetric characteristics of the specimens and ambient brightness). The computational and time burdens of acquisition by laser technique are lower than those by photogrammetric technique. The photogrammetry returns a textured model more suitable for carrying out the VSG. Visual strength grading performed on textured model is an effective methodology for working in a team even remotely. However, the survey of wane and cracks is a more time-consuming operation than standard Visual Inspection;
- Typical aspects of the ancient timber (double pith, biological decay, ring shake, mechanical damage) were identified through visual inspection, as well as LS and P. However, the criterion that considerably limits the VSG of ancient timber is the presence of wane. Indeed, this criterion has not been considered in the present work; large knots and slope of the grain have been the most recurrent defects respectively for Chestnut and Corsican Pine;
- From the application of NDT, it has been found that R_m and SWS are strictly correlated to timber density both for Chestnut and Pine. At the same time frequency seems to be not density dependent. Furthermore, for each specimen different values of MOE_{dyn} were determined by means of the application of acoustic and vibrational tests. However, in most cases the relative variation is less than 10%. A greater dispersion of MOE_{dyn} has been found for Corsican Pine. It is probably due to the heterogeneity of the quality of the material. Furthermore, for specimen 7 (PNL) MOE_{dyn} value was not affected by the high MC. This is probably due to the good characteristic of the member, as shown by the VSG results.

REFERENCES

- Abraldes, P., Cabaleiro, M., Sousa, H.S., Branco, J.M., 2022. Use of polar coordinates for improving the measurement of resistant cross-sections of existing timber elements combining laser scanner and drilling resistance tests. *Meas. J. Int. Meas. Confed.* 204, 1–13.
- Berti, S., Brunetti, M., Nocetti, M., Paletta, D., Ventre, A., 2015. The approach of Model Forest in the territory of Montagne; *Proc. of the XIV World Forestry Congress, Durban, South Africa, 2015*, 7–11.
- Brunetti, M., Nocetti, M., Burato, P., 2013. Strength properties of chestnut structural timber with wane. *Adv. Mater. Res.* 778, 377–384.
- Cruz, H., Yeomans, D., Tsakanika, E., Macchioni, N., Jorissen, A., Touza, M., Lourenço, P.B., 2015. Guidelines for on-site assessment of historic timber structures. *Int. J. Archit. Herit.* 9(3),277–289.
- Dackermann, U., Crews, K., Kasal, B., Li, J., Riggio, M., Rinn, F., Tannert, T., 2014. In situ assessment of structural timber using stress-wave measurements. *Mater. Struct. Constr.* 47, 787–803.
- Faggiano, B., Grippa, M.R., Marzo, A., Mazzolani, F.M., 2011. Experimental study for non-destructive mechanical evaluation of ancient chestnut timber. *J. Civ. Struct. Heal. Monit.* 1, 103–112.
- Faggiano, B., Marzo, A., Grippa, M.R., Iovane, G., Mazzolani, F.M., Calicchio, D., 2018. The inventory of structural typologies of timber floor slabs and roofs in the monumental built heritage: the case of the Royal Palace of Naples. *Int. J. Archit. Herit.* 12, 683–709.
- ICOMOS: ICOMOS Wood International Committee, Principles of conservation of the historic timber structures, General ICOMOS Assembly, Mexico City, 1999.
- Llana, D.F., Iñiguez-González, G., Diez, M.R., Arriaga, F., 2020. Nondestructive testing used on timber in Spain: A literature review. *Maderas Cienc. y Tecnol.* 22, 133–156.
- Nocetti, M., Aminti, G., Degl’Innocenti, M., Brunetti, M., 2021. Geometric representation of the irregular cross-section of old timber elements: Comparison of different approaches for mechanical characterisation. *Constr. Build. Mater.* 304, 124579.
- Nocetti, M., Bacher, M., Brunetti, M., Crivellaro, A., Van De Kuilen, J.W.G., 2010. Machine grading of Italian structural timber: Preliminary results on different wood species. In: *11th World Conf. Timber Eng. WCTE 2010, 20-24 June, Riva del Garda, Italy, 2010*, 285–291.

- Nowak, T.P., Jasięko, J., Hamrol-Bielecka, K., 2016. In situ assessment of structural timber using the resistance drilling method - Evaluation of usefulness. *Constr. Build. Mater.* 102, 403–415.
- Piazza, M. and Riggio, M., 2008. Visual strength-grading and NDT of timber in traditional structures. *J. Build. Apprais.* 3, 267–296.
- Riggio, M., Sandak, J., Franke, S., 2015. Application of imaging techniques for detection of defects, damage and decay in timber structures on-site, *Constr. Build. Mater.* 101(2),1241–1252.
- Rossitti, M., 2022. Action Research for the Conservation of Architectural Heritage in Inner Areas: Towards a Methodological Framework, *Lecture Notes in Networks and Systems. Springer Intern. Publishing.*
- Ruggieri, N., 2022. New Insights on the Borbone Construction System: a Peculiar 18th Century Retrofitting Solution for Earthquake Damaged Churches. *Int. J. Archit. Herit.* 16, 1289–1305.
- Ruggieri, N. and Serra, D. 2019. Il complesso Bernardino Telesio a Cosenza: Note storiche e costruttive. In: *Monère: rivista dei beni culturali e delle istituzioni politiche*, Il Menabò edizioni, Santa Maria a Vico (CE), Italy, 105–114.
- Stellacci, S. and Rato, V., 2021. Timber-Framing Construction in Herculaneum Archaeological Site: Characterisation and Main Reasons for its Diffusion. *Int. J. Archit. Herit.* 15, 1301–1319.
- Tampone, G. and Ruggieri, N., 2016. State-of-the-art technology on conservation of ancient roofs with timber structure. *J. Cult. Herit.* 22, 1019–1027.
- UNI 11035: 2010 Structural timber, Visual strength grading for structural timbers, Part 1: Terminology and measurements of features. Part 2: Visual strength grading rules and characteristics values for structural timber population.
- UNI 11119: 2004 Cultural heritage, Wooden artefacts, Load-bearing structures, On-site inspections for the diagnosis of timber members.

Failure analysis of ageing RC bridges: The cases of the Polcevera viaduct and the Capriogliola bridge

N. Scattarreggia, A. Orgnoni & G.M. Calvi
University School for Advanced Studies IUSS Pavia, Pavia, Italy

R. Pinho
Department of Civil Engineering and Architecture, University of Pavia, Pavia, Italy

D. Malomo
Department of Civil Engineering, McGill University, Montréal, Canada

M. Moratti
Studio Calvi Ltd, Pavia, Italy

ABSTRACT: Many existing bridges now have a life of more than 50 years and the recently occurred failures underline the need for many of these structures to be assessed and, if required, retrofitted, in order to avoid catastrophic collapses. The Applied Element Method is herein used to show as advanced numerical modelling that accounts for as-built structural details, construction stages, material deterioration effects and structural modifications over time, have the potential to predict the failure mechanism and study the sensitivity of complex structural schemes to external actions. To this end, the collapse of the Polcevera viaduct in Genoa (August 2018), and of the historical multi-span arch bridge of Capriogliola (April 2020) are reproduced. Comparisons between numerical results and evidence, indicate that an accurate knowledge of the as-built structural details and conservation may permit to point out potential criticalities and analyse the robustness of existing bridges to avoid the premature end of their life.

1 INTRODUCTION

After the Second World War the Italian government announced the need for (re-)constructing the infrastructural system of the country, introducing guidelines to regulate material and construction demands that promoted the use of affordable materials such as concrete. Therefore, many of the existing arch bridges, both in masonry and concrete, that were destroyed during the war were then rebuilt mainly using concrete. The evolvement from a national emergency situation to a new economic and commercial development stimulated and pushed for the introduction of innovative techniques, construction methods and structural systems. Prestressed concrete technology would have still been regarded as being in its infancy at the time, however, skilled designers such as Levi, Cestelli-Guidi, Pizzetti, Oberti and Zorzi started nonetheless to apply it to relatively long-span bridges (Iori & Poretti 2009). Solutions to problems related to creep, temperature variations, strand relaxation, redistribution effects in statically indeterminate structures, nonlinear and ultimate response, were only intuitively considered, and sometimes simply overlooked. Between 1956 and 1964 the 760 km “*Autostrada del Sole*” linking Milan to Rome and Naples was designed and built, with a total of 853 bridges and viaducts (in addition to 572 overpasses) and 38 tunnels needing to be constructed. It was only years later, with the development of dedicated software, that it became possible to model most of the aforementioned complex time-dependent effects.

Today, the road network of Italy counts around 839,629 km with approx. 60,000 bridges and viaducts, and is managed by four main operators. Almost 40-50% of these bridges have reached

their design life (ANAS 2021), which was typically between 50 and 100 years, and the majority are reinforced concrete (RC) and precast concrete (PC). In addition, the lack of government-enforced universal guidelines for the conservation of such complex infrastructural system, and thus the heterogeneity of the strategy adopted by each operator, has undoubtedly not contributed to an optimum management of the road network. Indeed, the critical condition of this aging infrastructure has recently been propelled onto the international stage due to the collapse of the Polcevera viaduct in Genoa, in August 2018, and is also well epitomized by the fact that a complete registry of existing bridges is currently still missing. Since then, however, further local and global failures of other Italian bridges of varying typologies, dimensions, and relevance have occurred, including the bridge of Capriogliola (Massa e Carrara, Italy), of significant historic value and strategic importance, which collapsed into the Magra river in April 2020. Considering the limited 2-year timespan from 2018 to 2020 alone, a relatively large number of local and global bridge failures have been reported in Italy (see Figure 1), which is quite alarming and highlights the need for an urgent assessment and rehabilitation of the road infrastructures.



Figure 1. Reported bridge failures in Italy in the 2-year timespan between 2018 and 2020. (Red coloured dots indicate failures reported by national media).

Thus, as underlined in recent guidelines e.g., CNR (2021), research is still strongly needed to investigate resistance, robustness and potential progressive collapse scenarios of deteriorated bridges, considering the interaction between continuous damage due to material degradation and discontinuous damage due to accidental events. As such, the present work aims to provide a contribution to a better understanding of the sensitivity to various external loadings (both standard and exceptional, due to natural and anthropic hazards) and input data (e.g., as-design vs. as-built structural details) of two structural scheme typologies; the arch bridge used in Capriogliola and the cable-stayed system adopted for the Polcevera viaduct. Use is made of the relatively innovative Applied Element Method (AEM, Meguro & Tagel-Din (2002)) structural modelling and analysis approach (as implemented in the computer program ELS (ASI 2020)), which has been shown to be capable of accurately modelling the response of bridge structures from their elastic behaviour up to debris distribution (e.g., Malomo et al. (2020)).

2 THE RC CABLE-STAYED BRIDGE OVER THE POLCEVERA RIVER: 51 YEARS OLD

2.1 Overview of its history

The viaduct over the Polcevera river in Genoa, Italy, was built between 1963 and 1967 and is widely known as Morandi bridge, taking the name of its designer, Riccardo Morandi. The complete viaduct had a total length of about 1100 m, with each of its twelve support points being

numbered sequentially from the Savona end (Figure 2), with piers 9, 10 and 11 constituting the so-called “balanced systems” passing over the Polcevera valley and railway tracks below.

The original design of the entire viaduct is described in e.g. Morandi (1967), being then revisited, in particular for what concerns its construction and loading history, in the work by Orgnoni et al. (2023a, b). As is common for structures of this type, the Polcevera viaduct was object of a number of maintenance operations during its lifetime (Rosati et al. 2020), among which, e.g., the substitution of the original steel guardrails with New Jersey barriers, the enlargement and strengthening of sidewalks in combination, and also addition of new asphalt layers.

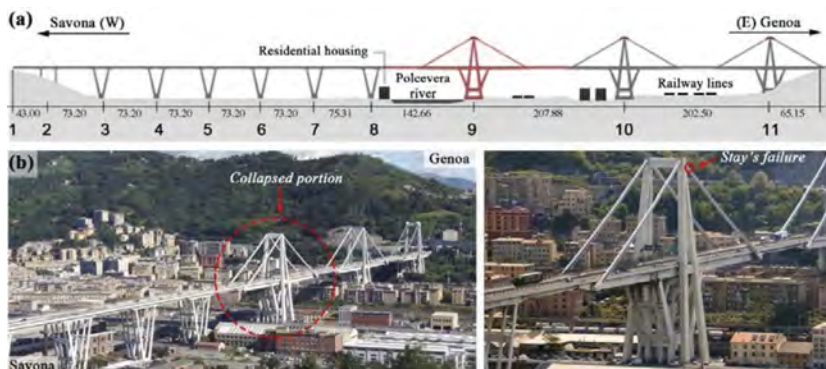


Figure 2. (a) Longitudinal schematic of the viaduct, (b) pre-collapse photos of the bridge and of pier 9.

2.2 The collapse in 2018, after 51 years of operativity

It was the balanced-system number 9 (shown in Figure 2) that collapsed on the 14th of August 2018. As is often the case in the aftermath of a structural collapse, the identification of the triggering event behind the observed stay failure remains an open question, with various qualitative hypotheses having been thus far formulated and discussed. Initial studies by Calvi et al. (2019) and Malomo et al. (2020) suggested the failure of one of its stays as a likely initiator of the observed collapse, an hypothesis that was subsequently confirmed by video footage (la Repubblica 2019) that clearly showed that the failure mechanism initiated with the occurrence of a rupture at the top end of the SE stay (see Figure 2). Subsequent forensics studies by Rosati et al. (2020) identified a number of previously unknown construction defects (e.g. heavily cluttered and congested layout of stays’ cables) and consequent (non-visible) material deterioration, underlining the noticeable mismatch between as-designed and as-built structural details. Pinho et al. (2023) have shown the influence of such construction defects on the residual capacity of the ruptured stay, highlighting as their combination with equally unforeseen exceptional load scenarios (such as e.g. impact of a falling coil and/or strong differential thermal effects) on the specific day of the collapse, could have indeed triggered the observed collapse.

2.3 Collapse analysis through the AEM-based model

The developed AEM bridge model shown in Figure 3 consisted in the assembly of approx. 100,000 elements for a total of 600,000 degrees-of-freedom. It was built based on pre-collapse building inspections, thus accounting for the as-built bridge geometry such as e.g. the twist of the antenna around its vertical axis and the stays in their catenary shape. The model featured a precise definition of acting loads, geometry, materials, and state of conservation at the time of the collapse (Scatarreggia et al. 2022a).

A number of numerical modelling studies, referenced throughout the present manuscript, have been carried out on this bridge by means of linear and nonlinear models, all reciprocally cross-validated, to investigate the impact of construction errors on the bridge conservation and stress-strain state at the time of the collapse, as well as the potential triggering factor of the stay’s failure. The results in Figure 4, taken from Scatarreggia et al. (2022a), show in particular

that the AEM model with as-built details (also including material deterioration) led to a failure mechanism noticeably different with respect to that obtained in initial studies by e.g. Calvi et al. (2019). Indeed, the model with the as-built details duplicated the collapse of the bridge portion in the immediate moments after the stay failure (see the comparison between numerical and as-observed counterpart in Figure 5), a result that could not be obtained in the earlier preliminary work by e.g. Calvi et al. (2019) and Malomo et al. (2020), where the actual as-built construction details, loading history and state of conservation were not yet fully known.

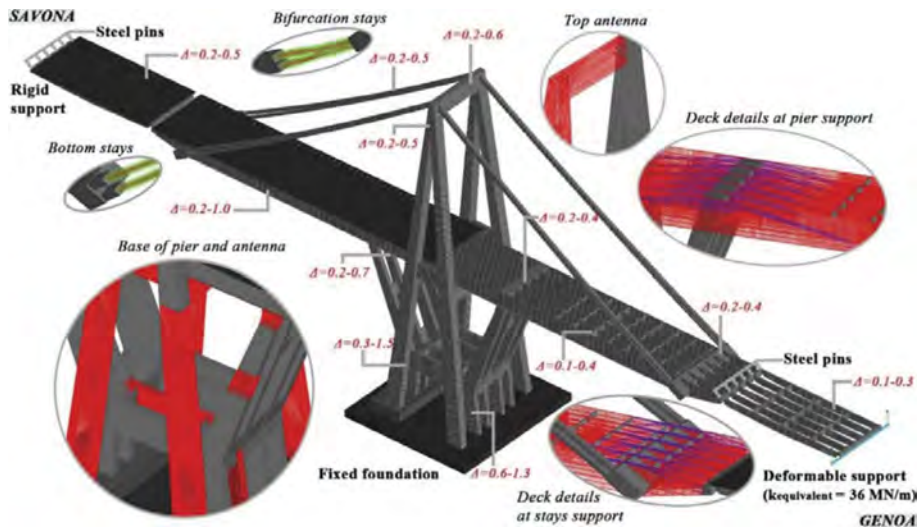


Figure 3. Mesh discretization (Δ indicates the average smallest and larger mesh dimension) adopted for various bridge parts, reinforcement details and restraints adopted in the AEM model.

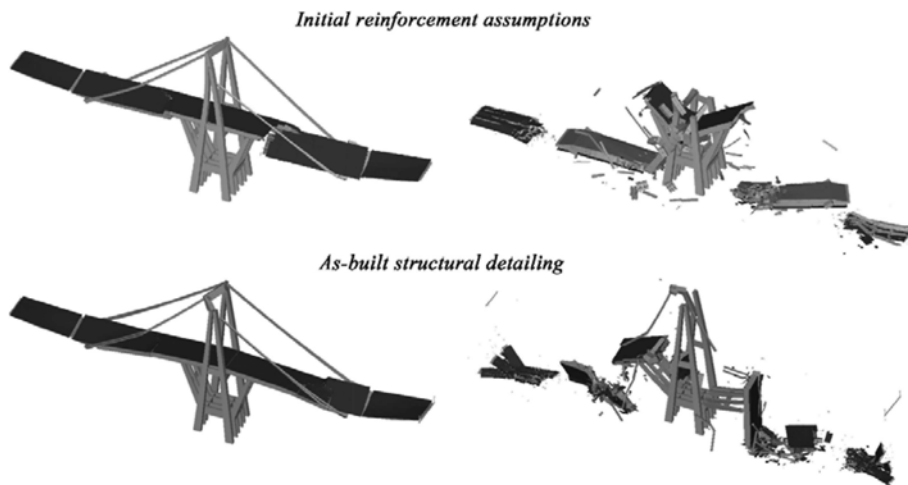


Figure 4. Frames of the collapse simulation induced by a stay failure, considering both the initially assumed (top) and as-built (bottom) structural details assumptions.

3 THE MULTI-SPAN RC ARCH BRIDGE OF CAPRIGLIOLA: 71 YEARS OLD

3.1 Overview of its history

The multi-span arch bridge over the Magra river, was first built in 1908, as a link between the two municipalities of Caprigliola and Albiano Magra, in Tuscany, Italy (see e.g. Ceradini

(1951)). It was designed by the Italian engineer Attilio Muggia, one of the Italian pioneers in the field of reinforced concrete. At that time, with its 260-m length, constituted by five 51-m spans, the bridge had the record of the longest bridge ever built worldwide. Unfortunately, it was bombed during the Second World War, and it thus had to be rebuilt between 1945 and 1949.

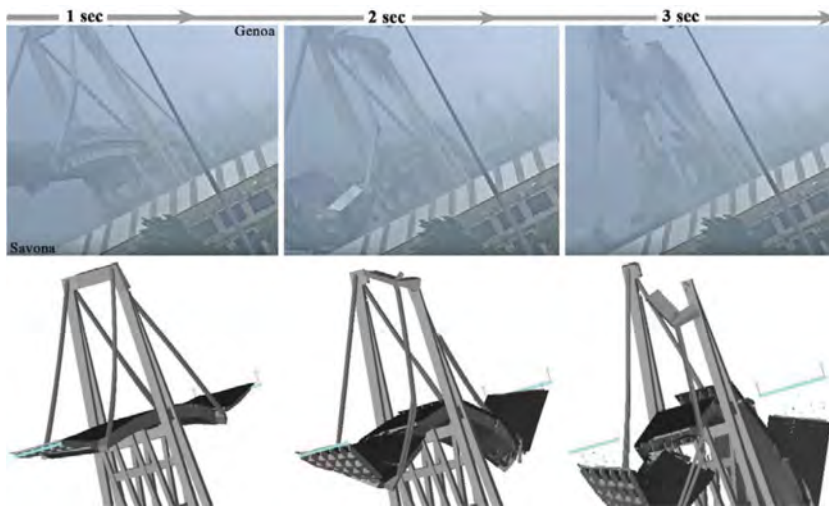


Figure 5. Comparison between the observed (top) and numerical collapse (below).

The new design was inspired by the engineer Robert Maillart, consisting of five variable-thickness slender RC arches that were supported on the existing original piers (Figure 6). It involved the change from a fixed-arch static scheme to a three-hinges arch bridge, as well as an increase of permanent loads due to carriage enlargement to meet the increase of traffic with respect to the time of its first construction. The static scheme change aimed at achieving a theoretically permanent state of compression in the arches, which would be a statically favourable characteristic, and deemed appropriate by the designers to manage potential settlements of the original foundations of the bombed bridge. Subsequently, during the 90's, to adapt the bridge to the road traffic of the twentieth century, the carriageway was enlarged by about 2 m (from 8 m to 10 m) and its thickness increased by about 0.35 m (as estimated from the post-collapse remains).

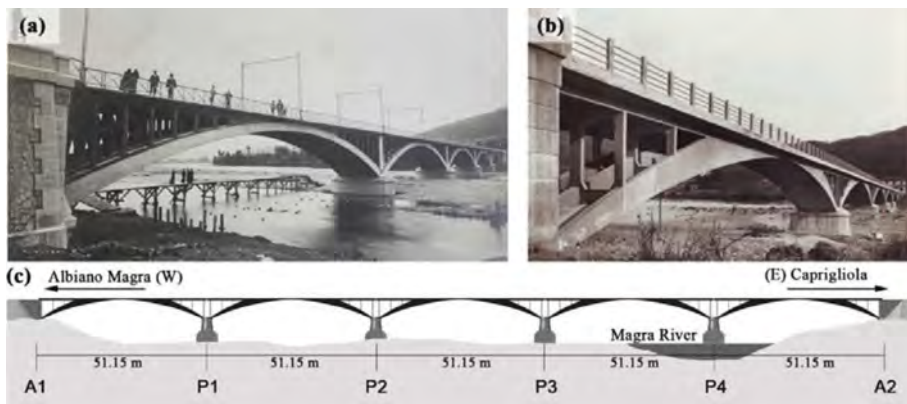


Figure 6. (a) Bridge over the Magra river built in the early '900, (b) bridge rebuilt in 1940's, and (c) schematic of the whole rebuilt bridge.

3.2 The collapse in 2020, after 71 years of operativity

On April 8th, 2020, around 10:20 am, after 71 years of operativity, the bridge suddenly collapsed (see Figure 7). Although the bridge was generally crossed by more than 2,000 vehicles per day, there was little traffic on that occasion due to travel restrictions in place due to the COVID-19 pandemic, and only minor injuries to two truck drivers were recorded. According to an eyewitness, who was driving on the bridge a few seconds before the event, localized damage, not well identified, would have spread rapidly starting from the Capriogliola side, causing a progressive domino-type of collapse.

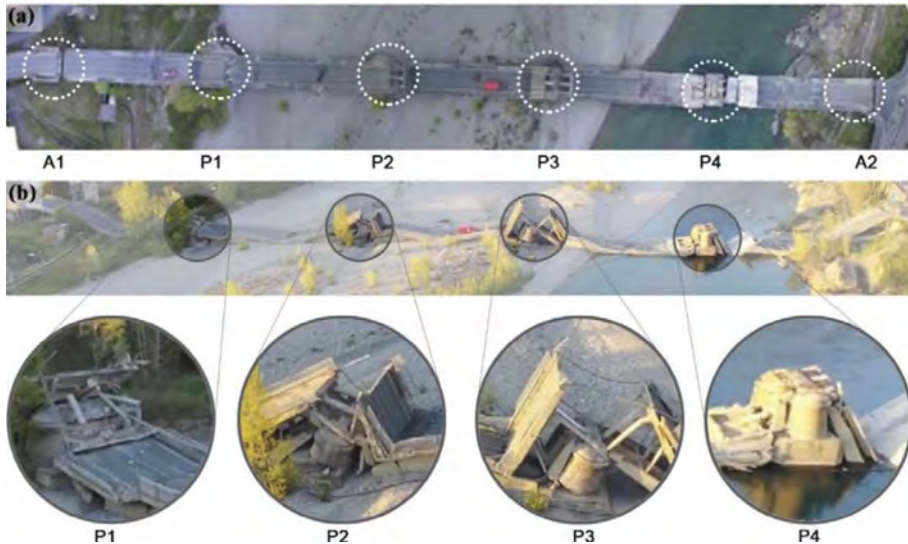


Figure 7. Post-collapse debris distribution: (a) top view, (b) global perspective view from the South.

Similarly to what happened after the collapse of the Morandi bridge, many qualitative hypotheses were formulated on the possible underlying collapse causes, among which (as described in Scattarreggia et al. (2022b); i) materials degradation, ii) foundations subsidence, iii) excessive loading, iv) a slow slope slippage on the Capriogliola side. However, to date, the actual cause, or, perhaps better and as usually happens, the contributing causes to the collapse are still unknown. Notwithstanding, from a preliminary analysis of Figure 7 it is readily possible to note that the residual rotations, with respect to the transversal axis of the bridge, of pier P2 and P3 towards abutment A2 are a clear indication that the progressive collapse of the bridge could not have started from the side of abutment A1, given that the piers could only have rotated towards the direction from where arch support became absent, and would suggest that something must have instead occurred on the opposite side, i.e. on Capriogliola side.

3.3 Collapse analysis through the AEM-based model

The AEM-based numerical model consisted of an assembly of approx. 100,000 elements for a single bridge span, shown in Figure 8 below. The model has been cross-validated using traditional 3D and 2D FE models, i.e. a 3D model in MidasFEA (MIDAS IT 2021), which eigenvalue analysis results were compared with onsite dynamic characterisation tests, and a 2D model in VecTor2 (VecTor Analysis Group 2020), as shown in Scattarreggia et al. (2022b). The analyses carried out indicated that the vertical load capacity of the bridge was well above the stresses induced by today's traffic loads, and hence notwithstanding the fact that the construction of the additional slab in the 90's had led to a considerable increase in stresses close to the pier-arch connections (+50%), the bridge was still capable of supporting a vertical load significantly higher than that acting at the time of the collapse. The potential deterioration of

the steel and concrete materials, hypothesized both independently as well as in combination, was not a critical factor for the collapse of the bridge under the action of vertical loads (assumed to be uniformly distributed).

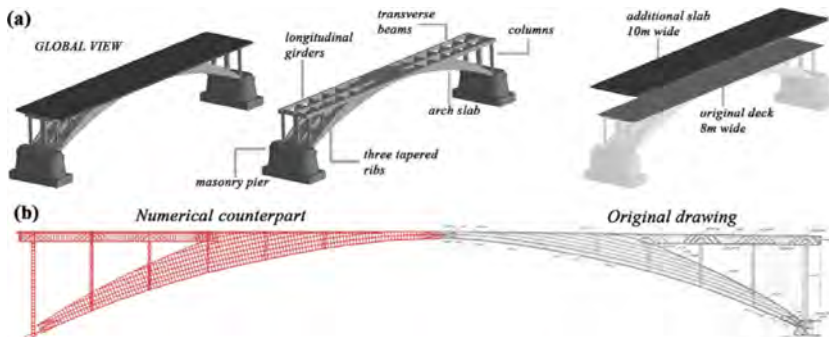


Figure 8. (a) AEM model of a single bridge span, with the nomenclature of main constituting components, and (b) comparison between original drawing reinforcement details and numerical counterpart.

On the contrary, small settlements/rotations at one end of an arch potentially induced on the piers in the riverbed by the erosive action of the river water, or near an abutment due to the thrust of slow slope slippage present on the Capriogliola side, would have had the potential to generate localized damage at critical sections near the pier-arch connection capable of inducing the failure. Such failure potential would have been further increased by the unintended variations in the height of the throat of RC hinges, which would have considerably reduced their rotational capacity compared to what it should have been for a 3-hinged arch bridge (theoretically iso-static), leading to a concentration of damage in correspondence of the critical section at pier-arch connection. Figure 9(a) shows the scenario following a failure in the span on the Capriogliola side at the most stressed section as inferred from the analyses considering small displacements/rotations of the pier/abutment on the Capriogliola side (as potentially induced by the recorded slow slope slippage). The final configuration of the debris predicted by the model (at 7.5 seconds in Figure 9(a)) is compatible with that observed on site (Figure 9(b)).

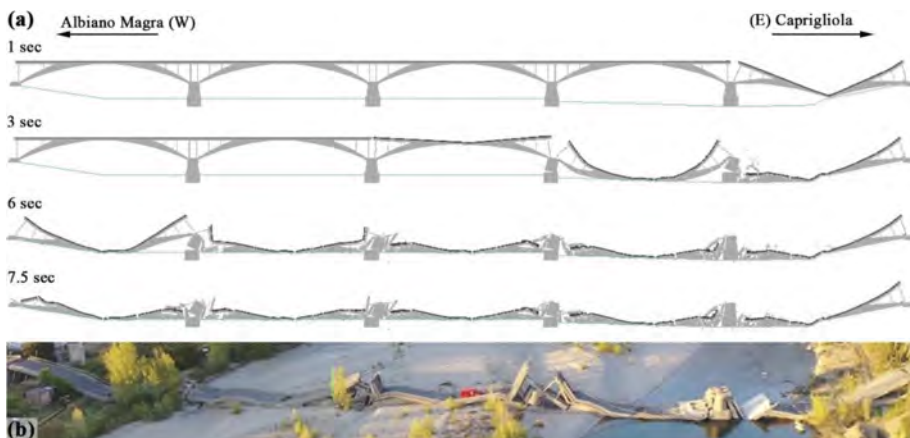


Figure 9. (a) Predicted progressive collapse mechanism of the entire bridge as triggered by a failure close to the pier-arch connection potentially caused by slope slippage at the abutment A2 and (b) observed debris.

4 CONCLUSIONS

The AEM seems to be a computational efficient numerical analysis method to study the response of quite complex and large RC bridge structures taking into consideration as-built

structural details as well as changes in loading and materials during the life of the structures. The application to the cable-stayed Polcevera viaduct and to the arch bridge of Capriogliola highlighted the criticalities of such bridge typologies. For what concerns the Morandi bridge, the innovative idea by Morandi of introducing only four main post-compressed stays, seemingly ingenious and effective, when combined with construction errors (that became known only after the collapse) and the consequent (non-visible) material deterioration throughout its life rendered the structure more vulnerable to potential exceptional load scenarios. In the case of the Capriogliola bridge, the idea of changing the initial fixed arch scheme into a three-hinges arch configuration, theoretically appropriate to render the bridge less sensitive to imposed foundation movements, when combined with initially unforeseen changes in the arch hinges throats and the years long slow slope slippage behind one of the abutments did inevitably render the bridge more susceptible to the type of complete collapse that was observed.

REFERENCES

- Applied Science International LLC (ASI). (2020). "Extreme Loading for Structures (2020)." Durham (NC), USA.
- Calvi, G. M., Moratti, M., O'Reilly, G. J., Scattarreggia, N., Monteiro, R., Malomo, D., Calvi, P. M. & Pinho, R. 2019. "Once upon a Time in Italy: The Tale of the Morandi Bridge." *Structural Engineering International*, 29 (2): 198–217. Taylor and Francis Ltd.
- Ceradini, G. 1951. "Esperienze su recenti ponti italiani di cemento armato: Esperienze sul ponte sul fiume Magra, fra Capriogliola ed Albiano." *Giornale del Genio Civile*, 1951.
- Consiglio Nazionale delle Ricerche (CNR) 2021. CNR DT-214/2018. *Guide to Design of Structures for Robustness*. Rome, Italy.
- Iori, T. & Poretti, S. 2009. "The golden age of 'Italian style' engineering." *Proceedings of the 3rd International Congress on Construction History*. Cottbus, Germany.
- Malomo, D., Scattarreggia, N., Orgnoni, A., Pinho, R., Moratti, M. & Calvi, G. M. 2020. "Numerical Study on the Collapse of the Morandi Bridge." *Journal of Performance of Constructed Facilities*, 34 (4): 04020044. American Society of Civil Engineers (ASCE).
- Meguro, K. & Tagel-Din, H. 2002. "Applied Element Method Used for Large Displacement Structural Analysis." *Journal of Natural Disaster Science*, 24(1), 25–34.
- MIDAS IT. 2021. "Midas FEA NX - Advanced Nonlinear and Detail Analysis System."
- Morandi, R. 1967. "Il viadotto del Polcevera dell'Autostrada Genova – Savona." *L'Industria Italiana del Cemento*, XXXVII, 849–872.
- Orgnoni, A., Pinho, R., Moratti M., Scattarreggia, N. & Calvi, G. M. 2023a. "Critical review and modelling of the construction sequence and loading history of the Morandi bridge." *International Journal of Bridge Engineering*, 10 (3).
- Orgnoni, A., Pinho, R., Calvi, G. M., Moratti, M., & Scattarreggia, N. 2023b. "Numerical dynamic characterization of concrete bridge stays." *Earthq Eng Struct Dyn*, submitted for publication.
- Pinho, R., Scattarreggia, N., Orgnoni, A., Lenzo, S. G., Grecchi, G., Moratti, M. & Calvi, G. M. 2023. "Forensic estimation of the residual capacity and imposed demand on a ruptured concrete bridge stay at the time of collapse." *Structures*, submitted for publication.
- la Repubblica. 2019. "Ponte Morandi, le immagini inedite della tragedia: il crollo ripreso dalla videosorveglianza - YouTube." Accessed September 2, 2021. https://www.youtube.com/watch?v=a-LfXohbn0U&ab_channel=LaRepubblica.
- Rosati, P., Losa, M., Valentini, R. & Tubaro S. 2020. *Secondo incidente probatorio - Procedimento Penale N. 7998/18 R.G.G.I.P. (N.10468/18 R.G.N.R.), Tribunale Ordinario di Genova, Genoa, Italy*.
- Scattarreggia, N., Galik, W., Calvi, P. M., Moratti, M., Orgnoni, A. & Pinho, R. 2022a. "Analytical and numerical analysis of the torsional response of the multi-cell deck of a collapsed cable-stayed bridge." *Eng Struct*, 265: 114412. Elsevier.
- Scattarreggia, N., Salomone, R., Moratti, M., Malomo, D., Pinho, R., & Calvi, G. M. 2022b. "Collapse analysis of the multi-span reinforced concrete arch bridge of Capriogliola, Italy." *Eng Struct*, 251: 113375. Elsevier.
- Scattarreggia, N., Orgnoni, A., Pinho, R., Moratti, M. & Calvi, G. M. 2023. "Numerical modelling of the impact of a falling object on a bridge deck." *Eng Fail Anal*, submitted for publication.
- VecTor Analysis Group. 2020. "VecTor2 – NLFEA program for the analysis of two-dimensional reinforced concrete membrane structures."

Digital fatigue test of flange-web welded details in guideway girders

C.S. Wang, X.G. Zhou, Y.Z. Wang & M.Y. Yang

Department of Bridge Engineering, College of Highways, Chang'an University, Xi'an, China

ABSTRACT: In order to investigate the long-term fatigue performance of the flange-web welded details of the guideway under eccentric loads, the digital fatigue tests of the flange-web welded details are carried out by using the extended finite element method (XFEM) and fracture mechanic theory. The results show a large welding residual tensile stress approaching to the yield stress of Q345 steel at the flange-web weld toes. Out-of-plane distortion will increase the local stress of steel structure under live load. The fatigue crack at the web is a mixed Mode I-II-III composite crack dominated by Mode I crack. This research determines the effect of residual tensile stress on distortion-induced fatigue behavior of this detail and the fatigue crack type under coupling actions. The design and construction of the guideway should avoid eccentric setting web, and the welding residual stress of fatigue-sensitive detail parts should be reduced by ultrasonic impact treatment.

1 INTRODUCTION

Fatigue cracks usually initiate at the weld in steel bridges, which can be divided into two types, including load-induced fatigue cracks and distortion-induced fatigue cracks, of which about 90% of fatigue cracks are caused by secondary stress due to out-of-plane distortion at fatigue details (Connor & Fisher 2006). Full-scale fatigue test proves that the fatigue life of vertical stiffener web gaps in steel girder bridges is affected by distortion ratio and nominal stress ratio (Wang et al. 2022). A new type of rubber-tyred tram transit system consisting of a rubber-tyred tram and guideway girder bridge is gradually being used in China. The guideway is composed of two I-girders connected by a transverse connection system. The running wheel of the rubber-tyred tram runs on the flange of I-girders because of lacking deck. Under the action of live loads, the distortion will cause high local flexural stresses and lead to the initiation and propagation of fatigue cracks at the flange-web welded details of the I-girder as shown in Figure 1.

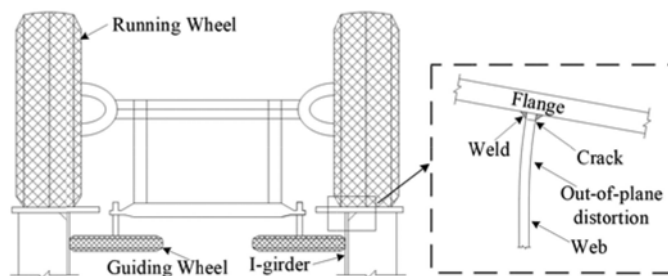


Figure 1. Out-of-plane distortion at the flange-web welding detail.

With the development of fracture mechanics theory and extended finite element method, the numerical simulation of fatigue crack propagation has made great progress. XFEM eliminates the need to remesh during simulated crack growth, greatly improving the solution efficiency

(Belytsehko & Black 1999; Stolarska et al. 2001). XFEM reflects the discontinuity of the crack through the special enriched functions, increasing the degree of freedom of element nodes around the crack (Moës et al. 1999). Compared with the traditional finite element method, XFEM can well simulate the mixed-mode cracks propagation of steel bridges (Wang et al. 2020). Based on the theory of linear elastic fracture mechanics (LFEM), Xiao et al. (2008) analyzed the fatigue stress under vehicle loads and estimated the life of the rib-to-deck joints in orthotropic steel decks. Zhan et al. (2017) simulated fatigue crack growth and evaluated the total fatigue life of components based on the XFEM. It was found that the crack propagation behavior and the predicted total fatigue life are consistent with the fatigue test results. XFEM has also been successfully applied to simulate fatigue cracking in steel bridges due to out-of-plane distortion (Mahmoud & Miller 2016; Wang et al 2017). Mahmoud and Miller (2016) used XFEM to explore the fatigue mechanism induced by out-of-plane distortion and determined the effectiveness of XFEM in simulating high-cycle fatigue crack growth.

The existence of welding residual stress has an important role in the fatigue crack propagation behavior in steel bridges. Barsoum (2009) confirmed that fatigue life predictions agree well with experimental results when residual stress is considered in crack propagation analysis. Wang et al. (2020) used the extended finite method of coupled welding residual stress field to numerically simulate the fatigue crack propagation of the I-girder web gap. The results show that the shape and propagation direction of the fatigue crack is consistent with the physical fatigue test results.

This paper researches the fatigue damage mechanism of flange-web welding details. The stress distribution of the flange-web welded detail is calculated considering the secondary stress caused by the out-of-plane distortion under fatigue loads. The welding residual stress field of fatigue details was obtained by simulating the flange-web fillet weld welding process. Fatigue crack propagation simulation under multi-field coupling is carried out to investigate the fatigue crack propagation mechanism of the flange-web weld toes under eccentric loads.

2 FATIGUE SIMULATION MODEL

Three-span continuous guideway girder is established based on the tram test line under construction. Flange-web welding fatigue detail is selected as the research object at the middle of the side span, as shown in Figure 2. For the full-bridge shell model, the total length is 89.9 m, with 2 intermediate supports (29.6 m+30 m+29.6 m). For the entity sub-model, the size of the fillet welds is 8×8 mm, and the dimensions of the flange and the web are 380×200×26 mm and 200×200×12 mm, respectively. Shell-solid coupling constraint is adopted between the solid sub-model and the full-bridge shell model, and the boundary conditions of the full-bridge model are shown in Figure 3.

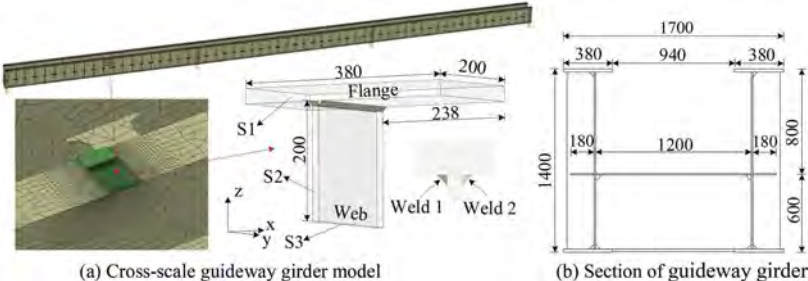


Figure 2. Three-span continuous guideway girder (Unit: mm).

The wheel track of the rubber-tyred tram is 1380 mm, and the wheelbase is 4200 mm. In operation by 4 vehicles as a group, the wheelbase between adjacent vehicles is 3800 mm.

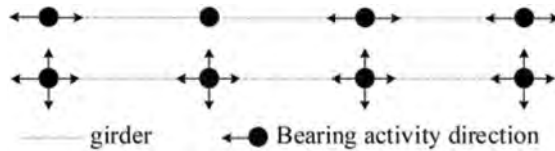


Figure 3. Boundary conditions of guideway girder.

The running wheel's load area is 195 mm × 130 mm on the guideway girder's flange plate, and the fixed axle load $P = 60$ kN. The fatigue load model adopts the vehicle formation in fixed personnel operation. Figure 4 gives the wheel load distribution of the rubber-tyred tram. And Figure 5 shows the relative position of the axle to the fatigue detail for longitudinal loading case 8.

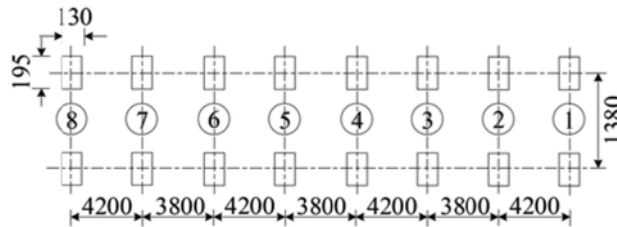


Figure 4. Fatigue load model (Unit: mm).

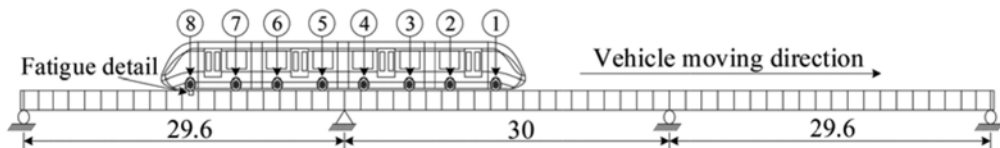


Figure 5. Longitudinal loading conditions (Unit: m).

3 FATIGUE CRACK PROPAGATION MECHANISM ANALYSIS

3.1 Live load stress analysis

The out-of-plane distortion of the flange-web welding details occurs below the load position, which causes large bending stress. Eight longitudinal working conditions are set up, and eight axles are applied to the flange plate above the fatigue details in turn (Figure 5). The stress component of the P1 path under live load is shown in Figure 6(a). Four paths are selected to characterize the stress field distribution caused by out-of-plane distortion under the most unfavorable conditions, as shown in Figure 6(b).

The stress extraction path is selected from the 1/2 section of the solid model. The starting point of the P1 path is the toe of weld 2 at the web, and the starting point of the P2 path is the toe of weld 2 at the flange plate. Similarly, the starting point of the P3 and P4 paths is the toe of weld 1. In the x -direction, the secondary stress caused by distortion drives tensile stress outside the web and compressive stress inside the web. The x -direction stress component is -49 MPa and -25 MPa at the starting point of P1 and P2, respectively. Without distortion, the x -direction stress component is -30 MPa at the weld toe.

3.2 Welding residual stress analysis

The welding residual stress is calculated by the thermal-stress sequential coupling method. For the thermal analysis, boundary conditions are not required to establish, and DC3D8 eight-node

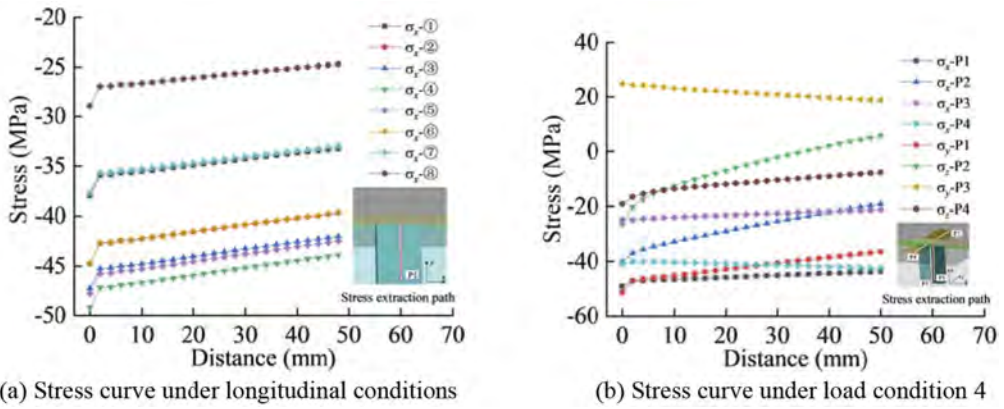


Figure 6. Live load stress distribution under longitudinal conditions.

linear hexahedron heat transfer elements are used to calculate the welding temperature field at the heat transfer analysis steps. In the thermo-mechanical analysis, the boundary conditions of the solid model are shown in Table 1. And the welding residual stress field is calculated by C3D8R eight-node linear hexahedron elements. The weld formation is simulated by model change in the welding process. The element size of the weld area is about 2 mm and away from the weld area is 4 mm. The thermal physical parameters of Q345 steel are shown in Figure 7.

Table 1. Thermal-force analysis model boundary condition.

Location	Constrain state	
	Weld 1	Weld 2
S1	$U_x = U_y = 0$	$U_x = U_y = 0$
S2	$U_x = U_y = 0$	$U_x = U_y = 0$
S3	$U_z = 0$	$U_z = 0$

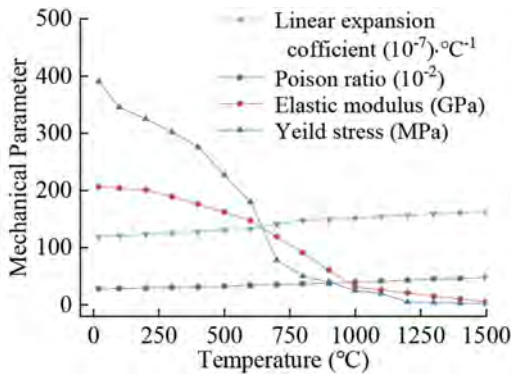


Figure 7. Material properties of Q345.

The web and flange of the guideway girder are connected by double-sided fillet welds, weld 1 on the inner side of the web and weld 2 on the outer side of the web. The welding heat source adopts the double ellipsoid heat source model, and the welding temperature field is shown in Figure 8. The temperature of the grey part is greater than the melting point of the steel (1450 °C) during the welding process. After welding, the temperature of the solid model is cooled to 20 °C.

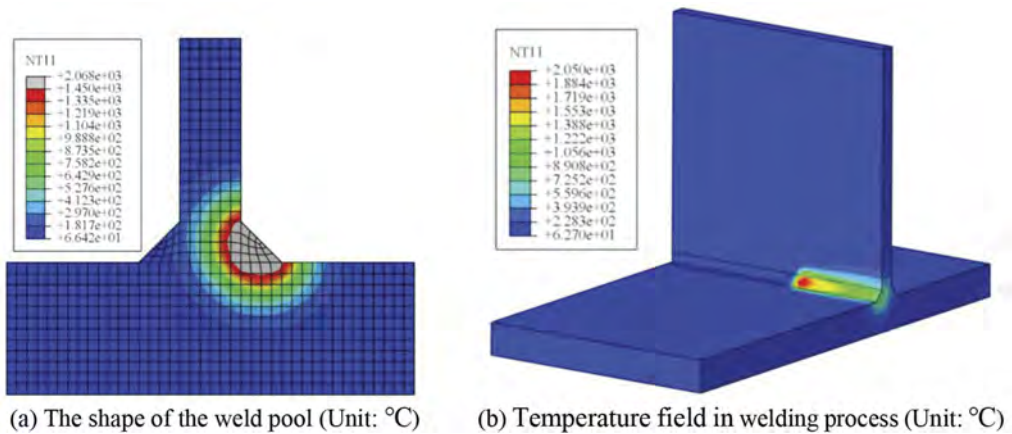


Figure 8. Welding temperature field.

In thermo-mechanical analysis, the welding temperature field is acted as a temperature load to the welding residual stress model with defined boundary conditions. After the welding is completed, there is a large welding residual tensile stress near the weld, which is close to the yield strength of the steel. And the Von Mises stress is shown in Figure 9(a). To accurately obtain the residual stress field distribution at the flange-web weld, the P1, P2, P3 and P4 stress extraction paths are selected for residual stress analysis, as shown in Figure 9(b). The x -direction stress component is 372 MPa and -49 MPa at the starting point of P1 and P2, respectively. In addition, the toe of weld 2 was mainly under cyclic compressive stress during the cyclic loading. Therefore, the flange-web welded details are vulnerable to fatigue cracking at the toe of weld 2.

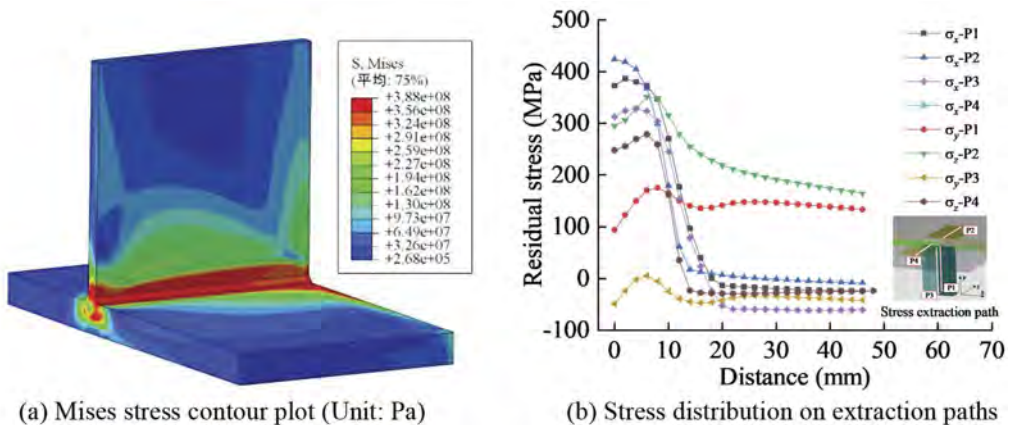


Figure 9. Welding residual stress distribution.

3.3 Fatigue crack growth analysis

When the residual stress is not considered, the weld toe is in a compressive state under vehicle load. In contrast, after the introduction of welding residual stress, this place is in a tension-tension state. As a result, fatigue cracks initiate and propagate there.

The crack propagation process in fatigue numerical simulation is characterized by strain energy release rate, calculated by the virtual crack closure technique (VCCT) (Shivakumar 1998). The classical Paris law is rewritten in the numerical fatigue simulation, and the fatigue crack propagation criterion is defined:

$$\frac{da}{dN} = c_1 \Delta G^{c_2} \quad (1)$$

where c_1 and c_2 are material parameters; ΔG is the strain energy release rate range. When $G_{th} < \Delta G < G_{pl}$, the crack will propagate stably under Paris law. Where G_{th} is the threshold of strain energy release rate; G_{pl} is the upper limit of strain energy release rate.

The initial fatigue crack size was assumed as $a_0/2c_0 = 0.5 \text{ mm}/2 \text{ mm}$, and the propagation path of the crack is shown in Figure 10. Figure 11 displays the variation in crack length on the web and flange surfaces during fatigue loading. When the initial fatigue crack begins to expand, the fatigue crack growth direction is deflected by 90 degrees. After 1.1 million times of fatigue loading, the fatigue crack propagates along the web simultaneously in the direction of the upper and lower flange plate. Until 1.6 million fatigue loadings, the fatigue crack penetrates the welds on both sides of the web, and the crack tip is semi-elliptical in the cross-section of the flange plate. The flange is penetrated by fatigue cracks during the 1.9 millionth fatigue loading. As shown in Figure 10(d), after 2.5 million cycles, the fatigue crack propagated to 70 mm, 48 mm and 96 mm in the web, top and bottom surfaces of the flange plate, respectively.

Figure 12 and Figure 13 show the cumulative strain energy release rates G_I , G_{II} and G_{III} in crack propagation process in the web and flange plate, respectively. As can be seen from Figure 12, mode I was the dominant crack mode, and G_{II}/G_I and G_{III}/G_I were respectively 0.07 and 0.15, with crack propagating along the web. As illustrated by Figure 13, G_{II}/G_I and G_{III}/G_I were respectively 0.07 and 0.15, with cracks propagating in the flange plate. And fatigue cracks in the flange plate Mode I.

4 CONCLUSIONS

Digital fatigue tests are conducted to investigate the mechanism of distortion-induced fatigue at flange-web welded details in guideway girder, based on XFEM and linear elastic fracture mechanics. The welding residual stress field and live load stress field are calculated. According to the analysis results, the following conclusions can be drawn:

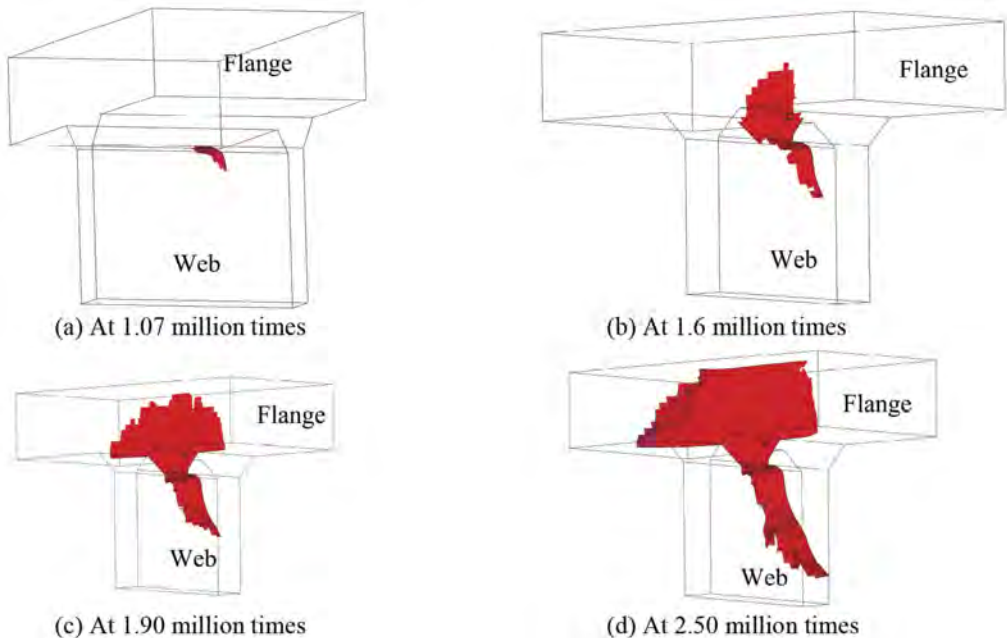


Figure 10. Propagation behavior of the crack.

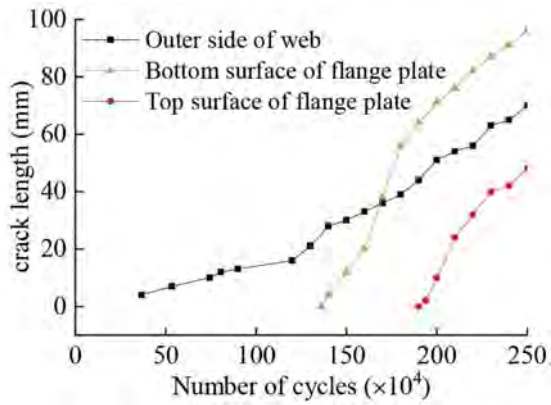


Figure 11. Fatigue crack length on web and flange surfaces.

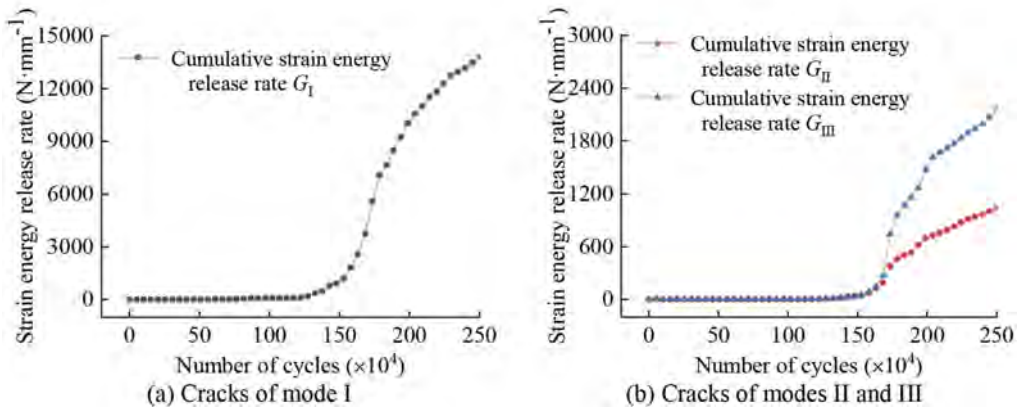


Figure 12. Cumulative strain energy release rate of crack propagation at web.

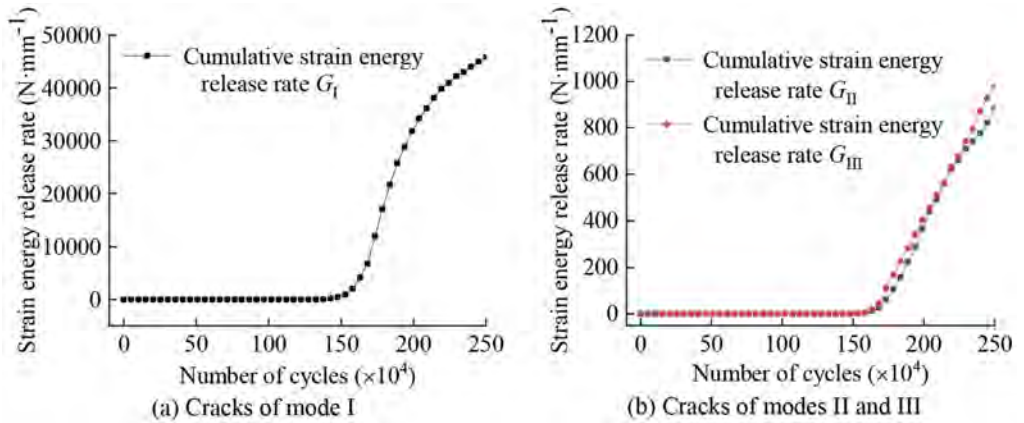


Figure 13. Cumulative strain energy release rate of crack propagation at the flange.

- (1) Fatigue cracks of flange-web welded details propagating at the web and flange plate are Mode I leading mixed-mode cracks of Modes I, II and III and Mode I, respectively. And the out-of-plane deflection occurs during the fatigue crack propagation at the web.
- (2) There is welding residual stress at the flange-web weld toes, and the von Mises stress peak is close to the yield stress of steel. After coupling the residual stress field, the compressive-compressive stress cycle caused by vehicle load is transformed into a tensile-tensile stress cycle in the fatigue details, which leads to the initiation and propagation of fatigue cracks. In the manufacture of guideway girders, the welding sequence should be optimized to reduce the welding residual stress, or the ultrasonic hammering technique should be used to hit the weld toe at fatigue details to reduce the influence of welding residual stress.
- (3) The distortion affects the local stress distribution of the steel bridges. The design of the guideway should avoid eccentric setting web or decrease the distance of adjacent vertical stiffeners to reduce out-of-plane distortion.

ACKNOWLEDGEMENT

The authors gratefully acknowledge the financial support provided by the Program of National Ten Thousand People Plan Science and Technology Innovation Leading Talents (W03020659), the Bridge Damage Resistance Design and Safety Maintenance Technology Innovation Team in Ministry of Transport of the People's Republic of China.

REFERENCES

- Belytschko, T. & Black, T. 1999. Elastic crack growth in finite elements with minimal remeshing. *International Journal for Numerical Methods in Engineering* 45(5): 601–620.
- Barsoum, Z. & Barsoum, I. 2009. Residual stress effects on fatigue life of welded structures using LEFM. *Engineering Failure Analysis* 1(16): 449–467.
- Connor, R. J. & Fisher, J. W. 2006. Identifying effective and ineffective retrofits for distortion fatigue cracking in steel bridges using field instrumentation. *Journal of Bridge Engineering* 11(6): 745–752.
- Moës, N. et al. 1999. A finite element method for crack growth without remeshing. *International Journal for Numerical Methods in Engineering* 46(1): 131–150.
- Mahmoud, H. N. & Miller, P. A. 2016. Distortion-induced fatigue cracks growth. *Journal of Bridge Engineering* 2(21): 04015041.
- Shivakumar, K. N. et al. 1988. A virtual crack-closure technique for calculating stress intensity factors for cracked three dimensional bodies. *International Journal of Fracture* 36(3): R43–R50.
- Stolarska, M. et al. 2001. Modelling crack growth by level sets in the extended finite element method. *International Journal for Numerical Methods in Engineering* 8: 51
- Wang, C. S. et al. 2017. Numerical fracture mechanical simulation of fatigue crack coupled propagation mechanism for the steel bridge deck. *China Journal of Highway and Transport* 30(3): 82–95. (in Chinese)
- Wang, C. S. et al. 2020. Numerical simulation of distortion-induced fatigue crack growth using extended finite element method. *Structure and Infrastructure Engineering* 1(16): 106–122.
- Wang, C. S. et al. 2022. Distortion-induced fatigue behavior of vertical stiffener web gaps in steel girder bridges. *Thin-Walled Structures* 180: 109892
- Xiao, Z. G. et al. 2008. Stress analyses and fatigue evaluation of rib-to-deck joints in steel orthotropic decks. *International Journal of Fatigue* 8(30): 1387–1397.
- Zhan, Z. X. et al. 2017. Continuum damage mechanics combined with the extended finite element method for the total life prediction of a metallic component. *International Journal of Mechanical Sciences* 124: 48–58.

3-D segmentation of concrete spalling in point cloud using unsupervised clustering and plane fitting

Y. Zhang

Aalto University, Espoo, Finland

B. Xia

Silo AI, Helsinki, Finland

ABSTRACT: Spalling is one of the typical damage types of concrete structures. Concrete spalling occurs with local concavity and volume loss, leading to a certain range of load capacity reduction. Recently, with the rapid development of structural health monitoring and non-destructive inspection technologies, it becomes possible to perform high-resolution measurements and capture rich details of civil structures. By using laser scanners, Lidar scanners, or photogrammetry techniques, dense point clouds of structural faces can be reconstructed. Those dense point cloudscan describe both global and local geometries of structures in detail, which can be further used for damage assessment. However, the researches on identifying and localizing structural damage on concrete structures based on PC processing are still limited. Therefore, in the article, we propose a method to segment concrete spalling in 3-D point clouds of concrete structures. Unsupervised clustering methods are used to segment the point cloud into several classes that represent different faces of the target structure or structural member. Then a plane is fitted to each class of the point cloud using the Least Squares method. Based on the distances from the points to the corresponding fitted plane, a threshold can be determined, and the points that are far off the plane can be identified and localized. Those identified points can be used to present concrete spalling damage. To validate the proposed method, an experiment was conducted on a reinforced concrete beam. The result shows that the volume loss of the concrete beam was successfully identified and localized. Using a distance threshold, the points of damage can be segmented from the point cloud. Therefore, the feasibility of the proposed method was fully demonstrated.

1 INTRODUCTION

Spalling is one of the most common types of damage on concrete structures. Spalling describes the cracked and delaminated areas of concrete. It is mainly caused by corrosion or oxidization of reinforcing rebar, freeze-thaw cycling, subpar quality concrete, improper curing, etc. Spalling leads to local volume loss and reduces the load-bearing capacity of concrete. It can spread on concrete structures and accelerate degradation. Therefore, spalling greatly affects the health state of concrete structures. Concrete with severe spalling damage had become a threat to public safety. To address this challenge, structural health monitoring (SHM) (Boller et al., 2009) and non-destructive testing (NDT) (Dwivedi et al., 2018) technologies can be used for acquiring information and analysing the health state of concrete structures.

Recently, SHM and NDT technologies have greatly powered the management and maintenance of civil structures. The advanced sensing technologies enable monitoring structural behaviours with enriched information, for instance, vibration (Zhang et al., 2019), image (Zhang and Li, 2022; Zhang et al., 2022), strain, temperature, and point cloud data of

structures can be acquired for further analyses. Long-term monitoring can accumulate large scale of monitoring data which provides a solid foundation for data-driven modelling methods, especially, machine learning (ML) and deep learning (DL) (LeCun et al., 2015; Goodfellow et al., 2016). These data-driven methods can be used for establishing mappings or functions to make predictions. The sensing technology and data-driven methods provide full potential for digging deeper into the concrete spalling issue.

The existing literature mainly discusses the detection and evaluation of concrete spalling using 2-D image processing and DL modelling (Cha et al., 2017). Deep learning models were trained by labelled images to output bounding boxes or segmented images. Areas with concrete spalling in image data are pointed out with bounding boxes or pixels with different colours. Such a method can perform a fast examination with satisfactory detection accuracy. However, researches on spalling quantification or quantitative analyses of spalling still remain insufficient.

As concrete spalling is generally with apparent volume losses, depth information is of great significance to analyse the damage. The commonly used methods that are based on 2-D image data cannot acquire depth information. Thus, a 3-D point cloud has great advantages to deal with depth-related issues, like quantitative analysis of concrete spalling. Indeed, acquiring point cloud data has become simplistic nowadays. Despite the expensive laser scanners for industrial applications, lidar scanners on portable devices or even photogrammetry techniques are quite handy tools to scan objects and generate point cloud data. Such a technological advance can also benefit the detection and evaluation of concrete spalling.

Overall, this article presents a method to perform 3-D segmentation of concrete spalling using point cloud processing, unsupervised clustering, and plane fitting. Those identified points can be used to detect concrete spalling damage in a rapid manner and provide the potential for further analyses.

2 METHODOLOGY

2.1 Overview of the proposed method

An overview of the proposed spalling segmentation method for point cloud data is shown in Figure 1. Point clouds can be generated in multiple approaches as mentioned in the introduction, for instance, laser scanning, Lidar scanning, photogrammetry (Mikhail et al., 2001), etc. In this study, photogrammetry was chosen because of its convenience and simplicity. Photos taken by ordinary commercial cameras are capable to be directly used for generating 3-D point clouds of the objects in the photos via the structure from motion (SfM) algorithm (Ullman, 1979; Özyeşil et al., 2017).

Raw point clouds generated by the above methods normally contain large numbers of points which represent the desired objects, backgrounds, and noises. To make the raw point clouds feasible to be clustered, applying pre-processing to the point clouds is necessary. The pre-processing includes cropping, down-sampling, and noise reduction. The cropping operation removes the undesired parts and leaves only the structure in the point cloud. Down-sampling reduces the number of points in the cloud, so that the computational speed can be significantly improved. Noise reduction can remove the outliers in the point cloud.

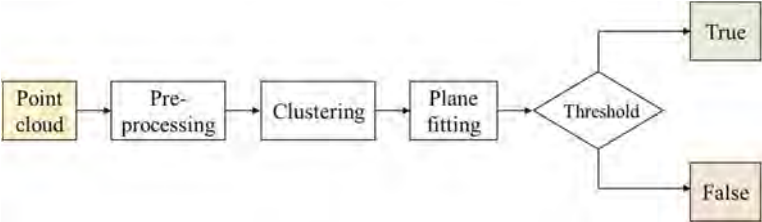


Figure 1. Flowchart of the proposed method.

The processed local point cloud with the region(s) of concrete spalling is clustered into several classes to represent different faces. Unsupervised learning algorithms, such as k -means, DBSCAN, etc., can be used for clustering. Then each cluster of the point cloud is fitted to a plane. Finally, by evaluating the distance from each point in the cloud to the fitted plane with a threshold, the points that are further away from the plane can be identified. As the points in the spalling regions are generally far off the fitted plane, the proposed method can achieve remarkable performance in detecting the points of spalling in the cloud of concrete structures.

2.2 Point cloud pre-processing

Voxel down sample can effectively reduce the number and the density of the point cloud. The algorithm has two steps. The points are embedded into voxels, and then each voxel outputs a point by averaging the coordinates of the embedded points in the voxel.

Statistical outlier removal algorithm removes the points that are further away from their neighbour points compared to the mean value of the entire point cloud. Two parameters of the algorithm are the number of neighbour points and the standard deviation of the mean distances across the point cloud.

2.3 Gaussian mixture model

Gaussian mixture model (GMM) is an efficient and powerful clustering algorithm (Press et al., 2007). It implements the expectation maximization (EM) algorithm (Dempster et al., 1977) for fitting and mixing Gaussian models. Then the fitted models can be used for clustering the data into a specific number of classes. To achieve robust performance, an initializer such as k -means (Hartigan & Wong, 1979), k -means ++ (Vassilvitskii & Arthur, 2006) can be used to initialize the weights, means, and precisions of the GMM. As GMM is a standard method, detailed descriptions are omitted in this article.

2.4 Plane fitting

Plane fitting of points is achieved by using the Least Squares method. Planes can be defined as Equation (1), in which the normal to the plane is $\langle A, B, C \rangle$. Equation (1) can also be simplified to Equation (2). Fitting 3-D points to a plane is calculating the optimal a , b , and c , which can be defined as an optimization problem described in Equations (3-6). In Equations (4), (6) and (7), x_i , y_i , and z_i are the coordinates of each point. The solution of a , b , and c for plan fitting can be finally obtained using Equation (7).

$$Ax + By + Cz + D = 0 \quad (1)$$

$$z = ax + by + c \quad (2)$$

$$a, b, c = \operatorname{argmin}(L) \quad (3)$$

$$L = \sum_{i=1}^n (ax_i + by_i + c - z_i)^2 \quad (4)$$

$$\begin{cases} \frac{\partial L}{\partial a} = 0 \\ \frac{\partial L}{\partial b} = 0 \\ \frac{\partial L}{\partial c} = 0 \end{cases} \quad (5)$$

$$\begin{pmatrix} \sum x_i^2 & \sum x_i y_i & \sum x_i \\ \sum x_i y_i & \sum y_i^2 & \sum y_i \\ \sum x_i & \sum y_i & n \end{pmatrix} \begin{pmatrix} a \\ b \\ c \end{pmatrix} = \begin{pmatrix} \sum z_i x_i \\ \sum z_i y_i \\ \sum z_i \end{pmatrix} \quad (6)$$

$$\begin{pmatrix} a \\ b \\ c \end{pmatrix} = \begin{pmatrix} \sum x_i^2 & \sum x_i y_i & \sum x_i \\ \sum x_i y_i & \sum y_i^2 & \sum y_i \\ \sum x_i & \sum y_i & n \end{pmatrix}^{-1} \begin{pmatrix} \sum z_i x_i \\ \sum z_i y_i \\ \sum z_i \end{pmatrix} \quad (7)$$

After that, the distance between each point to the fitted plane is calculated based on Equation (8). A threshold is manually assigned to evaluate whether the point is out of a plane. The out-of-plane points are then identified and localized as the points at the region(s) of concrete spalling.

$$d = \frac{|ax_0 + by_0 - z_0 + c|}{\sqrt{a^2 + b^2 + 1^2}} \quad (8)$$

3 EXPERIMENT SETTINGS

To validate the proposed method for 3-D segmentation of concrete spalling in a point cloud, an experiment was conducted on a reinforced concrete beam. One photo of the beam is shown in Figure 2. The length of the beam is 82 cm. Concrete volume loss is on one edge of the beam, as shown in Figure 3. The length of the damage is about 5 cm, and the depth of the damage is about 1 cm. Over 100 photos of the beam were taken from different perspectives for generating the 3D dense point cloud of the beam.

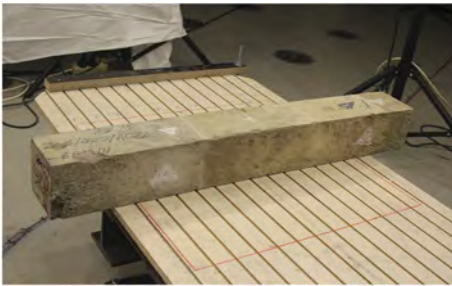


Figure 2. Photo of the concrete beam.



Figure 3. Spalling on the beam.

4 RESULTS

The 3-D dense point cloud of the scene was generated using an unordered photo set and the SfM algorithm, as shown in Figure 4. This procedure was realized using the Meshroom software (Griwodz et al., 2021). As the number of points is very large and the density of the point is too high, pre-processing was performed on the raw point cloud.



Figure 4. 3-D model of the scene generated by SfM.

The cropping operation was performed manually using MeshLab software (Cignoni et al., 2008). Then, voxel down sample and noise reduction were performed in Python environment and Open3D (Zhou et al., 2018). The parameters were determined by several rounds of trial and error. Figure 5 shows the cleaned local point cloud after the pre-processing. The point cloud describes three faces of the beam, because photos of the bottom face could not be taken and no point on the bottom face was generated in the 3-D reconstruction. The volume loss is presented clearly on the point cloud.

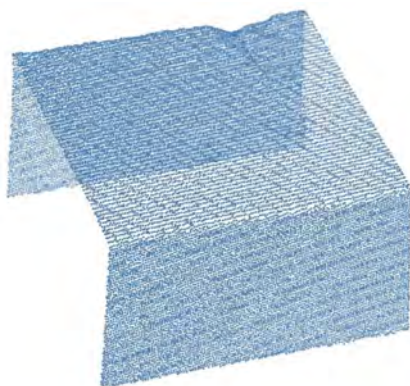


Figure 5. Cleaned local point cloud at the damage region.

The points in the local point cloud were then clustered into 3 classes for representing the three faces of the beam via the GMM algorithm which is included in the scikit-learn package (Pedregosa et al., 2011). The number of components is 3 because of the 3 faces. The covariance type is “tied” which means that all components share the same general covariance matrix. To achieve a robust performance of GMM clustering, the k -means algorithm was used as the initializer to initialize the weights, the means, and the precisions. The covariance type is tied, which means all components share the same general covariance matrix. The clustering result is shown in Figure 6, in which the points were accurately clustered based on the faces even at the damage region and edges, demonstrating the effectiveness of the GMM algorithm for this task. For structures with simpler geometries, directly using the k -means algorithm for clustering is also feasible, as proved in the article (Nakamizo and Nishio, 2022).

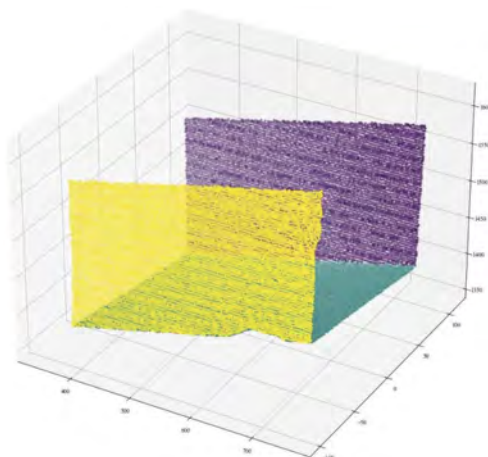


Figure 6. Result of clustering.

As the damage is at the edge of the beam, only the yellow and green point clusters are involved in the damage, as shown in Figure 7. Plane fitting and distance evaluation were performed on these two clusters respectively. Using the green cluster in Figure 8 as an example, the damage is clearly profiled.

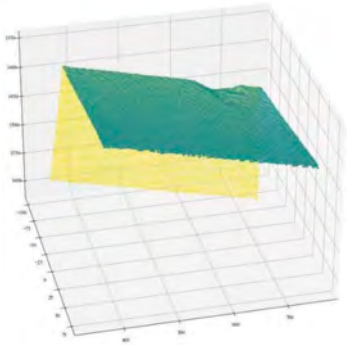


Figure 7. Two faces involved in the damage.

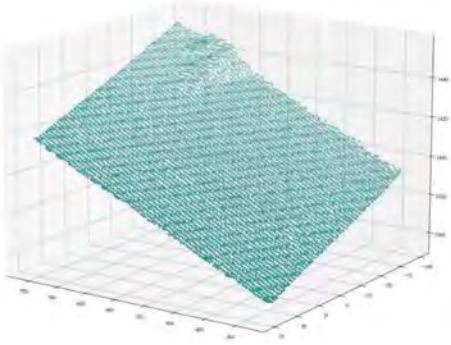


Figure 8. One of the two faces involved in the damage.

Implementing the plane fitting algorithm as introduced beforehand, a plane was accurately fitted to the green points, as shown in Figure 9. A side view of the green points and the corresponding plane was shown in Figure 10 to provide additional information about the result. The points at the damage region are out of plane clearly in Figure 10.

Subsequently, after several rounds of trial and error, a threshold of 1.5 mm was assigned to identify and localize the points at the damage region. Figure 11 shows the result of point segmentation, in which the points at the spalling region are successfully identified and marked with red colour.

Repeating the same procedure on the yellow point cluster and summarizing the results for each point cluster, the final result of the point segmentation at the spalling region was obtained, as shown in Figure 12. The result was demonstrated in three different perspectives in the subplots, and very high accuracy of point segmentation was achieved. Even though the depth of the concrete damage is about 7 mm which is relatively shallow, the remarkable point segmentation result can be achieved. In most other engineering cases which have concrete damage deeper than 7mm, better point segmentation results are expected.

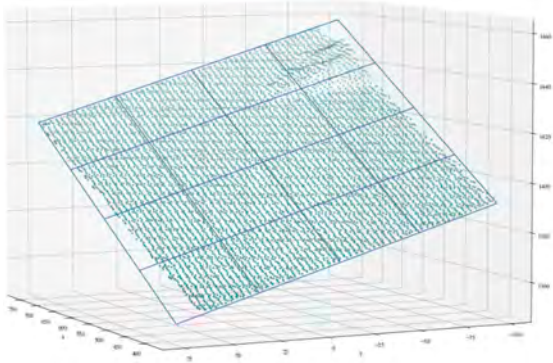


Figure 9. Result of plane fitting.

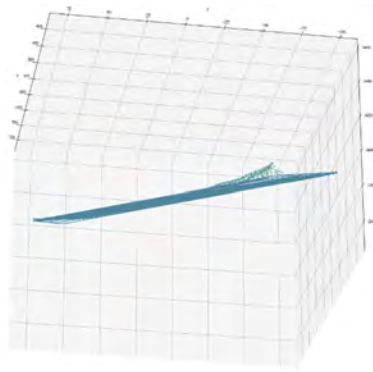


Figure 10. Side-view of the plane fitting result.

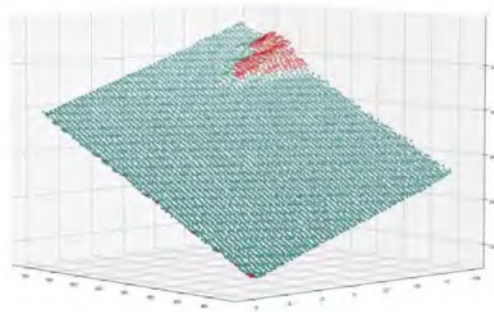


Figure 11. Identification of the points at the spalling region.

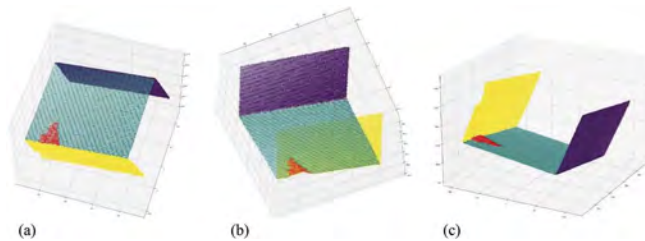


Figure 12. The final result of the point segmentation at the spalling region.

5 CONCLUSIONS

In this article, a simple yet efficient method for segmenting the points of spalling in the point cloud of concrete structure was proposed. The method combines GMM clustering, plane fitting, and distance evaluation. Through an experiment on a concrete beam, the effectiveness and feasibility of the proposed method were demonstrated.

As this research is in its beginning phase, currently the method includes several manual steps, such as cropping the raw point cloud and parameter tuning. The limitation of the method is that the distance threshold needs to be determined manually by trial and error. In our future work, the proposed method will be updated with more automatic processes and less manual intervention.

ACKNOWLEDGEMENT

The research is financially supported by the Academy of Finland (decision number: 339493).

REFERENCES

- Boller, C., Chang, F. K., & Fujino, Y. (Eds.). (2009). *Encyclopedia of structural health monitoring* (Vol. 1). New York: Wiley.
- Dempster, A. P., Laird, N. M., & Rubin, D. B. (1977). Maximum likelihood from incomplete data via the EM algorithm. *Journal of the Royal Statistical Society: Series B (Methodological)*, 39(1),1–22.
- Cha, Y. J., Choi, W., & Büyüköztürk, O. (2017). Deep learning-based crack damage detection using convolutional neural networks. *Computer-Aided Civil and Infrastructure Engineering*, 32(5),361–378.
- Cignoni, P., Callieri, M., Corsini, M., Dellepiane, M., Ganovelli, F., & Ranzuglia, G. (2008). Meshlab: an open-source mesh processing tool. In *Eurographics Italian chapter conference* (Vol. 2008, pp. 129–136).
- Dwivedi, S. K., Vishwakarma, M., & Soni, A. (2018). Advances and researches on non destructive testing: A review. *Materials Today: Proceedings*, 5(2),3690–3698.
- Griwodz, C., Gasparini, S., Calvet, L., Gurdjos, P., Castan, F., Maujean, B., ... & Lanthony, Y. (2021). AliceVision Meshroom: An open-source 3D reconstruction pipeline. In *Proceedings of the 12th ACM Multimedia Systems Conference* (pp. 241–247).
- Goodfellow, I., Bengio, Y., & Courville, A. (2016). *Deep learning*. MIT press.
- Hartigan, J. A., & Wong, M. A. (1979). Algorithm AS 136: A k-means clustering algorithm. *Journal of the royal statistical society. series c (applied statistics)*, 28(1),100–108.
- LeCun, Y., Bengio, Y., & Hinton, G. (2015). Deep learning. *nature*, 521(7553),436–444.
- Mikhail, E. M., Bethel, J. S., & McGlone, J. C. (2001). *Introduction to modern photogrammetry*. John Wiley & Sons.
- Nakamizo, T. & Nishio, M. (2022). Finite element modeling with shell element from 3D point clouds of thin-walled steel structural members (in Japanese). *Machine Learning Research*, 12, 2825–2830, 2011.
- Pedregosa, F., Varoquaux, G., Gramfort, A., Michel, V., Thirion, B., Grisel, O., ... & Duchesnay, E. (2011). Scikit-learn: Machine learning in Python. *the Journal of machine Learning research*, 12, 2825–2830.
- Press, W. H., Teukolsky, S. A., Vetterling, W. T., & Flannery, B. P. (2007). *Numerical recipes 3rd edition: The art of scientific computing*. Cambridge university press.
- Ullman, S. (1979). The interpretation of structure from motion. *Proceedings of the Royal Society of London. Series B. Biological Sciences*, 203(1153),405–426.
- Vassilvitskii, S., & Arthur, D. (2006). k-means++: The advantages of careful seeding. In *Proceedings of the eighteenth annual ACM-SIAM symposium on Discrete algorithms* (pp. 1027–1035).
- Zhang, Y., & Lin, W. (2022). Computer-vision-based differential remeshing for updating the geometry of finite element model. *Computer-Aided Civil and Infrastructure Engineering*, 37(2),185–203.
- Zhang, Y., Miyamori, Y., Mikami, S., & Saito, T. (2019). Vibration-based structural state identification by a 1-dimensional convolutional neural network. *Computer-Aided Civil and Infrastructure Engineering*, 34(9),822–839.
- Zhang, Y., Tang, Z., & Yang, R. (2022). Data anomaly detection for structural health monitoring by multi-view representation based on local binary patterns. *Measurement*, 202, 111804.
- Zhou, Q. Y., Park, J., & Koltun, V. (2018). Open3D: A modern library for 3D data processing. *arXiv preprint arXiv:1801.09847*.
- Özyeşil, O., Voroninski, V., Basri, R., & Singer, A. (2017). A survey of structure from motion*. *Acta Numerica*, 26, 305–364.

Fatigue assessment of complex welded connection in the large-span steel truss suspension bridge

G.Y. Xie

Hubei Communications Investment Group Co., Ltd, Wuhan, China

S.L. Ding

CCCC Second Highway Survey, Design and Research Institute Co., Ltd, Wuhan, China

H.J. Liu & C.S. Wang

Department of Bridge Engineering, College of Highways, Chang'an University, Xi'an, China

ABSTRACT: The integral joint of steel truss girder is widely used in the construction of modern large-span suspension bridges due to its advantages of simple course of manufacture and installation. However, the complex cross-section geometry and the inevitable existence of welding residual stress during the welding process, which would cause fatigue problems under the long process of cyclic vehicle loading. A framework for fatigue assessment of integral joints of steel truss girder in large-span suspension bridge is thus presented in this study. The main features of the framework include multi-scale finite element bridge model, vehicle induced stress, the simulation of complex welding residual stress field, and the crack propagation simulation of fatigue-prone details of integral joints. Based on the Linear Elastic Fracture Mechanics (LEFM) and Extended Finite Element Method (XFEM), the digital fatigue test was carried out. According to the digital fatigue test results, the cracking growth mode of fatigue-sensitive details of integral joints in steel truss girder were determined, and the fatigue damage characteristics of fatigue-prone details were analyzed. The results indicate that the developed framework is applicable and the Mixed-mode crack propagation law was identified in fatigue-prone details, and the fatigue growth life will be overestimated irrespective of the welding residual stress.

1 INTRODUCTION

In recent years, the steel truss girder is widely used in long-span highway or railway suspension bridges due to its light weight. The fully-welded integral joint are commonly used in steel truss girder for it can be prefabricated in the factory and simple installation. However, this kind of welded integral joints generally have complex cross welds, and large welding residual stress will exist around the fatigue details during the welding process. Under the superimposed of cyclic load and welding residual tensile stress, the fatigue cracks easily initiated and propagated in integral joints (Wang et al. 2013), which greatly affects the durability of long-span suspension bridges.

At present, the *S-N* curve method is mainly used to assess the fatigue life of integral joints (Cai et al. 2017, Liu et al. 2019, Wei et al. 2017), such as the nominal stress method, hot-spot stress method, effective notch stress method, etc. Both methods all ignore the initial crack of integral joints, and cannot describe the fatigue crack growth stage. Many studies have shown that the fracture mechanics evaluation method can be effectively used for the research on fatigue crack growth of steel bridges (Wang et al. 2019, Wang et al. 2020), overcoming the

deficiency that the traditional S-N curve method cannot consider the initial defects existing in actual structures. The fracture mechanics evaluation method can generally be divided into numerical methods and analytical methods. Because of simple application and avoiding complex analytic solution, the numerical method shows broad application prospects. Belytschko and Black (1999) of Northwestern University in the United States put forward a numerical solution method in 1999 - the Extended finite element method (XFEM). This method describes the discontinuous displacement of the crack surface and crack tip by adding displacement expansion terms during the crack growth simulation.

In this paper, the fatigue crack growth law of a out of plane deformation fatigue detail of a suspension bridge steel truss girder integral joint is studied. Based on the linear elastic fracture mechanics method (LEFM) and XFEM, the crack propagation law is analyzed by introducing an initial fatigue crack at the hot-spot. In addition, based on the sequential coupling principle, a refined numerical model was established to consider the welding residual stress. By comparison, the influence of welding residual stress on fatigue crack growth law and fatigue crack growth life was discussed, and the effectiveness of the numerical simulation method was verified.

2 CASE STUDY

A Double deck steel truss suspension bridge was selected for analysis, and the overall layout of the bridge is shown in Figure 1. The upper deck is a two-way 6-lane expressway with a total width of 33.5 m; the lower deck of the main bridge is a two-way 4-lane urban road with a total width of 25.0 m. Through stress characteristic analysis and fatigue sensitive details identification, the mid-span and short suspender area is selected for fatigue assessment.

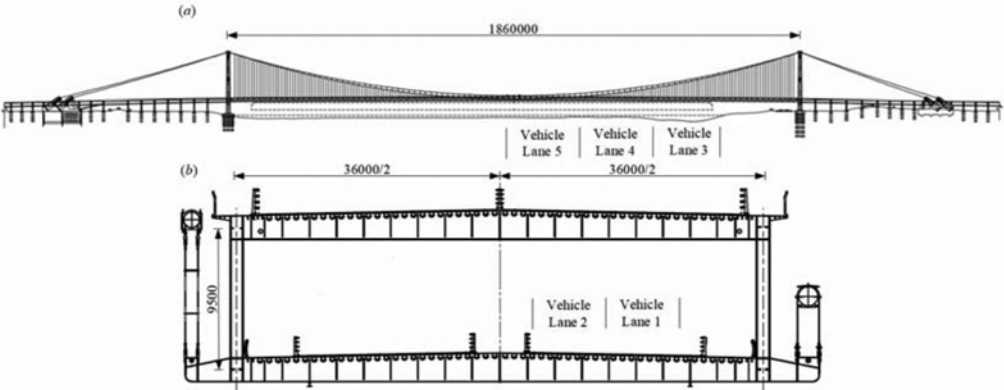


Figure 1. The layout of the bridge (Unit: mm): (a) bridge elevation; (b) cross section of stiffing girder.

3 FINITE ELEMENT ANALYSIS

3.1 Multi-scale bridge model

In order to display the characteristics of the whole bridge and the local fatigue detail geometric, a multi-scale finite element model is established. Firstly, the BEAM/TRUSS element is used to simulate the whole bridge except for the segmental double-layer steel truss girder, then the SHELL/SOLID element is used to establish the segmental double-layer steel truss girder. On the one hand, the fatigue detail geometry can only be simplified as a node when used SHELL element to simulate it. On the other hand, using SOLID elements to simulate all the double deck steel truss girder will lead to too many elements, which will affect the calculation efficiency. In order to accurately resolve the stress distribution around the fatigue details in

the integral joint and consider the calculation efficiency, a local area including fatigue details is selected in the segment model and the local area is established by using SOLID element, as shown in Figure 2(c). The shell element is used to simulate the remaining part of double deck steel truss girder. The selected fatigue detail for analysis are far away from the boundary area of the multi-scale model to ensure that the stress distribution of fatigue details is reasonable. To clarify the crack growth law at the fatigue detail, an elliptical initial crack is inserted at the hot-spot, and the crack length a is 0.5 mm, the crack depth c is 1.0 mm, as shown in Figure 2(d).

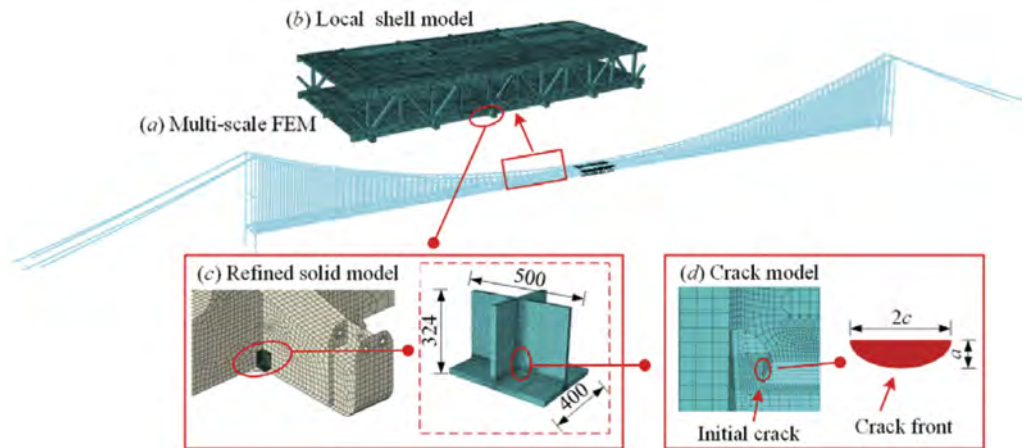


Figure 2. Multi-scale FEM of the suspension bridge (Unit: mm).

3.2 Welding process simulation

During the welding process simulation, the sequentially coupled thermo-mechanical analysis was adopted to predict the temperature history and welding residual stress distribution of the fatigue detail. The temperature field was calculated first, and then the temperature history of each node was imported as the initial state for the thermal stress analysis to obtain the distribution of WRS. A local refined three-dimension finite element model, including the fatigue detail was established, as shown in Figure 2(c). The 8-node hexahedral element DC3D8 and C3D8R were used to calculate the temperature history and WRS, respectively. The geometry and node number of the FEM are consistent, and only the element type is changed. The mesh size around the thermomechanical coupling region is set as 2mm and the symmetrical constraints is used in the thickness direction of all plates. As the material of the steel truss girder is Q420qd, the thermal performance parameter of Q390 high strengthen steel (Sun et al. 2016) was selected for conservative estimate the distribution of WRS. The welding wire material and the base metal are taken as the same material. To simulate the actual multi-layer welding situation, the multi-layer multi pass weld was simulated, and a cooling step is set between two adjacent welds to ensure a suitable interlayer temperature.

3.3 Fatigue loading

The FLM 2 is a double-truck model in Chinese design code for steel bridges (Ministry of Transport of the People's Republic of China 2015) to the fatigue design of members and connections, in which the longitudinal distance between two successive trucks is no less than 25.7 m, recommended in the specification. The spacing between two successive trucks is defined as the length between the last axle of the prior truck and the first axle of the rear truck. To obtain the stress response of the fatigue detail under truck loading, the FLM 2 was

used as the fatigue design loads in this paper, and the longitudinal distance between the two successive trucks was assumed as 25.7 m. The contact area between tires and pavement is defined as 0.35 m × 0.75 m considering the diffusion effect of asphalt pavement along the 45 degree angle.

4 MAJOR RESULTS AND DISCUSSION

4.1 Distribution of weld residual stress

In the thermal analysis, the heat source model will directly affect the accuracy of the temperature history as well as the WRS. A commonly used volumetric heat source model with a double ellipsoidal distribution proposed by Goldak et al. (1984) was applied to simulate the welding heating process. The heat source is expressed as follows:

$$q(x, y, z, t) = \frac{6\sqrt{3}f_f Q}{a_1 b c \sqrt{\pi}} e^{-3(z-vt-z_0)^2/a_1^2} e^{-3x^2/b^2} e^{-3y^2/c^2} \quad (1)$$

For the rear heat source:

$$q(x, y, z, t) = \frac{6\sqrt{3}f_r Q}{a_2 b c \sqrt{\pi}} e^{-3(z-vt-z_0)^2/a_2^2} e^{-3x^2/b^2} e^{-3y^2/c^2} \quad (2)$$

where f_1 and f_2 are constants of the heat deposited in the front and rear quadrants; Q is the heat input per unit time; v is the welding speed; t is the welding time; z_0 is the position of the heat source in the z -direction at the beginning. The heat source model geometric parameters a_1 , a_2 , b and c are independent and they can have different value.

To ensure complete penetration of weld during the welding heating process simulation, the heat source parameters were modified according to the melting pool geometry. Figure 3 shows the temperature field simulation results during welding process of the fifth and seventh weld. It can be seen from Figure 3 that the temperature in the weld area is the highest, and the molten pool geometry is basically consistent with that of the weld during welding process simulation, which demonstrates the selected heat source parameters are reasonable.

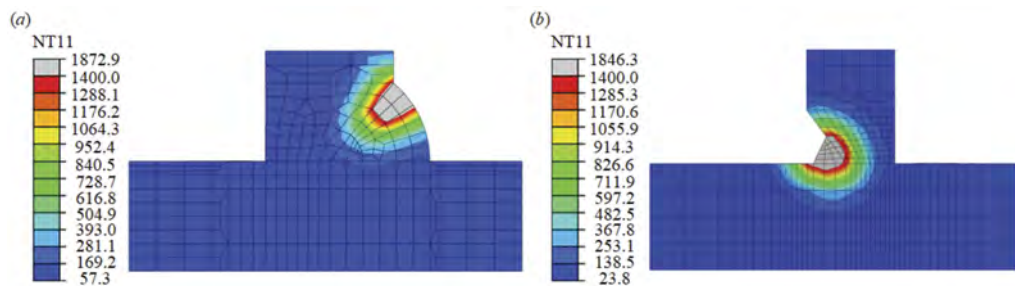


Figure 3. Simulated molten pool geometry and temperature contours (Unit: MPa): (a) $t = 2485.6$ s (welding process of fifth weld pass); (b) $t = 14525.5$ s (welding process of seventh weld pass).

After welding temperature field calculation, the temperature simulation results of each node are imported as the initial state to predict the WRS. The von Mises stress distribution results after the sixth weld cooling and final weld cooling are shown in Figure 4. It can be seen from the Figure 4 there is a large tensile WRS near the weld, and the maximum Mises stress is close to the yield strength of the steel Q420qd. In order to further analyze the WRS distribution at the fatigue crack growth location, the WRS distribution on different paths in the weld area is

extracted, as shown in Figure 5. It can be seen that the residual stress value near the corner continuous weld is about 100 MPa, and the WRS away from the corner weld increases gradually.

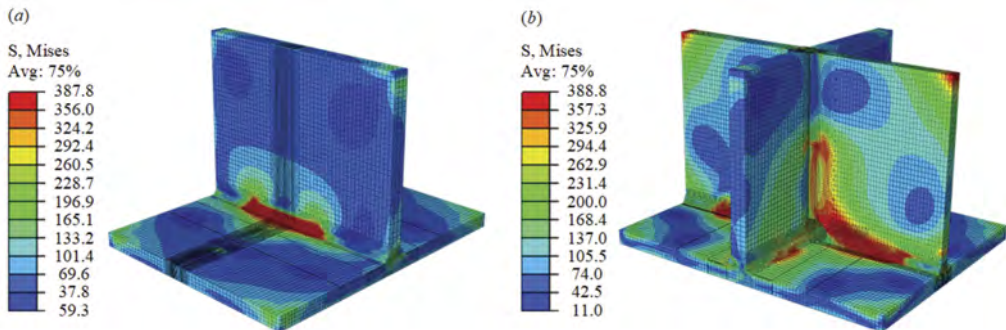


Figure 4. The simulated distribution of WRS (Unit: MPa): (a) after cooling of the sixth weld; (b) after final weld cooling.

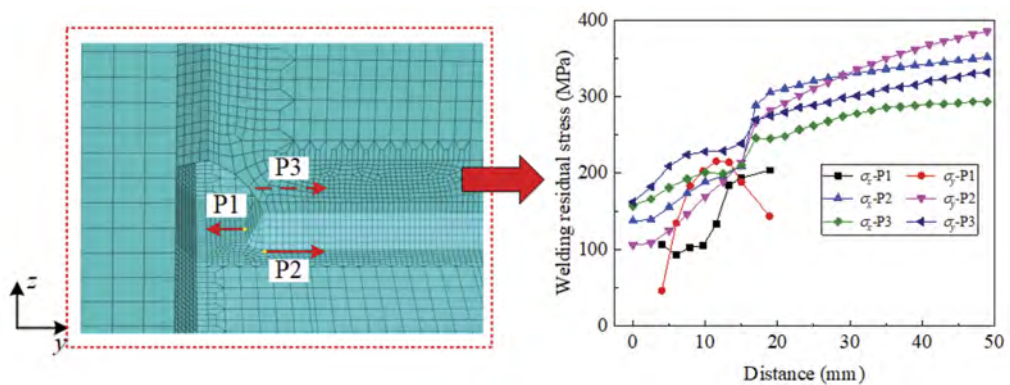


Figure 5. Distribution of WRS along extraction path during the simulation.

4.2 Stress response of typical fatigue detail

Various load conditions were designed to determine the most unfavorable loading conditions of FLM 2, as shown in Table 1. The stress responses at the fatigue details under different loading conditions without considering WRS are calculated respectively, as shown in Figure 6. It can be seen that the stress history presents a multi-peak distribution law. When the fatigue load truck is close to the fatigue detail position, the stress of the fatigue detail is maximum. Under all loading conditions, the stress amplitude of fatigue details under load case 5 is the largest and the maximum stress amplitude is 30.5 MPa.

4.3 Digital fatigue test results

Because physical fatigue test is expensive, digital fatigue test based on fracture mechanics method has been widely used in recent years. The existing research shows that Pairs model can well describe the crack growth law. To more accurately evaluate the crack growth rate of the selected fatigue detail, the Pairs model was adopted here, as shown in Equation 3.

Table 1. Designed load scenery of FLM 2.

Load cases	FLM 2 loading lane
Case 1	Vehicle lane 3
Case 2	Vehicle lane 1 and 3
Case 3	Vehicle lane 3 and 4
Case 4	Vehicle lane 1, 3 and 4
Case 5	Vehicle lane 1, 2, 3, and 4
Case 6	Vehicle lane 1,3, 4, and 5
Case 7	Vehicle lane 1
Case 8	Vehicle lane 1 and 2
Case 9	Vehicle lane 1, 2 and 3

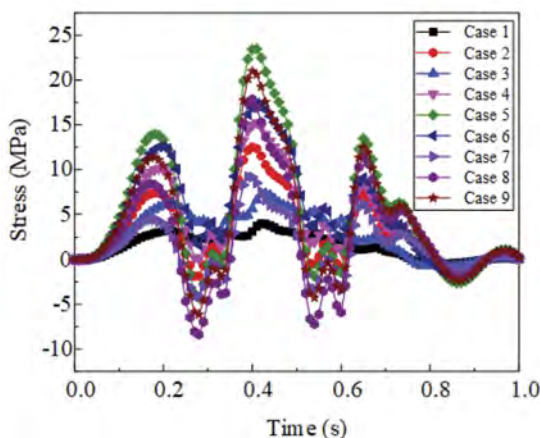


Figure 6. Stress time-history of fatigue detail without considering WRS.

$$\frac{da}{dN} = C(\Delta K)^m \quad (3)$$

where da/dN is the fatigue crack growth rate; C , m are the material constants; ΔK is the range of stress intensity factor.

4.3.1 Crack growth behaviors

In order to clarify the crack growth type at the hot-spot under cyclic FLM 2 loading, an energy based approach was adopted to calculate the deflection angle of the crack surface, the more detail of this method can be found in reference (Erdogan & Sih 1963). Figure 7 shows the fatigue crack growth path under the load case 5. It can be seen from the figures that, without considering the residual stress, the crack surface deflects along the length and depth direction during the crack growth process under cyclic load. After considering the WRS, the crack propagation trajectory basically does not change, indicating that the influence of residual stress on the crack growth type is negligible.

Further analysis shows that after the FLM 2 is loaded in 8.3 million cycles, the crack propagates about 9 mm and 24 mm along the depth respectively with and without considering the WRS. It is conservatively estimated that the crack growth rate will increase about 2.7 times considered the WRS.

4.3.2 Cumulative strain energy release rate

In order to further determine the crack growth law at the hot-spot, the cumulative strain energy release rate at the crack tip is compared, and the cumulative strain energy release rate is shown in

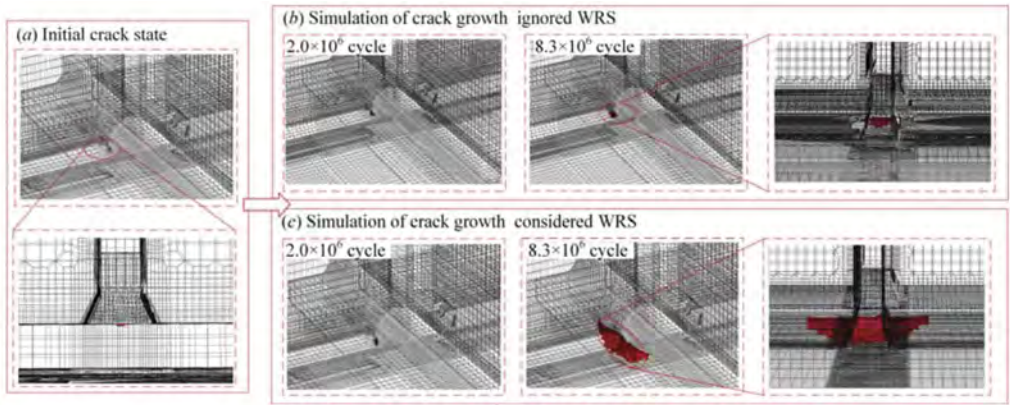


Figure 7. Comparison of crack growth simulation with and without considering WRS.

Figure 8. It can be seen that ΣG_I is far greater than ΣG_{II} and ΣG_{III} during the crack growth process. The value of $(\Sigma G_{III}\Sigma G_I)_{max}$ and $(\Sigma G_{III}\Sigma G_{II})_{max}$ without considering WRS is 4.8% and 5.8%, respectively. The value of $(\Sigma G_{III}\Sigma G_I)_{max}$ and $(\Sigma G_{III}\Sigma G_{II})_{max}$ with considering WRS is 15.4% and 23.5%, respectively. After considering the WRS, the strain energy release rate are significantly increased, The value of ΣG_I is much greater than that of ΣG_{II} and ΣG_{III} . To sum up, the crack growth mode is a mixed mode dominated by mode I with and without considering WRS.

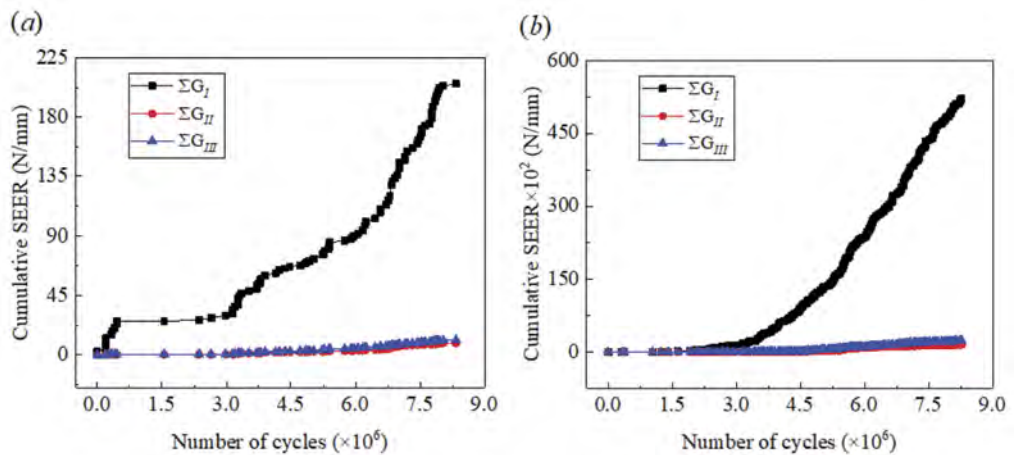


Figure 8. Cumulative strain energy release rate during the crack growth simulation: (a) without considering WRS; (b) considering WRS.

5 CONCLUSIONS

In this study, a framework for fatigue assessment of integral joints of steel truss girder in large-span suspension bridge has been proposed, including the multi-scale FEM model, vehicle induced stress, complex welding residual stress and crack growth simulation. Based on the LEM and XFEM, the full-scale digital fatigue test of integral joint of steel truss girder was carried out, and the main conclusions are summarized as follows:

- (1) To meet the actual welding process, the multi-layer multi pass weld was simulated. Based on the WRS simulation results, it was obtained that the WRS near the fatigue detail is about 100 MPa, which is about 23.8% of the yield stress of main truss material.

- (2) In full-scale digital fatigue test, the influence on crack growth rate is that ΣG_{III} is greater than ΣG_{II} , and ΣG_I is much larger than ΣG_{II} and ΣG_{III} . It can be concluded that the crack growth type is a mixed mode dominated by mode I with and without considering WRS.
- (3) During the most unfavorable cyclic loading condition of FLM 2, it is conservatively estimated that the crack growth rate will increase about 2.7 times considered the WRS, which indicated that the influence of welding residual stress on fatigue crack growth life cannot be ignored.

ACKNOWLEDGEMENT

The authors gratefully acknowledge the financial support provided by the Program of National Ten Thousand People Plan Science and Technology Innovation Leading Talents (W03020659), the Study On Reasonable Structure of Stiffened Girder and Fatigue Performance of Critical Joints.

REFERENCES

- Belytschko, T. & Black, T. 1999. Elastic crack growth in finite elements with minimal remeshing. *International Journal for Numerical Methods in Engineering* 45(5): 601–620.
- Cai, S. Y. et al. 2017. Fatigue life assessment of large scale T-jointed steel truss bridge components. *Journal of Constructional Steel Research* 133: 499–509.
- Erdogan, F. & Sih, G .C. 1963. On the crack extension in plates under plane loading and transverse shear. *Journal of Fluids Engineering* 85(4): 519–25.
- Goldak, J. et al. 1984. A new finite element model for welding heat sources. *Metallurgical Transactions B* 15: 299–305.
- Liu, Z. X. et al. 2019. Fatigue assessment of critical connections in a historic eyebar suspension bridge. *Journal of Performance of Constructed Facilities* 33(1): 04018091.
- Ministry of Transport of the People’s Republic of China. 2015. Highway steel bridge design code. Beijing: China Architecture & Building Press.
- Sun, J. M. et al. 2016. Numerical simulation of residual welding stress in multi-pass T-joint of thick Q390 high strength steel plate using instantaneous heat source. *Transactions of the China Welding Institution* 37(7): 31–34,38 (in Chinese).
- Wang, C. S. et al. 2013. Fatigue evaluation of a strengthened steel truss bridge. *Structural Engineering International* 23(4): 443–9.
- Wei, X. et al. 2017. Fatigue assessment and stress analysis of cope-hole details in welded joints of steel truss bridge. *International Journal of Fatigue* 100: 136–47.
- Wang, C. S. et al. 2019. Fatigue performance evaluation and cold reinforcement for old steel bridges. *Structural Engineering International* 29(4): 563–9.
- Wang, C. S. et al. 2020. Numerical simulation of distortion-induced fatigue crack growth using extended finite element method. *Structure and Infrastructure Engineering* 16(1): 106–22.

Life-cycle and evolution of tunnel equipment

G. Nodiroli, M. Katterbach & P. Klaus

Lombardi SA Ingegneri consulenti, Bellinzona-Giubiasco, Switzerland

D. Tillet

Lombardi Ingénierie SAS, Lyon, France

ABSTRACT: The equipment and systems of a tunnel are essential for the safe use of this particular transport route. These systems are often all but invisible for the user and only play a role in certain specific circumstances (in the event of unexpected incidents inside the tunnel). The equipment and systems in question have evolved enormously over the years and made a significant contribution to ongoing safety improvements (PDCA) and the avoidance of potential tragedies. The tunnel is a special environment where an incident such as a fire can suddenly endanger the lives of users and the integrity of the structure. The human factor remains the element that is the most difficult to control, while electromechanical devices have benefited from ongoing and favorable technological development. Today's devices and systems offer increased availability thanks to the introduction of redundancy concepts and deteriorated functionality, and contribute to a safer, less-interrupted management of tunnels.

1 INTRODUCTION

A tunnel has a different value depending on the perspective used to evaluate it. On an economic level, the tunnel may represent an investment that is amortised over the years, while from a sociological perspective a tunnel represents a communication route that shortens distances. On an engineering level, the construction of a tunnel is a technological challenge and the solution to an otherwise difficult if not impossible communication route. Tunnelling evolves over time, requirements change, technology advances rapidly and the expectations of generations change; what was done in the past is no longer accepted, and this also applies to tunnelling. Despite a very conservative approach to tunnel design and operation, it is now possible to apply innovative structural, equipment and functional solutions that bring a general benefit to the overall sustainability of this object. In addition to benefiting from technology directly, the tunnel can benefit from the indirect technological evolution of the users, vehicles that are becoming less polluting, intelligent and interconnected with time.

2 TECHNOLOGICAL EVOLUTION OF EQUIPMENT AND VEHICLES

The technological evolution of tunnel equipment draws on a number of wide-ranging aspects that, when taken together, facilitate the definition of a general evolutionary concept. The evolution of electromechanical equipment inevitably entails the evolution of materials and equipment, a reduction in energy consumption, the development of control and surveillance systems, which have seen major changes over the past few decades, and the evolution of modes of transport, which has also been significant over the same time frame.

2.1 *Evolution of materials and equipment*

The major link between the worlds of industry and tunnels is without question ventilation. Ventilation is a crucial installation when it comes to tunnel safety and, generally speaking, for any underground infrastructure. The evolution of this equipment has not been especially significant; capacities have increased and weights have been reduced, but the biggest change has been in the way these installations are managed. Without ventilation, it would be impossible to use these tunnels for road traffic – and it is often this very same ventilation that determines the degree to which usage is possible. Today, the ventilation can be controlled using sensors capable of measuring the speed and quality of the air very precisely, as well as the exact position of a fire, and all this extremely quickly and reliably. This information, rounded off by the intelligent and distributed control systems, facilitates the management of complex ventilation scenarios, including real-time management of various types of ventilators and associated equipment (dampers, motorized valves, etc.), all while operating a closed-loop control (PID-type controller) that adapts based on the data collected at a given moment inside the tunnel.

2.2 *Evolution of energy consumption*

Tunnels are major consumers of electrical energy, which is mainly necessary for lighting and ventilation (if present) and sometimes for air conditioning systems. Over the past few years, the greatest progress associated with the consumption of electricity has been achieved thanks to the LED technology used in lighting the tunnel and its auxiliary tunnels. Aside from lighting technology, another major development is associated with managing the intensity of the light generated by the lighting fixtures. The result of this is that it is now possible to adjust the setting of each lighting point individually via the control systems. It is now therefore possible to manage the equipment by optimising the energy to be consumed as part of an environmentally responsible approach so as to increase the sustainability of the tunnel.

2.3 *Evolution of the control and surveillance systems*

As with all systems in various fields of application, the tunnel has seen significant development in its control and surveillance systems. In just a few decades, technology has progressed from relay-based to intelligent automated systems. The various subsystems interact with one another in a coordinated way and react automatically to specific incidents (reflex-action concept).

All the information from the different systems is accessible at various levels, meaning that the complete functionality of the tunnel can be verified and managed from a distance, for example with remote video streams. The time required to alert the command centre of an incident is reduced to a minimum and is completely automated. The evolution of the control and surveillance systems has been facilitated by the processing power of the controllers used, the increasingly effective and secure communication networks, and digitisation, which now has an impact on almost all areas. The image below (Figure 1) shows in general terms how the field of application of the controllers (PLC) has been integrated with that of the computers to ultimately converge into integrated architecture. Even if it is possible to assert that the level of automation and surveillance attained thus far is high, development in other areas clearly demonstrates that this evolution is not complete, increasingly guiding us to intelligent interconnected systems and management of an ever-growing volume of data. Artificial intelligence, for example, is continuing to develop for Automatic Incident Detection (AID) systems in conjunction with real-time analysis of video images of the tunnel.

2.4 *Evolution of data processing*

Today, tunnel control and surveillance systems are able to access a lot of the data provided by modern sensors and actuators. However, the tendency to focus on the operational data that directly influence traffic management and infrastructure safety remains. Operating and auxiliary data provided by many sensors and actuators are recorded in databases within the various

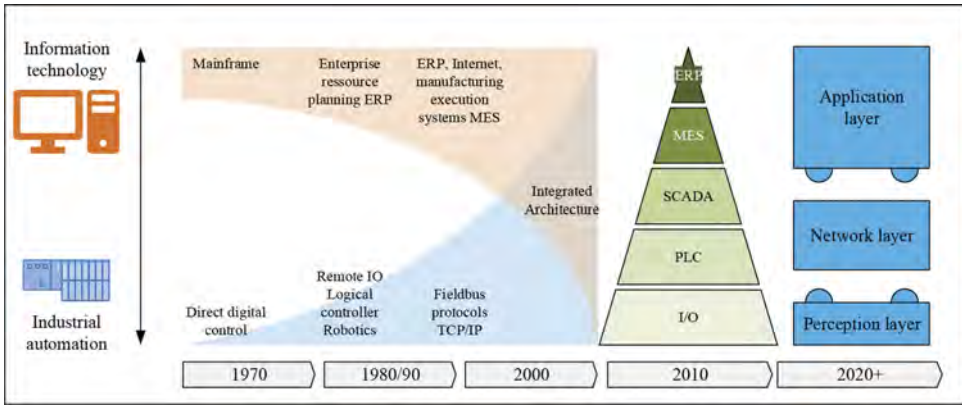


Figure 1. IT-IA convergence and system architectures.

installations' controllers and can be exported as tables or charts using the controller's own software. Recent developments in the processing of data have been moving towards the provision of all this information on an open, flexible platform where the various systems can interact with one another based on these data (Internet of Things – IoT). This platform allows us to access data and to implement applications that target a precise goal while using a program that is independent of the nature and type of controller, sensor or actuator. For example, opacity data from smoke detectors can be used to determine possible alarms inside the tunnel, data on the accumulation of dirt can be used to evaluate maintenance requirements, and measurements of opacity in time and space (provided by several detectors in different locations) facilitate the management of airflows within the tunnel associated with a specific incident. These three applications access data present on a single platform. Over time, it will be possible to add additional information to the platform and to create new applications without compromising what has already been achieved. The architecture of the Internet of Things is represented in a simple format in Figure 2 using two models of three and five layers (Figure 2).

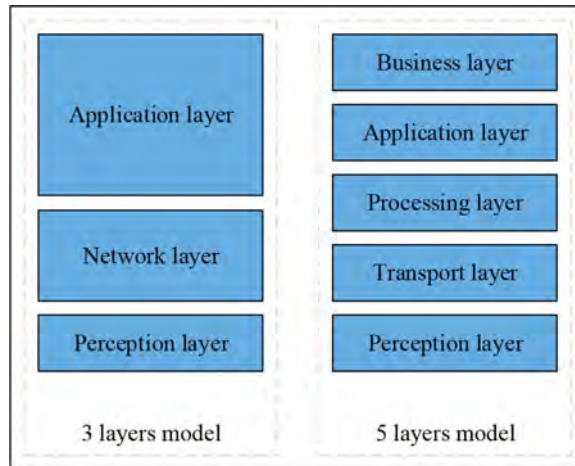


Figure 2. Architecture of IoT (three layers and five layers).

2.5 Evolution of modelling – BIM

The arrival of digitisation to the field of construction now offers the possibility of reproducing each individual component of a tunnel in a 3D model, but the use of this and the resulting innovation of processes represent the main challenge now both for engineers and the project

owner. Currently, a tunnel is represented using construction plans, usually in two dimensions. For the oldest structures, these exist exclusively in paper format. In practice, the representation of a tunnel consists of a significant number of documents in various formats that are then used in different ways depending on requirements. The evolution of digitisation has meant that it is increasingly common to use the “Building Information Modelling” (BIM) method within the context of design. This is a shared knowledge resource for information on a structure and represents a reliable basis for decisions throughout its life cycle – from the initial design and detailed development to implementation, maintenance and, ultimately, demolition. As for the management and maintenance of the installations, the BIM model may be extended during the object’s construction phases to include all relevant information on the installations, components, and operating and security systems. It is therefore possible to create an object’s digital twin, which can be used for management, training, inspection and maintenance activities.



Figure 3. BIM and IoT for tunneling life cycle management.

2.6 Evolution of vehicles

The evolution of vehicles for transporting goods and people is a topical subject that will give rise to significant changes in mobility over the short and medium term. Over the past few years, technology has facilitated a considerable reduction in harmful vehicle emissions and there is a clear prospect of ultimately achieving zero emissions for all vehicles in circulation. Regarding the tunnel, this change will require the modification of sanitary ventilation and various air quality sensors. In addition, the new vehicles behave in a different way to traditional combustion engine vehicles in the event of an incident, and the technological evolution of batteries and new fuels will likely lead to an increase in the potential energy of vehicles in transit and thus a different approach to managing the installations and response strategies of emergency services in the event of a fire.

Another central aspect associated with the technological evolution of vehicles concerns the level of automation in assisted driving. Here, we expect to reach the maximum level with completely autonomous guidance without a driver by 2050. The impact on safety inside the tunnel is significant. On the one hand, it is possible to eliminate human error while driving. On the other, it will be possible to evacuate the tunnel quickly and safely if a problem occurs within it. Several considerations can be raised in this respect:

Is it possible to equip the tunnel in a way that increases the effectiveness of assisted-driving systems (for level-four automation in particular)?

Once all vehicles are fitted with autonomous driving systems, will it be possible to dispense with or reduce certain installations within the tunnel?

It is clear that a major change in mobility towards a completely autonomous system will not happen in the immediate future. We will therefore face these developments and the associated maintenance of the tunnels and their operating and safety equipment progressively over the years to come.

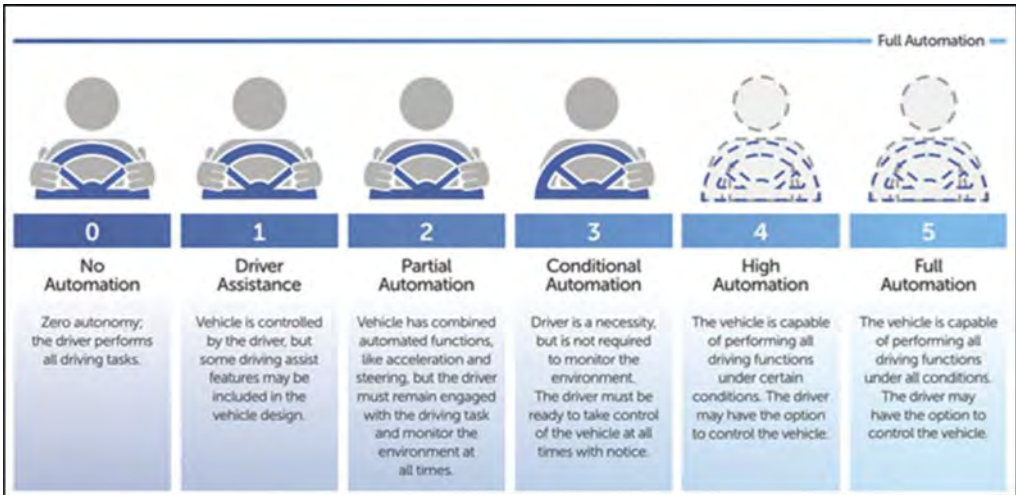


Figure 4. Description and comparison of automated vehicle levels.

Source: U.S. Department of Transportation, Automated Driving Systems 2.0, A Vision for Safety

3 MANAGEMENT OF THE TUNNEL'S LIFE CYCLE

The overall availability of the tunnel depends on a number of factors and, in specific cases, a lack of availability could lead to a temporary interruption of operation. The electromechanical equipment has little effect on the overall service life of a structure, but the correct management of these installations can improve day-to-day management, increase safety levels and limit facility closures. Moreover, the configuration and efficiency of the equipment facilitates the more efficient and sustainable use of a tunnel, with equipment that can be modified depending on a careful analysis of the general state of the construction.

Compared to the past, we now have a lot of data originating from various sources that determine the functional parameters of a structure. The challenge is therefore to find a platform (middleware) for data convergence where it would be possible to extrapolate the required information using adapted applications (predictive maintenance approach). In the following illustration, a platform (middleware) is shown that collects all data from various sources and makes them available to applications with a range of functionalities.

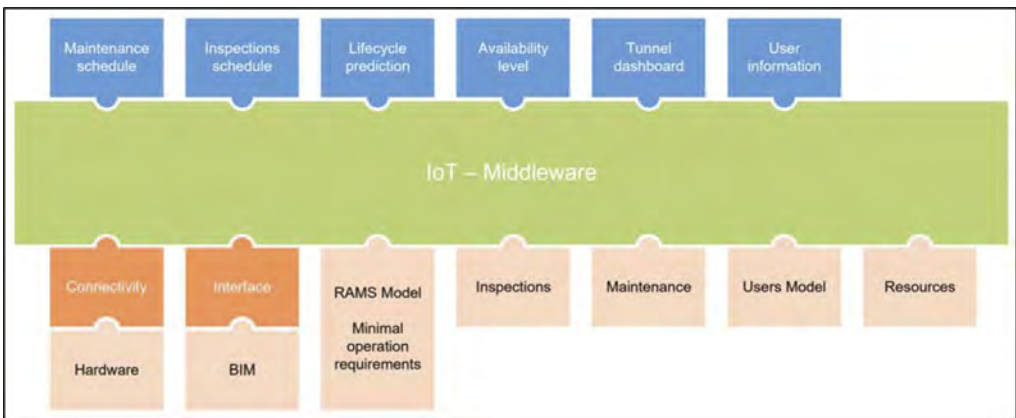


Figure 5. Example of an IoT model for tunnels.

3.1 *Source data*

Primarily, the following information (non-exhaustive list) can converge within the platform (middleware):

- Data from all devices installed in the tunnel, sensors and actuators, generally referred to as hardware.
- BIM model of the infrastructure that, aside from construction information, also contains hardware components.
- RAMS model (reliability, availability, maintainability and safety) defining the main parameters associated with the condition of the equipment when it comes to its reliability, availability, maintainability and degree of safety.
- Data originating from inspections and the condition of components.
- Feedback once maintenance has been conducted (use of a CMMS-type system – computerised maintenance management system).
- User model.
- Resources available for any management and maintenance activity for the construction.

3.2 *Basic platform (middleware) for data management*

Within IT projects, there is a very high risk that the predefined objectives will not be achieved or that there will simply be a delay. To implement a data management platform, it is therefore necessary to refer to existing models that are undergoing development and that can be expanded, improved and made more efficient without giving up what has already been implemented during previous phases. Today, we refer to these platforms in general terms as an “Internet of Things”. These platforms all have the basic characteristics for implementing a tool to manage a tunnel, a section or a full communication network:

- A database that can hold an unlimited number of different information types (data, documents, images, videos, etc.).
- Quick access to data.
- The possibility of expanding the information contained within the various data without compromising the existing data and without having to reconfigure the platform.

Generally speaking, it is necessary to have access to the data held on the platform without special restrictions while bearing in mind that the quantity and typology of the information will change over time depending on various technological developments. This type of platform thus facilitates the implementation of software without necessarily having to predict future uses of information during creation that are unknown at that point, with current availability and needs being the focus. This kind of approach is designed to avoid generating obstacles for the future evolution of applications.

3.3 *Applications*

The applications access the data stored in the middleware and codify the information necessary for the manager and owner of the infrastructure for the overall administration of the tunnel. The applications can be modified and expanded depending on requirements, and new applications can be implemented on the same platform in a fully independent manner. These applications may include the following functionalities (non-exhaustive list):

- Supporting maintenance, scheduling of servicing callouts, management of replacement parts, etc.
- Inspection planning.
- Prediction and planning of life cycles and various sections of the installation.
- Availability level constantly updated.
- Operational reliability level.
- Dashboard facilitating quick and complete access to all information related to the tunnel.
- Possible application allowing the provision of information to users.

4 LIFE CYCLE

A tunnel's life cycle is generally associated with the service life of the construction engineering infrastructure. During this time (which can be considered as lasting up to 100 years), the electromechanical equipment, which has an average life cycle of 20 years, requires refurbishment, rejuvenation and replacement work on several occasions. Preventive maintenance facilitates the extension of the service life and guarantees ongoing operation, but this is limited by specific components having conclusively reached the end of their service life.

In engineering, mathematical models are used to determine the parameters associated with a system's life cycle. These models are primarily used for design, but they can continue to be used to check on an ongoing basis that the system maintains its characteristics over time. Several approaches exist; the best known of these is RAMS (reliability, availability, maintainability and safety).

4.1 *RAMS analysis*

The abbreviation RAMS combines the key terms that characterise a system and its functionality.

Reliability is defined as the probability that a component or system will carry out its required function for a specified time provided that it is used within defined operational conditions. This is therefore the probability that it will not be subject to faults over time. Reliability is often associated with the quality of a product.

Availability is defined as the probability that a component or system will carry out its function at a given moment provided that it is used within defined operational conditions.

Maintainability is defined as the probability that a component or system will be able to be made operational again or repaired to a specified condition within a defined time frame provided that maintenance has been conducted in line with prescribed procedures.

As far as safety is concerned, a risk assessment helps to calculate the probability of harming people and structures. In general, this involves statistical indicators that provide probability values for which minimum threshold values are defined that must always be respected. In the event that these threshold values are not respected, it is possible to introduce specific measures that will have a positive impact on the calculation, making these values acceptable.

4.2 *Minimum operating conditions*

Minimum operating conditions define the minimum conditions with which a tunnel can be used, possible usage restrictions should optimal conditions not be respected and time limits within which anomalies must be corrected. Here, too, this involves a statistical analysis that limits the amount of time a component or system is unavailable. In extreme cases, a disruption could trigger a risk level that is too high to allow the tunnel to be used, forcing a temporary closure and bringing with it all the associated inconveniences. A tunnel may thus be allocated a nominal operational level, deteriorated levels and a closure level.

5 CONCLUSIONS

The tunnel is a special environment where an incident such as a fire can suddenly endanger the lives of users and the integrity of the structure. The human factor remains the element that is the most difficult to control, while electromechanical devices have benefited from ongoing and favourable technological development. Today's devices and systems offer increased availability thanks to the introduction of redundancy concepts and deteriorated functionality, and contribute to a safer, less-interrupted management of tunnels. At an operational level, it is possible to reduce the risk of fire by limiting the number of trips through a tunnel (typically for bidirectional tunnels) and carrying out checks on vehicles in transit (typically heavy-goods vehicles).

The life cycle of a tunnel is not only limited to its service life, but also considers the quality of service provided during this cycle. It is therefore important to be able to guarantee the correct

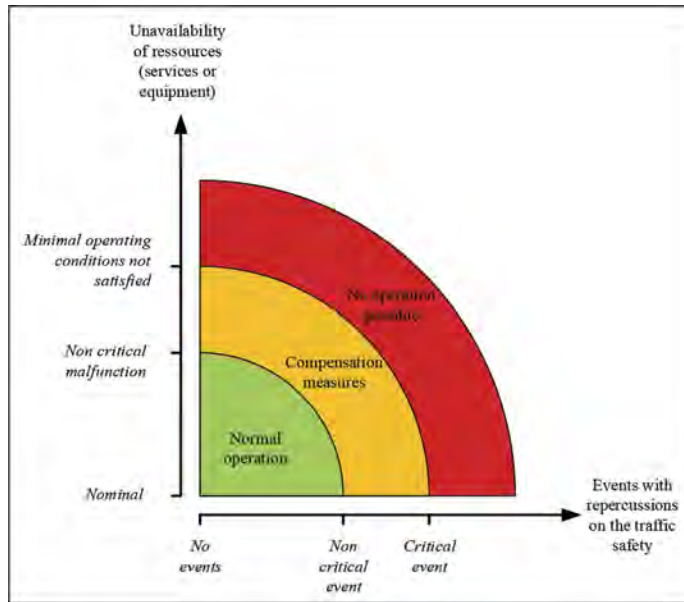


Figure 6. Different operating situations.

probability values derived from a RAMS analysis and to include information gained from inspections and maintenance within a comprehensive model that can provide the various stakeholders involved in management and administration with all information related to maintenance programmes, programmes concerned with updates and the replacement of components and systems, inspection programmes, and the overall forecasting of technical problems.

This information and these applications must form part of a communal platform that facilitates uniform access to the various levels based on this same information. The platform must be capable of evolving based on the technical development of equipment and users, meaning that it will be possible to keep up with IT developments employing opensource technologies that do not compromise portability and possible technological migrations. This platform includes various levels of specialisation – from the on-site maintenance supervisor to the control room operator, the infrastructure administrator, the head of security, the tunnel operator, the planners and executing companies, the mathematicians and safety engineers, the computer scientists, and the IT infrastructure managers. The management of a tunnel’s life cycle is not substantially different from the management of other types of structure in other fields. It is therefore possible to benefit from experience gained in other environments where managers have applied the concepts described above – in the generation and distribution of electricity (Smart Energy), for example, or in the field of manufacturing (Smart Manufacturing) in order to ultimately arrive at the Smart Tunnel.

REFERENCES

- Ebeling, Charles E. 2019. *An Introduction to Reliability and Maintainability Engineering*. Waveland Pr Inc; Reprint Edition.
- Hindawi. 2017. *Journal of Electrical and Computer Engineering*, Volume 2017, article ID 9324035, <https://doi.org/10.1155/2017/9324035>.
- Smith, David J. 2021. *Reliability, Maintainability and Risk: Practical Methods for Engineers*, Butterworth-Heinemann, 10th Edition.
- Wilkins, Neil. 2019. *Internet of Things*, Bravex Publications; Illustrated Edition.

A multi-phase survey approach for post-tensioned prestressed concrete bridge decks

Isabella Mazzatura, Silvia Caprili & Walter Salvatore

Department of Civil and Industrial Engineering (DICI), University of Pisa, Pisa, Italy

Alessio Lupoi

Department of Structural and Geotechnical Engineering, La Sapienza, Roma, Italy

Alessio Ficociello

SPERI, Engineering Design Firm, Roma, Italy

ABSTRACT: The assessment of existing structures is a crucial task upon which rely an efficient retrofit design. Bridges are ‘key elements’ of the infrastructural network, and ensuring their good serviceability is of paramount importance. In 2020, in Italy were enacted the ‘*Guidelines for the classification, risk management, safety evaluation and monitoring of existing bridges*’: the underlying philosophy is to deepen the analysis only on those bridges showing poor maintenance conditions. Prestressed concrete bridges with post-tensioned cables are one of the bridge typologies mostly affected by relevant structural issues and whose assessment is more complicated. In this research, a multiphase methodology is proposed, specifically to be applied to PT bridges. The method is organized in progressive levels of knowledges. The aim is to provide an answer about how to perform the safety assessment of these structures and how deep shall be the preliminary knowledge campaign to consider the PT bridge completely investigated.

1 INTRODUCTION

Bridges are crucial points in the infrastructural system, as their suboptimal functionality strongly affects the economic and social life of the community. The need to optimize the inspection and intervention procedures is, nowadays, a central issue especially in countries like Italy where several catastrophic events have occurred in recent decades. Since the Polcevera viaduct collapse (2018), both the professional and academic communities have been working on shared methodologies to optimize census and assessment; the overall effort led to the adoption of the ‘*Guidelines for the classification, risk management, safety assessment and monitoring of existing bridges*’ in 2020 (MIT CSLP 2020). The Italian Guidelines are organized into six deepening levels for the assessment. This multilevel approach allows to save resources and to optimize both inspections and interventions, since a lower risk level requires less analysis and a lower level of knowledge achieved for the infrastructure.

The first three assessment levels are required for all the structures: through Level 0 it is possible to carry out the census, Level 1 is devoted to the execution of in-situ visual inspections allowing to classify the infrastructures according to indications of Level 2. The Level 2 classification is the results of four different risks: the structural and geotechnical risk, the hydraulic risk, the seismic risk and the landslide risk. The so-derived ‘Attention Class’ allows the definition of a priority order of interventions and/or monitoring for considered infrastructures. All these evaluations can be performed by collecting data from the original documentation and

through only visual inspections. However, there are some situations where visual inspections only are not sufficient: this is the case of precast concrete bridges with post-tensioned cables (namely PT bridges).

PT bridges represent a consistent portion of the infrastructural system, especially of the highways' one. Their large number is due to the inherent advantages that this technology offered in comparison to the Reinforced Concrete (RC) one, as the possibility to gain longer spans using less materials, the easiness of construction phase thanks to the partial prefabrication and the repeatability of the static schemes. However, as the decades pass, the materials physiologically degrade, and the issue of inspection and evaluation becomes more and more urgent. The evaluation of the maintenance condition of a RC structure is relatively easy since the defectiveness is usually visible: the strong corrosion of rebars is often joined to the loss of the concrete cover or to a very serious degradation of it. On the other hand, PT structures may be affected by defects difficult to detect: for instance, since the steel cables are inside a duct, and the duct is inside the concrete section, with a cover usually thicker than that for ordinary reinforcement, it may be difficult to find corrosion defects on the cables. These situations may be defined as "*hidden defectiveness*" and in these cases a visual inspection cannot be sufficient to assess, even if in a preliminary evaluation, a PT bridge. The issue is complex being the hidden defects completely unknown and the critical questions are mainly two: how and where to perform inspections, i.e. which investigation technique shall be used and how many samples shall be analysed. The present research tries to give a general methodology to evaluate PT structures, from the preliminary to the accurate assessment.

2 THE MULTI-PHASE METHODOLOGY

The proposed methodology has been conceived referring to the Guidelines of the Federal Highway Administration (FHWA 2013), to the directions given by the Highways England in *CS 465 – Management of post-tensioned concrete bridges* (Highways England, 2020) and to the Italian Guidelines (MIT CSLP 2020).

The FHWA guidelines provide a method based on the adoption of destructive testing, which aims to assess the risk of PT bridges, and thus prioritize interventions and define a probable level of defectiveness. The determination of the number of samples to investigate is performed by assuming that the tests' results can be described with a hypergeometric distribution. The CS 465, on the other side, proposes a methodology for the management of inspections, monitoring and interventions on PT bridges carried out through a process including risk review, risk assessment and risk management. Suggestions are given about how to perform the tests, their best location and the most critical defects to be considered.

For PT systems, the Italian Guidelines 2020 proposes the so-called 'Special Inspections' (SI), giving indications about the mandatory information to collect, i.e. the individuation of the cables' trace, the localization of defects and their quantification and qualification, and how to perform the tests. Being the assessment of PT structures a relatively recent issue and lacking the knowledge about the technologies to employ and the way to perform an inspection campaign, more indications are needed.

A multi-phase methodology, following the approach of the Italian Guidelines and comprehensive of the suggestions given by FHWA and the Highways England, is then proposed (Figure 1). It works at subsequent levels of analysis: the more likely the presence of serious defectiveness, the more accurate the investigations. It means that it is not necessary to go through each phase for all the bridges, but only the most degraded ones need to be deeply assessed. The first two phases are mandatory for all the bridges: *phase 0* provides the knowledge of the structure and indications about the number of samples to investigate, *phase 1* provides for the overall assessment conditions through both non-destructive (ND) and semi-destructive (SD) testing, *Phase 2* consists in the deep analysis of the defectiveness individuated at the end of the phase 1 and, finally, *phase 3* is optional and contains suggestions for the global analysis of the bridge.

Two are the possible overall outcomes of the proposed procedure: (a) the classification of the bridge according to the LG as for all other bridge typologies or (b) the need for its accurate assessment. The classification shall be performed according to the Italian Guidelines, considering that the present methodology gives information only about the defectiveness level of the bridge. The accurate assessment is required only if the structure presents worrying defects. In the following, each phase will be discussed and deepened.

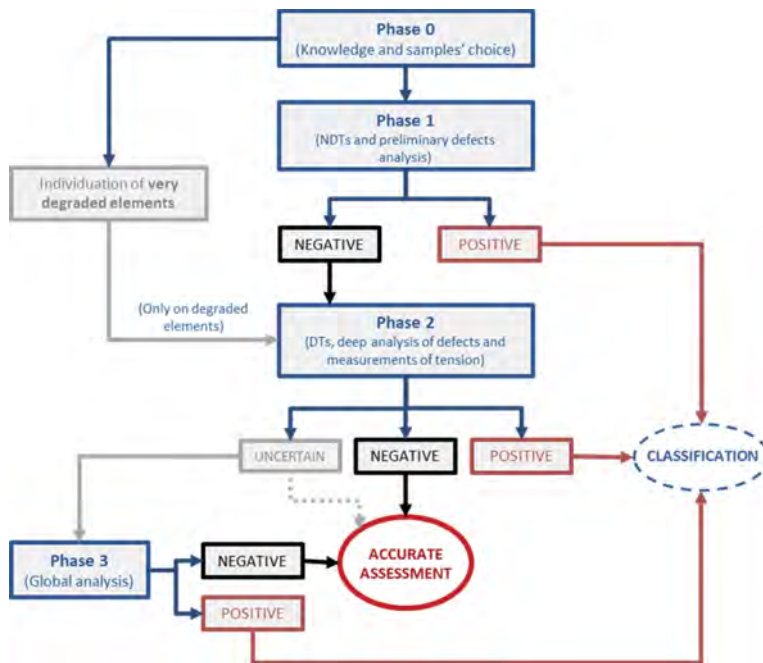


Figure 1. Logical flow of the proposed multi-phase methodology.

2.1 Phase 0: The knowledge

Phase 0 is devoted to the knowledge of the structure and can be divided into two main parts: (0a) the historical-critical analysis of the available documentation and (0b) the assessment of the conservation conditions through visual inspections. By completing these operations, all the required data to define the number of samples to investigate in the following steps, according to a method deriving from FHWA, are achieved. Besides, portions affected by high degradation - namely strong oxidation, or corrosion of the PT cables, if present - can be determined.

The historical-critical analysis (0a) is necessary to collect information about the type, the number and the trace of PT cables and relevant intervention/modifications after construction. In case of lack of original documents, on-site operations (geometrical surveys, non-destructive and/or destructive testing) shall be carried out: of course, the more unknowns, the more invasive will be the impact on the structure. Defectiveness (0b) shall be assessed according to Level 2 of the Italian Guidelines (MIT CSLP 2020), considering only beams and crossbeams belonging to the PT system, resulting in an overall defectiveness level strictly related to the one of each accounted component.

Once all the previous data are known, it is possible to proceed with the risk assessment, a necessary step to estimate the minimum number of samples to investigate. These two operations are based on the same hypothesis and follow the methodology proposed by the FHWA, with few integrations and adjustments required to match the Italian Guidelines.

To perform the risk assessment and therefore define the number of samples to investigate, it is necessary, as the FHWA proposes, to make some assumptions about the expected distribution of the defectiveness within the structure. The worst defect considered in this field is the one that may determine the corrosion of the cables; since the corrosion is most probable to occur in areas where the grouting is not complete, the investigations are focused on finding grouted/ungouted areas. Being these two outputs the only two possibilities and being the single investigation not able to provide the re-entry of the single test in the sample, the distribution can be described as hypergeometric.

The probability mass function of the hypergeometric distribution is then defined according to (1), being the main parameters n - the number of cables to be investigated, N - the total number of cables belonging to the same homogeneous group, k - the number of times in which the cables are ungrouted and $m = n/N \cdot 100$. By considering a homogeneous group of cables, in terms of geometrical and typological characteristics, the width N can be defined; by supposing a certain percentage of defective cables m (as described in the following) and by relating the probability of finding at least one defective cable ($k = 1$) to the concept of confidence in the outcome of the investigations and, therefore, establishing a confidence level, it is possible to determine the amplitude n of the sample to investigate.

The FHWA proposes to establish a probability/confidence level of 75%; being the planned investigations for Phase 2 ‘preliminary’, the same percentage is suggested to be adopted.

$$P(X = k) = \frac{\binom{m}{k} \binom{N - m}{n - k}}{\binom{N}{n}} \tag{1}$$

where m = defects present; n = number of cables to be investigated; N = total number of cables; k = times in which the cable is defective.

The assumed level m of defective elements depends on the risk level associated to the structure and on the structural impact associated to the tests to be performed. Three risk levels and three structural impact levels are then provided: *high*, *medium* and *low*. As showed in Figure 2, the risk level must be defined through the calculation of a probability index and of a confidence index, with values in the range 1÷5. The probability index depends on the presence of technical documentation, the length and type of PT cables and the actual defectiveness level of the structure, this last one defined as previously explained. The consequence index depends on the cost for restoring, the redundancy of the structure and its importance level, representing therefore a sort of exposure indicator.

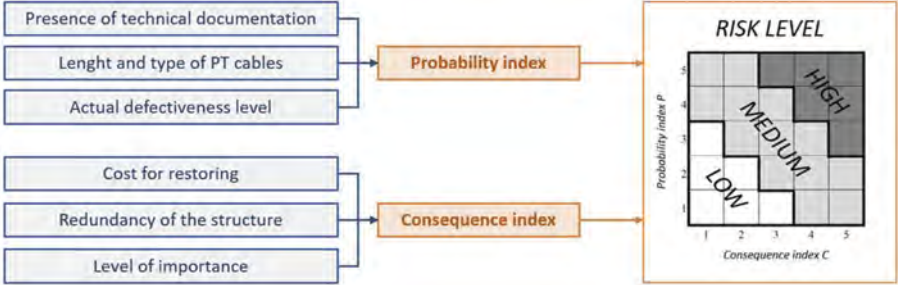


Figure 2. Definition of the risk level.

The number of samples deriving from the previous consideration must not include all the cables that present evident corrosion defects after a visual inspection. These samples must be deeply investigated directly by the analysis provided in the *Phase 2*.

In this context, one sample means one cable. A cable can be considered fully inspected if all the critical areas for the injection and therefore all the areas where the presence of defective grouting is most probable (Trejo et al. 2009), are investigated. Figure 3 shows the riskiest zone of a cable belonging to a simply supported post-tensioned beam: the anchorage zones, the midspan region and the zones in which there is a change in curvature. Finally, it is necessary to choose which sample to investigate. The suggestion is to investigate at most two cables for beam, to obtain a statistically significant result, and choosing the most defective beams belonging to the most defective spans.

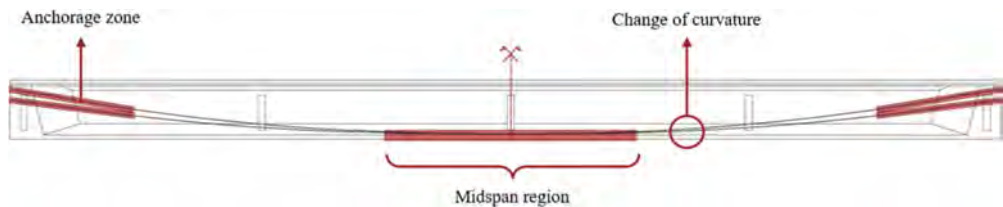


Figure 3. Areas to investigate in order to consider a sample (a cable) fully inspected.

2.2 Phase 1: Preliminary analysis

Phase 1 is devoted to the (1a) preliminary analysis of the defects through non-destructive (NDTs) or semi-destructive (SDTs) techniques and (1b) the definition of the corrosion probability of the concrete matrix.

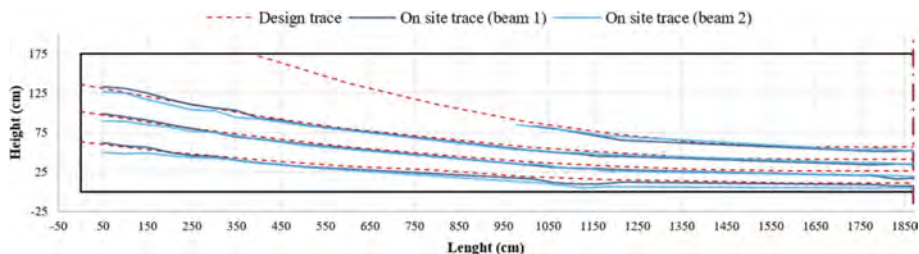


Figure 4. Individuation of cables' layout by using GPR technology (on site trace VS design trace).

The preliminary analysis of the defects (1a) aims to locate eventual deficiencies in the grouting. The definition of the cables' layout is then the preliminary necessary step and can be performed, for instance, through the Ground Penetrating Radar (GPR) technique (see Figure 4), strongly promoted and used by many researches (Terzioglu et al. 2018; Sławski, Kosno, and Świt 2016; Wai-Lok Lai, Dérobert, and Annan 2018). Of course, other possibilities can be explored if able to provide adequate and reliable results.

The individuation of defective grouting can be carried out by any test methodology of proven validity. In (Highways England 2020a) many proposals are given, such as the Impact Echo (IE), the Ultrasonic Echo (UE), the Ultrasonic Tomography (UT) and the X-rays scans. Even if in the academic and scientific world these technologies are well-known and widely tested (Giannopoulos et al. 2002; Sławski, Kosno, and Świt 2016; Terzioglu et al. 2018; Wai-Lok Lai, Dérobert, and Annan 2018), in the common practice there are still no consolidated procedures and protocols since the results of their application are often difficult to be interpreted and applied on-site. Keeping in mind the need for determining objective procedures and protocols for in-situ NDTs, the application of even more than one ND technique can be promoted (Terzioglu et al., 2018), or in combination with semi-destructive tests (e.g. endoscopic

investigations) more or less widely applied. Alternatively, it can be possible to apply only semi-destructive tests, but widely spreading them through the samples.

The definition of the corrosion probability (1b) can be performed preliminarily on the concrete matrix to evaluate the likelihood of occurrence of corrosive phenomena in the ordinary steel and in the metallic ducts. A high corrosion probability on these elements does not necessarily imply corrosion of the PT cables, as the opposite situation, but a low corrosion probability, together with the lack of ungrouted region, may indicate the good condition of the PT system. As suggested in (Highways England 2020b) the main factors to investigate, in this case, are: the width of the concrete cover, the depth of carbonatation, the concrete resistivity, the half-cell potential, the chloride, sulphate and alkali contents.

According to Figure 1, Phase 1 can give either ‘positive’ or ‘negative’ results. By adopting the classification of voids proposed by (Highways England 2020b) and reported in Table 1, a positive result means no voids or only small voids determined: namely, it is possible to consider that the structure, with the probability defined before, has no defects. On the other hand, if even one large void is found, or several medium voids and a high probability of corrosion is stated, it is not possible to consider the structure without defects and *Phase 2* becomes therefore necessary.

Table 1. Classification of voids according to (Highways England, 2020b).

Classification	Description
No void	Fully grouted
Small void	<50 mm length
Medium void	50-300 mm length
Large void	>300 mm length
UngROUTED	No evidence of grout

2.3 Phase 2: Deep analysis

Deep analysis of *Phase 2* is necessary when, from *Phase 1*, it is not possible to conclude that the structure has no deficiencies in the grouting, and/or when, from *Phase 0*, the presence of defects of oxidation/corrosion on the PT system is assessed by visual inspection. In-depth investigations must be then located in those areas emerged as defective from *Phase 1*, and/or on the degraded portions determined in *Phase 0*.

The primary objective is the damage evaluation in terms of cross-section reduction; therefore, samples through concrete excavation are required. If no corrosion/oxidation is stated after these operations, it is suggested to evaluate the corrosion probability of the grout by defining the cement content, the chloride ion concentration, the sulfate ion concentration, the alkalinity and the moisture content (Highways England 2020b). In addition, it is possible to evaluate the stress acting through the steel cable and/or the tensional state of the concrete cross-section, to indirectly assess the efficiency of the PT system and therefore exclude the presence of strong corrosion phenomena.

These evaluations can be performed in any way deemed effective by the current scientific literature. Some test methodologies can be suggested: for instance, to assess the stress acting through the wire/strand it is possible to perform the X-ray diffraction investigations, NDT usually adopted in the quality check of the manufacturing processes by the measure of residual stresses. Many researchers in last years confirm the reliability of this NDT (Carfagno et al. 1995; Morelli et al. 2021; Zanini, Faleschini, and Pellegrino 2022). The measure can be indirectly performed on the concrete section through the saw-cut method, which is basically a SDT relating the “released” deformation of the test area with the pre-existing tensional state; this methodology has been employed both on-site (Bagge, Nilimaa, and Elfgrén 2017;

Jakub Kral'ovanec, Moravčík, et al. 2021) and in laboratory (J Kral'ovanec and Moravčík 2021; Jakub Kral'ovanec, Bahleda, et al. 2021).



Figure 5. The picture in a) shows X-ray diffraction measurements on-site, while the picture b) shows the saw-cut method.

As well as for *Phase 1*, *Phase 2* can give either ‘positive’ or ‘negative’ results, but also the ‘uncertain’ condition is admitted. If no corrosion phenomena are detected and the probability of grout corrosion is negligible, it is possible to consider the structure, with the probability previously defined, not defective therefore going on with the classification according to Italian Guidelines. If corrosion phenomena are detected, or if large voids associated with a high corrosion probability are found, the accurate assessment of the structure is required. When the results of the investigations are difficult to interpret, or in any case, when the designer thinks that could be necessary, it is possible to go through the global analysis of the structure.

2.4 *Phase 3: Global analysis*

If the expert judgment is not able to completely exclude the presence of conditions that could compromise the safety of the whole structure or a part of it, or if there is the will of assessing the influence of certain detected damage on global behavior, it is possible to perform dynamic tests or static load tests. For this Phase too the final outputs can be positive or negative. Being these evaluations complex, it is not possible to generalize the cases in which it results a positive judgment instead of a negative one. The designer must have the responsibility in the assessment of the structure deriving from global analysis.

3 CONCLUSIONS

The present research aims to define a methodology for the design and execution of the in-situ inspection on precast concrete bridges with post-tensioned cables. This structural system is very complex to investigate as a consequence of the potential presence of hidden defectiveness: therefore, a multi-phase procedure organized into four different steps is proposed.

The procedure follows the same philosophy adopted by the Italian Guidelines, with the aim of optimizing time and economic resources for the inspection and the assessment of bridges: the higher the defectiveness, the deeper the evaluation and the more complex and reliable the tests’ methodologies required. For the methodology elaboration, reference has been also made to the indications provided by English and American Standards; in particular, the assumption for the determination of the number of samples to investigate is the same as the ones proposed by the FHWA. Many experimental campaigns are going to be planned and performed on existing case studies with the aim of validating the proposed procedure and providing in-depth indications about how to perform the accurate assessment of PT bridges.

REFERENCES

- Bagge, Niklas, Jonny Nilimaa, and Lennart Elfgren. 2017. "In-Situ Methods to Determine Residual Prestress Forces in Concrete Bridges." *Engineering Structures* 135 (March): 41–52. <https://doi.org/10.1016/j.engstruct.2016.12.059>.
- Carfagno, Michael G, Faired S Noorai, Michael E Brauss, and James A Pineault. 1995. "Extending the Lifespan of Structures." *IABSE Reports*. Vol. 73. <http://proceedings.spiedigitallibrary.org/>.
- FHWA. 2013. "Guidelines for Sampling, Assessing, and Restoring Defective Grout in Prestressed Concrete Bridge Post-Tensioning Ducts."
- Giannopoulos, Antonios, Paul Macintyre, Scott Rodgers, and Mike C Forde. 2002. "GPR Detection of Voids in Post-Tensioned Concrete Bridge Beams."
- Highways England. 2020a. "CS 464 - Non-Destructive Testing of Highways Structures."
- Highways England. 2020b. "CS 465 - Management of Post-Tensioned Concrete Bridges."
- Kraľovanec, J, and M Moravčík. 2021. "Numerical Verification of the Saw-Cut Method." *IOP Conference Series: Materials Science and Engineering* 1015 (1): 012031. <https://doi.org/10.1088/1757-899x/1015/1/012031>.
- Kraľovanec, Jakub, František Bahleda, Jozef Prokop, Martin Moravčík, and Miroslav Neslušán. 2021. "Verification of Actual Prestressing in Existing Pre-Tensioned Members." *Applied Sciences (Switzerland)* 11 (13). <https://doi.org/10.3390/app11135971>.
- Kraľovanec, Jakub, Martin Moravčík, Petra Bujňáková, and Jozef Jošt. 2021. "Indirect Determination of Residual Prestressing Force in Post-Tensioned Concrete Beam." *Materials* 14 (6). <https://doi.org/10.3390/ma14061338>.
- MIT CSLP. 2020. *Linee Guida per La Classificazione e Gestione Del Rischio, La Valutazione Della Sicurezza Ed Il Monitoraggio Dei Ponti Esistenti*.
- Morelli, Francesco, Ivan Panzera, Andrea Piscini, Walter Salvatore, Francesco Chichi, Gian Paolo Marconi, Daniele Maestrini, Massimo Gammino, and Michele Mori. 2021. "X-Ray Measure of Tensile Force in Post-Tensioned Steel Cables." *Construction and Building Materials* 305 (October). <https://doi.org/10.1016/j.conbuildmat.2021.124743>.
- Ślawski, Lukasz, Lukasz Kosno, and Grzegorz Świt. 2016. "Evaluation of Precast Pre-Post-Tensioned Concrete Bridge Beams with the Use of GPR Method." In *Procedia Engineering*, 156:443–50. Elsevier Ltd. <https://doi.org/10.1016/j.proeng.2016.08.319>.
- Terzioglu, Tevfik, Madhu M. Karthik, Stefan Hurlbaeus, Mary Beth D. Hueste, Stefan Maack, Jens Woestmann, Herbert Wiggenshauser, Martin Krause, Patrick K. Miller, and Larry D. Olson. 2018. "Nondestructive Evaluation of Grout Defects in Internal Tendons of Post-Tensioned Girders." *NDT and E International* 99 (October): 23–35. <https://doi.org/10.1016/j.ndteint.2018.05.013>.
- Trejo, David, Radhakrishna Pillai, Mary Beth, D Hueste, and Paolo Gardoni. 2009. "Parameters Influencing Corrosion and Tension Capacity of Post-Tensioning Strands." *ACI Materials Journal* 106 (March): 144–53. <https://www.researchgate.net/publication/289723918>.
- Wai-Lok Lai, Wallace, Xavier Dérobert, and Peter Annan. 2018. "A Review of Ground Penetrating Radar Application in Civil Engineering: A 30-Year Journey from Locating and Testing to Imaging and Diagnosis." *NDT and E International* 96 (June): 58–78. <https://doi.org/10.1016/j.ndteint.2017.04.002>.
- Zanini, Mariano Angelo, Flora Faleschini, and Carlo Pellegrino. 2022. "New Trends in Assessing the Prestress Loss in Post-Tensioned Concrete Bridges." *Frontiers in Built Environment* 8 (November). <https://doi.org/10.3389/fbuil.2022.956066>.

Super resolution of multi-channel ground penetrating radar volume data by zero-interpolated 3D kirchhoff migration

T. Imai & T. Mizutani

Institute of Industrial Science, the University of Tokyo, Meguro-Ku, Japan

ABSTRACT: On-vehicle multi-channel Ground Penetrating Radar is attracting much attention in infrastructure maintenance field. Besides the key benefits of high-speed 3D subsurface data acquisition, basic problems such as data discontinuity due to use of multiple antennas and sparse observation that arises aliasing have been a problem. This study proposes easily applicable but effective method to solve these problems. For the first issue, calibration in each channel was done by improved Sparse Blind Deconvolution (SBD) method proposed in previous research. It was found that disuse of low-intensity frequency band provides better estimation of transmitted waves. For the second issue, super resolution method was proposed. It interpolates zeros in between sparsely observed data and then apply synthetic aperture processing. Zero insertion is an operation that restores high frequencies, which makes it possible to restore frequency components above the Nyquist frequency under certain conditions. The method was confirmed to be effective on real data.

1 IMPORTANCE IN PRE-PROCESSING OF GPR VOLUME DATA

Infrastructures has been deteriorating worldwide and increasing inspection costs has becoming a concern. Shifting from breakdown maintenance that waits for structures' life limit without any repairing to preventive maintenance that extends service life by regular inspection plays an important role in controlling long-term management costs. In order to achieve this, establishment of early damage detection technology is necessary. Nowadays, Ground Penetrating Radar (GPR) has attracting much attention for inspection of road infrastructures. It obtains subsurface information by emitting electromagnetic waves and observing their reflection. Since the technology is completely non-contact, non-destructive and fast, it enables efficient maintenance of infrastructures.

Mainly two types of GPRs are used for different purposes. The first one is a ground-coupled hand-held type used for close inspection (Liu, Lin, Cui, Fan, Xie, & Spencer 2020; Dinh, Gucunski, Tran, Novo, & Nguyen 2021). It offers high-resolution images, and is also used for exploration of back and sides of structures. The second one is an on-vehicle multi-channel type, which is a main target of this study. It drives at maximum 80km/h and achieve high-speed data acquisition. Also, antenna elements are aligned transversely to the driving direction, thus provides 3D subsurface information.

Besides the key benefits, there are several issues regarding on-vehicle multi-channel GPR (Yamaguchi, Mizutani, Meguro, & Hirano 2022; Liu, Shi, Li, Liu, Meng, Du, & Chen 2021). First issue is lack of data consistency and continuity in the transverse direction, since it utilizes different antenna elements transmitting slightly different waveforms. In general, calibration by frequency domain deconvolution of observed data using transmitted wave is done for removing the inconsistency. For estimation of actual transmitted electromagnetic waves, Sparse Blind Deconvolution (SBD) method was proposed by (Jazayeri, Kazemi, & Kruse 2019). This method iteratively calculates sparse reflectivity and transmitted waveform from observed data. There remains problem of zero-division in the algorithm, that has to be solved.

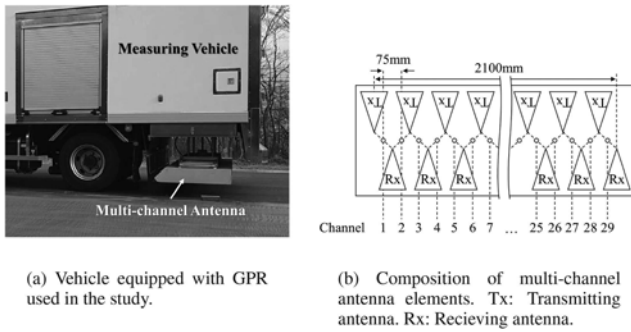


Figure 1. Equipment used for measurement and its composition.

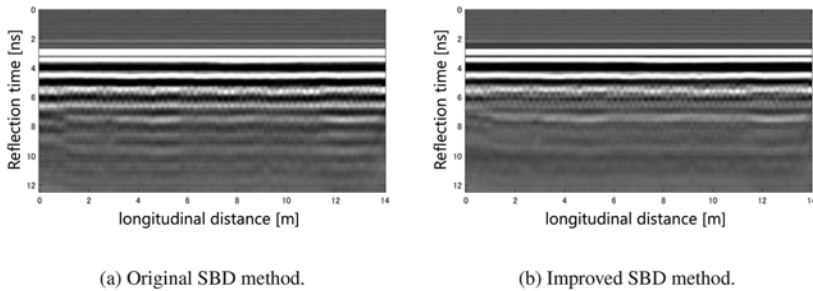


Figure 2. Comparison of calibrated data by original SBD method (previous research) and improved SBD (proposed).

Another issue is that it records data in a sparse spacing with 7 cm in the longitudinal direction for high-speed inspection. This sparse observation induces phenomena well-known as aliasing, and under data with 7 cm spacing acquisition, high-frequency waves under wavelength of 14 cm cannot be observed. Objects installed within structures at just similar intervals are the rebars. Knowing the rebar spacing helps to determine the structural strength of RC bridge decks. Also, damages often appears in the vicinity of rebars, therefore many studies has been conducted focusing on detection of rebars in GPR images (Wang, Zhou, Slabaugh, Zhai, & Fang 2011; Abouhad, Dawood, Jabri, Alsharqawi, & Zayed 2017). However, rebars in bridge decks are usually placed in 10 to 30 cm intervals, and of course there remains a risk that the information on rebars cannot be accurately extracted under aliasing. One major approach of increasing the radar image resolution is synthetic aperture processing, known as the term migration in subsurface exploration field. It is a method to converge diffraction curves, or hyperbolic responses seen in GPR images to a points. Preliminary investigation showed that migration sometimes does not recover the image with sparse observation, therefore further study is necessary.

The objective of this study is to propose a pre-processing method for on-vehicle multi-channel GPR. Composition is as follows. In section 2, appropriate updating methods in SBD algorithm to avoid zero-division problem is proposed. Section 3 focuses on proposal of super resolution of GPR image for resolution recovery. Application results of the proposed methods to in-service data will be shown in Section 4.

2 CALIBRATION OF ANTENNAS BY SPARSE BLIND DECONVOLUTION

Multi-channel GPR utilized in this study is composed of 29 (or 25) channels using 30 (or 26) antenna elements (Figure 1). It acquires data by Stepped-Frequency Continuous Wave (SFCW) system. The frequency of electromagnetic wave used was 50 MHz to 3030 MHz by a step of 20 MHz. Transmitted electromagnetic waves are desired be having an one-sided and narrow peak,

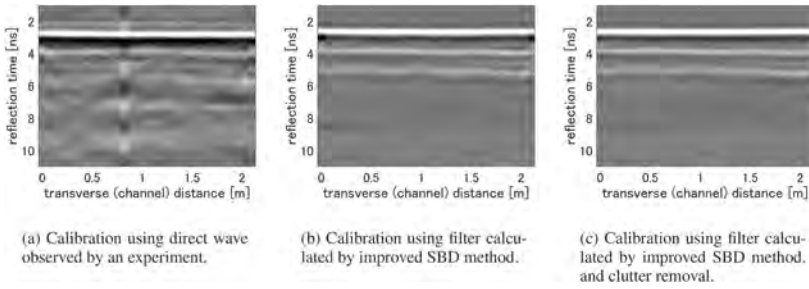


Figure 3. Changes in the transverse (channel) direction cross section image when using different calibration filters and clutter removal method.

for example the sinc function, but often this condition is not always satisfied. Therefore, the inverse convolution in the frequency domain is performed by the following equation:

$$\hat{y}_c = \frac{\hat{y}}{\hat{w}} \quad (1)$$

where, y is observed wave, w is transmitted wavelet and y_c is calibrated wave. $\hat{\cdot}$ indicates the Fourier Transform.

For estimation of the wavelet, SBD can be used. Here is a brief overview of SBD. Convolution of wavelet $w = (w[0], w[1], w[2], \dots, w[L-1])^T$ and reflectivity $r = (r[0], r[1], r[2], \dots, r[L-1])^T$ can be written in a matrix form:

$$y = Wr \quad (2)$$

where $y = (y[0], y[1], y[2], \dots, y[L-1])^T$ and W is circulant matrix constructed from wavelet vector w . In SBD, the reflectivity r and the transmitted wavelet w are obtained by alternately solving the following two equations:

$$r = \arg \min_r \|y - Wr\|_2^2 + \lambda_r \|r\|_1 \quad (3)$$

$$w = \arg \min_w \|y - R w\|_2^2 + \lambda_w \|w\|_2^2 \quad (4)$$

where R is circulant matrix constructed from reflectivity vector r . The first term in equation (3) is the fidelity term and the second term is the l_1 regularization term to assume sparsity in the reflectivity r . It is known that optimization problem with l_1 regularization term can be solved iteratively by Split Bregman Algorithm (Goldstein & Osher 2009). Equation (4) contains l_2 regularization term for maintaining smoothness of the estimated wavelet, and has a closed-form solution of:

$$w = (R^T R + \lambda_w I)^{-1} R y \quad (5)$$

and re-written in the frequency domain as:

$$\hat{w} = \frac{\hat{r}^* \odot \hat{y}}{\hat{r} + \lambda_w}, \quad (\hat{r} = \hat{r}^* \odot \hat{r}) \quad (6)$$

Here, $*$ is Hermitian transpose and \odot is Hadamard product. The wavelet is updated by taking average of the estimation results in each observation. However, Above solution has a problem when applied to calibration by equation (1). The problem occurs when the specific frequency-band components of the observed signal \hat{y} is close to zero. In this case \hat{w} also becomes close to zero, which causes zero-division providing unstable calibrated signal \hat{y}_c . In this study, a minor but effective approach of disusing a low-intensity frequency band for wavelet update was implemented. Certain threshold was set and the frequency band with amplitude below that threshold were disused. Comparison of calibrated data by equation (1) using wavelets calculated

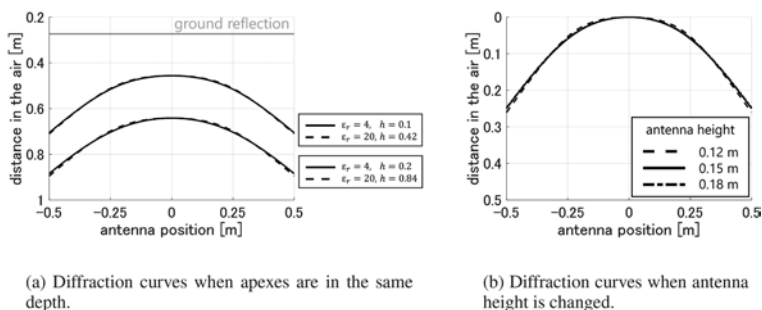


Figure 4. Comparison of ideal diffraction curves when changing the relative permittivity and the antenna height in the 2-layer model.

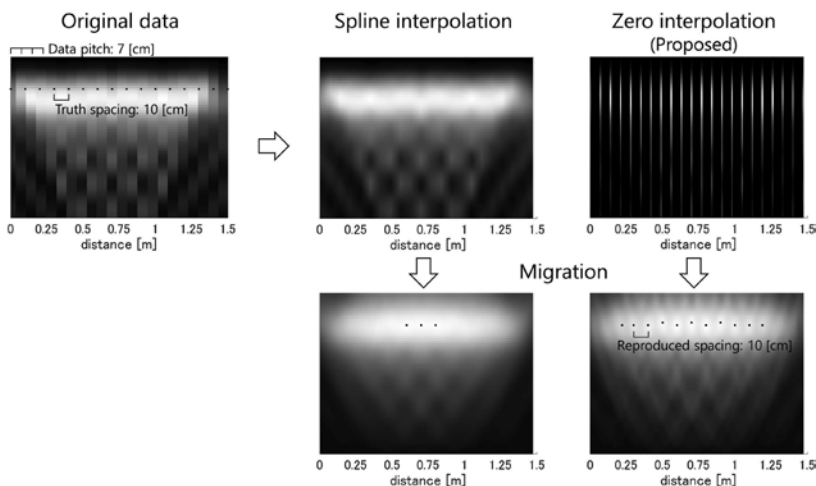


Figure 5. Simulation of super resolution.

by original method and the proposed disuse method is shown in Figure 2. Figure 2(a) calibrated by the original SBD method contains needless vibrations by poor estimation results in certain frequency band, while Figure 2(b) with the proposed method shows good estimation results.

Using the improved SBD method, Wavelets were estimated for each channel. Cross-sectional image of calibrated data in the transverse direction is shown in the center of Figure 3(b). Compared to the calibrated data using direct wave measured by an experiment (Figure 3(a)), it shows significantly clear image. The data was obtained from the RC bridge section, and rebar responses are recognized around 5 ns depth that were not visible in the left image. On the contrary to the favorable findings, slight clutter can be found in especially the edge of the center image. The clutter is stationary and it is presumed that this is attributed to reflection from the vehicle. Clutter was simply removed by subtracting only the components of variation in the transverse direction from the average image in the longitudinal direction (Figure 3(c)).

3 SUPER RESOLUTION OF GPR VOLUME DATA

3.1 Hyperbolic response with refraction

Electromagnetic waves are emitted spherically, and point-like objects are observed as hyperbolic diffraction curves in ground-penetrating radar images. Migration is an often-used

method for convergence of hyperbolic responses seen in GPR to a points, for improved visibility and resolution. Kirchhoff migration (Özdemir, Şevket Demirci, Yiğit, & Yilmaz 2014) is derived from the wave equation and can be applied as follows:

$$I(x, y, z) = \int \frac{\cos \theta}{r} \left(\frac{1}{c} E'(x, y, t = t_0) \right) dS \quad (7)$$

where E is observed signal and I is migrated image. t_0 represents the transmission time which is equal to the diffraction curve, and $\cos \theta$ indicates the radiant angle. To obtain appropriately converged images, accurate assumption of hyperbolic shape is required. Wave propagation using ground-coupled antennas can be explained by considering a two-layer model of air and soil (or concrete), and it can be formulated as follows:

$$f(x) = \frac{2}{c} \sqrt{(x - x_1)^2 + h^2} + \frac{2\sqrt{\epsilon_r}}{c} \sqrt{(x_1 - x_0)^2 + d^2} \quad (8)$$

$$\sin \theta_1 = \sqrt{\epsilon_r} \sin \theta_2 \quad (9)$$

where c is light velocity, ϵ_r is relative permittivity of the soil, d is the height of the antenna and d is the depth of the target object. (Persico, Leucci, Matera, de Giorgi, Soldovieri, Cataldo, Cannazza, & Benedetto 2015) stated that Snell's law (equation (9)) comes down to a quadratic equation and derived a closed-form solution.

They also made a qualitative discussion, stating that diffraction curves of objects at shallow depth does not change when observed by air-coupled GPR. This is explained by Fermat's principle of least time, where electromagnetic waves tend to pass the air layer than the soil layer. The theory support an important fact that relative permittivity of the propagating medium and depth of the object cannot be estimated from the diffraction curve. This disadvantage, however, inversely becomes an advantage in that migration can be applied using a single diffraction curve. In order to understand applicable limits, diffraction curves depending on various conditions were calculated. Since this study utilizes antennas with separated receiver and transmitter, diffraction curves were calculated by the following equation:

$$g(x; l) = f \left(\sqrt{\left(x - \frac{l_1}{2}\right)^2 + \left(y - \frac{l_2}{2}\right)^2} \right) + f \left(\sqrt{\left(x + \frac{l_1}{2}\right)^2 + \left(y + \frac{l_2}{2}\right)^2} \right) \quad (10)$$

where (x, y) is the longitudinal and transverse coordinate of antenna center and (l_1, l_2) is the distance of two antenna elements in each direction. Figure 4(a) shows changes of diffraction curves under conditions when apexes appear in the same reflection time. Two cases of relative permittivity $\epsilon_r = 4, 20$ are compared. When the depth of target is shallow around $0.1 \sim 0.2$ m, diffraction curves have almost no differences showing that migration can be applied using a unified curve.

Another important issue is undulation of data due to vehicle vibration. Changes in diffraction curves due to vertical displacement of the vehicle can have a effect on migration results. Diffraction curves under different antenna height conditions were compared. The curves showed less differences under the height variation of ± 3 cm (Figure 4(b)). According to the results, it is considered that the diffraction curve will be distorted by the same amount as the road surface variation in the image. For this reason, time-shifting of the A-scan signals for flattening the road surface reflection improves migration accuracy.

3.2 Kirchhoff migration for recovery from aliasing

Migration in discrete system is applied by similar processing of taking cross correlation with diffraction curve template. When data is sparsely observed, the data acquisition point is often not located directly above the point-like target object, and for this case, appropriate diffraction curve fitting cannot be implemented.

In this subsection, super resolution method for recovery of aliased GPR images based on zero-interpolated migration is proposed. The method is very simple: zeros are inserted in between sparsely observed data, then migration is processed. Simulation result of zero-interpolated migration compared with spline-interpolated migration is shown in Figure 5. Original data in the upper left figure expresses rebar response often seen in on-vehicle radar data image. It was produced by convolution of diffraction curve in 10 cm spacing, and sampled in 7cm pitch. Under this condition, apexes of diffraction curves are aliased and hard to recognize in the original data. The center and the right

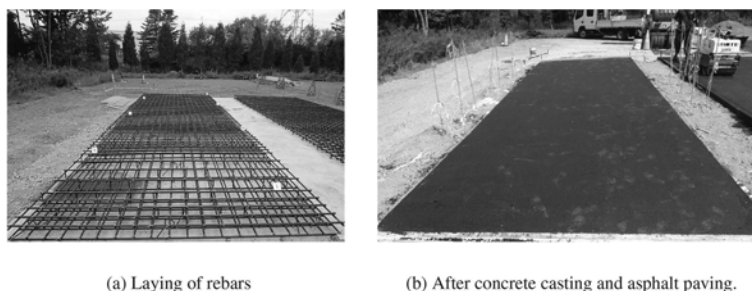


Figure 6. Photo of the experimental field where Data1 was measured.

Table 1. Parameters of antennas used for migration.

	Channel	Long. Dist.	Trans. Dist.	Height
Data1	29	47.5 cm	7.5 cm	15 cm
Data2	25	47.5 cm	7.5 cm	15 cm

figures shows interpolated data and migration results. Black dots in the migration data represent the local maxima points. The spline interpolated migration image hardly restores the black dots, whereas zero-interpolated migration produces black dots in accurately 10 cm spacing.

Zero-interpolated migration can be interpreted from mathematical point of views. As seen in the f-k migration (Stolt 1978), the synthetic aperture processing of GPR images can be interpreted in the frequency domain. For example, the simplest migration method is convolution with a single hyperbola, which can be represented in the frequency domain by multiplication of the spectrum. If the image is subjected to aliasing, of course the spectrum after migration does not contain any true frequency components. Spline interpolation is also impossible to recover the true frequency components since it is essentially a method of interpolating the image with a low-order polynomial function. On the contrary, zero interpolation in the time domain is equivalent to repetition of spectrum in the frequency domain. This allows the aliased spectrum restored to its true frequency again, symmetrically with respect to the Nyquist frequency. However, excessive interpolation also accentuates unwanted high-frequency noise, and a low-pass filter must be applied after zero-interpolated migration. In Figure 5, a filter with a cutoff frequency of 1/15 [1/m] is applied for high-frequency noise removal.

4 APPLICATION TO MEASUREMENT DATA

Super resolution by zero-interpolated migration was applied to real measurement data. Two volume images of different bridge decks were prepared. The first one (Data1) was with known rebar spacing: main rebar in 15 cm; and distribution rebar in 30 cm and 15 cm. Photos of the experimental field where Data1 was taken is shown in Figure 6. The other data (Data2) was acquired by driving an in-service bridge. The truth rebar spacing is unknown for Data2. The data was calibrated by the proposed method explained in Section 2. Road surface was flattened by time-shifting and 4 times zero-interpolation was applied.

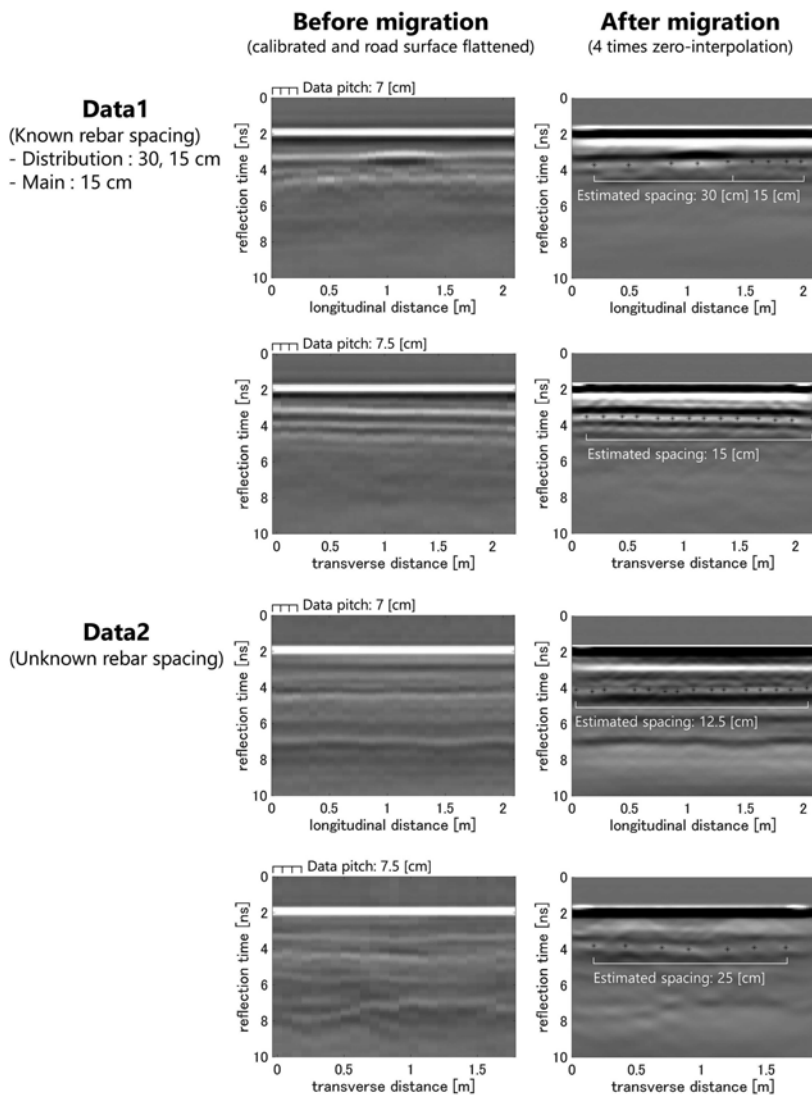


Figure 7. Super resolution of real volume data.

Precise calculation of diffraction curve requires distances of the Tx/Rx antenna elements in the longitudinal and transverse direction, and the height from the ground (equations (8) and (10)). The distance of the elements in the transverse direction is a known parameter and the height is obtained by actual measurement. Unknown parameter is only the distance in the longitudinal direction, and values that produces good migration result were chosen (Table 1). Relative permittivity was assumed to be 10 in the calculation.

Cross section images of original data and results of applying super resolution method is shown in Figure 7. While original images contain complex hyperbolic responses with unclear rebar apexes, super resolution provides easy-to-interpret images. Although these two sets of data may not have the same permittivity, the method worked well. This is based on discussion done in Section 3.1, and it could be concluded that the behavior of the real data follows the theory.

Black dots in the migrated images show local maxima points and only the depth that corresponding to the rebar response are extracted. For Data1, distribution rebars in the longitudinal

cross sectional image were seen in spacing of 30 cm and 15 cm; main rebar responses in the transverse image were recognized in 15 cm spacing. These were the same as the true rebar spacing, indicating that the migration worked effectively. Super resolution method also produced good results for Data2. Main rebars were seen in around 25 cm spacing with a little noise. Interestingly, distribution rebars appeared stably in a spacing of around 12.5 cm. The data was acquired at 7 cm intervals, which would normally not capture responses with a period of 14 cm or less, however this was overcome by super resolution.

5 CONCLUSION

In this study, mainly two methods regarding pre-processing of on-vehicle multi-channel GPR data were proposed. Both were easily applicable and strongly effective. Specifically, in Section 2, improvement of SBD method for calibration of data and maintaining smoothness in transverse direction images was introduced. Section 3 and Section 4 focused on recovery of true frequency component from aliased image. It was confirmed that the data acquired by on-vehicle GPR follows electromagnetic theory and possibility to avoid aliasing even in real data.

Also, various challenges remain. Firstly, clutter was removed by simple subtraction in the study, however, the mechanism is assumed to be complex and it needs to be solved comprehensively in conjunction with SBD and other methods. Secondly, there should be some limitations for recovery from aliased image and future study is needed for theoretical analysis. It would be also interesting to focus on engineering aspects that was not mentioned in the study such as automation of migration and rebar detection.

ACKNOWLEDGMENT

The authors are grateful to Mr. IGUCHI, Tatsuya, Mr. TAKEMOTO, Dai, and Mr. YAGISAWA, Kazuya from C.E.Management Integrated Laboratory Co.Ltd (C.E.O. SHIMODAIRA, Yuji) for designing and constructing the specimens.

REFERENCES

- Abouhamad, M., T. Dawood, A. Jabri, M. Alsharqawi, & T. Zayed (2017). Corrosiveness mapping of bridge decks using image-based analysis of gpr data. *Automation in Construction* 80, 104–117.
- Dinh, K., N. Gucunski, K. Tran, A. Novo, & T. Nguyen (2021). Full-resolution 3d imaging for concrete structures with dual-polarization gpr. *Automation in Construction* 125, 103652.
- Goldstein, T. & S. Osher (2009). The split bregman method for l1-regularized problems. *SIAM Journal on Imaging Sciences* 2(2), 323–343.
- Jazayeri, S., N. Kazemi, & S. Kruse (2019). Sparse blind deconvolution of ground penetrating radar data. *IEEE Transactions on Geoscience and Remote Sensing* 57(6), 3703–3712.
- Liu, H., C. Lin, J. Cui, L. Fan, X. Xie, & B. F. Spencer (2020). Detection and localization of rebar in concrete by deep learning using ground penetrating radar. *Automation in Construction* 118, 103279.
- Liu, H., Z. Shi, J. Li, C. Liu, X. Meng, Y. Du, & J. Chen (2021, 03). Detection of road cavities in urban cities by 3D ground-penetrating radar. *Geophysics* 86(3), WA25–WA33.
- Persico, R., G. Leucci, L. Matera, L. de Giorgi, F. Soldovieri, A. Cataldo, G. Cannazza, & E. D. Benedetto (2015). Effect of the height of the observation line on the diffraction curve in gpr prospecting. *Near Surface Geophysics* 13(3), 243–252.
- Stolt, R. H. (1978). Migration by fourier transform. *Geophysics* 43(1), 23–48.
- Wang, Z. W., M. Zhou, G. G. Slabaugh, J. Zhai, & T. Fang (2011). Automatic detection of bridge deck condition from ground penetrating radar images. *IEEE Transactions on Automation Science and Engineering* 8(3), 633–640.
- Yamaguchi, T., T. Mizutani, K. Meguro, & T. Hirano (2022). Detecting subsurface voids from gpr images by 3-d convolutional neural network using 2-d finite difference time domain method. *IEEE Journal of Selected Topics in Applied Earth Observations and Remote Sensing* 15, 3061–3073.
- Özdemir, C., Şevket Demirci, E. Yiğit, & B. Yılmaz (2014). A review on migration methods in b-scan ground penetrating radar imaging. *Mathematical Problems in Engineering* 2014, 1–16.

Crack growth suppression effect of SFRC overlay for root-deck fatigue in orthotropic steel deck

M.J.B. Uaje

Tokyo Metropolitan University, Tokyo, Japan
University of the Philippines Los Baños, Laguna, Philippines

J. Murakoshi

Tokyo Metropolitan University, Tokyo, Japan

ABSTRACT: A previous study demonstrated after 10 million cycles of 50 kN wheel loads that reinforcing a partial OSD specimen with SFRC overlay suppressed the crack growth propagation. To analytically evaluate the crack growth suppression effect of SFRC pavement reinforcement, several finite element models were developed, and semi-elliptical cracks with an aspect ratio of 0.15 were introduced at the root of the rib-to-deck weld. Using the displacement-matching approach for calculating the stress intensity factor (SIF) at the crack tip, the results showed that reinforcing a 12 mm thick deck plate with a 75 mm thick SFRC pavement lowers the SIF to about the level of the threshold value, confirming the experimental results.

1 INTRODUCTION

The orthotropic steel deck (OSD) is a deck system composed of a thin deck plate typically 12 to 16 mm in thickness and supported by closely spaced longitudinal ribs. The rib commonly takes a “U”-shape because of its effective torsional properties. It is used as a common deck system for long-span bridges and urban viaducts; however, its complicated welding details resulting in concentrated residual stresses make it susceptible to fatigue. Furthermore, with the increase in traffic volume and vehicle weights, fatigue cracks have been found in existing OSDs in Japan (JSCE 2010), and other countries such as Humen Bridge in China (Ji et al. 2013) and Temse Bridge in Belgium (Nagy et al. 2015). Root-deck cracks, which are one of the observed fatigue cracks in 12 mm thick deck plates under severe traffic condition, initiate from the root of the rib-to-deck weld and propagates through the deck. Previous studies confirmed the formation of the stress concentration at the rib-to-deck weld root, and these demonstrated that the steel fiber reinforced concrete (SFRC) pavement was effective in improving the stress condition (Murakoshi et al. 2019, Uaje & Murakoshi 2022). The latter study also confirmed that in the case of 75 mm thick SFRC pavement reinforcement, the debonding of adhesive increased the critical stress by only 15%. Furthermore, fatigue testing of the same specimen demonstrated the occurrence of root-deck cracks after subjecting it to at least 1 million cycles of 50 kN wheel load directly above the U-rib (Murakoshi et al. 2019). The current study aims to analytically clarify the crack growth suppression effect of SFRC pavement by introducing semi-elliptical cracks at the weld root and comparing the stress intensity factor (SIF) using the displacement-matching approach.

2 FINITE ELEMENT MODEL

2.1 Specimen

The finite element model developed in this study is based on the partial OSD specimen shown in Figure 1. The partial OSD specimen targeted the root-deck cracks at the cross beam since both field surveys (JSCE 2010) and previous fatigue testing (Murakoshi et al. 2012) showed

cracks occurring at the intersection of the cross beam and the U-rib. The thickness of the deck plate, U-rib, and cross beam web is 12, 6, and 12 mm, respectively (Figure 1). The deck plate is welded to the U-rib with one-sided fillet welds of leg length 8 mm and 75% weld penetration. Taking advantage of the symmetry of the specimen, only one-fourth of the OSD specimen was modeled. The software used was MSC Marc 2018.1.0.

In the calculation of the root stress in uncracked models, the modeling of the adhesive did not affect the stress condition significantly; hence the modeling technique adopted was to neglect the adhesive in favor of faster calculation time (Uaje & Murakoshi 2022). In the current study, on the other hand, it was found that the difference between the two methods resulted in a 7-12% difference in the SIF; therefore, the adhesive was considered in the modeling.

2.2 Modeling parameters

To save calculation time, the finite element model was divided into solid and shell elements, as shown in Figure 2. The upper portion, where the area of interest was located, was modeled as three-dimensional, eight-node, first-order, isoparametric solid elements. The lower portion was modeled as four-node, thick shell elements. Table 1 shows the properties of the materials used in the finite element model. The yield point σ_{yield} of the SM490YB steel is 355 MPa.

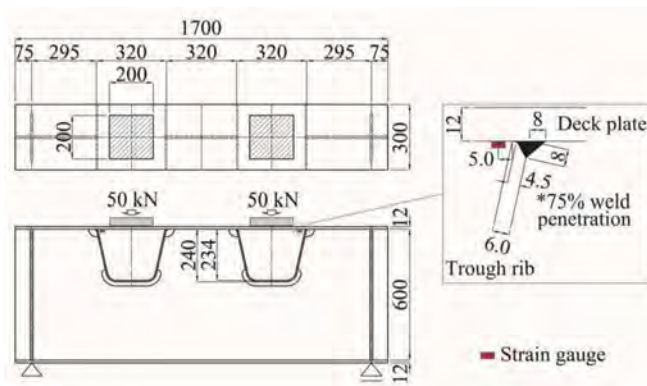


Figure 1. Unpaved OSD specimen from fatigue testing of Murakoshi et al. (2019). Dimensions in mm.

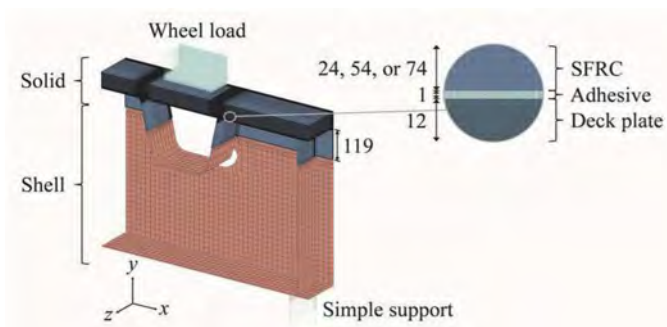


Figure 2. Finite element model of the specimen. Dimensions in mm.

A simple support was provided 75 mm from the end (Figure 2), following the specimen shown in Figure 1. The appropriate boundary conditions were applied accounting for the symmetry of the specimen. In the previous study (Murakoshi et al. 2019), the wheel load was simulated by the application of two-50 kN uniform load at each U-rib over a contact area of 200 by 200 mm through a rubber plate. The finite element model in this study was in turn loaded by

Table 1. Material properties.

Materials	Young's modulus	Poisson's ratio
	MPa	
Steel	200,000	0.30
SFRC pavement	40,000	0.20
Adhesive	2000	0.20

a pressure load of 1.25 MPa as shown in Figure 2. The design live load of the deck plate is 140 kN (considering impact to one side of the design T-load), which corresponds to a pressure load of 1.4 N/mm², and the test load is generally close to this value.

2.3 Crack geometry

In the previous fatigue testing (Murakoshi et al. 2019), before reinforcing the OSD specimen, semi-elliptical cracks initiating from the weld root were introduced by subjecting it to a wheel load of at least 1 million cycles. The previous study collected the crack data and established a linear relationship between the crack aspect ratio alb and a , where a and b are the depth and half-width of the semi-elliptical crack respectively. The crack depth a is not the actual depth of the crack, but rather the projected depth to the vertical plane. The same study conservatively chose the crack aspect ratio $alb = 0.15$, which corresponds to deep cracks, for the analysis. To maintain compatibility with the previous study, the current study utilized the same crack aspect ratio.

Figure 3 shows the typical crack modeling in the current study. Seven types of cracked models with crack depths of 2, 3, 4, 5, 6, 7, and 8 mm were developed. Although the actual crack initiates diagonally from the root and changes direction throughout the deck thickness, the introduced cracks at the weld root model were developed with a vertical orientation for simplicity. The crack surface was generated from two coincident nodes. Each pair of nodes along the crack surface had the same coordinates but were treated as separate nodes by the software. The mesh size from the crack tip to 0.30 mm of the crack plane was 0.025 by 0.025 by 0.25 mm. From 0.30 mm to 1.00 mm from the crack tip, the mesh size was set to 0.025 by 0.050 by 0.25 mm.

2.4 Strain comparison

To establish some consistency between the analytical models with the actual specimen, the strain ranges were compared. The gauge locations from testing which are focused on in this study are shown in Figure 1. It should be noted that this location is of interest because the analytical results exhibited more critical values from this location rather than that of the weld root locations near the midspan of the specimen. Murakoshi et al. (2019) attached the 3 mm strain gauges 5 mm away from the inner surface of the U-rib. Figure 4 shows the strain comparison for the analytical and testing strain ranges from both the unpaved and paved cases across various crack depths. For the uncracked case of the unpaved specimen, it can be observed that the strain ranges were close. For the cracked cases of the unpaved specimen, there is a discrepancy although the consistency of the general trend can be argued. This discrepancy may be mainly due to the simplified modeling of the crack. Furthermore, a wide variation can be observed in the testing strain range itself for the crack depth of approximately 9 mm. For the paved case, there were only two data points of comparison with one data point being close to the analytical trend and another with a significant discrepancy.

2.5 Analysis cases

The analysis discussion is divided into three sections. In Section 4.1, the pavement considered is SFRC. Pavement thicknesses of 25, 50, and 75 mm were chosen; however, the common practice in Japan is to reinforce the deck plate with either 50 or 75 mm thick SFRC pavement. The 25 mm thick SFRC pavement was included only as a theoretical comparison. In Section 4.2, the pavement type is also SFRC, but the debonding of the adhesive was considered. The debonding was accounted for by setting the Young's modulus of the four 0.25 mm layers of adhesive to near 0. i.e.

10 MPa. In Section 4.3, the pavement considered is asphalt, as it is a common overlay, and was included in this study for comparison. Deck plate thicknesses of 12 and 16 mm were considered to account for both the old and new thickness requirements. In the current Japanese design code,

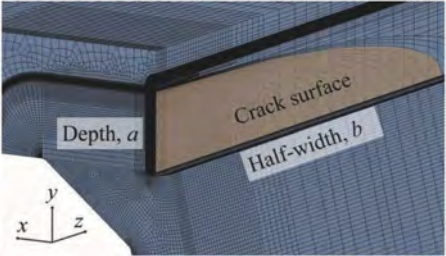


Figure 3. Typical crack modeling at the rib-to-deck weld with the crack surface exposed (8 mm deep crack model shown).

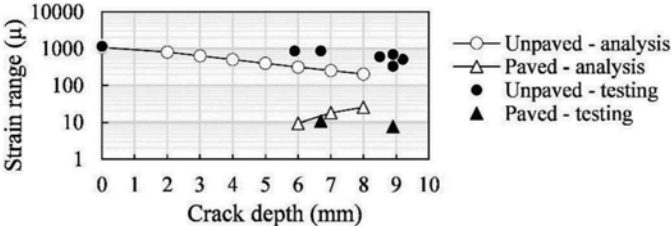


Figure 4. Strain comparison for analytical and testing strain ranges of unpaved and paved (75 mm thick SFRC) specimens.

the deck plate thickness requirement is 16 mm, but no scallop was specified as a structural detail (JRA 2017). Therefore, it should be noted that the 16 mm thick deck plate analytical model in this paper does not comply with the current design code in structural detail and is only a relative comparison of the effect of deck thickness. The 75 mm thick asphalt overlay is a common structural detail in bridges in Japan; hence, the results are presented for the same thickness. The disadvantage of asphalt for consideration of fatigue durability is its stiffness varies with temperature. In this study, three seasons were tested representing various temperatures, assuming the temperature for spring is the same for autumn. The Young’s modulus was set to 500, 1500, and 5000 MPa for summer, spring, and winter respectively, while the Poisson’s ratio for all cases of asphalt was set to 0.35 (Inokuchi et al. 2008).

3 STRESS INTENSITY FACTOR CALCULATION

3.1 Displacement-matching approach

Three modes exist to define the type of loading applied to a crack: Mode I, Mode II, and Mode III, which correspond to opening, in-plane shear, and out-of-plane shear respectively. Since a stress singularity tends to form at the crack tip, it is desirable to describe the crack tip condition by its amplitude, SIF. If the SIF K is determined, then all components of stress, strain, and displacement can be calculated, given the distance r from the crack tip, and angle θ from the horizontal at the opposite side of the crack. For Mode I, the SIF is defined by Equation 1 (Anderson 2005):

$$K_I = \lim_{r \rightarrow 0} \left[\frac{E u_y}{4(1 - \nu^2)} \sqrt{\frac{2\pi}{r}} \right] \tag{1}$$

where r is the distance from the crack tip; E is the Young’s modulus; u_y is the displacement perpendicular to the crack; and ν is the Poisson’s ratio. In lieu of obtaining the closed-form solution, the

SIF K_I can be obtained by calculating Equation 1 numerically. This study only focused on the Mode I SIF K_I , as the results demonstrated that it is the most dominant SIF. Hereon, this paper refers to the Mode I K_I as SIF, unless otherwise specified.

3.2 Crack-tip plasticity confirmation

To validate the applicability of Equation 1, the formation of crack-tip plasticity was examined. As the plastic zone at the crack tip becomes larger, the elastic analysis becomes more inaccurate (Anderson 2005). Hence, it would be desirable to confirm a minimal area of plasticity at the crack tip. Furthermore, the normal stress near the crack tip varies with $1/\sqrt{r}$, while the displacement near the crack tip varies with \sqrt{r} . In this section, it is demonstrated that all these conditions were met by the analytical model.

Figure 5a shows the relationship between the normal stress σ_{yy} in front of the crack tip (+x direction) and the distance from the crack tip for the unpaved 12 mm model with an 8 mm deep crack. In this section, the local coordinate system shown in Figure 5a is used. Taking the stress field for Mode I and the triaxial state due to plane strain, and substituting these equations to the von Mises yield criterion gives a normal stress at yield of $\sigma_{yy} = 887.5$ MPa for SM490YB, as outlined as well by Hattori et al. (2020). This means a normal stress above this value belongs to the plastic zone. As shown in Figure 5a, the plastic zone was formed up to about 0.09 mm from the crack tip. With respect to the crack dimensions (in this case, $a = 8$ mm; $b = 53.35$ mm), the plastic zone was relatively small. Furthermore, the singularity zone was confirmed to form up to 0.15 mm in front of the crack tip, as shown by the slope -1/2 on the logarithmic scale which corresponds to the normal stress varying with $1/\sqrt{r}$.

Figure 5b shows the relationship between the displacement perpendicular to the crack u_y of the crack-face node and its distance from the crack tip (-x direction). As shown, a singularity zone was formed up to 0.30 mm behind the crack tip. This zone was determined from the intersection with the line of slope 1/2 in the logarithmic scale, which corresponds to the displacement u_y varying with \sqrt{r} .

3.3 Stress intensity factor extrapolation

As the SIF is valid only to the crack-tip displacement field, the SIF should be taken only from the singularity zone. As shown in Figure 5b, the singularity zone for the 8 mm deep crack model reached up to 0.30 mm from the crack tip. For smaller cracks, the singularity zone had a longer range with the 2 mm deep crack model having the longest range of 1.20 mm. However, to maintain consistency across various models, the maximum range of 0.30 mm was considered for the calculation of the SIF.

In convergence studies by Anderson (2005), it was found that for the displacement-matching approach, the SIF should be extrapolated from crack-face nodes that are relatively close enough to the crack tip (i.e. singularity zone). However, Anderson (2005) stated that the inclusion of the first few nodes introduced some error with respect to the theoretical value. Therefore, in the current study, while taking the maximum range to be 0.30 mm from the crack tip, the range for SIF extrapolation was further narrowed by examining the consistency of the linearity between the argument of the limit in Equation 1 and the distance from the crack tip. Taking the range 0.125 to 0.30 mm resulted in a coefficient of determination R^2 of at least 0.96 for all sets of models including different pavement configurations. It should be noted that the closer the value of R^2 to 1.0, the greater the consistency of linearity is. Therefore, using the displacement-matching approach (Equation 1), the SIF was extrapolated from the range 0.125 to 0.30 mm from the crack tip.

4 ANALYTICAL RESULTS AND DISCUSSION

4.1 Effect of SFRC overlay thickness

Figure 6 shows the relationship between the SIF and crack depth for different thicknesses of SFRC pavement. It can be observed that the SIF increased across the crack depths except in the case of the unpaved condition wherein the SIF peaks at the 6 mm deep crack. This can be explained by the changing of the bending stress direction at the neutral axis in the deck plate. On unpaved models,

the neutral axis was located 5.9 mm from the bottom of the deck plate, as demonstrated by stress analysis on uncracked models. The neutral axis shifted to 8.8, 10.1, and 10.2 mm from the bottom of the deck plate for the 25, 50, and 75 mm thick SFRC pavement models respectively.

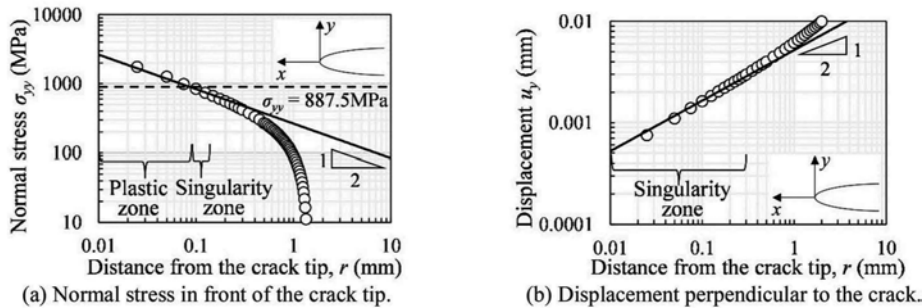


Figure 5. Crack-tip plasticity confirmation for the unpaved 12 mm thick deck plate model with an 8 mm deep crack.

In all cases of the uncracked models, the deck plate was in negative bending at the weld root location; hence, the weld root was in compression. However, it is assumed that there are residual tensile stresses resulting in net tension, which causes the crack to initiate.

Figure 7a shows the relationship between the SIF and SFRC pavement thickness for various crack depths. It should be noted that this figure shows the same data as Figure 6 but was reorganized to capture the influence of SFRC pavement thickness better. The other crack depths were removed as well for clarity. As the pavement thickness was increased, the SIF decreased. This is an expected behavior; since the SFRC pavement increased the rigidity of the deck system. Compared to the unpaved condition, the 50 mm SFRC pavement improved the SIF by at least 83% across the crack depths, while the 75 mm SFRC pavement improved the SIF by at least 88%. The Fatigue Design Recommendations for Steel Structures (JSSC 2012) states that the mean design threshold SIF, ΔK_{th} is equal to $76 \text{ N/mm}^{3/2}$ for the crack propagation design curve. A SIF below this threshold value means the crack is not likely to propagate. As shown in Figure 6, the SIF is below the threshold for crack depths of 2 to 3 mm ($\text{SIF} = 68 \text{ to } 73 \text{ N/mm}^{3/2}$). While the SIF for the model with crack depths 4 to 8 mm was above the threshold ($\text{SIF} = 77 \text{ to } 89 \text{ N/mm}^{3/2}$), it was still close; hence, theoretically, the crack may propagate, albeit very slowly. As for practical purposes though, it may be considered that the crack is not likely to propagate, as demonstrated by previous fatigue tests for 75 mm thick SFRC pavement reinforcement (Murakoshi et al. 2019). The previous fatigue testing showed that the remaining cracks (crack depth: 5.9 to 10.8 mm) did not propagate at 10 million cycles of 50 kN load after reinforcing the OSD specimen with SFRC pavement. The same study concluded that even for 50 mm thick SFRC pavement reinforcement (Analysis SIF for 8 mm deep crack = $128 \text{ N/mm}^{3/2}$), the cracks did not propagate. This further supports the argument that the propagation may be very slow for the 75 mm thick SFRC pavement reinforcement, and for practical purposes, sufficient to suppress the crack propagation.

4.2 Effect of adhesive debonding

Figure 7a shows the SIF of the base case wherein the Young's modulus of adhesive was set to full capacity. Figure 7b, on the other hand, shows the relationship between the SIF and SFRC pavement thickness of the case wherein the adhesive has debonded. The SIF of the debonding case increased by 60 to 87% across various crack depths and SFRC thicknesses. In particular, the SIF of the model with the 8 mm deep crack and 75 mm thick SFRC pavement increased from 89 to $153 \text{ N/mm}^{3/2}$, which is 101% higher than the threshold value ΔK_{th} . It is also above the SIF of the 50 mm thick SFRC pavement reinforcement (Analysis SIF = $128 \text{ N/mm}^{3/2}$) which did not show crack propagation in actual fatigue testing (Murakoshi et al. 2019). Therefore, there is no assurance in maintaining the crack suppression capacity of the 75 mm thick SFRC pavement if adhesive debonding occurs.

4.3 Effect of asphalt overlay rigidity

Figure 8a shows the relationship between SIF and asphalt rigidity for a 12 mm thick deck plate with a 75 mm thick asphalt overlay. The SIF was highest during summer and lowest during winter, which is an expected behavior based on stiffness across the seasons. For example, the SIF of a 75 mm thick asphalt on a 12 mm thick deck plate was at most 437 N/mm^{3/2} across crack depths during summer, at most 296 N/mm^{3/2} during spring, and at most 183 N/mm^{3/2} during winter, which are 475%, 290%, and 141% higher than the threshold ΔK_{th} respectively.

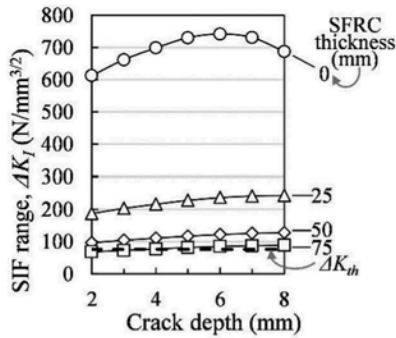


Figure 6. Relationship of SIF and crack depth for the 12 mm thick deck plate reinforced with SFRC pavement.

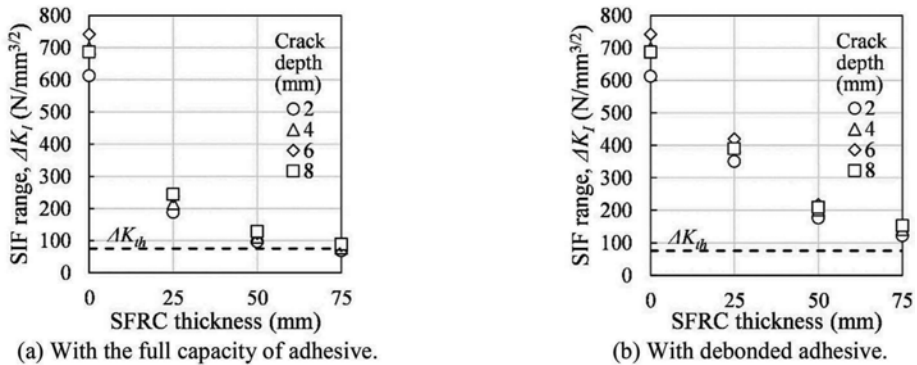


Figure 7. Relationship of SIF and SFRC pavement thickness across crack depths for 12 mm thick deck plate.

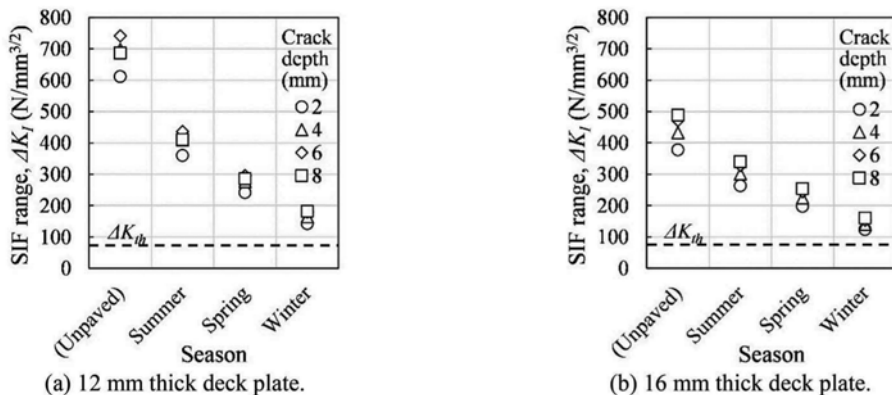


Figure 8. Relationship of SIF and asphalt rigidity for deck plate with 75 mm thick asphalt overlay.

Figure 8b shows the relationship between SIF and asphalt rigidity for a 16 mm thick deck plate with a 75 mm thick asphalt overlay. The SIF was at most $340 \text{ N/mm}^{3/2}$ during summer, at most $254 \text{ N/mm}^{3/2}$ during spring, and at most $161 \text{ N/mm}^{3/2}$ during winter, which are 347%, 234%, and 112% higher than the threshold ΔK_{th} . Hence, the SIF of the 75 mm thick asphalt in either the 12 or 16 mm thick deck plate during winter was still higher than that of the SFRC with debonded adhesive. In addition, this contribution from asphalt cannot be sustained during higher temperatures in other seasons.

5 CONCLUSIONS

Several finite element models were developed to analyze the crack suppression effect of SFRC pavement on a simply supported partial OSD specimen. Semi-elliptical cracks with an aspect ratio of 0.15 were introduced at the root of the rib-to-deck weld. A relatively small plastic zone, as well as a singularity zone, was confirmed at the crack tip, validating the use of the SIF for characterizing the stress condition. The SIF was then obtained from crack-face nodes 0.125 to 0.30 mm away from the crack tip using the displacement-matching method. The main results are enumerated as follows.

- (1) Reinforcing the OSD specimen with 75 mm thick SFRC pavement decreased the SIF to a level below the threshold ΔK_{th} for crack depths 2 to 3 mm, theoretically confirming that the crack is not likely to propagate. For crack depths of 4 to 8 mm, on the other hand, the SIF was still higher than the threshold, albeit close. Although theoretically the crack is likely to slowly propagate, previous fatigue testing supports that this is not the case. Therefore, for practical purposes, it can be considered that the crack still may not propagate.
- (2) The debonding of the adhesive that attached the SFRC pavement to the deck plate led to a 60 to 87% increase in the SIF across various crack depths and SFRC pavement configurations, making the SIF of the 75 mm thick SFRC pavement model significantly higher than the threshold value ΔK_{th} . Therefore, when the debonding of the adhesive occurs, a crack with any depth from 2 to 8 mm is theoretically likely to propagate.
- (3) The common deck detail of using an asphalt overlay helped in decreasing the SIF and was most effective at cold temperatures. However, even if a 75 mm thick asphalt overlay was used on either a 12 mm or 16 mm thick deck plate, the use of a debonded 75 mm thick SFRC pavement on a 12 mm thick deck plate still resulted in a lower SIF. Moreover, this contribution of asphalt weakens during higher temperatures, which makes it unreliable for crack suppression.

REFERENCES

- Anderson, T.L. 2005. *Fracture mechanics: Fundamentals and applications*. Florida: Taylor & Francis.
- Hattori, M., Tateishi, K., Takeshi, H. & Shimizu, M. 2020. Countermeasure effect of UHPFRC on fatigue cracks propagating from U-rib welds of orthotropic steel decks. *Journal of JSCE A1* 76(3): 542–559. (in Japanese)
- Inokuchi S., Uchida D., Kawabata A., Tamakoshi T. 2008. Influence of asphalt pavement failure on local stress of orthotropic steel decks. *Journal of Steel Construction Engineering* 15(59): 75–86. (in Japanese)
- Japan Road Association. 2017. *Japanese specifications for highway bridges*. (in Japanese)
- Japan Society of Civil Engineering. 2010. Fatigue of orthotropic steel bridge deck. *Steel Structures* 19. (in Japanese)
- Japan Society of Steel Construction. 2012. *Fatigue design recommendations for steel structures*. (in Japanese).
- Ji, B. Liu, R. Chen C., Maeno, H. & Xiongfei, C. 2013. Evaluation on root-deck fatigue of orthotropic steel bridge deck. *Journal of Constructional Steel Research* 90: 174–183.
- Murakoshi, J., Mori T., Haba S., Ono S., Sato A. & Takahashi, M. 2019. Retrofit effect of SFRC overlay on fatigue durability of orthotropic steel decks with cracks extending to deck plate. *Journal of JSCE A1* 75(2): 194–205. (in Japanese)
- Murakoshi, J., Yanadori, N., Ishizawa, T., Toyama, N. & Kosuge, T. 2012. Study on effect of deck thickness of orthotropic steel deck on fatigue durability (in Japanese). *Journal of Steel Construction Engineering* 19(75): 55–65. (in Japanese)
- Nagy, W., van Bogaert, P. & de Backer, H. 2015. LEM based fatigue design for welded connections in orthotropic steel bridge decks. *Procedia Engineering* 133: 758–769.
- Uaje, M.J.B. & Murakoshi, J. 2022. Numerical study on SFRC overlay for root-deck fatigue in orthotropic steel deck. *Proceedings of Constructional Steel* 30:314–322.

Refined perception and management of ring-wise deformation information for shield tunnels based on point cloud deep learning and BIM

Wei Lin, Xiongyao Xie, Biao Zhou & Pan Li
Tongji University, Shanghai, China

Cheng Wang
State Grid Shanghai Municipal Electric Power Company, Shanghai, China

ABSTRACT: The performance maintenance of shield tunnels is of more and more significance with a great number of shield tunnels being put into service. The perception of deformation is an essential part of shield tunnel performance assessment because of the correlation between deformation and all kinds of affecting factors during service. While due to the nature of shield tunnels, the perception of deformation based on the traditional method requires costly effort. For the refined perception of ring-wise deformation, which includes segment rotation and segment dislocation, an automated workflow for processing and managing the point cloud of tunnel lining has been proposed based on deep learning and BIM. An end-to-end deep learning model based on PointNet++ has been trained for the segmentation of ring-wise shield tunnel point clouds. With the proposed data normalization and augmentation method, the accuracy of the deep learning model can achieve promising results. Based on the ring-wise deformation pattern, a robust and efficient optimization algorithm for deformation extraction has been designed. The fusion of accurate data from point clouds and semantic information from BIM models enables the automatic calculation of all types of ring-wise deformation. The proposed methods and workflow provide novel perspectives of digitalization in the life-cycle maintenance for shield tunnels.

1 INSTRUCTION

The structural performance of shield tunnels is influenced by complex geotechnical and structural evolution during the life cycle, resulting in the lasting structural deformation process since as-built (Xie *et al.* 2021, Chang *et al.* 2022). The shield tunnel is a type of prefabricated assembled and long linear underground structure, constructed by joining lots of segments and rings. Due to the structural nature of shield tunnels, the deformation can be depicted as longitudinal deformation and transverse deformation (Yu *et al.* 2019). For each ring of shield tunnels, transverse deformation is the main concern when assessing life-cycle structural performance (Yang *et al.* 2018). Given the significance of ring-wise transverse deformation, varieties of methods and corresponding instruments have been proposed for data acquisition, such as total station, laser convergence gauge, tilt sensor (Chang *et al.* 2022), and optical-fiber sensors (Wang *et al.* 2019). However, the transverse deformation derived by the above methods is incomplete. The ring-wise transverse deformation of shield tunnels includes convergence, dislocation, and rotation (Dong *et al.* 2020). The above methods are designed for one of the deformation patterns and usually rely on instruments installed on the tunnel lining. Hence the measured transverse deformations are isolated between different deformation behaviors and are distributed at limited locations, which will result in poor information for life-cycle maintenance.

The development of laser scanning technology enables the efficient acquisition of large point cloud data during the life cycle of shield tunnels, in which detailed three-dimensional space information is included (Xie and Lu 2017, Lin *et al.* 2022). The advantages of laser

scanning also include the non-contact and non-destructive data acquisition process (Menendez *et al.* 2018). The segmentation of point cloud data, however, remains to be inefficient and labor-intensive (Yi *et al.* 2019). The promising feasibility of applying DL (deep learning) in the segmentation of shield tunnel point clouds has been shown (Zhang *et al.* 2022). While the application cases of DL in the shield tunnel point clouds are usually component-based systems rather than end-to-end models. In contrast, end-to-end models have the advantage of excellent performance, simplicity, and optimization (Li *et al.* 2022).

Lack of semantic information is another main challenge for interpreting and managing point clouds in the life cycle of infrastructure (Soilán *et al.* 2021). The deformation information between segments is implicitly included in the point cloud data. Consequently, it is difficult to extract deformation information without point-wise semantic information. The lack of semantic information will also result in the low re-usability of point cloud data in historical deformation analysis (Krijnen and Beetz 2017). The appearance of BIM enables information management and data exchange in the life-cycle of shield tunnels (Hegemann *et al.* 2020). While most researches concerning BIM in the field of shield tunnels focus on the design and construction phase (Ninic *et al.* 2021). The registration of geometric and semantic information for point clouds and BIM models is of obvious significance for infrastructure life-cycle data management (Shu *et al.* 2022), which has not been completely solved yet.

Given the challenges in the perception and management of deformation information for shield tunnels, this paper aims to advance digitalization in the life-cycle maintenance of shield tunnels utilizing DL and BIM. Point cloud datasets were labeled and the corresponding data processing algorithm was proposed. The deformation extraction method was then proposed based on a two-stage optimization algorithm for the semantic-rich point clouds. At last, an integrated and automatic workflow based on the proposed methods and BIM was proposed for the refined perception and management of ring-wise deformation of shield tunnels.

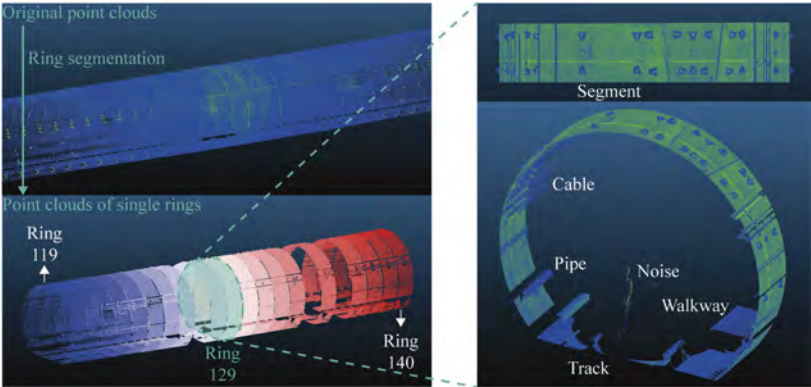


Figure 1. Ring segmentation of original point clouds.

2 SEMANTIC SEGMENTATION OF POINT CLOUDS

2.1 Point cloud scanning and labeling

The terrestrial laser scanning was performed in a station interval of a metro line, which consists of two parallel circle shield tunnels, namely upline and downline, from Wuxi. The point clouds were scanned by a Leica ScanStation C10, of which the modeled surface precision is within 2 mm. The coordinate systems of point clouds scanned from different scanning stations can be aligned by mutual targets. The point clouds of each shield tunnel ring can be segmented from the original point clouds, taking point clouds of upline between Ring 119 and Ring 140 for example, as shown in Figure 1. The point clouds of single rings contain the points generated by varieties of objects, such as segments, tracks, walkways, pipes, and cables, as also shown in Figure 1.

For point clouds of single rings, point-wise semantic labeling has been carried out. The labeled point clouds shown in Figure 2 can be used as datasets for DL training and testing. Given the assembled structural nature of shield tunnels, the segmentation of different segments is of great significance for deformation perception. Hence, point clouds for different segments are labeled separately. There are many utilities in the shield tunnels, which will bring disturbance in the point clouds. For the perception of structural deformation, segments are the actual concerned objects. One task of DL is to distinguish the points generated by other objects so that these undesired points can be removed. So the points of other different objects are labeled as the same, i.e., undesired points.

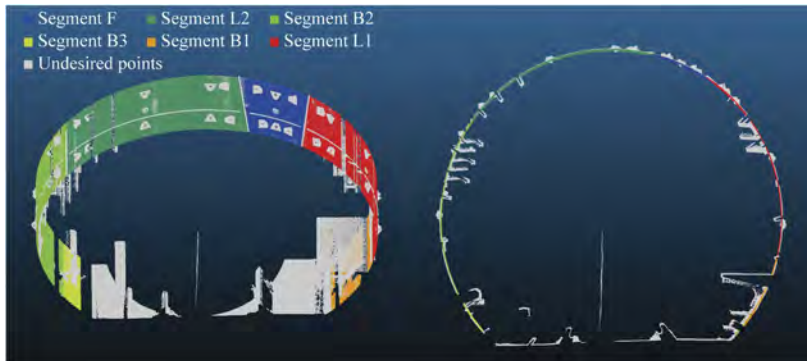


Figure 2. The labeled ring-wise point cloud.

2.2 Data normalization and augmentation

Data labeling is time-consuming and labor-intensive work. The number of valid datasets for DL may be very limited. Data augmentation is an important technique to reduce overfitting and improve DL performance, of which the outstanding examples include the models named AdaPC, PointAugment, and PointMixup. One feasible and economic way for data augmentation is to generate new datasets by rotating the points of real datasets. It's noted that unreasonable augmentation methods will result in invalid datasets, even harmful. For ring-wise point clouds of shield tunnels, a data augmentation method considering global and local rotation is proposed, as shown in Figure 3. The coordinate systems of point clouds are not specified when scanning. Hence, for the easier design of data processing and better performance of the DL model, the data should be normalized before the augmentation procedure. The point clouds of rings will be transformed into a unified Cartesian coordinate system for understandable spatial description and normative coordinate operation. In the unified Cartesian coordinate system, the y-axis denotes the vertically upward direction, the z-axis denotes the tunneling direction in the horizontal plane, and the x-axis is determined by the right-hand rule. The origin is the barycenter of the tunnel ring. For the chosen point cloud, the unified coordinate system is uniquely associated with the tunneling direction. The tunneling direction (denoted as d in Figure 3) can be represented by the vector of the cylindrical axis from the shape fitting of the point cloud.

After the data normalization, the data augmentation can be implemented by a unified data processing program. According to the design of shield tunnels, the slope and alignment of rings will differ. In the step of global rotation, the points will be rotated at random degrees around the x-axis and the y-axis respectively to generate different slopes and alignments. Local rotation is proposed to increase the diversity in the positions of non-structural objects. The points of non-structural objects will be rotated at random degrees around the vector of tunneling direction. The proposed method for data normalization and augmentation ensures highlighting the local features rather than the nonsense global features of the point clouds in the DL models.

2.3 DL model training and testing

The architecture of the end-to-end point cloud DL network adopted in this paper is PointNet ++ (Qi *et al.* 2017), which is popular and influential for point cloud understanding (Agapaki

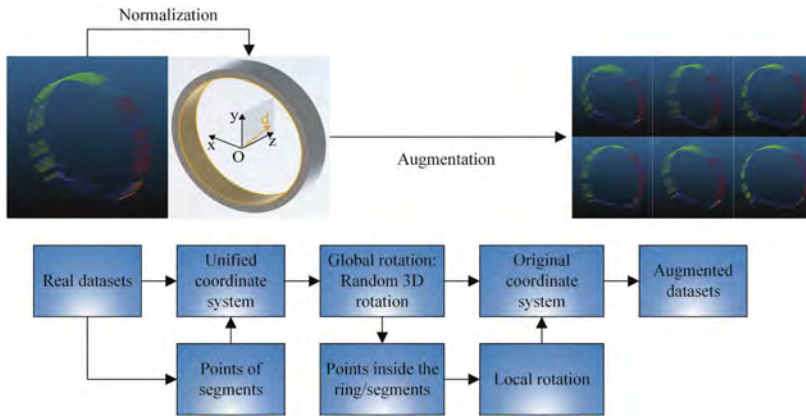


Figure 3. The workflow of the proposed data normalization and augmentation method.

Table 1. The number of points in the datasets.

Object	F	L2	B2	B3	B1	L1	Other objects
Number	3,136,410	7,498,800	3,693,890	925,909	3,389,710	8,618,730	11,885,100

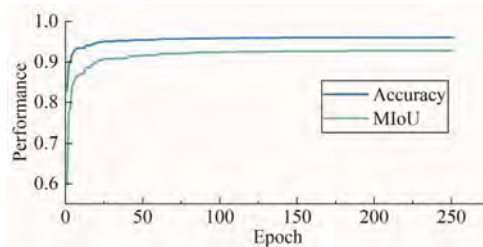


Figure 4. The segmentation performance of the trained model.

and Brilakis 2020). The end-to-end point cloud DL model allows inputting point clouds directly into the network without unrolling or other extra data processing. The multi-scale grouping algorithm is adopted in the DL model.

The real datasets and the augmented datasets will be used together for the training and testing of DL models. Scanned point clouds were labeled as the real datasets and then were augmented. As shown in Table 1, the point clouds of 2193 rings, including 39,148,549 points, were prepared for the model training and testing. Given the 80:20 rule, 80% of the datasets are utilized for model training and the remaining 20% of the datasets are leveraged for model testing. The optimized network architecture parameters were determined by comparing preliminary tests. The accuracy and MIoU (mean intersection over union) are adopted to evaluate the segmentation performance of the DL model, as shown in Figure 4. The best accuracy and MIoU on testing datasets reached 96.0% and 92.8% respectively. Promising segmentation performance was achieved, which is the basis for deformation perception.

3 PERCEPTION OF RING-WISE DEFORMATION

3.1 Ring-wise deformation pattern

The ring-wise deformation patterns of shield tunnels include rotation, dislocation, and convergence. Rotation denotes the relative rotation between two adjacent segments. Dislocation

denotes the relative dislocation along the radius direction. Besides, the segments will deform under the structural effect of axial force and moment. Convergence denotes the comprehensive influence of the three factors on the actual diameters of the rings, which usually occurs in the form of ovalization (Nuttens *et al.* 2014). The interpretation of numerical simulation and model experiments demonstrates that the rotation and dislocation, i.e., the deformation patterns happening at joints, constitute the main part of ring-wise deformation (Wang *et al.* 2021). Hence, the convergence is mainly contributed by rotation and dislocation, which can be extracted from point clouds.

A ring-wise deformation pattern for shield tunnels is proposed considering the rotation, dislocation, and consistency of segments, as shown in Figure 5. Taking the six-segment ring for example, the deformation is determined by 12 parameters of the rotation and dislocation, which are constrained by the consistency of the segments. The proposed ring-wise deformation pattern allows the representation of arbitrary ovalization or convergence induced by rotation and dislocation.

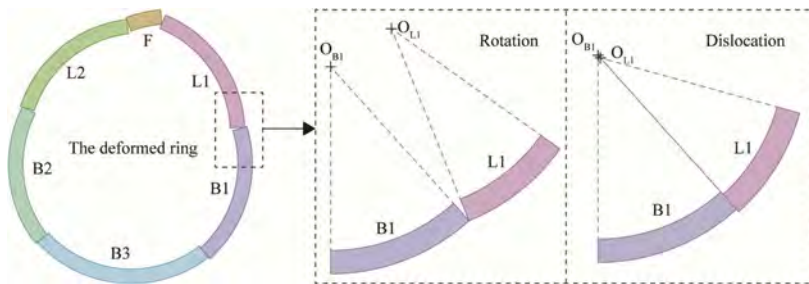


Figure 5. The ring-wise deformation pattern of shield tunnels.

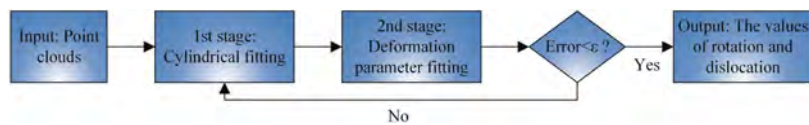


Figure 6. The workflow of the two-stage optimization algorithm for deformation extraction.

Table 2. The performance of the deformation extraction algorithm for the synthetic dataset.

Segment	F	L2	B2	B3	B1	L1	Maximum error
Ground truth of rotation/ $^{\circ}$	2.00	-0.30	0.40	0.20	-1.00	1.00	/
Extraction result of rotation/ $^{\circ}$	2.00	-0.31	0.40	0.20	-1.00	1.01	0.01
Ground truth of dislocation/mm	0.30	7.90	0.00	2.00	8.00	5.00	/
Extraction result of dislocation/mm	0.15	7.71	0.00	2.00	8.00	4.82	0.19

3.2 Deformation extraction algorithm

The high-resolution point clouds allow comprehensive descriptions of the deformation patterns. The point clouds with semantic information enable the automatic process of deformation extraction. The rotation and dislocation of each segment can be determined by the parameter fitting. Powered by the DL model and the deformation extraction method, an automatic perception method of ring-wise deformation is proposed. The workflow of the proposed algorithm for ring-wise deformation extraction is illustrated in Figure 6. A two-stage optimization method based on least squares is proposed for the fitting of 12 deformation parameters. The iteration of two-stage optimization is designed in the algorithm to ensure the overall accuracy of deformation extraction. Synthetic datasets generated by deformed ring

models with the designed deformation parameters were used to validate the performance of the deformation extraction. The performance of the proposed algorithm shows satisfying results, of which a case is listed in Table 2.

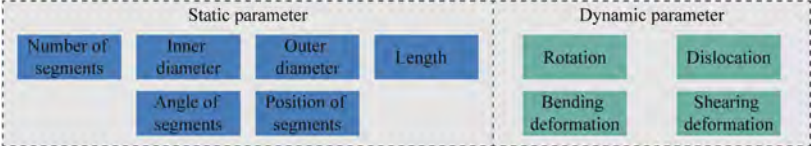


Figure 7. The parameters for modeling the ring-wise shield tunnels.

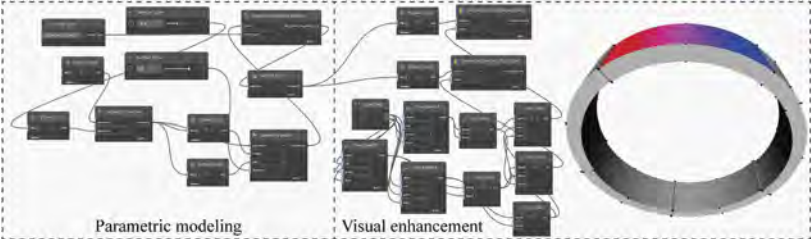


Figure 8. The codes and implemented results of parametric modeling and visual enhancement.

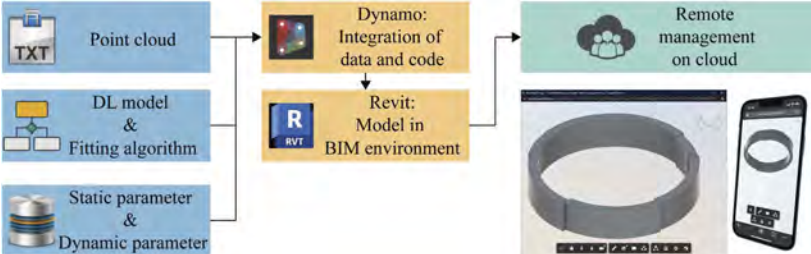


Figure 9. The management framework for data and information.

4 VISUALIZATION AND MANAGEMENT OF LIFE-CYCLE DEFORMATION INFORMATION

4.1 Parametric modeling of deformed shield tunnel rings

Due to the long-term behavior of life-cycle deformation, the models in the design and construction phase are not adequate to reflect the up-to-date deformation of shield tunnel rings. A parametric modeling method considering the rotation and dislocation of segments is proposed based on Revit and Dynamo. The demanded parameters for modeling the ring-wise shield tunnels are listed in Figure 7. The parameters can be classified into two types, namely static parameters and dynamic parameters. Static parameters reflect the inherent spatial properties of rings during the life cycle. While dynamic parameters reflect the up-to-date deformation information. For more elaborated models, the deformation behavior of the beam effect for segments can be further considered.

The proposed DL model and deformation extraction method can be coded as Python scripts and implemented in Dynamo. As a result, the proposed method can be embedded into the BIM environment, enhancing the level of automation and integration. Revit and Dynamo are also utilized to parametrically create and update BIM models of shield tunnel rings. Then, the ring-wise models can be defined automatically by static and dynamic parameters. The values of deformation are smaller than the size of shield tunnel rings, which brings difficulty

in observation. A visual enhancement algorithm was also proposed to explicitly display the deformation by RGB colors in the BIM environment. The proposed codes and implemented results in Revit are shown in Figure 8.

4.2 Management framework of point clouds and deformation information

Scanning data and deformation information are valuable digital assets in the life cycle of shield tunnels. A management framework combined with the BIM applications for data and information was designed to enhance data security and reusability, as shown in Figure 9. The semantic information is managed in the designed database. In the database, the historical deformation information is also stored so that the historical analysis will be convenient. The data and codes are integrated to model the deformed shield tunnel rings in Revit by Dynamo. The models can be uploaded to the cloud for remote management of shield tunnel performance.

5 CONCLUSIONS AND DISCUSSION

The data normalization and augmentation methods for ring-wise point clouds of shield tunnels are proposed to avoid the expensive effort of dataset scanning and labeling. Data normalization and augmentation will help reduce the demanded amount of scanning datasets. The segmentation performance of the end-to-end DL model trained by normalized and augmented datasets achieves promising results. The contribution of end-to-end DL in the workflow of deformation perception for the life-cycle maintenance of shield tunnels is illustrated. While the existing network architectures are not perfect and remain to be improved according to the characteristics of shield tunnel point clouds.

The ring-wise deformation pattern of shield tunnels considering the rotation and dislocation is analyzed. Based on the semantic-rich point clouds provided by the DL model, the deformation of each segment can be extracted based on the proposed two-stage optimization algorithm, which shows satisfying accuracy. The deformation behavior of the beam effect for segments can be further considered and extracted from point clouds. Despite the limitation, the proposed perception method of deformation is believed to be a promising supplement to existing measurement methods.

The data-driven parametric modeling is implemented by Dynamo with dynamic and static parameters as the input. The information supporting the life-cycle maintenance decision-making can be displayed in the models of deformed rings. In addition, a visual enhancement algorithm is proposed for the plain understanding of shield tunnel performance. The management framework of data and information ensures the level of automation in the workflow. For extension, the path for point clouds and deformation information to be expressed in the IFC framework should be further studied, for the unified information exchange.

The main interest of this paper is to explore the potential value of multi-discipline techniques in the life-cycle maintenance of shield tunnels. The practical application demonstrates that the life-cycle maintenance benefits from the digitalization of techniques adopted. Point clouds, DL, and BIM are believed to be the bases of the digital twin vision.

ACKNOWLEDGEMENT

This work was financially supported by National Natural Science Foundation of China (grant numbers 51978431 and 52038008), Shanghai Science and Technology Development Fund (grant number 20DZ1202004), and State Grid Shanghai Municipal Electric Power Company Science and Technology Project (grant number 52090W220001).

REFERENCES

Agapaki, E. and Brilakis, I., 2020. CLOI-NET: Class segmentation of industrial facilities' point cloud datasets. *Advanced Engineering Informatics*, 45, 101121.

- Chang, J., Huang, H., Zhang, D., Wu, H., and Yan, J., 2022. Transverse deformational behaviors of segmental lining during shield tunneling: A case study. *Structural Control and Health Monitoring*, 29, e3097.
- Dong, L., Yang, Z., Wang, Z., Ding, Y., and Qi, W., 2020. Study on internal force of tunnel segment by considering the influence of joints. *Advances in Materials Science and Engineering*, 2020, 1020732.
- Hegemann, F., Stascheit, J., and Maidl, U., 2020. As-built documentation of segmental lining rings in the BIM representation of tunnels. *Tunnelling and Underground Space Technology*, 106, 103582.
- Krijnen, T. and Beetz, J., 2017. An IFC schema extension and binary serialization format to efficiently integrate point cloud data into building models. *Advanced Engineering Informatics*, 33, 473–490.
- Li, L., Song, N., Sun, F., Liu, X., Wang, R., Yao, J., and Cao, S., 2022. Point2Roof: End-to-end 3D building roof modeling from airborne LiDAR point clouds. *ISPRS Journal of Photogrammetry and Remote Sensing*, 193, 17–28.
- Lin, W., Li, P., and Xie, X., 2022. A novel detection and assessment method for operational defects of pipe jacking tunnel based on 3D longitudinal deformation curve: A case study. *Sensors*, 22, 7648.
- Menendez, E., Victores, J.G., Montero, R., Martínez, S., and Balaguer, C., 2018. Tunnel structural inspection and assessment using an autonomous robotic system. *Automation in Construction*, 87, 117–126.
- Ninic, J., Alsahly, A., Vonthron, A., Bui, H.G., Koch, C., König, M., and Meschke, G., 2021. From digital models to numerical analysis for mechanised tunnelling: A fully automated design-through-analysis workflow. *Tunnelling and Underground Space Technology*, (107), 103622.
- Nuttens, T., Stal, C., De Backer, H., Schotte, K., Van Bogaert, P., and De Wulf, A., 2014. Methodology for the ovalization monitoring of newly built circular train tunnels based on laser scanning: Liefkenshoek Rail Link (Belgium). *Automation in Construction*, 43, 1–9.
- Qi, C.R., Yi, L., Su, H., and Guibas, L.J., 2017. PointNet++: Deep hierarchical feature learning on point sets in a metric space. In: *NIPS'17: Proceedings of the 31st International Conference on Neural Information Processing Systems*. 5105–5114.
- Shu, J., Zhang, C., Yu, K., Shoosharian, M., and Liang, P., 2022. IFC-based semantic modeling of damaged RC beams using 3D point clouds. *Structural Concrete*, 1–22.
- Soilán, M., Nóvoa, A., Sánchez-Rodríguez, A., Justo, A., and Riveiro, B., 2021. Fully automated methodology for the delineation of railway lanes and the generation of IFC alignment models using 3D point cloud data. *Automation in Construction*, 126, 103684.
- Wang, F., Shi, J., Huang, H., Zhang, D., and Liu, D., 2021. A horizontal convergence monitoring method based on wireless tilt sensors for shield tunnels with straight joints. *Structure and Infrastructure Engineering*, 17 (9), 1194–1209.
- Wang, T., Shi, B., and Zhu, Y., 2019. Structural monitoring and performance assessment of shield tunnels during the operation period, based on distributed optical-fiber sensors. *Symmetry*, 11, 940.
- Xie, X. and Lu, X., 2017. Development of a 3D modeling algorithm for tunnel deformation monitoring based on terrestrial laser scanning. *Underground Space*, 2, 16–29.
- Xie, X., Tian, H., Zhou, B., and Li, K., 2021. The life-cycle development and cause analysis of large diameter shield tunnel convergence in soft soil area. *Tunnelling and Underground Space Technology*, 107, 103680.
- Yang, Y., Zhou, B., Xie, X., and Liu, C., 2018. Characteristics and causes of cracking and damage of shield tunnel segmented lining in construction stage—a case study in Shanghai soft soil. *European Journal of Environmental and Civil Engineering*, 22, s213–s227.
- Yi, C., Lu, D., Xie, Q., Liu, S., Li, H., Wei, M., and Wang, J., 2019. Hierarchical tunnel modeling from 3D raw LiDAR point cloud. *Computer-Aided Design*, (114), 143–154.
- Yu, H., Cai, C., Bobet, A., Zhao, X., and Yuan, Y., 2019. Analytical solution for longitudinal bending stiffness of shield tunnels. *Tunnelling and Underground Space Technology*, 83, 27–34.
- Zhang, Z., Ji, A., Wang, K., and Zhang, L., 2022. UnrollingNet: An attention-based deep learning approach for the segmentation of large-scale point clouds of tunnels. *Automation in Construction*, 142, 104456.

Structural model updating of an existing concrete bridge based on load testing and monitoring data

A. Agredo Chávez, J. Gonzalez-Libreros, L. Elfgren & G. Sas
Luleå University of Technology, Luleå, Sweden

L. Capacci & F. Biondini
Politecnico di Milano, Milan, Italy

ABSTRACT: The backbone of European infrastructure was built after the end of the second World War and has reached, or is near to, the end of its nominal design life. This issue urges the development of structural assessment procedures that can provide infrastructure managers the information to make decisions for repairing, upgrading, or replacement. In this paper, a methodology based on load testing and Structural Health Monitoring (SHM) for the assessment of a 65-year-old prestressed concrete bridge located in Northern Sweden is presented. The retrieved data is used to develop and calibrate structural models with different levels of data completeness. The SHM procedure includes the evaluation of material properties by diagnostics, definition of the layout and installation of the instrumentation, test execution, and data analysis. A preliminary structural model is developed based only on the original design parameters, and it is sequentially updated with monitoring data retrieved during a performed proof loading test of the bridge.

1 INTRODUCTION

The existing infrastructure and built environment represent approximately 50% of the national wealth in most countries within Europe (Plos et al. 2017). The economic impact of aging and deterioration processes on all such systems is exceptionally high (Biondini & Frangopol 2016, Bagge 2020). Therefore, the need of an adequate structural assessment procedure is fundamental when managing bridges' integrity along their life cycle and their impact in infrastructures networks, where a high level of decision-making is required for effective management of resilient lifelines (Capacci et al. 2022). Hence, it is necessary to go beyond the traditional visual inspection to properly assess the necessary intervention on the structure (Casas & Gómez 2013). To cope with the need of retrieving timely and continuous data to assess the structure, Structural Health Monitoring (SHM) employing non-destructive tests has risen as a promising technique for damage assessment, structural evaluation, structural model updating and model verification (Sanayei et al. 2015). Numerical methods for structural analysis provide a solid groundwork to predict the structural behavior under different loading conditions, nevertheless, when these predictions are compared with experimental data, it is frequently found that the degree of correlation is not satisfactory to allow the further use of the model with confidence (Mottershead et al. 2011). One of the approaches to reduce this discrepancy is to modify the modelling assumptions using experimental data to overcome model parameter errors to generate an improved numerical model. This validated numerical model is then used in further predictions for alternative loading arrangements and distinct structural configurations to complete an adequate structural assessment (Mottershead 1993).

Thus, seeking to define an innovative approach for bridge management, a series of on-site evaluation and testing on the integrity of a 65-year-old prestressed concrete bridge (see Figure 1)

were carried out. The Kalix bridge was a prestressed concrete box girder bridge located in Northern Sweden, and it was constructed by the balanced cantilever method.



Figure 1. The old Kalix bridge in the foreground with foundations of the new bridge behind.

Considering it had reached the end of its lifetime, the bridge is currently being dismantled (as of January 2023) after the construction of a new bridge. The new structure is aimed to carry the increase of traffic loads in the area and both bearing capacity and geometry have been upgraded accordingly (Gonzalez-Libreros et al. 2022). The retrieved data will be then used to calibrate a structural model where the estimation of material properties by means of several core extraction and a proof loading test were performed with the aim of evaluating the structural response of the bridge under serviceability loading conditions.

2 KALIX BRIDGE

2.1 Description of the bridge

The Kalix bridge was a five (5) span prestressed concrete bridge, with total length of 283.6 m and 13 m wide. The structure is a single-box-girder with variable cross-section, as shown in Figure 2. The bridge shows complete symmetry (geometry and supports) at midspan, where the bridge halves are joined by a pendulum bearing as described in section 2.3. The bridge was dimensioned according to the 1955 Swedish provisional regulations and the prestressing system was ruled by DIN 4227 (Deutsche Norm Vorgespannt), obeying the German standard code for this bridge typology, initially patented and by Dyckerhoff & Widmann AG (Dinges 2009).

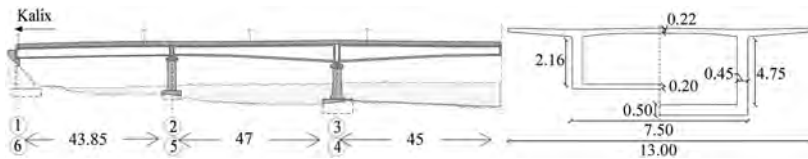


Figure 2. Kalix bridge lateral view (half of the bridge) and cross section geometry in meters.

2.2 Concrete cores extraction

According to the technical drawings retrieved from the Swedish Bridge and Tunnel Management system (BaTMan), the design concrete compressive strength for the superstructure was 45 MPa. Nevertheless, an extensive campaign of core extraction was performed as part of the material characterization. This allowed refining the knowledge on material mechanical properties to better calibrate the numerical model and improving model parameters uncertainties.

The extraction of concrete cores followed the schematic procedure shown in Figure 3 (red font). Different sections along the bridge were selected (from the outer span O_b , the inner span I_b , to the console C_b). The stages/batches used in the construction process were considered as a main criterion to choose the sections for core extraction and additional samples were obtained from regions in which the instrumentation was located (e.g., deflectometers). The instrumentation layout (black font) will be discussed in section 3.2.

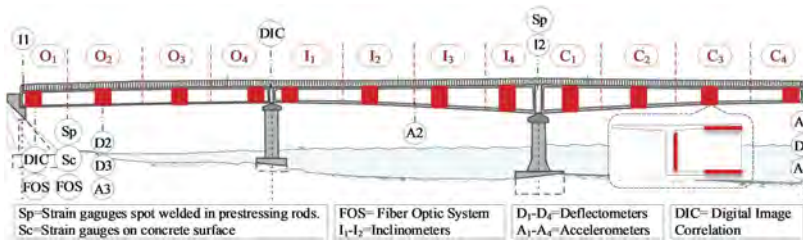


Figure 3. Kalix bridge instrumentation and core extraction layout.

In total, four sections per span were selected for core extraction (red zones), the number of sections chosen was constrained to 108 cores, since it allocated a significant amount of time and resources to obtain the samples. From each section, nine cores were obtained from the same element of the girder (either the wall, bottom, or top slab) as shown in the cross section drawing in Figure 3. Out of these nine cores, three are used for compression test, three to determine modulus of elasticity and three for fracture of energy. Currently, the tests are being performed at Luleå University of Technology (LTU) laboratory. A summary of the results for compressive strength obtained so far (as of January 2023) are shown in Table 1.

Table 1. Compressive strength results from core extraction MPa.

O ₁	O ₂	O ₃	O ₄	I ₁	I ₂	I ₃	I ₄	C ₁	C ₂	C ₃	C ₄
71.12	59.03	57.69	52.36	-	60.60	57.33	43.43	-	-	-	-
69.43	53.32	59.19	-	-	59.44	62.74	57.15	-	-	-	-
-	-	57.99	-	-	56.43	-	-	-	-	-	-
-	-	58.97	-	-	-	-	-	-	-	-	-
-	-	54.81	-	-	-	-	-	-	-	-	-

2.3 Boundary conditions

From the technical drawings and visits on site, initial boundary conditions were identified. It is important to stress out that the symmetry in geometry of the bridge includes the supports of each pillar as labelled in Figure 2. Continuity of the bridge is enforced by the continuous reinforcement along the bridge, no joint was constructed between the element's casting stages, except from the pendulum joint at the end of the balanced cantilever part. The support over pillars 1,2,5, and 6 were set to constraint vertical movement, meanwhile the support over pillars 3 and 4 constrained vertical a longitudinal displacement, allowing bending and torsional rotation.

The joint at the end of the cantilever segment consisted of two pendulum hinges, allowing for independent longitudinal displacement, and bending rotations of the two connected cantilever ends. However, the transversal and vertical displacements, as well as the torsional rotation, are forced to remain equal.

3 LOAD TESTS AND MONITORING

3.1 Proof-load test

The designed proof loading was performed at the beginning of January 2022, and it is extensively described elsewhere (Gonzalez-Libreros et al. 2022). It comprised three different load cases (Load case I, II and III), where the vehicles (see Figure 4(a)) were loaded with additional gravel material. Subsequently, they were placed in four different positions (position 1 to 4), giving a total combination of 36 different load patterns. For load case I, one vehicle was in the center of the cross section (see Figure 4(b)). Load case II consisted of two vehicles placed symmetrically with respect to the bridge axis. In load case III, four trucks were used and distributed in two rows with the same transversal layout as for case II.

Three different load levels were set with the aim to evaluate the serviceability state under low and high loading conditions for each load case. The levels were set at: 0%, 50% and 100% of the

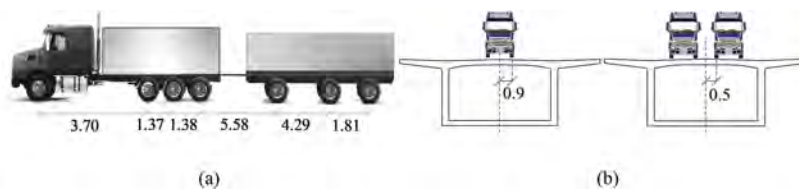


Figure 4. (a) Truck and Lorry dimensions in meters. (b) Truck position on the cross section in meters.

additional weight at which the truck can be loaded. It is important to note that for load cases II and III, the total weight applied to the structures need to be multiplied by two and four, respectively, due to the double layout of trucks on the cross section specified in Figure 4(b). Table 2 shows the weight per axle of a single truck and lorry for each load level.

Table 2. Weight in ton per axle in each load level for the vehicle shown in Figure 4 (a).

Load Level/Axle	A1	A2	A3	A4	A5	A6	A7	Total
Empty (0%)	5	4.3	4.8	0	3.8	0	4.8	22.7
Half (50%)	5.9	6	7	3.8	6.3	7	7	43
Full (100%)	5.9	9.7	9.4	7.2	8.9	10.9	10.9	62.9

Table 3 shows the four different positions along the length of the bridge that were set per every load case and load level to assess the bridge structural response under the loading condition. The time allocated for data recording per every position was five (5) minutes. This time was established to guarantee the stabilization of the readings and reduced the time of testing as it was performed under extremely low temperatures (-25°C).

Table 3. Truck location and main measurements during the proof loading.

Position	Location* and main measurement result
1	5.0 m from pier 6, shear strains
2	13.8 m from pier 6, maximum bending strains
3	42.0 m from pier 6, shear strains
4	47.0 m from pier 4, maximum displacement at hinge

*Measured from the given pier in direction from Kalix to Luleå.

3.2 Instrumentation

A measurement plan was designed to assess the bridge's behavior during the proof loading test. The deployed instrumentation shown in Figure 3 (black font) aimed to target: strains (in the pre-stressing bars S_p and concrete surface: S_c and DIC), displacements (D_1 - D_3), inclination (I_1 - I_2), and acceleration (A_1 - A_4). All the instrumentation was carefully chosen to feature resistance to temperatures up to (-30°C). Most of the measurements of the bridge were acquired at a sampling frequency 50 Hz, except for Fiber Optic Sensor (FOS's) strain measurement, which varies from (8.333 to 12.5 Hz). Temperature was measured at several locations using thermocouples type T distributed as follows: Two located into induced holes in the box-girder's walls, one located on the locker where the data acquisitions wires were being stored, one inside the concrete box girder and one located outside the box girder, in the top slab.

4 EXPERIMENTAL AND NUMERICAL RESULTS

4.1 Results from in-situ instrumentation

The three deflectometers displayed in Figure 3, consisted of two (2) optoNCDT located at mid-span between pillar 5 and 6, positioned in each flange side of the box girder and one (1) Noptel placed at the pendulum joint. The displacements retrieved from the proof loading test

performed showed, in general, a tendency to be stabilized during the measurement time of the testing as shown in the highlighted gray zone in Figure 5. This means that the time allocated for each load level allowed for instant deformations and the viscoelastic effects of the boundary conditions to be steadied.

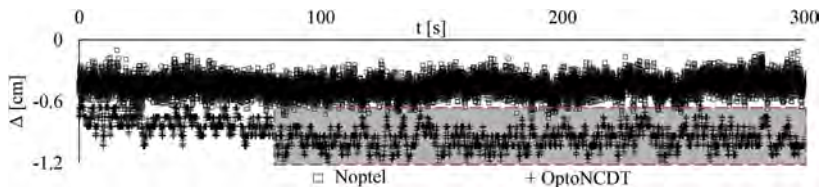


Figure 5. Deflection in time for Load case I with load level 0% measured by OptoNCDT and Noptel.

Figure 6 shows the data retrieved from the proof loading performed at position 2 from the OptoNCDT located at midspan between pillars 5 and 6, and Figure 7 represents the data read by the Noptel at the hinge (pendulum joint). Deflections recorded by the Noptel were significant lower to those read by the OptoNCDT due to the position of the loading level, therefore, for the sake of better appreciation of the data, the vertical axis of both OptoNCDT and Noptel were fitted as displayed in each load level. It is important to highlight that due to the constructions works aimed to the final stages of the new Kalix bridge and demolition of the old one from the contractor side, some load levels present disturbances on the displayed data or peaks at certain time in comparison with other load levels.

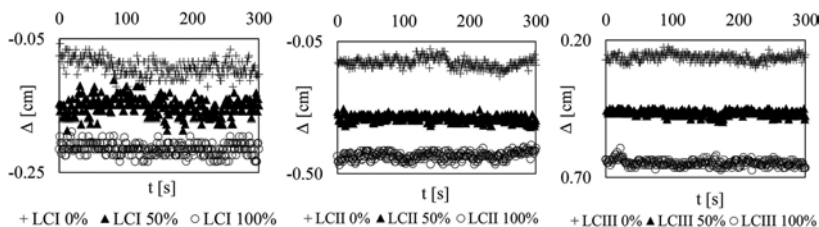


Figure 6. OptoNCDT deflections for load cases I, II and III.

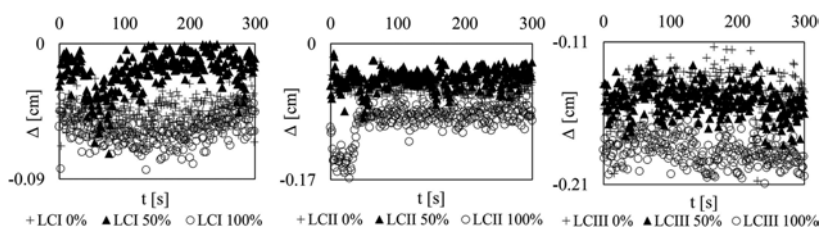


Figure 7. Noptel deflections for load cases I, II and III.

4.2 Calibration of numerical models

A linear elastic model was developed using Robot structural Analysis (Autodesk 2022), as shown in Figure 8. This model represents the Kalix bridge by means of continuous frame elements joined by a hinge which allows for independent longitudinal displacement and bending rotations of the two connected cantilever ends. The sectional and material properties were initially assigned based on the original design parameters. This model will enable to achieve the structural response evaluation under serviceability loading conditions replicating the proof loading test performed (see section 3.1).

The calibration of the numerical model followed an iterative procedure, as more information of the bridge is gathered, model updating is accomplished by progressively incorporating the new estimations into the structural model to meet model predictions with the retrieved testing data. First attempts of model updating showed that the modelled system was more

flexible than the behavior obtained in the testing, which is common for structures which visually showed a good condition throughout all the serviceability years (Faber et al. 2000). Therefore, in the calibration process, stiffness was adjusted to properly capture the on-site material properties and the actual mechanical behavior of the rigid diaphragm at the supports.



Figure 8. Structural model developed in Robot Structural Analysis (Autodesk 2022).

Before initiating the proof loading, all the instrumentation was zeroed to provide every device with a baseline reading when “no loading” was on the bridge. To achieve a validated model that resembles more closely the data display in section 4.1, an initial model (A) has been progressively modified as follows:

- Model A: Parameters are set following the information obtained from technical drawings materials (i.e., geometry, material properties, boundary conditions, etc).
- Model B: From model A, compressive strength is updated, following the core extraction and testing described in section 2.2.
- Model C: From the material update incorporated in model B, length offsets are then included at the abutments and mid-supports to account for the rigid diaphragm and transversal stiffening beams, causing a reduction of the elastic length of the element.

In the evaluation of results, only those retrieved for position 2 are displayed. Position 2 is of special interest in the evaluation of the bridge bending behavior as a previous condition assessment performed determined that the prestressing tendons in the bottom slab at this point have a utilization ratio in bending beyond 100%.

The displacement shape comparisons for half of the bridge between models A, B and C are shown in Figure 9, only load case III at position 2 is evaluated, where also the data recorded from the deflectometers OptoNCDT and Noptel are displayed. It is possible to observe how all the results obtained with different models, showed a resemblance of the structure’s proof loading deformed shape when comparing them with the measured data.

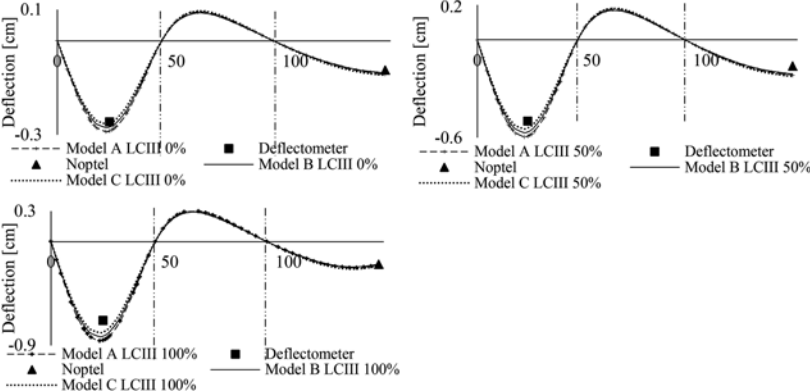


Figure 9. Deformed shape of progressive calibrated models (a) LCIII 0%. (b) LCIII 50%. (c) LCIII100%.

Tables 4 and 5 show the calibration results achieved when tuning material properties and boundary conditions, where $\Delta_{L/2}$ represents the displacement results at midspan between pillars 5 and 6 (OptoNCDT) and Δ_h represents the displacement results at the hinge (Noptel). In general, a good approximation is attained, where only in LCIII 50% results overpassed 20% of error at the hinge. The main reason for this is addressed that when performing that load level during the proof loading test, it was registered disturbances due to activities done by the contractor on the bridge, aimed to its demolition, modifying the recorded data in comparison to other load levels.

A better approximation was achieved for the first midspan from Kalix side than from the hinge, this may be related to a not accurate idealization of the pendulum joint behavior and additionally, to long-term deformations at the hinge associated to creep which is a well-known problem that bridges built by the balanced cantilever method undergo (Plos & Gylltoft 2006).

Table 4. Calibration results when comparing with OptoNCDT data.

	Model A			Model B		Model C	
	Δ	$\Delta_{L/2}$	error	$\Delta_{L/2}$	error	$\Delta_{L/2}$	error
	cm	cm	%	cm	%	cm	%
LCIII 0%	0.26	0.28	9.79	0.27	5.53	0.26	1.6
LCIII 50%	0.46	0.55	15.7	0.52	11.87	0.5	7.9
LCIII 100%	0.64	0.81	20.02	0.77	16.41	0.74	12.8

Table 5. Calibration results when comparing with Noptel data.

	Model A			Model B		Model C	
	Δ	Δ_h	error	Δ_h	error	Δ_h	error
	cm	cm	%	cm	%	cm	%
LCIII 0%	0.09	0.1	12.37	0.1	8.97	0.11	14.7
LCIII 50%	0.15	0.2	25.5	0.19	22.82	0.21	21.9
LCIII 100%	0.18	0.19	1.94	0.18	1.25	0.2	6.3

The longitudinal rotation retrieved by the inclinometers for the load case III 100% is presented Figure 10 (a). It is possible to appreciate how it was not feasible to achieve a steady rotation of the recorded data during the five minutes of the proof loading, especially, at the abutment. Main assumptions regarding not reaching steady readings are ascribed to viscoelastic effects of the boundary conditions. Therefore, an improvement of the boundary conditions should be performed which considers the instant deformations and the viscoelastic effects of the pillar and abutment.

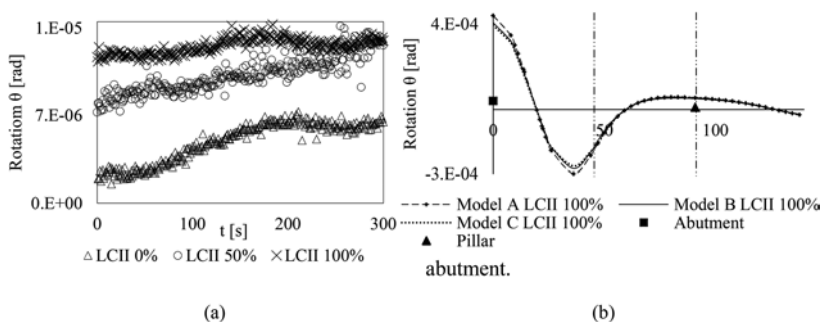


Figure 10. (a) Abutment rotation recorded in time. (b) Rotation achieved in numerical models.

All the data analysis and the results from the structural modelling showed how the actual structural response of the bridge under serviceability conditions was higher than the predicted with designed parameters by nearly 30%. This type of results is often attained and the main reasons ascribed are due to system effects, load redistribution, contribution of non-structural elements and bearings not performing in the expected way (Faber et al. 2000). It was also shown how the advantage of developing a structural model provides to decision makers a solid foundation to acknowledge the results coming from monitoring. Without an a-priori model based on designed parameters and as well as an updated model by parameter identification it would not be feasible to recommend options for corrective measures assertively (Ye et al. 2020).

5 CONCLUSIONS

This paper highlighted the importance of complementing proof-load testing and monitoring with structural models, particularly when the structure is subjected to external interference that could affect the quality of the monitored data. The presented case study investigated the structural performance of a 65-year-old prestressed concrete bridge located in Northern Sweden under serviceability loading conditions. The results and data gathered from the load testing indicated a stiffer structural response condition when compared with the numerical model built with parameters found on the technical drawings. This difference could be related to system effects, load redistribution, contribution of non-structural elements and bearings not performing in the expected way.

A better approximation was achieved for the first midspan from Kalix side than from the hinge, this may be related to the impact of long-term deformations at the pendulum joint associated to creep. Further studies should be performed to determine with a better degree of accurateness the boundary conditions that govern the structural response of the bridge. Moreover, the rotation did not reach steady readings during the five minutes of the proof loading, especially, at the abutment.

The progressive calibration process allowed to recognize how updating material properties and boundary conditions improved the structural model results when compared with monitored data at the same rate. The results obtained from the updates developed from model A to B (Young's modulus updated) improved in approximately 5%, when compared with testing data, which was nearly the same percentage when updates were introduced from model B to model C (Young modulus and boundary conditions updated). Therefore, structural monitoring and condition assessment should always account for methodologies to assess material properties and boundary conditions with the same level of importance.

REFERENCES

- Autodesk. 2022. Robot Structural Analysis Professional (2022). San Francisco, United States.
- Bagge, N. 2020. Demonstration and examination of procedures for successively improved structural assessment of concrete bridges. *Structural Concrete* 21: 1321–1344.
- Biondini, F. & Frangopol, D. M. 2016. Life-cycle performance of deteriorating structural systems under uncertainty: Review. *Journal of Structural Engineering* 142(9): 1–17. United States.
- Capacci, L., Biondini, F., & Frangopol, D. M. 2022. Resilience of aging structures and infrastructure systems with emphasis on seismic resilience of bridges and road networks. *Resilient Cities and Structures* 1(2): 23–41.
- Casas, J. R. & Gómez, J. D. 2013. Load rating of highway bridges by proof-loading. *KSCCE Journal of Civil Engineering* 17(3): 556–567.
- Dinges, T. 2009. The history of prestressed concrete: 1888 to 1963. *University of Kansas*. Lawrence: USA.
- Faber, M. H., Val, D. V., & Stewart, M. G. 2000. Proof load testing for bridge assessment and upgrading. *Engineering Structures* 22(12): 1677–1689.
- Gonzalez-Libreros, J.H., Wang, C., Agredo Chavez, A., Sarmiento, S., Tu, Y., Daescu, C.A. & Sas, G. 2022. Development of a bridge load test procedure for low temperature conditions. Casas, J.R., Frangopol, D.M., & Turmo, J. (eds.), *Bridge Safety, Maintenance, Management, Life-Cycle, Resilience and Sustainability: Proceedings of the Eleventh International Conference on Bridge Maintenance, Safety and Management (IABMAS 2022)*, Barcelona, Spain, July 11- 15 2022 (1st ed.)
- Mottershead, J.E., & Friswell, M.I. 1993. Model updating in structural dynamics. *Journal of Sound and Vibration* 167(2): 347–375.
- Mottershead, J. E., Link, M. & Friswell, M. I. 2011. The sensitivity method in finite element model updating: A tutorial. *Mechanical Systems and Signal Processing* 25(7): 2275–2296.
- Plos, M. & Gylltoft, K. 2006. Evaluation of shear capacity of a prestressed concrete box girder bridge using non-linear FEM. *Structural Engineering International: Journal of the International Association for Bridge and Structural Engineering (IABSE)* 16(3): 213–221.
- Sanayei, M., Khaloo, A., Gul, M., & Catbas, F. N. 2015. Automated finite element model updating of a scale bridge model using measured static and modal test data. *Engineering Structures* 102: 66–79.
- Shu, J., Plos, M., Zandi, K. & Lundgren, K. 2015. A multi-level structural assessment proposal for reinforced concrete bridge deck slabs. *Nordic Concrete Research*: 53–56.
- Ye, S., Lai, X., Bartoli, I., & Emin Aktan, A. 2020. Technology for condition and performance evaluation of highway bridges. *Journal of Civil Structural Health Monitoring* 10(4): 573–594.

Demolition of a 65-year-old box-girder prestressed concrete bridge located in Northern Sweden

C. Daescu

Luleå University of Technology, Luleå, Sweden
Politehnica University Timisoara, Timisoara, Romania

J. Gonzalez-Libreros, C. Wang, L. Elfgrén & G. Sas

Luleå University of Technology, Luleå, Sweden

L.B. Nilsson & T. Larsson

NCC, Stockholm, Sweden

P. Simonsson

Ramboll, Sweden

ABSTRACT: A new bridge was built in Kalix, northern Sweden, to replace the existing prestressed concrete box-girder bridge that had been in service for more than 60 years. The old bridge had a total length of 283.6 m divided in five spans: 43.9 m, 47.0 m, 94.0 m, 47.0 m, and 43.9 m. It was constructed using the balanced cantilever method with segments with a length of around 3.0 m. The need for replacement arose from recommendations extracted from an assessment of the old bridge state and capacity. In addition to the construction of the new bridge, its replacement prompted the need to evaluate and define the demolition procedure of the existing structure. The demolition procedure had to be carefully studied to avoid damages to the new bridge and stability related issues but also to avoid falling debris in the Kalix River, which is part of Natura 2000 protected area. In this paper, the different aspects considered for the development of the demolition strategy are discussed. These aspects include the use of bed-rock anchored tendons, intermediate support fixing at specific locations, and proper evaluation of position of the demolition equipment supported by the bridge, among others.

1 INTRODUCTION

Demolishing an existing bridge is always a challenge, especially if the bridge is located in a protected natural site; public discussions related to it represent all the time a good opportunity to share knowledge among the bridge engineers.

The initial plans of the bridge designed in 1955-1956 were studied in detail (Figure 1), to understand the structural details and construction phases involved in the initial built of the bridge.

2 PLAN FOR DEMOLITION

The existing bridge over the Kalix River is a five-span box-girder post-tensioned concrete bridge, built with balanced cantilevers (“*freivorbau*”). It was replaced by a new bridge in 2022.

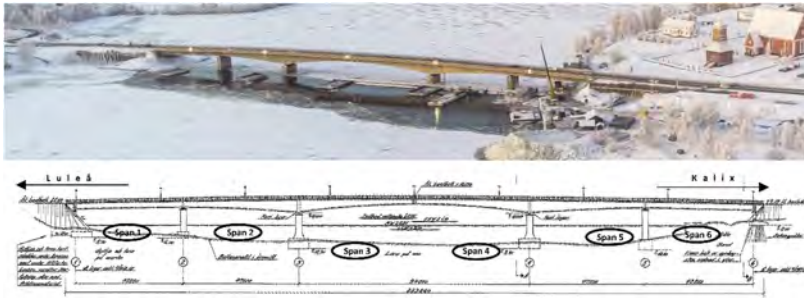


Figure 1. Kalix bridge lay-out.

The initial construction phases were studied in the old building plans and the demolishing procedure tried to follow similar de-construction steps (Daescu et al, 2022).

2.1 Spans 1 and 6

The initial building conditions involved the use of a general formwork solution, and it was estimated that the demolition procedure should have a similar approach. Of course, the input from the contractor was also considered carefully.

2.2 Spans 2-3 and 4-5

According to the original technical documentation, these spans of the bridge were constructed in $\approx 3.1\text{m}$ long sections. The evaluation of the demolition procedure considered the deconstruction of the bridge in a reversed-engineered process to the construction one.

The following are identified as critical points in the deconstruction procedure:

- Establishing the deconstruction phases, i.e., in what order and how large sections can be removed.
- Fixing the intermediate supports 3, 4 and evaluating the bending moment capacity of the intermediate support fixing system.
- De-coupling the bridge key-points., i.e., how to ensure safe transition between the two different statical systems, spans 1 and 6, and spans 2 3 and 4.
- Evaluating the footing condition during the deconstruction phases, i.e., how to prevent loss of stability at the foundation bedrock interface.

3 DEMOLITION DESIGN APPROACHES

Five demolition design approaches were studied to determine the optimum method for the demolition procedure. Modeling used the AxisVM software.

These five design approaches had to consider the following:

- Using a certain number of tendons anchored into the bedrock, to stabilize the bridge during deconstruction.
- Limiting the axial force in the bedrock anchors to avoid shear failure in the bridge.
- Fixing/blocking solutions for the existing pinned-supports.
- Checking the shear capacity of the bridge at the bedrock anchors fixing points.

The own weight of the demolition equipment (300kN) was included only in the 1st approach, but was left aside for the rest, since we needed to reduce the bending moments over the blocked supports 3 and 4 to a theoretical minimum value.

3.1 1st demolition design approach

The evaluation took into consideration removing $\approx 3.1\text{m}$ long sections, one by one, symmetrical to the supports 3 and 4, respectively; the aim was to evaluate the maximum axial force that can appear in the anchors (installed before process start, as sketched in Figure 2) due to the unbalance produced in the two cantilevers.

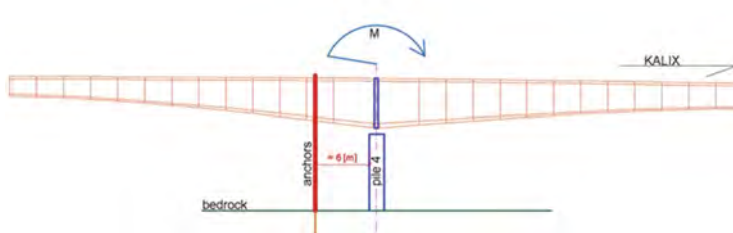


Figure 2. Studied anchoring system.

Figure 3 presents the variation of the axial stresses in the anchors, during the evolution of the demolition procedure (steps 1 ... 28, represented as blue segments).

From these results we can draw the conclusion that the required axial capacity of the tendon is about 17.6MN. Thus, the following issues raised:

- The tendon's capacity requirement is quite high, and a group of anchors might be necessary.
- The shear capacity of the bridge, at the position of the anchoring tendon is about 1.39MN, compared to the 17.6MN shear force applied by the anchor on each web in the bridge cross-section.

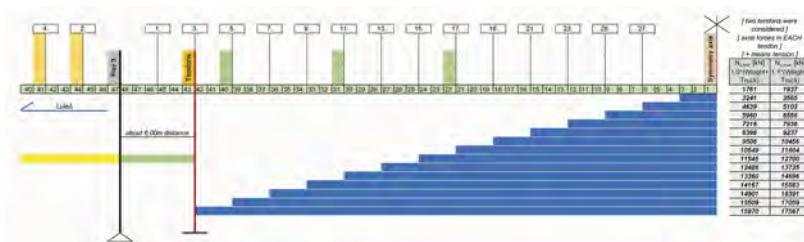


Figure 3. Variation of the axial stresses in the anchors – 1st approach.

3.2 2nd demolition design approach

The second approach involved placing anchors at about 9.3m distance (about three casting sections apart), meaning that on each side of the pier 3[4] should have three anchoring sections. Besides these tendons, in the final phase of the deconstruction, additional tendons should be installed closer to the pier 3[4], spaced at about 3m (at each casting section), as presented in Figure 4.

A maximum force of about 1.96MN resulted for anchor (+3) in the initial phase (step 00) of the demolition process, corresponding to the moment of the demolition of the decoupling sections. The rest of the steps, the maximum axial force in tendons was about 1.5MN.

This reduction in the axial force in the tendon leads to the following conclusions:

- The axial force in tendons is sufficiently small to be easily anchored.
- The utilization degree of the shear capacity of the bridge cross-section is about $1.96/1.39 \approx 141\%$ next to the tendon (+3).

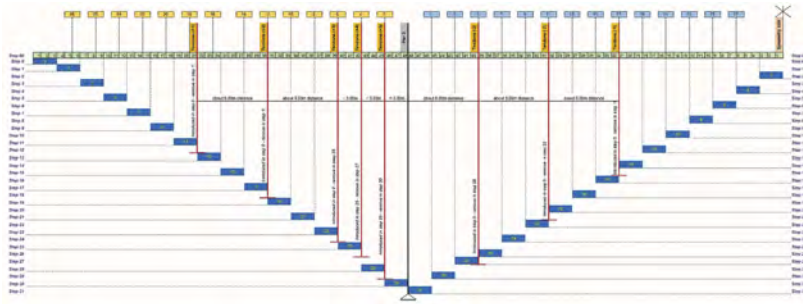


Figure 4. Variation of the axial stresses in the anchors – 2nd approach.

3.3 3rd demolition design approach

This approach is similar to the 2nd one, but we tried to reduce the necessary number of tendons and the axial forces in tendons by optimizing the deconstruction phases.

The evaluation procedure is illustrated in Figure 5; similarly, the blue cells indicate the cross-section to be demolished in a specific step (1 .. 27).

A maximum force of about 1.96MN was recorded for tendon (+3) in the initial phase (step 00) of the demolition process, corresponding to the moment of the demolition of the decoupling sections. The rest of the steps, the maximum axial force in tendons was about 0.68MN.

This reduction in the axial force in the tendon leads to the following conclusions:

- The axial force in tendons is sufficiently small to be easily anchored.
- The utilization degree of the shear capacity of the bridge cross-section is about $1.96/1.39 \approx 141\%$.
- The drawback of this solution is that there are still needed 16 tendons.
- It is necessary to use an additional system for the stabilization of the reinforced concrete wall inside the bridge, above the pier, in the final deconstruction phase.

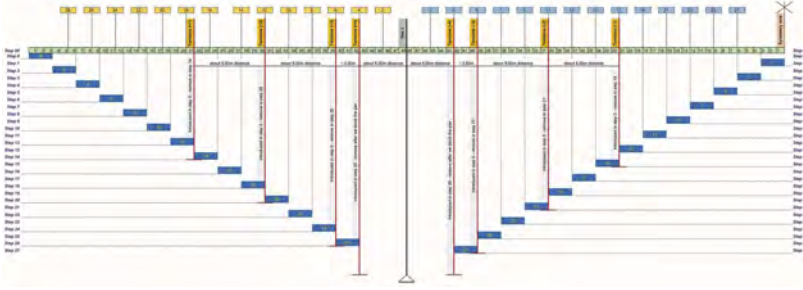


Figure 5. Variation of the axial stresses in the anchors – 3rd approach.

3.4 4th demolition design approach

This approach modifies the 3rd one by trying to reduce the necessary number of tendons and the axial forces in tendons by optimizing the deconstruction phases and by introducing a blocking system for the hinged support above the pier 3[4].

Besides these tendons, in the final phase of the deconstruction, additional laminated steel profiles should be used to block the hinged support above the pier 3[4], allowing the stabilization of the reinforced concrete wall inside the bridge, above the pier.

The evaluation is illustrated in Figure 6; similar to the previous figures, the blue cells indicate the cross-section to be demolished in a specific work step (1 .. 27).

A maximum force of about 1.96MN was recorded for tendon (+3) in the initial phase (step 00) of the demolition process, corresponding to the moment of the demolition of the decoupling sections. The rest of the steps, the maximum axial force in tendons was about 0.68MN.

This reduction in the axial force in the tendon leads to the following conclusions:

- The axial force in tendons is sufficiently small to be easily anchored.
- The utilization degree of the shear capacity of the bridge cross-section is about $1.96/1.39 \approx 141\%$.
- The additional system for the stabilization of the bridge in the final deconstruction phase consists of minimum 2 x HEB200 steel profiles located on both sides of each steel hinge (four hinges/pier). The maximum stress in the steel profiles is about 164N/mm^2 .

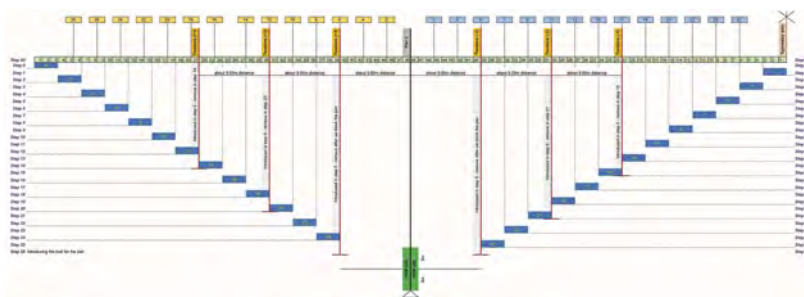


Figure 6. Variation of the axial stresses in the anchors – 4th approach.

3.5 5th demolition design approach

This last approach modifies the 4th one by trying once more to reduce the necessary number of tendons and the axial forces in tendons by optimizing the deconstruction phases and by introducing a slightly different blocking system for the hinged support above the pier [3][4]. Besides these tendons, from the initial phase of the deconstruction, on-site casted reinforced concrete should be used to block the hinged support above the pier [3][4], allowing the stabilization of the reinforced concrete wall inside the bridge, above the pier. This approach is illustrated in Figure 7; the blue cells indicate the cross-section to be demolished in a specific work step (1 . . .27).

Similar to the previous evaluations, a maximum force of about 1.15MN was recorded for tendon (+3) in the initial phase (step 00) of the demolition process, corresponding to the moment of the demolition of the decoupling sections. The rest of the steps, the maximum axial force in tendons was about 0.44MN.

This reduction in the axial force in the tendon leads to the following conclusions:

- The axial force in tendons is sufficiently small to be easily anchored.
- The utilization degree of the shear capacity of the bridge cross-section is about $1.15/1.39 \approx 83\%$.
- The additional system for the stabilization of the bridge in the final deconstruction phase consists of casted-in-place reinforced concrete walls, chemically anchored into the pillar.

3.6 Overview of the five studied approaches

These five studied cases evolved following the discussions with the general contractual for the demolishing works (NCC infrastructure). The request was to study the possibilities of using as less tendons as we could during the demolition process; for this purpose, step-by-step evaluation procedures were used. A general overview is presented in the Table 1.

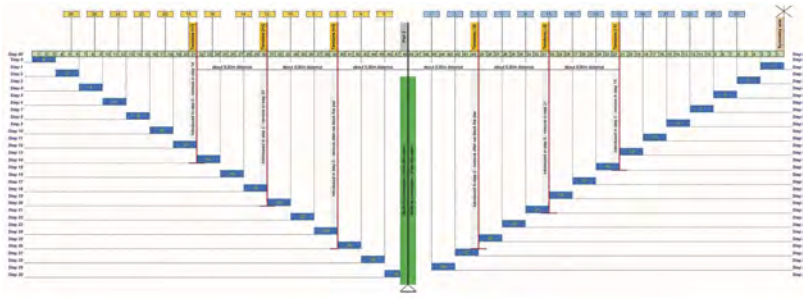


Figure 7. Variation of the axial stresses in the anchors – 5th approach.

Table 1. Results overview.

Approach	No. of tendons	Support 3[4] type	Anchor max. axial force [MN]	Bridge shear capacity [MN]
1 st	2	fixed*	17.6	1.39
2 nd	16	fixed*	1.50	1.39
3 rd	16	fixed*	1.42	1.39
4 th	12	fixed**	1.42	1.39
5 th	12	fixed**	1.14	1.39

*The fixed support is a result of the anchors balancing/preventing the rotation.

**Laminated profiles or cast-in place concrete blocking are used to block the rotation of the support.

4 INTERMEDIATE SUPPORT FIXING

There were studied two distinct fixing solutions:

- By using chemically anchored rebars and additional concreting.
- Fixing the hinge with the help of additional steel profiles.

4.1 Rebars and concrete

An estimated reinforcement ratio was computed, to design the necessary anchorage system to be applied.

The evaluation took into consideration removing ≈ 3.1 m long sections, one by one, symmetrical to the supports 3 and 4, respectively; the aim was to evaluate the maximum bending moment that can appear in the blocked support above the pier (installed before process start) due to the unbalance produced in the two cantilevers. In this way, one can establish the necessary tensioned reinforcement that can prevent the overturning of the support 3(4).

The variation of the bending moment in the support, during the deconstruction process was evaluated in a step-by-step approach.

As a conclusion for this scenario, the built-in support should be able to provide a minimum bending (overturning) capacity of about 1.9MNm/m.

The obtained bending (overturning) capacity of the system is evaluated to ≈ 2.45 MNm/m, using 2x4 Φ 28 S500 steel bars.

4.2 Laminated steel profiles

Laminated steel profiles were used to block the hinged support above the pier 3[4], allowing the stabilization of the reinforced concrete wall inside the bridge, above the pier. Each of the four hinges above the pier was blocked by using a pair of HEB200 laminated profiles. The additional

system used for the stabilization of the bridge in the final deconstruction phase managed to effectively block the hinge, while the maximum stress in the steel profiles is about 164 N/mm².

5 FOOTING EVALUATION

The original documents provide the following information:

- Geometry for the foundation system and for the piers.
- Load bearing capacity of the ground, considered in the initial design.

The aim is to estimate the variation in the pressure under the existing footing, based on the de-construction phases. For this, the 3D model used in the previous evaluations was completed with the pier and the foundation system, as presented in Figure 8.

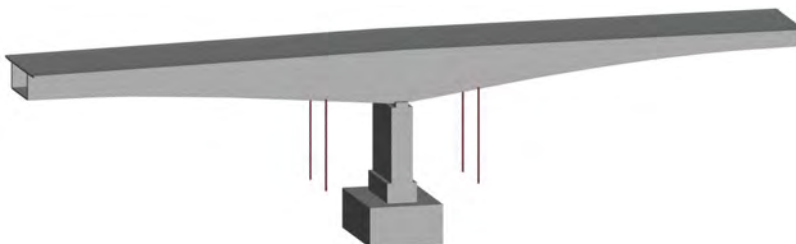


Figure 8. 3D model of the bridge, used for footing evaluation.

The start point of the analysis were the 4th and 5th approaches presented previously, but using the following hypotheses:

- there were used only two anchors on each side of the pier: Tendon (+3) and Tendon (-3).
- the surface support (between the footing and the soil) was considered with the rigidity $k_s = 100$ MN/m/m/m, to better observe the deformation of the footing, during the demolition phases.
- the connection between the bridge and the pier was considered as:
 - pinned in the 1st part of the analysis, to evaluate the pressure under the footing under the convoy loads.
 - pinned connection in the 2nd part of the analysis, to evaluate the pressure under the footing and stresses in anchors, during the de-construction phases.
 - moment connection in the 3rd part of the analysis, to evaluate the pressure under the footing and stresses in anchors, during the de-construction phases.

Table 2 presents the pressure funder the pier's footing, in all studied scenarios. Several standard convoys were used, according to Swedish TDOK code (2013).

Table 2. Footing pressure – convoy (j).

Scenario	Min pressure [kPa]	Max pressure [kPa]
no. 1	-334	-309
no. 2	-365	-309
no. 3	-375	-309

6 CONCLUSIONS

As expected, the study of the demolition procedures for the existing Kalix River bridge proved to be quite challenging. All the input data had to be chosen carefully, both in terms of

geometry materials and loads in order for the contractors to be able to have the optimal approach for the demolition (see Figure 9). For the studied case, additional considerations needed to be considered due to its location in a natural protection area. Among the parameters that were considered, it is possible to find: bridge stability, avoidance of undesirable movements during the demolition, bridge and footing capacity, and the selection of a demolition strategy that follows the construction process with the aim of counterbalancing the overturning moments during demolition.

Five different approaches were studied. These approaches provided a very carefully studied technical solution that included:

- Bed-rock anchored tendons, in a specific configuration, to keep the bridge segments in equilibrium at all stages.
- Careful evaluation of the shear capacity of the bridge webs, at the tendon's fixing points, to avoid local or global failure in bridge segments.
- Intermediate support fixing in the final stages of the de-construction.
- Precise positioning of the demolition equipment on the bridge – very important for the overall equilibrium of the structure.
- Footing evaluation to verify the changes in pressure due to the demolition process.



Figure 9. Kalix bridge during demolition, with anchors in place (courtesy of NCC Infrastructure).

Evaluation of the approaches showed that that even though only two anchors might be required to guarantee the stability of the structure (approach 1), the expected axial force is higher than the shear capacity of the bridge. Approaches 2-5 showed expected axial forces in the tendons obtained considerably lower than those of approach 1, however only for approach 5 they were lower than the bridge shear capacity.

ACKNOWLEDGEMENTS

This work has been funded by NCC Infrastructure, Division Civil Engineering, Sweden. The continuous feed-back of the NCC representative is also acknowledged here.

REFERENCES

- AxisVM - Structural Analysis & Design Software – www.axisvm.eu
- Daescu, C.A., Lundin, H., Sarmiento, S., Gonzalez-Libreros, J.H., Elfgrén, L. & Sas, G. (2022). Study of demolition strategies and preliminary plan for the case of the Kalix bridge. In J.R. Casas, D. M. Frangopol & J. Turmo (eds.), *Bridge Safety, Maintenance, Management, Life-Cycle, Resilience and Sustainability*. Proc. IABMAS 2022, Barcelona, Spain, July 11-15, Taylor & Francis. 8p.
- TDOK 2013:0267 - Bärighetsberäkning av broar (Capacity assessment of existing of bridges. In Swedish). Swedish Transport Administration.

Experimental study on constitutive law of stainless steel under multiaxial stress

E. Horisawa, K. Sugiura, Y. Kitane & Y. Goi

Graduate School of Engineering, Kyoto University, Kyoto, Japan

ABSTRACT: Stainless steel does not require painting and can contribute to the reduction of life cycle costs of structures. In general, material constitutive laws are essential to accurately evaluate the seismic behavior of structures in numerical analysis. In this study, the yield surface and flow rule of stainless steel were experimentally investigated to establish the multiaxial constitutive law. Axial forces and torques were applied to cylindrical specimens to represent various stress states. The yield surface of stainless steel in the plane of axial and shear stress were determined, and the evolution of plastic strain after yielding was observed. It was shown that austenitic grades exhibited isotropic yield surfaces, while duplex ones exhibited elliptical ones with an eccentricity of 0.7. It was also confirmed that the standard deviation of the direction of plastic strain propagation from the theoretical value is about 10 degrees, and the associated flow rule could be applied.

1 INTRODUCTION

Stainless steel is increasingly being used as the main material for civil engineering structures especially in severe corrosive environments due to its corrosion resistance. One of the reasons for adopting stainless steel is that it does not require periodic repainting which is necessary for typical steel structures. In addition, since stainless steel is theoretically 100% recyclable after use, making it an earth-friendly material from the perspective of effective utilization of global resources. Therefore, although the initial cost of stainless steel is high, it is possible to reduce the life cycle cost of structures (Gardner et al. 2007, Kere & Huang 2019).

To accurately simulate structural behaviour using analytical method such as finite element analysis, the material constitutive law that correctly expresses the relationship between stress and strain is essential. Regarding the constitutive law of stainless steel, several fundamental studies were reported so far. Under monotonic loading, classically Ramberg and Osgood proposed a stress strain equation with a round house shape, and it is now namely known as Ramberg-Osgood formulation (Ramberg & Osgood 1943, Hill 1944). The R-O curve has undergone various improvements to date, for instance, Arrayago et al. showed modified R-O curve (Arrayago et al. 2015). Apart from monotonic loading, studies in terms of the constitutive law under cyclic loading of tension-compression were also reported (Bondar et al. 2018). However, the plastic constitutive law of stainless steel under multiaxial stress such as tension in two axes and tension-torsion has rarely been studied so far due to the difficulty of testing.

Japan is one of the countries with the most frequent earthquakes in the world, and bridges built in the country must satisfy seismic design requirements. Since bridges are subject to repeated random loads during an earthquake, the stress generated in structures are not only simple tension-compression, but also complex multiaxial stress. Therefore, when investigating the seismic behavior of structures using finite element analysis, it is necessary to use material constitutive laws that are suitable for multiaxial stress states.

The plastic constitutive law under multiaxial stress is generally composed of the yield criterion, the flow rule, and the hardening rule, regardless of the material. The first item, yield criterion, represents the stress state at which virgin material yields under multiaxial stress, as typified by the Mises' yield criterion, and there are several studies on typical stainless steels (Wu & Yeh 1991). The second element, the flow rule, specifies a plastic strain path of the material after yielding, and can be classified into two cases: associated flow rule and non-associated flow rule. The last item, the hardening rule, is a rule that describes how the yield surface of a material changes once it has yielded, and is generally referred to as the isotropic, kinetic, or combined hardening rule. Research on this constitutive law of stainless steel has been conducted mainly in the field of plastic engineering, but there are almost no studies that have experimentally verified them in the study on bridges. By clarifying the exact constitutive equation of stainless steel, which has not been studied extensively, it will be possible to evaluate the seismic performance of stainless steel bridges and to rationalize them. They are expected to promote the spread of stainless steel bridges and labor-saving structures.

This study aims to establish a plastic constitutive law for stainless steel under multiaxial stress, and the experiments related to the yield criterion and the flow rule, which are two of the three components of the plastic constitutive law, were conducted. In addition, basic knowledge for establishing the constitutive law of stainless steel was obtained. This study also aimed Firstly, this proceeding introduces the experimental method for the yield criterion of stainless steel, and then presents the yield surface obtained by the experiment. Secondly, it is shown that the flow rule of stainless steel is associated with the yield condition by observing the plastic strain under multiaxial loading. Finally, a summary of these contents is presented at the end of this proceeding.

2 YIELD SURFACES

2.1 Materials and test pieces

The test to determine the yield surface was performed using two steel grades: the most common austenitic stainless steel SUS304 (EN 1.4301) and the nickel-saving duplex stainless steel SUS821L1 (JIS original). The mechanical properties and chemical compositions of these materials given by steel companies are shown in Tables 1 and 2, respectively. SUS821L1 has more than 1.6 times the yield strength and less than 1/4 of the nickel content of SUS304.

Specimens used for the test had a shape of a hollow cylinder with 20 mm in outer diameter, 18 mm in inner diameter, and 1 mm in thickness at the center part as shown in Figure 1. To apply torque to the specimen, end cross section of the specimen is D-shaped, consisting of a circular arc and a straight line. In the test, axial force was applied in the longitudinal direction of the specimen, and torque was applied around the longitudinal axis (in the direction of arrows in Figure 1). The outer diameter D and inner diameter d of the specimens were measured using a digital caliper prior to testing.

Table 1. Mechanical properties of stainless steels.

	Yield stress	Tensile stress	Elongation
	MPa	MPa	%
SUS304	277	591	60
SUS821L1	455	662	46

Table 2. Chemical compositions of stainless steels (%).

	C	Si	Mn	P	S	Ni	Cr	Co	Cu	N
SUS304	0.05	0.28	1.8	0.037	0.024	8.62	18.38	<1.0	-	-
SUS821L1	0.018	0.31	3.15	0.023	0.000	2.14	20.90	0.06	1.04	0.17

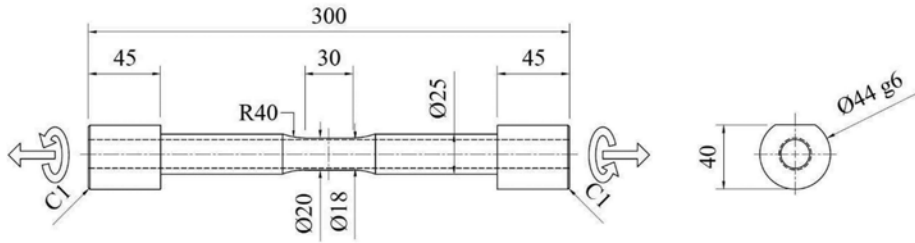


Figure 1. Nominal dimensions of test pieces (unit is mm).

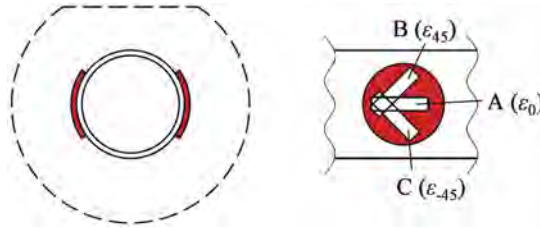


Figure 2. Strain gauge arrangement.

2.2 Stress and strain measurement

Axial force N and torque T were measured by load cells built into the testing machine as described below. Using these values, axial stress σ and shear stress τ acting on the parallel sections of the specimen were calculated using Equations 1 and 2.

$$\sigma = \frac{4N}{\pi(D^2 - d^2)} \quad (1)$$

$$\tau = \frac{16DT}{\pi(D^4 - d^4)} \quad (2)$$

The Mises's equivalent stress is as follows.

$$\sigma_{eq} = \sqrt{\sigma^2 + 3\tau^2} \quad (3)$$

Additionally, axial strain ε and shear strain γ of the specimen were measured by rosette gauges attached to the center part of the specimen as shown in Figure 2. Two triaxial strain gauges (FRA-5-11, TML) of a 5 mm gauge length were used for one specimen, with one gauge parallel to the longitudinal axis of the specimen and the other two gauges inclined at 45 degrees from the longitudinal axis. Referring to previous studies on shear strain measurement by strain gauges (Huang et al. 1993, Khan & Liang 2000, Khan et al. 2007), axial and shear strains of the specimen were calculated from these strain gauge readings using Equations 4 and 5.

$$\varepsilon = \varepsilon_0 \quad (4)$$

$$\gamma = \varepsilon_{45} - \varepsilon_{-45} \quad (5)$$

Using the elastic modulus E and shear modulus G in addition to the stresses and strains, the respective plastic strains and equivalent plastic strain when the material is isotropic are given by following Equations 6-8. Here, the elastic modulus and shear modulus were obtained by regression analysis of data with equivalent stress between 20 and 80 MPa.

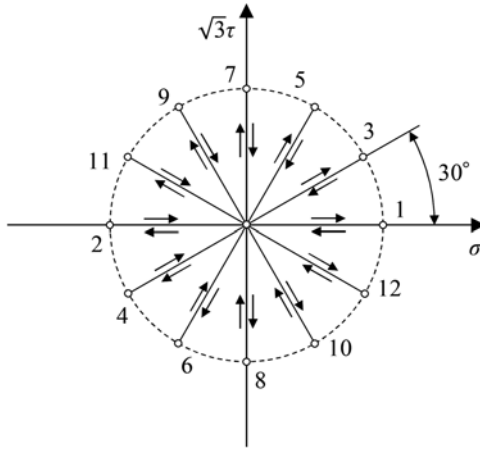


Figure 3. Schematic diagram of loading paths.



Figure 4. Specimen setup.

$$\varepsilon^p = \varepsilon - \frac{\sigma}{E} \quad (6)$$

$$\gamma^p = \gamma - \frac{\tau}{G} \quad (7)$$

$$\varepsilon_{eq}^p = \sqrt{(\varepsilon^p)^2 + \frac{(\gamma^p)^2}{3}} \quad (8)$$

2.3 Test procedure

Yield surfaces can be obtained by loading in any direction on the plane of axial and shear stresses and plotting the multiple yield stresses. Experimental methods for obtaining yield surfaces have been shown in previous studies (Štefan et al. 2021), and is also briefly explained here.

Figure 3 shows a schematic diagram of loading paths to obtain the yield surface. At the beginning of the test, only tensile stress is applied until the equivalent plastic strain reaches the offset strain ε_{off}^p which is defined as yielding (path 1 in the figure). After that, unloading is

performed to the origin of the $\sigma - \sqrt{3}\tau$ stress plane, and loading is performed again in the same way for compression indicated by path 2. Performing this procedure for the 12 paths shown in the figure, the yield surface is identified from 12 plots of yield stress.

An axial force-torsion multiaxial testing machine (EHF-10/TQ1, SHIMADZU) shown in Figure 4 was used for the above test. During the loading, axial force and torque speed were controlled so that the generated equivalent stress σ_{eq} was 2 MPa/s. In this study, the offset strain ϵ_{off} of 0.005%, which was used in some previous studies (Ishikawa & Sasaki 1988, Ishikawa 1997), was used as the definition of yielding. Preliminary experiments were conducted with a smaller ϵ_{off} of 0.0001%, confirming that the variability of the test results was much larger than the case with ϵ_{off} of 0.005%.

2.4 Results

The initial yield surface of the stainless steels obtained by the above test procedure are shown in Figures 5 and 6, and the Mises' yield criterion, which is the most common yield criterion, is indicated by a dashed line in Figure 5. In addition, Hill's equation (Hill 1948), which is an anisotropic yield function, is also shown in Figure 6. These yield criteria for the biaxial stress state of axial stress σ and shear stress τ in this study are expressed by the following equations.

$$f_{Mises} = \sqrt{\sigma^2 + 3\tau^2} - Y \quad (9)$$

$$f_{Hill} = \frac{\sigma^2}{\sigma_y^2} + \frac{\tau^2}{\tau_y^2} - 1 \quad (10)$$

where, Y is a general yield stress, σ_y and τ_y are yield stresses under pure axial or shear stress condition, respectively. Here, Y is the average of all loading paths, and the average of the two uniaxial stresses is used for each yield stress in Hill's yield function. It can be confirmed that the yield surface of SUS304 is consistent with the Mises' yield criterion, although the test data in the second quadrant is outside of the Mises' yield criterion. On the other hand, the yield surface of SUS821L1 shows an ellipse with a major diameter in the shear stress axis and an eccentricity of 0.7, which is in good agreement with Hill's anisotropic yield function. In addition, the standard deviation of the yield stress of SUS304 for the Mises' condition and that of SUS821L1 for the Hill's anisotropic condition were both 10 to 20 MPa. Duplex stainless steels exhibit anisotropy in the metallurgical structure due to the rolling process (Chalapathi et al.

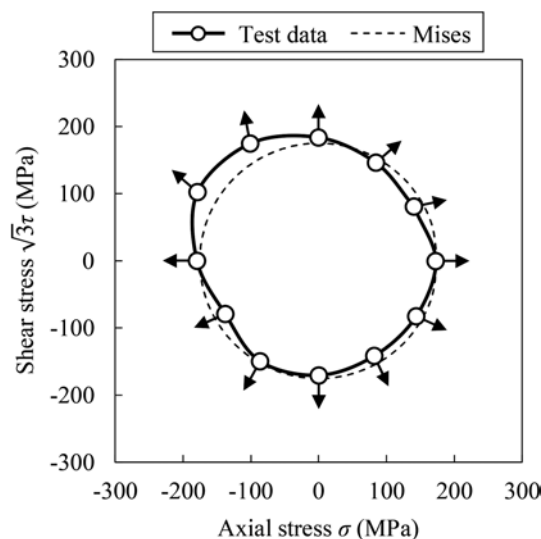


Figure 5. Measured yield surface of SUS304.

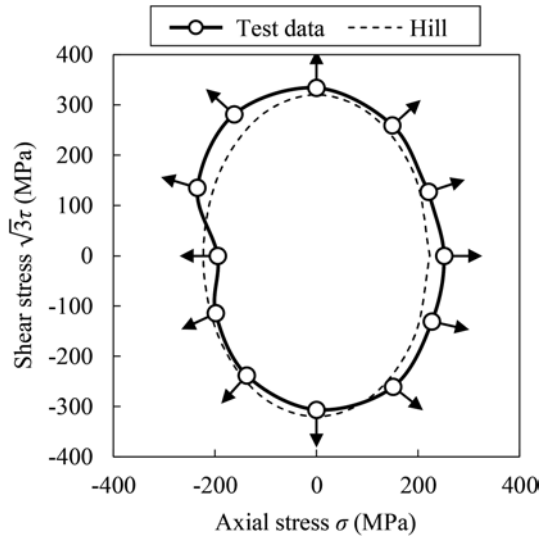


Figure 6. Measured yield surface of SUS821L1.

2022), and it is known that the tensile strength of plates also varies depending on the direction from which the specimens are taken (Horisawa et al. 2021). Since the steel bars in this study were manufactured by hot rolling, anisotropy in strength was also confirmed.

3 FLOW RULES

3.1 Methodology

The flow rule is a rule that describes the evolution of the plastic strain increment in a multiaxial stress state and is generally expressed by the following Equation 11.

$$d\varepsilon_{ij} = \frac{\partial f}{\partial \sigma_{ij}} d\lambda \quad (11)$$

where f is called the plastic potential, and $d\lambda$ is a positive constant. In this study, the test results are compared with the associated flow rule where f is the Mises' yield criterion or the Hill's yield function. This equation also indicates that the direction of plastic strain increment is perpendicular to the yield surface under the associated flow rule.

The flow rule for stainless steel is verified using the plastic strains measured during the initial yield surface identification tests described in Chapter 2. In the following section, the plastic strain paths obtained when loading was applied until the plastic strain of 0.005% are considered.

3.2 Result and discussion

The plastic strain paths of stainless steel observed in the tests are shown in Figures 7 and 8. The degrees in these figures represent the clockwise loading path angles shown in Figure 3, and the dashed lines represent the direction of plastic strain increment due to the associated flow rule using Mises' or Hill's yield criterion. The plastic strain paths of SUS304 can be seen to deviate clockwise from the associated flow rule in the first and second quadrants, whereas in the third and fourth quadrants, the results are in good agreement with the theoretical directions. From Figure 8, the ones of SUS821L1 evolved in directions generally close to the associated flow rule with Hill's equation as the plastic potential. Both results show the standard

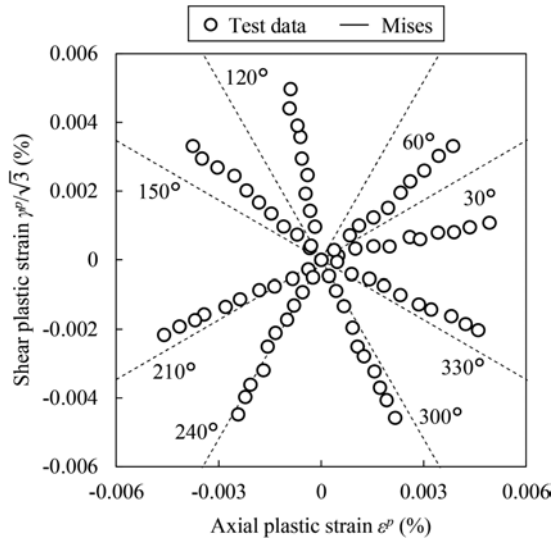


Figure 7. Plastic strain paths of SUS304.

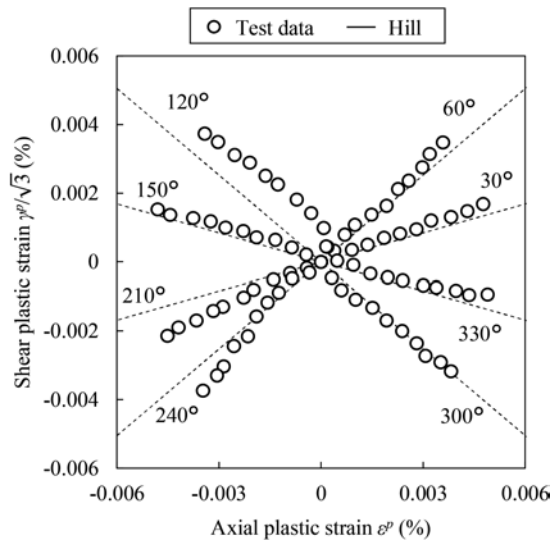


Figure 8. Plastic strain paths of SUS821L1.

deviation of around 10 degrees from the theoretical value, and the standard deviation in the direction for SUS821L1 was reduced from 16 degrees to 4 degrees by using Hill's yield criterion. These results show that with appropriate yield criterions, the plastic strain increments of stainless steel follow the associated flow rule.

The vectors of plastic strain increments on the yield surface obtained by regression of test result with the equivalent plastic strain from 0.004% to 0.005% of Figures 7 and 8 are shown as arrows in Figures 5 and 6. It is confirmed that the incremental plastic strain vectors for stainless steel are oriented normal to the yield surface. On the other hand, in regions where the difference between the vector and theoretical values is large, such as the second quadrant of SUS304, the yield surface is seen to be highly distorted, indicating that the perpendicularity to the experimental yield surface is maintained to some extent.

4 CONCLUSIONS

Toward the future development of multiaxial plastic constitutive equations for stainless steels, material tests on yield criteria and flow rules were conducted in this study. Yield stress and direction of plastic strain propagation were experimentally observed in each proportional loading path. The austenitic SUS304 satisfied the isotropic Mises yield criterion, and the duplex stainless steel SUS821L1 satisfied Hill's anisotropic yield function with predominant shear stress and the standard deviation of less than 20 MPa, based on yield surfaces specified under biaxial stress conditions of axial and shear stresses. In addition, the direction of the plastic strain increment on the yield surface is perpendicular to the yield surface for the two steel grades examined in this study, and the associated flow rule is satisfied. In the future, verification of the anisotropy of duplex stainless steels and material tests to define a hardening rule are planned. With these experiences, the goal of this study is to establish a material constitutive law for the rational design and the evaluation of seismic performance of stainless steel bridges that reduces its life cycle costs. The results of this study contributed to the construction of the material constitutive equation, which is a fundamental element for this purpose.

ACKNOWLEDGEMENTS

This work was supported by JST SPRING, Grant Number JPMJSP2110, and Association for Disaster Prevention Research.

REFERENCES

- Arrayago, I., Real, E. & Gardner, L. 2015. Description of stress-strain curves for stainless steel alloys, *Material and Design* 87: 540–552.
- Bondar, V. S., Dansin, V. D., Vu, L. D. & Duc, N. D. 2018. Constitutive modelling of cyclic plasticity deformation and low-high-cycle fatigue of stainless steel 304 uniaxial stress state 25(12): 1009–1017.
- Chalapathi, D., Sivaprasad, P. V., Chai & G., Kanjarla, A. K. 2022. Anisotropic work hardening behaviour in duplex stainless steel under uni-axial loading: Interplay between phase morphology and crystallographic texture, *Materials Science & Engineering A* 849: 143418.
- Gardner, L., Cruise, R.B., Sok, C.P., Krishnan, K. & Santos, J. M. D. 2007. Life cycle costing of metallic structures, *Proceedings of the Institution of Civil Engineers – Engineering Sustainability* 160(4): 167–177.
- Hill, H. N. 1944 Determination of stress-strain relations from “offset” yield strength values, *Technical Note No.927*, National Advisory Committee for Aeronautics.
- Hill, R. 1948. A theory of the yielding and plastic flow of anisotropic metals, *Proceedings of the Royal Society of London. Series A, Mathematical and Physical Sciences* 193(1033): 281–297.
- Horisawa, E., Sugiura, K. & Kitane, Y. 2021. Study on fatigue strength of lean duplex stainless steel base metal, *Steel Construction Engineering* 28(111): 107–117.
- Huang, S., Khan, A. S. & Yan, H. 1993. Shear measurement using strain gages under large deformation and rotation, *Experimental Mechanics* 33: 55–58.
- Ishikawa, H. & Sasaki, K. 1988. Yield surface of SUS304 under cyclic loading, *Transactions of the Japan Society of Mechanical Engineers Series A* 54(501): 1116–1123.
- Ishikawa, H. 1997. Subsequent yield surface probed from its current center, *International Journal of Plasticity* 13(6-7): 533–549.
- Kere, K. J. & Huang, Q. 2019. Life-cycle cost comparison of corrosion management strategies for steel bridges, *Journal of Bridge Engineering* 24(4): 04019007.
- Khan, A. S. & Liang, R. 2000. Behaviors of three BCC metals during non-proportional multi-axial loadings: experiments and modeling, *International Journal of Plasticity* 16: 1443–1458.
- Khan, A. S., Chen, X. & Abdel-Karim, M. 2007. Cyclic multiaxial and shear finite deformation response of OFHC: Part I, experimental results, *International Journal of Plasticity* 23: 1285–1306.
- Ramberg, W. & Osgood, W. R. 1943. Description of stress-strain curves by three parameters, *Technical Note No.902*, National Advisory Committee for Aeronautics.
- Štefan, J., Parma, S., Marek, R., Plešek, J., Ciocanel, C. & Feigenbaum, H. 2021. Overview of an experimental program for development of yield surfaces tracing method, *Applied Sciences* 11, 7606.
- Wu, H. C. & Yeh, W. C. 1991. On the experimental determination of yield surfaces and some results of annealed 304 stainless steel, *International Journal of Plasticity* 7: 803–826.

Structural behavior of UHPC transition segment of wind tower without ordinary reinforcement under serviceability limit state

L.R. Lin

College of Civil Engineering, Fuzhou University, Fuzhou, China

X. Zhang

CGN New Energy Holdings Co., Ltd, China

X.G. Wu

Key Lab of Structures Dynamic Behavior and Control of the Ministry of Education, Key Lab of Smart Prevention and Mitigation of Civil Engineering Disasters of the Ministry of the Industry and Information Technology, Harbin Institute of Technology, Harbin, China

X. Wang, X.S. Zhang & H. Wang

CGN New Energy Holdings Co., Ltd, China

ABSTRACT: The complexity of reinforcement and consequent corrosion of concrete have been technical issues of the transition segments of the hybrid wind turbine tower. A novel concrete transition segment using prestressed ultra-high performance concrete (UHPC) that does not necessitate ordinary reinforcement is applied to a 4.8MW H160 prestressed hybrid wind turbine tower. The mechanical behaviors of the transition segments only with reinforced concrete segment (T-C80RC) and the UHC140 segment without ordinary reinforcement (T-UHC140) are investigated using 3D finite element models. The comparative study shows that UHPC in T-UHC140 improves the overall mechanical performance.

1 INTRODUCTION

Offshore wind energy has attracted growing attention as a renewable wind energy source with increasing concern on global energy security (Lana 2021; McKenna 2022). A higher wind turbine tower (WTT) has the benefits of accessing sufficient and stable wind resources. Recently, the super-high WTT has been constructed using a hybrid WTT consisting of prestressed concrete section in the lower part and steel section in the upper part. The crux of the hybrid WTT for structural performance is the transition segment which connects the steel and concrete sections.

Ultra-high performance concrete (UHPC), with enhanced mechanical properties and durability, enables prestressed concrete structures that require reduced or no ordinary reinforcement (Yu 2020). It has been demonstrated that UHPC can improve flexural and shear properties, crack control capacity, and the ultimate bearing capacity of the prestressed structure even without ordinary reinforcement (Brian 2001; Ridha et al., 2018). It has also been shown that UHPC enables higher towers while reducing the cost of construction, transportation, and installation (Jammes 2009; Lewin and Sritharan 2010). Thus, it is promising to use the unreinforced prestressed UHPC segment for the transition segment of WTT to avoid the complex reinforcement and improve durability. Extensive research on the structural behavior of the prestressed UHPC transition segment without ordinary reinforcement is needed to exploit the advantages.

This paper investigates the performance of the transition segment of an offshore 4.8MW H160 wind turbine tower by comparing the behaviors between the transition segment of the

ordinary high-strength reinforced concrete segment (T-C80RC) and the transition segment of UHC140 segment without ordinary reinforcement (T-UHC140).

2 TRANSITION SEGMENT MODEL

2.1 Basic information

The structure of a 4.8 MW prestressed steel-concrete wind turbine tower with a height of 160 m is illustrated in Figure 1.

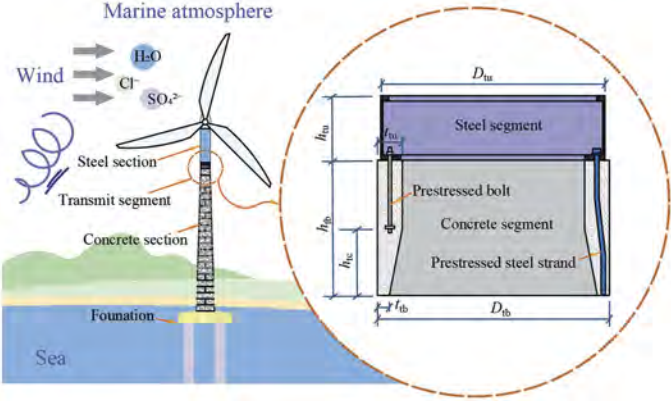


Figure 1. Transition segment (4.8MW H160).

The lower part of the structure (< 110.5 m) is a concrete section, and the upper part (≥ 110.5 m) is a steel section. The transition segment is mainly composed of a concrete segment and a steel segment. The steel segment is connected to the concrete segment by prestressed bolts and prestressed steel strands, which both pass through the concrete wall and are anchored at the bottom of the steel segment. The traditional transition segment (T-C80RC) uses a large amount of steel reinforcement, including horizontal circular reinforcement, vertical reinforcement, channel-strengthen reinforcement, and constructional reinforcement, as shown in Figure 2(a). In this study, a novel transition segment using UHPC (T-UHC140) without ordinary steel reinforcement is proposed. Figure 2(b) shows a sketch of the T-UHC140, and Table 1 summarizes the dimensions and the reinforcement ratio of the T-UHC140 segment. The material parameters used in this paper are listed in Table 2.

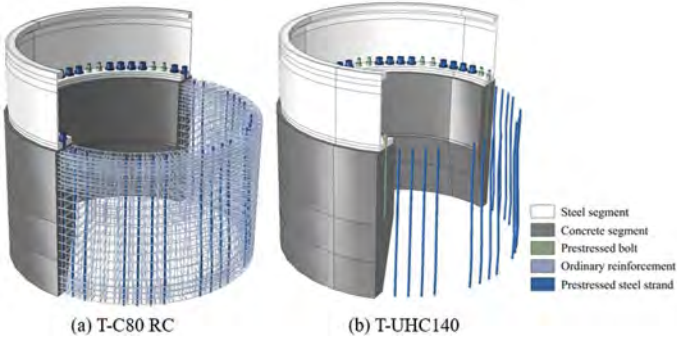


Figure 2. 3D view of transition segment.

Table 1. Dimensions and reinforcement ratio of transition segment.

Type*	D_{tu} (mm)	D_{tb} (mm)	t_{ru} (mm)	t_{tb} (mm)	h_{tb} (mm)	h_{tc} (mm)	h_{tu} (mm)	ρ_v (%)			
								R_{hc}	R_v	R_{cs}	R_c
T-C80RC	4180	4300	460	220	2500	1240	1500	0.84	0.60	0.55	0.85
T-UHC140								0	0	0	0

* T-C80RC is the transition segment with C80 reinforced concrete segment; T-UHC140 is the transition segment with UHC140 segment without ordinary reinforcement; D_{tu} , D_{tb} , t_{ru} , t_{tb} , h_{tb} , h_{tc} , and h_{tu} are indicated in Figure 1; R_{hc} is horizontal circular reinforcement; R_v is vertical reinforcement; R_{cs} is channel strengthen reinforcement; R_c is constructional reinforcement; and ρ_v is volume ratio of reinforcement.

Table 2. Material parameters of structural components.

Component*	Material	E (MPa)	ν	P (kg/m ³)	σ (MPa)	α (°C ⁻¹)
Concrete segment	C80	3.8×10^4	0.2	2400	-	-
	UHC140	4.6×10^4	0.2	2400	-	-
Ordinary reinforcement	HRB400	2.0×10^5	0.3	7900	360	-
Prestressed steel strand	1860 class 15.2mm	1.95×10^5	0.3	7900	1320	1.2×10^{-5}
Steel segment	Q355NE	2.0×10^5	0.3	7900	290	-
Prestressed bolt	10.9M56	2.0×10^5	0.3	7900	900	1.2×10^{-5}

* E is Young's modulus; ν is Poisson's ratio; ρ is density; σ is yield strength; and α is thermal expansion coefficient.

2.2 Constitutive model and concrete damage-plasticity model

The constitutive models of C80 high-strength concrete and UHC140 are shown in Figure 3. The constitutive model of C80 high-strength concrete is defined according to GB50010-2010. For C80 concrete, the standard value of compressive strength (f_{ck}) is 50.2 MPa, the standard value of tensile strength (f_{tk}) is 3.11 MPa, the design value of compressive strength (f_c) is 35.9 MPa, and the design value of tensile strength (f_t) is 2.22 MPa.

The constitutive models for uniaxial tensile and compression proposed by Du (Du 2014) are employed for UHC140. The test values in reference (Zhang 2020) are used for the compressive strength (f_{Uck}), the standard value of tensile strength (f_{Utk}), the design value of compressive strength (f_{Uc}), and the design value of tensile strength (f_{Ut}), which are 123.8 MPa, 7.27 MPa, 88.35 MPa, and 5.20 MPa, respectively. The maximum compressive and tensile strains are $3309\mu\epsilon$ and $1500\mu\epsilon$, respectively.

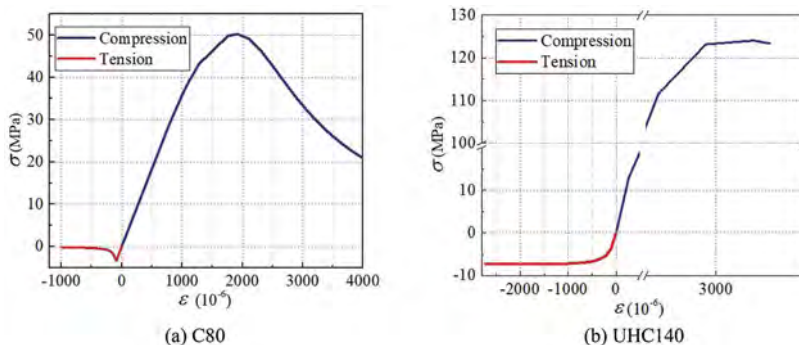


Figure 3. Concrete constitutive model.

The tensile and compressive damages of concrete are characterized by the concrete damage-plasticity model (CDPM). This model is capable of representing the crack formation and post-cracking behavior of reinforced concrete in stress-strain curves under compression and tension.

The CDPM parameters selected for C80 and UHC140 are shown in Table 3. The values of CDPM parameters for high-strength concrete have been widely used, while the values of CDPM parameters for UHPC varies depending on strength levels (Li 2009; Lee and Fenves 1998). The selected values of CDPM parameters for UHC140 are verified by comparing the numerical results from finite element models with experimental data.

Table 3. Concrete damage-plasticity model parameters.

Material	Dilation angle (°)	Eccentricity	f_{b0}/f_{c0}	K	Viscosity parameter
UHC140	28	0.1	1.16	0.667	0.005
C80	30	0.1	1.16	0.667	0.005

2.3 Load cases

Three load cases for a typical wind turbine tower are considered (Table 4). SLS-S1 is used to check the serviceability limit state in S1 level.

Table 4. Load cases for a wind turbine tower.

Case	M_x (kN·m)	M_y (kN·m)	M_z (kN·m)	F_x (kN)	F_y (kN)	F_z (kN)
SLS-S1	6583.9	41537.3	440.8	917.4	4.8	-5458.8

3 NUMERICAL RESULTS

3.1 Compressive stress level

Figure 4 shows the contours of the principal compressive stress in concrete segments of T-C80 RC and T-UHC140 for load case SLS-S. The compression zone is identified by negative sign, while the tension zone is identified by positive sign. The distribution patterns of principal stresses are similar between T-C80 RC and T-UHC140 segments. The volume ratios of elements in various stress levels are profiled in Figure 5, where the limit-state stress is defined as $\sigma_c/0.6f_{ck}$ and $\sigma_{Uc}/0.6f_{Uck}$. It is observed that all elements are positioned below 1 in the horizontal axis except only a few elements at the bolt hole due to the stress concentration, which implies that both T-C80 RC and T-UHC140 segments meet the design requirements for the serviceability limit state in SLS-S1. Further, most elements in T-UHC140 are distributed in the range of $\sigma_{Uc}/0.6f_{Uck} < 0.4$, while most elements in T-C80 RC are distributed in the range of $\sigma_c/0.6f_{ck} < 0.7$. Thus, T-UHPC140 has a lower compressive stress level and a higher stress safety margin than T-C80 RC, but concrete material in T-C80 RC more saturates the compressive performance.

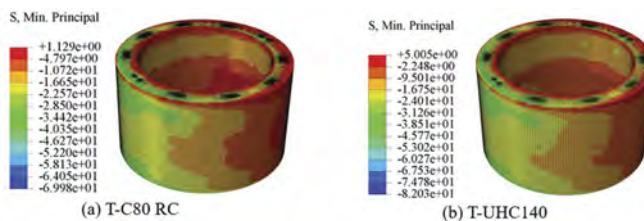


Figure 4. Principal compressive stress.

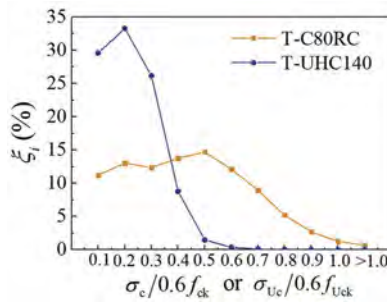


Figure 5. Volume ratio of various stress levels.

3.2 Tensile stress level and class of cracking control

Figure 6 shows the contours of the principal tensile stresses in T-C80 RC and T-UHPC140 segments for load case SLS-S. The tensile stress levels of concrete segment are not defined in current design codes, and cracks are usually allowed in the concrete segment under working condition. In this study, the tensile stress level is indexed by the volume ratio of elements in various stress intervals ξ_i . Figure 7 plots ξ_i profiles in terms of σ_t/f_{tk} and σ_{Ut}/f_{Utk} . It is found that the elements exceeding the requirement value of tensile strength appear at the bolt holes, where the stress concentration occurs. However, their volume ratio is less than 1%, which is negligible. Otherwise, the stress level (σ_t/f_{tk} or σ_{Ut}/f_{Utk}) is less than 1 and the values are relatively low, which indicates a low tensile stress in concrete segments of T-C80 RC and T-UHC140. In addition, T-UHC140 is manifested by a lower tensile stress level than T-C80 RC.

The class of crack control in the concrete segment of T-C80 RC and T-UHC140 can be classified as level 2 from GB50010-2010 [8], since the concrete tensile stress is lower than the concrete tensile strength. Because of the lower tensile stress, T-UHC140 facilitates a good crack control, which is even better than that of ordinary reinforced concrete.

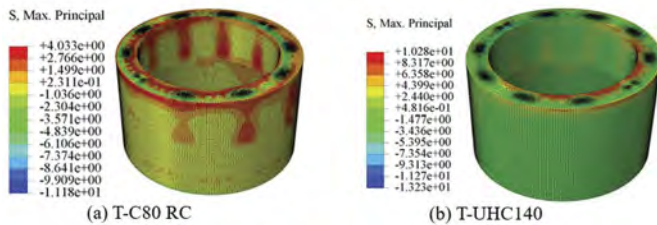


Figure 6. Principal tensile stress.

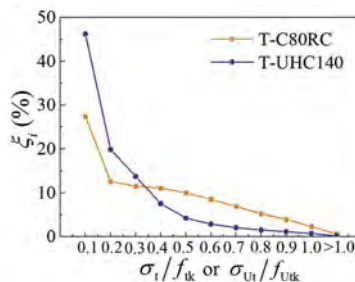


Figure 7. Volume ratio of various stress levels.

4 CONCLUSIONS

In this paper, a novel prestressed UHPC transition segment without ordinary reinforcement for super tall H160 wind turbine is proposed. In the transition segment of the tower, the prestressed UHC140 concrete segment without ordinary reinforcement can replace the prestressed C80 reinforced concrete segment. In load cases SLS-S1, the stress distribution of T-UHC140 and T-C80 RC is similar, while T-UHC140 possesses better mechanical properties and higher stress safety margin than T-C80 RC.

ACKNOWLEDGEMENTS

This work was supported by the National Natural Science Foundation of China (Grant number 52178195), Harbin city science and technology innovation talents special funds (2011RFLXG014), the open fund of Fujian Provincial Key Laboratory of Multi-disasters Prevention and Mitigation in Civil Engineerings (College of Civil Engineering, Fuzhou University).

REFERENCES

- Lana, J. 2021. Behaviour study of prestressed concrete wind-turbine tower in circular cross-section. *Engineering Structures* 227:111403.
- Weinand, J.M. 2022. High-resolution large-scale onshore wind energy assessments: A review of potential definitions, methodologies and future research needs. *Renewable Energy* 182:659–684.
- Yu, J. 2020. Experimental and multi-scale numerical investigation of ultra-high performance fiber reinforced concrete (UHPC) with different coarse aggregate content and fiber volume fraction. *Construction and Building Materials* 260:120444.
- Brian, F. 2001. FHWA gives superior marks to concrete bridge girder. *Civil Engineering Magazine* 71(10): 12–13.
- Ridha, M.M.S. & Sarsam, K.F. & Al-Shaarbaf, I.A.S. 2018. Experimental study and shear strength prediction for reactive powder concrete beams. *Case Studies in Construction Materials* 8:434–446.
- Jammes, F. 2009. *Design of Wind Turbines with Ultra-High Performance Concrete*. Cambridge. Massachusetts Institute of Technology.
- Lewin T, Sritharan S. 2010. *Design of 328-ft (100-m) Tall Wind Turbine Towers Using UHPC*. Iowa: Iowa State University.
- GB50010-2010. 2015. *Code for design of concrete structures*. Beijing: Architecture & Building Press.
- Du, R. 2014. *Study on ultimate bearing capacity of activated powder concrete beams and arches*. Fuzhou: Fuzhou University.
- Zhang, T. 2020. *Numerical simulation and experimental analysis of bending performance of reinforced ultra high performance concrete (UHPC) beams*. Wuhan: Wuhan University of Technology.
- Li, H. 2009. *Parameter identification for reactive powder concrete damage plasticity constitutive model and FEM verification*. Beijing: Beijing Jiaotong University.
- Lee, J. & Fenves, G.L. 1998. Plastic-damage model for cyclic loading of concrete structures. *Journal of Engineering Mechanics* 124(8): 892–900.

Applications of drone inspection and use of strain-hardening cementitious composites (ECC/SHCC) in lowering carbon footprint and lifecycle cost of bridges

D.K. Mishra, P. Ranjan & H. Sun
Raspect AI, Hong Kong SAR, PR China

J. Yu
Sun Yat-Sen University, Guangzhou, PR China

P.L. Ng
Vilnius Gediminas Technical University, Vilnius, Lithuania

ABSTRACT: Drone inspection is becoming quite common in condition monitoring of built infrastructure such as bridges. For the repair of defects identified from such inspection use of Engineered Cementitious Composites (ECC), also known as Strain-Hardening Cementitious Composites (SHCC), a class of advanced fibre-reinforced cement-based materials with ductile tensile properties can be effectively used as indicated in many structural applications over the last twenty years. In particular, their use in link slabs of the bridge decks as well as other structural elements in reinforced concrete and composite bridges is quite noteworthy. This paper reviews several such applications in light of the emerging challenges in bridge design requiring long service life and low life cycle costs throughout operation and maintenance. It is concluded that in spite of its higher initial material cost, the use of ECC/SHCC in bridge construction and repairs would result in lower life cycle costs, carbon footprint and better sustainability.

1 INTRODUCTION

Transportation infrastructure such as roads, bridges, ports, airports etc. are an integral part of the modern landscape. They form the lifeline of cities until they fail to serve the purpose for which they have been designed leading to a significant surge of social costs or even catastrophic accidents (National Academies of Sciences et al. (2020)). As per the American Society of Civil Engineers (ASCE) Infrastructure Report Card released in 2017 (ASCE (2017)), the U.S. has 614,387 bridges, almost four in 10 of which are 50 years or older. Out of them, 56,007 or 9.1% were structurally deficient. Many of the bridges are approaching the end of their design life. The estimate of the investment required for bridge rehabilitation in the US alone is at least US \$123 billion.

An estimated 6.3% of the total bridge deck area belonged to structurally deficient bridges in 2016, a small improvement from 9.5% in 2007 (Figure 1a). The situation in Europe is not much better which was tragically illustrated by the sudden collapse of the Morandi bridge in August 2018 in Genoa, Italy. Subsequently, it was revealed that a declining investment in routine inspection, repair and maintenance was a leading cause of the failure. The fast-developing economies of countries like India and China account for the bulk of the world's construction activities are also facing the challenge of fast-track building while ensuring durability, resiliency and sustainability, as illustrated in Figure 1b (Li (2019b)).

1.1 *Current challenges in bridge engineering*

The challenges faced by the infrastructure sector as a whole be it transportation (land, water, air), water (irrigation, drinking water), or power generation (thermal, nuclear, renewable etc.) - all have many common features such as design for long service life, the minimum cost of maintenance, minimum carbon footprint in both construction and operation etc. (Lepech and Li (2009)). A specific category of transportation infrastructure such as bridges has specific challenges that must be addressed. Among these, ensuring a long service life of up to and exceeding 100 years is a major challenge faced by engineers all over the world. Keoleian et al (Keoleian et al. (2005)) discussed a life cycle modelling-based concrete bridge design approach to compare the use of an ECC link slab to replace conventional steel expansion joint which is often a source of major damage needing frequent repairs. The demolition, repair, and recycling of materials and wastes from deteriorated infrastructure remain to be studied in detail. The development of low life cycle cost, low-carbon modular design is beneficial to the reduction of infrastructure deficiency (Kaewunruen et al. (2016)). ASCE (2017) recommended the following key actions to address the challenges of bridge infrastructure, among others.

- Increase funding from all levels of government to continue reducing the number of structurally deficient bridges, decrease the maintenance backlog, and address the large number of bridges that have passed or are approaching the end of their design life.
- Bridge owners should consider the costs across a bridge's entire life cycle to make smart design decisions and prioritize maintenance and rehabilitation.

1.2 *Drone inspection of bridges*

Drone (also referred to as unmanned aerial system, or UAS) inspection of bridges is an increasingly popular method being adopted by the engineering community worldwide (Shi et al. (2021); Azari et al. (2022)). Drones are able to provide a detailed view of the bridge, allowing engineers to identify any potential issues in the structure. Drone inspections are becoming more and more common as they offer a cost-effective way to inspect bridges quickly and accurately (see Figure 3). Drones provide an efficient way to inspect the bridge structure, allowing the inspector to quickly identify any potential issues. Drone inspections can provide a detailed overview of the bridge and identify any structural problems, such as cracks, corrosion, and deterioration. Additionally, drones are able to provide high-resolution images of the bridge, allowing for detailed analysis of the structure.

The use of drones for fracture-critical inspections is more challenging at present. Cameras and today's sensors still have little capability to see through dirt, debris, and corrosion which can hide critical defects. However, using the primary payloads of high-resolution visual and thermal imaging cameras, modern drones can identify most of the defects such as cracks, delamination, spalling, corrosion etc. That needs immediate attention. One of the challenges of data generated by a drone inspection is its voluminous nature which made it impossible to analyse using conventional manual methods. Machine learning and AI have made it possible to automate the processing of such voluminous data to identify the most common defects. An advantage of drone inspection of is the possibility for comparison of the inspection data collected at different points of time to estimate the change in the condition of the structure as illustrated in Figure 1b.

2 THE USE OF ECC/SHCC

Once the defects in the bridge are identified, the repair and maintenance require the selection of the right materials and methods for the best results. Innovation in new technologies, especially the development of materials such as fibre-reinforced composites is enabling bridges to be built stronger, last longer, require less maintenance and have a lower carbon footprint. As already discussed, Sensors and robots such as drones are being used in both new and old bridges for real-time or near real-time structural health monitoring so that problems can be identified and addressed earlier to improve public safety. To reduce the time for the construction or repair of bridges, prefabricated elements are being increasingly used. Engineered Cementitious

Composites (ECC) or Strain-Hardening Cementitious Composites (SHCC) is a class of fibre-reinforced cement-based composites that can be designed for a range of compressive strength while ensuring a requisite degree of tensile ductility (Li and Mishra (1996); Li (2008)).

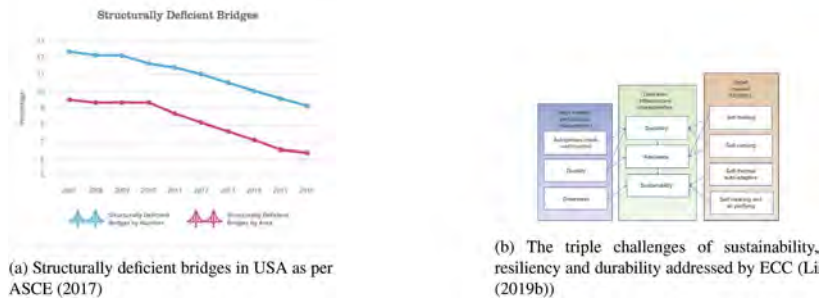


Figure 1. Structural design and sustainability.

As shown in Figure 3, the characteristic material property of ECC is reflected by its tensile stress-strain behaviour and cracking pattern. In contrast to the brittle nature of plain concrete which fails with a single crack under relatively low tensile stress, and the characteristic strain-softening behaviour of ordinary fibre-reinforced concrete, ECC continues to carry tensile stress beyond the first crack and even exhibits tensile strain-hardening accompanied by multiple micro-cracking phenomena. As a result, the average and maximum crack width of ECC is typically below 100 microns or less. These two unique properties of ECC, namely the high tensile strain capacity and inherent crack width control, can be effectively deployed in a number of structural applications to address major challenges faced by bridges, as discussed in previous sections. Figure 4 shows the graphical representation of a brief literature review undertaken to understand the state of progress in terms of the application of ECC/SHCC in real-life bridge scenarios using the connected papers' graphical representation. Table 1 gives a list of such applications taken from the textbook by Li (Li (2019a)).

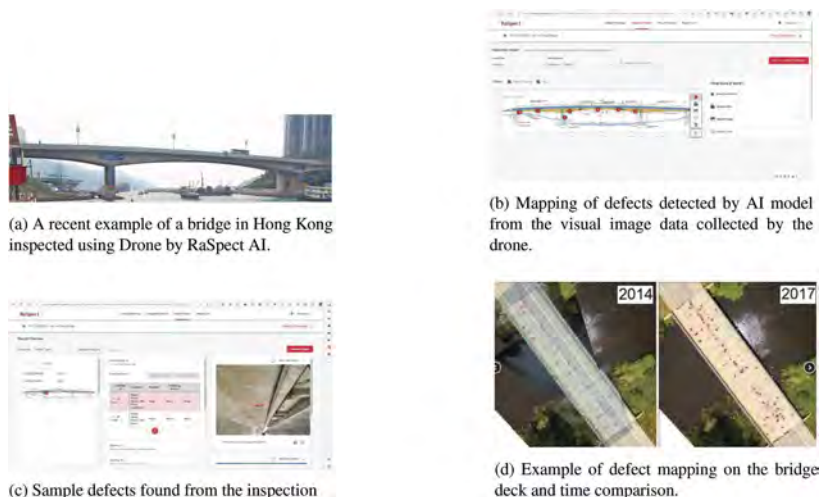


Figure 2. Moving towards drone-based monitoring.

2.1 Link slabs for bridge joints

Lack of watertight bridge joints leads to water leakage, which would cause premature deterioration and failure of the beam support zones, bearings, and underlying substructure elements. This is a major source of deterioration that requires frequent repairs. The application of ECC/

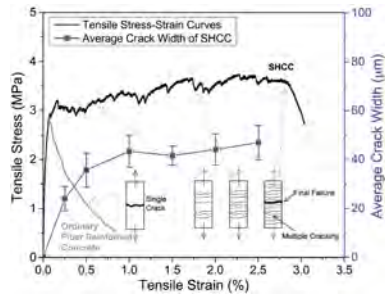


Figure 3. Typical tensile stress–strain behaviour of ECC with average crack-width data (Mishra, D K Yu, J Das, A Leung 2018).

Table 1. Application of ECC in transport infrastructure (bridge) [Li (2019a)].

Application	Problem Solved	ECC property utilized	Placement method
The bridge deck and road pavement link-slab retrofits	Reduce frequency and cost of bridge deck maintenance; Reduce traffic noise	Tensile ductility to accommodate thermal deformation; tight crack width; Fatigue resistance; wear durability	Cast-in-place or precast
Composite bridge deck	Reduce the risk of fatigue failure of steel deck; Reduce cost and weight	Tensile ductility; fatigue resistance	Cast-in-place
Patch repair of bridge deck	Reduce maintenance frequency and cost	Tensile ductility; durability against wheel loads and chloride environment	Cast-in-place
Rigid-frame railway bridge beam-column joint connection	Reduce steel reinforcement congestion	High shear capacity even without steel reinforcement	Precast in factory



Figure 4. Connected papers map showing (a) drone inspection of bridges, (b) application of ECC link slab in bridge deck joint linked to (Lepech and Li (2009)).

SHCC link slabs in place of conventional bridge joints offers an innovative solution to the problem. Lepech and Li (Keoleian et al. (2005)) developed a Life Cycle Assessment model specifically for bridge decks accounting for materials production and supply chain, construction and maintenance processes, construction-related logistics, and end-of-life management. The model indicated that the ECC/SHCC bridge deck system has significant advantages over conventional joints. It has 40% less life cycle energy consumption, 50% less solid waste generation, and 38% less raw material consumption. Based on the findings by (Keoleian et al. (2005)), construction-related traffic congestion was a dominant factor in life cycle cost assessment. The first ever real-life application of ECC link slab was launched at a bridge in Grove Street over the inter-state highway I-94 under the Michigan Department of Transportation (MDOT) (Lepech and Li (2009)). The performance of this bridge has been monitored ever since and it has been found to have performed exceedingly well throughout the reporting period up till 2015 (Li (2019a)).

Figure 5 shows a schematic of the link slab and a photograph of a similar bridge where an ECC link slab was implemented by the Virginia Department of Transport (VDOT) recently in 2018 (Walus and Engineer (2010)). According to (Thorkildsen et al. (2020)), the US Department of Transportation reports widespread practice of replacing conventional joints in bridge decks with link slabs by various state departments of transportation in New York, Maryland, Virginia and Massachusetts etc. Many of these applications including those in Virginia and Maryland reported successful use of ECC/SHCC and ultra-high-performance concrete (UHPC) in the construction of link slabs. Such applications are gaining popularity all over the world not only for joints at bridge decks (Hou et al. (2018)) but also in regular concrete road pavements (Zhang et al. (2017, 2010)). Compared to asphalt pavements, the driving comfort of concrete pavements is normally lower due to the existence of joints. The joints also reduce the durability of the reinforced concrete pavement due to susceptibility to infiltration of moisture and deicing salt etc. which in turn causes corrosion of reinforcement. Repair and maintenance cost is thus likely to increase with the presence of joints. By using low-shrinkage engineered cementitious composite (LSECC) strips in place of joints of conventional concrete pavement, it is possible to localize the fine cracks into the LSECC strip and significantly enhance long-term durability and reduce maintenance cost. This technique has been already applied to real-life projects in Japan (Rokugo (2010)) and China (Zhang et al. (2017, 2013)).

2.2 Bridge deck repair

Potholes on highway pavement surfaces, especially on concrete bridge decks have been arising concerns among transportation authorities and infrastructure/maintenance engineers. Asphalt pavements are notorious for their susceptibility to moisture ingress and the formation of potholes that require frequent repair. Concrete, on the other hand, is a longer-lasting alternative. However, it is also prone to cracking, delamination, and spalling and needs constant monitoring and repair. Bridge decks and pavements made of steel-reinforced concrete is additionally prone to corrosion-induced cracking and delamination. Dynamic loading from vehicular traffic causing fatigue is another major accelerating factor of such damage. Sahmaran and Li (Sahmaran et al. (2008)) showed that the high tensile ductility of ECC/SHCC can yield higher resistance to corrosion-induced spalling. It was also found that after 100k cycles of fatigue loading, the crack width in the reference concrete link slab specimen increased from 50 μm to greater than 0.6 mm, while the crack width in the ECC link slab remained close to 50 μm (Li (2008); Lepech and Li (2006a)) showed the superior performance of High Early Strength ECC (HES-ECC) as an overlay patch repair material under fatigue loading. Actually, one of the early applications of ECC was in patch repair of concrete pavements in which a high early strength ECC was deployed (Lepech and Li (2006b)). An ECC patch repair was carried out at the bridge deck of Curtis Road over highway M-14 in southern Michigan state in October 2002 in collaboration with the Michigan Department of Transportation (MDOT). In comparison with a side-by-side patch repaired with a conventional pre-packed commercial patching material, ECC performed far better. While in two years the conventional repair material had heavily deteriorated and had to be re-done, the ECC patch demonstrated desirable performance without much cracking and damage until the year 2007 when the entire bridge deck was re-laid. Another example of a real-life application of ECC for patch repair was carried out in November 2006. A HES-ECC patch repair was implemented at Ellsworth Road Bridge over highway US-23 (S07 of 81074) in Ann Arbor, Michigan (Lepech and Li (2006b)) with MDOT. The HES-ECC was a self-compacting mix and it was compared with the performance of a side-by-side patch done with Thoroc 10-60 (a commercial patch repair material). In the subsequent 2 to 3 years, the performance of ECC as a durable repair material was proven satisfactory in one of the harshest environments comprising effects of restrained shrinkage, freeze-thaw cycles, deicing salts, temperature fluctuations etc., in addition to heavy traffic loads. The damage in the ECC patch was minimal with maximum crack width remaining less than 100 μm in the ECC, as opposed to close to 2 mm in the control.

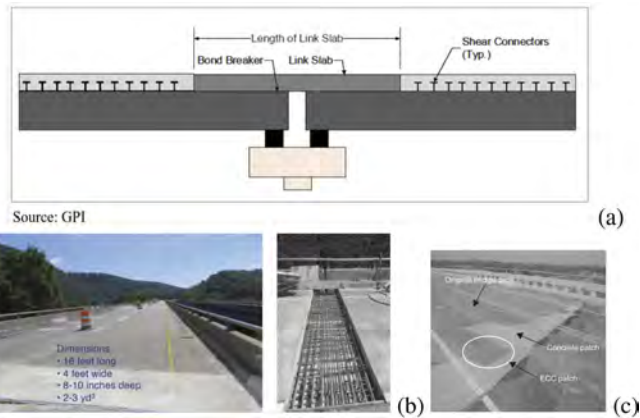


Figure 5. (a) Schematic of a typical full-depth link slab (Thorkildsen et al. (2020)) (b) Photograph of the ECC link slab on I-64 over Dunlap creek by VDOT (Walus and Engineer (2010)) (c) Photograph of the first patch repair using ECC on a bridge deck of Curtis Road in Ann Arbor, Michigan in 2002 (Li (2014)).

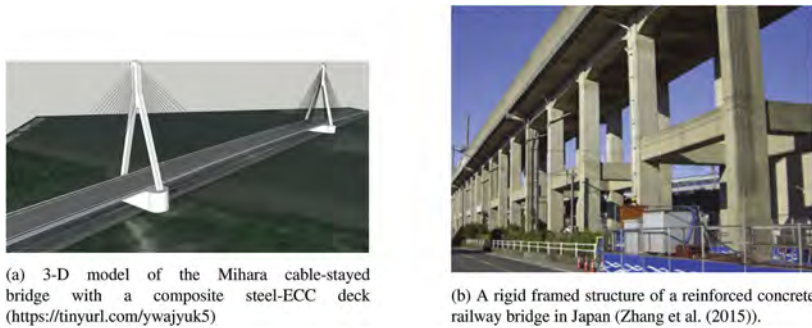


Figure 6. 3-D model and rigid structure.

2.3 Composite bridge deck

ECC/SHCC can be a suitable material for composite construction as shown by (Zhang et al. (2019)) where they have also taken into account the self-healing ability of ECC/SHCC which enhances its durability characteristics. A composite bridge deck taking advantage of the durability of ECC owing to its tight crack-control ability was designed and built in 2004 in Japan. The Mihara bridge in Hokkaido was a 962 m long cable-stayed bridge with a middle span of 340 m and a full deck area of 20,000 m^2 . It had a 38 mm thick ECC top layer to protect the steel deck underneath from corrosion. The bridge was opened to traffic in 2005 and it had a designed service life of 100 years. It is expected that the savings from reduced maintenance and repair costs would be substantial for the structure over its service life. Figure 6a shows a 3-D model of the bridge.

2.4 Strengthening bridge structure

ECC/SHCC has been proven to be a suitable material for applications where the structure is required to resist dynamic loads such as in an earthquake. Because of the high energy absorption capacity of ECC/SHCC stemming from its unique energy-dissipating failure mode, many researchers have used ECC/SHCC to form critical joints in structures subject to cyclic loading. It was concluded that ECC/SHCC outperforms conventional concrete in strengthening bridge structures (Li and Mishra (1996)). In a review paper, (Shang et al. (2019)) have cited a large number of studies that showed the advantages of ECC/SHCC as a repair material for structural strengthening over the conventional approach which uses fibre-reinforced plastics (FRP) and steel plates.

FRP is a brittle material and is prone to debonding from the substrate concrete, whereas steel plates are susceptible to corrosion. In a comprehensive experimental study, (Zhang et al. (2015)) showed the advantage of using ECC in mitigating the reinforcement congestion problem in beam-column joints designed as per the earthquake-resistant code requirements in Japan. At shear span to depth ratio $a/d = 2.8$, the shear capacity of the beams with and without stirrups increased by 20.6% and 107.6% respectively when using ECC in lieu of conventional concrete.

2.5 Other potential applications and scope for future research

Among other applications of ECC/SHCC that are in the domain of transportation in general are tunnel lining, repair of viaducts, structural strengthening of embankments and ports using FRP-reinforced or fabric-reinforced ECC/SHCC etc. Given the micromechanical design basis of ECC/SHCC, it can be tailored for individual situations by identifying the structural performance requirements and establishing a link with material properties. It is expected that in forthcoming years with the accumulation of more research data and field performance information, applications of ECC/SHCC combined with robotic inspection in real-life structures will get a big boost.

3 CONCLUSIONS

Robotic and drone inspection of bridge structures followed by the application of Engineered Cementitious Composites (ECC) or Strain-Hardening Cementitious Composites (SHCC) in repairs and other use in bridge engineering have been illustrated by citing real-life examples. This study indicates that advanced fibre-reinforced cement composites such as ECC/SHCC with their high tensile ductility and intrinsic tight crack width control can be utilized in both new and old bridges effectively. Such application can enhance structural safety and resilience while making concrete bridges more durable and thereby reducing their life cycle cost. Specifically, the following conclusions can be drawn:

- Robotic inspection of structures such as bridges using unmanned aerial vehicles commonly known as drones is becoming increasingly popular.
- identifying major and critical defects that need urgent attention is easier, less costly and safer using such methods.
- ECC/SHCC is an excellent material choice for long-lasting and durable repair of concrete pavements including bridge decks.
- Use of ECC/SHCC link slabs in place of conventional joints at bridge decks, as well as concrete pavements, can save maintenance costs, reduce traffic disruption and increase service life.
- Using ECC/SHCC in critical structural elements and joints can enhance the ductile performance of bridges under dynamic loads such as heavy traffic and earthquakes.
- Further accumulation of laboratory research and field performance data is beneficial to promote more ECC/SHCC applications in real-life structures.

ACKNOWLEDGEMENTS

Prof. Dhanada K. Mishra would like to thank KMBB College of Engineering and Technology for permitting his sabbatical at HKUST from September 2017 to January 2021. Dr. P.L. Ng would like to acknowledge the support from the European Regional Development Fund (Project no. 01.2.2-LMT-K-718-03-0010) under a grant agreement with the Research Council of Lithuania (LMTLT).

REFERENCES

- ASCE (2017). 2017 infrastructure report card. In *American Society of Civil Engineers*.
- Azari, H., O'Shea, D., and Campbell, J. (2022). Application of unmanned aerial systems for bridge inspection. *Transportation Research Record*, 2676(1):401–407.

- Hou, M., Hu, K., Yu, J., Dong, S., and Xu, S. (2018). Experimental study on ultra-high ductility cementitious composites applied to link slabs for jointless bridge decks. *Composite Structures*, 204:167–177.
- Kaewunruen, S., Sussman, J. M., and Matsumoto, A. (2016). Grand challenges in transportation and transit systems.
- Keoleian, G. A., Kendall, A., Dettling, J. E., Smith, V. M., Chandler, R. F., Lepech, M. D., and Li, V. C. (2005). Life cycle modeling of concrete bridge design: Comparison of engineered cementitious composite link slabs and conventional steel expansion joints. *Journal of infrastructure systems*, 11(1):51–60.
- Lepech, M. D. and Li, V. C. (2006a). Long term durability performance of engineered cementitious composites/langzeitbeständigkeit systematisch entwickelter zusammengesetzter zement gebundener werkstoffe. *Restoration of Buildings and Monuments*, 12(2):119–132.
- Lepech, M. D. and Li, V. C. (2006b). Long term durability performance of engineered cementitious composites/langzeitbeständigkeit systematisch entwickelter zusammengesetzter zement gebundener werkstoffe. *Restoration of Buildings and Monuments*, 12(2):119–132.
- Lepech, M. D. and Li, V. C. (2009). Application of ecc for bridge deck link slabs. *Materials and Structures*, 42(9):1185–1195.
- Li, M. (2014). Engineered cementitious composites for bridge decks. In *Advanced composites in bridge construction and repair*, pages 177–209. Elsevier.
- Li, V. C. (2008). Engineered cementitious composites (ecc) material, structural, and durability performance.
- Li, V. C. (2019a). *Engineered cementitious composites (ECC): bendable concrete for sustainable and resilient infrastructure*. Springer.
- Li, V. C. (2019b). High-performance and multifunctional cement-based composite material. *Engineering*, 5(2):250–260.
- Li, V. C. and Mishra, D. (1996). Structural applications of engineered cementitious composites. National Academies of Sciences, E., Medicine, et al. (2020). Critical issues in transportation 2019.
- Rokugo, K. (2010). Tension tests and structural applications of strain-hardening fiber-reinforced cementitious composites. *Fracture Mechanics of Concrete and Concrete Structures*, pages 1533–1540.
- Sahmaran, M., Li, V. C., and Andrade, C. (2008). Corrosion resistance performance of steel-reinforced engineered cementitious composite beams. *ACI Materials Journal*, 105(3):243.
- Shang, X.-Y., Yu, J.-T., Li, L.-Z., and Lu, Z.-D. (2019). Strengthening of rc structures by using engineered cementitious composites: A review. *Sustainability*, 11(12):3384.
- Shi, X., Olvera, A., Hamilton, C., Gao, E., Li, J., Utke, L., Petruska, A., Yu, Z., Udpa, L., Deng, Y., et al. (2021). Ai-enabled robotic nde for structural damage assessment and repair. *Materials Evaluation*, 79(7).
- Thorkildsen, E. T. et al. (2020). Case study: Eliminating bridge joints with link slabs-an overview of state practices. Technical report, United States. Federal Highway Administration.
- Walus, K. R. and Engineer, B. (2010). Dot design construction guidelines recent updates – bridge specifications. *National Steel Bridge Alliance Award*.
- Zhang, H., Lepech, M. D., Keoleian, G. A., Qian, S., and Li, V. C. (2010). Dynamic life-cycle modeling of pavement overlay systems: Capturing the impacts of users, construction, and roadway deterioration. *Journal of Infrastructure Systems*, 16(4):299–309.
- Zhang, J., Chen, Q., Wang, Z., Chen, C., Guo, Z., and Fu, Y. (2017). Design and construction of jointless concrete pavement. *Harbin Gongye Daxue Xuebao*, 49(03):68–73.
- Zhang, J., Wang, Z., and Ju, X. (2013). Application of ductile fiber reinforced cementitious composite in jointless concrete pavements. *Composites Part B: Engineering*, 50:224–231.
- Zhang, R., Matsumoto, K., Hirata, T., Ishizeki, Y., and Niwa, J. (2015). Application of pp-ecc in beam-column joint connections of rigid-framed railway bridges to reduce transverse reinforcements. *Engineering Structures*, 86:146–156.
- Zhang, Z., Hu, J., and Ma, H. (2019). Feasibility study of ecc with self-healing capacity applied on the long-span steel bridge deck overlay. *International Journal of Pavement Engineering*, 20(8):884–893.

Chloride-attack fragility curve: The probability of failure is estimated at a life expectancy

J.H. Kim, T.H. Han & D.J. Jeong

Korea Advanced Institute of Science and Technology, Daejeon, Republic of Korea

ABSTRACT: Chloride attack is one of the significant problems affecting the durability of concrete structures. The time for chloride ions arriving reinforcing bars is an indicator to predict service life in the view of the rebar corrosion. The diffusivity of chloride ions in concrete is a key factor for the prediction of service life, but it is inherently distributed at a large variation. Considering the diffusivity as a random variable allows us to analyze the inherent variation. A large number of mortar samples are subjected to a test measuring the diffusivity using a miniature device complying with NT BUILD 492. The statistical distribution of the diffusivity can be developed with the measurements. Applying Fick's 2nd law with the diffusivity results in calculating the probabilistic life span of a given structure. This study finally proposes chloride-attack fragility by evaluating the probability of failure at life expectancy.

1 INTRODUCTION

The durability of concrete is designed to have sufficient resistance to chloride attack. The chloride ions permeated in concrete break the passivation of reinforcing bars, which results in initiating their corrosion. Modeling the diffusion of chloride ions in concrete allows us to predict the time to the initiation of corrosion, and it is often referred to as service life (Alexander and Thomas 2015). In contrast with the deterministic prediction, a probabilistic approach on the modeling provides the range of expected time (Bentz 2003, Kwon *et al.* 2009). It is beneficial to manage the risk of corrosion.

Furthermore, for the risk quantification we need to consider aleatory and epistemic variabilities in the probabilistic approach (Electric Power Research Institute 2018). The former stems from randomness of a performance variable (Ait-Mokhtar *et al.* 2013), which cannot be removed in practice. The latter considers the uncertainty of the model or data describing the variable. Additional experiment or detailed analysis may reduce the epistemic variability on the variable. This paper proposes a chloride-attack fragility curve considering the two variabilities independently. The fragility curve provides the probability of failure (corrosion) at a specific age (time), where the confidence level considering the uncertainty variability is specified.

2 CHLORIDE-ATTACK FRAGILITY

2.1 Fragility curve

The probability of failure is evaluated by comparing the demand and capacity of concrete durability. The demand curve indicates the requirement for concrete that should be durable, while the capacity curve represents its performance. Both indexes are represented by the probabilistic density function of age (time).

The fragility accounts for the probability of which the demand exceeds the capacity of concrete durability, and it can be depicted by the overlapping area in Figure 1. The probability density of failure is given by

$$f_X(x) = P\{X < 1\} \quad (1)$$

where $X=R/L$. Here, the probabilistic variables R and L are the capacity (resistance) and demand (load) of concrete durability, respectively. We can presume that R and L are mutually independent. The fragility curve refers the cumulative distribution of the failure,

$$F_X(x) = P\{X < x\} = \int_{-\infty}^x f_X(\xi) d\xi \tag{2}$$

and it evaluates the non-exceedance probability at the specified age (x) of a concrete structure.

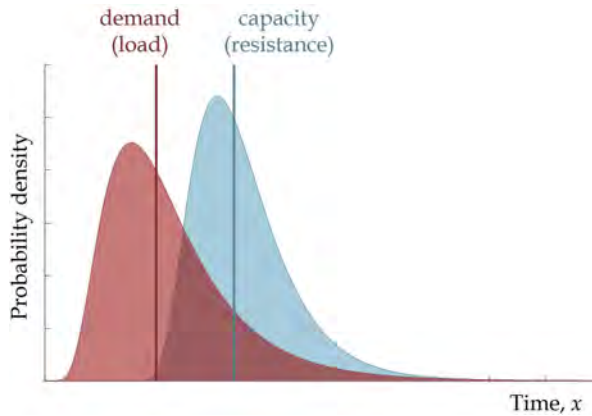


Figure 1. Demand and capacity represented by a probabilistic variable.

Assuming each of R and L curves follow a lognormal distribution, the probability of failure is also represented by a lognormal distribution: $X \sim \ln N(\mu_X, \sigma_X^2)$ where μ_X and σ_X are the mean and standard deviation of the natural logarithm of X , respectively. The probability is then understood by $\ln X = \ln R - \ln L$ complying with Eq. (1). The expectation and variance of X are calculated by

$$E\{X\} = \exp\left(\mu_X + \frac{\sigma_X^2}{2}\right) \tag{3}$$

and

$$\text{Var}\{X\} = (E\{X\})^2 (\exp \sigma_X^2 - 1) = (\exp \sigma_X^2 - 1) \exp(2\mu_X + \sigma_X^2) \tag{4}$$

respectively. The coefficient of variance is then

$$\text{CV}\{X\} = \sqrt{\exp \sigma_X^2 - 1} \approx \sigma_X \tag{5}$$

and sometimes it is simply estimated by σ_X . Lastly, the median is calculated by

$$\text{Med}\{X\} = x_m = \exp \mu_X \tag{6}$$

Normalizing the probability of failure allows us to easily evaluate it using the standard normal distribution,

$$Z = \frac{\ln X - \ln x_m}{\sigma_X} = \frac{\ln(X/x_m)}{\sigma_X} \tag{7}$$

for $Z \sim N(0,1)$. Its cumulative distribution $\Phi(z)$ is conveniently used with the standard normal table. The probability of failure in Eq. (1) and the fragility in Eq. (2) are then given by

$$f_X(x) = P\{\ln X < 0\} = \Phi\left(\frac{0 - \ln x_m}{\sigma_X}\right) = 1 - \Phi\left(\frac{\ln x_m}{\sigma_X}\right) \tag{8}$$

and

$$F_X(x) = P\{\ln X < \ln x\} = \Phi\left(\frac{\ln x - \ln x_m}{\sigma_X}\right) = \Phi\left(\frac{\ln(x/x_m)}{\sigma_X}\right) \quad (9)$$

respectively.

The aleatory and epistemic variabilities can be independently modelled using a double log-normal distribution (Electric Power Research Institute 2018). Taking the aleatory variability (randomness) for the non-exceedance probability allows us to have the true fragility of

$$F_X(x) = \Phi\left(\frac{\ln(x/x_m)}{\beta_R}\right) \quad (10)$$

where β_R is the coefficient for randomness. The estimator of fragility, $F(x)$, needs to be higher than the true fragility. The epistemic variability (uncertainty) addresses the confidence level of $Q = P\{F(x) > F_X(x)\}$, which is considered with an additional lognormal distribution. Assigning the true fragility to the median of the estimator finally provides it as

$$F(x) = \Phi\left(\frac{\ln(x/x_m) + \beta_U \Phi^{-1}(Q)}{\beta_R}\right) \quad (11)$$

where β_U is the coefficient for uncertainty.

Figure 2 shows the fragility curve considering the randomness and uncertainty of X . The uncertainty variability does not affect the fragility at the confidence level of $Q=50\%$, and it passes through the median of each estimator: $F(x)=F_X(x)$ since $\Phi^{-1}(0.5)=0$. For a higher confidence level, the fragility curve moves to left so that the prediction is conservative. The higher uncertainty (β_U) the fragility curves range wider. In contrast, the randomness (β_R) controls the slope of each fragility curve. The fragility curve lies down with a higher β_R .

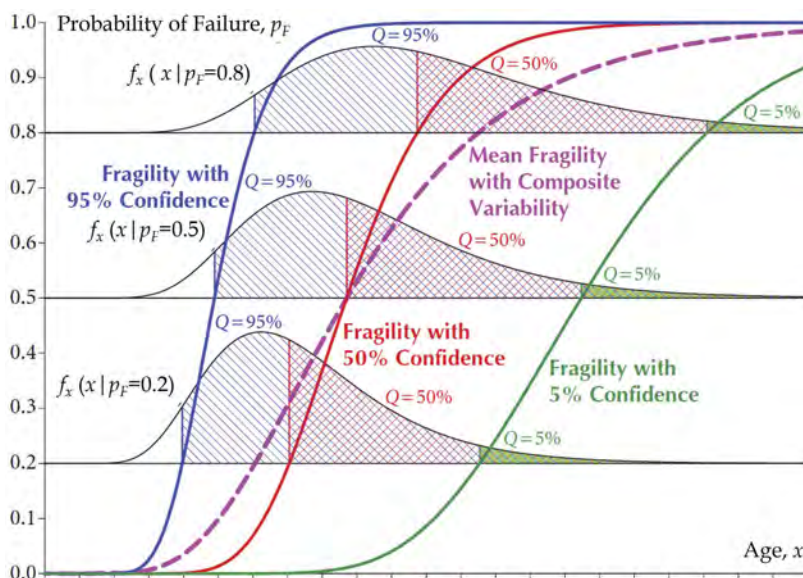


Figure 2. Fragility curve described by a double-lognormal distribution.

3 CHLORIDE-ATTACK FRAGILITY

3.1 Chloride diffusivity and its randomness

The diffusivity of chloride ion and its variation could be measured by the conventional test method (NT Build 492 1999). An experiment using miniature samples was conducted to collect

the variation on the chloride diffusivity. The sample was reduced to a cylinder having 30 mm-diameter and 30 mm-height while its original dimension was 100 mm in diameter and 50 mm high. The reduced dimension was fit to the samples of mortar; coarse aggregates were removed for the dimension. Beyond the dimension of the miniature sample, the procedure to measure the migration depth of chloride ions was the same with that specified in (NT Build 492 1999).

The diffusivity of chloride ion, D , was measured with 16 replicated samples of each mix. Table 1 reports the mix proportion of each mortar mix, where the effect of water-to-cement ratio was examined keeping the sand volume fraction of 58% constant. Type I Portland cement and ISO standard sand were used to produce the samples. In addition to the 30 mm-diameter cylinders for the diffusivity measurement, 40 mm cubes were made to measure the compressive strength of each mix. The strength and diffusivity were measured after the samples had been cured for 28 days. In the table, the mean and standard deviation of the diffusivity were reported. The diffusivity was thought to follow a normal distribution: $D \sim N(\mu_D, \sigma_D^2)$.

Table 1. Mix proportion of mortar samples.

Mix	Water-to-cement ratio	Sand-to-cement ratio	Strength, MPa	Diffusivity (D), $\times 10^{-12}$ m ² /s	
				Mean (μ_D)	Standard deviation (σ_D)
w/b=0.35	0.35	2.4	70.5	13.1	2.42
w/b=0.40	0.40	2.6	63.7	17.8	6.01
w/b=0.50	0.50	3.0	60.2	39.4	11.7

A lower water-to-cement ratio brought the increase in compressive strength and the decrease in diffusivity, as expected. The low water-to-cement ratio enhanced the mechanical resistance and durability of the mixes. Furthermore, it is worthwhile to note that the standard deviation of diffusivity decreased with a lower water-to-cement ratio. The randomness on the diffusivity weakens with the dense microstructure of mortar.

3.2 Uncertainty on critical chloride content

Chloride attack results in the corrosion of reinforcing bars. Passivation of steel breaks down with a certain amount of chloride ion, and consequently its oxidation accelerates leaving iron oxides consisting of rust. Therefore, the service life in terms of chloride attack is usually determined by the time of the passivation breakdown. A criterion for the determination can be stated: We expect corrosion when chloride concentration around the reinforcing bar increases up to a critical content so that the passivation breaks down.

The critical chloride content also shows variation. According to the recent review (Angst 2018), experiments on the critical chloride content, C_c , provided its mean and standard deviation as reported in Table 2. Given that the critical chloride content followed a lognormal distribution, Eqs. (3) and (4) calculated the mean and standard deviation of $\ln(C_c)$ by -0.32 and 0.67, respectively. The median was also calculated by $\text{Med}(C_c)=0.58\%$ using Eq. (6).

Table 2. Critical chloride content.

Critical chloride content (C_c), % by mass	
Mean	Standard deviation
0.91	0.69

On the other hand, in practice the critical chloride content is used as a deterministic variable. For example, $C_c=0.4\%$ is specified as the limit of endurable chloride content for a concrete structure. Its value can decrease with an emphasis on the durability of the structure. The uncertainty on the value of critical chloride content is therefore considered as the epistemic variability associating with the confidence level of the fragility curve.

3.3 Dataset to develop a fragility curve

Chloride-attack fragility curve develops by evaluating the probability of failure at a specific age. The failure due to chloride attack is defined when the migrated chloride content exceeds the critical chloride content with respect to the passivation breakdown. Fick's 2nd law predicts the chloride migration considering the diffusivity:

$$\frac{\partial c}{\partial t} = D \frac{\partial^2 c}{\partial r^2} \quad (12)$$

where $c(r,t)$ is the concentration of chloride at location r and time t . It is expressed in a unit of kg/m³. Given that the concrete is fully saturated having no chlorides, the chloride concentration starts to increase with the migration of chlorides on the external surface. The chloride concentration on the external surface is given by c_0 , and then the chloride concentration in concrete becomes

$$c(r, t) = c_0 \left(1 - \operatorname{erf} \frac{r}{2\sqrt{D \cdot t}} \right) \quad (13)$$

which is the solution of the diffusion equation in Eq. (12). The corrosion of reinforcing bar is declared if $c(r_0,t)=C_c$, where r_0 is the cover locating the reinforcing bar in concrete. Inverting Eq. (13) with respect to t allows us to have the service life of the concrete structure. It becomes a probabilistic variable represented by

$$X = \frac{r_0^2}{4D} \left(\operatorname{erf}^{-1} \left(1 - \frac{C_c}{c_0} \right) \right)^{-2} \quad (14)$$

Here, in this study, it was assumed that the external chloride content was $c_0=3\%$ considering the salinity of seawater and the cover was $r_0=40$ mm as an example.

The service life of X showed variation caused by the uncertainty of the critical chloride content (C_c) as well as the randomness of diffusivity (D). Both variabilities were anchored at the median of X , as described in the previous paragraph, where the fragility indicates 50% probability of failure at 50% confidence level. The aleatory variability (randomness) on the service life was first evaluated keeping 50% confidence. Taking the median of the critical chloride content, $\operatorname{Med}(C_c)=0.58\%$, made Eq. (14) have a probabilistic variable of D only. We have 3 sets of D according to the water-to-cement ratio, as reported in Table 1. A total of 100,000 samples could be produced by Monte-Carlo simulation on each $D \sim N(\mu_D, \sigma_D^2)$, and Eq. (14) resulted in 100,000 samples of X at $Q=50\%$. The coefficient of variance, $\operatorname{CV}\{X\}$ at $Q=50\%$, then approximated the coefficient for randomness (β_R) by Eq. (5)

Second, the epistemic variability (uncertainty) was evaluated at 50% probability of failure. Taking the median of diffusivity, $\operatorname{Med}(D)=13.1, 17.8, \text{ or } 39.4 \times 10^{-12}$ m²/s, leaves a probabilistic variable of C_c in Eq. (14). A total of 100,000 samples were produced by Monte-Carlo simulation on $C_c \sim \ln N(\mu_C, \sigma_C^2)$, and the service life of X at $p_F=50\%$ was calculated for each of the 3 medians of D . $\operatorname{CV}\{X\}$ at $p_F=50\%$ now approximated the coefficient for uncertainty (β_U). Table 3 reports the result of the calculation.

Table 3. Life span and its variation with respect to chloride attack.

Mix	$\operatorname{Med}\{D\},$ $\times 10^{-12}$ m ² /s	$\operatorname{Med}\{C_c\},$ %	x_m or $\operatorname{Med}\{X\},$ year	β_R or $\operatorname{CV}\{X\}$ at $Q=50\%$	β_U or $\operatorname{CV}\{X\}$ for $p_F=0.5$
w/b=0.35	13.1	0.58	9.83	0.35	1.84
w/b=0.40	17.8		5.87	0.71	1.84
w/b=0.50	39.4		1.56	0.60	1.85

3.4 Development of the fragility curve

Chloride-attack fragility curve by Eq. (11) can be developed using the median and the coefficients for randomness and uncertainty. The probability of failure predicts the extent of the corrosion. For example, 50% probability of failure represents the situation that half of reinforcing

bars in a concrete structure has been corroded. On the other hand, the confidence level accounts for the reliability on the prediction. Explaining the confidence level needs to define life expectancy: It is the age for which the prediction on the extent of corrosion is guaranteed at a confidence level. If the prediction on p_F is made at 50% confidence level, as an example, half of concrete structures within the life expectancy show a lower probability of failure than p_F .

Figure 3 shows the fragility curves of the mortar mixes produced by the water-to-cement ratio of 0.35, 0.4 or 0.5. A lower water-to-cement ratio pushes the fragility curve to right; the life expectancy increases. The median ($p_F=0.5$) of X at $Q=50\%$ confidence level is the representative value, which coincides with the service life of a deterministic approach. The chloride-attack fragility curve obtained by the probabilistic approach indicates the possibility of corrosion at a variety of confidence level. When the confidence level increases, the fragility curve moves to left. The life expectancy is calculated conservatively.

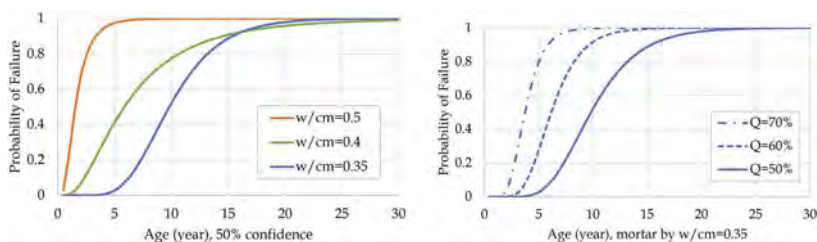


Figure 3. Chloride-attack fragility curve of the mortar mixes.

4 CONCLUSIONS

The chloride attack is a significant risk causing the corrosion of reinforcing bars, which results in diminishing the service life of concrete structures. The service life related to the chloride attack is generally predicted by calculating chloride diffusion through concrete cover. However, the variation on the prediction is not small. This paper proposes a chloride-attack fragility curve considering the aleatory and epistemic variabilities. The fragility curve represented by a double lognormal distribution considers both variabilities independently. The randomness on the chloride diffusivity through concrete is experimentally evaluated dispersing the probability of failure while the uncertainty on the critical chloride content for passivation breakdown is parameterized describing the confidence level. Finally, the life expectancy is provided indicating the age for which the prediction on the extent of corrosion is guaranteed at a confidence level.

REFERENCES

- Ait-Mokhtar, A., Belarbi, R., Benboudjema, F., Burlion, N., Capra, B., Carcassès, M., Colliat, J.B., Cussigh, F., Deby, F., Jacquemot, F., De Larrard, T., Lataste, J.F., Le Bescop, P., Pierre, M., Poyet, S., Rougeau, P., Rougelot, T., Sellier, A., Séménadisse, J., Torrenti, J.M., Trabelsi, A., Turcry, P., and Yanez-Godoy, H., 2013. Experimental investigation of the variability of concrete durability properties. *Cement and Concrete Research*, 45 (1), 21–36.
- Alexander, M. and Thomas, M., 2015. Service life prediction and performance testing - Current developments and practical applications. *Cement and Concrete Research*, 78, 155–164.
- Angst, U.M., 2018. Challenges and opportunities in corrosion of steel in concrete. *Materials and Structures/Materiaux et Constructions*, 51 (1), 1–20.
- Bentz, E.C., 2003. Probabilistic Modeling of Service Life for Structures Subjected to Chlorides. *ACI Materials Journal*, 100 (5), 391–397.
- Electric Power Research Institute, 2018. *Seismic Fragility and Seismic Margin Guidance for Seismic Probabilistic Risk Assessments*, EPRI 3002012994. Palo Alto, CA.
- Kwon, S.J., Na, U.J., Park, S.S., and Jung, S.H., 2009. Service life prediction of concrete wharves with early-aged crack: Probabilistic approach for chloride diffusion. *Structural Safety*, 31 (1), 75–83.
- NT Build 492, 1999. Concrete, mortar and cement-based repair materials: Chloride migration coefficient from non-steady-state migration experiments. *Measurement*, 1–8.

A review on electrodeposition repair of cracked reinforced concrete

Qian Zhang & Qing Chen

Key Laboratory of Advanced Civil Engineering Materials of Ministry of Education, School of Materials Science and Engineering, Tongji University, Shanghai, China

Haifeng Yang

Guangxi Key Laboratory of Disaster Prevention and Structural Safety, College of Civil Engineering and Architecture, Guangxi University, Nanning, China

ABSTRACT: Microcracks are virtually inevitable in reinforced concrete and will accelerate the deterioration of concrete structures. Repairing microcracks with traditional techniques is difficult, especially in an underwater environment. Electrodeposition repair is an effective technology for microcracks in aqueous conditions. This review summarizes the state of the art by discussing the repair electrolyte, introducing its numerical studies, and presenting the physical design of the repair device. The latest experimental details and relative patents of electrodeposition repair are collected. Electrodeposition repair technology exhibits great potential to enhance the durability and life cycle of concrete structures. Challenges and potential research directions are mentioned in the concluding remarks.

1 INTRODUCTION

Reinforced concrete is widely used in civil, tunneling, hydraulic, or marine engineering, etc. One of the factors affecting the durability of concrete materials is cracking. Due to the brittleness of the concrete composites, cracks inevitably occur when they are induced by load, temperature, erosion, or other factors (Jiang et al., 2020). Microcracks appear in the early stages of deterioration and seemingly pose a limited threat to engineering safety. However, microcracks are the primary pathways by which harmful ions enter the interior of concrete materials. Repairing microcracks with traditional techniques is difficult for those large-scale infrastructures because of many factors, like their massive amount or untouchable position. A self-healing conception of cementitious materials has been proposed owing to the reasons above. Current literature has reviewed those studies about autogenous healing or autonomous healing technology (Li et al., 2018). This study focuses on the most recent developments in electrodeposition repair.

Electrodeposition repair is an extrinsic healing technology (Sánchez et al., 2018) and is suitable for microcracks in aqueous conditions. Electrodeposition repair mainly relies on four key elements: the direct-current field, the anode (inert conductive materials), the cathode (steel bar), and the electrolyte (water environment). When direct current is applied, OH^- is produced around the cathode, and the cation (e.g. Ca^{2+} , Mg^{2+} , Zn^{2+}) gradually migrates to the cathode through microcracks. The electrodeposits (e.g. ZnO , $\text{Mg}(\text{OH})_2$) will form and fill the microcracks since the ion concentration reaches the solubility product (Zhang et al., 2021). In addition to this, the pH value in the crack will increase continuously with the time of power on, due to electrochemical reactions occurring. The harmful ions like Cl^- will be removed by the direct-current electric field. The details of electrodeposition repair were shown in Figure 1. Electrodeposition was first applied to the repair of concrete microcracks by Japanese scholars. In the late 1880s, Japan Seaport Research Institute (Port and Airport Research Institute) and Mitsui Engineering & Shipbuilding Company proposed a method of electrodeposition repair

for cracks in ocean engineering (Yokoda and Fukute, 1992). A series of studies relevant to the parameters and theory of electrodeposition were carried out subsequently.

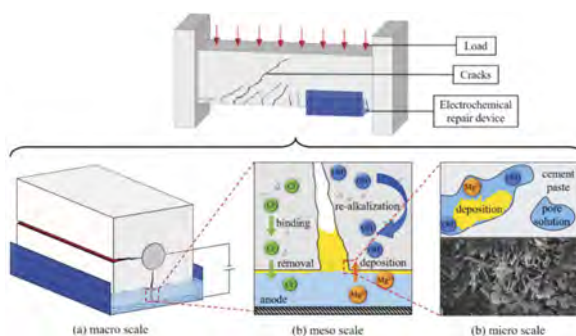


Figure 1. The process of electrodeposition repair (Meng et al., 2021).

2 REPAIR EFFECT AND INFLUENCING FACTORS

Normally, the repair effect is influenced by four aspects, and most research is also conducted from these perspectives:

2.1 *Electrode materials and geometry*

The anode material needs to be resistant to higher voltages, graphite and titanium is usually used as anode because of the low price and inert characteristic. Graphite anode is easily damaged during the test due to the low hardness and high brightness. Apart from that, graphite easily colors the objects that contacted with it. Therefore, titanium tends to be more popular than graphite in laboratory (Ryu, 2001). Taking the lightness and portability of anodes into account, titanium mesh is the most commonly used in laboratory investigations (Ryu, 2003).

The cathode material is steel bar. The most common type of steel is Q235, which has the dual advantage of being both inexpensive and simple to process. Q235 bar is also a commonly used steel in engineering. The diameter of the rebar depends on the size of the specimen, which is generally 5 mm to 8 mm (Zhang et al., 2021). The diameter of the rebar should be increased when the specimen is large. For the larger specimens simulating concrete beams, the steel cage is used as the cathode (Jiang et al., 2008).

2.2 *Current type and intensity*

Different sample sizes need different current values during repair. The current density is generally used to describe the current value. Current density refers to the current intensity per unit area perpendicular to the current direction. The current density at the crack position may be hundreds of times greater than that of the uncracked part. As a result, the electrochemical reaction at the crack is stronger, resulting in preferential deposits enrichment in the crack. The current density of electrodeposition is usually 0.5 A/mm^2 to 3.0 A/mm^2 . The general rule is that the higher the current, the faster the repair rate. However, the faster the deposits grow, the larger the grain size and the more loose the structure (Jin et al., 2019, Shen et al., 2020).

Some researchers (Chu et al., 2017, Chu et al., 2018) found that the repair effect is better when using pulse current. It may be that the concentration polarization of the electrolyte and the hydrogen evolution of the electrode can be alleviated during the intermittent time of the pulse current. When the specimens were repaired in ZnSO_4 solution by pulsed current, the deposits were interlaced and tightly bound to each other. While the sediment crystals under direct current had large sizes, random growth, and a loose structure. Moreover, deposits composition is not affected by the current type. However, in each pulse period, the current is zero

for a certain amount of time. In consequence, the total time of electrochemical reaction is shorter when using pulse current than that of direct current within the same repair time. In general, the effect of pulse current on electrodeposition is unclear and needs further research.

2.3 *Electrolyte type and concentration*

In most studies, single strong electrolyte solutions (MgCl_2 , ZnCl_2 , MgSO_4 , ZnSO_4 , etc.) were mainly used (Chu et al., 2014). Weak acid salts, such as acetate, are gradually accepted in order to avoid ion erosion. Existing investigations show that an electrolyte containing magnesium is the most effective solution when electrodeposition repair is conducted. The growth rate of deposits increases with the increase in electrolyte concentration. The concentration of electrolyte is generally 0.05 mol/L to 0.5 mol/L. The electrolyte should be replaced regularly during the experiment to avoid chemical reactions, evaporation, or other factors affecting the concentration of the electrolyte.

In consideration of the complex ion types in natural water environments, the coupling effects of Mg^{2+} and Ca^{2+} on the deposits were recently reported. $\text{Mg}(\text{OH})_2$ deposits on the cathode can form when $c(\text{Ca}^{2+}) < 0.0167 \text{ mol}\cdot\text{L}^{-1}$. $\text{Mg}(\text{OH})_2$ forms layered structures on the microscale. The mass and thickness of deposits increase as calcium concentration increases, while the volume of nanopores between the $\text{Mg}(\text{OH})_2$ layers decreases. Some small CaCO_3 crystal grains, including aragonite and calcite, precipitate in the layers. If $c(\text{Ca}^{2+}) > 0.05 \text{ mol}\cdot\text{L}^{-1}$, there will be portlandite in the deposits. Deposits on the cathode easily spall after the formation of portlandite (Li et al., 2021).

2.4 *Parameters of cement matrix*

The repair rate increases with the water-cement ratio of concrete (Jiang and Chu, 2005). Because the porosity of concrete will increase with a high water-cement ratio. Concrete matrix with high porosity will absorb more solutions, which leads to lower concrete resistivity. Meanwhile, the diffusion resistance of OH in the concrete also reduces. The repair rate decreases with the increase of concrete cover and crack width (Jiang and Chu, 2005). In addition to this, there are a few studies on concrete parameters. Most studies have focused on electrical parameters (Nishida et al., 2014) and numerical simulations (Chen et al., 2022a, Chen et al., 2020) of electrodeposition restorations.

3 LATEST RESEARCH

New investigations have been reported continuously because electrodeposition repair has a good prospect for cracked constructions in an aqueous environment. In this section, the recent progresses in electrodeposition repair are presented.

3.1 *Anode material*

The anode material in most studies was described as inert conductive materials such as graphite or titanium (Chu et al., 2020, Zhou et al., 2020). In fact, both graphite and pure titanium electrodes dissolve slightly in the electric field. When repairing a cracked reinforced concrete specimen, high voltage is often required because of the poor conductivity of concrete. Higher voltages easily cause the graphite and titanium to dissolve. The required voltage increases with the specimen volume, which makes the dissolution of the anode more visible. After the graphite is dissolved, black impurities will pollute the electrode and the deposits and affect the appearance and detection of the specimen.

For titanium cathodes, a passive film will first appear on the surface of the titanium electrode when the voltage is high. The passive film will reduce the conductivity of the electrode and affect the stability of the current. If the voltage is too high, pitting corrosion will occur on

the surface of the titanium electrode. It was found that titanium electrodes coated with ruthenium and iridium showed excellent corrosion resistance. The ruthenium-iridium coating can make the electrode completely resistant to corrosion during the electrodeposition repair process (Li et al., 2021, Chen et al., 2022b, Li et al., 2022).

3.2 Repair solution

A novel repair solution including $\text{Ca}(\text{CH}_3\text{COOH})_2$ and $\text{Al}_2(\text{SO}_4)_3$ was reported (Chen et al., 2022b). The innovation of this study is that the deposits are ettringite with an appropriate ratio of Ca^{2+} to Al^{3+} (Ca/Al). As one of the compositions of cement hydration products, ettringite exhibits better compatibility when it fills the microcracks. When the Ca/Al ratio is 1, gypsum is the main phase in the deposits. When the Ca/Al ratio is 3 or 5, the permeability coefficient decreased by roughly 4 orders of magnitude, and the crack closure time was lowered to 1 day after 7 days of repair. The products of all groups entered the whole fracture, and when the Ca/Al ratio is 5, the coverage ratio of the crack section can reach more than 60%. The morphology of the deposits in different Ca/Al ratio solutions is shown in Figure 2. The ettringite influenced by electric field shows extremely thin, acicular and elongated characteristics. An interlaced network structure generates because of the fibrous ettringite overlapped with each other. There are calcium crystal grains among the network, which make the netted texture denser. The microstructure of the deposits is shown in Figure 3.

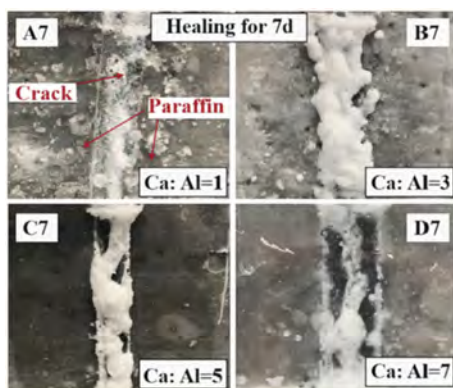


Figure 2. The morphology of the deposits in different Ca/Al ratio solutions.

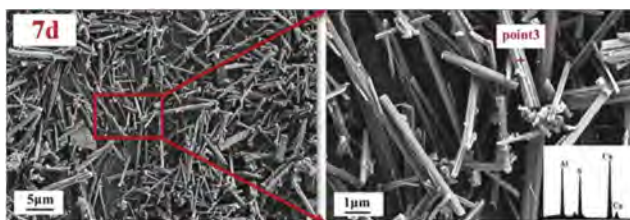


Figure 3. The microstructure of the deposits.

3.3 Additive agent

“Additive agent” in this part refers to the chemical substances added to the electrolyte to enhance the repair performance. The additive agent could be surfactant or complexing agent. Surfactant is a sort of amphiphilic molecule with hydrophilic and hydrophobic groups and can form ordered adsorption structures at the interface (Yasin et al., 2018). Hence, the

interface characteristics of the phase are modified. Complexing agents can form chelates with some metal ions. When the complexing agents are added to the repair solution, the chelate capacity may influence the migration of metal ions (El Bahi et al., 2020, Singh and Poolla, 2018). Accordingly, the surfactant and complexing agent are believed to facilitate the improvement of the quality of electrodeposition and optimize the crystal structures of deposits. The additive agents are commonly used in the electroplating industry, but there have been few studies in the electrodeposition repair field to date.

The effects of cetyltrimethylammonium bromide (CTAB) on electrodeposition repair was performed (Zeng et al., 2022). In $MgSO_4$ or $ZnSO_4$ electrolytes, the repair effect of crack specimens tended to first increase and then go down as CTAB content increased. Meanwhile, the adhesive strength between the steel bar and cement matrix, the Cl^- resistance, and the anti-corrosion ability of the steel bar were enhanced. The proper dosage (relative to the electrolyte volume) of CTAB is 1.00 vol%. CTAB enhances the repair effect by influencing the micromorphology rather than the components of deposits.

Sodium citrate, as a complexing agent, also enhances the repair effect (Zhu, 2021). In zinc acetate solution, the molar ratio of zinc ions to sodium citrate (Zn/SC) will affect the properties of the deposits. The deposits are zinc element and show low adhesion and a loose texture in the zinc acetate electrolyte without sodium citrate. When Zn/SC is between 3/2 and 3/6, the mass of deposits obviously increases. The adhesion ability and compactness of deposits are enhanced. The macroscopic morphology of deposits will not change when $Zn/SC > 3/6$. The reduction of Zn^{2+} is influenced by the sodium citrate solution. The formation of zinc hydroxide was promoted when the concentration of sodium citrate was more than twice that of zinc acetate. Citrate has a buffering effect on the pH value of repair solutions. Citrate keeps the pH value in a relatively stable state, which is more suitable for the electrodeposition repair of concrete.

3.4 Numerical study

A continuum damage-healing framework based on the multi-field coupling development process of the deposits was described (Zhu et al., 2021). The repair progress is affected by multiple fields such as electric fields, concentration fields, and transport-velocity fields. The electric fields were described by the current conservation equation, as Equation 1 showed. The ion transport process can be described by the Nernst-Planck equation, as Equation 2 showed. The consumption rate of Mg^{2+} in electrolyte can be described as Equation 3. The repair process will cause interface changes between the deposits and the electrolyte. The level set approach is used to monitor the growth of deposits, The ϕ of the cathode and anode is 0 and 1, respectively, as shown by Equation 4.

$$-\omega \nabla^2 V = Q \quad (1)$$

where ω = local voltage influenced by the ion concentration; and Q = external voltage influenced by the electrode interface reaction speed.

$$\frac{\partial c_i}{\partial t} - \nabla \cdot \left(D_i \nabla c_i + \frac{z_i e}{k_B} D_i c_i \nabla V \right) = R_i \quad (2)$$

where c_i = concentration of the i -th ion; D_i = diffusion coefficient of the i -th ion; z_i = valence of the i -th ion; k_B = Boltzmann constant; e = amount of elementary charge; ∇ = divergence; V = potential of the electrolyte; and R_i = source or sink term.

$$R_{Mg^{2+}} = k_1 (c_{Mg^{2+}} \cdot c_{OH^-}^2 - k_{sp1}) \quad (3)$$

where $R_{Mg^{2+}}$ = consumption rate; k_1 = constant of the precipitation reaction; and k_{sp1} = apparent solubility product constant of the Mg^{2+} .

$$\frac{\partial \phi}{\partial t} + \mathbf{u} \cdot \nabla \phi = \gamma \nabla \cdot \left(\varepsilon_{ls} \nabla \phi - \phi(1 - \phi) \frac{\nabla \phi}{|\nabla \phi|} \right) \quad (4)$$

where ϕ = reinitialization parameter \mathbf{u} = growing velocity field of deposits ε_{ls} = interface thickness of deposits; and γ = amount of reinitialization.

The generation processes were simulated by COMSOL. The filling process of deposits in cracks was displayed in Figure 4. The repair effect increased with the voltage, as shown in the figure, which is consistent with the experimental results as well. The influence of time, electrolyte concentrations, and voltages on the repair effect can be quantitatively obtained by the proposed models.

The simulation method can greatly shorten the test process and study the influence of various variables in a short amount of time. At present, there are few studies on the numerical simulation of electrodeposition repair.

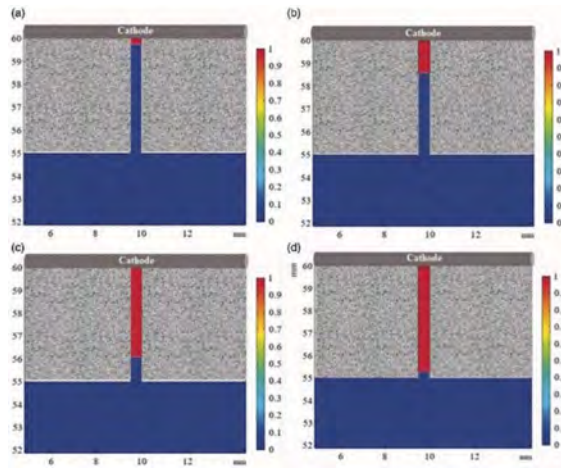


Figure 4. The generation of deposits at various voltages, (a) 3 V; (b) 5 V; (c) 8 V; (d) 10 V.

3.5 Repair device

An on-site repair device for underground structure leakage cracks was proposed (Chen et al., 2019), which is used to repair structural cracks of less than 2 mm. The device is shown in Figure 5 and comprises: (1) An adjustable DC power source used to generate adjustable weak current. (2) An electrolyte container sticking to the position of crack. (3) A ruthenium-iridium-titanium plate served as anode. Compared with the prior art, this device has the advantages of non-destructive repair, erosion reduction, repair adjustment, real-time monitoring, etc.

4 CHALLENGES AND POTENTIAL RESEARCH DIRECTIONS

To date, there are few engineering applications. It should be pointed out that, new challenges will appear when we conduct electrodeposition repair in engineering, such as:

- (1) Connecting steel bars and wires through a drill hole damages the structure to some extent, so more effective methods should be explored.
- (2) There is still no more accurate evaluation method of repair effect. It is only possible to visually measure whether the sediment has filled the crack and whether water is still seeping through the microcracks. Ultrasonic, acoustic emission, or other environmentally sensitive detecting technologies are not suitable for application in engineering.

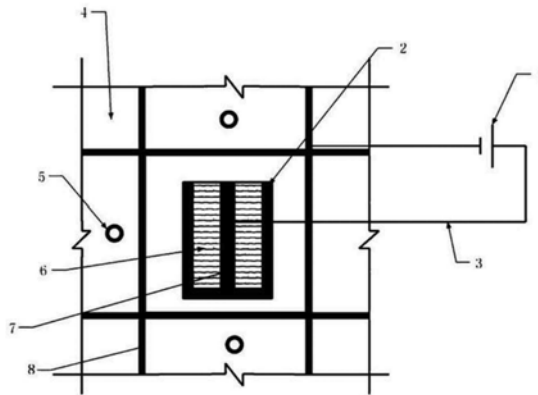


Figure 5. The structure of electrodeposition repair device. (1) Direct current power. (2) Electrolyte container. (3) Wires. (4) Wall surface with microcracks. (5) Reference electrode. (6) Electrolyte. (7) Anode. (8) Steel bar in the walls.

- (3) The temperature of the surrounding environment is critical. The rate of electrochemical deposition slows down at low temperatures.

5 CONCLUSIONS

This review reported the development of electrodeposition repair in the past three years, with a concentration on anode materials, repair solutions, additive agents, numerical studies, and repair devices. Electrodeposition repair shows great potential in a special condition, and its application scenarios have been expanding. Although a large-scale experimental test has been investigated, further research on how to promote engineering applications is required.

REFERENCES

- Chen, Q., Li, W. & Jiang, Z. (2022a) Theoretical estimation of the elastic moduli of self-healing concrete relevant to the evolution of cracks closing due to crystallization- and precipitation-based mechanism. *Journal of Building Engineering*, 58.
- Chen, Q., Liu, X., Zhu, H., Ju, J. W., Yongjian, X., Jiang, Z. & Yan, Z. (2020) Continuum damage-healing framework for the hydration induced self-healing of the cementitious composite. *International Journal of Damage Mechanics*, 30, 681–699.
- Chen, Q., Xie, L., Huang, A., Li, B., Sun, Y., Jiang, Z., Li, W. & Zhu, H. (2022b) Healing of concrete cracks by in-situ synthesis of ettringite induced by electric field. *Construction and Building Materials*, 352, 128685.
- Chen, Q., Zhu, H. & Zhu, Z. (2019) A kind of underground structure leakage crack site based on electro-deposition repair device and method. IN OFFICE, S. I. P. (Ed. China, Yang, Hongtai.
- Chu, H., Jiang, L., Song, Z., Xu, Y., Zhao, S. & Xiong, C. (2017) Repair of concrete crack by pulse electro-deposition technique. *Construction and Building Materials*, 148, 241–248.
- Chu, H., Jiang, L., Xiong, C., You, L. & Xu, N. (2014) Use of electrochemical method for repair of concrete cracks. *Construction and Building Materials*, 73, 58–66.
- Chu, H., Liang, Y., Guo, M.-Z., Zhu, Z., Zhao, S., Song, Z., Wang, L. & Jiang, L. (2020) Effect of electro-deposition on repair of cracks in reinforced concrete. *Construction and Building Materials*, 238, 117725.
- Chu, H., Wang, T., Jiang, L., Xu, Y., Song, Z., Xu, N. & Zhao, S. (2018) Effect of pulse parameters on deposition in concrete crack using pulse current electro-deposition. *Journal of Wuhan University of Technology-Mater. Sci. Ed.*, 33, 908–914.

- El Bahi, B., Galai, M., Cherkaoui, M. & Takenouti, H. (2020) Electrochemical deposition mechanism of copper-zinc-tin alloy and structural characterization. *Surfaces and Interfaces*, 19.
- Jiang, L. & Chu, H. (2005) Influence of concrete parameters on electrodeposition effect. *Advances in Science and Technology of Water Resources*, 25, 23–25.
- Jiang, Z., He, B., Zhu, X., Ren, Q. & Zhang, Y. (2020) State-of-the-art review on properties evolution and deterioration mechanism of concrete at cryogenic temperature. *Construction and Building Materials*, 257.
- Jiang, Z., Xing, F., Sun, Z. & Wang, P. (2008) Healing effectiveness of cracks rehabilitation in reinforced concrete using electrodeposition method. *Journal of Wuhan University of Technology-Mater. Sci. Ed.*, 23, 917–922.
- Jin, W., Peng, W., Mao, J., Wang, J., Fan, W. & Pan, C. (2019) Distribution characteristics of electrodeposition products of concrete cracks under different current densities. *Journal of Civil and Environmental Engineering*, 41, 127–133.
- Li, B., Jiang, Z., Chen, Q. & Li, C. (2022) Preparing Mg(OH)₂-based materials by electro-deposition method from magnesium- and calcium-rich brine simulant. *Desalination*, 527, 115580.
- Li, B., Jiang, Z., Zhou, G. & Chen, Q. (2021) The effect of Ca²⁺ concentrations on the characteristics of Mg(OH)₂-based building materials prepared in situ by electrodeposition. *Construction and Building Materials*, 271, 121523.
- Li, W., Dong, B., Yang, Z., Xu, J., Chen, Q., Li, H., Xing, F. & Jiang, Z. (2018) Recent Advances in Intrinsic Self-Healing Cementitious Materials. *Advanced Materials*, 30, e1705679.
- Meng, Z., Liu, Q.-F., She, W., Cai, Y., Yang, J. & Farjad Iqbal, M. (2021) Electrochemical deposition method for load-induced crack repair of reinforced concrete structures: A numerical study. *Engineering Structures*, 246, 112903.
- Nishida, T., Otsuki, N. & Saito, A. (2014) Development of improved electrodeposition method for repair of reinforced concrete structures. *Proceedings of the 4th International Conference on the Durability of Concrete Structures*. Purdue University, West Lafayette.
- Ryu, J. S. (2001) An experimental study on the repair of concrete crack by electrochemical technique. *Materials and Structures*, 34, 433–437.
- Ryu, J. S. (2003) Influence of crack width, cover depth, water-cement ratio and temperature on the formation of electrodeposits on the concrete surface. *Magazine of Concrete Research* 55, 35–40.
- Sánchez, M., Faria, P., Ferrara, L., Horszczaruk, E., Jonkers, H. M., Kwiecień, A., Mosa, J., Peled, A., Pereira, A. S., Snoeck, D., Stefanidou, M., Stryzewska, T. & Zając, B. (2018) External treatments for the preventive repair of existing constructions: A review. *Construction and Building Materials*, 193, 435–452.
- Shen, L., Xia, J. & Zhang, H. (2020) Review of the effect of electrochemical treatment on microstructure of concrete. *Concrete*, 366, 23–28.
- Singh, J. & Poolla, R. (2018) Effect of Complexing Agents on Properties of Electrodeposited InSb Thin Films. *Journal of Electronic Materials*, 47, 6848–6861.
- Yasin, G., Arif, M., Nizam, M. N., Shakeel, M., Khan, M. A., Khan, W. Q., Hassan, T. M., Abbas, Z., Farahbakhsh, I. & Zuo, Y. (2018) Effect of surfactant concentration in electrolyte on the fabrication and properties of nickel-graphene nanocomposite coating synthesized by electrochemical co-deposition. *RSC Advances*, 8, 20039–20047.
- Yokoda, M. & Fukute, T. (1992) Rehabilitation and protection of marine concrete structure member using electrodeposition method. *International RILEM/CSIRO/ACRA Conference on Rehabilitation of Concrete Member*. Melbourne.
- Zeng, Y. X., Zuo, Q. Y., Jiang, S., Guo, M. Z., Wang, T. & Chu, H. Q. (2022) Effect of CTAB on the healing of concrete cracks repaired by electrodeposition and the durability of repaired concrete. *Construction and Building Materials*, 326, 126757.
- Zhang, Q., Yuan, L., Zhou, Z. & Wang, J. (2021) Accelerating electrochemical repair rate for cracked cement composites: Effect of carbon nanofiber. *Construction and Building Materials*, 312, 125349.
- Zhou, Y., Liu, W., Chen, Q., Li, H., Zhu, H. & Ju, J. (2020) Multiphysics coupling model for the crack repairing process using electrochemical deposition. *Construction and Building Materials*, 264, 120625.
- Zhu, H., Chen, Q., Ju, J. W., Yan, Z. & Jiang, Z. (2021) Electrochemical deposition induced continuum damage-healing framework for the cementitious composite. *International Journal of Damage Mechanics*, 30, 945–963.
- Zhu, Z. (2021) Electrochemical deposition repair mechanism and meso transport model of underground structure concrete. *Materials Science and Engineering*. Shanghai, Tongji University.

The economic evaluation method of a foamed ceramics external wall panel based on full life-cycle theory

Z.W. Cao

*The Second Construction Limited Company of China Construction Eighth Engineering Division Jinan, China
School of Civil Engineering, Shandong University, Jinan, China*

H.B. Fang

The Second Construction Limited Company of China Construction Eighth Engineering Division Jinan, China

L. Tian

School of Civil Engineering, Shandong University, Jinan, China

ABSTRACT: The traditional external wall insulation system was flawed by its own material characteristics and structural design. Foamed ceramics had also been known as “solid waste gold” in the industry. Then a new kind of foamed ceramics external wall panel was proposed in this paper. The new kind of foamed ceramics external wall panel integrated the architectural function, structural function and decorative function, which could ensure the wall panel had the same duration as the building. In this paper, the economic evaluation method of the foamed ceramics external wall panel was proposed based on full life-cycle theory in order to provide a series of investment advices for the real estate developers and consumers. Through the analysis, it showed that the new kind of foamed ceramics external wall panel could be widely used in energy-saving residential areas, which was a good solution to contradiction between resource tension and consumption growth.

Keywords: Foamed ceramics, External wall panel, Low-carbon, Full life-cycle, Net present value method

1 GENERAL INSTRUCTIONS

1.1 *External wall insulation system*

Nowadays, the performance requirements of external wall become increasingly higher. The traditional external wall insulation system which was commonly known as the building’s coat was inherently flawed. First, traditional external wall insulation system was easy to fall off



Figure 1. Insulation system falls off.

which could lead to personnel safety accidents, as shown in Figure 1. Second, the construction quality of traditional external wall insulation system was hard to meet the requirement which could lead to short service life. With the progress of science and technology, people's demand for external wall was changing as well, and fire resistance and energy efficiency are gradually becoming the new demand for buildings.

Therefore, traditional external wall insulation system was forbidden in many Chinese provinces, a new kind of external wall insulation system called "Insulation-Structure Integration External Wall Insulation System" was strongly promoted due to its excellent performance. Insulation-Structure Integration External Wall Insulation System could not only utilize the new material perfectly, but also solve the problems of building energy saving and fire resistance. More importantly, it gradually realized the demand of the building market for insulation system with the same life of the building (Alfred A.Yee. 2016).

1.2 Exterior wall material

The material of insulation layer in traditional external wall insulation system could be divided into two parts, the organic combustible materials such as polystyrene and polyurethane, the inorganic non-combustible material such as rock wool. When cracks and hollow drum appeared during the usage phase of the insulation layer, the exposed organic insulation materials were highly susceptible to fire with toxic fumes which seriously affected the evacuation of personnel and fire rescue operation, as shown in Figure 2. In 2009, China's Ministry of Fire Protection proposed that only Class A fire-resistant material could be used in the insulation layer of external wall, however, no suitable material had been found which could combine the insulation function and fire-resistant function perfectly.



Figure 2. Fire incident caused by the insulation layer.

1.3 Research purpose

A new kind of foamed ceramics external wall panel which organically combined the foamed ceramics and the Insulation-Structure Integration External Wall Insulation System was proposed in this paper, as shown in Figure 3. The economic evaluation method of the foamed ceramics external wall panel was proposed based on full life-cycle theory. At last, a series of investment advices were provided for the real estate developers and consumers.

2 CONCEPT OF FOAMED CERAMICS EXTERNAL WALL PANEL

2.1 Foamed ceramics

Foamed ceramics had been called "solid waste gold" in the industry, the product had the advantages of light weight, high strength, fire resistance, water proof and moisture proof, heat insulation, sound insulation and noise reduction, green environmental protection, stable performance, good weather resistance, etc. Foamed ceramics were produced by recycling ceramic

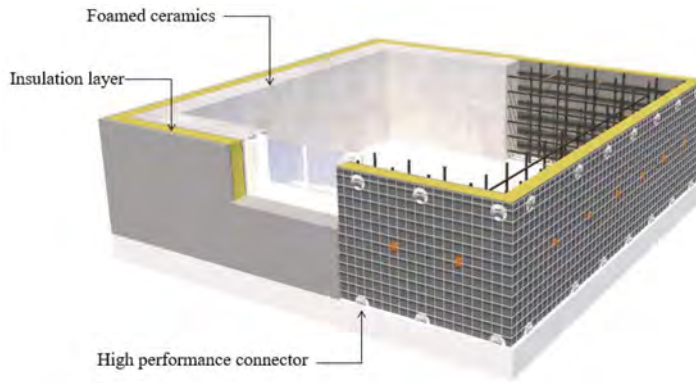


Figure 3. A new kind of foamed ceramics external wall panel.

tailings, fly ash, slag, coal mine stone, red mud, inorganic pollution and other industrial solid waste as the main raw materials, as shown in Figure 4. Precision-controlled foaming technology was used under 1200°C high-temperature roasting to produce a high porosity low-density closed-cell porcelain material which could reduce carbon emissions during cement production, building brick firing and transportation effectively. Moreover, foamed ceramic panels could achieve the same life as the building. There was no need to increase the cost of maintenance, renovation during the whole life cycle.



Figure 4. Foamed ceramics.

2.2 Advantages of foamed ceramics external wall panel

First, traditional external wall insulation system construction process was complex, and due to difference of the construction industry workers in skill and responsibility, construction quality was difficult to achieve the standard. At the same time, most design of the traditional external wall insulation system was completed, which led to the products not matching the buildings. In order to solve this technical difficulties, a digital service platform based on BIM information technology was provided to guide the preliminary architectural and structural design by establishing a stereotyped standard product library, which realized the integrated design of architecture, structure and decoration (Pons, O. 2010).

Second, China's construction industry was the largest in the world, and at the same time, it was also the largest carbon emitter in the world. Currently, the total building stock in China's cities and towns was about 65 billion square meters, and these buildings emitted about 2.1 billion tons of carbon dioxide in the process of use, accounting for 20% of the total carbon emissions in the world (Bonamente E, Merico M.C. 2014). Excessive carbon emissions would lead to the greenhouse effect, glacier melting, global warming and other serious environmental

problems. Therefore, the work of “carbon peaking and carbon neutral” had a long-term and far-reaching significance. Foamed ceramics were produced by recycling ceramic tailings, fly ash, slag, coal mine stone, red mud, inorganic pollution and other industrial solid waste as the main raw materials, which could reduce carbon emissions during cement production, building brick firing and transportation effectively.

At last, foamed ceramics external wall panel was of strategic importance to promote the green, intelligent and efficient synergistic development of the whole industrial chain of industrialized buildings and improved the core competitiveness of enterprises. Through the integrated design of insulation, structure and decoration, it could achieve 80% energy saving, 90% pollution reduction, 80% labor reduction and 50% reduction in construction period and it could help to realize the strategic goal of “double carbon” in the construction industry.

3 THE ECONOMIC EVALUATION OF FOAMED CERAMICS EXTERNAL WALL

3.1 Concept of full life-cycle

The whole life cycle for a building meant the whole process of material acquisition, manufacturing, transportation, installation construction, operation, maintenance and demolition of building systems.

The whole life cycle assessment was the economic evaluation of the environmental impact of the material and energy flow during the cycle of production, planning and design, construction and transportation, operation and maintenance, demolition and disposal of the building components, which was a comprehensive study of the economic, social and environmental benefits of the material.

The economic evaluation of external wall insulation system was to evaluate the energy efficiency of external wall insulation system from the economic point of view. The energy efficiency analysis of the system was carried out by applying the whole life cycle cost principle to reflect the economic benefits of the inputs and outputs of the system in the whole life cycle.

3.2 Cost component

The whole life cycle cost of a project is the cost of the external wall insulation system over its entire life cycle by adding up the various costs in net present value and subtracting the cash injection of, which could be calculated as follows:

$$LCC = I + \sum_{t=0}^T E + \sum_{t=0}^T M - S \quad (1)$$

where LCC =full life cycle cost; I =initial investment; E =operating cost; S =net salvage; T =full life cycle; t =time parameter; M =maintenance cost.

The heating fee could be calculated as follows:

$$P = K(t_i - t_w)ts \quad (2)$$

$$s = ab/1000Q\eta_1\eta_2 \quad (3)$$

where P =heating fee; K =heat transfer coefficient; t_i =indoor temperature; t_w =outdoor temperature; η_1 =efficiency of outdoor pipe network transmission; η_2 =boiler thermal efficiency.

3.3 Evaluation index

For the economic evaluation of building by using energy efficiency measures, there were two kinds of evaluation method (San-José Lombera JT, Garrucho Aprea I. 2010). One is the evaluation of an independent solution, the other one is the evaluation of multiple options (Luo Y. 2007). Absolute indicators were used for the evaluation of the economic feasibility of

an independent solution. The indicators of economic evaluation of an independent solution were usually *NPV*, *IRR*, investment profitability, payback period. Relative indicators were used for the mandatory selection of multiple mutually exclusive solutions including *NPV*, *IRR*, and *NAV*. From the perspective of real estate developers and consumers, *NPV* was used as an economic evaluation indicator, which could be calculated as follows:

$$NPV = \Delta P - \Delta I \tag{4}$$

where ΔP =net value of economic benefit; ΔI =net value of investment.

4 ACYTUAL CASE ANALYSIS

4.1 Case description

The following three insulation measures were proposed for a building in a certain area: (1) Non-insulation system; (2) Traditional external wall insulation system; (3) Foamed ceramics external wall system.

The life of residential building insulation materials was generally not less than 25 years, the above program of the initial investment, land use fees, planning and design fees were assumed to be the same in the same social resource environment. Annual maintenance and management costs for building insulation materials were estimated based on experience (Diana L, Thomas M.F. 2016). building insulation materials salvage value was depreciated on a straight-line basis at 5% depreciation rate. $t=152d$, $t_1=18^\circ C$, $t_w=-5.7^\circ C$, $a=200/t$, $b=3.4779$, $\eta_1=0.92$; $\eta_2=0.73$, $Q=0.2389kJ/kG$.

4.2 Case analysis

Economic comparison of three different insulation system about external wall was shown in Table1.

Table 1. Economic comparison of three different insulation system (CNY).

Insulation measures	Initial investment		Heating fee		Maintenance cost		Net salvage	
	<i>I</i>	Net value	<i>P</i>	Net value	<i>M</i>	Net value	<i>S</i>	Net value
Non-insulation	75	75	5.73	80.91	0.2	2.82	20.80	6.24
Traditional system	95	95	2.59	36.57	0.4	5.65	26.35	7.91
Foamed ceramics system	130	130	1.95	27.53	0.3	4.24	36.06	10.82

It can be seen from Table 1 that *LCC* of traditional system and foamed ceramics system were both less than that of non-insulation system, which indicated that insulation system was necessary for the building.

The *NPV* of foamed ceramics system and traditional system can be calculated as follows:

Foamed ceramics system:

$$NPV_1 = \Delta P_1 - \Delta I_1 = 58.18 \text{¥/m}^2$$

Traditional system:

$$NPV_2 = \Delta P_2 - \Delta I_2 = 36.54 \text{¥/m}^2$$

The payback life of foamed ceramics system and traditional system can be calculated as follows:

Foamed ceramics system:

$$T_1 = \frac{95}{80.91 - 36.57} = 2.14$$

$$T_2 = \frac{130}{80.91 - 27.53} = 2.44$$

Then, the economic benefits over the life cycle of foamed ceramics system was 1203.2¥, the economic benefits over the life cycle of traditional system was 1013.6¥.

5 CONCLUSIONS

In this paper, a new kind of foamed ceramics external wall panel which organically combined the foamed ceramics and the Insulation-Structure Integration External Wall Insulation System was proposed. Then, the economic evaluation method of the foamed ceramics external wall panel was proposed based on full life-cycle theory in order to provide a series of investment advices for the real estate developers and consumers. The results of this research project were summarized as follows.

- (1) Foamed ceramics external wall panel was of strategic importance to promote the green, intelligent and efficient synergistic development of the whole industrial chain of industrialized buildings due to its significant advantage.
- (2) *LCC* of traditional system and foamed ceramics system were both less than that of non-insulation system, which indicated that insulation system was necessary for the building.
- (3) Although the payback period of foamed ceramics system was a little bit longer than that of traditional system, foamed ceramics system had the long-term economic benefits over the full life cycle, which indicated that energy savings efficiency of foamed ceramics system was much better than that of traditional system.

REFERENCES

- Alfred A. Yee. 2016. Structural and economic benefits of precast concrete construction. *PCI Journal*: 78:34–42.
- Pons, O. 2010. Evolution of prefabricated technologies applied to building schools. *Informes De La Construcción*: 62(520): 15–26.
- Bonamente E, Merico M.C. 2014. Rinaldi S, et al. Environmental Impact of Industrial Prefabricated Buildings: Carbon and Energy Footprint Analysis Based on an LCA Approach. *Energy Procedia*: 61: 2841–2844.
- San-José Lombera JT, Garrucho Aprea I. 2010. A system approach to the environmental analysis of industrial buildings. *Building and Environment*, 45: 673–683.
- Luo Y. 2007. Decision support for prefabrication strategy selection on building systems. *The Pennsylvania State University*.
- Diana L, Thomas M.F. 2016. Analysis of Costs and Benefits of Panelized and Modular Prefabricated Homes. *Procedia Engineering*: 1291-1297.

Mechanical performance of steel plate combination beam bridge with clustered shear studs considering slip effect

Y.L. Yi

Anhui Transportation Holding Group Co.Ltd., Hefei, China

W.Y. Meng, N.N. Huo & X. Ruan

Tongji University, Shanghai, China

ABSTRACT: The mechanical property of composite girder bridges is significantly influenced by the mechanical performance of shear connectors. The slip between the deck plate and steel girders caused by deformed shear connectors will have an impact on the mechanical property of the entire bridge. The slip impact of the clustered shear studs is taken into account in this article in order to reflect the actual structural condition. The influence of this consideration on the force performance of the steel plate composite girder bridge is then examined by creating an ANSYS finite element model. The study focused on the deformation and stress distribution of a composite girder bridge, and the calculation analysis reveals that taking shear studs slippage into account will result in lower stress results in the deck plate and steel girder and higher overall deformation of the bridge. The longitudinal stress of the bridge deck is most significantly impacted by the shear studs connection performance, with a maximum stress variation of roughly 8%. The greatest deformation difference does not exceed 5%.

1 INTRODUCTION

Steel-concrete composite bridges select the proper material composition system in conjunction with the structural stressing characteristics and combines the benefits of both steel and concrete materials. It offers a significant benefit in many areas, including ease of construction, affordability, and beauty (Nie et al., 2012). Contrarily, shear studs are frequently used to connect the steel girders and concrete deck slab of steel-hybrid composite girder bridges, putting joint stress on every component of the structure. The mechanical qualities of the shear members, a crucial connecting component of the composite girder bridge, impact the structural performance of the entire structure, so it is crucial to research the various traits of shear studs.

The current research on shear studs focuses on two aspects: shear resistance of shear studs and slip effect.

Shear studs shear bearing capacity, tensile bearing capacity, tensile shear under the joint action of the bearing capacity and shear studs shear stiffness factors have been fully analyzed by researchers through push-out Test or finite element simulation, etc. for shear studs shear bearing capacity, tensile bearing capacity, tensile shear under the joint action of the bearing capacity and shear studs shear stiffness factors. The tensile strength, length, and diameter of shear studs, as well as the tensile strength and modulus of elasticity of concrete, are thought to be factors influencing shear performance (Amadio and Fragiaco, 2002, Moghimi and Ronagh, 2008, Qureshi et al., 2011, Shim et al., 2004, Zhou et al., 2014).

The study of the slip effect is mainly based on the finite element model, in which the shear studs deformation is considered to determine the slip at the interface of the composite beam, and then the slip effect on the force of the composite beam is analyzed. The general slip effect

will bring about the problems of increasing deflection, decreasing stiffness and decreasing load capacity of the composite beam(Gara et al., 2006, Spacone and El-Tawil, 2004, Su et al., 2016).

Comprehensive research has been undertaken, The shear performance of shear studs has been thoroughly researched; scholars have carried out numerous experiments and theoretical analyses, and the research is now more mature. However, there are still some issues with the study of the slip effect, such as the need for additional research on the impact of the ultimate load during operation and the slip effect on actual projects.

The layout of shear studs has changed recently along with the growth of assembly construction. The welded studs in the conventional composite girder structure are typically evenly and closely spaced at the point where the steel girder flange and concrete deck slab meet. However, this necessitates the lateral division of the prefabricated deck slab into many parts, reducing the structural integrity and delaying the construction process. As a result, a new type of studs arrangement is suggested, including cluster shear studs, uniformly and densely spaced shear studs in sections, and a cluster of shear studs at every other section of studs-free area on the steel girder flange. Two such types of shear studs arrangements are schematically depicted in Figure 1.

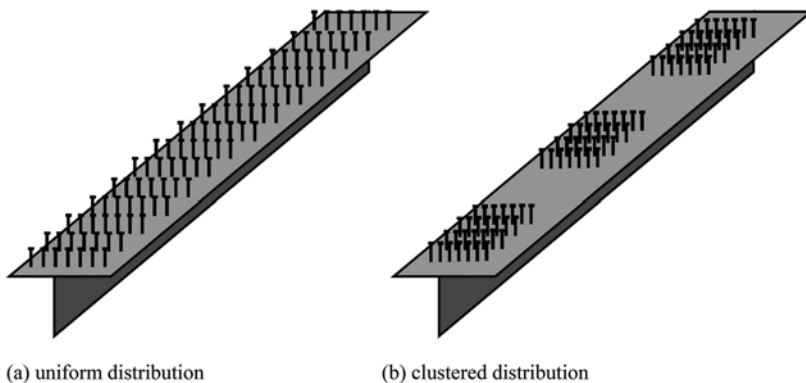


Figure 1. Layout of shear studs.

Compared with the uniform shear studs, clustered shear studs have significant advantages in bridge construction, construction design and other convenience.

- (1) The bridge transverse prestressing tendons pass easily through the studs-free zone set aside for each distance of cluster shear studs, which is suitable for the bridge transverse prestressing tendons through-length setup.
- (2) As industrial building has advanced, prefabricated deck plate technology has been included into the production of several coupled girder bridges. Cluster shear studs can erect the bridge deck by reserving holes in the shape of bridge deck plates, as opposed to evenly dispersed shear studs, which must erect the bridge deck in longitudinal and transverse blocks. This assures the prefabricated bridge deck's integrity. This ensures the prefabricated bridge deck's integrity and enhances structural performance.
- (3) Pre-drilled holes are typically used in composite girder bridges with cluster shear studs construction so that the steel girders can be attached to the deck plate later and pre-stress the deck plate more effectively.
- (4) The cluster shear studs structure also significantly increases construction efficiency, reduces the amount of in-situ concrete work, and makes it easier to replace the deck slab afterward, all of which are beneficial for bridge maintenance and operation.

2 BACKGROUND PROJECT

Study rely on the approach bridge project of Jiuwan Huihe Bridge of Guzhen-Bangbu Expressway Project. The main structure is composed of 50m simply supported steel plate combination girders and 35m continuous steel plate combination girders. The main girder adopts Q345qD I-beam straight web steel plate combination girder, and the concrete lane plate is connected with the steel main girder by clustered shear studs; the transverse connection of the main girder at the non-supporting point is in the form of small crossbeam with longitudinal spacing of 6.0m, the transverse connection of the middle pier is in the form of reinforced crossbeam, and the transverse connection of the split pier is in the form of large crossbeam. Large crossbeam form is used for the transverse connection of split piers. The steel main girders are "I" girders with a height of 2.5m for 50m span and 1.8m for 35m span, and the thickness of the steel girders is different according to the segmental length according to the different stresses. The bridge cross section is shown in Figure 2.

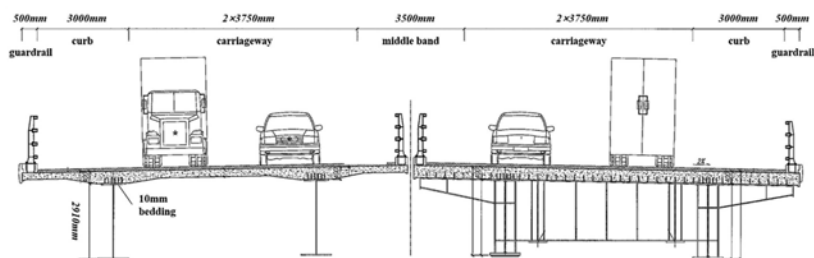


Figure 2. Bridge section (unit: cm).

The prefabricated travel lane slab is prefabricated in full width and connected by cast-in-place wet joints in the middle. The bridge deck plate is set with transverse prestressing tendons and pre-determined weld studs holes, and clustered shear studs are set on the upper flange of the corresponding steel girders at the weld studs holes and wet joints, and after the precast travel lane plate is positioned and installed, the weld studs holes and wet joint concrete are cast to connect with the steel girders. The precast travel lane slab is made of C50 concrete, the in-situ wet joint at the top of the pier of the middle pier is made of UHPC high-strength concrete, and the rest of the in-situ wet joints are made of C55 Compensating Shrinkage Concrete.

3 FINITE ELEMENT MODEL

3.1 Overview

In this paper, finite element analysis is used to determine the effect of slip effect on the mechanical properties of the composite beam bridge. The model is established based on the drawings of the 50m simply supported girder bridge in the approach bridge project of Jiuwan Hwoe River Special Bridge of Guzhen-Bengbu Expressway Project. The steel plate girders made of steel are supported by reinforced concrete bridge deck slabs. Combined with the material characteristics, the steel plate girder part adopts the plate unit model, and the bridge deck part adopts the solid model. The specific dimensions of the main beam, crossbeam, stiffener beam, deck slab and other components are input according to the design drawings, and the reinforcement distribution in the area of the drawings is referred to, and the reinforced concrete solid unit is established and the reinforcement distribution is input.

To study the response of various types of bridges under standard combinations, add the bridge self-weight, second phase load, vehicle load, and concrete shrinkage creep on the basis of taking the construction process into account. Then, analyze the precise degree to which the performance of clustered shear studs has an impact on structural performance.

Special attention is paid to the simulation of the spring unit for the shear studs the concrete deck slab to the steel beam, in which the stiffness of the spring unit is calculated based on the distribution of shear studs in the drawing to establish a calculation model considering relative slip. On the other hand, the spring unit is coupled at both ends to establish a calculation model without considering the relative slip. The details of the calculation model are shown in Figure 3 below.

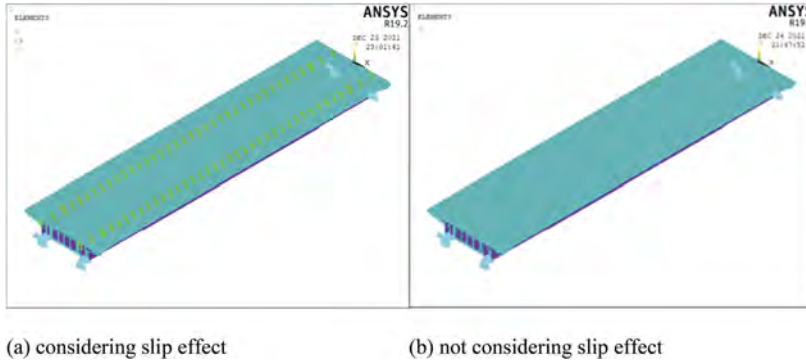


Figure 3. Finite element model.

3.2 Shear studs simulation method

The stiffness of the shear studs must be established for further study since the steel plate composite girder bridge's finite element model simulates the effect of shear studs on the connection between the concrete slab and the steel beam using spring units. Cluster shear studs employed in the background project have varying shear studs spacing from uniform shear studs, this variations will also have an impact on the group studs stiffness. A special study has been conducted to investigate the degree of stiffness reduction of the cluster studs effect.

3.2.1 Single studs shear stiffness

Regarding the shear stiffness of single shear studs, Spacone et al (Spacone and El-Tawil, 2004), combined with the launch tests of multiple groups of shear studs tests, expressed the shear stiffness of shear studs as the formula related to three parameters of shear studs shear bearing capacity (P_{max}), shear studs body diameter (d_{sh}), and concrete compressive strength (f_c).

$$K_i = \frac{P_{max}}{d_{sh}(\alpha - 0.0017f_c)} \quad (1)$$

The provisions of the European Code for Combined Structures (Eurocode 4) can be used to calculate the shear studs shear bearing capacity. Shear studs shear bearing capacity can be based on the shear studs body diameter (d_{sh}), concrete cylinder standard compressive strength (f_{ck}), shear studs material yield strength (f_y), concrete strength sub-factor (γ_{mc}), shear studs strength sub-factor (γ_{ms}) calculated from.

$$P_{max} = 0.36d_{sh}^2 \sqrt{f_{ck}E_c} / \gamma_{mc} \leq 0.7A_s f_y / r_{ms} \quad (2)$$

Combined with the specific parameters of shear studs used in the background project, 144KN can be calculated, and the shear stiffness of single studs is 374KN/mm.

3.2.2 Effect of shear studs spacing on shear stiffness

In the modeling procedure for cluster shear studs, a group of shear studs is treated as a spring unit to make the analysis simpler. Because the shear studs densities result in the discounted

stiffness, it is important to compute the mechanical properties of the cluster studs based on the mechanical properties of the single studs. The calculation technique must also take this into account. In other words, the shear stiffness of the group of studs will depend on the shear studs spacing.

Through a series of launch tests, some researchers(Huang et al., 2015) examined the force performance of various shear connector types. The results of the tests revealed that the average shear capacity per shear studs of cluster shear studs was 29% lower than that of single shear studs and the shear stiffness was 44% lower. Additionally, the force generated by a cluster of shear studs is clearly non-uniform; the stress is distributed in a “saddle-shaped” pattern from top to bottom. This reduces the bearing capacity of a single shear studs dramatically.Related numerical analysis demonstrates that: the single studs bearing capacity has a trend of first increasing and then decreasing with an increase in shear studs spacing; and the shear force direction of each row of shear studs establishes the distribution of the two large, small, and middle studs in a “saddle-shaped” pattern(Lu, 2015).

In order to quantitatively analyze the stiffness of a single shear studs group, the factors affecting the group studs stiffness can be included in two categories: the number of longitudinal rows of shear studs and the longitudinal spacing of shear studs.

Where the discount factor (ϕ) of the number of longitudinal rows of shear studs (n_p) for the group studs stiffness can be referred to the research results of Zhou Xuhong et al(Zhou et al., 2014). The following equation was used for the calculation.

$$\phi = \begin{cases} 1 & n_p \leq 3 \\ 1.0047 + 0.0071n_p - 0.0021n_p^2 & 3 < n_p \leq 7 \\ 1.0101 - 0.0117n_p - 0.0004n_p^2 & 7 < n_p \leq 15 \end{cases} \quad (3)$$

The discount factor (η) of shear studs longitudinal spacing for group studs stiffness can then be referred to the results of Okada et al.(Okada et al., 2006). The following equation was used to calculate: (where C_l is the ratio of shear studs spacing to diameter)

$$\begin{aligned} 3 \leq C_l < 13 \\ C25/30; \quad \eta &= 0.023C_l + 0.70 \\ C30/37; \quad \eta &= 0.021C_l + 0.73 \\ C40/50; \quad \eta &= 0.016C_l + 0.80 \\ C50/60; \quad \eta &= 0.013C_l + 0.84 \\ C_l \geq 13 \\ C25/30 \sim C50/60; \quad \eta &= 1.0 \end{aligned} \quad (4)$$

Therefore, taking into account the effect of the number of longitudinal rows of shear studs and shear longitudinal spacing on the stiffness of a single bundle of shear studs groups, the total stiffness (K) of a studs group consisting of n single studs (single studs stiffness of K_e):

$$K = \phi \times n \times K_e \quad (5)$$

For this project, the single bundle shear studs group consists of 30 shear studs, the longitudinal row number n_p is 5, so the longitudinal row number for the group studs stiffness discount factor ϕ is 0.98, the ratio of shear studs spacing to diameter C_l is 5.68, the corresponding stiffness discount factor η is 0.91. In summary, the single bundle shear studs group stiffness K is 10127.5 KN/mm. analyze the effect of slip effect on the structural performance of the bridge.

4 ANALYSIS OF SLIP EFFECTS

4.1 Bridge stress results

The variation of longitudinal stresses in the upper layer of the span deck slab along the bridge width with and without considering the relative slip under the standard combination of bridge self-weight, phase II load and vehicle load is shown in Figure 4.

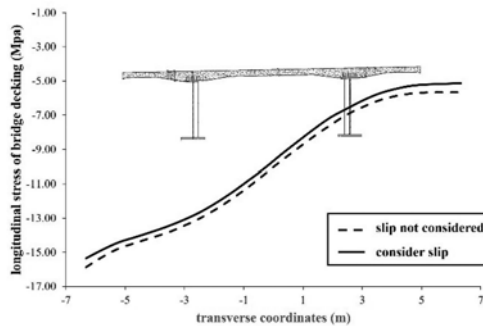


Figure 4. Change of longitudinal stress of bridge decking of mid span bridge deck along the bridge width.

Due to the vehicle deflection and double main girders, it can be seen from the figure that the trend of longitudinal stresses along the bridge width is the same, regardless of whether the slip is considered or not: the deflection increases from one side to the other of the cross-bridge. Considering the relative slip, the longitudinal stress of the bridge deck is greater than the longitudinal stress of the bridge deck without considering the relative slip, but the maximum ratio of the difference between the two stresses does not exceed 8%. It can be seen that the relative slip has a certain influence on the maximum compressive stress of the upper layer of the bridge deck plate, the bridge deck plate and shear studs direct vector, this effect is also the most direct.

The variation of longitudinal compressive stress along the bridge length for the upper edge of the steel main girders with and without considering relative slip under the standard combination of bridge self-weight, phase II load and vehicle load is shown in Figure 5.

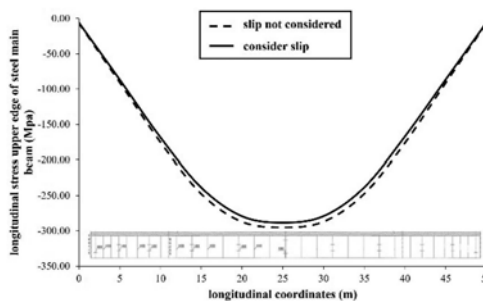


Figure 5. Longitudinal compressive stress of upper edge of steel main beam changes along the longitudinal direction.

When the main beam's longitudinal stress is examined, it can be seen that the change trend of compressive stress at the upper edge of the steel main beam is the same whether or not the slip action is taken into account. The stress at both ends is almost zero, and the stress near the span reaches the peak. This is because one side of the main beam is subjected to greater internal forces under the action of the vehicle deflection load. When relative slip is taken into account at the same time, the stress results are more unfavorable, and the difference between

the two is only 3%. Regarding the analysis of the steel main beam's force performance, the impact of taking shear studs slip into account is more constrained.

The variation of longitudinal tensile stresses along the length of the bridge for the lower edge of the steel main girders considering relative slip and without relative slip under the standard combination of bridge self-weight, phase II load and vehicle load is shown in Figure 6.

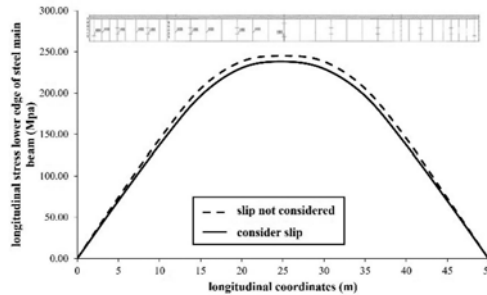


Figure 6. Longitudinal tensile stress of lower edge of steel main beam changes along the longitudinal direction.

One side of the main beam is subjected to greater internal forces as a result of the vehicle deflection load, so the longitudinal stress of this main beam is chosen. It can be seen that, whether or not the slip action is taken into account, the trend of the tensile stress at the lower edge of the steel main beam is the same: the stress at both ends is almost zero, and the stress near the span reaches the peak. The stress results of simultaneously taking into account relative slip are less beneficial, and the difference between the two is only 4%. The examination of the steel main beam's force performance is less affected by taking the shear studs slide effect into account.

4.2 Bridge deformation results

The variation of the bridge span displacement along the bridge width with and without considering the relative slip under the standard combination of the bridge self-weight, the second phase load and the vehicle load is shown in Figure 7.

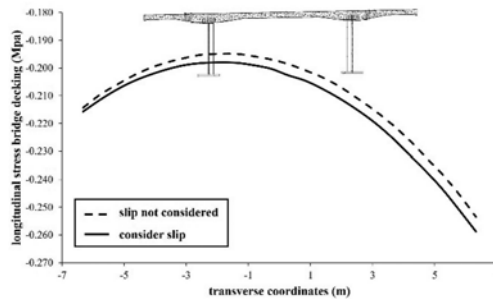


Figure 7. Variation of bridge displacement along bridge width.

The maximum displacement occurs in the mid-span region of the simply supported beam, and the displacement in the mid-span position is selected for both types of models. It can be found that the deflection on one side is greater than the other side under the action of vehicle deflection load, but whether to consider the effect of slip, the span mid displacement change trend is the same, both sides of the bridge displacement is larger, and because of the action of vehicle deflection load, the value of deflection on both sides is not equal. Also consider the relative slip displacement results are more unfavorable, and the difference between the two is

within 3%. The effect of considering shear studs slip is more limited for the bridge stiffness performance.

5 CONCLUSIONS

- (1) The deformation of shear pins in composite girder bridges will cause interface slip. A finite element analysis method to simulate interface slip is proposed in this paper to quantitatively evaluate the influence of interface slip on the overall stiffness and internal stress distribution of the bridges.
- (2) A 50m span composite beam bridge is used as the background for finite element analysis, and the results before and after considering the interface slip are compared. The interface slip of the combined girder bridge caused by the deformation of the set shear studs will have an effect on the stress and deformation of the bridge in both longitudinal and transverse directions.
- (3) The interface slip caused by the loading of the combined girder bridge during the operation phase will have a significant effect on the longitudinal compressive stresses on the deck slab and the top edge of the steel main girders, with or without the slip effect causing a stress gap of about 8%.
- (4) The interface slip generated by the load during the operation phase of the combined girder bridge will also have a limited effect on the bridge stiffness, which will lead to changes in the overall bridge deformation. The effect of whether to consider the slip effect on the above parameters does not exceed 5%.

ACKNOWLEDGMENTS

The paper was sponsored by the Research Project of Anhui Transportation Holding Group (GN2020-06-3051, GN2020-06-3052).

REFERENCES

- Amadio, C. & Fragiacomof, M. (2002) Effective width evaluation for steel–concrete composite beams. *Journal of Constructional Steel Research*, 58, 373–388.
- Gara, F., Ranzi, G. & Leoni, G. (2006) Displacement-based formulations for composite beams with longitudinal slip and vertical uplift. *International journal for numerical methods in engineering*, 65, 1197–1220.
- Huang, C., Zhang, Z., Zheng, Z. & Tan, Y. (2015) Force characteristics and failure mechanism experimental study of group-studs in steel-concrete composite structure. *Journal of Wuhan University of Technology*, 37, 100–105.
- Lu, W. (2015) Study on mechanical behavior and design method of steel-concrete composite pylon anchorage system with steel anchor box. *Chang An University*. Chang An University.
- Moghim, H. & Ronagh, H. R. (2008) Impact factors for a composite steel bridge using non-linear dynamic simulation. *International Journal of Impact Engineering*, 35, 1228–1243.
- Nie, J., Tao, M., Wu, L., Nie, X., Li, F. & Lei, F. (2012) Advances of research on steel-concrete composite bridges. *China Civil Engineering Journal*, 45, 110–122.
- Okada, J., Yoda, T. & Lebet, J.-P. (2006) A study of the grouped arrangements of stud connectors on shear strength behavior. *Structural Engineering/Earthquake Engineering*, 23, 75s–89s.
- Qureshi, J., Lam, D. & Ye, J. (2011) Effect of shear connector spacing and layout on the shear connector capacity in composite beams. *Journal of constructional steel research*, 67, 706–719.
- Shim, C.-S., Lee, P.-G. & Yoon, T.-Y. (2004) Static behavior of large stud shear connectors. *Engineering structures*, 26, 1853–1860.
- Spacone, E. & El-Tawil, S. (2004) Nonlinear analysis of steel-concrete composite structures: State of the art. *Journal of Structural Engineering*, 130, 159–168.
- Su, Q., Xue, Z., Li, C. & Jiang, X. (2016) Refined calculation of steel-concrete interface connection in composite girders. *Journal of Tongji University (Natural Science)*, 44, 1803–1809.
- Zhou, X., Lu, W., Di, J., Qin, F. & Zhao, M. (2014) Group studs effect and shear strength calculation method of group studs shear connector of steel anchor box. *China Journal of Highway and Transport*, 27, 33–45.

Risk-based prioritization of earthquake performance of RC buildings in Turkey by rapid visual scanning

M. Özdemir

Ağrı İbrahim Çeçen Universty, Ağrı, Turkey

ABSTRACT: In this paper, the rapid visual scanning method (PRDB) used in Turkey to predict the performance of RC buildings under the influence of earthquakes in a practical and fast way has been examined. In this context, 100 RC buildings that affected light, medium and heavy damage from the Afyon, Bingöl and Van earthquakes that occurred on different dates were examined and the success of the rapid visual scanning method applied was determined. At the same time, a computer program called EPA (Earthquake Performance Analysis) was developed in order to evaluate the parameters of the related data set faster, easier and without error. The results showed that rapid visual scanning method can be used for risk-based prioritization of buildings.

1 INTRODUCTION

Since the existence of the Earth, earthquakes have been occurring all over the world due to the movement of the earth's crust. In one of the countries most affected by the earthquake, Turkey. Located on the Alpine-Himalayan earthquake zone, which is one of the active earthquake zones, the country has been affected by large earthquakes in which thousands of lives and millions of dollars were lost before. According to the Earthquake Zones Map, 92% of the country is in earthquake zones and 95% of the country's population lives under earthquake hazard (KOERI, 2023). In the province of Kahramanmaraş in Turkey, earthquakes with a magnitude of $M_w=7.7$ on February 6, 2023 and with a magnitude of $M_w=7.6$ on February 7, 2023 occurred, approximately 10 thousand buildings were destroyed and more than 45 thousand lives were lost (DEMP, 2023). Between the years 1903-2014 in Turkey occurred in the range of $M = 6.0-11.0$ magnitude 119 earthquake. These earthquakes resulted in an average annual loss of 748 lives, 5291 damaged buildings and economic loss of \$ 721,610 dollars. These results clearly show the effect of earthquakes that may occur naturally and inevitably, unless the necessary measures are taken (Erdil & Ceylan, 2018).

Experience and statistics have shown the importance of determining the behavior of buildings under earthquake impact. Therefore, many studies have been carried out to determine the behavior of buildings under earthquake effects and these studies have been classified into three categories (FEMA P-154, 2015). These categories can be listed as rapid visual scanning methods (RVS), preliminary assessment methods (PAM) and detailed analyzes. Rapid visual scanning methods are quite simple and fast (Sucuoğlu & Yazgan, 2003). In this method, some parameters such as number of stories, irregularity information, structural system are obtained by making observations from outside without entering the building and then performance of the building against the earthquake effect is determined. PAM, which is another method, includes some different parameters which should be taken from the inside the building (material information, structural system element dimensions, etc.) in addition to the parameters used in RVS (Otani, 2000; Sucuoğlu et al., 2015; Kaplan et al., 2018; Boduroglu et al., 2004). Although this method (PAM) takes a little longer time-consuming than RVS, accuracy ratio is higher. The third and last method used to determine earthquake performance is detailed analysis. This method determines the performance of buildings against earthquake effects by performing linear and nonlinear analyzes (Harirchian & Lahmer, 2020a). Although this method

are highly accurate ratio, it take too time. When considering the thousands of buildings in which earthquake performance behavior should be determined, researchers have done many studies on RVS and PAM methods, which are called rapid assessment methods. The main purpose of these methods (RVS, PAM) is to risk-based prioritize buildings and to identify which buildings need detailed analysis. In this study, the rapid visual scanning method used in Turkey for risk-based prioritization of reinforced concrete buildings was examined.

1.1 Review on developed RVS methods

Rapid visual scanning methods are used to determine the risk priorities of buildings under the influence of earthquakes without the need for detailed analysis and structural analysis. All parameters used in RVS methods are collected by observing from the street without entering the buildings (Harirchian et al., 2020). The first visual scanning method was prepared in the USA in 1988 with the name “Rapid Visual Screening of Buildings for Potential Seismic Hazards: A Handbook” and was updated in 2002 and 2015 (FEMA P-154, 2015). Many countries such as Turkey (PDRB, 2019), Canada (NRC, 1993), New Zealand (NZSEE, 2017), India (IITK-GSDMA, 2005), Italy (GNDDT, 1993) have taken the FEMA P-154 method as a basis, they created RVS methods by adapting them to their seismic conditions and structural systems.

1.2 Purpose of the study

There are 2 main goals of this paper. The primary aim of the study is to obtain the seismic vulnerability scores of 100 RC buildings affected by earthquakes in different regions by using the visual scanning method used in Turkey and to prioritize the buildings according to these scores. At the same time, the percentage of success of the method will be obtained by comparing the risk-based prioritization and the real damage status of the structures. The second of these goals is to develop a computer program that can determine the earthquake performance status (damage scores) of buildings in a much shorter time and error without.

2 MATERIAL AND METHODS

2.1 Data set

The first of the datasets used was shaken by an earthquake with a depth of 5 km and a magnitude of $M_w = 7.2$ that occurred on October 23, 2011, then again on November 9, 2011, with a depth of 5 km and a magnitude of $M_w = 5.6$, and was shaken again by two major earthquakes. It was collected from the province of Van, which experienced an earthquake (DEMP, 2023). This dataset consists of 54 RC buildings. The second data set was selected from Bingöl province, which was shaken by an earthquake with a depth of 10 km and a magnitude of $M_w = 6.4$, which occurred on May 1, 2003 (KOERI, 2023). This dataset consists of 28 RC buildings and is taken from the SERU database (SERU, 2023). The third and last data set was selected from Afyon province, which was shaken by an earthquake with a depth of 7.6 km and a magnitude of $M_w = 5.8$, which occurred on February 3, 2002 (KOERI, 2023). This dataset consists of 18 RC buildings and is taken from the SERU database (SERU, 2023). The damage distribution of the collected data is shown in Table 1.

Table 1. The damage distribution of the collected data.

Damage State	Afyon	Bingöl	Van	Total
Light damage	4	15	0	19
Moderate damage	3	7	11	21
Severe damage	11	6	43	60
Total	18	28	54	100

2.2 Parameters

The number of stories, ground class, structural system type, seismic vulnerability, structure irregularity information and topographic structure parameters shown in Figure 1 from the RC buildings in the data sets were collected according to the conditions specified in Table 2 and the RC buildings were classified into damage classes (light damage, medium damage and heavily damaged).

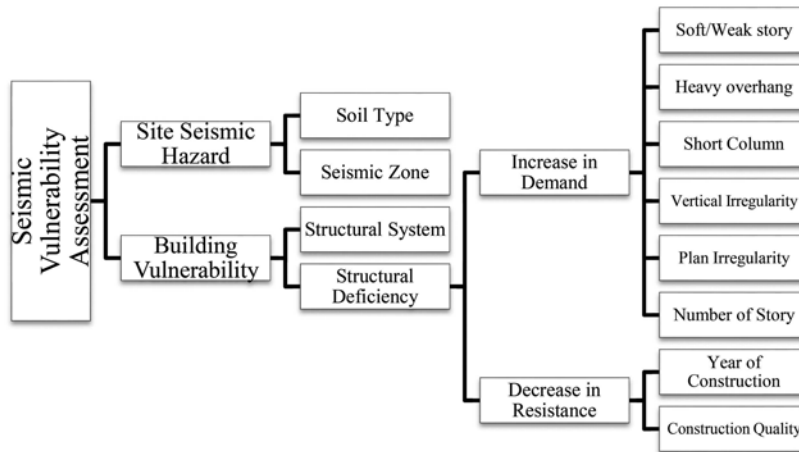


Figure 1. Parameters used in RVS methods in seismic vulnerability assessments of RC buildings.

Table 2. Parameter definitions and input features of reinforced concrete buildings collected for RVS studies.

Parameter	Description
No. of Story	Indicates the number of stories above ground
Structural System	By determining the structural system of the building, will be selected as one of the RC frame and RC frame and shear wall systems.
Soil Type	Determined according to ground survey reports
Vertical Irregularity	Columns and shear walls that do not continue along the height of the building create vertical irregularity
Plan Irregularity	It is defined as the geometrically not symmetrical plan and the irregular placement of vertical structural elements.
Short Column	Generally, ribbon window construction in industrial-type buildings or the absence of walls along the column creates the short column effect.
Heavy Overhang	The difference between the floor area on the ground and the floor area above the ground will be determined.
Construction Quality	Reflects the importance given to the quality of material and workmanship and the maintenance of the building.
Soft/Weak Story	It is expressed as the difference between story heights and the marked stiffness difference between stores.

All buildings in the data set are located in the 1st degree seismic zone according to the Turkey Earthquake Hazard Maps (TEHM, 2023), 48.96% of the buildings are Z2 ($760 < V_{S30} < 1500$), 49.48 are Z3 ($360 < V_{S30} < 760$) and 1.56 of them are on Z4 ($360 < V_{S30} < 760$) soil classes.

2.3 Methods

The method to be used within the scope of the study is to be used to determine the risky structures in Turkey, and the main purpose of the method is to determine the seismic vulnerability score of a building by giving penalty points according to the negative parameters (structure irregularity) it has, to a building that gets a starting score according to the structural system type, soil class and design spectral acceleration values. Then, these performance scores can be ranked among themselves and priority buildings with earthquake hazard can be determined. The method consists of 4 stages.

1. Determination of the building danger zone according to the design spectral acceleration coefficient (Sds) and ground class of the building whose seismic vulnerability will be determined (Table 3).

Table 3. Seismic danger zone (PDRB, 2019).

Danger Zone	Sds	Soil Class
I	$Sds \geq 1.0$	ZC/ZD/ZE
II	$Sds \geq 1.0$	ZA/ZB
	$1.0 \geq Sds \geq 0.75$	ZC/ZD/ZE
III	$1.0 \geq Sds \geq 0.75$	ZA/ZB
	$0.75 \geq Sds \geq 0.50$	ZC/ZD/ZE
IV	$0.75 \geq Sds \geq 0.50$	ZA/ZB
	$0.50 \geq Sds$	All soils

2. Determining the building base score (TP) according to the number of stories and seismic danger zone, and the structural system score (YSP) according to the number of stories and structural system type (Table 4).

Table 4. Base and structural score table (PDRB, 2019).

Total number of floors	Base score (TP)				Structural system score (YSP)	
	Danger zone				Structural system	
	I	II	III	IV	RCF	RCFW
1 and 2	90	120	160	195	0	100
3	80	100	140	170	0	85
4	70	90	130	160	0	75
5	60	80	110	135	0	65
6 and 7	50	65	90	110	0	55

3. Determining the parameters (structure irregularities, visual quality of the building) that will adversely affect the performance of the building against the earthquake effect and the scores of these negative parameters (Table 5).
4. Obtaining the seismic vulnerability score of the building according to the number 1 correlation and prioritizing the obtained scores based on risk.

$$PP = TP + \sum OPi + YSP \quad (1)$$

Table 5. Negativity parameter score (OP_i) table.

Total number of stories	Soft Storey	Apparent Quality	Heavy Overhangs	Vertical Irregularity	Irregularity/torsion effect in plan	Short Column	Topographic Effect
1 and 2	-10	-10	-10	-5	-5	-5	-3
3	-20	-10	-20	-10	-10	-5	-3
4	-30	-15	-30	-15	-10	-5	-3
5	-30	-25	-30	-15	-10	-5	-3
6 and 7	-30	-30	-30	-15	-10	-5	-3

3 RESULTS AND DISCUSSION

The seismic vulnerability scores of 100 RC buildings in the data set were determined according to the rapid visual scanning method (PDRB) used in Turkey. According to the results obtained, the rapid visual scanning method found 22% of the buildings at medium damage/risk, and 78% of them as severe damage/very risky. The method found none of the buildings to be slightly damaged/low risk (Figure 2).

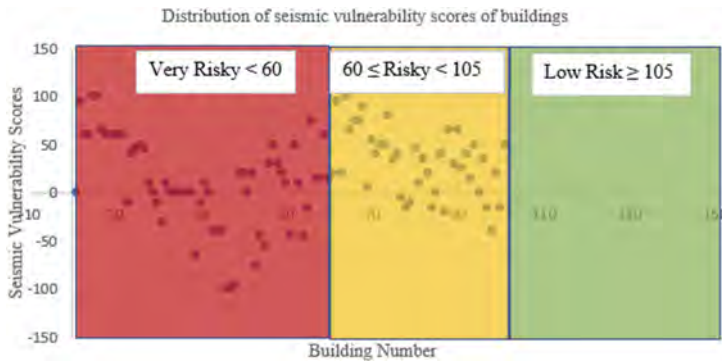


Figure 2. Distribution of seismic vulnerability scores of RC buildings.

When the actual damage conditions of the RC structures in the data set were compared with the results of the rapid visual scanning method, it was seen that the rapid visual scanning method predicted the seismic sensitivity status of 66% of the buildings correctly and 34% of

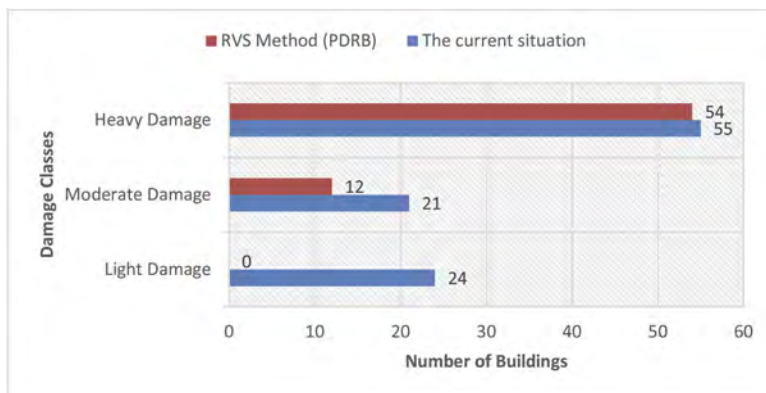


Figure 3. Number of buildings where the RVS method found the correct seismic vulnerability score.

them incorrectly. In addition, the method correctly predicted 98% of heavily damaged structures, correctly predicted 57% of moderately damaged structures, and it was seen that it could not predict any of the lightly damaged structures correctly (Figure 3).

The accuracy rate of 66% obtained with 11 parameters by scanning only from the street without entering the buildings is quite successful. At the same time, it has been seen that the method has high success in detecting heavily damaged buildings. However, the method failed to detect slightly damaged reinforced concrete structures. This situation leads to the conclusion that the method needs to be updated.

4 CONCLUSIONS

RC building stock in Turkey is quite high and the majority of this building stock consists of old buildings. It is not possible to examine all these older structures with detailed analysis methods. For this reason, risk-based prioritization of buildings is required and rapid visual scanning methods are used for this.

Within the scope of the study, the current damage conditions of 100 RC structures affected by earthquakes in different regions and rapid visual scanning results were compared and the success of the visual scanning method used in Turkey in the evaluation of seismic sensitivity of RC buildings was measured.

The data set used and the results obtained show that the relevant method has an accuracy of 66% in the evaluation of the seismic sensitivity of RC buildings, but it cannot detect the structures with little damage and moderate damage. It is considered that the method should be updated by increasing the number of buildings in the data set.

At the same time, as a result of the study, rapid visual scanning methods are thought to be an effective and useful method for risk-based prioritization of buildings.

REFERENCES

- ATC 21. 2015. Rapid Visual Screening of Buildings for Potential Seismic Hazards: A Handbook Second Edition, ATC-21. *Applied Technology Council*. USA.
- Bayraktar A. & Altunışık A.C. & Türker T, Karadeniz H. & Erdogdu S. & Angin Z. & Özşahin T.S. 2015. Structural performance evaluation of 90 RC buildings collapsed during the 2011 Van, Turkey. *Earthquakes. J Perform Constr Facil* 29(6):04014177
- Erdil, B. & Ceylan, H. 2018. Comparison of Walk-Down Procedures in Evaluating Seismic Vulnerability of RC Buildings in Turkey, *3rd International Mediterranean Science and Engineering Congress (IMSEC 2018)*, 24–26 Ekim 2018. Adana, Turkey.
- FEMA 154. 2015. Rapid Visual Screening of Buildings for potential seismic hazards: A Handbook, Federal Emergency Management Agency, Washington DC, USA.
- JBDDPA. 2001. Standard for seismic evaluation of existing reinforced concrete buildings (Version 2001). *The Japan Building Disaster Prevention Association*. Tokyo, Japan.
- KRDAE. 2019. Boğaziçi University Kandilli Observatory and Earthquake Research Institute <http://www.koeri.boun.edu.tr/simo/2/deprem-bilgileri/buyuk-depremler/>. Date of Access: 05.04.2019.
- Otani S. 2000. Seismic vulnerability assessment methods for buildings in Japan. *Earthq Eng Eng Seismol* 2(2):47–56.
- Özdemir M. Muvafık, M. 2019. Computer aided quick determination of earthquake performance of buildings by using street survey and preliminary assessment methods, *Van Yüzüncü Yıl University Institute of Science, VAN*.
- Özcebe, G. & Yüçemen, M. S. & Aydoğan, V. & Yakut, A. 2003. Preliminary Seismic Vulnerability Assessment of Existing Reinforced Concrete Buildings in Turkey. *Seismic Assessment and Rehabilitation of Existing Buildings*, 29–42.
- Structural Engineering Research Unit. 2017. Archival material from Afyon and Bingöl Earthquake database. Middle East Technical University, Ankara, Turkey. <http://www.seru.metu.edu.tr/archives.html>. Accessed 23 Oct 2017.

- Sucuoglu H. & Yazgan U. 2003. Simple survey procedures for seismic risk assessment in urban building stocks. *Seismic assessment and rehabilitation of existing buildings, earth and environmental sciences*. London: Kluwer Academic Publishers 29: 97–118.
- TEC2018 (Turkish Earthquake Resistant Code). 2018. Deprem Etkisi Altında Binaların Tasarımı İçin Esaslar (Specifications for Buildings to be Designed under Seismic Effect), *Turkish Ministry of Public Works and Settlement*, Ankara, Turkey.
- Yakut A. 2004. Preliminary Seismic Performance Assessment Procedure for Existing RC Buildings. *Engineering Structures*, 26, 1447–1461.

Chloride ingress of concrete structure considering the effect of early-age shrinkage

Y. Li & X. Ruan

Tongji University, Shanghai, China

T. Li & W.Y. Dou

Anhui Transportation Holding Group Co., Ltd., Anhui, China

ABSTRACT: Structural durability deterioration is a multiscale and multiphysics process and can be influenced by different factors. The influences of constructions initial status and the multiscale variation of concrete are also critical for the unexpected durability deterioration. Benefited from the development in concrete modeling, the progress in the shrinkage and durability are also prominent at meso-scale. In this paper, a comprehensive method is proposed combining the refined mesoscopic chloride ingress and the multiphysics shrinkage model. To investigate the influence of early-age shrinkage quantitatively, the numerical comparison between the 100-year chloride ingress with and without the shrinkage effect is conducted. With the modified diffusion coefficient, the ion concentration and the frontal depths of chloride ingress are all increased greatly. The extreme concentration under the 30mm concrete cover increases from 0.04kg/m^3 to 0.5kg/m^3 . The influence of different relative humidities in early-age curing is also investigated. With the drier curing environment, local tensile stress also increases greatly around the exposed surface, and the influenced area of chloride ingress is lager.

1 INTRODUCTION

The durability of reinforced concrete infrastructure is significant for structural safety and performance during long-term service. Many experiments focus on environmental exposure, substance transport, ingress resistance, and corrosion-induced crack to investigate the structural deterioration mechanisms. Various empirical functions are proposed at the beginning of this century for durability predictions. After decades of implementing the theory of durability design, the structural service performance is significantly improved with the higher strength of concrete material, the larger thickness of the concrete cover, and the introduction of specific protective measures. However, local disasters and damages can still be found in the infrastructural projects recently, which are much earlier than expected. Structural durability deterioration is a multiscale and multiphysics process and can be influenced by different factors (Li et al., 2022). Besides the factors like the coupling mechanism, the time-dependent environmental condition, or human activities, the influences of construction's initial status and the multiscale variation of concrete are also critical for unexpected durability deterioration (Hai-Long et al., 2016).

Early-age shrinkage is concrete's natural behavior after construction, leading to volume reduction and tensile strain in the cement mortar. Influenced by the water transport on the exposed surface and the mesostructure of concrete, the shrinkage behavior is non-uniform in concrete. The extreme tensile strain and the risk of local cracks can be found around the concrete surface and the narrow void between aggregates, leading to the higher diffusivity of environmental substances. So, it is necessary to investigate the influence of early-age shrinkage on the long-term durability of the reinforced concrete structure. Benefiting from the development in concrete modeling, the progress in shrinkage and durability are also prominent at the mesoscale recently (Li, Ruan, & Dou, 2023). The refined mesoscopic modeling method and the multiphysics shrinkage model can be introduced and combined herein for this comprehensive study.

DOI: 10.1201/9781003323020-501

This paper is organized as follows. Section 2 contains the comprehensive simulation for the long-term chloride ingress considering the influence of early-age shrinkage, which includes the modeling of concrete mesostructure, the multiphysics simulation of early-age shrinkage, and the solution of chloride ingress with modified diffusion coefficient. Section 3 contains the numerical comparison between the 100-year chloride ingress with and without the shrinkage effect, and the influence of different relative humidities in early-age curing is also investigated.

2 METHOD

2.1 Mesoscopic modeling

The mesostructure of concrete material is determined by the geometrical features of aggregates, the cement mortar is the continuous phase filling the void around aggregates, and the interfacial transition zone is the layer covering the particles with a thickness of around 30-80 μ m.

Mesoscopic modeling is to build the detailed sizes, shapes, positions, and orientations of aggregate particles. With the refined modeling method proposed by Ruan et al. (2019), the distribution of values of particle size, shape, and surface texture can be controlled based on the identification results based on real concrete sections in the framework as

$$S_{Agg} = \{P_{Agg}(D, \beta, T)\}. \quad (1)$$

where S_{Agg} is the set of aggregate particles and P_{Agg} is a single particle with properties such as particle size D , aspect ratio β , and surface texture T .

The three-level framework describes the parameter calculation method and the recommended distribution function. The equivalent particle size is related to the particle area, the Fuller grading solution can be controlled by the Walraven function (1980), the aspect ratio is the ratio of the particle length and width, and the value distribution can be described by the general extreme value distributions. The surface texture is controlled by different modeling algorithms to describe different aggregate types, where elliptical particles represent boulder aggregates and polygonal particles represent crushed stone aggregates.

In the detailed modeling, the sequence of particle sizes and aspect ratios are sampled following the corresponding probability distributions until the required aggregate content is reached. According to the types of aggregate material, the polygon shapes of particles are built with different numbers of vertices. Finally, the polygons are packed in a concrete model with random positions and orientations after checking the overlap between different particles.

2.2 Multiphysics shrinkage

The shrinkage of ordinary concrete includes self-shrinkage and drying shrinkage. The volume of hydration products is relatively smaller than that of the reactants, and the volume reduction caused by hydration is called self-shrinkage. Drying shrinkage is caused by changes in relative humidity (RH) and negative pressure in the capillary channels, which may be the result of the outward migration of moisture into the environment and water depletion in the hydration reaction. The shrinkage behavior occurs mainly within the cement mortar, and the aggregate effect is also important for the local mechanical response and moisture transport. As shrinkage increases, aggregate inhibits the behavior of the cement, limiting the apparent shrinkage but increasing the risk of internal microcracking.

During the multi-physical field shrinkage of concrete, self-shrinkage occurs with the hydration reaction, and drying shrinkage occurs in the unsaturated state of concrete. According to the distribution of moisture states in cement mortar, the shrinkage strain can be described as

$$\varepsilon_{cm}(x, t) = \begin{cases} \varepsilon_a, & H = 100\% \\ \varepsilon_a + \varepsilon_d, & H < 100\% \end{cases}, \quad x \in \Omega_{s,cm}, t \in \Omega_{t,sh}, \quad (2)$$

where both stages of the process can occur simultaneously in the same model, and the RH distribution is not uniform in space. ε_{cm} is the total shrinkage strain in the cement mortar; x is the spatial location $\Omega_{s,cm}$ in the cement mortar domain; t is the time point $\Omega_{T,sh}$ within the simulated shrinkage period; ε_a is the autogenous shrinkage controlled by the hydration reaction at RH, $H = 100\%$; ε_d is the drying shrinkage controlled by RH at $H < 100\%$. Based on the existing studies on the shrinkage mechanism of concrete, the self-shrinkage strain is mainly controlled by the hydration ratio, and the drying shrinkage strain is controlled by the moisture distribution in cement, which needs to consider both moisture migration and water consumption by hydration reaction.

2.3 Chloride ingress

Chloride ingress is one of the most serious mechanisms in the durability deterioration of the concrete structure. The behavior of ion transport can be described in Fick's diffusion law, and the density of ion flux is proportional to the gradient of concentration, which can be described as

$$\mathbf{J}_{cl} = -D_{Cl}\nabla c_{Cl}, \quad (3)$$

$$\frac{\partial c_{Cl}}{\partial t} = \nabla(D_{Cl}\nabla c_{Cl}), \quad (4)$$

where \mathbf{J} is the chloride ion diffusion flux ($\text{mol}/(\text{m}^2\cdot\text{d})$); D_{Cl} is the chloride ion diffusion coefficient (m^2/d); C_{Cl} is chloride ion content per unit volume of concrete (mol/m^3). To investigate the influence of mechanical status on the chloride ingress, the detailed diffusion coefficient can be modified according to the experimental regression by reference (Liu et al., 2020; Wang et al., 2018), see Figure 1. The detailed modification is presented as

$$D_{Cl,\sigma} = f(\sigma)D_{Cl,0}, \quad (5)$$

where $D_{Cl,\sigma}$ is the diffusion coefficient considering the mechanical influence; $f(\sigma)$ is the corresponding influence coefficient with the local stress σ , which can be calculated as

$$f(\sigma) = \begin{cases} 1.0 + 0.9598 \frac{\sigma}{\sigma_t} - 0.3608 \left(\frac{\sigma}{\sigma_t}\right)^2, & 0 < \sigma < 0.7\sigma_t \\ 1.0 - 1.6626 \frac{\sigma}{\sigma_c} + 2.2560 \left(\frac{\sigma}{\sigma_c}\right)^2, & 0.7\sigma_c < \sigma < 0 \end{cases}, \quad (6)$$

where σ is the local stress of cement mortar; σ_t and σ_c are the corresponding tensile and compressive strengths, respectively. So, the diffusion coefficient of cement mortar should be refined considering the detailed stress distribution.

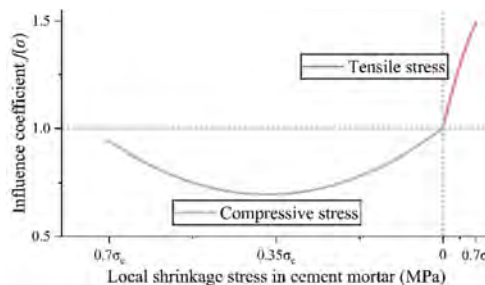


Figure 1. Influence coefficient of local shrinkage stress on the chloride diffusivity.

According to the detailed analysis requirement, the mesoscopic stress distribution caused by the shrinkage is transferred to the distribution of diffusion coefficient, and the chloride ingress during the long-term service is solved within the domain of cement mortar. The distribution of frontal depth and the probability of ion concentration can be analyzed and discussed.

3 SIMULATION

To investigate the influence of early-age shrinkage quantitatively, two 100mm×300mm models are built for comparison with the different considerations of shrinkage behavior. The basic properties of concrete material are set based on a bridge project. In the mesoscopic model, the aggregate area ratio is controlled at 45.3%. The aggregate sizes follow the Fuller grading design within the range from 5.0mm to 25.0mm, and as the crushed stone is used as aggregate, the particles are modeled with polygons. The triangle elements are unified in the cement mortar model, and in the concrete model, the sizes are refined greatly to reflect the detailed aggregate textures. For the early-age shrinkage, the related parameters are set based on the reference (Li, Ruan, Yi, et al., 2023), which is regressed from the free shrinkage test of cement and concrete specimens. For the long-term chloride ingress, the environmental boundary is considered as the exposure to de-icing solution in the cold regions. The basic diffusion coefficient of chloride ingress in cement mortar is determined as $6.246 \times 10^{-7} \text{ m}^2/\text{d}$ from the material test, and the mechanical influence is introduced as Equation (5).

Considering the 14-day shrinkage curing in the environment with 60% relative humidity (RH), the multiphysics shrinkage of the concrete specimen can be predicted, and the quantitative validation has been published in reference (Li, Ruan, Yi, et al., 2023). Extreme tensile stress occurs around the exposed surface, which can be even larger than the tensile strength of cement mortar in the thin layer covering the aggregates. For the 100-year chloride ingress, the time-dependent distributions of ion concentration are calculated considering the influence of shrinkage stress. The differences in the concentration distributions are remarkable, and the chloride ingress results after 20-year, 60-year, and 100-year services are compared, see Figure 2. Due to the tensile stress in the upper part of concrete shrinkage, the local diffusion coefficient is relatively larger, and the frontal depths of chloride ingress are much larger compared with normal simulations.

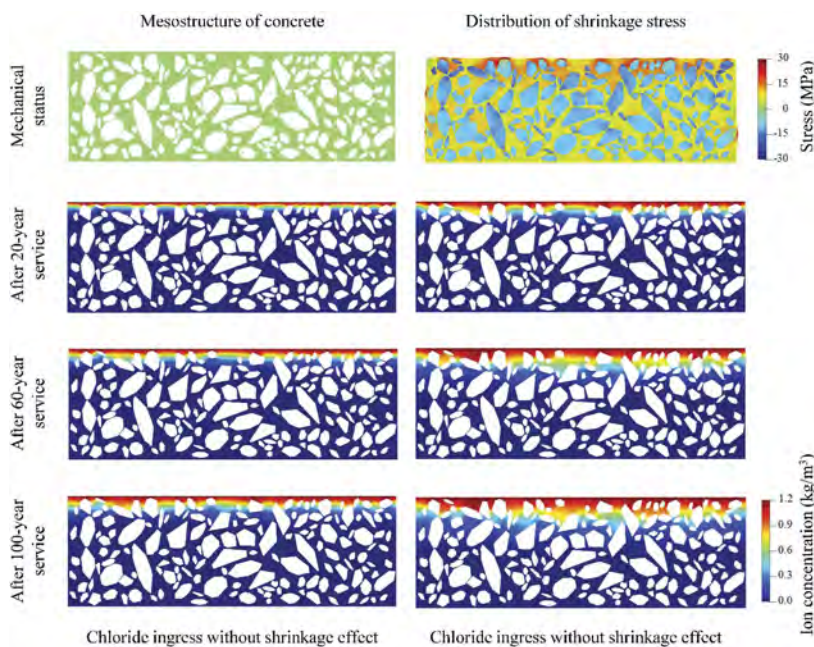


Figure 2. The distribution of ion concentration after 20-year, 60-year, and 100-year chloride ingress considering the influence of early-age shrinkage.

For the quantitative comparison between the two models, the probabilities in ion concentration at the 30mm depth under the exposed surface are analyzed, which is common to the designed thickness of the concrete cover. The local ion concentration is much higher after the consideration of stress distribution, which is reflected in the mean, 5% percentile, and 95%

percentile, see Figure 3. The extreme concentration at this depth can reach about 0.04kg/m^3 , and with the local enlarged diffusion coefficient, the extreme concentration can reach about 0.5kg/m^3 , which is larger than the critical concentration for reinforcement corrosion.

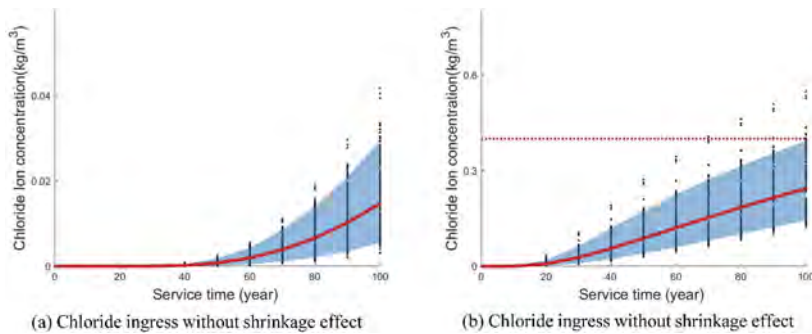


Figure 3. The time-dependent ion concentration on the reinforcement surface with the shrinkage effect.

With the proposed numerical method, the influence of different curing environments can also be discussed. The concrete shrinkage in the 40% RH, 60% RH, and 80% RH is simulated for the diffusion of influence coefficient on cement diffusivity. The eventual chloride ingress after 100-year service is analyzed and compared, see Figure 4. The influence of early-age shrinkage is important for the concrete long-term durability. With the drier curing environment, the deformation is larger around the exposed surface due to the drying shrinkage, and local tensile stress also increases greatly, which also influences long-term chloride ingress. With the RH of the curing environment decreasing from 80% to 40%, the influenced area of chloride ingress is larger, especially the part of cement mortar with large tensile stress.

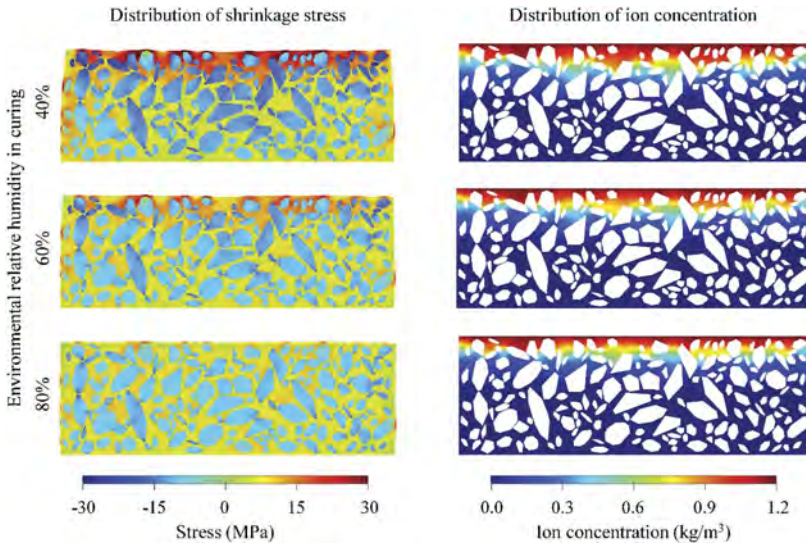


Figure 4. The distribution of ion concentration after 100-year service considering the 40%, 60%, and 80% RH in the early-age shrinkage.

For the quantitative comparison, the detailed ion concentrations under the concrete cover are extracted and compared with representative curves, see Figure 5. The extreme ion concentration increases from 0.4kg/m^3 to 0.7kg/m^3 , with the curing RH increasing from 40% to 80%. The variations of concentrations are also influenced by the early age shrinkages.

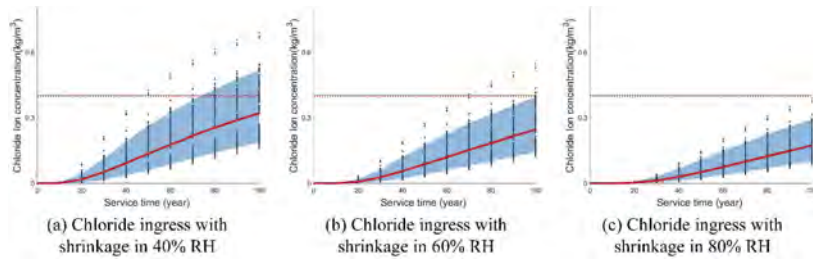


Figure 5. The time-dependent ion concentration on the reinforcement surface considering the different RHs in early-age shrinkage.

4 CONCLUSION

In this paper, a comprehensive method is proposed combining the refined mesoscopic chloride ingress and the multiphysics shrinkage model. To investigate the influence of early-age shrinkage quantitatively, the numerical comparison between the 100-year chloride ingress with and without the shrinkage effect is conducted. With the modified diffusion coefficient, the ion concentration and the frontal depths of chloride ingress are all increased greatly. The extreme concentration under the 30mm concrete cover increases from 0.04kg/m^3 to 0.5kg/m^3 .

The influence of different relative humidities in early-age curing is also investigated. With the drier curing environment, the deformation is larger around the exposed surface due to the drying shrinkage, and local tensile stress also increases greatly, which also influences long-term chloride ingress. The extreme ion concentration increases from 0.4kg/m^3 to 0.7kg/m^3 , with the curing RH increasing from 40% to 80%. The variations of concentrations are also influenced by the early age shrinkages.

ACKNOWLEDGEMENT

The support from the National Natural Science Foundations of China (Grant numbers 52078367), the Anhui Transportation Holding Group Research Project (Grant numbers JKKJ-2020-12), the China Scholarship Council (Grant numbers 202206260161) and the China Association for Science and Technology Outstanding Chinese and Foreign Youth Exchange Program (Grant numbers 0200151002) is gratefully acknowledged. The opinions and conclusions presented in this article are those of the authors and do not necessarily reflect the views of the sponsoring organizations.

REFERENCES

- Hai-Long, W., Jian-Guo, D., Xiao-Yan, S., & Xiao-Long, Z. (2016). Time-Dependent and Stress-Dependent Chloride Diffusivity of Concrete Subjected to Sustained Compressive Loading. *Journal of Materials in Civil Engineering*, 28(8), 04016059.
- Li, Y., Ruan, X., & Dou, W. (2023). Early age behavior of clustered shearing connector pocket in bridge composite girder. *Construction and Building Materials*, 368, 130465.
- Li, Y., Ruan, X., Yi, Y., & Xu, L. (2023). Multiphysics simulation for concrete early-age hydration behavior with mesoscopic modelling. *Construction and Building Materials*, 362, 129780.
- Li, Y., Ruan, X., Zhang, M., & Dou, W. (2022). RC structures life-cycle probabilistic evaluation method considering mesoscopic material uncertainty with chloride ingress. *Structure and Infrastructure Engineering*, 1–15.
- Liu, Y., Lin, P., & Ma, J. (2020). Diffusion Behavior of Chloride Ions in Concrete Box Girder under the Influence of Load and Carbonation. *Materials*, 13(9).
- Ruan, X., Li, Y., Jin, Z., Pan, Z., & Yin, Z. (2019). Modeling method of concrete material at mesoscale with refined aggregate shapes based on image recognition. *Construction and Building Materials*, 204, 562–575.
- Walraven, J. C. (1980). Aggregate interlock: A theoretical and experimental analysis.
- Wang, J., Su, H., & Du, J. (2018). Influence of coupled effects between flexural tensile stress and carbonation time on the carbonation depth of concrete. *Construction and Building Materials*, 190, 439–451.

Seismic performance evaluation of masonry infilled RC frame retrofitted with BRBs

R. Chelapramkandy & J. Ghosh

Indian Institute of Technology Bombay, Mumbai, Maharashtra, India

F. Freddi

University College London, London, UK

ABSTRACT: Reinforced concrete (RC) frames with unreinforced masonry infill represents a widely used construction typology across the globe, including regions characterized by moderate to high seismicity. These structures have been often designed before the introduction of modern seismic design codes, are characterized by low ductility and high seismic vulnerability and are in need for seismic retrofitting to meet the current safety standards. However, it is important to highlight that, although considered as non-structural elements, masonry infills can significantly affect the seismic response of the structure. However, their role on the seismic performance of retrofitted RC structures has been generally neglected in literature. Among the different retrofitting strategies, the use of buckling-restrained braces (BRBs) represents an effective solution to improve the seismic performance of existing RC structures. This study investigates the interaction between the BRBs and masonry infill on seismic response of a case study frame.

1 INTRODUCTION

Reinforced concrete (RC) frames with unreinforced masonry infills represent a widely used construction typology for building structures worldwide, including regions characterized by moderate to high seismicity (Dolšek & Fajfar, 2008; Akan et al. 2022). Historical and recent earthquakes have demonstrated the high vulnerability of these structures, especially when designed before the introduction of modern seismic design codes (i.e. low ductile frames) (Rossetto & Elnashai, 2003; Freddi et al. 2017; Freddi et al. 2021a). This highlights the urgent need to identify efficient and effective retrofit solutions for such structures to meet the life safety and damage limitation requirements. Among others, the use of dissipative braces represents an efficient strategy to improve the seismic performance of such low ductile buildings (Freddi et al. 2013; Gutiérrez-Urzúa & Freddi, 2022). The introduction of these braces creates a dual load path for the seismic input and increases strength, stiffness, and ductility of existing frames (Freddi et al. 2021b). Therefore, when introduced within existing frames, these braces can protect structural and non-structural building components from damage by reducing their seismic demand. Among others, buckling-restrained braces (BRBs) represent a type of dissipative devices in which a sleeve provides buckling resistance to an unbonded core that resists the axial stress, hence allowing the BRB's core to develop axial yielding in compression in addition to that in tension ensuring an almost symmetric hysteretic behavior (Freddi et al. 2021c).

Due to their brittle nature, the strength and stiffness of the masonry infills are often disregarded during the design process. However, it has been demonstrated that, from one side, they can significantly affect the seismic response of the structures; on the other side, their damage represents a significant percentage of the economic losses. For these reasons, several approaches are proposed in literature for simulating the presence of masonry infills within the

frame. Among others, a common strategy is to idealize the masonry infills as single or multiple compressive equivalent struts characterized by a highly nonlinear behavior (Crisafulli et al. 2000; Dolšek & Fajfar, 2008).

The present paper investigates the potential interactions between the retrofit system based on BRBs and the masonry infills. The numerical results provide some insights into the ability of BRBs in protecting not only the RC frame from damage but also the masonry infills. The paper is organized as follows: Section 2 describes the methodology followed for the definition of seismic fragility curves for the infilled and retrofitted infilled case study frames considering different damage states. Section 3 presents the finite element modeling strategy for the frame, the masonry infills, and the BRB devices. Section 4 presents the definition of damage states thresholds (using pushover analysis), the assessment of the seismic demand (using nonlinear time-history analysis) and the definition of seismic fragility curves for the infilled and retrofitted infilled frames. Finally, Section 5 presents the conclusions along with some future research directions.

2 METHODOLOGY

A three-story, three-bay masonry-infilled RC frame designed for gravity loads alone is selected as the case study structure and modeled in OpenSees (McKenna et al. 2000). The structure is retrofitted with BRBs following the procedure outlined in Freddi et al. (2021c). Nonlinear static analyses are performed for both infilled and retrofitted infilled RC frames to determine the damage state (DS) threshold values in terms of global engineering demand parameter (*EDP*). The maximum interstory drift ratio (IDR_{max}) is assumed as global *EDP* to synthetically describe the response of the structure, and the DS threshold values are estimated by mapping IDR_{max} to local *EDPs*, such as material strain and cross-section strength. Cloud analyses are successively performed considering a ground motion set to evaluate the seismic performance of the structure and subsequently determine the samples of structural demand by accounting for the record-to-record variability. Probabilistic seismic demand models (PSDMs) are successively derived for the IDR_{max} using the average spectral acceleration (Sa_{avg}) as the intensity measure (*IM*) (Baker & Jayaram, 2008; Eads et al. 2015). This *IM* is selected as it allows accounting for the natural period elongation that is typically observed in infilled frames as a consequence of the damage experienced by the infills during the earthquake. Moreover, it allows comparing fragility curves of structures characterized by different natural periods (i.e. the infilled and retrofitted infilled RC frames in this case). The Sa_{avg} is defined as the spectral acceleration averaged over a period band, as given in Equation (1).

$$Sa_{avg}(T_1, T_2, \dots, T_n) = \left(\prod_{i=1}^n Sa(T_i) \right)^{1/n} \quad (1)$$

where, $Sa(T_i)$ is the spectral acceleration at i^{th} period, and T_1, T_2, \dots, T_n are the ‘ n ’ periods of interest. In the present study, this period band is assumed to span from the natural period of the stiffest structure (i.e. the retrofitted infilled RC frames) to the natural period of the more flexible structure (i.e. the bare frame).

PSDMs are established by using bilinear regression models (Tubaldi et al. 2016; Freddi et al. 2017; O’Reilly & Monteiro, 2019; Aljawhari et al. 2021) based on the following expression:

$$\ln(EDP) = [a_1 + b_1 \times \ln(IM)]H_1 + [a_2 + b_2 \times \ln(IM)](1 - H_1) + \ln(\varepsilon) \quad (2)$$

where, $a_1, b_1, a_2,$ and b_2 are the regression coefficients, and H_1 is the step function with the value of $H_1 = 0$ when $IM > IM^*$ and value of $H_1 = 1$ when $IM \leq IM^*$, where IM^* is the intersection point of the two segments as shown in Figure 1. The value of the IM^* is obtained such that the fitted bilinear regressions maximize the goodness of fit coefficient (R^2) (Tubaldi et al. 2016).

Fragility curves are successively derived for the masonry-infilled RC frame with and without the BRBs. Fragility curves give the likelihood of meeting or exceeding a specific DS and

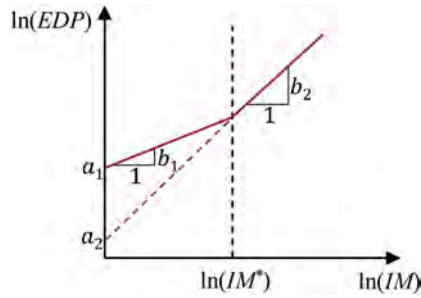


Figure 1. Bilinear probabilistic seismic demand model (PSDM) parameters.

are derived based on the PSDMs and DS threshold values according to the following expression:

$$P[DS|IM] = \Phi \left[\frac{\ln(EDP_{med}/S_C)}{\sqrt{\beta_{EDP|IM}^2 + \beta_C^2}} \right] \quad (3)$$

where, EDP_{med} and $\beta_{EDP|IM}$ are the median estimates of seismic demand and corresponding standard deviation, whereas S_C and β_C are the DS threshold value and corresponding standard deviation.

3 CASE STUDY

3.1 Case study description

A three-story, three-bay RC frame representative of non-seismically designed (low ductility) low-rise building is selected for case study purposes. Figure 2 shows the elevation view of the frame, which has a bay width of 5.49 m and an interstory height of 3.66 m. The beams have a rectangular section of 230 mm × 460 mm, while the columns have a square section of 300 mm × 300 mm. The reinforcement bars have a yield strength of 276 MPa, whereas the concrete has a compressive cube strength of 24 MPa. Experimental results for the global and local response of the case study structure are available in literature (Aycardi et al. 1994; Bracci et al. 1995) and allowed the validation of the numerical model of the frame in OpenSees. Additionally, Figure 2 shows the considered unreinforced masonry infill with openings of 18% of the infill area, and the dissipative braces (i.e. D1 to D3).

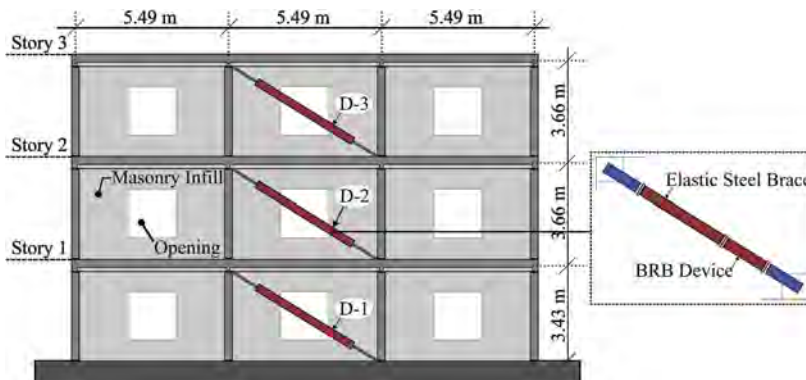


Figure 2. Case study infilled frame layout and placement of the dissipative braces.

3.2 Finite element modeling of the RC frame

The 2D model of the case study structure is developed in OpenSees. Columns and beams are modeled using the *beamWithHinges* element consisting of a central elastic part and two lateral portions with a specified length where a fiber approach is used to represent the nonlinear response of the section. The *Concrete02* and *Hysteretic* materials are used to model the concrete and longitudinal steel, respectively. The beam-to-column joints are modeled using four rigid off-sets and a two-node *zeroLength* rotational springs. Additionally, shear and axial column failure are also modeled in OpenSees within *zeroLength* nonlinear springs. More details on the numerical model of the frame can be found in Freddi et al. (2013), (2017), (2021c).

3.3 Finite element modeling of the masonry infills

Unreinforced masonry infills within the RC frame are modeled following the recommendations of Dolšek & Fajfar (2008). The equivalent single diagonal strut modeling method is used to simulate the masonry infill behavior (Crisafulli et al. 2000; Wu et al. 2022). According to Dolšek & Fajfar (2008), the initial stiffness of the masonry infill can be defined as follows:

$$K_i = \frac{G_w L_{in} t_w}{H_{in}} \quad (4)$$

where, H_{in} , L_{in} , and t_w represents the height, length, and thickness respectively of the infill, and G_w is the infill shear modulus. The maximum force F_m of the masonry infill is determined as:

$$F_m = 0.818 \frac{L_{in} t_w f_{tp}}{C_I} \left(1 + \sqrt{C_I^2 + 1} \right), \text{ where, } C_I = 1.925 \frac{L_{in}}{H_{in}} \quad (5)$$

where, f_{tp} is the cracking strength of the masonry infill, and C_I is the coefficient that takes into account the interaction between the infills and the surrounding frame.

Figure 3 shows the force-displacement back-bone curve of the masonry infill - represented by four branches. The thickness of the infill is considered as 100 mm, and the shear strength and the shear modulus of the masonry infills are adopted from Hak et al. (2012) as 0.31 MPa and 1089 MPa, respectively. According to Dolšek & Fajfar (2008), the cracking force of the masonry infill (F_c) is assumed to be 60% of the maximum force (F_m). For the infill with the window, the story drift corresponding to the maximum force is considered 0.15%, whereas the story drift corresponding to the infill collapse is considered five times the story drift at the maximum force. The present paper considers a residual force (F_r) of 5% of the maximum force. Window opening covering one-third of the horizontal length of infill is considered as shown in Figure 2. The parameter λ_0 is used to reduce the infill's strength and initial stiffness in order to account for the masonry infill's opening, defined according to Equation (6) (Dolšek & Fajfar, 2008; Troup et al. 2019)

$$\lambda_0 = 1 - \frac{1.5L_0}{L_{in}} \geq 0 \quad (6)$$

where, L_{in} and L_0 are, respectively, the total length of infill and horizontal length of openings.

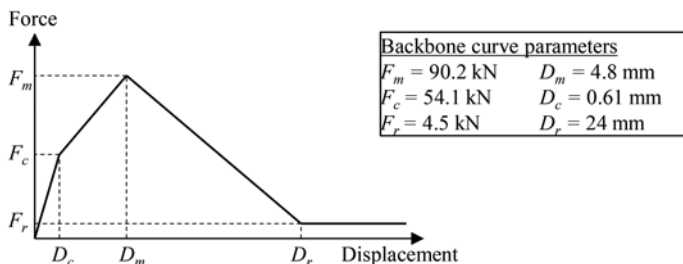


Figure 3. Lateral force-displacement envelope for the diagonal struts.

3.4 Finite element modeling of the Buckling-Restrained Braces (BRBs)

The design of the BRBs are based on the capacity curve of bare frame, and the retrofit design aims to double the retrofitted frame's base shear capacity (i.e. strength proportion coefficient $\alpha = 1$) (Freddi et al. (2021c)). The first mode shape of the retrofitted frame is maintained as same as that of the bare frame by properly proportioning the stiffness of BRBs in the frame, while the simultaneous yielding of the BRB device is ensured by properly proportioning the strength of BRBs among the stories. Each BRB consists of an elastic brace and a BRB device arranged in series. This study uses the *Steel02* material in OpenSees to model the BRB device. Additional details on the BRB design can be found in Freddi et al. (2021c). Table 1 lists the BRBs design properties where, F_c^i and K_c^i are the strength and stiffness, whereas $f_{y, BRB}$, L_{BRB} , and A_{BRB} are the yield strength, length, and area of cross-section of the BRB device core.

Table 1. Design properties of the BRBs and BRBs device core.

Story	F_c^i (kN)	K_c^i (kN/mm)	$f_{y, BRB}$ (MPa)	L_{BRB} (mm)	A_{BRB} (mm ²)
1	220.3	48.4	250	2815	881
2	189.6	32.6	250	3599	758
3	109.2	29.8	250	2270	437

4 SEISMIC FRAGILITY CURVES

4.1 Threshold mapping of damage states

Figure 4a shows the base shear vs. IDR_{max} results of the nonlinear static analyses performed for both the infilled and retrofitted infilled frames. The reduction in the base shear after attaining the peak value is related to the damage in the masonry infills. The DSs for the structural components are defined as Slight (S), Moderate (M), Extensive (E), and Complete (C) based on the distinct local responses of the structure listed in Table 2, along with the corresponding IDR_{max} at the onset of each DS. It is worthwhile to note that, due to the non-symmetric placement of the BRBs, nonlinear static analyses are carried out both in the positive and negative direction, providing slightly different capacity curves and DSs threshold values (marked in Figure 4a). Subsequently, the DS threshold values are taken as the average values from the two directions. For the infill panel, IDR_{max} value corresponding to the development of first crack on majority of infill at one floor is taken as threshold value corresponding to the Slight DS (SI). In order to incorporate the uncertainty in DS threshold estimation, a dispersion of 0.3 is assumed.

Table 2. Damage states description for infill panel, infilled frame and infilled frame retrofitted with BRBs.

Damage states	Description	Maximum IDR (%)	
		Infilled	Infilled + BRBs
Slight	50% of columns at one floor have yielded	0.57	0.52
Moderate	50% of columns at one floor experienced concrete crushing	1.33	1.52
Extensive	Average of Moderate and Complete	2.16	2.32
Complete	50% of columns at one floor experienced shear failure initiation	3.00	3.12
Slight	Infill panel Majority of infills at one floor develop first crack	0.019	0.019

4.2 Probabilistic seismic demand model

A set of 240 ground motion records from Baker et al. (2011) is used to perform the nonlinear time history analysis on the infilled frame and retrofitted infilled frame. The fundamental time period of the bare frame, infilled frame, and retrofitted infilled frame are 1.2s, 0.160s, and 0.156s, respectively. The period band considered for the calculation of the Sa_{avg} spans from 0.156s to 1.2s, with intervals of 0.1s. Figure 4b shows the bilinear PSDMs for both infilled frame and retrofitted infilled frame developed by following the approach discussed in Section 2. The results show a good fitting in both cases with R^2 values of 0.90 and 0.87. The expression of the bilinear PSDM, respectively, for the infilled and retrofitted infilled frames are as follows:

$$\ln[IDR_{max}(\%)] = [-1.17 + 1.02 \times \ln(Sa_{avg})]H_1 + [1.11 + 2.37 \times \ln(Sa_{avg})](1 - H_1) \quad (7)$$

$$\ln[IDR_{max}(\%)] = [-1.18 + 1.08 \times \ln(Sa_{avg})]H_1 + [0.46 + 2.50 \times \ln(Sa_{avg})](1 - H_1) \quad (8)$$

with values of IM^* , the intersection point of two segments, being equal to 0.18g and 0.32g for infilled and retrofitted infilled frames.

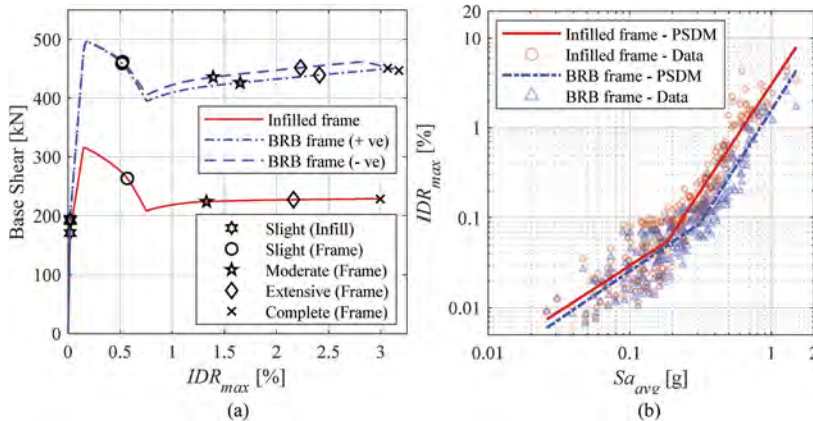


Figure 4. (a) Base shear vs. IDR_{max} curves and mapping of IDR_{max} values with different damage state thresholds; (b) Bilinear PSDMs of the infilled frame and retrofitted infilled frame.

4.3 Seismic fragility curves

Figure 5 shows the fragility curves for the infilled and retrofitted infilled frames. The median values of Sa_{avg} corresponding to different DSs are listed in Table 3. There is a significant decrease observed in the seismic fragility of the structural components after the retrofitting with BRBs, that is evident with the increases in the median values of Sa_{avg} for Slight, Moderate, Extensive, and Complete DS, respectively equal to 30%, 39%, 35%, and 32%. The advantages in protecting the infill panels from cracking is more modest. The comparison of the fragility curves shows an increase of 17% in the median values of Sa_{avg} for the Slight DS of the infill panels. This reduction in the seismic fragility shows the characteristics of the BRB device to provide a supplementary path to the lateral loads induced by the earthquake and to enhance the seismic performance by dissipating the earthquake energy. Moreover, a reduction in dispersion of 5.5% and 9.5% is observed, respectively, for the structural and non-structural components after the retrofitting with BRBs.

Table 3. Median values (in units of g) of lognormal fragility curves.

Structure type	Building frame				Infill panel
	Slight (S)	Moderate (M)	Extensive (E)	Complete (C)	Slight (SI)
Infilled frame	0.493	0.705	0.865	0.993	0.065
Infilled + BRB frame	0.641	0.984	1.166	1.312	0.076

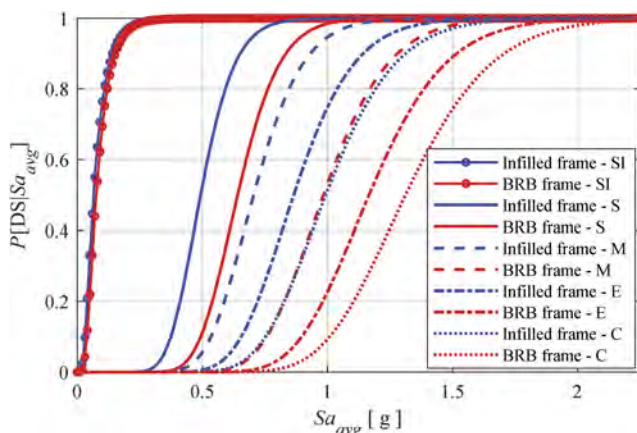


Figure 5. Seismic fragility curves of infilled and infilled frame retrofitted with BRBs.

5 CONCLUSIONS

The present study investigates the use of buckling-restrained braces (BRBs) for the seismic retrofitting of low ductility reinforced concrete (RC) frames. In particular the study focuses on the presence of masonry infills and their interaction with the BRBs. A three-story, three-bay masonry-infilled RC frame designed for gravity loads alone is selected as the case study structure and modeled in OpenSees. Masonry infills with openings are added to the model as single compressive diagonal struts in the two directions. Nonlinear static analyses were performed for both the infilled and retrofitted infilled frames for determining the DS thresholds, followed by the derivation of the PSDMs and fragility curves. The comparison of the fragility curves shows a significant improvement in the seismic performance of the structural components after the retrofitting with increases of the median Sa_{avg} values of 30%, 39%, 35%, and 32%, respectively for the Slight, Moderate, Extensive, and Complete DSs. A more modest increase (i.e. 17%) in the median value of Sa_{avg} was observed in the Slight DS of the infill panel. Future work may consider the different uncertainties for seismic evaluation of a retrofitted infilled frame and its life-cycle cost estimation.

REFERENCES

- Akan O.D., O'Reilly G.J., & Monteiro R. 2022. Simplified modelling and pushover analysis of infilled frame structures accounting for strut flexibility. *Earthquake Engineering and Structural Dynamics* 51 (6): 1383–1409.
- Aljawhari K., Gentile R., Freddi F., & Galasso C. 2021. Effects of ground-motion sequences on fragility and vulnerability of case-study reinforced concrete frames. *Bulletin of Earthquake Engineering* 19 (15): 6329–6359.
- Aycardi L.E., Mander J.B., & Reinhorn A.M. 1994. Seismic resistance of reinforced concrete frame structures designed only for gravity loads: Experimental performance of subassemblages. *ACI Materials Journal* 91 (5): 552–563.

- Baker J.W., & Jayaram N. 2008. Correlation of spectral acceleration values from NGA ground motion models. *Earthquake Spectra* 24 (1): 299–317.
- Baker J.W., Lin T., Shahu S.K., & Jayaram N. 2011. New Ground Motion Selection Procedures and Selected Motions for the PEER Transportation Research Program. *Pacific Earthquake Engineering Research Center*.
- Bracci J.M., Reinhorn A.M., & Mander J.B. 1995. Seismic resistance of reinforced concrete frame structures designed for gravity loads: performance of structural system. *ACI Materials Journal* 92 (5): 597–609.
- Crisafulli F.J., Carr A.J., & Park R. 2000. Analytical modelling of infilled frame structures - A general review. *Bulletin of the New Zealand Society for Earthquake Engineering* 33 (1): 30–47.
- Dolšek M., & Fajfar P. 2008. The effect of masonry infills on the seismic response of a four-storey reinforced concrete frame - a deterministic assessment. *Engineering Structures* 30 (7): 1991–2001.
- Eads L., Miranda E., & G. Lignos Dimitrios. 2015. Average spectral acceleration as an intensity measure for collapse risk assessment. *Earthquake Engineering & Structural Dynamics* 44: 2057–2073.
- Freddi F., Ghosh J., Kotoky N., & Raghunandan M. 2021c. Device uncertainty propagation in low-ductility RC frames retrofitted with BRBs for seismic risk mitigation. *Earthquake Engineering and Structural Dynamics* 50 (9): 2488–2509.
- Freddi F., Novelli V., Gentile R., Veliu E., Andreev S., Andonov A., Greco F., & Zhuleku E. 2021a. Observations from the 26th November 2019 Albania earthquake: the earthquake engineering field investigation team (EEFIT) mission. *Bulletin of Earthquake Engineering* 19 (5): 2013–2044.
- Freddi F., Padgett J.E., & Dall'Asta A. 2017. Probabilistic seismic demand modeling of local level response parameters of an RC frame. *Bulletin of Earthquake Engineering* 15 (1): 1–23.
- Freddi F., Tubaldi E., Ragni L., & Dall'Asta A. 2013. Probabilistic performance assessment of low-ductility reinforced concrete frames retrofitted with dissipative braces. *Earthquake Engineering & Structural Dynamics* 42: 993–1011.
- Freddi F., Tubaldi E., Zona A., & Dall'Asta A. 2021b. Seismic performance of dual systems coupling moment resisting and buckling-restrained braced frames. *Earthquake Engineering & Structural Dynamics* 50: 329–353.
- Gutiérrez-Urzúa F., & Freddi F. 2022. Influence of the design objectives on the seismic performance of steel moment resisting frames retrofitted with buckling restrained braces. *Earthquake Engineering & Structural Dynamics* 51: 3131–3153.
- Hak S., Morandi P., Magenes G., & Sullivan T.J. 2012. Damage control for clay masonry infills in the design of RC frame structures. *Journal of Earthquake Engineering* 16 (SUPPL. 1): 1–35.
- McKenna F., Fenves G.L., & Scott M.H. 2000. Open System for Earthquake Engineering Simulation. *Pacific Earthquake Engineering Research Center*
- O'Reilly G.J., & Monteiro R. 2019. Probabilistic models for structures with bilinear demand-intensity relationships. *Earthquake Engineering and Structural Dynamics* 48 (2): 253–268.
- Rossetto T., & Elnashai A. 2003. Derivation of vulnerability functions for European-type RC structures based on observational data. *Engineering Structures* 25 (10): 1241–1263.
- Troup L., Phillips R., Eckelman M.J., & Fannon D. 2019. Effect of window-to-wall ratio on measured energy consumption in US office buildings. *Energy and Buildings* 203: 109434.
- Tubaldi E., Freddi F., & Barbato M. 2016. Probabilistic seismic demand model for pounding risk assessment. *Earthquake Engineering & Structural Dynamics* 45: 1743–1758.
- Wu J.R., Di Sarno L., Freddi F., & D'Aniello M. 2022. Modelling of masonry infills in existing steel moment-resisting frames: Nonlinear force-displacement relationship. *Engineering Structures* 267.

LCA and EPD need digitalization

U.R. Pannuti

ICMQ S.p.A., Milan, Italy

ABSTRACT: The Italian Government has issued a message on the importance of digital investment when designing infrastructures included in the PNNR (National Resilience and Recovery Plan), approved by European Commission in June 2021. It calls for the verification of significant contributions for one or more environmental objectives embedded in the sustainability report, taking into account the life cycle of the infrastructure. The EPD (Environmental Product Declaration), based on the product LCA (Life Cycle Assessment), allows for estimating those environmental objectives. To design a sustainable building/infrastructure, disposing of products' information on their environmental impacts in a format is paramount so that they can be available and automatically importable into the building/infrastructure model in the LCA calculation software. On this matter, the digitization of environmental data and their integration on the BIM (Building Information Modeling) model could hit the target. This article reviews the benefits of EPD digitization and why LCA and EPD need it.

1 INTRODUCTION

Some European Countries have introduced mandatory LCA for new buildings into their national legislation. The United States, France and other countries are investing in requiring sustainability performances from products, while in Italy the new Decree on minimum environmental criteria for the design of new buildings, assigns a reward score for the designer that performs an LCA study for the building. This kind of LCA, unlike that of a simple product, can be performed if all the environmental impacts of materials that are installed into the building are already known. The document that shows the environmental impacts on the final user is the EPD, generally published in form of a pdf file. EPDs are released on the website of the Program Operator, the body that sets the rules for the verification and publication of EPDs. Since the environmental impacts of the products are listed in a pdf file, it may be difficult to read, write, and transfer them to the software for calculating the LCA of the building. The digitization of environmental impacts is why we stress the importance of having such data in a format useful for its integration with current technologies, such as BIM (Building Information Modelling), and legislative requirements. Moreover, BIM is strongly recommended by Italian law (see paragraph 3).

2 THE SITUATION IN EUROPE

To govern the EPD development process, the International Standard ISO 14025 “Environmental labels and declarations - Type III environmental declarations - Principles and procedures” (International Organization for Standardization 2006) requires a specific entity, named the Program Operator, to define the rules, according to the International Standard for:

- PCR (Product Category Rules) developing;

- LCA developing (general requirement);
- EPD developing (format and content);
- EPD verifying rules;
- EPD publishing.

The EPD has become a fundamental tool to demonstrate manufacturers' sustainability efforts and to drive growth in the construction sector. A few years ago, many major North-American building design Companies set the EPD as the only selection factor for their suppliers. Indeed, those who presented a product with EPD had the possibility of being chosen for building designs aimed at LEED submission (Leadership in energy and environmental design) (U.S. Green Building Council 2019), a rating system for the design, construction and management of sustainable high-performance buildings. In France, starting from January 2022, the LCA study is mandatory for new buildings.

Each European Country has an established Program Operator for EPDs verification and publication, which is the reason behind establishing Eco Platform, the European Association of leading Program Operators in the construction sector. One of its main objectives is to harmonize the EPDs verification process to facilitate the mutual recognition of EPDs. It is achieved by implementing a unique format (characterized by the Eco EPD logo), based on compliance with the EN 15804 Standard "Sustainability of construction works. Environmental product declarations. Core rules for the product category of construction products" (European Committee for Standardization 2012), which is mandatory to calculate the LCA of a construction product. Eco Platform is aware of the importance of having the EPDs in a simple format to spread the interchange process, so in 2020 it launched the Eco Portal to display all the digitalized EPDs. The used format is ILCD (International Life Cycle data)+EPD one, developed by the Indata Network technical group (International Open Data Network for sustainable construction), composed of different European Association members (also Italy). The format ILCD +EPD (see paragraph 6) has been considered as the most suitable for digitization software and comprehensive with all the information that could be gathered from an EPD.

3 THE NORMATIVE IN ITALY

The first step for the digitization process occurred with the publication of the Tender Code, Legislative Decree n. 50/2016 (Italian Government 2016), which introduced the use of electronic methodologies and tools. The Baratonno Decree or BIM Decree (Ministry of infrastructure and transport 2017) mandatorily requires the use of electronic methodologies and tools in the public tender with a modular approach over the years, depending on the economic value of works. It is the official introduction of the BIM into the design stage of an infrastructure. Similarly, starting in 2017, the Ministry for the Environment requires, for the construction of new buildings with the Decree on the Minimum Environmental Criteria (Ministry for the Environment 2017), the use of construction products that have a specific value of recycled content. This value must be verified through a number of methodologies, and among those, is the environmental product declaration published on EPDIItaly, the Italian Program Operator. Finally, the Italian Government and the ecological transition Ministry (already the environmental Ministry) are investing in the sustainability of the infrastructure/construction works with the PNRR. More than 25 billion € have been allocated for infrastructure, and the Guidelines for the PFTE (Economic Technical Feasibility Project) (Higher council of the Public works and Sustainable infrastructure and mobility 2021) have been developed in order to facilitate the PNRR implementation.

The sustainability concept is prominent in the PFTE, as the Report on Infrastructure Sustainability has become one of the mandatory elements to develop along the infrastructure design process. It's really an innovative element that links sustainability to the digitization needs, in order to design construction work in a modular approach, from the first stages.

Most of the elements of the Report are connected to environmental data of the products that will be included into the infrastructure and their assessment and digitalization help the process of infrastructure LCA calculation.

In fact the Report places particular emphasis on the LCA of infrastructure with certain environmental issues, such as:

- CO₂ calculation, with reference to Carbon footprint. The Carbon footprint calculation, performed by the designer, can be assessed by an independent third party such as an accredited Certification Body in compliance to ISO 14067 (International Organization for Standardization 2018).
- Verification of the LCA infrastructure. The designer can develop a LCA for the infrastructure. The assessment can be performed by an independent third party, in compliance to ISO 14040 (International Organization for Standardization 2006) and ISO 14044 (International Organization for Standardization 2006).

The above items could be calculated if the environmental data of materials that makes up the infrastructure are available. This kind of data are a prerogative of EPD development and must be available, at the early stages of the project, so that they can be used for the LCA of the infrastructure itself. No environmental impacts of construction products mean no LCA of infrastructure. The absence of environmental impact of the construction product means a LCA of the infrastructure can't be performed. This approach can only be pursued through a digital transformation of the use of data, towards which the Report is strongly pushing. The BIM approach is a methodology that addresses the needs mentioned above.

In the following paragraphs the author is going to explain how.

4 LCA AND BIM: A MARRIAGE MADE IN HEAVEN!

The connection of design activities allows designers to choose the appropriate building products and to manage any changes in real time. This approach constitutes the present and not the future for designers working in the field of digital information modelling, BIM.

In recent years, the design and realization of buildings and infrastructures have been the subject of various sustainability rating systems e.g. LEED or Envision (Institute for sustainable infrastructure 2012), a North American protocol for the sustainability of infrastructures, which is widespread in Italy. In this sense, the information provided by the manufacturers and their construction products is necessary to score the work. Indeed, the most widespread rating systems reward the availability of environmental information, right from the first phase of the project. In this sense, the simultaneous presence of an environmental information management system (such as the BIM) and an information communication tool (such as the Environmental Product Declaration EPD) is useful for optimizing the process of environmental information sharing between the various actors. Project development is thus simplified, facilitating possible revisions. The EPD allows, through clear and transparent communication and, above all, verified by an independent third party, data such as, for example:

- Global warming;
- Abiotic resource depletion - elements;
- Depletion of abiotic resources - fossil fuels;
- Acidification of soil and water;
- Ozone layer depletion;
- Eutrophication;
- Photochemical ozone creation.

The visibility of the environmental characteristics of these products for the life cycle of each of the phases and structure through a BIM system, is an opportunity for the manufacturer to be an active participant in the sustainable design of the building and infrastructure.

5 THE DIGITIZATION PROCESS

For the above stated reasons, it is appropriate that the environmental information is in a machine-readable format to facilitate import into the calculation software for the building/infrastructure LCA.

As already mentioned, Eco Platform has implemented a method of returning digital EPD data through a special portal called Eco Portal, through which the various Program Operators share their published EPDs. Indeed, the most representative international Program Operators have outlined a scenario in which the digitization of EPDs is a fundamental practice in EPD publication activities. For this reason, the Eco Portal, which publishes in digital format all the Eco EPDs published by the various Program Operators that have joined the initiative, allows users of the service to draw on a carnet of environmental data from all over Europe.

From now on, the Eco Portal will represent a further, internationally visible enhancement of the efforts made by manufacturers to develop an EPD. Their EPDs are visible on the Eco-Portal, following the digitization carried out by the Program Operator who published the EPD. The Eco-Portal allows access to the databases of the main Program Operators and also national databases. The Eco-Portal is linked to the web page of the Program Operator that finalized the digitization. The digitization process starts with the input of the EPD environmental data by the Program Operator or automatically by the manufacturer. The digitization software populates the Eco-Portal (see Table 1).

Table 1. The number of digitalized EPD into the Eco Portal.

Program Operator	Number*
EPD Norway	1704
Institut Bauen und Umwelt e.V.	616
EPD Danmark	544
BRE	319
EPDIItaly	284
International EPD System	236
MRPI	197
EPD Ireland	99
ITB/Other	77

* data as of September 2022.

Digitization carried out through the Eco-Portal entails several benefits:

- international visibility of a product's environmental data;
- significant reduction of effort in generating and reporting data;
- sharing of data in a single format (ILCD + EPD); this format combines the information contained in the EPD documentation, available in pdf format, with that required by the European Commission;
- common rules for data use, through the exchange of files in standard format (xml and csv, at the moment);
- future interaction, through special APIs (Application Programming Interfaces), with the main software for the development of the LCA of buildings;
- possibility for the user to use a special filter to identify: the language of the EPD, the country of origin, the manufacturer, the validity of the EPD, the originating Program Operator and, most importantly, the type of data (specific or average) to be used.

With the above advantage, the digitized EPD will be a reference for designers developing the LCA of the building or infrastructure, increasing the dissemination of environmental data of construction products.

The ILCD + EPD format contains more than 100 claims, among which we list the most relevant:

- adopted life cycle (cradle to gate, cradle to grave, . . .);
- mandatory information, such as EPD impact indicators for each life cycle stage;
- additional national information, such as recycled content, required by national legislation for buildings;
- other information that can be extracted from the EPD document (company name, production site, database, reference PCR, data collection period, functional unit, . . .);
- data verification and validation information (certification body, program operator, . . .).

The Program Operator transforms all entered data into a tabular format and, after a validation process carried out at the European level, assigns a unique code to the data set, thus making it visible and downloadable in xml/csv format from the online platform. EPD data feed the European Eco-Portal database for use online in building and infrastructure design systems.

The benefits of digital design can be visible in the building and infrastructure design process because, in addition to technical characteristics, environmental characteristics derived from an EPD can be available for each component material.

6 CONCLUSIONS

Many sudden changes are taking place in the construction industry in terms of sustainability and digitization, demonstrating their close interdependence. One cannot be separated from the other. After all, how would it be possible to build a smart highway, equipped with sensors to optimize traffic management, provide information to users and perform predictive maintenance, without a digital design model? Sustainability requires digitization.

And it is encouraging that the Italian government is also persuaded of this, sending out a message on the significance of the use of digital models in the design of infrastructures included in the National Resilience and Recovery Plan. The specific reference to the opportunity for contracting authorities to provide for the awarding of a bonus score in the design when using specific electronic methods and tools will enable the use of BIM to be expanded, speeding up the process of innovation needed to achieve those effectively measurable results in terms of environmental and social sustainability that Europe is asking us for. At the same time, greater digitization will guarantee higher levels of quality, ensuring greater time certainty and more precise cost control. Key factors for ensuring the economic sustainability of infrastructure.

The PFTE requires in the sustainability report the verification of certain environmental aspects that can be fulfilled by the EPD, the environmental identity card of the construction product, which could be available in a machine-readable format, increasing its use in the LCA calculation tool of buildings or infrastructures. Indeed, it is not possible to know the environmental impacts of a construction project if one does not have any knowledge of the environmental data of the construction products.

This will be very relevant in the coming years when the Italian investment plan will be relying on the shared use of digital modelling data for infrastructure design.

REFERENCES

- EN 15804 2019. Sustainability of construction works. Environmental product declarations. Core rules for the product category of construction products.
- Environmental Ministry 2017. Decreto 11 ottobre 2017. Criteri ambientali minimi per l'affidamento di servizi di progettazione e lavori per la nuova costruzione, ristrutturazione e manutenzione di edifici pubblici.
- Higher council of the Public works and Sustainable infrastructure and mobility 2021. Linee guida per la redazione del progetto di fattibilità tecnica ed economica da porre a base dell'affidamento di contratti pubblici di lavori del PNRR e del PNC (Art. 48, comma 7, del decreto-legge 31 maggio 2021, n. 77, convertito nella legge 29 luglio 2021, n. 108).

Institute for sustainable infrastructure 2012. Envision Protocol.

ISO 14025 2006. Environmental labels and declarations - Type III environmental declarations - Principles and procedures.

ISO 14040 2006. Environmental management — Life cycle assessment — Principles and framework.

ISO 14044 2006. Environmental management — Life cycle assessment — Requirements and guidelines.

ISO 14067 2018. Carbon Footprint of products.

Italian Government 2016. Decreto Legislativo del 18 aprile 2016, n. 50. Attuazione delle direttive 2014/23/UE, 2014/24/UE e 2014/25/UE sull'aggiudicazione dei contratti di concessione, sugli appalti pubblici e sulle procedure d'appalto degli enti erogatori nei settori dell'acqua, dell'energia, dei trasporti e dei servizi postali, nonché per il riordino della disciplina vigente in materia di contratti pubblici relativi a lavori, servizi e forniture.

Italian Government 2021. Piano Nazionale per la ripresa e la resilienza.

Ministry of Infrastructure and Transport 2017. Decreto n. 560 del 01/12/2017.

Orsenigo, L. 2021. La sostenibilità trascina la digitalizzazione. In ICMQ Notiziario n. 102:3.

Pannuti, U.R. 2017. Bim ed Epd: l'integrazione è possibile!. In ICMQ Notiziario n. 87:5.

Pannuti, U.R. 2020. Novità dall'Europa. In ICMQ Notiziario n. 100:17.

Pannuti, U.R. & Falbo A. 2019. La digitalizzazione delle EPD. In ICMQ Notiziario n. 95:12-13.

U.S. Green Building Council 2019. LEED v4 for Building Design and Construction.

Using monetization to harmonize life-cycle assessment and life-cycle cost analysis for green public procurement of pavement projects

B. Moins, D. Hernando, W. Van den bergh & A. Audenaert
University of Antwerp, Antwerp, Belgium

ABSTRACT: This research applies monetization to harmonize life cycle assessment (LCA) with life cycle cost analysis (LCCA) for implementation in the green public procurement of pavement projects. The monetized environmental impact (MEI) shows an excellent correlation with the net present value. As both indicators are expressed using the same unit, LCA and LCCA can be easily combined into a single sustainability indicator. The MEI is mainly determined by the impact of the upper asphalt layers. The structure with bitumen stabilized material (BSM) and no asphalt base has the lowest MEI, followed at a certain distance by the structure with unbound and lean asphalt bases. The cement-bound section and another BSM section show the highest MEI. Finally, a detailed hotspot analysis highlighted that climate change, particulate matter formation, and use of non-renewable energy resources contributed over 90% of the total MEI.

1 INTRODUCTION

Environmental awareness in pavement engineering and procurement is rapidly increasing. Additionally, sustainable practices that conserve nonrenewable resources and reduce waste streams are continuously supported by the pavement industry (Williams et al., 2019). This is progressively leading road agencies to the implementation of green public procurement (GPP). A way to help road agencies make informed decisions about the environmental impact of the pavement works they procure is to implement environmental indicators in GPP (Hernando et al., 2022). Furthermore, researchers clearly indicate that economic and environmental studies should focus on the long-term impact of projects as opposed to only impacts up to the construction phase (Moins et al., 2022). Two methods often used to describe the environmental and economic long-term impact are life cycle assessment (LCA) and life cycle cost analysis (LCCA), respectively.

However, most studies use LCA and LCCA separately or with little integration (França et al., 2021). Hence, it is important to harmonize LCA and LCCA to facilitate the transition from standard procurement to green procurement. Combining LCA and LCCA results can be difficult because both methods often use different methodological assumptions and indicators. For example, LCA studies often use multiple midpoint indicators for life cycle impact assessment (LCIA) whereas LCCA studies mostly use a single indicator to describe economic impact. Even though LCA studies can express the results using a single indicator when weighting is applied, it is not recommended by the ISO 14040 and 14044 standards on LCA as it increases the level of uncertainty. Nevertheless, it is commonly used in the interpretation phase as it can identify the most relevant impact categories and enables the aggregation of results (Amadei et al., 2021, Hernando et al., 2022).

One of the methods suitable for harmonizing LCA and LCCA is monetization, which expresses environmental impact using a single monetary value. As with LCCA, it is recommended

discounting future impacts in monetization using a social discount rate (Servaes et al., 2017, Zhang, 2017). In other words, using monetization to express the environmental impact is comparable to employing the net present value (NPV) for quantifying the economic impact.

There are various ways to monetize the external costs of environmental impacts. One subdivision includes the damage cost approach (DCAP), avoidance cost approach (ACAP), and replacement cost approach (RCAP) (Smith et al., 2020). DCAP values all damage caused by an externality and includes the social cost of carbon which values all damages to society because of climate. ACAP accounts for all externalities based on the total cost to reach a certain policy target. RCAP considers the cost of externalities based on the total cost to repair or replace the adverse impacts of those externalities. Another subdivision is based on the individuals' willingness to pay (WTP) or willingness to accept (WTA). WTP is the maximum amount an individual is willing to pay to avoid an undesirable change. Conversely, WTA is the minimum compensation an individual is willing to accept to consent to an undesirable change (Pizzol et al., 2015, Zhang, 2017). Literature shows that impacts according to WTA can be up to seven times higher than according to WTP because of income effect, bad-deal aversion, and study design (Arendt et al., 2020). However, note that all monetization methods have also been criticized because their link to income makes them wealth sensitive. Therefore, it is advised to discuss the geographical scope and use of equity weighing (Arendt et al., 2020).

To the authors' knowledge only a few studies combined pavement engineering with the monetization of environmental impacts. Their focus was mainly on monetizing social and safety aspects of the road user such as number of crashes, transportation related pollution, and road noise and not the impact of different pavement structures (Arter et al., 2021, Bi et al., 2019, Hofstetter and Müller-Wenk, 2005, Yang and Magalotti, 2016).

2 OBJECTIVE AND SCOPE

The first objective of this study is to examine the feasibility of expressing the environmental impact of a pavement project in monetary values to align with LCCA methodology. Another objective is to analyze the relationship between monetized environmental impact (MEI) and NPV using a test case. The third objective is to identify the individual materials/processes and impact indicators with the largest share in the overall MEI. All three objectives contribute to the ultimate goal of harmonizing LCA and LCCA so they can be combined in a single indicator.

3 MATERIALS AND METHODS

3.1 Description of the selected test case

Input from previous research was used as a test case for applying monetization. As shown in Figure 1, five alternative pavement structures with various base layers are considered, namely: unbound (UB), cement-bound (CB), lean asphalt (LA), bitumen stabilized material (BSM)

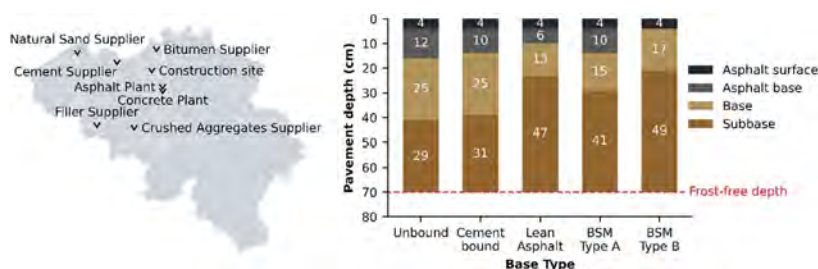


Figure 1. Overview of test track showing material suppliers, production locations, and considered pavement sections.

type A (asphalt base layer required), and BSM type B (no asphalt base layer needed). For the asphalt surface and asphalt base layer, AC10 and AC14 mixtures are used, respectively.

All structures were designed for a maximum traffic load of one million 100-kN equivalent single axle loads (ESALs) over a period of 20 years following local design guidelines (Awv, 2013, Awv, 2010). These reference structures alter layer thicknesses based on average material performance values per pavement layer. The assumption of the Flemish pavement design method is that the layer thickness of the reference structures is valid provided that each layer meets minimal material specifications. Thus, it is assumed that all alternatives will have the same service life.

Table 1 provides the material composition of the different pavement layers. Two different types of construction and demolition waste (CDW) are included: reclaimed asphalt pavement (RAP) and recycled concrete aggregate (RCA). From a recycling point of view, using RCA is preferred over RAP for UB and CB mixtures as higher recycling rates for RCA are allowed according to Flemish specifications.

Table 1. Material composition.

Base type	AC 10	AC 14	UB-base*	CB-base	LA-base	BSM-base
Crushed coarse aggregate [%]**	54.9	48.6			19.8	
Crushed fine aggregate [%]**	23.5	4.8				
Natural sand [%]**	9.4	3.8			26.1	
Added filler [%]**	6.1	1.9			0.1	
RAP [%]**		38.1			53.2	96.7
RCA [%]**			100	89.4		
Virgin bitumen [%]**	6.2	2.8			0.8	2.1
Portland cement (CEM III/A) [%]**				2.1		1.0
Water [%]**				8.5		0.2***

* This material is also used for the subbase.

** Percentage by total weight of mixture.

*** The BSM mix was designed with a water content of 5.7%; however, it was noticed the RAP was too moist during production. Therefore, the water content was reduced to 0.2%.

3.2 LCA methodology

3.2.1 Goal and scope

The functional unit of this research is: “1 m² of asphalt pavement designed according to Flemish specifications for a maximum traffic load of one million ESALs over 20 years”. The analysis period will be 40 years. This research will consider the environmental impact from raw material extraction up to and including the waste processing of RAP and RCA.

The environmental impact of RAP and RCA is modelled considering the end of waste (EOW) criteria for CDW aggregates proposed by the Joint Research Centre of the European Commission (Luis Delgado et al., 2009). These criteria allocate all impacts up to and including the crushing and sieving of the CDW to the waste product. The impact of transporting RAP and RCA after processing is allocated to the next life cycle. In Flanders most contractors process RAP and RCA at their own plant using mobile processing plants; therefore, RAP and RCA are burden free when entering a new life cycle as no further transportation to the production plant occurs.

Note that the system boundaries do not consider the impact associated with road users. Furthermore, small maintenance interventions such as crack filling are not considered as full rehabilitation (mill and replace) is more common in Flanders. Based on discussions with the Flemish pavement industry, rehabilitation intervals of 10 years, 20 years, and 40 years were considered for the asphalt surface course, asphalt base course, and base layer, respectively. Note that unless pavements are designed using a life-long approach (perpetual pavements), bases are designed to reach their distress limit at the end of the design period. This research did not consider perpetual pavements, so rehabilitation will be needed. LA and CB base types

are subjected to cracking and to a lesser extent permanent deformation. If the distress limit for cracking is reached, they must be fully replaced. BSM and UB (sub)bases are only subjected to permanent deformation, so they are not fully replaced. Therefore, only the full replacement of LA and CB bases is considered within the system boundaries.

3.2.2 Life Cycle Inventory (LCI)

The ecoinvent 3.8 database was accessed to couple primary data to the upstream supply chain data for all inputs except for bitumen, for which Eurobitume's LCI was used. Regarding transportation, primary data was used based on the locations of the suppliers, production sites and construction site, as shown in Figure 1. Unless otherwise indicated, all ecoinvent records were used in line with previous research (Moins et al., 2022).

The average energy consumption of the mobile cold recycling plant to produce the BSM was monitored during a test track: 0.26 l diesel per ton of BSM produced. To produce the CB base, the energy consumption of the ecoinvent dataset "*Lean concrete| production, with cement CEM III/A | Cut-off, U*" was copied. The required energy to produce the asphalt mixtures was determined using thermodynamics laws (Santos et al., 2018, Vandewalle et al., 2020). This resulted in the following energy consumptions:

- AC 10 surface = 298.8 MJ/ton
- AC 14 base = 298.6 MJ/ton
- LA base = 297.5 MJ/ton

Depending on the material type, a combination of equipment was modelled for the construction, deconstruction, and waste processing phases. All types of equipment were modelled using the same ecoinvent dataset, namely "*Machine operation, diesel, >= 74.57 kW*". However, their hourly fuel consumption was determined using the formula provided by the US Environmental Protection Agency for nonroad engine emissions modeling (Epa, 2002) and adjusted within the dataset. The following combinations were modelled:

- Construction:
 - Bitumen-bound and CB: Paver with two tandem rollers.
 - UB: Grader with a wheel loader and soil compactor.
 - BSM: Paver with one soil compactor and one tandem roller.
- Deconstruction:
 - LA: Milling machine and sweeper.
 - CB: Excavator with jackhammer and wheel loader.
- Waste processing:
 - All (except UB and BSM): Mobile jaw crusher with two wheel loaders.

3.2.3 Life Cycle Impact Assessment (LCIA)

A recent review on monetary valuation in LCA showed that a report written by Trinomics on behalf of the European Commission provides one of the most recent monetization methods available (Amadei et al., 2021). The approach starts with the environmental footprint (EF) LCIA method to determine the environmental impacts. With the emergence of environmental product declarations (EPDs) in mind, the EF v3.0 EN 15804 method was chosen as the LCIA method for this research as it uses the same environmental indicators and units.

Then, these environmental indicators are expressed in monetary value using the factors shown in Table 2, which also provides the corresponding cost approach. The framework in the report uses several sources to obtain the monetization factors including DG Move, the MMG method, ReCiPe, the Environmental Prices Handbook, as well as advice from the Joint Research Centre (JRC) of the European Commission. The monetization values were derived for the EU27 and adjusted to each country based on the relative 2018 gross domestic product per capita with an income elasticity assumption of 0.8 (Smith et al., 2020).

Note that the monetization values presented in the Trinomics report are provided in 2018 euros. It is recommended updating these values for inflation using the consumer price index (CPI) (Amadei et al., 2021). Therefore, the monetization values were recalculated as 2022 values. The values for the CPI indexes were obtained using the Eurostat database.

Monetizing environmental impacts requires one additional step to normal LCA studies: discounting the value of future impacts using a social discount rate, which is conform with LCCA studies. A 2017 update of the report describing monetization of the MMG method proposes a social discount rate of 3% (Servaes et al., 2017). This value is in line with the recommendations of the Flemish government. However, a literature review revealed that a value of 4% is the most used discount rate in LCCA studies focused on pavements (Moins et al., 2020). Therefore, this analysis will apply a discount rate of 4%. The monetized environmental impact (MEI) is determined using Equation 1:

$$MEI = \sum_{n=0}^{40} \sum_{i=1}^{15} \left(MF_i \times \frac{EI_{RM,i} + EI_{T,RM,i} + EI_{WP,i} + EI_{T,WP,i} + EI_{P,i} + EI_{T,site,i} + EI_{C,i} + EI_{DC,i}}{(1+r)^n} \right) \quad (1)$$

where MEI = monetized environmental impact; i = environmental indicator i; MF_i = adjusted central monetization value; n = year of impact; r = discount rate (4%); EI_{RM,i} = environmental impact from raw materials; EI_{T,RM,i} = environmental impact from raw material transportation; EI_{WP,i} = environmental impact from waste processing; EI_{T,WP,i} = environmental impact from transportation of secondary materials; EI_{P,i} = environmental impact from production; EI_{T,site,i} = environmental impact from transportation to the construction site; EI_{C,i} = environmental impact from construction; EI_{DC,i} = environmental impact from deconstruction.

Table 2. EU27 monetization values.

EF v3.0 EN 15804 indicator	Unit	Cost approach	Central monetization value [EUR ₂₀₁₈ /unit]	Adjusted central monetization value [EUR ₂₀₂₂ /unit]
1. Climate change	kg CO2-eq	ACAP	0.1025	0.1176
2. Ozone depletion	kg CFC-11 eq	DCAP	31.4	36.0
3. Ionising radiation, Human health	kBq U235 eq	DCAP	1.2E-03	1.4E-03
4. Photochemical ozone formation, Human health	kg NMVOC eq	DCAP	1.19	1.37
5. Particulate matter	Disease incidence	DCAP	784 126	899 583
6. Human toxicity, non-cancer	CTUh	DCAP	163 447	187 513
7. Human toxicity, cancer	CTUh	DCAP	902 616	1 035 520
8. Acidification	mol H+ eq	DCAP & ACAP	0.344	0.395
9. Eutrophication, freshwater	kg P eq	DCAP	1.92	2.20
10. Eutrophication, marine	kg N eq	DCAP	3.21	3.68
11. Ecotoxicity, freshwater	CTUe	DCAP	3.82E-05	4.38E-05
12. Land use (Soil quality index)	Dimensionless		1.75E-04	2.01E-04
13. Water use	m3 water eq	Resource depletion	4.99E-03	5.72E-03
14. Resource use, fossils	MJ	Resource depletion	1.30E-03	1.49E-03
15. Resource use, minerals and metals	kg Sb eq	Resource depletion	1.64	1.88

4 RESULTS AND DISCUSSION

The results of the LCA are shown in Figure 2. Part A illustrates the MEI per pavement structure and pavement layer. Even though the asphalt surface and asphalt base layer only account

for 6% to 23% of the entire pavement thickness depending on the structure, they account for 53% to 84% of the total MEI. This means that the environmental impact of pavement structures is mainly determined by the upper asphalt layers. As the BSM type B structure eliminates the asphalt base layer entirely, this structure has the lowest total MEI. The UB structure requires the thickest asphalt package; however, it does not have the highest impact because the EOW criteria result in a base layer with far lower impact than other bases. The LA structure shows a similar impact as the UB structure: the higher impact of the LA base cancels out with the lower impact of the thinner asphalt package. The CB and BSM type A structures have the highest overall impact.

The relationship between the environmental and economic impact expressed in monetary units is depicted in Figure 2b. There is an excellent linear correlation between the NPV and MEI, showing that both indicators provide the same conclusion. The ratio of the NPV to the MEI is 4.31 on average. In other words, if a single sustainability indicator were to be developed in GPP by aggregating LCA and LCCA results with a 50/50 contribution, MEI results should be multiplied by 4.31 before being added to the NPV.

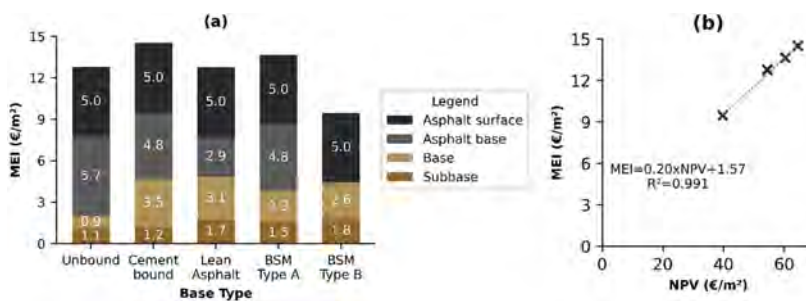


Figure 2. Results of the LCA: (a) MEI per base type and pavement layer, (b) Relationship between MEI and NPV.

The results of the detailed hotspot analysis are shown in Figure 3. Overall, three environmental indicators of the EF v3.0 EN15804 method are responsible for more than 90% of the MEI: climate change (CC), particulate matter formation (PMF), and use of non-renewable energy sources (UNRE). This is in line with previous research where global warming potential, fine particulate matter formation, and fossil resource scarcity accounted for over 85% of the single score of asphalt mixtures when ReCiPe 2016 (H) was used as the LCIA method (Hernando et al., 2022).

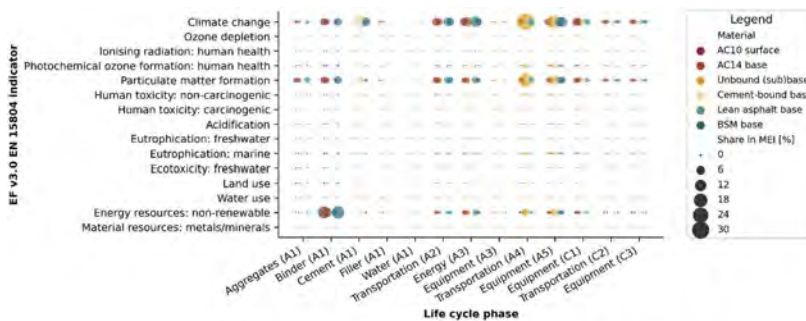


Figure 3. Detailed hotspot analysis of the MEI per life cycle phase and per environmental indicator.

Table 3 shows an overview of the three main hotspots per material type. The top three hotspots for the upper asphalt layers are mainly linked to the production impact of the mixtures:

bitumen production (A1), energy use (A3) and transportation of raw materials (A2). For the base layers, the hotspots mostly move further along the life cycle transportation to the construction site (A4) and use of construction equipment (A5). So, the main hotspots for individual life cycle phases depend on the type of material; however, almost all life cycle phases are highlighted in Table 3, except for the transportation (C2) and processing (C3) of waste. This shows the importance of considering the full life cycle in sustainability analyses.

Table 3. Top three environmental hotspots per material type.

Material	Share, Indicator, Process or Phase		
	#1 hotspot	#2 hotspot	#3 hotspot
AC10	16.8% UNRE Bitumen (A1)	7.1 % CC Energy (A3)	6.9% CC Transport (A2)
AC14	11.2% UNRE Bitumen (A1)	10.4% CC Energy (A3)	7.2% CC Equipment (C1)
UB base	31.9% CC Transport (A4)	21.1% PMF Transport (A4)	19.2% CC Equipment (A5)
CB base	20.0% CC Cement (A1)	15.0% CC Equipment (A5)	8.7% CC Transport (A4)
LA base	14.0% CC Energy (A3)	9.4% CC Equipment (A5)	8.0% CC Transport (A2)
BSM base	18.1% UNRE Bitumen (A1)	11.6% CC Equipment (A5)	8.0% CC Cement (A1)

5 CONCLUSIONS

The ultimate goal of this study was to harmonize LCA and LCCA so they could be combined in a single indicator. The first objective was to examine the feasibility of expressing the environmental impact of pavement project in monetary value to align with LCCA. An approach described by the European Commission was applied in this study, which uses monetization values for the EU27 zone. Literature concludes that geography is an important parameter to consider as monetization methods are mainly income sensitive. So, it is advised to adjust the monetization values based on the location of the study. However, once the correct values are computed, calculating the MEI can easily be aligned with an LCCA as it follows the same steps as determining the NPV.

The second objective was to study the relationship between the MEI and NPV using a test case. A comparison of five pavement structures with various base layers was used for this. The BSM type B had the lowest MEI (9.5 €/m² over 40 years). The UB and LA structures showed a similar impact of around 12.8 €/m² during the analysis period. Finally, MEIs of 13.7 €/m² and 14.5 €/m² were obtained for the BSM type A and CB structures, respectively. An excellent linear correlation between the NPV and MEI of the pavement sections was obtained, showing that both indicators provided the same conclusion. The NPV showed economic impacts in €/m² that were on average 4.31 times higher than the environmental impact of the MEI expressed using the same unit.

The final objective was to perform a hotspot analysis. The hotspot analysis showed that three environmental indicators were responsible for over 90% of the MEI: climate change, particulate matter formation, and use of non-renewable energy sources. This was in line with the 85% for the same three indicators when the ReCiPe single score was used in a prior study. Another important conclusion was drawn when individual materials and processes were evaluated. The three main hotspots depended on material type; however, when considering all findings, almost all life cycle phases were highlighted at least once, except for the transportation and processing of waste. This showed the importance of life cycle thinking, especially when waste materials were used since the hotspots tended to be appear more towards the end of the life cycle for base layers.

Of note, this research only applied one monetization method to a test case whereas literature shows that multiple methods exist. Therefore, as part of a sensitivity analysis, it is recommended testing multiple monetization methods and comparing how the results are affected depending on the method used. Furthermore, it is recommended that additional datapoints be added so that the ratio between the MEI and NPV can be calculated in a more detailed way. Afterwards, the effect of weighing and summing both indicators should be analyzed. This will

allow expressing environmental and economic impacts using a single value, making the selection of the most sustainable pavement alternative in GPP more straightforward.

REFERENCES

- Amadei, A. M., De Laurentiis, V. & Sala, S. (2021) A review of monetary valuation in life cycle assessment: State of the art and future needs. *Journal of Cleaner Production*, 329.
- Arendt, R., Bachmann, T. M., Motoshita, M., Bach, V. & Finkbeiner, M. (2020) Comparison of Different Monetization Methods in LCA: A Review. *Sustainability*, 12.
- Arter, C. A., Buonocore, J., Chang, C. & Arunachalam, S. (2021) Mortality-based damages per ton due to the on-road mobile sector in the Northeastern and Mid-Atlantic U.S. by region, vehicle class and precursor. *Environmental Research Letters*, 16.
- Awv (2010) Dienstorder MOW/AWV/2010/2: Standaardstructuren voor wegen met asfalt- en cementbetonverhardingen. Vlaamse overheid.
- Awv (2013) Dienstorder MOW/AWV/2013/17: Standaardstructuren voor wegen met schraalafsluitingen. Vlaamse overheid.
- Bi, Z., Keoleian, G. A., Lin, Z., Moore, M. R., Chen, K., Song, L. & Zhao, Z. (2019) Life cycle assessment and tempo-spatial optimization of deploying dynamic wireless charging technology for electric cars. *Transportation Research Part C: Emerging Technologies*, 100, 53–67.
- Epa (2002) Median Life, Annual Activity, and Load Factor Values for Nonroad Engine Emissions Modeling. Environmental Protection Agency.
- França, W. T., Barros, M. V., Salvador, R., De Francisco, A. C., Moreira, M. T. & Piekarski, C. M. (2021) Integrating life cycle assessment and life cycle cost: a review of environmental-economic studies. *The International Journal of Life Cycle Assessment*, 26, 244–274.
- Hernando, D., Moins, B., Van Den Bergh, W. & Audenaert, A. (2022) Identification of the Main Environmental Impact Categories Over the Life Cycle of Hot Mix Asphalt: An Application to Green Public Procurement. *Transportation Research Record*, 2676, 322–335.
- Hofstetter, P. & Müller-Wenk, R. (2005) Monetization of health damages from road noise with implications for monetizing health impacts in life cycle assessment. *Journal of Cleaner Production*, 13, 1235–1245.
- Luis Delgado, Ana Sofia Catarino, Peter Eder, Don Litten, Zheng Luo & Villanueva, A. (2009) End-of-Waste Criteria. European Commission Joint Research Centre.
- Moins, B., France, C., Van Den Bergh, W. & Audenaert, A. (2020) Implementing life cycle cost analysis in road engineering: A critical review on methodological framework choices. *Renewable and Sustainable Energy Reviews*, 133.
- Moins, B., Hernando, D., Buyle, M., France, C., Wim, V. & Audenaert, A. (2022) On the road again! An economic and environmental break-even and hotspot analysis of reclaimed asphalt pavement and rejuvenators. *Resources Conservation and Recycling*, 177.
- Pizzol, M., Weidema, B., Brandão, M. & Osset, P. (2015) Monetary valuation in Life Cycle Assessment: a review. *Journal of Cleaner Production*, 86, 170–179.
- Santos, J., Bressi, S., Cerezo, V., Lo Presti, D. & Dauvergne, M. (2018) Life cycle assessment of low temperature asphalt mixtures for road pavement surfaces: A comparative analysis. *Resources, Conservation and Recycling*, 138, 283–297.
- Servaes, R., De Nocker, L. & Debacker, W. (2017) Annex: Monetisation of the MMG method (update 2017). OVAM.
- Smith, M., Moerenhout, J., Thuring, M., De Regel, S. & Altmann, M. (2020) Final Report – External Costs: Energy costs, taxes and the impact of government interventions on investments. European Commission
- Vandewalle, D., Antunes, V., Neves, J. & Freire, A. C. (2020) Assessment of Eco-Friendly Pavement Construction and Maintenance Using Multi-Recycled RAP Mixtures. *Recycling*, 5.
- Williams, B. A., Willis, J. R. & Shacat, J. (2019) Asphalt Pavement Industry Survey on Recycled Materials and Warm-Mix Asphalt Usage: 2019. National Asphalt Pavement Association.
- Yang, X. & Magalotti, M. J. (2016) A Service Life Analysis of Roundabouts Retrofits for Signalized Intersections. *Procedia Engineering*, 145, 452–459.
- Zhang, Y. (2017) Taking the Time Characteristic into Account of Life Cycle Assessment: Method and Application for Buildings. *Sustainability*, 9.

Digital twins and sensor monitoring for alpine engineering structures: Applications for tunnels

A. Strauss, A. Beigel, F. Sattler & B. Täubling-Fruelex

Vienna Department of Civil Engineering and Natural Hazards, University of Natural Resources and Life Sciences, Vienna, Austria

C. Seywald

ÖBB-Infrastruktur AG, Streckenmanagement und Anlagenentwicklung, Fachbereich Bautechnik Tunnelbau, Vienna, Austria

H. Neuner & V. Kostjak

TU Wien, Department for Geodesy and Geoinformation, Vienna, Austria

D.M. Frangopol

Lehigh University, ATLSS Engineering Research Center, Bethlehem, PA, USA

ABSTRACT: Sensors create synergies in monitoring. The use of sensors to determine the reaction of a tunnel cross-section or tunnel maintenance to certain rock formations and to monitor construction and functional components is common practice in tunnelling today. Sensors can detect physical effects such as deformation, strain, vibration or temperature under real conditions that are not always easily described by numerical models. Nevertheless, given the complexity of modern tunnels and modern rehabilitation methods, as well as the interdependencies between components, comprehensive instrumentation can provide crucial insights for digital twin considerations. The aim of this contribution is to show how digital twins of tunnel cross-sections can be created using sensor monitoring information and what added value they can provide for cross-section performance assessment.

1 INTRODUCTION

Construction models, sometimes called digital twins, die at birth. An important goal is to bring these models back to life during the operational phase and maintenance of existing tunnels, especially during retrofits or interventions. Designers and tunnel operators invest a lot of time and money in creating analytical models to document the design of tunnel structures and rock formations and to perform simulations. The continuous use of a virtual model as a digital twin during operation is an excellent means of visualising all of the important components, performing analyses and calculations and improving the understanding and control of the long-term behaviour of the structural and functional components of the tunnel and rock formations during operation. In the preliminary study for the “MONTUN” project (Neuner et al., 2022, Strauss et al., 2022), a list of modern measurement systems (Strauss et al., 2020, Strauss et al., 2018) and software products for recording deformations in tunnel structures were compiled as a collaboration between the Austrian Federal Railways, the Vienna University of Technology, and the Vienna University of Natural Resources and Life Sciences. The most common system used in geodesy was the total station or laser tracker which has been in use for many years. The reason for this is that it can match newer innovations in terms of both accuracy and manageability. The second measurement system used was laser distance sensors which work on a similar principle to the tachymeter but without mirror reflection.

The inclinometer chain or “Shape Accel Array” (SAA) system, also provided by TU Wien, was mounted along the ring in the inner wall of the tunnel. The information from the continuous measurements of the monitoring systems provided an excellent basis for setting up a digital twin by means of Non-linear Finite Element models (Canestro et al., 2021, Slowik et al., 2021, Spyridis & Strauss, 2020).

2 FIELD TESTS

2.1 *Demonstration and monitoring systems*

The preliminary studies for this project were carried out by the Austrian Federal Railways, the Vienna University of Technology, and the Vienna University of Natural Resources and Life Sciences with the aim of analysing modern measuring systems used for the assessment of the monitoring of deformations in tunnel structures, see also Neuner et al., (2022). As a demonstrator for the filed investigations, the HABA reinforced concrete mouth profile 3600/2250 was used. It was manufactured according to ÖNORM EN 1916 and ÖNORM B5074 and has comparable geometric properties to real tunnel profiles. The profile was designed with 30 cm deep and 20 cm wide slots in the crown area, in the upper and lower strut area, in order to reduce the bending stiffness and thus generate significant 3D deformations which can occur in real tunnel shells. The loading processes were applied via tie rods. The HABA-Maul profile is a reinforced concrete profile C25/30 with $a = 4$ cm concrete cover and 36 pieces of $d = 8$ mm longitudinal reinforcement on the inner and outer circumference of the profile as well as a $d = 9$ mm per 8 cm ring reinforcement on the outer side and $d = 9$ mm per 6 cm on the inner side.

2.2 *Loading procedures & processes*

The mouth profile positioned on the HABA company site made it possible to apply a controlled load regime in predefined load steps in a relatively short time. Figure 1 provides more details regarding the load application (Beigel, 2023). In order to record the system response due to the loading processes the following monitoring systems were used. A Digital Image Correlation System DIC was used for the digital image correlation strain determination and the evaluation of out-of-plane displacements - profile deformation. A SAA inclinometer consists of a chain of individual inclinometers and was used for the measurement of inclination angles in the two main planes. Using an initial zero measurement, the SAA inclinometer can be used to derive displacements and deformations along the chain and thus the deformations of the mouth profile. A HBK Fibre Optic Inclinometer uses fibre brags along a lamella to monitor and measure the strains on defined points. From these measurements not only can the strains be derived but also the inclination angles and hence the profile deformation too. The load tests were carried out on the mouth profile on 7th February 2022, 9th February 2022 and 23rd February 2022. During the entire period from 7th February 2022 to 23rd February 2022, a continuous recording of the mouth profile deformations was made by means of SAA. The load test on 7th February 2022 was performed to a maximum load of 80 kN (4 x 20 kN threaded rod load) with the main objective of capturing the elastic system response and profile stiffness information for setting up the digital twin. The digital twin was then used to obtain a numerical prediction of the maximum load which was 400kN (4 x 100kN). Visible cracking on the inner surface of the mouth profile as well as on the outside of the stringers occurred for the first time at about 120kN. The load test on 9th February 2022 was carried out to a maximum load of 200 kN (4 x 50 kN threaded rod load) with the main objective of obtaining a non-elastic system response or initiating cracks to determine the suitability of the monitoring system for crack detection and plastic deformation. Further details on the analysis of the suitability of monitoring systems for tunnels that are renovated during operation can be found in Beigel, (2023).

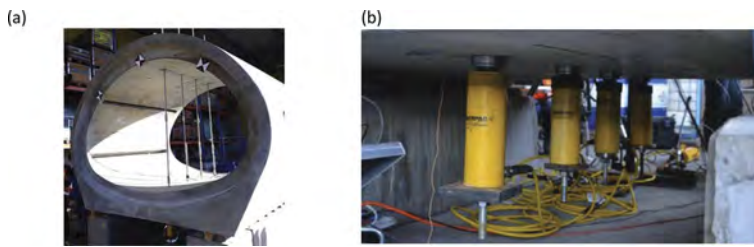


Figure 1. (a) Load application by means of strain-controlled threaded rods, (b) Load application by means of hydraulic presses.

3 DIGITAL TWIN ANALYSES

The digital twin of the mouth profile was constructed using a two-step approach: (a) the reproduction of the profile by means of a 2D non-linear finite element digital twin, and (b) the reproduction of the profile by means of a 3D non-linear finite element twin. The software solution used was ATENA Science from the company Červenka Consulting (Červenka et al., 2013). This two-stage procedure was chosen in order to obtain an understanding of the significant elements in the digital twin development in the first stage and to analyse the model updating procedure using the monitoring information in 2D and then transfer it to the 3D model. Figure 2(a) shows the digital twin model used in ATENA 2D and Figure 2(b) indicates the material properties. The reinforcement was characterised by a linear material model, the location of which is shown as solid black lines in the drawing. In addition to the classical Digital Twin updating of the material properties and the bearing conditions, e.g. by sequential updating procedures or sensitivity analyses, the updating of the geometrical positions of the reinforcement in the profile and of the depths of the subsequently inserted slots in the ridges and sidewall areas of the profile as well as the updating of the load application by using the monitoring information from the different loading phases were essential for this project.

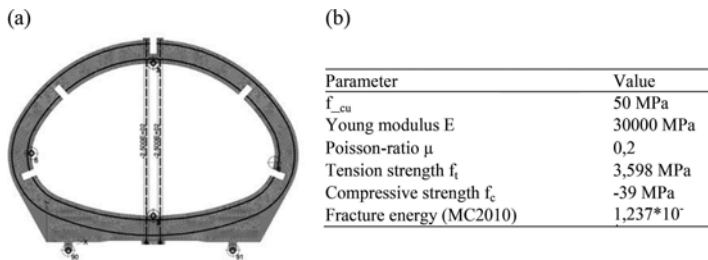


Figure 2. Nonlinear Finite Element 2D Digital Twin (a) Atena 2D Model, (b) Material parameters.

Besides other challenges, it was a crucial part of the digital twin setup process to model the load application effectively and realistically in order to allow the simulation of the load paths resulting from the test days.

The investigated applied load scenarios are shown in Figure 3, with (a) the force-controlled approach, (b) the approach with two external applied prestressed tendons, (c) the displacement-controlled approach, where only a one-sided loading in the ridge area was investigated in a first test.

A displacement-controlled variant using temperature loading and a force-controlled loading approach using a prestressing force was also investigated (Beigel, 2023). The Digital Twin simulation evaluated in the following is based on the force-controlled loading approach via two external preloads where the preload force was increased in specified steps. The fitting was performed using support points along the entire load path and for several displacement and force monitoring points within the profile. More details on the digital twin adjustment can be found in Beigel (2023).

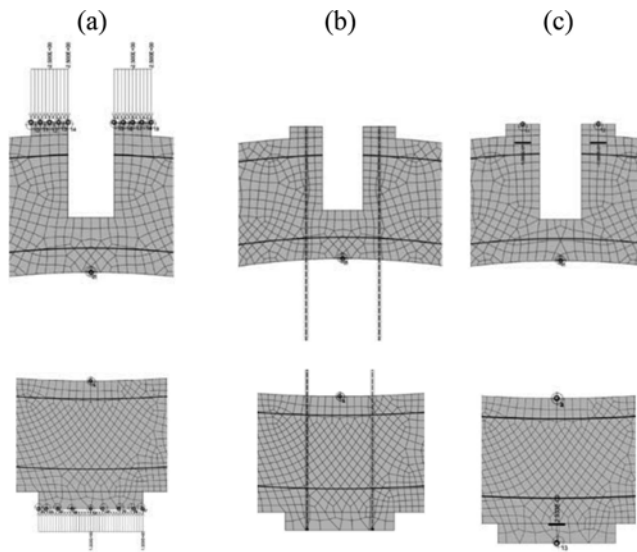


Figure 3. Digital Twin Details – Load transfer studies: (a) force-controlled, (b) coupling via external prestressing, (c) displacement-controlled.

Horizontal displacement in x-direction: With regard to the deformation of the profile, the horizontal displacements in defined points of the profile were of interest in a first approach especially since the deformation line of the mouth profile, which contained elements of yield joints and also rigid body movements, as well as the displacements in the bearing conditions could be detected. Figure 4 provides an overview of the results of the horizontal displacements in the x-direction. In particular, it shows (a) the tunnel cross-section with the measurement points and the corresponding coordinate system of the simulations, (b) the x-displacements for the 200 kN plane, (c) the force-displacement diagram for the x-displacement at point 25. In this diagram, the FE simulation is compared with the laser tracker (reference measurement) and the SAA. The diagram in Figure 4(d) shows the simulation results of the x-displacements at points 1, 17 and 25. Comparing the displacement at the load level of 80 kN before and after the maximum load of 200 kN shows plastic deformation. It can be seen that the deviations of the FE simulation from the reference measurement of the laser tracker are very small and thus very good results were achieved. The SAA measurement achieved a similar result compared to the laser tracker.

Vertical displacement in z-direction: In addition to the horizontal displacements at the defined points, the vertical displacements were also of significant importance for the comparison and updating of the model. Figure 5 provides the results of the displacements in the z-direction. Figure 5(b) shows the z-displacements occurring at Stage 80 kN. In Figure 5(c), a force-displacement diagram for the z-displacement at point 1 can be seen. The comparison of the laser tracker (reference measurement) and the SAA results show that they are in very strong agreement. It can be seen that the deviations of the NLFEA simulation from the reference measurement of the laser tracker are very small up to a load of 140 kN. From 140 kN to the load level of 200 kN, the simulation evokes a slightly stiffer system response than the reference measurement. However, the unloading load correlates very well with the reference measurement. The diagram in Figure 5(d) shows the simulation results of the z-displacements at points 1, 17 and 25. Comparing the z-displacement at the load level of 80 kN before and after the maximum load of 200 kN, a plastic deformation is evident.

Principal strains on the inner tunnel surface: The third important measurements, which were also used for the continuous updating process of the digital twin, were the main strains on the inner surface of the profile. Figure 6 shows the principal strains for the 200 kN level. In Figure 6(b), the minimal principal strains are shown while Figure 6(d) shows the maximal principal strains. It can be seen that the negative principal strains develop in the inner regions of the notches. In contrast,

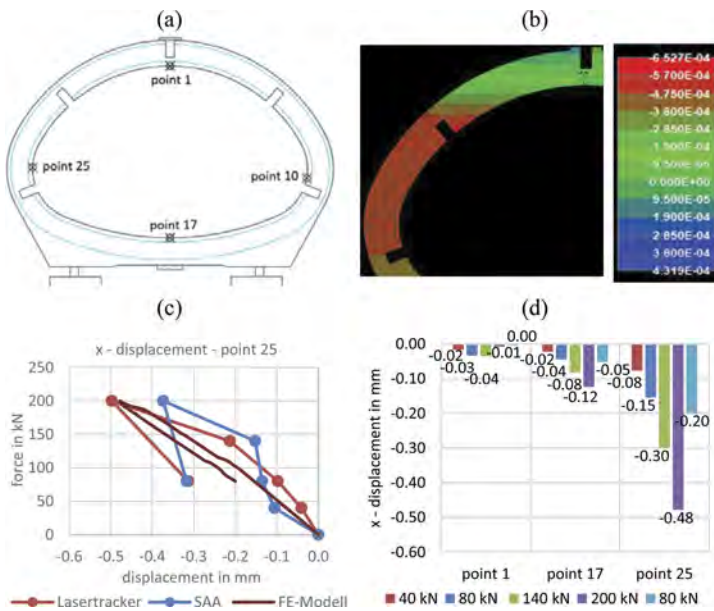


Figure 4. Digital Twin analyses of displacements in the x-direction (displacement controlled).

the positive principal strains occur at the interfaces opposite the notches, as expected. Figure 6(c) shows the simulation crack pattern at the 200 kN level with crack widths of up to 0.13 mm in the inner region of the flange notch. In addition, Figure 6(a) shows the crack in the ridge notch area caused by the test load.

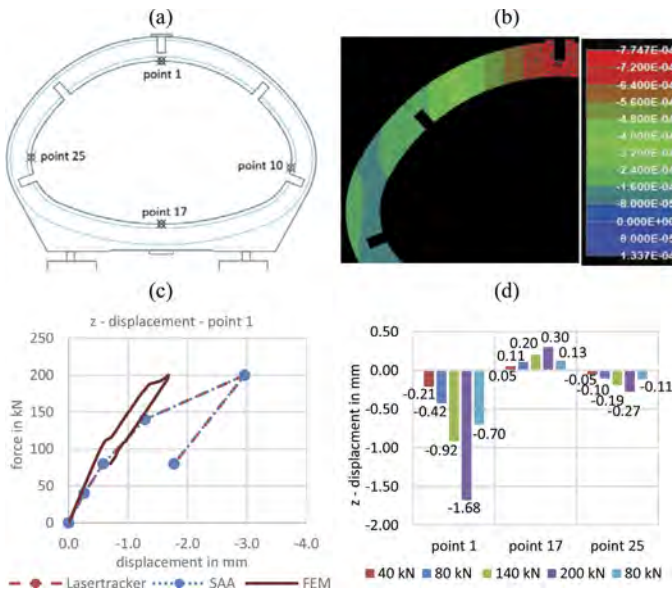


Figure 5. Digital Twin analyses of displacements in the x-direction (displacement controlled).

As Figure 6(a) clearly shows, massive cracks (“yield joint” formation) occurred next to the tie rods in the ridge area due to the reduction in cross-section and due to the deformation-controlled load application at a load level of 200kN. This could also be reproduced exactly with the ideally adjusted digital twin, as indicated in Figure 6(c) in the spatial crack pattern and in

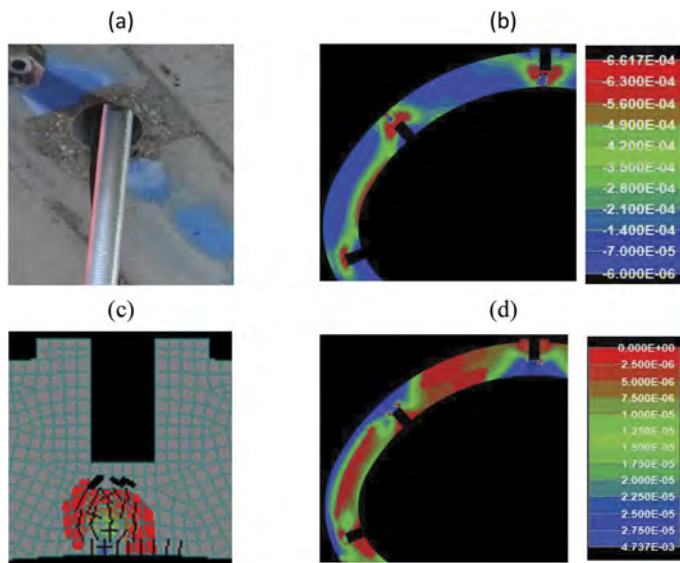


Figure 6. Principal strains and crack pattern at 200kN loading (displacement controlled).

Figure 6(b) and (d) in the compressive and tensile principal normal stress distributions. The modelled yield joint formation with the compression (red) and tension (blue) zones, which are also massive criss-crossed by cracks (black), showed a very good agreement with the monitored ones and could be analysed via digital twin in their spatial distribution and complexity in the further course of the load increase. The in-depth 2D and 3D analyses with the crack pattern analyses up to the ultimate load of 400 kN can be found in Beigel (2023).

4 DIGITAL TWIN ANALYSES AND MONITORING SYSTEMS

It became apparent from the analyses that the establishment of a digital twin for this tunnel profile required a multi-step process and several sensitivity analyses and adjustments of stiffness ratios and support conditions along the load path. The digital twin was ultimately able to contribute greatly to a detailed understanding of the behaviour of the imperfectly symmetrical tunnel cross-section as well as to the understanding of the level of approximations against the level of detailing and value of information as outlined in the new fib Model Code 2020. In particular, it was possible to set up the digital twin in relation to several monitoring systems and also to show the limits of the updating procedure against the monitoring ring uncertainties.

5 CONCLUSIONS

Several innovative monitoring systems and the Digital Twin Tuning process were investigated in controlled field trials for their suitability for use in tunnel retrofit processes. The studies have shown that accurate Digital Twin systems require a multi-stage updating process using information from advanced monitoring systems.

ACKNOWLEDGEMENTS

The authors thank the ÖBB Infra for funding the MONTUN Research Project. The authors also thank the fib COM3 “Existing Concrete Structures” for discussions and support and the IABSE TG1.4, and Czech Science Foundation, Czech Republic, under MAPA project number 22-00774S.

REFERENCES

- Beigel, A. 2023. Verifizierung innovativer Monitoringsysteme für Tunnelinstandsetzungen mittels digitaler Zwillingsanalysen. Vienna, Universität für Bodenkultur.
- Canestro, E., Strauss, A. & Helder, S. 2021. Multiscale modelling of the long-term performance of prestressed concrete structures – Case studies on T-Girder beams. *Engineering Structures*, 231, 111761.
- Červenka, V. Jendele, L. & Červenka, J. 2013. ATENA Program Documentation, Part I, Theory, Czechia: Červenka Consulting
- fib Model Code 2020, “Model Code for Concrete Structures”, (under review), 2023
- Neuner, H., Kostjak, V., Linzer, F., Loderer, W., Seywald, C., Strauss, A., Rigler, M. & Polt, M. 2022. Assessing Deformation Monitoring Systems For Supporting Structural Rehabilitation under Harsh Conditions. *EGU General Assembly 2022*. Vienna.
- Slowik, O., Novák, D., Novák, L. & Strauss, A. 2021. Stochastic modelling and assessment of long-span precast prestressed concrete elements failing in shear. *Engineering Structures*, 228, 111500.
- Spyridis, P. & Strauss, A. 2020. Robustness Assessment of Redundant Structural Systems Based on Design Provisions and Probabilistic Damage Analyses. *Buildings*, 10, 213.
- Strauss, A., Bergmeister, K., Novák, D. & Lehký, D. 2004. Stochastische Parameteridentifikation bei Konstruktionsbeton für die Betonerhaltung. *Beton- und Stahlbetonbau*, 99, 967–974.
- Strauss, A., Bien, J., Neuner, H., Harmening, C., Seywald, C., Österreicher, M., Voit, K., Pistone, E., Spyridis, P. & Bergmeister, K. 2020. Sensing and monitoring in tunnels testing and monitoring methods for the assessment of tunnels. *Structural Concrete*, 21, 1356–1376.
- Strauss, A., Castillo, P., Bergmeister, K., Krug, B., Wan-Wendner, R., Marcon, M., Matos, J. & Casas, J. R. 2018. Shear Performance Mechanism Description Using Digital Image Correlation. *Structural Engineering International*, 28, 338–346.
- Strauss, A., Frangopol, D. M. & Bergmeister, K. 2010. Assessment of Existing Structures Based on Identification. *Journal of Structural Engineering*, 136, 86–97.
- Strauss, A., Neuner, H., Rigler, M., Polt, M., Seywald, C., Kostjak, V., Linzer, F. & Loderer, W. 2022. Verification of the performance of reinforced concrete profiles of alpine infrastructure systems assisted by innovative monitoring. *EGU General Assembly 2022*. Vienna.

Life-cycle and sustainability impact of composite and combined concrete tunnel linings

P. Spyridis

TU Dortmund University, Dortmund, Germany

K. Bergmeister

University of Natural Resources and Life Sciences (BOKU), Vienna, Austria

ABSTRACT: Tunnels typically comprise large scale infrastructure projects, where a demand for an increased service life is present. On the other hand, temporary structures often do not need to be designed for a service life longer than a few years only or they can form part of the permanent structure. In addition to this, the use of composite or combined primary and secondary concrete tunnel linings (considering the conventional tunnelling approach) can significantly influence the CO₂ equivalent emissions footprint of tunnel projects – particularly during construction. The present paper discusses a reliability life-cycle based methodology to adjust safety factors used in the design of tunnel linings in order to reach a specified service life, i.e. a variation of the safety factors used leading to an analogous reliability level at the start of the structures' lifetime, which in turn provides a modification of the expected service life duration. Furthermore, the outcome of this approach is assessed in terms of sustainability under the spectrum of the recently introduced climate-change limit state. The results indicate the possibility to deploy a novel design concept which allows to improve a tunnel structure's profile holistically, i.e. with consideration of traditional design criteria such as construction costs and structural safety, but also acute future oriented needs such as the service life and the climate impacts of tunnel infrastructure.

1 INTRODUCTION

1.1 *Background situation*

Measurements and analyses in the last decades have confirmed the critical increase of greenhouse emissions and global average temperature, and consequently the possibility of an irreversible climate disruption in the immediate future. At the moment, intense efforts are devoted toward stabilising climate change, moreover within very narrow time margins, by posing accelerated reduction measures for CO₂ and other greenhouse emissions as well as similar environmental impacts in every human activity. This directs acute demands in the construction industry, which – accounting only for construction related emissions A1-A5 per EN 15978 (CEN 2012) – carries approximately 13% of annual global environmental impacts in terms of energy consumption and more than 20% in terms of construction material (mainly concrete and steel) production (GlobalABC 2021). Tunnelling is a rapidly increasing sector, with intensive energy and construction materials consumption, and – although it leads to overall environmentally beneficial solutions for many types of infrastructure – it is a major producer of climate change agents. Optimised tunnel and structural design concepts are therefore highly necessary, since they can vastly influence material consumption and facilitating resource-efficient construction layouts.

1.2 *Fundamentals of environmental impacts and sustainability in construction*

The environmental sustainability in construction can be assessed on the basis of the European standard EN 15978 (CEN 2012), and it is determined separately for operation and construction

stages and at different asset life cycle stages (modules). The scope of the modules is summarised in Table 1. Although various measures can be implemented for the environmental/climate impacts of construction, greenhouse gas emissions are represented herein as based on their equivalence of with CO₂ in terms of climate impact. This is a measurement scale developed and implemented by the United Nations' Intergovernmental Panel on Climate Change (IPCC 2021) to represent the influence of various gases on global warming. CO₂ equivalents are also referred to as "Global Warming Potential" (GWP) and abbreviated as CO₂-eq in mass units (kg). For a product (including construction products such as structural concrete constituents) these values can be found in its respective Environmental Product Declaration (EPD), which is defined by ISO 14025 (ISO 2020). Common Product Category Rules (PCR), i.e. guidance for EPD development, are outlined for the construction sector in Europe by EN 15804 (CEN 2019).

Table 1. Scope and classification to life cycle stages according to DIN EN 15978 (CEN 2012).

Life cycle stages:	Product stage	Construction process stage	Use stage	End of life stage	Benefits and loads beyond the system boundary
Modules	A1 – A3	A4 – A5	B1 – B7	C1 – C4	D
Construction phase	A1 Raw material supply A2 Transport A3 Manufacturing	A4 Transport A5 Construction and installation processes	B1 Use B2 Maintenance B3 Repair B4 Replacement B5 Refurbishment	C1 De-construction/ Demolition C2 Transport C3 Waste processing C4 Disposal	D Reuse, recovery and recycling potential
Operation Phase			B6 Operational energy B7 Operational water		

1.3 Climate Limit State – a novel design concept for sustainable structural design

Although significant progress has been made in measuring and reducing the emissions of construction products and materials by implementing alternative constituents as well as alternative energy sources for production, the application of overall climate efficient design concepts is still sporadic and inefficient with respect to the societal demands as these are expressed in governance targets for emission limits. In order to deliver transparent and measurable rating of ecological requirements in design, a new limit state termed "Climate Limit State (CLS)" has been proposed by Haist et al. (2022a, 2022b) for inclusion to structural design codes and standards. This is intended to complement the already established Ultimate Limit State (ULS), Serviceability Limit State (SLS) and Durability/Service Life thresholds. Moreover, this is placing the authority and responsibility of the climate impact reduction on the hands of the design engineers, who are also in turn driving forces for the specification of materials and the selection of construction techniques and technologies. The proposed CLS considers the CO₂-eq emissions resulting from construction but also the service life of the structure in an amortisation timeframe for emissions. The limit state is expressed as a proportion of whole-life emissions to a reference structure without emission mitigation measures and factors-in the allowable emission thresholds as required to decelerate or reverse global warming (Haist et al. 2022b). Account can then be made for low-emission materials, techniques and technologies, as well as optimised component detailing and dimensioning, but also on degradation processes, and it can apply at detail/component or structural system level (Haist et al. 2022a). The overall formulation of the CLS is provided on the example of a concrete member in Equation 1 and further explanatory details and examples can be retrieved from Haist et al. (2022a, 2022b). As seen, a vital and integrated element leading to increased sustainability rating is the length of the element's service life and the asset's life-cycle management programme.

$$CLS_{bm} = \frac{GWP_{eco,bm} \cdot \gamma_{GWP,eco} / t_{sl,eco,bm}}{GWP_{ref,bm} / t_{sl,design,bm}} \leq \alpha_{GWP} \quad (1)$$

where:

- CLS_{bm} : Climate Limit State Index for building members (bm)
- $GWP_{i,bm}$: Global Warming Potential of the building member (bm), in kg of CO₂-eq considering the considering the life cycle stages A1-A5, B1-B5 and C according to EN 15804 (CEN 2012), with i = eco or ref for ecologically optimised or reference member respectively
- $t_{sl,i,bm}$: Service life (sl) of the building member (bm), in years, respectively with i = eco and design, for optimised and reference member with typical/nominal service life.
- $\gamma_{GWP,eco}$: Partial safety factor for the building member's GWP considering uncertainties of the environmental impact
- α_{GWP} : target value of the year-specific GWP reduction to achieve climate protection goals in the concerned sector and geographical area

1.4 Proposed novelty and scope of the paper

The situation described above strongly advocates the need to reduce the GWP of materials related to the permanent and temporary support at the A1-A3 stages. But apart from this, it is possible to optimise the design life-cycle of the linings. In conventionally constructed tunnels, the standard method of a sprayed concrete lined tunnel (SCL) includes a temporary primary lining of sprayed concrete, a permanent cast-in-situ or sprayed secondary and a waterproofing membrane between them. The temporary lining is assumed to be used for the stabilisation of the underground excavation in the short-term in order to allow safe conditions for casting the long-term lining support. Over the last two decades, an innovative tunnel design philosophy has been established considering the traditionally primary lining as part of the long-term structure. According to (Spyridis 2014), a long service life for primary lining sharing the loading with the secondary lining can lead to a material reduction of 40-45% for tunnel construction, while the savings in concrete consequently result in additional savings in excavation volumes. Such design approaches have been successfully performed in the past, with examples including the recently completed London's Crossrail (Elisabeth line) (Spyridis et al. 2013), and the Brenner Base Tunnel (Bergmeister & Murr 2019). In the present study, plane-strain analyses with soil-structure interaction, including both the primary and secondary lining are carried out for a realistic SCL tunnel cross section. The design outcome is compared based on the GWP (CO₂-eq emissions), and the numerator of the Climate Limit State of Equation (1) in particular. The results enhance the argument that advanced analysis methods with consideration of the structure's life-cycle characteristics, can dramatically influence the linings' climate impact, and hence the overall impact of tunnel projects.

The tunnel structure selected for the comparative analyses is a conventionally excavated, non-circular, closed shell in soft ground. The dimensions of the excavation are approx. 13.5 by 10.0 m (width/height). The crown and water table depths are assumed at 25 m and 4 m from the surface respectively and the soil layers are: Made ground (0 - 7 m); Clay type 1 (7 - 38 m); Clay type 2 (38 - 46 m) – see also Figure 1. The primary and secondary linings are assumed to be sprayed and cast concrete respectively. Two design approaches are accounted for, namely with and without load sharing. In the first case, the primary lining remains as a load bearing element in composite action and load sharing with the secondary lining for the entire service life of the tunnel, and in the latter case the primary lining's service life is ended once the secondary lining is in place. The total GWP for each solution is calculated based on the required material quantities per the design. The service life spans are accordingly assumed at $t_{sl,prim} = 1$ year and $t_{sl,secd} = 120$ years.

2 PARTIAL SAFETY FACTORS ADJUSTMENT TO DESIGN SERVICE LIFE

The service life of a structure may be expressed in conjunction to its time-dependent performance level and be processed in the reliability discipline, as discussed by Frangopol et al. (2004) and as integrated in codified performance-based assessments (fib 2012) and tunnel project specifications (Bergmeister, 2012), considering the reliability level inherited to the structure at the very

beginning of its service life. A structure's service life can be defined as the "assumed period for which a structure or part of it is to be used for its intended purpose with anticipated maintenance but without major repair being necessary" (CEN 2002). Reliability can be inversely expressed by the failure probability per Equation 2 – with Φ , the cumulative function of the standard Normal distribution, and p_f the failure probability per annum. Based on Equation 5, and assuming statistical independence of annual failure events, the values of β_n for different reference periods (n in years) can be calculated solving Equation 3, and the structure's service life ends when the minimum acceptable (terminal) target reliability β_{TARGET} is reached.

$$\Phi(-\beta) = p_f \quad (2)$$

$$\Phi(\beta_n) = [\Phi(\beta_1)]^n \quad (3)$$

A simplified methodology to evaluate the design service life of a tunnel lining through an engineered scaling of the involved ULS partial safety factors is presented in detail by Spyridis (2014). This method uses a transformation of Cornell's expression of the reliability index β , i.e. based on mean values and standard deviations of the resistance and action stochastic variables, and the fractile-based expression of their characteristic values per Eurocode 0 (CEN 2002), and it yields the (combined) nominal safety factor γ_{nom} of a load-bearing structure per Equation 4 – with v_i the coefficient of variation ($v_i = \sigma_i / \mu_i$) for the load (S) and the resistance (R), and k the characteristic fractile value factor for the required statistical confidence and the test sample size.

$$\gamma_{nom} = \frac{1 - k \cdot v_R}{1 + k \cdot v_S} \cdot \frac{1 + \beta \cdot \sqrt{v_R^2 + v_S^2 - \beta^2 \cdot v_R^2 \cdot v_S^2}}{1 - \beta^2 \cdot v_R^2} \quad (4)$$

In the presented case study, the partial safety factors for steel and concrete material are set to $\gamma_s = 1.15$ and $\gamma_c = 1.50$ respectively. Adjusted load partial safety factors are used, namely $\gamma_{shor-term} = 1.10$ and $\gamma_{long-term} = 1.50$ following Spyridis (2013).

3 DETAILS OF SOIL-STRUCTURE INTERACTION MODELLING AND ANALYSIS

The numerical models implemented non-linear Mohr-Coulomb plasticity with a mesh of 5430 3-noded triangular solid material elements and 650 Timoshenko-beam elements to model the ground and the liners respectively. The analysis is performed in a plane-strain model by use of Rocscience FEM software. The used geotechnical parameters are presented in Table 2 below. These properties are chosen in coherence with previous project case studies, described in (Spyridis et al. 2016). The analysis procedure delivers the loads in the linings due to soil-structure equilibrium and it includes a total stress, undrained state in the temporary condition (i.e. soil is considered to be watertight due to the unloading compaction of clays) and then a switch to effective stress drained/ pore water pressure state for the long-term. To simulate the face advance stress relief and 3D arching effects during excavation, a 50 % relaxation employing the stiffness reduction method is implemented (Pöttler 1990). The analysis steps are summarised below:

- 1) In situ stress – nullified deformation equilibrium
- 2) Softening at the excavation area/simulated relaxation
- 3) Excavation (removal of cross-section soil elements) and installation of primary lining.
- 4) Installation of secondary lining
- 5) Application of porewater pressure
- 6) Switching to long-term drained parameters
- 7) Degradation (removal) of primary lining, i.e. long-term situation of secondary lining

For both the primary and secondary linings, the assumed thickness in the model is 300 mm each; although the design results in some adjustment for the lining thicknesses, these are not reiterated in the FEM analysis. The primary lining stiffness is assumed at 15 GPa to simulate the gradual simultaneous soil convergence and lining stiffness development (Pöttler, 1990), but the secondary lining it is set to 30 GPa. The linings are analysed as fully linear elastic materials and they are designed as plain unreinforced concrete or as concrete with a B500 rebar mesh of $\text{Ø}10/100$ and $\text{Ø}16/100$ mm for the primary and the secondary lining respectively.

4 LIFE-CYCLE BASED SUSTAINABILITY ANALYSIS

The GWP of the materials is calculated based on the weights of the constituents and published data (retrieved from Haist et al. (2022a) and online environmental declarations). For both sprayed and cast concrete the assumed cement type is Portland CEM I 42.5 R. For sprayed concrete, the proposed mix is derived from recipes in Ikumi et al. (2022), but both sprayed and cast mixes are deliberately selected with similar mixes of equivalent strength. The details are listed in Table 3 below. Based on these data, the following aggregate GWP values for the A1-A3 modules are calculated (note that the rebar quota is independent of the lining thickness):

Primary lining (Total perimeter: 37.5 m):	Concrete (sprayed)	391	kg CO ₂ -eq/m ³
	Bar reinforcement	10	kg CO ₂ -eq/m ²
Secondary lining (Total perimeter: 35.5 m):	Concrete (cast in situ)	405	kg CO ₂ -eq/m ³
	Bar reinforcement	25	kg CO ₂ -eq/m ²

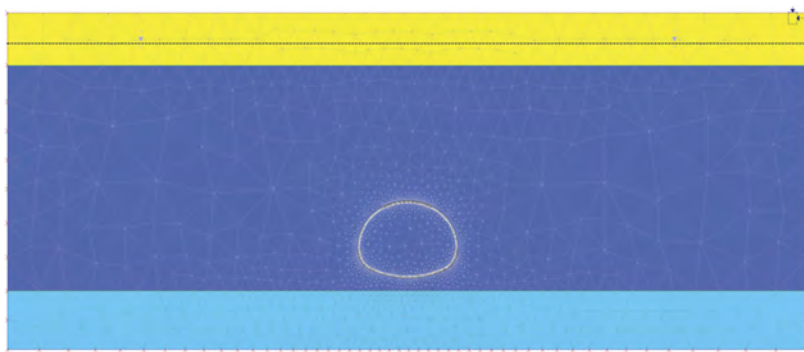


Figure 1. Overview of the plane-strain FE model.

Table 2. Input parameters for the FE model.

SOIL PROPERTIES		Made ground	Clay 1	Clay 2
Undr. Young's modulus	[MPa]	10	100	200
Drained Young's modulus	[MPa]	n/a	75	150
Undr. Poisson's ratio	[-]	0.20	0.45	0.45
Drained Poisson's ratio	[-]	n/a	0.20	0.2
Undr. Friction Angle	[°]	n/a	~ 0	~ 0
Drained Friction Angle	[°]	n/a	25	25
Undr. Shear Strength	[kPa]	n/a	100	200
Cohesion	[kPa]	n/a	15	15
Unit Weight	[kN/m ³]	20	20	20

Table 3. Concrete lining constituent materials; mass per concrete volumes and A1-A3 GWP per mass.

	Sprayed concrete Primary linings [kg/m ³]	Cast in situ concrete Secondary lining [kg/m ³]	GWP (Haist et al. 2022, online EPD) [kg CO ₂ -eq/kg]
Cement (CEM I 42.5 R)	450	500	0.81
Aggregates 0/4	1200	800	< 0.01
Aggregates 4/8	650	550	< 0.01
Aggregates 8/16	-	450	< 0.01
Water	200	200	< 0.01
Superplasticizer	4	-	1.88
Accelerators	8	-	2.28
Air-entrainer	2	-	0.53
Bar reinforcement B500	24.6 [kg/m ²]	63.1 [kg/m ²]	0.4

5 RESULTS

The FEM calculation results are expressed as the combination of normal forces and bending moments along the lining. A typical design practice for tunnel linings observes the applicable structural design codes and assumes that the linings behave as unit-width shell elements with axial/flexural load interaction. Given the fact that tunnel linings have a uniform thickness and reinforcement quantities, the design loads resulting from the analyses are compared against the structural capacity envelope of the lining which is represented in the form of interaction diagrams (hoop thrust against bending moment), also termed Capacity Limit Curves (CLC) (Spyridis et al. 2016). CLCs for structural concrete members are here produced in accordance to Eurocode 2 (CEN 2021). The CLCs of Figure 2 present all design combinations of axial forces and bending moments juxtaposed to the envelope of the cross-section's design capacity distinguishing the design assumption and dimensioned lining in a comprehensive graphical verification. Also, the lining thickness $d_{\text{prim}}/d_{\text{secd}}$ is noted. The design point (most onerous load pair coinciding with the CLC envelope) is defined by adjusting the concrete lining thickness, where two detailing concepts are implemented: (i) relying solely on plain unreinforced concrete, and (ii) relying on rebar mesh reinforced concrete. The data set name coding indicates the combination of the characteristics [Lining]-[Design concept]-[Detailing approach], with:

- Lining: Primary (Prim) /Secondary (Secd)
- Design concept: Individual life cycles (Ind)/Combined/Composite function (Com)
- Detailing: Concrete (Con)/Concrete and rebar (ConReb)

The lining dimensioning for each dataset are summarised in Table 4, along with the respective numerators of Equation (1), considering the GWP of the materials at A1-A3 life cycle stage per running meter, the service life of each solution being equal to the nominal service life $t_{\text{sl,prim}}$ or $t_{\text{sl,secd}}$, and assuming an overall safety factor of $\gamma_{\text{GWP}} = 1.0$. Table 4 is used as a basis for comparison between the different solutions on the basis of the assumptions clarified above.

Table 4. Concrete lining details and respective A1-A3 GWP assessments.

Dataset and analysis	Lining thickness (mm)	GWP in kg CO ₂ -eq per tunnel running meter			SUM
		Concrete	Rebar	Time adjustment (Eq. 1)	
Prim-Ind-Con	220	3226		3226	3277
Secd-Ind-Con	430	6182		52	
Prim-Ind-ConReb	210	3079	375	3454	3503
Secd-Ind-ConReb	340	5032	888	49	
Prim-Com-Con	320	4692		41	178
Secd-Com-Con	1100	15815		137	
Prim-Com-ConReb	290	4252	375	39	85
Secd-Com-ConReb	330	4745	888	47	

6 DISCUSSION: CLIMATE AND SUTAINABILITY OPTIMISATION IN TUNNELLING

The analysis above demonstrates a rational engineering and quantifiable procedure to assess the environmental impacts in tunnelling based on the A1-A3 (material) life cycle stages whilst predefining the expected service life of a structure also at the design stage and only accounting the reliability at delivery. The sustainability analysis is based on the widely accepted GWP metrics, and the newly introduced Climate Limit State. This is complemented by predefining appropriately selected safety factors in coherence with the initial structural design reliability threshold. This connotation is already made evident in the summary of results in Table 4: A governing effect in the analysis is the yearly apportionment of emissions and hence an amortisation of the environmental impacts over the service life of the tunnel. This life cycle effect has to be understood as a critical planning, design but also maintenance decision for any future tunnel project. At the same time, the Climate Limit State can be directly integrated into current structural design codes.

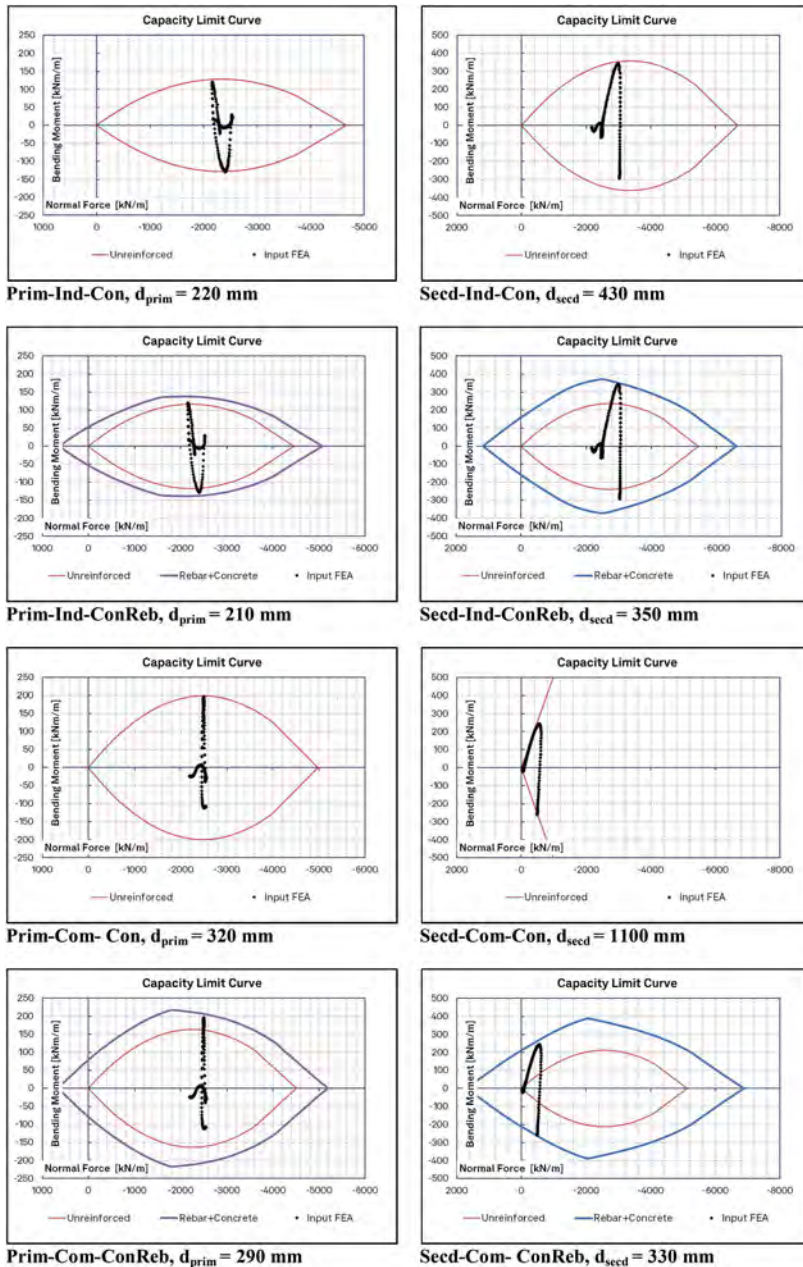


Figure 2. Capacity Limit Curves (CLC) for all analysed cases; see also the correspondence of the resulting lining thickness with the numerator in numerator of Equation (1).

As main takeaways of this study, it is briefly summarised that integrating the primary lining to the permanent, long-term support may require slightly higher dimensioning and possibly slightly higher quality control requirements in the initial phases of the project. However, this leads in this case to a reduction in life-cycle CO₂-eq. emissions by a tremendous 95 % or even more, compared to the standard approach of sacrificial primary lining. Moreover, the investigation demonstrates that enhancement of a lining's bending resistance by the use of rebar reinforcement allows a reduction of its thickness, which in turn can lead to a lower GWP as compared to completely unreinforced concrete.

This article explains a uniformly applicable methodology for a combined structural and sustainability assessments of tunnel structures which can immediately account for the above aspects. However, further insights should be gained on the aspects of structural, life cycle and sustainability engineering in tunnelling and infrastructure construction in the wider sense, with account on all asset phases (A1-D), reliability, quality, as well as material and construction technologies.

REFERENCES

- Bergmeister, K. & Murr, R. 2019. Optimierung des Konstruktionsbetons beim Brenner Basistunnel. *Beton-und Stahlbetonbau*, 114(12), pp.965–973.
- CEN - European Standards Committee. 2012. *EN 15978: 2012-10: Sustainability of construction works - Assessment of the environmental performance of buildings - Calculation method*, Brussels
- CEN - European Standards Committee. 2019. *EN 15804+A2: Sustainability of construction works - Environmental product declarations - Core rules for the product category of construction products*, Brussels
- CEN - European Standards Committee. 2021. *prEN 1992-1-1:2021: Eurocode 2: Design of concrete structures – Part 1-1: General rules* (draft), Brussels
- CEN - European Standards Committee 2002. *EN 1992-2002: Eurocode 0, “Basis of Design”*. Brussels
- Bergmeister, K. 2013. Life-cycle design for the world’s longest tunnel project. In Strauss, A., Frangopol, D.M., Bergmeister, K. (eds.), *Life-Cycle and Sustainability of Civil Infrastructure Systems*. Taylor and Francis, London.
- Frangopol, D.M., Kallen, M.J. & van Noortwijk, J.M. 2004. Probabilistic models for life-cycle performance of deteriorating structures: review and future directions. *Progress in Structural Engineering and Materials* 6(4), pp. 197–212.
- Fib - The International Federation for Structural Concrete. 2012. *fib - Bulletin N° 65: Model Code 2010 - Final draft, Volume 1*. Lausanne
- GlobalABC - Global Alliance for Buildings and Construction. 2021. *2021 Global Status Report for Buildings and Construction*. Nairobi
- Haist, M., Bergmeister, K., Curbach, M., Deiters, M.V., Forman, P., Gaganelis, G., Gerlach, J., Mark, P., Moffatt, J., Muller, C., Muller, H.S., Reiners, J., Schack, T., Scope, C., Tietze, M. & Voit, K. 2022b. Climate Limit State (CLS) for building structures - a possible companion of ULS, SLS and durability limit states. In: Proceedings 6th fib Congress June 2022 Oslo Norway, pp. 143–152
- Haist, M., Bergmeister, K., Curbach, M., Forman, P., Gaganelis, G., Gerlach, J., Mark, P., Moffatt, J., Muller, C., Muller, H.S., Reiners, J., Scope, C., Tietze, M. & Voit, K. 2022a. Nachhaltig konstruieren und bauen mit Beton. In K. Bergmeister, F. Fingerloos & J.-D. Wörner (eds.), *Beton Kalender 2022: Nachhaltigkeit, Digitalisierung, Instandhaltung*. pp. 421–531, Ernst und Sohn
- Ikumi, T., Salvador, R.P. & Aguado, A. 2022. Mix proportioning of sprayed concrete: A systematic literature review. *Tunnelling and Underground Space Technology*, 124, p.104456.
- IPCC - Intergovernmental Panel on Climate Change. 2021. *Climate Change 2021: The Physical Science Basis. Contribution of Working Group I to the Sixth Assessment Report of the Intergovernmental Panel on Climate Change*. Cambridge University Press.
- ISO - International Organization for Standardization. 2020. *ISO 14025:2006, Environmental labels and declarations – Type III environmental declarations – Principles and procedures* ISO, Geneva
- Pöttler, R. 1990. Time-dependent rock-shotcrete interaction, a numerical shortcut. *Computers and geotechnics*, 9(3), pp.149–169
- Spyridis, P. 2014. Adjustment of tunnel lining service life through appropriate safety factors. *Tunnelling and underground space technology*, 40, pp.324–332.
- Spyridis, P., Konstantis, S., & Gakis, A. 2016. Performance indicator of tunnel linings under geotechnical uncertainty. *Geomechanics and Tunnelling*, 9(2),158–164.
- Spyridis, P., Nasekhian, A. & Skalla, G. 2013. Design of SCL structures in London. *Geomechanics and Tunnelling*, 6(1), pp.66–80.

Assessing highway bridge scour reliability and risk under changing floods

N. Devineni & M. Ghosn

The City University of New York, New York, USA

ABSTRACT: Hydraulic events threaten highway bridge safety as more than 55% of bridge failures in the United States (U.S.) are attributed to floods. It is now well-documented that climate change could cause an increase in extreme precipitation leading to larger and more frequent floods in many U.S. regions. This study presents a systematic framework for the reliability analysis of bridges under future changing flood conditions. The bridge scour safety assessment process is demonstrated using a case study representing bridges over Schoharie Creek in Upstate New York, with more than 100 years of peak flow data and evidence of an increasing trend. Our results show that this trend could cause about an 18% increase in the probability of scour failure over the 75-year service life of bridges designed using current procedures. The reliability index for foundation scour should ideally surpass $\beta = 2.5$ to effectively lower the risk to acceptable levels.

1 INTRODUCTION

Wardhana and Hadipriono (2003) showed that flooding and scour contributed to almost 53% of all bridge failures in the U.S. between 1989 and 2000. Additionally, a study on the status of bridge failures in the U.S. from 1800 to 2009 conducted by Sharma and Mohan (2011) showed that floods caused the maximum number of bridge failures – accounting for 38% of the 1,814 failures that occurred in those years. In recent decades, floods have increased in intensity and frequency in the U.S., especially across the Northeast, Pacific Northwest, Midwest, and Great Plains (Slater and Villarini, 2016; Milly et al. 2005; Collins, 2009, Ahn and Palmer, 2015). Long-term analysis, based on over 100 years of peak flow records, also shows an increase in flooding in the northern half of the eastern prairies and parts of the midwest (Peterson et al. 2013). Particularly vulnerable to increased flooding are highway bridges that often form critical, if not unique, access links to many riverine communities. For example, Hurricane Irene in 2011 had cut off for several days a dozen towns in Upstate New York and Vermont from the outside world because of extensive flooding. The hurricane-induced floods led to entire collapses or caused damages to more than 300 bridges in Vermont alone, many of which were by flood-related foundation scour (Eckholm, 2011).

The American Association of State Highway and Transportation Officials (AASHTO) Load Resistance Factor Design (LRFD) specifications require that scour at bridge foundations be designed for 100-year peak floods. The corresponding 100-year design scour depth at bridge foundations is estimated based on the Federal Highway Administration's (FHWA) Hydraulic Engineering Circular No.18 (HEC-18) specifications (Richardson & Davis, 2012). An approximate 40% of U.S. bridges are over the age of 50 years (FHWA, 2015), implying that their scour design is based on the 100-year flood estimated from data before the 1970s. With recent increases in flooding across the U.S., there is a need to reassess and, if needed, update the 100-year design floods and the corresponding design scour depths to reflect new extreme conditions.

We introduce a framework to assess for the effect of long-term changes in flood intensities and update highway bridge scour depth estimation. Long-term changes in floods are detected and used in future flood modeling. Highway bridge scour depths are estimated using a reliability-based approach (Johnson and Dock, 1998; Johnson et al. 2015; NCHRP, 2007; Lagasse et al. 2013; NCHRP, 2013) that considers all the uncertainties associated with establishing bridge structure, foundation, loading characteristics, and scour modeling. This end-to-end bridge scour safety assessment process is

demonstrated using a case study representing a hypothetical bridge over the Schoharie Creek in Upstate New York for which more than 100 years of peak flow data is available.

2 DATA AND METHODS

2.1 Streamflow data

Peak streamflow data (the maximum instantaneous discharge) from the Schoharie Creek at Prattsville, NY (USGS gauge 1350000), was used in this study (NWIS, 2020). This gauging station is part of the Hydro-Climatic Data Network (HCDN) of the United States Geological Survey (USGS). Data from the HCDN stations are reportedly free of upstream regulation and diversion. The contributing drainage area of this station is 237 mi². Annual peak streamflow data (in cubic feet per second, cfs) is available for the 1908 to 2019 water years (Oct. 1 - Sept. 30).

2.2 Hypothetical bridge characteristics

AASHTO LRFD specifications are primarily designed for medium to short-span bridges. The hypothetical bridge, therefore, took a total span of 220 feet, assuming the channel below to have a width of roughly 200 feet. The three span (60'-100'-60') bridge is illustrated in Figure 1 and for the purpose of this study, each support column has an estimated diameter of 6 feet. The depth of foundation below the streambed which is susceptible to potential scouring is represented by, y_s .

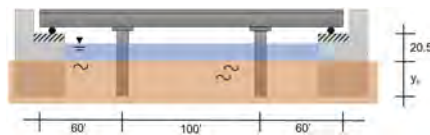


Figure 1. Profile of hypothetical bridge.

2.3 Methodology

2.3.1 Probability model and return levels

Lognormal, Log-Pearson Type III, and Generalized Extreme Value Distributions are commonly used and are reasonable, for modeling peak streamflow data (Stedinger et al. 1993). LPIII has been in use by Federal agencies since 1967 (USWRC, 1967). In this study, we used the Gumbel distribution (Type I Extreme Value Distribution) to have a minimum number of parameters that need to be estimated. The T-year design flood is estimated as follows:

$$Q_T = F^{-1}\left(1 - \frac{1}{T}\right) \quad (1)$$

where $F^{-1}(\cdot)$ is the inverse of the cumulative function of the selected probability distribution, and T is the return period for the flood event. In our case study, we are interested in the 100-year design flood. Hence, $Q_{100} = F^{-1}(0.99)$. Uncertainty in estimating the 100-year design flood is represented using a bootstrap sampling approach (Efron and Tibishirani, 1993).

2.3.2 Estimating bridge scour

The AASHTO LRFD specifications require that scour at bridge foundations be designed for the 100-year flood storm surge tide. The corresponding 100-year design scour depth at the bridge foundation is estimated following the procedure recommended by FHWA using HEC-18 (Richardson & Davis, 2012). The foundation should then be designed taking into consideration the design scour depth. This is achieved by placing the footings below the scour depth. This ensures that the lengths of piles, and their pile shafts, extend beyond the scour depth, where the remaining soil depth provides sufficient resistance against sliding failures and overturning, even after severe scour effects. The focus of this study is on local live-bed scour around bridge piers that, because of its cyclical nature, is the most unpredictable type of

scour. The HEC-18 design equation for local scour around bridge piers is a function of the flow depth, the pier nose shape, the angle of attack of the flow, the streambed conditions, the soil material size, the diameter of the pier, and the Froude number. The equation that is intended to predict the depth of maximum scour for design purposes is of the form:

$$y_{max} = 2y_0 K_1 K_2 K_3 K_4 \left(\frac{D}{y_0} \right)^{0.65} F_0^{0.43} \quad (2)$$

where y_{max} is the maximum depth of scour, y_0 is the depth of flow just upstream of the bridge pier excluding local scour, K_1 , K_2 , K_3 , and K_4 are coefficients that account for the nose shape of the pier, the angle between the direction of the flow and the direction of the pier, the streambed conditions, and the bed material size respectively, D is the pier diameter (Lagasse, 2013). F_0 is Froude's number and is defined by:

$$F_0 = \frac{V}{\sqrt{gy_0}} \quad (3)$$

where V is the mean flow velocity at the pier and g is the acceleration due to gravity. The flow depth, y_0 , and flow velocity, V , are related to the flow discharge rate, Q , and the shape of the channel represented by the cross-sectional area of the stream, A_0 . This relationship is given by:

$$Q = A_0 V \quad (4)$$

For a rectangular cross-section with a constant width, b , and flow depth y_0 , the relationship becomes:

$$Q = by_0 V \quad (5)$$

In this study, without a loss of generality, we assume that the channel cross-section is approximately rectangular. The relationship between the streamflow velocity, V , and the hydraulic radius that is related to the flow depth, y_0 , can be expressed using Manning's equation:

$$V = \frac{\Phi}{n} R^{(\frac{2}{3})} S^{(\frac{1}{2})} \quad (6)$$

where n is Manning's roughness coefficient, R is the hydraulic radius, and S is the slope of the streambed. Φ is a unit adjustment parameter equal to 1.486 when using U.S. units (feet and seconds). For SI units $\Phi = 1$. For a rectangular channel of width b , the hydraulic radius, R , can be calculated by:

$$R = \frac{by_0}{b + 2y_0} \quad (7)$$

Thus, the relationship between the flow rate, Q , and the flow depth, y_0 , is given from the equation:

$$Q = by_0 \frac{\Phi}{n} \left(\frac{by_0}{b + 2y_0} \right)^{(\frac{2}{3})} S^{(\frac{1}{2})} \quad (8)$$

Typical values for Manning's roughness coefficient, n , vary between 0.025 to 0.035 for earth (respectively for "good" condition and for a "weeds and stones" condition). It is noted that estimating the appropriate Manning roughness coefficient is associated with a high level of uncertainty. Researchers at Hydraulic Engineering Center (1986) determined that the roughness coefficient, n , follows a lognormal distribution with a CoV ranging from 20% to 35% (with an average value of 28%). Therefore, in this study, n is taken as a lognormal random variable with a mean equal to 0.025 and a coefficient of variation equal to 28%. It is also assumed that the slope, S , is known and thus the uncertainties in V are primarily due to the uncertainties in estimating n . As mentioned previously, we used Gumbel distribution to model the discharge rate, Q . Table 1 presents the values assumed for b , K_1 , K_2 , K_3 , K_4 , D , and S , for analyzing the hypothetical bridge.

Reliability analysis of a bridge pier under the effect of scour is proposed based on the work of Johnson (1995). This model is based on the observation that Equation 2 gives a conservative

estimate for the depth of the scour. The average ratio of the observed scour depth compared to the HEC-18 predicted depth was found by Johnson (1995) to be about 0.55. Also, the ratio of the true scour value over the predicted value has a CoV of 52%. This ratio is represented by a scour modeling variable, λ_{sc} , that is assumed to follow a normal distribution. Thus, according to Johnson (1995), the true scour value can be represented by an equation of the form:

$$y_{max} = 2\lambda_{sc}y_0K_1K_2K_3K_4\left(\frac{D}{y_0}\right)^{0.65}F_0^{0.43} \quad (9)$$

Table 1. Variables used in equation calculation.

Variable	Definition	Assumed Value
b	River/creek width	220 ft.
K ₁	Nose-shape of pier coefficient	1
K ₂	Angle of flow and pier coefficient	1
K ₃	Streambed condition coefficient	1.1
K ₄	Bed material size coefficient	1
D	Pier diameter	6 ft.
S	Slope of streambed	0.2%

Equation 9 assumes that the modeling variable, λ_{sc} is representative of the differences between the HEC-18 scour design equation and the true scour for all floods and rivers. It should be noted that Johnson (1995) also recommends that the factor K_3 , representing the effect of streambed conditions, should be treated as a random variable with a mean equal to 1.0 and a CoV equal to 5% to account for the possible variability of the streambed between floods. Table 2 summarizes the input data for the random variables appropriate for use with Equation 9. In this study, we assume that the scour depth is due to the single flood being analyzed and that the flooding period is always long enough for the maximum scour depth to be reached.

In summary, two equations are used to estimate bridge scour. Equation 2, as recommended by HEC-18, that estimates the maximum scour design depth given known deterministic values from Table 1. Equation 9, as proposed by Johnson (1995), that estimates the true scour depth under possible uncertainties that can arise from estimating peak streamflow, Q , Manning's roughness, n , and the bed condition factor, K_3 . In addition, Equation 9 includes a correction for the bias, λ_{sc} , between the predicted HC-18 scour when compared to the true scour. It is important to note that, while Equation 2 provides a deterministic estimate of the design scour depth, y_{design} , Equation 9 provides a range of values of the possible scour, $f(y_{max})$, when uncertainties are considered. Conjunctive use of the estimates computed from Equation 2 and Equation 9 enables us to develop the reliability analysis and extrapolate reliability indices (beta values).

Table 2. Input data for scour reliability analysis equations. Coefficient of Variation (CoV).

Variable	Definition	Mean Value	CoV	Distribution Type	Reference
Q	Peakflow	18790 cfs	80%	Gumbel	USGS NWIS (2020)
λ_{sc}	Observational bias	0.55	52%	Normal	Johnson (1995)
η	Manning's roughness coefficient	0.025	28%	Lognormal	HEC-18 (1986)
K ₃	Streambed condition coefficient	1.1	5%	Normal	Johnson (1995)

2.3.3 Reliability analysis

The purpose of reliability analysis is to study the level of bridge structural safety provided by the current AASHTO LRFD for flood-induced scour. The reliability analysis also examines how changes in the design criteria would affect the safety of bridge systems. We will use this information to calibrate appropriate load factors that adjust the design scour equation to meet different target reliability indices. We developed the reliability analysis by conjunctively

using Equation 2 and Equation 9. The bias-adjusted scour model described in Equation 9 is used in a Monte-Carlo simulation method along with bootstrapped simulations of the 100-year design flood, Q , to generate the probability distribution, $f(y_{max})$, of the true scour. From there, 10,000 realizations of maximum scour depths, y_{max} , were generated. The resulting 10,000 Monte-Carlo simulation-based y_{max} values constitute the probability distribution, $f(y_{max})$. We estimate the reliability curve, $P(Y_{max} > y_{max})$, from this distribution of y_{max} , where Y_{max} is the random variable that represents maximum scour under uncertainty. Such Monte-Carlo simulations are suitable for any random variable distribution type and failure equation. The HEC-18 scour equation, Equation 2, is used to compute the design depth, y_{design} . Note that y_{design} is based on the biased HEC-18 equation and will overestimate the depth. We compute the probability of exceeding this design depth from our reliability curve.

$$p_f = P(y_{max} > y_{design}) \quad (10)$$

In structural reliability, the probability of failure, p_f , is the probability that the resistance R (or the design scour depth) is less than, or equal to, the total applied load effect S (or the true scour depth due to possible uncertainties). Finally, the reliability index, or the beta factor, β , is computed as:

$$\beta = \phi^{-1}(-p_f) \quad (11)$$

where ϕ^{-1} , is the inverse of the standard normal distribution.

The reliability index, β , is often used as a measure of structural safety or risk. Assuming normal probability distributions, it gives the number of standard deviations that the mean margin of safety falls on the safe side. β in the range of 2 to 4 is usually specified for different structural applications (e.g., $\beta = 3.5$ was used to calibrate the Strength I limit state in AASHTO LRFD Specifications). These values usually correspond to the failure of a single component. If there is adequate redundancy, overall system reliability indices will be higher. Readers can find more detailed explanations of the reliability principles in published texts on structural reliability (e.g., Thoft-Christensen and Baker, 1982).

2.3.4 Modeling changing floods

We modeled the long-term trend in the peakflow dataset and assume that this long-term linear trend will continue into the future. By considering the 112 years of data as one dataset with some linear increase in peak streamflow across the decades, this trend can be extrapolated into the future using a modeling approach that estimates the parameters of Gumbel distribution which are allowed to change/increase with time.

The model is described as follows:

$$Q_t \sim \text{Gumbel}(a_t, b_t); t = 2021 : 2121 \quad (12)$$

$$a_t = 10370.83 + 51.71 * t \quad (13)$$

$$b_t = 5868.74 + 43.30 * t \quad (14)$$

Peak yearly flows (Q_t) are assumed to follow a Gumbel distribution with a location parameter (a_t) and scale parameter (b_t), which are both varying over time. The location parameter corresponds to the mean of the distribution and the scale parameter corresponds to the variance of the distribution. The model assumes that the location and the scale parameters are linearly changing over time. We used time (t) as an indicator for this change, but it can be substituted with Global Temperature or Global CO2 emissions data. If this trend in either the location or scale is significant based on the historical observed peak flow data, we assume that in the future, both mean (location) and variance (scale) will change over time and the model will simulate peak flow values from a Gumbel distribution with time-varying parameters. Given this model result, we can simulate future peak flows for a design life of 100 years from a Gumbel distribution whose location and scale parameters vary over time. An example of such realization for the next 100 years starting year 2021 is shown Figure 2. Also shown by a red circle in the realization is the maximum peak flow that may occur in the next 100-year time frame – a 1 in 100-year event, which related to the design flood for the future time frame. Notice that the worst event can occur anywhere in the

100-year time frame, and not always at the end of the design life. Such 100-year realizations can be simulated multiple times in a simulation mode and each time we can record the 1 in 100-year event (future design flood) as the worst event in the realized time frame. Multiple such simulated worst events (in the 100-year time frame) will form the probability distribution of the future design flood, which can then be used with the HEC-18 scour equations to assess the reliability and risk of the design scour depth.

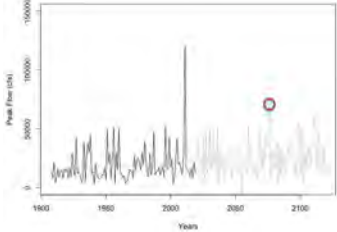


Figure 2. A 100-year realization of the future floods. Red circle shows the maximum flood in the period.

3 RESULTS AND ANALYSIS

3.1 Changes in design flood due to climate change

The results of the model fit to the observed peak flow data from 1908-2019 for the Schoharie Creek are given in Table 3.

Table 3. Climate model parameters.

Parameter	Estimate	Standard error	p-value
Location (intercept)	10371 cfs	1295 cfs	< 0.001
Location (time)	52 cfs/year	24 cfs/year	0.03
Scale (intercept)	5869 cfs	1211 cfs	< 0.001
Scale (time)	43 cfs/year	23 cfs/year	0.05

As we can see both the location and scale have their coefficients (β_a, β_b) to be statistically significant at the 90% and the 95% confidence level. The trend in the location parameter can be seen in the trend line in the plot in Figure 3a. Figure 3b is the density plot showing an initial look at the distribution of the historical and future design floods. The median of the distributions falls at about 48,000 cfs for the historic data, and about 85,000 cfs for the future simulated data. In essence suggesting a nearly 77% increase in expected extreme-event median in the coming 100 years. This increase will lead to a shift in the reliability and risk of bridge design which needs to be reassessed. Figure 3c shows the reliability-curves. They show a change between current anticipated risk based on historical data and future expected risk based on future simulation.

We then used Equation 11 to transform these exceedance probabilities into reliability indices or beta factors. Figure 3d shows these corresponding reliability indices computed from an inverse standard normal distribution for normalized critical depths (y/y_{design}). The normalization is done using HEC-18 design depths as the basis to get the load factors for critical scour depths. A load factor of 1 indicates that the foundation is designed to satisfy the foundation depth requirement of HEC-18. In essence, Figure 3d shows the safety (in terms of a reliability index) for a specific load factor applied on an initial HEC-18 required design scour. We can also use it to choose the load factors for a specified safety or reliability index.

Table 4 shows the Beta table derived from Figure 3d. It shows the calculated design depths with variance for the historical data as its entire 100 years, as well as for the future 100 years if an imposed linear trend is assumed. The base reliability index is approximately 1.4. In Table 4, the difference between HEC-18 and Beta=2.0 scour depths is about a 3 feet increase, whereas an increase from Beta=2.0 to Beta=2.5 is about an additional 3 feet, in both instances of observed

and predicted data. This indicates that given current reliability equations for scour design, a beta of 2.5 would require nearly five feet difference in height from initial designs. Ghosn and Lagasse (2013) have previously argued that a reliability index of 3 is justifiable based on their analysis of base reliability indices for wind loads and ship collision loads. They further recommend a load factor of 2 that would provide reliability in the range of 3. Our results corroborate their recommendations. We also highlight that the load factors are close to 2 for the future data at a reliability index of 3. This increase translates into an increase in the construction costs due to the additional anticipated depth. One can develop a long-term risk and economic assessment to investigate further the implications of the failure due to scour under climate change. This trade-off is important to consider when assessing the proper standard for scour design under climate change.

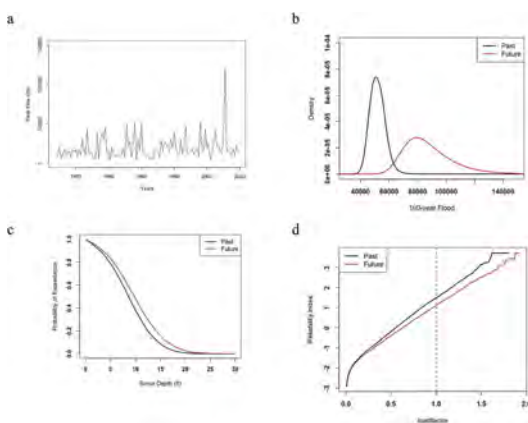


Figure 3. Observed trend in the peak flow data (a). Observed and future simulated 100-year design flood (b). Scour reliability curves based on observed and future simulated 100-year design flood (c). Load factor vs. reliability index (d).

Table 4. Reliability index comparison between historical and future events.

	HEC-18	$\beta = 2$	$\beta = 2.5$	$\beta = 3$
	Design Depth (ft)	Base Reliability Index (β)	Depth (ft)	Load Factor
Historical Data	15.58	1.49	18.22	1.17
Future Data		1.12	20.40	1.31

4 CONCLUSIONS

High-velocity flooding is known to be a major threat to highway bridge safety in the United States. Bridge reliability analysis is an important aspect of risk assessment because bridges can serve as critical access points to otherwise hard-to-reach cities and locations. Using data from Schoharie Creek at Prattsville, NY (USGS gauge 1350000) as a case study with over 100-years of peak streamflow data, we looked into various uncertainty models to better analyze the reliability of bridge foundation scour affected by climate change. Through HEC-18 standards on calculating scour depth based on anticipated peak streamflow, reliability curves were developed. Gumbel distribution were the basis for Monte-Carlo simulations along with uncertainties in bridge parameters for computing the probabilities of exceeding any designed scour depth. The reliability curves were then used to determine which design depths would lead to meeting specific values of target reliabilities.

Future research would include a deeper analysis of financial impacts, including better estimations of cost. The repair costs briefly emulated in this work hinge on the assumption of no total-bridge failure from any extreme event, but that is not always the case. By considering total failures as a possibility and developing bridge construction costs, one could develop Pareto trade-off curves to show the trade-off between repair costs, construction costs, and the implication of various reliability levels. This would entail further research into the history of bridges in the U.S. and their performance-based impact because the larger majority of bridges in the U.S. are nearing their design life expectancies.

REFERENCES

- “National Water Information System: Mapper.” *Water Resources of the United States-National Water Information System (NWIS) Mapper*, USGS, 22 July 2019.
- Collins, M. J., 2009: Evidence for changing flood risk in New England since the late 20th century. *J. Amer. Water Resour. Assoc.*, 45, 279–290.
- Eckholm, Erik. “Covered Bridges, Beloved Remnants of Another Era, Were Casualties, Too.” *The New York Times*, The New York Times, 1 Sept. 2011, www.nytimes.com/2011/09/01/us/01bridges.html.
- Efron, B. and Tibishirani, R.: *An Introduction to the Bootstrap*, Chapman and Hall, New York, 456 pp., 1993.
- Ghosn, M., Moses, F. & Wang J., 2003, Design of highway bridges for extreme events, NCHRP Report 489 Transportation Research Board, the National Academies, Washington DC. USA.
- Hydrologic Engineering Center (1986). “Accuracy of Computed Water Surface Profiles,” U.S. Army Corps of Engineers, DJohnson, Peggy A., and Daniel A. Dock. “Probabilistic bridge scour estimates.” *Journal of Hydraulic Engineering* 124.7 (1998): 750–754.
- Johnson P, Clopper P, Zevenbergen L, Lagasse P. Quantifying uncertainty and reliability in bridge scour estimations. *Journal of Hydraulic Engineering*, 2015, 141: 04015013
- Johnson, P.A. (1995). “Comparison of Pier Scour Equations Using Field Data,” ASCE, *Journal of Hydraulic Engineering*, Vol. 121(8), pp. 626–629.
- K.H. Ahn, R.N. Palmer, Trend and variability in observed hydrological extremes in the United States *J. Hydrol. Eng.*, 21 (2015).
- Lagasse, P. F., Ghosn, M., Johnson, P.A., Zevenbergen, L. W., Clopper, P. E., (2013) Risk-based approach for bridge scour prediction, NCHRP report 2013.
- Milly, P. C. D., K. A. Dunne, and A. V. Vecchia (2005), Global patterns of trends in streamflow and water availability in a changing climate, *Nature*, 438, 347–350, doi:10.1038/nature04312.
- National Academies of Sciences, Engineering, and Medicine 2007. *Risk-Based Management Guidelines for Scour at Bridges with Unknown Foundations*. Washington, DC: The National Academies Press. <https://doi.org/10.17226/23243>.
- National Academies of Sciences, Engineering, and Medicine 2013. *Reference Guide for Applying Risk and Reliability-Based Approaches for Bridge Scour Prediction*. Washington, DC: The National Academies Press. <https://doi.org/10.17226/22477>.
- Richardson EV, Davis SR (2012) Evaluating scour at bridges. Fifth Edition, Hydraulic Engineering Circular No. 18 (HEC-18), US Department of Transportation, Federal Highway Administration, Washington, DC, USA.
- Sharma, S., and Mohan, S.B. (2011) Status of bridge failures in the United States (1800-2009), 2011 Annual Meeting of the Transportation Research Board, Washington D.C.
- Slater, L. J., and Villarini, G. (2016), Recent trends in U.S. flood risk, *Geophys. Res. Lett.*, 43, 12,428–12,436, doi:10.1002/2016GL071199.
- Stedinger, J. Vogel, R., and Foufoula-Georgiou, E. (1993). *Frequency Analysis of Extreme Events*. Handbook of Hydrology. 18.
- T.C. Peterson, R.R. Heim Jr., R. Hirsch, D.P. Kaiser, H. Brooks, N.S. Diffenbaugh, R.M. Dole, J. P. Giovannetone, K. Guirguis, T.R. Karl, R.W. Katz, K. Kunkel, D. Lettenmaier, G.J.McCabe, C. J. Paciorek, K.R. Ryberg, S.Schubert, V.B.S. Silva, B.C. Stewart, A.V.Vecchia, G. Villarini, R. S. Vose, J. Walsh, M.Weher, D. Wolock, K. Wolter, C.A.Woodhouse, D. Wuebbles, Monitoring and understanding changes in heat waves, cold waves, floods and droughts in the United States—State of knowledge, *Bull. Am. Meteorol. Soc.* (2013), pp. 821–834
- Thoft-Christensen, P. and Baker, M.J. (1982) *Structural Reliability Theory and Its Applications*. Springer Verlag, Berlin. <https://doi.org/10.1007/978-3-642-68697-9>.
- U.S. Water Resources Council, 1967, A uniform technique for determining flood flow frequencies, Bulletin No. 15: U.S. Water Resources Council, Subcommittee on Hydrology, Washington, D.C.
- Wardhana, K., and Hadipriono, F.C. (2003) Analysis of recent bridge failures in the United States, *Journal of Performance of Constructed Facilities*, 17 (3) (2003), pp. 144–150.

Positive effects of aligned steel fiber using the electro-magnetic field on flexural behavior of reinforced UHPC beams

Y.M. Xiong, M. Yang, H. Shi & J. Zhao

School of Transportation, Southeast University, Nanjing, China

ABSTRACT: Ultra-High Performance Concrete (UHPC) has ultra-high tensile strength and toughness compared to normal concrete (NC), this advantage often benefits from the higher volume content of steel fibers. Some studies reported that the fibers are randomly distributed in the UHPC matrix, and the effectiveness of fibers is less than 40%. Increasing the fiber content has been proven to be an effective means to enhance the properties of materials, but the problems such as fiber agglomeration and local defects of materials will increase significantly. To solve the above problems, the aligned steel fiber UHPC (ASF-UHPC) was successfully developed by the theory of electromagnetism. The steel fibers aligned in UHPC matrix can optimize the fiber utilization efficiency, improve the material performance and reduce the unit cost. Meanwhile, a series of reinforced ASF-UHPC beams were cast by this method, and the bending test was conducted to study its flexural behavior, failure patterns, and load-deflection relationship. The relative fiber orientation in the reinforced beams was studied by CT 3D image technology, and the difference in flexural properties between ASF-UHPC beam and normal UHPC (N-UHPC) beam was analyzed from the point of view of the orientation of fibers. The research results show that the homogeneous magnetic field can optimize the fiber orientation in reinforced UHPC beams, and the fibers are parallel to the beam, which can improve the flexural load capacity. For instance, when the volumetric ratio of steel fibers is 2%, the flexural capacity of ASF-UHPC beam can be improved by about 24% at a low rebar ratio (0.016). Through the parametric analysis of different fiber volumetric ratios and fiber orientation, the enhancement efficiency of flexural capacity was studied, which provides reference value for improving the mechanical properties of UHPC material, reducing the cost of using UHPC and promoting carbon neutrality.

1 INTRODUCTION

Ultra-high Performance concrete (UHPC) is regarded as the best cementitious composite with superior characteristics such as high strength in compression and tension, ductility, and durability^[1]. However, the unit cost of raw materials always hindered its promotion, it is significant to develop the performance of materials and reduce the unit price. As fiber-reinforced cementitious composites, the mechanical characteristics of traditional concrete are greatly improved by mixing the fiber. The fiber reinforcing effect sourced from the relatively high volume content of steel fibers is the important reason of the superior performance of UHPC, but the enhancement in fiber volume can significantly increase the cost of raw materials^[2].

Therefore, optimizing the spatial state including direction and dosage of fibers is considered as an important means to improve the properties of UHPC materials. The research shows that the orientation and position of steel fibers in conventional steel fiber-reinforced cementing composites (SFRC) are randomly distributed, and the orientation efficiency coefficient in a certain direction is about 40%^[3]. The main way to improve the tensile properties and crack resistance of the cementitious matrix is to align the fibers.

In the present communication, the fiber alignment methods mainly include flow guidance and applied electromagnetic field^[4]. *Stähli P et al.* used the flow-properties of the fresh

(self-compacting) concrete to change the fiber distribution and orientation, which was regarded as the first time in aligning the fibers [5]. Subsequently, many scholars have studied the mechanical properties of UHPC by flow and casting methods, and these methods have drawn some interesting conclusions. *Zhang et al.* improved the device for UHPC casting to align steel fibers, the fibers aligned by self-flowing pouring, and most properties such as initial cracking strength, ultimate flexural strength and corresponding deflection of UHPC are increased significantly [6]. Subsequently, the influence of various flow fields on fiber orientation was analyzed by *Kang et al.*, and the mechanism of orientation through casting was explained [7]. However, it has been found that the UHPC flow will inevitably decay naturally during the flow process due to the conservation of energy, so, the efficiency of orientation will inevitably be unstable [8]. But more importantly, this method cannot be developed in the reinforcement structure with large numbers of densely laid-out steel rebar.

The method of external electromagnetic field to align the steel fibers was proposed by *Mu et. al.*, the paper points out that the orientation efficiency factor of steel fibers in cement mortar is about 0.90 [4]. However, there is still a key problem in the construction of engineering structures with this method, that is, the interference of the steel (such as steel rebar, profile steel, etc.) to the spatial magnetic field distribution. The typical manufacturing program of concrete structures is to first develop the template required for forming, then place the reinforced skeleton, and finally carry out the concrete pouring. Since the rebar is implanted inside the UHPC, the magnetic field must be applied after the UHPC is poured [9]. At this time, the magnetic field in the space region of the structure is bound to be affected by the steel skeleton. Therefore, it is very important to study the internal steel bar for the magnetized directional steel fiber UHPC beam.

The present study focuses on the orientation of steel fibers in freshly cast reinforced UHPC beams, and the possibility of making ASF-UHPC beams by electro-magnetic field. Firstly, the electromagnetic coils used for this study were designed. Then, the orientation of the fibers in the reinforced UHPC beam was scanned using X-ray images. Finally, the 4-point bending test was used to study the flexure mechanical properties of UHPC beams. Four UHPC beams with different fiber volume fractions and magnetic flux density (0mT and 40mT) were tested, and the flexural behaviors were discussed in terms of crack pattern, flexural moment, moment–deflection relationship, and failure mode.

2 DESIGN OF ELECTROMAGNETIC COIL

2.1 *Assembly of electro-magnetic coil*

Electromagnetic coil is a classical equipment used to produce a homogeneous electromagnetic field. A device capable of generating a unidirectional uniform magnetic field was developed, as shown in Figure 1. The test equipment includes a high conductivity copper conductor and a power supply, the wire is coated with a 0.2 mm thick polyether paint, which can effectively avoid short circuit problems and can withstand the high temperature of 120 °C, besides, and the power supply can convert 120V alternating current into 70V direct current. The skeleton of the coil is made of polymethyl methacrylate (PMMA). The PMMA frame has a circular inner space with a diameter of 200mm, which is sufficient to hold the UHPC specimens and ensure the test section is in a uniform magnetic field. During the operation of the electromagnetic coil, the internal magnetic field was measured by a Gauss meter at about 40mT.

3 UHPC BEAM MECHANICAL EXPERIMENT

3.1 *Materials and mixture proportions*

The P II 52.5 Portland cement produced by Nanjing Onoda company in accordance with the Chinese standard GB 175-2007 was used [10]. The mineral admixtures, including silica fume (SF), and fly ash (FA) were used to partially replace cement. The mix proportion of the UHPC dry mixture is summarized in Table 1. The aggregates consist of 80% coarse sand and 20% fine

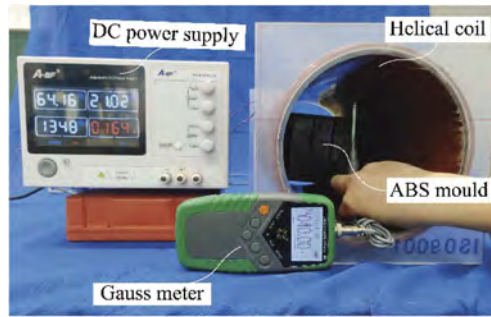


Figure 1. Details of the electromagnetic equipment.

sand with the particle size range of 380-830 μm and 180-380 μm , respectively. The polycarboxylic acid superplasticizer used in this study was provided by Jiangsu Sobute New Materials Co., Ltd. with a water reduction range of greater than 30% and a solid content of about 40%.

Table 1. Mix proportion of UHPC dry mixture (by weight ratio to cement).

Cementitious material					
Cement	Silica fume	Fly ash	Sand	Water	Superplasticizer
1	0.34	0.28	1.1	0.32	0.018

3.2 UHPC material properties

In order to study the mechanical properties of UHPC materials with different fiber volume fractions of 1.0%, 2.0%. Test up of UHPC material properties tests is shown in Figure 2. Three prismatic specimens (100 mm \times 100mm \times 300 mm) were poured to determine the basic compressive behavior of the materials, and three flexural specimens (100 mm \times 100 mm \times 400mm) were prepared to determine the flexural behavior. All test results are listed in Table 2.

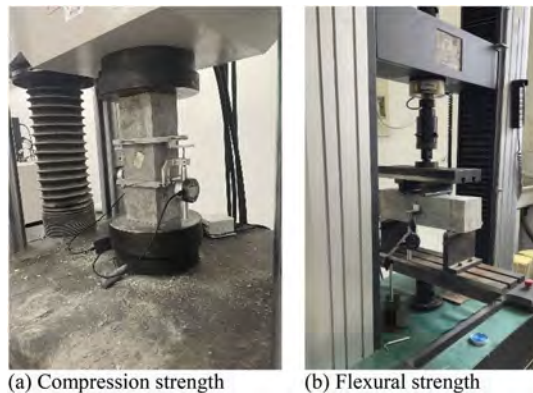


Figure 2. Test up of UHPC material properties tests.

Table 2. Material properties of the UHPC.

Material properties	Batch 1	Batch 2
Volume fraction of fiber (%)	1.0	2.0
Compressive strength (MPa)	105.75	119.56
Flexural strength (MPa)	11.80	18.83

3.3 Details of structural test specimen

In this test, the experimental program included tests on a total of 4 beam specimens are shown in Table 3, the all beams have rectangular cross sections of 100 mm × 100mm and length of 515 mm. The volume capacity of the electromagnetic coil is fixed, and the size of the beams is selected according to these conditions. It must be noted that the beam width was designed to satisfy the requirement that the adjacent longitudinal rebar spacing was greater than 1.5 times the steel fiber length, and the thickness of structural protective layer fulfills the code [11]. The beams were reinforced by Hot rolled ribbed steel reinforcements graded as HRB400, The mechanical properties of the steel reinforcement are shown in Table 4. Because the steel fibers can greatly improve the tensile strength of the cement matrix composites, all test beams were designed to have lower reinforcement ratios (less than or equal to 2%), the longitudinal reinforcement ratio ρ_s calculated by the equation of A_s/bd were set as 1.6 %. Since the oriented fiber technology increases fiber utilization efficiency, it is more meaningful to seek for mechanical properties with lower fiber content, the Volume fractions of fiber were set as 1.0 % and 2.0 %, respectively.

Beam specimens are divided into ASF-UHPC beam and N-UHPC studies. ASF-UHPC beam needs to be placed in the electromagnetic coil when the magnetic flux density is 40mT, the specimen number named M40. N-UHPC beam placed away from the electromagnetic coil, the ambient magnetic flux density is about 0mT, so specimen number named M0.

Table 3. Parameters used in the experimental program.

Specimen	F10M0	F10M40	F20M0	F20M40
Volume fraction of fiber (%)		1.0		2.0
Magnetic field intensity (mT)	0	40	0	40

Table 4. Properties of steel reinforcement bars.

Diameter d_s (mm)	Area A_{s1} (mm ²)	Elastic modulus E_s (GPa)	Yield strain ϵ_s (mm)	Yield strength f_y (MPa)	Ultimate strength σ_{ul} (MPa)
10	78.5	206.4	2348.7	483.6	640.2

3.4 The fabrication of the experimental beam

The production process of the UHPC experimental beams is as follows. Firstly, the assembly of the UHPC beam assembly is shown in Figure 3(a). A square groove made of ABS plastic was used as a mold for test beam casting. A pair of 1mm thick PVC plates fitted precisely to the dead end, and the spatial position of the steel bars are precisely controlled by means of preset scale lines.

Next, a forced mixer is used to mix the UHPC (Figure 3(b)). In order to avoid this unstable effect, the casting process adopts uniform casting along the long direction of the UHPC beam. The steel fibers in the UHPC matrix are closer to random distribution.

After finishing the UHPC casting process, a test beam was placed in the electromagnetic coil (Figure 1) to be magnetized while the same beam was placed in an ordinary environment, the time was controlled to 120s in this process. Then, all specimens were covered with preservative film and cured at curing chamber (20°C±2°C, HR≥95%) for 48 h. Finally, the specimens were cured in steam curing equipment (90°C±2°C, HR≥95%). After steam curing for 48 h, the specimens were gently cooled to ambient temperature for testing.

3.5 Loading procedures of beams

A four-point bending test with a pure bending length of 150 mm was performed on the UHPC beams, as shown in Figure 4. To obtain the deformation of the UHPC beams, three linear variable displacement transducers were arranged at the mid-span and supporting positions.

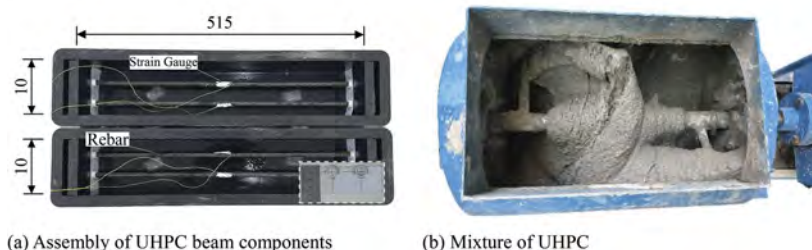


Figure 3. Details of test program (unit: mm).

In the initial loading stage, 5 kN was used as the first loading interval until the cracking load was reached. Then, 10kN was used as the second loading interval (adjusted according to the predicted bearing capacity). When the applied load reached 90% of the predicted ultimate load, the displacement in the mid-span was used to control the loading rate. The test ended once the load value was lower than 85% of the ultimate load. During the loading process, every loading stage was held for 5 min and the crack distribution, load, deflections, and strains were recorded simultaneously. The testing machine in laboratory controlled by an electrohydraulic servo loading system has sufficient accuracy to complete the test.

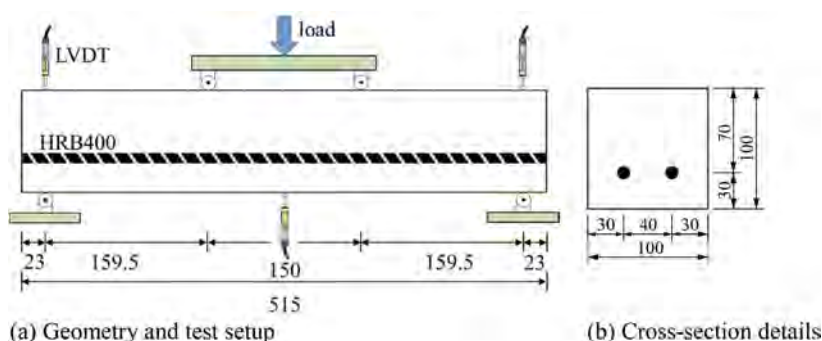


Figure 4. Details of test program (unit: mm).

4 RESULTS AND DISCUSSIONS

4.1 Magnetic orientation of fibers in UHPC

Use The distribution of fibers in UHPC detected by CT-ray is called the gold standard in this field ^[12]. In order to ensure the characterization accuracy of fiber distribution in UHPC, the measurement method should not be affected by the wall. In this study, the sample (100 mm × 100 mm × 50 mm) was cut to test the fiber distribution, as shown in Figure 5. The position of the rebar and the distribution of steel fibers can be seen in the section diagram. The cross-section of the steel bar looks regular, and the cross-section of the steel fiber is like a small dot, indicating that these components are vertically distributed with the cross-section of the sample.

The Micro-focused Computed Tomography (Y.CT Precision S) produced by YXLON was used to obtain the microstructure information of the sample. The identification of different materials from CT images is based on the density of the materials. The higher the density of the material, the higher the grayscale of the CT image. Because the density of steel fiber is much higher than other materials, so the image of steel fiber is easy to be extracted. The distribution features of steel fibers as shown in Figure 6.

The fiber distribution in the UHPC sample obtained by the classical concrete pouring method is shown in Figure 6(a), the reconstruction and qualitative visualization of 3D images

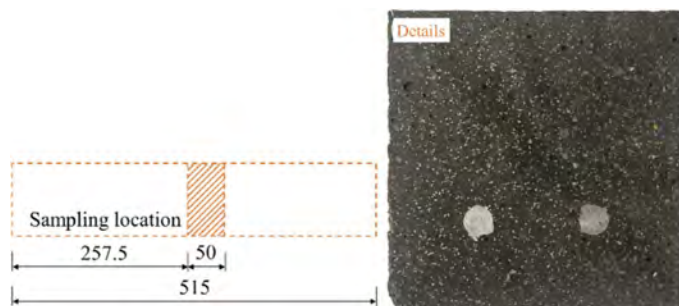


Figure 5. Sampling location of test sample (unit: mm).

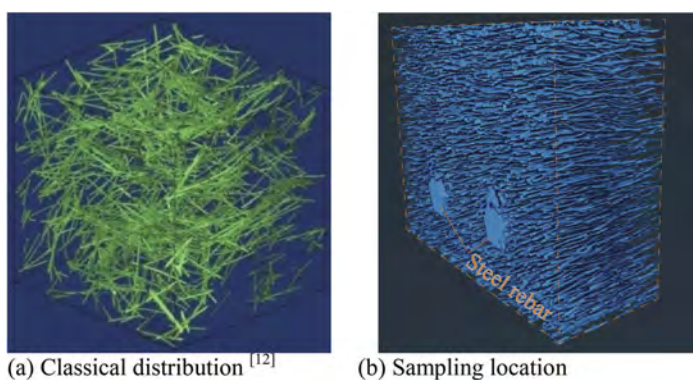


Figure 6. Fiber orientation in UHPC.

from micro-CT were reported by *Liu et al* [12]. As can be seen from the Figure 6(b), the fibers are uniformly distributed in the cement matrix, and the vector direction of the fibers is not clear. In bridge engineering, the direction of principal stress is often regular, and the random distribution of fibers has lower utilization efficiency.

In this study, the fiber distribution in the parts of the sampling location is shown in Figure 6 (b). It can be seen that the distribution characteristics of fibers in UHPC matrix. The two thicker parts represent the rebar bars in the picture, while the remaining small lines are the steel fibers. Obviously, the fibers in the UHPC matrix are distributed uniformly. It indicates that the orientation of the steel fiber in UHPC matrix is the same as that of the steel rebar, so it can coordinate with the steel bar to resist the tensile stress.

4.2 Load–deflection relationship and crack pattern

Figure 7 shows the four-point flexural test results of the reinforced UHPC beams. The left side of the figure shows the load mid-span deflection curve with different fiber volume fractions, and the deflection measurement has corrected the deformation of the test system. The corresponding mid-span cracking failure mode of the test beam is displayed on the right side of the figure. The direction of fracture development and the area of the largest cracks are in the pure bending location of the beam, which indicate that the test results are relatively reliable. With the increase of fiber content, the expression of the strain-hardening behavior of the material was higher. Although the bottom of the beam has narrow cracks at many positions during the loading, a large single crack is basically formed in the weak area.

The mechanical properties of UHPC beams structure are qualitatively analyzed by the load-deflection curve of the whole process, some key data are listed in Table 5. At the beginning of loading, the UHPC beam is in the elastic stage. The young's modulus of each beam can be

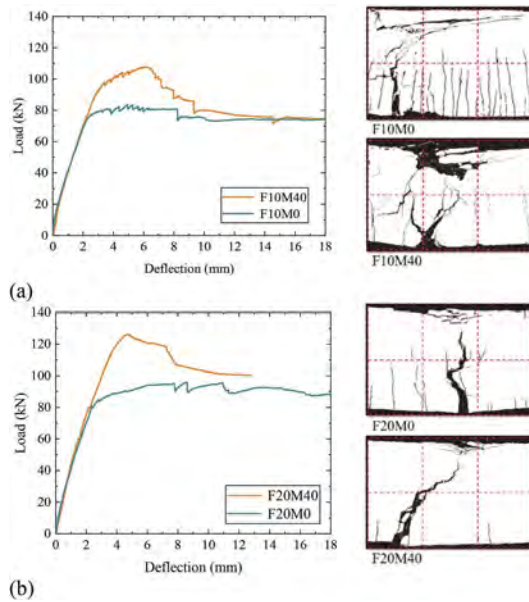


Figure 7. Load–deflection relationships and crack patterns.

deduced by applying the Euler-Bernoulli beam theory, Comparing classical UHPC beam with aligned steel fiber UHPC beam, the initial Young's modulus of these specimens is not much different. As can be seen from Table 5, aligning steel fibers provide approximately 20% (average) strength improvement over classical UHPC reinforced beams. Comparing the test results of 1% and 2% fiber volume content, it is not difficult to see that the strength index of the 1% directional steel fiber test beam (F10M40) is higher than the of 2% classical test beam (F20M0). That means that the method could halve the amount of steel fiber needed for the same mechanical performance material. So, the fiber alignment process significantly increased the yield load and peak load of each specimen, this could reduce the cost of UHPC and help spread green prefabricated UHPC structures.

Table 5. Summary of flexural test results for beams.

Name	Fiber volume fraction (%)	Yielding state		Peak state			
		P_y (kN)	Increase ratio (%)	D_y (mm)	P_p (kN)	Increase ratio (%)	D_p (mm)
F10M0	1.0	76.21		2.44	83.52		4.94
F10M40	1.0	94.53	19.4	3.15	107.77	22.5	6.10
F20M0	2.0	83.98	25.9	2.84	95.88	24.0	8.53
F20M40	2.0	113.40		3.62	126.24		4.74

* P_y = load at steel rebar yield, D_y = deflection at steel rebar yield, P_p = peak load, D_p = deflection at the peak.

5 CONCLUSIONS

This study starts from the aligning steel fibers using the electromagnetic field, the distribution characteristics of steel fibers in reinforced beams were studied, and the conclusions follow:

1. It is an effective and feasible method to align the steel fibers of UHPC reinforced beam with the magnetic field, the steel fibers can still keep parallel to the magnetic lines in the mid-span of the beam. This method can effectively drive the steel fibers in the UHPC reinforced beam parallel to the long direction of the beam, and improve the utilization efficiency of steel fibers in the UHPC matrix.
2. In reinforced beams, the steel fibers parallel to the stress direction in the mid-span of the beam, which can enhance the resistance to bending and tensile properties. Compared with the traditional UHPC reinforced beams, the oriented steel fibers can well strengthen the yield load and peak load of the beams.
3. Aligning the steel fibers by magnetic field has a large application space in UHPC structure and structure manufacturing under factory conditions. It can greatly reduce the unit cost and improve the structural carrying capacity without increasing the fiber content. This green manufacturing method using electro-magnetic field devices can be recycled and provide objective value for global carbon neutrality.

ACKNOWLEDGEMENTS

The study of this paper is financially supported by the Foundation Research Project of Jiangsu Province (Grant No. BK20221472), Innovative Project of Key Disciplines with Advantages and Characteristics of Key Laboratory for Safety Control of Bridge Engineering of Ministry of Education in Changsha University of Science and Technology (Grant No. 15KD01).

REFERENCES

- [1] Qin, J., Dai, F., *et al.* 2022. Development and characterization of magnesium phosphate cement based ultra-high performance concrete. *Composites Part B: Engineering*, 234, p.109694.
- [2] Yoo, D.Y., Kim, S., Park, G.J., Park, J.J. and Kim, S.W., 2017. Effects of fiber shape, aspect ratio, and volume fraction on flexural behavior of ultra-high-performance fiber-reinforced cement composites. *Composite Structures*, 174, pp.375–388.
- [3] Huang, H., Gao, X., Li, L. and Wang, H., 2018. Improvement effect of steel fiber orientation control on mechanical performance of UHPC. *Construction and Building Materials*, 188, pp.709–721.
- [4] Mu, R., Li, H., Qing, L., Lin, J. and Zhao, Q., 2017. Aligning steel fibers in cement mortar using electro-magnetic field. *Construction and Building Materials*, 131, pp.309–316.
- [5] Stähli, P., Custer, R. and van Mier, J.G., 2008. On flow properties, fibre distribution, fibre orientation and flexural behaviour of FRC. *Materials and structures*, 41(1), pp.189–196.
- [6] Zhang, Y., Zhu, Y., Qu, S., Kumar, A. and Shao, X., 2020. Improvement of flexural and tensile strength of layered-casting UHPC with aligned steel fibers. *Construction and Building Materials*, 251, p.118893.
- [7] Kang, S.T. and Kim, J.K., 2012. Numerical simulation of the variation of fiber orientation distribution during flow molding of ultra high performance cementitious composites (UHPC). *Cement and Concrete Composites*, 34(2), pp.208–217.
- [8] Alberti, M.G., Enfedaque, A. and Gálvez, J.C., 2017. On the prediction of the orientation factor and fibre distribution of steel and macro-synthetic fibres for fibre-reinforced concrete. *Cement and Concrete Composites*, 77, pp.29–48.
- [9] Yang, M., Tian, L., Yuan, Y. and Yang, Z., 2021. The study on composite trough beam with corrugated steel web wrapped with steel plate: Experiment and bending properties. *Journal of Constructional Steel Research*, 185, p.106853.
- [10] Wijffels, M.J.H., Wolfs, R.J.M., Suiker, A.S.J. and Salet, T.A.M., 2017. Magnetic orientation of steel fibres in self-compacting concrete beams: Effect on failure behaviour. *Cement and Concrete Composites*, 80, pp.342–355.
- [11] Khaksefidi, S., Ghalehnovi, M. and De Brito, J., 2021. Bond behaviour of high-strength steel rebars in normal (NSC) and ultra-high performance concrete (UHPC). *Journal of Building Engineering*, 33, p.101592.
- [12] Liu, J., Li, C., Liu, J., Cui, G. and Yang, Z., 2013. Study on 3D spatial distribution of steel fibers in fiber reinforced cementitious composites through micro-CT technique. *Construction and Building Materials*, 48, pp.656–661.

Service-life extension of transport infrastructure through structural health monitoring

M. Domaneschi & R. Cucuzza

Politecnico di Torino – DISEG, Turin, Italy

L. Martinelli

Politecnico di Milano – DICA, Milan, Italy

M. Noori

California Polytechnic State University, San Luis Obispo, USA

Visiting Professor, School of Civil Engineering, University of Leeds, Leeds, UK

ABSTRACT: Transportation Infrastructure systems are recognized as essential for economic development, territorial cohesion, and social transformation. Unfortunately, some of the key structural components of this massive system, such as bridges, are rapidly ageing, while load conditions are exceeding those for which these systems initially envisaged as they are subjected to different hazards, such as natural events or new man-made phenomena. Given that a substantial portion of the current bridge stock was constructed many decades ago, degradation phenomena and a rise in service conditions greater than those employed in the original design may have contributed to reducing the reliability level, if countermeasures are not adopted. Therefore, the assessment of the current state and the prediction of the future condition of Transportation Infrastructure, and their protection against external hazards, turn out to be essential. This contribution firstly focused on an in-depth study of the role of structural health monitoring in improving the structural resilience of transportation infrastructure and consequently its life-cycle. Subsequently, a practical example is provided to highlight the role of SHM toward structural resilience improvement for an Italian common transport infrastructure.

1 INTRODUCTION

With respect to a variety of causes, including corrosion brought on by severe weather conditions and fatigue damage, steel structures are vulnerable to time-dependent degradation and aging effects. Due to the extensive usage of steel bridges in many nations across the globe, the economic implications of these consequences are especially pertinent. Steel girders that are exposed to sea water and atmospheric corrosion deteriorate over time. In addition to other things, corrosion reduces the original thickness of connections and profiles, such as the web and flanges of steel I-girders. The damage affects the element's and section's structural characteristics owing to thickness decreases brought on by corrosion penetration (e.g. strength and stiffness) (Biondini & Frangopol 2016).

The issue of life-cycle of bridges with respect to degradation phenomena, such as corrosion and fatigue, has been investigated in the literature. The cumulative seismic damage and corrosion effects on bridges' life-cycle is deepened by Kumar et al. (2009) highlighting how the the cumulative seismic damage affects the structural reliability over time more than corrosion. The issue of corrosion deterioration effects on the seismic response of RC bridge piers has been also studied by Bartolozzi et al. (2022). The role played by bonding in the degradation of the seismic capacity has been highlighted.

With specific respect to transport infrastructure management, Kim et al. (2013) proposes a framework for structural inspection and maintenance planning, highlighting how the dependence between the appropriate maintenance and the damage degree. Aspects related to analysis and decision-making for assessing bridge life-cycle performance and cost have been deepened in Frangopol et al. (2017), considering also climate change and structural health monitoring. Life-cycle reliability, risk and resilience-based design of transportation infrastructures have been studied by Akiyama et al. (2020), highlighting the importance of studying both independent and interacting hazards to assess the bridge reliability (e.g. earthquake and tsunami, or landslide).

The relationship between structural health monitoring (SHM) and the life-cycle of bridges has been discussed in the literature, e.g. in the review work by Biondini & Frangopol (2016). Focusing on railway bridges, their reliability assessment and the role played by SHM has been studied by Vagnoli et al. (2018), comparing different types of structural health monitoring methods (e.g. model, non-model).

Despite the improvements in the knowledge provided by the existing literature, the impact of SHM in the life-cycle of transport infrastructures would need a further in-depth study. To this end, this contribution is offered; specifically to investigate how SHM can positively influence the resilience and, consequently, the life-cycle of bridge structures.

The next section brings together some aspects related to SHM toward structural resilience improvement. The following one provides an application example to highlight the relationship between structural health monitoring, resilience, and life-cycle.

2 SHM CONTRIBUTION TO STRUCTURAL RESILIENCE AND LIFE-CYCLE

2.1 *Diagnosis and prognosis*

Damage diagnosis enables decision-makers to be informed about the various forms of deterioration in civil engineering structures and the proper course of action to take in response to dangerous structural circumstances. Damage detection, localisation, quantification, and prognosis are the core stages of structural health monitoring (SHM) for damage diagnosis. The four stages may be described in more depth as follows:

- Phase 1: Determining if the building has been damaged.
- Phase 2: Phase 1 plus determining the geometric location of the damage.
- Phase 3 comprises Phase 2 and a calculation of the damage intensity.
- Phase 3 plus the assessment of the structure's remaining service life is Phase 4.

The first two steps serve as the primary pillars of the most used vibration-based damage diagnosis approaches (without the use of structural models). Phase 3 damage diagnosis may sometimes be accomplished by integrating vibration-based methods with a structural model. Phase 4 is still a difficult engineering challenge that needs interdisciplinary and predictive modelling skills, but it might provide enormous safety and financial advantages to the management of structures and infrastructure (Faravelli & Casciati 2004; Cheung et al. 2008; Domaneschi et al. 2017; Morgese et al. 2021).

A review of the literature on the many methods for spotting damage and keeping track of a structure's health based on changes in its observed dynamic characteristics is given by Doebling et al. in 1996. They are based on

- modifying modal features,
- altering dynamic flexibility,
- updating structural matrices while undergoing restricted optimization,
- nonlinear approaches,
- and neural network-based techniques.

Many of the techniques rely on a dataset of the undamaged structure as a baseline, while others need access to a comprehensive FEM of the structure to get more understanding and access to higher levels of data (e.g. quantification). The number of sensors in an SHM system has expanded over the last ten years due to significant advancements in growing processing

power and sensing technology, which in turn has led to an increase in the amount of data gathered. Advanced processing techniques are required to be used to handle this massive volume of data to transform the heterogeneous, multi-source data into various sorts of particular indications and enable efficient inspection, maintenance, and management choices. As a result, the scientific community has seen an increase in the usage of automated algorithms for data management, calculation, and structural (such as damage) detection.

Machine learning techniques, particularly deep learning algorithms, have been more useful and extensively used in vibration-based structural damage diagnostics because of their elegant performance and frequent, exacting correctness. The first involves data preparation (human involvement) to extract certain features or qualities, in contrast to the second, which may find a straight mapping from the initial inputs to the final outputs without the need for feature extraction. Deep learning is thus effectively used to handle massive volumes of data (big data) for many purposes (Avci et al. 2021).

In addition to Deep Learning, a combination of Wavelet and other time-frequency analysis and feature extraction techniques have been recently developed and applied for the processing of big data from sensor networks for the health assessment of bridge structures (Silik et al. 2022; Ghiasi et al. 2020).

2.2 *Structural resilience and dimensions*

Robustness, resourcefulness, redundancy, and rapidity are the four main components, or dimensions, of resilience, according to MCEER researchers (Bruneau & Reinhorn 2007). In detail: (1) Robustness refers to a structure's or an element's capacity to tolerate a certain amount of demand (such as damage) while retaining its usual degree of usefulness. Alternatively, one may refer to it as the idea of damage tolerance. (2) Redundancy, for instance, of load-bearing components: the capacity to create alternate load-supporting paths after the deterioration of the primary parts has a place (i.e., original elements that are replaceable); (3) Resourcefulness: The capacity to recognize problems, establish priorities, and gather materials when conditions pose a risk to the stability of the structure or one of its components; (4) Rapidity: The capacity to prioritize interventions and complete them as soon as possible to minimize losses, restore functioning, and stop additional interruptions.

There have been several studies published to help us understand structural resilience in buildings. The Resilience approach proposed by Cimellaro et al. (2010) for a condensed recovery plan is one example. The notion of immediate resilience is proposed in Domaneschi & Martinelli (2016) as being related to the automated function of certain components to make up for local out-of-services. Structural resilience has also been explored in many areas.

2.3 *SHM toward structural resilience*

The relationship between resilience and emerging digital technologies including the structure and infrastructure monitoring is a topic that has attracted the interest of the scientific community worldwide in recent years (Domaneschi et al. 2021; Wu et al. 2020).

Structural resilience is herein assumed as a Performance Indicator for life-cycle considerations of transport infrastructures accordingly with Biondini & Frangopol (2016). Following the identification of the four distinct SHM levels and the Resilience dimensions, a relationship between them can be drawn to show how the four SHM phases may be used as effective tools and methods for the assessment and enhancement of the Resilience dimensions (Domaneschi & Cucuzza 2023). Figure 1 reports the scheme with the conceptual connection between SHM phases and resilience dimensions.

If Damage Detection is taken into account as the initial level of the SHM, the information presented is the existence or absence of structural damage. It is impossible to provide any information about the location or severity of the damage. In this condition, the redundancy dimension of the same structure is directly related to the damaged state of the structure.

A redundant structure proves to be safer than a statically determined one, regardless of the sort of damage. Due to the structure's inherent lack of redundancy, the experience of the

Polcevera's Viaduct in Italy demonstrates that the issue of corrosion of the steel strands inside the concrete stays reasonably reflected the primary cause of the disaster (Domaneschi et al. 2021). For this reason, to implement the appropriate countermeasures, such as emergency measures (e.g. evacuation, traffic reduction, shutting of critical facilities), the simplest information on the presence of diseases in the structures through SHM techniques must be associated with the grade of redundancy of the structure.

Damage Localization, the second level of SHM, is related to the Rapidity dimension of resilience. The speed of the intervention and recovery stages is critical after the pathology has been identified and any localized or diffuse damage has been localized. In this situation, the SHM system may aid in decision-making to manage the emergency effectively while accelerating interventions that follow a prioritized plan.

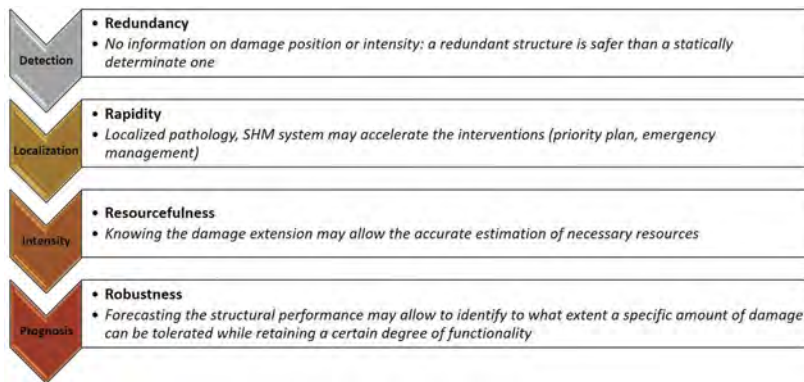


Figure 1. SHM toward structural resilience.

It is also possible to identify a connection between the Resourcefulness dimension and the third degree of Damage Intensity. The organizing and recovery phases are successfully supported by knowledge of the extent of the damage after disruptions, enabling the precise assessment of the resources that will be required.

The Prognosis level of SHM, the fourth level, is connected to the Robustness attribute of resilience. Given an evaluation of the structure's present state, the estimation of the structure's remaining life is the key subject. This SHM level attempts to predict the structural performance to withstand a given level of damage while maintaining its normal level of functionality, offering an indirect measure of structural robustness.

Thus, in light of this description and the relationships highlighted, the significance of implementing monitoring systems on structures and infrastructure to improve their resilience and safety, thereby extending their life cycle, becomes evident.

2.4 SHM toward resilience, quantitative aspects: Functionality and indices

The effect of degradation on the infrastructure is to affect and reduce its functionality. This is in association with loading conditions acting on the infrastructure, be they service actions or shocks such as severe weather conditions or medium to high intensity earthquakes. The reduction in functionality is the benchmark for calculating the infrastructure resilience (Vishwanath & Banerjee 2019).

Being able to take timely countermeasures to maintain the infrastructure before degradation significantly reduces functionality and thus becomes a critically important issue. SHM actions are intended in this direction, as they enable the restoration of functionality and thus improve infrastructure resilience. Depending on the level of SHM that can be developed on the infrastructure (from damage detection to prognosis), it will be possible to affect and improve resilience at different levels.

The detection of damage (SHM Phase 1) has a different weight on the further location information about the maintenance and functionality restoration of the infrastructure (Figure 2). And therefore, resilience R will also be positively affected by a more comprehensive SHM process that includes not only simple information about the presence of damage but also its location and quantification, to improve the speed of intervention and prepare resources for restoration as quickly as possible. A linear restoration curve has been shown in the figure for simplicity.

Moreover, Figure 2 highlights also the information related to the residual service life of the infrastructure, provided by the last and more complex SHM Phase related to predictive scenarios.

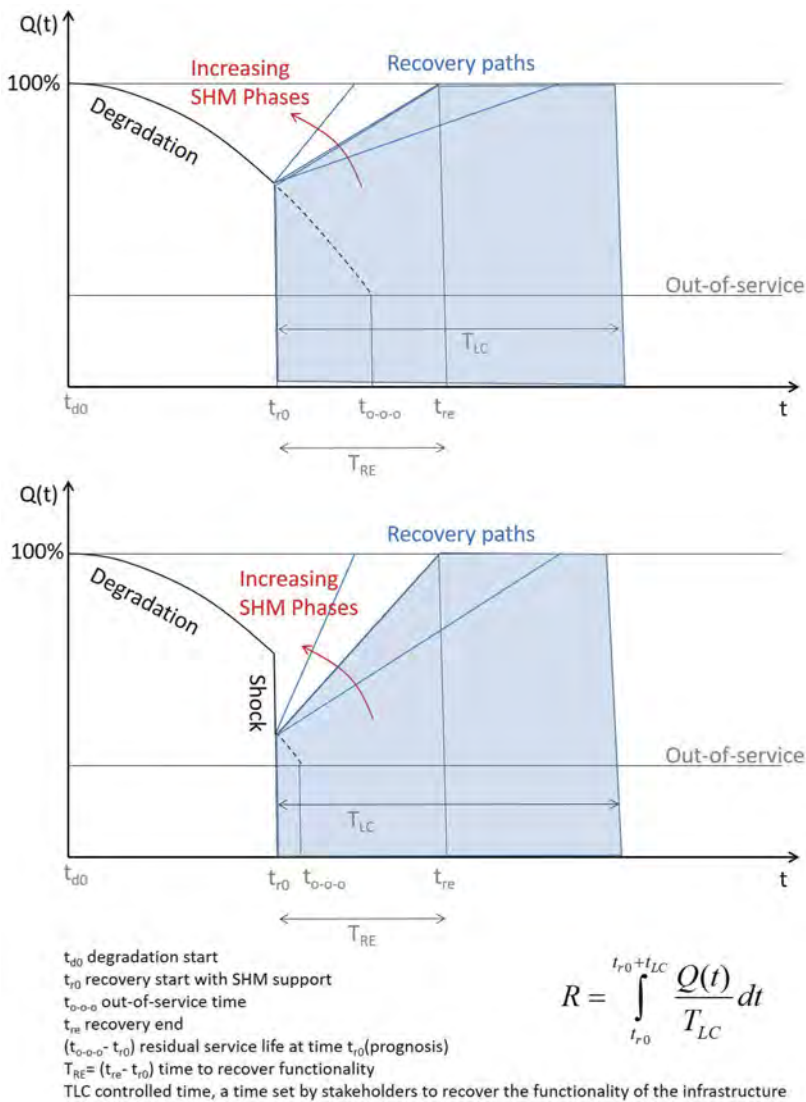


Figure 2. Resilience function: degradation only (top), and degradation with shock (bottom).

3 APPLICATION

This section provides an application example on resilience assessment of comparison between one condition without and another with a monitoring system for a reinforced concrete (RC) and prestressed concrete (PC) girder viaduct in Italy that is made up of 10 spans that are each 40 meters long. On Italian territory, this is a very frequent case study. It is a highway viaduct with three transit lanes that has been deteriorating for 20 years, starting from the time it was put into service, due to phenomena like, for instance, corrosion. A shock has been also considered, such as a significant earthquake that happened in the 20th year of the bridge's operation life.

Specialists and administrators with decades of experience in Italy's road infrastructure were consulted to quantify some useful parameters for the resilience evaluations presented in this section.

It is worth underlining that the present study is not focused on assessing the origin or the evolution of degradation; moreover, it is assumed that the monitoring system is able to detect, locate, and reasonably quantify the intensity of the damage. Figure 3 presents the functionality curves, representative of the two case studies under investigation, adopted for the present case study.

During the first 20 years after the viaduct is put into service, a reasonable reduction (roughly from 100% to 92%) in functionality due to various degradation phenomena in the structural components or, for example, even in the asphalt surface of the road, can be observed. In the 20th year an additional localized disturbance is superimposed, represented for example by an earthquake event that punctually and drastically reduces the functionality to 30% (i.e., a smaller transit lane in order to control and limit loads on the damaged infrastructure - one reduced transit lane open over three in total).

From this point, two different paths are highlighted: one represented by the infrastructure without a monitoring and damage detection system and the other where there is a monitoring system that can also locate and assess the intensity of damage with reasonable accuracy.

Both paths highlight common functionality recovery steps that can be represented by the following restoration actions: (i) opening of an alternative route outside the highway on district roads (37% functionality), (ii) widening of the already active highway lane to all vehicles (50% functionality), (iii) opening of a second highway lane (70% functionality), (iv) full opening of the infrastructure's lanes to the vehicle (95% functionality).

However, the presence of the monitoring system makes it possible to reduce the development time for some of the characteristic steps in the process of restoring functionality. In particular, it is reasonably possible to reduce the time for inspection and damage assessment from 2 months to 1 month.

The designer's choice (1 month) doesn't change, while the technical and economic feasibility design benefits from the more detailed and timely information provided by the implemented SHM system (estimated from 2 months to 1 month).

The administrative phase of publication of the call for bids did not change (1 month), while the final and executive design reasonably reduces the timelines from 2 to 1 month, again based on the quality of the information provided by the SHM system.

Finally, the intervention phase on the supports and structural components has also been speeded up from an estimated 10 months with the intervention of two teams working independently and simultaneously on the infrastructure to 6 months total.

The last phase of testing, estimated at 2 months, is assumed unchanged.

As a result of the considerations above, the resilience of the infrastructure for the case under consideration increases from the value of 0.57, without a monitoring system, to 0.71.

4 CONCLUSIONS

The research conducted in this paper delved into the relationship between structural health monitoring (SHM) and resilience, with a focus on how an efficient monitoring system can contribute to the improvement of structural resilience. Through the present exploration, it has

become apparent that monitoring activities have the potential to enhance the safety and resilience of structures and infrastructure, thereby prolonging their life cycle.

The development of a viaduct application has allowed to showcase the practical demonstration of the concepts discussed in this paper. By showing how monitoring activities can provide early warning signs of potential damage and enable rapid response to mitigate risks, it has been highlighted how an efficient monitoring system can be an essential tool in promoting the resilience of structures and infrastructure.

The analysis has also revealed that the effectiveness of a monitoring system in improving the resilience of structures and infrastructure is directly related to its ability to analyze damage-related factors and their evolution with increasing complexity. This requires not only the acquisition of data but also the capacity to interpret it and to identify the potential causes of damage, enabling preventative measures to be implemented before severe damage occurs.

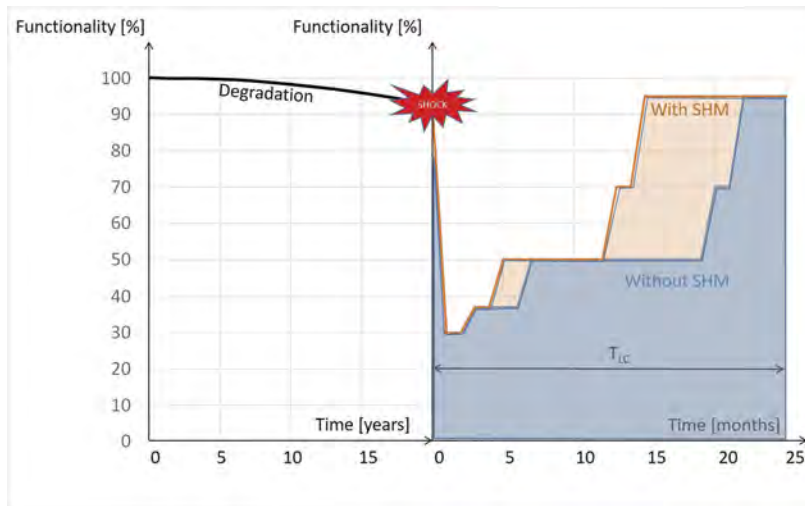


Figure 3. Viaduct application, resilience assessment: w/o and with SHM.

In conclusion, this research has highlighted the crucial role that monitoring activities can play in improving the resilience and safety of structures and infrastructure. By enhancing the capacity of monitoring systems to analyze damage-related factors with increasing depth and complexity, a more comprehensive understanding of structural health and enable the development of targeted interventions to mitigate risks and promote resilience can be provided.

REFERENCES

- Akiyama, M., Frangopol, D. & Ishibashi, H. Toward life-cycle reliability-, risk-and resilience-based design and assessment of bridges and bridge networks under independent and interacting hazards: emphasis on earthquake, tsunami and corrosion. *Structure And Infrastructure Engineering*. **16**, 26–50 (2020).
- Avci, O., Abdeljaber, O., Kiranyaz, S., Hussein, M., Gabbouj, M. & Inman, D. A review of vibration-based damage detection in civil structures: From traditional methods to Machine Learning and Deep Learning applications. *Mechanical Systems And Signal Processing*. **147** pp. 107077 (2021).
- Bartolozzi, M., Casas, J. & Domaneschi, M. Bond deterioration effects on corroded RC bridge pier in seismic zone. *Structural Concrete*. **23**, 51–66 (2022).
- Biondini, F. & Frangopol, D. Life-cycle performance of deteriorating structural systems under uncertainty: review. *Journal Of Structural Engineering*. **142**, F4016001 (2016).
- Bruneau, M. & Reinhorn, A. Exploring the concept of seismic resilience for acute care facilities. *Earthquake Spectra*. **23**, 41–62 (2007).

- Cheung, A., Cabrera, C., Sarabandi, P., Nair, K., Kiremidjian, A. & Wenzel, H. The application of statistical pattern recognition methods for damage detection to field data. *Smart Materials And Structures*. **17**, 065023 (2008).
- Cimellaro, G., Reinhorn, A. & Bruneau, M. Framework for analytical quantification of disaster resilience. *Engineering Structures*. **32**, 3639–3649 (2010).
- Doebbling, S., Farrar, C., Prime, M. & Shevitz, D. Damage identification and health monitoring of structural and mechanical systems from changes in their vibration characteristics: a literature review. (Los Alamos National Lab. (LANL), Los Alamos, NM (United States), 1996)
- Domaneschi, M., Cimellaro, G., Xie, L., Bruneau, M., Wu, Z., Didier, M., Noori, M., Mufti, A., Lu, X., Lu, X. & Others Present and future resilience research driven by science and technology. *International Journal Of Sustainable Materials And Structural Systems*. **5**, 50–89 (2021).
- Domaneschi, M. & Cucuzza, R. Structural Resilience through SHM: a critical review. In M. Noori, C. Rainieri, M. Domaneschi, V. Sarhosis, “Data Driven Methods for Civil Structural Health Monitoring and Resilience: Latest Developments and Applications”, CRC Press. In Press (2023).
- Domaneschi, M., Limongelli, M. & Martinelli, L. Vibration based damage localization using MEMS on a suspension bridge model. *Smart Struct. Syst.* **12**, 679–694 (2013).
- Domaneschi, M., Limongelli, M. & Martinelli, L. Wind-Driven Damage Localization on a Suspension Bridge. *Baltic Journal Of Road Bridge Engineering (Baltic Journal Of Road Bridge Engineering)*. **11** (2016).
- Domaneschi, M. & Martinelli, L. Earthquake-resilience-based control solutions for the extended benchmark cable-stayed bridge. *Journal Of Structural Engineering*. **142**, C4015009 (2016).
- Domaneschi, M., Pellecchia, C., De Iuliis, E., Cimellaro, G., Morgese, M., Khalil, A. & Ansari, F. Collapse analysis of the Polcevera viaduct by the applied element method. *Engineering Structures*. **214** pp. 110659 (2020).
- Domaneschi, M., Sigurdardottir, D. & Glisic, B. Damage detection on output-only monitoring of dynamic curvature in composite decks. *Structural Monitoring And Maintenance*. **4**, 1–15 (2017).
- Faravelli, L. & Casciati, S. Structural damage detection and localization by response change diagnosis. *Progress In Structural Engineering And Materials*. **6**, 104–115 (2004).
- Frangopol, D., Dong, Y. & Sabatino, S. Bridge life-cycle performance and cost: analysis, prediction, optimisation and decision-making. *Structures And Infrastructure Systems*. pp. 66–84 (2019).
- Ghiasi, R., Ghasemi, M., Noori, M. & Altabey, W. A non-parametric approach toward structural health monitoring for processing big data collected from the sensor network. *Experimental Vibration Analysis For Civil Structures*. pp. 419–426 (2020).
- Kim, S., Frangopol, D. & Soliman, M. Generalized probabilistic framework for optimum inspection and maintenance planning. *Journal Of Structural Engineering*. **139**, 435–447 (2013).
- Kumar, R., Gardoni, P. & Sanchez Silva, M. Effect of cumulative seismic damage and corrosion on the life-cycle cost of reinforced concrete bridges. *Earthquake Engineering Structural Dynamics*. **38**, 887–905 (2009).
- Martinelli, L. & Domaneschi, M. Effect of structural control on wind fatigue mitigation in suspension bridges. *International Journal Of Structural Engineering*. **8**, 289–307 (2017).
- Morgese, M., Domaneschi, M., Ansari, F., Cimellaro, G. & Inaudi, D. Improving Distributed Fiber-Optic Sensor Measures by Digital Image Correlation: Two-Stage Structural Health Monitoring. *ACI Structural Journal*. **118** (2021).
- Silik, A., Noori, M., Altabey, W., Dang, J., Ghiasi, R. & Wu, Z. Optimum wavelet selection for nonparametric analysis toward structural health monitoring for processing big data from sensor network: A comparative study. *Structural Health Monitoring*. **21**, 803–825 (2022).
- Sun, L., Shang, Z., Xia, Y., Bhowmick, S. & Nagarajaiah, S. Review of bridge structural health monitoring aided by big data and artificial intelligence: From condition assessment to damage detection. *Journal Of Structural Engineering*., 04020073 (2020).
- Vagnoli, M., Remenyte-Prescott, R. & Andrews, J. Railway bridge structural health monitoring and fault detection: State-of-the-art methods and future challenges. *Structural Health Monitoring*. **17**, 971–1007 (2018).
- Vishwanath, B. & Banerjee, S. Life-cycle resilience of aging bridges under earthquakes. *Journal Of Bridge Engineering*. **24**, 04019106 (2019).
- Wu, Z., Lu, X. & Noori, M. Resilience of Critical Infrastructure Systems: Emerging Developments and Future Challenges. (CRC Press, 2020).

Service-life extension of transport infrastructure through structural control

L. Martinelli

Politecnico di Milano – DICA, Milan, Italy

M. Domaneschi & R. Cucuzza

Politecnico di Torino – DISEG, Turin, Italy

M. Noori

California Polytechnic State University, San Luis Obispo, USA

Visiting Professor, School of Civil Engineering, University of Leeds, Leeds, UK

ABSTRACT: Transportation Infrastructure Systems are recognized as essential for economic development, territorial cohesion, and social transformation. Due to the increasing age of bridges, and given that a large part of the existing stock was built several decades ago, some of their key structural components, such as bridges, are getting older while loading conditions are often exceeding those initially envisaged as they are subjected to harsher natural events and growing levels of traffic. The increasing age of bridges, the deterioration phenomena and the increase in service conditions, exceeding those used in the initial design, contribute to reduce their reliability level. This contribution firstly explores the role that structural control can play, then it proposes a suitable measure for the formalization of this role within the life-cycle assessment of bridges and overcrossing structures. The effects of structural control are evaluated for the case study of a cable-supported bridge subjected to fatigue deterioration due to wind actions.

1 INTRODUCTION

Management of the life-cycle of products and components has received a great deal of attention starting from the first works that appeared at the half of the last century (SAIC 2006), evolving into a probabilistic approach (see the recent review in Biondini & Frangopol 2016 for applications to structures and infrastructures). In the field of structural engineering, a proper life-cycle assessment of a structure involves taking into account several time-variant aspects, ranging from the aging of the structure itself, to the evolution of the loading and the effects of maintenance and repair interventions. From the economic point of view, besides the cost of construction and maintenance of the structure, other aspects, often of greater importance, are also of interest, such as the social costs associated with the presence of an infrastructure and those related to its loss of functionality.

Transportation infrastructure systems are recognized as essential for an area's economic development, territorial cohesion, and social transformation. This opens up the issue of their aging. In many cases, some of their key structural components, such as bridges, are getting closer to their intended life while climate changes and society evolution are driving the loading conditions to exceed those initially envisaged at the design stage. In such scenario they can be indeed subjected to increasing hazards, such as natural events or manmade phenomena, and larger levels of traffic loads. Due to the increasing age of bridges, and given that a large part of the existing stock was built several decades ago (ASCE 2013), the deterioration phenomena and the increase in service condition loading, larger than those used in the initial design, might contribute to reducing the reliability level if countermeasures are not promptly taken. Therefore, the assessment of the current

state and the prediction of the future condition of bridges, as well as their protection against external hazards, has become an essential management challenge that needs to be addressed.

This work aims at contributing toward this practical goal by firstly exploring a suitable measure for the formalization of the role of structural control systems useful for the life-cycle assessment of bridges, and of overcrossing structures; subsequently, by evaluating the effects of structural control with reference to the case study of a cable-supported bridge subjected to fatigue deterioration due to wind action. The concepts explored are not restricted only to bridge structure, and can be applied, in principle, also to other structurally controlled structures.

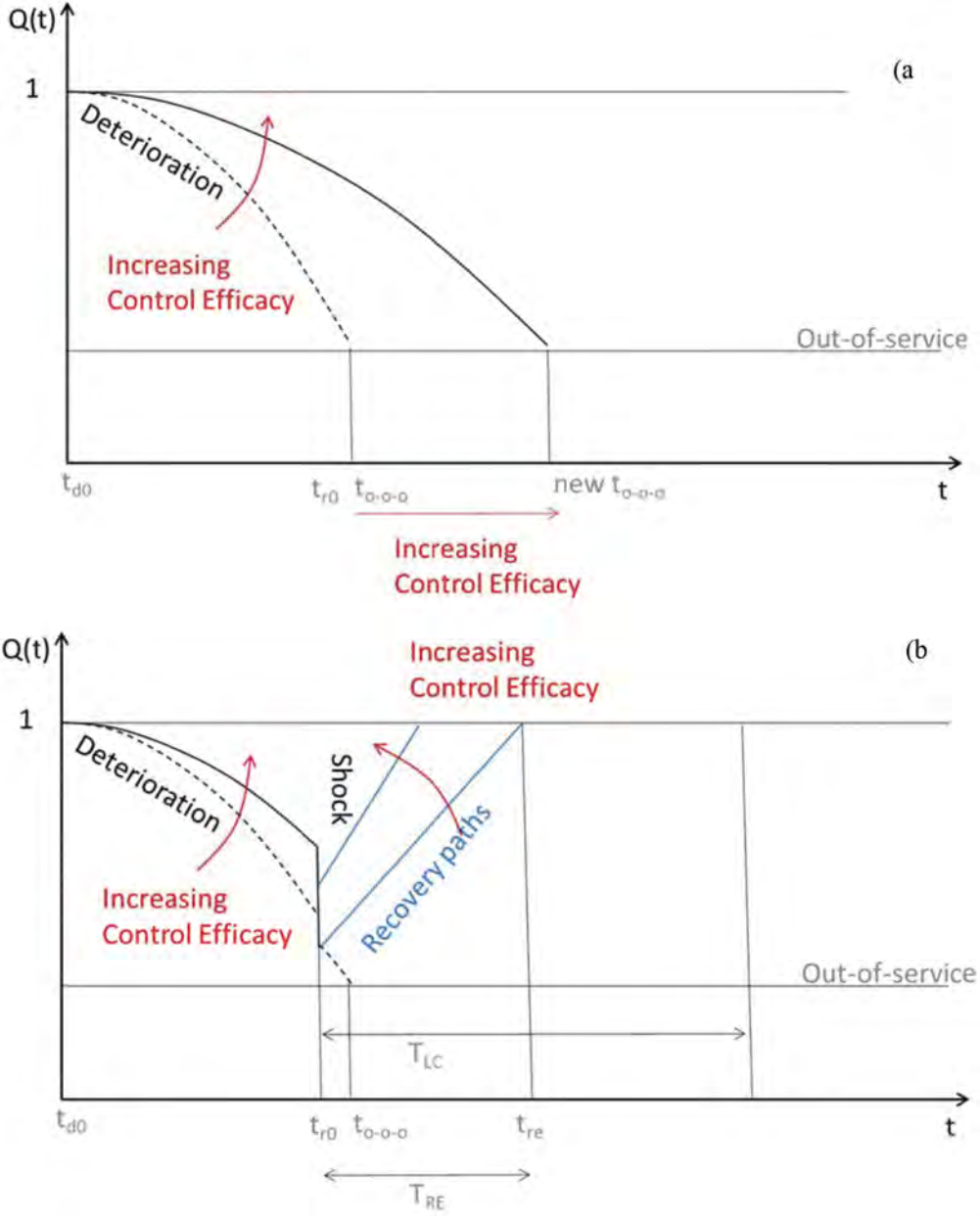


Figure 1. Graphical representation of the possible effects of Structural Control on the Functionality function: (a) in case no extreme events will happen; (b) in case of a single extreme event at time t_{r0} .

2 FORMALIZATION OF STRUCTURAL CONTROL EFFECTS ON THE LIFE CYCLE OF OF STRUCTURES

Structural Control refers to the application of techniques, such as active and passive control systems, to manage the structural behavior of a structure. The use of such techniques can have a significant impact on the life cycle analysis of a structure.

An important aspect of a Life-Cycle Assessment (LCA) is the ability to assess the system performance considering the aging and the deterioration of a system. This capability is a key constituent of LCA since the very purpose of an LCA exercise is usually to project into the future the life of a structure and assess the related costs.

Since Structural Control is able both to reduce the extreme values of the loading effects, as well as their variances (e.g. Casciati et al 2012), it will reduce damage, and hence it will extend the service life of the structure: time t_{o-o-o} (out-of-service time) in Figure 1a. Time t_{d0} , which is the time at which damage will start, can be, for practical purposes, assumed as the time at which the structure has been completed. The other marked time instants in Figure 1 make reference at the case in which a damaging extreme event will happen. They are: t_{re} = the time at end of recovery phase, $(t_{o-o-o} - t_{r0})$ = the residual service life after a shock at time t_{r0} , $T_{RE} = (t_{re} - t_{r0})$ = the time interval to recover full functionality, T_{LC} = a time interval limit set by the stakeholders to recover the functionality of the infrastructure.

In case of the occurrence of an extreme event at time t_{r0} Structural Control will have several positive effects since it will: a) reduce the structural deterioration up to time t_{r0} ; b) reduce the final deteriorated state of the structure after the extreme event occurs, since the structure will be found in a better shape in the controlled configuration with respect to the uncontrolled one; c) speed up the recovery rate, and shorten the recovery time T_{RE} of the structure, since being the structure in a better shape before the damaging event it will be less damaged after the occurrence of the extreme event and easier to repair. All these aspects will impact the Life-Cycle Assessment of the structure.

An indicator aimed to provide a comprehensive description of the time evolution of available structural resources, which includes besides deterioration also the possible occurrence of local and global failures, is the Functionality function $Q(t)$, which is at the base of the measure R of Resilience (see, e.g. Cimellaro et al. 2010). According to well known the definition in Manyena (2006), Resilience is the “intrinsic capacity of a system, community or society predisposed to a shock or stress to adapt and survive by changing its non-essential attributes and rebuilding itself”.

In essence, Resilience is related to the capability of a system to withstand the effects of extreme events and to recover efficiently the original performance and functionality (Bruneau et al. 2003). A well know measure R of Resilience is to defined R as the normalized area underneath the functionality function $Q(t)$ of a system (Figure 1):

$$R = \left(\frac{1}{T_{LC}} \right) \cdot \int_{t_{r0}}^{t_{r0}+T_{LC}} Q(t) dt \quad (1)$$

In Equation 1 the functionality function $Q(t)$ is a dimensionless function of time t that describes the level of functionality possessed by the structure, to a value of $Q(t) = 1$ it corresponds no loss-of-function for the system, while to a suitable small value of $Q(t)$, not necessarily zero if only a Serviceability Limit State has been exceeded, it corresponds the out-of-service of the system or of the structure; t_{r0} is the time at which recovery starts after a damaging event; T_{LC} is a time set by the stakeholders to recover the functionality of the infrastructure.

Aiming at applications within a Life Cycle Assessment procedure, in this work an extended version of the Resilience measure R is proposed which includes in Equation 1 the effects of Structural Control.

In the proposed definition the normalized area subtended by the functionality function $Q(t)$ is that from the time t_{d0} at which structural deterioration starts (see Figure 1b) to include all the life of the structure:

$$R = \left(\frac{1}{(t_{r0} - t_{d0} + T_{LC})} \right) \cdot \int_{t_{d0}}^{t_{r0} + T_{LC}} Q(t) dt \quad (2)$$

Since it is very difficult to precisely define the part of curve $Q(t)$ when a damaging process is in action, the curves in Figure 1 are only indicative. Note, however, that previous experience (Martinelli & Domaneschi 2017) pointed out that the specific shape of deterioration part of the functionality function $Q(t)$ is not changed by Structural Control, but the curve is made less steep as structural control will reduce damages and structural degrade.

3 APPLICATION OF STRUCTURAL CONTROL TO WIND-INDUCED FATIGUE LIFE

Long-span suspension bridges must satisfy reliability and safety requirements. Amongst these, Eurocode 3 (C.E.N. 2004) lists fatigue during the intended life of the structure.

Indeed, wind-induced motion has been recognized (Chen & Cai 2007, Seo & Caracoglia 2013, Seo & Caracoglia 2015, Sacconi et al. 2021, Zheng & Li 2022) as an important problem for long-span bridges, and cyclic loading stemming from wind fluid-structure interaction is regarded as an important issue.

The effects of Structural Control on the fatigue life of a suspension bridge under wind loading have been studied in Martinelli & Domaneschi (2017) with reference to a numerical model of a suspension bridge inspired by the Shimotsui-Seto Bridge, in Japan. The bridge model (Figure 2) has a total length of 1400 m, a span between the towers of 940 m, a towers height of 149 m, and a vertical distance of 31 m from the main girder to the foundations. The bridge has a steel truss main girder of rectangular transversal section of 30x13 m, width and thickness respectively. A complete description and validation of the model can be found in Domaneschi & Martinelli (2013a).

In the work by Martinelli & Domaneschi (2017), the standard deviation of the internal forces is assumed as a valuable parameter for evaluating fatigue effects in the main girder following general approaches of the existent literature, and typical structural details of the deck, having opposite characteristics in relation to fatigue life, are analyzed for fatigue failure using the stresses derived from the value of the wind induced bending moment in the main girder of the bridge. Prevention of fatigue damage is a complex problem that requires the identification and characterization of the structural element most prone to fatigue effects. Typical components suffering from fatigue are the connections between members of the structure, as the stresses are typically higher at these locations. The stress components in the connections depend, besides on the time history of the loading, also on the specific geometry, technology and typology of the connection itself.

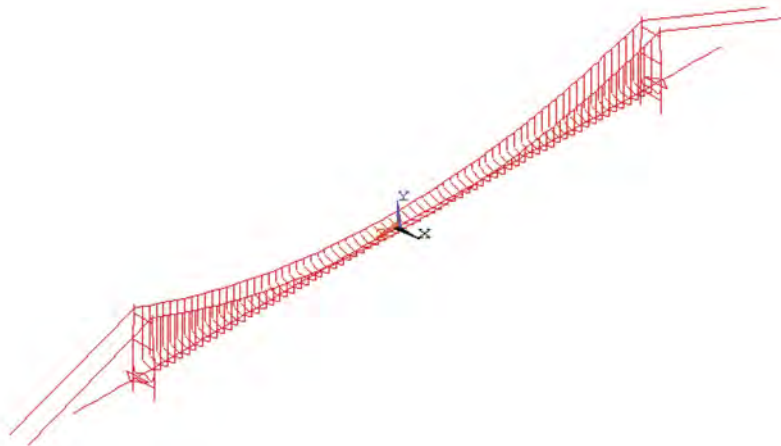


Figure 2. General view of the bridge model.

In the work by Martinelli & Domaneschi (2017) the representation of wind forces is based on the modeling of the drag force in time domain, as a completely non-linear force within the quasi-steady theory. For the lift force and the aerodynamic moment, instead, it is adopted a linearized form of the aerodynamic force and moment, with corrections for frequency-dependent loading using indicial functions. Details on the modelling of the wind loading, accounting for turbulence, can be found in Domaneschi & Martinelli (2013b).

All the wind interaction forces obviously depend on the wind velocity. The intensity of the wind loading is characterized through a representative statistical description of the average wind velocity as set forth in the IEC 61400-1 (2005) international standard, as this norm focuses specifically on applications that require a reliable statistics of the wind velocity.

The wind velocity mean value V over a time period of 10 min is assumed to follow the Rayleigh distribution, given as:

$$P_V(V_0) = 1 - \exp\left[-\pi\left(1 - \frac{V_0}{2V_a}\right)^2\right] \quad (3)$$

In Equation 3 $P_V(V_0)$ denotes the cumulative probability function for V (the probability that $V < V_0$) while V_a is the yearly average value of V .

This yearly average wind velocity value is derived from the value, V_{50} , relative to the extreme value, that has a recurrence period of 50 years, of the 10 min average wind speed. The relation between V_a and V_{50} adopted is the one proposed in IEC 61400-1: $V_a = 0.2 V_{50}$. With $V_{50} = 39.09$ m/s.

The value of V_{50} has been derived from the one, V_{150} , relative to the extreme 10 minutes mean velocity having a recurrence period of 150 years that was taken from the design specification for the bridge under study: $V_{150} = 43$ m/s.

The probability density function of the average 10 min wind velocity will be used in the following to describe the statistics of the wind loading for evaluating the occurrence of fatigue damage in selected structural details of the bridge deck.

In Martinelli & Domaneschi (2017) two hypothetical different details, having opposite characteristics in relation to fatigue life, were considered. A nominal stress component S was derived at a critical position in a deck connection from the lateral bending moment, M_y , in the girder on the base of the following linear law:

$$S = b_1 b_2 M_y \quad (4)$$

In Equation 4 the proportionality factor b_1 summarizes the effects of the deck connection details and of the girder section properties, while the factor b_2 scales the intensity of the input. Dependence on the other components of the main girder's internal forces is neglected.

A simple damage accumulation strategy, of the Miner's type (Committee on Fatigue and Fracture Reliability of the Committee on Structural Safety and Reliability of the Structural Division, American Society of Civil Engineers 1992) is then used to find the resulting effects of the constant amplitude cycles:

$$D = \sum_{i=1}^d D_{i,S_i} = \sum_{i=1}^d \frac{n_{i,S_i}}{N_{i,S_i}} \quad (5)$$

In Equation 5 D is the cumulated damage over the life of the structure, D_{i,S_i} is the fraction of damage suffered by the material due to a number n_{i,S_i} of cycles at stress level S_i while N_{i,S_i} is the fatigue strength (i.e. the number of cycles to failure at stress level S_i given by a so-called S-N curves). The S-N curves herein adopted are those reported in Eurocode 3 (fatigue) (C.E.N. 2004), and failure is assumed to occur when $D = 1$.

To better frame the impact of fatigue effects, the structural details studied were at the extremes of the sensitivity to fatigue effects among the details for which Eurocode 3 (fatigue) (C.E.N. 2004) gives direct guidance. The more sensitive detail is characterized by a constant stress amplitude $\Delta\sigma_C = 36$ MPa at $N = 2$ million cycles, with a yield strength of the steel $f_y = 430$ MPa. The less sensitive detail is characterized by $\Delta\sigma_C = 90$ MPa at $N = 2$ million cycles, with a yield strength of the steel $f_y = 430$ MPa.

3.1 Considered structural control settings

Different control settings are considered to assess the effects of Structural Control. These correspond to the ones already considered also in Martinelli & Domaneschi (2010). The control devices considered belong to the quite general fluid dynamic dampers family, able to perform either in a passive configuration or in a semi-active one. These control devices are positioned so that they connect the deck to the towers (Figure 3). Two orientations of the dampers are defined: transversal to the deck, denoted as TD, and longitudinal to the deck, indicated as LD. Transversal devices TD give a large contribution to the reduction of the deck transversal oscillations, while the LD devices help create a dissipative torque.

The three control settings considered are: passive-optimal (PO), passive-semi-active (SA), and uncontrolled (UNC). All controlled configurations comprise both TD and LD devices. The passive-semi-active configuration SA is obtained assuming that the transversal device TD can act as semi-active ones. The longitudinal devices LD are always of the passive type.

Figure 4 and 5 depict the degrading part of the functionality function $Q(t)$ due to wind-induced fatigue for the most sensitive structural detail ($\Delta\sigma_C = 36$ MPa at $N = 2$ million cycles) and for the least sensitive one ($\Delta\sigma_C = 90$ MPa at $N = 2$ million cycles). The degrading part corresponds to the time interval $t_{d0}=0 < t < t_{r0}=150$ years, and no extreme events have been assumed to happen. The curves in Figures 4 and 5 have been obtained by recalculating the data presented in Martinelli & Domaneschi (2017).

The effects of structural control are massively beneficial (Figure 4) for the most sensitive detail, showing a huge reduction in the predicted value of the damage. The curves in the figure are linear since the same distribution of average hourly wind velocity has been assumed for each year. Note that very little is gained in terms of fatigue life going from the passive optimal PO scheme to the semi-active SA one. With the hypotheses on the distribution of the wind velocity made, the uncontrolled structure life exceeds the 100 years mark.

The less sensitive detail, instead, has no problems (Figure 5) in reaching the intended design life of the structure, even in the uncontrolled case.

Application of Equation 2 to the curves in Figure 4 leads, for $t_{r0}+T_{LC} = 100$ years to a value of the extended Resilience $R = 0.5, 0.9, 0.9$ for the UNC, PO, SA cases, respectively, highlight as the proposed index can be useful in assessing the structure's resources within a Life Cycle Analysis.

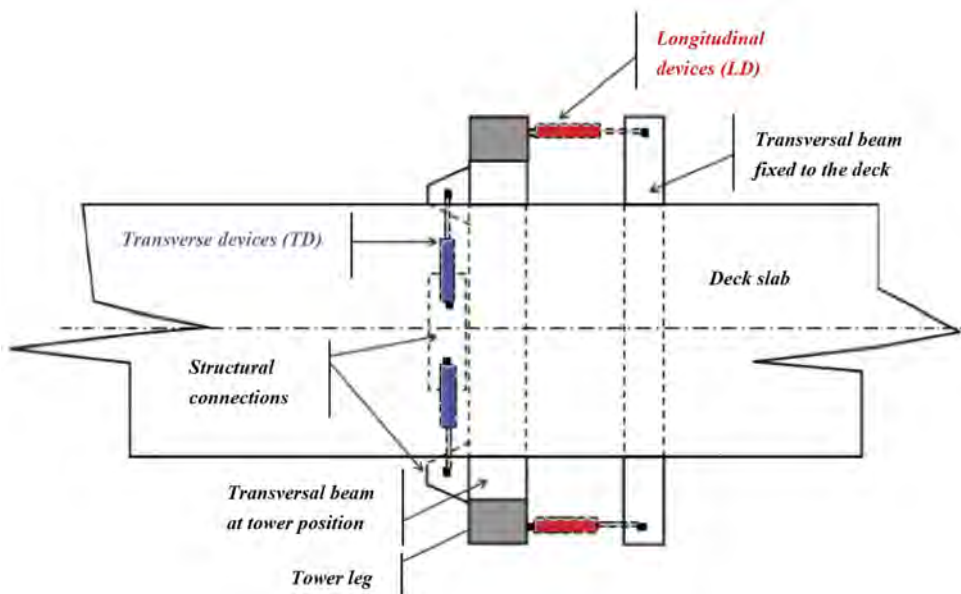


Figure 3. Top view of the deck at the towers, with the position of longitudinal LD and transversal TD devices.

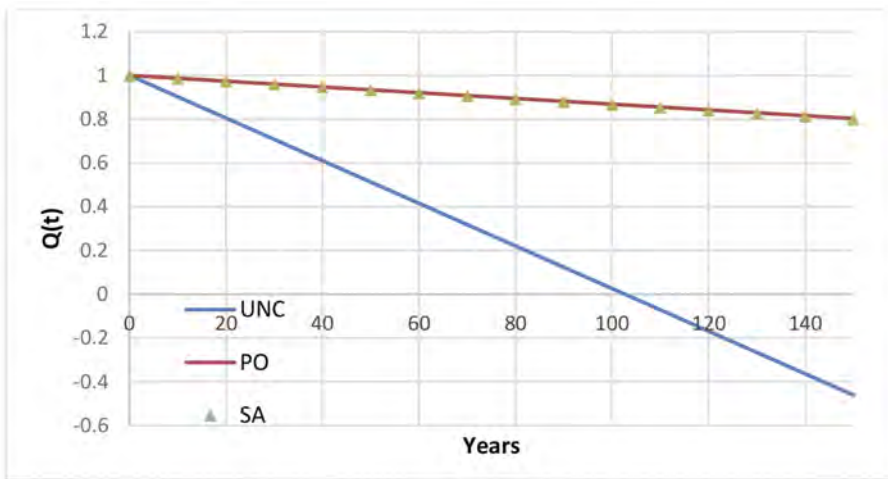


Figure 4. Deteriorating part of the functionality function $Q(t)$ due to wind-induced fatigue for the most sensitive structural detail.

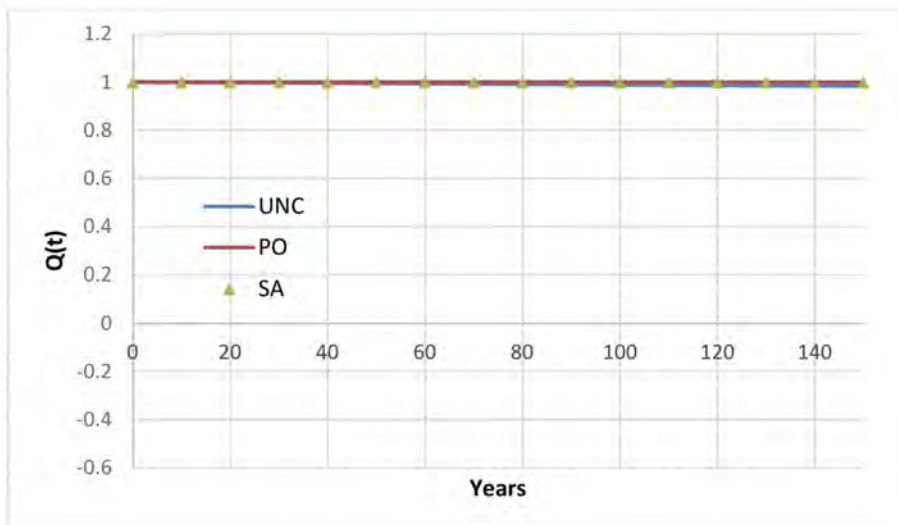


Figure 5. Deteriorating part of the functionality function $Q(t)$ due to wind-induced fatigue for the least sensitive structural detail.

4 CONCLUSIONS

Life cycle analysis involves assessing the environmental and economic impact of a structure over its entire life cycle, from construction to demolition. This analysis takes into account factors such as the use of materials, energy consumption, maintenance, and disposal. In this respect, structural control can be of help under several points of view.

Improved durability: Structural control techniques can help to minimize the impact of environmental factors such as wind, on the bridge structure. By reducing the damage caused by these factors, the bridge can last longer and require less frequent repairs and maintenance.

Increased safety: By monitoring and controlling the behavior of the bridge, structural control systems can help to detect and respond to any anomalies or potential failures before they

become serious safety concerns. This can help to minimize the risk of accidents and ensure the safety of users.

Reduced environmental impact: Structural control systems can help to minimize the use of materials and energy during construction and operation of the bridge. By reducing the amount of resources required, the environmental impact of the bridge can be minimized.

Improved cost-effectiveness: By reducing the need for maintenance and repairs, structural control can help to reduce the lifetime cost of the bridge. This can make the bridge more cost-effective and help to ensure that it provides value for money over its entire life cycle.

REFERENCES

- A.S.C.E. 2013. *Report card for America's infrastructure*. Reston, VA, (<http://www.infrastructurereportcard.org>).
- Biondini, F. & Frangopol D.M. 2016. Life-Cycle Performance of Deteriorating Structural Systems under Uncertainty: Review. *Journal of Structural Engineering*, ASCE, ISSN 0733-9445, 142(9):F4016001.
- Bruneau, M., Chang S.E., Eguchi R.T., Lee G.C., O'Rourke T.D., Reinhorn A.M., Shinozuka M., Tierney K., Wallace W.A., vonWinterfeldt D. 2003. A framework to quantitatively assess and enhance the seismic resilience of communities. *Earthquake Spectra*, 19(4): 733–752.
- Casciati, F., Rodellar, J., Yildirim, U. 2012. Active and semi-active control of structures – theory and applications: A review of recent advances. *Journal of Intelligent Material Systems and Structures*, 23(11) 1181–1195 DOI: 10.1177/1045389X12445029.
- C.E.N. 2004. *Eurocode 3. Design of steel structures (EN 1993-2: Steel bridges, EN 1993-1-9: Fatigue)*.
- Chen, S.R. & Cai, C.S. 2007. Equivalent Wheel Load Approach for Slender Cable-Stayed Bridge Fatigue Assessment under Traffic and Wind: Feasibility Study. *J Bridge Eng-ASCE*, 12: 755–764.
- Cimellaro, G. P., Reinhorn, A. M., and Bruneau, M. 2010. Framework for analytical quantification of disaster resilience. *Eng. Struct.*, 32(11): 3639–3649.
- Committee on Fatigue and Fracture Reliability of the Committee on Structural Safety and Reliability of the Structural Division, American Society of Civil Engineers. 1992. Fatigue reliability: variable amplitude loading. *ASCE Journal of the Structural division*, 108: 47–70.
- Domaneschi, M. & Martinelli, L. 2013a. Optimal Passive and Semi-active Control of a Wind Excited Suspension Bridge. *Struct Infrastruct E*, 9: 242–259.
- Domaneschi, M., Martinelli, L. 2013b. Refined Optimal Passive Control of Buffeting-induced Wind Loading of a Suspension Bridge. *Wind Struct*, 18: 1–20.
- Estes, A. C., & Frangopol, D. M. 2001. Bridge lifetime system reliability under multiple limit states. *J. Bridge Eng.*, 6(6): 523–528.
- Fumoto, K., Yamada, I., Moriyama, A., Yoki, Y. 2007. Fatigue design, evaluation and inspection for orthotropic steel decks on long-span bridges. In: *23th US - Japan Bridge Engineering Workshop*, Tsukuba JP, 2007.
- Hosomi, M., Kobayashi, H., Nitta, Y. 1997. Fatigue strength design for vortex-induced oscillation and buffeting of a bridge. *J Wind Eng Ind Aerod*, 67-68: 227–237.
- International Electrotechnical Commission. 2005. *IEC 61400-1 INTERNATIONAL STANDARD 2005-08. Wind turbines. Part 1: Design requirements*.
- Manyena, S. B. 2006. The concept of resilience revisited. *Disasters*, 30:434–50.
- Martinelli, L., Domaneschi, M. 2017. Effect of structural control on wind fatigue mitigation in suspension bridges. *International Journal of Structural Engineering*, 8(4): 289–307, DOI: 10.1504/IJSTRUCTE.2017.10010461.
- Sacconi, S., Ierimonti, L., Venanzi, I., Ubertini, F. 2021. Life-cycle cost analysis of bridges subjected to fatigue damage. *J Infrastruct Preserv Resil*, 2:25 <https://doi.org/10.1186/s43065-021-00040-3>.
- S.A.I.C. 2006. *Life Cycle Assessment: Principles & Practice*. EPA, pp. 88.
- Seo, D. W., Caracoglia, L. 2013. Estimating life-cycle monetary losses due to wind hazards: Fragility analysis of long-span bridges. *Engineering Structures* 56 (2013) 1593–1606.
- Seo, D. W., Caracoglia, L. 2015. Exploring the impact of “climate change” on lifetime replacement costs for long-span bridges prone to torsional flutter. *J. Wind Eng. Ind. Aerodyn.* 140(2015)1–9.
- Zheng, X. & Li, H. 2022. Life-cycle failure probability analysis of deteriorated RC bridges under multiple hazards of earthquakes and strong winds. *Earthq Eng & Eng Vib* (2022) 21: 811–823.

Digital Twin - solution in the digital age for improving critical infrastructure resilience to extreme events

M.Q. Tran, H.S. Sousa, E. Teixeira & J.C. Matos

Civil Engineering Department, ISISE, University of Minho, Guimarães, Portugal

H.T. Dang

University of Transport and Communications, Hanoi, Vietnam

ABSTRACT: Risk management is one of the approaches to improve the efficiency and safety of critical infrastructure against extreme events. This approach focuses on the design of robust CI and strong protection systems. In this way, the probability and consequences are minimized. However, extreme events are increasing in both number and severity. CIs (especially those built in the past) find it difficult to withstand and adapt to these extreme events. As a result, a recent dramatic shift has shifted from robust design to focus on preparedness, response, and resilience. Accordingly, CI can withstand the majority of adverse effects at higher-than-normal thresholds. In the event of destruction or damage, the CI can bounce back to normal operation more quickly with minimal resources. Increasing understanding and improving the resilience of CI to extreme events contribute to sustainable cities. Although considerable research has been conducted on the resilience of Critical Infrastructures systems over the years, it still has gaps. This paper applies the Digital Twin concept to the infrastructure domain to improve CI system resiliency. A comprehensive analysis of the critical infrastructure characteristics and resilience is implemented. The results show that the Digital Twin has the ability to fill research gaps, enhancing the resilience of critical infrastructure.

1 INTRODUCTION

A structure, system, or component that is crucial to the maintenance of a society's essential functions and whose disruption or destruction will have a negative impact on the society's ability to function sustainably is referred to as critical infrastructure. Critical infrastructures, as opposed to regular infrastructure, play a significant role in a nation's society. If there is a problem, a CI can cause disruption, affecting society and human activities.

The damage caused by extreme events can have enormous consequences. Disruptions in the operation of critical infrastructure can cause cascading failures, overloading the system. At the same time, it can lead to the collapse of all other infrastructures in a domino effect. To protect these lifelines during and after disruptive events, it is critical to strengthen the resilience of critical infrastructures to any type of disruption or disaster.

Critical infrastructure resilience is the ability to continue to deliver essential services reliably and with minimal disruption in the face of any extreme event (Royce Francis et al., 2014; AM Bento, Minh TQ, 2022). A system's resilience is determined by various factors, the most important of which are dynamic skills and rapid response strategies. Infrastructure resilience is increasingly valued and considered in design goals to enhance usability and sustainability for the entire system's development.

When a hazardous event occurs, risk management measures cannot be enough. With critical infrastructure at risk, reacting, responding, and accelerating recovery solutions is imperative. Critical social functions, critical infrastructure, must be restored or adjusted as quickly as

possible. The inability to completely eliminate disasters and the need to be prepared for major crises have led to views of having to “live with” extreme events (Minh TQ et al., 2022a). Resilience studies have gained global attention. Conventional infrastructure management mainly focuses on visual inspection, physical measurement, and expert evaluation of an infrastructure domain in isolation. Different approaches have been considered by many scientists (Ayyub, M. B et al., 2013; Bialas, A., 2016). However, these studies are limited by their consideration of different hazards, cascade effects and uncertain conditions, dealing with technical, organizational, economic and human domains as well as integration of time and space aspects.

M. Grieves first proposed the idea of digital twins as a concept for product lifecycle management in 2003 (Michael W. Grieves, 2003). Both academia and business are increasingly acknowledging the value of DT. Since the day it was first conceived and created until the present, DT has been used and put into practice, demonstrating its viability in a variety of industries, particularly product design, automatic production, manufacturing, automotive, and aviation (R.K Phanden et al., 2021; Minh TQ et al., 2022b).

Digital Twins are used as a comprehensive tool for monitoring, analyzing, controlling, and optimizing a system throughout its entire lifecycle. Because of ongoing digitization efforts, it is becoming increasingly possible to implement Digital Twins of large-scale systems. With its outstanding advantages, Digital Twins ensures a virtual copy in an up-to-date state. The Digital Twin concept, with its updated, integrated intelligent and adaptive functions and digital approaches, represents a potential approach to the field of infrastructure services. Virtual objects, when combined with the right tools, can improve the operational resiliency of infrastructure services.

Based on these initial assumptions, in this paper, the applicability of the Digital Twins concept is considered to improve the resiliency of critical infrastructure protection and operation against catastrophic events extreme. The Digital Twin paradigm is well suited for a framework that promotes increased resilience throughout the crisis life cycle.

2 RESILIENCE IN CRITICAL INFRASTRUCTURES

2.1 *Critical infrastructures*

Critical infrastructure is “the organizational structure and the physical and vital importance to the society and economy of a country”(Federal Republic of Germany, 2009). Their collapse or deterioration could result in protracted supply shortages, major disruptions to public safety and security, or other severe repercussions.” Specifically, the areas of energy, information and communication technology, water supply, and technical transport, as well as those of health, media and culture, food, finance, insurance, government, and administration, are seen as significant. In addition, some infrastructure networks, such as electricity or communication networks, cover entire continents and are interdependent across borders. Social engineering is deeply integrated and interacting with critical infrastructure. Increasingly complex and integrated infrastructures, networked societies, climate change, and worldwide political instability enhance the probability of dangerous situations in the medium and long term with critical infrastructure.

2.2 *Critical infrastructure resilience*

The concept of resilience is applied in many domains of research including ecology, psychology, eco-economics, and national security. . .(M. Wied et al., 2019). In the context of critical infrastructures, resilience refers to the capacity to continue delivering important services reliably and with few interruptions in the face of unspecified disturbances, as well as the capacity to regain full functioning after an impact. Accepting that not all future events are foreseeable and that unexpected occurrences will occur is essential to resilience (E. Hollnagel, 2010). In contrast to conventional risk management, which seeks to detect and restrict the effect of particular hazards, resilience management seeks to increase the system’s attributes so that it can better withstand threats future occurrences of any kind.

Resilience: subject resilience is closely related to vulnerability, the ability of the system to withstand disturbances caused by extreme events and to maintain the performance of the socio-economic, environmental, and physical components of the system. Resilience to extreme

events damages can be considered only in places with past events, since the main focus is on the experiences encountered during and after the extreme events. The resilience of the critical infrastructure layer depends on the characteristics of the system, as well as a set of dynamic skills and coping strategies, and recover. Overall, this highlights that resilience is not a given, purely static property, but can be actively enhanced and achieved.

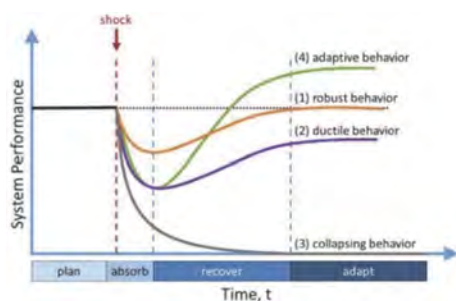


Figure 1. Infrastructure performance in the case of a disruption (P. Klimek et al., 2019).

As disruptions unfold, system performance fluctuates: first, system performance decreases as the impact of the shock is absorbed, then performance increases during the recovery phase, and finally, depending on system behavior, performance levels off at a lower, equal, or higher level than before the shock (Figure 1). In each of these stages, a distinct set of skills is needed and must be triggered in accordance with the circumstances. The theoretical framework of the resilience cycle describes this.

This cycle typically consists of a planning phase, an absorption phase, a recovery phase, and an adaptation phase. During the cycle, the system engages its resilience capabilities, some of them momentarily (e.g., robustness) and some continually (e.g., monitoring). A highly resilient system will learn from prior disruptions and system behavior, as well as repercussions, and incorporate adjustments to present processes or technology, leaving it better equipped to confront future disturbances when the cycle starts again (D. Rehak et al., 2019).

3 DIGITAL TWINS

3.1 *Digital twins*

Digital twin technology is a virtual digital model of an object, but unlike conventional digital simulations, this digital object is very intelligent and has the ability to acquire and analyze large data sources, and a variety of actual objects. There is a data flow between the virtual and the actual object, and through the sensors on the actual system, the virtual part is updated so that the state of the system can be monitored in real-time. In other words, Digital twin technology integrates Artificial Intelligence, Machine Learning and analyzes software with data to create a living digital simulation model that updates and changes as physical objects change. A digital twin continuously learns and updates from multiple sources to describe its near-real-time status, working conditions or location, thereby helping to make accurate diagnoses about the status of the device, and object when any abnormal changes occur. Digital twin greatly improves real-world objects (such as optimizing the design of airplanes, and cars, or automating and increasing the productivity of a production line), but at the same time improving itself based on newly updated data from real models.

3.2 *Properties of the digital twins*

There are many views on the components of the digital twin expressed under various definitions. However, essentially digital twin must consist of five parts: (i) the physical part, (ii) the virtual part, (iii) the connections, (iv) the data and (v) the services (Figure 2).

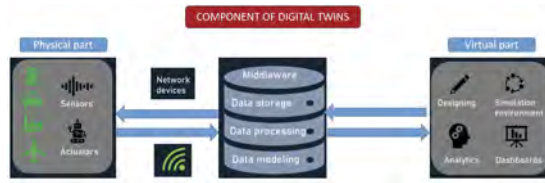


Figure 2. Components of digital twins (P. Klimek et al., 2019).

a. The physical part

One of the main parts of a digital twin is the real part of the object (the physical part). The physical objects in the digital twin are capable of perceiving the outside world. In other words, like the human senses, the real part of the digital twin is equipped with sensor systems to get real data. The object of study - for example, a bridge - is equipped with various sensors related to important functional areas. These sensors generate data about various aspects of a physical object's activity, such as energy output, temperature, weather conditions, and more. This data is then forwarded to a processing system and applied to the digital twins.

b. The virtual part

The virtual part of the digital twin are virtual models created by digital transformation that are reflected by the real object. Different from conventional simulation models, this model contains all the information about reality. The virtual part is always updated and changed according to the physical part. The virtual part is not simply an object that is established through conventional design models with the characteristics of shape and size. Traditional computer-aided engineering and design (CAD/CAE) modeling is often just the starting point of a DT.

c. The connections and data flow between physical part and virtual part

Actual objects constantly change in all aspects: quality, nature, characteristics, among others. Creating a digital model corresponding to a moment in time of a real object has been done many times before, but it is not considered a digital twin because there is no connection and data flow between physical part and virtual part.

The digital twin model is clearly distinguished from the digital model, and the digital shadow model interconnection and interactive flow of data between the parts. If the data flow between an existing physical object and a digital object is fully integrated in both directions, this constitutes the reference "Digital Twin" (A. Fuller et al., 2020)

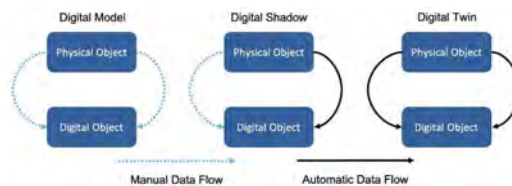


Figure 3. Digital model, shadow and twin (A. Fuller et al., 2020).

The connection and data flow between the real part and the virtual part form a closed loop. In there, the real data is transmitted from the sensor to the virtual part to help the model continuously update attributes. The virtual model also provides predictive cases, and possible scenarios, affecting human decisions to the real part. Two parallel data flow coexist, interact, and complement each other.

In the past years, technologies for cloud storage or internet of things or technologies for data transmission have not achieved the current achievements. It is very difficult to make the

connection between parts. However, now that these technologies have developed quite strongly, some technological barriers have been removed. The connection and data flow between real entities and virtual models is possible.

d. The services

Reviews show that digital twins can have applications in many areas. Main serviceability to the ability to integrate the real world into the virtual world. In the virtual world, people can perform tasks that are not possible in the real world. Destructive experiments, texture response perceptions, or full lifecycle reviews of an object can be visualized in the virtual world. Not only that, supporting important decisions greatly affects the real audience.

3.3 *Digital twins enabling technologies*

a. Technologies for physical objects

As discussed above, physical objects are an integral part of DT because they are data sources from the real world. Technologies implemented in the physical object make the DT aware of data such as geometrical shape, physical properties, and mechanical precision. Currently, sensor and measurement technologies deployed for DT include IoT sensing technology, reverse engineering, image recognition metrology, and particle sensing technology (Qi, Q et al., 2019).

b. Data construction and management technologies

The high-fidelity digital twin model contains a lot of complex information, including some data that needs to be stored intact, some data only a small part in the implementation process. Therefore, data construction and management technology is quite important in DT.

As we know, the data obtained is often multi-source and contains many noisy signals and messy arrangements. The purpose of data construction and management technology is to separate data that is valuable and meaningful to specific audiences from big data. The raw data will not be effective without cleaning, converting or reducing the size. Data construction and management can be divided into the following aspects: analytical visualization, data mining algorithms, and predictive analytics capabilities. Data mining and analysis algorithms will rely on AI to develop.

c. Virtual modeling technologies

Virtual modeling technologies allow users to visualize specific objects in the DT, while helping to manage information about geometry and texture response. Currently, there are many Computer-Aided Design (CAD) software that can display the geometric information of a physical object, such as UG, AutoCAD, SolidWorks, and Creo.

For the structure response side, many physics-based theories/models have been established to reveal the mapping relationship between input and behavior, such as computational fluid dynamics models (CFD), finite element modeling (FEM). Tao and Zhang suggest that behavioral models describe the mechanical correspondence of production equipment can be implemented specifically using finite element models and neural networks (Tao, F. and Zhang, M., 2017)

d. Connection and data transmission technologies

One of the most difficult issues to implement DT is the technology to connect and transfer data between the real and virtual parts. To realize real-time control and virtual-real state mapping, high-fidelity connection methods are needed for DT. Connection protocols for exchanging data between physical space and cyberspace are now strongly developed through different software and platforms.

Currently, wireless transmission methods including Zig-Bee, Bluetooth, Wi-fi, ultra-wideband are gradually replacing and becoming more modern. A series of application program interfaces (APIs) are commonly used to exchange data between different software to perform data transfer at the software level. Recently, 5G technology can be applied to meet the demand for high data rate, high reliability, high coverage and low latency.

4 DIGITAL TWINS FOR IMPROVING CRITICAL INFRASTRUCTURE RESILIENCE TO EXTREME EVENTS

A Digital Twin idea and framework applied to resilient critical infrastructures can help to synchronize existing research efforts and expedite the implementation of theoretical discoveries in a cost-effective way creative. This notion encompasses both Data Science and the digitally-created opportunities. A proposed model of Digital twins includes the main components and their interactions. This proposed model will be used to meet key requirements of the Digital Twin Conceptual Framework needed to increase resilience in critical infrastructures (Figure 4).

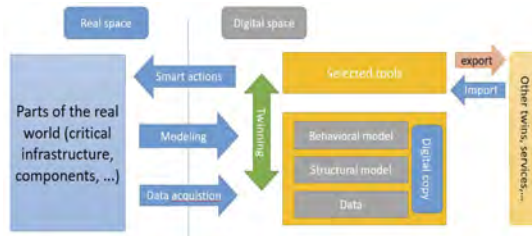


Figure 4. Proposal model structure of the digital twin concept with the real-world section to improving critical infrastructure resilience to extreme events.

The real-world segment may include any group of systems of interest, ranging from individual machine components to factories, buildings to cities, processes to complex interconnected systems-of-systems, and communities to networked socio-technical systems such as critical infrastructures. It is frequently referred to as an analog system, real system, or physical system, even if it may have software-implemented intelligent control systems. Depending on the use case, the system boundaries define the portion of the real world captured by the Digital Twin.

Initializing the virtual replica is the initial stage in establishing a Digital Twin, followed by modeling and data collection. Structural models, such as CAD models or component lists, describe the composition and features of the modeled section of the real world. They are accompanied by dynamic and functional behavioral models, such as simulation models or models built using machine learning or artificial intelligence. The structural model frequently serves as a semantic container for current and historical state data and behavioral models. The type and sophistication of the semantic container are determined by the intended use case and the nature of the data, which can range from raw sensor data and unstructured information such as natural language text or speech, non-normalized photographs, etc. to curated instances of data types, schema-bound data, and ontology-compliant data.

When designing the components of the DT system, the system boundaries of the real infrastructure under consideration must be established. Outside of the system’s limits, the external environment creates changes and disruptive occurrences that have an effect on the system. In addition, the purpose of the DT must be specified in order to extract the stakeholders, users, use cases, data sources, and design objectives for the replica and tools. In the first stage, relevant situations for each infrastructure type can be identified. For example, for urban facilities near rivers, extreme weather or floods situations are addressed. In subsequent iterations, the Digital Twin may be expanded to encompass other sorts of disruptions and services.

The federation of various Digital Twins allows regulatory requirements to be mapped to infrastructures. Along the import/export interfaces, regulatory processes and needs for data governance, privacy, and protection can be addressed. With the proper interfaces, system-of-systems can be linked to create similar virtual system-of-systems with a higher level of complexity and sector couplings. It is essential that the networked Digital Twins and their corresponding models accurately depict the emergent or self-organizing behavior of the actual system.

A Digital twins model is applied to the proposed critical infrastructure (Figure 5). This model consists of real part, imaginary part and full components as defined by Digital twins. Together they form a unified, functioning system. In accordance with this conceptual paradigm, a Digital

Twin that functions continuously and encompasses all stages of infrastructure operation, including regular operation and extreme occurrences, is continually operational.

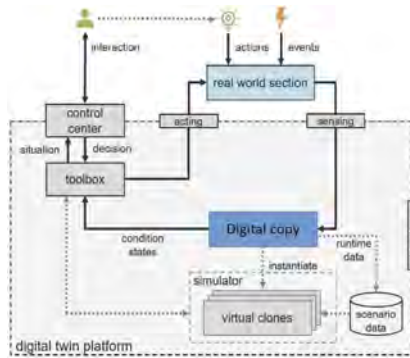


Figure 5. Digital twin conceptual model for infrastructure operation supporting improved resilience for extreme events.

The Digital Twins platform proposes for CI deployed in the cloud, using data collected from the real to update and connect to the virtual. At the heart of the architecture, virtual replicas receive and deliver data through streaming services and store that data in a database.

If necessary, Toolbox provides the ability to clone a virtual duplicate of critical infrastructure and initialize it to the present condition of the physical world. The digital twins are then utilized for forecasting and simulating alternative system configurations or interventions. In addition to new out-of-the-box actions advised by system specialists, optimization techniques may be employed to uncover system improvement opportunities. In addition, the replica is used to recreate the predicted sequence of events based on updated runtime and initialization data retrieved from historical records or the engineered scenario database.

The Control Center resembles an interface for stakeholders, directing each scenario and providing access to the toolset. It includes a situation room that has been augmented with the findings of Digital Twin monitoring and analysis. The control center can be accessed remotely, allowing stakeholders from diverse companies to take consistent action.

5 CONCLUSIONS

In this paper, the requirements for the operation and crisis management of critical infrastructures are presented, in order to improve their resilience to unforeseen events. The Digital Twin Model is a new, comprehensive, and effective approach to improving the resilience of critical infrastructure to extreme events.

Overall, applying the Digital Twin concept to critical infrastructure permits the development of new strategies and the study of past errors. This solution offers to play a significant role in tackling the issues faced by infrastructures and societies that are becoming increasingly complex and linked. The Digital Twin is the principal instrument for methodically driving resilience, as intelligent tools promote resilience.

Integrating many uncertain data sources and system model types into a Digital Twin architecture, evaluating smart technologies to help the recovery cycle, and ensuring the scalability and dependability of the IT platform are significant obstacles.

ACKNOWLEDGEMENT

This work was partly financed by FCT/MCTES through national funds (PIDDAC) under the R&D Unit Institute for Sustainability and Innovation in Structural Engineering (ISISE),

under reference UIDB/04029/2020. This research was supported by the doctoral Grant reference PRT/BD/154268/2022 financed by Portuguese Foundation for Science and Technology (FCT), under MIT Portugal Program (2022 MPP2030-FCT). This work was partially funded by InfraROB Project which has received funding from the European Union's Horizon 2020 research and innovation programme under grant agreement No. 955337. The second author acknowledges the funding by FCT through the Scientific Employment Stimulus - 4th Edition.

REFERENCES

- A. Fuller et al. (2020) 'Digital Twin: Enabling Technologies, Challenges and Open Research'. Available at: <https://doi.org/10.1109/ACCESS.2020.2998358>.
- AM Bento, Minh TQ (2022) 'Melhoria da precisão e otimização do método do índice de vulnerabilidade às cheias', *XX SILUBESA - Simpósio Luso-Bras. Eng. Sanitária E Ambient*, pp. 267–272. Available at: <https://www.aprh.pt/20silubesa/docs/XX-S>.
- Ayyub, M. B et al. (2013) 'Systems resilience for multihazard environments: Definition, metrics, and valuation for decision making', *Risk Anal.*, 34(2), pp. 340–355. Available at: <https://doi.org/10.1111/risa.12093>.
- Bialas, A. (2016) 'Risk management in critical infrastructure—Foundation for its sustainable work', 8(3). Available at: <https://doi.org/10.3390/su8030240>.
- D. Rehak et al. (2019) 'Complex approach to assessing resilience of critical infrastructure elements', *International J. Crit. Infrastruct. Prot.*, 25, pp. 125–138. Available at: <https://doi.org/10.1016/j.ijcip.2019.03.003>.
- E. Hollnagel (2010) 'Resilience Engineering in Practice: A Guidebook'.
- Federal Republic of Germany (2009) 'Federal Republic of Germany Federal Ministry of the Interior. National strategy for critical infrastructure protection (cip strategy)'. Available at: <https://www.qcert.org/sites/>.
- K. Costello et al. (2018) 'Gartner Identifies Five Emerging Technology Trends That Will Blur the Lines Between Human and Machine'. Available at: <https://www.gartner.com/en/newsroom/press-releases/2018-08-20-gartner-identifies-five-emerging-technology-trends-that-will-blur-the-lines-between-human-and-machine>.
- M. Wied et al. (2019) 'Conceptualizing resilience in engineering systems: An analysis of the literature', *Syst. Eng.*, 23 (1), pp. 3–13. Available at: <https://doi.org/10.1002/sys.21491>.
- Michael W. Grieves (2003) 'Virtually Intelligent Product Systems: Digital and Physical Twins', *Complex Syst. Eng. Theory Pract.*, pp. 175–200. Available at: <https://doi.org/10.2514/5.9781624105654.0175.0200>.
- Minh TQ et al. (2022a) 'Application of Artificial Intelligence (AI) in Flood Risk Forecasting'. Available at: http://www.ub.edu/wamyc/SEIO/IFCS2022_Book_Abstracts_v1.pdf#page=308.
- Minh TQ et al. (2022b) 'Opportunities and challenges of Digital Twins in Structural Health Monitoring', *Conf. 4th Int. Conf. Sustain. Civ. Eng.-ISCE2022* [Preprint].
- P. Klimek et al. (2019) 'Quantitative resilience assessment in emergency response reveals how organizations trade efficiency for redundancy', *Saf. Sci.*, 113, pp. 404–414. Available at: <https://doi.org/10.1016/j.ssci.2018.12.017>.
- Qi, Q et al. (2019) 'Enabling technologies and tools for DT', *J. Manuf. Syst.* [Preprint]. Available at: <https://doi.org/10.1016/j.jmsy.2019.10.001>.
- R.K Phanden et al. (2021) 'A review on simulation in digital twin for aerospace, manufacturing and robotics', *Mater. Today Proc.*, 38, pp. 174–178. Available at: <https://doi.org/10.1016/j.matpr.2020.06.446>.
- Royce Francis et al. (2014) 'A metric and frameworks for resilience analysis of engineered and infrastructure systems', *Reliability Engineering & System Safety*, 121, pp. 90–103. Available at: <https://doi.org/10.1016/j.res.2013.07.004>.
- Tao, F. and Zhang, M. (2017) 'Digital Twin Shop-Floor: A New Shop-Floor Paradigm Towards Smart Manufacturing'. Available at: <https://doi.org/10.1109/ACCESS.2017.2756069>.

Flood Vulnerability Index (FVI) of infrastructures for reducing adverse flood events

M.Q. Tran, H.S. Sousa, E. Teixeira & J.C. Matos

Civil Engineering Department, ISISE, University of Minho, Guimarães, Portugal

ABSTRACT: Floods disrupt peoples' lives and livelihoods worldwide and are one of the most common and severe natural hazards. The effects of flooding are devastating, especially in lower-income countries where the infrastructure, such as drainage and flood control systems, tends to be less developed or even un-existing. Flood vulnerability has the potential to support decision-makers in planning better measures to adapt to and mitigate the negative impacts of flooding. Assessing vulnerability to floods is often complicated because it involves many factors, sectors, and aspects. As a result, methods that simplify and improve flood vulnerability assessment are essential. Various approaches such as vulnerability curves, disaster loss data, computer modeling, and indicator-based methods have been investigated and well-accepted for assessing flood vulnerability. Reviewing these methods and contrasting their advantages and disadvantages is the goal of this study. After considering the methods comprehensively, the indicator-based approach provides a clearer picture of the overall flood vulnerability in each area. This study also provides a general and simple introduction to the indicator-based method to promote a better understanding of this method.

1 INTRODUCTION

1.1 *Floods and their effects*

Every time an extreme flood occurs, property, infrastructure, people, and animals are severely affected. Critical infrastructures such as bridges were swept away, and houses were submerged by flood water. In addition, the prolonged flood situation also affects agricultural activities. Floods, for example, can damage crops and reduce food supplies. Flash floods (a flood in which the water level rises very quickly when a large volume of water moves quickly from high to low terrain) are the number one weather-related cause of loss of human and animal lives. An indirect consequence of floods is the contamination of other resources. As an example, floods can disturb the public water supply by bringing waste from sewers, ponds, and landfills into the environment. Water pollution affects human health and spreads harmful viruses.

Floods may not be the most catastrophic event (unlike tsunamis or earthquakes), however they cause the most damage and affect most people. At the same time, Flood is also the most common of the disaster events. The number of floods between 2000 and 2019 accounted for 44% of all disasters. Meanwhile, all other negative events remained below 30% (Figure 1).

Along with global climate change, the number of flood events in the past two decades has increased markedly. During the period 1980-1999, the total number of flood events was 1389. Between 2000-2019, the number of flood occurrences increased to 3254 (Figure 2). It has been observed that flood events are increasing in frequency and intensity, with a 57% increase from the previous time period, constituting the largest increase in disaster events. Not only stopping there, the number of people affected by floods also accounts for the highest percentage. In the decade 2000-2019, floods affected up to 1.65 billion people, representing 41% of all disasters.

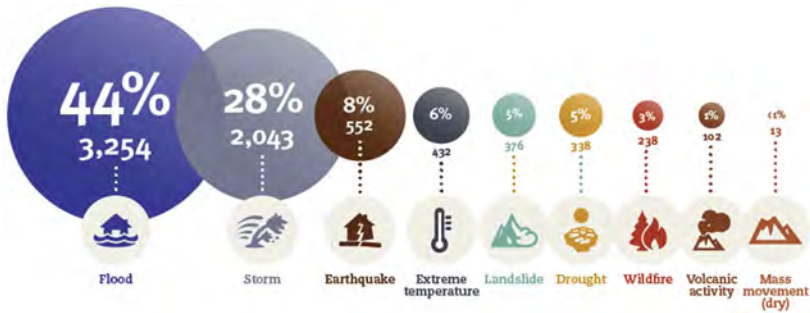


Figure 1. Percentage of occurrences of disasters from 2000-2019 (United Nations Office for Disaster Risk Reduction, 2019).

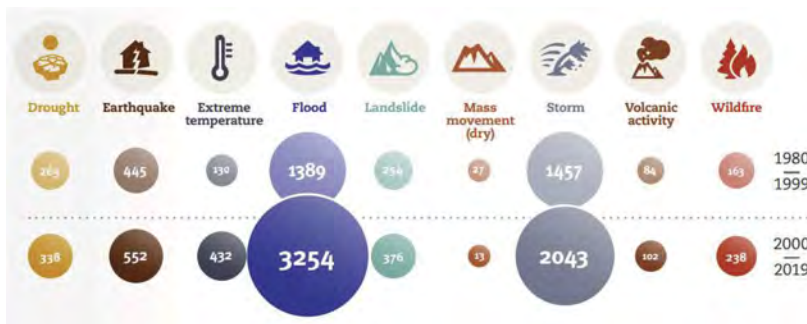


Figure 2. Total disaster events by type: 1980-1999 vs. 2000-2019 (United Nations Office for Disaster Risk Reduction, 2019).

1.2 Food risk and vulnerability

Flood events are becoming more frequent and severe in both intensity and frequency. Despite assessment, risk management and mitigation measures in recent years, flood impacts remain a serious problem. Floods are negatively impacting the economy and society worldwide at an alarming rate. Floods normally occur after prolonged signs from nature, such as heavy rain and high winds, or can arise suddenly and abnormally due to causes, such as hydroelectric dam failure, sudden flood discharge, among others. In previous studies, flood risk was considered as a problem to be assessed and remedied when the incident happened, not proactively (Z. Vojinovic, M.B. Abbott, 2012). With a new and more developed approach along with the advance of science and technology, nowadays, flood risk is deemed for management to propose solutions for prevention.

Currently, a clear definition of flood risk management does not exist. However, there is one most accepted and used definition: the potential for a community to be affected by a flood hazard depending on severity, vulnerability, and exposure (S.F. Balica, N.G. Wright, 2010; A. Bento, M.Q. Tran, H.S. Sousa, E. Teixeira, 2022; G. Cremen, C. Galasso, J. McCloskey, 2022; J.F.S. Barrionuevo, H.C. Noblejas and FF.J.C. Prados, 2022). In other words, flood risk is determined by three factors: (1) Hazards (H), (2) Exposure (E), and (3) Vulnerability (V). Figure 3 shows the relationship between the components and flood risk management.

The total elimination of a hazard (H) is impossible; thus flooding may occur in a specific region in the study and there might be no way to avoid it. Only forecasts based on hydrometeorological analysis can be used to minimize its effects. At the same time, exposure (E) to floods of human activities is natural, and people must appear in economic zones to participate in production activities, build new infrastructure, among others. Therefore, an important factor to tackle for flood risk management is related to vulnerability. Vulnerability (V) corresponds thus to the expected degree of harm under certain exposure conditions, susceptibility, and resilience.

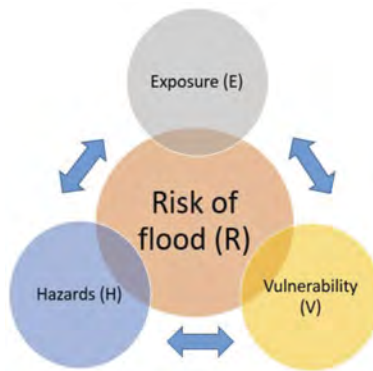


Figure 3. Relationship between flood risk management and its components.

Flood vulnerability is hence a key factor in flood risk assessment and damage assessment. This can be easily seen through the “butterfly effect” or the “domino effect”, where just a small fraction of the damage in a flood can lead to enormous consequences for a risk management concept.

2 APPROACHES AND METHODS FOR ASSESING VULNERABILITY TO FLOODS

There are many definitions of vulnerability, mentioned in many fields with many factors (Timmerman, 1981; Canon, 1994; Susan L. Cutter, 1996; Caroline, 1998; Alexander, 2012; W.E.Morrison, M.W. Nelson, J. F. Howard, E.J. Teeters, J.A. Hare, R.B. Griffis, J.D. Scott, and M.A. Alexander, 2015; Kumar, Bhattacharjya, 2020). Being vulnerability treated as an abstract concept, there is no consensus across industries, thereby the need to quantify it to better describe it. However, there are some similarities between the published studies. Therefore, vulnerability can be defined as the degree of loss or degradation of the deemed object (the system under consideration) before a harmful agent. For different fields of study, vulnerability can depend on several aspects, concerning the subject being considered. In the present study, flood vulnerability is mentioned and analyzed.

A number of flood vulnerability assessment methods have been developed by previous studies (J.F.S. Barrionuevo, H.C. Noblejas and FF.J.C.Prados, 2022), but the effectiveness of these methods is not high due to many factors. Vulnerability assessment methods are usually divided into the following basic groups: (i) vulnerability indicator method; (ii) vulnerability curve method; (iii) disaster loss data method; and (iv) modeling method.

The vulnerability indicator method is based on specifying vulnerability with a certain value through variables affecting vulnerability. Until now, this method has been widely used and preferred by policymakers. For flood vulnerability, indicators affecting the impact of floods on social, environmental, physical and economic aspects are considered. Usually, indicators are chosen by experts. However, for each region and each expert’s point of view, the indicators are often not the same or have little in common. This method is only useful for specific flood areas.

The vulnerability curve method is an approach based on the relationship between risk and related factors that depends on fully documented and published case study data. This group of methods uses variables in a specific area to evaluate, and build the damage curve step-by-step. Despite its accuracy, this method is rarely used due to space limitations (applicable only to a particular group with documented data) and consumes a lot of resources and efforts for conducting investigation, assessment and surveys. This approach is essentially founded on data from well-documented case studies so typically restricted to dwellings in a specific area.

Disaster loss data is a method for predicting future events and vulnerabilities by evaluating past data regarding losses. This method is not as accurate as desired, although quite easy to implement, due to the published loss data in a number of reliable sources (the national

information system, and the damage reports of the agencies). Damage and losses from flood events are recorded, from which damage predictions are performed. However, the data are not continuous and are often only comprehensive for severe floods, so predictions are often less accurate.

Modeling method considers the use of models, simulation evaluation, prediction of depth, height and flood pattern. Vulnerability assessment is carried out through model analysis results: predict flood prone locations, damage levels in each model area, forecast vulnerability according to a specified scale. This modeling approach can better assess vulnerability at a smaller scale than other methods, since it focuses on specific areas. In contrast, it is unable to describe a clear relationship between flood damage and forecast maps. The different vulnerability assessment methods each have their own advantages and disadvantages (Table 1).

Table 1. Advantages and disadvantages of vulnerability assessment methods.

Methods	Vulnerability indicator methods	Vulnerability curve methods	Disaster loss data methods	Modeling methods
Advantages	<ul style="list-style-type: none"> - Has specific, intuitive categorical value; - Widely researched and used; - Can evaluate in general or specific to each area. 	<ul style="list-style-type: none"> - Precise on the area under consideration since it was established on the basis of actual investigation. 	<ul style="list-style-type: none"> - Simple, easy to do thanks to finding open sources. 	<ul style="list-style-type: none"> - Very well applied to a specific area with full parameters.
Disadvantages	<ul style="list-style-type: none"> - Depends on several variables of many fields; - The choice of weights for the factors is controversial. 	<ul style="list-style-type: none"> - Takes a lot of time and effort; - Not applicable to different areas. 	<ul style="list-style-type: none"> - No significant accuracy. 	<ul style="list-style-type: none"> - Low accuracy in the absence of survey data; - Difficult to implement in a large area.

Flood vulnerability index methods (FVI) have proved to be more effective in recent studies (S.F. Balica, N.G. Wright, 2010; Nasiri et al., 2016; C.T. Van, D.Q. Tri, N.T. Son, T.T.T. Thao, D.T.H. Hoa, 2019). FVI assesses vulnerability not directly, but rather through various aspects of the main system. In this sense, it can be comprehensively reviewed and assessed in a large area, raising public awareness, and supporting the government in flood risk management. However, this method is less rigorous in the use of parameters. Parameters are selected based on the experts' opinions, often without regard to the importance of the parameters. In other words, the relevant parameters are all considered, and then calculated equally. At the same time, the flow and hydraulic conditions of the area are not analyzed in detail.

3 FLOOD VULNERABILITY INDEX (FVI)

As mentioned above, FVI provides a quick, reliable and relatively comprehensive flood vulnerability assessment method. Figure 4 schematizes its simple structure. This method uses sets of indicators covering all aspects of the area to assess flood vulnerability. The indicators used allow comparison of flood vulnerability in different areas. FVI can measure trends in changes in components, helping to identify and monitor the action priorities needed in flood response. These features provide strategically important information for flood risk planning and management.

a. FVI factors

Each component of vulnerability is assessed through three factors: exposure (E), susceptibility (S) and resilience (R). The interaction between vulnerability factors and components forms thus the foundation of the FVI method, illustrated in Figure 5.

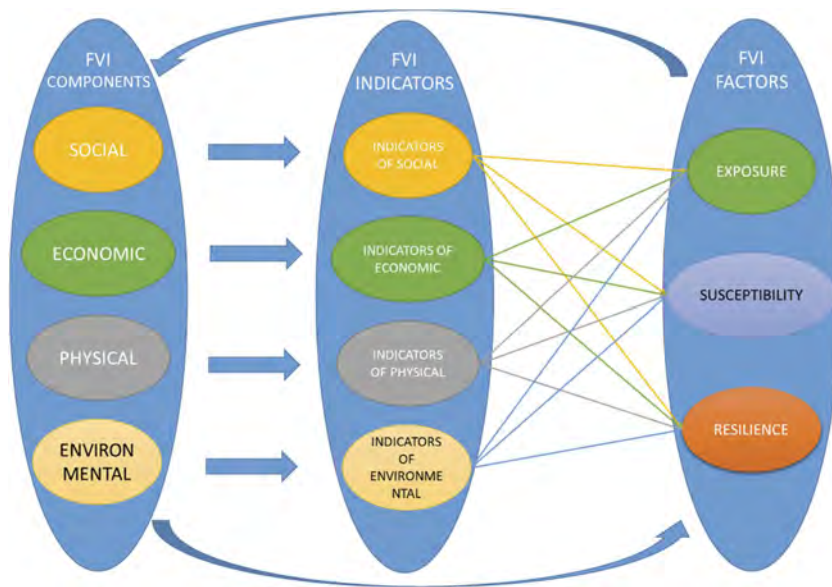


Figure 4. Flood vulnerability index (FVI) structure.

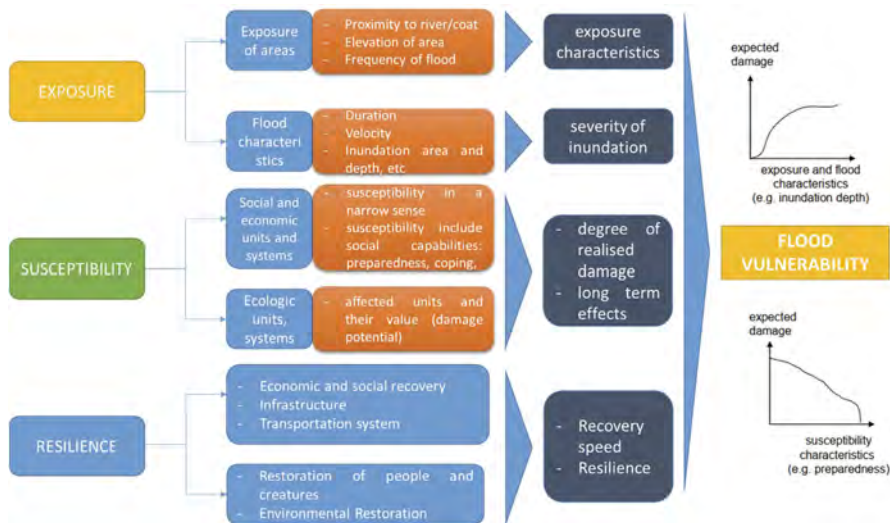


Figure 5. Factors to be used in flood vulnerability assessment.

The factors in a vulnerability assessment have a close relationship with each other and directly affect the total vulnerability index of the system. Two views, based on two mathematical relationships, have been studied and herein presented in Equations 1 and 2 (R F Connor, K Hiroki, 2005):

$$Vulnerability = \frac{Exposure \times Susceptibility}{Resilience} \quad (1)$$

$$Vulnerability = Exposure + Susceptibility - Resilience \quad (2)$$

In the proposed method, in order to directly identify the vulnerability values, Equation 3 was selected for implementation. Accordingly, Equation 2 becomes:

$$FVI_{total} = \frac{\left(\frac{E \times S}{R}\right)_{social} + \left(\frac{E \times S}{R}\right)_{economic} + \left(\frac{E \times S}{R}\right)_{environment} + \left(\frac{E \times S}{R}\right)_{physical}}{4} \quad (3)$$

b. FVI indicators

In a component, there are different aspects expressed through the parameters of the system. These parameters are characteristics of a certain region (i.e. the area under consideration). These parameters are commonly referred to as flood vulnerability indicators. In other words, flood vulnerability indicators are detailed components of the system that are considered in terms of social, economic, environmental, and physical components. However, within a system, there are many indicators, which may or may not be related to flooding vulnerability. Understanding and reviewing the indicators is thus essential to being able to make an accurate forecast.

Numerous studies have been conducted on selecting indicators to calculate flood vulnerability. The indicators depend quite heavily on the study area. By indepth analysis, the sets of indicators are increasingly reduced and optimized. These sets of indicators are quite concise and still provide the required accuracy (S.F. Balica, N.G. Wright, 2010). From 1993 to 1997, according to the detailed database of the World Bank, up to 1200 indicators were used to calculate and assess vulnerability (Albert Adriaanse, 1993). By 2007, (S.F. Balica; N. Douben; N. G. Wright, 2009) studied and improved the accuracy of the flood vulnerability index. From 80 considered indicators, 40 were analyzed and selected. Afterwards, (S.F. Balica, N.G. Wright, 2010) continued to study and subdivide the indexes for specific regions in the world, including: 20 for river basin scale, 22 for sub-catchment and 27 for urban area. In 2014, (N.T. Cam, 2014) proposed a weight-based flood vulnerability assessment method using 44 indices of components including 3 exposure indices, 28 susceptibility indices, and 13 resilience indices.

c. FVI components

In a system, the components social, economic, environmental and physical exist simultaneously. The social component provides indicators describing the social context, adaptive capacity, skills, knowledge, awareness and behavior of the constituents of the community at the considered geographical scales. The economic component represents the economic development level of the area under consideration. Economic indicators provide assessments of the capacity to produce and distribute goods and services affected by floods. The economic component is herein considered based on two points, When the economy develops and grows, the level of recovery and flood resistance increases, and also the potential damage increases. The environmental component provides criteria for damage to the environment caused by floods. Environmental activities, such as urbanization, industrialization, deforestation, and reforestation, among others, have been directly linked with flood vulnerability. The physical component refers to how physical conditions, either natural or human-made, can affect the vulnerability to flood of a given area. After obtaining the vulnerability indices of each of these components, the vulnerability can be assessed through the final index indicated in Equation 4:

$$FVI_{total} = \frac{FVI_{social} + FVI_{economic} + FVI_{environment} + FVI_{physical}}{4} \quad (4)$$

Through the FVI_{total} , information on the vulnerability of a certain geographical area is provided quickly, straightforwardly and reliably, since this index has given relatively complete consideration to the components of the system. Using the FVI_{total} , vulnerability levels can be compared across regions. By mapping vulnerability, flood risk reduction approaches can be designed and optimized. Along with that, identifying root causes of vulnerability provides essential information

for planning risk management and limiting flood damage. The extent of vulnerability to flood is determined by various sources. The most commonly used flood vulnerability scale is specified in Table 2.

Table 2. Flood Vulnerability Index (FVI_{total}) scale.

Level	FVI _{total}	Designation	Description
1	< 0.01	Little or no vulnerability to floods	Very small flood vulnerability, fast recovery area, high resilience, flood adaptive area, small exposure, an area that does not usually flood.
2	0.01 – 0.25	Low vulnerability to floods	This is an area where occasional floods occur. Components can be damaged but recover quickly, highly resistant.
3	0.25 – 0.5	Vulnerable to floods	The area is relatively prone to flooding. When having a flood, the vulnerable components are able to recover slowly, but gradually over the months, receiving the right amount of investment.
4	0.5 – 0.75	High vulnerability to floods	Flood frequency is relatively large, and flood level is high. This area is vulnerable to flooding, the resilience and adaptability is poor, and the restoration investment is very small.
5	0.75 - 1	Very high vulnerability to floods	High frequency of floods, high degree of flooding. This area is vulnerable to flooding, recovery is very slow, resilience and adaptation are poor, investment in restoration is very small, Budget is scarce

4 CONCLUSIONS

Vulnerability is an important aspect of assessing and mitigating the negative impacts of flooding events. The paper clarified the relationship between factors in flood vulnerability, from there, got an overview of the vulnerability. To minimize damage from floods or other negative events, it is necessary to reduce the vulnerability of communities and critical infrastructure by providing early warning, strengthening infrastructure, and taking countermeasures in the worst-case scenario.

There are many methods of assessing flood vulnerability, but each method has its own advantages and disadvantages. By analyzing the components and indicators of flood vulnerability, the paper proposes using FVI to flood vulnerability assessment, at the same time, providing a set of indicators to assess vulnerability.

The vulnerability method only contributes to mitigating the negative impacts of floods, however, it also has uncertainties due to the influence of many factors. These factors vary over both space and time, making it difficult to predict with complete accuracy.

ACKNOWLEDGEMENT

This work was partly financed by FCT/MCTES through national funds (PIDDAC) under the R&D Unit Institute for Sustainability and Innovation in Structural Engineering (ISISE), under reference UIDB/04029/2020. This work was partially funded by InfraROB Project which has received funding from the European Union’s Horizon 2020 research and innovation programme under grant agreement No. 955337. This work was partially funded by the provision of External Services to the Municipality of Viana do Castelo under the name “Sistema de Apoio à Gestão de Obras de Arte do Município de Viana do Castelo” with the reference ISISE and with funding from the Municipality of Viana do Castelo. M.Q.Tran was supported by the doctoral Grant reference PRT/BD/154268/2022 financed by Portuguese Foundation for Science and Technology (FCT), under MIT Portugal Program (2022 MPP2030-FCT). H.S.Sousa acknowledges the funding by FCT through the Scientific Employment Stimulus - 4th Edition.

REFERENCES

- A. Bento, M.Q. Tran, H.S. Sousa, E. Teixeira (2022) 'Melhoria da precisão e otimização do método do índice de vulnerabilidade às cheias', *XX SILUBESA - Simpósio Luso-Brasileiro de Engenharia Sanitária e Ambiental* [Preprint]. Available at: <https://www.aprh.pt/20silubesa/docs/XX-S>.
- Albert Adriaanse (1993) 'Environmental policy performance indicators: A study of the development of indicators for environmental policy in The Netherlands', *SDU* [Preprint].
- Alexander (2012) 'Models of Social Vulnerability to Disasters', *Open Edition Journals* [Preprint]. Available at: <https://doi.org/10.4000/rccsar.412>.
- Canon (1994) 'Vulnerability Analysis and the Explanation of "Natural" Disasters. In A. Varley (Ed.)', *Disasters, Development and Environment* [Preprint].
- Caroline (1998) 'The asset vulnerability framework: Reassessing urban poverty reduction strategies', *World Development* [Preprint]. Available at: [https://doi.org/10.1016/S0305-750X\(97\)10015-8](https://doi.org/10.1016/S0305-750X(97)10015-8).
- C.T. Van, D.Q. Tri, N.T. Son, T.T.T. Thao, D.T.H. Hoa (2019) 'Determining the vulnerability index in the context of high floods in An Giang province', *IOP Conf. Series: Earth and Environmental Science* [Preprint]. Available at: <https://doi.org/doi:10.1088/1755-1315/307/1/012015>.
- G. Cremen, C. Galasso, J. McCloskey (2022) 'Modelling and quantifying tomorrow's risks from natural hazards', *Science of The Total Environment* [Preprint]. Available at: <https://doi.org/10.1016/j.scitotenv.2021.152552>.
- J.F.S. Barrionuevo, H.C. Noblejas and FF.J.C. Prados (2022) 'Vulnerability to Flood Risk: A Methodological Proposal for Assessing the Isolation of the Population'. Available at: <https://doi.org/10.3390/land11020277>.
- Kumar, Bhattacharjya (2020) 'Review of different methods and techniques used for flood vulnerability analysis', *Natural Hazards and Earth System Sciences* [Preprint]. Available at: <https://doi.org/10.5194/nhess-2020-297>.
- Nasiri et al. (2016) 'An overview to flood vulnerability assessment methods', *Sustainable Water Resources Management* [Preprint]. Available at: <https://doi.org/10.1007/s40899-016-0051-x>.
- N.T. Cam (2014) 'Vulnerability assessment methods – theory and practice, *Tap chí Phát triển Khoa học và Công nghệ - Khoa học Tự nhiên (STDJNS)* Available at: <http://stdjns.scienceandtechnology.com.vn/index.php/stdjns>.
- R F Connor, K Hiroki (2005) 'Development of a method for assessing flood vulnerability', *Water Science & Technology* [Preprint]. Available at: <https://doi.org/10.2166/wst.2005.0109>.
- S. F. Balica; N. Douben; N. G. Wright (2009) 'Flood vulnerability indices at varying spatial scales', *Water Science & Technology*, 60(10):2571–80. Available at: <https://doi.org/10.2166/wst.2009.183>.
- S.F. Balica, N.G. Wright (2010) 'Reducing the complexity of the flood vulnerability index', *Environmental Hazards* [Preprint]. Available at: <https://doi.org/doi:10.3763/ehaz.2010.0043>.
- Susan L. Cutter (1996) 'Vulnerability to environmental hazards', *Progress in Human Geography* [Preprint]. Available at: <https://doi.org/10.1177/030913259602000407>.
- Timmerman (1981) 'Vulnerability, Resilience and the Collapse of Society'. Available at: <http://www.ilankelman.org/miscellany/Timmerman1981.pdf>.
- United Nations Office for Disaster Risk Reduction (2019) *Human cost of disasters - an overview of the last 20 years (2000-2019)*. Available at: <https://dds.cepal.org>.
- W.E. Morrison, M.W. Nelson, J. F. Howard, E.J. Teeters, J.A. Hare, R.B. Griffis, J.D. Scott, and M.A. Alexander (2015) 'Methodology for assessing the vulnerability of marine fish and shellfish species to a changing climate', *NOAA IR Home* [Preprint]. Available at: <https://doi.org/10.7289/V54X55TC>.
- Z. Vojinovic, M.B. Abbott (2012) *From Quantitative to Qualitative Flood Risk Assessment and Mitigation*. Available at: <https://www.iwapublishing.com/books/9781843393870/flood-risk-and-social-justice>.

Structural modeling and dynamic testing of high-speed railway bridges

M. Anghileri, L. Capacci & F. Biondini

Department of Civil and Environmental Engineering, Politecnico di Milano, Milan, Italy

L. Bernardini, C. Somaschini & M. Belloli

Department of Mechanical Engineering, Politecnico di Milano, Milan, Italy

ABSTRACT: This paper presents the validation of finite element models for modal analysis of prestressed concrete high-speed railway bridge decks. Structural modeling is developed with different levels of complexity using beam finite elements and three-dimensional solid finite elements. Geometrical and mechanical properties of the bridge decks are calibrated based on data gathered from both design technical documentation and outcomes of an experimental campaign, including non-destructive tests and laboratory tests. The results of finite element analyses are compared with the experimental outcomes based on dynamic modal tests to validate the structural models, collect information about the structural behavior and dynamic response of the bridge decks, and support the condition assessment of the railway bridges.

1 INTRODUCTION

Bridges are essential to transportation infrastructure systems and represent key components for economic and sustainable development of countries. It is therefore a priority to protect, maintain, and manage aging bridges over the entire life-cycle (ASCE 2021). An urgent need in many countries worldwide, including Italy, is related to knowledge about condition state and residual performance for huge stocks of aging bridges. This information is critical for public authorities and bridge owners to ensure effective bridge management based on a rational allocation of the available resources (Biondini and Frangopol 2016, 2019). Visual inspections, diagnostic activities, repair and maintenance interventions, and structural health monitoring may be adopted to gather information and data about the actual structural response and detect damage (Andrade and Alonso 2001, Frangopol et al. 2008, Malerba 2014). The results of these activities are crucial for a successful implementation in practice of life-cycle criteria and methods with the purpose of addressing future maintenance and management needs. They can also provide early warning of structural damage before significant repair or maintenance actions are planned (Frangopol and Soliman 2016). The importance of an integrated approach to gather data from inspections and diagnostic activities is also emphasized by recent codes of practice and guidelines (CSLLPP 2020).

This paper presents the validation of finite element models for modal analysis of concrete bridge decks as part of a more extensive activity for condition assessment and experimental testing of a group of viaducts along a high-speed railway line in Italy (Figure 1). The investigated bridges have been built between 1985 and 1989 and are characterized by prestressed concrete (PC) simply supported grillage decks and reinforced concrete (RC) bridge piers. The deck is composed by six longitudinal precast PC beams, five transversal RC beams (i.e., two outer and three inner beams), and a top RC slab. The viaducts along the railway line have a total length ranging from 67.20 m for a two-span viaduct to 1036.50 m for a 29-span viaduct. The span length is varying between 23.60 m and 36.50 m. The number of investigated grillage bridge decks is 126. The experimental campaign included a 12-span PC box-girder viaduct, for a total amount of 11 high-speed railway viaducts and 138 bridge decks investigated. The grillage bridge decks are investigated in this paper based on structural analysis and experimental dynamic modal tests.



Figure 1. High-speed railway bridges with PC grillage decks and RC piers.

2 INSPECTION-BASED CONDITION ASSESSMENT

Visual inspections represent fast activities and early assessment procedures to gather information about bridge condition state compared to diagnostic activities and structural health monitoring. However, results of visual inspections are generally affected by inspector subjectivity and may be limited by the accessibility to structural and non-structural components. On the other hand, the use of high-resolution cameras and drones can support inspection activities and judgments. Moreover, standardization of inspection activities by means of guidelines can significantly reduce uncertainties and subjectivity associated to inspectors and the results of visual inspections can also be efficiently used to update the reliability assessment of the system (Estes and Frangopol 2003). In this way, periodic visual inspections of infrastructural facilities may provide a preliminary indication of the actual structural deterioration state and its evolution in time. Nevertheless, this information is generally not sufficient to eventually plan maintenance and repair interventions.

For the bridge viaducts investigated in this paper, diagnostic activities have been combined with inspection activities to assess material characteristics, deterioration state, and residual structural performance. More specifically, non-destructive tests, such as rebound hammers and ultrasonic tests, have been used to estimate the mechanical characteristics of materials. Furthermore, laboratory tests on concrete cores and samples of reinforcing steel bars have been conducted to gather additional information about material characteristics and damage state. The condition state of the bridges is then quantified by performance indicators associated with the detected defects at various scales, from the elementary components of each grillage deck (i.e., longitudinal beams, transversal beams, and slab) up to the constitutive components of each bridge span module (i.e., deck, piers, and abutments). Statistical analysis has been carried out on the dataset of performance indicators with the aim of prioritizing further investigations and suggesting possible corrective interventions to better assess and ultimately improve the condition state of the most critical elements within the investigated bridge stock. The results of the extensive campaign of diagnostic activities have been also used to inform the development and calibration of the structural models presented in this paper.

3 DYNAMIC MODAL TESTS

The high-speed viaducts under investigation have been dynamically analyzed with the purpose to extract modal parameters and use them to further calibrate the finite element models. Due to the large number of bridges to be instrumented, a wireless sensor network has been adopted to enhance and speed up the entire experimental campaign. In fact, eleven different viaducts have been investigated, with a total amount of 138 spans dynamically assessed. Each studied span has been instrumented through a couple of sensors placed at midspan (Figure 2a). Furthermore, for each viaduct one span was instrumented also through a denser sensors setup (Figure 2b) in order to detect higher order modes. The sensing devices adopted consist of wireless accelerometers with MEMS technology (by LORD microstrain), with a full scale of 10g or 40g. Sensing devices with lower full scale have been positioned on the deck substructure, while the 40g accelerometers have been placed on railway track sleepers and used to identify the properties of the travelling railway vehicles (i.e., train type and speed). The sensors synchronization has been performed and controlled by their base station.

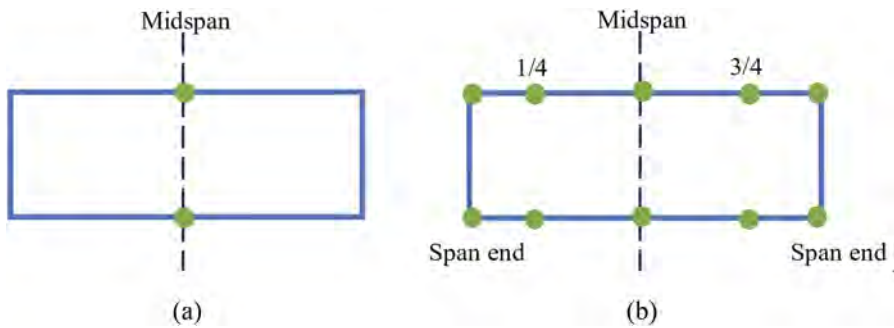


Figure 2. Sensors setup adopted during the dynamic experimental campaign: (a) basic setup; (b) denser setup. Accelerometers positions on the span are highlighted by green circles.

For each span, the accelerometers have been placed, together with the base station, on the bridge for a total amount of time ranging from 10 to 15 hours. In this way it has been possible to acquire an adequate number of train passages. The acquisition setup is collected in Table 1. Additional details regarding the experimental campaign can be found in Bernardini et al. (2021).

Table 1. Acquisition setup adopted during the experimental campaign.

Sampling frequency 10g accelerometers [Hz]	256
Sampling frequency 40g accelerometers [Hz]	1024
Trigger threshold for deck accelerometers (10g) [m/s^2]	0.05
Trigger threshold for track accelerometers (40g) [m/s^2]	0.5
Pre-trigger [s]	5
Minimum observation length [s]	40

The acquired signals contain both forced and free motions, as shown in Figure 3. The viaducts free decays, after train transit, have been used for modal analysis. Therefore, before being processed, the measured accelerations have been treated with the purpose to remove the forced motion (boxed in red in Figure 3) and retain only the free decay (boxed in green in Figure 3). Once the accelerations have been purged from the forced motion and the isolated free responses, collected during the testing interval, have been put in series one with each other, it has been possible to use the time series corresponding to each sensor composing the mesh as input for the commercial software ARTEMIS, used for modal identification. Therefore, modal parameters, namely eigenfrequencies, and the associated mode shapes and damping ratios, have been estimated.

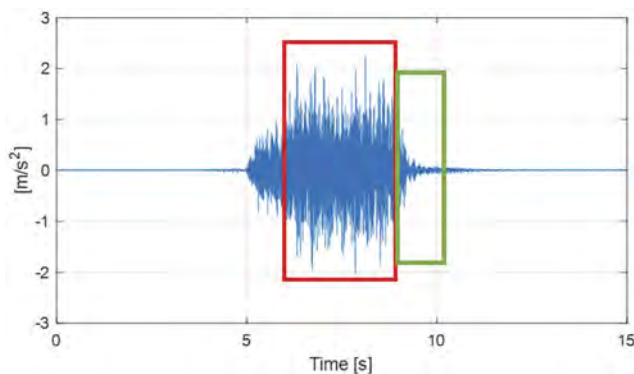


Figure 3. Example of recorded midspan deck acceleration. Forced motion boxed in red, free decay boxed in green.

4 FINITE ELEMENT MODELING AND VALIDATION

Structural modeling is developed with different levels of complexity adopting beam finite elements and three-dimensional (3D) solid finite elements. Geometrical and mechanical properties of the bridge decks are calibrated based on data gathered from design technical documentation and results from experimental activities which include non-destructive tests and laboratory tests. Moreover, the results of dynamic modal tests are used to validate the numerical models and investigate the dynamic response of the bridge decks.

Beam finite element models allow for an adequate balance between representativeness of the structural response and computational cost. This kind of modeling is particularly effective at representing the overall response of the structure and capture the role of the main structural elements (i.e., longitudinal and transversal beams).

3D solid finite element models are more effective to represent the actual bridge geometry, capture the local structural response at the stress-diffusion zones and incorporate local contributions to the stiffness properties of the structural system. These models are also a further support to validate the beam finite element models. On the other hand, they have a larger computational cost compared to beam models.

The definition of geometry, topology, boundary conditions, restraints, and mechanical properties of the finite element models based on the available technical documentation and data gathered from diagnostic activities is described in the following, along with the results of modal analyses with emphasis on the validation process based on the results of dynamic testing. Individual bridge deck spans are firstly considered for a preliminary calibration of the structural model with the experimental results. A joint model with two spans is hence considered to investigate the role of the railway track superstructure (e.g., ballast).

4.1 *Mechanical characteristics of concrete*

The mechanical characteristics of concrete have been assessed based on the results of the non-destructive sclerometric and ultrasonic experimental tests and laboratory compression tests on concrete samples. Table 2 reports the mean value of compressive cube strength and elastic modulus, along with the coefficient of variation (CoV) of the compressive cube strength, resulting from a statistical analysis combining the outcomes of non-destructive and destructive tests for one of the inspected bridge deck. Mean values have been assumed as nominal values and adopted in the validation process of the structural models.

Table 2. Statistical results from diagnostic activities.

Element	Mean compressive cube strength R_{cm} [MPa]	CoV(R_c)	Mean elastic modulus E_{cm} [MPa]
Longitudinal beams	61.18	3.12 %	35821
Transversal beams	42.77	6.29 %	32174

4.2 *Beam finite element modeling*

The cross-sectional geometry of the structural elements has been defined for the different bridge components based on design technical documentation and results of survey and inspection activities. Figure 4 shows an isometric view of the structural model with solid section of the longitudinal beams (Figure 4a) and transversal beams with collaborating top slab (Figure 4b).

The bearing support devices are modeled by rigid constraints. At the location of the unidirectional roller supports, the displacement components are constrained along vertical and transversal direction. At the location of the hinge supports, also longitudinal displacement component has been constrained.

For the structural (deck) and non-structural (ballast) masses density values of 2.5 t/m^3 and 9 t/m^3 , respectively, are assumed. The masses have been considered concentrated at the nodes and the portion of the mass at each node has been calculated in proportion to the corresponding influence area in the plan view.

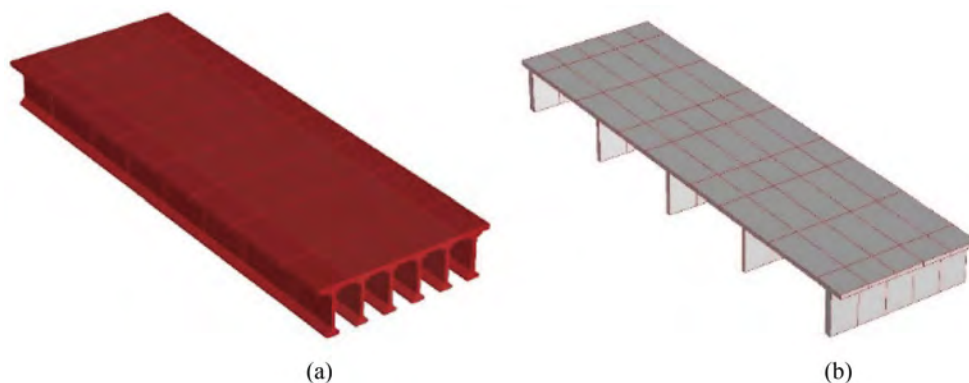


Figure 4. Isometric view of a beam model of the bridge deck: (a) longitudinal beams and (b) transversal beams with collaborating top slab.

Figure 5 shows the mode shapes of a bridge deck associated to first and second bending and torsional eigenfrequencies. Table 3 compares the first three natural frequencies obtained from both numerical analysis and experimental dynamic tests for one of the inspected bridges. The numerical vs experimental comparison allows to validate the numerical model of the bridge deck in terms of geometry, stiffness, and mass properties associated to the bridge members.

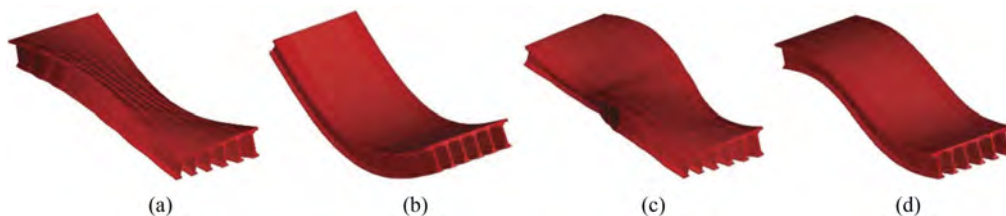


Figure 5. Natural vibration modes of the deck based on the beam modeling: (a) First torsional; (b) First flexural; (c) Second torsional; (d) Second flexural.

Table 3. Numerical vs experimental natural frequencies for a bridge deck.

Mode	Natural frequency [Hz]	
	Numerical	Experimental
First torsional	5.61	6.33
First flexural	5.63	5.92
Second torsional	19.94	19.88

4.3 Three-dimensional solid modeling

The 3D solid finite element modeling has been developed based on the volumetric sectional area reported in the design technical documentation of the different bridge deck members. Figure 6 shows a transversal section of the bridge deck with longitudinal beams (Figure 6a),

end ribs (Figure 6b), and stiffening transversal beams (Figure 6c) with collaborating top slab. The implementation of the structural model is based on the reference transversal sections that have been extruded along the longitudinal direction.

Figure 7 shows the 3D solid model, with a finite element discretization selected to guarantee adequate shape factor and aspect ratio (Figure 7a) and to accurately reproduce the tapered portions of the longitudinal beams adjacent to the transversal elements (Figure 7b). The model is mostly composed by hexahedral finite elements except for the elements that form the tapering portions of the longitudinal beams, which are based on tetrahedral elements with triangular or rectangular base. At location of the roller supports, the vertical and transversal displacement components have been constrained on the footprint of the support devices. At location of the hinge supports, also the longitudinal displacement components have been constrained.

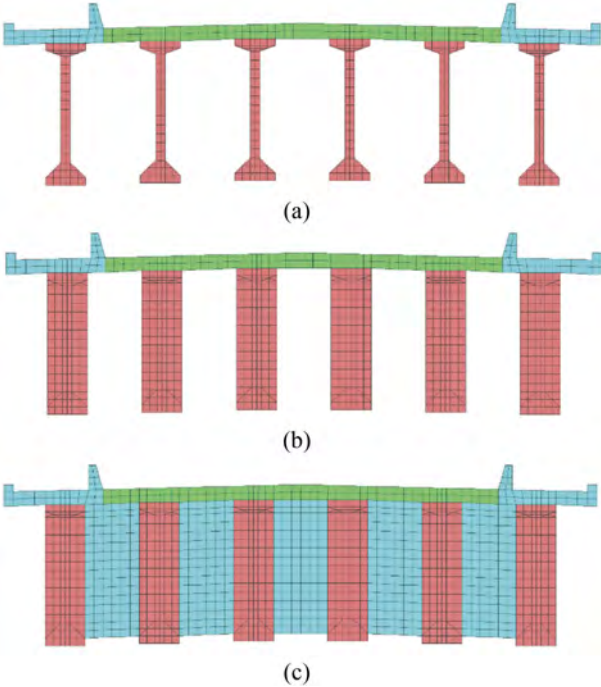


Figure 6. Transversal cross-sectional modeling and finite element discretization of the deck with (a) longitudinal beams, (b) end ribs, and (c) stiffening transversal beams with collaborating top slab.

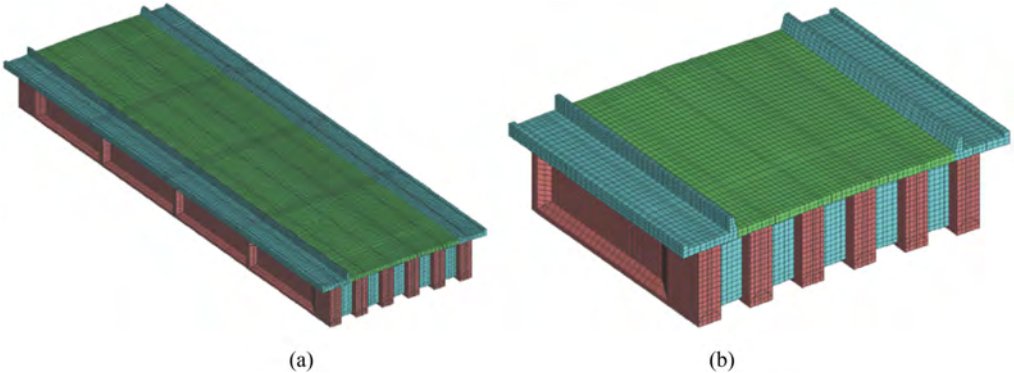


Figure 7. Three-dimensional solid model of the deck: (a) isometric view and (b) detail of the end region.

Figure 8 shows the natural vibration modes of a bridge deck associated to first and second bending and torsional modes. Table 4 compares the first three natural frequencies obtained from the two numerical models (i.e., beam and solid models) versus the experimental results.

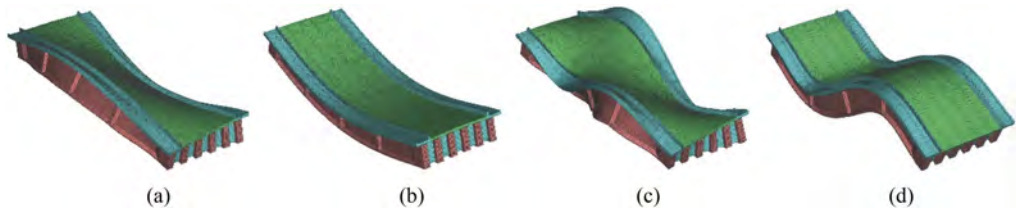


Figure 8. Natural vibration modes of the bridge deck based on the solid modeling: (a) First torsional; (b) First flexural; (c) Second torsional; (d) Second flexural.

Table 4. Numerical (beam and solid models) vs experimental natural frequencies of a bridge deck.

Mode	Natural frequency [Hz]		
	Numerical (Beam Modeling)	Numerical (Solid Modeling)	Experimental
First torsional	5.61	6.38	6.33
First flexural	5.63	5.28	5.92
Second torsional	19.94	20.50	19.88

This comparison indicates a good agreement between the two models, as well as between numerical and experimental results. These successful comparisons validate the numerical models and confirm the accuracy and effectiveness of the beam modeling of the grillage bridge deck, characterized by lower computational cost and easier management and interpretation of the overall structural response compared to a 3D solid modeling.

4.4 Modeling of railway tracks and interaction of bridge decks

The multi-span railway bridge superstructure participates in the structural response for both the contribution of non-structural elements (i.e., ballast and railway tracks) and for the interaction between adjacent bridge decks. The role of the railway tracks has been investigated with the 3D finite element model through the joint modeling of two adjacent spans of a viaduct. The railway tracks have been modeled with beam finite elements attached to the bridge deck by means of elastic links, that simulate the role of the ballast, with estimated stiffness of 190 MN/m^2 . Outside the bridge deck, for a length of 40 m beyond the deck ends, the elastic connection of the tracks has been attached to the ground. Figure 9 shows an overall isometric view of the model of two adjacent decks (Figure 9a) and a detail of the railway track-bridge deck connections

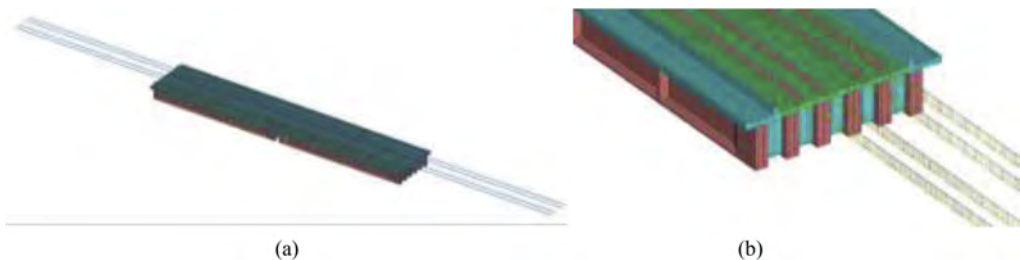


Figure 9. Modeling of railway tracks and interaction of adjacent bridge decks: (a) isometric view of two adjacent spans with railway tracks; (b) detail of the railway track-bridge deck connections.

(Figure 9b). As expected, it has been found that the role of the railway tracks in the structural response is quite limited and modal analysis conducted on this assembled structural model leads to negligible variations of natural frequencies due to this interaction.

5 CONCLUSIONS

This paper presented the validation of finite element models for modal analysis of concrete grillage bridge decks as part of a more extensive activity for condition assessment and experimental testing of a group of viaducts along a high-speed railway line in Italy. Structural modeling has been developed with different levels of complexity adopting beam finite elements and 3D solid finite elements. Geometry, topology, boundary conditions, restraints, and mechanical properties of the structural models have been based on the available technical documentation and data gathered from diagnostic activities, which include non-destructive tests and laboratory tests. Along with models of individual bridge decks, a joint model with two adjacent decks has been also considered to investigate the role of the railway track superstructure. The outcomes of dynamic modal tests have been hence used to validate the numerical models.

The results indicated good agreement between the two types of modeling, as well as between numerical and experimental results. These successful comparisons allowed to validate the numerical models and confirmed the accuracy and effectiveness of the beam modeling of the grillage bridge deck, characterized by lower computational cost and easier management and interpretation of the overall structural response compared to a 3D solid modeling. Finally, it has been found the role of the railway tracks in the structural response is quite limited, with negligible variations of the natural frequencies due to the railway track-bridge deck connections.

REFERENCES

- Andrade, C. and Alonso, C. 2001. On-site measurements of corrosion rate of reinforcements. *Construction and Building Materials*, Elsevier, 15(2-3), 141–145.
- ASCE 2021. *Report card for America's infrastructure*. America Society of Civil Engineers, Reston, VA, USA.
- Bernardini, L., Benedetti, L., Somaschini, C., Cazzulani, G., Belloli, M. 2021. SHM campaign on 138 spans of railway viaducts by means of OMA and wireless sensors network. *9th International Conference on Experimental Vibration Analysis for Civil Engineering Structures*, Tokyo, Japan, September 17-20, 2021.
- Biondini, F. and Frangopol, D. M. 2016. Life-cycle performance of deteriorating structural systems under uncertainty: Review. *Journal of Structural Engineering*, ASCE, 142 (9),F4016001.
- Biondini, F. and Frangopol, D. M., Eds. 2019. *Life-cycle design, assessment, and maintenance of structures and infrastructure systems*. America Society of Civil Engineers, Reston, VA, USA.
- CSLLPP (2020). *Linee guida per la classificazione e gestione del rischio, la valutazione della sicurezza ed il monitoraggio dei ponti esistenti*. Ministero delle Infrastrutture e dei Trasporti, Italy.
- Estes, A. C. and Frangopol, D. M. 2003. Updating bridge reliability based on bridge management systems visual inspection results. *Journal of Bridge Engineering*, ASCE, 8(6),374–382.
- Frangopol, D. M. and Soliman, M. 2016. Life-cycle of structural systems: recent achievements and future directions. *Structure and Infrastructure Engineering*, Taylor & Francis, 12(1),1–20.
- Frangopol, D. M., Strauss, A., and Kim, S. 2008. Bridge reliability assessment based on monitoring. *Journal of Bridge Engineering*, ASCE, 13(3),258–270.
- Malerba, P. G. 2014. Inspecting and repairing old bridges: Experiences and lessons. *Structure and Infrastructure Engineering*, Taylor & Francis, 10(4),443–470.

Seismic base isolation of Palazzo Partigiani in Perugia

F. Parisi

Department of Structures for Engineering and Architecture, University of Naples Federico II, Naples, Italy

T. Zordan

BOLINA Ingegneria, CEN-TC 340, Venice, Italy

A. Romano

BOLINA Ingegneria, Venice, Italy

ABSTRACT: Historic masonry buildings are often heavily damaged by earthquakes, resulting in huge loss of cultural heritage. Several studies have shown the effectiveness of seismic vulnerability mitigation via base isolation systems (BISs). This paper presents a major BIS project for seismic retrofitting of an existing strategic masonry building, which was built in the early 1950s in Perugia (Italy) and hosts the Umbria Region headquarters and other major public offices. The BIS design started from a historical investigation on the original design, fabrication and modifications of the masonry building. On-site experimental tests on both subsoil and masonry structure, as well as geometric surveys, were carried out, allowing a good knowledge of the building and calibration of three-dimensional structural models. The structural characteristics, historical value and public function of the building delineate a case study with considerable importance in the field of seismic isolation of existing masonry buildings.

Keywords: Seismic base isolation, Historic masonry buildings, Structural analysis, Construction

1 INTRODUCTION

Construction industry is among the largest global economy sectors, particularly if the most industrialized countries are considered. The uncertain nature of potentially harmful events (be they natural, anthropic or a combination of them), structural response of engineering facilities to such events, and consequences on property and people call for performance-based engineering methods and implementation of risk-based concepts in structural engineering (Dickson et al. 2012). In addition, a rational approach to disaster risk mitigation of civil infrastructure relies upon consideration of life-cycle performance of structures, accounting for aging and deterioration of materials, components and connections (Frangopol et al. 2004) as well as interaction with climate-change-related phenomena (Olsen 2015). Civil infrastructure is indeed meant to ease and protect human life, represent the welfare and heritage of people, and host a great part of the investments of both individuals and communities (DMRH 2017).

In the context of earthquake engineering, seismic design and retrofitting of structures is usually based on damage tolerance and control, taking advantage of the dissipation of inelastic materials and redistribution phenomena under strong ground motion. Nonetheless, seismic protection of strategic facilities must rely upon their ability to be operational under ground motion, allowing disaster emergency management and hence resilience of communities. None to slight damage is thus required to strategic structures, even if a strong earthquake occurs. This is in favor of a quick recovery process at both urban and regional scales, mitigating socioeconomic issues related to people dislocation away from their houses at least to allow safety checks on damaged structures.

Seismic base isolation, namely the idea of de-coupling the sub-structure from the super-structure through cutting and installation of specific devices able to lower the seismic demand on the superstructure (shifting the fundamental vibration period of the structure in the response spectrum towards longer periods associated with lower levels of acceleration) is an ancient technique based on self-construction (Figure 1) and empirical trial-and-error practice. Examples are known since the past in many earthquake-prone regions. In more recent times, starting from the early 1970s, base isolation has started becoming a standard for new construction in areas with medium-to-high seismicity. Accordingly, specific industrial products are constantly provided, certified and installed according to the rules of specifically oriented product standards (CEN 2009, Medeot & Zordan 2017, Zordan & Medeot 2020).



Figure 1. Seismic base isolation techniques: (a) general layout and (b, c) historic evidence based on self-construction.

Base isolation is known to be an effective tool in ensuring operation of structures and infrastructures hit by a severe earthquake, preventing damage to the super-structure and fully protecting non-structural components and content. In recent years, the possibility to provide also existing structures and infrastructures (and specifically buildings originally built with a fixed base) with base isolation has become a reality. After the earthquake that hit the city of L’Aquila (central Italy) in 2009, several applications of base isolation have taken place in Italy, mainly boosted by economic incentives introduced by the Italian government for reconstruction, in order to promote an increased and diffuse seismic resilience of the national built environment. Besides, innovation in seismic isolators is even more allowing effective disaster risk mitigation in masonry buildings located in developing countries (Losanno et al. 2021, 2022, 2023).

In this study, a major base isolation project for seismic retrofitting of an existing strategic masonry building with historical-architectural value is presented. After that key data on the original design, fabrication and modifications of the masonry building are collected, the paper illustrates the other phase of the knowledge process, which was based on-site experimental tests and geometric surveys. Then, three-dimensional (3D) modelling and response analysis of the masonry building are described, highlighting the significant benefits due to seismic base isolation. The paper ends with a short description of construction phases related to the creation of the base isolation system (BIS).

2 MAIN CHARACTERISTICS AND ON-SITE ASSESSMENT OF THE BUILDING

2.1 Short description of the building

The case-study building which was equipped with a BIS is Palazzo Partigiani in Perugia, Italy. That facility is a strategic building built in the early 1950s, mostly using unreinforced masonry as construction material but also other technologies. The building hosts the headquarters of Umbria Region, Perugia public prosecutor’s office and some offices of the Italian Ministry of

Infrastructure and Transportation. The building consists of five floor levels with L-shaped plan, which is approximately 1600 m² in size (Figure 2).

The structural design for the base isolation of the building began with a comprehensive historical investigation based on archival data and literature, which allowed the authors to assess how the building was conceptually designed and fabricated.



Figure 2. External views of Palazzo Partigiani in Perugia, Italy: (a) building at the end of construction in 1950; (b) building at present.

2.2 On-site assessment

A systematic survey of construction materials, together with an extensive campaign of investigations on geometry of foundations and on the superstructure, allowed the authors to achieve an exhaustive level of knowledge on the typological and mechanical characteristics of materials and construction details. First of all, the field activity showed how the building, in its seventy years of life, has undergone two main interventions; the former consisted of a superelevation of the building with the creation of a further storey; the latter was aimed at energy retrofitting.

An extensive campaign of non-destructive tests was carried out, particularly to identify the building portion made of masonry and the other fabricated with reinforced concrete (RC). Tomography, georadar and pacometer surveys were extensively used for this purpose (Figure 3).

Specimens were extracted and tested to determine the mechanical properties of concrete. Leeb rebound hardness tests were performed to identify the type of reinforcing steel (Figure 4).

Both single- and double-flat jack testing methods were implemented to measure compressive stresses and to evaluate the mechanical parameters of the masonry, respectively (Figure 5).

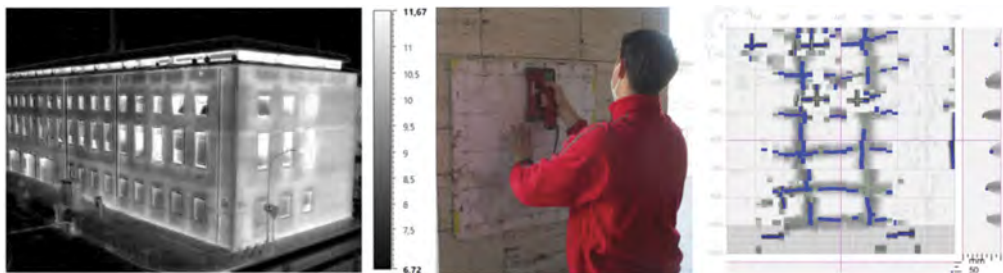


Figure 3. Termography, georadar and pacometer tests for identification of materials and structural components.



Figure 4. Leeb rebound hardness test and concrete samples.

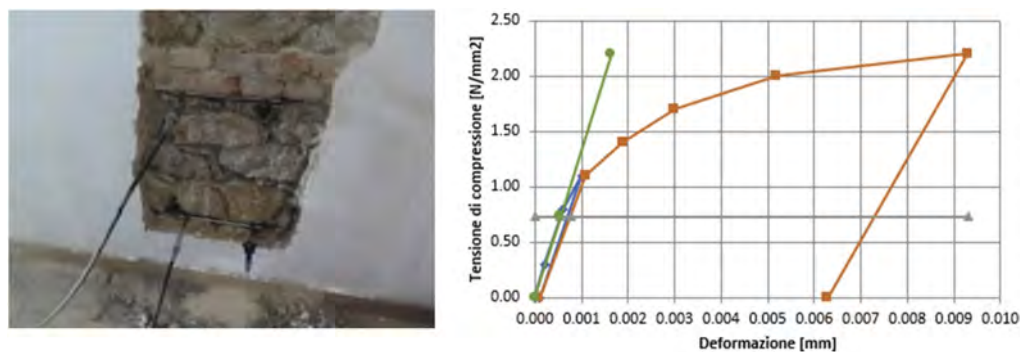


Figure 5. Double-flat jack testing and estimation of secant modulus of masonry.

Furthermore, pull-out tests on concrete were correlated to sample tests in order to obtain a general mapping of the actual properties of structural concrete (Figure 6).

Extensive endoscopy testing offered the chance to assess directly both the shape and appearance of elements, which otherwise would have been inaccessible to direct observation. This allowed the authors to carry out useful evaluations and to determine the exact sequence of layers in different parts of the structure (Figure 7).

The endoscopes gave also evidence of the state of conservation of materials and structural elements. Finally subsoil cores were extracted from boreholes, while deriving the geometry and consistence of the foundation system (Figure 8).



Figure 6. Pull-out tests.

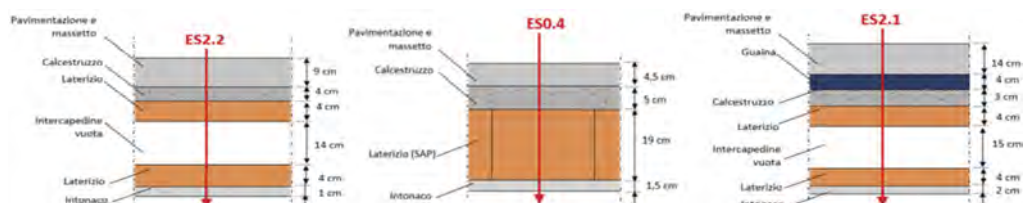


Figure 7. Endoscopy with direct assessment of different layers and degree of conservation of materials.



Figure 8. Subsoil cores obtained from boreholes and foundation assessment.

3 STRUCTURAL MODELLING AND ANALYSIS

Structural modelling and response analysis of Palazzo Partigiani were performed according to two alternative methods, namely, the equivalent frame (EF) modelling approach and the continuum-based finite element (FE) modelling approach based on the macro-modelling of masonry (Augenti & Parisi 2019). Two software packages were used for the above-mentioned modelling approaches, i.e. 3Muri and MasterSap. Specifically, the EF modelling approach was implemented for design and safety checking of the fixed-base structure (Figure 9a). Experimental data were effectively used to model mechanical properties of materials. Afterwards, the FE model was created and calibrated against the EF model in 3Muri, reproducing approximately the same natural periods, modal shapes, and participating masses.

Nonlinear static analysis with displacement control of the original fixed-base structure showed remarkable flaws in terms of seismic capacity, evidencing huge damage to the super-structure (Figure 10a) and insufficient displacement capacity at the ultimate limit state. Therefore, a target isolation period $T_{1,ISO} = 2.1$ s was defined, starting from a fixed-base fundamental period $T_{1,FB} = 0.5$ s, in order to design the base isolation system (Figure 10b). This latter consisted of a combination of different devices, namely 63 elastomeric bearings and 43 multidirectional rollers. Simple calculations allowed minimization of the eccentricity between the centers of mass and stiffness of the structure, as shown in Figure 11.

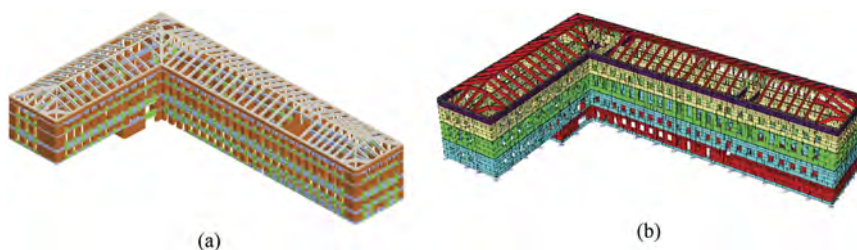


Figure 9. Structural models of the masonry building: (a) equivalent frame model for safety checks of the fixed-base structure and calibration of the continuum finite element model; (b) FE model for design of the base isolation system.

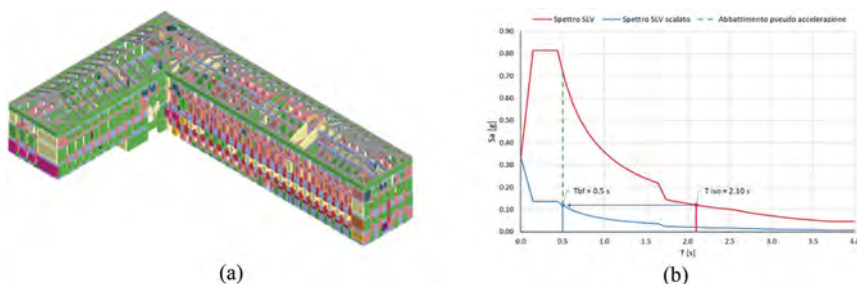


Figure 10. (a) Distribution of damage to the super-structure in fixed-base configuration and (b) identification of the base isolation target period.

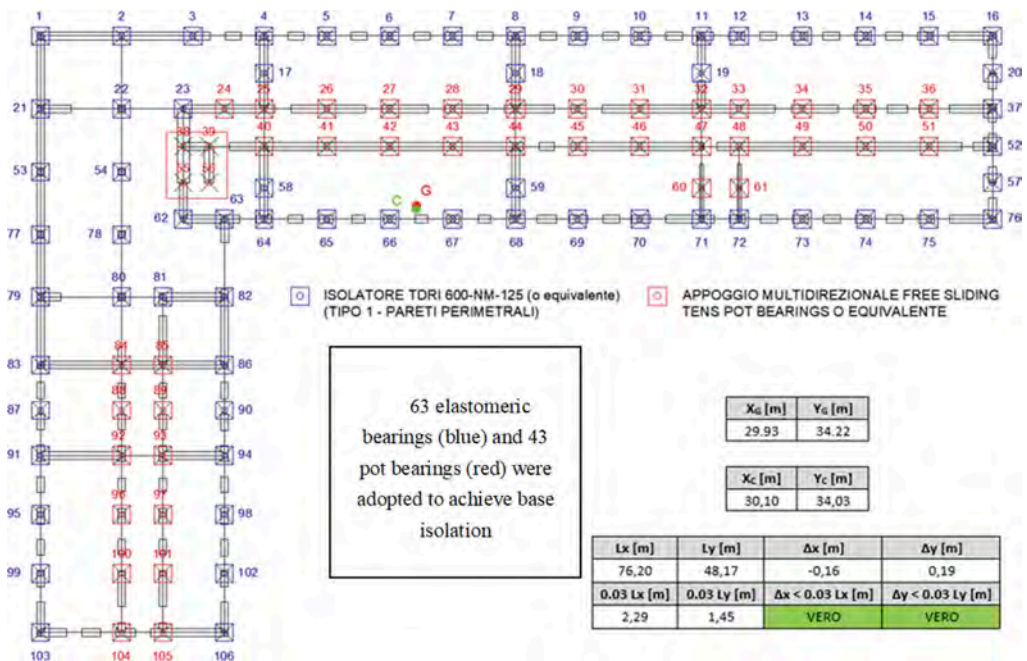


Figure 11. Layout of the elastomeric isolators and multidirectional rollers.

Despite the L-shaped plan of the building, the BIS produced an almost perfect decoupling of vibration modes in the two principal directions, as shown in Figure 12. The maximum displacement at the isolation level was found to be 162 mm, whereas the top roof displacement was estimated in 185mm. This produced a maximum relative displacement at the roof level equal to 230 mm, namely, a very small roof drift ratio. Consequently, no damage to the super-structure was found in the base isolated configuration, as outlined by safety checks in the base-isolated building (Figure 13). Thus, the BIS designed for Palazzo Partigiani allows a significant reduction in seismic demand on the super-structure, hence ensuring operation during strong earthquakes.

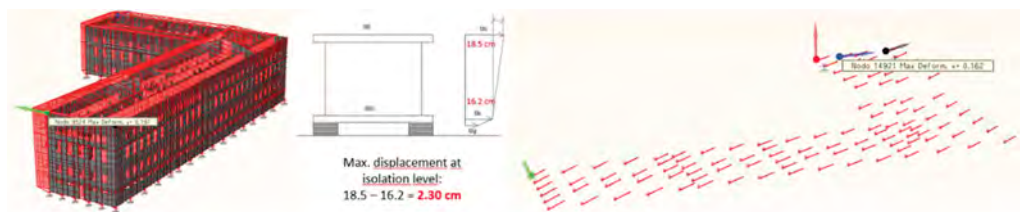


Figure 12. Maximum displacements predicted for the limit state of collapse.

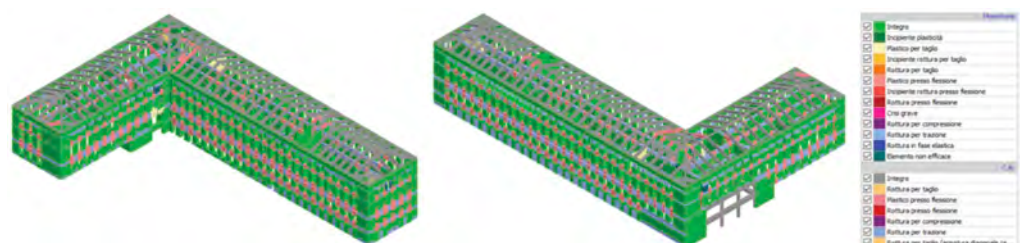


Figure 13. Outcomes of safety checks in structural elements of the base-isolated building.

4 FABRICATION OF THE BASE ISOLATION SYSTEM

The sequence of phases aiming to implement seismic base isolation at the level of the building foundation system is depicted in Figure 14. Specifically, the base isolation system was created through the following phases:

- Phase 1: Original site condition.
- Phase 2: Realization of a diaphragm wall.
- Phase 3: Cutting of masonry wall segments to create the isolation level.
- Phase 4: Fabrication of RC ring beams at the base of existing masonry walls, with removal of existing masonry (to get decoupling between sub-structure and super-structure) and final positioning of seismic isolators.
- Phase 5: Activation of the base isolation system and realization of finishes.

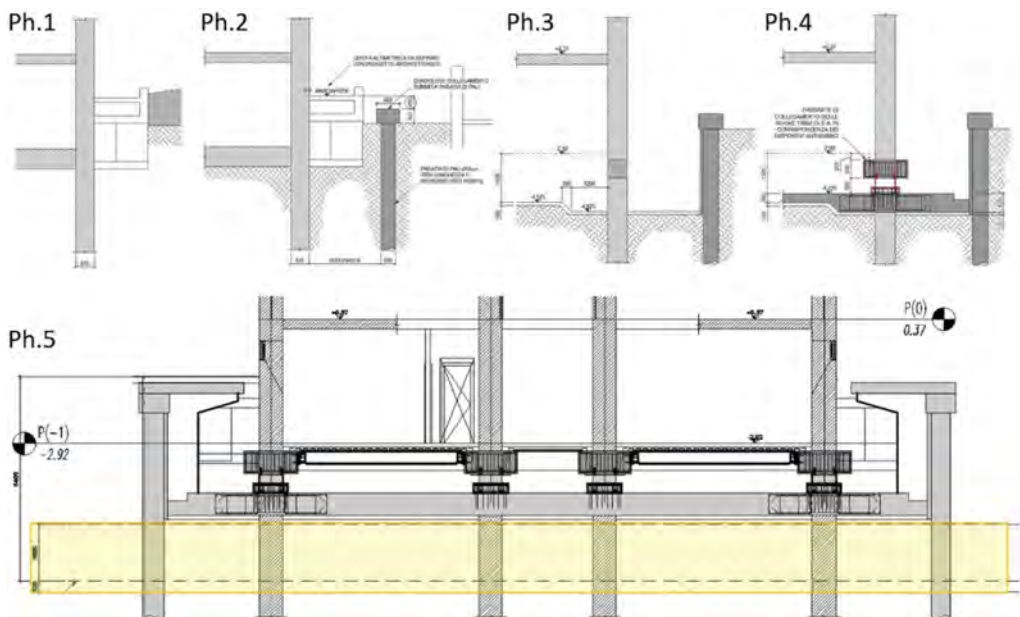


Figure 14. Construction phases for base isolation of the building.

5 CONCLUSIONS

In this paper, the base isolation of a strategic masonry building located in Perugia, Italy, has been presented. The building has architectural-historical value and hosts major public offices that are expected to be used to manage emergency operations after an earthquake. Therefore, the building was retrofitted with the aim of significantly reducing seismic demand on the super-structure, and hence damage. Key information on the building design, fabrication and modifications over time was collected, supporting the design of the base isolation system. On-site experimental tests and surveys were also conducted to assess materials, construction technologies, and detailing. Analysis results show that the isolation system allows the structure to significantly reduce lateral deformation under strong earthquakes, as well as to avoid damage to the super-structure. Ultimately, construction phases for creation of the base isolation system allows building operation during seismic retrofitting. The structural attributes, historical value and strategic role of the building outline a case study with significant importance in the field of seismic isolation of existing masonry buildings.

ACKNOWLEDGEMENTS

The authors would like to acknowledge Eng. Francesco Renò for his contribution given to this work during the preparation of his MSc thesis at University of Naples Federico II, Italy.

REFERENCES

- Augenti, N. & Parisi, F. 2019. *Teoria e Tecnica delle Strutture in Muratura*. Milano: Hoepli editore.
- CEN 2009. *EN 15129: Anti-Seismic Devices*. Brussels: European Committee for Standardization.
- Dickson, E., Baker, J., Hoorweg, D. & Tiwari, A. 2012. *Urban Risk Assessments - Understanding Disaster and Climate Risk in Cities*, Urban Development Series. Washington D.C.: The World Bank.
- DMRH – Disaster Management Reference Handbook*, 2017. Havana: Center for Excellence in Disaster Management & Humanitarian Assistance.
- Frangopol, D.M., Kallen, M.J. & Van Noortwijk, J.M. 2004. Probabilistic models for life-cycle performance of deteriorating structures: review and future directions. *Progress in Structural Engineering and Materials* 6(4): 197–212.
- Losanno, D., Ravichandran, N., Parisi, F., Calabrese, A. & Serino G. 2021. Seismic performance of a low-cost base isolation system for unreinforced brick masonry buildings in developing countries. *Soil Dynamics and Earthquake Engineering* 141: 106501.
- Losanno, D., Ravichandran, N. & Parisi F. 2022. Seismic fragility of base-isolated single-storey unreinforced masonry buildings equipped with classical and recycled rubber bearings in Himalayan regions. *Journal of Building Engineering* 45: 103648.
- Losanno, D., Ravichandran, N. & Parisi, F. 2023. Seismic fragility models for base-isolated unreinforced masonry buildings with fiber-reinforced elastomeric isolators. *Earthquake Engineering and Structural Dynamics* 52(2): 308–334.
- Medeot, R. & Zordan, T. 2017. EN15129: The new performance-oriented European standard on anti-seismic devices. *Proc. 16th World Conference on Earthquake Engineering*, ID3820, Santiago.
- Olsen, J.R. 2015. *Adapting Infrastructure and Civil Engineering Practice to a Changing Climate*. Reston: American Society of Civil Engineers.
- Zordan, T. & Medeot, R. 2020. Revision of EN15129. *Proc. 7th International Symposium on Life-Cycle Civil Engineering (IALCCE 2020)*, 2020, Shanghai.

Author Index

- Abdo, S. 3070
Abe, M. 541
Abe, W. 3372
Abu, A.K. 3054
Achenbach, M. 3292, 3380
Achillopoulou, D.V. 319, 1065
Acuña-Coll, N. 1853
Adachi, Y. 872
Adarne, M. 2473
Adey, B.T. 2112, 2120, 2541, 2573, 2580
Aguilar, M. 3649
Ahmadnia, A. 180
Ahrens, M.A. 1813
Ai, Q. 600
Aiello, M.A. 2789, 2820
Aizawa, M. 3086
Akahoshi, K. 562
Akiyama, M. 21, 509, 899, 1601
Akiyama, T. 3062
Akutagawa, S. 3664
Alaggio, R. 2746
Alahmad, A. 1729
AlBanwan, A. 3404
AlBehbehani, R. 3404
Alcocer, S.M. 2261
Alecci, V. 3704
AlFoudari, A. 3404
Alhamid, A.K. 1601
Al-Obaidi, S.M.J. 1217, 3094
Aloisio, A. 2746, 2762
Alonso, M.C. 2855
Alpen, M. 493
AlSanad, S. 2904
Altabey, W.A. 3808
Ames, I. 252, 268
Aminulai, H.O. 3340, 3348
Amir, A. 592, 2473
Amodio, S. 1360, 1400
An, Y. 1107
An, Y.H. 1127
Anastasopoulos, D. 391
Andrade, C. 2387
Andrews, J. 453
Andriotis, C.P. 523
Anghileri, M. 2001, 2061, 2069, 2085, 4163
Anjuna, S. 359
Anzlin, A. 1634
Aoki, K. 1601
Aoki, Y. 3062
Aoues, Y. 351
Apaydin, N.M. 2731
Apostolidi, E. 1721
Arena, M. 2017
Asgarpour, S. 973
Audenaert, A. 3206, 4092
Azzone, G. 2017
Bacic, M. 1634
Bai, H. 351
Bairán, J.M. 892, 3001, 3009
Bakker, A.M.R. 2591, 2598, 2612
Bakker, J.D. 981, 995, 1003
Baktheer, A. 3649
Ballio, F. 1993
Baniotopoulos, C. 1975
Barbosa, A.R. 1507
Barindelli, S. 2001
Barmpa, Z. 3252, 3260
Barneveld, A. 2605
Bartels, J.-H. 662
Bartoli, M. 2941
Bartsch, H. 1287
Basso, P. 3452
Bastien-Masse, M. 172
Beck, A.T. 268
Becker, T.C. 1481
Becks, H. 3649
Bednarska, D. 1241
Beer, M. 662, 670, 678
Beghini, A. 2631
Beigel, A. 4100
Bektas, K.E. 3198
Bel-Hadj, Y. 3688
Belletti, B. 2439, 2447, 2933
Bellin, S. 1323
Belloli, M. 4163
Bellotti, D. 2507
Beltrami, C. 2714, 3396, 3420, 3428, 3444, 3508, 3516
Bencardino, F. 1081
Bender, M. 3174
Benitz, Y. 407
Bento, N. 3078
Bercher, J.-F. 2227
Beretta, S. 2847
Berger, H. 2605
Bergmann, A. 2203, 2211
Bergmeister, K. 2269, 2959, 2975, 4107
Bernardi, P. 2439, 2447
Bernardini, L. 213, 237, 4163
Bertola, N. 1713
Bertolli, V. 2796, 2804
Bezak, B. 2531
Bi, S. 670
Bianchi, S. 2001
Biasioli, M. 3396
Bico, F.F. 2941
Bignozzi, M.C. 2831
Binder, F. 2363
Binnekamp, R. 949, 957
Biondini, F. 45, 883, 914, 1625, 1869, 2001, 2061, 2069, 2077, 2085, 2705, 3680, 3872, 3999, 4163
Bittencourt, T.N. 244, 252, 260, 268
Björnsson, I. 3904
Bletzinger, K.-U. 1821
Block, M. 2313, 2329
Bödefeld, J. 287, 548
Bodelier, C.J.J. 2598
Bolander, J.E. 1233

Bolzoni, F. 2847
 Bombace, A. 3508
 Bonassi, D. 3516
 Bong, J.K. 1265
 Bonoli, A. 2831
 Boothby, T.E. 1331
 Borlenghi, P. 1552, 1993
 Borrmann, A. 2321, 3634
 Botte, W. 57, 2371
 Boumakis, I. 2975, 2983
 Bramato, G. 2789
 Braml, Th. 3110, 3118
 Bredeveld, J. 2605
 Brenna, A. 2847
 Brescia, M. 3508
 Briseghella, B. 2746, 2754, 2762
 Broggi, M. 670, 678
 Brook, R. 3412
 Brouste, A. 1911
 Bruggi, M. 1315
 Brühwiler, E. 3, 1713
 Brunetti, M. 3920
 Bruschi, E. 1411, 1427
 Budi, L. 1489
 Burger, H. 3134
 Burlone, F. 3420
 Bussini, A. 931
 Buttgerreit, A. 2313
 Buyle, M. 3206
 Buzatu, R. 751, 1303
 Byers, B.S. 149
 Bysiec, D. 923

 Caddemi, S. 1590
 Caglayan, B.O. 367
 Cagliani, D. 3420
 Cagnoni, A. 2804
 Cai, M.B. 649
 Cai, Y. 1967
 Čairović, Đ. 1058
 Calabrese, A.S. 2796, 2804
 Caldera, S. 2001
 Calen, N. 2573
 Calì, I. 1590
 Calò, M. 1861
 Calvert, G. 453
 Calvi, G.M. 3927
 Cámara-Molina, J.C. 221
 Canali, F. 33
 Canestri, M. 2812
 Cannizzaro, F. 1590
 Cantero, D. 1895
 Cao, J.X. 649

 Cao, M. 2697
 Cao, R. 623
 Cao, S.G. 3864
 Cao, Z.W. 4051
 Capacci, L. 883, 914, 1625, 1869, 2001, 2705, 3999, 4163
 Capalbo, M. 3420
 Caprani, C. 1677
 Caprili, S. 2347, 3967
 Cardani, G. 1384
 Cardin, M.-A. 2565
 Carera, M.F. 3420
 Carhart, N. 2219
 Carnevale, M. 213
 Carrassi, A. 1169
 Carsana, M. 45, 2077
 Cartiaux, F.B. 1911, 2888
 Caruso, M. 931, 939, 2507
 Carvalho, C. 3078
 Carvalho, H. 244, 252, 260
 Casali, L. 2515, 2523
 Casarin, F. 1323
 Casas, J.R. 2347
 Cascini, L. 3793
 Caspeele, R. 57, 2371, 3070, 3244
 Cassiani, J.D. 3150
 Casti, L. 1625, 3420, 3872
 Castoro, C. 2762
 Castro, L.C.R. 3736
 Cattaneo, S. 2237, 2253
 Cauteruccio, G.F. 3920
 Cavalieri, F. 2507
 Çavdar, E. 1427
 Çazzulani, G. 2001
 Červenka, J. 3300
 Cesare, A.D. 1419
 Chabi, F. 2227
 Chamoin, L. 678
 Champion, L. 279
 Chan, R.S. 3142
 Chang, K. 2646
 Charlier, M. 2413
 Chaudhary, R.K. 3720
 Chávez, A.A. 3999
 Chelapramkandy, R. 4078
 Chen, A.R. 2663, 2678
 Chen, C.R. 2051
 Chen, D. 701
 Chen, H.-P. 2035
 Chen, J.B. 3777
 Chen, J. 2949
 Chen, L. 2178

 Chen, L.L. 2154
 Chen, Q. 4043
 Chen, Y. 533, 562
 Chen, Z. 1141, 1149
 Chen, Z.P. 1134
 Chen, Z.Y. 1127
 Cheng, J. 623, 1763
 Cheng, M. 1763, 1953
 Cheng, S.S. 3594
 Cheon, H.-Y. 90
 Chiaia, B. 2061
 Chisari, C. 1538
 Choffat, F. 1065
 Choi, S.-W. 3332
 Choi, Y. 477
 Chudoba, R. 3649
 Chung, D.H. 1265
 Chuo, S. 2112, 2120
 Cibelli, A. 1209, 1217
 Cilento, F. 1466
 Ciriello, C. 1466
 Classen, M. 3649
 Clauß, F. 1813
 Coccu, F. 2515
 Colas, A.S. 157
 Collina, A. 213, 237
 Colombi, P. 2796, 2804
 Colombo, M. 3856
 Colomés, O. 957
 Comaita, G. 3420
 Concu, G. 3308, 3816
 Contardi, A. 2295
 Contento, A. 2746, 2754
 Cordero, E.G. 188
 Coronelli, D. 33, 1331, 1338, 1344
 Cortese, A. 2447
 Corti, L. 2991
 Costa, G. 1693
 Couto, R. 939
 Craeye, B. 3206
 Crane, R. 2531
 Crippa, E. 3562
 Croce, P. 2481, 2497
 Cronin, L. 825
 Cucuzza, R. 4131, 4139
 Cui, H. 2911
 Curto, R. 1081
 Cusatis, G. 1225

 Dabbaghchian, I. 825
 Daescu, C. 4007
 Dafis, S. 2287
 Dakhili, K. 3174

Dal Lago, B. 2523
 Dall'Asta, A. 1499
 Damiani, A. 3562
 Damiani, F. 3420, 3508
 Dan, D. 3190
 Dang, H.T. 4147
 Davolio, M. 1217, 3094
 De Belie, N. 1169, 3094
 de Boer, A. 2873
 De Corte, W. 3244
 De Domenico, D. 2739
 de Graaf, S. 1003
 De la Fuente, A. 3602
 De Maio, F.V. 3452
 De Matteis, G. 1538
 De Pascale, B. 2831
 de Paula Filho, J.H. 2413
 de Raat, G.A. 989, 1003
 De Risi, R. 2219, 3800
 De Roeck, G. 391
 De Stefano, M. 3704
 de Vogel, B.Q. 1003
 degli Esposti, A. 2831
 Dehadray, H. 439
 del Castillo, C. 743
 Delgado, E. 415
 Derras, B. 2195
 Desbois, T. 157
 Devineni, N. 4115
 Devriendt, C. 3570, 3688
 De Wolf, C. 149
 Dhakal, R.P. 3054
 Di Dieco, G.D. 1507
 Di Carlo, F. 2941
 Di Luzio, G. 1209, 1217
 di Prisco, M. 1384, 3856
 di Summa, D. 1169, 3094
 Diamanti, M.V. 2847
 Diewald, F. 1827, 1842
 Ding, J.M. 2147, 2162
 Ding, L.C. 3777
 Ding, S.L. 3951
 Diniz, S.M.C. 3736
 Dinu, F. 767, 783, 791
 Dixit, M.K. 3126
 Dizaj, E.A. 3356, 3364
 Doan, T.P. 1935
 Domaneschi, M. 4131, 4139
 Dominiq, J. 783
 Donev, V. 3284
 Dong, Y. 1755, 1975
 Dong, Z. 2925
 Dou, W.Y. 4072
 Duan, L. 3896
 Duarte, N. 3001, 3009
 Dubina, D. 759, 783
 D'Angelo, M. 1993
 D'Antimo, M. 2413, 2421, 2429
 D'Antino, T. 2796, 2804
 D'Antuono, P. 3570
 D'Ayala, D. 3769
 Edler, P. 485
 Ehsani, R. 501
 El Ashri, M.S. 1352
 Elachachi, S.M. 3586
 El-Diraby, T. 1794
 Elfgrén, L. 3999, 4007
 Eliáš, J. 1225
 Elvarsson, A.B. 2541, 2580
 Emoto, H. 570
 Epple, N. 1805
 Eshkevari, S.S. 825
 Eskafi, M. 2549
 Esser, S. 2321
 Eyben, F. 1287
 Fabris, R. 1323
 Faddoul, A.G. 2128
 Faggiano, B. 3793, 3920
 Faleschini, F. 1021, 2455
 Fan, L. 3041
 Fan, P. 3594
 Fang, H. 195
 Fang, H.B. 4051
 Fang, J. 1115
 Fang, Q. 1368, 1530
 Farhan, N.S.D. 3808
 Faroz, S.A. 1661, 2355
 Fei, Y. 1141
 Feldmann, M. 1287
 Fenerci, A. 3672
 Feng, L.L. 2686
 Feng, Y.C. 3913
 Feraille, A. 157
 Ferguson, N.S. 3340, 3348
 Ferrara, L. 1169, 1209, 1217, 2531, 3094
 Ferrari, F. 2347
 Ferreira, E.C. 3492
 Ferretti, F. 2812
 Fiala, C. 3656
 Ficociello, A. 3967
 Fiorillo, G. 3492
 Fiorino, D.R. 3308
 Fischer, O. 3134
 Fivet, C. 172
 Fleischmann, C.M. 3054
 Flotzinger, J. 3110
 Fontana, C. 931
 Formichi, P. 2497
 Forth, K. 2321, 3634
 Fortunato, G. 3920
 Fossati, M. 3420
 Fox, M.J. 1450
 Fragkakis, N. 3252
 Franceschini, L. 2933
 Franco, A. 2820
 Frangopol, D.M. 21, 509, 515, 883, 1601, 1737, 1755, 1763, 4100
 Frattolillo, A. 2515
 Freddi, F. 4078
 Freitag, S. 485
 Frøseth, G.T. 1919
 Fu, C.Q. 2925
 Fu, J.L. 3864
 Fujii, Y. 615
 Fujishima, M. 1177
 Fukui, N. 570
 Fulco, A. 2523
 Fülöp, L. 743
 Furinghetti, M. 1458, 1474
 Furusato, Y. 1927
 Furuta, H. 578
 Futai, M.M. 244, 260, 268
 Gabbianelli, G. 1861
 Galano, R.M. 3142
 Galassi, S. 3704
 Galasso, C. 325
 Galvín, P. 221
 Gamino, A.L. 244
 Gammino, M. 2347
 Ganic, E. 1634
 Gao, H.O. 1953
 Gao, T. 1763
 Gao, W. 3832
 Gao, X. 2027
 Gara, F. 1515
 Garavaglia, E. 3460
 García, M. 892
 Gastaldi, M. 3025
 Gavin, K. 1634
 Gavriel, G. 1705, 2219, 3230
 Ge, S. 3610
 Gehlen, C. 1842, 3150
 Geier, R. 1721
 Genesis, G. 2245

Gentile, C. 1552, 1993
 Gentile, R. 325
 George, G. 359
 Gervasio, H. 2429
 Ghioni, M. 1582
 Ghosh, J. 311, 461, 1677, 4078
 Ghosh, S. 1661, 1677, 2355
 Ghosn, M. 69, 4115
 Giacalone, G. 3420, 3508
 Giacomello, G. 3752
 Giangregorio, M.C. 1338
 Gigante, A. 735
 Gilbert, M. 1360, 1376, 1400
 Giometti, D. 3396
 Giordano, P.F. 2009
 Gogolin, D. 2313
 Goi, Y. 857, 865, 872, 4015
 Gommolluch, S. 2313
 Gong, J.X. 2043
 González-Libberos, J. 3904, 3999, 4007
 Gordon, M. 149
 Gotou, H. 3062
 Grabke, S. 1821
 Granzner, M.F. 1721, 2722
 Grashorn, J. 678
 Greppi, R. 2820
 Grillanda, N. 1376
 Grilli, N. 3800
 Grosman, S. 1352, 1368, 1530
 Gu, X.L. 1107, 1115, 1122, 1127, 2949
 Gu, Y. 600
 Guglielmi, M. 2781
 Gündel, M. 493
 Gunner, S. 2219, 3800
 Gunturu, V.K.T. 2128
 Guo, S.S. 3594, 3626

 Habbaba, N. 2379
 Hafez, H. 3602
 Hagedorn, P. 1745
 Haiying, M. 2881
 Hájek, P. 3656
 Halding, P.S. 3158
 Hamer, M. 453
 Hamerslag, E.J.F. 2591, 2598
 Hamideh, S. 303
 Han, T.H. 4037
 Harsányi, P. 1097

 Hart, D. 3316
 Harte, A.M. 3610
 Hartmann, A. 965, 973, 981
 Haslbeck, M. 3110, 3118
 Hattori, H. 541
 Hayashi, G. 533, 555, 562
 Hayashi, H. 3324
 He, C. 433
 He, D.D. 3880
 He, H.F. 3594
 He, L.Q. 2754, 2762
 He, L. 1376
 He, Z. 433
 Hegger, J. 3649
 Helderweirt, S. 2371
 Helmus, M. 1249
 Heng, J. 1975
 Henry, M. 592, 2473, 2770
 Herban, S. 791
 Hernandez, E.M. 399
 Hernando, D. 4092
 Herrera, D. 469
 Herthogs, P. 3578
 Hertogh, M.J.C.M. 3214
 Herzfeldt, M. 3300
 Hiraoka, A. 555
 Hirohata, M. 631
 Hisazumi, K. 686
 Hlebec, N. 2363
 Hoffmann, M. 3276, 3284
 Hofmeyer, J. 2321
 Hollberg, A. 3634
 Horisawa, E. 4015
 Horiuchi, C. 2623, 2639, 2653
 Horiuchi, K. 1927
 Horn, J. 493
 Hradil, P. 743, 1295, 1303
 Huang, F.K. 641
 Huang, J.P. 2754, 2762
 Huo, N.N. 4057
 Huynh, T.C. 1158

 Iacobini, F. 1560
 Iannacone, L. 325
 Ientile, S. 2187
 Ierimonti, L. 2279
 Iitaka, Y. 570
 Ikeo, Y. 3436
 Imai, T. 3372, 3975
 Imperadori, M. 2405
 Ingling, B. 3316
 Iodice, F. 1560

 Ioka, R. 541
 Iovane, G. 3793, 3920
 Isfahani, F.T. 3396, 3420
 Ishibashi, H. 899
 Ishikawa, E. 3436
 Ishikawa, T. 608, 615, 3049
 Itasaka, K. 3049
 Iuorio, O. 127, 149, 735
 Iwama, K. 1185
 Iwanami, M. 3388, 3680
 Iyoda, T. 3268, 3436, 3500, 3547
 Izu, F. 3086
 Izzuddin, B.A. 1352, 1368, 1530

 Jaakkola, K. 1295
 Jaberansari, S. 2631
 Jafari, L. 1869
 Jäggle, E. 1842
 Jaimes-Quintanilla, M. 3476
 Jäkel, J.-I. 3712
 Janczyk, K. 1257
 Janda, A. 923
 Jang, N.G. 1265
 Janssens, Y.-A. 3688
 Jensen, J.S. 81
 Jeong, D.J. 4037
 Jiang, C. 1115, 1122
 Jiang, E.G. 1786
 Jiang, F. 631
 Jiang, J. 1149
 Jiang, W.J. 849
 Jiang, X. 600, 2147, 2154, 2162, 2170, 2178
 Jiang, Y. 1141, 2035
 Jiang, Z.L. 2925
 Jilissen, D.H.J.M. 135
 Jiménez-Barrera, M. 3476
 Joo, M.R. 3888
 Joshi, S. 439
 Jurina, L. 1344

 Kaewunruen, S. 1778, 1975
 Kajitani, Y. 717
 Kakeda, H. 3824
 Kalantari, S. 501
 Kamrath, P. 1270, 1278
 Kanazawa, S. 570
 Kane, A. 279
 Kang, J. 3896
 Kang, M.U. 447
 Kang, Z. 3896
 Karaki, G. 3728

Karmakar, S. 2355
 Karoumi, R. 229
 Karuk, V. 1427
 Kashani, M.M. 3340, 3348, 3356, 3364
 Katayama, T. 541
 Kato, M. 872
 Kato, S. 686
 Katterbach, M. 3959
 Kavoura, F. 799
 Kawai, K. 3033, 3086
 Kawabe, D. 809, 817, 833
 Kawamura, K. 584
 Kebig, T. 3174
 Kefalas, G. 2287
 Keshvari Fard, A. 1770
 Keßler, S. 2489
 Kessler, S. 2481, 2967, 3150
 Kesting, H. 1249
 Khan, M.S. 1661
 Khanmohammadi, M. 1869
 Kharoubi, Y. 3214
 Khorasani, M. 1073
 Kim, C.-W. 701, 809, 817, 833, 849, 857
 Kim, H.-K. 90
 Kim, J.H. 4037
 Kim, J.T. 1158
 Kim, S. 90
 Kim, I. 865
 Kiremidjian, A.S. 914, 1669
 Kitagawa, S. 833
 Kitahara, M. 662, 670
 Kitahara, T. 657, 670
 Kitane, Y. 865, 872, 4015
 Kitayama, S. 127
 Klaus, P. 3959
 Klemt-Albert, K. 3712
 Kloesgen, L. 3712
 Ko, S.S. 1265
 Kobayashi, Y. 3086
 Koenig, T. 3712
 Komarizadehasl, S. 415, 1685, 1729, 2881
 Komary, M. 1685, 1729
 Komon, K. 608
 Kondo, R. 725
 Kong, J.S. 477
 Kong, S. 623
 König, M. 1745, 2329
 Koniorczyk, M. 1241
 Kool, P. 229
 Koshimura, S. 899, 1601
 Kosic, M. 1634
 Kosse, S. 1745
 Kosta, A. 1065
 Kostjak, V. 1737, 4100
 Kotynia, R. 1050
 Kovacevic, M.S. 1634
 Kramer, N. 2605
 Kränkel, T. 1842, 3150
 Kromanis, R. 295
 Kuang, Y. 2911
 Kuhlmann, U. 3696
 Kuhnhenne, M. 1257
 Kunz, J. 1097
 Kwon, K. 477
 Lachat, A. 157
 Lahdensivu, J. 142
 Lai, F. 2531
 Lai, J. 533
 Lamarucciola, N. 1419
 Lambrechts, T.S.K. 165
 Lan, X.Z. 3848
 Lan, Y. 383
 Landi, F. 2481, 2489, 2497
 Landolfo, R. 775, 3793
 Larsson, T. 4007
 Lasri, O. 2009
 Lassman, R. 825
 Lau, K. 1877
 Law, K.H. 1669
 Lazoglu, A. 205
 Le Corvec, V. 1911
 Leander, J. 229
 Lee, C.-C. 1967
 Lee, E.-B. 3332
 Lee, Y.H. 447
 Lei, H. 2557
 Lei, X. 1755
 Lemos, J.V. 1523
 Lemosse, D. 351
 Leng, Y. 1141
 Leone, M. 2789
 Leoni, G. 1515
 Lepech, M.D. 1669
 Leu, L.J. 3523
 Leung, E. 2646
 Li, C. 3848
 Li, C.Q. 2557, 3238
 Li, F.L. 1201
 Li, J. 333, 2027
 Li, L. 3554
 Li, P.Y. 3880, 3896
 Li, P. 3991
 Li, Q. 3840
 Li, S.Y. 1786
 Li, T. 4072
 Li, W.B. 2035
 Li, X.B. 2043
 Li, X.Y. 3864
 Li, Y. 1961, 3041, 3880, 4072
 Li, Y.Q. 3913
 Li, Z. 374, 383
 Limongelli, M.P. 1653, 1693, 2009
 Lin, F.X. 2686
 Lin, L.R. 4023
 Lin, W. 374, 383, 3991
 Lin, Z. 2911
 Lindiri, S. 767
 Ling, H.W. 3626
 Liu, B. 817, 1392, 2178
 Liu, C. 3594, 3626
 Liu, F. 3744
 Liu, H.J. 3951
 Liu, P. 2154
 Liu, S. 3041
 Liu, Y. 623, 1107, 1763, 3041, 3785
 Liu, Z. 1149, 3664
 Lo, C.W. 641
 Loli, M. 2287
 Lollini, F. 3025
 Lombaert, G. 391, 2371
 Long, E. 2631
 Losanno, D. 1466
 Lotti, A. 422
 Lounis, Z. 1609, 1617
 Loverdos, D. 817
 Lozano, F. 1685
 Lozano Valcarcel, J.M. 3150
 Lozano-Galant, J.A. 415, 1685, 1729, 2881
 Lu, J. 3808
 Lu, W.L. 1201
 Lu, Y. 2379
 Lucherini, A. 3720
 Luiten, G.T. 1003
 Lukačević, I. 751
 Luo, B. 3554
 Lupoi, A. 3967
 Lv, Z.L. 2147
 Ma, R. 2663
 Ma, X.G. 3626
 Ma, X. 3664
 Maas, M. 3174
 Machner, A. 1842

Macorini, L. 1352, 1368, 1530
 Maekawa, K. 1185
 Maes, K. 391
 Maibaum, J. 2329
 Mak, S.-L. 1967
 Makhoul, N. 295, 1653, 2195, 3872
 Makrakis, N. 515
 Malavasi, M. 2447
 Maleska, T. 923
 Malomo, D. 3927
 Manzi, S. 2831
 Marano, G.C. 2762
 Marcucci, A. 1169
 Marí, A. 3001, 3009
 Mariani, F. 2279
 Mariata, D.J.M. 3484
 Marincu, C. 3190
 Marinković, S. 3602
 Marino, M. 3396
 Mark, P. 1813
 Marra, A.M. 3704
 Marra, M. 1435
 Marranzini, D. 3793, 3920
 Marrone, G. 2405
 Marsili, F. 287, 2481, 2489
 Martani, C. 2128, 2573
 Martignoni, F. 1169
 Martinelli, L. 4131, 4139
 Martinelli, P. 1384, 3856
 Martínez-Rodrigo, M.D. 221
 Marx, S. 205, 662, 1745
 Masi, A. 1029
 Masi, G. 2831
 Masunaga, K.M. 3268
 Matarazzo, T.J. 825
 Matos, J.C. 4147, 4155
 Matsuda, N. 3500
 Matsumoto, A. 3372
 Matsumoto, N. 608
 Matsuoka, K. 213, 237
 Matsuzaki, H. 906
 Matthys, S. 2371
 Mazzatura, I. 2347, 3967
 Mazzeo, M. 2739
 Mazzotti, C. 2812
 McGetrick, P.J. 3610
 Meda, A. 2941
 Medeiros, R. 2203, 2211
 Medina, C. 2439
 Mehrabi, A.B. 1877
 Mehranfar, H. 2112, 2120
 Mellios, N. 2269, 2967
 Meloni, D. 3816
 Menardo, F. 931
 Meng, W.Y. 4057
 Menna, C. 1466
 Merci, B. 3720
 Meschke, G. 485, 1834
 Meuleman, R. 1945
 Mezhov, A. 1193
 Mezzi, M. 2523
 Micallef, K. 2631
 Micelli, F. 2820
 Michelacci, A. 2831
 Mijic, A. 2565
 Milanese, D. 2447
 Milone, A. 775
 Mir Rangrez, Z.Y. 1677
 Miranda, P.S.T. 1885
 Mishra, D.K. 4029
 Mistretta, F. 2497
 Mitoulis, S.A. 2287
 Mitroulis, K. 2269
 Miura, T. 1177
 Miyagi, M. 2303
 Mizutani, D. 237, 2103
 Mizutani, M. 615
 Mizutani, T. 3975
 Mocellini, M. 1323
 Moctezuma, B. 2261
 Moghtadernejad, S. 2112, 2120
 Mohammed, A. 1642
 Moins, B. 4092
 Molaioni, F. 523, 2941
 Moliner, E. 221
 Molkens, T. 1945
 Montalbano, A. 1065
 Monteiro, L. 3618
 Monteiro, R. 939
 Monticelli, C. 180
 Moody, T. 3800
 Mooren, S.C.A. 973
 Morán A., J. 1983
 Morato, P.G. 1983
 Moratti, M. 3927
 Morè, R. 3516
 Moreira, L.S. 260
 Morgenstern, H. 3712
 Morici, M. 1515
 Moro, F. 2863
 Morosiuk, K. 3412
 Mosca, C. 188
 Mostofinejad, D. 1073
 Muciaccia, G. 1073, 2991
 Mudahemuka, E. 2303, 3531
 Mudge, F.J. 165
 Muhit, I.B. 817, 1392
 Müller, M. 2337
 Muller, S. 2531
 Muñoz, J.J. 2387
 Murakami, J. 541
 Murakoshi, J. 3983
 Murcia-Delso, J. 3001, 3009
 Mustafa, S. 1903
 Mustapha, S. 2379, 2896
 Mutiu, M. 759
 Nagae, T. 2103
 Nagaoka, S. 3388
 Nagayama, T. 686, 3832
 Nakamura, H. 1177
 Nakamura, R. 1927
 Nakamura, S. 3062
 Nakayama, K. 3388, 3680
 Nakazato, Y. 2103
 Namli, E. 3222
 Nanni, A. 1233
 Napolitano, M.S. 3516
 Naraniecki, H. 205
 Nascimbene, R. 2507
 Nash, W. 2531
 Nava, G.V. 1625
 Navarro, I.J. 2463
 Neagu, C. 767, 791
 Negendahl, K. 3158
 Neimeyer, T. 279
 Neuner, H. 1737, 4100
 Neves, L. 453
 Neves, L.C. 3412
 Ng, P.L. 4029
 Nicoletta, M. 3793
 Nicoletti, V. 1515
 Nicolò, M. 1169
 Nieborowski, S. 1745
 Niederleithinger, E. 1805
 Niero, L. 1567
 Nilsson, L.B. 4007
 Nincevic, K. 2975, 2983
 Ning, Y. 2678
 Nishida, T. 3033, 3086
 Nocetti, M. 3920
 Nodiroli, G. 3959
 Noland, J. 3316
 Nomura, Y. 578
 Noori, M. 3808, 4131, 4139
 Noppe, N. 3570
 Nord, T.S. 3672

Novák, D. 2697
 Novák, L. 2697
 Novotná, M. 3656
 Nucci, M. 2531
 Nuh, M. 119
 Nyman, J. 229

 Oba, N. 3324
 Ogawa, D. 686
 Ohsumi, M. 694
 Oikonomopoulou, E. 2245
 Okada, Y. 3539
 Okubo, N. 865
 Ólafsson, S. 1443
 Oller, E. 3001, 3009
 Ombres, L. 3920
 Omrani, I.A.N. 1241
 Ongpeng, J.M. 3142, 3166
 Onishi, H. 841, 3824
 Ono, K. 849
 Orgnoni, A. 3927
 Orlowsky, J. 2959
 Ormellese, M. 2847
 Orr, J. 119
 Orsenigo, L. 279
 Ortega-López, V. 2455
 Osmani, S. 3452
 Otárola, K. 325
 Oval, R. 119
 Ozakgul, K. 367
 Ozaki, S. 578
 Özçamur, U. 1427
 Özdemir, G. 1427
 Özdemir, M. 4065
 Ozer, I.E. 3198
 Öztürk, T. 3222
 O'Ceallaigh, C. 3610
 O'Mahoney, T. 2605

 Padgett, J.E. 341
 Padovani, F. 2705
 Paglia, C. 188
 Pakzad, S.N. 825
 Palic, S.S. 1634
 Palieraki, V. 2245, 2253
 Pan, Y. 3864
 Pan, Y.J. 2925
 Pan, Z.C. 2670
 Panchireddi, B. 461
 Panetsos, P. 3252, 3260
 Pannuti, U.R. 4086
 Pantoja, J.C. 1885
 Parisi, F. 1466, 4171
 Park, S.-E. 3332

 Parol, J. 2904
 Parsons, B. 279
 Pasetto, M. 3752
 Pasqualato, G. 2295
 Paulissen, J.H. 1003
 Pavese, A. 1450, 1458
 Pedeferra, M.P. 2847
 Pellegrino, C. 1021, 1546,
 1560, 1567, 2455
 Peng, W.Q. 1201
 Peng, Y.B. 3777
 Pešta, J. 3656
 Petroutsatou, K. 3252, 3260
 Pettorosso, C. 1411
 Petursson, H. 229
 Pham, H.G. 1481
 Pham, N.L. 1158
 Pham, Q.Q. 1158
 Phung, Q.T. 3070
 Piazzon, R. 1546
 Picciano, V. 1029
 Piccinin, R. 2975, 2983
 Pilia, E. 3308
 Pinho, R. 931, 939, 3927
 Piovano, G. 3396
 Piscini, A. 2347
 Plaza, P. 2439
 Poggi, C. 2796
 Ponzo, F.C. 1419
 Pourhosseini, H. 3182
 Pradeep Kumar, P. 3126
 Pregartner, T. 2975, 2983
 Pregolato, M. 1507, 1705,
 2219, 3230, 3800
 Previtali, M. 2009
 Prudhomme, B. 2888
 Psarropoulos, P.N. 515
 Pugliese, D. 3704
 Pukl, R. 2697, 3300
 Puppio, M.L. 2497, 2515
 Put, F. 3720

 Qian, J. 3664
 Qiang, X.H. 2147, 2154,
 2162, 2170
 Qiu, J.L. 1134
 Quaglino, V. 1411, 1427
 Quaranta, G. 2739
 Quattrone, A. 2061, 2093
 Quek, S.T. 649

 Rabbia, M. 3508, 3562
 Radaelli, E.O. 1344
 Radhakrishnan, N. 359

 Radović, A. 3602
 Radwan, S.M.I. 1217
 Raghunandan, M. 311
 Rahimi, A. 3468
 Rajić, A. 751
 Ramos, G. 415, 2881
 Randi, R.P. 3484
 Randl, N. 1037, 1044, 1089,
 1097
 Ranjan, P. 4029
 Rapticavoli, D. 1590
 Räsänen, A. 142
 Rashedi, M.R. 501
 Rasol, M. 2187
 Ratti, C. 825
 Raupach, M. 3712
 Ravasini, S. 2447, 2933
 Rayjada, S.P. 311
 Reale, S. 1450, 1458
 Rebecchi, G. 931
 Redaelli, E. 45, 2077
 Reimoser, T. 407
 Reiterer, M. 2722
 Ren, X.D. 3554
 Renne, N. 3206
 Reymer, S. 1745
 Reynders, E.P.B. 391
 Ribeiro, D. 252
 Ricci, D. 1560
 Rigo, P. 1983
 Rinaldi, Z. 523, 2941
 Rincon, R. 341
 Rivas, P. 3380
 Robbelein, K. 3570
 Robens-Radermacher, A.
 1193
 Robertson, I.N. 3102
 Rodrigues, L.G. 3412
 Rodrigues, P.Q. 1885
 Roghani, H. 1233
 Rogowski, J. 1050
 Roh, G.T. 447
 Romano, A. 4171
 Roman, O. 2541, 2580
 Romero, A. 221
 Rönquist, A. 1919
 Roohi, M. 333, 399
 Rosati, G. 2001, 2061, 2069
 Rosell, J.R. 2387
 Rosengren, P. 229
 Rosowsky, D. V. 399
 Rossi, E. 1037, 1044
 Rowsell, M. 2136
 Rozza, G. 3428

Ruan, X. 4057, 4072
 Ruggieri, N. 3920
 Rupakhety, R. 1443
 Russo, N. 3025
 Rymeš, J. 3300
 Ryota, S. 3531

Sabia, D. 2061, 2093
 Sadeghi, N. 3570
 Saenger, E.H. 1834
 Saha, D. 2355
 Saisi, A. 1552
 Saita, R. 841
 Saiyouri, N. 3618
 Salami, M.R. 3356, 3364
 Salazar L., P. 1983
 Saliba, J. 3618
 Salomone, R. 3420, 3508
 Salvatore, W. 2347, 3967
 Salvioni, J. 3420
 Sánchez, J. 2439
 Sanchez, L.F.M. 2203, 2211, 3484
 Sánchez-Garrido, A.J. 2463
 Sánchez-Silva, M. 1853
 Sanchez-Trujillo, C.A. 1805
 Santamaria, A. 2455
 Santarsiero, G. 1029
 Santi, P. 825
 Santinon, D. 1560
 Santoro, R. 2739
 Santos, A.C. 3484
 Santos, J. 965
 Santos, R.R. 244
 Sarhosis, V. 817, 1392
 Sardroud, J.M. 3182
 Sarkisian, M.P. 98, 2623, 2631, 2653
 Sarmiento, S. 3904
 Sartori, M. 1411
 Sas, G. 3904, 3999, 4007
 Sasaki, K. 3324
 Sasaki, T. 3824
 Sassoni, E. 2812
 Sassu, M. 2515
 Sato, T. 3760
 Sattler, F. 1737, 4100
 Savino, P. 2061, 2069, 2093
 Saygılı, Ö. 1523
 Scamardo, M. 2237
 Scarsi Napolitano, M. 3508
 Scattarreggia, N. 3927
 Schäfer, D. 2136
 Schäfer, M. 3174

Schiavi, L. 3025
 Schiessl-Pecka, A. 3150
 Schimanski, C.P. 2136
 Schmidt, F. 2187, 2227, 2287, 3872
 Schmidt, W. 1193
 Schmidt-Döhl, F. 3468
 Schmitt, A. 407
 Schneck, U. 2363
 Schneider, S. 1745
 Schoen, S. 485
 Scholten, H. 1003
 Schramm, N. 3134
 Schumann, R. 2136
 Sciancalepore, C. 2447
 Scozzese, F. 1499
 Sebastian, W. 3769
 Secchi, P. 2017
 Sechi, G. 3816
 Seetharam, S.C. 3070
 Segù, E. 2531
 Seiffert, A. 548
 Sekiya, H. 1903
 Semiao, J. 1911
 Senila, M. 767
 Sergi, G. 2839
 Sesana, M.M. 2397, 2405
 Seywald, C. 1737, 4100
 Shang, Y. 949
 Shekhar, S. 461
 Shen, H.J. 3626
 Shi, C. 351
 Shi, H. 4123
 Shim, C.S. 447
 Shin, R. 709, 2303, 3539
 Shinmura, N. 541
 Shinoda, K. 541
 Shiozaki, M. 584
 Shirkhani, H. 1609, 1617
 Shoji, G. 694, 717, 725
 Shook, D. 2623, 2646, 2653
 Shu, Y. 2170
 Shuku, T. 657
 Si, M. 649
 Siccardi, R. 1582
 Siedziako, B. 3672
 Silik, A. 3808
 Silimanotham, H. 2770
 Silva, A. 3078
 Silvestri, S. 1435
 Simões da Silva, L. 2429
 Simonsson, P. 4007
 Sinha, R. 3888
 Sirico, A. 2439, 2447

Skarmoutsos, G. 3696
 Smith, C.C. 1360, 1376, 1400
 Smits, J. 1945
 Soave, F. 3094
 Sobhkhiz, S. 1794
 Solari, C. 3452
 Somaschini, C. 213, 237, 4163
 Song, C. 1122
 Sotoudeh, P. 3492
 Soudijn, M.L. 2873
 Sousa, H.S. 4147, 4155
 Souza, E.F. 252, 268
 Spyridis, P. 2269, 2959, 2967, 4107
 Sresakoolchai, J. 1778
 Stagnitto, G. 1574, 1582
 Stamataki, N.K. 319
 Steenbrink, A.C. 957
 Steiner, M. 1089
 Štěpánek, P. 1058
 Stewart, M.G. 109
 Stipanovic, I. 1634
 Stouffs, R. 3578
 Sträter, N. 1813
 Strauss, A. 1721, 1737, 2363, 2722, 4100
 Stringer, M. 2639
 Strini, A. 3025
 Su, C. 2027
 Su, D. 3832
 Su, M.N. 1013
 Su, Q. 2178
 Sugimoto, Y. 841, 3824
 Sugiura, K. 865, 872, 4015
 Sun, H. 4029
 Sun, S.Y. 3017
 Sun, Y. 1729, 3785
 Sun, Y.X. 3523
 Suo, J. 2128
 Sutley, E. 303
 Suvarna, S. 2128
 Svecova, D. 3492

Ta, Q.B. 1158
 Taeby, M. 1877
 Takahara, R. 3372
 Takahashi, Y. 1185
 Takasu, A. 1935
 Takriti, A. 2967
 Taliercio, A. 1315
 Tang, F. 2911
 Tang, Y.D. 1201

Täubling-Fruleux, B. 1737, 4100
 Taylor, C. 2219, 3800
 Tehrani, F.M. 501
 ten Harmsen van der Beek, N.J.M. 2605
 Tephro, T. 3134
 TerMaath, S. 3316
 Teuffel, P.M. 165
 Teixeira, E. 4147, 4155
 Thienpont, T. 3244
 Thomas, D. 493
 Thöns, S. 1693, 3904
 Thorat, A. 439
 Tian, H. 3864
 Tian, L. 4051
 Tian, Y.Q. 2051
 Tillet, D. 3959
 Timothy, J.J. 1834, 1842
 Tizzani, F. 3578
 Togni, M. 3920
 Tolentino, D. 469
 Tominaga, T. 686
 Tondolo, F. 2061, 2069, 2093
 Tonelli, D. 422
 Torabian, F.T. 2714
 Torralba, V. 2881
 Torrent, R.J. 2863
 Torti, A. 2017
 Tošić, N. 3602
 Toska, K. 1021
 Tran, M.Q. 4147, 4155
 Trautwein, L.M. 3484
 Treiture, R. 995
 Trento, D. 2455
 Troian, R. 351
 Tryfonas, T. 2219
 Tsompanakis, Y. 515
 Tsuboi, A. 3824
 Tsunoda, H. 3062
 Tubaldi, E. 422, 1499
 Tully, P. 2219
 Tundalwar, M. 439
 Tuominen, K. 1295
 Turmo, J. 415, 1685, 1729, 2881
 Uaje, M.J.B. 3983
 Ubertini, F. 2279
 Ueno, M. 841
 Ulfarsson, G.F. 2549
 Umali, M.V. 3166
 Ummenhofer, T. 2337
 Unger, J.F. 1193
 Ungureanu, V. 751, 759, 1303
 Urbano, V.M. 2017
 Usman, A. 2515
 Vagdatli, T. 3252, 3260
 Vahedifard, F. 1642
 Valdés, M. 2515
 Valentino, J. 1376
 Valoti, D.O. 2077
 Valsecchi, R. 3452
 van Baaren, E.S. 2598, 2605
 Van Coile, R. 3244, 3720
 van de Lindt, J.W. 303, 333
 Van den bergh, W. 4092
 van den Bogaard, J. 3214
 van den Boomen, M. 3214
 Van Den Hende, K. 2371
 Van der Pijl, F. 965
 van Eck, G.J. 135
 van Gijzen, L. 2612
 van Heukelum, H.J. 957
 van Rossum, S. 2873
 Vangelisti, I. 2714, 3420, 3428, 3444, 3508
 Vantini, S. 2017
 Vardanega, P.J. 1705, 3230
 Vargas-Farias, A. 965
 Vargas-Sánchez, L. 3476
 Vecchi, A. 1560
 Veit-Egerer, R. 407
 Veljkovic, M. 799
 Venanzi, I. 2279
 Venclovský, J. 1058
 Ventura, G. 1029
 Vergano, F. 3396
 Vergoossen, R.P.H. 135
 Verre, S. 2781, 3920
 Vintzileou, E. 2245, 2253
 Viscuso, S. 180
 Vittone, M. 3420, 3508
 Vlasatá, B. 3656
 Voelkel, J. 1287
 Voet, E. 3688
 Voogt, H. 3642
 Voutsis, M. 3260
 Voyagaki, E. 2219, 3800
 Vu, G. 1834
 Vuong, H.T. 1935
 Wachsmann, A. 2329
 Wada, T. 541
 Wagemann, F. 3468
 Wahlström, M. 743
 Wallis, J. 3412
 Wang, B. 2663
 Wang, C. 3991, 4007
 Wang, C.S. 3880, 3896, 3913, 3935, 3951
 Wang, D.L. 2663, 2678
 Wang, G.S. 641
 Wang, H. 4023
 Wang, H.J. 3554
 Wang, L. 1141, 1967
 Wang, N. 2639, 2646
 Wang, S. 2178
 Wang, W. 303, 2557, 3238
 Wang, X. 3785, 4023
 Wang, Y. 1149
 Wang, Y. 1217
 Wang, Y. 3238
 Wang, Y.C. 1013
 Wang, Y.C. 2925
 Wang, Y.Z. 3935
 Wan-Wendner, R. 1217, 2975, 2983, 3070
 Watanabe, S. 865
 Weber, B. 3292, 3380
 Wedel, F. 1745
 Weijtjens, W. 3570, 3688
 Weil, M. 3688
 Wen, L.L. 2686
 Wen, Q.P. 2686
 Whyte, J. 2565
 Wickers, A. 493
 Widmer, N. 172
 Wijte, S.N.M. 165
 Windmann, S. 1745
 Wolfert, A.R.M. 949, 957
 Won, J.H. 1265
 Wrana, A. 2531
 Wu, H.L. 2147, 2162, 2170
 Wu, W.F. 3848
 Wu, X.G. 4023
 Wu, X.Y. 2043
 Wu, Y.F. 1786
 Wu, Y.P. 2162
 Wu, Z. 3808
 Xi, X. 2918
 Xia, B. 3943
 Xiang, C. 2678
 Xiao, S.W. 3554
 Xiao, X.W. 1127
 Xie, G.Y. 3951
 Xie, X. 3991
 Xin, H. 3785

Xin, J. 509
 Xiong, Y.M. 4123
 Xu, L.F. 1201
 Xu, Y.N. 3744
 Xue, J.Q. 2754, 2762
 Xue, K. 3832
 Xue, K. 3832
 Xue, Z. 3769

 Ya, D.T. 2686
 Yahiro, R. 3547
 Yamaguchi, E. 1927
 Yamaguchi, T. 533, 555,
 562
 Yamamoto, K. 709, 2303,
 3523, 3531, 3539
 Yamamoto, S. 694
 Yamato, Y. 578
 Yamazaki, H. 578
 Yáñez-Godoy, H. 3586,
 3618
 Yang, H. 4043
 Yang, M. 4123
 Yang, M.Y. 3913, 3935
 Yang, S.T. 2918
 Yang, W. 2557, 3238
 Yang, Y. 686
 Yang, Y.Y. 3523
 Yang, Z. 3041
 Yao, H. 833
 Yao, G.W. 1786
 Yassine, R. 2896
 Yasukawa, Y. 3324
 Ye, X. 1685
 Ye, Z. 3054

 Yepes, V. 2463
 Yi, Y.L. 4057
 Yilmaz, M.F. 367
 Yin, H. 825
 Yin, Z. 2918
 Yoshida, I. 1903
 Yoshii, C. 3680
 Yu, J. 4029
 Yu, Q.Q. 1127, 1134, 2949
 Yu, X.Y. 3744
 Yu, Y. 2027
 Yuan, X.-X. 1770
 Yuan, Y. 600, 3848
 Yukihiro, Y. 817
 Yuyama, A. 717

 Zabala-Vargas, S. 3476
 Zahedi, F. 3182
 Zaidman, I. 205
 Zakharenko, M. 1919
 Zampieri, P. 1546, 1560,
 1567, 1574, 1582
 Zanelli, A. 180
 Zani, G. 1384
 Zanini, M.A. 2455
 Zappani, A.A. 3920
 Zdrenghea, P.C. 791
 Zha, A. 2653
 Zhang, C. 649, 2178
 Zhang, D.W. 3626
 Zhang, F. 2918
 Zhang, G.F. 1786
 Zhang, H. 3664
 Zhang, J. 1609
 Zhang, J.J. 2670

 Zhang, L. 600
 Zhang, Q.L. 2170
 Zhang, Q. 4043
 Zhang, S.L. 649
 Zhang, W.P. 1107, 1127,
 1134, 2949
 Zhang, X. 4023
 Zhang, X.S. 4023
 Zhang, Y. 374, 383, 1961,
 3943
 Zhang, Z.J. 3840
 Zhao, B. 3832
 Zhao, J. 4123
 Zhelyazov, T. 1443
 Zheng, W. 584
 Zhou, B. 3991
 Zhou, F. 1967
 Zhou, S.N. 2762
 Zhou, X. 701, 3744
 Zhou, X.G. 3935
 Zhou, Z.J. 2051
 Zhu, C.H. 3896
 Zhu, L.X. 2051
 Zhu, X.M. 1013
 Zhu, Y.D. 1786
 Zinke, T. 1745, 2136,
 2337
 Zizi, M. 1538
 Zlámál, M. 1058
 Zonta, D. 422
 Zordan, T. 4171
 Zorzi, S. 422
 Zucca, M. 2497
 Zülfikar, A.C. 2731
 Zürbes, A. 3174